様式Ｃ－１８

先端加速器 LHC が切り拓くテラスケールの素粒子物理学

～真空と時空への新たな挑戦～

領域番号 2303

平成 23 年度～平成 27 年度科学研究費助成事業(科学研究費補助金)

（新学術領域研究(研究領域提案型)）研究成果報告書

平成 29 年 2 月

領域代表者　浅井祥仁

東京大学大学院理学系研究科教授

先端加速器 LHC が切り拓くテラスケールの素粒子物理学
～真空と時空への新たな挑戦～
平成 23 年度～平成 27 年度科学研究費助成事業(科学研究費補助金)
（新学術領域研究(研究領域提案型)）

領域ホームページ
http://www.icepp.s.u-tokyo.ac.jp/terascale/

目次

領域の概要 1

研究組織 1

領域の研究組織 1

領域の連携について 2

交付決定額 3

研究成果の概要 6

研究領域の目的 6

研究領域の成果 7

領域の貢献 17

当該学問分野及び関連学問分野への貢献度 17

研究計画に参画した若手研究者の成長の状況 18

総括班 21

総括班の研究組織 21

交付決定額 23

領域として開催した国際会議等 24

主要論文別刷 26

計画研究 A01 班「ヒッグス粒子の発見による素粒子の質量起源の解明」 81

研究組織 81

交付決定額 82

研究成果 83

主要論文別刷 90

計画研究 A02 班「超対称性の発見と大統一理論の実験的検証」 323

研究組織 323

交付決定額 324

研究成果 324

主要論文別刷 330

計画研究 A03 班「素粒子標準模型の精密検証で探るテラスケール物理現象」 571

研究組織 571

交付決定額 572

研究成果 573

主要論文別刷 580

計画研究 A04 班「トップクォークを用いた新しい素粒子現象の探索」 767
研究組織 767
交付決定額 768
研究成果 768
主要論文別刷 774
計画研究 A05 班「テラスケール物理の理論的研究」 909
研究組織 909
交付決定額 909
研究成果 910
主要論文別刷 920
計画研究 A06 班「LHC での発見が導く次世代エネルギーフロンティアの発展」 1037
研究組織 1037
交付決定額 1037
研究成果 1038
主要論文別刷 1044
計画研究 B01 班「LHC 時代の新しい初期宇宙像」 1125
研究組織 1125
交付決定額 1126
研究成果 1127
主要論文別刷 1134
計画研究 B02 班「テラスケール物理がもたらす新しい時空像」 1193
研究組織 1193
交付決定額 1193
研究成果 1194
主要論文別刷 1200
計画研究 B03 班「 テラスケールの物理から超弦理論への展開 」 1291
研究組織 1291
交付決定額 1292
研究成果 1293
主要論文別刷 1302
計画研究 B04 班「テラスケール物理における世代構造の研究」 1571
研究組織 1571
交付決定額 1572
研究成果 1572
主要論文別刷 1582

領域の概要

平成 23 年度～平成 27 年度に科学研究費助成事業(科学研究費補助金)の新学術領域研究(研究領域提案型)として実施された、領域名「先端加速器 LHC が切り拓くテラスケールの素粒子物理学～真空と時空への新たな挑戦」(領域番号 2303、領域略称「テラスケール物理」)の研究成果について報告する。

研究組織

本領域は総括班と 10 件の計画研究で構成されており、さらに平成 24 年度～平成 25 年度に 8 件、平成 26 年度～平成 27 年度に 5 件の公募研究を採択した。以下、研究組織の概要について表 2 及び表 3 に示す。各計画研究の組織の詳細についてはそれぞれの研究成果報告の部分に示す。領域代表者は浅井祥仁東京大学大学院理学系研究科教授がつとめた。

領域の研究組織

本領域は、LHC・アトラス実験でのテラスケール物理の研究（研究項目 A）を核に、宇宙、余剰次元、真空、超弦理論などの新しい展開を推進する研究（研究項目 B）の 2 つの研究項目で構成されている。

研究項目 A を推進するのが 6 つの計画研究(A01-06)である。
◎計画研究 A01(徳宿克夫(KEK))　　ヒッグス粒子の発見、次世代半導体検出器の開発
◎計画研究 A02(浅井祥仁(東京大)) 超対称性粒子や余剰次元などテラスケールでの新しい物理現象の探索、次世代加速器の基幹技術となる新しい超伝導技術の開発
◎計画研究 A03(藏重久弥(神戸大)) 標準理論の精密検証を通して、そのズレを探る、次世代の高放射線耐性、高速ミューオン検出器の開発
◎計画研究 A04(戸本誠(名古屋大)) トップクォークの詳細な研究、高速エレクトロニクスを用いた新しいトリガーシステムの開発
◎計画研究 A05(野尻美保子(KEK))　テラスケール物理の現象論的研究
◎計画研究 A06(駒宮幸男(東京大)) 次世代エネルギーフロンティア実験の準備研究、高性能カロリメータの開発研究

領域の概要

研究項目 B を推進するのが 4 つの計画研究(B01-04)である。
◎計画研究 B01(山口昌弘(東北大))　LHC 時代の新しい宇宙像
◎計画研究 B02(細谷裕(大阪大))　テラスケール物理がもたらす新しい時空像
◎計画研究 B03(渡利泰山(IPMU))　テラスケール物理から超弦理論への展開
◎計画研究 B04(久野純治(名古屋大))　テラスケール物理における世代構造の研究

領域の連携について

◎ 計画研究 A01,02 は、高い感度を有する直接探索による方法で、ヒッグス粒子や超対称性粒子などの標準理論を超えた新しい物理の直接発見を目指す。計画研究 A03,A04 は標準理論やトップクォークを精密に検証し、そのズレを探ることで新しい素粒子現象の発見を目指す。この方法は間接的であるが、特定のモデルに依存することなく、直接探索では見えないより高いエネルギースケールの物理を発見できる。このように直接・間接の二つの方法は相補的な研究で確実に新しい素粒子現象をとらえる。
◎ A01-A04 及び A06 各計画研究は、他の計画研究のバックグラウンドの理解や、検出器の効果の理解など共有すべきトピックスが多数ある。実験が行われている CERN に長期滞在している各計画研究の研究者が、毎月定期的に会合をもって、最新の検出器の状況や、解析の現状を共有している。(図中緑部の下側横の繋がり)
◎ 次世代のエネルギーフロンティア実験での超伝導加速器や検出器の基幹技術を、ただ開発するのではなく、LHC・アトラス実験での現場での実験経験にもとづいて開発を進めるところが本領域の大きな特徴である。成果や経験のフィードバックを絶えず行うために、各研究計画の中で情報を共有し、物理研究と基幹技術開発を平行に行う。(図中、緑部と肌色部を共有する様に計画研究を構成した。)
◎ 計画研究 A05 が、実験と理論を結びつける現象論的な研究である。テラスケールでの現象論的研究は、研究項目 A 及び B の両方と情報を常時交換しながら研究を進めている。
◎ 計画研究 A06 は、LHC でのテラスケール物理の成果を次世代実験に結びつける準備研究を行う。ヒッグスの発見からその背後のヒッグス・ポテンシャル解明への道筋を研究する。これと同時に次世代カロリメータ開発を行う。以上の 5 つで次期技術の主要なものをカバーする.
◎ 研究項目 B の成果は、宇宙、重力、真空・時空の融合と本領域の外に広がりを持つ。当該分野のみならず、関連分野へと広がっていく。
◎ 計画研究 B02, B03 は時空構造や超弦理論研究であり、top-down 型の研究を通して、テラスケールの物理を探る。
◎ 研究項目 B の各計画研究は、互いに協力しながら、関係する外国の研究者や国内の研究者を招待しミニワークショップを開催し、お互いの連携を深めている。このミニワークショップなど

には、研究項目 A の研究者も参加して最新の実験成果を発表すると同時に、新しい理論的な成果を取り込んで研究を進めている。(図中緑の上部の横の連携)
◎ 次世代の実験の基幹技術開発は、当該分野の発展に大きな寄与をするばかりでなく、超伝導、放射線耐性検出器などスピンオフが期待される。

交付決定額

本領域に配分された交付額を表 1 に示す。

表 1. 交付決定額（配分額）　（金額単位：円）

年度	直接経費	間接経費	合計
平成 23 年度	178,000,000	53,400,000	231,400,000
平成 24 年度	215,600,000	64,680,000	280,280,000
平成 25 年度	217,100,000	65,130,000	282,230,000
平成 26 年度	222,600,000	66,780,000	289,380,000
平成 27 年度	214,400,000	64,320,000	278,720,000
総計	1,047,700,000	314,310,000	1,362,010,000

表 2. 総括班及び計画研究の研究組織概要

研究項目	課題番号 研究課題名	研究期間	代表者氏名	所属機関 部局 職
X00 総括	先端加速器ＬＨＣが切り拓くテラスケールの素粒子物理学～真空と時空への新たな挑戦	平成 23 年度～ 平成 27 年度	浅井 祥仁	東京大学・大学院理学系研究科・教授
A01 計画	ヒッグス粒子の発見による素粒子の質量起源の解明	平成 23 年度～ 平成 27 年度	徳宿 克夫	大学共同利用機関法人高エネルギー加速器研究機構・素粒子原子核研究所・所長
A02 計画	超対称性の発見と大統一理論の実験的検証	平成 23 年度～ 平成 27 年度	浅井 祥仁	東京大学・大学院理学系研究科・教授
A03 計画	素粒子標準模型の精密検証で探るテラスケール物理現象	平成 23 年度～ 平成 27 年度	藏重 久弥	神戸大学・自然科学系先端融合研究環・教授
A04 計画	トップクォークを用いた新しい素粒子現象の探索	平成 23 年度～ 平成 27 年度	戸本 誠	名古屋大学・大学院理学研究科・准教授
A05 計画	テラスケール物理の理論的研究	平成 23 年度～ 平成 27 年度	野尻 美保子	大学共同利用機関法人高エネルギー加速器研究機構・素粒子原子核研究所・教授
A06 計画	ＬＨＣでの発見が導く次世代エネルギーフロンティアの発展	平成 23 年度～ 平成 27 年度	駒宮 幸男	東京大学・大学院理学系研究科・教授
B01 計画	ＬＨＣ時代の新しい初期宇宙像	平成 23 年度～ 平成 27 年度	山口 昌弘	東北大学・大学院理学研究科・教授
B02 計画	テラスケール物理がもたらす新しい時空像	平成 23 年度～ 平成 27 年度	細谷　裕	大阪大学・大学院理学研究科・教授
B03 計画	テラスケール物理から超弦理論への展開	平成 23 年度～ 平成 27 年度	渡利 泰山	東京大学・数物連携宇宙研究機構・特任准教授
B04 計画	テラスケール物理における世代構造の研究	平成 23 年度～ 平成 27 年度	久野 純治	名古屋大学・基礎理論研究センター・教授

表 3. 公募研究課題一覧

研究項目	研究課題名	研究期間	代表者氏名	所属機関・部局・職
公募研究	世界最高輝度 X 線を用いた真空の構造の研究	平成 26 年度～平成 27 年度	難波 俊雄	東京大学･素粒子物理国際研究センター・助教
公募研究	テラスケール余剰次元模型の性質についての現象論的研究	平成 26 年度～平成 27 年度	柿崎 充	富山大学･大学院理工学教育部理学領域・助教
公募研究	吸収層を用いる画期的ハドロンカロリメータの開発	平成 26 年度～平成 27 年度	竹下 徹	信州大学・理学部・教授
公募研究	標準ヒッグス結合のズレからテラスケールへ	平成 26 年度～平成 27 年度	津村 浩二	京都大学・大学院理学研究科・助教
公募研究	ミューオン異常磁気能率のアノマリーを説明する新物理の現象論的研究	平成 26 年度～平成 27 年度	戸部 和弘	名古屋大学･大学院理学研究科・准教授
公募研究	微細加工技術を用いた ATLAS ミューオン前方検出器の開発	平成 26 年度～平成 27 年度	越智 敦彦	神戸大学･大学院理学研究科・准教授
公募研究	重力波で探る新たな時空像	平成 26 年度～平成 27 年度	早田 次郎	神戸大学･大学院理学研究科・教授
公募研究	sub-eV 弱結合中性ボゾン探索へ向けた原子起因四光波混合の定量化	平成 26 年度～平成 27 年度	本間 謙輔	広島大学・大学院理学研究科・助教
公募研究	ジルコニウム９６を用いたニュートリノを放出しない２重ベータ崩壊事象の探索実験	平成 24 年度～平成 25 年度	福田 善之	宮城教育大学・教育学部・教授
公募研究	精密測定実験に基づくテラスケール素粒子模型の研究	平成 24 年度～平成 25 年度	曹 基哲	お茶の水女子大学･大学院人間文化創成科学研究科･教授
公募研究	ＬＨＣ後に必須な超微細分割カロリメータの検出器要素の基礎的研究	平成 24 年度～平成 25 年度	小寺 克茂	信州大学・理学部・研究員
公募研究	ゲージボソン３点結合の精密測定による新物理探索とそれを可能にするトリガーの研究	平成 24 年度～平成 25 年度	石野 雅也	京都大学・大学院理学研究科・准教授
公募研究	テラスケール弦模型の定式化と加速器実験での検証	平成 24 年度～平成 25 年度	北澤 敬章	首都大学東京・理工学研究科・助教

研究成果の概要

研究領域の目的

（研究領域の全体像）
◎本領域の目的は、ヒッグス粒子や超対称性粒子などの確実な発見を目指す。
◎その発見を核に、素粒子・時空・真空の新しい融合領域の生成を目指す。素粒子をプローブとして時空や真空を探り、新たな宇宙観や自然観の創成を目指す

（領域の研究目的）
1）先端加速器 LHC でのアトラス実験で、『テラスケール(TeV=10^{12}電子ボルトのエネルギースケール)』 の物理を直接研究することができる。**本領域の一つ目の研究目的は、このテラスケールに期待されているヒッグス粒子や超対称性粒子などの確実な発見**である。ヒッグス粒子や超対称性粒子の発見は、「物質」や「力」などの研究ばかりでなく、その容れ物である「真空」や「時空」の研究へと発展するものであり、本領域はこれらの発見をさらに推し進めて標準理論を超えた新しいパラダイムの構築を目指す。このため、**物理研究のみならず、最先端検出器の開発や新しい加速器技術の開発を通してエネルギーフロンティア**の更なる改善を図る。
2）これら**テラスケールでの実験的成果を核に、宇宙、時空の謎などの研究を、新しいパラダイムの中で大きく展開させ新しい研究領域を創造する**ことが第二の目的である。

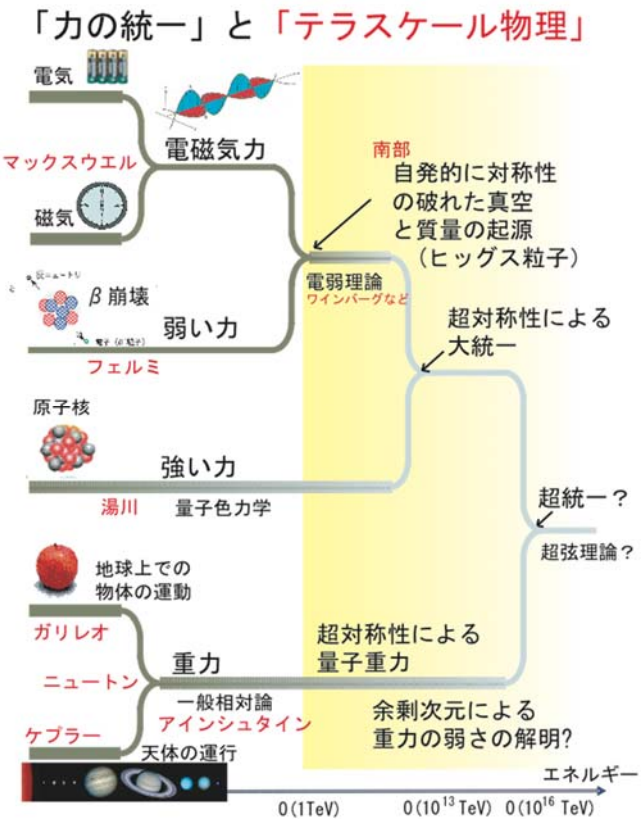

右図にテラスケールの物理の成果が大きな成果につながるものであることを示す。素粒子研究は「統一」の歴史そのものである。ヒッグス粒子の発見で、電磁気力と弱い力を統一し、質量の起源を解明することが出来る。超対称性粒子の発見は、強い力を含めた３つの力の大統一の証拠となる。超対称性や余剰次元は重力をも統一する（超統一）。

この様なテラスケールでの新しい物理の

発見は、素粒子物理学に大きく貢献するのみならず、宇宙の進化の解明など、科学全般への計り知れない貢献をもたらすものである。素粒子研究や宇宙研究の我が国の学術水準は、多くのノーベル物理学賞が示す様に高いものであるが、この成果により更に向上することができる。

また時間や空間は、我々の日常生活に密接に結びついた概念であり、超対称性の発見や余剰次元の研究を通して新しい「自然観」を創造することが期待される。

研究領域の成果

(1) ヒッグス粒子発見

本領域の一番大きな成果は、ヒッグス粒子の発見（右図は不変質量分布:ヒッグス粒子が ZZ を経由して 4 つのレプトンに崩壊した場合）と、質量の起源の解明(右下図)にある。測定されたヒッグス粒子の質量は、125.09±0.24GeV であり、すでに 0.2%の精度で決まった。ヒッグス粒子とゲージ粒子の結合のみならず、フェルミ粒子との結合が測定され、ヒッグス粒子がゲージ粒子とフェルミ粒子の質量の起源であることが分かった。また、第 2 世代の結合が弱いことも分かり、世代の理解をすすめることができた。今後はより測定精度を高め、質量起源の全貌を解明する為に、より詳細な研究が必要である。

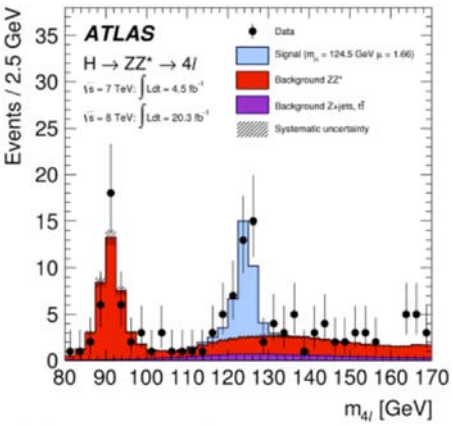

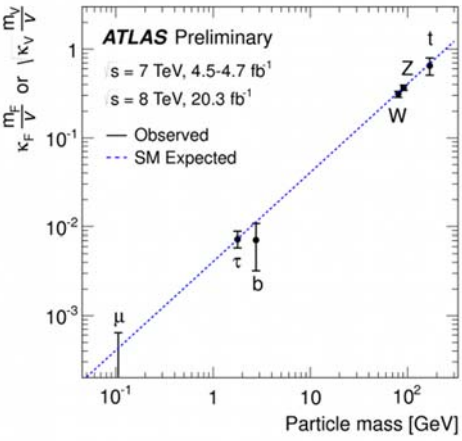

(2) 超対称性など標準理論を超える新しい素粒子現象に対する厳しい制限と新現象の可能性の示唆

新現象を確実に捉えるため、標準理論反応過程の精密検証と新現象の直接探索の両輪で研究を推進した。

◎超対称性粒子に対して厳しい制限（グルイーノに対して、約 1.5TeV より重い）が得られた。従来考えられていた超対称性理論のモデルやパラメーターに対する厳しい制約が得られ,ヒッグス粒子の質量とあいまって、ナチュラルネス（自然さ）を考え直す大きな成果となった。また暗黒物質に対する制限も厳しいものが得られた。

(3) ヒッグス粒子の発見は、真空が相転移しヒッグス場が凝縮した特殊な状態にあることの実験的な証拠

ヒッグス粒子の詳細な研究を通して、真空がどのような構造を持っているのかを調べ、宇宙の相

転移に関する知見が得られた。この質量は、この宇宙の状態が安定でなく、準安定な状態である可能性が指摘され、宇宙進化の重要な情報が得られた。
ヒッグスの３点結合測定に関し、次世代の ILC での精度がもたらす成果について新しい知見が得られた。CMB などの情報とあいまってインフレーションのモデルを絞ることができる。
125GeV のヒッグス粒子の存在と、超対称性などの新しい素粒子現象が 1 TeV より軽い領域にないことから、宇宙初期像や素粒子世代の研究に大きな影響を与えた。特に、ヒッグス粒子の質量スケールの自然さを問い直す新しい展開があった。（人間原理など）

(4) **LHC 高輝度実験・次世代エネルギーフロンティア実験の基盤技術の確立**

LHC 実験での経験から、高性能・耐放射線検出器、高速トリガーシステム、超伝導加速器技術に新たな知見が得られ、それを基に次世代の基盤技術の開発を行っている。より強い磁場を発生させることができる Nb_3Al 線材(右上図：ラザフォード線断面図、右下写真：試作した Nb_3Al 磁石)を開発し、放射線や機械的な強度耐性などを調べ設計に反映された。これらの技術は、次世代実験の鍵となる技術であり、J-PARC など広い応用への道筋ができた。

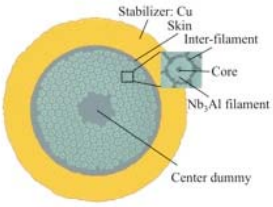

◎ビームのエミッタンスの向上にむけてビームサイズの精密測定技術を開発し、ATF で測定に用いられている。
半導体検出器、ミューオン検出器、高速トリガーシステム、カロリメータの主要な技術開発を行っている。例えば、n–in-p 型 pixel 検出器の開発、ミューオントリガーチェンバー、高速トラックトリガーシステム、High Level Trigger、カロリメータなどであり、ルミノシティーを１０倍に増強した HL-LHC や、次世代実験 ILC の検出器の基幹技術である。特に HL-LHC の検出器のグランドデザインとなる基幹技術の開発に成功した。これらは、LHC に限らず、エネルギーフロンティア実験全体に大きな貢献ができ、多くの応用が行われた。

以下各研究項目別の成果の概要を報告する。詳細については次章以降に述べる。

研究項目 A01 計画研究（ヒッグス粒子の発見による素粒子の質量起源の解明）

ヒッグス粒子を発見した。統計を増やして各崩壊モードの解析を行い、ヒッグス粒子が標準模型の予測する性質を持つことを確認した。標準模型を超えたヒッグス粒子の探索では兆候は確認されていない。
2012 年 7 月に、ヒッグス粒子と考えられる新粒子を発見でき、その後に収集したデータにより、この新粒子がヒッグス粒子であり、標準理論の予測する性質と合致していることが判明した。ヒ

ッグスの発見、スピン・パリティの解析に続き、全データを使った各崩壊モードでの解析と、超対称性粒子等で予想される他のヒッグス粒子の探索が進み、ほぼすべての解析が終了し論文として発表した。W,Z 及び γ への崩壊は確立し、フェルミ粒子への崩壊に関しては τ への崩壊が 4.5 σ で観測できている。一方で μ への崩壊は τ と同レベルでは観測されないことは確定できており、この粒子が二つのレプトン（二つの世代）を区別することを実験的に示した。ボトムへの崩壊や、トップクォークとの随伴生成の探索も進めている。これらのモードでは、標準理論のヒッグスと無矛盾であることを示すことができている。これらの測定結果から、この粒子が標準理論のヒッグスとよく合っていることを示せた。もう一つの LHC 実験である CMS 実験との共同解析も進み、0.2%精度の質量測定を達成した。結合定数に関する共同研究も進んでいる。発見したヒッグス粒子に加えて、新たな荷電及び中性ヒッグス粒子の探索も行った。残念ながら新しい粒子の兆候は得られていない。

次世代型シリコンピクセル検出器の開発を進めた。試作後、本実験で想定される放射線量を照射した。その後の性能評価を国内外の加速器施設におけるビームラインを用いて行い、十分な性能を確認した。

大面積の検出器を作る上でコストを下げられる n-in-p 型のシリコンセンサーの開発を進めた。センサーを試作後、放射線照射をした上で、国内外の加速器施設を使ったビームテストを行って、ピクセルの構造のどの部分が放射線損傷に弱いかを洗い出し、その改良を進め、弱点の克服にほぼ目処がついた。

研究項目 A02 計画研究（超対称性の発見と大統一理論の実験的検証）

生成･崩壊の事象トポロジー分類により､超対称性粒子探索を組織的に進めることを目標とした。発見には至らず、各チャンネルに厳しい制限を課した。一方、超対称性の存在を示唆する事象も確認した。

重心系エネルギー 13, 8, 7 TeV の陽子陽子衝突を用いて超対称性粒子の探索を進めた。Z/W+jets、ttbar+jets などの背景事象の高精度な見積り手法の開発も進め、第 3 世代スクォーク（超対称性クォークパートナー）質量下限 0.84TeV (於 13TeV)、グルイーノ、第 1,2 世代スクォーク質量下限 1.9TeV(於 8TeV)、電弱生成ゲージ粒子パートナー質量下限 0.4TeV（於 8TeV）などの厳しい制限を課した。一方で、複数ジェット＋消失エネルギー＋Z を要求するチャンネルでは 3 σ の超過事象数があることを確認。また 13TeV 衝突におけるグルイーノ・スクォーク対生成の 0 レプトン探索チャンネルでは、超対称性事象の可能性がある事象も複数確認されており、高エネルギー・高統計での追解析が急がれる。

長寿命粒子、高質量共鳴ピーク、その他特異な終状態など、超対称性以外の新粒子・現象の発見を目標とした。発見には至らず、各チャンネルに厳しい制限を課した。一方で、統計的有意な超過も確認した。

検出器中で崩壊する比較的長寿命の未知粒子、高質量領域の共鳴質量ピーク、その他特異な終状態など、超対称性以外の新粒子・現象の探索が行われ、多くのチャンネルに厳しい制限を課した。高質量領域では崩壊後のボソンが 2 本の近接したジェットに崩壊し、既存の手法では検出効率が下がる問題があったが、近接ジェットを再構成する新手法を開発し、8TeV 衝突で 2 ボソン共鳴の超過を 2.5σで確認した。高エネルギー・高統計での追解析が急がれる。

LHC 高輝度アップグレードに向けた磁石の開発、並びに次世代加速器用高磁場超電導磁石・線材の開発を目標にした。新開発の耐放射線線材を開発。線材を組み込んだ、2m 長モデル機の試作に成功し、冷却励磁試験を実施した。10T を超える高磁場磁石を製作し、励磁試験によりケーブル性能を評価した。

加速器開発: LHC 高輝度アップグレードに向けたビーム分離用大口径双極超電導磁石の開発を行い、電磁設計・機械構造設計などの基礎開発を進めた。2m 長モデル機を試作し、1.9K における冷却励磁試験を行った。同時に耐放射線性に優れた有機絶縁構造材料の開発を進めた。放射線照射による試験、並びに 2m 長モデル機に搭載し性能評価を行った。次世代高エネルギー加速器(FCC)計画に向けた、高磁場超電導磁石及び線材の開発も行った。10T を超える高磁場下でも臨界電流密度が安定する機械特性に優れた Nb3Al 線材に着目し研究開発を進めた。こちらはラザフォードケーブル（撚線）の試作に成功し、性能評価を行った。

研究項目 A03 計画研究（素粒子標準模型の精密検証で探るテラスケール物理現象）

弱ボゾン生成，ジェット生成などから LHC エネルギー領域での標準模型を精密検証し，同時に新物理探索のバックグランド理解を高めることを目標とした。パートン密度の新制限など標準模型の理解を深め，弱ボゾン融合生成や 4 レプトン崩壊など，ヒッグス粒子の測定感度を上げる測定ができた。

複数の弱ボゾン生成を通して標準模型の特徴的構造である弱ボゾンの 3 点・4 点ゲージ結合を精密測定し，また生成断面積の異常から新物理を探ることを目標とした。高精度の測定により，異常ゲージ結合に対し上限値を 1 桁以上更新した。また，新物理に感度の高い弱ボゾン同士の散乱を初めて観測した。

W/Z および WW,WZ,ZZ,2 光子生成断面積測定では最高で約 10%の精度で行い、理論予想値と矛盾しない結果を得た。これらの測定結果から、異常 3 点ゲージ結合カップリングとして、Tevatron/LEP の測定より 1 桁以上小さい上限値を得た。また，ヒッグス粒子生成と関連の深い Z

粒子の 4 レプトン崩壊，ベクトルボゾン融合過程などの散乱断面積を精密に測定した。
b-tagging の改良により、高 Pt を持つ Z 粒子の b 崩壊過程や、Bc+ 稀崩壊過程の測定を行った。ジェット生成反応の異なる重心系エネルギーでの断面積測定を行い、QCD Next Leading Order プロセスの計算結果との比較などによって、PDF 決定につなげた。

次世代の高ルミノシティーLHC 実験に対応した，事象を効率よく選別できるミューオントリガー検出器とトリガー回路の開発を目標とした。次のアップグレード用に放電を抑制したミューオントリガー検出器，トリガー論理と回路を開発した。より高ルミノシティー用の放射線耐性を持つ回路も開発した。

ミューオン検出器開発：　LHC フェーズ 1 アップグレードで計画されている ATLAS ミューオンスモールウィールでの Micromegas 検出器も開発を中心に行った。電極の構造・製造方法の開発を行い、アノードに高抵抗電極を用いることで、中性子による大きな電離損失事象に起因する放電を大幅に押さえられることがわかった。これを受けて，スモールウィールのプロトタイプの製作を行った。

トリガー開発：　スモールウィール検出器を用いたトリガーのためのアルゴリズム及びプロセッサーの開発を行った。LHC フェーズ 2 アップグレードで計画されている高ルミノシティー運転におけるミューオントリガーのために、ドリフトチューブを用いたアルゴリズムについて検討を行い、トリガーレートを削減できることを明らかにした。また、そのための高精度 TDC など放射線耐性をもつフロントエンド回路の開発を行った。

研究項目 A04 計画研究 （トップクォークを用いた新しい素粒子現象の探索）

重心系エネルギー 7、8、13TeV の陽子陽子衝突によるトップクォークの生成と崩壊を詳細に検証し（右図）、テラスケールに至るまで、摂動 QCD がトップクォーク対生成を良く記述する有効理論であることを立証した。また、高速飛跡再構成トリガーを新たに開発するなど、トリガーシステムを改良した。

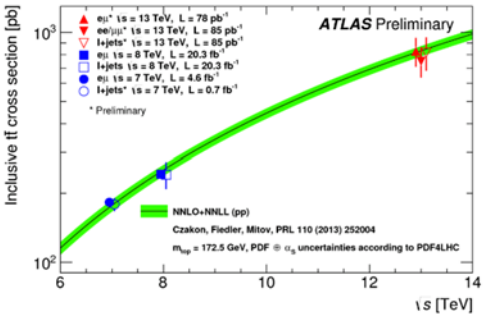

トップクォーク物理：　重心系エネルギー13TeV、8TeV, 7TeV の陽子陽子衝突による t クォーク対の生成断面積を、2 レプトン終状態事象（両方の t クォークの崩壊粒子に電子または μ 粒子が含まれる）を用いて精密に測定し、摂動 QCD がトップクォーク生成を良く記述する有効理論であることを立証した。

t クォークの崩壊による荷電レプトンと b クォークの角度差から、t→Wb 崩壊中の W 粒子の 3 種類の偏極度（FL, F0, FR）を測定した。F0 = 0.687±0.005, FR = 0.0017±0.0001（FL = 1 − F0

– FR）の結果は、V-A 型の弱い相互作用によって t クォークが崩壊する時の偏極度と無矛盾であることを示した。

重心系エネルギー7TeV の陽子陽子衝突による t クォーク対の生成断面積を τ had-レプトン事象（片方にハドロン崩壊をする τ 粒子、もう一方に電子また μ 粒子が含まれる）、全ハドロン事象（両方ともハドロンに崩壊する）を用いて測定し、標準模型と無矛盾であることを示した。

トリガー開発：　将来の高輝度 LHC 実験に向け、これまではトリガーに用いる必要のなかった精密飛跡検出器による μ 粒子トリガー回路の開発を行った。TDC 回路の基礎設計を終えた。

Run2 での導入を目指し、高速飛跡再構成トリガー(FTK)回路の開発と製作を行った。本計画研究によって開発する回路が ATLAS 実験の量産要請を満たすことを確認し、本研究によって構築したテストスタンドを用いて量産時の諸問題に対するフィードバックを行った結果、回路製作の量産を完遂させた。

t クォーク対生成事象の取得に重要な μ 粒子トリガーや電子トリガーの運動量閾値を 25GeV 程度の低い値に抑えつつ、トリガーレートを低く維持するアルゴリズムの開発に成功した。

研究項目 A05 計画研究（テラスケール物理の理論的研究）

QCD の理論特性を利用して新物理の探索感度を上げる研究をおこない、テラスケール物理探索の背景事象をより正しく理解することを目標とした。ジェットの構造や制動輻射に関する研究を行い, クォーク・グルーオン識別の向上や、ISR の性質を利用した背景事象の低減方法を明らかにした。標準模型の分布のズレから新粒子の断面積、崩壊パターン、スピン、質量を測定する新しい解析方法を考案することを目的とした。新物理の信号である高エネルギーのトップジェットから偏極を導き出す方法を明らかにするとともに、ISR の分布からスピンを明らかにする方法などを研究した。テラスケールでの新物理を新しいパラダイム（時空、宇宙など）に転換する研究を行い、この実験的検証にむけた現象論研究を目的とした。バリオン数生成、暗黒物質、ニュートリノ質量の生成機構とヒッグス粒子が関係する模型を網羅的に検討して、拡張模型を制限する方法を明らかにした。

検出手法の研究：　QCD の知見を用い a) QCD の高次過程の特性を利用して新粒子を発見する手法の考案 b)ジェットの種となるパートンがクォークかグルーオンかによって異なることを用いた、新粒子探索における S/N 向上方法の提案と理論的不定性の解明 c) Boost された top quark や重たいゲージ粒子から生成されるジェットの内部構造をもちいた scalar top や heavy boson の探索可能性の検討等を行った。

暗黒物質探索：　暗黒物質を含む模型について総合的に検討を行い、超対称模型、バリオン数生成と暗黒物質を関係づける模型、フェルミオンと暗黒物質のある系など、LHC での検証が可能である領域を明らかにした。

新物理の理論的検討：　ヒッグス粒子の発見に伴い、その性質の精密測定によって、新しい物

理の構造の手がかりを得ることが可能なのではないか期待された。Radion と Higgs の混合のあ Randall-Sundrum 模型, 超対称模型、Minimal composite Higgs 模型などについて、Higgs の生成、分岐比等の研究によって、広いパラメータ領域で新物理を明らかにできることを示した。また、兼村はヒッグスセクターの取り得る構造を輻射補正も含めて研究し ILC 実験や LHC 実験でその性質が明らかにできることを示した。また、電弱対称性の破れの背後の物理、標準理論で説明できない諸現象（暗黒物質、バリオン数生成、ニュートリノ質量）とヒッグス物理の関係を研究し、LHC Run2 等の将来実験を用いて検証可能である場合を明らかにした。

研究項目 A06 計画研究（LHC の発見が導く次世代エネルギーフロンティアの発展）

ILC での実用に向けたジェットエネルギー高精度測定用の稠密な電磁カロリメータを開発。素子の放射線耐性を、中性子を用いて精査した。ドイツで電子ビームを用いたプロトタイプの性能評価に成功した。
KEK の試験加速器 ATF2 において、電子ビームサイズを極限に抑え、鉛直方向世界最小サイズ 41nm の測定に成功した。フィードバックを用いたビームジッター抑制を英国や KEK と共同で行い成功した。
LHC で新粒子の事象候補があった。これらを ILC の実験で精査し物理の方向を見極める方法を開発した。

ILC ビーム収束系開発： local chromatic 補正と言うビームオプティクスを確立した。KEK の試験加速器 ATF2 において、世界で最小の縦方向ビームサイズ σy=41nm を達成した。2 バンチのビームを ATF でつくり 1 バンチ目の測定でフィードバックをかけ 2 バンチ目のビームジッターを減らすことに成功。

ILC のシリコン電磁カロリメータの詳細設計において安価でかつ性能を落とさないための素子のスペックを研究した。また、素子の放射線耐性を神戸大学の中性子ビームを用いて精査。十分な耐性があることを検証。ドイツ DESY においてプロトタイプのビームテストに成功。

τ の再構成は、重いヒッグスの CP 混合の決定に重要である。ILC での衝突点の位置、荷電粒子の軌道、$\pi 0$ からの光子の電磁カロリメータでのシャワー測定を用いて、いかなる τ 崩壊も再構成できることを証明。

研究項目 B01 計画研究（LHC 時代の新しい宇宙像）

実験結果に基づきテラスケールの素粒子模型を構築し、宇宙進化史への影響を明らかにすることを目標とした。ヒッグス粒子の質量を説明する超対称模型を複数構築し、暗黒物質の性質を中心

に宇宙進化史への影響を明らかにした。
標準模型を超える物理がもたらす宇宙進化への影響を明らかにすることを目標とした。超対称 Peccei-Quinn 模型の宇宙進化史について、宇宙初期の熱的プラズマの影響がアクシオンの超対称対の振る舞いに大きな影響を与えることを見つけることができた。
LHC 実験が示唆する物理に基づき、インフレーションに関する理解を進めることを目標とした。ヒッグス場がインフレーションを引き起こす可能性を追求し、運動項が重要となるインフレーション模型において実現できることを示した。

ヒッグス発見が超対称標準模型に与える示唆を研究：ヒッグス粒子質量を説明するには、超対称粒子が重いか、超対称標準模型を拡張する必要がある。①ゲージ一重項を加えた模型について詳細に研究し、Peccei-Quinn 対称性を持つ模型を構成、ヒッグスセクターの量子補正や混合によりヒッグス質量を実現できることを示し、暗黒物質の性質など宇宙論的影響を考察した。②超対称粒子の質量スケールが 10TeV にある可能性の重要性を指摘し、特に Wino 暗黒物質の場合、直接探査実験による検証可能性や、LHC における発見可能性を議論した。

超対称 Peccei-Quinn 模型に基づく宇宙論の研究： 超対称化された Peccei-Quinn 模型に基づく宇宙進化について、宇宙初期の熱的プラズマがアクシオンやその超対称対の運動に与える影響を考察し、特にアクシーノ場についてはプラズマとの相互作用がその運動に大きな影響を与え得ることを明らかにした。

ヒッグスインフレーション：運動項のヒッグス場自身への依存性を用いることでヒッグス粒子がインフレーションを引き起こす running kinetic inflation を提唱した。

研究項目 B02 計画研究（テラスケール物理がもたらす新しい時空像）

５次元時空ゲージヒッグス統合理論の構成を目標とした。期間中に達成した。低エネルギー実験や LHC 実験と無矛盾な SO(5)xU(1)統合理論を構成した。
14 TeV LHC 実験で検証できる予言を導くことを目標とした。ヒッグス粒子と標準模型粒子の結合は、標準模型とほぼ同じであるが、6TeV-10TeV 領域に、幅の大きい Z'(KK 粒子)が現れる事を予言した。ヒッグス粒子の自己相互作用も標準模型からずれるが、この検証は LHC では難しい。
ヒッグス場をもとにした新しい宇宙論の構築を目標とした。ヒッグスインフレーション理論を精密化した。ヒッグス場をもとにプランクスケールの物理が探れることを明らかにした。目標は概ね達成した。
ゲージヒッグス統合理論： ヒッグス場の正体を明らかにし、新しい時空像を探った。ヒッグス場が 5 次元目のゲージ場であるとする SO(5)xU(1)ゲージヒッグス統合理論が、低エネルギーや LHC での実験結果と整合すること、5 次元目があるにもかかわらず高次の量子補正が有限になること、6TeV-10TeV 領域に、幅の大きい Z'(KK 粒子)が現れることを示した。今後の LHC 実験で

５次元目が探索できることを示した。一般にゲージヒッグス統合のシナリオでは、高次元でのゲージ不変性により紫外発散が相殺し、ヒッグス粒子の質量の安定性や崩壊幅の有限性が保証され、超対称性理論にとって代わる理論的枠組みになることを示した。

また、ヒッグス場と重力との結合の結果、ヒッグス場によるインフレーションが可能となり、繰り込み群の解析から、プランクスケールまで標準理論を適用でき、超弦理論と結びつくことも示した。

研究項目 B03 計画研究（テラスケール物理の超弦理論への展開）

超弦理論のコンパクト化の文脈で初期宇宙、フレーバー構造を探求し、シナリオを絞りこむことを企図した。フレーバー、統一理論については、超弦理論で詰め切れるところまで達した。
超対称性と例外系代数がある時空の量子像の開拓。F-理論コンパクト化のモジュラー群の同定、弦理論双対性対応の対応関係の精密化などの成果が挙がった。
ハドロン高エネルギー散乱の非摂動的側面を扱う理論手法の開発においては、ハドロン内のパートンの（縦方向だけでない）３次元情報を捕まえる理論的枠組みを確立した。

A: 超弦理論の解の統計学。当科研費補助事業期間中、７本の連作論文(総計３７７ページ)において、超弦理論の解の統計を研究するための物理理論、数学的道具の開発を行い、実際の統計の結果をした。その結果、１）標準模型の U(1) ゲージ場を得るためには、「統一理論の低エネルギー有効理論として標準模型を得ること」がもっとも統計的に典型的であること、２）素粒子の世代数は統計的にガウス分布に従うこと、分散は O(1)、３）R-パリティの自発的破れの有効理論となる解は、超弦理論においては非常に稀であること、などがあげられる。

ハドロンの高エネルギー散乱を解析する理論的枠組みの構築。パートン同志の散乱であり大運動量移行が含まれる場合には、量子色力学を用いた理論計算が可能である。より一般のハドロン散乱過程で非摂動的な情報を扱える理論的枠組みを、AdS/CFT 対応を用いることによって目指す。2014 年の西尾・渡利の論文は Brower et.al.の 2006 年の論文で導入された理論を拡張し、ハドロン２体→２体の非弾性散乱を扱えるようにした。

この成果は、より一般のハドロンの ２体→N 体　の非弾性散乱を扱える理論を構築する上でのささやかな前進であると見ることができる。一方、この ２体→２体　非弾性、の理論の段階で、すでに ep → ep gamma(exclusive) の散乱過程の部分過程として含まれる、gamma (off shell) + p → gamma (on shell) + p に適用することができる。そして、この部分過程は、一般化されたパートン分布関数（GPD）というハドロンの非摂動的情報によって決定されることが知られている。このことを利用して、上記論文では、AdS/CFT 対応（holographic）原理を用いた一般化パートン分布関数の模型をも導いた。

研究項目 B04 計画研究（テラスケールにおける世代構造の研究）

テラスケール物理における世代構造をフレーバーの物理から制限を与え、それにより LHC 実験で模型の選別を行うことを目的とした。LHC 実験では明確な新物理の発見はなかったが、超対称模型、拡張ヒッグス模型などに対して、LHC 実験とフレーバーの物理から期待される新物理の可能性を明らかにした。
新しい素粒子像の構築を目的とした LHC 実験とフレーバーの物理から期待される新物理を外挿し、超対称大統一模型の現象論、超対称性の破れの起源、ニュートリノ質量起源の可能性を明らかにした。
宇宙の物質・反物質の非対称性の解明を目指した。拡張ヒッグス模型における電弱バリオン数生成の可能性を明らかにし、その検証の方法を明らかにした。世代対称性を課した超対称大統一模型においてレプトジェネシスが宇宙のバリオン数を説明できることを明らかにした。

中性子 EDM：　クォークの EDM、カラーEDM の中性子 EDM への寄与を QCD 和則、次元 6 までの CP 対称性を破る相互作用のウィルソン係数のくりこみ群の方程式の導出など、中性子の EDM の系統的な評価のための研究を行った。超対称模型、拡張ヒッグス模型などの標準模型を超える理論の EDM を評価し、模型に制限を与えるとともに、将来実験での検証の可能性の議論をした。

レプトンフレーバー研究：　超対称性シーソー模型におけるレプトンフレーバーを破る過程の研究を行った。ヒッグス質量をインプットとして，$\mu \to e\gamma$ や $\tau \to \mu\gamma$ などに対しどのような予言が得られるかを明らかにした。

拡張ヒッグス模型で電弱バリオン数生成を評価、現在のバリオン数を説明できる理論が電子、中性子の電気双極子能率の測定、ヒッグス粒子精密測定、新粒子探索により検証可能であることを示した。超対称性の破れが 100TeV 程度の超対称標準模型は発見されたヒッグス粒子の質量 125GeV を説明しうるが、この模型は超対称大統一模型に拡張した時、ゲージ結合定数の統一が改善すること、カラーヒッグス交換による陽子崩壊の問題が解消することを示した。超対称大統一模型の予言する X ボゾン交換による陽子崩壊に対する高次の量子補正を電弱スケールから大統一スケールまでの間の全てにおいて系統的に評価し、予言の信頼性を高めた。

公募研究

平成 24 年～平成 25 年に 5 件、平成 26 年～平成 27 年に 8 件の公募研究を採択した。
LHC 実験の高度化にむけた検出器開発に関するもの、LHC の実験結果の現象論的予測を研究計画 A05 とは別の角度から与えるもの、LHC の結果を受けて弦理論、重力波の理論など更に高エ

ネルギーの素粒子論との整合性を問う研究などが行われた。また、LHC の結果を受け、将来の国際リニアコライダー（ILC）を建設した際に用いられる検出器の開発、低・中エネルギー実験で探る真空構造など、LHC の物理に間接的に関係する研究も行われ、それぞれ一定の成果を収め、学術論文の形で研究結果を公開している。

領域の貢献

当該学問分野及び関連学問分野への貢献度

「ヒッグス粒子発見のインパクト」

本領域最大の成果であるヒッグス粒子の発見は当該素粒子分野に限らず、周辺分野まで含めその影響は極めて大きい。その重要性から発見翌年のノーベル物理学賞受賞へとつながった。ヒッグス粒子の発見、その後の性質測定により様々なことが分かって来ている。ヒッグス粒子の性質測定により、真空にはヒッグス場の凝縮状態が満ちており、これにより力を伝える粒子（ゲージ粒子）のみならず、物質粒子も質量を得ていることが判明した。ヒッグス場は素粒子の世代を明確に区別しており、大きな未解決問題である世代問題に足がかりができた。また、この真空の場の変化（相転移）により、初期宇宙が進化してきたことを初めて実験的に立証できた。今後の宇宙理論はヒッグス場の存在・測定された性質を前提に相転移前の宇宙の解明を目指して発展してゆく。またヒッグス粒子が軽かった(125GeV)ことは、標準模型を超える物理がテラ電子ボルトスケールに潜んでいることを示す。LHC 実験の長期計画、ILC 実験など、次世代の高エネルギー素粒子分野を牽引する加速器計画に対しても、具体的な強い方向付けを与えた。

「新粒子事象の兆候」

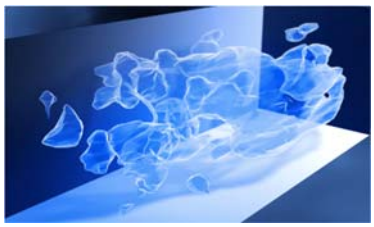

本領域最終年に 13TeV 衝突エネルギーで得られた幾つかの超過事象チャンネルから、宇宙・素粒子分野に大きな議論が巻き起こっている。高統計データにより存在が確認されれば、素粒子実験分野の将来計画を一気に具現化するインパクトをもつ。超対称性

粒子探索チャンネルで見られた超過事象は、宇宙暗黒物質など未解決問題の解明にも大きく寄与することが期待される。

「標準模型を超える物理の探索・標準模型の精密検証」

上述のように新物理の兆候は見られるが、一方で数多くの新物理探索チャンネルにおいて、新物理、特に従来考えられていた超対称性理論のモデルパラメータへの厳しい制限を得て、今後の探索領域を強く限定する成果を得た。特に、超対称性粒子探索など大きな消失エネルギーを用いるチャンネルからの制限より、宇宙暗黒物質の候補に対して強い制限を与える結果となり、非加速器実験による直接探索分野と相補的な暗黒物質研究が期待される。また、軽いヒッグス粒子の存在と新粒子未発見の事実は、これからの新たな物理模型構築の基本方針を大きく変更する成果となった。同時に精密測定による標準模型の精密検証、高統計データを用いた高次の標準模型過程が検証され、テラスケールにおける標準模型の有効領域が確認された。

「LHC 高輝度・次世代加速器開発による基盤技術の確立」

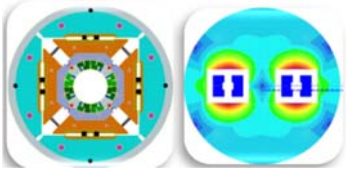

本領域では次世代加速器に向け、放射線耐性に優れ、高い磁場精度を保つ、超伝導素材開発が行われた。また、10T 以上の高電磁力線下での機械特性に優れた超伝導新素材の開発が行われた。これらの新たな超伝導加速器技術の知識・経験は我が国の加速器技術立国としての立場を不動のものにする影響力を持つ。

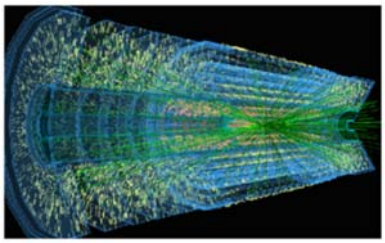

「次世代検出器開発」半導体検出器、ミューオン検出器等、アトラス実験の主要な構成検出器の高度化が進められた。これは次世代実験 ILC、その他の様々な実験で使われる検出器の基本設計に直接影響を及ぼす。

研究計画に参画した若手研究者の成長の状況

国際的に活躍する若手研究者の育成

若手研究者を最先端で競争の厳しい素粒子研究に従事させることで育成を行ってきた。実験が行われている CERN には、世界中から優秀な研究者が集まっている。若手研究者は、そのような環境である CERN に長期滞在し、諸外国の第一線の研究者と議論を重ね切磋琢磨することで、国際的に活躍する優秀な研究者に成長することができる。本領域の若手研究者はヒッグス粒子発見において、3 つの主要なチャンネルで解析責任者として現場を率いて発見という大きな成果をあげる活躍をした。そのほか多くの若手研究者(20 名以上)が解析や検出器の責任者として活躍をしてきた。

実験・理論の融合を通した若手研究者の育成

本領域の展開するテラスケール物理は、最先端の素粒子研究であると同時に、領域として実験・理論を融合した研究を推進してきた。若手研究者には研究会や勉強会を開催する(合計 11 回)などして実験と理論の両方の視点から研究を進める、他では得がたい研究環境を提供することを行ってきた。

博士研究員の雇用と育成

本領域の特徴として理論研究の博士研究員(17 名)を多く採用した。LHC・アトラス実験の Run1 の成果が出続けるなか、理論的に取り組むべき研究テーマは次々と生まれる。このような研究環境は単に若手研究者を引きつける魅力ある環境としてだけでなく若手研究者を優秀な研究者に育成する環境でもある。彼らの約 9 割はアカデミックな分野で教員(准教授 1 名, 講師 1 名, 助教 3 名)や研究員(10 名)として活躍している。また、実験の博士研究員 7 名は若手研究者として上述した成果をあげて、7 名全員がアカデミックな分野で教員(准教授 1 名, 助教 2 名)や研究員(4 名)として活躍している。

大学院生の育成

本領域では研究協力者として多くの大学院生を CERN という現場に中・長期に滞在させた。最先端の素粒子研究に従事することで、研究を直に学ぶ、経験することで将来のキャリアについて考える機会を与えてきた。修士号を取得した学生は 131 名で 57 名が進学、博士号を取得した学生は 70 名でそのうち 49 名はアカデミックの分野で活躍している。

最後に本領域に関わった若手研究者の動向をまとめる。非常勤の研究職であった研究者の約半数は常勤の職に就き、博士号を取得した多くの大学院生が非常勤の研究者として研究人生をスター

トさせていることが分かる。また、修士号のみを取得した大学院生は民間企業、官公庁などで活躍している。

本領域に関わった時点 → H28 年 4 月 1 日の時点	人数
研究職(常勤) → 研究職(常勤)（昇格など）	4
研究職(非常勤) → 研究職(常勤)	21
研究職(非常勤) → 研究職(非常勤)	19
研究職(非常勤) → その他(企業など)	2
大学院生 → 研究職(常勤)	5
大学院生 → 研究職(非常勤)	44
大学院生 → その他(企業など)	95

総括班

総括班の研究組織

(1)研究代表者
浅井　祥仁（ASAI, Shoji）
東京大学・理学系研究科・教授
研究者番号：60282505
研究全体の統括、計画研究 A02 代表

(3)連携研究者
徳宿　克夫（TOKUSHUKU, Katsuo）
高エネルギー加速器研究機構・素粒子原子核研究所・所長
研究者番号：80207547
計画研究 A01 代表

藏重　久弥（KURASHIGE, Hisaya）
神戸大学・自然科学系先端融合研究環・教授
研究者番号：20205181
計画研究 A03 代表

戸本 誠（TOMOTO, Makoto）
名古屋大学・大学院理学研究科・准教授
研究者番号：80432235
計画研究 A04 代表

野尻美保子　（NOJIRI, Mihoko）
大学共同利用機関法人・高エネルギー加速器研究機構・素粒子原子核機構・教授
研究者番号：30222201
計画研究 A05 代表

駒宮　幸男（KOMAMIYA, Sachio）
東京大学・大学院理学系研究科・教授
研究者番号：80126060

総括班

計画研究 A06 代表

山口　昌弘　(YAMAGUCHI, Masahiro)
東北大学・大学院理学研究科・教授
研究者番号：10222366
計画研究 B01 代表

細谷　裕（HOSOTANI, Yutaka）
大阪大学・大学院理学研究科・教授
研究者番号：50324744
計画研究 B02 代表

渡利　泰山（WATARI, Taizan）
東京大学　・カブリ数物連携宇宙研究機構・特任准教授
研究者番号：40451819
計画研究 B03 代表

久野純治（HISANO, Junji）
名古屋大学・基礎理論研究センター・教授
研究者番号：60300670
計画研究 B04 代表

横山　広美（YOKOYAMA, Hiromi）
東京大学・大学院理学系研究科・准教授
研究者番号：50401708
科学コミュニケーション担当

坂本　宏　(SAKAMOTO, Hiroshi)
東京大学・素粒子物理国際研究センター・教授
研究者番号：80178574
事務担当

交付決定額

総括班に配分された交付額を表 1 に示す。

表 1. 交付決定額（配分額）　（金額単位：円）

年度	直接経費	間接経費	合計
平成 23 年度	3,600,000	1,080,000	4,680,000
平成 24 年度	6,300,000	1,890,000	8,190,000
平成 25 年度	3,300,000	990,000	4,290,000
平成 26 年度	3,200,000	960,000	4,160,000
平成 27 年度	4,500,000	1,350,000	5,850,000
総計	20,900,000	6,270,000	27,170,000

領域ホームページ

領域が運用するホームページの URL は以下の通り

http://www.icepp.s.u-tokyo.ac.jp/terascale/

領域として開催した国際会議等

新学術領域研究会　テラスケール 2015 ～先端加速器 LHC が切り拓くテラスケールの素粒子物理学～
2015 年 12 月 21 日～23 日、東京工業大学大岡山キャンパス・レクチャーシアターで開催。
http://www.hep.phys.titech.ac.jp/atlas/terascale2015/index.html

新学術領域研究会　テラスケール研究会 ～先端加速器 LHC が切り拓くテラスケールの素粒子物理学～
2015 年 6 月 27 日、東京大学本郷キャンパスで開催。
http://www.icepp.s.u-tokyo.ac.jp/terascale/news/workshop201506.html

国際研究会「Computing in High Energy and Nuclear Physics 2015」
2015 年 4 月 13 日～17 日、沖縄科学技術大学院大学で開催。
http://chep2015.kek.jp/

新学術領域 「先端加速器 LHC が切り拓くテラスケールの素粒子物理学」研究会
2014 年 3 月 25 日～26 日、東京大学本郷キャンパスで開催。
http://www.icepp.s.u-tokyo.ac.jp/terascale/news/workshop201403.html

新学術領域研究会～真空と時空への新たな挑戦～
2013 年 5 月 23 日～25 日、名古屋大学で開催。
http://www.hepl.phys.nagoya-u.ac.jp/atlas/terascale2013/Welcome.html

国際研究会「Higgs Coupling 2012　(HC2012)」
2012 年 11 月 18 日～20 日、東京大学本郷キャンパスで開催。
http://www.icepp.s.u-tokyo.ac.jp/hc2012/

国際研究会「Hadron Collider Physics Symposium 2012」
2012 年 11 月 12 日～16 日、京都大学吉田キャンパス で開催。
http://www.icepp.s.u-tokyo.ac.jp/hcp2012/

一般公開講演会「ヒッグス粒子に迫る」

総括班

2012 年 9 月 1 日、東京大学安田講堂で開催。
http://www.icepp.s.u-tokyo.ac.jp/info/kouenkai2012_sep/

一般公開講演会「ヒッグス粒子の謎」
2012 年 3 月 31 日、東京大学安田講堂で開催。
http://www.icepp.s.u-tokyo.ac.jp/info/kouenkai2012/

国際研究会「Physics opportunities with LHC at 7 TeV」
2012 年 2 月 16 日～18 日、高エネルギー加速器研究機構 4 号館 で開催。
http://research.kek.jp/people/nojiri/shingakujyutu/index.html

研究会「先端加速器 LHC が切り拓くテラスケールの素粒子物理学」
2012 年 1 月 6 日～7 日、神戸大学で開催。
http://ppwww.phys.sci.kobe-u.ac.jp/TeraScale2012/

国際研究会「Extra Dimensions in the Era of the LHC」
2011 年 12 月 12 日～14 日、大阪大学シグマホールで開催。
https://sites.google.com/a/hetmail.phys.sci.osaka-u.ac.jp/edlhc11/

研究会「先端加速器 LHC が切り拓くテラスケールの素粒子物理学」
2012 年 1 月 6 日～7 日、神戸大学百年記念館 六甲ホールで開催。
http://ppwww.phys.sci.kobe-u.ac.jp/TeraScale2012/

主要論文別刷

[1] “Observation of a new particle in the search for the Standard Model Higgs boson with the ATLAS detector at the LHC”, Physics Letters B 716 (2012) 1–29

この論文はヒッグス粒子の発見を最初に報告したもので、領域の成果としてここに示す。2017 年 1 月段階で 6,900 回以上の被引用数を獲得している。

[2] “Evidence for the spin-0 nature of the Higgs boson using ATLAS data”, The ATLAS collaboration, Physics Letters B 726 (2013) 120-144.

この論文は新しく発見された粒子がヒッグス粒子であることを確認したものである。2017 年 1 月段階で 500 回近い被引用数を獲得している。

Physics Letters B 716 (2012) 1–29

Contents lists available at SciVerse ScienceDirect

Physics Letters B

www.elsevier.com/locate/physletb

Observation of a new particle in the search for the Standard Model Higgs boson with the ATLAS detector at the LHC ☆

ATLAS Collaboration *

This paper is dedicated to the memory of our ATLAS colleagues who did not live to see the full impact and significance of their contributions to the experiment.

ARTICLE INFO

Article history:
Received 31 July 2012
Received in revised form 8 August 2012
Accepted 11 August 2012
Available online 14 August 2012
Editor: W.-D. Schlatter

ABSTRACT

A search for the Standard Model Higgs boson in proton–proton collisions with the ATLAS detector at the LHC is presented. The datasets used correspond to integrated luminosities of approximately 4.8 fb^{-1} collected at $\sqrt{s} = 7$ TeV in 2011 and 5.8 fb^{-1} at $\sqrt{s} = 8$ TeV in 2012. Individual searches in the channels $H \to ZZ^{(*)} \to 4\ell$, $H \to \gamma\gamma$ and $H \to WW^{(*)} \to e\nu\mu\nu$ in the 8 TeV data are combined with previously published results of searches for $H \to ZZ^{(*)}$, $WW^{(*)}$, $b\bar{b}$ and $\tau^+\tau^-$ in the 7 TeV data and results from improved analyses of the $H \to ZZ^{(*)} \to 4\ell$ and $H \to \gamma\gamma$ channels in the 7 TeV data. Clear evidence for the production of a neutral boson with a measured mass of 126.0 ± 0.4 (stat) ± 0.4 (sys) GeV is presented. This observation, which has a significance of 5.9 standard deviations, corresponding to a background fluctuation probability of 1.7×10^{-9}, is compatible with the production and decay of the Standard Model Higgs boson.

© 2012 CERN. Published by Elsevier B.V. Open access under CC BY-NC-ND license.

1. Introduction

The Standard Model (SM) of particle physics [1–4] has been tested by many experiments over the last four decades and has been shown to successfully describe high energy particle interactions. However, the mechanism that breaks electroweak symmetry in the SM has not been verified experimentally. This mechanism [5–10], which gives mass to massive elementary particles, implies the existence of a scalar particle, the SM Higgs boson. The search for the Higgs boson, the only elementary particle in the SM that has not yet been observed, is one of the highlights of the Large Hadron Collider [11] (LHC) physics programme.

Indirect limits on the SM Higgs boson mass of $m_H < 158$ GeV at 95% confidence level (CL) have been set using global fits to precision electroweak results [12]. Direct searches at LEP [13], the Tevatron [14–16] and the LHC [17,18] have previously excluded, at 95% CL, a SM Higgs boson with mass below 600 GeV, apart from some mass regions between 116 GeV and 127 GeV.

Both the ATLAS and CMS Collaborations reported excesses of events in their 2011 datasets of proton–proton (pp) collisions at centre-of-mass energy $\sqrt{s} = 7$ TeV at the LHC, which were compatible with SM Higgs boson production and decay in the mass region 124–126 GeV, with significances of 2.9 and 3.1 standard deviations (σ), respectively [17,18]. The CDF and DØ experiments at the Tevatron have also recently reported a broad excess in the mass region 120–135 GeV; using the existing LHC constraints, the observed local significances for $m_H = 125$ GeV are 2.7σ for CDF [14], 1.1σ for DØ [15] and 2.8σ for their combination [16].

The previous ATLAS searches in 4.6–4.8 fb^{-1} of data at $\sqrt{s} = 7$ TeV are combined here with new searches for $H \to ZZ^{(*)} \to 4\ell$,[1] $H \to \gamma\gamma$ and $H \to WW^{(*)} \to e\nu\mu\nu$ in the 5.8–5.9 fb^{-1} of pp collision data taken at $\sqrt{s} = 8$ TeV between April and June 2012.

The data were recorded with instantaneous luminosities up to 6.8×10^{33} cm^{-2} s^{-1}; they are therefore affected by multiple pp collisions occurring in the same or neighbouring bunch crossings (pile-up). In the 7 TeV data, the average number of interactions per bunch crossing was approximately 10; the average increased to approximately 20 in the 8 TeV data. The reconstruction, identification and isolation criteria used for electrons and photons in the 8 TeV data are improved, making the $H \to ZZ^{(*)} \to 4\ell$ and $H \to \gamma\gamma$ searches more robust against the increased pile-up. These analyses were re-optimised with simulation and frozen before looking at the 8 TeV data.

In the $H \to WW^{(*)} \to \ell\nu\ell\nu$ channel, the increased pile-up deteriorates the event missing transverse momentum, E_T^{miss}, resolution, which results in significantly larger Drell–Yan background in the same-flavour final states. Since the $e\mu$ channel provides most of the sensitivity of the search, only this final state is used in the analysis of the 8 TeV data. The kinematic region in which a SM Higgs boson with a mass between 110 GeV and 140 GeV is

☆ © CERN for the benefit of the ATLAS Collaboration.

* *E-mail address:* atlas.publications@cern.ch.

[1] The symbol ℓ stands for electron or muon.

0370-2693/ © 2012 CERN. Published by Elsevier B.V. Open access under CC BY-NC-ND license.
http://dx.doi.org/10.1016/j.physletb.2012.08.020

searched for was kept blinded during the analysis optimisation, until satisfactory agreement was found between the observed and predicted numbers of events in control samples dominated by the principal backgrounds.

This Letter is organised as follows. The ATLAS detector is briefly described in Section 2. The simulation samples and the signal predictions are presented in Section 3. The analyses of the $H \to ZZ^{(*)} \to 4\ell$, $H \to \gamma\gamma$ and $H \to WW^{(*)} \to e\nu\mu\nu$ channels are described in Sections 4–6, respectively. The statistical procedure used to analyse the results is summarised in Section 7. The systematic uncertainties which are correlated between datasets and search channels are described in Section 8. The results of the combination of all channels are reported in Section 9, while Section 10 provides the conclusions.

2. The ATLAS detector

The ATLAS detector [19–21] is a multipurpose particle physics apparatus with forward-backward symmetric cylindrical geometry. The inner tracking detector (ID) consists of a silicon pixel detector, a silicon microstrip detector (SCT), and a straw-tube transition radiation tracker (TRT). The ID is surrounded by a thin superconducting solenoid which provides a 2 T magnetic field, and by high-granularity liquid-argon (LAr) sampling electromagnetic calorimetry. The electromagnetic calorimeter is divided into a central barrel (pseudorapidity[2] $|\eta| < 1.475$) and end-cap regions on either end of the detector ($1.375 < |\eta| < 2.5$ for the outer wheel and $2.5 < |\eta| < 3.2$ for the inner wheel). In the region matched to the ID ($|\eta| < 2.5$), it is radially segmented into three layers. The first layer has a fine segmentation in η to facilitate e/γ separation from π^0 and to improve the resolution of the shower position and direction measurements. In the region $|\eta| < 1.8$, the electromagnetic calorimeter is preceded by a presampler detector to correct for upstream energy losses. An iron-scintillator/tile calorimeter gives hadronic coverage in the central rapidity range ($|\eta| < 1.7$), while a LAr hadronic end-cap calorimeter provides coverage over $1.5 < |\eta| < 3.2$. The forward regions ($3.2 < |\eta| < 4.9$) are instrumented with LAr calorimeters for both electromagnetic and hadronic measurements. The muon spectrometer (MS) surrounds the calorimeters and consists of three large air-core superconducting magnets providing a toroidal field, each with eight coils, a system of precision tracking chambers, and fast detectors for triggering. The combination of all these systems provides charged particle measurements together with efficient and precise lepton and photon measurements in the pseudorapidity range $|\eta| < 2.5$. Jets and $E_{\mathrm{T}}^{\mathrm{miss}}$ are reconstructed using energy deposits over the full coverage of the calorimeters, $|\eta| < 4.9$.

3. Signal and background simulation samples

The SM Higgs boson production processes considered in this analysis are the dominant gluon fusion ($gg \to H$, denoted ggF), vector-boson fusion ($qq' \to qq'H$, denoted VBF) and Higgs-strahlung ($qq' \to WH, ZH$, denoted WH/ZH). The small contribution from the associated production with a $t\bar{t}$ pair ($q\bar{q}/gg \to t\bar{t}H$, denoted $t\bar{t}H$) is taken into account only in the $H \to \gamma\gamma$ analysis.

For the ggF process, the signal cross section is computed at up to next-to-next-to-leading order (NNLO) in QCD [22–28]. Next-to-leading order (NLO) electroweak (EW) corrections are applied [29,30], as well as QCD soft-gluon re-summations at up to next-to-next-to-leading logarithm (NNLL) [31]. These calculations, which are described in Refs. [32–35], assume factorisation between QCD and EW corrections. The transverse momentum, p_{T}, spectrum of the Higgs boson in the ggF process follows the HQT calculation [36], which includes QCD corrections at NLO and QCD soft-gluon re-summations up to NNLL; the effects of finite quark masses are also taken into account [37].

For the VBF process, full QCD and EW corrections up to NLO [38–41] and approximate NNLO QCD corrections [42] are used to calculate the cross section. Cross sections of the associated WH/ZH processes (VH) are calculated including QCD corrections up to NNLO [43–45] and EW corrections up to NLO [46]. The cross sections for the $t\bar{t}H$ process are estimated up to NLO QCD [47–51].

The total cross sections for SM Higgs boson production at the LHC with $m_H = 125$ GeV are predicted to be 17.5 pb for $\sqrt{s} = 7$ TeV and 22.3 pb for $\sqrt{s} = 8$ TeV [52,53].

The branching ratios of the SM Higgs boson as a function of m_H, as well as their uncertainties, are calculated using the HDECAY [54] and PROPHECY4F [55,56] programs and are taken from Refs. [52,53]. The interference in the $H \to ZZ^{(*)} \to 4\ell$ final states with identical leptons is taken into account [55,56,53].

The event generators used to model signal and background processes in samples of Monte Carlo (MC) simulated events are listed in Table 1. The normalisations of the generated samples are obtained from the state of the art calculations described above. Several different programs are used to generate the hard-scattering processes. To generate parton showers and their hadronisation, and to simulate the underlying event [66–68], PYTHIA6 [69] (for 7 TeV samples and 8 TeV samples produced with MadGraph [70,71] or AcerMC) or PYTHIA8 [72] (for other 8 TeV samples) are used. Alternatively, HERWIG [73] or SHERPA [74] are used to generate and hadronise parton showers, with the HERWIG underlying event simulation performed using JIMMY [75]. When PYTHIA6 or HERWIG are used, TAUOLA [76] and PHOTOS [77] are employed to describe tau lepton decays and additional photon radiation from charged leptons, respectively.

The following parton distribution function (PDF) sets are used: CT10 [78] for the POWHEG, MC@NLO, gg2WW and gg2ZZ samples; CTEQ6L1 [79] for the PYTHIA8, ALPGEN, AcerMC, MadGraph, HERWIG and SHERPA samples; and MRSTMCal [80] for the PYTHIA6 samples.

Acceptances and efficiencies are obtained mostly from full simulations of the ATLAS detector [81] using GEANT4 [82]. These simulations include a realistic modelling of the pile-up conditions observed in the data. Corrections obtained from measurements in

Table 1
Event generators used to model the signal and background processes. "PYTHIA" indicates that PYTHIA6 and PYTHIA8 are used for simulations of $\sqrt{s} = 7$ TeV and $\sqrt{s} = 8$ TeV data, respectively.

Process	Generator
ggF, VBF	POWHEG [57,58] + PYTHIA
WH, ZH, $t\bar{t}H$	PYTHIA
W + jets, Z/γ^* + jets	ALPGEN [59] + HERWIG
$t\bar{t}$, tW, tb	MC@NLO [60] + HERWIG
tqb	AcerMC [61] + PYTHIA
$q\bar{q} \to WW$	MC@NLO + HERWIG
$gg \to WW$	gg2WW [62] + HERWIG
$q\bar{q} \to ZZ$	POWHEG [63] + PYTHIA
$gg \to ZZ$	gg2ZZ [64] + HERWIG
WZ	MadGraph + PYTHIA, HERWIG
$W\gamma$ + jets	ALPGEN + HERWIG
$W\gamma^*$ [65]	MadGraph + PYTHIA
$q\bar{q}/gg \to \gamma\gamma$	SHERPA

[2] ATLAS uses a right-handed coordinate system with its origin at the nominal interaction point (IP) in the centre of the detector, and the z-axis along the beam line. The x-axis points from the IP to the centre of the LHC ring, and the y-axis points upwards. Cylindrical coordinates (r, ϕ) are used in the transverse plane, ϕ being the azimuthal angle around the beam line. Observables labelled "transverse" are projected into the x–y plane. The pseudorapidity is defined in terms of the polar angle θ as $\eta = -\ln\tan(\theta/2)$.

data are applied to account for small differences between data and simulation (e.g. large samples of W, Z and J/ψ decays are used to derive scale factors for lepton reconstruction and identification efficiencies).

4. $H \to ZZ^{(*)} \to 4\ell$ channel

The search for the SM Higgs boson through the decay $H \to ZZ^{(*)} \to 4\ell$, where $\ell = e$ or μ, provides good sensitivity over a wide mass range (110–600 GeV), largely due to the excellent momentum resolution of the ATLAS detector. This analysis searches for Higgs boson candidates by selecting two pairs of isolated leptons, each of which is comprised of two leptons with the same flavour and opposite charge. The expected cross section times branching ratio for the process $H \to ZZ^{(*)} \to 4\ell$ with $m_H = 125$ GeV is 2.2 fb for $\sqrt{s} = 7$ TeV and 2.8 fb for $\sqrt{s} = 8$ TeV.

The largest background comes from continuum $(Z^{(*)}/\gamma^*)(Z^{(*)}/\gamma^*)$ production, referred to hereafter as $ZZ^{(*)}$. For low masses there are also important background contributions from $Z+$jets and $t\bar{t}$ production, where charged lepton candidates arise either from decays of hadrons with b- or c-quark content or from mis-identification of jets.

The 7 TeV data have been re-analysed and combined with the 8 TeV data. The analysis is improved in several aspects with respect to Ref. [83] to enhance the sensitivity to a low-mass Higgs boson. In particular, the kinematic selections are revised, and the 8 TeV data analysis benefits from improvements in the electron reconstruction and identification. The expected signal significances for a Higgs boson with $m_H = 125$ GeV are 1.6σ for the 7 TeV data (to be compared with 1.25σ in Ref. [83]) and 2.1σ for the 8 TeV data.

4.1. Event selection

The data are selected using single-lepton or dilepton triggers. For the single-muon trigger, the p_T threshold is 18 GeV for the 7 TeV data and 24 GeV for the 8 TeV data, while for the single-electron trigger the transverse energy, E_T, threshold varies from 20 GeV to 22 GeV for the 7 TeV data and is 24 GeV for the 8 TeV data. For the dielectron triggers, the thresholds are 12 GeV for both electrons. For the dimuon triggers, the thresholds for the 7 TeV data are 10 GeV for each muon, while for the 8 TeV data the thresholds are 13 GeV. An additional asymmetric dimuon trigger is used in the 8 TeV data with thresholds 18 GeV and 8 GeV for the leading and sub-leading muon, respectively.

Muon candidates are formed by matching reconstructed ID tracks with either a complete track or a track-segment reconstructed in the MS [84]. The muon acceptance is extended with respect to Ref. [83] using tracks reconstructed in the forward region of the MS ($2.5 < |\eta| < 2.7$), which is outside the ID coverage. If both an ID and a complete MS track are present, the two independent momentum measurements are combined; otherwise the information of the ID or the MS is used alone. Electron candidates must have a well-reconstructed ID track pointing to an electromagnetic calorimeter cluster and the cluster should satisfy a set of identification criteria [85] that require the longitudinal and transverse shower profiles to be consistent with those expected for electromagnetic showers. Tracks associated with electromagnetic clusters are fitted using a Gaussian-Sum Filter [86], which allows for bremsstrahlung energy losses to be taken into account.

Each electron (muon) must satisfy $p_T > 7$ GeV ($p_T > 6$ GeV) and be measured in the pseudorapidity range $|\eta| < 2.47$ ($|\eta| < 2.7$). All possible quadruplet combinations with same-flavour opposite-charge lepton pairs are then formed. The most energetic lepton in the quadruplet must satisfy $p_T > 20$ GeV, and the second (third) lepton in p_T order must satisfy $p_T > 15$ GeV ($p_T > 10$ GeV). At least one of the leptons must satisfy the single-lepton trigger or one pair must satisfy the dilepton trigger requirements. The leptons are required to be separated from each other by $\Delta R = \sqrt{(\Delta\eta)^2 + (\Delta\phi)^2} > 0.1$ if they are of the same flavour and by $\Delta R > 0.2$ otherwise. The longitudinal impact parameters of the leptons along the beam axis are required to be within 10 mm of the reconstructed primary vertex. The primary vertex used for the event is defined as the reconstructed vertex with the highest $\sum p_T^2$ of associated tracks and is required to have at least three tracks with $p_T > 0.4$ GeV. To reject cosmic rays, muon tracks are required to have a transverse impact parameter, defined as the distance of closest approach to the primary vertex in the transverse plane, of less than 1 mm.

The same-flavour and opposite-charge lepton pair with an invariant mass closest to the Z boson mass (m_Z) in the quadruplet is referred to as the leading lepton pair. Its invariant mass, denoted by m_{12}, is required to be between 50 GeV and 106 GeV. The remaining same-flavour, opposite-charge lepton pair is the sub-leading lepton pair. Its invariant mass, m_{34}, is required to be in the range $m_{\min} < m_{34} < 115$ GeV, where the value of $m_{\min}$ depends on the reconstructed four-lepton invariant mass, $m_{4\ell}$. The value of $m_{\min}$ varies monotonically from 17.5 GeV at $m_{4\ell} = 120$ GeV to 50 GeV at $m_{4\ell} = 190$ GeV [87] and is constant above this value. All possible lepton pairs in the quadruplet that have the same flavour and opposite charge must satisfy $m_{\ell\ell} > 5$ GeV in order to reject backgrounds involving the production and decay of J/ψ mesons. If two or more quadruplets satisfy the above selection, the one with the highest value of m_{34} is selected. Four different analysis sub-channels, $4e$, $2e2\mu$, $2\mu 2e$ and 4μ, arranged by the flavour of the leading lepton pair, are defined.

Non-prompt leptons from heavy flavour decays, electrons from photon conversions and jets mis-identified as electrons have broader transverse impact parameter distributions than prompt leptons from Z boson decays and/or are non-isolated. Thus, the $Z+$jets and $t\bar{t}$ background contributions are reduced by applying a cut on the transverse impact parameter significance, defined as the transverse impact parameter divided by its uncertainty, d_0/σ_{d_0}. This is required to be less than 3.5 (6.5) for muons (electrons). The electron impact parameter is affected by bremsstrahlung and thus has a broader distribution.

In addition, leptons must satisfy isolation requirements based on tracking and calorimetric information. The normalised track isolation discriminant is defined as the sum of the transverse momenta of tracks inside a cone of size $\Delta R = 0.2$ around the lepton direction, excluding the lepton track, divided by the lepton p_T. The tracks considered in the sum are those compatible with the lepton vertex and have $p_T > 0.4$ GeV ($p_T > 1$ GeV) in the case of electron (muon) candidates. Each lepton is required to have a normalised track isolation smaller than 0.15. The normalised calorimetric isolation for electrons is computed as the sum of the E_T of positive-energy topological clusters [88] with a reconstructed barycentre falling within a cone of size $\Delta R = 0.2$ around the candidate electron cluster, divided by the electron E_T. The algorithm for topological clustering suppresses noise by keeping cells with a significant energy deposit and their neighbours. The summed energy of the cells assigned to the electron cluster is excluded, while a correction is applied to account for the electron energy deposited outside the cluster. The ambient energy deposition in the event from pile-up and the underlying event is accounted for using a calculation of the median transverse energy density from low-p_T jets [89,90]. The normalised calorimetric isolation for electrons is required to be less than 0.20. The normalised calorimetric isolation discriminant for muons is defined by the ratio to the p_T of the muon of the E_T sum of the calorimeter cells inside a cone of size

$\Delta R = 0.2$ around the muon direction minus the energy deposited by the muon. Muons are required to have a normalised calorimetric isolation less than 0.30 (0.15 for muons without an associated ID track). For both the track- and calorimeter-based isolation, any contributions arising from other leptons of the quadruplet are subtracted.

The combined signal reconstruction and selection efficiencies for a SM Higgs with $m_H = 125$ GeV for the 7 TeV (8 TeV) data are 37% (36%) for the 4μ channel, 20% (22%) for the $2e2\mu/2\mu2e$ channels and 15% (20%) for the $4e$ channel.

The 4ℓ invariant mass resolution is improved by applying a Z-mass constrained kinematic fit to the leading lepton pair for $m_{4\ell} < 190$ GeV and to both lepton pairs for higher masses. The expected width of the reconstructed mass distribution is dominated by the experimental resolution for $m_H < 350$ GeV, and by the natural width of the Higgs boson for higher masses (30 GeV at $m_H = 400$ GeV). The typical mass resolutions for $m_H = 125$ GeV are 1.7 GeV, 1.7 GeV/2.2 GeV and 2.3 GeV for the 4μ, $2e2\mu/2\mu2e$ and $4e$ sub-channels, respectively.

4.2. Background estimation

The expected background yield and composition are estimated using the MC simulation normalised to the theoretical cross section for $ZZ^{(*)}$ production and by methods using control regions from data for the $Z+$jets and $t\bar{t}$ processes. Since the background composition depends on the flavour of the sub-leading lepton pair, different approaches are taken for the $\ell\ell + \mu\mu$ and the $\ell\ell + ee$ final states. The transfer factors needed to extrapolate the background yields from the control regions defined below to the signal region are obtained from the MC simulation. The MC description of the selection efficiencies for the different background components has been verified with data.

The reducible $\ell\ell + \mu\mu$ background is dominated by $t\bar{t}$ and $Z+$jets (mostly $Zb\bar{b}$) events. A control region is defined by removing the isolation requirement on the leptons in the sub-leading pair, and by requiring that at least one of the sub-leading muons fails the transverse impact parameter significance selection. These modifications remove $ZZ^{(*)}$ contributions, and allow both the $t\bar{t}$ and $Z+$jets backgrounds to be estimated simultaneously using a fit to the m_{12} distribution. The $t\bar{t}$ background contribution is cross-checked by selecting a control sample of events with an opposite charge $e\mu$ pair with an invariant mass between 50 GeV and 106 GeV, accompanied by an opposite-charge muon pair. Events with a Z candidate decaying to a pair of electrons or muons in the aforementioned mass range are excluded. Isolation and transverse impact parameter significance requirements are applied only to the leptons of the $e\mu$ pair.

In order to estimate the reducible $\ell\ell + ee$ background, a control region is formed by relaxing the selection criteria for the electrons of the sub-leading pair. The different sources of electron background are then separated into categories consisting of non-prompt leptons from heavy flavour decays, electrons from photon conversions and jets mis-identified as electrons, using appropriate discriminating variables [91]. This method allows the sum of the $Z+$jets and $t\bar{t}$ background contributions to be estimated. As a cross-check, the same method is also applied to a similar control region containing same-charge sub-leading electron pairs. An additional cross-check of the $\ell\ell + ee$ background estimation is performed by using a control region with same-charge sub-leading electron pairs, where the three highest p_T leptons satisfy all the analysis criteria whereas the selection cuts are relaxed for the remaining electrons. All the cross-checks yield consistent results.

The data-driven background estimates are summarised in Table 2. The distribution of m_{34}, for events selected by the analysis except that the isolation and transverse impact parameter requirements for the sub-leading lepton pair are removed, is presented in Fig. 1.

Table 2
Summary of the estimated numbers of $Z+$jets and $t\bar{t}$ background events, for the $\sqrt{s} = 7$ TeV and $\sqrt{s} = 8$ TeV data in the entire phase-space of the analysis after the kinematic selections described in the text. The backgrounds are combined for the $2\mu2e$ and $4e$ channels, as discussed in the text. The first uncertainty is statistical, while the second is systematic.

Background	Estimated numbers of events	
	$\sqrt{s} = 7$ TeV	$\sqrt{s} = 8$ TeV
4μ		
$Z+$jets	$0.3 \pm 0.1 \pm 0.1$	$0.5 \pm 0.1 \pm 0.2$
$t\bar{t}$	$0.02 \pm 0.02 \pm 0.01$	$0.04 \pm 0.02 \pm 0.02$
$2e2\mu$		
$Z+$jets	$0.2 \pm 0.1 \pm 0.1$	$0.4 \pm 0.1 \pm 0.1$
$t\bar{t}$	$0.02 \pm 0.01 \pm 0.01$	$0.04 \pm 0.01 \pm 0.01$
$2\mu2e$		
$Z+$jets, $t\bar{t}$	$2.6 \pm 0.4 \pm 0.4$	$4.9 \pm 0.8 \pm 0.7$
$4e$		
$Z+$jets, $t\bar{t}$	$3.1 \pm 0.6 \pm 0.5$	$3.9 \pm 0.7 \pm 0.8$

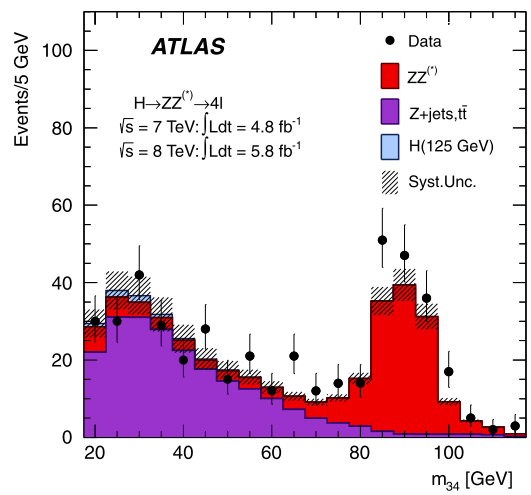

Fig. 1. Invariant mass distribution of the sub-leading lepton pair (m_{34}) for a sample defined by the presence of a Z boson candidate and an additional same-flavour electron or muon pair, for the combination of $\sqrt{s} = 7$ TeV and $\sqrt{s} = 8$ TeV data in the entire phase-space of the analysis after the kinematic selections described in the text. Isolation and transverse impact parameter significance requirements are applied to the leading lepton pair only. The MC is normalised to the data-driven background estimations. The relatively small contribution of a SM Higgs with $m_H = 125$ GeV in this sample is also shown.

4.3. Systematic uncertainties

The uncertainties on the integrated luminosities are determined to be 1.8% for the 7 TeV data and 3.6% for the 8 TeV data using the techniques described in Ref. [92].

The uncertainties on the lepton reconstruction and identification efficiencies and on the momentum scale and resolution are determined using samples of W, Z and J/ψ decays [85, 84]. The relative uncertainty on the signal acceptance due to the uncertainty on the muon reconstruction and identification efficiency is $\pm 0.7\%$ ($\pm 0.5\%/\pm 0.5\%$) for the 4μ ($2e2\mu/2\mu2e$) channel for $m_{4\ell} = 600$ GeV and increases to $\pm 0.9\%$ ($\pm 0.8\%/\pm 0.5\%$) for $m_{4\ell} = 115$ GeV. Similarly, the relative uncertainty on the signal acceptance due to the uncertainty on the electron reconstruction and identification efficiency is $\pm 2.6\%$ ($\pm 1.7\%/\pm 1.8\%$) for the $4e$ ($2e2\mu/2\mu2e$) channel for $m_{4\ell} = 600$ GeV and reaches $\pm 8.0\%$

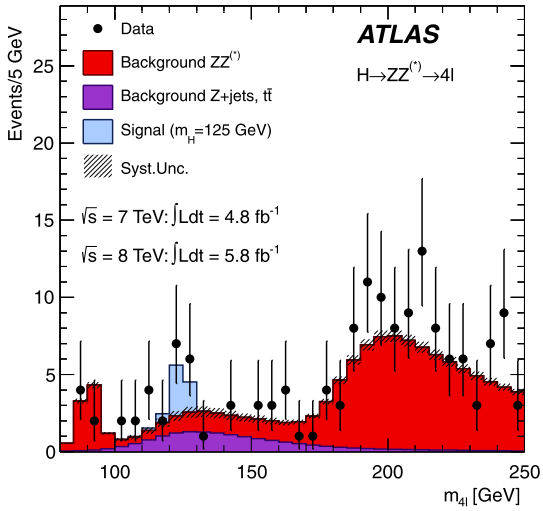

Fig. 2. The distribution of the four-lepton invariant mass, $m_{4\ell}$, for the selected candidates, compared to the background expectation in the 80–250 GeV mass range, for the combination of the $\sqrt{s} = 7$ TeV and $\sqrt{s} = 8$ TeV data. The signal expectation for a SM Higgs with $m_H = 125$ GeV is also shown.

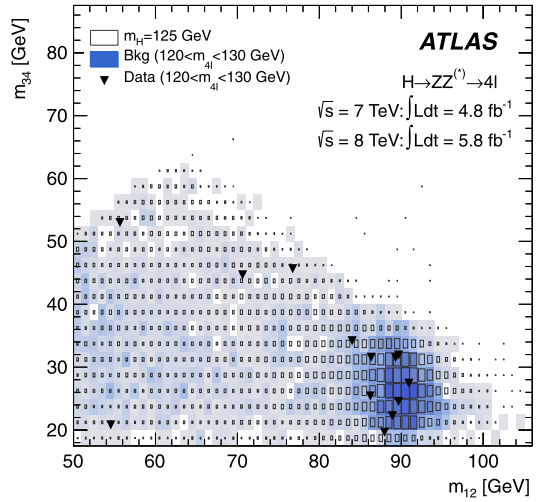

Fig. 3. Distribution of the m_{34} versus the m_{12} invariant mass, before the application of the Z-mass constrained kinematic fit, for the selected candidates in the $m_{4\ell}$ range 120–130 GeV. The expected distributions for a SM Higgs with $m_H = 125$ GeV (the sizes of the boxes indicate the relative density) and for the total background (the intensity of the shading indicates the relative density) are also shown.

Table 3
The numbers of expected signal ($m_H = 125$ GeV) and background events, together with the numbers of observed events in the data, in a window of size ±5 GeV around 125 GeV, for the combined $\sqrt{s} = 7$ TeV and $\sqrt{s} = 8$ TeV data.

	Signal	$ZZ^{(*)}$	$Z+$jets, $t\bar{t}$	Observed
4μ	2.09 ± 0.30	1.12 ± 0.05	0.13 ± 0.04	6
$2e2\mu/2\mu2e$	2.29 ± 0.33	0.80 ± 0.05	1.27 ± 0.19	5
$4e$	0.90 ± 0.14	0.44 ± 0.04	1.09 ± 0.20	2

(±2.3%/±7.6%) for $m_{4\ell} = 115$ GeV. The uncertainty on the electron energy scale results in an uncertainty of ±0.7% (±0.5%/±0.2%) on the mass scale of the $m_{4\ell}$ distribution for the $4e$ ($2e2\mu/2\mu2e$) channel. The impact of the uncertainties on the electron energy resolution and on the muon momentum resolution and scale are found to be negligible.

The theoretical uncertainties associated with the signal are described in detail in Section 8. For the SM $ZZ^{(*)}$ background, which is estimated from MC simulation, the uncertainty on the total yield due to the QCD scale uncertainty is ±5%, while the effect of the PDF and α_s uncertainties is ±4% (±8%) for processes initiated by quarks (gluons) [53]. In addition, the dependence of these uncertainties on the four-lepton invariant mass spectrum has been taken into account as discussed in Ref. [53]. Though a small excess of events is observed for $m_{4l} > 160$ GeV, the measured $ZZ^{(*)} \to 4\ell$ cross section [93] is consistent with the SM theoretical prediction. The impact of not using the theoretical constraints on the $ZZ^{(*)}$ yield on the search for a Higgs boson with $m_H < 2m_Z$ has been studied in Ref. [87] and has been found to be negligible. The impact of the interference between a Higgs signal and the non-resonant $gg \to ZZ^{(*)}$ background is small and becomes negligible for $m_H < 2m_Z$ [94].

4.4. Results

The expected distributions of $m_{4\ell}$ for the background and for a Higgs boson signal with $m_H = 125$ GeV are compared to the data in Fig. 2. The numbers of observed and expected events in a window of ±5 GeV around $m_H = 125$ GeV are presented for the combined 7 TeV and 8 TeV data in Table 3. The distribution of the m_{34} versus m_{12} invariant mass is shown in Fig. 3. The statistical interpretation of the excess of events near $m_{4\ell} = 125$ GeV in Fig. 2 is presented in Section 9.

5. $H \to \gamma\gamma$ channel

The search for the SM Higgs boson through the decay $H \to \gamma\gamma$ is performed in the mass range between 110 GeV and 150 GeV. The dominant background is SM diphoton production ($\gamma\gamma$); contributions also come from $\gamma +$ jet and jet + jet production with one or two jets mis-identified as photons (γj and jj) and from the Drell–Yan process. The 7 TeV data have been re-analysed and the results combined with those from the 8 TeV data. Among other changes to the analysis, a new category of events with two jets is introduced, which enhances the sensitivity to the VBF process. Higgs boson events produced by the VBF process have two forward jets, originating from the two scattered quarks, and tend to be devoid of jets in the central region. Overall, the sensitivity of the analysis has been improved by about 20% with respect to that described in Ref. [95].

5.1. Event selection

The data used in this channel are selected using a diphoton trigger [96], which requires two clusters formed from energy depositions in the electromagnetic calorimeter. An E_T threshold of 20 GeV is applied to each cluster for the 7 TeV data, while for the 8 TeV data the thresholds are increased to 35 GeV on the leading (the highest E_T) cluster and to 25 GeV on the sub-leading (the next-highest E_T) cluster. In addition, loose criteria are applied to the shapes of the clusters to match the expectations for electromagnetic showers initiated by photons. The efficiency of the trigger is greater than 99% for events passing the final event selection.

Events are required to contain at least one reconstructed vertex with at least two associated tracks with $p_T > 0.4$ GeV, as well as two photon candidates. Photon candidates are reconstructed in the fiducial region $|\eta| < 2.37$, excluding the calorimeter barrel/endcap transition region $1.37 \leqslant |\eta| < 1.52$. Photons that convert to electron–positron pairs in the ID material can have one or two reconstructed tracks matched to the clusters in the calorimeter. The photon reconstruction efficiency is about 97% for $E_T > 30$ GeV.

In order to account for energy losses upstream of the calorimeter and energy leakage outside of the cluster, MC simulation results are used to calibrate the energies of the photon candidates; there are separate calibrations for unconverted and converted

candidates. The calibration is refined by applying η-dependent correction factors, which are of the order of $\pm 1\%$, determined from measured $Z \to e^+e^-$ events. The leading (sub-leading) photon candidate is required to have $E_T > 40$ GeV (30 GeV).

Photon candidates are required to pass identification criteria based on shower shapes in the electromagnetic calorimeter and on energy leakage into the hadronic calorimeter [97]. For the 7 TeV data, this information is combined in a neural network, tuned to achieve a similar jet rejection as the cut-based selection described in Ref. [95], but with higher photon efficiency. For the 8 TeV data, cut-based criteria are used to ensure reliable photon performance for recently-recorded data. This cut-based selection has been tuned to be robust against pile-up by relaxing requirements on shower shape criteria more susceptible to pile-up, and tightening others. The photon identification efficiencies, averaged over η, range from 85% to above 95% for the E_T range under consideration.

To further suppress the jet background, an isolation requirement is applied. The isolation transverse energy is defined as the sum of the transverse energy of positive-energy topological clusters, as described in Section 4, within a cone of size $\Delta R = 0.4$ around the photon candidate, excluding the region within 0.125×0.175 in $\Delta\eta \times \Delta\phi$ around the photon barycentre. The distributions of the isolation transverse energy in data and simulation have been found to be in good agreement using electrons from $Z \to e^+e^-$ events and photons from $Z \to \ell^+\ell^-\gamma$ events. Remaining small differences are taken into account as a systematic uncertainty. Photon candidates are required to have an isolation transverse energy of less than 4 GeV.

5.2. Invariant mass reconstruction

The invariant mass of the two photons is evaluated using the photon energies measured in the calorimeter, the azimuthal angle ϕ between the photons as determined from the positions of the photons in the calorimeter, and the values of η calculated from the position of the identified primary vertex and the impact points of the photons in the calorimeter.

The primary vertex of the hard interaction is identified by combining the following information in a global likelihood: the directions of flight of the photons as determined using the longitudinal segmentation of the electromagnetic calorimeter (calorimeter pointing), the parameters of the beam spot, and the $\sum p_T^2$ of the tracks associated with each reconstructed vertex. In addition, for the 7 TeV data analysis, the reconstructed conversion vertex is used in the likelihood for converted photons with tracks containing hits in the silicon layers of the ID. The calorimeter pointing is sufficient to ensure that the contribution of the opening angle between the photons to the mass resolution is negligible. Using the calorimeter pointing alone, the resolution of the vertex z coordinate is ~ 15 mm, improving to ~ 6 mm for events with two reconstructed converted photons. The tracking information from the ID improves the identification of the vertex of the hard interaction, which is needed for the jet selection in the 2-jet category.

With the selection described in Section 5.1, in the diphoton invariant mass range between 100 GeV and 160 GeV, 23 788 and 35 251 diphoton candidates are observed in the 7 TeV and 8 TeV data samples, respectively.

Data-driven techniques [98] are used to estimate the numbers of $\gamma\gamma$, γj and jj events in the selected sample. The contribution from the Drell–Yan background is determined from a sample of $Z \to e^+e^-$ decays in data where either one or both electrons pass the photon selection. The measured composition of the selected sample is approximately 74%, 22%, 3% and 1% for the $\gamma\gamma$, γj, jj and Drell–Yan processes, respectively, demonstrating the dominance of the irreducible diphoton production. This decomposition is not directly used in the signal search; however, it is used to study the parameterisation of the background modelling.

5.3. Event categorisation

To increase the sensitivity to a Higgs boson signal, the events are separated into ten mutually exclusive categories having different mass resolutions and signal-to-background ratios. An exclusive category of events containing two jets improves the sensitivity to VBF. The other nine categories are defined by the presence or not of converted photons, η of the selected photons, and p_{Tt}, the component[3] of the diphoton p_T that is orthogonal to the axis defined by the difference between the two photon momenta [99,100].

Jets are reconstructed [101] using the anti-k_t algorithm [102] with radius parameter $R = 0.4$. At least two jets with $|\eta| < 4.5$ and $p_T > 25$ GeV are required in the 2-jet selection. In the analysis of the 8 TeV data, the p_T threshold is raised to 30 GeV for jets with $2.5 < |\eta| < 4.5$. For jets in the ID acceptance ($|\eta| < 2.5$), the fraction of the sum of the p_T of tracks, associated with the jet and matched to the selected primary vertex, with respect to the sum of the p_T of tracks associated with the jet (jet vertex fraction, JVF) is required to be at least 0.75. This requirement on the JVF reduces the number of jets from proton–proton interactions not associated with the primary vertex. Motivated by the VBF topology, three additional cuts are applied in the 2-jet selection: the difference of the pseudorapidity between the leading and sub-leading jets (tag jets) is required to be larger than 2.8, the invariant mass of the tag jets has to be larger than 400 GeV, and the azimuthal angle difference between the diphoton system and the system of the tag jets has to be larger than 2.6. About 70% of the signal events in the 2-jet category come from the VBF process.

The other nine categories are defined as follows: events with two unconverted photons are separated into *unconverted central* ($|\eta| < 0.75$ for both candidates) and *unconverted rest* (all other events), events with at least one converted photon are separated into *converted central* ($|\eta| < 0.75$ for both candidates), *converted transition* (at least one photon with $1.3 < |\eta| < 1.75$) and *converted rest* (all other events). Except for the *converted transition* category, each category is further divided by a cut at $p_{Tt} = 60$ GeV into two categories, *low* p_{Tt} and *high* p_{Tt}. MC studies show that signal events, particularly those produced via VBF or associated production (WH/ZH and $t\bar{t}H$), have on average larger p_{Tt} than background events. The number of data events in each category, as well as the sum of all the categories, which is denoted *inclusive*, are given in Table 4.

5.4. Signal modelling

The description of the Higgs boson signal is obtained from MC, as described in Section 3. The cross sections multiplied by the branching ratio into two photons are given in Table 4 for $m_H = 126.5$ GeV. The number of signal events produced via the ggF process is rescaled to take into account the expected destructive interference between the $gg \to \gamma\gamma$ continuum background and ggF [103], leading to a reduction of the production rate by 2–5% depending on m_H and the event category. For both the 7 TeV and 8 TeV MC samples, the fractions of ggF, VBF, WH, ZH and $t\bar{t}H$ production are approximately 88%, 7%, 3%, 2% and 0.5%, respectively, for $m_H = 126.5$ GeV.

In the simulation, the shower shape distributions are shifted slightly to improve the agreement with the data [97], and the

[3] $p_{Tt} = |(\mathbf{p}_T^{\gamma_1} + \mathbf{p}_T^{\gamma_2}) \times (\mathbf{p}_T^{\gamma_1} - \mathbf{p}_T^{\gamma_2})|/|\mathbf{p}_T^{\gamma_1} - \mathbf{p}_T^{\gamma_2}|$, where $\mathbf{p}_T^{\gamma_1}$ and $\mathbf{p}_T^{\gamma_2}$ are the transverse momenta of the two photons.

Table 4
Number of events in the data (N_D) and expected number of signal events (N_S) for $m_H = 126.5$ GeV from the $H \to \gamma\gamma$ analysis, for each category in the mass range 100–160 GeV. The mass resolution FWHM (see text) is also given for the 8 TeV data. The Higgs boson production cross section multiplied by the branching ratio into two photons ($\sigma \times B(H \to \gamma\gamma)$) is listed for $m_H = 126.5$ GeV. The statistical uncertainties on N_S and FWHM are less than 1%.

$\sqrt{s}$	7 TeV		8 TeV		
$\sigma \times B(H \to \gamma\gamma)$ [fb]	39		50		FWHM [GeV]
Category	N_D	N_S	N_D	N_S	
Unconv. central, low p_{Tt}	2054	10.5	2945	14.2	3.4
Unconv. central, high p_{Tt}	97	1.5	173	2.5	3.2
Unconv. rest, low p_{Tt}	7129	21.6	12 136	30.9	3.7
Unconv. rest, high p_{Tt}	444	2.8	785	5.2	3.6
Conv. central, low p_{Tt}	1493	6.7	2015	8.9	3.9
Conv. central, high p_{Tt}	77	1.0	113	1.6	3.5
Conv. rest, low p_{Tt}	8313	21.1	11 099	26.9	4.5
Conv. rest, high p_{Tt}	501	2.7	706	4.5	3.9
Conv. transition	3591	9.5	5140	12.8	6.1
2-jet	89	2.2	139	3.0	3.7
All categories (inclusive)	23 788	79.6	35 251	110.5	3.9

photon energy resolution is broadened (by approximately 1% in the barrel calorimeter and 1.2–2.1% in the end-cap regions) to account for small differences observed between $Z \to e^+e^-$ data and MC events. The signal yields expected for the 7 TeV and 8 TeV data samples are given in Table 4. The overall selection efficiency is about 40%.

The shape of the invariant mass of the signal in each category is modelled by the sum of a Crystal Ball function [104], describing the core of the distribution with a width σ_{CB}, and a Gaussian contribution describing the tails (amounting to $< 10\%$) of the mass distribution. The expected full-width-at-half-maximum (FWHM) is 3.9 GeV and σ_{CB} is 1.6 GeV for the inclusive sample. The resolution varies with event category (see Table 4); the FWHM is typically a factor 2.3 larger than σ_{CB}.

5.5. Background modelling

The background in each category is estimated from data by fitting the diphoton mass spectrum in the mass range 100–160 GeV with a selected model with free parameters of shape and normalisation. Different models are chosen for the different categories to achieve a good compromise between limiting the size of a potential bias while retaining good statistical power. A fourth-order Bernstein polynomial function [105] is used for the *unconverted rest* (*low* p_{Tt}), *converted rest* (*low* p_{Tt}) and *inclusive* categories, an exponential function of a second-order polynomial for the *unconverted central* (*low* p_{Tt}), *converted central* (*low* p_{Tt}) and *converted transition* categories, and an exponential function for all others.

Studies to determine the potential bias have been performed using large samples of simulated background events complemented by data-driven estimates. The background shapes in the simulation have been cross-checked using data from control regions. The potential bias for a given model is estimated, separately for each category, by performing a maximum likelihood fit to large samples of simulated background events in the mass range 100–160 GeV, of the sum of a signal plus the given background model. The signal shape is taken to follow the expectation for a SM Higgs boson; the signal yield is a free parameter of the fit. The potential bias is defined by the largest absolute signal yield obtained from the likelihood fit to the simulated background samples for hypothesised Higgs boson masses in the range 110–150 GeV. A pre-selection of background parameterisations is made by requiring that the potential bias, as defined above, is less than 20% of the statistical uncertainty on the fitted signal yield. The pre-selected parameterisation in each category with the best expected sensitivity for $m_H = 125$ GeV is selected as the background model.

The largest absolute signal yield as defined above is taken as the systematic uncertainty on the background model. It amounts to $\pm(0.2–4.6)$ and $\pm(0.3–6.8)$ events, depending on the category for the 7 TeV and 8 TeV data samples, respectively. In the final fit to the data (see Section 5.7) a signal-like term is included in the likelihood function for each category. This term incorporates the estimated potential bias, thus providing a conservative estimate of the uncertainty due to the background modelling.

5.6. Systematic uncertainties

Hereafter, in cases where two uncertainties are quoted, they refer to the 7 TeV and 8 TeV data, respectively. The dominant experimental uncertainty on the signal yield ($\pm 8\%$, $\pm 11\%$) comes from the photon reconstruction and identification efficiency, which is estimated with data using electrons from Z decays and photons from $Z \to \ell^+\ell^-\gamma$ events. Pile-up modelling also affects the expected yields and contributes to the uncertainty ($\pm 4\%$). Further uncertainties on the signal yield are related to the trigger ($\pm 1\%$), photon isolation ($\pm 0.4\%$, $\pm 0.5\%$) and luminosity ($\pm 1.8\%$, $\pm 3.6\%$). Uncertainties due to the modelling of the underlying event are $\pm 6\%$ for VBF and $\pm 30\%$ for other production processes in the 2-jet category. Uncertainties on the predicted cross sections and branching ratio are summarised in Section 8.

The uncertainty on the expected fractions of signal events in each category is described in the following. The uncertainty on the knowledge of the material in front of the calorimeter is used to derive the amount of possible event migration between the converted and unconverted categories ($\pm 4\%$). The uncertainty from pile-up on the population of the converted and unconverted categories is $\pm 2\%$. The uncertainty from the jet energy scale (JES) amounts to up to $\pm 19\%$ for the 2-jet category, and up to $\pm 4\%$ for the other categories. Uncertainties from the JVF modelling are $\pm 12\%$ (for the 8 TeV data) for the 2-jet category, estimated from $Z + 2$-jets events by comparing data and MC. Different PDFs and scale variations in the HqT calculations are used to derive possible event migration among categories ($\pm 9\%$) due to the modelling of the Higgs boson kinematics.

The total uncertainty on the mass resolution is $\pm 14\%$. The dominant contribution ($\pm 12\%$) comes from the uncertainty on the energy resolution of the calorimeter, which is determined from $Z \to e^+e^-$ events. Smaller contributions come from the imperfect knowledge of the material in front of the calorimeter, which affects the extrapolation of the calibration from electrons to photons ($\pm 6\%$), and from pile-up ($\pm 4\%$).

5.7. Results

The distributions of the invariant mass, $m_{\gamma\gamma}$, of the diphoton events, summed over all categories, are shown in Fig. 4(a) and (b). The result of a fit including a signal component fixed to $m_H = 126.5$ GeV and a background component described by a fourth-order Bernstein polynomial is superimposed.

The statistical analysis of the data employs an unbinned likelihood function constructed from those of the ten categories of the 7 TeV and 8 TeV data samples. To demonstrate the sensitivity of this likelihood analysis, Figs. 4(c) and (d) also show the mass spectrum obtained after weighting events with category-dependent factors reflecting the signal-to-background ratios. The weight w_i for events in category $i \in [1, 10]$ for the 7 TeV and 8 TeV data samples is defined to be $\ln(1 + S_i/B_i)$, where S_i is 90% of the expected signal for $m_H = 126.5$ GeV, and B_i is the integral, in

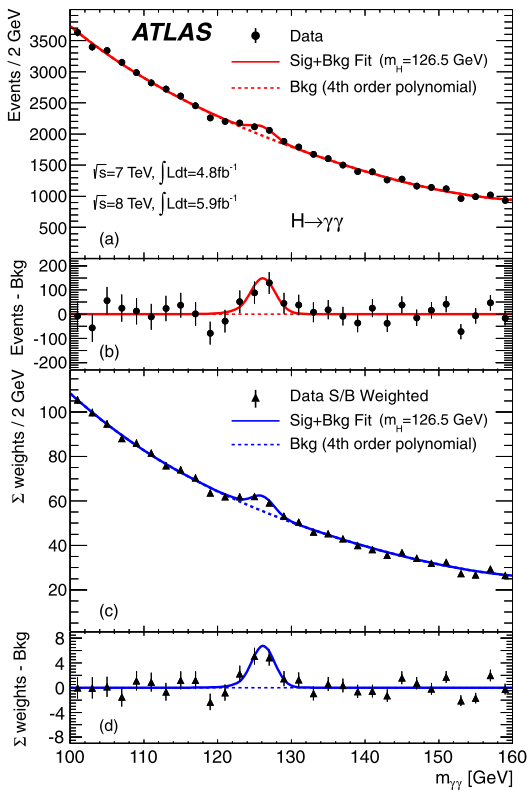

Fig. 4. The distributions of the invariant mass of diphoton candidates after all selections for the combined 7 TeV and 8 TeV data sample. The inclusive sample is shown in (a) and a weighted version of the same sample in (c); the weights are explained in the text. The result of a fit to the data of the sum of a signal component fixed to $m_H = 126.5$ GeV and a background component described by a fourth-order Bernstein polynomial is superimposed. The residuals of the data and weighted data with respect to the respective fitted background component are displayed in (b) and (d).

a window containing S_i, of a background-only fit to the data. The values S_i/B_i have only a mild dependence on m_H.

The statistical interpretation of the excess of events near $m_{\gamma\gamma} = 126.5$ GeV in Fig. 4 is presented in Section 9.

6. $H \to WW^{(*)} \to e\nu\mu\nu$ channel

The signature for this channel is two opposite-charge leptons with large transverse momentum and a large momentum imbalance in the event due to the escaping neutrinos. The dominant backgrounds are non-resonant WW, $t\bar{t}$, and Wt production, all of which have real W pairs in the final state. Other important backgrounds include Drell–Yan events ($pp \to Z/\gamma^{(*)} \to \ell\ell$) with $E_{\mathrm{T}}^{\mathrm{miss}}$ that may arise from mismeasurement, $W+$jets events in which a jet produces an object reconstructed as the second electron or muon, and $W\gamma$ events in which the photon undergoes a conversion. Boson pair production ($W\gamma^*/WZ^{(*)}$ and $ZZ^{(*)}$) can also produce opposite-charge lepton pairs with additional leptons that are not detected.

The analysis of the 8 TeV data presented here is focused on the mass range $110 < m_H < 200$ GeV. It follows the procedure used for the 7 TeV data, described in Ref. [106], except that more stringent criteria are applied to reduce the $W+$jets background and some selections have been modified to mitigate the impact of the higher instantaneous luminosity at the LHC in 2012. In particular, the higher luminosity results in a larger Drell–Yan background to the same-flavour final states, due to the deterioration of the missing transverse momentum resolution. For this reason, and the fact that the $e\mu$ final state provides more than 85% of the sensitivity of the search, the same-flavour final states have not been used in the analysis described here.

6.1. Event selection

For the 8 TeV $H \to WW^{(*)} \to e\nu\mu\nu$ search, the data are selected using inclusive single-muon and single-electron triggers. Both triggers require an isolated lepton with $p_{\mathrm{T}} > 24$ GeV. Quality criteria are applied to suppress non-collision backgrounds such as cosmic-ray muons, beam-related backgrounds, and noise in the calorimeters. The primary vertex selection follows that described in Section 4. Candidates for the $H \to WW^{(*)} \to e\nu\mu\nu$ search are pre-selected by requiring exactly two opposite-charge leptons of different flavours, with p_{T} thresholds of 25 GeV for the leading lepton and 15 GeV for the sub-leading lepton. Events are classified into two exclusive lepton channels depending on the flavour of the leading lepton, where $e\mu$ (μe) refers to events with a leading electron (muon). The dilepton invariant mass is required to be greater than 10 GeV.

The lepton selection and isolation have more stringent requirements than those used for the $H \to ZZ^{(*)} \to 4\ell$ analysis (see Section 4), to reduce the larger background from non-prompt leptons in the $\ell\nu\ell\nu$ final state. Electron candidates are selected using a combination of tracking and calorimetric information [85]; the criteria are optimised for background rejection, at the expense of some reduced efficiency. Muon candidates are restricted to those with matching MS and ID tracks [84], and therefore are reconstructed over $|\eta| < 2.5$. The isolation criteria require the scalar sums of the p_{T} of charged particles and of calorimeter topological clusters within $\Delta R = 0.3$ of the lepton direction (excluding the lepton itself) each to be less than 0.12–0.20 times the lepton p_{T}. The exact value differs between the criteria for tracks and calorimeter clusters, for both electrons and muons, and depends on the lepton p_{T}. Jet selections follow those described in Section 5.3, except that the JVF is required to be greater than 0.5.

Since two neutrinos are present in the signal final state, events are required to have large $E_{\mathrm{T}}^{\mathrm{miss}}$. $\mathbf{E}_{\mathrm{T}}^{\mathrm{miss}}$ is the negative vector sum of the transverse momenta of the reconstructed objects, including muons, electrons, photons, jets, and clusters of calorimeter cells not associated with these objects. The quantity $E_{\mathrm{T,rel}}^{\mathrm{miss}}$ used in this analysis is required to be greater than 25 GeV and is defined as: $E_{\mathrm{T,rel}}^{\mathrm{miss}} = E_{\mathrm{T}}^{\mathrm{miss}} \sin\Delta\phi_{\mathrm{min}}$, where $\Delta\phi_{\mathrm{min}}$ is $\min(\Delta\phi, \frac{\pi}{2})$, and $E_{\mathrm{T}}^{\mathrm{miss}}$ is the magnitude of the vector $\mathbf{E}_{\mathrm{T}}^{\mathrm{miss}}$. Here, $\Delta\phi$ is the angle between $\mathbf{E}_{\mathrm{T}}^{\mathrm{miss}}$ and the transverse momentum of the nearest lepton or jet with $p_{\mathrm{T}} > 25$ GeV. Compared to $E_{\mathrm{T}}^{\mathrm{miss}}$, $E_{\mathrm{T,rel}}^{\mathrm{miss}}$ has increased rejection power for events in which the $E_{\mathrm{T}}^{\mathrm{miss}}$ is generated by a neutrino in a jet or the mismeasurement of an object, since in those events the $\mathbf{E}_{\mathrm{T}}^{\mathrm{miss}}$ tends to point in the direction of the object. After the lepton isolation and $E_{\mathrm{T,rel}}^{\mathrm{miss}}$ requirements that define the pre-selected sample, the multijet background is negligible and the Drell–Yan background is much reduced. The Drell–Yan contribution becomes very small after the topological selections, described below, are applied.

The background rate and composition depend significantly on the jet multiplicity, as does the signal topology. Without accompanying jets, the signal originates almost entirely from the ggF process and the background is dominated by WW events. In contrast, when produced in association with two or more jets, the signal contains a much larger contribution from the VBF process compared to the ggF process, and the background is dominated by $t\bar{t}$ production. Therefore, to maximise the sensitivity to SM Higgs events, further selection criteria depending on the jet multiplicity are applied to the pre-selected sample. The data are subdivided into 0-jet, 1-jet and 2-jet search channels according to the number

of jets in the final state, with the 2-jet channel also including higher jet multiplicities.

Owing to spin correlations in the $WW^{(*)}$ system arising from the spin-0 nature of the SM Higgs boson and the V-A structure of the W boson decay vertex, the charged leptons tend to emerge from the primary vertex pointing in the same direction [107]. This kinematic feature is exploited for all jet multiplicities by requiring that $|\Delta\phi_{\ell\ell}| < 1.8$, and the dilepton invariant mass, $m_{\ell\ell}$, be less than 50 GeV for the 0-jet and 1-jet channels. For the 2-jet channel, the $m_{\ell\ell}$ upper bound is increased to 80 GeV.

In the 0-jet channel, the magnitude $p_{\mathrm{T}}^{\ell\ell}$ of the transverse momentum of the dilepton system, $\mathbf{p}_{\mathrm{T}}^{\ell\ell} = \mathbf{p}_{\mathrm{T}}^{\ell 1} + \mathbf{p}_{\mathrm{T}}^{\ell 2}$, is required to be greater than 30 GeV. This improves the rejection of the Drell–Yan background.

In the 1-jet channel, backgrounds from top quark production are suppressed by rejecting events containing a b-tagged jet, as determined using a b-tagging algorithm that uses a neural network and exploits the topology of weak decays of b- and c-hadrons [108]. The total transverse momentum, $p_{\mathrm{T}}^{\mathrm{tot}}$, defined as the magnitude of the vector sum $\mathbf{p}_{\mathrm{T}}^{\mathrm{tot}} = \mathbf{p}_{\mathrm{T}}^{\ell 1} + \mathbf{p}_{\mathrm{T}}^{\ell 2} + \mathbf{p}_{\mathrm{T}}^{j} + \mathbf{E}_{\mathrm{T}}^{\mathrm{miss}}$, is required to be smaller than 30 GeV to suppress top background events that have jets with p_{T} below the threshold defined for jet counting. In order to reject the background from $Z \to \tau\tau$, the $\tau\tau$ invariant mass, $m_{\tau\tau}$, is computed under the assumptions that the reconstructed leptons are τ lepton decay products. In addition the neutrinos produced in these decays are assumed to be the only source of $E_{\mathrm{T}}^{\mathrm{miss}}$ and to be collinear with the leptons [109]. Events with $|m_{\tau\tau} - m_Z| < 25$ GeV are rejected if the collinear approximation yields a physical solution.

The 2-jet selection follows the 1-jet selection described above, with the $p_{\mathrm{T}}^{\mathrm{tot}}$ definition modified to include all selected jets. Motivated by the VBF topology, several additional criteria are applied to the tag jets, defined as the two highest-p_{T} jets in the event. These are required to be separated in rapidity by a distance $|\Delta y_{jj}| > 3.8$ and to have an invariant mass, m_{jj}, larger than 500 GeV. Events with an additional jet with $p_{\mathrm{T}} > 20$ GeV between the tag jets ($y_{j1} < y < y_{j2}$) are rejected.

A transverse mass variable, m_{T} [110], is used to test for the presence of a signal for all jet multiplicities. This variable is defined as:

$$m_{\mathrm{T}} = \sqrt{\left(E_{\mathrm{T}}^{\ell\ell} + E_{\mathrm{T}}^{\mathrm{miss}}\right)^2 - \left|\mathbf{p}_{\mathrm{T}}^{\ell\ell} + \mathbf{E}_{\mathrm{T}}^{\mathrm{miss}}\right|^2},$$

where $E_{\mathrm{T}}^{\ell\ell} = \sqrt{|\mathbf{p}_{\mathrm{T}}^{\ell\ell}|^2 + m_{\ell\ell}^2}$. The statistical analysis of the data uses a fit to the m_{T} distribution in the signal region after the $\Delta\phi_{\ell\ell}$ requirement (see Section 6.4), which results in increased sensitivity compared to the analysis described in Ref. [111].

For a SM Higgs boson with $m_H = 125$ GeV, the cross section times branching ratio to the $e\nu\mu\nu$ final state is 88 fb for $\sqrt{s} = 7$ TeV, increasing to 112 fb at $\sqrt{s} = 8$ TeV. The combined acceptance times efficiency of the 8 TeV 0-jet and 1-jet selection relative to the ggF production cross section times branching ratio is about 7.4%. The acceptance times efficiency of the 8 TeV 2-jet selection relative to the VBF production cross section times branching ratio is about 14%. Both of these figures are based on the number of events selected before the final m_{T} criterion is applied (as described in Section 6.4).

6.2. Background normalisation and control samples

The leading backgrounds from SM processes producing two isolated high-p_{T} leptons are WW and top (in this section, "top" background always includes both $t\bar{t}$ and single top, unless otherwise noted). These are estimated using partially data-driven techniques based on normalising the MC predictions to the data in control regions dominated by the relevant background source. The $W+$jets background is estimated from data for all jet multiplicities. Only the small backgrounds from Drell–Yan and diboson processes other than WW, as well as the WW background for the 2-jet analysis, are estimated using MC simulation.

The control and validation regions are defined by selections similar to those used for the signal region but with some criteria reversed or modified to obtain signal-depleted samples enriched in a particular background. The term "validation region" distinguishes these regions from the control regions that are used to directly normalise the backgrounds. Some control regions have significant contributions from backgrounds other than the targeted one, which introduces dependencies among the background estimates. These correlations are fully incorporated in the fit to the m_{T} distribution. In the following sections, each background estimate is described after any others on which it depends. Hence, the largest background (WW) is described last.

6.2.1. $W+$jets background estimation

The $W+$jets background contribution is estimated using a control sample of events where one of the two leptons satisfies the identification and isolation criteria described in Section 6.1, and the other lepton fails these criteria but satisfies a loosened selection (denoted "anti-identified"). Otherwise, events in this sample are required to pass all the signal selections. The dominant contribution to this sample comes from $W+$jets events in which a jet produces an object that is reconstructed as a lepton. This object may be either a true electron or muon from the decay of a heavy quark, or else a product of the fragmentation identified as a lepton candidate.

The contamination in the signal region is obtained by scaling the number of events in the data control sample by a transfer factor. The transfer factor is defined here as the ratio of the number of identified lepton candidates passing all selections to the number of anti-identified leptons. It is calculated as a function of the anti-identified lepton p_{T} using a data sample dominated by QCD jet production (dijet sample) after subtracting the residual contributions from leptons produced by leptonic W and Z decays, as estimated from data. The small remaining lepton contamination, which includes $W\gamma^{(*)}/WZ^{(*)}$ events, is subtracted using MC simulation.

The processes producing the majority of same-charge dilepton events, $W+$jets, $W\gamma^{(*)}/WZ^{(*)}$ and $Z^{(*)}Z^{(*)}$, are all backgrounds in the opposite-charge signal region. $W+$jets and $W\gamma^{(*)}$ backgrounds are particularly important in a search optimised for a low Higgs boson mass hypothesis. Therefore, the normalisation and kinematic features of same-charge dilepton events are used to validate the predictions of these backgrounds. The predicted number of same-charge events after the $E_{\mathrm{T,rel}}^{\mathrm{miss}}$ and zero-jet requirements is 216 ± 7 (stat) ± 42 (syst), while 182 events are observed in the data. Satisfactory agreement between data and simulation is observed in various kinematic distributions, including those of $\Delta\phi_{\ell\ell}$ (see Fig. 5(a)) and the transverse mass.

6.2.2. Top control sample

In the 0-jet channel, the top quark background prediction is first normalised using events satisfying the pre-selection criteria described in Section 6.1. This sample is selected without jet multiplicity or b-tagging requirements, and the majority of events contain top quarks. Non-top contributions are subtracted using predictions from simulation, except for $W+$jets, which is estimated using data. After this normalisation is performed, the fraction of events with zero jets that pass all selections is evaluated. This fraction is small (about 3%), since the top quark decay $t \to Wb$

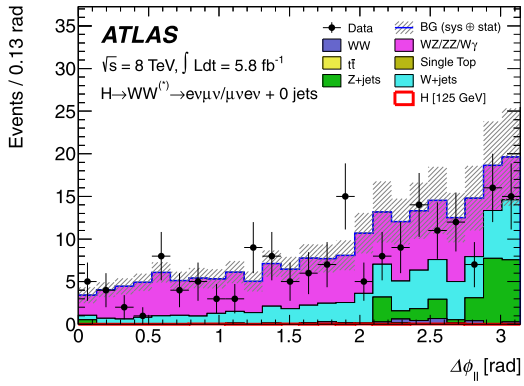

(a)

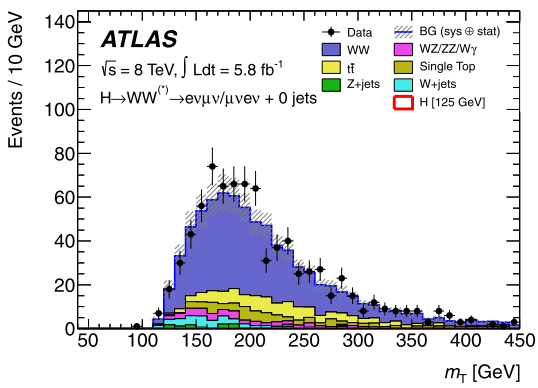

(b)

Fig. 5. Validation and control distributions for the $H \to WW^{(*)} \to e\nu\mu\nu$ analysis. (a) $\Delta\phi_{\ell\ell}$ distribution in the same-charge validation region after the $E_{\mathrm{T,rel}}^{\mathrm{miss}}$ and zero-jet requirements. (b) m_{T} distribution in the WW control region for the 0-jet channel. The $e\mu$ and μe final states are combined. The hashed area indicates the total uncertainty on the background prediction. The expected signal for $m_H = 125$ GeV is negligible and therefore not visible.

has a branching ratio of nearly 1. Predictions of this fraction from MC simulation are sensitive to theoretical uncertainties such as the modelling of initial- and final-state radiation, as well as experimental uncertainties, especially that on the jet energy scale. To reduce the impact of these uncertainties, the top quark background determination uses data from a b-tagged control region in which the one-to-two jet ratio is compared to the MC simulation [112]. The resulting correction factor to a purely MC-based background estimate after all selections amounts to 1.11 ± 0.06 (stat).

In the 1-jet and 2-jet analyses, the top quark background predictions are normalised to the data using control samples defined by reversing the b-jet veto and removing the requirements on $\Delta\phi_{\ell\ell}$ and $m_{\ell\ell}$. The $|\Delta y_{\mathrm{jj}}|$ and m_{jj} requirements are included in the definition of the 2-jet control region. The resulting samples are dominated by top quark events. The small contributions from other sources are taken into account using MC simulation and the data-driven $W+$jets estimate. Good agreement between data and MC simulation is observed for the total numbers of events and the shapes of the m_{T} distributions. The resulting normalisation factors are 1.11 ± 0.05 for the 1-jet control region and 1.01 ± 0.26 for the 2-jet control region. Only the statistical uncertainties are quoted.

6.2.3. WW control sample

The MC predictions of the WW background in the 0-jet and 1-jet analyses, summed over lepton flavours, are normalised using control regions defined with the same selections as for the signal region except that the $\Delta\phi_{\ell\ell}$ requirement is removed and the upper bound on $m_{\ell\ell}$ is replaced with a lower bound: $m_{\ell\ell} > 80$ GeV. The numbers of events and the shape of the m_{T} distribution in the control regions are in good agreement between data and MC, as shown in Fig. 5(b). WW production contributes about 70% of the events in the 0-jet control region and about 45% in the 1-jet region. Contaminations from sources other than WW are derived as for the signal region, including the data-driven $W+$jets and top estimates. The resulting normalisation factors with their associated statistical uncertainties are 1.06 ± 0.06 for the 0-jet control region and 0.99 ± 0.15 for the 1-jet control region.

6.3. Systematic uncertainties

The systematic uncertainties that have the largest impact on the sensitivity of the search are the theoretical uncertainties associated with the signal. These are described in Section 9. The main experimental uncertainties are associated with the JES, the jet energy resolution (JER), pile-up, $E_{\mathrm{T}}^{\mathrm{miss}}$, the b-tagging efficiency, the $W+$jets transfer factor, and the integrated luminosity. The largest uncertainties on the backgrounds include WW normalisation and modelling, top normalisation, and $W\gamma^{(*)}$ normalisation. The 2-jet systematic uncertainties are dominated by the statistical uncertainties in the data and the MC simulation, and are therefore not discussed further.

Variations of the jet energy scale within the systematic uncertainties can cause events to migrate between the jet bins. The uncertainty on the JES varies from $\pm 2\%$ to $\pm 9\%$ as a function of jet p_{T} and η for jets with $p_{\mathrm{T}} > 25$ GeV and $|\eta| < 4.5$ [101]. The largest impact of this uncertainty on the total signal (background) yield amounts to 7% (4%) in the 0-jet (1-jet) bin. The uncertainty on the JER is estimated from *in situ* measurements and it impacts mostly the 1-jet channel, where its effect on the total signal and background yields is 4% and 2%, respectively. An additional contribution to the JES uncertainty arises from pile-up, and is estimated to vary between $\pm 1\%$ and $\pm 5\%$ for multiple pp collisions in the same bunch crossing and up to $\pm 10\%$ for neighbouring bunch crossings. This uncertainty affects mainly the 1-jet channel, where its impact on the signal and background yields is 4% and 2%, respectively. JES and lepton momentum scale uncertainties are propagated to the $E_{\mathrm{T}}^{\mathrm{miss}}$ measurement. Additional contributions to the $E_{\mathrm{T}}^{\mathrm{miss}}$ uncertainties arise from jets with $p_{\mathrm{T}} < 20$ GeV and from low-energy calorimeter deposits not associated with reconstructed physics objects [113]. The impact of the $E_{\mathrm{T}}^{\mathrm{miss}}$ uncertainty on the total signal and background yields is $\sim 3\%$. The efficiency of the b-tagging algorithm is calibrated using samples containing muons reconstructed in the vicinity of jets [114]. The uncertainty on the b-jet tagging efficiency varies between $\pm 5\%$ and $\pm 18\%$ as a function of the jet p_{T}, and its impact on the total background yield is 10% for the 1-jet channel. The uncertainty in the $W+$jets transfer factor is dominated by differences in jet properties between dijet and $W+$jets events as observed in MC simulations. The total uncertainty on this background is approximately $\pm 40\%$, resulting in an uncertainty on the total background yield of 5%. The uncertainty on the integrated luminosity is $\pm 3.6\%$.

A fit to the distribution of m_{T} is performed in order to obtain the signal yield for each mass hypothesis (see Section 6.4). Most theoretical and experimental uncertainties do not produce statistically significant changes to the m_{T} distribution. The uncertainties that do produce significant changes of the distribution of m_{T} have no appreciable effect on the final results, with the exception of those associated with the WW background. In this case, an uncertainty is included to take into account differences in the distribution of m_{T} and normalisation observed between the MCFM [115], MC@NLO + HERWIG and POWHEG + PYTHIA

Table 5
The expected numbers of signal ($m_H = 125$ GeV) and background events after all selections, including a cut on the transverse mass of $0.75 m_H < m_T < m_H$ for $m_H = 125$ GeV. The observed numbers of events in data are also displayed. The $e\mu$ and μe channels are combined. The uncertainties shown are the combination of the statistical and all systematic uncertainties, taking into account the constraints from control samples. For the 2-jet analysis, backgrounds with fewer than 0.01 expected events are marked with '–'.

	0-jet	1-jet	2-jet
Signal	20 ± 4	5 ± 2	0.34 ± 0.07
WW	101 ± 13	12 ± 5	0.10 ± 0.14
$WZ^{(*)}/ZZ/W\gamma^{(*)}$	12 ± 3	1.9 ± 1.1	0.10 ± 0.10
$t\bar{t}$	8 ± 2	6 ± 2	0.15 ± 0.10
$tW/tb/tqb$	3.4 ± 1.5	3.7 ± 1.6	–
$Z/\gamma^* + \text{jets}$	1.9 ± 1.3	0.10 ± 0.10	–
$W + \text{jets}$	15 ± 7	2 ± 1	–
Total background	142 ± 16	26 ± 6	0.35 ± 0.18
Observed	185	38	0

generators. The potential impact of interference between resonant (Higgs-mediated) and non-resonant $gg \to WW$ diagrams [116] for $m_T > m_H$ was investigated and found to be negligible. The effect of the WW normalisation, modelling, and shape systematics on the total background yield is 9% for the 0-jet channel and 19% for the 1-jet channel. The uncertainty on the shape of the total background is dominated by the uncertainties on the normalisations of the individual backgrounds. The main uncertainties on the top background in the 0-jet analysis include those associated with interference effects between $t\bar{t}$ and single top, initial state an final state radiation, b-tagging, and JER. The impact on the total background yield in the 0-jet bin is 3%. For the 1-jet analysis, the impact of the top background on the total yield is 14%. Theoretical uncertainties on the $W\gamma$ background normalisation are evaluated for each jet bin using the procedure described in Ref. [117]. They are $\pm 11\%$ for the 0-jet bin and $\pm 50\%$ for the 1-jet bin. For $W\gamma^*$ with $m_{\ell\ell} < 7$ GeV, a k-factor of 1.3 ± 0.3 is applied to the MadGraph LO prediction based on the comparison with the MCFM NLO calculation. The k-factor for $W\gamma^*/WZ^{(*)}$ with $m_{\ell\ell} > 7$ GeV is 1.5 ± 0.5. These uncertainties affect mostly the 1-jet channel, where their impact on the total background yield is approximately 4%.

6.4. Results

Table 5 shows the numbers of events expected from a SM Higgs boson with $m_H = 125$ GeV and from the backgrounds, as well as the numbers of candidates observed in data, after application of all selection criteria plus an additional cut on m_T of $0.75 m_H < m_T < m_H$. The uncertainties shown in Table 5 include the systematic uncertainties discussed in Section 6.3, constrained by the use of the control regions discussed in Section 6.2. An excess of events relative to the background expectation is observed in the data.

Fig. 6 shows the distribution of the transverse mass after all selection criteria in the 0-jet and 1-jet channels combined, and for both lepton channels together.

The statistical analysis of the data employs a binned likelihood function constructed as the product of Poisson probability terms for the $e\mu$ channel and the μe channel. The mass-dependent cuts on m_T described above are not used. Instead, the 0-jet (1-jet) signal regions are subdivided into five (three) m_T bins. For the 2-jet signal region, only the results integrated over m_T are used, due to the small number of events in the final sample. The statistical interpretation of the observed excess of events is presented in Section 9.

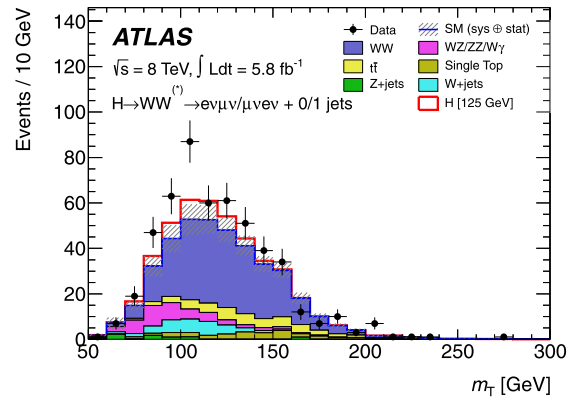

Fig. 6. Distribution of the transverse mass, m_T, in the 0-jet and 1-jet analyses with both $e\mu$ and μe channels combined, for events satisfying all selection criteria. The expected signal for $m_H = 125$ GeV is shown stacked on top of the background prediction. The $W + \text{jets}$ background is estimated from data, and WW and top background MC predictions are normalised to the data using control regions. The hashed area indicates the total uncertainty on the background prediction.

7. Statistical procedure

The statistical procedure used to interpret the data is described in Refs. [17,118–121]. The parameter of interest is the global signal strength factor μ, which acts as a scale factor on the total number of events predicted by the Standard Model for the Higgs boson signal. This factor is defined such that $\mu = 0$ corresponds to the background-only hypothesis and $\mu = 1$ corresponds to the SM Higgs boson signal in addition to the background. Hypothesised values of μ are tested with a statistic $\lambda(\mu)$ based on the profile likelihood ratio [122]. This test statistic extracts the information on the signal strength from a full likelihood fit to the data. The likelihood function includes all the parameters that describe the systematic uncertainties and their correlations.

Exclusion limits are based on the CL_s prescription [123]; a value of μ is regarded as excluded at 95% CL when CL_s is less than 5%. A SM Higgs boson with mass m_H is considered excluded at 95% confidence level (CL) when $\mu = 1$ is excluded at that mass. The significance of an excess in the data is first quantified with the local p_0, the probability that the background can produce a fluctuation greater than or equal to the excess observed in data. The equivalent formulation in terms of number of standard deviations, Z_l, is referred to as the local significance. The global probability for the most significant excess to be observed anywhere in a given search region is estimated with the method described in Ref. [124]. The ratio of the global to the local probabilities, the trials factor used to correct for the "look elsewhere" effect, increases with the range of Higgs boson mass hypotheses considered, the mass resolutions of the channels involved in the combination, and the significance of the excess.

The statistical tests are performed in steps of values of the hypothesised Higgs boson mass m_H. The asymptotic approximation [122] upon which the results are based has been validated with the method described in Ref. [17].

The combination of individual search sub-channels for a specific Higgs boson decay, and the full combination of all search channels, are based on the global signal strength factor μ and on the identification of the nuisance parameters that correspond to the correlated sources of systematic uncertainty described in Section 8.

8. Correlated systematic uncertainties

The individual search channels that enter the combination are summarised in Table 6.

Table 6
Summary of the individual channels entering the combination. The transition points between separately optimised m_H regions are indicated where applicable. In channels sensitive to associated production of the Higgs boson, V indicates a W or Z boson. The symbols $\otimes$ and $\oplus$ represent direct products and sums over sets of selection requirements, respectively.

Higgs boson decay	Subsequent decay	Sub-channels	m_H range [GeV]	$\int L dt$ [fb^{-1}]	Ref.
2011 $\sqrt{s} = 7$ TeV					
$H \to ZZ^{(*)}$	4ℓ	$\{4e, 2e2\mu, 2\mu 2e, 4\mu\}$	110–600	4.8	[87]
	$\ell\ell\nu\bar{\nu}$	$\{ee, \mu\mu\} \otimes$ {low, high pile-up}	200–280–600	4.7	[125]
	$\ell\ell q\bar{q}$	{b-tagged, untagged}	200–300–600	4.7	[126]
$H \to \gamma\gamma$	–	10 categories $\{p_{\mathrm{Tt}} \otimes \eta_\gamma \otimes$ conversion$\} \oplus$ {2-jet}	110–150	4.8	[127]
$H \to WW^{(*)}$	$\ell\nu\ell\nu$	$\{ee, e\mu/\mu e, \mu\mu\} \otimes$ {0-jet, 1-jet, 2-jet} $\otimes$ {low, high pile-up}	110–200–300–600	4.7	[106]
	$\ell\nu qq'$	$\{e, \mu\} \otimes$ {0-jet, 1-jet, 2-jet}	300–600	4.7	[128]
$H \to \tau\tau$	$\tau_{\mathrm{lep}}\tau_{\mathrm{lep}}$	$\{e\mu\} \otimes$ {0-jet} $\oplus \{\ell\ell\} \otimes$ {1-jet, 2-jet, VH}	110–150	4.7	[129]
	$\tau_{\mathrm{lep}}\tau_{\mathrm{had}}$	$\{e, \mu\} \otimes$ {0-jet} $\otimes \{E_{\mathrm{T}}^{\mathrm{miss}} < 20$ GeV, $E_{\mathrm{T}}^{\mathrm{miss}} \geqslant 20$ GeV$\}$ $\oplus \{e, \mu\} \otimes$ {1-jet} $\oplus \{\ell\} \otimes$ {2-jet}	110–150	4.7	
	$\tau_{\mathrm{had}}\tau_{\mathrm{had}}$	{1-jet}	110–150	4.7	
$VH \to Vbb$	$Z \to \nu\nu$	$E_{\mathrm{T}}^{\mathrm{miss}} \in$ {120–160, 160–200, $\geqslant$ 200 GeV}	110–130	4.6	[130]
	$W \to \ell\nu$	$p_{\mathrm{T}}^{W} \in$ {< 50, 50–100, 100–200, $\geqslant$ 200 GeV}	110–130	4.7	
	$Z \to \ell\ell$	$p_{\mathrm{T}}^{Z} \in$ {< 50, 50–100, 100–200, $\geqslant$ 200 GeV}	110–130	4.7	
2012 $\sqrt{s} = 8$ TeV					
$H \to ZZ^{(*)}$	4ℓ	$\{4e, 2e2\mu, 2\mu 2e, 4\mu\}$	110–600	5.8	[87]
$H \to \gamma\gamma$	–	10 categories $\{p_{\mathrm{Tt}} \otimes \eta_\gamma \otimes$ conversion$\} \oplus$ {2-jet}	110–150	5.9	[127]
$H \to WW^{(*)}$	$e\nu\mu\nu$	$\{e\mu, \mu e\} \otimes$ {0-jet, 1-jet, 2-jet}	110–200	5.8	[131]

The main uncorrelated systematic uncertainties are described in Sections 4–6 for the $H \to ZZ^{(*)} \to 4\ell$, $H \to \gamma\gamma$ and $H \to WW^{(*)} \to \ell\nu\ell\nu$ channels and in Ref. [17] for the other channels. They include the background normalisations or background model parameters from control regions or sidebands, the Monte Carlo simulation statistical uncertainties and the theoretical uncertainties affecting the background processes.

The main sources of correlated systematic uncertainties are the following.

1. *Integrated luminosity*: The uncertainty on the integrated luminosity is considered as fully correlated among channels and amounts to ±3.9% for the 7 TeV data [132,133], except for the $H \to ZZ^{(*)} \to 4\ell$ and $H \to \gamma\gamma$ channels which were re-analysed; the uncertainty is ±1.8% [92] for these channels. The uncertainty is ±3.6% for the 8 TeV data.

2. *Electron and photon trigger identification*: The uncertainties in the trigger and identification efficiencies are treated as fully correlated for electrons and photons.

3. *Electron and photon energy scales*: The electron and photon energy scales in the $H \to ZZ^{(*)} \to 4\ell$ and $H \to \gamma\gamma$ channels are described by five parameters, which provide a detailed account of the sources of systematic uncertainty. They are related to the calibration method, the presampler energy scale in the barrel and end-cap calorimeters, and the material description upstream of the calorimeters.

4. *Muon reconstruction*: The uncertainties affecting muons are separated into those related to the ID and MS, in order to obtain a better description of the correlated effects among channels using different muon identification criteria and different ranges of muon p_{T}.

5. *Jet energy scale and missing transverse energy*: The jet energy scale and jet energy resolution are affected by uncertainties which depend on the p_{T}, η, and flavour of the jet. A simplified scheme is used in which independent JES and JER nuisance parameters are associated with final states with significantly different kinematic selections and sensitivity to scattering processes with different kinematic distributions or flavour composition. This scheme includes a specific treatment for b-jets. The sensitivity of the results to various assumptions about the correlation between these sources of uncertainty has been found to be negligible. An uncorrelated component of the uncertainty on $E_{\mathrm{T}}^{\mathrm{miss}}$ is included, in addition to the JES uncertainty, which is due to low energy jet activity not associated with reconstructed physics objects.

6. *Theory uncertainties*: Correlated theoretical uncertainties affect mostly the signal predictions. The QCD scale uncertainties for $m_H = 125$ GeV amount to $^{+7\%}_{-8\%}$ for the ggF process, ±1% for the VBF and WH/ZH processes, and $^{+4\%}_{-9\%}$ for the $t\bar{t}H$ process [52,53]; the small dependence of these uncertainties on m_H is taken into account. The uncertainties on the predicted branching ratios amount to ±5%. The uncertainties related to the parton distribution functions amount to ±8% for the predominantly gluon-initiated ggF and $t\bar{t}H$ processes, and ±4% for the predominantly quark-initiated VBF and WH/ZH processes [78,134–136]. The theoretical uncertainty associated with the exclusive Higgs boson production process with additional jets in the $H \to \gamma\gamma$, $H \to WW^{(*)} \to \ell\nu\ell\nu$ and $H \to \tau^+\tau^-$ channels is estimated using the prescription of Refs. [53,117,118], with the noticeable difference that an explicit calculation of the gluon-fusion process at NLO using MCFM [137] in the 2-jet category reduces the uncertainty on this non-negligible contribution to 25%. An additional theoretical uncertainty on the signal normalisation of $\pm 150\% \times (m_H/\mathrm{TeV})^3$ (e.g. ±4% for $m_H = 300$ GeV) accounts for effects related to off-shell Higgs boson production and interference with other SM processes [53].

Sources of systematic uncertainty that affect both the 7 TeV and the 8 TeV data are taken as fully correlated. The uncertainties on background estimates based on control samples in the data are considered uncorrelated between the 7 TeV and 8 TeV data.

9. Results

The addition of the 8 TeV data for the $H \to ZZ^{(*)} \to 4\ell$, $H \to \gamma\gamma$ and $H \to WW^{(*)} \to e\nu\mu\nu$ channels, as well as the improvements to the analyses of the 7 TeV data in the first two of these channels, bring a significant gain in sensitivity in the low-mass region with respect to the previous combined search [17].

9.1. Excluded mass regions

The combined 95% CL exclusion limits on the production of the SM Higgs boson, expressed in terms of the signal strength parameter μ, are shown in Fig. 7(a) as a function of m_H. The expected 95% CL exclusion region covers the m_H range from 110 GeV to

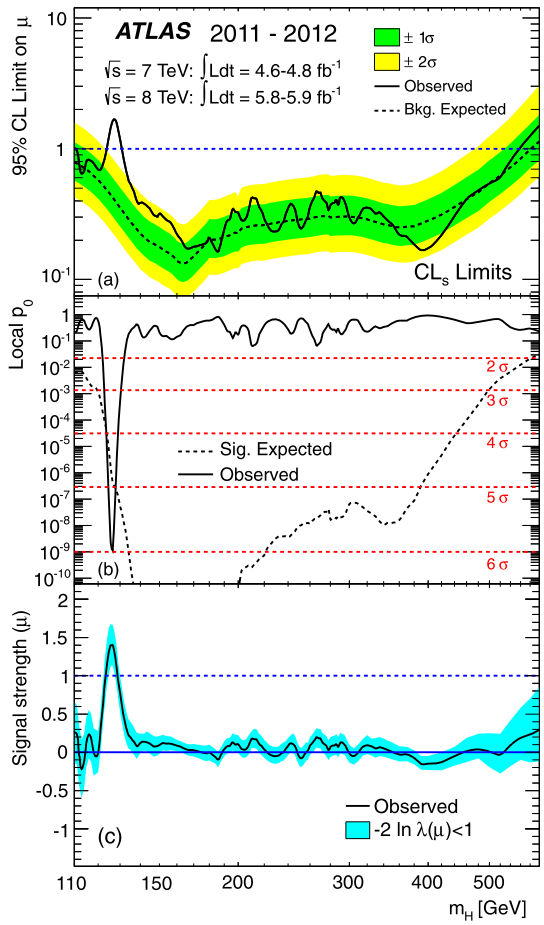

Fig. 7. Combined search results: (a) The observed (solid) 95% CL limits on the signal strength as a function of m_H and the expectation (dashed) under the background-only hypothesis. The dark and light shaded bands show the $\pm 1\sigma$ and $\pm 2\sigma$ uncertainties on the background-only expectation. (b) The observed (solid) local p_0 as a function of m_H and the expectation (dashed) for a SM Higgs boson signal hypothesis ($\mu = 1$) at the given mass. (c) The best-fit signal strength $\hat{\mu}$ as a function of m_H. The band indicates the approximate 68% CL interval around the fitted value.

582 GeV. The observed 95% CL exclusion regions are 111–122 GeV and 131–559 GeV. Three mass regions are excluded at 99% CL, 113–114, 117–121 and 132–527 GeV, while the expected exclusion range at 99% CL is 113–532 GeV.

9.2. Observation of an excess of events

An excess of events is observed near $m_H = 126$ GeV in the $H \to ZZ^{(*)} \to 4\ell$ and $H \to \gamma\gamma$ channels, both of which provide fully reconstructed candidates with high resolution in invariant mass, as shown in Figs. 8(a) and 8(b). These excesses are confirmed by the highly sensitive but low-resolution $H \to WW^{(*)} \to \ell\nu\ell\nu$ channel, as shown in Fig. 8(c).

The observed local p_0 values from the combination of channels, using the asymptotic approximation, are shown as a function of m_H in Fig. 7(b) for the full mass range and in Fig. 9 for the low mass range.

The largest local significance for the combination of the 7 and 8 TeV data is found for a SM Higgs boson mass hypothesis of $m_H = 126.5$ GeV, where it reaches 6.0σ, with an expected value in the presence of a SM Higgs boson signal at that mass of 4.9σ (see also Table 7). For the 2012 data alone, the maximum local significance for the $H \to ZZ^{(*)} \to 4\ell$, $H \to \gamma\gamma$ and $H \to WW^{(*)} \to$

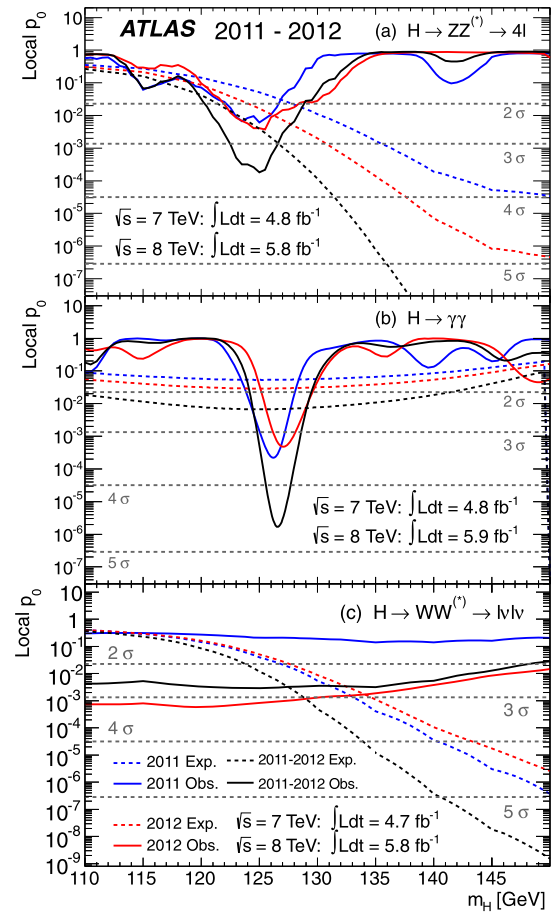

Fig. 8. The observed local p_0 as a function of the hypothesised Higgs boson mass for the (a) $H \to ZZ^{(*)} \to 4\ell$, (b) $H \to \gamma\gamma$ and (c) $H \to WW^{(*)} \to \ell\nu\ell\nu$ channels. The dashed curves show the expected local p_0 under the hypothesis of a SM Higgs boson signal at that mass. Results are shown separately for the $\sqrt{s} = 7$ TeV data (dark, blue in the web version), the $\sqrt{s} = 8$ TeV data (light, red in the web version), and their combination (black).

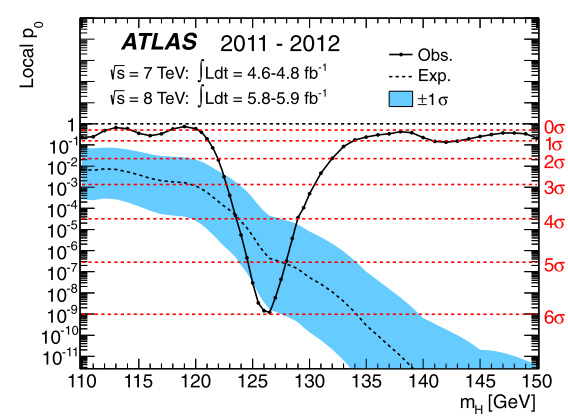

Fig. 9. The observed (solid) local p_0 as a function of m_H in the low mass range. The dashed curve shows the expected local p_0 under the hypothesis of a SM Higgs boson signal at that mass with its $\pm 1\sigma$ band. The horizontal dashed lines indicate the p-values corresponding to significances of 1 to 6 σ.

$e\nu\mu\nu$ channels combined is $4.9\,\sigma$, and occurs at $m_H = 126.5$ GeV (3.8σ expected).

The significance of the excess is mildly sensitive to uncertainties in the energy resolutions and energy scale systematic uncertainties for photons and electrons; the effect of the muon energy scale systematic uncertainties is negligible. The presence of these

Table 7
Characterisation of the excess in the $H \to ZZ^{(*)} \to 4\ell$, $H \to \gamma\gamma$ and $H \to WW^{(*)} \to \ell\nu\ell\nu$ channels and the combination of all channels listed in Table 6. The mass value $m_{\max}$ for which the local significance is maximum, the maximum observed local significance Z_l and the expected local significance $E(Z_l)$ in the presence of a SM Higgs boson signal at $m_{\max}$ are given. The best fit value of the signal strength parameter $\hat{\mu}$ at $m_H = 126$ GeV is shown with the total uncertainty. The expected and observed mass ranges excluded at 95% CL (99% CL, indicated by a *) are also given, for the combined $\sqrt{s} = 7$ TeV and $\sqrt{s} = 8$ TeV data.

Search channel	Dataset	$m_{\max}$ [GeV]	Z_l [σ]	$E(Z_l)$ [σ]	$\hat{\mu}(m_H = 126$ GeV)	Expected exclusion [GeV]	Observed exclusion [GeV]
$H \to ZZ^{(*)} \to 4\ell$	7 TeV	125.0	2.5	1.6	1.4 ± 1.1		
	8 TeV	125.5	2.6	2.1	1.1 ± 0.8		
	7 & 8 TeV	125.0	3.6	2.7	1.2 ± 0.6	124–164, 176–500	131–162, 170–460
$H \to \gamma\gamma$	7 TeV	126.0	3.4	1.6	2.2 ± 0.7		
	8 TeV	127.0	3.2	1.9	1.5 ± 0.6		
	7 & 8 TeV	126.5	4.5	2.5	1.8 ± 0.5	110–140	112–123, 132–143
$H \to WW^{(*)} \to \ell\nu\ell\nu$	7 TeV	135.0	1.1	3.4	0.5 ± 0.6		
	8 TeV	120.0	3.3	1.0	1.9 ± 0.7		
	7 & 8 TeV	125.0	2.8	2.3	1.3 ± 0.5	124–233	137–261
Combined	7 TeV	126.5	3.6	3.2	1.2 ± 0.4		
	8 TeV	126.5	4.9	3.8	1.5 ± 0.4		
	7 & 8 TeV	126.5	6.0	4.9	1.4 ± 0.3	110–582 113–532 (*)	111–122, 131–559 113–114, 117–121, 132–527 (*)

uncertainties, evaluated as described in Ref. [138], reduces the local significance to 5.9σ.

The global significance of a local 5.9σ excess anywhere in the mass range 110–600 GeV is estimated to be approximately 5.1σ, increasing to 5.3σ in the range 110–150 GeV, which is approximately the mass range not excluded at the 99% CL by the LHC combined SM Higgs boson search [139] and the indirect constraints from the global fit to precision electroweak measurements [12].

9.3. Characterising the excess

The mass of the observed new particle is estimated using the profile likelihood ratio $\lambda(m_H)$ for $H \to ZZ^{(*)} \to 4\ell$ and $H \to \gamma\gamma$, the two channels with the highest mass resolution. The signal strength is allowed to vary independently in the two channels, although the result is essentially unchanged when restricted to the SM hypothesis $\mu = 1$. The leading sources of systematic uncertainty come from the electron and photon energy scales and resolutions. The resulting estimate for the mass of the observed particle is 126.0 ± 0.4 (stat) ± 0.4 (sys) GeV.

The best-fit signal strength $\hat{\mu}$ is shown in Fig. 7(c) as a function of m_H. The observed excess corresponds to $\hat{\mu} = 1.4 \pm 0.3$ for $m_H = 126$ GeV, which is consistent with the SM Higgs boson hypothesis $\mu = 1$. A summary of the individual and combined best-fit values of the strength parameter for a SM Higgs boson mass hypothesis of 126 GeV is shown in Fig. 10, while more information about the three main channels is provided in Table 7.

In order to test which values of the strength and mass of a signal hypothesis are simultaneously consistent with the data, the profile likelihood ratio $\lambda(\mu, m_H)$ is used. In the presence of a strong signal, it will produce closed contours around the best-fit point $(\hat{\mu}, \hat{m}_H)$, while in the absence of a signal the contours will be upper limits on μ for all values of m_H.

Asymptotically, the test statistic $-2\ln\lambda(\mu, m_H)$ is distributed as a χ^2 distribution with two degrees of freedom. The resulting 68% and 95% CL contours for the $H \to \gamma\gamma$ and $H \to WW^{(*)} \to \ell\nu\ell\nu$ channels are shown in Fig. 11, where the asymptotic approximations have been validated with ensembles of pseudo-experiments. Similar contours for the $H \to ZZ^{(*)} \to 4\ell$ channel are also shown in Fig. 11, although they are only approximate confidence intervals due to the smaller number of candidates in this channel. These contours in the (μ, m_H) plane take into account uncertainties in the energy scale and resolution.

The probability for a single Higgs boson-like particle to produce resonant mass peaks in the $H \to ZZ^{(*)} \to 4\ell$ and $H \to \gamma\gamma$

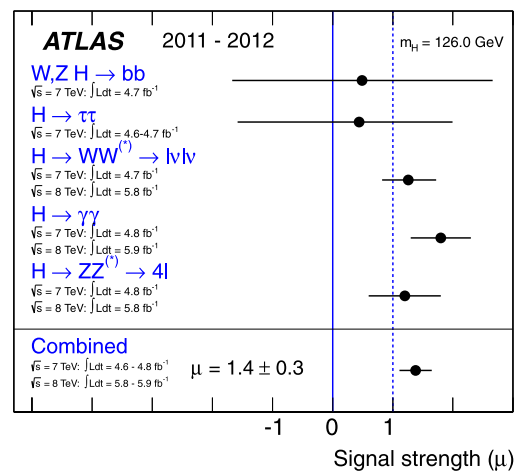

Fig. 10. Measurements of the signal strength parameter μ for $m_H = 126$ GeV for the individual channels and their combination.

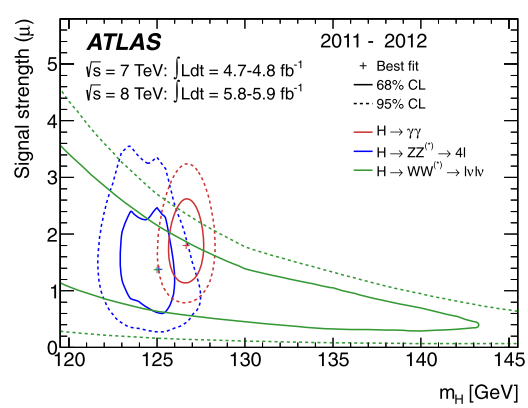

Fig. 11. Confidence intervals in the (μ, m_H) plane for the $H \to ZZ^{(*)} \to 4\ell$, $H \to \gamma\gamma$, and $H \to WW^{(*)} \to \ell\nu\ell\nu$ channels, including all systematic uncertainties. The markers indicate the maximum likelihood estimates $(\hat{\mu}, \hat{m}_H)$ in the corresponding channels (the maximum likelihood estimates for $H \to ZZ^{(*)} \to 4\ell$ and $H \to WW^{(*)} \to \ell\nu\ell\nu$ coincide).

channels separated by more than the observed mass difference, allowing the signal strengths to vary independently, is about 8%.

The contributions from the different production modes in the $H \to \gamma\gamma$ channel have been studied in order to assess any tension between the data and the ratios of the production cross

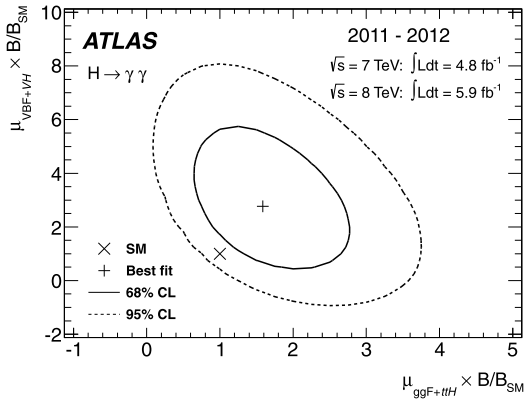

Fig. 12. Likelihood contours for the $H \to \gamma\gamma$ channel in the $(\mu_{\mathrm{ggF}+t\bar{t}H}, \mu_{\mathrm{VBF}+VH})$ plane including the branching ratio factor B/B_{SM}. The quantity $\mu_{\mathrm{ggF}+t\bar{t}H}$ ($\mu_{\mathrm{VBF}+VH}$) is a common scale factor for the ggF and $t\bar{t}H$ (VBF and VH) production cross sections. The best fit to the data (+) and 68% (full) and 95% (dashed) CL contours are also indicated, as well as the SM expectation (×).

sections predicted in the Standard Model. A new signal strength parameter μ_i is introduced for each production mode, defined by $\mu_i = \sigma_i/\sigma_{i,\mathrm{SM}}$. In order to determine the values of (μ_i, μ_j) that are simultaneously consistent with the data, the profile likelihood ratio $\lambda(\mu_i, \mu_j)$ is used with the measured mass treated as a nuisance parameter.

Since there are four Higgs boson production modes at the LHC, two-dimensional contours require either some μ_i to be fixed, or multiple μ_i to be related in some way. Here, μ_{ggF} and $\mu_{t\bar{t}H}$ have been grouped together as they scale with the $t\bar{t}H$ coupling in the SM, and are denoted by the common parameter $\mu_{\mathrm{ggF}+t\bar{t}H}$. Similarly, μ_{VBF} and μ_{VH} have been grouped together as they scale with the WWH/ZZH coupling in the SM, and are denoted by the common parameter $\mu_{\mathrm{VBF}+VH}$. Since the distribution of signal events among the 10 categories of the $H \to \gamma\gamma$ search is sensitive to these factors, constraints in the plane of $\mu_{\mathrm{ggF}+t\bar{t}H} \times B/B_{\mathrm{SM}}$ and $\mu_{\mathrm{VBF}+VH} \times B/B_{\mathrm{SM}}$, where B is the branching ratio for $H \to \gamma\gamma$, can be obtained (Fig. 12). Theoretical uncertainties are included so that the consistency with the SM expectation can be quantified. The data are compatible with the SM expectation at the $1.5\,\sigma$ level.

10. Conclusion

Searches for the Standard Model Higgs boson have been performed in the $H \to ZZ^{(*)} \to 4\ell$, $H \to \gamma\gamma$ and $H \to WW^{(*)} \to e\nu\mu\nu$ channels with the ATLAS experiment at the LHC using 5.8–5.9 fb^{-1} of pp collision data recorded during April to June 2012 at a centre-of-mass energy of 8 TeV. These results are combined with earlier results [17], which are based on an integrated luminosity of 4.6–4.8 fb^{-1} recorded in 2011 at a centre-of-mass energy of 7 TeV, except for the $H \to ZZ^{(*)} \to 4\ell$ and $H \to \gamma\gamma$ channels, which have been updated with the improved analyses presented here.

The Standard Model Higgs boson is excluded at 95% CL in the mass range 111–559 GeV, except for the narrow region 122–131 GeV. In this region, an excess of events with significance 5.9σ, corresponding to $p_0 = 1.7 \times 10^{-9}$, is observed. The excess is driven by the two channels with the highest mass resolution, $H \to ZZ^{(*)} \to 4\ell$ and $H \to \gamma\gamma$, and the equally sensitive but low-resolution $H \to WW^{(*)} \to \ell\nu\ell\nu$ channel. Taking into account the entire mass range of the search, 110–600 GeV, the global significance of the excess is 5.1σ, which corresponds to $p_0 = 1.7 \times 10^{-7}$.

These results provide conclusive evidence for the discovery of a new particle with mass 126.0 ± 0.4 (stat) ± 0.4 (sys) GeV. The signal strength parameter μ has the value 1.4 ± 0.3 at the fitted mass, which is consistent with the SM Higgs boson hypothesis $\mu = 1$. The decays to pairs of vector bosons whose net electric charge is zero identify the new particle as a neutral boson. The observation in the diphoton channel disfavours the spin-1 hypothesis [140, 141]. Although these results are compatible with the hypothesis that the new particle is the Standard Model Higgs boson, more data are needed to assess its nature in detail.

Acknowledgements

The results reported in this Letter would not have been possible without the outstanding performance of the LHC. We warmly thank CERN and the entire LHC exploitation team, including the operation, technical and infrastructure groups, and all the people who have contributed to the conception, design and construction of this superb accelerator. We thank also the support staff at our institutions without whose excellent contributions ATLAS could not have been successfully constructed or operated so efficiently.

We acknowledge the support of ANPCyT, Argentina; YerPhI, Armenia; ARC, Australia; BMWF, Austria; ANAS, Azerbaijan; SSTC, Belarus; CNPq and FAPESP, Brazil; NSERC, NRC and CFI, Canada; CERN; CONICYT, Chile; CAS, MOST and NSFC, China; COLCIENCIAS, Colombia; MSMT CR, MPO CR and VSC CR, Czech Republic; DNRF, DNSRC and Lundbeck Foundation, Denmark; EPLANET and ERC, European Union; IN2P3-CNRS, CEA-DSM/IRFU, France; GNAS, Georgia; BMBF, DFG, HGF, MPG and AvH Foundation, Germany; GSRT, Greece; ISF, MINERVA, GIF, DIP and Benoziyo Center, Israel; INFN, Italy; MEXT and JSPS, Japan; CNRST, Morocco; FOM and NWO, Netherlands; RCN, Norway; MNiSW, Poland; GRICES and FCT, Portugal; MERYS (MECTS), Romania; MES of Russia and ROSATOM, Russian Federation; JINR; MSTD, Serbia; MSSR, Slovakia; ARRS and MVZT, Slovenia; DST/NRF, South Africa; MICINN, Spain; SRC and Wallenberg Foundation, Sweden; SER, SNSF and Cantons of Bern and Geneva, Switzerland; NSC, Taiwan; TAEK, Turkey; STFC, the Royal Society and Leverhulme Trust, United Kingdom; DOE and NSF, United States of America.

The crucial computing support from all WLCG partners is acknowledged gratefully, in particular from CERN and the ATLAS Tier-1 facilities at TRIUMF (Canada), NDGF (Denmark, Norway, Sweden), CC-IN2P3 (France), KIT/GridKA (Germany), INFN-CNAF (Italy), NL-T1 (Netherlands), PIC (Spain), ASGC (Taiwan), RAL (UK) and BNL (USA) and in the Tier-2 facilities worldwide.

Open access

This article is published Open Access at sciencedirect.com. It is distributed under the terms of the Creative Commons Attribution License 3.0, which permits unrestricted use, distribution, and reproduction in any medium, provided the original authors and source are credited.

References

[1] S.L. Glashow, Nucl. Phys. 22 (4) (1961) 579.
[2] S. Weinberg, Phys. Rev. Lett. 19 (1967) 1264.
[3] A. Salam, in: N. Svartholm (Ed.), Proceedings of the Eighth Nobel Symposium, Almqvist & Wiksell, 1968, p. 367.
[4] G. 't Hooft, M. Veltman, Nucl. Phys. B 44 (1972) 189.
[5] F. Englert, R. Brout, Phys. Rev. Lett. 13 (1964) 321.
[6] P.W. Higgs, Phys. Lett. 12 (1964) 132.
[7] P.W. Higgs, Phys. Rev. Lett. 13 (1964) 508.
[8] G.S. Guralnik, C.R. Hagen, T.W.B. Kibble, Phys. Rev. Lett. 13 (1964) 585.
[9] P.W. Higgs, Phys. Rev. 145 (1966) 1156.
[10] T.W.B. Kibble, Phys. Rev. 155 (1967) 1554.
[11] L. Evans, P. Bryant (Eds.), LHC Machine, JINST, vol. 3, 2008, p. S08001.
[12] ALEPH, CDF, DØ, DELPHI, L3, OPAL, SLD Collaborations, the LEP Electroweak Working Group, the Tevatron Electroweak Working Group,

the SLD Electroweak and Heavy Flavour Groups, CERN-PH-EP-2010-095, arXiv:1012.2367 [hep-ex], 2010.
[13] ALEPH, DELPHI, L3 and OPAL Collaborations, Phys. Lett. B 565 (2003) 61.
[14] CDF Collaboration, T. Aaltonen, et al. Phys. Rev. Lett. (2012), in press, arXiv: 1207.1707 [hep-ex].
[15] DØ Collaboration, V.M. Abazov, et al. Phys. Rev. Lett. (2012), submitted for publication, arXiv:1207.6631 [hep-ex].
[16] CDF Collaboration, DØ Collaboration, Phys. Rev. Lett. (2012), submitted for publication, arXiv:1207.6436 [hep-ex].
[17] ATLAS Collaboration, Phys. Rev. D 86 (2012) 032003.
[18] CMS Collaboration, Phys. Lett. B 710 (2012) 26.
[19] ATLAS Collaboration, ATLAS: Letter of intent for a general-purpose pp experiment at the large hadron collider at CERN, CERN-LHCC-92-004 (1992).
[20] ATLAS Collaboration, The ATLAS Collaboration, ATLAS Technical Proposal for a General-Purpose pp Experiment at the Large Hadron Collider at CERN, CERN-LHCC-94-43 (1994).
[21] ATLAS Collaboration, JINST 3 (2008) S08003.
[22] H. Georgi, S. Glashow, M. Machacek, D.V. Nanopoulos, Phys. Rev. Lett. 40 (1978) 692.
[23] A. Djouadi, M. Spira, P.M. Zerwas, Phys. Lett. B 264 (1991) 440.
[24] S. Dawson, Nucl. Phys. B 359 (1991) 283.
[25] M. Spira, A. Djouadi, D. Graudenz, P.M. Zerwas, Nucl. Phys. B 453 (1995) 17.
[26] R. Harlander, W.B. Kilgore, Phys. Rev. Lett. 88 (2002) 201801.
[27] C. Anastasiou, K. Melnikov, Nucl. Phys. B 646 (2002) 220.
[28] V. Ravindran, J. Smith, W.L. van Neerven, Nucl. Phys. B 665 (2003) 325.
[29] U. Aglietti, R. Bonciani, G. Degrassi, A. Vicini, Phys. Lett. B 595 (2004) 432.
[30] S. Actis, G. Passarino, C. Sturm, S. Uccirati, Phys. Lett. B 670 (2008) 12.
[31] S. Catani, D. de Florian, M. Grazzini, P. Nason, JHEP 0307 (2003) 028.
[32] C. Anastasiou, R. Boughezal, F. Petriello, JHEP 0904 (2009) 003.
[33] D. de Florian, M. Grazzini, Higgs production at the LHC: Updated cross sections at $\sqrt{s} = 8$ TeV, arXiv:1206.4133 [hep-ph].
[34] C. Anastasiou, S. Buehler, F. Herzog, A. Lazopoulos, JHEP 1204 (2012) 004.
[35] J. Baglio, A. Djouadi, JHEP 1103 (2011) 055.
[36] D. de Florian, G. Ferrera, M. Grazzini, D. Tommasini, JHEP 1111 (2011) 064.
[37] P.S.E. Bagnaschi, G. Degrassi, A. Vicini, JHEP 1202 (2012) 88.
[38] R. Cahn, S. Dawson, Phys. Lett. B 136 (1984) 196;
R. Cahn, S. Dawson, Phys. Lett. B 138 (1984) 464 (Erratum).
[39] M. Ciccolini, A. Denner, S. Dittmaier, Phys. Rev. Lett. 99 (2007) 161803.
[40] M. Ciccolini, A. Denner, S. Dittmaier, Phys. Rev. D 77 (2008) 013002.
[41] K. Arnold, M. Bahr, G. Bozzi, F. Campanario, C. Englert, Comput. Phys. Commun. 180 (2009) 1661.
[42] P. Bolzoni, F. Maltoni, S.-O. Moch, M. Zaro, Phys. Rev. Lett. 105 (2010) 011801.
[43] S. Glashow, D.V. Nanopoulos, A. Yildiz, Phys. Rev. D 18 (1978) 1724.
[44] T. Han, S. Willenbrock, Phys. Lett. B 273 (1991) 167.
[45] O. Brein, A. Djouadi, R. Harlander, Phys. Lett. B 579 (2004) 149.
[46] M.L. Ciccolini, S. Dittmaier, M. Kramer, Phys. Rev. D 68 (2003) 073003.
[47] Z. Kunszt, Nucl. Phys. B 247 (1984) 339.
[48] W. Beenakker, et al., Phys. Rev. Lett. 87 (2001) 201805.
[49] W. Beenakker, et al., Nucl. Phys. B 653 (2003) 151.
[50] S. Dawson, L.H. Orr, L. Reina, D. Wackeroth, Phys. Rev. D 67 (2003) 071503.
[51] S. Dawson, C. Jackson, L.H. Orr, L. Reina, D. Wackeroth, Phys. Rev. D 68 (2003) 034022.
[52] S. Dittmaier, C. Mariotti, G. Passarino, R. Tanaka (Eds.), LHC Higgs Cross Section Working Group, Handbook of LHC Higgs cross sections: 1. Inclusive observables, CERN-2011-002, arXiv:1101.0593 [hep-ph], 2011.
[53] S. Dittmaier, C. Mariotti, G. Passarino, R. Tanaka (Eds.), LHC Higgs Cross Section Working Group, Handbook of LHC Higgs Cross Sections: 2. Differential Distributions, CERN-2012-002, arXiv:1201.3084 [hep-ph], 2012.
[54] A. Djouadi, J. Kalinowski, M. Spira, Comput. Phys. Commun. 108 (1998) 56.
[55] A. Bredenstein, A. Denner, S. Dittmaier, M.M. Weber, Phys. Rev. D 74 (2006) 013004.
[56] A. Bredenstein, A. Denner, S. Dittmaier, M.M. Weber, JHEP 0702 (2007) 080.
[57] S. Alioli, P. Nason, C. Oleari, E. Re, JHEP 0904 (2009) 002.
[58] P. Nason, C. Oleari, JHEP 1002 (2010) 037.
[59] M.L. Mangano, et al., JHEP 0307 (2003) 001.
[60] S. Frixione, B.R. Webber, JHEP 0206 (2002) 029;
S. Frixione, P. Nason, B.R. Webber, JHEP 0308 (2003) 007;
S. Frixione, E. Laenen, P. Motylinski, B.R. Webber, JHEP 0603 (2006) 092;
S. Frixione, E. Laenen, P. Motylinski, C. White, B.R. Webber, JHEP 0807 (2008) 029;
S. Frixione, F. Stoeckli, P. Torrielli, B.R. Webber, JHEP 1101 (2011) 053.
[61] B.P. Kersevan, E. Richter-Was, The Monte Carlo event generator AcerMC version 2.0 with interfaces to PYTHIA 6.2 and HERWIG 6.5, arXiv:hep-ph/0405247.
[62] T. Binoth, M. Ciccolini, N. Kauer, M. Krämer, JHEP 0612 (2006) 046.
[63] T. Melia, P. Nason, R. Rontsch, G. Zanderighi, JHEP 1111 (2011) 078.
[64] T. Binoth, N. Kauer, P. Mertsch, Gluon-induced QCD Corrections to $pp \to ZZ \to \ell\bar{\ell}\ell'\bar{\ell}'$, arXiv:0807.0024 [hep-ph].
[65] R.C. Gray, C. Kilic, M. Park, S. Somalwar, S. Thomas, Backgrounds to Higgs boson searches from $W\gamma^* \to l\nu l(l)$ asymmetric internal conversion, arXiv: 1110.1368 [hep-ph].
[66] ATLAS Collaborations, New ATLAS event generator tunes to 2010 data, ATL-PHYS-PUB-2011-008, http://cdsweb.cern.ch/record/1345343, 2011.
[67] ATLAS Collaborations, ATLAS tunes of PYTHIA 6 and Pythia 8 for MC11, ATL-PHYS-PUB-2011-009, http://cdsweb.cern.ch/record/1363300, 2011.
[68] ATLAS Collaborations, Further ATLAS tunes of PYTHIA6 and Pythia 8, ATL-PHYS-PUB-2011-014, http://cdsweb.cern.ch/record/1400677, 2011.
[69] T. Sjöstrand, S. Mrenna, P. Skands, JHEP 0605 (2006) 026.
[70] J. Alwall, et al., JHEP 0709 (2007) 028.
[71] J. Alwall, M. Herquet, F. Maltoni, O. Mattelaer, T. Stelzer, JHEP 1106 (2011) 128.
[72] T. Sjöstrand, S. Mrenna, P. Skands, Comput. Phys. Commun. 178 (2008) 852.
[73] G. Corcella, I. Knowles, G. Marchesini, S. Moretti, K. Odagiri, et al., JHEP 0101 (2001) 010.
[74] T. Gleisberg, et al., JHEP 0902 (2009) 007.
[75] J.M. Butterworth, J.R. Forshaw, M.H. Seymour, Z. Phys. C 72 (1996) 637.
[76] S. Jadach, Z. Was, R. Decker, J.H. Kuhn, Comput. Phys. Commun. 76 (1993) 361.
[77] P. Golonka, Z. Was, Eur. Phys. J. C 45 (2006) 97.
[78] H.-L. Lai, et al., Phys. Rev. D 82 (2010) 074024.
[79] P.M. Nadolsky, et al., Phys. Rev. D 78 (2008) 013004.
[80] A. Sherstnev, R.S. Thorne, Eur. Phys. J C 55 (2009) 553.
[81] ATLAS Collaboration, Eur. Phys. J. C 70 (2010) 823.
[82] S. Agostinelli, et al., Nucl. Instrum. Meth. A 506 (2003) 250.
[83] ATLAS Collaboration, Phys. Lett. B 710 (2012) 383.
[84] ATLAS Collaboration, Muon reconstruction efficiency in reprocessed 2010 LHC proton–proton collision data recorded with the ATLAS detector, ATLAS-CONF-2011-063, 2011, http://cdsweb.cern.ch/record/1345743.
[85] ATLAS Collaboration, Eur. Phys. J. C 72 (2012) 1909.
[86] ATLAS Collaboration, Improved electron reconstruction in ATLAS using the Gaussian Sum Filter-based model for bremsstrahlung, http://cdsweb.cern.ch/record/1449796.
[87] ATLAS Collaboration, Observation of an excess of events in the search for the Standard Model Higgs boson in the $H \to ZZ^{(*)} \to 4\ell$ channel with the ATLAS detector, ATLAS-CONF-2012-092, 2012, http://cdsweb.cern.ch/record/1460411.
[88] W. Lampl, S. Laplace, D. Lelas, P. Loch, H. Ma, S. Menke, S. Rajagopalan, D. Rousseau, S. Snyder, G. Unal, Calorimeter clustering algorithms: Description and performance, ATL-LARG-PUB-2008-002, 2008, http://cdsweb.cern.ch/record/1099735.
[89] M. Cacciari, G.P. Salam, Phys. Lett. B 659 (2008) 119.
[90] M. Cacciari, G.P. Salam, G. Soyez, Eur. Phys. J. C 72 (2012) 1896.
[91] ATLAS Collaboration, Phys. Lett. B 707 (2012) 438.
[92] ATLAS Collaboration, Improved luminosity determination in pp collisions at $\sqrt{s} = 7$ TeV using the ATLAS detector at the LHC, ATLAS-CONF-2012-080, 2012, http://cdsweb.cern.ch/record/1460392.
[93] ATLAS Collaboration, Measurement of the total ZZ production cross section in the four-lepton channel using 5.8 fb^{-1} of ATLAS data at $\sqrt{s} = 8$ TeV, ATLAS-CONF-2012-090, 2012, http://cdsweb.cern.ch/record/1460409.
[94] N. Kauer, G. Passarino, Inadequacy of zero-width approximation for a light Higgs boson signal, arXiv:1206.4803 [hep-ph].
[95] ATLAS Collaboration, Phys. Rev. Lett. 108 (2012) 111803.
[96] ATLAS Collaboration, Eur. Phys. J. C 72 (2012) 1849.
[97] ATLAS Collaboration, Phys. Rev. D 83 (2011) 052005.
[98] ATLAS Collaboration, Phys. Lett. B 705 (2011) 452.
[99] OPAL Collaboration, K. Ackerstaff, et al., Eur. Phys. J. C 4 (1998) 47.
[100] M. Vesterinen, T.R. Wyatt, Nucl. Instrum. Meth. A 602 (2009) 432.
[101] ATLAS Collaboration, Eur. Phys. J. C (2011), submitted for publication, arXiv: 1112.6426 [hep-ex].
[102] M. Cacciari, G.P. Salam, G. Soyez, JHEP 0804 (2008) 063.
[103] L.J. Dixon, M.S. Siu, Phys. Rev. Lett. 90 (2003) 252001.
[104] J. Gaiser, Charmonium spectroscopy from radiative decays of the J/Ψ and Ψ', Ph.D. Thesis No. SLAC-R-255, 1982.
[105] S.N. Bernstein, Comm. Soc. Math. Kharkov 13 (1912) 1.
[106] ATLAS Collaboration, Phys. Lett. B 716 (2012) 62, in this issue.
[107] M. Dittmar, H. Dreiner, Phys. Rev. D 55 (2007) 167.
[108] ATLAS Collaboration, Commissioning of the ATLAS high-performance b-tagging algorithms in the 7 TeV collision data, ATLAS-CONF-2011-102, 2011, http://cdsweb.cern.ch/record/1369219.
[109] R.K. Ellis, et al., Nucl. Phys. B 297 (1988) 221.
[110] A.J. Barr, B. Gripaios, C.G. Lester, JHEP 0907 (2009) 072.
[111] ATLAS Collaboration, Phys. Rev. Lett. 108 (2012) 111802.
[112] ATLAS Collaboration, Eur. Phys. J. C 71 (2011) 1728.
[113] ATLAS Collaboration, Eur. Phys. J. C 72 (2012) 1844.
[114] ATLAS Collaboration, Measurement of the b-tag efficiency in a sample of jets containing muons with 5 fb^{-1} of data from the ATLAS detector, ATLAS-CONF-2012-043, 2012, http://cdsweb.cern.ch/record/1435197.
[115] J.M. Campbell, R.K. Ellis, C. Williams, JHEP 1107 (2011) 018.
[116] J. Campbell, R. Ellis, C. Williams, JHEP 1110 (2011) 005.

[117] I. Stewart, F. Tackmann, Phys. Rev. D 85 (2012) 034011.
[118] ATLAS Collaboration, CMS Collaboration, Procedure for the LHC Higgs boson search combination in Summer 2011, ATL-PHYS-PUB-2011-011, CERN-CMS-NOTE-2011-005, 2011, http://cdsweb.cern.ch/record/1375842.
[119] L. Moneta, K. Belasco, K.S. Cranmer, S. Kreiss, A. Lazzaro, et al., The RooStats Project, PoS ACAT2010 (2010) 057, arXiv:1009.1003 [physics.data-an].
[120] K. Cranmer, G. Lewis, L. Moneta, A. Shibata, W. Verkerke, HistFactory: A tool for creating statistical models for use with RooFit and RooStats, CERN-OPEN-2012-016, 2012, http://cdsweb.cern.ch/record/1456844.
[121] W. Verkerke, D. Kirkby, The RooFit toolkit for data modeling, Tech. Rep., SLAC, Stanford, CA, June 2003, arXiv:physics/0306116 [physics.data-an].
[122] G. Cowan, K. Cranmer, E. Gross, O. Vitells, Eur. Phys. J. C 71 (2011) 1554.
[123] A.L. Read, J. Phys. G 28 (2002) 2693.
[124] E. Gross, O. Vitells, Eur. Phys. J. C 70 (2010) 525.
[125] ATLAS Collaboration, Phys. Lett. B (2012), submitted for publication, arXiv: 1205.6744 [hep-ex].
[126] ATLAS Collaboration, Phys. Lett. B (2012), submitted for publication, arXiv: 1206.2443 [hep-ex].
[127] ATLAS Collaboration, Observation of an excess of events in the search for the Standard Model Higgs boson in the gamma–gamma channel with the ATLAS detector, ATLAS-CONF-2012-091, 2012, http://cdsweb.cern.ch/record/1460410.
[128] ATLAS Collaboration, Phys. Lett. B (2012), submitted for publication, arXiv: 1206.6074 [hep-ex].
[129] ATLAS Collaboration, JHEP (2012), in press, arXiv:1206.5971 [hep-ex].
[130] ATLAS Collaboration, Phys. Lett. B (2012), submitted for publication, arXiv: 1207.0210 [hep-ex].
[131] ATLAS Collaboration, Observation of an excess of events in the search for the Standard Model Higgs Boson in the $H \to WW^{(*)} \to \ell\nu\ell\nu$ channel with the ATLAS detector, ATLAS-CONF-2012-098, 2012, http://cdsweb.cern.ch/record/1462530.
[132] ATLAS Collaboration, Eur. Phys. J. C 71 (2011) 1630.
[133] ATLAS Collaboration, Luminosity determination in pp collisions at $\sqrt{s} = 7$ TeV using the ATLAS detector in 2011, ATLAS-CONF-2011-116, 2011, http://cdsweb.cern.ch/record/1376384.
[134] M. Botje, J. Butterworth, A. Cooper-Sarkar, A. de Roeck, J. Feltesse, et al., The PDF4LHC Working Group interim recommendations, arXiv:1101.0538 [hep-ph].
[135] A. Martin, W. Stirling, R. Thorne, G. Watt, Eur. Phys. J. C 63 (2009) 189.
[136] R.D. Ball, et al., Nucl. Phys. B 849 (2011) 296.
[137] J.M. Campbell, R.K. Ellis, G. Zanderighi, JHEP 0610 (2006) 028.
[138] ATLAS Collaboration, Observation of an excess of events in the search for the Standard Model Higgs boson with the ATLAS detector at the LHC, ATLAS-CONF-2012-093, 2012, http://cdsweb.cern.ch/record/1460439.
[139] ATLAS Collaboration, CMS Collaboration, Combined Standard Model Higgs boson searches with up to 2.3 fb^{-1} of pp, collisions at $\sqrt{s} = 7$ TeV at the LHC, ATLAS-CONF-2011-157, CMS-PAS-HIG-11-023, 2011, http://cdsweb.cern.ch/record/1399599.
[140] L.D. Landau, Dokl. Akad. Nauk USSR 60 (1948) 207.
[141] C.N. Yang, Phys. Rev. 77 (1950) 242.

ATLAS Collaboration

G. Aad [48], T. Abajyan [21], B. Abbott [111], J. Abdallah [12], S. Abdel Khalek [115], A.A. Abdelalim [49], O. Abdinov [11], R. Aben [105], B. Abi [112], M. Abolins [88], O.S. AbouZeid [158], H. Abramowicz [153], H. Abreu [136], B.S. Acharya [164a,164b], L. Adamczyk [38], D.L. Adams [25], T.N. Addy [56], J. Adelman [176], S. Adomeit [98], P. Adragna [75], T. Adye [129], S. Aefsky [23], J.A. Aguilar-Saavedra [124b,a], M. Agustoni [17], M. Aharrouche [81], S.P. Ahlen [22], F. Ahles [48], A. Ahmad [148], M. Ahsan [41], G. Aielli [133a,133b], T. Akdogan [19a], T.P.A. Åkesson [79], G. Akimoto [155], A.V. Akimov [94], M.S. Alam [2], M.A. Alam [76], J. Albert [169], S. Albrand [55], M. Aleksa [30], I.N. Aleksandrov [64], F. Alessandria [89a], C. Alexa [26a], G. Alexander [153], G. Alexandre [49], T. Alexopoulos [10], M. Alhroob [164a,164c], M. Aliev [16], G. Alimonti [89a], J. Alison [120], B.M.M. Allbrooke [18], P.P. Allport [73], S.E. Allwood-Spiers [53], J. Almond [82], A. Aloisio [102a,102b], R. Alon [172], A. Alonso [79], F. Alonso [70], A. Altheimer [35], B. Alvarez Gonzalez [88], M.G. Alviggi [102a,102b], K. Amako [65], C. Amelung [23], V.V. Ammosov [128,*], S.P. Amor Dos Santos [124a], A. Amorim [124a,b], N. Amram [153], C. Anastopoulos [30], L.S. Ancu [17], N. Andari [115], T. Andeen [35], C.F. Anders [58b], G. Anders [58a], K.J. Anderson [31], A. Andreazza [89a,89b], V. Andrei [58a], M.-L. Andrieux [55], X.S. Anduaga [70], S. Angelidakis [9], P. Anger [44], A. Angerami [35], F. Anghinolfi [30], A. Anisenkov [107], N. Anjos [124a], A. Annovi [47], A. Antonaki [9], M. Antonelli [47], A. Antonov [96], J. Antos [144b], F. Anulli [132a], M. Aoki [101], S. Aoun [83], L. Aperio Bella [5], R. Apolle [118,c], G. Arabidze [88], I. Aracena [143], Y. Arai [65], A.T.H. Arce [45], S. Arfaoui [148], J.-F. Arguin [93], E. Arik [19a,*], M. Arik [19a], A.J. Armbruster [87], O. Arnaez [81], V. Arnal [80], C. Arnault [115], A. Artamonov [95], G. Artoni [132a,132b], D. Arutinov [21], S. Asai [155], S. Ask [28], B. Åsman [146a,146b], L. Asquith [6], K. Assamagan [25], A. Astbury [169], M. Atkinson [165], B. Aubert [5], E. Auge [115], K. Augsten [127], M. Aurousseau [145a], G. Avolio [163], R. Avramidou [10], D. Axen [168], G. Azuelos [93,d], Y. Azuma [155], M.A. Baak [30], G. Baccaglioni [89a], C. Bacci [134a,134b], A.M. Bach [15], H. Bachacou [136], K. Bachas [30], M. Backes [49], M. Backhaus [21], J. Backus Mayes [143], E. Badescu [26a], P. Bagnaia [132a,132b], S. Bahinipati [3], Y. Bai [33a], D.C. Bailey [158], T. Bain [158], J.T. Baines [129], O.K. Baker [176], M.D. Baker [25], S. Baker [77], P. Balek [126], E. Banas [39], P. Banerjee [93], Sw. Banerjee [173], D. Banfi [30], A. Bangert [150], V. Bansal [169], H.S. Bansil [18], L. Barak [172], S.P. Baranov [94], A. Barbaro Galtieri [15], T. Barber [48], E.L. Barberio [86], D. Barberis [50a,50b], M. Barbero [21], D.Y. Bardin [64], T. Barillari [99], M. Barisonzi [175], T. Barklow [143], N. Barlow [28], B.M. Barnett [129], R.M. Barnett [15], A. Baroncelli [134a], G. Barone [49], A.J. Barr [118], F. Barreiro [80], J. Barreiro Guimarães da Costa [57], P. Barrillon [115], R. Bartoldus [143], A.E. Barton [71], V. Bartsch [149], A. Basye [165], R.L. Bates [53], L. Batkova [144a], J.R. Batley [28], A. Battaglia [17], M. Battistin [30], F. Bauer [136], H.S. Bawa [143,e], S. Beale [98], T. Beau [78], P.H. Beauchemin [161], R. Beccherle [50a], P. Bechtle [21], H.P. Beck [17], A.K. Becker [175], S. Becker [98], M. Beckingham [138], K.H. Becks [175], A.J. Beddall [19c], A. Beddall [19c], S. Bedikian [176], V.A. Bednyakov [64], C.P. Bee [83], L.J. Beemster [105], M. Begel [25], S. Behar Harpaz [152], P.K. Behera [62], M. Beimforde [99],

C. Belanger-Champagne [85], P.J. Bell [49], W.H. Bell [49], G. Bella [153], L. Bellagamba [20a], M. Bellomo [30], A. Belloni [57], O. Beloborodova [107,f], K. Belotskiy [96], O. Beltramello [30], O. Benary [153], D. Benchekroun [135a], K. Bendtz [146a,146b], N. Benekos [165], Y. Benhammou [153], E. Benhar Noccioli [49], J.A. Benitez Garcia [159b], D.P. Benjamin [45], M. Benoit [115], J.R. Bensinger [23], K. Benslama [130], S. Bentvelsen [105], D. Berge [30], E. Bergeaas Kuutmann [42], N. Berger [5], F. Berghaus [169], E. Berglund [105], J. Beringer [15], P. Bernat [77], R. Bernhard [48], C. Bernius [25], F.U. Bernlochner [169], T. Berry [76], C. Bertella [83], A. Bertin [20a,20b], F. Bertolucci [122a,122b], M.I. Besana [89a,89b], G.J. Besjes [104], N. Besson [136], S. Bethke [99], W. Bhimji [46], R.M. Bianchi [30], M. Bianco [72a,72b], O. Biebel [98], S.P. Bieniek [77], K. Bierwagen [54], J. Biesiada [15], M. Biglietti [134a], H. Bilokon [47], M. Bindi [20a,20b], S. Binet [115], A. Bingul [19c], C. Bini [132a,132b], C. Biscarat [178], B. Bittner [99], K.M. Black [22], R.E. Blair [6], J.-B. Blanchard [136], G. Blanchot [30], T. Blazek [144a], I. Bloch [42], C. Blocker [23], J. Blocki [39], A. Blondel [49], W. Blum [81], U. Blumenschein [54], G.J. Bobbink [105], V.B. Bobrovnikov [107], S.S. Bocchetta [79], A. Bocci [45], C.R. Boddy [118], M. Boehler [48], J. Boek [175], N. Boelaert [36], J.A. Bogaerts [30], A. Bogdanchikov [107], A. Bogouch [90,*], C. Bohm [146a], J. Bohm [125], V. Boisvert [76], T. Bold [38], V. Boldea [26a], N.M. Bolnet [136], M. Bomben [78], M. Bona [75], M. Boonekamp [136], S. Bordoni [78], C. Borer [17], A. Borisov [128], G. Borissov [71], I. Borjanovic [13a], M. Borri [82], S. Borroni [87], V. Bortolotto [134a,134b], K. Bos [105], D. Boscherini [20a], M. Bosman [12], H. Boterenbrood [105], J. Bouchami [93], J. Boudreau [123], E.V. Bouhova-Thacker [71], D. Boumediene [34], C. Bourdarios [115], N. Bousson [83], A. Boveia [31], J. Boyd [30], I.R. Boyko [64], I. Bozovic-Jelisavcic [13b], J. Bracinik [18], P. Branchini [134a], G.W. Brandenburg [57], A. Brandt [8], G. Brandt [118], O. Brandt [54], U. Bratzler [156], B. Brau [84], J.E. Brau [114], H.M. Braun [175,*], S.F. Brazzale [164a,164c], B. Brelier [158], J. Bremer [30], K. Brendlinger [120], R. Brenner [166], S. Bressler [172], D. Britton [53], F.M. Brochu [28], I. Brock [21], R. Brock [88], F. Broggi [89a], C. Bromberg [88], J. Bronner [99], G. Brooijmans [35], T. Brooks [76], W.K. Brooks [32b], G. Brown [82], H. Brown [8], P.A. Bruckman de Renstrom [39], D. Bruncko [144b], R. Bruneliere [48], S. Brunet [60], A. Bruni [20a], G. Bruni [20a], M. Bruschi [20a], T. Buanes [14], Q. Buat [55], F. Bucci [49], J. Buchanan [118], P. Buchholz [141], R.M. Buckingham [118], A.G. Buckley [46], S.I. Buda [26a], I.A. Budagov [64], B. Budick [108], V. Büscher [81], L. Bugge [117], O. Bulekov [96], A.C. Bundock [73], M. Bunse [43], T. Buran [117], H. Burckhart [30], S. Burdin [73], T. Burgess [14], S. Burke [129], E. Busato [34], P. Bussey [53], C.P. Buszello [166], B. Butler [143], J.M. Butler [22], C.M. Buttar [53], J.M. Butterworth [77], W. Buttinger [28], S. Cabrera Urbán [167], D. Caforio [20a,20b], O. Cakir [4a], P. Calafiura [15], G. Calderini [78], P. Calfayan [98], R. Calkins [106], L.P. Caloba [24a], R. Caloi [132a,132b], D. Calvet [34], S. Calvet [34], R. Camacho Toro [34], P. Camarri [133a,133b], D. Cameron [117], L.M. Caminada [15], R. Caminal Armadans [12], S. Campana [30], M. Campanelli [77], V. Canale [102a,102b], F. Canelli [31,g], A. Canepa [159a], J. Cantero [80], R. Cantrill [76], L. Capasso [102a,102b], M.D.M. Capeans Garrido [30], I. Caprini [26a], M. Caprini [26a], D. Capriotti [99], M. Capua [37a,37b], R. Caputo [81], R. Cardarelli [133a], T. Carli [30], G. Carlino [102a], L. Carminati [89a,89b], B. Caron [85], S. Caron [104], E. Carquin [32b], G.D. Carrillo-Montoya [173], A.A. Carter [75], J.R. Carter [28], J. Carvalho [124a,h], D. Casadei [108], M.P. Casado [12], M. Cascella [122a,122b], C. Caso [50a,50b,*], A.M. Castaneda Hernandez [173,i], E. Castaneda-Miranda [173], V. Castillo Gimenez [167], N.F. Castro [124a], G. Cataldi [72a], P. Catastini [57], A. Catinaccio [30], J.R. Catmore [30], A. Cattai [30], G. Cattani [133a,133b], S. Caughron [88], V. Cavaliere [165], P. Cavalleri [78], D. Cavalli [89a], M. Cavalli-Sforza [12], V. Cavasinni [122a,122b], F. Ceradini [134a,134b], A.S. Cerqueira [24b], A. Cerri [30], L. Cerrito [75], F. Cerutti [47], S.A. Cetin [19b], A. Chafaq [135a], D. Chakraborty [106], I. Chalupkova [126], K. Chan [3], P. Chang [165], B. Chapleau [85], J.D. Chapman [28], J.W. Chapman [87], E. Chareyre [78], D.G. Charlton [18], V. Chavda [82], C.A. Chavez Barajas [30], S. Cheatham [85], S. Chekanov [6], S.V. Chekulaev [159a], G.A. Chelkov [64], M.A. Chelstowska [104], C. Chen [63], H. Chen [25], S. Chen [33c], X. Chen [173], Y. Chen [35], Y. Cheng [31], A. Cheplakov [64], R. Cherkaoui El Moursli [135e], V. Chernyatin [25], E. Cheu [7], S.L. Cheung [158], L. Chevalier [136], G. Chiefari [102a,102b], L. Chikovani [51a,*], J.T. Childers [30], A. Chilingarov [71], G. Chiodini [72a], A.S. Chisholm [18], R.T. Chislett [77], A. Chitan [26a], M.V. Chizhov [64], G. Choudalakis [31], S. Chouridou [137], I.A. Christidi [77], A. Christov [48], D. Chromek-Burckhart [30], M.L. Chu [151], J. Chudoba [125], G. Ciapetti [132a,132b], A.K. Ciftci [4a], R. Ciftci [4a], D. Cinca [34], V. Cindro [74], C. Ciocca [20a,20b], A. Ciocio [15], M. Cirilli [87], P. Cirkovic [13b], Z.H. Citron [172], M. Citterio [89a], M. Ciubancan [26a], A. Clark [49], P.J. Clark [46], R.N. Clarke [15], W. Cleland [123], J.C. Clemens [83], B. Clement [55], C. Clement [146a,146b], Y. Coadou [83], M. Cobal [164a,164c], A. Coccaro [138], J. Cochran [63], L. Coffey [23], J.G. Cogan [143], J. Coggeshall [165], E. Cogneras [178], J. Colas [5], S. Cole [106], A.P. Colijn [105], N.J. Collins [18], C. Collins-Tooth [53], J. Collot [55], T. Colombo [119a,119b], G. Colon [84], G. Compostella [99], P. Conde Muiño [124a], E. Coniavitis [166], M.C. Conidi [12], S.M. Consonni [89a,89b], V. Consorti [48],

S. Constantinescu [26a], C. Conta [119a,119b], G. Conti [57], F. Conventi [102a,j], M. Cooke [15], B.D. Cooper [77], A.M. Cooper-Sarkar [118], N.J. Cooper-Smith [76], K. Copic [15], T. Cornelissen [175], M. Corradi [20a], F. Corriveau [85,k], A. Cortes-Gonzalez [165], G. Cortiana [99], G. Costa [89a], M.J. Costa [167], D. Costanzo [139], D. Côté [30], L. Courneyea [169], G. Cowan [76], C. Cowden [28], B.E. Cox [82], K. Cranmer [108], F. Crescioli [122a,122b], M. Cristinziani [21], G. Crosetti [37a,37b], S. Crépé-Renaudin [55], C.-M. Cuciuc [26a], C. Cuenca Almenar [176], T. Cuhadar Donszelmann [139], M. Curatolo [47], C.J. Curtis [18], C. Cuthbert [150], P. Cwetanski [60], H. Czirr [141], P. Czodrowski [44], Z. Czyczula [176], S. D'Auria [53], M. D'Onofrio [73], A. D'Orazio [132a,132b], M.J. Da Cunha Sargedas De Sousa [124a], C. Da Via [82], W. Dabrowski [38], A. Dafinca [118], T. Dai [87], C. Dallapiccola [84], M. Dam [36], M. Dameri [50a,50b], D.S. Damiani [137], H.O. Danielsson [30], V. Dao [49], G. Darbo [50a], G.L. Darlea [26b], J.A. Dassoulas [42], W. Davey [21], T. Davidek [126], N. Davidson [86], R. Davidson [71], E. Davies [118,c], M. Davies [93], O. Davignon [78], A.R. Davison [77], Y. Davygora [58a], E. Dawe [142], I. Dawson [139], R.K. Daya-Ishmukhametova [23], K. De [8], R. de Asmundis [102a], S. De Castro [20a,20b], S. De Cecco [78], J. de Graat [98], N. De Groot [104], P. de Jong [105], C. De La Taille [115], H. De la Torre [80], F. De Lorenzi [63], L. de Mora [71], L. De Nooij [105], D. De Pedis [132a], A. De Salvo [132a], U. De Sanctis [164a,164c], A. De Santo [149], J.B. De Vivie De Regie [115], G. De Zorzi [132a,132b], W.J. Dearnaley [71], R. Debbe [25], C. Debenedetti [46], B. Dechenaux [55], D.V. Dedovich [64], J. Degenhardt [120], C. Del Papa [164a,164c], J. Del Peso [80], T. Del Prete [122a,122b], T. Delemontex [55], M. Deliyergiyev [74], A. Dell'Acqua [30], L. Dell'Asta [22], M. Della Pietra [102a,j], D. della Volpe [102a,102b], M. Delmastro [5], P. Delpierre [83], P.A. Delsart [55], C. Deluca [105], S. Demers [176], M. Demichev [64], B. Demirkoz [12,l], J. Deng [163], S.P. Denisov [128], D. Derendarz [39], J.E. Derkaoui [135d], F. Derue [78], P. Dervan [73], K. Desch [21], E. Devetak [148], P.O. Deviveiros [105], A. Dewhurst [129], B. DeWilde [148], S. Dhaliwal [158], R. Dhullipudi [25,m], A. Di Ciaccio [133a,133b], L. Di Ciaccio [5], C. Di Donato [102a,102b], A. Di Girolamo [30], B. Di Girolamo [30], S. Di Luise [134a,134b], A. Di Mattia [173], B. Di Micco [30], R. Di Nardo [47], A. Di Simone [133a,133b], R. Di Sipio [20a,20b], M.A. Diaz [32a], E.B. Diehl [87], J. Dietrich [42], T.A. Dietzsch [58a], S. Diglio [86], K. Dindar Yagci [40], J. Dingfelder [21], F. Dinut [26a], C. Dionisi [132a,132b], P. Dita [26a], S. Dita [26a], F. Dittus [30], F. Djama [83], T. Djobava [51b], M.A.B. do Vale [24c], A. Do Valle Wemans [124a,n], T.K.O. Doan [5], M. Dobbs [85], R. Dobinson [30,*], D. Dobos [30], E. Dobson [30,o], J. Dodd [35], C. Doglioni [49], T. Doherty [53], Y. Doi [65,*], J. Dolejsi [126], I. Dolenc [74], Z. Dolezal [126], B.A. Dolgoshein [96,*], T. Dohmae [155], M. Donadelli [24d], J. Donini [34], J. Dopke [30], A. Doria [102a], A. Dos Anjos [173], A. Dotti [122a,122b], M.T. Dova [70], J.D. Dowell [18], A.D. Doxiadis [105], A.T. Doyle [53], N. Dressnandt [120], M. Dris [10], J. Dubbert [99], S. Dube [15], E. Duchovni [172], G. Duckeck [98], D. Duda [175], A. Dudarev [30], F. Dudziak [63], M. Dührssen [30], I.P. Duerdoth [82], L. Duflot [115], M.-A. Dufour [85], L. Duguid [76], M. Dunford [58a], H. Duran Yildiz [4a], R. Duxfield [139], M. Dwuznik [38], F. Dydak [30], M. Düren [52], W.L. Ebenstein [45], J. Ebke [98], S. Eckweiler [81], K. Edmonds [81], W. Edson [2], C.A. Edwards [76], N.C. Edwards [53], W. Ehrenfeld [42], T. Eifert [143], G. Eigen [14], K. Einsweiler [15], E. Eisenhandler [75], T. Ekelof [166], M. El Kacimi [135c], M. Ellert [166], S. Elles [5], F. Ellinghaus [81], K. Ellis [75], N. Ellis [30], J. Elmsheuser [98], M. Elsing [30], D. Emeliyanov [129], R. Engelmann [148], A. Engl [98], B. Epp [61], J. Erdmann [54], A. Ereditato [17], D. Eriksson [146a], J. Ernst [2], M. Ernst [25], J. Ernwein [136], D. Errede [165], S. Errede [165], E. Ertel [81], M. Escalier [115], H. Esch [43], C. Escobar [123], X. Espinal Curull [12], B. Esposito [47], F. Etienne [83], A.I. Etienvre [136], E. Etzion [153], D. Evangelakou [54], H. Evans [60], L. Fabbri [20a,20b], C. Fabre [30], R.M. Fakhrutdinov [128], S. Falciano [132a], Y. Fang [173], M. Fanti [89a,89b], A. Farbin [8], A. Farilla [134a], J. Farley [148], T. Farooque [158], S. Farrell [163], S.M. Farrington [170], P. Farthouat [30], F. Fassi [167], P. Fassnacht [30], D. Fassouliotis [9], B. Fatholahzadeh [158], A. Favareto [89a,89b], L. Fayard [115], S. Fazio [37a,37b], R. Febbraro [34], P. Federic [144a], O.L. Fedin [121], W. Fedorko [88], M. Fehling-Kaschek [48], L. Feligioni [83], D. Fellmann [6], C. Feng [33d], E.J. Feng [6], A.B. Fenyuk [128], J. Ferencei [144b], W. Fernando [6], S. Ferrag [53], J. Ferrando [53], V. Ferrara [42], A. Ferrari [166], P. Ferrari [105], R. Ferrari [119a], D.E. Ferreira de Lima [53], A. Ferrer [167], D. Ferrere [49], C. Ferretti [87], A. Ferretto Parodi [50a,50b], M. Fiascaris [31], F. Fiedler [81], A. Filipčič [74], F. Filthaut [104], M. Fincke-Keeler [169], M.C.N. Fiolhais [124a,h], L. Fiorini [167], A. Firan [40], G. Fischer [42], M.J. Fisher [109], M. Flechl [48], I. Fleck [141], J. Fleckner [81], P. Fleischmann [174], S. Fleischmann [175], T. Flick [175], A. Floderus [79], L.R. Flores Castillo [173], M.J. Flowerdew [99], T. Fonseca Martin [17], A. Formica [136], A. Forti [82], D. Fortin [159a], D. Fournier [115], A.J. Fowler [45], H. Fox [71], P. Francavilla [12], M. Franchini [20a,20b], S. Franchino [119a,119b], D. Francis [30], T. Frank [172], M. Franklin [57], S. Franz [30], M. Fraternali [119a,119b], S. Fratina [120], S.T. French [28], C. Friedrich [42], F. Friedrich [44], R. Froeschl [30], D. Froidevaux [30], J.A. Frost [28], C. Fukunaga [156], E. Fullana Torregrosa [30],

B.G. Fulsom [143], J. Fuster [167], C. Gabaldon [30], O. Gabizon [172], S. Gadatsch [105], T. Gadfort [25], S. Gadomski [49], G. Gagliardi [50a,50b], P. Gagnon [60], C. Galea [98], B. Galhardo [124a], E.J. Gallas [118], V. Gallo [17], B.J. Gallop [129], P. Gallus [125], K.K. Gan [109], Y.S. Gao [143,e], A. Gaponenko [15], F. Garberson [176], M. Garcia-Sciveres [15], C. García [167], J.E. García Navarro [167], R.W. Gardner [31], N. Garelli [30], H. Garitaonandia [105], V. Garonne [30], C. Gatti [47], G. Gaudio [119a], B. Gaur [141], L. Gauthier [136], P. Gauzzi [132a,132b], I.L. Gavrilenko [94], C. Gay [168], G. Gaycken [21], E.N. Gazis [10], P. Ge [33d], Z. Gecse [168], C.N.P. Gee [129], D.A.A. Geerts [105], Ch. Geich-Gimbel [21], K. Gellerstedt [146a,146b], C. Gemme [50a], A. Gemmell [53], M.H. Genest [55], S. Gentile [132a,132b], M. George [54], S. George [76], P. Gerlach [175], A. Gershon [153], C. Geweniger [58a], H. Ghazlane [135b], N. Ghodbane [34], B. Giacobbe [20a], S. Giagu [132a,132b], V. Giakoumopoulou [9], V. Giangiobbe [12], F. Gianotti [30], B. Gibbard [25], A. Gibson [158], S.M. Gibson [30], M. Gilchriese [15], O. Gildemeister [30], D. Gillberg [29], A.R. Gillman [129], D.M. Gingrich [3,d], J. Ginzburg [153], N. Giokaris [9], M.P. Giordani [164c], R. Giordano [102a,102b], F.M. Giorgi [16], P. Giovannini [99], P.F. Giraud [136], D. Giugni [89a], M. Giunta [93], P. Giusti [20a], B.K. Gjelsten [117], L.K. Gladilin [97], C. Glasman [80], J. Glatzer [21], A. Glazov [42], K.W. Glitza [175], G.L. Glonti [64], J.R. Goddard [75], J. Godfrey [142], J. Godlewski [30], M. Goebel [42], T. Göpfert [44], C. Goeringer [81], C. Gössling [43], S. Goldfarb [87], T. Golling [176], A. Gomes [124a,b], L.S. Gomez Fajardo [42], R. Gonçalo [76], J. Goncalves Pinto Firmino Da Costa [42], L. Gonella [21], S. González de la Hoz [167], G. Gonzalez Parra [12], M.L. Gonzalez Silva [27], S. Gonzalez-Sevilla [49], J.J. Goodson [148], L. Goossens [30], P.A. Gorbounov [95], H.A. Gordon [25], I. Gorelov [103], G. Gorfine [175], B. Gorini [30], E. Gorini [72a,72b], A. Gorišek [74], E. Gornicki [39], B. Gosdzik [42], A.T. Goshaw [6], M. Gosselink [105], M.I. Gostkin [64], I. Gough Eschrich [163], M. Gouighri [135a], D. Goujdami [135c], M.P. Goulette [49], A.G. Goussiou [138], C. Goy [5], S. Gozpinar [23], I. Grabowska-Bold [38], P. Grafström [20a,20b], K.-J. Grahn [42], E. Gramstad [117], F. Grancagnolo [72a], S. Grancagnolo [16], V. Grassi [148], V. Gratchev [121], N. Grau [35], H.M. Gray [30], J.A. Gray [148], E. Graziani [134a], O.G. Grebenyuk [121], T. Greenshaw [73], Z.D. Greenwood [25,m], K. Gregersen [36], I.M. Gregor [42], P. Grenier [143], J. Griffiths [8], N. Grigalashvili [64], A.A. Grillo [137], S. Grinstein [12], Ph. Gris [34], Y.V. Grishkevich [97], J.-F. Grivaz [115], E. Gross [172], J. Grosse-Knetter [54], J. Groth-Jensen [172], K. Grybel [141], D. Guest [176], C. Guicheney [34], T. Guillemin [115], S. Guindon [54], U. Gul [53], J. Gunther [125], B. Guo [158], J. Guo [35], P. Gutierrez [111], N. Guttman [153], O. Gutzwiller [173], C. Guyot [136], C. Gwenlan [118], C.B. Gwilliam [73], A. Haas [143], S. Haas [30], C. Haber [15], H.K. Hadavand [8], D.R. Hadley [18], P. Haefner [21], F. Hahn [30], S. Haider [30], Z. Hajduk [39], H. Hakobyan [177], D. Hall [118], J. Haller [54], K. Hamacher [175], P. Hamal [113], K. Hamano [86], M. Hamer [54], A. Hamilton [145b,p], S. Hamilton [161], L. Han [33b], K. Hanagaki [116], K. Hanawa [160], M. Hance [15], C. Handel [81], P. Hanke [58a], J.R. Hansen [36], J.B. Hansen [36], J.D. Hansen [36], P.H. Hansen [36], P. Hansson [143], K. Hara [160], A.S. Hard [173], G.A. Hare [137], T. Harenberg [175], S. Harkusha [90], D. Harper [87], R.D. Harrington [46], O.M. Harris [138], J. Hartert [48], F. Hartjes [105], T. Haruyama [65], A. Harvey [56], S. Hasegawa [101], Y. Hasegawa [140], S. Hassani [136], S. Haug [17], M. Hauschild [30], R. Hauser [88], M. Havranek [21], C.M. Hawkes [18], R.J. Hawkings [30], A.D. Hawkins [79], T. Hayakawa [66], T. Hayashi [160], D. Hayden [76], C.P. Hays [118], H.S. Hayward [73], S.J. Haywood [129], S.J. Head [18], V. Hedberg [79], L. Heelan [8], S. Heim [88], B. Heinemann [15], S. Heisterkamp [36], L. Helary [22], C. Heller [98], M. Heller [30], S. Hellman [146a,146b], D. Hellmich [21], C. Helsens [12], R.C.W. Henderson [71], M. Henke [58a], A. Henrichs [54], A.M. Henriques Correia [30], S. Henrot-Versille [115], C. Hensel [54], T. Henß [175], C.M. Hernandez [8], Y. Hernández Jiménez [167], R. Herrberg [16], G. Herten [48], R. Hertenberger [98], L. Hervas [30], G.G. Hesketh [77], N.P. Hessey [105], E. Higón-Rodriguez [167], J.C. Hill [28], K.H. Hiller [42], S. Hillert [21], S.J. Hillier [18], I. Hinchliffe [15], E. Hines [120], M. Hirose [116], F. Hirsch [43], D. Hirschbuehl [175], J. Hobbs [148], N. Hod [153], M.C. Hodgkinson [139], P. Hodgson [139], A. Hoecker [30], M.R. Hoeferkamp [103], J. Hoffman [40], D. Hoffmann [83], M. Hohlfeld [81], M. Holder [141], S.O. Holmgren [146a], T. Holy [127], J.L. Holzbauer [88], T.M. Hong [120], L. Hooft van Huysduynen [108], S. Horner [48], J.-Y. Hostachy [55], S. Hou [151], A. Hoummada [135a], J. Howard [118], J. Howarth [82], I. Hristova [16], J. Hrivnac [115], T. Hryn'ova [5], P.J. Hsu [81], S.-C. Hsu [15], D. Hu [35], Z. Hubacek [127], F. Hubaut [83], F. Huegging [21], A. Huettmann [42], T.B. Huffman [118], E.W. Hughes [35], G. Hughes [71], M. Huhtinen [30], M. Hurwitz [15], N. Huseynov [64,q], J. Huston [88], J. Huth [57], G. Iacobucci [49], G. Iakovidis [10], M. Ibbotson [82], I. Ibragimov [141], L. Iconomidou-Fayard [115], J. Idarraga [115], P. Iengo [102a], O. Igonkina [105], Y. Ikegami [65], M. Ikeno [65], D. Iliadis [154], N. Ilic [158], T. Ince [99], J. Inigo-Golfin [30], P. Ioannou [9], M. Iodice [134a], K. Iordanidou [9], V. Ippolito [132a,132b], A. Irles Quiles [167], C. Isaksson [166], M. Ishino [67], M. Ishitsuka [157], R. Ishmukhametov [109], C. Issever [118], S. Istin [19a], A.V. Ivashin [128], W. Iwanski [39], H. Iwasaki [65], J.M. Izen [41], V. Izzo [102a], B. Jackson [120], J.N. Jackson [73], P. Jackson [1], M.R. Jaekel [30], V. Jain [60], K. Jakobs [48],

S. Jakobsen [36], T. Jakoubek [125], J. Jakubek [127], D.O. Jamin [151], D.K. Jana [111], E. Jansen [77], H. Jansen [30], A. Jantsch [99], M. Janus [48], G. Jarlskog [79], L. Jeanty [57], I. Jen-La Plante [31], D. Jennens [86], P. Jenni [30], A.E. Loevschall-Jensen [36], P. Jež [36], S. Jézéquel [5], M.K. Jha [20a], H. Ji [173], W. Ji [81], J. Jia [148], Y. Jiang [33b], M. Jimenez Belenguer [42], S. Jin [33a], O. Jinnouchi [157], M.D. Joergensen [36], D. Joffe [40], M. Johansen [146a,146b], K.E. Johansson [146a], P. Johansson [139], S. Johnert [42], K.A. Johns [7], K. Jon-And [146a,146b], G. Jones [170], R.W.L. Jones [71], T.J. Jones [73], C. Joram [30], P.M. Jorge [124a], K.D. Joshi [82], J. Jovicevic [147], T. Jovin [13b], X. Ju [173], C.A. Jung [43], R.M. Jungst [30], V. Juranek [125], P. Jussel [61], A. Juste Rozas [12], S. Kabana [17], M. Kaci [167], A. Kaczmarska [39], P. Kadlecik [36], M. Kado [115], H. Kagan [109], M. Kagan [57], E. Kajomovitz [152], S. Kalinin [175], L.V. Kalinovskaya [64], S. Kama [40], N. Kanaya [155], M. Kaneda [30], S. Kaneti [28], T. Kanno [157], V.A. Kantserov [96], J. Kanzaki [65], B. Kaplan [108], A. Kapliy [31], J. Kaplon [30], D. Kar [53], M. Karagounis [21], K. Karakostas [10], M. Karnevskiy [42], V. Kartvelishvili [71], A.N. Karyukhin [128], L. Kashif [173], G. Kasieczka [58b], R.D. Kass [109], A. Kastanas [14], M. Kataoka [5], Y. Kataoka [155], E. Katsoufis [10], J. Katzy [42], V. Kaushik [7], K. Kawagoe [69], T. Kawamoto [155], G. Kawamura [81], M.S. Kayl [105], S. Kazama [155], V.A. Kazanin [107], M.Y. Kazarinov [64], R. Keeler [169], P.T. Keener [120], R. Kehoe [40], M. Keil [54], G.D. Kekelidze [64], J.S. Keller [138], M. Kenyon [53], O. Kepka [125], N. Kerschen [30], B.P. Kerševan [74], S. Kersten [175], K. Kessoku [155], J. Keung [158], F. Khalil-zada [11], H. Khandanyan [146a,146b], A. Khanov [112], D. Kharchenko [64], A. Khodinov [96], A. Khomich [58a], T.J. Khoo [28], G. Khoriauli [21], A. Khoroshilov [175], V. Khovanskiy [95], E. Khramov [64], J. Khubua [51b], H. Kim [146a,146b], S.H. Kim [160], N. Kimura [171], O. Kind [16], B.T. King [73], M. King [66], R.S.B. King [118], J. Kirk [129], A.E. Kiryunin [99], T. Kishimoto [66], D. Kisielewska [38], T. Kitamura [66], T. Kittelmann [123], K. Kiuchi [160], E. Kladiva [144b], M. Klein [73], U. Klein [73], K. Kleinknecht [81], M. Klemetti [85], A. Klier [172], P. Klimek [146a,146b], A. Klimentov [25], R. Klingenberg [43], J.A. Klinger [82], E.B. Klinkby [36], T. Klioutchnikova [30], P.F. Klok [104], S. Klous [105], E.-E. Kluge [58a], T. Kluge [73], P. Kluit [105], S. Kluth [99], E. Kneringer [61], E.B.F.G. Knoops [83], A. Knue [54], B.R. Ko [45], T. Kobayashi [155], M. Kobel [44], M. Kocian [143], P. Kodys [126], K. Köneke [30], A.C. König [104], S. Koenig [81], L. Köpke [81], F. Koetsveld [104], P. Koevesarki [21], T. Koffas [29], E. Koffeman [105], L.A. Kogan [118], S. Kohlmann [175], F. Kohn [54], Z. Kohout [127], T. Kohriki [65], T. Koi [143], G.M. Kolachev [107,*], H. Kolanoski [16], V. Kolesnikov [64], I. Koletsou [89a], J. Koll [88], A.A. Komar [94], Y. Komori [155], T. Kondo [65], T. Kono [42,r], A.I. Kononov [48], R. Konoplich [108,s], N. Konstantinidis [77], R. Kopeliansky [152], S. Koperny [38], K. Korcyl [39], K. Kordas [154], A. Korn [118], A. Korol [107], I. Korolkov [12], E.V. Korolkova [139], V.A. Korotkov [128], O. Kortner [99], S. Kortner [99], V.V. Kostyukhin [21], S. Kotov [99], V.M. Kotov [64], A. Kotwal [45], C. Kourkoumelis [9], V. Kouskoura [154], A. Koutsman [159a], R. Kowalewski [169], T.Z. Kowalski [38], W. Kozanecki [136], A.S. Kozhin [128], V. Kral [127], V.A. Kramarenko [97], G. Kramberger [74], M.W. Krasny [78], A. Krasznahorkay [108], J.K. Kraus [21], S. Kreiss [108], F. Krejci [127], J. Kretzschmar [73], N. Krieger [54], P. Krieger [158], K. Kroeninger [54], H. Kroha [99], J. Kroll [120], J. Kroseberg [21], J. Krstic [13a], U. Kruchonak [64], H. Krüger [21], T. Kruker [17], N. Krumnack [63], Z.V. Krumshteyn [64], A. Kruse [173], T. Kubota [86], S. Kuday [4a], S. Kuehn [48], A. Kugel [58c], T. Kuhl [42], D. Kuhn [61], V. Kukhtin [64], Y. Kulchitsky [90], S. Kuleshov [32b], C. Kummer [98], M. Kuna [78], J. Kunkle [120], A. Kupco [125], H. Kurashige [66], M. Kurata [160], Y.A. Kurochkin [90], V. Kus [125], E.S. Kuwertz [147], M. Kuze [157], J. Kvita [142], R. Kwee [16], A. La Rosa [49], L. La Rotonda [37a,37b], L. Labarga [80], J. Labbe [5], S. Lablak [135a], C. Lacasta [167], F. Lacava [132a,132b], J. Lacey [29], H. Lacker [16], D. Lacour [78], V.R. Lacuesta [167], E. Ladygin [64], R. Lafaye [5], B. Laforge [78], T. Lagouri [176], S. Lai [48], E. Laisne [55], M. Lamanna [30], L. Lambourne [77], C.L. Lampen [7], W. Lampl [7], E. Lancon [136], U. Landgraf [48], M.P.J. Landon [75], V.S. Lang [58a], C. Lange [42], A.J. Lankford [163], F. Lanni [25], K. Lantzsch [175], S. Laplace [78], C. Lapoire [21], J.F. Laporte [136], T. Lari [89a], A. Larner [118], M. Lassnig [30], P. Laurelli [47], V. Lavorini [37a,37b], W. Lavrijsen [15], P. Laycock [73], T. Lazovich [57], O. Le Dortz [78], E. Le Guirriec [83], E. Le Menedeu [12], T. LeCompte [6], F. Ledroit-Guillon [55], H. Lee [105], J.S.H. Lee [116], S.C. Lee [151], L. Lee [176], M. Lefebvre [169], M. Legendre [136], F. Legger [98], C. Leggett [15], M. Lehmacher [21], G. Lehmann Miotto [30], X. Lei [7], M.A.L. Leite [24d], R. Leitner [126], D. Lellouch [172], B. Lemmer [54], V. Lendermann [58a], K.J.C. Leney [145b], T. Lenz [105], G. Lenzen [175], B. Lenzi [30], K. Leonhardt [44], S. Leontsinis [10], F. Lepold [58a], C. Leroy [93], J.-R. Lessard [169], C.G. Lester [28], C.M. Lester [120], J. Levêque [5], D. Levin [87], L.J. Levinson [172], A. Lewis [118], G.H. Lewis [108], A.M. Leyko [21], M. Leyton [16], B. Li [83], H. Li [148], H.L. Li [31], S. Li [33b,t], X. Li [87], Z. Liang [118,u], H. Liao [34], B. Liberti [133a], P. Lichard [30], M. Lichtnecker [98], K. Lie [165], W. Liebig [14], C. Limbach [21], A. Limosani [86], M. Limper [62], S.C. Lin [151,v], F. Linde [105], J.T. Linnemann [88], E. Lipeles [120], A. Lipniacka [14], T.M. Liss [165], D. Lissauer [25], A. Lister [49], A.M. Litke [137], C. Liu [29], D. Liu [151], H. Liu [87], J.B. Liu [87], K. Liu [33b,w], L. Liu [87], M. Liu [33b], Y. Liu [33b], M. Livan [119a,119b], S.S.A. Livermore [118],

A. Lleres [55], J. Llorente Merino [80], S.L. Lloyd [75], E. Lobodzinska [42], P. Loch [7], W.S. Lockman [137], T. Loddenkoetter [21], F.K. Loebinger [82], A. Loginov [176], C.W. Loh [168], T. Lohse [16], K. Lohwasser [48], M. Lokajicek [125], V.P. Lombardo [5], J.D. Long [87], R.E. Long [71], L. Lopes [124a], D. Lopez Mateos [57], J. Lorenz [98], N. Lorenzo Martinez [115], M. Losada [162], P. Loscutoff [15], F. Lo Sterzo [132a,132b], M.J. Losty [159a,*], X. Lou [41], A. Lounis [115], K.F. Loureiro [162], J. Love [6], P.A. Love [71], A.J. Lowe [143,e], F. Lu [33a], H.J. Lubatti [138], C. Luci [132a,132b], A. Lucotte [55], A. Ludwig [44], D. Ludwig [42], I. Ludwig [48], J. Ludwig [48], F. Luehring [60], G. Luijckx [105], W. Lukas [61], L. Luminari [132a], E. Lund [117], B. Lund-Jensen [147], B. Lundberg [79], J. Lundberg [146a,146b], O. Lundberg [146a,146b], J. Lundquist [36], M. Lungwitz [81], D. Lynn [25], E. Lytken [79], H. Ma [25], L.L. Ma [173], G. Maccarrone [47], A. Macchiolo [99], B. Maček [74], J. Machado Miguens [124a], R. Mackeprang [36], R.J. Madaras [15], H.J. Maddocks [71], W.F. Mader [44], R. Maenner [58c], T. Maeno [25], P. Mättig [175], S. Mättig [81], L. Magnoni [163], E. Magradze [54], K. Mahboubi [48], J. Mahlstedt [105], S. Mahmoud [73], G. Mahout [18], C. Maiani [136], C. Maidantchik [24a], A. Maio [124a,b], S. Majewski [25], Y. Makida [65], N. Makovec [115], P. Mal [136], B. Malaescu [30], Pa. Malecki [39], P. Malecki [39], V.P. Maleev [121], F. Malek [55], U. Mallik [62], D. Malon [6], C. Malone [143], S. Maltezos [10], V. Malyshev [107], S. Malyukov [30], R. Mameghani [98], J. Mamuzic [13b], A. Manabe [65], L. Mandelli [89a], I. Mandić [74], R. Mandrysch [16], J. Maneira [124a], A. Manfredini [99], P.S. Mangeard [88], L. Manhaes de Andrade Filho [24b], J.A. Manjarres Ramos [136], A. Mann [54], P.M. Manning [137], A. Manousakis-Katsikakis [9], B. Mansoulie [136], A. Mapelli [30], L. Mapelli [30], L. March [167], J.F. Marchand [29], F. Marchese [133a,133b], G. Marchiori [78], M. Marcisovsky [125], C.P. Marino [169], F. Marroquim [24a], Z. Marshall [30], F.K. Martens [158], L.F. Marti [17], S. Marti-Garcia [167], B. Martin [30], B. Martin [88], J.P. Martin [93], T.A. Martin [18], V.J. Martin [46], B. Martin dit Latour [49], S. Martin-Haugh [149], M. Martinez [12], V. Martinez Outschoorn [57], A.C. Martyniuk [169], M. Marx [82], F. Marzano [132a], A. Marzin [111], L. Masetti [81], T. Mashimo [155], R. Mashinistov [94], J. Masik [82], A.L. Maslennikov [107], I. Massa [20a,20b], G. Massaro [105], N. Massol [5], P. Mastrandrea [148], A. Mastroberardino [37a,37b], T. Masubuchi [155], P. Matricon [115], H. Matsunaga [155], T. Matsushita [66], C. Mattravers [118,c], J. Maurer [83], S.J. Maxfield [73], A. Mayne [139], R. Mazini [151], M. Mazur [21], L. Mazzaferro [133a,133b], M. Mazzanti [89a], J. Mc Donald [85], S.P. Mc Kee [87], A. McCarn [165], R.L. McCarthy [148], T.G. McCarthy [29], N.A. McCubbin [129], K.W. McFarlane [56,*], J.A. Mcfayden [139], G. Mchedlidze [51b], T. Mclaughlan [18], S.J. McMahon [129], R.A. McPherson [169,k], A. Meade [84], J. Mechnich [105], M. Mechtel [175], M. Medinnis [42], R. Meera-Lebbai [111], T. Meguro [116], R. Mehdiyev [93], S. Mehlhase [36], A. Mehta [73], K. Meier [58a], B. Meirose [79], C. Melachrinos [31], B.R. Mellado Garcia [173], F. Meloni [89a,89b], L. Mendoza Navas [162], Z. Meng [151,x], A. Mengarelli [20a,20b], S. Menke [99], E. Meoni [161], K.M. Mercurio [57], P. Mermod [49], L. Merola [102a,102b], C. Meroni [89a], F.S. Merritt [31], H. Merritt [109], A. Messina [30,y], J. Metcalfe [25], A.S. Mete [163], C. Meyer [81], C. Meyer [31], J.-P. Meyer [136], J. Meyer [174], J. Meyer [54], T.C. Meyer [30], S. Michal [30], L. Micu [26a], R.P. Middleton [129], S. Migas [73], L. Mijović [136], G. Mikenberg [172], M. Mikestikova [125], M. Mikuž [74], D.W. Miller [31], R.J. Miller [88], W.J. Mills [168], C. Mills [57], A. Milov [172], D.A. Milstead [146a,146b], D. Milstein [172], A.A. Minaenko [128], M. Miñano Moya [167], I.A. Minashvili [64], A.I. Mincer [108], B. Mindur [38], M. Mineev [64], Y. Ming [173], L.M. Mir [12], G. Mirabelli [132a], J. Mitrevski [137], V.A. Mitsou [167], S. Mitsui [65], P.S. Miyagawa [139], J.U. Mjörnmark [79], T. Moa [146a,146b], V. Moeller [28], K. Mönig [42], N. Möser [21], S. Mohapatra [148], W. Mohr [48], R. Moles-Valls [167], A. Molfetas [30], J. Monk [77], E. Monnier [83], J. Montejo Berlingen [12], F. Monticelli [70], S. Monzani [20a,20b], R.W. Moore [3], G.F. Moorhead [86], C. Mora Herrera [49], A. Moraes [53], N. Morange [136], J. Morel [54], G. Morello [37a,37b], D. Moreno [81], M. Moreno Llácer [167], P. Morettini [50a], M. Morgenstern [44], M. Morii [57], A.K. Morley [30], G. Mornacchi [30], J.D. Morris [75], L. Morvaj [101], H.G. Moser [99], M. Mosidze [51b], J. Moss [109], R. Mount [143], E. Mountricha [10,z], S.V. Mouraviev [94,*], E.J.W. Moyse [84], F. Mueller [58a], J. Mueller [123], K. Mueller [21], T.A. Müller [98], T. Mueller [81], D. Muenstermann [30], Y. Munwes [153], W.J. Murray [129], I. Mussche [105], E. Musto [102a,102b], A.G. Myagkov [128], M. Myska [125], O. Nackenhorst [54], J. Nadal [12], K. Nagai [160], R. Nagai [157], K. Nagano [65], A. Nagarkar [109], Y. Nagasaka [59], M. Nagel [99], A.M. Nairz [30], Y. Nakahama [30], K. Nakamura [155], T. Nakamura [155], I. Nakano [110], G. Nanava [21], A. Napier [161], R. Narayan [58b], M. Nash [77,c], T. Nattermann [21], T. Naumann [42], G. Navarro [162], H.A. Neal [87], P.Yu. Nechaeva [94], T.J. Neep [82], A. Negri [119a,119b], G. Negri [30], M. Negrini [20a], S. Nektarijevic [49], A. Nelson [163], T.K. Nelson [143], S. Nemecek [125], P. Nemethy [108], A.A. Nepomuceno [24a], M. Nessi [30,aa], M.S. Neubauer [165], M. Neumann [175], A. Neusiedl [81], R.M. Neves [108], P. Nevski [25], F.M. Newcomer [120], P.R. Newman [18], V. Nguyen Thi Hong [136], R.B. Nickerson [118],

R. Nicolaidou [136], B. Nicquevert [30], F. Niedercorn [115], J. Nielsen [137], N. Nikiforou [35], A. Nikiforov [16], V. Nikolaenko [128], I. Nikolic-Audit [78], K. Nikolics [49], K. Nikolopoulos [18], H. Nilsen [48], P. Nilsson [8], Y. Ninomiya [155], A. Nisati [132a], R. Nisius [99], T. Nobe [157], L. Nodulman [6], M. Nomachi [116], I. Nomidis [154], S. Norberg [111], M. Nordberg [30], P.R. Norton [129], J. Novakova [126], M. Nozaki [65], L. Nozka [113], I.M. Nugent [159a], A.-E. Nuncio-Quiroz [21], G. Nunes Hanninger [86], T. Nunnemann [98], E. Nurse [77], B.J. O'Brien [46], D.C. O'Neil [142], V. O'Shea [53], L.B. Oakes [98], F.G. Oakham [29,d], H. Oberlack [99], J. Ocariz [78], A. Ochi [66], S. Oda [69], S. Odaka [65], J. Odier [83], H. Ogren [60], A. Oh [82], S.H. Oh [45], C.C. Ohm [30], T. Ohshima [101], W. Okamura [116], H. Okawa [25], Y. Okumura [31], T. Okuyama [155], A. Olariu [26a], A.G. Olchevski [64], S.A. Olivares Pino [32a], M. Oliveira [124a,h], D. Oliveira Damazio [25], E. Oliver Garcia [167], D. Olivito [120], A. Olszewski [39], J. Olszowska [39], A. Onofre [124a,ab], P.U.E. Onyisi [31], C.J. Oram [159a], M.J. Oreglia [31], Y. Oren [153], D. Orestano [134a,134b], N. Orlando [72a,72b], I. Orlov [107], C. Oropeza Barrera [53], R.S. Orr [158], B. Osculati [50a,50b], R. Ospanov [120], C. Osuna [12], G. Otero y Garzon [27], J.P. Ottersbach [105], M. Ouchrif [135d], E.A. Ouellette [169], F. Ould-Saada [117], A. Ouraou [136], Q. Ouyang [33a], A. Ovcharova [15], M. Owen [82], S. Owen [139], V.E. Ozcan [19a], N. Ozturk [8], A. Pacheco Pages [12], C. Padilla Aranda [12], S. Pagan Griso [15], E. Paganis [139], C. Pahl [99], F. Paige [25], P. Pais [84], K. Pajchel [117], G. Palacino [159b], C.P. Paleari [7], S. Palestini [30], D. Pallin [34], A. Palma [124a], J.D. Palmer [18], Y.B. Pan [173], E. Panagiotopoulou [10], J.G. Panduro Vazquez [76], P. Pani [105], N. Panikashvili [87], S. Panitkin [25], D. Pantea [26a], A. Papadelis [146a], Th.D. Papadopoulou [10], A. Paramonov [6], D. Paredes Hernandez [34], W. Park [25,ac], M.A. Parker [28], F. Parodi [50a,50b], J.A. Parsons [35], U. Parzefall [48], S. Pashapour [54], E. Pasqualucci [132a], S. Passaggio [50a], A. Passeri [134a], F. Pastore [134a,134b,*], Fr. Pastore [76], G. Pásztor [49,ad], S. Pataraia [175], N. Patel [150], J.R. Pater [82], S. Patricelli [102a,102b], T. Pauly [30], M. Pecsy [144a], S. Pedraza Lopez [167], M.I. Pedraza Morales [173], S.V. Peleganchuk [107], D. Pelikan [166], H. Peng [33b], B. Penning [31], A. Penson [35], J. Penwell [60], M. Perantoni [24a], K. Perez [35,ae], T. Perez Cavalcanti [42], E. Perez Codina [159a], M.T. Pérez García-Estañ [167], V. Perez Reale [35], L. Perini [89a,89b], H. Pernegger [30], R. Perrino [72a], P. Perrodo [5], V.D. Peshekhonov [64], K. Peters [30], B.A. Petersen [30], J. Petersen [30], T.C. Petersen [36], E. Petit [5], A. Petridis [154], C. Petridou [154], E. Petrolo [132a], F. Petrucci [134a,134b], D. Petschull [42], M. Petteni [142], R. Pezoa [32b], A. Phan [86], P.W. Phillips [129], G. Piacquadio [30], A. Picazio [49], E. Piccaro [75], M. Piccinini [20a,20b], S.M. Piec [42], R. Piegaia [27], D.T. Pignotti [109], J.E. Pilcher [31], A.D. Pilkington [82], J. Pina [124a,b], M. Pinamonti [164a,164c], A. Pinder [118], J.L. Pinfold [3], B. Pinto [124a], C. Pizio [89a,89b], M. Plamondon [169], M.-A. Pleier [25], E. Plotnikova [64], A. Poblaguev [25], S. Poddar [58a], F. Podlyski [34], L. Poggioli [115], D. Pohl [21], M. Pohl [49], G. Polesello [119a], A. Policicchio [37a,37b], R. Polifka [158], A. Polini [20a], J. Poll [75], V. Polychronakos [25], D. Pomeroy [23], K. Pommès [30], L. Pontecorvo [132a], B.G. Pope [88], G.A. Popeneciu [26a], D.S. Popovic [13a], A. Poppleton [30], X. Portell Bueso [30], G.E. Pospelov [99], S. Pospisil [127], I.N. Potrap [99], C.J. Potter [149], C.T. Potter [114], G. Poulard [30], J. Poveda [60], V. Pozdnyakov [64], R. Prabhu [77], P. Pralavorio [83], A. Pranko [15], S. Prasad [30], R. Pravahan [25], S. Prell [63], K. Pretzl [17], D. Price [60], J. Price [73], L.E. Price [6], D. Prieur [123], M. Primavera [72a], K. Prokofiev [108], F. Prokoshin [32b], S. Protopopescu [25], J. Proudfoot [6], X. Prudent [44], M. Przybycien [38], H. Przysiezniak [5], S. Psoroulas [21], E. Ptacek [114], E. Pueschel [84], J. Purdham [87], M. Purohit [25,ac], P. Puzo [115], Y. Pylypchenko [62], J. Qian [87], A. Quadt [54], D.R. Quarrie [15], W.B. Quayle [173], F. Quinonez [32a], M. Raas [104], S. Raddum [117], V. Radeka [25], V. Radescu [42], P. Radloff [114], T. Rador [19a], F. Ragusa [89a,89b], G. Rahal [178], A.M. Rahimi [109], D. Rahm [25], S. Rajagopalan [25], M. Rammensee [48], M. Rammes [141], A.S. Randle-Conde [40], K. Randrianarivony [29], F. Rauscher [98], T.C. Rave [48], M. Raymond [30], A.L. Read [117], D.M. Rebuzzi [119a,119b], A. Redelbach [174], G. Redlinger [25], R. Reece [120], K. Reeves [41], E. Reinherz-Aronis [153], A. Reinsch [114], I. Reisinger [43], C. Rembser [30], Z.L. Ren [151], A. Renaud [115], M. Rescigno [132a], S. Resconi [89a], B. Resende [136], P. Reznicek [98], R. Rezvani [158], R. Richter [99], E. Richter-Was [5,af], M. Ridel [78], M. Rijpstra [105], M. Rijssenbeek [148], A. Rimoldi [119a,119b], L. Rinaldi [20a], R.R. Rios [40], I. Riu [12], G. Rivoltella [89a,89b], F. Rizatdinova [112], E. Rizvi [75], S.H. Robertson [85,k], A. Robichaud-Veronneau [118], D. Robinson [28], J.E.M. Robinson [82], A. Robson [53], J.G. Rocha de Lima [106], C. Roda [122a,122b], D. Roda Dos Santos [30], A. Roe [54], S. Roe [30], O. Røhne [117], S. Rolli [161], A. Romaniouk [96], M. Romano [20a,20b], G. Romeo [27], E. Romero Adam [167], N. Rompotis [138], L. Roos [78], E. Ros [167], S. Rosati [132a], K. Rosbach [49], A. Rose [149], M. Rose [76], G.A. Rosenbaum [158], E.I. Rosenberg [63], P.L. Rosendahl [14], O. Rosenthal [141], L. Rosselet [49], V. Rossetti [12], E. Rossi [132a,132b], L.P. Rossi [50a], M. Rotaru [26a], I. Roth [172], J. Rothberg [138], D. Rousseau [115], C.R. Royon [136], A. Rozanov [83], Y. Rozen [152], X. Ruan [33a,ag], F. Rubbo [12], I. Rubinskiy [42], N. Ruckstuhl [105], V.I. Rud [97], C. Rudolph [44], G. Rudolph [61], F. Rühr [7], A. Ruiz-Martinez [63],

L. Rumyantsev [64], Z. Rurikova [48], N.A. Rusakovich [64], J.P. Rutherfoord [7], P. Ruzicka [125], Y.F. Ryabov [121], M. Rybar [126], G. Rybkin [115], N.C. Ryder [118], A.F. Saavedra [150], I. Sadeh [153], H.F.-W. Sadrozinski [137], R. Sadykov [64], F. Safai Tehrani [132a], H. Sakamoto [155], G. Salamanna [75], A. Salamon [133a], M. Saleem [111], D. Salek [30], D. Salihagic [99], A. Salnikov [143], J. Salt [167], B.M. Salvachua Ferrando [6], D. Salvatore [37a,37b], F. Salvatore [149], A. Salvucci [104], A. Salzburger [30], D. Sampsonidis [154], B.H. Samset [117], A. Sanchez [102a,102b], V. Sanchez Martinez [167], H. Sandaker [14], H.G. Sander [81], M.P. Sanders [98], M. Sandhoff [175], T. Sandoval [28], C. Sandoval [162], R. Sandstroem [99], D.P.C. Sankey [129], A. Sansoni [47], C. Santamarina Rios [85], C. Santoni [34], R. Santonico [133a,133b], H. Santos [124a], J.G. Saraiva [124a], T. Sarangi [173], E. Sarkisyan-Grinbaum [8], F. Sarri [122a,122b], G. Sartisohn [175], O. Sasaki [65], Y. Sasaki [155], N. Sasao [67], I. Satsounkevitch [90], G. Sauvage [5,*], E. Sauvan [5], J.B. Sauvan [115], P. Savard [158,d], V. Savinov [123], D.O. Savu [30], L. Sawyer [25,m], D.H. Saxon [53], J. Saxon [120], C. Sbarra [20a], A. Sbrizzi [20a,20b], D.A. Scannicchio [163], M. Scarcella [150], J. Schaarschmidt [115], P. Schacht [99], D. Schaefer [120], U. Schäfer [81], A. Schaelicke [46], S. Schaepe [21], S. Schaetzel [58b], A.C. Schaffer [115], D. Schaile [98], R.D. Schamberger [148], A.G. Schamov [107], V. Scharf [58a], V.A. Schegelsky [121], D. Scheirich [87], M. Schernau [163], M.I. Scherzer [35], C. Schiavi [50a,50b], J. Schieck [98], M. Schioppa [37a,37b], S. Schlenker [30], P. Schmid [30], E. Schmidt [48], K. Schmieden [21], C. Schmitt [81], S. Schmitt [58b], M. Schmitz [21], B. Schneider [17], U. Schnoor [44], L. Schoeffel [136], A. Schoening [58b], A.L.S. Schorlemmer [54], M. Schott [30], D. Schouten [159a], J. Schovancova [125], M. Schram [85], C. Schroeder [81], N. Schroer [58c], M.J. Schultens [21], J. Schultes [175], H.-C. Schultz-Coulon [58a], H. Schulz [16], M. Schumacher [48], B.A. Schumm [137], Ph. Schune [136], C. Schwanenberger [82], A. Schwartzman [143], Ph. Schwegler [99], Ph. Schwemling [78], R. Schwienhorst [88], R. Schwierz [44], J. Schwindling [136], T. Schwindt [21], M. Schwoerer [5], G. Sciolla [23], W.G. Scott [129], J. Searcy [114], G. Sedov [42], E. Sedykh [121], S.C. Seidel [103], A. Seiden [137], F. Seifert [44], J.M. Seixas [24a], G. Sekhniaidze [102a], S.J. Sekula [40], K.E. Selbach [46], D.M. Seliverstov [121], B. Sellden [146a], G. Sellers [73], M. Seman [144b], N. Semprini-Cesari [20a,20b], C. Serfon [98], L. Serin [115], L. Serkin [54], R. Seuster [159a], H. Severini [111], A. Sfyrla [30], E. Shabalina [54], M. Shamim [114], L.Y. Shan [33a], J.T. Shank [22], Q.T. Shao [86], M. Shapiro [15], P.B. Shatalov [95], K. Shaw [164a,164c], D. Sherman [176], P. Sherwood [77], S. Shimizu [101], M. Shimojima [100], T. Shin [56], M. Shiyakova [64], A. Shmeleva [94], M.J. Shochet [31], D. Short [118], S. Shrestha [63], E. Shulga [96], M.A. Shupe [7], P. Sicho [125], A. Sidoti [132a], F. Siegert [48], Dj. Sijacki [13a], O. Silbert [172], J. Silva [124a], Y. Silver [153], D. Silverstein [143], S.B. Silverstein [146a], V. Simak [127], O. Simard [136], Lj. Simic [13a], S. Simion [115], E. Simioni [81], B. Simmons [77], R. Simoniello [89a,89b], M. Simonyan [36], P. Sinervo [158], N.B. Sinev [114], V. Sipica [141], G. Siragusa [174], A. Sircar [25], A.N. Sisakyan [64,*], S.Yu. Sivoklokov [97], J. Sjölin [146a,146b], T.B. Sjursen [14], L.A. Skinnari [15], H.P. Skottowe [57], K. Skovpen [107], P. Skubic [111], M. Slater [18], T. Slavicek [127], K. Sliwa [161], V. Smakhtin [172], B.H. Smart [46], L. Smestad [117], S.Yu. Smirnov [96], Y. Smirnov [96], L.N. Smirnova [97], O. Smirnova [79], B.C. Smith [57], D. Smith [143], K.M. Smith [53], M. Smizanska [71], K. Smolek [127], A.A. Snesarev [94], S.W. Snow [82], J. Snow [111], S. Snyder [25], R. Sobie [169,k], J. Sodomka [127], A. Soffer [153], C.A. Solans [167], M. Solar [127], J. Solc [127], E.Yu. Soldatov [96], U. Soldevila [167], E. Solfaroli Camillocci [132a,132b], A.A. Solodkov [128], O.V. Solovyanov [128], V. Solovyev [121], N. Soni [1], V. Sopko [127], B. Sopko [127], M. Sosebee [8], R. Soualah [164a,164c], A. Soukharev [107], S. Spagnolo [72a,72b], F. Spanò [76], W.R. Spearman [57], R. Spighi [20a], G. Spigo [30], R. Spiwoks [30], M. Spousta [126,ah], T. Spreitzer [158], B. Spurlock [8], R.D. St. Denis [53], J. Stahlman [120], R. Stamen [58a], E. Stanecka [39], R.W. Stanek [6], C. Stanescu [134a], M. Stanescu-Bellu [42], M.M. Stanitzki [42], S. Stapnes [117], E.A. Starchenko [128], J. Stark [55], P. Staroba [125], P. Starovoitov [42], R. Staszewski [39], A. Staude [98], P. Stavina [144a,*], G. Steele [53], P. Steinbach [44], P. Steinberg [25], I. Stekl [127], B. Stelzer [142], H.J. Stelzer [88], O. Stelzer-Chilton [159a], H. Stenzel [52], S. Stern [99], G.A. Stewart [30], J.A. Stillings [21], M.C. Stockton [85], K. Stoerig [48], G. Stoicea [26a], S. Stonjek [99], P. Strachota [126], A.R. Stradling [8], A. Straessner [44], J. Strandberg [147], S. Strandberg [146a,146b], A. Strandlie [117], M. Strang [109], E. Strauss [143], M. Strauss [111], P. Strizenec [144b], R. Ströhmer [174], D.M. Strom [114], J.A. Strong [76,*], R. Stroynowski [40], B. Stugu [14], I. Stumer [25,*], J. Stupak [148], P. Sturm [175], N.A. Styles [42], D.A. Soh [151,u], D. Su [143], HS. Subramania [3], R. Subramaniam [25], A. Succurro [12], Y. Sugaya [116], C. Suhr [106], M. Suk [126], V.V. Sulin [94], S. Sultansoy [4d], T. Sumida [67], X. Sun [55], J.E. Sundermann [48], K. Suruliz [139], G. Susinno [37a,37b], M.R. Sutton [149], Y. Suzuki [65], Y. Suzuki [66], M. Svatos [125], S. Swedish [168], I. Sykora [144a], T. Sykora [126], J. Sánchez [167], D. Ta [105], K. Tackmann [42], A. Taffard [163], R. Tafirout [159a], N. Taiblum [153], Y. Takahashi [101], H. Takai [25], R. Takashima [68], H. Takeda [66], T. Takeshita [140], Y. Takubo [65], M. Talby [83], A. Talyshev [107,f], M.C. Tamsett [25], K.G. Tan [86], J. Tanaka [155], R. Tanaka [115], S. Tanaka [131], S. Tanaka [65], A.J. Tanasijczuk [142],

K. Tani [66], N. Tannoury [83], S. Tapprogge [81], D. Tardif [158], S. Tarem [152], F. Tarrade [29], G.F. Tartarelli [89a], P. Tas [126], M. Tasevsky [125], E. Tassi [37a,37b], M. Tatarkhanov [15], Y. Tayalati [135d], C. Taylor [77], F.E. Taylor [92], G.N. Taylor [86], W. Taylor [159b], M. Teinturier [115], F.A. Teischinger [30], M. Teixeira Dias Castanheira [75], P. Teixeira-Dias [76], K.K. Temming [48], H. Ten Kate [30], P.K. Teng [151], S. Terada [65], K. Terashi [155], J. Terron [80], M. Testa [47], R.J. Teuscher [158,k], J. Therhaag [21], T. Theveneaux-Pelzer [78], S. Thoma [48], J.P. Thomas [18], E.N. Thompson [35], P.D. Thompson [18], P.D. Thompson [158], A.S. Thompson [53], L.A. Thomsen [36], E. Thomson [120], M. Thomson [28], W.M. Thong [86], R.P. Thun [87], F. Tian [35], M.J. Tibbetts [15], T. Tic [125], V.O. Tikhomirov [94], Y.A. Tikhonov [107,f], S. Timoshenko [96], E. Tiouchichine [83], P. Tipton [176], S. Tisserant [83], T. Todorov [5], S. Todorova-Nova [161], B. Toggerson [163], J. Tojo [69], S. Tokár [144a], K. Tokushuku [65], K. Tollefson [88], M. Tomoto [101], L. Tompkins [31], K. Toms [103], A. Tonoyan [14], C. Topfel [17], N.D. Topilin [64], I. Torchiani [30], E. Torrence [114], H. Torres [78], E. Torró Pastor [167], J. Toth [83,ad], F. Touchard [83], D.R. Tovey [139], T. Trefzger [174], L. Tremblet [30], A. Tricoli [30], I.M. Trigger [159a], G. Trilling [15], S. Trincaz-Duvoid [78], M.F. Tripiana [70], N. Triplett [25], W. Trischuk [158], B. Trocmé [55], C. Troncon [89a], M. Trottier-McDonald [142], M. Trzebinski [39], A. Trzupek [39], C. Tsarouchas [30], J.C.-L. Tseng [118], M. Tsiakiris [105], P.V. Tsiareshka [90], D. Tsionou [5,ai], G. Tsipolitis [10], S. Tsiskaridze [12], V. Tsiskaridze [48], E.G. Tskhadadze [51a], I.I. Tsukerman [95], V. Tsulaia [15], J.-W. Tsung [21], S. Tsuno [65], D. Tsybychev [148], A. Tua [139], A. Tudorache [26a], V. Tudorache [26a], J.M. Tuggle [31], M. Turala [39], D. Turecek [127], I. Turk Cakir [4e], E. Turlay [105], R. Turra [89a,89b], P.M. Tuts [35], A. Tykhonov [74], M. Tylmad [146a,146b], M. Tyndel [129], G. Tzanakos [9], K. Uchida [21], I. Ueda [155], R. Ueno [29], M. Ugland [14], M. Uhlenbrock [21], M. Uhrmacher [54], F. Ukegawa [160], G. Unal [30], A. Undrus [25], G. Unel [163], Y. Unno [65], D. Urbaniec [35], P. Urquijo [21], G. Usai [8], M. Uslenghi [119a,119b], L. Vacavant [83], V. Vacek [127], B. Vachon [85], S. Vahsen [15], J. Valenta [125], S. Valentinetti [20a,20b], A. Valero [167], S. Valkar [126], E. Valladolid Gallego [167], S. Vallecorsa [152], J.A. Valls Ferrer [167], R. Van Berg [120], P.C. Van Der Deijl [105], R. van der Geer [105], H. van der Graaf [105], R. Van Der Leeuw [105], E. van der Poel [105], D. van der Ster [30], N. van Eldik [30], P. van Gemmeren [6], I. van Vulpen [105], M. Vanadia [99], W. Vandelli [30], R. Vanguri [120], A. Vaniachine [6], P. Vankov [42], F. Vannucci [78], R. Vari [132a], T. Varol [84], D. Varouchas [15], A. Vartapetian [8], K.E. Varvell [150], V.I. Vassilakopoulos [56], F. Vazeille [34], T. Vazquez Schroeder [54], G. Vegni [89a,89b], J.J. Veillet [115], F. Veloso [124a], R. Veness [30], S. Veneziano [132a], A. Ventura [72a,72b], D. Ventura [84], M. Venturi [48], N. Venturi [158], V. Vercesi [119a], M. Verducci [138], W. Verkerke [105], J.C. Vermeulen [105], A. Vest [44], M.C. Vetterli [142,d], I. Vichou [165], T. Vickey [145b,aj], O.E. Vickey Boeriu [145b], G.H.A. Viehhauser [118], S. Viel [168], M. Villa [20a,20b], M. Villaplana Perez [167], E. Vilucchi [47], M.G. Vincter [29], E. Vinek [30], V.B. Vinogradov [64], M. Virchaux [136,*], J. Virzi [15], O. Vitells [172], M. Viti [42], I. Vivarelli [48], F. Vives Vaque [3], S. Vlachos [10], D. Vladoiu [98], M. Vlasak [127], A. Vogel [21], P. Vokac [127], G. Volpi [47], M. Volpi [86], G. Volpini [89a], H. von der Schmitt [99], H. von Radziewski [48], E. von Toerne [21], V. Vorobel [126], V. Vorwerk [12], M. Vos [167], R. Voss [30], T.T. Voss [175], J.H. Vossebeld [73], N. Vranjes [136], M. Vranjes Milosavljevic [105], V. Vrba [125], M. Vreeswijk [105], T. Vu Anh [48], R. Vuillermet [30], I. Vukotic [31], W. Wagner [175], P. Wagner [120], H. Wahlen [175], S. Wahrmund [44], J. Wakabayashi [101], S. Walch [87], J. Walder [71], R. Walker [98], W. Walkowiak [141], R. Wall [176], P. Waller [73], B. Walsh [176], C. Wang [45], F. Wang [173], H. Wang [173], H. Wang [33b,ak], J. Wang [151], J. Wang [55], R. Wang [103], S.M. Wang [151], T. Wang [21], A. Warburton [85], C.P. Ward [28], D.R. Wardrope [77], M. Warsinsky [48], A. Washbrook [46], C. Wasicki [42], I. Watanabe [66], P.M. Watkins [18], A.T. Watson [18], I.J. Watson [150], M.F. Watson [18], G. Watts [138], S. Watts [82], A.T. Waugh [150], B.M. Waugh [77], M.S. Weber [17], P. Weber [54], J.S. Webster [31], A.R. Weidberg [118], P. Weigell [99], J. Weingarten [54], C. Weiser [48], P.S. Wells [30], T. Wenaus [25], D. Wendland [16], Z. Weng [151,u], T. Wengler [30], S. Wenig [30], N. Wermes [21], M. Werner [48], P. Werner [30], M. Werth [163], M. Wessels [58a], J. Wetter [161], C. Weydert [55], K. Whalen [29], S.J. Wheeler-Ellis [163], A. White [8], M.J. White [86], S. White [122a,122b], S.R. Whitehead [118], D. Whiteson [163], D. Whittington [60], F. Wicek [115], D. Wicke [175], F.J. Wickens [129], W. Wiedenmann [173], M. Wielers [129], P. Wienemann [21], C. Wiglesworth [75], L.A.M. Wiik-Fuchs [48], P.A. Wijeratne [77], A. Wildauer [99], M.A. Wildt [42,r], I. Wilhelm [126], H.G. Wilkens [30], J.Z. Will [98], E. Williams [35], H.H. Williams [120], W. Willis [35], S. Willocq [84], J.A. Wilson [18], M.G. Wilson [143], A. Wilson [87], I. Wingerter-Seez [5], S. Winkelmann [48], F. Winklmeier [30], M. Wittgen [143], S.J. Wollstadt [81], M.W. Wolter [39], H. Wolters [124a,h], W.C. Wong [41], G. Wooden [87], B.K. Wosiek [39], J. Wotschack [30], M.J. Woudstra [82], K.W. Wozniak [39], K. Wraight [53], M. Wright [53], B. Wrona [73], S.L. Wu [173], X. Wu [49], Y. Wu [33b,al], E. Wulf [35], B.M. Wynne [46], S. Xella [36], M. Xiao [136], S. Xie [48], C. Xu [33b,z], D. Xu [139], B. Yabsley [150], S. Yacoob [145a,am], M. Yamada [65], H. Yamaguchi [155], Y. Yamaguchi [155], A. Yamamoto [65],

K. Yamamoto [63], S. Yamamoto [155], T. Yamamura [155], T. Yamanaka [155], T. Yamazaki [155], Y. Yamazaki [66], Z. Yan [22], H. Yang [87], H. Yang [173], U.K. Yang [82], Y. Yang [109], Z. Yang [146a,146b], S. Yanush [91], L. Yao [33a], Y. Yao [15], Y. Yasu [65], G.V. Ybeles Smit [130], J. Ye [40], S. Ye [25], M. Yilmaz [4c], R. Yoosoofmiya [123], K. Yorita [171], R. Yoshida [6], K. Yoshihara [155], C. Young [143], C.J. Young [118], S. Youssef [22], D. Yu [25], J. Yu [8], J. Yu [112], L. Yuan [66], A. Yurkewicz [106], M. Byszewski [30], B. Zabinski [39], R. Zaidan [62], A.M. Zaitsev [128], Z. Zajacova [30], L. Zanello [132a,132b], D. Zanzi [99], A. Zaytsev [25], C. Zeitnitz [175], M. Zeman [125], A. Zemla [39], C. Zendler [21], O. Zenin [128], T. Ženiš [144a], Z. Zinonos [122a,122b], D. Zerwas [115], G. Zevi della Porta [57], D. Zhang [33b,ak], H. Zhang [88], J. Zhang [6], X. Zhang [33d], Z. Zhang [115], L. Zhao [108], Z. Zhao [33b], A. Zhemchugov [64], J. Zhong [118], B. Zhou [87], N. Zhou [163], Y. Zhou [151], C.G. Zhu [33d], H. Zhu [42], J. Zhu [87], Y. Zhu [33b], X. Zhuang [98], V. Zhuravlov [99], D. Zieminska [60], N.I. Zimin [64], R. Zimmermann [21], S. Zimmermann [21], S. Zimmermann [48], M. Ziolkowski [141], R. Zitoun [5], L. Živković [35], V.V. Zmouchko [128,*], G. Zobernig [173], A. Zoccoli [20a,20b], M. zur Nedden [16], V. Zutshi [106], L. Zwalinski [30]

[1] *School of Chemistry and Physics, University of Adelaide, Adelaide, Australia*
[2] *Physics Department, SUNY Albany, Albany, NY, United States*
[3] *Department of Physics, University of Alberta, Edmonton, AB, Canada*
[4] [(a)] *Department of Physics, Ankara University, Ankara;* [(b)] *Department of Physics, Dumlupinar University, Kutahya;* [(c)] *Department of Physics, Gazi University, Ankara;* [(d)] *Division of Physics, TOBB University of Economics and Technology, Ankara;* [(e)] *Turkish Atomic Energy Authority, Ankara, Turkey*
[5] *LAPP, CNRS/IN2P3 and Université de Savoie, Annecy-le-Vieux, France*
[6] *High Energy Physics Division, Argonne National Laboratory, Argonne, IL, United States*
[7] *Department of Physics, University of Arizona, Tucson, AZ, United States*
[8] *Department of Physics, The University of Texas at Arlington, Arlington, TX, United States*
[9] *Physics Department, University of Athens, Athens, Greece*
[10] *Physics Department, National Technical University of Athens, Zografou, Greece*
[11] *Institute of Physics, Azerbaijan Academy of Sciences, Baku, Azerbaijan*
[12] *Institut de Física d'Altes Energies and Departament de Física de la Universitat Autònoma de Barcelona and ICREA, Barcelona, Spain*
[13] [(a)] *Institute of Physics, University of Belgrade, Belgrade;* [(b)] *Vinca Institute of Nuclear Sciences, University of Belgrade, Belgrade, Serbia*
[14] *Department for Physics and Technology, University of Bergen, Bergen, Norway*
[15] *Physics Division, Lawrence Berkeley National Laboratory and University of California, Berkeley, CA, United States*
[16] *Department of Physics, Humboldt University, Berlin, Germany*
[17] *Albert Einstein Center for Fundamental Physics and Laboratory for High Energy Physics, University of Bern, Bern, Switzerland*
[18] *School of Physics and Astronomy, University of Birmingham, Birmingham, United Kingdom*
[19] [(a)] *Department of Physics, Bogazici University, Istanbul;* [(b)] *Division of Physics, Dogus University, Istanbul;* [(c)] *Department of Physics Engineering, Gaziantep University, Gaziantep;* [(d)] *Department of Physics, Istanbul Technical University, Istanbul, Turkey*
[20] [(a)] *INFN Sezione di Bologna;* [(b)] *Dipartimento di Fisica, Università di Bologna, Bologna, Italy*
[21] *Physikalisches Institut, University of Bonn, Bonn, Germany*
[22] *Department of Physics, Boston University, Boston, MA, United States*
[23] *Department of Physics, Brandeis University, Waltham, MA, United States*
[24] [(a)] *Universidade Federal do Rio De Janeiro COPPE/EE/IF, Rio de Janeiro;* [(b)] *Federal University of Juiz de Fora (UFJF), Juiz de Fora;* [(c)] *Federal University of Sao Joao del Rei (UFSJ), Sao Joao del Rei;* [(d)] *Instituto de Fisica, Universidade de Sao Paulo, Sao Paulo, Brazil*
[25] *Physics Department, Brookhaven National Laboratory, Upton, NY, United States*
[26] [(a)] *National Institute of Physics and Nuclear Engineering, Bucharest;* [(b)] *University Politehnica Bucharest, Bucharest;* [(c)] *West University in Timisoara, Timisoara, Romania*
[27] *Departamento de Física, Universidad de Buenos Aires, Buenos Aires, Argentina*
[28] *Cavendish Laboratory, University of Cambridge, Cambridge, United Kingdom*
[29] *Department of Physics, Carleton University, Ottawa, ON, Canada*
[30] *CERN, Geneva, Switzerland*
[31] *Enrico Fermi Institute, University of Chicago, Chicago, IL, United States*
[32] [(a)] *Departamento de Física, Pontificia Universidad Católica de Chile, Santiago;* [(b)] *Departamento de Física, Universidad Técnica Federico Santa María, Valparaíso, Chile*
[33] [(a)] *Institute of High Energy Physics, Chinese Academy of Sciences, Beijing;* [(b)] *Department of Modern Physics, University of Science and Technology of China, Anhui;* [(c)] *Department of Physics, Nanjing University, Jiangsu;* [(d)] *School of Physics, Shandong University, Shandong, China*
[34] *Laboratoire de Physique Corpusculaire, Clermont Université and Université Blaise Pascal and CNRS/IN2P3, Clermont-Ferrand, France*
[35] *Nevis Laboratory, Columbia University, Irvington, NY, United States*
[36] *Niels Bohr Institute, University of Copenhagen, Kobenhavn, Denmark*
[37] [(a)] *INFN Gruppo Collegato di Cosenza;* [(b)] *Dipartimento di Fisica, Università della Calabria, Arcavata di Rende, Italy*
[38] *AGH University of Science and Technology, Faculty of Physics and Applied Computer Science, Krakow, Poland*
[39] *The Henryk Niewodniczanski Institute of Nuclear Physics, Polish Academy of Sciences, Krakow, Poland*
[40] *Physics Department, Southern Methodist University, Dallas, TX, United States*
[41] *Physics Department, University of Texas at Dallas, Richardson, TX, United States*
[42] *DESY, Hamburg and Zeuthen, Germany*
[43] *Institut für Experimentelle Physik IV, Technische Universität Dortmund, Dortmund, Germany*
[44] *Institut für Kern- und Teilchenphysik, Technical University Dresden, Dresden, Germany*
[45] *Department of Physics, Duke University, Durham, NC, United States*
[46] *SUPA – School of Physics and Astronomy, University of Edinburgh, Edinburgh, United Kingdom*
[47] *INFN Laboratori Nazionali di Frascati, Frascati, Italy*
[48] *Fakultät für Mathematik und Physik, Albert-Ludwigs-Universität, Freiburg, Germany*
[49] *Section de Physique, Université de Genève, Geneva, Switzerland*
[50] [(a)] *INFN Sezione di Genova;* [(b)] *Dipartimento di Fisica, Università di Genova, Genova, Italy*
[51] [(a)] *E. Andronikashvili Institute of Physics, Tbilisi State University, Tbilisi;* [(b)] *High Energy Physics Institute, Tbilisi State University, Tbilisi, Georgia*
[52] *II Physikalisches Institut, Justus-Liebig-Universität Giessen, Giessen, Germany*
[53] *SUPA – School of Physics and Astronomy, University of Glasgow, Glasgow, United Kingdom*
[54] *II Physikalisches Institut, Georg-August-Universität, Göttingen, Germany*
[55] *Laboratoire de Physique Subatomique et de Cosmologie, Université Joseph Fourier and CNRS/IN2P3 and Institut National Polytechnique de Grenoble, Grenoble, France*
[56] *Department of Physics, Hampton University, Hampton, VA, United States*

[57] Laboratory for Particle Physics and Cosmology, Harvard University, Cambridge, MA, United States
[58] [(a)] Kirchhoff-Institut für Physik, Ruprecht-Karls-Universität Heidelberg, Heidelberg; [(b)] Physikalisches Institut, Ruprecht-Karls-Universität Heidelberg, Heidelberg; [(c)] ZITI Institut für technische Informatik, Ruprecht-Karls-Universität Heidelberg, Mannheim, Germany
[59] Faculty of Applied Information Science, Hiroshima Institute of Technology, Hiroshima, Japan
[60] Department of Physics, Indiana University, Bloomington, IN, United States
[61] Institut für Astro- und Teilchenphysik, Leopold-Franzens-Universität, Innsbruck, Austria
[62] University of Iowa, Iowa City, IA, United States
[63] Department of Physics and Astronomy, Iowa State University, Ames, IA, United States
[64] Joint Institute for Nuclear Research, JINR Dubna, Dubna, Russia
[65] KEK, High Energy Accelerator Research Organization, Tsukuba, Japan
[66] Graduate School of Science, Kobe University, Kobe, Japan
[67] Faculty of Science, Kyoto University, Kyoto, Japan
[68] Kyoto University of Education, Kyoto, Japan
[69] Department of Physics, Kyushu University, Fukuoka, Japan
[70] Instituto de Física La Plata, Universidad Nacional de La Plata and CONICET, La Plata, Argentina
[71] Physics Department, Lancaster University, Lancaster, United Kingdom
[72] [(a)] INFN Sezione di Lecce; [(b)] Dipartimento di Matematica e Fisica, Università del Salento, Lecce, Italy
[73] Oliver Lodge Laboratory, University of Liverpool, Liverpool, United Kingdom
[74] Department of Physics, Jožef Stefan Institute and University of Ljubljana, Ljubljana, Slovenia
[75] School of Physics and Astronomy, Queen Mary University of London, London, United Kingdom
[76] Department of Physics, Royal Holloway University of London, Surrey, United Kingdom
[77] Department of Physics and Astronomy, University College London, London, United Kingdom
[78] Laboratoire de Physique Nucléaire et de Hautes Energies, UPMC and Université Paris-Diderot and CNRS/IN2P3, Paris, France
[79] Fysiska institutionen, Lunds universitet, Lund, Sweden
[80] Departamento de Fisica Teorica C-15, Universidad Autonoma de Madrid, Madrid, Spain
[81] Institut für Physik, Universität Mainz, Mainz, Germany
[82] School of Physics and Astronomy, University of Manchester, Manchester, United Kingdom
[83] CPPM, Aix-Marseille Université and CNRS/IN2P3, Marseille, France
[84] Department of Physics, University of Massachusetts, Amherst, MA, United States
[85] Department of Physics, McGill University, Montreal, QC, Canada
[86] School of Physics, University of Melbourne, Victoria, Australia
[87] Department of Physics, The University of Michigan, Ann Arbor, MI, United States
[88] Department of Physics and Astronomy, Michigan State University, East Lansing, MI, United States
[89] [(a)] INFN Sezione di Milano; [(b)] Dipartimento di Fisica, Università di Milano, Milano, Italy
[90] B.I. Stepanov Institute of Physics, National Academy of Sciences of Belarus, Minsk, Belarus
[91] National Scientific and Educational Centre for Particle and High Energy Physics, Minsk, Belarus
[92] Department of Physics, Massachusetts Institute of Technology, Cambridge, MA, United States
[93] Group of Particle Physics, University of Montreal, Montreal, QC, Canada
[94] P.N. Lebedev Institute of Physics, Academy of Sciences, Moscow, Russia
[95] Institute for Theoretical and Experimental Physics (ITEP), Moscow, Russia
[96] Moscow Engineering and Physics Institute (MEPhI), Moscow, Russia
[97] Skobeltsyn Institute of Nuclear Physics, Lomonosov Moscow State University, Moscow, Russia
[98] Fakultät für Physik, Ludwig-Maximilians-Universität München, München, Germany
[99] Max-Planck-Institut für Physik (Werner-Heisenberg-Institut), München, Germany
[100] Nagasaki Institute of Applied Science, Nagasaki, Japan
[101] Graduate School of Science and Kobayashi-Maskawa Institute, Nagoya University, Nagoya, Japan
[102] [(a)] INFN Sezione di Napoli; [(b)] Dipartimento di Scienze Fisiche, Università di Napoli, Napoli, Italy
[103] Department of Physics and Astronomy, University of New Mexico, Albuquerque, NM, United States
[104] Institute for Mathematics, Astrophysics and Particle Physics, Radboud University Nijmegen/Nikhef, Nijmegen, Netherlands
[105] Nikhef National Institute for Subatomic Physics and University of Amsterdam, Amsterdam, Netherlands
[106] Department of Physics, Northern Illinois University, DeKalb, IL, United States
[107] Budker Institute of Nuclear Physics, SB RAS, Novosibirsk, Russia
[108] Department of Physics, New York University, New York, NY, United States
[109] Ohio State University, Columbus, OH, United States
[110] Faculty of Science, Okayama University, Okayama, Japan
[111] Homer L. Dodge Department of Physics and Astronomy, University of Oklahoma, Norman, OK, United States
[112] Department of Physics, Oklahoma State University, Stillwater, OK, United States
[113] Palacký University, RCPTM, Olomouc, Czech Republic
[114] Center for High Energy Physics, University of Oregon, Eugene, OR, United States
[115] LAL, Université Paris-Sud and CNRS/IN2P3, Orsay, France
[116] Graduate School of Science, Osaka University, Osaka, Japan
[117] Department of Physics, University of Oslo, Oslo, Norway
[118] Department of Physics, Oxford University, Oxford, United Kingdom
[119] [(a)] INFN Sezione di Pavia; [(b)] Dipartimento di Fisica, Università di Pavia, Pavia, Italy
[120] Department of Physics, University of Pennsylvania, Philadelphia PA, United States
[121] Petersburg Nuclear Physics Institute, Gatchina, Russia
[122] [(a)] INFN Sezione di Pisa; [(b)] Dipartimento di Fisica E. Fermi, Università di Pisa, Pisa, Italy
[123] Department of Physics and Astronomy, University of Pittsburgh, Pittsburgh, PA, United States
[124] [(a)] Laboratorio de Instrumentacao e Fisica Experimental de Particulas – LIP, Lisboa, Portugal; [(b)] Departamento de Fisica Teorica y del Cosmos and CAFPE, Universidad de Granada, Granada, Spain
[125] Institute of Physics, Academy of Sciences of the Czech Republic, Praha, Czech Republic
[126] Faculty of Mathematics and Physics, Charles University in Prague, Praha, Czech Republic
[127] Czech Technical University in Prague, Praha, Czech Republic
[128] State Research Center Institute for High Energy Physics, Protvino, Russia
[129] Particle Physics Department, Rutherford Appleton Laboratory, Didcot, United Kingdom
[130] Physics Department, University of Regina, Regina, SK, Canada
[131] Ritsumeikan University, Kusatsu, Shiga, Japan
[132] [(a)] INFN Sezione di Roma I; [(b)] Dipartimento di Fisica, Università La Sapienza, Roma, Italy
[133] [(a)] INFN Sezione di Roma Tor Vergata; [(b)] Dipartimento di Fisica, Università di Roma Tor Vergata, Roma, Italy

[134] [(a)] INFN Sezione di Roma Tre; [(b)] Dipartimento di Fisica, Università Roma Tre, Roma, Italy
[135] [(a)] Faculté des Sciences Ain Chock, Réseau Universitaire de Physique des Hautes Energies – Université Hassan II, Casablanca; [(b)] Centre National de l'Energie des Sciences Techniques Nucleaires, Rabat; [(c)] Faculté des Sciences Semlalia, Université Cadi Ayyad, LPHEA-Marrakech; [(d)] Faculté des Sciences, Université Mohamed Premier and LPTPM, Oujda; [(e)] Faculté des sciences, Université Mohammed V-Agdal, Rabat, Morocco
[136] DSM/IRFU (Institut de Recherches sur les Lois Fondamentales de l'Univers), CEA Saclay (Commissariat a l'Energie Atomique), Gif-sur-Yvette, France
[137] Santa Cruz Institute for Particle Physics, University of California Santa Cruz, Santa Cruz, CA, United States
[138] Department of Physics, University of Washington, Seattle, WA, United States
[139] Department of Physics and Astronomy, University of Sheffield, Sheffield, United Kingdom
[140] Department of Physics, Shinshu University, Nagano, Japan
[141] Fachbereich Physik, Universität Siegen, Siegen, Germany
[142] Department of Physics, Simon Fraser University, Burnaby, BC, Canada
[143] SLAC National Accelerator Laboratory, Stanford, CA, United States
[144] [(a)] Faculty of Mathematics, Physics & Informatics, Comenius University, Bratislava, Slovak Republic; [(b)] Department of Subnuclear Physics, Institute of Experimental Physics of the Slovak Academy of Sciences, Kosice, Slovak Republic
[145] [(a)] Department of Physics, University of Johannesburg, Johannesburg; [(b)] School of Physics, University of the Witwatersrand, Johannesburg, South Africa
[146] [(a)] Department of Physics, Stockholm University; [(b)] The Oskar Klein Centre, Stockholm, Sweden
[147] Physics Department, Royal Institute of Technology, Stockholm, Sweden
[148] Departments of Physics & Astronomy and Chemistry, Stony Brook University, Stony Brook, NY, United States
[149] Department of Physics and Astronomy, University of Sussex, Brighton, United Kingdom
[150] School of Physics, University of Sydney, Sydney, Australia
[151] Institute of Physics, Academia Sinica, Taipei, Taiwan
[152] Department of Physics, Technion: Israel Institute of Technology, Haifa, Israel
[153] Raymond and Beverly Sackler School of Physics and Astronomy, Tel Aviv University, Tel Aviv, Israel
[154] Department of Physics, Aristotle University of Thessaloniki, Thessaloniki, Greece
[155] International Center for Elementary Particle Physics and Department of Physics, The University of Tokyo, Tokyo, Japan
[156] Graduate School of Science and Technology, Tokyo Metropolitan University, Tokyo, Japan
[157] Department of Physics, Tokyo Institute of Technology, Tokyo, Japan
[158] Department of Physics, University of Toronto, Toronto, ON, Canada
[159] [(a)] TRIUMF, Vancouver, BC; [(b)] Department of Physics and Astronomy, York University, Toronto, ON, Canada
[160] Faculty of Pure and Applied Sciences, University of Tsukuba, Tsukuba, Japan
[161] Department of Physics and Astronomy, Tufts University, Medford, MA, United States
[162] Centro de Investigaciones, Universidad Antonio Narino, Bogota, Colombia
[163] Department of Physics and Astronomy, University of California Irvine, Irvine, CA, United States
[164] [(a)] INFN Gruppo Collegato di Udine; [(b)] ICTP, Trieste; [(c)] Dipartimento di Chimica, Fisica e Ambiente, Università di Udine, Udine, Italy
[165] Department of Physics, University of Illinois, Urbana, IL, United States
[166] Department of Physics and Astronomy, University of Uppsala, Uppsala, Sweden
[167] Instituto de Física Corpuscular (IFIC) and Departamento de Física Atómica, Molecular y Nuclear and Departamento de Ingeniería Electrónica and Instituto de Microelectrónica de Barcelona (IMB-CNM), University of Valencia and CSIC, Valencia, Spain
[168] Department of Physics, University of British Columbia, Vancouver, BC, Canada
[169] Department of Physics and Astronomy, University of Victoria, Victoria, BC, Canada
[170] Department of Physics, University of Warwick, Coventry, United Kingdom
[171] Waseda University, Tokyo, Japan
[172] Department of Particle Physics, The Weizmann Institute of Science, Rehovot, Israel
[173] Department of Physics, University of Wisconsin, Madison, WI, United States
[174] Fakultät für Physik und Astronomie, Julius-Maximilians-Universität, Würzburg, Germany
[175] Fachbereich C Physik, Bergische Universität Wuppertal, Wuppertal, Germany
[176] Department of Physics, Yale University, New Haven, CT, United States
[177] Yerevan Physics Institute, Yerevan, Armenia
[178] Centre de Calcul de l'Institut National de Physique Nucléaire et de Physique des Particules (IN2P3), Villeurbanne, France

[a] Also at Laboratorio de Instrumentacao e Fisica Experimental de Particulas – LIP, Lisboa, Portugal.
[b] Also at Faculdade de Ciencias and CFNUL, Universidade de Lisboa, Lisboa, Portugal.
[c] Also at Particle Physics Department, Rutherford Appleton Laboratory, Didcot, United Kingdom.
[d] Also at TRIUMF, Vancouver, BC, Canada.
[e] Also at Department of Physics, California State University, Fresno, CA, United States.
[f] Also at Novosibirsk State University, Novosibirsk, Russia.
[g] Also at Fermilab, Batavia, IL, United States.
[h] Also at Department of Physics, University of Coimbra, Coimbra, Portugal.
[i] Also at Department of Physics, UASLP, San Luis Potosi, Mexico.
[j] Also at Università di Napoli Parthenope, Napoli, Italy.
[k] Also at Institute of Particle Physics (IPP), Canada.
[l] Also at Department of Physics, Middle East Technical University, Ankara, Turkey.
[m] Also at Louisiana Tech University, Ruston, LA, United States.
[n] Also at Dep Fisica and CEFITEC of Faculdade de Ciencias e Tecnologia, Universidade Nova de Lisboa, Caparica, Portugal.
[o] Also at Department of Physics and Astronomy, University College London, London, United Kingdom.
[p] Also at Department of Physics, University of Cape Town, Cape Town, South Africa.
[q] Also at Institute of Physics, Azerbaijan Academy of Sciences, Baku, Azerbaijan.
[r] Also at Institut für Experimentalphysik, Universität Hamburg, Hamburg, Germany.
[s] Also at Manhattan College, New York, NY, United States.
[t] Also at CPPM, Aix-Marseille Université and CNRS/IN2P3, Marseille, France.
[u] Also at School of Physics and Engineering, Sun Yat-sen University, Guanzhou, China.
[v] Also at Academia Sinica Grid Computing, Institute of Physics, Academia Sinica, Taipei, Taiwan.
[w] Also at Laboratoire de Physique Nucléaire et de Hautes Energies, UPMC and Université Paris-Diderot and CNRS/IN2P3, Paris, France.
[x] Also at School of Physics, Shandong University, Shandong, China.
[y] Also at Dipartimento di Fisica, Università La Sapienza, Roma, Italy.
[z] Also at DSM/IRFU (Institut de Recherches sur les Lois Fondamentales de l'Univers), CEA Saclay (Commissariat a l'Energie Atomique), Gif-sur-Yvette, France.
[aa] Also at Section de Physique, Université de Genève, Geneva, Switzerland.

[ab] Also at Departamento de Fisica, Universidade de Minho, Braga, Portugal.
[ac] Also at Department of Physics and Astronomy, University of South Carolina, Columbia, SC, United States.
[ad] Also at Institute for Particle and Nuclear Physics, Wigner Research Centre for Physics, Budapest, Hungary.
[ae] Also at California Institute of Technology, Pasadena, CA, United States.
[af] Also at Institute of Physics, Jagiellonian University, Krakow, Poland.
[ag] Also at LAL, Université Paris-Sud and CNRS/IN2P3, Orsay, France.
[ah] Also at Nevis Laboratory, Columbia University, Irvington, NY, United States.
[ai] Also at Department of Physics and Astronomy, University of Sheffield, Sheffield, United Kingdom.
[aj] Also at Department of Physics, Oxford University, Oxford, United Kingdom.
[ak] Also at Institute of Physics, Academia Sinica, Taipei, Taiwan.
[al] Also at Department of Physics, The University of Michigan, Ann Arbor, MI, United States.
[am] Also at Discipline of Physics, University of KwaZulu-Natal, Durban, South Africa.
[*] Deceased.

Physics Letters B 726 (2013) 120–144

Contents lists available at ScienceDirect

Physics Letters B

www.elsevier.com/locate/physletb

Evidence for the spin-0 nature of the Higgs boson using ATLAS data ☆

ATLAS Collaboration *

ARTICLE INFO

Article history:
Available online 16 August 2013
Editor: W.-D. Schlatter

Keywords:
Higgs boson
Spin
Parity

ABSTRACT

Studies of the spin and parity quantum numbers of the Higgs boson are presented, based on proton–proton collision data collected by the ATLAS experiment at the LHC. The Standard Model spin–parity $J^P = 0^+$ hypothesis is compared with alternative hypotheses using the Higgs boson decays $H \to \gamma\gamma$, $H \to ZZ^* \to 4\ell$ and $H \to WW^* \to \ell\nu\ell\nu$, as well as the combination of these channels. The analysed dataset corresponds to an integrated luminosity of 20.7 fb^{-1} collected at a centre-of-mass energy of $\sqrt{s} = 8$ TeV. For the $H \to ZZ^* \to 4\ell$ decay mode the dataset corresponding to an integrated luminosity of 4.6 fb^{-1} collected at $\sqrt{s} = 7$ TeV is included. The data are compatible with the Standard Model $J^P = 0^+$ quantum numbers for the Higgs boson, whereas all alternative hypotheses studied in this Letter, namely some specific $J^P = 0^-, 1^+, 1^-, 2^+$ models, are excluded at confidence levels above 97.8%. This exclusion holds independently of the assumptions on the coupling strengths to the Standard Model particles and in the case of the $J^P = 2^+$ model, of the relative fractions of gluon-fusion and quark–antiquark production of the spin-2 particle. The data thus provide evidence for the spin-0 nature of the Higgs boson, with positive parity being strongly preferred.

© 2013 CERN. Published by Elsevier B.V. All rights reserved.

1. Introduction

In 2012 the ATLAS and CMS Collaborations published the discovery of a new resonance [1,2] in the search for the Standard Model (SM) Higgs boson H [3–8]. The present experimental challenge is to compare its properties with the SM predictions for the Higgs boson. In the SM, the Higgs boson is a spin-0 and CP-even particle ($J^P = 0^+$). The Landau–Yang theorem forbids the direct decay of an on-shell spin-1 particle into a pair of photons [9, 10]. The spin-1 hypothesis is therefore strongly disfavoured by the observation of the $H \to \gamma\gamma$ decay. The CMS Collaboration has published a spin–parity study [11] based on the $H \to ZZ^*$ channel where the SM scalar hypothesis is favoured over the pseudoscalar hypothesis at a confidence level (CL) above 95%.

In this Letter the $J^P = 0^+$ hypothesis of the SM is compared to several alternative hypotheses with $J^P = 0^-, 1^+, 1^-, 2^+$. The measurements are based on the kinematic properties of the three final states $H \to \gamma\gamma$, $H \to ZZ^* \to 4\ell$ and $H \to WW^* \to \ell\nu\ell\nu$, where ℓ denotes an electron or a muon. For the alternative hypotheses leading order (LO) calculations are use to predict the kinematic properties. To improve the sensitivity to different spin–parity hypotheses, several final states are combined. To test the 0^- spin–parity hypothesis, only the $H \to ZZ^*$ decay mode is used, while for the 1^+ and 1^- hypotheses the $H \to ZZ^*$ and $H \to WW^*$ channels are combined. For the 2^+ study, all three decay modes are combined. It is assumed that only one single resonance contributes to the various decay modes considered in each combination.

The full dataset collected at $\sqrt{s} = 8$ TeV, corresponding to an integrated luminosity of 20.7 fb^{-1}, is analysed for all three channels. For the $H \to ZZ^*$ decay mode, a dataset corresponding to an integrated luminosity of 4.6 fb^{-1} collected at $\sqrt{s} = 7$ TeV is also included.

While for the SM Higgs boson the Lagrangian structure and its couplings are fully determined, the alternative hypotheses can be described by a wide variety of models, characterised by different structures and effective couplings. Several approaches to describe such signatures can be found in the literature [12–17]. In this Letter, the alternative model descriptions are based on Ref. [12], as described in Section 2. In Ref. [12], the production and decay of a generic boson with various J^P quantum numbers are described by defining the most general amplitudes consistent with Lorentz invariance, angular-momentum conservation, Bose symmetry and the unbroken symmetry of the $SU(3) \times SU(2) \times U(1)$ gauge group.

This Letter is published together with another one [18] reporting the ATLAS measurements of the couplings of the Higgs boson derived from the observed signal production and decay rates. In that Letter the measurement of the mass of the Higgs boson, based on the invariant mass spectra in the $H \to \gamma\gamma$ and $H \to ZZ^* \to 4\ell$ final states, is also reported. On the basis of that measurement, the observed final states are assumed to be produced in the decay of a single particle with a mass of 125.5 GeV [18]. The definitions of the physics objects used in the analyses, the simulation of the different backgrounds and the main systematic uncertainties are described in Ref. [18]. This Letter reports only aspects specific to

☆ © CERN for the benefit of the ATLAS Collaboration.

* *E-mail address:* atlas.publications@cern.ch.

0370-2693/ © 2013 CERN. Published by Elsevier B.V. All rights reserved.
http://dx.doi.org/10.1016/j.physletb.2013.08.026

the spin and parity analyses. The ATLAS Collaboration has made public a collection of conference notes that document in detail the analyses reported in this Letter [19–21].

The outline of this Letter is as follows: Section 2 describes the spin–parity models considered in all three channels and the signal Monte Carlo (MC) simulation samples used in the analyses. The statistical procedure used to test the different spin–parity hypotheses is presented in Section 3. Sections 4, 5 and 6 provide brief descriptions of the spin–parity analyses in the $H \to \gamma\gamma$, $H \to ZZ^*$ and $H \to WW^*$ decay modes. Finally, in Section 7, the combined results in terms of compatibility with several spin–parity hypotheses are presented.

2. Signal modelling and Monte Carlo samples

The interactions of spin-0, 1 and 2 resonances with Standard Model particles are described in Ref. [12] by Eqs. 2, 4 and 5 for bosons and by Eqs. 8, 9 and 10 for fermions. The choices of the boson and fermion couplings for the specific spin and parity models used in this analysis are presented in Table 1 of Ref. [12].

The implications of these choices are briefly summarised in the following. The quark–antiquark ($q\bar{q}$) annihilation production process is not considered in the case of $J^P = 0^-$, since its contribution is negligible compared to gluon fusion (gg). For the $J^P = 1^+$ and 1^- cases, only the quark–antiquark annihilation production process is considered, since the Landau–Yang theorem also forbids the production of a spin-1 particle through the fusion of two on-shell gluons. Given the large number of possible spin-2 models, a specific one, denoted by 2^+_m from Table 1 of Ref. [12], was chosen. This choice corresponds to a graviton-inspired tensor with minimal couplings to SM particles. In the 2^+_m boson rest frame, its polarisation states projected onto the parton collision axis can take only the values of ± 2 for the gluon-fusion process and ± 1 for the quark–antiquark annihilation process. For the spin-2 model, only these two production mechanisms are considered. The production of the 2^+_m boson is dominated by the gluon-fusion process with a contribution, at leading order in quantum chromodynamics (QCD), of about 4% from quark–antiquark annihilation [16,17]. This proportion could be significantly modified by higher-order QCD corrections. Since the experimental observables are sensitive to different polarisations, the studies were performed for several production admixtures by normalising the samples produced with the two different production processes in order to obtain samples of events corresponding to fractions, $f_{q\bar{q}}$, of $q\bar{q}$ annihilation ranging from 0% to 100% in steps of 25%. In the following, this model is referred to as $J^P = 2^+$.

The production and decay of the SM Higgs boson via the dominant gluon-fusion process is simulated using either the JHU Monte Carlo generator [12] for the $H \to ZZ^*$ process or the POWHEG [22] Monte Carlo generator for the $H \to \gamma\gamma$ and $H \to WW^*$ processes, each interfaced to PYTHIA8 [23] for parton showering and hadronisation. The production and decay of the $J^P = 0^-, 1^+, 1^-$ and 2^+ resonances are modelled using the JHU generator, interfaced to PYTHIA8 for parton showering and hadronisation.

The transverse momentum (p_T) distributions for the gluon-fusion signals produced with the JHU generator, which is leading-order in QCD, are weighted to reproduce the POWHEG+PYTHIA8 spectrum. The latter was tuned to reproduce the re-summed calculation of the HqT program [24]. It was checked that the distributions of all kinematic variables used for the spin–parity determination are compatible between the two MC generators after the re-weighting is applied. For the production process via $q\bar{q}$ annihilation, no re-weighting is applied.

The much smaller contributions from other production processes, namely vector-boson fusion and associated production, are also considered. For the $H \to \gamma\gamma$ channel, they are included in the analysis and simulated as described in Ref. [18]. For the $H \to ZZ^*$ channel, they are ignored because they do not affect the kinematic distributions used in the spin analysis. For the $H \to WW^*$ analysis, where only the $e\mu$ final state with no additional jet activity is considered, as described in Section 6, they contribute at a negligible level and are therefore ignored. It should be noted that for the resonance under study, dominant contributions via vector-boson fusion and associated production can be excluded based on the measurements presented in Ref. [18].

For the background processes, the simulated samples are the same as those used in the coupling analyses. A detailed list of the MC generators and samples is given in Ref. [18].

All MC samples are passed through a full simulation of the ATLAS detector [25] based on GEANT4 [26]. The simulation incorporates a model of the event pile-up conditions in the data, including the effects of multiple proton–proton collisions in in-time and nearby bunch crossings.

3. Statistical method

The analyses described in this Letter rely on discriminant observables chosen to be sensitive to the spin and parity of the signal while preserving the discrimination against the various backgrounds, as described in Sections 4, 5 and 6 for the three final states. A likelihood function $\mathcal{L}(J^P, \mu, \boldsymbol{\theta})$ that depends on the spin–parity assumption of the signal is constructed as a product of conditional probabilities over binned distributions of the discriminant observables in each channel:

$$\mathcal{L}\big(J^P, \mu, \boldsymbol{\theta}\big) = \prod_j^{N_{\text{chann.}}} \prod_i^{N_{\text{bins}}} P\big(N_{i,j} \,\big|\, \mu_j \cdot S_{i,j}^{(J^P)}(\boldsymbol{\theta}) + B_{i,j}(\boldsymbol{\theta})\big) \times \mathcal{A}_j(\boldsymbol{\theta}), \tag{1}$$

where μ_j represents the nuisance parameter associated with the signal rate in each channel j. The symbol $\boldsymbol{\theta}$ represents all other nuisance parameters. The likelihood function is therefore a product of Poisson distributions P corresponding to the observation of $N_{i,j}$ events in each bin i of the discriminant observable(s),[1] given the expectations for the signal, $S_{i,j}^{(J^P)}(\boldsymbol{\theta})$, and for the background, $B_{i,j}(\boldsymbol{\theta})$. Some of the nuisance parameters are constrained by auxiliary measurements through the functions $\mathcal{A}_j(\boldsymbol{\theta})$.

While for the SM Higgs boson the couplings to the SM particles are predicted, they are not known *a priori* for the alternative hypotheses, defined as J^P_{alt}. In order to be insensitive to such assumptions, the numbers of signal events in each channel and for each tested hypothesis are treated as an independent nuisance parameters in the likelihood.

The test statistic q used to distinguish between the two signal spin–parity hypotheses is based on a ratio of likelihoods:

$$q = \log \frac{\mathcal{L}(J^P = 0^+, \hat{\hat{\mu}}_{0^+}, \hat{\hat{\theta}}_{0^+})}{\mathcal{L}(J^P_{\text{alt}}, \hat{\hat{\mu}}_{J^P_{\text{alt}}}, \hat{\hat{\theta}}_{J^P_{\text{alt}}})}, \tag{2}$$

where $\mathcal{L}(J^P, \hat{\hat{\mu}}_{J^P}, \hat{\hat{\theta}}_{J^P})$ is the maximum likelihood estimator, evaluated under either the 0^+ or the J^P_{alt} spin–parity hypothesis. The $\hat{\hat{\mu}}_{J^P}$, $\hat{\hat{\theta}}_{J^P}$ represent the values of the signal strength and nuisance

[1] As explained in the following sections, the sensitivity for spin–parity separation is improved by a simultaneous fit to two discriminants in the $H \to \gamma\gamma$ and $H \to WW^*$ decay modes, while in the $H \to ZZ^*$ channel only one discriminant is used.

parameters fitted to the data under each J^P hypothesis. The distributions of the test statistic for each of the two hypotheses are obtained using ensemble tests (Monte Carlo pseudo-experiments). The generation of the pseudo-experiments uses the numbers of signal and background events in each channel obtained from maximum likelihood fits to data. In the fits of each pseudo-experiment, these and all other nuisance parameters are profiled, i.e. fitted to the value that maximises the likelihood for each value of the parameter of interest. When generating the distributions of the test statistic for a given spin–parity hypothesis, the signal strength μ is fixed to the value obtained in the fit to the data under the same spin–parity assumption. The distributions of q are used to determine the corresponding p_0-values $p_0(0^+)$ and $p_0(J^P_{\text{alt}})$. For a tested hypothesis J^P_{alt}, the observed (expected) p_0-values are obtained by integrating the corresponding test-statistic distributions above the observed value of q (above the median of the $J^P = 0^+ q$ distribution). When the measured data are in agreement with the tested hypothesis, the observed value of q is expected to be close to the median, corresponding to a p_0-value around 50%. Very small values of the integral of the J^P_{alt} distribution, corresponding to large values of q, are interpreted as the data being in disagreement with the tested hypothesis in favour of the SM hypothesis. An example of such distributions is shown in Section 7 for the 0^+ and 0^- hypotheses.

The exclusion of the alternative J^P_{alt} hypothesis in favour of the Standard Model 0^+ hypothesis is evaluated in terms of the corresponding $\text{CL}_s(J^P_{\text{alt}})$, defined as:

$$\text{CL}_s\left(J^P_{\text{alt}}\right) = \frac{p_0(J^P_{\text{alt}})}{1 - p_0(0^+)}. \tag{3}$$

4. $H \to \gamma\gamma$ analysis

The $H \to \gamma\gamma$ decay mode is sensitive to the spin of the Higgs boson through the measurement of the polar angular distribution of the photons in the resonance rest frame. For this channel, the SM spin hypothesis is compared only to the $J^P = 2^+$ hypothesis. Spin information can be extracted from the distribution of the absolute value of the cosine of the polar angle θ^* of the photons with respect to the z-axis of the Collins–Soper frame [27]:

$$\left|\cos\theta^*\right| = \frac{|\sinh(\Delta\eta^{\gamma\gamma})|}{\sqrt{1 + (p_{\text{T}}^{\gamma\gamma}/m_{\gamma\gamma})^2}} \frac{2p_{\text{T}}^{\gamma 1} p_{\text{T}}^{\gamma 2}}{m_{\gamma\gamma}^2}, \tag{4}$$

where $m_{\gamma\gamma}$ and $p_{\text{T}}^{\gamma\gamma}$ are the invariant mass and the transverse momentum of the photon pair, $\Delta\eta^{\gamma\gamma}$ is the separation in pseudorapidity of the two photons, and $p_{\text{T}}^{\gamma 1}$, $p_{\text{T}}^{\gamma 2}$ are the transverse momenta of the photons.

This channel has a large background, dominated by non-resonant diphoton production, whose distribution in $|\cos\theta^*|$ is intermediate between those expected for $J^P = 0^+$ and $J^P = 2^+$ states produced in gluon fusion. Two observables, $|\cos\theta^*|$ and $m_{\gamma\gamma}$, are used in the fit to data: $m_{\gamma\gamma}$ provides better separation power between the signal and the background, and $|\cos\theta^*|$ is sensitive to the spin.

The selected events contain two isolated photon candidates, as described in Ref. [18], but with the important difference that the kinematic requirements on the transverse momenta of the photons are proportional to $m_{\gamma\gamma}$. This choice reduces the correlation between $m_{\gamma\gamma}$ and $|\cos\theta^*|$ for the background to a negligible level. The selection requirements are set to $p_{\text{T}}^{\gamma 1} > 0.35 m_{\gamma\gamma}$ and $p_{\text{T}}^{\gamma 2} > 0.25 m_{\gamma\gamma}$. The fitted mass range is chosen to be 105 GeV $< m_{\gamma\gamma} <$ 160 GeV.

The intrinsic width of the resonance is assumed to be negligible compared to the detector resolution for both spin hypotheses. For this reason, the same probability density function is used to model the reconstructed mass spectra of both signal hypotheses, independent of the value of $|\cos\theta^*|$. The chosen function is the sum of a Crystal Ball [28] component, accounting for about 95% of the signal events, and a wider Gaussian component to model outlying events, as described in Ref. [18].

The $|\cos\theta^*|$ distributions of the signal, for either spin state, are obtained from simulated samples. The signal yields per $|\cos\theta^*|$ bin for a spin-0 particle are corrected for interference effects with the non-resonant diphoton background $gg \to \gamma\gamma$ [29]. The size of the correction is non-negligible only at high values of $|\cos\theta^*|$ and its value is taken as the systematic uncertainty on this effect. No interference between the spin-2 particle and the diphoton continuum background is assumed, since there are no theoretical models that describe it.

For the spin-2 state, the full size of the correction to the generated p_{T} spectrum of the diphoton system, described in Section 2, is taken as a systematic uncertainty.

The background distributions are derived directly from the observed data, using the two mass sidebands 105 GeV $< m_{\gamma\gamma} <$ 122 GeV and 130 GeV $< m_{\gamma\gamma} <$ 160 GeV, where the signal contribution is negligible. The background shape as a function of $m_{\gamma\gamma}$ is modelled by a fifth-order polynomial with coefficients fitted to the data. The background shape as a function of $|\cos\theta^*|$ is taken from the two mass sidebands, since the remaining correlation between the two observables is small. The statistical uncertainties affecting the determination of the $|\cos\theta^*|$ distribution from the sidebands are propagated into the signal region (SR), 122 GeV $< m_{\gamma\gamma} <$ 130 GeV, independently for each $|\cos\theta^*|$ bin. Detailed studies of the data in the sidebands, reported in [19], show that possible residual correlations between $m_{\gamma\gamma}$ and $|\cos\theta^*|$ are not significant compared to the statistical uncertainties. A study of the background, based on a large sample of simulated events using the SHERPA generator [30], indicates the presence of a residual correlation at the level of 0.6% for $|\cos\theta^*| < 0.8$ and 2% elsewhere. These values are treated as the systematic uncertainties due to possible correlations between $m_{\gamma\gamma}$ and $|\cos\theta^*|$.

The fit to data is carried out simultaneously in the signal region and the two sideband regions. In the signal region, the likelihood is a function of the two discriminant variables $m_{\gamma\gamma}$ and $|\cos\theta^*|$, while in the sidebands only $m_{\gamma\gamma}$ is considered.

The number of data events selected in the signal region is 14977, compared with a background estimate of about 14 300 events and an expected SM Higgs boson signal of about 370 events. Fig. 1 displays the data distribution for $|\cos\theta^*|$ in the signal region, overlaid with the signal and background components, fitted under the $J^P = 0^+$ hypothesis.

The likelihood function is fitted to data for both the spin-0 and spin-2 hypotheses with the signal and background normalisations treated as nuisance parameters. Fig. 2 shows the $|\cos\theta^*|$ distributions in the signal region, obtained after subtracting the estimated background, and compared with the expected distributions for spin-0 and spin-2 signals. The data points differ slightly between the two spin hypotheses, because the fitted background depends on the profiling of the nuisance parameters associated with the bin-by-bin systematic uncertainties.

5. $H \to ZZ^* \to 4\ell$ analysis

The $H \to ZZ^* \to 4\ell$ channel, where $\ell = e$ or μ, benefits from the presence of several observables dependent on spin and parity thanks to the full reconstruction of the four-lepton final state.

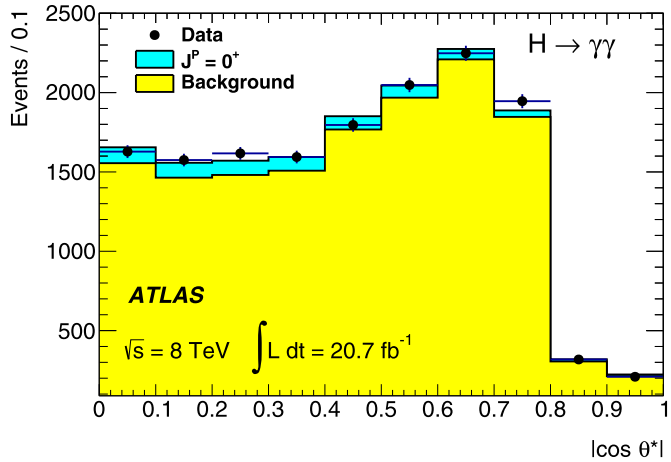

Fig. 1. Distribution of $|\cos\theta^*|$ for events in the signal region defined by 122 GeV $< m_{\gamma\gamma} <$ 130 GeV. The data (dots) are overlaid with the projection of the signal (blue/dark band) and background (yellow/light histogram) components obtained from the inclusive fit of the data under the spin-0 hypothesis.

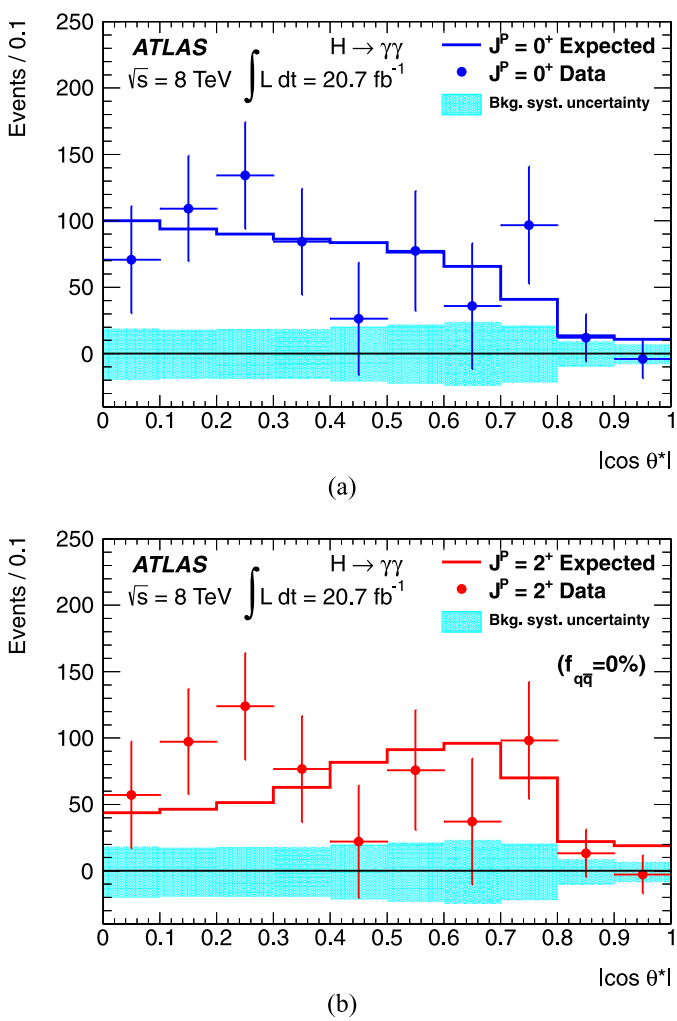

Fig. 2. Distributions of background-subtracted data in the signal region as a function of $|\cos\theta^*|$. The expected distributions for (a) spin-0 and (b) spin-2 signals produced by gluon fusion, normalised to the fitted number of signal events, are overlaid as solid lines. The cyan/grey bands around the horizontal lines at zero show the systematic uncertainties on the background modelling before the fits, which include the statistical uncertainties on the data sidebands.

The kinematic observables are the reconstructed masses of the two Z boson candidates and the five production and decay angles described in the following. The Z boson candidates are denoted hereafter as Z_1 and Z_2, where the index 1 refers to the lepton pair with the invariant mass closer to the central value of 91.1876 GeV of the Z boson mass [31]. Their respective masses are defined as m_{12} and m_{34}. The full definition of the production and decay angles as well as the description of their variation for different spin and parity values can be found in Ref. [20]. Here only a brief summary is given: θ_1 (θ_2) is the angle between the negatively charged final-state lepton in the Z_1 (Z_2) rest frame and the direction of flight of the Z_1 (Z_2) boson in the four-lepton rest frame. Φ is the angle between the decay planes defined by the two lepton pairs coming from the Z decays in the four-lepton rest frame. Φ_1 is the angle between the decay plane of the leading lepton pair and a plane defined by the momentum of the Z_1 in the four-lepton rest frame and the direction of the beam axis. θ^* is the production angle of the Z_1 defined in the four-lepton rest frame.

The lepton identification criteria and the analysis requirements follow the inclusive event selection described in Ref. [18]. To increase the sensitivity to the Higgs boson signal the final states are classified depending on the flavours of the lepton pairs. The events used to reconstruct the variables sensitive to the spin and parity of the resonance are selected in the region of reconstructed four-lepton invariant mass 115 GeV $< m_{4\ell} <$ 130 GeV, defined as the signal mass window.

After the analysis requirements 43 candidate events are selected in data in the signal mass window, compared with an expected background of about 16 events, dominated by the continuum ZZ^* process, and about 18 signal events for a SM Higgs boson with a mass of 125.5 GeV. The irreducible ZZ^* background is estimated from Monte Carlo simulation, normalised to NLO calculations, while the reducible $t\bar{t}$, $Zb\bar{b}$ and $Z+$jets backgrounds are estimated from corresponding control regions in data, as described in Ref. [18]. Fig. 3 shows the $\cos(\theta_1)$ and m_{34} distributions for events passing the full selection in the signal mass window.

In order to distinguish between pairs of spin and parity states, the reconstructed observables described above, namely the five angles and the two invariant masses, are combined using a multivariate discriminant based on a boosted decision tree (BDT) [32]. The BDT is trained on simulated signal events after full reconstruction and event selection. Dedicated discriminants are defined for the separation between the Standard Model $J^P = 0^+$ hypothesis and each of the considered alternative models, $J^P = 0^-, 1^+, 1^-, 2^+$. In the case of the spin-2 hypothesis, the studies are performed as a function of the $q\bar{q}$ production fraction, $f_{q\bar{q}}$.

The response of the BDT classifiers is evaluated separately for each pair of signal hypotheses, including the expected backgrounds from other SM processes. In addition, to improve the overall sensitivity, the BDT responses are evaluated separately for two $m_{4\ell}$ regions with high and low signal-over-background ratio (S/B): low (115–121 GeV and 127–130 GeV) and high (121–127 GeV).

Systematic uncertainties on the shapes of the BDT output and on the normalisations of the high and low S/B mass regions are considered. These are due to uncertainties on the lepton identification efficiencies, the lepton energy scale and its resolution. A systematic uncertainty of ±10% on the normalisation of the high and low S/B mass regions is applied to take into account the experimental uncertainty on the mass of the Higgs boson. The systematic uncertainties on the overall background yields and on the integrated luminosity are treated as described in Ref. [18]. Fig. 4 shows the BDT discriminant distributions for the $J^P = 0^+$ versus $J^P = 0^-$

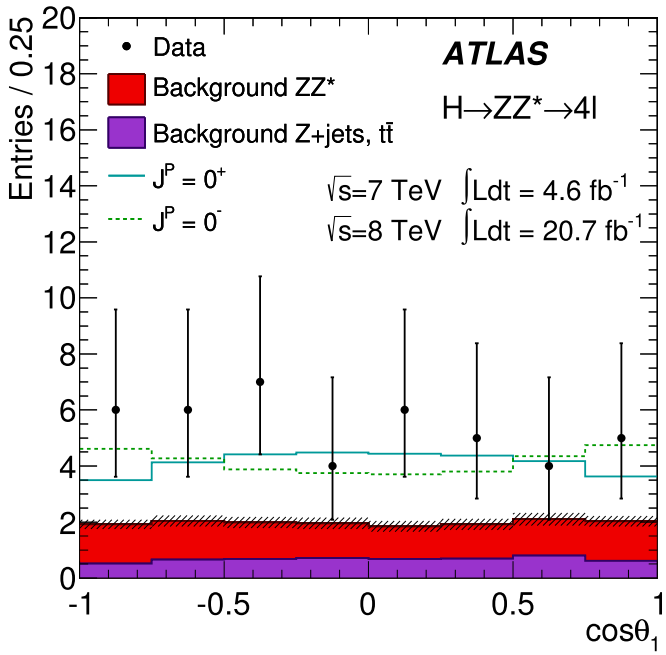

(a)

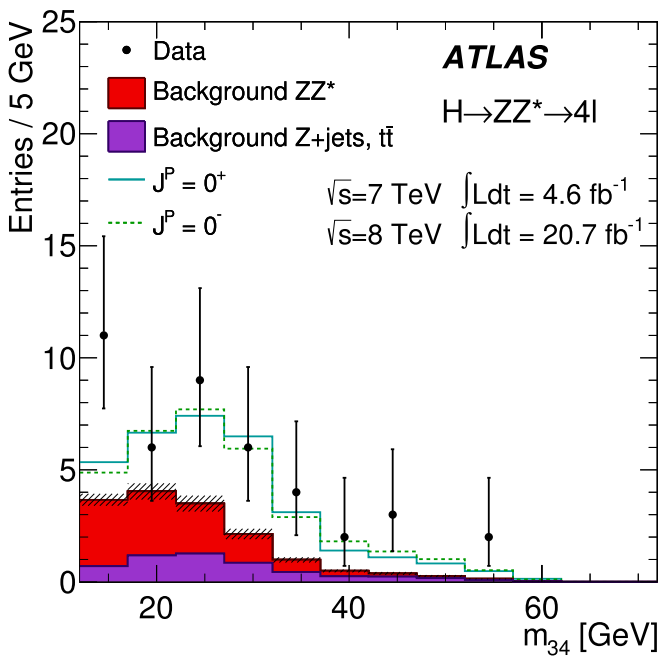

(b)

Fig. 3. Distributions of (a) $\cos(\theta_1)$ and (b) m_{34} for events passing the full selection in the signal mass window 115 GeV $< m_{4\ell} <$ 130 GeV for the combined $\sqrt{s} = 7$ TeV and $\sqrt{s} = 8$ TeV datasets. The expected contributions from the $J^P = 0^+$ (solid line) and $J^P = 0^-$ (dashed line) signal hypotheses, and the irreducible ZZ^* background are shown, together with the measured contribution from reducible non-ZZ^* backgrounds. The hatched areas represent the uncertainty on the background yields from statistical, experimental, and theoretical sources.

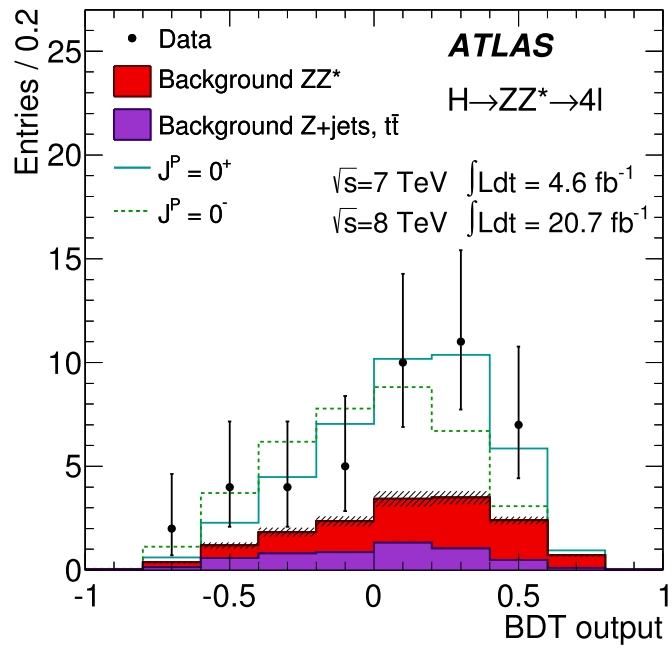

(a)

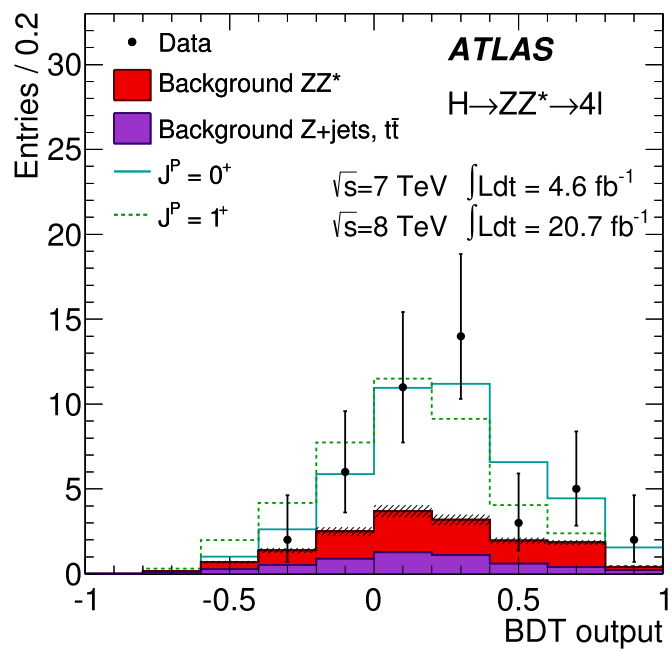

(b)

Fig. 4. Distributions of the BDT output for data (points with error bars) and expectations based on MC simulation (histograms). The distribution of each discriminant is shown for a pair of spin and parity hypotheses for the signal: $J^P = 0^+$ (solid line) and $J^P = 0^-$ (dashed line) in (a), $J^P = 0^+$ (solid line) and $J^P = 1^+$ (dashed line) in (b). The signal contribution for each of the two hypotheses is scaled using the profiled value of the signal strength. The hatched areas represent the uncertainty on the background yields from statistical, experimental, and theoretical sources.

and the $J^P = 0^+$ versus $J^P = 1^+$ hypotheses. The distribution of the BDT output is used as a discriminant observable in the likelihood defined in Section 3.

In addition to the BDT analysis an alternative approach based on the differential decay rate with respect to the angles and the masses, m_{12} and m_{34}, was also studied. These variables, corrected for detector acceptance and analysis selection effects, are used to construct a matrix-element-based discriminant. This alternative analysis yields results compatible with those obtained with the BDT, as described in detail in Ref. [20].

6. $H \to WW^* \to \ell\nu\ell\nu$ analysis

The analysis of the spin and parity in the $H \to WW^* \to \ell\nu\ell\nu$ channel is restricted to events containing two leptons of different flavour (one electron and one muon) and no observed jets with $p_T > 25$ GeV within $|\eta| < 2.5$ or with $p_T > 30$ GeV within $2.5 < |\eta| < 4.5$. The leading lepton is required to have $p_T > 25$ GeV and the sub-leading lepton $p_T > 15$ GeV. At least one of the two selected leptons is required to match a lepton that triggered the recording of the event.

The major sources of background after the dilepton selection are: $Z/\gamma^* +$ jets, diboson (WW, WZ/γ^*, ZZ/γ^*), top-quark ($t\bar{t}$ and single top) production, and W bosons produced in association with hadronic jets where a jet is misidentified as a lepton. The WW background also includes the small fraction of dibosons produced via gluon fusion. The requirement of two high-p_T isolated leptons significantly reduces the background contributions from fake leptons. Multi-jet and Z/γ^* events are suppressed by requiring relative missing transverse momentum[2] $E_{T,rel}^{miss}$ above 20 GeV.

Further lepton topological requirements are applied to optimise the sensitivity for the separation of different spin hypotheses, namely requirements on the dilepton invariant mass $m_{\ell\ell} < 80$ GeV, the transverse momentum of the dilepton system $p_T^{\ell\ell} > 20$ GeV and the azimuthal angular difference between leptons $\Delta\phi_{\ell\ell} < 2.8$ rad. This selection, which significantly reduces the WW continuum and Z/γ^* backgrounds, defines the signal region (SR).

The contributions from WW, top-quark and $Z +$ jets processes predicted by MC simulation are normalised to observed rates in control regions (CRs) dominated by the relevant background sources. The $Z +$ jets CR is defined by inverting the $\Delta\phi_{\ell\ell}$ requirement and removing the $p_T^{\ell\ell}$ one. The $Z +$ jets normalisation factor of 0.92 with a total uncertainty of ±8% is derived from this control region and applied to the simulated sample. The WW CR is defined using the same selection as for the SR except that the $\Delta\phi_{\ell\ell}$ requirement is removed and the $m_{\ell\ell}$ requirement is inverted. The resulting WW normalisation factor applied to the MC prediction is 1.08 with a total uncertainty of ±10%. The top-quark background is estimated as described in Ref. [18]. The ratio of the resulting prediction to the one from simulation alone is 1.07 with a total uncertainty of ±14%. The $W +$ jets background is estimated entirely from data. The shapes and normalisations of non-WW diboson backgrounds are estimated using simulation and cross-checked in a validation region [18]. The correlations introduced among the different background sources by the presence of other processes in the control regions are fully included in the statistical procedure to test the compatibility between data and the two spin hypotheses, as described in Section 3.

After the selection, the data SR contains 3615 events, with 170 events expected from the SM Higgs boson signal and about 3300 events from background processes, after their normalisation to data in the CRs.

Spin correlations between the decay products affect the $H \to WW^* \to \ell\nu\ell\nu$ event topologies by shaping the angular distributions of the leptons as well as the distributions of the lepton momenta and missing transverse energy. Due to the presence of two neutrinos in the event, a direct calculation of the various decay angles is not possible. Two of the most sensitive variables for measuring the spin of the Higgs boson are the dilepton invariant mass, $m_{\ell\ell}$, and the azimuthal separation of the two leptons, $\Delta\phi_{\ell\ell}$. Fig. 5 shows the distributions of both variables in the signal region. The distributions observed in the data agree well with the MC prediction for the expected SM $J^P = 0^+$ signal. The dilepton transverse momentum, $p_T^{\ell\ell}$, also has sensitivity to different spin hypotheses.

A BDT algorithm is used to distinguish between the spin hypotheses. In addition to the three variables mentioned above, the transverse mass of the dilepton and missing momentum system,

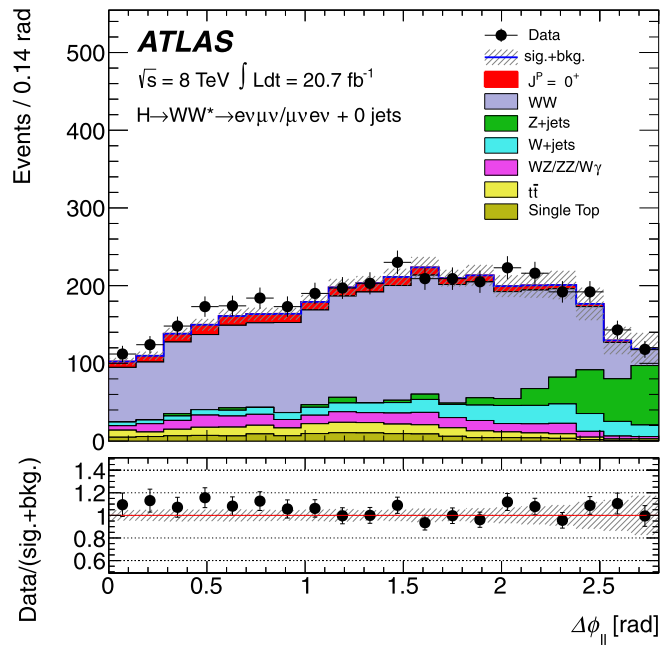

(a)

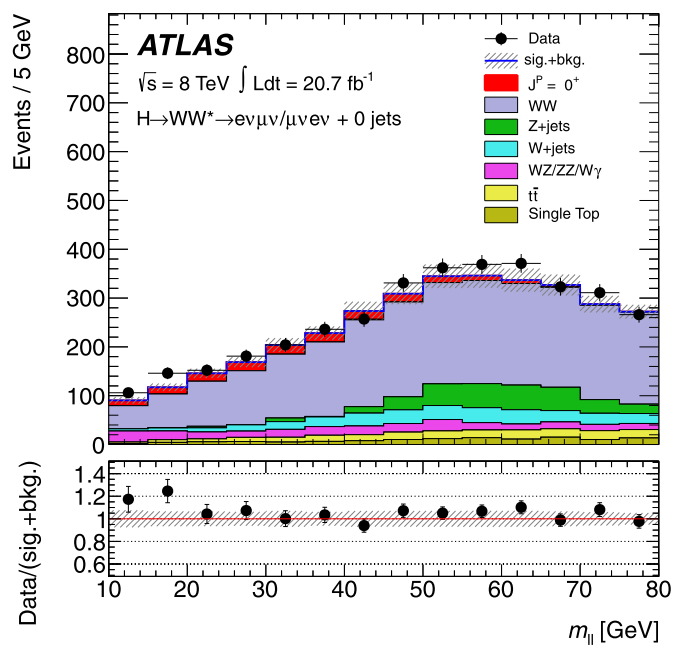

(b)

Fig. 5. Distributions of (a) $\Delta\phi_{\ell\ell}$ and (b) $m_{\ell\ell}$ in the signal region for $m_H = 125$ GeV and the $J^P = 0^+$ hypothesis. The signal is normalised to its SM expectation. In the lower part of the figures the ratio between data and the sum of signal and background is shown. The hatched areas represent the uncertainty on the signal and background yields from statistical, experimental, and theoretical sources.

[2] $E_{T,rel}^{miss} \equiv E_T^{miss} \cdot \sin\Delta\phi$, where $\Delta\phi$ is the azimuthal separation between the missing transverse momentum and the nearest reconstructed object (lepton or jet with $p_T > 25$ GeV) or $\pi/2$, whichever is smaller. The missing transverse energy E_T^{miss} is defined as the modulus of the missing transverse momentum.

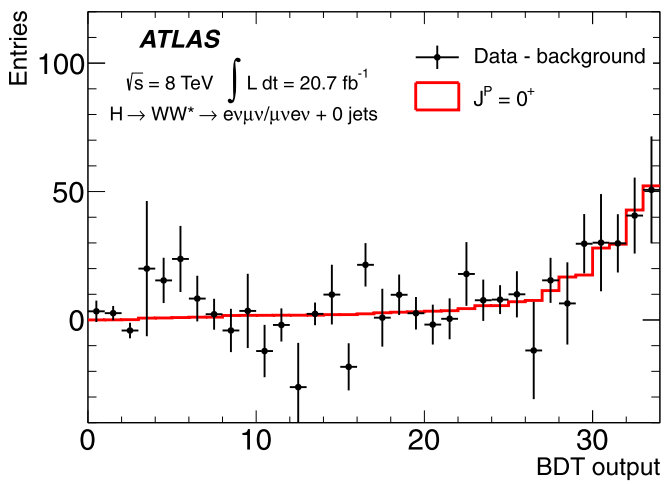

(a)

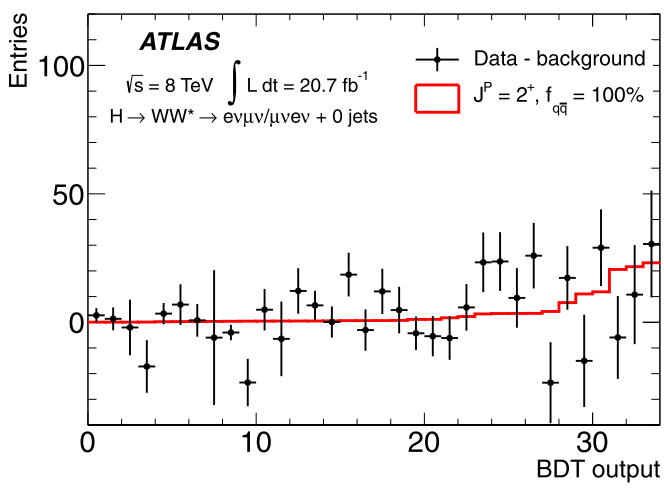

(b)

Fig. 6. One-dimensional distributions of the outputs of the BDT for the $H \to WW^*$ channel after background subtraction, using best-fit values for (a) $J^P = 0^+$ and (b) $J^P = 2^+$ with $f_{q\bar{q}} = 100\%$ hypotheses. In each case, the two-dimensional distribution of the two classifiers is remapped into a one-dimensional distribution, with the bins reordered in increasing number of expected signal events. Empty bins, defined as bins with expected content below 0.1, are removed.

m_T [18], is used in the BDT training as it provides a good separation between backgrounds and signals as well as some separation between the different spin hypotheses for the signals. Two separate BDT classifiers are developed for each hypothesis test: one classifier is trained to distinguish the $J^P = 0^+$ signal from the sum of all backgrounds while the second classifier separates the alternative spin–parity hypothesis ($J^P = 2^+$, 1^+ or 1^-) from the sum of all backgrounds. Background processes used to train both classifiers include WW, $t\bar{t}$ and single top, as well as WZ, ZZ, $W\gamma$, $W\gamma^*$, $W+$jets and $Z+$jets.

The resulting two-dimensional distribution of the two classifiers is then used in binned likelihood fits to test the data for compatibility with the presence of a $J^P = 0^+$, 1^+, 1^- or 2^+ particle in the data. The analysis of $J^P = 2^+$, including the retraining of the second classifier with the $J^P = 2^+$ sample as signal, is repeated for each of the five values of $f_{q\bar{q}}$. The BDT output distributions for data, after background subtraction, are shown in Fig. 6, after remapping the two-dimensional distribution of the two classifiers into a one-dimensional distribution.

The BDT relies on a good description of the input variables and their correlations. These were studied in detail and found to be well described by simulation [21]. In addition, dedicated studies were performed to verify that a BDT with the chosen four input variables is able to reliably separate the main backgrounds in a background-enriched region, and that the response is well modelled.

Two different categories of systematic uncertainties are considered: experimental or detector sources, such as the jet energy scale and resolution, or the lepton identification efficiencies, scale and resolution, as well as theoretical sources such as the estimation of the effect of higher-order contributions through variations of the QCD renormalisation and factorisation scales in the Monte Carlo simulation. The experimental uncertainties affect both the signal and background yields and are described in Ref. [18]. Monte Carlo samples with systematically varied parameters were analysed. Both the overall normalisation and shape distortions are included as nuisance parameters in the likelihood.

The WW background in the signal region is evaluated through extrapolation from a control region using the simulation. The theoretical uncertainties on the extrapolation parameter $\alpha = N_{SR}/N_{CR}$, the ratio of the number of events passing the signal region selection to the number passing the control region selection, are evaluated according to the prescription of Ref. [33]. Several sources of uncertainty on the normalisation are considered: uncertainties on the QCD renormalisation and factorisation scales, Parton Density Functions (PDF), the choice of Monte Carlo generator, and the underlying event and parton shower model. The total uncertainty on the extrapolation is $\pm 4.8\%$. Another important uncertainty arises from the shape modelling of the irreducible WW continuum background. The uncertainty on the shapes of the BDT discriminants is studied by varying the factorisation and renormalisation scales, by comparing the predictions of HERWIG [34] and PYTHIA8 leading-order parton shower programs, and by evaluating the uncertainties from the CT10 [35] PDF error set and combining them with the difference in central values between NNPDF [36] and CT10. An envelope for the predicted BDT shape for each discriminant is derived and included in the binned likelihood fit as a shape uncertainty.

7. Results

The SM $J^P = 0^+$ hypothesis is tested against several alternative spin–parity hypotheses using the analyses described in the previous sections. Using the statistical procedure described in Section 3, integral probabilities, the p_0-values, are determined to quantify the level of agreement of the data with different spin–parity hypotheses. When giving the confidence level associated with the rejection of a spin–parity hypothesis, the CL_s approach defined in Eq. (3) is used.

7.1. Systematic uncertainties

The sources of systematic uncertainty accounted for in the analyses of the individual channels are discussed in Sections 4, 5 and 6. In the combination, the correlations among the common sources of systematic uncertainties across channels are taken into account. Systematic uncertainties on electron and muon identification, reconstruction and trigger efficiencies, as well as on their energy and momentum resolution, are common to both the $H \to ZZ^*$ and $H \to WW^*$ channels. Systematic uncertainties on the energy scale of electrons and photons affect all three decay channels. It was also verified that the results presented in the following are insen-

sitive to variations of the Higgs boson mass within the measured accuracy of about ±0.6 GeV [18].

The overall impact of the systematic uncertainties is evaluated by comparing the baseline results of the likelihood fits obtained by profiling all nuisance parameters not directly measured from the data, with the results obtained by fixing them at their nominal values. For all tested hypotheses, the combined rejection significance is found to be degraded by less than 0.3σ when including all nuisance parameters in the fit with respect to fixing them at their nominal values.

The production mode has a significant impact on the underlying p_T spectrum of the Higgs boson. For signals produced through gluon fusion, the dependence on the p_T modelling was studied by comparing the discriminant observables before and after re-weighting the signal to the POWHEG+PYTHIA8 spectrum. However, the impact on the discriminant observables is found to be negligible compared to other sources of systematic uncertainty and therefore is neglected. For the $q\bar{q}$-initiated processes the p_T spectrum is expected to be softer than for processes produced via gluon fusion. Since no higher-order QCD predictions are available for the $q\bar{q}$ annihilation production process, no specific systematic uncertainty is assigned to the p_T spectrum of such signals. The impact of the large variation obtained by re-weighting the signals produced at leading order in $q\bar{q}$ annihilation for the $J^P = 2^+$ model to the POHWEG+PYTHIA8 gluon-fusion prediction was evaluated. The resulting weights increase from about unity at low transverse momentum to about four near 100 GeV. The $H \to WW^*$ and $H \to ZZ^*$ channels are almost insensitive to such re-weighting, which leads to changes in the BDT discriminant shapes of the order of a few percent. The $H \to \gamma\gamma$ channel is more sensitive to the signal p_T spectrum due to the impact on its acceptance at high $|\cos\theta^*|$ values. For this channel, the expected sensitivity for the spin-2 rejection is reduced by about 30% for $f_{q\bar{q}} = 100\%$, when the re-weighting is applied. Since the combined result for this case is dominated by the $H \to ZZ^*$ and $H \to WW^*$ channels, the overall impact of this re-weighting on the combined $J^P = 2^+$ rejection is negligible, below 0.1σ.

7.2. Test of SM $J^P = 0^+$ against $J^P = 0^-$

The distributions of the test statistics q from the $H \to ZZ^*$ channel for the $J^P = 0^+$ and 0^- hypotheses are shown in Fig. 7 together with the observed value.

The expected and observed rejections of the $J^P = 0^+$ and 0^- hypotheses are summarised in Table 1. The data are in agreement with the $J^P = 0^+$ hypothesis, while the 0^- hypothesis is excluded at 97.8% CL.

7.3. Test of SM $J^P = 0^+$ against $J^P = 1^+$

The expected and observed rejections of the $J^P = 0^+$ and 1^+ hypotheses in the $H \to ZZ^*$ and $H \to WW^*$ channels and their combination are summarised in Table 2. For both channels, the results are in agreement with the $J^P = 0^+$ hypothesis. In the $H \to ZZ^*$ channel, the 1^+ hypothesis is excluded at 99.8% CL, while in the $H \to WW^*$ channel, it is excluded at 92% CL. The combination excludes this hypothesis at 99.97% CL.

7.4. Test of SM $J^P = 0^+$ against $J^P = 1^-$

The expected and observed rejections of the $J^P = 0^+$ and 1^- hypotheses in the $H \to ZZ^*$ and $H \to WW^*$ channels and their combination are summarised in Table 3. For both channels, the results are in agreement with the $J^P = 0^+$ hypothesis. In the $H \to ZZ^*$ channel, the 1^- hypothesis is excluded at 94% CL. In the $H \to WW^*$ channel, the 1^- hypothesis is excluded at 98% CL. The combination excludes this hypothesis at 99.7% CL.

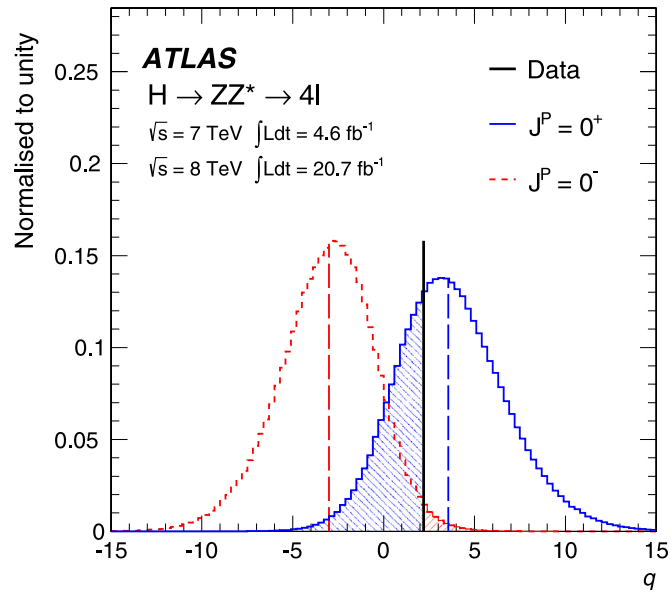

Fig. 7. Expected distributions of $q = \log(\mathcal{L}(J^P = 0^+)/\mathcal{L}(J^P = 0^-))$, the logarithm of the ratio of profiled likelihoods, under the $J^P = 0^+$ and 0^- hypotheses for the Standard Model $J^P = 0^+$ (blue/solid line distribution) or 0^- (red/dashed line distribution) signals. The observed value is indicated by the vertical solid line and the expected medians by the dashed lines. The coloured areas correspond to the integrals of the expected distributions up to the observed value and are used to compute the p_0-values for the rejection of each hypothesis.

7.5. Test of SM $J^P = 0^+$ against $J^P = 2^+$

The expected and observed rejections of the $J^P = 0^+$ and 2^+ hypotheses in the three channels are summarised in Table 4, for all $f_{q\bar{q}}$ values of the spin-2 particle considered. For all three channels, the results are in agreement with the spin-0 hypothesis. The results from the $H \to \gamma\gamma$ channel exclude a spin-2 particle produced via gluon fusion ($f_{q\bar{q}} = 0$) at 99.3% CL. The separation between the two spin hypotheses in this channel decreases with increasing $f_{q\bar{q}}$. For large values of $f_{q\bar{q}}$, the $|\cos\theta^*|$ distributions associated with the spin-0 and spin-2 signals become very similar. In the case of the $H \to ZZ^*$ channel, a separation slightly above one standard deviation is expected between the $J^P = 0^+$ and $J^P = 2^+$ hypotheses, with little dependence on the production mechanism. The $H \to WW^*$ channel has the opposite behaviour to the $H \to \gamma\gamma$ one, with the best expected rejection achieved for large values of $f_{q\bar{q}}$, as illustrated in Table 4. The results for the $H \to WW^*$ channel are also in agreement with the $J^P = 0^+$ hypothesis. The $J^P = 2^+$ hypothesis is excluded with a CL above 95%. The data are in better agreement with the $J^P = 0^+$ hypothesis over the full range of $f_{q\bar{q}}$.

Table 5 shows the expected and observed p_0-values for both the $J^P = 0^+$ and $J^P = 2^+$ hypotheses for the combination of the $H \to \gamma\gamma$, $H \to ZZ^*$ and $H \to WW^*$ channels. The test statistics calculated on data are compared to the corresponding expectations obtained from pseudo-experiments, as a function of $f_{q\bar{q}}$. The data are in good agreement with the Standard Model $J^P = 0^+$ hypothesis over the full $f_{q\bar{q}}$ range. Fig. 8 shows the comparison of the expected and observed CL_s values for the $J^P = 2^+$ rejection as a function of $f_{q\bar{q}}$. The observed exclusion of the $J^P = 2^+$ hypothesis in favour of the Standard Model $J^P = 0^+$ hypothesis exceeds 99.9% CL for all values of $f_{q\bar{q}}$.

Table 1
Summary of results for the 0^+ versus 0^- test in the $H \to ZZ^*$ channel. The expected p_0-values for rejecting the 0^+ and 0^- hypotheses (assuming the alternative hypothesis) are shown in the second and third columns. The fourth and fifth columns show the observed p_0-values, while the CL_s value for excluding the 0^- hypothesis is given in the last column.

Channel	0^- assumed Exp. $p_0(J^P = 0^+)$	0^+ assumed Exp. $p_0(J^P = 0^-)$	Obs. $p_0(J^P = 0^+)$	Obs. $p_0(J^P = 0^-)$	$\mathrm{CL}_s(J^P = 0^-)$
$H \to ZZ^*$	$1.5 \cdot 10^{-3}$	$3.7 \cdot 10^{-3}$	0.31	0.015	0.022

Table 2
Summary of results for the $J^P = 0^+$ versus 1^+ test in the $H \to ZZ^*$ and $H \to WW^*$ channels, as well as their combination. The expected p_0-values for rejecting the $J^P = 0^+$ and 1^+ hypotheses (assuming the alternative hypothesis) are shown in the second and third columns. The fourth and fifth columns show the observed p_0-values, while the CL_s values for excluding the 1^+ hypothesis are given in the last column.

Channel	1^+ assumed Exp. $p_0(J^P = 0^+)$	0^+ assumed Exp. $p_0(J^P = 1^+)$	Obs. $p_0(J^P = 0^+)$	Obs. $p_0(J^P = 1^+)$	$\mathrm{CL}_s(J^P = 1^+)$
$H \to ZZ^*$	$4.6 \cdot 10^{-3}$	$1.6 \cdot 10^{-3}$	0.55	$1.0 \cdot 10^{-3}$	$2.0 \cdot 10^{-3}$
$H \to WW^*$	0.11	0.08	0.70	0.02	0.08
Combination	$2.7 \cdot 10^{-3}$	$4.7 \cdot 10^{-4}$	0.62	$1.2 \cdot 10^{-4}$	$3.0 \cdot 10^{-4}$

Table 3
Summary of results for the $J^P = 0^+$ versus 1^- test in the $H \to ZZ^*$ and $H \to WW^*$ channels, as well as their combination. The expected p_0-values for rejecting the $J^P = 0^+$ and 1^- hypotheses (assuming the alternative hypothesis) are shown in the second and third columns. The fourth and fifth columns show the observed p_0-values, while the CL_s values for excluding the 1^- hypothesis are given in the last column.

Channel	1^- assumed Exp. $p_0(J^P = 0^+)$	0^+ assumed Exp. $p_0(J^P = 1^-)$	Obs. $p_0(J^P = 0^+)$	Obs. $p_0(J^P = 1^-)$	$\mathrm{CL}_s(J^P = 1^-)$
$H \to ZZ^*$	$0.9 \cdot 10^{-3}$	$3.8 \cdot 10^{-3}$	0.15	0.051	0.060
$H \to WW^*$	0.06	0.02	0.66	0.006	0.017
Combination	$1.4 \cdot 10^{-3}$	$3.6 \cdot 10^{-4}$	0.33	$1.8 \cdot 10^{-3}$	$2.7 \cdot 10^{-3}$

Table 4
Summary of results for the various fractions $f_{q\bar{q}}$ of the $q\bar{q}$ production of the spin-2 particle for the $H \to \gamma\gamma$ (top), $H \to ZZ^*$ (middle), and $H \to WW^*$ (bottom) channels. The expected p_0-values for rejecting the $J^P = 0^+$ and $J^P = 2^+$ hypotheses (assuming the alternative hypothesis) are shown in the second and third columns. The fourth and fifth columns show the observed p_0-values, while the CL_s values for excluding the $J^P = 2^+$ hypothesis are given in the last column.

$f_{q\bar{q}}$	2^+ assumed Exp. $p_0(J^P = 0^+)$	0^+ assumed Exp. $p_0(J^P = 2^+)$	Obs. $p_0(J^P = 0^+)$	Obs. $p_0(J^P = 2^+)$	$\mathrm{CL}_s(J^P = 2^+)$
			$H \to \gamma\gamma$		
100%	0.148	0.135	0.798	0.025	0.124
75%	0.319	0.305	0.902	0.033	0.337
50%	0.198	0.187	0.708	0.076	0.260
25%	0.052	0.039	0.609	0.021	0.054
0%	0.012	0.005	0.588	0.003	0.007
			$H \to ZZ^*$		
100%	0.102	0.082	0.962	0.001	0.026
75%	0.117	0.099	0.923	0.003	0.039
50%	0.129	0.113	0.943	0.002	0.035
25%	0.125	0.107	0.944	0.002	0.036
0%	0.099	0.092	0.532	0.079	0.169
			$H \to WW^*$		
100%	0.013	$3.6 \cdot 10^{-4}$	0.541	$1.7 \cdot 10^{-4}$	$3.6 \cdot 10^{-4}$
75%	0.028	0.003	0.586	0.001	0.003
50%	0.042	0.009	0.616	0.003	0.008
25%	0.048	0.019	0.622	0.008	0.020
0%	0.086	0.054	0.731	0.013	0.048

Table 5
Expected and observed p_0-values for the $J^P = 0^+$ and $J^P = 2^+$ hypotheses as a function of the fraction $f_{q\bar{q}}$ of the $q\bar{q}$ spin-2 production mechanism. The values are tabulated for the combination of the $H \to \gamma\gamma$, $H \to ZZ^*$ and $H \to WW^*$ channels. The CL_s values for excluding the $J^P = 2^+$ hypothesis are given in the last column.

$f_{q\bar{q}}$	2^+ assumed Exp. $p_0(J^P = 0^+)$	0^+ assumed Exp. $p_0(J^P = 2^+)$	Obs. $p_0(J^P = 0^+)$	Obs. $p_0(J^P = 2^+)$	$\mathrm{CL}_s(J^P = 2^+)$
100%	$3.0 \cdot 10^{-3}$	$8.8 \cdot 10^{-5}$	0.81	$1.6 \cdot 10^{-6}$	$0.8 \cdot 10^{-5}$
75%	$9.5 \cdot 10^{-3}$	$8.8 \cdot 10^{-4}$	0.81	$3.2 \cdot 10^{-5}$	$1.7 \cdot 10^{-4}$
50%	$1.3 \cdot 10^{-2}$	$2.7 \cdot 10^{-3}$	0.84	$8.6 \cdot 10^{-5}$	$5.3 \cdot 10^{-4}$
25%	$6.4 \cdot 10^{-3}$	$2.1 \cdot 10^{-3}$	0.80	$0.9 \cdot 10^{-4}$	$4.6 \cdot 10^{-4}$
0%	$2.1 \cdot 10^{-3}$	$5.5 \cdot 10^{-4}$	0.63	$1.5 \cdot 10^{-4}$	$4.2 \cdot 10^{-4}$

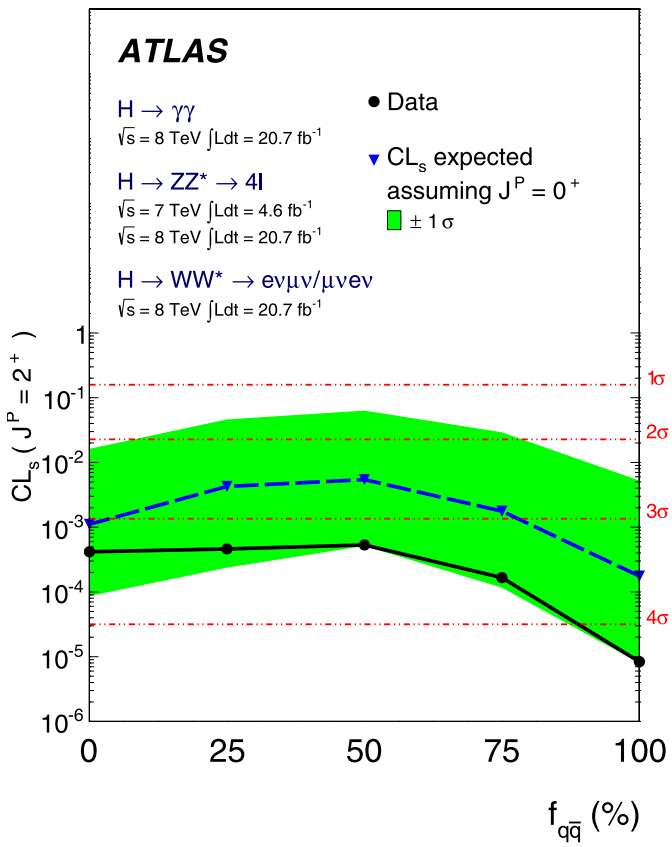

Fig. 8. Expected (blue triangles/dashed line) and observed (black circles/solid line) confidence levels, $\mathrm{CL}_s(J^P = 2^+)$, of the $J^P = 2^+$ hypothesis as a function of the fraction $f_{q\bar{q}}$ (see text) for the spin-2 particle. The green bands represent the 68% expected exclusion range for a signal with assumed $J^P = 0^+$. On the right y-axis, the corresponding numbers of Gaussian standard deviations are given, using the one-sided convention.

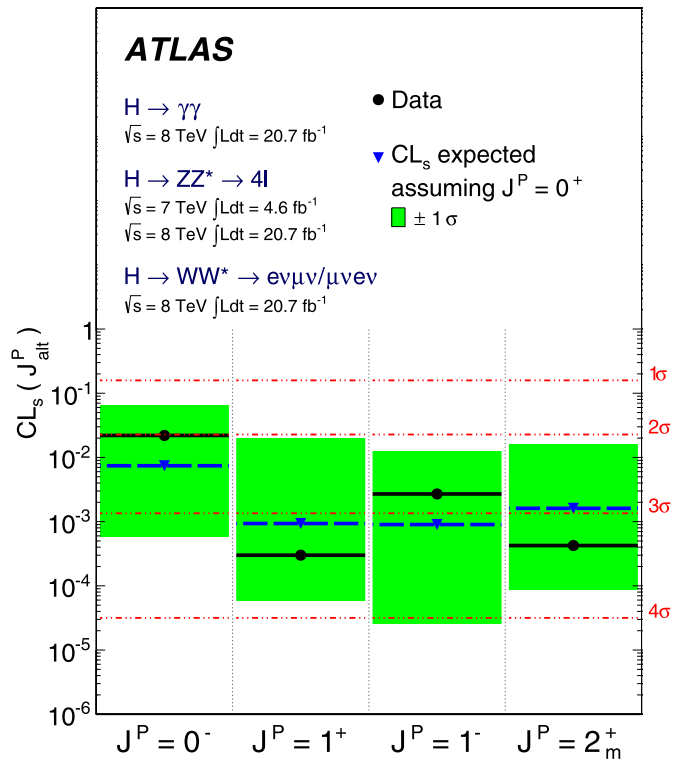

Fig. 9. Expected (blue triangles/dashed lines) and observed (black circles/solid lines) confidence level CL_s for alternative spin–parity hypotheses assuming a $J^P = 0^+$ signal. The green band represents the 68% $\mathrm{CL}_s(J^P_{\mathrm{alt}})$ expected exclusion range for a signal with assumed $J^P = 0^+$. For the spin-2 hypothesis, the results for the specific 2^+_m model, discussed in Section 2, are shown. On the right y-axis, the corresponding numbers of Gaussian standard deviations are given, using the one-sided convention.

7.6. Summary

The observed and expected CL_s values for the exclusion of the different spin–parity hypotheses are summarised in Fig. 9. For the spin-2 hypothesis, the CL_s value for the specific 2^+_m model, discussed in Section 2, is displayed.

8. Conclusions

The Standard Model $J^P = 0^+$ hypothesis for the Higgs boson has been compared to alternative spin–parity hypotheses using $\sqrt{s} = 8$ TeV (20.7 fb^{-1}) and 7 TeV (4.6 fb^{-1}) proton–proton collision data collected by the ATLAS experiment at the LHC. The Higgs boson decays $H \to \gamma\gamma$, $H \to ZZ^* \to 4\ell$ and $H \to WW^* \to \ell\nu\ell\nu$ have been used to test several specific alternative models, including $J^P = 0^-, 1^+, 1^-$ and a graviton-inspired $J^P = 2^+$ model with minimal couplings to SM particles. The data favour the Standard Model quantum numbers of $J^P = 0^+$. The 0^- hypothesis is rejected at 97.8% CL by using the $H \to ZZ^* \to 4\ell$ decay alone. The 1^+ and 1^- hypotheses are rejected with a CL of at least 99.7% by combining the $H \to ZZ^* \to 4\ell$ and $H \to WW^* \to \ell\nu\ell\nu$ channels. Finally, the $J^P = 2^+$ model is rejected at more than 99.9% CL by combining all three bosonic channels, $H \to \gamma\gamma$, $H \to ZZ^* \to 4\ell$ and $H \to WW^* \to \ell\nu\ell\nu$, independent of the assumed admixture of gluon-fusion and quark–antiquark production. All alternative models studied in this Letter are excluded without assumptions on the strength of the couplings of the Higgs boson to SM particles. These studies provide evidence for the spin-0 nature of the Higgs boson, with positive parity being strongly preferred.

Acknowledgements

We thank CERN for the very successful operation of the LHC, as well as the support staff from our institutions without whom ATLAS could not be operated efficiently.

We acknowledge the support of ANPCyT, Argentina; YerPhI, Armenia; ARC, Australia; BMWF and FWF, Austria; ANAS, Azerbaijan; SSTC, Belarus; CNPq and FAPESP, Brazil; NSERC, NRC and CFI, Canada; CERN; CONICYT, Chile; CAS, MOST and NSFC, China; COLCIENCIAS, Colombia; MSMT CR, MPO CR and VSC CR, Czech Republic; DNRF, DNSRC and Lundbeck Foundation, Denmark; EPLANET, ERC and NSRF, European Union; IN2P3-CNRS, CEA-DSM/IRFU, France; GNSF, Georgia; BMBF, DFG, HGF, MPG and AvH Foundation, Germany; GSRT and NSRF, Greece; ISF, MINERVA, GIF, DIP and Benoziyo Center, Israel; INFN, Italy; MEXT and JSPS, Japan; CNRST, Morocco; FOM and NWO, Netherlands; BRF and RCN, Norway; MNiSW, Poland; GRICES and FCT, Portugal; MERYS (MECTS), Romania; MES of Russia and ROSATOM, Russian Federation; JINR; MSTD, Serbia; MSSR, Slovakia; ARRS and MIZŠ, Slovenia; DST/NRF, South Africa; MICINN, Spain; SRC and Wallenberg Foundation, Sweden; SER, SNSF and Cantons of Bern and Geneva, Switzerland; NSC, Taiwan; TAEK, Turkey; STFC, the Royal Society and Leverhulme Trust, United Kingdom; DOE and NSF, United States of America.

The crucial computing support from all WLCG partners is acknowledged gratefully, in particular from CERN and the ATLAS Tier-1 facilities at TRIUMF (Canada), NDGF (Denmark, Norway, Sweden), CC-IN2P3 (France), KIT/GridKA (Germany), INFN-CNAF (Italy),

NL-T1 (Netherlands), PIC (Spain), ASGC (Taiwan), RAL (UK) and BNL (USA) and in the Tier-2 facilities worldwide.

Open access

This article is published Open Access at sciencedirect.com. It is distributed under the terms of the Creative Commons Attribution License 3.0, which permits unrestricted use, distribution, and reproduction in any medium, provided the original authors and source are credited.

References

[1] ATLAS Collaboration, Observation of a new particle in the search for the Standard Model Higgs boson with the ATLAS detector at the LHC, Phys. Lett. B 716 (2012) 1, arXiv:1207.7214 [hep-ex].
[2] CMS Collaboration, Observation of a new boson at a mass of 125 GeV with the CMS experiment at the LHC, Phys. Lett. B 716 (2012) 30, arXiv:1207.7235 [hep-ex].
[3] F. Englert, R. Brout, Broken symmetry and the mass of gauge vector mesons, Phys. Rev. Lett. 13 (1964) 321.
[4] P.W. Higgs, Broken symmetries, massless particles and gauge fields, Phys. Lett. 12 (1964) 132.
[5] P.W. Higgs, Broken symmetries and the masses of gauge bosons, Phys. Rev. Lett. 13 (1964) 508.
[6] G.S. Guralnik, C.R. Hagen, T.W.B. Kibble, Global conservation laws and massless particles, Phys. Rev. Lett. 13 (1964) 585.
[7] P.W. Higgs, Spontaneous symmetry breakdown without massless bosons, Phys. Rev. 145 (1966) 1156.
[8] T.W.B. Kibble, Symmetry breaking in non-Abelian gauge theories, Phys. Rev. 155 (1967) 1554.
[9] L.D. Landau, On the angular momentum of a two-photon system, Dokl. Akad. Nauk Ser. Fiz. 60 (1948) 207.
[10] C.-N. Yang, Selection rules for the dematerialization of a particle into two photons, Phys. Rev. 77 (1950) 242.
[11] CMS Collaboration, Study of the mass and spin–parity of the Higgs boson candidate via its decays to Z boson pairs, Phys. Rev. Lett. 110 (2013), arXiv:1212.6639 [hep-ex].
[12] Y. Gao, et al., Spin determination of single-produced resonances at hadron colliders, Phys. Rev. D 81 (2010) 075022, arXiv:1001.3396 [hep-ph].
[13] S. Bolognesi, et al., On the spin and parity of a single-produced resonance at the LHC, Phys. Rev. D 86 (2012) 095031, arXiv:1208.4018 [hep-ph].
[14] A. de Rujula, et al., Higgs look-alikes at the LHC, Phys. Rev. D 82 (2010) 013003, arXiv:1001.5300 [hep-ph].
[15] S.Y. Choi, D.J. Miller, M.M. Muhlleitner, P.M. Zerwas, Identifying the Higgs spin and parity in decays to Z pairs, Phys. Lett. B 553 (2003) 61, arXiv:hep-ph/0210077.
[16] P. de Aquino, K. Hagiwara, Q. Li, F. Maltoni, Simulating graviton production at hadron colliders, JHEP 1106 (2011) 132, arXiv:1101.5499 [hep-ph].
[17] J. Alwall, et al., MadGraph 5: Going beyond, JHEP 1106 (2011) 128, arXiv:1106.0522.
[18] ATLAS Collaboration, Measurements of Higgs boson production and couplings in diboson final states with the ATLAS detector at the LHC, Phys. Lett. B 726 (2013) 88, http://dx.doi.org/10.1016/j.physletb.2013.08.010.
[19] ATLAS Collaboration, Study of the spin of the Higgs-like boson in the two photon decay channel using 20.7 fb^{-1} of pp collisions collected at $\sqrt{s} =$ 8 TeV with the ATLAS detector, ATLAS-CONF-2013-029 (2013), http://cds.cern.ch/record/1527124.
[20] ATLAS Collaboration, Measurements of the properties of the Higgs-like boson in the four lepton decay channel with the ATLAS detector using 25 fb^{-1} of proton–proton collision data, ATLAS-CONF-2013-013 (2013), http://cds.cern.ch/record/1523699.
[21] ATLAS Collaboration, Study of the spin properties of the Higgs-like boson in the $H \to WW^{(*)} \to e\nu\mu\nu$ channel with 21 fb^{-1} of $\sqrt{s} = 8$ TeV data collected with the ATLAS detector, ATLAS-CONF-2013-031 (2013), http://cds.cern.ch/record/1527127.
[22] S. Alioli, P. Nason, C. Oleari, E. Re, NLO Higgs boson production via gluon fusion matched with shower in POWHEG, JHEP 0904 (2009) 002, arXiv:0812.0578 [hep-ph].
[23] T. Sjöstrand, S. Mrenna, P.Z. Skands, A brief introduction to PYTHIA 8.1, Comput. Phys. Commun. 178 (2008) 852, arXiv:0710.3820 [hep-ph].
[24] D. de Florian, G. Ferrera, M. Grazzini, D. Tommasini, Transverse-momentum resummation: Higgs boson production at the Tevatron and the LHC, JHEP 1111 (2011) 064, arXiv:1109.2109.
[25] ATLAS Collaboration, The ATLAS simulation infrastructure, Eur. Phys. J. C 70 (2010) 823, arXiv:1005.4568 [hep-ph].
[26] S. Agostinelli, et al., Geant4, a simulation toolkit, Nucl. Instrum. Meth. A 506 (2003) 250.
[27] J.C. Collins, D.E. Soper, Angular distribution of dileptons in high-energy hadron collisions, Phys. Rev. D 16 (1977) 2219–2225.
[28] M. Oreglia, PhD thesis, SLAC-R-0236, 1980, Appendix D.
[29] L.J. Dixon, M.S. Siu, Resonance-continuum interference in the diphoton Higgs signal at the LHC, Phys. Rev. Lett. 90 (2003) 252001, arXiv:hep-ph/0302233.
[30] T. Gleisberg, et al., Event generation with SHERPA 1.1, JHEP 0902 (2009) 007, arXiv:0811.4622 [hep-ph].
[31] J. Beringer, et al., Particle Data Group, Phys. Rev. D 86 (2012) 010001.
[32] A. Hoecker, et al., TMVA 4: Toolkit for multivariate data analysis with ROOT, arXiv:physics/0703039, 2009.
[33] LHC Higgs Cross Section Working Group, in: S. Dittmaier, C. Mariotti, G. Passarino, R. Tanaka (Eds.), Handbook of LHC Higgs Cross Sections: 2. Differential Distributions, CERN-2012-002, 2012, arXiv:1201.3084 [hep-ph].
[34] G. Corcella, et al., HERWIG 6: An event generator for hadron emission reactions with interfering gluons (including super-symmetric processes), JHEP 0101 (2001) 010, arXiv:hep-ph/0011363.
[35] H.-L. Lai, et al., New parton distributions for collider physics, Phys. Rev. D 82 (2010) 074024, arXiv:1007.2241 [hep-ph].
[36] R.D. Ball, et al., Impact of heavy quark masses on parton distributions and LHC phenomenology, Nucl. Phys. B 849 (2011) 296, arXiv:1101.1300 [hep-ph].

ATLAS Collaboration

G. Aad [48], T. Abajyan [21], B. Abbott [112], J. Abdallah [12], S. Abdel Khalek [116], O. Abdinov [11], R. Aben [106], B. Abi [113], M. Abolins [89], O.S. AbouZeid [159], H. Abramowicz [154], H. Abreu [137], Y. Abulaiti [147a,147b], B.S. Acharya [165a,165b,a], L. Adamczyk [38a], D.L. Adams [25], T.N. Addy [56], J. Adelman [177], S. Adomeit [99], T. Adye [130], S. Aefsky [23], J.A. Aguilar-Saavedra [125b,b], M. Agustoni [17], S.P. Ahlen [22], A. Ahmad [149], M. Ahsan [41], G. Aielli [134a,134b], T.P.A. Åkesson [80], G. Akimoto [156], A.V. Akimov [95], M.A. Alam [76], J. Albert [170], S. Albrand [55], M.J. Alconada Verzini [70], M. Aleksa [30], I.N. Aleksandrov [64], F. Alessandria [90a], C. Alexa [26a], G. Alexander [154], G. Alexandre [49], T. Alexopoulos [10], M. Alhroob [165a,165c], M. Aliev [16], G. Alimonti [90a], L. Alio [84], J. Alison [31], B.M.M. Allbrooke [18], L.J. Allison [71], P.P. Allport [73], S.E. Allwood-Spiers [53], J. Almond [83], A. Aloisio [103a,103b], R. Alon [173], A. Alonso [36], F. Alonso [70], A. Altheimer [35], B. Alvarez Gonzalez [89], M.G. Alviggi [103a,103b], K. Amako [65], Y. Amaral Coutinho [24a], C. Amelung [23], V.V. Ammosov [129,*], S.P. Amor Dos Santos [125a], A. Amorim [125a,c], S. Amoroso [48], N. Amram [154], C. Anastopoulos [30], L.S. Ancu [17], N. Andari [30], T. Andeen [35], C.F. Anders [58b], G. Anders [58a], K.J. Anderson [31], A. Andreazza [90a,90b], V. Andrei [58a], X.S. Anduaga [70], S. Angelidakis [9], P. Anger [44],

A. Angerami [35], F. Anghinolfi [30], A.V. Anisenkov [108], N. Anjos [125a], A. Annovi [47], A. Antonaki [9], M. Antonelli [47], A. Antonov [97], J. Antos [145b], F. Anulli [133a], M. Aoki [102], L. Aperio Bella [18], R. Apolle [119,d], G. Arabidze [89], I. Aracena [144], Y. Arai [65], A.T.H. Arce [45], S. Arfaoui [149], J-F. Arguin [94], S. Argyropoulos [42], E. Arik [19a,*], M. Arik [19a], A.J. Armbruster [88], O. Arnaez [82], V. Arnal [81], O. Arslan [21], A. Artamonov [96], G. Artoni [133a,133b], S. Asai [156], N. Asbah [94], S. Ask [28], B. Åsman [147a,147b], L. Asquith [6], K. Assamagan [25], R. Astalos [145a], A. Astbury [170], M. Atkinson [166], N.B. Atlay [142], B. Auerbach [6], E. Auge [116], K. Augsten [127], M. Aurousseau [146b], G. Avolio [30], D. Axen [169], G. Azuelos [94,e], Y. Azuma [156], M.A. Baak [30], C. Bacci [135a,135b], A.M. Bach [15], H. Bachacou [137], K. Bachas [155], M. Backes [30], M. Backhaus [21], J. Backus Mayes [144], E. Badescu [26a], P. Bagiacchi [133a,133b], P. Bagnaia [133a,133b], Y. Bai [33a], D.C. Bailey [159], T. Bain [35], J.T. Baines [130], O.K. Baker [177], S. Baker [77], P. Balek [128], F. Balli [137], E. Banas [39], Sw. Banerjee [174], D. Banfi [30], A. Bangert [151], V. Bansal [170], H.S. Bansil [18], L. Barak [173], S.P. Baranov [95], T. Barber [48], E.L. Barberio [87], D. Barberis [50a,50b], M. Barbero [84], D.Y. Bardin [64], T. Barillari [100], M. Barisonzi [176], T. Barklow [144], N. Barlow [28], B.M. Barnett [130], R.M. Barnett [15], A. Baroncelli [135a], G. Barone [49], A.J. Barr [119], F. Barreiro [81], J. Barreiro Guimarães da Costa [57], R. Bartoldus [144], A.E. Barton [71], V. Bartsch [150], A. Bassalat [116], A. Basye [166], R.L. Bates [53], L. Batkova [145a], J.R. Batley [28], M. Battistin [30], F. Bauer [137], H.S. Bawa [144,f], S. Beale [99], T. Beau [79], P.H. Beauchemin [162], R. Beccherle [50a], P. Bechtle [21], H.P. Beck [17], K. Becker [176], S. Becker [99], M. Beckingham [139], K.H. Becks [176], A.J. Beddall [19c], A. Beddall [19c], S. Bedikian [177], V.A. Bednyakov [64], C.P. Bee [84], L.J. Beemster [106], T.A. Beermann [176], M. Begel [25], C. Belanger-Champagne [86], P.J. Bell [49], W.H. Bell [49], G. Bella [154], L. Bellagamba [20a], A. Bellerive [29], M. Bellomo [30], A. Belloni [57], O.L. Beloborodova [108,g], K. Belotskiy [97], O. Beltramello [30], O. Benary [154], D. Benchekroun [136a], K. Bendtz [147a,147b], N. Benekos [166], Y. Benhammou [154], E. Benhar Noccioli [49], J.A. Benitez Garcia [160b], D.P. Benjamin [45], J.R. Bensinger [23], K. Benslama [131], S. Bentvelsen [106], D. Berge [30], E. Bergeaas Kuutmann [16], N. Berger [5], F. Berghaus [170], E. Berglund [106], J. Beringer [15], C. Bernard [22], P. Bernat [77], R. Bernhard [48], C. Bernius [78], F.U. Bernlochner [170], T. Berry [76], C. Bertella [84], F. Bertolucci [123a,123b], M.I. Besana [90a,90b], G.J. Besjes [105], O. Bessidskaia [147a,147b], N. Besson [137], S. Bethke [100], W. Bhimji [46], R.M. Bianchi [124], L. Bianchini [23], M. Bianco [72a,72b], O. Biebel [99], S.P. Bieniek [77], K. Bierwagen [54], J. Biesiada [15], M. Biglietti [135a], J. Bilbao De Mendizabal [49], H. Bilokon [47], M. Bindi [20a,20b], S. Binet [116], A. Bingul [19c], C. Bini [133a,133b], B. Bittner [100], C.W. Black [151], J.E. Black [144], K.M. Black [22], D. Blackburn [139], R.E. Blair [6], J.-B. Blanchard [137], T. Blazek [145a], I. Bloch [42], C. Blocker [23], J. Blocki [39], W. Blum [82,*], U. Blumenschein [54], G.J. Bobbink [106], V.S. Bobrovnikov [108], S.S. Bocchetta [80], A. Bocci [45], C.R. Boddy [119], M. Boehler [48], J. Boek [176], T.T. Boek [176], N. Boelaert [36], J.A. Bogaerts [30], A.G. Bogdanchikov [108], A. Bogouch [91,*], C. Bohm [147a], J. Bohm [126], V. Boisvert [76], T. Bold [38a], V. Boldea [26a], N.M. Bolnet [137], M. Bomben [79], M. Bona [75], M. Boonekamp [137], S. Bordoni [79], C. Borer [17], A. Borisov [129], G. Borissov [71], M. Borri [83], S. Borroni [42], J. Bortfeldt [99], V. Bortolotto [135a,135b], K. Bos [106], D. Boscherini [20a], M. Bosman [12], H. Boterenbrood [106], J. Bouchami [94], J. Boudreau [124], E.V. Bouhova-Thacker [71], D. Boumediene [34], C. Bourdarios [116], N. Bousson [84], S. Boutouil [136d], A. Boveia [31], J. Boyd [30], I.R. Boyko [64], I. Bozovic-Jelisavcic [13b], J. Bracinik [18], P. Branchini [135a], A. Brandt [8], G. Brandt [15], O. Brandt [54], U. Bratzler [157], B. Brau [85], J.E. Brau [115], H.M. Braun [176,*], S.F. Brazzale [165a,165c], B. Brelier [159], J. Bremer [30], K. Brendlinger [121], R. Brenner [167], S. Bressler [173], T.M. Bristow [146c], D. Britton [53], F.M. Brochu [28], I. Brock [21], R. Brock [89], F. Broggi [90a], C. Bromberg [89], J. Bronner [100], G. Brooijmans [35], T. Brooks [76], W.K. Brooks [32b], E. Brost [115], G. Brown [83], J. Brown [55], P.A. Bruckman de Renstrom [39], D. Bruncko [145b], R. Bruneliere [48], S. Brunet [60], A. Bruni [20a], G. Bruni [20a], M. Bruschi [20a], L. Bryngemark [80], T. Buanes [14], Q. Buat [55], F. Bucci [49], J. Buchanan [119], P. Buchholz [142], R.M. Buckingham [119], A.G. Buckley [46], S.I. Buda [26a], I.A. Budagov [64], B. Budick [109], F. Buehrer [48], L. Bugge [118], O. Bulekov [97], A.C. Bundock [73], M. Bunse [43], H. Burckhart [30], S. Burdin [73], T. Burgess [14], S. Burke [130], E. Busato [34],

V. Büscher [82], P. Bussey [53], C.P. Buszello [167], B. Butler [57], J.M. Butler [22], C.M. Buttar [53], J.M. Butterworth [77], W. Buttinger [28], A. Buzatu [53], M. Byszewski [10], S. Cabrera Urbán [168], D. Caforio [20a,20b], O. Cakir [4a], P. Calafiura [15], G. Calderini [79], P. Calfayan [99], R. Calkins [107], L.P. Caloba [24a], R. Caloi [133a,133b], D. Calvet [34], S. Calvet [34], R. Camacho Toro [49], P. Camarri [134a,134b], D. Cameron [118], L.M. Caminada [15], R. Caminal Armadans [12], S. Campana [30], M. Campanelli [77], V. Canale [103a,103b], F. Canelli [31], A. Canepa [160a], J. Cantero [81], R. Cantrill [76], T. Cao [40], M.D.M. Capeans Garrido [30], I. Caprini [26a], M. Caprini [26a], D. Capriotti [100], M. Capua [37a,37b], R. Caputo [82], R. Cardarelli [134a], T. Carli [30], G. Carlino [103a], L. Carminati [90a,90b], S. Caron [105], E. Carquin [32b], G.D. Carrillo-Montoya [146c], A.A. Carter [75], J.R. Carter [28], J. Carvalho [125a,h], D. Casadei [77], M.P. Casado [12], C. Caso [50a,50b,*], E. Castaneda-Miranda [146b], A. Castelli [106], V. Castillo Gimenez [168], N.F. Castro [125a], G. Cataldi [72a], P. Catastini [57], A. Catinaccio [30], J.R. Catmore [30], A. Cattai [30], G. Cattani [134a,134b], S. Caughron [89], V. Cavaliere [166], D. Cavalli [90a], M. Cavalli-Sforza [12], V. Cavasinni [123a,123b], F. Ceradini [135a,135b], B. Cerio [45], A.S. Cerqueira [24b], A. Cerri [15], L. Cerrito [75], F. Cerutti [15], A. Cervelli [17], S.A. Cetin [19b], A. Chafaq [136a], D. Chakraborty [107], I. Chalupkova [128], K. Chan [3], P. Chang [166], B. Chapleau [86], J.D. Chapman [28], J.W. Chapman [88], D.G. Charlton [18], V. Chavda [83], C.A. Chavez Barajas [30], S. Cheatham [86], S. Chekanov [6], S.V. Chekulaev [160a], G.A. Chelkov [64], M.A. Chelstowska [88], C. Chen [63], H. Chen [25], S. Chen [33c], X. Chen [174], Y. Chen [35], Y. Cheng [31], A. Cheplakov [64], R. Cherkaoui El Moursli [136e], V. Chernyatin [25,*], E. Cheu [7], L. Chevalier [137], V. Chiarella [47], G. Chiefari [103a,103b], J.T. Childers [30], A. Chilingarov [71], G. Chiodini [72a], A.S. Chisholm [18], R.T. Chislett [77], A. Chitan [26a], M.V. Chizhov [64], G. Choudalakis [31], S. Chouridou [9], B.K.B. Chow [99], I.A. Christidi [77], A. Christov [48], D. Chromek-Burckhart [30], M.L. Chu [152], J. Chudoba [126], G. Ciapetti [133a,133b], A.K. Ciftci [4a], R. Ciftci [4a], D. Cinca [62], V. Cindro [74], A. Ciocio [15], M. Cirilli [88], P. Cirkovic [13b], Z.H. Citron [173], M. Citterio [90a], M. Ciubancan [26a], A. Clark [49], P.J. Clark [46], R.N. Clarke [15], J.C. Clemens [84], B. Clement [55], C. Clement [147a,147b], Y. Coadou [84], M. Cobal [165a,165c], A. Coccaro [139], J. Cochran [63], S. Coelli [90a], L. Coffey [23], J.G. Cogan [144], J. Coggeshall [166], J. Colas [5], B. Cole [35], S. Cole [107], A.P. Colijn [106], C. Collins-Tooth [53], J. Collot [55], T. Colombo [58c], G. Colon [85], G. Compostella [100], P. Conde Muiño [125a], E. Coniavitis [167], M.C. Conidi [12], S.M. Consonni [90a,90b], V. Consorti [48], S. Constantinescu [26a], C. Conta [120a,120b], G. Conti [57], F. Conventi [103a,i], M. Cooke [15], B.D. Cooper [77], A.M. Cooper-Sarkar [119], N.J. Cooper-Smith [76], K. Copic [15], T. Cornelissen [176], M. Corradi [20a], F. Corriveau [86,j], A. Corso-Radu [164], A. Cortes-Gonzalez [12], G. Cortiana [100], G. Costa [90a], M.J. Costa [168], D. Costanzo [140], D. Côté [8], G. Cottin [32a], L. Courneyea [170], G. Cowan [76], B.E. Cox [83], K. Cranmer [109], S. Crépé-Renaudin [55], F. Crescioli [79], M. Cristinziani [21], G. Crosetti [37a,37b], C.-M. Cuciuc [26a], C. Cuenca Almenar [177], T. Cuhadar Donszelmann [140], J. Cummings [177], M. Curatolo [47], C. Cuthbert [151], H. Czirr [142], P. Czodrowski [44], Z. Czyczula [177], S. D'Auria [53], M. D'Onofrio [73], A. D'Orazio [133a,133b], M.J. Da Cunha Sargedas De Sousa [125a], C. Da Via [83], W. Dabrowski [38a], A. Dafinca [119], T. Dai [88], F. Dallaire [94], C. Dallapiccola [85], M. Dam [36], D.S. Damiani [138], A.C. Daniells [18], V. Dao [105], G. Darbo [50a], G.L. Darlea [26c], S. Darmora [8], J.A. Dassoulas [42], W. Davey [21], C. David [170], T. Davidek [128], E. Davies [119,d], M. Davies [94], O. Davignon [79], A.R. Davison [77], Y. Davygora [58a], E. Dawe [143], I. Dawson [140], R.K. Daya-Ishmukhametova [23], K. De [8], R. de Asmundis [103a], S. De Castro [20a,20b], S. De Cecco [79], J. de Graat [99], N. De Groot [105], P. de Jong [106], C. De La Taille [116], H. De la Torre [81], F. De Lorenzi [63], L. De Nooij [106], D. De Pedis [133a], A. De Salvo [133a], U. De Sanctis [165a,165c], A. De Santo [150], J.B. De Vivie De Regie [116], G. De Zorzi [133a,133b], W.J. Dearnaley [71], R. Debbe [25], C. Debenedetti [46], B. Dechenaux [55], D.V. Dedovich [64], J. Degenhardt [121], J. Del Peso [81], T. Del Prete [123a,123b], T. Delemontex [55], M. Deliyergiyev [74], A. Dell'Acqua [30], L. Dell'Asta [22], M. Della Pietra [103a,i], D. della Volpe [103a,103b], M. Delmastro [5], P.A. Delsart [55], C. Deluca [106], S. Demers [177], M. Demichev [64], A. Demilly [79], B. Demirkoz [12,k], S.P. Denisov [129], D. Derendarz [39], J.E. Derkaoui [136d], F. Derue [79], P. Dervan [73], K. Desch [21], P.O. Deviveiros [106],

A. Dewhurst [130], B. DeWilde [149], S. Dhaliwal [106], R. Dhullipudi [78,l], A. Di Ciaccio [134a,134b], L. Di Ciaccio [5], C. Di Donato [103a,103b], A. Di Girolamo [30], B. Di Girolamo [30], S. Di Luise [135a,135b], A. Di Mattia [153], B. Di Micco [135a,135b], R. Di Nardo [47], A. Di Simone [48], R. Di Sipio [20a,20b], M.A. Diaz [32a], E.B. Diehl [88], J. Dietrich [42], T.A. Dietzsch [58a], S. Diglio [87], K. Dindar Yagci [40], J. Dingfelder [21], F. Dinut [26a], C. Dionisi [133a,133b], P. Dita [26a], S. Dita [26a], F. Dittus [30], F. Djama [84], T. Djobava [51b], M.A.B. do Vale [24c], A. Do Valle Wemans [125a,m], T.K.O. Doan [5], D. Dobos [30], E. Dobson [77], J. Dodd [35], C. Doglioni [49], T. Doherty [53], T. Dohmae [156], Y. Doi [65,*], J. Dolejsi [128], Z. Dolezal [128], B.A. Dolgoshein [97,*], M. Donadelli [24d], J. Donini [34], J. Dopke [30], A. Doria [103a], A. Dos Anjos [174], A. Dotti [123a,123b], M.T. Dova [70], A.T. Doyle [53], M. Dris [10], J. Dubbert [88], S. Dube [15], E. Dubreuil [34], E. Duchovni [173], G. Duckeck [99], D. Duda [176], A. Dudarev [30], F. Dudziak [63], L. Duflot [116], M-A. Dufour [86], L. Duguid [76], M. Dührssen [30], M. Dunford [58a], H. Duran Yildiz [4a], M. Düren [52], M. Dwuznik [38a], J. Ebke [99], W. Edson [2], C.A. Edwards [76], N.C. Edwards [46], W. Ehrenfeld [21], T. Eifert [144], G. Eigen [14], K. Einsweiler [15], E. Eisenhandler [75], T. Ekelof [167], M. El Kacimi [136c], M. Ellert [167], S. Elles [5], F. Ellinghaus [82], K. Ellis [75], N. Ellis [30], J. Elmsheuser [99], M. Elsing [30], D. Emeliyanov [130], Y. Enari [156], O.C. Endner [82], R. Engelmann [149], A. Engl [99], J. Erdmann [177], A. Ereditato [17], D. Eriksson [147a], G. Ernis [176], J. Ernst [2], M. Ernst [25], J. Ernwein [137], D. Errede [166], S. Errede [166], E. Ertel [82], M. Escalier [116], H. Esch [43], C. Escobar [124], X. Espinal Curull [12], B. Esposito [47], F. Etienne [84], A.I. Etienvre [137], E. Etzion [154], D. Evangelakou [54], H. Evans [60], L. Fabbri [20a,20b], C. Fabre [30], G. Facini [30], R.M. Fakhrutdinov [129], S. Falciano [133a], Y. Fang [33a], M. Fanti [90a,90b], A. Farbin [8], A. Farilla [135a], T. Farooque [159], S. Farrell [164], S.M. Farrington [171], P. Farthouat [30], F. Fassi [168], P. Fassnacht [30], D. Fassouliotis [9], B. Fatholahzadeh [159], A. Favareto [90a,90b], L. Fayard [116], P. Federic [145a], O.L. Fedin [122], W. Fedorko [169], M. Fehling-Kaschek [48], L. Feligioni [84], C. Feng [33d], E.J. Feng [6], H. Feng [88], A.B. Fenyuk [129], J. Ferencei [145b], W. Fernando [6], S. Ferrag [53], J. Ferrando [53], V. Ferrara [42], A. Ferrari [167], P. Ferrari [106], R. Ferrari [120a], D.E. Ferreira de Lima [53], A. Ferrer [168], D. Ferrere [49], C. Ferretti [88], A. Ferretto Parodi [50a,50b], M. Fiascaris [31], F. Fiedler [82], A. Filipčič [74], M. Filipuzzi [42], F. Filthaut [105], M. Fincke-Keeler [170], K.D. Finelli [45], M.C.N. Fiolhais [125a,h], L. Fiorini [168], A. Firan [40], J. Fischer [176], M.J. Fisher [110], E.A. Fitzgerald [23], M. Flechl [48], I. Fleck [142], P. Fleischmann [175], S. Fleischmann [176], G.T. Fletcher [140], G. Fletcher [75], T. Flick [176], A. Floderus [80], L.R. Flores Castillo [174], A.C. Florez Bustos [160b], M.J. Flowerdew [100], T. Fonseca Martin [17], A. Formica [137], A. Forti [83], D. Fortin [160a], D. Fournier [116], H. Fox [71], P. Francavilla [12], M. Franchini [20a,20b], S. Franchino [30], D. Francis [30], M. Franklin [57], S. Franz [61], M. Fraternali [120a,120b], S. Fratina [121], S.T. French [28], C. Friedrich [42], F. Friedrich [44], D. Froidevaux [30], J.A. Frost [28], C. Fukunaga [157], E. Fullana Torregrosa [128], B.G. Fulsom [144], J. Fuster [168], C. Gabaldon [55], O. Gabizon [173], A. Gabrielli [20a,20b], A. Gabrielli [133a,133b], S. Gadatsch [106], T. Gadfort [25], S. Gadomski [49], G. Gagliardi [50a,50b], P. Gagnon [60], C. Galea [99], B. Galhardo [125a], E.J. Gallas [119], V. Gallo [17], B.J. Gallop [130], P. Gallus [127], G. Galster [36], K.K. Gan [110], R.P. Gandrajula [62], Y.S. Gao [144,f], F.M. Garay Walls [46], F. Garberson [177], C. García [168], J.E. García Navarro [168], M. Garcia-Sciveres [15], R.W. Gardner [31], N. Garelli [144], V. Garonne [30], C. Gatti [47], G. Gaudio [120a], B. Gaur [142], L. Gauthier [94], P. Gauzzi [133a,133b], I.L. Gavrilenko [95], C. Gay [169], G. Gaycken [21], E.N. Gazis [10], P. Ge [33d,n], Z. Gecse [169], C.N.P. Gee [130], D.A.A. Geerts [106], Ch. Geich-Gimbel [21], K. Gellerstedt [147a,147b], C. Gemme [50a], A. Gemmell [53], M.H. Genest [55], S. Gentile [133a,133b], M. George [54], S. George [76], D. Gerbaudo [164], A. Gershon [154], H. Ghazlane [136b], N. Ghodbane [34], B. Giacobbe [20a], S. Giagu [133a,133b], V. Giangiobbe [12], P. Giannetti [123a,123b], F. Gianotti [30], B. Gibbard [25], S.M. Gibson [76], M. Gilchriese [15], T.P.S. Gillam [28], D. Gillberg [30], A.R. Gillman [130], D.M. Gingrich [3,e], N. Giokaris [9], M.P. Giordani [165c], R. Giordano [103a,103b], F.M. Giorgi [16], P. Giovannini [100], P.F. Giraud [137], D. Giugni [90a], C. Giuliani [48], M. Giunta [94], B.K. Gjelsten [118], I. Gkialas [155,o], L.K. Gladilin [98], C. Glasman [81], J. Glatzer [21], A. Glazov [42], G.L. Glonti [64], M. Goblirsch-Kolb [100], J.R. Goddard [75], J. Godfrey [143], J. Godlewski [30], M. Goebel [42],

C. Goeringer [82], S. Goldfarb [88], T. Golling [177], D. Golubkov [129], A. Gomes [125a,c], L.S. Gomez Fajardo [42], R. Gonçalo [76], J. Goncalves Pinto Firmino Da Costa [42], L. Gonella [21], S. González de la Hoz [168], G. Gonzalez Parra [12], M.L. Gonzalez Silva [27], S. Gonzalez-Sevilla [49], J.J. Goodson [149], L. Goossens [30], P.A. Gorbounov [96], H.A. Gordon [25], I. Gorelov [104], G. Gorfine [176], B. Gorini [30], E. Gorini [72a,72b], A. Gorišek [74], E. Gornicki [39], A.T. Goshaw [6], C. Gössling [43], M.I. Gostkin [64], I. Gough Eschrich [164], M. Gouighri [136a], D. Goujdami [136c], M.P. Goulette [49], A.G. Goussiou [139], C. Goy [5], S. Gozpinar [23], H.M.X. Grabas [137], L. Graber [54], I. Grabowska-Bold [38a], P. Grafström [20a,20b], K-J. Grahn [42], E. Gramstad [118], F. Grancagnolo [72a], S. Grancagnolo [16], V. Grassi [149], V. Gratchev [122], H.M. Gray [30], J.A. Gray [149], E. Graziani [135a], O.G. Grebenyuk [122], Z.D. Greenwood [78,l], K. Gregersen [36], I.M. Gregor [42], P. Grenier [144], J. Griffiths [8], N. Grigalashvili [64], A.A. Grillo [138], K. Grimm [71], S. Grinstein [12,p], Ph. Gris [34], Y.V. Grishkevich [98], J.-F. Grivaz [116], J.P. Grohs [44], A. Grohsjean [42], E. Gross [173], J. Grosse-Knetter [54], J. Groth-Jensen [173], K. Grybel [142], F. Guescini [49], D. Guest [177], O. Gueta [154], C. Guicheney [34], E. Guido [50a,50b], T. Guillemin [116], S. Guindon [2], U. Gul [53], J. Gunther [127], J. Guo [35], S. Gupta [119], P. Gutierrez [112], N.G. Gutierrez Ortiz [53], N. Guttman [154], O. Gutzwiller [174], C. Guyot [137], C. Gwenlan [119], C.B. Gwilliam [73], A. Haas [109], C. Haber [15], H.K. Hadavand [8], P. Haefner [21], S. Hageboeck [21], Z. Hajduk [39], H. Hakobyan [178], D. Hall [119], G. Halladjian [62], K. Hamacher [176], P. Hamal [114], K. Hamano [87], M. Hamer [54], A. Hamilton [146a,q], S. Hamilton [162], L. Han [33b], K. Hanagaki [117], K. Hanawa [156], M. Hance [15], C. Handel [82], P. Hanke [58a], J.R. Hansen [36], J.B. Hansen [36], J.D. Hansen [36], P.H. Hansen [36], P. Hansson [144], K. Hara [161], A.S. Hard [174], T. Harenberg [176], S. Harkusha [91], D. Harper [88], R.D. Harrington [46], O.M. Harris [139], J. Hartert [48], F. Hartjes [106], A. Harvey [56], S. Hasegawa [102], Y. Hasegawa [141], S. Hassani [137], S. Haug [17], M. Hauschild [30], R. Hauser [89], M. Havranek [21], C.M. Hawkes [18], R.J. Hawkings [30], A.D. Hawkins [80], T. Hayashi [161], D. Hayden [89], C.P. Hays [119], H.S. Hayward [73], S.J. Haywood [130], S.J. Head [18], T. Heck [82], V. Hedberg [80], L. Heelan [8], S. Heim [121], B. Heinemann [15], S. Heisterkamp [36], J. Hejbal [126], L. Helary [22], C. Heller [99], M. Heller [30], S. Hellman [147a,147b], D. Hellmich [21], C. Helsens [30], J. Henderson [119], R.C.W. Henderson [71], A. Henrichs [177], A.M. Henriques Correia [30], S. Henrot-Versille [116], C. Hensel [54], G.H. Herbert [16], C.M. Hernandez [8], Y. Hernández Jiménez [168], R. Herrberg-Schubert [16], G. Herten [48], R. Hertenberger [99], L. Hervas [30], G.G. Hesketh [77], N.P. Hessey [106], R. Hickling [75], E. Higón-Rodriguez [168], J.C. Hill [28], K.H. Hiller [42], S. Hillert [21], S.J. Hillier [18], I. Hinchliffe [15], E. Hines [121], M. Hirose [117], D. Hirschbuehl [176], J. Hobbs [149], N. Hod [106], M.C. Hodgkinson [140], P. Hodgson [140], A. Hoecker [30], M.R. Hoeferkamp [104], J. Hoffman [40], D. Hoffmann [84], J.I. Hofmann [58a], M. Hohlfeld [82], S.O. Holmgren [147a], J.L. Holzbauer [89], T.M. Hong [121], L. Hooft van Huysduynen [109], J-Y. Hostachy [55], S. Hou [152], A. Hoummada [136a], J. Howard [119], J. Howarth [83], M. Hrabovsky [114], I. Hristova [16], J. Hrivnac [116], T. Hryn'ova [5], P.J. Hsu [82], S.-C. Hsu [139], D. Hu [35], X. Hu [25], Y. Huang [33a], Z. Hubacek [30], F. Hubaut [84], F. Huegging [21], A. Huettmann [42], T.B. Huffman [119], E.W. Hughes [35], G. Hughes [71], M. Huhtinen [30], T.A. Hülsing [82], M. Hurwitz [15], N. Huseynov [64,r], J. Huston [89], J. Huth [57], G. Iacobucci [49], G. Iakovidis [10], I. Ibragimov [142], L. Iconomidou-Fayard [116], J. Idarraga [116], P. Iengo [103a], O. Igonkina [106], Y. Ikegami [65], K. Ikematsu [142], M. Ikeno [65], D. Iliadis [155], N. Ilic [159], Y. Inamaru [66], T. Ince [100], P. Ioannou [9], M. Iodice [135a], K. Iordanidou [9], V. Ippolito [133a,133b], A. Irles Quiles [168], C. Isaksson [167], M. Ishino [67], M. Ishitsuka [158], R. Ishmukhametov [110], C. Issever [119], S. Istin [19a], A.V. Ivashin [129], W. Iwanski [39], H. Iwasaki [65], J.M. Izen [41], V. Izzo [103a], B. Jackson [121], J.N. Jackson [73], M. Jackson [73], P. Jackson [1], M.R. Jaekel [30], V. Jain [2], K. Jakobs [48], S. Jakobsen [36], T. Jakoubek [126], J. Jakubek [127], D.O. Jamin [152], D.K. Jana [112], E. Jansen [77], H. Jansen [30], J. Janssen [21], M. Janus [171], R.C. Jared [174], G. Jarlskog [80], L. Jeanty [57], G.-Y. Jeng [151], I. Jen-La Plante [31], D. Jennens [87], P. Jenni [48,s], J. Jentzsch [43], C. Jeske [171], S. Jézéquel [5], M.K. Jha [20a], H. Ji [174], W. Ji [82], J. Jia [149], Y. Jiang [33b], M. Jimenez Belenguer [42], S. Jin [33a], O. Jinnouchi [158], M.D. Joergensen [36], D. Joffe [40], K.E. Johansson [147a],

P. Johansson [140], S. Johnert [42], K.A. Johns [7], K. Jon-And [147a,147b], G. Jones [171], R.W.L. Jones [71], T.J. Jones [73], P.M. Jorge [125a], K.D. Joshi [83], J. Jovicevic [148], T. Agatonovic-Jovin [13b], X. Ju [174], C.A. Jung [43], R.M. Jungst [30], P. Jussel [61], A. Juste Rozas [12,p], M. Kaci [168], A. Kaczmarska [39], P. Kadlecik [36], M. Kado [116], H. Kagan [110], M. Kagan [57], E. Kajomovitz [153], S. Kalinin [176], S. Kama [40], N. Kanaya [156], M. Kaneda [30], S. Kaneti [28], T. Kanno [158], V.A. Kantserov [97], J. Kanzaki [65], B. Kaplan [109], A. Kapliy [31], D. Kar [53], K. Karakostas [10], N. Karastathis [10], M. Karnevskiy [82], S.N. Karpov [64], V. Kartvelishvili [71], A.N. Karyukhin [129], L. Kashif [174], G. Kasieczka [58b], R.D. Kass [110], A. Kastanas [14], Y. Kataoka [156], A. Katre [49], J. Katzy [42], V. Kaushik [7], K. Kawagoe [69], T. Kawamoto [156], G. Kawamura [54], S. Kazama [156], V.F. Kazanin [108], M.Y. Kazarinov [64], R. Keeler [170], P.T. Keener [121], R. Kehoe [40], M. Keil [54], J.S. Keller [139], H. Keoshkerian [5], O. Kepka [126], B.P. Kerševan [74], S. Kersten [176], K. Kessoku [156], J. Keung [159], F. Khalil-zada [11], H. Khandanyan [147a,147b], A. Khanov [113], D. Kharchenko [64], A. Khodinov [97], A. Khomich [58a], T.J. Khoo [28], G. Khoriauli [21], A. Khoroshilov [176], V. Khovanskiy [96], E. Khramov [64], J. Khubua [51b], H. Kim [147a,147b], S.H. Kim [161], N. Kimura [172], O. Kind [16], B.T. King [73], M. King [66], R.S.B. King [119], S.B. King [169], J. Kirk [130], A.E. Kiryunin [100], T. Kishimoto [66], D. Kisielewska [38a], T. Kitamura [66], T. Kittelmann [124], K. Kiuchi [161], E. Kladiva [145b], M. Klein [73], U. Klein [73], K. Kleinknecht [82], M. Klemetti [86], P. Klimek [147a,147b], A. Klimentov [25], R. Klingenberg [43], J.A. Klinger [83], E.B. Klinkby [36], T. Klioutchnikova [30], P.F. Klok [105], E.-E. Kluge [58a], P. Kluit [106], S. Kluth [100], E. Kneringer [61], E.B.F.G. Knoops [84], A. Knue [54], B.R. Ko [45], T. Kobayashi [156], M. Kobel [44], M. Kocian [144], P. Kodys [128], S. Koenig [82], P. Koevesarki [21], T. Koffas [29], E. Koffeman [106], L.A. Kogan [119], S. Kohlmann [176], F. Kohn [54], Z. Kohout [127], T. Kohriki [65], T. Koi [144], H. Kolanoski [16], I. Koletsou [90a], J. Koll [89], A.A. Komar [95,*], Y. Komori [156], T. Kondo [65], K. Köneke [48], A.C. König [105], T. Kono [42,t], R. Konoplich [109,u], N. Konstantinidis [77], R. Kopeliansky [153], S. Koperny [38a], L. Köpke [82], A.K. Kopp [48], K. Korcyl [39], K. Kordas [155], A. Korn [46], A.A. Korol [108], I. Korolkov [12], E.V. Korolkova [140], V.A. Korotkov [129], O. Kortner [100], S. Kortner [100], V.V. Kostyukhin [21], S. Kotov [100], V.M. Kotov [64], A. Kotwal [45], C. Kourkoumelis [9], V. Kouskoura [155], A. Koutsman [160a], R. Kowalewski [170], T.Z. Kowalski [38a], W. Kozanecki [137], A.S. Kozhin [129], V. Kral [127], V.A. Kramarenko [98], G. Kramberger [74], M.W. Krasny [79], A. Krasznahorkay [109], J.K. Kraus [21], A. Kravchenko [25], S. Kreiss [109], J. Kretzschmar [73], K. Kreutzfeldt [52], N. Krieger [54], P. Krieger [159], K. Kroeninger [54], H. Kroha [100], J. Kroll [121], J. Kroseberg [21], J. Krstic [13a], U. Kruchonak [64], H. Krüger [21], T. Kruker [17], N. Krumnack [63], Z.V. Krumshteyn [64], A. Kruse [174], M.K. Kruse [45], M. Kruskal [22], T. Kubota [87], S. Kuday [4a], S. Kuehn [48], A. Kugel [58c], T. Kuhl [42], V. Kukhtin [64], Y. Kulchitsky [91], S. Kuleshov [32b], M. Kuna [79], J. Kunkle [121], A. Kupco [126], H. Kurashige [66], M. Kurata [161], Y.A. Kurochkin [91], R. Kurumida [66], V. Kus [126], E.S. Kuwertz [148], M. Kuze [158], J. Kvita [143], R. Kwee [16], A. La Rosa [49], L. La Rotonda [37a,37b], L. Labarga [81], S. Lablak [136a], C. Lacasta [168], F. Lacava [133a,133b], J. Lacey [29], H. Lacker [16], D. Lacour [79], V.R. Lacuesta [168], E. Ladygin [64], R. Lafaye [5], B. Laforge [79], T. Lagouri [177], S. Lai [48], H. Laier [58a], E. Laisne [55], L. Lambourne [77], C.L. Lampen [7], W. Lampl [7], E. Lançon [137], U. Landgraf [48], M.P.J. Landon [75], V.S. Lang [58a], C. Lange [42], A.J. Lankford [164], F. Lanni [25], K. Lantzsch [30], A. Lanza [120a], S. Laplace [79], C. Lapoire [21], J.F. Laporte [137], T. Lari [90a], A. Larner [119], M. Lassnig [30], P. Laurelli [47], V. Lavorini [37a,37b], W. Lavrijsen [15], P. Laycock [73], B.T. Le [55], O. Le Dortz [79], E. Le Guirriec [84], E. Le Menedeu [12], T. LeCompte [6], F. Ledroit-Guillon [55], C.A. Lee [152], H. Lee [106], J.S.H. Lee [117], S.C. Lee [152], L. Lee [177], G. Lefebvre [79], M. Lefebvre [170], M. Legendre [137], F. Legger [99], C. Leggett [15], A. Lehan [73], M. Lehmacher [21], G. Lehmann Miotto [30], A.G. Leister [177], M.A.L. Leite [24d], R. Leitner [128], D. Lellouch [173], B. Lemmer [54], V. Lendermann [58a], K.J.C. Leney [146c], T. Lenz [106], G. Lenzen [176], B. Lenzi [30], R. Leone [7], K. Leonhardt [44], S. Leontsinis [10], C. Leroy [94], J-R. Lessard [170], C.G. Lester [28], C.M. Lester [121], J. Levêque [5], D. Levin [88], L.J. Levinson [173], A. Lewis [119], G.H. Lewis [109], A.M. Leyko [21], M. Leyton [16], B. Li [33b,v], B. Li [84], H. Li [149], H.L. Li [31], S. Li [45], X. Li [88], Z. Liang [119,w], H. Liao [34], B. Liberti [134a], P. Lichard [30], K. Lie [166], J. Liebal [21], W. Liebig [14], C. Limbach [21], A. Limosani [87],

M. Limper [62], S.C. Lin [152,x], F. Linde [106], B.E. Lindquist [149], J.T. Linnemann [89], E. Lipeles [121], A. Lipniacka [14], M. Lisovyi [42], T.M. Liss [166], D. Lissauer [25], A. Lister [169], A.M. Litke [138], B. Liu [152], D. Liu [152], J.B. Liu [33b], K. Liu [33b,y], L. Liu [88], M. Liu [45], M. Liu [33b], Y. Liu [33b], M. Livan [120a,120b], S.S.A. Livermore [119], A. Lleres [55], J. Llorente Merino [81], S.L. Lloyd [75], F. Lo Sterzo [133a,133b], E. Lobodzinska [42], P. Loch [7], W.S. Lockman [138], T. Loddenkoetter [21], F.K. Loebinger [83], A.E. Loevschall-Jensen [36], A. Loginov [177], C.W. Loh [169], T. Lohse [16], K. Lohwasser [48], M. Lokajicek [126], V.P. Lombardo [5], R.E. Long [71], L. Lopes [125a], D. Lopez Mateos [57], B. Lopez Paredes [140], J. Lorenz [99], N. Lorenzo Martinez [116], M. Losada [163], P. Loscutoff [15], M.J. Losty [160a,*], X. Lou [41], A. Lounis [116], J. Love [6], P.A. Love [71], A.J. Lowe [144,f], F. Lu [33a], H.J. Lubatti [139], C. Luci [133a,133b], A. Lucotte [55], D. Ludwig [42], I. Ludwig [48], J. Ludwig [48], F. Luehring [60], W. Lukas [61], L. Luminari [133a], E. Lund [118], J. Lundberg [147a,147b], O. Lundberg [147a,147b], B. Lund-Jensen [148], M. Lungwitz [82], D. Lynn [25], R. Lysak [126], E. Lytken [80], H. Ma [25], L.L. Ma [33d], G. Maccarrone [47], A. Macchiolo [100], B. Maček [74], J. Machado Miguens [125a], D. Macina [30], R. Mackeprang [36], R. Madar [48], R.J. Madaras [15], H.J. Maddocks [71], W.F. Mader [44], A. Madsen [167], M. Maeno [8], T. Maeno [25], L. Magnoni [164], E. Magradze [54], K. Mahboubi [48], J. Mahlstedt [106], S. Mahmoud [73], G. Mahout [18], C. Maiani [137], C. Maidantchik [24a], A. Maio [125a,c], S. Majewski [115], Y. Makida [65], N. Makovec [116], P. Mal [137,z], B. Malaescu [79], Pa. Malecki [39], V.P. Maleev [122], F. Malek [55], U. Mallik [62], D. Malon [6], C. Malone [144], S. Maltezos [10], V.M. Malyshev [108], S. Malyukov [30], J. Mamuzic [13b], L. Mandelli [90a], I. Mandić [74], R. Mandrysch [62], J. Maneira [125a], A. Manfredini [100], L. Manhaes de Andrade Filho [24b], J.A. Manjarres Ramos [137], A. Mann [99], P.M. Manning [138], A. Manousakis-Katsikakis [9], B. Mansoulie [137], R. Mantifel [86], L. Mapelli [30], L. March [168], J.F. Marchand [29], F. Marchese [134a,134b], G. Marchiori [79], M. Marcisovsky [126], C.P. Marino [170], C.N. Marques [125a], F. Marroquim [24a], Z. Marshall [15], L.F. Marti [17], S. Marti-Garcia [168], B. Martin [30], B. Martin [89], J.P. Martin [94], T.A. Martin [171], V.J. Martin [46], B. Martin dit Latour [49], H. Martinez [137], M. Martinez [12,p], S. Martin-Haugh [150], A.C. Martyniuk [170], M. Marx [83], F. Marzano [133a], A. Marzin [112], L. Masetti [82], T. Mashimo [156], R. Mashinistov [95], J. Masik [83], A.L. Maslennikov [108], I. Massa [20a,20b], N. Massol [5], P. Mastrandrea [149], A. Mastroberardino [37a,37b], T. Masubuchi [156], H. Matsunaga [156], T. Matsushita [66], P. Mättig [176], S. Mättig [42], J. Mattmann [82], C. Mattravers [119,d], J. Maurer [84], S.J. Maxfield [73], D.A. Maximov [108,g], R. Mazini [152], L. Mazzaferro [134a,134b], M. Mazzanti [90a], S.P. Mc Kee [88], A. McCarn [166], R.L. McCarthy [149], T.G. McCarthy [29], N.A. McCubbin [130], K.W. McFarlane [56,*], J.A. Mcfayden [140], G. Mchedlidze [51b], T. Mclaughlan [18], S.J. McMahon [130], R.A. McPherson [170,j], A. Meade [85], J. Mechnich [106], M. Mechtel [176], M. Medinnis [42], S. Meehan [31], R. Meera-Lebbai [112], S. Mehlhase [36], A. Mehta [73], K. Meier [58a], C. Meineck [99], B. Meirose [80], C. Melachrinos [31], B.R. Mellado Garcia [146c], F. Meloni [90a,90b], L. Mendoza Navas [163], A. Mengarelli [20a,20b], S. Menke [100], E. Meoni [162], K.M. Mercurio [57], S. Mergelmeyer [21], N. Meric [137], P. Mermod [49], L. Merola [103a,103b], C. Meroni [90a], F.S. Merritt [31], H. Merritt [110], A. Messina [30,aa], J. Metcalfe [25], A.S. Mete [164], C. Meyer [82], C. Meyer [31], J-P. Meyer [137], J. Meyer [30], J. Meyer [54], S. Michal [30], R.P. Middleton [130], S. Migas [73], L. Mijović [137], G. Mikenberg [173], M. Mikestikova [126], M. Mikuž [74], D.W. Miller [31], W.J. Mills [169], C. Mills [57], A. Milov [173], D.A. Milstead [147a,147b], D. Milstein [173], A.A. Minaenko [129], M. Miñano Moya [168], I.A. Minashvili [64], A.I. Mincer [109], B. Mindur [38a], M. Mineev [64], Y. Ming [174], L.M. Mir [12], G. Mirabelli [133a], T. Mitani [172], J. Mitrevski [138], V.A. Mitsou [168], S. Mitsui [65], P.S. Miyagawa [140], J.U. Mjörnmark [80], T. Moa [147a,147b], V. Moeller [28], S. Mohapatra [149], W. Mohr [48], S. Molander [147a,147b], R. Moles-Valls [168], A. Molfetas [30], K. Mönig [42], C. Monini [55], J. Monk [36], E. Monnier [84], J. Montejo Berlingen [12], F. Monticelli [70], S. Monzani [20a,20b], R.W. Moore [3], C. Mora Herrera [49], A. Moraes [53], N. Morange [62], J. Morel [54], D. Moreno [82], M. Moreno Llácer [168], P. Morettini [50a], M. Morgenstern [44], M. Morii [57], S. Moritz [82], A.K. Morley [148], G. Mornacchi [30], J.D. Morris [75], L. Morvaj [102], H.G. Moser [100], M. Mosidze [51b], J. Moss [110], R. Mount [144], E. Mountricha [10,ab],

S.V. Mouraviev [95,*], E.J.W. Moyse [85], R.D. Mudd [18], F. Mueller [58a], J. Mueller [124], K. Mueller [21], T. Mueller [28], T. Mueller [82], D. Muenstermann [49], Y. Munwes [154], J.A. Murillo Quijada [18], W.J. Murray [130], I. Mussche [106], E. Musto [153], A.G. Myagkov [129,ac], M. Myska [126], O. Nackenhorst [54], J. Nadal [12], K. Nagai [61], R. Nagai [158], Y. Nagai [84], K. Nagano [65], A. Nagarkar [110], Y. Nagasaka [59], M. Nagel [100], A.M. Nairz [30], Y. Nakahama [30], K. Nakamura [65], T. Nakamura [156], I. Nakano [111], H. Namasivayam [41], G. Nanava [21], A. Napier [162], R. Narayan [58b], M. Nash [77,d], T. Nattermann [21], T. Naumann [42], G. Navarro [163], H.A. Neal [88], P.Yu. Nechaeva [95], T.J. Neep [83], A. Negri [120a,120b], G. Negri [30], M. Negrini [20a], S. Nektarijevic [49], A. Nelson [164], T.K. Nelson [144], S. Nemecek [126], P. Nemethy [109], A.A. Nepomuceno [24a], M. Nessi [30,ad], M.S. Neubauer [166], M. Neumann [176], A. Neusiedl [82], R.M. Neves [109], P. Nevski [25], F.M. Newcomer [121], P.R. Newman [18], D.H. Nguyen [6], V. Nguyen Thi Hong [137], R.B. Nickerson [119], R. Nicolaidou [137], B. Nicquevert [30], J. Nielsen [138], N. Nikiforou [35], A. Nikiforov [16], V. Nikolaenko [129,ac], I. Nikolic-Audit [79], K. Nikolics [49], K. Nikolopoulos [18], P. Nilsson [8], Y. Ninomiya [156], A. Nisati [133a], R. Nisius [100], T. Nobe [158], L. Nodulman [6], M. Nomachi [117], I. Nomidis [155], S. Norberg [112], M. Nordberg [30], J. Novakova [128], M. Nozaki [65], L. Nozka [114], K. Ntekas [10], A.-E. Nuncio-Quiroz [21], G. Nunes Hanninger [87], T. Nunnemann [99], E. Nurse [77], B.J. O'Brien [46], F. O'grady [7], D.C. O'Neil [143], V. O'Shea [53], L.B. Oakes [99], F.G. Oakham [29,e], H. Oberlack [100], J. Ocariz [79], A. Ochi [66], M.I. Ochoa [77], S. Oda [69], S. Odaka [65], J. Odier [84], H. Ogren [60], A. Oh [83], S.H. Oh [45], C.C. Ohm [30], T. Ohshima [102], W. Okamura [117], H. Okawa [25], Y. Okumura [31], T. Okuyama [156], A. Olariu [26a], A.G. Olchevski [64], S.A. Olivares Pino [46], M. Oliveira [125a,h], D. Oliveira Damazio [25], E. Oliver Garcia [168], D. Olivito [121], A. Olszewski [39], J. Olszowska [39], A. Onofre [125a,ae], P.U.E. Onyisi [31,af], C.J. Oram [160a], M.J. Oreglia [31], Y. Oren [154], D. Orestano [135a,135b], N. Orlando [72a,72b], C. Oropeza Barrera [53], R.S. Orr [159], B. Osculati [50a,50b], R. Ospanov [121], G. Otero y Garzon [27], H. Otono [69], J.P. Ottersbach [106], M. Ouchrif [136d], E.A. Ouellette [170], F. Ould-Saada [118], A. Ouraou [137], K.P. Oussoren [106], Q. Ouyang [33a], A. Ovcharova [15], M. Owen [83], S. Owen [140], V.E. Ozcan [19a], N. Ozturk [8], K. Pachal [119], A. Pacheco Pages [12], C. Padilla Aranda [12], S. Pagan Griso [15], E. Paganis [140], C. Pahl [100], F. Paige [25], P. Pais [85], K. Pajchel [118], G. Palacino [160b], C.P. Paleari [7], S. Palestini [30], D. Pallin [34], A. Palma [125a], J.D. Palmer [18], Y.B. Pan [174], E. Panagiotopoulou [10], J.G. Panduro Vazquez [76], P. Pani [106], N. Panikashvili [88], S. Panitkin [25], D. Pantea [26a], A. Papadelis [147a], Th.D. Papadopoulou [10], K. Papageorgiou [155,o], A. Paramonov [6], D. Paredes Hernandez [34], M.A. Parker [28], F. Parodi [50a,50b], J.A. Parsons [35], U. Parzefall [48], S. Pashapour [54], E. Pasqualucci [133a], S. Passaggio [50a], A. Passeri [135a], F. Pastore [135a,135b,*], Fr. Pastore [76], G. Pásztor [49,ag], S. Pataraia [176], N.D. Patel [151], J.R. Pater [83], S. Patricelli [103a,103b], T. Pauly [30], J. Pearce [170], M. Pedersen [118], S. Pedraza Lopez [168], M.I. Pedraza Morales [174], S.V. Peleganchuk [108], D. Pelikan [167], H. Peng [33b], B. Penning [31], A. Penson [35], J. Penwell [60], D.V. Perepelitsa [35], T. Perez Cavalcanti [42], E. Perez Codina [160a], M.T. Pérez García-Estañ [168], V. Perez Reale [35], L. Perini [90a,90b], H. Pernegger [30], R. Perrino [72a], V.D. Peshekhonov [64], K. Peters [30], R.F.Y. Peters [54,ah], B.A. Petersen [30], J. Petersen [30], T.C. Petersen [36], E. Petit [5], A. Petridis [147a,147b], C. Petridou [155], E. Petrolo [133a], F. Petrucci [135a,135b], M. Petteni [143], R. Pezoa [32b], P.W. Phillips [130], G. Piacquadio [144], E. Pianori [171], A. Picazio [49], E. Piccaro [75], M. Piccinini [20a,20b], S.M. Piec [42], R. Piegaia [27], D.T. Pignotti [110], J.E. Pilcher [31], A.D. Pilkington [77], J. Pina [125a,c], M. Pinamonti [165a,165c,ai], A. Pinder [119], J.L. Pinfold [3], A. Pingel [36], B. Pinto [125a], C. Pizio [90a,90b], M.-A. Pleier [25], V. Pleskot [128], E. Plotnikova [64], P. Plucinski [147a,147b], S. Poddar [58a], F. Podlyski [34], R. Poettgen [82], L. Poggioli [116], D. Pohl [21], M. Pohl [49], G. Polesello [120a], A. Policicchio [37a,37b], R. Polifka [159], A. Polini [20a], C.S. Pollard [45], V. Polychronakos [25], D. Pomeroy [23], K. Pommès [30], L. Pontecorvo [133a], B.G. Pope [89], G.A. Popeneciu [26b], D.S. Popovic [13a], A. Poppleton [30], X. Portell Bueso [12], G.E. Pospelov [100], S. Pospisil [127], I.N. Potrap [64], C.J. Potter [150], C.T. Potter [115], G. Poulard [30], J. Poveda [60], V. Pozdnyakov [64], R. Prabhu [77], P. Pralavorio [84], A. Pranko [15], S. Prasad [30], R. Pravahan [25], S. Prell [63], D. Price [60], J. Price [73],

L.E. Price [6], D. Prieur [124], M. Primavera [72a], M. Proissl [46], K. Prokofiev [109], F. Prokoshin [32b], E. Protopapadaki [137], S. Protopopescu [25], J. Proudfoot [6], X. Prudent [44], M. Przybycien [38a], H. Przysiezniak [5], S. Psoroulas [21], E. Ptacek [115], E. Pueschel [85], D. Puldon [149], M. Purohit [25,aj], P. Puzo [116], Y. Pylypchenko [62], J. Qian [88], A. Quadt [54], D.R. Quarrie [15], W.B. Quayle [146c], D. Quilty [53], V. Radeka [25], V. Radescu [42], P. Radloff [115], F. Ragusa [90a,90b], G. Rahal [179], S. Rajagopalan [25], M. Rammensee [48], M. Rammes [142], A.S. Randle-Conde [40], C. Rangel-Smith [79], K. Rao [164], F. Rauscher [99], T.C. Rave [48], T. Ravenscroft [53], M. Raymond [30], A.L. Read [118], D.M. Rebuzzi [120a,120b], A. Redelbach [175], G. Redlinger [25], R. Reece [121], K. Reeves [41], A. Reinsch [115], I. Reisinger [43], M. Relich [164], C. Rembser [30], Z.L. Ren [152], A. Renaud [116], M. Rescigno [133a], S. Resconi [90a], B. Resende [137], P. Reznicek [99], R. Rezvani [94], R. Richter [100], E. Richter-Was [38b], M. Ridel [79], P. Rieck [16], M. Rijssenbeek [149], A. Rimoldi [120a,120b], L. Rinaldi [20a], R.R. Rios [40], E. Ritsch [61], I. Riu [12], G. Rivoltella [90a,90b], F. Rizatdinova [113], E. Rizvi [75], S.H. Robertson [86,j], A. Robichaud-Veronneau [119], D. Robinson [28], J.E.M. Robinson [83], A. Robson [53], J.G. Rocha de Lima [107], C. Roda [123a,123b], D. Roda Dos Santos [126], L. Rodrigues [30], A. Roe [54], S. Roe [30], O. Røhne [118], S. Rolli [162], A. Romaniouk [97], M. Romano [20a,20b], G. Romeo [27], E. Romero Adam [168], N. Rompotis [139], L. Roos [79], E. Ros [168], S. Rosati [133a], K. Rosbach [49], A. Rose [150], M. Rose [76], P.L. Rosendahl [14], O. Rosenthal [142], V. Rossetti [12], E. Rossi [133a,133b], L.P. Rossi [50a], R. Rosten [139], M. Rotaru [26a], I. Roth [173], J. Rothberg [139], D. Rousseau [116], C.R. Royon [137], A. Rozanov [84], Y. Rozen [153], X. Ruan [146c], F. Rubbo [12], I. Rubinskiy [42], N. Ruckstuhl [106], V.I. Rud [98], C. Rudolph [44], M.S. Rudolph [159], F. Rühr [7], A. Ruiz-Martinez [63], L. Rumyantsev [64], Z. Rurikova [48], N.A. Rusakovich [64], A. Ruschke [99], J.P. Rutherfoord [7], N. Ruthmann [48], P. Ruzicka [126], Y.F. Ryabov [122], M. Rybar [128], G. Rybkin [116], N.C. Ryder [119], A.F. Saavedra [151], A. Saddique [3], I. Sadeh [154], H.F-W. Sadrozinski [138], R. Sadykov [64], F. Safai Tehrani [133a], H. Sakamoto [156], G. Salamanna [75], A. Salamon [134a], M. Saleem [112], D. Salek [30], D. Salihagic [100], A. Salnikov [144], J. Salt [168], B.M. Salvachua Ferrando [6], D. Salvatore [37a,37b], F. Salvatore [150], A. Salvucci [105], A. Salzburger [30], D. Sampsonidis [155], A. Sanchez [103a,103b], J. Sánchez [168], V. Sanchez Martinez [168], H. Sandaker [14], H.G. Sander [82], M.P. Sanders [99], M. Sandhoff [176], T. Sandoval [28], C. Sandoval [163], R. Sandstroem [100], D.P.C. Sankey [130], A. Sansoni [47], C. Santoni [34], R. Santonico [134a,134b], H. Santos [125a], I. Santoyo Castillo [150], K. Sapp [124], A. Sapronov [64], J.G. Saraiva [125a], T. Sarangi [174], E. Sarkisyan-Grinbaum [8], B. Sarrazin [21], F. Sarri [123a,123b], G. Sartisohn [176], O. Sasaki [65], Y. Sasaki [156], N. Sasao [67], I. Satsounkevitch [91], G. Sauvage [5,*], E. Sauvan [5], J.B. Sauvan [116], P. Savard [159,e], V. Savinov [124], D.O. Savu [30], C. Sawyer [119], L. Sawyer [78,l], D.H. Saxon [53], J. Saxon [121], C. Sbarra [20a], A. Sbrizzi [3], T. Scanlon [30], D.A. Scannicchio [164], M. Scarcella [151], J. Schaarschmidt [116], P. Schacht [100], D. Schaefer [121], A. Schaelicke [46], S. Schaepe [21], S. Schaetzel [58b], U. Schäfer [82], A.C. Schaffer [116], D. Schaile [99], R.D. Schamberger [149], V. Scharf [58a], V.A. Schegelsky [122], D. Scheirich [88], M. Schernau [164], M.I. Scherzer [35], C. Schiavi [50a,50b], J. Schieck [99], C. Schillo [48], M. Schioppa [37a,37b], S. Schlenker [30], E. Schmidt [48], K. Schmieden [21], C. Schmitt [82], C. Schmitt [99], S. Schmitt [58b], B. Schneider [17], Y.J. Schnellbach [73], U. Schnoor [44], L. Schoeffel [137], A. Schoening [58b], A.L.S. Schorlemmer [54], M. Schott [82], D. Schouten [160a], J. Schovancova [126], M. Schram [86], C. Schroeder [82], N. Schroer [58c], N. Schuh [82], M.J. Schultens [21], H.-C. Schultz-Coulon [58a], H. Schulz [16], M. Schumacher [48], B.A. Schumm [138], Ph. Schune [137], A. Schwartzman [144], Ph. Schwegler [100], Ph. Schwemling [137], R. Schwienhorst [89], J. Schwindling [137], T. Schwindt [21], M. Schwoerer [5], F.G. Sciacca [17], E. Scifo [116], G. Sciolla [23], W.G. Scott [130], F. Scutti [21], J. Searcy [88], G. Sedov [42], E. Sedykh [122], S.C. Seidel [104], A. Seiden [138], F. Seifert [44], J.M. Seixas [24a], G. Sekhniaidze [103a], S.J. Sekula [40], K.E. Selbach [46], D.M. Seliverstov [122], G. Sellers [73], M. Seman [145b], N. Semprini-Cesari [20a,20b], C. Serfon [30], L. Serin [116], L. Serkin [54], T. Serre [84], R. Seuster [160a], H. Severini [112], F. Sforza [100], A. Sfyrla [30], E. Shabalina [54], M. Shamim [115], L.Y. Shan [33a], J.T. Shank [22], Q.T. Shao [87], M. Shapiro [15], P.B. Shatalov [96], K. Shaw [165a,165c], P. Sherwood [77], S. Shimizu [66], M. Shimojima [101], T. Shin [56], M. Shiyakova [64], A. Shmeleva [95], M.J. Shochet [31],

D. Short [119], S. Shrestha [63], E. Shulga [97], M.A. Shupe [7], S. Shushkevich [42], P. Sicho [126], D. Sidorov [113], A. Sidoti [133a], F. Siegert [48], Dj. Sijacki [13a], O. Silbert [173], J. Silva [125a], Y. Silver [154], D. Silverstein [144], S.B. Silverstein [147a], V. Simak [127], O. Simard [5], Lj. Simic [13a], S. Simion [116], E. Simioni [82], B. Simmons [77], R. Simoniello [90a,90b], M. Simonyan [36], P. Sinervo [159], N.B. Sinev [115], V. Sipica [142], G. Siragusa [175], A. Sircar [78], A.N. Sisakyan [64,*], S.Yu. Sivoklokov [98], J. Sjölin [147a,147b], T.B. Sjursen [14], L.A. Skinnari [15], H.P. Skottowe [57], K.Yu. Skovpen [108], P. Skubic [112], M. Slater [18], T. Slavicek [127], K. Sliwa [162], V. Smakhtin [173], B.H. Smart [46], L. Smestad [118], S.Yu. Smirnov [97], Y. Smirnov [97], L.N. Smirnova [98,ak], O. Smirnova [80], K.M. Smith [53], M. Smizanska [71], K. Smolek [127], A.A. Snesarev [95], G. Snidero [75], J. Snow [112], S. Snyder [25], R. Sobie [170,j], J. Sodomka [127], A. Soffer [154], D.A. Soh [152,w], C.A. Solans [30], M. Solar [127], J. Solc [127], E.Yu. Soldatov [97], U. Soldevila [168], E. Solfaroli Camillocci [133a,133b], A.A. Solodkov [129], O.V. Solovyanov [129], V. Solovyev [122], N. Soni [1], A. Sood [15], V. Sopko [127], B. Sopko [127], M. Sosebee [8], R. Soualah [165a,165c], P. Soueid [94], A.M. Soukharev [108], D. South [42], S. Spagnolo [72a,72b], F. Spanò [76], W.R. Spearman [57], R. Spighi [20a], G. Spigo [30], M. Spousta [128,al], T. Spreitzer [159], B. Spurlock [8], R.D. St. Denis [53], J. Stahlman [121], R. Stamen [58a], E. Stanecka [39], R.W. Stanek [6], C. Stanescu [135a], M. Stanescu-Bellu [42], M.M. Stanitzki [42], S. Stapnes [118], E.A. Starchenko [129], J. Stark [55], P. Staroba [126], P. Starovoitov [42], R. Staszewski [39], A. Staude [99], P. Stavina [145a,*], G. Steele [53], P. Steinbach [44], P. Steinberg [25], I. Stekl [127], B. Stelzer [143], H.J. Stelzer [89], O. Stelzer-Chilton [160a], H. Stenzel [52], S. Stern [100], G.A. Stewart [30], J.A. Stillings [21], M.C. Stockton [86], M. Stoebe [86], K. Stoerig [48], G. Stoicea [26a], S. Stonjek [100], A.R. Stradling [8], A. Straessner [44], J. Strandberg [148], S. Strandberg [147a,147b], A. Strandlie [118], E. Strauss [144], M. Strauss [112], P. Strizenec [145b], R. Ströhmer [175], D.M. Strom [115], R. Stroynowski [40], B. Stugu [14], I. Stumer [25,*], J. Stupak [149], P. Sturm [176], N.A. Styles [42], D. Su [144], HS. Subramania [3], R. Subramaniam [78], A. Succurro [12], Y. Sugaya [117], C. Suhr [107], M. Suk [127], V.V. Sulin [95], S. Sultansoy [4c], T. Sumida [67], X. Sun [55], J.E. Sundermann [48], K. Suruliz [140], G. Susinno [37a,37b], M.R. Sutton [150], Y. Suzuki [65], M. Svatos [126], S. Swedish [169], M. Swiatlowski [144], I. Sykora [145a], T. Sykora [128], D. Ta [106], K. Tackmann [42], A. Taffard [164], R. Tafirout [160a], N. Taiblum [154], Y. Takahashi [102], H. Takai [25], R. Takashima [68], H. Takeda [66], T. Takeshita [141], Y. Takubo [65], M. Talby [84], A.A. Talyshev [108,g], J.Y.C. Tam [175], M.C. Tamsett [78,am], K.G. Tan [87], J. Tanaka [156], R. Tanaka [116], S. Tanaka [132], S. Tanaka [65], A.J. Tanasijczuk [143], K. Tani [66], N. Tannoury [84], S. Tapprogge [82], S. Tarem [153], F. Tarrade [29], G.F. Tartarelli [90a], P. Tas [128], M. Tasevsky [126], T. Tashiro [67], E. Tassi [37a,37b], A. Tavares Delgado [125a], Y. Tayalati [136d], C. Taylor [77], F.E. Taylor [93], G.N. Taylor [87], W. Taylor [160b], M. Teinturier [116], F.A. Teischinger [30], M. Teixeira Dias Castanheira [75], P. Teixeira-Dias [76], K.K. Temming [48], H. Ten Kate [30], P.K. Teng [152], S. Terada [65], K. Terashi [156], J. Terron [81], M. Testa [47], R.J. Teuscher [159,j], J. Therhaag [21], T. Theveneaux-Pelzer [34], S. Thoma [48], J.P. Thomas [18], E.N. Thompson [35], P.D. Thompson [18], P.D. Thompson [159], A.S. Thompson [53], L.A. Thomsen [36], E. Thomson [121], M. Thomson [28], W.M. Thong [87], R.P. Thun [88,*], F. Tian [35], M.J. Tibbetts [15], T. Tic [126], V.O. Tikhomirov [95], Yu.A. Tikhonov [108,g], S. Timoshenko [97], E. Tiouchichine [84], P. Tipton [177], S. Tisserant [84], T. Todorov [5], S. Todorova-Nova [128], B. Toggerson [164], J. Tojo [69], S. Tokár [145a], K. Tokushuku [65], K. Tollefson [89], L. Tomlinson [83], M. Tomoto [102], L. Tompkins [31], K. Toms [104], A. Tonoyan [14], C. Topfel [17], N.D. Topilin [64], E. Torrence [115], H. Torres [79], E. Torró Pastor [168], J. Toth [84,ag], F. Touchard [84], D.R. Tovey [140], H.L. Tran [116], T. Trefzger [175], L. Tremblet [30], A. Tricoli [30], I.M. Trigger [160a], S. Trincaz-Duvoid [79], M.F. Tripiana [70], N. Triplett [25], W. Trischuk [159], B. Trocmé [55], C. Troncon [90a], M. Trottier-McDonald [143], M. Trovatelli [135a,135b], P. True [89], M. Trzebinski [39], A. Trzupek [39], C. Tsarouchas [30], J.C-L. Tseng [119], P.V. Tsiareshka [91], D. Tsionou [137], G. Tsipolitis [10], S. Tsiskaridze [12], V. Tsiskaridze [48], E.G. Tskhadadze [51a], I.I. Tsukerman [96], V. Tsulaia [15], J.-W. Tsung [21], S. Tsuno [65], D. Tsybychev [149], A. Tua [140], A. Tudorache [26a], V. Tudorache [26a], J.M. Tuggle [31], A.N. Tuna [121], S. Turchikhin [98,ak], D. Turecek [127], I. Turk Cakir [4d], R. Turra [90a,90b], P.M. Tuts [35], A. Tykhonov [74],

M. Tylmad [147a,147b], M. Tyndel [130], K. Uchida [21], I. Ueda [156], R. Ueno [29], M. Ughetto [84], M. Ugland [14], M. Uhlenbrock [21], F. Ukegawa [161], G. Unal [30], A. Undrus [25], G. Unel [164], F.C. Ungaro [48], Y. Unno [65], D. Urbaniec [35], P. Urquijo [21], G. Usai [8], A. Usanova [61], L. Vacavant [84], V. Vacek [127], B. Vachon [86], S. Vahsen [15], N. Valencic [106], S. Valentinetti [20a,20b], A. Valero [168], L. Valery [34], S. Valkar [128], E. Valladolid Gallego [168], S. Vallecorsa [49], J.A. Valls Ferrer [168], R. Van Berg [121], P.C. Van Der Deijl [106], R. van der Geer [106], H. van der Graaf [106], R. Van Der Leeuw [106], D. van der Ster [30], N. van Eldik [30], P. van Gemmeren [6], J. Van Nieuwkoop [143], I. van Vulpen [106], M. Vanadia [100], W. Vandelli [30], A. Vaniachine [6], P. Vankov [42], F. Vannucci [79], R. Vari [133a], E.W. Varnes [7], T. Varol [85], D. Varouchas [15], A. Vartapetian [8], K.E. Varvell [151], V.I. Vassilakopoulos [56], F. Vazeille [34], T. Vazquez Schroeder [54], J. Veatch [7], F. Veloso [125a], S. Veneziano [133a], A. Ventura [72a,72b], D. Ventura [85], M. Venturi [48], N. Venturi [159], V. Vercesi [120a], M. Verducci [139], W. Verkerke [106], J.C. Vermeulen [106], A. Vest [44], M.C. Vetterli [143,e], I. Vichou [166], T. Vickey [146c,an], O.E. Vickey Boeriu [146c], G.H.A. Viehhauser [119], S. Viel [169], R. Vigne [30], M. Villa [20a,20b], M. Villaplana Perez [168], E. Vilucchi [47], M.G. Vincter [29], V.B. Vinogradov [64], J. Virzi [15], O. Vitells [173], M. Viti [42], I. Vivarelli [48], F. Vives Vaque [3], S. Vlachos [10], D. Vladoiu [99], M. Vlasak [127], A. Vogel [21], P. Vokac [127], G. Volpi [47], M. Volpi [87], G. Volpini [90a], H. von der Schmitt [100], H. von Radziewski [48], E. von Toerne [21], V. Vorobel [128], M. Vos [168], R. Voss [30], J.H. Vossebeld [73], N. Vranjes [137], M. Vranjes Milosavljevic [106], V. Vrba [126], M. Vreeswijk [106], T. Vu Anh [48], R. Vuillermet [30], I. Vukotic [31], Z. Vykydal [127], W. Wagner [176], P. Wagner [21], S. Wahrmund [44], J. Wakabayashi [102], S. Walch [88], J. Walder [71], R. Walker [99], W. Walkowiak [142], R. Wall [177], P. Waller [73], B. Walsh [177], C. Wang [45], H. Wang [174], H. Wang [40], J. Wang [152], J. Wang [33a], K. Wang [86], R. Wang [104], S.M. Wang [152], T. Wang [21], X. Wang [177], A. Warburton [86], C.P. Ward [28], D.R. Wardrope [77], M. Warsinsky [48], A. Washbrook [46], C. Wasicki [42], I. Watanabe [66], P.M. Watkins [18], A.T. Watson [18], I.J. Watson [151], M.F. Watson [18], G. Watts [139], S. Watts [83], A.T. Waugh [151], B.M. Waugh [77], S. Webb [83], M.S. Weber [17], J.S. Webster [31], A.R. Weidberg [119], P. Weigell [100], J. Weingarten [54], C. Weiser [48], H. Weits [106], P.S. Wells [30], T. Wenaus [25], D. Wendland [16], Z. Weng [152,w], T. Wengler [30], S. Wenig [30], N. Wermes [21], M. Werner [48], P. Werner [30], M. Werth [164], M. Wessels [58a], J. Wetter [162], K. Whalen [29], A. White [8], M.J. White [87], R. White [32b], S. White [123a,123b], D. Whiteson [164], D. Whittington [60], D. Wicke [176], F.J. Wickens [130], W. Wiedenmann [174], M. Wielers [80,d], P. Wienemann [21], C. Wiglesworth [36], L.A.M. Wiik-Fuchs [21], P.A. Wijeratne [77], A. Wildauer [100], M.A. Wildt [42,t], I. Wilhelm [128], H.G. Wilkens [30], J.Z. Will [99], E. Williams [35], H.H. Williams [121], S. Williams [28], W. Willis [35,*], S. Willocq [85], J.A. Wilson [18], A. Wilson [88], I. Wingerter-Seez [5], S. Winkelmann [48], F. Winklmeier [30], M. Wittgen [144], T. Wittig [43], J. Wittkowski [99], S.J. Wollstadt [82], M.W. Wolter [39], H. Wolters [125a,h], W.C. Wong [41], G. Wooden [88], B.K. Wosiek [39], J. Wotschack [30], M.J. Woudstra [83], K.W. Wozniak [39], K. Wraight [53], M. Wright [53], B. Wrona [73], S.L. Wu [174], X. Wu [49], Y. Wu [88], E. Wulf [35], T.R. Wyatt [83], B.M. Wynne [46], S. Xella [36], M. Xiao [137], C. Xu [33b,ab], D. Xu [33a], L. Xu [33b,ao], B. Yabsley [151], S. Yacoob [146b,ap], M. Yamada [65], H. Yamaguchi [156], Y. Yamaguchi [156], A. Yamamoto [65], K. Yamamoto [63], S. Yamamoto [156], T. Yamamura [156], T. Yamanaka [156], K. Yamauchi [102], Y. Yamazaki [66], Z. Yan [22], H. Yang [33e], H. Yang [174], U.K. Yang [83], Y. Yang [110], Z. Yang [147a,147b], S. Yanush [92], L. Yao [33a], Y. Yasu [65], E. Yatsenko [42], K.H. Yau Wong [21], J. Ye [40], S. Ye [25], A.L. Yen [57], E. Yildirim [42], M. Yilmaz [4b], R. Yoosoofmiya [124], K. Yorita [172], R. Yoshida [6], K. Yoshihara [156], C. Young [144], C.J.S. Young [119], S. Youssef [22], D.R. Yu [15], J. Yu [8], J. Yu [113], L. Yuan [66], A. Yurkewicz [107], B. Zabinski [39], R. Zaidan [62], A.M. Zaitsev [129,ac], S. Zambito [23], L. Zanello [133a,133b], D. Zanzi [100], A. Zaytsev [25], C. Zeitnitz [176], M. Zeman [127], A. Zemla [39], O. Zenin [129], T. Ženiš [145a], D. Zerwas [116], G. Zevi della Porta [57], D. Zhang [88], H. Zhang [89], J. Zhang [6], L. Zhang [152], X. Zhang [33d], Z. Zhang [116], Z. Zhao [33b], A. Zhemchugov [64], J. Zhong [119], B. Zhou [88], N. Zhou [164], C.G. Zhu [33d], H. Zhu [42], J. Zhu [88], Y. Zhu [33b],

X. Zhuang [33a], A. Zibell [99], D. Zieminska [60], N.I. Zimin [64], C. Zimmermann [82], R. Zimmermann [21], S. Zimmermann [21], S. Zimmermann [48], Z. Zinonos [123a,123b], M. Ziolkowski [142], R. Zitoun [5], L. Živković [35], G. Zobernig [174], A. Zoccoli [20a,20b], M. zur Nedden [16], G. Zurzolo [103a,103b], V. Zutshi [107], L. Zwalinski [30]

[1] School of Chemistry and Physics, University of Adelaide, Adelaide, Australia
[2] Physics Department, SUNY Albany, Albany, NY, United States
[3] Department of Physics, University of Alberta, Edmonton, AB, Canada
[4] [(a)] Department of Physics, Ankara University, Ankara; [(b)] Department of Physics, Gazi University, Ankara; [(c)] Division of Physics, TOBB University of Economics and Technology, Ankara; [(d)] Turkish Atomic Energy Authority, Ankara, Turkey
[5] LAPP, CNRS/IN2P3 and Université de Savoie, Annecy-le-Vieux, France
[6] High Energy Physics Division, Argonne National Laboratory, Argonne, IL, United States
[7] Department of Physics, University of Arizona, Tucson, AZ, United States
[8] Department of Physics, The University of Texas at Arlington, Arlington, TX, United States
[9] Physics Department, University of Athens, Athens, Greece
[10] Physics Department, National Technical University of Athens, Zografou, Greece
[11] Institute of Physics, Azerbaijan Academy of Sciences, Baku, Azerbaijan
[12] Institut de Física d'Altes Energies and Departament de Física de la Universitat Autònoma de Barcelona, Barcelona, Spain
[13] [(a)] Institute of Physics, University of Belgrade, Belgrade; [(b)] Vinca Institute of Nuclear Sciences, University of Belgrade, Belgrade, Serbia
[14] Department for Physics and Technology, University of Bergen, Bergen, Norway
[15] Physics Division, Lawrence Berkeley National Laboratory and University of California, Berkeley, CA, United States
[16] Department of Physics, Humboldt University, Berlin, Germany
[17] Albert Einstein Center for Fundamental Physics and Laboratory for High Energy Physics, University of Bern, Bern, Switzerland
[18] School of Physics and Astronomy, University of Birmingham, Birmingham, United Kingdom
[19] [(a)] Department of Physics, Bogazici University, Istanbul; [(b)] Department of Physics, Dogus University, Istanbul; [(c)] Department of Physics Engineering, Gaziantep University, Gaziantep, Turkey
[20] [(a)] INFN Sezione di Bologna; [(b)] Dipartimento di Fisica e Astronomia, Università di Bologna, Bologna, Italy
[21] Physikalisches Institut, University of Bonn, Bonn, Germany
[22] Department of Physics, Boston University, Boston, MA, United States
[23] Department of Physics, Brandeis University, Waltham, MA, United States
[24] [(a)] Universidade Federal do Rio De Janeiro COPPE/EE/IF, Rio de Janeiro; [(b)] Federal University of Juiz de Fora (UFJF), Juiz de Fora; [(c)] Federal University of Sao Joao del Rei (UFSJ), Sao Joao del Rei; [(d)] Instituto de Fisica, Universidade de Sao Paulo, Sao Paulo, Brazil
[25] Physics Department, Brookhaven National Laboratory, Upton, NY, United States
[26] [(a)] National Institute of Physics and Nuclear Engineering, Bucharest; [(b)] National Institute for Research and Development of Isotopic and Molecular Technologies, Physics Department, Cluj Napoca; [(c)] University Politehnica Bucharest, Bucharest; [(d)] West University in Timisoara, Timisoara, Romania
[27] Departamento de Física, Universidad de Buenos Aires, Buenos Aires, Argentina
[28] Cavendish Laboratory, University of Cambridge, Cambridge, United Kingdom
[29] Department of Physics, Carleton University, Ottawa, ON, Canada
[30] CERN, Geneva, Switzerland
[31] Enrico Fermi Institute, University of Chicago, Chicago, IL, United States
[32] [(a)] Departamento de Física, Pontificia Universidad Católica de Chile, Santiago; [(b)] Departamento de Física, Universidad Técnica Federico Santa María, Valparaíso, Chile
[33] [(a)] Institute of High Energy Physics, Chinese Academy of Sciences, Beijing; [(b)] Department of Modern Physics, University of Science and Technology of China, Anhui; [(c)] Department of Physics, Nanjing University, Jiangsu; [(d)] School of Physics, Shandong University, Shandong; [(e)] Physics Department, Shanghai Jiao Tong University, Shanghai, China
[34] Laboratoire de Physique Corpusculaire, Clermont Université and Université Blaise Pascal and CNRS/IN2P3, Clermont-Ferrand, France
[35] Nevis Laboratory, Columbia University, Irvington, NY, United States
[36] Niels Bohr Institute, University of Copenhagen, Kobenhavn, Denmark
[37] [(a)] INFN Gruppo Collegato di Cosenza; [(b)] Dipartimento di Fisica, Università della Calabria, Rende, Italy
[38] [(a)] AGH University of Science and Technology, Faculty of Physics and Applied Computer Science, Krakow; [(b)] Marian Smoluchowski Institute of Physics, Jagiellonian University, Krakow, Poland
[39] The Henryk Niewodniczanski Institute of Nuclear Physics, Polish Academy of Sciences, Krakow, Poland
[40] Physics Department, Southern Methodist University, Dallas, TX, United States
[41] Physics Department, University of Texas at Dallas, Richardson, TX, United States
[42] DESY, Hamburg and Zeuthen, Germany
[43] Institut für Experimentelle Physik IV, Technische Universität Dortmund, Dortmund, Germany
[44] Institut für Kern- und Teilchenphysik, Technische Universität Dresden, Dresden, Germany
[45] Department of Physics, Duke University, Durham, NC, United States
[46] SUPA – School of Physics and Astronomy, University of Edinburgh, Edinburgh, United Kingdom
[47] INFN Laboratori Nazionali di Frascati, Frascati, Italy
[48] Fakultät für Mathematik und Physik, Albert-Ludwigs-Universität, Freiburg, Germany
[49] Section de Physique, Université de Genève, Geneva, Switzerland
[50] [(a)] INFN Sezione di Genova; [(b)] Dipartimento di Fisica, Università di Genova, Genova, Italy
[51] [(a)] E. Andronikashvili Institute of Physics, Iv. Javakhishvili Tbilisi State University, Tbilisi; [(b)] High Energy Physics Institute, Tbilisi State University, Tbilisi, Georgia
[52] II Physikalisches Institut, Justus-Liebig-Universität Giessen, Giessen, Germany
[53] SUPA – School of Physics and Astronomy, University of Glasgow, Glasgow, United Kingdom
[54] II Physikalisches Institut, Georg-August-Universität, Göttingen, Germany
[55] Laboratoire de Physique Subatomique et de Cosmologie, Université Joseph Fourier and CNRS/IN2P3 and Institut National Polytechnique de Grenoble, Grenoble, France
[56] Department of Physics, Hampton University, Hampton, VA, United States
[57] Laboratory for Particle Physics and Cosmology, Harvard University, Cambridge, MA, United States
[58] [(a)] Kirchhoff-Institut für Physik, Ruprecht-Karls-Universität Heidelberg, Heidelberg; [(b)] Physikalisches Institut, Ruprecht-Karls-Universität Heidelberg, Heidelberg; [(c)] ZITI Institut für technische Informatik, Ruprecht-Karls-Universität Heidelberg, Mannheim, Germany
[59] Faculty of Applied Information Science, Hiroshima Institute of Technology, Hiroshima, Japan
[60] Department of Physics, Indiana University, Bloomington, IN, United States

[61] Institut für Astro- und Teilchenphysik, Leopold-Franzens-Universität, Innsbruck, Austria
[62] University of Iowa, Iowa City, IA, United States
[63] Department of Physics and Astronomy, Iowa State University, Ames, IA, United States
[64] Joint Institute for Nuclear Research, JINR Dubna, Dubna, Russia
[65] KEK, High Energy Accelerator Research Organization, Tsukuba, Japan
[66] Graduate School of Science, Kobe University, Kobe, Japan
[67] Faculty of Science, Kyoto University, Kyoto, Japan
[68] Kyoto University of Education, Kyoto, Japan
[69] Department of Physics, Kyushu University, Fukuoka, Japan
[70] Instituto de Física La Plata, Universidad Nacional de La Plata and CONICET, La Plata, Argentina
[71] Physics Department, Lancaster University, Lancaster, United Kingdom
[72] [(a)] INFN Sezione di Lecce; [(b)] Dipartimento di Matematica e Fisica, Università del Salento, Lecce, Italy
[73] Oliver Lodge Laboratory, University of Liverpool, Liverpool, United Kingdom
[74] Department of Physics, Jožef Stefan Institute and University of Ljubljana, Ljubljana, Slovenia
[75] School of Physics and Astronomy, Queen Mary University of London, London, United Kingdom
[76] Department of Physics, Royal Holloway University of London, Surrey, United Kingdom
[77] Department of Physics and Astronomy, University College London, London, United Kingdom
[78] Louisiana Tech University, Ruston, LA, United States
[79] Laboratoire de Physique Nucléaire et de Hautes Energies, UPMC and Université Paris-Diderot and CNRS/IN2P3, Paris, France
[80] Fysiska institutionen, Lunds universitet, Lund, Sweden
[81] Departamento de Fisica Teorica C-15, Universidad Autonoma de Madrid, Madrid, Spain
[82] Institut für Physik, Universität Mainz, Mainz, Germany
[83] School of Physics and Astronomy, University of Manchester, Manchester, United Kingdom
[84] CPPM, Aix-Marseille Université and CNRS/IN2P3, Marseille, France
[85] Department of Physics, University of Massachusetts, Amherst, MA, United States
[86] Department of Physics, McGill University, Montreal, QC, Canada
[87] School of Physics, University of Melbourne, Victoria, Australia
[88] Department of Physics, The University of Michigan, Ann Arbor, MI, United States
[89] Department of Physics and Astronomy, Michigan State University, East Lansing, MI, United States
[90] [(a)] INFN Sezione di Milano; [(b)] Dipartimento di Fisica, Università di Milano, Milano, Italy
[91] B.I. Stepanov Institute of Physics, National Academy of Sciences of Belarus, Minsk, Belarus
[92] National Scientific and Educational Centre for Particle and High Energy Physics, Minsk, Belarus
[93] Department of Physics, Massachusetts Institute of Technology, Cambridge, MA, United States
[94] Group of Particle Physics, University of Montreal, Montreal, QC, Canada
[95] P.N. Lebedev Institute of Physics, Academy of Sciences, Moscow, Russia
[96] Institute for Theoretical and Experimental Physics (ITEP), Moscow, Russia
[97] Moscow Engineering and Physics Institute (MEPhI), Moscow, Russia
[98] D.V. Skobeltsyn Institute of Nuclear Physics, M.V. Lomonosov Moscow State University, Moscow, Russia
[99] Fakultät für Physik, Ludwig-Maximilians-Universität München, München, Germany
[100] Max-Planck-Institut für Physik (Werner-Heisenberg-Institut), München, Germany
[101] Nagasaki Institute of Applied Science, Nagasaki, Japan
[102] Graduate School of Science and Kobayashi–Maskawa Institute, Nagoya University, Nagoya, Japan
[103] [(a)] INFN Sezione di Napoli; [(b)] Dipartimento di Scienze Fisiche, Università di Napoli, Napoli, Italy
[104] Department of Physics and Astronomy, University of New Mexico, Albuquerque, NM, United States
[105] Institute for Mathematics, Astrophysics and Particle Physics, Radboud University Nijmegen/Nikhef, Nijmegen, Netherlands
[106] Nikhef National Institute for Subatomic Physics and University of Amsterdam, Amsterdam, Netherlands
[107] Department of Physics, Northern Illinois University, DeKalb, IL, United States
[108] Budker Institute of Nuclear Physics, SB RAS, Novosibirsk, Russia
[109] Department of Physics, New York University, New York, NY, United States
[110] Ohio State University, Columbus, OH, United States
[111] Faculty of Science, Okayama University, Okayama, Japan
[112] Homer L. Dodge Department of Physics and Astronomy, University of Oklahoma, Norman, OK, United States
[113] Department of Physics, Oklahoma State University, Stillwater, OK, United States
[114] Palacký University, RCPTM, Olomouc, Czech Republic
[115] Center for High Energy Physics, University of Oregon, Eugene, OR, United States
[116] LAL, Université Paris-Sud and CNRS/IN2P3, Orsay, France
[117] Graduate School of Science, Osaka University, Osaka, Japan
[118] Department of Physics, University of Oslo, Oslo, Norway
[119] Department of Physics, Oxford University, Oxford, United Kingdom
[120] [(a)] INFN Sezione di Pavia; [(b)] Dipartimento di Fisica, Università di Pavia, Pavia, Italy
[121] Department of Physics, University of Pennsylvania, Philadelphia, PA, United States
[122] Petersburg Nuclear Physics Institute, Gatchina, Russia
[123] [(a)] INFN Sezione di Pisa; [(b)] Dipartimento di Fisica E. Fermi, Università di Pisa, Pisa, Italy
[124] Department of Physics and Astronomy, University of Pittsburgh, Pittsburgh, PA, United States
[125] [(a)] Laboratorio de Instrumentacao e Fisica Experimental de Particulas – LIP, Lisboa, Portugal; [(b)] Departamento de Fisica Teorica y del Cosmos and CAFPE, Universidad de Granada, Granada, Spain
[126] Institute of Physics, Academy of Sciences of the Czech Republic, Praha, Czech Republic
[127] Czech Technical University in Prague, Praha, Czech Republic
[128] Faculty of Mathematics and Physics, Charles University in Prague, Praha, Czech Republic
[129] State Research Center Institute for High Energy Physics, Protvino, Russia
[130] Particle Physics Department, Rutherford Appleton Laboratory, Didcot, United Kingdom
[131] Physics Department, University of Regina, Regina, SK, Canada
[132] Ritsumeikan University, Kusatsu, Shiga, Japan
[133] [(a)] INFN Sezione di Roma I; [(b)] Dipartimento di Fisica, Università La Sapienza, Roma, Italy
[134] [(a)] INFN Sezione di Roma Tor Vergata; [(b)] Dipartimento di Fisica, Università di Roma Tor Vergata, Roma, Italy
[135] [(a)] INFN Sezione di Roma Tre; [(b)] Dipartimento di Matematica e Fisica, Università Roma Tre, Roma, Italy
[136] [(a)] Faculté des Sciences Ain Chock, Réseau Universitaire de Physique des Hautes Energies – Université Hassan II, Casablanca; [(b)] Centre National de l'Energie des Sciences Techniques Nucleaires, Rabat; [(c)] Faculté des Sciences Semlalia, Université Cadi Ayyad, LPHEA, Marrakech; [(d)] Faculté des Sciences, Université Mohamed Premier and LPTPM, Oujda; [(e)] Faculté des sciences, Université Mohammed V-Agdal, Rabat, Morocco

[137] DSM/IRFU (Institut de Recherches sur les Lois Fondamentales de l'Univers), CEA Saclay (Commissariat à l'Energie Atomique et aux Energies Alternatives), Gif-sur-Yvette, France
[138] Santa Cruz Institute for Particle Physics, University of California Santa Cruz, Santa Cruz, CA, United States
[139] Department of Physics, University of Washington, Seattle, WA, United States
[140] Department of Physics and Astronomy, University of Sheffield, Sheffield, United Kingdom
[141] Department of Physics, Shinshu University, Nagano, Japan
[142] Fachbereich Physik, Universität Siegen, Siegen, Germany
[143] Department of Physics, Simon Fraser University, Burnaby, BC, Canada
[144] SLAC National Accelerator Laboratory, Stanford, CA, United States
[145] [(a)] Faculty of Mathematics, Physics & Informatics, Comenius University, Bratislava; [(b)] Department of Subnuclear Physics, Institute of Experimental Physics of the Slovak Academy of Sciences, Kosice, Slovak Republic
[146] [(a)] Department of Physics, University of Cape Town, Cape Town; [(b)] Department of Physics, University of Johannesburg, Johannesburg; [(c)] School of Physics, University of the Witwatersrand, Johannesburg, South Africa
[147] [(a)] Department of Physics, Stockholm University; [(b)] The Oskar Klein Centre, Stockholm, Sweden
[148] Physics Department, Royal Institute of Technology, Stockholm, Sweden
[149] Departments of Physics & Astronomy and Chemistry, Stony Brook University, Stony Brook, NY, United States
[150] Department of Physics and Astronomy, University of Sussex, Brighton, United Kingdom
[151] School of Physics, University of Sydney, Sydney, Australia
[152] Institute of Physics, Academia Sinica, Taipei, Taiwan
[153] Department of Physics, Technion: Israel Institute of Technology, Haifa, Israel
[154] Raymond and Beverly Sackler School of Physics and Astronomy, Tel Aviv University, Tel Aviv, Israel
[155] Department of Physics, Aristotle University of Thessaloniki, Thessaloniki, Greece
[156] International Center for Elementary Particle Physics and Department of Physics, The University of Tokyo, Tokyo, Japan
[157] Graduate School of Science and Technology, Tokyo Metropolitan University, Tokyo, Japan
[158] Department of Physics, Tokyo Institute of Technology, Tokyo, Japan
[159] Department of Physics, University of Toronto, Toronto, ON, Canada
[160] [(a)] TRIUMF, Vancouver, BC; [(b)] Department of Physics and Astronomy, York University, Toronto, ON, Canada
[161] Faculty of Pure and Applied Sciences, University of Tsukuba, Tsukuba, Japan
[162] Department of Physics and Astronomy, Tufts University, Medford, MA, United States
[163] Centro de Investigaciones, Universidad Antonio Narino, Bogota, Colombia
[164] Department of Physics and Astronomy, University of California Irvine, Irvine, CA, United States
[165] [(a)] INFN Gruppo Collegato di Udine; [(b)] ICTP, Trieste; [(c)] Dipartimento di Chimica, Fisica e Ambiente, Università di Udine, Udine, Italy
[166] Department of Physics, University of Illinois, Urbana, IL, United States
[167] Department of Physics and Astronomy, University of Uppsala, Uppsala, Sweden
[168] Instituto de Física Corpuscular (IFIC) and Departamento de Física Atómica, Molecular y Nuclear and Departamento de Ingeniería Electrónica and Instituto de Microelectrónica de Barcelona (IMB-CNM), University of Valencia and CSIC, Valencia, Spain
[169] Department of Physics, University of British Columbia, Vancouver, BC, Canada
[170] Department of Physics and Astronomy, University of Victoria, Victoria, BC, Canada
[171] Department of Physics, University of Warwick, Coventry, United Kingdom
[172] Waseda University, Tokyo, Japan
[173] Department of Particle Physics, The Weizmann Institute of Science, Rehovot, Israel
[174] Department of Physics, University of Wisconsin, Madison, WI, United States
[175] Fakultät für Physik und Astronomie, Julius-Maximilians-Universität, Würzburg, Germany
[176] Fachbereich C Physik, Bergische Universität Wuppertal, Wuppertal, Germany
[177] Department of Physics, Yale University, New Haven, CT, United States
[178] Yerevan Physics Institute, Yerevan, Armenia
[179] Centre de Calcul de l'Institut National de Physique Nucléaire et de Physique des Particules (IN2P3), Villeurbanne, France

[a] Also at Department of Physics, King's College London, London, United Kingdom.
[b] Also at Laboratorio de Instrumentacao e Fisica Experimental de Particulas – LIP, Lisboa, Portugal.
[c] Also at Faculdade de Ciencias and CFNUL, Universidade de Lisboa, Lisboa, Portugal.
[d] Also at Particle Physics Department, Rutherford Appleton Laboratory, Didcot, United Kingdom.
[e] Also at TRIUMF, Vancouver, BC, Canada.
[f] Also at Department of Physics, California State University, Fresno, CA, United States.
[g] Also at Novosibirsk State University, Novosibirsk, Russia.
[h] Also at Department of Physics, University of Coimbra, Coimbra, Portugal.
[i] Also at Università di Napoli Parthenope, Napoli, Italy.
[j] Also at Institute of Particle Physics (IPP), Canada.
[k] Also at Department of Physics, Middle East Technical University, Ankara, Turkey.
[l] Also at Louisiana Tech University, Ruston, LA, United States.
[m] Also at Departamento de Fisica and CEFITEC of Faculdade de Ciencias e Tecnologia, Universidade Nova de Lisboa, Caparica, Portugal.
[n] Also at Department of Physics and Astronomy, Michigan State University, East Lansing, MI, United States.
[o] Also at Department of Financial and Management Engineering, University of the Aegean, Chios, Greece.
[p] Also at Institucio Catalana de Recerca i Estudis Avancats, ICREA, Barcelona, Spain.
[q] Also at Department of Physics, University of Cape Town, Cape Town, South Africa.
[r] Also at Institute of Physics, Azerbaijan Academy of Sciences, Baku, Azerbaijan.
[s] Also at CERN, Geneva, Switzerland.
[t] Also at Institut für Experimentalphysik, Universität Hamburg, Hamburg, Germany.
[u] Also at Manhattan College, New York, NY, United States.
[v] Also at Institute of Physics, Academia Sinica, Taipei, Taiwan.
[w] Also at School of Physics and Engineering, Sun Yat-sen University, Guanzhou, China.
[x] Also at Academia Sinica Grid Computing, Institute of Physics, Academia Sinica, Taipei, Taiwan.
[y] Also at Laboratoire de Physique Nucléaire et de Hautes Energies, UPMC and Université Paris-Diderot and CNRS/IN2P3, Paris, France.
[z] Also at School of Physical Sciences, National Institute of Science Education and Research, Bhubaneswar, India.
[aa] Also at Dipartimento di Fisica, Università La Sapienza, Roma, Italy.
[ab] Also at DSM/IRFU (Institut de Recherches sur les Lois Fondamentales de l'Univers), CEA Saclay (Commissariat à l'Energie Atomique et aux Energies Alternatives), Gif-sur-Yvette, France.

[ac] Also at Moscow Institute of Physics and Technology State University, Dolgoprudny, Russia.
[ad] Also at Section de Physique, Université de Genève, Geneva, Switzerland.
[ae] Also at Departamento de Fisica, Universidade de Minho, Braga, Portugal.
[af] Also at Department of Physics, The University of Texas at Austin, Austin, TX, United States.
[ag] Also at Institute for Particle and Nuclear Physics, Wigner Research Centre for Physics, Budapest, Hungary.
[ah] Also at DESY, Hamburg and Zeuthen, Germany.
[ai] Also at International School for Advanced Studies (SISSA), Trieste, Italy.
[aj] Also at Department of Physics and Astronomy, University of South Carolina, Columbia, SC, United States.
[ak] Also at Faculty of Physics, M.V. Lomonosov Moscow State University, Moscow, Russia.
[al] Also at Nevis Laboratory, Columbia University, Irvington, NY, United States.
[am] Also at Physics Department, Brookhaven National Laboratory, Upton, NY, United States.
[an] Also at Department of Physics, Oxford University, Oxford, United Kingdom.
[ao] Also at Department of Physics, The University of Michigan, Ann Arbor, MI, United States.
[ap] Also at Discipline of Physics, University of KwaZulu-Natal, Durban, South Africa.
[*] Deceased.

計画研究 A01 班

課題名「ヒッグス粒子の発見による素粒子の質量起源の解明」

研究組織

(1)研究代表者
徳宿　克夫（TOKUSHUKU, Katsuo）
高エネルギー加速器研究機構・素粒子原子核研究所・所長
研究者番号：80207547

(2)研究分担者
海野　義信（UNNO, Yoshinobu）
高エネルギー加速器研究機構・その他部局等・名誉教授
研究者番号：40151956

受川　史彦（UKEGAWA, Fumihiko）
筑波大学・数理物質科学研究科・教授
研究者番号：10312795

(3)連携研究者
津野　総司（TSUNO, Soshi）
高エネルギー加速器研究機構・素粒子原子核研究所・研究機関講師
研究者番号：30451834

増渕　達也（MASUBUCHI, Tatsuya）
東京大学・素粒子物理国際研究センター・特任助教
研究者番号：20512148

中村　浩二（NAKAMURA, Koji）
高エネルギー加速器研究機構・素粒子原子核研究所・助教
研究者番号：00554479

原　和彦（HARA, Kazuhiko）
筑波大学・数理物質科学研究科・講師
　研究者番号：20218613

岩崎　博行（IWASAKI, Hiroyuki）　H23-26
高エネルギー加速器研究機構・その他部局等・名誉教授
　研究者番号：40151724

高嶋　隆一（TAKASHIMA, Ryuichi）H23-26
京都教育大学・教育学部・准教授
　研究者番号：60163200

佐藤 構二（SATO, Koji）　H26-27
筑波大学・数理物質科学研究科・講師
　研究者番号：30422190

大川 英希（OKAWA Hideki）　H27
筑波大学・数理物質科学研究科・助教
　研究者番号：10746960

交付決定額

計画研究 A01 班に配分された交付額を表 1 に示す。

表 1. 交付決定額（配分額）　（金額単位：円）

年度	直接経費	間接経費	合計
平成 23 年度	35,800,000	10,740,000	46,540,000
平成 24 年度	41,200,000	12,360,000	53,560,000
平成 25 年度	44,000,000	13,200,000	57,200,000
平成 26 年度	39,900,000	11,970,000	51,870,000
平成 27 年度	31,700,000	9,510,000	41,210,000
総計	192,600,000	57,780,000	250,380,000

研究成果

1．研究開始当初の背景

素粒子物理学の根幹をなす「標準理論」では、ヒッグス機構とよばれる対称性の自発的な破れによって素粒子が質量を獲得すると考えられている。標準理論はクォークとレプトンの力学をよく説明するすぐれた理論であり、この対称性の破れの直接的証拠となるヒッグス粒子の探索を、様々な実験で長期にわたって進めてきたが未発見であった。スイス・CERN 研究所では、世界最高エネルギーでの陽子・陽子衝突を実現できる大型ハドロン衝突型加速器（LHC）が平成 21 年から稼働を開始した。この加速器は、ヒッグス粒子の発見を目的の一つに掲げて建設され、国際協力でアトラス実験が組織され、我々のグループも測定器の建設と実験準備を進めてきた。
標準理論が素粒子の力学を上手く説明する一方で、その範囲を超える現象が観測されている。例えば、神岡実験で確立したニュートリノ振動現象であり、また宇宙の大部分を占める暗黒エネルギーや暗黒物質である。これらは、標準理論を超える我々がまだ理解していない自然の枠組みがあることを示唆している。理論的にも、標準理論の枠内ではヒッグスの質量が摂動論的に不安定であると指摘されていた。このため、ヒッグス粒子を発見すればすべてが解決するというわけではないが、ヒッグス粒子の性質を精査することが、これらの問題点を理解する鍵となると考えられていた。

2．研究の目的

（1）LHC での陽子・陽子衝突実験で、ヒッグス粒子を直接発見し、ゲージ対称性の破れと質量の起源の謎の解明を目指す。
（2）発見したヒッグス粒子が、標準理論の予言するものであるかを精査することで、テラスケールの新しい物理の探索を進める。現在の真空の性質と宇宙の初期に起った相転移を理解し、宇宙がどのように進化してきたかの知見を得て新しい宇宙像を開拓する。
（3）ヒッグス粒子の精査にあたっては、高エネルギーで生成される短寿命の粒子の同定が重要になり、このためにはより精度の高い飛跡検出器を導入することが望ましい。平成 29 年あるいは 31 年頃にアトラス測定器の飛跡検出器入れ替えが検討されているので、この研究では、新しいピクセル型飛跡検出器の開発を物理の研究と並行して進め、将来のエネルギーフロンティア実験へ

の道筋を立てる。

3．研究の方法

平成 21 年から始まった LHC での陽子・陽子衝突実験を、ほぼ研究期間の 5 年間を通して遂行する。取得したデータからヒッグス粒子の探索を進め、発見できた場合はその性質を精査する。研究開始時点での予定では、重心系エネルギー7TeV での衝突実験から始め、平成 24 年までに積分ルミノシティ 5-7fb^{-1}が得られると想定していた。その後平成 25 年に LHC の運転を 1 年停止し、衝突エネルギーを設計値の 14TeV に上げるための準備を行い、平成 26－27 年の実験では設計値である重心系エネルギー14TeV で、合わせて 100fb^{-1}近く収集すると想定した。標準理論のヒッグス粒子が存在するのであれば、研究期間に発見を迅速に確認した上で、その性質の測定ができる。もし、ヒッグス粒子の徴候がない場合には、標準理論の考え方が違っていることになり、素粒子物理学に大きな波紋を投じることになると考えていた。
測定器開発では、n-in-p 型のピクセル検出器を製作し、外国のグループが開発した読み出しチップと接合（バンプボンディング）をして、性能を調べる。特に放射線損傷の影響を定量的に研究し、バイアス電圧の安定供給の性能などを調べる。狭いバンプボンディング間隔（50μm あるいはそれ以下）での安定接合技術をつかむ。

ピクセルセンサーのデザインでは、将来のヒッグス精密測定のためにどのようなサイズのピクセルが必要かを、シミュレーションをもとに検討を行う。アトラス実験グループ全体の動きを見ながら、次世代検出器の必要パラメータ（ピクセルの形状、厚さなど）の検討をする。

4．研究成果

実際の LHC の運転は、目標をはるかに超えて積分ルミノシティを得ることができ、既に平成 23 年中に 7TeV で 5fb^{-1}、平成 24 年には重心エネルギーを 8TeV に上げて 23fb^{-1} のデータを収集できた。

これらのデータにより、平成 24 年 7 月に質量 125GeV 付近に新粒子を発見し、その崩壊のパターンからこれがヒッグス粒子であることを確信した（論文[5,6],図 1)。LHC スケジュールは 8TeV 運転での実験を当初の予定より少し長くし、このエネルギーでの衝突データから、ヒッグスの性質をできるだけ引き出す方向で予定を修正した。その分平成 25-26 年度は加速器と測定器の改修のための長期シャットダウンとすることになった。これにより、以下に述べるようにヒッグス粒子に関して多くの知見を研究期間内に得ることができた。

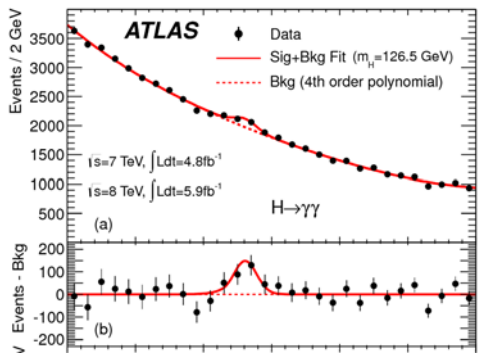

図 1：ヒッグス粒子が 2 光子に崩壊することを示した実験結果（論文[6]）

平成 27 年度に重心系 13TeV で実験を再開した。加速器の調整が時間かかったが 3fb^{-1} のデータを収集でき、高いエネルギー衝突エネルギーで、125GeV のヒッグス粒子の確認を進めるとともに、さらに別のヒッグス粒子が存在しないかという探索を開始することができた。加速器・実験装置の面では長期シャットダウンでの改善により、今後の 3 年間でこのエネルギーで 100fb^{-1} のデータをためられる見通しとともに、ヒッグス粒子の性質の精査に関しても解析手法等を期間内に確立することができた。

まず得られた全体像を簡単にまとめると、発見した新粒子は、標準理論の予想するヒッグス粒子の性質と非常によくあっており、測定精度の範囲内では有意なずれは見られていない、そして複数のヒッグス粒子があるかどうかの探索も進めているが有意な発見はなかった、という結論になる。

本研究の大きな成果はヒッグス機構を伴う標準理論の正しさを確立した。

ヒッグス粒子の質量は約 125GeV で、様々な崩壊モードを観測できる領域であり、これによって、ヒッグス粒子の精査が、標準理論を超える理論を構築するための重要な実験手段となることを示した。

一方で、これまで標準理論を超える現象を理解する直接的なヒントはヒッグス粒子の測定及び、新粒子の探索のどちらからも得られておらず、研究当初考えていたよりはテラスケールの物理を理解することが単純でないことがわかった。標準理論が非常に高いエネルギーまで成り立つという可能性もあり、これまでの素粒子論・宇宙論的に大きな見直しを迫る実験的結果を与えた。

以下にこれまでにわかったヒッグス粒子の性質をより詳しく述べる。新粒子の発見後、この粒子のスピン・ パリティの解析を行い、ヒッグス粒子と同じで、スピンはゼロで正のパリティとほぼ確定し、この時点でヒッグス粒子であると確信した（論文[4]）。

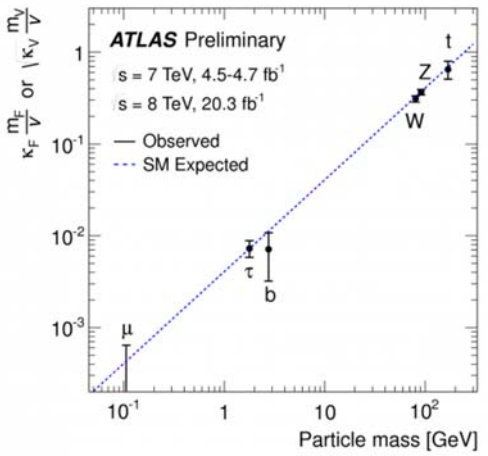

図 2：ヒッグス粒子と他の粒子との結合の強さのまとめ

全データを使った各崩壊モードでの解析と、超対称性粒子等で予想される他のヒッグス粒子の探索が進み、ほぼすべての解析が終了し論文として発表した。W,Z 及び γ への崩壊は確立し、フェルミ粒子への崩壊に関しては τ への崩壊が 4.5σ で観測できている（論文[3]）。一方で μ への崩壊は τ と同レベルでは観測されないことは確定できており、この粒子が二つのレプトン（二つの世代）を区別することを実験的に示し、ここでもヒッグス粒子の特質を明らかにした。

ボトムへの崩壊や、トップクォークとの随伴生成の探索も進めている。これらのモードでは、標準理論のヒッグスと無矛盾であることを示すことができている。各粒子への崩壊をまとめたのを図 2 に示し、各粒子との結合の強さが質量と強く関係するという、ヒッグス粒子の特徴をよく捉えている。

もう一つの LHC 実験である CMS 実験との共同解析も進み、0.2%精度の質量測定を達成した（論文[2]）。結合定数に関する共同研究も暫定結果を平成 25 年の国際会議で発表し、平成 28 年 6 月に論文投稿した。

発見したヒッグス粒子に加えて、新たな荷電及び中性ヒッグス粒子の探索も行った。残念ながら新しい粒子の兆候は得られていない。13TeV の衝突データで二光子への崩壊モードで 750GeV 付近にやや超過がみられることを、平成 27 年 12 月のセミナーで公表し、大きな反響をよんでいるが、まだ統計的には有意でなく、これが今後のデータ収集と共にどうなるかが楽しみである。

ピクセル検出器の開発では、半導体素子自体の開発とともに、放射線照射テスト時の被ばくを軽減するために自動化するシステムを構築するなど、開発環境を大きく改善した。

バイアス電圧の配線レイアウト等を替えた試作機を作りテストを繰り返すことで、

放射線損傷後 飛跡検出効率が落ちる原因を究明し、放射線損傷後でも検出効率 99%を維持している事をビームテストで確認した（論文[1],図 3）。

また、薄型センサー／薄型読み出しチップ（厚み150/150 μm)の接合（バンプボンディング）においても、バンプ接合不良を発生させる原因を特定し安定した接合技術を確立した。
これらにより、将来の高輝度 LHC でのヒックス粒子の精密測定に導入するピクセル検出器の開発を基本的な部分を完了することができた。

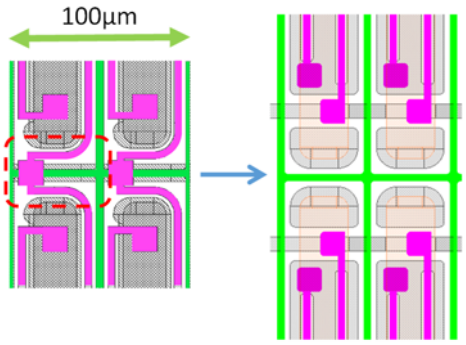

図 3　ピクセル検出器の改善前後のレイアウト。右の赤線で囲んだ部分が放射線照射後に検出効率が落ちることを実験的に示し、改善した。

5．主な発表論文等

（研究代表者、研究分担者及び連携研究者には下線）
〔雑誌論文〕（計　90 件）
(主な物のみ掲載：ATLAS　Collaboration の論文には、研究代表者・研究分担者・連携研究者をすべて含む)

[1]Development of n^{+}-in-p planar pixel sensors for very high radiation environments, designed to retain high efficiency after irradiation.”; Y. Unno et al. to be published in Nucl. Instru. Meth. A (2016), DOI:10.1016/j.nima.2016.04.039

[2]“Combined measurement of the Higgs Boson mass in pp collisions at √s =7 and 8 TeV with the ATLAS and CMS experiments”; (The ATLAS and CMS Collaboration) Phys. Rev. Lett. 114 (2015) 191803, DOI:10.1103/PhysRevLett.114.191803

[3] “Evidence for the Higgs-boson Yukawa coupling to tau leptons with the ATLAS detector”; G Aad et al. (ATLAS Collaboration) JHEP 04 (2015) 117, DOI:10.1007/JHEP04(2015)117

[4] “Evidence for the spin-0 nature of the Higgs boson using ATLAS data”; G Aad et al. (ATLAS Collaboration) Phys. Lett. B738 (2013) 120-144, DOI:10.1016/j.physletb.2013.08.026

[5] “A Massive Particle Consistent with the Standard Model Higgs Boson observed with the ATLAS Detector at the Large Hadron Collider” ; G.Aad, et al.(ATLAS Collaboration), Science

338 (2012) 1232005 査読有、DOI:10.1126/science.1232005

[6] “Observation of a new particle in the search for the Standard Model Higgs boson with the ATLAS detector at the LHC” ; G.Aad et al. (ATLAS Collaboration) Phys. Lett. B716 (2012) 1-29, DOI:10.1016/j.physletb.2012.08.020

〔学会発表〕（計　77 件）
（主なもののみ掲載）
[1]“New ATLAS Higgs physics results”, T. Masubuchi, CERN Seminar 7/Oct/2015, CERN, Geneva(Switzerland).

[2]“Planar p-type pixel and strip sensors development for HL-LHC in Japan” Y. Unno, 9th "Trento" Workshop on Advanced Silicon Radiation Detectors, 26-28/Feb/2014, Genova(Italy).

[3]“Mass measurement in H->gamma gamma in ATLAS”, Y. Yamaguchi, Higgs Hunting 2013, 25/July/2013 LAL, Paris(France).

[4]“Searches for a Light Higgs boson at ATLAS” T. Masubuchi, Physics at LHC (pLHC2012), 4-9/June/2012 TRIUMF, Vancouver(Canada).

〔図書〕（計　3 件）
（主なもののみ掲載）
[1] Y.Unno et al. Elsevier B.V. “Proceedings, 6th International Workshop on Semiconductor Pixel Detectors for Particles and Imaging (PIXEL2012) Inawashiro, Japan, September 3-7, 2012”、2013 年、総ページ数 334 ページ

〔産業財産権〕
○出願状況（計　0 件）

○取得状況（計 0 件）

〔その他〕
[1]「宇宙の物質はどのようにできたのか　素粒子から生命へ」, 日本物理学会 (編集) (徳宿克夫、他), 日本評論社。　（日本物理学会主催の一般シンポジウム講演（2013 年 8 月））

[2]一般向け講演会「科学と音楽の饗宴」2012 年 11 月 10 日（茨城県つくば市ノバホール）「質量の起源とヒッグス粒子—理論と実験の成果」　小林誠、徳宿克夫　約 800 名が参加

[3]一般向け講演会「世紀の大ニュース『ヒッグス粒子』って何？」2012 年 9 月 1 日（茨城県つくば市筑波大学春日キャンパス春日講堂）　金信弘，原和彦　約 200 名が参加

ホームページ等
ATLAS 実験日本グループのＷｅｂ
http://atlas.kek.jp/index.html
ATLAS 実験の一般向けＷｅｂ（英語）
http://atlas.ch/
ATLAS 実験の物理成果のＷｅｂ（英語）
https://twiki.cern.ch/twiki/bin/view/AtlasPublic

主要論文別刷

[1] “Measurements of the Higgs boson production and decay rates and constraints on its couplings from a combined ATLAS and CMS analysis of the LHC pp collision data at $\sqrt{s}$ = 7 and 8 TeV”, The ATLAS and CMS collaborations, Journal of High Energy Physics, JHEP08 (2016) 045.

[2] “Development of n^+-in-p planar pixel sensors for extremely high radiation environments, designed to retain high efficiency after irradiation”, Y. Unno et al., Nuclear Instruments and Methods in Physics Research A831(2016)122–132.

[3] “Combined Measurement of the Higgs Boson Mass in pp Collisions at $\sqrt{s}$ = 7 and 8 TeV with the ATLAS and CMS Experiments”, G. Aad et al., the ATLAS and CMS collaborations, Physical Review Letters PRL 114, 191803 (2015).

[4] “Evidence for the Higgs-boson Yukawa coupling to tau leptons with the ATLAS detector”, The ATLAS collaboration, Journal of High Energy Physics JHEP04 (2015) 117.

[5] “Evidence for the spin-0 nature of the Higgs boson using ATLAS data”, The ATLAS collaboration, Physics Letters B 726 (2013) 120-144.
(総括班主要論文別刷に掲示)

Published for SISSA by Springer

Received: *June 8, 2016*
Accepted: *July 18, 2016*
Published: *August 5, 2016*

Measurements of the Higgs boson production and decay rates and constraints on its couplings from a combined ATLAS and CMS analysis of the LHC pp collision data at $\sqrt{s} = 7$ and 8 TeV

The ATLAS and CMS collaborations

E-mail: atlas.publications@cern.ch, cms-publication-committee-chair@cern.ch

Abstract: Combined ATLAS and CMS measurements of the Higgs boson production and decay rates, as well as constraints on its couplings to vector bosons and fermions, are presented. The combination is based on the analysis of five production processes, namely gluon fusion, vector boson fusion, and associated production with a W or a Z boson or a pair of top quarks, and of the six decay modes $H \to ZZ, WW$, $\gamma\gamma, \tau\tau, bb$, and $\mu\mu$. All results are reported assuming a value of 125.09 GeV for the Higgs boson mass, the result of the combined measurement by the ATLAS and CMS experiments. The analysis uses the CERN LHC proton-proton collision data recorded by the ATLAS and CMS experiments in 2011 and 2012, corresponding to integrated luminosities per experiment of approximately $5\,\mathrm{fb}^{-1}$ at $\sqrt{s} = 7$ TeV and $20\,\mathrm{fb}^{-1}$ at $\sqrt{s} = 8$ TeV. The Higgs boson production and decay rates measured by the two experiments are combined within the context of three generic parameterisations: two based on cross sections and branching fractions, and one on ratios of coupling modifiers. Several interpretations of the measurements with more model-dependent parameterisations are also given. The combined signal yield relative to the Standard Model prediction is measured to be 1.09 ± 0.11. The combined measurements lead to observed significances for the vector boson fusion production process and for the $H \to \tau\tau$ decay of 5.4 and 5.5 standard deviations, respectively. The data are consistent with the Standard Model predictions for all parameterisations considered.

Keywords: Hadron-Hadron scattering (experiments), Higgs physics

ArXiv ePrint: 1606.02266

Open Access, Copyright CERN,
for the benefit of the ATLAS-CMS Collaboration.
Article funded by SCOAP^3.

doi:10.1007/JHEP08(2016)045

JHEP08(2016)045

Contents

1 Introduction **1**

2 Higgs boson phenomenology and interpretation framework **2**
- 2.1 Higgs boson production and decay 3
- 2.2 Signal Monte Carlo simulation 5
- 2.3 Signal strengths 7
- 2.4 Coupling modifiers 8

3 Combination procedure and experimental inputs **11**
- 3.1 Overview of input analyses 12
- 3.2 Statistical treatment 13
- 3.3 Treatment of systematic uncertainties 14
- 3.4 Analysis modifications for the combination 17

4 Generic parameterisations of experimental results **18**
- 4.1 Parameterisations using cross sections and branching fractions 20
  - 4.1.1 Parameterisation using independent products of cross sections and branching fractions 20
  - 4.1.2 Parameterisation using ratios of cross sections and branching fractions 23
- 4.2 Parameterisation using ratios of coupling modifiers 30

5 Measurements of signal strengths **30**
- 5.1 Global signal strength 32
- 5.2 Signal strengths of individual production processes and decay channels 33
- 5.3 Boson- and fermion-mediated production processes 36
- 5.4 Search for mass-degenerate states with different coupling structures 38

6 Constraints on Higgs boson couplings **41**
- 6.1 Parameterisations allowing contributions from BSM particles in loops and in decays 42
- 6.2 Parameterisation assuming SM structure of the loops and no BSM decays 42
- 6.3 Parameterisations related to the fermion sector 46
  - 6.3.1 Probing the up- and down-type fermion symmetry 47
  - 6.3.2 Probing the lepton and quark symmetry 48
- 6.4 Fermion and vector boson couplings 49

7 Summary **56**

A Correlation matrices **59**

B Breakdown of systematic uncertainties **59**

JHEP08(2016)045

C Likelihood scans for coupling modifier parameterisations **66**

The ATLAS collaboration **76**

The CMS collaboration **93**

1 Introduction

The elucidation of the mechanism of electroweak (EW) symmetry breaking has been one of the main goals driving the design of the ATLAS [1] and CMS [2] experiments at the CERN LHC. In the Standard Model (SM) of particle physics [3–6], the breaking of the symmetry is achieved through the introduction of a complex doublet scalar field, leading to the prediction of the existence of one physical neutral scalar particle, commonly known as the Higgs boson [7–12]. Through Yukawa interactions, the Higgs scalar field can also account for fermion masses [4, 13]. While the SM does not predict the value of the Higgs boson mass, m_H, the production cross sections and decay branching fractions (B) of the Higgs boson can be precisely calculated once its mass is known.

In 2012, the ATLAS and CMS Collaborations reported the observation of a new particle with a mass of approximately 125 GeV and Higgs-boson-like properties [14–16]. Subsequent results from both experiments, summarised in refs. [17–21], established that all measurements of the properties of the new particle, including its spin, CP properties, and coupling strengths to SM particles, are consistent within the uncertainties with those expected for the SM Higgs boson. ATLAS and CMS have published a combined measurement of the Higgs boson mass [22], using LHC Run 1 data for the $H \to \gamma\gamma$ and $H \to ZZ$ channels, where Run 1 indicates the LHC proton-proton (pp) data taking period in 2011 and 2012 at centre-of-mass energies $\sqrt{s} = 7$ and 8 TeV. The combined mass measurement is

$$m_H = 125.09 \pm 0.21(\text{stat.}) \pm 0.11(\text{syst.})\ \text{GeV}, \tag{1.1}$$

where the total uncertainty is dominated by the statistical component. The Higgs boson mass is assumed to be $m_H = 125.09$ GeV for all analyses presented in this paper.

This paper reports the first ATLAS and CMS combined measurements of the Higgs boson production and decay rates as well as constraints on its couplings to SM particles. These measurements yield the most precise and comprehensive experimental results on these quantities to date. The main production processes studied are gluon fusion (ggF), vector boson fusion (VBF), and associated production with vector bosons (WH and ZH, denoted together as VH) or a pair of top quarks (ttH). The decay channels considered are those to bosons, $H \to ZZ$, $H \to WW$, and $H \to \gamma\gamma$; and to fermions, $H \to \tau\tau$, $H \to bb$, and $H \to \mu\mu$. Throughout this paper, Z and W indicate both real and virtual vector bosons, and no distinction is made between particles and antiparticles.

All analyses used in the combination are based on the complete Run 1 collision data collected by the ATLAS and CMS experiments. These data correspond to integrated luminosities per experiment of approximately 5 fb^{-1} at $\sqrt{s} =$ 7 TeV (recorded in 2011)

JHEP08(2016)045

and 20 fb^{-1} at $\sqrt{s}$ = 8 TeV (recorded in 2012). The results of the ATLAS and CMS individual combinations based on the Run 1 data are reported in refs. [17, 18].

Unless otherwise stated, in this paper it is assumed, as in refs. [17, 18], that the particle under study is a single SM-like Higgs boson state, i.e. a CP-even scalar particle with the tensor coupling structure of the SM for its interactions. The Higgs boson width, predicted to be approximately 4 MeV in the SM, is assumed to be small enough that the narrow-width approximation is valid and that the Higgs boson production and decay mechanisms can be factorised. These assumptions are corroborated by tests of the spin and CP properties of the Higgs boson [20, 21] and by studies of its width [18, 23–25]. The Higgs boson signal modelling is based on the hypothesis of a SM Higgs boson in terms of its production and decay kinematics. Measurements of differential production cross sections [26–29] support these assumptions within the current statistical uncertainties. The inherent model dependence related to these hypotheses applies to all results presented here; the reliance on this model has a negligible impact for small deviations from the SM, but could be important for significant deviations from the SM predictions.

The results presented here for each experiment separately are slightly different from those reported in refs. [17, 18]. Some small variations with respect to the earlier results are related to a different choice for the value of the Higgs boson mass. Other differences arise from minor modifications to the signal parameterisation and to the treatment of systematic uncertainties. These modifications are introduced in the present analysis to allow a fully consistent and correlated treatment of the dominant theoretical uncertainties in the signal modelling between the two experiments.

This paper is organised as described below. Section 2 briefly reviews the theoretical calculations of Higgs boson production and decay, and the modelling of the Higgs boson signal in Monte Carlo (MC) simulation; it also introduces the formalisms of signal strengths and coupling modifiers used for the interpretation of the data. Section 3 gives an overview of the analyses included in this combination, describes the statistical procedure used, together with the treatment of systematic uncertainties, and summarises modifications to the individual analyses for the combination. Section 4 describes the parameterisation of the measured signal yields in generic terms and reports the results using three distinct parameterisations. Section 5 compares the measured Higgs boson yields to the SM predictions for different production processes and decay modes, and reports the results of a test for the possible presence of multiple mass-degenerate states. Section 6 studies the couplings of the Higgs boson to probe for possible deviations from the SM predictions, using various assumptions motivated in many cases by beyond the SM (BSM) physics scenarios. Finally, section 7 presents a summary of the results.

2 Higgs boson phenomenology and interpretation framework

This section briefly reviews Higgs boson phenomenology and introduces the most important aspects of the interpretation framework used to combine the measurements and to assess their compatibility with the SM predictions. The dominant production processes and major decay modes of the SM Higgs boson, along with the theoretical predictions for the cross sections and branching fractions, are presented. The main features of the MC generators used to simulate Higgs boson production and decay in each experiment are described. Finally,

JHEP08(2016)045

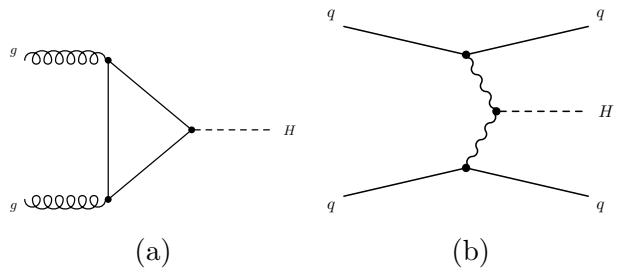

Figure 1. Examples of leading-order Feynman diagrams for Higgs boson production via the (a) ggF and (b) VBF production processes.

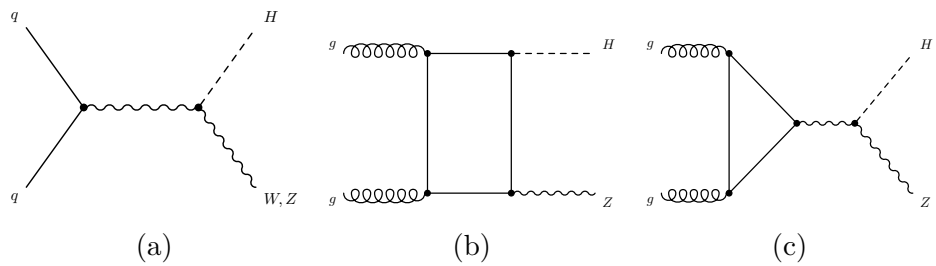

Figure 2. Examples of leading-order Feynman diagrams for Higgs boson production via the (a) $qq \to VH$ and (b, c) $gg \to ZH$ production processes.

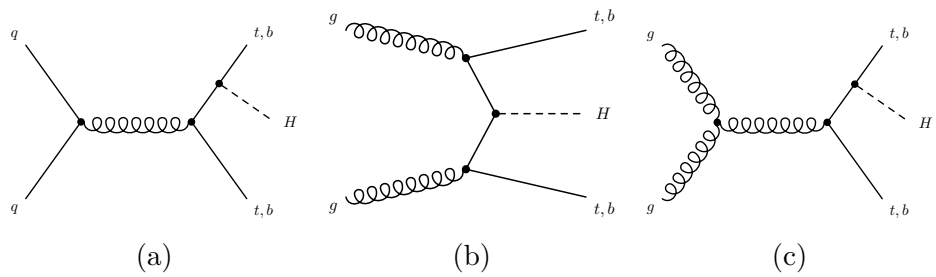

Figure 3. Examples of leading-order Feynman diagrams for Higgs boson production via the $qq/gg \to ttH$ and $qq/gg \to bbH$ processes.

the formalisms of two widely used frameworks, based on signal strengths and coupling modifiers, for the interpretation of the Higgs boson measurements at the LHC, are introduced.

2.1 Higgs boson production and decay

In the SM, Higgs boson production at the LHC mainly occurs through the following processes, listed in order of decreasing cross section at the Run 1 centre-of-mass energies:

- gluon fusion production $gg \to H$ (figure 1a);
- vector boson fusion production $qq \to qqH$ (figure 1b);
- associated production with a W boson, $qq \to WH$ (figure 2a), or with a Z boson, $pp \to ZH$, including a small ($\sim 8\%$) but less precisely known contribution from $gg \to ZH$ ($ggZH$) (figures 2a, 2b, and 2c);
- associated production with a pair of top quarks, $qq, gg \to ttH$ (figure 3).

JHEP08(2016)045

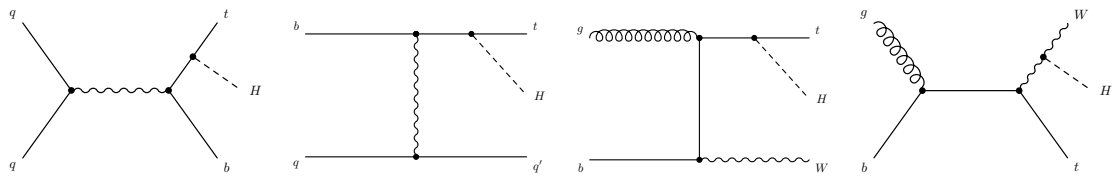

(a) (b) (c) (d)

Figure 4. Examples of leading-order Feynman diagrams for Higgs boson production in association with a single top quark via the (a, b) tHq and (c, d) tHW production processes.

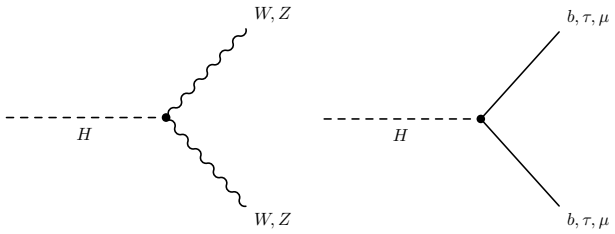

(a) (b)

Figure 5. Examples of leading-order Feynman diagrams for Higgs boson decays (a) to W and Z bosons and (b) to fermions.

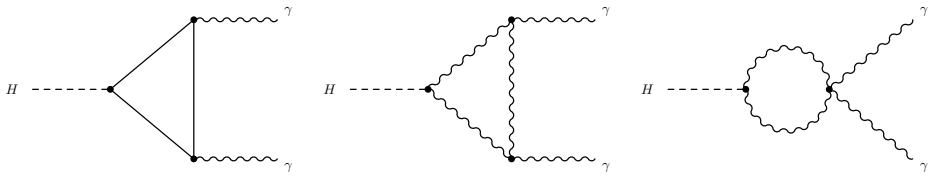

(a) (b) (c)

Figure 6. Examples of leading-order Feynman diagrams for Higgs boson decays to a pair of photons.

Other less important production processes in the SM, which are not the target of a direct search but are included in the combination, are $qq, gg \to bbH$ (bbH), also shown in figure 3, and production in association with a single top quark (tH), shown in figure 4. The latter process proceeds through either $qq/qb \to tHb/tHq'$ (tHq) (figures 4a and 4b) or $gb \to tHW$ (tHW) (figures 4c and 4d) production.

Examples of leading-order (LO) Feynman diagrams for the Higgs boson decays considered in the combination are shown in figures 5 and 6. The decays to W and Z bosons (figure 5a) and to fermions (figure 5b) proceed through tree-level processes whereas the $H \to \gamma\gamma$ decay is mediated by W boson or heavy quark loops (figure 6).

The SM Higgs boson production cross sections and decay branching fractions are taken from refs. [30–32] and are based on the extensive theoretical work documented in refs. [33–77]. The inclusive cross sections and branching fractions for the most important production and decay modes are summarised with their overall uncertainties in tables 1 and 2 for a

JHEP08(2016)045

Production process	Cross section [pb] $\sqrt{s} = 7$ TeV	$\sqrt{s} = 8$ TeV	Order of calculation
ggF	15.0 ± 1.6	19.2 ± 2.0	NNLO(QCD) + NLO(EW)
VBF	1.22 ± 0.03	1.58 ± 0.04	NLO(QCD+EW) + APPROX. NNLO(QCD)
WH	0.577 ± 0.016	0.703 ± 0.018	NNLO(QCD) + NLO(EW)
ZH	0.334 ± 0.013	0.414 ± 0.016	NNLO(QCD) + NLO(EW)
$[ggZH]$	0.023 ± 0.007	0.032 ± 0.010	NLO(QCD)
ttH	0.086 ± 0.009	0.129 ± 0.014	NLO(QCD)
tH	0.012 ± 0.001	0.018 ± 0.001	NLO(QCD)
bbH	0.156 ± 0.021	0.203 ± 0.028	5FS NNLO(QCD) + 4FS NLO(QCD)
Total	17.4 ± 1.6	22.3 ± 2.0	

Table 1. Standard Model predictions for the Higgs boson production cross sections together with their theoretical uncertainties. The value of the Higgs boson mass is assumed to be $m_H = 125.09$ GeV and the predictions are obtained by linear interpolation between those at 125.0 and 125.1 GeV from ref. [32] except for the tH cross section, which is taken from ref. [78]. The $pp \to ZH$ cross section, calculated at NNLO in QCD, includes both the quark-initiated, i.e. $qq \to ZH$ or $qg \to ZH$, and the $gg \to ZH$ contributions. The contribution from the $gg \to ZH$ production process, calculated only at NLO in QCD and indicated separately in brackets, is given with a theoretical uncertainty assumed to be 30%. The uncertainties in the cross sections are evaluated as the sum in quadrature of the uncertainties resulting from variations of the QCD scales, parton distribution functions, and α_s. The uncertainty in the tH cross section is calculated following the procedure of ref. [79]. The order of the theoretical calculations for the different production processes is also indicated. In the case of bbH production, the values are given for the mixture of five-flavour (5FS) and four-flavour (4FS) schemes recommended in ref. [74].

Higgs boson mass $m_H = 125.09$ GeV. The SM predictions of the branching fractions for $H \to gg, cc$, and $Z\gamma$ are included for completeness. Although not an explicit part of the searches, they impact the combination through their contributions to the Higgs boson width and, at a small level, through their expected yields in some of the individual analyses.

2.2 Signal Monte Carlo simulation

All analyses use MC samples to model the Higgs boson production and decay kinematics, to estimate the acceptance and selection efficiency, and to describe the distributions of variables used to discriminate between signal and background events. The main features of the signal simulation are summarised here; for more details, the reader is referred to the individual publications:

- for ggF and VBF production, both experiments use POWHEG [80–84] for the event generation, interfaced either to PYTHIA8 [85] (ATLAS) or PYTHIA6.4 [86] (CMS) for the simulation of the parton shower, the hadronisation, and the underlying event, collectively referred to in the following as UEPS.

JHEP08(2016)045

Decay mode	Branching fraction [%]
$H \to bb$	57.5 ± 1.9
$H \to WW$	21.6 ± 0.9
$H \to gg$	8.56 ± 0.86
$H \to \tau\tau$	6.30 ± 0.36
$H \to cc$	2.90 ± 0.35
$H \to ZZ$	2.67 ± 0.11
$H \to \gamma\gamma$	0.228 ± 0.011
$H \to Z\gamma$	0.155 ± 0.014
$H \to \mu\mu$	0.022 ± 0.001

Table 2. Standard Model predictions for the decay branching fractions of a Higgs boson with a mass of 125.09 GeV, together with their uncertainties [32]. Included are decay modes that are either directly studied or important for the combination because of their contributions to the Higgs boson width.

- for WH and ZH production, both experiments use LO event generators for all quark-initiated processes, namely Pythia8 in ATLAS and Pythia6.4 in CMS. A prominent exception is the $H \to bb$ decay channel, for which ATLAS uses Powheg interfaced to Pythia8, while CMS uses Powheg interfaced to Herwig++ [87]. The $ggZH$ production process is also considered, even though it contributes only approximately 8% of the total ZH production cross section in the SM, because it is expected to yield a relatively hard Higgs boson transverse momentum (p_{T}) spectrum, enhancing the contribution to the most sensitive categories in the $H \to bb$ decay channel. Both experiments therefore include $ggZH$ production as a separate process in the VH analysis for the $H \to bb$ channel. ATLAS uses Powheg interfaced to Pythia8 while CMS uses a reweighted $qq \to ZH$ sample to model the $ggZH$ contribution, including next-to-leading order (NLO) effects [66, 67]. For the other channels, the contribution from this process is only accounted for as a correction to the overall signal cross section.

- for ttH production, ATLAS uses the NLO calculation of the HELAC-Oneloop package [88] interfaced to Powheg, often referred to as Powhel [89], while CMS simulates this process with the LO Pythia6.4 program.

- within the SM, the contribution from tH production to analyses searching for ttH production is small, but in certain BSM scenarios it may become large through interference effects (see section 2.4). The tH production processes are simulated in both experiments using MadGraph5_aMC@NLO [79] interfaced to Herwig++ in the case of tHW production, while the tHq production process is simulated using

JHEP08(2016)045

MadGraph [90] interfaced to Pythia8 in ATLAS and MadGraph5_aMC@NLO interfaced to Pythia6.4 in CMS.

- finally, bbH production contributes approximately 1% to the total Higgs boson cross section in the SM. It is studied using Pythia8 in ATLAS and Pythia6.4 and MadGraph5_aMC@NLO in CMS, for the categories most sensitive to this production process in the various channels. Given that the selection efficiencies of bbH production are similar to those of the ggF process, the latter process is used to model the bbH signal for all decay channels, with an approximate correction to account for the difference in overall efficiency.

Table 3 summarises the event generators used by ATLAS and CMS for the $\sqrt{s} = 8\,\text{TeV}$ data analyses. For each production process and decay mode, the cross section and branching fraction used correspond to the higher-order state-of-the-art theoretical calculations, namely the values given in tables 1 and 2.

Furthermore, the p_{T} distribution of the Higgs boson in the ggF process, which in many cases affects categorisation and selection efficiencies, is reweighted to match the HRes2.1 prediction [45–47], which accounts for next-to-next-to-leading-order (NNLO) and next-to-next-to-leading-logarithmic (NNLL) QCD corrections. In addition, the Higgs boson p_{T} spectrum in $gg \to H$ events with two or more jets is reweighted to match the prediction of the Powheg MiNLO H+2-jet generator [91]. This consistent treatment by the two experiments of the most prominent theoretical aspects of Higgs boson production and decay is quite important since all theoretical uncertainties in the various signal processes described in table 3 are treated as correlated for the combination (see section 3). The impact of using different generators for the less sensitive channels is negligible compared to their dominant sources of uncertainty.

2.3 Signal strengths

The signal strength μ, defined as the ratio of the measured Higgs boson rate to its SM prediction, is used to characterise the Higgs boson yields. For a specific production process and decay mode $i \to H \to f$, the signal strengths for the production, μ_i, and for the decay, μ^f, are defined as

$$\mu_i = \frac{\sigma_i}{(\sigma_i)_{\text{SM}}} \quad \text{and} \quad \mu^f = \frac{\text{B}^f}{(\text{B}^f)_{\text{SM}}}. \tag{2.1}$$

Here σ_i ($i = gg\text{F}, \text{VBF}, WH, ZH, ttH$) and B^f ($f = ZZ, WW, \gamma\gamma, \tau\tau, bb, \mu\mu$) are respectively the production cross section for $i \to H$ and the decay branching fraction for $H \to f$. The subscript "SM" refers to their respective SM predictions, so by definition, $\mu_i = 1$ and $\mu^f = 1$ in the SM. Since σ_i and B^f cannot be separated without additional assumptions, only the product of μ_i and μ^f can be measured experimentally, leading to a signal strength μ_i^f for the combined production and decay:

$$\mu_i^f = \frac{\sigma_i \cdot \text{B}^f}{(\sigma_i)_{\text{SM}} \cdot (\text{B}^f)_{\text{SM}}} = \mu_i \cdot \mu^f. \tag{2.2}$$

JHEP08(2016)045

Production process	Event generator	
	ATLAS	CMS
ggF	Powheg [80–84]	Powheg
VBF	Powheg	Powheg
WH	Pythia8 [85]	Pythia6.4 [86]
ZH ($qq \to ZH$ or $qg \to ZH$)	Pythia8	Pythia6.4
$ggZH$ ($gg \to ZH$)	Powheg	See text
ttH	Powhel [88]	Pythia6.4
tHq ($qb \to tHq$)	MadGraph [90]	aMC@NLO [79]
tHW ($gb \to tHW$)	aMC@NLO	aMC@NLO
bbH	Pythia8	Pythia6.4, aMC@NLO

Table 3. Summary of the event generators used by ATLAS and CMS to model the Higgs boson production processes and decay channels at $\sqrt{s} = 8\,\text{TeV}$.

The ATLAS and CMS data are combined and analysed using this signal strength formalism and the results are presented in section 5. For all these signal strength fits, as well as for the generic parameterisations presented in section 4.1, the parameterisations of the expected yields in each analysis category are performed with a set of assumptions, which are needed because some production processes or decay modes, which are not specifically searched for, contribute to other channels. These assumptions are the following: for the production processes, the bbH signal strength is assumed to be the same as for ggF, the tH signal strength is assumed to be the same as for ttH, and the $ggZH$ signal strength is assumed to be the same as for quark-initiated ZH production; for the Higgs boson decays, the $H \to gg$ and $H \to cc$ signal strengths are assumed to be the same as for $H \to bb$ decays, and the $H \to Z\gamma$ signal strength is assumed to be the same as for $H \to \gamma\gamma$ decays.

2.4 Coupling modifiers

Based on a LO-motivated framework [32] (κ-framework), coupling modifiers have been proposed to interpret the LHC data by introducing specific modifications of the Higgs boson couplings related to BSM physics. Within the assumptions already mentioned in section 1, the production and decay of the Higgs boson can be factorised, such that the cross section times branching fraction of an individual channel $\sigma(i \to H \to f)$ contributing to a measured signal yield can be parameterised as:

$$\sigma_i \cdot \mathrm{B}^f = \frac{\sigma_i(\vec{\kappa}) \cdot \Gamma^f(\vec{\kappa})}{\Gamma_H}, \tag{2.3}$$

where Γ_H is the total width of the Higgs boson and Γ^f is the partial width for Higgs boson decay to the final state f. A set of coupling modifiers, $\vec{\kappa}$, is introduced to parameterise

JHEP08(2016)045

possible deviations from the SM predictions of the Higgs boson couplings to SM bosons and fermions. For a given production process or decay mode, denoted "j", a coupling modifier κ_j is defined such that:

$$\kappa_j^2 = \sigma_j/\sigma_j^{\mathrm{SM}} \quad \text{or} \quad \kappa_j^2 = \Gamma^j/\Gamma^j_{\mathrm{SM}}, \tag{2.4}$$

where all κ_j values equal unity in the SM; here, by construction, the SM cross sections and branching fractions include the best available higher-order QCD and EW corrections. This higher-order accuracy is not necessarily preserved for κ_j values different from unity, but the dominant higher-order QCD corrections factorise to a large extent from any rescaling of the coupling strengths and are therefore assumed to remain valid over the entire range of κ_j values considered in this paper. Different production processes and decay modes probe different coupling modifiers, as can be visualised from the Feynman diagrams shown in figures 1–6. Individual coupling modifiers, corresponding to tree-level Higgs boson couplings to the different particles, are introduced, as well as two effective coupling modifiers, κ_g and κ_γ, which describe the loop processes for ggF production and $H \to \gamma\gamma$ decay. This is possible because BSM particles that might be present in these loops are not expected to appreciably change the kinematics of the corresponding process. The $gg \to H$ and $H \to \gamma\gamma$ loop processes can thus be studied, either through these effective coupling modifiers, thereby providing sensitivity to potential BSM particles in the loops, or through the coupling modifiers corresponding to the SM particles. In contrast, the $gg \to ZH$ process, which occurs at LO through box and triangular loop diagrams (figures 2b and 2c), is always taken into account, within the limitations of the framework, by resolving the loop in terms of the corresponding coupling modifiers, κ_Z and κ_t.

Contributions from interference effects between the different diagrams provide some sensitivity to the relative signs of the Higgs boson couplings to different particles. As discussed in section 6.4, such effects are potentially largest for the $H \to \gamma\gamma$ decays, but may also be significant in the case of $ggZH$ and tH production. The ggF production process, when resolved in terms of its SM structure, provides sensitivity, although limited, to the relative signs of κ_t and κ_b through the t–b interference. The relative signs of the coupling modifiers κ_τ and κ_μ with respect to other coupling modifiers are not considered in this paper, since the current sensitivity to possible interference terms is negligible.

As an example of the possible size of such interference effects, the tH cross section is small in the SM, approximately 14% of the ttH cross section, because of destructive interference between diagrams involving the couplings to the W boson and the top quark, as shown in table 4. However, the interference becomes constructive for negative values of the product $\kappa_W \cdot \kappa_t$. In the specific case where $\kappa_W \cdot \kappa_t = -1$, the tHW and tHq cross sections increase by factors of 6 and 13, respectively, so that the tH process displays some sensitivity to the relative sign between the W boson and top quark couplings, despite its small SM cross section.

The relations among the coupling modifiers, the production cross sections σ_i, and partial decay widths Γ^f are derived within this context, as shown in table 4, and are used as a parameterisation to extract the coupling modifiers from the measurements. The coefficients are derived from Higgs production cross sections and decay rates evaluated including the

JHEP08(2016)045

Production	Loops	Interference	Effective scaling factor	Resolved scaling factor
$\sigma(gg\mathrm{F})$	✓	t–b	κ_g^2	$1.06 \cdot \kappa_t^2 + 0.01 \cdot \kappa_b^2 - 0.07 \cdot \kappa_t \kappa_b$
$\sigma(\mathrm{VBF})$	—	—		$0.74 \cdot \kappa_W^2 + 0.26 \cdot \kappa_Z^2$
$\sigma(WH)$	—	—		κ_W^2
$\sigma(qq/qg \to ZH)$	—	—		κ_Z^2
$\sigma(gg \to ZH)$	✓	t–Z		$2.27 \cdot \kappa_Z^2 + 0.37 \cdot \kappa_t^2 - 1.64 \cdot \kappa_Z \kappa_t$
$\sigma(ttH)$	—	—		κ_t^2
$\sigma(gb \to tHW)$	—	t–W		$1.84 \cdot \kappa_t^2 + 1.57 \cdot \kappa_W^2 - 2.41 \cdot \kappa_t \kappa_W$
$\sigma(qq/qb \to tHq)$	—	t–W		$3.40 \cdot \kappa_t^2 + 3.56 \cdot \kappa_W^2 - 5.96 \cdot \kappa_t \kappa_W$
$\sigma(bbH)$	—	—		κ_b^2
Partial decay width				
Γ^{ZZ}	—	—		κ_Z^2
Γ^{WW}	—	—		κ_W^2
$\Gamma^{\gamma\gamma}$	✓	t–W	κ_γ^2	$1.59 \cdot \kappa_W^2 + 0.07 \cdot \kappa_t^2 - 0.66 \cdot \kappa_W \kappa_t$
$\Gamma^{\tau\tau}$	—	—		κ_τ^2
Γ^{bb}	—	—		κ_b^2
$\Gamma^{\mu\mu}$	—	—		κ_μ^2
Total width ($\mathrm{B_{BSM}} = 0$)				
Γ_H	✓	—	κ_H^2	$0.57 \cdot \kappa_b^2 + 0.22 \cdot \kappa_W^2 + 0.09 \cdot \kappa_g^2 +$ $0.06 \cdot \kappa_\tau^2 + 0.03 \cdot \kappa_Z^2 + 0.03 \cdot \kappa_c^2 +$ $0.0023 \cdot \kappa_\gamma^2 + 0.0016 \cdot \kappa_{(Z\gamma)}^2 +$ $0.0001 \cdot \kappa_s^2 + 0.00022 \cdot \kappa_\mu^2$

Table 4. Higgs boson production cross sections σ_i, partial decay widths Γ^f, and total decay width (in the absence of BSM decays) parameterised as a function of the κ coupling modifiers as discussed in the text, including higher-order QCD and EW corrections to the inclusive cross sections and decay partial widths. The coefficients in the expression for Γ_H do not sum exactly to unity because some contributions that are negligible or not relevant to the analyses presented in this paper are not shown.

JHEP08(2016)045

best available higher-order QCD and EW corrections (up to NNLO QCD and NLO EW precision), as indicated in tables 1 and 2. The numerical values are obtained from ref. [32] and are given for $\sqrt{s} = 8$ TeV and $m_H = 125.09$ GeV (they are similar for $\sqrt{s} = 7$ TeV). The current LHC data are insensitive to the coupling modifiers κ_c and κ_s, and have limited sensitivity to κ_μ. Thus, in the following, it is assumed that κ_c varies as κ_t, κ_s as κ_b, and κ_μ as κ_τ. Other coupling modifiers (κ_u, κ_d, and κ_e) are irrelevant for the combination provided they are of order unity. When probing the total width, the partial decay width Γ^{gg} is assumed to vary as κ_g^2. These assumptions are not the same as those described for the signal strength framework in section 2.3, so the two parameterisations are only approximately equivalent. The two sets of assumptions have a negligible impact on the measurements reported here provided that the unmeasured parameters do not deviate strongly from unity.

Changes in the values of the couplings will result in a variation of the Higgs boson width. A new modifier, κ_H, defined as $\kappa_H^2 = \sum_j \mathrm{B}_{\mathrm{SM}}^j \kappa_j^2$ and assumed to be positive without loss of generality, is introduced to characterise this variation. In the case where the SM decays of the Higgs boson are the only ones allowed, the relation $\kappa_H^2 = \Gamma_H/\Gamma_H^{\mathrm{SM}}$ holds. If instead deviations from the SM are introduced in the decays, the width Γ_H can be expressed as:

$$\Gamma_H = \frac{\kappa_H^2 \cdot \Gamma_H^{\mathrm{SM}}}{1 - \mathrm{B}_{\mathrm{BSM}}}, \tag{2.5}$$

where $\mathrm{B}_{\mathrm{BSM}}$ indicates the total branching fraction into BSM decays. Such BSM decays can be of three types: decays into BSM particles that are invisible to the detector because they do not appreciably interact with ordinary matter, decays into BSM particles that are not detected because they produce event topologies that are not searched for, or modifications of the decay branching fractions into SM particles in the case of channels that are not directly measured, such as $H \to cc$. Although direct and indirect experimental constraints on the Higgs boson width exist, they are either model dependent or are not stringent enough to constrain the present fits, and are therefore not included in the combinations. Since Γ_H is not experimentally constrained in a model-independent manner with sufficient precision, only ratios of coupling strengths can be measured in the most generic parameterisation considered in the κ-framework.

3 Combination procedure and experimental inputs

The individual ATLAS and CMS analyses of the Higgs boson production and decay rates are combined using the profile likelihood method described in section 3.2. The combination is based on simultaneous fits to the data from both experiments taking into account the correlations between systematic uncertainties within each experiment and between the two experiments. The analyses included in the combination, the statistical procedure used, the treatment of systematic uncertainties, and the changes made to the analyses for the combination are summarised in this section.

JHEP08(2016)045

3.1 Overview of input analyses

The individual analyses included in the combination were published separately by each experiment. Most of these analyses examine a specific Higgs boson decay mode, with categories related to the various production processes. They are $H \to \gamma\gamma$ [92, 93], $H \to ZZ$ [94, 95], $H \to WW$ [96–98], $H \to \tau\tau$ [99, 100], $H \to bb$ [101, 102], and $H \to \mu\mu$ [103, 104]. The ttH production process was also studied separately [78, 105–108] and the results are included in the combination. The $H \to \mu\mu$ analysis is included in the combination fit only for the measurement of the corresponding decay signal strength reported in section 5.2 and for the specific parameterisation of the coupling analysis described in section 6.2. It provides constraints on the coupling of the Higgs boson to second-generation fermions, but offers no relevant constraints for other parameterisations. The ATLAS [17] and CMS [18] individual combined publications take into account other results, such as upper limits on the $H \to Z\gamma$ decay [109, 110], results on VBF production in the $H \to bb$ decay channel [111], constraints on off-shell Higgs boson production [23, 24], and upper limits on invisible Higgs boson decays [112–114]. These results are not considered further here since they were not included in both combined publications of the individual experiments. In the case of the $H \to bb$ decay mode, the ggF production process is not considered by either experiment because of the overwhelming QCD multijet background.

Almost all input analyses are based on the concept of event categorisation. For each decay mode, events are classified in different categories, based on their kinematic characteristics and their detailed properties. This categorisation increases the sensitivity of the analysis and also allows separation of the different production processes on the basis of exclusive selections that identify the decay products of the particles produced in association with the Higgs boson: W or Z boson decays, VBF jets, and so on. A total of approximately 600 exclusive categories addressing the five production processes explicitly considered are defined for the five main decay channels. The exception is $H \to bb$, for which only the VH and ttH production processes are used in the combination for the reasons stated above.

The signal yield in a category k, $n_{\text{signal}}(k)$, can be expressed as a sum over all possible Higgs boson production processes i, with cross section σ_i, and decay modes f, with branching fraction B^f:

$$\begin{aligned} n_{\text{signal}}(k) &= \mathcal{L}(k) \cdot \sum_i \sum_f \left\{ \sigma_i \cdot A_i^{f,\mathrm{SM}}(k) \cdot \varepsilon_i^f(k) \cdot \mathrm{B}^f \right\} \\ &= \mathcal{L}(k) \cdot \sum_i \sum_f \mu_i \mu^f \left\{ \sigma_i^{\mathrm{SM}} \cdot A_i^{f,\mathrm{SM}}(k) \cdot \varepsilon_i^f(k) \cdot \mathrm{B}_{\mathrm{SM}}^f \right\}, \end{aligned} \tag{3.1}$$

where $\mathcal{L}(k)$ represents the integrated luminosity, $A_i^{f,\mathrm{SM}}(k)$ the detector acceptance assuming SM Higgs boson production and decay, and $\varepsilon_i^f(k)$ the overall selection efficiency for the signal category k. The symbols μ_i and μ^f are the production and decay signal strengths, respectively, defined in section 2.3. As eq. (3.1) shows, the measurements considered in this paper are only sensitive to the products of the cross sections and branching fractions, $\sigma_i \cdot \mathrm{B}^f$.

In the ideal case, each category would only contain signal events from a given production process and decay mode. Most decay modes approach this ideal case, but, in the

JHEP08(2016)045

case of the production processes, the categories are much less pure and there is significant cross-contamination in most channels.

3.2 Statistical treatment

The overall statistical methodology used in the combination to extract the parameters of interest in various parameterisations is the same as that used for the individual ATLAS and CMS combinations, as published in refs. [17, 18]. It was developed by the ATLAS and CMS Collaborations and is described in ref. [115]. Some details of this procedure are important for this combination and are briefly reviewed here.

The statistical treatment of the data is based on the standard LHC data modelling and handling toolkits: RooFit [116], RooStats [117], and HistFactory [118]. The parameters of interest, $\vec{\alpha}$, e.g. signal strengths (μ), coupling modifiers (κ), production cross sections, branching fractions, or ratios of the above quantities, are estimated, together with their corresponding confidence intervals, via the profile likelihood ratio test statistic $\Lambda(\vec{\alpha})$ [119]. The latter depends on one or more parameters of interest, as well as on the nuisance parameters, $\vec{\theta}$, which reflect various experimental or theoretical uncertainties:

$$\Lambda(\vec{\alpha}) = \frac{L\big(\vec{\alpha}\,,\,\hat{\hat{\vec{\theta}}}(\vec{\alpha})\big)}{L(\hat{\vec{\alpha}},\hat{\vec{\theta}})}. \tag{3.2}$$

The likelihood functions in the numerator and denominator of this equation are constructed using products of signal and background probability density functions (pdfs) of the discriminating variables. The pdfs are obtained from simulation for the signal and from both data and simulation for the background, as described in refs. [17, 18]. The vectors $\hat{\vec{\alpha}}$ and $\hat{\vec{\theta}}$ represent the unconditional maximum likelihood estimates of the parameter values, while $\hat{\hat{\vec{\theta}}}$ denotes the conditional maximum likelihood estimate for given values of the parameters of interest $\vec{\alpha}$. Systematic uncertainties and their correlations are a subset of the nuisance parameters $\vec{\theta}$, described by likelihood functions associated with the estimate of the corresponding parameter.

As an example of a specific choice of parameters of interest, the parameterisation considered in section 6.4 assumes that all fermion couplings are scaled by κ_F and all weak vector boson couplings by κ_V. The likelihood ratio is therefore a function of the two parameters of interest, κ_F and κ_V, and the profile likelihood ratio is expressed as:

$$\Lambda(\kappa_F,\kappa_V) = \frac{L\big(\kappa_F,\kappa_V,\hat{\hat{\vec{\theta}}}(\kappa_F,\kappa_V)\big)}{L(\hat{\kappa}_F,\hat{\kappa}_V,\hat{\vec{\theta}})}\,. \tag{3.3}$$

Likelihood fits are performed to determine the parameters of interest and their uncertainties, using the data to obtain the observed values and Asimov data sets to determine the predicted values in the SM. An Asimov data set [119] is a pseudo-data distribution that is equal to the signal plus background prediction for given values of the parameters of interest and of all nuisance parameters, and does not include statistical fluctuations. It is a representative data set of a given parameterisation that yields a result corresponding

JHEP08(2016)045

to the median of an ensemble of pseudo-experiments generated from the same parameterisation. A pre-fit Asimov data set is meant to represent the predictions of the theory, and all parameters are fixed to their estimates prior to the fit to the data.

These fits are rather challenging, involving many parameters of interest and a very large number of nuisance parameters. All the fit results were independently cross-checked to a very high level of precision by ATLAS and CMS, both for the combination and for the individual results. In particular, fine likelihood scans of all the parameters of interest were inspected to verify the convergence and stability of the fits.

For all results presented in this paper, unless otherwise stated, the negative log-likelihood estimator $q(\vec{\alpha}) = -2\ln\Lambda(\vec{\alpha})$ is assumed to follow a χ^2 distribution (asymptotic approximation). The 1σ and 2σ confidence level (CL) intervals for one-dimensional measurements are defined by requiring $q(\alpha_i) = 1$ and $q(\alpha_i) = 4$, respectively. In the case of disjoint intervals, the uncertainties corresponding only to the interval around the best fit value with $q(\alpha_i) < 1$ are also given for some parameterisations. The 68% (95%) confidence level regions for two-dimensional scans are defined at $q(\alpha_i) = 2.30$ (5.99). For the derivation of the upper limit on $\mathrm{B_{BSM}}$ in section 6.1, the test statistic $\tilde{t}(\alpha)$ of ref. [119] is used to account for the constraint $\alpha = \mathrm{B_{BSM}} \geq 0$. This is equivalent to the confidence interval estimation method of ref. [120]. The upper limit at 95% CL corresponds to $\tilde{t}(\alpha) = 3.84$. The p-values, characterising the compatibility of a fit result with a given hypothesis, are likewise computed in the asymptotic approximation.

3.3 Treatment of systematic uncertainties

The treatment of the systematic uncertainties and of their correlations is a crucial aspect of the combination of Higgs boson coupling measurements. The details of the chosen methodology for treating systematic uncertainties, characterised by nuisance parameters, are given in ref. [115]. The combined analysis presented here incorporates approximately 4200 nuisance parameters. A large fraction of these are statistical in nature, i.e. related to the finite size of the simulated samples used to model the expected signals and backgrounds, but are classified as part of the systematic uncertainties, as described below.

Nuisance parameters can be associated with a single analysis category or can be correlated between categories, channels, and/or experiments. A very important and delicate part of this combination is the estimation of the correlations between the various sources of systematic uncertainty, both between the various channels and between the two experiments. The correlations within each experiment are modelled following the procedure adopted for their individual combinations. The systematic uncertainties that are correlated between the two experiments are theoretical systematic uncertainties affecting the signal yield, certain theoretical systematic uncertainties in the background predictions, and a part of the experimental uncertainty related to the measurement of the integrated luminosity.

The main sources of theoretical uncertainties affecting the signal yield are the following: missing higher-order QCD corrections (estimated through variation of the QCD scales, i.e. renormalisation and factorisation scale) and uncertainties in parton distribution functions (PDF), in the treatment of UEPS, and in Higgs boson branching fractions.

JHEP08(2016)045

These uncertainties apply both to the inclusive cross sections and to the acceptances and selection efficiencies in the various categories. The PDF uncertainties in the inclusive rates are correlated between the two experiments for a given production process, but are treated as uncorrelated between different processes, except for the WH, ZH, and VBF production processes, where they are assumed to be fully correlated. A cross-check with the full PDF correlation matrix, as given in ref. [32], yields differences no larger than 1% for the generic parameterisations discussed in section 4. Similarly, QCD scale and UEPS uncertainties are assumed to be correlated between the two experiments in the same production processes and to be uncorrelated between different processes. The effects of correlations between Higgs boson branching fractions were determined to be negligible in general, and are ignored in the fits, except for the uncertainties in the branching fractions to WW and ZZ, which are assumed to be fully correlated. When measuring ratios, however, there are cases, e.g. the measurements of ratios of coupling modifiers described in section 4.2, where such uncertainties become the dominant theoretical uncertainties, and in these cases the full branching fraction correlation model specified in ref. [32] was applied. Other theoretical uncertainties in the signal acceptance and selection efficiencies are also usually small. They are estimated and treated in very different manners by the two experiments and therefore are assumed to be uncorrelated between ATLAS and CMS. It was verified that treating them as correlated would have a negligible impact on the results.

Whereas the signal selection criteria are quite inclusive in most channels, this is not the case for the backgrounds, which are often restricted to very limited regions of phase space and which are often treated differently by the two experiments. For these reasons, the ATLAS and CMS background modelling uncertainties cannot be easily correlated, even though such correlations should be considered for channels where they represent significant contributions to the overall systematic uncertainty. Obvious examples are those where the background estimates are obtained from simulation, as is the case for the ZZ continuum background in the $H \to ZZ$ channel, and for the ttW and ttZ backgrounds in the ttH multi-lepton channel. For these two cases, the background cross section uncertainties are treated as fully correlated between the two experiments. Other more complex examples are the WW continuum background in the $H \to WW$ channel, the $ttbb$ background in the $ttH, H \to bb$ channel, and the Wbb background in the $WH, H \to bb$ channel. In these cases, it was verified that the choice of not implementing correlations in the background modelling uncertainties between the two experiments has only a small impact on the measurements. The most significant impact was found for the $ttbb$ background in the $ttH, H \to bb$ channel, for which the choice of different correlation models between the two experiments yields an impact below 10% of the total uncertainty in the signal strength measurement in this specific channel.

Finally, all experimental systematic uncertainties are treated independently by the two experiments, reflecting independent assessments of these uncertainties, except for the integrated luminosity uncertainties, which are treated as partially correlated through the contribution arising from the imperfect knowledge of the beam currents in the LHC accelerator.

JHEP08(2016)045

The various sources of uncertainties can be broadly classified in four groups:

1. uncertainties (labelled as "stat" in the following) that are statistical in nature. In addition to the data, these include the statistical uncertainties in certain background control regions and certain fit parameters used to describe backgrounds measured from data, but they exclude the finite size of MC simulation samples;

2. theoretical uncertainties affecting the Higgs boson signal (labelled as "thsig" in the following);

3. theoretical uncertainties affecting background processes only (these are not correlated with any of the signal theoretical uncertainties and are labelled as "thbgd" in the following);

4. all other uncertainties (labelled as "expt" in the following), which include the experimental uncertainties and those related to the finite size of the MC simulation samples.

Some of the results are provided with a full breakdown of the uncertainties into these four categories, but, in most cases, the uncertainties are divided only into their statistical and systematic (syst) components. In some cases, as in section 4, when considering ratios of cross sections or coupling strengths, the theoretical systematic uncertainties are very small, because the signal normalisation uncertainties, which are in general dominant, do not affect the measurements. The precision with which the uncertainties and their components are quoted is typically of order 1% relative to the SM prediction.

As mentioned above, the Higgs boson mass is fixed, for all results reported in this paper, at the measured value of 125.09 GeV. The impact of the Higgs boson mass uncertainty (± 0.24 GeV) on the measurements has two main sources. One is the dependence of the $\sigma \cdot \mathrm{B}$ product on the mass. This dependence has an impact only on the measurements of the signal strengths and of the coupling modifiers, in which the SM signal yield predictions enter directly. The associated uncertainties are up to 4% for the signal strengths and 2% for the coupling modifiers. The other source of uncertainty is the dependence of the measured yields on the mass, arising from the fit to the mass spectra in the high-resolution $H \to \gamma\gamma$ and $H \to ZZ$ decay channels. In principle, this uncertainty affects all the measurements, including those related to the generic parameterisations, and is expected to be of the same order as the first one, namely 1% to 2%. In practice, since the measured masses in the $H \to \gamma\gamma$ and $H \to ZZ$ decay channels, resulting from the combination of ATLAS and CMS data, agree within 100 MeV, this uncertainty is less than 1% for all combined ATLAS and CMS measurements reported in this paper. Additional uncertainties of approximately 1% in the measurements of the Higgs boson signal strengths and coupling modifiers arise from the uncertainty in the LHC beam energy, which is estimated to be 0.66% at 8 TeV [121]. The uncertainties in the Higgs boson mass and the LHC beam energy are much smaller than the statistical uncertainties in the measurements and are neglected in the following.

JHEP08(2016)045

3.4 Analysis modifications for the combination

There are some differences in the treatment of signal and background in the combined analysis compared to the published analyses from each experiment. The differences are larger for CMS than for ATLAS, mainly because the CMS analyses were published earlier, before some refinements for the SM Higgs boson predictions were made available. The main differences are the following:

- ATLAS now uses the Stewart-Tackmann prescription [48] for the jet bin uncertainties in the $H \to WW$ channel instead of the jet-veto-efficiency procedure [49];
- CMS now includes the bbH, tH, and $ggZH$ production processes in the signal model for all the channels in which they are relevant;
- CMS now uses the signal cross section calculations from ref. [32] for all channels;
- CMS now adopts a unified prescription for the treatment of the Higgs boson p_{T} in the ggF production process, as described in section 2.2;
- The cross sections for the dominant backgrounds were adjusted to the most recent theoretical calculations in the cases where they are estimated from simulation (ZZ background in the $H \to ZZ$ channel and ttZ and ttW backgrounds in the ttH channels);
- Both experiments have adopted the same correlation scheme for some of the signal theoretical uncertainties: for example, the treatment of the PDF uncertainties in the signal production cross sections now follows a common scheme for all decay channels, as described in section 3.3.

The total effect of these modifications is small, both for the expected and observed results. All measurements differ from the individual combined results by less than approximately 10% of the total uncertainty for CMS and by even less for ATLAS.

Table 5 gives an overview of the Higgs boson decay and production processes that are combined in the following. To provide a snapshot of the relative importance of the various channels, the results from the analysis presented in this paper (tables 12 and 13 in section 5.2) are shown separately for each experiment, as measurements of the overall signal strengths μ, for each of the six decay channels and for the ttH production process. The total observed and expected statistical significances for $m_H = 125.09$ GeV are also shown, except for the $H \to \mu\mu$ channel, which has very low sensitivity. These results are quite close to those published for the individual analyses by each experiment, which are cited in table 5. For several decay channels, these refer only to the most sensitive analyses, e.g. the VH analysis for the $H \to bb$ decay channel. Even though they are less sensitive, the ttH analyses have a contribution from all the decay channels, and this is one of the reasons for quoting this production process specifically in this table. As stated above, the differences between the analysis in this paper and the published ones are also in part due to the different values assumed for the Higgs boson mass, and to adjustments in the various analyses for the purposes of this combination, mostly in terms of the signal modelling and of the treatment of the correlations of the signal theoretical uncertainties between different channels.

JHEP08(2016)045

Channel	References for individual publications		Signal strength [μ] from results in this paper (section 5.2)		Signal significance [σ]	
	ATLAS	CMS	ATLAS	CMS	ATLAS	CMS
$H \to \gamma\gamma$	[92]	[93]	$1.14\,^{+0.27}_{-0.25}$	$1.11\,^{+0.25}_{-0.23}$	5.0	5.6
			$\left(^{+0.26}_{-0.24}\right)$	$\left(^{+0.23}_{-0.21}\right)$	(4.6)	(5.1)
$H \to ZZ$	[94]	[95]	$1.52\,^{+0.40}_{-0.34}$	$1.04\,^{+0.32}_{-0.26}$	7.6	7.0
			$\left(^{+0.32}_{-0.27}\right)$	$\left(^{+0.30}_{-0.25}\right)$	(5.6)	(6.8)
$H \to WW$	[96, 97]	[98]	$1.22\,^{+0.23}_{-0.21}$	$0.90\,^{+0.23}_{-0.21}$	6.8	4.8
			$\left(^{+0.21}_{-0.20}\right)$	$\left(^{+0.23}_{-0.20}\right)$	(5.8)	(5.6)
$H \to \tau\tau$	[99]	[100]	$1.41\,^{+0.40}_{-0.36}$	$0.88\,^{+0.30}_{-0.28}$	4.4	3.4
			$\left(^{+0.37}_{-0.33}\right)$	$\left(^{+0.31}_{-0.29}\right)$	(3.3)	(3.7)
$H \to bb$	[101]	[102]	$0.62\,^{+0.37}_{-0.37}$	$0.81\,^{+0.45}_{-0.43}$	1.7	2.0
			$\left(^{+0.39}_{-0.37}\right)$	$\left(^{+0.45}_{-0.43}\right)$	(2.7)	(2.5)
$H \to \mu\mu$	[103]	[104]	$-0.6\,^{+3.6}_{-3.6}$	$0.9\,^{+3.6}_{-3.5}$		
			$\left(^{+3.6}_{-3.6}\right)$	$\left(^{+3.3}_{-3.2}\right)$		
ttH production	[78, 105, 106]	[108]	$1.9\,^{+0.8}_{-0.7}$	$2.9\,^{+1.0}_{-0.9}$	2.7	3.6
			$\left(^{+0.7}_{-0.7}\right)$	$\left(^{+0.9}_{-0.8}\right)$	(1.6)	(1.3)

Table 5. Overview of the decay channels analysed in this paper. The ttH production process, which has contributions from all decay channels, is also shown. To show the relative importance of the various channels, the results from the combined analysis presented in this paper for $m_H = 125.09$ GeV (tables 12 and 13 in section 5.2) are reported as observed signal strengths μ with their measured uncertainties. The expected uncertainties are shown in parentheses. Also shown are the observed statistical significances, together with the expected significances in parentheses, except for the $H \to \mu\mu$ channel, which has very low sensitivity. For most decay channels, only the most sensitive analyses are quoted as references, e.g. the ggF and VBF analyses for the $H \to WW$ decay channel or the VH analysis for the $H \to bb$ decay channel. Although not exactly the same, the results are close to those from the individual publications, in which slightly different values for the Higgs boson mass were assumed and in which the signal modelling and signal uncertainties were slightly different, as discussed in the text.

4 Generic parameterisations of experimental results

This section describes three generic parameterisations and presents their results. The first two are based on cross sections and branching fractions, either expressed as independent products $\sigma_i \cdot \mathrm{B}^f$ for each channel $i \to H \to f$, or as ratios of cross sections and branching fractions plus one reference $\sigma_i \cdot \mathrm{B}^f$ product. In these parameterisations, the theoretical uncertainties in the signal inclusive cross sections for the various production processes do not affect the measured observables, in contrast to measurements of signal strengths, such

JHEP08(2016)045

σ and B ratio parameterisation	Coupling modifier ratio parameterisation
$\sigma(gg \to H \to ZZ)$	$\kappa_{gZ} = \kappa_g \cdot \kappa_Z/\kappa_H$
$\sigma_{\mathrm{VBF}}/\sigma_{gg\mathrm{F}}$	
$\sigma_{WH}/\sigma_{gg\mathrm{F}}$	
$\sigma_{ZH}/\sigma_{gg\mathrm{F}}$	$\lambda_{Zg} = \kappa_Z/\kappa_g$
$\sigma_{ttH}/\sigma_{gg\mathrm{F}}$	$\lambda_{tg} = \kappa_t/\kappa_g$
$\mathrm{B}^{WW}/\mathrm{B}^{ZZ}$	$\lambda_{WZ} = \kappa_W/\kappa_Z$
$\mathrm{B}^{\gamma\gamma}/\mathrm{B}^{ZZ}$	$\lambda_{\gamma Z} = \kappa_\gamma/\kappa_Z$
$\mathrm{B}^{\tau\tau}/\mathrm{B}^{ZZ}$	$\lambda_{\tau Z} = \kappa_\tau/\kappa_Z$
$\mathrm{B}^{bb}/\mathrm{B}^{ZZ}$	$\lambda_{bZ} = \kappa_b/\kappa_Z$

Table 6. Parameters of interest in the two generic parameterisations described in sections 4.1.2 and 4.2. For both parameterisations, the $gg \to H \to ZZ$ channel is chosen as a reference, expressed through the first row in the table. All other measurements are expressed as ratios of cross sections or branching fractions in the first column and of coupling modifiers in the second column. There are fewer parameters of interest in the case of the coupling parameterisation, in which the ratios of cross sections for the WH, ZH, and VBF processes can all be expressed as functions of the two parameters, λ_{Zg} and λ_{WZ}. The slightly different additional assumptions in each parameterisation are discussed in the text.

as those described in section 2.3. These analyses lead to the most model-independent results presented in this paper and test, with minimal assumptions, the compatibility of the measurements with the SM. The third generic parameterisation is derived from the one described in section 2.4 and is based on ratios of coupling modifiers. None of these parameterisations incorporate any assumption about the Higgs boson total width other than the narrow-width approximation. Some theoretical and experimental systematic uncertainties largely cancel in the parameterisations involving ratios but at the current level of sensitivity the impact is small.

Table 6 gives an overview of the parameters of interest for the two generic parameterisations involving ratios which are described in more detail in sections 4.1.2 and 4.2. The first row makes explicit that the $gg \to H \to ZZ$ channel is chosen as a reference. The $\lambda_{Zg} = \kappa_Z/\kappa_g$ term in the fourth row is related to the ratio of the ZH and ggF production cross sections. Once $\lambda_{WZ} = \kappa_W/\kappa_Z$ is also specified, the VBF, WH, and ZH production cross sections are fully defined. This explains the smaller number of independent parameters of interest in the coupling modifier ratio parameterisation compared to the parameterisation based mostly on ratios of cross sections and branching fractions. In addition, these two parameterisations rely on slightly different assumptions and approximations, which are summarised in sections 2.3 and 2.4. These approximations are due to the fact that one cannot experimentally constrain all possible Higgs boson production processes and decay modes, in particular those that are expected to be small in the SM, but might be enhanced, should specific BSM physics scenarios be realised in nature.

JHEP08(2016)045

Production process	Decay channel				
	$H \to \gamma\gamma$	$H \to ZZ$	$H \to WW$	$H \to \tau\tau$	$H \to bb$
ggF	$(\sigma \cdot \mathrm{B})^{\gamma\gamma}_{gg\mathrm{F}}$	$(\sigma \cdot \mathrm{B})^{ZZ}_{gg\mathrm{F}}$	$(\sigma \cdot \mathrm{B})^{WW}_{gg\mathrm{F}}$	$(\sigma \cdot \mathrm{B})^{\tau\tau}_{gg\mathrm{F}}$	–
VBF	$(\sigma \cdot \mathrm{B})^{\gamma\gamma}_{\mathrm{VBF}}$	$(\sigma \cdot \mathrm{B})^{ZZ}_{\mathrm{VBF}}$	$(\sigma \cdot \mathrm{B})^{WW}_{\mathrm{VBF}}$	$(\sigma \cdot \mathrm{B})^{\tau\tau}_{\mathrm{VBF}}$	–
WH	$(\sigma \cdot \mathrm{B})^{\gamma\gamma}_{WH}$	$(\sigma \cdot \mathrm{B})^{ZZ}_{WH}$	$(\sigma \cdot \mathrm{B})^{WW}_{WH}$	$(\sigma \cdot \mathrm{B})^{\tau\tau}_{WH}$	$(\sigma \cdot \mathrm{B})^{bb}_{WH}$
ZH	$(\sigma \cdot \mathrm{B})^{\gamma\gamma}_{ZH}$	$(\sigma \cdot \mathrm{B})^{ZZ}_{ZH}$	$(\sigma \cdot \mathrm{B})^{WW}_{ZH}$	$(\sigma \cdot \mathrm{B})^{\tau\tau}_{ZH}$	$(\sigma \cdot \mathrm{B})^{bb}_{ZH}$
ttH	$(\sigma \cdot \mathrm{B})^{\gamma\gamma}_{ttH}$	$(\sigma \cdot \mathrm{B})^{ZZ}_{ttH}$	$(\sigma \cdot \mathrm{B})^{WW}_{ttH}$	$(\sigma \cdot \mathrm{B})^{\tau\tau}_{ttH}$	$(\sigma \cdot \mathrm{B})^{bb}_{ttH}$

Table 7. The signal parameterisation used to express the $\sigma_i \cdot \mathrm{B}^f$ values for each specific channel $i \to H \to f$. The values labelled with a "–" are not measured and are therefore fixed to the SM predictions.

4.1 Parameterisations using cross sections and branching fractions

4.1.1 Parameterisation using independent products of cross sections and branching fractions

In a very generic approach, one can extract for each specific channel $i \to H \to f$ a measurement of the product $\sigma_i \cdot \mathrm{B}^f$ and then compare it to the theoretical prediction. Based on all the categories considered in the various analyses and on the five production processes (ggF, VBF, WH, ZH, and ttH) and five main decay channels ($H \to ZZ$, $H \to WW$, $H \to \gamma\gamma$, $H \to \tau\tau$, and $H \to bb$) considered in this paper, there are in principle 25 such independent products to be measured. In practice, as already mentioned, the ggF and VBF production processes are not probed in the case of the $H \to bb$ decay mode and are assumed to have the values predicted by the SM, so the fit is performed with 23 parameters of interest, which are specified in table 7. The individual experiments cannot provide constraints on all the parameters of interest because of the low overall expected and observed yields in the current data. Even when combining the ATLAS and CMS data, the ZH, WH, and ttH production processes cannot be measured with meaningful precision in the $H \to ZZ$ decay channel. The fit results are therefore quoted only for the remaining 20 parameters and for the combined ATLAS and CMS data.

JHEP08(2016)045

Production process		Decay mode														
		$H \to \gamma\gamma$ [fb]			$H \to ZZ$ [fb]			$H \to WW$ [pb]			$H \to \tau\tau$ [fb]			$H \to bb$ [pb]		
		Best fit value	Uncertainty Stat	Uncertainty Syst	Best fit value	Uncertainty Stat	Uncertainty Syst	Best fit value	Uncertainty Stat	Uncertainty Syst	Best fit value	Uncertainty Stat	Uncertainty Syst	Best fit value	Uncertainty Stat	Uncertainty Syst
ggF	Measured	$48.0\ ^{+10.0}_{-9.7}$	$^{+9.4}_{-9.4}$	$^{+3.2}_{-2.3}$	$580\ ^{+170}_{-160}$	$^{+170}_{-160}$	$^{+40}_{-40}$	$3.5\ ^{+0.7}_{-0.7}$	$^{+0.5}_{-0.5}$	$^{+0.5}_{-0.5}$	$1300\ ^{+700}_{-700}$	$^{+400}_{-400}$	$^{+500}_{-500}$	–		
		$\left(^{+9.7}_{-9.5}\right)$	$\left(^{+9.4}_{-9.4}\right)$	$\left(^{+2.5}_{-1.6}\right)$	$\left(^{+150}_{-130}\right)$	$\left(^{+140}_{-130}\right)$	$\left(^{+30}_{-20}\right)$	$\left(^{+0.7}_{-0.7}\right)$	$\left(^{+0.5}_{-0.5}\right)$	$\left(^{+0.5}_{-0.5}\right)$	$\left(^{+700}_{-700}\right)$	$\left(^{+400}_{-400}\right)$	$\left(^{+500}_{-500}\right)$	–		
	Predicted	44 ± 5			510 ± 60			4.1 ± 0.5			1210 ± 140			11.0 ± 1.2		
	Ratio	$1.10\ ^{+0.23}_{-0.22}$	$^{+0.22}_{-0.21}$	$^{+0.07}_{-0.05}$	$1.13\ ^{+0.34}_{-0.31}$	$^{+0.33}_{-0.30}$	$^{+0.09}_{-0.07}$	$0.84\ ^{+0.17}_{-0.17}$	$^{+0.12}_{-0.12}$	$^{+0.12}_{-0.11}$	$1.0\ ^{+0.6}_{-0.6}$	$^{+0.4}_{-0.4}$	$^{+0.4}_{-0.4}$	–		
VBF	Measured	$4.6\ ^{+1.9}_{-1.8}$	$^{+1.8}_{-1.7}$	$^{+0.6}_{-0.5}$	$3\ ^{+46}_{-26}$	$^{+46}_{-25}$	$^{+7}_{-7}$	$0.39\ ^{+0.14}_{-0.13}$	$^{+0.13}_{-0.12}$	$^{+0.07}_{-0.05}$	$125\ ^{+39}_{-37}$	$^{+34}_{-32}$	$^{+19}_{-18}$	–		
		$\left(^{+1.8}_{-1.6}\right)$	$\left(^{+1.7}_{-1.6}\right)$	$\left(^{+0.5}_{-0.4}\right)$	$\left(^{+60}_{-39}\right)$	$\left(^{+60}_{-39}\right)$	$\left(^{+8}_{-5}\right)$	$\left(^{+0.15}_{-0.13}\right)$	$\left(^{+0.13}_{-0.12}\right)$	$\left(^{+0.07}_{-0.06}\right)$	$\left(^{+39}_{-37}\right)$	$\left(^{+34}_{-32}\right)$	$\left(^{+19}_{-18}\right)$	–		
	Predicted	3.60 ± 0.20			42.2 ± 2.0			0.341 ± 0.017			100 ± 6			0.91 ± 0.04		
	Ratio	$1.3\ ^{+0.5}_{-0.5}$	$^{+0.5}_{-0.5}$	$^{+0.2}_{-0.1}$	$0.1\ ^{+1.1}_{-0.6}$	$^{+1.1}_{-0.6}$	$^{+0.2}_{-0.2}$	$1.2\ ^{+0.4}_{-0.4}$	$^{+0.4}_{-0.3}$	$^{+0.2}_{-0.2}$	$1.3\ ^{+0.4}_{-0.4}$	$^{+0.3}_{-0.3}$	$^{+0.2}_{-0.2}$	–		
WH	Measured	$0.7\ ^{+2.1}_{-1.9}$	$^{+2.1}_{-1.8}$	$^{+0.3}_{-0.3}$	–			$0.24\ ^{+0.18}_{-0.16}$	$^{+0.15}_{-0.14}$	$^{+0.10}_{-0.08}$	$-64\ ^{+64}_{-61}$	$^{+55}_{-50}$	$^{+32}_{-34}$	$0.42\ ^{+0.21}_{-0.20}$	$^{+0.17}_{-0.16}$	$^{+0.12}_{-0.11}$
		$\left(^{+1.9}_{-1.8}\right)$	$\left(^{+1.9}_{-1.8}\right)$	$\left(^{+0.1}_{-0.1}\right)$	–			$\left(^{+0.16}_{-0.14}\right)$	$\left(^{+0.14}_{-0.13}\right)$	$\left(^{+0.08}_{-0.07}\right)$	$\left(^{+67}_{-64}\right)$	$\left(^{+60}_{-54}\right)$	$\left(^{+30}_{-32}\right)$	$\left(^{+0.22}_{-0.21}\right)$	$\left(^{+0.18}_{-0.17}\right)$	$\left(^{+0.12}_{-0.11}\right)$
	Predicted	1.60 ± 0.09			18.8 ± 0.9			0.152 ± 0.007			44.3 ± 2.8			0.404 ± 0.017		
	Ratio	$0.5\ ^{+1.3}_{-1.2}$	$^{+1.3}_{-1.1}$	$^{+0.2}_{-0.2}$	–			$1.6\ ^{+1.2}_{-1.0}$	$^{+1.0}_{-0.9}$	$^{+0.6}_{-0.5}$	$-1.4\ ^{+1.4}_{-1.4}$	$^{+1.2}_{-1.1}$	$^{+0.7}_{-0.8}$	$1.0\ ^{+0.5}_{-0.5}$	$^{+0.4}_{-0.4}$	$^{+0.3}_{-0.3}$

JHEP08(2016)045

Production process		Decay mode														
		$H \to \gamma\gamma$ [fb]			$H \to ZZ$ [fb]			$H \to WW$ [pb]			$H \to \tau\tau$ [fb]			$H \to bb$ [pb]		
		Best fit value	Uncertainty Stat	Uncertainty Syst	Best fit value	Uncertainty Stat	Uncertainty Syst	Best fit value	Uncertainty Stat	Uncertainty Syst	Best fit value	Uncertainty Stat	Uncertainty Syst	Best fit value	Uncertainty Stat	Uncertainty Syst
ZH	Measured	$0.5\ ^{+2.9}_{-2.4}$	$^{+2.8}_{-2.3}$	$^{+0.5}_{-0.2}$		–		$0.53\ ^{+0.23}_{-0.20}$	$^{+0.21}_{-0.19}$	$^{+0.10}_{-0.07}$	$58\ ^{+56}_{-47}$	$^{+52}_{-44}$	$^{+20}_{-16}$	$0.08\ ^{+0.09}_{-0.09}$	$^{+0.08}_{-0.08}$	$^{+0.04}_{-0.04}$
		$\left(^{+2.3}_{-1.9}\right)$	$\left(^{+2.3}_{-1.9}\right)$	$\left(^{+0.1}_{-0.1}\right)$		–		$\left(^{+0.17}_{-0.14}\right)$	$\left(^{+0.16}_{-0.14}\right)$	$\left(^{+0.05}_{-0.04}\right)$	$\left(^{+49}_{-40}\right)$	$\left(^{+46}_{-38}\right)$	$\left(^{+16}_{-12}\right)$	$\left(^{+0.10}_{-0.09}\right)$	$\left(^{+0.09}_{-0.08}\right)$	$\left(^{+0.05}_{-0.04}\right)$
	Predicted	0.94 ± 0.06			11.1 ± 0.6			0.089 ± 0.005			26.1 ± 1.8			0.238 ± 0.012		
	Ratio	$0.5\ ^{+3.0}_{-2.5}$	$^{+3.0}_{-2.5}$	$^{+0.5}_{-0.2}$		–		$5.9\ ^{+2.6}_{-2.2}$	$^{+2.3}_{-2.1}$	$^{+1.1}_{-0.8}$	$2.2\ ^{+2.2}_{-1.8}$	$^{+2.0}_{-1.7}$	$^{+0.8}_{-0.6}$	$0.4\ ^{+0.4}_{-0.4}$	$^{+0.3}_{-0.3}$	$^{+0.2}_{-0.2}$
ttH	Measured	$0.64\ ^{+0.48}_{-0.38}$	$^{+0.48}_{-0.38}$	$^{+0.07}_{-0.04}$		–		$0.14\ ^{+0.05}_{-0.05}$	$^{+0.04}_{-0.04}$	$^{+0.03}_{-0.03}$	$-15\ ^{+30}_{-26}$	$^{+26}_{-22}$	$^{+15}_{-15}$	$0.08\ ^{+0.07}_{-0.07}$	$^{+0.04}_{-0.04}$	$^{+0.06}_{-0.06}$
		$\left(^{+0.45}_{-0.34}\right)$	$\left(^{+0.44}_{-0.33}\right)$	$\left(^{+0.10}_{-0.05}\right)$		–		$\left(^{+0.04}_{-0.04}\right)$	$\left(^{+0.04}_{-0.04}\right)$	$\left(^{+0.02}_{-0.02}\right)$	$\left(^{+31}_{-26}\right)$	$\left(^{+26}_{-22}\right)$	$\left(^{+16}_{-13}\right)$	$\left(^{+0.07}_{-0.06}\right)$	$\left(^{+0.04}_{-0.04}\right)$	$\left(^{+0.06}_{-0.05}\right)$
	Predicted	0.294 ± 0.035			3.4 ± 0.4			0.0279 ± 0.0032			8.1 ± 1.0			0.074 ± 0.008		
	Ratio	$2.2\ ^{+1.6}_{-1.3}$	$^{+1.6}_{-1.3}$	$^{+0.2}_{-0.1}$		–		$5.0\ ^{+1.8}_{-1.7}$	$^{+1.5}_{-1.5}$	$^{+1.0}_{-0.9}$	$-1.9\ ^{+3.7}_{-3.3}$	$^{+3.2}_{-2.7}$	$^{+1.9}_{-1.8}$	$1.1\ ^{+1.0}_{-1.0}$	$^{+0.5}_{-0.5}$	$^{+0.8}_{-0.8}$

Table 8. Best fit values of $\sigma_i \cdot \mathrm{B}^f$ for each specific channel $i \to H \to f$, as obtained from the generic parameterisation with 23 parameters for the combination of the ATLAS and CMS measurements, using the $\sqrt{s} = 7$ and 8 TeV data. The cross sections are given for $\sqrt{s} = 8$ TeV, assuming the SM values for $\sigma_i(7\text{ TeV})/\sigma_i(8\text{ TeV})$. The results are shown together with their total uncertainties and their breakdown into statistical and systematic components. The expected uncertainties in the measurements are displayed in parentheses. The SM predictions [32] and the ratios of the results to these SM predictions are also shown. The values labelled with a "–" are either not measured with a meaningful precision and therefore not quoted, in the case of the $H \to ZZ$ decay channel for the WH, ZH, and ttH production processes, or not measured at all and therefore fixed to their corresponding SM predictions, in the case of the $H \to bb$ decay mode for the ggF and VBF production processes.

JHEP08(2016)045

Table 8 presents, for the combination of ATLAS and CMS, the fit results for each $\sigma_i \cdot \mathrm{B}^f$ product along with its statistical and systematic uncertainties. The corresponding SM predictions are also given. The ratios of the fit results to SM predictions are included in table 8 and displayed in figure 7. Figure 7 additionally shows the theoretical uncertainties in the SM predictions for the fitted parameters. In almost all cases, the dominant uncertainty is statistical. The results presented in table 8 and figure 7 clearly exhibit which decay modes are probed best for each production process, and conversely which production processes are probed best for each decay mode. With the current sensitivity of the combination, six of the $\sigma_i \cdot \mathrm{B}^f$ products can be measured with a precision better than 40%, namely the $H \to \gamma\gamma$, $H \to ZZ$, and $H \to WW$ decay modes for the ggF production process, and the $H \to \gamma\gamma$, $H \to WW$, and $H \to \tau\tau$ decay modes for the VBF production process. Because of the sizeable cross-contamination between the ggF and VBF categories, the corresponding results are significantly anticorrelated, as illustrated by the measured correlation matrix in figure 27 of appendix A.

4.1.2 Parameterisation using ratios of cross sections and branching fractions

If there is only one Higgs boson, each row or column in table 7 can be derived from the others by identical ratios of cross sections for the rows and of branching fractions for the columns. Therefore, in a second generic approach, ratios of cross sections and of branching fractions can be extracted from a combined fit to the data by normalising the yield of any specific channel $i \to H \to f$ to a reference process. In this paper, the $gg \to H \to ZZ$ channel is chosen as the reference because it has very little background and is one of the channels with the smallest overall and systematic uncertainties. The $gg \to H \to WW$ channel, which has the smallest overall uncertainty but larger systematic uncertainties, is used as an alternate reference for comparison, and the corresponding results are reported in appendix B.

The product of the cross section and the branching fraction of $i \to H \to f$ can then be expressed using the ratios as:

$$\sigma_i \cdot \mathrm{B}^f = \sigma(gg \to H \to ZZ) \cdot \left(\frac{\sigma_i}{\sigma_{gg\mathrm{F}}}\right) \cdot \left(\frac{\mathrm{B}^f}{\mathrm{B}^{ZZ}}\right), \tag{4.1}$$

where $\sigma(gg \to H \to ZZ) = \sigma_{gg\mathrm{F}} \cdot \mathrm{B}^{ZZ}$ in the narrow-width approximation. With $\sigma(gg \to H \to ZZ)$ constraining the overall normalisation, the ratios in eq. (4.1) can be determined separately, based on the five production processes (ggF, VBF, WH, ZH, and ttH) and five decay modes ($H \to ZZ$, $H \to WW$, $H \to \gamma\gamma$, $H \to \tau\tau$, and $H \to bb$). The combined fit results can be presented as a function of nine parameters of interest: one reference cross section times branching fraction, $\sigma(gg \to H \to ZZ)$, four ratios of production cross sections, $\sigma_i/\sigma_{gg\mathrm{F}}$, and four ratios of branching fractions, $\mathrm{B}^f/\mathrm{B}^{ZZ}$, as reported in the left column of table 6.

Expressing the measurements through ratios of cross sections and branching fractions has the advantage that the ratios are independent of the theoretical predictions for the inclusive production cross sections and decay branching fractions of the Higgs boson. In particular, they are not subject to the dominant signal theoretical uncertainties in the inclusive cross sections for the various production processes. These measurements will

JHEP08(2016)045

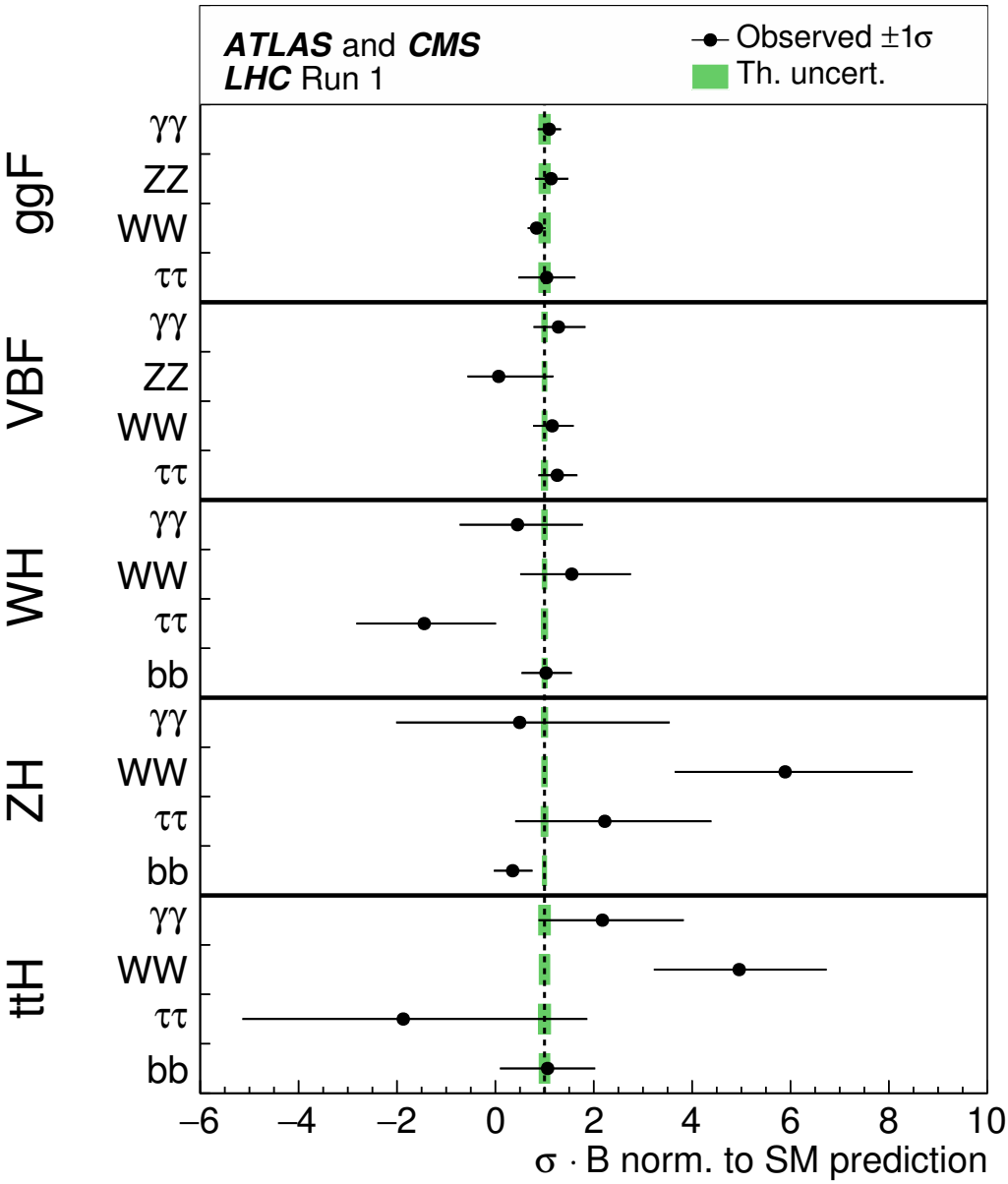

Figure 7. Best fit values of $\sigma_i \cdot \mathrm{B}^f$ for each specific channel $i \to H \to f$, as obtained from the generic parameterisation with 23 parameters for the combination of the ATLAS and CMS measurements. The error bars indicate the 1σ intervals. The fit results are normalised to the SM predictions for the various parameters and the shaded bands indicate the theoretical uncertainties in these predictions. Only 20 parameters are shown because some are either not measured with a meaningful precision, in the case of the $H \to ZZ$ decay channel for the WH, ZH, and ttH production processes, or not measured at all and therefore fixed to their corresponding SM predictions, in the case of the $H \to bb$ decay mode for the ggF and VBF production processes.

JHEP08(2016)045

Parameter	SM prediction	Best fit value	Uncertainty Stat	Uncertainty Syst	Best fit value	Uncertainty Stat	Uncertainty Syst	Best fit value	Uncertainty Stat	Uncertainty Syst
		ATLAS+CMS			ATLAS			CMS		
$\sigma(gg \to H \to ZZ)$ [pb]	0.51 ± 0.06	$0.59\,^{+0.11}_{-0.10}$	$^{+0.11}_{-0.10}$	$^{+0.02}_{-0.02}$	$0.77\,^{+0.19}_{-0.17}$	$^{+0.19}_{-0.16}$	$^{+0.05}_{-0.03}$	$0.44\,^{+0.14}_{-0.12}$	$^{+0.13}_{-0.11}$	$^{+0.05}_{-0.03}$
		$\left(^{+0.11}_{-0.10}\right)$	$\left(^{+0.11}_{-0.09}\right)$	$\left(^{+0.03}_{-0.02}\right)$	$\left(^{+0.16}_{-0.14}\right)$	$\left(^{+0.16}_{-0.13}\right)$	$\left(^{+0.03}_{-0.02}\right)$	$\left(^{+0.15}_{-0.13}\right)$	$\left(^{+0.15}_{-0.13}\right)$	$\left(^{+0.04}_{-0.03}\right)$
$\sigma_{\mathrm{VBF}}/\sigma_{gg\mathrm{F}}$	0.082 ± 0.009	$0.109\,^{+0.034}_{-0.027}$	$^{+0.029}_{-0.024}$	$^{+0.018}_{-0.013}$	$0.079\,^{+0.035}_{-0.026}$	$^{+0.030}_{-0.023}$	$^{+0.019}_{-0.012}$	$0.138\,^{+0.073}_{-0.051}$	$^{+0.061}_{-0.046}$	$^{+0.039}_{-0.023}$
		$\left(^{+0.029}_{-0.024}\right)$	$\left(^{+0.024}_{-0.020}\right)$	$\left(^{+0.016}_{-0.012}\right)$	$\left(^{+0.042}_{-0.031}\right)$	$\left(^{+0.036}_{-0.028}\right)$	$\left(^{+0.022}_{-0.014}\right)$	$\left(^{+0.043}_{-0.033}\right)$	$\left(^{+0.037}_{-0.029}\right)$	$\left(^{+0.023}_{-0.015}\right)$
$\sigma_{WH}/\sigma_{gg\mathrm{F}}$	0.037 ± 0.004	$0.031\,^{+0.028}_{-0.026}$	$^{+0.024}_{-0.022}$	$^{+0.015}_{-0.014}$	$0.054\,^{+0.036}_{-0.026}$	$^{+0.031}_{-0.023}$	$^{+0.020}_{-0.013}$	$0.005\,^{+0.044}_{-0.037}$	$^{+0.037}_{-0.028}$	$^{+0.023}_{-0.024}$
		$\left(^{+0.021}_{-0.017}\right)$	$\left(^{+0.019}_{-0.015}\right)$	$\left(^{+0.011}_{-0.007}\right)$	$\left(^{+0.033}_{-0.022}\right)$	$\left(^{+0.029}_{-0.020}\right)$	$\left(^{+0.015}_{-0.009}\right)$	$\left(^{+0.032}_{-0.022}\right)$	$\left(^{+0.027}_{-0.020}\right)$	$\left(^{+0.017}_{-0.010}\right)$
$\sigma_{ZH}/\sigma_{gg\mathrm{F}}$	0.0216 ± 0.0024	$0.066\,^{+0.039}_{-0.031}$	$^{+0.032}_{-0.025}$	$^{+0.023}_{-0.018}$	$0.013\,^{+0.028}_{-0.014}$	$^{+0.021}_{-0.012}$	$^{+0.018}_{-0.007}$	$0.123\,^{+0.076}_{-0.053}$	$^{+0.063}_{-0.046}$	$^{+0.044}_{-0.026}$
		$\left(^{+0.016}_{-0.011}\right)$	$\left(^{+0.014}_{-0.010}\right)$	$\left(^{+0.009}_{-0.004}\right)$	$\left(^{+0.027}_{-0.014}\right)$	$\left(^{+0.023}_{-0.013}\right)$	$\left(^{+0.014}_{-0.005}\right)$	$\left(^{+0.024}_{-0.013}\right)$	$\left(^{+0.020}_{-0.012}\right)$	$\left(^{+0.014}_{-0.006}\right)$
$\sigma_{ttH}/\sigma_{gg\mathrm{F}}$	0.0067 ± 0.0010	$0.022\,^{+0.007}_{-0.006}$	$^{+0.005}_{-0.005}$	$^{+0.004}_{-0.003}$	$0.013\,^{+0.007}_{-0.005}$	$^{+0.005}_{-0.004}$	$^{+0.004}_{-0.003}$	$0.034\,^{+0.016}_{-0.012}$	$^{+0.012}_{-0.010}$	$^{+0.010}_{-0.006}$
		$\left(^{+0.004}_{-0.004}\right)$	$\left(^{+0.003}_{-0.003}\right)$	$\left(^{+0.003}_{-0.002}\right)$	$\left(^{+0.006}_{-0.004}\right)$	$\left(^{+0.005}_{-0.004}\right)$	$\left(^{+0.004}_{-0.003}\right)$	$\left(^{+0.007}_{-0.005}\right)$	$\left(^{+0.005}_{-0.004}\right)$	$\left(^{+0.004}_{-0.004}\right)$
$\mathrm{B}^{WW}/\mathrm{B}^{ZZ}$	$8.09 \pm < 0.01$	$6.7\,^{+1.6}_{-1.3}$	$^{+1.5}_{-1.2}$	$^{+0.6}_{-0.5}$	$6.5\,^{+2.1}_{-1.6}$	$^{+2.0}_{-1.4}$	$^{+0.8}_{-0.6}$	$7.1\,^{+2.9}_{-2.1}$	$^{+2.6}_{-1.8}$	$^{+1.3}_{-0.9}$
		$\left(^{+2.2}_{-1.7}\right)$	$\left(^{+2.0}_{-1.6}\right)$	$\left(^{+0.9}_{-0.7}\right)$	$\left(^{+3.5}_{-2.4}\right)$	$\left(^{+3.3}_{-2.2}\right)$	$\left(^{+1.2}_{-0.9}\right)$	$\left(^{+3.2}_{-2.2}\right)$	$\left(^{+2.9}_{-2.0}\right)$	$\left(^{+1.4}_{-1.0}\right)$
$\mathrm{B}^{\gamma\gamma}/\mathrm{B}^{ZZ}$	0.0854 ± 0.0010	$0.069\,^{+0.018}_{-0.014}$	$^{+0.018}_{-0.014}$	$^{+0.004}_{-0.003}$	$0.062\,^{+0.024}_{-0.018}$	$^{+0.023}_{-0.017}$	$^{+0.007}_{-0.005}$	$0.079\,^{+0.034}_{-0.023}$	$^{+0.032}_{-0.023}$	$^{+0.010}_{-0.006}$
		$\left(^{+0.025}_{-0.019}\right)$	$\left(^{+0.024}_{-0.019}\right)$	$\left(^{+0.006}_{-0.004}\right)$	$\left(^{+0.040}_{-0.027}\right)$	$\left(^{+0.039}_{-0.027}\right)$	$\left(^{+0.010}_{-0.006}\right)$	$\left(^{+0.035}_{-0.025}\right)$	$\left(^{+0.034}_{-0.024}\right)$	$\left(^{+0.008}_{-0.005}\right)$
$\mathrm{B}^{\tau\tau}/\mathrm{B}^{ZZ}$	2.36 ± 0.05	$1.8\,^{+0.6}_{-0.5}$	$^{+0.5}_{-0.4}$	$^{+0.3}_{-0.2}$	$2.2\,^{+1.1}_{-0.7}$	$^{+0.9}_{-0.6}$	$^{+0.6}_{-0.4}$	$1.6\,^{+0.9}_{-0.6}$	$^{+0.8}_{-0.5}$	$^{+0.5}_{-0.3}$
		$\left(^{+0.9}_{-0.7}\right)$	$\left(^{+0.8}_{-0.6}\right)$	$\left(^{+0.5}_{-0.3}\right)$	$\left(^{+1.5}_{-1.0}\right)$	$\left(^{+1.3}_{-0.9}\right)$	$\left(^{+0.8}_{-0.5}\right)$	$\left(^{+1.2}_{-0.9}\right)$	$\left(^{+1.0}_{-0.7}\right)$	$\left(^{+0.7}_{-0.4}\right)$
$\mathrm{B}^{bb}/\mathrm{B}^{ZZ}$	21.5 ± 1.0	$4.2\,^{+4.4}_{-2.6}$	$^{+2.8}_{-2.0}$	$^{+3.4}_{-1.6}$	$9.6\,^{+10.1}_{-5.7}$	$^{+7.4}_{-4.4}$	$^{+6.9}_{-3.6}$	$3.7\,^{+4.1}_{-2.4}$	$^{+3.1}_{-2.0}$	$^{+2.7}_{-1.4}$
		$\left(^{+16.8}_{-9.0}\right)$	$\left(^{+13.9}_{-7.9}\right)$	$\left(^{+9.5}_{-4.4}\right)$	$\left(^{+29.3}_{-11.8}\right)$	$\left(^{+24.2}_{-10.5}\right)$	$\left(^{+16.6}_{-5.3}\right)$	$\left(^{+29.4}_{-11.9}\right)$	$\left(^{+23.4}_{-10.4}\right)$	$\left(^{+17.8}_{-5.9}\right)$

Table 9. Best fit values of $\sigma(gg \to H \to ZZ)$, $\sigma_i/\sigma_{gg\mathrm{F}}$, and $\mathrm{B}^f/\mathrm{B}^{ZZ}$, as obtained from the generic parameterisation with nine parameters for the combined analysis of the $\sqrt{s} = 7$ and 8 TeV data. The values involving cross sections are given for $\sqrt{s} = 8$ TeV, assuming the SM values for $\sigma_i(7\text{ TeV})/\sigma_i(8\text{ TeV})$. The results are reported for the combination of ATLAS and CMS and also separately for each experiment, together with their total uncertainties and their breakdown into statistical and systematic components. The expected uncertainties in the measurements are displayed in parentheses. The SM predictions [32] are also shown with their total uncertainties.

therefore remain valid when, for example, improved theoretical calculations of Higgs boson production cross sections become available. The remaining theoretical uncertainties are those related to the acceptances and selection efficiencies in the various categories, for which SM Higgs boson production and decay kinematics are assumed in the simulation, based on the MC generators discussed in section 2.2.

Table 9 shows the results of the fit to the data with a breakdown of the uncertainties into their statistical and systematic components. The full breakdown of the uncertainties into the four components is shown in table 20 of appendix B, while the measured correlation matrix can be found in figure 28 of appendix A. The results are shown for the combination of ATLAS and CMS and also separately for each experiment. They are illustrated in figure 8, where the fit result for each parameter is normalised to the corresponding SM prediction. Also shown in figure 8 are the theoretical uncertainties in the SM predictions for the fitted parameters. For the ratios of branching fractions, the theoretical uncertainties in the predictions are barely visible since they are below 5%. Compared to the results of the fit of table 8, where the ggF parameters are independent for each decay mode, the uncertainties

JHEP08(2016)045

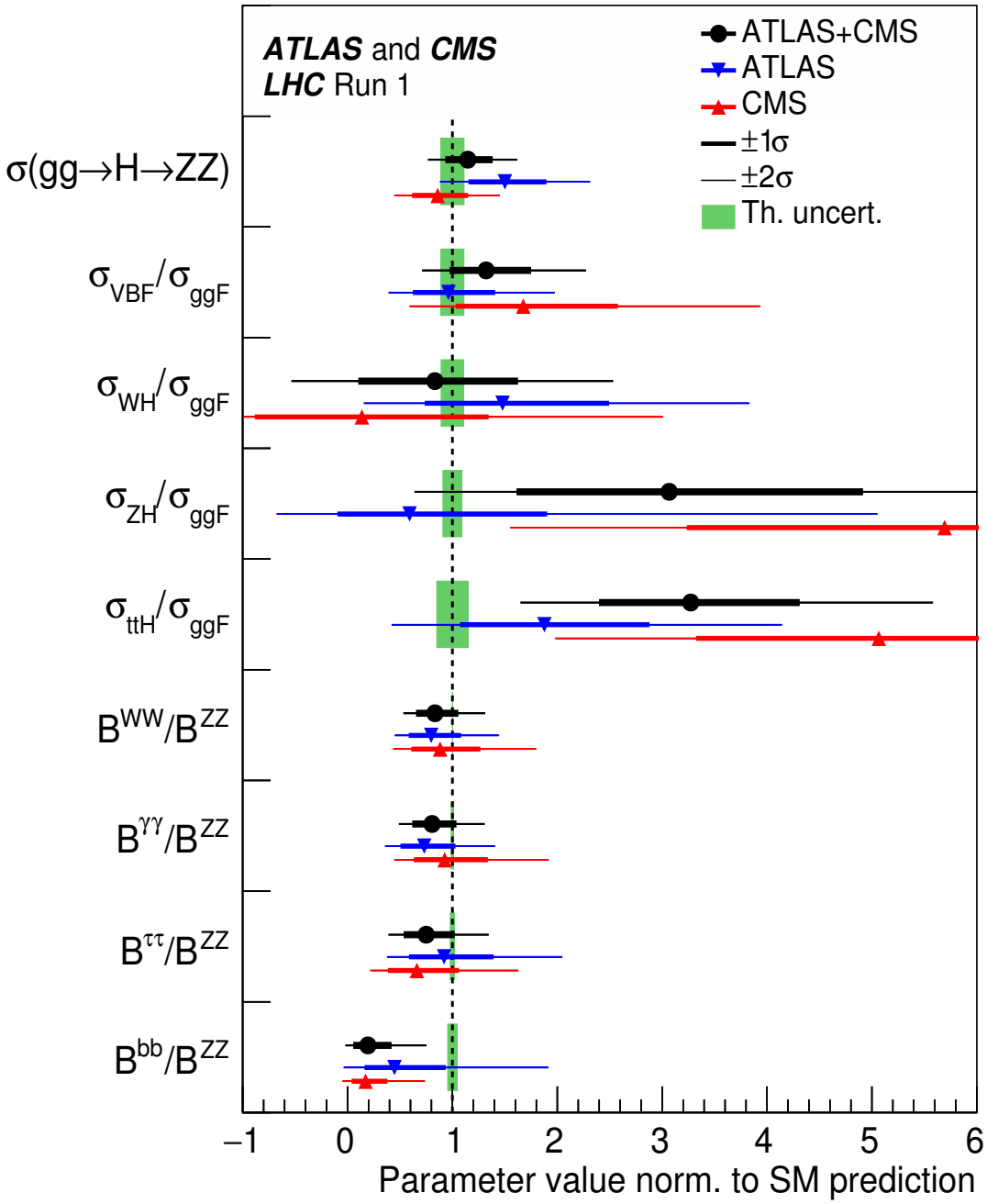

Figure 8. Best fit values of the $\sigma(gg \to H \to ZZ)$ cross section and of ratios of cross sections and branching fractions, as obtained from the generic parameterisation with nine parameters and tabulated in table 9 for the combination of the ATLAS and CMS measurements. Also shown are the results from each experiment. The values involving cross sections are given for $\sqrt{s} = 8\,\text{TeV}$, assuming the SM values for $\sigma_i(7\ \text{TeV})/\sigma_i(8\ \text{TeV})$. The error bars indicate the 1σ (thick lines) and 2σ (thin lines) intervals. The fit results are normalised to the SM predictions for the various parameters and the shaded bands indicate the theoretical uncertainties in these predictions.

JHEP08(2016)045

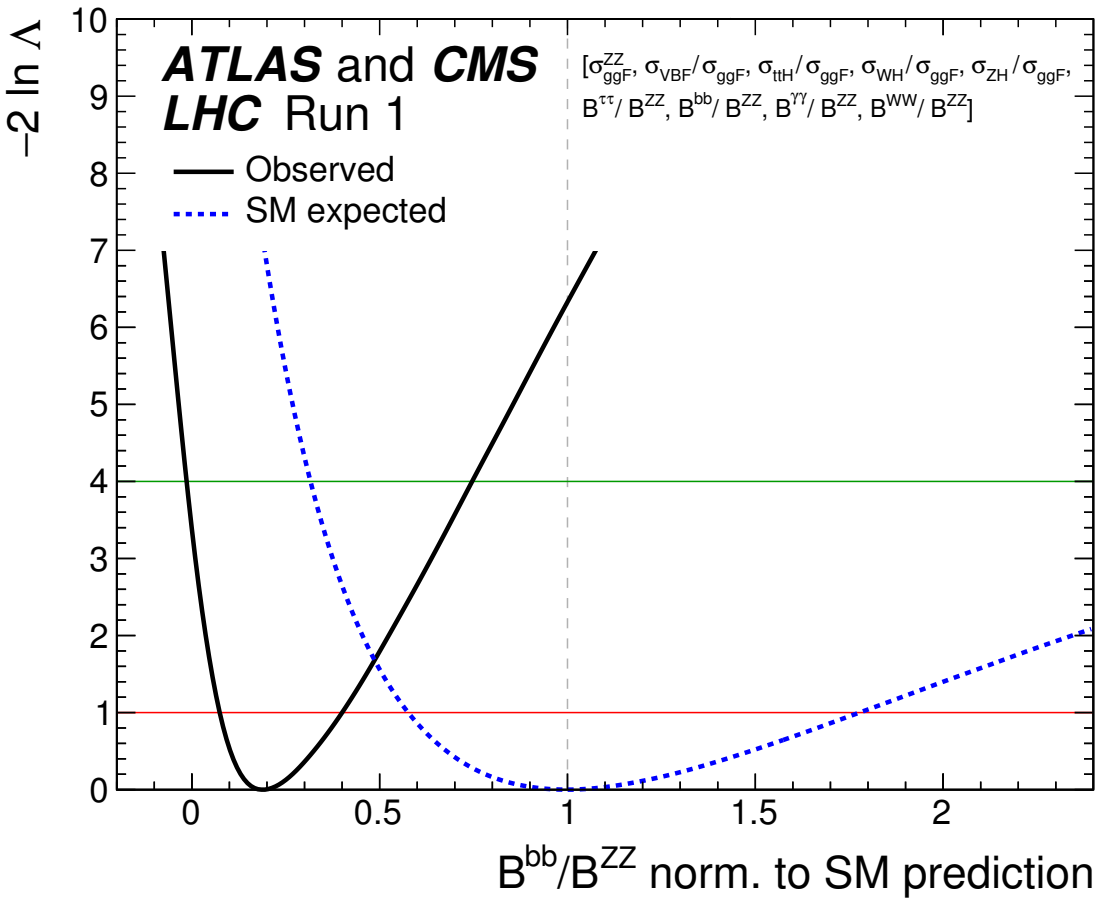

Figure 9. Observed (solid line) and expected (dashed line) negative log-likelihood scan of the $\mathrm{B}^{bb}/\mathrm{B}^{ZZ}$ parameter normalised to the corresponding SM prediction. All the other parameters of interest are also varied in the minimisation procedure. The red (green) horizontal line at the $-2\Delta\ln\Lambda$ value of 1 (4) indicates the value of the profile likelihood ratio corresponding to a 1σ (2σ) CL interval for the parameter of interest, assuming the asymptotic χ^2 distribution of the test statistic. The vertical dashed line indicates the SM prediction.

in $\sigma(gg \to H \to ZZ)$ are reduced by almost a factor of two in table 9, owing to the contributions from the other decay channels (mainly $H \to \gamma\gamma$ and $H \to WW$). The total uncertainty in $\sigma(gg \to H \to ZZ)$ is approximately 18%, with its main contribution coming from the statistical uncertainty. The total relative systematic uncertainty is only ∼4%. Appendix B shows the results obtained when choosing the $H \to WW$ decay mode as an alternative reference process. This yields a smaller total uncertainty of approximately 15% in $\sigma(gg \to H \to WW)$, but with a much larger contribution of ∼11% from the systematic uncertainties. The ratios $\sigma_{\mathrm{VBF}}/\sigma_{gg\mathrm{F}}$, $\mathrm{B}^{WW}/\mathrm{B}^{ZZ}$, $\mathrm{B}^{\gamma\gamma}/\mathrm{B}^{ZZ}$, and $\mathrm{B}^{\tau\tau}/\mathrm{B}^{ZZ}$ are measured with relative uncertainties of 30–40%.

The p-value of the compatibility between the data and the SM predictions is 16%. Most measurements are consistent with the SM predictions within less than 2σ; however, the

JHEP08(2016)045

Parameter	Best fit value	Uncertainty Stat	Uncertainty Syst	Best fit value	Uncertainty Stat	Uncertainty Syst	Best fit value	Uncertainty Stat	Uncertainty Syst
	ATLAS+CMS			ATLAS			CMS		
κ_{gZ}	$1.09\,^{+0.11}_{-0.11}$	$^{+0.09}_{-0.09}$	$^{+0.06}_{-0.06}$	$1.20\,^{+0.16}_{-0.15}$	$^{+0.14}_{-0.14}$	$^{+0.08}_{-0.07}$	$0.99\,^{+0.14}_{-0.13}$	$^{+0.12}_{-0.12}$	$^{+0.07}_{-0.06}$
	$\left(^{+0.11}_{-0.11}\right)$	$\left(^{+0.09}_{-0.09}\right)$	$\left(^{+0.06}_{-0.05}\right)$	$\left(^{+0.15}_{-0.15}\right)$	$\left(^{+0.14}_{-0.13}\right)$	$\left(^{+0.07}_{-0.06}\right)$	$\left(^{+0.14}_{-0.14}\right)$	$\left(^{+0.13}_{-0.12}\right)$	$\left(^{+0.07}_{-0.06}\right)$
λ_{Zg}	$1.27\,^{+0.23}_{-0.20}$	$^{+0.18}_{-0.16}$	$^{+0.15}_{-0.12}$	$1.07\,^{+0.26}_{-0.22}$	$^{+0.21}_{-0.18}$	$^{+0.15}_{-0.11}$	$1.47\,^{+0.45}_{-0.34}$	$^{+0.35}_{-0.28}$	$^{+0.28}_{-0.20}$
	$\left(^{+0.20}_{-0.17}\right)$	$\left(^{+0.15}_{-0.14}\right)$	$\left(^{+0.12}_{-0.10}\right)$	$\left(^{+0.28}_{-0.23}\right)$	$\left(^{+0.23}_{-0.20}\right)$	$\left(^{+0.16}_{-0.11}\right)$	$\left(^{+0.27}_{-0.23}\right)$	$\left(^{+0.21}_{-0.19}\right)$	$\left(^{+0.16}_{-0.13}\right)$
λ_{tg}	$1.78\,^{+0.30}_{-0.27}$	$^{+0.21}_{-0.20}$	$^{+0.21}_{-0.18}$	$1.40\,^{+0.34}_{-0.33}$	$^{+0.25}_{-0.24}$	$^{+0.23}_{-0.23}$	$-2.26\,^{+0.50}_{-0.53}$	$^{+0.43}_{-0.39}$	$^{+0.26}_{-0.36}$
	$\left(^{+0.28}_{-0.38}\right)$	$\left(^{+0.20}_{-0.30}\right)$	$\left(^{+0.20}_{-0.24}\right)$	$\left(^{+0.38}_{-0.54}\right)$	$\left(^{+0.28}_{-0.39}\right)$	$\left(^{+0.25}_{-0.37}\right)$	$\left(^{+0.42}_{-0.64}\right)$	$\left(^{+0.31}_{-0.42}\right)$	$\left(^{+0.28}_{-0.49}\right)$
λ_{WZ}	$0.88\,^{+0.10}_{-0.09}$	$^{+0.09}_{-0.08}$	$^{+0.04}_{-0.04}$	$0.92\,^{+0.14}_{-0.12}$	$^{+0.13}_{-0.11}$	$^{+0.05}_{-0.05}$	$-0.85\,^{+0.13}_{-0.15}$	$^{+0.11}_{-0.13}$	$^{+0.06}_{-0.07}$
	$\left(^{+0.12}_{-0.10}\right)$	$\left(^{+0.11}_{-0.09}\right)$	$\left(^{+0.05}_{-0.04}\right)$	$\left(^{+0.18}_{-0.15}\right)$	$\left(^{+0.17}_{-0.13}\right)$	$\left(^{+0.06}_{-0.06}\right)$	$\left(^{+0.17}_{-0.14}\right)$	$\left(^{+0.15}_{-0.13}\right)$	$\left(^{+0.07}_{-0.06}\right)$
$\lvert\lambda_{\gamma Z}\rvert$	$0.89\,^{+0.11}_{-0.10}$	$^{+0.10}_{-0.09}$	$^{+0.04}_{-0.03}$	$0.87\,^{+0.15}_{-0.13}$	$^{+0.15}_{-0.13}$	$^{+0.05}_{-0.04}$	$0.91\,^{+0.17}_{-0.14}$	$^{+0.16}_{-0.14}$	$^{+0.05}_{-0.04}$
	$\left(^{+0.13}_{-0.12}\right)$	$\left(^{+0.13}_{-0.11}\right)$	$\left(^{+0.04}_{-0.03}\right)$	$\left(^{+0.20}_{-0.17}\right)$	$\left(^{+0.20}_{-0.17}\right)$	$\left(^{+0.06}_{-0.04}\right)$	$\left(^{+0.18}_{-0.16}\right)$	$\left(^{+0.18}_{-0.15}\right)$	$\left(^{+0.05}_{-0.04}\right)$
$\lvert\lambda_{\tau Z}\rvert$	$0.85\,^{+0.13}_{-0.12}$	$^{+0.12}_{-0.10}$	$^{+0.07}_{-0.06}$	$0.96\,^{+0.21}_{-0.18}$	$^{+0.18}_{-0.15}$	$^{+0.11}_{-0.09}$	$0.78\,^{+0.20}_{-0.17}$	$^{+0.17}_{-0.15}$	$^{+0.10}_{-0.09}$
	$\left(^{+0.17}_{-0.15}\right)$	$\left(^{+0.14}_{-0.13}\right)$	$\left(^{+0.09}_{-0.08}\right)$	$\left(^{+0.27}_{-0.23}\right)$	$\left(^{+0.23}_{-0.19}\right)$	$\left(^{+0.14}_{-0.12}\right)$	$\left(^{+0.23}_{-0.20}\right)$	$\left(^{+0.19}_{-0.17}\right)$	$\left(^{+0.12}_{-0.11}\right)$
$\lvert\lambda_{bZ}\rvert$	$0.58\,^{+0.16}_{-0.20}$	$^{+0.12}_{-0.17}$	$^{+0.10}_{-0.10}$	$0.61\,^{+0.24}_{-0.24}$	$^{+0.20}_{-0.19}$	$^{+0.14}_{-0.16}$	$0.47\,^{+0.26}_{-0.17}$	$^{+0.23}_{-0.13}$	$^{+0.13}_{-0.12}$
	$\left(^{+0.25}_{-0.22}\right)$	$\left(^{+0.21}_{-0.20}\right)$	$\left(^{+0.13}_{-0.10}\right)$	$\left(^{+0.36}_{-0.29}\right)$	$\left(^{+0.31}_{-0.26}\right)$	$\left(^{+0.18}_{-0.13}\right)$	$\left(^{+0.38}_{-0.37}\right)$	$\left(^{+0.32}_{-0.34}\right)$	$\left(^{+0.20}_{-0.16}\right)$

Table 10. Best fit values of $\kappa_{gZ} = \kappa_g \cdot \kappa_Z/\kappa_H$ and of the ratios of coupling modifiers, as defined in the parameterisation studied in the context of the κ-framework, from the combined analysis of the $\sqrt{s} = 7$ and 8 TeV data. The results are shown for the combination of ATLAS and CMS and also separately for each experiment, together with their total uncertainties and their breakdown into statistical and systematic components. The uncertainties in λ_{tg} and λ_{WZ}, for which a negative solution is allowed, are calculated around the overall best fit value. The combined 1σ CL intervals are $\lambda_{tg} = [-2.00, -1.59] \cup [1.50, 2.07]$ and $\lambda_{WZ} = [-0.96, -0.82] \cup [0.80, 0.98]$. The expected uncertainties in the measurements are displayed in parentheses. For those parameters with no sensitivity to the sign, only the absolute values are shown.

production cross section ratio $\sigma_{ttH}/\sigma_{gg\mathrm{F}}$ relative to the SM ratio is measured to be $3.3^{+1.0}_{-0.9}$, corresponding to an excess of approximately 3.0σ relative to the SM prediction. This excess is mainly due to the multi-lepton categories. The ratio $\sigma_{ZH}/\sigma_{gg\mathrm{F}}$ relative to the SM ratio is measured to be $3.2^{+1.8}_{-1.4}$, with the observed excess mainly due to the ZH, $H \to WW$ measurements. The ratio of branching fractions $\mathrm{B}^{bb}/\mathrm{B}^{ZZ}$ is measured to be $0.19^{+0.21}_{-0.12}$ relative to the SM prediction. In this parameterisation, the high values found for the production cross section ratios for the ZH and ttH processes induce a low value for the $H \to bb$ decay branching fraction because the $H \to bb$ decay mode does not contribute to the observed excesses. The likelihood scan of the $\mathrm{B}^{bb}/\mathrm{B}^{ZZ}$ parameter is very asymmetric, as shown in figure 9, resulting in an overall deficit of approximately 2.5σ relative to the SM prediction. This deviation is anticorrelated with the ones quoted above for the $\sigma_{ttH}/\sigma_{gg\mathrm{F}}$ and $\sigma_{ZH}/\sigma_{gg\mathrm{F}}$ production cross section ratios, as shown in figure 28 of appendix A.

JHEP08(2016)045

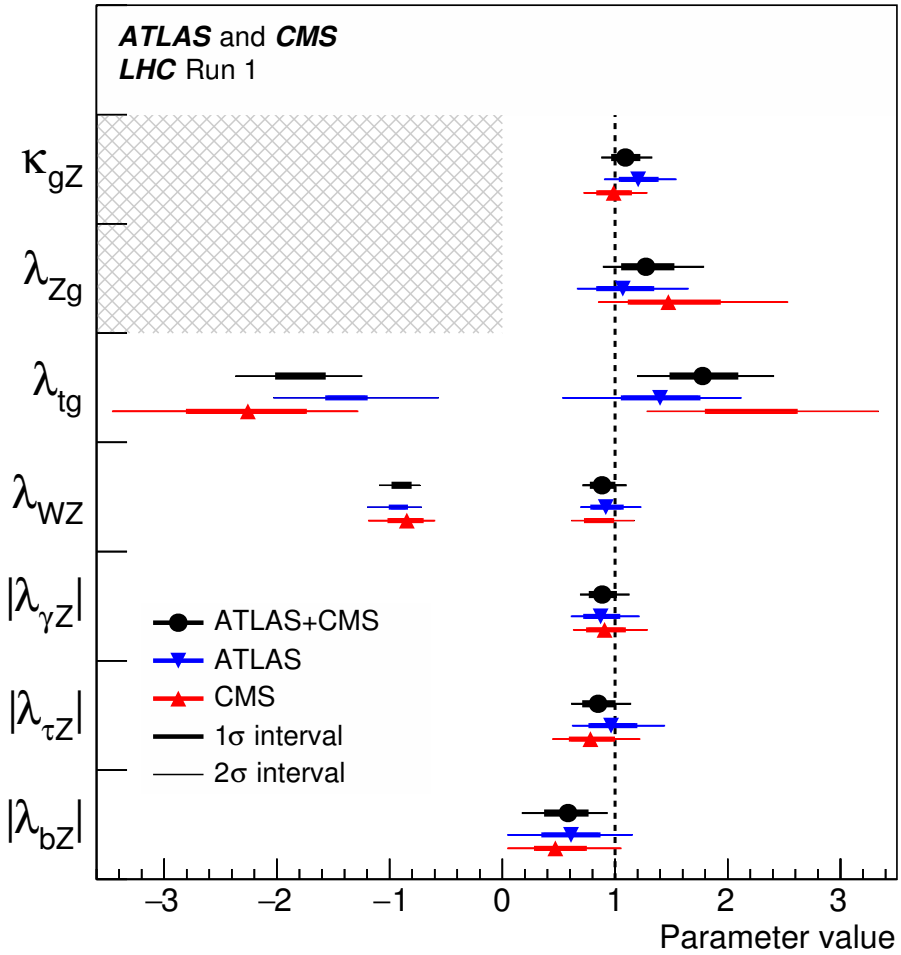

Figure 10. Best fit values of ratios of Higgs boson coupling modifiers, as obtained from the generic parameterisation described in the text and as tabulated in table 10 for the combination of the ATLAS and CMS measurements. Also shown are the results from each experiment. The error bars indicate the 1σ (thick lines) and 2σ (thin lines) intervals. The hatched areas indicate the non-allowed regions for the parameters that are assumed to be positive without loss of generality. For those parameters with no sensitivity to the sign, only the absolute values are shown.

In the various fits, the combination of the 7 and 8 TeV data is performed assuming that the ratios of the production cross sections at 7 and 8 TeV are the same as in the SM. One can introduce as free parameters in the fit the ratios of the production cross sections at 7 and 8 TeV of the five main production processes: $\sigma_i(7\text{TeV})/\sigma_i(8\text{TeV})$. Given the limited size of the data samples at 7 TeV, only the ggF and VBF ratios can be extracted with a meaningful precision. The results are: $\sigma_{gg\text{F}}(7\text{ TeV})/\sigma_{gg\text{F}}(8\text{ TeV}) = 1.12^{+0.33}_{-0.29}$ and $\sigma_{\text{VBF}}(7\text{ TeV})/\sigma_{\text{VBF}}(8\text{ TeV}) = 0.37^{+0.49}_{-0.43}$. Both values are consistent with the SM predictions of $\sigma_{gg\text{F}}(7\text{ TeV})/\sigma_{gg\text{F}}(8\text{ TeV}) = 0.78$ and $\sigma_{\text{VBF}}(7\text{ TeV})/\sigma_{\text{VBF}}(8\text{ TeV}) = 0.77$.

JHEP08(2016)045

4.2 Parameterisation using ratios of coupling modifiers

The parameterisation using the Higgs boson coupling modifiers is based on the κ-framework described in section 2.4 and the parameters of interest are listed in the right column of table 6. The cross section times branching fraction for the $gg \to H \to ZZ$ channel is parameterised as a function of $\kappa_{gZ} = \kappa_g \cdot \kappa_Z/\kappa_H$, where κ_g is the effective coupling modifier of the Higgs boson to the gluon in ggF production, which in the SM occurs mainly through loops involving top and bottom quarks. The $\lambda_{Zg} = \kappa_Z/\kappa_g$ parameter is probed by the measurements of VBF and ZH production, while the measurements of the ttH production process are sensitive to $\lambda_{tg} = \kappa_t/\kappa_g$. Three of the decay modes, namely $H \to WW$, $H \to \tau\tau$, and $H \to bb$, probe the three ratios $\lambda_{WZ} = \kappa_W/\kappa_Z$, $\lambda_{\tau Z} = \kappa_\tau/\kappa_Z$, and $\lambda_{bZ} = \kappa_b/\kappa_Z$, through their respective ratios to the $H \to ZZ$ branching fraction. The remaining decay mode, $H \to \gamma\gamma$, which in the SM occurs through loops involving predominantly the top quark and the W boson, is sensitive to the ratio $\lambda_{\gamma Z} = \kappa_\gamma/\kappa_Z$. In this parameterisation, $\lambda_{WZ} = \kappa_W/\kappa_Z$ is also probed by the VBF, WH, and ZH production processes. Without any loss of generality, the signs of κ_Z and κ_g can be assumed to be the same, constraining λ_{Zg} and κ_{gZ} to be positive.

Table 10 shows the results of the fit to the data with a breakdown of uncertainties into their statistical and systematic components, while the complete breakdown of the uncertainties into the four components is shown in table 22 of appendix B. The measured correlation matrix can be found in figure 29 of appendix A. The coupling modifiers are assumed to be the same at the two centre-of-mass energies, as in the parameterisation based on the ratios of cross sections and branching fractions. Figure 10 illustrates the complete ranges of allowed values with their total uncertainties, including the negative ranges allowed for λ_{WZ} and λ_{tg}, the two parameters chosen to illustrate possible interference effects due to $ggZH$ or tH production. Figure 11 shows the likelihood scan results for these two parameters for the combination of ATLAS and CMS, both for the observed and expected results. As described in section 2.4, the interference terms are responsible for the small asymmetry between the likelihood curves for the positive and negative values of the parameters of interest. In both cases, the best fit values correspond to the positive sign, but the sensitivity to the interference terms remains small. Appendix C, with the specific example of λ_{bZ} (shown in figure 31), describes how the four possible sign combinations between λ_{WZ} and λ_{tg} may impact the best fit value and the uncertainty in the other parameters of interest. The p-value of the compatibility between the data and the SM predictions is 13%. All results are consistent with the SM predictions within less than 2σ, except those for λ_{tg} and λ_{bZ}, which exhibit deviations from the SM similar to those reported and explained in section 4.1.2 for the measurement of the ratios of the ttH and ggF production cross sections, and of the ratios of the bb and ZZ decay branching fractions.

5 Measurements of signal strengths

Section 4.1 presents the results from generic parameterisations, expressed in terms of cross sections and branching fractions. This section probes more specific parameterisations, with additional assumptions. Results for these parameterisations are presented, starting with

JHEP08(2016)045

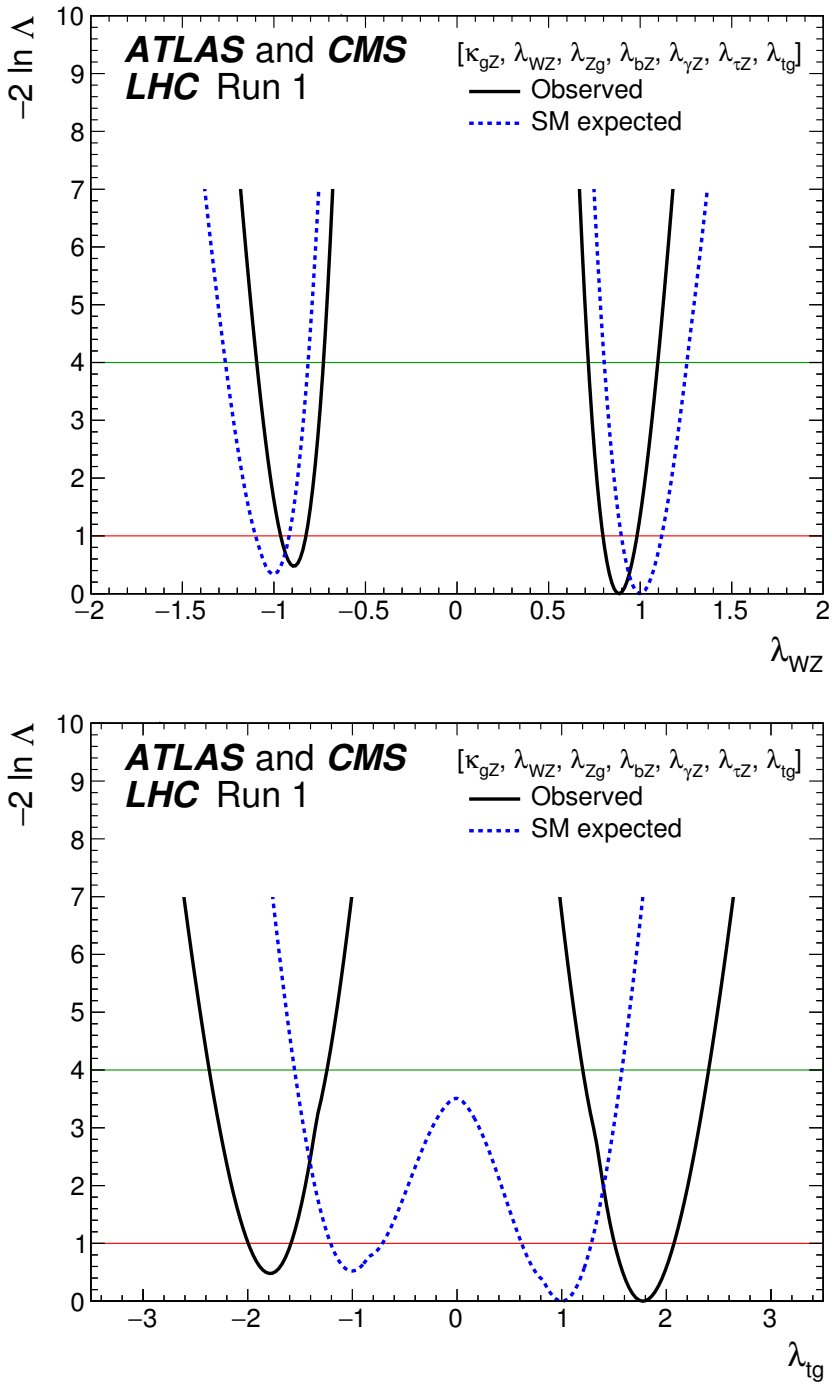

Figure 11. Observed (solid line) and expected (dashed line) negative log-likelihood scans for λ_{WZ} (top) and λ_{tg} (bottom), the two parameters of figure 10 that are of interest in the negative range in the generic parameterisation of ratios of Higgs boson coupling modifiers described in the text. All the other parameters of interest from the list in the legend are also varied in the minimisation procedure. The red (green) horizontal lines at the $-2\Delta \ln \Lambda$ value of 1 (4) indicate the value of the profile likelihood ratio corresponding to a 1σ (2σ) CL interval for the parameter of interest, assuming the asymptotic χ^2 distribution of the test statistic.

JHEP08(2016)045

	Best fit μ	Uncertainty				
		Total	Stat	Expt	Thbgd	Thsig
ATLAS + CMS (measured)	1.09	$^{+0.11}_{-0.10}$	$^{+0.07}_{-0.07}$	$^{+0.04}_{-0.04}$	$^{+0.03}_{-0.03}$	$^{+0.07}_{-0.06}$
ATLAS + CMS (expected)		$^{+0.11}_{-0.10}$	$^{+0.07}_{-0.07}$	$^{+0.04}_{-0.04}$	$^{+0.03}_{-0.03}$	$^{+0.07}_{-0.06}$
ATLAS (measured)	1.20	$^{+0.15}_{-0.14}$	$^{+0.10}_{-0.10}$	$^{+0.06}_{-0.06}$	$^{+0.04}_{-0.04}$	$^{+0.08}_{-0.07}$
ATLAS (expected)		$^{+0.14}_{-0.13}$	$^{+0.10}_{-0.10}$	$^{+0.06}_{-0.05}$	$^{+0.04}_{-0.04}$	$^{+0.07}_{-0.06}$
CMS (measured)	0.97	$^{+0.14}_{-0.13}$	$^{+0.09}_{-0.09}$	$^{+0.05}_{-0.05}$	$^{+0.04}_{-0.03}$	$^{+0.07}_{-0.06}$
CMS (expected)		$^{+0.14}_{-0.13}$	$^{+0.09}_{-0.09}$	$^{+0.05}_{-0.05}$	$^{+0.04}_{-0.03}$	$^{+0.08}_{-0.06}$

Table 11. Measured global signal strength μ and its total uncertainty, together with the breakdown of the uncertainty into its four components as defined in section 3.3. The results are shown for the combination of ATLAS and CMS, and separately for each experiment. The expected uncertainty, with its breakdown, is also shown.

the most restrictive one using a single parameter of interest, which was used to assess the sensitivity of the experimental analyses to the presence of a Higgs boson at the time of its discovery. Section 5.4 describes the test of a hypothesis that two or more neutral Higgs bosons might be present with similar masses.

5.1 Global signal strength

The simplest and most restrictive signal strength parameterisation is to assume that the values of the signal strengths μ_i^f, as defined in eq. (2.2), are the same for all production processes i and decay channels f. In this case, the SM predictions of signal yields in all categories are scaled by a global signal strength μ. Such a parameterisation provides the simplest test of the compatibility of the experimental data with the SM predictions. A fit to the ATLAS and CMS data at $\sqrt{s} = 7$ and 8 TeV with μ as the parameter of interest results in the best fit value:

$$\mu = 1.09^{+0.11}_{-0.10} = 1.09^{+0.07}_{-0.07}\ (\text{stat})\ ^{+0.04}_{-0.04}\ (\text{expt})\ ^{+0.03}_{-0.03}\ (\text{thbgd})^{+0.07}_{-0.06}\ (\text{thsig}),$$

where the breakdown of the uncertainties into their four components is performed as described in section 3.3. The overall systematic uncertainty of $^{+0.09}_{-0.08}$ is larger than the statistical uncertainty and its largest component is the theoretical uncertainty in the ggF cross section. This result is consistent with the SM prediction of $\mu = 1$ within less than 1σ and the p-value of the compatibility between the data and the SM predictions is 40%. This result is shown in table 11, together with that from each experiment, including the breakdown of the uncertainties into their four components. The expected uncertainties and their breakdown are also given.

JHEP08(2016)045

Production process	ATLAS+CMS	ATLAS	CMS
$\mu_{gg\mathrm{F}}$	$1.03\,^{+0.16}_{-0.14}$ $\left(^{+0.16}_{-0.14}\right)$	$1.26\,^{+0.23}_{-0.20}$ $\left(^{+0.21}_{-0.18}\right)$	$0.84\,^{+0.18}_{-0.16}$ $\left(^{+0.20}_{-0.17}\right)$
μ_{VBF}	$1.18\,^{+0.25}_{-0.23}$ $\left(^{+0.24}_{-0.23}\right)$	$1.21\,^{+0.33}_{-0.30}$ $\left(^{+0.32}_{-0.29}\right)$	$1.14\,^{+0.37}_{-0.34}$ $\left(^{+0.36}_{-0.34}\right)$
μ_{WH}	$0.89\,^{+0.40}_{-0.38}$ $\left(^{+0.41}_{-0.39}\right)$	$1.25\,^{+0.56}_{-0.52}$ $\left(^{+0.56}_{-0.53}\right)$	$0.46\,^{+0.57}_{-0.53}$ $\left(^{+0.60}_{-0.57}\right)$
μ_{ZH}	$0.79\,^{+0.38}_{-0.36}$ $\left(^{+0.39}_{-0.36}\right)$	$0.30\,^{+0.51}_{-0.45}$ $\left(^{+0.55}_{-0.51}\right)$	$1.35\,^{+0.58}_{-0.54}$ $\left(^{+0.55}_{-0.51}\right)$
μ_{ttH}	$2.3\,^{+0.7}_{-0.6}$ $\left(^{+0.5}_{-0.5}\right)$	$1.9\,^{+0.8}_{-0.7}$ $\left(^{+0.7}_{-0.7}\right)$	$2.9\,^{+1.0}_{-0.9}$ $\left(^{+0.9}_{-0.8}\right)$

Table 12. Measured signal strengths μ and their total uncertainties for different Higgs boson production processes. The results are shown for the combination of ATLAS and CMS, and separately for each experiment, for the combined $\sqrt{s} = 7$ and 8 TeV data. The expected uncertainties in the measurements are displayed in parentheses. These results are obtained assuming that the Higgs boson branching fractions are the same as in the SM.

5.2 Signal strengths of individual production processes and decay channels

The global signal strength is the most precisely measured Higgs boson coupling-related observable, but this simple parameterisation is very model dependent, since all Higgs boson production and decay measurements are combined assuming that all their ratios are the same as in the SM. The compatibility of the measurements with the SM can be tested in a less model-dependent way by relaxing these assumptions separately for the production cross sections and the decay branching fractions.

Assuming the SM values for the Higgs boson branching fractions, namely $\mu^f = 1$ in eq. (3.1), the five main Higgs boson production processes are explored with independent signal strengths: $\mu_{gg\mathrm{F}}$, μ_{VBF}, μ_{WH}, μ_{ZH}, and μ_{ttH}. A combined analysis of the ATLAS and CMS data is performed with these five signal strengths as parameters of interest. The results are shown in table 12 for the combined $\sqrt{s} = 7$ and 8 TeV data sets. The signal strengths at the two energies are assumed to be the same for each production process. Figure 12 illustrates these results with their total uncertainties. The p-value of the compatibility between the data and the SM predictions is 24%.

JHEP08(2016)045

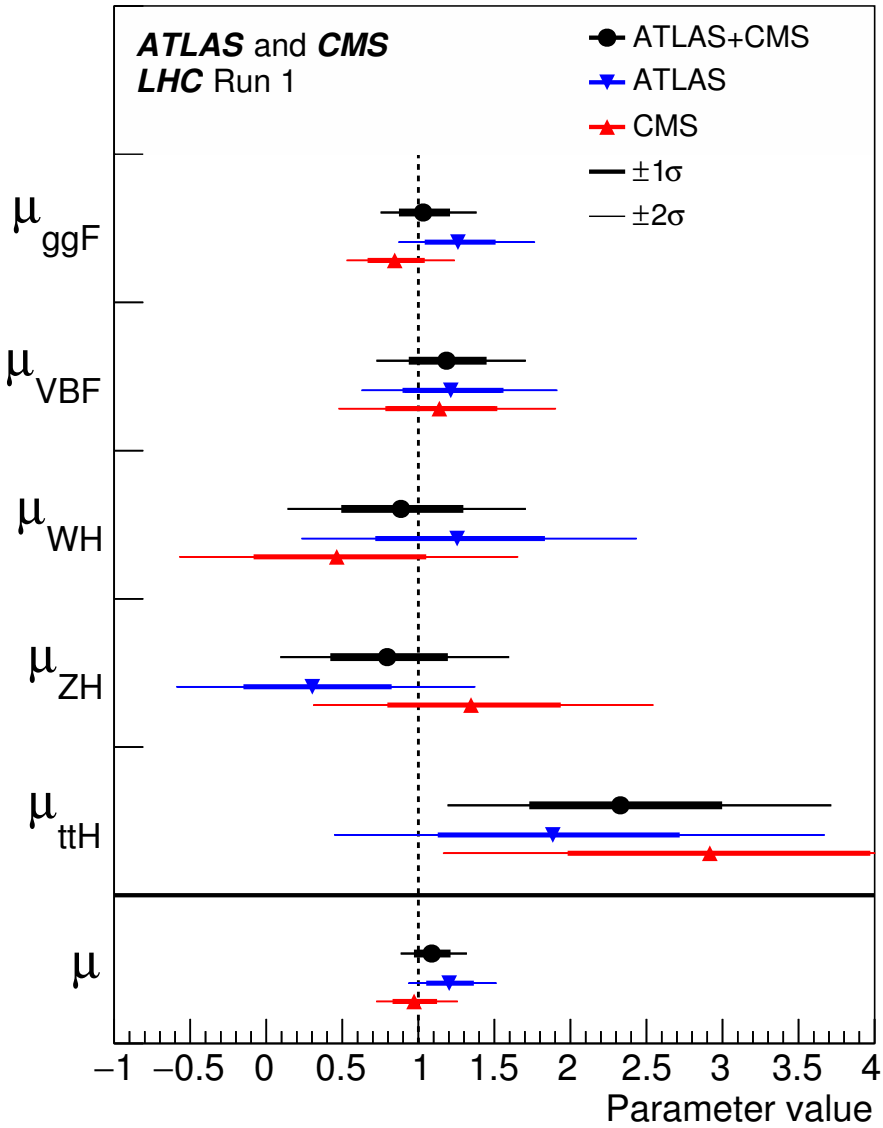

Figure 12. Best fit results for the production signal strengths for the combination of ATLAS and CMS data. Also shown are the results from each experiment. The error bars indicate the 1σ (thick lines) and 2σ (thin lines) intervals. The measurements of the global signal strength μ are also shown.

Higgs boson decays are also studied with six independent signal strengths, one for each decay channel included in the combination, assuming that the Higgs boson production cross sections are the same as in the SM. Unlike the production signal strengths, these decay-based signal strengths are independent of the collision centre-of-mass energy and therefore the $\sqrt{s} = 7$ and 8 TeV data sets can be combined without additional assumptions. Table 13 and figure 13 present the best fit results for the combination of ATLAS and CMS, and separately for each experiment (the results for $\mu^{\mu\mu}$ are only reported in table 13). The p-value of the compatibility between the data and the SM predictions is 75%.

JHEP08(2016)045

Decay channel	ATLAS+CMS	ATLAS	CMS
$\mu^{\gamma\gamma}$	$1.14\,^{+0.19}_{-0.18}$ $\left(^{+0.18}_{-0.17}\right)$	$1.14\,^{+0.27}_{-0.25}$ $\left(^{+0.26}_{-0.24}\right)$	$1.11\,^{+0.25}_{-0.23}$ $\left(^{+0.23}_{-0.21}\right)$
μ^{ZZ}	$1.29\,^{+0.26}_{-0.23}$ $\left(^{+0.23}_{-0.20}\right)$	$1.52\,^{+0.40}_{-0.34}$ $\left(^{+0.32}_{-0.27}\right)$	$1.04\,^{+0.32}_{-0.26}$ $\left(^{+0.30}_{-0.25}\right)$
μ^{WW}	$1.09\,^{+0.18}_{-0.16}$ $\left(^{+0.16}_{-0.15}\right)$	$1.22\,^{+0.23}_{-0.21}$ $\left(^{+0.21}_{-0.20}\right)$	$0.90\,^{+0.23}_{-0.21}$ $\left(^{+0.23}_{-0.20}\right)$
$\mu^{\tau\tau}$	$1.11\,^{+0.24}_{-0.22}$ $\left(^{+0.24}_{-0.22}\right)$	$1.41\,^{+0.40}_{-0.36}$ $\left(^{+0.37}_{-0.33}\right)$	$0.88\,^{+0.30}_{-0.28}$ $\left(^{+0.31}_{-0.29}\right)$
μ^{bb}	$0.70\,^{+0.29}_{-0.27}$ $\left(^{+0.29}_{-0.28}\right)$	$0.62\,^{+0.37}_{-0.37}$ $\left(^{+0.39}_{-0.37}\right)$	$0.81\,^{+0.45}_{-0.43}$ $\left(^{+0.45}_{-0.43}\right)$
$\mu^{\mu\mu}$	$0.1\,^{+2.5}_{-2.5}$ $\left(^{+2.4}_{-2.3}\right)$	$-0.6\,^{+3.6}_{-3.6}$ $\left(^{+3.6}_{-3.6}\right)$	$0.9\,^{+3.6}_{-3.5}$ $\left(^{+3.3}_{-3.2}\right)$

Table 13. Measured signal strengths μ and their total uncertainties for different Higgs boson decay channels. The results are shown for the combination of ATLAS and CMS, and separately for each experiment, for the combined $\sqrt{s} = 7$ and 8 TeV data. The expected uncertainties in the measurements are displayed in parentheses. These results are obtained assuming that the Higgs boson production process cross sections at $\sqrt{s} = 7$ and 8 TeV are the same as in the SM.

JHEP08(2016)045

From the combined likelihood scans it is possible to evaluate the significances for the observation of the different production processes and decay channels. The combination of the data from the two experiments corresponds to summing their recorded integrated luminosities and consequently increases the sensitivity by approximately a factor of $\sqrt{2}$, since the theoretical uncertainties in the Higgs boson signal are only weakly relevant for this evaluation and all the other significant uncertainties are uncorrelated between the two experiments. The results are reported in table 14 for all production processes and decay channels, except for those that have already been clearly observed, namely the ggF production process and the $H \to ZZ$, $H \to WW$, and $H \to \gamma\gamma$ decay channels. The combined significances for the observation of the VBF production process and of the $H \to \tau\tau$ decay are each above 5σ, and the combined significance for the VH production process is above 3σ. The combined significance for the ttH process is 4.4σ, whereas only 2.0σ is expected, corresponding to a measured excess of 2.3σ with respect to the SM prediction.

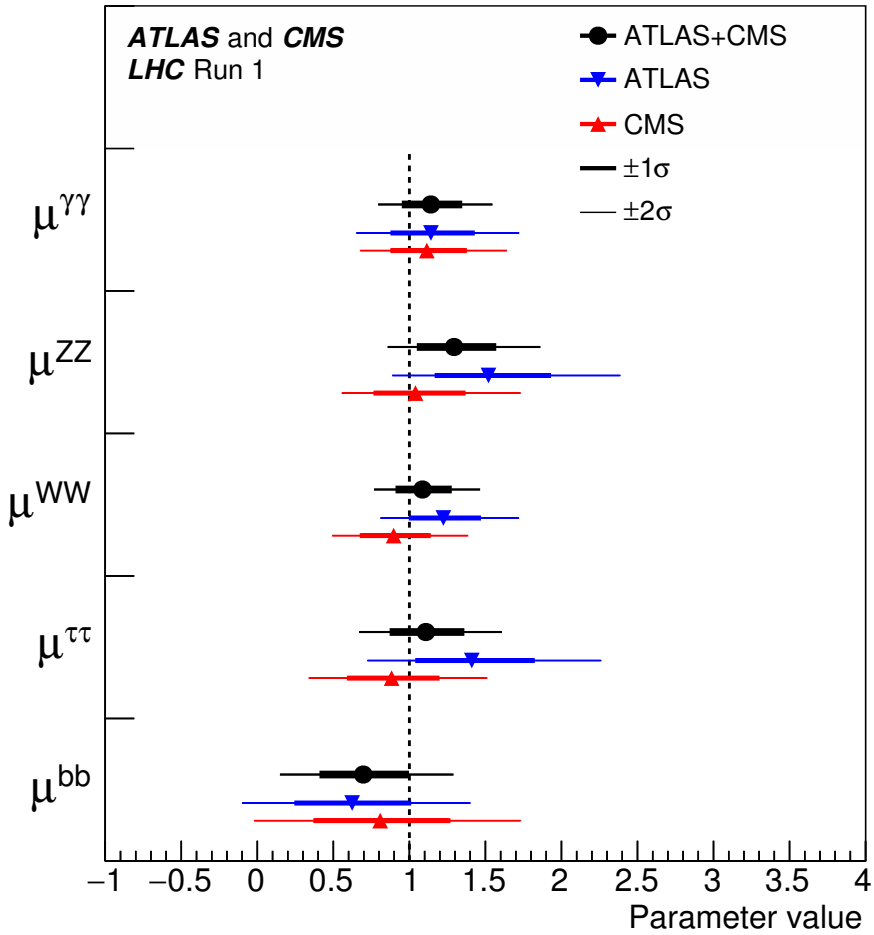

Figure 13. Best fit results for the decay signal strengths for the combination of ATLAS and CMS data (the results for $\mu^{\mu\mu}$ are reported in table 13). Also shown are the results from each experiment. The error bars indicate the 1σ (thick lines) and 2σ (thin lines) intervals.

5.3 Boson- and fermion-mediated production processes

The Higgs boson production processes can be associated with Higgs boson couplings to either fermions (ggF and ttH) or vector bosons (VBF, WH, and ZH). Potential deviations of these couplings from the SM predictions can be tested by using a parameterisation with two signal strengths for each decay channel f: $\mu_F^f = \mu_{gg\mathrm{F}+ttH}^f$ for the fermion-mediated production processes and $\mu_V^f = \mu_{\mathrm{VBF}+VH}^f$ for the vector-boson-mediated production processes. The branching fraction cancels in the ratio μ_V^f/μ_F^f that can be formed for each Higgs boson decay channel. Two fits are performed for the combination of ATLAS and CMS, and also separately for each experiment. The first is a ten-parameter fit of μ_F^f and μ_V^f for each of the five decay channels, while the second is a six-parameter fit of μ_V/μ_F and μ_F^f for each of the five decay channels.

JHEP08(2016)045

Production process	Measured significance (σ)	Expected significance (σ)
VBF	5.4	4.6
WH	2.4	2.7
ZH	2.3	2.9
VH	3.5	4.2
ttH	4.4	2.0
Decay channel		
$H \to \tau\tau$	5.5	5.0
$H \to bb$	2.6	3.7

Table 14. Measured and expected significances for the observation of Higgs boson production processes and decay channels for the combination of ATLAS and CMS. Not included are the ggF production process and the $H \to ZZ$, $H \to WW$, and $H \to \gamma\gamma$ decay channels, which have already been clearly observed. All results are obtained constraining the decay branching fractions to their SM values when considering the production processes, and constraining the production cross sections to their SM values when studying the decays.

Figure 14 shows the 68% CL region for the ten-parameter fit of the five decay channels included in the combination of the ATLAS and CMS measurements. These results are obtained by combining the $\sqrt{s} = 7$ and 8 TeV data, assuming that μ_F^f and μ_V^f are the same at the two energies. The SM predictions of $\mu_F^f = 1$ and $\mu_V^f = 1$ lie within the 68% CL regions of all these measurements. Combinations of these regions would require assumptions about the branching fractions and are therefore not performed. Table 15 reports the best fit values and the total uncertainties for all the parameters of the fits, together with the expected uncertainties for the combination of ATLAS and CMS. The p-values of the compatibility between the data and the SM predictions are 90% and 75% for the ten-parameter and six-parameter fits, respectively. The six-parameter fit, without any additional assumptions about the Higgs boson branching fractions, yields: $\mu_V/\mu_F = 1.09^{+0.36}_{-0.28}$, in agreement with the SM.

JHEP08(2016)045

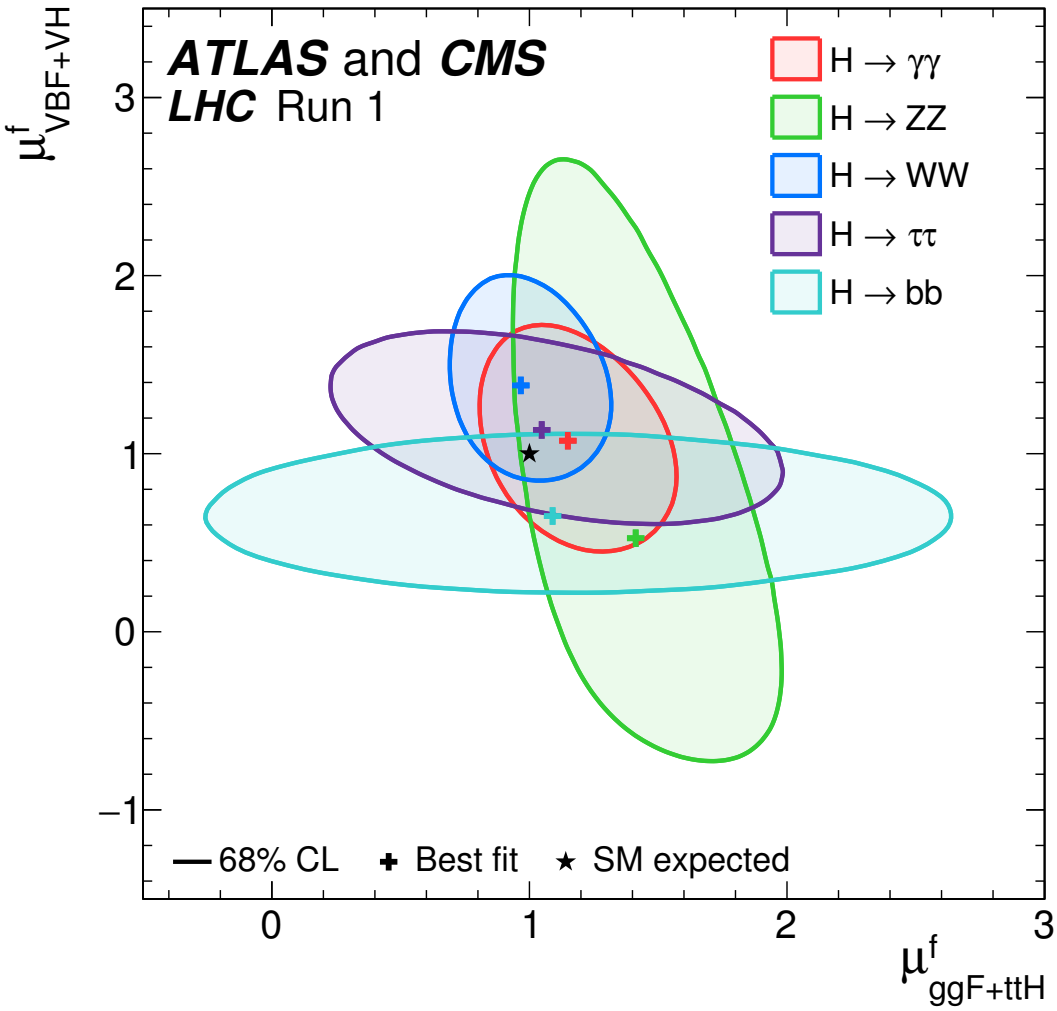

Figure 14. Negative log-likelihood contours at 68% CL in the $(\mu^f_{gg\mathrm{F}+ttH}, \mu^f_{\mathrm{VBF}+VH})$ plane for the combination of ATLAS and CMS, as obtained from the ten-parameter fit described in the text for each of the five decay channels $H \to ZZ$, $H \to WW$, $H \to \gamma\gamma$, $H \to \tau\tau$, and $H \to bb$. The best fit values obtained for each of the five decay channels are also shown, together with the SM expectation.

5.4 Search for mass-degenerate states with different coupling structures

One important assumption underlying all the results reported elsewhere in this paper is that the observations are due to the presence of a single particle with well defined mass that has been precisely measured [22]. This section addresses the case in which the observed signal could be due to the presence of two or more particles with similar masses, such that they cannot be resolved within the current precision of the mass measurements in the different channels. Several BSM models predict, for example, a superposition of states with indistinguishable mass values [122–125], possibly with different coupling structures to the SM particles. With such an assumption, it may be possible to distinguish between single and multiple states by measuring the cross sections of individual production processes

JHEP08(2016)045

Parameter	ATLAS+CMS Measured	ATLAS+CMS Expected uncertainty	ATLAS Measured	CMS Measured
Ten-parameter fit of μ_F^f and μ_V^f				
$\mu_V^{\gamma\gamma}$	$1.05^{+0.44}_{-0.41}$	$^{+0.41}_{-0.38}$	$0.69^{+0.63}_{-0.58}$	$1.37^{+0.62}_{-0.56}$
μ_V^{ZZ}	$0.47^{+1.37}_{-0.92}$	$^{+1.16}_{-0.84}$	$0.24^{+1.60}_{-0.93}$	$1.45^{+2.32}_{-2.29}$
μ_V^{WW}	$1.38^{+0.41}_{-0.37}$	$^{+0.38}_{-0.35}$	$1.56^{+0.52}_{-0.46}$	$1.08^{+0.65}_{-0.58}$
$\mu_V^{\tau\tau}$	$1.12^{+0.37}_{-0.35}$	$^{+0.38}_{-0.35}$	$1.29^{+0.58}_{-0.53}$	$0.88^{+0.49}_{-0.45}$
μ_V^{bb}	$0.65^{+0.31}_{-0.29}$	$^{+0.32}_{-0.30}$	$0.50^{+0.39}_{-0.37}$	$0.85^{+0.47}_{-0.44}$
$\mu_F^{\gamma\gamma}$	$1.16^{+0.27}_{-0.24}$	$^{+0.25}_{-0.23}$	$1.30^{+0.37}_{-0.33}$	$1.00^{+0.33}_{-0.30}$
μ_F^{ZZ}	$1.42^{+0.37}_{-0.33}$	$^{+0.29}_{-0.25}$	$1.74^{+0.51}_{-0.44}$	$0.96^{+0.53}_{-0.41}$
μ_F^{WW}	$0.98^{+0.22}_{-0.20}$	$^{+0.21}_{-0.19}$	$1.10^{+0.29}_{-0.26}$	$0.84^{+0.27}_{-0.24}$
$\mu_F^{\tau\tau}$	$1.06^{+0.60}_{-0.56}$	$^{+0.56}_{-0.53}$	$1.72^{+1.24}_{-1.12}$	$0.89^{+0.67}_{-0.63}$
μ_F^{bb}	$1.15^{+0.99}_{-0.94}$	$^{+0.90}_{-0.86}$	$1.52^{+1.16}_{-1.09}$	$0.11^{+1.85}_{-1.90}$
Six-parameter fit of global μ_V/μ_F and of μ_F^f				
μ_V/μ_F	$1.09^{+0.36}_{-0.28}$	$^{+0.34}_{-0.27}$	$0.92^{+0.40}_{-0.30}$	$1.31^{+0.68}_{-0.47}$
$\mu_F^{\gamma\gamma}$	$1.10^{+0.23}_{-0.21}$	$^{+0.21}_{-0.19}$	$1.17^{+0.32}_{-0.28}$	$1.01^{+0.29}_{-0.25}$
μ_F^{ZZ}	$1.27^{+0.28}_{-0.24}$	$^{+0.24}_{-0.20}$	$1.55^{+0.43}_{-0.35}$	$0.98^{+0.32}_{-0.26}$
μ_F^{WW}	$1.06^{+0.21}_{-0.18}$	$^{+0.19}_{-0.17}$	$1.25^{+0.28}_{-0.24}$	$0.84^{+0.25}_{-0.21}$
$\mu_F^{\tau\tau}$	$1.05^{+0.33}_{-0.27}$	$^{+0.33}_{-0.27}$	$1.50^{+0.64}_{-0.48}$	$0.74^{+0.38}_{-0.29}$
μ_F^{bb}	$0.64^{+0.37}_{-0.28}$	$^{+0.45}_{-0.34}$	$0.67^{+0.58}_{-0.41}$	$0.63^{+0.53}_{-0.35}$

Table 15. Results of the ten-parameter fit of $\mu_F^f = \mu_{gg\mathrm{F}+ttH}^f$ and $\mu_V^f = \mu_{\mathrm{VBF}+VH}^f$ for each of the five decay channels, and of the six-parameter fit of the global ratio $\mu_V/\mu_F = \mu_{\mathrm{VBF}+VH}/\mu_{gg\mathrm{F}+ttH}$ together with μ_F^f for each of the five decay channels. The results are shown for the combination of ATLAS and CMS, together with their measured and expected uncertainties. The measured results are also shown separately for each experiment.

JHEP08(2016)045

General matrix parameterisation: rank($\mathcal{M}$) = 5					
	$H \to \gamma\gamma$	$H \to ZZ$	$H \to WW$	$H \to \tau\tau$	$H \to bb$
ggF	$\mu^{\gamma\gamma}_{gg\mathrm{F}}$	$\mu^{ZZ}_{gg\mathrm{F}}$	$\mu^{WW}_{gg\mathrm{F}}$	$\mu^{\tau\tau}_{gg\mathrm{F}}$	$\mu^{bb}_{gg\mathrm{F}}$
VBF	$\lambda^{\gamma\gamma}_{\mathrm{VBF}}\,\mu^{\gamma\gamma}_{gg\mathrm{F}}$	$\lambda^{ZZ}_{\mathrm{VBF}}\,\mu^{ZZ}_{gg\mathrm{F}}$	$\lambda^{WW}_{\mathrm{VBF}}\,\mu^{WW}_{gg\mathrm{F}}$	$\lambda^{\tau\tau}_{\mathrm{VBF}}\,\mu^{\tau\tau}_{gg\mathrm{F}}$	$\lambda^{bb}_{\mathrm{VBF}}\,\mu^{bb}_{gg\mathrm{F}}$
WH	$\lambda^{\gamma\gamma}_{WH}\,\mu^{\gamma\gamma}_{gg\mathrm{F}}$	$\lambda^{ZZ}_{WH}\,\mu^{ZZ}_{gg\mathrm{F}}$	$\lambda^{WW}_{WH}\,\mu^{WW}_{gg\mathrm{F}}$	$\lambda^{\tau\tau}_{WH}\,\mu^{\tau\tau}_{gg\mathrm{F}}$	$\lambda^{bb}_{WH}\,\mu^{bb}_{gg\mathrm{F}}$
ZH	$\lambda^{\gamma\gamma}_{ZH}\,\mu^{\gamma\gamma}_{gg\mathrm{F}}$	$\lambda^{ZZ}_{ZH}\,\mu^{ZZ}_{gg\mathrm{F}}$	$\lambda^{WW}_{ZH}\,\mu^{WW}_{gg\mathrm{F}}$	$\lambda^{\tau\tau}_{ZH}\,\mu^{\tau\tau}_{gg\mathrm{F}}$	$\lambda^{bb}_{ZH}\,\mu^{bb}_{gg\mathrm{F}}$
ttH	$\lambda^{\gamma\gamma}_{ttH}\,\mu^{\gamma\gamma}_{gg\mathrm{F}}$	$\lambda^{ZZ}_{ttH}\,\mu^{ZZ}_{gg\mathrm{F}}$	$\lambda^{WW}_{ttH}\,\mu^{WW}_{gg\mathrm{F}}$	$\lambda^{\tau\tau}_{ttH}\,\mu^{\tau\tau}_{gg\mathrm{F}}$	$\lambda^{bb}_{ttH}\,\mu^{bb}_{gg\mathrm{F}}$
Single-state matrix parameterisation: rank($\mathcal{M}$) = 1					
	$H \to \gamma\gamma$	$H \to ZZ$	$H \to WW$	$H \to \tau\tau$	$H \to bb$
ggF	$\mu^{\gamma\gamma}_{gg\mathrm{F}}$	$\mu^{ZZ}_{gg\mathrm{F}}$	$\mu^{WW}_{gg\mathrm{F}}$	$\mu^{\tau\tau}_{gg\mathrm{F}}$	$\mu^{bb}_{gg\mathrm{F}}$
VBF	$\lambda_{\mathrm{VBF}}\,\mu^{\gamma\gamma}_{gg\mathrm{F}}$	$\lambda_{\mathrm{VBF}}\,\mu^{ZZ}_{gg\mathrm{F}}$	$\lambda_{\mathrm{VBF}}\,\mu^{WW}_{gg\mathrm{F}}$	$\lambda_{\mathrm{VBF}}\,\mu^{\tau\tau}_{gg\mathrm{F}}$	$\lambda_{\mathrm{VBF}}\,\mu^{bb}_{gg\mathrm{F}}$
WH	$\lambda_{WH}\,\mu^{\gamma\gamma}_{gg\mathrm{F}}$	$\lambda_{WH}\,\mu^{ZZ}_{gg\mathrm{F}}$	$\lambda_{WH}\,\mu^{WW}_{gg\mathrm{F}}$	$\lambda_{WH}\,\mu^{\tau\tau}_{gg\mathrm{F}}$	$\lambda_{WH}\,\mu^{bb}_{gg\mathrm{F}}$
ZH	$\lambda_{ZH}\,\mu^{\gamma\gamma}_{gg\mathrm{F}}$	$\lambda_{ZH}\,\mu^{ZZ}_{gg\mathrm{F}}$	$\lambda_{ZH}\,\mu^{WW}_{gg\mathrm{F}}$	$\lambda_{ZH}\,\mu^{\tau\tau}_{gg\mathrm{F}}$	$\lambda_{ZH}\,\mu^{bb}_{gg\mathrm{F}}$
ttH	$\lambda_{ttH}\,\mu^{\gamma\gamma}_{gg\mathrm{F}}$	$\lambda_{ttH}\,\mu^{ZZ}_{gg\mathrm{F}}$	$\lambda_{ttH}\,\mu^{WW}_{gg\mathrm{F}}$	$\lambda_{ttH}\,\mu^{\tau\tau}_{gg\mathrm{F}}$	$\lambda_{ttH}\,\mu^{bb}_{gg\mathrm{F}}$

Table 16. The two signal parameterisations used to scale the expected yields of the 5×5 combinations of production processes and decay modes. The first parameterisation corresponds to the most general case with 25 independent parameters, while the second parameterisation corresponds to that expected for a single Higgs boson state. As explained in the text for the case of the general matrix parameterisation, the two parameters $\mu^{bb}_{gg\mathrm{F}}$ and $\lambda^{bb}_{\mathrm{VBF}}$ are set to unity in the fits, since the current analyses are not able to constrain them.

independently for each decay mode, as described in section 4.1.1. Several methods have been proposed to assess the compatibility of the data with a single state [126, 127]. A test for the possible presence of overlapping Higgs boson states is performed, based on a profile likelihood ratio suggested in ref. [128]. This test accounts both for missing measurements, such as the $H \to bb$ decay mode in the ggF and VBF production processes, and for uncertainties in the measurements, including their correlations.

The 25 possible combinations resulting from five production processes times five decay modes can be parameterised using a 5×5 matrix $\mathcal{M}$ in two ways:

- allowing full freedom for all yields except the two mentioned above, which are not addressed in the combined analyses, leading to 23 free parameters, similarly to the fit performed for all products of cross sections times branching fractions and presented in section 4.1.1;
- assuming that all yields originate from five production processes and five decay modes, leading to nine free parameters, as shown in table 6, similarly to the fit performed for one reference cross section times branching fraction and eight ratios of cross sections and branching fractions, described in section 4.1.2.

There is a direct relation between the rank of the 5×5 matrix $\mathcal{M}$ and the number of degenerate states. More specifically, if the observations are due to a single state, the

JHEP08(2016)045

matrix can be obtained from one of its rows by using one common multiplier per row and therefore rank($\mathcal{M}$) = 1, in contrast to rank($\mathcal{M}$) = 5 in the most general case. The two parameterisations of $\mathcal{M}$ used in this test are shown in table 16. They are both expressed in terms of $\mu^j_{gg\mathrm{F}}$, defined as in eq. (2.2). Then, for the general case, the other parameters are $\lambda^j_i = \mu^j_i/\mu^j_{gg\mathrm{F}}$, whereas for the rank($\mathcal{M}$) = 1 case the other parameters are $\lambda_i = \mu_i/\mu_{gg\mathrm{F}}$. In this section, the index i runs over the VBF, WH, ZH, and ttH production processes and the index j runs over the five decay modes. The two statistical parameterisations are nested since the second one can be obtained from the first by imposing $\lambda^j_i = \lambda_i$. The SM prediction corresponds to the rank($\mathcal{M}$) =1 case, where $\mu^j_{gg\mathrm{F}} = \lambda_i = \lambda^j_i = 1$.

In contrast to the fits described previously, all the parameters of interest are constrained to be positive for the fits performed in this section. This choice to restrict the parameter space to the physically meaningful region improves the convergence of the fits. The results of the fits to the data are consistent with those presented in section 4.1 for the two similar parameterisations and are not reported here.

In order to quantify the compatibility of the data with the single-state hypothesis, a profile likelihood ratio test statistic, q_λ, is built that compares the hypothesis of a single-state matrix with rank($\mathcal{M}$) = 1 to the general hypothesis with rank($\mathcal{M}$) = 5:

$$q_\lambda = -2 \ln \frac{L(\mathrm{data}|\lambda^j_i = \hat{\lambda}_i, \hat{\mu}^j_{gg\mathrm{F}})}{L(\mathrm{data}|\hat{\lambda}^j_i, \hat{\mu}'^j_{gg\mathrm{F}})}, \tag{5.1}$$

where $\hat{\mu}^j_{gg\mathrm{F}}$ and $\hat{\mu}'^j_{gg\mathrm{F}}$ represent the best fit values of the parameters of interest, respectively for the single-state and general hypotheses. The observed value of q_λ in data is compared with the expected distribution, as obtained from pseudo-data samples randomly generated from the best fit values of the rank($\mathcal{M}$) =1 hypothesis. The p-value of the data with the single-state hypothesis is (29±2)%, where the uncertainty reflects the finite number of pseudo-data samples generated, and does not show any significant departure from the single-state hypothesis. The p-values obtained for the individual experiments are 58% and 33% for ATLAS and CMS, respectively. These p-values can only be considered as the results of compatibility tests with the single-state hypothesis, represented by the rank($\mathcal{M}$) = 1 parameterisation described above.

6 Constraints on Higgs boson couplings

Section 4.2 discusses the fit results from the most generic parameterisation in the context of the κ-framework. This section probes more specific parameterisations with additional assumptions. In the following, results from a few selected parameterisations, with increasingly restrictive assumptions, are presented. The results are obtained from the combined fits to the $\sqrt{s}$ = 7 and 8 TeV data assuming that the coupling modifiers are the same at the two energies.

JHEP08(2016)045

6.1 Parameterisations allowing contributions from BSM particles in loops and in decays

As discussed in sections 2 and 3, the rates of Higgs boson production in the various decay modes are inversely proportional to the Higgs boson width, which is sensitive to potential invisible or undetected decay modes predicted by BSM theories. To directly measure the individual coupling modifiers, an assumption about the Higgs boson width is necessary. Two possible scenarios are considered in this section: the first leaves B_{BSM} free, provided that $B_{BSM} \geq 0$, but assumes that $|\kappa_W| \leq 1$ and $|\kappa_Z| \leq 1$ and that the signs of κ_W and κ_Z are the same, assumptions denoted $|\kappa_V| \leq 1$ in the following; the second assumes $B_{BSM} = 0$. The constraints assumed in the first scenario are compatible with a wide range of BSM physics, which may become manifest in the loop-induced processes of $gg \to H$ production and $H \to \gamma\gamma$ decay. These processes are particularly sensitive to loop contributions from new heavy particles, carrying electric or colour charge, or both, and such new physics can be probed using the effective coupling modifiers κ_g and κ_γ. Furthermore, potential deviations from the SM of the tree-level couplings to ordinary particles are parameterised with their respective coupling modifiers. The parameters of interest in the fits to data are thus the seven independent coupling modifiers, κ_Z, κ_W, κ_t, κ_τ, κ_b, κ_g, and κ_γ, one for each SM particle involved in the production processes and decay modes studied, plus B_{BSM} in the case of the first fit. Here and in section 6.2, the coupling modifier κ_t is assumed to be positive, without any loss of generality.

Figure 15 and table 17 show the results of the two fits, assuming either $|\kappa_V| \leq 1$ and $B_{BSM} \geq 0$ or $B_{BSM} = 0$. In the former case, an upper limit of $B_{BSM} = 0.34$ at 95% CL is obtained, compared to an expected upper limit of 0.39. The corresponding negative log-likelihood scan is shown in figure 16. Appendix C describes how the two possible sign combinations between κ_W and κ_Z impact the likelihood scan of B_{BSM} for the observed and expected results, as illustrated in figure 32. The p-value of the compatibility between the data and the SM predictions is 11% with the assumption that $B_{BSM} = 0$.

Another fit, motivated, for example, by BSM scenarios with new heavy particles that may contribute to loop processes in Higgs boson production or decay, assumes that all the couplings to SM particles are the same as in the SM, that there are no BSM decays ($B_{BSM} = 0$), and that only the gluon-gluon production and $\gamma\gamma$ decay loops may be affected by the presence of additional particles. The results of this fit, which has only the effective coupling modifiers κ_γ and κ_g as free parameters, with all other coupling modifiers fixed to their SM values of unity, are shown in figure 17. The point $\kappa_\gamma = 1$ and $\kappa_g = 1$ lies within the 68% CL region and the p-value of the compatibility between the data and the SM predictions is 82%.

6.2 Parameterisation assuming SM structure of the loops and no BSM decays

In this section it is assumed that there are no new particles in the loops entering ggF production and $H \to \gamma\gamma$ decay. This assumption is supported by the measurements of the effective coupling modifiers κ_g and κ_γ, which are consistent with the SM predictions. The cross section for ggF production and the branching fraction for the $H \to \gamma\gamma$ decay are expressed in terms of the coupling modifiers of the SM particles in the loops, as indicated

JHEP08(2016)045

Parameter	ATLAS+CMS Measured	ATLAS+CMS Expected uncertainty	ATLAS Measured	CMS Measured
Parameterisation assuming $\lvert\kappa_V\rvert \leq 1$ and $\mathrm{B_{BSM}} \geq 0$				
κ_Z	1.00 $[0.92, 1.00]$	$[-1.00, -0.89]\cup$ $[0.89, 1.00]$	1.00 $[-0.97, -0.94]\cup$ $[0.86, 1.00]$	-1.00 $[-1.00, -0.84]\cup$ $[0.90, 1.00]$
κ_W	0.90 $[0.81, 0.99]$	$[-1.00, -0.90]\cup$ $[0.89, 1.00]$	0.92 $[-0.88, -0.84]\cup$ $[0.79, 1.00]$	-0.84 $[-1.00, -0.71]\cup$ $[0.76, 0.98]$
κ_t	$1.43^{+0.23}_{-0.22}$	$^{+0.27}_{-0.32}$	$1.31^{+0.35}_{-0.33}$	$1.45^{+0.42}_{-0.32}$
$\lvert\kappa_\tau\rvert$	$0.87^{+0.12}_{-0.11}$	$^{+0.14}_{-0.15}$	$0.97^{+0.21}_{-0.17}$	$0.79^{+0.20}_{-0.16}$
$\lvert\kappa_b\rvert$	$0.57^{+0.16}_{-0.16}$	$^{+0.19}_{-0.23}$	$0.61^{+0.24}_{-0.26}$	$0.49^{+0.26}_{-0.19}$
$\lvert\kappa_g\rvert$	$0.81^{+0.13}_{-0.10}$	$^{+0.17}_{-0.14}$	$0.94^{+0.23}_{-0.16}$	$0.69^{+0.21}_{-0.13}$
$\lvert\kappa_\gamma\rvert$	$0.90^{+0.10}_{-0.09}$	$^{+0.10}_{-0.12}$	$0.87^{+0.15}_{-0.14}$	$0.89^{+0.17}_{-0.13}$
$\mathrm{B_{BSM}}$	$0.00^{+0.16}$	$^{+0.19}$	$0.00^{+0.25}$	$0.03^{+0.26}$
Parameterisation assuming $\mathrm{B_{BSM}} = 0$				
κ_Z	-0.98 $[-1.08, -0.88]\cup$ $[0.94, 1.13]$	$[-1.01, -0.87]\cup$ $[0.89, 1.11]$	1.01 $[-1.09, -0.85]\cup$ $[0.87, 1.15]$	-0.99 $[-1.14, -0.84]\cup$ $[0.94, 1.19]$
κ_W	0.87 $[0.78, 1.00]$	$[-1.08, -0.90]\cup$ $[0.88, 1.11]$	0.92 $[-0.94, -0.85]\cup$ $[0.78, 1.05]$	0.84 $[-0.99, -0.74]\cup$ $[0.71, 1.01]$
κ_t	$1.40^{+0.24}_{-0.21}$	$^{+0.26}_{-0.39}$	$1.32^{+0.31}_{-0.33}$	$1.51^{+0.33}_{-0.32}$
$\lvert\kappa_\tau\rvert$	$0.84^{+0.15}_{-0.11}$	$^{+0.16}_{-0.15}$	$0.97^{+0.19}_{-0.19}$	$0.77^{+0.18}_{-0.15}$
$\lvert\kappa_b\rvert$	$0.49^{+0.27}_{-0.15}$	$^{+0.25}_{-0.28}$	$0.61^{+0.26}_{-0.31}$	$0.47^{+0.34}_{-0.19}$
$\lvert\kappa_g\rvert$	$0.78^{+0.13}_{-0.10}$	$^{+0.17}_{-0.14}$	$0.94^{+0.18}_{-0.17}$	$0.67^{+0.14}_{-0.12}$
$\lvert\kappa_\gamma\rvert$	$0.87^{+0.14}_{-0.09}$	$^{+0.12}_{-0.13}$	$0.88^{+0.15}_{-0.15}$	$0.89^{+0.19}_{-0.13}$

Table 17. Fit results for two parameterisations allowing BSM loop couplings discussed in the text: the first one assumes that $|\kappa_V| \leq 1$, where κ_V denotes κ_Z or κ_W, and that $\mathrm{B_{BSM}} \geq 0$, while the second one assumes that there are no additional BSM contributions to the Higgs boson width, i.e. $\mathrm{B_{BSM}} = 0$. The results for the combination of ATLAS and CMS are reported with their measured and expected uncertainties. Also shown are the results from each experiment. For the parameters with both signs allowed, the 1σ intervals are shown on a second line. When a parameter is constrained and reaches a boundary, namely $\mathrm{B_{BSM}} = 0$, the uncertainty is not indicated. For those parameters with no sensitivity to the sign, only the absolute values are shown.

JHEP08(2016)045

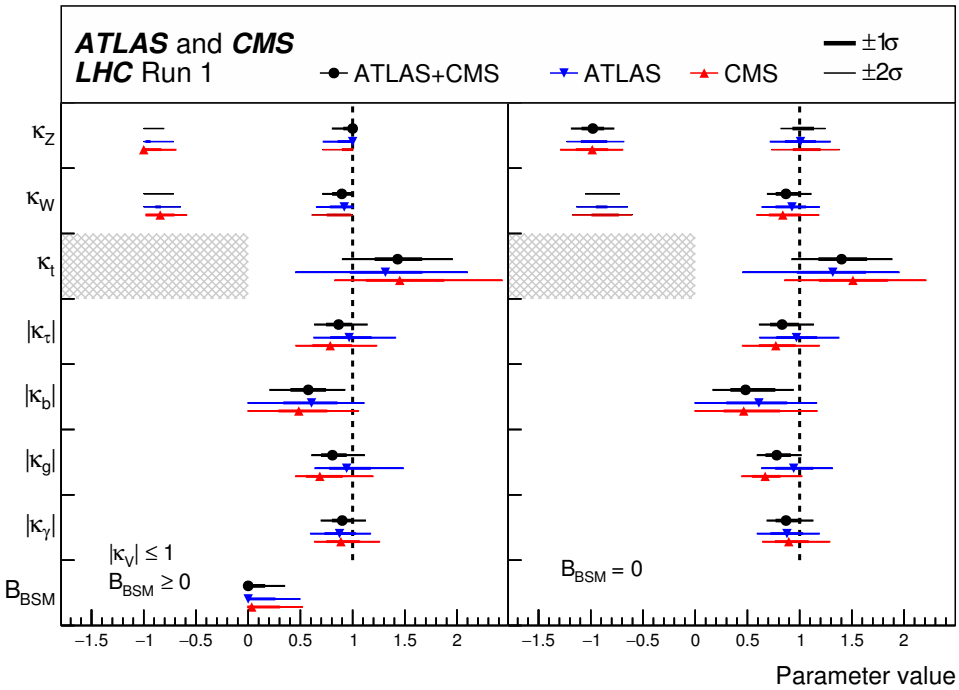

Figure 15. Fit results for two parameterisations allowing BSM loop couplings discussed in the text: the first one assumes that $B_{BSM} \geq 0$ and that $|\kappa_V| \leq 1$, where κ_V denotes κ_Z or κ_W, and the second one assumes that there are no additional BSM contributions to the Higgs boson width, i.e. $B_{BSM} = 0$. The measured results for the combination of ATLAS and CMS are reported together with their uncertainties, as well as the individual results from each experiment. The hatched areas show the non-allowed regions for the κ_t parameter, which is assumed to be positive without loss of generality. The error bars indicate the 1σ (thick lines) and 2σ (thin lines) intervals. When a parameter is constrained and reaches a boundary, namely $|\kappa_V| = 1$ or $B_{BSM} = 0$, the uncertainty is not defined beyond this boundary. For those parameters with no sensitivity to the sign, only the absolute values are shown.

in table 4. This leads to a parameterisation with six free coupling modifiers: κ_W, κ_Z, κ_t, κ_τ, κ_b, and κ_μ; the results of the $H \to \mu\mu$ analysis are included for this specific case. In this more constrained fit, it is also assumed that $B_{BSM} = 0$.

Figure 18 and table 18 show the results of the fit for the combination of ATLAS and CMS, and separately for each experiment. Compared to the results from the fitted decay signal strengths (table 13) or the global signal strength $\mu = 1.09 \pm 0.11$ (section 5.1), this fit yields values of the coupling modifiers lower than those predicted by the SM. This is a consequence of the low value of κ_b, as measured by the combination of ATLAS and CMS and by each experiment. A low value of κ_b decreases the total Higgs boson width through the dominant Γ^{bb} partial decay width, and, as a consequence, the measured values of all the coupling modifiers decrease, such that the values of $\sigma_i(\vec{\kappa}) \cdot B^f$ remain consistent with the observed signal yields. The p-value of the compatibility between the data and the SM predictions is 74%.

JHEP08(2016)045

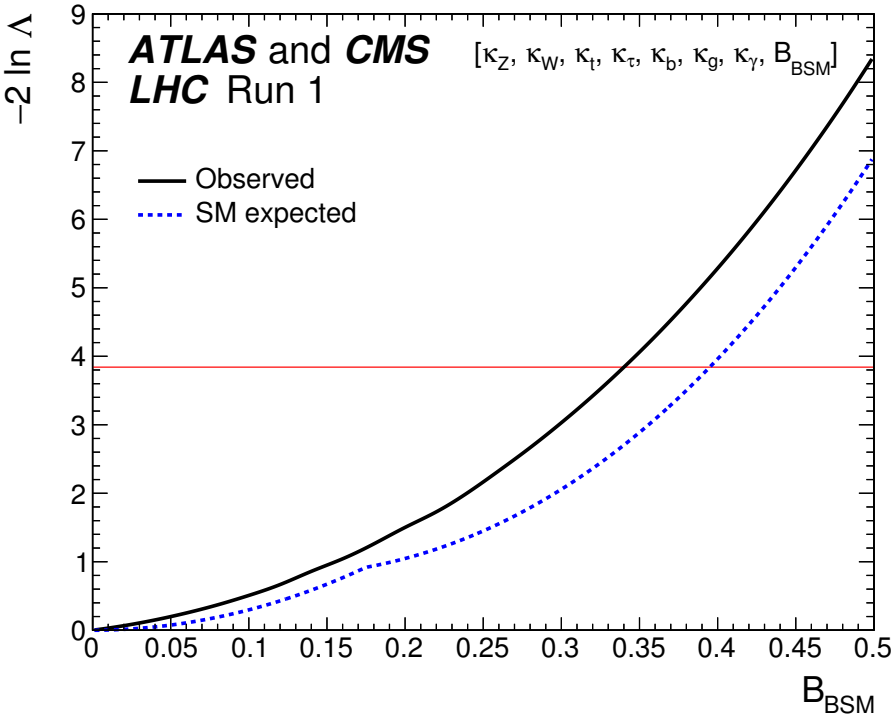

Figure 16. Observed (solid line) and expected (dashed line) negative log-likelihood scan of B_{BSM}, shown for the combination of ATLAS and CMS when allowing additional BSM contributions to the Higgs boson width. The results are shown for the parameterisation with the assumptions that $|\kappa_V| \leq 1$ and $B_{BSM} \geq 0$ in figure 15. All the other parameters of interest from the list in the legend are also varied in the minimisation procedure. The red horizontal line at 3.84 indicates the log-likelihood variation corresponding to the 95% CL upper limit, as discussed in section 3.2.

A different view of the relation between the fitted coupling modifiers and the SM predictions is presented in figure 19. New parameters are derived from the coupling modifiers, to make explicit the dependence on the particle masses: linear for the Yukawa couplings to the fermions and quadratic for the gauge couplings of the Higgs boson to the weak vector bosons. These new parameters are all assumed in this case to be positive. For fermions with mass $m_{F,i}$, the parameters are $\kappa_{F,i} \cdot y_{F,i}/\sqrt{2} = \kappa_{F,i} \cdot m_{F,i}/v$, where $y_{F,i}$ is the Yukawa coupling strength, assuming a SM Higgs boson with a mass of 125.09 GeV, and $v = 246$ GeV is the vacuum expectation value of the Higgs field. For the weak vector bosons with mass $m_{V,i}$, the new parameters are $\sqrt{\kappa_{V,i} \cdot g_{V,i}/2v} = \sqrt{\kappa_{V,i}} \cdot m_{V,i}/v$, where $g_{V,i}$ is the absolute Higgs boson gauge coupling strength. The linear scaling of these new parameters as a function of the particle masses observed in figure 19 indicates qualitatively the compatibility of the measurements with the SM. For the b quark, the running mass evaluated at a scale equal to m_H, $m_b(m_H) = 2.76$ GeV, is used.

Following the phenomenological model suggested in ref. [129], the coupling modifiers can also be expressed as a function of a mass scaling parameter ϵ, with a value $\epsilon = 0$ in the SM, and a free parameter M, equal to v in the SM: $\kappa_{F,i} = v \cdot m_{F,i}^{\epsilon}/M^{1+\epsilon}$ and $\kappa_{V,i} =$

JHEP08(2016)045

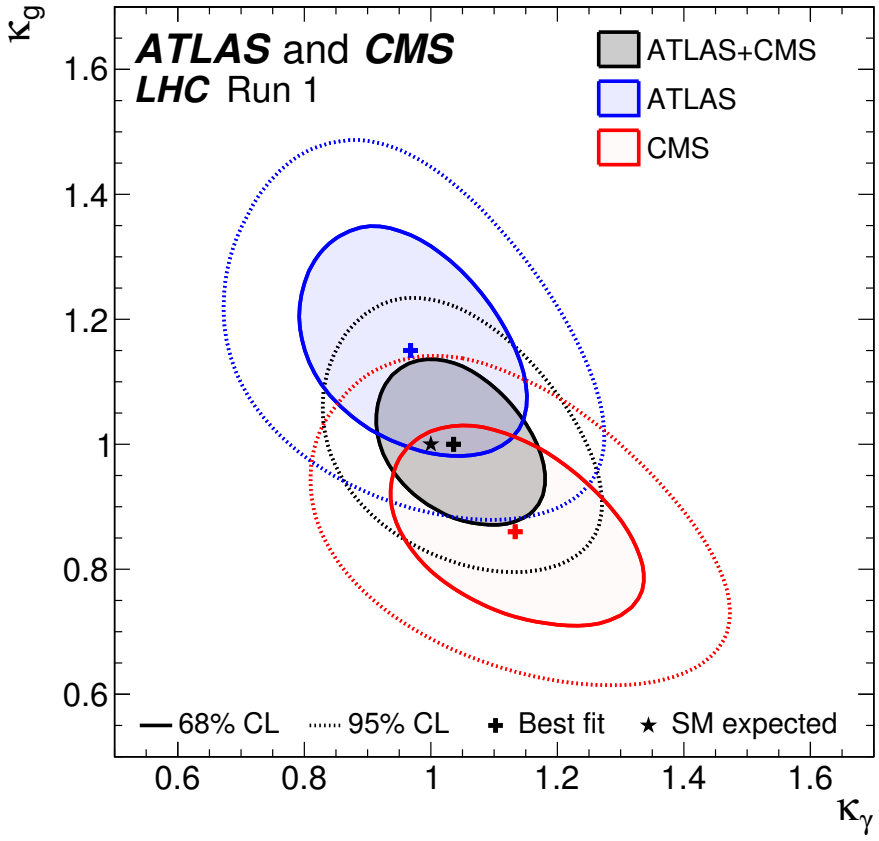

Figure 17. Negative log-likelihood contours at 68% and 95% CL in the (κ_γ, κ_g) plane for the combination of ATLAS and CMS and for each experiment separately, as obtained from the fit to the parameterisation constraining all the other coupling modifiers to their SM values and assuming $\mathrm{B_{BSM}} = 0$.

$v \cdot m_{V,i}^{2\epsilon}/M^{1+2\epsilon}$. A fit is then performed with the same assumptions as those of table 18 with ϵ and M as parameters of interest. The results for the combination of ATLAS and CMS are $\epsilon = 0.023^{+0.029}_{-0.027}$ and $M = 233^{+13}_{-12}$ GeV, and are compatible with the SM predictions. Figure 19 shows the results of this fit with its corresponding 68% and 95% CL bands.

6.3 Parameterisations related to the fermion sector

Common coupling modifications for up-type fermions versus down-type fermions or for leptons versus quarks are predicted by many extensions of the SM. One such class of theoretically well motivated models is the 2HDM [130].

The ratios of the coupling modifiers are tested in the most generic parameterisation proposed in ref. [32], in which the total Higgs boson width is also allowed to vary. The main parameters of interest for these tests are $\lambda_{du} = \kappa_d/\kappa_u$ for the up- and down-type fermion symmetry, and $\lambda_{lq} = \kappa_l/\kappa_q$ for the lepton and quark symmetry, where both are allowed to be positive or negative. In this parameterisation, the loops are resolved in terms of their expected SM contributions.

JHEP08(2016)045

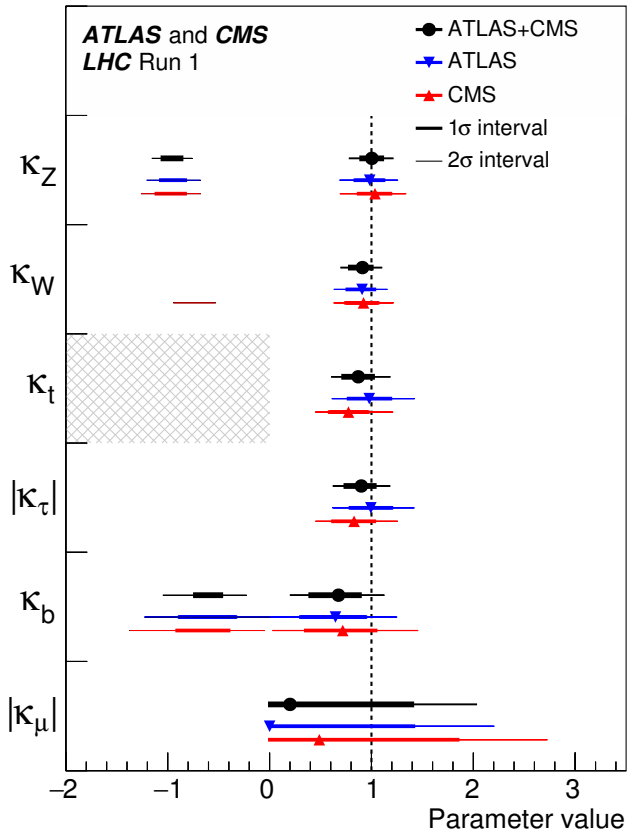

Figure 18. Best fit values of parameters for the combination of ATLAS and CMS data, and separately for each experiment, for the parameterisation assuming the absence of BSM particles in the loops, $B_{BSM} = 0$. The hatched area indicates the non-allowed region for the parameter that is assumed to be positive without loss of generality. The error bars indicate the 1σ (thick lines) and 2σ (thin lines) intervals. When a parameter is constrained and reaches a boundary, namely $|\kappa_\mu| = 0$, the uncertainty is not defined beyond this boundary. For those parameters with no sensitivity to the sign, only the absolute values are shown.

6.3.1 Probing the up- and down-type fermion symmetry

The free parameters for this test are: $\lambda_{du} = \kappa_d/\kappa_u$, $\lambda_{Vu} = \kappa_V/\kappa_u$, and $\kappa_{uu} = \kappa_u \cdot \kappa_u/\kappa_H$, where this latter term is positive definite since κ_H is always assumed to be positive. The up-type fermion couplings are mainly probed by the ggF production process, the $H \to \gamma\gamma$ decay channel, and to a certain extent the ttH production process. The down-type fermion couplings are mainly probed by the $H \to bb$ and $H \to \tau\tau$ decays. A small sensitivity to the relative sign arises from the interference between top and bottom quarks in the gluon fusion loop.

The results of the fit are reported in table 19 and figure 20. The p-value of the compatibility between the data and the SM predictions is 72%. The likelihood scan for the λ_{du} parameter is shown in figure 21 for the combination of ATLAS and CMS. Negative values for the parameter λ_{Vu} are excluded by more than 4σ.

JHEP08(2016)045

Parameter	ATLAS+CMS Measured	ATLAS+CMS Expected uncertainty	ATLAS Measured	CMS Measured
κ_Z	1.00		0.98	1.03
	$[-1.05, -0.86]\cup$	$[-1.00, -0.88]\cup$	$[-1.07, -0.83]\cup$	$[-1.11, -0.83]\cup$
	$[0.90, 1.11]$	$[0.90, 1.10]$	$[0.84, 1.12]$	$[0.87, 1.19]$
κ_W	$0.91^{+0.10}_{-0.12}$	$^{+0.10}_{-0.11}$	$0.91^{+0.12}_{-0.15}$	$0.92^{+0.14}_{-0.17}$
κ_t	$0.87^{+0.15}_{-0.15}$	$^{+0.15}_{-0.18}$	$0.98^{+0.21}_{-0.20}$	$0.77^{+0.20}_{-0.18}$
$\lvert\kappa_\tau\rvert$	$0.90^{+0.14}_{-0.16}$	$^{+0.15}_{-0.14}$	$0.99^{+0.20}_{-0.20}$	$0.83^{+0.20}_{-0.21}$
κ_b	0.67		0.64	0.71
	$[-0.73, -0.47]\cup$	$[-1.24, -0.76]\cup$	$[-0.89, -0.33]\cup$	$[-0.91, -0.40]\cup$
	$[0.40, 0.89]$	$[0.74, 1.24]$	$[0.30, 0.94]$	$[0.35, 1.04]$
$\lvert\kappa_\mu\rvert$	$0.2^{+1.2}$	$^{+0.9}$	$0.0^{+1.4}$	$0.5^{+1.4}$

Table 18. Fit results for the parameterisation assuming the absence of BSM particles in the loops ($B_{BSM} = 0$). The results with their measured and expected uncertainties are reported for the combination of ATLAS and CMS, together with the individual results from each experiment. For the parameters with both signs allowed, the 1σ CL intervals are shown on a second line. When a parameter is constrained and reaches a boundary, namely $|\kappa_\mu| = 0$, the uncertainty is not indicated. For those parameters with no sensitivity to the sign, only the absolute values are shown.

6.3.2 Probing the lepton and quark symmetry

The parameterisation for this test is very similar to that of section 6.3.1, which probes the up- and down-type fermion symmetry. In this case, the free parameters are $\lambda_{lq} = \kappa_l/\kappa_q$, $\lambda_{Vq} = \kappa_V/\kappa_q$, and $\kappa_{qq} = \kappa_q \cdot \kappa_q/\kappa_H$, where the latter term is positive definite, like κ_{uu}. The quark couplings are mainly probed by the ggF process, the $H \to \gamma\gamma$ and $H \to bb$ decays, and to a lesser extent by the ttH process. The lepton couplings are probed by the $H \to \tau\tau$ decays. The results are expected, however, to be insensitive to the relative sign of the couplings, because there is no sizeable lepton-quark interference in any of the relevant Higgs boson production processes and decay modes. Only the absolute value of the λ_{lq} parameter is therefore considered in the fit.

The results of the fit are reported in table 19 and figure 22. The p-value of the compatibility between the data and the SM predictions is 79%. The likelihood scan for the λ_{lq} parameter is shown in figure 23 for the combination of ATLAS and CMS. Negative values for the parameter λ_{Vq} are excluded by more than 4σ.

JHEP08(2016)045

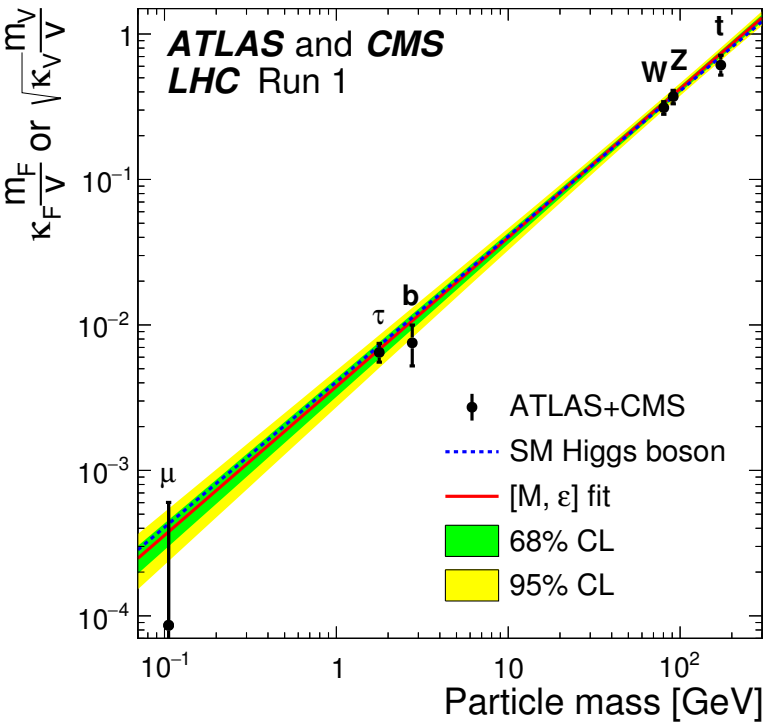

Figure 19. Best fit values as a function of particle mass for the combination of ATLAS and CMS data in the case of the parameterisation described in the text, with parameters defined as $\kappa_F \cdot m_F/v$ for the fermions, and as $\sqrt{\kappa_V} \cdot m_V/v$ for the weak vector bosons, where $v = 246$ GeV is the vacuum expectation value of the Higgs field. The dashed (blue) line indicates the predicted dependence on the particle mass in the case of the SM Higgs boson. The solid (red) line indicates the best fit result to the $[M, \epsilon]$ phenomenological model of ref. [129] with the corresponding 68% and 95% CL bands.

6.4 Fermion and vector boson couplings

The last and most constrained parameterisation studied in this section is motivated by the intrinsic difference between the Higgs boson couplings to weak vector bosons, which originate from the breaking of the EW symmetry, and the Yukawa couplings to the fermions. Similarly to section 6.2, it is assumed in this section that there are no new particles in the loops (ggF production process and $H \to \gamma\gamma$ decay mode) and that there are no BSM decays, i.e. $B_{BSM} = 0$. Vector and fermion coupling modifiers, κ_V and κ_F, are defined such that $\kappa_Z = \kappa_W = \kappa_V$ and $\kappa_t = \kappa_\tau = \kappa_b = \kappa_F$. These definitions can be applied either globally, yielding two parameters, or separately for each of the five decay channels, yielding ten parameters κ_V^f and κ_F^f (following the notation related to Higgs boson decays used for the signal strength parameterisation). Two fits are performed: a two-parameter fit as a function of κ_V and κ_F, and a ten-parameter fit as a function of κ_V^f and κ_F^f for each decay channel.

As explained in section 2.4 and shown explicitly in table 4, the Higgs boson production cross sections and partial decay widths are only sensitive to products of coupling modifiers and not to their absolute sign. Any sensitivity to the relative sign between κ_V and κ_F

JHEP08(2016)045

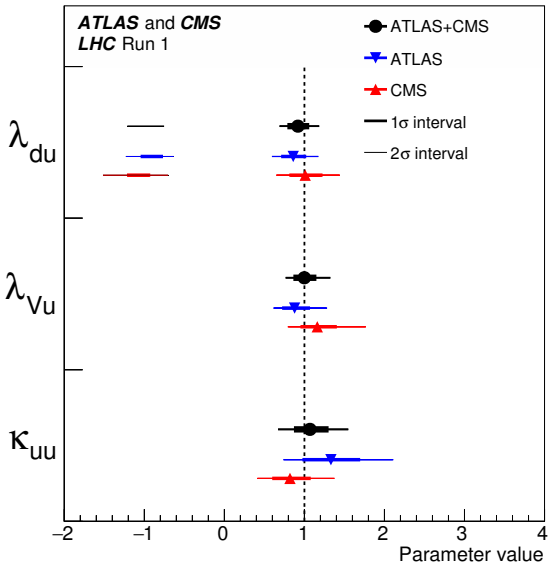

Figure 20. Best fit values of parameters for the combination of ATLAS and CMS data, and separately for each experiment, for the parameterisation testing the up- and down-type fermion coupling ratios. The error bars indicate the 1σ (thick lines) and 2σ (thin lines) intervals. The parameter κ_{uu} is positive definite since κ_H is always assumed to be positive. Negative values for the parameter λ_{Vu} are excluded by more than 4σ.

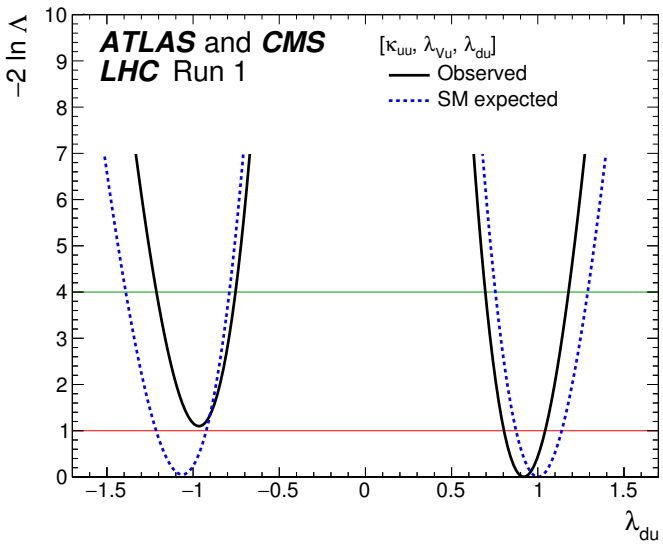

Figure 21. Observed (solid line) and expected (dashed line) negative log-likelihood scan of the λ_{du} parameter, probing the ratios of coupling modifiers for up-type versus down-type fermions for the combination of ATLAS and CMS. The other parameters of interest from the list in the legend are also varied in the minimisation procedure. The red (green) horizontal line at the $-2\Delta\ln\Lambda$ value of 1 (4) indicates the value of the profile likelihood ratio corresponding to a 1σ (2σ) CL interval for the parameter of interest, assuming the asymptotic χ^2 distribution of the test statistic.

JHEP08(2016)045

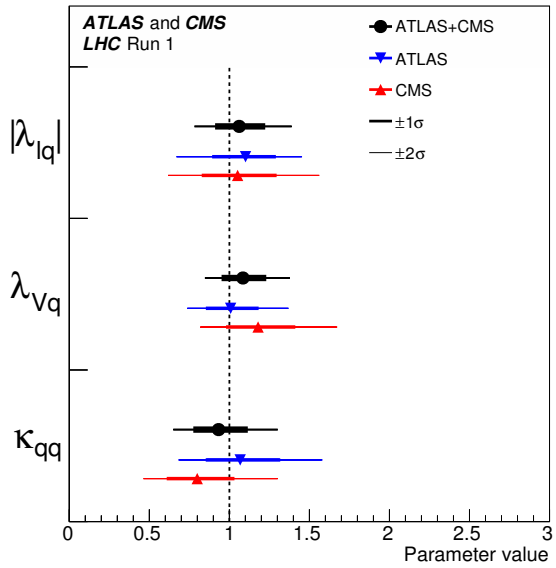

Figure 22. Best fit values of parameters for the combination of ATLAS and CMS data, and separately for each experiment, for the parameterisation testing the lepton and quark coupling ratios. The error bars indicate the 1σ (thick lines) and 2σ (thin lines) intervals. For the parameter λ_{lq}, for which there is no sensitivity to the sign, only the absolute values are shown. The parameter κ_{qq} is positive definite since κ_H is always assumed to be positive. Negative values for the parameter λ_{Vq} are excluded by more than 4σ.

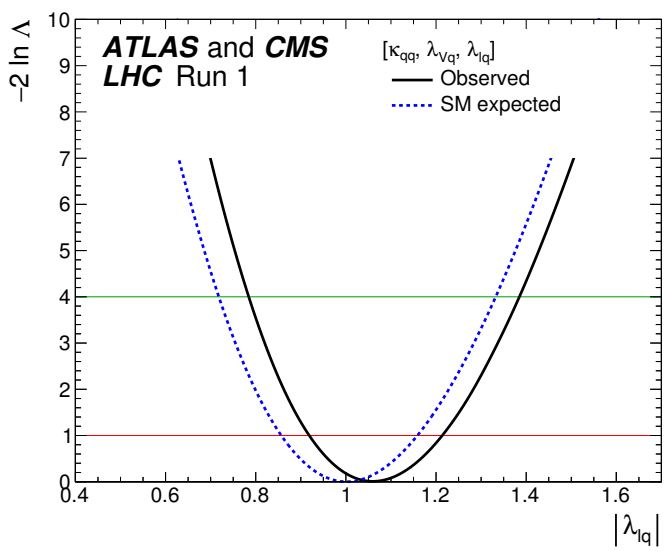

Figure 23. Observed (solid line) and expected (dashed line) negative log-likelihood scan of the λ_{lq} parameter, probing the ratios of coupling modifiers for leptons versus quarks for the combination of ATLAS and CMS. The other parameters of interest from the list in the legend are also varied in the minimisation procedure. The red (green) horizontal line at the $-2\Delta \ln \Lambda$ value of 1 (4) indicates the value of the profile likelihood ratio corresponding to a 1σ (2σ) CL interval for the parameter of interest, assuming the asymptotic χ^2 distribution of the test statistic.

JHEP08(2016)045

Parameter	ATLAS+CMS Measured	ATLAS+CMS Expected uncertainty	ATLAS Measured	CMS Measured
λ_{du}	0.92		0.86	1.01
	$[0.80, 1.04]$	$[-1.21, -0.92]\cup$ $[0.87, 1.14]$	$[-1.03, -0.78]\cup$ $[0.73, 1.01]$	$[-1.20, -0.94]\cup$ $[0.83, 1.21]$
λ_{Vu}	$1.00^{+0.13}_{-0.12}$	$^{+0.20}_{-0.12}$	$0.88^{+0.18}_{-0.14}$	$1.16^{+0.23}_{-0.19}$
κ_{uu}	$1.07^{+0.22}_{-0.18}$	$^{+0.20}_{-0.27}$	$1.33^{+0.35}_{-0.34}$	$0.82^{+0.24}_{-0.21}$
$\lvert\lambda_{lq}\rvert$	$1.06^{+0.15}_{-0.14}$	$^{+0.16}_{-0.14}$	$1.10^{+0.20}_{-0.18}$	$1.05^{+0.24}_{-0.22}$
λ_{Vq}	$1.09^{+0.14}_{-0.13}$	$^{+0.13}_{-0.12}$	$1.01^{+0.17}_{-0.15}$	$1.18^{+0.22}_{-0.19}$
κ_{qq}	$0.93^{+0.17}_{-0.15}$	$^{+0.18}_{-0.16}$	$1.07^{+0.24}_{-0.21}$	$0.80^{+0.22}_{-0.18}$

Table 19. Summary of fit results for the two parameterisations probing the ratios of coupling modifiers for up-type versus down-type fermions and for leptons versus quarks. The results for the combination of ATLAS and CMS are reported together with their measured and expected uncertainties. Also shown are the results from each experiment. The parameters κ_{uu} and κ_{qq} are both positive definite since κ_H is always assumed to be positive. For the parameter λ_{du}, for which both signs are allowed, the 1σ CL intervals are shown on a second line. For the parameter λ_{lq}, for which there is no sensitivity to the sign, only the absolute values are shown. Negative values for the parameters λ_{Vu} and λ_{Vq} are excluded by more than 4σ.

can only occur through interference terms, either in the $H \to \gamma\gamma$ decays, through the t–W interference in the $\gamma\gamma$ decay loop, or in $ggZH$ or tH production. Without any loss of generality, this parameterisation assumes that one of the two coupling modifiers, namely κ_V (or κ_V^f), is positive.

The combined ATLAS and CMS results are shown in figure 24 for the individual channels and their combination. The individual decay channels are seen to be compatible with each other only for positive values of κ_F^f. The incompatibility between the channels for negative values of κ_F^f arises mostly from the $H \to \gamma\gamma$, $H \to WW$, and $H \to ZZ$ channels. Nonetheless, the best fit values for most of the individual channels correspond to negative values of κ_F^f. However, the best fit value from the global fit yields $\kappa_F \geq 0$, a result that is driven by the large asymmetry between the positive and negative coupling ratios in the case of $H \to \gamma\gamma$ decays.

The fact that, for four of the five individual channels, the best fit values correspond to $\kappa_F^f \leq 0$ is not significant, as shown by the likelihood curves in figures 25 (a-e). The $H \to bb$ decay channel displays the largest expected sensitivity, mostly arising from the contribution of the $ggZH$ process, and the best fit value of κ_F^{bb} is positive. For all other decay modes, a small sensitivity arises because of the tH process. The excess observed in the combination of the two experiments for the ttH production process induces a preference for a relative

JHEP08(2016)045

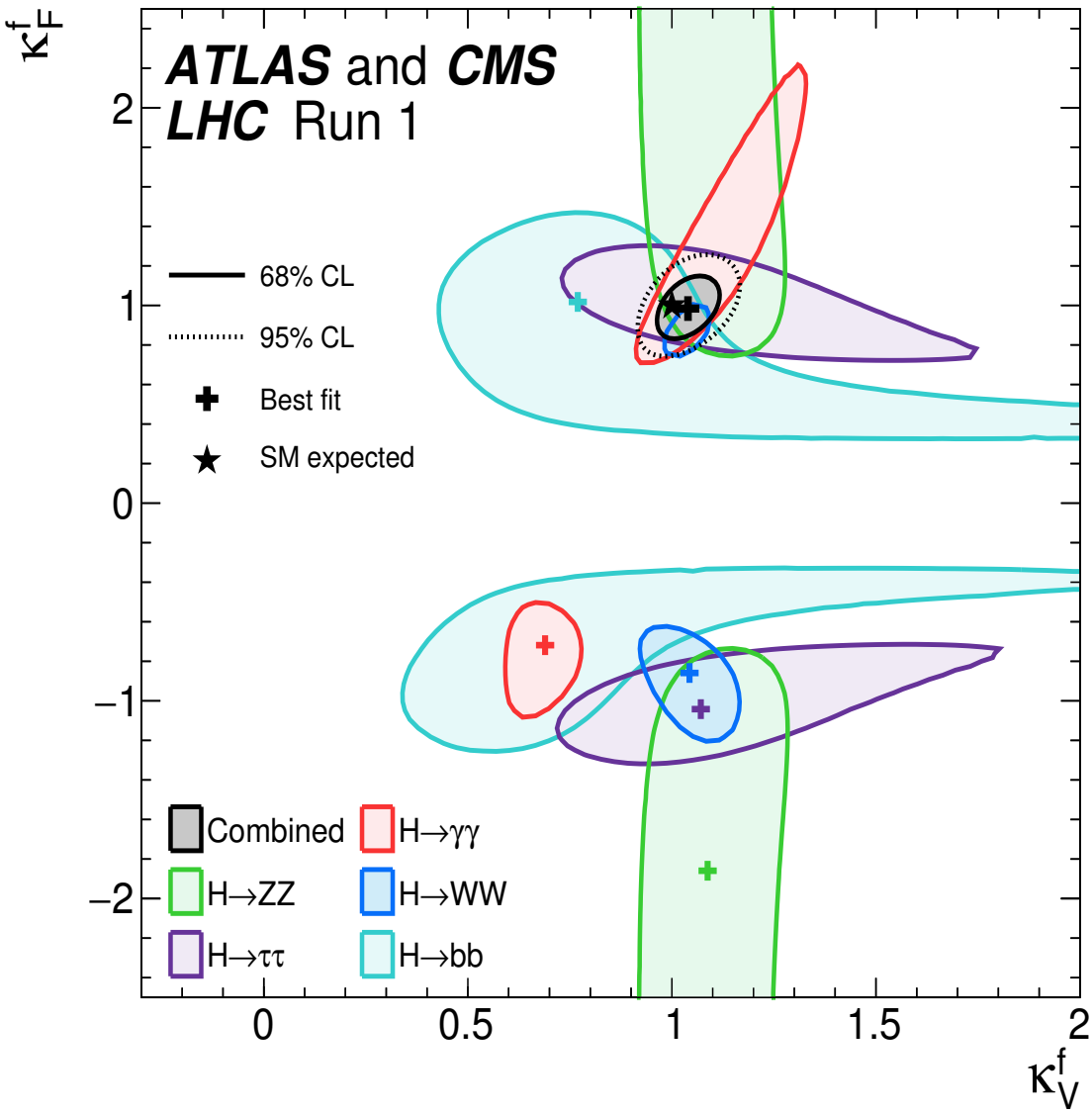

Figure 24. Negative log-likelihood contours at 68% and 95% CL in the (κ_F^f, κ_V^f) plane for the combination of ATLAS and CMS and for the individual decay channels, as well as for their combination (κ_F versus κ_V shown in black), without any assumption about the sign of the coupling modifiers. The other two quadrants (not shown) are symmetric with respect to the point (0,0).

JHEP08(2016)045

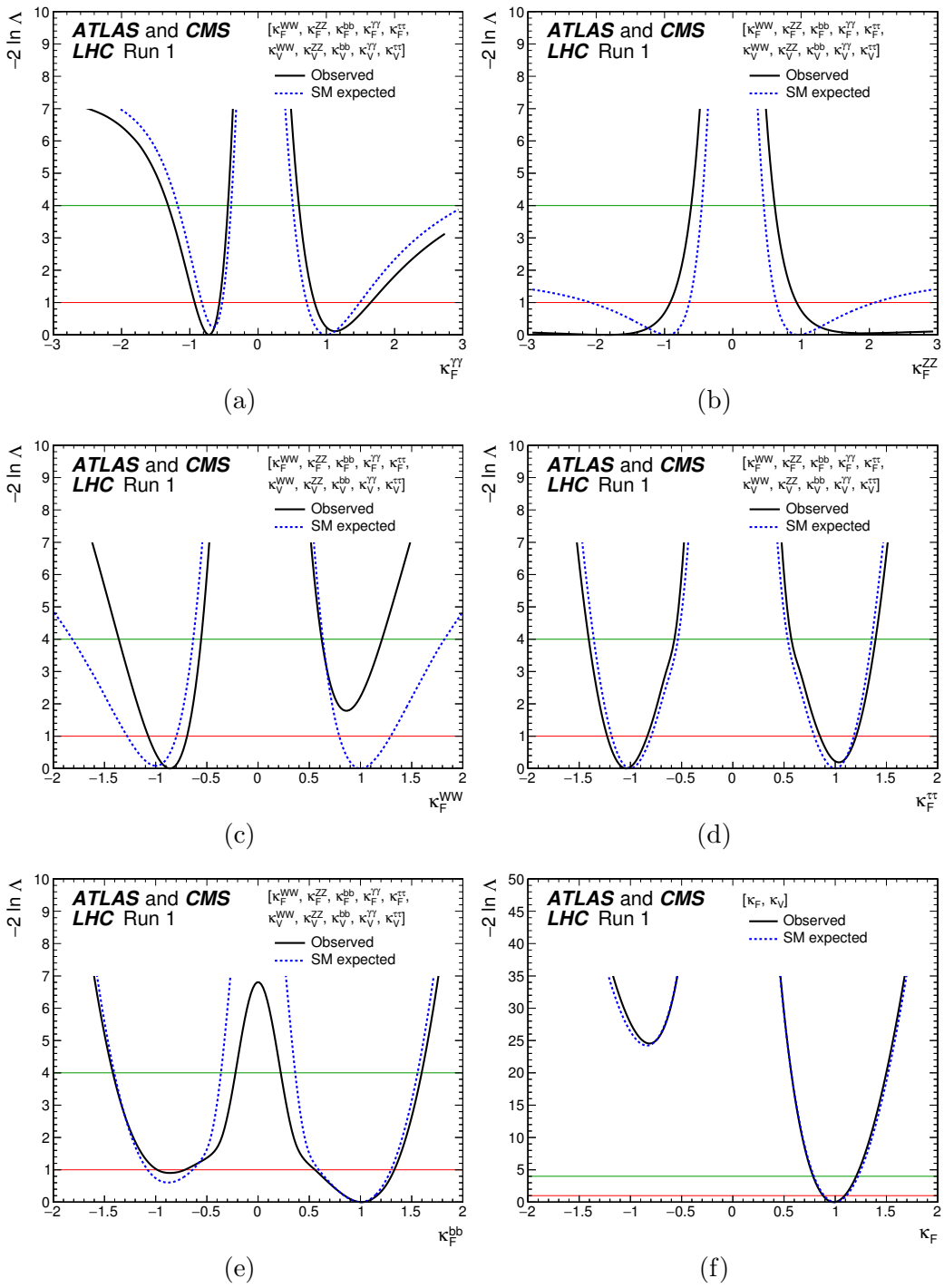

Figure 25. Observed (solid line) and expected (dashed line) negative log-likelihood scans for the five κ_F^f parameters, corresponding to each individual decay channel, and for the global κ_F parameter, corresponding to the combination of all decay channels: (a) $\kappa_F^{\gamma\gamma}$, (b) κ_F^{ZZ}, (c) κ_F^{WW}, (d) $\kappa_F^{\tau\tau}$, (e) κ_F^{bb}, and (f) κ_F. All the other parameters of interest from the list in the legends are also varied in the minimisation procedure. The red (green) horizontal lines at the $-2\Delta\ln\Lambda$ value of 1 (4) indicate the value of the profile likelihood ratio corresponding to a 1σ (2σ) CL interval for the parameter of interest, assuming the asymptotic χ^2 distribution of the test statistic.

JHEP08(2016)045

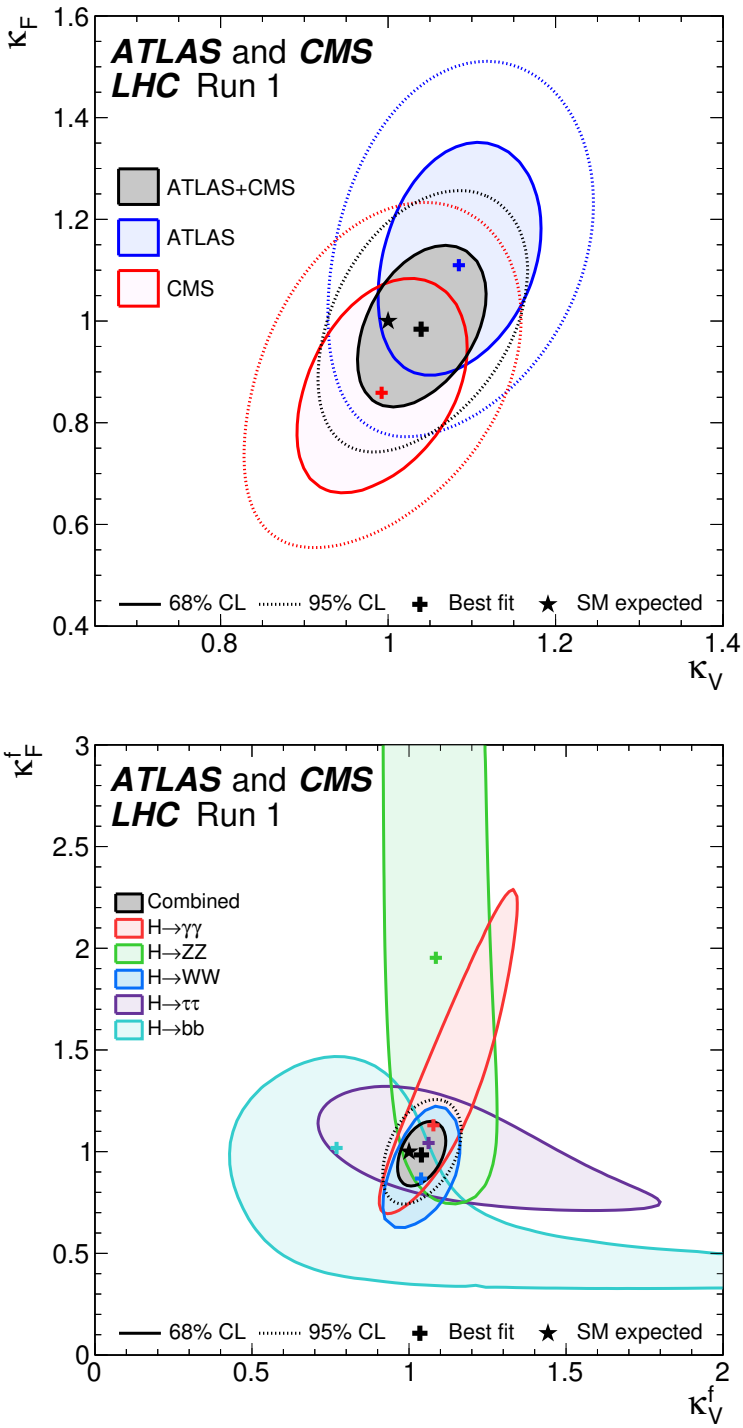

Figure 26. Top: negative log-likelihood contours at 68% and 95% CL in the (κ_F, κ_V) plane on an enlarged scale for the combination of ATLAS and CMS and for the global fit of all channels. Also shown are the contours obtained for each experiment separately. Bottom: negative log-likelihood contours at 68% CL in the (κ_F^f, κ_V^f) plane for the combination of ATLAS and CMS and for the individual decay channels as well as for their global combination (κ_F versus κ_V), assuming that all coupling modifiers are positive.

JHEP08(2016)045

negative sign between the two coupling modifiers, which increases significantly the tH cross section and thereby provides a better fit to the data. The only visible difference between the two minima at positive and negative values of κ_F^f is observed for the $H \to WW$ channel.

As stated above, the channel most affected by the relative sign of the couplings is the $H \to \gamma\gamma$ decay channel: because of the negative t–W interference in the $\gamma\gamma$ loop, the $H \to \gamma\gamma$ partial width would be much larger if the sign of $\kappa_F^{\gamma\gamma}$ were opposite to that of $\kappa_V^{\gamma\gamma}$. When combining the $H \to \gamma\gamma$ decay channel with all the other channels, the opposite sign case is excluded by almost 5σ, as can be inferred from figure 25 (f).

Figure 26 (top) presents, on an enlarged scale, the results of the scan for the global coupling modifiers as well as those obtained separately for each experiment. For completeness, additional likelihood scans are performed for the two global coupling modifiers and for those of each decay channel, assuming in all cases that κ_F and κ_V are both positive. The results of these scans are shown in figure 26 (bottom). The most precise determination of κ_F^f and κ_V^f is obtained from the $H \to WW$ decay channel because it is the only one that provides significant constraints on both parameters, through the measurements of the ggF and VBF production processes. The difference in size between the $H \to WW$ confidence regions obtained for $\kappa_F^f \geq 0$ in figure 24 and figure 26 (bottom), where it is explicitly assumed that $\kappa_F^f \geq 0$, is due to the fact that the negative log-likelihood contours are evaluated using as a reference the minima obtained from different likelihood fits. The combination of all decay modes provides significant additional constraints. All results are in agreement with the SM prediction, $\kappa_F^f = 1$ and $\kappa_V^f = 1$, and the p-value of the compatibility between the data and the SM predictions is 59%.

7 Summary

An extensive set of combined ATLAS and CMS measurements of the Higgs boson production and decay rates is presented, and a number of constraints on its couplings to vector bosons and fermions are derived based on various sets of assumptions. The combination is based on the analysis of approximately 600 categories of selected events, concerning five production processes, ggF, VBF, WH, ZH, and ttH, where ggF and VBF refer, respectively, to production through the gluon fusion and vector boson fusion processes; and six decay channels, $H \to ZZ, WW, \gamma\gamma, \tau\tau, bb$, and $\mu\mu$. All results are reported assuming a value of 125.09 GeV for the Higgs boson mass, the result of the combined Higgs boson mass measurement by the two experiments [22]. The analysis uses the LHC proton-proton collision data sets recorded by the ATLAS and CMS detectors in 2011 and 2012, corresponding to integrated luminosities per experiment of approximately 5 fb^{-1} at $\sqrt{s} = 7$ TeV and 20 fb^{-1} at $\sqrt{s} = 8$ TeV. This paper presents the final Higgs boson coupling combined results from ATLAS and CMS based on the LHC Run 1 data.

The combined analysis is sensitive to the couplings of the Higgs boson to the weak vector bosons and to the heavier fermions (top quarks, b quarks, τ leptons, and – marginally – muons). The analysis is also sensitive to the effective couplings of the Higgs boson to the photon and the gluon. At the LHC, only products of cross sections and branching fractions are measured, so the width of the Higgs boson cannot be probed without assumptions be-

JHEP08(2016)045

yond the main one used for all measurements presented here, namely that the Higgs boson production and decay kinematics are close to those predicted by the Standard Model (SM). In general, the combined analysis presented in this paper provides a significant improvement with respect to the individual combinations published by each experiment separately. The precision of the results improves in most cases by a factor of approximately $1/\sqrt{2}$, as one would expect for the combination of two largely uncorrelated measurements based on similar-size data samples. A few illustrative results are summarised below.

For the first time, results are shown for the most generic parameterisation of the observed event yields in terms of products of Higgs boson production cross sections times branching fractions, separately for each of 20 measurable (σ_i, B^f) pairs of production processes and decay modes. These measurements do not rely on theoretical predictions for the inclusive cross sections and the uncertainties are mostly dominated by their statistical component. In the context of this parameterisation, one can test whether the observed yields arise from more than one Higgs boson, all with experimentally indistinguishable masses, but possibly with different coupling structures to the SM particles. The data are compatible with the hypothesis of a single Higgs boson, yielding a p-value of 29%.

Fits to the observed event yields are also performed without any assumption about the Higgs boson width in the context of two other generic parameterisations. The first parameterisation is in terms of ratios of production cross sections and branching fractions, together with the reference cross section of the process $gg \to H \to ZZ$. All results are compatible with the SM. The best relative precision, of about 30%, is achieved for the ratio of cross sections $\sigma_{\mathrm{VBF}}/\sigma_{gg\mathrm{F}}$ and for the ratios of branching fractions $\mathrm{B}^{WW}/\mathrm{B}^{ZZ}$ and $\mathrm{B}^{\gamma\gamma}/\mathrm{B}^{ZZ}$. A relative precision of around 40% is achieved for the ratio of branching fractions $\mathrm{B}^{\tau\tau}/\mathrm{B}^{ZZ}$. The second parameterisation is in terms of ratios of coupling modifiers, together with one parameter expressing the $gg \to H \to ZZ$ reference process in terms of these modifiers. The ratios of coupling modifiers are measured with precisions of approximately 10–20%, where the improvement in precision in this second parameterisation arises because the signal yields are expressed as squares or products of these coupling modifiers.

All measurements based on the generic parameterisations are compatible between the two experiments and with the predictions of the SM. The potential presence of physics beyond the SM (BSM) is also probed using specific parameterisations. With minimal additional assumptions, the overall branching fraction of the Higgs boson into BSM decays is determined to be less than 34% at 95% CL. This constraint applies to invisible decays into BSM particles, decays into BSM particles that are not detected as such, and modifications of the decays into SM particles that are not directly measured by the experiments.

The combined signal yield relative to the SM expectation is measured to be 1.09 ± 0.07 (stat) ± 0.08 (syst), where the systematic uncertainty is dominated by the theoretical uncertainty in the inclusive cross sections. The measured (expected) significance for the direct observation of the VBF production process is at the level of 5.4σ (4.6σ), while that for the $H \to \tau\tau$ decay channel is at the level of 5.5σ (5.0σ).

JHEP08(2016)045

Acknowledgments

We thank CERN for the very successful operation of the LHC, as well as the support staff from our institutions without whom ATLAS and CMS could not be operated efficiently.

We acknowledge the support of ANPCyT (Argentina); YerPhI (Armenia); ARC (Australia); BMWFW and FWF (Austria); ANAS (Azerbaijan); SSTC (Belarus); FNRS and FWO (Belgium); CNPq, CAPES, FAPERJ, and FAPESP (Brazil); MES (Bulgaria); NSERC, NRC, and CFI (Canada); CERN; CONICYT (Chile); CAS, MoST, and NSFC (China); COLCIENCIAS (Colombia); MSES and CSF (Croatia); RPF (Cyprus); MSMT CR, MPO CR, and VSC CR (Czech Republic); DNRF and DNSRC (Denmark); MoER, ERC IUT, and ERDF (Estonia); Academy of Finland, MEC, and HIP (Finland); CEA and CNRS/IN2P3 (France); GNSF (Georgia); BMBF , DFG, HGF, and MPG (Germany); GSRT (Greece); RGC (Hong Kong SAR, China); OTKA and NIH (Hungary); DAE and DST (India); IPM (Iran); SFI (Ireland); ISF, I-CORE, and Benoziyo Center (Israel); INFN (Italy); MEXT and JSPS (Japan); JINR; MSIP, and NRF (Republic of Korea); LAS (Lithuania); MOE and UM (Malaysia); BUAP, CINVESTAV, CONACYT, LNS, SEP, and UASLP-FAI (Mexico); CNRST (Morocco); FOM and NWO (Netherlands); MBIE (New Zealand); RCN (Norway); PAEC (Pakistan); MNiSW, MSHE, NCN, and NSC (Poland); FCT (Portugal); MNE/IFA (Romania); MES of Russia, MON, NRC KI, RosAtom, RAS, and RFBR (Russian Federation); MESTD (Serbia); MSSR (Slovakia); ARRS and MIZŠ (Slovenia); DST/NRF (South Africa); MINECO, SEIDI, and CPAN (Spain); SRC and Wallenberg Foundation (Sweden); ETH Board, ETH Zurich, PSI, SERI, SNSF, UniZH, and Cantons of Bern, Geneva and Zurich (Switzerland); MOST (Taipei); ThEPCenter, IPST, STAR, and NSTDA (Thailand); TUBITAK and TAEK (Turkey); NASU and SFFR (Ukraine); STFC (United Kingdom); DOE and NSF (United States of America).

In addition, individual groups and members have received support from BELSPO, FRIA, and IWT (Belgium); BCKDF, the Canada Council, CANARIE, CRC, Compute Canada, FQRNT, and the Ontario Innovation Trust (Canada); the Leventis Foundation (Cyprus); MEYS (Czech Republic); EPLANET, ERC, FP7, Horizon 2020, and Marie Skłodowska-Curie Actions (European Union); Investissements d'Avenir Labex and Idex, ANR, Région Auvergne and Fondation Partager le Savoir (France); AvH Foundation (Germany); the Herakleitos, Thales, and Aristeia programmes co-financed by EU-ESF and the Greek NSRF (Greece); CSIR (India); BSF, GIF, and Minerva (Israel); BRF (Norway); the HOMING PLUS programme of the FPS, co-financed from the EU Regional Development Fund, the Mobility Plus programme of the MSHE, and the OPUS programme of the NSC (Poland); the NPRP by Qatar NRF (Qatar); Generalitat de Catalunya, Generalitat Valenciana, and the Programa Clarín-COFUND del Principado de Asturias (Spain); the Rachadapisek Sompot Fund for Postdoctoral Fellowship, Chulalongkorn University, and the Chulalongkorn Academic into Its 2nd Century Project Advancement Project (Thailand); the Royal Society and Leverhulme Trust (United Kingdom); the A. P. Sloan Foundation and the Welch Foundation (United States of America).

The crucial computing support from all WLCG partners is acknowledged gratefully, in particular from CERN and the Tier-1 facilities at TRIUMF (Canada), NDGF (Den-

JHEP08(2016)045

mark, Norway, Sweden), CC-IN2P3 (France), KIT/GridKA (Germany), INFN-CNAF (Italy), NL-T1 (Netherlands), RRC-KI and JINR (Russian Federation), PIC (Spain), ASGC (Taipei), RAL (U.K.), and BNL and FNAL (U.S.A.), and from the Tier-2 facilities worldwide.

A Correlation matrices

Figures 27, 28 and 29 show the correlation matrices obtained from the fits to the generic parameterisations described respectively in sections 4.1.1, 4.1.2, and 4.2. The correlation coefficients are evaluated around the best fit values, using the second derivatives of the negative log-likelihood ratio.

In the case of the parameterisation using 23 products of cross sections times branching fractions, most of the parameters are uncorrelated, as shown in figure 27. Some significant anticorrelations are present however, because of cross-contamination between different channels. These can be seen in the ggF versus VBF production processes for all decay modes, in the WH versus ZH production processes for the $H \to \gamma\gamma$ decay mode, and in the $H \to WW$ versus $H \to \tau\tau$ decay modes for the ttH production process.

In contrast, for the two parameterisations based on ratios shown in figures 28 and 29, correlations are present for all pairs of parameters. For example, in each of these parameterisations, the first parameter is anticorrelated to most of the others, which are all expressed as ratios of cross sections, branching fractions, or coupling modifiers, because it is directly correlated to the denominators of these ratios.

These correlation matrices are constructed as symmetric at the observed best fit values of the parameters of interest, and therefore are not fully representative of the asymmetric uncertainties observed in certain parameterisations, as shown for example in figure 9. The derivation of the results for a specific parameterisation, with additional assumptions compared to a more generic one, from the fit results and the covariance matrix of this more generic parameterisation, is therefore not straightforward. This is one of the reasons for quoting the best fit results in sections 5 and 6 for a wide range of parameterisations, beyond the more generic ones discussed in section 4.

B Breakdown of systematic uncertainties

The results of the generic parameterisation of section 4.1.2, in terms of ratios of cross sections and branching fractions, with $gg \to H \to ZZ$ as the reference channel, are shown with the full breakdown of the uncertainties in table 20. The corresponding results for a similar parameterisation, with $gg \to H \to WW$ as reference, are shown in table 21 and illustrated in figure 30. The parameters corresponding to ratios of cross sections are identical in each of these parameterisations, and they are included in both tables for convenience, as are the two ratios, $\mathrm{B}^{WW}/\mathrm{B}^{ZZ}$ and $\mathrm{B}^{ZZ}/\mathrm{B}^{WW}$. Finally, the results of the generic parameterisation of section 4.2, in terms of ratios of coupling modifiers, are shown with the full breakdown of the uncertainties in table 22.

JHEP08(2016)045

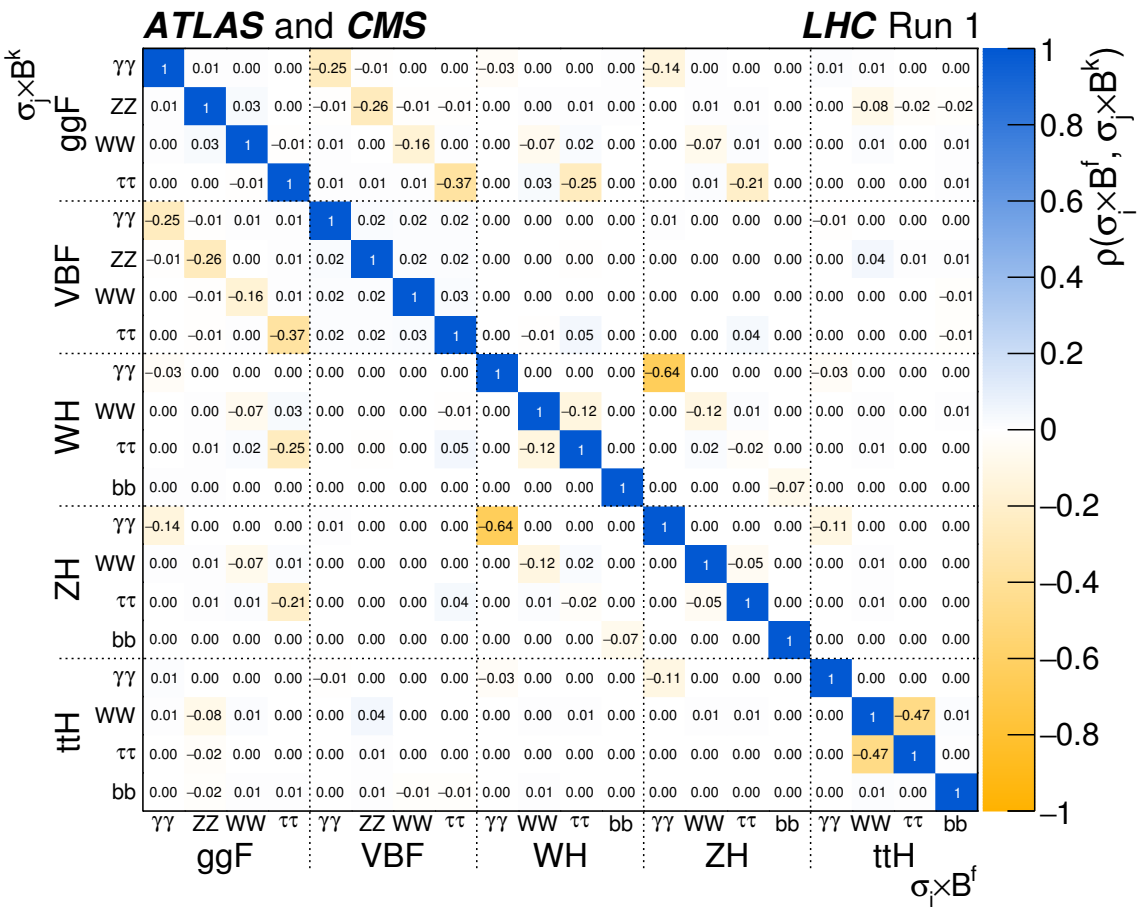

Figure 27. Correlation matrix obtained from the fit combining the ATLAS and CMS data using the generic parameterisation with 23 parameters described in section 4.1.1. Only 20 parameters are shown because the other three, corresponding to the $H \to ZZ$ decay channel for the WH, ZH, and ttH production processes, are not measured with a meaningful precision.

JHEP08(2016)045

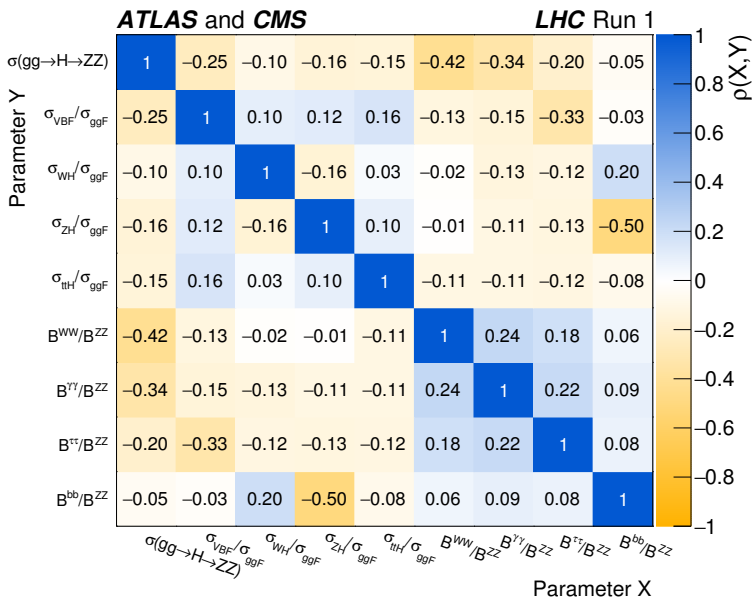

Figure 28. Correlation matrix obtained from the fit combining the ATLAS and CMS data using the generic parameterisation with nine parameters described in section 4.1.2.

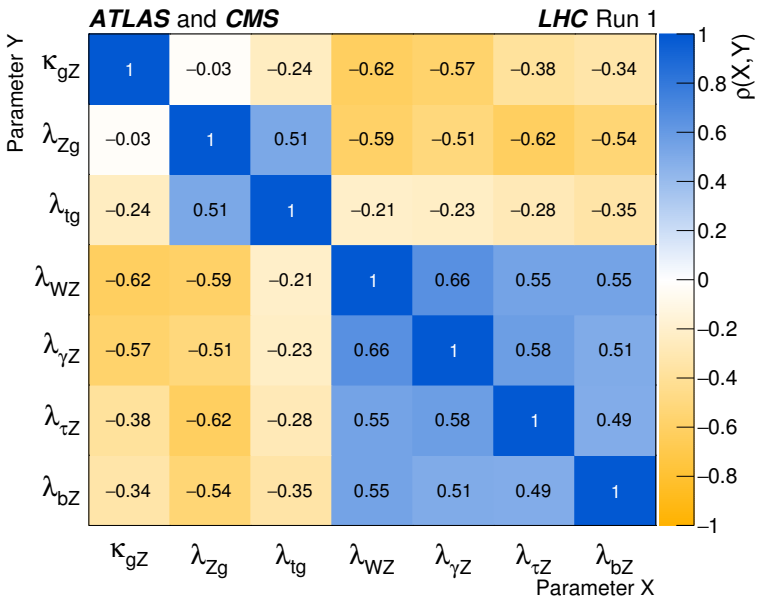

Figure 29. Correlation matrix obtained from the fit combining the ATLAS and CMS data using the generic parameterisation with seven parameters described in section 4.2.

JHEP08(2016)045

Parameter	SM prediction	Best fit value	Uncertainty Stat	Uncertainty Expt	Uncertainty Thbgd	Uncertainty Thsig	Best fit value	Uncertainty Stat	Uncertainty Expt	Uncertainty Thbgd	Uncertainty Thsig	Best fit value	Uncertainty Stat	Uncertainty Expt	Uncertainty Thbgd	Uncertainty Thsig
		ATLAS+CMS					ATLAS					CMS				
$\sigma(gg \to$	0.51 ± 0.06	$0.59\,^{+0.11}_{-0.10}$	$^{+0.11}_{-0.10}$	$^{+0.02}_{-0.01}$	$^{+0.01}_{-0.01}$	$^{+0.01}_{-0.01}$	$0.77\,^{+0.19}_{-0.17}$	$^{+0.19}_{-0.16}$	$^{+0.04}_{-0.03}$	$^{+0.02}_{-0.02}$	$^{+0.01}_{-0.01}$	$0.44\,^{+0.14}_{-0.12}$	$^{+0.13}_{-0.11}$	$^{+0.04}_{-0.03}$	$^{+0.01}_{-0.01}$	$^{+0.02}_{-0.01}$
$H \to ZZ)$ [pb]		$\left(^{+0.11}_{-0.10}\right)$	$\left(^{+0.11}_{-0.09}\right)$	$\left(^{+0.02}_{-0.02}\right)$	$\left(^{+0.01}_{-0.01}\right)$	$\left(^{+0.01}_{-0.01}\right)$	$\left(^{+0.16}_{-0.14}\right)$	$\left(^{+0.16}_{-0.13}\right)$	$\left(^{+0.03}_{-0.02}\right)$	$\left(^{+0.01}_{-0.01}\right)$	$\left(^{+0.01}_{-0.01}\right)$	$\left(^{+0.15}_{-0.13}\right)$	$\left(^{+0.15}_{-0.13}\right)$	$\left(^{+0.03}_{-0.02}\right)$	$\left(^{+0.01}_{-0.01}\right)$	$\left(^{+0.02}_{-0.01}\right)$
$\sigma_{\mathrm{VBF}}/\sigma_{gg\mathrm{F}}$	0.082 ± 0.009	$0.109\,^{+0.034}_{-0.027}$	$^{+0.029}_{-0.024}$	$^{+0.013}_{-0.009}$	$^{+0.006}_{-0.004}$	$^{+0.010}_{-0.008}$	$0.079\,^{+0.035}_{-0.026}$	$^{+0.030}_{-0.023}$	$^{+0.014}_{-0.009}$	$^{+0.008}_{-0.005}$	$^{+0.009}_{-0.006}$	$0.138\,^{+0.073}_{-0.051}$	$^{+0.061}_{-0.046}$	$^{+0.033}_{-0.019}$	$^{+0.014}_{-0.006}$	$^{+0.015}_{-0.010}$
		$\left(^{+0.029}_{-0.024}\right)$	$\left(^{+0.024}_{-0.020}\right)$	$\left(^{+0.012}_{-0.009}\right)$	$\left(^{+0.005}_{-0.003}\right)$	$\left(^{+0.009}_{-0.007}\right)$	$\left(^{+0.042}_{-0.031}\right)$	$\left(^{+0.036}_{-0.028}\right)$	$\left(^{+0.016}_{-0.010}\right)$	$\left(^{+0.010}_{-0.006}\right)$	$\left(^{+0.011}_{-0.008}\right)$	$\left(^{+0.043}_{-0.033}\right)$	$\left(^{+0.037}_{-0.029}\right)$	$\left(^{+0.020}_{-0.012}\right)$	$\left(^{+0.006}_{-0.003}\right)$	$\left(^{+0.010}_{-0.008}\right)$
$\sigma_{WH}/\sigma_{gg\mathrm{F}}$	0.037 ± 0.004	$0.031\,^{+0.028}_{-0.026}$	$^{+0.024}_{-0.022}$	$^{+0.012}_{-0.012}$	$^{+0.008}_{-0.008}$	$^{+0.003}_{-0.002}$	$0.054\,^{+0.036}_{-0.026}$	$^{+0.031}_{-0.023}$	$^{+0.012}_{-0.008}$	$^{+0.014}_{-0.009}$	$^{+0.007}_{-0.004}$	$0.005\,^{+0.044}_{-0.037}$	$^{+0.037}_{-0.028}$	$^{+0.021}_{-0.023}$	$^{+0.010}_{-0.008}$	$^{+0.003}_{-0.001}$
		$\left(^{+0.021}_{-0.017}\right)$	$\left(^{+0.019}_{-0.015}\right)$	$\left(^{+0.008}_{-0.005}\right)$	$\left(^{+0.007}_{-0.005}\right)$	$\left(^{+0.002}_{-0.002}\right)$	$\left(^{+0.033}_{-0.022}\right)$	$\left(^{+0.029}_{-0.020}\right)$	$\left(^{+0.010}_{-0.006}\right)$	$\left(^{+0.011}_{-0.006}\right)$	$\left(^{+0.005}_{-0.002}\right)$	$\left(^{+0.032}_{-0.022}\right)$	$\left(^{+0.027}_{-0.020}\right)$	$\left(^{+0.014}_{-0.008}\right)$	$\left(^{+0.009}_{-0.006}\right)$	$\left(^{+0.003}_{-0.001}\right)$
$\sigma_{ZH}/\sigma_{gg\mathrm{F}}$	0.0216 ± 0.0024	$0.066\,^{+0.039}_{-0.031}$	$^{+0.032}_{-0.025}$	$^{+0.018}_{-0.012}$	$^{+0.014}_{-0.012}$	$^{+0.005}_{-0.003}$	$0.013\,^{+0.028}_{-0.014}$	$^{+0.021}_{-0.012}$	$^{+0.013}_{-0.005}$	$^{+0.013}_{-0.005}$	$^{+0.003}_{-0.002}$	$0.123\,^{+0.076}_{-0.053}$	$^{+0.063}_{-0.046}$	$^{+0.038}_{-0.022}$	$^{+0.019}_{-0.013}$	$^{+0.009}_{-0.005}$
		$\left(^{+0.016}_{-0.011}\right)$	$\left(^{+0.014}_{-0.010}\right)$	$\left(^{+0.006}_{-0.003}\right)$	$\left(^{+0.006}_{-0.003}\right)$	$\left(^{+0.002}_{-0.001}\right)$	$\left(^{+0.027}_{-0.014}\right)$	$\left(^{+0.023}_{-0.013}\right)$	$\left(^{+0.009}_{-0.003}\right)$	$\left(^{+0.011}_{-0.004}\right)$	$\left(^{+0.003}_{-0.001}\right)$	$\left(^{+0.024}_{-0.013}\right)$	$\left(^{+0.020}_{-0.012}\right)$	$\left(^{+0.010}_{-0.004}\right)$	$\left(^{+0.009}_{-0.004}\right)$	$\left(^{+0.002}_{-0.001}\right)$
$\sigma_{ttH}/\sigma_{gg\mathrm{F}}$	0.0067 ± 0.0010	$0.0220\,^{+0.0068}_{-0.0057}$	$^{+0.0055}_{-0.0048}$	$^{+0.0031}_{-0.0023}$	$^{+0.0023}_{-0.0020}$	$^{+0.0014}_{-0.0010}$	$0.0126\,^{+0.0066}_{-0.0053}$	$^{+0.0052}_{-0.0042}$	$^{+0.0031}_{-0.0023}$	$^{+0.0024}_{-0.0020}$	$^{+0.0013}_{-0.0007}$	$0.0340\,^{+0.0158}_{-0.0116}$	$^{+0.0121}_{-0.0097}$	$^{+0.0085}_{-0.0051}$	$^{+0.0048}_{-0.0036}$	$^{+0.0026}_{-0.0015}$
		$\left(^{+0.0042}_{-0.0035}\right)$	$\left(^{+0.0033}_{-0.0027}\right)$	$\left(^{+0.0018}_{-0.0013}\right)$	$\left(^{+0.0020}_{-0.0019}\right)$	$\left(^{+0.0005}_{-0.0003}\right)$	$\left(^{+0.0061}_{-0.0045}\right)$	$\left(^{+0.0047}_{-0.0035}\right)$	$\left(^{+0.0026}_{-0.0017}\right)$	$\left(^{+0.0027}_{-0.0022}\right)$	$\left(^{+0.0008}_{-0.0004}\right)$	$\left(^{+0.0066}_{-0.0054}\right)$	$\left(^{+0.0051}_{-0.0038}\right)$	$\left(^{+0.0027}_{-0.0016}\right)$	$\left(^{+0.0032}_{-0.0034}\right)$	$\left(^{+0.0006}_{-0.0002}\right)$
$\mathrm{B}^{WW}/\mathrm{B}^{ZZ}$	$8.09 \pm < 0.01$	$6.7\,^{+1.6}_{-1.3}$	$^{+1.5}_{-1.2}$	$^{+0.4}_{-0.3}$	$^{+0.4}_{-0.3}$	$^{+0.3}_{-0.2}$	$6.5\,^{+2.1}_{-1.6}$	$^{+2.0}_{-1.4}$	$^{+0.6}_{-0.4}$	$^{+0.5}_{-0.4}$	$^{+0.3}_{-0.2}$	$7.1\,^{+2.9}_{-2.1}$	$^{+2.6}_{-1.8}$	$^{+1.0}_{-0.7}$	$^{+0.7}_{-0.5}$	$^{+0.4}_{-0.3}$
		$\left(^{+2.2}_{-1.7}\right)$	$\left(^{+2.0}_{-1.6}\right)$	$\left(^{+0.7}_{-0.5}\right)$	$\left(^{+0.5}_{-0.4}\right)$	$\left(^{+0.3}_{-0.2}\right)$	$\left(^{+3.5}_{-2.4}\right)$	$\left(^{+3.3}_{-2.2}\right)$	$\left(^{+0.9}_{-0.6}\right)$	$\left(^{+0.8}_{-0.6}\right)$	$\left(^{+0.4}_{-0.3}\right)$	$\left(^{+3.2}_{-2.2}\right)$	$\left(^{+2.9}_{-2.0}\right)$	$\left(^{+1.1}_{-0.8}\right)$	$\left(^{+0.7}_{-0.5}\right)$	$\left(^{+0.5}_{-0.4}\right)$
$\mathrm{B}^{\gamma\gamma}/\mathrm{B}^{ZZ}$	0.0854 ± 0.0010	$0.069\,^{+0.018}_{-0.014}$	$^{+0.018}_{-0.014}$	$^{+0.003}_{-0.002}$	$^{+0.002}_{-0.001}$	$^{+0.002}_{-0.002}$	$0.062\,^{+0.024}_{-0.018}$	$^{+0.023}_{-0.017}$	$^{+0.007}_{-0.004}$	$^{+0.002}_{-0.001}$	$^{+0.003}_{-0.002}$	$0.079\,^{+0.034}_{-0.023}$	$^{+0.032}_{-0.023}$	$^{+0.009}_{-0.005}$	$^{+0.003}_{-0.002}$	$^{+0.004}_{-0.003}$
		$\left(^{+0.025}_{-0.019}\right)$	$\left(^{+0.024}_{-0.019}\right)$	$\left(^{+0.005}_{-0.003}\right)$	$\left(^{+0.002}_{-0.001}\right)$	$\left(^{+0.003}_{-0.002}\right)$	$\left(^{+0.040}_{-0.027}\right)$	$\left(^{+0.039}_{-0.027}\right)$	$\left(^{+0.008}_{-0.005}\right)$	$\left(^{+0.003}_{-0.002}\right)$	$\left(^{+0.004}_{-0.003}\right)$	$\left(^{+0.035}_{-0.025}\right)$	$\left(^{+0.034}_{-0.024}\right)$	$\left(^{+0.007}_{-0.004}\right)$	$\left(^{+0.002}_{-0.001}\right)$	$\left(^{+0.004}_{-0.003}\right)$
$\mathrm{B}^{\tau\tau}/\mathrm{B}^{ZZ}$	2.36 ± 0.05	$1.77\,^{+0.59}_{-0.46}$	$^{+0.52}_{-0.41}$	$^{+0.27}_{-0.20}$	$^{+0.05}_{-0.04}$	$^{+0.06}_{-0.04}$	$2.17\,^{+1.07}_{-0.74}$	$^{+0.89}_{-0.64}$	$^{+0.53}_{-0.35}$	$^{+0.16}_{-0.10}$	$^{+0.17}_{-0.09}$	$1.56\,^{+0.90}_{-0.61}$	$^{+0.78}_{-0.54}$	$^{+0.45}_{-0.26}$	$^{+0.07}_{-0.05}$	$^{+0.07}_{-0.04}$
		$\left(^{+0.90}_{-0.68}\right)$	$\left(^{+0.75}_{-0.58}\right)$	$\left(^{+0.47}_{-0.33}\right)$	$\left(^{+0.08}_{-0.06}\right)$	$\left(^{+0.10}_{-0.06}\right)$	$\left(^{+1.54}_{-0.98}\right)$	$\left(^{+1.30}_{-0.86}\right)$	$\left(^{+0.76}_{-0.44}\right)$	$\left(^{+0.22}_{-0.12}\right)$	$\left(^{+0.22}_{-0.10}\right)$	$\left(^{+1.23}_{-0.86}\right)$	$\left(^{+1.03}_{-0.73}\right)$	$\left(^{+0.66}_{-0.44}\right)$	$\left(^{+0.04}_{-0.03}\right)$	$\left(^{+0.12}_{-0.07}\right)$
$\mathrm{B}^{bb}/\mathrm{B}^{ZZ}$	21.5 ± 1.0	$4.2\,^{+4.4}_{-2.6}$	$^{+2.8}_{-2.0}$	$^{+2.3}_{-1.1}$	$^{+2.5}_{-1.2}$	$^{+0.4}_{-0.2}$	$9.6\,^{+10.1}_{-5.7}$	$^{+7.4}_{-4.4}$	$^{+4.5}_{-2.4}$	$^{+5.1}_{-2.7}$	$^{+1.3}_{-0.5}$	$3.7\,^{+4.1}_{-2.4}$	$^{+3.1}_{-2.0}$	$^{+1.8}_{-0.9}$	$^{+1.9}_{-1.1}$	$^{+0.4}_{-0.2}$
		$\left(^{+16.8}_{-9.0}\right)$	$\left(^{+13.9}_{-7.9}\right)$	$\left(^{+6.3}_{-2.8}\right)$	$\left(^{+6.7}_{-3.3}\right)$	$\left(^{+2.1}_{-0.9}\right)$	$\left(^{+29.3}_{-11.8}\right)$	$\left(^{+24.2}_{-10.5}\right)$	$\left(^{+10.9}_{-3.3}\right)$	$\left(^{+11.8}_{-4.0}\right)$	$\left(^{+4.0}_{-1.2}\right)$	$\left(^{+29.4}_{-11.9}\right)$	$\left(^{+23.4}_{-10.4}\right)$	$\left(^{+12.7}_{-3.8}\right)$	$\left(^{+12.2}_{-4.4}\right)$	$\left(^{+2.5}_{-0.9}\right)$

Table 20. Best fit values of $\sigma(gg \to H \to ZZ)$, $\sigma_i/\sigma_{gg\mathrm{F}}$, and $\mathrm{B}^f/\mathrm{B}^{ZZ}$ from the combined analysis of the $\sqrt{s} = 7$ and 8 TeV data. The values involving cross sections are given for $\sqrt{s} = 8$ TeV, assuming the SM values for $\sigma_i(7\ \ \mathrm{TeV})/\sigma_i(8\ \ \mathrm{TeV})$. The results are shown for the combination of ATLAS and CMS, and also separately for each experiment, together with their total uncertainties and their breakdown into the four components described in the text. The expected total uncertainties in the measurements are also shown in parentheses. The SM predictions [32] are shown with their total uncertainties.

JHEP08(2016)045

Parameter	SM prediction	Best fit value	Uncertainty Stat	Uncertainty Expt	Uncertainty Thbgd	Uncertainty Thsig	Best fit value	Uncertainty Stat	Uncertainty Expt	Uncertainty Thbgd	Uncertainty Thsig	Best fit value	Uncertainty Stat	Uncertainty Expt	Uncertainty Thbgd	Uncertainty Thsig
		ATLAS+CMS					ATLAS					CMS				
$\sigma(gg \to$	4.1 ± 0.5	$4.0\,^{+0.6}_{-0.6}$	$^{+0.5}_{-0.5}$	$^{+0.3}_{-0.3}$	$^{+0.2}_{-0.2}$	$^{+0.2}_{-0.1}$	$5.0\,^{+1.0}_{-0.9}$	$^{+0.7}_{-0.7}$	$^{+0.4}_{-0.4}$	$^{+0.4}_{-0.4}$	$^{+0.2}_{-0.2}$	$3.1\,^{+0.8}_{-0.8}$	$^{+0.6}_{-0.6}$	$^{+0.5}_{-0.4}$	$^{+0.3}_{-0.3}$	$^{+0.2}_{-0.1}$
$H \to WW)$ [pb]		$\left(^{+0.7}_{-0.6}\right)$	$\left(^{+0.5}_{-0.5}\right)$	$\left(^{+0.3}_{-0.3}\right)$	$\left(^{+0.3}_{-0.3}\right)$	$\left(^{+0.2}_{-0.1}\right)$	$\left(^{+0.9}_{-0.9}\right)$	$\left(^{+0.7}_{-0.7}\right)$	$\left(^{+0.4}_{-0.4}\right)$	$\left(^{+0.4}_{-0.4}\right)$	$\left(^{+0.2}_{-0.1}\right)$	$\left(^{+0.9}_{-0.9}\right)$	$\left(^{+0.6}_{-0.6}\right)$	$\left(^{+0.5}_{-0.5}\right)$	$\left(^{+0.4}_{-0.3}\right)$	$\left(^{+0.2}_{-0.2}\right)$
$\sigma_{\mathrm{VBF}}/\sigma_{gg\mathrm{F}}$	0.082 ± 0.009	$0.109\,^{+0.034}_{-0.027}$	$^{+0.028}_{-0.024}$	$^{+0.013}_{-0.009}$	$^{+0.006}_{-0.004}$	$^{+0.011}_{-0.008}$	$0.079\,^{+0.035}_{-0.026}$	$^{+0.030}_{-0.023}$	$^{+0.015}_{-0.009}$	$^{+0.008}_{-0.005}$	$^{+0.009}_{-0.006}$	$0.137\,^{+0.072}_{-0.051}$	$^{+0.061}_{-0.046}$	$^{+0.032}_{-0.018}$	$^{+0.014}_{-0.006}$	$^{+0.016}_{-0.010}$
		$\left(^{+0.029}_{-0.024}\right)$	$\left(^{+0.024}_{-0.020}\right)$	$\left(^{+0.012}_{-0.009}\right)$	$\left(^{+0.005}_{-0.003}\right)$	$\left(^{+0.009}_{-0.007}\right)$	$\left(^{+0.042}_{-0.031}\right)$	$\left(^{+0.036}_{-0.028}\right)$	$\left(^{+0.016}_{-0.010}\right)$	$\left(^{+0.010}_{-0.006}\right)$	$\left(^{+0.011}_{-0.008}\right)$	$\left(^{+0.043}_{-0.033}\right)$	$\left(^{+0.037}_{-0.029}\right)$	$\left(^{+0.020}_{-0.012}\right)$	$\left(^{+0.006}_{-0.003}\right)$	$\left(^{+0.010}_{-0.008}\right)$
$\sigma_{WH}/\sigma_{gg\mathrm{F}}$	0.037 ± 0.004	$0.030\,^{+0.028}_{-0.026}$	$^{+0.024}_{-0.022}$	$^{+0.012}_{-0.012}$	$^{+0.008}_{-0.008}$	$^{+0.003}_{-0.002}$	$0.054\,^{+0.037}_{-0.026}$	$^{+0.031}_{-0.023}$	$^{+0.012}_{-0.008}$	$^{+0.014}_{-0.009}$	$^{+0.007}_{-0.003}$	$0.005\,^{+0.043}_{-0.037}$	$^{+0.037}_{-0.028}$	$^{+0.021}_{-0.023}$	$^{+0.010}_{-0.008}$	$^{+0.003}_{-0.001}$
		$\left(^{+0.021}_{-0.017}\right)$	$\left(^{+0.019}_{-0.015}\right)$	$\left(^{+0.008}_{-0.005}\right)$	$\left(^{+0.007}_{-0.005}\right)$	$\left(^{+0.003}_{-0.002}\right)$	$\left(^{+0.032}_{-0.022}\right)$	$\left(^{+0.029}_{-0.020}\right)$	$\left(^{+0.010}_{-0.006}\right)$	$\left(^{+0.011}_{-0.006}\right)$	$\left(^{+0.004}_{-0.002}\right)$	$\left(^{+0.032}_{-0.022}\right)$	$\left(^{+0.027}_{-0.020}\right)$	$\left(^{+0.014}_{-0.008}\right)$	$\left(^{+0.009}_{-0.006}\right)$	$\left(^{+0.003}_{-0.001}\right)$
$\sigma_{ZH}/\sigma_{gg\mathrm{F}}$	0.0216 ± 0.0024	$0.066\,^{+0.039}_{-0.031}$	$^{+0.032}_{-0.025}$	$^{+0.018}_{-0.013}$	$^{+0.014}_{-0.012}$	$^{+0.005}_{-0.003}$	$0.013\,^{+0.028}_{-0.013}$	$^{+0.021}_{-0.008}$	$^{+0.013}_{-0.011}$	$^{+0.013}_{-0.006}$	$^{+0.003}_{-0.002}$	$0.123\,^{+0.075}_{-0.052}$	$^{+0.062}_{-0.046}$	$^{+0.037}_{-0.021}$	$^{+0.018}_{-0.013}$	$^{+0.009}_{-0.005}$
		$\left(^{+0.016}_{-0.011}\right)$	$\left(^{+0.014}_{-0.010}\right)$	$\left(^{+0.006}_{-0.003}\right)$	$\left(^{+0.006}_{-0.003}\right)$	$\left(^{+0.002}_{-0.001}\right)$	$\left(^{+0.027}_{-0.014}\right)$	$\left(^{+0.023}_{-0.013}\right)$	$\left(^{+0.009}_{-0.003}\right)$	$\left(^{+0.011}_{-0.004}\right)$	$\left(^{+0.003}_{-0.001}\right)$	$\left(^{+0.024}_{-0.013}\right)$	$\left(^{+0.020}_{-0.012}\right)$	$\left(^{+0.010}_{-0.004}\right)$	$\left(^{+0.009}_{-0.004}\right)$	$\left(^{+0.002}_{-0.001}\right)$
$\sigma_{ttH}/\sigma_{gg\mathrm{F}}$	0.0067 ± 0.0010	$0.0220\,^{+0.0068}_{-0.0057}$	$^{+0.0055}_{-0.0048}$	$^{+0.0031}_{-0.0023}$	$^{+0.0023}_{-0.0020}$	$^{+0.0014}_{-0.0010}$	$0.0126\,^{+0.0066}_{-0.0053}$	$^{+0.0052}_{-0.0042}$	$^{+0.0031}_{-0.0023}$	$^{+0.0024}_{-0.0020}$	$^{+0.0013}_{-0.0007}$	$0.0340\,^{+0.0157}_{-0.0116}$	$^{+0.0121}_{-0.0096}$	$^{+0.0085}_{-0.0050}$	$^{+0.0048}_{-0.0036}$	$^{+0.0026}_{-0.0015}$
		$\left(^{+0.0042}_{-0.0035}\right)$	$\left(^{+0.0033}_{-0.0027}\right)$	$\left(^{+0.0018}_{-0.0013}\right)$	$\left(^{+0.0020}_{-0.0019}\right)$	$\left(^{+0.0005}_{-0.0003}\right)$	$\left(^{+0.0060}_{-0.0045}\right)$	$\left(^{+0.0047}_{-0.0035}\right)$	$\left(^{+0.0026}_{-0.0017}\right)$	$\left(^{+0.0027}_{-0.0022}\right)$	$\left(^{+0.0008}_{-0.0004}\right)$	$\left(^{+0.0067}_{-0.0054}\right)$	$\left(^{+0.0051}_{-0.0038}\right)$	$\left(^{+0.0027}_{-0.0016}\right)$	$\left(^{+0.0032}_{-0.0034}\right)$	$\left(^{+0.0006}_{-0.0002}\right)$
$\mathrm{B}^{ZZ}/\mathrm{B}^{WW}$	$0.124 \pm < 0.001$	$0.148\,^{+0.035}_{-0.029}$	$^{+0.032}_{-0.027}$	$^{+0.010}_{-0.007}$	$^{+0.009}_{-0.006}$	$^{+0.006}_{-0.004}$	$0.155\,^{+0.050}_{-0.039}$	$^{+0.045}_{-0.036}$	$^{+0.016}_{-0.009}$	$^{+0.014}_{-0.008}$	$^{+0.007}_{-0.005}$	$0.140\,^{+0.057}_{-0.041}$	$^{+0.049}_{-0.038}$	$^{+0.023}_{-0.012}$	$^{+0.016}_{-0.008}$	$^{+0.009}_{-0.005}$
		$\left(^{+0.033}_{-0.027}\right)$	$\left(^{+0.029}_{-0.025}\right)$	$\left(^{+0.011}_{-0.007}\right)$	$\left(^{+0.009}_{-0.006}\right)$	$\left(^{+0.005}_{-0.003}\right)$	$\left(^{+0.050}_{-0.037}\right)$	$\left(^{+0.045}_{-0.035}\right)$	$\left(^{+0.014}_{-0.008}\right)$	$\left(^{+0.014}_{-0.007}\right)$	$\left(^{+0.006}_{-0.004}\right)$	$\left(^{+0.048}_{-0.035}\right)$	$\left(^{+0.041}_{-0.033}\right)$	$\left(^{+0.019}_{-0.010}\right)$	$\left(^{+0.013}_{-0.007}\right)$	$\left(^{+0.009}_{-0.005}\right)$
$\mathrm{B}^{\gamma\gamma}/\mathrm{B}^{WW}$	0.01056 ± 0.00010	$0.0102\,^{+0.0022}_{-0.0019}$	$^{+0.0020}_{-0.0017}$	$^{+0.0008}_{-0.0005}$	$^{+0.0006}_{-0.0004}$	$^{+0.0004}_{-0.0003}$	$0.0097\,^{+0.0031}_{-0.0025}$	$^{+0.0026}_{-0.0023}$	$^{+0.0013}_{-0.0008}$	$^{+0.0008}_{-0.0005}$	$^{+0.0006}_{-0.0004}$	$0.0111\,^{+0.0039}_{-0.0029}$	$^{+0.0033}_{-0.0027}$	$^{+0.0018}_{-0.0010}$	$^{+0.0012}_{-0.0006}$	$^{+0.0006}_{-0.0004}$
		$\left(^{+0.0025}_{-0.0020}\right)$	$\left(^{+0.0021}_{-0.0019}\right)$	$\left(^{+0.0009}_{-0.0006}\right)$	$\left(^{+0.0007}_{-0.0005}\right)$	$\left(^{+0.0005}_{-0.0003}\right)$	$\left(^{+0.0037}_{-0.0029}\right)$	$\left(^{+0.0032}_{-0.0027}\right)$	$\left(^{+0.0014}_{-0.0008}\right)$	$\left(^{+0.0011}_{-0.0006}\right)$	$\left(^{+0.0007}_{-0.0005}\right)$	$\left(^{+0.0036}_{-0.0027}\right)$	$\left(^{+0.0030}_{-0.0025}\right)$	$\left(^{+0.0015}_{-0.0008}\right)$	$\left(^{+0.0011}_{-0.0005}\right)$	$\left(^{+0.0007}_{-0.0004}\right)$
$\mathrm{B}^{\tau\tau}/\mathrm{B}^{WW}$	0.292 ± 0.006	$0.26\,^{+0.08}_{-0.06}$	$^{+0.06}_{-0.05}$	$^{+0.04}_{-0.03}$	$^{+0.02}_{-0.01}$	$^{+0.01}_{-0.01}$	$0.34\,^{+0.14}_{-0.10}$	$^{+0.11}_{-0.09}$	$^{+0.08}_{-0.06}$	$^{+0.03}_{-0.02}$	$^{+0.03}_{-0.02}$	$0.22\,^{+0.11}_{-0.08}$	$^{+0.09}_{-0.07}$	$^{+0.06}_{-0.04}$	$^{+0.02}_{-0.01}$	$^{+0.01}_{-0.01}$
		$\left(^{+0.09}_{-0.08}\right)$	$\left(^{+0.07}_{-0.06}\right)$	$\left(^{+0.06}_{-0.04}\right)$	$\left(^{+0.02}_{-0.01}\right)$	$\left(^{+0.01}_{-0.01}\right)$	$\left(^{+0.15}_{-0.11}\right)$	$\left(^{+0.12}_{-0.09}\right)$	$\left(^{+0.09}_{-0.06}\right)$	$\left(^{+0.03}_{-0.02}\right)$	$\left(^{+0.03}_{-0.01}\right)$	$\left(^{+0.13}_{-0.10}\right)$	$\left(^{+0.10}_{-0.08}\right)$	$\left(^{+0.08}_{-0.06}\right)$	$\left(^{+0.03}_{-0.01}\right)$	$\left(^{+0.02}_{-0.01}\right)$
$\mathrm{B}^{bb}/\mathrm{B}^{WW}$	2.66 ± 0.12	$0.61\,^{+0.64}_{-0.38}$	$^{+0.39}_{-0.29}$	$^{+0.34}_{-0.16}$	$^{+0.37}_{-0.18}$	$^{+0.05}_{-0.02}$	$1.50\,^{+1.54}_{-0.90}$	$^{+1.06}_{-0.66}$	$^{+0.73}_{-0.42}$	$^{+0.82}_{-0.43}$	$^{+0.20}_{-0.09}$	$0.52\,^{+0.54}_{-0.34}$	$^{+0.39}_{-0.27}$	$^{+0.25}_{-0.13}$	$^{+0.28}_{-0.14}$	$^{+0.05}_{-0.02}$
		$\left(^{+2.01}_{-1.09}\right)$	$\left(^{+1.63}_{-0.93}\right)$	$\left(^{+0.78}_{-0.35}\right)$	$\left(^{+0.84}_{-0.42}\right)$	$\left(^{+0.23}_{-0.10}\right)$	$\left(^{+3.49}_{-1.38}\right)$	$\left(^{+2.83}_{-1.20}\right)$	$\left(^{+1.37}_{-0.42}\right)$	$\left(^{+1.45}_{-0.52}\right)$	$\left(^{+0.45}_{-0.14}\right)$	$\left(^{+3.57}_{-1.46}\right)$	$\left(^{+2.78}_{-1.25}\right)$	$\left(^{+1.58}_{-0.49}\right)$	$\left(^{+1.56}_{-0.58}\right)$	$\left(^{+0.26}_{-0.10}\right)$

Table 21. Best fit values of $\sigma(gg \to H \to WW)$, $\sigma_i/\sigma_{gg\mathrm{F}}$, and $\mathrm{B}^f/\mathrm{B}^{WW}$ from the combined analysis of the $\sqrt{s} = 7$ and 8 TeV data. The values involving cross sections are given for $\sqrt{s} = 8$ TeV, assuming the SM values for $\sigma_i(7\ \mathrm{TeV})/\sigma_i(8\ \mathrm{TeV})$. The results are shown for the combination of ATLAS and CMS, and also separately for each experiment, together with their total uncertainties and their breakdown into the four components described in the text. The expected total uncertainties in the measurements are also shown in parentheses. The SM predictions [32] are shown with their total uncertainties.

JHEP08(2016)045

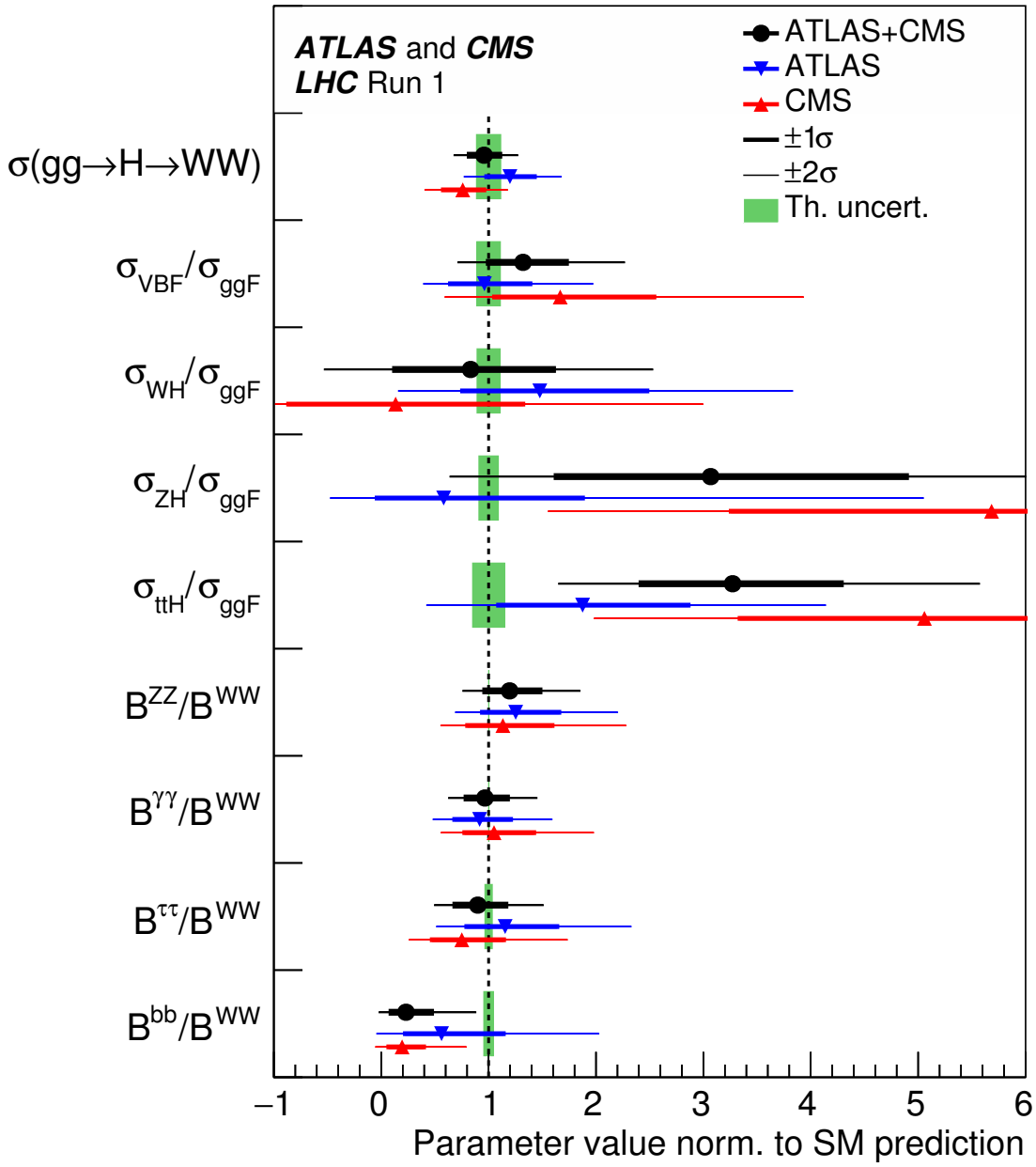

Figure 30. Best fit values of the $gg \to H \to WW$ cross section and of ratios of cross sections and branching fractions, as obtained from the generic parameterisation described in section 4.1.2 and as tabulated in table 21 for the combination of the ATLAS and CMS measurements. Also shown are the results from each experiment. The values involving cross sections are given for $\sqrt{s} = 8\,\text{TeV}$, assuming the SM values for $\sigma_i(7\ \text{TeV})/\sigma_i(8\ \text{TeV})$. The error bars indicate the 1σ (thick lines) and 2σ (thin lines) intervals. In this figure, the fit results are normalised to the SM predictions for the various parameters and the shaded bands indicate the theoretical uncertainties in these predictions.

JHEP08(2016)045

Parameter	Best fit value	Uncertainty Stat	Uncertainty Expt	Uncertainty Thbgd	Uncertainty Thsig	Best fit value	Uncertainty Stat	Uncertainty Expt	Uncertainty Thbgd	Uncertainty Thsig	Best fit value	Uncertainty Stat	Uncertainty Expt	Uncertainty Thbgd	Uncertainty Thsig
	ATLAS+CMS					ATLAS					CMS				
κ_{gZ}	$1.09\,^{+0.11}_{-0.11}$	$^{+0.09}_{-0.09}$	$^{+0.02}_{-0.02}$	$^{+0.00}_{-0.01}$	$^{+0.06}_{-0.05}$	$1.20\,^{+0.16}_{-0.15}$	$^{+0.14}_{-0.14}$	$^{+0.03}_{-0.03}$	$^{+0.02}_{-0.02}$	$^{+0.07}_{-0.06}$	$0.99\,^{+0.14}_{-0.13}$	$^{+0.12}_{-0.12}$	$^{+0.03}_{-0.04}$	$^{+0.01}_{-0.01}$	$^{+0.06}_{-0.04}$
	$\left(^{+0.11}_{-0.11}\right)$	$\left(^{+0.09}_{-0.09}\right)$	$\left(^{+0.02}_{-0.02}\right)$	$\left(^{+0.01}_{-0.01}\right)$	$\left(^{+0.06}_{-0.05}\right)$	$\left(^{+0.15}_{-0.15}\right)$	$\left(^{+0.14}_{-0.13}\right)$	$\left(^{+0.03}_{-0.03}\right)$	$\left(^{+0.01}_{-0.02}\right)$	$\left(^{+0.06}_{-0.05}\right)$	$\left(^{+0.14}_{-0.14}\right)$	$\left(^{+0.13}_{-0.12}\right)$	$\left(^{+0.03}_{-0.03}\right)$	$\left(^{+0.01}_{-0.01}\right)$	$\left(^{+0.06}_{-0.05}\right)$
λ_{Zg}	$1.27\,^{+0.23}_{-0.20}$	$^{+0.18}_{-0.16}$	$^{+0.10}_{-0.07}$	$^{+0.06}_{-0.05}$	$^{+0.10}_{-0.08}$	$1.07\,^{+0.26}_{-0.22}$	$^{+0.21}_{-0.18}$	$^{+0.10}_{-0.06}$	$^{+0.07}_{-0.06}$	$^{+0.09}_{-0.07}$	$1.47\,^{+0.45}_{-0.34}$	$^{+0.35}_{-0.28}$	$^{+0.22}_{-0.14}$	$^{+0.11}_{-0.10}$	$^{+0.13}_{-0.09}$
	$\left(^{+0.20}_{-0.17}\right)$	$\left(^{+0.15}_{-0.14}\right)$	$\left(^{+0.08}_{-0.06}\right)$	$\left(^{+0.05}_{-0.04}\right)$	$\left(^{+0.08}_{-0.07}\right)$	$\left(^{+0.28}_{-0.23}\right)$	$\left(^{+0.23}_{-0.20}\right)$	$\left(^{+0.10}_{-0.07}\right)$	$\left(^{+0.09}_{-0.05}\right)$	$\left(^{+0.09}_{-0.07}\right)$	$\left(^{+0.27}_{-0.23}\right)$	$\left(^{+0.21}_{-0.19}\right)$	$\left(^{+0.12}_{-0.09}\right)$	$\left(^{+0.07}_{-0.05}\right)$	$\left(^{+0.09}_{-0.07}\right)$
λ_{tg}	$1.78\,^{+0.30}_{-0.27}$	$^{+0.21}_{-0.20}$	$^{+0.13}_{-0.11}$	$^{+0.09}_{-0.09}$	$^{+0.14}_{-0.11}$	$1.40\,^{+0.34}_{-0.33}$	$^{+0.25}_{-0.24}$	$^{+0.14}_{-0.15}$	$^{+0.12}_{-0.14}$	$^{+0.14}_{-0.09}$	$-2.26\,^{+0.50}_{-0.53}$	$^{+0.43}_{-0.39}$	$^{+0.22}_{-0.23}$	$^{+0.04}_{-0.18}$	$^{+0.14}_{-0.21}$
	$\left(^{+0.28}_{-0.38}\right)$	$\left(^{+0.20}_{-0.30}\right)$	$\left(^{+0.11}_{-0.13}\right)$	$\left(^{+0.14}_{-0.20}\right)$	$\left(^{+0.09}_{-0.05}\right)$	$\left(^{+0.38}_{-0.54}\right)$	$\left(^{+0.28}_{-0.39}\right)$	$\left(^{+0.14}_{-0.22}\right)$	$\left(^{+0.18}_{-0.29}\right)$	$\left(^{+0.11}_{-0.06}\right)$	$\left(^{+0.42}_{-0.64}\right)$	$\left(^{+0.31}_{-0.42}\right)$	$\left(^{+0.16}_{-0.22}\right)$	$\left(^{+0.21}_{-0.43}\right)$	$\left(^{+0.11}_{-0.06}\right)$
λ_{WZ}	$0.88\,^{+0.10}_{-0.09}$	$^{+0.09}_{-0.08}$	$^{+0.03}_{-0.03}$	$^{+0.03}_{-0.02}$	$^{+0.02}_{-0.01}$	$0.92\,^{+0.14}_{-0.12}$	$^{+0.13}_{-0.11}$	$^{+0.04}_{-0.03}$	$^{+0.03}_{-0.03}$	$^{+0.02}_{-0.02}$	$-0.85\,^{+0.13}_{-0.15}$	$^{+0.11}_{-0.13}$	$^{+0.05}_{-0.06}$	$^{+0.04}_{-0.04}$	$^{+0.01}_{-0.03}$
	$\left(^{+0.12}_{-0.10}\right)$	$\left(^{+0.11}_{-0.09}\right)$	$\left(^{+0.04}_{-0.03}\right)$	$\left(^{+0.03}_{-0.03}\right)$	$\left(^{+0.02}_{-0.01}\right)$	$\left(^{+0.18}_{-0.15}\right)$	$\left(^{+0.17}_{-0.13}\right)$	$\left(^{+0.04}_{-0.04}\right)$	$\left(^{+0.04}_{-0.04}\right)$	$\left(^{+0.02}_{-0.02}\right)$	$\left(^{+0.17}_{-0.14}\right)$	$\left(^{+0.15}_{-0.13}\right)$	$\left(^{+0.06}_{-0.05}\right)$	$\left(^{+0.03}_{-0.03}\right)$	$\left(^{+0.03}_{-0.02}\right)$
$\lvert\lambda_{\gamma Z}\rvert$	$0.89\,^{+0.11}_{-0.10}$	$^{+0.10}_{-0.09}$	$^{+0.03}_{-0.02}$	$^{+0.01}_{-0.02}$	$^{+0.02}_{-0.01}$	$0.87\,^{+0.15}_{-0.13}$	$^{+0.15}_{-0.13}$	$^{+0.04}_{-0.04}$	$^{+0.02}_{-0.01}$	$^{+0.02}_{-0.02}$	$0.91\,^{+0.17}_{-0.14}$	$^{+0.16}_{-0.14}$	$^{+0.04}_{-0.03}$	$^{+0.02}_{-0.02}$	$^{+0.02}_{-0.02}$
	$\left(^{+0.13}_{-0.12}\right)$	$\left(^{+0.13}_{-0.11}\right)$	$\left(^{+0.03}_{-0.02}\right)$	$\left(^{+0.01}_{-0.01}\right)$	$\left(^{+0.02}_{-0.01}\right)$	$\left(^{+0.20}_{-0.17}\right)$	$\left(^{+0.20}_{-0.17}\right)$	$\left(^{+0.05}_{-0.03}\right)$	$\left(^{+0.03}_{-0.01}\right)$	$\left(^{+0.02}_{-0.02}\right)$	$\left(^{+0.18}_{-0.16}\right)$	$\left(^{+0.18}_{-0.15}\right)$	$\left(^{+0.04}_{-0.03}\right)$	$\left(^{+0.01}_{-0.01}\right)$	$\left(^{+0.02}_{-0.02}\right)$
$\lvert\lambda_{\tau Z}\rvert$	$0.85\,^{+0.13}_{-0.12}$	$^{+0.12}_{-0.10}$	$^{+0.07}_{-0.06}$	$^{+0.01}_{-0.02}$	$^{+0.02}_{-0.01}$	$0.96\,^{+0.21}_{-0.18}$	$^{+0.18}_{-0.15}$	$^{+0.10}_{-0.09}$	$^{+0.04}_{-0.03}$	$^{+0.03}_{-0.02}$	$0.78\,^{+0.20}_{-0.17}$	$^{+0.17}_{-0.15}$	$^{+0.10}_{-0.08}$	$^{+0.01}_{-0.02}$	$^{+0.02}_{-0.01}$
	$\left(^{+0.17}_{-0.15}\right)$	$\left(^{+0.14}_{-0.13}\right)$	$\left(^{+0.09}_{-0.08}\right)$	$\left(^{+0.02}_{-0.02}\right)$	$\left(^{+0.02}_{-0.02}\right)$	$\left(^{+0.27}_{-0.23}\right)$	$\left(^{+0.23}_{-0.19}\right)$	$\left(^{+0.13}_{-0.11}\right)$	$\left(^{+0.04}_{-0.03}\right)$	$\left(^{+0.04}_{-0.02}\right)$	$\left(^{+0.23}_{-0.20}\right)$	$\left(^{+0.19}_{-0.17}\right)$	$\left(^{+0.12}_{-0.11}\right)$	$\left(^{+0.02}_{-0.01}\right)$	$\left(^{+0.02}_{-0.02}\right)$
$\lvert\lambda_{bZ}\rvert$	$0.58\,^{+0.16}_{-0.20}$	$^{+0.12}_{-0.17}$	$^{+0.07}_{-0.06}$	$^{+0.07}_{-0.07}$	$^{+0.03}_{-0.04}$	$0.61\,^{+0.24}_{-0.24}$	$^{+0.20}_{-0.19}$	$^{+0.09}_{-0.12}$	$^{+0.10}_{-0.10}$	$^{+0.04}_{-0.03}$	$0.47\,^{+0.26}_{-0.17}$	$^{+0.23}_{-0.13}$	$^{+0.06}_{-0.07}$	$^{+0.11}_{-0.08}$	$^{+0.00}_{-0.04}$
	$\left(^{+0.25}_{-0.22}\right)$	$\left(^{+0.21}_{-0.20}\right)$	$\left(^{+0.09}_{-0.07}\right)$	$\left(^{+0.08}_{-0.05}\right)$	$\left(^{+0.06}_{-0.05}\right)$	$\left(^{+0.36}_{-0.29}\right)$	$\left(^{+0.31}_{-0.26}\right)$	$\left(^{+0.12}_{-0.09}\right)$	$\left(^{+0.11}_{-0.08}\right)$	$\left(^{+0.08}_{-0.05}\right)$	$\left(^{+0.38}_{-0.37}\right)$	$\left(^{+0.32}_{-0.34}\right)$	$\left(^{+0.15}_{-0.11}\right)$	$\left(^{+0.11}_{-0.09}\right)$	$\left(^{+0.07}_{-0.07}\right)$

Table 22. Best fit values of $\kappa_{gZ} = \kappa_g \cdot \kappa_Z/\kappa_H$ and of the ratios of coupling modifiers, as defined in the most generic parameterisation described in the context of the κ framework, from the combined analysis of the $\sqrt{s} = 7$ and 8 TeV data. The results are shown for the combination of ATLAS and CMS and also separately for each experiment, together with their total uncertainties and their breakdown into the four components described in the text. The uncertainties in λ_{tg} and λ_{WZ}, for which a negative solution is allowed, are calculated around the overall best fit value. The combined 1σ CL intervals are $\lambda_{tg} = [-2.00, -1.59] \cup [1.50, 2.07]$ and $\lambda_{WZ} = [-0.96, -0.82] \cup [0.80, 0.98]$. The expected total uncertainties in the measurements are also shown in parentheses. For those parameters with no sensitivity to the sign, only the absolute values are shown.

JHEP08(2016)045

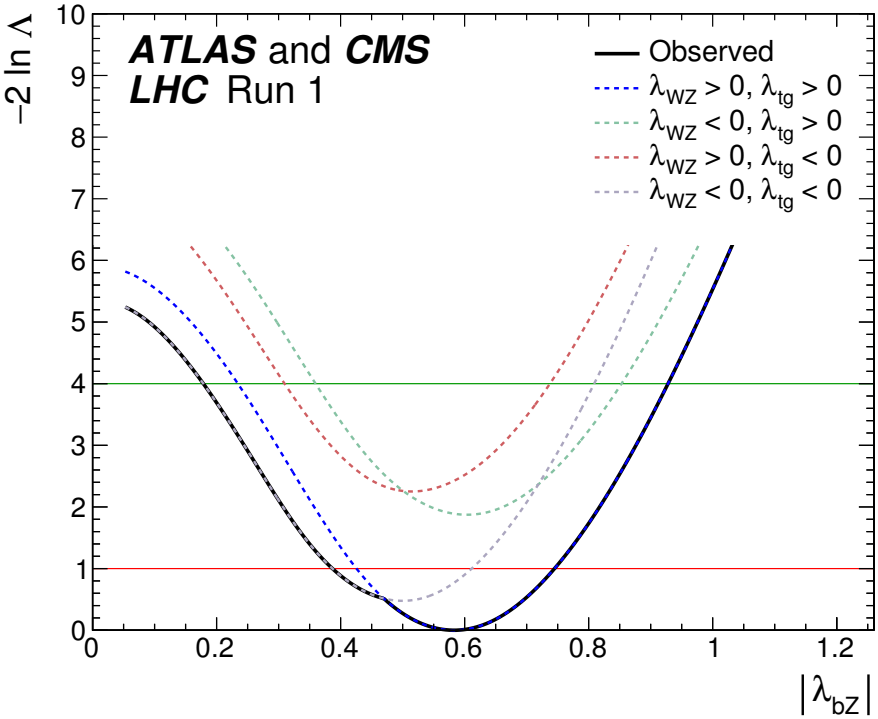

Figure 31. Negative log-likelihood scan for λ_{bZ} showing the minima obtained when considering all sign combinations (solid line) and each specific one separately (dashed lines).

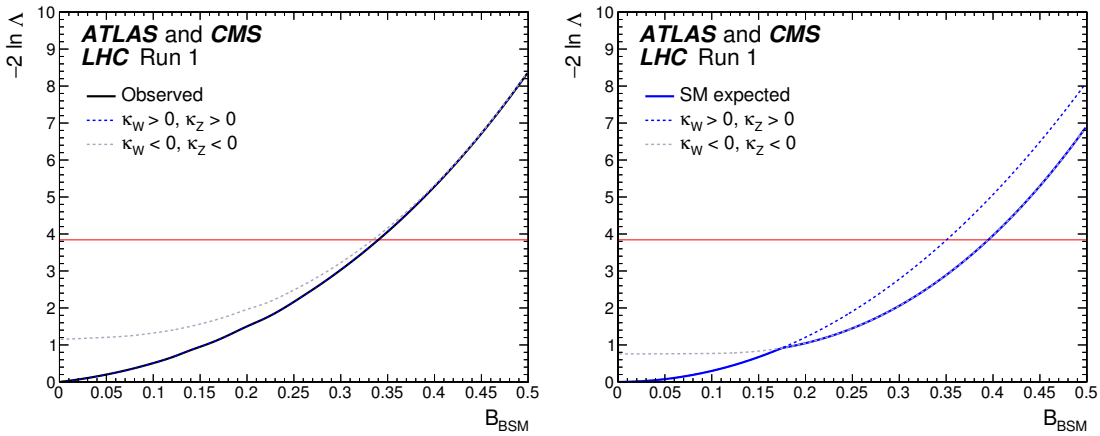

Figure 32. Observed (left) and expected (right) negative log-likelihood scan for B_{BSM}, the minima obtained when considering both sign combinations (solid line) and each specific one separately (dashed lines).

C Likelihood scans for coupling modifier parameterisations

For the results based on certain coupling modifier parameterisations described in sections 4.2 and 6, it is necessary to account for the relative signs between parameters that

JHEP08(2016)045

modify the rates of certain signal production processes and decay modes through interference effects. For example, in the generic parameterisation in terms of ratios of coupling modifiers, the signs of λ_{Zg}, λ_{WZ}, and λ_{tg} affect the rates of tH production through t–W interference, and of $ggZH$ production through t–Z interference. The parameters λ_{Zg} and, as a consequence, κ_{gZ} are assumed to be positive without loss of generality. From this follows that there are four relevant sign combinations of λ_{WZ} and λ_{tg}, which must be evaluated when performing all likelihood scans. An example is given in figure 31 for $|\lambda_{bZ}|$, with a separate curve shown for each sign combination. Each sign hypothesis gives rise to a distinct local minimum. As the negative log-likelihood for each case is determined relative to a common reference point, it is possible to identify the global minimum. For this parameterisation, the SM sign hypothesis ($\lambda_{WZ} > 0, \lambda_{tg} > 0$) corresponds to this global minimum. A new negative log-likelihood curve is defined as the envelope of the ones obtained for the different sign hypotheses, by taking the smallest value of $-2\ln\Lambda$ from the different sign hypotheses as a function of the parameter being considered in the scan. This curve, indicated by the solid line in figure 31, is used to determine the uncertainties and the confidence intervals. In the case of the example chosen here, but also more generally, this procedure results in larger confidence intervals than would be found from the ($\lambda_{WZ} > 0, \lambda_{tg} > 0$) hypothesis alone.

Another example of the effect of the different sign combinations is given in figure 32, which shows the observed and expected negative log-likelihood scans for $\mathrm{B_{BSM}}$ using the parameterisation described in section 6.1. Given that in this parameterisation, opposite signs of κ_W and κ_Z are not considered, only two sign combination hypotheses, $\kappa_W > 0, \kappa_Z > 0$ and $\kappa_W < 0, \kappa_Z < 0$, are evaluated. In the expected negative log-likelihood curve, a transition between the two hypotheses occurs at $\mathrm{B_{BSM}} \approx 0.175$. This has the effect of increasing the expected 95% CL upper limit on $\mathrm{B_{BSM}}$ from 0.35, when considering only the $\kappa_W > 0, \kappa_Z > 0$ case, to 0.39, once both sign combinations are considered.

Open Access. This article is distributed under the terms of the Creative Commons Attribution License (CC-BY 4.0), which permits any use, distribution and reproduction in any medium, provided the original author(s) and source are credited.

References

[1] ATLAS collaboration, *The ATLAS experiment at the CERN Large Hadron Collider*, 2008 *JINST* **3** S08003 [INSPIRE].

[2] CMS collaboration, *The CMS experiment at the CERN LHC*, 2008 *JINST* **3** S08004 [INSPIRE].

[3] S.L. Glashow, *Partial-symmetries of weak interactions*, *Nucl. Phys.* **22** (1961) 579 [INSPIRE].

[4] S. Weinberg, *A model of leptons*, *Phys. Rev. Lett.* **19** (1967) 1264 [INSPIRE].

[5] A. Salam, *Weak and electromagnetic interactions*, in *Elementary particle physics: relativistic groups and analyticity. Proceedings of the* 8th *Nobel symposium*, N. Svartholm ed., Almqvist & Wiskell, (1968) [INSPIRE].

JHEP08(2016)045

[6] G. 't Hooft and M.J.G. Veltman, *Regularization and renormalization of gauge fields*, *Nucl. Phys.* **B 44** (1972) 189 [INSPIRE].

[7] F. Englert and R. Brout, *Broken symmetry and the mass of gauge vector mesons*, *Phys. Rev. Lett.* **13** (1964) 321 [INSPIRE].

[8] P.W. Higgs, *Broken symmetries, massless particles and gauge fields*, *Phys. Lett.* **12** (1964) 132 [INSPIRE].

[9] P.W. Higgs, *Broken symmetries and the masses of gauge bosons*, *Phys. Rev. Lett.* **13** (1964) 508 [INSPIRE].

[10] G.S. Guralnik, C.R. Hagen and T.W.B. Kibble, *Global conservation laws and massless particles*, *Phys. Rev. Lett.* **13** (1964) 585 [INSPIRE].

[11] P.W. Higgs, *Spontaneous symmetry breakdown without massless bosons*, *Phys. Rev.* **145** (1966) 1156 [INSPIRE].

[12] T.W.B. Kibble, *Symmetry breaking in non-Abelian gauge theories*, *Phys. Rev.* **155** (1967) 1554 [INSPIRE].

[13] Y. Nambu and G. Jona-Lasinio, *Dynamical model of elementary particles based on an analogy with superconductivity.* 1, *Phys. Rev.* **122** (1961) 345 [INSPIRE].

[14] ATLAS collaboration, *Observation of a new particle in the search for the Standard Model Higgs boson with the ATLAS detector at the LHC*, *Phys. Lett.* **B 716** (2012) 1 [arXiv:1207.7214] [INSPIRE].

[15] CMS collaboration, *Observation of a new boson at a mass of* 125 *GeV with the CMS experiment at the LHC*, *Phys. Lett.* **B 716** (2012) 30 [arXiv:1207.7235] [INSPIRE].

[16] CMS collaboration, *Observation of a new boson with mass near* 125 *GeV in pp collisions at* $\sqrt{s} = 7$ *and* 8 *TeV*, *JHEP* **06** (2013) 081 [arXiv:1303.4571] [INSPIRE].

[17] ATLAS collaboration, *Measurements of the Higgs boson production and decay rates and coupling strengths using pp collision data at* $\sqrt{s} = 7$ *and* 8 *TeV in the ATLAS experiment*, *Eur. Phys. J.* **C 76** (2016) 6 [arXiv:1507.04548] [INSPIRE].

[18] CMS collaboration, *Precise determination of the mass of the Higgs boson and tests of compatibility of its couplings with the Standard Model predictions using proton collisions at* 7 *and* 8 *TeV*, *Eur. Phys. J.* **C 75** (2015) 212 [arXiv:1412.8662] [INSPIRE].

[19] CMS collaboration, *Study of the mass and spin-parity of the Higgs boson candidate via its decays to Z boson pairs*, *Phys. Rev. Lett.* **110** (2013) 081803 [arXiv:1212.6639] [INSPIRE].

[20] ATLAS collaboration, *Evidence for the spin-*0 *nature of the Higgs boson using ATLAS data*, *Phys. Lett.* **B 726** (2013) 120 [arXiv:1307.1432] [INSPIRE].

[21] CMS collaboration, *Constraints on the spin-parity and anomalous HVV couplings of the Higgs boson in proton collisions at* 7 *and* 8 *TeV*, *Phys. Rev.* **D 92** (2015) 012004 [arXiv:1411.3441] [INSPIRE].

[22] ATLAS and CMS collaborations, *Combined measurement of the Higgs boson mass in pp collisions at* $\sqrt{s} = 7$ *and* 8 *TeV with the ATLAS and CMS experiments*, *Phys. Rev. Lett.* **114** (2015) 191803 [arXiv:1503.07589] [INSPIRE].

[23] ATLAS collaboration, *Constraints on the off-shell Higgs boson signal strength in the high-mass ZZ and WW final states with the ATLAS detector*, *Eur. Phys. J.* **C 75** (2015) 335 [arXiv:1503.01060] [INSPIRE].

JHEP08(2016)045

[24] CMS collaboration, *Constraints on the Higgs boson width from off-shell production and decay to Z-boson pairs*, *Phys. Lett.* **B 736** (2014) 64 [arXiv:1405.3455] [INSPIRE].

[25] CMS collaboration, *Limits on the Higgs boson lifetime and width from its decay to four charged leptons*, *Phys. Rev.* **D 92** (2015) 072010 [arXiv:1507.06656] [INSPIRE].

[26] ATLAS collaboration, *Measurements of fiducial and differential cross sections for Higgs boson production in the diphoton decay channel at $\sqrt{s} = 8$ TeV with ATLAS*, *JHEP* **09** (2014) 112 [arXiv:1407.4222] [INSPIRE].

[27] ATLAS collaboration, *Fiducial and differential cross sections of Higgs boson production measured in the four-lepton decay channel in pp collisions at $\sqrt{s} = 8$ TeV with the ATLAS detector*, *Phys. Lett.* **B 738** (2014) 234 [arXiv:1408.3226] [INSPIRE].

[28] CMS collaboration, *Measurement of differential cross sections for Higgs boson production in the diphoton decay channel in pp collisions at $\sqrt{s} = 8$ TeV*, *Eur. Phys. J.* **C 76** (2016) 13 [arXiv:1508.07819] [INSPIRE].

[29] CMS collaboration, *Measurement of differential and integrated fiducial cross sections for Higgs boson production in the four-lepton decay channel in pp collisions at $\sqrt{s} = 7$ and 8 TeV*, *JHEP* **04** (2016) 005 [arXiv:1512.08377] [INSPIRE].

[30] LHC Higgs Cross section Working Group collaboration, S. Dittmaier et al., *Handbook of LHC Higgs cross sections: 1. Inclusive observables*, CERN-2011-002, CERN, Geneva Switzerland (2011) [arXiv:1101.0593] [INSPIRE].

[31] LHC Higgs Cross Section Working Group collaboration, S. Dittmaier et al., *Handbook of LHC Higgs cross sections: 2. Differential distributions*, CERN-2012-002, CERN, Geneva Switzerland (2012) [arXiv:1201.3084] [INSPIRE].

[32] LHC Higgs Cross Section Working Group collaboration, J.R. Andersen et al., *Handbook of LHC Higgs cross sections: 3. Higgs properties*, CERN-2013-004, CERN, Geneva Switzerland (2013) [FERMILAB-CONF-13-667-T] [arXiv:1307.1347] [INSPIRE].

[33] H.M. Georgi, S.L. Glashow, M.E. Machacek and D.V. Nanopoulos, *Higgs bosons from two gluon annihilation in proton proton collisions*, *Phys. Rev. Lett.* **40** (1978) 692 [INSPIRE].

[34] A. Djouadi, M. Spira and P.M. Zerwas, *Production of Higgs bosons in proton colliders: QCD corrections*, *Phys. Lett.* **B 264** (1991) 440 [INSPIRE].

[35] S. Dawson, *Radiative corrections to Higgs boson production*, *Nucl. Phys.* **B 359** (1991) 283 [INSPIRE].

[36] M. Spira, A. Djouadi, D. Graudenz and P.M. Zerwas, *Higgs boson production at the LHC*, *Nucl. Phys.* **B 453** (1995) 17 [hep-ph/9504378] [INSPIRE].

[37] R.V. Harlander and W.B. Kilgore, *Next-to-next-to-leading order Higgs production at hadron colliders*, *Phys. Rev. Lett.* **88** (2002) 201801 [hep-ph/0201206] [INSPIRE].

[38] C. Anastasiou and K. Melnikov, *Higgs boson production at hadron colliders in NNLO QCD*, *Nucl. Phys.* **B 646** (2002) 220 [hep-ph/0207004] [INSPIRE].

[39] V. Ravindran, J. Smith and W.L. van Neerven, *NNLO corrections to the total cross-section for Higgs boson production in hadron hadron collisions*, *Nucl. Phys.* **B 665** (2003) 325 [hep-ph/0302135] [INSPIRE].

[40] S. Catani, D. de Florian, M. Grazzini and P. Nason, *Soft gluon resummation for Higgs boson production at hadron colliders*, *JHEP* **07** (2003) 028 [hep-ph/0306211] [INSPIRE].

JHEP08(2016)045

[41] S. Actis, G. Passarino, C. Sturm and S. Uccirati, *NLO electroweak corrections to Higgs boson production at hadron colliders*, *Phys. Lett.* **B 670** (2008) 12 [arXiv:0809.1301] [INSPIRE].

[42] C. Anastasiou, R. Boughezal and F. Petriello, *Mixed QCD-electroweak corrections to Higgs boson production in gluon fusion*, *JHEP* **04** (2009) 003 [arXiv:0811.3458] [INSPIRE].

[43] D. de Florian and M. Grazzini, *Higgs production through gluon fusion: updated cross sections at the Tevatron and the LHC*, *Phys. Lett.* **B 674** (2009) 291 [arXiv:0901.2427] [INSPIRE].

[44] D. de Florian and M. Grazzini, *Higgs production at the LHC: updated cross sections at* $\sqrt{s} = 8$ *TeV*, *Phys. Lett.* **B 718** (2012) 117 [arXiv:1206.4133] [INSPIRE].

[45] G. Bozzi, S. Catani, D. de Florian and M. Grazzini, *Transverse-momentum resummation and the spectrum of the Higgs boson at the LHC*, *Nucl. Phys.* **B 737** (2006) 73 [hep-ph/0508068] [INSPIRE].

[46] D. de Florian, G. Ferrera, M. Grazzini and D. Tommasini, *Transverse-momentum resummation: Higgs boson production at the Tevatron and the LHC*, *JHEP* **11** (2011) 064 [arXiv:1109.2109] [INSPIRE].

[47] M. Grazzini and H. Sargsyan, *Heavy-quark mass effects in Higgs boson production at the LHC*, *JHEP* **09** (2013) 129 [arXiv:1306.4581] [INSPIRE].

[48] I.W. Stewart and F.J. Tackmann, *Theory uncertainties for Higgs and other searches using jet bins*, *Phys. Rev.* **D 85** (2012) 034011 [arXiv:1107.2117] [INSPIRE].

[49] A. Banfi, P.F. Monni, G.P. Salam and G. Zanderighi, *Higgs and Z-boson production with a jet veto*, *Phys. Rev. Lett.* **109** (2012) 202001 [arXiv:1206.4998] [INSPIRE].

[50] J.R. Ellis, M.K. Gaillard and D.V. Nanopoulos, *A phenomenological profile of the Higgs boson*, *Nucl. Phys.* **B 106** (1976) 292 [INSPIRE].

[51] A. Djouadi, J. Kalinowski and M. Spira, *HDECAY: a program for Higgs boson decays in the Standard Model and its supersymmetric extension*, *Comput. Phys. Commun.* **108** (1998) 56 [hep-ph/9704448] [INSPIRE].

[52] A. Bredenstein, A. Denner, S. Dittmaier and M.M. Weber, *Precise predictions for the Higgs-boson decay* $H \to WW/ZZ \to 4$ *leptons*, *Phys. Rev.* **D 74** (2006) 013004 [hep-ph/0604011] [INSPIRE].

[53] A. Bredenstein, A. Denner, S. Dittmaier and M.M. Weber, *Radiative corrections to the semileptonic and hadronic Higgs-boson decays* $H \to WW/ZZ \to 4$ *fermions*, *JHEP* **02** (2007) 080 [hep-ph/0611234] [INSPIRE].

[54] A. Denner, S. Heinemeyer, I. Puljak, D. Rebuzzi and M. Spira, *Standard Model Higgs-boson branching ratios with uncertainties*, *Eur. Phys. J.* **C 71** (2011) 1753 [arXiv:1107.5909] [INSPIRE].

[55] R.N. Cahn and S. Dawson, *Production of very massive Higgs bosons*, *Phys. Lett.* **B 136** (1984) 196 [*Erratum ibid.* **B 138** (1984) 464] [INSPIRE].

[56] M. Ciccolini, A. Denner and S. Dittmaier, *Strong and electroweak corrections to the production of Higgs +2 jets via weak interactions at the LHC*, *Phys. Rev. Lett.* **99** (2007) 161803 [arXiv:0707.0381] [INSPIRE].

JHEP08(2016)045

[57] M. Ciccolini, A. Denner and S. Dittmaier, *Electroweak and QCD corrections to Higgs production via vector-boson fusion at the LHC*, *Phys. Rev.* **D 77** (2008) 013002 [arXiv:0710.4749] [INSPIRE].

[58] P. Bolzoni, F. Maltoni, S.-O. Moch and M. Zaro, *Higgs boson production via vector-boson fusion at NNLO in QCD*, *Phys. Rev. Lett.* **105** (2010) 011801 [arXiv:1003.4451] [INSPIRE].

[59] M. Botje et al., *The PDF4LHC working group interim recommendations*, arXiv:1101.0538 [INSPIRE].

[60] H.-L. Lai et al., *New parton distributions for collider physics*, *Phys. Rev.* **D 82** (2010) 074024 [arXiv:1007.2241] [INSPIRE].

[61] A.D. Martin, W.J. Stirling, R.S. Thorne and G. Watt, *Parton distributions for the LHC*, *Eur. Phys. J.* **C 63** (2009) 189 [arXiv:0901.0002] [INSPIRE].

[62] R.D. Ball et al., *A first unbiased global NLO determination of parton distributions and their uncertainties*, *Nucl. Phys.* **B 838** (2010) 136 [arXiv:1002.4407] [INSPIRE].

[63] S.L. Glashow, D.V. Nanopoulos and A. Yildiz, *Associated production of Higgs bosons and Z particles*, *Phys. Rev.* **D 18** (1978) 1724 [INSPIRE].

[64] O. Brein, A. Djouadi and R. Harlander, *NNLO QCD corrections to the Higgs-strahlung processes at hadron colliders*, *Phys. Lett.* **B 579** (2004) 149 [hep-ph/0307206] [INSPIRE].

[65] A. Denner, S. Dittmaier, S. Kallweit and A. Mück, *Electroweak corrections to Higgs-strahlung off W/Z bosons at the Tevatron and the LHC with HAWK*, *JHEP* **03** (2012) 075 [arXiv:1112.5142] [INSPIRE].

[66] C. Englert, M. McCullough and M. Spannowsky, *Gluon-initiated associated production boosts Higgs physics*, *Phys. Rev.* **D 89** (2014) 013013 [arXiv:1310.4828] [INSPIRE].

[67] G. Ferrera, M. Grazzini and F. Tramontano, *Associated ZH production at hadron colliders: the fully differential NNLO QCD calculation*, *Phys. Lett.* **B 740** (2015) 51 [arXiv:1407.4747] [INSPIRE].

[68] R. Raitio and W.W. Wada, *Higgs boson production at large transverse momentum in QCD*, *Phys. Rev.* **D 19** (1979) 941 [INSPIRE].

[69] W. Beenakker, S. Dittmaier, M. Krämer, B. Plumper, M. Spira and P.M. Zerwas, *NLO QCD corrections to $t\bar{t}H$ production in hadron collisions*, *Nucl. Phys.* **B 653** (2003) 151 [hep-ph/0211352] [INSPIRE].

[70] S. Dawson, C. Jackson, L.H. Orr, L. Reina and D. Wackeroth, *Associated Higgs production with top quarks at the Large Hadron Collider: NLO QCD corrections*, *Phys. Rev.* **D 68** (2003) 034022 [hep-ph/0305087] [INSPIRE].

[71] R.V. Harlander and W.B. Kilgore, *Higgs boson production in bottom quark fusion at next-to-next-to leading order*, *Phys. Rev.* **D 68** (2003) 013001 [hep-ph/0304035] [INSPIRE].

[72] S. Dittmaier, M. Krämer and M. Spira, *Higgs radiation off bottom quarks at the Tevatron and the CERN LHC*, *Phys. Rev.* **D 70** (2004) 074010 [hep-ph/0309204] [INSPIRE].

[73] S. Dawson, C.B. Jackson, L. Reina and D. Wackeroth, *Exclusive Higgs boson production with bottom quarks at hadron colliders*, *Phys. Rev.* **D 69** (2004) 074027 [hep-ph/0311067] [INSPIRE].

JHEP08(2016)045

[74] R. Harlander, M. Krämer and M. Schumacher, *Bottom-quark associated Higgs-boson production: reconciling the four- and five-flavour scheme approach*, arXiv:1112.3478 [INSPIRE].

[75] M. Farina, C. Grojean, F. Maltoni, E. Salvioni and A. Thamm, *Lifting degeneracies in Higgs couplings using single top production in association with a Higgs boson*, *JHEP* **05** (2013) 022 [arXiv:1211.3736] [INSPIRE].

[76] D. Zeppenfeld, R. Kinnunen, A. Nikitenko and E. Richter-Was, *Measuring Higgs boson couplings at the CERN LHC*, *Phys. Rev.* **D 62** (2000) 013009 [hep-ph/0002036] [INSPIRE].

[77] M. Dührssen, S. Heinemeyer, H. Logan, D. Rainwater, G. Weiglein and D. Zeppenfeld, *Extracting Higgs boson couplings from CERN LHC data*, *Phys. Rev.* **D 70** (2004) 113009 [hep-ph/0406323] [INSPIRE].

[78] ATLAS collaboration, *Search for $H \to \gamma\gamma$ produced in association with top quarks and constraints on the Yukawa coupling between the top quark and the Higgs boson using data taken at 7 TeV and 8 TeV with the ATLAS detector*, *Phys. Lett.* **B 740** (2015) 222 [arXiv:1409.3122] [INSPIRE].

[79] J. Alwall et al., *The automated computation of tree-level and next-to-leading order differential cross sections and their matching to parton shower simulations*, *JHEP* **07** (2014) 079 [arXiv:1405.0301] [INSPIRE].

[80] P. Nason, *A new method for combining NLO QCD with shower Monte Carlo algorithms*, *JHEP* **11** (2004) 040 [hep-ph/0409146] [INSPIRE].

[81] S. Frixione, P. Nason and C. Oleari, *Matching NLO QCD computations with parton shower simulations: the POWHEG method*, *JHEP* **11** (2007) 070 [arXiv:0709.2092] [INSPIRE].

[82] S. Alioli, P. Nason, C. Oleari and E. Re, *NLO Higgs boson production via gluon fusion matched with shower in POWHEG*, *JHEP* **04** (2009) 002 [arXiv:0812.0578] [INSPIRE].

[83] S. Alioli, P. Nason, C. Oleari and E. Re, *A general framework for implementing NLO calculations in shower Monte Carlo programs: the POWHEG BOX*, *JHEP* **06** (2010) 043 [arXiv:1002.2581] [INSPIRE].

[84] E. Bagnaschi, G. Degrassi, P. Slavich and A. Vicini, *Higgs production via gluon fusion in the POWHEG approach in the SM and in the MSSM*, *JHEP* **02** (2012) 088 [arXiv:1111.2854] [INSPIRE].

[85] T. Sjöstrand, S. Mrenna and P.Z. Skands, *A brief introduction to PYTHIA* 8.1, *Comput. Phys. Commun.* **178** (2008) 852 [arXiv:0710.3820] [INSPIRE].

[86] T. Sjöstrand, S. Mrenna and P.Z. Skands, *PYTHIA* 6.4 *physics and manual*, *JHEP* **05** (2006) 026 [hep-ph/0603175] [INSPIRE].

[87] M. Bahr et al., *HERWIG++ physics and manual*, *Eur. Phys. J.* **C 58** (2008) 639 [arXiv:0803.0883] [INSPIRE].

[88] G. Bevilacqua et al., *HELAC-NLO*, *Comput. Phys. Commun.* **184** (2013) 986 [arXiv:1110.1499] [INSPIRE].

[89] M.V. Garzelli, A. Kardos, C.G. Papadopoulos and Z. Trócsányi, *Standard Model Higgs boson production in association with a top anti-top pair at NLO with parton showering*, *Europhys. Lett.* **96** (2011) 11001 [arXiv:1108.0387] [INSPIRE].

JHEP08(2016)045

[90] F. Maltoni and T. Stelzer, *MadEvent: automatic event generation with MadGraph*, *JHEP* **02** (2003) 027 [hep-ph/0208156] [INSPIRE].

[91] J.M. Campbell, R.K. Ellis and G. Zanderighi, *Next-to-leading order Higgs +2 jet production via gluon fusion*, *JHEP* **10** (2006) 028 [hep-ph/0608194] [INSPIRE].

[92] ATLAS collaboration, *Measurement of Higgs boson production in the diphoton decay channel in pp collisions at center-of-mass energies of 7 and 8 TeV with the ATLAS detector*, *Phys. Rev.* **D 90** (2014) 112015 [arXiv:1408.7084] [INSPIRE].

[93] CMS collaboration, *Observation of the diphoton decay of the Higgs boson and measurement of its properties*, *Eur. Phys. J.* **C 74** (2014) 3076 [arXiv:1407.0558] [INSPIRE].

[94] ATLAS collaboration, *Measurements of Higgs boson production and couplings in the four-lepton channel in pp collisions at center-of-mass energies of 7 and 8 TeV with the ATLAS detector*, *Phys. Rev.* **D 91** (2015) 012006 [arXiv:1408.5191] [INSPIRE].

[95] CMS collaboration, *Measurement of the properties of a Higgs boson in the four-lepton final state*, *Phys. Rev.* **D 89** (2014) 092007 [arXiv:1312.5353] [INSPIRE].

[96] ATLAS collaboration, *Observation and measurement of Higgs boson decays to WW^* with the ATLAS detector*, *Phys. Rev.* **D 92** (2015) 012006 [arXiv:1412.2641] [INSPIRE].

[97] ATLAS collaboration, *Study of $(W/Z)H$ production and Higgs boson couplings using $H \to WW^*$ decays with the ATLAS detector*, *JHEP* **08** (2015) 137 [arXiv:1506.06641] [INSPIRE].

[98] CMS collaboration, *Measurement of Higgs boson production and properties in the WW decay channel with leptonic final states*, *JHEP* **01** (2014) 096 [arXiv:1312.1129] [INSPIRE].

[99] ATLAS collaboration, *Evidence for the Higgs-boson Yukawa coupling to τ leptons with the ATLAS detector*, *JHEP* **04** (2015) 117 [arXiv:1501.04943] [INSPIRE].

[100] CMS collaboration, *Evidence for the 125 GeV Higgs boson decaying to a pair of τ leptons*, *JHEP* **05** (2014) 104 [arXiv:1401.5041] [INSPIRE].

[101] ATLAS collaboration, *Search for the $b\bar{b}$ decay of the Standard Model Higgs boson in associated $(W/Z)H$ production with the ATLAS detector*, *JHEP* **01** (2015) 069 [arXiv:1409.6212] [INSPIRE].

[102] CMS collaboration, *Search for the Standard Model Higgs boson produced in association with a W or a Z boson and decaying to bottom quarks*, *Phys. Rev.* **D 89** (2014) 012003 [arXiv:1310.3687] [INSPIRE].

[103] ATLAS collaboration, *Search for the Standard Model Higgs boson decay to $\mu^+\mu^-$ with the ATLAS detector*, *Phys. Lett.* **B 738** (2014) 68 [arXiv:1406.7663] [INSPIRE].

[104] CMS collaboration, *Search for a standard model-like Higgs boson in the $\mu^+\mu^-$ and e^+e^- decay channels at the LHC*, *Phys. Lett.* **B 744** (2015) 184 [arXiv:1410.6679] [INSPIRE].

[105] ATLAS collaboration, *Search for the Standard Model Higgs boson produced in association with top quarks and decaying into $b\bar{b}$ in pp collisions at $\sqrt{s} = 8$ TeV with the ATLAS detector*, *Eur. Phys. J.* **C 75** (2015) 349 [arXiv:1503.05066] [INSPIRE].

[106] ATLAS collaboration, *Search for the associated production of the Higgs boson with a top quark pair in multilepton final states with the ATLAS detector*, *Phys. Lett.* **B 749** (2015) 519 [arXiv:1506.05988] [INSPIRE].

JHEP08(2016)045

[107] CMS collaboration, *Search for the Standard Model Higgs boson produced in association with a top-quark pair in pp collisions at the LHC*, *JHEP* **05** (2013) 145 [arXiv:1303.0763] [INSPIRE].

[108] CMS collaboration, *Search for the associated production of the Higgs boson with a top-quark pair*, *JHEP* **09** (2014) 087 [*Erratum ibid.* **10** (2014) 106] [arXiv:1408.1682] [INSPIRE].

[109] ATLAS collaboration, *Search for Higgs boson decays to a photon and a Z boson in pp collisions at* $\sqrt{s} = 7$ *and* 8 *TeV with the ATLAS detector*, *Phys. Lett.* **B 732** (2014) 8 [arXiv:1402.3051] [INSPIRE].

[110] CMS collaboration, *Search for a Higgs boson decaying into a Z and a photon in pp collisions at* $\sqrt{s} = 7$ *and* 8 *TeV*, *Phys. Lett.* **B 726** (2013) 587 [arXiv:1307.5515] [INSPIRE].

[111] CMS collaboration, *Search for the Standard Model Higgs boson produced through vector boson fusion and decaying to* $b\bar{b}$, *Phys. Rev.* **D 92** (2015) 032008 [arXiv:1506.01010] [INSPIRE].

[112] ATLAS collaboration, *Search for invisible decays of a Higgs boson produced in association with a Z boson in ATLAS*, *Phys. Rev. Lett.* **112** (2014) 201802 [arXiv:1402.3244] [INSPIRE].

[113] ATLAS collaboration, *Search for invisible decays of the Higgs boson produced in association with a hadronically decaying vector boson in pp collisions at* $\sqrt{s} = 8$ *TeV with the ATLAS detector*, *Eur. Phys. J.* **C 75** (2015) 337 [arXiv:1504.04324] [INSPIRE].

[114] CMS collaboration, *Search for invisible decays of Higgs bosons in the vector boson fusion and associated ZH production modes*, *Eur. Phys. J.* **C 74** (2014) 2980 [arXiv:1404.1344] [INSPIRE].

[115] ATLAS and CMS collaborations, *Procedure for the LHC Higgs boson search combination in summer* 2011, ATL-PHYS-PUB-2011-011, CERN-CMS-NOTE-2011-005, CERN, Geneva Switzerland (2011).

[116] W. Verkerke and D.P. Kirkby, *The RooFit toolkit for data modeling*, *eConf* **C 0303241** (2003) MOLT007 [physics/0306116] [INSPIRE].

[117] L. Moneta et al., *The RooStats project*, PoS(ACAT2010)057 [arXiv:1009.1003] [INSPIRE].

[118] K. Cranmer et al., *HistFactory: a tool for creating statistical models for use with RooFit and RooStats*, CERN-OPEN-2012-016, CERN, Geneva Switzerland (2012).

[119] G. Cowan, K. Cranmer, E. Gross and O. Vitells, *Asymptotic formulae for likelihood-based tests of new physics*, *Eur. Phys. J.* **C 71** (2011) 1554 [*Erratum ibid.* **C 73** (2013) 2501] [arXiv:1007.1727] [INSPIRE].

[120] G.J. Feldman and R.D. Cousins, *A unified approach to the classical statistical analysis of small signals*, *Phys. Rev.* **D 57** (1998) 3873 [physics/9711021] [INSPIRE].

[121] J. Wenninger, *Energy calibration of the LHC beams at* 4 *TeV*, CERN-ATS-2013-40, CERN, Geneva Switzerland (2013).

[122] J.F. Gunion, Y. Jiang and S. Kraml, *Could two NMSSM Higgs bosons be present near* 125 *GeV?*, *Phys. Rev.* **D 86** (2012) 071702 [arXiv:1207.1545] [INSPIRE].

[123] B. Grzadkowski, J.F. Gunion and M. Toharia, *Higgs-radion interpretation of the LHC data?*, *Phys. Lett.* **B 712** (2012) 70 [arXiv:1202.5017] [INSPIRE].

JHEP08(2016)045

[124] A. Drozd, B. Grzadkowski, J.F. Gunion and Y. Jiang, *Two-Higgs-doublet models and enhanced rates for a* 125 *GeV Higgs*, *JHEP* **05** (2013) 072 [arXiv:1211.3580] [INSPIRE].

[125] P.M. Ferreira, R. Santos, H.E. Haber and J.P. Silva, *Mass-degenerate Higgs bosons at* 125 *GeV in the two-Higgs-doublet model*, *Phys. Rev.* **D 87** (2013) 055009 [arXiv:1211.3131] [INSPIRE].

[126] J.F. Gunion, Y. Jiang and S. Kraml, *Diagnosing degenerate Higgs bosons at* 125 *GeV*, *Phys. Rev. Lett.* **110** (2013) 051801 [arXiv:1208.1817] [INSPIRE].

[127] Y. Grossman, Z. Surujon and J. Zupan, *How to test for mass degenerate Higgs resonances*, *JHEP* **03** (2013) 176 [arXiv:1301.0328] [INSPIRE].

[128] A. David, J. Heikkilä and G. Petrucciani, *Searching for degenerate Higgs bosons*, *Eur. Phys. J.* **C 75** (2015) 49 [arXiv:1409.6132] [INSPIRE].

[129] J. Ellis and T. You, *Updated global analysis of Higgs couplings*, *JHEP* **06** (2013) 103 [arXiv:1303.3879] [INSPIRE].

[130] T.D. Lee, *A theory of spontaneous T violation*, *Phys. Rev.* **D 8** (1973) 1226 [INSPIRE].

JHEP08(2016)045

The ATLAS collaboration

G. Aad[87], B. Abbott[114], J. Abdallah[65], O. Abdinov[12], B. Abeloos[118], R. Aben[108], O.S. AbouZeid[138], N.L. Abraham[150], H. Abramowicz[154], H. Abreu[153], R. Abreu[117], Y. Abulaiti[147a,147b], B.S. Acharya[164a,164b,a], L. Adamczyk[40a], D.L. Adams[27], J. Adelman[109], S. Adomeit[101], T. Adye[132], A.A. Affolder[76], T. Agatonovic-Jovin[14], J. Agricola[56], J.A. Aguilar-Saavedra[127a,127f], S.P. Ahlen[24], F. Ahmadov[67,b], G. Aielli[134a,134b], H. Akerstedt[147a,147b], T.P.A. Åkesson[83], A.V. Akimov[97], G.L. Alberghi[22a,22b], J. Albert[169], S. Albrand[57], M.J. Alconada Verzini[73], M. Aleksa[32], I.N. Aleksandrov[67], C. Alexa[28b], G. Alexander[154], T. Alexopoulos[10], M. Alhroob[114], M. Aliev[75a,75b], G. Alimonti[93a], J. Alison[33], S.P. Alkire[37], B.M.M. Allbrooke[150], B.W. Allen[117], P.P. Allport[19], A. Aloisio[105a,105b], A. Alonso[38], F. Alonso[73], C. Alpigiani[139], M. Alstaty[87], B. Alvarez Gonzalez[32], D. Álvarez Piqueras[167], M.G. Alviggi[105a,105b], B.T. Amadio[16], K. Amako[68], Y. Amaral Coutinho[26a], C. Amelung[25], D. Amidei[91], S.P. Amor Dos Santos[127a,127c], A. Amorim[127a,127b], S. Amoroso[32], G. Amundsen[25], C. Anastopoulos[140], L.S. Ancu[51], N. Andari[109], T. Andeen[11], C.F. Anders[60b], G. Anders[32], J.K. Anders[76], K.J. Anderson[33], A. Andreazza[93a,93b], V. Andrei[60a], S. Angelidakis[9], I. Angelozzi[108], P. Anger[46], A. Angerami[37], F. Anghinolfi[32], A.V. Anisenkov[110,c], N. Anjos[13], A. Annovi[125a,125b], M. Antonelli[49], A. Antonov[99], J. Antos[145b], F. Anulli[133a], M. Aoki[68], L. Aperio Bella[19], G. Arabidze[92], Y. Arai[68], J.P. Araque[127a], A.T.H. Arce[47], F.A. Arduh[73], J-F. Arguin[96], S. Argyropoulos[65], M. Arik[20a], A.J. Armbruster[144], L.J. Armitage[78], O. Arnaez[32], H. Arnold[50], M. Arratia[30], O. Arslan[23], A. Artamonov[98], G. Artoni[121], S. Artz[85], S. Asai[156], N. Asbah[44], A. Ashkenazi[154], B. Åsman[147a,147b], L. Asquith[150], K. Assamagan[27], R. Astalos[145a], M. Atkinson[166], N.B. Atlay[142], K. Augsten[129], G. Avolio[32], B. Axen[16], M.K. Ayoub[118], G. Azuelos[96,d], M.A. Baak[32], A.E. Baas[60a], M.J. Baca[19], H. Bachacou[137], K. Bachas[75a,75b], M. Backes[32], M. Backhaus[32], P. Bagiacchi[133a,133b], P. Bagnaia[133a,133b], Y. Bai[35a], J.T. Baines[132], O.K. Baker[176], E.M. Baldin[110,c], P. Balek[130], T. Balestri[149], F. Balli[137], W.K. Balunas[123], E. Banas[41], Sw. Banerjee[173,e], A.A.E. Bannoura[175], L. Barak[32], E.L. Barberio[90], D. Barberis[52a,52b], M. Barbero[87], T. Barillari[102], T. Barklow[144], N. Barlow[30], S.L. Barnes[86], B.M. Barnett[132], R.M. Barnett[16], Z. Barnovska[5], A. Baroncelli[135a], G. Barone[25], A.J. Barr[121], L. Barranco Navarro[167], F. Barreiro[84], J. Barreiro Guimarães da Costa[35a], R. Bartoldus[144], A.E. Barton[74], P. Bartos[145a], A. Basalaev[124], A. Bassalat[118], R.L. Bates[55], S.J. Batista[159], J.R. Batley[30], M. Battaglia[138], M. Bauce[133a,133b], F. Bauer[137], H.S. Bawa[144,f], J.B. Beacham[112], M.D. Beattie[74], T. Beau[82], P.H. Beauchemin[162], P. Bechtle[23], H.P. Beck[18,g], K. Becker[121], M. Becker[85], M. Beckingham[170], C. Becot[111], A.J. Beddall[20e], A. Beddall[20b], V.A. Bednyakov[67], M. Bedognetti[108], C.P. Bee[149], L.J. Beemster[108], T.A. Beermann[32], M. Begel[27], J.K. Behr[44], C. Belanger-Champagne[89], A.S. Bell[80], G. Bella[154], L. Bellagamba[22a], A. Bellerive[31], M. Bellomo[88], K. Belotskiy[99], O. Beltramello[32], N.L. Belyaev[99], O. Benary[154], D. Benchekroun[136a], M. Bender[101], K. Bendtz[147a,147b], N. Benekos[10], Y. Benhammou[154], E. Benhar Noccioli[176], J. Benitez[65], D.P. Benjamin[47], J.R. Bensinger[25], S. Bentvelsen[108], L. Beresford[121], M. Beretta[49], D. Berge[108], E. Bergeaas Kuutmann[165], N. Berger[5], J. Beringer[16], S. Berlendis[57], N.R. Bernard[88], C. Bernius[111], F.U. Bernlochner[23], T. Berry[79], P. Berta[130], C. Bertella[85], G. Bertoli[147a,147b], F. Bertolucci[125a,125b], I.A. Bertram[74], C. Bertsche[44], D. Bertsche[114], G.J. Besjes[38], O. Bessidskaia Bylund[147a,147b], M. Bessner[44], N. Besson[137], C. Betancourt[50], S. Bethke[102], A.J. Bevan[78], W. Bhimji[16], R.M. Bianchi[126], L. Bianchini[25], M. Bianco[32], O. Biebel[101], D. Biedermann[17], R. Bielski[86], N.V. Biesuz[125a,125b], M. Biglietti[135a], J. Bilbao De Mendizabal[51], H. Bilokon[49], M. Bindi[56], S. Binet[118], A. Bingul[20b], C. Bini[133a,133b], S. Biondi[22a,22b], D.M. Bjergaard[47], C.W. Black[151], J.E. Black[144], K.M. Black[24], D. Blackburn[139], R.E. Blair[6], J.-B. Blanchard[137], J.E. Blanco[79], T. Blazek[145a], I. Bloch[44], C. Blocker[25],

JHEP08(2016)045

W. Blum[85,*], U. Blumenschein[56], S. Blunier[34a], G.J. Bobbink[108], V.S. Bobrovnikov[110,c], S.S. Bocchetta[83], A. Bocci[47], C. Bock[101], M. Boehler[50], D. Boerner[175], J.A. Bogaerts[32], D. Bogavac[14], A.G. Bogdanchikov[110], C. Bohm[147a], V. Boisvert[79], P. Bokan[14], T. Bold[40a], A.S. Boldyrev[164a,164c], M. Bomben[82], M. Bona[78], M. Boonekamp[137], A. Borisov[131], G. Borissov[74], J. Bortfeldt[101], D. Bortoletto[121], V. Bortolotto[62a,62b,62c], K. Bos[108], D. Boscherini[22a], M. Bosman[13], J.D. Bossio Sola[29], J. Boudreau[126], J. Bouffard[2], E.V. Bouhova-Thacker[74], D. Boumediene[36], C. Bourdarios[118], S.K. Boutle[55], A. Boveia[32], J. Boyd[32], I.R. Boyko[67], J. Bracinik[19], A. Brandt[8], G. Brandt[56], O. Brandt[60a], U. Bratzler[157], B. Brau[88], J.E. Brau[117], H.M. Braun[175,*], W.D. Breaden Madden[55], K. Brendlinger[123], A.J. Brennan[90], L. Brenner[108], R. Brenner[165], S. Bressler[172], T.M. Bristow[48], D. Britton[55], D. Britzger[44], F.M. Brochu[30], I. Brock[23], R. Brock[92], G. Brooijmans[37], T. Brooks[79], W.K. Brooks[34b], J. Brosamer[16], E. Brost[117], J.H Broughton[19], P.A. Bruckman de Renstrom[41], D. Bruncko[145b], R. Bruneliere[50], A. Bruni[22a], G. Bruni[22a], BH Brunt[30], M. Bruschi[22a], N. Bruscino[23], P. Bryant[33], L. Bryngemark[83], T. Buanes[15], Q. Buat[143], P. Buchholz[142], A.G. Buckley[55], I.A. Budagov[67], F. Buehrer[50], M.K. Bugge[120], O. Bulekov[99], D. Bullock[8], H. Burckhart[32], S. Burdin[76], C.D. Burgard[50], B. Burghgrave[109], K. Burka[41], S. Burke[132], I. Burmeister[45], E. Busato[36], D. Büscher[50], V. Büscher[85], P. Bussey[55], J.M. Butler[24], C.M. Buttar[55], J.M. Butterworth[80], P. Butti[108], W. Buttinger[27], A. Buzatu[55], A.R. Buzykaev[110,c], S. Cabrera Urbán[167], D. Caforio[129], V.M. Cairo[39a,39b], O. Cakir[4a], N. Calace[51], P. Calafiura[16], A. Calandri[87], G. Calderini[82], P. Calfayan[101], L.P. Caloba[26a], D. Calvet[36], S. Calvet[36], T.P. Calvet[87], R. Camacho Toro[33], S. Camarda[32], P. Camarri[134a,134b], D. Cameron[120], R. Caminal Armadans[166], C. Camincher[57], S. Campana[32], M. Campanelli[80], A. Camplani[93a,93b], A. Campoverde[149], V. Canale[105a,105b], A. Canepa[160a], M. Cano Bret[35e], J. Cantero[115], R. Cantrill[127a], T. Cao[42], M.D.M. Capeans Garrido[32], I. Caprini[28b], M. Caprini[28b], M. Capua[39a,39b], R. Caputo[85], R.M. Carbone[37], R. Cardarelli[134a], F. Cardillo[50], I. Carli[130], T. Carli[32], G. Carlino[105a], L. Carminati[93a,93b], S. Caron[107], E. Carquin[34b], G.D. Carrillo-Montoya[32], J.R. Carter[30], J. Carvalho[127a,127c], D. Casadei[19], M.P. Casado[13,h], M. Casolino[13], D.W. Casper[163], E. Castaneda-Miranda[146a], R. Castelijn[108], A. Castelli[108], V. Castillo Gimenez[167], N.F. Castro[127a,i], A. Catinaccio[32], J.R. Catmore[120], A. Cattai[32], J. Caudron[85], V. Cavaliere[166], E. Cavallaro[13], D. Cavalli[93a], M. Cavalli-Sforza[13], V. Cavasinni[125a,125b], F. Ceradini[135a,135b], L. Cerda Alberich[167], B.C. Cerio[47], A.S. Cerqueira[26b], A. Cerri[150], L. Cerrito[78], F. Cerutti[16], M. Cerv[32], A. Cervelli[18], S.A. Cetin[20d], A. Chafaq[136a], D. Chakraborty[109], S.K. Chan[59], Y.L. Chan[62a], P. Chang[166], J.D. Chapman[30], D.G. Charlton[19], A. Chatterjee[51], C.C. Chau[159], C.A. Chavez Barajas[150], S. Che[112], S. Cheatham[74], A. Chegwidden[92], S. Chekanov[6], S.V. Chekulaev[160a], G.A. Chelkov[67,j], M.A. Chelstowska[91], C. Chen[66], H. Chen[27], K. Chen[149], S. Chen[35c], S. Chen[156], X. Chen[35f], Y. Chen[69], H.C. Cheng[91], H.J Cheng[35a], Y. Cheng[33], A. Cheplakov[67], E. Cheremushkina[131], R. Cherkaoui El Moursli[136e], V. Chernyatin[27,*], E. Cheu[7], L. Chevalier[137], V. Chiarella[49], G. Chiarelli[125a,125b], G. Chiodini[75a], A.S. Chisholm[19], A. Chitan[28b], M.V. Chizhov[67], K. Choi[63], A.R. Chomont[36], S. Chouridou[9], B.K.B. Chow[101], V. Christodoulou[80], D. Chromek-Burckhart[32], J. Chudoba[128], A.J. Chuinard[89], J.J. Chwastowski[41], L. Chytka[116], G. Ciapetti[133a,133b], A.K. Ciftci[4a], D. Cinca[55], V. Cindro[77], I.A. Cioara[23], A. Ciocio[16], F. Cirotto[105a,105b], Z.H. Citron[172], M. Citterio[93a], M. Ciubancan[28b], A. Clark[51], B.L. Clark[59], M.R. Clark[37], P.J. Clark[48], R.N. Clarke[16], C. Clement[147a,147b], Y. Coadou[87], M. Cobal[164a,164c], A. Coccaro[51], J. Cochran[66], L. Coffey[25], L. Colasurdo[107], B. Cole[37], A.P. Colijn[108], J. Collot[57], T. Colombo[32], G. Compostella[102], P. Conde Muiño[127a,127b], E. Coniavitis[50], S.H. Connell[146b], I.A. Connelly[79], V. Consorti[50], S. Constantinescu[28b], G. Conti[32], F. Conventi[105a,k], M. Cooke[16], B.D. Cooper[80], A.M. Cooper-Sarkar[121], K.J.R. Cormier[159], T. Cornelissen[175], M. Corradi[133a,133b], F. Corriveau[89,l], A. Corso-Radu[163],

JHEP08(2016)045

A. Cortes-Gonzalez[13], G. Cortiana[102], G. Costa[93a], M.J. Costa[167], D. Costanzo[140], G. Cottin[30], G. Cowan[79], B.E. Cox[86], K. Cranmer[111], S.J. Crawley[55], G. Cree[31], S. Crépé-Renaudin[57], F. Crescioli[82], W.A. Cribbs[147a,147b], M. Crispin Ortuzar[121], M. Cristinziani[23], V. Croft[107], G. Crosetti[39a,39b], T. Cuhadar Donszelmann[140], J. Cummings[176], M. Curatolo[49], J. Cúth[85], C. Cuthbert[151], H. Czirr[142], P. Czodrowski[3], G. D'amen[22a,22b], S. D'Auria[55], M. D'Onofrio[76], M.J. Da Cunha Sargedas De Sousa[127a,127b], C. Da Via[86], W. Dabrowski[40a], T. Dado[145a], T. Dai[91], O. Dale[15], F. Dallaire[96], C. Dallapiccola[88], M. Dam[38], J.R. Dandoy[33], N.P. Dang[50], A.C. Daniells[19], N.S. Dann[86], M. Danninger[168], M. Dano Hoffmann[137], V. Dao[50], G. Darbo[52a], S. Darmora[8], J. Dassoulas[3], A. Dattagupta[63], W. Davey[23], C. David[169], T. Davidek[130], M. Davies[154], P. Davison[80], E. Dawe[90], I. Dawson[140], R.K. Daya-Ishmukhametova[88], K. De[8], R. de Asmundis[105a], A. De Benedetti[114], S. De Castro[22a,22b], S. De Cecco[82], N. De Groot[107], P. de Jong[108], H. De la Torre[84], F. De Lorenzi[66], A. De Maria[56], D. De Pedis[133a], A. De Salvo[133a], U. De Sanctis[150], A. De Santo[150], J.B. De Vivie De Regie[118], W.J. Dearnaley[74], R. Debbe[27], C. Debenedetti[138], D.V. Dedovich[67], N. Dehghanian[3], I. Deigaard[108], M. Del Gaudio[39a,39b], J. Del Peso[84], T. Del Prete[125a,125b], D. Delgove[118], F. Deliot[137], C.M. Delitzsch[51], M. Deliyergiyev[77], A. Dell'Acqua[32], L. Dell'Asta[24], M. Dell'Orso[125a,125b], M. Della Pietra[105a,k], D. della Volpe[51], M. Delmastro[5], P.A. Delsart[57], C. Deluca[108], D.A. DeMarco[159], S. Demers[176], M. Demichev[67], A. Demilly[82], S.P. Denisov[131], D. Denysiuk[137], D. Derendarz[41], J.E. Derkaoui[136d], F. Derue[82], P. Dervan[76], K. Desch[23], C. Deterre[44], K. Dette[45], P.O. Deviveiros[32], A. Dewhurst[132], S. Dhaliwal[25], A. Di Ciaccio[134a,134b], L. Di Ciaccio[5], W.K. Di Clemente[123], C. Di Donato[133a,133b], A. Di Girolamo[32], B. Di Girolamo[32], B. Di Micco[135a,135b], R. Di Nardo[32], A. Di Simone[50], R. Di Sipio[159], D. Di Valentino[31], C. Diaconu[87], M. Diamond[159], F.A. Dias[48], M.A. Diaz[34a], E.B. Diehl[91], J. Dietrich[17], S. Diglio[87], A. Dimitrievska[14], J. Dingfelder[23], P. Dita[28b], S. Dita[28b], F. Dittus[32], F. Djama[87], T. Djobava[53b], J.I. Djuvsland[60a], M.A.B. do Vale[26c], D. Dobos[32], M. Dobre[28b], C. Doglioni[83], T. Dohmae[156], J. Dolejsi[130], Z. Dolezal[130], B.A. Dolgoshein[99,*], M. Donadelli[26d], S. Donati[125a,125b], P. Dondero[122a,122b], J. Donini[36], J. Dopke[132], A. Doria[105a], M.T. Dova[73], A.T. Doyle[55], E. Drechsler[56], M. Dris[10], Y. Du[35d], J. Duarte-Campderros[154], E. Duchovni[172], G. Duckeck[101], O.A. Ducu[96,m], D. Duda[108], A. Dudarev[32], L. Duflot[118], L. Duguid[79], M. Dührssen[32], M. Dumancic[172], M. Dunford[60a], H. Duran Yildiz[4a], M. Düren[54], A. Durglishvili[53b], D. Duschinger[46], B. Dutta[44], M. Dyndal[44], C. Eckardt[44], K.M. Ecker[102], R.C. Edgar[91], N.C. Edwards[48], T. Eifert[32], G. Eigen[15], K. Einsweiler[16], T. Ekelof[165], M. El Kacimi[136c], V. Ellajosyula[87], M. Ellert[165], S. Elles[5], F. Ellinghaus[175], A.A. Elliot[169], N. Ellis[32], J. Elmsheuser[27], M. Elsing[32], D. Emeliyanov[132], Y. Enari[156], O.C. Endner[85], M. Endo[119], J.S. Ennis[170], J. Erdmann[45], A. Ereditato[18], G. Ernis[175], J. Ernst[2], M. Ernst[27], S. Errede[166], E. Ertel[85], M. Escalier[118], H. Esch[45], C. Escobar[126], B. Esposito[49], A.I. Etienvre[137], E. Etzion[154], H. Evans[63], A. Ezhilov[124], F. Fabbri[22a,22b], L. Fabbri[22a,22b], G. Facini[33], R.M. Fakhrutdinov[131], S. Falciano[133a], R.J. Falla[80], J. Faltova[130], Y. Fang[35a], M. Fanti[93a,93b], A. Farbin[8], A. Farilla[135a], C. Farina[126], T. Farooque[13], S. Farrell[16], S.M. Farrington[170], P. Farthouat[32], F. Fassi[136e], P. Fassnacht[32], D. Fassouliotis[9], M. Faucci Giannelli[79], A. Favareto[52a,52b], W.J. Fawcett[121], L. Fayard[118], O.L. Fedin[124,n], W. Fedorko[168], S. Feigl[120], L. Feligioni[87], C. Feng[35d], E.J. Feng[32], H. Feng[91], A.B. Fenyuk[131], L. Feremenga[8], P. Fernandez Martinez[167], S. Fernandez Perez[13], J. Ferrando[55], A. Ferrari[165], P. Ferrari[108], R. Ferrari[122a], D.E. Ferreira de Lima[60b], A. Ferrer[167], D. Ferrere[51], C. Ferretti[91], A. Ferretto Parodi[52a,52b], F. Fiedler[85], A. Filipčič[77], M. Filipuzzi[44], F. Filthaut[107], M. Fincke-Keeler[169], K.D. Finelli[151], M.C.N. Fiolhais[127a,127c], L. Fiorini[167], A. Firan[42], A. Fischer[2], C. Fischer[13], J. Fischer[175], W.C. Fisher[92], N. Flaschel[44], I. Fleck[142], P. Fleischmann[91], G.T. Fletcher[140], R.R.M. Fletcher[123], T. Flick[175], A. Floderus[83], L.R. Flores Castillo[62a], M.J. Flowerdew[102], G.T. Forcolin[86], A. Formica[137], A. Forti[86],

JHEP08(2016)045

A.G. Foster[19], D. Fournier[118], H. Fox[74], S. Fracchia[13], P. Francavilla[82], M. Franchini[22a,22b], D. Francis[32], L. Franconi[120], M. Franklin[59], M. Frate[163], M. Fraternali[122a,122b], D. Freeborn[80], S.M. Fressard-Batraneanu[32], F. Friedrich[46], D. Froidevaux[32], J.A. Frost[121], C. Fukunaga[157], E. Fullana Torregrosa[85], T. Fusayasu[103], J. Fuster[167], C. Gabaldon[57], O. Gabizon[175], A. Gabrielli[22a,22b], A. Gabrielli[16], G.P. Gach[40a], S. Gadatsch[32], S. Gadomski[51], G. Gagliardi[52a,52b], L.G. Gagnon[96], P. Gagnon[63], C. Galea[107], B. Galhardo[127a,127c], E.J. Gallas[121], B.J. Gallop[132], P. Gallus[129], G. Galster[38], K.K. Gan[112], J. Gao[35b,87], Y. Gao[48], Y.S. Gao[144,f], F.M. Garay Walls[48], C. García[167], J.E. García Navarro[167], M. Garcia-Sciveres[16], R.W. Gardner[33], N. Garelli[144], V. Garonne[120], A. Gascon Bravo[44], C. Gatti[49], A. Gaudiello[52a,52b], G. Gaudio[122a], B. Gaur[142], L. Gauthier[96], I.L. Gavrilenko[97], C. Gay[168], G. Gaycken[23], E.N. Gazis[10], Z. Gecse[168], C.N.P. Gee[132], Ch. Geich-Gimbel[23], M.P. Geisler[60a], C. Gemme[52a], M.H. Genest[57], C. Geng[35b,o], S. Gentile[133a,133b], S. George[79], D. Gerbaudo[13], A. Gershon[154], S. Ghasemi[142], H. Ghazlane[136b], M. Ghneimat[23], B. Giacobbe[22a], S. Giagu[133a,133b], P. Giannetti[125a,125b], B. Gibbard[27], S.M. Gibson[79], M. Gignac[168], M. Gilchriese[16], T.P.S. Gillam[30], D. Gillberg[31], G. Gilles[175], D.M. Gingrich[3,d], N. Giokaris[9], M.P. Giordani[164a,164c], F.M. Giorgi[22a], F.M. Giorgi[17], P.F. Giraud[137], P. Giromini[59], D. Giugni[93a], F. Giuli[121], C. Giuliani[102], M. Giulini[60b], B.K. Gjelsten[120], S. Gkaitatzis[155], I. Gkialas[155], E.L. Gkougkousis[118], L.K. Gladilin[100], C. Glasman[84], J. Glatzer[32], P.C.F. Glaysher[48], A. Glazov[44], M. Goblirsch-Kolb[102], J. Godlewski[41], S. Goldfarb[91], T. Golling[51], D. Golubkov[131], A. Gomes[127a,127b,127d], R. Gonçalo[127a], J. Goncalves Pinto Firmino Da Costa[137], L. Gonella[19], A. Gongadze[67], S. González de la Hoz[167], G. Gonzalez Parra[13], S. Gonzalez-Sevilla[51], L. Goossens[32], P.A. Gorbounov[98], H.A. Gordon[27], I. Gorelov[106], B. Gorini[32], E. Gorini[75a,75b], A. Gorišek[77], E. Gornicki[41], A.T. Goshaw[47], C. Gössling[45], M.I. Gostkin[67], C.R. Goudet[118], D. Goujdami[136c], A.G. Goussiou[139], N. Govender[146b,p], E. Gozani[153], L. Graber[56], I. Grabowska-Bold[40a], P.O.J. Gradin[57], P. Grafström[22a,22b], J. Gramling[51], E. Gramstad[120], S. Grancagnolo[17], V. Gratchev[124], H.M. Gray[32], E. Graziani[135a], Z.D. Greenwood[81,q], C. Grefe[23], K. Gregersen[80], I.M. Gregor[44], P. Grenier[144], K. Grevtsov[5], J. Griffiths[8], A.A. Grillo[138], K. Grimm[74], S. Grinstein[13,r], Ph. Gris[36], J.-F. Grivaz[118], S. Groh[85], J.P. Grohs[46], E. Gross[172], J. Grosse-Knetter[56], G.C. Grossi[81], Z.J. Grout[150], L. Guan[91], W. Guan[173], J. Guenther[129], F. Guescini[51], D. Guest[163], O. Gueta[154], E. Guido[52a,52b], T. Guillemin[5], S. Guindon[2], U. Gul[55], C. Gumpert[32], J. Guo[35e], Y. Guo[35b,o], S. Gupta[121], G. Gustavino[133a,133b], P. Gutierrez[114], N.G. Gutierrez Ortiz[80], C. Gutschow[46], C. Guyot[137], C. Gwenlan[121], C.B. Gwilliam[76], A. Haas[111], C. Haber[16], H.K. Hadavand[8], N. Haddad[136e], A. Hadef[87], P. Haefner[23], S. Hageböck[23], Z. Hajduk[41], H. Hakobyan[177,*], M. Haleem[44], J. Haley[115], G. Halladjian[92], G.D. Hallewell[87], K. Hamacher[175], P. Hamal[116], K. Hamano[169], A. Hamilton[146a], G.N. Hamity[140], P.G. Hamnett[44], L. Han[35b], K. Hanagaki[68,s], K. Hanawa[156], M. Hance[138], B. Haney[123], P. Hanke[60a], R. Hanna[137], J.B. Hansen[38], J.D. Hansen[38], M.C. Hansen[23], P.H. Hansen[38], K. Hara[161], A.S. Hard[173], T. Harenberg[175], F. Hariri[118], S. Harkusha[94], R.D. Harrington[48], P.F. Harrison[170], F. Hartjes[108], N.M. Hartmann[101], M. Hasegawa[69], Y. Hasegawa[141], A. Hasib[114], S. Hassani[137], S. Haug[18], R. Hauser[92], L. Hauswald[46], M. Havranek[128], C.M. Hawkes[19], R.J. Hawkings[32], D. Hayden[92], C.P. Hays[121], J.M. Hays[78], H.S. Hayward[76], S.J. Haywood[132], S.J. Head[19], T. Heck[85], V. Hedberg[83], L. Heelan[8], S. Heim[123], T. Heim[16], B. Heinemann[16], J.J. Heinrich[101], L. Heinrich[111], C. Heinz[54], J. Hejbal[128], L. Helary[24], S. Hellman[147a,147b], C. Helsens[32], J. Henderson[121], R.C.W. Henderson[74], Y. Heng[173], S. Henkelmann[168], A.M. Henriques Correia[32], S. Henrot-Versille[118], G.H. Herbert[17], Y. Hernández Jiménez[167], G. Herten[50], R. Hertenberger[101], L. Hervas[32], G.G. Hesketh[80], N.P. Hessey[108], J.W. Hetherly[42], R. Hickling[78], E. Higón-Rodriguez[167], E. Hill[169], J.C. Hill[30], K.H. Hiller[44], S.J. Hillier[19], I. Hinchliffe[16],

JHEP08(2016)045

E. Hines[123], R.R. Hinman[16], M. Hirose[158], D. Hirschbuehl[175], J. Hobbs[149], N. Hod[160a], M.C. Hodgkinson[140], P. Hodgson[140], A. Hoecker[32], M.R. Hoeferkamp[106], F. Hoenig[101], M. Hohlfeld[85], D. Hohn[23], T.R. Holmes[16], M. Homann[45], T.M. Hong[126], B.H. Hooberman[166], W.H. Hopkins[117], Y. Horii[104], A.J. Horton[143], J-Y. Hostachy[57], S. Hou[152], A. Hoummada[136a], J. Howarth[44], M. Hrabovsky[116], I. Hristova[17], J. Hrivnac[118], T. Hryn'ova[5], A. Hrynevich[95], C. Hsu[146c], P.J. Hsu[152,t], S.-C. Hsu[139], D. Hu[37], Q. Hu[35b], Y. Huang[44], Z. Hubacek[129], F. Hubaut[87], F. Huegging[23], T.B. Huffman[121], E.W. Hughes[37], G. Hughes[74], M. Huhtinen[32], T.A. Hülsing[85], P. Huo[149], N. Huseynov[67,b], J. Huston[92], J. Huth[59], G. Iacobucci[51], G. Iakovidis[27], I. Ibragimov[142], L. Iconomidou-Fayard[118], E. Ideal[176], Z. Idrissi[136e], P. Iengo[32], O. Igonkina[108,u], T. Iizawa[171], Y. Ikegami[68], M. Ikeno[68], Y. Ilchenko[11,v], D. Iliadis[155], N. Ilic[144], T. Ince[102], G. Introzzi[122a,122b], P. Ioannou[9,*], M. Iodice[135a], K. Iordanidou[37], V. Ippolito[59], M. Ishino[70], M. Ishitsuka[158], R. Ishmukhametov[112], C. Issever[121], S. Istin[20a], F. Ito[161], J.M. Iturbe Ponce[86], R. Iuppa[134a,134b], W. Iwanski[41], H. Iwasaki[68], J.M. Izen[43], V. Izzo[105a], S. Jabbar[3], B. Jackson[123], M. Jackson[76], P. Jackson[1], V. Jain[2], K.B. Jakobi[85], K. Jakobs[50], S. Jakobsen[32], T. Jakoubek[128], D.O. Jamin[115], D.K. Jana[81], E. Jansen[80], R. Jansky[64], J. Janssen[23], M. Janus[56], G. Jarlskog[83], N. Javadov[67,b], T. Javůrek[50], F. Jeanneau[137], L. Jeanty[16], J. Jejelava[53a,w], G.-Y. Jeng[151], D. Jennens[90], P. Jenni[50,x], J. Jentzsch[45], C. Jeske[170], S. Jézéquel[5], H. Ji[173], J. Jia[149], H. Jiang[66], Y. Jiang[35b], S. Jiggins[80], J. Jimenez Pena[167], S. Jin[35a], A. Jinaru[28b], O. Jinnouchi[158], P. Johansson[140], K.A. Johns[7], W.J. Johnson[139], K. Jon-And[147a,147b], G. Jones[170], R.W.L. Jones[74], S. Jones[7], T.J. Jones[76], J. Jongmanns[60a], P.M. Jorge[127a,127b], J. Jovicevic[160a], X. Ju[173], A. Juste Rozas[13,r], M.K. Köhler[172], A. Kaczmarska[41], M. Kado[118], H. Kagan[112], M. Kagan[144], S.J. Kahn[87], E. Kajomovitz[47], C.W. Kalderon[121], A. Kaluza[85], S. Kama[42], A. Kamenshchikov[131], N. Kanaya[156], S. Kaneti[30], L. Kanjir[77], V.A. Kantserov[99], J. Kanzaki[68], B. Kaplan[111], L.S. Kaplan[173], A. Kapliy[33], D. Kar[146c], K. Karakostas[10], A. Karamaoun[3], N. Karastathis[10], M.J. Kareem[56], E. Karentzos[10], M. Karnevskiy[85], S.N. Karpov[67], Z.M. Karpova[67], K. Karthik[111], V. Kartvelishvili[74], A.N. Karyukhin[131], K. Kasahara[161], L. Kashif[173], R.D. Kass[112], A. Kastanas[15], Y. Kataoka[156], C. Kato[156], A. Katre[51], J. Katzy[44], K. Kawagoe[72], T. Kawamoto[156], G. Kawamura[56], S. Kazama[156], V.F. Kazanin[110,c], R. Keeler[169], R. Kehoe[42], J.S. Keller[44], J.J. Kempster[79], K Kentaro[104], H. Keoshkerian[159], O. Kepka[128], B.P. Kerševan[77], S. Kersten[175], R.A. Keyes[89], F. Khalil-zada[12], A. Khanov[115], A.G. Kharlamov[110,c], T.J. Khoo[51], V. Khovanskiy[98], E. Khramov[67], J. Khubua[53b,y], S. Kido[69], H.Y. Kim[8], S.H. Kim[161], Y.K. Kim[33], N. Kimura[155], O.M. Kind[17], B.T. King[76], M. King[167], S.B. King[168], J. Kirk[132], A.E. Kiryunin[102], T. Kishimoto[69], D. Kisielewska[40a], F. Kiss[50], K. Kiuchi[161], O. Kivernyk[137], E. Kladiva[145b], M.H. Klein[37], M. Klein[76], U. Klein[76], K. Kleinknecht[85], P. Klimek[147a,147b], A. Klimentov[27], R. Klingenberg[45], J.A. Klinger[140], T. Klioutchnikova[32], E.-E. Kluge[60a], P. Kluit[108], S. Kluth[102], J. Knapik[41], E. Kneringer[64], E.B.F.G. Knoops[87], A. Knue[55], A. Kobayashi[156], D. Kobayashi[158], T. Kobayashi[156], M. Kobel[46], M. Kocian[144], P. Kodys[130], T. Koffas[31], E. Koffeman[108], T. Koi[144], H. Kolanoski[17], M. Kolb[60b], I. Koletsou[5], A.A. Komar[97,*], Y. Komori[156], T. Kondo[68], N. Kondrashova[44], K. Köneke[50], A.C. König[107], T. Kono[68,z], R. Konoplich[111,aa], N. Konstantinidis[80], R. Kopeliansky[63], S. Koperny[40a], L. Köpke[85], A.K. Kopp[50], K. Korcyl[41], K. Kordas[155], A. Korn[80], A.A. Korol[110,c], I. Korolkov[13], E.V. Korolkova[140], O. Kortner[102], S. Kortner[102], T. Kosek[130], V.V. Kostyukhin[23], A. Kotwal[47], A. Kourkoumeli-Charalampidi[155], C. Kourkoumelis[9], V. Kouskoura[27], A.B. Kowalewska[41], R. Kowalewski[169], T.Z. Kowalski[40a], C. Kozakai[156], W. Kozanecki[137], A.S. Kozhin[131], V.A. Kramarenko[100], G. Kramberger[77], D. Krasnopevtsev[99], A. Krasznahorkay[32], J.K. Kraus[23], A. Kravchenko[27], M. Kretz[60c], J. Kretzschmar[76], K. Kreutzfeldt[54], P. Krieger[159], K. Krizka[33], K. Kroeninger[45], H. Kroha[102], J. Kroll[123], J. Kroseberg[23], J. Krstic[14], U. Kruchonak[67], H. Krüger[23], N. Krumnack[66],

JHEP08(2016)045

A. Kruse[173], M.C. Kruse[47], M. Kruskal[24], T. Kubota[90], H. Kucuk[80], S. Kuday[4b], J.T. Kuechler[175], S. Kuehn[50], A. Kugel[60c], F. Kuger[174], A. Kuhl[138], T. Kuhl[44], V. Kukhtin[67], R. Kukla[137], Y. Kulchitsky[94], S. Kuleshov[34b], M. Kuna[133a,133b], T. Kunigo[70], A. Kupco[128], H. Kurashige[69], Y.A. Kurochkin[94], V. Kus[128], E.S. Kuwertz[169], M. Kuze[158], J. Kvita[116], T. Kwan[169], D. Kyriazopoulos[140], A. La Rosa[102], J.L. La Rosa Navarro[26d], L. La Rotonda[39a,39b], C. Lacasta[167], F. Lacava[133a,133b], J. Lacey[31], H. Lacker[17], D. Lacour[82], V.R. Lacuesta[167], E. Ladygin[67], R. Lafaye[5], B. Laforge[82], T. Lagouri[176], S. Lai[56], S. Lammers[63], W. Lampl[7], E. Lançon[137], U. Landgraf[50], M.P.J. Landon[78], V.S. Lang[60a], J.C. Lange[13], A.J. Lankford[163], F. Lanni[27], K. Lantzsch[23], A. Lanza[122a], S. Laplace[82], C. Lapoire[32], J.F. Laporte[137], T. Lari[93a], F. Lasagni Manghi[22a,22b], M. Lassnig[32], P. Laurelli[49], W. Lavrijsen[16], A.T. Law[138], P. Laycock[76], T. Lazovich[59], M. Lazzaroni[93a,93b], B. Le[90], O. Le Dortz[82], E. Le Guirriec[87], E.P. Le Quilleuc[137], M. LeBlanc[169], T. LeCompte[6], F. Ledroit-Guillon[57], C.A. Lee[27], S.C. Lee[152], L. Lee[1], G. Lefebvre[82], M. Lefebvre[169], F. Legger[101], C. Leggett[16], A. Lehan[76], G. Lehmann Miotto[32], X. Lei[7], W.A. Leight[31], A. Leisos[155,ab], A.G. Leister[176], M.A.L. Leite[26d], R. Leitner[130], D. Lellouch[172], B. Lemmer[56], K.J.C. Leney[80], T. Lenz[23], B. Lenzi[32], R. Leone[7], S. Leone[125a,125b], C. Leonidopoulos[48], S. Leontsinis[10], G. Lerner[150], C. Leroy[96], A.A.J. Lesage[137], C.G. Lester[30], M. Levchenko[124], J. Levêque[5], D. Levin[91], L.J. Levinson[172], M. Levy[19], A.M. Leyko[23], M. Leyton[43], B. Li[35b,o], H. Li[149], H.L. Li[33], L. Li[47], L. Li[35e], Q. Li[35a], S. Li[47], X. Li[86], Y. Li[142], Z. Liang[35a], B. Liberti[134a], A. Liblong[159], P. Lichard[32], K. Lie[166], J. Liebal[23], W. Liebig[15], A. Limosani[151], S.C. Lin[152,ac], T.H. Lin[85], B.E. Lindquist[149], A.E. Lionti[51], E. Lipeles[123], A. Lipniacka[15], M. Lisovyi[60b], T.M. Liss[166], A. Lister[168], A.M. Litke[138], B. Liu[152,ad], D. Liu[152], H. Liu[91], H. Liu[27], J. Liu[87], J.B. Liu[35b], K. Liu[87], L. Liu[166], M. Liu[47], M. Liu[35b], Y.L. Liu[35b], Y. Liu[35b], M. Livan[122a,122b], A. Lleres[57], J. Llorente Merino[35a], S.L. Lloyd[78], F. Lo Sterzo[152], E. Lobodzinska[44], P. Loch[7], W.S. Lockman[138], F.K. Loebinger[86], A.E. Loevschall-Jensen[38], K.M. Loew[25], A. Loginov[176], T. Lohse[17], K. Lohwasser[44], M. Lokajicek[128], B.A. Long[24], J.D. Long[166], R.E. Long[74], L. Longo[75a,75b], K.A. Looper[112], L. Lopes[127a], D. Lopez Mateos[59], B. Lopez Paredes[140], I. Lopez Paz[13], A. Lopez Solis[82], J. Lorenz[101], N. Lorenzo Martinez[63], M. Losada[21], P.J. Lösel[101], X. Lou[35a], A. Lounis[118], J. Love[6], P.A. Love[74], H. Lu[62a], N. Lu[91], H.J. Lubatti[139], C. Luci[133a,133b], A. Lucotte[57], C. Luedtke[50], F. Luehring[63], W. Lukas[64], L. Luminari[133a], O. Lundberg[147a,147b], B. Lund-Jensen[148], D. Lynn[27], R. Lysak[128], E. Lytken[83], V. Lyubushkin[67], H. Ma[27], L.L. Ma[35d], Y. Ma[35d], G. Maccarrone[49], A. Macchiolo[102], C.M. Macdonald[140], B. Maček[77], J. Machado Miguens[123,127b], D. Madaffari[87], R. Madar[36], H.J. Maddocks[165], W.F. Mader[46], A. Madsen[44], J. Maeda[69], S. Maeland[15], T. Maeno[27], A. Maevskiy[100], E. Magradze[56], J. Mahlstedt[108], C. Maiani[118], C. Maidantchik[26a], A.A. Maier[102], T. Maier[101], A. Maio[127a,127b,127d], S. Majewski[117], Y. Makida[68], N. Makovec[118], B. Malaescu[82], Pa. Malecki[41], V.P. Maleev[124], F. Malek[57], U. Mallik[65], D. Malon[6], C. Malone[144], S. Maltezos[10], S. Malyukov[32], J. Mamuzic[167], G. Mancini[49], B. Mandelli[32], L. Mandelli[93a], I. Mandić[77], J. Maneira[127a,127b], L. Manhaes de Andrade Filho[26b], J. Manjarres Ramos[160b], A. Mann[101], B. Mansoulie[137], J.D. Mansour[35a], R. Mantifel[89], M. Mantoani[56], S. Manzoni[93a,93b], L. Mapelli[32], G. Marceca[29], L. March[51], G. Marchiori[82], M. Marcisovsky[128], M. Marjanovic[14], D.E. Marley[91], F. Marroquim[26a], S.P. Marsden[86], Z. Marshall[16], S. Marti-Garcia[167], B. Martin[92], T.A. Martin[170], V.J. Martin[48], B. Martin dit Latour[15], M. Martinez[13,r], S. Martin-Haugh[132], V.S. Martoiu[28b], A.C. Martyniuk[80], M. Marx[139], A. Marzin[32], L. Masetti[85], T. Mashimo[156], R. Mashinistov[97], J. Masik[86], A.L. Maslennikov[110,c], I. Massa[22a,22b], L. Massa[22a,22b], P. Mastrandrea[5], A. Mastroberardino[39a,39b], T. Masubuchi[156], P. Mättig[175], J. Mattmann[85], J. Maurer[28b], S.J. Maxfield[76], D.A. Maximov[110,c], R. Mazini[152], S.M. Mazza[93a,93b], N.C. Mc Fadden[106], G. Mc Goldrick[159], S.P. Mc Kee[91], A. McCarn[91], R.L. McCarthy[149], T.G. McCarthy[31], L.I. McClymont[80], E.F. McDonald[90], K.W. McFarlane[58,*], J.A. Mcfayden[80],

JHEP08(2016)045

G. Mchedlidze[56], S.J. McMahon[132], R.A. McPherson[169,l], M. Medinnis[44], S. Meehan[139], S. Mehlhase[101], A. Mehta[76], K. Meier[60a], C. Meineck[101], B. Meirose[43], D. Melini[167], B.R. Mellado Garcia[146c], M. Melo[145a], F. Meloni[18], A. Mengarelli[22a,22b], S. Menke[102], E. Meoni[162], S. Mergelmeyer[17], P. Mermod[51], L. Merola[105a,105b], C. Meroni[93a], F.S. Merritt[33], A. Messina[133a,133b], J. Metcalfe[6], A.S. Mete[163], C. Meyer[85], C. Meyer[123], J-P. Meyer[137], J. Meyer[108], H. Meyer Zu Theenhausen[60a], F. Miano[150], R.P. Middleton[132], S. Miglioranzi[52a,52b], L. Mijović[23], G. Mikenberg[172], M. Mikestikova[128], M. Mikuž[77], M. Milesi[90], A. Milic[64], D.W. Miller[33], C. Mills[48], A. Milov[172], D.A. Milstead[147a,147b], A.A. Minaenko[131], Y. Minami[156], I.A. Minashvili[67], A.I. Mincer[111], B. Mindur[40a], M. Mineev[67], Y. Ming[173], L.M. Mir[13], K.P. Mistry[123], T. Mitani[171], J. Mitrevski[101], V.A. Mitsou[167], A. Miucci[51], P.S. Miyagawa[140], J.U. Mjörnmark[83], T. Moa[147a,147b], K. Mochizuki[96], S. Mohapatra[37], S. Molander[147a,147b], R. Moles-Valls[23], R. Monden[70], M.C. Mondragon[92], K. Mönig[44], J. Monk[38], E. Monnier[87], A. Montalbano[149], J. Montejo Berlingen[32], F. Monticelli[73], S. Monzani[93a,93b], R.W. Moore[3], N. Morange[118], D. Moreno[21], M. Moreno Llácer[56], P. Morettini[52a], D. Mori[143], T. Mori[156], M. Morii[59], M. Morinaga[156], V. Morisbak[120], S. Moritz[85], A.K. Morley[151], G. Mornacchi[32], J.D. Morris[78], S.S. Mortensen[38], L. Morvaj[149], M. Mosidze[53b], J. Moss[144], K. Motohashi[158], R. Mount[144], E. Mountricha[27], S.V. Mouraviev[97,*], E.J.W. Moyse[88], S. Muanza[87], R.D. Mudd[19], F. Mueller[102], J. Mueller[126], R.S.P. Mueller[101], T. Mueller[30], D. Muenstermann[74], P. Mullen[55], G.A. Mullier[18], F.J. Munoz Sanchez[86], J.A. Murillo Quijada[19], W.J. Murray[170,132], H. Musheghyan[56], M. Muškinja[77], A.G. Myagkov[131,ae], M. Myska[129], B.P. Nachman[144], O. Nackenhorst[51], K. Nagai[121], R. Nagai[68,z], K. Nagano[68], Y. Nagasaka[61], K. Nagata[161], M. Nagel[50], E. Nagy[87], A.M. Nairz[32], Y. Nakahama[32], K. Nakamura[68], T. Nakamura[156], I. Nakano[113], H. Namasivayam[43], R.F. Naranjo Garcia[44], R. Narayan[11], D.I. Narrias Villar[60a], I. Naryshkin[124], T. Naumann[44], G. Navarro[21], R. Nayyar[7], H.A. Neal[91], P.Yu. Nechaeva[97], T.J. Neep[86], P.D. Nef[144], A. Negri[122a,122b], M. Negrini[22a], S. Nektarijevic[107], C. Nellist[118], A. Nelson[163], S. Nemecek[128], P. Nemethy[111], A.A. Nepomuceno[26a], M. Nessi[32,af], M.S. Neubauer[166], M. Neumann[175], R.M. Neves[111], P. Nevski[27], P.R. Newman[19], D.H. Nguyen[6], T. Nguyen Manh[96], R.B. Nickerson[121], R. Nicolaidou[137], J. Nielsen[138], A. Nikiforov[17], V. Nikolaenko[131,ae], I. Nikolic-Audit[82], K. Nikolopoulos[19], J.K. Nilsen[120], P. Nilsson[27], Y. Ninomiya[156], A. Nisati[133a], R. Nisius[102], T. Nobe[156], L. Nodulman[6], M. Nomachi[119], I. Nomidis[31], T. Nooney[78], S. Norberg[114], M. Nordberg[32], N. Norjoharuddeen[121], O. Novgorodova[46], S. Nowak[102], M. Nozaki[68], L. Nozka[116], K. Ntekas[10], E. Nurse[80], F. Nuti[90], F. O'grady[7], D.C. O'Neil[143], A.A. O'Rourke[44], V. O'Shea[55], F.G. Oakham[31,d], H. Oberlack[102], T. Obermann[23], J. Ocariz[82], A. Ochi[69], I. Ochoa[37], J.P. Ochoa-Ricoux[34a], S. Oda[72], S. Odaka[68], H. Ogren[63], A. Oh[86], S.H. Oh[47], C.C. Ohm[16], H. Ohman[165], H. Oide[32], H. Okawa[161], Y. Okumura[33], T. Okuyama[68], A. Olariu[28b], L.F. Oleiro Seabra[127a], S.A. Olivares Pino[48], D. Oliveira Damazio[27], A. Olszewski[41], J. Olszowska[41], A. Onofre[127a,127e], K. Onogi[104], P.U.E. Onyisi[11,v], M.J. Oreglia[33], Y. Oren[154], D. Orestano[135a,135b], N. Orlando[62b], R.S. Orr[159], B. Osculati[52a,52b], R. Ospanov[86], G. Otero y Garzon[29], H. Otono[72], M. Ouchrif[136d], F. Ould-Saada[120], A. Ouraou[137], K.P. Oussoren[108], Q. Ouyang[35a], M. Owen[55], R.E. Owen[19], V.E. Ozcan[20a], N. Ozturk[8], K. Pachal[143], A. Pacheco Pages[13], C. Padilla Aranda[13], M. Pagáčová[50], S. Pagan Griso[16], F. Paige[27], P. Pais[88], K. Pajchel[120], G. Palacino[160b], S. Palestini[32], M. Palka[40b], D. Pallin[36], A. Palma[127a,127b], E.St. Panagiotopoulou[10], C.E. Pandini[82], J.G. Panduro Vazquez[79], P. Pani[147a,147b], S. Panitkin[27], D. Pantea[28b], L. Paolozzi[51], Th.D. Papadopoulou[10], K. Papageorgiou[155], A. Paramonov[6], D. Paredes Hernandez[176], A.J. Parker[74], M.A. Parker[30], K.A. Parker[140], F. Parodi[52a,52b], J.A. Parsons[37], U. Parzefall[50], V.R. Pascuzzi[159], E. Pasqualucci[133a], S. Passaggio[52a], F. Pastore[135a,135b,*], Fr. Pastore[79], G. Pásztor[31,ag], S. Pataraia[175], J.R. Pater[86], T. Pauly[32],

JHEP08(2016)045

J. Pearce[169], B. Pearson[114], L.E. Pedersen[38], M. Pedersen[120], S. Pedraza Lopez[167], R. Pedro[127a,127b], S.V. Peleganchuk[110,c], D. Pelikan[165], O. Penc[128], C. Peng[35a], H. Peng[35b], J. Penwell[63], B.S. Peralva[26b], M.M. Perego[137], D.V. Perepelitsa[27], E. Perez Codina[160a], L. Perini[93a,93b], H. Pernegger[32], S. Perrella[105a,105b], R. Peschke[44], V.D. Peshekhonov[67], K. Peters[44], R.F.Y. Peters[86], B.A. Petersen[32], T.C. Petersen[38], E. Petit[57], A. Petridis[1], C. Petridou[155], P. Petroff[118], E. Petrolo[133a], M. Petrov[121], F. Petrucci[135a,135b], N.E. Pettersson[88], A. Peyaud[137], R. Pezoa[34b], P.W. Phillips[132], G. Piacquadio[144], E. Pianori[170], A. Picazio[88], E. Piccaro[78], M. Piccinini[22a,22b], M.A. Pickering[121], R. Piegaia[29], J.E. Pilcher[33], A.D. Pilkington[86], A.W.J. Pin[86], M. Pinamonti[164a,164c,ah], J.L. Pinfold[3], A. Pingel[38], S. Pires[82], H. Pirumov[44], M. Pitt[172], L. Plazak[145a], M.-A. Pleier[27], V. Pleskot[85], E. Plotnikova[67], P. Plucinski[92], D. Pluth[66], R. Poettgen[147a,147b], L. Poggioli[118], D. Pohl[23], G. Polesello[122a], A. Poley[44], A. Policicchio[39a,39b], R. Polifka[159], A. Polini[22a], C.S. Pollard[55], V. Polychronakos[27], K. Pommès[32], L. Pontecorvo[133a], B.G. Pope[92], G.A. Popeneciu[28c], D.S. Popovic[14], A. Poppleton[32], S. Pospisil[129], K. Potamianos[16], I.N. Potrap[67], C.J. Potter[30], C.T. Potter[117], G. Poulard[32], J. Poveda[32], V. Pozdnyakov[67], M.E. Pozo Astigarraga[32], P. Pralavorio[87], A. Pranko[16], S. Prell[66], D. Price[86], L.E. Price[6], M. Primavera[75a], S. Prince[89], M. Proissl[48], K. Prokofiev[62c], F. Prokoshin[34b], S. Protopopescu[27], J. Proudfoot[6], M. Przybycien[40a], D. Puddu[135a,135b], D. Puldon[149], M. Purohit[27,ai], P. Puzo[118], J. Qian[91], G. Qin[55], Y. Qin[86], A. Quadt[56], W.B. Quayle[164a,164b], M. Queitsch-Maitland[86], D. Quilty[55], S. Raddum[120], V. Radeka[27], V. Radescu[60b], S.K. Radhakrishnan[149], P. Radloff[117], P. Rados[90], F. Ragusa[93a,93b], G. Rahal[178], J.A. Raine[86], S. Rajagopalan[27], M. Rammensee[32], C. Rangel-Smith[165], M.G. Ratti[93a,93b], F. Rauscher[101], S. Rave[85], T. Ravenscroft[55], I. Ravinovich[172], M. Raymond[32], A.L. Read[120], N.P. Readioff[76], M. Reale[75a,75b], D.M. Rebuzzi[122a,122b], A. Redelbach[174], G. Redlinger[27], R. Reece[138], K. Reeves[43], L. Rehnisch[17], J. Reichert[123], H. Reisin[29], C. Rembser[32], H. Ren[35a], M. Rescigno[133a], S. Resconi[93a], O.L. Rezanova[110,c], P. Reznicek[130], R. Rezvani[96], R. Richter[102], S. Richter[80], E. Richter-Was[40b], O. Ricken[23], M. Ridel[82], P. Rieck[17], C.J. Riegel[175], J. Rieger[56], O. Rifki[114], M. Rijssenbeek[149], A. Rimoldi[122a,122b], M. Rimoldi[18], L. Rinaldi[22a], B. Ristić[51], E. Ritsch[32], I. Riu[13], F. Rizatdinova[115], E. Rizvi[78], C. Rizzi[13], S.H. Robertson[89,l], A. Robichaud-Veronneau[89], D. Robinson[30], J.E.M. Robinson[44], A. Robson[55], C. Roda[125a,125b], Y. Rodina[87], A. Rodriguez Perez[13], D. Rodriguez Rodriguez[167], S. Roe[32], C.S. Rogan[59], O. Røhne[120], A. Romaniouk[99], M. Romano[22a,22b], S.M. Romano Saez[36], E. Romero Adam[167], N. Rompotis[139], M. Ronzani[50], L. Roos[82], E. Ros[167], S. Rosati[133a], K. Rosbach[50], P. Rose[138], O. Rosenthal[142], N.-A. Rosien[56], V. Rossetti[147a,147b], E. Rossi[105a,105b], L.P. Rossi[52a], J.H.N. Rosten[30], R. Rosten[139], M. Rotaru[28b], I. Roth[172], J. Rothberg[139], D. Rousseau[118], C.R. Royon[137], A. Rozanov[87], Y. Rozen[153], X. Ruan[146c], F. Rubbo[144], M.S. Rudolph[159], F. Rühr[50], A. Ruiz-Martinez[31], Z. Rurikova[50], N.A. Rusakovich[67], A. Ruschke[101], H.L. Russell[139], J.P. Rutherfoord[7], N. Ruthmann[32], Y.F. Ryabov[124], M. Rybar[166], G. Rybkin[118], S. Ryu[6], A. Ryzhov[131], G.F. Rzehorz[56], A.F. Saavedra[151], G. Sabato[108], S. Sacerdoti[29], H.F-W. Sadrozinski[138], R. Sadykov[67], F. Safai Tehrani[133a], P. Saha[109], M. Sahinsoy[60a], M. Saimpert[137], T. Saito[156], H. Sakamoto[156], Y. Sakurai[171], G. Salamanna[135a,135b], A. Salamon[134a,134b], J.E. Salazar Loyola[34b], D. Salek[108], P.H. Sales De Bruin[139], D. Salihagic[102], A. Salnikov[144], J. Salt[167], D. Salvatore[39a,39b], F. Salvatore[150], A. Salvucci[62a], A. Salzburger[32], D. Sammel[50], D. Sampsonidis[155], A. Sanchez[105a,105b], J. Sánchez[167], V. Sanchez Martinez[167], H. Sandaker[120], R.L. Sandbach[78], H.G. Sander[85], M. Sandhoff[175], C. Sandoval[21], R. Sandstroem[102], D.P.C. Sankey[132], M. Sannino[52a,52b], A. Sansoni[49], C. Santoni[36], R. Santonico[134a,134b], H. Santos[127a], I. Santoyo Castillo[150], K. Sapp[126], A. Sapronov[67], J.G. Saraiva[127a,127d], B. Sarrazin[23], O. Sasaki[68], Y. Sasaki[156], K. Sato[161], G. Sauvage[5,*], E. Sauvan[5], G. Savage[79], P. Savard[159,d],

JHEP08(2016)045

C. Sawyer[132], L. Sawyer[81,q], J. Saxon[33], C. Sbarra[22a], A. Sbrizzi[22a,22b], T. Scanlon[80], D.A. Scannicchio[163], M. Scarcella[151], V. Scarfone[39a,39b], J. Schaarschmidt[172], P. Schacht[102], B.M. Schachtner[101], D. Schaefer[32], R. Schaefer[44], J. Schaeffer[85], S. Schaepe[23], S. Schaetzel[60b], U. Schäfer[85], A.C. Schaffer[118], D. Schaile[101], R.D. Schamberger[149], V. Scharf[60a], V.A. Schegelsky[124], D. Scheirich[130], M. Schernau[163], C. Schiavi[52a,52b], S. Schier[138], C. Schillo[50], M. Schioppa[39a,39b], S. Schlenker[32], K. Schmieden[32], C. Schmitt[85], S. Schmitt[44], S. Schmitz[85], B. Schneider[160a], U. Schnoor[50], L. Schoeffel[137], A. Schoening[60b], B.D. Schoenrock[92], E. Schopf[23], M. Schott[85], J. Schovancova[8], S. Schramm[51], M. Schreyer[174], N. Schuh[85], M.J. Schultens[23], H.-C. Schultz-Coulon[60a], H. Schulz[17], M. Schumacher[50], B.A. Schumm[138], Ph. Schune[137], A. Schwartzman[144], T.A. Schwarz[91], Ph. Schwegler[102], H. Schweiger[86], Ph. Schwemling[137], R. Schwienhorst[92], J. Schwindling[137], T. Schwindt[23], G. Sciolla[25], F. Scuri[125a,125b], F. Scutti[90], J. Searcy[91], P. Seema[23], S.C. Seidel[106], A. Seiden[138], F. Seifert[129], J.M. Seixas[26a], G. Sekhniaidze[105a], K. Sekhon[91], S.J. Sekula[42], D.M. Seliverstov[124,*], N. Semprini-Cesari[22a,22b], C. Serfon[120], L. Serin[118], L. Serkin[164a,164b], M. Sessa[135a,135b], R. Seuster[169], H. Severini[114], T. Sfiligoj[77], F. Sforza[32], A. Sfyrla[51], E. Shabalina[56], N.W. Shaikh[147a,147b], L.Y. Shan[35a], R. Shang[166], J.T. Shank[24], M. Shapiro[16], P.B. Shatalov[98], K. Shaw[164a,164b], S.M. Shaw[86], A. Shcherbakova[147a,147b], C.Y. Shehu[150], P. Sherwood[80], L. Shi[152,aj], S. Shimizu[69], C.O. Shimmin[163], M. Shimojima[103], M. Shiyakova[67,ak], A. Shmeleva[97], D. Shoaleh Saadi[96], M.J. Shochet[33], S. Shojaii[93a,93b], S. Shrestha[112], E. Shulga[99], M.A. Shupe[7], P. Sicho[128], P.E. Sidebo[148], O. Sidiropoulou[174], D. Sidorov[115], A. Sidoti[22a,22b], F. Siegert[46], Dj. Sijacki[14], J. Silva[127a,127d], S.B. Silverstein[147a], V. Simak[129], O. Simard[5], Lj. Simic[14], S. Simion[118], E. Simioni[85], B. Simmons[80], D. Simon[36], M. Simon[85], P. Sinervo[159], N.B. Sinev[117], M. Sioli[22a,22b], G. Siragusa[174], S.Yu. Sivoklokov[100], J. Sjölin[147a,147b], T.B. Sjursen[15], M.B. Skinner[74], H.P. Skottowe[59], P. Skubic[114], M. Slater[19], T. Slavicek[129], M. Slawinska[108], K. Sliwa[162], R. Slovak[130], V. Smakhtin[172], B.H. Smart[5], L. Smestad[15], J. Smiesko[145a], S.Yu. Smirnov[99], Y. Smirnov[99], L.N. Smirnova[100,al], O. Smirnova[83], M.N.K. Smith[37], R.W. Smith[37], M. Smizanska[74], K. Smolek[129], A.A. Snesarev[97], S. Snyder[27], R. Sobie[169,l], F. Socher[46], A. Soffer[154], D.A. Soh[152], G. Sokhrannyi[77], C.A. Solans Sanchez[32], M. Solar[129], E.Yu. Soldatov[99], U. Soldevila[167], A.A. Solodkov[131], A. Soloshenko[67], O.V. Solovyanov[131], V. Solovyev[124], P. Sommer[50], H. Son[162], H.Y. Song[35b,am], A. Sood[16], A. Sopczak[129], V. Sopko[129], V. Sorin[13], D. Sosa[60b], C.L. Sotiropoulou[125a,125b], R. Soualah[164a,164c], A.M. Soukharev[110,c], D. South[44], B.C. Sowden[79], S. Spagnolo[75a,75b], M. Spalla[125a,125b], M. Spangenberg[170], F. Spanò[79], D. Sperlich[17], F. Spettel[102], R. Spighi[22a], G. Spigo[32], L.A. Spiller[90], M. Spousta[130], R.D. St. Denis[55,*], A. Stabile[93a], R. Stamen[60a], S. Stamm[17], E. Stanecka[41], R.W. Stanek[6], C. Stanescu[135a], M. Stanescu-Bellu[44], M.M. Stanitzki[44], S. Stapnes[120], E.A. Starchenko[131], G.H. Stark[33], J. Stark[57], P. Staroba[128], P. Starovoitov[60a], S. Stärz[32], R. Staszewski[41], P. Steinberg[27], B. Stelzer[143], H.J. Stelzer[32], O. Stelzer-Chilton[160a], H. Stenzel[54], G.A. Stewart[55], J.A. Stillings[23], M.C. Stockton[89], M. Stoebe[89], G. Stoicea[28b], P. Stolte[56], S. Stonjek[102], A.R. Stradling[8], A. Straessner[46], M.E. Stramaglia[18], J. Strandberg[148], S. Strandberg[147a,147b], A. Strandlie[120], M. Strauss[114], P. Strizenec[145b], R. Ströhmer[174], D.M. Strom[117], R. Stroynowski[42], A. Strubig[107], S.A. Stucci[18], B. Stugu[15], N.A. Styles[44], D. Su[144], J. Su[126], R. Subramaniam[81], S. Suchek[60a], Y. Sugaya[119], M. Suk[129], V.V. Sulin[97], S. Sultansoy[4c], T. Sumida[70], S. Sun[59], X. Sun[35a], J.E. Sundermann[50], K. Suruliz[150], G. Susinno[39a,39b], M.R. Sutton[150], S. Suzuki[68], M. Svatos[128], M. Swiatlowski[33], I. Sykora[145a], T. Sykora[130], D. Ta[50], C. Taccini[135a,135b], K. Tackmann[44], J. Taenzer[159], A. Taffard[163], R. Tafirout[160a], N. Taiblum[154], H. Takai[27], R. Takashima[71], T. Takeshita[141], Y. Takubo[68], M. Talby[87], A.A. Talyshev[110,c], K.G. Tan[90], J. Tanaka[156], R. Tanaka[118], S. Tanaka[68], B.B. Tannenwald[112], S. Tapia Araya[34b], S. Tapprogge[85], S. Tarem[153], G.F. Tartarelli[93a], P. Tas[130], M. Tasevsky[128], T. Tashiro[70],

JHEP08(2016)045

E. Tassi[39a,39b], A. Tavares Delgado[127a,127b], Y. Tayalati[136d], A.C. Taylor[106], G.N. Taylor[90], P.T.E. Taylor[90], W. Taylor[160b], F.A. Teischinger[32], P. Teixeira-Dias[79], K.K. Temming[50], D. Temple[143], H. Ten Kate[32], P.K. Teng[152], J.J. Teoh[119], F. Tepel[175], S. Terada[68], K. Terashi[156], J. Terron[84], S. Terzo[102], M. Testa[49], R.J. Teuscher[159,l], T. Theveneaux-Pelzer[87], J.P. Thomas[19], J. Thomas-Wilsker[79], E.N. Thompson[37], P.D. Thompson[19], A.S. Thompson[55], L.A. Thomsen[176], E. Thomson[123], M. Thomson[30], M.J. Tibbetts[16], R.E. Ticse Torres[87], V.O. Tikhomirov[97,an], Yu.A. Tikhonov[110,c], S. Timoshenko[99], P. Tipton[176], S. Tisserant[87], K. Todome[158], T. Todorov[5,*], S. Todorova-Nova[130], J. Tojo[72], S. Tokár[145a], K. Tokushuku[68], E. Tolley[59], L. Tomlinson[86], M. Tomoto[104], L. Tompkins[144,ao], K. Toms[106], B. Tong[59], E. Torrence[117], H. Torres[143], E. Torró Pastor[139], J. Toth[87,ap], F. Touchard[87], D.R. Tovey[140], T. Trefzger[174], A. Tricoli[27], I.M. Trigger[160a], S. Trincaz-Duvoid[82], M.F. Tripiana[13], W. Trischuk[159], B. Trocmé[57], A. Trofymov[44], C. Troncon[93a], M. Trottier-McDonald[16], M. Trovatelli[169], L. Truong[164a,164c], M. Trzebinski[41], A. Trzupek[41], J.C-L. Tseng[121], P.V. Tsiareshka[94], G. Tsipolitis[10], N. Tsirintanis[9], S. Tsiskaridze[13], V. Tsiskaridze[50], E.G. Tskhadadze[53a], K.M. Tsui[62a], I.I. Tsukerman[98], V. Tsulaia[16], S. Tsuno[68], D. Tsybychev[149], A. Tudorache[28b], V. Tudorache[28b], A.N. Tuna[59], S.A. Tupputi[22a,22b], S. Turchikhin[100,al], D. Turecek[129], D. Turgeman[172], R. Turra[93a,93b], A.J. Turvey[42], P.M. Tuts[37], M. Tyndel[132], G. Ucchielli[22a,22b], I. Ueda[156], R. Ueno[31], M. Ughetto[147a,147b], F. Ukegawa[161], G. Unal[32], A. Undrus[27], G. Unel[163], F.C. Ungaro[90], Y. Unno[68], C. Unverdorben[101], J. Urban[145b], P. Urquijo[90], P. Urrejola[85], G. Usai[8], A. Usanova[64], L. Vacavant[87], V. Vacek[129], B. Vachon[89], C. Valderanis[101], E. Valdes Santurio[147a,147b], N. Valencic[108], S. Valentinetti[22a,22b], A. Valero[167], L. Valery[13], S. Valkar[130], S. Vallecorsa[51], J.A. Valls Ferrer[167], W. Van Den Wollenberg[108], P.C. Van Der Deijl[108], R. van der Geer[108], H. van der Graaf[108], N. van Eldik[153], P. van Gemmeren[6], J. Van Nieuwkoop[143], I. van Vulpen[108], M.C. van Woerden[32], M. Vanadia[133a,133b], W. Vandelli[32], R. Vanguri[123], A. Vaniachine[6], P. Vankov[108], G. Vardanyan[177], R. Vari[133a], E.W. Varnes[7], T. Varol[42], D. Varouchas[82], A. Vartapetian[8], K.E. Varvell[151], J.G. Vasquez[176], F. Vazeille[36], T. Vazquez Schroeder[89], J. Veatch[56], L.M. Veloce[159], F. Veloso[127a,127c], S. Veneziano[133a], A. Ventura[75a,75b], M. Venturi[169], N. Venturi[159], A. Venturini[25], V. Vercesi[122a], M. Verducci[133a,133b], W. Verkerke[108], J.C. Vermeulen[108], A. Vest[46,aq], M.C. Vetterli[143,d], O. Viazlo[83], I. Vichou[166], T. Vickey[140], O.E. Vickey Boeriu[140], G.H.A. Viehhauser[121], S. Viel[16], L. Vigani[121], R. Vigne[64], M. Villa[22a,22b], M. Villaplana Perez[93a,93b], E. Vilucchi[49], M.G. Vincter[31], V.B. Vinogradov[67], C. Vittori[22a,22b], I. Vivarelli[150], S. Vlachos[10], M. Vlasak[129], M. Vogel[175], P. Vokac[129], G. Volpi[125a,125b], M. Volpi[90], H. von der Schmitt[102], E. von Toerne[23], V. Vorobel[130], K. Vorobev[99], M. Vos[167], R. Voss[32], J.H. Vossebeld[76], N. Vranjes[14], M. Vranjes Milosavljevic[14], V. Vrba[128], M. Vreeswijk[108], R. Vuillermet[32], I. Vukotic[33], Z. Vykydal[129], P. Wagner[23], W. Wagner[175], H. Wahlberg[73], S. Wahrmund[46], J. Wakabayashi[104], J. Walder[74], R. Walker[101], W. Walkowiak[142], V. Wallangen[147a,147b], C. Wang[35c], C. Wang[35d,87], F. Wang[173], H. Wang[16], H. Wang[42], J. Wang[44], J. Wang[151], K. Wang[89], R. Wang[6], S.M. Wang[152], T. Wang[23], T. Wang[37], X. Wang[176], C. Wanotayaroj[117], A. Warburton[89], C.P. Ward[30], D.R. Wardrope[80], A. Washbrook[48], P.M. Watkins[19], A.T. Watson[19], M.F. Watson[19], G. Watts[139], S. Watts[86], B.M. Waugh[80], S. Webb[85], M.S. Weber[18], S.W. Weber[174], J.S. Webster[6], A.R. Weidberg[121], B. Weinert[63], J. Weingarten[56], C. Weiser[50], H. Weits[108], P.S. Wells[32], T. Wenaus[27], T. Wengler[32], S. Wenig[32], N. Wermes[23], M. Werner[50], P. Werner[32], M. Wessels[60a], J. Wetter[162], K. Whalen[117], N.L. Whallon[139], A.M. Wharton[74], A. White[8], M.J. White[1], R. White[34b], D. Whiteson[163], F.J. Wickens[132], W. Wiedenmann[173], M. Wielers[132], P. Wienemann[23], C. Wiglesworth[38], L.A.M. Wiik-Fuchs[23], A. Wildauer[102], F. Wilk[86], H.G. Wilkens[32], H.H. Williams[123], S. Williams[108], C. Willis[92], S. Willocq[88], J.A. Wilson[19], I. Wingerter-Seez[5], F. Winklmeier[117],

JHEP08(2016)045

O.J. Winston[150], B.T. Winter[23], M. Wittgen[144], J. Wittkowski[101], S.J. Wollstadt[85], M.W. Wolter[41], H. Wolters[127a,127c], B.K. Wosiek[41], J. Wotschack[32], M.J. Woudstra[86], K.W. Wozniak[41], M. Wu[57], M. Wu[33], S.L. Wu[173], X. Wu[51], Y. Wu[91], T.R. Wyatt[86], B.M. Wynne[48], S. Xella[38], D. Xu[35a], L. Xu[27], B. Yabsley[151], S. Yacoob[146a], R. Yakabe[69], D. Yamaguchi[158], Y. Yamaguchi[119], A. Yamamoto[68], S. Yamamoto[156], T. Yamanaka[156], K. Yamauchi[104], Y. Yamazaki[69], Z. Yan[24], H. Yang[35e], H. Yang[173], Y. Yang[152], Z. Yang[15], W-M. Yao[16], Y.C. Yap[82], Y. Yasu[68], E. Yatsenko[5], K.H. Yau Wong[23], J. Ye[42], S. Ye[27], I. Yeletskikh[67], A.L. Yen[59], E. Yildirim[85], K. Yorita[171], R. Yoshida[6], K. Yoshihara[123], C. Young[144], C.J.S. Young[32], S. Youssef[24], D.R. Yu[16], J. Yu[8], J.M. Yu[91], J. Yu[66], L. Yuan[69], S.P.Y. Yuen[23], I. Yusuff[30,ar], B. Zabinski[41], R. Zaidan[35d], A.M. Zaitsev[131,ae], N. Zakharchuk[44], J. Zalieckas[15], A. Zaman[149], S. Zambito[59], L. Zanello[133a,133b], D. Zanzi[90], C. Zeitnitz[175], M. Zeman[129], A. Zemla[40a], J.C. Zeng[166], Q. Zeng[144], K. Zengel[25], O. Zenin[131], T. Ženiš[145a], D. Zerwas[118], D. Zhang[91], F. Zhang[173], G. Zhang[35b,am], H. Zhang[35c], J. Zhang[6], L. Zhang[50], R. Zhang[23], R. Zhang[35b,as], X. Zhang[35d], Z. Zhang[118], X. Zhao[42], Y. Zhao[35d], Z. Zhao[35b], A. Zhemchugov[67], J. Zhong[121], B. Zhou[91], C. Zhou[47], L. Zhou[37], L. Zhou[42], M. Zhou[149], N. Zhou[35f], C.G. Zhu[35d], H. Zhu[35a], J. Zhu[91], Y. Zhu[35b], X. Zhuang[35a], K. Zhukov[97], A. Zibell[174], D. Zieminska[63], N.I. Zimine[67], C. Zimmermann[85], S. Zimmermann[50], Z. Zinonos[56], M. Zinser[85], M. Ziolkowski[142], L. Živković[14], G. Zobernig[173], A. Zoccoli[22a,22b], M. zur Nedden[17], G. Zurzolo[105a,105b] and L. Zwalinski[32]

[1] *Department of Physics, University of Adelaide, Adelaide, Australia*
[2] *Physics Department, SUNY Albany, Albany NY, United States of America*
[3] *Department of Physics, University of Alberta, Edmonton AB, Canada*
[4] [(a)] *Department of Physics, Ankara University, Ankara;* [(b)] *Istanbul Aydin University, Istanbul;* [(c)] *Division of Physics, TOBB University of Economics and Technology, Ankara, Turkey*
[5] *LAPP, CNRS/IN2P3 and Université Savoie Mont Blanc, Annecy-le-Vieux, France*
[6] *High Energy Physics Division, Argonne National Laboratory, Argonne IL, United States of America*
[7] *Department of Physics, University of Arizona, Tucson AZ, United States of America*
[8] *Department of Physics, The University of Texas at Arlington, Arlington TX, United States of America*
[9] *Physics Department, University of Athens, Athens, Greece*
[10] *Physics Department, National Technical University of Athens, Zografou, Greece*
[11] *Department of Physics, The University of Texas at Austin, Austin TX, United States of America*
[12] *Institute of Physics, Azerbaijan Academy of Sciences, Baku, Azerbaijan*
[13] *Institut de Física d'Altes Energies (IFAE), The Barcelona Institute of Science and Technology, Barcelona, Spain*
[14] *Institute of Physics, University of Belgrade, Belgrade, Serbia*
[15] *Department for Physics and Technology, University of Bergen, Bergen, Norway*
[16] *Physics Division, Lawrence Berkeley National Laboratory and University of California, Berkeley CA, United States of America*
[17] *Department of Physics, Humboldt University, Berlin, Germany*
[18] *Albert Einstein Center for Fundamental Physics and Laboratory for High Energy Physics, University of Bern, Bern, Switzerland*
[19] *School of Physics and Astronomy, University of Birmingham, Birmingham, United Kingdom*
[20] [(a)] *Department of Physics, Bogazici University, Istanbul;* [(b)] *Department of Physics Engineering, Gaziantep University, Gaziantep;* [(d)] *Istanbul Bilgi University, Faculty of Engineering and Natural Sciences, Istanbul;* [(e)] *Bahcesehir University, Faculty of Engineering and Natural Sciences, Istanbul, Turkey*
[21] *Centro de Investigaciones, Universidad Antonio Narino, Bogota, Colombia*
[22] [(a)] *INFN Sezione di Bologna;* [(b)] *Dipartimento di Fisica e Astronomia, Università di Bologna, Bologna, Italy*

JHEP08(2016)045

[23] *Physikalisches Institut, University of Bonn, Bonn, Germany*
[24] *Department of Physics, Boston University, Boston MA, United States of America*
[25] *Department of Physics, Brandeis University, Waltham MA, United States of America*
[26] [(a)] *Universidade Federal do Rio De Janeiro COPPE/EE/IF, Rio de Janeiro;* [(b)] *Electrical Circuits Department, Federal University of Juiz de Fora (UFJF), Juiz de Fora;* [(c)] *Federal University of Sao Joao del Rei (UFSJ), Sao Joao del Rei;* [(d)] *Instituto de Fisica, Universidade de Sao Paulo, Sao Paulo, Brazil*
[27] *Physics Department, Brookhaven National Laboratory, Upton NY, United States of America*
[28] [(a)] *Transilvania University of Brasov, Brasov;* [(b)] *National Institute of Physics and Nuclear Engineering, Bucharest;* [(c)] *National Institute for Research and Development of Isotopic and Molecular Technologies, Physics Department, Cluj Napoca;* [(d)] *University Politehnica Bucharest, Bucharest;* [(e)] *West University in Timisoara, Timisoara, Romania*
[29] *Departamento de Física, Universidad de Buenos Aires, Buenos Aires, Argentina*
[30] *Cavendish Laboratory, University of Cambridge, Cambridge, United Kingdom*
[31] *Department of Physics, Carleton University, Ottawa ON, Canada*
[32] *CERN, Geneva, Switzerland*
[33] *Enrico Fermi Institute, University of Chicago, Chicago IL, United States of America*
[34] [(a)] *Departamento de Física, Pontificia Universidad Católica de Chile, Santiago;* [(b)] *Departamento de Física, Universidad Técnica Federico Santa María, Valparaíso, Chile*
[35] [(a)] *Institute of High Energy Physics, Chinese Academy of Sciences, Beijing;* [(b)] *Department of Modern Physics, University of Science and Technology of China, Anhui;* [(c)] *Department of Physics, Nanjing University, Jiangsu;* [(d)] *School of Physics, Shandong University, Shandong;* [(e)] *Department of Physics and Astronomy, Shanghai Key Laboratory for Particle Physics and Cosmology, Shanghai Jiao Tong University, Shanghai; (also affiliated with PKU-CHEP);* [(f)] *Physics Department, Tsinghua University, Beijing 100084, China*
[36] *Laboratoire de Physique Corpusculaire, Clermont Université and Université Blaise Pascal and CNRS/IN2P3, Clermont-Ferrand, France*
[37] *Nevis Laboratory, Columbia University, Irvington NY, United States of America*
[38] *Niels Bohr Institute, University of Copenhagen, Kobenhavn, Denmark*
[39] [(a)] *INFN Gruppo Collegato di Cosenza, Laboratori Nazionali di Frascati;* [(b)] *Dipartimento di Fisica, Università della Calabria, Rende, Italy*
[40] [(a)] *AGH University of Science and Technology, Faculty of Physics and Applied Computer Science, Krakow;* [(b)] *Marian Smoluchowski Institute of Physics, Jagiellonian University, Krakow, Poland*
[41] *Institute of Nuclear Physics Polish Academy of Sciences, Krakow, Poland*
[42] *Physics Department, Southern Methodist University, Dallas TX, United States of America*
[43] *Physics Department, University of Texas at Dallas, Richardson TX, United States of America*
[44] *DESY, Hamburg and Zeuthen, Germany*
[45] *Institut für Experimentelle Physik IV, Technische Universität Dortmund, Dortmund, Germany*
[46] *Institut für Kern- und Teilchenphysik, Technische Universität Dresden, Dresden, Germany*
[47] *Department of Physics, Duke University, Durham NC, United States of America*
[48] *SUPA - School of Physics and Astronomy, University of Edinburgh, Edinburgh, United Kingdom*
[49] *INFN Laboratori Nazionali di Frascati, Frascati, Italy*
[50] *Fakultät für Mathematik und Physik, Albert-Ludwigs-Universität, Freiburg, Germany*
[51] *Section de Physique, Université de Genève, Geneva, Switzerland*
[52] [(a)] *INFN Sezione di Genova;* [(b)] *Dipartimento di Fisica, Università di Genova, Genova, Italy*
[53] [(a)] *E. Andronikashvili Institute of Physics, Iv. Javakhishvili Tbilisi State University, Tbilisi;* [(b)] *High Energy Physics Institute, Tbilisi State University, Tbilisi, Georgia*
[54] *II Physikalisches Institut, Justus-Liebig-Universität Giessen, Giessen, Germany*
[55] *SUPA - School of Physics and Astronomy, University of Glasgow, Glasgow, United Kingdom*
[56] *II Physikalisches Institut, Georg-August-Universität, Göttingen, Germany*
[57] *Laboratoire de Physique Subatomique et de Cosmologie, Université Grenoble-Alpes, CNRS/IN2P3, Grenoble, France*

JHEP08(2016)045

[58] Department of Physics, Hampton University, Hampton VA, United States of America
[59] Laboratory for Particle Physics and Cosmology, Harvard University, Cambridge MA, United States of America
[60] [(a)] Kirchhoff-Institut für Physik, Ruprecht-Karls-Universität Heidelberg, Heidelberg; [(b)] Physikalisches Institut, Ruprecht-Karls-Universität Heidelberg, Heidelberg; [(c)] ZITI Institut für technische Informatik, Ruprecht-Karls-Universität Heidelberg, Mannheim, Germany
[61] Faculty of Applied Information Science, Hiroshima Institute of Technology, Hiroshima, Japan
[62] [(a)] Department of Physics, The Chinese University of Hong Kong, Shatin, N.T., Hong Kong; [(b)] Department of Physics, The University of Hong Kong, Hong Kong; [(c)] Department of Physics, The Hong Kong University of Science and Technology, Clear Water Bay, Kowloon, Hong Kong, China
[63] Department of Physics, Indiana University, Bloomington IN, United States of America
[64] Institut für Astro- und Teilchenphysik, Leopold-Franzens-Universität, Innsbruck, Austria
[65] University of Iowa, Iowa City IA, United States of America
[66] Department of Physics and Astronomy, Iowa State University, Ames IA, United States of America
[67] Joint Institute for Nuclear Research, JINR Dubna, Dubna, Russia
[68] KEK, High Energy Accelerator Research Organization, Tsukuba, Japan
[69] Graduate School of Science, Kobe University, Kobe, Japan
[70] Faculty of Science, Kyoto University, Kyoto, Japan
[71] Kyoto University of Education, Kyoto, Japan
[72] Department of Physics, Kyushu University, Fukuoka, Japan
[73] Instituto de Física La Plata, Universidad Nacional de La Plata and CONICET, La Plata, Argentina
[74] Physics Department, Lancaster University, Lancaster, United Kingdom
[75] [(a)] INFN Sezione di Lecce; [(b)] Dipartimento di Matematica e Fisica, Università del Salento, Lecce, Italy
[76] Oliver Lodge Laboratory, University of Liverpool, Liverpool, United Kingdom
[77] Department of Physics, Jožef Stefan Institute and University of Ljubljana, Ljubljana, Slovenia
[78] School of Physics and Astronomy, Queen Mary University of London, London, United Kingdom
[79] Department of Physics, Royal Holloway University of London, Surrey, United Kingdom
[80] Department of Physics and Astronomy, University College London, London, United Kingdom
[81] Louisiana Tech University, Ruston LA, United States of America
[82] Laboratoire de Physique Nucléaire et de Hautes Energies, UPMC and Université Paris-Diderot and CNRS/IN2P3, Paris, France
[83] Fysiska institutionen, Lunds universitet, Lund, Sweden
[84] Departamento de Fisica Teorica C-15, Universidad Autonoma de Madrid, Madrid, Spain
[85] Institut für Physik, Universität Mainz, Mainz, Germany
[86] School of Physics and Astronomy, University of Manchester, Manchester, United Kingdom
[87] CPPM, Aix-Marseille Université and CNRS/IN2P3, Marseille, France
[88] Department of Physics, University of Massachusetts, Amherst MA, United States of America
[89] Department of Physics, McGill University, Montreal QC, Canada
[90] School of Physics, University of Melbourne, Victoria, Australia
[91] Department of Physics, The University of Michigan, Ann Arbor MI, United States of America
[92] Department of Physics and Astronomy, Michigan State University, East Lansing MI, United States of America
[93] [(a)] INFN Sezione di Milano; [(b)] Dipartimento di Fisica, Università di Milano, Milano, Italy
[94] B.I. Stepanov Institute of Physics, National Academy of Sciences of Belarus, Minsk, Republic of Belarus
[95] National Scientific and Educational Centre for Particle and High Energy Physics, Minsk, Republic of Belarus
[96] Group of Particle Physics, University of Montreal, Montreal QC, Canada
[97] P.N. Lebedev Physical Institute of the Russian Academy of Sciences, Moscow, Russia
[98] Institute for Theoretical and Experimental Physics (ITEP), Moscow, Russia
[99] National Research Nuclear University MEPhI, Moscow, Russia

JHEP08(2016)045

[100] *D.V. Skobeltsyn Institute of Nuclear Physics, M.V. Lomonosov Moscow State University, Moscow, Russia*
[101] *Fakultät für Physik, Ludwig-Maximilians-Universität München, München, Germany*
[102] *Max-Planck-Institut für Physik (Werner-Heisenberg-Institut), München, Germany*
[103] *Nagasaki Institute of Applied Science, Nagasaki, Japan*
[104] *Graduate School of Science and Kobayashi-Maskawa Institute, Nagoya University, Nagoya, Japan*
[105] [(a)] *INFN Sezione di Napoli;* [(b)] *Dipartimento di Fisica, Università di Napoli, Napoli, Italy*
[106] *Department of Physics and Astronomy, University of New Mexico, Albuquerque NM, United States of America*
[107] *Institute for Mathematics, Astrophysics and Particle Physics, Radboud University Nijmegen/Nikhef, Nijmegen, Netherlands*
[108] *Nikhef National Institute for Subatomic Physics and University of Amsterdam, Amsterdam, Netherlands*
[109] *Department of Physics, Northern Illinois University, DeKalb IL, United States of America*
[110] *Budker Institute of Nuclear Physics, SB RAS, Novosibirsk, Russia*
[111] *Department of Physics, New York University, New York NY, United States of America*
[112] *Ohio State University, Columbus OH, United States of America*
[113] *Faculty of Science, Okayama University, Okayama, Japan*
[114] *Homer L. Dodge Department of Physics and Astronomy, University of Oklahoma, Norman OK, United States of America*
[115] *Department of Physics, Oklahoma State University, Stillwater OK, United States of America*
[116] *Palacký University, RCPTM, Olomouc, Czech Republic*
[117] *Center for High Energy Physics, University of Oregon, Eugene OR, United States of America*
[118] *LAL, Univ. Paris-Sud, CNRS/IN2P3, Université Paris-Saclay, Orsay, France*
[119] *Graduate School of Science, Osaka University, Osaka, Japan*
[120] *Department of Physics, University of Oslo, Oslo, Norway*
[121] *Department of Physics, Oxford University, Oxford, United Kingdom*
[122] [(a)] *INFN Sezione di Pavia;* [(b)] *Dipartimento di Fisica, Università di Pavia, Pavia, Italy*
[123] *Department of Physics, University of Pennsylvania, Philadelphia PA, United States of America*
[124] *National Research Centre "Kurchatov Institute" B.P.Konstantinov Petersburg Nuclear Physics Institute, St. Petersburg, Russia*
[125] [(a)] *INFN Sezione di Pisa;* [(b)] *Dipartimento di Fisica E. Fermi, Università di Pisa, Pisa, Italy*
[126] *Department of Physics and Astronomy, University of Pittsburgh, Pittsburgh PA, United States of America*
[127] [(a)] *Laboratório de Instrumentação e Física Experimental de Partículas - LIP, Lisboa;* [(b)] *Faculdade de Ciências, Universidade de Lisboa, Lisboa;* [(c)] *Department of Physics, University of Coimbra, Coimbra;* [(d)] *Centro de Física Nuclear da Universidade de Lisboa, Lisboa;* [(e)] *Departamento de Fisica, Universidade do Minho, Braga;* [(f)] *Departamento de Fisica Teorica y del Cosmos and CAFPE, Universidad de Granada, Granada (Spain);* [(g)] *Dep Fisica and CEFITEC of Faculdade de Ciencias e Tecnologia, Universidade Nova de Lisboa, Caparica, Portugal*
[128] *Institute of Physics, Academy of Sciences of the Czech Republic, Praha, Czech Republic*
[129] *Czech Technical University in Prague, Praha, Czech Republic*
[130] *Faculty of Mathematics and Physics, Charles University in Prague, Praha, Czech Republic*
[131] *State Research Center Institute for High Energy Physics (Protvino), NRC KI, Russia*
[132] *Particle Physics Department, Rutherford Appleton Laboratory, Didcot, United Kingdom*
[133] [(a)] *INFN Sezione di Roma;* [(b)] *Dipartimento di Fisica, Sapienza Università di Roma, Roma, Italy*
[134] [(a)] *INFN Sezione di Roma Tor Vergata;* [(b)] *Dipartimento di Fisica, Università di Roma Tor Vergata, Roma, Italy*
[135] [(a)] *INFN Sezione di Roma Tre;* [(b)] *Dipartimento di Matematica e Fisica, Università Roma Tre, Roma, Italy*
[136] [(a)] *Faculté des Sciences Ain Chock, Réseau Universitaire de Physique des Hautes Energies - Université Hassan II, Casablanca;* [(b)] *Centre National de l'Energie des Sciences Techniques*

JHEP08(2016)045

Nucleaires, Rabat; [(c)] *Faculté des Sciences Semlalia, Université Cadi Ayyad, LPHEA-Marrakech;* [(d)] *Faculté des Sciences, Université Mohamed Premier and LPTPM, Oujda;* [(e)] *Faculté des sciences, Université Mohammed V, Rabat, Morocco*

[137] *DSM/IRFU (Institut de Recherches sur les Lois Fondamentales de l'Univers), CEA Saclay (Commissariat à l'Energie Atomique et aux Energies Alternatives), Gif-sur-Yvette, France*

[138] *Santa Cruz Institute for Particle Physics, University of California Santa Cruz, Santa Cruz CA, United States of America*

[139] *Department of Physics, University of Washington, Seattle WA, United States of America*

[140] *Department of Physics and Astronomy, University of Sheffield, Sheffield, United Kingdom*

[141] *Department of Physics, Shinshu University, Nagano, Japan*

[142] *Fachbereich Physik, Universität Siegen, Siegen, Germany*

[143] *Department of Physics, Simon Fraser University, Burnaby BC, Canada*

[144] *SLAC National Accelerator Laboratory, Stanford CA, United States of America*

[145] [(a)] *Faculty of Mathematics, Physics & Informatics, Comenius University, Bratislava;* [(b)] *Department of Subnuclear Physics, Institute of Experimental Physics of the Slovak Academy of Sciences, Kosice, Slovak Republic*

[146] [(a)] *Department of Physics, University of Cape Town, Cape Town;* [(b)] *Department of Physics, University of Johannesburg, Johannesburg;* [(c)] *School of Physics, University of the Witwatersrand, Johannesburg, South Africa*

[147] [(a)] *Department of Physics, Stockholm University;* [(b)] *The Oskar Klein Centre, Stockholm, Sweden*

[148] *Physics Department, Royal Institute of Technology, Stockholm, Sweden*

[149] *Departments of Physics & Astronomy and Chemistry, Stony Brook University, Stony Brook NY, United States of America*

[150] *Department of Physics and Astronomy, University of Sussex, Brighton, United Kingdom*

[151] *School of Physics, University of Sydney, Sydney, Australia*

[152] *Institute of Physics, Academia Sinica, Taipei, Taiwan*

[153] *Department of Physics, Technion: Israel Institute of Technology, Haifa, Israel*

[154] *Raymond and Beverly Sackler School of Physics and Astronomy, Tel Aviv University, Tel Aviv, Israel*

[155] *Department of Physics, Aristotle University of Thessaloniki, Thessaloniki, Greece*

[156] *International Center for Elementary Particle Physics and Department of Physics, The University of Tokyo, Tokyo, Japan*

[157] *Graduate School of Science and Technology, Tokyo Metropolitan University, Tokyo, Japan*

[158] *Department of Physics, Tokyo Institute of Technology, Tokyo, Japan*

[159] *Department of Physics, University of Toronto, Toronto ON, Canada*

[160] [(a)] *TRIUMF, Vancouver BC;* [(b)] *Department of Physics and Astronomy, York University, Toronto ON, Canada*

[161] *Faculty of Pure and Applied Sciences, and Center for Integrated Research in Fundamental Science and Engineering, University of Tsukuba, Tsukuba, Japan*

[162] *Department of Physics and Astronomy, Tufts University, Medford MA, United States of America*

[163] *Department of Physics and Astronomy, University of California Irvine, Irvine CA, United States of America*

[164] [(a)] *INFN Gruppo Collegato di Udine, Sezione di Trieste, Udine;* [(b)] *ICTP, Trieste;* [(c)] *Dipartimento di Chimica, Fisica e Ambiente, Università di Udine, Udine, Italy*

[165] *Department of Physics and Astronomy, University of Uppsala, Uppsala, Sweden*

[166] *Department of Physics, University of Illinois, Urbana IL, United States of America*

[167] *Instituto de Fisica Corpuscular (IFIC) and Departamento de Fisica Atomica, Molecular y Nuclear and Departamento de Ingeniería Electrónica and Instituto de Microelectrónica de Barcelona (IMB-CNM), University of Valencia and CSIC, Valencia, Spain*

[168] *Department of Physics, University of British Columbia, Vancouver BC, Canada*

[169] *Department of Physics and Astronomy, University of Victoria, Victoria BC, Canada*

[170] *Department of Physics, University of Warwick, Coventry, United Kingdom*

JHEP08(2016)045

[171] *Waseda University, Tokyo, Japan*
[172] *Department of Particle Physics, The Weizmann Institute of Science, Rehovot, Israel*
[173] *Department of Physics, University of Wisconsin, Madison WI, United States of America*
[174] *Fakultät für Physik und Astronomie, Julius-Maximilians-Universität, Würzburg, Germany*
[175] *Fakultät für Mathematik und Naturwissenschaften, Fachgruppe Physik, Bergische Universität Wuppertal, Wuppertal, Germany*
[176] *Department of Physics, Yale University, New Haven CT, United States of America*
[177] *Yerevan Physics Institute, Yerevan, Armenia*
[178] *Centre de Calcul de l'Institut National de Physique Nucléaire et de Physique des Particules (IN2P3), Villeurbanne, France*

[a] *Also at Department of Physics, King's College London, London, United Kingdom*
[b] *Also at Institute of Physics, Azerbaijan Academy of Sciences, Baku, Azerbaijan*
[c] *Also at Novosibirsk State University, Novosibirsk, Russia*
[d] *Also at TRIUMF, Vancouver BC, Canada*
[e] *Also at Department of Physics & Astronomy, University of Louisville, Louisville, KY, United States of America*
[f] *Also at Department of Physics, California State University, Fresno CA, United States of America*
[g] *Also at Department of Physics, University of Fribourg, Fribourg, Switzerland*
[h] *Also at Departament de Fisica de la Universitat Autonoma de Barcelona, Barcelona, Spain*
[i] *Also at Departamento de Fisica e Astronomia, Faculdade de Ciencias, Universidade do Porto, Portugal*
[j] *Also at Tomsk State University, Tomsk, Russia*
[k] *Also at Universita di Napoli Parthenope, Napoli, Italy*
[l] *Also at Institute of Particle Physics (IPP), Canada*
[m] *Also at National Institute of Physics and Nuclear Engineering, Bucharest, Romania*
[n] *Also at Department of Physics, St. Petersburg State Polytechnical University, St. Petersburg, Russia*
[o] *Also at Department of Physics, The University of Michigan, Ann Arbor MI, United States of America*
[p] *Also at Centre for High Performance Computing, CSIR Campus, Rosebank, Cape Town, South Africa*
[q] *Also at Louisiana Tech University, Ruston LA, United States of America*
[r] *Also at Institucio Catalana de Recerca i Estudis Avancats, ICREA, Barcelona, Spain*
[s] *Also at Graduate School of Science, Osaka University, Osaka, Japan*
[t] *Also at Department of Physics, National Tsing Hua University, Taiwan*
[u] *Also at Institute for Mathematics, Astrophysics and Particle Physics, Radboud University Nijmegen/Nikhef, Nijmegen, Netherlands*
[v] *Also at Department of Physics, The University of Texas at Austin, Austin TX, United States of America*
[w] *Also at Institute of Theoretical Physics, Ilia State University, Tbilisi, Georgia*
[x] *Also at CERN, Geneva, Switzerland*
[y] *Also at Georgian Technical University (GTU),Tbilisi, Georgia*
[z] *Also at Ochadai Academic Production, Ochanomizu University, Tokyo, Japan*
[aa] *Also at Manhattan College, New York NY, United States of America*
[ab] *Also at Hellenic Open University, Patras, Greece*
[ac] *Also at Academia Sinica Grid Computing, Institute of Physics, Academia Sinica, Taipei, Taiwan*
[ad] *Also at School of Physics, Shandong University, Shandong, China*
[ae] *Also at Moscow Institute of Physics and Technology State University, Dolgoprudny, Russia*
[af] *Also at Section de Physique, Université de Genève, Geneva, Switzerland*
[ag] *Also at Eotvos Lorand University, Budapest, Hungary*
[ah] *Also at International School for Advanced Studies (SISSA), Trieste, Italy*

JHEP08(2016)045

[ai] *Also at Department of Physics and Astronomy, University of South Carolina, Columbia SC, United States of America*
[aj] *Also at School of Physics and Engineering, Sun Yat-sen University, Guangzhou, China*
[ak] *Also at Institute for Nuclear Research and Nuclear Energy (INRNE) of the Bulgarian Academy of Sciences, Sofia, Bulgaria*
[al] *Also at Faculty of Physics, M.V.Lomonosov Moscow State University, Moscow, Russia*
[am] *Also at Institute of Physics, Academia Sinica, Taipei, Taiwan*
[an] *Also at National Research Nuclear University MEPhI, Moscow, Russia*
[ao] *Also at Department of Physics, Stanford University, Stanford CA, United States of America*
[ap] *Also at Institute for Particle and Nuclear Physics, Wigner Research Centre for Physics, Budapest, Hungary*
[aq] *Also at Flensburg University of Applied Sciences, Flensburg, Germany*
[ar] *Also at University of Malaya, Department of Physics, Kuala Lumpur, Malaysia*
[as] *Also at CPPM, Aix-Marseille Université and CNRS/IN2P3, Marseille, France*
[*] *Deceased*

JHEP08(2016)045

The CMS collaboration

Yerevan Physics Institute, Yerevan, Armenia

V. Khachatryan, A.M. Sirunyan, A. Tumasyan

Institut für Hochenergiephysik der OeAW, Wien, Austria

W. Adam, E. Asilar, T. Bergauer, J. Brandstetter, E. Brondolin, M. Dragicevic, J. Erö, M. Flechl, M. Friedl, R. Frühwirth[1], V.M. Ghete, C. Hartl, N. Hörmann, J. Hrubec, M. Jeitler[1], A. König, I. Krätschmer, D. Liko, T. Matsushita, I. Mikulec, D. Rabady, N. Rad, B. Rahbaran, H. Rohringer, J. Schieck[1], J. Strauss, W. Treberer-Treberspurg, W. Waltenberger, C.-E. Wulz[1]

National Centre for Particle and High Energy Physics, Minsk, Belarus

V. Mossolov, N. Shumeiko, J. Suarez Gonzalez

Universiteit Antwerpen, Antwerpen, Belgium

S. Alderweireldt, E.A. De Wolf, X. Janssen, A. Knutsson, J. Lauwers, M. Van De Klundert, H. Van Haevermaet, P. Van Mechelen, N. Van Remortel, A. Van Spilbeeck

Vrije Universiteit Brussel, Brussel, Belgium

S. Abu Zeid, F. Blekman, J. D'Hondt, N. Daci, I. De Bruyn, K. Deroover, N. Heracleous, S. Lowette, S. Moortgat, L. Moreels, A. Olbrechts, Q. Python, S. Tavernier, W. Van Doninck, P. Van Mulders, I. Van Parijs

Université Libre de Bruxelles, Bruxelles, Belgium

H. Brun, C. Caillol, B. Clerbaux, G. De Lentdecker, H. Delannoy, G. Fasanella, L. Favart, R. Goldouzian, A. Grebenyuk, G. Karapostoli, T. Lenzi, A. Léonard, J. Luetic, T. Maerschalk, A. Marinov, A. Randle-conde, T. Seva, C. Vander Velde, P. Vanlaer, R. Yonamine, F. Zenoni, F. Zhang[2]

Ghent University, Ghent, Belgium

A. Cimmino, T. Cornelis, D. Dobur, A. Fagot, G. Garcia, M. Gul, J. Mccartin, D. Poyraz, S. Salva, R. Schöfbeck, M. Tytgat, W. Van Driessche, E. Yazgan, N. Zaganidis

Université Catholique de Louvain, Louvain-la-Neuve, Belgium

C. Beluffi[3], O. Bondu, S. Brochet, G. Bruno, A. Caudron, L. Ceard, S. De Visscher, C. Delaere, M. Delcourt, L. Forthomme, B. Francois, A. Giammanco, A. Jafari, P. Jez, M. Komm, V. Lemaitre, A. Magitteri, A. Mertens, M. Musich, C. Nuttens, K. Piotrzkowski, L. Quertenmont, M. Selvaggi, M. Vidal Marono, S. Wertz

Université de Mons, Mons, Belgium

N. Beliy

Centro Brasileiro de Pesquisas Fisicas, Rio de Janeiro, Brazil

W.L. Aldá Júnior, F.L. Alves, G.A. Alves, L. Brito, M. Correa Martins Junior, C. Hensel, A. Moraes, M.E. Pol, P. Rebello Teles

JHEP08(2016)045

Universidade do Estado do Rio de Janeiro, Rio de Janeiro, Brazil
E. Belchior Batista Das Chagas, W. Carvalho, J. Chinellato[4], A. Custódio, E.M. Da Costa, G.G. Da Silveira, D. De Jesus Damiao, C. De Oliveira Martins, S. Fonseca De Souza, L.M. Huertas Guativa, H. Malbouisson, D. Matos Figueiredo, C. Mora Herrera, L. Mundim, H. Nogima, W.L. Prado Da Silva, A. Santoro, A. Sznajder, E.J. Tonelli Manganote[4], A. Vilela Pereira

Universidade Estadual Paulista [a], Universidade Federal do ABC [b], São Paulo, Brazil
S. Ahuja[a], C.A. Bernardes[b], S. Dogra[a], T.R. Fernandez Perez Tomei[a], E.M. Gregores[b], P.G. Mercadante[b], C.S. Moon[a,5], S.F. Novaes[a], Sandra S. Padula[a], D. Romero Abad[b], J.C. Ruiz Vargas

Institute for Nuclear Research and Nuclear Energy, Sofia, Bulgaria
A. Aleksandrov, R. Hadjiiska, P. Iaydjiev, M. Rodozov, S. Stoykova, G. Sultanov, M. Vutova

University of Sofia, Sofia, Bulgaria
A. Dimitrov, I. Glushkov, L. Litov, B. Pavlov, P. Petkov

Beihang University, Beijing, China
W. Fang[6]

Institute of High Energy Physics, Beijing, China
M. Ahmad, J.G. Bian, G.M. Chen, H.S. Chen, M. Chen, Y. Chen[7], T. Cheng, R. Du, C.H. Jiang, D. Leggat, Z. Liu, F. Romeo, S.M. Shaheen, A. Spiezia, J. Tao, C. Wang, Z. Wang, H. Zhang, J. Zhao

State Key Laboratory of Nuclear Physics and Technology, Peking University, Beijing, China
C. Asawatangtrakuldee, Y. Ban, Q. Li, S. Liu, Y. Mao, S.J. Qian, D. Wang, Z. Xu

Universidad de Los Andes, Bogota, Colombia
C. Avila, A. Cabrera, L.F. Chaparro Sierra, C. Florez, J.P. Gomez, C.F. González Hernández, J.D. Ruiz Alvarez, J.C. Sanabria

University of Split, Faculty of Electrical Engineering, Mechanical Engineering and Naval Architecture, Split, Croatia
N. Godinovic, D. Lelas, I. Puljak, P.M. Ribeiro Cipriano

University of Split, Faculty of Science, Split, Croatia
Z. Antunovic, M. Kovac

Institute Rudjer Boskovic, Zagreb, Croatia
V. Brigljevic, D. Ferencek, K. Kadija, S. Micanovic, L. Sudic

University of Cyprus, Nicosia, Cyprus
A. Attikis, G. Mavromanolakis, J. Mousa, C. Nicolaou, F. Ptochos, P.A. Razis, H. Rykaczewski

JHEP08(2016)045

Charles University, Prague, Czech Republic
M. Finger[8], M. Finger Jr.[8]

Universidad San Francisco de Quito, Quito, Ecuador
E. Carrera Jarrin

Academy of Scientific Research and Technology of the Arab Republic of Egypt, Egyptian Network of High Energy Physics, Cairo, Egypt
A.A. Abdelalim[9,10], E. El-khateeb[11], M.A. Mahmoud[12,13], A. Radi[13,11]

National Institute of Chemical Physics and Biophysics, Tallinn, Estonia
B. Calpas, M. Kadastik, M. Murumaa, L. Perrini, M. Raidal, A. Tiko, C. Veelken

Department of Physics, University of Helsinki, Helsinki, Finland
P. Eerola, J. Pekkanen, M. Voutilainen

Helsinki Institute of Physics, Helsinki, Finland
J. Härkönen, J.K. Heikkilä, V. Karimäki, R. Kinnunen, T. Lampén, K. Lassila-Perini, S. Lehti, T. Lindén, P. Luukka, T. Peltola, J. Tuominiemi, E. Tuovinen, L. Wendland

Lappeenranta University of Technology, Lappeenranta, Finland
J. Talvitie, T. Tuuva

DSM/IRFU, CEA/Saclay, Gif-sur-Yvette, France
M. Besancon, F. Couderc, M. Dejardin, D. Denegri, B. Fabbro, J.L. Faure, C. Favaro, F. Ferri, S. Ganjour, S. Ghosh, A. Givernaud, P. Gras, G. Hamel de Monchenault, P. Jarry, I. Kucher, E. Locci, M. Machet, J. Malcles, J. Rander, A. Rosowsky, M. Titov, A. Zghiche

Laboratoire Leprince-Ringuet, Ecole Polytechnique, IN2P3-CNRS, Palaiseau, France
A. Abdulsalam, I. Antropov, S. Baffioni, F. Beaudette, P. Busson, L. Cadamuro, E. Chapon, C. Charlot, O. Davignon, R. Granier de Cassagnac, M. Jo, S. Lisniak, P. Miné, I.N. Naranjo, M. Nguyen, C. Ochando, G. Ortona, P. Paganini, P. Pigard, S. Regnard, R. Salerno, Y. Sirois, T. Strebler, Y. Yilmaz, A. Zabi

Institut Pluridisciplinaire Hubert Curien, Université de Strasbourg, Université de Haute Alsace Mulhouse, CNRS/IN2P3, Strasbourg, France
J.-L. Agram[14], J. Andrea, A. Aubin, D. Bloch, J.-M. Brom, M. Buttignol, E.C. Chabert, N. Chanon, C. Collard, E. Conte[14], X. Coubez, J.-C. Fontaine[14], D. Gelé, U. Goerlach, A.-C. Le Bihan, J.A. Merlin[15], K. Skovpen, P. Van Hove

Centre de Calcul de l'Institut National de Physique Nucleaire et de Physique des Particules, CNRS/IN2P3, Villeurbanne, France
S. Gadrat

Université de Lyon, Université Claude Bernard Lyon 1, CNRS-IN2P3, Institut de Physique Nucléaire de Lyon, Villeurbanne, France
S. Beauceron, C. Bernet, G. Boudoul, E. Bouvier, C.A. Carrillo Montoya, R. Chierici, D. Contardo, B. Courbon, P. Depasse, H. El Mamouni, J. Fan, J. Fay, S. Gascon,

JHEP08(2016)045

M. Gouzevitch, G. Grenier, B. Ille, F. Lagarde, I.B. Laktineh, M. Lethuillier, L. Mirabito, A.L. Pequegnot, S. Perries, A. Popov[16], D. Sabes, V. Sordini, M. Vander Donckt, P. Verdier, S. Viret

Georgian Technical University, Tbilisi, Georgia

T. Toriashvili[17]

Tbilisi State University, Tbilisi, Georgia

Z. Tsamalaidze[8]

RWTH Aachen University, I. Physikalisches Institut, Aachen, Germany

C. Autermann, S. Beranek, L. Feld, A. Heister, M.K. Kiesel, K. Klein, M. Lipinski, A. Ostapchuk, M. Preuten, F. Raupach, S. Schael, C. Schomakers, J.F. Schulte, J. Schulz, T. Verlage, H. Weber, V. Zhukov[16]

RWTH Aachen University, III. Physikalisches Institut A, Aachen, Germany

M. Brodski, E. Dietz-Laursonn, D. Duchardt, M. Endres, M. Erdmann, S. Erdweg, T. Esch, R. Fischer, A. Güth, T. Hebbeker, C. Heidemann, K. Hoepfner, S. Knutzen, M. Merschmeyer, A. Meyer, P. Millet, S. Mukherjee, M. Olschewski, K. Padeken, P. Papacz, T. Pook, M. Radziej, H. Reithler, M. Rieger, F. Scheuch, L. Sonnenschein, D. Teyssier, S. Thüer

RWTH Aachen University, III. Physikalisches Institut B, Aachen, Germany

V. Cherepanov, Y. Erdogan, G. Flügge, F. Hoehle, B. Kargoll, T. Kress, A. Künsken, J. Lingemann, A. Nehrkorn, A. Nowack, I.M. Nugent, C. Pistone, O. Pooth, A. Stahl[15]

Deutsches Elektronen-Synchrotron, Hamburg, Germany

M. Aldaya Martin, I. Asin, K. Beernaert, O. Behnke, U. Behrens, A.A. Bin Anuar, K. Borras[18], A. Campbell, P. Connor, C. Contreras-Campana, F. Costanza, C. Diez Pardos, G. Dolinska, G. Eckerlin, D. Eckstein, T. Eichhorn, E. Gallo[19], J. Garay Garcia, A. Geiser, A. Gizhko, J.M. Grados Luyando, P. Gunnellini, A. Harb, J. Hauk, M. Hempel[20], H. Jung, A. Kalogeropoulos, O. Karacheban[20], M. Kasemann, J. Keaveney, J. Kieseler, C. Kleinwort, I. Korol, W. Lange, A. Lelek, J. Leonard, K. Lipka, A. Lobanov, W. Lohmann[20], R. Mankel, I.-A. Melzer-Pellmann, A.B. Meyer, G. Mittag, J. Mnich, A. Mussgiller, E. Ntomari, D. Pitzl, R. Placakyte, A. Raspereza, B. Roland, M.Ö. Sahin, P. Saxena, T. Schoerner-Sadenius, C. Seitz, S. Spannagel, N. Stefaniuk, K.D. Trippkewitz, G.P. Van Onsem, R. Walsh, C. Wissing

University of Hamburg, Hamburg, Germany

V. Blobel, M. Centis Vignali, A.R. Draeger, T. Dreyer, J. Erfle, E. Garutti, K. Goebel, D. Gonzalez, M. Görner, J. Haller, M. Hoffmann, R.S. Höing, A. Junkes, R. Klanner, R. Kogler, N. Kovalchuk, T. Lapsien, T. Lenz, I. Marchesini, D. Marconi, M. Meyer, M. Niedziela, D. Nowatschin, J. Ott, F. Pantaleo[15], T. Peiffer, A. Perieanu, N. Pietsch, J. Poehlsen, C. Sander, C. Scharf, P. Schleper, E. Schlieckau, A. Schmidt, S. Schumann, J. Schwandt, H. Stadie, G. Steinbrück, F.M. Stober, M. Stöver, H. Tholen, D. Troendle, E. Usai, L. Vanelderen, A. Vanhoefer, B. Vormwald

JHEP08(2016)045

Institut für Experimentelle Kernphysik, Karlsruhe, Germany

C. Barth, C. Baus, J. Berger, E. Butz, T. Chwalek, F. Colombo, W. De Boer, A. Dierlamm, S. Fink, R. Friese, M. Giffels, A. Gilbert, D. Haitz, F. Hartmann[15], S.M. Heindl, U. Husemann, I. Katkov[16], A. Kornmayer[15], P. Lobelle Pardo, B. Maier, H. Mildner, M.U. Mozer, T. Müller, Th. Müller, M. Plagge, G. Quast, K. Rabbertz, S. Röcker, F. Roscher, M. Schröder, G. Sieber, H.J. Simonis, R. Ulrich, J. Wagner-Kuhr, S. Wayand, M. Weber, T. Weiler, S. Williamson, C. Wöhrmann, R. Wolf

Institute of Nuclear and Particle Physics (INPP), NCSR Demokritos, Aghia Paraskevi, Greece

G. Anagnostou, G. Daskalakis, T. Geralis, V.A. Giakoumopoulou, A. Kyriakis, D. Loukas, I. Topsis-Giotis

National and Kapodistrian University of Athens, Athens, Greece

A. Agapitos, S. Kesisoglou, A. Panagiotou, N. Saoulidou, E. Tziaferi

University of Ioánnina, Ioánnina, Greece

I. Evangelou, G. Flouris, C. Foudas, P. Kokkas, N. Loukas, N. Manthos, I. Papadopoulos, E. Paradas

MTA-ELTE Lendület CMS Particle and Nuclear Physics Group, Eötvös Loránd University

N. Filipovic

Wigner Research Centre for Physics, Budapest, Hungary

G. Bencze, C. Hajdu, P. Hidas, D. Horvath[21], F. Sikler, V. Veszpremi, G. Vesztergombi[22], A.J. Zsigmond

Institute of Nuclear Research ATOMKI, Debrecen, Hungary

N. Beni, S. Czellar, J. Karancsi[23], J. Molnar, Z. Szillasi

University of Debrecen, Debrecen, Hungary

M. Bartók[22], A. Makovec, P. Raics, Z.L. Trocsanyi, B. Ujvari

National Institute of Science Education and Research, Bhubaneswar, India

S. Bahinipati, S. Choudhury[24], P. Mal, K. Mandal, A. Nayak[25], D.K. Sahoo, N. Sahoo, S.K. Swain

Panjab University, Chandigarh, India

S. Bansal, S.B. Beri, V. Bhatnagar, R. Chawla, R. Gupta, U.Bhawandeep, A.K. Kalsi, A. Kaur, M. Kaur, R. Kumar, A. Mehta, M. Mittal, J.B. Singh, G. Walia

University of Delhi, Delhi, India

Ashok Kumar, A. Bhardwaj, B.C. Choudhary, R.B. Garg, S. Keshri, A. Kumar, S. Malhotra, M. Naimuddin, N. Nishu, K. Ranjan, R. Sharma, V. Sharma

JHEP08(2016)045

Saha Institute of Nuclear Physics, Kolkata, India

R. Bhattacharya, S. Bhattacharya, K. Chatterjee, S. Dey, S. Dutt, S. Dutta, S. Ghosh, N. Majumdar, A. Modak, K. Mondal, S. Mukhopadhyay, S. Nandan, A. Purohit, A. Roy, D. Roy, S. Roy Chowdhury, S. Sarkar, M. Sharan, S. Thakur

Indian Institute of Technology Madras, Madras, India

P.K. Behera

Bhabha Atomic Research Centre, Mumbai, India

R. Chudasama, D. Dutta, V. Jha, V. Kumar, A.K. Mohanty[15], P.K. Netrakanti, L.M. Pant, P. Shukla, A. Topkar

Tata Institute of Fundamental Research-A, Mumbai, India

T. Aziz, S. Dugad, G. Kole, B. Mahakud, S. Mitra, G.B. Mohanty, N. Sur, B. Sutar

Tata Institute of Fundamental Research-B, Mumbai, India

S. Banerjee, S. Bhowmik[26], R.K. Dewanjee, S. Ganguly, M. Guchait, Sa. Jain, S. Kumar, M. Maity[26], G. Majumder, K. Mazumdar, B. Parida, T. Sarkar[26], N. Wickramage[27]

Indian Institute of Science Education and Research (IISER), Pune, India

S. Chauhan, S. Dube, A. Kapoor, K. Kothekar, A. Rane, S. Sharma

Institute for Research in Fundamental Sciences (IPM), Tehran, Iran

H. Bakhshiansohi, H. Behnamian, S. Chenarani[28], E. Eskandari Tadavani, S.M. Etesami[28], A. Fahim[29], M. Khakzad, M. Mohammadi Najafabadi, M. Naseri, S. Paktinat Mehdiabadi, F. Rezaei Hosseinabadi, B. Safarzadeh[30], M. Zeinali

University College Dublin, Dublin, Ireland

M. Felcini, M. Grunewald

INFN Sezione di Bari [a], Università di Bari [b], Politecnico di Bari [c], Bari, Italy

M. Abbrescia[a,b], C. Calabria[a,b], C. Caputo[a,b], A. Colaleo[a], D. Creanza[a,c], L. Cristella[a,b], N. De Filippis[a,c], M. De Palma[a,b], L. Fiore[a], G. Iaselli[a,c], G. Maggi[a,c], M. Maggi[a], G. Miniello[a,b], S. My[a,b], S. Nuzzo[a,b], A. Pompili[a,b], G. Pugliese[a,c], R. Radogna[a,b], A. Ranieri[a], G. Selvaggi[a,b], L. Silvestris[a,15], R. Venditti[a,b]

INFN Sezione di Bologna [a], Università di Bologna [b], Bologna, Italy

G. Abbiendi[a], C. Battilana, D. Bonacorsi[a,b], S. Braibant-Giacomelli[a,b], L. Brigliadori[a,b], R. Campanini[a,b], P. Capiluppi[a,b], A. Castro[a,b], F.R. Cavallo[a], S.S. Chhibra[a,b], G. Codispoti[a,b], M. Cuffiani[a,b], G.M. Dallavalle[a], F. Fabbri[a], A. Fanfani[a,b], D. Fasanella[a,b], P. Giacomelli[a], C. Grandi[a], L. Guiducci[a,b], S. Marcellini[a], G. Masetti[a], A. Montanari[a], F.L. Navarria[a,b], A. Perrotta[a], A.M. Rossi[a,b], T. Rovelli[a,b], G.P. Siroli[a,b], N. Tosi[a,b,15]

INFN Sezione di Catania [a], Università di Catania [b], Catania, Italy

S. Albergo[a,b], M. Chiorboli[a,b], S. Costa[a,b], A. Di Mattia[a], F. Giordano[a,b], R. Potenza[a,b], A. Tricomi[a,b], C. Tuve[a,b]

JHEP08(2016)045

INFN Sezione di Firenze [a], Università di Firenze [b], Firenze, Italy

G. Barbagli[a], V. Ciulli[a,b], C. Civinini[a], R. D'Alessandro[a,b], E. Focardi[a,b], V. Gori[a,b], P. Lenzi[a,b], M. Meschini[a], S. Paoletti[a], G. Sguazzoni[a], L. Viliani[a,b,15]

INFN Laboratori Nazionali di Frascati, Frascati, Italy

L. Benussi, S. Bianco, F. Fabbri, D. Piccolo, F. Primavera[15]

INFN Sezione di Genova [a], Università di Genova [b], Genova, Italy

V. Calvelli[a,b], F. Ferro[a], M. Lo Vetere[a,b], M.R. Monge[a,b], E. Robutti[a], S. Tosi[a,b]

INFN Sezione di Milano-Bicocca [a], Università di Milano-Bicocca [b], Milano, Italy

L. Brianza, M.E. Dinardo[a,b], S. Fiorendi[a,b], S. Gennai[a], A. Ghezzi[a,b], P. Govoni[a,b], S. Malvezzi[a], R.A. Manzoni[a,b,15], B. Marzocchi[a,b], D. Menasce[a], L. Moroni[a], M. Paganoni[a,b], D. Pedrini[a], S. Pigazzini, S. Ragazzi[a,b], T. Tabarelli de Fatis[a,b]

INFN Sezione di Napoli [a], Università di Napoli 'Federico II' [b], Napoli, Italy, Università della Basilicata [c], Potenza, Italy, Università G. Marconi [d], Roma, Italy

S. Buontempo[a], N. Cavallo[a,c], G. De Nardo, S. Di Guida[a,d,15], M. Esposito[a,b], F. Fabozzi[a,c], A.O.M. Iorio[a,b], G. Lanza[a], L. Lista[a], S. Meola[a,d,15], M. Merola[a], P. Paolucci[a,15], C. Sciacca[a,b], F. Thyssen

INFN Sezione di Padova [a], Università di Padova [b], Padova, Italy, Università di Trento [c], Trento, Italy

P. Azzi[a,15], N. Bacchetta[a], L. Benato[a,b], D. Bisello[a,b], A. Boletti[a,b], R. Carlin[a,b], A. Carvalho Antunes De Oliveira[a,b], P. Checchia[a], M. Dall'Osso[a,b], P. De Castro Manzano[a], T. Dorigo[a], U. Dosselli[a], F. Gasparini[a,b], U. Gasparini[a,b], A. Gozzelino[a], S. Lacaprara[a], M. Margoni[a,b], A.T. Meneguzzo[a,b], J. Pazzini[a,b,15], N. Pozzobon[a,b], P. Ronchese[a,b], F. Simonetto[a,b], E. Torassa[a], M. Tosi[a,b], M. Zanetti, P. Zotto[a,b], A. Zucchetta[a,b], G. Zumerle[a,b]

INFN Sezione di Pavia [a], Università di Pavia [b], Pavia, Italy

A. Braghieri[a], A. Magnani[a,b], P. Montagna[a,b], S.P. Ratti[a,b], V. Re[a], C. Riccardi[a,b], P. Salvini[a], I. Vai[a,b], P. Vitulo[a,b]

INFN Sezione di Perugia [a], Università di Perugia [b], Perugia, Italy

L. Alunni Solestizi[a,b], G.M. Bilei[a], D. Ciangottini[a,b], L. Fanò[a,b], P. Lariccia[a,b], R. Leonardi[a,b], G. Mantovani[a,b], M. Menichelli[a], A. Saha[a], A. Santocchia[a,b]

INFN Sezione di Pisa [a], Università di Pisa [b], Scuola Normale Superiore di Pisa [c], Pisa, Italy

K. Androsov[a,31], P. Azzurri[a,15], G. Bagliesi[a], J. Bernardini[a], T. Boccali[a], R. Castaldi[a], M.A. Ciocci[a,31], R. Dell'Orso[a], S. Donato[a,c], G. Fedi, A. Giassi[a], M.T. Grippo[a,31], F. Ligabue[a,c], T. Lomtadze[a], L. Martini[a,b], A. Messineo[a,b], F. Palla[a], A. Rizzi[a,b], A. Savoy-Navarro[a,32], P. Spagnolo[a], R. Tenchini[a], G. Tonelli[a,b], A. Venturi[a], P.G. Verdini[a]

JHEP08(2016)045

INFN Sezione di Roma [a], Università di Roma [b], Roma, Italy

L. Barone[a,b], F. Cavallari[a], M. Cipriani[a,b], G. D'imperio[a,b,15], D. Del Re[a,b,15], M. Diemoz[a], S. Gelli[a,b], C. Jorda[a], E. Longo[a,b], F. Margaroli[a,b], P. Meridiani[a], G. Organtini[a,b], R. Paramatti[a], F. Preiato[a,b], S. Rahatlou[a,b], C. Rovelli[a], F. Santanastasio[a,b]

INFN Sezione di Torino [a], Università di Torino [b], Torino, Italy, Università del Piemonte Orientale [c], Novara, Italy

N. Amapane[a,b], R. Arcidiacono[a,c,15], S. Argiro[a,b], M. Arneodo[a,c], N. Bartosik[a], R. Bellan[a,b], C. Biino[a], N. Cartiglia[a], M. Costa[a,b], R. Covarelli[a,b], A. Degano[a,b], N. Demaria[a], L. Finco[a,b], B. Kiani[a,b], C. Mariotti[a], S. Maselli[a], E. Migliore[a,b], V. Monaco[a,b], E. Monteil[a,b], M.M. Obertino[a,b], L. Pacher[a,b], N. Pastrone[a], M. Pelliccioni[a], G.L. Pinna Angioni[a,b], F. Ravera[a,b], A. Romero[a,b], M. Ruspa[a,c], R. Sacchi[a,b], K. Shchelina[a,b], V. Sola[a], A. Solano[a,b], A. Staiano[a], P. Traczyk[a,b]

INFN Sezione di Trieste [a], Università di Trieste [b], Trieste, Italy

S. Belforte[a], V. Candelise[a,b], M. Casarsa[a], F. Cossutti[a], G. Della Ricca[a,b], C. La Licata[a,b], A. Schizzi[a,b], A. Zanetti[a]

Kyungpook National University, Daegu, Korea

D.H. Kim, G.N. Kim, M.S. Kim, S. Lee, S.W. Lee, Y.D. Oh, S. Sekmen, D.C. Son, Y.C. Yang

Chonbuk National University, Jeonju, Korea

H. Kim, A. Lee

Hanyang University, Seoul, Korea

J.A. Brochero Cifuentes, T.J. Kim

Korea University, Seoul, Korea

S. Cho, S. Choi, Y. Go, D. Gyun, S. Ha, B. Hong, Y. Jo, Y. Kim, B. Lee, K. Lee, K.S. Lee, S. Lee, J. Lim, S.K. Park, Y. Roh

Seoul National University, Seoul, Korea

J. Almond, J. Kim, S.B. Oh, S.h. Seo, U.K. Yang, H.D. Yoo, G.B. Yu

University of Seoul, Seoul, Korea

M. Choi, H. Kim, H. Kim, J.H. Kim, J.S.H. Lee, I.C. Park, G. Ryu, M.S. Ryu

Sungkyunkwan University, Suwon, Korea

Y. Choi, J. Goh, D. Kim, E. Kwon, J. Lee, I. Yu

Vilnius University, Vilnius, Lithuania

V. Dudenas, A. Juodagalvis, J. Vaitkus

National Centre for Particle Physics, Universiti Malaya, Kuala Lumpur, Malaysia

I. Ahmed, Z.A. Ibrahim, J.R. Komaragiri, M.A.B. Md Ali[33], F. Mohamad Idris[34], W.A.T. Wan Abdullah, M.N. Yusli, Z. Zolkapli

JHEP08(2016)045

Centro de Investigacion y de Estudios Avanzados del IPN, Mexico City, Mexico
E. Casimiro Linares, H. Castilla-Valdez, E. De La Cruz-Burelo, I. Heredia-De La Cruz[35], A. Hernandez-Almada, R. Lopez-Fernandez, J. Mejia Guisao, A. Sanchez-Hernandez

Universidad Iberoamericana, Mexico City, Mexico
S. Carrillo Moreno, F. Vazquez Valencia

Benemerita Universidad Autonoma de Puebla, Puebla, Mexico
I. Pedraza, H.A. Salazar Ibarguen, C. Uribe Estrada

Universidad Autónoma de San Luis Potosí, San Luis Potosí, Mexico
A. Morelos Pineda

University of Auckland, Auckland, New Zealand
D. Krofcheck

University of Canterbury, Christchurch, New Zealand
P.H. Butler

National Centre for Physics, Quaid-I-Azam University, Islamabad, Pakistan
A. Ahmad, M. Ahmad, Q. Hassan, H.R. Hoorani, W.A. Khan, T. Khurshid, S. Qazi, M. Waqas

National Centre for Nuclear Research, Swierk, Poland
H. Bialkowska, M. Bluj, B. Boimska, T. Frueboes, M. Górski, M. Kazana, K. Nawrocki, K. Romanowska-Rybinska, M. Szleper, P. Zalewski

Institute of Experimental Physics, Faculty of Physics, University of Warsaw, Warsaw, Poland
K. Bunkowski, A. Byszuk[36], K. Doroba, A. Kalinowski, M. Konecki, J. Krolikowski, M. Misiura, M. Olszewski, M. Walczak

Laboratório de Instrumentação e Física Experimental de Partículas, Lisboa, Portugal
P. Bargassa, C. Beirão Da Cruz E Silva, A. Di Francesco, P. Faccioli, P.G. Ferreira Parracho, M. Gallinaro, J. Hollar, N. Leonardo, L. Lloret Iglesias, M.V. Nemallapudi, J. Rodrigues Antunes, J. Seixas, O. Toldaiev, D. Vadruccio, J. Varela, P. Vischia

Joint Institute for Nuclear Research, Dubna, Russia
S. Afanasiev, M. Gavrilenko, I. Golutvin, I. Gorbunov, V. Karjavin, G. Kozlov, A. Lanev, A. Malakhov, V. Matveev[37,38], P. Moisenz, V. Palichik, V. Perelygin, M. Savina, S. Shmatov, S. Shulha, N. Skatchkov, V. Smirnov, N. Voytishin, A. Zarubin

Petersburg Nuclear Physics Institute, Gatchina (St. Petersburg), Russia
L. Chtchipounov, V. Golovtsov, Y. Ivanov, V. Kim[39], E. Kuznetsova[40], V. Murzin, V. Oreshkin, V. Sulimov, A. Vorobyev

Institute for Nuclear Research, Moscow, Russia
Yu. Andreev, A. Dermenev, S. Gninenko, N. Golubev, A. Karneyeu, M. Kirsanov, N. Krasnikov, A. Pashenkov, D. Tlisov, A. Toropin

JHEP08(2016)045

Institute for Theoretical and Experimental Physics, Moscow, Russia

V. Epshteyn, V. Gavrilov, N. Lychkovskaya, V. Popov, I. Pozdnyakov, G. Safronov, A. Spiridonov, M. Toms, E. Vlasov, A. Zhokin

National Research Nuclear University 'Moscow Engineering Physics Institute' (MEPhI), Moscow, Russia

R. Chistov, O. Markin, V. Rusinov

P.N. Lebedev Physical Institute, Moscow, Russia

V. Andreev, M. Azarkin[38], I. Dremin[38], M. Kirakosyan, A. Leonidov[38], S.V. Rusakov, A. Terkulov

Skobeltsyn Institute of Nuclear Physics, Lomonosov Moscow State University, Moscow, Russia

A. Baskakov, A. Belyaev, E. Boos, V. Bunichev, M. Dubinin[41], L. Dudko, A. Ershov, A. Gribushin, V. Klyukhin, O. Kodolova, I. Lokhtin, I. Miagkov, S. Obraztsov, S. Petrushanko, V. Savrin

State Research Center of Russian Federation, Institute for High Energy Physics, Protvino, Russia

I. Azhgirey, I. Bayshev, S. Bitioukov, D. Elumakhov, V. Kachanov, A. Kalinin, D. Konstantinov, V. Krychkine, V. Petrov, R. Ryutin, A. Sobol, S. Troshin, N. Tyurin, A. Uzunian, A. Volkov

University of Belgrade, Faculty of Physics and Vinca Institute of Nuclear Sciences, Belgrade, Serbia

P. Adzic[42], P. Cirkovic, D. Devetak, J. Milosevic, V. Rekovic

Centro de Investigaciones Energéticas Medioambientales y Tecnológicas (CIEMAT), Madrid, Spain

J. Alcaraz Maestre, E. Calvo, M. Cerrada, M. Chamizo Llatas, N. Colino, B. De La Cruz, A. Delgado Peris, A. Escalante Del Valle, C. Fernandez Bedoya, J.P. Fernández Ramos, J. Flix, M.C. Fouz, P. Garcia-Abia, O. Gonzalez Lopez, S. Goy Lopez, J.M. Hernandez, M.I. Josa, E. Navarro De Martino, A. Pérez-Calero Yzquierdo, J. Puerta Pelayo, A. Quintario Olmeda, I. Redondo, L. Romero, M.S. Soares

Universidad Autónoma de Madrid, Madrid, Spain

J.F. de Trocóniz, M. Missiroli, D. Moran

Universidad de Oviedo, Oviedo, Spain

J. Cuevas, J. Fernandez Menendez, I. Gonzalez Caballero, E. Palencia Cortezon, S. Sanchez Cruz, J.M. Vizan Garcia

Instituto de Física de Cantabria (IFCA), CSIC-Universidad de Cantabria, Santander, Spain

I.J. Cabrillo, A. Calderon, J.R. Castiñeiras De Saa, E. Curras, M. Fernandez, J. Garcia-Ferrero, G. Gomez, A. Lopez Virto, J. Marco, C. Martinez Rivero, F. Matorras,

JHEP08(2016)045

J. Piedra Gomez, T. Rodrigo, A. Ruiz-Jimeno, L. Scodellaro, N. Trevisani, I. Vila, R. Vilar Cortabitarte

CERN, European Organization for Nuclear Research, Geneva, Switzerland

D. Abbaneo, E. Auffray, G. Auzinger, M. Bachtis, P. Baillon, A.H. Ball, D. Barney, P. Bloch, A. Bocci, A. Bonato, C. Botta, T. Camporesi, R. Castello, M. Cepeda, G. Cerminara, M. D'Alfonso, D. d'Enterria, A. Dabrowski, V. Daponte, A. David, M. De Gruttola, F. De Guio, A. De Roeck, E. Di Marco[43], M. Dobson, M. Dordevic, B. Dorney, T. du Pree, D. Duggan, M. Dünser, N. Dupont, A. Elliott-Peisert, S. Fartoukh, G. Franzoni, J. Fulcher, W. Funk, D. Gigi, K. Gill, M. Girone, F. Glege, S. Gundacker, M. Guthoff, J. Hammer, P. Harris, J. Hegeman, V. Innocente, P. Janot, H. Kirschenmann, V. Knünz, M.J. Kortelainen, K. Kousouris, M. Krammer[1], P. Lecoq, C. Lourenço, M.T. Lucchini, N. Magini, L. Malgeri, M. Mannelli, A. Martelli, F. Meijers, S. Mersi, E. Meschi, F. Moortgat, S. Morovic, M. Mulders, H. Neugebauer, S. Orfanelli[44], L. Orsini, L. Pape, E. Perez, M. Peruzzi, A. Petrilli, G. Petrucciani, A. Pfeiffer, M. Pierini, A. Racz, T. Reis, G. Rolandi[45], M. Rovere, M. Ruan, H. Sakulin, J.B. Sauvan, C. Schäfer, C. Schwick, M. Seidel, A. Sharma, P. Silva, M. Simon, P. Sphicas[46], J. Steggemann, M. Stoye, Y. Takahashi, D. Treille, A. Triossi, A. Tsirou, V. Veckalns[47], G.I. Veres[22], N. Wardle, A. Zagozdzinska[36], W.D. Zeuner

Paul Scherrer Institut, Villigen, Switzerland

W. Bertl, K. Deiters, W. Erdmann, R. Horisberger, Q. Ingram, H.C. Kaestli, D. Kotlinski, U. Langenegger, T. Rohe

Institute for Particle Physics, ETH Zurich, Zurich, Switzerland

F. Bachmair, L. Bäni, L. Bianchini, B. Casal, G. Dissertori, M. Dittmar, M. Donegà, P. Eller, C. Grab, C. Heidegger, D. Hits, J. Hoss, G. Kasieczka, P. Lecomte[†], W. Lustermann, B. Mangano, M. Marionneau, P. Martinez Ruiz del Arbol, M. Masciovecchio, M.T. Meinhard, D. Meister, F. Micheli, P. Musella, F. Nessi-Tedaldi, F. Pandolfi, J. Pata, F. Pauss, G. Perrin, L. Perrozzi, M. Quittnat, M. Rossini, M. Schönenberger, A. Starodumov[48], M. Takahashi, V.R. Tavolaro, K. Theofilatos, R. Wallny

Universität Zürich, Zurich, Switzerland

T.K. Aarrestad, C. Amsler[49], L. Caminada, M.F. Canelli, V. Chiochia, A. De Cosa, C. Galloni, A. Hinzmann, T. Hreus, B. Kilminster, C. Lange, J. Ngadiuba, D. Pinna, G. Rauco, P. Robmann, D. Salerno, Y. Yang

National Central University, Chung-Li, Taiwan

T.H. Doan, Sh. Jain, R. Khurana, M. Konyushikhin, C.M. Kuo, W. Lin, Y.J. Lu, A. Pozdnyakov, S.S. Yu

National Taiwan University (NTU), Taipei, Taiwan

Arun Kumar, P. Chang, Y.H. Chang, Y.W. Chang, Y. Chao, K.F. Chen, P.H. Chen, C. Dietz, F. Fiori, Y. Hsiung, Y.F. Liu, R.-S. Lu, M. Miñano Moya, E. Paganis, A. Psallidas, J.f. Tsai, Y.M. Tzeng

JHEP08(2016)045

Chulalongkorn University, Faculty of Science, Department of Physics, Bangkok, Thailand

B. Asavapibhop, G. Singh, N. Srimanobhas, N. Suwonjandee

Cukurova University, Adana, Turkey

A. Adiguzel, M.N. Bakirci[50], S. Damarseckin, Z.S. Demiroglu, C. Dozen, I. Dumanoglu, S. Girgis, G. Gokbulut, Y. Guler, E. Gurpinar, I. Hos, E.E. Kangal[51], A. Kayis Topaksu, G. Onengut[52], K. Ozdemir[53], D. Sunar Cerci[54], B. Tali[54], C. Zorbilmez

Middle East Technical University, Physics Department, Ankara, Turkey

B. Bilin, S. Bilmis, B. Isildak[55], G. Karapinar[56], M. Yalvac, M. Zeyrek

Bogazici University, Istanbul, Turkey

E. Gülmez, M. Kaya[57], O. Kaya[58], E.A. Yetkin[59], T. Yetkin[60]

Istanbul Technical University, Istanbul, Turkey

A. Cakir, K. Cankocak, S. Sen[61], F.I. Vardarlı

Institute for Scintillation Materials of National Academy of Science of Ukraine, Kharkov, Ukraine

B. Grynyov

National Scientific Center, Kharkov Institute of Physics and Technology, Kharkov, Ukraine

L. Levchuk, P. Sorokin

University of Bristol, Bristol, United Kingdom

R. Aggleton, F. Ball, L. Beck, J.J. Brooke, D. Burns, E. Clement, D. Cussans, H. Flacher, J. Goldstein, M. Grimes, G.P. Heath, H.F. Heath, J. Jacob, L. Kreczko, C. Lucas, Z. Meng, D.M. Newbold[62], S. Paramesvaran, A. Poll, T. Sakuma, S. Seif El Nasr-storey, S. Senkin, D. Smith, V.J. Smith

Rutherford Appleton Laboratory, Didcot, United Kingdom

K.W. Bell, A. Belyaev[63], C. Brew, R.M. Brown, L. Calligaris, D. Cieri, D.J.A. Cockerill, J.A. Coughlan, K. Harder, S. Harper, E. Olaiya, D. Petyt, C.H. Shepherd-Themistocleous, A. Thea, I.R. Tomalin, T. Williams

Imperial College, London, United Kingdom

M. Baber, R. Bainbridge, O. Buchmuller, A. Bundock, D. Burton, S. Casasso, M. Citron, D. Colling, L. Corpe, P. Dauncey, G. Davies, A. De Wit, M. Della Negra, P. Dunne, A. Elwood, D. Futyan, Y. Haddad, G. Hall, G. Iles, R. Lane, C. Laner, R. Lucas[62], L. Lyons, A.-M. Magnan, S. Malik, L. Mastrolorenzo, J. Nash, A. Nikitenko[48], J. Pela, B. Penning, M. Pesaresi, D.M. Raymond, A. Richards, A. Rose, C. Seez, A. Tapper, K. Uchida, M. Vazquez Acosta[64], T. Virdee[15], S.C. Zenz

Brunel University, Uxbridge, United Kingdom

J.E. Cole, P.R. Hobson, A. Khan, P. Kyberd, D. Leslie, I.D. Reid, P. Symonds, L. Teodorescu, M. Turner

JHEP08(2016)045

Baylor University, Waco, U.S.A.
A. Borzou, K. Call, J. Dittmann, K. Hatakeyama, H. Liu, N. Pastika

The University of Alabama, Tuscaloosa, U.S.A.
O. Charaf, S.I. Cooper, C. Henderson, P. Rumerio

Boston University, Boston, U.S.A.
D. Arcaro, A. Avetisyan, T. Bose, D. Gastler, D. Rankin, C. Richardson, J. Rohlf, L. Sulak, D. Zou

Brown University, Providence, U.S.A.
G. Benelli, E. Berry, D. Cutts, A. Ferapontov, A. Garabedian, J. Hakala, U. Heintz, O. Jesus, E. Laird, G. Landsberg, Z. Mao, M. Narain, S. Piperov, S. Sagir, E. Spencer, R. Syarif

University of California, Davis, Davis, U.S.A.
R. Breedon, G. Breto, D. Burns, M. Calderon De La Barca Sanchez, S. Chauhan, M. Chertok, J. Conway, R. Conway, P.T. Cox, R. Erbacher, C. Flores, G. Funk, M. Gardner, W. Ko, R. Lander, C. Mclean, M. Mulhearn, D. Pellett, J. Pilot, F. Ricci-Tam, S. Shalhout, J. Smith, M. Squires, D. Stolp, M. Tripathi, S. Wilbur, R. Yohay

University of California, Los Angeles, U.S.A.
R. Cousins, P. Everaerts, A. Florent, J. Hauser, M. Ignatenko, D. Saltzberg, E. Takasugi, V. Valuev, M. Weber

University of California, Riverside, Riverside, U.S.A.
K. Burt, R. Clare, J. Ellison, J.W. Gary, G. Hanson, J. Heilman, P. Jandir, E. Kennedy, F. Lacroix, O.R. Long, M. Malberti, M. Olmedo Negrete, M.I. Paneva, A. Shrinivas, H. Wei, S. Wimpenny, B. R. Yates

University of California, San Diego, La Jolla, U.S.A.
J.G. Branson, G.B. Cerati, S. Cittolin, R.T. D'Agnolo, M. Derdzinski, R. Gerosa, A. Holzner, R. Kelley, D. Klein, J. Letts, I. Macneill, D. Olivito, S. Padhi, M. Pieri, M. Sani, V. Sharma, S. Simon, M. Tadel, A. Vartak, S. Wasserbaech[65], C. Welke, J. Wood, F. Würthwein, A. Yagil, G. Zevi Della Porta

University of California, Santa Barbara, Santa Barbara, U.S.A.
R. Bhandari, J. Bradmiller-Feld, C. Campagnari, A. Dishaw, V. Dutta, K. Flowers, M. Franco Sevilla, P. Geffert, C. George, F. Golf, L. Gouskos, J. Gran, R. Heller, J. Incandela, N. Mccoll, S.D. Mullin, A. Ovcharova, J. Richman, D. Stuart, I. Suarez, C. West, J. Yoo

California Institute of Technology, Pasadena, U.S.A.
D. Anderson, A. Apresyan, J. Bendavid, A. Bornheim, J. Bunn, Y. Chen, J. Duarte, A. Mott, H.B. Newman, C. Pena, M. Spiropulu, J.R. Vlimant, S. Xie, R.Y. Zhu

Carnegie Mellon University, Pittsburgh, U.S.A.
M.B. Andrews, V. Azzolini, A. Calamba, B. Carlson, T. Ferguson, M. Paulini, J. Russ, M. Sun, H. Vogel, I. Vorobiev

JHEP08(2016)045

University of Colorado Boulder, Boulder, U.S.A.

J.P. Cumalat, W.T. Ford, F. Jensen, A. Johnson, M. Krohn, T. Mulholland, K. Stenson, S.R. Wagner

Cornell University, Ithaca, U.S.A.

J. Alexander, J. Chaves, J. Chu, S. Dittmer, N. Mirman, G. Nicolas Kaufman, J.R. Patterson, A. Rinkevicius, A. Ryd, L. Skinnari, W. Sun, S.M. Tan, Z. Tao, J. Thom, J. Tucker, P. Wittich

Fairfield University, Fairfield, U.S.A.

D. Winn

Fermi National Accelerator Laboratory, Batavia, U.S.A.

S. Abdullin, M. Albrow, G. Apollinari, S. Banerjee, L.A.T. Bauerdick, A. Beretvas, J. Berryhill, P.C. Bhat, G. Bolla, K. Burkett, J.N. Butler, H.W.K. Cheung, F. Chlebana, S. Cihangir, M. Cremonesi, V.D. Elvira, I. Fisk, J. Freeman, E. Gottschalk, L. Gray, D. Green, S. Grünendahl, O. Gutsche, D. Hare, R.M. Harris, S. Hasegawa, J. Hirschauer, Z. Hu, B. Jayatilaka, S. Jindariani, M. Johnson, U. Joshi, B. Klima, B. Kreis, S. Lammel, J. Linacre, D. Lincoln, R. Lipton, T. Liu, R. Lopes De Sá, J. Lykken, K. Maeshima, J.M. Marraffino, S. Maruyama, D. Mason, P. McBride, P. Merkel, S. Mrenna, S. Nahn, C. Newman-Holmes[†], V. O'Dell, K. Pedro, O. Prokofyev, G. Rakness, L. Ristori, E. Sexton-Kennedy, A. Soha, W.J. Spalding, L. Spiegel, S. Stoynev, N. Strobbe, L. Taylor, S. Tkaczyk, N.V. Tran, L. Uplegger, E.W. Vaandering, C. Vernieri, M. Verzocchi, R. Vidal, M. Wang, H.A. Weber, A. Whitbeck

University of Florida, Gainesville, U.S.A.

D. Acosta, P. Avery, P. Bortignon, D. Bourilkov, A. Brinkerhoff, A. Carnes, M. Carver, D. Curry, S. Das, R.D. Field, I.K. Furic, J. Konigsberg, A. Korytov, P. Ma, K. Matchev, H. Mei, P. Milenovic[66], G. Mitselmakher, D. Rank, L. Shchutska, D. Sperka, L. Thomas, J. Wang, S. Wang, J. Yelton

Florida International University, Miami, U.S.A.

S. Linn, P. Markowitz, G. Martinez, J.L. Rodriguez

Florida State University, Tallahassee, U.S.A.

A. Ackert, J.R. Adams, T. Adams, A. Askew, S. Bein, B. Diamond, S. Hagopian, V. Hagopian, K.F. Johnson, A. Khatiwada, H. Prosper, A. Santra, M. Weinberg

Florida Institute of Technology, Melbourne, U.S.A.

M.M. Baarmand, V. Bhopatkar, S. Colafranceschi[67], M. Hohlmann, H. Kalakhety, D. Noonan, T. Roy, F. Yumiceva

University of Illinois at Chicago (UIC), Chicago, U.S.A.

M.R. Adams, L. Apanasevich, D. Berry, R.R. Betts, I. Bucinskaite, R. Cavanaugh, O. Evdokimov, L. Gauthier, C.E. Gerber, D.J. Hofman, P. Kurt, C. O'Brien, I.D. Sandoval Gonzalez, P. Turner, N. Varelas, Z. Wu, M. Zakaria, J. Zhang

JHEP08(2016)045

The University of Iowa, Iowa City, U.S.A.

B. Bilki[68], W. Clarida, K. Dilsiz, S. Durgut, R.P. Gandrajula, M. Haytmyradov, V. Khristenko, J.-P. Merlo, H. Mermerkaya[69], A. Mestvirishvili, A. Moeller, J. Nachtman, H. Ogul, Y. Onel, F. Ozok[70], A. Penzo, C. Snyder, E. Tiras, J. Wetzel, K. Yi

Johns Hopkins University, Baltimore, U.S.A.

I. Anderson, B. Blumenfeld, A. Cocoros, N. Eminizer, D. Fehling, L. Feng, A.V. Gritsan, P. Maksimovic, M. Osherson, J. Roskes, U. Sarica, M. Swartz, M. Xiao, Y. Xin, C. You

The University of Kansas, Lawrence, U.S.A.

A. Al-bataineh, P. Baringer, A. Bean, J. Bowen, C. Bruner, J. Castle, R.P. Kenny III, A. Kropivnitskaya, D. Majumder, W. Mcbrayer, M. Murray, S. Sanders, R. Stringer, J.D. Tapia Takaki, Q. Wang

Kansas State University, Manhattan, U.S.A.

A. Ivanov, K. Kaadze, S. Khalil, M. Makouski, Y. Maravin, A. Mohammadi, L.K. Saini, N. Skhirtladze, S. Toda

Lawrence Livermore National Laboratory, Livermore, U.S.A.

D. Lange, F. Rebassoo, D. Wright

University of Maryland, College Park, U.S.A.

C. Anelli, A. Baden, O. Baron, A. Belloni, B. Calvert, S.C. Eno, C. Ferraioli, J.A. Gomez, N.J. Hadley, S. Jabeen, R.G. Kellogg, T. Kolberg, J. Kunkle, Y. Lu, A.C. Mignerey, Y.H. Shin, A. Skuja, M.B. Tonjes, S.C. Tonwar

Massachusetts Institute of Technology, Cambridge, U.S.A.

A. Apyan, R. Barbieri, A. Baty, R. Bi, K. Bierwagen, S. Brandt, W. Busza, I.A. Cali, Z. Demiragli, L. Di Matteo, G. Gomez Ceballos, M. Goncharov, D. Gulhan, D. Hsu, Y. Iiyama, G.M. Innocenti, M. Klute, D. Kovalskyi, K. Krajczar, Y.S. Lai, Y.-J. Lee, A. Levin, P.D. Luckey, A.C. Marini, C. Mcginn, C. Mironov, S. Narayanan, X. Niu, C. Paus, C. Roland, G. Roland, J. Salfeld-Nebgen, G.S.F. Stephans, K. Sumorok, K. Tatar, M. Varma, D. Velicanu, J. Veverka, J. Wang, T.W. Wang, B. Wyslouch, M. Yang, V. Zhukova

University of Minnesota, Minneapolis, U.S.A.

A.C. Benvenuti, R.M. Chatterjee, B. Dahmes, A. Evans, A. Finkel, A. Gude, P. Hansen, S. Kalafut, S.C. Kao, K. Klapoetke, Y. Kubota, Z. Lesko, J. Mans, S. Nourbakhsh, N. Ruckstuhl, R. Rusack, N. Tambe, J. Turkewitz

University of Mississippi, Oxford, U.S.A.

J.G. Acosta, S. Oliveros

University of Nebraska-Lincoln, Lincoln, U.S.A.

E. Avdeeva, R. Bartek, K. Bloom, S. Bose, D.R. Claes, A. Dominguez, C. Fangmeier, R. Gonzalez Suarez, R. Kamalieddin, D. Knowlton, I. Kravchenko, F. Meier, J. Monroy, J.E. Siado, G.R. Snow, B. Stieger

JHEP08(2016)045

State University of New York at Buffalo, Buffalo, U.S.A.
M. Alyari, J. Dolen, J. George, A. Godshalk, C. Harrington, I. Iashvili, J. Kaisen, A. Kharchilava, A. Kumar, A. Parker, S. Rappoccio, B. Roozbahani

Northeastern University, Boston, U.S.A.
G. Alverson, E. Barberis, D. Baumgartel, M. Chasco, A. Hortiangtham, A. Massironi, D.M. Morse, D. Nash, T. Orimoto, R. Teixeira De Lima, D. Trocino, R.-J. Wang, D. Wood

Northwestern University, Evanston, U.S.A.
S. Bhattacharya, K.A. Hahn, A. Kubik, J.F. Low, N. Mucia, N. Odell, B. Pollack, M.H. Schmitt, K. Sung, M. Trovato, M. Velasco

University of Notre Dame, Notre Dame, U.S.A.
N. Dev, M. Hildreth, K. Hurtado Anampa, C. Jessop, D.J. Karmgard, N. Kellams, K. Lannon, N. Marinelli, F. Meng, C. Mueller, Y. Musienko[37], M. Planer, A. Reinsvold, R. Ruchti, N. Rupprecht, G. Smith, S. Taroni, N. Valls, M. Wayne, M. Wolf, A. Woodard

The Ohio State University, Columbus, U.S.A.
J. Alimena, L. Antonelli, J. Brinson, B. Bylsma, L.S. Durkin, S. Flowers, B. Francis, A. Hart, C. Hill, R. Hughes, W. Ji, B. Liu, W. Luo, D. Puigh, M. Rodenburg, B.L. Winer, H.W. Wulsin

Princeton University, Princeton, U.S.A.
S. Cooperstein, O. Driga, P. Elmer, J. Hardenbrook, P. Hebda, J. Luo, D. Marlow, T. Medvedeva, M. Mooney, J. Olsen, C. Palmer, P. Piroué, D. Stickland, C. Tully, A. Zuranski

University of Puerto Rico, Mayaguez, U.S.A.
S. Malik

Purdue University, West Lafayette, U.S.A.
A. Barker, V.E. Barnes, D. Benedetti, S. Folgueras, L. Gutay, M.K. Jha, M. Jones, A.W. Jung, K. Jung, D.H. Miller, N. Neumeister, B.C. Radburn-Smith, X. Shi, J. Sun, A. Svyatkovskiy, F. Wang, W. Xie, L. Xu

Purdue University Calumet, Hammond, U.S.A.
N. Parashar, J. Stupak

Rice University, Houston, U.S.A.
A. Adair, B. Akgun, Z. Chen, K.M. Ecklund, F.J.M. Geurts, M. Guilbaud, W. Li, B. Michlin, M. Northup, B.P. Padley, R. Redjimi, J. Roberts, J. Rorie, Z. Tu, J. Zabel

University of Rochester, Rochester, U.S.A.
B. Betchart, A. Bodek, P. de Barbaro, R. Demina, Y.t. Duh, T. Ferbel, M. Galanti, A. Garcia-Bellido, J. Han, O. Hindrichs, A. Khukhunaishvili, K.H. Lo, P. Tan, M. Verzetti

Rutgers, The State University of New Jersey, Piscataway, U.S.A.
J.P. Chou, E. Contreras-Campana, Y. Gershtein, T.A. Gómez Espinosa, E. Halkiadakis, M. Heindl, D. Hidas, E. Hughes, S. Kaplan, R. Kunnawalkam Elayavalli, S. Kyriacou,

JHEP08(2016)045

A. Lath, K. Nash, H. Saka, S. Salur, S. Schnetzer, D. Sheffield, S. Somalwar, R. Stone, S. Thomas, P. Thomassen, M. Walker

University of Tennessee, Knoxville, U.S.A.
M. Foerster, J. Heideman, G. Riley, K. Rose, S. Spanier, K. Thapa

Texas A&M University, College Station, U.S.A.
O. Bouhali[71], A. Castaneda Hernandez[71], A. Celik, M. Dalchenko, M. De Mattia, A. Delgado, S. Dildick, R. Eusebi, J. Gilmore, T. Huang, E. Juska, T. Kamon[72], V. Krutelyov, R. Mueller, Y. Pakhotin, R. Patel, A. Perloff, L. Perniè, D. Rathjens, A. Rose, A. Safonov, A. Tatarinov, K.A. Ulmer

Texas Tech University, Lubbock, U.S.A.
N. Akchurin, C. Cowden, J. Damgov, C. Dragoiu, P.R. Dudero, J. Faulkner, S. Kunori, K. Lamichhane, S.W. Lee, T. Libeiro, S. Undleeb, I. Volobouev, Z. Wang

Vanderbilt University, Nashville, U.S.A.
A.G. Delannoy, S. Greene, A. Gurrola, R. Janjam, W. Johns, C. Maguire, A. Melo, H. Ni, P. Sheldon, S. Tuo, J. Velkovska, Q. Xu

University of Virginia, Charlottesville, U.S.A.
M.W. Arenton, P. Barria, B. Cox, J. Goodell, R. Hirosky, A. Ledovskoy, H. Li, C. Neu, T. Sinthuprasith, X. Sun, Y. Wang, E. Wolfe, F. Xia

Wayne State University, Detroit, U.S.A.
C. Clarke, R. Harr, P.E. Karchin, P. Lamichhane, J. Sturdy

University of Wisconsin - Madison, Madison, WI, U.S.A.
D.A. Belknap, S. Dasu, L. Dodd, S. Duric, B. Gomber, M. Grothe, M. Herndon, A. Hervé, P. Klabbers, A. Lanaro, A. Levine, K. Long, R. Loveless, I. Ojalvo, T. Perry, G.A. Pierro, G. Polese, T. Ruggles, A. Savin, A. Sharma, N. Smith, W.H. Smith, D. Taylor, P. Verwilligen, N. Woods

†: Deceased
1: Also at Vienna University of Technology, Vienna, Austria
2: Also at State Key Laboratory of Nuclear Physics and Technology, Peking University, Beijing, China
3: Also at Institut Pluridisciplinaire Hubert Curien, Université de Strasbourg, Université de Haute Alsace Mulhouse, CNRS/IN2P3, Strasbourg, France
4: Also at Universidade Estadual de Campinas, Campinas, Brazil
5: Also at Centre National de la Recherche Scientifique (CNRS) - IN2P3, Paris, France
6: Also at Université Libre de Bruxelles, Bruxelles, Belgium
7: Also at Deutsches Elektronen-Synchrotron, Hamburg, Germany
8: Also at Joint Institute for Nuclear Research, Dubna, Russia
9: Also at Helwan University, Cairo, Egypt
10: Now at Zewail City of Science and Technology, Zewail, Egypt
11: Also at Ain Shams University, Cairo, Egypt
12: Also at Fayoum University, El-Fayoum, Egypt

JHEP08(2016)045

13: Now at British University in Egypt, Cairo, Egypt
14: Also at Université de Haute Alsace, Mulhouse, France
15: Also at CERN, European Organization for Nuclear Research, Geneva, Switzerland
16: Also at Skobeltsyn Institute of Nuclear Physics, Lomonosov Moscow State University, Moscow, Russia
17: Also at Tbilisi State University, Tbilisi, Georgia
18: Also at RWTH Aachen University, III. Physikalisches Institut A, Aachen, Germany
19: Also at University of Hamburg, Hamburg, Germany
20: Also at Brandenburg University of Technology, Cottbus, Germany
21: Also at Institute of Nuclear Research ATOMKI, Debrecen, Hungary
22: Also at MTA-ELTE Lendület CMS Particle and Nuclear Physics Group, Eötvös Loránd University, Budapest, Hungary
23: Also at University of Debrecen, Debrecen, Hungary
24: Also at Indian Institute of Science Education and Research, Bhopal, India
25: Also at Institute of Physics, Bhubaneswar, India
26: Also at University of Visva-Bharati, Santiniketan, India
27: Also at University of Ruhuna, Matara, Sri Lanka
28: Also at Isfahan University of Technology, Isfahan, Iran
29: Also at University of Tehran, Department of Engineering Science, Tehran, Iran
30: Also at Plasma Physics Research Center, Science and Research Branch, Islamic Azad University, Tehran, Iran
31: Also at Università degli Studi di Siena, Siena, Italy
32: Also at Purdue University, West Lafayette, U.S.A.
33: Also at International Islamic University of Malaysia, Kuala Lumpur, Malaysia
34: Also at Malaysian Nuclear Agency, MOSTI, Kajang, Malaysia
35: Also at Consejo Nacional de Ciencia y Tecnología, Mexico city, Mexico
36: Also at Warsaw University of Technology, Institute of Electronic Systems, Warsaw, Poland
37: Also at Institute for Nuclear Research, Moscow, Russia
38: Now at National Research Nuclear University 'Moscow Engineering Physics Institute' (MEPhI), Moscow, Russia
39: Also at St. Petersburg State Polytechnical University, St. Petersburg, Russia
40: Also at University of Florida, Gainesville, U.S.A.
41: Also at California Institute of Technology, Pasadena, U.S.A.
42: Also at Faculty of Physics, University of Belgrade, Belgrade, Serbia
43: Also at INFN Sezione di Roma; Università di Roma, Roma, Italy
44: Also at National Technical University of Athens, Athens, Greece
45: Also at Scuola Normale e Sezione dell'INFN, Pisa, Italy
46: Also at National and Kapodistrian University of Athens, Athens, Greece
47: Also at Riga Technical University, Riga, Latvia
48: Also at Institute for Theoretical and Experimental Physics, Moscow, Russia
49: Also at Albert Einstein Center for Fundamental Physics, Bern, Switzerland
50: Also at Gaziosmanpasa University, Tokat, Turkey
51: Also at Mersin University, Mersin, Turkey
52: Also at Cag University, Mersin, Turkey
53: Also at Piri Reis University, Istanbul, Turkey
54: Also at Adiyaman University, Adiyaman, Turkey
55: Also at Ozyegin University, Istanbul, Turkey
56: Also at Izmir Institute of Technology, Izmir, Turkey

JHEP08(2016)045

57: Also at Marmara University, Istanbul, Turkey
58: Also at Kafkas University, Kars, Turkey
59: Also at Istanbul Bilgi University, Istanbul, Turkey
60: Also at Yildiz Technical University, Istanbul, Turkey
61: Also at Hacettepe University, Ankara, Turkey
62: Also at Rutherford Appleton Laboratory, Didcot, United Kingdom
63: Also at School of Physics and Astronomy, University of Southampton, Southampton, United Kingdom
64: Also at Instituto de Astrofísica de Canarias, La Laguna, Spain
65: Also at Utah Valley University, Orem, U.S.A.
66: Also at University of Belgrade, Faculty of Physics and Vinca Institute of Nuclear Sciences, Belgrade, Serbia
67: Also at Facoltà Ingegneria, Università di Roma, Roma, Italy
68: Also at Argonne National Laboratory, Argonne, U.S.A.
69: Also at Erzincan University, Erzincan, Turkey
70: Also at Mimar Sinan University, Istanbul, Istanbul, Turkey
71: Also at Texas A&M University at Qatar, Doha, Qatar
72: Also at Kyungpook National University, Daegu, Korea

JHEP08(2016)045

Nuclear Instruments and Methods in Physics Research A 831 (2016) 122–132

Contents lists available at ScienceDirect

Nuclear Instruments and Methods in Physics Research A

journal homepage: www.elsevier.com/locate/nima

Development of n^+-in-p planar pixel sensors for extremely high radiation environments, designed to retain high efficiency after irradiation

Y. Unno [b,*], S. Kamada [a], K. Yamamura [a], Y. Ikegami [b], K. Nakamura [b], Y. Takubo [b], R. Takashima [c], J. Tojo [d], T. Kono [e], K. Hanagaki [f,b], K. Yajima [f], Y. Yamauchi [f], M. Hirose [g], Y. Homma [g], O. Jinnouchi [g], K. Kimura [g], K. Motohashi [g], S. Sato [g], H. Sawai [g], K. Todome [g], D. Yamaguchi [g], K. Hara [h,i], Kz. Sato [h], Kj. Sato [h,i], M. Hagihara [h], S. Iwabuchi [h]

[a] Solid State Div., Hamamatsu Photonics K.K., 1126-1, Ichino-cho, Higashi-ku, Hamamatsu-shi, Shizuoka 435-8558, Japan
[b] Institute of Particle and Nuclear Study, KEK, Oho 1-1, Tsukuba, Ibaraki 305-0801, Japan
[c] Department of Science Education, Kyoto University of Education, Kyoto 612-8522, Japan
[d] Department of Physics, Faculty of Science, Kyushu University, 744 Motooka, Nishi-ku, Fukuoka 819-0395, Japan
[e] Ochadai Academic Production, Ochanomizu University, 2-1-1, Otsuka, Bunkyo-ku, Tokyo, 112-8610, Japan
[f] Department of Physics, Osaka University, Machikaneyama-cho 1-1, Toyonaka-shi, Osaka 560-0043, Japan
[g] Institute of Science and Engineering, Tokyo Institute of Technology, Ookayama 2-12-1, Meguro-ku, Tokyo 152-8551, Japan
[h] Institute of Pure and Applied Sciences, University of Tsukuba, Tsukuba, Ibaraki 305-9751, Japan
[i] Center for Integrated Research in Fundamental Science and Engineering, University of Tsukuba, Tsukuba, Ibaraki 305-8571, Japan

ARTICLE INFO

Article history:
Received 9 December 2015
Received in revised form
11 April 2016
Accepted 13 April 2016
Available online 23 April 2016

Keywords:
n-in-p
p-type
Pixel
Silicon
Radiation damage
HL-LHC

ABSTRACT

We have developed n^+-in-p pixel sensors to obtain highly radiation tolerant sensors for extremely high radiation environments such as those found at the high-luminosity LHC. We have designed novel pixel structures to eliminate the sources of efficiency loss under the bias rails after irradiation by removing the bias rail out of the boundary region and routing the bias resistors inside the area of the pixel electrodes. After irradiation by protons with the fluence of approximately 3×10^{15} n_{eq}/cm^2, the pixel structure with the polysilicon bias resistor and the bias rails removed far away from the boundary shows an efficiency loss of <0.5% per pixel at the boundary region, which is as efficient as the pixel structure without a biasing structure. The pixel structure with the bias rails at the boundary and the widened p-stop's underneath the bias rail also exhibits an improved loss of approximately 1% per pixel at the boundary region. We have elucidated the physical mechanisms behind the efficiency loss under the bias rail with TCAD simulations. The efficiency loss is due to the interplay of the bias rail acting as a charge collecting electrode with the region of low electric field in the silicon near the surface at the boundary. The region acts as a "shield" for the electrode. After irradiation, the strong applied electric field nearly eliminates the region. The TCAD simulations have shown that wide p-stop and large $Si–SiO_2$ interface charge (inversion layer, specifically) act to shield the weighting potential. The pixel sensor of the old design irradiated by γ-rays at 2.4 MGy is confirmed to exhibit only a slight efficiency loss at the boundary.

© 2016 Elsevier B.V. All rights reserved.

1. Introduction

We have developed radiation-tolerant, planar-process, position-sensitive, silicon sensors in p-type 6-inch silicon wafers for applications in extremely high radiation environments [1–3] where radiation damage is generated by charged and neutral particles passing through the silicon sensors. Since the silicon bulk stays as p-type after irradiation, the p-type sensor requires lithographic processing only in the p–n junction side, simplifying the fabrication and leading to low device cost. Reading the signals out from the n-side enables the operation of the sensor without completely depleting the bulk and makes the sensor highly radiation tolerant. The planar silicon fabrication process is well established in the industry and is a cost-effective solution for large volume device production.

Extremely high radiation environments are found in the large hadron collider (LHC) [4]. The LHC accelerator complex is planned to be upgraded to High Luminosity LHC (HL-LHC) [5] to reach a

* Corresponding author.
E-mail address: yoshinobu.unno@kek.jp (Y. Unno).

http://dx.doi.org/10.1016/j.nima.2016.04.039
0168-9002/© 2016 Elsevier B.V. All rights reserved.

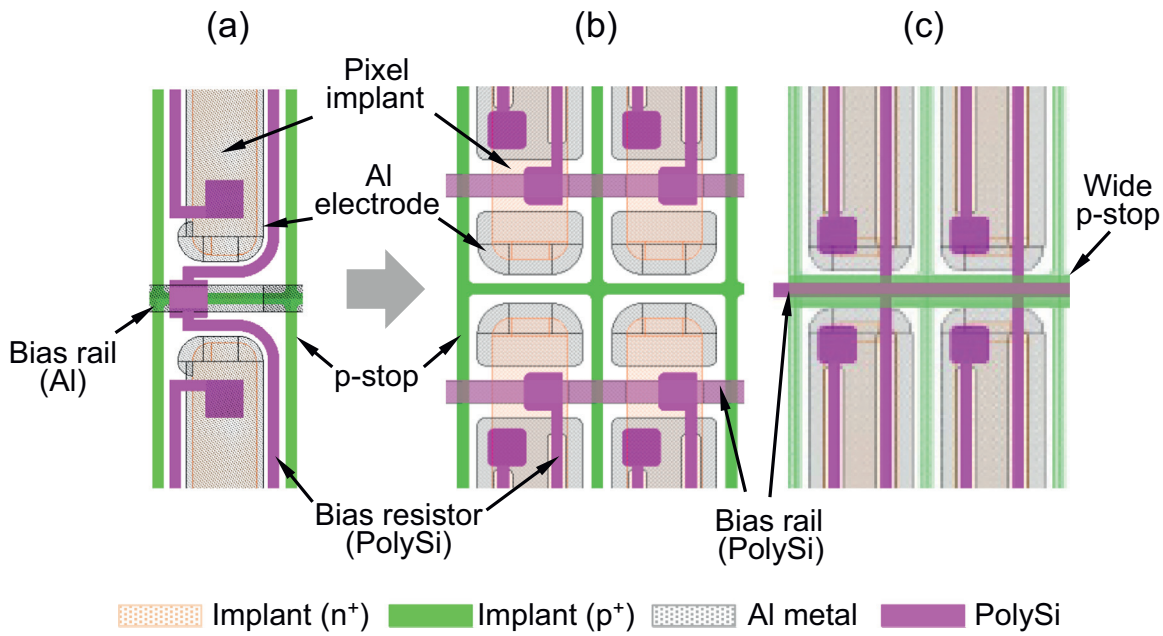

Fig. 1. Pixel structures: (a) old structure in wafer layout #2, (b) Type 10 and (c) Type 13 in wafer layout #4 .

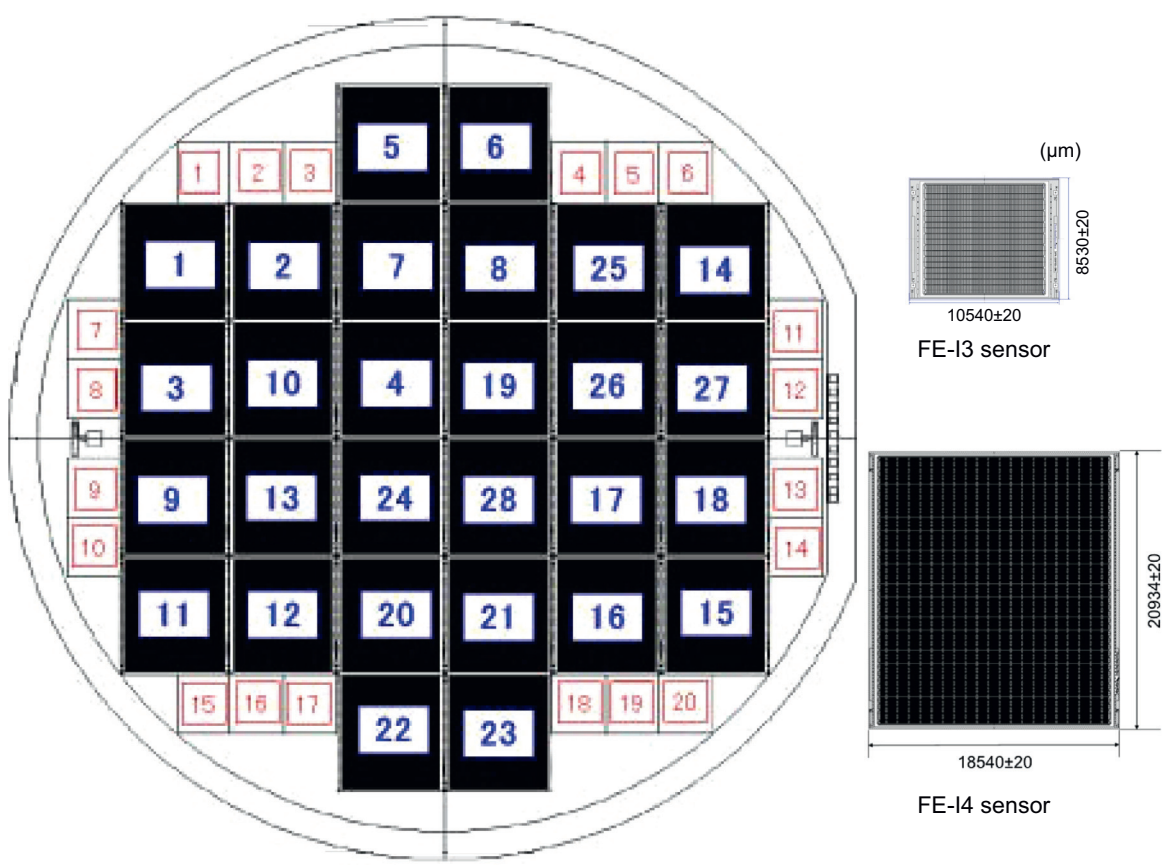

Fig. 2. Wafer layout #4 in 6-inch wafer, with 28 of ATLAS FE-I4 singles and 20 of FE-I3 singles of pixel sensors. Each FE-I4 and FE-I3 pixel sensor is 18.54×20.93 and 10.54×8.53 mm^2 in chip size, with a 336×80 and 160×18 matrix of 50×250 and 50×400 μm^2 pixels, respectively, with unique pixel structure per sensor.

higher collision rate (5×10^{34} cm^{-2}s^{-1} with "luminosity leveling") and consequently obtain an increase of one order in magnitude in the number of accumulated events (3000 fb^{-1}). The upgrade is scheduled during the LHC shutdown during the years 2024–2026. Our study primarily aims to develop a planar pixel sensor for the ATLAS detector, which is a general-purpose detector at a collision point in the LHC ring [6], that will be upgraded for the HL-LHC [7]. Considering a safety factor of 2, the sensor must cope with a radiation specified: the accumulated flow of particles ("fluence") of approximately 2×10^{16} 1 MeV-neutrons equivalent (n_{eq})/cm^2 and 3×10^{15} n_{eq}/cm^2 at a radius of 4 cm for the inner pixel layers and at 15 cm for the outer pixel layers, respectively [8].

Table 1
Specifications of wafer layout #4 of n^+-in-p pixel sensors.

Silicon wafer diameter	6 inch (150 mm)
Wafer type	p-type, float zone (FZ)
Crystal orientation	⟨100⟩
Resistivity	3–7 kΩ cm
Thickness	320 μm
Thinned	150 μm
Number FE-I4 sensors	28
Number FE-I3 sensors	20

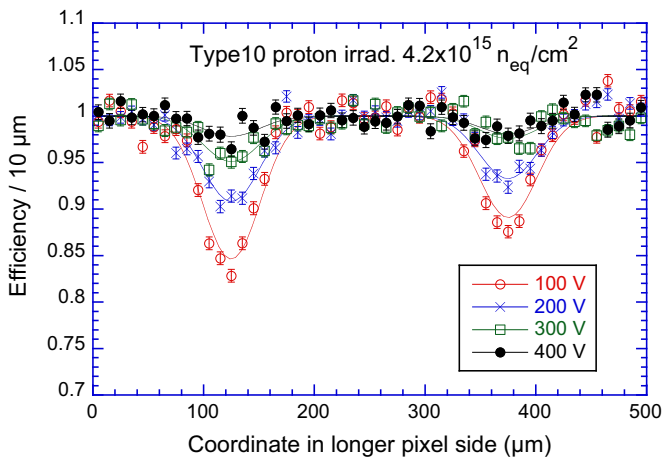

Fig. 3. Efficiency mapping over two pixel regions projected on the long pixel side. Pixel boundaries of the bias rail side and the no bias rail side are at 125 and 375 μm, respectively.

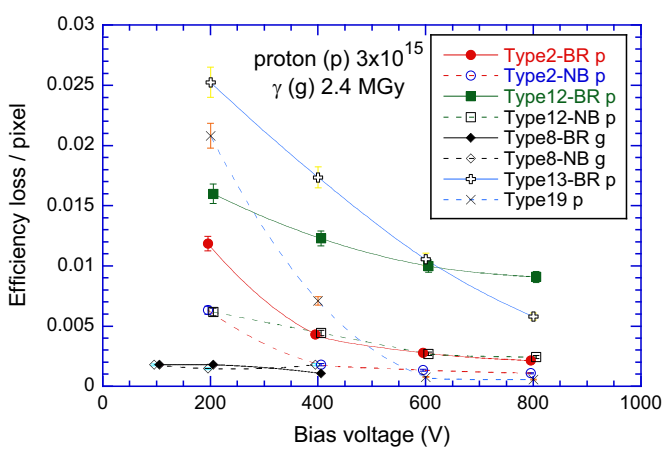

Fig. 4. Efficiency loss per pixel as a function of bias voltage in the bias rail (BR, filled) and the no bias bail (NB, open) regions, of Types 2 (Large offset, circle) and 12 (Small offset, square) pixel structures after proton irradiation of 3×10^{15} n_{eq}/cm^2, Type 8 (Old, diamond) after γ irradiation of 2.4 MGy. Those data of Types 13 (Wide p-stop, vertical cross) and 19 (No bias, cross) after proton irradiation [16] are reproduced together.

2. KEK/HPK n^+-in-p pixel sensors

2.1. Pixel structure – "Old" design (wafer layout #2)

We have previously produced n^+-in-p pixel sensors[1] in 6-inch wafers (hereafter referred to as "wafer layout #2") [2]. The sensors were bump bonded to the ATLAS pixel readout ASIC, FE-I4 [9], irradiated at a fluence of 2×10^{15} n_{eq}/cm^2 with 23 MeV protons at KIT [10], and tested by beam tests before and after the irradiation [11]. Several issues were identified on the basis of the results of these experiments.

The pixel structure of interest in the wafer layout #2 is shown in Fig. 1(a) (hereafter referred to as "Old" structure). Although the individual pixels are to be DC coupled to the readout ASIC, we have designed a connection of bias potential to the individual pixels to

[1] The superscript, +, indicates that the density of the material is higher than that of the silicon bulk.

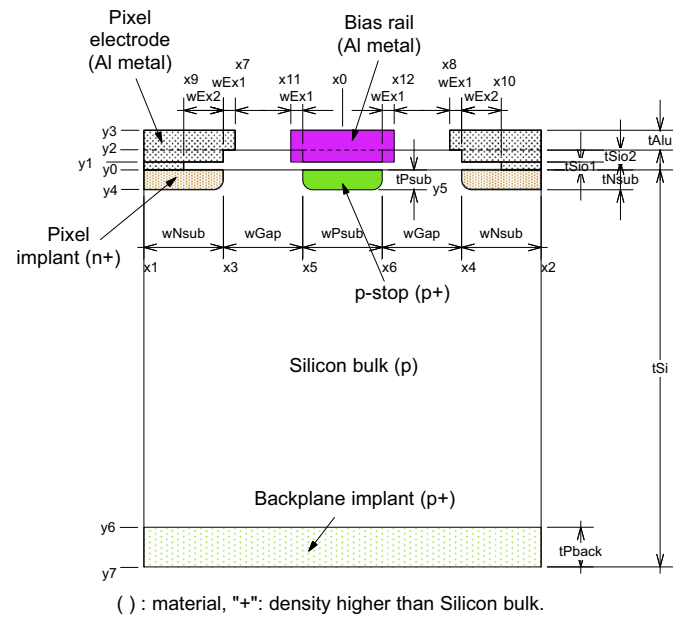

Fig. 5. TCAD 2D geometry of the pixel boundary region with the bias rail.

Table 2
Parameters before and after irradiation in TCAD simulations.

Parameter	Non-irrad.	Irrad.
Fluence (n_{eq}/cm^2)	0	3×10^{15}
Effective space charge concentration (p-type), N_{eff} (cm^{-3})	2.6×10^{12}	2.5×10^{13}
Full depletion voltage, V_{dep} (V)	44	430
Applied bias voltage, V_{op} (V)	100	430
Leakage current, I_{leak} (a.u.)	1	$\sim 10^3$
Surface density of interface charge, Q_f (cm^{-2})	1×10^{10}	1×10^{12}

(a.u: arbitrary unit)

Table 3
Geometry parameters used in TCAD simulations.

Parameter	Value
Silicon thickness (*tSi*)	150 μm
Bulk type	p-type
Pixel: implant type	n-type
Dopant concentration	1×10^{19} cm^{-3}
Implant width, depth (*wNsub*, *tNsub*)	50, 1 μm
Metal electrode	Al, DC-coupled
Overhang (*wEx*1)	2 μm
p-stop: implant type	p-type
Dopant concentration	1×10^{16} cm^{-3}
Implant width (*wPsub*), narrow/wide	4 / 8 μm
Implant depth (*tPsub*=*tNsub*)	1 μm
Gap to Pixel implant (*wGap*), wide/narrow	9.5/6.5 μm
Bias rail: metal, thickness	Al, 1.8 μm
Overhang, wide/narrow (*wEx*1, −2 × *wEx*1)	2/−4 μm
Insulator thickness (*tSio*1)	0.2 μm
Backplane implant, thickness (*tPback*)	p-type, 3 μm
Dopant concentration	1×10^{18} cm^{-3}

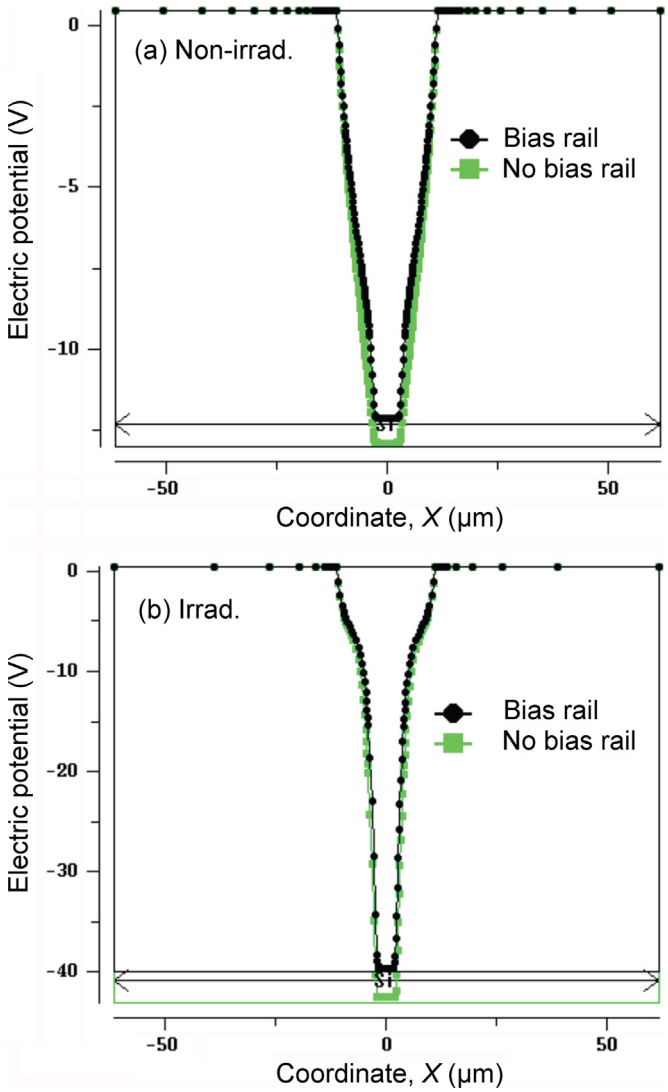

Fig. 6. Electric potential near the surface under the bias rail, with bias rail (black circle) and without bias rail (light-color square): (a) before irradiation (Non-irrad.) and (b) after irradiation (Irrad.).

test the sensor without bump bonding to the ASIC. We use a bias resistor made of polysilicon material to connect the individual pixels to a bias rail common to a row of pixel pairs. The bias rail was made of polysilicon in the design. Addition of a biasing network is a complication in the pixel structure but the quality control of the sensors would save time and cost at later assembly stages.

In the old design, the bias rail runs in the middle of the boundary of a pair of pixels, which is shown horizontally in the figure, and the bias resistors are routed to the pixel implants by encircling outside the pixels. The bias rail runs over the narrow trace of p^+ implant in the surface of silicon, called "p-stop". The p-stop is required to separate the n^+ pixel implants. The bias rail and the p-stop are separated spatially and electrically by the SiO_2 surface passivation. The width of the p-stop was chosen to be narrow according to the analysis of the designs [12]. The width of the bias rail is wider than that of the p-stop to reduce the electric field at the edge of the p-stop.

Efficiency loss was observed for this layout. The loss of efficiency was most pronounced under the bias rails, and was smaller but still noticeable under the bias resistors, compared to the loss at the pixel boundaries in the opposite side where no bias rail exists.

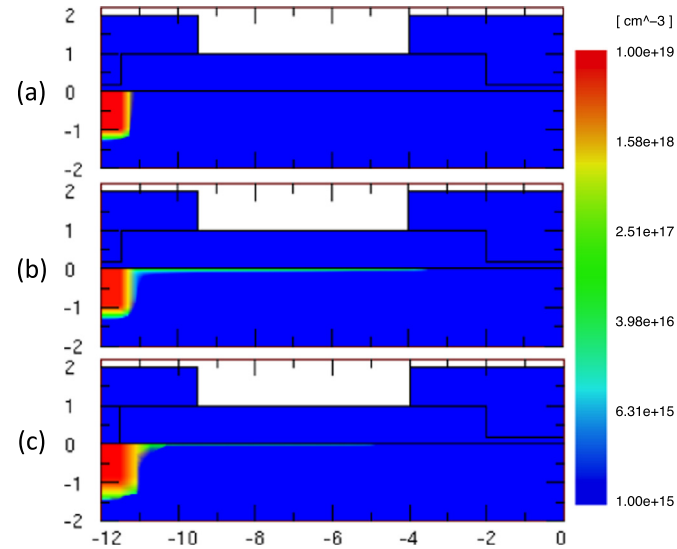

Fig. 7. Electron density in the surface of silicon simulated with TCAD: (a) before irradiation, $Q_f = 1 \times 10^{10}$ cm^{-2}, bias voltage -100 V, (b) the same as (a) but $Q_f = 1 \times 10^{12}$ cm^{-2}, and (c) after irradiation, $Q_f = 1 \times 10^{12}$ cm^{-2}, bias voltage -430 V. The color scale is in the unit of volume density (cm^{-3}). (For interpretation of the references to color in this figure caption, the reader is referred to the web version of this paper.)

In the absence of irradiation, the loss was negligible.

2.2. Optimization of pixel structures – novel design (wafer layout #4)

We have then designed novel pixel structures to optimize the pixel structures to mitigate the problems found for sensors with wafer layout #2. The structures of special interest are shown in Fig. 1, (b) Type 10 and (c) Type 13 in wafer layout #4. The physical mechanisms behind the efficiency loss, especially the difference between before and after irradiation, have been investigated and are presented in Section 4. Phenomenologically, we hypothesized that removal of the bias rails out of the boundary region and the placement of the bias rails and bias resistor traces in the area of and over the pixel implantation to shield them from the silicon underneath will mitigate the efficiency loss. In Type10 (hereafter referred to as "Large offset"), the common bias rail for a pair of rows of pixels is split into individual bias rails per a row of pixels, the bias rails are removed far away from the boundary, and the bias rails and the bias resistors are routed in the area of and over the pixel implantation. In Type13 (hereafter referred to as "Wide p-stop"), the common bias rails are kept at the boundaries, but their width is smaller and the width of the p-stop is wider, which is based on the hypothesis that the p-stop may function as a shield for the bias rail.

The novel pixel structures are laid out in wafer layout #4 as shown in Fig. 2 in two types of sensors: FE-I4 (18.54×20.93 mm^2) with a matrix of 336×80 of 50×250 μm^2 pixels [9] and FE-I3 (10.54×8.53 mm^2) with 160×18 of 50×400 μm^2 pixels [13]. The detailed description of the novel pixel designs is given in Appendix A along with relevant tables and figures. No additional cost is associated with the novel pixel structures in fabrication as the PolySi process has already been included.

Typical parameters of the wafer layout #4 are summarized in Table 1. The thickness of the raw wafers is 320 μm. After the fabrication of the front side, the thin sensors are fabricated by thinning the rear of the wafer to a thickness of 150 μm, followed by an additional process for the rear.

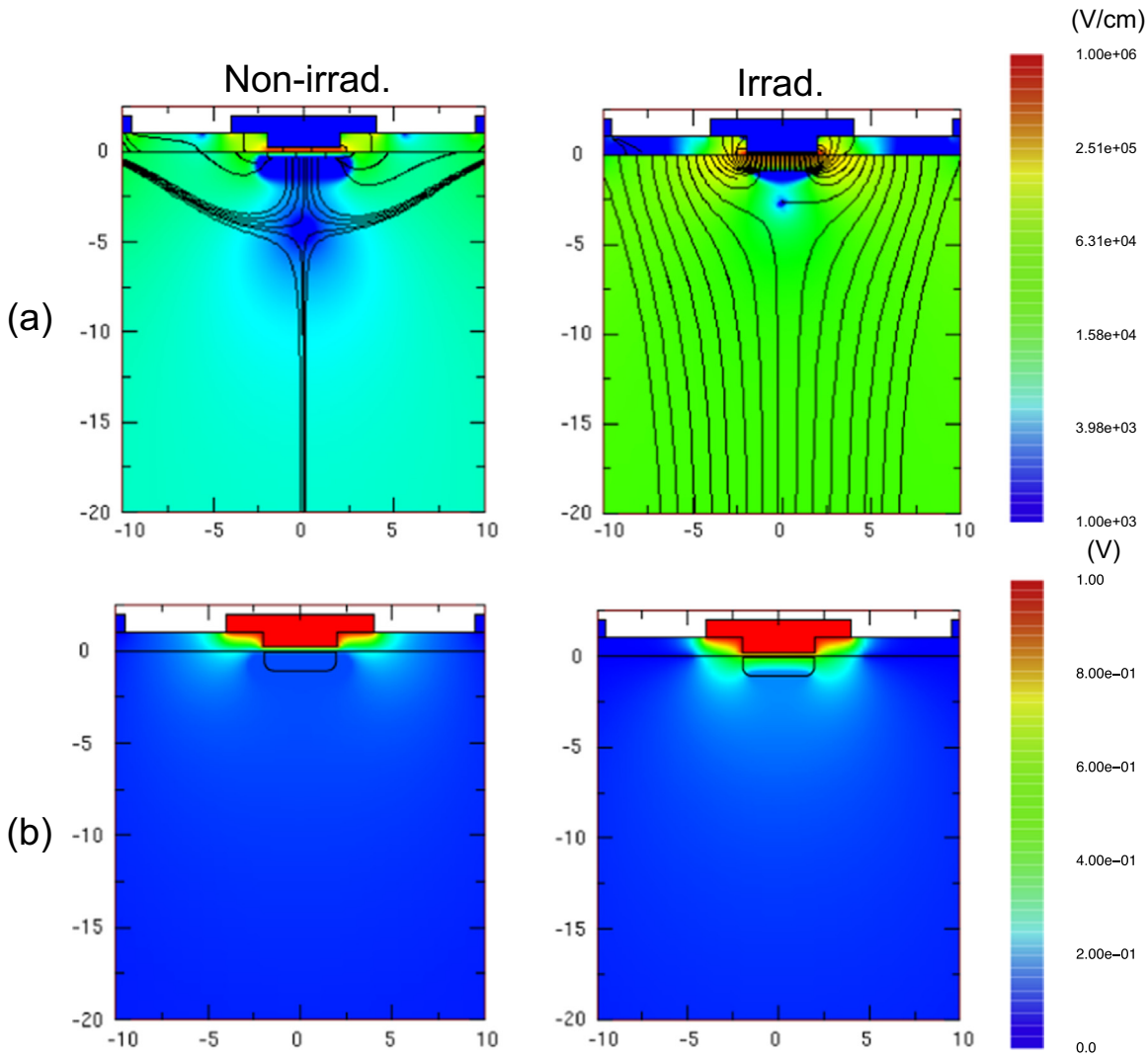

Fig. 8. 2D maps of the fields in the vicinity of bias rail, before and after irradiation in the left and right column, and in the rows of (a) electric field E overlaid with flow lines and (b) weighting potential of the bias rail V_{qA}, respectively.

3. Results with test beams

Pixel sensors with the novel pixel structures were irradiated at a fluence of 3 to 5×10^{15} n_{eq}/cm^2 with 70 MeV protons at CYRIC [14]. The samples were irradiated in an irradiation box attached to an X–Y stage to scan the beam uniformly over the samples. The samples were cooled to -15 °C during the irradiation with the cold nitrogen gas from a liquid nitrogen dewar, and after irradiation stored cold in a freezer. A pixel sensor of the old design was irradiated with γ rays at a dose of 2.4 MGy at TARRI [15]. These irradiated samples were then tested using test beams at DESY with 4 GeV electrons and/or CERN with 120 GeV π's [16,17]. Based on the energy of the beam particles, together with the distance between the telescope planes and the device under test (DUT), the pointing resolution of the beam particles at the DUT plane was approximately 30 and 8 μm at DESY and CERN, respectively.

3.1. Efficiency mapping over pixel boundaries

An example of the improvement of the novel pixel structure is illustrated in Fig. 3, using an efficiency mapping over two pixel regions projected on the long pixel side. The DUT is KEK46 and 150 μm thick with the Type 10 pixel structure, irradiated at 4.18×10^{15} n_{eq}/cm^2 and tested at DESY. The boundary of the bias rail side (Bias rail (hereafter referred to as BR)) is at 125 μm and the opposite side (No bias rail (hereafter referred to as NB)) is at 375 μm. The curves are fit to the data for guidance. The width of the efficiency loss is dominated by the pointing resolution. The efficiency losses in the BR and NB boundaries are nearly symmetric; the effect of the bias rail is nearly eliminated. In the plot, the efficiencies of the central region of the pixels are normalized to unity since the absolute efficiency was not reliable due to a technical issue in this test beam.

3.2. Efficiency loss per pixel – comparison of pixel structures

The efficiency loss at the boundary can be quantified as an "efficiency loss per pixel" by fitting a Gaussian function to the efficiency mapping over the pixel boundaries and dividing the integrated "area" of the Gaussian by the length of two pixels. The calculation of "area" eliminates the difference in the pointing resolutions at DESY and CERN. A compilation of the efficiency loss per pixel at the boundaries is shown in Fig. 4 for the DUT's of KEK84ch1 (150 μm, Type 2, p 3.03×10^{15}), KEK71ch3 (150 μm, Type 12, p 3.08×10^{15}), KEK93 (320 μm, Type 8, γ 2.4 MGy), using the CERN data and KEK49ch3 (150 μm, Type 13, p 3.20×10^{15}) and KEK53ch3 (150 μm, Type 19, p 2.35×10^{15}) using the DESY data. The letters "p" and "g" in the legend

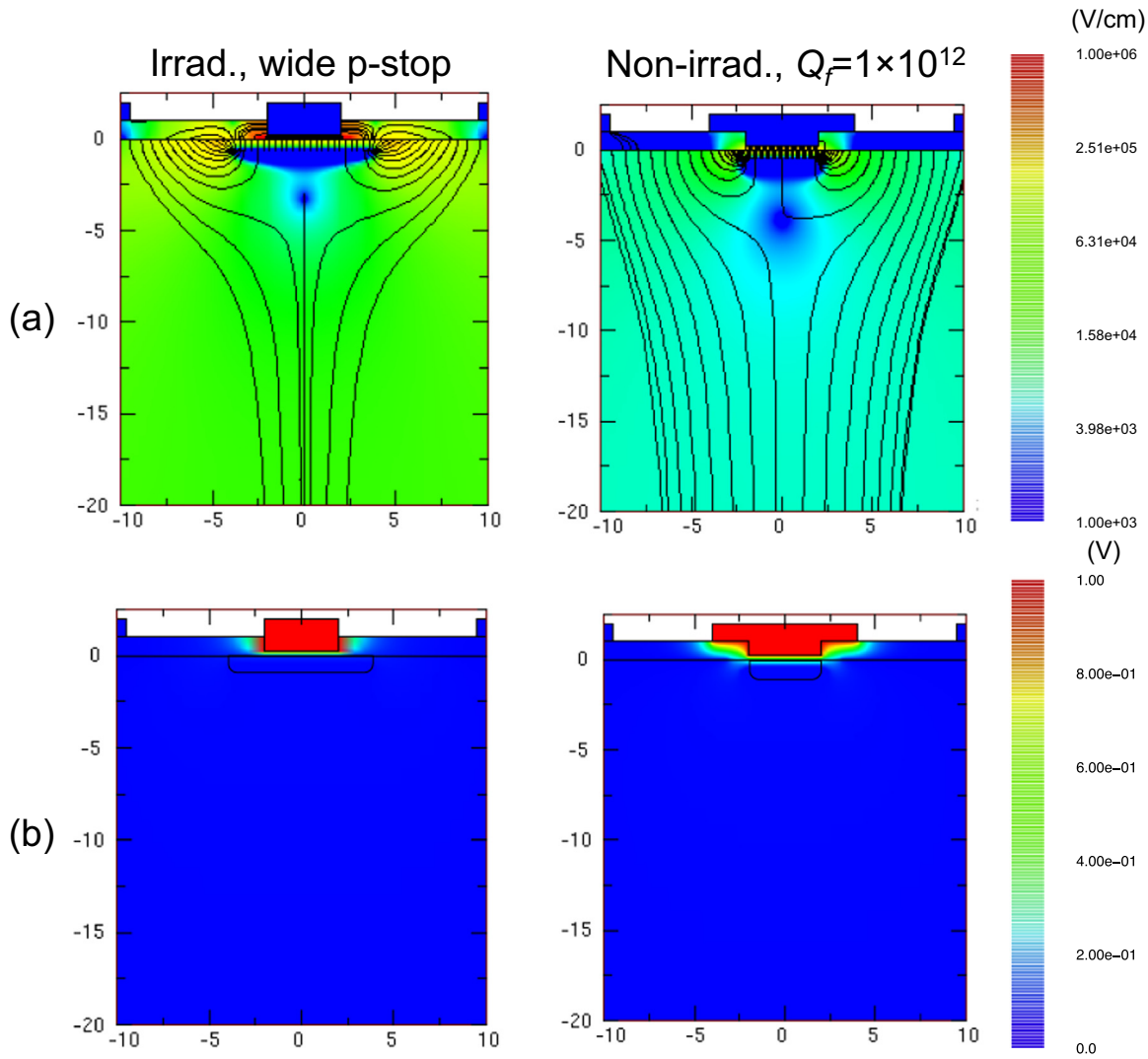

Fig. 9. 2D maps of the fields in the vicinity of bias rail of the wide p-stop geometry after irradiation and the narrow p-stop geometry before irradiation with the interface charge as that after irradiation in the left and right column, and in the rows of (a) electric field E overlaid with flow lines and (b) weighting potential of the bias rail V_{qA}, respectively.

indicate the proton and the γ irradiation, respectively. The efficiency losses at the boundary of the bias rail side or the no bias rail side are indicated with the BR (with solid line) or NB (with dashed line), respectively. The pixel structure of Type 2 is an equivalent of Type 10 but the bias rail is made from an aluminum material. Type 12 is a variation of Type 10 with the bias rails set at the edges of the pixels (hereafter referred to as "Small offset"). Type 8 is an equivalent of the old structure. Type 19 is the reference with no bias structure and represents the best case. The details of the pixel structures are presented in Appendix A.

There is a noticeable difference in bias voltage dependence between the DUT's of the CERN (Types 2 and 12) and DESY data (Types 13 and 19). The difference has been traced to the difference in the bias voltage dependence of the pulse height distribution, most likely due to different tunings of the readout ASICs at different bias voltages. This difference can be removed by normalizing the NB data points by each other because the NB side is basically the same as the no bias structure.

On the basis of Fig. 4, we have evaluated the pixel structure of the bias rail side (BR), finding that

(1) Type 2 (Large offset) is as good as NB (No bias) side, the loss is <0.5% per pixel at the bias voltage >400 V,
(2) Type 12 (Small offset) and Type 13 (Wide p-stop) are similarly good, the loss is approximately 1% at >600 V,
(3) These pixel structures exhibit greatly improved efficiency loss, compared with the ≥3% loss of the "old" design [16], and
(4) γ irradiation has no effect on the efficiency loss under the bias rail.

The result (4) especially indicates that the efficiency loss under the bias rail is not caused by the surface charge in the Si–SiO_2 interface but caused by the radiation damage in the silicon bulk.

4. Understanding the underlying physics

We have used a semiconductor technology CAD (TCAD) program, ENEXSS [18], to calculate the electric fields in detail, including the effect of trapped charges in the interface. The region of the pixel boundary with the bias rail is modeled and implemented as a 2D geometry in the TCAD simulations as shown in Fig. 5. We have approximated the conditions before and after irradiation with three parameters according to the method elaborated in Ref. [19]: effective space charge concentration (N_{eff}) and leakage current (I_{leak}) in the silicon bulk, and fixed interface charge (Q_f) at the

Table 4
Variation of pixel structure of FE-I4 sensors in wafer layout #4.

Type no.	Pixel size (μm^2)	Bump pad	Bias type	PolySi routing	Bias rail	Bias rail offset	p-stop width	Bias rail material	Comment
(1)	50×250	End	PolySi	Inside	1	Large	Narrow	Al	
(2)					2				
(3)					1	Small			
(4)					2				
(5)					1	None	Wide		
(6)				Inside[a]					
(7)				Outside					
(8)							Narrow		Old default
9				Inside	1	Large	Narrow	PolySi	
10					2				New default
11					1	Small			
12					2				
13					1	None	Wide		
14							Narrow		
(15)			PT	–	Straight			Al	
(16)							Wide		
(17)					Zigzag	Small	Narrow		
(18)						Large			
19			None		–	–		–	
(20)	25×500	End	PT	–	Straight	None	Wide	Al	
(21)			PolySi	Inside[b]	1				
22					2	Large	Narrow	PolySi	
(23)		Center	PT	–	Zigzag			Al	
(24)			PolySi	Inside[b]	2	Small			
(25)						Large			
26								PolySi	
27		Staggered			1				
28		End	None	–	–	–		–	

[a] No opening in the DC-Al metal of the pixel implant under the PolySi trace.
[b] PolySi is routed along one side of the perimeter of pixel implant.

Table 5
Variation of pixel structure of FE-I3 sensors in wafer layout #4.

Type no.	Pixel size (μm^2)	Bump pad	Bias type	PolySi routing	Bias rail	Bias rail offset	p-stop width	Bias rail material	FE-I4 sensor equivalent
(1)	50×400	End	PolySi	Inside	2	Large	Narrow	Al	Type(2)
(2)						Small			Type(4)
(3)					1	None	Wide		Type(5)
(4)				Inside[a]					Type(6)
(5)				Outside					Type(7)
(6)							Narrow		Type(8)
7				Inside	2	Large		PolySi	Type10
8						Small			Type12
9					1	None	Wide		Type13
(10)			PT	–	Straight			Al	Type(16)
(11)					Zigzag	Small	Narrow		Type(17)
(12)						Large			Type(18)
13			None		–	–		–	Type19
(14)	25×800	End	PT	–	Straight	None	Wide	Al	Type(20)
(15)			PolySi	Inside[b]	1				Type(21)
16					2	Large	Narrow	PolySi	Type22
(17)		Center	PT	–	Zigzag	Large		Al	Type(23)
(18)			PolySi	Inside[b]	2	Small			Type(24)
19		Staggered			1	Large		PolySi	Type27
20		End	None	–	–	–		–	Type28

[a] No opening in the DC-Al metal of the pixel implant under the PolySi trace.
[b] PolySi is routed along one side of the perimeter of pixel implant.

boundary between the silicon bulk and the surface SiO_2. After irradiation, space charge concentration, leakage current, and fixed interface charge are taken to be increased by one order, three orders, and two orders of magnitude, respectively, caused by displacement and ionization damages. The parameters before and after irradiation are summarized in Table 2, in columns of "Non-irrad." and "Irrad.", respectively (hereafter referred to as Non-irrad. and Irrad.). The values of the geometry parameters are summarized in Table 3.

4.1. Effect of electric potential of the bias rail

In the DUTs with polysilicon bias resistors, the pixel electrode is connected to the bias rail through the polysilicon resistor. The pixel electrode is connected to the virtual ground of ASIC and thus the bias rail is at the ground potential. We used TCAD simulations to determine the electric field in the boundary region near the surface of the silicon (1 μm below the surface of silicon in the TCAD geometry) with and without the bias rail. The electric

potentials before and after irradiation are shown in Fig. 6(a) and (b) for the narrow p-stop geometry (widths of bias rail and p-stop being 8 and 4 μm), with the Non-irrad. (bias voltage of −100 V) and the Irrad. (−430 V) conditions, respectively. The data obtained with and without the bias rail are shown by filled circles and squares, respectively. The existence of the ground potential induced a difference of approximately 1 V over the electric potential of 16 V before irradiation and of 2 V over 42 V after irradiation at the location of the bias rail. The differences are small and the fractions to the total potential are similar before and after irradiation. The difference of the interface charge before and after irradiation generates a subtle difference in the shape of the electric potential between the p-stop and the pixel electrode, but only slightly influences the values of the potentials with and without the bias rail. The existence or non-existence of the ground potential does not appear to be the source of efficiency loss at the boundary.

4.2. Charge induced on the bias rail

A moving charge in the presence of any number of electrodes kept at constant voltages induces a mirror charge on the electrodes according to Ramo's theorem:

$$Q_A = q \cdot V_{qA}, \tag{1}$$

where Q_A is the charge induced on an electrode A, q is the charge at a given position, and V_{qA} is the "weighting potential" of the electrode A at the position of the charge q. In a finite time, with a fast readout electronics, instantaneous induced current i_A is represented by the gradient of V_{qA} along the direction of motion multiplied by the drift velocity:

$$i_A = q \cdot \frac{dV_{qA}}{dt} = q \cdot \left(\frac{\partial V_{qA}}{\partial x}\frac{dx}{dt}\right) = q \cdot \vec{v} \cdot \overrightarrow{\frac{\partial V_{qA}}{\partial x}} = q \cdot \mu \vec{E} \cdot \overrightarrow{\frac{\partial V_{qA}}{\partial x}}, \tag{2}$$

where μ is the charge carrier mobility and E is the electric field. Although the current has to be integrated to evaluate the charge, an insight into the physics can be obtained qualitatively and visually from the maps of the electric field E, the flow lines of the electric field representing the drifting paths of the charge carriers, and the weighting potential V_{qA}.

Since the drifting carriers do not terminate on the bias rail, the current induced on the bias rail is bipolar. The collection time of charge carriers (electrons in n^+ electrode) is in the order of 10 ns. Since we use a fast-shaping amplifier (peaking time of approximately 20 ns), the early part of the bipolar signal will result in a finite amount of charges induced on the bias rail. Thus, it is natural to expect that charge will be lost to the bias rail, causing efficiency loss. However, it is unclear why we observe efficiency loss only after irradiation and not prior to it.

4.3. Visualization of the fields and predictions by TCAD

The weighting potential is independent of the space charge distribution and actual voltages, however, it depends on the geometry of the electrodes and the resulting electric field. In a semiconductor device the actual shape of the electrode is bias dependent due to the change in depletion volume, for instance. In the p-type device the effective extent of the n^+ electrode is bias dependent due to the existence of inversion layer in the n-side surface of silicon. The radiation damage by charged particles on the surface of device leaves positive fixed charge at the interface of Si–SiO_2. The inversion layer is created by the electric potential of the positive fixed charges that repels the holes from the silicon surface. The potential of the fixed interface charge is partially compensated by the potential at the surface of silicon generated by the bias voltage (see Fig. 6), thus the extent of the inversion layer is bias dependent.

Using the geometry setup and the conditions described above, we extract two-dimensional maps of fields. The inversion layer is indeed simulated in the TCAD as shown as the electron density in the surface of silicon in Fig. 7, (a) before irradiation (with Non-irrad. condition: $Q_f = 1 \times 10^{10}$ cm^{-2}, bias voltage −100 V), (b) as same as (a) but $Q_f = 1 \times 10^{12}$ cm^{-2}, and (c) after irradiation (with Irrad. condition: $Q_f = 1 \times 10^{12}$ cm^{-2}, bias voltage −430 V). There is little inversion layer before irradiation due to the low density of the interface charge. The inversion layer is visible with the interface charge density after irradiation; extends from the n^+ electrode toward the p-stop (edge at −2 μm) approximately to −3 and −5 μm with the bias voltage of −100 V and −430 V, respectively. Visual thickness of the layers in the plots should be due to the resolution of the calculation and plotting.

The weighting potential of the electrode of interest is calculated from the difference of the two maps of the electric potential: the map with the setup and that obtained by adding 1 V to the electrode of interest over the setup. The remnant is the potential where the selected electrode at unit potential, all other electrodes at zero potential. The extracted fields are shown in Fig. 8 for the narrow p-stop geometry in the rows of (a) electric field E overlaid with flow lines of the field and (b) weighting potential of the bias rail V_{qA}, in the columns of before (Non-irrad., −100 V) and after irradiation (Irrad., −430 V), respectively.

Examination of Fig. 8 shows that there are several distinctive differences between the fields before and after irradiation. Prior to irradiation, the electric field shows a large blob of low electric field region under the bias rail/p-stop, the flow lines of the electric field, i.e., the path of drifting carriers are deflected from the low electric field region toward the pixel electrodes distinctly, and the intensity of the weighing potential of the bias rail is not extending in the area and vicinity of the low electric field region. The area of low electric field region appears to function as a shield against the drift paths and the weighting potential. After irradiation, the blob of low electric field region under the bias rail becomes minute, the flow lines are not deflected very much, and the intensity of the weighting potential extends more near to the bias rail and more toward the backplane. The shrinkage of the blob is caused by the strong electric field generated by the large bias voltage applied to cope with the space charge (N_{eff}) increased by the radiation damage in the silicon bulk. The extent of the inversion layer shields the weighting potential to remain in the vicinity of the bias rail.

The charge induced on the bias rail is determined by the interplay of the weighting potential and the path of drifting carriers. By overlaying the flow lines over the weighting potentials, we observe that before irradiation the drifting carriers from most of the bulk do not pass high intensity region of the weighting potential, but after irradiation drifting carriers especially from the bulk under the bias rail pass through. On the basis of the visualization, we conclude that the charge induced on the bias rail is small (almost zero) before irradiation but finite after irradiation.

The TCAD simulations have also predicted only a slight efficiency loss in the pixel structure with the wide p-stop geometry (widths of bias rail and p-stop being 4 and 8 μm) after irradiation, and in the old pixel structure after γ irradiation. Fig. 9 shows in the rows of (a) electric field overlaid with flow lines and (b) weighting potential, in the columns of the cases of wide p-stop geometry after irradiation (Irrad., wide p-stop) and of narrow p-stop geometry before irradiation but with the interface charge as that after irradiation (Non-irrad., $Q_f = 1 \times 10^{12}$ cm^{-2}), respectively. The latter scenario corresponds to the case of γ irradiation. In both cases, the weighting potentials are very low and uniform over a wide region including under the bias rail/p-stop region. The low electric field

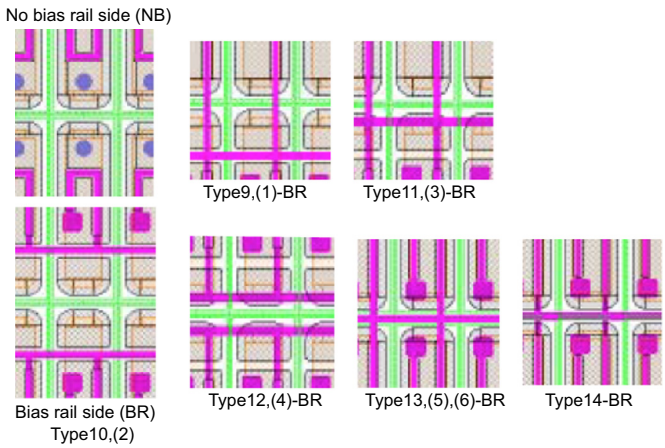

Fig. 10. Pixel structures in wafer layout #4 of Types 1–6 and 9–14 with variations of number of bias rails and their locations. Bias rail is made of polysilicon (Types 9–14) or aluminum (Types 1–6).

region under the p-stop and the extent of the inversion layer are nearly overlapping, thus seem to shield the weighting potential against extending into the silicon bulk. The γ irradiation study was motivated by the TCAD prediction.

5. Summary

We have developed n^+-in-p pixel sensors, using planar process in p-type 6-inch silicon wafers to obtain highly radiation tolerant sensors for extremely high radiation environments such those found in HL-LHC. We have designed novel pixel structures – wafer layout #4 – to eliminate the efficiency loss at the pixel boundary observed in the old pixel structure of the wafer layout #2, especially after irradiation. The new pixel sensors were irradiated with protons at a fluence of approximately 3×10^{15} n_{eq}/cm^2 at CYRIC or with γ rays at a dose of 2.4 MGy at TARRI, and evaluated with test beams at CERN and DESY.

- Among the novel pixel structures tested, the best pixel structure to retain high efficiency after irradiation is the one with "Large offset" where the bias rails removed far away from the boundary and the polysilicon biasing resistor routed inside the pixel implant region, achieving an efficiency loss of <0.5% per pixel at the boundary, as efficient as that without the bias rail.
- If offsetting the bias rail were not applicable, the one with "Wide p-stop" geometry could be an alternate solution, achieving a loss of approximately 1% per pixel at the boundary.

We have also obtained an understanding of the physics underlying the efficiency loss under the bias rail with TCAD simulations, by simulating the electric fields, especially the weighting potential of the bias rail.

- The efficiency loss is due to the loss of charge induced on the bias rail.
- The difference of the charge induced on the bias rail before and after irradiation is caused by the difference of the region of low electric field under the bias rail together with the extent of the inversion layer in the surface of silicon.
- Before irradiation, a large blob of low electric field region under the bias rail makes the weighting potential very low in the area and vicinity, deflects drifting carries out of high intensity region of the weighting potential.
- After irradiation, the blob becomes minute due to strong electric field in the radiation-damaged silicon, which together with the extent of the inversion layer makes the weighting potential to extend more into the silicon under the bias rail, makes drifting carriers especially from the region under the bias rail to pass through high intensity region of the weighting potential.
- The TCAD simulations have also shown that wide p-stop and large Si–SiO_2 interface charge (inversion layer, specifically) act to shield the weighting potential against extending into the silicon bulk. The pixel sensor with old pixel structures irradiated with γ rays has confirmed little efficiency loss at the boundary.

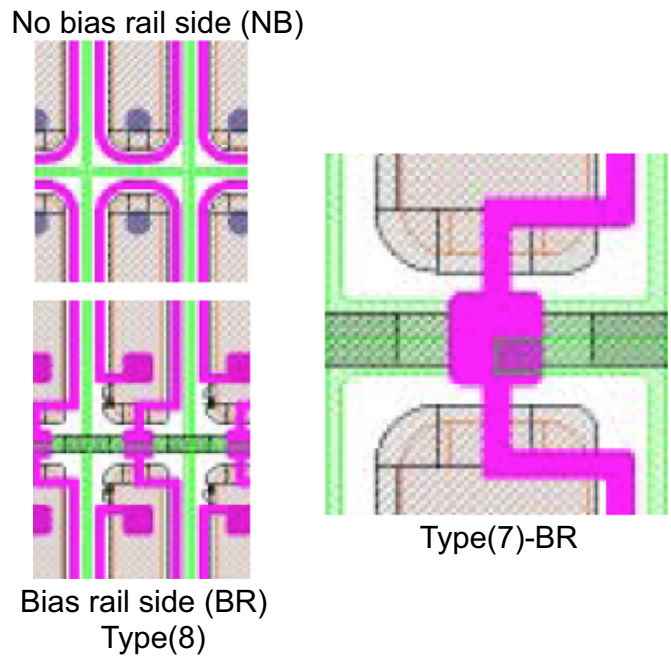

Fig. 11. Pixel structures in wafer layout #4: Type 8 with polysilicon bias resistor routing outside the pixel implant with the width of p-stop narrower than the width of bias rail (narrow p-stop, old design), and Type 7 with wide p-stop.

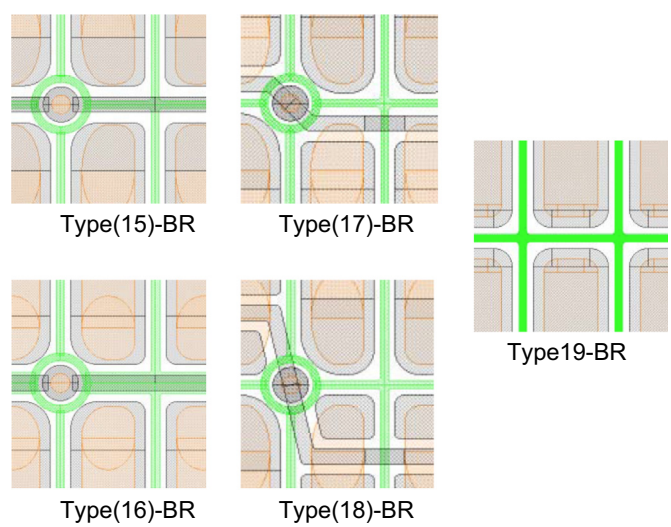

Fig. 12. Pixel structures of punch-through (PT) bias resistor in wafer layout #4: Types 15 and 16 with narrow and wide p-stop, and 17 and 18 with small and large offset of bias rails, respectively. Type 19 is without a biasing structure.

Acknowledgments

The irradiations were performed, with protons at Cyclotron and

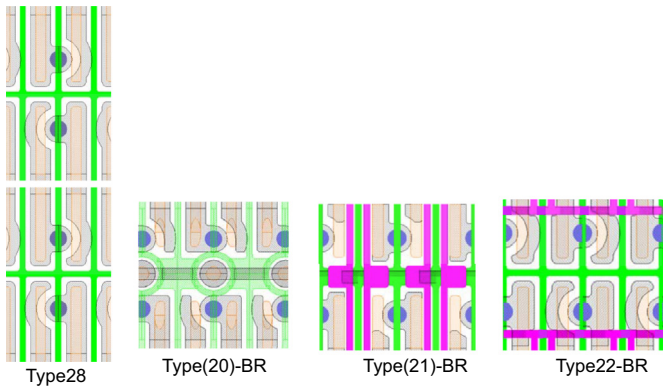

Fig. 13. Pixel structures of the 25 × 500 μm^2 pixel size with the bump bonding pads at the end of the pixels in wafer layout #4: Type 28 without a biasing structure, 20 with PT biasing and wide p-stop, 21 with PolySi biasing and wide p-stop, and 22 with PolySi biasing and large offset of bias rails.

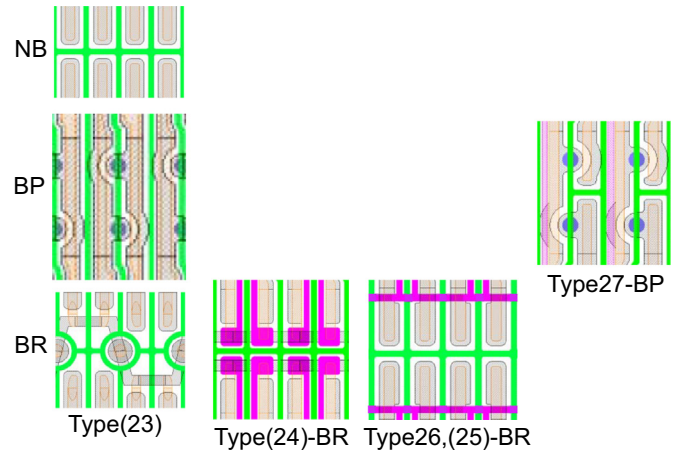

Fig. 14. Pixel structures of the 25 × 500 μm^2 pixel size with the bump bonding pads at the central region of the pixels or at staggered pixels in wafer layout #4: Type 23 with PT biasing and small offset of zigzag bias rail, 24 with PolySi biasing and small offset of bias rails, 26 and 25 with PolySi biasing and large offset of bias rails, and 27 with PolySi biasing with half-pitch (250 μm) staggered pixels.

Radioisotope Center (CYRIC), Tohoku University, with Y. Sakemi, M. Ito, and T. Wakui, and with γ at Takasaki Advanced Radiation Research Institute, Japan Atomic Energy Agency. The research was supported and financed in part by the Japan Society for Promoting Science KAKENHI-A Grant number 20244038 and KAKENHI-C Grant number 20540291, the Ministry of Education, Culture, Sports, Science and Technology – Japan, KAKENHI for Research on Priority Area Grant number 20025007 and for Scientific Research on Innovative Areas Grant number 23104002.

Appendix A. Pixel structures in wafer layout #4

In the wafer layout #4 (Fig. 2), we have designed several variations of the structures to investigate and evaluate the novel pixel structures in FE-I4 and FE-I3 pixel sensors. The characteristics of 28 variations in the FE-I4 pixel sensors and 20 in that of the FE-I3 pixel sensors are summarized in Tables 4 and 5, respectively. The material of the bias rail is either polysilicon (referred to as "PolySi") or aluminum (referred to as "Al"). The pixel structure with the Al bias rail is symbolized with the type number in parenthesis. The detailed views of the pixel structures are shown in Figs. 10–14. The pixel structures of bias rail side and no bias rail side are labelled with BR and NB, respectively.

A.1. FE-I4 sensors

The 19 variations from Types 1 to 19 are fabricated using a pixel size of 50 × 250 μm^2 (column "Pixel size" in the tables, Figs. 10–12). The 9 variations from Types 20 to 28 are fabricated with a pixel size of 25 × 500 μm^2, mating to the same grid of the bump pads of the FE-I4 readout ASIC, splitting the 50 μm of short pixel direction into two 25 μm pixels and merging two pixels to 500-μm-long pixels in the long pixel direction to study a finer pitch of the pixels (Figs. 13 and 14).

In the 50 × 250 μm^2 pixels, the location of the bump pads (column "Bump pad") is always at the end of pixel electrodes (referred to as "End", e.g. Fig. 10) in the NB side for Types 1–19. In the 25 × 500 μm^2 pixels, the locations of the bump pads are, (1) at the end of pixel electrodes for Type 20, etc. (Fig. 13), (2) at the center of pixel electrodes (referred to as "Center" in the tables, BP in Fig. 14) for Type 23, etc., or (3) at the center and the end alternately (referred to as "Staggered") for Type 27 (Fig. 14) to make the pixel electrodes to be staggered by half pitch in the long pixel direction. The staggered pixel layout is used to evaluate improvements in position resolution in the long pixel direction because more two-cluster hits are expected in the 25 μm pixels than in the 50 μm pixels.

The bias resistor is either formed with a resistive trace of polysilicon material, approximately 5 kΩ/μm (column "Bias type", referred to as "PolySi") or a punch-through structure with a narrow gap, approximately 18 μm between a bias dot (n^+ implant) and the pixel electrodes (n^+ implant) (referred to as "PT"). The PolySi resistor is routed (column "PolySi routing") to place the trace either "inside" the area of pixel electrode (Fig. 10) to mitigate the efficiency loss under the trace or "outside" the pixel area for Types 7 and 8 (Fig. 11) as a reference to the old design.

One approach for the removal of the bias rail out of the boundary region is to use two bias rails for a pair of pixel rows (column "Bias rail"), placing them in the pixel area largely away from the boundary (referred to as "Large offset", column "Bias rail offset", e.g. Fig. 10 Type 10) or just over the edge of the pixel electrode (referred to as "Small offset", Fig. 10 Type 12). The other is to keep one bias rail at the boundary (referred to as "None") but to increase the width of the p-stop under the bias rail while keeping the width of the bias rail narrow (referred to as "Wide", column "p-stop width", Fig. 10 Type 13), otherwise narrow (referred to as "Narrow", Fig. 10 Type 14).

In the case of PT structures, one PT dot is shared by four pixels in a pair of pixel rows to which one bias rail is placed [20]. The bias rail is either straight (referred to as "Straight", column "Bias rail") with the wide p-stop under the bias rail ("Wide", column "p-stop width") or zigzags ("Zigzag", column "Bias rail") by passing through the bias dot and then being largely removed away from the boundary region ("Large offset", column "Bias rail offset") or just over the edge of the pixel electrode ("Small offset", Fig. 12).

The material of the bias rail is listed in the column "Bias rail material". Historically, Al has been used. The resistance of the biasing network is a source of electrical noise (parallel noise). Larger resistance gives smaller noise, leading to our preference to "PolySi".

The similar structures of PolySi and PT are implemented in the 25 × 500 μm^2 pixels (Types 20–28, Figs. 13 and 14). The pixel structure without the biasing network ("None", column "Bias type") is used as the reference due to it showing the best performance (Type 19, Fig. 12 for the 50 × 250 μm^2 and Type 28, Fig. 13 for the 25 × 500 μm^{2}pixels).

A.2. FE-I3 sensors

The characteristics of the variations in the FE-I3 pixel sensors

are summarized in Table 5. The pixel structures are limited to 20 variations due to the available space in the wafer layout. The 13 variations from Type 1 to 13 used $50 \times 400\ \mu m^2$ pixels. The 7 variations from Type 14 to 20 used $25 \times 800\ \mu m^2$ pixels. The basic structures are copied from the FE-I4 pixel structures. The pixel structures equivalent to the FE-I4 sensors are listed in the "FE-I4 sensor equivalent" column in Table 5.

References

[1] S. Terada, et al., Nucl. Instrum. Methods Phys. Res. Sect. A 383 (1996) 159–165.
[2] Y. Unno, et al., Nucl. Instrum. Methods Phys. Res. Sect. A 699 (2013) 72–77.
[3] Y. Unno, et al., Nucl. Instrum. Methods Phys. Res. Sect. A 765 (2014) 80–90.
[4] K.A. Olive et al. (Particle Data Group), Chin. Phys. C 38 (2014) 090001, page 395, High Energy Collider Parameters, column of LHC.
[5] 〈http://hilumilhc.web.cern.ch/HiLumiLHC/index.html〉(accessed on December 2015).
[6] ATLAS Collaboration, J. Instrum. 3 (2008) S08003.
[7] ATLAS Collaboration, Letter of Intent for the Phase-II Upgrade of the ATLAS Experiment, CERN-LHCC-2012-022; LHCC-I-023.
[8] S. Baranov, et al., Atlas Radiation Background Task Force Summary Document, ATL-GEN-2005-001.
[9] M. Garcia-Sciveres, et al., Nucl. Instrum. Methods Phys. Res. Sect. A 636 (Suppl.) (2011) S155–S159.
[10] Irradiation Center Karlsruhe, Karlsruhe Institutes of Technology (KIT), Hermann-von-Helmholtz-Platz 1, Building 401, D-76344 Eggenstein-Leopoldshafen, Germany.
[11] K. Motohashi, et al., Nucl. Instrum. Methods Phys. Res. Sect. A 765 (2014) 125–129.
[12] Y. Unno, et al., in: Proceedings of Science, Vertex 2011, p. 024.
[13] I. Peric, et al., Nucl. Instrum. Methods Phys. Res. A 565 (2006) 178–187.
[14] Cyclotron and Radio Isotope Center (CYRIC), Tohoku University, Aoba 6-3, Aoba-ku, Sendai-shi, Miyagi-ken 980-8578, Japan.
[15] Takasaki Advanced Radiation Research Institute (TARRI), Japan Atomic Energy Agency, 1233 Watanuki-cho, Takasaki-shi, Gunma-ken 370-1292.
[16] K. Nakamura, et al., J. Instrum. 10 (2015) C06008.
[17] K. Kimura, et al., Test-beam evaluation of newly developed n^+-in-p planar pixel sensors aiming for use in very high radiation environment, in these proceedings, http://dx.doi.org/10.1016/j.nima.2016.04.004.
[18] Hyper Environment for Exploration of Semiconductor Simulation (ENEXSS), developed by a consortium, Semiconductor Leading Edge Technologies, Inc. (SELETE), 2006/4–2011/3.
[19] Y. Unno, et al., Nucl. Instrum. Methods Phys. Res. Sect. A 731 (2013) 183–188.
[20] Y. Unno, et al., Nucl. Instrum. Methods Phys. Res. Sect. A 650 (2011) 129–135.

Combined Measurement of the Higgs Boson Mass in pp Collisions at $\sqrt{s} = 7$ and 8 TeV with the ATLAS and CMS Experiments

G. Aad *et al.*[*]

(ATLAS Collaboration)[†]
(CMS Collaboration)[‡]

(Received 25 March 2015; published 14 May 2015)

A measurement of the Higgs boson mass is presented based on the combined data samples of the ATLAS and CMS experiments at the CERN LHC in the $H \to \gamma\gamma$ and $H \to ZZ \to 4\ell$ decay channels. The results are obtained from a simultaneous fit to the reconstructed invariant mass peaks in the two channels and for the two experiments. The measured masses from the individual channels and the two experiments are found to be consistent among themselves. The combined measured mass of the Higgs boson is $m_H = 125.09 \pm 0.21\,(\mathrm{stat}) \pm 0.11\,(\mathrm{syst})$ GeV.

DOI: 10.1103/PhysRevLett.114.191803 PACS numbers: 14.80.Bn, 13.85.Qk

The study of the mechanism of electroweak symmetry breaking is one of the principal goals of the CERN LHC program. In the standard model (SM), this symmetry breaking is achieved through the introduction of a complex doublet scalar field, leading to the prediction of the Higgs boson H [1–6], whose mass m_H is, however, not predicted by the theory. In 2012, the ATLAS and CMS Collaborations at the LHC announced the discovery of a particle with Higgs-boson-like properties and a mass of about 125 GeV [7–9]. The discovery was based primarily on mass peaks observed in the $\gamma\gamma$ and $ZZ \to \ell^+\ell^-\ell'^+\ell'^-$ (denoted $H \to ZZ \to 4\ell$ for simplicity) decay channels, where one or both of the Z bosons can be off shell and where ℓ and ℓ' denote an electron or muon. With m_H known, all properties of the SM Higgs boson, such as its production cross section and partial decay widths, can be predicted. Increasingly precise measurements [10–13] have established that all observed properties of the new particle, including its spin, parity, and coupling strengths to SM particles are consistent within the uncertainties with those expected for the SM Higgs boson.

The ATLAS and CMS Collaborations have independently measured m_H using the samples of proton-proton collision data collected in 2011 and 2012, commonly referred to as LHC Run 1. The analyzed samples correspond to approximately 5 fb^{-1} of integrated luminosity at $\sqrt{s} = 7$ TeV, and 20 fb^{-1} at $\sqrt{s} = 8$ TeV, for each experiment. Combined results in the context of the separate experiments, as well as those in the individual channels, are presented in Refs. [12,14–16].

This Letter describes a combination of the Run 1 data from the two experiments, leading to improved precision for m_H. Besides its intrinsic importance as a fundamental parameter, improved knowledge of m_H yields more precise predictions for the other Higgs boson properties. Furthermore, the combined mass measurement provides a first step towards combinations of other quantities, such as the couplings. In the SM, m_H is related to the values of the masses of the W boson and top quark through loop-induced effects. Taking into account other measured SM quantities, the comparison of the measurements of the Higgs boson, W boson, and top quark masses can be used to directly test the consistency of the SM [17] and thus to search for evidence of physics beyond the SM.

The combination is performed using only the $H \to \gamma\gamma$ and $H \to ZZ \to 4\ell$ decay channels, because these two channels offer the best mass resolution. Interference between the Higgs boson signal and the continuum background is expected to produce a downward shift of the signal peak relative to the true value of m_H. The overall effect in the $H \to \gamma\gamma$ channel [18–20] is expected to be a few tens of MeV for a Higgs boson with a width near the SM value, which is small compared to the current precision. The effect in the $H \to ZZ \to 4\ell$ channel is expected to be much smaller [21]. The effects of the interference on the mass spectra are neglected in this Letter.

The ATLAS and CMS detectors [22,23] are designed to precisely reconstruct charged leptons, photons, hadronic jets, and the imbalance of momentum transverse to the direction of the beams. The two detectors are based on different technologies requiring different reconstruction and calibration methods. Consequently, they are subject to different sources of systematic uncertainty.

The $H \to \gamma\gamma$ channel is characterized by a narrow resonant signal peak containing several hundred events per experiment above a large falling continuum background. The overall signal-to-background ratio is a few

[*]Full author list given at the end of the article.

Published by the American Physical Society under the terms of the Creative Commons Attribution 3.0 License. Further distribution of this work must maintain attribution to the author(s) and the published article's title, journal citation, and DOI.

 © 2015 CERN, for the ATLAS and CMS Collab.

percent. Both experiments divide the $H \to \gamma\gamma$ events into different categories depending on the signal purity and mass resolution, as a means to improve sensitivity. While CMS uses the same analysis procedure for the measurement of the Higgs boson mass and couplings [15], ATLAS implements separate analyses for the couplings [24] and for the mass [14]; the latter analysis classifies events in a manner that reduces the expected systematic uncertainties in m_H.

The $H \to ZZ \to 4\ell$ channel yields only a few tens of signal events per experiment, but has very little background, resulting in a signal-to-background ratio larger than 1. The events are analyzed separately depending on the flavor of the lepton pairs. To extract m_H, ATLAS employs a two-dimensional (2D) fit to the distribution of the four-lepton mass and a kinematic discriminant introduced to reject the main background, which arises from ZZ continuum production. The CMS procedure is based on a three-dimensional fit, utilizing the four-lepton mass distribution, a kinematic discriminant, and the estimated event-by-event uncertainty in the four-lepton mass. Both analyses are optimized for the mass measurement and neither attempts to distinguish between different Higgs boson production mechanisms.

There are only minor differences in the parametrizations used for the present combination compared to those used for the combination of the two channels by the individual experiments. These differences have almost no effect on the results.

The measurement of m_H, along with its uncertainty, is based on the maximization of profile-likelihood ratios $\Lambda(\boldsymbol{\alpha})$ in the asymptotic regime [25,26]:

$$\Lambda(\boldsymbol{\alpha}) = \frac{L(\boldsymbol{\alpha}, \hat{\hat{\boldsymbol{\theta}}}(\boldsymbol{\alpha}))}{L(\hat{\boldsymbol{\alpha}}, \hat{\boldsymbol{\theta}})}, \tag{1}$$

where L represents the likelihood function, $\boldsymbol{\alpha}$ the parameters of interest, and $\boldsymbol{\theta}$ the nuisance parameters. There are three types of nuisance parameters: those corresponding to systematic uncertainties, the fitted parameters of the background models, and any unconstrained signal model parameters not relevant to the particular hypothesis under test. Systematic uncertainties are discussed below. The other two types of nuisance parameters are incorporated into the statistical uncertainty. The $\boldsymbol{\theta}$ terms are profiled, i.e., for each possible value of a parameter of interest (e.g., m_H), all nuisance parameters are refitted to maximize L. The $\hat{\boldsymbol{\alpha}}$ and $\hat{\boldsymbol{\theta}}$ terms denote the unconditional maximum likelihood estimates of the best-fit values for the parameters, while $\hat{\hat{\boldsymbol{\theta}}}(\boldsymbol{\alpha})$ is the conditional maximum likelihood estimate for given parameter values $\boldsymbol{\alpha}$.

The likelihood functions L are constructed using signal and background probability density functions (PDFs) that depend on the discriminating variables: for the $H \to \gamma\gamma$ channel, the diphoton mass, and, for the $H \to ZZ \to 4\ell$ channel, the four-lepton mass (for CMS, also its uncertainty) and the kinematic discriminant. The signal PDFs are derived from samples of Monte Carlo (MC) simulated events. For the $H \to ZZ \to 4\ell$ channel, the background PDFs are determined using a combination of simulation and data control regions. For the $H \to \gamma\gamma$ channel, the background PDFs are obtained directly from the fit to the data. The profile-likelihood fits to the data are performed as a function of m_H and the signal-strength scale factors defined below. The fitting framework is implemented independently by ATLAS and CMS, using the ROOFIT [27], ROOSTATS [28], and HISTFACTORY [29] data modeling and handling packages.

Despite the current agreement between the measured Higgs boson properties and the SM predictions, it is pertinent to perform a mass measurement that is as independent as possible of SM assumptions. For this purpose, three signal-strength scale factors are introduced and profiled in the fit, thus reducing the dependence of the results on assumptions about the Higgs boson couplings and about the variation of the production cross section (σ) times branching fraction (BF) with the mass. The signal strengths are defined as $\mu = (\sigma_{\rm expt} \times {\rm BF}_{\rm expt})/(\sigma_{\rm SM} \times {\rm BF}_{\rm SM})$, representing the ratio of the cross section times branching fraction in the experiment to the corresponding SM expectation for the different production and decay modes. Two factors, $\mu^{\gamma\gamma}_{ggF+t\bar{t}H}$ and $\mu^{\gamma\gamma}_{{\rm VBF}+VH}$, are used to scale the signal strength in the $H \to \gamma\gamma$ channel. The production processes involving Higgs boson couplings to fermions, namely gluon fusion (ggF) and associated production with a top quark-antiquark pair ($t\bar{t}H$), are scaled with the $\mu^{\gamma\gamma}_{ggF+t\bar{t}H}$ factor. The production processes involving couplings to vector bosons, namely vector boson fusion (VBF) and associated production with a vector boson (VH), are scaled with the $\mu^{\gamma\gamma}_{{\rm VBF}+VH}$ factor. The third factor $\mu^{4\ell}$ is used to scale the signal strength in the $H \to ZZ \to 4\ell$ channel. Only a single signal-strength parameter is used for $H \to ZZ \to 4\ell$ events because the m_H measurement in this case is found to exhibit almost no sensitivity to the different production mechanisms.

The procedure based on the two scale factors $\mu^{\gamma\gamma}_{ggF+t\bar{t}H}$ and $\mu^{\gamma\gamma}_{{\rm VBF}+VH}$ for the $H \to \gamma\gamma$ channel was previously employed by CMS [15] but not by ATLAS. Instead, ATLAS relied on a single $H \to \gamma\gamma$ signal-strength scale factor. The additional degree of freedom introduced by ATLAS for the present study results in a shift of about 40 MeV in the ATLAS $H \to \gamma\gamma$ result, leading to a shift of 20 MeV in the ATLAS combined mass measurement.

The individual signal strengths $\mu^{\gamma\gamma}_{ggF+t\bar{t}H}$, $\mu^{\gamma\gamma}_{{\rm VBF}+VH}$, and $\mu^{4\ell}$ are assumed to be the same for ATLAS and CMS, and are profiled in the combined fit for m_H. The corresponding profile-likelihood ratio is

$$\Lambda(m_H) = \frac{L[m_H, \hat{\hat{\mu}}^{\gamma\gamma}_{ggF+t\bar{t}H}(m_H), \hat{\hat{\mu}}^{\gamma\gamma}_{{\rm VBF}+VH}(m_H), \hat{\hat{\mu}}^{4\ell}(m_H), \hat{\hat{\boldsymbol{\theta}}}(m_H)]}{L(\hat{m}_H, \hat{\mu}^{\gamma\gamma}_{ggF+t\bar{t}H}, \hat{\mu}^{\gamma\gamma}_{{\rm VBF}+VH}, \hat{\mu}^{4\ell}, \hat{\boldsymbol{\theta}})}. \tag{2}$$

Slightly more complex fit models are used, as described below, to perform additional compatibility tests between the different decay channels and between the results from ATLAS and CMS.

Combining the ATLAS and CMS data for the $H \to \gamma\gamma$ and $H \to ZZ \to 4\ell$ channels according to the above procedure, the mass of the Higgs boson is determined to be

$$m_H = 125.09 \pm 0.24 \text{ GeV} = 125.09 \pm 0.21\,(\text{stat}) \pm 0.11\,(\text{syst}) \text{ GeV}, \quad (3)$$

where the total uncertainty is obtained from the width of a negative log-likelihood ratio scan with all parameters profiled. The statistical uncertainty is determined by fixing all nuisance parameters to their best-fit values, except for the three signal-strength scale factors and the $H \to \gamma\gamma$ background function parameters, which are profiled. The systematic uncertainty is determined by subtracting in quadrature the statistical uncertainty from the total uncertainty. Equation (3) shows that the uncertainties in the m_H measurement are dominated by the statistical term, even when the Run 1 data sets of ATLAS and CMS are combined. Figure 1 shows the negative log-likelihood ratio scans as a function of m_H, with all nuisance parameters profiled (solid curves), and with the nuisance parameters fixed to their best-fit values (dashed curves).

The signal strengths at the measured value of m_H are found to be $\mu^{\gamma\gamma}_{ggF+t\bar{t}H} = 1.15^{+0.28}_{-0.25}$, $\mu^{\gamma\gamma}_{\text{VBF}+VH} = 1.17^{+0.58}_{-0.53}$, and $\mu^{4\ell} = 1.40^{+0.30}_{-0.25}$. The combined overall signal strength

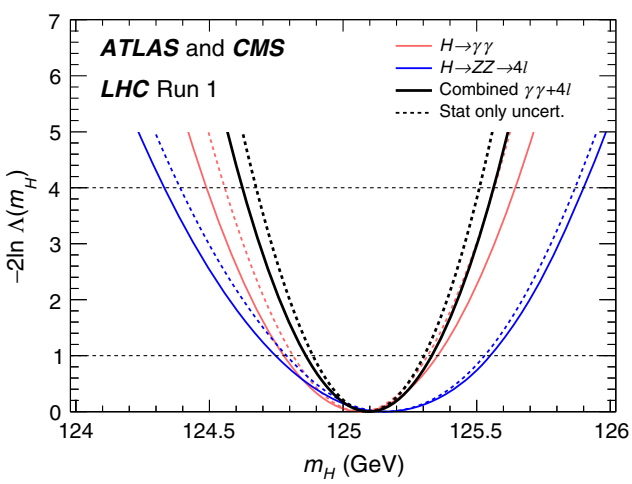

FIG. 1 (color online). Scans of twice the negative log-likelihood ratio $-2\ln\Lambda(m_H)$ as functions of the Higgs boson mass m_H for the ATLAS and CMS combination of the $H \to \gamma\gamma$ (red), $H \to ZZ \to 4\ell$ (blue), and combined (black) channels. The dashed curves show the results accounting for statistical uncertainties only, with all nuisance parameters associated with systematic uncertainties fixed to their best-fit values. The 1 and 2 standard deviation limits are indicated by the intersections of the horizontal lines at 1 and 4, respectively, with the log-likelihood scan curves.

μ (with $\mu^{\gamma\gamma}_{ggF+t\bar{t}H} = \mu^{\gamma\gamma}_{\text{VBF}+VH} = \mu^{4\ell} \equiv \mu$) is $\mu = 1.24^{+0.18}_{-0.16}$. The results reported here for the signal strengths are not expected to have the same sensitivity, nor exactly the same values, as those that would be extracted from a combined analysis optimized for the coupling measurements.

The combined ATLAS and CMS results for m_H in the separate $H \to \gamma\gamma$ and $H \to ZZ \to 4\ell$ channels are

$$m_H^{\gamma\gamma} = 125.07 \pm 0.29 \text{ GeV} = 125.07 \pm 0.25\,(\text{stat}) \pm 0.14\,(\text{syst}) \text{ GeV} \quad (4)$$

and

$$m_H^{4\ell} = 125.15 \pm 0.40 \text{ GeV} = 125.15 \pm 0.37\,(\text{stat}) \pm 0.15\,(\text{syst}) \text{ GeV}. \quad (5)$$

The corresponding likelihood ratio scans are shown in Fig. 1. For the $H \to ZZ \to 4\ell$ channel, the systematic uncertainty is dominated by the absolute scale uncertainty in the momentum measurement for the muons and in the momentum and energy measurements for the electrons. Large samples ($> 10^7$ events) of dilepton decays of the J/ψ, $\Upsilon(nS)$, and Z resonances are used by both experiments to evaluate the absolute scales and to correct for residual misalignments in the inner tracker systems [14,16]. The systematic uncertainty in the ATLAS m_H result from $H \to ZZ \to 4\ell$ decays was conservatively set to 60 MeV in Ref. [14] to account for the limited numerical precision in its estimate. A more precise procedure, resulting in a reduced systematic uncertainty of 40 MeV, is used here. For CMS, conservative systematic uncertainties of 0.1% for the $H \to ZZ \to 4\mu$ and $2\mu 2e$ channels, and 0.3% for the $H \to ZZ \to 4e$ channel, were obtained in Ref. [16] and are used here.

A summary of the results from the individual analyses and their combination is presented in Fig. 2.

The observed uncertainties in the combined measurement can be compared with expectations. The latter are evaluated by generating two Asimov data sets [26], where an Asimov data set is a representative event sample that provides both the median expectation for an experimental result and its expected statistical variation, in the asymptotic approximation, without the need for an extensive MC-based calculation. The first Asimov data set is a "prefit" sample, generated using $m_H = 125.0$ GeV and the SM predictions for the couplings, with all nuisance parameters fixed to their nominal values. The second Asimov data set is a "postfit" sample, in which m_H, the three signal strengths $\mu^{\gamma\gamma}_{ggF+t\bar{t}H}$, $\mu^{\gamma\gamma}_{\text{VBF}+VH}$, and $\mu^{4\ell}$, and all nuisance parameters are fixed to their best-fit estimates from the data. The expected uncertainties for the combined mass are

$$\delta m_{H\,\text{prefit}} = \pm 0.24 \text{ GeV} = \pm 0.22\,(\text{stat}) \pm 0.10\,(\text{syst}) \text{ GeV} \quad (6)$$

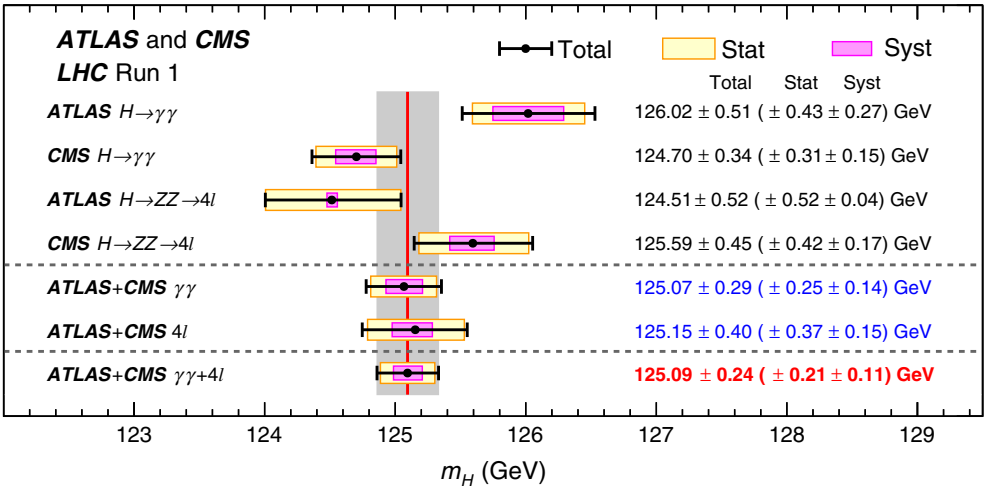

FIG. 2 (color online). Summary of Higgs boson mass measurements from the individual analyses of ATLAS and CMS and from the combined analysis presented here. The systematic (narrower, magenta-shaded bands), statistical (wider, yellow-shaded bands), and total (black error bars) uncertainties are indicated. The (red) vertical line and corresponding (gray) shaded column indicate the central value and the total uncertainty of the combined measurement, respectively.

for the prefit case and

$$\delta m_{H\,\mathrm{postfit}} = \pm 0.22\ \mathrm{GeV} = \pm 0.19\,(\mathrm{stat}) \pm 0.10\,(\mathrm{syst})\ \mathrm{GeV} \qquad (7)$$

for the postfit case, which are both very similar to the observed uncertainties reported in Eq. (3).

Constraining all signal yields to their SM predictions results in an m_H value that is about 70 MeV larger than the nominal result with a comparable uncertainty. The increase in the central value reflects the combined effect of the higher-than-expected $H \to ZZ \to 4\ell$ measured signal strength and the increase of the $H \to ZZ$ branching fraction with m_H. Thus, the fit assuming SM couplings forces the mass to a higher value in order to accommodate the value $\mu = 1$ expected in the SM.

Since the discovery, both experiments have improved their understanding of the electron, photon, and muon measurements [16,30–34], leading to a significant reduction of the systematic uncertainties in the mass measurement. Nevertheless, the treatment and understanding of systematic uncertainties is an important aspect of the individual measurements and their combination. The combined analysis incorporates approximately 300 nuisance parameters. Among these, approximately 100 are fitted parameters describing the shapes and normalizations of the background models in the $H \to \gamma\gamma$ channel, including a number of discrete parameters that allow the functional form in each of the CMS $H \to \gamma\gamma$ analysis categories to be changed [35]. Of the remaining almost 200 nuisance parameters, most correspond to experimental or theoretical systematic uncertainties.

Based on the results from the individual experiments, the dominant systematic uncertainties for the combined m_H result are expected to be those associated with the energy or momentum scale and its resolution: for the photons in the $H \to \gamma\gamma$ channel and for the electrons and muons in the $H \to ZZ \to 4\ell$ channel [14–16]. These uncertainties are assumed to be uncorrelated between the two experiments since they are related to the specific characteristics of the detectors as well as to the calibration procedures, which are fully independent except for negligible effects due to the use of the common Z boson mass [36] to specify the absolute energy and momentum scales. Other experimental systematic uncertainties [14–16] are similarly assumed to be uncorrelated between the two experiments. Uncertainties in the theoretical predictions and in the measured integrated luminosities are treated as fully and partially correlated, respectively.

To evaluate the relative importance of the different sources of systematic uncertainty, the nuisance parameters are grouped according to their correspondence to three broad classes of systematic uncertainty: (1) uncertainties in the energy or momentum scale and resolution for photons, electrons, and muons ("scale"), (2) theoretical uncertainties, e.g., uncertainties in the Higgs boson cross section and branching fractions, and in the normalization of SM background processes ("theory"), (3) other experimental uncertainties ("other").

First, the total uncertainty is obtained from the full profile-likelihood scan, as explained above. Next, parameters associated with the scale terms are fixed and a new scan is performed. Then, in addition to the scale terms, the parameters associated with the theory terms are fixed and a scan performed. Finally, in addition, the other parameters are fixed and a scan performed. Thus the fits are performed iteratively, with the different classes of nuisance parameters cumulatively held fixed to their best-fit values. The uncertainties associated with the different classes of nuisance parameters are defined by the difference in quadrature

between the uncertainties resulting from consecutive scans. The statistical uncertainty is determined from the final scan, with all nuisance parameters associated with systematic terms held fixed, as explained above. The result is

$$m_H = 125.09 \pm 0.21\,(\text{stat}) \pm 0.11\,(\text{scale}) \pm 0.02\,(\text{other}) \pm 0.01\,(\text{theory})\ \text{GeV}, \tag{8}$$

from which it is seen that the systematic uncertainty is indeed dominated by the energy and momentum scale terms. The result in Eq. (8) is consistent with the values of m_H derived from the less precise WW and $\tau\tau$ Higgs boson decay modes [37–40].

The relative importance of the various sources of systematic uncertainty is further investigated by dividing the nuisance parameters into yet-finer groups, with each group associated with a specific underlying effect, and evaluating the impact of each group on the overall mass uncertainty. The matching of nuisance parameters to an effect is not strictly rigorous because nuisance parameters in the two experiments do not always represent exactly the same effect and in some cases multiple effects are related to the same nuisance parameter. Nevertheless, the relative impact of the different effects can be explored. A few experiment-specific groups of nuisance parameters are defined. For example, ATLAS includes a group of nuisance parameters to account for the inaccuracy of the background modeling for the $H \to \gamma\gamma$ channel. To model this background, ATLAS uses specific analytic functions in each category [14] while CMS simultaneously considers different background parametrizations [35]. The systematic uncertainty in m_H related to the background modeling in CMS is estimated to be negligible [15].

The impact of groups of nuisance parameters is evaluated starting from the contribution of each individual nuisance parameter to the total uncertainty. This contribution is defined as the mass shift δm_H observed when reevaluating the profile-likelihood ratio after fixing the nuisance parameter in question to its best-fit value increased or decreased by 1 standard deviation (σ) in its distribution. For a nuisance parameter whose PDF is a Gaussian distribution, this shift corresponds to the contribution of that particular nuisance parameter to the final uncertainty. The impact of a group of nuisance parameters is estimated by summing in quadrature the contributions from the individual parameters.

The impacts δm_H due to each of the considered effects are listed in Table I. The results are reported for the four individual channels, both for the data and (in parentheses) the prefit Asimov data set. The row labeled "Systematic uncertainty (sum in quadrature)" shows the total sums in quadrature of the individual terms in the table. The row labeled "Systematic uncertainty (nominal)" shows the corresponding total systematic uncertainties derived using the subtraction in quadrature method discussed in connection with Eq. (3). The two methods to evaluate the total systematic uncertainty are seen to agree within 10 MeV, which is comparable with the precision of the estimates. The two rightmost columns of Table I list the contribution of each group of nuisance parameters to the uncertainties in the combined mass measurement, for ATLAS and CMS separately.

The statistical and total uncertainties are summarized in the bottom section of Table I. Since the weight of a channel in the final combination is determined by the inverse of the squared uncertainty, the approximate relative weights for the combined result are 19% ($H \to \gamma\gamma$) and 18% ($H \to ZZ \to 4\ell$) for ATLAS, and 40% ($H \to \gamma\gamma$) and 23% ($H \to ZZ \to 4\ell$) for CMS. These weights are reported in the last row of Table I, along with the expected values.

Figure 3 presents the impact of each group of nuisance parameters on the total systematic uncertainty in the mass measurement of ATLAS, CMS, and the combination. For the individual ATLAS and CMS measurements, the results in Fig. 3 are approximately equivalent to the sum in quadrature of the respective δm_H terms in Table I multiplied by their analysis weights, after normalizing these weights to correspond to either ATLAS only or CMS only. The ATLAS and CMS combined results in Fig. 3 are the sum in quadrature of the combined results in Table I.

The results in Table I and Fig. 3 establish that the largest systematic effects for the mass uncertainty are those related to the determination of the energy scale of the photons, followed by those associated with the determination of the electron and muon momentum scales. Since the CMS $H \to \gamma\gamma$ channel has the largest weight in the combination, its impact on the systematic uncertainty of the combined result is largest.

The mutual compatibility of the m_H results from the four individual channels is tested using a likelihood ratio with four masses in the numerator and a common mass in the denominator, and thus three degrees of freedom. The three signal strengths are profiled in both the numerator and denominator as in Eq. (1). The resulting compatibility, defined as the asymptotic p value of the fit, is 10%. Allowing the ATLAS and CMS signal strengths to vary independently yields a compatibility of 7%. This latter fit results in an m_H value that is 40 MeV larger than the nominal result.

The compatibility of the combined ATLAS and CMS mass measurement in the $H \to \gamma\gamma$ channel with the combined measurement in the $H \to ZZ \to 4\ell$ channel is evaluated using the variable $\Delta m_{\gamma Z} \equiv m_H{}^{\gamma\gamma} - m_H{}^{4\ell}$ as the parameter of interest, with all other parameters, including m_H, profiled. Similarly, the compatibility of the ATLAS combined mass measurement in the two channels with the CMS combined measurement in the two channels is evaluated using the variable $\Delta m^{\text{expt}} \equiv m_H^{\text{ATLAS}} - m_H^{\text{CMS}}$. The observed results, $\Delta m_{\gamma Z} = -0.1 \pm 0.5$ GeV and $\Delta m^{\text{expt}} = 0.4 \pm 0.5$ GeV, are both consistent with zero within 1σ. The difference between the mass values in

TABLE I. Systematic uncertainties δm_H (see text) associated with the indicated effects for each of the four input channels, and the corresponding contributions of ATLAS and CMS to the systematic uncertainties of the combined result. "ECAL" refers to the electromagnetic calorimeters. The numbers in parentheses indicate expected values obtained from the prefit Asimov data set discussed in the text. The uncertainties for the combined result are related to the values of the individual channels through the relative weight of the individual channel in the combination, which is proportional to the inverse of the respective uncertainty squared. The top section of the table divides the sources of systematic uncertainty into three classes, which are discussed in the text. The bottom section of the table shows the total systematic uncertainties estimated by adding the individual contributions in quadrature, the total systematic uncertainties evaluated using the nominal method discussed in the text, the statistical uncertainties, the total uncertainties, and the analysis weights, illustrative of the relative weight of each channel in the combined m_H measurement.

	Uncertainty in ATLAS results (GeV): observed (expected)		Uncertainty in CMS results (GeV): observed (expected)		Uncertainty in combined result (GeV): observed (expected)	
	$H \to \gamma\gamma$	$H \to ZZ \to 4\ell$	$H \to \gamma\gamma$	$H \to ZZ \to 4\ell$	ATLAS	CMS
Scale uncertainties:						
ATLAS ECAL nonlinearity or CMS photon nonlinearity	0.14 (0.16)	···	0.10 (0.13)	···	0.02 (0.04)	0.05 (0.06)
Material in front of ECAL	0.15 (0.13)	···	0.07 (0.07)	···	0.03 (0.03)	0.04 (0.03)
ECAL longitudinal response	0.12 (0.13)	···	0.02 (0.01)	···	0.02 (0.03)	0.01 (0.01)
ECAL lateral shower shape	0.09 (0.08)	···	0.06 (0.06)	···	0.02 (0.02)	0.03 (0.03)
Photon energy resolution	0.03 (0.01)	···	0.01 (<0.01)	···	0.02 (<0.01)	<0.01 (<0.01)
ATLAS $H \to \gamma\gamma$ vertex and conversion reconstruction	0.05 (0.05)	···	···	···	0.01 (0.01)	···
$Z \to ee$ calibration	0.05 (0.04)	0.03 (0.02)	0.05 (0.05)	···	0.02 (0.01)	0.02 (0.02)
CMS electron energy scale and resolution	···	···	···	0.12 (0.09)	···	0.03 (0.02)
Muon momentum scale and resolution	···	0.03 (0.04)	···	0.11 (0.10)	<0.01 (0.01)	0.05 (0.02)
Other uncertainties:						
ATLAS $H \to \gamma\gamma$ background modeling	0.04 (0.03)	···	···	···	0.01 (0.01)	···
Integrated luminosity	0.01 (<0.01)	<0.01 (<0.01)	0.01 (<0.01)	<0.01 (<0.01)	0.01 (<0.01)	
Additional experimental systematic uncertainties	0.03 (<0.01)	<0.01 (<0.01)	0.02 (<0.01)	0.01 (<0.01)	0.01 (<0.01)	0.01 (<0.01)
Theory uncertainties:	<0.01 (<0.01)	<0.01 (<0.01)	0.02 (<0.01)	< 0.01 (<0.01)	0.01 (<0.01)	
Systematic uncertainty (sum in quadrature)	0.27 (0.27)	0.04 (0.04)	0.15 (0.17)	0.16 (0.13)	0.11 (0.10)	
Systematic uncertainty (nominal)	0.27 (0.27)	0.04 (0.05)	0.15 (0.17)	0.17 (0.14)	0.11 (0.10)	
Statistical uncertainty	0.43 (0.45)	0.52 (0.66)	0.31 (0.32)	0.42 (0.57)	0.21 (0.22)	
Total uncertainty	0.51 (0.52)	0.52 (0.66)	0.34 (0.36)	0.45 (0.59)	0.24 (0.24)	
Analysis weights	19% (22%)	18% (14%)	40% (46%)	23% (17%)	···	

the two experiments is $\Delta m_{\gamma\gamma}^{\rm expt} = 1.3 \pm 0.6$ GeV (2.1σ) for the $H \to \gamma\gamma$ channel and $\Delta m_{4\ell}^{\rm expt} = -0.9 \pm 0.7$ GeV (1.3σ) for the $H \to ZZ \to 4\ell$ channel. The combined results exhibit a greater degree of compatibility than the results from the individual decay channels because the $\Delta m^{\rm expt}$ value has opposite signs in the two channels.

The compatibility of the signal strengths from ATLAS and CMS is evaluated through the ratios $\lambda^{\rm expt} = \mu^{\rm ATLAS}/\mu^{\rm CMS}$, $\lambda_F^{\rm expt} = \mu_{ggF+t\bar{t}H}^{\gamma\gamma\rm ATLAS}/\mu_{ggF+t\bar{t}H}^{\gamma\gamma\rm CMS}$, and $\lambda_{4\ell}^{\rm expt} = \mu^{4\ell\rm ATLAS}/\mu^{4\ell\rm CMS}$. For this purpose, each ratio is individually taken to be the parameter of interest, with all other nuisance parameters profiled, including the remaining two ratios for the first two tests. We find $\lambda^{\rm expt} = 1.21^{+0.30}_{-0.24}$, $\lambda_F^{\rm expt} = 1.3^{+0.8}_{-0.5}$, and $\lambda_{4\ell}^{\rm expt} = 1.3^{+0.5}_{-0.4}$, all of which are consistent with unity within 1σ. The ratio $\lambda_V^{\rm expt} = \mu_{\rm VBF+VH}^{\gamma\gamma\rm ATLAS}/\mu_{\rm VBF+VH}^{\gamma\gamma\rm CMS}$ is omitted because the ATLAS mass measurement in the $H \to \gamma\gamma$ channel is not sensitive to $\mu_{\rm VBF+VH}^{\gamma\gamma}/\mu_{ggF+t\bar{t}H}^{\gamma\gamma}$.

The correlation between the signal strength and the measured mass is explored with 2D likelihood scans as functions of μ and m_H. The three signal strengths are assumed to be the same: $\mu_{ggF+t\bar{t}H}^{\gamma\gamma} = \mu_{\rm VBF+VH}^{\gamma\gamma} = \mu^{4\ell} \equiv \mu$, and thus the ratios of the production cross sections times branching fractions are constrained to the SM

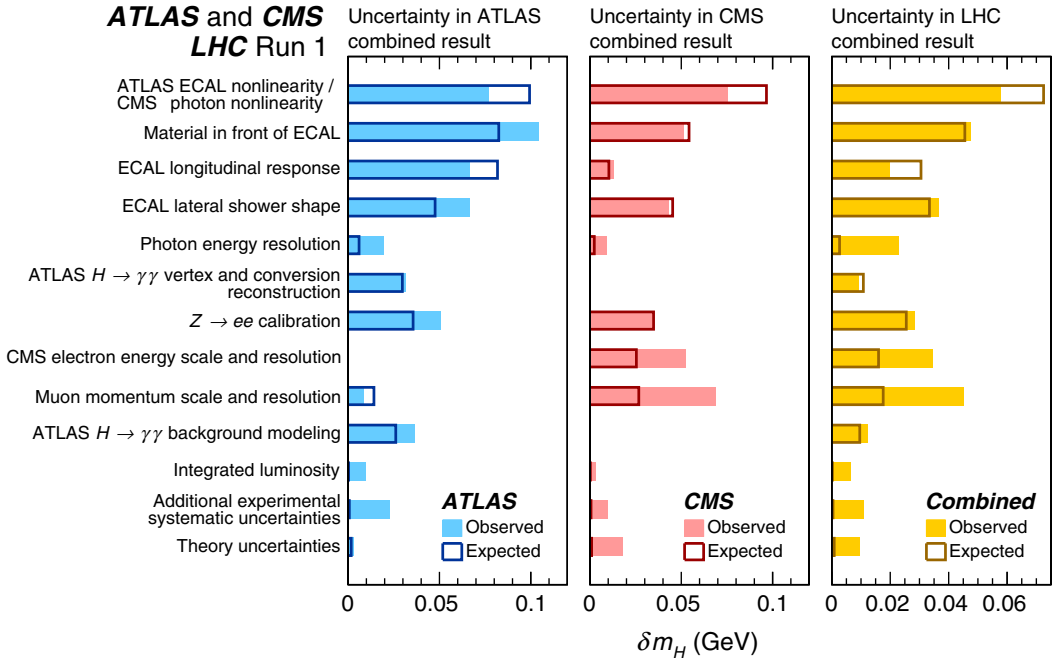

FIG. 3 (color online). The impacts δm_H (see text) of the nuisance parameter groups in Table I on the ATLAS (left), CMS (center), and combined (right) mass measurement uncertainty. The observed (expected) results are shown by the solid (empty) bars.

predictions. Assuming that the negative log-likelihood ratio $-2\ln\Lambda(\mu, m_H)$ is distributed as a χ^2 variable with two degrees of freedom, the 68% confidence level (C.L.) confidence regions are shown in Fig. 4 for each individual measurement, as well as for the combined result.

In summary, a combined measurement of the Higgs boson mass is performed in the $H \to \gamma\gamma$ and $H \to ZZ \to 4\ell$ channels using the LHC Run 1 data sets of the ATLAS and CMS experiments, with minimal reliance on the assumption that the Higgs boson behaves as predicted by the SM.

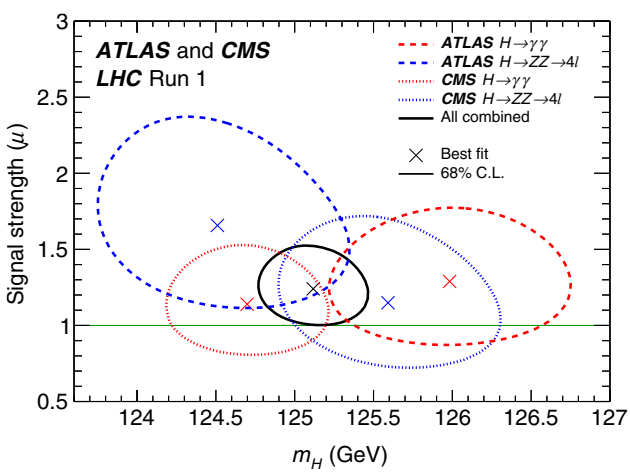

FIG. 4 (color online). Summary of likelihood scans in the 2D plane of signal strength μ versus Higgs boson mass m_H for the ATLAS and CMS experiments. The 68% C.L. confidence regions of the individual measurements are shown by the dashed curves and of the overall combination by the solid curve. The markers indicate the respective best-fit values. The SM signal strength is indicated by the horizontal line at $\mu = 1$.

The result is

$$\begin{aligned} m_H &= 125.09 \pm 0.24 \text{ GeV} \\ &= 125.09 \pm 0.21\,(\text{stat}) \pm 0.11\,(\text{syst}) \text{ GeV}, \end{aligned} \tag{9}$$

where the total uncertainty is dominated by the statistical term, with the systematic uncertainty dominated by effects related to the photon, electron, and muon energy or momentum scales and resolutions. Compatibility tests are performed to ascertain whether the measurements are consistent with each other, both between the different decay channels and between the two experiments. All tests on the combined results indicate consistency of the different measurements within 1σ, while the four Higgs boson mass measurements in the two channels of the two experiments agree within 2σ. The combined measurement of the Higgs boson mass improves upon the results from the individual experiments and is the most precise measurement to date of this fundamental parameter of the newly discovered particle.

We thank CERN for the very successful operation of the LHC, as well as the support staff from our institutions without whom ATLAS and CMS could not be operated efficiently. We acknowledge the support of ANPCyT (Argentina); YerPhI (Armenia); ARC (Australia); BMWFW and FWF (Austria); ANAS (Azerbaijan); SSTC (Belarus); FNRS and FWO (Belgium); CNPq, CAPES, FAPERJ, and FAPESP (Brazil); MES

(Bulgaria); NSERC, NRC, and CFI (Canada); CERN; CONICYT (Chile); CAS, MoST, and NSFC (China); COLCIENCIAS (Colombia); MSES and CSF (Croatia); RPF (Cyprus); MSMT CR, MPO CR, and VSC CR (Czech Republic); DNRF, DNSRC, and Lundbeck Foundation (Denmark); MoER, ERC IUT, and ERDF (Estonia); EPLANET, ERC, and NSRF (European Union); Academy of Finland, MEC, and HIP (Finland); CEA, CNRS/IN2P3 (France); GNSF (Georgia); BMBF, DFG, HGF, MPG, and AvH Foundation (Germany); GSRT and NSRF (Greece); RGC (Hong Kong SAR, China); OTKA and NIH (Hungary); DAE and DST (India); IPM (Iran); SFI (Ireland); ISF, MINERVA, GIF, I-CORE, and Benoziyo Center (Israel); INFN (Italy); MEXT and JSPS (Japan); JINR; MSIP, and NRF (Republic of Korea); LAS (Lithuania); MOE and UM (Malaysia); CINVESTAV, CONACYT, SEP, and UASLP-FAI (Mexico); CNRST (Morocco); FOM and NWO (Netherlands); MBIE (New Zealand); BRF and RCN (Norway); PAEC (Pakistan); MNiSW, MSHE, NCN, and NSC (Poland); GRICES and FCT (Portugal); MNE/IFA (Romania); MES of Russia, MON, RosAtom, RAS, and RFBR (Russian Federation); MSTD and MESTD (Serbia); MSSR (Slovakia); ARRS and MIZŠ (Slovenia); DST/NRF (South Africa); MINECO, SEIDI, and CPAN (Spain); SRC and Wallenberg Foundation (Sweden); ETH Board, ETH Zurich, PSI, SER, SNSF, UniZH, and Cantons of Bern, Genève, and Zurich (Switzerland); NSC (Taipei); MST (Taiwan); ThEPCenter, IPST, STAR, and NSTDA (Thailand); TUBITAK and TAEK (Turkey); NASU and SFFR (Ukraine); STFC and the Royal Society and Leverhulme Trust (U.K.); DOE and NSF (U.S.). In addition, we gratefully acknowledge the crucial computing support from all WLCG partners, in particular from CERN and the Tier-1 and Tier-2 facilities worldwide.

[1] F. Englert and R. Brout, Broken Symmetry and the Mass of Gauge Vector Mesons, Phys. Rev. Lett. **13**, 321 (1964).

[2] P. W. Higgs, Broken symmetries, massless particles and gauge fields, Phys. Lett. **12**, 132 (1964).

[3] P. W. Higgs, Broken Symmetries and the Masses of Gauge Bosons, Phys. Rev. Lett. **13**, 508 (1964).

[4] G. S. Guralnik, C. R. Hagen, and T. W. B. Kibble, Global Conservation Laws and Massless Particles, Phys. Rev. Lett. **13**, 585 (1964).

[5] P. W. Higgs, Spontaneous symmetry breakdown without massless bosons, Phys. Rev. **145**, 1156 (1966).

[6] T. W. B. Kibble, Symmetry breaking in non-Abelian gauge theories, Phys. Rev. **155**, 1554 (1967).

[7] ATLAS Collaboration, Observation of a new particle in the search for the Standard Model Higgs boson with the ATLAS detector at the LHC, Phys. Lett. B **716**, 1 (2012).

[8] CMS Collaboration, Observation of a new boson at a mass of 125 GeV with the CMS experiment at the LHC, Phys. Lett. B **716**, 30 (2012).

[9] CMS Collaboration, Observation of a new boson with mass near 125 GeV in pp collisions at $\sqrt{s} = 7$ and 8 TeV, J. High Energy Phys. 06 (2013) 081.

[10] ATLAS Collaboration, Measurements of Higgs boson production and couplings in diboson final states with the ATLAS detector at the LHC, Phys. Lett. B **726**, 88 (2013).

[11] ATLAS Collaboration, Evidence for the spin-0 nature of the Higgs boson using ATLAS data, Phys. Lett. B **726**, 120 (2013).

[12] CMS Collaboration, Precise determination of the mass of the Higgs boson and tests of compatibility of its couplings with the standard model predictions using proton collisions at 7 and 8 TeV, arXiv:1412.8662 [Eur. Phys. J. C (to be published)].

[13] CMS Collaboration, Constraints on the spin-parity and anomalous HVV couplings of the Higgs boson in proton collisions at 7 and 8 TeV, arXiv:1411.3441 [Phys. Rev. D (to be published)].

[14] ATLAS Collaboration, Measurement of the Higgs boson mass from the $H \to \gamma\gamma$ and $H \to ZZ^* \to 4\ell$ channels in pp collisions at center-of-mass energies of 7 and 8 TeV with the ATLAS detector, Phys. Rev. D **90**, 052004 (2014).

[15] CMS Collaboration, Observation of the diphoton decay of the 125 GeV Higgs boson and measurement of its properties, Eur. Phys. J. C **74**, 3076 (2014).

[16] CMS Collaboration, Measurement of the properties of a Higgs boson in the four-lepton final state, Phys. Rev. D **89**, 092007 (2014).

[17] M. Baak *et al.* (Gfitter Group), The global electroweak fit at NNLO and prospects for the LHC and ILC, Eur. Phys. J. C **74**, 3046 (2014).

[18] L. J. Dixon and M. S. Siu, Resonance-Continuum Interference in the Diphoton Higgs Signal at the LHC, Phys. Rev. Lett. **90**, 252001 (2003).

[19] S. P. Martin, Shift in the LHC Higgs diphoton mass peak from interference with background, Phys. Rev. D **86**, 073016 (2012).

[20] L. J. Dixon and Y. Li, Bounding the Higgs Boson Width through Interferometry, Phys. Rev. Lett. **111**, 111802 (2013).

[21] N. Kauer and G. Passarino, Inadequacy of zero-width approximation for a light Higgs boson signal, J. High Energy Phys. 08 (2012) 116.

[22] ATLAS Collaboration, The ATLAS experiment at the CERN Large Hadron Collider, J. Instrum. **3**, S08003 (2008).

[23] CMS Collaboration, The CMS experiment at the CERN LHC, J. Instrum. **3**, S08004 (2008).

[24] ATLAS Collaboration, Measurement of Higgs boson production in the diphoton decay channel in pp collisions at center-of-mass energies of 7 and 8 TeV with the ATLAS detector, Phys. Rev. D **90**, 112015 (2014).

[25] ATLAS and CMS Collaborations, "Procedure for the LHC Higgs boson search combination in Summer 2011," Tech. Rep. CMS NOTE 2011/005, ATL-PHYS-PUB 2011-11, 2011 (http://cds.cern.ch/record/1379837).

[26] G. Cowan, K. Cranmer, E. Gross, and O. Vitells, Asymptotic formulae for likelihood-based tests of new physics, Eur. Phys. J. C **71**, 1554 (2011).

[27] W. Verkerke and D. P. Kirkby, The ROOFIT toolkit for data modeling, in Proceedings of the 13th International

Conference for Computing in High-Energy and Nuclear Physics (CHEP03), 2003, CHEP-2003-MOLT007, arXiv:physics/0306116.

[28] L. Moneta, K. Belasco, K. S. Cranmer, A. Lazzaro, D. Piparo, G. Schott, W. Verkerke, and M. Wolf, The ROOSTATS Project, in Proceedings of the 13th International Workshop on Advanced Computing and Analysis Techniques in Physics Research (ACAT2010) (SISSA, 2010), Proc. Sci., ACAT2010 (2010) 057 [arXiv:1009.1003].

[29] K. Cranmer, G. Lewis, L. Moneta, A. Shibata, and W. Verkerke (ROOT), "HISTFACTORY: A tool for creating statistical models for use with ROOFIT and ROOSTATS," Tech. Rep. CERN-OPEN-2012-016, 2012 (http://cds.cern.ch/record/1456844).

[30] ATLAS Collaboration, Electron and photon energy calibration with the ATLAS detector using LHC Run 1 data, Eur. Phys. J. C **74**, 3071 (2014).

[31] ATLAS Collaboration, Measurement of the muon reconstruction performance of the ATLAS detector using 2011 and 2012 LHC proton-proton collision data, Eur. Phys. J. C **74**, 3130 (2014).

[32] CMS Collaboration, Performance of CMS muon reconstruction in pp collision events at $\sqrt{s} = 7$ TeV, J. Instrum. **7**, P10002 (2012).

[33] CMS Collaboration, Performance of electron reconstruction and selection with the CMS detector in proton-proton collisions at $\sqrt{s} = 8$ TeV, arXiv:1502.02701 [J. Instrum. (to be published)].

[34] CMS Collaboration, Performance of photon reconstruction and identification with the CMS detector in proton-proton collisions at $\sqrt{s} = 8$ TeV, arXiv:1502.02702.

[35] P. D. Dauncey, M. Kenzie, N. Wardle, and G. J. Davies, Handling uncertainties in background shapes: The discrete profiling method, J. Instrum. **10**, P04015 (2015).

[36] ALEPH, DELPHI, L3, OPAL, SLD Collaborations, LEP Electroweak Working Group, and SLD Electroweak and Heavy Flavour Groups, Precision electroweak measurements on the Z resonance, Phys. Rep. **427**, 257 (2006).

[37] ATLAS Collaboration, Observation and measurement of Higgs boson decays to WW^* with the ATLAS detector, arXiv:1412.2641 [Phys. Rev. D (to be published)].

[38] ATLAS Collaboration, Evidence for the Higgs-boson Yukawa coupling to tau leptons with the ATLAS detector, J. High Energy Phys. 04 (2015) 117.

[39] CMS Collaboration, Measurement of Higgs boson production and properties in the WW decay channel with leptonic final states, J. High Energy Phys. 01 (2014) 096.

[40] CMS Collaboration, Evidence for the 125 GeV Higgs boson decaying to a pair of τ leptons, J. High Energy Phys. 05 (2014) 104.

G. Aad,[85,†] B. Abbott,[113,†] J. Abdallah,[151,†] O. Abdinov,[11,†] R. Aben,[107,†] M. Abolins,[90,†] O. S. AbouZeid,[158,†] H. Abramowicz,[153,†] H. Abreu,[152,†] R. Abreu,[30,†] Y. Abulaiti,[146a,146b,†] B. S. Acharya,[164a,164b,b,†] L. Adamczyk,[38a,†] D. L. Adams,[25,†] J. Adelman,[108,†] S. Adomeit,[100,†] T. Adye,[131,†] A. A. Affolder,[74,†] T. Agatonovic-Jovin,[13,†] J. A. Aguilar-Saavedra,[126a,126f,†] S. P. Ahlen,[22,†] F. Ahmadov,[65,c,†] G. Aielli,[133a,133b,†] H. Akerstedt,[146a,146b,†] T. P. A. Åkesson,[81,†] G. Akimoto,[155,†] A. V. Akimov,[96,†] G. L. Alberghi,[20a,20b,†] J. Albert,[169,†] S. Albrand,[55,†] M. J. Alconada Verzini,[71,†] M. Aleksa,[30,†] I. N. Aleksandrov,[65,†] C. Alexa,[26a,†] G. Alexander,[153,†] T. Alexopoulos,[10,†] M. Alhroob,[113,†] G. Alimonti,[91a,†] L. Alio,[85,†] J. Alison,[31,†] S. P. Alkire,[35,†] B. M. M. Allbrooke,[18,†] P. P. Allport,[74,†] A. Aloisio,[104a,104b,†] A. Alonso,[36,†] F. Alonso,[71,†] C. Alpigiani,[76,†] A. Altheimer,[35,†] B. Alvarez Gonzalez,[30,†] D. Álvarez Piqueras,[167,†] M. G. Alviggi,[104a,104b,†] B. T. Amadio,[15,†] K. Amako,[66,†] Y. Amaral Coutinho,[24a,†] C. Amelung,[23,†] D. Amidei,[89,†] S. P. Amor Dos Santos,[126a,126c,†] A. Amorim,[126a,126b,†] S. Amoroso,[48,†] N. Amram,[153,†] G. Amundsen,[23,†] C. Anastopoulos,[139,†] L. S. Ancu,[49,†] N. Andari,[30,†] T. Andeen,[35,†] C. F. Anders,[58b,†] G. Anders,[30,†] J. K. Anders,[74,†] K. J. Anderson,[31,†] A. Andreazza,[91a,91b,†] V. Andrei,[58a,†] S. Angelidakis,[9,†] I. Angelozzi,[107,†] P. Anger,[44,†] A. Angerami,[35,†] F. Anghinolfi,[30,†] A. V. Anisenkov,[109,d,†] N. Anjos,[12,†] A. Annovi,[124a,124b,†] M. Antonelli,[47,†] A. Antonov,[98,†] J. Antos,[144b,†] F. Anulli,[132a,†] M. Aoki,[66,†] L. Aperio Bella,[18,†] G. Arabidze,[90,†] Y. Arai,[66,†] J. P. Araque,[126a,†] A. T. H. Arce,[45,†] F. A. Arduh,[71,†] J-F. Arguin,[95,†] S. Argyropoulos,[42,†] M. Arik,[19a,†] A. J. Armbruster,[30,†] O. Arnaez,[30,†] V. Arnal,[82,†] H. Arnold,[48,†] M. Arratia,[28,†] O. Arslan,[21,†] A. Artamonov,[97,†] G. Artoni,[23,†] S. Asai,[155,†] N. Asbah,[42,†] A. Ashkenazi,[153,†] B. Åsman,[146a,146b,†] L. Asquith,[149,†] K. Assamagan,[25,†] R. Astalos,[144a,†] M. Atkinson,[165,†] N. B. Atlay,[141,†] B. Auerbach,[6,†] K. Augsten,[128,†] M. Aurousseau,[145b,†] G. Avolio,[30,†] B. Axen,[15,†] M. K. Ayoub,[117,†] G. Azuelos,[95,e,†] M. A. Baak,[30,†] A. E. Baas,[58a,†] C. Bacci,[134a,134b,†] H. Bachacou,[136,†] K. Bachas,[154,†] M. Backes,[30,†] M. Backhaus,[30,†] E. Badescu,[26a,†] P. Bagiacchi,[132a,132b,†] P. Bagnaia,[132a,132b,†] Y. Bai,[33a,†] T. Bain,[35,†] J. T. Baines,[131,†] O. K. Baker,[176,†] P. Balek,[129,†] T. Balestri,[148,†] F. Balli,[84,†] E. Banas,[39,†] Sw. Banerjee,[173,†] A. A. E. Bannoura,[175,†] H. S. Bansil,[18,†] L. Barak,[30,†] S. P. Baranov,[96,†] E. L. Barberio,[88,†] D. Barberis,[50a,50b,†] M. Barbero,[85,†] T. Barillari,[101,†] M. Barisonzi,[164a,164b,†] T. Barklow,[143,†] N. Barlow,[28,†] S. L. Barnes,[84,†] B. M. Barnett,[131,†] R. M. Barnett,[15,†] Z. Barnovska,[5,†] A. Baroncelli,[134a,†] G. Barone,[49,†] A. J. Barr,[120,†] F. Barreiro,[82,†] J. Barreiro Guimarães da Costa,[57,†] R. Bartoldus,[143,†] A. E. Barton,[72,†]

P. Bartos,[144a,†] A. Bassalat,[117,†] A. Basye,[165,†] R. L. Bates,[53,†] S. J. Batista,[158,†] J. R. Batley,[28,†] M. Battaglia,[137,†] M. Bauce,[132a,132b,†] F. Bauer,[136,†] H. S. Bawa,[143,f,†] J. B. Beacham,[111,†] M. D. Beattie,[72,†] T. Beau,[80,†] P. H. Beauchemin,[161,†] R. Beccherle,[124a,124b,†] P. Bechtle,[21,†] H. P. Beck,[17,g,†] K. Becker,[120,†] M. Becker,[83,†] S. Becker,[100,†] M. Beckingham,[170,†] C. Becot,[117,†] A. J. Beddall,[19c,†] A. Beddall,[19c,†] V. A. Bednyakov,[65,†] C. P. Bee,[148,†] L. J. Beemster,[107,†] T. A. Beermann,[175,†] M. Begel,[25,†] J. K. Behr,[120,†] C. Belanger-Champagne,[87,†] W. H. Bell,[49,†] G. Bella,[153,†] L. Bellagamba,[20a,†] A. Bellerive,[29,†] M. Bellomo,[86,†] K. Belotskiy,[98,†] O. Beltramello,[30,†] O. Benary,[153,†] D. Benchekroun,[135a,†] M. Bender,[100,†] K. Bendtz,[146a,146b,†] N. Benekos,[10,†] Y. Benhammou,[153,†] E. Benhar Noccioli,[49,†] J. A. Benitez Garcia,[159b,†] D. P. Benjamin,[45,†] J. R. Bensinger,[23,†] S. Bentvelsen,[107,†] L. Beresford,[120,†] M. Beretta,[47,†] D. Berge,[107,†] E. Bergeaas Kuutmann,[166,†] N. Berger,[5,†] F. Berghaus,[169,†] J. Beringer,[15,†] C. Bernard,[22,†] N. R. Bernard,[86,†] C. Bernius,[110,†] F. U. Bernlochner,[21,†] T. Berry,[77,†] P. Berta,[129,†] C. Bertella,[83,†] G. Bertoli,[146a,146b,†] F. Bertolucci,[124a,124b,†] C. Bertsche,[113,†] D. Bertsche,[113,†] M. I. Besana,[91a,†] G. J. Besjes,[106,†] O. Bessidskaia Bylund,[146a,146b,†] M. Bessner,[42,†] N. Besson,[136,†] C. Betancourt,[48,†] S. Bethke,[101,†] A. J. Bevan,[76,†] W. Bhimji,[46,†] R. M. Bianchi,[125,†] L. Bianchini,[23,†] M. Bianco,[30,†] O. Biebel,[100,†] S. P. Bieniek,[78,†] M. Biglietti,[134a,†] J. Bilbao De Mendizabal,[49,†] H. Bilokon,[47,†] M. Bindi,[54,†] S. Binet,[117,†] A. Bingul,[19c,†] C. Bini,[132a,132b,†] C. W. Black,[150,†] J. E. Black,[143,†] K. M. Black,[22,†] D. Blackburn,[138,†] R. E. Blair,[6,†] J.-B. Blanchard,[136,†] J. E. Blanco,[77,†] T. Blazek,[144a,†] I. Bloch,[42,†] C. Blocker,[23,†] W. Blum,[83,a,†] U. Blumenschein,[54,†] G. J. Bobbink,[107,†] V. S. Bobrovnikov,[109,d,†] S. S. Bocchetta,[81,†] A. Bocci,[45,†] C. Bock,[100,†] M. Boehler,[48,†] J. A. Bogaerts,[30,†] A. G. Bogdanchikov,[109,†] C. Bohm,[146a,†] V. Boisvert,[77,†] T. Bold,[38a,†] V. Boldea,[26a,†] A. S. Boldyrev,[99,†] M. Bomben,[80,†] M. Bona,[76,†] M. Boonekamp,[136,†] A. Borisov,[130,†] G. Borissov,[72,†] S. Borroni,[42,†] J. Bortfeldt,[100,†] V. Bortolotto,[60a–60c,†] K. Bos,[107,†] D. Boscherini,[20a,†] M. Bosman,[12,†] J. Boudreau,[125,†] J. Bouffard,[2,†] E. V. Bouhova-Thacker,[72,†] D. Boumediene,[34,†] C. Bourdarios,[117,†] N. Bousson,[114,†] A. Boveia,[30,†] J. Boyd,[30,†] I. R. Boyko,[65,†] I. Bozic,[13,†] J. Bracinik,[18,†] A. Brandt,[8,†] G. Brandt,[54,†] O. Brandt,[58a,†] U. Bratzler,[156,†] B. Brau,[86,†] J. E. Brau,[116,†] H. M. Braun,[175,a,†] S. F. Brazzale,[164a,164c,†] K. Brendlinger,[122,†] A. J. Brennan,[88,†] L. Brenner,[107,†] R. Brenner,[166,†] S. Bressler,[172,†] K. Bristow,[145c,†] T. M. Bristow,[46,†] D. Britton,[53,†] D. Britzger,[42,†] F. M. Brochu,[28,†] I. Brock,[21,†] R. Brock,[90,†] J. Bronner,[101,†] G. Brooijmans,[35,†] T. Brooks,[77,†] W. K. Brooks,[32b,†] J. Brosamer,[15,†] E. Brost,[116,†] J. Brown,[55,†] P. A. Bruckman de Renstrom,[39,†] D. Bruncko,[144b,†] R. Bruneliere,[48,†] A. Bruni,[20a,†] G. Bruni,[20a,†] M. Bruschi,[20a,†] L. Bryngemark,[81,†] T. Buanes,[14,†] Q. Buat,[142,†] P. Buchholz,[141,†] A. G. Buckley,[53,†] S. I. Buda,[26a,†] I. A. Budagov,[65,†] F. Buehrer,[48,†] L. Bugge,[119,†] M. K. Bugge,[119,†] O. Bulekov,[98,†] D. Bullock,[8,†] H. Burckhart,[30,†] S. Burdin,[74,†] B. Burghgrave,[108,†] S. Burke,[131,†] I. Burmeister,[43,†] E. Busato,[34,†] D. Büscher,[48,†] V. Büscher,[83,†] P. Bussey,[53,†] C. P. Buszello,[166,†] J. M. Butler,[22,†] A. I. Butt,[3,†] C. M. Buttar,[53,†] J. M. Butterworth,[78,†] P. Butti,[107,†] W. Buttinger,[25,†] A. Buzatu,[53,†] R. Buzykaev,[109,d,†] S. Cabrera Urbán,[167,†] D. Caforio,[128,†] V. M. Cairo,[37a,37b,†] O. Cakir,[4a,†] P. Calafiura,[15,†] A. Calandri,[136,†] G. Calderini,[80,†] P. Calfayan,[100,†] L. P. Caloba,[24a,†] D. Calvet,[34,†] S. Calvet,[34,†] R. Camacho Toro,[31,†] S. Camarda,[42,†] P. Camarri,[133a,133b,†] D. Cameron,[119,†] L. M. Caminada,[15,†] R. Caminal Armadans,[12,†] S. Campana,[30,†] M. Campanelli,[78,†] A. Campoverde,[148,†] V. Canale,[104a,104b,†] A. Canepa,[159a,†] M. Cano Bret,[76,†] J. Cantero,[82,†] R. Cantrill,[126a,†] T. Cao,[40,†] M. D. M. Capeans Garrido,[30,†] I. Caprini,[26a,†] M. Caprini,[26a,†] M. Capua,[37a,37b,†] R. Caputo,[83,†] R. Cardarelli,[133a,†] T. Carli,[30,†] G. Carlino,[104a,†] L. Carminati,[91a,91b,†] S. Caron,[106,†] E. Carquin,[32a,†] G. D. Carrillo-Montoya,[8,†] J. R. Carter,[28,†] J. Carvalho,[126a,126c,†] D. Casadei,[78,†] M. P. Casado,[12,†] M. Casolino,[12,†] E. Castaneda-Miranda,[145b,†] A. Castelli,[107,†] V. Castillo Gimenez,[167,†] N. F. Castro,[126a,h,†] P. Catastini,[57,†] A. Catinaccio,[30,†] J. R. Catmore,[119,†] A. Cattai,[30,†] J. Caudron,[83,†] V. Cavaliere,[165,†] D. Cavalli,[91a,†] M. Cavalli-Sforza,[12,†] V. Cavasinni,[124a,124b,†] F. Ceradini,[134a,134b,†] B. C. Cerio,[45,†] K. Cerny,[129,†] A. S. Cerqueira,[24b,†] A. Cerri,[149,†] L. Cerrito,[76,†] F. Cerutti,[15,†] M. Cerv,[30,†] A. Cervelli,[17,†] S. A. Cetin,[19b,†] A. Chafaq,[135a,†] D. Chakraborty,[108,†] I. Chalupkova,[129,†] P. Chang,[165,†] B. Chapleau,[87,†] J. D. Chapman,[28,†] D. G. Charlton,[18,†] C. C. Chau,[158,†] C. A. Chavez Barajas,[149,†] S. Cheatham,[152,†] A. Chegwidden,[90,†] S. Chekanov,[6,†] S. V. Chekulaev,[159a,†] G. A. Chelkov,[65,i,†] M. A. Chelstowska,[89,†] C. Chen,[64,†] H. Chen,[25,†] K. Chen,[148,†] L. Chen,[33d,j,†] S. Chen,[33c,†] X. Chen,[33f,†] Y. Chen,[67,†] H. C. Cheng,[89,†] Y. Cheng,[31,†] A. Cheplakov,[65,†] E. Cheremushkina,[130,†] R. Cherkaoui El Moursli,[135e,†] V. Chernyatin,[25,a,†] E. Cheu,[7,†] L. Chevalier,[136,†] V. Chiarella,[47,†] J. T. Childers,[6,†] G. Chiodini,[73a,†] A. S. Chisholm,[18,†] R. T. Chislett,[78,†] A. Chitan,[26a,†] M. V. Chizhov,[65,†] K. Choi,[61,†] S. Chouridou,[9,†] B. K. B. Chow,[100,†] V. Christodoulou,[78,†] D. Chromek-Burckhart,[30,†] M. L. Chu,[151,†] J. Chudoba,[127,†] A. J. Chuinard,[87,†] J. J. Chwastowski,[39,†] L. Chytka,[115,†] G. Ciapetti,[132a,132b,†] A. K. Ciftci,[4a,†] D. Cinca,[53,†] V. Cindro,[75,†] I. A. Cioara,[21,†] A. Ciocio,[15,†] Z. H. Citron,[172,†] M. Ciubancan,[26a,†] A. Clark,[49,†] B. L. Clark,[57,†] P. J. Clark,[46,†] R. N. Clarke,[15,†] W. Cleland,[125,†] C. Clement,[146a,146b,†] Y. Coadou,[85,†] M. Cobal,[164a,164c,†] A. Coccaro,[138,†] J. Cochran,[64,†] L. Coffey,[23,†]

J. G. Cogan,[143,†] B. Cole,[35,†] S. Cole,[108,†] A. P. Colijn,[107,†] J. Collot,[55,†] T. Colombo,[58c,†] G. Compostella,[101,†] P. Conde Muiño,[126a,126b,†] E. Coniavitis,[48,†] S. H. Connell,[145b,†] I. A. Connelly,[77,†] S. M. Consonni,[91a,91b,†] V. Consorti,[48,†] S. Constantinescu,[26a,†] C. Conta,[121a,121b,†] G. Conti,[30,†] F. Conventi,[104a,k,†] M. Cooke,[15,†] B. D. Cooper,[78,†] A. M. Cooper-Sarkar,[120,†] T. Cornelissen,[175,†] M. Corradi,[20a,†] F. Corriveau,[87,l,†] A. Corso-Radu,[163,†] A. Cortes-Gonzalez,[12,†] G. Cortiana,[101,†] G. Costa,[91a,†] M. J. Costa,[167,†] D. Costanzo,[139,†] D. Côté,[8,†] G. Cottin,[28,†] G. Cowan,[77,†] B. E. Cox,[84,†] K. Cranmer,[110,†] G. Cree,[29,†] S. Crépé-Renaudin,[55,†] F. Crescioli,[80,†] W. A. Cribbs,[146a,146b,†] M. Crispin Ortuzar,[120,†] M. Cristinziani,[21,†] V. Croft,[106,†] G. Crosetti,[37a,37b,†] T. Cuhadar Donszelmann,[139,†] J. Cummings,[176,†] M. Curatolo,[47,†] C. Cuthbert,[150,†] H. Czirr,[141,†] P. Czodrowski,[3,†] S. D'Auria,[53,†] M. D'Onofrio,[74,†] M. J. Da Cunha Sargedas De Sousa,[126a,126b,†] C. Da Via,[84,†] W. Dabrowski,[38a,†] A. Dafinca,[120,†] T. Dai,[89,†] O. Dale,[14,†] F. Dallaire,[95,†] C. Dallapiccola,[86,†] M. Dam,[36,†] J. R. Dandoy,[31,†] N. P. Dang,[48,†] A. C. Daniells,[18,†] M. Danninger,[168,†] M. Dano Hoffmann,[136,†] V. Dao,[48,†] G. Darbo,[50a,†] S. Darmora,[8,†] J. Dassoulas,[3,†] A. Dattagupta,[61,†] W. Davey,[21,†] C. David,[169,†] T. Davidek,[129,†] E. Davies,[120,m,†] M. Davies,[153,†] P. Davison,[78,†] Y. Davygora,[58a,†] E. Dawe,[88,†] I. Dawson,[139,†] R. K. Daya-Ishmukhametova,[86,†] K. De,[8,†] R. de Asmundis,[104a,†] S. De Castro,[20a,20b,†] S. De Cecco,[80,†] N. De Groot,[106,†] P. de Jong,[107,†] H. De la Torre,[82,†] F. De Lorenzi,[64,†] L. De Nooij,[107,†] D. De Pedis,[132a,†] A. De Salvo,[132a,†] U. De Sanctis,[149,†] A. De Santo,[149,†] J. B. De Vivie De Regie,[117,†] W. J. Dearnaley,[72,†] R. Debbe,[25,†] C. Debenedetti,[137,†] D. V. Dedovich,[65,†] I. Deigaard,[107,†] J. Del Peso,[82,†] T. Del Prete,[124a,124b,†] D. Delgove,[117,†] F. Deliot,[136,†] C. M. Delitzsch,[49,†] M. Deliyergiyev,[75,†] A. Dell'Acqua,[30,†] L. Dell'Asta,[22,†] M. Dell'Orso,[124a,124b,†] M. Della Pietra,[104a,k,†] D. della Volpe,[49,†] M. Delmastro,[5,†] P. A. Delsart,[55,†] C. Deluca,[107,†] D. A. DeMarco,[158,†] S. Demers,[176,†] M. Demichev,[65,†] A. Demilly,[80,†] S. P. Denisov,[130,†] D. Derendarz,[39,†] J. E. Derkaoui,[135d,†] F. Derue,[80,†] P. Dervan,[74,†] K. Desch,[21,†] C. Deterre,[42,†] P. O. Deviveiros,[30,†] A. Dewhurst,[131,†] S. Dhaliwal,[107,†] A. Di Ciaccio,[133a,133b,†] L. Di Ciaccio,[5,†] A. Di Domenico,[132a,132b,†] C. Di Donato,[104a,104b,†] A. Di Girolamo,[30,†] B. Di Girolamo,[30,†] A. Di Mattia,[152,†] B. Di Micco,[134a,134b,†] R. Di Nardo,[47,†] A. Di Simone,[48,†] R. Di Sipio,[158,†] D. Di Valentino,[29,†] C. Diaconu,[85,†] M. Diamond,[158,†] F. A. Dias,[46,†] M. A. Diaz,[32a,†] E. B. Diehl,[89,†] J. Dietrich,[16,†] S. Diglio,[85,†] A. Dimitrievska,[13,†] J. Dingfelder,[21,†] P. Dita,[26a,†] S. Dita,[26a,†] F. Dittus,[30,†] F. Djama,[85,†] T. Djobava,[51b,†] J. I. Djuvsland,[58a,†] M. A. B. do Vale,[24c,†] D. Dobos,[30,†] M. Dobre,[26a,†] C. Doglioni,[49,†] T. Dohmae,[155,†] J. Dolejsi,[129,†] Z. Dolezal,[129,†] B. A. Dolgoshein,[98,a,†] M. Donadelli,[24d,†] S. Donati,[124a,124b,†] P. Dondero,[121a,121b,†] J. Donini,[34,†] J. Dopke,[131,†] A. Doria,[104a,†] M. T. Dova,[71,†] A. T. Doyle,[53,†] E. Drechsler,[54,†] M. Dris,[10,†] E. Dubreuil,[34,†] E. Duchovni,[172,†] G. Duckeck,[100,†] O. A. Ducu,[26a,85,†] D. Duda,[175,†] A. Dudarev,[30,†] L. Duflot,[117,†] L. Duguid,[77,†] M. Dührssen,[30,†] M. Dunford,[58a,†] H. Duran Yildiz,[4a,†] M. Düren,[52,†] A. Durglishvili,[51b,†] D. Duschinger,[44,†] M. Dyndal,[38a,†] C. Eckardt,[42,†] K. M. Ecker,[101,†] R. C. Edgar,[89,†] W. Edson,[2,†] N. C. Edwards,[46,†] W. Ehrenfeld,[21,†] T. Eifert,[30,†] G. Eigen,[14,†] K. Einsweiler,[15,†] T. Ekelof,[166,†] M. El Kacimi,[135c,†] M. Ellert,[166,†] S. Elles,[5,†] F. Ellinghaus,[83,†] A. A. Elliot,[169,†] N. Ellis,[30,†] J. Elmsheuser,[100,†] M. Elsing,[30,†] D. Emeliyanov,[131,†] Y. Enari,[155,†] O. C. Endner,[83,†] M. Endo,[118,†] R. Engelmann,[148,†] J. Erdmann,[43,†] A. Ereditato,[17,†] G. Ernis,[175,†] J. Ernst,[2,†] M. Ernst,[25,†] S. Errede,[165,†] E. Ertel,[83,†] M. Escalier,[117,†] H. Esch,[43,†] C. Escobar,[125,†] B. Esposito,[47,†] A. I. Etienvre,[136,†] E. Etzion,[153,†] H. Evans,[61,†] A. Ezhilov,[123,†] L. Fabbri,[20a,20b,†] G. Facini,[31,†] R. M. Fakhrutdinov,[130,†] S. Falciano,[132a,†] R. J. Falla,[78,†] J. Faltova,[129,†] Y. Fang,[33a,†] M. Fanti,[91a,91b,†] A. Farbin,[8,†] A. Farilla,[134a,†] T. Farooque,[12,†] S. Farrell,[15,†] S. M. Farrington,[170,†] P. Farthouat,[30,†] F. Fassi,[135e,†] P. Fassnacht,[30,†] D. Fassouliotis,[9,†] M. Faucci Giannelli,[77,†] A. Favareto,[50a,50b,†] L. Fayard,[117,†] P. Federic,[144a,†] O. L. Fedin,[123,n,†] W. Fedorko,[168,†] S. Feigl,[30,†] L. Feligioni,[85,†] C. Feng,[33d,†] E. J. Feng,[6,†] H. Feng,[89,†] A. B. Fenyuk,[130,†] P. Fernandez Martinez,[167,†] S. Fernandez Perez,[30,†] S. Ferrag,[53,†] J. Ferrando,[53,†] A. Ferrari,[166,†] P. Ferrari,[107,†] R. Ferrari,[121a,†] D. E. Ferreira de Lima,[53,†] A. Ferrer,[167,†] D. Ferrere,[49,†] C. Ferretti,[89,†] A. Ferretto Parodi,[50a,50b,†] M. Fiascaris,[31,†] F. Fiedler,[83,†] A. Filipčič,[75,†] M. Filipuzzi,[42,†] F. Filthaut,[106,†] M. Fincke-Keeler,[169,†] K. D. Finelli,[150,†] M. C. N. Fiolhais,[126a,126c,†] L. Fiorini,[167,†] A. Firan,[40,†] A. Fischer,[2,†] C. Fischer,[12,†] J. Fischer,[175,†] W. C. Fisher,[90,†] E. A. Fitzgerald,[23,†] M. Flechl,[48,†] I. Fleck,[141,†] P. Fleischmann,[89,†] S. Fleischmann,[175,†] G. T. Fletcher,[139,†] G. Fletcher,[76,†] T. Flick,[175,†] A. Floderus,[81,†] L. R. Flores Castillo,[60a,†] M. J. Flowerdew,[101,†] A. Formica,[136,†] A. Forti,[84,†] D. Fournier,[117,†] H. Fox,[72,†] S. Fracchia,[12,†] P. Francavilla,[80,†] M. Franchini,[20a,20b,†] D. Francis,[30,†] L. Franconi,[119,†] M. Franklin,[57,†] M. Fraternali,[121a,121b,†] D. Freeborn,[78,†] S. T. French,[28,†] F. Friedrich,[44,†] D. Froidevaux,[30,†] J. A. Frost,[120,†] C. Fukunaga,[156,†] E. Fullana Torregrosa,[83,†] B. G. Fulsom,[143,†] J. Fuster,[167,†] C. Gabaldon,[55,†] O. Gabizon,[175,†] A. Gabrielli,[20a,20b,†] A. Gabrielli,[132a,132b,†] S. Gadatsch,[107,†] S. Gadomski,[49,†] G. Gagliardi,[50a,50b,†] P. Gagnon,[61,†] C. Galea,[106,†] B. Galhardo,[126a,126c,†] E. J. Gallas,[120,†] B. J. Gallop,[131,†] P. Gallus,[128,†] G. Galster,[36,†] K. K. Gan,[111,†] J. Gao,[33b,85,†] Y. Gao,[46,†] Y. S. Gao,[143,f,†] F. M. Garay Walls,[46,†] F. Garberson,[176,†] C. García,[167,†] J. E. García Navarro,[167,†] M. Garcia-Sciveres,[15,†]

R. W. Gardner,[31,†] N. Garelli,[143,†] V. Garonne,[119,†] C. Gatti,[47,†] A. Gaudiello,[50a,50b,†] G. Gaudio,[121a,†] B. Gaur,[141,†] L. Gauthier,[95,†] P. Gauzzi,[132a,132b,†] I. L. Gavrilenko,[96,†] C. Gay,[168,†] G. Gaycken,[21,†] E. N. Gazis,[10,†] P. Ge,[33d,†] Z. Gecse,[168,†] C. N. P. Gee,[131,†] D. A. A. Geerts,[107,†] Ch. Geich-Gimbel,[21,†] M. P. Geisler,[58a,†] C. Gemme,[50a,†] M. H. Genest,[55,†] S. Gentile,[132a,132b,†] M. George,[54,†] S. George,[77,†] D. Gerbaudo,[163,†] A. Gershon,[153,†] H. Ghazlane,[135b,†] B. Giacobbe,[20a,†] S. Giagu,[132a,132b,†] V. Giangiobbe,[12,†] P. Giannetti,[124a,124b,†] B. Gibbard,[25,†] S. M. Gibson,[77,†] M. Gilchriese,[15,†] T. P. S. Gillam,[28,†] D. Gillberg,[30,†] G. Gilles,[34,†] D. M. Gingrich,[3,e,†] N. Giokaris,[9,†] M. P. Giordani,[164a,164c,†] F. M. Giorgi,[20a,†] F. M. Giorgi,[16,†] P. F. Giraud,[136,†] P. Giromini,[47,†] D. Giugni,[91a,†] C. Giuliani,[48,†] M. Giulini,[58b,†] B. K. Gjelsten,[119,†] S. Gkaitatzis,[154,†] I. Gkialas,[154,†] E. L. Gkougkousis,[117,†] L. K. Gladilin,[99,†] C. Glasman,[82,†] J. Glatzer,[30,†] P. C. F. Glaysher,[46,†] A. Glazov,[42,†] M. Goblirsch-Kolb,[101,†] J. R. Goddard,[76,†] J. Godlewski,[39,†] S. Goldfarb,[89,†] T. Golling,[49,†] D. Golubkov,[130,†] A. Gomes,[126a,126b,126d,†] R. Gonçalo,[126a,†] J. Goncalves Pinto Firmino Da Costa,[136,†] L. Gonella,[21,†] S. González de la Hoz,[167,†] G. Gonzalez Parra,[12,†] S. Gonzalez-Sevilla,[49,†] L. Goossens,[30,†] P. A. Gorbounov,[97,†] H. A. Gordon,[25,†] I. Gorelov,[105,†] B. Gorini,[30,†] E. Gorini,[73a,73b,†] A. Gorišek,[75,†] E. Gornicki,[39,†] A. T. Goshaw,[45,†] C. Gössling,[43,†] M. I. Gostkin,[65,†] D. Goujdami,[135c,†] A. G. Goussiou,[138,†] N. Govender,[145b,†] H. M. X. Grabas,[137,†] L. Graber,[54,†] I. Grabowska-Bold,[38a,†] P. Grafström,[20a,20b,†] K-J. Grahn,[42,†] J. Gramling,[49,†] E. Gramstad,[119,†] S. Grancagnolo,[16,†] V. Grassi,[148,†] V. Gratchev,[123,†] H. M. Gray,[30,†] E. Graziani,[134a,†] Z. D. Greenwood,[79,o,†] K. Gregersen,[78,†] I. M. Gregor,[42,†] P. Grenier,[143,†] J. Griffiths,[8,†] A. A. Grillo,[137,†] K. Grimm,[72,†] S. Grinstein,[12,p,†] Ph. Gris,[34,†] J.-F. Grivaz,[117,†] J. P. Grohs,[44,†] A. Grohsjean,[42,†] E. Gross,[172,†] J. Grosse-Knetter,[54,†] G. C. Grossi,[79,†] Z. J. Grout,[149,†] L. Guan,[33b,†] J. Guenther,[128,†] F. Guescini,[49,†] D. Guest,[176,†] O. Gueta,[153,†] E. Guido,[50a,50b,†] T. Guillemin,[117,†] S. Guindon,[2,†] U. Gul,[53,†] C. Gumpert,[44,†] J. Guo,[33e,†] S. Gupta,[120,†] P. Gutierrez,[113,†] N. G. Gutierrez Ortiz,[53,†] C. Gutschow,[44,†] C. Guyot,[136,†] C. Gwenlan,[120,†] C. B. Gwilliam,[74,†] A. Haas,[110,†] C. Haber,[15,†] H. K. Hadavand,[8,†] N. Haddad,[135e,†] P. Haefner,[21,†] S. Hageböck,[21,†] Z. Hajduk,[39,†] H. Hakobyan,[177,†] M. Haleem,[42,†] J. Haley,[114,†] D. Hall,[120,†] G. Halladjian,[90,†] G. D. Hallewell,[85,†] K. Hamacher,[175,†] P. Hamal,[115,†] K. Hamano,[169,†] M. Hamer,[54,†] A. Hamilton,[145a,†] G. N. Hamity,[145c,†] P. G. Hamnett,[42,†] L. Han,[33b,†] K. Hanagaki,[118,†] K. Hanawa,[155,†] M. Hance,[15,†] P. Hanke,[58a,†] R. Hanna,[136,†] J. B. Hansen,[36,†] J. D. Hansen,[36,†] M. C. Hansen,[21,†] P. H. Hansen,[36,†] K. Hara,[160,†] A. S. Hard,[173,†] T. Harenberg,[175,†] F. Hariri,[117,†] S. Harkusha,[92,†] R. D. Harrington,[46,†] P. F. Harrison,[170,†] F. Hartjes,[107,†] M. Hasegawa,[67,†] S. Hasegawa,[103,†] Y. Hasegawa,[140,†] A. Hasib,[113,†] S. Hassani,[136,†] S. Haug,[17,†] R. Hauser,[90,†] L. Hauswald,[44,†] M. Havranek,[127,†] C. M. Hawkes,[18,†] R. J. Hawkings,[30,†] A. D. Hawkins,[81,†] T. Hayashi,[160,†] D. Hayden,[90,†] C. P. Hays,[120,†] J. M. Hays,[76,†] H. S. Hayward,[74,†] S. J. Haywood,[131,†] S. J. Head,[18,†] T. Heck,[83,†] V. Hedberg,[81,†] L. Heelan,[8,†] S. Heim,[122,†] T. Heim,[175,†] B. Heinemann,[15,†] L. Heinrich,[110,†] J. Hejbal,[127,†] L. Helary,[22,†] S. Hellman,[146a,146b,†] D. Hellmich,[21,†] C. Helsens,[30,†] J. Henderson,[120,†] R. C. W. Henderson,[72,†] Y. Heng,[173,†] C. Hengler,[42,†] A. Henrichs,[176,†] A. M. Henriques Correia,[30,†] S. Henrot-Versille,[117,†] G. H. Herbert,[16,†] Y. Hernández Jiménez,[167,†] R. Herrberg-Schubert,[16,†] G. Herten,[48,†] R. Hertenberger,[100,†] L. Hervas,[30,†] G. G. Hesketh,[78,†] N. P. Hessey,[107,†] J. W. Hetherly,[40,†] R. Hickling,[76,†] E. Higón-Rodriguez,[167,†] E. Hill,[169,†] J. C. Hill,[28,†] K. H. Hiller,[42,†] S. J. Hillier,[18,†] I. Hinchliffe,[15,†] E. Hines,[122,†] R. R. Hinman,[15,†] M. Hirose,[157,†] D. Hirschbuehl,[175,†] J. Hobbs,[148,†] N. Hod,[107,†] M. C. Hodgkinson,[139,†] P. Hodgson,[139,†] A. Hoecker,[30,†] M. R. Hoeferkamp,[105,†] F. Hoenig,[100,†] M. Hohlfeld,[83,†] D. Hohn,[21,†] T. R. Holmes,[15,†] T. M. Hong,[122,†] L. Hooft van Huysduynen,[110,†] W. H. Hopkins,[116,†] Y. Horii,[103,†] A. J. Horton,[142,†] J-Y. Hostachy,[55,†] S. Hou,[151,†] A. Hoummada,[135a,†] J. Howard,[120,†] J. Howarth,[42,†] M. Hrabovsky,[115,†] I. Hristova,[16,†] J. Hrivnac,[117,†] T. Hryn'ova,[5,†] A. Hrynevich,[93,†] C. Hsu,[145c,†] P. J. Hsu,[151,q,†] S.-C. Hsu,[138,†] D. Hu,[35,†] Q. Hu,[33b,†] X. Hu,[89,†] Y. Huang,[42,†] Z. Hubacek,[30,†] F. Hubaut,[85,†] F. Huegging,[21,†] T. B. Huffman,[120,†] E. W. Hughes,[35,†] G. Hughes,[72,†] M. Huhtinen,[30,†] T. A. Hülsing,[83,†] N. Huseynov,[65,c,†] J. Huston,[90,†] J. Huth,[57,†] G. Iacobucci,[49,†] G. Iakovidis,[25,†] I. Ibragimov,[141,†] L. Iconomidou-Fayard,[117,†] E. Ideal,[176,†] Z. Idrissi,[135e,†] P. Iengo,[30,†] O. Igonkina,[107,†] T. Iizawa,[171,†] Y. Ikegami,[66,†] K. Ikematsu,[141,†] M. Ikeno,[66,†] Y. Ilchenko,[31,r,†] D. Iliadis,[154,†] N. Ilic,[143,†] Y. Inamaru,[67,†] T. Ince,[101,†] P. Ioannou,[9,†] M. Iodice,[134a,†] K. Iordanidou,[35,†] V. Ippolito,[57,†] A. Irles Quiles,[167,†] C. Isaksson,[166,†] M. Ishino,[68,†] M. Ishitsuka,[157,†] R. Ishmukhametov,[111,†] C. Issever,[120,†] S. Istin,[19a,†] J. M. Iturbe Ponce,[84,†] R. Iuppa,[133a,133b,†] J. Ivarsson,[81,†] W. Iwanski,[39,†] H. Iwasaki,[66,†] J. M. Izen,[41,†] V. Izzo,[104a,†] S. Jabbar,[3,†] B. Jackson,[122,†] M. Jackson,[74,†] P. Jackson,[1,†] M. R. Jaekel,[30,†] V. Jain,[2,†] K. Jakobs,[48,†] S. Jakobsen,[30,†] T. Jakoubek,[127,†] J. Jakubek,[128,†] D. O. Jamin,[151,†] D. K. Jana,[79,†] E. Jansen,[78,†] R. W. Jansky,[62,†] J. Janssen,[21,†] M. Janus,[170,†] G. Jarlskog,[81,†] N. Javadov,[65,c,†] T. Javůrek,[48,†] L. Jeanty,[15,†] J. Jejelava,[51a,s,†] G.-Y. Jeng,[150,†] D. Jennens,[88,†] P. Jenni,[48,t,†] J. Jentzsch,[43,†] C. Jeske,[170,†] S. Jézéquel,[5,†] H. Ji,[173,†] J. Jia,[148,†] Y. Jiang,[33b,†] S. Jiggins,[78,†] J. Jimenez Pena,[167,†] S. Jin,[33a,†] A. Jinaru,[26a,†] O. Jinnouchi,[157,†] M. D. Joergensen,[36,†] P. Johansson,[139,†] K. A. Johns,[7,†]

K. Jon-And,[146a,146b,†] G. Jones,[170,†] R. W. L. Jones,[72,†] T. J. Jones,[74,†] J. Jongmanns,[58a,†] P. M. Jorge,[126a,126b,†] K. D. Joshi,[84,†] J. Jovicevic,[159a,†] X. Ju,[173,†] C. A. Jung,[43,†] P. Jussel,[62,†] A. Juste Rozas,[12,p,†] M. Kaci,[167,†] A. Kaczmarska,[39,†] M. Kado,[117,†] H. Kagan,[111,†] M. Kagan,[143,†] S. J. Kahn,[85,†] E. Kajomovitz,[45,†] C. W. Kalderon,[120,†] S. Kama,[40,†] A. Kamenshchikov,[130,†] N. Kanaya,[155,†] M. Kaneda,[30,†] S. Kaneti,[28,†] V. A. Kantserov,[98,†] J. Kanzaki,[66,†] B. Kaplan,[110,†] A. Kapliy,[31,†] D. Kar,[53,†] K. Karakostas,[10,†] A. Karamaoun,[3,†] N. Karastathis,[10,107,†] M. J. Kareem,[54,†] M. Karnevskiy,[83,†] S. N. Karpov,[65,†] Z. M. Karpova,[65,†] K. Karthik,[110,†] V. Kartvelishvili,[72,†] A. N. Karyukhin,[130,†] L. Kashif,[173,†] R. D. Kass,[111,†] A. Kastanas,[14,†] Y. Kataoka,[155,†] A. Katre,[49,†] J. Katzy,[42,†] K. Kawagoe,[70,†] T. Kawamoto,[155,†] G. Kawamura,[54,†] S. Kazama,[155,†] V. F. Kazanin,[109,d,†] M. Y. Kazarinov,[65,†] R. Keeler,[169,†] R. Kehoe,[40,†] J. S. Keller,[42,†] J. J. Kempster,[77,†] H. Keoshkerian,[84,†] O. Kepka,[127,†] B. P. Kerševan,[75,†] S. Kersten,[175,†] R. A. Keyes,[87,†] F. Khalil-zada,[11,†] H. Khandanyan,[146a,146b,†] A. Khanov,[114,†] A. G. Kharlamov,[109,d,†] T. J. Khoo,[28,†] V. Khovanskiy,[97,†] E. Khramov,[65,†] J. Khubua,[51b,u,†] H. Y. Kim,[8,†] H. Kim,[146a,146b,†] S. H. Kim,[160,†] Y. Kim,[31,†] N. Kimura,[154,†] O. M. Kind,[16,†] B. T. King,[74,†] M. King,[167,†] R. S. B. King,[120,†] S. B. King,[168,†] J. Kirk,[131,†] A. E. Kiryunin,[101,†] T. Kishimoto,[67,†] D. Kisielewska,[38a,†] F. Kiss,[48,†] K. Kiuchi,[160,†] O. Kivernyk,[136,†] E. Kladiva,[144b,†] M. H. Klein,[35,†] M. Klein,[74,†] U. Klein,[74,†] K. Kleinknecht,[83,†] P. Klimek,[146a,146b,†] A. Klimentov,[25,†] R. Klingenberg,[43,†] J. A. Klinger,[84,†] T. Klioutchnikova,[30,†] E.-E. Kluge,[58a,†] P. Kluit,[107,†] S. Kluth,[101,†] E. Kneringer,[62,†] E. B. F. G. Knoops,[85,†] A. Knue,[53,†] A. Kobayashi,[155,†] D. Kobayashi,[157,†] T. Kobayashi,[155,†] M. Kobel,[44,†] M. Kocian,[143,†] P. Kodys,[129,†] T. Koffas,[29,†] E. Koffeman,[107,†] L. A. Kogan,[120,†] S. Kohlmann,[175,†] Z. Kohout,[128,†] T. Kohriki,[66,†] T. Koi,[143,†] H. Kolanoski,[16,†] I. Koletsou,[5,†] A. A. Komar,[96,a,*] Y. Komori,[155,†] T. Kondo,[66,†] N. Kondrashova,[42,†] K. Köneke,[48,†] A. C. König,[106,†] S. König,[83,†] T. Kono,[66,v,†] R. Konoplich,[110,w,†] N. Konstantinidis,[78,†] R. Kopeliansky,[152,†] S. Koperny,[38a,†] L. Köpke,[83,†] A. K. Kopp,[48,†] K. Korcyl,[39,†] K. Kordas,[154,†] A. Korn,[78,†] A. A. Korol,[109,d,†] I. Korolkov,[12,†] E. V. Korolkova,[139,†] O. Kortner,[101,†] S. Kortner,[101,†] T. Kosek,[129,†] V. V. Kostyukhin,[21,†] V. M. Kotov,[65,†] A. Kotwal,[45,†] A. Kourkoumeli-Charalampidi,[154,†] C. Kourkoumelis,[9,†] V. Kouskoura,[25,†] A. Koutsman,[159a,†] R. Kowalewski,[169,†] T. Z. Kowalski,[38a,†] W. Kozanecki,[136,†] A. S. Kozhin,[130,†] V. A. Kramarenko,[99,†] G. Kramberger,[75,†] D. Krasnopevtsev,[98,†] A. Krasznahorkay,[30,†] J. K. Kraus,[21,†] A. Kravchenko,[25,†] S. Kreiss,[110,†] M. Kretz,[58c,†] J. Kretzschmar,[74,†] K. Kreutzfeldt,[52,†] P. Krieger,[158,†] K. Krizka,[31,†] K. Kroeninger,[43,†] H. Kroha,[101,†] J. Kroll,[122,†] J. Kroseberg,[21,†] J. Krstic,[13,†] U. Kruchonak,[65,†] H. Krüger,[21,†] N. Krumnack,[64,†] Z. V. Krumshteyn,[65,†] A. Kruse,[173,†] M. C. Kruse,[45,†] M. Kruskal,[22,†] T. Kubota,[88,†] H. Kucuk,[78,†] S. Kuday,[4b,†] S. Kuehn,[48,†] A. Kugel,[58c,†] F. Kuger,[174,†] A. Kuhl,[137,†] T. Kuhl,[42,†] V. Kukhtin,[65,†] Y. Kulchitsky,[92,†] S. Kuleshov,[32b,†] M. Kuna,[132a,132b,†] T. Kunigo,[68,†] A. Kupco,[127,†] H. Kurashige,[67,†] Y. A. Kurochkin,[92,†] R. Kurumida,[67,†] V. Kus,[127,†] E. S. Kuwertz,[169,†] M. Kuze,[157,†] J. Kvita,[115,†] T. Kwan,[169,†] D. Kyriazopoulos,[139,†] A. La Rosa,[49,†] J. L. La Rosa Navarro,[24d,†] L. La Rotonda,[37a,37b,†] C. Lacasta,[167,†] F. Lacava,[132a,132b,†] J. Lacey,[29,†] H. Lacker,[16,†] D. Lacour,[80,†] V. R. Lacuesta,[167,†] E. Ladygin,[65,†] R. Lafaye,[5,†] B. Laforge,[80,†] T. Lagouri,[176,†] S. Lai,[48,†] L. Lambourne,[78,†] S. Lammers,[61,†] C. L. Lampen,[7,†] W. Lampl,[7,†] E. Lançon,[136,†] U. Landgraf,[48,†] M. P. J. Landon,[76,†] V. S. Lang,[58a,†] J. C. Lange,[12,†] A. J. Lankford,[163,†] F. Lanni,[25,†] K. Lantzsch,[30,†] S. Laplace,[80,†] C. Lapoire,[30,†] J. F. Laporte,[136,†] T. Lari,[91a,†] F. Lasagni Manghi,[20a,20b,†] M. Lassnig,[30,†] P. Laurelli,[47,†] W. Lavrijsen,[15,†] A. T. Law,[137,†] P. Laycock,[74,†] O. Le Dortz,[80,†] E. Le Guirriec,[85,†] E. Le Menedeu,[12,†] M. LeBlanc,[169,†] T. LeCompte,[6,†] F. Ledroit-Guillon,[55,†] C. A. Lee,[145b,†] S. C. Lee,[151,†] L. Lee,[1,†] G. Lefebvre,[80,†] M. Lefebvre,[169,†] F. Legger,[100,†] C. Leggett,[15,†] A. Lehan,[74,†] G. Lehmann Miotto,[30,†] X. Lei,[7,†] W. A. Leight,[29,†] A. Leisos,[154,†] A. G. Leister,[176,†] M. A. L. Leite,[24d,†] R. Leitner,[129,†] D. Lellouch,[172,†] B. Lemmer,[54,†] K. J. C. Leney,[78,†] T. Lenz,[21,†] B. Lenzi,[30,†] R. Leone,[7,†] S. Leone,[124a,124b,†] C. Leonidopoulos,[46,†] S. Leontsinis,[10,†] C. Leroy,[95,†] C. G. Lester,[28,†] M. Levchenko,[123,†] J. Levêque,[5,†] D. Levin,[89,†] L. J. Levinson,[172,†] M. Levy,[18,†] A. Lewis,[120,†] A. M. Leyko,[21,†] M. Leyton,[41,†] B. Li,[33b,x,†] H. Li,[148,†] H. L. Li,[31,†] L. Li,[45,†] L. Li,[33e,†] S. Li,[45,†] Y. Li,[33c,y,†] Z. Liang,[137,†] H. Liao,[34,†] B. Liberti,[133a,†] A. Liblong,[158,†] P. Lichard,[30,†] K. Lie,[165,†] J. Liebal,[21,†] W. Liebig,[14,†] C. Limbach,[21,†] A. Limosani,[150,†] S. C. Lin,[151,z,†] T. H. Lin,[83,†] F. Linde,[107,†] B. E. Lindquist,[148,†] J. T. Linnemann,[90,†] E. Lipeles,[122,†] A. Lipniacka,[14,†] M. Lisovyi,[58b,†] T. M. Liss,[165,†] D. Lissauer,[25,†] A. Lister,[168,†] A. M. Litke,[137,†] B. Liu,[151,aa,†] D. Liu,[151,†] J. Liu,[85,†] J. B. Liu,[33b,†] K. Liu,[85,†] L. Liu,[165,†] M. Liu,[45,†] M. Liu,[33b,†] Y. Liu,[33b,†] M. Livan,[121a,121b,†] A. Lleres,[55,†] J. Llorente Merino,[82,†] S. L. Lloyd,[76,†] F. Lo Sterzo,[151,†] E. Lobodzinska,[42,†] P. Loch,[7,†] W. S. Lockman,[137,†] F. K. Loebinger,[84,†] A. E. Loevschall-Jensen,[36,†] A. Loginov,[176,†] T. Lohse,[16,†] K. Lohwasser,[42,†] M. Lokajicek,[127,†] B. A. Long,[22,†] J. D. Long,[89,†] R. E. Long,[72,†] K. A. Looper,[111,†] L. Lopes,[126a,†] D. Lopez Mateos,[57,†] B. Lopez Paredes,[139,†] I. Lopez Paz,[12,†] J. Lorenz,[100,†] N. Lorenzo Martinez,[61,†] M. Losada,[162,†] P. Loscutoff,[15,†] P. J. Lösel,[100,†] X. Lou,[33a,†] A. Lounis,[117,†] J. Love,[6,†] P. A. Love,[72,†] N. Lu,[89,†] H. J. Lubatti,[138,†] C. Luci,[132a,132b,†] A. Lucotte,[55,†] F. Luehring,[61,†]

W. Lukas,[62,†] L. Luminari,[132a,†] O. Lundberg,[146a,146b,†] B. Lund-Jensen,[147,†] D. Lynn,[25,†] R. Lysak,[127,†] E. Lytken,[81,†] H. Ma,[25,†] L. L. Ma,[33d,†] G. Maccarrone,[47,†] A. Macchiolo,[101,†] C. M. Macdonald,[139,†] J. Machado Miguens,[122,126b,†] D. Macina,[30,†] D. Madaffari,[85,†] R. Madar,[34,†] H. J. Maddocks,[72,†] W. F. Mader,[44,†] A. Madsen,[166,†] S. Maeland,[14,†] T. Maeno,[25,†] A. Maevskiy,[99,†] E. Magradze,[54,†] K. Mahboubi,[48,†] J. Mahlstedt,[107,†] C. Maiani,[136,†] C. Maidantchik,[24a,†] A. A. Maier,[101,†] T. Maier,[100,†] A. Maio,[126a,126b,126d,†] S. Majewski,[116,†] Y. Makida,[66,†] N. Makovec,[117,†] B. Malaescu,[80,†] Pa. Malecki,[39,†] V. P. Maleev,[123,†] F. Malek,[55,†] U. Mallik,[63,†] D. Malon,[6,†] C. Malone,[143,†] S. Maltezos,[10,†] V. M. Malyshev,[109,†] S. Malyukov,[30,†] J. Mamuzic,[42,†] G. Mancini,[47,†] B. Mandelli,[30,†] L. Mandelli,[91a,†] I. Mandić,[75,†] R. Mandrysch,[63,†] J. Maneira,[126a,126b,†] A. Manfredini,[101,†] L. Manhaes de Andrade Filho,[24b,†] J. Manjarres Ramos,[159b,†] A. Mann,[100,†] P. M. Manning,[137,†] A. Manousakis-Katsikakis,[9,†] B. Mansoulie,[136,†] R. Mantifel,[87,†] M. Mantoani,[54,†] L. Mapelli,[30,†] L. March,[145c,†] G. Marchiori,[80,†] M. Marcisovsky,[127,†] C. P. Marino,[169,†] M. Marjanovic,[13,†] F. Marroquim,[24a,†] S. P. Marsden,[84,†] Z. Marshall,[15,†] L. F. Marti,[17,†] S. Marti-Garcia,[167,†] B. Martin,[90,†] T. A. Martin,[170,†] V. J. Martin,[46,†] B. Martin dit Latour,[14,†] M. Martinez,[12,p,†] S. Martin-Haugh,[131,†] V. S. Martoiu,[26a,†] A. C. Martyniuk,[78,†] M. Marx,[138,†] F. Marzano,[132a,†] A. Marzin,[30,†] L. Masetti,[83,†] T. Mashimo,[155,†] R. Mashinistov,[96,†] J. Masik,[84,†] A. L. Maslennikov,[109,d,†] I. Massa,[20a,20b,†] L. Massa,[20a,20b,†] N. Massol,[5,†] P. Mastrandrea,[148,†] A. Mastroberardino,[37a,37b,†] T. Masubuchi,[155,†] P. Mättig,[175,†] J. Mattmann,[83,†] J. Maurer,[26a,†] S. J. Maxfield,[74,†] D. A. Maximov,[109,d,†] R. Mazini,[151,†] S. M. Mazza,[91a,91b,†] L. Mazzaferro,[133a,133b,†] G. Mc Goldrick,[158,†] S. P. Mc Kee,[89,†] A. McCarn,[89,†] R. L. McCarthy,[148,†] T. G. McCarthy,[29,†] N. A. McCubbin,[131,†] K. W. McFarlane,[56,a,†] J. A. Mcfayden,[78,†] G. Mchedlidze,[54,†] S. J. McMahon,[131,†] R. A. McPherson,[169,l,†] M. Medinnis,[42,†] S. Meehan,[145a,†] S. Mehlhase,[100,†] A. Mehta,[74,†] K. Meier,[58a,†] C. Meineck,[100,†] B. Meirose,[41,†] B. R. Mellado Garcia,[145c,†] F. Meloni,[17,†] A. Mengarelli,[20a,20b,†] S. Menke,[101,†] E. Meoni,[161,†] K. M. Mercurio,[57,†] S. Mergelmeyer,[21,†] P. Mermod,[49,†] L. Merola,[104a,104b,†] C. Meroni,[91a,†] F. S. Merritt,[31,†] A. Messina,[132a,132b,†] J. Metcalfe,[25,†] A. S. Mete,[163,†] C. Meyer,[83,†] C. Meyer,[122,†] J-P. Meyer,[136,†] J. Meyer,[107,†] R. P. Middleton,[131,†] S. Miglioranzi,[164a,164c,†] L. Mijović,[21,†] G. Mikenberg,[172,†] M. Mikestikova,[127,†] M. Mikuž,[75,†] M. Milesi,[88,†] A. Milic,[30,†] D. W. Miller,[31,†] C. Mills,[46,†] A. Milov,[172,†] D. A. Milstead,[146a,146b,†] A. A. Minaenko,[130,†] Y. Minami,[155,†] I. A. Minashvili,[65,†] A. I. Mincer,[110,†] B. Mindur,[38a,†] M. Mineev,[65,†] Y. Ming,[173,†] L. M. Mir,[12,†] T. Mitani,[171,†] J. Mitrevski,[100,†] V. A. Mitsou,[167,†] A. Miucci,[49,†] P. S. Miyagawa,[139,†] J. U. Mjörnmark,[81,†] T. Moa,[146a,146b,†] K. Mochizuki,[85,†] S. Mohapatra,[35,†] W. Mohr,[48,†] S. Molander,[146a,146b,†] R. Moles-Valls,[167,†] K. Mönig,[42,†] C. Monini,[55,†] J. Monk,[36,†] E. Monnier,[85,†] J. Montejo Berlingen,[12,†] F. Monticelli,[71,†] S. Monzani,[132a,132b,†] R. W. Moore,[3,†] N. Morange,[117,†] D. Moreno,[162,†] M. Moreno Llácer,[54,†] P. Morettini,[50a,†] M. Morgenstern,[44,†] M. Morii,[57,†] M. Morinaga,[155,†] V. Morisbak,[119,†] S. Moritz,[83,†] A. K. Morley,[147,†] G. Mornacchi,[30,†] J. D. Morris,[76,†] S. S. Mortensen,[36,†] A. Morton,[53,†] L. Morvaj,[103,†] M. Mosidze,[51b,†] J. Moss,[111,†] K. Motohashi,[157,†] R. Mount,[143,†] E. Mountricha,[25,†] S. V. Mouraviev,[96,a,†] E. J. W. Moyse,[86,†] S. Muanza,[85,†] R. D. Mudd,[18,†] F. Mueller,[101,†] J. Mueller,[125,†] K. Mueller,[21,†] R. S. P. Mueller,[100,†] T. Mueller,[28,†] D. Muenstermann,[49,†] P. Mullen,[53,†] Y. Munwes,[153,†] J. A. Murillo Quijada,[18,†] W. J. Murray,[170,131,†] H. Musheghyan,[54,†] E. Musto,[152,†] A. G. Myagkov,[130,bb,†] M. Myska,[128,†] O. Nackenhorst,[54,†] J. Nadal,[54,†] K. Nagai,[120,†] R. Nagai,[157,†] Y. Nagai,[85,†] K. Nagano,[66,†] A. Nagarkar,[111,†] Y. Nagasaka,[59,†] K. Nagata,[160,†] M. Nagel,[101,†] E. Nagy,[85,†] A. M. Nairz,[30,†] Y. Nakahama,[30,†] K. Nakamura,[66,†] T. Nakamura,[155,†] I. Nakano,[112,†] H. Namasivayam,[41,†] R. F. Naranjo Garcia,[42,†] R. Narayan,[31,†] T. Naumann,[42,†] G. Navarro,[162,†] R. Nayyar,[7,†] H. A. Neal,[89,†] P.Yu. Nechaeva,[96,†] T. J. Neep,[84,†] P. D. Nef,[143,†] A. Negri,[121a,121b,†] M. Negrini,[20a,†] S. Nektarijevic,[106,†] C. Nellist,[117,†] A. Nelson,[163,†] S. Nemecek,[127,†] P. Nemethy,[110,†] A. A. Nepomuceno,[24a,†] M. Nessi,[30,cc,†] M. S. Neubauer,[165,†] M. Neumann,[175,†] R. M. Neves,[110,†] P. Nevski,[25,†] P. R. Newman,[18,†] D. H. Nguyen,[6,†] R. B. Nickerson,[120,†] R. Nicolaidou,[136,†] B. Nicquevert,[30,†] J. Nielsen,[137,†] N. Nikiforou,[35,†] A. Nikiforov,[16,†] V. Nikolaenko,[130,bb,†] I. Nikolic-Audit,[80,†] K. Nikolopoulos,[18,†] J. K. Nilsen,[119,†] P. Nilsson,[25,†] Y. Ninomiya,[155,†] A. Nisati,[132a,†] R. Nisius,[101,†] T. Nobe,[157,†] M. Nomachi,[118,†] I. Nomidis,[29,†] T. Nooney,[76,†] S. Norberg,[113,†] M. Nordberg,[30,†] O. Novgorodova,[44,†] S. Nowak,[101,†] M. Nozaki,[66,†] L. Nozka,[115,†] K. Ntekas,[10,†] G. Nunes Hanninger,[88,†] T. Nunnemann,[100,†] E. Nurse,[78,†] F. Nuti,[88,†] B. J. O'Brien,[46,†] F. O'grady,[7,†] D. C. O'Neil,[142,†] V. O'Shea,[53,†] F. G. Oakham,[29,e,†] H. Oberlack,[101,†] T. Obermann,[21,†] J. Ocariz,[80,†] A. Ochi,[67,†] I. Ochoa,[78,†] J. P. Ochoa-Ricoux,[32a,†] S. Oda,[70,†] S. Odaka,[66,†] H. Ogren,[61,†] A. Oh,[84,†] S. H. Oh,[45,†] C. C. Ohm,[15,†] H. Ohman,[166,†] H. Oide,[30,†] W. Okamura,[118,†] H. Okawa,[160,†] Y. Okumura,[31,†] T. Okuyama,[155,†] A. Olariu,[26a,†] S. A. Olivares Pino,[46,†] D. Oliveira Damazio,[25,†] E. Oliver Garcia,[167,†] A. Olszewski,[39,†] J. Olszowska,[39,†] A. Onofre,[126a,126e,†] P. U. E. Onyisi,[31,r,†] C. J. Oram,[159a,†] M. J. Oreglia,[31,†] Y. Oren,[153,†] D. Orestano,[134a,134b,†] N. Orlando,[154,†] C. Oropeza Barrera,[53,†] R. S. Orr,[158,†] B. Osculati,[50a,50b,†] R. Ospanov,[84,†]

G. Otero y Garzon,[27,†] H. Otono,[70,†] M. Ouchrif,[135d,†] E. A. Ouellette,[169,†] F. Ould-Saada,[119,†] A. Ouraou,[136,†] K. P. Oussoren,[107,†] Q. Ouyang,[33a,†] A. Ovcharova,[15,†] M. Owen,[53,†] R. E. Owen,[18,†] V. E. Ozcan,[19a,†] N. Ozturk,[8,†] K. Pachal,[142,†] A. Pacheco Pages,[12,†] C. Padilla Aranda,[12,†] M. Pagáčová,[48,†] S. Pagan Griso,[15,†] E. Paganis,[139,†] C. Pahl,[101,†] F. Paige,[25,†] P. Pais,[86,†] K. Pajchel,[119,†] G. Palacino,[159b,†] S. Palestini,[30,†] M. Palka,[38b,†] D. Pallin,[34,†] A. Palma,[126a,126b,†] Y. B. Pan,[173,†] E. Panagiotopoulou,[10,†] C. E. Pandini,[80,†] J. G. Panduro Vazquez,[77,†] P. Pani,[146a,146b,†] S. Panitkin,[25,†] D. Pantea,[26a,†] L. Paolozzi,[49,†] Th.D. Papadopoulou,[10,†] K. Papageorgiou,[154,†] A. Paramonov,[6,†] D. Paredes Hernandez,[154,†] M. A. Parker,[28,†] K. A. Parker,[139,†] F. Parodi,[50a,50b,†] J. A. Parsons,[35,†] U. Parzefall,[48,†] E. Pasqualucci,[132a,†] S. Passaggio,[50a,†] F. Pastore,[134a,134b,a,†] Fr. Pastore,[77,†] G. Pásztor,[29,†] S. Pataraia,[175,†] N. D. Patel,[150,†] J. R. Pater,[84,†] T. Pauly,[30,†] J. Pearce,[169,†] B. Pearson,[113,†] L. E. Pedersen,[36,†] M. Pedersen,[119,†] S. Pedraza Lopez,[167,†] R. Pedro,[126a,126b,†] S. V. Peleganchuk,[109,†] D. Pelikan,[166,†] H. Peng,[33b,†] B. Penning,[31,†] J. Penwell,[61,†] D. V. Perepelitsa,[25,†] E. Perez Codina,[159a,†] M. T. Pérez García-Estañ,[167,†] L. Perini,[91a,91b,†] H. Pernegger,[30,†] S. Perrella,[104a,104b,†] R. Peschke,[42,†] V. D. Peshekhonov,[65,†] K. Peters,[30,†] R. F. Y. Peters,[84,†] B. A. Petersen,[30,†] T. C. Petersen,[36,†] E. Petit,[42,†] A. Petridis,[146a,146b,†] C. Petridou,[154,†] E. Petrolo,[132a,†] F. Petrucci,[134a,134b,†] N. E. Pettersson,[157,†] R. Pezoa,[32b,†] P. W. Phillips,[131,†] G. Piacquadio,[143,†] E. Pianori,[170,†] A. Picazio,[49,†] E. Piccaro,[76,†] M. Piccinini,[20a,20b,†] M. A. Pickering,[120,†] R. Piegaia,[27,†] D. T. Pignotti,[111,†] J. E. Pilcher,[31,†] A. D. Pilkington,[84,†] J. Pina,[126a,126b,126d,†] M. Pinamonti,[164a,164c,dd,†] J. L. Pinfold,[3,†] A. Pingel,[36,†] B. Pinto,[126a,†] S. Pires,[80,†] M. Pitt,[172,†] C. Pizio,[91a,91b,†] L. Plazak,[144a,†] M.-A. Pleier,[25,†] V. Pleskot,[129,†] E. Plotnikova,[65,†] P. Plucinski,[146a,146b,†] D. Pluth,[64,†] R. Poettgen,[83,†] L. Poggioli,[117,†] D. Pohl,[21,†] G. Polesello,[121a,†] A. Policicchio,[37a,37b,†] R. Polifka,[158,†] A. Polini,[20a,†] C. S. Pollard,[53,†] V. Polychronakos,[25,†] K. Pommès,[30,†] L. Pontecorvo,[132a,†] B. G. Pope,[90,†] G. A. Popeneciu,[26b,†] D. S. Popovic,[13,†] A. Poppleton,[30,†] S. Pospisil,[128,†] K. Potamianos,[15,†] I. N. Potrap,[65,†] C. J. Potter,[149,†] C. T. Potter,[116,†] G. Poulard,[30,†] J. Poveda,[30,†] V. Pozdnyakov,[65,†] P. Pralavorio,[85,†] A. Pranko,[15,†] S. Prasad,[30,†] S. Prell,[64,†] D. Price,[84,†] L. E. Price,[6,†] M. Primavera,[73a,†] S. Prince,[87,†] M. Proissl,[46,†] K. Prokofiev,[60c,†] F. Prokoshin,[32b,†] E. Protopapadaki,[136,†] S. Protopopescu,[25,†] J. Proudfoot,[6,†] M. Przybycien,[38a,†] E. Ptacek,[116,†] D. Puddu,[134a,134b,†] E. Pueschel,[86,†] D. Puldon,[148,†] M. Purohit,[25,ee,†] P. Puzo,[117,†] J. Qian,[89,†] G. Qin,[53,†] Y. Qin,[84,†] A. Quadt,[54,†] D. R. Quarrie,[15,†] W. B. Quayle,[164a,164b,†] M. Queitsch-Maitland,[84,†] D. Quilty,[53,†] S. Raddum,[119,†] V. Radeka,[25,†] V. Radescu,[42,†] S. K. Radhakrishnan,[148,†] P. Radloff,[116,†] P. Rados,[88,†] F. Ragusa,[91a,91b,†] G. Rahal,[178,†] S. Rajagopalan,[25,†] M. Rammensee,[30,†] C. Rangel-Smith,[166,†] F. Rauscher,[100,†] S. Rave,[83,†] T. Ravenscroft,[53,†] M. Raymond,[30,†] A. L. Read,[119,†] N. P. Readioff,[74,†] D. M. Rebuzzi,[121a,121b,†] A. Redelbach,[174,†] G. Redlinger,[25,†] R. Reece,[137,†] K. Reeves,[41,†] L. Rehnisch,[16,†] H. Reisin,[27,†] M. Relich,[163,†] C. Rembser,[30,†] H. Ren,[33a,†] A. Renaud,[117,†] M. Rescigno,[132a,†] S. Resconi,[91a,†] O. L. Rezanova,[109,d,†] P. Reznicek,[129,†] R. Rezvani,[95,†] R. Richter,[101,†] S. Richter,[78,†] E. Richter-Was,[38b,†] O. Ricken,[21,†] M. Ridel,[80,†] P. Rieck,[16,†] C. J. Riegel,[175,†] J. Rieger,[54,†] M. Rijssenbeek,[148,†] A. Rimoldi,[121a,121b,†] L. Rinaldi,[20a,†] B. Ristić,[49,†] E. Ritsch,[62,†] I. Riu,[12,†] F. Rizatdinova,[114,†] E. Rizvi,[76,†] S. H. Robertson,[87,l,†] A. Robichaud-Veronneau,[87,†] D. Robinson,[28,†] J. E. M. Robinson,[84,†] A. Robson,[53,†] C. Roda,[124a,124b,†] S. Roe,[30,†] O. Røhne,[119,†] S. Rolli,[161,†] A. Romaniouk,[98,†] M. Romano,[20a,20b,†] S. M. Romano Saez,[34,†] E. Romero Adam,[167,†] N. Rompotis,[138,†] M. Ronzani,[48,†] L. Roos,[80,†] E. Ros,[167,†] S. Rosati,[132a,†] K. Rosbach,[48,†] P. Rose,[137,†] P. L. Rosendahl,[14,†] O. Rosenthal,[141,†] V. Rossetti,[146a,146b,†] E. Rossi,[104a,104b,†] L. P. Rossi,[50a,†] R. Rosten,[138,†] M. Rotaru,[26a,†] I. Roth,[172,†] J. Rothberg,[138,†] D. Rousseau,[117,†] C. R. Royon,[136,†] A. Rozanov,[85,†] Y. Rozen,[152,†] X. Ruan,[145c,†] F. Rubbo,[143,†] I. Rubinskiy,[42,†] V. I. Rud,[99,†] C. Rudolph,[44,†] M. S. Rudolph,[158,†] F. Rühr,[48,†] A. Ruiz-Martinez,[30,†] Z. Rurikova,[48,†] N. A. Rusakovich,[65,†] A. Ruschke,[100,†] H. L. Russell,[138,†] J. P. Rutherfoord,[7,†] N. Ruthmann,[48,†] Y. F. Ryabov,[123,†] M. Rybar,[129,†] G. Rybkin,[117,†] N. C. Ryder,[120,†] A. F. Saavedra,[150,†] G. Sabato,[107,†] S. Sacerdoti,[27,†] A. Saddique,[3,†] H. F-W. Sadrozinski,[137,†] R. Sadykov,[65,†] F. Safai Tehrani,[132a,†] M. Saimpert,[136,†] H. Sakamoto,[155,†] Y. Sakurai,[171,†] G. Salamanna,[134a,134b,†] A. Salamon,[133a,†] M. Saleem,[113,†] D. Salek,[107,†] P. H. Sales De Bruin,[138,†] D. Salihagic,[101,†] A. Salnikov,[143,†] J. Salt,[167,†] D. Salvatore,[37a,37b,†] F. Salvatore,[149,†] A. Salvucci,[106,†] A. Salzburger,[30,†] D. Sampsonidis,[154,†] A. Sanchez,[104a,104b,†] J. Sánchez,[167,†] V. Sanchez Martinez,[167,†] H. Sandaker,[14,†] R. L. Sandbach,[76,†] H. G. Sander,[83,†] M. P. Sanders,[100,†] M. Sandhoff,[175,†] C. Sandoval,[162,†] R. Sandstroem,[101,†] D. P. C. Sankey,[131,†] M. Sannino,[50a,50b,†] A. Sansoni,[47,†] C. Santoni,[34,†] R. Santonico,[133a,133b,†] H. Santos,[126a,†] I. Santoyo Castillo,[149,†] K. Sapp,[125,†] A. Sapronov,[65,†] J. G. Saraiva,[126a,126d,†] B. Sarrazin,[21,†] O. Sasaki,[66,†] Y. Sasaki,[155,†] K. Sato,[160,†] G. Sauvage,[5,a,†] E. Sauvan,[5,†] G. Savage,[77,†] P. Savard,[158,e,†] C. Sawyer,[120,†] L. Sawyer,[79,o,†] J. Saxon,[31,†] C. Sbarra,[20a,†] A. Sbrizzi,[20a,20b,†] T. Scanlon,[78,†] D. A. Scannicchio,[163,†] M. Scarcella,[150,†] V. Scarfone,[37a,37b,†] J. Schaarschmidt,[172,†] P. Schacht,[101,†] D. Schaefer,[30,†] R. Schaefer,[42,†] J. Schaeffer,[83,†] S. Schaepe,[21,†] S. Schaetzel,[58b,†] U. Schäfer,[83,†] A. C. Schaffer,[117,†] D. Schaile,[100,†] R. D. Schamberger,[148,†] V. Scharf,[58a,†]

V. A. Schegelsky,[123,†] D. Scheirich,[129,†] M. Schernau,[163,†] C. Schiavi,[50a,50b,†] C. Schillo,[48,†] M. Schioppa,[37a,37b,†] S. Schlenker,[30,†] E. Schmidt,[48,†] K. Schmieden,[30,†] C. Schmitt,[83,†] S. Schmitt,[58b,†] S. Schmitt,[42,†] B. Schneider,[159a,†] Y. J. Schnellbach,[74,†] U. Schnoor,[44,†] L. Schoeffel,[136,†] A. Schoening,[58b,†] B. D. Schoenrock,[90,†] E. Schopf,[21,†] A. L. S. Schorlemmer,[54,†] M. Schott,[83,†] D. Schouten,[159a,†] J. Schovancova,[8,†] S. Schramm,[158,†] M. Schreyer,[174,†] C. Schroeder,[83,†] N. Schuh,[83,†] M. J. Schultens,[21,†] H.-C. Schultz-Coulon,[58a,†] H. Schulz,[16,†] M. Schumacher,[48,†] B. A. Schumm,[137,†] Ph. Schune,[136,†] C. Schwanenberger,[84,†] A. Schwartzman,[143,†] T. A. Schwarz,[89,†] Ph. Schwegler,[101,†] Ph. Schwemling,[136,†] R. Schwienhorst,[90,†] J. Schwindling,[136,†] T. Schwindt,[21,†] M. Schwoerer,[5,†] F. G. Sciacca,[17,†] E. Scifo,[117,†] G. Sciolla,[23,†] F. Scuri,[124a,124b,†] F. Scutti,[21,†] J. Searcy,[89,†] G. Sedov,[42,†] E. Sedykh,[123,†] P. Seema,[21,†] S. C. Seidel,[105,†] A. Seiden,[137,†] F. Seifert,[128,†] J. M. Seixas,[24a,†] G. Sekhniaidze,[104a,†] K. Sekhon,[89,†] S. J. Sekula,[40,†] K. E. Selbach,[46,†] D. M. Seliverstov,[123,a,†] N. Semprini-Cesari,[20a,20b,†] C. Serfon,[30,†] L. Serin,[117,†] L. Serkin,[164a,164b,†] T. Serre,[85,†] M. Sessa,[134a,134b,†] R. Seuster,[159a,†] H. Severini,[113,†] T. Sfiligoj,[75,†] F. Sforza,[101,†] A. Sfyrla,[30,†] E. Shabalina,[54,†] M. Shamim,[116,†] L. Y. Shan,[33a,†] R. Shang,[165,†] J. T. Shank,[22,†] M. Shapiro,[15,†] P. B. Shatalov,[97,†] K. Shaw,[164a,164b,†] S. M. Shaw,[84,†] A. Shcherbakova,[146a,146b,†] C. Y. Shehu,[149,†] P. Sherwood,[78,†] L. Shi,[151,ff,†] S. Shimizu,[67,†] C. O. Shimmin,[163,†] M. Shimojima,[102,†] M. Shiyakova,[65,†] A. Shmeleva,[96,†] D. Shoaleh Saadi,[95,†] M. J. Shochet,[31,†] S. Shojaii,[91a,91b,†] S. Shrestha,[111,†] E. Shulga,[98,†] M. A. Shupe,[7,†] S. Shushkevich,[42,†] P. Sicho,[127,†] O. Sidiropoulou,[174,†] D. Sidorov,[114,†] A. Sidoti,[20a,20b,†] F. Siegert,[44,†] Dj. Sijacki,[13,†] J. Silva,[126a,126d,†] Y. Silver,[153,†] S. B. Silverstein,[146a,†] V. Simak,[128,†] O. Simard,[5,†] Lj. Simic,[13,†] S. Simion,[117,†] E. Simioni,[83,†] B. Simmons,[78,†] D. Simon,[34,†] R. Simoniello,[91a,91b,†] P. Sinervo,[158,†] N. B. Sinev,[116,†] G. Siragusa,[174,†] A. N. Sisakyan,[65,a,†] S.Yu. Sivoklokov,[99,†] J. Sjölin,[146a,146b,†] T. B. Sjursen,[14,†] M. B. Skinner,[72,†] H. P. Skottowe,[57,†] P. Skubic,[113,†] M. Slater,[18,†] T. Slavicek,[128,†] M. Slawinska,[107,†] K. Sliwa,[161,†] V. Smakhtin,[172,†] B. H. Smart,[46,†] L. Smestad,[14,†] S.Yu. Smirnov,[98,†] Y. Smirnov,[98,†] L. N. Smirnova,[99,gg,†] O. Smirnova,[81,†] M. N. K. Smith,[35,†] R. W. Smith,[35,†] M. Smizanska,[72,†] K. Smolek,[128,†] A. A. Snesarev,[96,†] G. Snidero,[76,†] S. Snyder,[25,†] R. Sobie,[169,l,†] F. Socher,[44,†] A. Soffer,[153,†] D. A. Soh,[151,ff,†] C. A. Solans,[30,†] M. Solar,[128,†] J. Solc,[128,†] E.Yu. Soldatov,[98,†] U. Soldevila,[167,†] A. A. Solodkov,[130,†] A. Soloshenko,[65,†] O. V. Solovyanov,[130,†] V. Solovyev,[123,†] P. Sommer,[48,†] H. Y. Song,[33b,†] N. Soni,[1,†] A. Sood,[15,†] A. Sopczak,[128,†] B. Sopko,[128,†] V. Sopko,[128,†] V. Sorin,[12,†] D. Sosa,[58b,†] M. Sosebee,[8,†] C. L. Sotiropoulou,[124a,124b,†] R. Soualah,[164a,164c,†] P. Soueid,[95,†] A. M. Soukharev,[109,d,†] D. South,[42,†] B. C. Sowden,[77,†] S. Spagnolo,[73a,73b,†] M. Spalla,[124a,124b,†] F. Spanò,[77,†] W. R. Spearman,[57,†] F. Spettel,[101,†] R. Spighi,[20a,†] G. Spigo,[30,†] L. A. Spiller,[88,†] M. Spousta,[129,†] T. Spreitzer,[158,†] R. D. St. Denis,[53,a,†] S. Staerz,[44,†] J. Stahlman,[122,†] R. Stamen,[58a,†] S. Stamm,[16,†] E. Stanecka,[39,†] C. Stanescu,[134a,†] M. Stanescu-Bellu,[42,†] M. M. Stanitzki,[42,†] S. Stapnes,[119,†] E. A. Starchenko,[130,†] J. Stark,[55,†] P. Staroba,[127,†] P. Starovoitov,[42,†] R. Staszewski,[39,†] P. Stavina,[144a,a,†] P. Steinberg,[25,†] B. Stelzer,[142,†] H. J. Stelzer,[30,†] O. Stelzer-Chilton,[159a,†] H. Stenzel,[52,†] S. Stern,[101,†] G. A. Stewart,[53,†] J. A. Stillings,[21,†] M. C. Stockton,[87,†] M. Stoebe,[87,†] G. Stoicea,[26a,†] P. Stolte,[54,†] S. Stonjek,[101,†] A. R. Stradling,[8,†] A. Straessner,[44,†] M. E. Stramaglia,[17,†] J. Strandberg,[147,†] S. Strandberg,[146a,146b,†] A. Strandlie,[119,†] E. Strauss,[143,†] M. Strauss,[113,†] P. Strizenec,[144b,†] R. Ströhmer,[174,†] D. M. Strom,[116,†] R. Stroynowski,[40,†] A. Strubig,[106,†] S. A. Stucci,[17,†] B. Stugu,[14,†] N. A. Styles,[42,†] D. Su,[143,†] J. Su,[125,†] R. Subramaniam,[79,†] A. Succurro,[12,†] Y. Sugaya,[118,†] C. Suhr,[108,†] M. Suk,[128,†] V. V. Sulin,[96,†] S. Sultansoy,[4c,†] T. Sumida,[68,†] S. Sun,[57,†] X. Sun,[33a,†] J. E. Sundermann,[48,†] K. Suruliz,[149,†] G. Susinno,[37a,37b,†] M. R. Sutton,[149,†] S. Suzuki,[66,†] Y. Suzuki,[66,†] M. Svatos,[127,†] S. Swedish,[168,†] M. Swiatlowski,[143,†] I. Sykora,[144a,†] T. Sykora,[129,†] D. Ta,[90,†] C. Taccini,[134a,134b,†] K. Tackmann,[42,†] J. Taenzer,[158,†] A. Taffard,[163,†] R. Tafirout,[159a,†] N. Taiblum,[153,†] H. Takai,[25,†] R. Takashima,[69,†] H. Takeda,[67,†] T. Takeshita,[140,†] Y. Takubo,[66,†] M. Talby,[85,†] A. A. Talyshev,[109,d,†] J. Y. C. Tam,[174,†] K. G. Tan,[88,†] J. Tanaka,[155,†] R. Tanaka,[117,†] S. Tanaka,[66,†] B. B. Tannenwald,[111,†] N. Tannoury,[21,†] S. Tapprogge,[83,†] S. Tarem,[152,†] F. Tarrade,[29,†] G. F. Tartarelli,[91a,†] P. Tas,[129,†] M. Tasevsky,[127,†] T. Tashiro,[68,†] E. Tassi,[37a,37b,†] A. Tavares Delgado,[126a,126b,†] Y. Tayalati,[135d,†] F. E. Taylor,[94,†] G. N. Taylor,[88,†] W. Taylor,[159b,†] F. A. Teischinger,[30,†] M. Teixeira Dias Castanheira,[76,†] P. Teixeira-Dias,[77,†] K. K. Temming,[48,†] H. Ten Kate,[30,†] P. K. Teng,[151,†] J. J. Teoh,[118,†] F. Tepel,[175,†] S. Terada,[66,†] K. Terashi,[155,†] J. Terron,[82,†] S. Terzo,[101,†] M. Testa,[47,†] R. J. Teuscher,[158,l,†] J. Therhaag,[21,†] T. Theveneaux-Pelzer,[34,†] J. P. Thomas,[18,†] J. Thomas-Wilsker,[77,†] E. N. Thompson,[35,†] P. D. Thompson,[18,†] R. J. Thompson,[84,†] A. S. Thompson,[53,†] L. A. Thomsen,[36,†] E. Thomson,[122,†] M. Thomson,[28,†] R. P. Thun,[89,a,†] M. J. Tibbetts,[15,†] R. E. Ticse Torres,[85,†] V. O. Tikhomirov,[96,hh,†] Yu.A. Tikhonov,[109,d,†] S. Timoshenko,[98,†] E. Tiouchichine,[85,†] P. Tipton,[176,†] S. Tisserant,[85,†] T. Todorov,[5,a,†] S. Todorova-Nova,[129,†] J. Tojo,[70,†] S. Tokár,[144a,†] K. Tokushuku,[66,†] K. Tollefson,[90,†] E. Tolley,[57,†] L. Tomlinson,[84,†] M. Tomoto,[103,†] L. Tompkins,[143,ii,†] K. Toms,[105,†] E. Torrence,[116,†] H. Torres,[142,†] E. Torró Pastor,[167,†] J. Toth,[85,jj,†] F. Touchard,[85,†] D. R. Tovey,[139,†] T. Trefzger,[174,†]

L. Tremblet,[30,†] A. Tricoli,[30,†] I. M. Trigger,[159a,†] S. Trincaz-Duvoid,[80,†] M. F. Tripiana,[12,†] W. Trischuk,[158,†] B. Trocmé,[55,†] C. Troncon,[91a,†] M. Trottier-McDonald,[15,†] M. Trovatelli,[134a,134b,†] P. True,[90,†] L. Truong,[164a,164c,†] M. Trzebinski,[39,†] A. Trzupek,[39,†] C. Tsarouchas,[30,†] J.C-L. Tseng,[120,†] P. V. Tsiareshka,[92,†] D. Tsionou,[154,†] G. Tsipolitis,[10,†] N. Tsirintanis,[9,†] S. Tsiskaridze,[12,†] V. Tsiskaridze,[48,†] E. G. Tskhadadze,[51a,†] I. I. Tsukerman,[97,†] V. Tsulaia,[15,†] S. Tsuno,[66,†] D. Tsybychev,[148,†] A. Tudorache,[26a,†] V. Tudorache,[26a,†] A. N. Tuna,[122,†] S. A. Tupputi,[20a,20b,†] S. Turchikhin,[99,gg,†] D. Turecek,[128,†] R. Turra,[91a,91b,†] A. J. Turvey,[40,†] P. M. Tuts,[35,†] A. Tykhonov,[49,†] M. Tylmad,[146a,146b,†] M. Tyndel,[131,†] I. Ueda,[155,†] R. Ueno,[29,†] M. Ughetto,[146a,146b,†] M. Ugland,[14,†] M. Uhlenbrock,[21,†] F. Ukegawa,[160,†] G. Unal,[30,†] A. Undrus,[25,†] G. Unel,[163,†] F. C. Ungaro,[48,†] Y. Unno,[66,†] C. Unverdorben,[100,†] J. Urban,[144b,†] P. Urquijo,[88,†] P. Urrejola,[83,†] G. Usai,[8,†] A. Usanova,[62,†] L. Vacavant,[85,†] V. Vacek,[128,†] B. Vachon,[87,†] C. Valderanis,[83,†] N. Valencic,[107,†] S. Valentinetti,[20a,20b,†] A. Valero,[167,†] L. Valery,[12,†] S. Valkar,[129,†] E. Valladolid Gallego,[167,†] S. Vallecorsa,[49,†] J. A. Valls Ferrer,[167,†] W. Van Den Wollenberg,[107,†] P. C. Van Der Deijl,[107,†] R. van der Geer,[107,†] H. van der Graaf,[107,†] R. Van Der Leeuw,[107,†] N. van Eldik,[152,†] P. van Gemmeren,[6,†] J. Van Nieuwkoop,[142,†] I. van Vulpen,[107,†] M. C. van Woerden,[30,†] M. Vanadia,[132a,132b,†] W. Vandelli,[30,†] R. Vanguri,[122,†] A. Vaniachine,[6,†] F. Vannucci,[80,†] G. Vardanyan,[177,†] R. Vari,[132a,†] E. W. Varnes,[7,†] T. Varol,[40,†] D. Varouchas,[80,†] A. Vartapetian,[8,†] K. E. Varvell,[150,†] F. Vazeille,[34,†] T. Vazquez Schroeder,[87,†] J. Veatch,[7,†] L. M. Veloce,[158,†] F. Veloso,[126a,126c,†] T. Velz,[21,†] S. Veneziano,[132a,†] A. Ventura,[73a,73b,†] D. Ventura,[86,†] M. Venturi,[169,†] N. Venturi,[158,†] A. Venturini,[23,†] V. Vercesi,[121a,†] M. Verducci,[132a,132b,†] W. Verkerke,[107,†] J. C. Vermeulen,[107,†] A. Vest,[44,†] M. C. Vetterli,[142,e,†] O. Viazlo,[81,†] I. Vichou,[165,†] T. Vickey,[139,†] O. E. Vickey Boeriu,[139,†] G. H. A. Viehhauser,[120,†] S. Viel,[15,†] R. Vigne,[30,†] M. Villa,[20a,20b,†] M. Villaplana Perez,[91a,91b,†] E. Vilucchi,[47,†] M. G. Vincter,[29,†] V. B. Vinogradov,[65,†] I. Vivarelli,[149,†] F. Vives Vaque,[3,†] S. Vlachos,[10,†] D. Vladoiu,[100,†] M. Vlasak,[128,†] M. Vogel,[32a,†] P. Vokac,[128,†] G. Volpi,[124a,124b,†] M. Volpi,[88,†] H. von der Schmitt,[101,†] H. von Radziewski,[48,†] E. von Toerne,[21,†] V. Vorobel,[129,†] K. Vorobev,[98,†] M. Vos,[167,†] R. Voss,[30,†] J. H. Vossebeld,[74,†] N. Vranjes,[13,†] M. Vranjes Milosavljevic,[13,†] V. Vrba,[127,†] M. Vreeswijk,[107,†] R. Vuillermet,[30,†] I. Vukotic,[31,†] Z. Vykydal,[128,†] P. Wagner,[21,†] W. Wagner,[175,†] H. Wahlberg,[71,†] S. Wahrmund,[44,†] J. Wakabayashi,[103,†] J. Walder,[72,†] R. Walker,[100,†] W. Walkowiak,[141,†] C. Wang,[33c,†] F. Wang,[173,†] H. Wang,[15,†] H. Wang,[40,†] J. Wang,[42,†] J. Wang,[33a,†] K. Wang,[87,†] R. Wang,[6,†] S. M. Wang,[151,†] T. Wang,[21,†] X. Wang,[176,†] C. Wanotayaroj,[116,†] A. Warburton,[87,†] C. P. Ward,[28,†] D. R. Wardrope,[78,†] M. Warsinsky,[48,†] A. Washbrook,[46,†] C. Wasicki,[42,†] P. M. Watkins,[18,†] A. T. Watson,[18,†] I. J. Watson,[150,†] M. F. Watson,[18,†] G. Watts,[138,†] S. Watts,[84,†] B. M. Waugh,[78,†] S. Webb,[84,†] M. S. Weber,[17,†] S. W. Weber,[174,†] J. S. Webster,[31,†] A. R. Weidberg,[120,†] B. Weinert,[61,†] J. Weingarten,[54,†] C. Weiser,[48,†] H. Weits,[107,†] P. S. Wells,[30,†] T. Wenaus,[25,†] T. Wengler,[30,†] S. Wenig,[30,†] N. Wermes,[21,†] M. Werner,[48,†] P. Werner,[30,†] M. Wessels,[58a,†] J. Wetter,[161,†] K. Whalen,[29,†] A. M. Wharton,[72,†] A. White,[8,†] M. J. White,[1,†] R. White,[32b,†] S. White,[124a,124b,†] D. Whiteson,[163,†] F. J. Wickens,[131,†] W. Wiedenmann,[173,†] M. Wielers,[131,†] P. Wienemann,[21,†] C. Wiglesworth,[36,†] L. A. M. Wiik-Fuchs,[21,†] A. Wildauer,[101,†] H. G. Wilkens,[30,†] H. H. Williams,[122,†] S. Williams,[107,†] C. Willis,[90,†] S. Willocq,[86,†] A. Wilson,[89,†] J. A. Wilson,[18,†] I. Wingerter-Seez,[5,†] F. Winklmeier,[116,†] B. T. Winter,[21,†] M. Wittgen,[143,†] J. Wittkowski,[100,†] S. J. Wollstadt,[83,†] M. W. Wolter,[39,†] H. Wolters,[126a,126c,†] B. K. Wosiek,[39,†] J. Wotschack,[30,†] M. J. Woudstra,[84,†] K. W. Wozniak,[39,†] M. Wu,[55,†] M. Wu,[31,†] S. L. Wu,[173,†] X. Wu,[49,†] Y. Wu,[89,†] T. R. Wyatt,[84,†] B. M. Wynne,[46,†] S. Xella,[36,†] D. Xu,[33a,†] L. Xu,[33b,kk,†] B. Yabsley,[150,†] S. Yacoob,[145b,ll,†] R. Yakabe,[67,†] M. Yamada,[66,†] Y. Yamaguchi,[118,†] A. Yamamoto,[66,†] S. Yamamoto,[155,†] T. Yamanaka,[155,†] K. Yamauchi,[103,†] Y. Yamazaki,[67,†] Z. Yan,[22,†] H. Yang,[33e,†] H. Yang,[173,†] Y. Yang,[151,†] L. Yao,[33a,†] W-M. Yao,[15,†] Y. Yasu,[66,†] E. Yatsenko,[5,†] K. H. Yau Wong,[21,†] J. Ye,[40,†] S. Ye,[25,†] I. Yeletskikh,[65,†] A. L. Yen,[57,†] E. Yildirim,[42,†] K. Yorita,[171,†] R. Yoshida,[6,†] K. Yoshihara,[122,†] C. Young,[143,†] C. J. S. Young,[30,†] S. Youssef,[22,†] D. R. Yu,[15,†] J. Yu,[8,†] J. M. Yu,[89,†] J. Yu,[114,†] L. Yuan,[67,†] A. Yurkewicz,[108,†] I. Yusuff,[28,mm,†] B. Zabinski,[39,†] R. Zaidan,[63,†] A. M. Zaitsev,[130,bb,†] J. Zalieckas,[14,†] A. Zaman,[148,†] S. Zambito,[57,†] L. Zanello,[132a,132b,†] D. Zanzi,[88,†] C. Zeitnitz,[175,†] M. Zeman,[128,†] A. Zemla,[38a,†] K. Zengel,[23,†] O. Zenin,[130,†] T. Ženiš,[144a,†] D. Zerwas,[117,†] D. Zhang,[89,†] F. Zhang,[173,†] J. Zhang,[6,†] L. Zhang,[48,†] R. Zhang,[33b,†] X. Zhang,[33d,†] Z. Zhang,[117,†] X. Zhao,[40,†] Y. Zhao,[33d,117,†] Z. Zhao,[33b,†] A. Zhemchugov,[65,†] J. Zhong,[120,†] B. Zhou,[89,†] C. Zhou,[45,†] L. Zhou,[35,†] L. Zhou,[40,†] N. Zhou,[163,†] C. G. Zhu,[33d,†] H. Zhu,[33a,†] J. Zhu,[89,†] Y. Zhu,[33b,†] X. Zhuang,[33a,†] K. Zhukov,[96,†] A. Zibell,[174,†] D. Zieminska,[61,†] N. I. Zimine,[65,†] C. Zimmermann,[83,†] S. Zimmermann,[48,†] Z. Zinonos,[54,†] M. Zinser,[83,†] M. Ziolkowski,[141,†] L. Živković,[13,†] G. Zobernig,[173,†] A. Zoccoli,[20a,20b,†] M. zur Nedden,[16,†] G. Zurzolo,[104a,104b,†] L. Zwalinski,[30,†] V. Khachatryan,[179,‡] A. M. Sirunyan,[179,‡] A. Tumasyan,[179,‡] W. Adam,[180,‡] E. Asilar,[180,‡] T. Bergauer,[180,‡] J. Brandstetter,[180,‡] E. Brondolin,[180,‡] M. Dragicevic,[180,‡] J. Erö,[180,‡] M. Flechl,[180,‡] M. Friedl,[180,‡] R. Frühwirth,[180,nn,‡] V. M. Ghete,[180,‡] C. Hartl,[180,‡] N. Hörmann,[180,‡] J. Hrubec,[180,‡] M. Jeitler,[180,nn,‡] V. Knünz,[180,‡] A. König,[180,‡]

M. Krammer,[180,nn,‡] I. Krätschmer,[180,‡] D. Liko,[180,‡] T. Matsushita,[180,‡] I. Mikulec,[180,‡] D. Rabady,[180,oo,‡] B. Rahbaran,[180,‡] H. Rohringer,[180,‡] J. Schieck,[180,nn,‡] R. Schöfbeck,[180,‡] J. Strauss,[180,‡] W. Treberer-Treberspurg,[180,‡] W. Waltenberger,[180,‡] C.-E. Wulz,[180,nn,‡] V. Mossolov,[181,‡] N. Shumeiko,[181,‡] J. Suarez Gonzalez,[181,‡] S. Alderweireldt,[182,‡] T. Cornelis,[182,‡] E. A. De Wolf,[182,‡] X. Janssen,[182,‡] A. Knutsson,[182,‡] J. Lauwers,[182,‡] S. Luyckx,[182,‡] S. Ochesanu,[182,‡] R. Rougny,[182,‡] M. Van De Klundert,[182,‡] H. Van Haevermaet,[182,‡] P. Van Mechelen,[182,‡] N. Van Remortel,[182,‡] A. Van Spilbeeck,[182,‡] S. Abu Zeid,[183,‡] F. Blekman,[183,‡] J. D'Hondt,[183,‡] N. Daci,[183,‡] I. De Bruyn,[183,‡] K. Deroover,[183,‡] N. Heracleous,[183,‡] J. Keaveney,[183,‡] S. Lowette,[183,‡] L. Moreels,[183,‡] A. Olbrechts,[183,‡] Q. Python,[183,‡] D. Strom,[183,‡] S. Tavernier,[183,‡] W. Van Doninck,[183,‡] P. Van Mulders,[183,‡] G. P. Van Onsem,[183,‡] I. Van Parijs,[183,‡] P. Barria,[184,‡] C. Caillol,[184,‡] B. Clerbaux,[184,‡] G. De Lentdecker,[184,‡] H. Delannoy,[184,‡] D. Dobur,[184,‡] G. Fasanella,[184,‡] L. Favart,[184,‡] A. P. R. Gay,[184,‡] A. Grebenyuk,[184,‡] T. Lenzi,[184,‡] A. Léonard,[184,‡] T. Maerschalk,[184,‡] A. Mohammadi,[184,‡] L. Perniè,[184,‡] A. Randle-conde,[184,‡] T. Reis,[184,‡] T. Seva,[184,‡] L. Thomas,[184,‡] C. Vander Velde,[184,‡] P. Vanlaer,[184,‡] J. Wang,[184,‡] R. Yonamine,[184,‡] F. Zenoni,[184,‡] F. Zhang,[184,pp,‡] K. Beernaert,[185,‡] L. Benucci,[185,‡] A. Cimmino,[185,‡] S. Crucy,[185,‡] A. Fagot,[185,‡] G. Garcia,[185,‡] M. Gul,[185,‡] J. Mccartin,[185,‡] A. A. Ocampo Rios,[185,‡] D. Poyraz,[185,‡] D. Ryckbosch,[185,‡] S. Salva Diblen,[185,‡] M. Sigamani,[185,‡] N. Strobbe,[185,‡] M. Tytgat,[185,‡] W. Van Driessche,[185,‡] E. Yazgan,[185,‡] N. Zaganidis,[185,‡] S. Basegmez,[186,‡] C. Beluffi,[186,qq,‡] O. Bondu,[186,‡] G. Bruno,[186,‡] R. Castello,[186,‡] A. Caudron,[186,‡] L. Ceard,[186,‡] G. G. Da Silveira,[186,‡] C. Delaere,[186,‡] D. Favart,[186,‡] L. Forthomme,[186,‡] A. Giammanco,[186,rr,‡] J. Hollar,[186,‡] A. Jafari,[186,‡] P. Jez,[186,‡] M. Komm,[186,‡] V. Lemaitre,[186,‡] A. Mertens,[186,‡] C. Nuttens,[186,‡] L. Perrini,[186,‡] A. Pin,[186,‡] K. Piotrzkowski,[186,‡] A. Popov,[186,ss,‡] L. Quertenmont,[186,‡] M. Selvaggi,[186,‡] M. Vidal Marono,[186,‡] N. Beliy,[187,‡] T. Caebergs,[187,‡] G. H. Hammad,[187,‡] W. L. Aldá Júnior,[188,‡] G. A. Alves,[188,‡] L. Brito,[188,‡] M. Correa Martins Junior,[188,‡] T. Dos Reis Martins,[188,‡] C. Hensel,[188,‡] C. Mora Herrera,[188,‡] A. Moraes,[188,‡] M. E. Pol,[188,‡] P. Rebello Teles,[188,‡] E. Belchior Batista Das Chagas,[189,‡] W. Carvalho,[189,‡] J. Chinellato,[189,tt,‡] A. Custódio,[189,‡] E. M. Da Costa,[189,‡] D. De Jesus Damiao,[189,‡] C. De Oliveira Martins,[189,‡] S. Fonseca De Souza,[189,‡] L. M. Huertas Guativa,[189,‡] H. Malbouisson,[189,‡] D. Matos Figueiredo,[189,‡] L. Mundim,[189,‡] H. Nogima,[189,‡] W. L. Prado Da Silva,[189,‡] A. Santoro,[189,‡] A. Sznajder,[189,‡] E. J. Tonelli Manganote,[189,tt,‡] A. Vilela Pereira,[189,‡] S. Ahuja,[190a,‡] C. A. Bernardes,[190b,‡] A. De Souza Santos,[190b,‡] S. Dogra,[190a,‡] T. R. Fernandez Perez Tomei,[190a,‡] E. M. Gregores,[190b,‡] P. G. Mercadante,[190b,‡] C. S. Moon,[190a,uu,‡] S. F. Novaes,[190a,‡] Sandra S. Padula,[190a,‡] D. Romero Abad,[190a,‡] J. C. Ruiz Vargas,[190a,‡] A. Aleksandrov,[191,‡] V. Genchev,[191,oo,‡] R. Hadjiiska,[191,‡] P. Iaydjiev,[191,‡] A. Marinov,[191,‡] S. Piperov,[191,‡] M. Rodozov,[191,‡] S. Stoykova,[191,‡] G. Sultanov,[191,‡] M. Vutova,[191,‡] A. Dimitrov,[192,‡] I. Glushkov,[192,‡] L. Litov,[192,‡] B. Pavlov,[192,‡] P. Petkov,[192,‡] M. Ahmad,[193,‡] J. G. Bian,[193,‡] G. M. Chen,[193,‡] H. S. Chen,[193,‡] M. Chen,[193,‡] T. Cheng,[193,‡] R. Du,[193,‡] C. H. Jiang,[193,‡] R. Plestina,[193,vv,‡] F. Romeo,[193,‡] S. M. Shaheen,[193,‡] J. Tao,[193,‡] C. Wang,[193,‡] Z. Wang,[193,‡] H. Zhang,[193,‡] C. Asawatangtrakuldee,[194,‡] Y. Ban,[194,‡] G. Chen,[194,‡] Q. Li,[194,‡] S. Liu,[194,‡] Y. Mao,[194,‡] S. J. Qian,[194,‡] D. Wang,[194,‡] M. Wang,[194,‡] Q. Wang,[194,‡] Z. Xu,[194,‡] D. Yang,[194,‡] Z. Zhang,[194,‡] W. Zou,[194,‡] C. Avila,[195,‡] A. Cabrera,[195,‡] L. F. Chaparro Sierra,[195,‡] C. Florez,[195,‡] J. P. Gomez,[195,‡] B. Gomez Moreno,[195,‡] J. C. Sanabria,[195,‡] N. Godinovic,[196,‡] D. Lelas,[196,‡] D. Polic,[196,‡] I. Puljak,[196,‡] Z. Antunovic,[197,‡] M. Kovac,[197,‡] V. Brigljevic,[198,‡] K. Kadija,[198,‡] J. Luetic,[198,‡] L. Sudic,[198,‡] A. Attikis,[199,‡] G. Mavromanolakis,[199,‡] J. Mousa,[199,‡] C. Nicolaou,[199,‡] F. Ptochos,[199,‡] P. A. Razis,[199,‡] H. Rykaczewski,[199,‡] M. Bodlak,[200,‡] M. Finger,[200,ww,‡] M. Finger Jr.,[200,ww,‡] A. Ali,[201,xx,yy,‡] R. Aly,[201,zz,‡] S. Aly,[201,zz,‡] Y. Assran,[201,aaa,‡] A. Ellithi Kamel,[201,bbb,‡] A. Lotfy,[201,ccc,‡] M. A. Mahmoud,[201,ccc,‡] R. Masod,[201,xx,‡] A. Radi,[201,yy,xx,‡] B. Calpas,[202,‡] M. Kadastik,[202,‡] M. Murumaa,[202,‡] M. Raidal,[202,‡] A. Tiko,[202,‡] C. Veelken,[202,‡] P. Eerola,[203,‡] J. Pekkanen,[203,‡] M. Voutilainen,[203,‡] J. Härkönen,[204,‡] V. Karimäki,[204,‡] R. Kinnunen,[204,‡] T. Lampén,[204,‡] K. Lassila-Perini,[204,‡] S. Lehti,[204,‡] T. Lindén,[204,‡] P. Luukka,[204,‡] T. Mäenpää,[204,‡] T. Peltola,[204,‡] E. Tuominen,[204,‡] J. Tuominiemi,[204,‡] E. Tuovinen,[204,‡] L. Wendland,[204,‡] J. Talvitie,[205,‡] T. Tuuva,[205,‡] M. Besancon,[206,‡] F. Couderc,[206,‡] M. Dejardin,[206,‡] D. Denegri,[206,‡] B. Fabbro,[206,‡] J. L. Faure,[206,‡] C. Favaro,[206,‡] F. Ferri,[206,‡] S. Ganjour,[206,‡] A. Givernaud,[206,‡] P. Gras,[206,‡] G. Hamel de Monchenault,[206,‡] P. Jarry,[206,‡] E. Locci,[206,‡] M. Machet,[206,‡] J. Malcles,[206,‡] J. Rander,[206,‡] A. Rosowsky,[206,‡] M. Titov,[206,‡] A. Zghiche,[206,‡] S. Baffioni,[207,‡] F. Beaudette,[207,‡] P. Busson,[207,‡] L. Cadamuro,[207,‡] E. Chapon,[207,‡] C. Charlot,[207,‡] T. Dahms,[207,‡] O. Davignon,[207,‡] N. Filipovic,[207,‡] A. Florent,[207,‡] R. Granier de Cassagnac,[207,‡] S. Lisniak,[207,‡] L. Mastrolorenzo,[207,‡] P. Miné,[207,‡] I. N. Naranjo,[207,‡] M. Nguyen,[207,‡] C. Ochando,[207,‡] G. Ortona,[207,‡] P. Paganini,[207,‡] S. Regnard,[207,‡] R. Salerno,[207,‡] J. B. Sauvan,[207,‡] Y. Sirois,[207,‡] T. Strebler,[207,‡] Y. Yilmaz,[207,‡] A. Zabi,[207,‡] J.-L. Agram,[208,ddd,‡] J. Andrea,[208,‡] A. Aubin,[208,‡] D. Bloch,[208,‡] J.-M. Brom,[208,‡] M. Buttignol,[208,‡] E. C. Chabert,[208,‡] N. Chanon,[208,‡] C. Collard,[208,‡] E. Conte,[208,ddd,‡] J.-C. Fontaine,[208,ddd,‡] D. Gelé,[208,‡]

U. Goerlach,[208,‡] C. Goetzmann,[208,‡] A.-C. Le Bihan,[208,‡] J. A. Merlin,[208,oo,‡] K. Skovpen,[208,‡] P. Van Hove,[208,‡] S. Gadrat,[209,‡] S. Beauceron,[210,‡] C. Bernet,[210,‡] G. Boudoul,[210,‡] E. Bouvier,[210,‡] S. Brochet,[210,‡] C. A. Carrillo Montoya,[210,‡] J. Chasserat,[210,‡] R. Chierici,[210,‡] D. Contardo,[210,‡] B. Courbon,[210,‡] P. Depasse,[210,‡] H. El Mamouni,[210,‡] J. Fan,[210,‡] J. Fay,[210,‡] S. Gascon,[210,‡] M. Gouzevitch,[210,‡] B. Ille,[210,‡] I. B. Laktineh,[210,‡] M. Lethuillier,[210,‡] L. Mirabito,[210,‡] A. L. Pequegnot,[210,‡] S. Perries,[210,‡] J. D. Ruiz Alvarez,[210,‡] D. Sabes,[210,‡] L. Sgandurra,[210,‡] V. Sordini,[210,‡] M. Vander Donckt,[210,‡] P. Verdier,[210,‡] S. Viret,[210,‡] H. Xiao,[210,‡] Z. Tsamalaidze,[211,ww,‡] C. Autermann,[212,‡] S. Beranek,[212,‡] M. Bontenackels,[212,‡] M. Edelhoff,[212,‡] L. Feld,[212,‡] A. Heister,[212,‡] M. K. Kiesel,[212,‡] K. Klein,[212,‡] M. Lipinski,[212,‡] A. Ostapchuk,[212,‡] M. Preuten,[212,‡] F. Raupach,[212,‡] J. Sammet,[212,‡] S. Schael,[212,‡] J. F. Schulte,[212,‡] T. Verlage,[212,‡] H. Weber,[212,‡] B. Wittmer,[212,‡] V. Zhukov,[212,ss,‡] M. Ata,[213,‡] M. Brodski,[213,‡] E. Dietz-Laursonn,[213,‡] D. Duchardt,[213,‡] M. Endres,[213,‡] M. Erdmann,[213,‡] S. Erdweg,[213,‡] T. Esch,[213,‡] R. Fischer,[213,‡] A. Güth,[213,‡] T. Hebbeker,[213,‡] C. Heidemann,[213,‡] K. Hoepfner,[213,‡] D. Klingebiel,[213,‡] S. Knutzen,[213,‡] P. Kreuzer,[213,‡] M. Merschmeyer,[213,‡] A. Meyer,[213,‡] P. Millet,[213,‡] M. Olschewski,[213,‡] K. Padeken,[213,‡] P. Papacz,[213,‡] T. Pook,[213,‡] M. Radziej,[213,‡] H. Reithler,[213,‡] M. Rieger,[213,‡] F. Scheuch,[213,‡] L. Sonnenschein,[213,‡] D. Teyssier,[213,‡] S. Thüer,[213,‡] V. Cherepanov,[214,‡] Y. Erdogan,[214,‡] G. Flügge,[214,‡] H. Geenen,[214,‡] M. Geisler,[214,‡] W. Haj Ahmad,[214,‡] F. Hoehle,[214,‡] B. Kargoll,[214,‡] T. Kress,[214,‡] Y. Kuessel,[214,‡] A. Künsken,[214,‡] J. Lingemann,[214,oo,‡] A. Nehrkorn,[214,‡] A. Nowack,[214,‡] I. M. Nugent,[214,‡] C. Pistone,[214,‡] O. Pooth,[214,‡] A. Stahl,[214,‡] M. Aldaya Martin,[215,‡] I. Asin,[215,‡] N. Bartosik,[215,‡] O. Behnke,[215,‡] U. Behrens,[215,‡] A. J. Bell,[215,‡] K. Borras,[215,‡] A. Burgmeier,[215,‡] A. Cakir,[215,‡] L. Calligaris,[215,‡] A. Campbell,[215,‡] S. Choudhury,[215,‡] F. Costanza,[215,‡] C. Diez Pardos,[215,‡] G. Dolinska,[215,‡] S. Dooling,[215,‡] T. Dorland,[215,‡] G. Eckerlin,[215,‡] D. Eckstein,[215,‡] T. Eichhorn,[215,‡] G. Flucke,[215,‡] E. Gallo,[215,‡] J. Garay Garcia,[215,‡] A. Geiser,[215,‡] A. Gizhko,[215,‡] P. Gunnellini,[215,‡] J. Hauk,[215,‡] M. Hempel,[215,eee,‡] H. Jung,[215,‡] A. Kalogeropoulos,[215,‡] O. Karacheban,[215,eee,‡] M. Kasemann,[215,‡] P. Katsas,[215,‡] J. Kieseler,[215,‡] C. Kleinwort,[215,‡] I. Korol,[215,‡] W. Lange,[215,‡] J. Leonard,[215,‡] K. Lipka,[215,‡] A. Lobanov,[215,‡] W. Lohmann,[215,eee,‡] R. Mankel,[215,‡] I. Marfin,[215,eee,‡] I.-A. Melzer-Pellmann,[215,‡] A. B. Meyer,[215,‡] G. Mittag,[215,‡] J. Mnich,[215,‡] A. Mussgiller,[215,‡] S. Naumann-Emme,[215,‡] A. Nayak,[215,‡] E. Ntomari,[215,‡] H. Perrey,[215,‡] D. Pitzl,[215,‡] R. Placakyte,[215,‡] A. Raspereza,[215,‡] P. M. Ribeiro Cipriano,[215,‡] B. Roland,[215,‡] M. Ö. Sahin,[215,‡] J. Salfeld-Nebgen,[215,‡] P. Saxena,[215,‡] T. Schoerner-Sadenius,[215,‡] M. Schröder,[215,‡] C. Seitz,[215,‡] S. Spannagel,[215,‡] K. D. Trippkewitz,[215,‡] C. Wissing,[215,‡] V. Blobel,[216,‡] M. Centis Vignali,[216,‡] A. R. Draeger,[216,‡] J. Erfle,[216,‡] E. Garutti,[216,‡] K. Goebel,[216,‡] D. Gonzalez,[216,‡] M. Görner,[216,‡] J. Haller,[216,‡] M. Hoffmann,[216,‡] R. S. Höing,[216,‡] A. Junkes,[216,‡] R. Klanner,[216,‡] R. Kogler,[216,‡] T. Lapsien,[216,‡] T. Lenz,[216,‡] I. Marchesini,[216,‡] D. Marconi,[216,‡] D. Nowatschin,[216,‡] J. Ott,[216,‡] F. Pantaleo,[216,oo,‡] T. Peiffer,[216,‡] A. Perieanu,[216,‡] N. Pietsch,[216,‡] J. Poehlsen,[216,‡] D. Rathjens,[216,‡] C. Sander,[216,‡] H. Schettler,[216,‡] P. Schleper,[216,‡] E. Schlieckau,[216,‡] A. Schmidt,[216,‡] J. Schwandt,[216,‡] M. Seidel,[216,‡] V. Sola,[216,‡] H. Stadie,[216,‡] G. Steinbrück,[216,‡] H. Tholen,[216,‡] D. Troendle,[216,‡] E. Usai,[216,‡] L. Vanelderen,[216,‡] A. Vanhoefer,[216,‡] M. Akbiyik,[217,‡] C. Amstutz,[217,‡] C. Barth,[217,‡] C. Baus,[217,‡] J. Berger,[217,‡] C. Beskidt,[217,‡] C. Böser,[217,‡] E. Butz,[217,‡] R. Caspart,[217,‡] T. Chwalek,[217,‡] F. Colombo,[217,‡] W. De Boer,[217,‡] A. Descroix,[217,‡] A. Dierlamm,[217,‡] R. Eber,[217,‡] M. Feindt,[217,‡] S. Fink,[217,‡] M. Fischer,[217,‡] F. Frensch,[217,‡] B. Freund,[217,‡] R. Friese,[217,‡] D. Funke,[217,‡] M. Giffels,[217,‡] A. Gilbert,[217,‡] D. Haitz,[217,‡] T. Harbaum,[217,‡] M. A. Harrendorf,[217,‡] F. Hartmann,[217,oo,‡] U. Husemann,[217,‡] F. Kassel,[217,oo,‡] I. Katkov,[217,ss,‡] A. Kornmayer,[217,oo,‡] S. Kudella,[217,‡] P. Lobelle Pardo,[217,‡] B. Maier,[217,‡] H. Mildner,[217,‡] M. U. Mozer,[217,‡] T. Müller,[217,‡] Th. Müller,[217,‡] M. Plagge,[217,‡] M. Printz,[217,‡] G. Quast,[217,‡] K. Rabbertz,[217,‡] S. Röcker,[217,‡] F. Roscher,[217,‡] I. Shvetsov,[217,‡] G. Sieber,[217,‡] H. J. Simonis,[217,‡] F. M. Stober,[217,‡] R. Ulrich,[217,‡] J. Wagner-Kuhr,[217,‡] S. Wayand,[217,‡] T. Weiler,[217,‡] S. Williamson,[217,‡] C. Wöhrmann,[217,‡] R. Wolf,[217,‡] G. Anagnostou,[218,‡] G. Daskalakis,[218,‡] T. Geralis,[218,‡] V. A. Giakoumopoulou,[218,‡] A. Kyriakis,[218,‡] D. Loukas,[218,‡] A. Markou,[218,‡] A. Psallidas,[218,‡] I. Topsis-Giotis,[218,‡] A. Agapitos,[219,‡] S. Kesisoglou,[219,‡] A. Panagiotou,[219,‡] N. Saoulidou,[219,‡] E. Tziaferi,[219,‡] I. Evangelou,[220,‡] G. Flouris,[220,‡] C. Foudas,[220,‡] P. Kokkas,[220,‡] N. Loukas,[220,‡] N. Manthos,[220,‡] I. Papadopoulos,[220,‡] E. Paradas,[220,‡] J. Strologas,[220,‡] G. Bencze,[221,‡] C. Hajdu,[221,‡] A. Hazi,[221,‡] P. Hidas,[221,‡] D. Horvath,[221,fff,‡] F. Sikler,[221,‡] V. Veszpremi,[221,‡] G. Vesztergombi,[221,ggg,‡] A. J. Zsigmond,[221,‡] N. Beni,[222,‡] S. Czellar,[222,‡] J. Karancsi,[222,hhh,‡] J. Molnar,[222,‡] Z. Szillasi,[222,‡] M. Bartók,[223,iii,‡] A. Makovec,[223,‡] P. Raics,[223,‡] Z. L. Trocsanyi,[223,‡] B. Ujvari,[223,‡] P. Mal,[224,‡] K. Mandal,[224,‡] N. Sahoo,[224,‡] S. K. Swain,[224,‡] S. Bansal,[225,‡] S. B. Beri,[225,‡] V. Bhatnagar,[225,‡] R. Chawla,[225,‡] R. Gupta,[225,‡] U. Bhawandeep,[225,‡] A. K. Kalsi,[225,‡] A. Kaur,[225,‡] M. Kaur,[225,‡] R. Kumar,[225,‡] A. Mehta,[225,‡] M. Mittal,[225,‡] N. Nishu,[225,‡] J. B. Singh,[225,‡] G. Walia,[225,‡] Ashok Kumar,[226,‡] Arun Kumar,[226,‡] A. Bhardwaj,[226,‡] B. C. Choudhary,[226,‡] R. B. Garg,[226,‡] A. Kumar,[226,‡] S. Malhotra,[226,‡] M. Naimuddin,[226,‡] K. Ranjan,[226,‡] R. Sharma,[226,‡] V. Sharma,[226,‡] S. Banerjee,[227,‡] S. Bhattacharya,[227,‡]

K. Chatterjee,[227,‡] S. Dey,[227,‡] S. Dutta,[227,‡] Sa. Jain,[227,‡] Sh. Jain,[227,‡] R. Khurana,[227,‡] N. Majumdar,[227,‡] A. Modak,[227,‡] K. Mondal,[227,‡] S. Mukherjee,[227,‡] S. Mukhopadhyay,[227,‡] A. Roy,[227,‡] D. Roy,[227,‡] S. Roy Chowdhury,[227,‡] S. Sarkar,[227,‡] M. Sharan,[227,‡] A. Abdulsalam,[228,‡] R. Chudasama,[228,‡] D. Dutta,[228,‡] V. Jha,[228,‡] V. Kumar,[228,‡] A. K. Mohanty,[228,oo,‡] L. M. Pant,[228,‡] P. Shukla,[228,‡] A. Topkar,[228,‡] T. Aziz,[229,‡] S. Banerjee,[229,‡] S. Bhowmik,[229,jjj,‡] R. M. Chatterjee,[229,‡] R. K. Dewanjee,[229,‡] S. Dugad,[229,‡] S. Ganguly,[229,‡] S. Ghosh,[229,‡] M. Guchait,[229,‡] A. Gurtu,[229,kkk,‡] G. Kole,[229,‡] S. Kumar,[229,‡] B. Mahakud,[229,‡] M. Maity,[229,jjj,‡] G. Majumder,[229,‡] K. Mazumdar,[229,‡] S. Mitra,[229,‡] G. B. Mohanty,[229,‡] B. Parida,[229,‡] T. Sarkar,[229,jjj,‡] K. Sudhakar,[229,‡] N. Sur,[229,‡] B. Sutar,[229,‡] N. Wickramage,[229,lll,‡] S. Sharma,[230,‡] H. Bakhshiansohi,[231,‡] H. Behnamian,[231,‡] S. M. Etesami,[231,mmm,‡] A. Fahim,[231,nnn,‡] R. Goldouzian,[231,‡] M. Khakzad,[231,‡] M. Mohammadi Najafabadi,[231,‡] M. Naseri,[231,‡] S. Paktinat Mehdiabadi,[231,‡] F. Rezaei Hosseinabadi,[231,‡] B. Safarzadeh,[231,ooo,‡] M. Zeinali,[231,‡] M. Felcini,[232,‡] M. Grunewald,[232,‡] M. Abbrescia,[233a,233b,‡] C. Calabria,[233a,233b,‡] C. Caputo,[233a,233b,‡] S. S. Chhibra,[233a,233b,‡] A. Colaleo,[233a,‡] D. Creanza,[233a,233c,‡] L. Cristella,[233a,233b,‡] N. De Filippis,[233a,233c,‡] M. De Palma,[233a,233b,‡] L. Fiore,[233a,‡] G. Iaselli,[233a,233c,‡] G. Maggi,[233a,233c,‡] M. Maggi,[233a,‡] G. Miniello,[233a,233b,‡] S. My,[233a,233c,‡] S. Nuzzo,[233a,233b,‡] A. Pompili,[233a,233b,‡] G. Pugliese,[233a,233c,‡] R. Radogna,[233a,233b,‡] A. Ranieri,[233a,‡] G. Selvaggi,[233a,233b,‡] L. Silvestris,[233a,oo,‡] R. Venditti,[233a,233b,‡] P. Verwilligen,[233a,‡] G. Abbiendi,[234a,‡] C. Battilana,[234a,oo,‡] A. C. Benvenuti,[234a,‡] D. Bonacorsi,[234a,234b,‡] S. Braibant-Giacomelli,[234a,234b,‡] L. Brigliadori,[234a,234b,‡] R. Campanini,[234a,234b,‡] P. Capiluppi,[234a,234b,‡] A. Castro,[234a,234b,‡] F. R. Cavallo,[234a,‡] G. Codispoti,[234a,234b,‡] M. Cuffiani,[234a,234b,‡] G. M. Dallavalle,[234a,‡] F. Fabbri,[234a,‡] A. Fanfani,[234a,234b,‡] D. Fasanella,[234a,234b,‡] P. Giacomelli,[234a,‡] C. Grandi,[234a,‡] L. Guiducci,[234a,234b,‡] S. Marcellini,[234a,‡] G. Masetti,[234a,‡] A. Montanari,[234a,‡] F. L. Navarria,[234a,234b,‡] A. Perrotta,[234a,‡] A. M. Rossi,[234a,234b,‡] T. Rovelli,[234a,234b,‡] G. P. Siroli,[234a,234b,‡] N. Tosi,[234a,234b,‡] R. Travaglini,[234a,234b,‡] G. Cappello,[235a,‡] M. Chiorboli,[235a,235b,‡] S. Costa,[235a,235b,‡] F. Giordano,[235a,‡] R. Potenza,[235a,235b,‡] A. Tricomi,[235a,235b,‡] C. Tuve,[235a,235b,‡] G. Barbagli,[236a,‡] V. Ciulli,[236a,236b,‡] C. Civinini,[236a,‡] R. D'Alessandro,[236a,236b,‡] E. Focardi,[236a,236b,‡] S. Gonzi,[236a,236b,‡] V. Gori,[236a,236b,‡] P. Lenzi,[236a,236b,‡] M. Meschini,[236a,‡] S. Paoletti,[236a,‡] G. Sguazzoni,[236a,‡] A. Tropiano,[236a,236b,‡] L. Viliani,[236a,236b,‡] L. Benussi,[237,‡] S. Bianco,[237,‡] F. Fabbri,[237,‡] D. Piccolo,[237,‡] V. Calvelli,[238a,238b,‡] F. Ferro,[238a,‡] M. Lo Vetere,[238a,238b,‡] E. Robutti,[238a,‡] S. Tosi,[238a,238b,‡] M. E. Dinardo,[239a,239b,‡] S. Fiorendi,[239a,239b,‡] S. Gennai,[239a,‡] R. Gerosa,[239a,239b,‡] A. Ghezzi,[239a,239b,‡] P. Govoni,[239a,239b,‡] S. Malvezzi,[239a,‡] R. A. Manzoni,[239a,239b,‡] B. Marzocchi,[239a,239b,oo,‡] D. Menasce,[239a,‡] L. Moroni,[239a,‡] M. Paganoni,[239a,239b,‡] D. Pedrini,[239a,‡] S. Ragazzi,[239a,239b,‡] N. Redaelli,[239a,‡] T. Tabarelli de Fatis,[239a,239b,‡] S. Buontempo,[240a,‡] N. Cavallo,[240a,240c,‡] S. Di Guida,[240a,240d,oo,‡] M. Esposito,[240a,240b,‡] F. Fabozzi,[240a,240c,‡] A. O. M. Iorio,[240a,240b,‡] G. Lanza,[240a,‡] L. Lista,[240a,‡] S. Meola,[240a,240d,oo,‡] M. Merola,[240a,‡] P. Paolucci,[240a,oo,‡] C. Sciacca,[240a,240b,‡] F. Thyssen,[240a,‡] P. Azzi,[241a,oo,‡] N. Bacchetta,[241a,‡] D. Bisello,[241a,241b,‡] A. Branca,[241a,241b,‡] R. Carlin,[241a,241b,‡] A. Carvalho Antunes De Oliveira,[241a,241b,‡] P. Checchia,[241a,‡] M. Dall'Osso,[241a,241b,oo,‡] T. Dorigo,[241a,‡] U. Dosselli,[241a,‡] F. Gasparini,[241a,241b,‡] U. Gasparini,[241a,241b,‡] A. Gozzelino,[241a,‡] K. Kanishchev,[241a,241c,‡] S. Lacaprara,[241a,‡] M. Margoni,[241a,241b,‡] A. T. Meneguzzo,[241a,241b,‡] J. Pazzini,[241a,241b,‡] N. Pozzobon,[241a,241b,‡] P. Ronchese,[241a,241b,‡] F. Simonetto,[241a,241b,‡] E. Torassa,[241a,‡] M. Tosi,[241a,241b,‡] M. Zanetti,[241a,‡] P. Zotto,[241a,241b,‡] A. Zucchetta,[241a,241b,oo,‡] G. Zumerle,[241a,241b,‡] A. Braghieri,[242a,‡] M. Gabusi,[242a,242b,‡] A. Magnani,[242a,‡] S. P. Ratti,[242a,242b,‡] V. Re,[242a,‡] C. Riccardi,[242a,242b,‡] P. Salvini,[242a,‡] I. Vai,[242a,‡] P. Vitulo,[242a,242b,‡] L. Alunni Solestizi,[243a,243b,‡] M. Biasini,[243a,243b,‡] G. M. Bilei,[243a,‡] D. Ciangottini,[243a,243b,oo,‡] L. Fanò,[243a,243b,‡] P. Lariccia,[243a,243b,‡] G. Mantovani,[243a,243b,‡] M. Menichelli,[243a,‡] A. Saha,[243a,‡] A. Santocchia,[243a,243b,‡] A. Spiezia,[243a,243b,‡] K. Androsov,[244a,ppp,‡] P. Azzurri,[244a,‡] G. Bagliesi,[244a,‡] J. Bernardini,[244a,‡] T. Boccali,[244a,‡] G. Broccolo,[244a,244c,‡] R. Castaldi,[244a,‡] M. A. Ciocci,[244a,ppp,‡] R. Dell'Orso,[244a,‡] S. Donato,[244a,244c,oo,‡] G. Fedi,[244a,‡] L. Foà,[244a,244c,,‡] A. Giassi,[244a,‡] M. T. Grippo,[244a,ppp,‡] F. Ligabue,[244a,244c,‡] T. Lomtadze,[244a,‡] L. Martini,[244a,244b,‡] A. Messineo,[244a,244b,‡] F. Palla,[244a,‡] A. Rizzi,[244a,244b,‡] A. Savoy-Navarro,[244a,qqq,‡] A. T. Serban,[244a,‡] P. Spagnolo,[244a,‡] P. Squillacioti,[244a,ppp,‡] R. Tenchini,[244a,‡] G. Tonelli,[244a,244b,‡] A. Venturi,[244a,‡] P. G. Verdini,[244a,‡] L. Barone,[245a,245b,‡] F. Cavallari,[245a,‡] G. D'imperio,[245a,245b,oo,‡] D. Del Re,[245a,245b,‡] M. Diemoz,[245a,‡] S. Gelli,[245a,245b,‡] C. Jorda,[245a,‡] E. Longo,[245a,245b,‡] F. Margaroli,[245a,245b,‡] P. Meridiani,[245a,‡] F. Micheli,[245a,245b,‡] G. Organtini,[245a,245b,‡] R. Paramatti,[245a,‡] F. Preiato,[245a,245b,‡] S. Rahatlou,[245a,245b,‡] C. Rovelli,[245a,‡] F. Santanastasio,[245a,245b,‡] P. Traczyk,[245a,245b,oo,‡] N. Amapane,[246a,246b,‡] R. Arcidiacono,[246a,246c,‡] S. Argiro,[246a,246b,‡] M. Arneodo,[246a,246c,‡] R. Bellan,[246a,246b,‡] C. Biino,[246a,‡] N. Cartiglia,[246a,‡] M. Costa,[246a,246b,‡] R. Covarelli,[246a,246b,‡] A. Degano,[246a,246b,‡] N. Demaria,[246a,‡] L. Finco,[246a,246b,oo,‡] B. Kiani,[246a,246b,‡] C. Mariotti,[246a,‡] S. Maselli,[246a,‡] E. Migliore,[246a,246b,‡] V. Monaco,[246a,246b,‡] E. Monteil,[246a,246b,‡] M. Musich,[246a,‡] M. M. Obertino,[246a,246b,‡] L. Pacher,[246a,246b,‡] N. Pastrone,[246a,‡] M. Pelliccioni,[246a,‡] G. L. Pinna Angioni,[246a,246b,‡]

F. Ravera,[246a,246b,‡] A. Romero,[246a,246b,‡] M. Ruspa,[246a,246c,‡] R. Sacchi,[246a,246b,‡] A. Solano,[246a,246b,‡] A. Staiano,[246a,‡] U. Tamponi,[246a,‡] S. Belforte,[247a,‡] V. Candelise,[247a,247b,oo,‡] M. Casarsa,[247a,‡] F. Cossutti,[247a,‡] G. Della Ricca,[247a,247b,‡] B. Gobbo,[247a,‡] C. La Licata,[247a,247b,‡] M. Marone,[247a,247b,‡] A. Schizzi,[247a,247b,‡] T. Umer,[247a,247b,‡] A. Zanetti,[247a,‡] S. Chang,[248,‡] A. Kropivnitskaya,[248,‡] S. K. Nam,[248,‡] D. H. Kim,[249,‡] G. N. Kim,[249,‡] M. S. Kim,[249,‡] D. J. Kong,[249,‡] S. Lee,[249,‡] Y. D. Oh,[249,‡] A. Sakharov,[249,‡] D. C. Son,[249,‡] J. A. Brochero Cifuentes,[250,‡] H. Kim,[250,‡] T. J. Kim,[250,‡] M. S. Ryu,[250,‡] S. Song,[251,‡] S. Choi,[252,‡] Y. Go,[252,‡] D. Gyun,[252,‡] B. Hong,[252,‡] M. Jo,[252,‡] H. Kim,[252,‡] Y. Kim,[252,‡] B. Lee,[252,‡] K. Lee,[252,‡] K. S. Lee,[252,‡] S. Lee,[252,‡] S. K. Park,[252,‡] Y. Roh,[252,‡] H. D. Yoo,[253,‡] M. Choi,[254,‡] J. H. Kim,[254,‡] J. S. H. Lee,[254,‡] I. C. Park,[254,‡] G. Ryu,[254,‡] Y. Choi,[255,‡] Y. K. Choi,[255,‡] J. Goh,[255,‡] D. Kim,[255,‡] E. Kwon,[255,‡] J. Lee,[255,‡] I. Yu,[255,‡] A. Juodagalvis,[256,‡] J. Vaitkus,[256,‡] Z. A. Ibrahim,[257,‡] J. R. Komaragiri,[257,‡] M. A. B. Md Ali,[257,rrr,‡] F. Mohamad Idris,[257,‡] W. A. T. Wan Abdullah,[257,‡] E. Casimiro Linares,[258,‡] H. Castilla-Valdez,[258,‡] E. De La Cruz-Burelo,[258,‡] I. Heredia-de La Cruz,[258,sss,‡] A. Hernandez-Almada,[258,‡] R. Lopez-Fernandez,[258,‡] A. Sanchez-Hernandez,[258,‡] S. Carrillo Moreno,[259,‡] F. Vazquez Valencia,[259,‡] S. Carpinteyro,[260,‡] I. Pedraza,[260,‡] H. A. Salazar Ibarguen,[260,‡] A. Morelos Pineda,[261,‡] D. Krofcheck,[262,‡] P. H. Butler,[263,‡] S. Reucroft,[263,‡] A. Ahmad,[264,‡] M. Ahmad,[264,‡] Q. Hassan,[264,‡] H. R. Hoorani,[264,‡] W. A. Khan,[264,‡] T. Khurshid,[264,‡] M. Shoaib,[264,‡] H. Bialkowska,[265,‡] M. Bluj,[265,‡] B. Boimska,[265,‡] T. Frueboes,[265,‡] M. Górski,[265,‡] M. Kazana,[265,‡] K. Nawrocki,[265,‡] K. Romanowska-Rybinska,[265,‡] M. Szleper,[265,‡] P. Zalewski,[265,‡] G. Brona,[266,‡] K. Bunkowski,[266,‡] K. Doroba,[266,‡] A. Kalinowski,[266,‡] M. Konecki,[266,‡] J. Krolikowski,[266,‡] M. Misiura,[266,‡] M. Olszewski,[266,‡] M. Walczak,[266,‡] P. Bargassa,[267,‡] C. Beirão Da Cruz E Silva,[267,‡] A. Di Francesco,[267,‡] P. Faccioli,[267,‡] P. G. Ferreira Parracho,[267,‡] M. Gallinaro,[267,‡] L. Lloret Iglesias,[267,‡] F. Nguyen,[267,‡] J. Rodrigues Antunes,[267,‡] J. Seixas,[267,‡] O. Toldaiev,[267,‡] D. Vadruccio,[267,‡] J. Varela,[267,‡] P. Vischia,[267,‡] S. Afanasiev,[268,‡] P. Bunin,[268,‡] M. Gavrilenko,[268,‡] I. Golutvin,[268,‡] I. Gorbunov,[268,‡] A. Kamenev,[268,‡] V. Karjavin,[268,‡] V. Konoplyanikov,[268,‡] A. Lanev,[268,‡] A. Malakhov,[268,‡] V. Matveev,[268,ttt,‡] P. Moisenz,[268,‡] V. Palichik,[268,‡] V. Perelygin,[268,‡] S. Shmatov,[268,‡] S. Shulha,[268,‡] N. Skatchkov,[268,‡] V. Smirnov,[268,‡] T. Toriashvili,[268,uuu,‡] A. Zarubin,[268,‡] V. Golovtsov,[269,‡] Y. Ivanov,[269,‡] V. Kim,[269,vvv,‡] E. Kuznetsova,[269,‡] P. Levchenko,[269,‡] V. Murzin,[269,‡] V. Oreshkin,[269,‡] I. Smirnov,[269,‡] V. Sulimov,[269,‡] L. Uvarov,[269,‡] S. Vavilov,[269,‡] A. Vorobyev,[269,‡] Yu. Andreev,[270,‡] A. Dermenev,[270,‡] S. Gninenko,[270,‡] N. Golubev,[270,‡] A. Karneyeu,[270,‡] M. Kirsanov,[270,‡] N. Krasnikov,[270,‡] A. Pashenkov,[270,‡] D. Tlisov,[270,‡] A. Toropin,[270,‡] V. Epshteyn,[271,‡] V. Gavrilov,[271,‡] N. Lychkovskaya,[271,‡] V. Popov,[271,‡] I. Pozdnyakov,[271,‡] G. Safronov,[271,‡] A. Spiridonov,[271,‡] E. Vlasov,[271,‡] A. Zhokin,[271,‡] V. Andreev,[272,‡] M. Azarkin,[272,www,‡] I. Dremin,[272,www,‡] M. Kirakosyan,[272,‡] A. Leonidov,[272,www,‡] G. Mesyats,[272,‡] S. V. Rusakov,[272,‡] A. Vinogradov,[272,‡] A. Baskakov,[273,‡] A. Belyaev,[273,‡] E. Boos,[273,‡] V. Bunichev,[273,‡] M. Dubinin,[273,xxx,‡] L. Dudko,[273,‡] A. Ershov,[273,‡] A. Gribushin,[273,‡] V. Klyukhin,[273,‡] O. Kodolova,[273,‡] I. Lokhtin,[273,‡] I. Myagkov,[273,‡] S. Obraztsov,[273,‡] S. Petrushanko,[273,‡] V. Savrin,[273,‡] I. Azhgirey,[274,‡] I. Bayshev,[274,‡] S. Bitioukov,[274,‡] V. Kachanov,[274,‡] A. Kalinin,[274,‡] D. Konstantinov,[274,‡] V. Krychkine,[274,‡] V. Petrov,[274,‡] R. Ryutin,[274,‡] A. Sobol,[274,‡] L. Tourtchanovitch,[274,‡] S. Troshin,[274,‡] N. Tyurin,[274,‡] A. Uzunian,[274,‡] A. Volkov,[274,‡] P. Adzic,[275,yyy,‡] M. Ekmedzic,[275,‡] J. Milosevic,[275,‡] V. Rekovic,[275,‡] J. Alcaraz Maestre,[276,‡] E. Calvo,[276,‡] M. Cerrada,[276,‡] M. Chamizo Llatas,[276,‡] N. Colino,[276,‡] B. De La Cruz,[276,‡] A. Delgado Peris,[276,‡] D. Domínguez Vázquez,[276,‡] A. Escalante Del Valle,[276,‡] C. Fernandez Bedoya,[276,‡] J. P. Fernández Ramos,[276,‡] J. Flix,[276,‡] M. C. Fouz,[276,‡] P. Garcia-Abia,[276,‡] O. Gonzalez Lopez,[276,‡] S. Goy Lopez,[276,‡] J. M. Hernandez,[276,‡] M. I. Josa,[276,‡] E. Navarro De Martino,[276,‡] A. Pérez-Calero Yzquierdo,[276,‡] J. Puerta Pelayo,[276,‡] A. Quintario Olmeda,[276,‡] I. Redondo,[276,‡] L. Romero,[276,‡] M. S. Soares,[276,‡] C. Albajar,[277,‡] J. F. de Trocóniz,[277,‡] M. Missiroli,[277,‡] D. Moran,[277,‡] H. Brun,[278,‡] J. Cuevas,[278,‡] J. Fernandez Menendez,[278,‡] S. Folgueras,[278,‡] I. Gonzalez Caballero,[278,‡] E. Palencia Cortezon,[278,‡] J. M. Vizan Garcia,[278,‡] I. J. Cabrillo,[279,‡] A. Calderon,[279,‡] J. R. Castiñeiras De Saa,[279,‡] J. Duarte Campderros,[279,‡] M. Fernandez,[279,‡] G. Gomez,[279,‡] A. Graziano,[279,‡] A. Lopez Virto,[279,‡] J. Marco,[279,‡] R. Marco,[279,‡] C. Martinez Rivero,[279,‡] F. Matorras,[279,‡] F. J. Munoz Sanchez,[279,‡] J. Piedra Gomez,[279,‡] T. Rodrigo,[279,‡] A. Y. Rodríguez-Marrero,[279,‡] A. Ruiz-Jimeno,[279,‡] L. Scodellaro,[279,‡] I. Vila,[279,‡] R. Vilar Cortabitarte,[279,‡] D. Abbaneo,[280,‡] E. Auffray,[280,‡] G. Auzinger,[280,‡] M. Bachtis,[280,‡] P. Baillon,[280,‡] A. H. Ball,[280,‡] D. Barney,[280,‡] A. Benaglia,[280,‡] J. Bendavid,[280,‡] L. Benhabib,[280,‡] J. F. Benitez,[280,‡] G. M. Berruti,[280,‡] P. Bloch,[280,‡] A. Bocci,[280,‡] A. Bonato,[280,‡] C. Botta,[280,‡] H. Breuker,[280,‡] T. Camporesi,[280,‡] G. Cerminara,[280,‡] S. Colafranceschi,[280,zzz,‡] M. D'Alfonso,[280,‡] D. d'Enterria,[280,‡] A. Dabrowski,[280,‡] V. Daponte,[280,‡] A. David,[280,‡] M. De Gruttola,[280,‡] F. De Guio,[280,‡] A. De Roeck,[280,‡] S. De Visscher,[280,‡] E. Di Marco,[280,‡] M. Dobson,[280,‡] M. Dordevic,[280,‡] T. du Pree,[280,‡] N. Dupont-Sagorin,[280,‡] A. Elliott-Peisert,[280,‡] G. Franzoni,[280,‡] W. Funk,[280,‡] D. Gigi,[280,‡] K. Gill,[280,‡] D. Giordano,[280,‡]

M. Girone,[280,‡] F. Glege,[280,‡] R. Guida,[280,‡] S. Gundacker,[280,‡] M. Guthoff,[280,‡] J. Hammer,[280,‡] M. Hansen,[280,‡] P. Harris,[280,‡] J. Hegeman,[280,‡] V. Innocente,[280,‡] P. Janot,[280,‡] H. Kirschenmann,[280,‡] M. J. Kortelainen,[280,‡] K. Kousouris,[280,‡] K. Krajczar,[280,‡] P. Lecoq,[280,‡] C. Lourenço,[280,‡] M. T. Lucchini,[280,‡] N. Magini,[280,‡] L. Malgeri,[280,‡] M. Mannelli,[280,‡] J. Marrouche,[280,‡] A. Martelli,[280,‡] L. Masetti,[280,‡] F. Meijers,[280,‡] S. Mersi,[280,‡] E. Meschi,[280,‡] F. Moortgat,[280,‡] S. Morovic,[280,‡] M. Mulders,[280,‡] M. V. Nemallapudi,[280,‡] H. Neugebauer,[280,‡] S. Orfanelli,[280,aaaa,‡] L. Orsini,[280,‡] L. Pape,[280,‡] E. Perez,[280,‡] A. Petrilli,[280,‡] G. Petrucciani,[280,‡] A. Pfeiffer,[280,‡] D. Piparo,[280,‡] A. Racz,[280,‡] G. Rolandi,[280,bbbb,‡] M. Rovere,[280,‡] M. Ruan,[280,‡] H. Sakulin,[280,‡] C. Schäfer,[280,‡] C. Schwick,[280,‡] A. Sharma,[280,‡] P. Silva,[280,‡] M. Simon,[280,‡] P. Sphicas,[280,cccc,‡] D. Spiga,[280,‡] J. Steggemann,[280,‡] B. Stieger,[280,‡] M. Stoye,[280,‡] Y. Takahashi,[280,‡] D. Treille,[280,‡] A. Tsirou,[280,‡] G. I. Veres,[280,ggg,‡] N. Wardle,[280,‡] H. K. Wöhri,[280,‡] A. Zagozdzinska,[280,dddd,‡] W. D. Zeuner,[280,‡] W. Bertl,[281,‡] K. Deiters,[281,‡] W. Erdmann,[281,‡] R. Horisberger,[281,‡] Q. Ingram,[281,‡] H. C. Kaestli,[281,‡] D. Kotlinski,[281,‡] U. Langenegger,[281,‡] T. Rohe,[281,‡] F. Bachmair,[282,‡] L. Bäni,[282,‡] L. Bianchini,[282,‡] M. A. Buchmann,[282,‡] B. Casal,[282,‡] G. Dissertori,[282,‡] M. Dittmar,[282,‡] M. Donegà,[282,‡] M. Dünser,[282,‡] P. Eller,[282,‡] C. Grab,[282,‡] C. Heidegger,[282,‡] D. Hits,[282,‡] J. Hoss,[282,‡] G. Kasieczka,[282,‡] W. Lustermann,[282,‡] B. Mangano,[282,‡] A. C. Marini,[282,‡] M. Marionneau,[282,‡] P. Martinez Ruiz del Arbol,[282,‡] M. Masciovecchio,[282,‡] D. Meister,[282,‡] P. Musella,[282,‡] F. Nessi-Tedaldi,[282,‡] F. Pandolfi,[282,‡] J. Pata,[282,‡] F. Pauss,[282,‡] L. Perrozzi,[282,‡] M. Peruzzi,[282,‡] M. Quittnat,[282,‡] M. Rossini,[282,‡] A. Starodumov,[282,eeee,‡] M. Takahashi,[282,‡] V. R. Tavolaro,[282,‡] K. Theofilatos,[282,‡] R. Wallny,[282,‡] H. A. Weber,[282,‡] T. K. Aarrestad,[283,‡] C. Amsler,[283,ffff,‡] M. F. Canelli,[283,‡] V. Chiochia,[283,‡] A. De Cosa,[283,‡] C. Galloni,[283,‡] A. Hinzmann,[283,‡] T. Hreus,[283,‡] B. Kilminster,[283,‡] C. Lange,[283,‡] J. Ngadiuba,[283,‡] D. Pinna,[283,‡] P. Robmann,[283,‡] F. J. Ronga,[283,‡] D. Salerno,[283,‡] S. Taroni,[283,‡] Y. Yang,[283,‡] M. Cardaci,[284,‡] K. H. Chen,[284,‡] T. H. Doan,[284,‡] C. Ferro,[284,‡] M. Konyushikhin,[284,‡] C. M. Kuo,[284,‡] W. Lin,[284,‡] Y. J. Lu,[284,‡] R. Volpe,[284,‡] S. S. Yu,[284,‡] P. Chang,[285,‡] Y. H. Chang,[285,‡] Y. W. Chang,[285,‡] Y. Chao,[285,‡] K. F. Chen,[285,‡] P. H. Chen,[285,‡] C. Dietz,[285,‡] F. Fiori,[285,‡] U. Grundler,[285,‡] W.-S. Hou,[285,‡] Y. Hsiung,[285,‡] Y. F. Liu,[285,‡] R.-S. Lu,[285,‡] M. Miñano Moya,[285,‡] E. Petrakou,[285,‡] J. f. Tsai,[285,‡] Y. M. Tzeng,[285,‡] R. Wilken,[285,‡] B. Asavapibhop,[286,‡] K. Kovitanggoon,[286,‡] G. Singh,[286,‡] N. Srimanobhas,[286,‡] N. Suwonjandee,[286,‡] A. Adiguzel,[287,‡] S. Cerci,[287,gggg,‡] C. Dozen,[287,‡] S. Girgis,[287,‡] G. Gokbulut,[287,‡] Y. Guler,[287,‡] E. Gurpinar,[287,‡] I. Hos,[287,‡] E. E. Kangal,[287,hhhh,‡] A. Kayis Topaksu,[287,‡] G. Onengut,[287,iiii,‡] K. Ozdemir,[287,jjjj,‡] S. Ozturk,[287,kkkk,‡] B. Tali,[287,gggg,‡] H. Topakli,[287,kkkk,‡] M. Vergili,[287,‡] C. Zorbilmez,[287,‡] I. V. Akin,[288,‡] B. Bilin,[288,‡] S. Bilmis,[288,‡] B. Isildak,[288,llll,‡] G. Karapinar,[288,mmmm,‡] U. E. Surat,[288,‡] M. Yalvac,[288,‡] M. Zeyrek,[288,‡] E. A. Albayrak,[289,nnnn,‡] E. Gülmez,[289,‡] M. Kaya,[289,oooo,‡] O. Kaya,[289,pppp,‡] T. Yetkin,[289,qqqq,‡] K. Cankocak,[290,‡] S. Sen,[290,rrrr,‡] F. I. Vardarlı,[290,‡] B. Grynyov,[291,‡] L. Levchuk,[292,‡] P. Sorokin,[292,‡] R. Aggleton,[293,‡] F. Ball,[293,‡] L. Beck,[293,‡] J. J. Brooke,[293,‡] E. Clement,[293,‡] D. Cussans,[293,‡] H. Flacher,[293,‡] J. Goldstein,[293,‡] M. Grimes,[293,‡] G. P. Heath,[293,‡] H. F. Heath,[293,‡] J. Jacob,[293,‡] L. Kreczko,[293,‡] C. Lucas,[293,‡] Z. Meng,[293,‡] D. M. Newbold,[293,ssss,‡] S. Paramesvaran,[293,‡] A. Poll,[293,‡] T. Sakuma,[293,‡] S. Seif El Nasr-storey,[293,‡] S. Senkin,[293,‡] D. Smith,[293,‡] V. J. Smith,[293,‡] K. W. Bell,[294,‡] A. Belyaev,[294,tttt,‡] C. Brew,[294,‡] R. M. Brown,[294,‡] D. J. A. Cockerill,[294,‡] J. A. Coughlan,[294,‡] K. Harder,[294,‡] S. Harper,[294,‡] E. Olaiya,[294,‡] D. Petyt,[294,‡] C. H. Shepherd-Themistocleous,[294,‡] A. Thea,[294,‡] I. R. Tomalin,[294,‡] T. Williams,[294,‡] W. J. Womersley,[294,‡] S. D. Worm,[294,‡] M. Baber,[295,‡] R. Bainbridge,[295,‡] O. Buchmuller,[295,‡] A. Bundock,[295,‡] D. Burton,[295,‡] S. Casasso,[295,‡] M. Citron,[295,‡] D. Colling,[295,‡] L. Corpe,[295,‡] N. Cripps,[295,‡] P. Dauncey,[295,‡] G. Davies,[295,‡] A. De Wit,[295,‡] M. Della Negra,[295,‡] P. Dunne,[295,‡] A. Elwood,[295,‡] W. Ferguson,[295,‡] J. Fulcher,[295,‡] D. Futyan,[295,‡] G. Hall,[295,‡] G. Iles,[295,‡] G. Karapostoli,[295,‡] M. Kenzie,[295,‡] R. Lane,[295,‡] R. Lucas,[295,ssss,‡] L. Lyons,[295,‡] A.-M. Magnan,[295,‡] S. Malik,[295,‡] J. Nash,[295,‡] A. Nikitenko,[295,eeee,‡] J. Pela,[295,‡] M. Pesaresi,[295,‡] K. Petridis,[295,‡] D. M. Raymond,[295,‡] A. Richards,[295,‡] A. Rose,[295,‡] C. Seez,[295,‡] P. Sharp,[295,,‡] A. Tapper,[295,‡] K. Uchida,[295,‡] M. Vazquez Acosta,[295,uuuu,‡] T. Virdee,[295,‡] S. C. Zenz,[295,‡] J. E. Cole,[296,‡] P. R. Hobson,[296,‡] A. Khan,[296,‡] P. Kyberd,[296,‡] D. Leggat,[296,‡] D. Leslie,[296,‡] I. D. Reid,[296,‡] P. Symonds,[296,‡] L. Teodorescu,[296,‡] M. Turner,[296,‡] A. Borzou,[297,‡] J. Dittmann,[297,‡] K. Hatakeyama,[297,‡] A. Kasmi,[297,‡] H. Liu,[297,‡] N. Pastika,[297,‡] O. Charaf,[298,‡] S. I. Cooper,[298,‡] C. Henderson,[298,‡] P. Rumerio,[298,‡] A. Avetisyan,[299,‡] T. Bose,[299,‡] C. Fantasia,[299,‡] D. Gastler,[299,‡] P. Lawson,[299,‡] D. Rankin,[299,‡] C. Richardson,[299,‡] J. Rohlf,[299,‡] J. St. John,[299,‡] L. Sulak,[299,‡] D. Zou,[299,‡] J. Alimena,[300,‡] E. Berry,[300,‡] S. Bhattacharya,[300,‡] D. Cutts,[300,‡] N. Dhingra,[300,‡] A. Ferapontov,[300,‡] A. Garabedian,[300,‡] U. Heintz,[300,‡] E. Laird,[300,‡] G. Landsberg,[300,‡] Z. Mao,[300,‡] M. Narain,[300,‡] S. Sagir,[300,‡] T. Sinthuprasith,[300,‡] R. Breedon,[301,‡] G. Breto,[301,‡] M. Calderon De La Barca Sanchez,[301,‡] S. Chauhan,[301,‡] M. Chertok,[301,‡] J. Conway,[301,‡] R. Conway,[301,‡] P. T. Cox,[301,‡] R. Erbacher,[301,‡] M. Gardner,[301,‡] W. Ko,[301,‡] R. Lander,[301,‡] M. Mulhearn,[301,‡] D. Pellett,[301,‡] J. Pilot,[301,‡] F. Ricci-Tam,[301,‡] S. Shalhout,[301,‡] J. Smith,[301,‡] M. Squires,[301,‡] D. Stolp,[301,‡] M. Tripathi,[301,‡]

S. Wilbur,[301,‡] R. Yohay,[301,‡] R. Cousins,[302,‡] P. Everaerts,[302,‡] C. Farrell,[302,‡] J. Hauser,[302,‡] M. Ignatenko,[302,‡] G. Rakness,[302,‡] D. Saltzberg,[302,‡] E. Takasugi,[302,‡] V. Valuev,[302,‡] M. Weber,[302,‡] K. Burt,[303,‡] R. Clare,[303,‡] J. Ellison,[303,‡] J. W. Gary,[303,‡] G. Hanson,[303,‡] J. Heilman,[303,‡] M. Ivova Rikova,[303,‡] P. Jandir,[303,‡] E. Kennedy,[303,‡] F. Lacroix,[303,‡] O. R. Long,[303,‡] A. Luthra,[303,‡] M. Malberti,[303,‡] M. Olmedo Negrete,[303,‡] A. Shrinivas,[303,‡] S. Sumowidagdo,[303,‡] H. Wei,[303,‡] S. Wimpenny,[303,‡] J. G. Branson,[304,‡] G. B. Cerati,[304,‡] S. Cittolin,[304,‡] R. T. D'Agnolo,[304,‡] A. Holzner,[304,‡] R. Kelley,[304,‡] D. Klein,[304,‡] J. Letts,[304,‡] I. Macneill,[304,‡] D. Olivito,[304,‡] S. Padhi,[304,‡] M. Pieri,[304,‡] M. Sani,[304,‡] V. Sharma,[304,‡] S. Simon,[304,‡] M. Tadel,[304,‡] Y. Tu,[304,‡] A. Vartak,[304,‡] S. Wasserbaech,[304,vvvv,‡] C. Welke,[304,‡] F. Würthwein,[304,‡] A. Yagil,[304,‡] G. Zevi Della Porta,[304,‡] D. Barge,[305,‡] J. Bradmiller-Feld,[305,‡] C. Campagnari,[305,‡] A. Dishaw,[305,‡] V. Dutta,[305,‡] K. Flowers,[305,‡] M. Franco Sevilla,[305,‡] P. Geffert,[305,‡] C. George,[305,‡] F. Golf,[305,‡] L. Gouskos,[305,‡] J. Gran,[305,‡] J. Incandela,[305,‡] C. Justus,[305,‡] N. Mccoll,[305,‡] S. D. Mullin,[305,‡] J. Richman,[305,‡] D. Stuart,[305,‡] I. Suarez,[305,‡] W. To,[305,‡] C. West,[305,‡] J. Yoo,[305,‡] D. Anderson,[306,‡] A. Apresyan,[306,‡] A. Bornheim,[306,‡] J. Bunn,[306,‡] Y. Chen,[306,‡] J. Duarte,[306,‡] A. Mott,[306,‡] H. B. Newman,[306,‡] C. Pena,[306,‡] M. Pierini,[306,‡] M. Spiropulu,[306,‡] J. R. Vlimant,[306,‡] S. Xie,[306,‡] R. Y. Zhu,[306,‡] V. Azzolini,[307,‡] A. Calamba,[307,‡] B. Carlson,[307,‡] T. Ferguson,[307,‡] Y. Iiyama,[307,‡] M. Paulini,[307,‡] J. Russ,[307,‡] M. Sun,[307,‡] H. Vogel,[307,‡] I. Vorobiev,[307,‡] J. P. Cumalat,[308,‡] W. T. Ford,[308,‡] A. Gaz,[308,‡] F. Jensen,[308,‡] A. Johnson,[308,‡] M. Krohn,[308,‡] T. Mulholland,[308,‡] U. Nauenberg,[308,‡] J. G. Smith,[308,‡] K. Stenson,[308,‡] S. R. Wagner,[308,‡] J. Alexander,[309,‡] A. Chatterjee,[309,‡] J. Chaves,[309,‡] J. Chu,[309,‡] S. Dittmer,[309,‡] N. Eggert,[309,‡] N. Mirman,[309,‡] G. Nicolas Kaufman,[309,‡] J. R. Patterson,[309,‡] A. Rinkevicius,[309,‡] A. Ryd,[309,‡] L. Skinnari,[309,‡] L. Soffi,[309,‡] W. Sun,[309,‡] S. M. Tan,[309,‡] W. D. Teo,[309,‡] J. Thom,[309,‡] J. Thompson,[309,‡] J. Tucker,[309,‡] Y. Weng,[309,‡] P. Wittich,[309,‡] S. Abdullin,[310,‡] M. Albrow,[310,‡] J. Anderson,[310,‡] G. Apollinari,[310,‡] L. A. T. Bauerdick,[310,‡] A. Beretvas,[310,‡] J. Berryhill,[310,‡] P. C. Bhat,[310,‡] G. Bolla,[310,‡] K. Burkett,[310,‡] J. N. Butler,[310,‡] H. W. K. Cheung,[310,‡] F. Chlebana,[310,‡] S. Cihangir,[310,‡] V. D. Elvira,[310,‡] I. Fisk,[310,‡] J. Freeman,[310,‡] E. Gottschalk,[310,‡] L. Gray,[310,‡] D. Green,[310,‡] S. Grünendahl,[310,‡] O. Gutsche,[310,‡] J. Hanlon,[310,‡] D. Hare,[310,‡] R. M. Harris,[310,‡] J. Hirschauer,[310,‡] B. Hooberman,[310,‡] Z. Hu,[310,‡] S. Jindariani,[310,‡] M. Johnson,[310,‡] U. Joshi,[310,‡] A. W. Jung,[310,‡] B. Klima,[310,‡] B. Kreis,[310,‡] S. Kwan,[310,‡] S. Lammel,[310,‡] J. Linacre,[310,‡] D. Lincoln,[310,‡] R. Lipton,[310,‡] T. Liu,[310,‡] R. Lopes De Sá,[310,‡] J. Lykken,[310,‡] K. Maeshima,[310,‡] J. M. Marraffino,[310,‡] V. I. Martinez Outschoorn,[310,‡] S. Maruyama,[310,‡] D. Mason,[310,‡] P. McBride,[310,‡] P. Merkel,[310,‡] K. Mishra,[310,‡] S. Mrenna,[310,‡] S. Nahn,[310,‡] C. Newman-Holmes,[310,‡] V. O'Dell,[310,‡] O. Prokofyev,[310,‡] E. Sexton-Kennedy,[310,‡] A. Soha,[310,‡] W. J. Spalding,[310,‡] L. Spiegel,[310,‡] L. Taylor,[310,‡] S. Tkaczyk,[310,‡] N. V. Tran,[310,‡] L. Uplegger,[310,‡] E. W. Vaandering,[310,‡] C. Vernieri,[310,‡] M. Verzocchi,[310,‡] R. Vidal,[310,‡] A. Whitbeck,[310,‡] F. Yang,[310,‡] H. Yin,[310,‡] D. Acosta,[311,‡] P. Avery,[311,‡] P. Bortignon,[311,‡] D. Bourilkov,[311,‡] A. Carnes,[311,‡] M. Carver,[311,‡] D. Curry,[311,‡] S. Das,[311,‡] G. P. Di Giovanni,[311,‡] R. D. Field,[311,‡] M. Fisher,[311,‡] I. K. Furic,[311,‡] J. Hugon,[311,‡] J. Konigsberg,[311,‡] A. Korytov,[311,‡] J. F. Low,[311,‡] P. Ma,[311,‡] K. Matchev,[311,‡] H. Mei,[311,‡] P. Milenovic,[311,wwww,‡] G. Mitselmakher,[311,‡] L. Muniz,[311,‡] D. Rank,[311,‡] L. Shchutska,[311,‡] M. Snowball,[311,‡] D. Sperka,[311,‡] S. j. Wang,[311,‡] J. Yelton,[311,‡] S. Hewamanage,[312,‡] S. Linn,[312,‡] P. Markowitz,[312,‡] G. Martinez,[312,‡] J. L. Rodriguez,[312,‡] A. Ackert,[313,‡] J. R. Adams,[313,‡] T. Adams,[313,‡] A. Askew,[313,‡] J. Bochenek,[313,‡] B. Diamond,[313,‡] J. Haas,[313,‡] S. Hagopian,[313,‡] V. Hagopian,[313,‡] K. F. Johnson,[313,‡] A. Khatiwada,[313,‡] H. Prosper,[313,‡] V. Veeraraghavan,[313,‡] M. Weinberg,[313,‡] V. Bhopatkar,[314,‡] M. Hohlmann,[314,‡] H. Kalakhety,[314,‡] D. Mareskas-palcek,[314,‡] T. Roy,[314,‡] F. Yumiceva,[314,‡] M. R. Adams,[315,‡] L. Apanasevich,[315,‡] D. Berry,[315,‡] R. R. Betts,[315,‡] I. Bucinskaite,[315,‡] R. Cavanaugh,[315,‡] O. Evdokimov,[315,‡] L. Gauthier,[315,‡] C. E. Gerber,[315,‡] D. J. Hofman,[315,‡] P. Kurt,[315,‡] C. O'Brien,[315,‡] I. D. Sandoval Gonzalez,[315,‡] C. Silkworth,[315,‡] P. Turner,[315,‡] N. Varelas,[315,‡] Z. Wu,[315,‡] M. Zakaria,[315,‡] B. Bilki,[316,xxxx,‡] W. Clarida,[316,‡] K. Dilsiz,[316,‡] S. Durgut,[316,‡] R. P. Gandrajula,[316,‡] M. Haytmyradov,[316,‡] V. Khristenko,[316,‡] J.-P. Merlo,[316,‡] H. Mermerkaya,[316,yyyy,‡] A. Mestvirishvili,[316,‡] A. Moeller,[316,‡] J. Nachtman,[316,‡] H. Ogul,[316,‡] Y. Onel,[316,‡] F. Ozok,[316,nnnn,‡] A. Penzo,[316,‡] C. Snyder,[316,‡] P. Tan,[316,‡] E. Tiras,[316,‡] J. Wetzel,[316,‡] K. Yi,[316,‡] I. Anderson,[317,‡] B. A. Barnett,[317,‡] B. Blumenfeld,[317,‡] D. Fehling,[317,‡] L. Feng,[317,‡] A. V. Gritsan,[317,‡] P. Maksimovic,[317,‡] C. Martin,[317,‡] K. Nash,[317,‡] M. Osherson,[317,‡] M. Swartz,[317,‡] M. Xiao,[317,‡] Y. Xin,[317,‡] P. Baringer,[318,‡] A. Bean,[318,‡] G. Benelli,[318,‡] C. Bruner,[318,‡] J. Gray,[318,‡] R. P. Kenny III,[318,‡] D. Majumder,[318,‡] M. Malek,[318,‡] M. Murray,[318,‡] D. Noonan,[318,‡] S. Sanders,[318,‡] R. Stringer,[318,‡] Q. Wang,[318,‡] J. S. Wood,[318,‡] I. Chakaberia,[319,‡] A. Ivanov,[319,‡] K. Kaadze,[319,‡] S. Khalil,[319,‡] M. Makouski,[319,‡] Y. Maravin,[319,‡] L. K. Saini,[319,‡] N. Skhirtladze,[319,‡] I. Svintradze,[319,‡] S. Toda,[319,‡] D. Lange,[320,‡] F. Rebassoo,[320,‡] D. Wright,[320,‡] C. Anelli,[321,‡] A. Baden,[321,‡] O. Baron,[321,‡] A. Belloni,[321,‡] B. Calvert,[321,‡] S. C. Eno,[321,‡] C. Ferraioli,[321,‡] J. A. Gomez,[321,‡] N. J. Hadley,[321,‡] S. Jabeen,[321,‡] R. G. Kellogg,[321,‡] T. Kolberg,[321,‡] J. Kunkle,[321,‡] Y. Lu,[321,‡]

A. C. Mignerey,[321,‡] K. Pedro,[321,‡] Y. H. Shin,[321,‡] A. Skuja,[321,‡] M. B. Tonjes,[321,‡] S. C. Tonwar,[321,‡] A. Apyan,[322,‡] R. Barbieri,[322,‡] A. Baty,[322,‡] K. Bierwagen,[322,‡] S. Brandt,[322,‡] W. Busza,[322,‡] I. A. Cali,[322,‡] L. Di Matteo,[322,‡] G. Gomez Ceballos,[322,‡] M. Goncharov,[322,‡] D. Gulhan,[322,‡] G. M. Innocenti,[322,‡] M. Klute,[322,‡] D. Kovalskyi,[322,‡] Y. S. Lai,[322,‡] Y.-J. Lee,[322,‡] A. Levin,[322,‡] P. D. Luckey,[322,‡] C. Mcginn,[322,‡] X. Niu,[322,‡] C. Paus,[322,‡] D. Ralph,[322,‡] C. Roland,[322,‡] G. Roland,[322,‡] G. S. F. Stephans,[322,‡] K. Sumorok,[322,‡] M. Varma,[322,‡] D. Velicanu,[322,‡] J. Veverka,[322,‡] J. Wang,[322,‡] T. W. Wang,[322,‡] B. Wyslouch,[322,‡] M. Yang,[322,‡] V. Zhukova,[322,‡] B. Dahmes,[323,‡] A. Finkel,[323,‡] A. Gude,[323,‡] P. Hansen,[323,‡] S. Kalafut,[323,‡] S. C. Kao,[323,‡] K. Klapoetke,[323,‡] Y. Kubota,[323,‡] Z. Lesko,[323,‡] J. Mans,[323,‡] S. Nourbakhsh,[323,‡] N. Ruckstuhl,[323,‡] R. Rusack,[323,‡] N. Tambe,[323,‡] J. Turkewitz,[323,‡] J. G. Acosta,[324,‡] S. Oliveros,[324,‡] E. Avdeeva,[325,‡] K. Bloom,[325,‡] S. Bose,[325,‡] D. R. Claes,[325,‡] A. Dominguez,[325,‡] C. Fangmeier,[325,‡] R. Gonzalez Suarez,[325,‡] R. Kamalieddin,[325,‡] J. Keller,[325,‡] D. Knowlton,[325,‡] I. Kravchenko,[325,‡] J. Lazo-Flores,[325,‡] F. Meier,[325,‡] J. Monroy,[325,‡] F. Ratnikov,[325,‡] J. E. Siado,[325,‡] G. R. Snow,[325,‡] M. Alyari,[326,‡] J. Dolen,[326,‡] J. George,[326,‡] A. Godshalk,[326,‡] I. Iashvili,[326,‡] J. Kaisen,[326,‡] A. Kharchilava,[326,‡] A. Kumar,[326,‡] S. Rappoccio,[326,‡] G. Alverson,[327,‡] E. Barberis,[327,‡] D. Baumgartel,[327,‡] M. Chasco,[327,‡] A. Hortiangtham,[327,‡] A. Massironi,[327,‡] D. M. Morse,[327,‡] D. Nash,[327,‡] T. Orimoto,[327,‡] R. Teixeira De Lima,[327,‡] D. Trocino,[327,‡] R.-J. Wang,[327,‡] D. Wood,[327,‡] J. Zhang,[327,‡] K. A. Hahn,[328,‡] A. Kubik,[328,‡] N. Mucia,[328,‡] N. Odell,[328,‡] B. Pollack,[328,‡] A. Pozdnyakov,[328,‡] M. Schmitt,[328,‡] S. Stoynev,[328,‡] K. Sung,[328,‡] M. Trovato,[328,‡] M. Velasco,[328,‡] S. Won,[328,‡] A. Brinkerhoff,[329,‡] N. Dev,[329,‡] M. Hildreth,[329,‡] C. Jessop,[329,‡] D. J. Karmgard,[329,‡] N. Kellams,[329,‡] K. Lannon,[329,‡] S. Lynch,[329,‡] N. Marinelli,[329,‡] F. Meng,[329,‡] C. Mueller,[329,‡] Y. Musienko,[329,ttt,‡] T. Pearson,[329,‡] M. Planer,[329,‡] R. Ruchti,[329,‡] G. Smith,[329,‡] N. Valls,[329,‡] M. Wayne,[329,‡] M. Wolf,[329,‡] A. Woodard,[329,‡] L. Antonelli,[330,‡] J. Brinson,[330,‡] B. Bylsma,[330,‡] L. S. Durkin,[330,‡] S. Flowers,[330,‡] A. Hart,[330,‡] C. Hill,[330,‡] R. Hughes,[330,‡] K. Kotov,[330,‡] T. Y. Ling,[330,‡] B. Liu,[330,‡] W. Luo,[330,‡] D. Puigh,[330,‡] M. Rodenburg,[330,‡] B. L. Winer,[330,‡] H. W. Wulsin,[330,‡] O. Driga,[331,‡] P. Elmer,[331,‡] J. Hardenbrook,[331,‡] P. Hebda,[331,‡] S. A. Koay,[331,‡] P. Lujan,[331,‡] D. Marlow,[331,‡] T. Medvedeva,[331,‡] M. Mooney,[331,‡] J. Olsen,[331,‡] C. Palmer,[331,‡] P. Piroué,[331,‡] X. Quan,[331,‡] H. Saka,[331,‡] D. Stickland,[331,‡] C. Tully,[331,‡] J. S. Werner,[331,‡] A. Zuranski,[331,‡] V. E. Barnes,[332,‡] D. Benedetti,[332,‡] D. Bortoletto,[332,‡] L. Gutay,[332,‡] M. K. Jha,[332,‡] M. Jones,[332,‡] K. Jung,[332,‡] M. Kress,[332,‡] N. Leonardo,[332,‡] D. H. Miller,[332,‡] N. Neumeister,[332,‡] F. Primavera,[332,‡] B. C. Radburn-Smith,[332,‡] X. Shi,[332,‡] I. Shipsey,[332,‡] D. Silvers,[332,‡] J. Sun,[332,‡] A. Svyatkovskiy,[332,‡] F. Wang,[332,‡] W. Xie,[332,‡] L. Xu,[332,‡] J. Zablocki,[332,‡] N. Parashar,[333,‡] J. Stupak,[333,‡] A. Adair,[334,‡] B. Akgun,[334,‡] Z. Chen,[334,‡] K. M. Ecklund,[334,‡] F. J. M. Geurts,[334,‡] M. Guilbaud,[334,‡] W. Li,[334,‡] B. Michlin,[334,‡] M. Northup,[334,‡] B. P. Padley,[334,‡] R. Redjimi,[334,‡] J. Roberts,[334,‡] J. Rorie,[334,‡] Z. Tu,[334,‡] J. Zabel,[334,‡] B. Betchart,[335,‡] A. Bodek,[335,‡] P. de Barbaro,[335,‡] R. Demina,[335,‡] Y. Eshaq,[335,‡] T. Ferbel,[335,‡] M. Galanti,[335,‡] A. Garcia-Bellido,[335,‡] P. Goldenzweig,[335,‡] J. Han,[335,‡] A. Harel,[335,‡] O. Hindrichs,[335,‡] A. Khukhunaishvili,[335,‡] G. Petrillo,[335,‡] M. Verzetti,[335,‡] L. Demortier,[336,‡] S. Arora,[337,‡] A. Barker,[337,‡] J. P. Chou,[337,‡] C. Contreras-Campana,[337,‡] E. Contreras-Campana,[337,‡] D. Duggan,[337,‡] D. Ferencek,[337,‡] Y. Gershtein,[337,‡] R. Gray,[337,‡] E. Halkiadakis,[337,‡] D. Hidas,[337,‡] E. Hughes,[337,‡] S. Kaplan,[337,‡] R. Kunnawalkam Elayavalli,[337,‡] A. Lath,[337,‡] S. Panwalkar,[337,‡] M. Park,[337,‡] S. Salur,[337,‡] S. Schnetzer,[337,‡] D. Sheffield,[337,‡] S. Somalwar,[337,‡] R. Stone,[337,‡] S. Thomas,[337,‡] P. Thomassen,[337,‡] M. Walker,[337,‡] M. Foerster,[338,‡] G. Riley,[338,‡] K. Rose,[338,‡] S. Spanier,[338,‡] A. York,[338,‡] O. Bouhali,[339,zzzz,‡] A. Castaneda Hernandez,[339,‡] M. Dalchenko,[339,‡] M. De Mattia,[339,‡] A. Delgado,[339,‡] S. Dildick,[339,‡] R. Eusebi,[339,‡] W. Flanagan,[339,‡] J. Gilmore,[339,‡] T. Kamon,[339,aaaaa,‡] V. Krutelyov,[339,‡] R. Montalvo,[339,‡] R. Mueller,[339,‡] I. Osipenkov,[339,‡] Y. Pakhotin,[339,‡] R. Patel,[339,‡] A. Perloff,[339,‡] J. Roe,[339,‡] A. Rose,[339,‡] A. Safonov,[339,‡] A. Tatarinov,[339,‡] K. A. Ulmer,[339,oo,‡] N. Akchurin,[340,‡] C. Cowden,[340,‡] J. Damgov,[340,‡] C. Dragoiu,[340,‡] P. R. Dudero,[340,‡] J. Faulkner,[340,‡] S. Kunori,[340,‡] K. Lamichhane,[340,‡] S. W. Lee,[340,‡] T. Libeiro,[340,‡] S. Undleeb,[340,‡] I. Volobouev,[340,‡] E. Appelt,[341,‡] A. G. Delannoy,[341,‡] S. Greene,[341,‡] A. Gurrola,[341,‡] R. Janjam,[341,‡] W. Johns,[341,‡] C. Maguire,[341,‡] Y. Mao,[341,‡] A. Melo,[341,‡] P. Sheldon,[341,‡] B. Snook,[341,‡] S. Tuo,[341,‡] J. Velkovska,[341,‡] Q. Xu,[341,‡] M. W. Arenton,[342,‡] S. Boutle,[342,‡] B. Cox,[342,‡] B. Francis,[342,‡] J. Goodell,[342,‡] R. Hirosky,[342,‡] A. Ledovskoy,[342,‡] H. Li,[342,‡] C. Lin,[342,‡] C. Neu,[342,‡] E. Wolfe,[342,‡] J. Wood,[342,‡] F. Xia,[342,‡] C. Clarke,[343,‡] R. Harr,[343,‡] P. E. Karchin,[343,‡] C. Kottachchi Kankanamge Don,[343,‡] P. Lamichhane,[343,‡] J. Sturdy,[343,‡] D. A. Belknap,[344,‡] D. Carlsmith,[344,‡] M. Cepeda,[344,‡] A. Christian,[344,‡] S. Dasu,[344,‡] L. Dodd,[344,‡] S. Duric,[344,‡] E. Friis,[344,‡] B. Gomber,[344,‡] R. Hall-Wilton,[344,‡] M. Herndon,[344,‡] A. Hervé,[344,‡] P. Klabbers,[344,‡] A. Lanaro,[344,‡] A. Levine,[344,‡] K. Long,[344,‡] R. Loveless,[344,‡] A. Mohapatra,[344,‡] I. Ojalvo,[344,‡] T. Perry,[344,‡] G. A. Pierro,[344,‡] G. Polese,[344,‡] I. Ross,[344,‡] T. Ruggles,[344,‡] T. Sarangi,[344,‡] A. Savin,[344,‡] A. Sharma,[344,‡] N. Smith,[344,‡] W. H. Smith,[344,‡] D. Taylor,[344,‡] and N. Woods[344,‡]

(ATLAS Collaboration)†
(CMS Collaboration)‡

[1]Department of Physics, University of Adelaide, Adelaide, Australia
[2]Physics Department, SUNY Albany, Albany, New York, USA
[3]Department of Physics, University of Alberta, Edmonton, Alberta, Canada
[4a]Department of Physics, Ankara University, Ankara, Turkey
[4b]Istanbul Aydin University, Istanbul, Turkey
[4c]Division of Physics, TOBB University of Economics and Technology, Ankara, Turkey
[5]LAPP, CNRS/IN2P3 and Université Savoie Mont Blanc, Annecy-le-Vieux, France
[6]High Energy Physics Division, Argonne National Laboratory, Argonne, Illinois, USA
[7]Department of Physics, University of Arizona, Tucson, Arizona, USA
[8]Department of Physics, The University of Texas at Arlington, Arlington, Texas, USA
[9]Physics Department, University of Athens, Athens, Greece
[10]Physics Department, National Technical University of Athens, Zografou, Greece
[11]Institute of Physics, Azerbaijan Academy of Sciences, Baku, Azerbaijan
[12]Institut de Física d'Altes Energies and Departament de Física de la Universitat Autònoma de Barcelona, Barcelona, Spain
[13]Institute of Physics, University of Belgrade, Belgrade, Serbia
[14]Department for Physics and Technology, University of Bergen, Bergen, Norway
[15]Physics Division, Lawrence Berkeley National Laboratory and University of California, Berkeley, California, USA
[16]Department of Physics, Humboldt University, Berlin, Germany
[17]Albert Einstein Center for Fundamental Physics and Laboratory for High Energy Physics, University of Bern, Bern, Switzerland
[18]School of Physics and Astronomy, University of Birmingham, Birmingham, United Kingdom
[19a]Department of Physics, Bogazici University, Istanbul, Turkey
[19b]Department of Physics, Dogus University, Istanbul, Turkey
[19c]Department of Physics Engineering, Gaziantep University, Gaziantep, Turkey
[20a]INFN Sezione di Bologna, Bologna, Italy
[20b]Dipartimento di Fisica e Astronomia, Università di Bologna, Bologna, Italy
[21]Physikalisches Institut, University of Bonn, Bonn, Germany
[22]Department of Physics, Boston University, Boston, Massachusetts, USA
[23]Department of Physics, Brandeis University, Waltham, Massachusetts, USA
[24a]Universidade Federal do Rio De Janeiro COPPE/EE/IF, Rio de Janeiro, Brazil
[24b]Electrical Circuits Department, Federal University of Juiz de Fora (UFJF), Juiz de Fora, Brazil
[24c]Federal University of Sao Joao del Rei (UFSJ), Sao Joao del Rei, Brazil
[24d]Instituto de Fisica, Universidade de Sao Paulo, Sao Paulo, Brazil
[25]Physics Department, Brookhaven National Laboratory, Upton, New York, USA
[26a]National Institute of Physics and Nuclear Engineering, Bucharest, Romania
[26b]National Institute for Research and Development of Isotopic and Molecular Technologies, Physics Department, Cluj Napoca, Romania
[26c]University Politehnica Bucharest, Bucharest, Romania
[26d]West University in Timisoara, Timisoara, Romania
[27]Departamento de Física, Universidad de Buenos Aires, Buenos Aires, Argentina
[28]Cavendish Laboratory, University of Cambridge, Cambridge, United Kingdom
[29]Department of Physics, Carleton University, Ottawa, Ontario, Canada
[30]CERN, Geneva, Switzerland
[31]Enrico Fermi Institute, University of Chicago, Chicago, Illinois, USA
[32a]Departamento de Física, Pontificia Universidad Católica de Chile, Santiago, Chile
[32b]Departamento de Física, Universidad Técnica Federico Santa María, Valparaíso, Chile
[33a]Institute of High Energy Physics, Chinese Academy of Sciences, Beijing, China
[33b]Department of Modern Physics, University of Science and Technology of China, Anhui, China
[33c]Department of Physics, Nanjing University, Jiangsu, China
[33d]School of Physics, Shandong University, Shandong, China
[33e]Department of Physics and Astronomy, Shanghai Key Laboratory for Particle Physics and Cosmology, Shanghai Jiao Tong University, Shanghai, China
[33f]Physics Department, Tsinghua University, Beijing 100084, China
[34]Laboratoire de Physique Corpusculaire, Clermont Université and Université Blaise Pascal and CNRS/IN2P3, Clermont-Ferrand, France
[35]Nevis Laboratory, Columbia University, Irvington, New York, USA
[36]Niels Bohr Institute, University of Copenhagen, Kobenhavn, Denmark

[37a]INFN Gruppo Collegato di Cosenza, Laboratori Nazionali di Frascati, Frascati, Italy
[37b]Dipartimento di Fisica, Università della Calabria, Rende, Italy
[38a]AGH University of Science and Technology, Faculty of Physics and Applied Computer Science, Krakow, Poland
[38b]Marian Smoluchowski Institute of Physics, Jagiellonian University, Krakow, Poland
[39]Institute of Nuclear Physics Polish Academy of Sciences, Krakow, Poland
[40]Physics Department, Southern Methodist University, Dallas, Texas, USA
[41]Physics Department, University of Texas at Dallas, Richardson, Texas, USA
[42]DESY, Hamburg and Zeuthen, Germany
[43]Institut für Experimentelle Physik IV, Technische Universität Dortmund, Dortmund, Germany
[44]Institut für Kern- und Teilchenphysik, Technische Universität Dresden, Dresden, Germany
[45]Department of Physics, Duke University, Durham, North Carolina, USA
[46]SUPA-School of Physics and Astronomy, University of Edinburgh, Edinburgh, United Kingdom
[47]INFN Laboratori Nazionali di Frascati, Frascati, Italy
[48]Fakultät für Mathematik und Physik, Albert-Ludwigs-Universität, Freiburg, Germany
[49]Section de Physique, Université de Genève, Geneva, Switzerland
[50a]INFN Sezione di Genova, Genova, Italy
[50b]Dipartimento di Fisica, Università di Genova, Genova, Italy
[51a]E. Andronikashvili Institute of Physics, Iv. Javakhishvili Tbilisi State University, Tbilisi, Georgia
[51b]High Energy Physics Institute, Tbilisi State University, Tbilisi, Georgia
[52]II Physikalisches Institut, Justus-Liebig-Universität Giessen, Giessen, Germany
[53]SUPA-School of Physics and Astronomy, University of Glasgow, Glasgow, United Kingdom
[54]II Physikalisches Institut, Georg-August-Universität, Göttingen, Germany
[55]Laboratoire de Physique Subatomique et de Cosmologie, Université Grenoble-Alpes, CNRS/IN2P3, Grenoble, France
[56]Department of Physics, Hampton University, Hampton, Virginia, USA
[57]Laboratory for Particle Physics and Cosmology, Harvard University, Cambridge, Massachusetts, USA
[58a]Kirchhoff-Institut für Physik, Ruprecht-Karls-Universität Heidelberg, Heidelberg, Germany
[58b]Physikalisches Institut, Ruprecht-Karls-Universität Heidelberg, Heidelberg, Germany
[58c]ZITI Institut für technische Informatik, Ruprecht-Karls-Universität Heidelberg, Mannheim, Germany
[59]Faculty of Applied Information Science, Hiroshima Institute of Technology, Hiroshima, Japan
[60a]Department of Physics, The Chinese University of Hong Kong, Shatin, N.T., Hong Kong, China
[60b]Department of Physics, The University of Hong Kong, Hong Kong, China
[60c]Department of Physics, The Hong Kong University of Science and Technology, Clear Water Bay, Kowloon, Hong Kong, China
[61]Department of Physics, Indiana University, Bloomington, Indiana, USA
[62]Institut für Astro- und Teilchenphysik, Leopold-Franzens-Universität, Innsbruck, Austria
[63]University of Iowa, Iowa City, Iowa, USA
[64]Department of Physics and Astronomy, Iowa State University, Ames, Iowa, USA
[65]Joint Institute for Nuclear Research, JINR Dubna, Dubna, Russia
[66]KEK, High Energy Accelerator Research Organization, Tsukuba, Japan
[67]Graduate School of Science, Kobe University, Kobe, Japan
[68]Faculty of Science, Kyoto University, Kyoto, Japan
[69]Kyoto University of Education, Kyoto, Japan
[70]Department of Physics, Kyushu University, Fukuoka, Japan
[71]Instituto de Física La Plata, Universidad Nacional de La Plata and CONICET, La Plata, Argentina
[72]Physics Department, Lancaster University, Lancaster, United Kingdom
[73a]INFN Sezione di Lecce, Lecce, Italy
[73b]Dipartimento di Matematica e Fisica, Università del Salento, Lecce, Italy
[74]Oliver Lodge Laboratory, University of Liverpool, Liverpool, United Kingdom
[75]Department of Physics, Jožef Stefan Institute and University of Ljubljana, Ljubljana, Slovenia
[76]School of Physics and Astronomy, Queen Mary University of London, London, United Kingdom
[77]Department of Physics, Royal Holloway University of London, Surrey, United Kingdom
[78]Department of Physics and Astronomy, University College London, London, United Kingdom
[79]Louisiana Tech University, Ruston, Louisiana, USA
[80]Laboratoire de Physique Nucléaire et de Hautes Energies, UPMC and Université Paris-Diderot and CNRS/IN2P3, Paris, France
[81]Fysiska institutionen, Lunds universitet, Lund, Sweden
[82]Departamento de Fisica Teorica C-15, Universidad Autonoma de Madrid, Madrid, Spain
[83]Institut für Physik, Universität Mainz, Mainz, Germany
[84]School of Physics and Astronomy, University of Manchester, Manchester, United Kingdom
[85]CPPM, Aix-Marseille Université and CNRS/IN2P3, Marseille, France
[86]Department of Physics, University of Massachusetts, Amherst, Massachusetts, USA
[87]Department of Physics, McGill University, Montreal, Quebec, Canada

[88]School of Physics, University of Melbourne, Victoria, Australia
[89]Department of Physics, The University of Michigan, Ann Arbor, Michigan, USA
[90]Department of Physics and Astronomy, Michigan State University, East Lansing, Michigan, USA
[91a]INFN Sezione di Milano, Milano, Italy
[91b]Dipartimento di Fisica, Università di Milano, Milano, Italy
[92]B.I. Stepanov Institute of Physics, National Academy of Sciences of Belarus, Minsk, Republic of Belarus
[93]National Scientific and Educational Centre for Particle and High Energy Physics, Minsk, Republic of Belarus
[94]Department of Physics, Massachusetts Institute of Technology, Cambridge, Massachusetts, USA
[95]Group of Particle Physics, University of Montreal, Montreal, Quebec, Canada
[96]P.N. Lebedev Institute of Physics, Academy of Sciences, Moscow, Russia
[97]Institute for Theoretical and Experimental Physics (ITEP), Moscow, Russia
[98]National Research Nuclear University MEPhI, Moscow, Russia
[99]D.V. Skobeltsyn Institute of Nuclear Physics, M.V. Lomonosov Moscow State University, Moscow, Russia
[100]Fakultät für Physik, Ludwig-Maximilians-Universität München, München, Germany
[101]Max-Planck-Institut für Physik (Werner-Heisenberg-Institut), München, Germany
[102]Nagasaki Institute of Applied Science, Nagasaki, Japan
[103]Graduate School of Science and Kobayashi-Maskawa Institute, Nagoya University, Nagoya, Japan
[104a]INFN Sezione di Napoli, Napoli, Italy
[104b]Dipartimento di Fisica, Università di Napoli, Napoli, Italy
[105]Department of Physics and Astronomy, University of New Mexico, Albuquerque, New Mexico, USA
[106]Institute for Mathematics, Astrophysics and Particle Physics, Radboud University Nijmegen/Nikhef, Nijmegen, Netherlands
[107]Nikhef National Institute for Subatomic Physics and University of Amsterdam, Amsterdam, Netherlands
[108]Department of Physics, Northern Illinois University, DeKalb, Illinois, USA
[109]Budker Institute of Nuclear Physics, SB RAS, Novosibirsk, Russia
[110]Department of Physics, New York University, New York, New York, USA
[111]The Ohio State University, Columbus, Ohio, USA
[112]Faculty of Science, Okayama University, Okayama, Japan
[113]Homer L. Dodge Department of Physics and Astronomy, University of Oklahoma, Norman, Oklahoma, USA
[114]Department of Physics, Oklahoma State University, Stillwater, Oklahoma, USA
[115]Palacký University, RCPTM, Olomouc, Czech Republic
[116]Center for High Energy Physics, University of Oregon, Eugene, Oregon, USA
[117]LAL, Université Paris-Sud and CNRS/IN2P3, Orsay, France
[118]Graduate School of Science, Osaka University, Osaka, Japan
[119]Department of Physics, University of Oslo, Oslo, Norway
[120]Department of Physics, Oxford University, Oxford, United Kingdom
[121a]INFN Sezione di Pavia, Pavia, Italy
[121b]Dipartimento di Fisica, Università di Pavia, Pavia, Italy
[122]Department of Physics, University of Pennsylvania, Philadelphia, Pennsylvania, USA
[123]National Research Centre "Kurchatov Institute" B.P.Konstantinov Petersburg Nuclear Physics Institute, St. Petersburg, Russia
[124a]INFN Sezione di Pisa, Pisa, Italy
[124b]Dipartimento di Fisica E. Fermi, Università di Pisa, Pisa, Italy
[125]Department of Physics and Astronomy, University of Pittsburgh, Pittsburgh, Pennsylvania, USA
[126a]Laboratorio de Instrumentacao e Fisica Experimental de Particulas-LIP, Lisboa, Portugal
[126b]Faculdade de Ciências, Universidade de Lisboa, Lisboa, Portugal
[126c]Department of Physics, University of Coimbra, Coimbra, Portugal
[126d]Centro de Física Nuclear da Universidade de Lisboa, Lisboa, Portugal
[126e]Departamento de Fisica, Universidade do Minho, Braga, Portugal
[126f]Departamento de Fisica Teorica y del Cosmos and CAFPE, Universidad de Granada, Granada (Spain), Portugal
[126g]Dep Fisica and CEFITEC of Faculdade de Ciencias e Tecnologia, Universidade Nova de Lisboa, Caparica, Portugal
[127]Institute of Physics, Academy of Sciences of the Czech Republic, Praha, Czech Republic
[128]Czech Technical University in Prague, Praha, Czech Republic
[129]Faculty of Mathematics and Physics, Charles University in Prague, Praha, Czech Republic
[130]State Research Center Institute for High Energy Physics, Protvino, Russia
[131]Particle Physics Department, Rutherford Appleton Laboratory, Didcot, United Kingdom
[132a]INFN Sezione di Roma, Roma, Italy
[132b]Dipartimento di Fisica, Sapienza Università di Roma, Roma, Italy
[133a]INFN Sezione di Roma Tor Vergata, Roma, Italy
[133b]Dipartimento di Fisica, Università di Roma Tor Vergata, Roma, Italy
[134a]INFN Sezione di Roma Tre, Roma, Italy
[134b]Dipartimento di Matematica e Fisica, Università Roma Tre, Roma, Italy

[135a]Faculté des Sciences Ain Chock, Réseau Universitaire de Physique des Hautes Energies-Université Hassan II, Casablanca, Morocco
[135b]Centre National de l'Energie des Sciences Techniques Nucleaires, Rabat, Morocco
[135c]Faculté des Sciences Semlalia, Université Cadi Ayyad, LPHEA-Marrakech, Morocco
[135d]Faculté des Sciences, Université Mohamed Premier and LPTPM, Oujda, Morocco
[135e]Faculté des sciences, Université Mohammed V-Agdal, Rabat, Morocco
[136]DSM/IRFU (Institut de Recherches sur les Lois Fondamentales de l'Univers), CEA Saclay (Commissariat à l'Energie Atomique et aux Energies Alternatives), Gif-sur-Yvette, France
[137]Santa Cruz Institute for Particle Physics, University of California Santa Cruz, Santa Cruz, California, USA
[138]Department of Physics, University of Washington, Seattle, Washington, USA
[139]Department of Physics and Astronomy, University of Sheffield, Sheffield, United Kingdom
[140]Department of Physics, Shinshu University, Nagano, Japan
[141]Fachbereich Physik, Universität Siegen, Siegen, Germany
[142]Department of Physics, Simon Fraser University, Burnaby, British Columbia, Canada
[143]SLAC National Accelerator Laboratory, Stanford, California, USA
[144a]Faculty of Mathematics, Physics & Informatics, Comenius University, Bratislava, Slovak Republic
[144b]Department of Subnuclear Physics, Institute of Experimental Physics of the Slovak Academy of Sciences, Kosice, Slovak Republic
[145a]Department of Physics, University of Cape Town, Cape Town, South Africa
[145b]Department of Physics, University of Johannesburg, Johannesburg, South Africa
[145c]School of Physics, University of the Witwatersrand, Johannesburg, South Africa
[146a]Department of Physics, Stockholm University, Sweden
[146b]The Oskar Klein Centre, Stockholm, Sweden
[147]Physics Department, Royal Institute of Technology, Stockholm, Sweden
[148]Departments of Physics & Astronomy and Chemistry, Stony Brook University, Stony Brook, New York, USA
[149]Department of Physics and Astronomy, University of Sussex, Brighton, United Kingdom
[150]School of Physics, University of Sydney, Sydney, Australia
[151]Institute of Physics, Academia Sinica, Taipei, Taiwan
[152]Department of Physics, Technion: Israel Institute of Technology, Haifa, Israel
[153]Raymond and Beverly Sackler School of Physics and Astronomy, Tel Aviv University, Tel Aviv, Israel
[154]Department of Physics, Aristotle University of Thessaloniki, Thessaloniki, Greece
[155]International Center for Elementary Particle Physics and Department of Physics, The University of Tokyo, Tokyo, Japan
[156]Graduate School of Science and Technology, Tokyo Metropolitan University, Tokyo, Japan
[157]Department of Physics, Tokyo Institute of Technology, Tokyo, Japan
[158]Department of Physics, University of Toronto, Toronto, Ontario, Canada
[159a]TRIUMF, Vancouver, British Columbia, Canada
[159b]Department of Physics and Astronomy, York University, Toronto, Ontario, Canada
[160]Faculty of Pure and Applied Sciences, University of Tsukuba, Tsukuba, Japan
[161]Department of Physics and Astronomy, Tufts University, Medford, Massachusetts, USA
[162]Centro de Investigaciones, Universidad Antonio Narino, Bogota, Colombia
[163]Department of Physics and Astronomy, University of California Irvine, Irvine, California, USA
[164a]INFN Gruppo Collegato di Udine, Sezione di Trieste, Udine, Italy
[164b]ICTP, Trieste, Italy
[164c]Dipartimento di Chimica, Fisica e Ambiente, Università di Udine, Udine, Italy
[165]Department of Physics, University of Illinois, Urbana, Illinois, USA
[166]Department of Physics and Astronomy, University of Uppsala, Uppsala, Sweden
[167]Instituto de Física Corpuscular (IFIC) and Departamento de Física Atómica, Molecular y Nuclear and Departamento de Ingeniería Electrónica and Instituto de Microelectrónica de Barcelona (IMB-CNM), University of Valencia and CSIC, Valencia, Spain
[168]Department of Physics, University of British Columbia, Vancouver, British Columbia, Canada
[169]Department of Physics and Astronomy, University of Victoria, Victoria, British Columbia, Canada
[170]Department of Physics, University of Warwick, Coventry, United Kingdom
[171]Waseda University, Tokyo, Japan
[172]Department of Particle Physics, The Weizmann Institute of Science, Rehovot, Israel
[173]Department of Physics, University of Wisconsin, Madison, Wisconsin, USA
[174]Fakultät für Physik und Astronomie, Julius-Maximilians-Universität, Würzburg, Germany
[175]Fachbereich C Physik, Bergische Universität Wuppertal, Wuppertal, Germany
[176]Department of Physics, Yale University, New Haven, Connecticut, USA
[177]Yerevan Physics Institute, Yerevan, Armenia
[178]Centre de Calcul de l'Institut National de Physique Nucléaire et de Physique des Particules (IN2P3), Villeurbanne, France
[179]Yerevan Physics Institute, Yerevan, Armenia
[180]Institut für Hochenergiephysik der OeAW, Wien, Austria

[181]National Centre for Particle and High Energy Physics, Minsk, Belarus
[182]Universiteit Antwerpen, Antwerpen, Belgium
[183]Vrije Universiteit Brussel, Brussel, Belgium
[184]Université Libre de Bruxelles, Bruxelles, Belgium
[185]Ghent University, Ghent, Belgium
[186]Université Catholique de Louvain, Louvain-la-Neuve, Belgium
[187]Université de Mons, Mons, Belgium
[188]Centro Brasileiro de Pesquisas Fisicas, Rio de Janeiro, Brazil
[189]Universidade do Estado do Rio de Janeiro, Rio de Janeiro, Brazil
[190a]Universidade Estadual Paulista, São Paulo, Brazil
[190b]Universidade Federal do ABC, São Paulo, Brazil
[191]Institute for Nuclear Research and Nuclear Energy, Sofia, Bulgaria
[192]University of Sofia, Sofia, Bulgaria
[193]Institute of High Energy Physics, Beijing, China
[194]State Key Laboratory of Nuclear Physics and Technology, Peking University, Beijing, China
[195]Universidad de Los Andes, Bogota, Colombia
[196]University of Split, Faculty of Electrical Engineering, Mechanical Engineering and Naval Architecture, Split, Croatia
[197]University of Split, Faculty of Science, Split, Croatia
[198]Institute Rudjer Boskovic, Zagreb, Croatia
[199]University of Cyprus, Nicosia, Cyprus
[200]Charles University, Prague, Czech Republic
[201]Academy of Scientific Research and Technology of the Arab Republic of Egypt, Egyptian Network of High Energy Physics, Cairo, Egypt
[202]National Institute of Chemical Physics and Biophysics, Tallinn, Estonia
[203]Department of Physics, University of Helsinki, Helsinki, Finland
[204]Helsinki Institute of Physics, Helsinki, Finland
[205]Lappeenranta University of Technology, Lappeenranta, Finland
[206]DSM/IRFU, CEA/Saclay, Gif-sur-Yvette, France
[207]Laboratoire Leprince-Ringuet, Ecole Polytechnique, IN2P3-CNRS, Palaiseau, France
[208]Institut Pluridisciplinaire Hubert Curien, Université de Strasbourg, Université de Haute Alsace Mulhouse, CNRS/IN2P3, Strasbourg, France
[209]Centre de Calcul de l'Institut National de Physique Nucleaire et de Physique des Particules, CNRS/IN2P3, Villeurbanne, France
[210]Université de Lyon, Université Claude Bernard Lyon 1, CNRS-IN2P3, Institut de Physique Nucléaire de Lyon, Villeurbanne, France
[211]Institute of High Energy Physics and Informatization, Tbilisi State University, Tbilisi, Georgia
[212]RWTH Aachen University, I. Physikalisches Institut, Aachen, Germany
[213]RWTH Aachen University, III. Physikalisches Institut A, Aachen, Germany
[214]RWTH Aachen University, III. Physikalisches Institut B, Aachen, Germany
[215]Deutsches Elektronen-Synchrotron, Hamburg, Germany
[216]University of Hamburg, Hamburg, Germany
[217]Institut für Experimentelle Kernphysik, Karlsruhe, Germany
[218]Institute of Nuclear and Particle Physics (INPP), NCSR Demokritos, Aghia Paraskevi, Greece
[219]University of Athens, Athens, Greece
[220]University of Ioánnina, Ioánnina, Greece
[221]Wigner Research Centre for Physics, Budapest, Hungary
[222]Institute of Nuclear Research ATOMKI, Debrecen, Hungary
[223]University of Debrecen, Debrecen, Hungary
[224]National Institute of Science Education and Research, Bhubaneswar, India
[225]Panjab University, Chandigarh, India
[226]University of Delhi, Delhi, India
[227]Saha Institute of Nuclear Physics, Kolkata, India
[228]Bhabha Atomic Research Centre, Mumbai, India
[229]Tata Institute of Fundamental Research, Mumbai, India
[230]Indian Institute of Science Education and Research (IISER), Pune, India
[231]Institute for Research in Fundamental Sciences (IPM), Tehran, Iran
[232]University College Dublin, Dublin, Ireland
[233a]INFN Sezione di Bari, Bari, Italy
[233b]Università di Bari, Bari, Italy
[233c]Politecnico di Bari, Bari, Italy
[234a]INFN Sezione di Bologna, Bologna, Italy
[234b]Università di Bologna, Bologna, Italy

[235a]INFN Sezione di Catania, Catania, Italy
[235b]Università di Catania, Catania, Italy
[235c]CSFNSM, Catania, Italy
[236a]INFN Sezione di Firenze, Firenze, Italy
[236b]Università di Firenze, Firenze, Italy
[237]INFN Laboratori Nazionali di Frascati, Frascati, Italy
[238a]INFN Sezione di Genova, Genova, Italy
[238b]Università di Genova, Genova, Italy
[239a]INFN Sezione di Milano-Bicocca, Milano, Italy
[239b]Università di Milano-Bicocca, Milano, Italy
[240a]INFN Sezione di Napoli, Napoli, Italy
[240b]Università di Napoli "Federico II," Napoli, Italy
[240c]Università della Basilicata, Roma, Italy
[240d]Università G. Marconi, Roma, Italy
[241a]INFN Sezione di Padova, Padova, Italy
[241b]Università di Padova, Padova, Italy
[241c]Università di Trento, Trento, Italy
[242a]INFN Sezione di Pavia, Pavia, Italy
[242b]Università di Pavia, Pavia, Italy
[243a]INFN Sezione di Perugia, Perugia, Italy
[243b]Università di Perugia, Perugia, Italy
[244a]INFN Sezione di Pisa, Pisa, Italy
[244b]Università di Pisa, Pisa, Italy
[244c]Scuola Normale Superiore di Pisa, Pisa, Italy
[245a]INFN Sezione di Roma, Roma, Italy
[245b]Università di Roma, Roma, Italy
[246a]INFN Sezione di Torino, Novara, Italy
[246b]Università di Torino, Novara, Italy
[246c]Università del Piemonte Orientale, Novara, Italy
[247a]INFN Sezione di Trieste, Trieste, Italy
[247b]Università di Trieste, Trieste, Italy
[248]Kangwon National University, Chunchon, Korea
[249]Kyungpook National University, Daegu, Korea
[250]Chonbuk National University, Jeonju, Korea
[251]Chonnam National University, Institute for Universe and Elementary Particles, Kwangju, Korea
[252]Korea University, Seoul, Korea
[253]Seoul National University, Seoul, Korea
[254]University of Seoul, Seoul, Korea
[255]Sungkyunkwan University, Suwon, Korea
[256]Vilnius University, Vilnius, Lithuania
[257]National Centre for Particle Physics, Universiti Malaya, Kuala Lumpur, Malaysia
[258]Centro de Investigacion y de Estudios Avanzados del IPN, Mexico City, Mexico
[259]Universidad Iberoamericana, Mexico City, Mexico
[260]Benemerita Universidad Autonoma de Puebla, Puebla, Mexico
[261]Universidad Autónoma de San Luis Potosí, San Luis Potosí, Mexico
[262]University of Auckland, Auckland, New Zealand
[263]University of Canterbury, Christchurch, New Zealand
[264]National Centre for Physics, Quaid-I-Azam University, Islamabad, Pakistan
[265]National Centre for Nuclear Research, Swierk, Poland
[266]Institute of Experimental Physics, Faculty of Physics, University of Warsaw, Warsaw, Poland
[267]Laboratório de Instrumentação e Física Experimental de Partículas, Lisboa, Portugal
[268]Joint Institute for Nuclear Research, Dubna, Russia
[269]Petersburg Nuclear Physics Institute, Gatchina (St. Petersburg), Russia
[270]Institute for Nuclear Research, Moscow, Russia
[271]Institute for Theoretical and Experimental Physics, Moscow, Russia
[272]P.N. Lebedev Physical Institute, Moscow, Russia
[273]Skobeltsyn Institute of Nuclear Physics, Lomonosov Moscow State University, Moscow, Russia
[274]State Research Center of Russian Federation, Institute for High Energy Physics, Protvino, Russia
[275]University of Belgrade, Faculty of Physics and Vinca Institute of Nuclear Sciences, Belgrade, Serbia
[276]Centro de Investigaciones Energéticas Medioambientales y Tecnológicas (CIEMAT), Madrid, Spain

[277]Universidad Autónoma de Madrid, Madrid, Spain
[278]Universidad de Oviedo, Oviedo, Spain
[279]Instituto de Física de Cantabria (IFCA), CSIC-Universidad de Cantabria, Santander, Spain
[280]CERN, European Organization for Nuclear Research, Geneva, Switzerland
[281]Paul Scherrer Institut, Villigen, Switzerland
[282]Institute for Particle Physics, ETH Zurich, Zurich, Switzerland
[283]Universität Zürich, Zurich, Switzerland
[284]National Central University, Chung-Li, Taiwan
[285]National Taiwan University (NTU), Taipei, Taiwan
[286]Chulalongkorn University, Faculty of Science, Department of Physics, Bangkok, Thailand
[287]Cukurova University, Adana, Turkey
[288]Middle East Technical University, Physics Department, Ankara, Turkey
[289]Bogazici University, Istanbul, Turkey
[290]Istanbul Technical University, Istanbul, Turkey
[291]Institute for Scintillation Materials of National Academy of Science of Ukraine, Kharkov, Ukraine
[292]National Scientific Center, Kharkov Institute of Physics and Technology, Kharkov, Ukraine
[293]University of Bristol, Bristol, United Kingdom
[294]Rutherford Appleton Laboratory, Didcot, United Kingdom
[295]Imperial College, London, United Kingdom
[296]Brunel University, Uxbridge, United Kingdom
[297]Baylor University, Waco, Texas, USA
[298]The University of Alabama, Tuscaloosa, Alabama, USA
[299]Boston University, Boston, Massachusetts, USA
[300]Brown University, Providence, Rhode Island, USA
[301]University of California, Davis, Davis, California, USA
[302]University of California, Los Angeles, Los Angeles, California, USA
[303]University of California, Riverside, Riverside, California, USA
[304]University of California, San Diego, La Jolla, California, USA
[305]University of California, Santa Barbara, Santa Barbara, California, USA
[306]California Institute of Technology, Pasadena, California, USA
[307]Carnegie Mellon University, Pittsburgh, Pennsylvania, USA
[308]University of Colorado at Boulder, Boulder, Colorado, USA
[309]Cornell University, Ithaca, New York, USA
[310]Fermi National Accelerator Laboratory, Batavia, Illinois, USA
[311]University of Florida, Gainesville, Florida, USA
[312]Florida International University, Miami, Florida, USA
[313]Florida State University, Tallahassee, Florida, USA
[314]Florida Institute of Technology, Melbourne, Florida, USA
[315]University of Illinois at Chicago (UIC), Chicago, Illinois, USA
[316]The University of Iowa, Iowa City, Iowa, USA
[317]Johns Hopkins University, Baltimore, Maryland, USA
[318]The University of Kansas, Lawrence, Kansas, USA
[319]Kansas State University, Manhattan, Kansas, USA
[320]Lawrence Livermore National Laboratory, Livermore, California, USA
[321]University of Maryland, College Park, Maryland, USA
[322]Massachusetts Institute of Technology, Cambridge, Massachusetts, USA
[323]University of Minnesota, Minneapolis, Minnesota, USA
[324]University of Mississippi, Oxford, Mississippi, USA
[325]University of Nebraska-Lincoln, Lincoln, Nebraska, USA
[326]State University of New York at Buffalo, Buffalo, New York, USA
[327]Northeastern University, Boston, Massachusetts, USA
[328]Northwestern University, Evanston, Illinois, USA
[329]University of Notre Dame, Notre Dame, Indiana, USA
[330]The Ohio State University, Columbus, Ohio, USA
[331]Princeton University, Princeton, New Jersey, USA
[332]Purdue University, West Lafayette, Indiana, USA
[333]Purdue University Calumet, Hammond, Indiana, USA
[334]Rice University, Houston, Texas, USA
[335]University of Rochester, Rochester, New York, USA
[336]The Rockefeller University, New York, New York, USA

[337]Rutgers, The State University of New Jersey, Piscataway, New Jersey, USA
[338]University of Tennessee, Knoxville, Tennessee, USA
[339]Texas A&M University, College Station, Maryland, USA
[340]Texas Tech University, Lubbock, Texas, USA
[341]Vanderbilt University, Nashville, Tennessee, USA
[342]University of Virginia, Charlottesville, Virginia, USA
[343]Wayne State University, Detroit, Michigan, USA
[344]University of Wisconsin, Madison, Wisconsin, USA

[a]Deceased.
[b]Also at Department of Physics, King's College London, London, United Kingdom.
[c]Also at Institute of Physics, Azerbaijan Academy of Sciences, Baku, Azerbaijan.
[d]Also at Novosibirsk State University, Novosibirsk, Russia.
[e]Also at TRIUMF, Vancouver, BC, Canada.
[f]Also at Department of Physics, California State University, Fresno, CA, USA.
[g]Also at Department of Physics, University of Fribourg, Fribourg, Switzerland.
[h]Also at Departamento de Fisica e Astronomia, Faculdade de Ciencias, Universidade do Porto, Portugal.
[i]Also at Tomsk State University, Tomsk, Russia.
[j]Also at CPPM, Aix-Marseille Université and CNRS/IN2P3, Marseille, France.
[k]Also at Università di Napoli Parthenope, Napoli, Italy.
[l]Also at Institute of Particle Physics (IPP), Canada.
[m]Also at Particle Physics Department, Rutherford Appleton Laboratory, Didcot, United Kingdom.
[n]Also at Department of Physics, St. Petersburg State Polytechnical University, St. Petersburg, Russia.
[o]Also at Louisiana Tech University, Ruston, LA, USA.
[p]Also at Institucio Catalana de Recerca i Estudis Avancats, ICREA, Barcelona, Spain.
[q]Also at Department of Physics, National Tsing Hua University, Taiwan.
[r]Also at Department of Physics, The University of Texas at Austin, Austin, TX, USA.
[s]Also at Institute of Theoretical Physics, Ilia State University, Tbilisi, Georgia.
[t]Also at CERN, Geneva, Switzerland.
[u]Also at Georgian Technical University (GTU),Tbilisi, Georgia.
[v]Also at Ochadai Academic Production, Ochanomizu University, Tokyo, Japan.
[w]Also at Manhattan College, New York, NY, USA.
[x]Also at Institute of Physics, Academia Sinica, Taipei, Taiwan.
[y]Also at LAL, Université Paris-Sud and CNRS/IN2P3, Orsay, France.
[z]Also at Academia Sinica Grid Computing, Institute of Physics, Academia Sinica, Taipei, Taiwan.
[aa]Also at School of Physics, Shandong University, Shandong, China.
[bb]Also at Moscow Institute of Physics and Technology State University, Dolgoprudny, Russia.
[cc]Also at Section de Physique, Université de Genève, Geneva, Switzerland.
[dd]Also at International School for Advanced Studies (SISSA), Trieste, Italy.
[ee]Also at Department of Physics and Astronomy, University of South Carolina, Columbia, SC, USA.
[ff]Also at School of Physics and Engineering, Sun Yat-sen University, Guangzhou, China.
[gg]Also at Faculty of Physics, M.V.Lomonosov Moscow State University, Moscow, Russia.
[hh]Also at National Research Nuclear University MEPhI, Moscow, Russia.
[ii]Also at Department of Physics, Stanford University, Stanford, CA, USA.
[jj]Also at Institute for Particle and Nuclear Physics, Wigner Research Centre for Physics, Budapest, Hungary.
[kk]Also at Department of Physics, The University of Michigan, Ann Arbor, MI, USA.
[ll]Also at Discipline of Physics, University of KwaZulu-Natal, Durban, South Africa.
[mm]Also at University of Malaya, Department of Physics, Kuala Lumpur, Malaysia.
[nn]Also at Vienna University of Technology, Vienna, Austria.
[oo]Also at CERN, European Organization for Nuclear Research, Geneva, Switzerland.
[pp]Also at State Key Laboratory of Nuclear Physics and Technology, Peking University, Beijing, China.
[qq]Also at Institut Pluridisciplinaire Hubert Curien, Université de Strasbourg, Université de Haute Alsace Mulhouse, CNRS/IN2P3, Strasbourg, France.
[rr]Also at National Institute of Chemical Physics and Biophysics, Tallinn, Estonia.
[ss]Also at Skobeltsyn Institute of Nuclear Physics, Lomonosov Moscow State University, Moscow, Russia.
[tt]Also at Universidade Estadual de Campinas, Campinas, Brazil.
[uu]Also at Centre National de la Recherche Scientifique (CNRS)–IN2P3, Paris, France.
[vv]Also at Laboratoire Leprince-Ringuet, Ecole Polytechnique, IN2P3–CNRS, Palaiseau, France.
[ww]Also at Joint Institute for Nuclear Research, Dubna, Russia.
[xx]Also at Ain Shams University, Cairo, Egypt.

[yy]Also at British University in Egypt, Cairo, Egypt.
[zz]Also at Helwan University, Cairo, Egypt.
[aaa]Also at Suez University, Suez, Egypt.
[bbb]Also at Cairo University, Cairo, Egypt.
[ccc]Also at Fayoum University, El-Fayoum, Egypt.
[ddd]Also at Université de Haute Alsace, Mulhouse, France.
[eee]Also at Brandenburg University of Technology, Cottbus, Germany.
[fff]Also at Institute of Nuclear Research ATOMKI, Debrecen, Hungary.
[ggg]Also at Eötvös Loránd University, Budapest, Hungary.
[hhh]Also at University of Debrecen, Debrecen, Hungary.
[iii]Also at Wigner Research Centre for Physics, Budapest, Hungary.
[jjj]Also at University of Visva-Bharati, Santiniketan, India.
[kkk]Also at King Abdulaziz University, Jeddah, Saudi Arabia.
[lll]Also at University of Ruhuna, Matara, Sri Lanka.
[mmm]Also at Isfahan University of Technology, Isfahan, Iran.
[nnn]Also at University of Tehran, Department of Engineering Science, Tehran, Iran.
[ooo]Also at Plasma Physics Research Center, Science and Research Branch, Islamic Azad University, Tehran, Iran.
[ppp]Also at Università degli Studi di Siena, Siena, Italy.
[qqq]Also at Purdue University, West Lafayette, IN, USA.
[rrr]Also at International Islamic University of Malaysia, Kuala Lumpur, Malaysia.
[sss]Also at Consejo National de Ciencia y Tecnologia, Mexico, Mexico.
[ttt]Also at Institute for Nuclear Research, Moscow, Russia.
[uuu]Also at Institute of High Energy Physics and Informatization, Tbilisi State University, Tbilisi, Georgia.
[vvv]Also at St. Petersburg State Polytechnical University, St. Petersburg, Russia.
[www]Also at National Research Nuclear University 'Moscow Engineering Physics Institute' (MEPhI), Moscow, Russia.
[xxx]Also at California Institute of Technology, Pasadena, CA, USA.
[yyy]Also at Faculty of Physics, University of Belgrade, Belgrade, Serbia.
[zzz]Also at Facoltà Ingegneria, Università di Roma, Roma, Italy.
[aaaa]Also at National Technical University of Athens, Athens, Greece.
[bbbb]Also at Scuola Normale e Sezione dell'INFN, Pisa, Italy.
[cccc]Also at University of Athens, Athens, Greece.
[dddd]Also at Warsaw University of Technology, Institute of Electronic Systems, Warsaw, Poland.
[eeee]Also at Institute for Theoretical and Experimental Physics, Moscow, Russia.
[ffff]Also at Albert Einstein Center for Fundamental Physics, Bern, Switzerland.
[gggg]Also at Adiyaman University, Adiyaman, Turkey.
[hhhh]Also at Mersin University, Mersin, Turkey.
[iiii]Also at Cag University, Mersin, Turkey.
[jjjj]Also at Piri Reis University, Istanbul, Turkey.
[kkkk]Also at Gaziosmanpasa University, Tokat, Turkey.
[llll]Also at Ozyegin University, Istanbul, Turkey.
[mmmm]Also at Izmir Institute of Technology, Izmir, Turkey.
[nnnn]Also at Mimar Sinan University, Istanbul, Istanbul, Turkey.
[oooo]Also at Marmara University, Istanbul, Turkey.
[pppp]Also at Kafkas University, Kars, Turkey.
[qqqq]Also at Yildiz Technical University, Istanbul, Turkey.
[rrrr]Also at Hacettepe University, Ankara, Turkey.
[ssss]Also at Rutherford Appleton Laboratory, Didcot, United Kingdom.
[tttt]Also at School of Physics and Astronomy, University of Southampton, Southampton, United Kingdom.
[uuuu]Also at Instituto de Astrofísica de Canarias, La Laguna, Spain.
[vvvv]Also at Utah Valley University, Orem, UT, USA.
[wwww]Also at University of Belgrade, Faculty of Physics and Vinca Institute of Nuclear Sciences, Belgrade, Serbia.
[xxxx]Also at Argonne National Laboratory, Argonne, IL, USA.
[yyyy]Also at Erzincan University, Erzincan, Turkey.
[zzzz]Also at Texas A&M University at Qatar, Doha, Qatar.
[aaaaa]Also at Kyungpook National University, Daegu, Korea.

Published for SISSA by Springer

Received: *January 21, 2015*
Accepted: *March 30, 2015*
Published: *April 21, 2015*

Evidence for the Higgs-boson Yukawa coupling to tau leptons with the ATLAS detector

The ATLAS collaboration

E-mail: atlas.publications@cern.ch

Abstract: Results of a search for $H \to \tau\tau$ decays are presented, based on the full set of proton-proton collision data recorded by the ATLAS experiment at the LHC during 2011 and 2012. The data correspond to integrated luminosities of $4.5\,\mathrm{fb}^{-1}$ and $20.3\,\mathrm{fb}^{-1}$ at centre-of-mass energies of $\sqrt{s} = 7\,\mathrm{TeV}$ and $\sqrt{s} = 8\,\mathrm{TeV}$ respectively. All combinations of leptonic ($\tau \to \ell\nu\bar{\nu}$ with $\ell = e, \mu$) and hadronic ($\tau \to$ hadrons ν) tau decays are considered. An excess of events over the expected background from other Standard Model processes is found with an observed (expected) significance of 4.5 (3.4) standard deviations. This excess provides evidence for the direct coupling of the recently discovered Higgs boson to fermions. The measured signal strength, normalised to the Standard Model expectation, of $\mu = 1.43\,^{+0.43}_{-0.37}$ is consistent with the predicted Yukawa coupling strength in the Standard Model.

Keywords: Hadron-Hadron Scattering

ArXiv ePrint: 1501.04943

Open Access, Copyright CERN,
for the benefit of the ATLAS Collaboration.
Article funded by SCOAP^3.

doi:10.1007/JHEP04(2015)117

JHEP04(2015)117

Contents

1 Introduction **2**

2 The ATLAS detector and object reconstruction **3**

3 Data and simulated samples **5**

4 Event selection and categorisation **7**
- 4.1 Event selection 7
- 4.2 Analysis categories 11
- 4.3 Higgs boson candidate mass reconstruction 13

5 Boosted decision trees **13**

6 Background estimation **19**
- 6.1 Background from $Z \to \tau\tau$ production 19
- 6.2 Background from misidentified leptons or hadronically decaying taus 21
- 6.3 $Z \to ee$ and $Z \to \mu\mu$ background 23
- 6.4 W+jets background 24
- 6.5 Background from top-quark production 24
- 6.6 Diboson background 25
- 6.7 Contributions from other Higgs boson decays 25
- 6.8 Validation of background estimates 25

7 Systematic uncertainties **27**
- 7.1 Experimental uncertainties 27
- 7.2 Background modelling uncertainties 28
- 7.3 Theoretical uncertainties 29

8 Signal extraction procedure **32**

9 Results **39**

10 Cross-check with cut-based analysis **43**

11 Conclusions **49**

The ATLAS collaboration **58**

JHEP04(2015)117

1 Introduction

The investigation of the origin of electroweak symmetry breaking and, related to this, the experimental confirmation of the Brout-Englert-Higgs mechanism [1–6] is one of the prime goals of the physics programme at the Large Hadron Collider (LHC) [7]. With the discovery of a Higgs boson with a mass of approximately 125 GeV by the ATLAS [8] and CMS [9] collaborations, an important milestone has been reached. More precise measurements of the properties of the discovered particle [10, 11] as well as tests of the spin-parity quantum numbers [12–14] continue to be consistent with the predictions for the Standard Model (SM) Higgs boson.

These measurements rely predominantly on studies of the bosonic decay modes, $H \to \gamma\gamma$, $H \to ZZ^*$ and $H \to WW^*$. To establish the mass generation mechanism for fermions as implemented in the SM, it is of prime importance to demonstrate the direct coupling of the Higgs boson to fermions and the proportionality of its strength to mass [15]. The most promising candidate decay modes are the decays into tau leptons, $H \to \tau\tau$, and bottom quarks (b-quarks), $H \to b\bar{b}$. Due to the high background, the search for decays to $b\bar{b}$ is restricted to Higgs bosons produced in modes which have a more distinct signature but a lower cross-section, such as H production with an associated vector boson. The smaller rate of these processes in the presence of still large background makes their detection challenging. More favourable signal-to-background conditions are expected for $H \to \tau\tau$ decays. Recently, the CMS Collaboration published evidence for $H \to \tau\tau$ decays at a significance in terms of standard deviations of 3.2σ [16], and an excess corresponding to a significance of 2.1σ in the search for $H \to b\bar{b}$ decays [17]. The combination of channels provides evidence for fermionic couplings with a significance of 3.8σ [18]. The yield of events in the search for $H \to b\bar{b}$ decays observed by the ATLAS Collaboration has a signal significance of 1.4σ [19]. The Tevatron experiments have observed an excess corresponding to 2.8σ in the $H \to b\bar{b}$ search [20].

In this paper, the results of a search for $H \to \tau\tau$ decays are presented, based on the full proton-proton dataset collected by the ATLAS experiment during the 2011 and 2012 data-taking periods, corresponding to integrated luminosities of 4.5 fb^{-1} at a centre-of-mass energy of $\sqrt{s} = 7$ TeV and 20.3 fb^{-1} at $\sqrt{s} = 8$ TeV. These results supersede the earlier upper limits on the cross section times the branching ratio obtained with the 7 TeV data [21]. All combinations of leptonic ($\tau \to \ell\nu\bar{\nu}$ with $\ell = e, \mu$) and hadronic ($\tau \to$ hadrons ν) tau decays are considered.[1] The corresponding three analysis channels are denoted by $\tau_{\rm lep}\tau_{\rm lep}$, $\tau_{\rm lep}\tau_{\rm had}$, and $\tau_{\rm had}\tau_{\rm had}$ in the following. The search is designed to be sensitive to the major production processes of a SM Higgs boson, i.e. production via gluon fusion (ggF) [22], vector-boson fusion (VBF) [23], and associated production (VH) with $V = W$ or Z. These production processes lead to different final-state signatures, which are exploited by defining an event categorisation. Two dedicated categories are considered to achieve both a good signal-to-background ratio and good resolution for the reconstructed $\tau\tau$ invariant mass. The VBF category, enriched in events produced via vector-boson fusion,

[1] Throughout this paper the inclusion of charge-conjugate decay modes is implied.

JHEP04(2015)117

is defined by the presence of two jets with a large separation in pseudorapidity.[2] The boosted category contains events where the reconstructed Higgs boson candidate has a large transverse momentum. It is dominated by events produced via gluon fusion with additional jets from gluon radiation. In view of the signal-to-background conditions, and in order to exploit correlations between final-state observables, a multivariate analysis technique, based on boosted decision trees (BDTs) [24–26], is used to extract the final results. As a cross-check, a separate analysis where cuts on kinematic variables are applied is carried out.

2 The ATLAS detector and object reconstruction

The ATLAS detector [27] is a multi-purpose detector with a cylindrical geometry. It comprises an inner detector (ID) surrounded by a thin superconducting solenoid, a calorimeter system and an extensive muon spectrometer in a toroidal magnetic field. The ID tracking system consists of a silicon pixel detector, a silicon microstrip detector (SCT), and a transition radiation tracker (TRT). It provides precise position and momentum measurements for charged particles and allows efficient identification of jets containing b-hadrons (b-jets) in the pseudorapidity range $|\eta| < 2.5$. The ID is immersed in a 2 T axial magnetic field and is surrounded by high-granularity lead/liquid-argon (LAr) sampling electromagnetic calorimeters which cover the pseudorapidity range $|\eta| < 3.2$. A steel/scintillator tile calorimeter provides hadronic energy measurements in the central pseudorapidity range ($|\eta| < 1.7$). In the forward regions ($1.5 < |\eta| < 4.9$), the system is complemented by two end-cap calorimeters using LAr as active material and copper or tungsten as absorbers. The muon spectrometer (MS) surrounds the calorimeters and consists of three large superconducting eight-coil toroids, a system of tracking chambers, and detectors for triggering. The deflection of muons is measured within $|\eta| < 2.7$ by three layers of precision drift tubes, and cathode strip chambers in the innermost layer for $|\eta| > 2.0$. The trigger chambers consist of resistive plate chambers in the barrel ($|\eta| < 1.05$) and thin-gap chambers in the end-cap regions ($1.05 < |\eta| < 2.4$).

A three-level trigger system [28] is used to select events. A hardware-based Level-1 trigger uses a subset of detector information to reduce the event rate to a value to 75 kHz or less. The rate of accepted events is then reduced to about 400 Hz by two software-based trigger levels, Level-2 and the Event Filter.

The reconstruction of the basic physics objects used in this analysis is described in the following. The primary vertex referenced below is chosen as the proton-proton vertex candidate with the highest sum of the squared transverse momenta of all associated tracks.

Electron candidates are reconstructed from energy clusters in the electromagnetic calorimeters matched to a track in the ID. They are required to have a transverse en-

[2] The ATLAS experiment uses a right-handed coordinate system with its origin at the nominal interaction point (IP) in the centre of the detector and the z-axis along the beam direction. The x-axis points from the IP to the centre of the LHC ring, and the y-axis points upward. Cylindrical coordinates (r, ϕ) are used in the transverse (x, y) plane, ϕ being the azimuthal angle around the beam direction. The pseudorapidity is defined in terms of the polar angle θ as $\eta = -\ln\tan(\theta/2)$. The distance ΔR in the η–ϕ space is defined as $\Delta R = \sqrt{(\Delta\eta)^2 + (\Delta\phi)^2}$.

JHEP04(2015)117

ergy, $E_{\mathrm{T}} = E \sin\theta$, greater than 15 GeV, to be within the pseudorapidity range $|\eta| < 2.47$, and to satisfy the medium shower shape and track selection criteria defined in ref. [29]. Candidates found in the transition region between the end-cap and barrel calorimeters ($1.37 < |\eta| < 1.52$) are not considered. Typical reconstruction and identification efficiencies for electrons satisfying these selection criteria range between 80% and 90% depending on E_{T} and η.

Muon candidates are reconstructed using an algorithm [30] that combines information from the ID and the MS. The distance between the z-position of the point of closest approach of the muon inner-detector track to the beam-line and the z-coordinate of the primary vertex is required to be less than 1 cm. This requirement reduces the contamination due to cosmic-ray muons and beam-induced backgrounds. Muon quality criteria such as inner detector hit requirements are applied to achieve a precise measurement of the muon momentum and reduce the misidentification rate. Muons are required to have a momentum in the transverse plane $p_{\mathrm{T}} > 10$ GeV and to be within $|\eta| < 2.5$. Typical efficiencies for muons satisfying these selection criteria are above 95% [30].

Jets are reconstructed using the anti-k_t jet clustering algorithm [31, 32] with a radius parameter $R = 0.4$, taking topological energy clusters [33] in the calorimeters as inputs. Jet energies are corrected for the contribution of multiple interactions using a technique based on jet area [34] and are calibrated using p_{T}- and η-dependent correction factors determined from data and simulation [35–37]. Jets are required to be reconstructed in the range $|\eta| < 4.5$ and to have $p_{\mathrm{T}} > 30$ GeV. To reduce the contamination of jets by additional interactions in the same or neighbouring bunch crossings (pile-up), tracks originating from the primary vertex must contribute a large fraction of the p_{T} when summing the scalar p_{T} of all tracks in the jet. This jet vertex fraction (JVF) is required to be at least 75% (50%) for jets with $|\eta| < 2.4$ in the 7 TeV (8 TeV) dataset. Moreover, for the 8 TeV dataset, the JVF selection is applied only to jets with $p_{\mathrm{T}} < 50$ GeV. Jets with no associated tracks are retained.

In the pseudorapidity range $|\eta| < 2.5$, b-jets are selected using a tagging algorithm [38]. The b-jet tagging algorithm has an efficiency of 60–70% for b-jets in simulated $t\bar{t}$ events. The corresponding light-quark jet misidentification probability is 0.1–1%, depending on the jet's p_{T} and η.

Hadronically decaying tau leptons are reconstructed starting from clusters of energy in the electromagnetic and hadronic calorimeters. The τ_{had}[3] reconstruction is seeded by the anti-k_t jet finding algorithm with a radius parameter $R = 0.4$. Jet-specific cleaning selection such as the JVF requirement is not needed for the tau candidate seeds, due to stricter vertex requirements. Tracks with $p_{\mathrm{T}} > 1$ GeV within a cone of radius 0.2 around the cluster barycentre are matched to the τ_{had} candidate, and the τ_{had} charge is determined from the sum of the charges of its associated tracks. The rejection of jets is provided in a separate identification step using discriminating variables based on tracks with $p_{\mathrm{T}} > 1$ GeV and the energy deposited in calorimeter cells found in the core region ($\Delta R < 0.2$) and in the region $0.2 < \Delta R < 0.4$ around the τ_{had} candidate's direction. Such discriminating variables

[3] In the following, the τ_{had} symbol always refers to the visible decay products of the τ hadronic decay.

JHEP04(2015)117

are combined in a boosted decision tree and three working points, labelled tight, medium and loose [39], are defined, corresponding to different τ_{had} identification efficiency values.

In this analysis, τ_{had} candidates with $p_{\text{T}} > 20$ GeV and $|\eta| < 2.47$ are used. The τ_{had} candidates are required to have charge ± 1, and must be 1- or 3-track (prong) candidates. In addition, a sample without the charge and track multiplicity requirements is retained for background modelling in the $\tau_{\text{had}}\tau_{\text{had}}$ channel, as described in section 6.2. The identification efficiency for τ_{had} candidates satisfying the medium criteria is of the order of 55–60%. Dedicated criteria [39] to separate τ_{had} candidates from misidentified electrons are also applied, with a selection efficiency for true τ_{had} decays of 95%. The probability to misidentify a jet with $p_{\text{T}} > 20$ GeV as a τ_{had} candidate is typically 1–2%.

Following their reconstruction, candidate leptons, hadronically decaying taus and jets may point to the same energy deposits in the calorimeters (within $\Delta R < 0.2$). Such overlaps are resolved by selecting objects in the following order of priority (from highest to lowest): muons, electrons, τ_{had}, and jet candidates. For all channels, the leptons that are considered in overlap removal with τ_{had} candidates need to only satisfy looser criteria than those defined above, to reduce misidentified τ_{had} candidates from leptons. The p_{T} threshold of muons considered in overlap removal is also lowered to 4 GeV.

The missing transverse momentum (with magnitude $E_{\text{T}}^{\text{miss}}$) is reconstructed using the energy deposits in calorimeter cells calibrated according to the reconstructed physics objects (e, γ, τ_{had}, jets and μ) with which they are associated [40]. The transverse momenta of reconstructed muons are included in the $E_{\text{T}}^{\text{miss}}$ calculation, with the energy deposited by these muons in the calorimeters taken into account. The energy from calorimeter cells not associated with any physics objects is scaled by a soft-term vertex fraction and also included in the $E_{\text{T}}^{\text{miss}}$ calculation. This fraction is the ratio of the summed scalar p_{T} of tracks from the primary vertex not matched with objects to the summed scalar p_{T} of all tracks in the event also not matched to objects. This method allows to achieve a more accurate reconstruction of the $E_{\text{T}}^{\text{miss}}$ in high pile-up conditions [41].

3 Data and simulated samples

After data quality requirements, the integrated luminosities of the samples used are 4.5 fb^{-1} at $\sqrt{s} = 7$ TeV and 20.3 fb^{-1} at $\sqrt{s} = 8$ TeV.

Samples of signal and background events were simulated using various Monte Carlo (MC) generators, as summarised in table 1. The generators used for the simulation of the hard-scattering process and the model used for the simulation of the parton shower, of the hadronisation and of the underlying-event activity are listed. In addition, the cross section values to which the simulation is normalised and the perturbative order in QCD of the respective calculations are provided.

The signal contributions considered include the three main processes for Higgs boson production at the LHC: ggF, VBF, and associated VH production processes. The contributions from the associated $t\bar{t}H$ production process are found to be small and are neglected. The ggF and VBF production processes are simulated with Powheg [42–45] interfaced to Pythia8 [46]. In the Powheg event generator, the CT10 [47] parameter-

JHEP04(2015)117

isation of the parton distribution functions (PDFs) is used. The overall normalisation of the ggF process is taken from a calculation at next-to-next-to-leading-order (NNLO) [48–53] in QCD, including soft-gluon resummation up to next-to-next-to-leading logarithm terms (NNLL) [54]. Next-to-leading order (NLO) electroweak (EW) corrections are also included [55, 56]. Production by VBF is normalised to a cross section calculated with full NLO QCD and EW corrections [57–59] with an approximate NNLO QCD correction applied [60]. The associated VH production process is simulated with Pythia8. The Cteq6L1 [61] parameterisation of PDFs is used for the Pythia8 event generator. The predictions for VH production are normalised to cross sections calculated at NNLO in QCD [62], with NLO EW radiative corrections [63] applied.

Additional corrections to the shape of the generated p_{T} distribution of Higgs bosons produced via ggF are applied to match the distribution from a calculation at NNLO including the NNLL corrections provided by the HRes2.1 [64] program. In this calculation, the effects of finite masses of the top and bottom quarks [64, 65] are included and dynamical renormalisation and factorisation scales, $\mu_{\mathrm{R}}, \mu_{\mathrm{F}} = \sqrt{m_H^2 + p_{\mathrm{T}}^2}$, are used. A reweighting is performed separately for events with no more than one jet at particle level and for events with two or more jets. In the latter case, the Higgs boson p_{T} spectrum is reweighted to match the MinLo HJJ predictions [66]. The reweighting is derived such that the inclusive Higgs boson p_{T} spectrum and the p_{T} spectrum of events with at least two jets match the HRes2.1 and MinLo HJJ predictions respectively, and that the jet multiplicities are in agreement with (N)NLO calculations from JetVHeto [67–69].

The NLO EW corrections for VBF production depend on the p_{T} of the Higgs boson, varying from a few percent at low p_{T} to $\sim 20\%$ at $p_{\mathrm{T}} = 300$ GeV [70]. The p_{T} spectrum of the VBF-produced Higgs boson is therefore reweighted, based on the difference between the Powheg+Pythia calculation and the Hawk [57, 58] calculation which includes these corrections.

The main and largely irreducible $Z/\gamma^* \to \tau\tau$ background is modelled using $Z/\gamma^* \to \mu\mu$ events from data,[4] where the muon tracks and associated energy depositions in the calorimeters are replaced by the corresponding simulated signatures of the final-state particles of the tau decay. In this approach, essential features such as the modelling of the kinematics of the produced boson, the modelling of the hadronic activity of the event (jets and underlying event) as well as contributions from pile-up are taken from data. Thereby the dependence on the simulation is minimised and only the τ decays and the detector response to the tau-lepton decay products are based on simulation. By requiring two isolated, high-energy muons with opposite charge and a dimuon invariant mass $m_{\mu\mu} > 40$ GeV, $Z \to \mu\mu$ events can be selected from the data with high efficiency and purity. To replace the muons in the selected events, all tracks associated with the muons are removed and calorimeter cell energies associated with the muons are corrected by subtracting the corresponding energy depositions in a single simulated $Z \to \mu\mu$ event with the same kinematics. Finally, both the track information and the calorimeter cell energies from a simulated $Z \to \tau\tau$ decay are

[4] These processes are hereafter for simplicity denoted by $Z \to \tau\tau$ and $Z \to \mu\mu$ respectively, even though the whole continuum above and below the Z peak is considered.

JHEP04(2015)117

added to the data event. The decays of the tau leptons are simulated by Tauola [71]. The tau lepton kinematics are matched to the kinematics of the muons they are replacing, including polarisation and spin correlations [72], and the mass difference between the muons and the tau leptons is accounted for. This hybrid sample is referred to as embedded data in the following.

Other background processes are simulated using different generators, each interfaced to Pythia [46, 73] or Herwig [74, 75] to provide the parton shower, hadronisation and the modelling of the underlying event, as indicated in table 1. For the Herwig samples, the decays of tau leptons are also simulated using Tauola [71]. Photon radiation from charged leptons for all samples is provided by Photos [76]. The samples for W/Z+jets production are generated with Alpgen [77], employing the MLM matching scheme [78] between the hard process (calculated with LO matrix elements for up to five partons) and the parton shower. For WW production, the loop-induced $gg \to WW$ process is also generated, using the gg2WW [79] program. In the AcerMC [80], Alpgen, and Herwig event generators, the Cteq6L1 parameterisation of the PDFs is used, while the CT10 parameterisation is used for the generation of events with gg2WW. The normalisation of these background contributions is either estimated from control regions using data, as described in section 6, or the cross sections quoted in table 1 are used.

For all samples, a full simulation of the ATLAS detector response [81] using the Geant4 program [82] was performed. In addition, events from minimum-bias interactions were simulated using the AU2 [83] parameter tuning of Pythia8. The AU2 tune includes the set of optimized parameters for the parton shower, hadronisation, and multiple parton interactions. They are overlaid on the simulated signal and background events according to the luminosity profile of the recorded data. The contributions from these pile-up interactions are simulated both within the same bunch crossing as the hard-scattering process and in neighbouring bunch crossings. Finally, the resulting simulated events are processed through the same reconstruction programs as the data.

4 Event selection and categorisation

4.1 Event selection

Single lepton, dilepton and di-τ_{had} triggers were used to select the events for the analysis. A summary of the triggers used by each channel at the two centre-of-mass energies is reported in table 2. Due to the increasing luminosity and the different pile-up conditions, the online p_{T} thresholds increased during data-taking in 2011 and again for 2012, and more stringent identification requirements were applied for the data-taking in 2012. The p_{T} requirements on the objects in the analysis are usually 2 GeV higher than the trigger requirements, to ensure that the trigger is fully efficient.

In addition to applying criteria to ensure that the detector was functioning properly, requirements to increase the purity and quality of the data sample are applied by rejecting non-collision events such as cosmic rays and beam-halo events. At least one reconstructed vertex is required with at least four associated tracks with $p_{\text{T}} > 400$ MeV and a posi-

JHEP04(2015)117

Signal ($m_H = 125$ GeV)	MC generator	$\sigma \times \mathcal{B}$ [pb] $\sqrt{s} = 8$ TeV		
ggF, $H \to \tau\tau$	POWHEG [42–45] + PYTHIA8 [46]	1.22	NNLO+NNLL	[48–53, 84]
VBF, $H \to \tau\tau$	POWHEG + PYTHIA8	0.100	(N)NLO	[57–59, 84]
WH, $H \to \tau\tau$	PYTHIA8	0.0445	NNLO	[62, 84]
ZH, $H \to \tau\tau$	PYTHIA8	0.0262	NNLO	[62, 84]
Background	**MC generator**	**$\sigma \times \mathcal{B}$ [pb] $\sqrt{s} = 8$ TeV**		
$W(\to \ell\nu)$, $(\ell = e, \mu, \tau)$	ALPGEN [77]+PYTHIA8	36800	NNLO	[85, 86]
$Z/\gamma^*(\to \ell\ell)$, 60 GeV$< m_{\ell\ell} <$ 2 TeV	ALPGEN+PYTHIA8	3910	NNLO	[85, 86]
$Z/\gamma^*(\to \ell\ell)$, 10 GeV$< m_{\ell\ell} <$ 60 GeV	ALPGEN+HERWIG [87]	13000	NNLO	[85, 86]
VBF $Z/\gamma^*(\to \ell\ell)$	SHERPA [88]	1.1	LO	[88]
$t\bar{t}$	POWHEG + PYTHIA8	$253^\dagger$	NNLO+NNLL	[89–94]
Single top : Wt	POWHEG + PYTHIA8	$22^\dagger$	NNLO	[95]
Single top : s-channel	POWHEG + PYTHIA8	$5.6^\dagger$	NNLO	[96]
Single top : t-channel	AcerMC [80]+PYTHIA6 [73]	$87.8^\dagger$	NNLO	[97]
$q\bar{q} \to WW$	ALPGEN+HERWIG	$54^\dagger$	NLO	[98]
$gg \to WW$	GG2WW [79]+HERWIG	$1.4^\dagger$	NLO	[79]
WZ, ZZ	HERWIG	$30^\dagger$	NLO	[98]
$H \to WW$	same as for $H \to \tau\tau$ signal	$4.7^\dagger$		

Table 1. Monte Carlo generators used to model the signal and the background processes at $\sqrt{s} = 8$ TeV. The cross sections times branching fractions ($\sigma \times \mathcal{B}$) used for the normalisation of some processes (many of these are subsequently normalised to data) are included in the last column together with the perturbative order of the QCD calculation. For the signal processes the $H \to \tau\tau$ SM branching ratio is included, and for the W and Z/γ^* background processes the branching ratios for leptonic decays ($\ell = e, \mu, \tau$) of the bosons are included. For all other background processes, inclusive cross sections are quoted (marked with a †).

tion consistent with the beam spot. It has been verified that, after object selection cuts, contributions from other primary vertices are negligible.

With respect to the object identification requirements described in section 2, tighter criteria are applied to address the different background contributions and compositions in the different analysis channels. Higher p_{T} thresholds are applied to electrons, muons, and τ_{had} candidates according to the trigger conditions satisfied by the event, as listed in table 2. For the channels involving leptonic tau decays, $\tau_{\mathrm{lep}}\tau_{\mathrm{lep}}$ and $\tau_{\mathrm{lep}}\tau_{\mathrm{had}}$, additional isolation criteria for electrons and muons, based on tracking and calorimeter information, are used to suppress the background from misidentified jets or from semileptonic decays of charm and bottom hadrons. The calorimeter isolation variable $I(E_{\mathrm{T}}, \Delta R)$ is defined

JHEP04(2015)117

$\sqrt{s} = 7$ TeV				
Trigger	Trigger level thresholds, p_{T} [GeV]	Analysis level thresholds [GeV]		
		$\tau_{\mathrm{lep}}\tau_{\mathrm{lep}}$	$\tau_{\mathrm{lep}}\tau_{\mathrm{had}}$	$\tau_{\mathrm{had}}\tau_{\mathrm{had}}$
Single electron	20−22	$e\mu$: $p_{\mathrm{T}}^{e} > 22-24$, $p_{\mathrm{T}}^{\mu} > 10$	$e\tau$: $p_{\mathrm{T}}^{e} > 25$, $p_{\mathrm{T}}^{\tau} > 20$	–
Single muon	18	$\mu\mu$: $p_{\mathrm{T}}^{\mu_1} > 20$, $p_{\mathrm{T}}^{\mu_2} > 10$; $e\mu$: $p_{\mathrm{T}}^{\mu} > 20$, $p_{\mathrm{T}}^{e} > 15$	$\mu\tau$: $p_{\mathrm{T}}^{\mu} > 22$, $p_{\mathrm{T}}^{\tau} > 20$	–
Di-electron	12/12	ee: $p_{\mathrm{T}}^{e_1} > 15$, $p_{\mathrm{T}}^{e_2} > 15$	–	–
Di-τ_{had}	29/20	–	–	$\tau\tau$: $p_{\mathrm{T}}^{\tau_1} > 35$, $p_{\mathrm{T}}^{\tau_2} > 25$
$\sqrt{s} = 8$ TeV				
Trigger	Trigger level thresholds, p_{T} [GeV]	Analysis level thresholds [GeV]		
		$\tau_{\mathrm{lep}}\tau_{\mathrm{lep}}$	$\tau_{\mathrm{lep}}\tau_{\mathrm{had}}$	$\tau_{\mathrm{had}}\tau_{\mathrm{had}}$
Single electron	24	$e\mu$: $p_{\mathrm{T}}^{e} > 26$, $p_{\mathrm{T}}^{\mu} > 10$; ee: $p_{\mathrm{T}}^{e_1} > 26$, $p_{\mathrm{T}}^{e_2} > 15$	$e\tau$: $p_{\mathrm{T}}^{e} > 26$, $p_{\mathrm{T}}^{\tau} > 20$	–
Single muon	24	–	$\mu\tau$: $p_{\mathrm{T}}^{\mu} > 26$, $p_{\mathrm{T}}^{\tau} > 20$	–
Di-electron	12/12	ee: $p_{\mathrm{T}}^{e_1} > 15$, $p_{\mathrm{T}}^{e_2} > 15$	–	–
Di-muon	18/8	$\mu\mu$: $p_{\mathrm{T}}^{\mu_1} > 20$, $p_{\mathrm{T}}^{\mu_2} > 10$	–	–
Electron+muon	12/8	$e\mu$: $p_{\mathrm{T}}^{e} > 15$, $p_{\mathrm{T}}^{\mu} > 10$	–	–
Di-τ_{had}	29/20	–	–	$\tau\tau$: $p_{\mathrm{T}}^{\tau_1} > 35$, $p_{\mathrm{T}}^{\tau_2} > 25$

Table 2. Summary of the triggers used to select events for the different analysis channels at the two centre-of-mass energies. The transverse momentum thresholds applied at trigger level and in the analysis are listed. When more than one trigger is used, a logical OR is taken and the trigger efficiencies are calculated accordingly.

JHEP04(2015)117

		$\tau_{\rm lep}\tau_{\rm lep}$	$\tau_{\rm lep}\tau_{\rm had}$
Electrons	7 TeV	$I(p_{\rm T}, 0.4) < 0.06$ $I(E_{\rm T}, 0.2) < 0.08$	$I(p_{\rm T}, 0.4) < 0.06$ $I(E_{\rm T}, 0.2) < 0.06$
	8 TeV	$I(p_{\rm T}, 0.4) < 0.17$ $I(E_{\rm T}, 0.2) < 0.09$	$I(p_{\rm T}, 0.4) < 0.06$ $I(E_{\rm T}, 0.2) < 0.06$
Muons	7 TeV	$I(p_{\rm T}, 0.4) < 0.06$ $I(E_{\rm T}, 0.2) < 0.04$	$I(p_{\rm T}, 0.4) < 0.06$ $I(E_{\rm T}, 0.2) < 0.06$
	8 TeV	$I(p_{\rm T}, 0.4) < 0.18$ $I(E_{\rm T}, 0.2) < 0.09$	$I(p_{\rm T}, 0.4) < 0.06$ $I(E_{\rm T}, 0.2) < 0.06$

Table 3. Summary of isolation requirements applied for the selection of isolated electrons and muons at the two centre-of-mass energies. The isolation variables are defined in the text.

as the sum of the total transverse energy in the calorimeter in a cone of size ΔR around the electron cluster or the muon track, divided by the $E_{\rm T}$ of the electron cluster or the $p_{\rm T}$ of the muon respectively. The track-based isolation $I(p_{\rm T}, \Delta R)$ is defined as the sum of the transverse momenta of tracks within a cone of ΔR around the electron or muon track, divided by the $E_{\rm T}$ of the electron cluster or the muon $p_{\rm T}$ respectively. The isolation requirements applied are slightly different for the two centre-of-mass energies and are listed in table 3.

In the $\tau_{\rm had}\tau_{\rm had}$ channel, isolated taus are selected by requiring that there are no tracks with $p_{\rm T} > 0.5$ GeV in an isolation region of $0.2 < \Delta R < 0.6$ around the tau direction. This requirement leads to a 12% (4%) efficiency loss for hadronic taus, while 30% (10%) of contamination from jets is rejected in 8 (7) TeV data.

After the basic lepton selection, further channel-dependent cuts are applied, as detailed in the following. The full event selection is summarised in table 4.

The $\tau_{\rm lep}\tau_{\rm lep}$ channel: exactly two isolated leptons with opposite-sign (OS) electric charges, passing the $p_{\rm T}$ threshold listed in table 2, are required. Events containing a $\tau_{\rm had}$ candidate are vetoed. For the $\tau_{\rm had}$ candidates considered, the criteria used to reject electrons misidentified as $\tau_{\rm had}$ candidates are tightened to a working-point of 85% signal efficiency [39].

In addition to the irreducible $Z \to \tau\tau$ background, sizeable background contributions from $Z \to \ell\ell$ and from $t\bar{t}$ production are expected in this channel. Background contributions from Z decays, but also from low mass resonances (charmonium and bottomonium), are rejected by requirements on the invariant mass $m_{\tau\tau}^{\rm vis}$ of the visible tau decay products, on the angle $\Delta\phi_{\ell\ell}$ between the two leptons in the transverse plane and on $E_{\rm T}^{\rm miss}$. To reject the large $Z \to \ell\ell$ contribution in events with same-flavour (SF) leptons ($ee, \mu\mu$), more stringent cuts on the visible mass and on $E_{\rm T}^{\rm miss}$ are applied for these events than for events with different-flavour (DF) leptons ($e\mu$). For SF final states, an additional variable named *high-$p_{\rm T}$ objects* $E_{\rm T}^{\rm miss}$ ($E_{\rm T}^{\rm miss,HPTO}$) is also used to reject background from Z/γ^* production. It is calculated from the high-$p_{\rm T}$ objects in the event, i.e. from the two leptons and from jets with $p_{\rm T} > 25$ GeV. Due to the presence of real neutrinos, the two $E_{\rm T}^{\rm miss}$ variables

JHEP04(2015)117

are strongly correlated for signal events but only loosely correlated for background from $Z \to ee$ and $Z \to \mu\mu$ decays.

To further suppress background contributions from misidentified leptons[5] a minimum value of the scalar sum of the transverse momenta of the two leptons is required. Contributions from $t\bar{t}$ events are further reduced by rejecting events with a b-jet with $p_{\mathrm{T}} > 25$ GeV.

Within the collinear approximation [99], i.e. assuming that the tau directions are given by the directions of the visible tau decay products and that the momenta of the neutrinos constitute the missing transverse momentum, the tau momenta can be reconstructed. For tau decays, the fractions of the tau momenta carried by the visible decay products,[6] $x_{\tau,i} = p_{\mathrm{vis},i}/(p_{\mathrm{vis},i} + p_{\mathrm{mis},i})$, with $i = 1, 2$, are expected to lie in the interval $0 < x_{\tau,i} < 1$, and hence corresponding requirements are applied to further reject non-tau background contributions.

Finally, to avoid overlap between this analysis and the search for $H \to WW^* \to \ell\nu\ell\nu$ decays, the $\tau\tau$ mass in the collinear approximation is required to satisfy the condition $m_{\tau\tau}^{\mathrm{coll}} > m_Z - 25$ GeV.

The $\tau_{\mathrm{lep}}\tau_{\mathrm{had}}$ channel: exactly one isolated lepton and one τ_{had} candidate with OS charges, passing the p_{T} thresholds listed in table 2, are required. The criteria used to reject electrons misidentified as τ_{had} are also tightened in this channel to a working-point of 85% signal efficiency [39].

The production of W+jets and of top quarks constitute the dominant reducible background in this channel. To substantially reduce the W+jets contribution, a cut on the transverse mass[7] constructed from the lepton and the missing transverse momentum is applied and events with $m_{\mathrm{T}} > 70$ GeV are rejected. Contributions from $t\bar{t}$ events are reduced by rejecting events with a b-jet with $p_{\mathrm{T}} > 30$ GeV.

The $\tau_{\mathrm{had}}\tau_{\mathrm{had}}$ channel: one isolated medium τ_{had} candidate and one isolated tight τ_{had} candidate with OS charges are required. Events with electron or muon candidates are rejected. For all data, the missing transverse momentum must satisfy $E_{\mathrm{T}}^{\mathrm{miss}} > 20$ GeV and its direction must either be between the two visible τ_{had} candidates in ϕ or within $\Delta\phi < \pi/4$ of the nearest τ_{had} candidate. To further reduce the background from multijet production, additional cuts on the ΔR and pseudorapidity separation $\Delta\eta$ between the two τ_{had} candidates are applied.

With these selections, there is no overlap between the individual channels.

4.2 Analysis categories

To exploit signal-sensitive event topologies, two analysis categories are defined in an exclusive way.

[5] Misidentified leptons and τ_{had} candidates are also referred to as "fake" in this paper.

[6] The variable p_{vis} is defined as the total momentum of the visible decay products of the tau lepton while p_{mis} is defined as the momentum of the neutrino system reconstructed using the collinear approximation.

[7] $m_{\mathrm{T}} = \sqrt{2p_{\mathrm{T}}^{\ell}\, E_{\mathrm{T}}^{\mathrm{miss}} \cdot (1 - \cos\Delta\phi)}$, where $\Delta\phi$ is the azimuthal separation between the directions of the lepton and the missing transverse momentum.

JHEP04(2015)117

Channel	Preselection cuts
$\tau_{\text{lep}}\tau_{\text{lep}}$	Exactly two isolated opposite-sign leptons Events with τ_{had} candidates are rejected 30 GeV $< m_{\tau\tau}^{\text{vis}} < 100$ (75) GeV for DF (SF) events $\Delta\phi_{\ell\ell} < 2.5$ $E_{\text{T}}^{\text{miss}} > 20$ (40) GeV for DF (SF) events $E_{\text{T}}^{\text{miss,HPTO}} > 40$ GeV for SF events $p_{\text{T}}^{\ell_1} + p_{\text{T}}^{\ell_2} > 35$ GeV Events with a b-tagged jet with $p_{\text{T}} > 25$ GeV are rejected $0.1 < x_{\tau_1}, x_{\tau_2} < 1$ $m_{\tau\tau}^{\text{coll}} > m_Z - 25$ GeV
$\tau_{\text{lep}}\tau_{\text{had}}$	Exactly one isolated lepton and one medium τ_{had} candidate with opposite charges $m_{\text{T}} < 70$ GeV Events with a b-tagged jet with $p_{\text{T}} > 30$ GeV are rejected
$\tau_{\text{had}}\tau_{\text{had}}$	One isolated medium and one isolated tight opposite-sign τ_{had}-candidate Events with leptons are vetoed $E_{\text{T}}^{\text{miss}} > 20$ GeV $E_{\text{T}}^{\text{miss}}$ points between the two visible taus in ϕ, or $\min[\Delta\phi(\tau, E_{\text{T}}^{\text{miss}})] < \pi/4$ $0.8 < \Delta R(\tau_{\text{had}_1}, \tau_{\text{had}_2}) < 2.4$ $\Delta\eta(\tau_{\text{had}_1}, \tau_{\text{had}_2}) < 1.5$
Channel	VBF category selection cuts
$\tau_{\text{lep}}\tau_{\text{lep}}$	At least two jets with $p_{\text{T}}^{j_1} > 40$ GeV and $p_{\text{T}}^{j_2} > 30$ GeV $\Delta\eta(j_1, j_2) > 2.2$
$\tau_{\text{lep}}\tau_{\text{had}}$	At least two jets with $p_{\text{T}}^{j_1} > 50$ GeV and $p_{\text{T}}^{j_2} > 30$ GeV $\Delta\eta(j_1, j_2) > 3.0$ $m_{\tau\tau}^{\text{vis}} > 40$ GeV
$\tau_{\text{had}}\tau_{\text{had}}$	At least two jets with $p_{\text{T}}^{j_1} > 50$ GeV and $p_{\text{T}}^{j_2} > 30$ GeV $p_{\text{T}}^{j_2} > 35$ GeV for jets with $\lvert\eta\rvert > 2.4$ $\Delta\eta(j_1, j_2) > 2.0$
Channel	Boosted category selection cuts
$\tau_{\text{lep}}\tau_{\text{lep}}$	At least one jet with $p_{\text{T}} > 40$ GeV
All	Failing the VBF selection $p_{\text{T}}^{H} > 100$ GeV

Table 4. Summary of the event selection for the three analysis channels. The requirements used in both the preselection and for the definition of the analysis categories are given. The labels (1) and (2) refer to the leading (highest p_{T}) and subleading final-state objects (leptons, τ_{had}, jets). The variables are defined in the text.

- The VBF category targets events with a Higgs boson produced via vector boson fusion and is characterised by the presence of two high-p_{T} jets with a large pseudorapidity separation (see table 4). The $\Delta\eta(j_1, j_2)$ requirement is applied to the two highest-p_{T} jets in the event. In the $\tau_{\text{lep}}\tau_{\text{had}}$ channel, there is an additional requirement that $m_{\tau\tau}^{\text{vis}} > 40$ GeV, to eliminate low-mass Z/γ^* events. Although this category is dominated by VBF events, it also includes smaller contributions from ggF and VH production.

- The boosted category targets events with a boosted Higgs boson produced via ggF.

JHEP04(2015)117

Higgs boson candidates are therefore required to have large transverse momentum, $p_{\mathrm{T}}^{H} > 100$ GeV. The p_{T}^{H} is reconstructed using the vector sum of the missing transverse momentum and the transverse momentum of the visible tau decay products. In the $\tau_{\mathrm{lep}}\tau_{\mathrm{lep}}$ channel, at least one jet with $p_{\mathrm{T}} > 40$ GeV is required. The jet requirement selects a region of the phase space where the $E_{\mathrm{T}}^{\mathrm{miss}}$ of same-flavour events is well modelled by simulation. In order to define an orthogonal category, events passing the VBF category selection are not considered. This category also includes small contributions from VBF and VH production.

While these categories are conceptually identical across the three channels, differences in the dominant background contributions require different selection criteria. For both categories, the requirement on jets is inclusive and additional jets, apart from those passing the category requirements, are allowed.

For the $\tau_{\mathrm{had}}\tau_{\mathrm{had}}$ channel, the so-called *rest category* is used as a control region. In this category, events passing the preselection requirements but not passing the VBF or boosted category selections are considered. This category is used to constrain the $Z \to \tau\tau$ and multijet background contributions. The signal contamination in this category is negligible.

4.3 Higgs boson candidate mass reconstruction

The di-tau invariant mass ($m_{\tau\tau}^{\mathrm{MMC}}$) is reconstructed using the missing mass calculator (MMC) [100]. This requires solving an underconstrained system of equations for six to eight unknowns, depending on the number of neutrinos in the $\tau\tau$ final state. These unknowns include the x-, y-, and z-components of the momentum carried by the neutrinos for each of the two tau leptons in the event, and the invariant mass of the two neutrinos from any leptonic tau decays. The calculation uses the constraints from the measured x- and y-components of the missing transverse momentum, and the visible masses of both tau candidates. A scan is performed over the two components of the missing transverse momentum vector and the yet undetermined variables. Each scan point is weighted by its probability according to the $E_{\mathrm{T}}^{\mathrm{miss}}$ resolution and the tau decay topologies. The estimator for the $\tau\tau$ mass is defined as the most probable value of the scan points.

The MMC algorithm provides a solution for ∼99% of the $H \to \tau\tau$ and $Z \to \tau\tau$ events. This is a distinct advantage compared to the mass calculation using the collinear approximation where the failure rate is higher due to the implicit collinearity assumptions. The small loss rate of about 1% for signal events is due to large fluctuations of the $E_{\mathrm{T}}^{\mathrm{miss}}$ measurement or other scan variables.

Figure 1 shows reconstructed $m_{\tau\tau}^{\mathrm{MMC}}$ mass distributions for $H \to \tau\tau$ and $Z \to \tau\tau$ events in the $\tau_{\mathrm{lep}}\tau_{\mathrm{had}}$ VBF and boosted categories. The mass resolution, defined as the ratio between the full width at half maximum (FWHM) and the peak value of the mass distribution (m_{peak}), is found to be $\approx 30\%$ for all categories and channels.

5 Boosted decision trees

Boosted decision trees are used in each category to extract the Higgs boson signal from the large number of background events. Decision trees [24] recursively partition the parameter

JHEP04(2015)117

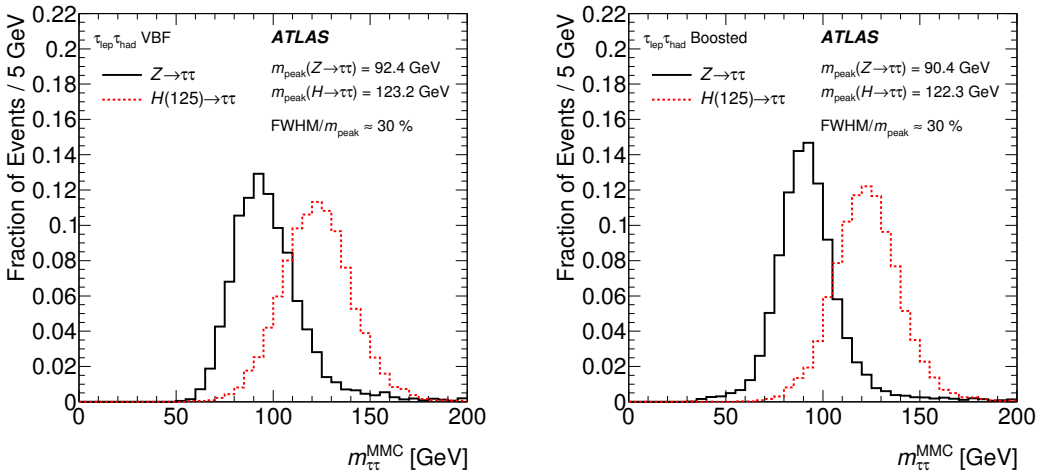

(a) (b)

Figure 1. The reconstructed invariant $\tau\tau$ mass, $m_{\tau\tau}^{\mathrm{MMC}}$ for $H \to \tau\tau$ ($m_H = 125$ GeV) and $Z \to \tau\tau$ events in MC simulation and embedding respectively, for events passing (a) the VBF category selection and (b) the boosted category selection in the $\tau_{\mathrm{lep}}\tau_{\mathrm{had}}$ channel.

space into multiple regions where signal or background purities are enhanced. Boosting is a method which improves the performance and stability of decision trees and involves the combination of many trees into a single final discriminant [25, 26]. After boosting, the final score undergoes a transformation to map the scores on the interval -1 to $+1$. The most signal-like events have scores near 1 while the most background-like events have scores near -1.

Separate BDTs are trained for each analysis category and channel with signal and background samples, described in section 6, at $\sqrt{s} = 8$ TeV. They are then applied to the analysis of the data at both centre-of-mass energies. The separate training naturally exploits differences in event kinematics between different Higgs boson production modes. It also allows different discriminating variables to be used to address the different background compositions in each channel. A large set of potential variables was investigated, in each channel separately, and only those variables which led to an improved discrimination performance of the BDT were kept. For the training in the VBF category, only a VBF Higgs production signal sample is used, while training in the boosted category uses ggF, VBF, and VH signal samples. The Higgs boson mass is chosen to be $m_H = 125$ GeV for all signal samples. The BDT input variables used at both centre-of-mass energies are listed in table 5. Most of these variables have straightforward definitions, and the more complex ones are defined in the following.

- $\Delta R(\tau_1, \tau_2)$: the distance ΔR between the two leptons, between the lepton and τ_{had}, or between the two τ_{had} candidates, depending on the decay mode.

- $p_{\mathrm{T}}^{\mathrm{Total}}$: magnitude of the vector sum of the transverse momenta of the visible tau decay products, the two leading jets, and $E_{\mathrm{T}}^{\mathrm{miss}}$.

JHEP04(2015)117

- Sum p_{T}: scalar sum of the p_{T} of the visible components of the tau decay products and of the jets.

- $E_{\mathrm{T}}^{\mathrm{miss}}\phi$ centrality: a variable that quantifies the relative angular position of the missing transverse momentum with respect to the visible tau decay products in the transverse plane. The transverse plane is transformed such that the direction of the tau decay products are orthogonal, and that the smaller ϕ angle between the tau decay products defines the positive quadrant of the transformed plane. The $E_{\mathrm{T}}^{\mathrm{miss}}\phi$ centrality is defined as the sum of the x- and y-components of the $E_{\mathrm{T}}^{\mathrm{miss}}$ unit vector in this transformed plane.

- Sphericity: a variable that describes the isotropy of the energy flow in the event [101]. It is based on the quadratic momentum tensor

$$S^{\alpha\beta} = \frac{\sum_i p_i^{\alpha} p_i^{\beta}}{\sum_i |\vec{p_i}^2|}. \tag{5.1}$$

  In this equation, α and β are the indices of the tensor. The summation is performed over the momenta of the selected leptons and jets in the event. The sphericity of the event (S) is then defined in terms of the two smallest eigenvalues of this tensor, λ_2 and λ_3,

$$S = \frac{3}{2}(\lambda_2 + \lambda_3). \tag{5.2}$$

- $\min(\Delta\eta_{\ell_1\ell_2,\mathrm{jets}})$: the minimum $\Delta\eta$ between the dilepton system and either of the two jets.

- Object η centrality: a variable that quantifies the η position of an object (an isolated lepton, a τ_{had} candidate or a jet) with respect to the two leading jets in the event. It is defined as

$$C_{\eta_1,\eta_2}(\eta) = \exp\left[\frac{-4}{(\eta_1-\eta_2)^2}\left(\eta - \frac{\eta_1+\eta_2}{2}\right)^2\right], \tag{5.3}$$

  where η, η_1 and η_2 are the pseudorapidities of the object and the two leading jets respectively. This variable has a value of 1 when the object is halfway in η between the two jets, 1/e when the object is aligned with one of the jets, and $< 1/\mathrm{e}$ when the object is not between the jets in η. In the $\tau_{\mathrm{lep}}\tau_{\mathrm{lep}}$ channel the η centrality of a third jet in the event, $C_{\eta_1,\eta_2}(\eta_{j_3})$, and the product of the η centralities of the two leptons are used as BDT input variables, while in the $\tau_{\mathrm{lep}}\tau_{\mathrm{had}}$ channel the η centrality of the lepton, $C_{\eta_1,\eta_2}(\eta_\ell)$, is used, and in the $\tau_{\mathrm{had}}\tau_{\mathrm{had}}$ channel the η centrality of each τ, $C_{\eta_1,\eta_2}(\eta_{\tau_1})$ and $C_{\eta_1,\eta_2}(\eta_{\tau_2})$, is used. Events with only two jets are assigned a dummy value of -0.5 for $C_{\eta_1,\eta_2}(\eta_{j_3})$.

Among these variables the most discriminating ones include $m_{\tau\tau}^{\mathrm{MMC}}$, $\Delta R(\tau_1,\tau_2)$ and $\Delta\eta(j_1,j_2)$. Figures 2 and 3 show the distributions of selected BDT input variables. For the VBF category, the distributions of $\Delta\eta(j_1,j_2)$ and centrality variables are shown for all three channels. For the boosted category, the distributions of $\Delta R(\tau_1,\tau_2)$ and $E_{\mathrm{T}}^{\mathrm{miss}}\phi$

JHEP04(2015)117

Variable	VBF			Boosted		
	$\tau_{\rm lep}\tau_{\rm lep}$	$\tau_{\rm lep}\tau_{\rm had}$	$\tau_{\rm had}\tau_{\rm had}$	$\tau_{\rm lep}\tau_{\rm lep}$	$\tau_{\rm lep}\tau_{\rm had}$	$\tau_{\rm had}\tau_{\rm had}$
$m_{\tau\tau}^{\rm MMC}$	•	•	•	•	•	•
$\Delta R(\tau_1, \tau_2)$	•	•	•		•	•
$\Delta\eta(j_1, j_2)$	•	•	•			
m_{j_1,j_2}	•	•	•			
$\eta_{j_1} \times \eta_{j_2}$		•	•			
$p_{\rm T}^{\rm Total}$		•	•			
Sum $p_{\rm T}$					•	•
$p_{\rm T}^{\tau_1}/p_{\rm T}^{\tau_2}$					•	•
$E_{\rm T}^{\rm miss}\phi$ centrality		•	•	•	•	•
m_{ℓ,ℓ,j_1}				•		
m_{ℓ_1,ℓ_2}				•		
$\Delta\phi(\ell_1, \ell_2)$				•		
Sphericity				•		
$p_{\rm T}^{\ell_1}$				•		
$p_{\rm T}^{j_1}$				•		
$E_{\rm T}^{\rm miss}/p_{\rm T}^{\ell_2}$				•		
$m_{\rm T}$		•			•	
$\min(\Delta\eta_{\ell_1\ell_2,\rm jets})$	•					
$C_{\eta_1,\eta_2}(\eta_{\ell_1}) \cdot C_{\eta_1,\eta_2}(\eta_{\ell_2})$	•					
$C_{\eta_1,\eta_2}(\eta_\ell)$		•				
$C_{\eta_1,\eta_2}(\eta_{j_3})$	•					
$C_{\eta_1,\eta_2}(\eta_{\tau_1})$			•			
$C_{\eta_1,\eta_2}(\eta_{\tau_2})$			•			

Table 5. Discriminating variables used in the training of the BDT for each channel and category at $\sqrt{s} = 8$ TeV. The more complex variables are described in the text. The filled circles indicate which variables are used in each case.

centrality are shown for the $\tau_{\rm lep}\tau_{\rm had}$ and $\tau_{\rm had}\tau_{\rm had}$ channels, and the distribution of the $p_{\rm T}$ of the leading jet and the sphericity are shown for the $\tau_{\rm lep}\tau_{\rm lep}$ channel. For all distributions, the data are compared to the predicted SM backgrounds at $\sqrt{s} = 8$ TeV. The corresponding uncertainties are indicated by the shaded bands. All input distributions are well described, giving confidence that the background models (from simulation and data) describe well the relevant input variables of the BDT. Similarly, good agreement is found for the distributions at $\sqrt{s} = 7$ TeV.

JHEP04(2015)117

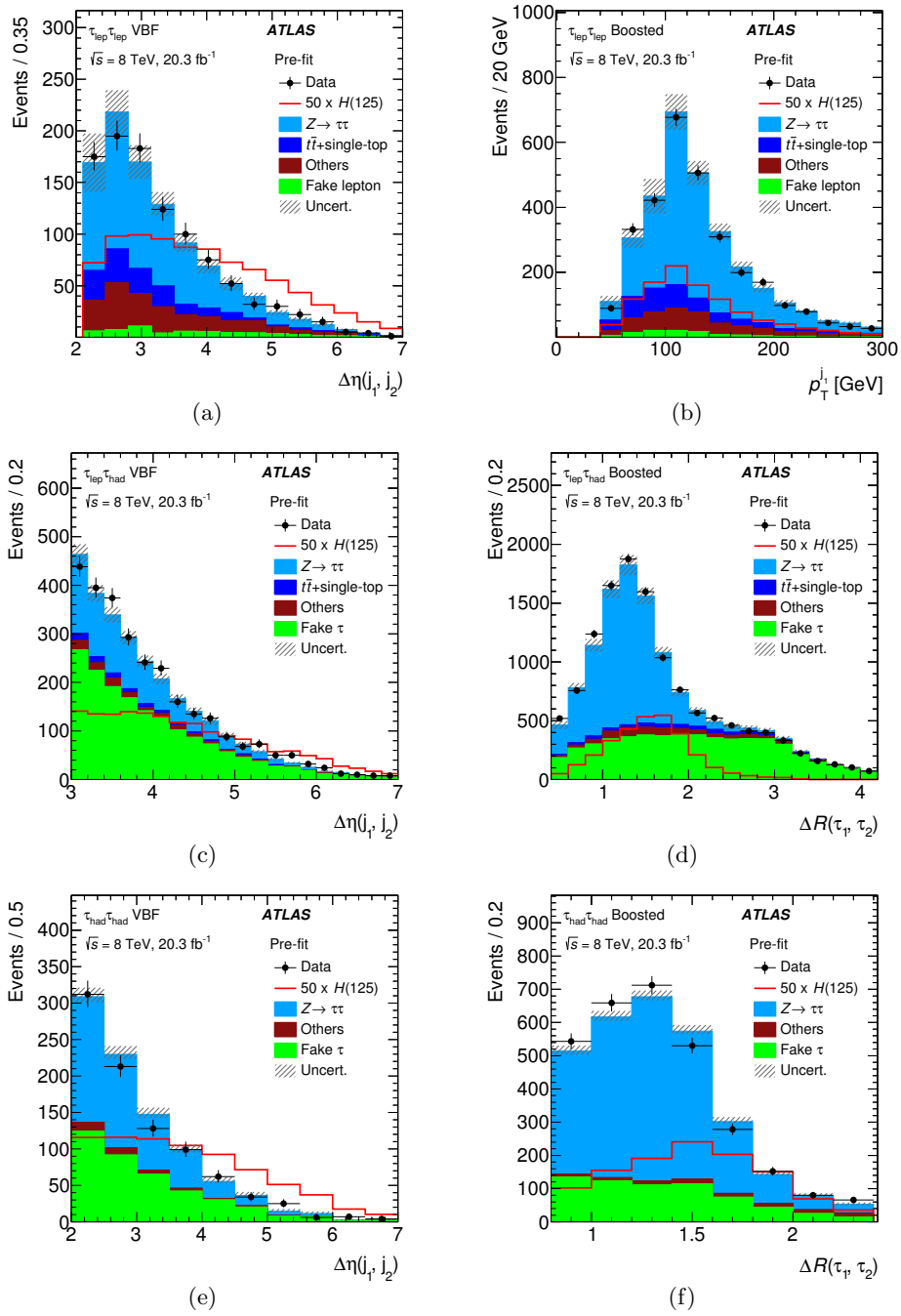

Figure 2. Distributions of important BDT input variables for the three channels and the two categories (VBF, left) and (boosted, right) for data collected at $\sqrt{s} = 8$ TeV. The distributions are shown for (a) the separation in pseudorapidity of the jets, $\Delta\eta(j_1, j_2)$, and (b) the transverse momentum of the leading jet $p_{\mathrm{T}}^{j_1}$ in the $\tau_{\mathrm{lep}}\tau_{\mathrm{lep}}$ channel, for (c) $\Delta\eta(j_1, j_2)$ and (d) $\Delta R(\tau_1, \tau_2)$, the distance ΔR between the lepton and τ_{had}, in the $\tau_{\mathrm{lep}}\tau_{\mathrm{had}}$ channel and for (e) $\Delta\eta(j_1, j_2)$ and (f) $\Delta R(\tau_1, \tau_2)$, the distance ΔR between the two τ_{had} candidates, in the $\tau_{\mathrm{had}}\tau_{\mathrm{had}}$ channel. The contributions from a Standard Model Higgs boson with $m_H = 125$ GeV are superimposed, multiplied by a factor of 50. These figures use background predictions made without the global fit defined in section 8. The error band includes statistical and pre-fit systematic uncertainties.

JHEP04(2015)117

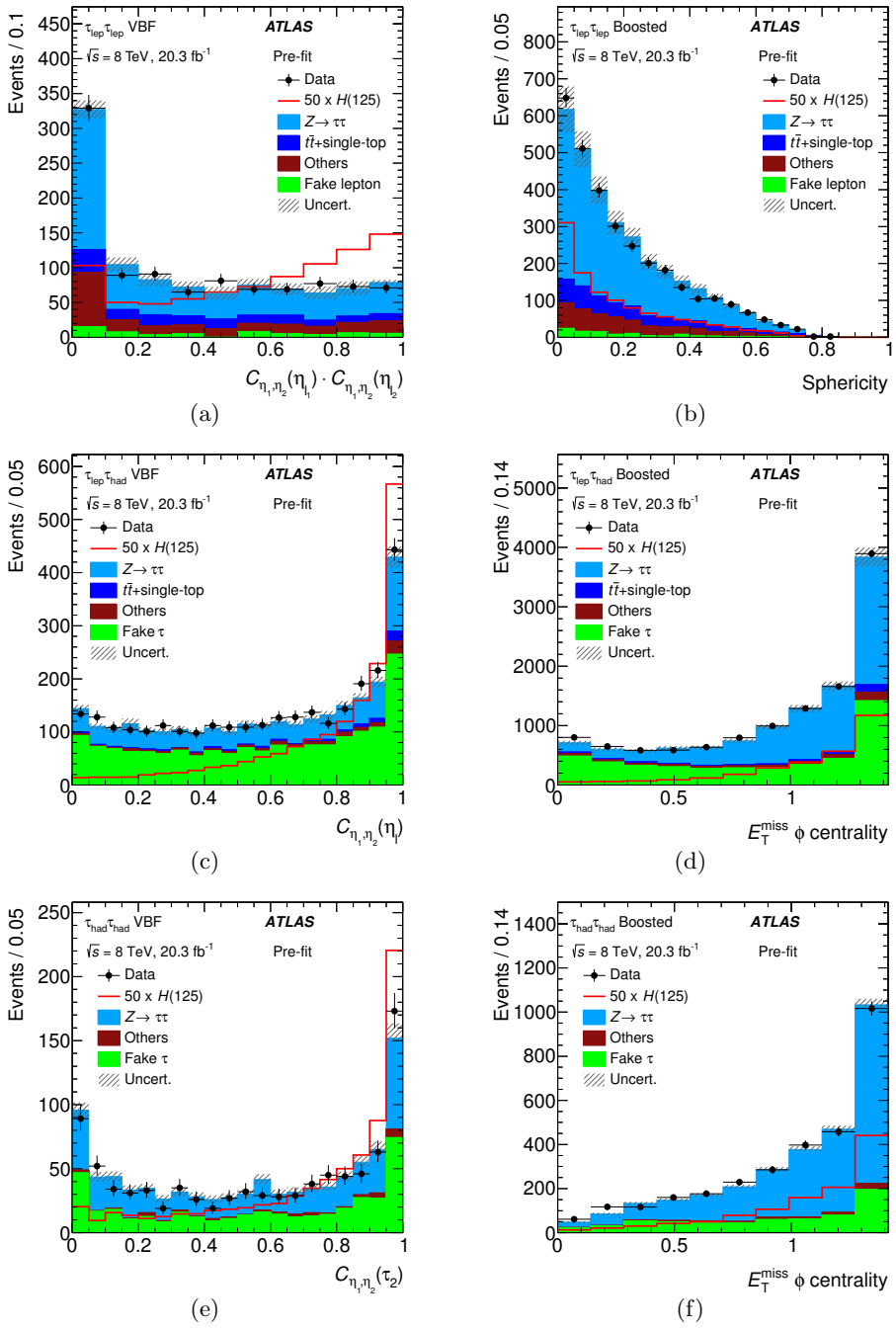

Figure 3. Distributions of important BDT input variables for the three channels and the two categories (VBF, left) and (boosted, right) for data collected at $\sqrt{s} = 8$ TeV. The distributions are shown for (a) the product of the lepton centralities, $C_{\eta_1,\eta_2}(\eta_{\ell_1}) \cdot C_{\eta_1,\eta_2}(\eta_{\ell_2})$, and (b) the sphericity in the $\tau_{\rm lep}\tau_{\rm lep}$ channel, for (c) the centrality of the lepton, $C_{\eta_1,\eta_2}(\eta_\ell)$, and (d) the $E_{\rm T}^{\rm miss}\phi$ centrality in the $\tau_{\rm lep}\tau_{\rm had}$ channel, and for (e) the centrality of the subleading tau, $C_{\eta_1,\eta_2}(\eta_{\tau_2})$, and (f) the $E_{\rm T}^{\rm miss}\phi$ centrality in the $\tau_{\rm had}\tau_{\rm had}$ channel. The contributions from a Standard Model Higgs boson with $m_H = 125$ GeV are superimposed, multiplied by a factor of 50. These figures use background predictions made without the global fit defined in section 8. The error band includes statistical and pre-fit systematic uncertainties.

JHEP04(2015)117

6 Background estimation

The different final-state topologies of the three analysis channels have different background compositions which necessitate different strategies for the background estimation. In general, the number of expected background events and the associated kinematic distributions are derived from a mixture of data-driven methods and simulation. The normalisation of several important background contributions is performed by comparing the simulated samples of individual background sources to data in regions which only have a small or negligible contamination from signal or other background events. The control regions used in the analysis are summarised in table 6.

Common to all channels is the dominant $Z \to \tau\tau$ background, for which the kinematic distributions are taken from data by employing the embedding technique, as described in section 3. Background contributions from jets that are misidentified as hadronically decaying taus (fake backgrounds) are estimated by using either a *fake-factor* method or samples of non-isolated τ_{had} candidates. Likewise, samples of non-isolated leptons are used to estimate fake-lepton contributions from jets or hadronically decaying taus and leptons from other sources, such as heavy-quark decays.[8]

Contributions from various other physics processes with leptons and/or τ_{had} candidates in the final state are estimated using the simulation, normalised to the theoretical cross sections, as given in table 1. A more detailed discussion of the estimation of the various background components in the different channels is given in the following.

6.1 Background from $Z \to \tau\tau$ production

A reliable modelling of the irreducible $Z \to \tau\tau$ background is an important ingredient of the analysis. It has been shown in other ATLAS analyses that existing Z+jets Monte Carlo simulation needs to be reweighted to model data correctly [102–104]. Additionally, it is not possible to select a sufficiently pure and signal-free $Z \to \tau\tau$ control sample from data to model the background in the signal region. Therefore this background is estimated using embedded data, as described in section 3. This procedure was extensively validated using both data and simulation. To validate the subtraction procedure of the muon cell energies and tracks from data and the subsequent embedding of the corresponding information from simulation, the muons in $Z \to \mu\mu$ events are replaced by simulated muons. The calorimeter isolation energy in a cone of $\Delta R = 0.3$ around the muons from data before and after embedding is compared in figure 4(a). Good agreement is found, which indicates that no deterioration (e.g. possible energy biases) in the muon environment is introduced. Another important test validates the embedding of more complex $Z \to \tau\tau$ events, which can only be performed in the simulation. To achieve a meaningful validation, the same MC generator with identical settings was used to simulate both the $Z \to \mu\mu$ and $Z \to \tau\tau$ events. The sample of embedded events is corrected for the bias due to the trigger, reconstruction and acceptance of the original muons. These corrections are determined from data as a function of p_{T}^{μ} and $\eta(\mu)$, and allow the acceptance of the original selection to be corrected. The tau decay products are treated like any other objects obtained from the simulation, with one

[8] For simplicity, leptons from heavy-quark decays are considered as fake leptons in the following.

JHEP04(2015)117

Process	$\tau_{\text{lep}}\tau_{\text{lep}}$	$\tau_{\text{lep}}\tau_{\text{had}}$	$\tau_{\text{had}}\tau_{\text{had}}$
$Z \to \ell\ell$-enriched	$80 < m_{\tau\tau}^{\text{vis}} < 100$ GeV (same-flavour)		
Top control region	Invert b-jet veto	Invert b-jet veto and $m_{\text{T}} > 40$ GeV	
Rest category			Pass preselection, Fail VBF and Boosted selections
$Z \to \tau\tau$-enriched	$m_{\tau\tau}^{\text{HPTO}} < 100$ GeV	$m_{\text{T}} < 40$ GeV and $m_{\tau\tau}^{\text{MMC}} < 110$ GeV	
Fake-enriched	Same sign τ decay products	Same sign τ decay products	
W-enriched		$m_{\text{T}} > 70$ GeV	
Mass sideband			$m_{\tau\tau}^{\text{MMC}} < 110$ GeV or $m_{\tau\tau}^{\text{MMC}} > 150$ GeV

Table 6. Summary and definition of the control regions used in the analysis. The requirements shown represent modifications to the signal region requirements. All other selections are applied as for the corresponding signal regions. The variable $m_{\tau\tau}^{\text{HPTO}}$ is the invariant mass of the $\tau\tau$-system obtained using the collinear approximation and the same objects as used in $E_{\text{T}}^{\text{miss,HPTO}}$. Each control region listed is actually two control regions, corresponding to the VBF or boosted categories, with the exception of the rest category. The first three control regions listed are used in the global fit defined in section 8.

JHEP04(2015)117

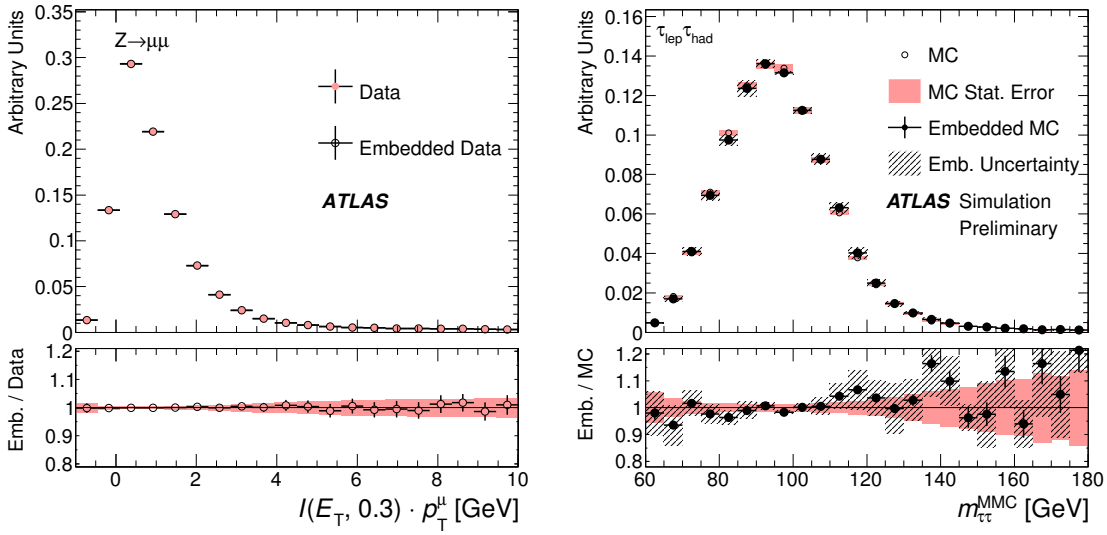

(a) (b)

Figure 4. (a) The distribution of the calorimeter isolation energy $I(E_{\mathrm{T}}, 0.3) \cdot p_{\mathrm{T}}^{\mu}$ within a cone of radius $\Delta R = 0.3$ around the muons in $Z \to \mu\mu$ events from data, before and after the embedding of simulated muons. (b) The distribution of the reconstructed invariant $\tau\tau$ mass, $m_{\tau\tau}^{\mathrm{MMC}}$, in the $\tau_{\mathrm{lep}}\tau_{\mathrm{had}}$ final state, for simulated $Z \to \tau\tau$ events, compared to the one obtained from simulated $Z \to \mu\mu$ events after tau embedding. The ratios of the values before and after the embedding and between the embedded $Z \to \mu\mu$ and $Z \to \tau\tau$ events are given in (a) and (b) respectively. The errors in (a) and (b) on the ratios (points) represent the statistical uncertainties, while the systematic uncertainties are indicated by the hatched bands in (b). The shaded bands represent the statistical uncertainties from the $Z \to \mu\mu$ data events in (a) and from the $Z \to \tau\tau$ simulation in (b).

important difference due to the absence of trigger simulation in this sample. Trigger effects are parameterised from the simulation as a function of the tau decay product p_{T}. After replacing the muons with simulated taus, kinematic distributions of the embedded sample can be directly compared to the fully simulated ones. As an example, the reconstructed invariant mass, $m_{\tau\tau}^{\mathrm{MMC}}$, is shown in figure 4(b), for the $\tau_{\mathrm{lep}}\tau_{\mathrm{had}}$ final state. Good agreement is found and the observed differences are covered by the systematic uncertainties. Similarly, good agreement is found for other variables, such as the missing transverse momentum, the kinematic variables of the hadronically decaying tau lepton or of the associated jets in the event. A direct comparison of the $Z \to \tau\tau$ background in data and the modelling using the embedding technique also shows good agreement. This can be seen in several kinematic quantity distributions, which are dominated by $Z \to \tau\tau$ events, shown in figure 2.

The normalisation of this background process is taken from the final fit described in section 8. The normalisation is independent for the $\tau_{\mathrm{lep}}\tau_{\mathrm{lep}}$, $\tau_{\mathrm{lep}}\tau_{\mathrm{had}}$, and $\tau_{\mathrm{had}}\tau_{\mathrm{had}}$ analysis channels.

6.2 Background from misidentified leptons or hadronically decaying taus

For the $\tau_{\mathrm{lep}}\tau_{\mathrm{lep}}$ channel, all background sources resulting from misidentified leptons are treated together. In this approach, contributions from multijet and W+jets production,

JHEP04(2015)117

as well as the part of the $t\bar{t}$ background resulting from decays to leptons and hadrons ($t\bar{t} \to \ell\nu b\, qqb$) are included. A control sample is defined in data by inverting the isolation requirements for one of the two leptons, while applying all other signal region requirements. The contributions from other background channels (dileptonic $t\bar{t}$ decays ($t\bar{t} \to \ell\nu b\, \ell\nu b$), $Z \to ee$, $Z \to \mu\mu$, and diboson production) are obtained from the simulation and are subtracted. From this control sample a template is created. The normalisation factor is obtained by fitting the p_{T} distribution of the subleading lepton at an early stage of the preselection.

For the $\tau_{\mathrm{lep}}\tau_{\mathrm{had}}$ channel, the fake-factor method is used to derive estimates for the multijet, W+jets, Z+jets, and semileptonic $t\bar{t}$ background events that pass the $\tau_{\mathrm{lep}}\tau_{\mathrm{had}}$ selection due to a misidentified τ_{had} candidate. The fake factor is defined as the ratio of the number of jets identified as medium τ_{had} candidates to the number satisfying the loose, but not the medium, criteria. Since the fake factor depends on the type of parton initiating the jet and on the p_{T} of the jet, it is determined as a function of p_{T} separately for samples enriched in quark- and gluon-initiated jets. In addition, the fake factor is found to be different for 1-track and 3-track candidates. Three different, quark-jet dominated samples are used separately for the W+jets, $t\bar{t}$ and Z+jets background components. They are defined by selecting the high-m_{T} region ($m_{\mathrm{T}} > 70$ GeV), by inverting the b-jet veto and by requiring two leptons with an invariant mass consistent with m_Z (80 GeV $< m_{\ell\ell} <$ 100 GeV) respectively. In addition, a multijet sample dominated by gluon-initiated jets is selected by relaxing the lepton identification and requiring it to satisfy the loose identification criteria. The derived fake factors are found to vary from 0.124 (0.082) for $p_{\mathrm{T}} = 20$ GeV to 0.088 (0.038) for $p_{\mathrm{T}} = 150$ GeV for 1-track (3-track) candidates in the VBF category. The corresponding values for the boosted category are 0.146 (0.084) for $p_{\mathrm{T}} = 20$ GeV and 0.057 (0.033) for $p_{\mathrm{T}} = 150$ GeV. To obtain the fake-background estimate for the VBF and boosted signal regions, these factors are then applied, weighted by the expected relative W+jets, Z+jets, multijet, and $t\bar{t}$ fractions, to the events in regions defined by applying the selections of the corresponding signal region, except that the τ_{had} candidate is required to pass the loose and to fail the medium τ_{had} identification. As an example, the good agreement between data and background estimates is shown in figure 5(a) for the reconstructed $\tau\tau$ mass for events in the high-m_{T} region, which is dominated by W+jets production.

For the $\tau_{\mathrm{had}}\tau_{\mathrm{had}}$ channel, the multijet background is modelled using a template extracted from data that pass the VBF or boosted category selection, where, however, the taus fail the isolation and opposite-sign charge requirements (the number-of-tracks requirement is not enforced). The normalisation of the multijet background is first determined by performing a simultaneous fit of the multijet (modelled by the data sample just mentioned) and $Z \to \tau\tau$ (modelled by embedding) templates after the preselection cuts. The fit is performed for the distribution of the difference in pseudorapidity between the two hadronic tau candidates, $\Delta\eta(\tau_{\mathrm{had}}, \tau_{\mathrm{had}})$. The signal contribution is expected to be small in this category. The agreement between data and the background estimate for this distribution is shown in figure 5(b) for the rest category defined in section 4. The preselection normalisation is used as a reference point and starting value for the global fit (see below) and is used for validation plots. The final normalisations of the two important background components,

JHEP04(2015)117

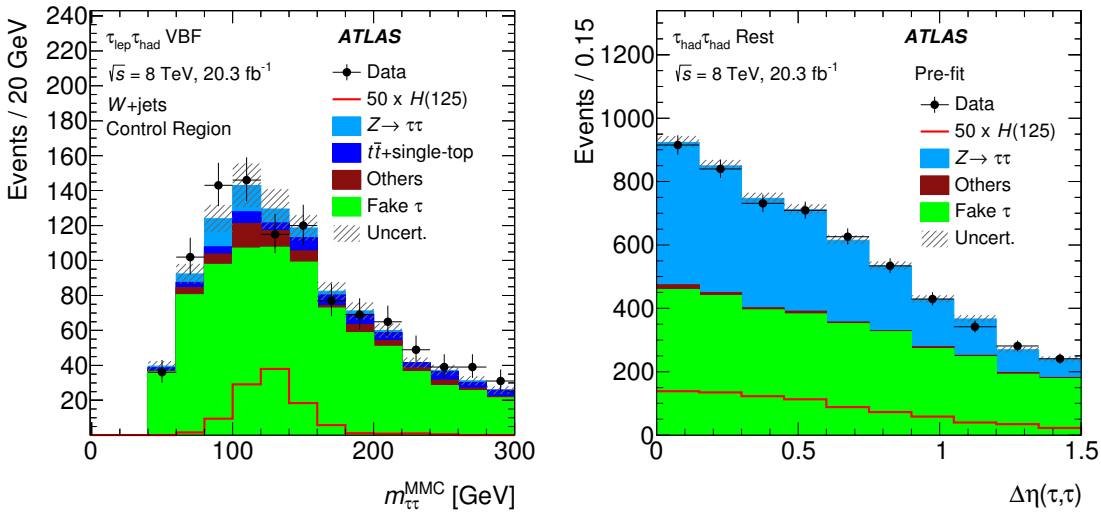

(a) (b)

Figure 5. (a) The distribution of the reconstructed invariant $\tau\tau$ mass, $m_{\tau\tau}^{\mathrm{MMC}}$, for events in the W+jets control region, for the $\tau_{\mathrm{lep}}\tau_{\mathrm{had}}$ channel. (b) The separation in pseudorapidity of the τ_{had} candidates, $\Delta\eta(\tau_{\mathrm{had}}, \tau_{\mathrm{had}})$, for the $\tau_{\mathrm{had}}\tau_{\mathrm{had}}$ channel in the rest control region. The expected SM Higgs boson signal contribution is superimposed, multiplied by a factor 50. These figures use background predictions made without the global fit defined in section 8. The error band includes statistical and pre-fit systematic uncertainties.

from multijet and $Z \to \tau\tau$ events, are extracted from the final global fit, as described in section 8, in which the $\Delta\eta(\tau_{\mathrm{had}}, \tau_{\mathrm{had}})$ distribution for the rest category is included.

6.3 $Z \to ee$ and $Z \to \mu\mu$ background

The Drell-Yan $Z/\gamma^* \to ee$ and $Z/\gamma^* \to \mu\mu$ background channels are important contributions to the final states with two same-flavour leptons. They also contribute to the other channels. As described below, a simulation based on Alpgen is used to estimate these background sources. Correction factors are applied to account for differences between data and simulation.

In the $\tau_{\mathrm{lep}}\tau_{\mathrm{lep}}$ channel, the Alpgen simulation is normalised to the data in the Z-mass control region, 80 GeV $< m_{\ell\ell} <$ 100 GeV, for each category, and separately for $Z \to ee$ and $Z \to \mu\mu$ events. The normalisation factors are determined from the final fit described in section 8. The distribution of the reconstructed $\tau\tau$ mass for events in this control region is shown in figure 6(a).

In the $\tau_{\mathrm{lep}}\tau_{\mathrm{had}}$ channel, the $Z \to ee$ and $Z \to \mu\mu$ background estimates are also based on simulation. The corrections applied for a τ_{had} candidate depend on whether it originates from a lepton from the Z boson decay or from a jet. In the first case, corrections from data, derived from dedicated tag-and-probe studies, are applied to account for the difference in the rate of misidentified τ_{had} candidates resulting from leptons [21, 105]. This is particularly important for $Z \to ee$ events with a misidentified τ_{had} candidate originating from a true electron. In the second case, the fake-factor method described in section 6.2 is applied.

JHEP04(2015)117

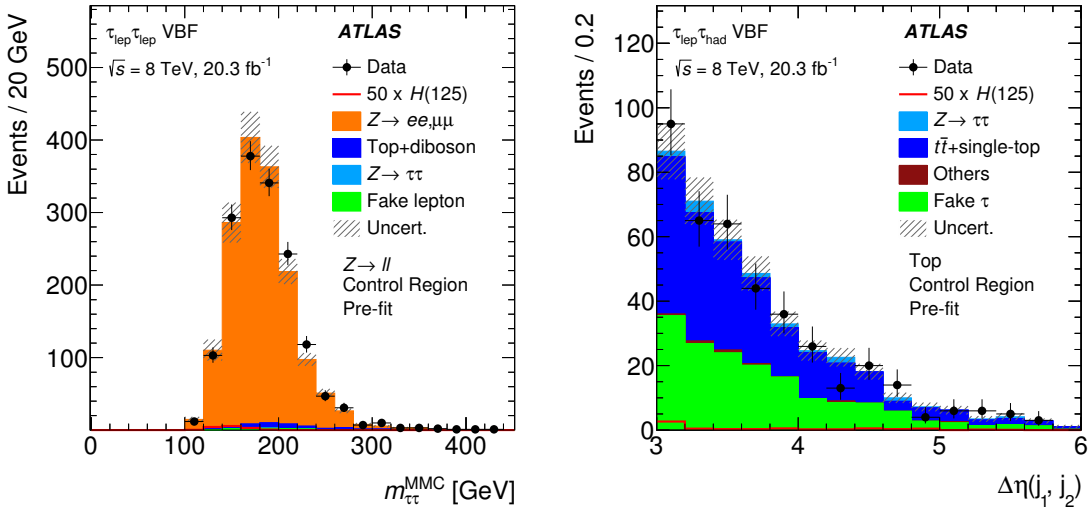

(a) (b)

Figure 6. (a) The distribution of the reconstructed invariant $\tau\tau$ mass, $m_{\tau\tau}^{\mathrm{MMC}}$, for events in the $Z \to \ell\ell$ control region, for the $\tau_{\mathrm{lep}}\tau_{\mathrm{lep}}$ channel. (b) The distribution of the separation in pseudorapidity of the two leading jets, $\Delta\eta(j_1, j_2)$, for events in the top control region, for the $\tau_{\mathrm{lep}}\tau_{\mathrm{had}}$ channel. This figure uses background predictions made without the global fit defined in section 8. The error band includes statistical and pre-fit systematic uncertainties.

In the $\tau_{\mathrm{had}}\tau_{\mathrm{had}}$ channel, the contribution of this background is very small and is taken from simulation.

6.4 W+jets background

Events with W bosons and jets constitute a background to all channels since leptonic W decays can feed into all signatures when the true lepton is accompanied by a jet which is falsely identified as a τ_{had} or a lepton candidate. This process can also contribute via semileptonic heavy quark decays that provide identified leptons.

As stated in section 6.2, for the $\tau_{\mathrm{lep}}\tau_{\mathrm{lep}}$ and $\tau_{\mathrm{lep}}\tau_{\mathrm{had}}$ channels, the W+jets contributions are determined with data-driven methods. For the $\tau_{\mathrm{had}}\tau_{\mathrm{had}}$ channel, the $W \to \tau_{\mathrm{had}}\nu$ background is estimated from simulation. A correction is applied to account for differences in the τ_{had} misidentification probability between data and simulation.

6.5 Background from top-quark production

Background contributions from $t\bar{t}$ and single top-quark production, where leptons or hadronically decaying taus appear in decays of top quarks, are estimated from simulation in the $\tau_{\mathrm{lep}}\tau_{\mathrm{lep}}$ and $\tau_{\mathrm{lep}}\tau_{\mathrm{had}}$ channels. The normalisation is obtained from data control regions defined by requiring a b-jet instead of a b-veto. In the $\tau_{\mathrm{lep}}\tau_{\mathrm{had}}$ channel, a large value of the transverse mass m_{T} is also required, to enhance the background from top-quark production and to suppress the signal contribution. This background is also found to be small for the $\tau_{\mathrm{had}}\tau_{\mathrm{had}}$ channel and it is estimated using simulation. The distribution of $\Delta\eta(j_1, j_2)$ for events in the top control region, for the $\tau_{\mathrm{lep}}\tau_{\mathrm{had}}$ channel, is shown in figure 6(b).

JHEP04(2015)117

Channel	Background	Scale factors (CR) VBF	Boosted
$\tau_{\text{lep}}\tau_{\text{lep}}$	Top	0.99 ± 0.07	1.01 ± 0.05
	$Z \to ee$	0.91 ± 0.16	0.98 ± 0.10
	$Z \to \mu\mu$	0.97 ± 0.13	0.96 ± 0.08
$\tau_{\text{lep}}\tau_{\text{had}}$	Top	0.84 ± 0.08	0.96 ± 0.04

Table 7. The scale factors calculated in control regions (CR) for background normalisation. Only the statistical uncertainties are given. The background contributions shown in validation plots use the normalisation predicted from simulation multiplied by the corresponding scale factor. Final normalisations are taken from the global fit, described in section 8.

6.6 Diboson background

The production of pairs of vector bosons (W^+W^-, ZZ and $W^\pm Z$), with subsequent decays to leptons or jets, contributes especially to the background in the $\tau_{\text{lep}}\tau_{\text{lep}}$ channel. For all analysis channels, these contributions are estimated from simulation, normalised to the NLO cross sections indicated in table 1.

6.7 Contributions from other Higgs boson decays

In the $\tau_{\text{lep}}\tau_{\text{lep}}$ channel, a non-negligible contribution from $H \to WW \to \ell\nu\ell\nu$ exists and this process is considered as background. Its contribution is estimated for $m_H = 125$ GeV using simulation. The corresponding signal cross section is assumed to be the SM value and is indicated in table 1.

6.8 Validation of background estimates

As described above, the normalisation for important background sources that are modelled with simulation are determined by fitting to data in control regions. These normalisations are compared in table 7 to predictions based on the theoretical cross sections for the 8 TeV analysis. In most cases, the values obtained are compatible with unity within the statistical uncertainties shown. For the top control region in the VBF category of the $\tau_{\text{lep}}\tau_{\text{had}}$ channel, the value is also in agreement with unity if the experimental and theoretical systematic uncertainties are included. The control-region normalisations are used for validation plots, and they are used as starting values in the final global fit described in section 8. The global fit does not change any of these normalisations by more than 2%.

It is important to verify that the BDT output distributions in data control regions are well described after the various background determinations. Figure 7 shows distributions from important control regions for the $\sqrt{s} = 8$ TeV dataset, i.e. the Z-enriched control regions for the $\tau_{\text{lep}}\tau_{\text{lep}}$ and $\tau_{\text{lep}}\tau_{\text{had}}$ channels, and the reconstructed $\tau\tau$ invariant mass sideband control region (defined as $m_{\tau\tau}^{\text{MMC}} < 100$ GeV or $m_{\tau\tau}^{\text{MMC}} > 150$ GeV) for the $\tau_{\text{had}}\tau_{\text{had}}$ channel. The distributions are shown for both the VBF and the boosted categories. All distributions are found to be well described, within the systematic uncertainties.

JHEP04(2015)117

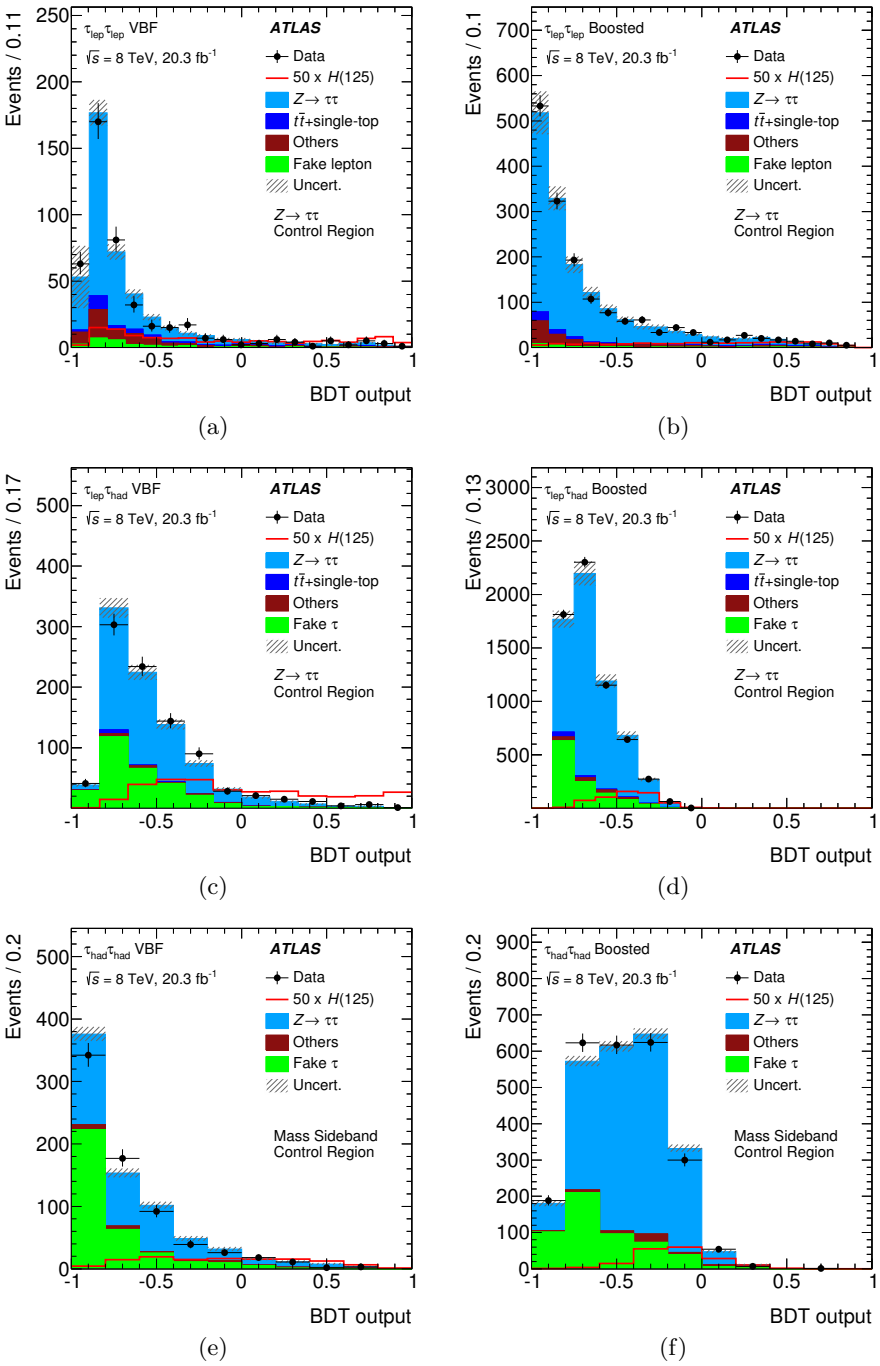

Figure 7. Distributions of the BDT output for data collected at $\sqrt{s} = 8$ TeV, compared to the expected background contributions in important control regions. The distributions are shown for the VBF (left) and boosted (right) categories (a,b) for the $Z \to \tau\tau$-enriched control region in the $\tau_{\rm lep}\tau_{\rm lep}$ channel, (c,d) for the $Z \to \tau\tau$-enriched control region in the $\tau_{\rm lep}\tau_{\rm had}$ channel and (e,f) for the $\tau\tau$ invariant mass sideband control region in the $\tau_{\rm had}\tau_{\rm had}$ channel. The contributions from a Standard Model Higgs boson with $m_H = 125$ GeV are superimposed, multiplied by a factor of 50. These figures use background predictions made without the global fit defined in section 8. The error band includes statistical and pre-fit systematic uncertainties.

JHEP04(2015)117

7 Systematic uncertainties

The numbers of expected signal and background events, the input variables to the BDT, and thereby the BDT output and the final discrimination between signal and background are affected by systematic uncertainties. They are discussed below, grouped into three categories: experimental uncertainties, background modelling uncertainties, and theoretical uncertainties. For all uncertainties, the effects on both the total signal and background yields and on the shape of the BDT output distribution are evaluated. Table 8 gives a summary of the systematic uncertainties and their impact on the number of expected events for the signal and the total background for the analysis of the data taken at $\sqrt{s} = 8$ TeV. The dominant sources that affect the shape of the BDT output distribution are marked in the table. All uncertainties are treated either as fully correlated or uncorrelated across channels. The latter are also marked in table 8. The effects of the systematic uncertainties at $\sqrt{s} = 7$ TeV are found to be similar and are not discussed here. The inclusion of the uncertainties in the profile likelihood global fit is described in section 8 and the effect of the most significant systematic uncertainties is presented in table 13.

7.1 Experimental uncertainties

The major experimental systematic uncertainties result from uncertainties on efficiencies for triggering, object reconstruction and identification, as well as from uncertainties on the energy scale and resolution of jets, hadronically decaying taus and leptons. In general, the effects resulting from lepton-related uncertainties are smaller than those from jets and taus. They are not discussed in detail, however, their impact is included in table 8. In addition, uncertainties on the luminosity affect the number of signal and background events from simulation.

- Luminosity: the uncertainty on the integrated luminosity is ±2.8% for the 8 TeV dataset and ±1.8% for the 7 TeV dataset. It is determined from a calibration of the luminosity scale derived from beam-separation scans performed in 2011 and 2012 using the method described in ref. [106].

- Efficiencies: the efficiencies for triggering, reconstructing and identifying electrons, muons, and τ_{had} candidates are measured in data using tag-and-probe techniques. The uncertainties on the τ_{had} identification efficiency are ±(2–3)% for 1-prong and ±(3–5)% for 3-prong tau decays [39]. The b-jet tagging efficiency has been measured from data using $t\bar{t}$ events, where both top quarks decay to leptons, with a total uncertainty of about ±2% for jets with transverse momenta up to 100 GeV [38, 107]. The MC samples used are corrected for differences in these efficiencies between data and simulation and the associated uncertainties are propagated through the analysis.

- Energy scales: the uncertainties on the jet energy scale (JES) arise from several sources. These include, among others, varied response due to the jet flavour composition (quark- versus gluon-initiated jets), pile-up, η intercalibration, and detector

JHEP04(2015)117

response and modelling of in situ jet calibration [35, 36]. The impact of the JES uncertainty in this analysis is reduced because many of the background components are estimated using data. The tau energy scale is obtained by fitting the reconstructed visible mass for $Z \to \tau\tau$ events in data, which can be selected with a satisfactory purity. It is measured with a precision of ±(2–4)% [108]. Since systematic uncertainties on the energy scales of all objects affect the reconstructed missing transverse momentum, it is recalculated after each variation is applied. The scale uncertainty on $E_{\mathrm{T}}^{\mathrm{miss}}$ due to the energy in calorimeter cells not associated with physics objects is also taken into account.

- Energy resolutions: systematic uncertainties on the energy resolution of taus, electrons, muons, jets, and $E_{\mathrm{T}}^{\mathrm{miss}}$ affect the final discriminant. The effects resulting from uncertainties on the tau energy resolution are small. The impact of changes in the amount of material (inactive material in the detector, e.g. support structures), in the hadronic shower model and in the underlying-event tune were studied in the simulation. They result in systematic uncertainties below 1% on the tau energy resolution. The jet energy resolution is determined by in situ measurements, as described in ref. [109], and affects signal modelling and background components modelled by the simulation. The uncertainty of the resolution on $E_{\mathrm{T}}^{\mathrm{miss}}$ is estimated by evaluating the energy resolution of each of the $E_{\mathrm{T}}^{\mathrm{miss}}$ terms. The largest impact results from the soft term (see section 2), arising both from the MC modelling and the effects of pile-up. It is evaluated using simulated $Z(\to \mu\mu)$+jets events.

7.2 Background modelling uncertainties

The most significant systematic uncertainties on the background estimation techniques, as described in section 6, are detailed in the following for the three decay modes considered.

In the $\tau_{\mathrm{lep}}\tau_{\mathrm{lep}}$ channel, systematic uncertainties on the shape and normalisation of fake-lepton background sources are estimated by comparing samples of same-sign lepton events that pass and fail the lepton isolation criteria. These uncertainties amount to ±33% (±20%) at 8 TeV and ±10.5% (±13%) at 7 TeV for the boosted (VBF) category. The extrapolation uncertainty for the $Z \to \ell\ell$ background is obtained by varying the $m_{\ell\ell}$ window that defines the control region for this background, and amounts to about ±6%. The corresponding extrapolation uncertainty for top-quark background sources is ±(3–6)%, obtained from the differences in event yields in the top-quark control regions when using different MC generators. Neither of these extrapolation uncertainties is significant for the final result. The dominant uncertainties on the normalisation of the $t\bar{t}$ background, obtained from the global fit, are the systematic uncertainties on the b-jet tagging efficiency and the jet energy scale.

In the $\tau_{\mathrm{lep}}\tau_{\mathrm{had}}$ channel, an important systematic uncertainty on the background determination comes from the estimated fake background, for which several sources of systematic uncertainty are considered. The statistical uncertainty on the effective fake factor is ±4.3% (±2.3%) in the 8 TeV VBF (boosted) category, and about ±22% (±11%) in the 7 TeV VBF (boosted) category. The dominant systematic uncertainty on the methodology itself arises

JHEP04(2015)117

from the composition of the combined fake background (W+jets, Z+jets, multijet, and $t\bar{t}$ fractions), which is largely estimated based on simulated event samples as explained in section 6.2. The uncertainty is estimated by varying each fractional contribution by ±50%, which affects the effective fake factor by ±3% (±6%) and by ±10% (±15%) in the 8 TeV and 7 TeV boosted (VBF) categories respectively. As a closure test, the method was also applied in a region of data where the lepton and τ_{had} candidate have the same charge, rich in fake τ_{had} candidates. Very good agreement was observed between data and the method's prediction, so that no additional in situ uncertainty was deemed necessary. In addition, the uncertainties on the normalisation of the $t\bar{t}$ background are important. As in the case of the $\tau_{\text{lep}}\tau_{\text{lep}}$ channel, the dominant contribution obtained from the global fit originates from systematic uncertainties on the b-jet tagging efficiency and the jet energy scale, along with statistical uncertainties on the observed data in the respective control regions.

In the $\tau_{\text{had}}\tau_{\text{had}}$ channel, the major background from multijet production is determined using a data-driven template method. The default multijet template, derived from a sample in data where the τ_{had} candidates fail the isolation and opposite-sign charge requirements, is compared with an alternative template derived from a sample where the τ_{had} candidates fail just the opposite-sign charge requirement. The normalisation of the alternative template is fixed to that of the default template at preselection; the alternative multijet template is propagated into the various categories and gives a different set of yields from the default template. This difference, along with the difference in shape between the two templates, constitutes the systematic uncertainty on the background estimate. This leads to an overall multijet yield variation of 10% (3%) in the VBF (boosted) category at $\sqrt{s} = 8$ TeV and of 10% (30%) in the VBF (boosted) category $\sqrt{s} = 7$ TeV. However, there is a very strong shape dependence, such that the uncertainties on the BDT output are much larger at higher output values.

For the embedding method used in all channels, the major systematic uncertainties are related to the selection of $Z \to \mu\mu$ events in data and to the subtraction of the muon energy deposits in the calorimeters. The selection uncertainties are estimated by varying the muon isolation criteria in the selection from the nominal value of $I(p_{\text{T}}, 0.2) < 0.2$ (see section 4) to tighter ($I(p_{\text{T}}, 0.4) < 0.06$ and $I(E_{\text{T}}, 0.2) < 0.04$) and looser (no isolation requirements) values. The muon-related cell energies to be subtracted are varied within ±20% (±30%) for the 8 TeV (7 TeV) data. In addition, systematic uncertainties on the corrections for trigger and reconstruction efficiencies are taken into account. Due to the combination of single-lepton and dilepton triggers used, the uncertainties are largest for the $\tau_{\text{lep}}\tau_{\text{lep}}$ channel. All experimental systematic uncertainties relating to the embedded τ decay products (such as tau energy scale or identification uncertainties) are applied normally. The combined effect of all uncertainties on the signal and background yields is included in table 8. Because the $Z \to \tau\tau$ normalisation is determined in the final fit, the impact on the final result is much smaller.

7.3 Theoretical uncertainties

Theoretical uncertainties are estimated for the signal and for all background contributions modelled with the simulation. Since the major background contributions, from $Z \to \tau\tau$

JHEP04(2015)117

Source	Relative signal and background variations [%]											
	$\tau_{\rm lep}\tau_{\rm lep}$ VBF		$\tau_{\rm lep}\tau_{\rm lep}$ Boosted		$\tau_{\rm lep}\tau_{\rm had}$ VBF		$\tau_{\rm lep}\tau_{\rm had}$ Boosted		$\tau_{\rm had}\tau_{\rm had}$ VBF		$\tau_{\rm had}\tau_{\rm had}$ Boosted	
	S	B	S	B	S	B	S	B	S	B	S	B
Experimental												
Luminosity	± 2.8	± 0.1	± 2.8	± 0.1	± 2.8	± 0.1	± 2.8	± 0.1	± 2.8	± 0.1	± 2.8	± 0.1
Tau trigger*	—	—	—	—	—	—	—	—	$^{+7.7}_{-8.8}$	< 0.1	$^{+7.8}_{-8.9}$	< 0.1
Tau identification	—	—	—	—	± 3.3	± 1.2	± 3.3	± 1.8	± 6.6	± 3.8	± 6.6	± 5.1
Lepton ident. and trigger*	$^{+1.4}_{-2.1}$	$^{+1.3}_{-1.7}$	$^{+1.4}_{-2.1}$	$^{+1.1}_{-1.5}$	± 1.8	± 0.5	± 1.8	± 0.8	—	—	—	—
b-tagging	± 1.3	± 1.6	± 1.6	± 1.6	< 0.1	± 0.2	± 0.4	± 0.2	—	—	—	—
τ energy scale†	—	—	—	—	± 2.4	± 1.3	± 2.4	± 0.9	± 2.9	± 2.5	± 2.9	± 2.5
Jet energy scale and resolution†	$^{+8.5}_{-9.1}$	± 9.2	$^{+4.7}_{-4.9}$	$^{+3.7}_{-3.0}$	$^{+9.5}_{-8.7}$	± 1.0	± 3.9	± 0.4	$^{+10.1}_{-8.0}$	± 0.3	$^{+5.1}_{-6.2}$	± 0.2
$E_{\rm T}^{\rm miss}$ soft scale & resolution	$^{+0.0}_{-0.2}$	$^{+0.0}_{-1.2}$	$^{+0.0}_{-0.1}$	$^{+0.0}_{-1.2}$	$^{+0.8}_{-0.3}$	± 0.2	± 0.4	< 0.1	± 0.5	± 0.2	± 0.1	< 0.1
Background Model												
Modelling of fake backgrounds*†	—	± 1.2	—	± 1.2	—	± 2.6	—	± 2.6	—	± 5.2	—	± 0.6
Embedding†	—	$^{+3.8}_{-4.3}$	—	$^{+6.0}_{-6.5}$	—	± 1.5	—	± 1.2	—	± 2.2	—	± 3.3
$Z \to \ell\ell$ normalisation*	—	± 2.1	—	± 0.7	—	—	—	—	—	—	—	–
Theoretical												
Higher-order QCD corrections †	$^{+11.3}_{-9.1}$	± 0.2	$^{+19.8}_{-15.3}$	± 0.2	$^{+9.7}_{-7.6}$	± 0.2	$^{+19.3}_{-14.7}$	± 0.2	$^{+10.7}_{-8.2}$	< 0.1	$^{+20.3}_{-15.4}$	< 0.1
UE/PS	± 1.8	< 0.1	± 5.9	< 0.1	± 3.8	< 0.1	± 2.9	< 0.1	± 4.6	< 0.1	± 3.8	< 0.1
Generator modelling	± 2.3	< 0.1	± 1.2	< 0.1	± 2.7	< 0.1	± 1.3	< 0.1	± 2.4	< 0.1	± 1.2	< 0.1
EW corrections	± 1.1	< 0.1	± 0.4	< 0.1	± 1.3	< 0.1	± 0.4	< 0.1	± 1.1	< 0.1	± 0.4	< 0.1
PDF †	$^{+4.5}_{-5.8}$	± 0.3	$^{+6.2}_{-8.0}$	± 0.2	$^{+3.9}_{-3.6}$	± 0.2	$^{+6.6}_{-6.1}$	± 0.2	$^{+4.3}_{-4.0}$	± 0.2	$^{+6.3}_{-5.8}$	± 0.1
BR ($H \to \tau\tau$)	± 5.7	—	± 5.7	—	± 5.7	—	± 5.7	—	± 5.7	—	± 5.7	—

Table 8. Impact of systematic uncertainties on the total signal, S, (sum of all production modes) and on the sum of all background estimates, B, for each of the three channels and the two signal categories for the analysis of the data taken at $\sqrt{s} = 8$ TeV. Each systematic uncertainty is assumed to be correlated across the analysis channels, except those marked with a *. Uncertainties that affect the shape of the BDT-output distribution in a non-negligible way are marked with a †. All values are given before the global fit. The notation UE/PS refers to the underlying event and parton shower modelling.

JHEP04(2015)117

and misidentification of hadronically decaying τ leptons, are estimated using data-driven methods, they are not affected by these uncertainties. Uncertainties on the signal cross sections are assigned from missing higher-order corrections, from uncertainties in the PDFs, and from uncertainties in the modelling of the underlying event.

For VBF and VH Higgs boson production cross sections, the uncertainties due to missing higher-order QCD corrections are estimated by varying the factorisation and renormalisation scales by factors of two around the nominal scale m_W, as prescribed by the LHC Higgs Cross section Working Group [110]. The resulting uncertainties range from $\pm 2\%$ to $\pm 4\%$, depending on the process and the category-specific selection considered. In addition, a 2% uncertainty related to the inclusion of the NLO EWK corrections (see section 3) is assigned.

For Higgs boson production via ggF, the uncertainties on the cross sections due to missing higher order QCD corrections are estimated by varying the renormalisation and factorisation scales around the central values $\mu_{\mathrm{R}} = \mu_{\mathrm{F}} = \sqrt{m_H^2 + p_{\mathrm{T}}^2}$ in the NLO cross section calculations of $H + 1$-jet and $H + 2$-jet production. In the calculation of the uncertainties, appropriate cuts on the Higgs p_{T} ($p_{\mathrm{T}}^H > 100$ GeV) and on the jet kinematics $(\Delta\eta, p_{\mathrm{T}})$ are applied at parton level for the boosted and VBF categories respectively. The resulting uncertainties on the ggF contributions are found to be about $\pm 24\%$ in the boosted category and $\pm 23\%$ in the VBF category. The ggF contribution is dominant in the boosted category, whereas it is only about 20% of the signal in the VBF category. Since the two categories are exclusive, their anti-correlation is taken into account following the prescription in ref. [111].

In the present analysis, no explicit veto on jets is applied in the VBF selection, but enough kinematical information is provided as input to the BDT so that the high BDT-output region corresponds to a more exclusive region, where the probability of finding a third jet is reduced. Since the cross section for gluon-fusion events produced with a third jet is only known at LO, this could introduce a large uncertainty on the gluon-fusion contamination in the highest (and most sensitive) BDT-output bins. The uncertainty on the BDT shape of the ggF contribution is evaluated using the MCFM Monte Carlo program [98], which calculates $H + 3$ jets at LO. Scale variations induce changes of the ggF contribution in the highest BDT bin of about $\pm 30\%$. They are taken into account in the final fit.

Uncertainties related to the simulation of the underlying event and parton shower are estimated by comparing the acceptance from POWHEG+PYTHIA to POWHEG+HERWIG for both VBF and ggF Higgs boson production modes. Differences in the signal yields range from $\pm 1\%$ to $\pm 8\%$ for the VBF and from $\pm 1\%$ to $\pm 9\%$ for ggF production, depending on the channel and category. The BDT-score distribution of the POWHEG+PYTHIA and POWHEG+HERWIG samples are compatible with each other within statistical uncertainties.

The PDF uncertainties are estimated by studying the change in the acceptance when using different PDF sets or varying the CT10 PDF set within its uncertainties. The standard VBF POWHEG sample and a MC@NLO [112] ggF sample, both generated with the CT10 PDFs, are reweighted to the MSTW2008NLO [113], NNPDF [114] and the

JHEP04(2015)117

CT10 eigen-tunes parameterisation. The largest variation in acceptance for each category is used as a constant PDF uncertainty; it varies between approximately ±4.5% and ±6% for ggF production and between about ±0.8% and ±1.0% for VBF production. A shape uncertainty is also included to cover any difference between the BDT score in the default sample and the reweighted ones. The uncertainty on the total cross section for the VBF, VH and ggF production modes due to the PDFs is also considered.

Variations in the acceptance for different Monte Carlo generators are also included, comparing Powheg+Herwig samples to MC@NLO+Herwig samples for ggF, and to aMC@NLO+Herwig [115] samples for VBF. The generator modelling uncertainty is around ±2% for ggF and ±4% for VBF productions modes.

Finally, an uncertainty on the decay branching ratio, $\mathrm{BR}(H \to \tau\tau)$, of ±5.7% [70] affects the signal rates.

The theoretical systematic uncertainties on the background predictions taken from the simulation are evaluated by applying the same procedures as used for the signal samples. Uncertainties resulting from the choice of QCD scales, PDF parameterisation and underlying-event model are estimated. The results are reported in table 8.

8 Signal extraction procedure

The BDT output in the six analysis categories provides the final discrimination between signal and background for both the 7 and 8 TeV datasets. A maximum-likelihood fit is performed on all categories simultaneously to extract the signal strength, μ, defined as the ratio of the measured signal yield to the Standard Model expectation. The value $\mu = 0$ ($\mu = 1$) corresponds to the absence (presence) of a Higgs boson signal with the SM production cross section. The statistical analysis of the data employs a binned likelihood function $\mathcal{L}(\mu, \vec{\theta})$, constructed as the product of Poisson probability terms, to estimate μ.

The impact of systematic uncertainties on the signal and background expectations is described by nuisance parameters, $\vec{\theta}$, which are each parameterised by a Gaussian or log-normal constraint. The expected numbers of signal and background events in each bin are functions of $\vec{\theta}$. The test statistic q_μ is then constructed according to the profile likelihood ratio: $q_\mu = -2\ln[\mathcal{L}(\mu, \hat{\hat{\vec{\theta}}})/\mathcal{L}(\hat{\mu}, \hat{\vec{\theta}})]$, where $\hat{\mu}$ and $\hat{\vec{\theta}}$ are the parameters that maximise the likelihood, and $\hat{\hat{\vec{\theta}}}$ are the nuisance parameter values that maximise the likelihood for a given μ. This test statistic is used to measure the compatibility of the background-only hypothesis with the observed data.

The likelihood is maximised on the BDT distributions in the signal regions, with information from control regions included to constrain background normalisations. The fit includes the event yields from the $Z \to \ell\ell$ and top control regions in the $\tau_{\mathrm{lep}}\tau_{\mathrm{lep}}$ channel, and from the top control region of the $\tau_{\mathrm{lep}}\tau_{\mathrm{had}}$ channel; furthermore the $\Delta\eta(\tau_{\mathrm{had}}, \tau_{\mathrm{had}})$ distribution in the rest control region of the $\tau_{\mathrm{had}}\tau_{\mathrm{had}}$ channel is also included.

The $Z \to \tau\tau$ background is constrained primarily in the signal regions, due to the difference between the BDT distributions for $Z \to \tau\tau$ events and the signal. For the $\tau_{\mathrm{had}}\tau_{\mathrm{had}}$ channel, the $Z \to \tau\tau$ and multijet background rates are constrained by the simultaneous

JHEP04(2015)117

fit of the two signal regions and the $\Delta\eta(\tau_{\rm had}\tau_{\rm had})$ distribution in the rest category control region. The top and $Z \to \ell\ell$ background components for the $\tau_{\rm lep}\tau_{\rm lep}$ and $\tau_{\rm lep}\tau_{\rm had}$ channels are also allowed to float freely, but are primarily constrained by the inclusion of the respective control regions.

As described in section 7, a large number of systematic uncertainties, taken into account via nuisance parameters, affect the final results. It is important to investigate the behaviour of the global fit and in particular to investigate how far the nuisance parameters are pulled away from their nominal values and how well their uncertainties are constrained. Furthermore, it is important to understand which systematic uncertainties have the most impact on the final result. For this purpose a ranking of nuisance parameters is introduced. For each parameter, the fit is performed again with the parameter fixed to its fitted value shifted up or down by its fitted uncertainty, with all the other parameters allowed to vary. The ranking obtained for those nuisance parameters contributing most to the uncertainty on the signal strength is shown in figure 8 for the combined fit of the three channels at the two centre-of-mass energies. The parameters contributing most are those related to the jet energy scale, the normalisation uncertainties for $Z \to \tau\tau$ and top-quark events, and the tau energy scale. The uncertainties on the jet energy scale are decomposed into several uncorrelated components (among others: η intercalibration of different calorimeter regions, jet energy response, and response to jets of different flavour). In addition, theoretical uncertainties on the branching ratio BR $(H \to \tau\tau)$ are found to have a significant impact. In general, good agreement is found between the pre-fit and post-fit values for these nuisance parameters and neither large pulls nor large constraints are observed.

The distributions of the BDT discriminants for all channels and categories for the data at 8 TeV are shown in figure 9, with background normalisations, signal normalisation, and nuisance parameters adjusted by the profile likelihood global fit.

The results for the numbers of fitted signal and background events, split into the various contributions, are summarised in tables 9, 10 and 11 for the three channels separately, for the dataset collected at 8 TeV centre-of-mass energy. In addition to the total number of events, the expected number of events in each of the two highest BDT output bins is given. The number of events observed in the data is also included. Within the uncertainties, good agreement is observed between the data and the model predictions for the sum of background components and a Standard Model Higgs boson with $m_H = 125$ GeV.

JHEP04(2015)117

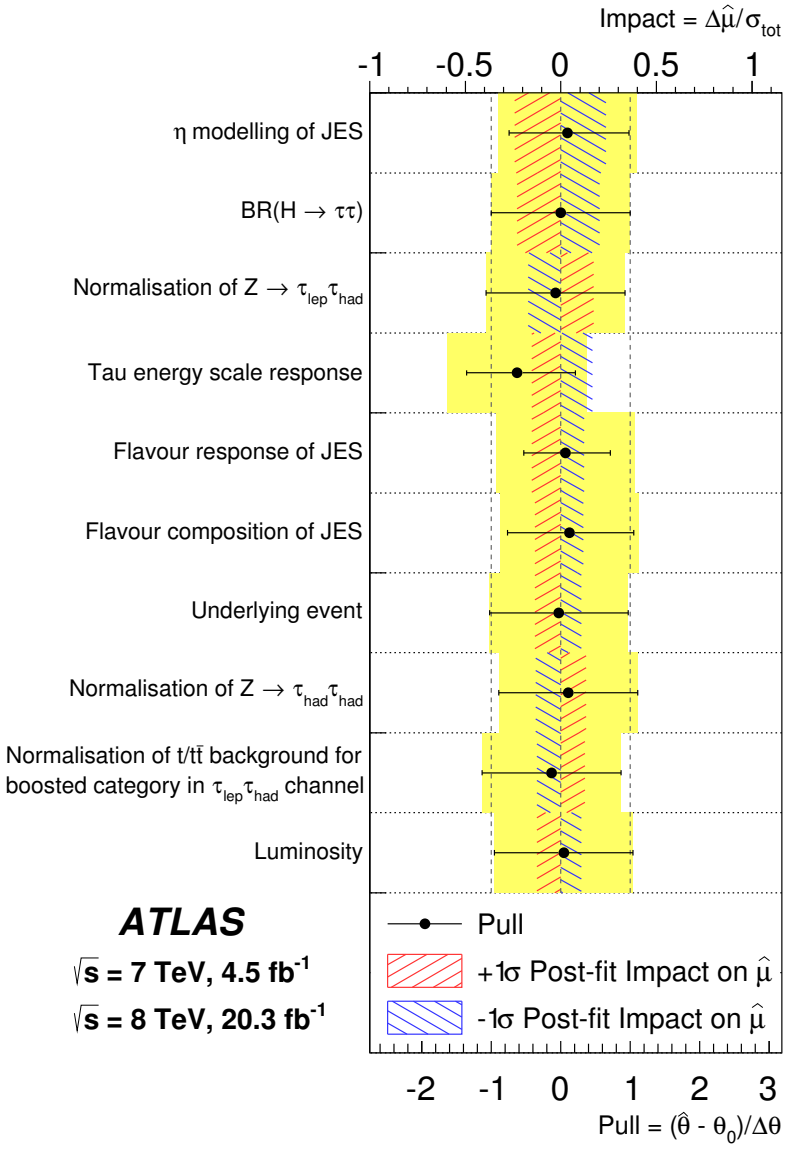

Figure 8. Impact of systematic uncertainties on the fitted signal-strength parameter $\hat{\mu}$ for the combined fit for all channels and both centre-of-mass energies. The systematic uncertainties are listed in decreasing order of their impact on $\hat{\mu}$ on the y-axis. The hatched blue and red boxes show the variations of $\hat{\mu}$ with respect to the total error on μ, $\sigma_{\rm tot}$, referring to the top x-axis, when fixing the corresponding individual nuisance parameter θ to its post-fit value $\hat{\theta}$ modified upwards or downwards by its post-fit uncertainty, and repeating the fit. The filled circles, referring to the bottom x-axis, show the pulls of the fitted nuisance parameters, i.e. the deviations of the fitted parameters $\hat{\theta}$ from their nominal values θ_0, normalised to their nominal uncertainties $\Delta\theta$. The black lines show the post-fit uncertainties of the nuisance parameters, relative to their nominal uncertainties, which are indicated by the yellow band. The jet energy scale uncertainties are decomposed into uncorrelated components.

JHEP04(2015)117

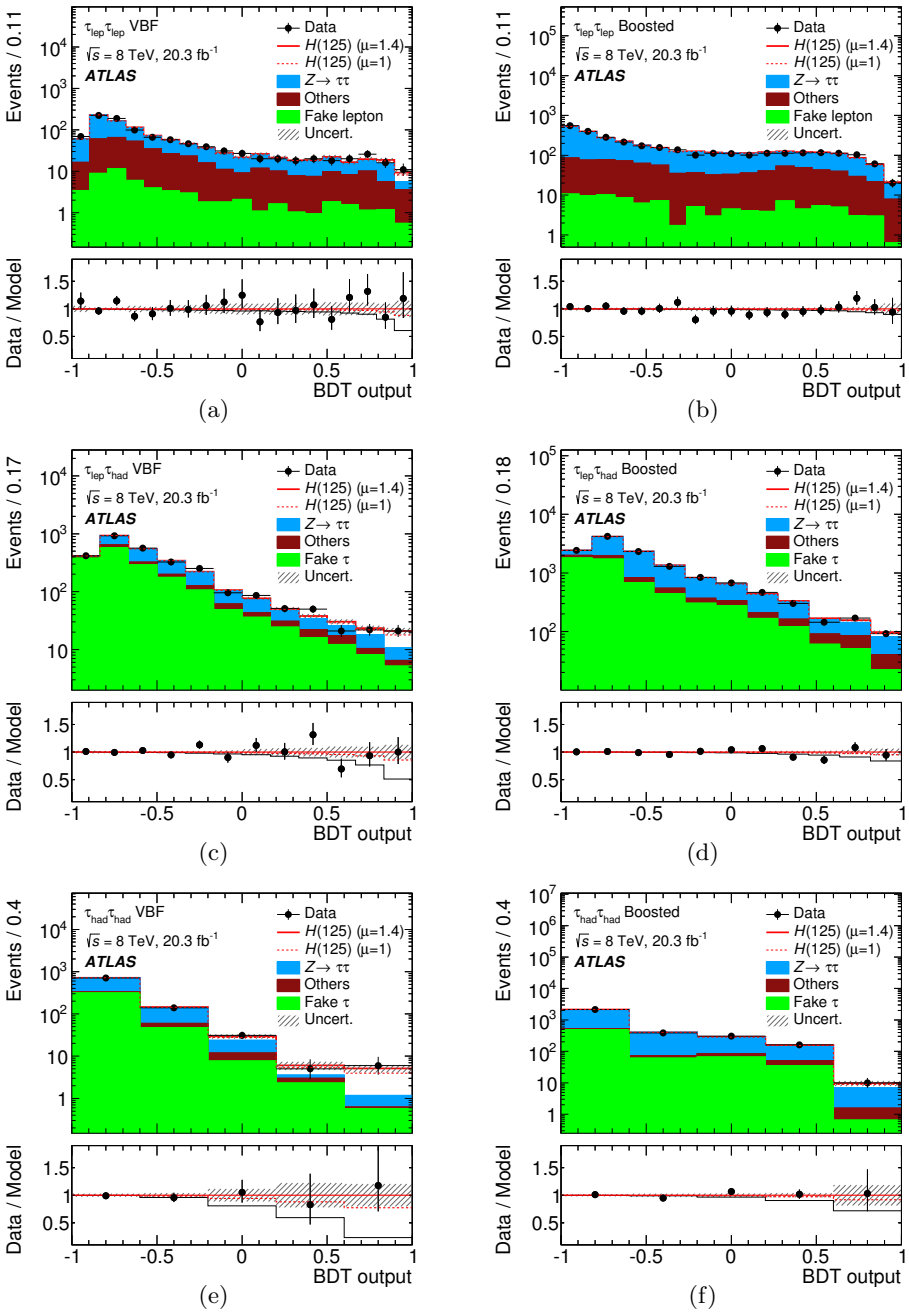

Figure 9. Distributions of the BDT discriminants for the data taken at $\sqrt{s} = 8$ TeV in the signal regions of the VBF (left) and boosted (right) categories for the $\tau_{\rm lep}\tau_{\rm lep}$ (top), $\tau_{\rm lep}\tau_{\rm had}$ (middle), and $\tau_{\rm had}\tau_{\rm had}$ (bottom) channels. The Higgs boson signal ($m_H = 125$ GeV) is shown stacked with a signal strength of $\mu = 1$ (dashed line) and $\mu = 1.4$ (solid line). The background predictions are determined in the global fit (that gives $\mu = 1.4$). The size of the statistical and systematic normalisation uncertainties is indicated by the hashed band. The ratios of the data to the model (background plus Higgs boson contributions with $\mu = 1.4$) are shown in the lower panels. The dashed red and the solid black lines represent the changes in the model when $\mu = 1.0$ or $\mu = 0$ are assumed respectively.

JHEP04(2015)117

Process/Category	VBF			Boosted		
BDT output bin	All bins	Second to last bin	Last bin	All bins	Second to last bin	Last bin
$Z \to \tau\tau$	589 ± 24	9.7 ± 1.0	1.99 ± 0.34	2190 ± 80	33.7 ± 2.3	11.3 ± 1.3
Fake background	57 ± 12	1.2 ± 0.6	0.55 ± 0.35	100 ± 40	2.9 ± 1.3	0.6 ± 0.4
Top	131 ± 19	0.9 ± 0.4	0.89 ± 0.33	380 ± 50	9.8 ± 2.1	4.3 ± 1.0
Others	196 ± 17	3.0 ± 0.4	1.7 ± 0.6	400 ± 40	8.3 ± 1.6	2.6 ± 0.7
ggF: $H \to WW$ $(m_H = 125$ GeV)	2.9 ± 0.8	0.12 ± 0.04	0.11 ± 0.04	7.7 ± 2.3	0.43 ± 0.13	0.24 ± 0.08
VBF: $H \to WW$	3.4 ± 0.4	0.40 ± 0.06	0.38 ± 0.08	1.65 ± 0.18	0.102 ± 0.017	< 0.1
$WH: \ H \to WW$	< 0.1	< 0.1	< 0.1	0.90 ± 0.10	< 0.1	< 0.1
$ZH: \ H \to WW$	< 0.1	< 0.1	< 0.1	0.59 ± 0.07	< 0.1	< 0.1
ggF: $H \to \tau\tau$ $(m_H = 125\,\text{GeV})$	9.8 ± 3.4	0.73 ± 0.26	0.35 ± 0.14	21 ± 8	2.4 ± 0.9	1.3 ± 0.5
VBF: $H \to \tau\tau$	13.3 ± 4.0	2.7 ± 0.7	3.3 ± 0.9	5.5 ± 1.5	0.95 ± 0.26	0.49 ± 0.13
$WH: \ H \to \tau\tau$	0.25 ± 0.07	< 0.1	< 0.1	3.8 ± 1.0	0.44 ± 0.12	0.22 ± 0.06
$ZH: \ H \to \tau\tau$	0.14 ± 0.04	< 0.1	< 0.1	2.0 ± 0.5	0.21 ± 0.06	0.113 ± 0.031
Total background	980 ± 22	15.4 ± 1.8	5.6 ± 1.4	3080 ± 50	55 ± 4	19.2 ± 2.1
Total signal	24 ± 6	3.5 ± 0.9	3.6 ± 1.0	33 ± 10	4.0 ± 1.2	2.1 ± 0.6
Data	1014	16	11	3095	61	20

Table 9. The predicted post-fit event yields in the $\tau_{\text{lep}}\tau_{\text{lep}}$ channel for $m_H = 125$ GeV for the total number of events and for the two highest bins of the BDT distributions for the data taken at $\sqrt{s} = 8$ TeV. The background normalisations, signal normalisation, and their uncertainties represent the post-fit values (see text). The uncertainties on the total background and total signal represent the full statistical and systematic uncertainty, while the uncertainties on the individual background components represent the full systematic uncertainty only.

JHEP04(2015)117

Process/Category	VBF			Boosted		
BDT output bin	All bins	Second to last bin	Last bin	All bins	Second to last bin	Last bin
Fake background	1680 ± 50	8.2 ± 0.9	5.2 ± 0.7	5640 ± 160	51.0 ± 2.5	22.3 ± 1.8
$Z \to \tau\tau$	877 ± 29	7.6 ± 0.9	4.2 ± 0.7	6210 ± 170	57.5 ± 2.8	41.1 ± 3.2
Top	82 ± 15	0.3 ± 0.4	0.5 ± 0.4	380 ± 50	12 ± 4	4.8 ± 1.5
$Z \to \ell\ell(\ell \to \tau_{\text{had}})$	54 ± 26	1.0 ± 0.7	0.30 ± 0.28	200 ± 50	13 ± 4	8.6 ± 3.5
Diboson	63 ± 11	1.0 ± 0.4	0.48 ± 0.20	430 ± 40	9.7 ± 2.2	4.7 ± 1.6
ggF: $H \to \tau\tau$ ($m_H = 125$ GeV)	16 ± 6	1.0 ± 0.4	1.2 ± 0.6	60 ± 20	9.2 ± 3.2	10.1 ± 3.4
VBF: $H \to \tau\tau$	31 ± 8	4.5 ± 1.1	9.1 ± 2.2	16 ± 4	2.5 ± 0.6	2.9 ± 0.7
$WH: \ H \to \tau\tau$	0.6 ± 0.4	< 0.1	< 0.1	9.1 ± 2.3	1.3 ± 0.4	1.9 ± 0.5
$ZH: \ H \to \tau\tau$	0.16 ± 0.07	< 0.1	< 0.1	4.6 ± 1.2	0.77 ± 0.20	0.93 ± 0.24
Total background	2760 ± 40	18.1 ± 2.3	10.7 ± 2.7	12860 ± 110	143 ± 6	82 ± 6
Total signal	48 ± 12	5.5 ± 1.3	10.3 ± 2.5	89 ± 26	14 ± 4	16 ± 4
Data	2830	22	21	12952	170	92

Table 10. The predicted post-fit event yields in the $\tau_{\text{lep}}\tau_{\text{had}}$ channel for $m_H = 125$ GeV for the total number of events and for the two highest bins of the BDT distributions for the data taken at $\sqrt{s} = 8$ TeV. The background normalisations, signal normalisation, and their uncertainties represent the post-fit values (see text). The uncertainties on the total background and total signal represent the full statistical and systematic uncertainty, while the uncertainties on the individual background components represent the full systematic uncertainty only.

JHEP04(2015)117

Process/Category	VBF			Boosted		
BDT output bin	All bins	Second to last bin	Last bin	All bins	Second to last bin	Last bin
Fake background	370 ± 18	2.3 ± 0.9	0.57 ± 0.29	645 ± 26	35 ± 4	0.65 ± 0.33
Others	37 ± 5	0.67 ± 0.22	< 0.1	89 ± 11	15.9 ± 2.0	0.92 ± 0.22
$Z \to \tau\tau$	475 ± 16	0.6 ± 0.7	0.6 ± 0.4	2230 ± 70	93 ± 4	5.4 ± 1.6
ggF: $H \to \tau\tau$ ($m_H = 125\,\text{GeV}$)	8.0 ± 2.7	0.67 ± 0.23	0.53 ± 0.20	21 ± 8	9.1 ± 3.3	1.6 ± 0.6
VBF: $H \to \tau\tau$	12.0 ± 3.1	1.8 ± 0.5	3.4 ± 0.9	6.3 ± 1.6	2.8 ± 0.7	0.52 ± 0.13
$WH : H \to \tau\tau$	0.25 ± 0.07	< 0.1	< 0.1	4.0 ± 1.1	1.9 ± 0.5	0.41 ± 0.11
$ZH : \ H \to \tau\tau$	0.16 ± 0.04	< 0.1	< 0.1	2.4 ± 0.6	1.13 ± 0.30	0.23 ± 0.06
Total background	883 ± 18	3.6 ± 1.3	1.2 ± 1.0	2960 ± 50	143 ± 6	7.0 ± 1.8
Total signal	20 ± 5	2.5 ± 0.6	3.9 ± 1.0	34 ± 10	15 ± 4	2.7 ± 0.8
Data	892	5	6	3020	161	10

Table 11. The predicted post-fit event yields in the $\tau_{\text{had}}\tau_{\text{had}}$ channel for $m_H = 125$ GeV for the total number of events and for the two highest bins of the BDT distributions for the data taken at $\sqrt{s} = 8$ TeV. The background normalisations, signal normalisation, and their uncertainties represent the post-fit values (see text). The uncertainties on the total background and total signal represent the full statistical and systematic uncertainty, while the uncertainties on the individual background components represent the full systematic uncertainty only.

JHEP04(2015)117

9 Results

As explained in the previous section, the observed signal strength is determined from a global maximum likelihood fit to the BDT output distributions in data, with nuisance parameters that are either free or constrained. The results are extracted for each channel and for each category individually as well as for combinations of categories and for the overall combination.

At the value of the Higgs boson mass obtained from the combination of the ATLAS $H \to \gamma\gamma$ and $H \to ZZ^*$ measurements [116], $m_H = 125.36$ GeV, the signal strength obtained from the combined $H \to \tau\tau$ analysis is:

$$\mu = 1.43\ ^{+0.27}_{-0.26}(\text{stat.})\ ^{+0.32}_{-0.25}(\text{syst.})\ \pm 0.09(\text{theory syst.}).$$

The systematic uncertainties are split into two groups: systematic uncertainties (syst.) including all experimental effects as well as theoretical uncertainties on the signal region acceptance, such as those due to the QCD scales, the PDF choice, and the underlying event and parton shower; and, separately, theoretical uncertainties on the inclusive Higgs boson production cross section and $H \to \tau\tau$ branching ratio (theory syst.). The results for each individual channel and for each category as well as for their combination are shown in figure 10. They are based on the full dataset, however, separate combined results are given for the two centre-of-mass energies.

The probability p_0 of obtaining a result at least as signal-like as observed in the data if no signal were present is calculated using the test statistic $q_{\mu=0} = -2\ln(\mathcal{L}(0,\hat{\hat{\vec{\theta}}})/\mathcal{L}(\hat{\mu},\hat{\vec{\theta}}))$ in the asymptotic approximation [117]. For $m_H = 125.36$ GeV, the observed p_0 value is 2.7×10^{-6}, which corresponds to a deviation from the background-only hypothesis of 4.5σ. This can be compared to an expected significance of 3.4σ. This provides evidence at the level of 4.5σ for the decay of the Higgs boson into tau leptons. Table 12 shows the expected and observed significances for the signal strength measured in each channel separately.

Figure 11 shows the expected and observed number of events, in bins of $\log_{10}(S/B)$, for all signal region bins. Here, S/B is the signal-to-background ratio calculated assuming $\mu = 1.4$ for each BDT bin in the signal regions. The expected signal yield for both $\mu = 1$ and the best-fit value $\mu = 1.4$ for $m_H = 125$ GeV is shown on top of the background prediction from the best-fit values. The background expectation where the signal-strength parameter is fixed to $\mu = 0$ is also shown for comparison.

To visualise the compatibility of this excess of events above background predictions with the SM Higgs boson at $m_H = 125$ GeV, a weighted distribution of events as a function of $m_{\tau\tau}^{\text{MMC}}$ is shown in figure 12. The events are weighted by a factor of $\ln(1 + S/B)$, which enhances the events compatible with the signal hypothesis. The excess of events in this mass distribution is consistent with the expectation for a Standard Model Higgs boson with $m_H = 125$ GeV. The distributions for the predicted excess in data over the background are also shown for alternative SM Higgs boson mass hypotheses of $m_H = 110$ GeV and $m_H = 150$ GeV. The data favour a Higgs boson mass of $m_H = 125$ GeV and are less consistent with the other masses considered.

JHEP04(2015)117

Channel and Category	Expected Significance (σ)	Observed Significance (σ)
$\tau_{\text{lep}}\tau_{\text{lep}}$ VBF	1.15	1.88
$\tau_{\text{lep}}\tau_{\text{lep}}$ Boosted	0.57	1.72
$\tau_{\text{lep}}\tau_{\text{lep}}$ Total	1.25	2.40
$\tau_{\text{lep}}\tau_{\text{had}}$ VBF	2.11	2.23
$\tau_{\text{lep}}\tau_{\text{had}}$ Boosted	1.11	1.01
$\tau_{\text{lep}}\tau_{\text{had}}$ Total	2.33	2.33
$\tau_{\text{had}}\tau_{\text{had}}$ VBF	1.70	2.23
$\tau_{\text{had}}\tau_{\text{had}}$ Boosted	0.82	2.56
$\tau_{\text{had}}\tau_{\text{had}}$ Total	1.99	3.25
Combined	3.43	4.54

Table 12. The expected and observed significances of the signal in each channel and category for the combined 7 and 8 TeV datasets.

Source of Uncertainty	Uncertainty on μ
Signal region statistics (data)	$^{+0.27}_{-0.26}$
Jet energy scale	$\pm$ 0.13
Tau energy scale	$\pm$ 0.07
Tau identification	$\pm$ 0.06
Background normalisation	$\pm$ 0.12
Background estimate stat.	$\pm$ 0.10
BR ($H \to \tau\tau$)	$\pm$ 0.08
Parton shower/Underlying event	$\pm$ 0.04
PDF	$\pm$ 0.03
Total sys.	$^{+0.33}_{-0.26}$
Total	$^{+0.43}_{-0.37}$

Table 13. Important sources of uncertainty on the measured signal-strength parameter μ. The contributions are given as absolute uncertainties on the best-fit value of $\mu = 1.43$. Various sub-components are combined assuming no correlations.

As discussed in section 8, the dominant uncertainties on the measurement of the signal-strength parameters include statistical uncertainties on the data from the signal regions, uncertainties on the jet and tau energy scales, uncertainties on the normalisation of the $Z \to \tau\tau$ and $t\bar{t}$ background components as well as theoretical uncertainties. The contributions of each of these significant sources to the uncertainty of the measured signal strength are summarised in table 13.

JHEP04(2015)117

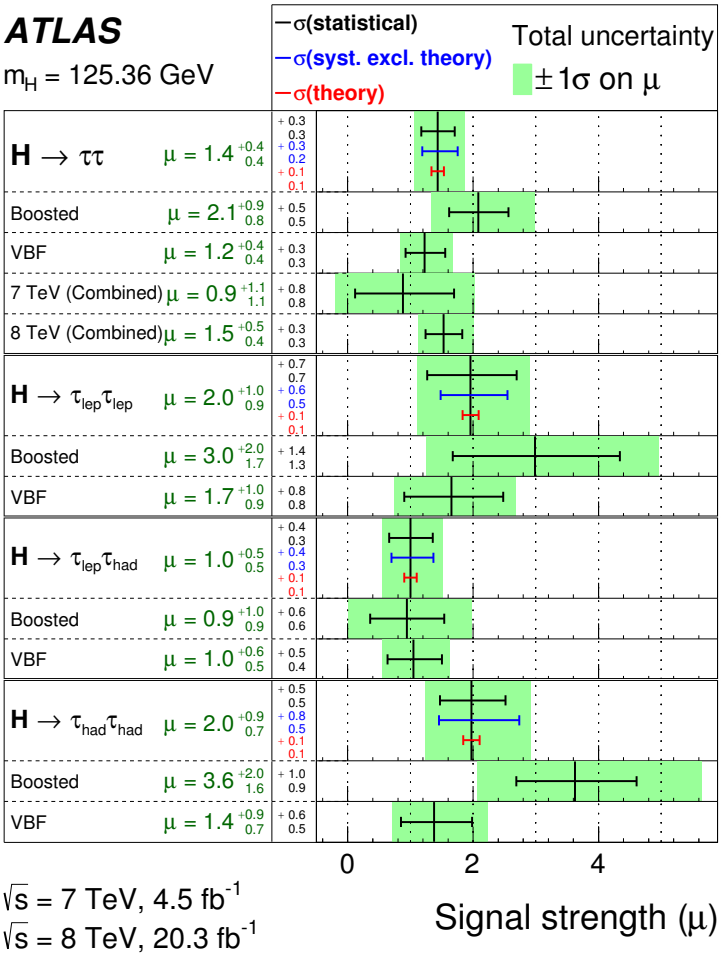

Figure 10. The best-fit value for the signal strength μ in the individual channels and their combination for the full ATLAS datasets at $\sqrt{s} = 7$ TeV and $\sqrt{s} = 8$ TeV. The total $\pm 1\sigma$ uncertainty is indicated by the shaded green band, with the individual contributions from the statistical uncertainty (top, black), the experimental systematic uncertainty (middle, blue), and the theory uncertainty (bottom, red) on the signal cross section (from QCD scale, PDF, and branching ratios) shown by the error bars and printed in the central column.

The normalisation uncertainties on the $Z \to \tau\tau$ embedded sample are correlated across the categories in each respective channel. The global fit also constrains the normalisation for $Z \to \tau\tau$ more strongly than for the $Z \to \ell\ell$ and top-quark background components, as the low BDT-score region is dominated by $Z \to \tau\tau$ events.

The measurement of the overall signal strength discussed above does not give direct information on the relative contributions of the different production mechanisms. Therefore, the signal strengths of different production processes contributing to the $H \to \tau\tau$ decay mode are determined, exploiting the sensitivity offered by the use of the event categories in the analyses of the three channels. The data are fitted separating the vector-boson-mediated VBF and VH processes from gluon-mediated ggF processes. Two signal strength parameters, $\mu^{\tau\tau}_{ggF}$ and $\mu^{\tau\tau}_{\mathrm{VBF}+VH}$, which scale the SM-predicted rates to those ob-

JHEP04(2015)117

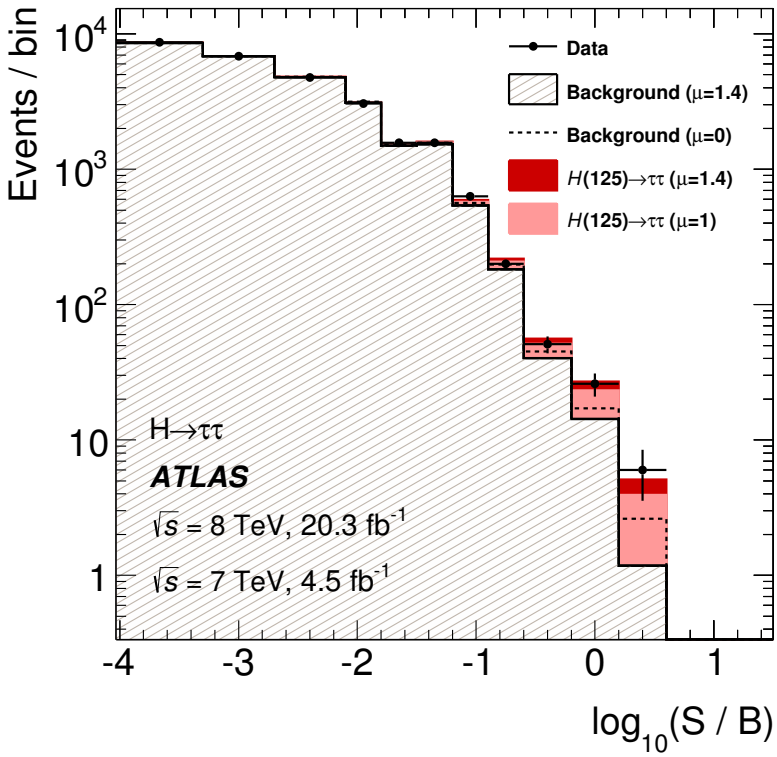

Figure 11. Event yields as a function of $\log_{10}(S/B)$, where S (signal yield) and B (background yield) are taken from the BDT output bin of each event, assuming a signal strength $\mu = 1.4$. Events in all categories are included. The predicted background is obtained from the global fit (with $\mu = 1.4$), and signal yields are shown for $m_H = 125$ GeV at $\mu = 1$ and $\mu = 1.4$ (the best-fit value). The background-only distribution (dashed line) is obtained from the global fit, with μ fixed at zero.

served, are introduced. The two-dimensional 68% and 95% confidence level (CL) contours in the plane of $\mu^{\tau\tau}_{ggF}$ and $\mu^{\tau\tau}_{\mathrm{VBF}+VH}$ [84] are shown in figure 13 for $m_H = 125.36$ GeV. The best-fit values are

$$\mu^{\tau\tau}_{ggF} = 2.0 \ \pm 0.8(\text{stat.}) \ ^{+1.2}_{-0.8}(\text{syst.}) \ \pm 0.3(\text{theory syst.})$$

and

$$\mu^{\tau\tau}_{\mathrm{VBF}+VH} = 1.24 \ ^{+0.49}_{-0.45}(\text{stat.}) \ ^{+0.31}_{-0.29}(\text{syst.}) \ \pm 0.08(\text{theory syst.}),$$

in agreement with the predictions from the Standard Model. The two results are strongly anti-correlated (correlation coefficient of -48%). The observed (expected) significances of the $\mu^{\tau\tau}_{ggF}$ and $\mu^{\tau\tau}_{\mathrm{VBF}+VH}$ signal strengths are 1.74σ (0.95σ) and 2.25σ (1.72σ) respectively.

A total cross section times branching ratio for $H \to \tau\tau$ with $m_H = 125$ GeV can also be measured. The central value is obtained from the product of the measured μ and the predicted cross section used to define it. The uncertainties are similarly obtained by scaling the uncertainties on μ by the predicted cross section, noting that theoretical uncertainties on the inclusive cross section cancel between μ and the predicted cross section and thus are not included for the production processes under consideration. These include the

JHEP04(2015)117

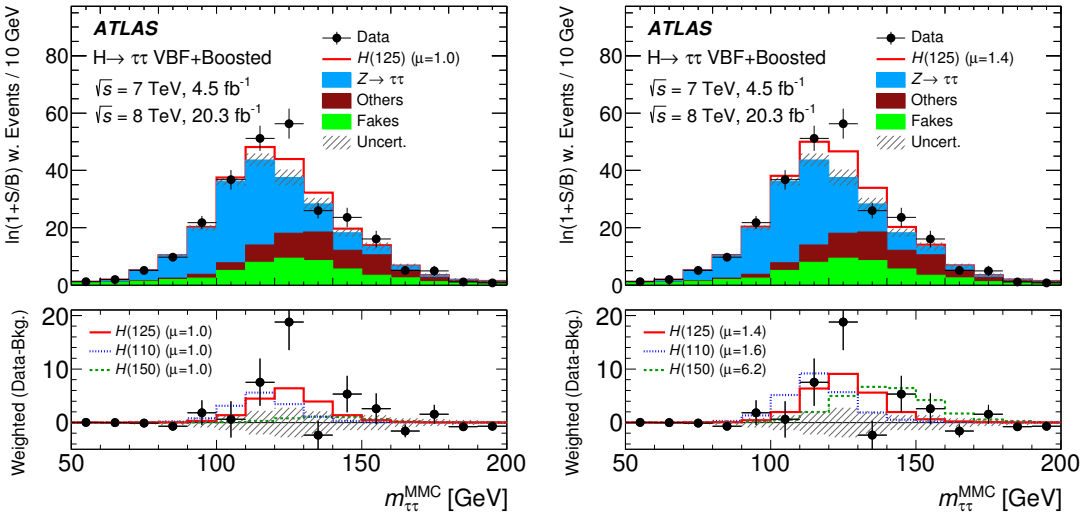

(a) (b)

Figure 12. Distributions of the reconstructed invariant $\tau\tau$ mass, $m_{\tau\tau}^{\mathrm{MMC}}$, where events are weighted by $\ln(1 + S/B)$ for all channels. These weights are determined by the signal (S) and background (B) predictions for each BDT bin. The bottom panel in each plot shows the difference between weighted data events and weighted background events (black points), compared to the weighted signal yields. The background predictions are obtained from the global fit with the $m_H = 125$ GeV signal hypothesis (signal strength $\mu = 1.4$). The $m_H = 125$ GeV signal is plotted with a solid red line, and, for comparison, signals for $m_H = 110$ GeV (blue) and $m_H = 150$ GeV (green) are also shown. The signal normalisations are taken from fits to data with the corresponding signal mass hypotheses, and the fitted μ values are given in the figure. The signal strengths are shown for the Standard Model expectations ($\mu = 1$) in (a), while in (b) the best-fit values are used.

uncertainties on the inclusive cross section due to the QCD scale and the PDF choice as well as the uncertainty on the branching ratio $H \to \tau\tau$; however, theoretical uncertainties on the acceptance of the signal regions from the QCD scale and PDF choice are retained, along with the uncertainties due to underlying event and parton shower, and the electroweak correction on VBF production. Table 14 gives the measured values for the total cross section at 7 and at 8 TeV, as well as the measured values at 8 TeV for gluon fusion production and for VBF and VH production separately.

10 Cross-check with cut-based analysis

The search for the SM Higgs boson presented above is cross-checked for the dataset collected at $\sqrt{s} = 8$ TeV in an analysis where cuts on kinematic variables are applied. This search uses improved definitions of event categories and an improved fit model with respect to results previously published for the $\sqrt{s} = 7$ TeV dataset [21]. To allow a straightforward comparison of results, the multivariate and cut-based analyses have common components. The two analyses are performed for the same three channels, $\tau_{\mathrm{lep}}\tau_{\mathrm{lep}}$, $\tau_{\mathrm{lep}}\tau_{\mathrm{had}}$ and $\tau_{\mathrm{had}}\tau_{\mathrm{had}}$, they use the same preselection and share the same strategy for the estimation of background contributions and systematic uncertainties. As in the multivariate analysis, the irreducible

JHEP04(2015)117

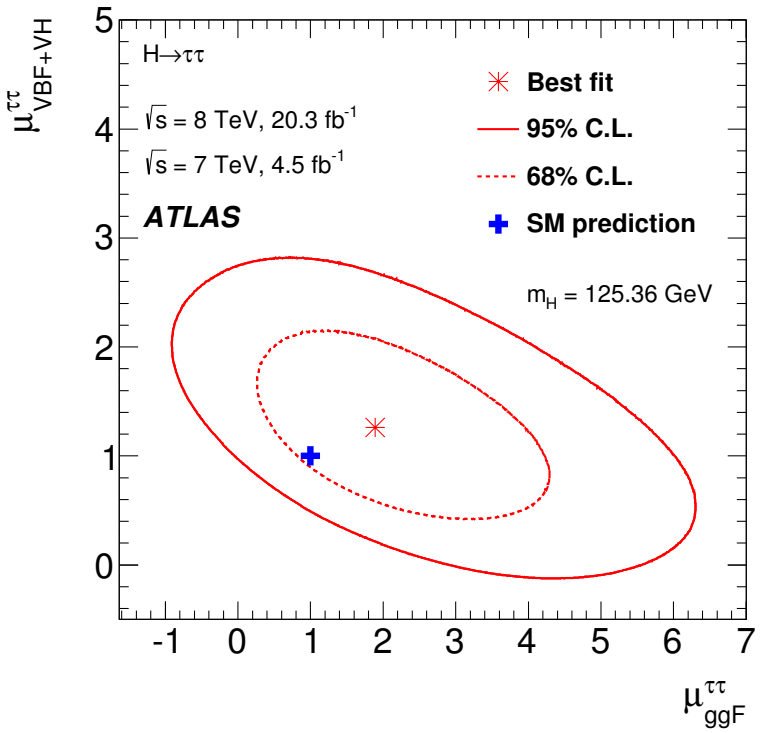

Figure 13. Likelihood contours for the combination of all channels in the ($\mu^{\tau\tau}_{ggF}$, $\mu^{\tau\tau}_{\mathrm{VBF}+VH}$) plane. The signal strength μ is the ratio of the measured signal yield to the Standard Model expectation, for each production mode. The 68% and 95% CL contours are shown as dashed and solid lines respectively, for $m_H = 125.36$ GeV. The SM expectation is shown by a filled plus symbol, and the best fit to the data is shown as a star.

	Measured $\sigma\times$BR [pb]	Predicted $\sigma\times$BR [pb]
7 TeV	$1.0\ ^{+0.9}_{-0.8}(\mathrm{stat.})^{+0.9}_{-0.8}(\mathrm{syst.})$	1.09 ± 0.11
8 TeV	$2.1 \pm 0.4(\mathrm{stat.})^{+0.5}_{-0.4}(\mathrm{syst.})$	1.39 ± 0.14
Gluon fusion, 8 TeV	$1.7 \pm 1.1(\mathrm{stat.})^{+1.5}_{-1.1}(\mathrm{syst.})$	1.22 ± 0.14
VBF+VH, 8 TeV	$0.26 \pm 0.09(\mathrm{stat.})^{+0.06}_{-0.05}(\mathrm{syst.})$	0.17 ± 0.01

Table 14. Measured and predicted total cross section times branching ratio for $H \to \tau\tau$ with $m_H = 125$ GeV, at 7 TeV and at 8 TeV for all production modes, as well as for gluon fusion and for VBF and VH production separately, at 8 TeV only. The theoretical predictions are obtained as described in section 3.

JHEP04(2015)117

$Z \to \tau\tau$ background is estimated using the embedding procedure and the reducible ones are estimated using similar data-driven methods, as described in section 6. Finally, the same statistical methods are used to extract the results, although these are applied to different discriminating variables. While the multivariate analysis performs a fit to the BDT output distribution, the cut-based analysis relies on a fit to the $\tau\tau$ invariant mass distribution. The $\tau\tau$ invariant mass is calculated using the missing mass calculator, as described in section 4.3. The analysis is not designed to be sensitive to a specific value of the Higgs boson mass m_H. The use of the mass as the discriminating variable is motivated not only by its power to separate the irreducible $Z \to \tau\tau$ background from signal, but also by its sensitivity to the mass of the signal itself.

In the cut-based analysis, a categorisation is performed similar to that in the multivariate analysis, i.e. VBF and boosted categories are defined. To increase the separation power, subcategories are introduced for the $\tau_{\text{lep}}\tau_{\text{had}}$ and $\tau_{\text{had}}\tau_{\text{had}}$ channels. These subcategories target events produced via the same production mode, but select different phase-space regions with different signal-to-background ratios. With this strategy the most sensitive subcategories have a small number of events, but a high signal-to-background ratio. Although the combined sensitivity is dominated by the few highly sensitive subcategories, the others are important not just to increase the sensitivity but also to constrain the various background components.

An overview of the defined categories in the three channels is given in table 15. In all channels, the event categorisation is designed by splitting events first according to the production mode, either VBF-like or boosted ggF-like, and second, for the $\tau_{\text{lep}}\tau_{\text{had}}$ and $\tau_{\text{had}}\tau_{\text{had}}$ channels, by signal-to-background ratio. The events accepted in the VBF categories pass a common selection that requires the presence of the two forward jets distinctive of VBF production. In the $\tau_{\text{lep}}\tau_{\text{had}}$ channel, tight and loose *VBF* subcategories are defined, via cuts on the mass of the dijet system, m_{jj}, and p_{T}^{H}, the transverse momentum of the Higgs boson candidate. In the $\tau_{\text{had}}\tau_{\text{had}}$ channel, the variables used to select the most sensitive categories for both production modes are p_{T}^{H} and the separation $\Delta R(\tau_1, \tau_2)$ between the two τ_{had} candidates. In the VBF-like events, correlations between the invariant mass of the selected jets m_{jj} and $\Delta\eta_{jj}$ of the jets characteristic of VBF production are also used. The subcategory with the highest purity is the *VBF high-*p_{T}^{H} subcategory, where tight cuts on p_{T}^{H} and $\Delta R(\tau_1, \tau_2)$ reject almost all non-resonant background sources. The other two VBF-like subcategories are distinguished by a different signal-to-background ratio due to a tighter selection applied to the forward jets. For the $\tau_{\text{had}}\tau_{\text{had}}$ channel, boosted subcategories are also defined. The division is based on the same cuts on p_{T}^{H} and $\Delta R(\tau_1, \tau_2)$ as used in the VBF high-p_{T}^{H} category. Events with low transverse momentum are not used in any category because in such events the signal cannot be effectively distinguished from background channels. The proportion of the signal yield produced via VBF in the VBF-like subcategories is found to be 80% in the $\tau_{\text{lep}}\tau_{\text{lep}}$ channel, between 67% and 85% in the $\tau_{\text{lep}}\tau_{\text{had}}$ channel and between 58% and 78% in the $\tau_{\text{had}}\tau_{\text{had}}$ channel.

The final results are derived from the combined fit of the $m_{\tau\tau}$ distributions observed in the various subcategories. The number of fitted signal and background events in each channel and category is given in table 16. The combined mass distribution for the three

JHEP04(2015)117

Channel	VBF category selection criteria		
$\tau_{\mathrm{lep}}\tau_{\mathrm{lep}}$	At least two jets with $p_{\mathrm{T}}^{j_1} > 40$ GeV and $p_{\mathrm{T}}^{j_2} > 30$ GeV $\lvert\Delta\eta_{j_1,j_2}\rvert > 3.0$ $m_{j_1,j_2} > 400$ GeV b-jet veto for jets with $p_{\mathrm{T}} > 25$ GeV Jet veto: no additional jet with $p_{\mathrm{T}} > 25$ GeV within $\lvert\eta\rvert < 2.4$		
$\tau_{\mathrm{lep}}\tau_{\mathrm{had}}$	At least two jets with $p_{\mathrm{T}}^{j_1} > 40$ GeV and $p_{\mathrm{T}}^{j_2} > 30$ GeV $E_{\mathrm{T}}^{\mathrm{miss}} >$ 20 GeV $\lvert\Delta\eta_{j_1,j_2}\rvert > 3.0$ and $\eta(j_1)\cdot\eta(j_2) < 0$, $m_{j_1,j_2} > 300$ GeV $p_{\mathrm{T}}^{\mathrm{Total}} = \lvert\vec{p}_{\mathrm{T}}^{\,\ell} + \vec{p}_{\mathrm{T}}^{\,\tau_{\mathrm{had}}} + \vec{p}_{\mathrm{T}}^{\,j_1} + \vec{p}_{\mathrm{T}}^{\,j_2} + \vec{E}_{\mathrm{T}}^{\mathrm{miss}}\rvert < 30$ GeV b-jet veto for jets with $p_{\mathrm{T}} > 30$ GeV $\min(\eta_{(j_1)},\eta_{(j_2)}) < \eta_{(\ell)},\eta_{(\tau_{\mathrm{had}})} < \max(\eta_{(\mathrm{j}_1)},\eta_{(\mathrm{j}_2)})$		
	VBF tight $m_{j_1,j_2} > 500$ GeV $p_{\mathrm{T}}^{H} > 100$ GeV $p_{\mathrm{T}}^{\tau_{\mathrm{had}}} > 30$ GeV $m_{\mathrm{vis}} > 40$ GeV	**VBF loose** Non tight VBF	
$\tau_{\mathrm{had}}\tau_{\mathrm{had}}$	At least two jets with $p_{\mathrm{T}}^{j_1} > 50$ GeV and $p_{\mathrm{T}}^{j_2} > 30$ GeV $\lvert\Delta\eta(\tau_1,\tau_2)\rvert < 1.5$ $\lvert\Delta\eta_{j_1,j_2}\rvert > 2.6$ and $m_{j_1,j_2} > 250$ GeV $\min(\eta_{(j_1)},\eta_{(j_2)}) < \eta_{(\tau_1)},\eta_{(\tau_2)} < \max(\eta_{(j_1)},\eta_{(j_2)})$		
	VBF high p_{T}^{H} $\Delta R(\tau_1,\tau_2) < 1.5$ and $p_{\mathrm{T}}^{H} > 140$ GeV	**VBF low p_{T}^{H}, tight** $\Delta R(\tau_1,\tau_2) > 1.5$ or $p_{\mathrm{T}}^{H} < 140$ GeV $m_{j_1,j_2}[\mathrm{GeV}] > (-250\cdot\lvert\Delta\eta_{\mathrm{j}_1,\mathrm{j}_2}\rvert + 1550)$	**VBF low p_{T}^{H}, loose** $\Delta R(\tau_1,\tau_2) > 1.5$ or $p_{\mathrm{T}}^{H} < 140$ GeV $m_{j_1,j_2}[\mathrm{GeV}] < (-250\cdot\lvert\Delta\eta_{\mathrm{j}_1,\mathrm{j}_2}\rvert + 1550)$
Channel	Boosted category selection criteria		
$\tau_{\mathrm{lep}}\tau_{\mathrm{lep}}$	Exclude events passing the VBF selection $p_{\mathrm{T}}^{H} > 100$ GeV b-jet veto for jets with $p_{\mathrm{T}} > 25$ GeV		
$\tau_{\mathrm{lep}}\tau_{\mathrm{had}}$	Exclude events passing the VBF selection $E_{\mathrm{T}}^{\mathrm{miss}} > 20$ GeV $p_{\mathrm{T}}^{H} > 100$ GeV $p_{\mathrm{T}}(\tau_{\mathrm{had}}) > 30$ GeV b-jet veto for jets with $p_{\mathrm{T}} > 30$ GeV		
$\tau_{\mathrm{had}}\tau_{\mathrm{had}}$	Exclude events passing the VBF selection $\Delta\eta(\tau_1,\tau_2) < 1.5$ $p_{\mathrm{T}}^{H} > 100$ GeV		
	Boosted high p_{T}^{H} $\Delta R(\tau_1,\tau_2) < 1.5$ and $p_{\mathrm{T}}^{H} > 140$ GeV	**Boosted low p_{T}^{H}** $\Delta R(\tau_1,\tau_2) > 1.5$ or $p_{\mathrm{T}}^{H} < 140$ GeV	

Table 15. Summary of the selection criteria used to define the VBF and boosted subcategories in the cut-based analysis for the three analysis channels. The labels (1) and (2) refer to the leading (highest p_{T}) and subleading final-state objects (leptons, τ_{had}, jets). The variables are defined in the text.

JHEP04(2015)117

$\tau_{\rm lep}\tau_{\rm lep}$	VBF			Boosted	
Total signal	11 ± 4			38 ± 13	
Total background	130 ± 7			3400 ± 64	
Data	152			3428	
$\tau_{\rm lep}\tau_{\rm had}$	Tight VBF	Loose VBF		Boosted	
Signal	8.8 ± 3	17 ± 6		52 ± 17	
Background	52 ± 4	398 ± 17		4399 ± 73	
Data	62	407		4435	
$\tau_{\rm had}\tau_{\rm had}$	VBF high $p_{\rm T}^H$	VBF low $p_{\rm T}^H$		Boosted	
		tight	loose	high $p_{\rm T}^H$	low $p_{\rm T}^H$
Signal	5.7 ± 1.9	5.2 ± 1.9	3.7 ± 1.3	17 ± 6	20 ± 7
Background	59 ± 4	86 ± 5	156 ± 7	1155 ± 28	2130 ± 41
Data	65	94	157	1204	2121

Table 16. The measured signal and background yields of the cut-based analysis at $\sqrt{s} = 8$ TeV in the $\tau_{\rm lep}\tau_{\rm lep}$, $\tau_{\rm lep}\tau_{\rm had}$ and $\tau_{\rm had}\tau_{\rm had}$ channels for $m_H = 125$ GeV. The normalisations and uncertainties are taken from the global fit. The uncertainties on the predicted yields reflect the full statistical and systematic uncertainties.

channels is shown in figure 14, where events are weighted by $\ln(1 + S/B)$, based on the signal and background content of their channel and category. An excess of events above the expected SM background is visible in the mass region around 125 GeV.

The signal strengths extracted in the three analysis channels and their combination are given in table 17. This cut-based analysis also provides evidence for $H \to \tau\tau$ decays, giving a combined signal strength of

$$\mu_{\rm Cut-based} = 1.43\ ^{+0.36}_{-0.35}(\text{stat.})\ ^{+0.41}_{-0.33}(\text{syst.})\ \pm 0.10(\text{theory syst.})$$

for $m_H = 125.36$ GeV. For comparison, the results obtained in the multivariate analysis for the dataset at $\sqrt{s} = 8$ TeV are also included in table 17. Good agreement between the results of the two analyses is found for the individual channels as well as for their combination. To further quantify the level of agreement, the correlation ρ and the uncertainties on the differences between the μ values obtained, i.e. $\Delta\mu \pm \delta(\Delta\mu)$, were evaluated using the so-called jackknife technique [118, 119]. Using this method, the correlation between the μ values obtained in the two analyses is found to be between 0.55 and 0.75 for each of the three analysis channels. The results of the analyses are found to be fully compatible, with deviations $\Delta\mu/\delta(\Delta\mu)$ below 1 for all analysis channels as well as for the combined result.

The probability p_0 of obtaining a result at least as signal-like as observed if no signal were present is shown as a function of the mass in figure 15 for the cut-based analysis for the combined dataset at $\sqrt{s} = 8$ TeV. The observed p_0 values show a shallow minimum around 125 GeV, corresponding to a significance of 3.2σ. The expected significance for the cut-based analysis is superimposed on the figure and reaches a significance of 2.5σ at $m_H = 125.36$ GeV. The corresponding significance values for the multivariate analysis for

JHEP04(2015)117

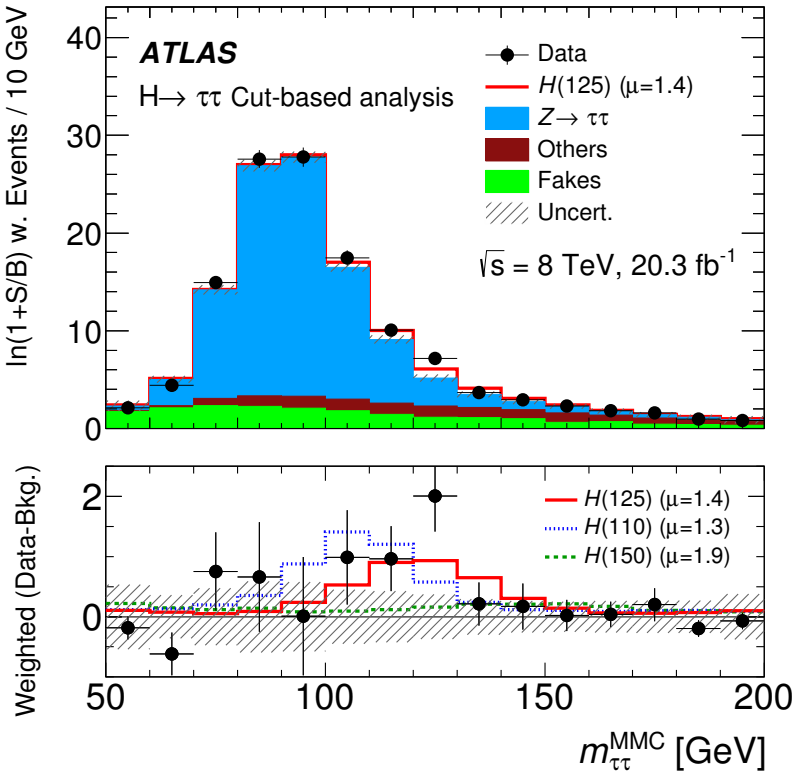

Figure 14. Distribution of the reconstructed invariant $\tau\tau$ mass, $m_{\tau\tau}^{\mathrm{MMC}}$, for the sum of all channels in the cut-based analysis for the data taken at $\sqrt{s} = 8$ TeV. The events are weighted by a factor of $\ln(1 + S/B)$ based on the signal (S) and background (B) yields in each category. The bottom panel shows the difference between weighted data events and weighted background events (black points), compared to the weighted signal yields. The background predictions are obtained from the global fit with the $m_H = 125$ GeV signal hypothesis (signal strength $\mu = 1.4$). The $m_H = 125$ GeV signal is plotted as a solid red line, and, for comparison, signals for $m_H = 110$ GeV (blue) and $m_H = 150$ GeV (green) are also shown. The signal normalisations are taken from fits to data with the corresponding signal mass hypotheses and the fitted μ values are given in the figure.

	Fitted μ values		
	$\sqrt{s}$	Multivariate analysis	Cut-based analysis
$\tau_{\mathrm{lep}}\tau_{\mathrm{lep}}$	8 TeV	$1.9^{+1.0}_{-0.9}$	$3.2^{+1.4}_{-1.3}$
$\tau_{\mathrm{lep}}\tau_{\mathrm{had}}$	8 TeV	$1.1^{+0.6}_{-0.5}$	$0.7^{+0.7}_{-0.6}$
$\tau_{\mathrm{had}}\tau_{\mathrm{had}}$	8 TeV	$1.8^{+0.9}_{-0.7}$	$1.6^{+0.9}_{-0.7}$
All channels	8 TeV	$1.53^{+0.47}_{-0.41}$	$1.43^{+0.55}_{-0.49}$

Table 17. Fitted values of the signal strength for the different channels at $\sqrt{s} = 8$ TeV for the multivariate and cut-based analyses, measured at m_H=125.36 GeV. The results for the combinations of all channels are also given. The total uncertainties (statistical and systematic) are quoted.

JHEP04(2015)117

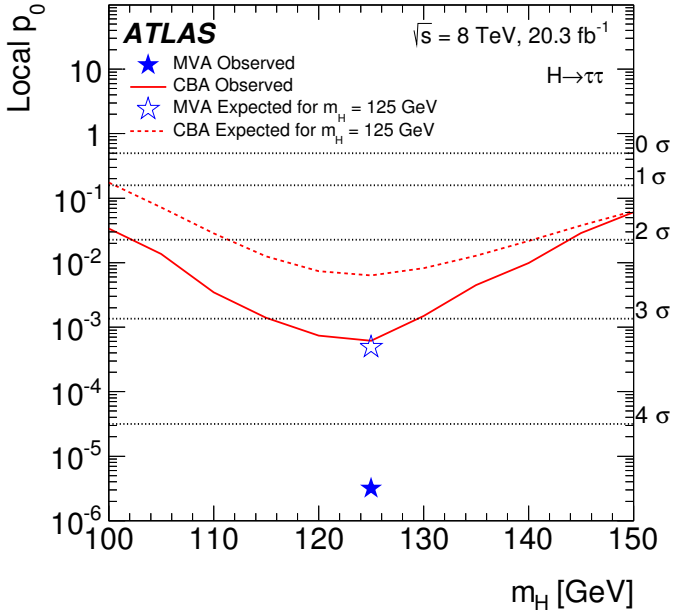

Figure 15. Observed (solid red) and expected (dashed red) p_0 values as a function of m_H for the combination of all channels in the cut-based analysis (CBA) for the data taken at $\sqrt{s} = 8$ TeV. The expected p_0 values are given for the background-only hypothesis. The corresponding observed and expected p_0 values for the multivariate analysis (MVA) are indicated for $m_H = 125$ GeV by a full and open star respectively. The axis labels on the right hand side and the dotted lines display the significance in units of Gaussian standard deviations.

the dataset at $\sqrt{s} = 8$ TeV are found to be 4.5σ (observed) and 3.3σ (expected). They are also indicated in the figure.

Given the mass sensitivity of the cut-based analysis, a two-dimensional likelihood fit for the signal strength μ and the mass m_H is performed. The mass points are tested in steps of 5 GeV in the range between 100 GeV and 150 GeV. The best fit value is found at $\mu = 1.4$ and $m_H = 125$ GeV. The result is shown in the (m_H, μ) plane in figure 16 together with the 68% and 95% CL contours. This result indicates that the observation is compatible with the decay of a Standard Model Higgs boson with a mass of 125 GeV.

11 Conclusions

Evidence for decays of the recently discovered Higgs boson into pairs of tau leptons is presented. The analysis is based on the full set of proton-proton collision data recorded by the ATLAS experiment at the LHC during Run 1. The data correspond to integrated luminosities of 4.5 fb^{-1} and 20.3 fb^{-1} at centre-of-mass energies of $\sqrt{s} = 7$ TeV and $\sqrt{s} =$ 8 TeV respectively. All combinations of leptonic and hadronic tau decay channels are included and event categories selecting both the vector boson fusion and highly boosted $\tau\tau$ signatures are considered in a multivariate analysis. An excess of events over the expected background from other Standard Model processes is found with an observed (expected) significance of 4.5 (3.4) standard deviations. This excess is consistent with resulting from

JHEP04(2015)117

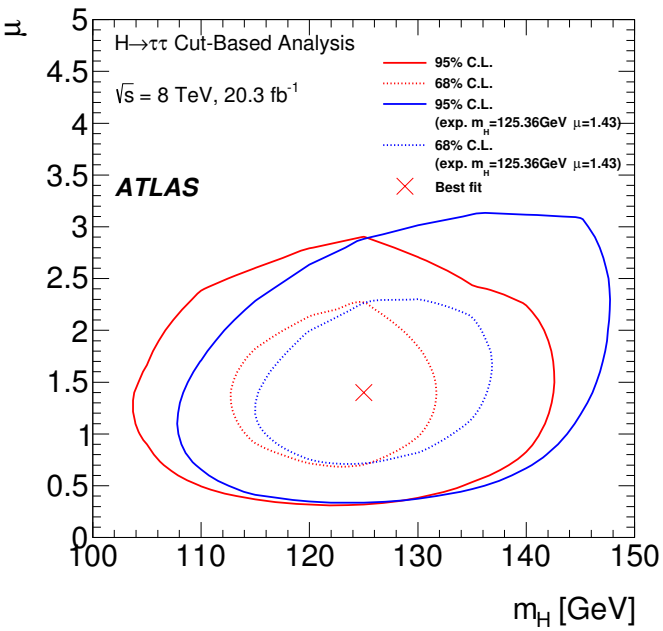

Figure 16. The results of the two-dimensional likelihood fit in the (m_H, μ) plane for the cut-based analysis for the data taken at $\sqrt{s} = 8$ TeV. The signal strength μ is the ratio of the measured signal yield to the Standard Model expectation. The 68% and 95% CL contours are shown as dashed and solid red lines respectively. The best-fit value is indicated as a red cross. The dashed and solid blue lines correspond to the expected 68% and 95% CL contours for $m_H = 125.36$ GeV and $\mu = 1.43$.

$H \to \tau\tau$ decays with $m_H = 125.36$ GeV. The measured signal strength, normalised to the Standard Model expectation, is

$$\mu = 1.43\ ^{+0.27}_{-0.26}(\text{stat.})\ ^{+0.32}_{-0.25}(\text{syst.})\ \pm 0.09(\text{theory syst.}).$$

This value is consistent with the predicted Yukawa coupling strength of the Higgs boson in the Standard Model.

The results of the multivariate analysis are cross-checked for the data collected at $\sqrt{s} = 8$ TeV using a cut-based analysis. The results confirm the findings of the multivariate analysis, and an excess with a compatible signal strength is found. A two-dimensional fit of the signal strength μ and m_H in the cut-based analysis indicates that the observed excess is compatible with the $\tau\tau$ decay of the Higgs boson with a mass of 125 GeV.

Acknowledgments

We thank CERN for the very successful operation of the LHC, as well as the support staff from our institutions without whom ATLAS could not be operated efficiently.

We acknowledge the support of ANPCyT, Argentina; YerPhI, Armenia; ARC, Australia; BMWFW and FWF, Austria; ANAS, Azerbaijan; SSTC, Belarus; CNPq and FAPESP, Brazil; NSERC, NRC and CFI, Canada; CERN; CONICYT, Chile; CAS, MOST and NSFC, China; COLCIENCIAS, Colombia; MSMT CR, MPO CR and VSC CR,

JHEP04(2015)117

Czech Republic; DNRF, DNSRC and Lundbeck Foundation, Denmark; EPLANET, ERC and NSRF, European Union; IN2P3-CNRS, CEA-DSM/IRFU, France; GNSF, Georgia; BMBF, DFG, HGF, MPG and AvH Foundation, Germany; GSRT and NSRF, Greece; RGC, Hong Kong SAR, China; ISF, MINERVA, GIF, I-CORE and Benoziyo Center, Israel; INFN, Italy; MEXT and JSPS, Japan; CNRST, Morocco; FOM and NWO, Netherlands; BRF and RCN, Norway; MNiSW and NCN, Poland; GRICES and FCT, Portugal; MNE/IFA, Romania; MES of Russia and ROSATOM, Russian Federation; JINR; MSTD, Serbia; MSSR, Slovakia; ARRS and MIZŠ, Slovenia; DST/NRF, South Africa; MINECO, Spain; SRC and Wallenberg Foundation, Sweden; SER, SNSF and Cantons of Bern and Geneva, Switzerland; NSC, Taiwan; TAEK, Turkey; STFC, the Royal Society and Leverhulme Trust, United Kingdom; DOE and NSF, United States of America.

The crucial computing support from all WLCG partners is acknowledged gratefully, in particular from CERN and the ATLAS Tier-1 facilities at TRIUMF (Canada), NDGF (Denmark, Norway, Sweden), CC-IN2P3 (France), KIT/GridKA (Germany), INFN-CNAF (Italy), NL-T1 (Netherlands), PIC (Spain), ASGC (Taiwan), RAL (U.K.) and BNL (USA) and in the Tier-2 facilities worldwide.

Open Access. This article is distributed under the terms of the Creative Commons Attribution License (CC-BY 4.0), which permits any use, distribution and reproduction in any medium, provided the original author(s) and source are credited.

References

[1] F. Englert and R. Brout, *Broken symmetry and the mass of gauge vector mesons*, *Phys. Rev. Lett.* **13** (1964) 321 [INSPIRE].

[2] P.W. Higgs, *Broken symmetries, massless particles and gauge fields*, *Phys. Lett.* **12** (1964) 132 [INSPIRE].

[3] P.W. Higgs, *Broken symmetries and the masses of gauge bosons*, *Phys. Rev. Lett.* **13** (1964) 508 [INSPIRE].

[4] G.S. Guralnik, C.R. Hagen and T.W.B. Kibble, *Global conservation laws and massless particles*, *Phys. Rev. Lett.* **13** (1964) 585 [INSPIRE].

[5] P.W. Higgs, *Spontaneous symmetry breakdown without massless bosons*, *Phys. Rev.* **145** (1966) 1156 [INSPIRE].

[6] T.W.B. Kibble, *Symmetry breaking in nonAbelian gauge theories*, *Phys. Rev.* **155** (1967) 1554 [INSPIRE].

[7] L. Evans and P. Bryant, *LHC machine*, 2008 *JINST* **3** S08001 [INSPIRE].

[8] ATLAS collaboration, *Observation of a new particle in the search for the Standard Model Higgs boson with the ATLAS detector at the LHC*, *Phys. Lett.* **B 716** (2012) 1 [arXiv:1207.7214] [INSPIRE].

[9] CMS collaboration, *Observation of a new boson at a mass of* 125 *GeV with the CMS experiment at the LHC*, *Phys. Lett.* **B 716** (2012) 30 [arXiv:1207.7235] [INSPIRE].

[10] ATLAS collaboration, *Measurements of Higgs boson production and couplings in diboson final states with the ATLAS detector at the LHC*, *Phys. Lett.* **B 726** (2013) 88 [arXiv:1307.1427] [INSPIRE].

[11] CMS collaboration, *Observation of a new boson with mass near* 125 *GeV in pp collisions at* $\sqrt{s} = 7$ *and* 8 *TeV*, *JHEP* **06** (2013) 081 [arXiv:1303.4571] [INSPIRE].

[12] ATLAS collaboration, *Evidence for the spin-0 nature of the Higgs boson using ATLAS data*, *Phys. Lett.* **B 726** (2013) 120 [arXiv:1307.1432] [INSPIRE].

[13] CMS collaboration, *Study of the mass and spin-parity of the Higgs boson candidate via its decays to Z boson pairs*, *Phys. Rev. Lett.* **110** (2013) 081803 [arXiv:1212.6639] [INSPIRE].

[14] CMS collaboration, *Constraints on the spin-parity and anomalous HVV couplings of the Higgs boson in proton collisions at* 7 *and* 8 *TeV*, arXiv:1411.3441 [INSPIRE].

[15] S. Weinberg, *A model of leptons*, *Phys. Rev. Lett.* **19** (1967) 1264 [INSPIRE].

[16] CMS collaboration, *Evidence for the* 125 *GeV Higgs boson decaying to a pair of* τ *leptons*, *JHEP* **05** (2014) 104 [arXiv:1401.5041] [INSPIRE].

[17] CMS collaboration, *Search for the standard model Higgs boson produced in association with a W or a Z boson and decaying to bottom quarks*, *Phys. Rev.* **D 89** (2014) 012003 [arXiv:1310.3687] [INSPIRE].

[18] CMS collaboration, *Evidence for the direct decay of the* 125 *GeV Higgs boson to fermions*, *Nature Phys.* **10** (2014) 557 [arXiv:1401.6527] [INSPIRE].

[19] ATLAS collaboration, *Search for the* $b\bar{b}$ *decay of the standard model Higgs boson in associated* $(W/Z)H$ *production with the ATLAS detector*, *JHEP* **01** (2015) 069 [arXiv:1409.6212] [INSPIRE].

[20] CDF, D0 collaboration, T. Aaltonen et al., *Evidence for a particle produced in association with weak bosons and decaying to a bottom-antibottom quark pair in Higgs boson searches at the Tevatron*, *Phys. Rev. Lett.* **109** (2012) 071804 [arXiv:1207.6436] [INSPIRE].

[21] ATLAS collaboration, *Search for the standard model Higgs boson in the H to* $\tau^+\tau^-$ *decay mode in* $\sqrt{s} = 7$ *TeV pp collisions with ATLAS*, *JHEP* **09** (2012) 070 [arXiv:1206.5971] [INSPIRE].

[22] S. Alioli, P. Nason, C. Oleari and E. Re, *NLO Higgs boson production via gluon fusion matched with shower in POWHEG*, *JHEP* **04** (2009) 002 [arXiv:0812.0578] [INSPIRE].

[23] P. Nason and C. Oleari, *NLO Higgs boson production via vector-boson fusion matched with shower in POWHEG*, *JHEP* **02** (2010) 037 [arXiv:0911.5299] [INSPIRE].

[24] L. Breiman, J. Friedman, R. Olshen and C. Stone, *Classification and regression trees*, Chapman & Hall, New York U.S.A. (1984).

[25] J. Friedman, *Stochastic gradient boosting*, *Comput. Stat. Data Anal.* **38** (2002) 367.

[26] Y. Freund and R. E. Schapire, *A decision-theoretic generalization of on-line learning and an application to boosting*, *J. Comput. Syst. Sci.* **55** (1997) 119.

[27] ATLAS collaboration, *The ATLAS experiment at the CERN Large Hadron Collider*, 2008 *JINST* **3** S08003 [INSPIRE].

[28] ATLAS collaboration, *Performance of the ATLAS trigger system in 2010*, *Eur. Phys. J.* **C 72** (2012) 1849 [arXiv:1110.1530] [INSPIRE].

[29] ATLAS collaboration, *Electron reconstruction and identification efficiency measurements with the ATLAS detector using the 2011 LHC proton-proton collision data*, *Eur. Phys. J.* **C 74** (2014) 2941 [arXiv:1404.2240] [INSPIRE].

[30] ATLAS collaboration, *Measurement of the muon reconstruction performance of the ATLAS detector using 2011 and 2012 LHC proton-proton collision data*, *Eur. Phys. J.* **C 74** (2014) 3130 [arXiv:1407.3935] [INSPIRE].

JHEP04(2015)117

[31] M. Cacciari, G.P. Salam and G. Soyez, *The anti-k_t jet clustering algorithm*, *JHEP* **04** (2008) 063 [arXiv:0802.1189] [INSPIRE].

[32] M. Cacciari and G.P. Salam, *Dispelling the N^3 myth for the k_t jet-finder*, *Phys. Lett.* **B 641** (2006) 57 [hep-ph/0512210] [INSPIRE].

[33] W. Lampl et al., *Calorimeter clustering algorithms: description and performance*, ATL-LARG-PUB-2008-002 (2008).

[34] M. Cacciari and G.P. Salam, *Pileup subtraction using jet areas*, *Phys. Lett.* **B 659** (2008) 119 [arXiv:0707.1378] [INSPIRE].

[35] ATLAS collaboration, *Jet energy measurement with the ATLAS detector in proton-proton collisions at $\sqrt{s} = 7$ TeV*, *Eur. Phys. J.* **C 73** (2013) 2304 [arXiv:1112.6426] [INSPIRE].

[36] ATLAS collaboration, *Jet energy measurement and its systematic uncertainty in proton-proton collisions at $\sqrt{s} = 7$ TeV with the ATLAS detector*, *Eur. Phys. J.* **C 75** (2015) 17 [arXiv:1406.0076] [INSPIRE].

[37] ATLAS collaboration, *Single hadron response measurement and calorimeter jet energy scale uncertainty with the ATLAS detector at the LHC*, *Eur. Phys. J.* **C 73** (2013) 2305 [arXiv:1203.1302] [INSPIRE].

[38] ATLAS collaboration, *Calibration of the performance of b-tagging for c and light-flavour jets in the 2012 ATLAS data*, ATLAS-CONF-2014-046 (2014).

[39] ATLAS collaboration, *Identification and energy calibration of hadronically decaying tau leptons with the ATLAS experiment in pp collisions at $\sqrt{s} = 8$ TeV*, arXiv:1412.7086 [INSPIRE].

[40] ATLAS collaboration, *Performance of missing transverse momentum reconstruction in proton-proton collisions at 7 TeV with ATLAS*, *Eur. Phys. J.* **C 72** (2012) 1844 [arXiv:1108.5602] [INSPIRE].

[41] ATLAS collaboration, *Performance of missing transverse momentum reconstruction in ATLAS studied in proton-proton collisions recorded in 2012 at 8 TeV*, ATLAS-CONF-2013-082 (2013).

[42] P. Nason, *A new method for combining NLO QCD with shower Monte Carlo algorithms*, *JHEP* **11** (2004) 040 [hep-ph/0409146] [INSPIRE].

[43] S. Frixione, P. Nason and C. Oleari, *Matching NLO QCD computations with parton shower simulations: the POWHEG method*, *JHEP* **11** (2007) 070 [arXiv:0709.2092] [INSPIRE].

[44] S. Alioli, P. Nason, C. Oleari and E. Re, *A general framework for implementing NLO calculations in shower Monte Carlo programs: the POWHEG BOX*, *JHEP* **06** (2010) 043 [arXiv:1002.2581] [INSPIRE].

[45] E. Bagnaschi, G. Degrassi, P. Slavich and A. Vicini, *Higgs production via gluon fusion in the POWHEG approach in the SM and in the MSSM*, *JHEP* **02** (2012) 088 [arXiv:1111.2854] [INSPIRE].

[46] T. Sjöstrand, S. Mrenna and P.Z. Skands, *A brief introduction to PYTHIA 8.1*, *Comput. Phys. Commun.* **178** (2008) 852 [arXiv:0710.3820] [INSPIRE].

[47] H.-L. Lai et al., *New parton distributions for collider physics*, *Phys. Rev.* **D 82** (2010) 074024 [arXiv:1007.2241] [INSPIRE].

[48] A. Djouadi, M. Spira and P.M. Zerwas, *Production of Higgs bosons in proton colliders: QCD corrections*, *Phys. Lett.* **B 264** (1991) 440 [INSPIRE].

[49] S. Dawson, *Radiative corrections to Higgs boson production*, *Nucl. Phys.* **B 359** (1991) 283 [INSPIRE].

JHEP04(2015)117

[50] M. Spira, A. Djouadi, D. Graudenz and P.M. Zerwas, *Higgs boson production at the LHC*, *Nucl. Phys.* **B 453** (1995) 17 [hep-ph/9504378] [INSPIRE].

[51] R.V. Harlander and W.B. Kilgore, *Next-to-next-to-leading order Higgs production at hadron colliders*, *Phys. Rev. Lett.* **88** (2002) 201801 [hep-ph/0201206] [INSPIRE].

[52] C. Anastasiou and K. Melnikov, *Higgs boson production at hadron colliders in NNLO QCD*, *Nucl. Phys.* **B 646** (2002) 220 [hep-ph/0207004] [INSPIRE].

[53] V. Ravindran, J. Smith and W.L. van Neerven, *NNLO corrections to the total cross-section for Higgs boson production in hadron hadron collisions*, *Nucl. Phys.* **B 665** (2003) 325 [hep-ph/0302135] [INSPIRE].

[54] S. Catani, D. de Florian, M. Grazzini and P. Nason, *Soft gluon resummation for Higgs boson production at hadron colliders*, *JHEP* **07** (2003) 028 [hep-ph/0306211] [INSPIRE].

[55] U. Aglietti, R. Bonciani, G. Degrassi and A. Vicini, *Two loop light fermion contribution to Higgs production and decays*, *Phys. Lett.* **B 595** (2004) 432 [hep-ph/0404071] [INSPIRE].

[56] S. Actis, G. Passarino, C. Sturm and S. Uccirati, *NLO electroweak corrections to Higgs boson production at hadron colliders*, *Phys. Lett.* **B 670** (2008) 12 [arXiv:0809.1301] [INSPIRE].

[57] M. Ciccolini, A. Denner and S. Dittmaier, *Strong and electroweak corrections to the production of Higgs + 2-jets via weak interactions at the LHC*, *Phys. Rev. Lett.* **99** (2007) 161803 [arXiv:0707.0381] [INSPIRE].

[58] M. Ciccolini, A. Denner and S. Dittmaier, *Electroweak and QCD corrections to Higgs production via vector-boson fusion at the LHC*, *Phys. Rev.* **D 77** (2008) 013002 [arXiv:0710.4749] [INSPIRE].

[59] K. Arnold et al., *VBFNLO: a parton level Monte Carlo for processes with electroweak bosons*, *Comput. Phys. Commun.* **180** (2009) 1661 [arXiv:0811.4559] [INSPIRE].

[60] P. Bolzoni, F. Maltoni, S.-O. Moch and M. Zaro, *Higgs production via vector-boson fusion at NNLO in QCD*, *Phys. Rev. Lett.* **105** (2010) 011801 [arXiv:1003.4451] [INSPIRE].

[61] J. Pumplin et al., *New generation of parton distributions with uncertainties from global QCD analysis*, *JHEP* **07** (2002) 012 [hep-ph/0201195] [INSPIRE].

[62] O. Brein, A. Djouadi and R. Harlander, *NNLO QCD corrections to the Higgs-strahlung processes at hadron colliders*, *Phys. Lett.* **B 579** (2004) 149 [hep-ph/0307206] [INSPIRE].

[63] M.L. Ciccolini, S. Dittmaier and M. Krämer, *Electroweak radiative corrections to associated WH and ZH production at hadron colliders*, *Phys. Rev.* **D 68** (2003) 073003 [hep-ph/0306234] [INSPIRE].

[64] M. Grazzini and H. Sargsyan, *Heavy-quark mass effects in Higgs boson production at the LHC*, *JHEP* **09** (2013) 129 [arXiv:1306.4581] [INSPIRE].

[65] D. de Florian, G. Ferrera, M. Grazzini and D. Tommasini, *Higgs boson production at the LHC: transverse momentum resummation effects in the $H \to 2\gamma$, $H \to WW \to l\nu l\nu$ and $H \to ZZ \to 4l$ decay modes*, *JHEP* **06** (2012) 132 [arXiv:1203.6321] [INSPIRE].

[66] J.M. Campbell, R.K. Ellis and G. Zanderighi, *Next-to-leading order Higgs + 2 jet production via gluon fusion*, *JHEP* **10** (2006) 028 [hep-ph/0608194] [INSPIRE].

[67] A. Banfi, P.F. Monni, G.P. Salam and G. Zanderighi, *Higgs and Z-boson production with a jet veto*, *Phys. Rev. Lett.* **109** (2012) 202001 [arXiv:1206.4998] [INSPIRE].

[68] A. Banfi, G.P. Salam and G. Zanderighi, *NLL+NNLO predictions for jet-veto efficiencies in Higgs-boson and Drell-Yan production*, *JHEP* **06** (2012) 159 [arXiv:1203.5773] [INSPIRE].

JHEP04(2015)117

[69] A. Banfi, P.F. Monni and G. Zanderighi, *Quark masses in Higgs production with a jet veto*, *JHEP* **01** (2014) 097 [arXiv:1308.4634] [INSPIRE].

[70] LHC Higgs Cross Section Working Group, S. Dittmaier et al., *Handbook of LHC Higgs cross sections: 2. Differential distributions*, arXiv:1201.3084 [INSPIRE].

[71] S. Jadach, Z. Was, R. Decker and J.H. Kuhn, *The τ decay library TAUOLA: version 2.4*, *Comput. Phys. Commun.* **76** (1993) 361 [INSPIRE].

[72] Z. Czyczula, T. Przedzinski and Z. Was, *TauSpinner program for studies on spin effect in τ production at the LHC*, *Eur. Phys. J.* **C 72** (2012) 1988 [arXiv:1201.0117] [INSPIRE].

[73] T. Sjöstrand, S. Mrenna and P.Z. Skands, *PYTHIA 6.4 physics and manual*, *JHEP* **05** (2006) 026 [hep-ph/0603175] [INSPIRE].

[74] G. Marchesini et al., *HERWIG 5.1 — A Monte Carlo event generator for simulating hadron emission reactions with interfering gluons*, *Comput. Phys. Commun.* **67** (1992) 465.

[75] G. Corcella et al., *HERWIG 6: an event generator for hadron emission reactions with interfering gluons (including supersymmetric processes)*, *JHEP* **01** (2001) 010 [hep-ph/0011363] [INSPIRE].

[76] N. Davidson, T. Przedzinski and Z. Was, *PHOTOS interface in C++: technical and physics documentation*, arXiv:1011.0937 [INSPIRE].

[77] M.L. Mangano, M. Moretti, F. Piccinini, R. Pittau and A.D. Polosa, *ALPGEN, a generator for hard multiparton processes in hadronic collisions*, *JHEP* **07** (2003) 001 [hep-ph/0206293] [INSPIRE].

[78] M.L. Mangano, M. Moretti and R. Pittau, *Multijet matrix elements and shower evolution in hadronic collisions: $Wb\bar{b}$ + n jets as a case study*, *Nucl. Phys.* **B 632** (2002) 343 [hep-ph/0108069] [INSPIRE].

[79] T. Binoth, M. Ciccolini, N. Kauer and M. Krämer, *Gluon-induced W-boson pair production at the LHC*, *JHEP* **12** (2006) 046 [hep-ph/0611170] [INSPIRE].

[80] B.P. Kersevan and E. Richter-Was, *The Monte Carlo event generator AcerMC versions 2.0 to 3.8 with interfaces to PYTHIA 6.4, HERWIG 6.5 and ARIADNE 4.1*, *Comput. Phys. Commun.* **184** (2013) 919 [hep-ph/0405247] [INSPIRE].

[81] ATLAS collaboration, *The ATLAS simulation infrastructure*, *Eur. Phys. J.* **C 70** (2010) 823 [arXiv:1005.4568] [INSPIRE].

[82] GEANT4 collaboration, S. Agostinelli et al., *GEANT4: a simulation toolkit*, *Nucl. Instrum. Meth.* **A 506** (2003) 250 [INSPIRE].

[83] ATLAS collaboration, *Summary of ATLAS PYTHIA 8 tunes*, ATL-PHYS-PUB-2012-003 (2012).

[84] LHC Higgs Cross Section Working Group, S. Heinemeyer et al., *Handbook of LHC Higgs cross sections: 3. Higgs properties*, arXiv:1307.1347 [INSPIRE].

[85] S. Catani, L. Cieri, G. Ferrera, D. de Florian and M. Grazzini, *Vector boson production at hadron colliders: a fully exclusive QCD calculation at NNLO*, *Phys. Rev. Lett.* **103** (2009) 082001 [arXiv:0903.2120] [INSPIRE].

[86] S. Catani and M. Grazzini, *An NNLO subtraction formalism in hadron collisions and its application to Higgs boson production at the LHC*, *Phys. Rev. Lett.* **98** (2007) 222002 [hep-ph/0703012] [INSPIRE].

[87] G. Corcella et al., *HERWIG 6.5 release note*, hep-ph/0210213 [INSPIRE].

JHEP04(2015)117

[88] T. Gleisberg et al., *Event generation with SHERPA 1.1*, *JHEP* **02** (2009) 007 [arXiv:0811.4622] [INSPIRE].

[89] M. Cacciari, M. Czakon, M. Mangano, A. Mitov and P. Nason, *Top-pair production at hadron colliders with next-to-next-to-leading logarithmic soft-gluon resummation*, *Phys. Lett.* **B 710** (2012) 612 [arXiv:1111.5869] [INSPIRE].

[90] P. Bärnreuther, M. Czakon and A. Mitov, *Percent level precision physics at the Tevatron: first genuine NNLO QCD corrections to $q\bar{q} \to t\bar{t} + X$*, *Phys. Rev. Lett.* **109** (2012) 132001 [arXiv:1204.5201] [INSPIRE].

[91] M. Czakon and A. Mitov, *NNLO corrections to top-pair production at hadron colliders: the all-fermionic scattering channels*, *JHEP* **12** (2012) 054 [arXiv:1207.0236] [INSPIRE].

[92] M. Czakon and A. Mitov, *NNLO corrections to top pair production at hadron colliders: the quark-gluon reaction*, *JHEP* **01** (2013) 080 [arXiv:1210.6832] [INSPIRE].

[93] M. Czakon, P. Fiedler and A. Mitov, *Total top-quark pair-production cross section at hadron colliders through $O(\alpha_s^4)$*, *Phys. Rev. Lett.* **110** (2013) 252004 [arXiv:1303.6254] [INSPIRE].

[94] M. Czakon and A. Mitov, *Top++: a program for the calculation of the top-pair cross-section at hadron colliders*, *Comput. Phys. Commun.* **185** (2014) 2930 [arXiv:1112.5675] [INSPIRE].

[95] N. Kidonakis, *Two-loop soft anomalous dimensions for single top quark associated production with a W^- or H^-*, *Phys. Rev.* **D 82** (2010) 054018 [arXiv:1005.4451] [INSPIRE].

[96] N. Kidonakis, *NNLL resummation for s-channel single top quark production*, *Phys. Rev.* **D 81** (2010) 054028 [arXiv:1001.5034] [INSPIRE].

[97] N. Kidonakis, *Next-to-next-to-leading-order collinear and soft gluon corrections for t-channel single top quark production*, *Phys. Rev.* **D 83** (2011) 091503 [arXiv:1103.2792] [INSPIRE].

[98] J.M. Campbell, R.K. Ellis and C. Williams, *Vector boson pair production at the LHC*, *JHEP* **07** (2011) 018 [arXiv:1105.0020] [INSPIRE].

[99] R. Ellis et al., *Higgs decay to $\tau^+\tau^-$: a possible signature of intermediate mass Higgs bosons at high energy hadron colliders*, *Nucl. Phys.* **297** (1988) 221.

[100] A. Elagin, P. Murat, A. Pranko and A. Safonov, *A new mass reconstruction technique for resonances decaying to di-τ*, *Nucl. Instrum. Meth.* **A 654** (2011) 481 [arXiv:1012.4686] [INSPIRE].

[101] G. Hanson et al., *Evidence for Jet Structure in Hadron Production by e^+e^- Annihilation*, *Phys. Rev. Lett.* **35** (1975) 1609 [INSPIRE].

[102] ATLAS collaboration, *Measurement of the production cross section of jets in association with a Z boson in pp collisions at $\sqrt{s} = 7$ TeV with the ATLAS detector*, *JHEP* **07** (2013) 032 [arXiv:1304.7098] [INSPIRE].

[103] ATLAS collaboration, *Measurement of the Z/γ^* boson transverse momentum distribution in pp collisions at $\sqrt{s} = 7$ TeV with the ATLAS detector*, *JHEP* **09** (2014) 145 [arXiv:1406.3660] [INSPIRE].

[104] ATLAS collaboration, *Measurement of the electroweak production of dijets in association with a Z-boson and distributions sensitive to vector boson fusion in proton-proton collisions at $\sqrt{s} = 8$ TeV using the ATLAS detector*, *JHEP* **04** (2014) 031 [arXiv:1401.7610] [INSPIRE].

[105] ATLAS collaboration, *Measurement of the $Z \to \tau\tau$ cross section with the ATLAS detector*, *Phys. Rev.* **D 84** (2011) 112006 [arXiv:1108.2016] [INSPIRE].

JHEP04(2015)117

[106] ATLAS collaboration, *Improved luminosity determination in pp collisions at $\sqrt{s} = 7$ TeV using the ATLAS detector at the LHC*, *Eur. Phys. J.* **C 73** (2013) 2518 [arXiv:1302.4393] [INSPIRE].

[107] ATLAS collaboration, *Calibration of b-tagging using dileptonic top pair events in a combinatorial likelihood approach with the ATLAS experiment*, ATLAS-CONF-2014-004 (2014).

[108] ATLAS collaboration, *Determination of the τ energy scale and the associated systematic uncertainty in proton-proton collisions at $\sqrt{s} = 8$ TeV with the ATLAS detector at the LHC in 2012*, ATLAS-CONF-2013-044 (2013).

[109] ATLAS collaboration, *Jet energy resolution in proton-proton collisions at $\sqrt{s} = 7$ TeV recorded in 2010 with the ATLAS detector*, *Eur. Phys. J.* **C 73** (2013) 2306 [arXiv:1210.6210] [INSPIRE].

[110] LHC Higgs Cross Section Working Group, S. Dittmaier et al., *Handbook of LHC Higgs cross sections: 1. Inclusive observables*, arXiv:1101.0593 [INSPIRE].

[111] I.W. Stewart and F.J. Tackmann, *Theory uncertainties for Higgs and other searches using jet bins*, *Phys. Rev.* **D 85** (2012) 034011 [arXiv:1107.2117] [INSPIRE].

[112] S. Frixione and B.R. Webber, *Matching NLO QCD computations and parton shower simulations*, *JHEP* **06** (2002) 029 [hep-ph/0204244] [INSPIRE].

[113] A.D. Martin, W.J. Stirling, R.S. Thorne and G. Watt, *Parton distributions for the LHC*, *Eur. Phys. J.* **C 63** (2009) 189 [arXiv:0901.0002] [INSPIRE].

[114] R.D. Ball et al., *Impact of heavy quark masses on parton distributions and LHC phenomenology*, *Nucl. Phys.* **B 849** (2011) 296 [arXiv:1101.1300] [INSPIRE].

[115] J. Alwall et al., *The automated computation of tree-level and next-to-leading order differential cross sections and their matching to parton shower simulations*, *JHEP* **07** (2014) 079 [arXiv:1405.0301] [INSPIRE].

[116] ATLAS collaboration, *Measurement of the Higgs boson mass from the $H \to \gamma\gamma$ and $H \to ZZ^* \to 4\ell$ channels with the ATLAS detector using $25\,fb^{-1}$ of pp collision data*, *Phys. Rev.* **D 90** (2014) 052004 [arXiv:1406.3827] [INSPIRE].

[117] G. Cowan, K. Cranmer, E. Gross and O. Vitells, *Asymptotic formulae for likelihood-based tests of new physics*, *Eur. Phys. J.* **C 71** (2011) 1554 [*Erratum ibid.* **C 73** (2013) 2501] [arXiv:1007.1727] [INSPIRE].

[118] B. Efron and C. Stein, *The Jackknife estimate of variance*, *Ann. Statist.* **9** (1981) 586.

[119] G. Bohm and G. Zech, *Introduction to statistics and data analysis for physicists*, 2nd revised edition, Verlag Deutsches Elektronen-Synchrotron, Hamburg, Germany (2014).

JHEP04(2015)117

The ATLAS collaboration

G. Aad[85], B. Abbott[113], J. Abdallah[152], S. Abdel Khalek[117], O. Abdinov[11], R. Aben[107], B. Abi[114], M. Abolins[90], O.S. AbouZeid[159], H. Abramowicz[154], H. Abreu[153], R. Abreu[30], Y. Abulaiti[147a,147b], B.S. Acharya[165a,165b,a], L. Adamczyk[38a], D.L. Adams[25], J. Adelman[108], S. Adomeit[100], T. Adye[131], T. Agatonovic-Jovin[13a], J.A. Aguilar-Saavedra[126a,126f], M. Agustoni[17], S.P. Ahlen[22], F. Ahmadov[65,b], G. Aielli[134a,134b], H. Akerstedt[147a,147b], T.P.A. Åkesson[81], G. Akimoto[156], A.V. Akimov[96], G.L. Alberghi[20a,20b], J. Albert[170], S. Albrand[55], M.J. Alconada Verzini[71], M. Aleksa[30], I.N. Aleksandrov[65], C. Alexa[26a], G. Alexander[154], G. Alexandre[49], T. Alexopoulos[10], M. Alhroob[113], G. Alimonti[91a], L. Alio[85], J. Alison[31], B.M.M. Allbrooke[18], L.J. Allison[72], P.P. Allport[74], A. Aloisio[104a,104b], A. Alonso[36], F. Alonso[71], C. Alpigiani[76], A. Altheimer[35], B. Alvarez Gonzalez[90], D. Álvarez Piqueras[168], M.G. Alviggi[104a,104b], K. Amako[66], Y. Amaral Coutinho[24a], C. Amelung[23], D. Amidei[89], S.P. Amor Dos Santos[126a,126c], A. Amorim[126a,126b], S. Amoroso[48], N. Amram[154], G. Amundsen[23], C. Anastopoulos[140], L.S. Ancu[49], N. Andari[30], T. Andeen[35], C.F. Anders[58b], G. Anders[30], K.J. Anderson[31], A. Andreazza[91a,91b], V. Andrei[58a], X.S. Anduaga[71], S. Angelidakis[9], I. Angelozzi[107], P. Anger[44], A. Angerami[35], F. Anghinolfi[30], A.V. Anisenkov[109,c], N. Anjos[12], A. Annovi[47], M. Antonelli[47], A. Antonov[98], J. Antos[145b], F. Anulli[133a], M. Aoki[66], L. Aperio Bella[18], G. Arabidze[90], Y. Arai[66], J.P. Araque[126a], A.T.H. Arce[45], F.A. Arduh[71], J-F. Arguin[95], S. Argyropoulos[42], M. Arik[19a], A.J. Armbruster[30], O. Arnaez[30], V. Arnal[82], H. Arnold[48], M. Arratia[28], O. Arslan[21], A. Artamonov[97], G. Artoni[23], S. Asai[156], N. Asbah[42], A. Ashkenazi[154], B. Åsman[147a,147b], L. Asquith[150], K. Assamagan[25], R. Astalos[145a], M. Atkinson[166], N.B. Atlay[142], B. Auerbach[6], K. Augsten[128], M. Aurousseau[146b], G. Avolio[30], B. Axen[15], G. Azuelos[95,d], Y. Azuma[156], M.A. Baak[30], A.E. Baas[58a], C. Bacci[135a,135b], H. Bachacou[137], K. Bachas[155], M. Backes[30], M. Backhaus[30], E. Badescu[26a], P. Bagiacchi[133a,133b], P. Bagnaia[133a,133b], Y. Bai[33a], T. Bain[35], J.T. Baines[131], O.K. Baker[177], P. Balek[129], F. Balli[84], E. Banas[39], Sw. Banerjee[174], A.A.E. Bannoura[176], H.S. Bansil[18], L. Barak[173], S.P. Baranov[96], E.L. Barberio[88], D. Barberis[50a,50b], M. Barbero[85], T. Barillari[101], M. Barisonzi[176], T. Barklow[144], N. Barlow[28], S.L. Barnes[84], B.M. Barnett[131], R.M. Barnett[15], Z. Barnovska[5], A. Baroncelli[135a], G. Barone[49], A.J. Barr[120], F. Barreiro[82], J. Barreiro Guimarães da Costa[57], R. Bartoldus[144], A.E. Barton[72], P. Bartos[145a], V. Bartsch[150], A. Bassalat[117], A. Basye[166], R.L. Bates[53], S.J. Batista[159], J.R. Batley[28], M. Battaglia[138], M. Battistin[30], F. Bauer[137], H.S. Bawa[144,e], J.B. Beacham[111], M.D. Beattie[72], T. Beau[80], P.H. Beauchemin[162], R. Beccherle[124a,124b], P. Bechtle[21], H.P. Beck[17,f], K. Becker[120], S. Becker[100], M. Beckingham[171], C. Becot[117], A.J. Beddall[19c], A. Beddall[19c], S. Bedikian[177], V.A. Bednyakov[65], C.P. Bee[149], L.J. Beemster[107], T.A. Beermann[176], M. Begel[25], K. Behr[120], C. Belanger-Champagne[87], P.J. Bell[49], W.H. Bell[49], G. Bella[154], L. Bellagamba[20a], A. Bellerive[29], M. Bellomo[86], K. Belotskiy[98], O. Beltramello[30], O. Benary[154], D. Benchekroun[136a], K. Bendtz[147a,147b], N. Benekos[166], Y. Benhammou[154], E. Benhar Noccioli[49], J.A. Benitez Garcia[160b], D.P. Benjamin[45], J.R. Bensinger[23], S. Bentvelsen[107], D. Berge[107], E. Bergeaas Kuutmann[167], N. Berger[5], F. Berghaus[170], J. Beringer[15], C. Bernard[22], N.R. Bernard[86], C. Bernius[110], F.U. Bernlochner[21], T. Berry[77], P. Berta[129], C. Bertella[83], G. Bertoli[147a,147b], F. Bertolucci[124a,124b], C. Bertsche[113], D. Bertsche[113], M.I. Besana[91a], G.J. Besjes[106], O. Bessidskaia Bylund[147a,147b], M. Bessner[42], N. Besson[137], C. Betancourt[48], S. Bethke[101], A.J. Bevan[76], W. Bhimji[46], R.M. Bianchi[125], L. Bianchini[23], M. Bianco[30], O. Biebel[100], S.P. Bieniek[78], K. Bierwagen[54], M. Biglietti[135a], J. Bilbao De Mendizabal[49], H. Bilokon[47], M. Bindi[54], S. Binet[117], A. Bingul[19c], C. Bini[133a,133b], C.W. Black[151], J.E. Black[144], K.M. Black[22], D. Blackburn[139], R.E. Blair[6], J.-B. Blanchard[137], T. Blazek[145a], I. Bloch[42], C. Blocker[23], W. Blum[83,*], U. Blumenschein[54], G.J. Bobbink[107], V.S. Bobrovnikov[109,c], S.S. Bocchetta[81], A. Bocci[45], C. Bock[100], C.R. Boddy[120], M. Boehler[48], T.T. Boek[176], J.A. Bogaerts[30], A.G. Bogdanchikov[109], A. Bogouch[92,*], C. Bohm[147a], V. Boisvert[77], T. Bold[38a], V. Boldea[26a], A.S. Boldyrev[99], M. Bomben[80], M. Bona[76], M. Boonekamp[137], A. Borisov[130], G. Borissov[72], S. Borroni[42], J. Bortfeldt[100], V. Bortolotto[60a], K. Bos[107], D. Boscherini[20a], M. Bosman[12], H. Boterenbrood[107], J. Boudreau[125], J. Bouffard[2],

JHEP04(2015)117

E.V. Bouhova-Thacker[72], D. Boumediene[34], C. Bourdarios[117], N. Bousson[114], S. Boutouil[136d], A. Boveia[31], J. Boyd[30], I.R. Boyko[65], I. Bozic[13a], J. Bracinik[18], A. Brandt[8], G. Brandt[15], O. Brandt[58a], U. Bratzler[157], B. Brau[86], J.E. Brau[116], H.M. Braun[176,*], S.F. Brazzale[165a,165c], B. Brelier[159], K. Brendlinger[122], A.J. Brennan[88], R. Brenner[167], S. Bressler[173], K. Bristow[146c], T.M. Bristow[46], D. Britton[53], F.M. Brochu[28], I. Brock[21], R. Brock[90], J. Bronner[101], G. Brooijmans[35], T. Brooks[77], W.K. Brooks[32b], J. Brosamer[15], E. Brost[116], J. Brown[55], P.A. Bruckman de Renstrom[39], D. Bruncko[145b], R. Bruneliere[48], S. Brunet[61], A. Bruni[20a], G. Bruni[20a], M. Bruschi[20a], L. Bryngemark[81], T. Buanes[14], Q. Buat[143], F. Bucci[49], P. Buchholz[142], A.G. Buckley[53], S.I. Buda[26a], I.A. Budagov[65], F. Buehrer[48], L. Bugge[119], M.K. Bugge[119], O. Bulekov[98], A.C. Bundock[74], H. Burckhart[30], S. Burdin[74], B. Burghgrave[108], S. Burke[131], I. Burmeister[43], E. Busato[34], D. Büscher[48], V. Büscher[83], P. Bussey[53], C.P. Buszello[167], B. Butler[57], J.M. Butler[22], A.I. Butt[3], C.M. Buttar[53], J.M. Butterworth[78], P. Butti[107], W. Buttinger[28], A. Buzatu[53], M. Byszewski[10], S. Cabrera Urbán[168], D. Caforio[20a,20b], O. Cakir[4a], P. Calafiura[15], A. Calandri[137], G. Calderini[80], P. Calfayan[100], L.P. Caloba[24a], D. Calvet[34], S. Calvet[34], R. Camacho Toro[49], S. Camarda[42], D. Cameron[119], L.M. Caminada[15], R. Caminal Armadans[12], S. Campana[30], M. Campanelli[78], A. Campoverde[149], V. Canale[104a,104b], A. Canepa[160a], M. Cano Bret[76], J. Cantero[82], R. Cantrill[126a], T. Cao[40], M.D.M. Capeans Garrido[30], I. Caprini[26a], M. Caprini[26a], M. Capua[37a,37b], R. Caputo[83], R. Cardarelli[134a], T. Carli[30], G. Carlino[104a], L. Carminati[91a,91b], S. Caron[106], E. Carquin[32a], G.D. Carrillo-Montoya[146c], J.R. Carter[28], J. Carvalho[126a,126c], D. Casadei[78], M.P. Casado[12], M. Casolino[12], E. Castaneda-Miranda[146b], A. Castelli[107], V. Castillo Gimenez[168], N.F. Castro[126a], P. Catastini[57], A. Catinaccio[30], J.R. Catmore[119], A. Cattai[30], G. Cattani[134a,134b], J. Caudron[83], V. Cavaliere[166], D. Cavalli[91a], M. Cavalli-Sforza[12], V. Cavasinni[124a,124b], F. Ceradini[135a,135b], B.C. Cerio[45], K. Cerny[129], A.S. Cerqueira[24b], A. Cerri[150], L. Cerrito[76], F. Cerutti[15], M. Cerv[30], A. Cervelli[17], S.A. Cetin[19b], A. Chafaq[136a], D. Chakraborty[108], I. Chalupkova[129], P. Chang[166], B. Chapleau[87], J.D. Chapman[28], D. Charfeddine[117], D.G. Charlton[18], C.C. Chau[159], C.A. Chavez Barajas[150], S. Cheatham[153], A. Chegwidden[90], S. Chekanov[6], S.V. Chekulaev[160a], G.A. Chelkov[65,g], M.A. Chelstowska[89], C. Chen[64], H. Chen[25], K. Chen[149], L. Chen[33d,h], S. Chen[33c], X. Chen[33f], Y. Chen[67], H.C. Cheng[89], Y. Cheng[31], A. Cheplakov[65], E. Cheremushkina[130], R. Cherkaoui El Moursli[136e], V. Chernyatin[25,*], E. Cheu[7], L. Chevalier[137], V. Chiarella[47], G. Chiefari[104a,104b], J.T. Childers[6], A. Chilingarov[72], G. Chiodini[73a], A.S. Chisholm[18], R.T. Chislett[78], A. Chitan[26a], M.V. Chizhov[65], S. Chouridou[9], B.K.B. Chow[100], D. Chromek-Burckhart[30], M.L. Chu[152], J. Chudoba[127], J.J. Chwastowski[39], L. Chytka[115], G. Ciapetti[133a,133b], A.K. Ciftci[4a], R. Ciftci[4a], D. Cinca[53], V. Cindro[75], A. Ciocio[15], Z.H. Citron[173], M. Citterio[91a], M. Ciubancan[26a], A. Clark[49], P.J. Clark[46], R.N. Clarke[15], W. Cleland[125], J.C. Clemens[85], C. Clement[147a,147b], Y. Coadou[85], M. Cobal[165a,165c], A. Coccaro[139], J. Cochran[64], L. Coffey[23], J.G. Cogan[144], B. Cole[35], S. Cole[108], A.P. Colijn[107], J. Collot[55], T. Colombo[58c], G. Compostella[101], P. Conde Muiño[126a,126b], E. Coniavitis[48], S.H. Connell[146b], I.A. Connelly[77], S.M. Consonni[91a,91b], V. Consorti[48], S. Constantinescu[26a], C. Conta[121a,121b], G. Conti[30], F. Conventi[104a,i], M. Cooke[15], B.D. Cooper[78], A.M. Cooper-Sarkar[120], N.J. Cooper-Smith[77], K. Copic[15], T. Cornelissen[176], M. Corradi[20a], F. Corriveau[87,j], A. Corso-Radu[164], A. Cortes-Gonzalez[12], G. Cortiana[101], G. Costa[91a], M.J. Costa[168], D. Costanzo[140], D. Côté[8], G. Cottin[28], G. Cowan[77], B.E. Cox[84], K. Cranmer[110], G. Cree[29], S. Crépé-Renaudin[55], F. Crescioli[80], W.A. Cribbs[147a,147b], M. Crispin Ortuzar[120], M. Cristinziani[21], V. Croft[106], G. Crosetti[37a,37b], T. Cuhadar Donszelmann[140], J. Cummings[177], M. Curatolo[47], C. Cuthbert[151], H. Czirr[142], P. Czodrowski[3], S. D'Auria[53], M. D'Onofrio[74], M.J. Da Cunha Sargedas De Sousa[126a,126b], C. Da Via[84], W. Dabrowski[38a], A. Dafinca[120], T. Dai[89], O. Dale[14], F. Dallaire[95], C. Dallapiccola[86], M. Dam[36], A.C. Daniells[18], M. Danninger[169], M. Dano Hoffmann[137], V. Dao[48], G. Darbo[50a], S. Darmora[8], J. Dassoulas[74], A. Dattagupta[61], W. Davey[21], C. David[170], T. Davidek[129], E. Davies[120,k], M. Davies[154], O. Davignon[80], A.R. Davison[78], P. Davison[78], Y. Davygora[58a], E. Dawe[143], I. Dawson[140], R.K. Daya-Ishmukhametova[86], K. De[8], R. de Asmundis[104a], S. De Castro[20a,20b], S. De Cecco[80],

JHEP04(2015)117

N. De Groot[106], P. de Jong[107], H. De la Torre[82], F. De Lorenzi[64], L. De Nooij[107], D. De Pedis[133a], A. De Salvo[133a], U. De Sanctis[150], A. De Santo[150], J.B. De Vivie De Regie[117], W.J. Dearnaley[72], R. Debbe[25], C. Debenedetti[138], B. Dechenaux[55], D.V. Dedovich[65], I. Deigaard[107], J. Del Peso[82], T. Del Prete[124a,124b], F. Deliot[137], C.M. Delitzsch[49], M. Deliyergiyev[75], A. Dell'Acqua[30], L. Dell'Asta[22], M. Dell'Orso[124a,124b], M. Della Pietra[104a,i], D. della Volpe[49], M. Delmastro[5], P.A. Delsart[55], C. Deluca[107], D.A. DeMarco[159], S. Demers[177], M. Demichev[65], A. Demilly[80], S.P. Denisov[130], D. Derendarz[39], J.E. Derkaoui[136d], F. Derue[80], P. Dervan[74], K. Desch[21], C. Deterre[42], P.O. Deviveiros[30], A. Dewhurst[131], S. Dhaliwal[107], A. Di Ciaccio[134a,134b], L. Di Ciaccio[5], A. Di Domenico[133a,133b], C. Di Donato[104a,104b], A. Di Girolamo[30], B. Di Girolamo[30], A. Di Mattia[153], B. Di Micco[135a,135b], R. Di Nardo[47], A. Di Simone[48], R. Di Sipio[20a,20b], D. Di Valentino[29], F.A. Dias[46], M.A. Diaz[32a], E.B. Diehl[89], J. Dietrich[16], T.A. Dietzsch[58a], S. Diglio[85], A. Dimitrievska[13a], J. Dingfelder[21], P. Dita[26a], S. Dita[26a], F. Dittus[30], F. Djama[85], T. Djobava[51b], J.I. Djuvsland[58a], M.A.B. do Vale[24c], D. Dobos[30], C. Doglioni[49], T. Doherty[53], T. Dohmae[156], J. Dolejsi[129], Z. Dolezal[129], B.A. Dolgoshein[98,*], M. Donadelli[24d], S. Donati[124a,124b], P. Dondero[121a,121b], J. Donini[34], J. Dopke[131], A. Doria[104a], M.T. Dova[71], A.T. Doyle[53], E. Drechsler[54], M. Dris[10], J. Dubbert[89], S. Dube[15], E. Dubreuil[34], E. Duchovni[173], G. Duckeck[100], O.A. Ducu[26a], D. Duda[176], A. Dudarev[30], F. Dudziak[64], L. Duflot[117], L. Duguid[77], M. Dührssen[30], M. Dunford[58a], H. Duran Yildiz[4a], M. Düren[52], A. Durglishvili[51b], D. Duschinger[44], M. Dwuznik[38a], M. Dyndal[38a], J. Ebke[100], W. Edson[2], N.C. Edwards[46], W. Ehrenfeld[21], T. Eifert[30], G. Eigen[14], K. Einsweiler[15], T. Ekelof[167], M. El Kacimi[136c], M. Ellert[167], S. Elles[5], F. Ellinghaus[83], A.A. Elliot[170], N. Ellis[30], J. Elmsheuser[100], M. Elsing[30], D. Emeliyanov[131], Y. Enari[156], O.C. Endner[83], M. Endo[118], R. Engelmann[149], J. Erdmann[43], A. Ereditato[17], D. Eriksson[147a], G. Ernis[176], J. Ernst[2], M. Ernst[25], J. Ernwein[137], S. Errede[166], E. Ertel[83], M. Escalier[117], H. Esch[43], C. Escobar[125], B. Esposito[47], A.I. Etienvre[137], E. Etzion[154], H. Evans[61], A. Ezhilov[123], L. Fabbri[20a,20b], G. Facini[31], R.M. Fakhrutdinov[130], S. Falciano[133a], R.J. Falla[78], J. Faltova[129], Y. Fang[33a], M. Fanti[91a,91b], A. Farbin[8], A. Farilla[135a], T. Farooque[12], S. Farrell[15], S.M. Farrington[171], P. Farthouat[30], F. Fassi[136e], P. Fassnacht[30], D. Fassouliotis[9], A. Favareto[50a,50b], L. Fayard[117], P. Federic[145a], O.L. Fedin[123,l], W. Fedorko[169], S. Feigl[30], L. Feligioni[85], C. Feng[33d], E.J. Feng[6], H. Feng[89], A.B. Fenyuk[130], P. Fernandez Martinez[168], S. Fernandez Perez[30], S. Ferrag[53], J. Ferrando[53], A. Ferrari[167], P. Ferrari[107], R. Ferrari[121a], D.E. Ferreira de Lima[53], A. Ferrer[168], D. Ferrere[49], C. Ferretti[89], A. Ferretto Parodi[50a,50b], M. Fiascaris[31], F. Fiedler[83], A. Filipčič[75], M. Filipuzzi[42], F. Filthaut[106], M. Fincke-Keeler[170], K.D. Finelli[151], M.C.N. Fiolhais[126a,126c], L. Fiorini[168], A. Firan[40], A. Fischer[2], J. Fischer[176], W.C. Fisher[90], E.A. Fitzgerald[23], M. Flechl[48], I. Fleck[142], P. Fleischmann[89], S. Fleischmann[176], G.T. Fletcher[140], G. Fletcher[76], T. Flick[176], A. Floderus[81], L.R. Flores Castillo[60a], M.J. Flowerdew[101], A. Formica[137], A. Forti[84], D. Fournier[117], H. Fox[72], S. Fracchia[12], P. Francavilla[80], M. Franchini[20a,20b], S. Franchino[30], D. Francis[30], L. Franconi[119], M. Franklin[57], M. Fraternali[121a,121b], S.T. French[28], C. Friedrich[42], F. Friedrich[44], D. Froidevaux[30], J.A. Frost[120], C. Fukunaga[157], E. Fullana Torregrosa[83], B.G. Fulsom[144], J. Fuster[168], C. Gabaldon[55], O. Gabizon[176], A. Gabrielli[20a,20b], A. Gabrielli[133a,133b], S. Gadatsch[107], S. Gadomski[49], G. Gagliardi[50a,50b], P. Gagnon[61], C. Galea[106], B. Galhardo[126a,126c], E.J. Gallas[120], B.J. Gallop[131], P. Gallus[128], G. Galster[36], K.K. Gan[111], J. Gao[33b], Y.S. Gao[144,e], F.M. Garay Walls[46], F. Garberson[177], C. García[168], J.E. García Navarro[168], M. Garcia-Sciveres[15], R.W. Gardner[31], N. Garelli[144], V. Garonne[30], C. Gatti[47], G. Gaudio[121a], B. Gaur[142], L. Gauthier[95], P. Gauzzi[133a,133b], I.L. Gavrilenko[96], C. Gay[169], G. Gaycken[21], E.N. Gazis[10], P. Ge[33d], Z. Gecse[169], C.N.P. Gee[131], D.A.A. Geerts[107], Ch. Geich-Gimbel[21], K. Gellerstedt[147a,147b], C. Gemme[50a], A. Gemmell[53], M.H. Genest[55], S. Gentile[133a,133b], M. George[54], S. George[77], D. Gerbaudo[164], A. Gershon[154], H. Ghazlane[136b], N. Ghodbane[34], B. Giacobbe[20a], S. Giagu[133a,133b], V. Giangiobbe[12], P. Giannetti[124a,124b], F. Gianotti[30], B. Gibbard[25], S.M. Gibson[77], M. Gilchriese[15], T.P.S. Gillam[28], D. Gillberg[30], G. Gilles[34], D.M. Gingrich[3,d], N. Giokaris[9], M.P. Giordani[165a,165c], R. Giordano[104a,104b], F.M. Giorgi[20a], F.M. Giorgi[16], P.F. Giraud[137], D. Giugni[91a], C. Giuliani[48], M. Giulini[58b],

JHEP04(2015)117

B.K. Gjelsten[119], S. Gkaitatzis[155], I. Gkialas[155], E.L. Gkougkousis[117], L.K. Gladilin[99], C. Glasman[82], J. Glatzer[30], P.C.F. Glaysher[46], A. Glazov[42], G.L. Glonti[62], M. Goblirsch-Kolb[101], J.R. Goddard[76], J. Godlewski[30], S. Goldfarb[89], T. Golling[49], D. Golubkov[130], A. Gomes[126a,126b,126d], L.S. Gomez Fajardo[42], R. Gonçalo[126a], J. Goncalves Pinto Firmino Da Costa[137], L. Gonella[21], S. González de la Hoz[168], G. Gonzalez Parra[12], S. Gonzalez-Sevilla[49], L. Goossens[30], P.A. Gorbounov[97], H.A. Gordon[25], I. Gorelov[105], B. Gorini[30], E. Gorini[73a,73b], A. Gorišek[75], E. Gornicki[39], A.T. Goshaw[45], C. Gössling[43], M.I. Gostkin[65], M. Gouighri[136a], D. Goujdami[136c], M.P. Goulette[49], A.G. Goussiou[139], C. Goy[5], H.M.X. Grabas[138], L. Graber[54], I. Grabowska-Bold[38a], P. Grafström[20a,20b], K-J. Grahn[42], J. Gramling[49], E. Gramstad[119], S. Grancagnolo[16], V. Grassi[149], V. Gratchev[123], H.M. Gray[30], E. Graziani[135a], O.G. Grebenyuk[123], Z.D. Greenwood[79,m], K. Gregersen[78], I.M. Gregor[42], P. Grenier[144], J. Griffiths[8], A.A. Grillo[138], K. Grimm[72], S. Grinstein[12,n], Ph. Gris[34], Y.V. Grishkevich[99], J.-F. Grivaz[117], J.P. Grohs[44], A. Grohsjean[42], E. Gross[173], J. Grosse-Knetter[54], G.C. Grossi[134a,134b], Z.J. Grout[150], L. Guan[33b], J. Guenther[128], F. Guescini[49], D. Guest[177], O. Gueta[154], C. Guicheney[34], E. Guido[50a,50b], T. Guillemin[117], S. Guindon[2], U. Gul[53], C. Gumpert[44], J. Guo[35], S. Gupta[120], P. Gutierrez[113], N.G. Gutierrez Ortiz[53], C. Gutschow[78], N. Guttman[154], C. Guyot[137], C. Gwenlan[120], C.B. Gwilliam[74], A. Haas[110], C. Haber[15], H.K. Hadavand[8], N. Haddad[136e], P. Haefner[21], S. Hageböck[21], Z. Hajduk[39], H. Hakobyan[178], M. Haleem[42], J. Haley[114], D. Hall[120], G. Halladjian[90], G.D. Hallewell[85], K. Hamacher[176], P. Hamal[115], K. Hamano[170], M. Hamer[54], A. Hamilton[146a], S. Hamilton[162], G.N. Hamity[146c], P.G. Hamnett[42], L. Han[33b], K. Hanagaki[118], K. Hanawa[156], M. Hance[15], P. Hanke[58a], R. Hanna[137], J.B. Hansen[36], J.D. Hansen[36], P.H. Hansen[36], K. Hara[161], A.S. Hard[174], T. Harenberg[176], F. Hariri[117], S. Harkusha[92], R.D. Harrington[46], P.F. Harrison[171], F. Hartjes[107], M. Hasegawa[67], S. Hasegawa[103], Y. Hasegawa[141], A. Hasib[113], S. Hassani[137], S. Haug[17], M. Hauschild[30], R. Hauser[90], M. Havranek[127], C.M. Hawkes[18], R.J. Hawkings[30], A.D. Hawkins[81], T. Hayashi[161], D. Hayden[90], C.P. Hays[120], J.M. Hays[76], H.S. Hayward[74], S.J. Haywood[131], S.J. Head[18], T. Heck[83], V. Hedberg[81], L. Heelan[8], S. Heim[122], T. Heim[176], B. Heinemann[15], L. Heinrich[110], J. Hejbal[127], L. Helary[22], C. Heller[100], M. Heller[30], S. Hellman[147a,147b], D. Hellmich[21], C. Helsens[30], J. Henderson[120], R.C.W. Henderson[72], Y. Heng[174], C. Hengler[42], A. Henrichs[177], A.M. Henriques Correia[30], S. Henrot-Versille[117], G.H. Herbert[16], Y. Hernández Jiménez[168], R. Herrberg-Schubert[16], G. Herten[48], R. Hertenberger[100], L. Hervas[30], G.G. Hesketh[78], N.P. Hessey[107], R. Hickling[76], E. Higón-Rodriguez[168], E. Hill[170], J.C. Hill[28], K.H. Hiller[42], S.J. Hillier[18], I. Hinchliffe[15], E. Hines[122], R.R. Hinman[15], M. Hirose[158], D. Hirschbuehl[176], J. Hobbs[149], N. Hod[107], M.C. Hodgkinson[140], P. Hodgson[140], A. Hoecker[30], M.R. Hoeferkamp[105], F. Hoenig[100], D. Hoffmann[85], M. Hohlfeld[83], T.R. Holmes[15], T.M. Hong[122], L. Hooft van Huysduynen[110], W.H. Hopkins[116], Y. Horii[103], A.J. Horton[143], J-Y. Hostachy[55], S. Hou[152], A. Hoummada[136a], J. Howard[120], J. Howarth[42], M. Hrabovsky[115], I. Hristova[16], J. Hrivnac[117], T. Hryn'ova[5], A. Hrynevich[93], C. Hsu[146c], P.J. Hsu[152,o], S.-C. Hsu[139], D. Hu[35], X. Hu[89], Y. Huang[42], Z. Hubacek[30], F. Hubaut[85], F. Huegging[21], T.B. Huffman[120], E.W. Hughes[35], G. Hughes[72], M. Huhtinen[30], T.A. Hülsing[83], M. Hurwitz[15], N. Huseynov[65,b], J. Huston[90], J. Huth[57], G. Iacobucci[49], G. Iakovidis[10], I. Ibragimov[142], L. Iconomidou-Fayard[117], E. Ideal[177], Z. Idrissi[136e], P. Iengo[104a], O. Igonkina[107], T. Iizawa[172], Y. Ikegami[66], K. Ikematsu[142], M. Ikeno[66], Y. Ilchenko[31,p], D. Iliadis[155], N. Ilic[159], Y. Inamaru[67], T. Ince[101], P. Ioannou[9], M. Iodice[135a], K. Iordanidou[9], V. Ippolito[57], A. Irles Quiles[168], C. Isaksson[167], M. Ishino[68], M. Ishitsuka[158], R. Ishmukhametov[111], C. Issever[120], S. Istin[19a], J.M. Iturbe Ponce[84], R. Iuppa[134a,134b], J. Ivarsson[81], W. Iwanski[39], H. Iwasaki[66], J.M. Izen[41], V. Izzo[104a], B. Jackson[122], M. Jackson[74], P. Jackson[1], M.R. Jaekel[30], V. Jain[2], K. Jakobs[48], S. Jakobsen[30], T. Jakoubek[127], J. Jakubek[128], D.O. Jamin[152], D.K. Jana[79], E. Jansen[78], H. Jansen[30], J. Janssen[21], M. Janus[171], G. Jarlskog[81], N. Javadov[65,b], T. Javůrek[48], L. Jeanty[15], J. Jejelava[51a,q], G.-Y. Jeng[151], D. Jennens[88], P. Jenni[48,r], J. Jentzsch[43], C. Jeske[171], S. Jézéquel[5], H. Ji[174], J. Jia[149], Y. Jiang[33b], M. Jimenez Belenguer[42], S. Jin[33a], A. Jinaru[26a], O. Jinnouchi[158],

JHEP04(2015)117

M.D. Joergensen[36], P. Johansson[140], K.A. Johns[7], K. Jon-And[147a,147b], G. Jones[171], R.W.L. Jones[72], T.J. Jones[74], J. Jongmanns[58a], P.M. Jorge[126a,126b], K.D. Joshi[84], J. Jovicevic[148], X. Ju[174], C.A. Jung[43], P. Jussel[62], A. Juste Rozas[12,n], M. Kaci[168], A. Kaczmarska[39], M. Kado[117], H. Kagan[111], M. Kagan[144], E. Kajomovitz[45], C.W. Kalderon[120], S. Kama[40], A. Kamenshchikov[130], N. Kanaya[156], M. Kaneda[30], S. Kaneti[28], V.A. Kantserov[98], J. Kanzaki[66], B. Kaplan[110], A. Kapliy[31], D. Kar[53], K. Karakostas[10], A. Karamaoun[3], N. Karastathis[10], M.J. Kareem[54], M. Karnevskiy[83], S.N. Karpov[65], Z.M. Karpova[65], K. Karthik[110], V. Kartvelishvili[72], A.N. Karyukhin[130], L. Kashif[174], G. Kasieczka[58b], R.D. Kass[111], A. Kastanas[14], Y. Kataoka[156], A. Katre[49], J. Katzy[42], V. Kaushik[7], K. Kawagoe[70], T. Kawamoto[156], G. Kawamura[54], S. Kazama[156], V.F. Kazanin[109], M.Y. Kazarinov[65], R. Keeler[170], R. Kehoe[40], M. Keil[54], J.S. Keller[42], J.J. Kempster[77], H. Keoshkerian[5], O. Kepka[127], B.P. Kerševan[75], S. Kersten[176], K. Kessoku[156], J. Keung[159], R.A. Keyes[87], F. Khalil-zada[11], H. Khandanyan[147a,147b], A. Khanov[114], A. Kharlamov[109], A. Khodinov[98], A. Khomich[58a], T.J. Khoo[28], G. Khoriauli[21], V. Khovanskiy[97], E. Khramov[65], J. Khubua[51b], H.Y. Kim[8], H. Kim[147a,147b], S.H. Kim[161], N. Kimura[155], O. Kind[16], B.T. King[74], M. King[168], R.S.B. King[120], S.B. King[169], J. Kirk[131], A.E. Kiryunin[101], T. Kishimoto[67], D. Kisielewska[38a], F. Kiss[48], K. Kiuchi[161], E. Kladiva[145b], M. Klein[74], U. Klein[74], K. Kleinknecht[83], P. Klimek[147a,147b], A. Klimentov[25], R. Klingenberg[43], J.A. Klinger[84], T. Klioutchnikova[30], P.F. Klok[106], E.-E. Kluge[58a], P. Kluit[107], S. Kluth[101], E. Kneringer[62], E.B.F.G. Knoops[85], A. Knue[53], D. Kobayashi[158], T. Kobayashi[156], M. Kobel[44], M. Kocian[144], P. Kodys[129], T. Koffas[29], E. Koffeman[107], L.A. Kogan[120], S. Kohlmann[176], Z. Kohout[128], T. Kohriki[66], T. Koi[144], H. Kolanoski[16], I. Koletsou[5], J. Koll[90], A.A. Komar[96,*], Y. Komori[156], T. Kondo[66], N. Kondrashova[42], K. Köneke[48], A.C. König[106], S. König[83], T. Kono[66,s], R. Konoplich[110,t], N. Konstantinidis[78], R. Kopeliansky[153], S. Koperny[38a], L. Köpke[83], A.K. Kopp[48], K. Korcyl[39], K. Kordas[155], A. Korn[78], A.A. Korol[109,c], I. Korolkov[12], E.V. Korolkova[140], V.A. Korotkov[130], O. Kortner[101], S. Kortner[101], V.V. Kostyukhin[21], V.M. Kotov[65], A. Kotwal[45], A. Kourkoumeli-Charalampidi[155], C. Kourkoumelis[9], V. Kouskoura[25], A. Koutsman[160a], R. Kowalewski[170], T.Z. Kowalski[38a], W. Kozanecki[137], A.S. Kozhin[130], V.A. Kramarenko[99], G. Kramberger[75], D. Krasnopevtsev[98], A. Krasznahorkay[30], J.K. Kraus[21], A. Kravchenko[25], S. Kreiss[110], M. Kretz[58c], J. Kretzschmar[74], K. Kreutzfeldt[52], P. Krieger[159], K. Krizka[31], K. Kroeninger[43], H. Kroha[101], J. Kroll[122], J. Kroseberg[21], J. Krstic[13a], U. Kruchonak[65], H. Krüger[21], N. Krumnack[64], Z.V. Krumshteyn[65], A. Kruse[174], M.C. Kruse[45], M. Kruskal[22], T. Kubota[88], H. Kucuk[78], S. Kuday[4c], S. Kuehn[48], A. Kugel[58c], F. Kuger[175], A. Kuhl[138], T. Kuhl[42], V. Kukhtin[65], Y. Kulchitsky[92], S. Kuleshov[32b], M. Kuna[133a,133b], T. Kunigo[68], A. Kupco[127], H. Kurashige[67], Y.A. Kurochkin[92], R. Kurumida[67], V. Kus[127], E.S. Kuwertz[148], M. Kuze[158], J. Kvita[115], D. Kyriazopoulos[140], A. La Rosa[49], L. La Rotonda[37a,37b], C. Lacasta[168], F. Lacava[133a,133b], J. Lacey[29], H. Lacker[16], D. Lacour[80], V.R. Lacuesta[168], E. Ladygin[65], R. Lafaye[5], B. Laforge[80], T. Lagouri[177], S. Lai[48], H. Laier[58a], L. Lambourne[78], S. Lammers[61], C.L. Lampen[7], W. Lampl[7], E. Lançon[137], U. Landgraf[48], M.P.J. Landon[76], V.S. Lang[58a], A.J. Lankford[164], F. Lanni[25], K. Lantzsch[30], S. Laplace[80], C. Lapoire[21], J.F. Laporte[137], T. Lari[91a], F. Lasagni Manghi[20a,20b], M. Lassnig[30], P. Laurelli[47], W. Lavrijsen[15], A.T. Law[138], P. Laycock[74], O. Le Dortz[80], E. Le Guirriec[85], E. Le Menedeu[12], T. LeCompte[6], F. Ledroit-Guillon[55], C.A. Lee[146b], H. Lee[107], S.C. Lee[152], L. Lee[1], G. Lefebvre[80], M. Lefebvre[170], F. Legger[100], C. Leggett[15], A. Lehan[74], G. Lehmann Miotto[30], X. Lei[7], W.A. Leight[29], A. Leisos[155], A.G. Leister[177], M.A.L. Leite[24d], R. Leitner[129], D. Lellouch[173], B. Lemmer[54], K.J.C. Leney[78], T. Lenz[21], G. Lenzen[176], B. Lenzi[30], R. Leone[7], S. Leone[124a,124b], C. Leonidopoulos[46], S. Leontsinis[10], C. Leroy[95], C.G. Lester[28], C.M. Lester[122], M. Levchenko[123], J. Levêque[5], D. Levin[89], L.J. Levinson[173], M. Levy[18], A. Lewis[120], A.M. Leyko[21], M. Leyton[41], B. Li[33b,u], B. Li[85], H. Li[149], H.L. Li[31], L. Li[45], L. Li[33e], S. Li[45], Y. Li[33c,v], Z. Liang[138], H. Liao[34], B. Liberti[134a], P. Lichard[30], K. Lie[166], J. Liebal[21], W. Liebig[14], C. Limbach[21], A. Limosani[151], S.C. Lin[152,w], T.H. Lin[83], F. Linde[107], B.E. Lindquist[149], J.T. Linnemann[90], E. Lipeles[122], A. Lipniacka[14], M. Lisovyi[42], T.M. Liss[166], D. Lissauer[25], A. Lister[169], A.M. Litke[138], B. Liu[152],

JHEP04(2015)117

D. Liu[152], J. Liu[85], J.B. Liu[33b], K. Liu[33b,x], L. Liu[89], M. Liu[45], M. Liu[33b], Y. Liu[33b], M. Livan[121a,121b], A. Lleres[55], J. Llorente Merino[82], S.L. Lloyd[76], F. Lo Sterzo[152], E. Lobodzinska[42], P. Loch[7], W.S. Lockman[138], F.K. Loebinger[84], A.E. Loevschall-Jensen[36], A. Loginov[177], T. Lohse[16], K. Lohwasser[42], M. Lokajicek[127], B.A. Long[22], J.D. Long[89], R.E. Long[72], K.A. Looper[111], L. Lopes[126a], D. Lopez Mateos[57], B. Lopez Paredes[140], I. Lopez Paz[12], J. Lorenz[100], N. Lorenzo Martinez[61], M. Losada[163], P. Loscutoff[15], X. Lou[33a], A. Lounis[117], J. Love[6], P.A. Love[72], A.J. Lowe[144,e], F. Lu[33a], N. Lu[89], H.J. Lubatti[139], C. Luci[133a,133b], A. Lucotte[55], F. Luehring[61], W. Lukas[62], L. Luminari[133a], O. Lundberg[147a,147b], B. Lund-Jensen[148], M. Lungwitz[83], D. Lynn[25], R. Lysak[127], E. Lytken[81], H. Ma[25], L.L. Ma[33d], G. Maccarrone[47], A. Macchiolo[101], J. Machado Miguens[126a,126b], D. Macina[30], D. Madaffari[85], R. Madar[48], H.J. Maddocks[72], W.F. Mader[44], A. Madsen[167], M. Maeno[8], T. Maeno[25], A. Maevskiy[99], E. Magradze[54], K. Mahboubi[48], J. Mahlstedt[107], S. Mahmoud[74], C. Maiani[137], C. Maidantchik[24a], A.A. Maier[101], A. Maio[126a,126b,126d], S. Majewski[116], Y. Makida[66], N. Makovec[117], P. Mal[137,y], B. Malaescu[80], Pa. Malecki[39], V.P. Maleev[123], F. Malek[55], U. Mallik[63], D. Malon[6], C. Malone[144], S. Maltezos[10], V.M. Malyshev[109], S. Malyukov[30], J. Mamuzic[13b], B. Mandelli[30], L. Mandelli[91a], I. Mandić[75], R. Mandrysch[63], J. Maneira[126a,126b], A. Manfredini[101], L. Manhaes de Andrade Filho[24b], J. Manjarres Ramos[160b], A. Mann[100], P.M. Manning[138], A. Manousakis-Katsikakis[9], B. Mansoulie[137], R. Mantifel[87], M. Mantoani[54], L. Mapelli[30], L. March[146c], J.F. Marchand[29], G. Marchiori[80], M. Marcisovsky[127], C.P. Marino[170], M. Marjanovic[13a], F. Marroquim[24a], S.P. Marsden[84], Z. Marshall[15], L.F. Marti[17], S. Marti-Garcia[168], B. Martin[30], B. Martin[90], T.A. Martin[171], V.J. Martin[46], B. Martin dit Latour[14], H. Martinez[137], M. Martinez[12,n], S. Martin-Haugh[131], A.C. Martyniuk[78], M. Marx[139], F. Marzano[133a], A. Marzin[30], L. Masetti[83], T. Mashimo[156], R. Mashinistov[96], J. Masik[84], A.L. Maslennikov[109,c], I. Massa[20a,20b], L. Massa[20a,20b], N. Massol[5], P. Mastrandrea[149], A. Mastroberardino[37a,37b], T. Masubuchi[156], P. Mättig[176], J. Mattmann[83], J. Maurer[26a], S.J. Maxfield[74], D.A. Maximov[109,c], R. Mazini[152], S.M. Mazza[91a,91b], L. Mazzaferro[134a,134b], G. Mc Goldrick[159], S.P. Mc Kee[89], A. McCarn[89], R.L. McCarthy[149], T.G. McCarthy[29], N.A. McCubbin[131], K.W. McFarlane[56,*], J.A. Mcfayden[78], G. Mchedlidze[54], S.J. McMahon[131], R.A. McPherson[170,j], J. Mechnich[107], M. Medinnis[42], S. Meehan[31], S. Mehlhase[100], A. Mehta[74], K. Meier[58a], C. Meineck[100], B. Meirose[41], C. Melachrinos[31], B.R. Mellado Garcia[146c], F. Meloni[17], A. Mengarelli[20a,20b], S. Menke[101], E. Meoni[162], K.M. Mercurio[57], S. Mergelmeyer[21], N. Meric[137], P. Mermod[49], L. Merola[104a,104b], C. Meroni[91a], F.S. Merritt[31], H. Merritt[111], A. Messina[30,z], J. Metcalfe[25], A.S. Mete[164], C. Meyer[83], C. Meyer[122], J-P. Meyer[137], J. Meyer[30], R.P. Middleton[131], S. Migas[74], S. Miglioranzi[165a,165c], L. Mijović[21], G. Mikenberg[173], M. Mikestikova[127], M. Mikuž[75], A. Milic[30], D.W. Miller[31], C. Mills[46], A. Milov[173], D.A. Milstead[147a,147b], A.A. Minaenko[130], Y. Minami[156], I.A. Minashvili[65], A.I. Mincer[110], B. Mindur[38a], M. Mineev[65], Y. Ming[174], L.M. Mir[12], G. Mirabelli[133a], T. Mitani[172], J. Mitrevski[100], V.A. Mitsou[168], A. Miucci[49], P.S. Miyagawa[140], J.U. Mjörnmark[81], T. Moa[147a,147b], K. Mochizuki[85], S. Mohapatra[35], W. Mohr[48], S. Molander[147a,147b], R. Moles-Valls[168], K. Mönig[42], C. Monini[55], J. Monk[36], E. Monnier[85], J. Montejo Berlingen[12], F. Monticelli[71], S. Monzani[133a,133b], R.W. Moore[3], N. Morange[63], D. Moreno[163], M. Moreno Llácer[54], P. Morettini[50a], M. Morgenstern[44], M. Morii[57], M. Morinaga[156], V. Morisbak[119], S. Moritz[83], A.K. Morley[148], G. Mornacchi[30], J.D. Morris[76], A. Morton[42], L. Morvaj[103], H.G. Moser[101], M. Mosidze[51b], J. Moss[111], K. Motohashi[158], R. Mount[144], E. Mountricha[25], S.V. Mouraviev[96,*], E.J.W. Moyse[86], S. Muanza[85], R.D. Mudd[18], F. Mueller[58a], J. Mueller[125], K. Mueller[21], T. Mueller[28], D. Muenstermann[49], P. Mullen[53], Y. Munwes[154], J.A. Murillo Quijada[18], W.J. Murray[171,131], H. Musheghyan[54], E. Musto[153], A.G. Myagkov[130,aa], M. Myska[128], O. Nackenhorst[54], J. Nadal[54], K. Nagai[120], R. Nagai[158], Y. Nagai[85], K. Nagano[66], A. Nagarkar[111], Y. Nagasaka[59], K. Nagata[161], M. Nagel[101], A.M. Nairz[30], Y. Nakahama[30], K. Nakamura[66], T. Nakamura[156], I. Nakano[112], H. Namasivayam[41], G. Nanava[21], R.F. Naranjo Garcia[42], R. Narayan[58b], T. Nattermann[21], T. Naumann[42], G. Navarro[163], R. Nayyar[7], H.A. Neal[89], P.Yu. Nechaeva[96], T.J. Neep[84],

JHEP04(2015)117

P.D. Nef[144], A. Negri[121a,121b], G. Negri[30], M. Negrini[20a], S. Nektarijevic[49], C. Nellist[117], A. Nelson[164], T.K. Nelson[144], S. Nemecek[127], P. Nemethy[110], A.A. Nepomuceno[24a], M. Nessi[30,ab], M.S. Neubauer[166], M. Neumann[176], R.M. Neves[110], P. Nevski[25], P.R. Newman[18], D.H. Nguyen[6], R.B. Nickerson[120], R. Nicolaidou[137], B. Nicquevert[30], J. Nielsen[138], N. Nikiforou[35], A. Nikiforov[16], V. Nikolaenko[130,aa], I. Nikolic-Audit[80], K. Nikolics[49], K. Nikolopoulos[18], P. Nilsson[25], Y. Ninomiya[156], A. Nisati[133a], R. Nisius[101], T. Nobe[158], M. Nomachi[118], I. Nomidis[29], S. Norberg[113], M. Nordberg[30], O. Novgorodova[44], S. Nowak[101], M. Nozaki[66], L. Nozka[115], K. Ntekas[10], G. Nunes Hanninger[88], T. Nunnemann[100], E. Nurse[78], F. Nuti[88], B.J. O'Brien[46], F. O'grady[7], D.C. O'Neil[143], V. O'Shea[53], F.G. Oakham[29,d], H. Oberlack[101], T. Obermann[21], J. Ocariz[80], A. Ochi[67], I. Ochoa[78], S. Oda[70], S. Odaka[66], H. Ogren[61], A. Oh[84], S.H. Oh[45], C.C. Ohm[15], H. Ohman[167], H. Oide[30], W. Okamura[118], H. Okawa[161], Y. Okumura[31], T. Okuyama[156], A. Olariu[26a], A.G. Olchevski[65], S.A. Olivares Pino[46], D. Oliveira Damazio[25], E. Oliver Garcia[168], A. Olszewski[39], J. Olszowska[39], A. Onofre[126a,126e], P.U.E. Onyisi[31,p], C.J. Oram[160a], M.J. Oreglia[31], Y. Oren[154], D. Orestano[135a,135b], N. Orlando[73a,73b], C. Oropeza Barrera[53], R.S. Orr[159], B. Osculati[50a,50b], R. Ospanov[122], G. Otero y Garzon[27], H. Otono[70], M. Ouchrif[136d], E.A. Ouellette[170], F. Ould-Saada[119], A. Ouraou[137], K.P. Oussoren[107], Q. Ouyang[33a], A. Ovcharova[15], M. Owen[84], V.E. Ozcan[19a], N. Ozturk[8], K. Pachal[120], A. Pacheco Pages[12], C. Padilla Aranda[12], M. Pagáčová[48], S. Pagan Griso[15], E. Paganis[140], C. Pahl[101], F. Paige[25], P. Pais[86], K. Pajchel[119], G. Palacino[160b], S. Palestini[30], M. Palka[38b], D. Pallin[34], A. Palma[126a,126b], J.D. Palmer[18], Y.B. Pan[174], E. Panagiotopoulou[10], J.G. Panduro Vazquez[77], P. Pani[107], N. Panikashvili[89], S. Panitkin[25], D. Pantea[26a], L. Paolozzi[134a,134b], Th.D. Papadopoulou[10], K. Papageorgiou[155], A. Paramonov[6], D. Paredes Hernandez[155], M.A. Parker[28], F. Parodi[50a,50b], J.A. Parsons[35], U. Parzefall[48], E. Pasqualucci[133a], S. Passaggio[50a], A. Passeri[135a], F. Pastore[135a,135b,*], Fr. Pastore[77], G. Pásztor[29], S. Pataraia[176], N.D. Patel[151], J.R. Pater[84], S. Patricelli[104a,104b], T. Pauly[30], J. Pearce[170], L.E. Pedersen[36], M. Pedersen[119], S. Pedraza Lopez[168], R. Pedro[126a,126b], S.V. Peleganchuk[109], D. Pelikan[167], H. Peng[33b], B. Penning[31], J. Penwell[61], D.V. Perepelitsa[25], E. Perez Codina[160a], M.T. Pérez García-Estañ[168], L. Perini[91a,91b], H. Pernegger[30], S. Perrella[104a,104b], R. Peschke[42], V.D. Peshekhonov[65], K. Peters[30], R.F.Y. Peters[84], B.A. Petersen[30], T.C. Petersen[36], E. Petit[42], A. Petridis[147a,147b], C. Petridou[155], E. Petrolo[133a], F. Petrucci[135a,135b], N.E. Pettersson[158], R. Pezoa[32b], P.W. Phillips[131], G. Piacquadio[144], E. Pianori[171], A. Picazio[49], E. Piccaro[76], M. Piccinini[20a,20b], M.A. Pickering[120], R. Piegaia[27], D.T. Pignotti[111], J.E. Pilcher[31], A.D. Pilkington[78], J. Pina[126a,126b,126d], M. Pinamonti[165a,165c,ac], A. Pinder[120], J.L. Pinfold[3], A. Pingel[36], B. Pinto[126a], S. Pires[80], M. Pitt[173], C. Pizio[91a,91b], L. Plazak[145a], M.-A. Pleier[25], V. Pleskot[129], E. Plotnikova[65], P. Plucinski[147a,147b], D. Pluth[64], S. Poddar[58a], F. Podlyski[34], R. Poettgen[83], L. Poggioli[117], D. Pohl[21], M. Pohl[49], G. Polesello[121a], A. Policicchio[37a,37b], R. Polifka[159], A. Polini[20a], C.S. Pollard[53], V. Polychronakos[25], K. Pommès[30], L. Pontecorvo[133a], B.G. Pope[90], G.A. Popeneciu[26b], D.S. Popovic[13a], A. Poppleton[30], S. Pospisil[128], K. Potamianos[15], I.N. Potrap[65], C.J. Potter[150], C.T. Potter[116], G. Poulard[30], J. Poveda[30], V. Pozdnyakov[65], P. Pralavorio[85], A. Pranko[15], S. Prasad[30], S. Prell[64], D. Price[84], J. Price[74], L.E. Price[6], D. Prieur[125], M. Primavera[73a], S. Prince[87], M. Proissl[46], K. Prokofiev[60c], F. Prokoshin[32b], E. Protopapadaki[137], S. Protopopescu[25], J. Proudfoot[6], M. Przybycien[38a], H. Przysiezniak[5], E. Ptacek[116], D. Puddu[135a,135b], E. Pueschel[86], D. Puldon[149], M. Purohit[25,ad], P. Puzo[117], J. Qian[89], G. Qin[53], Y. Qin[84], A. Quadt[54], D.R. Quarrie[15], W.B. Quayle[165a,165b], M. Queitsch-Maitland[84], D. Quilty[53], A. Qureshi[160b], V. Radeka[25], V. Radescu[42], S.K. Radhakrishnan[149], P. Radloff[116], P. Rados[88], F. Ragusa[91a,91b], G. Rahal[179], S. Rajagopalan[25], M. Rammensee[30], C. Rangel-Smith[167], K. Rao[164], F. Rauscher[100], S. Rave[83], T.C. Rave[48], T. Ravenscroft[53], M. Raymond[30], A.L. Read[119], N.P. Readioff[74], D.M. Rebuzzi[121a,121b], A. Redelbach[175], G. Redlinger[25], R. Reece[138], K. Reeves[41], L. Rehnisch[16], H. Reisin[27], M. Relich[164], C. Rembser[30], H. Ren[33a], Z.L. Ren[152], A. Renaud[117], M. Rescigno[133a], S. Resconi[91a], O.L. Rezanova[109,c], P. Reznicek[129], R. Rezvani[95], R. Richter[101], E. Richter-Was[38b], M. Ridel[80], P. Rieck[16], J. Rieger[54], M. Rijssenbeek[149], A. Rimoldi[121a,121b], L. Rinaldi[20a],

JHEP04(2015)117

E. Ritsch[62], I. Riu[12], F. Rizatdinova[114], E. Rizvi[76], S.H. Robertson[87,j], A. Robichaud-Veronneau[87], D. Robinson[28], J.E.M. Robinson[84], A. Robson[53], C. Roda[124a,124b], L. Rodrigues[30], S. Roe[30], O. Røhne[119], S. Rolli[162], A. Romaniouk[98], M. Romano[20a,20b], E. Romero Adam[168], N. Rompotis[139], M. Ronzani[48], L. Roos[80], E. Ros[168], S. Rosati[133a], K. Rosbach[49], M. Rose[77], P. Rose[138], P.L. Rosendahl[14], O. Rosenthal[142], V. Rossetti[147a,147b], E. Rossi[104a,104b], L.P. Rossi[50a], R. Rosten[139], M. Rotaru[26a], I. Roth[173], J. Rothberg[139], D. Rousseau[117], C.R. Royon[137], A. Rozanov[85], Y. Rozen[153], X. Ruan[146c], F. Rubbo[12], I. Rubinskiy[42], V.I. Rud[99], C. Rudolph[44], M.S. Rudolph[159], F. Rühr[48], A. Ruiz-Martinez[30], Z. Rurikova[48], N.A. Rusakovich[65], A. Ruschke[100], H.L. Russell[139], J.P. Rutherfoord[7], N. Ruthmann[48], Y.F. Ryabov[123], M. Rybar[129], G. Rybkin[117], N.C. Ryder[120], A.F. Saavedra[151], G. Sabato[107], S. Sacerdoti[27], A. Saddique[3], H.F-W. Sadrozinski[138], R. Sadykov[65], F. Safai Tehrani[133a], H. Sakamoto[156], Y. Sakurai[172], G. Salamanna[135a,135b], A. Salamon[134a], M. Saleem[113], D. Salek[107], P.H. Sales De Bruin[139], D. Salihagic[101], A. Salnikov[144], J. Salt[168], D. Salvatore[37a,37b], F. Salvatore[150], A. Salvucci[106], A. Salzburger[30], D. Sammel[48], D. Sampsonidis[155], A. Sanchez[104a,104b], J. Sánchez[168], V. Sanchez Martinez[168], H. Sandaker[14], R.L. Sandbach[76], H.G. Sander[83], M.P. Sanders[100], M. Sandhoff[176], T. Sandoval[28], C. Sandoval[163], R. Sandstroem[101], D.P.C. Sankey[131], A. Sansoni[47], C. Santoni[34], R. Santonico[134a,134b], H. Santos[126a], I. Santoyo Castillo[150], K. Sapp[125], A. Sapronov[65], J.G. Saraiva[126a,126d], B. Sarrazin[21], G. Sartisohn[176], O. Sasaki[66], Y. Sasaki[156], K. Sato[161], G. Sauvage[5,*], E. Sauvan[5], P. Savard[159,d], D.O. Savu[30], C. Sawyer[120], L. Sawyer[79,m], D.H. Saxon[53], J. Saxon[31], C. Sbarra[20a], A. Sbrizzi[20a,20b], T. Scanlon[78], D.A. Scannicchio[164], M. Scarcella[151], V. Scarfone[37a,37b], J. Schaarschmidt[173], P. Schacht[101], D. Schaefer[30], R. Schaefer[42], S. Schaepe[21], S. Schaetzel[58b], U. Schäfer[83], A.C. Schaffer[117], D. Schaile[100], R.D. Schamberger[149], V. Scharf[58a], V.A. Schegelsky[123], D. Scheirich[129], M. Schernau[164], C. Schiavi[50a,50b], J. Schieck[100], C. Schillo[48], M. Schioppa[37a,37b], S. Schlenker[30], E. Schmidt[48], K. Schmieden[30], C. Schmitt[83], S. Schmitt[58b], B. Schneider[17], Y.J. Schnellbach[74], U. Schnoor[44], L. Schoeffel[137], A. Schoening[58b], B.D. Schoenrock[90], A.L.S. Schorlemmer[54], M. Schott[83], D. Schouten[160a], J. Schovancova[25], S. Schramm[159], M. Schreyer[175], C. Schroeder[83], N. Schuh[83], M.J. Schultens[21], H.-C. Schultz-Coulon[58a], H. Schulz[16], M. Schumacher[48], B.A. Schumm[138], Ph. Schune[137], C. Schwanenberger[84], A. Schwartzman[144], T.A. Schwarz[89], Ph. Schwegler[101], Ph. Schwemling[137], R. Schwienhorst[90], J. Schwindling[137], T. Schwindt[21], M. Schwoerer[5], F.G. Sciacca[17], E. Scifo[117], G. Sciolla[23], F. Scuri[124a,124b], F. Scutti[21], J. Searcy[89], G. Sedov[42], E. Sedykh[123], P. Seema[21], S.C. Seidel[105], A. Seiden[138], F. Seifert[128], J.M. Seixas[24a], G. Sekhniaidze[104a], S.J. Sekula[40], K.E. Selbach[46], D.M. Seliverstov[123,*], G. Sellers[74], N. Semprini-Cesari[20a,20b], C. Serfon[30], L. Serin[117], L. Serkin[54], T. Serre[85], R. Seuster[160a], H. Severini[113], T. Sfiligoj[75], F. Sforza[101], A. Sfyrla[30], E. Shabalina[54], M. Shamim[116], L.Y. Shan[33a], R. Shang[166], J.T. Shank[22], M. Shapiro[15], P.B. Shatalov[97], K. Shaw[165a,165b], A. Shcherbakova[147a,147b], C.Y. Shehu[150], P. Sherwood[78], L. Shi[152,ae], S. Shimizu[67], C.O. Shimmin[164], M. Shimojima[102], M. Shiyakova[65], A. Shmeleva[96], D. Shoaleh Saadi[95], M.J. Shochet[31], S. Shojaii[91a,91b], D. Short[120], S. Shrestha[111], E. Shulga[98], M.A. Shupe[7], S. Shushkevich[42], P. Sicho[127], O. Sidiropoulou[155], D. Sidorov[114], A. Sidoti[133a], F. Siegert[44], Dj. Sijacki[13a], J. Silva[126a,126d], Y. Silver[154], D. Silverstein[144], S.B. Silverstein[147a], V. Simak[128], O. Simard[5], Lj. Simic[13a], S. Simion[117], E. Simioni[83], B. Simmons[78], D. Simon[34], R. Simoniello[91a,91b], P. Sinervo[159], N.B. Sinev[116], G. Siragusa[175], A. Sircar[79], A.N. Sisakyan[65,*], S.Yu. Sivoklokov[99], J. Sjölin[147a,147b], T.B. Sjursen[14], H.P. Skottowe[57], P. Skubic[113], M. Slater[18], T. Slavicek[128], M. Slawinska[107], K. Sliwa[162], V. Smakhtin[173], B.H. Smart[46], L. Smestad[14], S.Yu. Smirnov[98], Y. Smirnov[98], L.N. Smirnova[99,af], O. Smirnova[81], K.M. Smith[53], M. Smith[35], M. Smizanska[72], K. Smolek[128], A.A. Snesarev[96], G. Snidero[76], S. Snyder[25], R. Sobie[170,j], F. Socher[44], A. Soffer[154], D.A. Soh[152,ae], C.A. Solans[30], M. Solar[128], J. Solc[128], E.Yu. Soldatov[98], U. Soldevila[168], A.A. Solodkov[130], A. Soloshenko[65], O.V. Solovyanov[130], V. Solovyev[123], P. Sommer[48], H.Y. Song[33b], N. Soni[1], A. Sood[15], A. Sopczak[128], B. Sopko[128], V. Sopko[128], V. Sorin[12], M. Sosebee[8], R. Soualah[165a,165c], P. Soueid[95], A.M. Soukharev[109,c], D. South[42], S. Spagnolo[73a,73b], F. Spanò[77], W.R. Spearman[57],

JHEP04(2015)117

F. Spettel[101], R. Spighi[20a], G. Spigo[30], L.A. Spiller[88], M. Spousta[129], T. Spreitzer[159], R.D. St. Denis[53,*], S. Staerz[44], J. Stahlman[122], R. Stamen[58a], S. Stamm[16], E. Stanecka[39], C. Stanescu[135a], M. Stanescu-Bellu[42], M.M. Stanitzki[42], S. Stapnes[119], E.A. Starchenko[130], J. Stark[55], P. Staroba[127], P. Starovoitov[42], R. Staszewski[39], P. Stavina[145a,*], P. Steinberg[25], B. Stelzer[143], H.J. Stelzer[30], O. Stelzer-Chilton[160a], H. Stenzel[52], S. Stern[101], G.A. Stewart[53], J.A. Stillings[21], M.C. Stockton[87], M. Stoebe[87], G. Stoicea[26a], P. Stolte[54], S. Stonjek[101], A.R. Stradling[8], A. Straessner[44], M.E. Stramaglia[17], J. Strandberg[148], S. Strandberg[147a,147b], A. Strandlie[119], E. Strauss[144], M. Strauss[113], P. Strizenec[145b], R. Ströhmer[175], D.M. Strom[116], R. Stroynowski[40], A. Strubig[106], S.A. Stucci[17], B. Stugu[14], N.A. Styles[42], D. Su[144], J. Su[125], R. Subramaniam[79], A. Succurro[12], Y. Sugaya[118], C. Suhr[108], M. Suk[128], V.V. Sulin[96], S. Sultansoy[4d], T. Sumida[68], S. Sun[57], X. Sun[33a], J.E. Sundermann[48], K. Suruliz[150], G. Susinno[37a,37b], M.R. Sutton[150], Y. Suzuki[66], M. Svatos[127], S. Swedish[169], M. Swiatlowski[144], I. Sykora[145a], T. Sykora[129], D. Ta[90], C. Taccini[135a,135b], K. Tackmann[42], J. Taenzer[159], A. Taffard[164], R. Tafirout[160a], N. Taiblum[154], H. Takai[25], R. Takashima[69], H. Takeda[67], T. Takeshita[141], Y. Takubo[66], M. Talby[85], A.A. Talyshev[109,c], J.Y.C. Tam[175], K.G. Tan[88], J. Tanaka[156], R. Tanaka[117], S. Tanaka[132], S. Tanaka[66], A.J. Tanasijczuk[143], B.B. Tannenwald[111], N. Tannoury[21], S. Tapprogge[83], S. Tarem[153], F. Tarrade[29], G.F. Tartarelli[91a], P. Tas[129], M. Tasevsky[127], T. Tashiro[68], E. Tassi[37a,37b], A. Tavares Delgado[126a,126b], Y. Tayalati[136d], F.E. Taylor[94], G.N. Taylor[88], W. Taylor[160b], F.A. Teischinger[30], M. Teixeira Dias Castanheira[76], P. Teixeira-Dias[77], K.K. Temming[48], H. Ten Kate[30], P.K. Teng[152], J.J. Teoh[118], F. Tepel[176], S. Terada[66], K. Terashi[156], J. Terron[82], S. Terzo[101], M. Testa[47], R.J. Teuscher[159,j], J. Therhaag[21], T. Theveneaux-Pelzer[34], J.P. Thomas[18], J. Thomas-Wilsker[77], E.N. Thompson[35], P.D. Thompson[18], R.J. Thompson[84], A.S. Thompson[53], L.A. Thomsen[36], E. Thomson[122], M. Thomson[28], W.M. Thong[88], R.P. Thun[89,*], F. Tian[35], M.J. Tibbetts[15], V.O. Tikhomirov[96,ag], Yu.A. Tikhonov[109,c], S. Timoshenko[98], E. Tiouchichine[85], P. Tipton[177], S. Tisserant[85], T. Todorov[5,*], S. Todorova-Nova[129], J. Tojo[70], S. Tokár[145a], K. Tokushuku[66], K. Tollefson[90], E. Tolley[57], L. Tomlinson[84], M. Tomoto[103], L. Tompkins[31], K. Toms[105], N.D. Topilin[65], E. Torrence[116], H. Torres[143], E. Torró Pastor[168], J. Toth[85,ah], F. Touchard[85], D.R. Tovey[140], H.L. Tran[117], T. Trefzger[175], L. Tremblet[30], A. Tricoli[30], I.M. Trigger[160a], S. Trincaz-Duvoid[80], M.F. Tripiana[12], W. Trischuk[159], B. Trocmé[55], C. Troncon[91a], M. Trottier-McDonald[15], M. Trovatelli[135a,135b], P. True[90], M. Trzebinski[39], A. Trzupek[39], C. Tsarouchas[30], J.C-L. Tseng[120], P.V. Tsiareshka[92], D. Tsionou[137], G. Tsipolitis[10], N. Tsirintanis[9], S. Tsiskaridze[12], V. Tsiskaridze[48], E.G. Tskhadadze[51a], I.I. Tsukerman[97], V. Tsulaia[15], S. Tsuno[66], D. Tsybychev[149], A. Tudorache[26a], V. Tudorache[26a], A.N. Tuna[122], S.A. Tupputi[20a,20b], S. Turchikhin[99,af], D. Turecek[128], I. Turk Cakir[4c], R. Turra[91a,91b], A.J. Turvey[40], P.M. Tuts[35], A. Tykhonov[49], M. Tylmad[147a,147b], M. Tyndel[131], I. Ueda[156], R. Ueno[29], M. Ughetto[85], M. Ugland[14], M. Uhlenbrock[21], F. Ukegawa[161], G. Unal[30], A. Undrus[25], G. Unel[164], F.C. Ungaro[48], Y. Unno[66], C. Unverdorben[100], J. Urban[145b], D. Urbaniec[35], P. Urquijo[88], G. Usai[8], A. Usanova[62], L. Vacavant[85], V. Vacek[128], B. Vachon[87], N. Valencic[107], S. Valentinetti[20a,20b], A. Valero[168], L. Valery[34], S. Valkar[129], E. Valladolid Gallego[168], S. Vallecorsa[49], J.A. Valls Ferrer[168], W. Van Den Wollenberg[107], P.C. Van Der Deijl[107], R. van der Geer[107], H. van der Graaf[107], R. Van Der Leeuw[107], D. van der Ster[30], N. van Eldik[30], P. van Gemmeren[6], J. Van Nieuwkoop[143], I. van Vulpen[107], M.C. van Woerden[30], M. Vanadia[133a,133b], W. Vandelli[30], R. Vanguri[122], A. Vaniachine[6], P. Vankov[42], F. Vannucci[80], G. Vardanyan[178], R. Vari[133a], E.W. Varnes[7], T. Varol[86], D. Varouchas[80], A. Vartapetian[8], K.E. Varvell[151], F. Vazeille[34], T. Vazquez Schroeder[54], J. Veatch[7], F. Veloso[126a,126c], T. Velz[21], S. Veneziano[133a], A. Ventura[73a,73b], D. Ventura[86], M. Venturi[170], N. Venturi[159], A. Venturini[23], V. Vercesi[121a], M. Verducci[133a,133b], W. Verkerke[107], J.C. Vermeulen[107], A. Vest[44], M.C. Vetterli[143,d], O. Viazlo[81], I. Vichou[166], T. Vickey[146c,ai], O.E. Vickey Boeriu[146c], G.H.A. Viehhauser[120], S. Viel[169], R. Vigne[30], M. Villa[20a,20b], M. Villaplana Perez[91a,91b], E. Vilucchi[47], M.G. Vincter[29], V.B. Vinogradov[65], J. Virzi[15], I. Vivarelli[150], F. Vives Vaque[3], S. Vlachos[10], D. Vladoiu[100], M. Vlasak[128], A. Vogel[21], M. Vogel[32a], P. Vokac[128], G. Volpi[124a,124b],

JHEP04(2015)117

M. Volpi[88], H. von der Schmitt[101], H. von Radziewski[48], E. von Toerne[21], V. Vorobel[129], K. Vorobev[98], M. Vos[168], R. Voss[30], J.H. Vossebeld[74], N. Vranjes[137], M. Vranjes Milosavljevic[13a], V. Vrba[127], M. Vreeswijk[107], T. Vu Anh[48], R. Vuillermet[30], I. Vukotic[31], Z. Vykydal[128], P. Wagner[21], W. Wagner[176], H. Wahlberg[71], S. Wahrmund[44], J. Wakabayashi[103], J. Walder[72], R. Walker[100], W. Walkowiak[142], R. Wall[177], P. Waller[74], B. Walsh[177], C. Wang[33c], C. Wang[45], F. Wang[174], H. Wang[15], H. Wang[40], J. Wang[42], J. Wang[33a], K. Wang[87], R. Wang[105], S.M. Wang[152], T. Wang[21], X. Wang[177], C. Wanotayaroj[116], A. Warburton[87], C.P. Ward[28], D.R. Wardrope[78], M. Warsinsky[48], A. Washbrook[46], C. Wasicki[42], P.M. Watkins[18], A.T. Watson[18], I.J. Watson[151], M.F. Watson[18], G. Watts[139], S. Watts[84], B.M. Waugh[78], S. Webb[84], M.S. Weber[17], S.W. Weber[175], J.S. Webster[31], A.R. Weidberg[120], B. Weinert[61], J. Weingarten[54], C. Weiser[48], H. Weits[107], P.S. Wells[30], T. Wenaus[25], D. Wendland[16], Z. Weng[152,ae], T. Wengler[30], S. Wenig[30], N. Wermes[21], M. Werner[48], P. Werner[30], M. Wessels[58a], J. Wetter[162], K. Whalen[29], A. White[8], M.J. White[1], R. White[32b], S. White[124a,124b], D. Whiteson[164], D. Wicke[176], F.J. Wickens[131], W. Wiedenmann[174], M. Wielers[131], P. Wienemann[21], C. Wiglesworth[36], L.A.M. Wiik-Fuchs[21], P.A. Wijeratne[78], A. Wildauer[101], M.A. Wildt[42,aj], H.G. Wilkens[30], H.H. Williams[122], S. Williams[28], C. Willis[90], S. Willocq[86], A. Wilson[89], J.A. Wilson[18], I. Wingerter-Seez[5], F. Winklmeier[116], B.T. Winter[21], M. Wittgen[144], J. Wittkowski[100], S.J. Wollstadt[83], M.W. Wolter[39], H. Wolters[126a,126c], B.K. Wosiek[39], J. Wotschack[30], M.J. Woudstra[84], K.W. Wozniak[39], M. Wright[53], M. Wu[55], S.L. Wu[174], X. Wu[49], Y. Wu[89], T.R. Wyatt[84], B.M. Wynne[46], S. Xella[36], M. Xiao[137], D. Xu[33a], L. Xu[33b,ak], B. Yabsley[151], S. Yacoob[146b,al], R. Yakabe[67], M. Yamada[66], H. Yamaguchi[156], Y. Yamaguchi[118], A. Yamamoto[66], S. Yamamoto[156], T. Yamamura[156], T. Yamanaka[156], K. Yamauchi[103], Y. Yamazaki[67], Z. Yan[22], H. Yang[33e], H. Yang[174], Y. Yang[111], S. Yanush[93], L. Yao[33a], W-M. Yao[15], Y. Yasu[66], E. Yatsenko[42], K.H. Yau Wong[21], J. Ye[40], S. Ye[25], I. Yeletskikh[65], A.L. Yen[57], E. Yildirim[42], M. Yilmaz[4b], K. Yorita[172], R. Yoshida[6], K. Yoshihara[156], C. Young[144], C.J.S. Young[30], S. Youssef[22], D.R. Yu[15], J. Yu[8], J.M. Yu[89], J. Yu[114], L. Yuan[67], A. Yurkewicz[108], I. Yusuff[28,am], B. Zabinski[39], R. Zaidan[63], A.M. Zaitsev[130,aa], A. Zaman[149], S. Zambito[23], L. Zanello[133a,133b], D. Zanzi[88], C. Zeitnitz[176], M. Zeman[128], A. Zemla[38a], K. Zengel[23], O. Zenin[130], T. Ženiš[145a], D. Zerwas[117], G. Zevi della Porta[57], D. Zhang[89], F. Zhang[174], H. Zhang[90], J. Zhang[6], L. Zhang[152], R. Zhang[33b], X. Zhang[33d], Z. Zhang[117], X. Zhao[40], Y. Zhao[33d], Z. Zhao[33b], A. Zhemchugov[65], J. Zhong[120], B. Zhou[89], C. Zhou[45], L. Zhou[35], L. Zhou[40], N. Zhou[164], C.G. Zhu[33d], H. Zhu[33a], J. Zhu[89], Y. Zhu[33b], X. Zhuang[33a], K. Zhukov[96], A. Zibell[175], D. Zieminska[61], N.I. Zimine[65], C. Zimmermann[83], R. Zimmermann[21], S. Zimmermann[21], S. Zimmermann[48], Z. Zinonos[54], M. Ziolkowski[142], G. Zobernig[174], A. Zoccoli[20a,20b], M. zur Nedden[16], G. Zurzolo[104a,104b], L. Zwalinski[30]

[1] Department of Physics, University of Adelaide, Adelaide, Australia
[2] Physics Department, SUNY Albany, Albany NY, United States of America
[3] Department of Physics, University of Alberta, Edmonton AB, Canada
[4] [(a)] Department of Physics, Ankara University, Ankara; [(b)] Department of Physics, Gazi University, Ankara; [(c)] Istanbul Aydin University, Istanbul; [(d)] Division of Physics, TOBB University of Economics and Technology, Ankara, Turkey
[5] LAPP, CNRS/IN2P3 and Université de Savoie, Annecy-le-Vieux, France
[6] High Energy Physics Division, Argonne National Laboratory, Argonne IL, United States of America
[7] Department of Physics, University of Arizona, Tucson AZ, United States of America
[8] Department of Physics, The University of Texas at Arlington, Arlington TX, United States of America
[9] Physics Department, University of Athens, Athens, Greece
[10] Physics Department, National Technical University of Athens, Zografou, Greece
[11] Institute of Physics, Azerbaijan Academy of Sciences, Baku, Azerbaijan
[12] Institut de Física d'Altes Energies and Departament de Física de la Universitat Autònoma de Barcelona, Barcelona, Spain

JHEP04(2015)117

[13] [(a)] Institute of Physics, University of Belgrade, Belgrade; [(b)] Vinca Institute of Nuclear Sciences, University of Belgrade, Belgrade, Serbia
[14] Department for Physics and Technology, University of Bergen, Bergen, Norway
[15] Physics Division, Lawrence Berkeley National Laboratory and University of California, Berkeley CA, United States of America
[16] Department of Physics, Humboldt University, Berlin, Germany
[17] Albert Einstein Center for Fundamental Physics and Laboratory for High Energy Physics, University of Bern, Bern, Switzerland
[18] School of Physics and Astronomy, University of Birmingham, Birmingham, United Kingdom
[19] [(a)] Department of Physics, Bogazici University, Istanbul; [(b)] Department of Physics, Dogus University, Istanbul; [(c)] Department of Physics Engineering, Gaziantep University, Gaziantep, Turkey
[20] [(a)] INFN Sezione di Bologna; [(b)] Dipartimento di Fisica e Astronomia, Università di Bologna, Bologna, Italy
[21] Physikalisches Institut, University of Bonn, Bonn, Germany
[22] Department of Physics, Boston University, Boston MA, United States of America
[23] Department of Physics, Brandeis University, Waltham MA, United States of America
[24] [(a)] Universidade Federal do Rio De Janeiro COPPE/EE/IF, Rio de Janeiro; [(b)] Electrical Circuits Department, Federal University of Juiz de Fora (UFJF), Juiz de Fora; [(c)] Federal University of Sao Joao del Rei (UFSJ), Sao Joao del Rei; [(d)] Instituto de Fisica, Universidade de Sao Paulo, Sao Paulo, Brazil
[25] Physics Department, Brookhaven National Laboratory, Upton NY, United States of America
[26] [(a)] National Institute of Physics and Nuclear Engineering, Bucharest; [(b)] National Institute for Research and Development of Isotopic and Molecular Technologies, Physics Department, Cluj Napoca; [(c)] University Politehnica Bucharest, Bucharest; [(d)] West University in Timisoara, Timisoara, Romania
[27] Departamento de Física, Universidad de Buenos Aires, Buenos Aires, Argentina
[28] Cavendish Laboratory, University of Cambridge, Cambridge, United Kingdom
[29] Department of Physics, Carleton University, Ottawa ON, Canada
[30] CERN, Geneva, Switzerland
[31] Enrico Fermi Institute, University of Chicago, Chicago IL, United States of America
[32] [(a)] Departamento de Física, Pontificia Universidad Católica de Chile, Santiago; [(b)] Departamento de Física, Universidad Técnica Federico Santa María, Valparaíso, Chile
[33] [(a)] Institute of High Energy Physics, Chinese Academy of Sciences, Beijing; [(b)] Department of Modern Physics, University of Science and Technology of China, Anhui; [(c)] Department of Physics, Nanjing University, Jiangsu; [(d)] School of Physics, Shandong University, Shandong; [(e)] Physics Department, Shanghai Jiao Tong University, Shanghai; [(f)] Physics Department, Tsinghua University, Beijing 100084, China
[34] Laboratoire de Physique Corpusculaire, Clermont Université and Université Blaise Pascal and CNRS/IN2P3, Clermont-Ferrand, France
[35] Nevis Laboratory, Columbia University, Irvington NY, United States of America
[36] Niels Bohr Institute, University of Copenhagen, Kobenhavn, Denmark
[37] [(a)] INFN Gruppo Collegato di Cosenza, Laboratori Nazionali di Frascati; [(b)] Dipartimento di Fisica, Università della Calabria, Rende, Italy
[38] [(a)] AGH University of Science and Technology, Faculty of Physics and Applied Computer Science, Krakow; [(b)] Marian Smoluchowski Institute of Physics, Jagiellonian University, Krakow, Poland
[39] The Henryk Niewodniczanski Institute of Nuclear Physics, Polish Academy of Sciences, Krakow, Poland
[40] Physics Department, Southern Methodist University, Dallas TX, United States of America
[41] Physics Department, University of Texas at Dallas, Richardson TX, United States of America
[42] DESY, Hamburg and Zeuthen, Germany
[43] Institut für Experimentelle Physik IV, Technische Universität Dortmund, Dortmund, Germany

JHEP04(2015)117

[44] Institut für Kern- und Teilchenphysik, Technische Universität Dresden, Dresden, Germany
[45] Department of Physics, Duke University, Durham NC, United States of America
[46] SUPA - School of Physics and Astronomy, University of Edinburgh, Edinburgh, United Kingdom
[47] INFN Laboratori Nazionali di Frascati, Frascati, Italy
[48] Fakultät für Mathematik und Physik, Albert-Ludwigs-Universität, Freiburg, Germany
[49] Section de Physique, Université de Genève, Geneva, Switzerland
[50] [(a)] INFN Sezione di Genova; [(b)] Dipartimento di Fisica, Università di Genova, Genova, Italy
[51] [(a)] E. Andronikashvili Institute of Physics, Iv. Javakhishvili Tbilisi State University, Tbilisi; [(b)] High Energy Physics Institute, Tbilisi State University, Tbilisi, Georgia
[52] II Physikalisches Institut, Justus-Liebig-Universität Giessen, Giessen, Germany
[53] SUPA - School of Physics and Astronomy, University of Glasgow, Glasgow, United Kingdom
[54] II Physikalisches Institut, Georg-August-Universität, Göttingen, Germany
[55] Laboratoire de Physique Subatomique et de Cosmologie, Université Grenoble-Alpes, CNRS/IN2P3, Grenoble, France
[56] Department of Physics, Hampton University, Hampton VA, United States of America
[57] Laboratory for Particle Physics and Cosmology, Harvard University, Cambridge MA, United States of America
[58] [(a)] Kirchhoff-Institut für Physik, Ruprecht-Karls-Universität Heidelberg, Heidelberg; [(b)] Physikalisches Institut, Ruprecht-Karls-Universität Heidelberg, Heidelberg; [(c)] ZITI Institut für technische Informatik, Ruprecht-Karls-Universität Heidelberg, Mannheim, Germany
[59] Faculty of Applied Information Science, Hiroshima Institute of Technology, Hiroshima, Japan
[60] [(a)] Department of Physics, The Chinese University of Hong Kong, Shatin, N.T., Hong Kong; [(b)] Department of Physics, The University of Hong Kong, Hong Kong; [(c)] Department of Physics, The Hong Kong University of Science and Technology, Clear Water Bay, Kowloon, Hong Kong, China
[61] Department of Physics, Indiana University, Bloomington IN, United States of America
[62] Institut für Astro- und Teilchenphysik, Leopold-Franzens-Universität, Innsbruck, Austria
[63] University of Iowa, Iowa City IA, United States of America
[64] Department of Physics and Astronomy, Iowa State University, Ames IA, United States of America
[65] Joint Institute for Nuclear Research, JINR Dubna, Dubna, Russia
[66] KEK, High Energy Accelerator Research Organization, Tsukuba, Japan
[67] Graduate School of Science, Kobe University, Kobe, Japan
[68] Faculty of Science, Kyoto University, Kyoto, Japan
[69] Kyoto University of Education, Kyoto, Japan
[70] Department of Physics, Kyushu University, Fukuoka, Japan
[71] Instituto de Física La Plata, Universidad Nacional de La Plata and CONICET, La Plata, Argentina
[72] Physics Department, Lancaster University, Lancaster, United Kingdom
[73] [(a)] INFN Sezione di Lecce; [(b)] Dipartimento di Matematica e Fisica, Università del Salento, Lecce, Italy
[74] Oliver Lodge Laboratory, University of Liverpool, Liverpool, United Kingdom
[75] Department of Physics, Jožef Stefan Institute and University of Ljubljana, Ljubljana, Slovenia
[76] School of Physics and Astronomy, Queen Mary University of London, London, United Kingdom
[77] Department of Physics, Royal Holloway University of London, Surrey, United Kingdom
[78] Department of Physics and Astronomy, University College London, London, United Kingdom
[79] Louisiana Tech University, Ruston LA, United States of America
[80] Laboratoire de Physique Nucléaire et de Hautes Energies, UPMC and Université Paris-Diderot and CNRS/IN2P3, Paris, France
[81] Fysiska institutionen, Lunds universitet, Lund, Sweden
[82] Departamento de Fisica Teorica C-15, Universidad Autonoma de Madrid, Madrid, Spain
[83] Institut für Physik, Universität Mainz, Mainz, Germany
[84] School of Physics and Astronomy, University of Manchester, Manchester, United Kingdom
[85] CPPM, Aix-Marseille Université and CNRS/IN2P3, Marseille, France
[86] Department of Physics, University of Massachusetts, Amherst MA, United States of America

JHEP04(2015)117

[87] Department of Physics, McGill University, Montreal QC, Canada
[88] School of Physics, University of Melbourne, Victoria, Australia
[89] Department of Physics, The University of Michigan, Ann Arbor MI, United States of America
[90] Department of Physics and Astronomy, Michigan State University, East Lansing MI, United States of America
[91] [(a)] INFN Sezione di Milano; [(b)] Dipartimento di Fisica, Università di Milano, Milano, Italy
[92] B.I. Stepanov Institute of Physics, National Academy of Sciences of Belarus, Minsk, Republic of Belarus
[93] National Scientific and Educational Centre for Particle and High Energy Physics, Minsk, Republic of Belarus
[94] Department of Physics, Massachusetts Institute of Technology, Cambridge MA, United States of America
[95] Group of Particle Physics, University of Montreal, Montreal QC, Canada
[96] P.N. Lebedev Institute of Physics, Academy of Sciences, Moscow, Russia
[97] Institute for Theoretical and Experimental Physics (ITEP), Moscow, Russia
[98] National Research Nuclear University MEPhI, Moscow, Russia
[99] D.V. Skobeltsyn Institute of Nuclear Physics, M.V. Lomonosov Moscow State University, Moscow, Russia
[100] Fakultät für Physik, Ludwig-Maximilians-Universität München, München, Germany
[101] Max-Planck-Institut für Physik (Werner-Heisenberg-Institut), München, Germany
[102] Nagasaki Institute of Applied Science, Nagasaki, Japan
[103] Graduate School of Science and Kobayashi-Maskawa Institute, Nagoya University, Nagoya, Japan
[104] [(a)] INFN Sezione di Napoli; [(b)] Dipartimento di Fisica, Università di Napoli, Napoli, Italy
[105] Department of Physics and Astronomy, University of New Mexico, Albuquerque NM, United States of America
[106] Institute for Mathematics, Astrophysics and Particle Physics, Radboud University Nijmegen/Nikhef, Nijmegen, Netherlands
[107] Nikhef National Institute for Subatomic Physics and University of Amsterdam, Amsterdam, Netherlands
[108] Department of Physics, Northern Illinois University, DeKalb IL, United States of America
[109] Budker Institute of Nuclear Physics, SB RAS, Novosibirsk, Russia
[110] Department of Physics, New York University, New York NY, United States of America
[111] Ohio State University, Columbus OH, United States of America
[112] Faculty of Science, Okayama University, Okayama, Japan
[113] Homer L. Dodge Department of Physics and Astronomy, University of Oklahoma, Norman OK, United States of America
[114] Department of Physics, Oklahoma State University, Stillwater OK, United States of America
[115] Palacký University, RCPTM, Olomouc, Czech Republic
[116] Center for High Energy Physics, University of Oregon, Eugene OR, United States of America
[117] LAL, Université Paris-Sud and CNRS/IN2P3, Orsay, France
[118] Graduate School of Science, Osaka University, Osaka, Japan
[119] Department of Physics, University of Oslo, Oslo, Norway
[120] Department of Physics, Oxford University, Oxford, United Kingdom
[121] [(a)] INFN Sezione di Pavia; [(b)] Dipartimento di Fisica, Università di Pavia, Pavia, Italy
[122] Department of Physics, University of Pennsylvania, Philadelphia PA, United States of America
[123] Petersburg Nuclear Physics Institute, Gatchina, Russia
[124] [(a)] INFN Sezione di Pisa; [(b)] Dipartimento di Fisica E. Fermi, Università di Pisa, Pisa, Italy
[125] Department of Physics and Astronomy, University of Pittsburgh, Pittsburgh PA, United States of America
[126] [(a)] Laboratorio de Instrumentacao e Fisica Experimental de Particulas - LIP, Lisboa; [(b)] Faculdade de Ciências, Universidade de Lisboa, Lisboa; [(c)] Department of Physics, University of Coimbra, Coimbra; [(d)] Centro de Física Nuclear da Universidade de Lisboa, Lisboa; [(e)] Departamento de

JHEP04(2015)117

Fisica, Universidade do Minho, Braga; [(f)] Departamento de Fisica Teorica y del Cosmos and CAFPE, Universidad de Granada, Granada (Spain); [(g)] Dep Fisica and CEFITEC of Faculdade de Ciencias e Tecnologia, Universidade Nova de Lisboa, Caparica, Portugal
[127] Institute of Physics, Academy of Sciences of the Czech Republic, Praha, Czech Republic
[128] Czech Technical University in Prague, Praha, Czech Republic
[129] Faculty of Mathematics and Physics, Charles University in Prague, Praha, Czech Republic
[130] State Research Center Institute for High Energy Physics, Protvino, Russia
[131] Particle Physics Department, Rutherford Appleton Laboratory, Didcot, United Kingdom
[132] Ritsumeikan University, Kusatsu, Shiga, Japan
[133] [(a)] INFN Sezione di Roma; [(b)] Dipartimento di Fisica, Sapienza Università di Roma, Roma, Italy
[134] [(a)] INFN Sezione di Roma Tor Vergata; [(b)] Dipartimento di Fisica, Università di Roma Tor Vergata, Roma, Italy
[135] [(a)] INFN Sezione di Roma Tre; [(b)] Dipartimento di Matematica e Fisica, Università Roma Tre, Roma, Italy
[136] [(a)] Faculté des Sciences Ain Chock, Réseau Universitaire de Physique des Hautes Energies - Université Hassan II, Casablanca; [(b)] Centre National de l'Energie des Sciences Techniques Nucleaires, Rabat; [(c)] Faculté des Sciences Semlalia, Université Cadi Ayyad, LPHEA-Marrakech; [(d)] Faculté des Sciences, Université Mohamed Premier and LPTPM, Oujda; [(e)] Faculté des sciences, Université Mohammed V-Agdal, Rabat, Morocco
[137] DSM/IRFU (Institut de Recherches sur les Lois Fondamentales de l'Univers), CEA Saclay (Commissariat à l'Energie Atomique et aux Energies Alternatives), Gif-sur-Yvette, France
[138] Santa Cruz Institute for Particle Physics, University of California Santa Cruz, Santa Cruz CA, United States of America
[139] Department of Physics, University of Washington, Seattle WA, United States of America
[140] Department of Physics and Astronomy, University of Sheffield, Sheffield, United Kingdom
[141] Department of Physics, Shinshu University, Nagano, Japan
[142] Fachbereich Physik, Universität Siegen, Siegen, Germany
[143] Department of Physics, Simon Fraser University, Burnaby BC, Canada
[144] SLAC National Accelerator Laboratory, Stanford CA, United States of America
[145] [(a)] Faculty of Mathematics, Physics & Informatics, Comenius University, Bratislava; [(b)] Department of Subnuclear Physics, Institute of Experimental Physics of the Slovak Academy of Sciences, Kosice, Slovak Republic
[146] [(a)] Department of Physics, University of Cape Town, Cape Town; [(b)] Department of Physics, University of Johannesburg, Johannesburg; [(c)] School of Physics, University of the Witwatersrand, Johannesburg, South Africa
[147] [(a)] Department of Physics, Stockholm University; [(b)] The Oskar Klein Centre, Stockholm, Sweden
[148] Physics Department, Royal Institute of Technology, Stockholm, Sweden
[149] Departments of Physics & Astronomy and Chemistry, Stony Brook University, Stony Brook NY, United States of America
[150] Department of Physics and Astronomy, University of Sussex, Brighton, United Kingdom
[151] School of Physics, University of Sydney, Sydney, Australia
[152] Institute of Physics, Academia Sinica, Taipei, Taiwan
[153] Department of Physics, Technion: Israel Institute of Technology, Haifa, Israel
[154] Raymond and Beverly Sackler School of Physics and Astronomy, Tel Aviv University, Tel Aviv, Israel
[155] Department of Physics, Aristotle University of Thessaloniki, Thessaloniki, Greece
[156] International Center for Elementary Particle Physics and Department of Physics, The University of Tokyo, Tokyo, Japan
[157] Graduate School of Science and Technology, Tokyo Metropolitan University, Tokyo, Japan
[158] Department of Physics, Tokyo Institute of Technology, Tokyo, Japan
[159] Department of Physics, University of Toronto, Toronto ON, Canada
[160] [(a)] TRIUMF, Vancouver BC; [(b)] Department of Physics and Astronomy, York University, Toronto ON, Canada

JHEP04(2015)117

[161] Faculty of Pure and Applied Sciences, University of Tsukuba, Tsukuba, Japan
[162] Department of Physics and Astronomy, Tufts University, Medford MA, United States of America
[163] Centro de Investigaciones, Universidad Antonio Narino, Bogota, Colombia
[164] Department of Physics and Astronomy, University of California Irvine, Irvine CA, United States of America
[165] [(a)] INFN Gruppo Collegato di Udine, Sezione di Trieste, Udine; [(b)] ICTP, Trieste; [(c)] Dipartimento di Chimica, Fisica e Ambiente, Università di Udine, Udine, Italy
[166] Department of Physics, University of Illinois, Urbana IL, United States of America
[167] Department of Physics and Astronomy, University of Uppsala, Uppsala, Sweden
[168] Instituto de Física Corpuscular (IFIC) and Departamento de Física Atómica, Molecular y Nuclear and Departamento de Ingeniería Electrónica and Instituto de Microelectrónica de Barcelona (IMB-CNM), University of Valencia and CSIC, Valencia, Spain
[169] Department of Physics, University of British Columbia, Vancouver BC, Canada
[170] Department of Physics and Astronomy, University of Victoria, Victoria BC, Canada
[171] Department of Physics, University of Warwick, Coventry, United Kingdom
[172] Waseda University, Tokyo, Japan
[173] Department of Particle Physics, The Weizmann Institute of Science, Rehovot, Israel
[174] Department of Physics, University of Wisconsin, Madison WI, United States of America
[175] Fakultät für Physik und Astronomie, Julius-Maximilians-Universität, Würzburg, Germany
[176] Fachbereich C Physik, Bergische Universität Wuppertal, Wuppertal, Germany
[177] Department of Physics, Yale University, New Haven CT, United States of America
[178] Yerevan Physics Institute, Yerevan, Armenia
[179] Centre de Calcul de l'Institut National de Physique Nucléaire et de Physique des Particules (IN2P3), Villeurbanne, France

[a] Also at Department of Physics, King's College London, London, United Kingdom
[b] Also at Institute of Physics, Azerbaijan Academy of Sciences, Baku, Azerbaijan
[c] Also at Novosibirsk State University, Novosibirsk, Russia
[d] Also at TRIUMF, Vancouver BC, Canada
[e] Also at Department of Physics, California State University, Fresno CA, United States of America
[f] Also at Department of Physics, University of Fribourg, Fribourg, Switzerland
[g] Also at Tomsk State University, Tomsk, Russia
[h] Also at CPPM, Aix-Marseille Université and CNRS/IN2P3, Marseille, France
[i] Also at Università di Napoli Parthenope, Napoli, Italy
[j] Also at Institute of Particle Physics (IPP), Canada
[k] Also at Particle Physics Department, Rutherford Appleton Laboratory, Didcot, United Kingdom
[l] Also at Department of Physics, St. Petersburg State Polytechnical University, St. Petersburg, Russia
[m] Also at Louisiana Tech University, Ruston LA, United States of America
[n] Also at Institucio Catalana de Recerca i Estudis Avancats, ICREA, Barcelona, Spain
[o] Also at Department of Physics, National Tsing Hua University, Taiwan
[p] Also at Department of Physics, The University of Texas at Austin, Austin TX, United States of America
[q] Also at Institute of Theoretical Physics, Ilia State University, Tbilisi, Georgia
[r] Also at CERN, Geneva, Switzerland
[s] Also at Ochadai Academic Production, Ochanomizu University, Tokyo, Japan
[t] Also at Manhattan College, New York NY, United States of America
[u] Also at Institute of Physics, Academia Sinica, Taipei, Taiwan
[v] Also at LAL, Université Paris-Sud and CNRS/IN2P3, Orsay, France
[w] Also at Academia Sinica Grid Computing, Institute of Physics, Academia Sinica, Taipei, Taiwan
[x] Also at Laboratoire de Physique Nucléaire et de Hautes Energies, UPMC and Université Paris-Diderot and CNRS/IN2P3, Paris, France

JHEP04(2015)117

[y] Also at School of Physical Sciences, National Institute of Science Education and Research, Bhubaneswar, India
[z] Also at Dipartimento di Fisica, Sapienza Università di Roma, Roma, Italy
[aa] Also at Moscow Institute of Physics and Technology State University, Dolgoprudny, Russia
[ab] Also at section de Physique, Université de Genève, Geneva, Switzerland
[ac] Also at International School for Advanced Studies (SISSA), Trieste, Italy
[ad] Also at Department of Physics and Astronomy, University of South Carolina, Columbia SC, United States of America
[ae] Also at School of Physics and Engineering, Sun Yat-sen University, Guangzhou, China
[af] Also at Faculty of Physics, M.V.Lomonosov Moscow State University, Moscow, Russia
[ag] Also at National Research Nuclear University MEPhI, Moscow, Russia
[ah] Also at Institute for Particle and Nuclear Physics, Wigner Research Centre for Physics, Budapest, Hungary
[ai] Also at Department of Physics, Oxford University, Oxford, United Kingdom
[aj] Also at Institut für Experimentalphysik, Universität Hamburg, Hamburg, Germany
[ak] Also at Department of Physics, The University of Michigan, Ann Arbor MI, United States of America
[al] Also at Discipline of Physics, University of KwaZulu-Natal, Durban, South Africa
[am] Also at University of Malaya, Department of Physics, Kuala Lumpur, Malaysia
[*] Deceased

JHEP04(2015)117

計画研究 A02 班

課題名「超対称性の発見と大統一理論の実験的検証」

研究組織

(1)研究代表者
浅井　祥仁（ASAI, Shoji）
東京大学・理学系研究科・教授
研究者番号：60282505

(2)研究分担者
中本　建志（NAKAMOTO, Tatsushi）
高エネルギー加速器研究機構・超伝導低温工学センター・教授
研究者番号：20290851

田中　純一（TANAKA, Junichi）
東京大学・素粒子物理国際研究センター・准教授
研究者番号：80376699

陣内　修（JINNOUCHI, Osamu）
東京工業大学・理学院・准教授
研究者番号：50360566

(3)連携研究者
山本　明（YAMAMOTO, Akira）
高エネルギー加速器研究機構・加速器研究施設 加速器第六研究系・研究員
研究者番号：30113418

佐々木　憲一（SASAKI, Kenichi）
高エネルギー加速器研究機構・超伝導低温工学センター・准教授
研究者番号：70322831

菊池　章弘（KIKUCHI, Akihiro）
物質・材料研究機構・超電導線材ユニット・主席研究員
研究者番号：5034877

横山　広美（YOKOYAMA, Hiromi）
東京大学・理学系研究科・准教授
研究者番号：50401708

交付決定額

計画研究 A02 班に配分された交付額を表 1 に示す。

表 1. 交付決定額（配分額）　（金額単位：円）

年度	直接経費	間接経費	合計
平成 23 年度	43,600,000	13,080,000	56,680,000
平成 24 年度	48,600,000	14,580,000	63,180,000
平成 25 年度	49,900,000	14,970,000	64,870,000
平成 26 年度	47,200,000	14,160,000	61,360,000
平成 27 年度	47,100,000	14,130,000	61,230,000
総計	236,400,000	70,920,000	307,320,000

研究成果

1．研究開始当初の背景

素粒子標準理論はこれまで電弱エネルギースケールにおいて高精度に検証されてきた。しかし、標準理論は暗黒物質を含まないなど観測との矛盾や、階層性問題など幾つかの理論的な課題を抱えており、より本質的な基礎理論が存在すると考えられている。その中で最も有望視されているのが、超対称性理論である。TeV 領域における新しい素粒子現象、特に新粒子群の発見が、LEP などの精密測定、3 つの力の大統一、暗黒物質、階層性問題の解決などから予言されている。超対

称性粒子探索は CERN の LHC 加速器と国際共同実験 ATLAS 検出器を用いて行う。本計画研究開始の前年にはパイロット実験が行われ、研究代表者を中心とした解析チームにより、超対称性粒子の低質量領域を棄却することに成功した。本計画研究は、開始前年度の経験・実績を踏まえ、データ量が大幅に増加する平成 23 年から本格的な探索を開始した。

また本研究で得られる研究成果は次世代実験計画に大きなインパクトを持つ。それらの計画で期待される物理と加速器スペックの策定を行い、次世代の加速器開発を進めることが重要である。これにより、本計画研究で得られた物理成果を発展させることができる。

２．研究の目的

4 つの目的がある。

（1）LHC アトラス実験で、超対称性など、標準理論を超える新しい素粒子現象を直接的に発見することである。探索対象が未知なため、探索は特定の現象論モデルに依存しないよう、観測事象のイベント・トポロジーを基本とした直接探索を系統的に行う。これにより確実な発見を目指す。

（2）背景事象量の評価を、実験データを用いて行う。この研究は(1)の発見に不可欠であると同時に、他の実験系の研究班にとっても、共通に重要な要素となる。

（3）次世代加速器に向けた新しい超伝導素材の開発を行う。また耐放射線性能、高磁場実現を両立させることのできる、次世代超伝導磁石を開発する。プロトタイプ磁石を制作し、性能評価をする。

（4）理論系の計画研究班と共同で得られた成果を元に、新しい素粒子像を創生する。B01 班とは、本研究の新物理と宇宙の暗黒物質との関係、宇宙進化に与えた影響を探る B02, B03 班との共同研究により、超対称性が導く新たな時空像、数学構造を発展させる。

３．研究の方法

平成 23 年、平成 24 年はそれぞれ衝突エネルギー7TeV,8TeV での運転が行われた。それぞれ約 5 fb^{-1}, 20 fb^{-1} の積分ルミノシティに相当する高品質データを収集した。

（1）検出器の理解を進める。特にハドロン・ジェットのエネルギー較正、検出器ノイズや宇宙線事象の除去、消失運動量の算出手法や較正について、精度の向上を目指す。背景事象量を実験データから直接見積り、その不定性を評価する。

（2）超対称性や余剰次元などの信号を、ジェット数、レプトン数、b-jet 数、消失エネルギーの大小などにより、事象トポロジー毎に分類し、系統的な探索を置こなう。

（3）超伝導加速器用の新しい Nb_3Al 超伝導線の開発を行う。超伝導材を機械的に固定する樹脂を選定する。放射線耐性が期待できるシアネートエステル樹脂の性能評価を行う。

更に最終年度の平成 27 年には、衝突エネルギーが倍増され 13TeV での運転を行った。
（4）エネルギー増強により、新物理への感度が上がった。直接探索を組織的に展開し、超対称性粒子や新しい素粒子現象の兆候を確認する。
（5）LHC 高輝度アップグレードを念頭に、強磁場双極超伝導磁石の設計と試作を行い、冷却励磁試験などを通して性能評価を行う。

４．研究成果

LHC 加速器の陽子・陽子衝突を用いて行った。平成 24 年までの 7、8TeV 衝突エネルギー用いた第一実験期(Run1)と、平成 27,28 年の 13TeV を用いた第二実験期(Run2)の結果を合わせて報告する。但し本計画研究では、平成 27 年の段階で、幾つかの探索チャンネルに 3σ程度の超過が見られており、物理信号であるかどうか見極めるために、補助事業の期間を延長することとした。従ってここでは平成 28 年前半の結果も含む。

（1）超対称性粒子探索に対する厳しい制限：
観測事象のイベント・トポロジーに探索チャンネルを分類し、組織的な探索を展開した。また背景事象の見積りをシミュレーションによるものに加えて、実験データを用いたものも導入し、評価の不定性を著しく抑えることに成功した。

これらの手法の開発・調整は平成 24 年までに大きな進展が見られた。同様の手法を平成 27 年にも用いて探索を進めた。

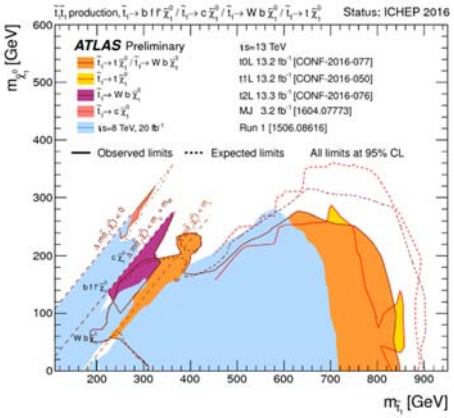

図 1.

(a) Run1 で発見されたヒッグス粒子の質量 125GeV を実現するために、第 3 世代超対称クォーク（スカラートップ等）が 1TeV 以下程度に軽い、というのが自然に期待される。広域な質量領域に渡り、軽いスカラートップの存在を棄却する結果となった。0.85 TeV の制限を設けた(図 1)。

(b) 強い相互作用により生成されるグルイーノ・スクォークを多数ジェット＋消失エネルギー解析により、高統計データを用いて行われた。グルイーノ質量＝スクォーク質量の仮定で 1.85TeV の厳しい制限を設けた(図 2)。

(c) 電弱相互作用によるゲージーノ生成も統計の増加に伴い重要なチャンネルとなった。複数のレプトンを要求する解析では、様々な崩壊過程を考慮して広範囲に渡る質量領域を棄却した。

（2）超対称性粒子以外の新粒子・現象も含む事象に対する厳しい制限

(a) 飛跡検出器の理解が進み、検出器内で崩壊するような長寿命の新粒子探索が可能になった。飛跡が検出器内で消失する事象や、崩壊バーテックスが検出器中央からずれるような特異な事象の探索を進めた(図 3)。

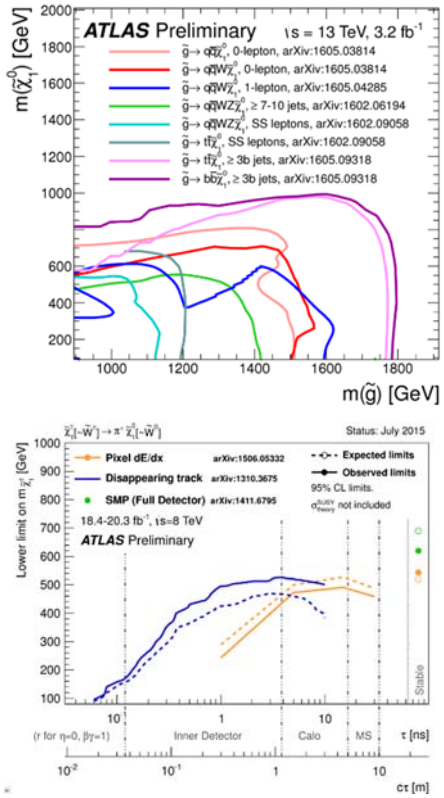

図 3.

(b) レプトン対生成や 2 本ジェット等の不変質量分布を用いた、余剰次元模型や、その他幾つかの新しい理論体系が予言する新粒子に対して、直接探索を行った。余剰次元模型の一つである RS 模型が予言する重力子に対しては、3.2TeV の下限を設けた。

(c) マイクロ・ブラックホール生成、ベクターライク・クォーク等、特異な終状態をもつ新物理の探索も行った。これまでのところ、背景事象からの超過は見られていない。

（3）加速器開発：LHC 高輝度アップグレードに向けたビーム分離用大口径双極超伝導磁石の開発を行い、電磁設計・機械構造設計などの基礎開発を進めた。2m 長モデル機を試作し、1.9K における冷却励磁試験を行った。また、耐放射線性に優れた有機絶縁構造材料の開発を進めた。放射線照射による試験、並びに 2m 長モデル機に搭載して性能評価を行った。

次世代高エネルギー加速器（FCC）計画に向けた、高磁場超電導磁石及び、線材の開発も行った。10T（テスラ）を超える高磁場下でも臨界電流密度が安定する機械特性に優れた Nb_3Al 線材に着目し研究開発を進めた。こちらはラザフォードケーブル（撚線）の試作に成功し、その性能評価を行った。

（4）総括班が主催して開催した「テラスケール研究会」は 11 回に及び、2 回/年のペースで行われた。領域全域に渡る議論が、長日に渡り行われるが、特に超対称性探索、新粒子探索、暗黒物質、時空構造に関する議論を実験・理論間で展開することができた。理論・実験合同研究から発展した論文も出版された。

5．主な発表論文等

（研究代表者、研究分担者及び連携研究者には下線）

〔雑誌論文〕（計 122 件）

(代表論文のみ掲載：ATLAS　Collaboration の論文には、研究代表者・研究分担者・連携研究者の内アトラス実験関係者を全て含む)

[1]“Summary of the searches for squarks and gluinos using √s = 8 TeV *pp* collisions with the ATLAS experiment at LHC”; The ATLAS collaboration, JHEP10(2015)054、査読有、DOI: 10.1007/JHEP10(2015)054

[2]“ATLAS Run1 searches for direct pair production of third-generation squarks at the Large Hadron Collider”; The ATLAS collaboration, Euro. Phys. J. C (2015) 75: 510. 、査読有、DOI:10.1140/epjc/
s10052-015-3726-9

[3]“Search for the elecroweak production of supersymmetric particles in √s = 8 TeV *pp* collisions with the ATLAS detector” ; The ATLAS collaboration, Phys.Rev.D93,052002、査読有、DOI:http://
dx.doi.org/10.1103/PhysRevD.93.052002

[4] “Search for massive long-lived particles using multitrack displaced vertices of displaced lepton pairs in pp collisions ” ; The ATLAS collaboration, Phys.Rev.D93,052002、査読有, DOI:http://dx.doi.org/10.1103/PhysRevD.92.072004

[5]“Model Magnet Development of D1 Beam Separation Dipole for the HL-LHC Upgrade”, T. Nakamoto, M. Sugano, Q. Xu et al., IEEE Trans. Appl. Supercond., 25, No.3 (2015) 4000505, 査読有

〔学会発表〕

（主なもののみ掲載）

[1]“Beyond the SM Higgs searches”, J.Tanaka, 4-th Annual Large Hadron Collider Physics Conference 2016, 13-19/June/2016, Lund (Sweden).

[2]“New physics searches at the LHC: where do we go with run II?” O.Jinnouchi, TeV Particle Astrophysics 2015, , 26-30/Oct/2015, Kashiwa(Japan).

[3]“SUSY searches at the LHC”, S. Asai, 27th Recontres de Blois ,31/May - 5/June/2015, Blois(France).

[4]“Searches for BSM and Higgs boson at LHC”, O. Jinnouchi, International Workshop on Grand Unified Theories, 15-17/March/2012,　Kyoto(Japan).

[5]“Search for the Standard Model Higgs boson at ATLAS”, J.Tanaka, Les Rencontres de Physique de la Vallee d’Aoste, 26/Feb-3/Mar/2012, La Thuile (Italy)

[6]“R&D Efforts towards High Field Accelerator Magnets at KEK”, T. Nakamoto, 22nd International Conference on Magnet Technology (MT-22) , September 12-16, 2011, Marseille (France).

〔図書〕（計 2 件）
（主なもののみ掲載）
[1]「LHC の物理　ヒッグス粒子発見とその後の展開」浅井祥仁（著）共立出版、物理学最前線シリーズ 7，134 頁，2016 年

[2]「ヒッグス粒子の謎」浅井祥仁（著）祥伝社新書、203 頁，2012 年

〔産業財産権〕
○出願状況（計　0 件）

○取得状況（計 0 件）

主要論文別刷

[1]“Summary of the searches for squarks and gluinos using $\sqrt{s}$ = 8 TeV pp collisions with the ATLAS experiment at LHC”; The ATLAS collaboration, JHEP10(2015)054、査読有、DOI: 10.1007/JHEP10(2015)054

[2]“ATLAS Run1 searches for direct pair production of third-generation squarks at the Large Hadron Collider”; The ATLAS collaboration, Euro. Phys. J. C (2015) 75: 510. 、査読有、DOI:10.1140/epjc/s10052-015-3726-9

[3]“Search for the elecroweak production of supersymmetric particles in $\sqrt{s}$ = 8 TeV pp collisions with the ATLAS detector”；The ATLAS collaboration, Phys.Rev.D93,052002、査読有、DOI:http://dx.doi.org/10.1103/PhysRevD.93.052002

[4] “Search for massive long-lived particles using multitrack displaced vertices of displaced lepton pairs in pp collisions ”；The ATLAS collaboration, Phys.Rev.D93,052002、査読有, DOI:http://dx.doi.org/10.1103/PhysRevD.92.072004

[5]“Model Magnet Development of D1 Beam Separation Dipole for the HL-LHC Upgrade”, T. Nakamoto, M. Sugano, Q. Xu et al., IEEE Trans. Appl. Supercond., 25, No.3 (2015) 4000505, 査読有

Published for SISSA by Springer

Received: *July 21, 2015*
Accepted: *September 9, 2015*
Published: *October 8, 2015*

Summary of the searches for squarks and gluinos using $\sqrt{s} = 8$ TeV pp collisions with the ATLAS experiment at the LHC

The ATLAS collaboration

E-mail: atlas.publications@cern.ch

Abstract: A summary is presented of ATLAS searches for gluinos and first- and second-generation squarks in final states containing jets and missing transverse momentum, with or without leptons or b-jets, in the $\sqrt{s} = 8$ TeV data set collected at the Large Hadron Collider in 2012. This paper reports the results of new interpretations and statistical combinations of previously published analyses, as well as a new analysis. Since no significant excess of events over the Standard Model expectation is observed, the data are used to set limits in a variety of models. In all the considered simplified models that assume R-parity conservation, the limit on the gluino mass exceeds 1150 GeV at 95% confidence level, for an LSP mass smaller than 100 GeV. Furthermore, exclusion limits are set for left-handed squarks in a phenomenological MSSM model, a minimal Supergravity/Constrained MSSM model, R-parity-violation scenarios, a minimal gauge-mediated supersymmetry breaking model, a natural gauge mediation model, a non-universal Higgs mass model with gaugino mediation and a minimal model of universal extra dimensions.

Keywords: Supersymmetry, Hadron-Hadron Scattering

ArXiv ePrint: 1507.05525

Open Access, Copyright CERN,
for the benefit of the ATLAS Collaboration.
Article funded by SCOAP[3].

doi:10.1007/JHEP10(2015)054

JHEP10(2015)054

Contents

1 Introduction **1**

2 SUSY models **3**
- 2.1 Phenomenological models 4
  - 2.1.1 A phenomenological MSSM model 4
  - 2.1.2 Minimal Supergravity/Constrained MSSM and bilinear R-parity-violation models 5
  - 2.1.3 Minimal gauge-mediated supersymmetry breaking model 5
  - 2.1.4 Natural gauge mediation model 6
  - 2.1.5 Non-universal Higgs mass models with gaugino mediation 6
  - 2.1.6 Minimal Universal Extra Dimensions model 7
- 2.2 Simplified models 7
  - 2.2.1 Direct decays of squarks and gluinos 7
  - 2.2.2 One-step decays of squarks and gluinos 9
  - 2.2.3 Two-step decays of squarks and gluinos 9
  - 2.2.4 Gluino decays via third-generation squarks 11

3 The ATLAS detector and data sample **13**

4 Monte Carlo simulated samples **14**

5 Object reconstruction and identification **16**

6 Analysis strategy **17**

7 Experimental signatures **19**
- 7.1 Final states with high-p_{T} jets, missing transverse momentum and no electrons or muons 20
- 7.2 Final states with high-p_{T} jets, missing transverse momentum and at least one electron or muon 24
- 7.3 Final states with high-p_{T} jets, missing transverse momentum and at least one hadronically decaying tau lepton 27
- 7.4 Final states with many b-jets and missing transverse momentum 27

8 Systematic uncertainties **28**

9 Results for the new signal regions **29**

10 Combination strategy **30**

JHEP10(2015)054

11 Limits in SUSY models **32**
11.1 Limits in phenomenological models 35
11.1.1 A phenomenological MSSM model 35
11.1.2 Minimal Supergravity/Constrained MSSM and bilinear R-parity-violation models 35
11.1.3 Minimal gauge-mediated supersymmetry breaking model 38
11.1.4 Natural gauge mediation model 38
11.1.5 Non-universal Higgs mass model with gaugino mediation 38
11.1.6 Minimal Universal Extra Dimension model 38
11.2 Limits in simplified models 40
11.2.1 Direct decays of squarks and gluinos 40
11.2.2 One-step decays of squarks and gluinos 42
11.2.3 Two-step decays of squarks and gluinos 46
11.2.4 Gluino decays via third-generation squarks 50

12 Conclusions **56**

A Extension of the $\tilde{g} \to t\bar{t}\tilde{\chi}_1^0$ simplified model to include decays with off-shell top quarks **57**

B Summary of selection criteria **58**

C 0-lepton Razor analysis details **58**
C.1 The Razor variables 60
C.2 Signal regions 65
C.3 Control and validation regions for SM background processes 67

The ATLAS collaboration **83**

1 Introduction

Supersymmetry (SUSY) [1–9] is a generalization of space-time symmetries that predicts new bosonic partners for the fermions and new fermionic partners for the bosons of the Standard Model (SM). If R-parity is conserved [10–13], SUSY particles (called sparticles) are produced in pairs and the lightest supersymmetric particle (LSP) is stable. The scalar partners of the left- and right-handed quarks, the squarks ($\tilde{q}_{\mathrm{L}}$ and $\tilde{q}_{\mathrm{R}}$ which mix to form two mass eigenstates $\tilde{q}_1$ and $\tilde{q}_2$, ordered by increasing mass), and the fermionic partners of the gluons, gluinos ($\tilde{g}$), could be produced in strong interaction processes at the Large Hadron Collider (LHC) [14] and decay via cascades ending with a stable LSP. The rest of the cascade would yield final states with multiple jets and possibly leptons arising from the decay of sleptons ($\tilde{\ell}$), the superpartners of leptons, or W, Z and Higgs (h) bosons originating from the decays of charginos ($\tilde{\chi}^{\pm}$) or neutralinos ($\tilde{\chi}^0$), where the charginos and neutralinos

JHEP10(2015)054

are the mass eigenstates formed from the linear superpositions of the superpartners of the charged and neutral electroweak and Higgs bosons. In the Minimal Supersymmetric extension of the Standard Model (MSSM) [10–13, 15], there are four charginos, $\tilde{\chi}_1^{\pm}$ and $\tilde{\chi}_2^{\pm}$, and four neutralinos, $\tilde{\chi}_i^0$ ($i = 1$ to 4, ordered by increasing mass); unless stated otherwise, this is assumed in the following. In a large variety of models, the LSP is the lightest neutralino ($\tilde{\chi}_1^0$), which interacts weakly and is a possible candidate for dark matter [16]. Undetected $\tilde{\chi}_1^0$ LSPs would result in substantial missing transverse momentum ($\boldsymbol{E}_{\mathrm{T}}^{\mathrm{miss}}$, with magnitude $E_{\mathrm{T}}^{\mathrm{miss}}$). Significant $E_{\mathrm{T}}^{\mathrm{miss}}$ can also arise in R-parity-violating (RPV) scenarios in which the LSP decays to final states containing neutrinos or in scenarios where neutrinos are present in the cascade decay chains of the produced SUSY particles. Significant mass splitting between the top squark (stop) mass eigenstates $\tilde{t}_1$ and $\tilde{t}_2$ is possible due to the large top Yukawa coupling.[1] Because of the SM weak isospin symmetry the mass of the left-handed bottom squark (sbottom, $\tilde{b}_{\mathrm{L}}$) is tied to the mass of the left-handed stop ($\tilde{t}_{\mathrm{L}}$), and as a consequence the lightest sbottom ($\tilde{b}_1$) and stop ($\tilde{t}_1$) could be produced via the strong interaction with relatively large cross-sections at the LHC, either through direct pair production or in the decay of pair-produced gluinos.

The ATLAS experiment [17] performed several searches for supersymmetric particles in Run 1. No statistically significant excesses of events compared to the predictions of the Standard Model were observed. Therefore the results were expressed as model-independent limits on the production cross-sections of new particles and limits in the parameter space of supersymmetric or simplified models.

The large cross-sections of squark and gluino production in strong interaction processes offer sensitivity to a broad range of SUSY models. This paper provides a summary of the results from inclusive searches for gluinos and first- and second-generation squarks performed by ATLAS, using data from proton-proton (pp) collisions at a centre-of-mass energy of 8 TeV collected during Run 1 of the LHC. The results for direct production of third-generation squarks are reported elsewhere [18]. In addition to summarizing already published searches for squarks and gluinos, this paper presents new signal regions, new interpretations and statistical combinations of those searches, as well as an additional search using the Razor variable set [19], thus improving the sensitivity to supersymmetric models. In order to differentiate strongly produced SUSY events from the SM background, the searches typically require high $E_{\mathrm{T}}^{\mathrm{miss}}$ due to the presence of the LSP and possibly neutrinos, several high-p_{T} jets and large deposited transverse energy. They are further classified according to the presence of leptons and b-jets. A first class of searches applies a veto on leptons [20–22], a second considers final states containing electrons and muons [23–25], and a third requires tau leptons in the final state [26]. A fourth class of searches concentrates on final states containing multiple b-jets [27].

The paper is organized as follows. Section 2 summarizes the SUSY signals in the strong production of gluinos and light-flavour squarks. Section 3 describes the ATLAS experiment and the data sample used, and section 4 the Monte Carlo (MC) simulation samples used for

[1] The masses of the $\tilde{t}_1$ and $\tilde{t}_2$ are the eigenvalues of the stop mass matrix. The stop mass matrix involves the top quark Yukawa coupling in the off-diagonal elements, which typically induces a large mass splitting.

JHEP10(2015)054

background and signal modelling. The physics object reconstruction and identification are presented in section 5. A description of the analysis strategy is given in section 6, and the experimental signatures are presented in section 7. A summary of systematic uncertainties is presented in section 8. Results obtained using the new signal regions with selections similar to those used in previous publications as well as the new analysis using the Razor variable set are reported in section 9. The strategy used for the combination of the results from different analyses is discussed in section 10. Limits in phenomenological and simplified models are presented in section 11. Section 12 is devoted to a summary and conclusions.

2 SUSY models

Since no superpartners of any of the SM particles have been observed, SUSY, if realized in nature, must be a broken symmetry with a mechanism for breaking the symmetry taking place at a higher energy scale. It is difficult to construct a realistic model of spontaneously broken low-energy supersymmetry where the SUSY breaking arises solely as a consequence of the interactions of the particles of the MSSM [28–30]. Therefore, it is often assumed that the SUSY breaking originates in a "hidden" sector, and its effects are transmitted to the MSSM by some unknown mechanism. Various such mechanisms have been proposed, such as gravity-mediated SUSY breaking (SUGRA) [31–36], gauge-mediated SUSY breaking (GMSB) [37–42] and anomaly-mediated SUSY breaking (AMSB) [43, 44]. As a result, these models consider only a small part of the parameter space of the more general MSSM. In such SUSY models, the particle spectrum is typically specified by fixing parameters at the high scale. In order to translate this set of parameters into physically meaningful quantities that describe physics near the electroweak scale, it is necessary to evolve them using their renormalization group equations.

Another approach to constraining SUSY at the electroweak scale is to use simplified models [45, 46] which are based on an effective Lagrangian that only describes a small set of kinematically accessible particles, interactions, production cross-sections and branching ratios. The simplest case corresponds to considering one specific SUSY production process with a fixed decay chain.

Several classes of phenomenological and simplified models, as well as a minimal Universal Extra Dimensions (mUED) scenario [47, 48], covering different combinations of physics objects in the final state, are considered in this paper. Unless otherwise specified, R-parity is assumed to be conserved and the lightest neutralino, $\tilde{\chi}_1^0$, is taken to be the LSP. The phenomenological models include a scenario for the phenomenological MSSM (pMSSM) [49–51], minimal Supergravity/Constrained MSSM (mSUGRA/CMSSM) [31–36], bilinear R-parity violation (bRPV) [52], a minimal gauge-mediated supersymmetry breaking model (mGMSB) [37–42], natural gauge mediation (nGM) [53], and a non-universal Higgs mass model with gaugino mediation (NUHMG) [54]. The simplified models presented here include the pair production of gluinos or first- and second-generation squarks with various hypotheses for their decay chains (direct, one-step or two-step decay), as well as gluino decays via real or virtual third-generation squarks. Direct decays are those where the considered SUSY particles decay directly into SM particles and the LSP, e.g., $\tilde{q} \to q\tilde{\chi}_1^0$.

JHEP10(2015)054

One-step (two-step) decays refer to the cases where the decays occur via one (two) intermediate on-shell SUSY particle(s), e.g., $\tilde{q} \to q\tilde{\chi}_1^{\pm} \to qW\tilde{\chi}_1^0$ ($\tilde{q} \to q\tilde{\chi}_1^{\pm} \to qW\tilde{\chi}_2^0 \to qWZ\tilde{\chi}_1^0$). In gluino decays via third-generation squarks, gluinos undergo a one-step decay to a stop or sbottom such as $\tilde{g} \to t\tilde{t} \to tt\tilde{\chi}_1^0$, or decay directly to final states containing top or bottom quarks, for example $\tilde{g} \to tt\tilde{\chi}_1^0$ if the stop is off-shell. In these simplified models, all supersymmetric particles which do not directly enter the production and decay chain are effectively decoupled, i.e. with masses set above a few TeV. The list of models considered is not comprehensive, and the searches presented here are sensitive to a larger class of decay patterns, mass combinations and hierarchies.

2.1 Phenomenological models

2.1.1 A phenomenological MSSM model

In the pMSSM scenario, no specific theoretical assumption is introduced at the scale of Grand Unification Theories (GUT), or associated with a SUSY breaking mechanism. A short list of experimentally motivated considerations is used to reduce the 120 parameters of the MSSM to 19 real, weak-scale parameters:

- R-parity is exactly conserved,
- there are no new sources of CP violation beyond that already present in the quark mixing matrix,
- Minimal Flavour Violation [55] is imposed at the electroweak scale,
- the first two generations of squarks and sleptons with the same quantum numbers are mass-degenerate, and their Yukawa couplings are too small to affect sparticle production or precision observables.

The remaining 19 independent parameters are: 10 squark and slepton masses, the gaugino masses (M_1, M_2, M_3, associated with the $\mathrm{U(1)_Y}$, $\mathrm{SU(2)_L}$, $\mathrm{SU(3)_C}$ gauge groups, respectively), the higgsino mass parameter (μ), the ratio ($\tan\beta$) of the vacuum expectation values of the two Higgs fields, the mass of the pseudoscalar Higgs boson (m_A), and the trilinear couplings for the third generation (A_b, A_t and A_τ) [49].

In the pMSSM model considered here only the left-handed squarks of the first two generations, the two lightest neutralinos $\tilde{\chi}_2^0$ and $\tilde{\chi}_1^0$, and the lightest chargino $\tilde{\chi}_1^{\pm}$ are assumed to be within kinematic reach. Three gluino masses are considered, $m_{\tilde{g}} = 1.6$, 2.2 and 3.0 TeV, while the masses of all other SUSY particles are kinematically decoupled with masses set to 5 TeV. The parameter $\tan\beta$ is set to 4. The model is further specified by four parameters: $m_{\tilde{q}_\mathrm{L}}$, μ, and M_1 and M_2, from which $m_{\tilde{\chi}_1^0}$, $m_{\tilde{\chi}_2^0}$ and $m_{\tilde{\chi}_1^{\pm}}$ can be calculated. Either M_1 is fixed to 60 GeV and M_2 is varied independently, or M_1 is varied and M_2 is set to $(M_1 + m_{\tilde{q}_\mathrm{L}})/2$.

Left-handed squarks can be pair produced only via t-channel gluino exchange. They can undergo a direct $\tilde{q}_\mathrm{L} \to q\tilde{\chi}_1^0$ decay, or one-step decays: $\tilde{q}_\mathrm{L} \to q + \tilde{\chi}_2^0 \to q + Z/h + \tilde{\chi}_1^0$ or $\tilde{q}_\mathrm{L} \to q + \tilde{\chi}_1^{\pm} \to q + W^{\pm} + \tilde{\chi}_1^0$. Here the lightest Higgs boson h is assumed to have the SM

JHEP10(2015)054

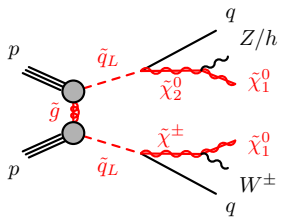

Figure 1. Example of a one-step decay topology of the left-handed squark in the phenomenological MSSM.

decay branching fractions, and its mass is set to 125 GeV. The $\tilde{\chi}_1^\pm$ always decays to $W^\pm$ and $\tilde{\chi}_1^0$ (figure 1). The branching fraction to a left-handed squark via the one-step decay with $\tilde{\chi}_2^0$ ($\tilde{\chi}_1^\pm$) is $\sim$ 30% (65%). The branching fraction of the $\tilde{\chi}_2^0 \to h\tilde{\chi}_1^0$ decay is between 70% and 90% depending on $m_{\tilde{q}_L}$.

2.1.2 Minimal Supergravity/Constrained MSSM and bilinear R-parity-violation models

The mSUGRA/CMSSM model is specified by five parameters: a universal scalar mass (m_0), a universal gaugino mass ($m_{1/2}$) , a universal trilinear scalar coupling (A_0), all defined at the grand unification scale, $\tan\beta$, and the sign of the higgsino mass parameter (μ). The dependence of the SUSY particle mass spectrum on these five parameters is such that all masses increase with increasing $m_{1/2}$, while squark and slepton masses also depend on m_0. In the mSUGRA/CMSSM model studied here the values $\tan\beta = 30$, $A_0 = -2m_0$ and $\mu > 0$ are chosen, such that the lightest scalar Higgs boson mass is approximately 125 GeV in a large fraction of the (m_0, $m_{1/2}$) parameter space studied.

The bRPV scenario uses the same parameters as the mSUGRA/CMSSM model, but R-parity violation is allowed through the bilinear terms[2] $\epsilon_i L_i H_2$, whose coupling parameters are determined by a fit to neutrino oscillation data [56] under the tree-level dominance scenario [57]. In this scenario, the $\tilde{\chi}_1^0$ LSP decays promptly to $W\mu$, $W\tau$, $Z\nu_\tau$ or $h\nu_\tau$ (where the $W/Z/h$ boson can either be on- or off-shell) with branching fractions which are weakly dependent on m_0 and $m_{1/2}$ and are typically on the order of 20–40%, 20–40%, 20–30% and 0–20%, respectively.

2.1.3 Minimal gauge-mediated supersymmetry breaking model

In gauge-mediated SUSY breaking models, the LSP is a very light gravitino ($\tilde{G}$). The mGMSB model is described by six parameters: the SUSY-breaking mass scale felt by the low-energy sector (Λ), the mass of the SUSY breaking messengers (M_{mess}), the number of SU(5) messenger fields (N_5), $\tan\beta$, μ and the gravitino coupling scale factor (C_{grav}) which determines the lifetime of the next-to-lightest SUSY particle (NLSP). Four parameters are fixed to the values previously used in refs. [58–60]: $M_{\text{mess}} = 250$ TeV, $N_5 = 3$, $\mu > 0$ and $C_{\text{grav}} = 1$. With this choice of parameters the production of squark and/or gluino pairs is

[2] In this notation, L_i indicates a lepton SU(2)-doublet superfield, the Higgs SU(2)-doublet superfield H_2 contains the Higgs field that couples to up-type quarks, and the ϵ_i parameters have dimension of mass.

JHEP10(2015)054

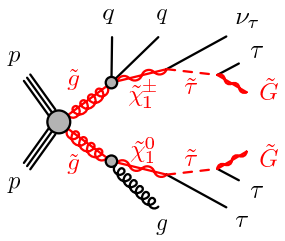

Figure 2. Example of a gluino-pair production followed by the two possible decay chains within the nGM scenario.

expected to dominate over other SUSY processes at the LHC. These SUSY particles decay into the NLSP, which subsequently decays to the LSP. The experimental signatures are largely determined by the nature of the NLSP: this can be either the lightest stau ($\tilde{\tau}$), a selectron or a smuon ($\tilde{\ell}$), the lightest neutralino ($\tilde{\chi}_1^0$), or a sneutrino ($\tilde{\nu}$), leading to final states usually containing tau leptons, light leptons ($\ell = e, \mu$), photons, or neutrinos, respectively.

2.1.4 Natural gauge mediation model

In the nGM scenario, which assumes general gauge mediation [61, 62], the phenomenology depends on the nature of the NLSP [63, 64]. Various models assume that the mass hierarchies of squarks and sleptons are generated by the same physics responsible for breaking SUSY (for example refs. [65, 66]). Typically in these models the third generation of squarks and sleptons is lighter than the other two, and together with the fact that sleptons only acquire small masses through hypercharge interactions in gauge mediation, this leads to a stau NLSP. In the model considered here, it is also assumed that the gluino is the only light coloured sparticle. All squark and slepton mass parameters are set to 2.5 TeV except the lightest stau mass, $m_{\tilde{\tau}}$, which is assumed to be smaller. The parameters M_1 and M_2 are also set to 2.5 TeV, while all trilinear coupling terms are set to zero. The value of μ is set to 400 GeV to ensure that strong production dominates in the parameter space studied. This leaves the gluino mass M_3 and the stau mass $m_{\tilde{\tau}}$ as the only free parameters. The chosen value of the μ parameter sets the masses of the $\tilde{\chi}_1^\pm$, $\tilde{\chi}_1^0$ and $\tilde{\chi}_2^0$, which are almost mass-degenerate. The only light sparticles in the model are the stau, a light gluino, higgsino-dominated charginos and neutralinos, and a very light gravitino LSP. Therefore, the strong production process allowed in this model is gluino-pair production followed by the three possible decay chains: $\tilde{g} \to g\tilde{\chi}_{1,2}^0 \to g\tilde{\tau}\tau \to g\tau\tau\tilde{G}$, $\tilde{g} \to q\bar{q}\tilde{\chi}_{1,2}^0 \to q\bar{q}\tilde{\tau}\tau \to q\bar{q}\tau\tau\tilde{G}$ and $\tilde{g} \to qq\tilde{\chi}_1^\pm \to qq\nu_\tau\tilde{\tau} \to qq\nu_\tau\tau\tilde{G}$ (figure 2), where the final-state quarks are almost exclusively top or bottom quarks. A range of signals with varying gluino and stau masses is studied. The lightest Higgs boson mass is specifically set to 125 GeV.

2.1.5 Non-universal Higgs mass models with gaugino mediation

The NUHMG model is specified with parameters $m_0 = 0$, $\tan\beta = 10$, $\mu > 0$, $m_{H_2}^2 = 0$, and A_0 chosen to maximize the mass of the lightest Higgs boson. The ranges of the two remaining free parameters of the model, $m_{1/2}$ and $m_{H_1}^2$, are chosen such that the NSLP is a tau sneutrino with properties satisfying Big Bang nucleosynthesis constraints [54]. The

JHEP10(2015)054

Diagram	Production	Parameters	Mass relation	Branching ratio	Result
figure 3(a)	$\tilde{q}\tilde{q}$	$m_{\tilde{q}}, m_{\tilde{\chi}_1^0}$	$m_{\tilde{q}} > m_{\tilde{\chi}_1^0}$	$\mathrm{BR}(\tilde{q} \to q\tilde{\chi}_1^0) = 1$	figure 18
figure 3(b)	$\tilde{g}\tilde{q}$	$m_{\tilde{g}}, m_{\tilde{\chi}_1^0}$	$m_{\tilde{q}} = 0.96\ m_{\tilde{g}} > m_{\tilde{\chi}_1^0}$	$\mathrm{BR}(\tilde{q} \to q\tilde{\chi}_1^0) = 1$ $\mathrm{BR}(\tilde{g} \to \tilde{q}q) = 1$	figure 20(a)
		$m_{\tilde{q}}, m_{\tilde{g}}$	$m_{\tilde{\chi}_1^0} = (0, 395, 695)$ GeV	If $m(\tilde{g}) > m(\tilde{q})$: $\mathrm{BR}(\tilde{q} \to q\tilde{\chi}_1^0) = 1$, $\mathrm{BR}(\tilde{g} \to \tilde{q}q) = 1$ If $m(\tilde{q}) > m(\tilde{g})$: $\mathrm{BR}(\tilde{g} \to qq\tilde{\chi}_1^0) = 1$, $\mathrm{BR}(\tilde{q} \to \tilde{g}q) = 1$	figure 20(b)
figure 3(c)	$\tilde{g}\tilde{g}$	$m_{\tilde{g}}, m_{\tilde{\chi}_1^0}$	$m_{\tilde{g}} > m_{\tilde{\chi}_1^0}$	$\mathrm{BR}(\tilde{g} \to qq\tilde{\chi}_1^0) = 1$	figure 19
figure 3(d)	$\tilde{g}\tilde{g}$	$m_{\tilde{g}}$	$m_{\tilde{\chi}_1^0} = 0$	$\mathrm{BR}(\tilde{g} \to g\tilde{\chi}_1^0) = 1$	figure 21(a)
		$m_{\tilde{\chi}_1^0}$	$m_{\tilde{g}} = 850$ GeV		figure 21(b)

Table 1. Simplified models of squark and gluino production with direct decays to $\tilde{\chi}_1^0$. For each model the diagram of the decay topology, the model parameters and assumptions about mass relations and branching ratios are listed. The last column refers to the experimental results presented in section 11.2. Horizontal dashed lines separate different mass or branching ratio assumptions within a model.

squared mass terms of the two Higgs doublets, $m_{H_1}^2$ and $m_{H_2}^2$, are defined at the unification scale. This model is characterized by significant cross-sections for $\tilde{q}$ and $\tilde{g}$ production. The gluino decays mainly to a light quark/squark pair $q\tilde{q}$ ($\approx 50\%$), but also to $t\tilde{t}$ ($\approx 30\%$) or $b\tilde{b}$ ($\approx 20\%$), while the squark multi-step decays typically involve charginos, neutralinos and/or sleptons.

2.1.6 Minimal Universal Extra Dimensions model

The mUED model is the minimal extension of the SM with one additional universal spatial dimension. In this non-SUSY model, the Kaluza-Klein (KK) quark excitation's decay chain to the lightest KK particle, the KK photon, gives a signature very similar to the supersymmetric decay chain of a squark to the lightest neutralino. The properties of the model depend on two parameters: the compactification radius R_c and the cut-off scale Λ. This cut-off is interpreted as the scale at which some new physics underlying the effective non-renormalizable UED framework becomes relevant. The Higgs boson mass is fixed to 125 GeV.

2.2 Simplified models

The details of the simplified models considered are given below and summarized in tables 1–3.

2.2.1 Direct decays of squarks and gluinos

Simplified models with direct decay of the pair-produced strongly interacting supersymmetric particles assume the production of gluino pairs with decoupled squarks, light-flavour

JHEP10(2015)054

Diagram	Production	Parameters	Mass relation	Branching ratio	Result
figure 4(a)	$\tilde{q}\tilde{q}$	$m_{\tilde{q}}, m_{\tilde{\chi}_1^0}$	$m_{\tilde{\chi}_1^\pm} = (m_{\tilde{q}} + m_{\tilde{\chi}_1^0})/2$	$\mathrm{BR}(\tilde{q} \to qW\tilde{\chi}_1^0) = 1$	figure 22(a)
		$m_{\tilde{q}}$	$m_{\tilde{\chi}_1^0} = 60\,\mathrm{GeV}$		figure 22(b)
		$x = \Delta m(\tilde{\chi}_1^\pm, \tilde{\chi}_1^0)/\Delta m(\tilde{q}, \tilde{\chi}_1^0)$			
figure 4(b)	$\tilde{g}\tilde{g}$	$m_{\tilde{g}}, m_{\tilde{\chi}_1^0}$	$m_{\tilde{\chi}_1^\pm} = (m_{\tilde{g}} + m_{\tilde{\chi}_1^0})/2$	$\mathrm{BR}(\tilde{g} \to qqW\tilde{\chi}_1^0) = 1$	figure 23(a)
		$m_{\tilde{g}}$	$m_{\tilde{\chi}_1^0} = 60\,\mathrm{GeV}$		figure 23(b)
		$x = \Delta m(\tilde{\chi}_1^\pm, \tilde{\chi}_1^0)/\Delta m(\tilde{g}, \tilde{\chi}_1^0)$			
figure 5(a)	$\tilde{q}\tilde{q}$	$m_{\tilde{q}}, m_{\tilde{\chi}_1^0}$	$m_{\tilde{\chi}_1^\pm, \tilde{\chi}_2^0} = (m_{\tilde{q}} + m_{\tilde{\chi}_1^0})/2$	$\mathrm{BR}(\tilde{q} \to q(\ell\nu/\ell\ell)\tilde{\chi}_1^0) = 1$	figure 26
			$m_{\tilde{\ell},\tilde{\nu}} = (m_{\tilde{\chi}_1^\pm, \tilde{\chi}_2^0} + m_{\tilde{\chi}_1^0})/2$	$\ell \equiv (e, \mu)$	
				$\mathrm{BR}(\tilde{q} \to q(\tau\nu/\tau\tau/\nu\nu)\tilde{\chi}_1^0) = 1$	figure 28
				$\ell \equiv \tau$	
figure 5(b)	$\tilde{q}\tilde{q}$	$m_{\tilde{q}}, m_{\tilde{\chi}_1^0}$	$m_{\tilde{\chi}_1^\pm} = (m_{\tilde{q}} + m_{\tilde{\chi}_1^0})/2$	$\mathrm{BR}(\tilde{q} \to qWZ\tilde{\chi}_1^0) = 1$	figure 24
			$m_{\tilde{\chi}_2^0} = (m_{\tilde{\chi}_1^\pm} + m_{\tilde{\chi}_1^0})/2$		
figure 5(c)	$\tilde{g}\tilde{g}$	$m_{\tilde{g}}, m_{\tilde{\chi}_1^0}$	$m_{\tilde{\chi}_1^\pm, \tilde{\chi}_2^0} = (m_{\tilde{g}} + m_{\tilde{\chi}_1^0})/2$	$\mathrm{BR}(\tilde{g} \to qq(\ell\nu/\ell\ell)\tilde{\chi}_1^0) = 1$	figure 27
			$m_{\tilde{\ell},\tilde{\nu}} = (m_{\tilde{\chi}_1^\pm, \tilde{\chi}_2^0} + m_{\tilde{\chi}_1^0})/2$	$\ell \equiv (e, \mu)$	
				$\mathrm{BR}(\tilde{g} \to qq(\tau\nu/\tau\tau/\nu\nu)\tilde{\chi}_1^0) = 1$	figure 29
				$\ell \equiv \tau$	
figure 5(d)	$\tilde{g}\tilde{g}$	$m_{\tilde{g}}, m_{\tilde{\chi}_1^0}$	$m_{\tilde{\chi}_1^\pm} = (m_{\tilde{g}} + m_{\tilde{\chi}_1^0})/2$	$\mathrm{BR}(\tilde{g} \to qqWZ\tilde{\chi}_1^0) = 1$	figure 25
			$m_{\tilde{\chi}_2^0} = (m_{\tilde{\chi}_1^\pm} + m_{\tilde{\chi}_1^0})/2$		

Table 2. Simplified models of squark and gluino production with one- and two-step decays to $\tilde{\chi}_1^0$. For each model the diagram of the decay topology, the model parameters and assumptions about mass relations and branching ratios are listed. The last column refers to the experimental results presented in section 11.2. Horizontal dashed lines separate different mass or branching ratio assumptions within a model.

JHEP10(2015)054

squark pairs with decoupled gluinos, or light-flavour squarks and gluinos; all other superpartners except the lightest neutralino are decoupled. This assumption forces squarks or gluinos to decay directly to quarks or gluons and the lightest neutralino, as shown in figure 3. In the case of squark-gluino production, the masses of the light-flavour squarks are set to 0.96 times the mass of the gluino as suggested in refs. [67, 68], and gluinos can decay via on-shell squarks as $\tilde{g} \to \tilde{q}q \to qq\tilde{\chi}_1^0$. For models with decoupled gluinos two scenarios have been considered: a scenario with eight mass-degenerate light-flavour squarks ($\tilde{q}_\mathrm{L}$ and $\tilde{q}_\mathrm{R}$, with $\tilde{q} = \tilde{u}, \tilde{d}, \tilde{s}, \tilde{c}$), or a scenario with only one accessible light-flavour squark [69]. Changing the number of light-flavoured squarks affects only the cross-section but not the kinematics of the events. The free parameters in these models are $m_{\tilde{q}}$ or $m_{\tilde{g}}$, and $m_{\tilde{\chi}_1^0}$.

An additional set of simplified models with direct decay of pair-produced gluinos assumes that all squarks and sleptons are much heavier than the gluino, which remains relatively light and decays promptly into a gluon and a neutralino [70], as shown in figure 3(d). The free parameters in these models are $m_{\tilde{g}}$ and $m_{\tilde{\chi}_1^0}$.

Diagram	Parameters	Mass relation	Branching ratio	Result
figure 6(a)	$m_{\tilde{g}}, m_{\tilde{t}_1}$	$m_{\tilde{g}} > m_{\tilde{t}_1} + m_t$ $m_{\tilde{\chi}_1^0} = 60\,\text{GeV}$	$\text{BR}(\tilde{g} \to \tilde{t}_1 t) = 1$ $\text{BR}(\tilde{t}_1 \to t\tilde{\chi}_1^0) = 1$	figure 31
figure 6(b)	$m_{\tilde{g}}, m_{\tilde{t}_1}$	$m_{\tilde{g}} > m_{\tilde{t}_1} + m_t$ $m_{\tilde{\chi}_1^\pm} = 2m_{\tilde{\chi}_1^0}$ $m_{\tilde{\chi}_1^0} = 60\,\text{GeV}$	$\text{BR}(\tilde{g} \to \tilde{t}_1 t) = 1$ $\text{BR}(\tilde{t}_1 \to b\tilde{\chi}_1^\pm) = 1$ $\text{BR}(\tilde{\chi}_1^\pm \to W^*\tilde{\chi}_1^0) = 1$	figure 32
figure 6(c)	$m_{\tilde{g}}, m_{\tilde{t}_1}$	$m_{\tilde{g}} > m_{\tilde{t}_1} + m_t$ $m_{\tilde{\chi}_1^0} = m_{\tilde{t}_1} - 20\,\text{GeV}$	$\text{BR}(\tilde{g} \to \tilde{t}_1 t) = 1$ $\text{BR}(\tilde{t}_1 \to c\tilde{\chi}_1^0) = 1$	figure 33
figure 6(d)	$m_{\tilde{g}}, m_{\tilde{t}_1}$	$m_{\tilde{g}} > m_{\tilde{t}_1} + m_t$	$\text{BR}(\tilde{g} \to \tilde{t}_1 t) = 1$ $\text{BR}(\tilde{t}_1 \to sb) = 1$	figure 34
figure 7	$m_{\tilde{g}}, m_{\tilde{b}_1}$	$m_{\tilde{g}} > m_{\tilde{b}_1} + m_b$ $m_{\tilde{\chi}_1^0} = 60\,\text{GeV}$	$\text{BR}(\tilde{g} \to \tilde{b}_1 b) = 1$ $\text{BR}(\tilde{b}_1 \to b\tilde{\chi}_1^0) = 1$	figure 35
figure 8(a)	$m_{\tilde{g}}, m_{\tilde{\chi}_1^0}$	$m_{\tilde{g}} \ll m_{\tilde{t}_1}$	If $m_{\tilde{g}} > 2m_t + m_{\tilde{\chi}_1^0}$: $\text{BR}(\tilde{g} \to t\bar{t}\tilde{\chi}_1^0) = 1$ If $m_{\tilde{g}} < 2m_t + m_{\tilde{\chi}_1^0}$: $\text{BR}(\tilde{g} \to tWb\tilde{\chi}_1^0)+\text{BR}(\tilde{g} \to WbWb\tilde{\chi}_1^0) = 1$	figure 30
figure 8(b)	$m_{\tilde{g}}, m_{\tilde{\chi}_1^0}$	$2m_b + m_{\tilde{\chi}_1^0} < m_{\tilde{g}} \ll m_{\tilde{b}_1}$	$\text{BR}(\tilde{g} \to b\bar{b}\tilde{\chi}_1^0) = 1$	figure 36
figure 8(c)	$m_{\tilde{g}}, m_{\tilde{\chi}_1^0}$	$m_b + m_t + m_{\tilde{\chi}_1^\pm} < m_{\tilde{g}} \ll m_{\tilde{t}_1}, m_{\tilde{b}_1}$ $m_{\tilde{\chi}_1^\pm} = m_{\tilde{\chi}_1^0} + 2\,\text{GeV}$	$\text{BR}(\tilde{g} \to tb\tilde{\chi}_1^\pm) = 1$ $\text{BR}(\tilde{\chi}_1^\pm \to \tilde{\chi}_1^0 ff') = 1$	figure 37

Table 3. Simplified models of gluino pair production with decays via third-generation squarks. For each model the diagram of the decay topology, the model parameters and assumptions about mass relations and branching ratios are listed. The last column refers to the experimental results presented in section 11.2. Horizontal dashed lines separate different mass or branching ratio assumptions within a model.

2.2.2 One-step decays of squarks and gluinos

Simplified models with one-step decays of the pair-produced squarks or gluinos assume that these particles decay via the $\tilde{\chi}_1^\pm$ into a W boson and the $\tilde{\chi}_1^0$, as shown in figure 4. The free parameters in these models are $m_{\tilde{q}}$ or $m_{\tilde{g}}$, and either $m_{\tilde{\chi}_1^\pm}$ with a fixed $m_{\tilde{\chi}_1^0} = 60\,\text{GeV}$ or $m_{\tilde{\chi}_1^0}$ with $m_{\tilde{\chi}_1^\pm} = (m_{\tilde{g}/\tilde{q}} + m_{\tilde{\chi}_1^0})/2$.

2.2.3 Two-step decays of squarks and gluinos

Two categories of simplified models with two-step decays of squarks and gluinos are considered: models with and without sleptons.

In the two-step models with sleptons the pair-produced squarks or gluinos decay with equal probability to either the lightest chargino or the next-to-lightest neutralino ($\tilde{\chi}_2^0$). These subsequently decay via left-handed sleptons (or sneutrinos) which then further decay into a lepton (or neutrino) and the lightest neutralino. In these models, the free parameters are the mass of the initially produced particle and the mass of the lightest neutralino. The

JHEP10(2015)054

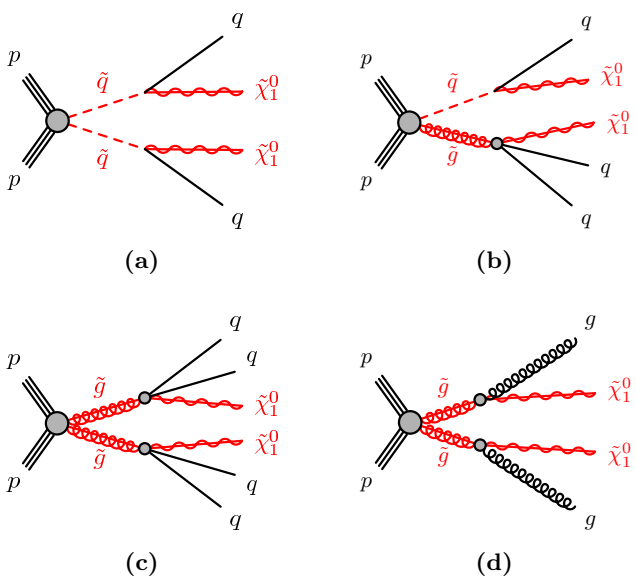

Figure 3. The decay topologies of (a) squark-pair production, (b) squark-gluino production or (c,d) gluino-pair production, in the simplified models with direct decays.

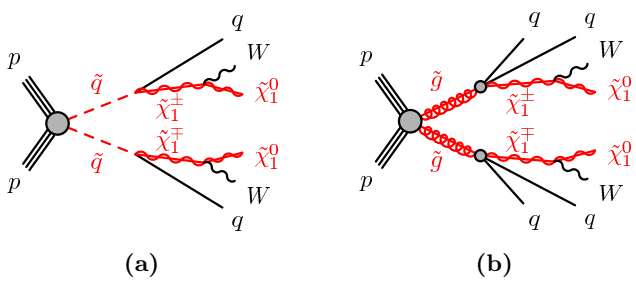

Figure 4. The decay topologies of (a) squark- or (b) gluino-pair production, in the simplified models with one-step decays.

masses of the intermediate charginos or neutralinos are equal and set to be $m_{\tilde{\chi}_1^\pm,\tilde{\chi}_2^0} = (m_{\tilde{g}/\tilde{q}} + m_{\tilde{\chi}_1^0})/2$, while the slepton and sneutrino masses are set to be $m_{\tilde{\ell}_L,\tilde{\nu}} = (m_{\tilde{\chi}_1^\pm/\tilde{\chi}_2^0} + m_{\tilde{\chi}_1^0})/2$. All three slepton flavours are mass-degenerate in this model. A separate model in which the slepton is exclusively a $\tilde{\tau}$ is also considered.

In the second category, two-step models without sleptons, the initial supersymmetric particle decays via the lightest chargino, which itself decays into a W boson and the next-to-lightest neutralino. The latter finally decays into a Z boson and the lightest neutralino. The lightest chargino mass is fixed at $m_{\tilde{\chi}_1^\pm} = (m_{\tilde{g}/\tilde{q}} + m_{\tilde{\chi}_1^0})/2$ and the next-to-lightest neutralino mass is set to be $m_{\tilde{\chi}_2^0} = (m_{\tilde{\chi}_1^\pm} + m_{\tilde{\chi}_1^0})/2$.

These two categories of simplified models with two-step decays of squarks and gluinos are illustrated in figure 5.

JHEP10(2015)054

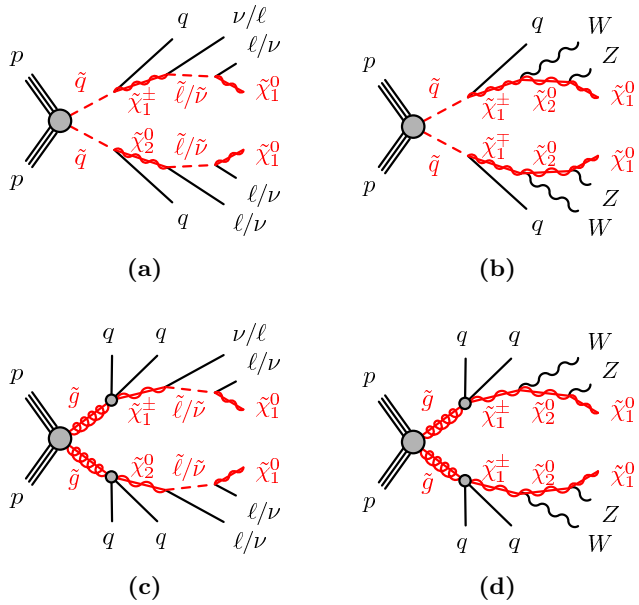

Figure 5. Examples of decay topologies of (a, b) squark- or (c, d) gluino-pair production, in the simplified models with two-step decays with (left) or without (right) sleptons.

2.2.4 Gluino decays via third-generation squarks

Two classes of simplified models with gluino decays via third-generation squarks are considered. In the first, the lightest stop or sbottom is lighter than the gluino, such that $\tilde{t}_1$ or $\tilde{b}_1$ are produced via gluino-pair production followed by $\tilde{g} \to \tilde{t}_1 t$ or $\tilde{g} \to \tilde{b}_1 b$ decays. Gluino-stop models within this class assume that the $\tilde{t}_1$ is the lightest squark while all other squarks are heavier than the gluino, and $m_{\tilde{g}} > m_{\tilde{t}_1} + m_t$ such that the branching ratio for $\tilde{g} \to \tilde{t}_1 t$ decays is 100%. Top squarks are assumed to decay via either $\tilde{t}_1 \to t\tilde{\chi}_1^0$, $\tilde{t}_1 \to b\tilde{\chi}_1^\pm$, $\tilde{t}_1 \to c\tilde{\chi}_1^0$, or via $\tilde{t}_1 \to sb$ with R-parity and baryon number violation, as illustrated in figure 6. For the model with the $\tilde{t}_1 \to b\tilde{\chi}_1^\pm$ decay, the chargino mass is assumed to be twice the mass of the neutralino, and the chargino decays into a neutralino and a W boson. In the model with the $\tilde{t}_1 \to c\tilde{\chi}_1^0$ decay, which proceeds via a loop and is most relevant when the $\tilde{t}_1 \to bW\tilde{\chi}_1^0$ decay is kinematically forbidden, the mass gap between the $\tilde{t}_1$ and the lightest neutralino is fixed to 20 GeV. Using gluino-pair production to probe this decay is particularly interesting because it is complementary to the direct pair production of $\tilde{t}_1$, which is more difficult to extract from the background for this specific decay mode [21]. Gluino-sbottom models within this class assume that the $\tilde{b}_1$ is the lightest squark, all other squarks are heavier than the gluino, and $m_{\tilde{g}} > m_{\tilde{b}_1} + m_b$ such that the branching ratio for $\tilde{g} \to \tilde{b}_1 b$ decays is 100%. The bottom squarks are assumed to decay exclusively via $\tilde{b}_1 \to b\tilde{\chi}_1^0$ (figure 7).

In the second class of simplified models with gluino decays via top or bottom squarks, all sparticles apart from the gluino and the neutralino have masses well above the TeV scale such that the $\tilde{t}_1$ or the $\tilde{b}_1$ are only produced off-shell via prompt decay of the gluinos and have little impact on the kinematics of the final state. For the gluino-off-shell-stop model illustrated in figure 8(a), the $\tilde{t}_1$ is assumed to be the lightest squark, but $m_{\tilde{g}} < m_{\tilde{t}_1}$. A three-

JHEP10(2015)054

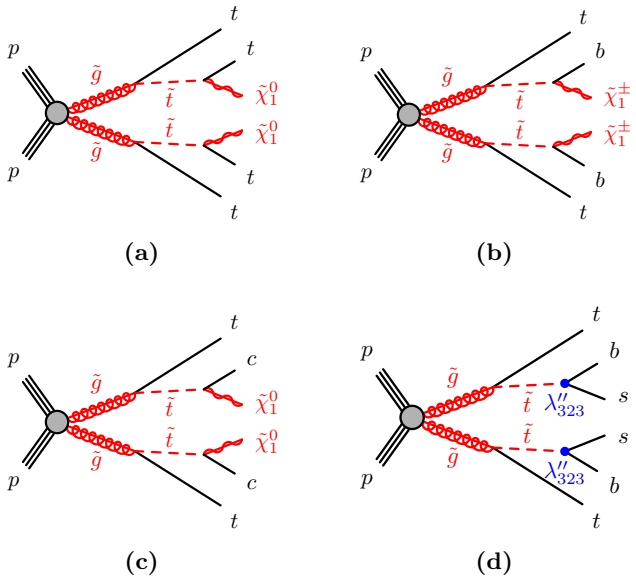

Figure 6. Decay topologies in the gluino-stop simplified models with the top squark decays: (a) $\tilde{t}_1 \to t\tilde{\chi}_1^0$, (b) $\tilde{t}_1 \to b\tilde{\chi}_1^{\pm}$, (c) $\tilde{t}_1 \to c\tilde{\chi}_1^0$ and (d) $\tilde{t}_1 \to sb$ with R-parity and baryon number violation, with a strength determined by the parameter λ''_{323}.

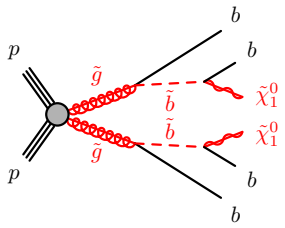

Figure 7. The decay topology in the gluino-sbottom simplified models, with the bottom squark decay $\tilde{b}_1 \to b\tilde{\chi}_1^0$.

body decay $\tilde{g} \to t\bar{t}\tilde{\chi}_1^0$ via an off-shell stop is assumed for the gluino with a branching ratio of 100%. For the configuration $m_{\tilde{g}} < 2m_t + m_{\tilde{\chi}_1^0}$, decays of the gluino involve an off-shell top quark, e.g. the four-body decay $\tilde{g} \to tWb\tilde{\chi}_1^0$. Only four- and five-body decays of this type are considered, because for higher multiplicities the gluinos do not decay promptly. For the gluino-off-shell-sbottom model shown in figure 8(b), the $\tilde{b}_1$ is assumed to be the lightest squark but with $m_{\tilde{g}} < m_{\tilde{b}_1}$. A three-body decay $\tilde{g} \to b\bar{b}\tilde{\chi}_1^0$ via an off-shell sbottom is assumed for the gluino with a branching ratio of 100%. In the gluino-off-shell-stop/sbottom model illustrated in figure 8(c), the $\tilde{b}_1$ and $\tilde{t}_1$ are the lightest squarks, with $m_{\tilde{g}} < m_{\tilde{b}_1,\tilde{t}_1}$. Pair production of gluinos is the only process taken into account, with gluinos decaying via off-shell stops or sbottoms, and a branching ratio of 100% assumed for $\tilde{t}_1 \to b + \tilde{\chi}_1^{\pm}$ and $\tilde{b}_1 \to t + \tilde{\chi}_1^{\pm}$ decays. The mass difference between charginos and neutralinos is set to 2 GeV, such that the fermions produced in $\tilde{\chi}_1^{\pm} \to \tilde{\chi}_1^0 + ff'$ decays do not contribute to the event selection, and gluino decays result in effective three-body decays $bt\tilde{\chi}_1^0$.

JHEP10(2015)054

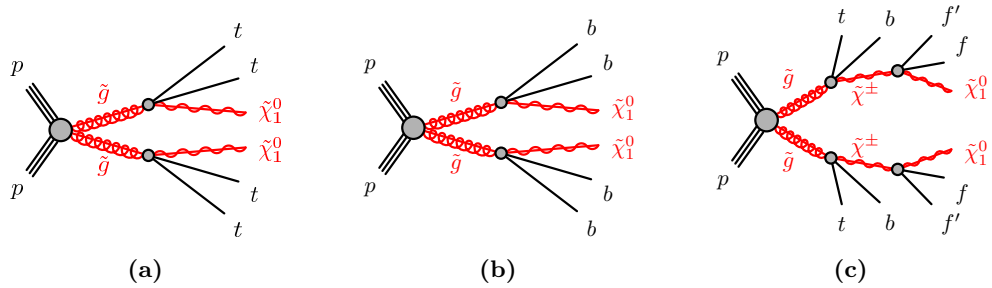

Figure 8. The decay topologies in the (a) gluino-off-shell-stop, (b) gluino-off-shell-sbottom and (c) gluino-off-shell-stop/sbottom simplified models.

3 The ATLAS detector and data sample

The ATLAS detector [17] is a multi-purpose particle physics detector with a forward-backward symmetric cylindrical geometry and nearly 4π coverage in solid angle.[3] The inner tracking detector (ID) consists of pixel and silicon microstrip detectors covering the pseudorapidity region $|\eta| < 2.5$, surrounded by a transition radiation tracker (TRT) which enhances electron identification in the region $|\eta| < 2.0$. The ID is surrounded by a thin superconducting solenoid providing an axial 2 T magnetic field and by a fine-granularity lead/liquid-argon (LAr) electromagnetic calorimeter covering $|\eta| < 3.2$. A steel/scintillator-tile calorimeter provides hadronic coverage in the central pseudorapidity range ($|\eta| < 1.7$). The endcap and forward regions ($1.5 < |\eta| < 4.9$) of the hadronic calorimeter are made of LAr active layers with either copper or tungsten as the absorber material. An extensive muon spectrometer with an air-core toroid magnet system surrounds the calorimeters. Three layers of high-precision tracking chambers provide coverage in the range $|\eta| < 2.7$, while dedicated fast chambers allow triggering in the region $|\eta| < 2.4$. The ATLAS trigger system [71] consists of three levels; the first level (L1) is a hardware-based system, while the second and third levels are software-based systems and are together called the High Level Trigger (HLT).

The data used in these searches were collected from March to December 2012 with the LHC operating at a centre-of-mass energy of 8 TeV. After the application of beam, detector and data quality requirements, the total integrated luminosity ranges from 20.1 to 20.3 fb^{-1}, depending on the triggers used for the event selection, with a relative uncertainty of $\pm 2.8\%$. The uncertainty is derived following the methodology detailed in ref. [72]. During the data-taking period, the peak instantaneous luminosity per LHC fill was typically $7 \times 10^{33}\,\mathrm{cm}^{-2}\mathrm{s}^{-1}$, while the average number of pp interactions per LHC bunch crossing ranged from approximately 6 to 40, with a mean value of 21. In order to maximize the efficiency of selecting the various final states used by the analyses included in this paper, different

[3] ATLAS uses a right-handed coordinate system with its origin at the nominal interaction point in the centre of the detector. The positive x-axis is defined by the direction from the interaction point to the centre of the LHC ring, with the positive y-axis pointing upwards, while the beam direction defines the z-axis. Cylindrical coordinates (r, ϕ) are used in the transverse plane, ϕ being the azimuthal angle around the z-axis. The pseudorapidity η is defined in terms of the polar angle θ by $\eta = -\ln\tan(\theta/2)$.

JHEP10(2015)054

triggers or combinations of triggers were used: $E_{\mathrm{T}}^{\mathrm{miss}}$ triggers, multi-jet triggers, combined $E_{\mathrm{T}}^{\mathrm{miss}}$ +jet, lepton+$E_{\mathrm{T}}^{\mathrm{miss}}$ or lepton+jet+$E_{\mathrm{T}}^{\mathrm{miss}}$ triggers, single-lepton or dilepton triggers. Details of the trigger selections used in the published ATLAS searches included in this paper are not discussed here and can be found in the corresponding publications [20–27].

4 Monte Carlo simulated samples

The simulated event samples for the SM backgrounds are summarized in table 4, together with the choices of Monte Carlo generator, cross-section calculation, set of tunable parameters (tune) used for the underlying event and parton distribution functions (PDFs). The Powheg-Box+Pythia $t\bar{t}$ sample is used for all analyses except for the analysis that requires high jet multiplicities (at least seven to at least ten jets) and large missing transverse momentum [22], which uses the Sherpa $t\bar{t}$ sample. The Sherpa Drell-Yan samples have a lepton filter requiring $p_{\mathrm{T}}^{\ell_1(\ell_2)} > 9$ (5) GeV and $|\eta^{\ell_1(\ell_2)}| < 2.8$. This filter prevents its use in analyses requiring the presence of soft leptons in the final state. Such analyses instead use Alpgen samples with a lepton p_{T} threshold at 5 GeV. When using the baseline Powheg-Box+Pythia top quark pair production sample, in some of the analyses events are reweighted in bins of $p_{\mathrm{T}}(t\bar{t})$ to match the top quark pair differential cross-section measured in ATLAS data [73, 74]. The exact usage of MC simulated samples together with the additional samples used to assess modelling uncertainties are detailed in the corresponding publication of each analysis.

Signal samples for the pMSSM, mSUGRA, mGMSB, nGM and mUED models, as well as the samples for the simplified models of gluino-mediated top squark production (for $m_{\tilde{g}} - m_{\tilde{\chi}_1^0} > 2m_t$) are generated with Herwig++ 2.5.2 [106]. Samples for all the other simplified models are generated with up to one extra parton in the matrix element using Madgraph 5 1.3.33 interfaced to Pythia 6.426. The MLM matching scheme [107] is applied with a scale parameter that is set to a quarter of the mass of the lightest sparticle in the hard-scattering matrix element, with a maximum value of 500 GeV. The signal samples used for the bRPV and NUHMG models are generated with Pythia 6.426.

For the gluino-off-shell-stop model in the region $m_{\tilde{g}} - m_{\tilde{\chi}_1^0} < 2m_t$, the production of gluino pairs is generated with Madgraph 5 1.3.33. The events are subsequently combined with separately generated gluino decays $\tilde{g} \to f\bar{f}'f''\bar{f}'''b\bar{b}\tilde{\chi}_1^0$ based on the full matrix element amplitude (also using Madgraph), preserving spin-dependent distributions. A summary of the studies related to event generation in this model can be found in appendix A. Potential effects of the gluino lifetime (displaced decays, hadronization), which are strongly model dependent, have been neglected.

The ATLAS underlying-event tune AUET2B [80] is used for Madgraph 5 and Pythia 6 samples while the UE-EE-3C tune [108] is used for Herwig++ samples. The parton distribution functions from CTEQ6L1 [81] are used for all signal samples.

For all except the mUED sample, the signal cross-sections are calculated to next-to-leading order in the strong coupling constant, including the resummation of soft gluon emission at next-to-leading-logarithmic accuracy (NLO+NLL) [109–113]. In each case the nominal cross-section and its uncertainty are taken from an ensemble of cross-section

JHEP10(2015)054

Process	Generator	Cross-section order in α_s	Tune	PDF set
$W(\to \ell\nu)$+jets	Sherpa 1.4.1 [75]	NNLO [76]	Sherpa default	CT10 [77]
$Z/\gamma^*(\to \ell\ell)$+jets	Sherpa 1.4.1	NNLO [76]	Sherpa default	CT10
Drell-Yan ($8 < m_{\ell\ell} < 40$ GeV)	Sherpa 1.4.1	NNLO [78]	Sherpa default	CT10
$Z/\gamma^*(\to \ell\ell)$ + jets ($10 < m_{\ell\ell} < 60$ GeV)	Alpgen 2.14 [79] + Herwig 6.520 [82, 83] + Jimmy [84]	NNLO [78]	AUET2 [80]	CTEQ6L1 [81]
γ+jets	Sherpa 1.4.1	LO	Sherpa default	CT10
$t\bar{t}$	Powheg-Box 1.0 [85–87] + Pythia 6.426 [90]	NNLO+NNLL [88, 89]	Perugia2011C [91, 92]	CT10
$t\bar{t}$	Sherpa 1.4.1	NNLO+NNLL	Sherpa default	CT10
Single top				
t-channel	AcerMC 3.8 [93] + Pythia 6.426	NNLO+NNLL [94]	AUET2B [95]	CTEQ6L1
s-channel, Wt	mc@nlo 4.03 [96, 97] + Herwig 6.520	NNLO+NNLL [98, 99]	AUET2B	CT10
$t\bar{t}$ +W/Z boson	Madgraph 5 1.3.28 [100] + Pythia 6.426	NLO [101–103]	AUET2B	CTEQ6L1
Dibosons WW, WZ, ZZ, $W\gamma$ and $Z\gamma$	Sherpa 1.4.1	NLO [104, 105]	Sherpa default	CT10

Table 4. The Standard Model background Monte Carlo simulation samples used in this paper. The generators, the order in α_s of cross-section calculations used for yield normalization (leading order (LO), next-to-leading order (NLO), next-to-next-to-leading order (NNLO), next-to-next-to-leading logarithm (NNLL)), tunes used for the underlying event and PDF sets are shown. For the γ+jets process the LO cross-section is taken directly from the MC generator.

predictions using different PDF sets and factorization and renormalization scales, as described in ref. [114]. For the mUED model, the cross-section is taken at leading order from Herwig++. For the mSUGRA/CMSSM and NUHMG samples, Susy-Hit [115] and Sdecay 1.3b [116], interfaced to the Softsusy 3.1.6 spectrum generator [117], are used to calculate the sparticle mass spectra and decay tables, and to ensure consistent electroweak symmetry breaking.

The decays of tau leptons are simulated directly in the generators in the case of event samples produced with Sherpa, Herwig++ 2.5.2 and Pythia 8.165, while in all other cases Tauola 2.4 [118, 119] is used.

Standard Model background samples are passed through either the full ATLAS detector simulation [120] based on Geant4 [121], or through a fast simulation using a parameterization of the performance of the ATLAS electromagnetic and hadronic calorimeters [122] and Geant4 elsewhere; the latter applies to $W/Z/\gamma$+jets samples with boson $p_T < 280$ GeV and Powheg-Box+Pythia $t\bar{t}$ samples. All SUSY signal samples are passed through the fast simulation, with the exception of the mSUGRA/CMSSM model samples which are produced with the Geant4 simulation. The fast simulation of SUSY signal

JHEP10(2015)054

events was validated against full GEANT4 simulation for several signal models. Differing pile-up (multiple pp interactions in the same or neighbouring bunch-crossings) conditions as a function of the instantaneous luminosity are taken into account by overlaying simulated minimum-bias events (simulated using PYTHIA 8 with the MSTW2008LO PDF set [123] and the A2 tune [95]) onto the hard-scattering process and reweighting events according to the distribution of the mean number of interactions observed in data.

5 Object reconstruction and identification

This paper summarizes different analyses which are combined to improve the sensitivity to a variety of possible topologies originating from the production and decay of squarks and gluinos. Although different event selections are used among these analyses, they share common definitions of the reconstructed objects. Analysis-specific exceptions to these definitions are detailed in the corresponding publication of each analysis.

The reconstructed primary vertex of the event is required to be consistent with the beamspot envelope and to have at least five associated tracks with $p_{\mathrm{T}} > 400\,\mathrm{MeV}$. When more than one such vertex is found, the vertex with the largest $\sum p_{\mathrm{T}}^2$ of the associated tracks is chosen.

Jet candidates are reconstructed using the anti-k_t jet clustering algorithm [124, 125] with a radius parameter of 0.4. The inputs to this algorithm are topological clusters [126, 127] of calorimeter cells seeded by those with energy significantly above the measured noise (topoclusters). The local cluster weighting (LCW) calibration method [127, 128] is used to classify topoclusters as being either of electromagnetic or hadronic origin, and based on this classification it applies energy corrections derived from MC simulations and measurements in data. The jets are corrected for energy from pile-up using the method suggested in ref. [129]: a contribution equal to the product of the jet area and the median energy density of the event is subtracted from the jet energy [130]. Further corrections, referred to as the jet energy scale (JES) corrections, are derived from MC simulation and data and used to calibrate on average the energies of jets to the scale of their constituent particles [127, 131]. Only jet candidates with $p_{\mathrm{T}} > 20\,\mathrm{GeV}$ and $|\eta| < 4.5$ after all corrections are retained. To remove events with jets from detector noise and non-collision backgrounds, events are rejected if they include jets failing to satisfy the "loose" quality criteria described in ref. [127].

A neural-network-based algorithm [132] is used to identify jets containing a b-hadron (b-jets). It uses as inputs the output weights of several algorithms exploiting the impact parameter of the inner detector tracks, secondary vertex reconstruction and the topology of b- and c-hadron decays inside the jet. The algorithm used has an efficiency of 70% for tagging b-jets, determined with simulated $t\bar{t}$ events [133]. For this efficiency, the algorithm provides a rejection factor of approximately 140 for light-quark and gluon jets, and of approximately 5 for charm jets [134]. Candidate b-jets are required to have $p_{\mathrm{T}} > 40\,\mathrm{GeV}$ and $|\eta| < 2.5$.

Electrons are reconstructed from energy clusters in the electromagnetic calorimeter matched to tracks in the inner detector [135] and are required to have $p_{\mathrm{T}} > 10\,\mathrm{GeV}$ and $|\eta| < 2.47$. The preselected electron candidates are required to pass a variant of the "medium" selection [135], which was modified in 2012 to reduce the impact of pile-up.

JHEP10(2015)054

Photon candidates, which in the analyses presented are used only for the measurement of the missing transverse momentum, are required to have $p_{\mathrm{T}} > 10\,\mathrm{GeV}$ and $|\eta| < 1.37$ or $1.52 < |\eta| < 2.47$, to satisfy photon shower shape and electron rejection criteria [136], and to be isolated.

Muon candidates are formed by combining information from the muon spectrometer and inner tracking detectors [137]. The preselected muon candidates are required to have $p_{\mathrm{T}} > 10\,\mathrm{GeV}$ and $|\eta| < 2.4$ or 2.5, depending on the analysis.

Reconstruction of hadronically decaying tau leptons starts from jets with $p_{\mathrm{T}} > 10\,\mathrm{GeV}$ [138], and an η- and p_{T}-dependent energy calibration to the tau energy scale for hadronic decays is applied [139]. Tau lepton candidates must have one or three associated track(s) with a charge sum of ± 1, and satisfy $p_{\mathrm{T}} > 20\,\mathrm{GeV}$ and $|\eta| < 2.5$. The "loose" and "medium" working points [138] are used and correspond to efficiencies of approximately 70% and 60%, independent of p_{T}, with rejection factors of 10 and 20 against jets misidentified as tau candidates, respectively.

After these selections, ambiguities between candidate jets with $|\eta| < 2.8$ and leptons (electrons and muons) are resolved as follows. First, any such jet candidate lying within a distance $\Delta R = \sqrt{(\Delta\eta)^2 + (\Delta\phi)^2} = 0.2$ of a preselected electron is discarded; then any lepton candidate within a distance $\Delta R = 0.4$ of any surviving jet candidate is discarded. In analyses requiring the presence of one lepton (electron or muon) in the final state, electrons are also required to be well separated from muon candidates with $\Delta R(e, \mu) > 0.01$. If two preselected electrons are found within an angular distance $\Delta R(e, e) = 0.05$ of each other, only the electron with the higher p_{T} is kept. Finally, in the analyses that require the presence of at least one or two opposite-sign leptons in the final state, any event containing a preselected electron in the transition region between the barrel and endcap electromagnetic calorimeters, $1.37 < |\eta| < 1.52$, is rejected.

The measurement of the missing transverse momentum vector is based on the transverse momenta of all electron, photon, jet and muon candidates, and all calorimeter energy clusters not associated with such objects [140]. Fully calibrated electrons and photons with $p_{\mathrm{T}} > 10\,\mathrm{GeV}$ and jets with $p_{\mathrm{T}} > 20\,\mathrm{GeV}$ are used. Energy deposits not associated with these objects are also taken into account in the $\boldsymbol{E}_{\mathrm{T}}^{\mathrm{miss}}$ calculation using an energy-flow algorithm that considers calorimeter energy deposits as well as ID tracks [141]. In the $E_{\mathrm{T}}^{\mathrm{miss}}$ measurement tau leptons are not distinguished from jets and it has been checked that this does not introduce a bias in any kinematic variables used in the analyses.

Corrections derived from data control samples are applied to account for differences between data and simulation for the lepton trigger and reconstruction efficiencies, momentum/energy scale and resolution, and for the efficiency and mis-tag rate for tagging jets originating from b-quarks.

6 Analysis strategy

A search for squarks and gluinos under various decay mode assumptions necessitates many different event selections targeting the wide range of experimental signatures. This section summarizes the common analysis strategy and statistical techniques that are employed in

JHEP10(2015)054

all searches included in this paper. Signal regions (SRs) are defined using the Monte Carlo simulation of the signal processes and the SM backgrounds, and are optimized to maximize the expected significance for each model considered. To estimate the SM backgrounds in a consistent and robust fashion, corresponding control regions (CRs) are defined for each of the signal regions. They are chosen to be non-overlapping with the SR selections in order to provide independent data samples enriched in particular background sources. The CR selections are optimized to have negligible SUSY signal contamination for the models under investigation, while minimizing as much as possible the systematic uncertainties arising from the extrapolation of the CR event yields to the expectations in the SR. Cross-checks of the background estimates are performed using several validation regions (VRs) selected with requirements such that these regions do not overlap with the CR and SR selections, again with a low probability of signal contamination.

Several classes of profile likelihood fits that utilize the observed numbers of events in the various regions are employed in the analyses [142]. In some analyses, the shape of a final discriminating variable in the SRs is also used. A background-only fit is used to determine the compatibility of the observed event yield in each SR with the corresponding SM background expectation. This fit uses as constraints only the observed event yields or the shape of the discriminating variable distributions from the CRs associated with the SR, but not the SR itself. It is assumed that signal events from physics beyond the Standard Model (BSM) do not contribute to these yields. The numbers of observed and predicted events in each of these CRs are described using Poisson probability density functions. The systematic uncertainties and the MC statistical uncertainties on the expected values are included in the fit as nuisance parameters which are constrained by Gaussian distributions with widths corresponding to the sizes of the uncertainties considered and Poisson distributions, respectively. Correlations of a given nuisance parameter across the various regions, between the various backgrounds, and possibly the signal, are taken into account. The product of the various probability density functions forms the likelihood, which the fit maximizes by adjusting the inputs to the fit and the nuisance parameters. The inputs to the fit for each of the SRs are the number of events observed in each of the CRs, and the corresponding number of events expected from simulation, the extrapolation factors obtained from the simulation which relate the number of predicted SM background events in their associated CR to that predicted in the SR, and the number of events predicted by the simulation in each region for the other background processes. The background fit results are cross-checked in validation regions. The data in the validation regions are not used to constrain the fits; they are only used to compare the results of the fits to statistically independent observations.

A model-independent fit is used to set upper limits on the number of BSM signal events in each SR. This fit proceeds in the same way as the background-only fit, except that the number of events observed in the SR is added as an input to the fit, and the BSM signal strength, constrained to be non-negative, is added as a free parameter. The observed and expected upper limits at 95% confidence level (CL) on the number of events from BSM phenomena for each signal region ($S^{95}_{\rm obs}$ and $S^{95}_{\rm exp}$) are derived using the $CL_{\rm S}$ prescription [143], neglecting any possible signal contamination in the control regions; an uncertainty on $S^{95}_{\rm exp}$ is also computed from the $\pm 1\sigma$ uncertainty on the expectation. These

JHEP10(2015)054

limits, when normalized by the integrated luminosity of the data sample, may be interpreted as upper limits on the visible cross-section of BSM physics ($\langle\epsilon\sigma\rangle^{95}_{\rm obs}$), where the visible cross-section is defined as the product of production cross-section, acceptance and efficiency. The model-independent fit is also used to compute the one-sided p-value (p_0) of the background-only hypothesis which quantifies the statistical significance of an excess.

Model-dependent fits are used to set exclusion limits on the signal cross-sections for specific SUSY models. Such a fit proceeds in the same way as the model-independent fit, except that signal contamination in the CRs is taken into account as well as the yield in the signal region and, in some analyses, the model shape information. Correlations between signal and background systematic uncertainties are taken into account where appropriate. The systematic uncertainties on the signal expectations originating from detector effects and the theoretical uncertainties on the signal acceptance are included in the fit. The impact of the theoretical uncertainties on the signal cross-section is shown on the limit plots obtained (section 11). Numbers quoted in the text are evaluated from the observed exclusion limit based on the nominal signal cross-section minus its 1σ theoretical uncertainty.

Background-only and model-independent fit results are presented in this paper only for new analyses or signal regions which are not available in earlier ATLAS publications. In the context of this publication, model-dependent exclusion fits for various simplified and phenomenological models are combined to include results from different searches for each model individually, in order to maximize the expected exclusion reach for each model. Where possible a full statistical combination of non-overlapping searches is applied, as explained in section 10.

7 Experimental signatures

This paper summarizes and combines the results of several individual inclusive squark and gluino analyses previously published by the ATLAS experiment. Each of these searches uses one or more sets of signal regions targeting specific experimental signatures which originate from different squark or gluino decay modes and mass hierarchies. Several extensions to the previously published searches in the form of additional signal regions are also included, along with one new analysis channel. The full list of searches and their signal regions used in this paper is presented in table 5, together with the corresponding references. The details of the signal region selections for all searches listed in table 5 can be found in appendix B. The details of the control and validation region selections, together with the strategies used for the estimation of the background processes, can be found in the corresponding publications. The new analysis and extended signal regions, which are also presented in table 5, are discussed in more detail in the subsequent subsections. Each signal region is referred to with an acronym, listed in table 5, indicating the analysis origin, so for example the '2jl' region from the 0-lepton + 2–6 jets + $E_{\rm T}^{\rm miss}$ analysis is referred to as '0L_2jl'. The correspondence between the searches and the various models probed is provided in table 6 and a summary of the limits in simplified models presented in the respective papers is given in table 7. The 0-lepton + 2–6 jets + $E_{\rm T}^{\rm miss}$ and 1-lepton (soft+hard) + jets +

JHEP10(2015)054

Short analysis name and corresponding reference	Acronym	Signal region name
Monojet [21]	MONOJ	M1, M2, M3
0-lepton + 2–6 jets + $E_{\mathrm{T}}^{\mathrm{miss}}$ [20]	0L	2jl, 2jm, 2jt, 2jW, 3j, 4jW, 4jl-, 4jl, 4jm, 4jt, 5j, 6jl, 6jm, 6jt, 6jt+
0-lepton + 4–5 jets + $E_{\mathrm{T}}^{\mathrm{miss}}$ ($\star$)	0L	4jt+, 5jt
0-lepton + 7–10 jets + $E_{\mathrm{T}}^{\mathrm{miss}}$ [22]	MULTJ	8j50, 9j50, 10j50 (multi-jet+flavour stream), 7j80, 8j80, (multi-jet+flavour stream), 8j50, 9j50, 10j50 (multi-jet+M_J^{Σ} stream)
0-lepton Razor ($\bullet$)	0LRaz	$\mathrm{SR}_{\mathrm{loose}}$, $\mathrm{SR}_{\mathrm{tight}}$
1-lepton (soft+hard) + jets + $E_{\mathrm{T}}^{\mathrm{miss}}$ [23]	1L(S,H)	3-jet/5-jet/3-jet inclusive (soft lepton), 3-jet/5-jet/6-jet (hard lepton)
1-lepton (hard) + 7 jets + $E_{\mathrm{T}}^{\mathrm{miss}}$ ($\star$)	1L(H)	7-jet
2-leptons (soft) + jets + $E_{\mathrm{T}}^{\mathrm{miss}}$ [23]	2L(S)	2-jet (soft dimuon)
2-leptons (hard) + jets + $E_{\mathrm{T}}^{\mathrm{miss}}$ [23]	2LRaz	$\leq$ 2-jet/3-jet
2-leptons off-Z [24]	2L-offZ	SR-2j-bveto, SR-2j-btag, SR-4j-bveto, SR-4j-btag, SR-loose
Same-sign dileptons or 3-leptons + jets + $E_{\mathrm{T}}^{\mathrm{miss}}$ [25]	SS/3L	SR3b, SR0b, SR1b, SR3Llow, SR3Lhigh
Taus + jets + $E_{\mathrm{T}}^{\mathrm{miss}}$ [26]	TAU	1τ (Loose, Tight), 2τ (Inclusive, GMSB, nGM, bRPV), $\tau + l$ (GMSB, nGM, bRPV, mSUGRA)
0/1-lepton + 3b-jets + $E_{\mathrm{T}}^{\mathrm{miss}}$ [27]	0/1L3B	SR-0l-4j-A, SR-0l-4j-B, SR-0l-4j-C, SR-0l-7j-A , SR-0l-7j-B, SR-0l-7j-C, SR-1l-6j-A, SR-1l-6j-B, SR-1l-6j-C

Table 5. List of analysis names referring to the experimental signatures addressed, with references to the appropriate publications; their acronyms; and all signal region names. The new analysis is denoted with ($\bullet$), while the extended signal regions are denoted with ($\star$). The details of the signal region selections for all searches listed in the table can be found in appendix B.

$E_{\mathrm{T}}^{\mathrm{miss}}$ statistical combination, referred to as (0+1)-lepton combination, is used to probe the models for which both analyses have comparable sensitivity.

7.1 Final states with high-p_{T} jets, missing transverse momentum and no electrons or muons

Several searches to address final states without electrons or muons, containing high-p_{T} jets and missing transverse momentum, have been performed in ATLAS. These searches are split according to the jet multiplicity into three categories: searches with at least one, two to six and seven to ten jets. They are presented in table 5 as Monojet, 0-lepton + 2–6 jets + $E_{\mathrm{T}}^{\mathrm{miss}}$ (extended with two additional signal regions) and 0-lepton + 7–10 jets + $E_{\mathrm{T}}^{\mathrm{miss}}$, respectively. Events with reconstructed electrons or muons are vetoed in these searches. A new search using kinematic variables, known as Razor variables [19], which provide longitudinal and transverse information about each event (listed as 0-lepton Razor in table 5), has also been performed and is included in the results presented in this paper.

JHEP10(2015)054

Model	(0+1)-lepton combination	MONOJ	0L	MULTJ	0LRaz	1L(S,H)	1L(H)	2L(S)	2LRaz	2L-offZ	SS/3L	TAU	0/1L3B
pMSSM			✓										
mSUGRA/CMSSM	✓			✓			✓				✓	✓	✓
mSUGRA/CMSSM with bRPV			✓	✓		✓	✓				✓	✓	
mGMSB											✓	✓	
nGM			✓			✓						✓	
NUHMG	✓												
mUED			✓			✓		✓	✓		✓		
$\tilde{q}\tilde{q}$ production, $\tilde{q} \to q\tilde{\chi}_1^0$		✓	✓		✓								
$\tilde{g}\tilde{g}$ production, $\tilde{g} \to qq\tilde{\chi}_1^0$			✓										
$\tilde{q}\tilde{g}$ production, $\tilde{q} \to q\tilde{\chi}_1^0$, $\tilde{g} \to qq\tilde{\chi}_1^0$			✓										
$\tilde{g}\tilde{g}$ production, $\tilde{g} \to g\tilde{\chi}_1^0$			✓										
$\tilde{q}\tilde{q}$ production, $\tilde{q} \to qW\tilde{\chi}_1^0$	✓												
$\tilde{g}\tilde{g}$ production, $\tilde{g} \to qqW\tilde{\chi}_1^0$	✓			✓							✓		
$\tilde{q}\tilde{q}$ production, $\tilde{q} \to q(\ell\ell/\ell\nu/\nu\nu)\tilde{\chi}_1^0$	✓								✓	✓	✓		
$\tilde{g}\tilde{g}$ production, $\tilde{g} \to qq(\ell\ell/\ell\nu/\nu\nu)\tilde{\chi}_1^0$	✓			✓		✓			✓	✓	✓		
$\tilde{q}\tilde{q}$ production, $\tilde{q} \to q(\tau\tau/\tau\nu/\nu\nu)\tilde{\chi}_1^0$												✓	
$\tilde{g}\tilde{g}$ production, $\tilde{g} \to qq(\tau\tau/\tau\nu/\nu\nu)\tilde{\chi}_1^0$												✓	
$\tilde{q}\tilde{q}$ production, $\tilde{q} \to qWZ\tilde{\chi}_1^0$			✓								✓		
$\tilde{g}\tilde{g}$ production, $\tilde{g} \to qqWZ\tilde{\chi}_1^0$	✓			✓							✓		
$\tilde{g}\tilde{g}$ production, $\tilde{g} \to t\bar{t}\tilde{\chi}_1^0$ (off-shell stop)				✓		✓					✓		✓
$\tilde{g}\tilde{g}$ production, $\tilde{g} \to \tilde{t}_1 t$, $\tilde{t}_1 \to t\tilde{\chi}_1^0$				✓									✓
$\tilde{g}\tilde{g}$ production, $\tilde{g} \to \tilde{t}_1 t$, $\tilde{t}_1 \to b\tilde{\chi}_1^\pm$											✓		✓
$\tilde{g}\tilde{g}$ production, $\tilde{g} \to \tilde{t}_1 t$, $\tilde{t}_1 \to c\tilde{\chi}_1^0$	✓										✓		
$\tilde{g}\tilde{g}$ production, $\tilde{g} \to \tilde{t}_1 t$, $\tilde{t}_1 \to bs$				✓							✓		
$\tilde{g}\tilde{g}$ production, $\tilde{g} \to tb\tilde{\chi}_1^0$													✓
$\tilde{g}\tilde{g}$ production, $\tilde{g} \to b\bar{b}\tilde{\chi}_1^0$ (off-shell sbottom)			✓										✓
$\tilde{g}\tilde{g}$ production, $\tilde{g} \to \tilde{b}_1 b$, $\tilde{b}_1 \to b\tilde{\chi}_1^0$													✓

Table 6. Searches used to probe each of the phenomenological models described in section 2.1 and simplified models described in section 2.2.

JHEP10(2015)054

Analysis acronym	Process	95% CL limit	Assumptions
0L [20]	$\tilde{g}\tilde{g}$, $\tilde{g} \to g\tilde{\chi}_1^0$, $\tilde{g} \to qq\tilde{\chi}_1^0$	$m_{\tilde{g}} > 1330\,\text{GeV}$	$m_{\tilde{\chi}_1^0} = 0\,\text{GeV}$
	$\tilde{q}\tilde{q}$, $\tilde{q} \to q\tilde{\chi}_1^0$	$m_{\tilde{q}} > 850\,\text{GeV}$	$m_{\tilde{\chi}_1^0} = 0\,\text{GeV}$, mass degenerate $\tilde{q}$
	$\tilde{q}\tilde{q}$, $\tilde{q} \to q\tilde{\chi}_1^0$	$m_{\tilde{q}} > 440\,\text{GeV}$	$m_{\tilde{\chi}_1^0} = 0\,\text{GeV}$, single flavour $\tilde{q}$
	$\tilde{g}\tilde{g}$, $\tilde{g} \to qqW\tilde{\chi}_1^0$	$m_{\tilde{g}} > 1100\,\text{GeV}$	$m_{\tilde{\chi}_1^0} = 0\,\text{GeV}$
	$\tilde{q}\tilde{q}$, $\tilde{q} \to qW\tilde{\chi}_1^0$	$m_{\tilde{q}} > 700\,\text{GeV}$	$m_{\tilde{\chi}_1^0} = 0\,\text{GeV}$
	$\tilde{g}\tilde{g}$, $\tilde{g} \to \tilde{t}_1 t$, $\tilde{t}_1 \to c\tilde{\chi}_1^0$	$m_{\tilde{g}} > 1100\,\text{GeV}$	$m_{\tilde{t}_1} = 400\,\text{GeV}$, $m_{\tilde{\chi}_1^0} = m_{\tilde{t}_1} - 20\,\text{GeV}$
MULTJ [22]	$\tilde{g}\tilde{g}$, $\tilde{g} \to t\bar{t}\tilde{\chi}_1^0$	$m_{\tilde{g}} > 1100\,\text{GeV}$	$m_{\tilde{\chi}_1^0} < 350\,\text{GeV}$
	$\tilde{g}\tilde{g}$, $\tilde{g} \to qqW\tilde{\chi}_1^0$	$m_{\tilde{g}} > 1000\,\text{GeV}$	$m_{\tilde{\chi}_1^0} < 200\,\text{GeV}$
	$\tilde{g}\tilde{g}$, $\tilde{g} \to qqWZ\tilde{\chi}_1^0$	$m_{\tilde{g}} > 1100\,\text{GeV}$	$m_{\tilde{\chi}_1^0} < 300\,\text{GeV}$
1L(S,H),	$\tilde{g}\tilde{g}$, $\tilde{g} \to qqW\tilde{\chi}_1^0$	$m_{\tilde{g}} > 1200\,\text{GeV}$	$x = \Delta m(\chi_1^\pm, \tilde{\chi}_1^0)/\Delta m(\tilde{g}, \tilde{\chi}_1^0) = 1/2$, $m_{\tilde{\chi}_1^0} = 60\,\text{GeV}$
2L(S),	$\tilde{q}\tilde{q}$, $\tilde{q} \to qW\tilde{\chi}_1^0$	$m_{\tilde{q}} > 700\,\text{GeV}$	$x = \Delta m(\chi_1^\pm, \tilde{\chi}_1^0)/\Delta m(\tilde{q}, \tilde{\chi}_1^0) = 1/2$, $m_{\tilde{\chi}_1^0} < 200\,\text{GeV}$
2LRaz [23]	$\tilde{g}\tilde{g}$, $\tilde{g} \to qq\ell\nu\tilde{\chi}_1^0$	$m_{\tilde{g}} > 1320\,\text{GeV}$	$m_{\tilde{\chi}_1^0} = 100\,\text{GeV}$
	$\tilde{q}\tilde{q}$, $\tilde{q} \to q\ell\nu\tilde{\chi}_1^0$	$m_{\tilde{q}} > 840\,\text{GeV}$	$m_{\tilde{\chi}_1^0} = 40\,\text{GeV}$
	$\tilde{g}\tilde{g}$, $\tilde{g} \to \tilde{t}_1 t$, $\tilde{t}_1 \to c\tilde{\chi}_1^0$	$m_{\tilde{g}} > 1200\,\text{GeV}$	$m_{\tilde{t}_1} = 200\,\text{GeV}$, $m_{\tilde{\chi}_1^0} = m_{\tilde{t}_1} - 20\,\text{GeV}$
	$\tilde{g}\tilde{g}$, $\tilde{g} \to qqWZ\tilde{\chi}_1^0$	$m_{\tilde{g}} > 1140\,\text{GeV}$	$m_{\tilde{\chi}_1^0} < 200\,\text{GeV}$
2L-offZ [24]	$\tilde{g}\tilde{g}$, $\tilde{g} \to qq(\ell\ell/\ell\nu/\nu\nu)\tilde{\chi}_1^0$	$m_{\tilde{g}} > 1170\,\text{GeV}$	$m_{\tilde{\chi}_1^0} = 50\,\text{GeV}$
	$\tilde{q}\tilde{q}$, $\tilde{q} \to q(\ell\ell/\ell\nu/\nu\nu)\tilde{\chi}_1^0$	$m_{\tilde{g}} > 780\,\text{GeV}$	$m_{\tilde{\chi}_1^0} = 50\,\text{GeV}$
SS/3L [25]	$\tilde{g}\tilde{g}$, $\tilde{g} \to t\bar{t}\tilde{\chi}_1^0$	$m_{\tilde{g}} > 950\,\text{GeV}$	
	$\tilde{g}\tilde{g}$, $\tilde{g} \to \tilde{t}_1 t$, $\tilde{t}_1 \to sb$	$m_{\tilde{g}} > 850\,\text{GeV}$	
	$\tilde{g}\tilde{g}$, $\tilde{g} \to qqW\tilde{\chi}_1^0$	$m_{\tilde{g}} > 860\,\text{GeV}$	$m_{\tilde{\chi}_1^0} < 400\,\text{GeV}$
	$\tilde{g}\tilde{g}$, $\tilde{g} \to qqWZ\tilde{\chi}_1^0$	$m_{\tilde{g}} > 1040\,\text{GeV}$	$m_{\tilde{\chi}_1^0} < 520\,\text{GeV}$
	$\tilde{q}\tilde{q}$, $\tilde{q} \to qWZ\tilde{\chi}_1^0$	$m_{\tilde{q}} > 670\,\text{GeV}$	$m_{\tilde{\chi}_1^0} < 300\,\text{GeV}$
	$\tilde{g}\tilde{g}$, $\tilde{g} \to qq(\ell\ell/\ell\nu/\nu\nu)\tilde{\chi}_1^0$	$m_{\tilde{g}} > 1200\,\text{GeV}$	$m_{\tilde{\chi}_1^0} < 660\,\text{GeV}$
	$\tilde{q}\tilde{q}$, $\tilde{q} \to q(\ell\ell/\ell\nu/\nu\nu)\tilde{\chi}_1^0$	$m_{\tilde{g}} > 780\,\text{GeV}$	$m_{\tilde{\chi}_1^0} < 460\,\text{GeV}$
TAU [26]	$\tilde{g}\tilde{g}$, $\tilde{g} \to qq(\tau\tau/\tau\nu/\nu\nu)\tilde{\chi}_1^0$	$m_{\tilde{g}} > 1090\,\text{GeV}$	nGM model, $\tilde{\tau}$ is NLSP
0/1L3B [27]	$\tilde{g}\tilde{g}$, $\tilde{g} \to t\bar{t}\tilde{\chi}_1^0$	$m_{\tilde{g}} > 1340\,\text{GeV}$	$m_{\tilde{\chi}_1^0} < 400\,\text{GeV}$

Table 7. The 95% CL exclusion limits obtained in published ATLAS searches listed in table 5 for the indicated processes and related assumptions. A dedicated search for $\tilde{c}\tilde{c}$ pair production [144] excludes charm squark masses up to 490 GeV for $m_{\tilde{\chi}_1^0} < 200\,\text{GeV}$ (95% CL).

The monojet (MONOJ) analysis, originally designed to search for direct production of top squarks ($\tilde{t}$), each decaying into a charm quark and a neutralino ($\tilde{\chi}_1^0$) [21], targets final states characterized by at least one high-p_T jet (with $p_\text{T} > 150\,\text{GeV}$ and $|\eta| < 2.8$) and large missing transverse momentum. Signal regions have been specifically optimized for models with a very small mass difference ($\leq 20\,\text{GeV}$) between the top squark and the neutralino. The event selection makes use of the presence of initial-state radiation (ISR) jets to identify signal events, and the squark-pair system is boosted, leading to large E_T^miss. Three signal regions which are based only on different selection criteria related to the jet p_T and E_T^miss have been used to bring additional sensitivity to models with very small mass differences between SUSY particles. These signal regions do not impose any criteria to specifically select events originating from the top squarks and as such they can be used to select events in which squarks are produced in pairs and decay directly via $\tilde{q} \to q\tilde{\chi}_1^0$ with a small $\tilde{q}$–$\tilde{\chi}_1^0$ mass difference.

JHEP10(2015)054

Signal region name	**0L_4jt+**	**0L_5jt**
Number of jets $\geq$	4	5
$E_{\mathrm{T}}^{\mathrm{miss}}/m_{\mathrm{eff}}^{N_{\mathrm{j}}} \geq$	0.30	0.15
$m_{\mathrm{eff}}^{\mathrm{incl}}$ [GeV] $\geq$	2200	1900

Table 8. Additional 0L signal regions optimized to increase the sensitivity of the search for left-handed squarks within the pMSSM.

The 0-lepton + 2–6 jets + $E_{\mathrm{T}}^{\mathrm{miss}}$ (0L) search [20] targets final states where each initial squark yields one jet and $E_{\mathrm{T}}^{\mathrm{miss}}$ and each initial gluino yields two jets and $E_{\mathrm{T}}^{\mathrm{miss}}$. Additional decay modes can include the production of charginos via $\tilde{q} \to q\tilde{\chi}_1^{\pm}$ and $\tilde{g} \to q\bar{q}\tilde{\chi}_1^{\pm}$, where the subsequent decay of these charginos to a W boson and $\tilde{\chi}_1^0$ can lead to final states with larger jet multiplicity. The search strategy is optimized for various squark and gluino masses, for a range of models. Fifteen inclusive signal regions are characterized by increasing the minimum jet-multiplicity from two to six (for jets with $p_{\mathrm{T}} > 40\,\mathrm{GeV}$ and $|\eta| < 2.8$), and are based on different selection criteria on the effective mass $m_{\mathrm{eff}}^{\mathrm{incl}}$, defined as the scalar sum of $E_{\mathrm{T}}^{\mathrm{miss}}$ and the p_{T} of the jets; the ratio of $E_{\mathrm{T}}^{\mathrm{miss}}/m_{\mathrm{eff}}^{N_{\mathrm{j}}}$, where $m_{\mathrm{eff}}^{N_{\mathrm{j}}}$ is m_{eff} constructed from only the leading N_{j} jets; and the minimum azimuthal angle between jets and $E_{\mathrm{T}}^{\mathrm{miss}}$. Two of the signal regions are designed to improve sensitivity to models with the cascade $\tilde{q}$ or $\tilde{g}$ decay via $\tilde{\chi}_1^{\pm}$ to W and $\tilde{\chi}_1^0$, in cases where the $\tilde{\chi}_1^{\pm}$ is nearly degenerate in mass with the $\tilde{q}$ or $\tilde{g}$. These signal regions place additional requirements on the invariant masses $m(W_{\mathrm{cand}})$ of the candidate W bosons reconstructed from a single high-mass jet, or from a pair of jets.

Following the same analysis strategy, two additional signal regions are included in this paper, which are optimized to increase the sensitivity of the 0L search for left-handed squarks within the pMSSM model described in section 2. These two signal regions target the two one-step decays of $\tilde{q}_{\mathrm{L}}$, $\tilde{q}_{\mathrm{L}} \to q\tilde{\chi}^{\pm} \to qW^{\pm}\tilde{\chi}_1^0$ and $\tilde{q}_{\mathrm{L}} \to q\tilde{\chi}_2^0 \to q(Z/h)\tilde{\chi}_1^0$ and are obtained by optimizing on two variables, $E_{\mathrm{T}}^{\mathrm{miss}}/m_{\mathrm{eff}}^{N_{\mathrm{j}}}$ and $m_{\mathrm{eff}}^{\mathrm{incl}}$, in the channels with at least four or at least five jets. All other selection criteria are exactly the same as for the corresponding channels described in the original publication. The two new signal regions, named 4jt+ and 5jt following the naming convention from ref. [20], are summarized in table 8.

A high jet multiplicity is expected from the decays of gluino pairs via a top squark, or via squarks involving the production of $\tilde{\chi}^{\pm}$ and $\tilde{\chi}_2^0$ in their decay chain, and is the main topology targeted by the 0-lepton + 7–10 jets + $E_{\mathrm{T}}^{\mathrm{miss}}$ (MULTJ) analysis [22]. The sensitivity of the search is enhanced by the subdivision into two categories. First, in the multi-jet+flavour stream, an event classification based on the number of jets ($p_{\mathrm{T}} > 50\,\mathrm{GeV}$ and $|\eta| < 2$) and number of b-jets ($p_{\mathrm{T}} > 40\,\mathrm{GeV}$ and $|\eta| < 2.5$) gives enhanced sensitivity to models which predict either more or fewer b-jets than the SM background. In the second category (multi-jet+M_J^{Σ} stream), which targets models with large numbers of objects in the final state, the jets reconstructed with the jet radius parameter $R = 0.4$ are reclustered into large composite jets using the anti-k_t algorithm with $R = 1.0$. The event variable M_J^{Σ} is computed as the sum of the masses of the composite jets: $M_J^{\Sigma} \equiv \sum_j m_j^{R=1.0}$, where the composite jets satisfy $p_{\mathrm{T}}^{R=1.0} > 100\,\mathrm{GeV}$ and $|\eta^{R=1.0}| < 1.5$. In total, nineteen signal regions

JHEP10(2015)054

	0LRaz_SR$_{\text{loose}}$	**0LRaz_SR$_{\text{tight}}$**
$E_{\text{T}}^{\text{miss}}$ [GeV] >	160	
$p_{\text{T}}^{\text{jet}_{1,2}}$ [GeV] >	150	200
$\Delta\phi(\text{jet}_{1,2}, E_{\text{T}}^{\text{miss}})$ >	0.4	1.4
R >	0.5	0.6
M_R' [GeV] >	700	900

Table 9. Overview of the selection criteria for the two signal regions used by the 0LRaz analysis. The 0LRaz_SR$_{\text{tight}}$ targets high masses of the heavy produced sparticle, and the 0LRaz_SR$_{\text{loose}}$ targets small mass splittings between the heavy produced sparticle and the LSP. Details of the construction of Razor variables $M_R^{'}$ and R can be found in appendix C.1.

are defined, based on different selection criteria on the total number of jets, number of b-jets, $E_{\text{T}}^{\text{miss}}/\sqrt{H_{\text{T}}}$ (where H_{T} is the scalar sum of the p_{T} of all jets) and on the event variable M_J^{Σ}.

The Razor variable set is designed to group together visible final-state particles associated with heavy produced sparticles, and in doing so contains information about the mass scale of those sparticles. The events are selected using a combination of $E_{\text{T}}^{\text{miss}}$ triggers which are fully efficient for the event selections considered in this search. The new 0-lepton Razor (0LRaz) analysis presented here selects events with at least two high-p_{T} jets and $E_{\text{T}}^{\text{miss}}$. The baseline object selection and event cleaning, as well as the choice of MC generators for SM background processes and the approach for calculating systematic uncertainties exactly follow those of the 0L search [20]. Two signal regions are identified by optimizing criteria on the Razor variables to give the best expected sensitivity in the model with squark pair production followed by the direct decay of the squarks. One signal region, SR$_{\text{loose}}$, targets models with small mass splittings which typically have softer visible objects, while the other signal region, SR$_{\text{tight}}$, is designed to target models with high squark masses which typically contain harder visible objects. Appendix C describes in detail the construction of the event variables, optimization strategy for these signal regions and corresponding control and validation regions, explicitly showing the distributions of the variables used for the selection, and the impact of the selection on the expected SM background and signal yields. An overview of the selection criteria for the two signal regions used in this search is given in table 9.

7.2 Final states with high-p_{T} jets, missing transverse momentum and at least one electron or muon

Three types of searches addressing decays of squarks and gluinos in events containing electrons or muons, jets and missing transverse momentum are summarized here: searches with at least one isolated lepton, which have been extended with an additional signal region with high jet multiplicity, a search with two same-flavour opposite-sign leptons inconsistent with Z boson decay (off-Z search), and searches in final states with a same-sign lepton pair or at least three leptons.

JHEP10(2015)054

The 1-lepton (soft+hard)/2-leptons + jets + $E_{\mathrm{T}}^{\mathrm{miss}}$ (1L(S,H), 2L(S), 2LRaz) searches [23] require the presence of at least one isolated lepton (electron or muon) in the decay chains of strongly produced squarks or gluinos. Different categories of events are defined in order to cover a broad parameter space: first the events are separated by different requirements on the transverse momentum of the leptons, either using an electron or muon with p_{T} >25 GeV in the hard lepton selection, or an electron (muon) with $p_{\mathrm{T}} > 7$ (6) GeV in the soft lepton selection. Each of these selections is further subdivided into a single-lepton and a dilepton search channel. The soft and hard lepton channels are designed to be complementary, and are more sensitive to supersymmetric spectra with small or large mass splittings, respectively, while the different lepton multiplicities cover different production and decay modes. To enhance the sensitivity to gluino or squark production, high and low jet multiplicity signal regions, respectively, are defined. The single-lepton channels (1L(S,H)) use a statistically independent set of events, compared to the 0L search, allowing the statistical combination of the two searches in the models for which it is relevant. The hard dilepton channel (2LRaz) targets gluino and first- and second-generation squark production, as well as mUED searches. This channel uses a Razor variable set and is not designed to search for signal events in which a real Z boson is present. In all search channels except the soft dimuon channel (2L(S)), two separate selections are performed for each jet multiplicity: one single-bin signal region optimized for discovery reach, which is also used to place limits on the visible cross-section, and one signal region which is binned in an appropriate variable in order to exploit the expected shape of the distribution of signal events when placing model-dependent limits.

An additional signal region with one hard lepton (electron or muon), high jet multiplicity and $E_{\mathrm{T}}^{\mathrm{miss}}$, referred to as 1L(H)_7-jet in table 5, is considered in this paper. The selection is based on looser missing transverse momentum selection criteria compared to the value used in ref. [23] together with the requirement for high jet multiplicity, which is suggested in refs. [145, 146] in the search for natural SUSY. The 1L(H)_7-jet signal region selection follows the concepts of the 1L(H) analysis [23], only modifying the criteria for the signal, validation and control regions to take into account a selection of events with at least seven jets in the final state. Due to these changes, a re-evaluation of the systematic uncertainties, in particular of the theoretical uncertainties on the background, is also performed. The selection criteria are summarized in table 10.

The 2-leptons off-Z (2L-offZ) search [24] targets events where the final state same-flavour opposite-sign leptons originate from the decay $\tilde{\chi}_2^0 \to \ell^+\ell^-\tilde{\chi}_1^0$, where $\tilde{\chi}_2^0$ is produced in the decays of squarks and gluinos, e.g. $\tilde{q} \to q\tilde{\chi}_2^0$ and $\tilde{g} \to qq\tilde{\chi}_2^0$. Compared to the decay $Z \to \ell^+\ell^-$, which leads to a peak in the $m_{\ell\ell}$ distribution around the Z boson mass, the decay $\tilde{\chi}_2^0 \to \ell^+\ell^-\tilde{\chi}_1^0$ leads to a rising distribution in $m_{\ell\ell}$ that terminates at an endpoint ("edge") [147] because events with larger $m_{\ell\ell}$ values are kinematically forbidden. Four signal regions are defined by requirements on jet multiplicity, b-tagged jet multiplicity and $E_{\mathrm{T}}^{\mathrm{miss}}$. The selection criteria are optimized for the simplified models of pair-produced squarks or gluinos followed by their two-step decays with sleptons, described in section 2.2.2. The signal regions with a b-jet veto provide the best sensitivity in the two-step simplified models considered here, since the signal b-jet content is lower than that of the dominant $t\bar{t}$ background. Signal regions with a requirement of at least one b-tagged jet

JHEP10(2015)054

	1L(H)_7-jet	**1L(H)_WR_7-jet**	**1L(H)_TR_7-jet**	**1L(H)_VR_7-jet $E_{\mathrm{T}}^{\mathrm{miss}}$**	**1L(H)_VR_7-jet m_{T}**
N_{lep}	$== 1$				
$p_{\mathrm{T}}^{\ell_1}$ [GeV]	> 25 (20)				
$p_{\mathrm{T}}^{\ell_2}$ [GeV]	< 10				
N_{jet}	≥ 7				
$p_{\mathrm{T}}^{\mathrm{jet}}$ [GeV]	$> 80, 25, 25, 25, 25, 25, 25$				
$\mathrm{N}_{b-\mathrm{tag}}$	–	$== 0$	≥ 1	–	–
$E_{\mathrm{T}}^{\mathrm{miss}}$ [GeV]	> 180	$\in[100, 180]$	$\in[100, 180]$	$\in[180, 500]$	$\in[100, 180]$
m_{T} [GeV]	> 120	$\in[40, 80]$	$\in[40, 120]$	$\in[60, 120]$	$\in[120, 320]$
$m_{\mathrm{eff}}^{\mathrm{incl}}$ [GeV]	> 750				

Table 10. Overview of the selection criteria for the 1L(H) + 7 jets + $E_{\mathrm{T}}^{\mathrm{miss}}$ analysis, for the signal region (1L(H)_7-jet), W+jets and semileptonic $t\bar{t}$ control regions (1L(H)_WR_7-jet and 1L(H)_TR_7-jet respectively) and two validation regions used to cross-check the background estimates (1L(H)_VR_7-jet $E_{\mathrm{T}}^{\mathrm{miss}}$ and 1L(H)_VR_7-jet m_{T}). The p_{T} selections for leptons are given for electrons (muons).

JHEP10(2015)054

target other signal models not explicitly considered here, such as those with bottom squarks that are lighter than the other squark flavours. One signal region with similar requirements to those used by the CMS experiment in a comparable search [148] which reported an excess of events above the SM background with a significance of 2.6 standard deviations, is also used for comparison purposes. No evidence for an excess is observed in this region.

Another leptonic search channel [25] is used for an analysis of final states with multiple jets, and either two leptons of the same electric charge or at least three leptons (SS/3L). The motivation for searches using these final states is that pair-produced gluinos have the same probability to decay to pairs of leptons with the same charge as with opposite charge. Squark production (directly in pairs or through $\tilde{g}\tilde{g}$ or $\tilde{g}\tilde{q}$ production with subsequent $\tilde{g} \to q\tilde{q}$ decay) can also lead to same-sign lepton or three-lepton signatures when the squarks decay in cascades involving top quarks, charginos, neutralinos or sleptons. Requiring a pair of leptons with the same electric charge largely suppresses the background coming from the SM processes, giving a very clean and powerful signature to search for new physics processes. It also allows the use of relatively loose kinematic requirements on $E_{\mathrm{T}}^{\mathrm{miss}}$, increasing the sensitivity to scenarios with small mass differences between SUSY particles or with R-parity violation. Five statistically independent signal regions are defined: two signal regions requiring same-sign leptons and b-jets (optimized for gluino decays via top squarks), a complementary signal region requiring a b-jet veto (optimized for the gluino decays via first- and second-generation squarks), and two signal regions requiring three leptons (designed for scenarios characterized by multi-step decays).

7.3 Final states with high-p_{T} jets, missing transverse momentum and at least one hadronically decaying tau lepton

A search for squarks and gluinos in events with large missing transverse momentum, jets and at least one hadronically decaying tau lepton [26] is motivated by naturalness arguments [149, 150], and by the assumption that light sleptons could play a role in the co-annihilation with neutralinos in the early universe [151]. In particular, models with light tau sleptons are consistent with dark-matter searches [152]. Four distinct topologies are studied in order to optimize the tau + jets + $E_{\mathrm{T}}^{\mathrm{miss}}$ (TAU) search for various models: one hadronically decaying tau (1τ) or two or more hadronically decaying taus (2τ) in the final state with no additional light leptons (e/μ) and one or more tau leptons with exactly one lepton (one electron ($\tau+e$) or muon ($\tau+\mu$)). The different topologies (1τ, 2τ and $\tau+\ell$, where ℓ is electron or muon) have been optimized separately, and, where relevant, are statistically combined to increase the analysis sensitivity. The same signal regions are used for additional model interpretations, not presented in ref. [26]. These are simplified models of squark- or gluino-pair production where the squark or gluino undergoes a two-step cascade decay via sleptons, as shown in figures 5(a) and 5(c), where the sleptons are assumed to be exclusively staus, since the first two generations of sleptons and sneutrinos are kinematically decoupled.

7.4 Final states with many b-jets and missing transverse momentum

A search requiring at least three b-jets [27] is one of the most sensitive searches to various SUSY models favoured by naturalness arguments, where top or bottom quarks are produced

JHEP10(2015)054

in the gluino decay chains. The search is carried out in statistically independent zero- and one-lepton channels (0/1L3B) which are combined to maximize the sensitivity. Three sets of signal regions, two for the zero-lepton channel and one for the one-lepton channel, are defined to enhance the sensitivity to the various models considered. They are characterized by having relatively hard $E_{\mathrm{T}}^{\mathrm{miss}}$ requirements and at least four, six or seven jets, amongst which at least three are required to be b-jets. Signal regions with zero leptons and at least four jets target SUSY models with sbottoms in the decay chain, while the one-lepton and the zero-lepton signal regions with at least six or seven jets aim to probe SUSY models where top-quark-enriched final states are expected.

8 Systematic uncertainties

Systematic uncertainties on background estimates in all searches included in this paper arise from the use of transfer factors which relate observations in the control regions to background expectations in the signal regions, and from the MC modelling of minor backgrounds. Since CRs are designed to be kinematically as close as possible to the SRs, many sources of systematic uncertainty largely cancel. In searches which include leptons in the final state, systematic uncertainties also impact the estimation of jets misidentified as leptons or of non-prompt leptons. The full details of all sources of systematic uncertainty and their impact on background predictions for each search included in this paper can be found in the corresponding original publication. Only the dominant uncertainties on the background estimations, common to all searches, are mentioned here.

Since at least one high-p_{T} jet and significant missing transverse momentum are present in all searches summarized in this paper, the primary common sources of systematic uncertainty for the SM backgrounds estimated with transfer factors derived from MC simulation are the JES and the jet energy resolution (JER). The theoretical modelling of background processes and the limited number of data events in the CRs and in the MC simulation are also typically important.

The JES uncertainty is estimated from a combination of simulation, test beam data and in-situ measurements [127, 153], and depends on the p_{T} and η of the jet. Additional contributions accounting for the jet-flavour composition, the calorimeter response to different jet flavours, pile-up and b-jet calibration uncertainties are also taken into account. Uncertainties on the JER are obtained with an in-situ measurement [154] of the jet transverse momentum balance in dijet events. Uncertainties in jet measurements are propagated to the $E_{\mathrm{T}}^{\mathrm{miss}}$, and additional subdominant uncertainties on $E_{\mathrm{T}}^{\mathrm{miss}}$ arising from the contribution from energy deposits not associated with reconstructed objects are also included. In signal regions designed for searches based on large jet multiplicities these uncertainties can be as large as 30% of the estimated background yield in the SRs.

Searches requiring the presence of tau leptons in the final state are subject to additional systematic uncertainties from the tau energy scale [139] and the tau lepton identification [138]. The uncertainties from the jet and tau energy scales are the largest experimental uncertainties in these searches, being as large as 13% and 8% of the estimated background yield respectively, and are treated as uncorrelated, since the calibration methods differ.

JHEP10(2015)054

In searches that require the presence of b-jets in the final state, the uncertainty associated with flavour-tagging efficiencies is evaluated by varying the p_{T}- and flavour-dependent correction factors applied to each jet in the simulation within a range that reflects the systematic uncertainty on the measured tagging efficiencies and mistag rates. This uncertainty varies between 10% and 16% in the different SRs requiring at least three b-jets in the final state.

Uncertainties arising from the theoretical modelling of background processes are typically evaluated by comparing the estimates to those obtained with different MC generators. The uncertainty due to the factorization and renormalization scales is computed by varying these scales up and down by a factor of two with respect to the nominal setting. Uncertainties from PDFs are computed following the PDF4LHC recommendations [155]. These uncertainties vary across the different searches and in some signal regions are the dominant source of systematic uncertainties.

The same sources of experimental uncertainty apply to the signal acceptance. Several theoretical uncertainties on the acceptance for the various signal models are taken into account. These uncertainties are estimated using the Madgraph5+Pythia6 samples by varying the following parameters up and down by a factor of two: the Madgraph scale used to determine the event-by-event renormalization and factorization scale, the parameters used to determine the scales for initial- and final-state QCD radiation and the parameters used for jet matching. The uncertainty on the modelling of initial-state radiation plays an important role in simplified models with small mass differences in the decay cascade, and is as large as 20–30% in such regions. For all models, except the mUED model, the NLO+NLL cross-section uncertainty is taken from an envelope of cross-section predictions using different PDF sets and factorization and renormalization scales, as described in ref. [114]. The mUED model cross-sections are based on a calculation at LO in QCD, and the events are generated with a leading-order MC event generator. No theoretical uncertainties on the acceptance are considered for this case.

The overall background uncertainties for the two new signal regions defined in the 0LRaz search are estimated to be 6% in the 0LRaz_SR$_{\mathrm{loose}}$ signal region and 9% in the 0LRaz_SR$_{\mathrm{tight}}$ signal region. These uncertainties are dominated by the modelling of the Z+jets process and by the uncertainties on diboson production due to renormalization and factorization scales and PDF uncertainties for which a conservative uniform 50% uncertainty is applied. In the additional signal region for the 1-lepton (hard) + jets + $E_{\mathrm{T}}^{\mathrm{miss}}$ analysis, 1L(H)_7-jet, the overall background uncertainty is estimated to be 35%, and it is dominated by the modelling of the $t\bar{t}$ process in the events with high jet multiplicity. The estimated background uncertainties in the two additional signal regions for the 0-lepton + 2–6 jets + $E_{\mathrm{T}}^{\mathrm{miss}}$ analysis, 0L_4jt+ and 0L_5jt, are consistent with the uncertainties obtained for the two closest signal regions (4jt and 5j) from the original publication [20].

9 Results for the new signal regions

The number of events observed in the data and expected from SM processes are shown for all new signal regions in tables 11, 12 and 13. Table 11 summarizes the results for the two

JHEP10(2015)054

additional signal regions for the 0L analysis. Table 12 displays the equivalent results for the two signal regions of the new 0LRaz analysis, and those for the additional region of the 1L(H) analysis are shown in table 13. All results are determined using the background-only fit. The pre-fit background expectations are also shown in the tables, for comparison purposes. The prediction of the W/Z+jets background processes by the simulation prior to the fit is found to be overestimated in the phase space of interest and is consequently decreased by the fit. This is consistent with the behaviour observed in previous publications probing a similar phase space [20]. In all new signal regions presented in this paper the number of events observed is consistent with the post-fit SM expectations. The observed and expected upper limits at 95% CL on the number of BSM events ($S^{95}_{\rm obs}$ and $S^{95}_{\rm exp}$), together with the upper limits on the visible cross-section of BSM physics ($\langle\epsilon\sigma\rangle^{95}_{\rm obs}$) and the p-value for the background-only hypothesis, are also presented in the tables 11–13. The confidence levels are calculated with the $CL_{\rm S}$ prescription [143]. For an observed number of events lower than expected, the p-value is truncated at 0.5.

10 Combination strategy

Statistical combinations of the analyses, as listed in table 6, are performed in order to increase the exclusion reach in several SUSY models in which at least two analyses designed to be statistically independent in their signal and control region definitions provide comparable sensitivities. The conditions are satisfied for a combination of the 1L(S,H) and 0L searches. These analyses search for squarks and gluinos in final states containing jets and missing transverse momentum, either with at least one isolated electron or muon (1L(S,H)), or applying an explicit veto on events containing electrons or muons (0L). They are statistically independent due to a veto on any electron or muon with $p_{\rm T} > 10\,$GeV in the case of the 0L search, and requiring an electron or muon with $p_{\rm T}(e/\mu) > 25\,$GeV (hard single-lepton) or $p_{\rm T}(e/\mu) > 7/6\,$GeV (soft single-lepton) in the case of the 1L(S,H) search. It has been checked explicitly that the difference in lepton-$p_{\rm T}$ thresholds in the 0L and soft single-lepton analyses does not result in events selected by both analyses. The control regions used to estimate contributions from W+jets and top backgrounds used by the 0L search have been slightly modified with respect to the original regions [20] such that events which are selected by the respective control regions in the 1L(S,H) analyses are vetoed. This modification ensures complete statistical independence of the three analyses, which can therefore be combined where relevant.

The statistical combination is obtained from the individual likelihoods of the analyses involved. In the case of the 0L analysis the likelihood for the signal region that provides the best expected $CL_{\rm S}$ value for the signal model considered, and its corresponding control regions, is chosen. The choice of this signal region can vary as a function of sparticle masses. For the 1L(S,H) analyses, all the available signal regions are statistically independent and hence a single likelihood that describes all of them serves as input for the combination procedure. Some of the systematic uncertainties can be correlated when building the combined likelihood. The correlated uncertainties in the combination procedure are the luminosity uncertainty, the uncertainty on the SUSY cross-sections,

JHEP10(2015)054

Signal region	**0L_4jt+**	**0L_5jt**
Expected background events before the fit		
$t\bar{t}$ (+ V) + single top	0.37	2.9
W+jets	0.75	4.5
Z/γ^*+jets	2.1	4.8
Diboson	–	0.32
Fitted background events		
$t\bar{t}$ (+ V) + single top	0.39 ± 0.32	3.0 ± 1.8
W+jets	0.55 ± 0.33	2.0 ± 1.5
Z/γ^*+jets	$0.10^{+0.17}_{-0.10}$	1.7 ± 0.9
Diboson	–	0.32 ± 0.16
Multi-jet	–	$0.58^{+0.73}_{-0.58}$
Total background	1.04 ± 0.43	7.6 ± 1.9
Observed events	0	8
$\langle\epsilon\sigma\rangle^{95}_{\rm obs}$[fb]	0.17	0.40
$S^{95}_{\rm obs}$	3.4	8.2
$S^{95}_{\rm exp}$	$3.5^{+1.3}_{-0.5}$	$7.5^{+3.1}_{-2.0}$
$p(s=0)$	0.50	0.35

Table 11. The background expectations before the fit and the background fit results for the new 0L signal regions. Negligible contributions are marked as '–'. The uncertainties shown combine the statistical uncertainties on the event samples with the systematic uncertainties. Also shown are the 95% CL upper limits on the visible cross-section ($\langle\epsilon\sigma\rangle^{95}_{\rm obs}$) and on the number of signal events ($S^{95}_{\rm obs}$). The expected upper limit on the number of signal events ($S^{95}_{\rm exp}$) is calculated from the expected number of background events after fit, with uncertainties indicating the $\pm 1\sigma$ deviations from the expectation. The p-value ($p(s=0)$) is also presented in the table.

b-tagging uncertainties, and the jet energy resolution and $E_{\rm T}^{\rm miss}$-related uncertainties. Other systematic uncertainties, such as theoretical uncertainties, are not correlated, e.g. the uncertainties due to different Monte Carlo generators used in the analyses considered. The jet energy scale uncertainty, which is subdominant, is not correlated due to the use of different prescriptions in the analyses involved. The combination of the analyses was carefully validated by ensuring that the combined likelihood did not lead to artificial correlations between fit parameters or major changes in post-fit values of nuisance parameters with respect to the individual analysis fits discussed in refs. [20, 23].

Figures 9 and 10 show the result of the combination of the 1L(S,H) and 0L analyses for both squark-pair and gluino-pair production for the one-step decays of squarks and gluinos described in section 2.2.2. The limits obtained improve the results of the separate analyses, reaching higher $\tilde{\chi}^0_1$ mass and approximately 50 GeV higher squark or gluino mass

JHEP10(2015)054

Signal region	**0LRaz_SR**$_{\text{loose}}$	**0LRaz_SR**$_{\text{tight}}$
Expected background events before the fit		
$t\bar{t}$	138	1.8
Single top	23.9	1.6
$t\bar{t}+V$	4.7	0.2
W+jets	794	49
Z+jets	762	58
Diboson	112	10
Fitted background events		
$t\bar{t}$	117 ± 22	1.7 ± 0.5
Single top	24.9 ± 2.6	1.8 ± 0.3
$t\bar{t}+V$	3.7 ± 1.0	0.20 ± 0.07
W+jets	454 ± 40	27.0 ± 3.0
Z+jets	618 ± 76	45 ± 6
Diboson	94 ± 49	10 ± 5
Multi-jet	14 ± 13	2.4 ± 2.4
Total background	1326 ± 84	88 ± 8
Observed events	1322	74
$\langle\epsilon\sigma\rangle^{95}_{\text{obs}}$[fb]	6.17	0.83
S^{95}_{obs}	125.3	16.8
S^{95}_{exp}	$135.1^{+64.8}_{-42.2}$	$24.3^{+9.9}_{-6.9}$
$p(s=0)$	0.49	0.50

Table 12. The background expectations before the fit and the background fit results for the 0LRaz analysis. Negligible contributions are marked as '–'. The uncertainties shown combine the statistical uncertainties on the event samples with the systematic uncertainties. Also shown are the 95% CL upper limits on the visible cross-section ($\langle\epsilon\sigma\rangle^{95}_{\text{obs}}$) and on the number of signal events (S^{95}_{obs}). The expected upper limit on the number of signal events (S^{95}_{exp}) is calculated from the expected number of background events after fit, with uncertainties indicating the $\pm 1\sigma$ deviations from the expectation. The p-value ($p(s=0)$) is also presented in the table.

for massless neutralinos. The combined limit also approaches the diagonal $m(\tilde{\chi}^0_1) = m(\tilde{q}, \tilde{g})$ closer than the individual analyses.

11 Limits in SUSY models

This section summarizes the exclusion limits placed in the various phenomenological and simplified models described in section 2 (there is a one-to-one correspondence between the subsections of section 2 and this section). The analyses and corresponding signal

JHEP10(2015)054

Signal region	**1L(H)_7-jet**
Expected background events before the fit	
$t\bar{t}$	81
Single top	3.4
$t\bar{t}+V$	2.8
W+jets	11
Z+jets	0.59
Diboson	2.7
Fitted background events	
$t\bar{t}$	56 ± 27
Single top	3.4 ± 2.2
$t\bar{t}+V$	2.8 ± 1.0
W+jets	8 ± 4
Z+jets	0.59 ± 0.17
Diboson	2.7 ± 1.5
Multi-jet	2.4 ± 2.3
Total background	76 ± 27
Observed events	68
$\langle\epsilon\sigma\rangle^{95}_{\text{obs}}$[fb]	2.06
S^{95}_{obs}	41.9
S^{95}_{exp}	45^{+12}_{-10}
$p(s=0)$	0.5

Table 13. The background expectations before the fit and the background fit results for the new 1L(H) signal region. An overview of the selection criteria for the signal, validation and control regions used in this analysis is given in table 10. The uncertainties shown combine the statistical uncertainties on the event samples with the systematic uncertainties. Also shown are the 95% CL upper limits on the visible cross-section ($\langle\epsilon\sigma\rangle^{95}_{\text{obs}}$) and on the number of signal events (S^{95}_{obs}). The expected upper limit on the number of signal events (S^{95}_{exp}) is calculated from the expected number of background events after fit, with uncertainties indicating the $\pm 1\sigma$ deviations from the expectation. The p-value ($p(s=0)$) is also presented in the table.

JHEP10(2015)054

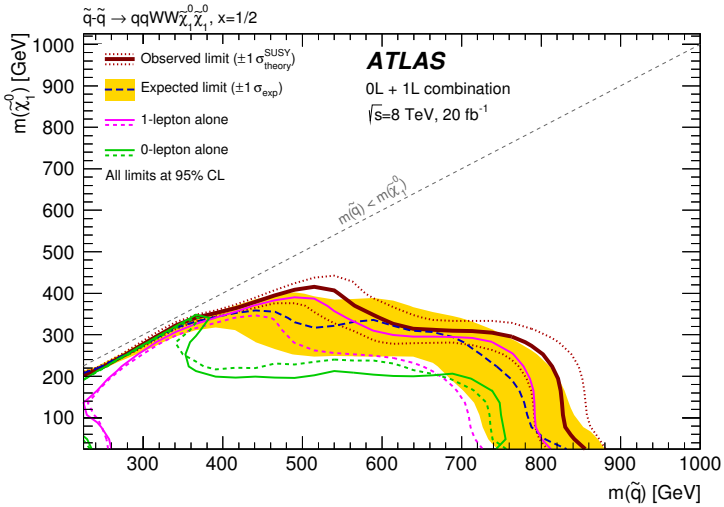

Figure 9. Observed and expected exclusion limits for simplified models of squark-pair production with one-step decays via the $\tilde{\chi}_1^{\pm}$ into a W boson and the $\tilde{\chi}_1^0$. The mass of the $\tilde{\chi}_1^{\pm}$ is chosen to be between the $m_{\tilde{q}}$ and $m_{\tilde{\chi}_1^0}$ and is determined by $x = (m_{\tilde{\chi}_1^{\pm}} - m_{\tilde{\chi}_1^0})/(m_{\tilde{q}} - m_{\tilde{\chi}_1^0}) = 1/2$. Squark and neutralino masses in the area below the observed limit are excluded at 95% CL. The yellow band includes all experimental uncertainties; the red dotted lines indicate the theory uncertainty on the cross-section. The individual limits from the 0L and the 1L(S,H) analyses are overlaid in green and magenta, respectively.

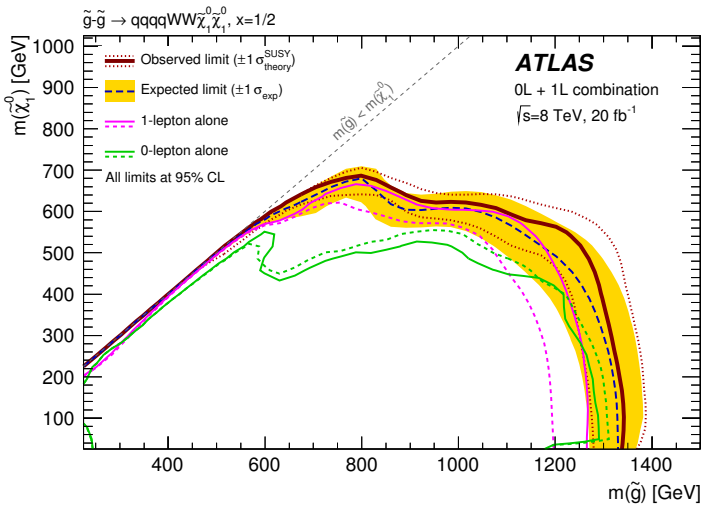

Figure 10. Observed and expected exclusion limits for simplified models of gluino-pair production with decays via the $\tilde{\chi}_1^{\pm}$ into a W boson and the $\tilde{\chi}_1^0$. The mass of the $\tilde{\chi}_1^{\pm}$ is chosen to be between the $m_{\tilde{g}}$ and $m_{\tilde{\chi}_1^0}$ and is determined by $x = (m_{\tilde{\chi}_1^{\pm}} - m_{\tilde{\chi}_1^0})/(m_{\tilde{g}} - m_{\tilde{\chi}_1^0}) = 1/2$. Gluino and neutralino masses in the area below the observed limit are excluded at 95% CL. The yellow band includes all experimental uncertainties; the red dotted lines indicate the theory uncertainty on the cross-section. The individual limits from the 0L and the 1L(S,H) analyses are overlaid in green and magenta, respectively.

JHEP10(2015)054

regions are referred to by their acronyms defined in table 5. An overview of all searches used to probe the phenomenological models described in section 2.1 and the simplified models described in section 2.2 is given in table 6. A limit obtained from the statistical combination of 1L(S,H) and 0L analyses is presented for models for which both analyses have comparable sensitivity and is used as a single contribution to the final combined limit. The final combined observed and expected 95% CL exclusion limits are obtained from the signal regions belonging to the contributing analyses that provide the best expected CL_{S} value. Expected limits from the individual analyses which contribute to the final combined limits are also presented for comparison. The $\pm 1\sigma^{\mathrm{SUSY}}_{\mathrm{theory}}$ lines around the observed limits in the figures are obtained by changing the signal cross-section by one standard deviation ($\pm 1\sigma$), as described in section 8. All mass limits on supersymmetric particles quoted later in this section are derived from the $-1\sigma^{\mathrm{SUSY}}_{\mathrm{theory}}$ line.

11.1 Limits in phenomenological models

This section summarizes the exclusion limits placed on the phenomenological models described in section 2.1.

11.1.1 A phenomenological MSSM model

The measurements are interpreted in a phenomenological MSSM model, which possesses three parameters: $m_{\tilde{q}_{\mathrm{L}}}$, M_1 and M_2, where M_1 and M_2 are the masses associated with the bino and wino fields. For the exclusion limits in figure 11 either M_1 is fixed to 60 GeV and M_2 is varied independently, or M_1 is varied and M_2 is set to $M_2 = (M_1 + m_{\tilde{q}_{\mathrm{L}}})/2$. The figures show limits in the $(m_{\tilde{q}}, m_{\tilde{\chi}^{\pm}_1, \tilde{\chi}^0_2})$ and $(m_{\tilde{q}}, m_{\tilde{\chi}^0_1})$ planes, for various gluino masses, as obtained from the 0L analysis with the additional 0L_4jt+ and 0L_5jt signal regions optimized specifically for this model. As expected, for the relatively light gluino mass of 1600 GeV, a large range of squark masses (up to 1500 GeV) and $\tilde{\chi}^{\pm}_1/\tilde{\chi}^0_2$ masses (up to 1150 GeV) can be excluded. The exclusion reach decreases with increasing gluino mass.

11.1.2 Minimal Supergravity/Constrained MSSM and bilinear R-parity-violation models

The exclusion limits in the (m_0, $m_{1/2}$) mSUGRA/CMSSM plane with $\tan\beta = 30$, $A_0 = -2m_0$ and $\mu > 0$ are shown in figure 12. In the parameter space region with m_0 values smaller than about 1800 GeV the best sensitivity is obtained with the (0+1)-lepton combination, which slightly improves the individual limit obtained by the 0L_3jt signal region from the 0L search. For high m_0 values, final states with four top quarks dominate, and consequently the best sensitivity is provided by the 0/1L3B search. This search excludes gluino masses smaller than 1280 GeV.

The exclusion limits for the RPV model, which uses the same parameters as the mSUGRA/CMSSM but allows for bilinear R-parity-violating terms in the superpotential resulting in an unstable LSP, are shown in the (m_0, $m_{1/2}$) plane in figure 13. The best sensitivity is provided by the TAU and the SS/3L searches. For m_0 values smaller than approximately 750 GeV the sensitivity is dominated by the TAU search which excludes $m_{1/2}$ values up to 680 GeV using the combination of all final states considered in the search. At

JHEP10(2015)054

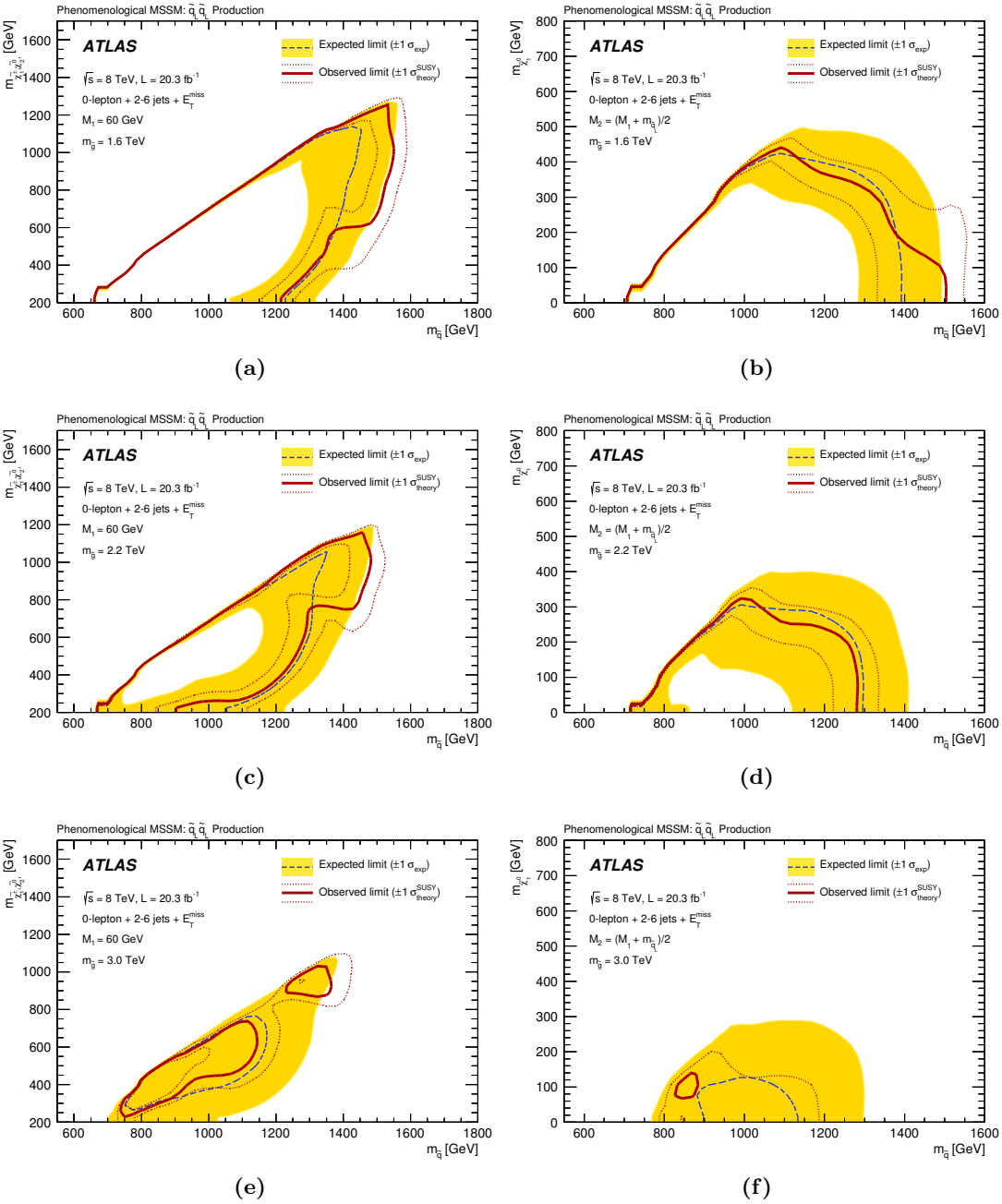

Figure 11. 95% CL exclusion limits in the pMSSM considered in the search for left-handed squarks, with mass parameters M_1 and M_2, which are associated with the bino and wino masses, respectively. The limits are obtained from the 0L analysis with the additional 0L_4jt+ and 0L_5jt signal regions optimized specifically for this model. The parameter set considered here has either (a, c, e) $M_1 = 60\,\text{GeV}$ and M_2 varying or (b, d, f) $M_2 = (M_1 + m_{\tilde{q}_L})/2$ and M_1 varying. For each M_1, M_2 combination three gluino masses are considered, $m_{\tilde{g}} = 1600, 2200, 3000\,\text{GeV}$. Gluino pair production is not included. The solid red line and the dashed blue line show respectively the combined observed and expected 95% CL exclusion limits.

JHEP10(2015)054

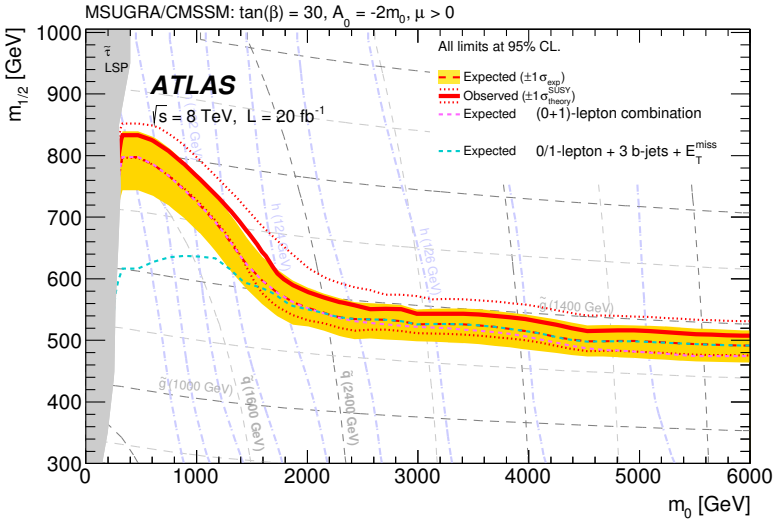

Figure 12. Exclusion limits in the (m_0, $m_{1/2}$) plane for the mSUGRA/CMSSM model. The solid red line and the dashed red line show respectively the combined observed and expected 95% CL exclusion limits. Expected limits from the individual analyses which contribute to the final combined limits are also shown for comparison.

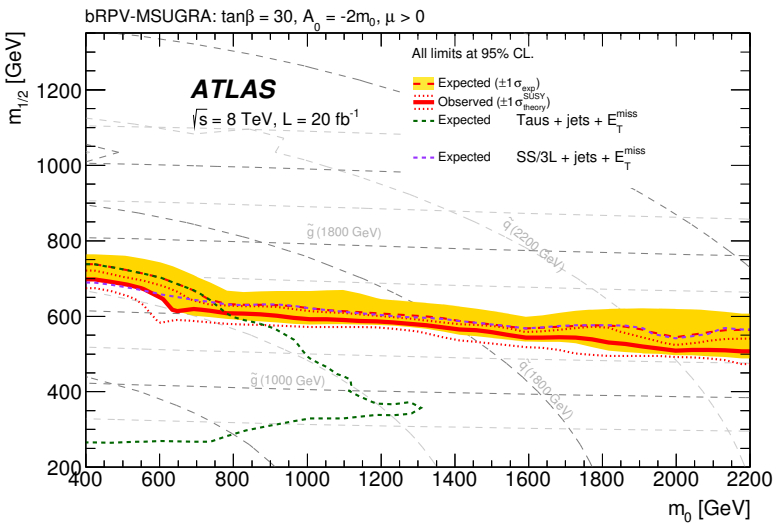

Figure 13. Exclusion limits in the (m_0, $m_{1/2}$) plane for the bRPV model. The solid red line and the dashed red line show respectively the combined observed and expected 95% CL exclusion limits. Expected limits from the individual analyses which contribute to the final combined limits are also shown for comparison.

high m_0 values the best sensitivity is provided by the SS/3L_SR3b signal region from the SS/3L search, which excludes values of $m_{1/2}$ between 200 GeV and 490 GeV. For m_0 values below 2200 GeV, signal models with $m_{1/2} < 200$ GeV are not considered because the lepton acceptance is significantly reduced due to the increased LSP lifetime in that region.

JHEP10(2015)054

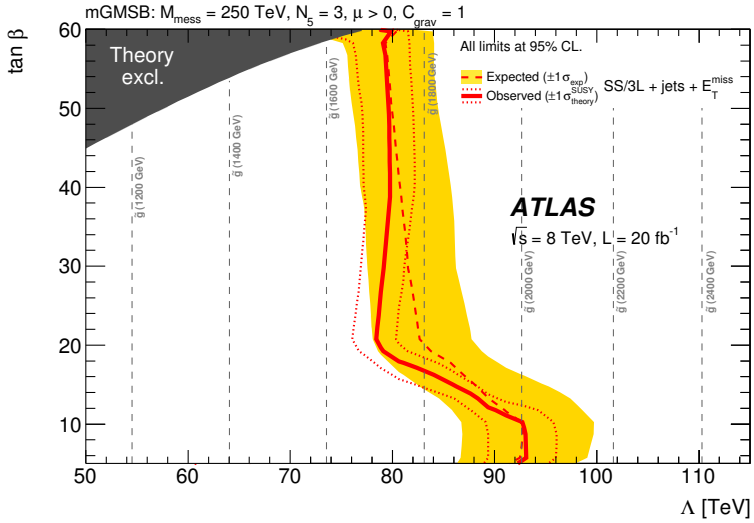

Figure 14. Exclusion limits in the (Λ, tan β) plane for the mGMSB model. The solid red line and the dashed red line show respectively the combined observed and expected 95% CL exclusion limits. The region of small Λ and large tan β just above the exclusion limit is excluded theoretically since it leads to tachyonic states.

11.1.3 Minimal gauge-mediated supersymmetry breaking model

The observed and expected limits for the mGMSB scenario are shown in figure 14, in the plane defined by the SUSY breaking scale Λ and the tan β value. The region of small Λ and large tan β just above the exclusion limit is excluded theoretically since it leads to tachyonic states. The SS/3L search provides the best sensitivity for this model and excludes values of Λ up to about 75 TeV.

11.1.4 Natural gauge mediation model

The limits obtained for the nGM scenario are shown in figure 15 in the ($m_{\tilde{\tau}}$, $m_{\tilde{g}}$) plane. The best limits are obtained by the 1L(S,H) and TAU searches, resulting in an exclusion of gluino masses below approximately 1100 GeV independent of the $\tilde{\tau}$ mass.

11.1.5 Non-universal Higgs mass model with gaugino mediation

The exclusion limits in the context of a NUHMG model with parameters $m_0 = 0$, tan β = 10, $\mu > 0$ and $m^2_{H_2} = 0$ are shown in the ($m^2_{H_1}$, $m_{1/2}$) plane in figure 16. They are provided by the (0+1)-lepton combination. A band in the ($m^2_{H_1}$, $m_{1/2}$) plane can be excluded, extending up to the ranges $2000 \times 10^3\,\mathrm{GeV}^2 < m^2_{H_1} < 5400 \times 10^3\,\mathrm{GeV}^2$ and $450\,\mathrm{GeV} < m_{1/2} < 620\,\mathrm{GeV}$.

11.1.6 Minimal Universal Extra Dimension model

Finally, the limits obtained for the mUED scenario are shown in figure 17 in the ($1/R_c$, ΛR_c) plane. The 2L(S), 2LRaz and SS/3L searches provide competitive sensitivities for this model in which the mass spectrum is naturally degenerate and the decay chain of the

JHEP10(2015)054

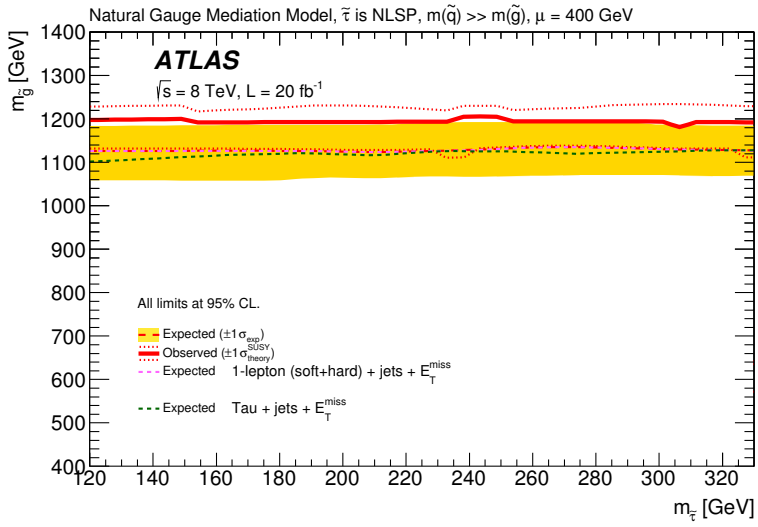

Figure 15. Exclusion limits in the $(m_{\tilde{\tau}}, m_{\tilde{g}})$ plane for the nGM model. The solid red line and the dashed red line show respectively the combined observed and expected 95% CL exclusion limits. Expected limits from the individual analyses which contribute to the final combined limits are also shown for comparison.

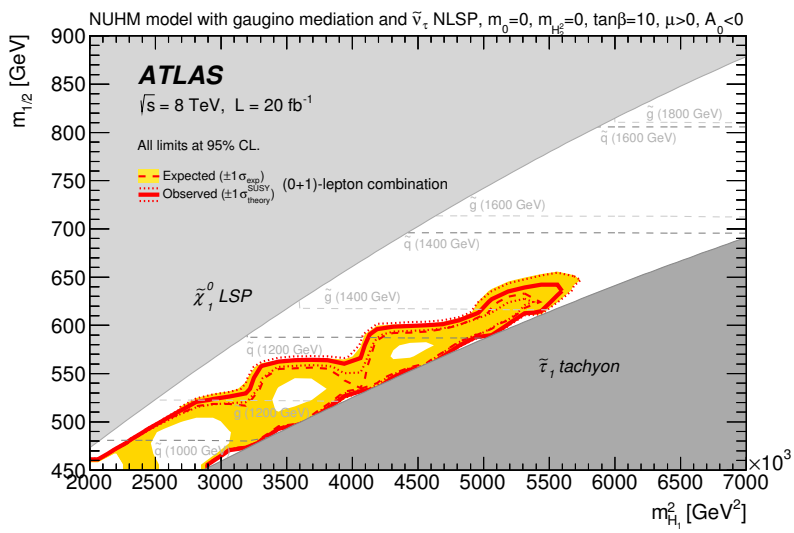

Figure 16. Exclusion limits in the $(m^2_{H_1}, m_{1/2})$ plane for the NUHMG model. The solid red line and the dashed red line show respectively the combined observed and expected 95% CL exclusion limits.

JHEP10(2015)054

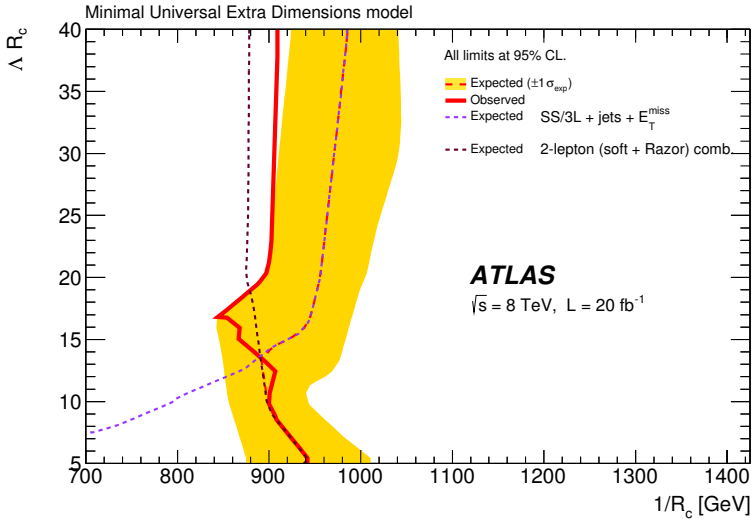

Figure 17. Exclusion limits in the $(1/R_c, \Lambda R_c)$ plane for the mUED model. The solid red line and the dashed red line show respectively the combined observed and expected 95% CL exclusion limits. Expected limits from the individual analyses which contribute to the final combined limits are also shown for comparison.

Kaluza-Klein (KK) quark excitation to the lightest KK particle, the KK photon, gives a signature very similar to the supersymmetric decay chain of a squark via cascades involving top quarks, charginos, neutralinos or sleptons, which can subsequently produce many leptons. In the region where the cut-off scale times radius (ΛR_c) is smaller than 13, the combined exclusion is dominated by the 2L(S) and 2LRaz searches which are combined based on the best expected CL_S value, while in the remaining regions of the parameter space the final exclusion is dominated by the SS/3L_SR3Lhigh and SS/3L_SR0b signal regions from the SS/3L search. Values of $1/R_c$ below 850 GeV are excluded.

11.2 Limits in simplified models

11.2.1 Direct decays of squarks and gluinos

This section summarizes the exclusion limits in simplified models with direct decays of gluinos and squarks of the first and second generation described in section 2.2.1. Here and in sections 11.2.2 and 11.2.3, unless otherwise stated, the eight light-flavoured squarks are always assumed to be mass-degenerate.

Figure 18 shows the exclusion limits in simplified models with squark-pair production and subsequent direct squark decays to a quark and the lightest neutralino. The expected limits from the three most sensitive searches (0L, MONOJ and 0LRaz) are presented individually along with the combined expected and observed exclusion limits. The 0L and 0LRaz analyses yield in general higher expected mass limits, but the MONOJ search provides the best sensitivity close to the diagonal line, in the region of parameter space where the mass difference between the squark and the lightest neutralino is small. From the observed limits, neutralino masses below about 280 GeV can be excluded for squark masses

JHEP10(2015)054

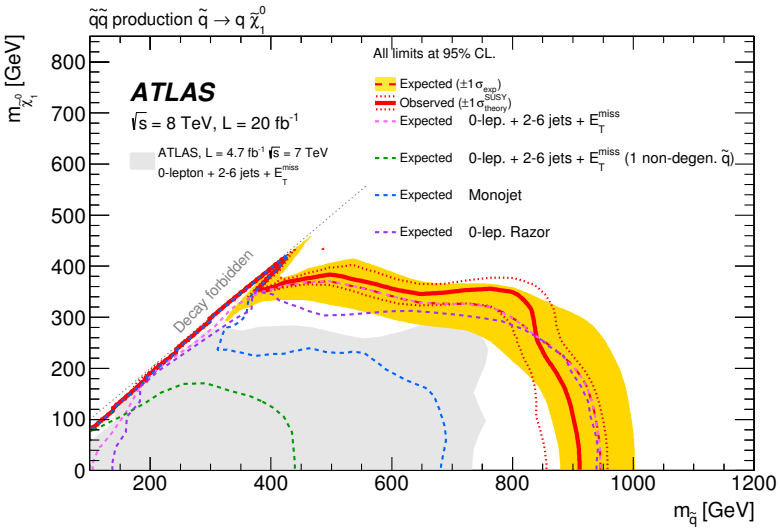

Figure 18. Exclusion limits in the mass plane of the lightest neutralino and first- and second-generation squarks assuming squark-pair production and direct decays $\tilde{q} \rightarrow q\tilde{\chi}_1^0$. The solid red line and the dashed red line show respectively the combined observed and expected 95% CL exclusion limits. Expected limits from the individual analyses which contribute to the final combined limits are also shown for comparison. A previous result from ATLAS [156] using 7 TeV proton-proton collisions is represented by the shaded (grey) area. A limit obtained with the 0L search [20] in a scenario with only one light-flavour squark produced is also presented for completeness.

up to 800 GeV, and for a neutralino mass of 100 GeV squark masses are excluded below 850 GeV. In a scenario with only one light-flavour squark produced, which affects only the cross-section but not the kinematics of the events, a lower limit on the squark mass of 440 GeV is obtained with the 0L search [20].

Another example of a direct decay is shown in figure 19, taken from ref. [20], where gluino-pair production with the subsequent decay $\tilde{g} \rightarrow qq\tilde{\chi}_1^0$ is considered. Due to the higher production cross-sections compared to the squark-pair production, higher mass limits can be obtained. For gluino masses up to about 1000 GeV, neutralino masses can be excluded below about 500 GeV or close to the kinematic limit near the diagonal. For small neutralino masses the observed limit is as large as 1330 GeV.

A simplified model of $\tilde{q}\tilde{g}$ strong production with the direct decays of squarks $\tilde{q} \rightarrow q\tilde{\chi}_1^0$ and gluinos $\tilde{g} \rightarrow qq\tilde{\chi}_1^0$ is considered in figure 20, taken from ref. [20], for the 0L analysis. The squark mass is fixed at $0.96m_{\tilde{g}}$ in figure 20(a), and gluinos can decay via on-shell squarks as $\tilde{g} \rightarrow \tilde{q}q \rightarrow qq\tilde{\chi}_1^0$. The exclusion limit for the neutralino mass is very close to the kinematic limit near the diagonal line and reaches 700 GeV for gluino masses up to 1200 GeV. For a massless neutralino, gluino masses below 1500 GeV are excluded.

Figure 20(b) expresses the mass limits in the $(m_{\tilde{g}}, m_{\tilde{q}})$ plane in the model with combined production of squark pairs, gluino pairs, and of squark-gluino pairs, for different assumptions on the neutralino mass: $m_{\tilde{\chi}_1^0} = 0$ GeV, 395 GeV or 695 GeV. Depending on the mass hierarchy, the $\tilde{g} \rightarrow \tilde{q}q$ and $\tilde{q} \rightarrow \tilde{g}q$ one-step decays are taken into account. The masses of all other supersymmetric particles are set outside the kinematic reach. A lower limit of 1650 GeV for equal squark and gluino mass is found for the scenario with a massless $\tilde{\chi}_1^0$.

JHEP10(2015)054

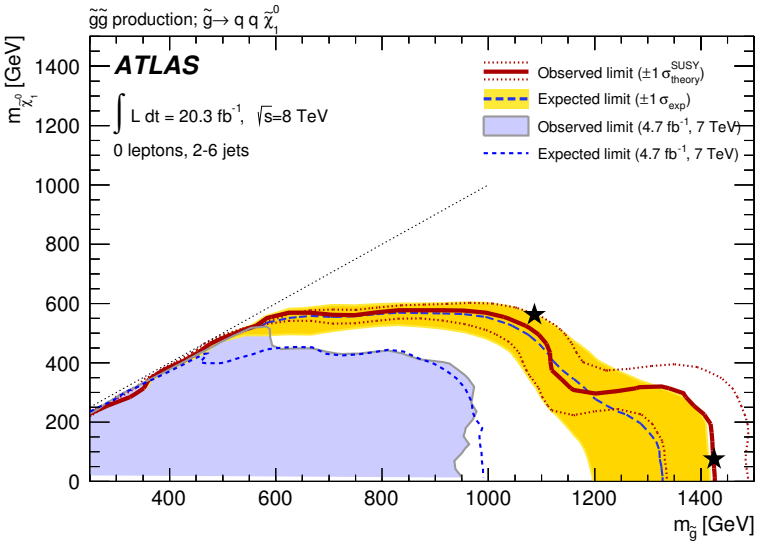

Figure 19. Exclusion limits in the mass plane of the lightest neutralino and the gluino for gluino-pair production with direct decay $\tilde{g} \to qq\tilde{\chi}_1^0$ taken from the 0L search [20]. The solid red line and the dashed blue line show respectively the observed and expected 95% CL exclusion limits. The star symbols indicates two benchmark models which are investigated in more detail in the publication. A previous result from ATLAS [156] using 7 TeV proton-proton collisions is represented by the shaded (light blue) area.

Figure 21 shows the cross-section times branching ratio limits for gluino-pair production with direct gluino decays to a gluon and the lightest neutralino based on the 0L search. For a massless neutralino (figure 21(a)), gluino masses below 1250 GeV can be excluded. The result can also be used to obtain lower mass limits on $\tilde{\chi}_1^0$, e.g. 550 GeV for a gluino mass of 850 GeV (figure 21(b)). The cross-section exclusion for the $\tilde{g} \to g\tilde{\chi}_1^0$ model is very similar to that for the $\tilde{q} \to q\tilde{\chi}_1^0$ as would be expected if there is not much difference between quark- and gluon-initiated jets.

11.2.2 One-step decays of squarks and gluinos

This section presents the limits in simplified models with one-step decays of squarks and gluinos described in section 2.2.2.

Figure 22 shows the exclusion limits for squark-pair production where the squark decays via an intermediate chargino (one step) to a quark, W boson and neutralino. For the model presented in figure 22(a) the chargino mass is fixed at $m_{\tilde{\chi}_1^\pm} = (m_{\tilde{q}} + m_{\tilde{\chi}_1^0})/2$ and the result is shown in the $(m_{\tilde{q}}, m_{\tilde{\chi}_1^0})$ plane. The best sensitivity is obtained by the (0+1)-lepton combination. Neutralino masses up to 370 GeV are excluded. For a neutralino mass of 100 GeV, squark masses are excluded below 790 GeV. Figure 22(b) shows the exclusion limits in the $(m_{\tilde{q}}, x)$ plane, where x is defined as $x = \Delta m(\tilde{\chi}_1^\pm, \tilde{\chi}_1^0)/\Delta m(\tilde{q}, \tilde{\chi}_1^0)$, in models in which the neutralino mass is fixed at 60 GeV. Squark masses are excluded up to 830 GeV for the most favourable x values. The 1L(S,H) search yields stronger limits than the 0L analysis for most of the parameter space of both types of models.

JHEP10(2015)054

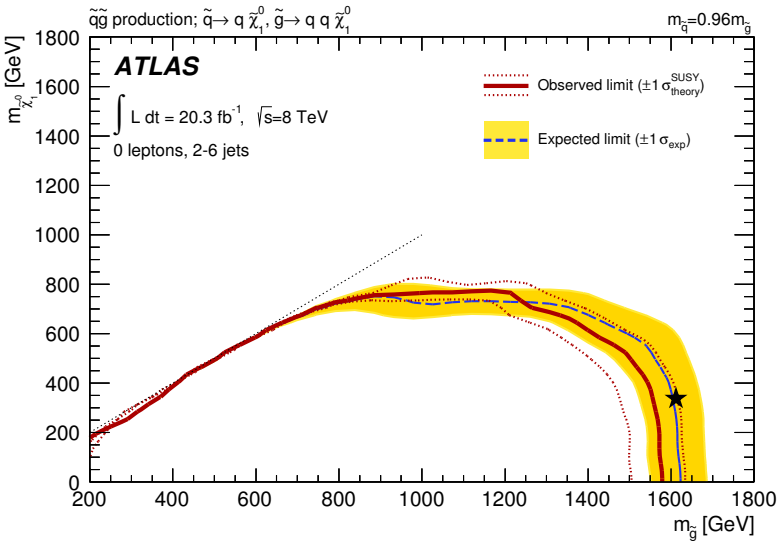

(a)

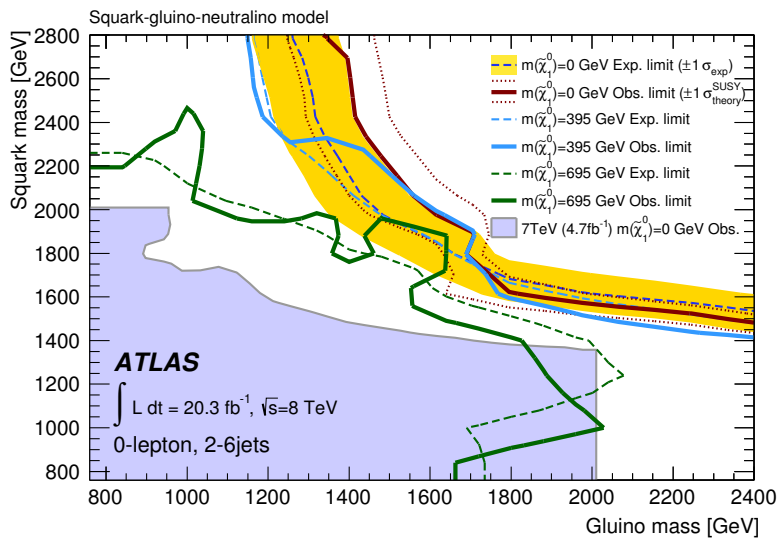

(b)

Figure 20. Exclusion limits on the production of a first- or second-generation squark and a gluino with direct decays of both particles, taken from the 0L search [20]. The solid red line and the dashed blue line show respectively the observed and expected 95% CL exclusion limits. The squark mass is fixed at 0.96 $m_{\tilde{g}}$ in (a) and allowed to vary freely in (b) with three assumptions on the neutralino mass of 0, 395 GeV or 695 GeV. The black star indicates a benchmark model as discussed in ref. [20]. Previous results for a massless neutralino from ATLAS at 7 TeV [156] are represented by the shaded (light blue) area. The 7 TeV results are valid for squark or gluino masses below 2000 GeV, the mass range studied for that analysis.

JHEP10(2015)054

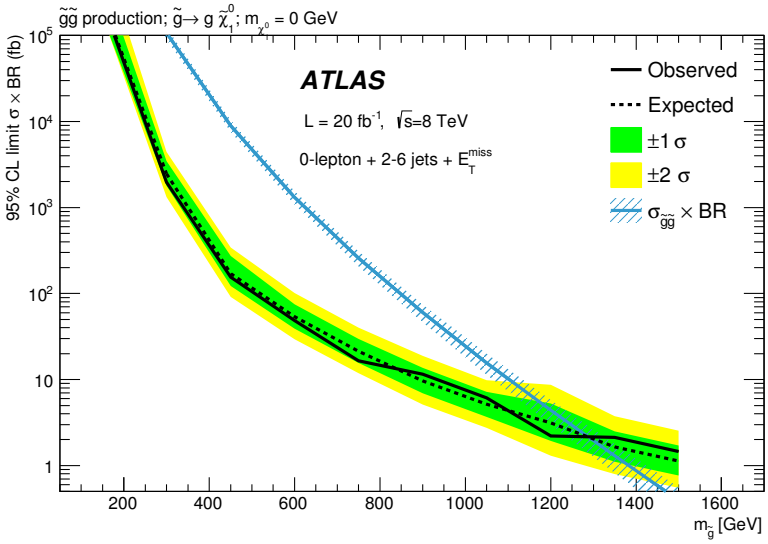

(a)

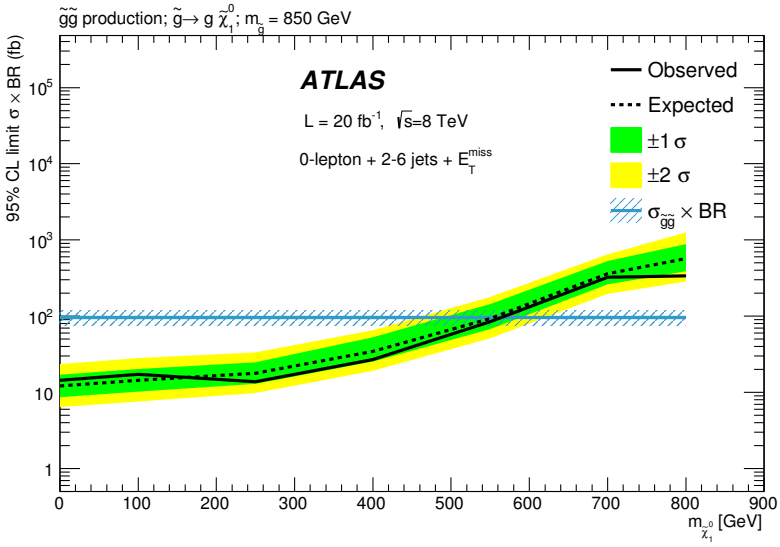

(b)

Figure 21. Limits at 95% CL on the production cross-section times branching ratio for gluino-pair production with direct decay of gluino to gluon and the lightest neutralino for (a) a massless neutralino as a function of the gluino mass, and (b) as a function of the $\tilde{\chi}_1^0$ mass for a fixed gluino mass of $m_{\tilde{g}} = 850\,\text{GeV}$. The solid black line shows the observed limit and the dashed line the expected limit. The solid medium dark (blue) line indicates the theoretical cross-section times branching ratio. The hatched (blue) bands around the theoretical σ·BR curves denote the scale and PDF uncertainties.

JHEP10(2015)054

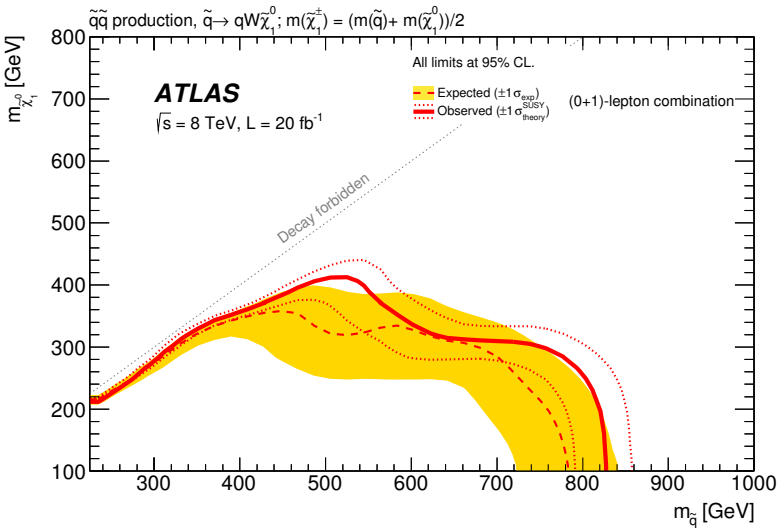

(a)

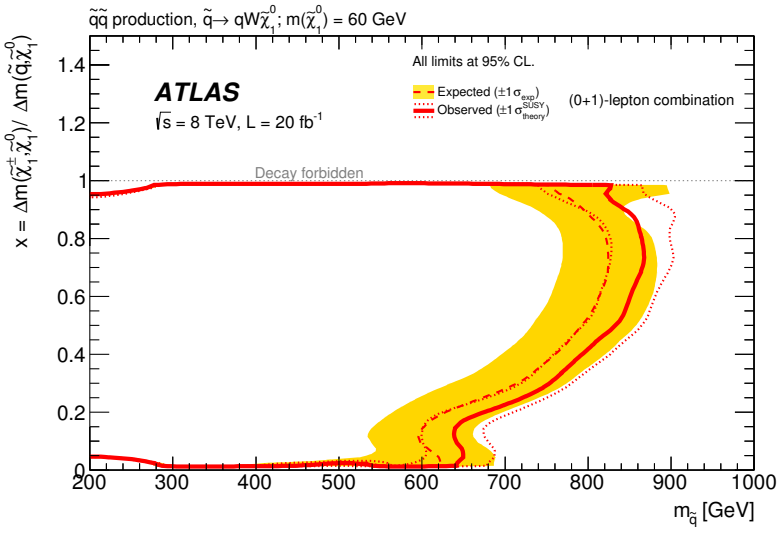

(b)

Figure 22. Exclusion limits for squark-pair production with a one-step decay via an intermediate chargino into $qW\tilde{\chi}_1^0$. Figure (a) shows the limits in the $(m_{\tilde{q}}, m_{\tilde{\chi}_1^0})$ plane for a chargino mass fixed at $m_{\tilde{\chi}_1^\pm} = (m_{\tilde{q}} + m_{\tilde{\chi}_1^0})/2$. Alternatively (b), the neutralino mass is fixed at 60 GeV and exclusion limits are given for $x = \Delta m(\tilde{\chi}_1^\pm, \tilde{\chi}_1^0)/\Delta m(\tilde{q}, \tilde{\chi}_1^0)$ as function of the squark mass. The solid red line and the dashed red line show respectively the combined observed and expected 95% CL exclusion limits.

JHEP10(2015)054

The results of the searches for gluino-pair production with a one-step decay via an intermediate chargino into $qqW\tilde{\chi}_1^0$ are shown in figure 23. Figure 23(a) shows the limit for a chargino mass fixed at $m_{\tilde{\chi}_1^\pm} = (m_{\tilde{g}} + m_{\tilde{\chi}_1^0})/2$, where the (0+1)-lepton combination provides the best sensitivity. For a neutralino mass of 100 GeV, gluino masses below 1270 GeV are excluded. Neutralino masses are excluded below 480 GeV for gluino masses up to 1200 GeV. Fixing the neutralino mass at 60 GeV (figure 23(b)), one obtains limits on the variable $x = \Delta m(\tilde{\chi}_1^\pm, \tilde{\chi}_1^0)/\Delta m(\tilde{g}, \tilde{\chi}_1^0)$. Nearly the whole range $0 < x < 1$ is excluded for gluino masses below 1100 GeV.

11.2.3 Two-step decays of squarks and gluinos

This section presents the limits in simplified models with two-step decays of squarks and gluinos described in section 2.2.3.

Exclusion limits for squark-pair production with a subsequent two-step squark decay via a chargino and neutralino to $qWZ\tilde{\chi}_1^0$ are shown in figure 24. Results are obtained with two searches, the 0L and the SS/3L searches. The 0L search is mainly sensitive in the low-mass region of 240 GeV $< m_{\tilde{q}} <$ 300 GeV, whereas the SS/3L search is most sensitive for squark masses between 450 and 650 GeV, where $\tilde{\chi}_1^0$ masses below 250 GeV are excluded.

Exclusion limits in a simplified model of gluino-pair production with a subsequent two-step gluino decay via a chargino and neutralino to $qqWZ\tilde{\chi}_1^0$ are shown in figure 25. The results are obtained with the (0+1)-lepton combination, MULTJ, and the SS/3L searches. The (0+1)-lepton combination provides the highest $\tilde{\chi}_1^0$ mass limits at low gluino masses. For the intermediate range around $m_{\tilde{g}} \approx 900$ GeV the SS/3L search is most sensitive, while for high gluino masses the best limits are obtained by the MULTJ analysis. For gluino masses below 500 GeV, $\tilde{\chi}_1^0$ masses are excluded up to the kinematic limit indicated by the diagonal line, and in the range 500 GeV $< m_{\tilde{g}} <$ 1000 GeV lower limits on $\tilde{\chi}_1^0$ masses are set around 400 GeV. For $m_{\tilde{\chi}_1^0} = 100$ GeV, gluino masses are excluded below 1150 GeV.

Another example of a simplified model with squark-pair production is considered in figure 26, where squarks decay through a two-step process via a chargino or neutralino and a slepton into final states with jets, leptons and missing transverse momentum. Figure 26 shows the exclusion limits in the $(m_{\tilde{q}}, m_{\tilde{\chi}_1^0})$ plane, for which the best results are obtained by the 2LRaz and the SS/3L searches. Masses for the lightest neutralino can be excluded nearly up to the kinematic limit (diagonal line) for squark masses below 630 GeV. For $\tilde{\chi}_1^0$ masses below 100 GeV, squark masses can be excluded below 820 GeV.

Similarly, a simplified model with gluino-pair production is considered in figure 27, where gluinos decay through a two-step process via a chargino or neutralino and sleptons into final states with jets, leptons and missing transverse momentum. Figure 27 shows the exclusion limits in the $(m_{\tilde{g}}, m_{\tilde{\chi}_1^0})$ plane. The combined 1L(S,H)+2LRaz searches based on the best expected CL_{S} value and the SS/3L search provide the best sensitivities for this model. Masses for the lightest neutralino can be excluded nearly up to the kinematic limit (diagonal line) for gluino masses below 600 GeV. For $\tilde{\chi}_1^0$ masses below 100 GeV, gluino masses can be excluded below 1320 GeV.

A further example of a simplified model of squark-pair production and decay through a two-step process is shown in figure 28, where squarks decay via charginos or neutralinos

JHEP10(2015)054

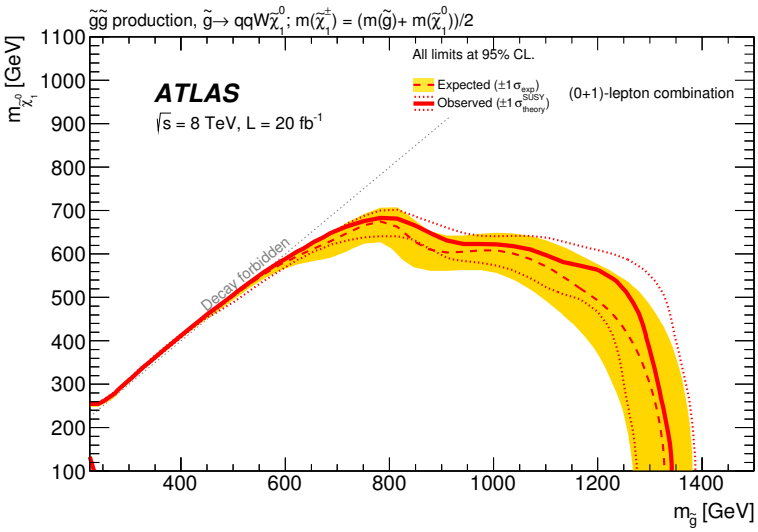

(a)

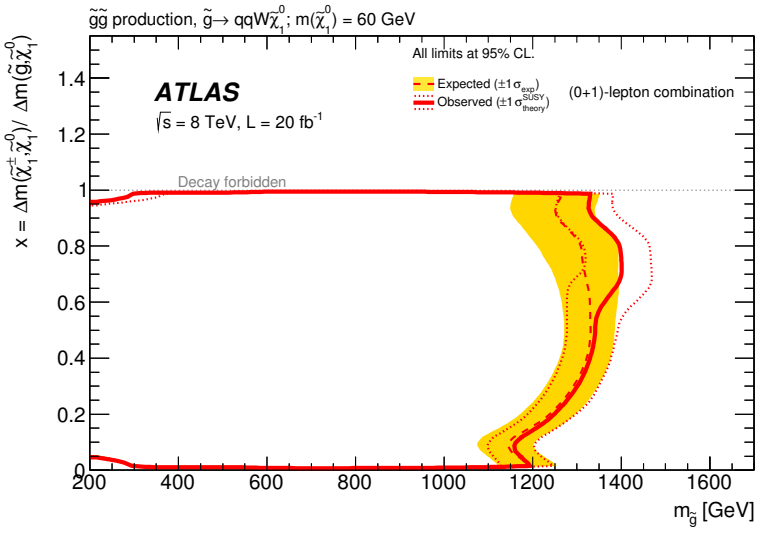

(b)

Figure 23. Exclusion limits for gluino-pair production with a one-step decay via an intermediate chargino into $qqW\tilde{\chi}_1^0$. Figure (a) shows the limits in the $(m_{\tilde{g}}, m_{\tilde{\chi}_1^0})$ plane for a chargino mass fixed at $m_{\tilde{\chi}_1^\pm} = (m_{\tilde{g}} + m_{\tilde{\chi}_1^0})/2$. Alternatively (b), the neutralino mass is fixed at 60 GeV and exclusion limits are given for $x = \Delta m(\tilde{\chi}_1^\pm, \tilde{\chi}_1^0)/\Delta m(\tilde{g}, \tilde{\chi}_1^0)$ as function of the gluino mass. The solid red line and the dashed red line show respectively the combined observed and expected 95% CL exclusion limits.

JHEP10(2015)054

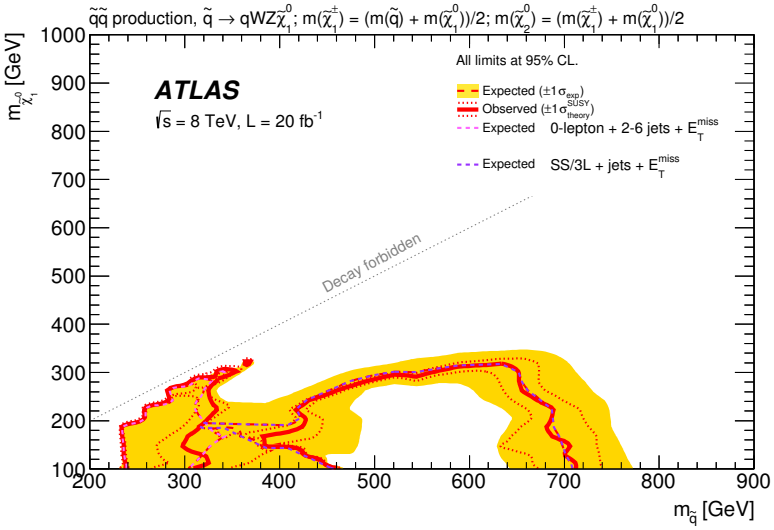

Figure 24. Exclusion limits in the $(m_{\tilde{q}}, m_{\tilde{\chi}_1^0})$ plane for a simplified model of first- and second-generation squark-pair production with two-step decay into $qqWWZZ\tilde{\chi}_1^0\tilde{\chi}_1^0$ and missing transverse momentum. The solid red line and the dashed red line show respectively the combined observed and expected 95% CL exclusion limits. Expected limits from the individual analyses which contribute to the final combined limits are also shown for comparison.

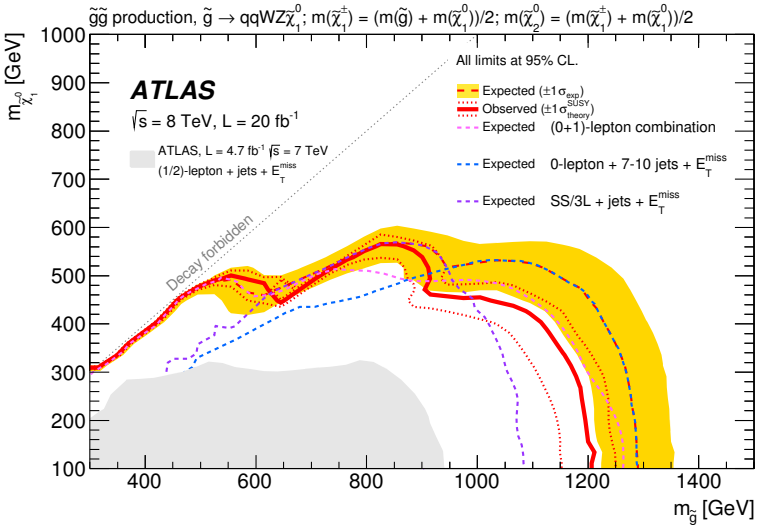

Figure 25. Exclusion limits in the $(m_{\tilde{g}}, m_{\tilde{\chi}_1^0})$ plane for a simplified model of gluino-pair production with two-step decay into $qqq'q'WWZZ\tilde{\chi}_1^0\tilde{\chi}_1^0$ and missing transverse momentum. The solid red line and the dashed red line show respectively the combined observed and expected 95% CL exclusion limits. Expected limits from the individual analyses which contribute to the final combined limits are also shown for comparison. A previous result from ATLAS [60] using 7 TeV proton-proton collisions is represented by the shaded (grey) area.

JHEP10(2015)054

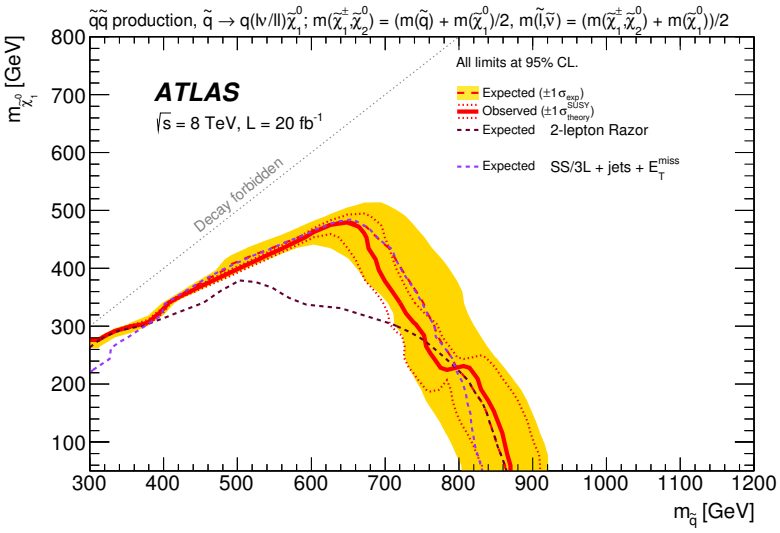

Figure 26. Exclusion limits in the $(m_{\tilde{q}}, m_{\tilde{\chi}_1^0})$ plane for a simplified model of squark-pair production with two-step decay into jets, leptons and missing transverse momentum via sleptons. The solid red line and the dashed red line show respectively the combined observed and expected 95% CL exclusion limits. Expected limits from the individual analyses which contribute to the final combined limits are also shown for comparison.

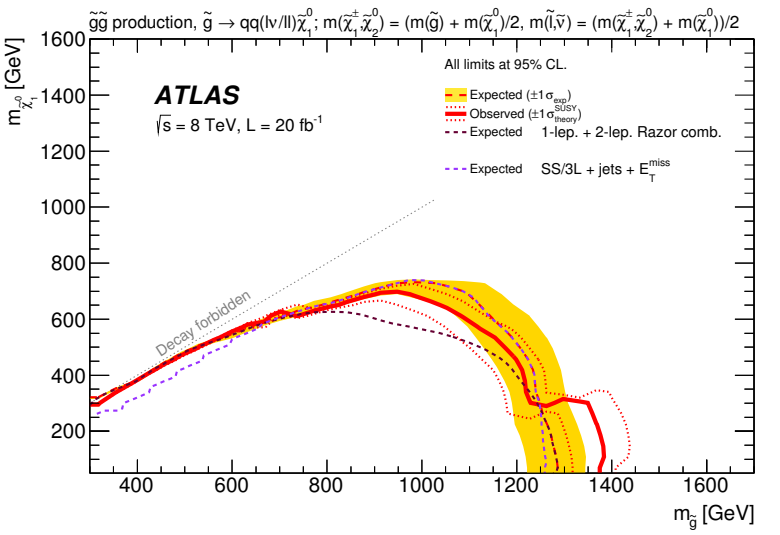

Figure 27. Exclusion limits in the $(m_{\tilde{g}}, m_{\tilde{\chi}_1^0})$ plane for a simplified model of gluino-pair production with two-step decay into jets, leptons and missing transverse momentum via sleptons. The solid red line and the dashed red line show respectively the combined observed and expected 95% CL exclusion limits. Expected limits from the individual analyses which contribute to the final combined limits are also shown for comparison.

JHEP10(2015)054

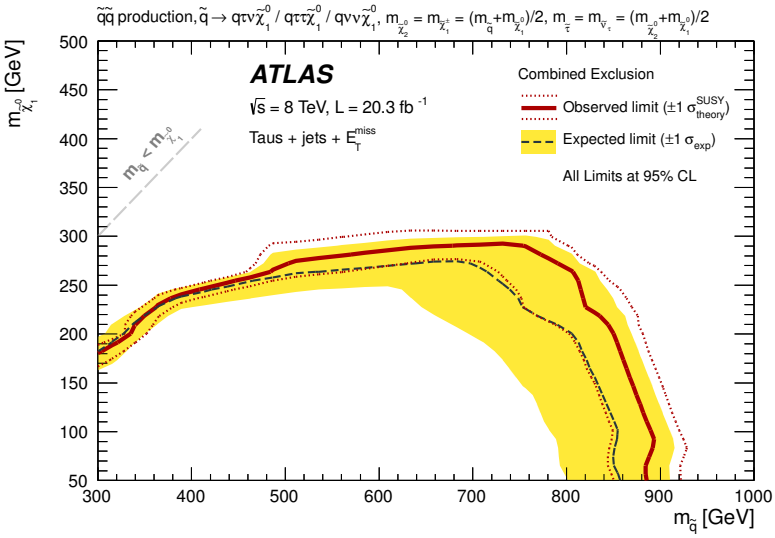

Figure 28. 95% CL exclusion limits in the $(m_{\tilde{q}}, m_{\tilde{\chi}_1^0})$ plane for a simplified model of squark-pair production with two-step decay via staus. The solid red line and the dashed black line show respectively the observed and expected 95% CL exclusion limits.

and staus. The exclusion limits obtained by the TAU search are indicated in the $(m_{\tilde{q}}, m_{\tilde{\chi}_1^0})$ plane. For light $\tilde{\chi}_1^0$ masses around 50 GeV, squark masses below 850 GeV are excluded; and for light squark masses of 300 GeV, neutralino masses below 170 GeV are excluded.

A simplified model of gluino-pair production and decay through a two-step process is shown in figure 29, where gluinos decay via charginos or neutralinos and staus. The exclusion limits obtained by the TAU search are indicated in the $(m_{\tilde{g}}, m_{\tilde{\chi}_1^0})$ plane. For light $\tilde{\chi}_1^0$ masses around 100 GeV, gluino masses below 1220 GeV are excluded; and for light gluino masses of 400 GeV, neutralino masses below 280 GeV are excluded.

11.2.4 Gluino decays via third-generation squarks

This section summarizes the exclusion limits placed in the various simplified models with gluino decays via third-generation squarks described in section 2.2.4.

The combined expected and observed exclusion limits for the gluino-off-shell-stop models are given in the $(m_{\tilde{g}}, m_{\tilde{\chi}_1^0})$ plane in figure 30, where a 100% branching ratio for the decay $\tilde{g} \to t\bar{t}^{(*)}\tilde{\chi}_1^0$ via an off-shell stop is assumed. In the regions where $m_{\tilde{g}} < 2m_t + m_{\tilde{\chi}_1^0}$, the three-body decays $(\tilde{g} \to t\bar{t}\tilde{\chi}_1^0)$ are replaced by the more complex multi-body decays proceeding via off-shell top quarks and W bosons, as discussed in appendix A. The best sensitivity for this model is provided by the 0/1L3B and the SS/3L searches. In the regions of parameter space where the mass difference between the gluino and the lightest neutralino is small, the most sensitive search is the SS/3L, and the sensitivity is dominated by the SS/3L_SR3b signal region. In the regions with a large mass splitting between the gluino and the neutralino, where hard jets and large $E_{\mathrm{T}}^{\mathrm{miss}}$ are expected, the sensitivity is dominated by the 0/1L3B_SR-0l-7j signal regions from the 0/1L3B search. For these models, gluino masses below about 1310 GeV are excluded for $m_{\tilde{\chi}_1^0} < 400$ GeV.

JHEP10(2015)054

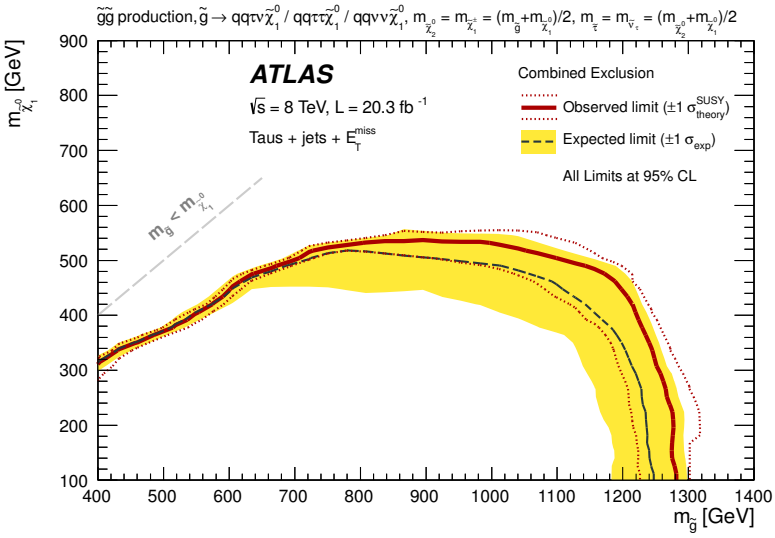

Figure 29. 95% CL exclusion limits in the $(m_{\tilde{g}}, m_{\tilde{\chi}_1^0})$ plane for a simplified model of gluino-pair production with two-step decay via staus. The solid red line and the dashed black line show respectively the observed and expected 95% CL exclusion limits.

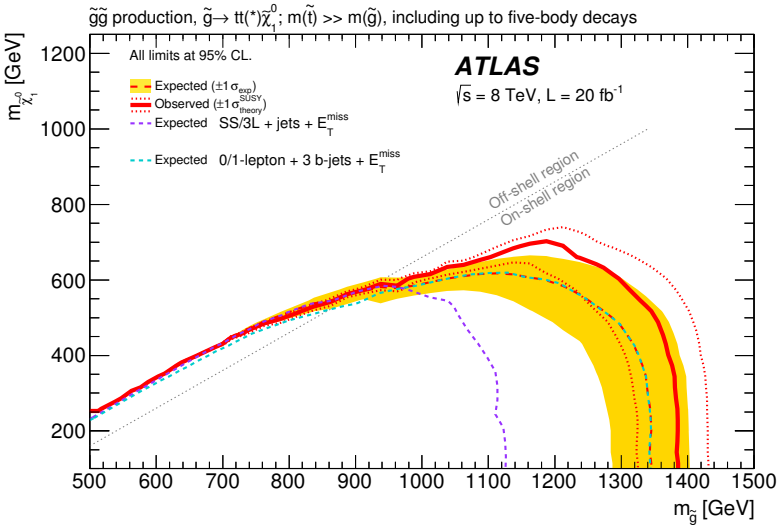

Figure 30. Exclusion limits in the $(m_{\tilde{g}}, m_{\tilde{\chi}_1^0})$ plane for the gluino-off-shell-stop simplified models in which the pair-produced gluinos decay via an off-shell stop, as $\tilde{g} \to t\bar{t}\tilde{\chi}_1^0$. In the region below the grey dashed line labelled "On-shell region", $m_{\tilde{g}} > 2m_t + m_{\tilde{\chi}_1^0}$ and thus gluinos decay to two real top quarks. In the "Off-shell region", $m_{\tilde{g}} < 2m_t + m_{\tilde{\chi}_1^0}$ and the decays of the gluino involve an off-shell top quark. Only four-body ($\tilde{g} \to tWb\tilde{\chi}_1^0$) and five-body ($\tilde{g} \to WbWb\tilde{\chi}_1^0$) decays are considered because for higher multiplicities the gluinos do not decay promptly. The solid red line and the dashed red line show respectively the combined observed and expected 95% CL exclusion limits. Expected limits from the individual analyses which contribute to the final combined limits are also shown for comparison.

JHEP10(2015)054

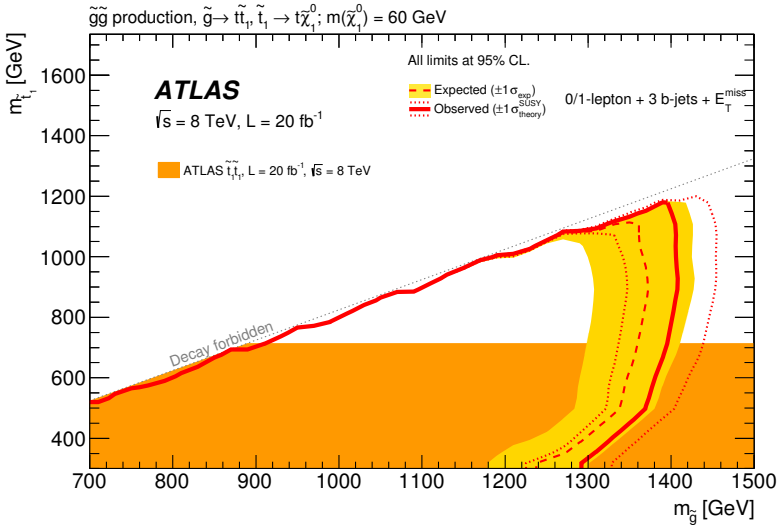

Figure 31. Exclusion limits in the $(m_{\tilde{g}}, m_{\tilde{t}_1})$ plane for the gluino-stop simplified models in which the top squarks are produced in the decay of pair-produced gluinos and decay via $\tilde{t}_1 \to t\tilde{\chi}_1^0$. The neutralino mass is set to 60 GeV. The solid red line and the dashed red line show respectively the combined observed and expected 95% CL exclusion limits. Also shown for reference is the limit from the ATLAS search for direct stop-pair production [18].

The exclusion limits for the gluino-stop simplified models are given in the $(m_{\tilde{g}}, m_{\tilde{t}_1})$ plane in figure 31. The $\tilde{t}_1$ is assumed to be the lightest squark while all other squarks are heavier than the gluino, and $m_{\tilde{g}} > m_{\tilde{t}_1} + m_t$ such that the branching ratio is 100% for $\tilde{g} \to \tilde{t}_1 t$ decays, and the top squark decays as $\tilde{t}_1 \to t\tilde{\chi}_1^0$. The 0/1L3B search provides the best sensitivity in these models, excluding gluino masses below 1220 GeV for stop masses up to 1000 GeV. Limits for the same class of simplified models, but assuming the $\tilde{t}_1 \to b\tilde{\chi}_1^\pm$ decay of the top squark, are also given in the $(m_{\tilde{g}}, m_{\tilde{t}_1})$ plane, and summarized in figure 32. The mass of the lightest neutralino in these models is set to 60 GeV, and the mass of the chargino is assumed to be twice the mass of the neutralino. The chargino decays into a neutralino and a virtual W boson. The strongest limits are provided by the 0/1L3B search. Compared to the models where the top squark decays via $\tilde{t}_1 \to t\tilde{\chi}_1^0$, presented in figure 31, the sensitivity in these models is lower for most of the parameter space where soft $E_{\mathrm{T}}^{\mathrm{miss}}$ and jets are expected from the chargino decay $\tilde{\chi}_1^\pm \to W^*\tilde{\chi}_1^0$. Gluino masses below 1180 GeV are excluded for stop masses up to 1000 GeV in these models.

Another possible decay of the top squark, $\tilde{t}_1 \to c\tilde{\chi}_1^0$, is considered within the same class of simplified models, with the mass difference between the $\tilde{t}_1$ and the lightest neutralino fixed to 20 GeV. The (0+1)-lepton combination provides the best sensitivity in these models. The 1L(S,H) search is complementary to the 0L search in that the expected limit for the single-lepton search is able to cover higher top squark masses at intermediate gluino masses (e.g. 80 GeV higher at $m_{\tilde{g}} = 900$ GeV). The resulting exclusion limit is presented in the $(m_{\tilde{g}}, m_{\tilde{t}_1})$ plane in figure 33, and reaches gluino masses up to 1260 GeV.

JHEP10(2015)054

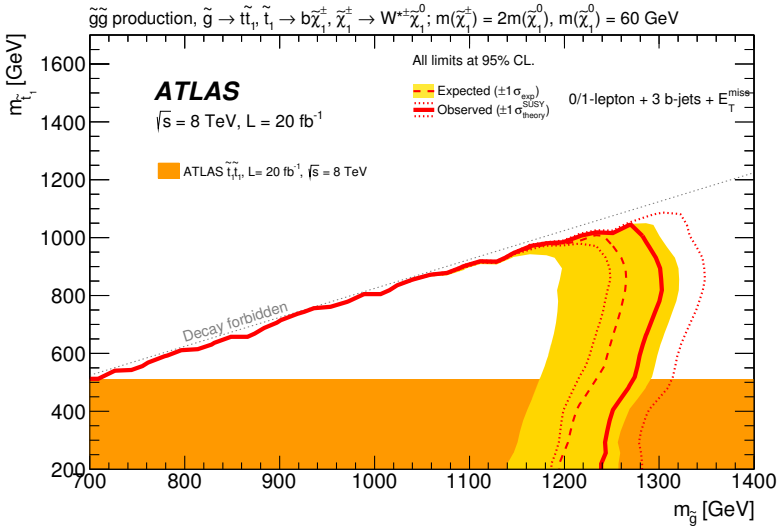

Figure 32. Exclusion limits in the $(m_{\tilde{g}}, m_{\tilde{t}_1})$ plane for the gluino-stop simplified models in which the top squarks are produced in the decay of pair-produced gluinos and decay via $\tilde{t}_1 \to b\tilde{\chi}_1^{\pm}$. The neutralino mass is set to 60 GeV and the mass of the chargino is assumed to be twice the mass of the neutralino. The solid red line and the dashed red line show respectively the combined observed and expected 95% CL exclusion limits. Also shown for reference is the limit from the ATLAS search for direct stop-pair production [18].

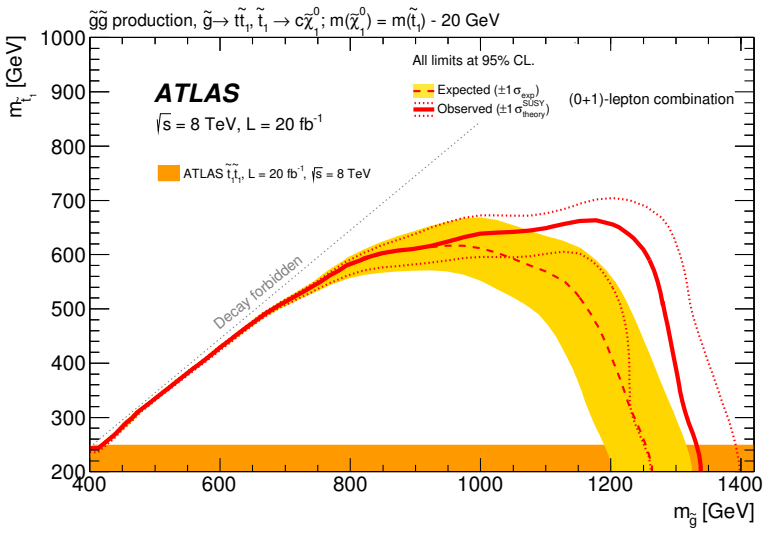

Figure 33. Exclusion limits in the $(m_{\tilde{g}}, m_{\tilde{t}_1})$ plane for the gluino-stop simplified models in which the top squarks are produced in the decay of pair-produced gluinos and decay via $\tilde{t}_1 \to c + \tilde{\chi}_1^0$. The mass difference between the $\tilde{t}_1$ and the lightest neutralino is fixed to 20 GeV. The solid red line and the dashed red line show respectively the combined observed and expected 95% CL exclusion limits. Also shown for reference is the limit from the ATLAS search for direct stop-pair production [18].

JHEP10(2015)054

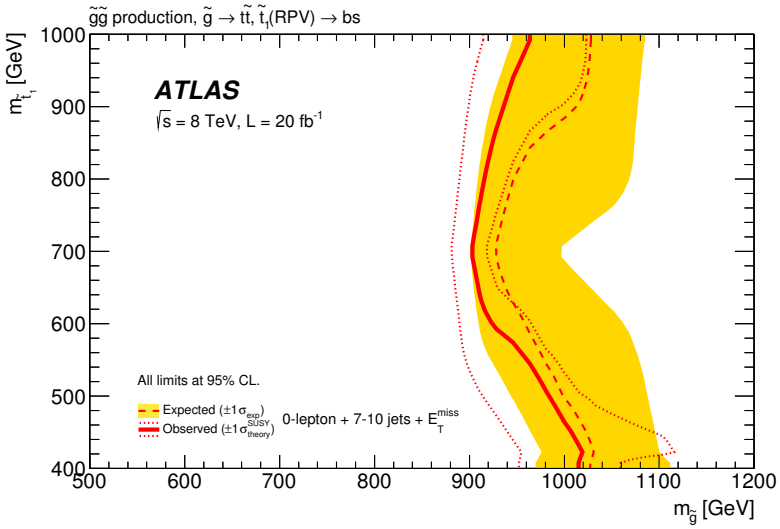

Figure 34. Exclusion limits in the $(m_{\tilde{g}}, m_{\tilde{t}_1})$ plane for the gluino-stop simplified models in which the top squarks are produced in the decay of pair-produced gluinos and decay via R-parity and baryon number violation $\tilde{t}_1 \to sb$. The solid red line and the dashed red line show respectively the combined observed and expected 95% CL exclusion limits. Expected limits from the individual analyses which contribute to the final combined limits are also shown for comparison.

A simplified model is also considered, in which the top squark decay, $\tilde{t}_1 \to sb$, involves R-parity and baryon number violation. The result is presented in the $(m_{\tilde{g}}, m_{\tilde{t}_1})$ plane in figure 34, where the best limit is obtained by the MULTJ search. Gluino masses below 880 GeV are excluded for top squark masses ranging from 400 GeV to 1000 GeV.

The sensitivity in the gluino-sbottom simplified models in which the branching ratio for $\tilde{g} \to \tilde{b}_1 b$ decays is 100% and the bottom squarks are assumed to decay exclusively via $\tilde{b}_1 \to b\tilde{\chi}_1^0$ is provided only by the 0/1L3B search [27] and the result is presented for completeness in figure 35. The search excludes gluino masses below 1200 GeV for sbottom masses up to about 1100 GeV.

The limits for the gluino-off-shell-sbottom simplified models, which assume 100% branching ratio for the gluino three-body decay $\tilde{g} \to b\bar{b}\tilde{\chi}_1^0$ via an off-shell sbottom, are given in the $(m_{\tilde{g}}, m_{\tilde{\chi}_1^0})$ plane in figure 36. The best sensitivities are provided by two searches, the 0/1L3B and the 0L search. The former is the most sensitive search in regions of the parameter space with a large mass splitting between the gluino and the lightest neutralino, and the latter in regions with a small mass splitting where softer jets and smaller $E_{\mathrm{T}}^{\mathrm{miss}}$ are expected in the final state. In these models, gluino masses below 1250 GeV are excluded for $m_{\tilde{\chi}_1^0} < 400$ GeV while neutralino masses below 600 GeV are excluded in the gluino mass range between 700 and 1200 GeV.

The sensitivity in the gluino-off-shell-stop/sbottom simplified models in which gluinos decay via virtual stops or sbottoms is provided only by the 0/1L3B search [27]. Here the mass difference between the particles is set such that the gluino decays result in an effectively three-body final state $(bt\tilde{\chi}_1^0)$. The exclusion limit is presented in figure 37 for completeness. For neutralino masses of 500 GeV, gluino masses are excluded between 750 and 1250 GeV.

JHEP10(2015)054

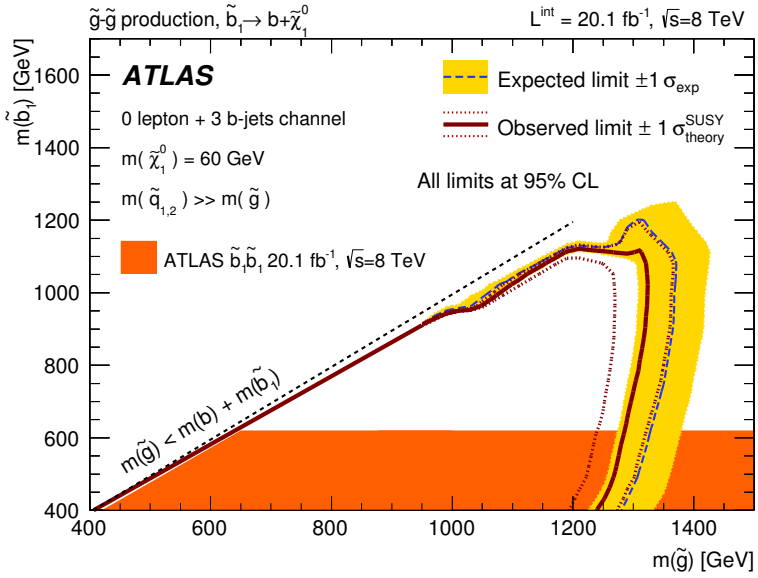

Figure 35. Exclusion limits in the $(m_{\tilde{g}}, m_{\tilde{b}_1})$ plane for the gluino-sbottom simplified models, taken from ref. [27]. Also shown for reference is the limit from the ATLAS search for direct sbottom-pair production [18].

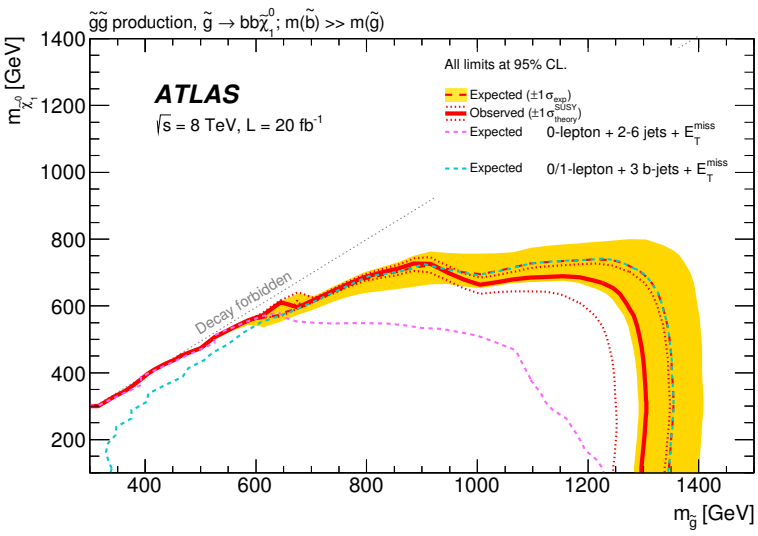

Figure 36. Exclusion limits in the $(m_{\tilde{g}}, m_{\tilde{\chi}_1^0})$ plane for the gluino-off-shell-sbottom simplified models in which the pair-produced gluinos decay via an off-shell sbottom as $\tilde{g} \to b\bar{b}\tilde{\chi}_1^0$. The solid red line and the dashed red line show respectively the combined observed and expected 95% CL exclusion limits. Expected limits from the individual analyses which contribute to the final combined limits are also shown for comparison.

JHEP10(2015)054

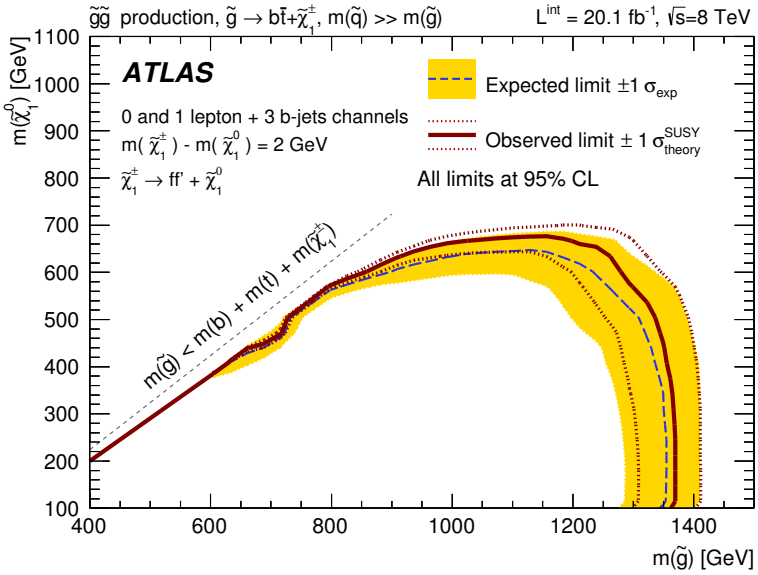

Figure 37. Exclusion limits in the $(m_{\tilde{g}}, m_{\tilde{\chi}_1^0})$ plane for the gluino-off-shell-stop/sbottom simplified models, taken from ref. [27].

12 Conclusions

A search for squarks and gluinos in inclusive final states containing high-p_{T} jets and missing transverse momentum, with or without leptons or b-jets, is presented. The data were recorded in 2012 by the ATLAS experiment with $\sqrt{s} = 8$ TeV proton-proton collisions at the Large Hadron Collider, with a total integrated luminosity up to 20.3 fb^{-1}. Earlier ATLAS searches have been extended and combined with new search techniques, thus improving the sensitivity for supersymmetric models. Good agreement is found with the predictions from SM processes. The data are therefore used to set exclusion limits for a variety of simplified and phenomenological SUSY models.

Limits in simplified models with gluinos and squarks of the first and second generations are derived for direct and one- or two-step decays of squarks and gluinos, and gluino decays via third-generation squarks. In all the considered simplified models that assume R-parity conservation, the limit on the gluino mass exceeds 1150 GeV at 95% CL, for an LSP mass smaller than 100 GeV. Additional limits are set in a phenomenological MSSM model used in the search for left-handed squarks, a minimal Supergravity/Constrained MSSM model, R-parity-violation scenarios, a minimal gauge-mediated supersymmetry breaking model, a natural gauge mediation model, a non-universal Higgs mass model with gaugino mediation and a minimal model of universal extra dimensions. These limits are either new or extend the region of parameter space excluded by previous searches with the ATLAS detector.

Acknowledgments

We thank CERN for the very successful operation of the LHC, as well as the support staff from our institutions without whom ATLAS could not be operated efficiently.

JHEP10(2015)054

We acknowledge the support of ANPCyT, Argentina; YerPhI, Armenia; ARC, Australia; BMWFW and FWF, Austria; ANAS, Azerbaijan; SSTC, Belarus; CNPq and FAPESP, Brazil; NSERC, NRC and CFI, Canada; CERN; CONICYT, Chile; CAS, MOST and NSFC, China; COLCIENCIAS, Colombia; MSMT CR, MPO CR and VSC CR, Czech Republic; DNRF, DNSRC and Lundbeck Foundation, Denmark; EPLANET, ERC and NSRF, European Union; IN2P3-CNRS, CEA-DSM/IRFU, France; GNSF, Georgia; BMBF, DFG, HGF, MPG and AvH Foundation, Germany; GSRT and NSRF, Greece; RGC, Hong Kong SAR, China; ISF, MINERVA, GIF, I-CORE and Benoziyo Center, Israel; INFN, Italy; MEXT and JSPS, Japan; CNRST, Morocco; FOM and NWO, Netherlands; BRF and RCN, Norway; MNiSW and NCN, Poland; GRICES and FCT, Portugal; MNE/IFA, Romania; MES of Russia and NRC KI, Russian Federation; JINR; MSTD, Serbia; MSSR, Slovakia; ARRS and MIZŠ, Slovenia; DST/NRF, South Africa; MINECO, Spain; SRC and Wallenberg Foundation, Sweden; SER, SNSF and Cantons of Bern and Geneva, Switzerland; NSC, Taiwan; TAEK, Turkey; STFC, the Royal Society and Leverhulme Trust, United Kingdom; DOE and NSF, United States of America.

The crucial computing support from all WLCG partners is acknowledged gratefully, in particular from CERN and the ATLAS Tier-1 facilities at TRIUMF (Canada), NDGF (Denmark, Norway, Sweden), CC-IN2P3 (France), KIT/GridKA (Germany), INFN-CNAF (Italy), NL-T1 (Netherlands), PIC (Spain), ASGC (Taiwan), RAL (U.K.) and BNL (U.S.A.) and in the Tier-2 facilities worldwide.

A Extension of the $\tilde{g} \to t\bar{t}\tilde{\chi}_1^0$ simplified model to include decays with off-shell top quarks

In this appendix, further details are provided about the extension of the gluino-mediated off-shell stop model $\tilde{g} \to t\bar{t}\tilde{\chi}_1^0$ to the region $m_t + m_W + m_b \leq m_{\tilde{g}} - m_{\tilde{\chi}_1^0} \leq 2m_t$, where three-body decays are replaced by more complex multi-body decays proceeding via off-shell top quarks and W bosons. This region is delimited by the kinematic boundaries corresponding to three- and four-body gluino decays. In principle, the extension could have been performed up to mass gaps as small as $m_{\tilde{g}} - m_{\tilde{\chi}_1^0} \geq 2m_b$, but it was found that for a 100% branching ratio hypothesis for the $\tilde{g} \to t\bar{t}\tilde{\chi}_1^0$ mode, mass gaps smaller than the four-body kinematic bound quickly lead to large gluino lifetimes, resulting in displaced gluino decays. This is verified even in the scenario leading to the smallest gluino lifetime ($m_{\tilde{t}_1} = m_{\tilde{g}}$, $\tilde{t}_1 = \tilde{t}_R$). Since the results of the various searches reported in this paper are all based on prompt objects, the expected sensitivity to these scenarios with small mass gaps is very small, and they are addressed by dedicated searches [157]. Therefore, the probed parameter space is limited to $m_{\tilde{g}} - m_{\tilde{\chi}_1^0} \geq m_t + m_W + m_b$.

Despite the restriction of the model parameter space to regions where four-body gluino decays $\tilde{g} \to tWb\tilde{\chi}_1^0$ are always kinematically allowed, more complex decays (mainly five-body) can occur concurrently with a significant branching ratio, and even become dominant when the mass gap approaches its lower bound. Consideration of these alternative decay modes also sometimes leads to large differences in kinematic distributions of the decay products. For example, the b-quark in the decay $\tilde{g} \to tWb\tilde{\chi}_1^0$ becomes too soft for ex-

JHEP10(2015)054

perimental detection when $m_{\tilde{g}} \approx m_t + m_W + m_b + m_{\tilde{\chi}_1^0}$, whereas it can still get sizeable momentum in the alternative decay $\tilde{g} \to WWbb\tilde{\chi}_1^0$. Since the most sensitive searches for this model rely on selections with at least three b-jets, one can see that the acceptance of these selections would vanish at the kinematic bound if considering only four-body decays, although it is not the case thanks to the alternative decay modes. To summarize, quantitative studies showed that it is important to consider at least the five-body decay as well in this region of the parameter space.

Finally, signal events were generated following a configuration defined and validated by comparing generator predictions for several observables in a region at low neutralino mass where only three-body decays contribute. The reference was provided by Herwig++ (the generator used for the $m_{\tilde{g}} - m_{\tilde{\chi}_1^0} > 2m_t$ region of this scenario), characterized notably by the use of a matrix element amplitude for the gluino decay, and the preservation of spin correlation between the decay products. It was first observed that narrow-width approximations for the gluino decay compared poorly to the reference, hence imposing the need for decay amplitudes computed from matrix elements for the four- and five-body decays, and as a consequence the choice of the Madgraph generator. However, the computing requirements to obtain the amplitude associated with such a $2 \to 10\,(+1)$ hard process (with an extra parton) are too demanding. An approximation is used instead, consisting in the separate generation of pair-produced gluinos, and gluino decays into fermions $\tilde{g} \to f\bar{f}'f''\bar{f}'''bb\tilde{\chi}_1^0$. The two stages are then combined by boosting the gluino decay products according to the gluino's directions and momenta defined by the hard process, while preserving the gluino spin orientations. The use of the inclusive seven-body gluino decay, instead of the minimally required five-body decay, came at no additional computing cost and allowed, in particular, proper propagation of the various spin correlations along the gluino decay chain. This setup provided agreement with the reference at the level of 5%, for the shapes of various generator-level kinematic distributions (a few of which are presented in figure 38), as well as for fiducial acceptances of typical event selections used as signal regions in the relevant SUSY searches.

B Summary of selection criteria

Tables 14–22 summarize the selection criteria for signal regions listed in table 5 which have been defined in previous ATLAS publications [20–27].

C 0-lepton Razor analysis details

Many kinematical variables have been used to search for SUSY at hadron colliders, typically making use of the expected heavy mass scale of the SUSY particles produced, and the missing transverse momentum originating from the LSP. The analysis described here searches for squarks in final states with high-p_{T} jets, missing transverse momentum and no electrons or muons, using the Razor variable set [19]. These variables provide longitudinal and transverse information about each event, contribute to the rejection of the background from the multi-jet processes that dominate hadronic collisions, and can be used as an approximation of the mass scale of the produced particles.

JHEP10(2015)054

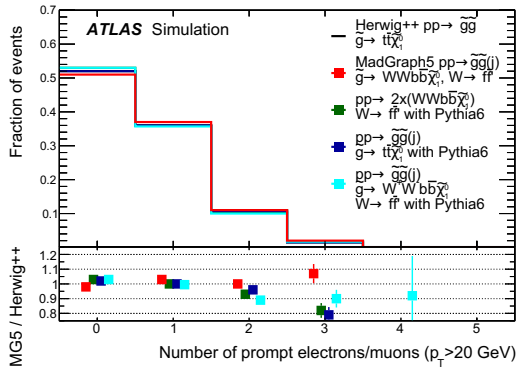

(a) Distribution of the number of prompt leptons (electrons and muons), $p_{\mathrm{T}} > 20\,\mathrm{GeV}$, $|\eta| < 2.5$.

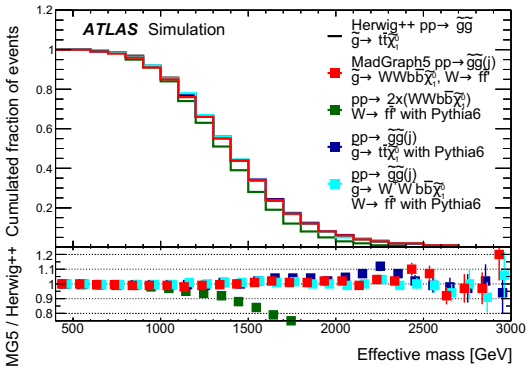

(b) Cumulative distribution of the effective mass built from selected leptons, jets and non-interacting particles.

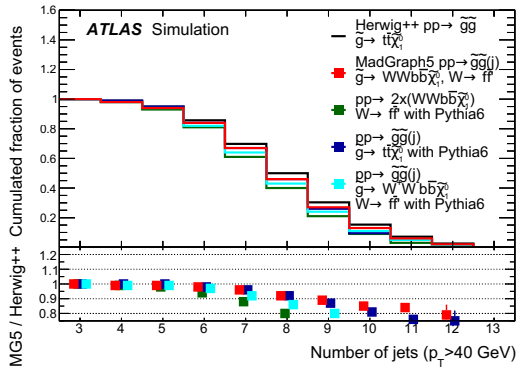

(c) Cumulative distribution of the number of jets (anti-k_t algorithm, $R = 0.4$), $p_{\mathrm{T}} > 40\,\mathrm{GeV}$, $|\eta| < 2.8$.

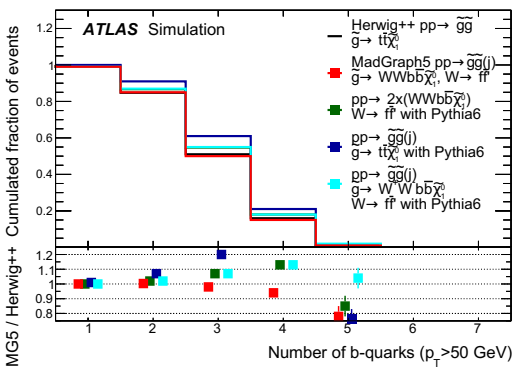

(d) Cumulative distribution of the number of b-quarks, $p_{\mathrm{T}} > 50\,\mathrm{GeV}$, $|\eta| < 2.5$.

Figure 38. Validation of the MADGRAPH5+PYTHIA6 setup used to generate five-body gluino decays $\tilde{g} \to W^+W^-b\bar{b}\tilde{\chi}_1^0$: kinematic distributions obtained with the nominal configuration (red markers) are compared to the reference HERWIG++ sample (black), for a signal scenario featuring only three-body gluino decays $\tilde{g} \to t\bar{t}\tilde{\chi}_1^0$ ($m_{\tilde{g}} = 1\,\mathrm{TeV}$, $m_{\tilde{\chi}_1^0} = 100\,\mathrm{GeV}$). A few alternative (and simpler) generator configurations are also shown (other coloured markers), but they fail to reach a satisfactory level of agreement with the reference, for the typical signal region requirements (cf. SR3b in table 20). The distributions are built from the outgoing particles provided by the generators.

The basic analysis approach relies on the definition of statistically independent regions in the Razor variable phase space, R and M'_R, explained in details in the remainder of this section, that are rich in SUSY-like events, and other regions, each dominated by one SM background component. Following the strategy explained in section 6, the Monte Carlo expectations are normalized to the data in each background control region, and those normalization factors are then transferred to the MC prediction in the SUSY signal regions. The baseline object selection and event cleaning, as well as the choice of MC generators for SM background processes and the approach for calculating systematic uncertainties exactly follow those of the 0-lepton + 2–6 jets + $E_{\mathrm{T}}^{\mathrm{miss}}$ (0L) search [20], and are not discussed here.

JHEP10(2015)054

Requirement	Signal region		
	M1	**M2**	**M3**
Jets preselection	At most three jets with $p_{\mathrm{T}} > 30$ GeV and $\lvert\eta\rvert < 2.8$		
$p_{\mathrm{T}}^{\mathrm{jet}_1}$ [GeV] >	280	340	450
$E_{\mathrm{T}}^{\mathrm{miss}}$ [GeV] >	220	340	450
$\Delta\phi(\mathrm{jet}, \boldsymbol{E}_{\mathrm{T}}^{\mathrm{miss}})$ >	0.4		

Table 14. Selection criteria used to define the three signal regions in the search with at least one high-p_{T} jet and large missing transverse momentum (Monojet) [21]. The azimuthal separation $\Delta\phi(\mathrm{jet}, \boldsymbol{E}_{\mathrm{T}}^{\mathrm{miss}})$ is calculated between the missing transverse momentum direction and each of the selected jets.

C.1 The Razor variables

The Razor variable set is designed to group together visible final-state particles associated with heavy produced sparticles, and in doing so contains information about the mass scale of the directly produced sparticles. The final-state jets are grouped into two hemispheres called "mega-jets", where all visible objects from one side of the di-sparticle decay are collected together to create a single four-vector, representing the decay products of a single sparticle. The mega-jet construction involves iterating over all possible combinations of the four-vectors of the visible reconstructed objects, with the favoured combination being that which minimizes the sum of the squared masses of the mega-jet four-vectors. Using this mega-jet configuration, with some simplifying assumptions (e.g. symmetric sparticle production), the rest frame of the sparticles (the so-called "R-frame" described in ref. [19]) can be reconstructed, and a characteristic mass M'_R can be defined in this frame:

$$M'_R = \sqrt{(j_{1,E} + j_{2,E})^2 - (j_{1,\mathrm{L}} + j_{2,\mathrm{L}})^2}, \tag{C.1}$$

where $j_{i,\mathrm{L}}$ denotes the longitudinal momentum, and $j_{i,E}$ the energy in the R-frame, of the mega-jet i.

To help reduce the SM backgrounds, a second variable, M_{T}^R, is defined that includes information about the transverse quantities, including the total missing transverse momentum and its angular distance to the two mega-jets. In the di-sparticle decay there are two mega-jets, each with associated $E_{\mathrm{T}}^{\mathrm{miss}}$ from the escaping LSPs. Assigning half of the missing transverse momentum per event to each of the LSPs, M_{T}^R is defined as

$$M_{\mathrm{T}}^R = \sqrt{\frac{E_{\mathrm{T}}^{\mathrm{miss}}(j_{1,\mathrm{T}} + j_{2,\mathrm{T}}) - \boldsymbol{E}_{\mathrm{T}}^{\mathrm{miss}} \cdot (\boldsymbol{j}_{1,\mathrm{T}} + \boldsymbol{j}_{2,\mathrm{T}})}{2}}, \tag{C.2}$$

where $\boldsymbol{j}_{i,\mathrm{T}}$ denotes the transverse momentum of the mega-jet i. The variable M_{T}^R is designed such that for small values of $E_{\mathrm{T}}^{\mathrm{miss}}$, M_{T}^R is also small. If the multi-jet event were perfectly re-

JHEP10(2015)054

Requirement	Signal region					
	2jl	**2jm**	**2jt**	**2jW**	**3j**	**4jW**
$E_{\mathrm{T}}^{\mathrm{miss}}$ [GeV] >	160					
$p_{\mathrm{T}}^{\mathrm{jet}_1}$ [GeV] >	130					
$p_{\mathrm{T}}^{\mathrm{jet}_2}$ [GeV] >	60					
$p_{\mathrm{T}}^{\mathrm{jet}_3}$ [GeV] >	–				60	40
$p_{\mathrm{T}}^{\mathrm{jet}_4}$ [GeV] >	–					40
$\Delta\phi(\mathrm{jet}_{1,2,(3)}, \boldsymbol{E}_{\mathrm{T}}^{\mathrm{miss}})_{\mathrm{min}}$ >	0.4					
$\Delta\phi(\mathrm{jet}_{i>3}, \boldsymbol{E}_{\mathrm{T}}^{\mathrm{miss}})_{\mathrm{min}}$ >	–					0.2
W candidates	–			$2(W \to j)$	–	$(W \to j) + (W \to jj)$
$E_{\mathrm{T}}^{\mathrm{miss}}/\sqrt{H_{\mathrm{T}}}$ [GeV$^{1/2}$] >	8	15		–		
$E_{\mathrm{T}}^{\mathrm{miss}}/m_{\mathrm{eff}}^{N_{\mathrm{j}}}$ >	–			0.25	0.3	0.35
$m_{\mathrm{eff}}^{\mathrm{incl}}$ [GeV] >	800	1200	1600	1800	2200	1100

Requirement	Signal region								
	4jl-	**4jl**	**4jm**	**4jt**	**5j**	**6jl**	**6jm**	**6jt**	**6jt+**
$E_{\mathrm{T}}^{\mathrm{miss}}$ [GeV] >	160								
$p_{\mathrm{T}}^{\mathrm{jet}_1}$ [GeV] >	130								
$p_{\mathrm{T}}^{\mathrm{jet}_2}$ [GeV] >	60								
$p_{\mathrm{T}}^{\mathrm{jet}_3}$ [GeV] >	60								
$p_{\mathrm{T}}^{\mathrm{jet}_4}$ [GeV] >	60								
$p_{\mathrm{T}}^{\mathrm{jet}_5}$ [GeV] >	–				60				
$p_{\mathrm{T}}^{\mathrm{jet}_6}$ [GeV] >	–					60			
$\Delta\phi(\mathrm{jet}_{1,2,(3)}, \boldsymbol{E}_{\mathrm{T}}^{\mathrm{miss}})_{\mathrm{min}}$ >	0.4								
$\Delta\phi(\mathrm{jet}_{i>3}, \boldsymbol{E}_{\mathrm{T}}^{\mathrm{miss}})_{\mathrm{min}}$ >	0.2								
$E_{\mathrm{T}}^{\mathrm{miss}}/\sqrt{H_{\mathrm{T}}}$ [GeV$^{1/2}$] >	10		–						
$E_{\mathrm{T}}^{\mathrm{miss}}/m_{\mathrm{eff}}^{N_{\mathrm{j}}}$ >	–		0.4	0.25	0.2			0.25	0.15
$m_{\mathrm{eff}}^{\mathrm{incl}}$ [GeV] >	700	1000	1300	2200	1200	900	1200	1500	1700

Table 15. Selection criteria used to define the fifteen signal regions in the search with at least two to at least six jets, significant $E_{\mathrm{T}}^{\mathrm{miss}}$ and the absence of isolated electrons or muons (0-lepton + 2–6 jets + $E_{\mathrm{T}}^{\mathrm{miss}}$) [20]. Each signal region is labelled with the inclusive jet multiplicity considered ('2j', '3j', etc.) together with the degree of background rejection. The latter is denoted by labels 'l-' ('very loose'), 'l' ('loose'), 'm' ('medium'), 't' ('tight') and 't+' ('very tight'). The $E_{\mathrm{T}}^{\mathrm{miss}}/m_{\mathrm{eff}}^{N_{\mathrm{j}}}$ requirement in any N_{j}-jet channel uses a value of m_{eff} constructed from only the leading N_{j} jets ($m_{\mathrm{eff}}^{N_{\mathrm{j}}}$). The final $m_{\mathrm{eff}}^{\mathrm{incl}}$ selection, which is used to define the signal regions, includes all jets with $p_{\mathrm{T}} > 40\,\mathrm{GeV}$. The variable H_{T} is defined as the scalar sum of the transverse momenta of all jets with $p_{\mathrm{T}} > 40\,\mathrm{GeV}$. The azimuthal separation $\Delta\phi(\mathrm{jet}, \boldsymbol{E}_{\mathrm{T}}^{\mathrm{miss}})_{\mathrm{min}}$ is defined to be the smallest of the azimuthal separations between $\boldsymbol{E}_{\mathrm{T}}^{\mathrm{miss}}$ and the reconstructed jets. In SR 2jW and SR 4jW a requirement $60\,\mathrm{GeV} < m(W_{\mathrm{cand}}) < 100\,\mathrm{GeV}$ is placed on the masses of candidate resolved or unresolved hadronically decaying W bosons. Candidate W bosons are reconstructed from single high-mass jets (unresolved candidates; $W \to j$ in the table) or from pairs of jets (resolved candidates; $W \to jj$ in the table.

JHEP10(2015)054

Requirement	Signal regions in multi-jet + flavour stream												
	8j50			**9j50**			**10j50**	**7j80**			**8j80**		
$\|\eta\|^{\text{jet}} <$	2.0												
$p_{\text{T}}^{\text{jet}}$ [GeV] $>$	50							80					
N_{jet}	$= 8$			$= 9$			≥ 10	$= 7$			≥ 8		
$N_{b-\text{jet}}$ ($p_{\text{T}} > 40\,\text{GeV}, \|\eta\| < 2.5$)	0	1	≥ 2	0	1	≥ 2	—	0	1	≥ 2	0	1	≥ 2
$E_{\text{T}}^{\text{miss}}/\sqrt{H_{\text{T}}}$ [GeV$^{1/2}$] $>$	4												

Requirement	Signal regions in multi-jet + M_J^{Σ} stream		
	8j50	**9j50**	**10j50**
$\|\eta\|^{\text{jet}} <$	2.8		
$p_{\text{T}}^{\text{jet}}$ [GeV] $>$	50		
N_{jet}	≥ 8	≥ 9	≥ 10
M_J^{Σ} [GeV]	> 340 and > 420 for each case		
$E_{\text{T}}^{\text{miss}}/\sqrt{H_{\text{T}}}$ [GeV$^{1/2}$] $>$	4		

Table 16. Selection criteria used to define the nineteen signal regions in the search with at least seven to at least ten jets, significant $E_{\text{T}}^{\text{miss}}$ and the absence of isolated electrons or muons (0-lepton + 7–10 jets + $E_{\text{T}}^{\text{miss}}$) [22]. The four-momenta of the R=0.4 jets satisfying $p_{\text{T}} > 20\,\text{GeV}$ and $|\eta| < 2.8$ are used as inputs to a second iteration of the anti-k_t jet algorithm, this time using the larger distance parameter R=1.0. The resulting larger objects are denoted as composite jets. The selection variable M_J^{Σ} is then defined to be the sum of the masses of the composite jets: $M_J^{\Sigma} \equiv \sum_j m_j^{R=1.0}$, where the sum is over the composite jets that satisfy $p_{\text{T}}^{R=1.0} > 100\,\text{GeV}$ and $|\eta^{R=1.0}| < 1.5$. The variable H_{T} is defined as the scalar sum of p_{T} of all jets with $p_{\text{T}} > 40\,\text{GeV}$ and $|\eta| <2.8$.

constructed then $E_{\text{T}}^{\text{miss}} = 0$ and M_{T}^R would also be zero, while in the case where a jet is mis-calibrated, the fake $\boldsymbol{E}_{\text{T}}^{\text{miss}}$ tends to align with one of the mega-jets (that are back-to-back), also creating small values of M_{T}^R. For SUSY-like events where the mega-jets tend not to be back-to-back, and their vector sum is opposite to the $\boldsymbol{E}_{\text{T}}^{\text{miss}}$, the quantity M_{T}^R is large. The kinematic endpoint of M_{T}^R is the mass difference between the heavy and the light sparticles.

Finally, the razor variable is defined as:

$$R = \frac{M_{\text{T}}^R}{M_R'}. \tag{C.3}$$

For SUSY-like events, when the mass splitting between the heavier and light sparticles is large, M_R' peaks near the mass of the heavier sparticle and M_{T}^R has a kinematical endpoint at the mass of the heavier sparticle. For SM processes, R tends to have a low value, while it tends to have a broad distribution centred around 0.5 for SUSY-like events. Thus R can be used as a discriminant between signal and background.

JHEP10(2015)054

Requirement	Signal region			
	Single-bin (binned) soft single-lepton			**Soft dimuon**
	3-jet	**5-jet**	**3-jet inclusive**	**2-jet**
N_ℓ	1 electron or muon			2 muons
p_{T}^{ℓ}[GeV]	[7,25] for electron, [6,25] for muon			[6,25]
Lepton veto	No additional electron or muon with $p_{\mathrm{T}} > 7\,\mathrm{GeV}$ or $6\,\mathrm{GeV}$, respectively			
$m_{\mu\mu}$ [GeV]	–	–	–	[15,60]
N_{jet}	[3,4]	≥ 5	≥ 3	≥ 2
$p_{\mathrm{T}}{}^{\mathrm{jet}}$[GeV] >	180, 25, 25	180, 25, 25, 25, 25	130, 100, 25	80, 25
$N_{b-\mathrm{jet}}$	–	–	0	0
$E_{\mathrm{T}}^{\mathrm{miss}}$ [GeV] >	400	300	180	
m_{T} [GeV] >	100		120	40
$E_{\mathrm{T}}^{\mathrm{miss}}/m_{\mathrm{eff}}^{\mathrm{incl}}$ >	0.3 (0.1)		0.1	0.3
$\Delta R_{\mathrm{min}}(\mathrm{jet},\ell)$ >	1.0	–	–	1.0 (2nd muon)
Binned variable	($E_{\mathrm{T}}^{\mathrm{miss}}/m_{\mathrm{eff}}^{\mathrm{incl}}$ in 4 bins)			–
Bin width	(0.1, 4th is inclusive)			–

Requirement	Signal region		
	Single-bin (binned) hard single-lepton		
	3-jet	**5-jet**	**6-jet**
N_ℓ	1 electron or muon		
p_{T}^{ℓ}[GeV] >	25		
Lepton veto	$p_{\mathrm{T}}{}^{2^{\mathrm{nd}}\mathrm{lepton}} < 10\,\mathrm{GeV}$		
N_{jet}	≥ 3	≥ 5	≥ 6
$p_{\mathrm{T}}{}^{\mathrm{jet}}$[GeV] >	80, 80, 30	80, 50, 40, 40, 40	80, 50, 40, 40, 40, 40
Jet veto	($p_{\mathrm{T}}{}^{5^{\mathrm{th}}\mathrm{jet}} < 40\,\mathrm{GeV}$)	($p_{\mathrm{T}}{}^{6^{\mathrm{th}}\mathrm{jet}} < 40\,\mathrm{GeV}$)	–
$E_{\mathrm{T}}^{\mathrm{miss}}$ [GeV] >	500 (300)	300	350 (250)
m_{T} [GeV] >	150	200 (150)	150
$E_{\mathrm{T}}^{\mathrm{miss}}/m_{\mathrm{eff}}^{\mathrm{excl}}$ >	0.3	–	–
$m_{\mathrm{eff}}^{\mathrm{incl}}$ [GeV] >	1400 (800)		600
Binned variable	($m_{\mathrm{eff}}^{\mathrm{incl}}$ in 4 bins)		($E_{\mathrm{T}}^{\mathrm{miss}}$ in 3 bins)
Bin width	(200 GeV, 4th is inclusive)		(100 GeV, 3rd is inclusive)

Table 17. Selection criteria used to define the signal regions in the search requiring at least one isolated lepton (1-lepton (soft+hard) + jets + $E_{\mathrm{T}}^{\mathrm{miss}}$) and in the search requiring two soft muons (2-leptons + jets + $E_{\mathrm{T}}^{\mathrm{miss}}$) [23]. For each jet multiplicity in the single-lepton channel, two sets of requirements are defined: one single-bin signal region optimized for discovery reach, which is also used to place limits on the visible cross-section, and one signal region which is binned in an appropriate variable in order to exploit the expected shape of the distribution of signal events when placing model-dependent limits. The requirements of the binned signal region are shown in parentheses when they differ from those of the single-bin signal region. The transverse mass (m_{T}) of the lepton (ℓ) and $\boldsymbol{E}_{\mathrm{T}}^{\mathrm{miss}}$ is defined as $m_{\mathrm{T}} = \sqrt{2p_{\mathrm{T}}^{\ell}E_{\mathrm{T}}^{\mathrm{miss}}(1-\cos[\Delta\phi(\vec{\ell},\boldsymbol{E}_{\mathrm{T}}^{\mathrm{miss}})])}$. The inclusive effective mass ($m_{\mathrm{eff}}^{\mathrm{inc}}$) is computed as the scalar sum of the p_{T} of the lepton(s), the jets and $E_{\mathrm{T}}^{\mathrm{miss}}$: $m_{\mathrm{eff}}^{\mathrm{inc}} = \sum_{i=1}^{N_\ell} p_{\mathrm{T},i}^{\ell} + \sum_{j=1}^{N_{\mathrm{jet}}} p_{\mathrm{T},j} + E_{\mathrm{T}}^{\mathrm{miss}}$, where the index i identifies all the signal leptons and the index j all the signal jets in the event. The exclusive effective mass ($m_{\mathrm{eff}}^{\mathrm{excl}}$) is defined in a similar way to $m_{\mathrm{eff}}^{\mathrm{inc}}$, with the exception that only the three leading signal jets are considered. The minimum angular separation ΔR_{min} calculated between the signal lepton ℓ and all preselected jets is used to reduce the background coming from misidentified or non-prompt leptons in the soft-lepton signal region with three jets and in the soft dimuon signal region. In the latter case, the subleading signal muon is used to compute ΔR_{min}.

JHEP10(2015)054

Requirement	Signal region			
	Single-bin (binned) hard dilepton			
	Low-multiplicity ($\leq$ 2-jet)		**3-jet**	
	$ee/\mu\mu$	$e\mu$	$ee/\mu\mu$	$e\mu$
N_ℓ	2, 2 of opposite sign or ≥ 2			
p_{T}^{ℓ}[GeV] $>$	14,10			
$N_{\ell\ell}$ with 81$<m_{\ell\ell}<$101 GeV	0	–	0	–
N_{jet}	≤ 2		≥ 3	
p_{T} ^{jet} [GeV] $>$	50,50		50, 50, 50	
$N_{b-\mathrm{jet}}$	0			
R	$>$0.5		$>$0.35	
$M_R^{'}$ [GeV] $>$	600 (400 in 8 bins)		800 (800 in 5 bins)	
$M_R^{'}$ bin width [GeV]	(100, the last is inclusive)			

Table 18. Selection criteria used to define the signal regions in the search requiring two hard leptons (2-leptons + jets + $E_{\mathrm{T}}^{\mathrm{miss}}$) [23]. For each jet multiplicity two sets of requirements are defined: one single-bin signal region optimized for discovery reach, which is also used to place limits on the visible cross-section, and one signal region which is binned in an appropriate variable in order to exploit the expected shape of the distribution of signal events when placing model-dependent limits. The requirements of the binned signal region are shown in parentheses when they differ from those of the single-bin signal region. Details of the construction of Razor variables $M_R^{'}$ and R can be found in the appendix C.1. In this case, mega-jets are constructed using the final-state jets and leptons.

Requirement	Signal region				
	SR-2j-bveto	**SR-2j-btag**	**SR-4j-bveto**	**SR-4j-btag**	**SR-loose**
$N_{\mathrm{jet}} \geq$	≥ 2	≥ 2	≥ 4	≥ 4	(2, $\geq$ 3)
$N_{b-\mathrm{jet}}$	$= 0$	≥ 1	$= 0$	≥ 1	—
$E_{\mathrm{T}}^{\mathrm{miss}}$ [GeV] $>$	200	200	200	200	(150, 100)
$m_{\ell\ell}$ [GeV] $\notin$	[80, 110]	[80, 110]	[80, 110]	[80, 110]	[80, 110]

Table 19. Selection criteria used to define the signal regions in the search requiring two same-flavour opposite-sign electrons or muons (2-leptons off-Z) [24]. If more than two leptons are present, the two with the largest values of p_{T} are selected. The leading lepton in the event must have $p_{\mathrm{T}} > 25$ GeV and the subleading lepton is required to have $p_{\mathrm{T}} > 20$ GeV. These two leptons are used to define the dilepron invariant mass, $m_{\ell\ell}$. In addition, one SR with the same requirements as those used in the CMS search [148], which reported an excess of events above the SM background with a significance of 2.6 standard deviations, is defined (SR-loose) for comparison purposes.

JHEP10(2015)054

Requirement	Signal region				
	SR3b	**SR0b**	**SR1b**	**SR3Llow**	**SR3Lhigh**
Leptons	SS or 3L	SS	SS	3L	3L
$N_{b-\text{jet}}$	≥ 3	=0	≥ 1	-	-
$N_{\text{jet}} \geq$	5	3	3	4	4
$E_{\text{T}}^{\text{miss}}$ [GeV]		> 150	> 150	$50 < E_{\text{T}}^{\text{miss}} < 150$	> 150
m_{T} [GeV] $>$	-	100	-	-	-
Veto	-	-	SR3b	Z boson, SR3b	SR3b
m_{eff} [GeV] $>$	350	400	700	400	400

Table 20. Selection criteria used to define the signal regions in the search with multiple jets, and either two leptons of the same electric charge (same-sign leptons) or at least three leptons (SS/3L + jets + $E_{\text{T}}^{\text{miss}}$) [25]. The effective mass (m_{eff}) is computed from all selected leptons and selected jets in event, as $m_{\text{eff}} = \sum_{i=1}^{N_\ell} p_{\text{T},i}^{\ell} + \sum_{j=1}^{N_{\text{jet}}} p_{\text{T},j} + E_{\text{T}}^{\text{miss}}$. The transverse mass ($m_{\text{T}}$) is computed from the highest-p_{T} lepton (ℓ_1) and $\boldsymbol{E}_{\text{T}}^{\text{miss}}$ as $m_{\text{T}} = \sqrt{2p_{\text{T}}^{\ell_1} E_{\text{T}}^{\text{miss}}(1 - \cos[\Delta\phi(\vec{\ell_1}, \boldsymbol{E}_{\text{T}}^{\text{miss}})])}$.

C.2 Signal regions

The SUSY models targeted by this search are expected to have final states characterized by the presence of jets, missing transverse momentum, and no leptons. In the simplest case of squark-pair production with direct decays to quarks and neutralinos, there are at least two jets visible in the detector, so the baseline inclusive signal regions require at least two jets. This is also the minimum number of visible objects in the final state necessary to construct the Razor variables. Figure 39 shows the values of R and M_R' for two simplified model signal points, one with $m_{\tilde{q}} = 450\,\text{GeV}$ and $m_{\text{LSP}} = 400\,\text{GeV}$, where the $\Delta m = 50\,\text{GeV}$ is small (referred to as small-Δm_{signal}) and the other with $m_{\tilde{q}} = 850\,\text{GeV}$ and $m_{\text{LSP}} = 100\,\text{GeV}$, where the $\Delta m = 750\,\text{GeV}$ is large (referred to as large-Δm_{signal}), after requiring no leptons and at least two jets in the final state.

Since the variable M_R' is related to the mass difference between the squark and the neutralino, going from the small-Δm_{signal} to the large-Δm_{signal}, the events tend to populate higher M_R' regions. Extending this to all points of the model with squark-pair production followed by the direct decay of squarks, the average value of M_R' is approximately constant for a fixed mass splitting between the LSP and the squark, and increases with increasing Δm, while the average R-value tends to be around 0.5.

To select events for this search, the combination of two $E_{\text{T}}^{\text{miss}}$ triggers, which are fully efficient in events having offline reconstructed $E_{\text{T}}^{\text{miss}} > 160\,\text{GeV}$ is used. Two signal regions which target different regions of the $(m_{\tilde{q}}, m_{\tilde{\chi}_1^0})$ plane are defined: SR_{loose} and SR_{tight}. Signal region SR_{loose} has a lower requirement on R and targets regions of the $(m_{\tilde{q}}, m_{\tilde{\chi}_1^0})$ plane with small mass splitting, which typically have softer visible objects. Signal region SR_{tight} was chosen to target high squark masses which typically contain harder visible objects. An overview of the selection criteria for these two signal regions is given in table 9.

JHEP10(2015)054

Requirement	Signal region	
	1τ **Loose SR**	1τ **Tight SR**
Taus	$N_\tau^{\text{medium}} = 1$ $p_{\text{T}} > 30\,\text{GeV}$	
$\Delta\phi(\text{jet}_{1,2}, \boldsymbol{E}_{\text{T}}^{\text{miss}}) >$	0.4	
$\Delta\phi(\tau, \boldsymbol{E}_{\text{T}}^{\text{miss}}) >$	0.2	
m_{T}^{τ} [GeV] $>$	140	
$E_{\text{T}}^{\text{miss}}$ [GeV] $>$	200	300
H_{T} [GeV] $>$	800	1000

Requirement	Signal region			
	2τ **Inclusive SR**	2τ **GMSB SR**	2τ **nGM SR**	2τ **bRPV SR**
Taus	$N_\tau^{\text{loose}} \geq 2$ $p_{\text{T}} > 20\,\text{GeV}$			
$\Delta\phi(\text{jet}_{1,2}, \boldsymbol{E}_{\text{T}}^{\text{miss}}) \geq$	0.3			
$m_{\text{T}}^{\tau_1} + m_{\text{T}}^{\tau_2}$ [GeV] $\geq$	150	250	250	150
$H_{\text{T}}^{2\text{j}}$ [GeV] $>$	1000	1000	600	1000
$N_{\text{jet}} \geq$	-	4		

Requirement	Signal region			
	$\tau{+}\ell$ **GMSB SR**	$\tau{+}\ell$ **nGM SR**	$\tau{+}\ell$ **bRPV SR**	$\tau{+}\ell$ **mSUGRA SR**
Taus	$N_\tau^{\text{loose}} \geq 1$ $p_{\text{T}} > 20\,\text{GeV}$			
$N_\ell =$	1			
m_{T}^{ℓ} [GeV] $>$	100			
m_{eff} [GeV] $>$	1700	-	1300	-
$E_{\text{T}}^{\text{miss}}$ [GeV] $>$	-	350	-	300
$N_{\text{jet}} \geq$	-	3	4	3

Table 21. Selection criteria used to define the signal regions in the search requiring large missing transverse momentum, jets and at least one hadronically decaying tau lepton (taus + jets + $E_{\text{T}}^{\text{miss}}$) [26]. The transverse mass m_{T}^{τ} is formed from the $\boldsymbol{E}_{\text{T}}^{\text{miss}}$ and the p_{T} of the tau lepton in the 1τ channel as: $m_{\text{T}}^{\tau} = \sqrt{2p_{\text{T}}^{\tau}E_{\text{T}}^{\text{miss}}(1-\cos(\Delta\phi(\tau, \boldsymbol{E}_{\text{T}}^{\text{miss}})))}$. In addition, the variable $m_{\text{T}}^{\tau_1}+m_{\text{T}}^{\tau_2}$ is used as a discriminating variable in the 2τ channel. The transverse mass m_{T}^{ℓ} is similarly formed from the $\boldsymbol{E}_{\text{T}}^{\text{miss}}$ and the p_{T} of the light leptons. The variable H_{T} is defined as the scalar sum of the transverse momenta of the tau, light lepton and jets ($p_{\text{T}}^{\text{jet}} > 30\,\text{GeV}$): $H_{\text{T}} = \sum_{i=1}^{N_\ell} p_{\text{T}}^{\ell} + \sum_{j=1}^{N_\tau} p_{\text{T}}^{\tau} + \sum_{k=1}^{N_{\text{jet}}} p_{\text{T}}^{\text{jet}}$. The variable $H_{\text{T}}^{2\text{j}}$ is defined as the scalar sum of the transverse momenta of the tau and light lepton candidates, and the two jets with the largest transverse momenta in the event: $H_{\text{T}}^{2\text{j}} = \sum_{i=1}^{N_\ell} p_{\text{T}}^{\ell} + \sum_{j=1}^{N_\tau} p_{\text{T}}^{\tau} + \sum_{k=1,2} p_{\text{T}}^{\text{jet}_k}$. The effective mass ($m_{\text{eff}}$) is defined as $m_{\text{eff}} = H_{\text{T}}^{2\text{j}}+E_{\text{T}}^{\text{miss}}$.

JHEP10(2015)054

Requirement	Signal region					
	SR-0ℓ-4j-A	**SR-0ℓ-4j-B**	**SR-0ℓ-4j-C***	**SR-0ℓ-7j-A**	**SR-0ℓ-7j-B**	**SR-0ℓ-7j-C**
Baseline 0-lepton selection	lepton veto, $p_{\mathrm{T}}^{\mathrm{jet}_1} > 90\,\mathrm{GeV}$, $E_{\mathrm{T}}^{\mathrm{miss}} > 150\,\mathrm{GeV}$					
N jets (p_{T} [GeV]) $\geq$	4 (50)	4 (50)	4 (30)	7 (30)	7 (30)	7 (30)
$E_{\mathrm{T}}^{\mathrm{miss}}$ [GeV] $>$	250	350	400	200	350	250
$m_{\mathrm{eff}}^{\mathrm{incl}}$ [GeV] $>$	-	-	-	1000	1000	1500
$m_{\mathrm{eff}}^{\mathrm{4j}}$ [GeV] $>$	1300	1100	1100	-	-	-
$E_{\mathrm{T}}^{\mathrm{miss}}/\sqrt{H_{\mathrm{T}}^{\mathrm{4j}}}$ [$\sqrt{\mathrm{GeV}}$] $>$	-	-	16	-	-	-

Requirement	Signal region		
	SR-1ℓ-6j-A	**SR-1ℓ-6j-B**	**SR-1ℓ-6j-C**
Baseline 1-lepton selection	$\geqslant 1$ signal lepton (e,μ), $p_{\mathrm{T}}^{\mathrm{jet}_1} > 90\,\mathrm{GeV}$, $E_{\mathrm{T}}^{\mathrm{miss}} > 150\,\mathrm{GeV}$		
N jets (p_{T} [GeV]) $\geq$	6 (30)	6 (30)	6 (30)
$E_{\mathrm{T}}^{\mathrm{miss}}$ [GeV] $>$	175	225	275
m_{T}[GeV] $>$	140	140	160
$m_{\mathrm{eff}}^{\mathrm{incl}}$ [GeV] $>$	700	800	900

Table 22. Selection criteria used to define the signal regions in the search that requires at least three jets tagged as b-jets, no or at least one lepton, jets and large missing transverse momentum (0/1-lepton + 3b-jets + $E_{\mathrm{T}}^{\mathrm{miss}}$) [27]. The jet p_{T} threshold requirements are also applied to b-jets. The notation SR-0ℓ-4j-C* means that the leading jet is required to fail the b-tagging requirements, in order to target the region close to the kinematic boundary in the gluino-sbottom simplified models. In the 0-lepton selection, the inclusive effective mass $m_{\mathrm{eff}}^{\mathrm{incl}}$ is defined as the scalar sum of the $E_{\mathrm{T}}^{\mathrm{miss}}$ and the p_{T} of all jets with $p_{\mathrm{T}} > 30\,\mathrm{GeV}$. In the 1-lepton selection the $m_{\mathrm{eff}}^{\mathrm{incl}}$ is defined as for the 0-lepton selection with the addition of the p_{T} of all selected leptons with $p_{\mathrm{T}} > 20\,\mathrm{GeV}$. The exclusive effective mass ($m_{\mathrm{eff}}^{\mathrm{4j}}$) is defined as the scalar sum of the $E_{\mathrm{T}}^{\mathrm{miss}}$ and the p_{T} of the four leading jets. The transverse mass (m_{T}) is computed from the leading lepton and the missing transverse momentum. The variable $H_{\mathrm{T}}^{\mathrm{4j}}$ is defined as the scalar sum of the transverse momenta of the four leading jets.

C.3 Control and validation regions for SM background processes

The dominant SM background processes which contribute to the event counts in the signal regions are: Z+jets, W+jets, top quark pairs, and multiple jets. For each of these processes a dedicated control region is defined. The production of boson (W/Z) pairs in which at least one boson decays to charged leptons and/or neutrinos (referred to as 'dibosons' below), the single-top production, and the $t\bar{t}+W/Z$ boson production are small components of the total background and are estimated with MC simulated data.

Figure 40 shows the values of R and M_R' for the major SM backgrounds in this search. As previously discussed, the SM backgrounds tend to occupy regions with lower values of M_R' and R, which is taken into account while defining control regions for the main background processes. A summary of the selection criteria used to define the control and validation regions in this search is shown in table 23.

The largest potential background for a search with no leptons is expected to originate from the QCD-induced multi-jet event. However, the Razor variables were constructed

JHEP10(2015)054

Preselection				
Exactly two opposite-sign, same-flavour electrons or muons	Exactly one electron or muon	Exactly one electron or muon	No leptons	No leptons
–	No b-jets	At least one b-jet	–	–
$66 < m(\ell\ell) < 116\,\text{GeV}$	–	–	$p_{\text{T}}^{\text{jet}_{1,2}} > 150\,\text{GeV}$	$p_{\text{T}}^{\text{jet}_{1,2}} > 200\,\text{GeV}$
$E_{\text{T}}^{\text{miss}'} = E_{\text{T}}^{\text{miss}} + p_{\text{T}}(\ell\ell)$	Treat lepton as a jet	Treat lepton as a jet	–	–
0LRaz_CRZ	**0LRaz_CRW**	**0LRaz_CRT**	**0LRaz_CRQ**$_{\text{loose}}$	**0LRaz_CRQ**$_{\text{tight}}$
–	–	–	$\Delta\phi(p_{\text{T}}^{\text{jet}_2}, E_{\text{T}}^{\text{miss}}) < 0.2$	$\Delta\phi(p_{\text{T}}^{\text{jet}_2}, E_{\text{T}}^{\text{miss}}) < 0.2$
$0.3 < R < 0.55$	$0.3 < R < 0.55$	$0.3 < R < 0.55$	$0.35 < R < 0.45$	$0.5 < R < 0.55$
$M_R' > 800\,\text{GeV}$	$M_R' > 800\,\text{GeV}$	$M_R' > 800\,\text{GeV}$	$M_R' > 1000\,\text{GeV}$	$M_R' > 1000\,\text{GeV}$
0LRaz_VRZ	**0LRaz_VRW**	**0LRaz_VRT**	**0LRaz_VRQ**$_{\text{loose}}$	**0LRaz_VRQ**$_{\text{tight}}$
–	–	–	$\Delta\phi(p_{\text{T}}^{\text{jet}_2}, E_{\text{T}}^{\text{miss}}) < 0.4$	$\Delta\phi(p_{\text{T}}^{\text{jet}_2}, E_{\text{T}}^{\text{miss}}) < 1.4$
$0.55 < R < 1.0$	$0.55 < R < 1.0$	$0.55 < R < 1.0$	$0.45 < R < 0.5$	$0.55 < R < 0.6$
$400 < M_R' < 1000\,\text{GeV}$	$400 < M_R' < 1000\,\text{GeV}$	$400 < M_R' < 1000\,\text{GeV}$	$M_R' > 900\,\text{GeV}$	$M_R' > 900\,\text{GeV}$

Table 23. Overview of the selection criteria for the Z+jets, W+jets, semileptonic $t\bar{t}$ and multi-jet control regions (0LRaz_CRZ, 0LRaz_CRW, 0LRaz_CRT and 0LRaz_CRQ$_{\text{loose/tight}}$ respectively) and the corresponding validation regions (0LRaz_VRZ, 0LRaz_VRW, 0LRaz_VRT, 0LRaz_VRQ$_{\text{loose/tight}}$) used by the 0-lepton Razor analysis. Details of the construction of Razor variables $M_R^{'}$ and R can be found in the appendix C.1.

JHEP10(2015)054

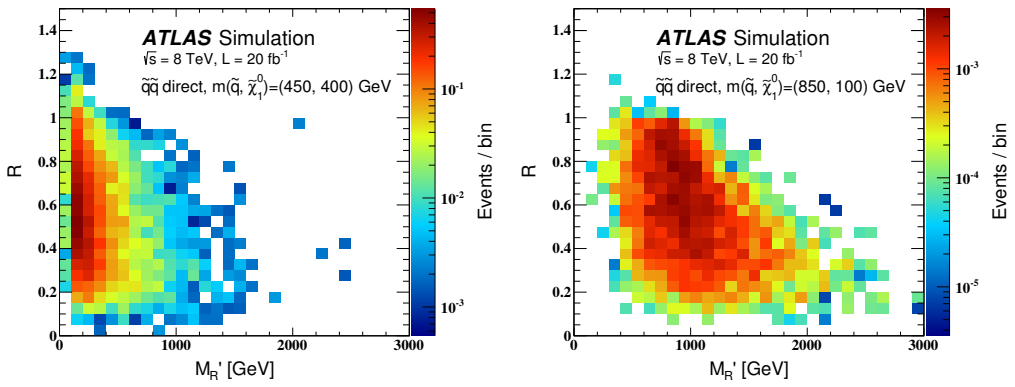

(a) (b)

Figure 39. Distributions of the Razor variable R versus the characteristic mass in the R-frame M'_R for two points of the simplified model with squark-pair production assuming the direct decay of squarks, after requiring no leptons and at least two jets. Figure (a) shows the case where $m_{\tilde{q}} = 450\,\text{GeV}$ and $m_{\text{LSP}} = 400\,\text{GeV}$, and (b) where $m_{\tilde{q}} = 850\,\text{GeV}$ and $m_{\text{LSP}} = 100\,\text{GeV}$.

to be able to distinguish this background from a SUSY-like signal, which minimizes the contribution of the multi-jet events after the SR event selection has been applied. To estimate the contribution of multi-jet background events in the final signal region selection, a data-driven technique [156], which applies a resolution function to well-measured multi-jet events in order to estimate the impact of jet energy mis-measurement and heavy-flavour semileptonic decays on $E_{\text{T}}^{\text{miss}}$ and other variables, is used. Two dedicated control regions, $\text{CRQ}_{\text{loose}}$ and $\text{CRQ}_{\text{tight}}$, which use different selection criteria on R and $\Delta\phi(p_T^{j2}, E_{\text{T}}^{\text{miss}})$, correspond to the loose and tight signal regions respectively, and select samples of events with similar kinematics to the SR but enriched in multi-jet background events.

Since the QCD multi-jet background is significantly reduced by use of the Razor variables, the largest remaining backgrounds come from the production of W/Z bosons with additional jets and semileptonic $t\bar{t}$ decays, where the leptons can be mis-reconstructed as jets, non-prompt or be outside the lepton identification criteria. For each of these backgrounds a control region, rich in the respective process, is defined. The trigger requirements for these lepton-rich control regions follow those used by the corresponding control regions for the the 0L search [20]. The Razor variables are used to preselect a region which is dominated by the particular process. Following this preselection, to control the $t\bar{t}$ background, the control region CRT requires at least one jet tagged as a b-jet and exactly one electron or muon, while the W+jets control region, CRW, applies a veto on the presence of b-jets and requires exactly one electron or muon. In both cases the lepton is treated as a jet in the reconstruction of the Razor variables. This treatment of leptons as jets is motivated by the observation that ∼75% of W($\rightarrow \ell\nu$)+jets and semileptonic $t\bar{t}$ events appearing in the SRs possess leptons which have fake jets, either through the misidentification of electrons or by the production of tau leptons decaying hadronically (identification of hadronic tau decays is not used in this analysis). The Z+jets control region, CRZ, is required to have exactly two opposite-sign same-flavour leptons. The Z+jets contribution to the signal region largely originates from Z decays to neutrinos. To mimic the behaviour of $Z \rightarrow \nu\nu$ in the

JHEP10(2015)054

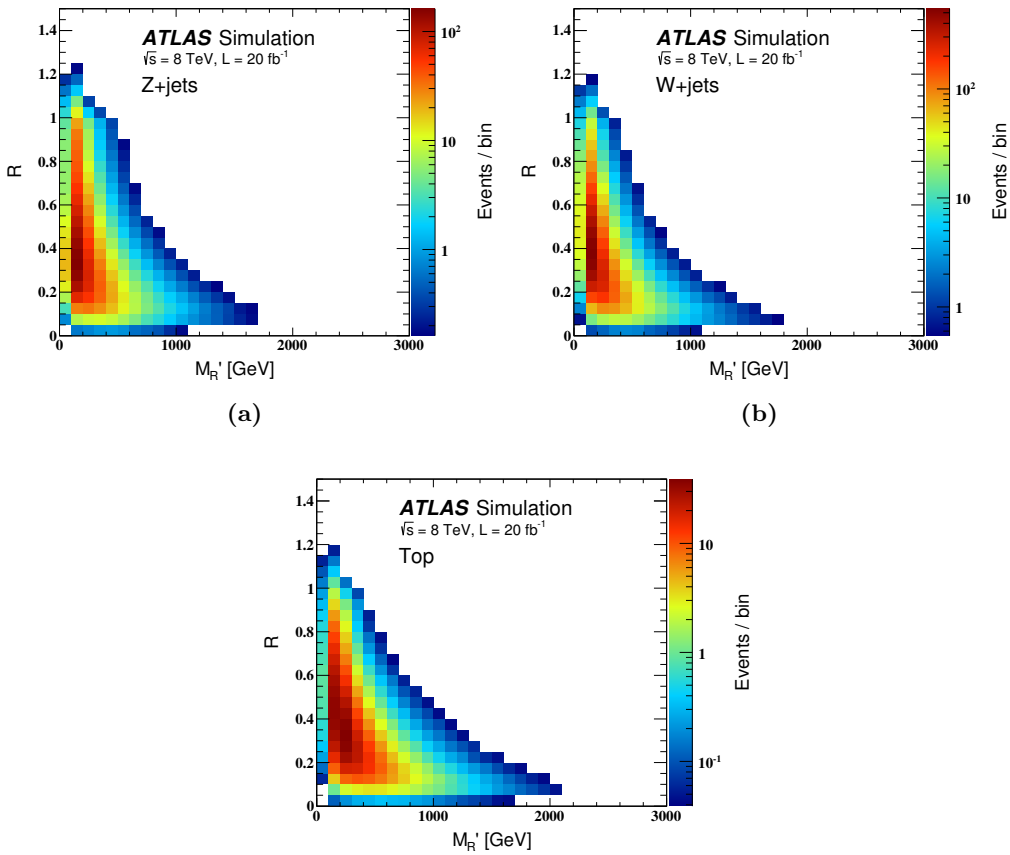

(a) (b) (c)

Figure 40. Distributions of the Razor variable R versus the characteristic mass in the R-frame M'_R for the dominant Standard Model backgrounds: (a) Z+jets, (b) W+jets and (c) $t\bar{t}$, after requiring no-leptons and at least two jets in the final state.

control region, the two leptons have been treated as invisible and are used to re-calculate $\boldsymbol{E}_{\mathrm{T}}^{\mathrm{miss}}$ as $\boldsymbol{E}_{\mathrm{T}}^{\mathrm{miss}'} = \boldsymbol{E}_{\mathrm{T}}^{\mathrm{miss}} + \boldsymbol{p}_{\mathrm{T}}(\ell\ell)$ with the invariant mass of the leptons falling within a Z-mass window, $66 < m(\ell\ell) < 116$ GeV. The Razor variables are also calculated with this methodology where the leptons are treated as invisible objects.

To validate the normalization parameters extracted in the background control regions, validation regions VRZ, VRW, VRT, $\mathrm{VRQ}_{\mathrm{loose}}$ and $\mathrm{VRQ}_{\mathrm{tight}}$ for Z+jets, W+jets, $t\bar{t}$ and multi-jet backgrounds respectively, are defined (table 23). These validation regions are statistically independent from the signal and control regions previously defined, and are expected to have minimal contribution from any signal, if present.

Following the definition of the control and validation regions, the backgrounds from Z+jets, W+jets, $t\bar{t}$ and multi-jet processes are estimated by using the background-only fit, as described in section 6. Figures 41 and 42 show the M'_R distributions for these control and validation regions after the fit. Good agreement is seen between the fitted and observed yields in all regions.

JHEP10(2015)054

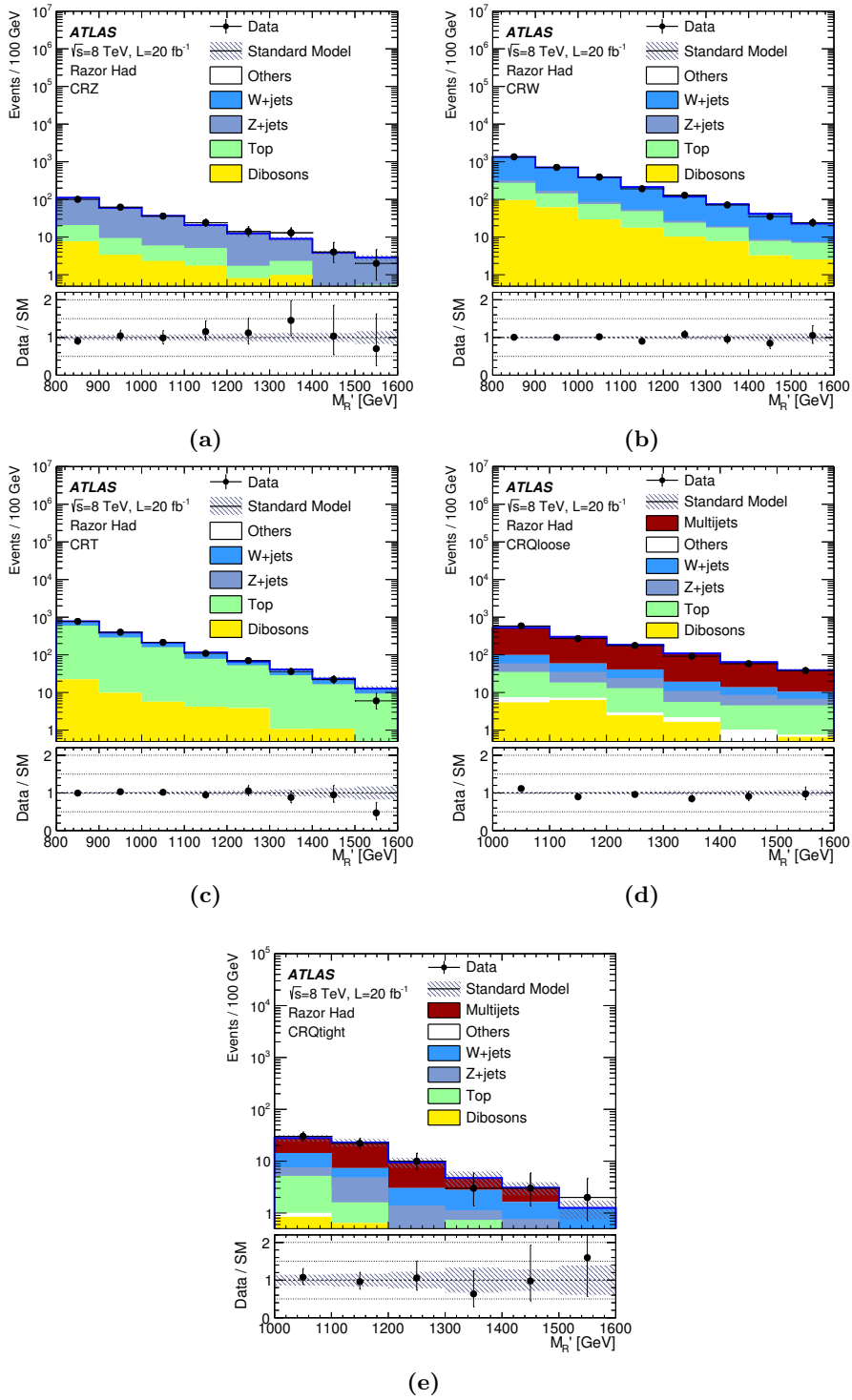

Figure 41. Observed M'_R distributions in control regions for (a) Z+jets, (b) W+jets, (c) $t\bar{t}$ and multi-jet backgrounds for (d) loose and (e) tight selection. The "Top" label includes all top-quark-related backgrounds ($t\bar{t}$, single top and $t\bar{t}+V$), while the "Others" includes the contributions of the jets misidentified as leptons or of non-prompt leptons, and the γ+jets background which is estimated with MC simulated data. All distributions are after the background-only fit has been performed.

JHEP10(2015)054

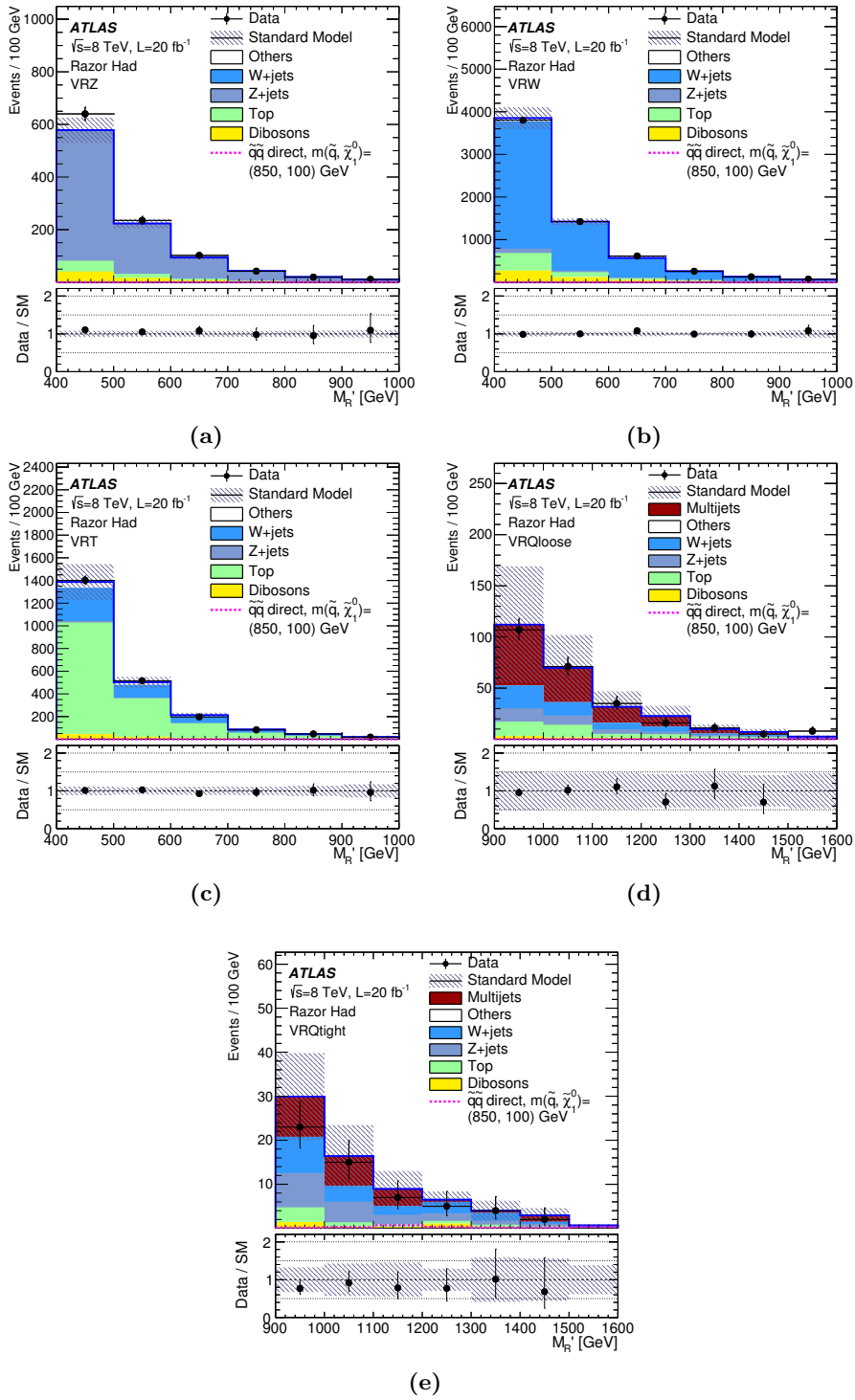

Figure 42. Observed M'_R distributions in validation regions for (a) Z+jets, (b) W+jets, (c) $t\bar{t}$ and multi-jet backgrounds for (d) loose and (e) tight selection. The "Top" label includes all top-quark-related backgrounds ($t\bar{t}$, single top and $t\bar{t}+V$), while the "Others" includes the contributions of the jets misidentified as leptons or of non-prompt leptons, and the γ+jets background which is estimated with MC simulated data. All distributions are after the background-only fit has been performed.

JHEP10(2015)054

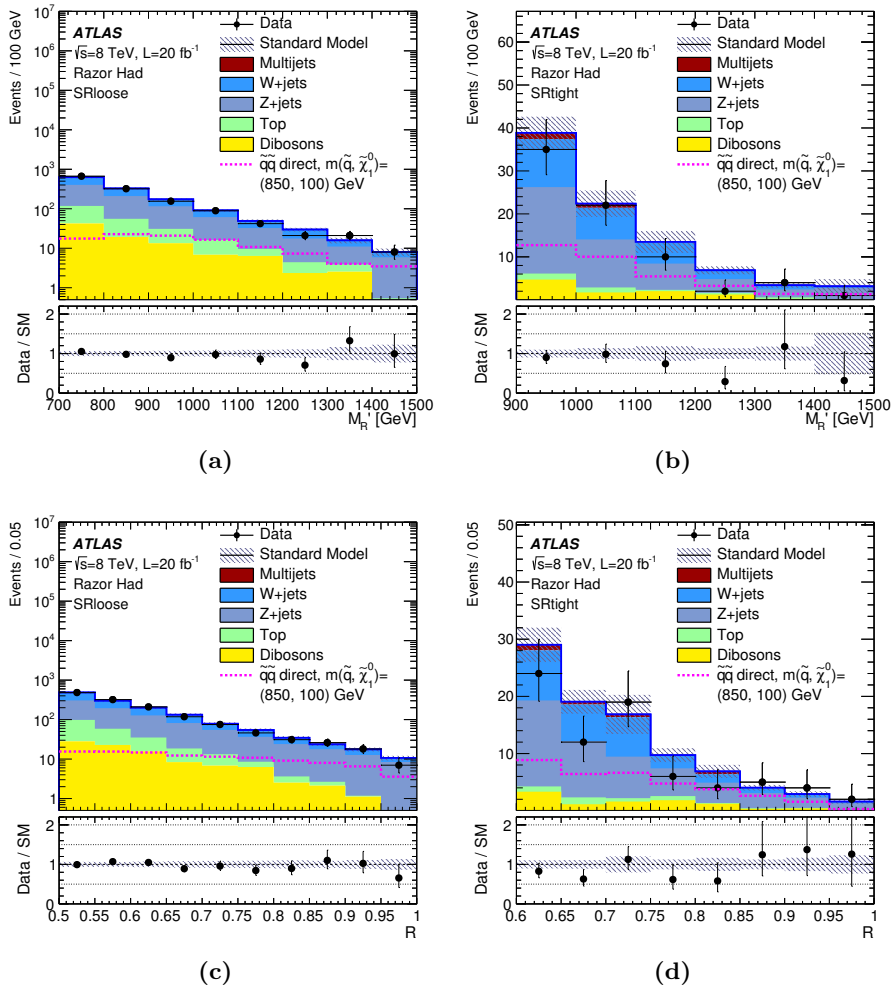

Figure 43. Observed (a, c) M'_R and (b, d) R distributions in (a, b) loose and (c, d) tight signal region selections listed in table 9. The "Top" label includes all top-quark-related backgrounds ($t\bar{t}$, single top and $t\bar{t}+V$). All distributions are after the background-only fit has been performed.

The Razor variable distributions, M'_R and R, for the SM backgrounds and a simplified model point with large-Δm_{signal} are shown in figure 43 for SR_{loose} and SR_{tight}.

Open Access. This article is distributed under the terms of the Creative Commons Attribution License (CC-BY 4.0), which permits any use, distribution and reproduction in any medium, provided the original author(s) and source are credited.

References

[1] H. Miyazawa, *Baryon number changing currents*, *Prog. Theor. Phys.* **36** (1966) 1266 [INSPIRE].

[2] P. Ramond, *Dual theory for free fermions*, *Phys. Rev.* **D 3** (1971) 2415 [INSPIRE].

JHEP10(2015)054

[3] Yu. A. Golfand and E.P. Likhtman, *Extension of the algebra of Poincaré group generators and violation of p invariance*, *JETP Lett.* **13** (1971) 323 [*Pisma Zh. Eksp. Teor. Fiz.* **13** (1971) 452] [INSPIRE].

[4] A. Neveu and J.H. Schwarz, *Factorizable dual model of pions*, *Nucl. Phys.* **B 31** (1971) 86 [INSPIRE].

[5] A. Neveu and J.H. Schwarz, *Quark model of dual pions*, *Phys. Rev.* **D 4** (1971) 1109 [INSPIRE].

[6] J.-L. Gervais and B. Sakita, *Field theory interpretation of supergauges in dual models*, *Nucl. Phys.* **B 34** (1971) 632 [INSPIRE].

[7] D.V. Volkov and V.P. Akulov, *Is the neutrino a Goldstone particle?*, *Phys. Lett.* **B 46** (1973) 109 [INSPIRE].

[8] J. Wess and B. Zumino, *A Lagrangian model invariant under supergauge transformations*, *Phys. Lett.* **B 49** (1974) 52 [INSPIRE].

[9] J. Wess and B. Zumino, *Supergauge transformations in four-dimensions*, *Nucl. Phys.* **B 70** (1974) 39 [INSPIRE].

[10] P. Fayet, *Supersymmetry and weak, electromagnetic and strong interactions*, *Phys. Lett.* **B 64** (1976) 159 [INSPIRE].

[11] P. Fayet, *Spontaneously broken supersymmetric theories of weak, electromagnetic and strong interactions*, *Phys. Lett.* **B 69** (1977) 489 [INSPIRE].

[12] G.R. Farrar and P. Fayet, *Phenomenology of the production, decay and detection of new hadronic states associated with supersymmetry*, *Phys. Lett.* **B 76** (1978) 575 [INSPIRE].

[13] P. Fayet, *Relations between the masses of the superpartners of leptons and quarks, the Goldstino couplings and the neutral currents*, *Phys. Lett.* **B 84** (1979) 416 [INSPIRE].

[14] L. Evans and P. Bryant, *LHC machine*, 2008 *JINST* **3** S08001 [INSPIRE].

[15] S. Dimopoulos and H. Georgi, *Softly broken supersymmetry and* SU(5), *Nucl. Phys.* **B 193** (1981) 150 [INSPIRE].

[16] H. Goldberg, *Constraint on the photino mass from cosmology*, *Phys. Rev. Lett.* **50** (1983) 1419 [*Erratum ibid.* **103** (2009) 099905] [INSPIRE].

[17] ATLAS collaboration, *The ATLAS experiment at the CERN Large Hadron Collider*, 2008 *JINST* **3** S08003 [INSPIRE].

[18] ATLAS collaboration, *ATLAS Run 1 searches for direct pair production of third-generation squarks at the Large Hadron Collider*, submitted to *Eur. Phys. J.* (2015) [arXiv:1506.08616] [INSPIRE].

[19] C. Rogan, *Kinematical variables towards new dynamics at the LHC*, [arXiv:1006.2727] [INSPIRE].

[20] ATLAS collaboration, *Search for squarks and gluinos with the ATLAS detector in final states with jets and missing transverse momentum using* $\sqrt{s} = 8$ *TeV proton-proton collision data*, *JHEP* **09** (2014) 176 [arXiv:1405.7875] [INSPIRE].

[21] ATLAS collaboration, *Search for pair-produced third-generation squarks decaying via charm quarks or in compressed supersymmetric scenarios in pp collisions at* $\sqrt{s} = 8$ *TeV with the ATLAS detector*, *Phys. Rev.* **D 90** (2014) 052008 [arXiv:1407.0608] [INSPIRE].

JHEP10(2015)054

[22] ATLAS collaboration, *Search for new phenomena in final states with large jet multiplicities and missing transverse momentum at $\sqrt{s} = 8$ TeV proton-proton collisions using the ATLAS experiment*, *JHEP* **10** (2013) 130 [*Erratum ibid.* **01** (2014) 109] [arXiv:1308.1841] [INSPIRE].

[23] ATLAS collaboration, *Search for squarks and gluinos in events with isolated leptons, jets and missing transverse momentum at $\sqrt{s} = 8$ TeV with the ATLAS detector*, *JHEP* **04** (2015) 116 [arXiv:1501.03555] [INSPIRE].

[24] ATLAS collaboration, *Search for supersymmetry in events containing a same-flavour opposite-sign dilepton pair, jets and large missing transverse momentum in $\sqrt{s} = 8$ TeV pp collisions with the ATLAS detector*, *Eur. Phys. J.* **C 75** (2015) 318 [arXiv:1503.03290] [INSPIRE].

[25] ATLAS collaboration, *Search for supersymmetry at $\sqrt{s} = 8$ TeV in final states with jets and two same-sign leptons or three leptons with the ATLAS detector*, *JHEP* **06** (2014) 035 [arXiv:1404.2500] [INSPIRE].

[26] ATLAS collaboration, *Search for supersymmetry in events with large missing transverse momentum, jets and at least one τ lepton in $20\,\mathrm{fb}^{-1}$ of $\sqrt{s} = 8$ TeV proton-proton collision data with the ATLAS detector*, *JHEP* **09** (2014) 103 [arXiv:1407.0603] [INSPIRE].

[27] ATLAS collaboration, *Search for strong production of supersymmetric particles in final states with missing transverse momentum and at least three b-jets at $\sqrt{s} = 8$ TeV proton-proton collisions with the ATLAS detector*, *JHEP* **10** (2014) 024 [arXiv:1407.0600] [INSPIRE].

[28] P. Fayet and J. Iliopoulos, *Spontaneously broken supergauge symmetries and Goldstone spinors*, *Phys. Lett.* **B 51** (1974) 461 [INSPIRE].

[29] P. Fayet, *Supergauge invariant extension of the Higgs mechanism and a model for the electron and its neutrino*, *Nucl. Phys.* **B 90** (1975) 104 [INSPIRE].

[30] L. O'Raifeartaigh, *Spontaneous symmetry breaking for chiral scalar superfields*, *Nucl. Phys.* **B 96** (1975) 331 [INSPIRE].

[31] A.H. Chamseddine, R.L. Arnowitt and P. Nath, *Locally supersymmetric grand unification*, *Phys. Rev. Lett.* **49** (1982) 970 [INSPIRE].

[32] R. Barbieri, S. Ferrara and C.A. Savoy, *Gauge models with spontaneously broken local supersymmetry*, *Phys. Lett.* **B 119** (1982) 343 [INSPIRE].

[33] L.E. Ibáñez, *Locally supersymmetric* SU(5) *grand unification*, *Phys. Lett.* **B 118** (1982) 73 [INSPIRE].

[34] L.J. Hall, J.D. Lykken and S. Weinberg, *Supergravity as the messenger of supersymmetry breaking*, *Phys. Rev.* **D 27** (1983) 2359 [INSPIRE].

[35] N. Ohta, *Grand unified theories based on local supersymmetry*, *Prog. Theor. Phys.* **70** (1983) 542 [INSPIRE].

[36] G.L. Kane, C.F. Kolda, L. Roszkowski and J.D. Wells, *Study of constrained minimal supersymmetry*, *Phys. Rev.* **D 49** (1994) 6173 [hep-ph/9312272] [INSPIRE].

[37] M. Dine and W. Fischler, *A phenomenological model of particle physics based on supersymmetry*, *Phys. Lett.* **B 110** (1982) 227 [INSPIRE].

JHEP10(2015)054

[38] L. Álvarez-Gaumé, M. Claudson and M.B. Wise, *Low-energy supersymmetry*, Nucl. Phys. **B 207** (1982) 96 [INSPIRE].

[39] C.R. Nappi and B.A. Ovrut, *Supersymmetric extension of the* SU(3) × SU(2) × U(1) *model*, Phys. Lett. **B 113** (1982) 175 [INSPIRE].

[40] M. Dine and A.E. Nelson, *Dynamical supersymmetry breaking at low-energies*, Phys. Rev. **D 48** (1993) 1277 [hep-ph/9303230] [INSPIRE].

[41] M. Dine, A.E. Nelson and Y. Shirman, *Low-energy dynamical supersymmetry breaking simplified*, Phys. Rev. **D 51** (1995) 1362 [hep-ph/9408384] [INSPIRE].

[42] M. Dine, A.E. Nelson, Y. Nir and Y. Shirman, *New tools for low-energy dynamical supersymmetry breaking*, Phys. Rev. **D 53** (1996) 2658 [hep-ph/9507378] [INSPIRE].

[43] G.F. Giudice, M.A. Luty, H. Murayama and R. Rattazzi, *Gaugino mass without singlets*, JHEP **12** (1998) 027 [hep-ph/9810442] [INSPIRE].

[44] L. Randall and R. Sundrum, *Out of this world supersymmetry breaking*, Nucl. Phys. **B 557** (1999) 79 [hep-th/9810155] [INSPIRE].

[45] J. Alwall, P. Schuster and N. Toro, *Simplified models for a first characterization of new physics at the LHC*, Phys. Rev. **D 79** (2009) 075020 [arXiv:0810.3921] [INSPIRE].

[46] LHC New Physics Working Group collaboration, D. Alves, *Simplified models for LHC new physics searches*, J. Phys. **G 39** (2012) 105005 [arXiv:1105.2838] [INSPIRE].

[47] T. Appelquist, H.-C. Cheng and B.A. Dobrescu, *Bounds on universal extra dimensions*, Phys. Rev. **D 64** (2001) 035002 [hep-ph/0012100] [INSPIRE].

[48] H.-C. Cheng, K.T. Matchev and M. Schmaltz, *Bosonic supersymmetry? Getting fooled at the CERN LHC*, Phys. Rev. **D 66** (2002) 056006 [hep-ph/0205314] [INSPIRE].

[49] MSSM Working Group collaboration, A. Djouadi et al., *The Minimal Supersymmetric Standard Model: group summary report*, hep-ph/9901246 [INSPIRE].

[50] C.F. Berger, J.S. Gainer, J.L. Hewett and T.G. Rizzo, *Supersymmetry without prejudice*, JHEP **02** (2009) 023 [arXiv:0812.0980] [INSPIRE].

[51] M.W. Cahill-Rowley, J.L. Hewett, S. Hoeche, A. Ismail and T.G. Rizzo, *The new look pMSSM with neutralino and gravitino LSPs*, Eur. Phys. J. **C 72** (2012) 2156 [arXiv:1206.4321] [INSPIRE].

[52] S. Roy and B. Mukhopadhyaya, *Some implications of a supersymmetric model with R-parity breaking bilinear interactions*, Phys. Rev. **D 55** (1997) 7020 [hep-ph/9612447] [INSPIRE].

[53] J. Barnard, B. Farmer, T. Gherghetta and M. White, *Natural gauge mediation with a bino NLSP at the LHC*, Phys. Rev. Lett. **109** (2012) 241801 [arXiv:1208.6062] [INSPIRE].

[54] L. Covi and S. Kraml, *Collider signatures of gravitino dark matter with a sneutrino NLSP*, JHEP **08** (2007) 015 [hep-ph/0703130] [INSPIRE].

[55] G. D'Ambrosio, G.F. Giudice, G. Isidori and A. Strumia, *Minimal flavor violation: an effective field theory approach*, Nucl. Phys. **B 645** (2002) 155 [hep-ph/0207036] [INSPIRE].

[56] D.F. Carvalho, M.E. Gomez and J.C. Romao, *Charged lepton flavor violation in supersymmetry with bilinear R-parity violation*, Phys. Rev. **D 65** (2002) 093013 [hep-ph/0202054] [INSPIRE].

JHEP10(2015)054

[57] Y. Grossman and S. Rakshit, *Neutrino masses in R-parity violating supersymmetric models*, *Phys. Rev.* **D 69** (2004) 093002 [hep-ph/0311310] [INSPIRE].

[58] ATLAS collaboration, *Search for supersymmetry with jets, missing transverse momentum and at least one hadronically decaying τ lepton in proton-proton collisions at $\sqrt{s} = 7$ TeV with the ATLAS detector*, *Phys. Lett.* **B 714** (2012) 197 [arXiv:1204.3852] [INSPIRE].

[59] ATLAS collaboration, *Search for events with large missing transverse momentum, jets and at least two tau leptons in 7 TeV proton-proton collision data with the ATLAS detector*, *Phys. Lett.* **B 714** (2012) 180 [arXiv:1203.6580] [INSPIRE].

[60] ATLAS collaboration, *Further search for supersymmetry at $\sqrt{s} = 7$ TeV in final states with jets, missing transverse momentum and isolated leptons with the ATLAS detector*, *Phys. Rev.* **D 86** (2012) 092002 [arXiv:1208.4688] [INSPIRE].

[61] P. Meade, N. Seiberg and D. Shih, *General gauge mediation*, *Prog. Theor. Phys. Suppl.* **177** (2009) 143 [arXiv:0801.3278] [INSPIRE].

[62] M. Buican, P. Meade, N. Seiberg and D. Shih, *Exploring general gauge mediation*, *JHEP* **03** (2009) 016 [arXiv:0812.3668] [INSPIRE].

[63] J. Barnard, B. Farmer, T. Gherghetta and M. White, *Natural gauge mediation with a bino NLSP at the LHC*, *Phys. Rev. Lett.* **109** (2012) 241801 [arXiv:1208.6062] [INSPIRE].

[64] M. Asano, H.D. Kim, R. Kitano and Y. Shimizu, *Natural supersymmetry at the LHC*, *JHEP* **12** (2010) 019 [arXiv:1010.0692] [INSPIRE].

[65] M. Gabella, T. Gherghetta and J. Giedt, *A gravity dual and LHC study of single-sector supersymmetry breaking*, *Phys. Rev.* **D 76** (2007) 055001 [arXiv:0704.3571] [INSPIRE].

[66] N. Craig, M. McCullough and J. Thaler, *Flavor mediation delivers natural SUSY*, *JHEP* **06** (2012) 046 [arXiv:1203.1622] [INSPIRE].

[67] T.J. LeCompte and S.P. Martin, *Large Hadron Collider reach for supersymmetric models with compressed mass spectra*, *Phys. Rev.* **D 84** (2011) 015004 [arXiv:1105.4304] [INSPIRE].

[68] T.J. LeCompte and S.P. Martin, *Compressed supersymmetry after* $1\,\mathrm{fb}^{-1}$ *at the Large Hadron Collider*, *Phys. Rev.* **D 85** (2012) 035023 [arXiv:1111.6897] [INSPIRE].

[69] R. Mahbubani, M. Papucci, G. Perez, J.T. Ruderman and A. Weiler, *Light nondegenerate squarks at the LHC*, *Phys. Rev. Lett.* **110** (2013) 151804 [arXiv:1212.3328] [INSPIRE].

[70] M. Toharia and J.D. Wells, *Gluino decays with heavier scalar superpartners*, *JHEP* **02** (2006) 015 [hep-ph/0503175] [INSPIRE].

[71] ATLAS collaboration, *Performance of the ATLAS trigger system in* 2010, *Eur. Phys. J.* **C 72** (2012) 1849 [arXiv:1110.1530] [INSPIRE].

[72] ATLAS collaboration, *Improved luminosity determination in pp collisions at $\sqrt{s} = 7$ TeV using the ATLAS detector at the LHC*, *Eur. Phys. J.* **C 73** (2013) 2518 [arXiv:1302.4393] [INSPIRE].

[73] ATLAS collaboration, *Measurements of top quark pair relative differential cross-sections with ATLAS in pp collisions at $\sqrt{s} = 7$ TeV*, *Eur. Phys. J.* **C 73** (2013) 2261 [arXiv:1207.5644] [INSPIRE].

JHEP10(2015)054

[74] ATLAS collaboration, *Measurements of normalized differential cross sections for $t\bar{t}$ production in pp collisions at $\sqrt{s} = 7$ TeV using the ATLAS detector*, Phys. Rev. **D 90** (2014) 072004 [arXiv:1407.0371] [INSPIRE].

[75] T. Gleisberg et al., *Event generation with SHERPA* 1.1, JHEP **02** (2009) 007 [arXiv:0811.4622] [INSPIRE].

[76] S. Catani, L. Cieri, G. Ferrera, D. de Florian and M. Grazzini, *Vector boson production at hadron colliders: a fully exclusive QCD calculation at NNLO*, Phys. Rev. Lett. **103** (2009) 082001 [arXiv:0903.2120] [INSPIRE].

[77] H.-L. Lai et al., *New parton distributions for collider physics*, Phys. Rev. **D 82** (2010) 074024 [arXiv:1007.2241] [INSPIRE].

[78] K. Melnikov and F. Petriello, *Electroweak gauge boson production at hadron colliders through $O(\alpha_s^2)$*, Phys. Rev. **D 74** (2006) 114017 [hep-ph/0609070] [INSPIRE].

[79] M.L. Mangano, M. Moretti, F. Piccinini, R. Pittau and A.D. Polosa, *ALPGEN, a generator for hard multiparton processes in hadronic collisions*, JHEP **07** (2003) 001 [hep-ph/0206293] [INSPIRE].

[80] ATLAS collaboration, *New ATLAS event generator tunes to* 2010 *data*, ATL-PHYS-PUB-2011-008, CERN, Geneva Switzerland (2011).

[81] J. Pumplin et al., *New generation of parton distributions with uncertainties from global QCD analysis*, JHEP **07** (2002) 012 [hep-ph/0201195] [INSPIRE].

[82] G. Corcella et al., *HERWIG* 6*: an event generator for hadron emission reactions with interfering gluons (including supersymmetric processes)*, JHEP **01** (2001) 010 [hep-ph/0011363] [INSPIRE].

[83] G. Corcella et al., *HERWIG* 6.5 *release note*, hep-ph/0210213 [INSPIRE].

[84] J.M. Butterworth, J.R. Forshaw and M.H. Seymour, *Multiparton interactions in photoproduction at HERA*, Z. Phys. **C 72** (1996) 637 [hep-ph/9601371] [INSPIRE].

[85] P. Nason, *A new method for combining NLO QCD with shower Monte Carlo algorithms*, JHEP **11** (2004) 040 [hep-ph/0409146] [INSPIRE].

[86] S. Frixione, P. Nason and C. Oleari, *Matching NLO QCD computations with parton shower simulations: the POWHEG method*, JHEP **11** (2007) 070 [arXiv:0709.2092] [INSPIRE].

[87] S. Alioli, P. Nason, C. Oleari and E. Re, *A general framework for implementing NLO calculations in shower Monte Carlo programs: the POWHEG BOX*, JHEP **06** (2010) 043 [arXiv:1002.2581] [INSPIRE].

[88] M. Czakon, P. Fiedler and A. Mitov, *Total top-quark pair-production cross section at hadron colliders through $O(\alpha_s^4)$*, Phys. Rev. Lett. **110** (2013) 252004 [arXiv:1303.6254] [INSPIRE].

[89] M. Czakon and A. Mitov, *Top++: a program for the calculation of the top-pair cross-section at hadron colliders*, Comput. Phys. Commun. **185** (2014) 2930 [arXiv:1112.5675] [INSPIRE].

[90] T. Sjöstrand, S. Mrenna and P.Z. Skands, *PYTHIA* 6.4 *physics and manual*, JHEP **05** (2006) 026 [hep-ph/0603175] [INSPIRE].

[91] B. Cooper, J. Katzy, M.L. Mangano, A. Messina, L. Mijovic and P. Skands, *Importance of a consistent choice of α_s in the matching of ALPGEN and PYTHIA*, Eur. Phys. J. **C 72** (2012) 2078 [arXiv:1109.5295] [INSPIRE].

JHEP10(2015)054

[92] P.Z. Skands, *Tuning Monte Carlo generators: the Perugia tunes*, *Phys. Rev.* **D 82** (2010) 074018 [arXiv:1005.3457] [INSPIRE].

[93] B.P. Kersevan and E. Richter-Was, *The Monte Carlo event generator AcerMC versions* 2.0 *to* 3.8 *with interfaces to PYTHIA* 6.4*, HERWIG* 6.5 *and ARIADNE* 4.1, *Comput. Phys. Commun.* **184** (2013) 919 [hep-ph/0405247] [INSPIRE].

[94] N. Kidonakis, *Next-to-next-to-leading-order collinear and soft gluon corrections for t-channel single top quark production*, *Phys. Rev.* **D 83** (2011) 091503 [arXiv:1103.2792] [INSPIRE].

[95] ATLAS collaboration, *Further ATLAS tunes of PYTHIA*6 *and PYTHIA*8, ATL-PHYS-PUB-2011-014, CERN, Geneva Switzerland (2011).

[96] S. Frixione and B.R. Webber, *Matching NLO QCD computations and parton shower simulations*, *JHEP* **06** (2002) 029 [hep-ph/0204244] [INSPIRE].

[97] S. Frixione, P. Nason and B.R. Webber, *Matching NLO QCD and parton showers in heavy flavor production*, *JHEP* **08** (2003) 007 [hep-ph/0305252] [INSPIRE].

[98] N. Kidonakis, *NNLL resummation for s-channel single top quark production*, *Phys. Rev.* **D 81** (2010) 054028 [arXiv:1001.5034] [INSPIRE].

[99] N. Kidonakis, *Two-loop soft anomalous dimensions for single top quark associated production with a* W^- *or* H^-, *Phys. Rev.* **D 82** (2010) 054018 [arXiv:1005.4451] [INSPIRE].

[100] J. Alwall, M. Herquet, F. Maltoni, O. Mattelaer and T. Stelzer, *MadGraph* 5*: going beyond*, *JHEP* **06** (2011) 128 [arXiv:1106.0522] [INSPIRE].

[101] A. Lazopoulos, T. McElmurry, K. Melnikov and F. Petriello, *Next-to-leading order QCD corrections to* $t\bar{t}Z$ *production at the LHC*, *Phys. Lett.* **B 666** (2008) 62 [arXiv:0804.2220] [INSPIRE].

[102] M.V. Garzelli, A. Kardos, C.G. Papadopoulos and Z. Trócsányi, $t\bar{t}W^{\pm}$ *and* $t\bar{t}Z$ *hadroproduction at NLO accuracy in QCD with parton shower and hadronization effects*, *JHEP* **11** (2012) 056 [arXiv:1208.2665] [INSPIRE].

[103] J.M. Campbell and R.K. Ellis, $t\bar{t}W^{\pm}$ *production and decay at NLO*, *JHEP* **07** (2012) 052 [arXiv:1204.5678] [INSPIRE].

[104] J.M. Campbell and R.K. Ellis, *An update on vector boson pair production at hadron colliders*, *Phys. Rev.* **D 60** (1999) 113006 [hep-ph/9905386] [INSPIRE].

[105] J.M. Campbell, R.K. Ellis and C. Williams, *Vector boson pair production at the LHC*, *JHEP* **07** (2011) 018 [arXiv:1105.0020] [INSPIRE].

[106] M. Bahr et al., *HERWIG++ physics and manual*, *Eur. Phys. J.* **C 58** (2008) 639 [arXiv:0803.0883] [INSPIRE].

[107] M.L. Mangano, M. Moretti, F. Piccinini and M. Treccani, *Matching matrix elements and shower evolution for top-quark production in hadronic collisions*, *JHEP* **01** (2007) 013 [hep-ph/0611129] [INSPIRE].

[108] S. Gieseke, C. Rohr and A. Siodmok, *Colour reconnections in HERWIG++*, *Eur. Phys. J.* **C 72** (2012) 2225 [arXiv:1206.0041] [INSPIRE].

[109] W. Beenakker, R. Hopker, M. Spira and P.M. Zerwas, *Squark and gluino production at hadron colliders*, *Nucl. Phys.* **B 492** (1997) 51 [hep-ph/9610490] [INSPIRE].

JHEP10(2015)054

[110] A. Kulesza and L. Motyka, *Threshold resummation for squark-antisquark and gluino-pair production at the LHC*, Phys. Rev. Lett. **102** (2009) 111802 [arXiv:0807.2405] [INSPIRE].

[111] A. Kulesza and L. Motyka, *Soft gluon resummation for the production of gluino-gluino and squark-antisquark pairs at the LHC*, Phys. Rev. **D 80** (2009) 095004 [arXiv:0905.4749] [INSPIRE].

[112] W. Beenakker et al., *Soft-gluon resummation for squark and gluino hadroproduction*, JHEP **12** (2009) 041 [arXiv:0909.4418] [INSPIRE].

[113] W. Beenakker et al., *Squark and gluino hadroproduction*, Int. J. Mod. Phys. **A 26** (2011) 2637 [arXiv:1105.1110] [INSPIRE].

[114] M. Krämer et al., *Supersymmetry production cross sections in pp collisions at* $\sqrt{s} = 7$ *TeV*, arXiv:1206.2892 [INSPIRE].

[115] A. Djouadi, M.M. Muhlleitner and M. Spira, *Decays of supersymmetric particles: the program SUSY-HIT (SUspect-SdecaY-HDECAY-InTerface)*, Acta Phys. Polon. **B 38** (2007) 635 [hep-ph/0609292] [INSPIRE].

[116] M. Muhlleitner, A. Djouadi and Y. Mambrini, *SDECAY: a fortran code for the decays of the supersymmetric particles in the MSSM*, Comput. Phys. Commun. **168** (2005) 46 [hep-ph/0311167] [INSPIRE].

[117] B.C. Allanach, *SOFTSUSY: a program for calculating supersymmetric spectra*, Comput. Phys. Commun. **143** (2002) 305 [hep-ph/0104145] [INSPIRE].

[118] S. Jadach, Z. Was, R. Decker and J.H. Kuhn, *The tau decay library TAUOLA: version* 2.4, Comput. Phys. Commun. **76** (1993) 361 [INSPIRE].

[119] P. Golonka, B. Kersevan, T. Pierzchala, E. Richter-Was, Z. Was and M. Worek, *The Tauola photos F environment for the TAUOLA and PHOTOS packages: release* 2, Comput. Phys. Commun. **174** (2006) 818 [hep-ph/0312240] [INSPIRE].

[120] ATLAS collaboration, *The ATLAS simulation infrastructure*, Eur. Phys. J. **C 70** (2010) 823 [arXiv:1005.4568] [INSPIRE].

[121] GEANT4 collaboration, S. Agostinelli et al., *GEANT4: a simulation toolkit*, Nucl. Instrum. Meth. **A 506** (2003) 250 [INSPIRE].

[122] ATLAS collaboration, *The simulation principle and performance of the ATLAS fast calorimeter simulation FastCaloSim*, ATL-PHYS-PUB-2010-013, CERN, Geneva Switzerland (2010).

[123] A. Sherstnev and R.S. Thorne, *Parton distributions for LO generators*, Eur. Phys. J. **C 55** (2008) 553 [arXiv:0711.2473] [INSPIRE].

[124] M. Cacciari, G.P. Salam and G. Soyez, *The anti-*k_t *jet clustering algorithm*, JHEP **04** (2008) 063 [arXiv:0802.1189] [INSPIRE].

[125] M. Cacciari and G.P. Salam, *Dispelling the* N^3 *myth for the* k_t *jet-finder*, Phys. Lett. **B 641** (2006) 57 [hep-ph/0512210] [INSPIRE].

[126] W. Lampl et al., *Calorimeter clustering algorithms: description and performance*, ATL-LARG-PUB-2008-002, CERN, Geneva Switzerland (2008).

[127] ATLAS collaboration, *Jet energy measurement and its systematic uncertainty in proton-proton collisions at* $\sqrt{s} = 7$ *TeV with the ATLAS detector*, Eur. Phys. J. **C 75** (2015) 17 [arXiv:1406.0076] [INSPIRE].

JHEP10(2015)054

[128] C. Issever, K. Borras and D. Wegener, *An improved weighting algorithm to achieve software compensation in a fine grained LAr calorimeter*, *Nucl. Instrum. Meth.* **A 545** (2005) 803 [physics/0408129] [INSPIRE].

[129] M. Cacciari and G.P. Salam, *Pileup subtraction using jet areas*, *Phys. Lett.* **B 659** (2008) 119 [arXiv:0707.1378] [INSPIRE].

[130] ATLAS collaboration, *Pile-up subtraction and suppression for jets in ATLAS*, ATLAS-CONF-2013-083, CERN, Geneva Switzerland (2013).

[131] ATLAS collaboration, *Jet energy scale and its systematic uncertainty in proton-proton collisions at* $\sqrt{s} = 7$ *TeV with ATLAS* 2011 *data*, ATLAS-CONF-2013-004, CERN, Geneva Switzerland (2013).

[132] ATLAS collaboration, *Commissioning of the ATLAS high-performance b-tagging algorithms in the* 7 *TeV collision data*, ATLAS-CONF-2011-102, CERN, Geneva Switzerland (2011).

[133] ATLAS collaboration, *Calibration of b-tagging using dileptonic top pair events in a combinatorial likelihood approach with the ATLAS experiment*, ATLAS-CONF-2014-004, CERN, Geneva Switzerland (2014).

[134] ATLAS collaboration, *Calibration of the performance of b-tagging for c and light-flavour jets in the* 2012 *ATLAS data*, ATLAS-CONF-2014-046, CERN, Geneva Switzerland (2014).

[135] ATLAS collaboration, *Electron reconstruction and identification efficiency measurements with the ATLAS detector using the* 2011 *LHC proton-proton collision data*, *Eur. Phys. J.* **C 74** (2014) 2941 [arXiv:1404.2240] [INSPIRE].

[136] ATLAS collaboration, *Measurements of the photon identification efficiency with the ATLAS detector using* $4.9\,\mathrm{fb}^{-1}$ *of pp collision data collected in* 2011, ATLAS-CONF-2012-123, CERN, Geneva Switzerland (2012).

[137] ATLAS collaboration, *Muon reconstruction efficiency and momentum resolution of the ATLAS experiment in proton-proton collisions at* $\sqrt{s} = 7$ *TeV in* 2010, *Eur. Phys. J.* **C 74** (2014) 3034 [arXiv:1404.4562] [INSPIRE].

[138] ATLAS collaboration, *Identification of the hadronic decays of tau leptons in* 2012 *data with the ATLAS detector*, ATLAS-CONF-2013-064, CERN, Geneva Switzerland (2013).

[139] ATLAS collaboration, *Determination of the tau energy scale and the associated systematic uncertainty in proton-proton collisions at* $\sqrt{s} = 8$ *TeV with the ATLAS detector at the LHC in* 2012, ATLAS-CONF-2013-044, CERN, Geneva Switzerland (2013).

[140] ATLAS collaboration, *Performance of missing transverse momentum reconstruction in proton-proton collisions at* 7 *TeV with ATLAS*, *Eur. Phys. J.* **C 72** (2012) 1844 [arXiv:1108.5602] [INSPIRE].

[141] ATLAS collaboration, *Performance of missing transverse momentum reconstruction in ATLAS studied in proton-proton collisions recorded in* 2012 *at* 8 *TeV*, ATLAS-CONF-2013-082, CERN, Geneva Switzerland (2013).

[142] M. Baak, G.J. Besjes, D. Côte, A. Koutsman, J. Lorenz and D. Short, *HistFitter software framework for statistical data analysis*, *Eur. Phys. J.* **C 75** (2015) 153 [arXiv:1410.1280] [INSPIRE].

[143] A.L. Read, *Presentation of search results: the* CL_s *technique*, *J. Phys.* **G 28** (2002) 2693 [INSPIRE].

JHEP10(2015)054

[144] ATLAS collaboration, *Search for scalar charm quark pair production in pp collisions at $\sqrt{s} = 8$ TeV with the ATLAS detector*, *Phys. Rev. Lett.* **114** (2015) 161801 [arXiv:1501.01325] [INSPIRE].

[145] M. Lisanti, P. Schuster, M. Strassler and N. Toro, *Study of LHC searches for a lepton and many jets*, *JHEP* **11** (2012) 081 [arXiv:1107.5055] [INSPIRE].

[146] J.A. Evans, Y. Kats, D. Shih and M.J. Strassler, *Toward full LHC coverage of natural supersymmetry*, *JHEP* **07** (2014) 101 [arXiv:1310.5758] [INSPIRE].

[147] I. Hinchliffe, F.E. Paige, M.D. Shapiro, J. Soderqvist and W. Yao, *Precision SUSY measurements at CERN LHC*, *Phys. Rev.* **D 55** (1997) 5520 [hep-ph/9610544] [INSPIRE].

[148] CMS collaboration, *Search for physics beyond the standard model in events with two leptons, jets and missing transverse momentum in pp collisions at $\sqrt{s} = 8$ TeV*, *JHEP* **04** (2015) 124 [arXiv:1502.06031] [INSPIRE].

[149] R. Barbieri and G.F. Giudice, *Upper bounds on supersymmetric particle masses*, *Nucl. Phys.* **B 306** (1988) 63 [INSPIRE].

[150] B. de Carlos and J.A. Casas, *One loop analysis of the electroweak breaking in supersymmetric models and the fine tuning problem*, *Phys. Lett.* **B 309** (1993) 320 [hep-ph/9303291] [INSPIRE].

[151] J.R. Ellis, T. Falk, K.A. Olive and M. Srednicki, *Calculations of neutralino-stau coannihilation channels and the cosmologically relevant region of MSSM parameter space*, *Astropart. Phys.* **13** (2000) 181 [*Erratum ibid.* **15** (2001) 413] [hep-ph/9905481] [INSPIRE].

[152] D. Albornoz Vasquez, G. Bélanger and C. Boehm, *Revisiting light neutralino scenarios in the MSSM*, *Phys. Rev.* **D 84** (2011) 095015 [arXiv:1108.1338] [INSPIRE].

[153] ATLAS collaboration, *Single hadron response measurement and calorimeter jet energy scale uncertainty with the ATLAS detector at the LHC*, *Eur. Phys. J.* **C 73** (2013) 2305 [arXiv:1203.1302] [INSPIRE].

[154] ATLAS collaboration, *Jet energy resolution in proton-proton collisions at $\sqrt{s} = 7$ TeV recorded in* 2010 *with the ATLAS detector*, *Eur. Phys. J.* **C 73** (2013) 2306 [arXiv:1210.6210] [INSPIRE].

[155] M. Botje et al., *The PDF4LHC working group interim recommendations*, arXiv:1101.0538 [INSPIRE].

[156] ATLAS collaboration, *Search for squarks and gluinos with the ATLAS detector in final states with jets and missing transverse momentum using* $4.7\,\mathrm{fb}^{-1}$ *of $\sqrt{s} = 7$ TeV proton-proton collision data*, *Phys. Rev.* **D 87** (2013) 012008 [arXiv:1208.0949] [INSPIRE].

[157] ATLAS collaboration, *Limits on metastable gluinos from ATLAS SUSY searches at* 8 *TeV*, ATLAS-CONF-2014-037, CERN, Geneva Switzerland (2014).

JHEP10(2015)054

The ATLAS collaboration

G. Aad[85], B. Abbott[113], J. Abdallah[151], O. Abdinov[11], R. Aben[107], M. Abolins[90], O.S. AbouZeid[158], H. Abramowicz[153], H. Abreu[152], R. Abreu[116], Y. Abulaiti[146a,146b], B.S. Acharya[164a,164b,a], L. Adamczyk[38a], D.L. Adams[25], J. Adelman[108], S. Adomeit[100], T. Adye[131], A.A. Affolder[74], T. Agatonovic-Jovin[13], J. Agricola[54], J.A. Aguilar-Saavedra[126a,126f], S.P. Ahlen[22], F. Ahmadov[65,b], G. Aielli[133a,133b], H. Akerstedt[146a,146b], T.P.A. Åkesson[81], A.V. Akimov[96], G.L. Alberghi[20a,20b], J. Albert[169], S. Albrand[55], M.J. Alconada Verzini[71], M. Aleksa[30], I.N. Aleksandrov[65], C. Alexa[26a], G. Alexander[153], T. Alexopoulos[10], M. Alhroob[113], G. Alimonti[91a], L. Alio[85], J. Alison[31], S.P. Alkire[35], B.M.M. Allbrooke[149], P.P. Allport[74], A. Aloisio[104a,104b], A. Alonso[36], F. Alonso[71], C. Alpigiani[76], A. Altheimer[35], B. Alvarez Gonzalez[30], D. Álvarez Piqueras[167], M.G. Alviggi[104a,104b], B.T. Amadio[15], K. Amako[66], Y. Amaral Coutinho[24a], C. Amelung[23], D. Amidei[89], S.P. Amor Dos Santos[126a,126c], A. Amorim[126a,126b], S. Amoroso[48], N. Amram[153], G. Amundsen[23], C. Anastopoulos[139], L.S. Ancu[49], N. Andari[108], T. Andeen[35], C.F. Anders[58b], G. Anders[30], J.K. Anders[74], K.J. Anderson[31], A. Andreazza[91a,91b], V. Andrei[58a], S. Angelidakis[9], I. Angelozzi[107], P. Anger[44], A. Angerami[35], F. Anghinolfi[30], A.V. Anisenkov[109,c], N. Anjos[12], A. Annovi[124a,124b], M. Antonelli[47], A. Antonov[98], J. Antos[144b], F. Anulli[132a], M. Aoki[66], L. Aperio Bella[18], G. Arabidze[90], Y. Arai[66], J.P. Araque[126a], A.T.H. Arce[45], F.A. Arduh[71], J-F. Arguin[95], S. Argyropoulos[42], M. Arik[19a], A.J. Armbruster[30], O. Arnaez[30], V. Arnal[82], H. Arnold[48], M. Arratia[28], O. Arslan[21], A. Artamonov[97], G. Artoni[23], S. Asai[155], N. Asbah[42], A. Ashkenazi[153], B. Åsman[146a,146b], L. Asquith[149], K. Assamagan[25], R. Astalos[144a], M. Atkinson[165], N.B. Atlay[141], K. Augsten[128], M. Aurousseau[145b], G. Avolio[30], B. Axen[15], M.K. Ayoub[117], G. Azuelos[95,d], M.A. Baak[30], A.E. Baas[58a], M.J. Baca[18], C. Bacci[134a,134b], H. Bachacou[136], K. Bachas[154], M. Backes[30], M. Backhaus[30], P. Bagiacchi[132a,132b], P. Bagnaia[132a,132b], Y. Bai[33a], T. Bain[35], J.T. Baines[131], O.K. Baker[176], E.M. Baldin[109,c], P. Balek[129], T. Balestri[148], F. Balli[84], E. Banas[39], Sw. Banerjee[173], A.A.E. Bannoura[175], H.S. Bansil[18], L. Barak[30], E.L. Barberio[88], D. Barberis[50a,50b], M. Barbero[85], T. Barillari[101], M. Barisonzi[164a,164b], T. Barklow[143], N. Barlow[28], S.L. Barnes[84], B.M. Barnett[131], R.M. Barnett[15], Z. Barnovska[5], A. Baroncelli[134a], G. Barone[23], A.J. Barr[120], F. Barreiro[82], J. Barreiro Guimarães da Costa[57], R. Bartoldus[143], A.E. Barton[72], P. Bartos[144a], A. Basalaev[123], A. Bassalat[117], A. Basye[165], R.L. Bates[53], S.J. Batista[158], J.R. Batley[28], M. Battaglia[137], M. Bauce[132a,132b], F. Bauer[136], H.S. Bawa[143,e], J.B. Beacham[111], M.D. Beattie[72], T. Beau[80], P.H. Beauchemin[161], R. Beccherle[124a,124b], P. Bechtle[21], H.P. Beck[17,f], K. Becker[120], M. Becker[83], S. Becker[100], M. Beckingham[170], C. Becot[117], A.J. Beddall[19b], A. Beddall[19b], V.A. Bednyakov[65], C.P. Bee[148], L.J. Beemster[107], T.A. Beermann[175], M. Begel[25], J.K. Behr[120], C. Belanger-Champagne[87], W.H. Bell[49], G. Bella[153], L. Bellagamba[20a], A. Bellerive[29], M. Bellomo[86], K. Belotskiy[98], O. Beltramello[30], O. Benary[153], D. Benchekroun[135a], M. Bender[100], K. Bendtz[146a,146b], N. Benekos[10], Y. Benhammou[153], E. Benhar Noccioli[49], J.A. Benitez Garcia[159b], D.P. Benjamin[45], J.R. Bensinger[23], S. Bentvelsen[107], L. Beresford[120], M. Beretta[47], D. Berge[107], E. Bergeaas Kuutmann[166], N. Berger[5], F. Berghaus[169], J. Beringer[15], C. Bernard[22], N.R. Bernard[86], C. Bernius[110], F.U. Bernlochner[21], T. Berry[77], P. Berta[129], C. Bertella[83], G. Bertoli[146a,146b], F. Bertolucci[124a,124b], C. Bertsche[113], D. Bertsche[113], M.I. Besana[91a], G.J. Besjes[36], O. Bessidskaia Bylund[146a,146b], M. Bessner[42], N. Besson[136], C. Betancourt[48], S. Bethke[101], A.J. Bevan[76], W. Bhimji[15], R.M. Bianchi[125], L. Bianchini[23], M. Bianco[30], O. Biebel[100], D. Biedermann[16], S.P. Bieniek[78], M. Biglietti[134a], J. Bilbao De Mendizabal[49], H. Bilokon[47], M. Bindi[54], S. Binet[117], A. Bingul[19b], C. Bini[132a,132b], S. Biondi[20a,20b], C.W. Black[150], J.E. Black[143], K.M. Black[22], D. Blackburn[138], R.E. Blair[6], J.-B. Blanchard[136],

JHEP10(2015)054

J.E. Blanco[77], T. Blazek[144a], I. Bloch[42], C. Blocker[23], W. Blum[83,*], U. Blumenschein[54], G.J. Bobbink[107], V.S. Bobrovnikov[109,c], S.S. Bocchetta[81], A. Bocci[45], C. Bock[100], M. Boehler[48], J.A. Bogaerts[30], D. Bogavac[13], A.G. Bogdanchikov[109], C. Bohm[146a], V. Boisvert[77], T. Bold[38a], V. Boldea[26a], A.S. Boldyrev[99], M. Bomben[80], M. Bona[76], M. Boonekamp[136], A. Borisov[130], G. Borissov[72], S. Borroni[42], J. Bortfeldt[100], V. Bortolotto[60a,60b,60c], K. Bos[107], D. Boscherini[20a], M. Bosman[12], J. Boudreau[125], J. Bouffard[2], E.V. Bouhova-Thacker[72], D. Boumediene[34], C. Bourdarios[117], N. Bousson[114], A. Boveia[30], J. Boyd[30], I.R. Boyko[65], I. Bozic[13], J. Bracinik[18], A. Brandt[8], G. Brandt[54], O. Brandt[58a], U. Bratzler[156], B. Brau[86], J.E. Brau[116], H.M. Braun[175,*], S.F. Brazzale[164a,164c], W.D. Breaden Madden[53], K. Brendlinger[122], A.J. Brennan[88], L. Brenner[107], R. Brenner[166], S. Bressler[172], K. Bristow[145c], T.M. Bristow[46], D. Britton[53], D. Britzger[42], F.M. Brochu[28], I. Brock[21], R. Brock[90], J. Bronner[101], G. Brooijmans[35], T. Brooks[77], W.K. Brooks[32b], J. Brosamer[15], E. Brost[116], J. Brown[55], P.A. Bruckman de Renstrom[39], D. Bruncko[144b], R. Bruneliere[48], A. Bruni[20a], G. Bruni[20a], M. Bruschi[20a], N. Bruscino[21], L. Bryngemark[81], T. Buanes[14], Q. Buat[142], P. Buchholz[141], A.G. Buckley[53], S.I. Buda[26a], I.A. Budagov[65], F. Buehrer[48], L. Bugge[119], M.K. Bugge[119], O. Bulekov[98], D. Bullock[8], H. Burckhart[30], S. Burdin[74], C.D. Burgard[48], B. Burghgrave[108], S. Burke[131], I. Burmeister[43], E. Busato[34], D. Büscher[48], V. Büscher[83], P. Bussey[53], J.M. Butler[22], A.I. Butt[3], C.M. Buttar[53], J.M. Butterworth[78], P. Butti[107], W. Buttinger[25], A. Buzatu[53], A.R. Buzykaev[109,c], S. Cabrera Urbán[167], D. Caforio[128], V.M. Cairo[37a,37b], O. Cakir[4a], N. Calace[49], P. Calafiura[15], A. Calandri[136], G. Calderini[80], P. Calfayan[100], L.P. Caloba[24a], D. Calvet[34], S. Calvet[34], R. Camacho Toro[31], S. Camarda[42], P. Camarri[133a,133b], D. Cameron[119], R. Caminal Armadans[165], S. Campana[30], M. Campanelli[78], A. Campoverde[148], V. Canale[104a,104b], A. Canepa[159a], M. Cano Bret[33e], J. Cantero[82], R. Cantrill[126a], T. Cao[40], M.D.M. Capeans Garrido[30], I. Caprini[26a], M. Caprini[26a], M. Capua[37a,37b], R. Caputo[83], R. Cardarelli[133a], F. Cardillo[48], T. Carli[30], G. Carlino[104a], L. Carminati[91a,91b], S. Caron[106], E. Carquin[32a], G.D. Carrillo-Montoya[30], J.R. Carter[28], J. Carvalho[126a,126c], D. Casadei[78], M.P. Casado[12], M. Casolino[12], E. Castaneda-Miranda[145b], A. Castelli[107], V. Castillo Gimenez[167], N.F. Castro[126a,g], P. Catastini[57], A. Catinaccio[30], J.R. Catmore[119], A. Cattai[30], J. Caudron[83], V. Cavaliere[165], D. Cavalli[91a], M. Cavalli-Sforza[12], V. Cavasinni[124a,124b], F. Ceradini[134a,134b], B.C. Cerio[45], K. Cerny[129], A.S. Cerqueira[24b], A. Cerri[149], L. Cerrito[76], F. Cerutti[15], M. Cerv[30], A. Cervelli[17], S.A. Cetin[19c], A. Chafaq[135a], D. Chakraborty[108], I. Chalupkova[129], P. Chang[165], J.D. Chapman[28], D.G. Charlton[18], C.C. Chau[158], C.A. Chavez Barajas[149], S. Cheatham[152], A. Chegwidden[90], S. Chekanov[6], S.V. Chekulaev[159a], G.A. Chelkov[65,h], M.A. Chelstowska[89], C. Chen[64], H. Chen[25], K. Chen[148], L. Chen[33d,i], S. Chen[33c], X. Chen[33f], Y. Chen[67], H.C. Cheng[89], Y. Cheng[31], A. Cheplakov[65], E. Cheremushkina[130], R. Cherkaoui El Moursli[135e], V. Chernyatin[25,*], E. Cheu[7], L. Chevalier[136], V. Chiarella[47], G. Chiarelli[124a,124b], G. Chiodini[73a], A.S. Chisholm[18], R.T. Chislett[78], A. Chitan[26a], M.V. Chizhov[65], K. Choi[61], S. Chouridou[9], B.K.B. Chow[100], V. Christodoulou[78], D. Chromek-Burckhart[30], J. Chudoba[127], A.J. Chuinard[87], J.J. Chwastowski[39], L. Chytka[115], G. Ciapetti[132a,132b], A.K. Ciftci[4a], D. Cinca[53], V. Cindro[75], I.A. Cioara[21], A. Ciocio[15], Z.H. Citron[172], M. Ciubancan[26a], A. Clark[49], B.L. Clark[57], P.J. Clark[46], R.N. Clarke[15], W. Cleland[125], C. Clement[146a,146b], Y. Coadou[85], M. Cobal[164a,164c], A. Coccaro[138], J. Cochran[64], L. Coffey[23], J.G. Cogan[143], L. Colasurdo[106], B. Cole[35], S. Cole[108], A.P. Colijn[107], J. Collot[55], T. Colombo[58c], G. Compostella[101], P. Conde Muiño[126a,126b], E. Coniavitis[48], S.H. Connell[145b], I.A. Connelly[77], S.M. Consonni[91a,91b], V. Consorti[48], S. Constantinescu[26a], C. Conta[121a,121b], G. Conti[30], F. Conventi[104a,j], M. Cooke[15], B.D. Cooper[78], A.M. Cooper-Sarkar[120], T. Cornelissen[175], M. Corradi[20a], F. Corriveau[87,k], A. Corso-Radu[163], A. Cortes-Gonzalez[12], G. Cortiana[101], G. Costa[91a], M.J. Costa[167], D. Costanzo[139], D. Côté[8], G. Cottin[28], G. Cowan[77], B.E. Cox[84], K. Cranmer[110], G. Cree[29],

JHEP10(2015)054

S. Crépé-Renaudin[55], F. Crescioli[80], W.A. Cribbs[146a,146b], M. Crispin Ortuzar[120], M. Cristinziani[21], V. Croft[106], G. Crosetti[37a,37b], T. Cuhadar Donszelmann[139], J. Cummings[176], M. Curatolo[47], C. Cuthbert[150], H. Czirr[141], P. Czodrowski[3], S. D'Auria[53], M. D'Onofrio[74], M.J. Da Cunha Sargedas De Sousa[126a,126b], C. Da Via[84], W. Dabrowski[38a], A. Dafinca[120], T. Dai[89], O. Dale[14], F. Dallaire[95], C. Dallapiccola[86], M. Dam[36], J.R. Dandoy[31], N.P. Dang[48], A.C. Daniells[18], M. Danninger[168], M. Dano Hoffmann[136], V. Dao[48], G. Darbo[50a], S. Darmora[8], J. Dassoulas[3], A. Dattagupta[61], W. Davey[21], C. David[169], T. Davidek[129], E. Davies[120,l], M. Davies[153], P. Davison[78], Y. Davygora[58a], E. Dawe[88], I. Dawson[139], R.K. Daya-Ishmukhametova[86], K. De[8], R. de Asmundis[104a], A. De Benedetti[113], S. De Castro[20a,20b], S. De Cecco[80], N. De Groot[106], P. de Jong[107], H. De la Torre[82], F. De Lorenzi[64], L. De Nooij[107], D. De Pedis[132a], A. De Salvo[132a], U. De Sanctis[149], A. De Santo[149], J.B. De Vivie De Regie[117], W.J. Dearnaley[72], R. Debbe[25], C. Debenedetti[137], D.V. Dedovich[65], I. Deigaard[107], J. Del Peso[82], T. Del Prete[124a,124b], D. Delgove[117], F. Deliot[136], C.M. Delitzsch[49], M. Deliyergiyev[75], A. Dell'Acqua[30], L. Dell'Asta[22], M. Dell'Orso[124a,124b], M. Della Pietra[104a,j], D. della Volpe[49], M. Delmastro[5], P.A. Delsart[55], C. Deluca[107], D.A. DeMarco[158], S. Demers[176], M. Demichev[65], A. Demilly[80], S.P. Denisov[130], D. Derendarz[39], J.E. Derkaoui[135d], F. Derue[80], P. Dervan[74], K. Desch[21], C. Deterre[42], P.O. Deviveiros[30], A. Dewhurst[131], S. Dhaliwal[23], A. Di Ciaccio[133a,133b], L. Di Ciaccio[5], A. Di Domenico[132a,132b], C. Di Donato[104a,104b], A. Di Girolamo[30], B. Di Girolamo[30], A. Di Mattia[152], B. Di Micco[134a,134b], R. Di Nardo[47], A. Di Simone[48], R. Di Sipio[158], D. Di Valentino[29], C. Diaconu[85], M. Diamond[158], F.A. Dias[46], M.A. Diaz[32a], E.B. Diehl[89], J. Dietrich[16], S. Diglio[85], A. Dimitrievska[13], J. Dingfelder[21], P. Dita[26a], S. Dita[26a], F. Dittus[30], F. Djama[85], T. Djobava[51b], J.I. Djuvsland[58a], M.A.B. do Vale[24c], D. Dobos[30], M. Dobre[26a], C. Doglioni[81], T. Dohmae[155], J. Dolejsi[129], Z. Dolezal[129], B.A. Dolgoshein[98,*], M. Donadelli[24d], S. Donati[124a,124b], P. Dondero[121a,121b], J. Donini[34], J. Dopke[131], A. Doria[104a], M.T. Dova[71], A.T. Doyle[53], E. Drechsler[54], M. Dris[10], E. Dubreuil[34], E. Duchovni[172], G. Duckeck[100], O.A. Ducu[26a,85], D. Duda[107], A. Dudarev[30], L. Duflot[117], L. Duguid[77], M. Dührssen[30], M. Dunford[58a], H. Duran Yildiz[4a], M. Düren[52], A. Durglishvili[51b], D. Duschinger[44], M. Dyndal[38a], C. Eckardt[42], K.M. Ecker[101], R.C. Edgar[89], W. Edson[2], N.C. Edwards[46], W. Ehrenfeld[21], T. Eifert[30], G. Eigen[14], K. Einsweiler[15], T. Ekelof[166], M. El Kacimi[135c], M. Ellert[166], S. Elles[5], F. Ellinghaus[175], A.A. Elliot[169], N. Ellis[30], J. Elmsheuser[100], M. Elsing[30], D. Emeliyanov[131], Y. Enari[155], O.C. Endner[83], M. Endo[118], J. Erdmann[43], A. Ereditato[17], G. Ernis[175], J. Ernst[2], M. Ernst[25], S. Errede[165], E. Ertel[83], M. Escalier[117], H. Esch[43], C. Escobar[125], B. Esposito[47], A.I. Etienvre[136], E. Etzion[153], H. Evans[61], A. Ezhilov[123], L. Fabbri[20a,20b], G. Facini[31], R.M. Fakhrutdinov[130], S. Falciano[132a], R.J. Falla[78], J. Faltova[129], Y. Fang[33a], M. Fanti[91a,91b], A. Farbin[8], A. Farilla[134a], T. Farooque[12], S. Farrell[15], S.M. Farrington[170], P. Farthouat[30], F. Fassi[135e], P. Fassnacht[30], D. Fassouliotis[9], M. Faucci Giannelli[77], A. Favareto[50a,50b], L. Fayard[117], P. Federic[144a], O.L. Fedin[123,m], W. Fedorko[168], S. Feigl[30], L. Feligioni[85], C. Feng[33d], E.J. Feng[6], H. Feng[89], A.B. Fenyuk[130], L. Feremenga[8], P. Fernandez Martinez[167], S. Fernandez Perez[30], J. Ferrando[53], A. Ferrari[166], P. Ferrari[107], R. Ferrari[121a], D.E. Ferreira de Lima[53], A. Ferrer[167], D. Ferrere[49], C. Ferretti[89], A. Ferretto Parodi[50a,50b], M. Fiascaris[31], F. Fiedler[83], A. Filipčič[75], M. Filipuzzi[42], F. Filthaut[106], M. Fincke-Keeler[169], K.D. Finelli[150], M.C.N. Fiolhais[126a,126c], L. Fiorini[167], A. Firan[40], A. Fischer[2], C. Fischer[12], J. Fischer[175], W.C. Fisher[90], E.A. Fitzgerald[23], N. Flaschel[42], I. Fleck[141], P. Fleischmann[89], S. Fleischmann[175], G.T. Fletcher[139], G. Fletcher[76], R.R.M. Fletcher[122], T. Flick[175], A. Floderus[81], L.R. Flores Castillo[60a], M.J. Flowerdew[101], A. Formica[136], A. Forti[84], D. Fournier[117], H. Fox[72], S. Fracchia[12], P. Francavilla[80], M. Franchini[20a,20b], D. Francis[30], L. Franconi[119], M. Franklin[57], M. Frate[163], M. Fraternali[121a,121b], D. Freeborn[78], S.T. French[28], F. Friedrich[44], D. Froidevaux[30],

JHEP10(2015)054

J.A. Frost[120], C. Fukunaga[156], E. Fullana Torregrosa[83], B.G. Fulsom[143], T. Fusayasu[102], J. Fuster[167], C. Gabaldon[55], O. Gabizon[175], A. Gabrielli[20a,20b], A. Gabrielli[132a,132b], G.P. Gach[38a], S. Gadatsch[30], S. Gadomski[49], G. Gagliardi[50a,50b], P. Gagnon[61], C. Galea[106], B. Galhardo[126a,126c], E.J. Gallas[120], B.J. Gallop[131], P. Gallus[128], G. Galster[36], K.K. Gan[111], J. Gao[33b,85], Y. Gao[46], Y.S. Gao[143,e], F.M. Garay Walls[46], F. Garberson[176], C. García[167], J.E. García Navarro[167], M. Garcia-Sciveres[15], R.W. Gardner[31], N. Garelli[143], V. Garonne[119], C. Gatti[47], A. Gaudiello[50a,50b], G. Gaudio[121a], B. Gaur[141], L. Gauthier[95], P. Gauzzi[132a,132b], I.L. Gavrilenko[96], C. Gay[168], G. Gaycken[21], E.N. Gazis[10], P. Ge[33d], Z. Gecse[168], C.N.P. Gee[131], Ch. Geich-Gimbel[21], M.P. Geisler[58a], C. Gemme[50a], M.H. Genest[55], S. Gentile[132a,132b], M. George[54], S. George[77], D. Gerbaudo[163], A. Gershon[153], S. Ghasemi[141], H. Ghazlane[135b], B. Giacobbe[20a], S. Giagu[132a,132b], V. Giangiobbe[12], P. Giannetti[124a,124b], B. Gibbard[25], S.M. Gibson[77], M. Gilchriese[15], T.P.S. Gillam[28], D. Gillberg[30], G. Gilles[34], D.M. Gingrich[3,d], N. Giokaris[9], M.P. Giordani[164a,164c], F.M. Giorgi[20a], F.M. Giorgi[16], P.F. Giraud[136], P. Giromini[47], D. Giugni[91a], C. Giuliani[48], M. Giulini[58b], B.K. Gjelsten[119], S. Gkaitatzis[154], I. Gkialas[154], E.L. Gkougkousis[117], L.K. Gladilin[99], C. Glasman[82], J. Glatzer[30], P.C.F. Glaysher[46], A. Glazov[42], M. Goblirsch-Kolb[101], J.R. Goddard[76], J. Godlewski[39], S. Goldfarb[89], T. Golling[49], D. Golubkov[130], A. Gomes[126a,126b,126d], R. Gonçalo[126a], J. Goncalves Pinto Firmino Da Costa[136], L. Gonella[21], S. González de la Hoz[167], G. Gonzalez Parra[12], S. Gonzalez-Sevilla[49], L. Goossens[30], P.A. Gorbounov[97], H.A. Gordon[25], I. Gorelov[105], B. Gorini[30], E. Gorini[73a,73b], A. Gorišek[75], E. Gornicki[39], A.T. Goshaw[45], C. Gössling[43], M.I. Gostkin[65], D. Goujdami[135c], A.G. Goussiou[138], N. Govender[145b], E. Gozani[152], H.M.X. Grabas[137], L. Graber[54], I. Grabowska-Bold[38a], P.O.J. Gradin[166], P. Grafström[20a,20b], K-J. Grahn[42], J. Gramling[49], E. Gramstad[119], S. Grancagnolo[16], V. Gratchev[123], H.M. Gray[30], E. Graziani[134a], Z.D. Greenwood[79,n], K. Gregersen[78], I.M. Gregor[42], P. Grenier[143], J. Griffiths[8], A.A. Grillo[137], K. Grimm[72], S. Grinstein[12,o], Ph. Gris[34], J.-F. Grivaz[117], J.P. Grohs[44], A. Grohsjean[42], E. Gross[172], J. Grosse-Knetter[54], G.C. Grossi[79], Z.J. Grout[149], L. Guan[89], J. Guenther[128], F. Guescini[49], D. Guest[176], O. Gueta[153], E. Guido[50a,50b], T. Guillemin[117], S. Guindon[2], U. Gul[53], C. Gumpert[44], J. Guo[33e], Y. Guo[33b], S. Gupta[120], G. Gustavino[132a,132b], P. Gutierrez[113], N.G. Gutierrez Ortiz[78], C. Gutschow[44], C. Guyot[136], C. Gwenlan[120], C.B. Gwilliam[74], A. Haas[110], C. Haber[15], H.K. Hadavand[8], N. Haddad[135e], P. Haefner[21], S. Hageböck[21], Z. Hajduk[39], H. Hakobyan[177], M. Haleem[42], J. Haley[114], D. Hall[120], G. Halladjian[90], G.D. Hallewell[85], K. Hamacher[175], P. Hamal[115], K. Hamano[169], A. Hamilton[145a], G.N. Hamity[139], P.G. Hamnett[42], L. Han[33b], K. Hanagaki[66,p], K. Hanawa[155], M. Hance[15], P. Hanke[58a], R. Hanna[136], J.B. Hansen[36], J.D. Hansen[36], M.C. Hansen[21], P.H. Hansen[36], K. Hara[160], A.S. Hard[173], T. Harenberg[175], F. Hariri[117], S. Harkusha[92], R.D. Harrington[46], P.F. Harrison[170], F. Hartjes[107], M. Hasegawa[67], S. Hasegawa[103], Y. Hasegawa[140], A. Hasib[113], S. Hassani[136], S. Haug[17], R. Hauser[90], L. Hauswald[44], M. Havranek[127], C.M. Hawkes[18], R.J. Hawkings[30], A.D. Hawkins[81], T. Hayashi[160], D. Hayden[90], C.P. Hays[120], J.M. Hays[76], H.S. Hayward[74], S.J. Haywood[131], S.J. Head[18], T. Heck[83], V. Hedberg[81], L. Heelan[8], S. Heim[122], T. Heim[175], B. Heinemann[15], L. Heinrich[110], J. Hejbal[127], L. Helary[22], S. Hellman[146a,146b], D. Hellmich[21], C. Helsens[12], J. Henderson[120], R.C.W. Henderson[72], Y. Heng[173], C. Hengler[42], A. Henrichs[176], A.M. Henriques Correia[30], S. Henrot-Versille[117], G.H. Herbert[16], Y. Hernández Jiménez[167], R. Herrberg-Schubert[16], G. Herten[48], R. Hertenberger[100], L. Hervas[30], G.G. Hesketh[78], N.P. Hessey[107], J.W. Hetherly[40], R. Hickling[76], E. Higón-Rodriguez[167], E. Hill[169], J.C. Hill[28], K.H. Hiller[42], S.J. Hillier[18], I. Hinchliffe[15], E. Hines[122], R.R. Hinman[15], M. Hirose[157], D. Hirschbuehl[175], J. Hobbs[148], N. Hod[107], M.C. Hodgkinson[139], P. Hodgson[139], A. Hoecker[30], M.R. Hoeferkamp[105], F. Hoenig[100], M. Hohlfeld[83], D. Hohn[21], T.R. Holmes[15], M. Homann[43], T.M. Hong[125], L. Hooft van Huysduynen[110], W.H. Hopkins[116], Y. Horii[103], A.J. Horton[142],

JHEP10(2015)054

J-Y. Hostachy[55], S. Hou[151], A. Hoummada[135a], J. Howard[120], J. Howarth[42], M. Hrabovsky[115], I. Hristova[16], J. Hrivnac[117], T. Hryn'ova[5], A. Hrynevich[93], C. Hsu[145c], P.J. Hsu[151,q], S.-C. Hsu[138], D. Hu[35], Q. Hu[33b], X. Hu[89], Y. Huang[42], Z. Hubacek[128], F. Hubaut[85], F. Huegging[21], T.B. Huffman[120], E.W. Hughes[35], G. Hughes[72], M. Huhtinen[30], T.A. Hülsing[83], N. Huseynov[65,b], J. Huston[90], J. Huth[57], G. Iacobucci[49], G. Iakovidis[25], I. Ibragimov[141], L. Iconomidou-Fayard[117], E. Ideal[176], Z. Idrissi[135e], P. Iengo[30], O. Igonkina[107], T. Iizawa[171], Y. Ikegami[66], K. Ikematsu[141], M. Ikeno[66], Y. Ilchenko[31,r], D. Iliadis[154], N. Ilic[143], T. Ince[101], G. Introzzi[121a,121b], P. Ioannou[9], M. Iodice[134a], K. Iordanidou[35], V. Ippolito[57], A. Irles Quiles[167], C. Isaksson[166], M. Ishino[68], M. Ishitsuka[157], R. Ishmukhametov[111], C. Issever[120], S. Istin[19a], J.M. Iturbe Ponce[84], R. Iuppa[133a,133b], J. Ivarsson[81], W. Iwanski[39], H. Iwasaki[66], J.M. Izen[41], V. Izzo[104a], S. Jabbar[3], B. Jackson[122], M. Jackson[74], P. Jackson[1], M.R. Jaekel[30], V. Jain[2], K. Jakobs[48], S. Jakobsen[30], T. Jakoubek[127], J. Jakubek[128], D.O. Jamin[114], D.K. Jana[79], E. Jansen[78], R. Jansky[62], J. Janssen[21], M. Janus[54], G. Jarlskog[81], N. Javadov[65,b], T. Javůrek[48], L. Jeanty[15], J. Jejelava[51a,s], G.-Y. Jeng[150], D. Jennens[88], P. Jenni[48,t], J. Jentzsch[43], C. Jeske[170], S. Jézéquel[5], H. Ji[173], J. Jia[148], Y. Jiang[33b], S. Jiggins[78], J. Jimenez Pena[167], S. Jin[33a], A. Jinaru[26a], O. Jinnouchi[157], M.D. Joergensen[36], P. Johansson[139], K.A. Johns[7], K. Jon-And[146a,146b], G. Jones[170], R.W.L. Jones[72], T.J. Jones[74], J. Jongmanns[58a], P.M. Jorge[126a,126b], K.D. Joshi[84], J. Jovicevic[159a], X. Ju[173], C.A. Jung[43], P. Jussel[62], A. Juste Rozas[12,o], M. Kaci[167], A. Kaczmarska[39], M. Kado[117], H. Kagan[111], M. Kagan[143], S.J. Kahn[85], E. Kajomovitz[45], C.W. Kalderon[120], S. Kama[40], A. Kamenshchikov[130], N. Kanaya[155], S. Kaneti[28], V.A. Kantserov[98], J. Kanzaki[66], B. Kaplan[110], L.S. Kaplan[173], A. Kapliy[31], D. Kar[145c], K. Karakostas[10], A. Karamaoun[3], N. Karastathis[10,107], M.J. Kareem[54], E. Karentzos[10], M. Karnevskiy[83], S.N. Karpov[65], Z.M. Karpova[65], K. Karthik[110], V. Kartvelishvili[72], A.N. Karyukhin[130], L. Kashif[173], R.D. Kass[111], A. Kastanas[14], Y. Kataoka[155], C. Kato[155], A. Katre[49], J. Katzy[42], K. Kawagoe[70], T. Kawamoto[155], G. Kawamura[54], S. Kazama[155], V.F. Kazanin[109,c], R. Keeler[169], R. Kehoe[40], J.S. Keller[42], J.J. Kempster[77], H. Keoshkerian[84], O. Kepka[127], B.P. Kerševan[75], S. Kersten[175], R.A. Keyes[87], F. Khalil-zada[11], H. Khandanyan[146a,146b], A. Khanov[114], A.G. Kharlamov[109,c], T.J. Khoo[28], V. Khovanskiy[97], E. Khramov[65], J. Khubua[51b,u], S. Kido[67], H.Y. Kim[8], S.H. Kim[160], Y.K. Kim[31], N. Kimura[154], O.M. Kind[16], B.T. King[74], M. King[167], S.B. King[168], J. Kirk[131], A.E. Kiryunin[101], T. Kishimoto[67], D. Kisielewska[38a], F. Kiss[48], K. Kiuchi[160], O. Kivernyk[136], E. Kladiva[144b], M.H. Klein[35], M. Klein[74], U. Klein[74], K. Kleinknecht[83], P. Klimek[146a,146b], A. Klimentov[25], R. Klingenberg[43], J.A. Klinger[139], T. Klioutchnikova[30], E.-E. Kluge[58a], P. Kluit[107], S. Kluth[101], J. Knapik[39], E. Kneringer[62], E.B.F.G. Knoops[85], A. Knue[53], A. Kobayashi[155], D. Kobayashi[157], T. Kobayashi[155], M. Kobel[44], M. Kocian[143], P. Kodys[129], T. Koffas[29], E. Koffeman[107], L.A. Kogan[120], S. Kohlmann[175], Z. Kohout[128], T. Kohriki[66], T. Koi[143], H. Kolanoski[16], I. Koletsou[5], A.A. Komar[96,*], Y. Komori[155], T. Kondo[66], N. Kondrashova[42], K. Köneke[48], A.C. König[106], T. Kono[66], R. Konoplich[110,v], N. Konstantinidis[78], R. Kopeliansky[152], S. Koperny[38a], L. Köpke[83], A.K. Kopp[48], K. Korcyl[39], K. Kordas[154], A. Korn[78], A.A. Korol[109,c], I. Korolkov[12], E.V. Korolkova[139], O. Kortner[101], S. Kortner[101], T. Kosek[129], V.V. Kostyukhin[21], V.M. Kotov[65], A. Kotwal[45], A. Kourkoumeli-Charalampidi[154], C. Kourkoumelis[9], V. Kouskoura[25], A. Koutsman[159a], R. Kowalewski[169], T.Z. Kowalski[38a], W. Kozanecki[136], A.S. Kozhin[130], V.A. Kramarenko[99], G. Kramberger[75], D. Krasnopevtsev[98], M.W. Krasny[80], A. Krasznahorkay[30], J.K. Kraus[21], A. Kravchenko[25], S. Kreiss[110], M. Kretz[58c], J. Kretzschmar[74], K. Kreutzfeldt[52], P. Krieger[158], K. Krizka[31], K. Kroeninger[43], H. Kroha[101], J. Kroll[122], J. Kroseberg[21], J. Krstic[13], U. Kruchonak[65], H. Krüger[21], N. Krumnack[64], A. Kruse[173], M.C. Kruse[45], M. Kruskal[22], T. Kubota[88], H. Kucuk[78], S. Kuday[4b], S. Kuehn[48], A. Kugel[58c], F. Kuger[174], A. Kuhl[137], T. Kuhl[42], V. Kukhtin[65], Y. Kulchitsky[92], S. Kuleshov[32b], M. Kuna[132a,132b], T. Kunigo[68], A. Kupco[127], H. Kurashige[67], Y.A. Kurochkin[92], V. Kus[127],

JHEP10(2015)054

E.S. Kuwertz[169], M. Kuze[157], J. Kvita[115], T. Kwan[169], D. Kyriazopoulos[139], A. La Rosa[137], J.L. La Rosa Navarro[24d], L. La Rotonda[37a,37b], C. Lacasta[167], F. Lacava[132a,132b], J. Lacey[29], H. Lacker[16], D. Lacour[80], V.R. Lacuesta[167], E. Ladygin[65], R. Lafaye[5], B. Laforge[80], T. Lagouri[176], S. Lai[54], L. Lambourne[78], S. Lammers[61], C.L. Lampen[7], W. Lampl[7], E. Lançon[136], U. Landgraf[48], M.P.J. Landon[76], V.S. Lang[58a], J.C. Lange[12], A.J. Lankford[163], F. Lanni[25], K. Lantzsch[30], A. Lanza[121a], S. Laplace[80], C. Lapoire[30], J.F. Laporte[136], T. Lari[91a], F. Lasagni Manghi[20a,20b], M. Lassnig[30], P. Laurelli[47], W. Lavrijsen[15], A.T. Law[137], P. Laycock[74], T. Lazovich[57], O. Le Dortz[80], E. Le Guirriec[85], E. Le Menedeu[12], M. LeBlanc[169], T. LeCompte[6], F. Ledroit-Guillon[55], C.A. Lee[145b], S.C. Lee[151], L. Lee[1], G. Lefebvre[80], M. Lefebvre[169], F. Legger[100], C. Leggett[15], A. Lehan[74], G. Lehmann Miotto[30], X. Lei[7], W.A. Leight[29], A. Leisos[154,w], A.G. Leister[176], M.A.L. Leite[24d], R. Leitner[129], D. Lellouch[172], B. Lemmer[54], K.J.C. Leney[78], T. Lenz[21], B. Lenzi[30], R. Leone[7], S. Leone[124a,124b], C. Leonidopoulos[46], S. Leontsinis[10], C. Leroy[95], C.G. Lester[28], M. Levchenko[123], J. Levêque[5], D. Levin[89], L.J. Levinson[172], M. Levy[18], A. Lewis[120], A.M. Leyko[21], M. Leyton[41], B. Li[33b,x], H. Li[148], H.L. Li[31], L. Li[45], L. Li[33e], S. Li[45], X. Li[84], Y. Li[33c,y], Z. Liang[137], H. Liao[34], B. Liberti[133a], A. Liblong[158], P. Lichard[30], K. Lie[165], J. Liebal[21], W. Liebig[14], C. Limbach[21], A. Limosani[150], S.C. Lin[151,z], T.H. Lin[83], F. Linde[107], B.E. Lindquist[148], J.T. Linnemann[90], E. Lipeles[122], A. Lipniacka[14], M. Lisovyi[58b], T.M. Liss[165], D. Lissauer[25], A. Lister[168], A.M. Litke[137], B. Liu[151,aa], D. Liu[151], H. Liu[89], J. Liu[85], J.B. Liu[33b], K. Liu[85], L. Liu[165], M. Liu[45], M. Liu[33b], Y. Liu[33b], M. Livan[121a,121b], A. Lleres[55], J. Llorente Merino[82], S.L. Lloyd[76], F. Lo Sterzo[151], E. Lobodzinska[42], P. Loch[7], W.S. Lockman[137], F.K. Loebinger[84], A.E. Loevschall-Jensen[36], A. Loginov[176], T. Lohse[16], K. Lohwasser[42], M. Lokajicek[127], B.A. Long[22], J.D. Long[89], R.E. Long[72], K.A. Looper[111], L. Lopes[126a], D. Lopez Mateos[57], B. Lopez Paredes[139], I. Lopez Paz[12], J. Lorenz[100], N. Lorenzo Martinez[61], M. Losada[162], P. Loscutoff[15], P.J. Lösel[100], X. Lou[33a], A. Lounis[117], J. Love[6], P.A. Love[72], N. Lu[89], H.J. Lubatti[138], C. Luci[132a,132b], A. Lucotte[55], F. Luehring[61], W. Lukas[62], L. Luminari[132a], O. Lundberg[146a,146b], B. Lund-Jensen[147], D. Lynn[25], R. Lysak[127], E. Lytken[81], H. Ma[25], L.L. Ma[33d], G. Maccarrone[47], A. Macchiolo[101], C.M. Macdonald[139], B. Maček[75], J. Machado Miguens[122,126b], D. Macina[30], D. Madaffari[85], R. Madar[34], H.J. Maddocks[72], W.F. Mader[44], A. Madsen[166], J. Maeda[67], S. Maeland[14], T. Maeno[25], A. Maevskiy[99], E. Magradze[54], K. Mahboubi[48], J. Mahlstedt[107], C. Maiani[136], C. Maidantchik[24a], A.A. Maier[101], T. Maier[100], A. Maio[126a,126b,126d], S. Majewski[116], Y. Makida[66], N. Makovec[117], B. Malaescu[80], Pa. Malecki[39], V.P. Maleev[123], F. Malek[55], U. Mallik[63], D. Malon[6], C. Malone[143], S. Maltezos[10], V.M. Malyshev[109], S. Malyukov[30], J. Mamuzic[42], G. Mancini[47], B. Mandelli[30], L. Mandelli[91a], I. Mandić[75], R. Mandrysch[63], J. Maneira[126a,126b], A. Manfredini[101], L. Manhaes de Andrade Filho[24b], J. Manjarres Ramos[159b], A. Mann[100], A. Manousakis-Katsikakis[9], B. Mansoulie[136], R. Mantifel[87], M. Mantoani[54], L. Mapelli[30], L. March[145c], G. Marchiori[80], M. Marcisovsky[127], C.P. Marino[169], M. Marjanovic[13], D.E. Marley[89], F. Marroquim[24a], S.P. Marsden[84], Z. Marshall[15], L.F. Marti[17], S. Marti-Garcia[167], B. Martin[90], T.A. Martin[170], V.J. Martin[46], B. Martin dit Latour[14], M. Martinez[12,o], S. Martin-Haugh[131], V.S. Martoiu[26a], A.C. Martyniuk[78], M. Marx[138], F. Marzano[132a], A. Marzin[30], L. Masetti[83], T. Mashimo[155], R. Mashinistov[96], J. Masik[84], A.L. Maslennikov[109,c], I. Massa[20a,20b], L. Massa[20a,20b], N. Massol[5], P. Mastrandrea[148], A. Mastroberardino[37a,37b], T. Masubuchi[155], P. Mättig[175], J. Mattmann[83], J. Maurer[26a], S.J. Maxfield[74], D.A. Maximov[109,c], R. Mazini[151], S.M. Mazza[91a,91b], L. Mazzaferro[133a,133b], G. Mc Goldrick[158], S.P. Mc Kee[89], A. McCarn[89], R.L. McCarthy[148], T.G. McCarthy[29], N.A. McCubbin[131], K.W. McFarlane[56,*], J.A. Mcfayden[78], G. Mchedlidze[54], S.J. McMahon[131], R.A. McPherson[169,k], M. Medinnis[42], S. Meehan[145a], S. Mehlhase[100], A. Mehta[74], K. Meier[58a], C. Meineck[100], B. Meirose[41], B.R. Mellado Garcia[145c], F. Meloni[17], A. Mengarelli[20a,20b],

JHEP10(2015)054

S. Menke[101], E. Meoni[161], K.M. Mercurio[57], S. Mergelmeyer[21], P. Mermod[49], L. Merola[104a,104b], C. Meroni[91a], F.S. Merritt[31], A. Messina[132a,132b], J. Metcalfe[25], A.S. Mete[163], C. Meyer[83], C. Meyer[122], J-P. Meyer[136], J. Meyer[107], H. Meyer Zu Theenhausen[58a], R.P. Middleton[131], S. Miglioranzi[164a,164c], L. Mijović[21], G. Mikenberg[172], M. Mikestikova[127], M. Mikuž[75], M. Milesi[88], A. Milic[30], D.W. Miller[31], C. Mills[46], A. Milov[172], D.A. Milstead[146a,146b], A.A. Minaenko[130], Y. Minami[155], I.A. Minashvili[65], A.I. Mincer[110], B. Mindur[38a], M. Mineev[65], Y. Ming[173], L.M. Mir[12], T. Mitani[171], J. Mitrevski[100], V.A. Mitsou[167], A. Miucci[49], P.S. Miyagawa[139], J.U. Mjörnmark[81], T. Moa[146a,146b], K. Mochizuki[85], S. Mohapatra[35], W. Mohr[48], S. Molander[146a,146b], R. Moles-Valls[21], K. Mönig[42], C. Monini[55], J. Monk[36], E. Monnier[85], J. Montejo Berlingen[12], F. Monticelli[71], S. Monzani[132a,132b], R.W. Moore[3], N. Morange[117], D. Moreno[162], M. Moreno Llácer[54], P. Morettini[50a], D. Mori[142], M. Morii[57], M. Morinaga[155], V. Morisbak[119], S. Moritz[83], A.K. Morley[150], G. Mornacchi[30], J.D. Morris[76], S.S. Mortensen[36], A. Morton[53], L. Morvaj[103], M. Mosidze[51b], J. Moss[111], K. Motohashi[157], R. Mount[143], E. Mountricha[25], S.V. Mouraviev[96,*], E.J.W. Moyse[86], S. Muanza[85], R.D. Mudd[18], F. Mueller[101], J. Mueller[125], R.S.P. Mueller[100], T. Mueller[28], D. Muenstermann[49], P. Mullen[53], G.A. Mullier[17], J.A. Murillo Quijada[18], W.J. Murray[170,131], H. Musheghyan[54], E. Musto[152], A.G. Myagkov[130,ab], M. Myska[128], B.P. Nachman[143], O. Nackenhorst[54], J. Nadal[54], K. Nagai[120], R. Nagai[157], Y. Nagai[85], K. Nagano[66], A. Nagarkar[111], Y. Nagasaka[59], K. Nagata[160], M. Nagel[101], E. Nagy[85], A.M. Nairz[30], Y. Nakahama[30], K. Nakamura[66], T. Nakamura[155], I. Nakano[112], H. Namasivayam[41], R.F. Naranjo Garcia[42], R. Narayan[31], D.I. Narrias Villar[58a], T. Naumann[42], G. Navarro[162], R. Nayyar[7], H.A. Neal[89], P.Yu. Nechaeva[96], T.J. Neep[84], P.D. Nef[143], A. Negri[121a,121b], M. Negrini[20a], S. Nektarijevic[106], C. Nellist[117], A. Nelson[163], S. Nemecek[127], P. Nemethy[110], A.A. Nepomuceno[24a], M. Nessi[30,ac], M.S. Neubauer[165], M. Neumann[175], R.M. Neves[110], P. Nevski[25], P.R. Newman[18], D.H. Nguyen[6], R.B. Nickerson[120], R. Nicolaidou[136], B. Nicquevert[30], J. Nielsen[137], N. Nikiforou[35], A. Nikiforov[16], V. Nikolaenko[130,ab], I. Nikolic-Audit[80], K. Nikolopoulos[18], J.K. Nilsen[119], P. Nilsson[25], Y. Ninomiya[155], A. Nisati[132a], R. Nisius[101], T. Nobe[155], M. Nomachi[118], I. Nomidis[29], T. Nooney[76], S. Norberg[113], M. Nordberg[30], O. Novgorodova[44], S. Nowak[101], M. Nozaki[66], L. Nozka[115], K. Ntekas[10], G. Nunes Hanninger[88], T. Nunnemann[100], E. Nurse[78], F. Nuti[88], B.J. O'Brien[46], F. O'grady[7], D.C. O'Neil[142], V. O'Shea[53], F.G. Oakham[29,d], H. Oberlack[101], T. Obermann[21], J. Ocariz[80], A. Ochi[67], I. Ochoa[78], J.P. Ochoa-Ricoux[32a], S. Oda[70], S. Odaka[66], H. Ogren[61], A. Oh[84], S.H. Oh[45], C.C. Ohm[15], H. Ohman[166], H. Oide[30], W. Okamura[118], H. Okawa[160], Y. Okumura[31], T. Okuyama[66], A. Olariu[26a], S.A. Olivares Pino[46], D. Oliveira Damazio[25], E. Oliver Garcia[167], A. Olszewski[39], J. Olszowska[39], A. Onofre[126a,126e], P.U.E. Onyisi[31,r], C.J. Oram[159a], M.J. Oreglia[31], Y. Oren[153], D. Orestano[134a,134b], N. Orlando[154], C. Oropeza Barrera[53], R.S. Orr[158], B. Osculati[50a,50b], R. Ospanov[84], G. Otero y Garzon[27], H. Otono[70], M. Ouchrif[135d], F. Ould-Saada[119], A. Ouraou[136], K.P. Oussoren[107], Q. Ouyang[33a], A. Ovcharova[15], M. Owen[53], R.E. Owen[18], V.E. Ozcan[19a], N. Ozturk[8], K. Pachal[142], A. Pacheco Pages[12], C. Padilla Aranda[12], M. Pagáčová[48], S. Pagan Griso[15], E. Paganis[139], F. Paige[25], P. Pais[86], K. Pajchel[119], G. Palacino[159b], S. Palestini[30], M. Palka[38b], D. Pallin[34], A. Palma[126a,126b], Y.B. Pan[173], E. Panagiotopoulou[10], C.E. Pandini[80], J.G. Panduro Vazquez[77], P. Pani[146a,146b], S. Panitkin[25], D. Pantea[26a], L. Paolozzi[49], Th.D. Papadopoulou[10], K. Papageorgiou[154], A. Paramonov[6], D. Paredes Hernandez[154], M.A. Parker[28], K.A. Parker[139], F. Parodi[50a,50b], J.A. Parsons[35], U. Parzefall[48], E. Pasqualucci[132a], S. Passaggio[50a], F. Pastore[134a,134b,*], Fr. Pastore[77], G. Pásztor[29], S. Pataraia[175], N.D. Patel[150], J.R. Pater[84], T. Pauly[30], J. Pearce[169], B. Pearson[113], L.E. Pedersen[36], M. Pedersen[119], S. Pedraza Lopez[167], R. Pedro[126a,126b], S.V. Peleganchuk[109,c], D. Pelikan[166], O. Penc[127], C. Peng[33a], H. Peng[33b], B. Penning[31], J. Penwell[61], D.V. Perepelitsa[25], E. Perez Codina[159a], M.T. Pérez García-Estañ[167], L. Perini[91a,91b], H. Pernegger[30],

JHEP10(2015)054

S. Perrella[104a,104b], R. Peschke[42], V.D. Peshekhonov[65], K. Peters[30], R.F.Y. Peters[84], B.A. Petersen[30], T.C. Petersen[36], E. Petit[42], A. Petridis[1], C. Petridou[154], P. Petroff[117], E. Petrolo[132a], F. Petrucci[134a,134b], N.E. Pettersson[157], R. Pezoa[32b], P.W. Phillips[131], G. Piacquadio[143], E. Pianori[170], A. Picazio[49], E. Piccaro[76], M. Piccinini[20a,20b], M.A. Pickering[120], R. Piegaia[27], D.T. Pignotti[111], J.E. Pilcher[31], A.D. Pilkington[84], J. Pina[126a,126b,126d], M. Pinamonti[164a,164c,ad], J.L. Pinfold[3], A. Pingel[36], S. Pires[80], H. Pirumov[42], M. Pitt[172], C. Pizio[91a,91b], L. Plazak[144a], M.-A. Pleier[25], V. Pleskot[129], E. Plotnikova[65], P. Plucinski[146a,146b], D. Pluth[64], R. Poettgen[146a,146b], L. Poggioli[117], D. Pohl[21], G. Polesello[121a], A. Poley[42], A. Policicchio[37a,37b], R. Polifka[158], A. Polini[20a], C.S. Pollard[53], V. Polychronakos[25], K. Pommès[30], L. Pontecorvo[132a], B.G. Pope[90], G.A. Popeneciu[26b], D.S. Popovic[13], A. Poppleton[30], S. Pospisil[128], K. Potamianos[15], I.N. Potrap[65], C.J. Potter[149], C.T. Potter[116], G. Poulard[30], J. Poveda[30], V. Pozdnyakov[65], P. Pralavorio[85], A. Pranko[15], S. Prasad[30], S. Prell[64], D. Price[84], L.E. Price[6], M. Primavera[73a], S. Prince[87], M. Proissl[46], K. Prokofiev[60c], F. Prokoshin[32b], E. Protopapadaki[136], S. Protopopescu[25], J. Proudfoot[6], M. Przybycien[38a], E. Ptacek[116], D. Puddu[134a,134b], E. Pueschel[86], D. Puldon[148], M. Purohit[25,ae], P. Puzo[117], J. Qian[89], G. Qin[53], Y. Qin[84], A. Quadt[54], D.R. Quarrie[15], W.B. Quayle[164a,164b], M. Queitsch-Maitland[84], D. Quilty[53], S. Raddum[119], V. Radeka[25], V. Radescu[42], S.K. Radhakrishnan[148], P. Radloff[116], P. Rados[88], F. Ragusa[91a,91b], G. Rahal[178], S. Rajagopalan[25], M. Rammensee[30], C. Rangel-Smith[166], F. Rauscher[100], S. Rave[83], T. Ravenscroft[53], M. Raymond[30], A.L. Read[119], N.P. Readioff[74], D.M. Rebuzzi[121a,121b], A. Redelbach[174], G. Redlinger[25], R. Reece[137], K. Reeves[41], L. Rehnisch[16], J. Reichert[122], H. Reisin[27], M. Relich[163], C. Rembser[30], H. Ren[33a], A. Renaud[117], M. Rescigno[132a], S. Resconi[91a], O.L. Rezanova[109,c], P. Reznicek[129], R. Rezvani[95], R. Richter[101], S. Richter[78], E. Richter-Was[38b], O. Ricken[21], M. Ridel[80], P. Rieck[16], C.J. Riegel[175], J. Rieger[54], M. Rijssenbeek[148], A. Rimoldi[121a,121b], L. Rinaldi[20a], B. Ristić[49], E. Ritsch[30], I. Riu[12], F. Rizatdinova[114], E. Rizvi[76], S.H. Robertson[87,k], A. Robichaud-Veronneau[87], D. Robinson[28], J.E.M. Robinson[42], A. Robson[53], C. Roda[124a,124b], S. Roe[30], O. Røhne[119], S. Rolli[161], A. Romaniouk[98], M. Romano[20a,20b], S.M. Romano Saez[34], E. Romero Adam[167], N. Rompotis[138], M. Ronzani[48], L. Roos[80], E. Ros[167], S. Rosati[132a], K. Rosbach[48], P. Rose[137], P.L. Rosendahl[14], O. Rosenthal[141], V. Rossetti[146a,146b], E. Rossi[104a,104b], L.P. Rossi[50a], J.H.N. Rosten[28], R. Rosten[138], M. Rotaru[26a], I. Roth[172], J. Rothberg[138], D. Rousseau[117], C.R. Royon[136], A. Rozanov[85], Y. Rozen[152], X. Ruan[145c], F. Rubbo[143], I. Rubinskiy[42], V.I. Rud[99], C. Rudolph[44], M.S. Rudolph[158], F. Rühr[48], A. Ruiz-Martinez[30], Z. Rurikova[48], N.A. Rusakovich[65], A. Ruschke[100], H.L. Russell[138], J.P. Rutherfoord[7], N. Ruthmann[48], Y.F. Ryabov[123], M. Rybar[165], G. Rybkin[117], N.C. Ryder[120], A.F. Saavedra[150], G. Sabato[107], S. Sacerdoti[27], A. Saddique[3], H.F-W. Sadrozinski[137], R. Sadykov[65], F. Safai Tehrani[132a], M. Sahinsoy[58a], M. Saimpert[136], T. Saito[155], H. Sakamoto[155], Y. Sakurai[171], G. Salamanna[134a,134b], A. Salamon[133a], J.E. Salazar Loyola[32b], M. Saleem[113], D. Salek[107], P.H. Sales De Bruin[138], D. Salihagic[101], A. Salnikov[143], J. Salt[167], D. Salvatore[37a,37b], F. Salvatore[149], A. Salvucci[60a], A. Salzburger[30], D. Sammel[48], D. Sampsonidis[154], A. Sanchez[104a,104b], J. Sánchez[167], V. Sanchez Martinez[167], H. Sandaker[119], R.L. Sandbach[76], H.G. Sander[83], M.P. Sanders[100], M. Sandhoff[175], C. Sandoval[162], R. Sandstroem[101], D.P.C. Sankey[131], M. Sannino[50a,50b], A. Sansoni[47], C. Santoni[34], R. Santonico[133a,133b], H. Santos[126a], I. Santoyo Castillo[149], K. Sapp[125], A. Sapronov[65], J.G. Saraiva[126a,126d], B. Sarrazin[21], O. Sasaki[66], Y. Sasaki[155], K. Sato[160], G. Sauvage[5,*], E. Sauvan[5], G. Savage[77], P. Savard[158,d], C. Sawyer[131], L. Sawyer[79,n], J. Saxon[31], C. Sbarra[20a], A. Sbrizzi[20a,20b], T. Scanlon[78], D.A. Scannicchio[163], M. Scarcella[150], V. Scarfone[37a,37b], J. Schaarschmidt[172], P. Schacht[101], D. Schaefer[30], R. Schaefer[42], J. Schaeffer[83], S. Schaepe[21], S. Schaetzel[58b], U. Schäfer[83], A.C. Schaffer[117], D. Schaile[100], R.D. Schamberger[148],

JHEP10(2015)054

V. Scharf[58a], V.A. Schegelsky[123], D. Scheirich[129], M. Schernau[163], C. Schiavi[50a,50b], C. Schillo[48], M. Schioppa[37a,37b], S. Schlenker[30], E. Schmidt[48], K. Schmieden[30], C. Schmitt[83], S. Schmitt[58b], S. Schmitt[42], B. Schneider[159a], Y.J. Schnellbach[74], U. Schnoor[44], L. Schoeffel[136], A. Schoening[58b], B.D. Schoenrock[90], E. Schopf[21], A.L.S. Schorlemmer[54], M. Schott[83], D. Schouten[159a], J. Schovancova[8], S. Schramm[49], M. Schreyer[174], C. Schroeder[83], N. Schuh[83], M.J. Schultens[21], H.-C. Schultz-Coulon[58a], H. Schulz[16], M. Schumacher[48], B.A. Schumm[137], Ph. Schune[136], C. Schwanenberger[84], A. Schwartzman[143], T.A. Schwarz[89], Ph. Schwegler[101], H. Schweiger[84], Ph. Schwemling[136], R. Schwienhorst[90], J. Schwindling[136], T. Schwindt[21], F.G. Sciacca[17], E. Scifo[117], G. Sciolla[23], F. Scuri[124a,124b], F. Scutti[21], J. Searcy[89], G. Sedov[42], E. Sedykh[123], P. Seema[21], S.C. Seidel[105], A. Seiden[137], F. Seifert[128], J.M. Seixas[24a], G. Sekhniaidze[104a], K. Sekhon[89], S.J. Sekula[40], D.M. Seliverstov[123,*], N. Semprini-Cesari[20a,20b], C. Serfon[30], L. Serin[117], L. Serkin[164a,164b], T. Serre[85], M. Sessa[134a,134b], R. Seuster[159a], H. Severini[113], T. Sfiligoj[75], F. Sforza[30], A. Sfyrla[30], E. Shabalina[54], M. Shamim[116], L.Y. Shan[33a], R. Shang[165], J.T. Shank[22], M. Shapiro[15], P.B. Shatalov[97], K. Shaw[164a,164b], S.M. Shaw[84], A. Shcherbakova[146a,146b], C.Y. Shehu[149], P. Sherwood[78], L. Shi[151,af], S. Shimizu[67], C.O. Shimmin[163], M. Shimojima[102], M. Shiyakova[65], A. Shmeleva[96], D. Shoaleh Saadi[95], M.J. Shochet[31], S. Shojaii[91a,91b], S. Shrestha[111], E. Shulga[98], M.A. Shupe[7], S. Shushkevich[42], P. Sicho[127], P.E. Sidebo[147], O. Sidiropoulou[174], D. Sidorov[114], A. Sidoti[20a,20b], F. Siegert[44], Dj. Sijacki[13], J. Silva[126a,126d], Y. Silver[153], S.B. Silverstein[146a], V. Simak[128], O. Simard[5], Lj. Simic[13], S. Simion[117], E. Simioni[83], B. Simmons[78], D. Simon[34], R. Simoniello[91a,91b], P. Sinervo[158], N.B. Sinev[116], M. Sioli[20a,20b], G. Siragusa[174], A.N. Sisakyan[65,*], S.Yu. Sivoklokov[99], J. Sjölin[146a,146b], T.B. Sjursen[14], M.B. Skinner[72], H.P. Skottowe[57], P. Skubic[113], M. Slater[18], T. Slavicek[128], M. Slawinska[107], K. Sliwa[161], V. Smakhtin[172], B.H. Smart[46], L. Smestad[14], S.Yu. Smirnov[98], Y. Smirnov[98], L.N. Smirnova[99,ag], O. Smirnova[81], M.N.K. Smith[35], R.W. Smith[35], M. Smizanska[72], K. Smolek[128], A.A. Snesarev[96], G. Snidero[76], S. Snyder[25], R. Sobie[169,k], F. Socher[44], A. Soffer[153], D.A. Soh[151,af], C.A. Solans[30], M. Solar[128], J. Solc[128], E.Yu. Soldatov[98], U. Soldevila[167], A.A. Solodkov[130], A. Soloshenko[65], O.V. Solovyanov[130], V. Solovyev[123], P. Sommer[48], H.Y. Song[33b], N. Soni[1], A. Sood[15], A. Sopczak[128], B. Sopko[128], V. Sopko[128], V. Sorin[12], D. Sosa[58b], M. Sosebee[8], C.L. Sotiropoulou[124a,124b], R. Soualah[164a,164c], A.M. Soukharev[109,c], D. South[42], B.C. Sowden[77], S. Spagnolo[73a,73b], M. Spalla[124a,124b], F. Spanò[77], W.R. Spearman[57], D. Sperlich[16], F. Spettel[101], R. Spighi[20a], G. Spigo[30], L.A. Spiller[88], M. Spousta[129], T. Spreitzer[158], R.D. St. Denis[53,*], S. Staerz[44], J. Stahlman[122], R. Stamen[58a], S. Stamm[16], E. Stanecka[39], C. Stanescu[134a], M. Stanescu-Bellu[42], M.M. Stanitzki[42], S. Stapnes[119], E.A. Starchenko[130], J. Stark[55], P. Staroba[127], P. Starovoitov[58a], R. Staszewski[39], P. Stavina[144a,*], P. Steinberg[25], B. Stelzer[142], H.J. Stelzer[30], O. Stelzer-Chilton[159a], H. Stenzel[52], G.A. Stewart[53], J.A. Stillings[21], M.C. Stockton[87], M. Stoebe[87], G. Stoicea[26a], P. Stolte[54], S. Stonjek[101], A.R. Stradling[8], A. Straessner[44], M.E. Stramaglia[17], J. Strandberg[147], S. Strandberg[146a,146b], A. Strandlie[119], E. Strauss[143], M. Strauss[113], P. Strizenec[144b], R. Ströhmer[174], D.M. Strom[116], R. Stroynowski[40], A. Strubig[106], S.A. Stucci[17], B. Stugu[14], N.A. Styles[42], D. Su[143], J. Su[125], R. Subramaniam[79], A. Succurro[12], Y. Sugaya[118], C. Suhr[108], M. Suk[128], V.V. Sulin[96], S. Sultansoy[4c], T. Sumida[68], S. Sun[57], X. Sun[33a], J.E. Sundermann[48], K. Suruliz[149], G. Susinno[37a,37b], M.R. Sutton[149], S. Suzuki[66], M. Svatos[127], M. Swiatlowski[143], I. Sykora[144a], T. Sykora[129], D. Ta[90], C. Taccini[134a,134b], K. Tackmann[42], J. Taenzer[158], A. Taffard[163], R. Tafirout[159a], N. Taiblum[153], H. Takai[25], R. Takashima[69], H. Takeda[67], T. Takeshita[140], Y. Takubo[66], M. Talby[85], A.A. Talyshev[109,c], J.Y.C. Tam[174], K.G. Tan[88], J. Tanaka[155], R. Tanaka[117], S. Tanaka[66], B.B. Tannenwald[111], N. Tannoury[21], S. Tapprogge[83], S. Tarem[152], F. Tarrade[29], G.F. Tartarelli[91a], P. Tas[129], M. Tasevsky[127], T. Tashiro[68], E. Tassi[37a,37b], A. Tavares Delgado[126a,126b], Y. Tayalati[135d],

JHEP10(2015)054

F.E. Taylor[94], G.N. Taylor[88], W. Taylor[159b], F.A. Teischinger[30], M. Teixeira Dias Castanheira[76], P. Teixeira-Dias[77], K.K. Temming[48], D. Temple[142], H. Ten Kate[30], P.K. Teng[151], J.J. Teoh[118], F. Tepel[175], S. Terada[66], K. Terashi[155], J. Terron[82], S. Terzo[101], M. Testa[47], R.J. Teuscher[158,k], T. Theveneaux-Pelzer[34], J.P. Thomas[18], J. Thomas-Wilsker[77], E.N. Thompson[35], P.D. Thompson[18], R.J. Thompson[84], A.S. Thompson[53], L.A. Thomsen[176], E. Thomson[122], M. Thomson[28], R.P. Thun[89,*], M.J. Tibbetts[15], R.E. Ticse Torres[85], V.O. Tikhomirov[96,ah], Yu.A. Tikhonov[109,c], S. Timoshenko[98], E. Tiouchichine[85], P. Tipton[176], S. Tisserant[85], K. Todome[157], T. Todorov[5], S. Todorova-Nova[129], J. Tojo[70], S. Tokár[144a], K. Tokushuku[66], K. Tollefson[90], E. Tolley[57], L. Tomlinson[84], M. Tomoto[103], L. Tompkins[143,ai], K. Toms[105], E. Torrence[116], H. Torres[142], E. Torró Pastor[138], J. Toth[85,aj], F. Touchard[85], D.R. Tovey[139], T. Trefzger[174], L. Tremblet[30], A. Tricoli[30], I.M. Trigger[159a], S. Trincaz-Duvoid[80], M.F. Tripiana[12], W. Trischuk[158], B. Trocmé[55], C. Troncon[91a], M. Trottier-McDonald[15], M. Trovatelli[169], P. True[90], L. Truong[164a,164c], M. Trzebinski[39], A. Trzupek[39], C. Tsarouchas[30], J.C-L. Tseng[120], P.V. Tsiareshka[92], D. Tsionou[154], G. Tsipolitis[10], N. Tsirintanis[9], S. Tsiskaridze[12], V. Tsiskaridze[48], E.G. Tskhadadze[51a], I.I. Tsukerman[97], V. Tsulaia[15], S. Tsuno[66], D. Tsybychev[148], A. Tudorache[26a], V. Tudorache[26a], A.N. Tuna[122], S.A. Tupputi[20a,20b], S. Turchikhin[99,ag], D. Turecek[128], R. Turra[91a,91b], A.J. Turvey[40], P.M. Tuts[35], A. Tykhonov[49], M. Tylmad[146a,146b], M. Tyndel[131], I. Ueda[155], R. Ueno[29], M. Ughetto[146a,146b], M. Ugland[14], F. Ukegawa[160], G. Unal[30], A. Undrus[25], G. Unel[163], F.C. Ungaro[48], Y. Unno[66], C. Unverdorben[100], J. Urban[144b], P. Urquijo[88], P. Urrejola[83], G. Usai[8], A. Usanova[62], L. Vacavant[85], V. Vacek[128], B. Vachon[87], C. Valderanis[83], N. Valencic[107], S. Valentinetti[20a,20b], A. Valero[167], L. Valery[12], S. Valkar[129], E. Valladolid Gallego[167], S. Vallecorsa[49], J.A. Valls Ferrer[167], W. Van Den Wollenberg[107], P.C. Van Der Deijl[107], R. van der Geer[107], H. van der Graaf[107], N. van Eldik[152], P. van Gemmeren[6], J. Van Nieuwkoop[142], I. van Vulpen[107], M.C. van Woerden[30], M. Vanadia[132a,132b], W. Vandelli[30], R. Vanguri[122], A. Vaniachine[6], F. Vannucci[80], G. Vardanyan[177], R. Vari[132a], E.W. Varnes[7], T. Varol[40], D. Varouchas[80], A. Vartapetian[8], K.E. Varvell[150], F. Vazeille[34], T. Vazquez Schroeder[87], J. Veatch[7], L.M. Veloce[158], F. Veloso[126a,126c], T. Velz[21], S. Veneziano[132a], A. Ventura[73a,73b], D. Ventura[86], M. Venturi[169], N. Venturi[158], A. Venturini[23], V. Vercesi[121a], M. Verducci[132a,132b], W. Verkerke[107], J.C. Vermeulen[107], A. Vest[44], M.C. Vetterli[142,d], O. Viazlo[81], I. Vichou[165], T. Vickey[139], O.E. Vickey Boeriu[139], G.H.A. Viehhauser[120], S. Viel[15], R. Vigne[62], M. Villa[20a,20b], M. Villaplana Perez[91a,91b], E. Vilucchi[47], M.G. Vincter[29], V.B. Vinogradov[65], I. Vivarelli[149], F. Vives Vaque[3], S. Vlachos[10], D. Vladoiu[100], M. Vlasak[128], M. Vogel[32a], P. Vokac[128], G. Volpi[124a,124b], M. Volpi[88], H. von der Schmitt[101], H. von Radziewski[48], E. von Toerne[21], V. Vorobel[129], K. Vorobev[98], M. Vos[167], R. Voss[30], J.H. Vossebeld[74], N. Vranjes[13], M. Vranjes Milosavljevic[13], V. Vrba[127], M. Vreeswijk[107], R. Vuillermet[30], I. Vukotic[31], Z. Vykydal[128], P. Wagner[21], W. Wagner[175], H. Wahlberg[71], S. Wahrmund[44], J. Wakabayashi[103], J. Walder[72], R. Walker[100], W. Walkowiak[141], C. Wang[151], F. Wang[173], H. Wang[15], H. Wang[40], J. Wang[42], J. Wang[33a], K. Wang[87], R. Wang[6], S.M. Wang[151], T. Wang[21], T. Wang[35], X. Wang[176], C. Wanotayaroj[116], A. Warburton[87], C.P. Ward[28], D.R. Wardrope[78], A. Washbrook[46], C. Wasicki[42], P.M. Watkins[18], A.T. Watson[18], I.J. Watson[150], M.F. Watson[18], G. Watts[138], S. Watts[84], B.M. Waugh[78], S. Webb[84], M.S. Weber[17], S.W. Weber[174], J.S. Webster[31], A.R. Weidberg[120], B. Weinert[61], J. Weingarten[54], C. Weiser[48], H. Weits[107], P.S. Wells[30], T. Wenaus[25], T. Wengler[30], S. Wenig[30], N. Wermes[21], M. Werner[48], P. Werner[30], M. Wessels[58a], J. Wetter[161], K. Whalen[116], A.M. Wharton[72], A. White[8], M.J. White[1], R. White[32b], S. White[124a,124b], D. Whiteson[163], F.J. Wickens[131], W. Wiedenmann[173], M. Wielers[131], P. Wienemann[21], C. Wiglesworth[36], L.A.M. Wiik-Fuchs[21], A. Wildauer[101], H.G. Wilkens[30], H.H. Williams[122], S. Williams[107], C. Willis[90], S. Willocq[86],

JHEP10(2015)054

A. Wilson[89], J.A. Wilson[18], I. Wingerter-Seez[5], F. Winklmeier[116], B.T. Winter[21], M. Wittgen[143], J. Wittkowski[100], S.J. Wollstadt[83], M.W. Wolter[39], H. Wolters[126a,126c], B.K. Wosiek[39], J. Wotschack[30], M.J. Woudstra[84], K.W. Wozniak[39], M. Wu[55], M. Wu[31], S.L. Wu[173], X. Wu[49], Y. Wu[89], T.R. Wyatt[84], B.M. Wynne[46], S. Xella[36], D. Xu[33a], L. Xu[33b,ak], B. Yabsley[150], S. Yacoob[145a], R. Yakabe[67], M. Yamada[66], D. Yamaguchi[157], Y. Yamaguchi[118], A. Yamamoto[66], S. Yamamoto[155], T. Yamanaka[155], K. Yamauchi[103], Y. Yamazaki[67], Z. Yan[22], H. Yang[33e], H. Yang[173], Y. Yang[151], W-M. Yao[15], Y. Yasu[66], E. Yatsenko[5], K.H. Yau Wong[21], J. Ye[40], S. Ye[25], I. Yeletskikh[65], A.L. Yen[57], E. Yildirim[42], K. Yorita[171], R. Yoshida[6], K. Yoshihara[122], C. Young[143], C.J.S. Young[30], S. Youssef[22], D.R. Yu[15], J. Yu[8], J.M. Yu[89], J. Yu[114], L. Yuan[67], S.P.Y. Yuen[21], A. Yurkewicz[108], I. Yusuff[28,al], B. Zabinski[39], R. Zaidan[63], A.M. Zaitsev[130,ab], J. Zalieckas[14], A. Zaman[148], S. Zambito[57], L. Zanello[132a,132b], D. Zanzi[88], C. Zeitnitz[175], M. Zeman[128], A. Zemla[38a], Q. Zeng[143], K. Zengel[23], O. Zenin[130], T. Ženiš[144a], D. Zerwas[117], D. Zhang[89], F. Zhang[173], H. Zhang[33c], J. Zhang[6], L. Zhang[48], R. Zhang[33b], X. Zhang[33d], Z. Zhang[117], X. Zhao[40], Y. Zhao[33d,117], Z. Zhao[33b], A. Zhemchugov[65], J. Zhong[120], B. Zhou[89], C. Zhou[45], L. Zhou[35], L. Zhou[40], N. Zhou[33f], C.G. Zhu[33d], H. Zhu[33a], J. Zhu[89], Y. Zhu[33b], X. Zhuang[33a], K. Zhukov[96], A. Zibell[174], D. Zieminska[61], N.I. Zimine[65], C. Zimmermann[83], S. Zimmermann[48], Z. Zinonos[54], M. Zinser[83], M. Ziolkowski[141], L. Živković[13], G. Zobernig[173], A. Zoccoli[20a,20b], M. zur Nedden[16], G. Zurzolo[104a,104b] and L. Zwalinski[30].

[1] *Department of Physics, University of Adelaide, Adelaide, Australia*
[2] *Physics Department, SUNY Albany, Albany NY, United States of America*
[3] *Department of Physics, University of Alberta, Edmonton AB, Canada*
[4] [(a)] *Department of Physics, Ankara University, Ankara;* [(b)] *Istanbul Aydin University, Istanbul;* [(c)] *Division of Physics, TOBB University of Economics and Technology, Ankara, Turkey*
[5] *LAPP, CNRS/IN2P3 and Université Savoie Mont Blanc, Annecy-le-Vieux, France*
[6] *High Energy Physics Division, Argonne National Laboratory, Argonne IL, United States of America*
[7] *Department of Physics, University of Arizona, Tucson AZ, United States of America*
[8] *Department of Physics, The University of Texas at Arlington, Arlington TX, United States of America*
[9] *Physics Department, University of Athens, Athens, Greece*
[10] *Physics Department, National Technical University of Athens, Zografou, Greece*
[11] *Institute of Physics, Azerbaijan Academy of Sciences, Baku, Azerbaijan*
[12] *Institut de Física d'Altes Energies and Departament de Física de la Universitat Autònoma de Barcelona, Barcelona, Spain*
[13] *Institute of Physics, University of Belgrade, Belgrade, Serbia*
[14] *Department for Physics and Technology, University of Bergen, Bergen, Norway*
[15] *Physics Division, Lawrence Berkeley National Laboratory and University of California, Berkeley CA, United States of America*
[16] *Department of Physics, Humboldt University, Berlin, Germany*
[17] *Albert Einstein Center for Fundamental Physics and Laboratory for High Energy Physics, University of Bern, Bern, Switzerland*
[18] *School of Physics and Astronomy, University of Birmingham, Birmingham, United Kingdom*
[19] [(a)] *Department of Physics, Bogazici University, Istanbul;* [(b)] *Department of Physics Engineering, Gaziantep University, Gaziantep;* [(c)] *Department of Physics, Dogus University, Istanbul, Turkey*
[20] [(a)] *INFN Sezione di Bologna;* [(b)] *Dipartimento di Fisica e Astronomia, Università di Bologna, Bologna, Italy*
[21] *Physikalisches Institut, University of Bonn, Bonn, Germany*
[22] *Department of Physics, Boston University, Boston MA, United States of America*
[23] *Department of Physics, Brandeis University, Waltham MA, United States of America*
[24] [(a)] *Universidade Federal do Rio De Janeiro COPPE/EE/IF, Rio de Janeiro;* [(b)] *Electrical Circuits Department, Federal University of Juiz de Fora (UFJF), Juiz de Fora;* [(c)] *Federal University of Sao*

JHEP10(2015)054

Joao del Rei (UFSJ), Sao Joao del Rei; [(d)] *Instituto de Fisica, Universidade de Sao Paulo, Sao Paulo, Brazil*

[25] *Physics Department, Brookhaven National Laboratory, Upton NY, United States of America*

[26] [(a)] *National Institute of Physics and Nuclear Engineering, Bucharest;* [(b)] *National Institute for Research and Development of Isotopic and Molecular Technologies, Physics Department, Cluj Napoca;* [(c)] *University Politehnica Bucharest, Bucharest;* [(d)] *West University in Timisoara, Timisoara, Romania*

[27] *Departamento de Física, Universidad de Buenos Aires, Buenos Aires, Argentina*

[28] *Cavendish Laboratory, University of Cambridge, Cambridge, United Kingdom*

[29] *Department of Physics, Carleton University, Ottawa ON, Canada*

[30] *CERN, Geneva, Switzerland*

[31] *Enrico Fermi Institute, University of Chicago, Chicago IL, United States of America*

[32] [(a)] *Departamento de Física, Pontificia Universidad Católica de Chile, Santiago;* [(b)] *Departamento de Física, Universidad Técnica Federico Santa María, Valparaíso, Chile*

[33] [(a)] *Institute of High Energy Physics, Chinese Academy of Sciences, Beijing;* [(b)] *Department of Modern Physics, University of Science and Technology of China, Anhui;* [(c)] *Department of Physics, Nanjing University, Jiangsu;* [(d)] *School of Physics, Shandong University, Shandong;* [(e)] *Department of Physics and Astronomy, Shanghai Key Laboratory for Particle Physics and Cosmology, Shanghai Jiao Tong University, Shanghai;* [(f)] *Physics Department, Tsinghua University, Beijing 100084, China*

[34] *Laboratoire de Physique Corpusculaire, Clermont Université and Université Blaise Pascal and CNRS/IN2P3, Clermont-Ferrand, France*

[35] *Nevis Laboratory, Columbia University, Irvington NY, United States of America*

[36] *Niels Bohr Institute, University of Copenhagen, Kobenhavn, Denmark*

[37] [(a)] *INFN Gruppo Collegato di Cosenza, Laboratori Nazionali di Frascati;* [(b)] *Dipartimento di Fisica, Università della Calabria, Rende, Italy*

[38] [(a)] *AGH University of Science and Technology, Faculty of Physics and Applied Computer Science, Krakow;* [(b)] *Marian Smoluchowski Institute of Physics, Jagiellonian University, Krakow, Poland*

[39] *Institute of Nuclear Physics Polish Academy of Sciences, Krakow, Poland*

[40] *Physics Department, Southern Methodist University, Dallas TX, United States of America*

[41] *Physics Department, University of Texas at Dallas, Richardson TX, United States of America*

[42] *DESY, Hamburg and Zeuthen, Germany*

[43] *Institut für Experimentelle Physik IV, Technische Universität Dortmund, Dortmund, Germany*

[44] *Institut für Kern- und Teilchenphysik, Technische Universität Dresden, Dresden, Germany*

[45] *Department of Physics, Duke University, Durham NC, United States of America*

[46] *SUPA - School of Physics and Astronomy, University of Edinburgh, Edinburgh, United Kingdom*

[47] *INFN Laboratori Nazionali di Frascati, Frascati, Italy*

[48] *Fakultät für Mathematik und Physik, Albert-Ludwigs-Universität, Freiburg, Germany*

[49] *Section de Physique, Université de Genève, Geneva, Switzerland*

[50] [(a)] *INFN Sezione di Genova;* [(b)] *Dipartimento di Fisica, Università di Genova, Genova, Italy*

[51] [(a)] *E. Andronikashvili Institute of Physics, Iv. Javakhishvili Tbilisi State University, Tbilisi;* [(b)] *High Energy Physics Institute, Tbilisi State University, Tbilisi, Georgia*

[52] *II Physikalisches Institut, Justus-Liebig-Universität Giessen, Giessen, Germany*

[53] *SUPA - School of Physics and Astronomy, University of Glasgow, Glasgow, United Kingdom*

[54] *II Physikalisches Institut, Georg-August-Universität, Göttingen, Germany*

[55] *Laboratoire de Physique Subatomique et de Cosmologie, Université Grenoble-Alpes, CNRS/IN2P3, Grenoble, France*

[56] *Department of Physics, Hampton University, Hampton VA, United States of America*

[57] *Laboratory for Particle Physics and Cosmology, Harvard University, Cambridge MA, United States of America*

[58] [(a)] *Kirchhoff-Institut für Physik, Ruprecht-Karls-Universität Heidelberg, Heidelberg;* [(b)] *Physikalisches Institut, Ruprecht-Karls-Universität Heidelberg, Heidelberg;* [(c)] *ZITI Institut für*

JHEP10(2015)054

technische Informatik, Ruprecht-Karls-Universität Heidelberg, Mannheim, Germany
[59] Faculty of Applied Information Science, Hiroshima Institute of Technology, Hiroshima, Japan
[60] [(a)] Department of Physics, The Chinese University of Hong Kong, Shatin, N.T., Hong Kong; [(b)] Department of Physics, The University of Hong Kong, Hong Kong; [(c)] Department of Physics, The Hong Kong University of Science and Technology, Clear Water Bay, Kowloon, Hong Kong, China
[61] Department of Physics, Indiana University, Bloomington IN, United States of America
[62] Institut für Astro- und Teilchenphysik, Leopold-Franzens-Universität, Innsbruck, Austria
[63] University of Iowa, Iowa City IA, United States of America
[64] Department of Physics and Astronomy, Iowa State University, Ames IA, United States of America
[65] Joint Institute for Nuclear Research, JINR Dubna, Dubna, Russia
[66] KEK, High Energy Accelerator Research Organization, Tsukuba, Japan
[67] Graduate School of Science, Kobe University, Kobe, Japan
[68] Faculty of Science, Kyoto University, Kyoto, Japan
[69] Kyoto University of Education, Kyoto, Japan
[70] Department of Physics, Kyushu University, Fukuoka, Japan
[71] Instituto de Física La Plata, Universidad Nacional de La Plata and CONICET, La Plata, Argentina
[72] Physics Department, Lancaster University, Lancaster, United Kingdom
[73] [(a)] INFN Sezione di Lecce; [(b)] Dipartimento di Matematica e Fisica, Università del Salento, Lecce, Italy
[74] Oliver Lodge Laboratory, University of Liverpool, Liverpool, United Kingdom
[75] Department of Physics, Jožef Stefan Institute and University of Ljubljana, Ljubljana, Slovenia
[76] School of Physics and Astronomy, Queen Mary University of London, London, United Kingdom
[77] Department of Physics, Royal Holloway University of London, Surrey, United Kingdom
[78] Department of Physics and Astronomy, University College London, London, United Kingdom
[79] Louisiana Tech University, Ruston LA, United States of America
[80] Laboratoire de Physique Nucléaire et de Hautes Energies, UPMC and Université Paris-Diderot and CNRS/IN2P3, Paris, France
[81] Fysiska institutionen, Lunds universitet, Lund, Sweden
[82] Departamento de Fisica Teorica C-15, Universidad Autonoma de Madrid, Madrid, Spain
[83] Institut für Physik, Universität Mainz, Mainz, Germany
[84] School of Physics and Astronomy, University of Manchester, Manchester, United Kingdom
[85] CPPM, Aix-Marseille Université and CNRS/IN2P3, Marseille, France
[86] Department of Physics, University of Massachusetts, Amherst MA, United States of America
[87] Department of Physics, McGill University, Montreal QC, Canada
[88] School of Physics, University of Melbourne, Victoria, Australia
[89] Department of Physics, The University of Michigan, Ann Arbor MI, United States of America
[90] Department of Physics and Astronomy, Michigan State University, East Lansing MI, United States of America
[91] [(a)] INFN Sezione di Milano; [(b)] Dipartimento di Fisica, Università di Milano, Milano, Italy
[92] B.I. Stepanov Institute of Physics, National Academy of Sciences of Belarus, Minsk, Republic of Belarus
[93] National Scientific and Educational Centre for Particle and High Energy Physics, Minsk, Republic of Belarus
[94] Department of Physics, Massachusetts Institute of Technology, Cambridge MA, United States of America
[95] Group of Particle Physics, University of Montreal, Montreal QC, Canada
[96] P.N. Lebedev Institute of Physics, Academy of Sciences, Moscow, Russia
[97] Institute for Theoretical and Experimental Physics (ITEP), Moscow, Russia
[98] National Research Nuclear University MEPhI, Moscow, Russia
[99] D.V. Skobeltsyn Institute of Nuclear Physics, M.V. Lomonosov Moscow State University, Moscow, Russia
[100] Fakultät für Physik, Ludwig-Maximilians-Universität München, München, Germany

JHEP10(2015)054

[101] *Max-Planck-Institut für Physik (Werner-Heisenberg-Institut), München, Germany*
[102] *Nagasaki Institute of Applied Science, Nagasaki, Japan*
[103] *Graduate School of Science and Kobayashi-Maskawa Institute, Nagoya University, Nagoya, Japan*
[104] [(a)] *INFN Sezione di Napoli;* [(b)] *Dipartimento di Fisica, Università di Napoli, Napoli, Italy*
[105] *Department of Physics and Astronomy, University of New Mexico, Albuquerque NM, United States of America*
[106] *Institute for Mathematics, Astrophysics and Particle Physics, Radboud University Nijmegen/Nikhef, Nijmegen, Netherlands*
[107] *Nikhef National Institute for Subatomic Physics and University of Amsterdam, Amsterdam, Netherlands*
[108] *Department of Physics, Northern Illinois University, DeKalb IL, United States of America*
[109] *Budker Institute of Nuclear Physics, SB RAS, Novosibirsk, Russia*
[110] *Department of Physics, New York University, New York NY, United States of America*
[111] *Ohio State University, Columbus OH, United States of America*
[112] *Faculty of Science, Okayama University, Okayama, Japan*
[113] *Homer L. Dodge Department of Physics and Astronomy, University of Oklahoma, Norman OK, United States of America*
[114] *Department of Physics, Oklahoma State University, Stillwater OK, United States of America*
[115] *Palacký University, RCPTM, Olomouc, Czech Republic*
[116] *Center for High Energy Physics, University of Oregon, Eugene OR, United States of America*
[117] *LAL, Université Paris-Sud and CNRS/IN2P3, Orsay, France*
[118] *Graduate School of Science, Osaka University, Osaka, Japan*
[119] *Department of Physics, University of Oslo, Oslo, Norway*
[120] *Department of Physics, Oxford University, Oxford, United Kingdom*
[121] [(a)] *INFN Sezione di Pavia;* [(b)] *Dipartimento di Fisica, Università di Pavia, Pavia, Italy*
[122] *Department of Physics, University of Pennsylvania, Philadelphia PA, United States of America*
[123] *National Research Centre "Kurchatov Institute" B.P.Konstantinov Petersburg Nuclear Physics Institute, St. Petersburg, Russia*
[124] [(a)] *INFN Sezione di Pisa;* [(b)] *Dipartimento di Fisica E. Fermi, Università di Pisa, Pisa, Italy*
[125] *Department of Physics and Astronomy, University of Pittsburgh, Pittsburgh PA, United States of America*
[126] [(a)] *Laboratório de Instrumentação e Física Experimental de Partículas - LIP, Lisboa;* [(b)] *Faculdade de Ciências, Universidade de Lisboa, Lisboa;* [(c)] *Department of Physics, University of Coimbra, Coimbra;* [(d)] *Centro de Física Nuclear da Universidade de Lisboa, Lisboa;* [(e)] *Departamento de Fisica, Universidade do Minho, Braga;* [(f)] *Departamento de Fisica Teorica y del Cosmos and CAFPE, Universidad de Granada, Granada (Spain);* [(g)] *Dep Fisica and CEFITEC of Faculdade de Ciencias e Tecnologia, Universidade Nova de Lisboa, Caparica, Portugal*
[127] *Institute of Physics, Academy of Sciences of the Czech Republic, Praha, Czech Republic*
[128] *Czech Technical University in Prague, Praha, Czech Republic*
[129] *Faculty of Mathematics and Physics, Charles University in Prague, Praha, Czech Republic*
[130] *State Research Center Institute for High Energy Physics, Protvino, Russia*
[131] *Particle Physics Department, Rutherford Appleton Laboratory, Didcot, United Kingdom*
[132] [(a)] *INFN Sezione di Roma;* [(b)] *Dipartimento di Fisica, Sapienza Università di Roma, Roma, Italy*
[133] [(a)] *INFN Sezione di Roma Tor Vergata;* [(b)] *Dipartimento di Fisica, Università di Roma Tor Vergata, Roma, Italy*
[134] [(a)] *INFN Sezione di Roma Tre;* [(b)] *Dipartimento di Matematica e Fisica, Università Roma Tre, Roma, Italy*
[135] [(a)] *Faculté des Sciences Ain Chock, Réseau Universitaire de Physique des Hautes Energies - Université Hassan II, Casablanca;* [(b)] *Centre National de l'Energie des Sciences Techniques Nucleaires, Rabat;* [(c)] *Faculté des Sciences Semlalia, Université Cadi Ayyad, LPHEA-Marrakech;* [(d)] *Faculté des Sciences, Université Mohamed Premier and LPTPM, Oujda;* [(e)] *Faculté des sciences, Université Mohammed V-Agdal, Rabat, Morocco*

JHEP10(2015)054

[136] *DSM/IRFU (Institut de Recherches sur les Lois Fondamentales de l'Univers), CEA Saclay (Commissariat à l'Energie Atomique et aux Energies Alternatives), Gif-sur-Yvette, France*
[137] *Santa Cruz Institute for Particle Physics, University of California Santa Cruz, Santa Cruz CA, United States of America*
[138] *Department of Physics, University of Washington, Seattle WA, United States of America*
[139] *Department of Physics and Astronomy, University of Sheffield, Sheffield, United Kingdom*
[140] *Department of Physics, Shinshu University, Nagano, Japan*
[141] *Fachbereich Physik, Universität Siegen, Siegen, Germany*
[142] *Department of Physics, Simon Fraser University, Burnaby BC, Canada*
[143] *SLAC National Accelerator Laboratory, Stanford CA, United States of America*
[144] [(a)] *Faculty of Mathematics, Physics & Informatics, Comenius University, Bratislava;* [(b)] *Department of Subnuclear Physics, Institute of Experimental Physics of the Slovak Academy of Sciences, Kosice, Slovak Republic*
[145] [(a)] *Department of Physics, University of Cape Town, Cape Town;* [(b)] *Department of Physics, University of Johannesburg, Johannesburg;* [(c)] *School of Physics, University of the Witwatersrand, Johannesburg, South Africa*
[146] [(a)] *Department of Physics, Stockholm University;* [(b)] *The Oskar Klein Centre, Stockholm, Sweden*
[147] *Physics Department, Royal Institute of Technology, Stockholm, Sweden*
[148] *Departments of Physics & Astronomy and Chemistry, Stony Brook University, Stony Brook NY, United States of America*
[149] *Department of Physics and Astronomy, University of Sussex, Brighton, United Kingdom*
[150] *School of Physics, University of Sydney, Sydney, Australia*
[151] *Institute of Physics, Academia Sinica, Taipei, Taiwan*
[152] *Department of Physics, Technion: Israel Institute of Technology, Haifa, Israel*
[153] *Raymond and Beverly Sackler School of Physics and Astronomy, Tel Aviv University, Tel Aviv, Israel*
[154] *Department of Physics, Aristotle University of Thessaloniki, Thessaloniki, Greece*
[155] *International Center for Elementary Particle Physics and Department of Physics, The University of Tokyo, Tokyo, Japan*
[156] *Graduate School of Science and Technology, Tokyo Metropolitan University, Tokyo, Japan*
[157] *Department of Physics, Tokyo Institute of Technology, Tokyo, Japan*
[158] *Department of Physics, University of Toronto, Toronto ON, Canada*
[159] [(a)] *TRIUMF, Vancouver BC;* [(b)] *Department of Physics and Astronomy, York University, Toronto ON, Canada*
[160] *Faculty of Pure and Applied Sciences, University of Tsukuba, Tsukuba, Japan*
[161] *Department of Physics and Astronomy, Tufts University, Medford MA, United States of America*
[162] *Centro de Investigaciones, Universidad Antonio Narino, Bogota, Colombia*
[163] *Department of Physics and Astronomy, University of California Irvine, Irvine CA, United States of America*
[164] [(a)] *INFN Gruppo Collegato di Udine, Sezione di Trieste, Udine;* [(b)] *ICTP, Trieste;* [(c)] *Dipartimento di Chimica, Fisica e Ambiente, Università di Udine, Udine, Italy*
[165] *Department of Physics, University of Illinois, Urbana IL, United States of America*
[166] *Department of Physics and Astronomy, University of Uppsala, Uppsala, Sweden*
[167] *Instituto de Física Corpuscular (IFIC) and Departamento de Física Atómica, Molecular y Nuclear and Departamento de Ingeniería Electrónica and Instituto de Microelectrónica de Barcelona (IMB-CNM), University of Valencia and CSIC, Valencia, Spain*
[168] *Department of Physics, University of British Columbia, Vancouver BC, Canada*
[169] *Department of Physics and Astronomy, University of Victoria, Victoria BC, Canada*
[170] *Department of Physics, University of Warwick, Coventry, United Kingdom*
[171] *Waseda University, Tokyo, Japan*
[172] *Department of Particle Physics, The Weizmann Institute of Science, Rehovot, Israel*
[173] *Department of Physics, University of Wisconsin, Madison WI, United States of America*

JHEP10(2015)054

[174] Fakultät für Physik und Astronomie, Julius-Maximilians-Universität, Würzburg, Germany
[175] Fachbereich C Physik, Bergische Universität Wuppertal, Wuppertal, Germany
[176] Department of Physics, Yale University, New Haven CT, United States of America
[177] Yerevan Physics Institute, Yerevan, Armenia
[178] Centre de Calcul de l'Institut National de Physique Nucléaire et de Physique des Particules (IN2P3), Villeurbanne, France

[a] Also at Department of Physics, King's College London, London, United Kingdom
[b] Also at Institute of Physics, Azerbaijan Academy of Sciences, Baku, Azerbaijan
[c] Also at Novosibirsk State University, Novosibirsk, Russia
[d] Also at TRIUMF, Vancouver BC, Canada
[e] Also at Department of Physics, California State University, Fresno CA, United States of America
[f] Also at Department of Physics, University of Fribourg, Fribourg, Switzerland
[g] Also at Departamento de Fisica e Astronomia, Faculdade de Ciencias, Universidade do Porto, Portugal
[h] Also at Tomsk State University, Tomsk, Russia
[i] Also at CPPM, Aix-Marseille Université and CNRS/IN2P3, Marseille, France
[j] Also at Universita di Napoli Parthenope, Napoli, Italy
[k] Also at Institute of Particle Physics (IPP), Canada
[l] Also at Particle Physics Department, Rutherford Appleton Laboratory, Didcot, United Kingdom
[m] Also at Department of Physics, St. Petersburg State Polytechnical University, St. Petersburg, Russia
[n] Also at Louisiana Tech University, Ruston LA, United States of America
[o] Also at Institucio Catalana de Recerca i Estudis Avancats, ICREA, Barcelona, Spain
[p] Also at Graduate School of Science, Osaka University, Osaka, Japan
[q] Also at Department of Physics, National Tsing Hua University, Taiwan
[r] Also at Department of Physics, The University of Texas at Austin, Austin TX, United States of America
[s] Also at Institute of Theoretical Physics, Ilia State University, Tbilisi, Georgia
[t] Also at CERN, Geneva, Switzerland
[u] Also at Georgian Technical University (GTU),Tbilisi, Georgia
[v] Also at Manhattan College, New York NY, United States of America
[w] Also at Hellenic Open University, Patras, Greece
[x] Also at Institute of Physics, Academia Sinica, Taipei, Taiwan
[y] Also at LAL, Université Paris-Sud and CNRS/IN2P3, Orsay, France
[z] Also at Academia Sinica Grid Computing, Institute of Physics, Academia Sinica, Taipei, Taiwan
[aa] Also at School of Physics, Shandong University, Shandong, China
[ab] Also at Moscow Institute of Physics and Technology State University, Dolgoprudny, Russia
[ac] Also at section de Physique, Université de Genève, Geneva, Switzerland
[ad] Also at International School for Advanced Studies (SISSA), Trieste, Italy
[ae] Also at Department of Physics and Astronomy, University of South Carolina, Columbia SC, United States of America
[af] Also at School of Physics and Engineering, Sun Yat-sen University, Guangzhou, China
[ag] Also at Faculty of Physics, M.V.Lomonosov Moscow State University, Moscow, Russia
[ah] Also at National Research Nuclear University MEPhI, Moscow, Russia
[ai] Also at Department of Physics, Stanford University, Stanford CA, United States of America
[aj] Also at Institute for Particle and Nuclear Physics, Wigner Research Centre for Physics, Budapest, Hungary
[ak] Also at Department of Physics, The University of Michigan, Ann Arbor MI, United States of America
[al] Also at University of Malaya, Department of Physics, Kuala Lumpur, Malaysia
[*] Deceased

JHEP10(2015)054

Eur. Phys. J. C (2015) 75:510
DOI 10.1140/epjc/s10052-015-3726-9

THE EUROPEAN PHYSICAL JOURNAL C

Regular Article - Experimental Physics

ATLAS Run 1 searches for direct pair production of third-generation squarks at the Large Hadron Collider

ATLAS Collaboration*

CERN, 1211 Geneva 23, Switzerland

Received: 30 June 2015 / Accepted: 8 October 2015 / Published online: 29 October 2015
© CERN for the benefit of the ATLAS collaboration 2015. This article is published with open access at Springerlink.com

Abstract This paper reviews and extends searches for the direct pair production of the scalar supersymmetric partners of the top and bottom quarks in proton–proton collisions collected by the ATLAS collaboration during the LHC Run 1. Most of the analyses use 20 fb^{-1} of collisions at a centre-of-mass energy of $\sqrt{s} = 8$ TeV, although in some case an additional 4.7 fb^{-1} of collision data at $\sqrt{s} = 7$ TeV are used. New analyses are introduced to improve the sensitivity to specific regions of the model parameter space. Since no evidence of third-generation squarks is found, exclusion limits are derived by combining several analyses and are presented in both a simplified model framework, assuming simple decay chains, as well as within the context of more elaborate phenomenological supersymmetric models.

Contents

1 Introduction . . . 1
2 Third-generation squark phenomenology . . . 2
3 General discussion of the analysis strategy . . . 4
4 Interpretations in simplified models . . . 5
4.1 Stop decays with no charginos in the decay chain 5
4.2 Stop decays with a chargino in the decay chain . 8
4.3 Limits on pair production of $\tilde{t}_2$ . . . 10
4.4 Sbottom decays . . . 11
5 Interpretations in pMSSM models . . . 11
6 Conclusions . . . 17
A The ATLAS detector and object reconstruction . . . 18
B Analyses used in the paper . . . 19
B.1 Review of already published signal regions . . . 19
B.2 Description of the new signal regions . . . 22
B.2.1 Final states with two leptons at intermediate values of m_{T2}(WW) . . . 23
B.2.2 Final states containing two top quarks and a Higgs boson (t2t1h) . . . 25
B.2.3 Final states containing two b-jets, a charged lepton, and missing transverse momentum (tb) 27
C Further details of the statistical combination of the t0L and t1L signal regions . . . 30
D Signal generation details . . . 33
References . . . 34

* e-mail: atlas.publications@cern.ch

1 Introduction

In a theory with broken supersymmetry (SUSY) [1–9], the mass scale of the supersymmetric particles is undetermined. However, for SUSY to provide a solution to the hierarchy problem [10–13] some of the new SUSY particles masses are typically required to be below about one TeV [14,15], hence they could be within the reach of the LHC.

The scalar partners of the right-handed and left-handed chiral components of the top-quark state ($\tilde{t}_R$ and $\tilde{t}_L$ respectively) are among these particles. In many supersymmetric models, the large Yukawa coupling of the top quark to the Higgs sector makes the Higgs boson mass sensitive to the masses of the scalar top (referred to as stop in the following) states, such that, to avoid fine tuning, their masses are often required to be light. The $\tilde{t}_R$ and $\tilde{t}_L$ components mix to form the mass eigenstates $\tilde{t}_1$ and $\tilde{t}_2$, $\tilde{t}_1$ being defined as the lighter of the two. The scalar superpartner of the left-handed chiral component of the bottom quark ($\tilde{b}_L$) belongs to the same weak isospin doublet as the $\tilde{t}_L$, hence they usually share the same supersymmetry-breaking mass parameter: a light stop can therefore imply the existence of a light scalar bottom. The lightest sbottom mass eigenstate is referred to as $\tilde{b}_1$.

The ATLAS and CMS collaborations have searched for direct production of stops and sbottoms [16–35] using about 4.7 fb^{-1} of data from the proton–proton collisions produced by the LHC at $\sqrt{s} = 7$ TeV and 20 fb^{-1} at $\sqrt{s} = 8$ TeV. These searches have found no evidence of third-generation squark signals, leading to exclusion limits in many SUSY models. The aim of this paper is to sum-

marise the sensitivity of the ATLAS experiment to R-parity-conserving[1] [38–42] models including the direct pair production of stops and sbottoms using the full $\sqrt{s} = 8$ TeV proton–proton collision dataset collected during Run 1 of the LHC.[2] The third-generation squarks are assumed to decay to the stable lightest supersymmetric particle (LSP) directly or through one or more intermediate stages. The analyses considered are those previously published by the ATLAS collaboration on the topic, together with new ones designed to increase the sensitivity to scenarios not optimally covered so far. A wide range of SUSY scenarios are studied by combining different analyses to improve the global sensitivity.

The paper is organised as follows: Sect. 2 briefly reviews the expected phenomenology of third-generation squark production and decay; Sect. 3 reviews the general analysis approach followed by the ATLAS collaboration for SUSY searches; Sects. 4 and 5 present the exclusion limits obtained in specific models by combining the results of several analyses. Two different types of models have been considered: simplified models, where the third-generation squarks are assumed to decay into typically one or two different final states, and more complex phenomenological supersymmetric models, where the stop and sbottom have many allowed decay channels. Conclusions are drawn in Sect. 6.

For the sake of brevity, the body of the paper provides no details of the ATLAS detector and object reconstruction, of the analyses used in the limit derivation, or of how the signal Monte Carlo simulation samples were generated. However, a comprehensive set of appendices is provided to supply additional information to the interested reader. Appendix A briefly summarises the layout of the ATLAS detector and the general principles used in the reconstruction of electrons, muons, jets, jets containing b-hadrons (b-jets), and the missing transverse momentum vector $\mathbf{p}_{\mathrm{T}}^{\mathrm{miss}}$ (whose magnitude is referred to as $E_{\mathrm{T}}^{\mathrm{miss}}$). Appendix B discusses the analyses used to derive the exclusion limits presented in Sects. 4 and 5. The analyses that have already been published are only briefly reviewed, while those presented for the first time in this paper are discussed in detail. Appendix C provides further details of a combination of analyses which is performed for the first time in this paper. Finally, Appendix D provides details about the generation and simulation of the signal Monte Carlo samples used to derive the limits presented.

2 Third-generation squark phenomenology

The cross section for direct stop pair production in proton–proton collisions at $\sqrt{s} = 8$ TeV as a function of the stop mass as calculated with PROSPINO [43,44] is shown in Fig. 1a. It is calculated to next-to-leading order accuracy in the strong coupling constant, adding the resummation of soft gluon emission at next-to-leading-logarithmic accuracy (NLO+NLL) [45–47]. In this paper, the nominal cross section and its uncertainty are taken from an envelope of cross-section predictions using different parton distribution function (PDF) sets and factorisation and renormalisation scales described in Ref. [44]. The difference in cross section between the sbottom and stop pair production is known to be small [46], hence the values of Fig. 1a are used for both.

Searches for direct production of stops and sbottoms by the ATLAS collaboration have covered several possible final-state topologies. The experimental signatures used to identify these processes depend on the masses of the stop or sbottom, on the masses of the other supersymmetric particles they can decay into, and on other parameters of the model, such as the stop and sbottom left–right mixing and the mixing between the gaugino and higgsino states in the chargino–neutralino sector.

Assuming that the lightest supersymmetric particle is a stable neutralino ($\tilde{\chi}_1^0$), and that no other supersymmetric particle plays a significant role in the sbottom decay, the decay chain of the sbottom is simply $\tilde{b}_1 \rightarrow b\tilde{\chi}_1^0$ (Fig. 2a).

A significantly more complex phenomenology has to be considered for the stop, depending on its mass and on the $\tilde{\chi}_1^0$ mass. Figure 1b shows the three main regions in the $m_{\tilde{t}_1}$–$m_{\tilde{\chi}_1^0}$ plane that are taken into account. They are identified by different values of $\Delta m(\tilde{t}_1, \tilde{\chi}_1^0) = m_{\tilde{t}_1} - m_{\tilde{\chi}_1^0}$. In the region where $\Delta m(\tilde{t}_1, \tilde{\chi}_1^0) > m_t$, the favoured decay is $\tilde{t}_1 \rightarrow t\tilde{\chi}_1^0$ (Fig. 2b). The region where $m_W + m_b < \Delta m(\tilde{t}_1, \tilde{\chi}_1^0) < m_t$ is characterised by the three-body decay[3] ($\tilde{t}_1 \rightarrow Wb\tilde{\chi}_1^0$ through an off-shell top quark, Fig. 2c). The region where the value of $\Delta m(\tilde{t}_1, \tilde{\chi}_1^0)$ drops below $m_W + m_b$, sees the four-body decay $\tilde{t}_1 \rightarrow bff'\tilde{\chi}_1^0$, (where f and f' indicate generic fermions coming from the decay of an off-shell W boson, Fig. 2d) competing with the flavour-changing decay[4] $\tilde{t}_1 \rightarrow c\tilde{\chi}_1^0$ of Fig. 2e; the dominant decay depends on the details of the supersymmetric model chosen [50].

If the third-generation squark decay involves more SUSY particles (other than the $\tilde{\chi}_1^0$), then additional dependencies on

[1] It is also assumed that the decay of the third-generation squarks is prompt: long-lived and metastable stops/sbottoms are discussed elsewhere [36,37].

[2] The analysis exploiting the measurement of the $t\bar{t}$ cross section discussed in this paper also uses 4.7 fb^{-1} of proton–proton collisions at $\sqrt{s} = 7$ TeV.

[3] In scenarios that depart from the minimal flavour violation assumption, flavour-changing decays like $\tilde{t}_1 \rightarrow c\tilde{\chi}_1^0$ or $\tilde{t}_1 \rightarrow u\tilde{\chi}_1^0$ could have a significant branching ratio up to $\Delta m(\tilde{t}_1, \tilde{\chi}_1^0) \sim 100$ GeV [48].

[4] The decay $\tilde{t}_1 \rightarrow u\tilde{\chi}_1^0$, in the assumption of minimal flavour violation [49], is further suppressed with respect to $\tilde{t}_1 \rightarrow c\tilde{\chi}_1^0$ by corresponding factors of the CKM matrix.

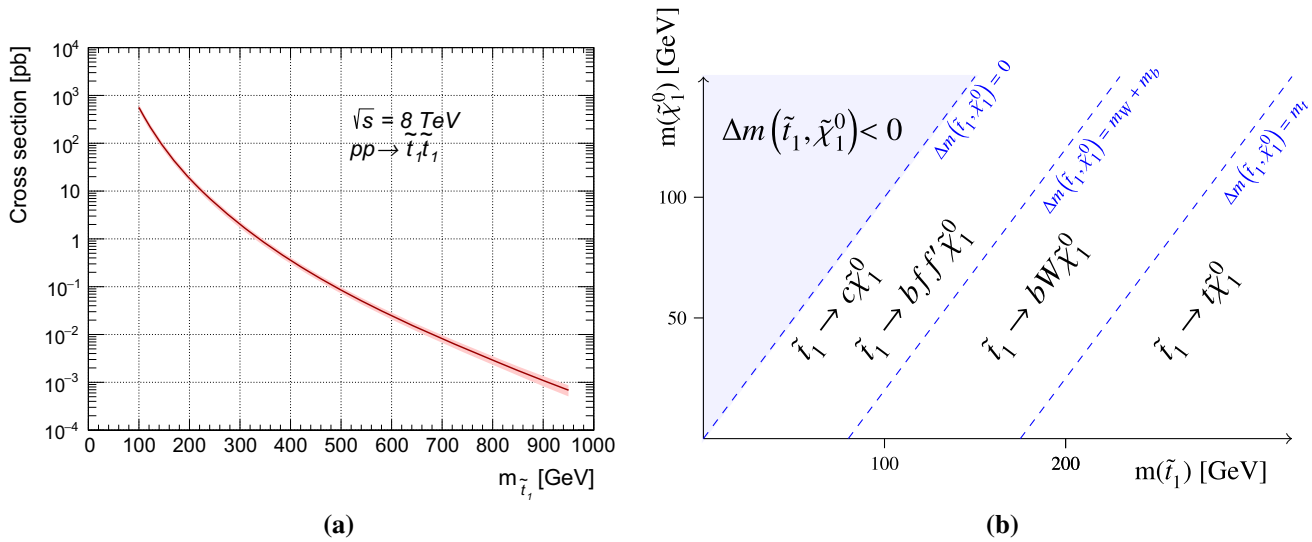

Fig. 1 **a** Direct stop pair production cross section at $\sqrt{s} = 8$ TeV as a function of the stop mass. The band around the cross section curve illustrates the uncertainty (which is everywhere about 15–20 %) on the cross section due to scale and PDF variations. **b** Illustration of stop decay modes in the plane spanned by the masses of the stop ($\tilde{t}_1$) and the lightest neutralino ($\tilde{\chi}_1^0$), where the latter is assumed to be the lightest supersymmetric particle and the only one present among the decay products. The *dashed blue lines* indicate thresholds separating regions where different processes dominate

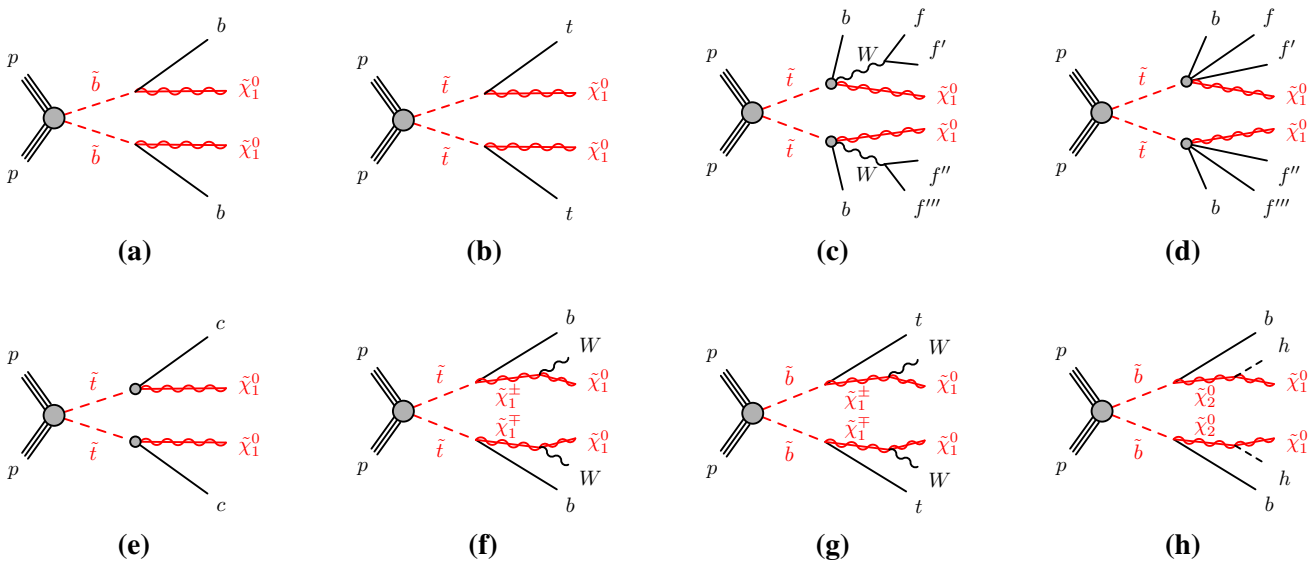

Fig. 2 Diagrams of $\tilde{t}_1$ and $\tilde{b}_1$ pair production and decays considered as simplified models: **a** $\tilde{b}_1\tilde{b}_1 \to b\tilde{\chi}_1^0 b\tilde{\chi}_1^0$; **b** $\tilde{t}_1\tilde{t}_1 \to t\tilde{\chi}_1^0 t\tilde{\chi}_1^0$; **c** three-body decay; **d** four-body decay; **e** $\tilde{t}_1\tilde{t}_1 \to c\tilde{\chi}_1^0 c\tilde{\chi}_1^0$; **f** $\tilde{t}_1\tilde{t}_1 \to b\tilde{\chi}_1^\pm b\tilde{\chi}_1^\pm$; **g** $\tilde{b}_1\tilde{b}_1 \to t\tilde{\chi}_1^\pm t\tilde{\chi}_1^\pm$; **h** $\tilde{b}_1\tilde{b}_1 \to b\tilde{\chi}_2^0 b\tilde{\chi}_2^0$. The diagrams do not show "mixed" decays, in which the two pair-produced third-generation squarks decay to different final states

SUSY parameters arise. For example, if the lightest chargino ($\tilde{\chi}_1^\pm$) is the next-to-lightest supersymmetric particle (NLSP), then the stop tends to have a significant branching ratio for $\tilde{t}_1 \to b\tilde{\chi}_1^\pm$ (Fig. 2f), or, for the sbottom, $\tilde{b}_1 \to t\tilde{\chi}_1^\pm$ if kinematically allowed (Fig. 2g). The presence of additional particles in the decay chain makes the phenomenology depend on their masses. Several possible scenarios have been considered, the most common ones being the gauge-universality inspired $m_{\tilde{\chi}_1^\pm} = 2m_{\tilde{\chi}_1^0}$, favoured, for example, in mSUGRA/CMSSM models [51–56]; other interpretations include the case of a chargino almost degenerate with the neutralino, a chargino almost degenerate with the squark, or a chargino of fixed mass. Another possible decay channel considered for the sbottom is $\tilde{b}_1 \to b\tilde{\chi}_2^0 \to bh\tilde{\chi}_1^0$ (Fig. 2h), which occurs in scenarios with a large higgsino component of the two lightest neutralinos.

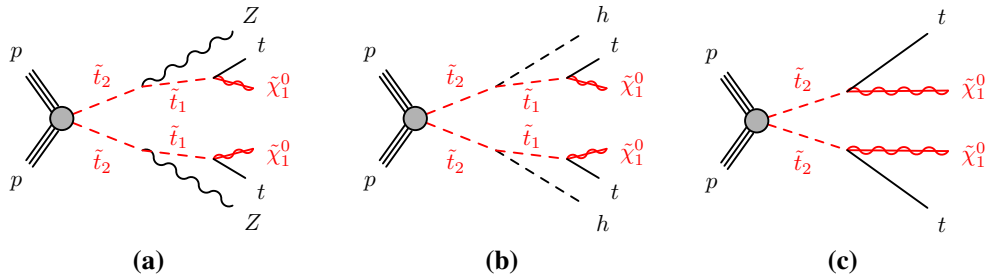

Fig. 3 Diagrams of $\tilde{t}_2$ decays considered as simplified models: **a** $\tilde{t}_2\tilde{t}_2 \rightarrow \tilde{t}_1 Z \tilde{t}_1 Z$; **b** $\tilde{t}_2\tilde{t}_2 \rightarrow \tilde{t}_1 h \tilde{t}_1 h$; **c** $\tilde{t}_2\tilde{t}_2 \rightarrow t\tilde{\chi}_1^0 t\tilde{\chi}_1^0$. The *diagrams* do not show "mixed" decays, in which the two pair-produced third-generation squarks decay to different final states. The decay $\tilde{t}_2 \rightarrow \gamma\tilde{t}_1$ is not an allowed process

Despite the lower production cross section and similar final states to $\tilde{t}_1$, the heavier stop state ($\tilde{t}_2$) pair production has also been studied: the search for it becomes interesting in scenarios where the detection of $\tilde{t}_1$ pair production becomes difficult (for example if $\Delta m(\tilde{t}_1, \tilde{\chi}_1^0) \sim m_t$). The diagrams of the investigated processes are shown in Fig. 3.

Two types of SUSY models are used to interpret the results in terms of exclusion limits. The simplified model approach assumes that either a stop or a sbottom pair is produced and that they decay into well-defined final states, involving one or two decay channels. Simplified models are used to optimise the analyses for a specific final-state topology, rather than the complex (and model-dependent) mixture of different topologies that would arise from a SUSY model involving many possible allowed production and decay channels. The sensitivity to simplified models is discussed in Sect. 4.

More complete phenomenological minimal supersymmetric extensions of the Standard Model (pMSSM in the following [57]) are also considered, to assess the performance of the analyses in scenarios where the stop and sbottom typically have many allowed decay channels with competing branching ratios. Three different sets of pMSSM models are considered, which take into account experimental constraints from LHC direct searches, satisfying the Higgs boson mass and dark-matter relic density constraints, or additional constraints arising from considerations of naturalness. The sensitivity to these models is discussed in Sect. 5.

3 General discussion of the analysis strategy

The rich phenomenology of third-generation supersymmetric particles requires several event selections to target the wide range of possible topologies. A common analysis strategy and common statistical techniques, which are extensively described in Ref. [58], are employed.

Signal regions (SR) are defined, which target one specific model and SUSY particle mass range. The event selection is optimised by relying on the Monte Carlo simulation of both the Standard Model (SM) background production processes and the signal itself. The optimisation process aims to maximise the expected significance for discovery or exclusion for each of the models considered.

For each SR, multiple control regions (CR) are defined: they are used to constrain the normalisation of the most relevant SM production processes and to validate the MC predictions of the shapes of distributions of the kinematic variables used in the analysis. The event selection of the CRs is mutually exclusive with that of the SRs. It is, however, chosen to be as close as possible to that of the signal region while keeping the signal contamination small, and such that the event yield is dominated by one specific background process.

A likelihood function is built as the product of Poisson probability functions, describing the observed and expected number of events in the control and signal regions. The observed numbers of events in the various CRs and SRs are used in a combined profile likelihood fit [59] to determine the expected SM background yields for each of the SRs. Systematic uncertainties are treated as nuisance parameters in the fit and are constrained with Gaussian functions with standard deviation equal to their value. The fit procedure takes into account correlations in the yield predictions between different regions due to common background normalisation parameters and systematic uncertainties, as well as contamination from SUSY signal events, when a particular model is considered for exclusion.

The full procedure is validated by comparing the background predictions and the shapes of the distributions of the key analysis variables from the fit results to those observed in dedicated validation regions (VRs), which are defined to be orthogonal to, and kinematically similar, to the signal regions, with low potential contamination from signal.

After successful validation, the observed yields in the signal regions are compared to the prediction. The profile likelihood ratio statistic is used first to verify the SM background-only hypothesis, and, if no significant excess is observed, to exclude the signal-plus-background hypothesis in specific signal models. A signal model is said to be excluded at 95 % confidence level (CL) if the CL_s [60,61] of the profile likeli-

hood ratio statistics of the signal-plus-background hypothesis is below 0.05.

Several publications, targeting specific stop and sbottom final-state topologies, were published by the ATLAS collaboration at the end of the proton–proton collision run at $\sqrt{s} = 8$ TeV, using a total integrated luminosity of about 20 fb^{-1}. Each of these papers defined one or more sets of signal regions optimised for different simplified models with different mass hierarchies and decay modes for the stop and/or sbottom. A few additional signal regions, focusing on regions of the parameter space not well covered by existing analyses have been defined since then. All signal regions that are used in this paper are discussed in detail in Appendix B, while Table 1 introduces their names and the targeted models. Each analysis is identified by a short acronym defined in the second column of Table 1. The signal region names of previously published analyses are retained, but, to avoid confusion and to ease the bookkeeping, the analysis acronym is prepended to their names. For example, SRA1 from the t0L analysis of Ref. [16], which is a search for stop pair production in channels with no leptons in the final state, is referred to as t0L-SRA1.

4 Interpretations in simplified models

The use of simplified models for analysis optimisation and result interpretation has become more and more common in the last years. The attractive feature of this approach is that it focuses on a specific final-state topology, rather than on a complex (and often heavily model-dependent) mixture of several different topologies: only a few SUSY particles are assumed to be produced in the proton–proton collision – often just one type – and only a few decay channels are assumed to be allowed. In the remainder of this section, several exclusion limits derived in different supersymmetric simplified models are presented. Details about how the MC signal samples used for the limit derivations were produced are available in Appendix D.

4.1 Stop decays with no charginos in the decay chain

A first series of simplified models is considered. It includes direct stop pair production as the only SUSY production process, and assumes that no supersymmetric particle other than the $\tilde{t}_1$ itself and the LSP, taken to be the lightest neutralino $\tilde{\chi}_1^0$, is involved in the decay. Under this assumption, there is little model dependence left in the stop phenomenology, as discussed in Sect. 2. The stop decay modes are defined mainly by the mass separation $\Delta m(\tilde{t}_1, \tilde{\chi}_1^0)$ between the stop and the neutralino, as shown in Fig. 1b. The corresponding diagrams are shown in Fig. 2.

Figure 4 shows the 95 % CL exclusion limits obtained in the $m_{\tilde{t}_1} - m_{\tilde{\chi}_1^0}$ plane by the relevant analyses listed in Table 1 and discussed in Appendix B, or by their combination. A detailed discussion of which analysis is relevant in each range of $\Delta m(\tilde{t}_1, \tilde{\chi}_1^0)$ follows.

$\boldsymbol{\Delta m(\tilde{t}_1, \tilde{\chi}_1^0) < m_W + m_b}$ This kinematic region is characterised by the presence of two competing decays: the flavour-violating decay $\tilde{t}_1 \to c\tilde{\chi}_1^0$ (Fig. 2e) and the four-body decay $\tilde{t}_1 \to bff'\tilde{\chi}_1^0$ (Fig. 2d). Which one of the two becomes dominant depends on the model details, in particular on the mass separation between the stop and the neutralino, and on the amount of flavour violation allowed in the model [50]. Several analyses have sensitivity in this region of the $m_{\tilde{t}_1} - m_{\tilde{\chi}_1^0}$ plane. The monojet-like signal regions (tc-M1-3) dominate the sensitivity in the region with $\Delta m(\tilde{t}_1, \tilde{\chi}_1^0) \gtrsim m_b$, regardless of the decay of the stop pair, which goes undetected: their selection is based on the presence of an initial-state radiation (ISR) jet recoiling against the stop-pair system, which is assumed to be invisible. At larger values of $\Delta m(\tilde{t}_1, \tilde{\chi}_1^0)$, signal regions requiring the presence of a c-tagged jet (tc-C1-2) complement the monojet-like signal regions by targeting the $\tilde{t}_1 \to c\tilde{\chi}_1^0$ decay. Limits on four-body decays can be set using signal regions which include low transverse momentum electrons and muons (t1L-bCa_low and WW).

The limits reported in Fig. 4 for these values of Δm all assume that the branching ratio of the stop decay into either $\tilde{t}_1 \to c\tilde{\chi}_1^0$ or $\tilde{t}_1 \to bff'\tilde{\chi}_1^0$ is 100 %. However, this assumption can be relaxed, and exclusion limits derived as a function of the branching ratio of the $\tilde{t}_1 \to c\tilde{\chi}_1^0$ decay, BR($\tilde{t}_1 \to c\tilde{\chi}_1^0$), assuming that BR($\tilde{t}_1 \to c\tilde{\chi}_1^0$) + BR($\tilde{t}_1 \to bff'\tilde{\chi}_1^0$) = 1. Two different scenarios, with $\Delta m(\tilde{t}_1, \tilde{\chi}_1^0) = 10, 80$ GeV, are considered. The first compressed scenario is characterised by low-p_T stop decay products, and the set of signal regions which have sensitivity is the tc-M, independently of the decay of the stop. In the second scenario, the phase space available for the $\tilde{t}_1$ decay is larger, and the full set of tc-M, tc-C, t1L-bCa_low, t1L-bCa_med and WW-SR selections have different sensitivity, depending on BR($\tilde{t}_1 \to c\tilde{\chi}_1^0$).

The cross-section limit is derived by combining the analyses discussed above. The SR giving the lowest expected exclusion CL$_s$ for each signal model and for each value of BR($\tilde{t} \to c\tilde{\chi}_1^0$) is chosen.

Figure 5 shows the result of these combinations. For $\Delta m(\tilde{t}_1, \tilde{\chi}_1^0) = 10$ GeV, the sensitivity is completely dominated by the tc-M signal regions, hence no significant dependence on BR($\tilde{t} \to c\tilde{\chi}_1^0$) is observed. In this case, stop masses up to about 250 GeV are excluded. For $\Delta m(\tilde{t}_1, \tilde{\chi}_1^0) = 80$ GeV, the sensitivity is dominated by the tc-C signal regions at high values of BR($\tilde{t} \to c\tilde{\chi}_1^0$). For lower values of BR($\tilde{t} \to c\tilde{\chi}_1^0$), the "soft-lepton" and WW signal regions both become competitive, the latter yielding a higher sensitivity at smaller

Table 1 Summary of the ATLAS analyses and signal regions used in this paper. Each signal region is identified by the acronym of the corresponding analysis followed by the original name of the signal region defined either in the published paper or in Appendix B.2. A dash in the signal region name column indicates that the analysis does not use the concept of signal region

Analysis name and corresponding reference	Analysis acronym	Original signal region name	Model targeted
Multijet final states [16]	t0L	SRA1-4	$\tilde{t}_1 \to t\tilde{\chi}_1^0$
		SRB	
		SRC1-3	$\tilde{t}_1\tilde{t}_1 \to bt\tilde{\chi}_1^0\tilde{\chi}_1^\pm$ with $m_{\tilde{\chi}_1^\pm} = 2m_{\tilde{\chi}_1^0}$
One-lepton final states [17]	t1L	tN_diag	$\tilde{t}_1 \to t\tilde{\chi}_1^0$ with $m_{\tilde{t}_1} \sim m_t + m_{\tilde{\chi}_1^0}$
		tN_med, tN_high, tN_boost	$\tilde{t}_1 \to t\tilde{\chi}_1^0$
		bCa_low, bCa_med, bCb_med1,	$\tilde{t}_1 \to b\tilde{\chi}_1^\pm$
		bCb_high, bCb_med2, bCc_diag	
		bCd_bulk, bCd_high1, bCd_high2	
		3body	$\tilde{t}_1 \to bW\tilde{\chi}_1^0$ (three-body decay)
		tNbC_mix	$\tilde{t}_1\tilde{t}_1 \to bt\tilde{\chi}_1^0\tilde{\chi}_1^\pm$ with $m_{\tilde{\chi}_1^\pm} = 2m_{\tilde{\chi}_1^0}$
Two-lepton final states [18]	t2L	L90, L100, L110, L120, H160	$\tilde{t}_1 \to b\tilde{\chi}_1^\pm$, three-body decay
		M1-4	$\tilde{t}_1 \to t\tilde{\chi}_1^0$
Final states from compressed stop decays [19]	tc	M1-3	$\tilde{t}_1/\tilde{b}_1 \to$ anything with $m_{\tilde{t}_1} \sim m_{\tilde{\chi}_1^0}$
		C1-2	$\tilde{t}_1 \to c\tilde{\chi}_1^0$
Final states with a Z boson [20]	t2t1Z	SR2A, SR2B, SR2C, SR3A, SR3B	$\tilde{t}_2 \to \tilde{t}_1 Z$ and $\tilde{t}_2 \to \tilde{t}_1 h$
Final states with two b-jets and $E_{\mathrm{T}}^{\mathrm{miss}}$ [21]	b0L	SRA, SRB	$\tilde{b}_1 \to b\tilde{\chi}_1^0$ and $\tilde{t}_1 \to b\tilde{\chi}_1^\pm$ with $m_{\tilde{\chi}_1^\pm} \sim m_{\tilde{\chi}_1^0}$
Final states with two leptons at intermediate m_{T2} (Appendix B.2.1)	WW	SR1–7	$\tilde{t}_1 \to b\tilde{\chi}_1^\pm$ with $m_{\tilde{\chi}_1^\pm} = m_{\tilde{t}_1} - 10$ GeV and
			$\tilde{t}_1 \to b\ell\nu\tilde{\chi}_1^0$ (three- and four-body decays)
Final states containing two top quarks and a Higgs boson (Appendix B.2.2)	t2t1h	–	$\tilde{t}_2 \to \tilde{t}_1 h$
Final states containing a top and a b-quark (Appendix B.2.3)	tb	SR1-5	$\tilde{t}_1\tilde{t}_1 \to b\tilde{\chi}_1^\pm t\tilde{\chi}_1^0$ with $m_{\tilde{\chi}_1^\pm} \sim m_{\tilde{\chi}_1^0}$ and pMSSM models
Final states with three b-jets [62]	g3b	SR-0ℓ-4j-A, SR-0ℓ-4j-B, SR-0ℓ-4j-C,	Gluino-mediated $\tilde{t}_1$ and $\tilde{b}_1$ production,
		SR-0ℓ-7j-A, SR-0ℓ-7j-B, SR-0ℓ-7j-C,	$\tilde{b}_1 \to \tilde{\chi}_2^0 b \to \tilde{\chi}_1^0 hb$
		SR-1ℓ-6j-A, SR-1ℓ-6j-B, SR-1ℓ-7j-C	
Strongly produced final states with two same-sign or three leptons [63]	SS3L	SR3b, SR0b, SR1b,	Generic gluino and squark production, $\tilde{b}_1 \to t\tilde{\chi}_1^\pm$
		SR3Llow, S3Lhigh	
Spin correlation in $t\bar{t}$ production events [64]	SC	–	$\tilde{t}_1 \to t\tilde{\chi}_1^0$ with $m_{\tilde{t}_1} \sim m_t + m_{\tilde{\chi}_1^0}$
$t\bar{t}$ production cross section [65]	xsec	–	$\tilde{t}_1 \to t\tilde{\chi}_1^0$, three-body decay

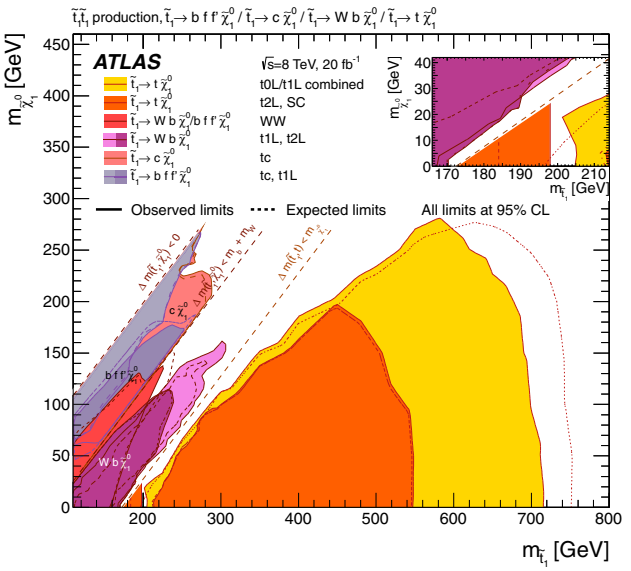

Fig. 4 Summary of the ATLAS Run 1 searches for direct stop pair production in models where no supersymmetric particle other than the $\tilde{t}_1$ and the $\tilde{\chi}_1^0$ is involved in the $\tilde{t}_1$ decay. The 95 % CL exclusion limits are shown in the $m_{\tilde{t}_1}$–$m_{\tilde{\chi}_1^0}$ mass plane. The *dashed* and *solid lines* show the expected and observed limits, respectively, including all uncertainties except the theoretical signal cross-section uncertainty (PDF and scale). Four decay modes are considered separately with a branching ratio of 100 %: $\tilde{t}_1 \rightarrow t\tilde{\chi}_1^0$, where the $\tilde{t}_1$ is mostly $\tilde{t}_R$, for $\Delta m(\tilde{t}_1, \tilde{\chi}_1^0) > m_t$; $\tilde{t}_1 \rightarrow Wb\tilde{\chi}_1^0$ (three-body decay) for $m_W + m_b < \Delta m(\tilde{t}_1, \tilde{\chi}_1^0) < m_t$; $\tilde{t}_1 \rightarrow c\tilde{\chi}_1^0$ and $\tilde{t}_1 \rightarrow bff'\tilde{\chi}_1^0$ (four-body decay) for $\Delta m(\tilde{t}_1, \tilde{\chi}_1^0) < m_W + m_b$. The latter two decay modes are superimposed

values of the stop mass. The maximum excluded stop mass ranges from about 180 GeV for $\mathrm{BR}(\tilde{t} \rightarrow c\tilde{\chi}_1^0) = 25\,\%$ to about 270 GeV for $\mathrm{BR}(\tilde{t} \rightarrow c\tilde{\chi}_1^0) = 100\,\%$.

$\boldsymbol{m_W + m_b < \Delta m(\tilde{t}_1, \tilde{\chi}_1^0) < m_t}$ In this case, the three-body decay of Fig. 2c is dominant. The signal regions that are sensitive to this decay are the dedicated signal region defined in the analysis selecting one-lepton final states (the t1L-3body) and the combination of several signal regions from the analysis selecting two-lepton final states, the t2L. The exclusion limits shown in Fig. 4 assume $\mathrm{BR}(\tilde{t}_1 \rightarrow bW\tilde{\chi}_1^0) = 1$. The WW signal regions are found to be sensitive to the kinematic region separating the three-body from the four-body stop decay region.

$\boldsymbol{\Delta m(\tilde{t}_1, \tilde{\chi}_1^0) \sim m_t}$ In this case, the neutralinos are produced with low p_{T}, and the kinematic properties of the signal are similar to those of SM $t\bar{t}$ production. Exclusion limits in this region were obtained by two analyses performing precision SM measurements. The first one is the measurement of the $t\bar{t}$ inclusive production cross section $\sigma_{t\bar{t}}$. Limits on $\tilde{t}_1$ pair production were already set in Ref. [65], which measured $\sigma_{t\bar{t}}$ in the different-flavour, opposite-sign channel $e\mu$. They were derived assuming a $\tilde{t}_1$ decay into an on-shell top quark, $\tilde{t}_1 \rightarrow t\tilde{\chi}_1^0$. An extension of the limits into the three-body stop decay is discussed in Appendix B.1. For a massless neutralino, the analysis excludes stop masses from about 150 GeV to about m_t. The limit deteriorates for higher neutralino masses, mainly because of the softer b-jet spectrum and the consequent loss in acceptance. The second analysis considered is that of the top quark spin correlation (SC) which considers SM $t\bar{t}$ production with decays to final states containing two leptons (electrons or muons). The shape and normalisation of the distribution of the azimuthal angle between the two leptons is sensitive to the spin of the produced particles,

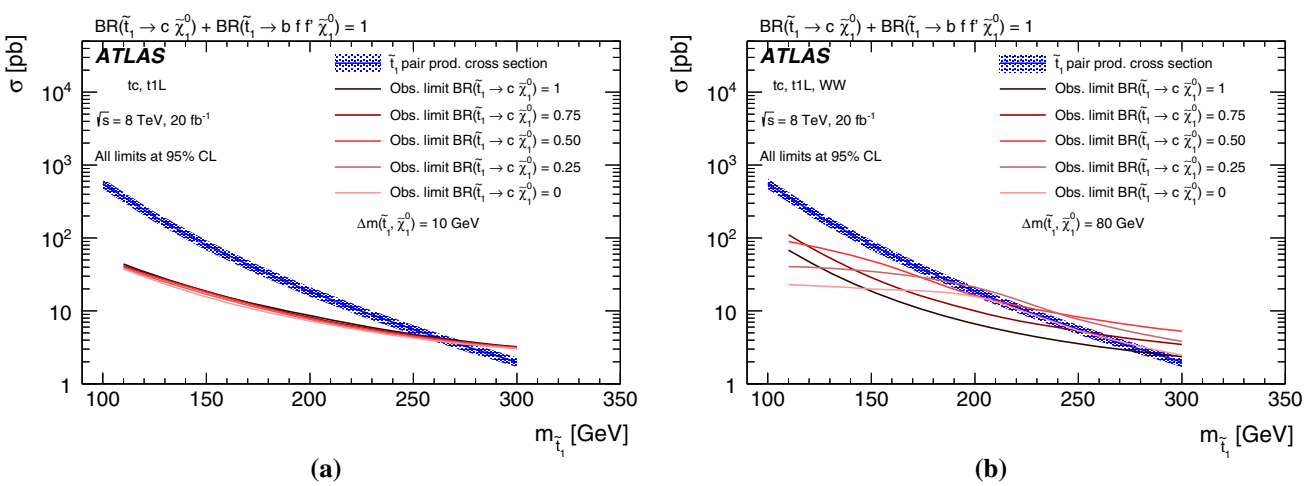

Fig. 5 Upper limits on the stop pair production cross sections for different values of the BRs for the decays $\tilde{t}_1 \rightarrow c\tilde{\chi}_1^0$ and $\tilde{t}_1 \rightarrow ff'b\tilde{\chi}_1^0$. Signal points with $\Delta m(\tilde{t}_1, \tilde{\chi}_1^0)$ of 10 GeV (**a**) and 80 GeV (**b**) are shown. The limits quoted are taken from the best performing, based on expected exclusion CL_s, signal regions from the tc-M, tc-C, t1L-bCa_low and WW analyses at each mass point. The *blue line* and corresponding *hashed band* correspond to the mean value and uncertainty on the production cross section of the stop as a function of its mass. The *pink lines*, whose *darkness* indicate the value of $\mathrm{BR}(\tilde{t} \rightarrow c\tilde{\chi}_1^0)$ according to the legend, indicate the observed limit on the production cross section

hence it allows the analysis to differentiate between stop pair and $t\bar{t}$ production. The limit obtained is shown in the bottom middle (dark orange) of the inset of Fig. 4. A small region of $\Delta m(\tilde{t}_1, \tilde{\chi}_1^0) \approx 180$ GeV is excluded with this measurement assuming a small neutralino mass.

$\boldsymbol{\Delta m(\tilde{t}_1, \tilde{\chi}_1^0) > m_t}$ In this kinematic region, the decay $\tilde{t}_1 \rightarrow t\tilde{\chi}_1^0$ (see Fig. 2b) is dominant. The best results in this region are obtained by a statistical combination of the results of the multijet (t0L) and one-lepton (t1L) analyses. They both have dedicated signal regions targeting this scenario and the expected sensitivity is comparable for the two analyses. The number of required leptons makes the two signal regions mutually exclusive.

To maximise the sensitivity to the $\tilde{t}_1 \rightarrow t\tilde{\chi}_1^0$ decays a statistical combination of the t0L and t1L signal regions is performed. The details of the combination are given in Appendix C and the final limit is shown in Fig. 4 by the largest shaded region (yellow). The expected limit on the stop mass is about 50 GeV higher at low $m_{\tilde{\chi}_1^0}$ than in the individual analyses. The observed limit is increased by roughly the same amount and stop masses between 200 and 700 GeV are excluded for small neutralino masses.[5]

A similar combination is performed to target a scenario where the stop can decay as $\tilde{t}_1 \rightarrow t\tilde{\chi}_1^0$ with branching ratio x and as $\tilde{t}_1 \rightarrow b\tilde{\chi}_1^\pm$ with branching ratio $1-x$. Assuming gauge universality, the mass of the chargino is set to be twice that of the neutralino. Neutralino masses below 50 GeV are not considered, to take into account limits on the lightest chargino mass obtained at LEP [66–70]. The exclusion limits are derived for $x = 75, 50, 25$ and 0 %.[6] Regardless of the branching ratio considered, it is always assumed that $m_{\tilde{t}_1} > m_t + m_{\tilde{\chi}_1^0}$ and $m_{\tilde{t}_1} > m_b + m_{\tilde{\chi}_1^\pm}$, such that the two decays $\tilde{t} \rightarrow t\tilde{\chi}_1^0$ and $\tilde{t} \rightarrow b\tilde{\chi}_1^\pm$ are both kinematically allowed. A statistical combination, identical to the one described above, is used for $x = 75$ %. For smaller values of x, no combined fit is performed, as the sensitivity is dominated by the t1L analysis almost everywhere: rather either the t0L or the t1L analysis is used, depending which one gives the smaller expected CL_s value.

Figure 6 shows the result of the combination in the $m_{\tilde{t}_1} - m_{\tilde{\chi}_1^0}$ plane. The limit is improved, with respect to the individual analyses, by about 50 GeV for $m_{\tilde{\chi}_1^0} = 50$ GeV and $x = 75$ %. For other x values, the t1L analysis is used on the full plane, with the exception of the point at the highest stop mass for $m_{\tilde{\chi}_1^0} = 50$ GeV at $x = 50$ and 25 %. Stop masses below 500 GeV are excluded for $m_{\tilde{\chi}_1^0} < 160$ GeV for any value of x.

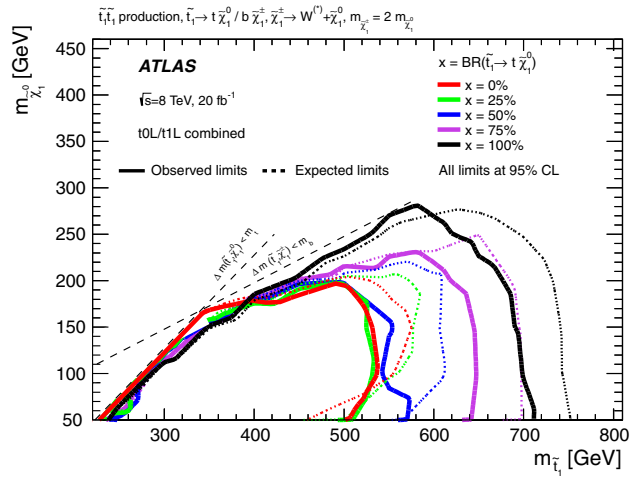

Fig. 6 Combined exclusion limits assuming that the stop decays through $\tilde{t}_1 \rightarrow t\tilde{\chi}_1^0$ with different branching ratios x and through $\tilde{t}_1 \rightarrow b\tilde{\chi}_1^\pm$ with branching ratios $1-x$. The limits assume $m_{\tilde{\chi}_1^\pm} = 2m_{\tilde{\chi}_1^0}$, and values of x from 0 to 100 % are considered. For each branching ratio, the observed (with *solid lines*) and expected (with *dashed lines*) limits are shown

4.2 Stop decays with a chargino in the decay chain

In the pMSSM, unless the higgsino–gaugino mass parameters are related by $M_1 \ll \mu, M_2$, the mass difference between the lightest neutralino and the lightest chargino cannot be too large. The mass hierarchy $m_{\tilde{\chi}_1^0} < m_{\tilde{\chi}_1^\pm} < m_{\tilde{t}_1}$ is, hence, well motivated, leading to the decay chain shown in Fig. 2f.

If additional particles beside the stop and the lightest neutralino take part in the stop decay, the stop phenomenology quickly becomes complex. Even if the chargino is the only other relevant SUSY particle, the stop phenomenology depends on the chargino mass, on the stop left–right mixing, and on the composition of the neutralino and chargino in terms of bino, wino and higgsino states.

Figure 7 shows the exclusion limits obtained by the analyses listed in Table 1 and discussed in Appendix B if a branching ratio of 100 % for $\tilde{t} \rightarrow b\tilde{\chi}_1^\pm$ is assumed. The exclusion limits are presented in a number of $m_{\tilde{t}_1}$–$m_{\tilde{\chi}_1^0}$ planes, each characterised by a different hypothesis on the chargino mass. For all scenarios considered, the chargino is assumed to decay as $\tilde{\chi}_1^\pm \rightarrow W^{(*)}\tilde{\chi}_1^0$, where the $(*)$ indicates a possibly virtual W boson.

$\boldsymbol{\Delta m(\tilde{\chi}_1^\pm, \tilde{\chi}_1^0) = 5, 20}$ **GeV** This scenario assumes that the difference in mass between the lightest chargino and the neutralino is small (Fig. 7a), which is a rather common feature of models where, for example, the LSP has a large wino or higgsino component. Two hypotheses have been considered,

[5] This result holds if the top quark produced in the $\tilde{t}_1$ decay has a right-handed chirality. The dependence of the individual limits on the top quark chirality is discussed in Refs. [16,17].

[6] A value of $x = 0$ % is in fact not achievable in a real supersymmetric model. Nevertheless, this value has been considered as the limiting case of a simplified model.

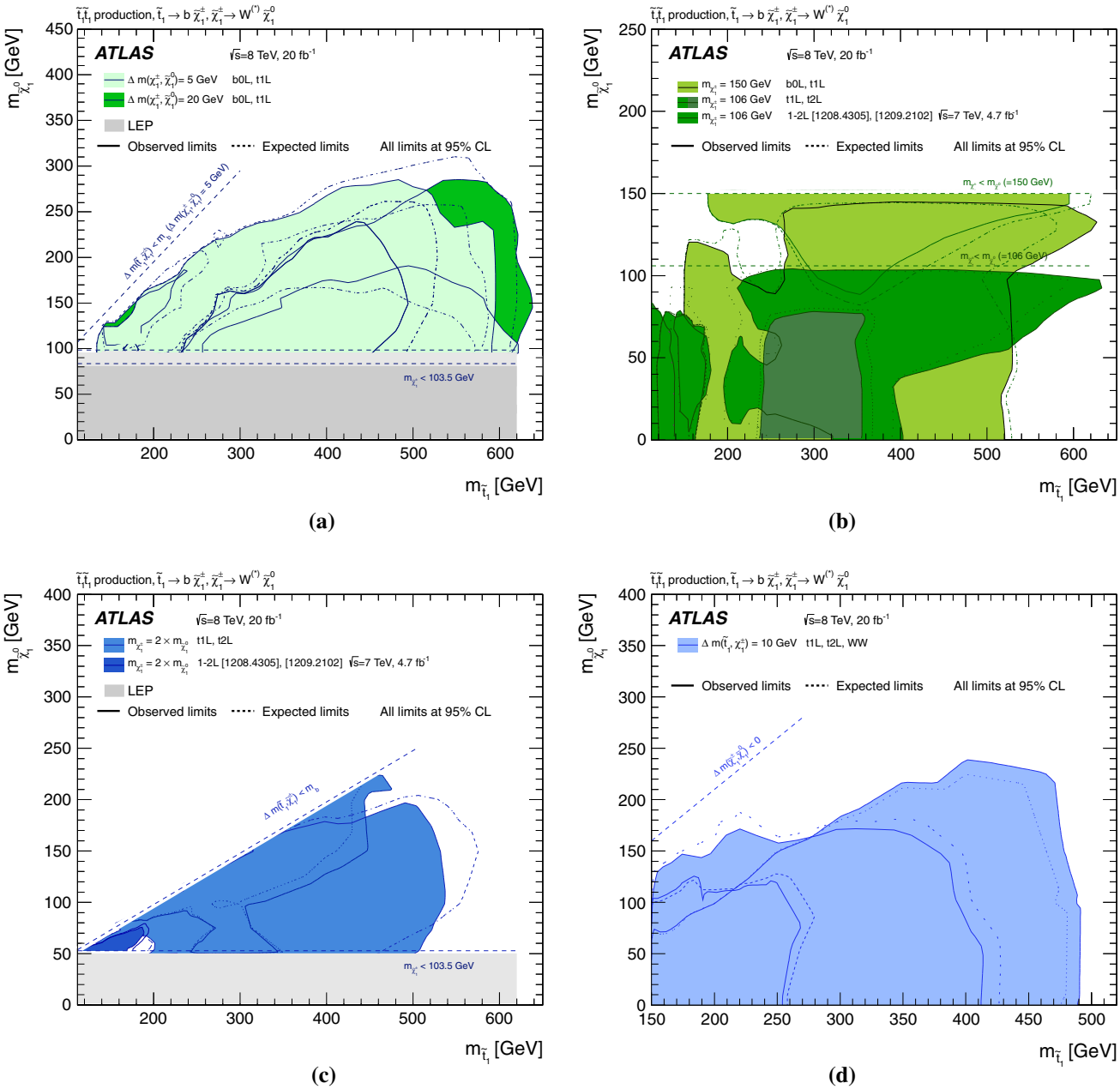

Fig. 7 Summary of the ATLAS Run 1 searches for direct stop pair production in models where the decay mode $\tilde{t}_1 \rightarrow b\tilde{\chi}_1^{\pm}$ with $\tilde{\chi}_1^{\pm} \rightarrow W^*\tilde{\chi}_1^0$ is assumed with a branching ratio of 100 %. Various hypotheses on the $\tilde{t}_1$, $\tilde{\chi}_1^{\pm}$, and $\tilde{\chi}_1^0$ mass hierarchy are used. Exclusion limits at 95 % CL are shown in the $\tilde{t}_1 - \tilde{\chi}_1^0$ mass plane. The *dashed* and *solid lines* show the expected and observed limits, respectively, including all uncertainties except the theoretical signal cross-section uncertainty (PDF and scale). Wherever not superseded by any $\sqrt{s} = 8$ TeV analysis, results obtained by analyses using 4.7 fb^{-1} of proton–proton collision data taken at $\sqrt{s} = 7$ TeV are also shown, with the corresponding reference. The four *plots* correspond to interpretations of **a** the b0L and t1L soft-lepton analyses in two scenarios ($\Delta m(\tilde{\chi}_1^{\pm}, \tilde{\chi}_1^0) = 5$ GeV in *light green* and $\Delta m(\tilde{\chi}_1^{\pm}, \tilde{\chi}_1^0) = 20$ GeV in *dark green*), for a total of four limits; **b** the b0L, t1L and t2L analyses in scenarios with a fixed chargino mass $m_{\tilde{\chi}_1^{\pm}} = 106$ GeV (*dark green*) and $m_{\tilde{\chi}_1^{\pm}} = 150$ GeV (*light green*); **c** the t1L and t2L analyses in scenarios with $m_{\tilde{\chi}_1^{\pm}} = 2m_{\tilde{\chi}_1^0}$; **d** interpretations of the t1L, t2L and WW analyses in senarios with $\Delta m\left(\tilde{t}_1, \tilde{\chi}_1^{\pm}\right) = 10$ GeV

with $\Delta m(\tilde{\chi}_1^{\pm}, \tilde{\chi}_1^0) = 5$ GeV and $\Delta m(\tilde{\chi}_1^{\pm}, \tilde{\chi}_1^0) = 20$ GeV. For both, the complete decay chain is $\tilde{t}_1 \rightarrow b\tilde{\chi}_1^{\pm} \rightarrow bff'\tilde{\chi}_1^0$, where the transverse momenta of the fermions f and f' depend on $\Delta m(\tilde{\chi}_1^{\pm}, \tilde{\chi}_1^0)$ and on the stop mass, given the dependency on the chargino boost. If $\Delta m(\tilde{\chi}_1^{\pm}, \tilde{\chi}_1^0) = 5$ GeV, the fermions have momenta too low to be efficiently reconstructed. The observed final state then consists of two b-jets and $E_{\mathrm{T}}^{\mathrm{miss}}$. This final state is the direct target of the b0L signal

regions. For $\Delta m(\tilde{\chi}_1^{\pm}, \tilde{\chi}_1^0) = 20$ GeV, the signal efficiencies of the b0L signal regions decrease because of the lepton and jet veto applied. The t1L signal regions with soft leptons, instead, gain in sensitivity, profiting from the higher transverse momentum of the fermions from the off-shell W decay produced in the chargino decay.

$\boldsymbol{m_{\tilde{\chi}_1^{\pm}} = 106, 150}$ **GeV** This scenario (Fig. 7b) assumes a fixed chargino mass. The SR yielding the lowest expected exclusion CL_s for this scenario depends on the value of $\Delta m(\tilde{\chi}_1^{\pm}, \tilde{\chi}_1^0)$. For $\Delta m(\tilde{\chi}_1^{\pm}, \tilde{\chi}_1^0) < 20$ GeV, the b0L signal regions provide the best sensitivity; for larger values of $\Delta m(\tilde{\chi}_1^{\pm}, \tilde{\chi}_1^0)$, the t1L and t2L signal regions provide better sensitivity because of the same mechanism as in the $\Delta m(\tilde{\chi}_1^{\pm}, \tilde{\chi}_1^0) = 5, 20$ GeV scenario above. The exclusion extends up to about 600 GeV for small values of $\Delta m(\tilde{\chi}_1^{\pm}, \tilde{\chi}_1^0)$. A region of the parameter space with $m_{\tilde{t}_1}$ up to about 260 GeV and $m_{\tilde{\chi}_1^0}$ between 100 GeV and $m_{\tilde{\chi}_1^{\pm}}$ is not yet excluded.

$\boldsymbol{m_{\tilde{\chi}_1^{\pm}} = 2m_{\tilde{\chi}_1^0}}$ Inspired by gauge-universality considerations, the third scenario (Fig. 7c) is characterised by a relatively large $\Delta m(\tilde{\chi}_1^{\pm}, \tilde{\chi}_1^0)$. The t2L signal regions dominate the sensitivity for $m_{\tilde{t}_1} \sim m_{\tilde{\chi}_1^{\pm}}$. The sensitivity of the dedicated t1L-bC is dominant in a large region of the plane, and determines the exclusion reach for moderate to large values of $\Delta m(\tilde{t}_1, \tilde{\chi}_1^0)$.

$\boldsymbol{\Delta m(\tilde{t}_1, \tilde{\chi}_1^{\pm}) = 10}$ **GeV** The fourth scenario (Fig. 7d) assumes a rather compressed $\tilde{t}_1 - \tilde{\chi}_1^{\pm}$ spectrum. The region at low $m_{\tilde{t}_1}$ and large $m_{\tilde{\chi}_1^0}$ is characterised by low mass separations between all particles involved, and it is best covered by the t1L-bCc_diag, the t1L soft lepton, and the WW signal regions. At larger values of the stop mass, the leptons emitted in the $\tilde{\chi}_1^{\pm}$ decay have larger p_{T}, and the t2L signal regions provide the best sensitivity.

$\boldsymbol{m_{\tilde{t}_1} = 300}$ **GeV** The final scenario considered is one where the stop mass is fixed at 300 GeV, and the exclusion limits are expressed in the $m_{\tilde{\chi}_1^{\pm}}$–$m_{\tilde{\chi}_1^0}$ plane. In the case of the compressed scenario, corresponding to a small mass difference $\Delta m(\tilde{\chi}_1^{\pm}, \tilde{\chi}_1^0)$, the fermions from the $W^{(*)}$ decay can escape detection and only the two b-jets and $E_{\mathrm{T}}^{\mathrm{miss}}$ would be identified in the final state. Thus, the b0L signal regions are expected to have a large sensitivity in this case, while for larger values of $\Delta m(\tilde{\chi}_1^{\pm}, \tilde{\chi}_1^0)$, the lepton can be observed, yielding a final-state signature investigated by the t1L soft-lepton signal region. A combination of the b0L and t1L signal regions is performed by choosing, for each point of the plane, the SR giving the lowest CL_s for expected exclusion. The result, reported in Fig. 8, shows that a large portion of the plane is excluded, with the exception of a region where the mass separations between the $\tilde{t}_1$, the $\tilde{\chi}_1^{\pm}$ and the $\tilde{\chi}_1^0$ are small.

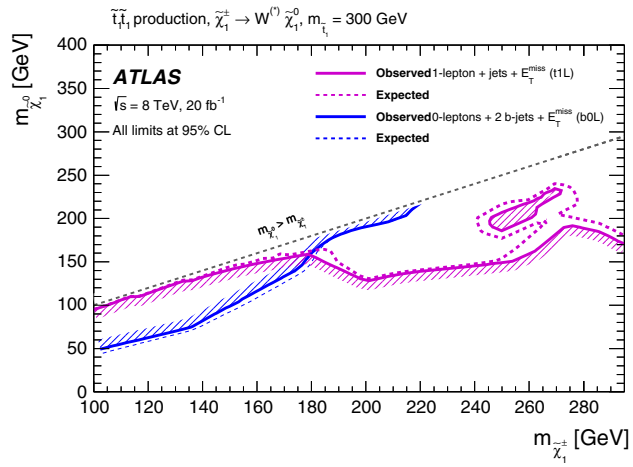

Fig. 8 Exclusion limits assuming that the stop decays through $\tilde{t}_1 \to b + \tilde{\chi}_1^{\pm} \to b + W^{(*)} + \tilde{\chi}_1^0$ with branching ratio of 100 % assuming a fixed stop mass of $m_{\tilde{t}_1} = 300$ GeV. The region *below the purple line* and *above the blue line*, indicated by a *light shading*, is excluded

Summarising, in the simplified models with $\tilde{t}_1 \to b\tilde{\chi}_1^{\pm} \to bW^{(*)}\tilde{\chi}_1^0$, stop masses up to 450–600 GeV are generally excluded. Scenarios where $\Delta m(\tilde{t}_1, \tilde{\chi}_1^0)$ is small are particularly difficult to exclude and in these compressed scenarios, stop masses as low as 200 GeV are still allowed (Fig. 7b). A small unexcluded area is also left for a small region around $(m_{\tilde{t}_1}, m_{\tilde{\chi}_1^{\pm}}, m_{\tilde{\chi}_1^0}) = (180, 100, 50)$ GeV (Fig. 7c), where the sensitivity of the analyses is poor because the signal kinematics are similar to SM $t\bar{t}$ production.

4.3 Limits on pair production of $\tilde{t}_2$

Although the pair production of $\tilde{t}_1$ has a cross section larger than that of $\tilde{t}_2$, and although the decay patterns of the two particles can be similar, it can be convenient to search for the latter in regions where the sensitivity to the former is limited. This is the case, for example, in the region where $\Delta m(\tilde{t}_1, \tilde{\chi}_1^0) \sim m_t$ of Fig. 4, where the separation of $\tilde{t}_1$ pair production from SM top quark pair production is difficult. The t2t1Z and t2t1h analyses are designed to detect $\tilde{t}_2$ pair production in this region of the $m_{\tilde{t}_1} - m_{\tilde{\chi}_1^0}$ plane, followed by the decays $\tilde{t}_2 \to \tilde{t}_1 Z$ and $\tilde{t}_2 \to \tilde{t}_1 h$. The Higgs boson h is assumed to have a mass of 125 GeV and SM branching ratios.

The exclusion limits were first derived in a scenario in which the pair-produced $\tilde{t}_2$ decays either through $\tilde{t}_2 \to Z\tilde{t}_1$ with a branching ratio of 100 % (Fig. 3a), or through $\tilde{t}_2 \to h\tilde{t}_1$ (again with a branching ratio of 100 %; Fig. 3b). In both cases, the $\tilde{t}_1$ is assumed to decay through $\tilde{t}_1 \to t\tilde{\chi}_1^0$, and its mass is set to be 180 GeV above that of the neutralino (assumed to be the LSP), which is the region not excluded in Fig. 4. The final state contains two top quarks, two neutralinos, and either two Z or two h bosons.

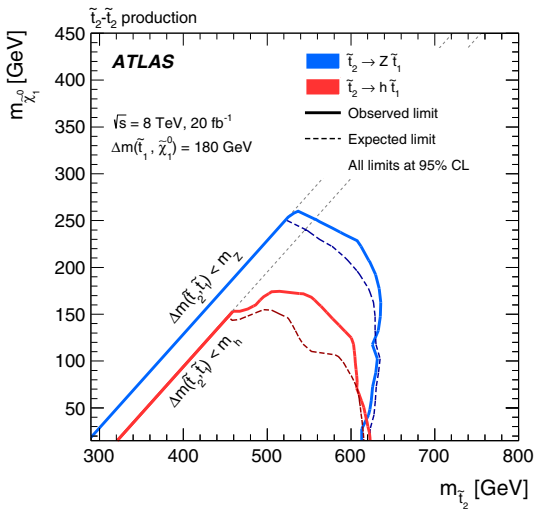

Fig. 9 Exclusion limits at 95 % CL in the scenario where $\tilde{t}_2$ pair production is assumed, followed by the decay $\tilde{t}_2 \to Z\tilde{t}_1$ (*blue*) or $\tilde{t}_2 \to \tilde{t}_1 h$ (*red*) and then by $\tilde{t}_1 \to t\tilde{\chi}_1^0$ with a branching ratio of 100 %, as a function of the $\tilde{t}_2$ and $\tilde{\chi}_1^0$ mass. The $\tilde{t}_1$ mass is determined by the relation $m_{\tilde{t}_1} - m_{\tilde{\chi}_1^0} = 180$ GeV. The *dashed lines* indicate the expected limit and the *solid lines* indicate the observed limit

Figure 9 shows the exclusion limits for the t2t1h and the t2t1Z analyses. In both cases, a limit on $m_{\tilde{t}_2}$ is set at about 600 GeV for a massless neutralino. In the case of a $\tilde{t}_2$ decay through a Higgs boson, the limit covers neutralino masses lower than in the case of the decay through a Z boson.

The assumption on the branching ratio of the $\tilde{t}_2$ has also been relaxed, and limits have been derived assuming that the three decays $\tilde{t}_2 \to Z\tilde{t}_1$, $\tilde{t}_2 \to h\tilde{t}_1$ and $\tilde{t}_2 \to t\tilde{\chi}_1^0$ (Fig. 3c) are the only possible ones. The limits are shown in Fig. 10 as a function of the three BRs, for different combinations of the $\tilde{t}_2$ and $\tilde{\chi}_1^0$ masses. Three analyses have been considered: the t2t1Z, t2t1h and the combination of the t0L and t1L discussed in Sect. 4.1.[7] The three analyses have complementary sensitivities. Together, they exclude $\tilde{t}_2$ pair production with a mass of 350 and 500 GeV for $m_{\tilde{\chi}_1^0} = 20$ GeV. A non-excluded region appears for $m_{\tilde{t}_2} = 500$ GeV if larger $\tilde{\chi}_1^0$ masses are considered.

4.4 Sbottom decays

Under the assumption that no supersymmetric particle takes part in the sbottom decay apart from the lightest neutralino, the sbottom decays as $\tilde{b}_1 \to b\tilde{\chi}_1^0$ with a branching ratio of 100 % (Fig. 2a). The final state arising from sbottom pair production hence contains two b-jets and $E_{\mathrm{T}}^{\mathrm{miss}}$. The b0L signal regions were explicitly optimised to be sensitive to this scenario. In case of a mass degeneracy between the sbottom and the neutralino, the general consideration that the monojet-like tc-M selection is almost insensitive to the details of the decay of the produced particles still holds: the tc-M signal regions offer the best sensitivity for scenarios where $m_{\tilde{b}_1} \sim m_{\tilde{\chi}_1^0}$.

Figure 11 shows the limits of the tc and b0L analyses on the $m_{\tilde{b}_1} - m_{\tilde{\chi}_1^0}$ plane. The monojet-like (tc-M) SRs exclude models up to a value of $m_{\tilde{b}_1} \sim m_{\tilde{\chi}_1^0} \sim 280$ GeV. Sbottom masses are excluded up to about 600 GeV for neutralino masses below about 250 GeV.

If other supersymmetric particles enter into the decay chain, then multiple decay channels would be allowed. Similarly to the stop, the case in which other neutralinos or charginos have a mass below the sbottom is well motivated. The branching ratios of the sbottom to the different decay channels depend on the supersymmetric particle mass hierarchy, on the mixing of the left–right components of the sbottom, and on the composition of the charginos and neutralinos in terms of bino, wino, and higgsino states.

An exclusion limit is derived under the assumption that the sbottom decays with a branching ratio of 100 % into $\tilde{b}_1 \to t\tilde{\chi}_1^{\pm}$ (Fig. 2g). The chargino is assumed to decay through $\tilde{\chi}_1^{\pm} \to W^{(*)}\tilde{\chi}_1^0$ with a branching ratio of 100 %. The final state is a complex one, and offers many handles for background rejection: it potentially contains up to ten jets, two b-jets, and up to four leptons. The limits of Fig. 12a, shown in the $m_{\tilde{b}_1} - m_{\tilde{\chi}_1^0}$ plane, were obtained by using the three-lepton signal regions SS3L, either fixing the mass of the neutralino to $m_{\tilde{\chi}_1^0} = 60$ GeV or by making the assumption that $m_{\tilde{\chi}_1^{\pm}} = 2m_{\tilde{\chi}_1^0}$. In the two scenarios considered, sbottom masses up to about 440 GeV are excluded, with a mild dependency on the neutralino mass.

The last case considered is one where the pair-produced sbottoms decay through $\tilde{b}_1 \to b\tilde{\chi}_2^0$, followed by the decay of $\tilde{\chi}_2^0$ into a $\tilde{\chi}_1^0$ and a SM-like Higgs boson h (Fig. 2h). The final state contains up to six b-jets, four of which are produced by the two Higgs bosons decays. Since multiple b-jets are present in the final state, the three-b-jets signal regions (g3b) are used to place limits in this model.

The limit, derived as a function of $m_{\tilde{b}_1}$ and $m_{\tilde{\chi}_2^0}$ assuming a fixed neutralino mass of $\tilde{\chi}_1^0 = 60$ GeV, is shown in Fig. 12b. Sbottom masses between about 300 and 650 GeV are excluded for $\tilde{\chi}_2^0$ masses above 250 GeV.

5 Interpretations in pMSSM models

The interpretation of the results in simplified models is useful to assess the sensitivity of each signal region to a specific topology. However, this approach fails to test signal regions on the complexity of the stop and sbottom phenomenology

[7] For the combination of the t0L and t1L analyses, the limits extracted for the $\tilde{t}_1 \to t\tilde{\chi}_1^0$ decay with branching ratio of 100 % have simply been rescaled by appropriate factors depending on the branching ratio of $\tilde{t}_2 \to t\tilde{\chi}_1^0$ considered here.

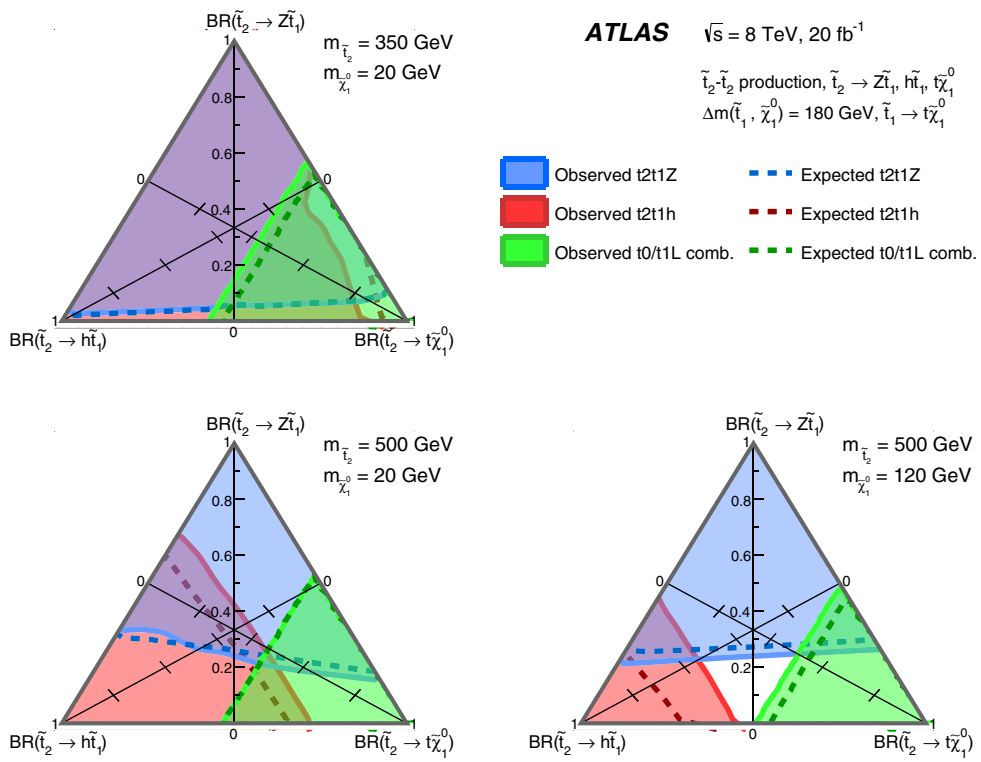

Fig. 10 Exclusion limits as a function of the $\tilde{t}_2$ branching ratio for $\tilde{t}_2 \rightarrow \tilde{t}_1 h$, $\tilde{t}_2 \rightarrow \tilde{t}_1 Z$ and $\tilde{t}_2 \rightarrow t\tilde{\chi}_1^0$. The *blue*, *red* and *green limit* refers to the t2t1Z, t2t1h and combination of t0L and t1L analyses respectively. The limits are given for three different values of the $\tilde{t}_2$ and $\tilde{\chi}_1^0$ masses

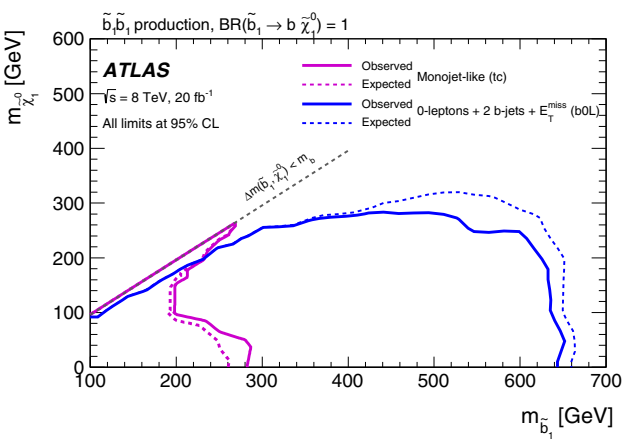

Fig. 11 Observed (*solid lines*) and expected (*dashed lines*) 95 % CL limits on sbottom pair production where the sbottom is assumed to decay as $\tilde{b}_1 \rightarrow b\tilde{\chi}_1^0$ with a branching ratio of 100 %. The *purple lines* refer to the limit of the tc analysis, while the *blue lines* refer to the b0L analysis

that appears in a realistic SUSY model. To this extent, the signal regions are used to derive exclusion limits in the context of specific pMSSM models.

The pMSSM [57] is obtained from the more general MSSM by making assumptions based on experimental results:

- No new source of CP violation beyond the Standard Model. New sources of CP violation are constrained by experimental limits on the electron and neutron electric dipole moments.
- No flavour-changing neutral currents. This is implemented by requiring that the matrices for the sfermion masses and trilinear couplings are diagonal.
- First- and second-generation universality. The soft-SUSY-breaking mass parameters and the trilinear couplings for the first and second generation are assumed to be the same based on experimental data from, e.g., the neutral kaon system [71].

With the above assumptions, and with the choice of a neutralino as the LSP, the pMSSM adds 19 free parameters on top of those of the SM. The complete set of pMSSM parameters is shown in Table 2.

A full assessment of the ATLAS sensitivity to a scan of the 19-parameters space has been performed in Ref. [72]. Here, a set of additional hypotheses are made, to focus on the sensitivity to a specific, well-motivated set of models with enhanced third generation squark production:

- The common masses of the first- and second-generation squarks have been set to a multi-TeV scale, making these quarks irrelevant for the processes studied at the energies investigated in this paper. This choice is motivated by the

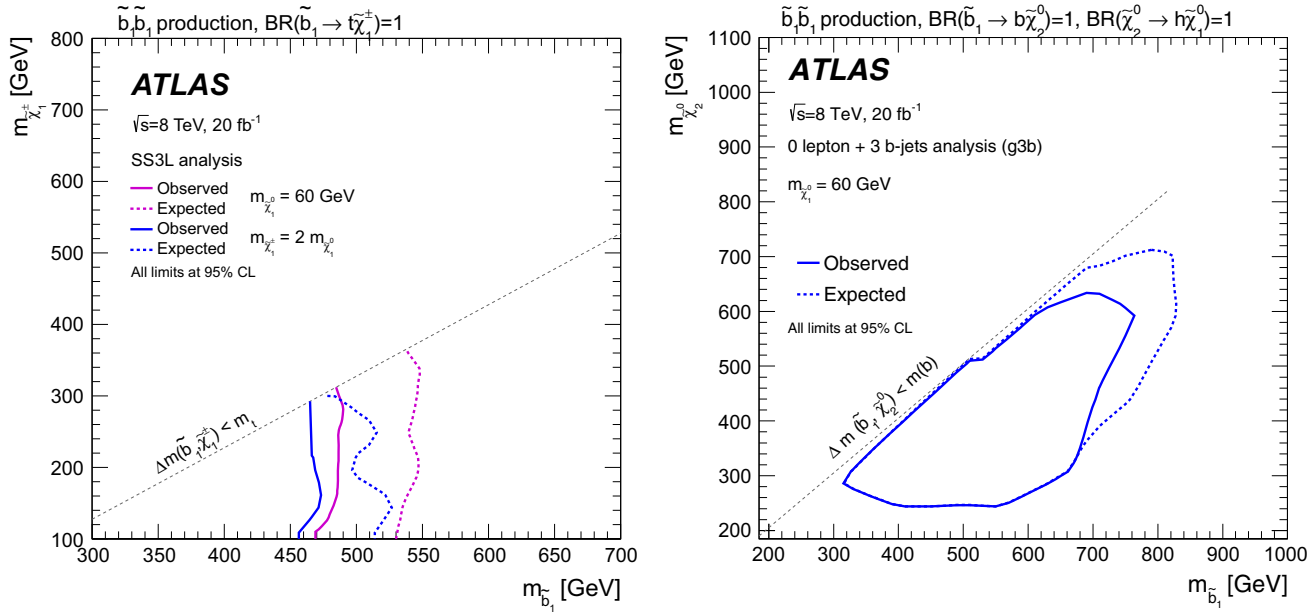

(a) **(b)**

Fig. 12 Exclusion limits at 95 % CL for a scenario where sbottoms are pair produced and decay as **a** $\tilde{b}_1 \to t\tilde{\chi}_1^{\pm}$ with a BR of 100 % or **b** $\tilde{b}_1 \to b\tilde{\chi}_2^0$ with a BR of 100 %. The signal regions used in **a** are the SS3L, and two different models are considered: a fixed neutralino mass of 60 GeV (in *purple*) or $m_{\tilde{\chi}_1^{\pm}} = 2m_{\tilde{\chi}_1^0}$ (in *blue*). The limits are shown in the $m_{\tilde{b}_1}$–$m_{\tilde{\chi}_1^{\pm}}$ plane. The signal regions used in **b** are the g3b-SR-0j. A fixed neutralino mass of 60 GeV is assumed, and the limit is shown in the $m_{\tilde{b}_1}$–$m_{\tilde{\chi}_2^0}$ plane

Table 2 Description of the 19 additional parameters of the pMSSM model with a neutralino LSP

Parameter	Description
$m_{\tilde{u}R}, m_{\tilde{d}R}, m_{\tilde{q}L1}, m_{\tilde{e}R}, m_{\tilde{\ell}L1}$	First- and second-generation common mass parameters
$m_{\tilde{b}R}, m_{\tilde{t}R}, m_{\tilde{q}L3}, m_{\tilde{\tau}R}, m_{\tilde{\ell}L3}$	Third-generation mass parameters
M_1, M_2, M_3	Gaugino mass parameters
A_b, A_τ, A_t	Trilinear couplings
μ, M_A	Higgs/higgsino mass parameters
$\tan\beta$	Ratio of vacuum expectation values of the two Higgs doublets

absence of any signal from squark or gluino production in dedicated SUSY searches performed by the ATLAS [62,63,73–76] and CMS [29,34,77–82] collaborations.

- All slepton mass parameters have been set to the same scale as the first- and second-generation squarks. This choice has no specific experimental or theoretical motivation, and should be regarded as an assumption.
- A decoupling limit with $M_A = 3$ TeV and large $\tan\beta$ values ($\tan\beta > 15$) has been assumed. This is partially motivated by results of the LHC searches for higher mass Higgs boson states [83,84].
- For $\tan\beta \gg 1$, the Higgs boson mass depends heavily on the product of the stop-mass parameters $M_S = \sqrt{m_{\tilde{t}_1} m_{\tilde{t}_2}}$ and the mixing between the left- and right-handed states $X_t = A_t - \mu/\tan\beta$ [85]. The stop sector is therefore completely fixed, given the Higgs boson mass, the value of X_t and one of the two stop mass parameters.[8]
- The trilinear couplings A_b in the sbottom sector are found to have limited impact on the phenomenology, and are therefore set to zero.
- The gluino mass parameter M_3 is set such to evade LHC constraints on gluino-pair production.

These assumptions reduce the number of additional free parameters of the model to the mass parameters of the electroweak sector (μ, M_1, M_2) and two of the three third-generation squark mass parameters ($m_{\tilde{q}L3}, m_{\tilde{t}R}, m_{\tilde{b}R}$). All the assumptions made either have a solid experimental basis, or are intended to simplify the interpretation in terms of direct production of stops and sbottoms (as, for example, the assumption on the slepton mass parameters).

Three types of models have been chosen, that, by implementing in different ways constraints arising from naturalness arguments and the dark-matter relic density measurement, further reduce the number of parameters to be scanned over. They are described below, and summarised in Table 3

[8] In particular, a minimum value of $M_S \sim 800$ GeV is allowed if the maximal mixing condition $X_t/M_S = \sqrt{6}$ is realised.

Table 3 Details of parameters scanned in the three pMSSM models used for interpretations. The settings of additional parameters that are fixed for each model are also given together with the main production and decay channels targeted

Model name	Parameters scanned	Other parameter settings	Production channels	Typical decays
Naturalness-inspired pMSSM	350 GeV $< m_{\tilde{q}L3} <$ 900 GeV	$M_2 = 3\mu$	$pp \to \tilde{t}_1\tilde{t}_1$	For $\mu = 110$ GeV, $m_{\tilde{q}L3} = 400$ GeV
	100 GeV $< \mu < m_{\tilde{q}L3} - 150$ GeV	$m_{\tilde{t}_R}$ such that $M_S = 800$ GeV	$pp \to \tilde{b}_1\tilde{b}_1$	$\tilde{t}_1 \to t\tilde{\chi}_1^0$ (33 %); $\tilde{t}_1 \to t\tilde{\chi}_2^0$ (36 %)
		A_t such that $X_t/M_S = \sqrt{6}$		$\tilde{t}_1 \to b\tilde{\chi}_1^\pm$ (26 %); $\tilde{b}_1 \to t\tilde{\chi}_1^\pm$ (70 %)
				$\tilde{b}_1 \to b\tilde{\chi}_1^0$ (16 %); $\tilde{b}_1 \to b\tilde{\chi}_2^0$ (13 %)
Well-tempered neutralino pMSSM	310 GeV $< m_{\tilde{q}L3} <$ 810 GeV		$pp \to \tilde{t}_1\tilde{t}_1$	For $M_1 = 110$ GeV, $m_{\tilde{q}L3} = 410$ GeV
	110 GeV $< M_1 < m_{\tilde{q}L3} - 50$ GeV		$pp \to \tilde{b}_1\tilde{b}_1$	$\tilde{t}_1 \to t\tilde{\chi}_2^0$ (35 %); $\tilde{t}_1 \to t\tilde{\chi}_3^0$ (38 %)
		$\mu \sim -M_1$		$\tilde{t}_1 \to b\tilde{\chi}_1^\pm$ (20 %); $\tilde{b}_1 \to t\tilde{\chi}_1^\pm$ (85 %)
				$\tilde{b}_1 \to \tilde{t}_1 W$ (6 %); $\tilde{b}_1 \to b\tilde{\chi}_2^0$ (4 %)
		Similar to naturalness-inspired		
	260 GeV $< m_{\tilde{t}_R} <$ 760 GeV	for A_t, $m_{\tilde{t}_R}$ or $m_{\tilde{q}L3}$, M_3	$pp \to \tilde{t}_1\tilde{t}_1$	For $M_1 = 110$ GeV, $m_{\tilde{t}_R} = 410$ GeV
	110 GeV $< M_1 < m_{\tilde{q}L3} - 50$ GeV			$\tilde{t}_1 \to t\tilde{\chi}_2^0$ (17 %); $\tilde{t}_1 \to t\tilde{\chi}_3^0$ (19 %)
				$\tilde{t}_1 \to t\tilde{\chi}_1^0$ (6.7 %); $\tilde{t}_1 \to b\tilde{\chi}_1^\pm$ (57 %)
h/Z-enriched pMSSM	250 GeV $< m_{\tilde{b}_R} <$ 750 GeV	$M_1 = 100$ GeV; $M_2 = \mu$	$pp \to \tilde{b}_1\tilde{b}_1$	For $\mu = 300$ GeV, $m_{\tilde{b}_R} = 400$ GeV
	100 GeV $< \mu < m_{\tilde{b}_R}$	$m_{\tilde{t}_R} = 1.6$ TeV; $m_{\tilde{q}L3} = 1.2$ TeV		$\tilde{b}_1 \to b\tilde{\chi}_1^0$ (37 %); $\tilde{b}_1 \to b\tilde{\chi}_2^0$ (39 %)
		A_t fixed by $m_h \sim 125$ GeV		$\tilde{b}_1 \to b\tilde{\chi}_3^0$ (23 %)
				$\tilde{\chi}_2^0 \to Z\tilde{\chi}_1^0$ (29 %); $\tilde{\chi}_2^0 \to h\tilde{\chi}_1^0$ (71 %)
				$\tilde{\chi}_3^0 \to Z\tilde{\chi}_1^0$ (85 %); $\tilde{\chi}_3^0 \to h\tilde{\chi}_1^0$ (15 %)
	500 GeV $< m_{\tilde{q}L3} <$ 800 GeV	$M_1 = 100$ GeV; $M_2 = 1$ TeV	$pp \to \tilde{t}_1\tilde{t}_1$	For $\mu = 300$ GeV, $m_{\tilde{q}L3} = 600$ GeV
	100 GeV $< M_1 < m_{\tilde{q}L3}$ GeV	$m_{\tilde{b}_R} = 3$ TeV; $m_{\tilde{t}_R} = 2$ TeV	$pp \to \tilde{b}_1\tilde{b}_1$	$\tilde{t}_1 \to t\tilde{\chi}_2^0$ (46 %); $\tilde{t}_1 \to t\tilde{\chi}_3^0$ (39 %)
		A_t fixed by $m_h \sim 125$ GeV		$\tilde{t}_1 \to b\tilde{\chi}_1^\pm$ (11 %); $\tilde{b}_1 \to t\tilde{\chi}_1^\pm$ (87 %)
				$\tilde{\chi}_2^0 \to Z\tilde{\chi}_1^0$ (24 %); $\tilde{\chi}_2^0 \to h\tilde{\chi}_1^0$ (76 %)
				$\tilde{\chi}_3^0 \to Z\tilde{\chi}_1^0$ (88 %); $\tilde{\chi}_3^0 \to h\tilde{\chi}_1^0$ (12 %)

together with additional information on the most relevant production and decay channels.

Naturalness-inspired pMSSM The model is inspired by naturalness criteria, which require a value of μ in the range of a few hundred GeV, favour stop masses below one TeV, place weak constraints on the gluino mass and give no constraints on the mass of other SUSY particles [86]. The exclusion limits are determined as a function of the higgsino mass parameter μ and the left-handed squark mass parameter $m_{\tilde{q}L3}$. The parameter $m_{\tilde{q}L3}$ is scanned in the range 350 GeV $< m_{\tilde{q}L3} <$ 900 GeV. The parameter μ is scanned in the range 100 GeV $< \mu < m_{\tilde{q}L3} - 150$ GeV, where the lower bound is determined by limits on the chargino mass arising from LEP [66–70]. The right-handed stop mass parameter $m_{\tilde{t}R}$ and the stop mixing parameter X_t are determined by choosing the maximal mixing scenario $X_t/M_S = \sqrt{6}$ and by the requirement of having a Higgs boson mass of about 125 GeV. The other squark and slepton masses, as well as the bino mass parameter M_1, are set to 3 TeV. The wino mass parameter M_2 is set such that $M_2 = 3\mu$. The gluino mass parameter M_3 is set to 1.7 TeV.

With this choice of the model parameters, the spectrum is characterised by two light neutralinos $(\tilde{\chi}_1^0, \tilde{\chi}_2^0)$ and one chargino $(\tilde{\chi}_1^\pm)$, all with masses of the order of μ, a light $\tilde{b}_1$ with a mass of the order of $m_{\tilde{q}L3}$, and a light $\tilde{t}_1$ with mass of the order of $m_{\tilde{q}L3}$ up to $m_{\tilde{q}L3} \sim 700$ GeV (the constraint on M_S does not allow the mass of $\tilde{t}_1$ to increase beyond about 650 GeV). The production processes considered are direct pair production of $\tilde{b}_1$ and $\tilde{t}_1$ with similar masses. Because of the abundance of light higgsino states, many different decays can occur.

Well-tempered neutralino pMSSM The models are designed to loosely satisfy dark-matter thermal-relic density constraints ($0.09 < \Omega_c h^2 < 0.15$, where h is the Hubble constant), while keeping fine tuning (defined as in Ref. [87]) to less than 1 %. The exclusion limits are determined as a function of M_1 and $m_{\tilde{q}L3}$, or M_1 and $m_{\tilde{t}R}$, with $\mu \sim -M_1$ in both cases to satisfy the dark-matter constraints through the presence of well-tempered neutralinos [88]. The constraints on the Higgs boson mass are satisfied in a way similar to the naturalness-inspired pMSSM model above. All other parameters are the same as in the naturalness-inspired pMSSM model. These models tend to have three neutralinos and two charginos with masses lower than $\tilde{t}_1$ or $\tilde{b}_1$, giving rise to a diverse phenomenology.

h/Z-enriched pMSSM These models are defined such that Higgs and Z bosons are produced abundantly in the SUSY particles' decay chains. The assumption of $M_1 = 100$ GeV ensures the presence of a bino-like neutralino LSP, while $M_3 = 2.5$ TeV ensures that direct gluino production is highly suppressed compared to third-generation squark production. Two sets of models have been defined: in the first one, μ and the right-handed sbottom mass parameter $m_{\tilde{b}R}$ are scanned while keeping $M_2 = \mu$, $m_{\tilde{q}L3} = 1.2$ TeV, $m_{\tilde{t}R} = 1.6$ TeV; in the second one, μ and $m_{\tilde{q}L3}$ are scanned while keeping $M_2 = 1$ TeV, $m_{\tilde{b}R} = 3$ TeV, $m_{\tilde{t}R} = 2$ TeV. The former is dominated by sbottom pair production, while both sbottom and stop pair production are relevant for the latter. Stop mixing parameters are chosen with maximal mixing to satisfy Higgs boson mass constraints. In these models, the decays of the third generation squarks into the heavier neutralino states ($\tilde{\chi}_2^0$ and $\tilde{\chi}_3^0$) are followed by decays to the lightest neutralino with the emission of a Z or a h boson. Typically the $\tilde{\chi}_2^0$ ($\tilde{\chi}_3^0$) decays into a Z boson 30 % (85 %) of the times, and into a Higgs boson 70 % (15 %) of the times. The subsequent decays of the Higgs boson into b-quark pairs (happening with the same branching ratio as in the Standard Model) lead to final states rich in b-jets.

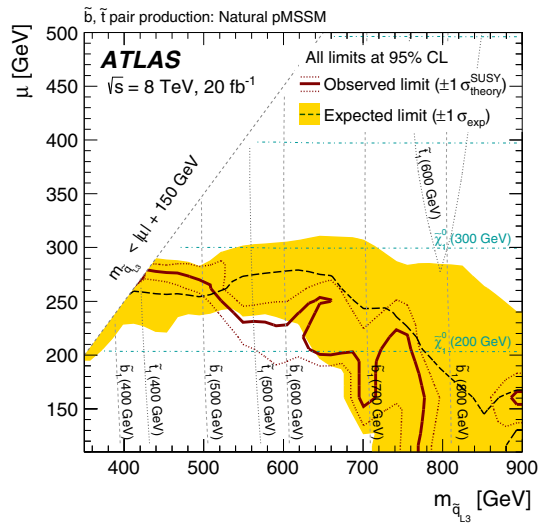

Fig. 13 Expected and observed 95 % CL exclusion limits for the naturalness-inspired set of pMSSM models from the combination t0L, t1L and tb analyses using the signal region yielding the smallest CL_s value for the signal-plus-background hypothesis. The *dashed black line* indicates the expected limit, and the *yellow band* indicates the $\pm 1\sigma$ uncertainties, which include all uncertainties except the theoretical uncertainties in the signal. The *red solid line* indicates the observed limit, and the *red dotted lines* indicate the sensitivity to $\pm 1\sigma$ variations of the signal theoretical uncertainties. The *dashed* and *dotted grey lines* indicate a constant value of the stop and sbottom masses, while the *dashed light-blue line* indicates a constant value of the neutralino mass

Exclusion limits for these pMSSM models are determined by combining many of the SRs defined for the searches discussed in this paper (t0L, t1L, tb,[9] t2t1Z, g3b, tc). For each

[9] The tb signal region, discussed in detail in Appendix B.2.3, implement a one-lepton selection, designed to be sensitive to final states containing a top quark, a b-quark and E_T^{miss}. It complements the selections of the $t0L$ and $t1L$ signal regions targeting ttE_T^{miss} final states.

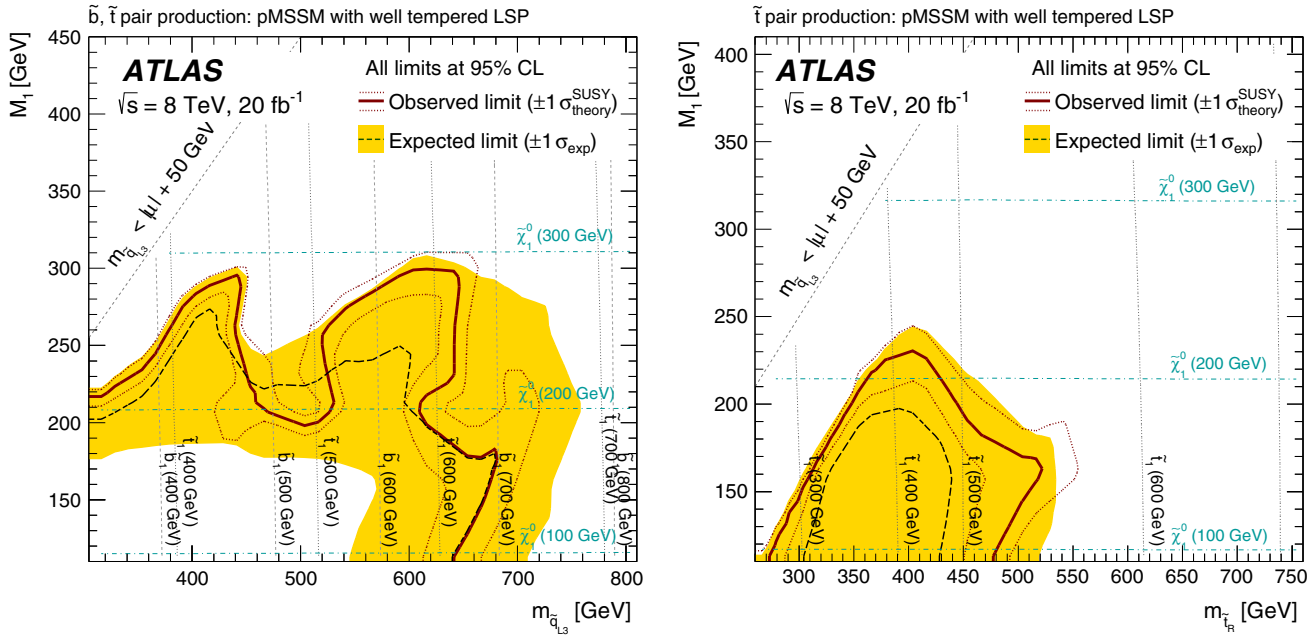

(a) **(b)**

Fig. 14 Expected and observed 95 % CL exclusion limits for the pMSSM model with well-tempered neutralinos as a function of M_1 and **a** $m_{\tilde{q}L3}$ or **b** $m_{\tilde{t}_R}$. The limit of **a** is obtained as the combination of the t0L, t1L, tb and SS3L analyses, while the t0L analysis is used for **b**. The signal region yielding the smallest CL_s value for the signal-plus-background hypothesis is used for each point. The *dashed black line* indicates the expected limit, and the *yellow band* indicates the $\pm 1\sigma$ uncertainties, which include all uncertainties except the theoretical uncertainties in the signal. The *red solid line* indicates the observed limit, and the *red dotted lines* indicate the sensitivity to $\pm 1\sigma$ variations of the signal theoretical. The *dashed* and *dotted grey lines* indicate a constant value of the stop and sbottom masses, while the *dashed light-blue line* indicates a constant value of the neutralino mass

set of parameters the individual 95 % CL expected limit is evaluated. The combined exclusion contour is determined by choosing, for each model point, the signal region having the smallest expected CL_s value of the test statistic for the signal-plus-background hypothesis.

Figure 13 shows the exclusion limit for the naturalness-inspired set of pMSSM models based on the t0L, t1L and tb analyses. The t0L and t1L analyses have a similar expected sensitivity. These SRs were optimised assuming a 100 % BR for $\tilde{t}_1 \rightarrow t\tilde{\chi}_1^0$ or $\tilde{t}_1 \rightarrow b\tilde{\chi}_1^{\pm}$, while for these pMSSM models, the stop decays to $\tilde{t}_1 \rightarrow t\tilde{\chi}_1^0$, $\tilde{t}_1 \rightarrow b\tilde{\chi}_1^{\pm}$ and $\tilde{t}_1 \rightarrow b\tilde{\chi}_2^0$ with similar branching ratios (and the sbottom to both $\tilde{b}_1 \rightarrow b\tilde{\chi}_1^0$ and $\tilde{b}_1 \rightarrow t\tilde{\chi}_1^{\pm}$). The tb signal regions, discussed in detail in Appendix B.2.3, are designed to be sensitive to final states containing a top quark, a b-quark and missing transverse momentum and address such mixed-decay scenarios by requiring a lower jet multiplicity.

The signal regions that dominate the sensitivity are the tb, t0L-SRC1 and t1L-bCd_bulk at low values of $m_{\tilde{q}L3}$, and tb, t0L-SRA1, t0L-SRA2 and t1L-tNbC_mix at intermediate and high values of $m_{\tilde{q}L3}$. The excluded region for models with $m_{\tilde{q}L3} \sim 900$ GeV and $\mu \sim 150$ GeV is due to the saturation of $m_{\tilde{t}_1}$ at high $m_{\tilde{q}L3}$ values: to satisfy the Higgs boson mass constraint requires $M_S \sim 800$ GeV, hence $m_{\tilde{t}_1}$ at $m_{\tilde{q}L3} \sim 900$ GeV is smaller than that at $m_{\tilde{q}L3} \sim 800$ GeV. The large fluctuations of the observed limit with respect to the expected one are due to transitions between different signal regions providing the best expected exclusion in different regions of the plane.

Figure 14a, b show the exclusion limit obtained for the set of pMSSM models with well-tempered neutralinos as a function of $m_{\tilde{q}L3}$ and $m_{\tilde{t}R}$, respectively. In both cases, the exclusion is largely dominated by the t0L analysis. For Fig. 14a, the signal region dominating the sensitivity at low $m_{\tilde{q}L3}$ is t0L-SRC1, while at higher $m_{\tilde{q}L3}$ values t0L-SRA1 and t0L-SRA2 dominate the sensitivity. The drop in sensitivity at $m_{\tilde{q}L3} = 410$ GeV, $M_1 = 260$ GeV is due to the opening of the $\tilde{t}_1 \rightarrow t\tilde{\chi}_2^0$ and $\tilde{t}_1 \rightarrow t\tilde{\chi}_3^0$ transition, kinematically suppressed for smaller values of the difference $m_{\tilde{q}L3} - M_1$. Such decays introduce more intermediate states in the decay, effectively reducing the transverse momenta of the final state objects. The large fluctuations of the observed limit are again due to transitions between different signal regions. For Fig. 14b, the sensitivity is entirely dominated by the various t0L-SRC. The difference in sensitivity between these two scenarios is due to the presence of both a stop and

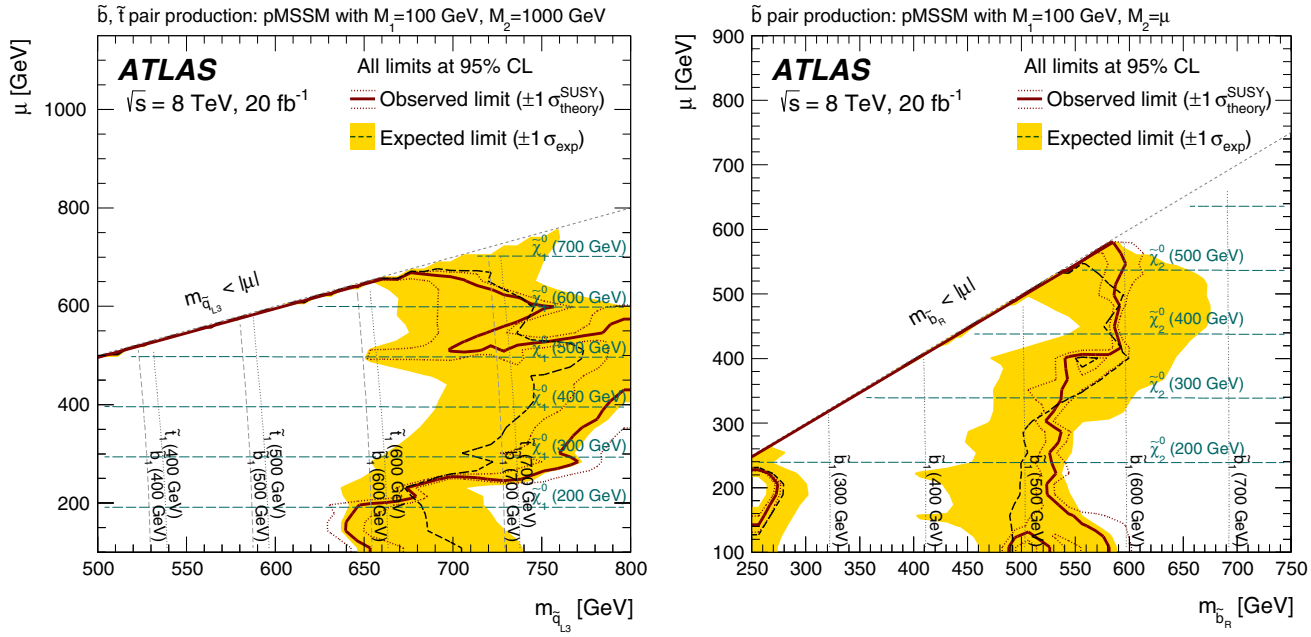

(a) (b)

Fig. 15 Expected and observed 95 % CL exclusion limits for the set of h/Z-enriched pMSSM models as a function of μ and **a** $m_{\tilde{q}L3}$ and **b** $m_{\tilde{b}_R}$. The limit of **a** is obtained as the combination of the t0L, g3b, t2t1Z and SS3L analyses, while the t0L, t2t1Z and tb analysis are used for **b**. The signal region yielding the smallest CL_s value for the signal-plus-background hypothesis is used for each point. The *dashed black line* indicates the expected limit, and the *yellow band* indicates the $\pm 1\sigma$ uncertainties, which include all uncertainties except the theoretical uncertainties in the signal. The *red solid line* indicates the observed limit, and the *red dotted lines* indicate the sensitivity to $\pm 1\sigma$ variations of the signal theoretical. The *dashed* and *dotted grey lines* indicate a constant value of the stop and sbottom masses, while the *dashed light-blue line* indicates a constant value of the neutralino mass

a sbottom for small $m_{\tilde{q}L3}$, while only a stop is present for low values of $m_{\tilde{t}R}$.

Finally, Fig. 15a, b show the exclusion limit obtained for the set of h/Z-enriched pMSSM models. These models yield large b-jet multiplicities to the final state through direct sbottom decays, top-quark decays and $\tilde{\chi}_2^0 \rightarrow h/Z\tilde{\chi}_1^0$. The exclusion is dominated by the t0L and g3b analyses for Fig. 15a and by and the t0L analysis for Fig. 15b.

More informations about the limits obtained, including the SLHA files for the points mentioned in Table 3, can be found in Refs. [89] and [90].

6 Conclusions

The search programme of the ATLAS collaboration for the direct pair production of stops and sbottoms is summarised and extended by new analyses targeting scenarios not optimally covered by previously published searches. The paper is based on 20 fb^{-1} of proton–proton collisions collected at the LHC by ATLAS in 2012 at a centre-of-mass energy $\sqrt{s}$ = 8 TeV. Exclusion limits in the context of simplified models are presented. In general, stop and sbottom masses up to several hundred GeV are excluded, although the exclusion limits significantly weaken in the presence of compressed SUSY mass spectra or multiple allowed decay chains. Three classes of pMSSM models, based on general arguments of Higgs boson mass naturalness and compatibility with the observed dark-matter relic density have also been studied and exclusion limits have been set. Large regions of the considered parameter space are excluded.

We thank CERN for the very successful operation of the LHC, as well as the support staff from our institutions without whom ATLAS could not be operated efficiently.

Acknowledgments We acknowledge the support of ANPCyT, Argentina; YerPhI, Armenia; ARC, Australia; BMWFW and FWF, Austria; ANAS, Azerbaijan; SSTC, Belarus; CNPq and FAPESP, Brazil; NSERC, NRC and CFI, Canada; CERN; CONICYT, Chile; CAS, MOST and NSFC, China; COLCIENCIAS, Colombia; MSMT CR, MPO CR and VSC CR, Czech Republic; DNRF, DNSRC and Lundbeck Foundation, Denmark; EPLANET, ERC and NSRF, European Union; IN2P3-CNRS, CEA-DSM/IRFU, France; GNSF, Georgia; BMBF, DFG, HGF, MPG and AvH Foundation, Germany; GSRT and NSRF, Greece; RGC, Hong Kong SAR, China; ISF, MINERVA, GIF, I-CORE and Benoziyo Center, Israel; INFN, Italy; MEXT and JSPS, Japan; CNRST, Morocco; FOM and NWO, Netherlands; BRF and RCN, Norway; MNiSW and NCN, Poland; GRICES and FCT, Portugal; MNE/IFA, Romania; MES of Russia and NRC KI, Russian Federation; JINR; MSTD, Serbia; MSSR, Slovakia; ARRS and MIZŠ, Slovenia; DST/NRF, South Africa; MINECO, Spain; SRC and Wallenberg Foundation, Sweden; SER, SNSF and Cantons of Bern and

Geneva, Switzerland; NSC, Taiwan; TAEK, Turkey; STFC, the Royal Society and Leverhulme Trust, UK; DOE and NSF, USA.The crucial computing support from all WLCG partners is acknowledged gratefully, in particular from CERN and the ATLAS Tier-1 facilities at TRIUMF (Canada), NDGF (Denmark, Norway, Sweden), CC-IN2P3 (France), KIT/GridKA (Germany), INFN-CNAF (Italy), NL-T1 (Netherlands), PIC (Spain), ASGC (Taiwan), RAL (UK) and BNL (USA) and in the Tier-2 facilities worldwide.

Open Access This article is distributed under the terms of the Creative Commons Attribution 4.0 International License (http://creativecommons.org/licenses/by/4.0/), which permits unrestricted use, distribution, and reproduction in any medium, provided you give appropriate credit to the original author(s) and the source, provide a link to the Creative Commons license, and indicate if changes were made.
Funded by SCOAP[3].

A The ATLAS detector and object reconstruction

The ATLAS detector [91] consists of inner tracking devices surrounded by a superconducting solenoid, electromagnetic and hadronic calorimeters and a muon spectrometer immersed in a toroidal magnetic field. The inner detector (ID), in combination with a superconducting solenoid magnet with a central field of 2 T, provides precision tracking and momentum measurements of charged particles in a pseudorapidity[10] range $|\eta| < 2.5$. The ID consists of a silicon pixel detector, a silicon microstrip detector and a straw tube tracker ($|\eta| < 2.0$) that also provides transition radiation measurements for electron identification. A high-granularity electromagnetic calorimeter system, with acceptance covering $|\eta| < 3.2$, uses liquid argon (LAr) as the active medium. A scintillator-tile calorimeter provides hadronic coverage for $|\eta| < 1.7$. The end-cap and forward regions, spanning $1.5 < |\eta| < 4.9$, are instrumented with LAr electromagnetic and hadronic calorimeters. The muon spectrometer has separate trigger and high-precision tracking chambers which provide trigger coverage for $|\eta| < 2.4$ and muon identification and momentum measurements for $|\eta| < 2.7$.

The data sample used in this analysis was taken during the period from March to December 2012 with the LHC operating at a pp centre-of-mass energy of $\sqrt{s} = 8$ TeV.[11] Following requirements based on beam, detector conditions and data quality, the complete dataset corresponds to an integrated luminosity of 20.3 fb^{-1}, with an associated uncertainty of 2.8 %. The uncertainty is derived following the same methodology as that detailed in Ref. [92]. Events used in the analyses presented in this paper were selected using the ATLAS three-level trigger following different chains based on the signatures being considered. A common set of cleaning cuts, aimed at rejecting events heavily contaminated by non-collision backgrounds, or events containing badly measured or fake jets is applied to all analyses.

The experimental signature of third-generation supersymmetric particles includes the production of b-jets in association with missing transverse momentum and possibly additional jets and charged leptons. Different signatures are investigated in this paper to gain sensitivity to a variety of possible topologies arising from the production and decay of stops and sbottoms. Different event selections share common definitions of the final reconstructed objects, which are detailed in the remainder of this Appendix. Analysis-specific departures from those definitions are detailed for each case in Appendix B or in the specific analysis paper.

The reconstructed primary vertex [93] is required to be consistent with the luminous region and to have at least five associated tracks with $p_{\mathrm{T}} > 400$ MeV; when more than one such vertex is found, the vertex with the largest summed p_{T}^2 of the associated tracks is chosen.

Jets are constructed from three-dimensional clusters of noise-suppressed calorimeter cells [94] using the anti-k_t algorithm [95–97] with a distance parameter $R = 0.4$ and calibrated with a local cluster weighting algorithm [98]. An area-dependent correction is applied for energy from additional proton–proton collisions based on an estimate of the pileup activity in a given event using the method proposed in Ref. [99]. Jets are calibrated as discussed in Ref. [100] and required to have $p_{\mathrm{T}} > 20$ GeV and $|\eta| < 4.5$. Events containing jets arising from detector noise, cosmic-ray muons, or other non-collision sources are removed from consideration [100].

Jets arising from a b-quark fragmentation and within the acceptance of the inner detector ($|\eta| < 2.5$) are identified with an algorithm that exploits both the track impact parameters and secondary vertex information [101]; this algorithm is based on a neural network using the output weights of the IP3D, JetFitter+IP3D, and SV1 algorithms (defined in Refs. [102,103]). A lower cut on the output of the neural network defines the b-tagged jets. Three different working points are used, with a nominal efficiency of 60, 70 and 80 % as evaluated on simulated top quark pair production events. The corresponding rejection factors against jets originating from light (c) quarks are 25 (3), 135 (5) and 600 (8).

Electrons are reconstructed from energy clusters in the electromagnetic calorimeter matched to a track in the inner detector [104] and are required to have $|\eta| < 2.47$. Several criteria, including calorimeter shower shape, quality

[10] ATLAS uses a right-handed system with its origin at the nominal interaction point (IP) in the centre of the detector and the z-axis along the beam pipe. The x-axis points from the IP to the centre of the LHC ring, and the y-axis points upward. Cylindrical coordinates (r, ϕ) are used in the transverse plane, ϕ being the azimuthal angle around the beam pipe. The pseudorapidity is defined in terms of the polar angle θ as $\eta = -\ln\tan(\theta/2)$. The distance ΔR in the η–ϕ space is defined as $\Delta R = \sqrt{(\Delta\eta)^2 + (\Delta\phi)^2}$.

[11] The limits derived using a measurement of the $t\bar{t}$ production cross section discussed in Sect. 4.1 and Appendix B.1 also uses 4.7 fb^{-1} of pp collisions data collected at a centre-of-mass energy of $\sqrt{s} = 7$ TeV.

of the match between the track and the cluster, and the amount of transition radiation emitted in the TRT detector, are used to define three selections with decreasing efficiency and increasing purity, named respectively 'loose', 'medium' and 'tight' [104]. These three electron selections are used throughout this paper in the definitions of various signal and control regions. Muons, which are identified either as a combined track in the muon spectrometer and inner detector systems, or as an inner detector track matched with a muon spectrometer track segment [105,106], are required to have $|\eta| < 2.4$.

Electrons and muons (generically referred to by the symbol ℓ) are usually required to have transverse momentum $p_{\mathrm{T}} > 10$ GeV. For specific scenarios with compressed mass spectra, low-p_{T} leptons are expected and the p_{T} threshold is lowered to 6 GeV for muons and to 7 GeV for electrons.

The missing transverse momentum $\mathbf{p}_{\mathrm{T}}^{\mathrm{miss}}$ (with magnitude $E_{\mathrm{T}}^{\mathrm{miss}}$) is the negative vector sum of the p_{T} measured in the clusters of calorimeter cells, which are calibrated according to their associated reconstructed object (e.g. jets and electrons), and the p_{T} of the muons. Calorimeter cells not associated with any reconstructed object are also used in the calculation of $\mathbf{p}_{\mathrm{T}}^{\mathrm{miss}}$. The missing transverse momentum from the tracking system (denoted by $\mathbf{p}_{\mathrm{T}}^{\mathrm{miss,track}}$, with magnitude $E_{\mathrm{T}}^{\mathrm{miss,track}}$) is computed from the vector sum of the reconstructed inner detector tracks with $p_{\mathrm{T}} > 500$ MeV and $|\eta| < 2.5$, associated with the primary vertex in the event.

B Analyses used in the paper

Several signal regions are used in this paper, either standalone or in combination with others, to derive exclusion limits in the many models considered. This Appendix provides a review of the already published analyses and a more extended documentation of the signal regions not previously published.

B.1 Review of already published signal regions

The discussion of analyses that have already been published is reduced to a summary for the sake of brevity. Table 1 provides a reference to the papers where full details of the signal, control and validation region selections, together with the strategies adopted for the estimation of the background processes are found.

Multijet final states (t0L) The analysis is designed to be sensitive to final states arising from all-hadronic decays of directly pair-produced stops [16]. Two sets of signal regions were optimised to maximise the sensitivity to topologies arising from $\tilde{t}_1 \to t\tilde{\chi}_1^0$ decays, assumed to happen with a branching ratio of one. The first set of signal regions, named t0L-SRA, assumes that both top quark hadronic decays can be fully resolved by indentifying the six final-state jets. The SM background [dominated by $t\bar{t}$ and $Z+$ heavy flavour (HF) jets production] is rejected based on the presence of two hadronic systems consistent with top quarks and large $E_{\mathrm{T}}^{\mathrm{miss}}$. The second set of signal regions, named t0L-SRB targets a similar scenario, but aims at topologies where the top quarks have a large boost, and some of the decay products are merged into a single jet. The event selection is designed to select final states with a maximum of five $R = 0.4$ anti-k_t jets, to be mutually exclusive with t0L-SRA, and relies on the presence of $R = 0.8$ and $R = 1.2$ anti-k_t jets containing the hadronic decay products of the two top quarks. The jet masses, the transverse mass of the $E_{\mathrm{T}}^{\mathrm{miss}}$ and the nearest b-jet, and other variables are used to discriminate against the dominant SM $t\bar{t}$, Z + HF jets and W + HF jets production background processes.

Finally, a third set of signal regions, named t0L-SRC, is designed to increase the analysis sensitivity to the decay $\tilde{t}_1 \to b\tilde{\chi}_1^{\pm}$. The presence of the intermediate chargino state tends to decrease the jet multiplicity: these signal regions require five anti-k_t jets with $R = 0.4$, and base the signal selection on a set of transverse mass variables aimed at rejecting the dominant SM $t\bar{t}$ production process.

One-lepton final states (t1L) The large number of signal regions defined in this analysis stems from the variety and complexity of the possible stop final states considered [17]. All signal regions are characterised by the presence of one lepton, a second-lepton veto, a minimum of two jets and large $E_{\mathrm{T}}^{\mathrm{miss}}$. A first set of four signal regions (t1L-tN) were optimised assuming a branching ratio of 100 % for the decay $\tilde{t} \to t\tilde{\chi}_1^0$. These signal regions aim at having sensitivity to different $\Delta m(\tilde{t}, \tilde{\chi}_1^0)$, in particular t1L-tN_diag targets scenarios with small $\Delta m(\tilde{t}_1, \tilde{\chi}_1^0)$ and makes use of the shape information of the $E_{\mathrm{T}}^{\mathrm{miss}}$ and m_{T} distributions.[12] The t1L-tN_boost SR targets models with the largest $\Delta m(\tilde{t}, \tilde{\chi}_1^0)$, where the top quark produced by the stop decay has a large boost and large-R jets are used to reconstruct the top quark decays.

The decay $\tilde{t} \to \tilde{\chi}_1^{\pm} b$ introduces additional degrees of freedom in the decay. The final-state kinematics is largely driven by the mass separation between the stop and the chargino $\Delta m(\tilde{t}, \tilde{\chi}_1^{\pm})$, and by that between the chargino and the neutralino $\Delta m(\tilde{\chi}_1^{\pm}, \tilde{\chi}_1^0)$. Several signal regions, identified by the

[12] The transverse mass m_{T} of the lepton with transverse momentum $\mathbf{p}_{\mathrm{T}}$ and the missing transverse momentum vector $\mathbf{p}_{\mathrm{T}}^{\mathrm{miss}}$ with magnitude $E_{\mathrm{T}}^{\mathrm{miss}}$ is defined as

$$m_{\mathrm{T}} = \sqrt{2\left(|\mathbf{p}_{\mathrm{T}}| E_{\mathrm{T}}^{\mathrm{miss}} - \mathbf{p}_{\mathrm{T}} \cdot \mathbf{p}_{\mathrm{T}}^{\mathrm{miss}}\right)} \quad (1)$$

and it is extensively used in one-lepton final states to reject SM background processes containing a W boson decaying leptonically.

prefix t1L-bC were designed and optimised depending on the mass hierarchy and, consequently, on the different kinematics of the lepton and b-jets.

The four signal regions t1L-bCa_low, t1L-bCa_med, t1L-bCb_med1 and t1L-bCb_high target small values of $\Delta m(\tilde{\chi}_1^{\pm}, \tilde{\chi}_1^0)$ and have the common feature of making use of a dedicated soft-lepton selection: muons and electrons are identified down to a p_{T} threshold of 6 and 7 GeV, respectively, requiring a special treatment for the estimate of possible background processes arising from lepton misidentification. They are collectively referred to as "soft-lepton" signal regions. Both t1L-bCa signal regions require a hard ISR jet to boost the stop pair system and produce a sizeable $E_{\mathrm{T}}^{\mathrm{miss}}$. The t1L-bCb targets large values of $\Delta m(\tilde{t}_1, \tilde{\chi}_1^{\pm})$ and exploits the presence of two relatively hard b-jets in the event.

The signal region t1L-bCc_diag targets a mass hierarchy complementary to that of the t1L-bCb. The small value of $\Delta m(\tilde{t}, \tilde{\chi}_1^{\pm})$ gives rise to soft b-jets that go undetected, hence b-tagged jets are vetoed for this region.

Topologies arising from scenarios where both $\Delta m(\tilde{t}, \tilde{\chi}_1^{\pm})$ and $\Delta m(\tilde{\chi}_1^{\pm}, \tilde{\chi}_1^0)$ are sizeable are targeted by the three t1L-bCd regions: they all require four jets in the final state, are characterised by different b-jet multiplicities, and apply different selections on the $E_{\mathrm{T}}^{\mathrm{miss}}$, m_{T} and am_{T2}[13] variables. A veto on additional isolated tracks and τ lepton candidates identified with loose criteria helps to suppress the dominant SM background from dileptonic $t\bar{t}$ decays.

The last two signal regions listed in Table 1, t1L-3body and t1L-tNbC_mix, were optimised for two additional possible scenarios. If $\Delta m(\tilde{t}, \tilde{\chi}_1^0) < m_t$ and the mass hierarchy or the model parameters suppress the decay through a chargino, then the dominant stop decay is $\tilde{t} \rightarrow bW\tilde{\chi}_1^0$, through an off-shell top quark (three-body decay). The dedicated signal region relies on the shape information from the m_{T} and am_{T2} variable distributions. Finally, t1L-tNbC_mix is designed to recover sensitivity in scenarios where the stop is assumed to decay with similar probabilities to $t\tilde{\chi}_1^0$ and $b\tilde{\chi}_1^{\pm}$: the selection aims to reject the dominant dileptonic $t\bar{t}$ background by making use of the topness [109] variable.

Two-lepton final states (t2L) If the SUSY mass hierarchy forbids the presence of sleptons in the stop decay chain, final states containing two leptons (e or μ) and a large amount of $E_{\mathrm{T}}^{\mathrm{miss}}$ would arise from stop pair production. The main background is given by SM processes containing two W bosons in the final state (mainly $t\bar{t}$ and WW) [18]. To discriminate the stop signal from the SM background, the stransverse mass variable m_{T2} [107,108] is used. The stransverse mass, computed using the two leptons as visible particles and the missing transverse momentum vector, exhibits a kinematical end-point at m_W for most SM processes. Because of the presence of additional $E_{\mathrm{T}}^{\mathrm{miss}}$ due to the LSP, the end-point for a SUSY signal can be at larger values, depending on the mass separation between the particles involved in the decay. The analysis is optimised assuming $\tilde{t}_1 \rightarrow \tilde{\chi}_1^{\pm} b$ with BR = 100 % and $\Delta m(\tilde{\chi}_1^{\pm}, \tilde{\chi}_1^0) > m_W$, but it is also sensitive to the three-body decay mode of the stop. To derive exclusion limits, five signal regions (t2L) have been defined, requiring different jet multiplicities and different m_{T2} thresholds. A selection requiring two b-jets and based on m_{T2} computed using them as visible particles is sensitive to the chargino decay mode with $\Delta m(\tilde{t}_1, \tilde{\chi}_1^{\pm}) > m_t$. Finally, a multivariate discriminant is built which targets the $\tilde{t}_1 \rightarrow t\tilde{\chi}_1^0$ decay mode.

Final states from compressed stop decays (tc) If the difference in mass between the stop and the neutralino is smaller than the W boson mass, then the only possible decay channels are $\tilde{t} \rightarrow \tilde{\chi}_1^0 c$ or $\tilde{t} \rightarrow W^* b$, where the decay products of the off-shell W^* would, in general, be soft. This analysis [19] has defined two sets of signal regions, both optimised for the $\tilde{t} \rightarrow \tilde{\chi}_1^0 c$ decay. A common preselection requires the presence of a high-p_{T} jet, large $E_{\mathrm{T}}^{\mathrm{miss}}$ and applies a lepton veto. The first set of signal regions named tc-M, targets scenarios with the stop mass almost degenerate with the neutralino mass, and applies a selection that exploits a monojet-like signature arising from the presence of an ISR jet. Three different signal regions have been designed, characterised by increasing thresholds on the leading jet p_{T} and $E_{\mathrm{T}}^{\mathrm{miss}}$. The second set of signal regions, named tc-C, targets less compressed scenarios, and exploits the presence of jets originating from the fragmentation of c-quarks in the final state. A dedicated c-tagging algorithm was used to reject the dominant SM background processes arising mostly from $t\bar{t}$ and $Z \rightarrow \nu\bar{\nu}$ (produced in association with heavy-flavour jets) production. As in the case of the tc-M signal regions, different thresholds on the leading jet p_{T} and on $E_{\mathrm{T}}^{\mathrm{miss}}$ are used to identify a looser and a tighter tc-C region.

Final states with a Z boson (t2t1Z) A Z boson can be emitted in the decay of $\tilde{t}_2 \rightarrow \tilde{t}_1 Z$, producing final states with large lepton multiplicities. It can be useful to look for $\tilde{t}_2$ (rather than $\tilde{t}_1$) production if, for example, the mass of $\tilde{t}_1$ is very close to the sum of the top quark and neutralino masses, which would lead to $\tilde{t}_1$ pair production final states difficult to distinguish from SM $t\bar{t}$ production. Models are investigated with $\Delta m(\tilde{t}_1, \tilde{\chi}_1^0) = 180$ GeV with the decay $\tilde{t}_1 \rightarrow t\tilde{\chi}_1^0$. The final state would contain, beyond the Z boson, several jets arising from the $\tilde{t}_1$ decay. Similar final states can be obtained in GMSB models where the Z boson is emitted

[13] The asymmetric stransverse mass variable is a variant of the stransverse mass variable [107,108] defined to efficiently reject dileptonic $t\bar{t}$ decays. It assumes that the undetected particle is the W boson for the branch with the lost lepton and the neutrino is the missing particle for the branch with the observed charged lepton. For the dileptonic $t\bar{t}$events, am_{T2} is bounded from above by the top quark mass, whereas new physics can exceed this bound.

in the $\tilde{\chi}_1^0 \to \tilde{G}Z$ decay if the gravitino $\tilde{G}$ is the LSP and the neutralino the NLSP.

This analysis [20] defines five different signal regions divided into two sets. The first set, named t2t1Z-SR2, requires two same-flavour leptons whose invariant mass is consistent with that of a Z boson, m_Z, and at least one b-tagged jet. The three signal regions are characterised by the different selection thresholds applied to the $E_{\mathrm{T}}^{\mathrm{miss}}$, to the transverse momentum of the dilepton system $p_{\mathrm{T}}(\ell\ell)$ and to the jet multiplicity. The second set of signal regions, named t2t1Z-SR3, requires three leptons, two of which must form an opposite-sign same-flavour pair whose invariant mass is consistent with m_Z. Both signal regions require at least five jets, among which at least one has to be b-tagged. The two signal regions are characterised by the different selection thresholds applied to $p_{\mathrm{T}}(\ell\ell)$ and to the leading lepton p_{T}.

Final states with two b-jets and $E_{\mathrm{T}}^{\mathrm{miss}}$ (b0L) This signature arises naturally from the sbottom decay $\tilde{b}_1 \to b\tilde{\chi}_1^0$. Moreover, one expects the same final state from $\tilde{t}_1 \to \tilde{\chi}_1^{\pm} b$ followed by $\tilde{\chi}_1^{\pm} \to ff'\tilde{\chi}_1^0$ in the limit of small $\Delta m(\tilde{\chi}_1^{\pm}, \tilde{\chi}_1^0)$. This analysis [21] defines two sets of signal regions, b0L-SRA and b0L-SRB, targeting scenarios with large and small squark–neutralino mass separations, respectively.

The event selection of b0L-SRA requires large $E_{\mathrm{T}}^{\mathrm{miss}}$, exactly two b-jets and vetoes the presence of additional jets; the rejection of the SM $t\bar{t}$production background is carried out by making use of the contransverse mass [110] of the two b-jets. Its distributions shows a kinematical end-point at about 135 GeV for $t\bar{t}$ production, while extending to higher values for the signal.

A selection relying on the presence of an ISR jet is instead needed if the third-generation squark mass is almost degenerate with that of the neutralino. This is the purpose of b0L-SRB, which selects a hard, non-b-tagged leading jet recoiling against the squark pair system. The selection includes the requirement of two b-tagged jets, a veto on additional hadronic activity, and the presence of large $E_{\mathrm{T}}^{\mathrm{miss}}$.

Final states with three b-jets (g3b) This analysis [62] is designed to search for gluino-mediated sbottom and stop production in events with no leptons or one lepton (electron or muon) in the final state. However, it was found to have sensitivity for direct $\tilde{b}_1$ production followed by $\tilde{b}_1 \to \tilde{\chi}_2^0 b \to \tilde{\chi}_1^0 hb$, where h is the SM Higgs boson with mass $m_h = 125$ GeV, and also sensitivity to some of the pMSSM models considered in this paper. Such final states are characterised by a large multiplicity of b-jets both in $\tilde{g}\tilde{g} \to \tilde{t}_1\tilde{t}_1 tt$ and $\tilde{g}\tilde{g} \to \tilde{b}_1\tilde{b}_1 bb$ where there are up to four b-jets in the final state.

Three sets of signal regions have been designed to target different mass hierarchies of the gluino-mediated sbottom and stop production models. All signal regions have at least four jets with $p_{\mathrm{T}} > 30$ GeV, three identified b-jets, large $E_{\mathrm{T}}^{\mathrm{miss}}$ and a large m_{eff}, defined as the scalar sum of the p_{T} of the jets and $E_{\mathrm{T}}^{\mathrm{miss}}$.

Strongly produced final states with two same sign or three leptons (SS3L) Final states containing many leptons or same-sign (SS) leptons can arise from the pair production of gluinos and squarks, when the produced particles decay to the LSP through multiple intermediate stages, or when several top quarks appear as part of the decay chain. The analysis was developed for the gluino-mediated stop production process $\tilde{g}\tilde{g} \to \tilde{t}_1\tilde{t}_1 tt$ followed by $\tilde{t}_1 \to t\tilde{\chi}_1^0$, which can yield final states containing up to four leptons, including SS pairs. Similar final states arise from the sbottom decay $\tilde{b}_1 \to t\tilde{\chi}_1^{\pm}$, which are studied in this paper.

This analysis [63] concentrates on final states containing either three leptons or a SS lepton pair produced in association with many jets. Five signal regions (identified by the prefix SS3L) are defined, which are characterised by different light- and heavy-flavour jet multiplicities, high selection thresholds on $E_{\mathrm{T}}^{\mathrm{miss}}$ and m_{eff}, and different thresholds on the transverse mass of the lepton with the highest transverse momentum and the $E_{\mathrm{T}}^{\mathrm{miss}}$.

Spin correlation in $t\bar{t}$ production events (SC) If the mass of the $\tilde{t}_1$ is such that $m_{\tilde{t}_1} \sim m_{\tilde{\chi}_1^0} + m_t$, the final-state kinematics are similar to that of Standard Model $t\bar{t}$ production. One possible approach is to derive exclusion limits on the stop mass by performing SM precision measurements. This analysis has measured the azimuthal angle difference between the two leptons arising from the dileptonic $t\bar{t}$ decay [64]. The events are required to contain, beside the two leptons, at least two additional jets, one of which is required to be b-tagged. In events containing two leptons of the same flavour, the Z production background is suppressed by applying a selection on the dilepton invariant mass. The distribution of the azimuthal angle between the two leptons is sensitive to the spin correlations of the $t\bar{t}$ system: it is hence used to extract limits on possible contaminations from direct scalar top production events.

$t\bar{t}$ production cross section (xsec) The measurement of the $t\bar{t}$ production cross section using events containing two different-flavour leptons $e\mu$ and b-tagged jets is used in Ref. [65] to extract limits on the direct pair production of $\tilde{t}_1$ with mass close to the top quark. The assumed decay is $\tilde{t}_1 \to t\tilde{\chi}_1^0$.

The $t\bar{t}$ production cross section $\sigma_{t\bar{t}}$ is obtained by using the equations

$$N_1 = L\sigma_{t\bar{t}}\epsilon_{e\mu}2\epsilon_b(1 - C_b\epsilon_b) + N_1^{\mathrm{bkg}} \quad (2)$$

$$N_2 = L\sigma_{t\bar{t}}\epsilon_{e\mu}C_b\epsilon_b^2 + N_2^{\mathrm{bkg}} \quad (3)$$

where N_1 and N_2 are the number of events with two different flavour leptons having exactly one or two b-tagged jets, respectively, L is the integrated luminosity, $\epsilon_{e\mu}$ the efficiency for a $t\bar{t}$ event to pass the lepton selection, ϵ_b is the probability of having a b-jet within acceptance and for it to be tagged, C_b is a correlation coefficient which is close to unity, and N_1^{bkg} and N_2^{bkg} are the number of events with one or two b-tagged jets from SM events different from $t\bar{t}$ production. The values of $\sigma_{t\bar{t}}$ and ϵ_b are extracted from the data by solving the two simultaneous Eqs. (2) and (3), avoiding the need to estimate ϵ_b from simulation.

Stop-pair production events with $m_{\tilde{t}_1} > m_t + m_{\tilde{\chi}_1^0}$ have similar $\epsilon_{e\mu}$ and b-jet kinematics to SM $t\bar{t}$ production events, so the fitted value of ϵ_b in a combined sample is compatible with that from $t\bar{t}$ production events alone, and the fitted cross section corresponds closely to the sum of $t\bar{t}$ and stop-pair production cross sections. Limits on stop pair production are extracted by calculating 95 % CL limits on the stop pair production signal strength μ (defined as the ratio of the obtained stop cross section to the theoretical prediction) based on the comparison of the measured cross section with that predicted for SM $t\bar{t}$ production events alone. A 95 % CL signal strength smaller than unity for a given signal point implies its exclusion.

This interpretation, which made use of collision data with both $\sqrt{s} = 7$ and 8 TeV, is extended here to the three-body decay $\tilde{t}_1 \to Wb\tilde{\chi}_1^0$. The main difference with respect to the scenario considered in Ref. [65] is that the three-body decay tends to yield b-jets with lower p_{T}, leading to a fitted ϵ_b for the combined sample which is different from that expected for $t\bar{t}$ events alone. The limits obtained are summarised in Fig. 16 for a neutralino mass of 1 GeV. A 95 % CL limit that excludes stop masses below 175 GeV is obtained. The figure also shows the effect on the limit of a "sneaky top squark" scenario [111]: the presence of a $\tilde{t}_1$ with mass similar to that of the top quark could bias the measurement of the top-quark mass itself. The bias in the top-mass measurement introduced by the existence of a $\tilde{t}_1$ with mass $m_{\tilde{t}_1} = 170$ GeV depends on the analysis technique and channel, and was evaluated to be at most 1 GeV for the two- and three-dimensional template techniques used in the ATLAS top mass measurement in the lepton+jets channel [112]. The effect of a potential bias of 1 and 2.5 GeV on the top-mass measurement was studied by recalculating the observed 95 % CL limit on μ when reducing the predicted SM $t\bar{t}$ production cross section from the baseline value of $m_t = 172.5 \pm 1.0$ GeV to those obtained for top mass central values of 173.5 and 175 GeV. The corresponding limit on the stop mass is reduced by about 5 and 15 GeV, respectively.

The dependence of the exclusion limits on the neutralino mass was studied and found to be important: the effect of an increasing neutralino mass is to decrease the p_{T} of the b-jets,

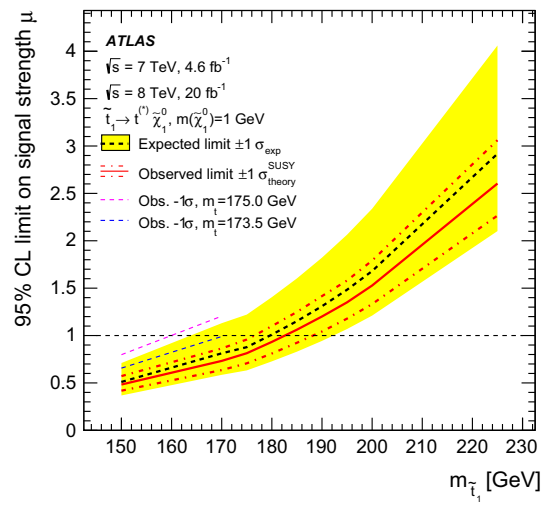

Fig. 16 Expected and observed 95 % CL limits on the signal strength μ (defined as the ratio of the obtained stop cross section to the theoretical prediction) for the production of $\tilde{t}_1$ pairs as a function of $m_{\tilde{t}_1}$. The stop is assumed to decay as $\tilde{t}_1 \to t\tilde{\chi}_1^0$ or through its three-body decay depending on its mass. The neutralino is assumed to have a mass of 1 GeV. The *black dotted line* shows the expected limit with $\pm 1\sigma$ uncertainty band *shaded in yellow*, taking into account all uncertainties except the theoretical cross-section uncertainties on the signal. The *red solid line* shows the observed limit, with *dotted lines* indicating the changes as the nominal signal cross section is scaled *up* and *down* by its theoretical uncertainty. The *short blue* and *purple dashed lines* indicate how the observed limits with the signal cross section reduced by one standard deviation of its theoretical uncertainty for $m_{\tilde{t}_1} < m_t$ when the top quark mass is assumed instead to be 173.5 ± 1.0 and 175.0 ± 1.0 GeV

and hence to lower the value of ϵ_b for the stop pair production signal. For a neutralino mass of 30 GeV, only a small range of stop masses around 150 GeV is excluded.

The sensitivity of the $t\bar{t}$ cross-section measurement to $\tilde{t}_1$ pair production assuming a branching ratio of 100 % into $\tilde{t}_1 \to b\tilde{\chi}_1^{\pm}$, followed by $\tilde{\chi}_1^{\pm} \to W^{(*)}\tilde{\chi}_1^0$ with $m_{\tilde{\chi}_1^{\pm}} = 2m_{\tilde{\chi}_1^0}$ was also investigated. The presence of the intermediate chargino state tends to lower the p_{T} of the leptons and of the b-jets significantly, hence decreasing both $\epsilon_{e\mu}$ and ϵ_b. No exclusion limit can be derived for this scenario.

Summarising, the limits on stop pair production obtained in Ref. [65] have been extended by considering the stop three-body decay. Stop masses between 150 GeV and m_t can be excluded for a neutralino mass of 1 GeV. The exclusion holds provided that any bias in the top-quark mass measurement by a nearby stop is not significant. Studies indicate that this potential bias would affect the limit on the stop mass by less than 5 GeV.

B.2 Description of the new signal regions

New analyses were developed to target topologies and regions of the SUSY parameter space not well covered

by previously published signal regions. They are identified throughout this paper and in Table 1 with the acronym WW, tb and t2t1h. Their contribution to the exclusion limits derived both in simplified and pMSSM models is outlined in Sects. 4 and 5 respectively. In this Appendix, further details about these analyses are provided for the interested reader. Additional informations about selection efficiencies, sensitivities of the different signal regions and individual limit plots, please refer to Refs. [89,90].

B.2.1 Final states with two leptons at intermediate values of $m_{T2}(WW)$

The measurement of the production cross section of non-resonant WW pairs in the two-lepton channel at the LHC [113–115] has given rise to theoretical speculations [116–118] which interpret the possible excess as due to the production of a light stop. The mass hierarchy favoured by these speculations includes a $\tilde{t}_1$ with mass around 200 GeV, a $\tilde{\chi}_1^{\pm}$ degenerate with it, and $m_{\tilde{\chi}_1^{\pm}} - m_{\tilde{\chi}_1^0}$ of a few tens of GeV: possible hadronic decay products of the $\tilde{t}_1 \to b\tilde{\chi}_1^{\pm}$ transition would have low p_{T} and would allow the events to survive the tight jet-veto selections applied in the SM cross-section measurement. Dedicated signal regions, defined by requiring two different-flavour opposite-sign leptons in the final states, are designed to have maximum sensitivity to such scenarios. The approach is also sensitive to scenarios where the stop decays predominantly through the three-body $\tilde{t}_1 \to bW\tilde{\chi}_1^0$ or four-body $\tilde{t}_1 \to b\ell\nu\tilde{\chi}_1^0$ decay.

MC simulated events are used to model the signal and to describe all backgrounds that produce two prompt leptons from W, Z or h decay. For processes whose predicted yield in the signal regions is small, or whose topology resembles very closely that of the signal, making it hard to define a proper control region, the background estimate is fully based on MC simulation. For $t\bar{t}$, Z + jets and WW production processes, which are the dominant backgrounds, the acceptance of the signal regions selection is estimated with MC simulation, while the normalisation is estimated in dedicated control regions. The MC samples used are the same as in Ref. [18].

The identification criteria for electrons, muons and jets follow the strategy defined in Appendix A: baseline electrons, which are used in the estimation of the fake-lepton background, are selected by applying the "medium" identification criteria. Signal electrons are identified using the "tight" criteria, and they are further required to be isolated. Signal muons correspond to baseline muons with an additional calorimeter- and track-based isolation requirement applied. Jets that have $|\eta| < 2.5$ and $p_{\mathrm{T}} > 20$ GeV are used for the event selection, although all jets up to $|\eta| < 4.5$ are retained for the computation of the missing transverse momentum.

Candidate stop production events, preselected by the same trigger and data quality requirements used in Ref. [18], are further required to contain one electron and one muon of opposite charge, with an invariant mass $m_{\ell\ell} > 20$ GeV. The leading (in p_{T}) and next-to-leading leptons are required to have $p_{\mathrm{T}} > 25$ GeV and $p_{\mathrm{T}} > 20$ GeV, respectively.

At this stage of the selection, the background is dominated by production of top-quark pairs and $Z \to \tau\tau$, followed by WW and Wt production.

A requirement of $m_{\mathrm{T2}} > 20$ GeV, where m_{T2} is the stransverse mass of the two leptons, strongly reduces the $Z \to \tau\tau$ background, which is expected to have a kinematical end-point at $m_{\mathrm{T2}} = m_{\tau}$. The ratio R_1 of the $E_{\mathrm{T}}^{\mathrm{miss}}$ and the effective mass, defined as the scalar p_{T} sum of the $E_{\mathrm{T}}^{\mathrm{miss}}$, the leptons and the jets, is useful in suppressing the $t\bar{t}$ background, which is typically characterised by a larger hadronic activity than in signal events. The selection chosen is $R_1 > 0.3 + m_{\mathrm{eff}}$ (with m_{eff} in TeV).

After the above selections, the SM background is dominated by WW production. Two differences between this process and the stop pair production signal are further exploited: firstly, the WW production is dominated by quark-antiquark scattering, while stop pair production is mostly initiated by gluon-gluon processes, and secondly the stop pair production signal has four invisible (two neutralinos and two neutrinos) and two undetected (the two b-jets) objects, while the WW process has only two. The first difference implies a higher longitudinal boost of the system emerging from the hard scattering in signal events than in background events. The variable

$$\Delta X = 2\left|\frac{(p_z(\ell_1) + p_z(\ell_2))}{\sqrt{s}}\right| \tag{4}$$

was defined in Ref. [119], and it is an estimator of the boost. The second difference implies a higher $E_{\mathrm{T}}^{\mathrm{miss}}$ for signal events. This is exploited by making use of

$$R_2 = \frac{E_{\mathrm{T}}^{\mathrm{miss}}}{E_{\mathrm{T}}^{\mathrm{miss}} + p_{\mathrm{T}}(\ell_1) + p_{\mathrm{T}}(\ell_2)}. \tag{5}$$

Finally, the variable $\cos\theta_{\mathrm{b}}$, the cosine of the angle between the direction of motion of one of the two leptons and the beam axis in the centre-of-mass frame of the two visible leptons [119], is sensitive to the spin of the produced particles, hence it provides additional rejection power against the WW production process.

A set of seven signal regions were optimised for the discovery of stop pair production, with the stop decaying either as $\tilde{t}_1 \to \tilde{\chi}_1^{\pm}b$ with a branching ratio of 100 % (assuming $m_{\tilde{t}_1} - m_{\tilde{\chi}_1^{\pm}} < 10$ GeV), or as $\tilde{t}_1 \to bW^{(*)}\tilde{\chi}_1^0$. The definitions of the signal regions are shown in Table 4.

Table 4 Summary of signal regions used in the analysis. The upper part of the table shows the preselection requirements

SR	WW-SR1	WW-SR2	WW-SR3	WW-SR4	WW-SR5	WW-SR6	WW-SR7
$p_T(\ell_1)$	>25 GeV						
$p_T(\ell_2)$	>20 GeV						
R_1	$>0.3 + m_{\text{eff}}$ (TeV)						
m_{T2}	>20 GeV						
ΔX	<0.02						
R_2	>0.5						
$\lvert\cos\theta_b\rvert$	<0.8	<0.8	<0.8	–	–	<0.8	–
m_{T2}	<45 GeV	>25, <55 GeV	–	>70 GeV	>90 GeV	>25, <70 GeV	>80 GeV

The background from non-prompt leptons originating from heavy-quark decays or from photon conversions in the signal regions, or from hadrons misidentified as leptons (collectively referred to as fake leptons in the following), is estimated as in Ref. [18].

Specific control regions, whose event yield is expected to be dominated by each of these production processes, are defined and included in the fit to constrain the normalisation parameters. The control region CRT for $t\bar{t}$ production is defined by changing the following selections with respect to the signal regions: $m_{T2} > 35$ GeV, $R_1 < 0.3$. Its purity is 92 %. The CR for WW production (CRW) is defined by $m_{T2} > 35$ GeV, $\Delta X > 0.04$, and has a purity of 72 %. Finally, the CR for Z + jets (CRZ) is defined by $m_{T2} < 20$ GeV, 30 GeV $< m_{\ell\ell} <$ 80 GeV, with a purity of 86 %. The normalisation factors of the WW, $t\bar{t}$, Z + jets production processes (μ_{WW}, $\mu_{t\bar{t}}$ and μ_Z respectively) are determined by a combined profile likelihood fit. When testing the signal-plus-background hypothesis for rejection, the fit takes automatically into account the signal contamination in the control regions. For signal scenarios considering light ($m_{\tilde{t}_1} < 150$ GeV) stops decaying through $\tilde{t}_1 \to bW^{(*)}\tilde{\chi}_1^0$, the signal contamination becomes so large that μ_{WW} becomes unrealistically low. For such cases the fit is performed excluding CRW and taking the normalisation of the WW background from MC simulation.

Systematic uncertainties, affecting both the modelling of the detector response (detector-related systematic uncertainties) and the theoretical prediction of the cross sections and acceptances of the background processes (theory-related systematic uncertainties) affect the predicted rates in the signal regions. Their classification and estimation follows closely those defined in Ref. [18]. A few differences, discussed in the following, exist on the estimation of the theory-related uncertainties. The total uncertainty on the yield of the WW production process is composed of three terms: the uncertainty on the NLO hard-scattering calculation is taken to be the difference between the prediction of POWHEG and aMC@NLO both using PYTHIA for the parton shower; the uncertainty addressing the choice of the parton-shower model is estimated as the difference of the aMC@NLO predictions showered either with HERWIG or PYTHIA; the uncertainty due to the choice of the renormalisation and factorisation scale is evaluated by changing the scales independently by a factor of two or one-half and taking the maximum difference. The estimated relative uncertainties on the signal region yields are about 6 % in SR1–SR4 and SR6; 11 % in SR7 and 29 % in SR5. Similar comparisons performed on the WZ and ZZ process yield uncertainties ranging from 30 to 45 % depending on the signal region considered. Additional systematic uncertainties are assigned to the small expected yields from Z + jets production (80 %), Wt (50–100 % depending on the SR considered), and non-prompt lepton background.

Table 5 Normalisation factors for the $t\bar{t}$, WW and Z + jets background processes obtained by the combined fit to the control region yields. The uncertainties include systematic and statistical uncertainties

Normalisation factor	Value
$\mu_{t\bar{t}}$	0.94 ± 0.05
μ_{WW}	1.01 ± 0.11
μ_Z	0.95 ± 0.62

The values of the normalisation factors obtained when performing the fit to the control regions only are shown in Table 5.

The overall predictions of the fit are compared to the data in dedicated validation region that are kinematically close to the signal region. They are defined by applying the preselection requirements of Table 4 with the additional selections shown in Table 6. The m_{T2} distribution in WW-VR2 and WW-VRT is shown in Fig. 17.

For all signal regions, the expected background yield is dominated by production of WW (35 % in SR1 to 66 % in SR4). Other important background processes are Z + jets in SR1 (20 %), non-prompt leptons in SR2 (12 %), $t\bar{t}$ in all other SR, with contributions of about 10 %. The distributions of E_T^{miss} and m_{T2} in the signal region WW-SR3 are shown in Fig. 18.

Table 6 Summary of the validation regions used in the WW analysis. The preselection requirements of Table 4 are also applied in all three validation regions

WW-VR1	WW-VR2	WW-VRT
–	–	$0.3 < R_1 < 0.3 + m_{\text{eff}}$ (TeV)
$0.02 < \lvert\Delta X\rvert < 0.04$	$\Delta X < 0.02$	$\Delta X < 0.02$
$R_2 > 0.5$	$R_2 < 0.5$	$R_2 > 0.5$
$\lvert\cos\theta_b\rvert < 0.8$	$\lvert\cos\theta_b\rvert < 0.8$	$\lvert\cos\theta_b\rvert < 0.8$

Table 7 compares the predicted and observed numbers of events in each of the signal regions. No excess above the SM prediction is observed, hence the results are first used to derive model-independent 95 % CL exclusion limits on the minimum number of events beyond the Standard Model in the signal region assuming no signal contamination in the control regions, and then to extract limits on $\sigma_{\text{vis}} = \sigma \times \epsilon \times \mathcal{A}$, where σ is the cross section for non-SM processes, ϵ is the selection efficiency and $\mathcal{A}$ is the selection acceptance. These limits are also reported in Table 7. Finally, 95 % CL exclusion limits are derived in specific supersymmetric models of direct pair production of stops. The first exclusion limit (Fig. 19a) is derived in a model where the stop is assumed to decay as $\tilde{t}_1 \to b\tilde{\chi}_1^{\pm}$ with a branching ratio of 100 %, followed by the decay of the chargino into the neutralino, assumed to be the stable LSP, through $\tilde{\chi}_1^{\pm} \to W^{(*)}\tilde{\chi}_1^0$. The chargino mass is assumed to satisfy the relation $m_{\tilde{\chi}_1^{\pm}} = m_{\tilde{t}_1} - 10$ GeV, and the limit is derived in the $m_{\tilde{t}_1}$–$m_{\tilde{\chi}_1^0}$ plane. Stop masses up to about 250 GeV are excluded, almost independently of the neutralino mass. The second limit is derived in a model where the $\tilde{t}_1$ decays through its three-body or four-body decay (depending on its mass and on that of the neutralino) into $\tilde{t}_1 \to b\ell\nu\tilde{\chi}_1^0$ with a branching ratio of 100 %, under the assumption that the decay happens through an off-shell top quark and an on- or off-shell W boson. The limit is shown in Fig. 19b and fills a gap between the exclusions of the t2L and t1L analyses.

B.2.2 Final states containing two top quarks and a Higgs boson (t2t1h)

If the lightest stop has a mass such that $\Delta m(\tilde{t}_1, \tilde{\chi}_1^0) \sim m_t$, the sensitivity of the searches for the production of a $\tilde{t}_1$ pair is greatly reduced. One of the approaches followed is to search for direct pair production of $\tilde{t}_2$ instead. This is the strategy used, for example, by the t2t1Z analysis, whose signal regions were optimised to detect the decay of a pair-produced $\tilde{t}_2$ followed by the decay $\tilde{t}_2 \to Z\tilde{t}_1$.

Inspired by the search for a SM Higgs boson produced in association with a top quark pair, a search was developed and optimised for the decay $\tilde{t}_2 \to h\tilde{t}_1$, where the Higgs boson is assumed to have SM properties, and the $\tilde{t}_1$ is assumed to decay as $\tilde{t}_1 \to t\tilde{\chi}_1^0$ with a BR of 100 %. The final state is hence characterised by a large jet multiplicity, by the presence of many b-jets from the top quark and Higgs boson decays and by $E_{\text{T}}^{\text{miss}}$ associated with the presence of neutrinos from semileptonic decays of the top quark and of neutralinos.

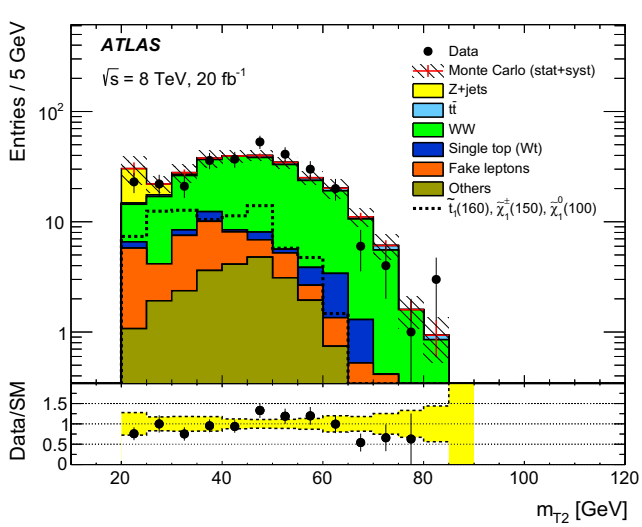

(a)

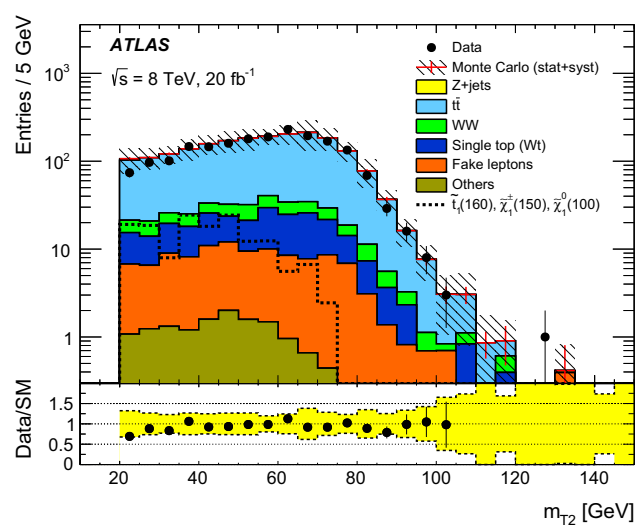

(b)

Fig. 17 Distribution of the stransverse mass m_{T2} in the **a** WW-VR2 and **b** WW-VRT regions defined in the text. The contributions from all SM processes are shown as a *histogram stack*. The component labelled as "Fake leptons" includes the estimate of the background from non-prompt leptons. The expected signal for a model of stop pair production with the stop decaying as $\tilde{t}_1 \to b\tilde{\chi}_1^{\pm} \to b\ell^{\pm}\nu\tilde{\chi}_1^0$ with $m_{\tilde{t}_1} = 160$ GeV, $m_{\tilde{\chi}_1^{\pm}} = 150$ GeV and $m_{\tilde{\chi}_1^0} = 100$ GeV is also shown. The *lower panels* show the ratio between the data and the SM prediction; the *yellow band* includes statistical and systematic uncertainties on the SM prediction

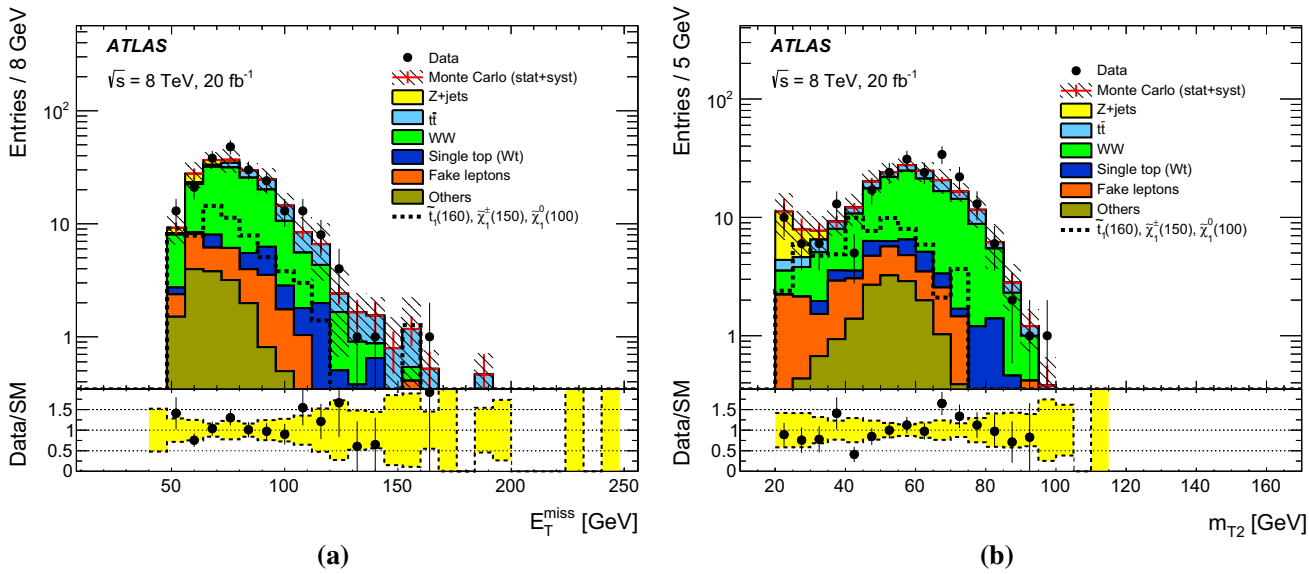

(a) (b)

Fig. 18 Distribution of the **a** magnitude of missing transverse momentum $E_{\mathrm{T}}^{\mathrm{miss}}$ and **b** stransverse mass m_{T2} in WW-SR3. The contributions from all SM processes are shown as a *histogram stack*. The component labelled as "Fake leptons" includes the estimate of the background from non-prompt leptons. The expected signal for a model of stop pair production with the stop decaying into $\tilde{t}_1 \rightarrow b\tilde{\chi}_1^{\pm} \rightarrow b\ell^{\pm}\nu\tilde{\chi}_1^0$ with $m_{\tilde{t}_1} = 160$ GeV, $m_{\tilde{\chi}_1^{\pm}} = 150$ GeV and $m_{\tilde{\chi}_1^0} = 100$ GeV is also shown. The *lower panels* show the ratio between the data and the SM prediction; the *yellow band* includes statistical and systematic uncertainties on the SM prediction

Table 7 Observed (Obs) and predicted (Exp) numbers of events in the signal regions of the WW analysis, together with the 95 % CL upper limits on the observed and expected number of signal events (S_{obs}^{95} and S_{exp}^{95}, respectively), and on the visible cross section ($\langle\epsilon\sigma\rangle_{\mathrm{obs}}^{95}$)

Signal channel	Obs	Exp	S_{obs}^{95}	S_{exp}^{95}	$\langle\epsilon\sigma\rangle_{\mathrm{obs}}^{95}$(fb)
SR1	40	47 ± 14	22.6	$25.2^{+9.4}_{-4.3}$	1.12
SR2	71	80 ± 13	25.3	$27.8^{+11.5}_{-4.1}$	1.24
SR3	215	203 ± 27	48.4	$46.6^{+4.9}_{-6.9}$	2.38
SR4	88	81 ± 11	35.1	$28.8^{+11.0}_{-5.4}$	1.73
SR5	4	3.4 ± 0.9	6.2	$5.7^{+2.1}_{-1.4}$	0.30
SR6	160	154 ± 19	45.6	$43.8^{+19.3}_{-14.4}$	2.25
SR7	21	23 ± 4	12.4	$13.4^{+4.8}_{-3.4}$	0.61

The selection of electrons, muons, jets and b-jets follows the principles outlined in Appendix A. The specific choices made for the p_{T} and pseudorapidity thresholds and working points of the final-state objects, as well as the trigger selection, are the same as those in Ref. [120]. The selection requires the presence of exactly one electron or muon with $p_{\mathrm{T}} > 25$ GeV, $E_{\mathrm{T}}^{\mathrm{miss}} > 50$ GeV, at least six jets with $p_{\mathrm{T}} > 25$ GeV and $|\eta| < 2.5$, of which at least two are required to be b-tagged. The working point chosen for the b-tagging is such that the efficiency to tag b-jets (evaluated on a MC sample of $t\bar{t}$ production) is about 70 %.

The modelling of the production of $t\bar{t}$ pairs in association with heavy flavour ($t\bar{t}$+HF) is of key relevance in this analysis. A detailed categorisation of $t\bar{t}$+HF is made for the purpose of comparisons with different generators and of the propagation of systematic uncertainties on the different heavy-flavour components. The categorisation is also used to reweight the different flavour components of the $t\bar{t}$+jets background to obtain a better modelling. These categorisation and reweighting procedures are discussed in detail in Ref. [120]. In particular, the $t\bar{t} + b\bar{b}$ component, which is simulated with POWHEG, is reweighted to a full NLO calculation [121] performed in SHERPA 1.4.1+OpenLoops [122,123]. The reweighting is done at generator level using a number of kinematic variables such as the top quark p_{T}, $t\bar{t}$ system p_{T}, ΔR and p_{T} of the dijet system not coming from the top-quark decay. A different reweighting is applied to the $t\bar{t} + c\bar{c}$ and $t\bar{t}$+ light-jets components, which is based on the ratio of the differential cross sections at $\sqrt{s} = 7$ TeV obtained in data and simulation as a function of the top quark p_{T} and $t\bar{t}$ system p_{T} [124].

The selected events are categorised into different channels, depending on the number of b-tagged jets (two,

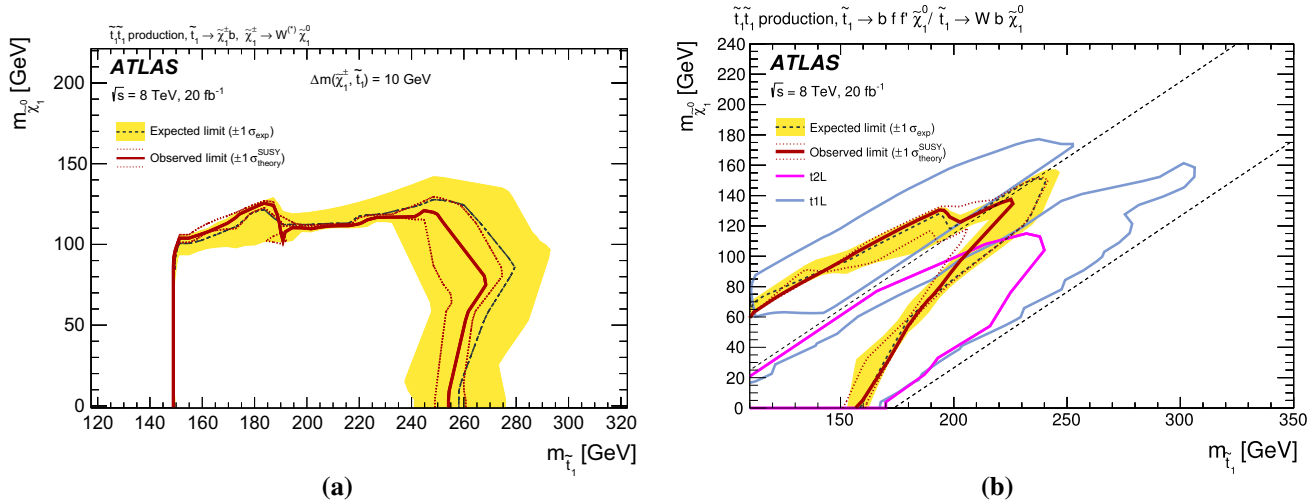

Fig. 19 Exclusion limits at 95 % CL in the scenario where both pair-produced stop decay exclusively via **a** $\tilde{t}_1 \rightarrow b\tilde{\chi}_1^{\pm}$ followed by $\tilde{\chi}_1^{\pm} \rightarrow W\tilde{\chi}_1^0$, with $\Delta m(\tilde{t}_1, \tilde{\chi}_1^{\pm}) = 10$ GeV, and **b** three-body or four-body decay (depending on the neutralino and stop mass). The *black dashed line* indicates the expected limit, and the *yellow band* indicates the $\pm 1\sigma$ uncertainties, which include all uncertainties except the theoretical uncertainties in the signal. The *red solid line* indicates the observed limit, and the *red dotted lines* indicate the sensitivity to $\pm 1\sigma$ variations of the signal theoretical uncertainties. For **b**, the observed limits achieved by the t1L and t2L analyses are also shown, and the *straight dashed lines* correspond to $\Delta m(\tilde{t}_1, \tilde{\chi}_1^0) = m_W + m_b$ and $\Delta m(\tilde{t}_1, \tilde{\chi}_1^0) = m_t$

three or at least four). The channel with at least four b-jets has the largest signal-to-background ratio. The channels with two and three b-tagged jets are used to calibrate the $t\bar{t}$+jets background prediction and constrain the associated systematic uncertainties, which, in the channel with at least four b-tagged jets, are dominated by the b-tagging, jet energy scale, and $t\bar{t}$+jets heavy-flavour content uncertainties.

For a given b-tag multiplicity, events are further categorised depending on the value of the transverse mass m_{T} of the lepton and the missing transverse momentum. A "low-m_{T}" ("high-m_{T}") region is defined by the requirement $m_{\mathrm{T}} < 120$ GeV ($m_{\mathrm{T}} > 120$ GeV).

The final discriminating variable used is $H_{\mathrm{T}}^{\mathrm{nolep}}$, defined as the scalar sum of $E_{\mathrm{T}}^{\mathrm{miss}}$ and the transverse momenta of all selected jets. The signal is searched for by performing a binned likelihood fit to the $H_{\mathrm{T}}^{\mathrm{nolep}}$ distribution simultaneously in the six channels defined (low/high-m_{T} for three bins in b-tagged jet multiplicity). The binning used for the $H_{\mathrm{T}}^{\mathrm{nolep}}$ distributions is that used in Fig. 20, where the background estimate both before and after the fit is compared to the data in the high-m_{T} region. The dominant post-fit uncertainties are those on the absolute normalisation of the $t\bar{t} + b\bar{b}$ and $t\bar{t} + c\bar{c}$ processes.

The full list of detector systematic uncertainties considered, discussed in detail in Ref. [120], includes, beside a total uncertainty of 2.8 % on the integrated luminosity, systematic uncertainties on the identification efficiency and energy scale uncertainty of the leptons, reconstruction efficiency and energy scale and resolution uncertainties for jets, b-tagging efficiency and mis-tag rate uncertainties. Further modelling uncertainties are considered, which include, beside production cross-section uncertainties for W/Z+jets, single top and $t\bar{t}$, dedicated uncertainties on the NLO calculation of the $t\bar{t}+b\bar{b}$ process and on the modelling of the $t\bar{t}+c\bar{c}$ component.

No significant excess above the expected background is observed, hence 95 % CL limits are derived in a model where $\tilde{t}_2$ production is assumed, followed by the decay $\tilde{t}_2 \rightarrow \tilde{t}_1 h$ (with a branching ratio of 100 %) and $\tilde{t}_1 \rightarrow t\tilde{\chi}_1^0$ (again with a branching fraction of 100 %).[14] The limit is derived as a function of the $\tilde{t}_2$ and $\tilde{\chi}_1^0$ masses, under the assumption that $\Delta m(\tilde{t}_1, \tilde{\chi}_1^0) = 180$ GeV, and it is presented in Sect. 4.3.

B.2.3 Final states containing two b-jets, a charged lepton, and missing transverse momentum (tb)

Several phenomenological models, where both $\tilde{\chi}_1^{\pm}$ and $\tilde{\chi}_1^0$ are lighter than the stop (or the sbottom), allow for the $\tilde{t}_1 \rightarrow t\tilde{\chi}_1^0$, $\tilde{t}_1 \rightarrow b\tilde{\chi}_1^{\pm}$ and $\tilde{b}_1 \rightarrow b\tilde{\chi}_1^0$, $\tilde{b}_1 \rightarrow t\tilde{\chi}_1^{\pm}$ decay channels to be open with competing branching ratios. Naturalness arguments require the higgsino mass parameter μ to be smaller than a few hundred GeV, while they impose virtually no constraint on the bino and wino mass parameters M_1 and M_2. If $\mu \ll M_1, M_2$, then the lightest chargino and neutralino masses are both of the order of μ and hence $\Delta m(\tilde{\chi}_1^{\pm}, \tilde{\chi}_1^0)$ is small. Therefore, pair production of stops can lead to

[14] Production of $\tilde{t}_1$ pairs is also included in the simplified models. The acceptance of the selection for such events is very small. Nevertheless, this component is considered as signal in the statistical analysis.

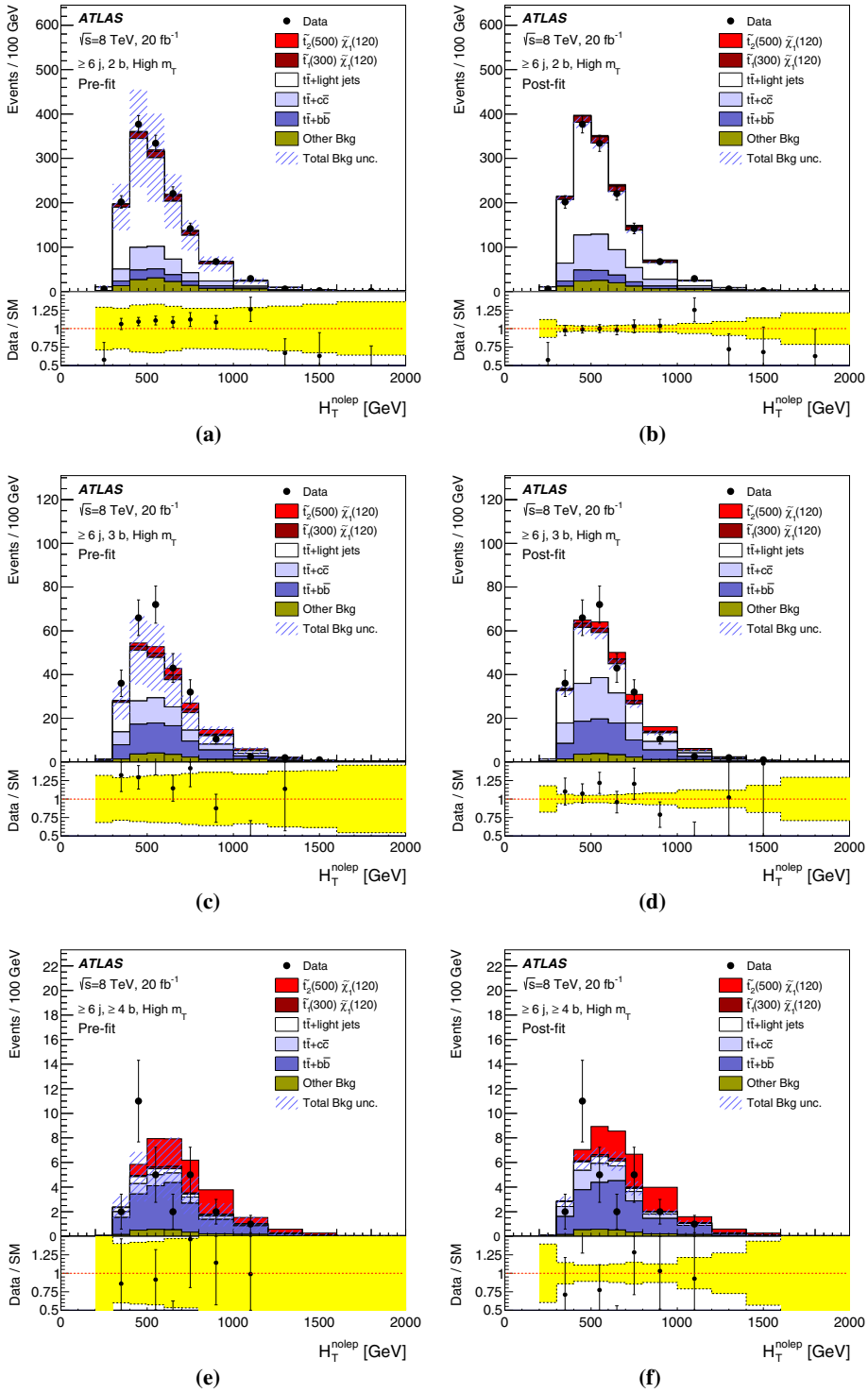

Fig. 20 Comparison between data and prediction for the distribution of $H_{\mathrm{T}}^{\mathrm{nolep}}$, defined as the scalar sum of the missing transverse momentum and the transverse momenta of all selected jets, in the high-m_{T} channels considered: (*top*) two b-tagged jets, (*middle*) three b-tagged jets and (*bottom*) four b-tagged jets, (*left*) before and (*right*) after the combined fit to data under the background-only hypothesis. The expected signal contributions from $\tilde{t}_1$ and $\tilde{t}_2$ pair production, assuming $m_{\tilde{t}_2} = 500$ GeV, $m_{\tilde{t}_1} = 300$ GeV, $m_{\tilde{\chi}_1^0} = 120$ GeV and a branching ratio of 100 % for $\tilde{t}_2 \to h\tilde{t}_1$ are also shown added to the stack (*red histograms*, in *dark* red the contribution from direct $\tilde{t}_1$ pair production). The *bottom panel* displays the ratio of the data to the total background prediction. The *hashed area* represents the statistical and systematics uncertainty on the background

$\tilde{t}_1\tilde{t}_1 \to t\tilde{\chi}_1^0 b\tilde{\chi}_1^{\pm} \to tb\tilde{\chi}_1^0\tilde{\chi}_1^0 ff'$, where f and f' represents low-p_{T} fermions emitted through $\tilde{\chi}_1^{\pm} \to ff'\tilde{\chi}_1^0$. Assuming both f and f' are too soft to be detected, the final state is characterised by the presence of a top quark, a bottom quark, and neutralinos escaping the detector. Similarly, $\tilde{b}_1$ pair production can lead to the same final state. Dedicated SRs are defined that target this topology, which is not well covered by the t0L and t1L signal regions aimed at final states containing $t\bar{t}E_{\mathrm{T}}^{\mathrm{miss}}$ and the b0L signal regions targeting $b\bar{b}E_{\mathrm{T}}^{\mathrm{miss}}$ final states.

Both the leptonic and hadronic decays of the top quark have been studied, and the leptonic channel was found to give a better sensitivity to the signal models of interest. The dominant SM background processes in the signal regions are

Table 8 Summary of signal regions used by the tb analysis

SR	tb-SRIn1	tb-SRIn2	tb-SRIn3	tb-SREx1
b-jets	2 b-jets; p_{T} >25 GeV			
1 lepton	p_{T} >25 GeV			
	$\lvert\eta\rvert < 2.5$ (2.47) for μ (e)			
$E_{\mathrm{T}}^{\mathrm{miss}}$ (GeV)	>200	>120	>220	>160
m_{T} (GeV)	>140	>140	>180	>120
m_{eff} (GeV)	>300	>450	>650	>300
am_{T2} (GeV)	>180	>200	>180	>180
$m_{b\ell}^{\mathrm{min}}$ (GeV)	<170			
$\Delta\phi_{\mathrm{min}}^{b}$	>0.4			
$E_{\mathrm{T}}^{\mathrm{miss}}$ significance (GeV$^{1/2}$)	>8	>12	>5	>10
N_{xjets}	–	–	–	<2

semileptonic $t\bar{t}$ and single top production. The SM background is evaluated using a combination of Monte Carlo and partially data-driven techniques.

Events are selected online by a trigger requiring the presence of one electron or muon. The online selection thresholds are such that the plateau efficiency is reached for lepton transverse momenta of 25 GeV.

The identification criteria for electrons, muons, jets and $E_{\mathrm{T}}^{\mathrm{miss}}$ follow the principles outlined in Appendix A. In particular, electrons and muons are required to be isolated: the scalar p_{T} sum of tracks in a cone $\Delta R = 0.2$ around the electron (muon) is required to be smaller than 10 % of the electron transverse momentum (1.2 GeV). The electron or muon track is excluded from the sum. The b-tagging algorithm is used at an operating point with 70 % efficiency in simulated top-quark pair production events. Signal regions are defined as detailed in Table 8, requiring one and only one electron or muon, two b-tagged jets and a large $E_{\mathrm{T}}^{\mathrm{miss}}$. Three of the SRs, labelled tb–SRin have no additional jet veto applied, while one of them (tb-SREx1) has a veto requirement on the number of jets (N_{xjets}) with p_{T} >50 GeV in addition to the two leading b-tagged jets. The final SR optimisation is performed by using selections on the momenta of the objects, the m_{T} and the m_{eff} variables. In addition, the following kinematic variables are used in the event selection:

- $\Delta\phi_{\mathrm{min}}^{b}$: the minimum azimuthal distance between the closest b-tagged jet and the $E_{\mathrm{T}}^{\mathrm{miss}}$. This variable is used to remove multijet backgrounds with a cut of $\Delta\phi_{\mathrm{min}}^{b} > 0.4$.
- m_{eff}: the scalar sum of the p_{T} of the two b-jets (with $p_{\mathrm{T}} > 25$ GeV and $\lvert\eta\rvert < 2.8$) plus at most one light jet (with $p_{\mathrm{T}} > 25$ GeV and $\lvert\eta\rvert < 2.5$) and the $E_{\mathrm{T}}^{\mathrm{miss}}$. The number of light jets, n, included in this sum depends on the signal region under study, although $n = 1$ was mostly used.
- $E_{\mathrm{T}}^{\mathrm{miss}}$ significance: the ratio of the $E_{\mathrm{T}}^{\mathrm{miss}}$ to the square root of H_{T}, which is the scalar sum of the p_{T} of the two b-jets plus one light jet with $p_{\mathrm{T}} > 25$ GeV and $\lvert\eta\rvert < 2.8$.
- m_{T}: the transverse mass of the lepton and the missing transverse momentum vector.
- m_{bb}: the invariant mass of the two b-tagged jets.
- $m_{b\ell}$: the invariant mass of a b-tagged jet and the charged lepton. This variable is bounded from above at m_t in $t\bar{t}$ production events. Since two jets are b-tagged the variables $m_{b\ell}$ (1) and $m_{b\ell}$ (2) are defined to indicate the invariant mass constructed with the leading and subleading b-jet respectively. The variable $m_{b\ell}^{\mathrm{min}}$ is also defined to indicate the minimum between $m_{b\ell}$ (1) and $m_{b\ell}$ (2).
- am_{T2}: the asymmetric stransverse mass [108] is a kinematic variable which can be used to separate processes in which two decays giving missing transverse momentum occur. It is defined as follows:

$$am_{\mathrm{T2}}^{2}(\chi) = \min_{\not{\mathbf{q}}_{\mathrm{T}}^{(1)}+\not{\mathbf{q}}_{\mathrm{T}}^{(2)}=\not{\mathbf{p}}_{\mathrm{T}}} \times [\max\{m_{\mathrm{T}}^{2}(\mathbf{p}_{\mathrm{T}}(v_1), \not{\mathbf{q}}_{\mathrm{T}}{}^{(1)}; \chi), m_{\mathrm{T}}^{2}(\mathbf{p}_{\mathrm{T}}(v_2), \not{\mathbf{q}}_{\mathrm{T}}^{(2)}; \chi)\}] \quad (6)$$

where $\mathbf{p}_{\mathrm{T}}(v_i)$ are reconstructed transverse momentum vectors, $\not{\mathbf{q}}_{\mathrm{T}}^{(i)}$ represent the missing transverse momenta from the two decays, with a total missing transverse momentum, $\not{\mathbf{p}}_{\mathrm{T}}$, and χ is a free parameter representing the unknown neutralino mass, which is assumed to be zero in the calculation. The am_{T2} variable is calculated with different choices for $\mathbf{p}_{\mathrm{T}}(v_1)$ and $\mathbf{p}_{\mathrm{T}}(v_2)$, depending on the value of $m_{b\ell}$ (n) ($n = 1, 2$), the invariant mass of the nth b-tagged jet b_n and the lepton:

  - if $m_{b\ell}(i) < 170$ GeV and $m_{b\ell}(j) > 170$ GeV, then am_{T2} is calculated with $v_1 = b_i + \ell$ and $v_2 = b_j$;
  - if $m_{b\ell}(1) < 170$ GeV and $m_{b\ell}(2) < 170$ GeV, then am_{T2} is evaluated using the two possible combinations for v_1 and v_2, and the minimum is used;

– it both $m_{b\ell}(1) > 170$ GeV and $m_{b\ell}(2) > 170$ GeV the event is rejected.

The case of both $m_{b\ell}$ (1) and $m_{b\ell}$ (2) exceeding 170 GeV is irrelevant: only events with the minimum value of $m_{b\ell}$ smaller than 170 GeV populate the control, validation and signal regions.

The optimisation is carried out using both a pMSSM signal model and simplified models where $\Delta m(\tilde{\chi}_1^{\pm}, \tilde{\chi}_1^0) = 5$ or 10 GeV. In the case of the pMSSM model, additional non-b-tagged jets are expected in the final state via the production of other SUSY particles, hence the optimisation points to SRs with no requirement on the N_{xjets} variable (tb-SRIn). In the case of the simplified models, additional jets come only from initial- or final-state radiation, and as a consequence a strict selection on N_{xjets} is applied as in the selection tb-SREx1.

The main SM backgrounds are top-pair production, W production in association with heavy-flavour jets and single-top production. The MC cross section is used to normalise the single-top background and all the other minor SM backgrounds, such as Z+jets, diboson production, $t\bar{t}$+W and $t\bar{t}$+Z. The normalisation factors of the $t\bar{t}$ and W + jets backgrounds are determined by a combined profile-likelihood fit. Specific control regions, whose event yield is expected to be dominated by each of these production processes, are defined and included in the fit to constrain the normalisation parameters. The $t\bar{t}$ control regions (CRT) are defined by inverting the selection on am_{T2}, requiring am_{T2} <160 (180) GeV for the inclusive (exclusive) SRs. The purity of the $t\bar{t}$ process in the CRTs is in excess of 95 %. The W + jets control regions (CRW) are defined by requiring m_{T} <120 GeV. For the control regions corresponding to the tb-SRIn, events with one b-tagged jet are included in the CRW. Top quark pair production dominates the CRWs, with a W + jets purity of 30 % or better. The normalisation factors μ_W and $\mu_{t\bar{t}}$ are presented in Table 9. The background model is then validated using validation regions, where little signal contamination is expected.

The distributions of the variable am_{T2} in the four SRs are shown in Fig. 21 together with the expected distribution from some of the signal models used to optimise the analysis. Table 10 compares the predicted and observed numbers of events in each of the signal regions. No excess above the SM prediction is observed, hence the results are first used to derive model-independent 95 % CL exclusion limits on the number of events beyond the Standard Model in the signal region, and then to extract limits on $\sigma_{\text{vis}} = \sigma \times \epsilon \times \mathcal{A}$, where σ is the cross section for non-SM processes, ϵ is the selection efficiency and $\mathcal{A}$ is the selection acceptance. All these limits are also reported in Table 10.

Since the number of events observed agrees with the SM predictions, 95 % CL exclusion limits are derived in specific supersymmetric models of direct pair production of stops. Simplified models were simulated with the two decays $\tilde{t}_1 \to t\tilde{\chi}_1^0, \tilde{t}_1 \to b\tilde{\chi}_1^{\pm}$ each having a 50 % BR for values of $\Delta m(\tilde{\chi}_1^{\pm}, \tilde{\chi}_1^0) = 5, 20$ GeV. Furthermore, by using a weighted combination of these simplified models with models corresponding to a 100 % BR in either $\tilde{t}_1 \to t\tilde{\chi}_1^0$ or $\tilde{t}_1 \to b\tilde{\chi}_1^{\pm}$, limits can be obtained for any value of the stop BR. Figure 22 shows the exclusion limits for BR($\tilde{t}_1 \to t\tilde{\chi}_1^0$) = 25, 50 and 75 % for the two values of $\Delta m(\tilde{\chi}_1^{\pm}, \tilde{\chi}_1^0)$ considered.

Finally, 95 % CL exclusion limits are also derived for a natural pMSSM model and are presented in Fig. 23

Table 9 Background scale factors for the $t\bar{t}$and W samples, as obtained by the background fit. The errors include both the statistical and systematics uncertainties

Norm. factor	SRinA	SRinB	SRinC	SRexA
$\mu_{t\bar{t}}$	1.06 ± 0.07	1.12 ± 0.09	0.94 ± 0.21	1.06 ± 0.07
μ_W	0.92 ± 0.20	0.61 ± 0.23	0.93 ± 0.27	1.10 ± 0.34

C Further details of the statistical combination of the t0L and t1L signal regions

This section provides additional details on the combination of the t0L and t1L signal regions targeting scenarios in which the stop decays into either $\tilde{t}_1 \to t\tilde{\chi}_1^0$ or the mixed case where $\tilde{t}_1 \to t\tilde{\chi}_1^0$ and $\tilde{t}_1 \to b\tilde{\chi}_1^{\pm}$ are both allowed, as discussed in Sect. 4.1

The statistical combination of the two analyses is performed by running the combined fit simultaneously on the control and signal regions of the two analyses. The detector systematic uncertainties are treated as correlated by using, for each of the uncertainties considered, a single nuisance parameter. The supersymmetric signal parameter strength used is the same for the two analyses, while the normalisation parameters for the background processes are kept independent in each analysis.[15] The nuisance parameters associated with modelling uncertainties of the various processes are also kept independent.

The control regions of the two analyses are not mutually exclusive: the events that belong to both a CR of t0L and one of t1L are, at most about 2 % of the total number of events of the t0L CR. The strategy adopted is to remove them from the corresponding t0L CR for the combination. It has been verified that such removal does not affect the individual results of the t0L analysis.

[15] The choice is motivated by the fact that the phase-space regions in which the two analyses determine the normalisation parameters of the $t\bar{t}$, Z + jets and W + jets (for t0L) and $t\bar{t}$ and W + jets (for t1L) are characterised by different kinematic selections and jet multiplicities.

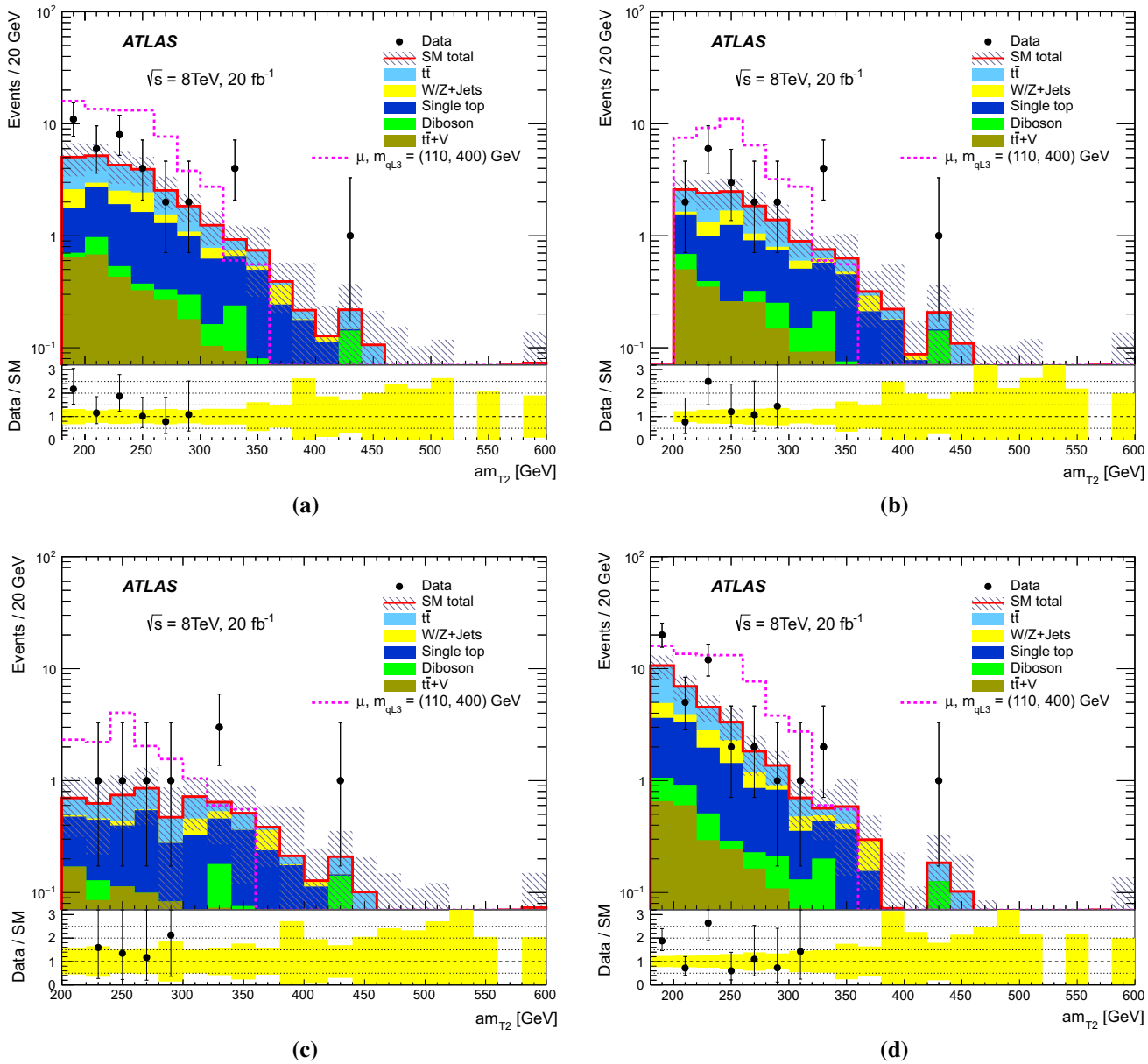

Fig. 21 Distribution of the asymmetric stransverse mass am_{T2} in the **a** SRinA, **b** SRinB (*top right*), **c** SRinC and **d** SRexA defined in the text. The contributions from all SM processes are shown as a *histogram stack*. The contribution from signal points studied by this analysis are also shown. The *lower panels* show the ratio between the data and the SM prediction; the band includes statistical and systematic uncertainties on the SM prediction

Table 10 Observed (Obs) and predicted (Exp) numbers of events in the signal regions of the tb analysis, together with the 95 % CL upper limits on the observed and expected number of signal events (S^{95}_{obs} and S^{95}_{exp} respectively), and on the visible cross section ($\langle\epsilon\sigma\rangle^{95}_{\mathrm{obs}}$)

Signal channel	Obs	Exp	S^{95}_{obs}	S^{95}_{exp}	$\langle\epsilon\sigma\rangle^{95}_{\mathrm{obs}}$ (fb)
SRinA	38	27 ± 7	28.5	$19.3^{+7.0}_{-6.1}$	1.41
SRinB	20	14.1 ± 2.8	16.3	$10.7^{+4.5}_{-2.6}$	0.81
SRinC	10	7.1 ± 2.9	11.9	$9.8^{+3.3}_{-2.4}$	0.58
SRexA	46	31 ± 7	32.1	$20.3^{+8.0}_{-3.6}$	1.58

For each combination performed, the fit setup is validated by checking that the background normalisation parameters obtained are compatible with those obtained separately by the two analyses, by verifying that no additional constraint on the nuisance parameters is introduced with respect to the individual fits, and by checking that no artificial correlation is introduced between any of the fit parameters.

The 95 % CL limit derived from the combination is shown in Fig. 24, where the combined limit is compared to the individual limits obtained by the t0L and t1L analyses independently.

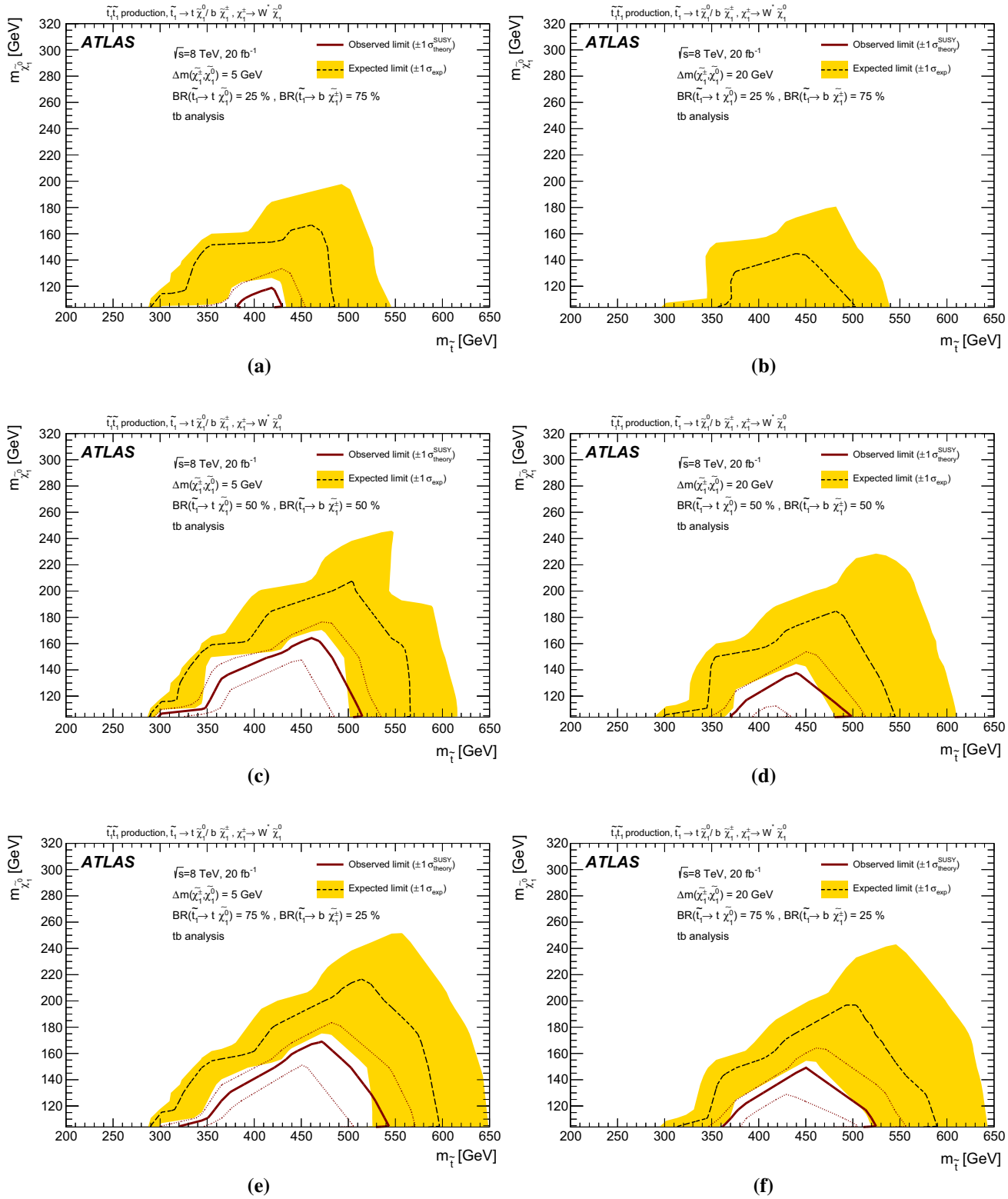

Fig. 22 Exclusion limits at 95 % CL from the tb signal regions for simplified models with stop decays into both $\tilde{t}_1 \rightarrow t\tilde{\chi}_1^0$ and $\tilde{t}_1 \rightarrow b\tilde{\chi}_1^{\pm}$ and for $\mathrm{BR}(\tilde{t}_1 \rightarrow t\tilde{\chi}_1^0) = 25, 50, 75$ % (in *descending rows*) for the grids $\Delta m(\tilde{\chi}_1^{\pm}, \tilde{\chi}_1^0) = 5, 20$ (*left*, *right columns*). The *black dashed line* indicates the expected limit, and the *yellow band* indicates the $\pm 1\sigma$ uncertainties, which include all uncertainties except the theoretical uncertainties in the signal. The *red solid line* indicates the observed limit, and the *red dotted lines* indicate the sensitivity to $\pm 1\sigma$ variations of the signal theoretical uncertainties. For each point the SR giving the best expected significance is used

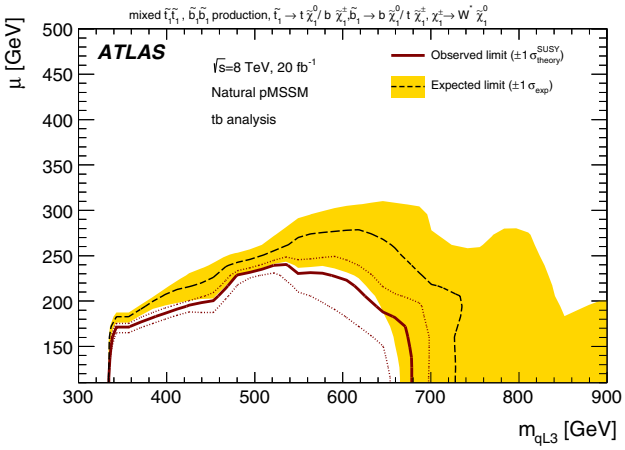

Fig. 23 Exclusion limits at 95 % CL from the tb signal regions for the natural pMSSM model. The *black dashed line* indicates the expected limit, and the *yellow band* indicates the $\pm 1\sigma$ uncertainties, which include all uncertainties except the theoretical uncertainties in the signal. The *red solid line* indicates the observed limit, and the *red dotted lines* indicate the sensitivity to $\pm 1\sigma$ variations of the signal theoretical uncertainties. For each point the SR giving the best expected significance is used

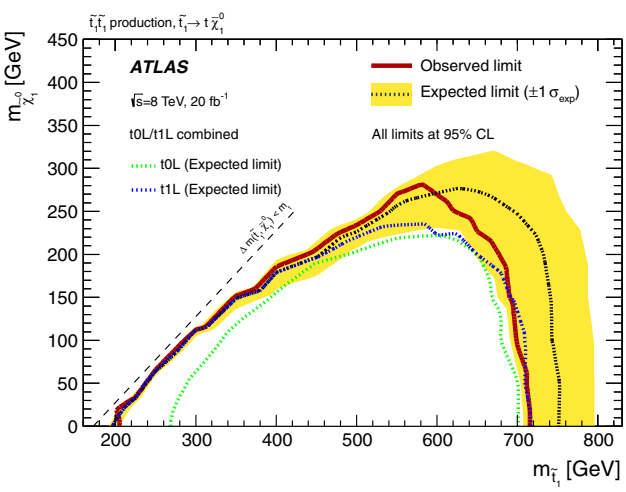

Fig. 24 Combined exclusion limits at 95 % CL in the scenario where both stops decay exclusively via $\tilde{t}_1 \rightarrow t\tilde{\chi}_1^0$. The *black dashed line* indicates the expected limit, and the *yellow band* indicates the $\pm 1\sigma$ uncertainties, which include all uncertainties except the theoretical uncertainties in the signal. The *red solid line* indicates the observed limit. For comparison the *dotted green* and *blue lines* show the expected limits from the standalone t0L and t1L analyses

D Signal generation details

Several SUSY models are considered throughout this paper. This section provides the details of how these signal models are generated. For all SUSY models discussed below, the detector response is simulated by passing the generated events through a detector simulation [125] based on GEANT4 [126] or through a fast simulation using a parametric response to the showers in the electromagnetic and hadronic calorimeters [127] and GEANT4-based simulation elsewhere. All samples are produced with a varying number of simulated minimum-bias interactions overlaid on the hard-scattering event to account for multiple pp interactions in the same or nearby bunch crossings (pileup). The simulation is reweighted to match the number of minimum bias interactions in data, which varies between approximately 10 and 30 interactions in each bunch crossing. Corrections are applied to the simulated samples to account for differences between data and simulation for the trigger and reconstruction efficiencies, momentum scale and resolution of the final-state objects, including the efficiency of identifying jets originating from the fragmentation of b-quarks, together with the probability for mis-tagging light-flavour and charm quarks.

Simplified models The signal samples for the scenario where both stops decay to a top quark and a neutralino are generated using Herwig++ 2.5.2 [128] interfaced to PYTHIA 6.426 [129]. The neutralino is fixed to be a pure bino, enhancing the decay of the $\tilde{t}_R$ component of $\tilde{t}_1$ to a right-handed top quark. Signal samples where the two stops decay as $\tilde{t}_1 \rightarrow b\tilde{\chi}_1^{\pm}$ are generated with MadGraph 5.1.4.8 [130]. For models where the W boson is on-shell, the $\tilde{t}_1$ decay is treated by MadGraph, while if the W is off-shell, PYTHIA is used to decay the $\tilde{t}_1$. In these samples, the $\tilde{t}_1$ is assumed to be mostly a $\tilde{t}_L$, and the chargino is assumed to decay through $\tilde{\chi}_1^{\pm} \rightarrow W^{(*)}b$ with a branching ratio of 100 %. Several assumptions about the chargino masses are considered as described in the body of the paper.

Models in which the stop is assumed to decay either as $\tilde{t}_1 \rightarrow t\tilde{\chi}_1^0$ or $\tilde{t}_1 \rightarrow b\tilde{\chi}_1^{\pm}$ with different branching ratios are obtained by appropriately weighting three samples: one where both stops decay through $\tilde{t}_1 \rightarrow t\tilde{\chi}_1^0$, a second one where both stops decay through $\tilde{t}_1 \rightarrow b\tilde{\chi}_1^{\pm}$, and a third one, where one of the two pair-produced stops decays as $\tilde{t}_1 \rightarrow t\tilde{\chi}_1^0$ and the other one decays as $\tilde{t}_1 \rightarrow b\tilde{\chi}_1^{\pm}$. This last sample is generated with MadGraph, the $\tilde{t}_1$ is assumed to be a maximal mixing of $\tilde{t}_L$ and $\tilde{t}_R$. The mass of the chargino in this sample satisfies the gauge-universality relation $m_{\tilde{\chi}_1^{\pm}} = 2m_{\tilde{\chi}_1^0}$.

The three-body stop decay samples are generated with Herwig++, which performs the matrix element calculation of the three-body decay. The four-body stop decay samples are generated with MadGraph.

For all samples considered, the mass of the bottom quark is fixed to 4.8 GeV and its width is assumed to be zero.

The samples where both stops decay as $\tilde{t}_1 \rightarrow c\tilde{\chi}_1^0$ are generated with MadGraph, with one additional parton from the matrix element. Similarly to the case of the limit derived as a function of the stop branching ratio into $\tilde{t}_1 \rightarrow t\tilde{\chi}_1^0$,

the samples with both stops decaying as $\tilde{t}_1 \rightarrow c\tilde{\chi}_1^0$ and those where both stops decay through the four-body decay are appropriately weighted and combined with a third sample where one stop decays as $\tilde{t}_1 \rightarrow c\tilde{\chi}_1^0$ and the other decays through the four-body decay to produce a sample of arbitrary branching ratio into $\tilde{t}_1 \rightarrow c\tilde{\chi}_1^0$ (assuming that $\tilde{t}_1 \rightarrow c\tilde{\chi}_1^0$ and the four-body decay are the only possible stop decays). Such mixed samples are also generated with MadGraph.

Sbottom pair production samples are also all produced with MadGraph interfaced to PYTHIA, and no more than one additional parton is added to the matrix element. The PDF set used for all signal samples is CTEQ6L1 [131].

pMSSM models In all cases, the particle spectra are generated with SOFTSUSY 3.3.3 [132], while sparticles decays are calculated with SUSY-HIT [133] (SDECAY 1.3b and HDECAY 3.4). The simulated signal events are generated using Herwig++ 2.6.3 [128] with the CTEQ6L1 PDF set.

References

1. H. Miyazawa, Prog. Theor. Phys. **36**(6), 1266–1276 (1966)
2. P. Ramond, Phys. Rev. D **3**, 2415–2418 (1971)
3. Y. Golfand, E. Likhtman, JETP Lett. **13**, 323–326 (1971)
4. A. Neveu, J.H. Schwarz, Nucl. Phys. B **31**, 86–112 (1971)
5. A. Neveu, J.H. Schwarz, Phys. Rev. D **4**, 1109–1111 (1971)
6. J. Gervais, B. Sakita, Nucl. Phys. B **34**, 632–639 (1971)
7. D. Volkov, V. Akulov, Phys. Lett. B **46**, 109–110 (1973)
8. J. Wess, B. Zumino, Phys. Lett. B **49**, 52–54 (1974)
9. J. Wess, B. Zumino, Nucl. Phys. B **70**, 39–50 (1974)
10. S. Weinberg, Phys. Rev. D **13**, 974–996 (1976)
11. E. Gildener, Phys. Rev. D **14**, 1667–1672 (1976)
12. S. Weinberg, Phys. Rev. D **19**, 1277–1280 (1979)
13. L. Susskind, Phys. Rev. D **20**, 2619–2625 (1979)
14. R. Barbieri, G. Giudice, Nucl. Phys. B **306**, 63–76 (1988)
15. B. de Carlos, J. Casas, Phys. Lett. B **309**, 320–328 (1993). arXiv:hep-ph/9303291
16. ATLAS Collaboration, JHEP **09**, 015 (2014). arXiv:1406.1122 [hep-ex]
17. ATLAS Collaboration, JHEP **1411**, 118 (2014). arXiv:1407.0583 [hep-ex]
18. ATLAS Collaboration, JHEP **1406**, 124 (2014). arXiv:1403.4853 [hep-ex]
19. ATLAS Collaboration, Phys. Rev. D **90**(5), 052008 (2014). arXiv:1407.0608 [hep-ex]
20. ATLAS Collaboration, Eur. Phys. J. C **74**, 2883 (2014). arXiv:1403.5222 [hep-ex]
21. ATLAS Collaboration, JHEP **1310**, 189 (2013). arXiv:1308.2631 [hep-ex]
22. ATLAS Collaboration, Phys. Lett. B **715**, 44–60 (2012). arXiv:1204.6736 [hep-ex]
23. ATLAS Collaboration, Phys. Rev. Lett. **109**, 211802 (2012). arXiv:1208.1447 [hep-ex]
24. ATLAS Collaboration, Eur. Phys. J. C **72**, 2237 (2012). arXiv:1208.4305 [hep-ex]
25. ATLAS Collaboration, JHEP **11**, 094 (2012). arXiv:1209.4186 [hep-ex]
26. ATLAS Collaboration, Phys. Lett. B **720**, 13–31 (2013). arXiv:1209.2102 [hep-ex]
27. CMS Collaboration, Phys. Rev. Lett. **111**(8), 081802 (2013). arXiv:1212.6961 [hep-ex]
28. CMS Collaboration, JHEP **01**, 077 (2013). arXiv:1210.8115 [hep-ex]
29. CMS Collaboration, Eur. Phys. J. C **73**, 2568 (2013). arXiv:1303.2985 [hep-ex]
30. CMS Collaboration, Eur. Phys. J. C **73**, 2677 (2013). arXiv:1308.1586 [hep-ex]
31. CMS Collaboration, Phys. Rev. Lett. **112**, 161802 (2014). arXiv:1312.3310 [hep-ex]
32. CMS Collaboration. arXiv:1503.08037 [hep-ex]
33. CMS Collaboration, Phys. Lett. B **736**, 371–397 (2014). arXiv:1405.3886 [hep-ex]
34. CMS Collaboration, Phys. Lett. B **745**, 5–28 (2015). arXiv:1412.4109 [hep-ex]
35. CMS Collaboration, JHEP **1303**, 037 (2013). arXiv:1212.6194 [hep-ex]
36. ATLAS Collaboration, JHEP **1501**, 068 (2015). arXiv:1411.6795 [hep-ex]
37. ATLAS Collaboration, Phys. Rev. D **88**(11), 112003 (2013). arXiv:1310.6584 [hep-ex]
38. P. Fayet, Phys. Lett. B **64**, 159–162 (1976)
39. P. Fayet, Phys. Lett. B **69**, 489–494 (1977)
40. G.R. Farrar, P. Fayet, Phys. Lett. B **76**, 575–579 (1978)
41. P. Fayet, Phys. Lett. B **84**, 416–420 (1979)
42. S. Dimopoulos, H. Georgi, Nucl. Phys. B **193**, 150–162 (1981)
43. W. Beenakker, R. Höpker, M. Spira (1996). arXiv:hep-ph/9611232
44. M. Krämer et al. arXiv:1206.2892 [hep-ph]
45. W. Beenakker et al., Nucl. Phys. B **515**, 3–14 (1998)
46. W. Beenakker et al., JHEP **08**, 098 (2010). arXiv:1006.4771 [hep-ph]
47. W. Beenakker et al., Int. J. Mod. Phys. A **26**, 2637–2664 (2011)
48. R. Grober, M. Muhlleitner, E. Popenda, A. Wlotzka. arXiv:1502.05935 [hep-ph]
49. G. D'Ambrosio, G. Giudice, G. Isidori, A. Strumia, Nucl. Phys. B **645**, 155–187 (2002). arXiv:hep-ph/0207036
50. R. Grober, M. Muhlleitner, E. Popenda, A. Wlotzka. arXiv:1408.4662 [hep-ph]
51. A.H. Chamseddine, R. Arnowitt, P. Nath, Phys. Rev. Lett. **49**, 970 (1982)
52. R. Barbieri, S. Ferrara, C.A. Savoy, Phys. Lett. B **119**, 343 (1982)
53. L.E. Ibanez, Phys. Lett. B **118**, 73 (1982)
54. L.J. Hall, J.D. Lykken, S. Weinberg, Phys. Rev. D **27**, 2359–2378 (1983)
55. N. Ohta, Prog. Theor. Phys. **70**, 542 (1983)
56. G.L. Kane, C.F. Kolda, L. Roszkowski, J.D. Wells, Phys. Rev. D **49**, 6173–6210 (1994)
57. MSSM Working Group Collaboration, A. Djouadi et al. arXiv:hep-ph/9901246
58. M. Baak et al., Eur. Phys. J. C **75**(4), 153 (2015). arXiv:1410.1280 [hep-ex]
59. G. Cowan, K. Cranmer, E. Gross, O. Vitells, Eur. Phys. J. C **71**, 1554 (2011). arXiv:1007.1727 [physics.data-an]
60. T. Junk, Nucl. Instrum. Methods A **434**, 435–443 (1999). arXiv:hep-ex/9902006
61. A.L. Read, J. Phys. G **28**, 2693–2704 (2002)
62. ATLAS Collaboration, JHEP **1410**, 24 (2014). arXiv:1407.0600 [hep-ex]
63. ATLAS Collaboration, JHEP **1406**, 035 (2014). arXiv:1404.2500 [hep-ex]
64. ATLAS Collaboration, Phys. Rev. Lett. **114**(14), 142001 (2015). arXiv:1412.4742 [hep-ex]
65. ATLAS Collaboration, Eur. Phys. J. C **74**(10), 3109 (2014). arXiv:1406.5375 [hep-ex]

66. LEP SUSY Working Group (Aleph, Delphi, L3, Opal), Notes lepsusywg/01-03.1 and 04-02.1. (2004). http://lepsusy.web.cern.ch/lepsusy/. Accessed 20 Oct 2015
67. ALEPH Collaboration, A. Heister et al., Phys. Lett. B **583**, 247–263 (2004)
68. DELPHI Collaboration, J. Abdallah et al., Eur. Phys. J. C **31**, 421–479 (2003). arXiv:hep-ex/0311019
69. L3 Collaboration, M. Acciarri et al., Phys. Lett. B **472**, 420–433 (2000). arXiv:hep-ex/9910007
70. OPAL Collaboration, G. Abbiendi et al., Eur. Phys. J. C **35**, 1–20 (2004). arXiv:hep-ex/0401026
71. M. Ciuchini et al., JHEP **9810**, 008 (1998). arXiv:hep-ph/9808328
72. ATLAS Collaboration, JHEP (2015). arXiv:1508.06608 [hep-ex]
73. ATLAS Collaboration, JHEP **1409**, 176 (2014). arXiv:1405.7875 [hep-ex]
74. ATLAS Collaboration, JHEP **1504**, 116 (2015). arXiv:1501.03555 [hep-ex]
75. ATLAS Collaboration, JHEP **1310**, 130 (2013). arXiv:1308.1841 [hep-ex]
76. ATLAS Collaboration, Phys. Rev. Lett. **114**(16), 161801 (2015). arXiv:1501.01325 [hep-ex]
77. CMS Collaboration, JHEP **1505**, 078 (2015). arXiv:1502.04358 [hep-ex]
78. CMS Collaboration, JHEP **1401**, 163 (2014). arXiv:1311.6736
79. CMS Collaboration, Phys. Rev. D **91**, 052018 (2015). arXiv:1502.00300 [hep-ex]
80. CMS Collaboration, JHEP **1406**, 055 (2014). arXiv:1402.4770 [hep-ex]
81. CMS Collaboration, Phys. Lett. B **733**, 328–353 (2014). arXiv:1311.4937 [hep-ex]
82. CMS Collaboration, Phys. Lett. B **725**, 243–270 (2013). arXiv:1305.2390 [hep-ex]
83. ATLAS Collaboration, JHEP **1411**, 056 (2014). arXiv:1409.6064 [hep-ex]
84. CMS Collaboration, JHEP **1410**, 160 (2014). arXiv:1408.3316 [hep-ex]
85. A. Delgado et al., Eur. Phys. J. C **73**(3), 2370 (2013). arXiv:1212.6847 [hep-ph]
86. M. Papucci, J.T. Ruderman, A. Weiler, JHEP **1209**, 035 (2012). arXiv:1110.6926 [hep-ph]
87. M.W. Cahill-Rowley, J.L. Hewett, A. Ismail, T.G. Rizzo, Phys. Rev. D **86**, 075015 (2012). arXiv:1206.5800 [hep-ph]
88. N. Arkani-Hamed, A. Delgado, G. Giudice, Nucl. Phys. B **741**, 108–130 (2006). arXiv:hep-ph/0601041
89. (2015). https://atlas.web.cern.ch/Atlas/GROUPS/PHYSICS/PAPERS/SUSY-2014-07/hepdata_info.pdf. Accessed 20 Oct 2015
90. The Durham HepData Project (2015). http://hepdata.cedar.ac.uk/view/ins1380183. Accessed 20 Oct 2015
91. ATLAS Collaboration, JINST **3**, S08003 (2008)
92. ATLAS Collaboration, Eur. Phys. J. C **73**, 2518 (2013). arXiv:1302.4393 [hep-ex]
93. ATLAS Collaboration, ATLAS-CONF-2010-069 (2010). http://cdsweb.cern.ch/record/1281344. Accessed 20 Oct 2015
94. W. Lampl et al., ATL-LARG-PUB-2008-002 (2008). http://cdsweb.cern.ch/record/1099735. Accessed 20 Oct 2015
95. M. Cacciari, G.P. Salam, G. Soyez, JHEP **04**, 063 (2008). arXiv:0802.1189 [hep-ph]
96. M. Cacciari, G.P. Salam, Phys. Lett. B **641**, 57–61 (2006). arXiv:hep-ph/0512210
97. M. Cacciari, G.P. Salam, G. Soyez, Eur. Phys. J. C **72**, 1896 (2012). arXiv:1111.6097 [hep-ph]
98. C. Issever, K. Borras, D. Wegener, Nucl. Instrum. Methods A **545**, 803–812 (2005). arXiv:physics/0408129
99. M. Cacciari, G.P. Salam, Phys. Lett. B **659**, 119–126 (2008). arXiv:0707.1378 [hep-ph]
100. ATLAS Collaboration, Eur. Phys. J. C **73**, 2304 (2013). arXiv:1112.6426 [hep-ex]
101. ATLAS Collaboration, ATLAS-CONF-2012-043 (2012). http://cdsweb.cern.ch/record/1435197. Accessed 20 Oct 2015
102. ATLAS Collaboration, ATLAS-CONF-2011-089 (2011). http://cdsweb.cern.ch/record/1356198. Accessed 20 Oct 2015
103. ATLAS Collaboration, ATLAS-CONF-2011-102 (2011). http://cdsweb.cern.ch/record/1369219. Accessed 20 Oct 2015
104. ATLAS Collaboration, Eur. Phys. J. C **72**, 1909 (2012). arXiv:1110.3174 [hep-ex]
105. ATLAS Collaboration, ATLAS-CONF-2011-021 (2011). http://cdsweb.cern.ch/record/1336750. Accessed 20 Oct 2015
106. ATLAS Collaboration, ATLAS-CONF-2011-063 (2011). http://cdsweb.cern.ch/record/1345743. Accessed 20 Oct 2015
107. C. Lester, D. Summers, Phys. Lett. B **463**, 99–103 (1999). arXiv:hep-ph/9906349
108. A. Barr, C. Lester, P. Stephens, J. Phys. G **29**, 2343–2363 (2003). arXiv:hep-ph/0304226
109. M.L. Graesser, J. Shelton, Phys. Rev. Lett. **111**(12), 121802 (2013). arXiv:1212.4495 [hep-ph]
110. D.R. Tovey, JHEP **0804**, 034 (2008). arXiv:0802.2879 [hep-ph]
111. T. Eifert, B. Nachman, Phys. Lett. B **743**, 218–223 (2015). arXiv:1410.7025 [hep-ph]
112. ATLAS Collaboration, Eur. Phys. J. C **75**(7), 330 (2015). arXiv:1503.05427 [hep-ex]
113. ATLAS Collaboration, Phys. Lett. B **712**, 289–308 (2012). arXiv:1203.6232 [hep-ex]
114. CMS Collaboration, Eur. Phys. J. C **73**(10), 2610 (2013). arXiv:1306.1126 [hep-ex]
115. CMS Collaboration, Phys. Lett. B **721**, 190–211 (2013). arXiv:1301.4698 [hep-ex]
116. K. Rolbiecki, K. Sakurai, JHEP **1309**, 004 (2013). arXiv:1303.5696 [hep-ph]
117. J.S. Kim, K. Rolbiecki, K. Sakurai, J. Tattersall, JHEP **1412**, 010 (2014). arXiv:1406.0858 [hep-ph]
118. D. Curtin, P. Meade, P.-J. Tien, Phys. Rev. D **90**(11), 115012 (2014). arXiv:1406.0848 [hep-ph]
119. T. Melia, JHEP **1201**, 143 (2012). arXiv:1110.6185 [hep-ph]
120. ATLAS Collaboration, Eur. Phys. J. C **75**(7), 349 (2015). arXiv:1503.05066 [hep-ex]
121. F. Cascioli et al., Phys. Lett. B **734**, 210–214 (2014). arXiv:1309.5912 [hep-ph]
122. T. Gleisberg et al., JHEP **02**, 007 (2009). arXiv:0811.4622 [hep-ph]
123. F. Cascioli, P. Maierhofer, S. Pozzorini, Phys. Rev. Lett. **108**, 111601 (2012). arXiv:1111.5206 [hep-ph]
124. ATLAS Collaboration, Phys. Rev. D **90**(7), 072004 (2014). arXiv:1407.0371 [hep-ex]
125. ATLAS Collaboration, Eur. Phys. J. C **70**, 823–874 (2010). arXiv:1005.4568 [physics.ins-det]
126. GEANT4 Collaboration, S. Agostinelli et al., Nucl. Instrum. Methods A **506**, 250–303 (2003)
127. ATLAS Collaboration, ATL-PHYS-PUB-2010-013 (2010). http://cdsweb.cern.ch/record/1300517. Accessed 20 Oct 2015
128. M. Bähr et al., Eur. Phys. J. C **58**, 639–707 (2008). arXiv:0803.0883 [hep-ph]
129. T. Sjöstrand, S. Mrenna, P.Z. Skands, JHEP **05**, 026 (2006). arXiv:hep-ph/0603175
130. J. Alwall et al., JHEP **06**, 128 (2011). arXiv:1106.0522 [hep-ph]
131. J. Pumplin et al., JHEP **07**, 012 (2002). arXiv:hep-ph/0201195
132. B. Allanach, Comput. Phys. Commun. **143**, 305–331 (2002). arXiv:hep-ph/0104145
133. A. Djouadi, M.M. Muhlleitner, M. Spira, Acta Phys. Polon. B **38**, 635–644 (2007). arXiv:hep-ph/0609292

ATLAS Collaboration

G. Aad[85], B. Abbott[113], J. Abdallah[151], O. Abdinov[11], R. Aben[107], M. Abolins[90], O. S. AbouZeid[158], H. Abramowicz[153], H. Abreu[152], R. Abreu[116], Y. Abulaiti[146a,146b], B. S. Acharya[164a,164b,a], L. Adamczyk[38a], D. L. Adams[25], J. Adelman[108], S. Adomeit[100], T. Adye[131], A. A. Affolder[74], T. Agatonovic-Jovin[13], J. Agricola[54], J. A. Aguilar-Saavedra[126a,126f], S. P. Ahlen[22], F. Ahmadov[65,b], G. Aielli[133a,133b], H. Akerstedt[146a,146b], T. P. A. Åkesson[81], A. V. Akimov[96], G. L. Alberghi[20a,20b], J. Albert[169], S. Albrand[55], M. J. Alconada Verzini[71], M. Aleksa[30], I. N. Aleksandrov[65], C. Alexa[26a], G. Alexander[153], T. Alexopoulos[10], M. Alhroob[113], G. Alimonti[91a], L. Alio[85], J. Alison[31], S. P. Alkire[35], B. M. M. Allbrooke[149], P. P. Allport[74], A. Aloisio[104a,104b], A. Alonso[36], F. Alonso[71], C. Alpigiani[76], A. Altheimer[35], B. Alvarez Gonzalez[30], D. Álvarez Piqueras[167], M. G. Alviggi[104a,104b], B. T. Amadio[15], K. Amako[66], Y. Amaral Coutinho[24a], C. Amelung[23], D. Amidei[89], S. P. Amor Dos Santos[126a,126c], A. Amorim[126a,126b], S. Amoroso[48], N. Amram[153], G. Amundsen[23], C. Anastopoulos[139], L. S. Ancu[49], N. Andari[108], T. Andeen[35], C. F. Anders[58b], G. Anders[30], J. K. Anders[74], K. J. Anderson[31], A. Andreazza[91a,91b], V. Andrei[58a], S. Angelidakis[9], I. Angelozzi[107], P. Anger[44], A. Angerami[35], F. Anghinolfi[30], A. V. Anisenkov[109,c], N. Anjos[12], A. Annovi[124a,124b], M. Antonelli[47], A. Antonov[98], J. Antos[144b], F. Anulli[132a], M. Aoki[66], L. Aperio Bella[18], G. Arabidze[90], Y. Arai[66], J. P. Araque[126a], A. T. H. Arce[45], F. A. Arduh[71], J-F. Arguin[95], S. Argyropoulos[42], M. Arik[19a], A. J. Armbruster[30], O. Arnaez[30], V. Arnal[82], H. Arnold[48], M. Arratia[28], O. Arslan[21], A. Artamonov[97], G. Artoni[23], S. Asai[155], N. Asbah[42], A. Ashkenazi[153], B. Åsman[146a,146b], L. Asquith[149], K. Assamagan[25], R. Astalos[144a], M. Atkinson[165], N. B. Atlay[141], B. Auerbach[6], K. Augsten[128], M. Aurousseau[145b], G. Avolio[30], B. Axen[15], M. K. Ayoub[117], G. Azuelos[95,d], M. A. Baak[30], A. E. Baas[58a], M. J. Baca[18], C. Bacci[134a,134b], H. Bachacou[136], K. Bachas[154], M. Backes[30], M. Backhaus[30], P. Bagiacchi[132a,132b], P. Bagnaia[132a,132b], Y. Bai[33a], T. Bain[35], J. T. Baines[131], O. K. Baker[176], E. M. Baldin[109,c], P. Balek[129], T. Balestri[148], F. Balli[84], E. Banas[39], Sw. Banerjee[173], A. A. E. Bannoura[175], H. S. Bansil[18], L. Barak[30], E. L. Barberio[88], D. Barberis[50a,50b], M. Barbero[85], T. Barillari[101], M. Barisonzi[164a,164b], T. Barklow[143], N. Barlow[28], S. L. Barnes[84], B. M. Barnett[131], R. M. Barnett[15], Z. Barnovska[5], A. Baroncelli[134a], G. Barone[23], A. J. Barr[120], F. Barreiro[82], J. Barreiro Guimarães da Costa[57], R. Bartoldus[143], A. E. Barton[72], P. Bartos[144a], A. Basalaev[123], A. Bassalat[117], A. Basye[165], R. L. Bates[53], S. J. Batista[158], J. R. Batley[28], M. Battaglia[137], M. Bauce[132a,132b], F. Bauer[136], H. S. Bawa[143,e], J. B. Beacham[111], M. D. Beattie[72], T. Beau[80], P. H. Beauchemin[161], R. Beccherle[124a,124b], P. Bechtle[21], H. P. Beck[17,f], K. Becker[120], M. Becker[83], S. Becker[100], M. Beckingham[170], C. Becot[117], A. J. Beddall[19b], A. Beddall[19b], V. A. Bednyakov[65], C. P. Bee[148], L. J. Beemster[107], T. A. Beermann[175], M. Begel[25], J. K. Behr[120], C. Belanger-Champagne[87], W. H. Bell[49], G. Bella[153], L. Bellagamba[20a], A. Bellerive[29], M. Bellomo[86], K. Belotskiy[98], O. Beltramello[30], O. Benary[153], D. Benchekroun[135a], M. Bender[100], K. Bendtz[146a,146b], N. Benekos[10], Y. Benhammou[153], E. Benhar Noccioli[49], J. A. Benitez Garcia[159b], D. P. Benjamin[45], J. R. Bensinger[23], S. Bentvelsen[107], L. Beresford[120], M. Beretta[47], D. Berge[107], E. Bergeaas Kuutmann[166], N. Berger[5], F. Berghaus[169], J. Beringer[15], C. Bernard[22], N. R. Bernard[86], C. Bernius[110], F. U. Bernlochner[21], T. Berry[77], P. Berta[129], C. Bertella[83], G. Bertoli[146a,146b], F. Bertolucci[124a,124b], C. Bertsche[113], D. Bertsche[113], M. I. Besana[91a], G. J. Besjes[36], O. Bessidskaia Bylund[146a,146b], M. Bessner[42], N. Besson[136], C. Betancourt[48], S. Bethke[101], A. J. Bevan[76], W. Bhimji[15], R. M. Bianchi[125], L. Bianchini[23], M. Bianco[30], O. Biebel[100], D. Biedermann[16], S. P. Bieniek[78], M. Biglietti[134a], J. Bilbao De Mendizabal[49], H. Bilokon[47], M. Bindi[54], S. Binet[117], A. Bingul[19b], C. Bini[132a,132b], S. Biondi[20a,20b], C. W. Black[150], J. E. Black[143], K. M. Black[22], D. Blackburn[138], R. E. Blair[6], J.-B. Blanchard[136], J. E. Blanco[77], T. Blazek[144a], I. Bloch[42], C. Blocker[23], W. Blum[83,*], U. Blumenschein[54], G. J. Bobbink[107], V. S. Bobrovnikov[109,c], S. S. Bocchetta[81], A. Bocci[45], C. Bock[100], M. Boehler[48], J. A. Bogaerts[30], D. Bogavac[13], A. G. Bogdanchikov[109], C. Bohm[146a], V. Boisvert[77], T. Bold[38a], V. Boldea[26a], A. S. Boldyrev[99], M. Bomben[80], M. Bona[76], M. Boonekamp[136], A. Borisov[130], G. Borissov[72], S. Borroni[42], J. Bortfeldt[100], V. Bortolotto[60a,60b,60c], K. Bos[107], D. Boscherini[20a], M. Bosman[12], J. Boudreau[125], J. Bouffard[2], E. V. Bouhova-Thacker[72], D. Boumediene[34], C. Bourdarios[117], N. Bousson[114], A. Boveia[30], J. Boyd[30], I. R. Boyko[65], I. Bozic[13], J. Bracinik[18], A. Brandt[8], G. Brandt[54], O. Brandt[58a], U. Bratzler[156], B. Brau[86], J. E. Brau[116], H. M. Braun[175,*], S. F. Brazzale[164a,164c], W. D. Breaden Madden[53], K. Brendlinger[122], A. J. Brennan[88], L. Brenner[107], R. Brenner[166], S. Bressler[172], K. Bristow[145c], T. M. Bristow[46], D. Britton[53], D. Britzger[42], F. M. Brochu[28], I. Brock[21], R. Brock[90], J. Bronner[101], G. Brooijmans[35], T. Brooks[77], W. K. Brooks[32b], J. Brosamer[15], E. Brost[116], J. Brown[55], P. A. Bruckman de Renstrom[39], D. Bruncko[144b], R. Bruneliere[48], A. Bruni[20a], G. Bruni[20a], M. Bruschi[20a], N. Bruscino[21], L. Bryngemark[81], T. Buanes[14], Q. Buat[142], P. Buchholz[141], A. G. Buckley[53], S. I. Buda[26a], I. A. Budagov[65], F. Buehrer[48], L. Bugge[119], M. K. Bugge[119], O. Bulekov[98], D. Bullock[8], H. Burckhart[30], S. Burdin[74], B. Burghgrave[108], S. Burke[131], I. Burmeister[43], E. Busato[34], D. Büscher[48], V. Büscher[83], P. Bussey[53], J. M. Butler[22], A. I. Butt[3], C. M. Buttar[53], J. M. Butterworth[78], P. Butti[107], W. Buttinger[25], A. Buzatu[53], A. R. Buzykaev[109,c], S. Cabrera Urbán[167], D. Caforio[128], V. M. Cairo[37a,37b], O. Cakir[4a],

N. Calace[49], P. Calafiura[15], A. Calandri[136], G. Calderini[80], P. Calfayan[100], L. P. Caloba[24a], D. Calvet[34], S. Calvet[34], R. Camacho Toro[31], S. Camarda[42], P. Camarri[133a,133b], D. Cameron[119], R. Caminal Armadans[165], S. Campana[30], M. Campanelli[78], A. Campoverde[148], V. Canale[104a,104b], A. Canepa[159a], M. Cano Bret[33e], J. Cantero[82], R. Cantrill[126a], T. Cao[40], M. D. M. Capeans Garrido[30], I. Caprini[26a], M. Caprini[26a], M. Capua[37a,37b], R. Caputo[83], R. Cardarelli[133a], F. Cardillo[48], T. Carli[30], G. Carlino[104a], L. Carminati[91a,91b], S. Caron[106], E. Carquin[32a], G. D. Carrillo-Montoya[8], J. R. Carter[28], J. Carvalho[126a,126c], D. Casadei[78], M. P. Casado[12], M. Casolino[12], E. Castaneda-Miranda[145b], A. Castelli[107], V. Castillo Gimenez[167], N. F. Castro[126a,g], P. Catastini[57], A. Catinaccio[30], J. R. Catmore[119], A. Cattai[30], J. Caudron[83], V. Cavaliere[165], D. Cavalli[91a], M. Cavalli-Sforza[12], V. Cavasinni[124a,124b], F. Ceradini[134a,134b], B. C. Cerio[45], K. Cerny[129], A. S. Cerqueira[24b], A. Cerri[149], L. Cerrito[76], F. Cerutti[15], M. Cerv[30], A. Cervelli[17], S. A. Cetin[19c], A. Chafaq[135a], D. Chakraborty[108], I. Chalupkova[129], P. Chang[165], J. D. Chapman[28], D. G. Charlton[18], C. C. Chau[158], C. A. Chavez Barajas[149], S. Cheatham[152], A. Chegwidden[90], S. Chekanov[6], S. V. Chekulaev[159a], G. A. Chelkov[65,h], M. A. Chelstowska[89], C. Chen[64], H. Chen[25], K. Chen[148], L. Chen[33d,i], S. Chen[33c], X. Chen[33f], Y. Chen[67], H. C. Cheng[89], Y. Cheng[31], A. Cheplakov[65], E. Cheremushkina[130], R. Cherkaoui El Moursli[135e], V. Chernyatin[25,*], E. Cheu[7], L. Chevalier[136], V. Chiarella[47], G. Chiarelli[124a,124b], J. T. Childers[6], G. Chiodini[73a], A. S. Chisholm[18], R. T. Chislett[78], A. Chitan[26a], M. V. Chizhov[65], K. Choi[61], S. Chouridou[9], B. K. B. Chow[100], V. Christodoulou[78], D. Chromek-Burckhart[30], J. Chudoba[127], A. J. Chuinard[87], J. J. Chwastowski[39], L. Chytka[115], G. Ciapetti[132a,132b], A. K. Ciftci[4a], D. Cinca[53], V. Cindro[75], I. A. Cioara[21], A. Ciocio[15], Z. H. Citron[172], M. Ciubancan[26a], A. Clark[49], B. L. Clark[57], P. J. Clark[46], R. N. Clarke[15], W. Cleland[125], C. Clement[146a,146b], Y. Coadou[85], M. Cobal[164a,164c], A. Coccaro[138], J. Cochran[64], L. Coffey[23], J. G. Cogan[143], L. Colasurdo[106], B. Cole[35], S. Cole[108], A. P. Colijn[107], J. Collot[55], T. Colombo[58c], G. Compostella[101], P. Conde Muiño[126a,126b], E. Coniavitis[48], S. H. Connell[145b], I. A. Connelly[77], S. M. Consonni[91a,91b], V. Consorti[48], S. Constantinescu[26a], C. Conta[121a,121b], G. Conti[30], F. Conventi[104a,j], M. Cooke[15], B. D. Cooper[78], A. M. Cooper-Sarkar[120], T. Cornelissen[175], M. Corradi[20a], F. Corriveau[87,k], A. Corso-Radu[163], A. Cortes-Gonzalez[12], G. Cortiana[101], G. Costa[91a], M. J. Costa[167], D. Costanzo[139], D. Côté[8], G. Cottin[28], G. Cowan[77], B. E. Cox[84], K. Cranmer[110], G. Cree[29], S. Crépé-Renaudin[55], F. Crescioli[80], W. A. Cribbs[146a,146b], M. Crispin Ortuzar[120], M. Cristinziani[21], V. Croft[106], G. Crosetti[37a,37b], T. Cuhadar Donszelmann[139], J. Cummings[176], M. Curatolo[47], C. Cuthbert[150], H. Czirr[141], P. Czodrowski[3], S. D'Auria[53], M. D'Onofrio[74], M. J. Da Cunha Sargedas De Sousa[126a,126b], C. Da Via[84], W. Dabrowski[38a], A. Dafinca[120], T. Dai[89], O. Dale[14], F. Dallaire[95], C. Dallapiccola[86], M. Dam[36], J. R. Dandoy[31], N. P. Dang[48], A. C. Daniells[18], M. Danninger[168], M. Dano Hoffmann[136], V. Dao[48], G. Darbo[50a], S. Darmora[8], J. Dassoulas[3], A. Dattagupta[61], W. Davey[21], C. David[169], T. Davidek[129], E. Davies[120,l], M. Davies[153], P. Davison[78], Y. Davygora[58a], E. Dawe[88], I. Dawson[139], R. K. Daya-Ishmukhametova[86], K. De[8], R. de Asmundis[104a], A. De Benedetti[113], S. De Castro[20a,20b], S. De Cecco[80], N. De Groot[106], P. de Jong[107], H. De la Torre[82], F. De Lorenzi[64], L. De Nooij[107], D. De Pedis[132a], A. De Salvo[132a], U. De Sanctis[149], A. De Santo[149], J. B. De Vivie De Regie[117], W. J. Dearnaley[72], R. Debbe[25], C. Debenedetti[137], D. V. Dedovich[65], I. Deigaard[107], J. Del Peso[82], T. Del Prete[124a,124b], D. Delgove[117], F. Deliot[136], C. M. Delitzsch[49], M. Deliyergiyev[75], A. Dell'Acqua[30], L. Dell'Asta[22], M. Dell'Orso[124a,124b], M. Della Pietra[104a,j], D. della Volpe[49], M. Delmastro[5], P. A. Delsart[55], C. Deluca[107], D. A. DeMarco[158], S. Demers[176], M. Demichev[65], A. Demilly[80], S. P. Denisov[130], D. Derendarz[39], J. E. Derkaoui[135d], F. Derue[80], P. Dervan[74], K. Desch[21], C. Deterre[42], P. O. Deviveiros[30], A. Dewhurst[131], S. Dhaliwal[23], A. Di Ciaccio[133a,133b], L. Di Ciaccio[5], A. Di Domenico[132a,132b], C. Di Donato[104a,104b], A. Di Girolamo[30], B. Di Girolamo[30], A. Di Mattia[152], B. Di Micco[134a,134b], R. Di Nardo[47], A. Di Simone[48], R. Di Sipio[158], D. Di Valentino[29], C. Diaconu[85], M. Diamond[158], F. A. Dias[46], M. A. Diaz[32a], E. B. Diehl[89], J. Dietrich[16], S. Diglio[85], A. Dimitrievska[13], J. Dingfelder[21], P. Dita[26a], S. Dita[26a], F. Dittus[30], F. Djama[85], T. Djobava[51b], J. I. Djuvsland[58a], M. A. B. do Vale[24c], D. Dobos[30], M. Dobre[26a], C. Doglioni[81], T. Dohmae[155], J. Dolejsi[129], Z. Dolezal[129], B. A. Dolgoshein[98,*], M. Donadelli[24d], S. Donati[124a,124b], P. Dondero[121a,121b], J. Donini[34], J. Dopke[131], A. Doria[104a], M. T. Dova[71], A. T. Doyle[53], E. Drechsler[54], M. Dris[10], E. Dubreuil[34], E. Duchovni[172], G. Duckeck[100], O. A. Ducu[26a,85], D. Duda[107], A. Dudarev[30], L. Duflot[117], L. Duguid[77], M. Dührssen[30], M. Dunford[58a], H. Duran Yildiz[4a], M. Düren[52], A. Durglishvili[51b], D. Duschinger[44], M. Dyndal[38a], C. Eckardt[42], K. M. Ecker[101], R. C. Edgar[89], W. Edson[2], N. C. Edwards[46], W. Ehrenfeld[21], T. Eifert[30], G. Eigen[14], K. Einsweiler[15], T. Ekelof[166], M. El Kacimi[135c], M. Ellert[166], S. Elles[5], F. Ellinghaus[175], A. A. Elliot[169], N. Ellis[30], J. Elmsheuser[100], M. Elsing[30], D. Emeliyanov[131], Y. Enari[155], O. C. Endner[83], M. Endo[118], J. Erdmann[43], A. Ereditato[17], G. Ernis[175], J. Ernst[2], M. Ernst[25], S. Errede[165], E. Ertel[83], M. Escalier[117], H. Esch[43], C. Escobar[125], B. Esposito[47], A. I. Etienvre[136], E. Etzion[153], H. Evans[61], A. Ezhilov[123], L. Fabbri[20a,20b], G. Facini[31], R. M. Fakhrutdinov[130], S. Falciano[132a], R. J. Falla[78], J. Faltova[129], Y. Fang[33a], M. Fanti[91a,91b], A. Farbin[8], A. Farilla[134a], T. Farooque[12], S. Farrell[15], S. M. Farrington[170], P. Farthouat[30], F. Fassi[135e], P. Fassnacht[30], D. Fassouliotis[9], M. Faucci Giannelli[77], A. Favareto[50a,50b], L. Fayard[117], P. Federic[144a], O. L. Fedin[123,m], W. Fedorko[168], S. Feigl[30], L. Feligioni[85], C. Feng[33d],

E. J. Feng[6], H. Feng[89], A. B. Fenyuk[130], L. Feremenga[8], P. Fernandez Martinez[167], S. Fernandez Perez[30], J. Ferrando[53], A. Ferrari[166], P. Ferrari[107], R. Ferrari[121a], D. E. Ferreira de Lima[53], A. Ferrer[167], D. Ferrere[49], C. Ferretti[89], A. Ferretto Parodi[50a,50b], M. Fiascaris[31], F. Fiedler[83], A. Filipčič[75], M. Filipuzzi[42], F. Filthaut[106], M. Fincke-Keeler[169], K. D. Finelli[150], M. C. N. Fiolhais[126a,126c], L. Fiorini[167], A. Firan[40], A. Fischer[2], C. Fischer[12], J. Fischer[175], W. C. Fisher[90], E. A. Fitzgerald[23], N. Flaschel[42], I. Fleck[141], P. Fleischmann[89], S. Fleischmann[175], G. T. Fletcher[139], G. Fletcher[76], R. R. M. Fletcher[122], T. Flick[175], A. Floderus[81], L. R. Flores Castillo[60a], M. J. Flowerdew[101], A. Formica[136], A. Forti[84], D. Fournier[117], H. Fox[72], S. Fracchia[12], P. Francavilla[80], M. Franchini[20a,20b], D. Francis[30], L. Franconi[119], M. Franklin[57], M. Frate[163], M. Fraternali[121a,121b], D. Freeborn[78], S. T. French[28], F. Friedrich[44], D. Froidevaux[30], J. A. Frost[120], C. Fukunaga[156], E. Fullana Torregrosa[83], B. G. Fulsom[143], T. Fusayasu[102], J. Fuster[167], C. Gabaldon[55], O. Gabizon[175], A. Gabrielli[20a,20b], A. Gabrielli[132a,132b], G. P. Gach[38a], S. Gadatsch[107], S. Gadomski[49], G. Gagliardi[50a,50b], P. Gagnon[61], C. Galea[106], B. Galhardo[126a,126c], E. J. Gallas[120], B. J. Gallop[131], P. Gallus[128], G. Galster[36], K. K. Gan[111], J. Gao[33b,85], Y. Gao[46], Y. S. Gao[143,e], F. M. Garay Walls[46], F. Garberson[176], C. García[167], J. E. García Navarro[167], M. Garcia-Sciveres[15], R. W. Gardner[31], N. Garelli[143], V. Garonne[119], C. Gatti[47], A. Gaudiello[50a,50b], G. Gaudio[121a], B. Gaur[141], L. Gauthier[95], P. Gauzzi[132a,132b], I. L. Gavrilenko[96], C. Gay[168], G. Gaycken[21], E. N. Gazis[10], P. Ge[33d], Z. Gecse[168], C. N. P. Gee[131], D. A. A. Geerts[107], Ch. Geich-Gimbel[21], M. P. Geisler[58a], C. Gemme[50a], M. H. Genest[55], S. Gentile[132a,132b], M. George[54], S. George[77], D. Gerbaudo[163], A. Gershon[153], S. Ghasemi[141], H. Ghazlane[135b], B. Giacobbe[20a], S. Giagu[132a,132b], V. Giangiobbe[12], P. Giannetti[124a,124b], B. Gibbard[25], S. M. Gibson[77], M. Gilchriese[15], T. P. S. Gillam[28], D. Gillberg[30], G. Gilles[34], D. M. Gingrich[3,d], N. Giokaris[9], M. P. Giordani[164a,164c], F. M. Giorgi[20a], F. M. Giorgi[16], P. F. Giraud[136], P. Giromini[47], D. Giugni[91a], C. Giuliani[48], M. Giulini[58b], B. K. Gjelsten[119], S. Gkaitatzis[154], I. Gkialas[154], E. L. Gkougkousis[117], L. K. Gladilin[99], C. Glasman[82], J. Glatzer[30], P. C. F. Glaysher[46], A. Glazov[42], M. Goblirsch-Kolb[101], J. R. Goddard[76], J. Godlewski[39], S. Goldfarb[89], T. Golling[49], D. Golubkov[130], A. Gomes[126a,126b,126d], R. Gonçalo[126a], J. Goncalves Pinto Firmino Da Costa[136], L. Gonella[21], S. González de la Hoz[167], G. Gonzalez Parra[12], S. Gonzalez-Sevilla[49], L. Goossens[30], P. A. Gorbounov[97], H. A. Gordon[25], I. Gorelov[105], B. Gorini[30], E. Gorini[73a,73b], A. Gorišek[75], E. Gornicki[39], A. T. Goshaw[45], C. Gössling[43], M. I. Gostkin[65], D. Goujdami[135c], A. G. Goussiou[138], N. Govender[145b], E. Gozani[152], H. M. X. Grabas[137], L. Graber[54], I. Grabowska-Bold[38a], P. O. J. Gradin[166], P. Grafström[20a,20b], K-J. Grahn[42], J. Gramling[49], E. Gramstad[119], S. Grancagnolo[16], V. Grassi[148], V. Gratchev[123], H. M. Gray[30], E. Graziani[134a], Z. D. Greenwood[79,n], K. Gregersen[78], I. M. Gregor[42], P. Grenier[143], J. Griffiths[8], A. A. Grillo[137], K. Grimm[72], S. Grinstein[12,o], Ph. Gris[34], J.-F. Grivaz[117], J. P. Grohs[44], A. Grohsjean[42], E. Gross[172], J. Grosse-Knetter[54], G. C. Grossi[79], Z. J. Grout[149], L. Guan[89], J. Guenther[128], F. Guescini[49], D. Guest[176], O. Gueta[153], E. Guido[50a,50b], T. Guillemin[117], S. Guindon[2], U. Gul[53], C. Gumpert[44], J. Guo[33e], Y. Guo[33b], S. Gupta[120], G. Gustavino[132a,132b], P. Gutierrez[113], N. G. Gutierrez Ortiz[78], C. Gutschow[44], C. Guyot[136], C. Gwenlan[120], C. B. Gwilliam[74], A. Haas[110], C. Haber[15], H. K. Hadavand[8], N. Haddad[135e], P. Haefner[21], S. Hageböck[21], Z. Hajduk[39], H. Hakobyan[177], M. Haleem[42], J. Haley[114], D. Hall[120], G. Halladjian[90], G. D. Hallewell[85], K. Hamacher[175], P. Hamal[115], K. Hamano[169], M. Hamer[54], A. Hamilton[145a], G. N. Hamity[145c], P. G. Hamnett[42], L. Han[33b], K. Hanagaki[66,p], K. Hanawa[155], M. Hance[15], P. Hanke[58a], R. Hanna[136], J. B. Hansen[36], J. D. Hansen[36], M. C. Hansen[21], P. H. Hansen[36], K. Hara[160], A. S. Hard[173], T. Harenberg[175], F. Hariri[117], S. Harkusha[92], R. D. Harrington[46], P. F. Harrison[170], F. Hartjes[107], M. Hasegawa[67], S. Hasegawa[103], Y. Hasegawa[140], A. Hasib[113], S. Hassani[136], S. Haug[17], R. Hauser[90], L. Hauswald[44], M. Havranek[127], C. M. Hawkes[18], R. J. Hawkings[30], A. D. Hawkins[81], T. Hayashi[160], D. Hayden[90], C. P. Hays[120], J. M. Hays[76], H. S. Hayward[74], S. J. Haywood[131], S. J. Head[18], T. Heck[83], V. Hedberg[81], L. Heelan[8], S. Heim[122], T. Heim[175], B. Heinemann[15], L. Heinrich[110], J. Hejbal[127], L. Helary[22], S. Hellman[146a,146b], D. Hellmich[21], C. Helsens[12], J. Henderson[120], R. C. W. Henderson[72], Y. Heng[173], C. Hengler[42], A. Henrichs[176], A. M. Henriques Correia[30], S. Henrot-Versille[117], G. H. Herbert[16], Y. Hernández Jiménez[167], R. Herrberg-Schubert[16], G. Herten[48], R. Hertenberger[100], L. Hervas[30], G. G. Hesketh[78], N. P. Hessey[107], J. W. Hetherly[40], R. Hickling[76], E. Higón-Rodriguez[167], E. Hill[169], J. C. Hill[28], K. H. Hiller[42], S. J. Hillier[18], I. Hinchliffe[15], E. Hines[122], R. R. Hinman[15], M. Hirose[157], D. Hirschbuehl[175], J. Hobbs[148], N. Hod[107], M. C. Hodgkinson[139], P. Hodgson[139], A. Hoecker[30], M. R. Hoeferkamp[105], F. Hoenig[100], M. Hohlfeld[83], D. Hohn[21], T. R. Holmes[15], M. Homann[43], T. M. Hong[125], L. Hooft van Huysduynen[110], W. H. Hopkins[116], Y. Horii[103], A. J. Horton[142], J-Y. Hostachy[55], S. Hou[151], A. Hoummada[135a], J. Howard[120], J. Howarth[42], M. Hrabovsky[115], I. Hristova[16], J. Hrivnac[117], T. Hryn'ova[5], A. Hrynevich[93], C. Hsu[145c], P. J. Hsu[151,q], S.-C. Hsu[138], D. Hu[35], Q. Hu[33b], X. Hu[89], Y. Huang[42], Z. Hubacek[128], F. Hubaut[85], F. Huegging[21], T. B. Huffman[120], E. W. Hughes[35], G. Hughes[72], M. Huhtinen[30], T. A. Hülsing[83], N. Huseynov[65,b], J. Huston[90], J. Huth[57], G. Iacobucci[49], G. Iakovidis[25], I. Ibragimov[141], L. Iconomidou-Fayard[117], E. Ideal[176], Z. Idrissi[135e], P. Iengo[30], O. Igonkina[107], T. Iizawa[171], Y. Ikegami[66], K. Ikematsu[141], M. Ikeno[66], Y. Ilchenko[31,r], D. Iliadis[154], N. Ilic[143], T. Ince[101], G. Introzzi[121a,121b], P. Ioannou[9], M. Iodice[134a], K. Iordanidou[35], V. Ippolito[57], A. Irles Quiles[167], C. Isaksson[166], M. Ishino[68], M. Ishitsuka[157],

R. Ishmukhametov[111], C. Issever[120], S. Istin[19a], J. M. Iturbe Ponce[84], R. Iuppa[133a,133b], J. Ivarsson[81], W. Iwanski[39], H. Iwasaki[66], J. M. Izen[41], V. Izzo[104a], S. Jabbar[3], B. Jackson[122], M. Jackson[74], P. Jackson[1], M. R. Jaekel[30], V. Jain[2], K. Jakobs[48], S. Jakobsen[30], T. Jakoubek[127], J. Jakubek[128], D. O. Jamin[114], D. K. Jana[79], E. Jansen[78], R. Jansky[62], J. Janssen[21], M. Janus[170], G. Jarlskog[81], N. Javadov[65,b], T. Javůrek[48], L. Jeanty[15], J. Jejelava[51a,s], G.-Y. Jeng[150], D. Jennens[88], P. Jenni[48,t], J. Jentzsch[43], C. Jeske[170], S. Jézéquel[5], H. Ji[173], J. Jia[148], Y. Jiang[33b], S. Jiggins[78], J. Jimenez Pena[167], S. Jin[33a], A. Jinaru[26a], O. Jinnouchi[157], M. D. Joergensen[36], P. Johansson[139], K. A. Johns[7], K. Jon-And[146a,146b], G. Jones[170], R. W. L. Jones[72], T. J. Jones[74], J. Jongmanns[58a], P. M. Jorge[126a,126b], K. D. Joshi[84], J. Jovicevic[159a], X. Ju[173], C. A. Jung[43], P. Jussel[62], A. Juste Rozas[12,o], M. Kaci[167], A. Kaczmarska[39], M. Kado[117], H. Kagan[111], M. Kagan[143], S. J. Kahn[85], E. Kajomovitz[45], C. W. Kalderon[120], S. Kama[40], A. Kamenshchikov[130], N. Kanaya[155], S. Kaneti[28], V. A. Kantserov[98], J. Kanzaki[66], B. Kaplan[110], L. S. Kaplan[173], A. Kapliy[31], D. Kar[53], K. Karakostas[10], A. Karamaoun[3], N. Karastathis[10,107], M. J. Kareem[54], E. Karentzos[10], M. Karnevskiy[83], S. N. Karpov[65], Z. M. Karpova[65], K. Karthik[110], V. Kartvelishvili[72], A. N. Karyukhin[130], L. Kashif[173], R. D. Kass[111], A. Kastanas[14], Y. Kataoka[155], A. Katre[49], J. Katzy[42], K. Kawagoe[70], T. Kawamoto[155], G. Kawamura[54], S. Kazama[155], V. F. Kazanin[109,c], R. Keeler[169], R. Kehoe[40], J. S. Keller[42], J. J. Kempster[77], H. Keoshkerian[84], O. Kepka[127], B. P. Kerševan[75], S. Kersten[175], R. A. Keyes[87], F. Khalil-zada[11], H. Khandanyan[146a,146b], A. Khanov[114], A. G. Kharlamov[109,c], T. J. Khoo[28], V. Khovanskiy[97], E. Khramov[65], J. Khubua[51b,u], H. Y. Kim[8], H. Kim[146a,146b], S. H. Kim[160], Y. Kim[31], N. Kimura[154], O. M. Kind[16], B. T. King[74], M. King[167], S. B. King[168], J. Kirk[131], A. E. Kiryunin[101], T. Kishimoto[67], D. Kisielewska[38a], F. Kiss[48], K. Kiuchi[160], O. Kivernyk[136], E. Kladiva[144b], M. H. Klein[35], M. Klein[74], U. Klein[74], K. Kleinknecht[83], P. Klimek[146a,146b], A. Klimentov[25], R. Klingenberg[43], J. A. Klinger[139], T. Klioutchnikova[30], E.-E. Kluge[58a], P. Kluit[107], S. Kluth[101], J. Knapik[39], E. Kneringer[62], E. B. F. G. Knoops[85], A. Knue[53], A. Kobayashi[155], D. Kobayashi[157], T. Kobayashi[155], M. Kobel[44], M. Kocian[143], P. Kodys[129], T. Koffas[29], E. Koffeman[107], L. A. Kogan[120], S. Kohlmann[175], Z. Kohout[128], T. Kohriki[66], T. Koi[143], H. Kolanoski[16], I. Koletsou[5], A. A. Komar[96,*], Y. Komori[155], T. Kondo[66], N. Kondrashova[42], K. Köneke[48], A. C. König[106], T. Kono[66], R. Konoplich[110,v], N. Konstantinidis[78], R. Kopeliansky[152], S. Koperny[38a], L. Köpke[83], A. K. Kopp[48], K. Korcyl[39], K. Kordas[154], A. Korn[78], A. A. Korol[109,c], I. Korolkov[12], E. V. Korolkova[139], O. Kortner[101], S. Kortner[101], T. Kosek[129], V. V. Kostyukhin[21], V. M. Kotov[65], A. Kotwal[45], A. Kourkoumeli-Charalampidi[154], C. Kourkoumelis[9], V. Kouskoura[25], A. Koutsman[159a], R. Kowalewski[169], T. Z. Kowalski[38a], W. Kozanecki[136], A. S. Kozhin[130], V. A. Kramarenko[99], G. Kramberger[75], D. Krasnopevtsev[98], M. W. Krasny[80], A. Krasznahorkay[30], J. K. Kraus[21], A. Kravchenko[25], S. Kreiss[110], M. Kretz[58c], J. Kretzschmar[74], K. Kreutzfeldt[52], P. Krieger[158], K. Krizka[31], K. Kroeninger[43], H. Kroha[101], J. Kroll[122], J. Kroseberg[21], J. Krstic[13], U. Kruchonak[65], H. Krüger[21], N. Krumnack[64], A. Kruse[173], M. C. Kruse[45], M. Kruskal[22], T. Kubota[88], H. Kucuk[78], S. Kuday[4b], S. Kuehn[48], A. Kugel[58c], F. Kuger[174], A. Kuhl[137], T. Kuhl[42], V. Kukhtin[65], Y. Kulchitsky[92], S. Kuleshov[32b], M. Kuna[132a,132b], T. Kunigo[68], A. Kupco[127], H. Kurashige[67], Y. A. Kurochkin[92], V. Kus[127], E. S. Kuwertz[169], M. Kuze[157], J. Kvita[115], T. Kwan[169], D. Kyriazopoulos[139], A. La Rosa[137], J. L. La Rosa Navarro[24d], L. La Rotonda[37a,37b], C. Lacasta[167], F. Lacava[132a,132b], J. Lacey[29], H. Lacker[16], D. Lacour[80], V. R. Lacuesta[167], E. Ladygin[65], R. Lafaye[5], B. Laforge[80], T. Lagouri[176], S. Lai[54], L. Lambourne[78], S. Lammers[61], C. L. Lampen[7], W. Lampl[7], E. Lançon[136], U. Landgraf[48], M. P. J. Landon[76], V. S. Lang[58a], J. C. Lange[12], A. J. Lankford[163], F. Lanni[25], K. Lantzsch[30], A. Lanza[121a], S. Laplace[80], C. Lapoire[30], J. F. Laporte[136], T. Lari[91a], F. Lasagni Manghi[20a,20b], M. Lassnig[30], P. Laurelli[47], W. Lavrijsen[15], A. T. Law[137], P. Laycock[74], T. Lazovich[57], O. Le Dortz[80], E. Le Guirriec[85], E. Le Menedeu[12], M. LeBlanc[169], T. LeCompte[6], F. Ledroit-Guillon[55], C. A. Lee[145b], S. C. Lee[151], L. Lee[1], G. Lefebvre[80], M. Lefebvre[169], F. Legger[100], C. Leggett[15], A. Lehan[74], G. Lehmann Miotto[30], X. Lei[7], W. A. Leight[29], A. Leisos[154,w], A. G. Leister[176], M. A. L. Leite[24d], R. Leitner[129], D. Lellouch[172], B. Lemmer[54], K. J. C. Leney[78], T. Lenz[21], B. Lenzi[30], R. Leone[7], S. Leone[124a,124b], C. Leonidopoulos[46], S. Leontsinis[10], G. Lerner[149], C. Leroy[95], C. G. Lester[28], M. Levchenko[123], J. Levêque[5], D. Levin[89], L. J. Levinson[172], M. Levy[18], A. Lewis[120], A. M. Leyko[21], M. Leyton[41], B. Li[33b,x], H. Li[148], H. L. Li[31], L. Li[45], L. Li[33e], S. Li[45], Y. Li[33c,y], Z. Liang[137], H. Liao[34], B. Liberti[133a], A. Liblong[158], P. Lichard[30], K. Lie[165], J. Liebal[21], W. Liebig[14], C. Limbach[21], A. Limosani[150], S. C. Lin[151,z], T. H. Lin[83], F. Linde[107], B. E. Lindquist[148], J. T. Linnemann[90], E. Lipeles[122], A. Lipniacka[14], M. Lisovyi[58b], T. M. Liss[165], D. Lissauer[25], A. Lister[168], A. M. Litke[137], B. Liu[151,aa], D. Liu[151], H. Liu[89], J. Liu[85], J. B. Liu[33b], K. Liu[85], L. Liu[165], M. Liu[45], M. Liu[33b], Y. Liu[33b], M. Livan[121a,121b], A. Lleres[55], J. Llorente Merino[82], S. L. Lloyd[76], F. Lo Sterzo[151], E. Lobodzinska[42], P. Loch[7], W. S. Lockman[137], F. K. Loebinger[84], A. E. Loevschall-Jensen[36], A. Loginov[176], T. Lohse[16], K. Lohwasser[42], M. Lokajicek[127], B. A. Long[22], J. D. Long[89], R. E. Long[72], K. A. Looper[111], L. Lopes[126a], D. Lopez Mateos[57], B. Lopez Paredes[139], I. Lopez Paz[12], J. Lorenz[100], N. Lorenzo Martinez[61], M. Losada[162], P. Loscutoff[15], P. J. Lösel[100], X. Lou[33a], A. Lounis[117], J. Love[6], P. A. Love[72], N. Lu[89], H. J. Lubatti[138], C. Luci[132a,132b], A. Lucotte[55], F. Luehring[61], W. Lukas[62], L. Luminari[132a], O. Lundberg[146a,146b], B. Lund-Jensen[147], D. Lynn[25], R. Lysak[127], E. Lytken[81], H. Ma[25], L. L. Ma[33d], G. Maccarrone[47],

A. Macchiolo[101], C. M. Macdonald[139], J. Machado Miguens[122,126b], D. Macina[30], D. Madaffari[85], R. Madar[34], H. J. Maddocks[72], W. F. Mader[44], A. Madsen[166], S. Maeland[14], T. Maeno[25], A. Maevskiy[99], E. Magradze[54], K. Mahboubi[48], J. Mahlstedt[107], C. Maiani[136], C. Maidantchik[24a], A. A. Maier[101], T. Maier[100], A. Maio[126a,126b,126d], S. Majewski[116], Y. Makida[66], N. Makovec[117], B. Malaescu[80], Pa. Malecki[39], V. P. Maleev[123], F. Malek[55], U. Mallik[63], D. Malon[6], C. Malone[143], S. Maltezos[10], V. M. Malyshev[109], S. Malyukov[30], J. Mamuzic[42], G. Mancini[47], B. Mandelli[30], L. Mandelli[91a], I. Mandić[75], R. Mandrysch[63], J. Maneira[126a,126b], A. Manfredini[101], L. Manhaes de Andrade Filho[24b], J. Manjarres Ramos[159b], A. Mann[100], P. M. Manning[137], A. Manousakis-Katsikakis[9], B. Mansoulie[136], R. Mantifel[87], M. Mantoani[54], L. Mapelli[30], L. March[145c], G. Marchiori[80], M. Marcisovsky[127], C. P. Marino[169], M. Marjanovic[13], D. E. Marley[89], F. Marroquim[24a], S. P. Marsden[84], Z. Marshall[15], L. F. Marti[17], S. Marti-Garcia[167], B. Martin[90], T. A. Martin[170], V. J. Martin[46], B. Martin dit Latour[14], M. Martinez[12,o], S. Martin-Haugh[131], V. S. Martoiu[26a], A. C. Martyniuk[78], M. Marx[138], F. Marzano[132a], A. Marzin[30], L. Masetti[83], T. Mashimo[155], R. Mashinistov[96], J. Masik[84], A. L. Maslennikov[109,c], I. Massa[20a,20b], L. Massa[20a,20b], N. Massol[5], P. Mastrandrea[148], A. Mastroberardino[37a,37b], T. Masubuchi[155], P. Mättig[175], J. Mattmann[83], J. Maurer[26a], S. J. Maxfield[74], D. A. Maximov[109,c], R. Mazini[151], S. M. Mazza[91a,91b], L. Mazzaferro[133a,133b], G. Mc Goldrick[158], S. P. Mc Kee[89], A. McCarn[89], R. L. McCarthy[148], T. G. McCarthy[29], N. A. McCubbin[131], K. W. McFarlane[56,*], J. A. Mcfayden[78], G. Mchedlidze[54], S. J. McMahon[131], R. A. McPherson[169,k], M. Medinnis[42], S. Meehan[145a], S. Mehlhase[100], A. Mehta[74], K. Meier[58a], C. Meineck[100], B. Meirose[41], B. R. Mellado Garcia[145c], F. Meloni[17], A. Mengarelli[20a,20b], S. Menke[101], E. Meoni[161], K. M. Mercurio[57], S. Mergelmeyer[21], P. Mermod[49], L. Merola[104a,104b], C. Meroni[91a], F. S. Merritt[31], A. Messina[132a,132b], J. Metcalfe[25], A. S. Mete[163], C. Meyer[83], C. Meyer[122], J-P. Meyer[136], J. Meyer[107], R. P. Middleton[131], S. Miglioranzi[164a,164c], L. Mijović[21], G. Mikenberg[172], M. Mikestikova[127], M. Mikuž[75], M. Milesi[88], A. Milic[30], D. W. Miller[31], C. Mills[46], A. Milov[172], D. A. Milstead[146a,146b], A. A. Minaenko[130], Y. Minami[155], I. A. Minashvili[65], A. I. Mincer[110], B. Mindur[38a], M. Mineev[65], Y. Ming[173], L. M. Mir[12], T. Mitani[171], J. Mitrevski[100], V. A. Mitsou[167], A. Miucci[49], P. S. Miyagawa[139], J. U. Mjörnmark[81], T. Moa[146a,146b], K. Mochizuki[85], S. Mohapatra[35], W. Mohr[48], S. Molander[146a,146b], R. Moles-Valls[21], K. Mönig[42], C. Monini[55], J. Monk[36], E. Monnier[85], J. Montejo Berlingen[12], F. Monticelli[71], S. Monzani[132a,132b], R. W. Moore[3], N. Morange[117], D. Moreno[162], M. Moreno Llácer[54], P. Morettini[50a], M. Morgenstern[44], D. Mori[142], M. Morii[57], M. Morinaga[155], V. Morisbak[119], S. Moritz[83], A. K. Morley[150], G. Mornacchi[30], J. D. Morris[76], S. S. Mortensen[36], A. Morton[53], L. Morvaj[103], M. Mosidze[51b], J. Moss[111], K. Motohashi[157], R. Mount[143], E. Mountricha[25], S. V. Mouraviev[96,*], E. J. W. Moyse[86], S. Muanza[85], R. D. Mudd[18], F. Mueller[101], J. Mueller[125], R. S. P. Mueller[100], T. Mueller[28], D. Muenstermann[49], P. Mullen[53], G. A. Mullier[17], J. A. Murillo Quijada[18], W. J. Murray[170,131], H. Musheghyan[54], E. Musto[152], A. G. Myagkov[130,ab], M. Myska[128], B. P. Nachman[143], O. Nackenhorst[54], J. Nadal[54], K. Nagai[120], R. Nagai[157], Y. Nagai[85], K. Nagano[66], A. Nagarkar[111], Y. Nagasaka[59], K. Nagata[160], M. Nagel[101], E. Nagy[85], A. M. Nairz[30], Y. Nakahama[30], K. Nakamura[66], T. Nakamura[155], I. Nakano[112], H. Namasivayam[41], R. F. Naranjo Garcia[42], R. Narayan[31], T. Naumann[42], G. Navarro[162], R. Nayyar[7], H. A. Neal[89], P. Yu. Nechaeva[96], T. J. Neep[84], P. D. Nef[143], A. Negri[121a,121b], M. Negrini[20a], S. Nektarijevic[106], C. Nellist[117], A. Nelson[163], S. Nemecek[127], P. Nemethy[110], A. A. Nepomuceno[24a], M. Nessi[30,ac], M. S. Neubauer[165], M. Neumann[175], R. M. Neves[110], P. Nevski[25], P. R. Newman[18], D. H. Nguyen[6], R. B. Nickerson[120], R. Nicolaidou[136], B. Nicquevert[30], J. Nielsen[137], N. Nikiforou[35], A. Nikiforov[16], V. Nikolaenko[130,ab], I. Nikolic-Audit[80], K. Nikolopoulos[18], J. K. Nilsen[119], P. Nilsson[25], Y. Ninomiya[155], A. Nisati[132a], R. Nisius[101], T. Nobe[155], M. Nomachi[118], I. Nomidis[29], T. Nooney[76], S. Norberg[113], M. Nordberg[30], O. Novgorodova[44], S. Nowak[101], M. Nozaki[66], L. Nozka[115], K. Ntekas[10], G. Nunes Hanninger[88], T. Nunnemann[100], E. Nurse[78], F. Nuti[88], B. J. O'Brien[46], F. O'grady[7], D. C. O'Neil[142], V. O'Shea[53], F. G. Oakham[29,d], H. Oberlack[101], T. Obermann[21], J. Ocariz[80], A. Ochi[67], I. Ochoa[78], J. P. Ochoa-Ricoux[32a], S. Oda[70], S. Odaka[66], H. Ogren[61], A. Oh[84], S. H. Oh[45], C. C. Ohm[15], H. Ohman[166], H. Oide[30], W. Okamura[118], H. Okawa[160], Y. Okumura[31], T. Okuyama[66], A. Olariu[26a], S. A. Olivares Pino[46], D. Oliveira Damazio[25], E. Oliver Garcia[167], A. Olszewski[39], J. Olszowska[39], A. Onofre[126a,126e], P. U. E. Onyisi[31,r], C. J. Oram[159a], M. J. Oreglia[31], Y. Oren[153], D. Orestano[134a,134b], N. Orlando[154], C. Oropeza Barrera[53], R. S. Orr[158], B. Osculati[50a,50b], R. Ospanov[84], G. Otero y Garzon[27], H. Otono[70], M. Ouchrif[135d], E. A. Ouellette[169], F. Ould-Saada[119], A. Ouraou[136], K. P. Oussoren[107], Q. Ouyang[33a], A. Ovcharova[15], M. Owen[53], R. E. Owen[18], V. E. Ozcan[19a], N. Ozturk[8], K. Pachal[142], A. Pacheco Pages[12], C. Padilla Aranda[12], M. Pagáčová[48], S. Pagan Griso[15], E. Paganis[139], F. Paige[25], P. Pais[86], K. Pajchel[119], G. Palacino[159b], S. Palestini[30], M. Palka[38b], D. Pallin[34], A. Palma[126a,126b], Y. B. Pan[173], E. Panagiotopoulou[10], C. E. Pandini[80], J. G. Panduro Vazquez[77], P. Pani[146a,146b], S. Panitkin[25], D. Pantea[26a], L. Paolozzi[49], Th. D. Papadopoulou[10], K. Papageorgiou[154], A. Paramonov[6], D. Paredes Hernandez[154], M. A. Parker[28], K. A. Parker[139], F. Parodi[50a,50b], J. A. Parsons[35], U. Parzefall[48], E. Pasqualucci[132a], S. Passaggio[50a], F. Pastore[134a,134b,*], Fr. Pastore[77], G. Pásztor[29], S. Pataraia[175], N. D. Patel[150], J. R. Pater[84], T. Pauly[30], J. Pearce[169], B. Pearson[113], L. E. Pedersen[36], M. Pedersen[119], S. Pedraza Lopez[167], R. Pedro[126a,126b], S. V. Peleganchuk[109,c],

D. Pelikan[166], O. Penc[127], C. Peng[33a], H. Peng[33b], B. Penning[31], J. Penwell[61], D. V. Perepelitsa[25], E. Perez Codina[159a], M. T. Pérez García-Estañ[167], L. Perini[91a,91b], H. Pernegger[30], S. Perrella[104a,104b], R. Peschke[42], V. D. Peshekhonov[65], K. Peters[30], R. F. Y. Peters[84], B. A. Petersen[30], T. C. Petersen[36], E. Petit[42], A. Petridis[146a,146b], C. Petridou[154], P. Petroff[117], E. Petrolo[132a], F. Petrucci[134a,134b], N. E. Pettersson[157], R. Pezoa[32b], P. W. Phillips[131], G. Piacquadio[143], E. Pianori[170], A. Picazio[49], E. Piccaro[76], M. Piccinini[20a,20b], M. A. Pickering[120], R. Piegaia[27], D. T. Pignotti[111], J. E. Pilcher[31], A. D. Pilkington[84], J. Pina[126a,126b,126d], M. Pinamonti[164a,164c,ad], J. L. Pinfold[3], A. Pingel[36], B. Pinto[126a], S. Pires[80], H. Pirumov[42], M. Pitt[172], C. Pizio[91a,91b], L. Plazak[144a], M.-A. Pleier[25], V. Pleskot[129], E. Plotnikova[65], P. Plucinski[146a,146b], D. Pluth[64], R. Poettgen[146a,146b], L. Poggioli[117], D. Pohl[21], G. Polesello[121a], A. Poley[42], A. Policicchio[37a,37b], R. Polifka[158], A. Polini[20a], C. S. Pollard[53], V. Polychronakos[25], K. Pommès[30], L. Pontecorvo[132a], B. G. Pope[90], G. A. Popeneciu[26b], D. S. Popovic[13], A. Poppleton[30], S. Pospisil[128], K. Potamianos[15], I. N. Potrap[65], C. J. Potter[149], C. T. Potter[116], G. Poulard[30], J. Poveda[30], V. Pozdnyakov[65], P. Pralavorio[85], A. Pranko[15], S. Prasad[30], S. Prell[64], D. Price[84], L. E. Price[6], M. Primavera[73a], S. Prince[87], M. Proissl[46], K. Prokofiev[60c], F. Prokoshin[32b], E. Protopapadaki[136], S. Protopopescu[25], J. Proudfoot[6], M. Przybycien[38a], E. Ptacek[116], D. Puddu[134a,134b], E. Pueschel[86], D. Puldon[148], M. Purohit[25,ae], P. Puzo[117], J. Qian[89], G. Qin[53], Y. Qin[84], A. Quadt[54], D. R. Quarrie[15], W. B. Quayle[164a,164b], M. Queitsch-Maitland[84], D. Quilty[53], S. Raddum[119], V. Radeka[25], V. Radescu[42], S. K. Radhakrishnan[148], P. Radloff[116], P. Rados[88], F. Ragusa[91a,91b], G. Rahal[178], S. Rajagopalan[25], M. Rammensee[30], C. Rangel-Smith[166], F. Rauscher[100], S. Rave[83], T. Ravenscroft[53], M. Raymond[30], A. L. Read[119], N. P. Readioff[74], D. M. Rebuzzi[121a,121b], A. Redelbach[174], G. Redlinger[25], R. Reece[137], K. Reeves[41], L. Rehnisch[16], J. Reichert[122], H. Reisin[27], M. Relich[163], C. Rembser[30], H. Ren[33a], A. Renaud[117], M. Rescigno[132a], S. Resconi[91a], O. L. Rezanova[109,c], P. Reznicek[129], R. Rezvani[95], R. Richter[101], S. Richter[78], E. Richter-Was[38b], O. Ricken[21], M. Ridel[80], P. Rieck[16], C. J. Riegel[175], J. Rieger[54], M. Rijssenbeek[148], A. Rimoldi[121a,121b], L. Rinaldi[20a], B. Ristić[49], E. Ritsch[30], I. Riu[12], F. Rizatdinova[114], E. Rizvi[76], S. H. Robertson[87,k], A. Robichaud-Veronneau[87], D. Robinson[28], J. E. M. Robinson[42], A. Robson[53], C. Roda[124a,124b], S. Roe[30], O. Røhne[119], S. Rolli[161], A. Romaniouk[98], M. Romano[20a,20b], S. M. Romano Saez[34], E. Romero Adam[167], N. Rompotis[138], M. Ronzani[48], L. Roos[80], E. Ros[167], S. Rosati[132a], K. Rosbach[48], P. Rose[137], P. L. Rosendahl[14], O. Rosenthal[141], V. Rossetti[146a,146b], E. Rossi[104a,104b], L. P. Rossi[50a], R. Rosten[138], M. Rotaru[26a], I. Roth[172], J. Rothberg[138], D. Rousseau[117], C. R. Royon[136], A. Rozanov[85], Y. Rozen[152], X. Ruan[145c], F. Rubbo[143], I. Rubinskiy[42], V. I. Rud[99], C. Rudolph[44], M. S. Rudolph[158], F. Rühr[48], A. Ruiz-Martinez[30], Z. Rurikova[48], N. A. Rusakovich[65], A. Ruschke[100], H. L. Russell[138], J. P. Rutherfoord[7], N. Ruthmann[48], Y. F. Ryabov[123], M. Rybar[165], G. Rybkin[117], N. C. Ryder[120], A. F. Saavedra[150], G. Sabato[107], S. Sacerdoti[27], A. Saddique[3], H. F-W. Sadrozinski[137], R. Sadykov[65], F. Safai Tehrani[132a], M. Saimpert[136], T. Saito[155], H. Sakamoto[155], Y. Sakurai[171], G. Salamanna[134a,134b], A. Salamon[133a], M. Saleem[113], D. Salek[107], P. H. Sales De Bruin[138], D. Salihagic[101], A. Salnikov[143], J. Salt[167], D. Salvatore[37a,37b], F. Salvatore[149], A. Salvucci[106], A. Salzburger[30], D. Sammel[48], D. Sampsonidis[154], A. Sanchez[104a,104b], J. Sánchez[167], V. Sanchez Martinez[167], H. Sandaker[119], R. L. Sandbach[76], H. G. Sander[83], M. P. Sanders[100], M. Sandhoff[175], C. Sandoval[162], R. Sandstroem[101], D. P. C. Sankey[131], M. Sannino[50a,50b], A. Sansoni[47], C. Santoni[34], R. Santonico[133a,133b], H. Santos[126a], I. Santoyo Castillo[149], K. Sapp[125], A. Sapronov[65], J. G. Saraiva[126a,126d], B. Sarrazin[21], O. Sasaki[66], Y. Sasaki[155], K. Sato[160], G. Sauvage[5,*], E. Sauvan[5], G. Savage[77], P. Savard[158,d], C. Sawyer[131], L. Sawyer[79,n], J. Saxon[31], C. Sbarra[20a], A. Sbrizzi[20a,20b], T. Scanlon[78], D. A. Scannicchio[163], M. Scarcella[150], V. Scarfone[37a,37b], J. Schaarschmidt[172], P. Schacht[101], D. Schaefer[30], R. Schaefer[42], J. Schaeffer[83], S. Schaepe[21], S. Schaetzel[58b], U. Schäfer[83], A. C. Schaffer[117], D. Schaile[100], R. D. Schamberger[148], V. Scharf[58a], V. A. Schegelsky[123], D. Scheirich[129], M. Schernau[163], C. Schiavi[50a,50b], C. Schillo[48], M. Schioppa[37a,37b], S. Schlenker[30], E. Schmidt[48], K. Schmieden[30], C. Schmitt[83], S. Schmitt[58b], S. Schmitt[42], B. Schneider[159a], Y. J. Schnellbach[74], U. Schnoor[44], L. Schoeffel[136], A. Schoening[58b], B. D. Schoenrock[90], E. Schopf[21], A. L. S. Schorlemmer[54], M. Schott[83], D. Schouten[159a], J. Schovancova[8], S. Schramm[49], M. Schreyer[174], C. Schroeder[83], N. Schuh[83], M. J. Schultens[21], H.-C. Schultz-Coulon[58a], H. Schulz[16], M. Schumacher[48], B. A. Schumm[137], Ph. Schune[136], C. Schwanenberger[84], A. Schwartzman[143], T. A. Schwarz[89], Ph. Schwegler[101], H. Schweiger[84], Ph. Schwemling[136], R. Schwienhorst[90], J. Schwindling[136], T. Schwindt[21], F. G. Sciacca[17], E. Scifo[117], G. Sciolla[23], F. Scuri[124a,124b], F. Scutti[21], J. Searcy[89], G. Sedov[42], E. Sedykh[123], P. Seema[21], S. C. Seidel[105], A. Seiden[137], F. Seifert[128], J. M. Seixas[24a], G. Sekhniaidze[104a], K. Sekhon[89], S. J. Sekula[40], D. M. Seliverstov[123,*], N. Semprini-Cesari[20a,20b], C. Serfon[30], L. Serin[117], L. Serkin[164a,164b], T. Serre[85], M. Sessa[134a,134b], R. Seuster[159a], H. Severini[113], T. Sfiligoj[75], F. Sforza[30], A. Sfyrla[30], E. Shabalina[54], M. Shamim[116], L. Y. Shan[33a], R. Shang[165], J. T. Shank[22], M. Shapiro[15], P. B. Shatalov[97], K. Shaw[164a,164b], S. M. Shaw[84], A. Shcherbakova[146a,146b], C. Y. Shehu[149], P. Sherwood[78], L. Shi[151,af], S. Shimizu[67], C. O. Shimmin[163], M. Shimojima[102], M. Shiyakova[65], A. Shmeleva[96], D. Shoaleh Saadi[95], M. J. Shochet[31], S. Shojaii[91a,91b], S. Shrestha[111], E. Shulga[98], M. A. Shupe[7], S. Shushkevich[42], P. Sicho[127], P. E. Sidebo[147], O. Sidiropoulou[174], D. Sidorov[114], A. Sidoti[20a,20b], F. Siegert[44], Dj. Sijacki[13], J. Silva[126a,126d],

Y. Silver[153], S. B. Silverstein[146a], V. Simak[128], O. Simard[5], Lj. Simic[13], S. Simion[117], E. Simioni[83], B. Simmons[78], D. Simon[34], R. Simoniello[91a,91b], P. Sinervo[158], N. B. Sinev[116], M. Sioli[20a,20b], G. Siragusa[174], A. N. Sisakyan[65,*], S. Yu. Sivoklokov[99], J. Sjölin[146a,146b], T. B. Sjursen[14], M. B. Skinner[72], H. P. Skottowe[57], P. Skubic[113], M. Slater[18], T. Slavicek[128], M. Slawinska[107], K. Sliwa[161], V. Smakhtin[172], B. H. Smart[46], L. Smestad[14], S. Yu. Smirnov[98], Y. Smirnov[98], L. N. Smirnova[99,ag], O. Smirnova[81], M. N. K. Smith[35], R. W. Smith[35], M. Smizanska[72], K. Smolek[128], A. A. Snesarev[96], G. Snidero[76], S. Snyder[25], R. Sobie[169,k], F. Socher[44], A. Soffer[153], D. A. Soh[151,af], C. A. Solans[30], M. Solar[128], J. Solc[128], E. Yu. Soldatov[98], U. Soldevila[167], A. A. Solodkov[130], A. Soloshenko[65], O. V. Solovyanov[130], V. Solovyev[123], P. Sommer[48], H. Y. Song[33b], N. Soni[1], A. Sood[15], A. Sopczak[128], B. Sopko[128], V. Sopko[128], V. Sorin[12], D. Sosa[58b], M. Sosebee[8], C. L. Sotiropoulou[124a,124b], R. Soualah[164a,164c], A. M. Soukharev[109,c], D. South[42], B. C. Sowden[77], S. Spagnolo[73a,73b], M. Spalla[124a,124b], F. Spanò[77], W. R. Spearman[57], D. Sperlich[16], F. Spettel[101], R. Spighi[20a], G. Spigo[30], L. A. Spiller[88], M. Spousta[129], T. Spreitzer[158], R. D. St. Denis[53,*], S. Staerz[44], J. Stahlman[122], R. Stamen[58a], S. Stamm[16], E. Stanecka[39], C. Stanescu[134a], M. Stanescu-Bellu[42], M. M. Stanitzki[42], S. Stapnes[119], E. A. Starchenko[130], J. Stark[55], P. Staroba[127], P. Starovoitov[42], R. Staszewski[39], P. Stavina[144a,*], P. Steinberg[25], B. Stelzer[142], H. J. Stelzer[30], O. Stelzer-Chilton[159a], H. Stenzel[52], G. A. Stewart[53], J. A. Stillings[21], M. C. Stockton[87], M. Stoebe[87], G. Stoicea[26a], P. Stolte[54], S. Stonjek[101], A. R. Stradling[8], A. Straessner[44], M. E. Stramaglia[17], J. Strandberg[147], S. Strandberg[146a,146b], A. Strandlie[119], E. Strauss[143], M. Strauss[113], P. Strizenec[144b], R. Ströhmer[174], D. M. Strom[116], R. Stroynowski[40], A. Strubig[106], S. A. Stucci[17], B. Stugu[14], N. A. Styles[42], D. Su[143], J. Su[125], R. Subramaniam[79], A. Succurro[12], Y. Sugaya[118], C. Suhr[108], M. Suk[128], V. V. Sulin[96], S. Sultansoy[4c], T. Sumida[68], S. Sun[57], X. Sun[33a], J. E. Sundermann[48], K. Suruliz[149], G. Susinno[37a,37b], M. R. Sutton[149], S. Suzuki[66], M. Svatos[127], S. Swedish[168], M. Swiatlowski[143], I. Sykora[144a], T. Sykora[129], D. Ta[90], C. Taccini[134a,134b], K. Tackmann[42], J. Taenzer[158], A. Taffard[163], R. Tafirout[159a], N. Taiblum[153], H. Takai[25], R. Takashima[69], H. Takeda[67], T. Takeshita[140], Y. Takubo[66], M. Talby[85], A. A. Talyshev[109,c], J. Y. C. Tam[174], K. G. Tan[88], J. Tanaka[155], R. Tanaka[117], S. Tanaka[66], B. B. Tannenwald[111], N. Tannoury[21], S. Tapprogge[83], S. Tarem[152], F. Tarrade[29], G. F. Tartarelli[91a], P. Tas[129], M. Tasevsky[127], T. Tashiro[68], E. Tassi[37a,37b], A. Tavares Delgado[126a,126b], Y. Tayalati[135d], F. E. Taylor[94], G. N. Taylor[88], W. Taylor[159b], F. A. Teischinger[30], M. Teixeira Dias Castanheira[76], P. Teixeira-Dias[77], K. K. Temming[48], H. Ten Kate[30], P. K. Teng[151], J. J. Teoh[118], F. Tepel[175], S. Terada[66], K. Terashi[155], J. Terron[82], S. Terzo[101], M. Testa[47], R. J. Teuscher[158,k], T. Theveneaux-Pelzer[34], J. P. Thomas[18], J. Thomas-Wilsker[77], E. N. Thompson[35], P. D. Thompson[18], R. J. Thompson[84], A. S. Thompson[53], L. A. Thomsen[176], E. Thomson[122], M. Thomson[28], R. P. Thun[89,*], M. J. Tibbetts[15], R. E. Ticse Torres[85], V. O. Tikhomirov[96,ah], Yu. A. Tikhonov[109,c], S. Timoshenko[98], E. Tiouchichine[85], P. Tipton[176], S. Tisserant[85], K. Todome[157], T. Todorov[5,*], S. Todorova-Nova[129], J. Tojo[70], S. Tokár[144a], K. Tokushuku[66], K. Tollefson[90], E. Tolley[57], L. Tomlinson[84], M. Tomoto[103], L. Tompkins[143,ai], K. Toms[105], E. Torrence[116], H. Torres[142], E. Torró Pastor[167], J. Toth[85,aj], F. Touchard[85], D. R. Tovey[139], T. Trefzger[174], L. Tremblet[30], A. Tricoli[30], I. M. Trigger[159a], S. Trincaz-Duvoid[80], M. F. Tripiana[12], W. Trischuk[158], B. Trocmé[55], C. Troncon[91a], M. Trottier-McDonald[15], M. Trovatelli[169], P. True[90], L. Truong[164a,164c], M. Trzebinski[39], A. Trzupek[39], C. Tsarouchas[30], J. C-L. Tseng[120], P. V. Tsiareshka[92], D. Tsionou[154], G. Tsipolitis[10], N. Tsirintanis[9], S. Tsiskaridze[12], V. Tsiskaridze[48], E. G. Tskhadadze[51a], I. I. Tsukerman[97], V. Tsulaia[15], S. Tsuno[66], D. Tsybychev[148], A. Tudorache[26a], V. Tudorache[26a], A. N. Tuna[122], S. A. Tupputi[20a,20b], S. Turchikhin[99,ag], D. Turecek[128], R. Turra[91a,91b], A. J. Turvey[40], P. M. Tuts[35], A. Tykhonov[49], M. Tylmad[146a,146b], M. Tyndel[131], I. Ueda[155], R. Ueno[29], M. Ughetto[146a,146b], M. Ugland[14], M. Uhlenbrock[21], F. Ukegawa[160], G. Unal[30], A. Undrus[25], G. Unel[163], F. C. Ungaro[48], Y. Unno[66], C. Unverdorben[100], J. Urban[144b], P. Urquijo[88], P. Urrejola[83], G. Usai[8], A. Usanova[62], L. Vacavant[85], V. Vacek[128], B. Vachon[87], C. Valderanis[83], N. Valencic[107], S. Valentinetti[20a,20b], A. Valero[167], L. Valery[12], S. Valkar[129], E. Valladolid Gallego[167], S. Vallecorsa[49], J. A. Valls Ferrer[167], W. Van Den Wollenberg[107], P. C. Van Der Deijl[107], R. van der Geer[107], H. van der Graaf[107], R. Van Der Leeuw[107], N. van Eldik[152], P. van Gemmeren[6], J. Van Nieuwkoop[142], I. van Vulpen[107], M. C. van Woerden[30], M. Vanadia[132a,132b], W. Vandelli[30], R. Vanguri[122], A. Vaniachine[6], F. Vannucci[80], G. Vardanyan[177], R. Vari[132a], E. W. Varnes[7], T. Varol[40], D. Varouchas[80], A. Vartapetian[8], K. E. Varvell[150], F. Vazeille[34], T. Vazquez Schroeder[87], J. Veatch[7], L. M. Veloce[158], F. Veloso[126a,126c], T. Velz[21], S. Veneziano[132a], A. Ventura[73a,73b], D. Ventura[86], M. Venturi[169], N. Venturi[158], A. Venturini[23], V. Vercesi[121a], M. Verducci[132a,132b], W. Verkerke[107], J. C. Vermeulen[107], A. Vest[44], M. C. Vetterli[142,d], O. Viazlo[81], I. Vichou[165], T. Vickey[139], O. E. Vickey Boeriu[139], G. H. A. Viehhauser[120], S. Viel[15], R. Vigne[62], M. Villa[20a,20b], M. Villaplana Perez[91a,91b], E. Vilucchi[47], M. G. Vincter[29], V. B. Vinogradov[65], I. Vivarelli[149], F. Vives Vaque[3], S. Vlachos[10], D. Vladoiu[100], M. Vlasak[128], M. Vogel[32a], P. Vokac[128], G. Volpi[124a,124b], M. Volpi[88], H. von der Schmitt[101], H. von Radziewski[48], E. von Toerne[21], V. Vorobel[129], K. Vorobev[98], M. Vos[167], R. Voss[30], J. H. Vossebeld[74], N. Vranjes[13], M. Vranjes Milosavljevic[13], V. Vrba[127], M. Vreeswijk[107], R. Vuillermet[30], I. Vukotic[31], Z. Vykydal[128], P. Wagner[21], W. Wagner[175], H. Wahlberg[71], S. Wahrmund[44], J. Wakabayashi[103], J. Walder[72], R. Walker[100], W. Walkowiak[141], C. Wang[151], F. Wang[173], H. Wang[15], H. Wang[40], J. Wang[42], J. Wang[33a], K. Wang[87], R. Wang[6],

S. M. Wang[151], T. Wang[21], T. Wang[35], X. Wang[176], C. Wanotayaroj[116], A. Warburton[87], C. P. Ward[28], D. R. Wardrope[78], M. Warsinsky[48], A. Washbrook[46], C. Wasicki[42], P. M. Watkins[18], A. T. Watson[18], I. J. Watson[150], M. F. Watson[18], G. Watts[138], S. Watts[84], B. M. Waugh[78], S. Webb[84], M. S. Weber[17], S. W. Weber[174], J. S. Webster[31], A. R. Weidberg[120], B. Weinert[61], J. Weingarten[54], C. Weiser[48], H. Weits[107], P. S. Wells[30], T. Wenaus[25], T. Wengler[30], S. Wenig[30], N. Wermes[21], M. Werner[48], P. Werner[30], M. Wessels[58a], J. Wetter[161], K. Whalen[116], A. M. Wharton[72], A. White[8], M. J. White[1], R. White[32b], S. White[124a,124b], D. Whiteson[163], F. J. Wickens[131], W. Wiedenmann[173], M. Wielers[131], P. Wienemann[21], C. Wiglesworth[36], L. A. M. Wiik-Fuchs[21], A. Wildauer[101], H. G. Wilkens[30], H. H. Williams[122], S. Williams[107], C. Willis[90], S. Willocq[86], A. Wilson[89], J. A. Wilson[18], I. Wingerter-Seez[5], F. Winklmeier[116], B. T. Winter[21], M. Wittgen[143], J. Wittkowski[100], S. J. Wollstadt[83], M. W. Wolter[39], H. Wolters[126a,126c], B. K. Wosiek[39], J. Wotschack[30], M. J. Woudstra[84], K. W. Wozniak[39], M. Wu[55], M. Wu[31], S. L. Wu[173], X. Wu[49], Y. Wu[89], T. R. Wyatt[84], B. M. Wynne[46], S. Xella[36], D. Xu[33a], L. Xu[33b,ak], B. Yabsley[150], S. Yacoob[145a], R. Yakabe[67], M. Yamada[66], Y. Yamaguchi[118], A. Yamamoto[66], S. Yamamoto[155], T. Yamanaka[155], K. Yamauchi[103], Y. Yamazaki[67], Z. Yan[22], H. Yang[33e], H. Yang[173], Y. Yang[151], W-M. Yao[15], Y. Yasu[66], E. Yatsenko[5], K. H. Yau Wong[21], J. Ye[40], S. Ye[25], I. Yeletskikh[65], A. L. Yen[57], E. Yildirim[42], K. Yorita[171], R. Yoshida[6], K. Yoshihara[122], C. Young[143], C. J. S. Young[30], S. Youssef[22], D. R. Yu[15], J. Yu[8], J. M. Yu[89], J. Yu[114], L. Yuan[67], S. P. Y. Yuen[21], A. Yurkewicz[108], I. Yusuff[28,al], B. Zabinski[39], R. Zaidan[63], A. M. Zaitsev[130,ab], J. Zalieckas[14], A. Zaman[148], S. Zambito[57], L. Zanello[132a,132b], D. Zanzi[88], C. Zeitnitz[175], M. Zeman[128], A. Zemla[38a], K. Zengel[23], O. Zenin[130], T. Ženiš[144a], D. Zerwas[117], D. Zhang[89], F. Zhang[173], H. Zhang[33c], J. Zhang[6], L. Zhang[48], R. Zhang[33b], X. Zhang[33d], Z. Zhang[117], X. Zhao[40], Y. Zhao[33d,117], Z. Zhao[33b], A. Zhemchugov[65], J. Zhong[120], B. Zhou[89], C. Zhou[45], L. Zhou[35], L. Zhou[40], N. Zhou[163], C. G. Zhu[33d], H. Zhu[33a], J. Zhu[89], Y. Zhu[33b], X. Zhuang[33a], K. Zhukov[96], A. Zibell[174], D. Zieminska[61], N. I. Zimine[65], C. Zimmermann[83], S. Zimmermann[48], Z. Zinonos[54], M. Zinser[83], M. Ziolkowski[141], L. Živković[13], G. Zobernig[173], A. Zoccoli[20a,20b], M. zur Nedden[16], G. Zurzolo[104a,104b], L. Zwalinski[30]

[1] Department of Physics, University of Adelaide, Adelaide, Australia
[2] Physics Department, SUNY Albany, Albany, NY, USA
[3] Department of Physics, University of Alberta, Edmonton, AB, Canada
[4] [(a)]Department of Physics, Ankara University, Ankara, Turkey; [(b)]Istanbul Aydin University, Istanbul, Turkey; [(c)]Division of Physics, TOBB University of Economics and Technology, Ankara, Turkey
[5] LAPP, CNRS/IN2P3 and Université Savoie Mont Blanc, Annecy-le-Vieux, France
[6] High Energy Physics Division, Argonne National Laboratory, Argonne, IL, USA
[7] Department of Physics, University of Arizona, Tucson, AZ, USA
[8] Department of Physics, The University of Texas at Arlington, Arlington, TX, USA
[9] Physics Department, University of Athens, Athens, Greece
[10] Physics Department, National Technical University of Athens, Zografou, Greece
[11] Institute of Physics, Azerbaijan Academy of Sciences, Baku, Azerbaijan
[12] Institut de Física d'Altes Energies and Departament de Física de la Universitat Autònoma de Barcelona, Barcelona, Spain
[13] Institute of Physics, University of Belgrade, Belgrade, Serbia
[14] Department for Physics and Technology, University of Bergen, Bergen, Norway
[15] Physics Division, Lawrence Berkeley National Laboratory and University of California, Berkeley, CA, USA
[16] Department of Physics, Humboldt University, Berlin, Germany
[17] Albert Einstein Center for Fundamental Physics and Laboratory for High Energy Physics, University of Bern, Bern, Switzerland
[18] School of Physics and Astronomy, University of Birmingham, Birmingham, UK
[19] [(a)]Department of Physics, Bogazici University, Istanbul, Turkey; [(b)]Department of Physics Engineering, Gaziantep University, Gaziantep, Turkey; [(c)]Department of Physics, Dogus University, Istanbul, Turkey
[20] [(a)]INFN Sezione di Bologna, Bologna, Italy; [(b)]Dipartimento di Fisica e Astronomia, Università di Bologna, Bologna, Italy
[21] Physikalisches Institut, University of Bonn, Bonn, Germany
[22] Department of Physics, Boston University, Boston, MA, USA
[23] Department of Physics, Brandeis University, Waltham, MA, USA
[24] [(a)]Universidade Federal do Rio De Janeiro COPPE/EE/IF, Rio de Janeiro, Brazil; [(b)]Electrical Circuits Department, Federal University of Juiz de Fora (UFJF), Juiz de Fora, Brazil; [(c)]Federal University of Sao Joao del Rei (UFSJ), Sao Joao del Rei, Brazil; [(d)]Instituto de Fisica, Universidade de Sao Paulo, São Paulo, Brazil
[25] Physics Department, Brookhaven National Laboratory, Upton, NY, USA

[26] [(a)]National Institute of Physics and Nuclear Engineering, Bucharest, Romania; [(b)]Physics Department, National Institute for Research and Development of Isotopic and Molecular Technologies, Cluj Napoca, Romania; [(c)]University Politehnica Bucharest, Bucharest, Romania; [(d)]West University in Timisoara, Timisoara, Romania
[27] Departamento de Física, Universidad de Buenos Aires, Buenos Aires, Argentina
[28] Cavendish Laboratory, University of Cambridge, Cambridge, UK
[29] Department of Physics, Carleton University, Ottawa, ON, Canada
[30] CERN, Geneva, Switzerland
[31] Enrico Fermi Institute, University of Chicago, Chicago, IL, USA
[32] [(a)]Departamento de Física, Pontificia Universidad Católica de Chile, Santiago, Chile; [(b)]Departamento de Física, Universidad Técnica Federico Santa María, Valparaiso, Chile
[33] [(a)]Institute of High Energy Physics, Chinese Academy of Sciences, Beijing, China; [(b)]Department of Modern Physics, University of Science and Technology of China, Hefei, Anhui, China; [(c)]Department of Physics, Nanjing University, Nanjing, Jiangsu, China; [(d)]School of Physics, Shandong University, Shandong, China; [(e)]Shanghai Key Laboratory for Particle Physics and Cosmology, Department of Physics and Astronomy, Shanghai Jiao Tong University, Shanghai, China; [(f)]Physics Department, Tsinghua University, Beijing 100084, China
[34] Laboratoire de Physique Corpusculaire, Clermont Université and Université Blaise Pascal and CNRS/IN2P3, Clermont-Ferrand, France
[35] Nevis Laboratory, Columbia University, Irvington, NY, USA
[36] Niels Bohr Institute, University of Copenhagen, Copenhagen, Denmark
[37] [(a)]INFN Gruppo Collegato di Cosenza, Laboratori Nazionali di Frascati, Frascati, Italy; [(b)]Dipartimento di Fisica, Università della Calabria, Rende, Italy
[38] [(a)]AGH University of Science and Technology, Faculty of Physics and Applied Computer Science, Kraków, Poland; [(b)]Marian Smoluchowski Institute of Physics, Jagiellonian University, Kraków, Poland
[39] Institute of Nuclear Physics, Polish Academy of Sciences, Kraków, Poland
[40] Physics Department, Southern Methodist University, Dallas, TX, USA
[41] Physics Department, University of Texas at Dallas, Richardson, TX, USA
[42] DESY, Hamburg and Zeuthen, Germany
[43] Institut für Experimentelle Physik IV, Technische Universität Dortmund, Dortmund, Germany
[44] Institut für Kern- und Teilchenphysik, Technische Universität Dresden, Dresden, Germany
[45] Department of Physics, Duke University, Durham, NC, USA
[46] SUPA-School of Physics and Astronomy, University of Edinburgh, Edinburgh, UK
[47] INFN Laboratori Nazionali di Frascati, Frascati, Italy
[48] Fakultät für Mathematik und Physik, Albert-Ludwigs-Universität, Freiburg, Germany
[49] Section de Physique, Université de Genève, Geneva, Switzerland
[50] [(a)]INFN Sezione di Genova, Genoa, Italy; [(b)]Dipartimento di Fisica, Università di Genova, Genoa, Italy
[51] [(a)]E. Andronikashvili Institute of Physics, Iv. Javakhishvili Tbilisi State University, Tbilisi, Georgia; [(b)]High Energy Physics Institute, Tbilisi State University, Tbilisi, Georgia
[52] II Physikalisches Institut, Justus-Liebig-Universität Giessen, Giessen, Germany
[53] SUPA-School of Physics and Astronomy, University of Glasgow, Glasgow, UK
[54] II Physikalisches Institut, Georg-August-Universität, Göttingen, Germany
[55] Laboratoire de Physique Subatomique et de Cosmologie, Université Grenoble-Alpes, CNRS/IN2P3, Grenoble, France
[56] Department of Physics, Hampton University, Hampton, VA, USA
[57] Laboratory for Particle Physics and Cosmology, Harvard University, Cambridge, MA, USA
[58] [(a)]Kirchhoff-Institut für Physik, Ruprecht-Karls-Universität Heidelberg, Heidelberg, Germany; [(b)]Physikalisches Institut, Ruprecht-Karls-Universität Heidelberg, Heidelberg, Germany; [(c)]ZITI Institut für technische Informatik, Ruprecht-Karls-Universität Heidelberg, Mannheim, Germany
[59] Faculty of Applied Information Science, Hiroshima Institute of Technology, Hiroshima, Japan
[60] [(a)]Department of Physics, The Chinese University of Hong Kong, Shatin, NT, Hong Kong; [(b)]Department of Physics, The University of Hong Kong, Hong Kong, Hong Kong; [(c)]Department of Physics, The Hong Kong University of Science and Technology, Clear Water Bay, Kowloon, Hong Kong, China
[61] Department of Physics, Indiana University, Bloomington, IN, USA
[62] Institut für Astro- und Teilchenphysik, Leopold-Franzens-Universität, Innsbruck, Austria
[63] University of Iowa, Iowa City, IA, USA

[64] Department of Physics and Astronomy, Iowa State University, Ames, IA, USA
[65] Joint Institute for Nuclear Research, JINR Dubna, Dubna, Russia
[66] KEK, High Energy Accelerator Research Organization, Tsukuba, Japan
[67] Graduate School of Science, Kobe University, Kobe, Japan
[68] Faculty of Science, Kyoto University, Kyoto, Japan
[69] Kyoto University of Education, Kyoto, Japan
[70] Department of Physics, Kyushu University, Fukuoka, Japan
[71] Instituto de Física La Plata, Universidad Nacional de La Plata and CONICET, La Plata, Argentina
[72] Physics Department, Lancaster University, Lancaster, UK
[73] [(a)]INFN Sezione di Lecce, Lecce, Italy; [(b)]Dipartimento di Matematica e Fisica, Università del Salento, Lecce, Italy
[74] Oliver Lodge Laboratory, University of Liverpool, Liverpool, UK
[75] Department of Physics, Jožef Stefan Institute and University of Ljubljana, Ljubljana, Slovenia
[76] School of Physics and Astronomy, Queen Mary University of London, London, UK
[77] Department of Physics, Royal Holloway University of London, Surrey, UK
[78] Department of Physics and Astronomy, University College London, London, UK
[79] Louisiana Tech University, Ruston, LA, USA
[80] Laboratoire de Physique Nucléaire et de Hautes Energies, UPMC and Université Paris-Diderot and CNRS/IN2P3, Paris, France
[81] Fysiska institutionen, Lunds universitet, Lund, Sweden
[82] Departamento de Fisica Teorica C-15, Universidad Autonoma de Madrid, Madrid, Spain
[83] Institut für Physik, Universität Mainz, Mainz, Germany
[84] School of Physics and Astronomy, University of Manchester, Manchester, UK
[85] CPPM, Aix-Marseille Université and CNRS/IN2P3, Marseille, France
[86] Department of Physics, University of Massachusetts, Amherst, MA, USA
[87] Department of Physics, McGill University, Montreal, QC, Canada
[88] School of Physics, University of Melbourne, Melbourne, VIC, Australia
[89] Department of Physics, The University of Michigan, Ann Arbor, MI, USA
[90] Department of Physics and Astronomy, Michigan State University, East Lansing, MI, USA
[91] [(a)]INFN Sezione di Milano, Milan, Italy; [(b)]Dipartimento di Fisica, Università di Milano, Milan, Italy
[92] B.I. Stepanov Institute of Physics, National Academy of Sciences of Belarus, Minsk, Republic of Belarus
[93] National Scientific and Educational Centre for Particle and High Energy Physics, Minsk, Republic of Belarus
[94] Department of Physics, Massachusetts Institute of Technology, Cambridge, MA, USA
[95] Group of Particle Physics, University of Montreal, Montreal, QC, Canada
[96] P.N. Lebedev Institute of Physics, Academy of Sciences, Moscow, Russia
[97] Institute for Theoretical and Experimental Physics (ITEP), Moscow, Russia
[98] National Research Nuclear University MEPhI, Moscow, Russia
[99] D.V. Skobeltsyn Institute of Nuclear Physics, M.V. Lomonosov Moscow State University, Moscow, Russia
[100] Fakultät für Physik, Ludwig-Maximilians-Universität München, Munich, Germany
[101] Max-Planck-Institut für Physik (Werner-Heisenberg-Institut), Munich, Germany
[102] Nagasaki Institute of Applied Science, Nagasaki, Japan
[103] Graduate School of Science and Kobayashi-Maskawa Institute, Nagoya University, Nagoya, Japan
[104] [(a)]INFN Sezione di Napoli, Naples, Italy; [(b)]Dipartimento di Fisica, Università di Napoli, Naples, Italy
[105] Department of Physics and Astronomy, University of New Mexico, Albuquerque, NM, USA
[106] Institute for Mathematics, Astrophysics and Particle Physics, Radboud University Nijmegen/Nikhef, Nijmegen, The Netherlands
[107] Nikhef National Institute for Subatomic Physics and University of Amsterdam, Amsterdam, The Netherlands
[108] Department of Physics, Northern Illinois University, De Kalb, IL, USA
[109] Budker Institute of Nuclear Physics, SB RAS, Novosibirsk, Russia
[110] Department of Physics, New York University, New York, NY, USA
[111] Ohio State University, Columbus, OH, USA
[112] Faculty of Science, Okayama University, Okayama, Japan
[113] Homer L. Dodge Department of Physics and Astronomy, University of Oklahoma, Norman, OK, USA
[114] Department of Physics, Oklahoma State University, Stillwater, OK, USA

[115] Palacký University, RCPTM, Olomouc, Czech Republic
[116] Center for High Energy Physics, University of Oregon, Eugene, OR, USA
[117] LAL, Université Paris-Sud and CNRS/IN2P3, Orsay, France
[118] Graduate School of Science, Osaka University, Osaka, Japan
[119] Department of Physics, University of Oslo, Oslo, Norway
[120] Department of Physics, Oxford University, Oxford, UK
[121] [(a)]INFN Sezione di Pavia, Pavia, Italy; [(b)]Dipartimento di Fisica, Università di Pavia, Pavia, Italy
[122] Department of Physics, University of Pennsylvania, Philadelphia, PA, USA
[123] National Research Centre "Kurchatov Institute" B.P.Konstantinov, Petersburg Nuclear Physics Institute, St. Petersburg, Russia
[124] [(a)]INFN Sezione di Pisa, Pisa, Italy; [(b)]Dipartimento di Fisica E. Fermi, Università di Pisa, Pisa, Italy
[125] Department of Physics and Astronomy, University of Pittsburgh, Pittsburgh, PA, USA
[126] [(a)]Laboratório de Instrumentação e Física Experimental de Partículas-LIP, Lisbon, Portugal; [(b)]Faculdade de Ciências, Universidade de Lisboa, Lisbon, Portugal; [(c)]Department of Physics, University of Coimbra, Coimbra, Portugal; [(d)]Centro de Física Nuclear da Universidade de Lisboa, Lisbon, Portugal; [(e)]Departamento de Fisica, Universidade do Minho, Braga, Portugal; [(f)]Departamento de Fisica Teorica y del Cosmos and CAFPE, Universidad de Granada, Granada, Spain; [(g)]Dep Fisica and CEFITEC of Faculdade de Ciencias e Tecnologia, Universidade Nova de Lisboa, Caparica, Portugal
[127] Institute of Physics, Academy of Sciences of the Czech Republic, Prague, Czech Republic
[128] Czech Technical University in Prague, Prague, Czech Republic
[129] Faculty of Mathematics and Physics, Charles University in Prague, Prague, Czech Republic
[130] State Research Center Institute for High Energy Physics, Protvino, Russia
[131] Particle Physics Department, Rutherford Appleton Laboratory, Didcot, UK
[132] [(a)]INFN Sezione di Roma, Rome, Italy; [(b)]Dipartimento di Fisica, Sapienza Università di Roma, Rome, Italy
[133] [(a)]INFN Sezione di Roma Tor Vergata, Rome, Italy; [(b)]Dipartimento di Fisica, Università di Roma Tor Vergata, Rome, Italy
[134] [(a)]INFN Sezione di Roma Tre, Rome, Italy; [(b)]Dipartimento di Matematica e Fisica, Università Roma Tre, Rome, Italy
[135] [(a)]Faculté des Sciences Ain Chock, Réseau Universitaire de Physique des Hautes Energies-Université Hassan II, Casablanca, Morocco; [(b)]Centre National de l'Energie des Sciences Techniques Nucleaires, Rabat, Morocco; [(c)]Faculté des Sciences Semlalia, Université Cadi Ayyad, LPHEA-Marrakech, Marrakech, Morocco; [(d)]Faculté des Sciences, Université Mohamed Premier and LPTPM, Oujda, Morocco; [(e)]Faculté des Sciences, Université Mohammed V-Agdal, Rabat, Morocco
[136] DSM/IRFU (Institut de Recherches sur les Lois Fondamentales de l'Univers), CEA Saclay (Commissariat à l'Energie Atomique et aux Energies Alternatives), Gif-sur-Yvette, France
[137] Santa Cruz Institute for Particle Physics, University of California Santa Cruz, Santa Cruz, CA, USA
[138] Department of Physics, University of Washington, Seattle, WA, USA
[139] Department of Physics and Astronomy, University of Sheffield, Sheffield, UK
[140] Department of Physics, Shinshu University, Nagano, Japan
[141] Fachbereich Physik, Universität Siegen, Siegen, Germany
[142] Department of Physics, Simon Fraser University, Burnaby, BC, Canada
[143] SLAC National Accelerator Laboratory, Stanford, CA, USA
[144] [(a)]Faculty of Mathematics, Physics and Informatics, Comenius University, Bratislava, Slovak Republic; [(b)]Department of Subnuclear Physics, Institute of Experimental Physics of the Slovak Academy of Sciences, Kosice, Slovak Republic
[145] [(a)]Department of Physics, University of Cape Town, Cape Town, South Africa; [(b)]Department of Physics, University of Johannesburg, Johannesburg, South Africa; [(c)]School of Physics, University of the Witwatersrand, Johannesburg, South Africa
[146] [(a)]Department of Physics, Stockholm University, Stockholm, Sweden; [(b)]The Oskar Klein Centre, Stockholm, Sweden
[147] Physics Department, Royal Institute of Technology, Stockholm, Sweden
[148] Departments of Physics and Astronomy and Chemistry, Stony Brook University, Stony Brook, NY, USA
[149] Department of Physics and Astronomy, University of Sussex, Brighton, UK
[150] School of Physics, University of Sydney, Sydney, Australia
[151] Institute of Physics, Academia Sinica, Taipei, Taiwan
[152] Department of Physics, Technion: Israel Institute of Technology, Haifa, Israel

[153] Raymond and Beverly Sackler School of Physics and Astronomy, Tel Aviv University, Tel Aviv, Israel
[154] Department of Physics, Aristotle University of Thessaloniki, Thessaloníki, Greece
[155] International Center for Elementary Particle Physics and Department of Physics, The University of Tokyo, Tokyo, Japan
[156] Graduate School of Science and Technology, Tokyo Metropolitan University, Tokyo, Japan
[157] Department of Physics, Tokyo Institute of Technology, Tokyo, Japan
[158] Department of Physics, University of Toronto, Toronto, ON, Canada
[159] [(a)]TRIUMF, Vancouver, BC, Canada; [(b)]Department of Physics and Astronomy, York University, Toronto, ON, Canada
[160] Faculty of Pure and Applied Sciences, University of Tsukuba, Tsukuba, Japan
[161] Department of Physics and Astronomy, Tufts University, Medford, MA, USA
[162] Centro de Investigaciones, Universidad Antonio Narino, Bogotá, Colombia
[163] Department of Physics and Astronomy, University of California Irvine, Irvine, CA, USA
[164] [(a)]INFN Gruppo Collegato di Udine, Sezione di Trieste, Udine, Italy; [(b)]ICTP, Trieste, Italy; [(c)]Dipartimento di Chimica Fisica e Ambiente, Università di Udine, Udine, Italy
[165] Department of Physics, University of Illinois, Urbana, IL, USA
[166] Department of Physics and Astronomy, University of Uppsala, Uppsala, Sweden
[167] Instituto de Física Corpuscular (IFIC) and Departamento de Física Atómica, Molecular y Nuclear and Departamento de Ingeniería Electrónica and Instituto de Microelectrónica de Barcelona (IMB-CNM), University of Valencia and CSIC, Valencia, Spain
[168] Department of Physics, University of British Columbia, Vancouver, BC, Canada
[169] Department of Physics and Astronomy, University of Victoria, Victoria, BC, Canada
[170] Department of Physics, University of Warwick, Coventry, UK
[171] Waseda University, Tokyo, Japan
[172] Department of Particle Physics, The Weizmann Institute of Science, Rehovot, Israel
[173] Department of Physics, University of Wisconsin, Madison, WI, USA
[174] Fakultät für Physik und Astronomie, Julius-Maximilians-Universität, Würzburg, Germany
[175] Fachbereich C Physik, Bergische Universität Wuppertal, Wuppertal, Germany
[176] Department of Physics, Yale University, New Haven, CT, USA
[177] Yerevan Physics Institute, Yerevan, Armenia
[178] Centre de Calcul de l'Institut National de Physique Nucléaire et de Physique des Particules (IN2P3), Villeurbanne, France

[a] Also at Department of Physics, King's College London, London, UK
[b] Also at Institute of Physics, Azerbaijan Academy of Sciences, Baku, Azerbaijan
[c] Also at Novosibirsk State University, Novosibirsk, Russia
[d] Also at TRIUMF, Vancouver, BC, Canada
[e] Also at Department of Physics, California State University, Fresno, CA, USA
[f] Also at Department of Physics, University of Fribourg, Fribourg, Switzerland
[g] Also at Departamento de Fisica e Astronomia, Faculdade de Ciencias, Universidade do Porto, Porto, Portugal
[h] Also at Tomsk State University, Tomsk, Russia
[i] Also at CPPM, Aix-Marseille Université and CNRS/IN2P3, Marseille, France
[j] Also at Universita di Napoli Parthenope, Naples, Italy
[k] Also at Institute of Particle Physics (IPP), Waterloo, Canada
[l] Also at Particle Physics Department, Rutherford Appleton Laboratory, Didcot, UK
[m] Also at Department of Physics, St. Petersburg State Polytechnical University, St. Petersburg, Russia
[n] Also at Louisiana Tech University, Ruston, LA, USA
[o] Also at Institucio Catalana de Recerca i Estudis Avancats, ICREA, Barcelona, Spain
[p] Also at Graduate School of Science, Osaka University, Osaka, Japan
[q] Also at Department of Physics, National Tsing Hua University, Taiwan
[r] Also at Department of Physics, The University of Texas at Austin, Austin, TX, USA
[s] Also at Institute of Theoretical Physics, Ilia State University, Tbilisi, Georgia
[t] Also at CERN, Geneva, Switzerland
[u] Also at Georgian Technical University (GTU), Tbilisi, Georgia
[v] Also at Manhattan College, New York, NY, USA
[w] Also at Hellenic Open University, Patras, Greece

[x] Also at Institute of Physics, Academia Sinica, Taipei, Taiwan
[y] Also at LAL, Université Paris-Sud and CNRS/IN2P3, Orsay, France
[z] Also at Academia Sinica Grid Computing, Institute of Physics, Academia Sinica, Taipei, Taiwan
[aa] Also at School of Physics, Shandong University, Shandong, China
[ab] Also at Moscow Institute of Physics and Technology State University, Dolgoprudny, Russia
[ac] Also at Section de Physique, Université de Genève, Geneva, Switzerland
[ad] Also at International School for Advanced Studies (SISSA), Trieste, Italy
[ae] Also at Department of Physics and Astronomy, University of South Carolina, Columbia, SC, USA
[af] Also at School of Physics and Engineering, Sun Yat-sen University, Guangzhou, China
[ag] Also at Faculty of Physics, M.V.Lomonosov Moscow State University, Moscow, Russia
[ah] Also at National Research Nuclear University MEPhI, Moscow, Russia
[ai] Also at Department of Physics, Stanford University, Stanford, CA, USA
[aj] Also at Institute for Particle and Nuclear Physics, Wigner Research Centre for Physics, Budapest, Hungary
[ak] Also at Department of Physics, The University of Michigan, Ann Arbor, MI, USA
[al] Also at University of Malaya, Department of Physics, Kuala Lumpur, Malaysia
* Deceased

PHYSICAL REVIEW D **93,** 052002 (2016)

Search for the electroweak production of supersymmetric particles in $\sqrt{s} = 8$ TeV pp collisions with the ATLAS detector

G. Aad *et al.*[*]
(ATLAS Collaboration)
(Received 23 September 2015; published 4 March 2016)

The ATLAS experiment has performed extensive searches for the electroweak production of charginos, neutralinos, and staus. This article summarizes and extends the search for electroweak supersymmetry with new analyses targeting scenarios not covered by previously published searches. New searches use vector-boson fusion production, initial-state radiation jets, and low-momentum lepton final states, as well as multivariate analysis techniques to improve the sensitivity to scenarios with small mass splittings and low-production cross sections. Results are based on 20 fb^{-1} of proton-proton collision data at $\sqrt{s} = 8$ TeV recorded with the ATLAS experiment at the Large Hadron Collider. No significant excess beyond Standard Model expectations is observed. The new and existing searches are combined and interpreted in terms of 95% confidence-level exclusion limits in simplified models, where a single production process and decay mode is assumed, as well as within phenomenological supersymmetric models.

DOI: 10.1103/PhysRevD.93.052002

I. INTRODUCTION

Supersymmetry (SUSY) [1–9] is a space-time symmetry that postulates for each Standard Model (SM) particle the existence of a partner state whose spin differs by one-half unit. The introduction of these new SUSY particles (sparticles) provides a potential solution to the hierarchy problem [10–13]. If R-parity is conserved [14–18], as assumed in this article, sparticles are always produced in pairs and the lightest supersymmetric particle (LSP) emerges as a stable dark-matter candidate.

The charginos and neutralinos are mixtures of the bino, winos, and higgsinos, collectively referred to as the electroweakinos, that are superpartners of the U(1), SU(2) gauge bosons and the Higgs bosons, respectively. Their mass eigenstates are referred to as $\tilde{\chi}_i^{\pm}$ ($i = 1, 2$) and $\tilde{\chi}_j^0$ ($j = 1, 2, 3, 4$) in order of increasing mass. The direct production of charginos, neutralinos, and sleptons ($\tilde{\ell}$) through electroweak (EW) interactions may dominate the SUSY production at the Large Hadron Collider (LHC) if the masses of the gluinos and squarks are large. Previous searches for electroweak SUSY production at ATLAS targeted the production of $\tilde{\ell}^+\tilde{\ell}^-$, $\tilde{\tau}^+\tilde{\tau}^-$, $\tilde{\chi}_1^+\tilde{\chi}_1^-$ (decaying through $\tilde{\ell}$ or W bosons), $\tilde{\chi}_1^{\pm}\tilde{\chi}_2^0$ (decaying through $\tilde{\ell}$ or W and Z/h bosons), and $\tilde{\chi}_2^0\tilde{\chi}_3^0$ (decaying through $\tilde{\ell}$ or Z bosons) [19–23], and found no significant excess beyond SM expectations. These searches are typically sensitive to scenarios where there is a relatively large $O(m_{W,Z})$ splitting between the produced sparticles and the LSP, leaving uncovered territory for smaller mass splittings.

This article addresses EW SUSY production based on the 20.3 fb^{-1} of $\sqrt{s} = 8$ TeV proton-proton collisions collected by the ATLAS experiment in 2012. A series of new analyses targeting regions in parameter space not covered by previous ATLAS analyses [19–23] are presented. The results from new and published searches are combined and reinterpreted to provide the final 8 TeV ATLAS limits on the production of EW SUSY particles in a variety of models. The dependence of the limits on the mass of the intermediate slepton in models of electroweakino production with $\tilde{\ell}$-mediated decays is also studied, thus generalizing the results of Refs. [19–21].

In cases where the LSP is wino or higgsino dominated, the lighter electroweakino states $\tilde{\chi}_1^{\pm}$, $\tilde{\chi}_2^0$ can have mass differences with the $\tilde{\chi}_1^0$ ranging from a few GeV to a few tens of GeV, depending on the values of the other parameters in the mixing matrix [24]. In particular, in naturalness-inspired models [25,26] the higgsino must be light, so the $\tilde{\chi}_1^0$, $\tilde{\chi}_2^0$, and $\tilde{\chi}_1^{\pm}$ are usually higgsino-dominated and have a small mass splitting. Therefore, a situation with a light $\tilde{\chi}_1^0$ approximately mass degenerate with the $\tilde{\chi}_1^{\pm}$ and $\tilde{\chi}_2^0$ has a strong theoretical motivation. A relatively low mass splitting between the produced sparticles and the LSP (referred to as compressed scenarios) results in low-momentum decay products that are difficult to reconstruct efficiently, and probing these signatures is experimentally challenging. The new analyses introduced in this article improve the sensitivity to the compressed spectra. The two- and three-lepton searches for $\tilde{\chi}_1^+\tilde{\chi}_1^-$ and $\tilde{\chi}_1^{\pm}\tilde{\chi}_2^0$ production in Refs. [19,20] are extended by lowering the transverse momentum threshold on reconstructed leptons, and by boosting the electroweak SUSY system through the

[*]Full author list given at the end of the article.

Published by the American Physical Society under the terms of the Creative Commons Attribution 3.0 License. Further distribution of this work must maintain attribution to the author(s) and the published article's title, journal citation, and DOI.

 © 2016 CERN, for the ATLAS Collaboration

requirement of QCD initial state radiation (ISR). The search for the vector-boson fusion (VBF) production of $\tilde{\chi}_1^{\pm}\tilde{\chi}_1^{\pm}$ uses the signature of a same-sign light lepton (e, μ) pair with two jets to probe compressed spectra.

In many SUSY scenarios with large $\tan\beta$, the stau ($\tilde{\tau}$) is lighter than the selectron and smuon [27], resulting in tau-rich final states. Coannihilation processes [28] favor a light $\tilde{\tau}$ that has a small mass splitting with a bino LSP, as it can set the relic density to the observed value [29]. An additional new search is presented here, which uses a final state with two hadronically decaying τ leptons and multivariate techniques to improve the sensitivity to direct $\tilde{\tau}$ production compared to the search presented in Ref. [22].

Searches for the electroweak production of SUSY particles have been conducted at the Tevatron [30,31] and by the CMS Collaboration [32–34]. At LEP [35–39], searches set lower limits of 103.5 GeV, 99.9 GeV, 94.6 GeV, and 86.6 GeV at 95% confidence level (CL) on the mass of promptly decaying charginos, selectrons, smuons, and staus, respectively. For the interval $0.1 \lesssim \Delta m(\tilde{\chi}_1^{\pm}, \tilde{\chi}_1^0) \lesssim 3$ GeV, the chargino mass limit set by LEP degrades to 91.9 GeV. The slepton mass limits from LEP assume gaugino mass unification, which is not assumed in the results presented here.

The article is organized as follows: Sec. II describes the signal models studied in this article; Sec. III provides a brief description of the ATLAS detector; Secs. IV and V outline the Monte Carlo (MC) simulation and event selection, respectively; Sec. VI discusses the analysis strategy common to all analyses studied in this article; Sec. VII presents the direct stau production search; Sec. VIII presents the compressed spectra searches in direct production; Sec. IX presents the search for same-sign chargino-pair production via VBF; Sec. X provides a global overview of the results of the ATLAS searches for electroweakino production at 8 TeV, integrating the results of the new analyses with published analyses in the framework of several relevant signal models; and finally conclusions are drawn in Sec. XI.

II. SUSY SCENARIOS

The SUSY scenarios considered in this article can be divided into two categories: simplified models and phenomenological models. The simplified models [40] target the production of charginos, neutralinos, and sleptons, where the masses and the decay modes of the relevant particles are the only free parameters. In each of the simplified models, a single production process with a fixed decay chain is considered for optimization of the event selection and interpretation of the results. To illustrate the range of applicability of the searches, several classes of phenomenological models that consider all relevant SUSY production and decay processes are also used to interpret the results. These models include the five-dimensional EW phenomenological minimal supersymmetric standard model (pMSSM) [41], the nonuniversal Higgs masses (NUHM) model [42,43], and a gauge-mediated SUSY breaking (GMSB) model [44–49].

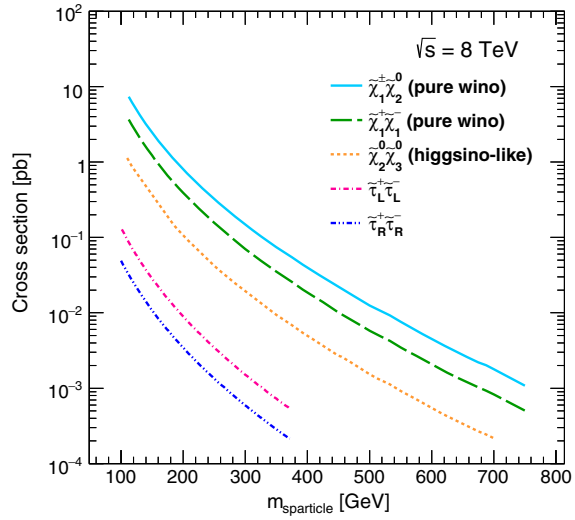

FIG. 1. The production cross sections for the simplified models of the direct production of $\tilde{\chi}_1^{+}\tilde{\chi}_1^{-}$, $\tilde{\chi}_1^{\pm}\tilde{\chi}_2^0$ [where $m(\tilde{\chi}_1^{\pm}) = m(\tilde{\chi}_2^0)$], $\tilde{\chi}_2^0\tilde{\chi}_3^0$ [where $m(\tilde{\chi}_2^0) = m(\tilde{\chi}_3^0)$], and $\tilde{\tau}^{+}\tilde{\tau}^{-}$ studied in this article. The left-handed and right-handed stau-pair production cross sections are shown separately.

R-parity is assumed to be conserved in all SUSY scenarios considered in this article. The LSP is assumed to be the lightest neutralino $\tilde{\chi}_1^0$ except in the GMSB scenarios, where it is the gravitino $\tilde{G}$. The next-to-LSP (NLSP) is usually one or more of the charginos, neutralinos, or sleptons. All SUSY particles are assumed to decay promptly, with the exception of the LSP, which is stable. Finally, SUSY particles that are not considered in a given model are decoupled by setting their masses to values inaccessible at the LHC.

Unless stated otherwise, signal cross sections are calculated to next-to-leading order (NLO) in the strong coupling constant using PROSPINO2 [50] and are shown in Fig. 1 for a number of selected simplified-model production modes. The cross sections for the production of charginos and neutralinos are in agreement with the NLO calculations matched to resummation at next-to-leading logarithmic (NLL) accuracy (NLO + NLL) within about 2% [51–53]. The nominal cross section and the uncertainty are taken from the center and spread, respectively, of the envelope of cross-section predictions using different parton distribution function (PDF) sets and factorization and renormalization scales, as described in Ref. [54].

A. Direct stau-pair production simplified model

Two simplified models describing the direct production of $\tilde{\tau}^{+}\tilde{\tau}^{-}$ are used in this article: one considers stau partners of the left-handed τ lepton ($\tilde{\tau}_L$), and a second considers stau partners of the right-handed τ lepton ($\tilde{\tau}_R$). In both models,

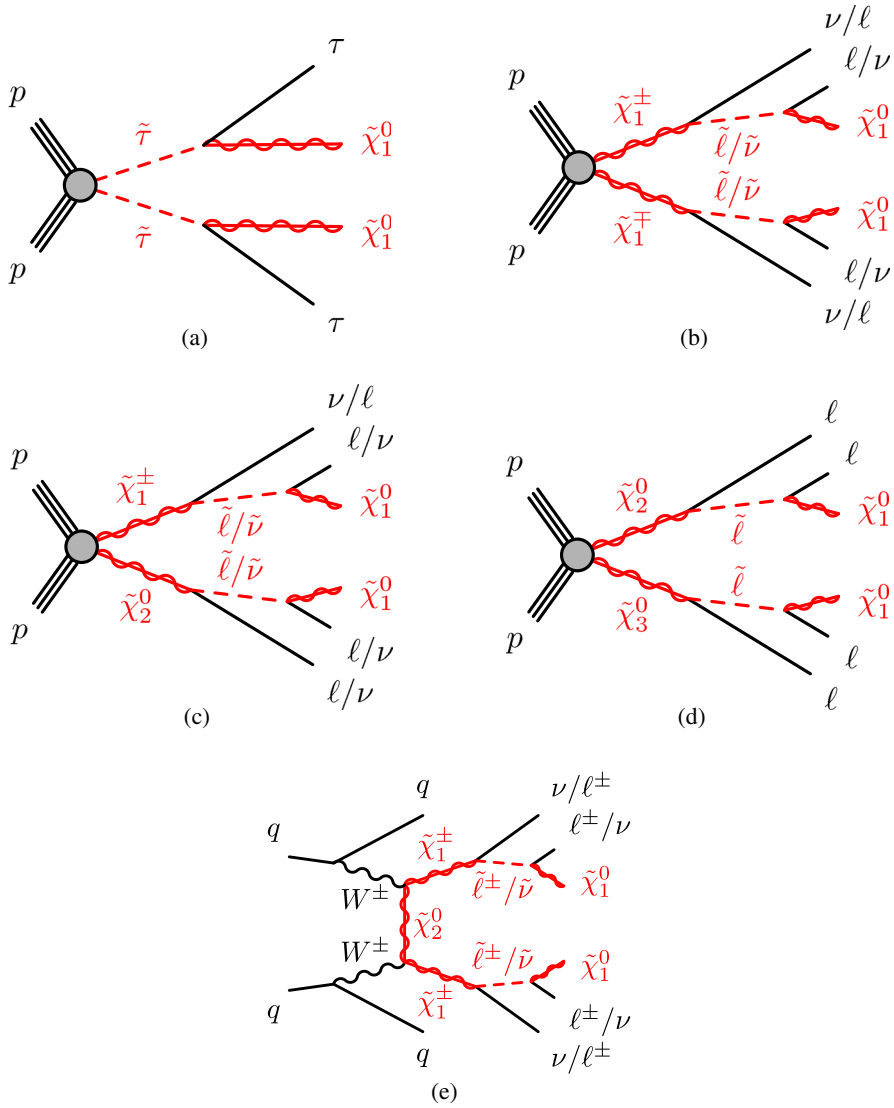

FIG. 2. The diagrams for the simplified models of the direct pair production of staus and the direct production of $\tilde{\chi}_1^+\tilde{\chi}_1^-$, $\tilde{\chi}_1^\pm\tilde{\chi}_2^0$, and $\tilde{\chi}_2^0\tilde{\chi}_3^0$, and the VBF production of $\tilde{\chi}_1^\pm\tilde{\chi}_1^\pm$ studied in this article. All three generations are included in the definition of $\tilde{\ell}/\tilde{\nu}$, except for the direct production of $\tilde{\chi}_2^0\tilde{\chi}_3^0$ where only the first two generations are assumed. The different decay modes are discussed in the text.

the stau decays with a branching fraction of 100% to the SM tau lepton and the LSP. The diagram for this model can be seen in Fig. 2(a).

B. Direct chargino-pair, chargino-neutralino, and neutralino-pair production simplified models

In the simplified models describing the direct production of $\tilde{\chi}_1^+\tilde{\chi}_1^-$ and $\tilde{\chi}_1^\pm\tilde{\chi}_2^0$, both the $\tilde{\chi}_1^\pm$ and $\tilde{\chi}_2^0$ are assumed to be pure wino and mass degenerate, while the $\tilde{\chi}_1^0$ is assumed to be pure bino. However, it is possible to reinterpret the results from these simplified models by assuming different compositions of the $\tilde{\chi}_1^0$, $\tilde{\chi}_2^0$, and $\tilde{\chi}_1^\pm$ for the same masses of the states. Two different scenarios for the decays of the $\tilde{\chi}_1^\pm$ and $\tilde{\chi}_2^0$ are considered, as shown in Figs. 2(b) and 2(c):

(i) $\tilde{\chi}_1^+\tilde{\chi}_1^-/\tilde{\chi}_1^\pm\tilde{\chi}_2^0$ *production with* $\tilde{\ell}_L$*-mediated decays:* The $\tilde{\chi}_1^\pm$ and $\tilde{\chi}_2^0$ decay with a branching fraction of 1/6 via $\tilde{e}_L$, $\tilde{\mu}_L$, $\tilde{\tau}_L$, $\tilde{\nu}_e$, $\tilde{\nu}_\mu$, or $\tilde{\nu}_\tau$ with masses $m_{\tilde{\nu}_\ell} = m_{\tilde{\ell}_L} = x(m_{\tilde{\chi}_1^\pm} - m_{\tilde{\chi}_1^0}) + m_{\tilde{\chi}_1^0}$ with $x = 0.05$, 0.25, 0.5, 0.75, or 0.95,

(ii) $\tilde{\chi}_1^\pm\tilde{\chi}_2^0$ *production with* $\tilde{\tau}_L$*-mediated decay:* The first- and second-generation sleptons and sneutrinos are assumed to be very heavy, so that the $\tilde{\chi}_1^\pm$ and $\tilde{\chi}_2^0$ decay with a branching fraction of 1/2 via $\tilde{\tau}_L$ or $\tilde{\nu}_\tau$ with masses $m_{\tilde{\nu}_\tau} = m_{\tilde{\tau}_L} = 0.5(m_{\tilde{\chi}_1^\pm} + m_{\tilde{\chi}_1^0})$.

In the simplified models considered here, the slepton mass is assumed to lie between the $\tilde{\chi}_1^0$ and $\tilde{\chi}_1^\pm/\tilde{\chi}_2^0$ masses, which increases the branching fraction to leptonic final states compared to scenarios without sleptons.

The compressed spectra searches in this article are less sensitive to scenarios where the $\tilde{\chi}_1^\pm/\tilde{\chi}_2^0$ decay through SM W, Z, or Higgs bosons, as the branching fraction to leptonic final states is significantly suppressed. The results of the ATLAS searches for $\tilde{\chi}_1^+\tilde{\chi}_1^-$ production with WW-mediated decays [19], $\tilde{\chi}_1^\pm\tilde{\chi}_2^0$ production with WZ-mediated decays [20], and $\tilde{\chi}_1^\pm\tilde{\chi}_2^0$ production with Wh-mediated decays [23] are summarized in Sec. X E. In these scenarios with decays mediated by SM bosons, the W, Z, and h bosons are assumed to decay with SM branching fractions.

In the simplified models of the direct production of $\tilde{\chi}_2^0\tilde{\chi}_3^0$, the $\tilde{\chi}_2^0$ and $\tilde{\chi}_3^0$ are assumed to be pure higgsino and mass degenerate, while the $\tilde{\chi}_1^0$ is assumed to be pure bino. The $\tilde{\chi}_2^0$ and $\tilde{\chi}_3^0$ are assumed to decay with a branching fraction of one-half via $\tilde{e}_R$, $\tilde{\mu}_R$ with mass $m_{\tilde{\ell}_R} = x(m_{\tilde{\chi}_2^0} - m_{\tilde{\chi}_1^0}) + m_{\tilde{\chi}_1^0}$ with $x = 0.05$, 0.25, 0.5, 0.75, or 0.95 ($\tilde{\chi}_2^0\tilde{\chi}_3^0$ production with $\tilde{\ell}_R$-mediated decay). The associated diagram is shown in Fig. 2(d). In this $\tilde{\chi}_2^0\tilde{\chi}_3^0$ simplified model, the choice of right-handed sleptons in the decay chain ensures high lepton multiplicities in the final state while suppressing the leptonic branching fraction of any associated chargino, thus enhancing the rate of four-lepton events with respect to events with lower lepton multiplicities.

C. Simplified model of same-sign chargino-pair production via vector-boson fusion

A simplified model for $\tilde{\chi}_1^\pm\tilde{\chi}_1^\pm$ production via VBF [55,56] is also considered. As in the case of direct production, the $\tilde{\chi}_1^\pm$ is assumed to be pure wino, and mass degenerate with the $\tilde{\chi}_2^0$, and the $\tilde{\chi}_1^0$ is assumed to be pure bino. The $\tilde{\chi}_1^\pm$ decays with a branching fraction of 1/6 via $\tilde{e}_L$, $\tilde{\mu}_L$, $\tilde{\tau}_L$, $\tilde{\nu}_e$, $\tilde{\nu}_\mu$, or $\tilde{\nu}_\tau$ with masses $m_{\tilde{\nu}_\ell} = m_{\tilde{\ell}_L} = 0.5(m_{\tilde{\chi}_1^\pm} + m_{\tilde{\chi}_1^0})$. The diagram for $\tilde{\chi}_1^\pm\tilde{\chi}_1^\pm$ production via VBF, where the sparticles are produced along with two jets, is shown in Fig. 2(e). The jets are widely separated in pseudorapidity[1] η and have a relatively high dijet invariant mass m_{jj}. Because of the VBF topology, the charginos are often boosted in the transverse plane, forcing the decay products to be more collinear and energetic, even in highly compressed spectra. This feature of VBF production makes it a good candidate to probe compressed SUSY scenarios that are experimentally difficult to explore via the direct production modes. The signal cross sections are calculated to leading order (LO) in the strong coupling constant using MadGraph 5-1.3.33 [57] (more details on the cross-section calculation are given in the Appendix). The uncertainties on the signal cross sections are calculated by using different PDF sets (2%) and by varying the renormalization and factorization scales between 0.5 and 2 times the nominal values (6%) [58]. For a $\tilde{\chi}_1^\pm$ with mass of 120 GeV, the cross section for $\tilde{\chi}_1^\pm\tilde{\chi}_1^\pm$ production in association with two jets satisfying the criteria $m_{jj} > 350$ GeV and $|\Delta\eta_{jj}| > 1.6$ is 1.1 fb. For the assumed mixings in the chargino-neutralino sector, and the mass values considered in the analysis, the cross section for $\tilde{\chi}_1^\pm\tilde{\chi}_1^\pm$ VBF production is found to be independent of the $\tilde{\chi}_1^0$ mass.

[1]ATLAS uses a right-handed coordinate system with its origin at the nominal interaction point (IP) in the center of the detector and the z axis along the beam pipe. The x axis points from the IP to the center of the LHC ring, and the y axis points upward. Cylindrical coordinates (r, ϕ) are used in the transverse plane, ϕ being the azimuthal angle around the z axis. The pseudorapidity is defined in terms of the polar angle θ as $\eta = -\ln\tan(\theta/2)$.

D. Phenomenological minimal supersymmetric standard model

The analysis results are interpreted in a pMSSM scenario. The masses of the sfermions, the gluino, and the CP-odd Higgs boson are set to high values (2 TeV, 2 TeV, and 500 GeV, respectively), thus decoupling the production of these particles and allowing only the direct production of charginos and neutralinos decaying via SM gauge bosons and the lightest Higgs boson. The remaining four parameters, the ratio of the expectation values of the two Higgs doublets ($\tan\beta$), the gaugino mass parameters M_1 and M_2, and the higgsino mass parameter μ, determine the phenomenology of direct electroweak SUSY production. For the analysis presented here, μ and M_2 are treated as free parameters. The remaining parameters are fixed to $\tan\beta = 10$ and $M_1 = 50$ GeV, so that the relic dark-matter density is below the cosmological bound [29] across most of the μ-M_2 grid. The lightest Higgs boson has a mass close to 125 GeV, which is set by tuning the mixing in the top squark sector, and decays to SUSY as well as SM particles where kinematically allowed.

E. Two-parameter nonuniversal Higgs masses model

Radiatively driven natural SUSY [59] allows the Z and Higgs boson masses to be close to 100 GeV, with gluino and squark masses beyond the TeV scale. In the two-parameter NUHM model (NUHM2) that is considered in this article, the direct production of charginos and neutralinos is dominant in a large area of the parameter space considered. The mass hierarchy, composition, and production cross section of the SUSY particles are governed by the universal soft SUSY-breaking scalar mass m_0, the soft SUSY-breaking gaugino mass $m_{1/2}$, the trilinear SUSY-breaking parameter A_0, the pseudoscalar Higgs boson mass m_A, $\tan\beta$, and μ. Both μ and $m_{1/2}$ are treated as free parameters, and the other parameters are fixed to $m_0 = 5$ TeV, $A_0 = -1.6m_0$, $\tan\beta = 15$, $m_A = 1$ TeV, and $\mathrm{sign}(\mu) > 0$. These conditions ensure a low level of electroweak fine-tuning, while keeping the lightest Higgs boson mass close to 125 GeV and the squark masses to a few TeV. The gluino mass typically satisfies $m_{\tilde{g}} \simeq 2.5m_{1/2}$. For low gluino masses, the production of strongly interacting

SUSY particles dominates; as the gluino mass increases, the production of electroweakinos becomes more important. The charginos and neutralinos decay via W, Z, and Higgs bosons.

F. Gauge-mediated SUSY breaking model

Minimal GMSB models are described by six parameters: the SUSY-breaking mass scale in the low-energy sector (Λ), the messenger mass (M_{mess}), the number of SU(5) messenger fields (N_5), the scale factor for the gravitino mass (C_{grav}), $\tan\beta$, and μ. In the model presented here, Λ and $\tan\beta$ are treated as free parameters, and the remaining parameters are fixed to $M_{\mathrm{mess}} = 250$ TeV, $N_5 = 3$, $C_{\mathrm{grav}} = 1$, and $\mathrm{sign}(\mu) > 0$. For high Λ values, the EW production of SUSY particles dominates over other SUSY processes. In most of the relevant parameter space, the NLSP is the $\tilde{\tau}$ for large values of $\tan\beta$ ($\tan\beta > 20$), and the final states contain two, three, or four tau leptons. In the region where the mass difference between the stau and selectron/smuon is smaller than the sum of the tau and the electron/muon masses, the stau, selectron, and smuon decay directly into the LSP and a lepton, defining the phenomenology. The charginos and neutralinos decay as $\tilde{\chi}_1^{\pm} \to W^{\pm}\tilde{\chi}_1^0$ and $\tilde{\chi}_2^0 \to Z\tilde{\chi}_1^0$, where the $\tilde{\chi}_1^0$ decays as $\tilde{\chi}_1^0 \to \ell^{\pm}\tilde{\ell}^{\mp} \to \ell^+\ell^-\tilde{G}$ and the LSP is the gravitino $\tilde{G}$.

III. THE ATLAS DETECTOR

The ATLAS detector [60] is a multipurpose particle physics detector with forward-backward symmetric cylindrical geometry. The inner tracking detector (ID) covers $|\eta| < 2.5$ and consists of a silicon pixel detector, a semiconductor microstrip detector, and a transition radiation tracker. The ID is surrounded by a thin superconducting solenoid providing a 2 T axial magnetic field. A high-granularity lead/liquid-argon sampling calorimeter measures the energy and the position of electromagnetic showers within $|\eta| < 3.2$. Sampling calorimeters with liquid argon as the active medium are also used to measure hadronic showers in the end cap ($1.5 < |\eta| < 3.2$) and forward ($3.1 < |\eta| < 4.9$) regions, while a steel/scintillator tile calorimeter measures hadronic showers in the central region ($|\eta| < 1.7$). The muon spectrometer (MS) surrounds the calorimeters and consists of three large superconducting air-core toroid magnets, each with eight coils, a system of precision tracking chambers ($|\eta| < 2.7$), and fast trigger chambers ($|\eta| < 2.4$). A three-level trigger system [61] selects events to be recorded for off-line analysis.

IV. MONTE CARLO SIMULATION

Monte Carlo generators are used to simulate SM processes and new physics signals. The SM processes considered are those that can lead to leptonic signatures. Details of the signal and background MC simulation samples used in this article, as well as the order of cross-section calculations in perturbative QCD used for yield normalization, are shown in Table I.

For all MC simulation samples, the propagation of particles through the ATLAS detector is modeled with Geant 4 [96] using the full ATLAS detector simulation [97], or a fast simulation using a parametric response of the electromagnetic and hadronic calorimeters [98] and Geant 4 elsewhere. The effect of multiple proton-proton collisions in the same or nearby beam bunch crossings (in-time and out-of-time pileup) is incorporated into the simulation by overlaying additional minimum-bias events generated with Pythia -8 onto hard-scatter events. Simulated events are weighted to match the distribution of the mean number of interactions per bunch crossing in data and are reconstructed in the same manner as data. The simulated MC samples are corrected to account for differences with respect to the data in the heavy-flavor quark jet selection efficiencies and misidentification probabilities, lepton efficiencies, tau misidentification probabilities, as well as the energy and momentum measurements of leptons and jets. The $\tilde{\chi}_1^+\tilde{\chi}_1^-$ ($\tilde{\chi}_1^{\pm}\tilde{\chi}_2^0$) signal samples simulated with Herwig++ are reweighted to match the $\tilde{\chi}_1^+\tilde{\chi}_1^-$ ($\tilde{\chi}_1^{\pm}\tilde{\chi}_2^0$) system transverse momentum distribution obtained from the MadGraph samples that are generated with an additional parton in the matrix element to give a better description of the ISR.

V. EVENT RECONSTRUCTION

Events recorded during stable data-taking conditions are analyzed if the reconstructed primary vertex has five or more tracks with transverse momentum $p_{\mathrm{T}} > 400$ GeV associated with it. The primary vertex of an event is identified as the vertex with the highest $\Sigma {p_{\mathrm{T}}}^2$ of associated tracks. After the application of beam, detector, and data-quality requirements, the total luminosity considered in these analyses corresponds to 20.3 fb^{-1} (20.1 fb^{-1} for the direct stau production analysis due to a different trigger requirement).

Electron candidates are required to have $|\eta| < 2.47$ and $p_{\mathrm{T}} > 7$ GeV, where the p_{T} and η are determined from the calibrated clustered energy deposits in the electromagnetic calorimeter and the matched ID track, respectively. Electrons must satisfy "medium" identification criteria, following Ref. [99]. Muon candidates are reconstructed by combining tracks in the ID and tracks in the MS [100], and are required to have $|\eta| < 2.5$ and $p_{\mathrm{T}} > 5$ GeV. Events containing one or more muons that have transverse impact parameter with respect to the primary vertex $|d_0| > 0.2$ mm or longitudinal impact parameter with respect to the primary vertex $|z_0| > 1$ mm are rejected to suppress cosmic-ray muon background. In the direct stau production analysis, and the two-lepton compressed spectra analyses, electrons and muons are required to have $p_{\mathrm{T}} > 10$ GeV.

Jets are reconstructed with the anti-k_t algorithm [101] with a radius parameter of $R = 0.4$. Three-dimensional

TABLE I. The MC simulation samples used in this article for background and signal estimates. Shown are the generator type, the order of cross-section calculations used for yield normalization, the names of the sets of tunable parameters (tunes) used for the underlying-event generation, and the PDF sets.

Process	Generator + fragmentation/hadronization	Cross section	Tune	PDF set
Diboson (VV)				
W^+W^-, WZ, ZZ	POWHEG BOX-r2129 [62,63] + PYTHIA-8.165 [64] (or + PYTHIA-6.426)	NLO QCD with MCFM-6.2 [65,66]	AU2 [67]	CT10 [68]
$W^\pm W^\pm$	SHERPA-1.4.0 [69]	NLO	(SHERPA internal)	CT10
$W^\pm W^\pm$ via vector-boson fusion	SHERPA-1.4.0	NLO	(SHERPA internal)	CT10
ZZ, W^+W^- via gluon fusion (*not incl. in)* POWHEG BOX)	gg2VV [70] + HERWIG-6.520	NLO	AUET2B [71]	CT10
$W\gamma$, $Z\gamma$	SHERPA-1.4.1	NLO	(SHERPA internal)	CT10
Triboson (VVV)				
WWW, ZWW	MADGRAPH5-1.3.33 + PYTHIA-6.426	NLO [72]	AUET2B	CTEQ6L1 [73]
Higgs				
Via gluon fusion	POWHEGBOX-r2092 + PYTHIA-8.165	NNLO + NNLL QCD, NLO EW [74]	AU2	CT10
Via vector-boson fusion	POWHEG BOX-r2092 + PYTHIA-8.165	NNLO QCD, NLO EW [74]	AU2	CT10
Associated W/Z production	PYTHIA-8.165	NNLO QCD, NLO EW [74]	AU2	CTEQ6L1
Associated $t\bar{t}$-production	PYTHIA-8.165	NNLO QCD [74]	AU2	CTEQ6L1
Top + Boson $t\bar{t}V$				
$t\bar{t}W$, $t\bar{t}Z$	ALPGEN-2.14 [75] HERWIG-6.520	NLO [76,77]	AUET2B	CTEQ6L1
$t\bar{t}WW$	MADGRAPH 5-1.3.33 + PYTHIA-6.426	NLO [77]	AUET2B	CTEQ6L1
$\mathbf{t\bar{t}}$	POWHEG BOX-r2129 + PYTHIA-6.426	NNLO + NNLL [78–83]	PERUGIA2011C [84]	CT10
Single top				
t-channel	ACERMC-38 [85] + PYTHIA-6.426	NNLO + NNLL [86]	AUET2B	CTEQ6L1
s-channel, Wt	MC@NLO-4.06 [87,88] + HERWIG-6.520	NNLO + NNLL [89,90]	AUET2B	CT10
tZ	MADGRAPH 5-1.5.11 + PYTHIA-6.426	NLO [91]	AUET2B	CTEQ6L1
W + jets, Z + jets	ALPGEN-2.14 + PYTHIA-6.426 (or + HERWIG-6.520) or SHERPA-1.4.0	NNLO QCD using DYNNLO-1.1 [92] with MSTW2008 NNLO [93] NNLO QCD using DYNNLO-1.1 with MSTW2008 NNLO	PERUGIA 2011C	CTEQ6L1 CT10
Low-mass resonances				
J/Ψ, Υ	PYTHIA -8.165	NLO	AU2	CTEQ6L1
SUSY signal				
$\tilde{\tau}\tilde{\tau}$, $\tilde{\chi}_1^+\tilde{\chi}_1^-$, $\tilde{\chi}_1^\pm\tilde{\chi}_2^0$ simplified models	HERWIG + + -2.5.2 [94]	NLO using PROSPINO2 [50]	UE-EE-3 [95]	CTEQ6L1
$\tilde{\chi}_2^0\tilde{\chi}_3^0$ simplified models	MADGRAPH 5-1.5.12 + PYTHIA-6.426	NLO using PROSPINO2	AUET2B	CTEQ6L1
VBF $\tilde{\chi}_1^+\tilde{\chi}_1^-$ simplified models	MADGRAPH 5_aMC@NLO-2.1.1 + PYTHIA -6.426	LO using MADGRAPH 5-1.3.33 [57]	AUET2B	CTEQ6L1
NUHM2, GMSB	HERWIG + + -2.5.2	NLO using PROSPINO2	UE-EE-3	CTEQ6L1

calorimeter energy clusters are used as input to the jet reconstruction. The clusters are calibrated using the local hadronic calibration [102], which gives different weights to the energy deposits from the electromagnetic and hadronic components of the showers. The final jet energy calibration corrects the calorimeter response to the particle-level jet energy [102,103], where correction factors are obtained from simulation and then refined and validated using data. Corrections for in-time and out-of-time pileup are also applied based on the jet area method [102]. Central jets must have $|\eta| < 2.4$ and $p_T > 20$ GeV, and a "jet vertex fraction" (JVF) [102] larger than 0.5 if $p_T < 50$ GeV. The JVF is the p_T-weighted fraction of the tracks in the jet that are associated with the primary vertex. Requiring large JVF values suppresses jets from pileup. Forward jets are those with $2.4 < |\eta| < 4.5$ and $p_T > 30$ GeV. Events containing jets failing to satisfy the quality criteria described in Ref. [102] are rejected to suppress events with large calorimeter noise and noncollision backgrounds.

Central jets are identified as containing b-hadrons (referred to as b-tagged) using a multivariate technique based on quantities related to reconstructed secondary vertices. The chosen working point of the b-tagging algorithm [104] correctly identifies b-hadrons in simulated $t\bar{t}$ samples with an efficiency of 80%, with a light-flavor jet misidentification probability of about 4% and a c-jet misidentification probability of about 30%.

Hadronically decaying τ leptons (τ_{had}) are reconstructed using jets described above with $|\eta| < 2.47$ and a lower p_T threshold of 10 GeV. The τ_{had} reconstruction algorithm uses information about the tracks within $\Delta R \equiv \sqrt{(\Delta\phi)^2 + (\Delta\eta)^2} = 0.2$ of the seed jet, in addition to the electromagnetic and hadronic shower shapes in the calorimeters. The τ_{had} candidates are required to have one or three associated tracks (prongs), as τ leptons predominantly decay to either one or three charged pions together with a neutrino and often additional neutral pions. The τ_{had} candidates are required to have $p_T > 20$ GeV and unit total charge of their constituent tracks. A boosted decision tree algorithm (BDT) uses discriminating track and cluster variables to optimize τ_{had} identification, where "loose," "medium," and "tight" working points are defined [105]. Electrons misidentified as τ_{had} candidates are vetoed using transition radiation and calorimeter information. The τ_{had} candidates are corrected to the τ energy scale [105] using an η- and p_T-dependent calibration. Kinematic variables built using taus in this article use only the visible decay products from the hadronically decaying tau.

The missing transverse momentum is the negative vector sum of the transverse momenta of all muons with $p_T > 10$ GeV, electrons with $p_T > 10$ GeV, photons with $p_T > 10$ GeV [99], jets with $p_T > 20$ GeV, and calibrated calorimeter energy clusters with $|\eta| < 4.9$ not associated with these objects. Hadronically decaying τ leptons are included in the E_T^{miss} calculation as jets. Clusters associated with electrons, photons, and jets are calibrated to the scale of the corresponding objects. Calorimeter energy clusters not associated with these objects are calibrated using both calorimeter and tracker information [106]. For jets, the calibration includes the pileup correction described above, while the JVF requirement is not considered when selecting jet candidates.

To avoid potential ambiguities among objects, "tagged" leptons are candidate leptons separated from each other and from jets in the following order:

(1) If two electron candidates are reconstructed with $\Delta R < 0.1$, the lower energy candidate is discarded.
(2) Jets within $\Delta R = 0.2$ of an electron candidate, and τ_{had} candidates within $\Delta R = 0.2$ of an electron or muon, are discarded.
(3) Electron and muon candidates are discarded if found within $\Delta R = 0.4$ of a remaining jet to suppress leptons from semileptonic decays of c- and b-hadrons.
(4) To reject bremsstrahlung from muons, $e\mu$ ($\mu\mu$) pairs are discarded if the two leptons are within $\Delta R = 0.01$ (0.05) of one another.
(5) Jets found within $\Delta R = 0.2$ of a "signal" τ lepton (see below) are discarded.

Finally, to suppress low-mass decays, if tagged electrons and muons form a same-flavor opposite-sign (SFOS) pair with $m_{\mathrm{SFOS}} < 2$ GeV, both leptons in the pair are discarded.

Tagged leptons satisfying additional identification criteria are called signal leptons. To maximize the search sensitivity, some analyses presented in this article require different additional criteria for signal leptons, and these are highlighted where necessary. Signal τ leptons must satisfy medium identification criteria [105], while for the final signal-region selections, both the medium and tight criteria are used. Unless stated otherwise, signal electrons (muons) are tagged electrons (muons) for which the scalar sum of the transverse momenta of tracks within a cone of $\Delta R = 0.3$ around the lepton candidate is less than 16% (12%) of the lepton p_T. Tracks used for the electron (muon) isolation requirement defined above are those that have $p_T > 0.4$ (1.0) GeV and $|z_0| < 2$ mm with respect to the primary vertex of the event. Tracks of the leptons themselves as well as tracks closer in z_0 to another vertex (that is not the primary vertex) are not included. The isolation requirements are imposed to reduce the contributions from semileptonic decays of hadrons and jets misidentified as leptons. Signal electrons must also satisfy tight identification criteria [99], and the sum of the extra transverse energy deposits in the calorimeter (corrected for pileup effects) within a cone of $\Delta R = 0.3$ around the electron candidate must be less than 18% of the electron p_T. To further suppress electrons and muons originating from secondary vertices, the d_0 normalized to its uncertainty is required to be small, with $|d_0|/\sigma(d_0) < 5(3)$, and $|z_0 \sin\theta| < 0.4$ mm (1 mm) for electrons (muons).

TABLE II. The triggers used in the analyses and the off-line p_T threshold used, ensuring that the lepton(s) or E_T^{miss} triggering the event are in the plateau region of the trigger efficiency. Where multiple triggers are listed for an analysis, events are used if any of the triggers is passed. Muons are triggered within a restricted range of $|\eta| < 2.4$.

Trigger	p_T threshold [GeV]	Analysis
Single τ	150	Direct stau production
Double τ	40,25	
Single isolated e	25	Compressed spectra $\ell^+\ell^-$, 3ℓ
Single isolated μ	25	
Double e	14,14 25,10	Compressed spectra $\ell^+\ell^-$, $\ell^\pm\ell^\pm$, 3ℓ
Double μ	14,14 18,10	Compressed spectra $\ell^+\ell^-$, $\ell^\pm\ell^\pm$, 3ℓ
Triple e	20,9,9	Compressed spectra 3ℓ
Triple μ	7,7,7 19,5,5	Compressed spectra 3ℓ
Combined $e\mu$	$14(e)$,$10(\mu)$ $18(\mu)$,$10(e)$ $9(e)$, $9(e)$, $7(\mu)$ $9(e)$, $7(\mu)$, $7(\mu)$	Compressed spectra 3ℓ
E_T^{miss}	120	Chargino production via VBF

Events must satisfy the relevant trigger for the analysis and satisfy the corresponding p_T-threshold requirements shown in Table II.

VI. GENERAL ANALYSIS STRATEGY

The broad range of EW SUSY scenarios considered by the ATLAS experiment is accompanied by a large number of experimental signatures: from the two-tau signature from direct stau production to three-lepton signatures from $\tilde{\chi}_1^\pm\tilde{\chi}_2^0$ production. As much as possible the individual analyses follow a common approach. Signal regions (SR) are defined to target one or more EW SUSY scenarios, using kinematic variables with good signal-background separation, as described in Sec. VI A. The optimization of key selection variables is performed by maximizing the expected sensitivity to the signal model. A common background estimation strategy is used for the analyses in this article: the main SM backgrounds are estimated by normalizing MC simulation samples to data in dedicated control regions (CRs); backgrounds due to nonprompt and fake leptons are derived from data as outlined in Sec. VI B, while small backgrounds are estimated purely using MC simulation samples. The HistFitter [107] software framework is used in all analyses for constraining the background normalizations and the statistical interpretation of the results.

The CRs are defined with kinematic properties similar to the SRs, yet are disjoint from the SR, and have high purity for the background process under consideration. The CRs are designed in a way that minimizes the contamination from the signal model, and cross contamination between multiple CRs is taken into account in the normalization to data. To validate the modeling of the SM backgrounds, the yields and shapes of key kinematic variables are compared to data in validation regions (VR). The VRs are defined to be close to, yet disjoint from the SR and CR, and be dominated by the background process under consideration. The VRs are designed such that the contamination from the signal model is low. Three different fit configurations are used. The "background-only fit" is used for estimating the expected background in the SRs and VRs using observations in the CRs, with no assumptions made on any signal model. In the absence of an observed excess of events in one or more signal regions, the "model-dependent signal fit" is used to set exclusion limits in a particular model, where the signal contribution from the particular model that is being tested is taken into account in all CR and SR. Finally, in the "model-independent signal fit," both the CRs and SRs are used in the same manner as for the model-dependent signal fit, but signal contamination is not accounted for in the CRs. A likelihood function is built as the product of Poisson probability functions, describing the observed and expected number of events in the CRs and SRs. The observed number of events in various CRs and SRs are used in a combined profile likelihood fit to determine the expected SM background yields in each of the SRs. The systematic uncertainties on the expected background yields described in Sec. VI C are included as nuisance parameters, constrained to be Gaussian with a width determined by the size of the uncertainty. Correlations between control and signal regions, and background processes, are taken into account with common nuisance parameters. The free parameters and the nuisance parameters are determined by maximizing the product of the Poisson probability functions and the Gaussian constraints on the nuisance parameters.

After the background modeling is understood and validated, the predicted background in the SR is compared to the observed data. In order to quantify the probability for the background-only hypothesis to fluctuate to the observed number of events or higher, the one-sided p_0-value is calculated. For this calculation, the profile likelihood ratio is used as a test statistic to exclude the signal-plus-background hypothesis if no significant excess is observed. A signal model can be excluded at 95% CL if the CL_s [108] of the signal plus background hypothesis is < 0.05. For each signal region, the expected and observed upper limits at 95% CL on the number of beyond-the-SM

events ($S^{95}_{\rm exp}$ and $S^{95}_{\rm obs}$) are calculated using the model-independent signal fit. The 95% CL upper limits on the signal cross section times efficiency ($\langle\epsilon\sigma\rangle^{95}_{\rm obs}$) and the CL_b value for the background-only hypothesis are also calculated for each analysis in this article.

A. Event variables

A large set of discriminating variables is used in the analysis strategies presented here. The following kinematic variables are defined and their use in the various analyses is detailed in Secs. VII–IX:

$p_{\rm T}^X$ The transverse momentum of a reconstructed object X.

$\Delta\phi(X,Y)$, $\Delta\eta(X,Y)$ The separation in ϕ or η between two reconstructed objects X and Y, e.g. $\Delta\phi(E_{\rm T}^{\rm miss},\ell)$.

$|\Delta\eta_{jj}|$ The separation in η between the leading two jets.

$E_{\rm T}^{\rm miss}$ The magnitude of the missing transverse momentum in the event.

$E_{\rm T}^{\rm miss,rel}$ The quantity $E_{\rm T}^{\rm miss,rel}$ is defined as

$$E_{\rm T}^{\rm miss,rel} = \begin{cases} E_{\rm T}^{\rm miss} & \text{if } \Delta\phi(E_{\rm T}^{\rm miss},\ell/j) \geq \pi/2 \\ E_{\rm T}^{\rm miss} \times \sin\Delta\phi(E_{\rm T}^{\rm miss},\ell/j) & \text{if } \Delta\phi(E_{\rm T}^{\rm miss},\ell/j) < \pi/2 \end{cases}, \tag{1}$$

where $\Delta\phi(E_{\rm T}^{\rm miss},\ell/j)$ is the azimuthal angle between the direction of $E_{\rm T}^{\rm miss}$ and that of the nearest electron, muon, or central jet.

$p_{\rm T}^{\ell\ell}$ The transverse momentum of the two-lepton system.

$H_{\rm T}$ The scalar sum of the transverse momenta of the leptons and jets in the event.

$m_{\rm T}$ The transverse mass formed using the $E_{\rm T}^{\rm miss}$ and the leading lepton or tau in the event

$$m_{\rm T}(\vec{p}_{\rm T}^{\,\ell/\tau}, E_{\rm T}^{\rm miss}) = \sqrt{2{p_{\rm T}}^{\ell/\tau}E_{\rm T}^{\rm miss} - 2\vec{p}_{\rm T}^{\,\ell/\tau}\cdot E_{\rm T}^{\rm miss}}. \tag{2}$$

In the three-lepton analysis, the lepton not forming the SFOS lepton pair with mass closest to the Z boson mass is used. In cases where the second lepton or tau is used, the variable is labeled as $m_{\rm T}^X$, where X is the object used with the $E_{\rm T}^{\rm miss}$ to form the transverse mass.

$m_{\rm SFOS}$ The invariant mass of the SFOS lepton pair in the event. In the three-lepton analysis, the SFOS pair with mass closest to the Z boson mass is used.

$m_{\rm SFOS}^{\rm min}$ The lowest $m_{\rm SFOS}$ value among the possible SFOS combinations.

$m_{\ell\ell\ell}$ The three-lepton invariant mass.

$m_{\tau\tau}$ The two-tau invariant mass.

$m_{\rm T2}$ The "stransverse mass" is calculated as

$$m_{\rm T2} = \min_{\vec{q}_{\rm T}}[\max(m_{\rm T}({\vec{p}_{\rm T}}^{\ell 1/\tau 1},\vec{q}_{\rm T}), m_{\rm T}({\vec{p}_{\rm T}}^{\ell 2/\tau 2}, E_{\rm T}^{\rm miss}-\vec{q}_{\rm T}))], \tag{3}$$

where $\ell 1/\tau 1$ and $\ell 2/\tau 2$ denote the highest- and second-highest-$p_{\rm T}$ leptons or taus in the event, respectively, and $\vec{q}_{\rm T}$ is a test transverse vector that minimizes the larger of the two transverse masses

m_{T}. The m_{T2} distribution has a kinematic end point for events where two massive pair-produced particles each decay to two particles, one of which is detected and the other escapes undetected [109,110].

m_{eff} The scalar sum of the transverse momenta of the signal leptons, taus, jets, and $E_{\mathrm{T}}^{\mathrm{miss}}$ in the event

$$m_{\mathrm{eff}} = E_{\mathrm{T}}^{\mathrm{miss}} + \Sigma p_{\mathrm{T}}{}^{\mathrm{leptons}} + \Sigma p_{\mathrm{T}}{}^{\mathrm{taus}} + \Sigma p_{\mathrm{T}}{}^{\mathrm{jets}}. \tag{4}$$

In the case of the two-tau analysis, only the sum of the $E_{\mathrm{T}}^{\mathrm{miss}}$ and two taus is used.

R_2 The quantity R_2 is defined as

$$R_2 = \frac{E_{\mathrm{T}}^{\mathrm{miss}}}{E_{\mathrm{T}}^{\mathrm{miss}} + p_{\mathrm{T}}{}^{\ell 1} + p_{\mathrm{T}}{}^{\ell 2}}. \tag{5}$$

The R_2 distribution is shifted toward unity for signal events compared to the background, due to the existence of the LSPs that results in a larger $E_{\mathrm{T}}^{\mathrm{miss}}$.

M_{Δ}^{R}, $\Delta\phi_{R}^{\beta}$ The super-razor quantities M_{Δ}^{R} and $\Delta\phi_{R}^{\beta}$ are defined in Ref. [111]. These variables are motivated by the generic process of the pair production of two massive particles, each decaying into a set of visible and invisible particles (i.e. $\tilde{\chi}_1^{\pm} \to \ell\nu_{\ell}\tilde{\chi}_1^0$). Similar to m_{T2}, M_{Δ}^{R} is sensitive to the squared mass difference of the pair-produced massive particle and the invisible particle, via a kinematic end point. These two variables are expected to provide a similar performance for discriminating the signal from the background. For systems where the invisible particle has a mass that is comparable to the pair-produced massive particle (i.e. compressed spectra), the variable $\Delta\phi_{R}^{\beta}$ has a pronounced peak near π. The effect is magnified as the spectrum becomes more and more compressed, making this variable a good discriminator for compressed spectra searches.

B. Common reducible background estimation

Electron and muon candidates can be classified into three main types, depending on their origin: "real" leptons are prompt and isolated leptons from a W or Z boson, a prompt tau, or a SUSY particle decay; "fake" leptons can originate from a misidentified light-flavor quark or gluon jet (referred to as "light flavor"); "nonprompt" leptons can originate from a semileptonic decay of a heavy-flavor quark, from the decay of a meson, or from an electron from a photon conversion. The background due to nonprompt and fake electrons and muons, collectively referred to as "reducible," is commonly estimated using the matrix method described in Ref. [112]. The matrix method extracts the number of events with one or two fake or nonprompt leptons from a system of linear equations relating the number of events with two signal or tagged leptons (before signal lepton identification requirements are applied) to the number of events with two candidates that are either real, fake, or nonprompt. The coefficients of the linear equations are functions of the real-lepton identification efficiencies and of the fake and nonprompt lepton misidentification probabilities, both defined as a fraction of the corresponding tagged leptons satisfying the signal lepton requirements.

The real-lepton identification efficiencies are obtained from MC simulation samples in the region under consideration to account for detailed kinematic dependencies and are multiplied by correction factors to account for residual differences with respect to the data. The correction factors are obtained from a control region rich in $Z \to e^+e^-$ and $Z \to \mu^+\mu^-$ decays. The fake and nonprompt lepton misidentification probabilities are calculated as the weighted averages of the corrected type- and process-dependent misidentification probabilities defined below according to their relative contributions in a given signal or validation region. The type- and process-dependent misidentification probabilities for each relevant fake and nonprompt lepton type (heavy-flavor, light-flavor, or conversion) and for each reducible background process are corrected using the ratio ("correction factor") of the misidentification probability in data to that in simulation obtained from dedicated control samples. The correction factors are assumed to be independent of the selected regions and of any potential composition or kinematic differences. For nonprompt electrons and muons from heavy-flavor quark decays, the correction factor is measured in a $b\bar{b}$-dominated control sample. The correction factor for the conversion candidates is determined in events with a converted photon radiated from a muon in $Z \to \mu\mu$ decays.

C. Common systematic uncertainties

Several sources of systematic uncertainty are considered for the SM background estimates and signal yield predictions. When the MC simulation samples are normalized to data yields in the CR, there is a partial cancellation of both the experimental and theoretical modeling systematic uncertainties.

The experimental systematic uncertainties affecting the simulation-based estimates include the following: the uncertainties due to the jet energy scale and resolution [100,102]; the uncertainties due to the lepton energy scale, energy resolution, and identification efficiency [99,100,105]; the uncertainty due to the hadronic tau misidentification probability [105]; the uncertainty on the $E_{\mathrm{T}}^{\mathrm{miss}}$ from energy deposits not associated with reconstructed objects ($E_{\mathrm{T}}^{\mathrm{miss}}$ soft-term resolution) [106]; and the uncertainties due to b-tagging efficiency and mistag probability [104]. The uncertainty on the integrated luminosity is $\pm 2.8\%$ and is derived following the same methodology as that detailed in Ref. [113]. The uncertainty due to the modeling of the pileup in the MC simulation samples is estimated by varying the distribution of the number of interactions per bunch crossing overlaid in the MC samples by $\pm 10\%$. An uncertainty is applied to MC samples to cover differences in efficiency observed between the trigger in data and the MC trigger simulation.

The systematic uncertainties due to the limitations in theoretical models or calculations affecting the simulation-based background estimates include the cross-section uncertainties that are estimated by varying the renormalization and factorization scales and the PDFs, and the acceptance uncertainties due to PDFs and the choice of MC generator and parton shower. The cross-section uncertainties for the irreducible backgrounds used here are 30% for $t\bar{t}V$ [76,77], 50% for tZ, 5% for ZZ, 7% for WZ, and 100% for the triboson samples. For the Higgs boson samples, a 20% uncertainty is used for VH and VBF production, while a 100% uncertainty is assigned to $t\bar{t}H$ and Higgs boson production via gluon fusion [74]. For the $\tilde{\chi}_1^+\tilde{\chi}_1^-$ and $\tilde{\chi}_1^\pm\tilde{\chi}_2^0$ signal simulations that are sensitive to ISR, the impact of the choice of renormalization scales, factorization scales, the scale for the first emission in the so-called MLM matching scheme [114], and MLM matching scale are evaluated by varying these individually between 0.5 and 2 times the nominal values in MadGraph.

VII. DIRECT STAU PRODUCTION

This section presents a search for direct stau-pair production with subsequent decay into final states with two taus and $E_{\mathrm{T}}^{\mathrm{miss}}$. The search for direct stau production is very challenging, as the final state is difficult to trigger on and to separate from the SM background. In Ref. [22], the best observed upper limit on the direct stau production cross section was found for a stau mass of 80 GeV and a massless $\tilde{\chi}_1^0$, where the theoretical cross section at NLO is 0.07 (0.17) pb for right-handed (left-handed) stau-pair production and the excluded cross section is 0.22 (0.28) pb. This analysis is an update of Ref. [22], using a multivariate analysis technique instead of a simple cut-based method to improve the sensitivity to direct stau-pair production.

A. Event selection

Events are selected using the basic reconstruction, object, and event selection criteria described in Sec. V. In addition, if taus form an SFOS pair with $m_{\mathrm{SFOS}} < 12$ GeV, the event is rejected. Events with exactly two hadronically decaying tau candidates are selected, where the two tau candidates are required to have opposite-sign (OS) charge. At least one tau must satisfy the tight tau identification BDT requirement, and events with additional tagged light leptons are vetoed. Events must satisfy either the single-tau or ditau trigger criteria, as described in Sec. V.

To suppress events from Z boson decays, events are rejected if the invariant mass of the tau pair lies within ± 10 GeV of the peak value of 81 GeV for Z boson candidates.[2] To suppress background from events containing a top quark, events with b-tagged jets are vetoed. To further select SUSY events from direct stau production and suppress WW and $t\bar{t}$ production, m_{T2} is calculated using the two taus and the $E_{\mathrm{T}}^{\mathrm{miss}}$ in the event. The additional requirement of $m_{\mathrm{T2}} > 30$ GeV is applied to select events for the training and optimization of the multivariate analysis (MVA).

After applying the preselection listed above, both the signal and background MC samples are split in two. Half is used for the BDT training and the other half for testing. Twelve variables with good discriminatory power are considered as input for the BDT training procedure: $E_{\mathrm{T}}^{\mathrm{miss}}$, m_{eff}, m_{T2}, $m_{\tau\tau}$, $\Delta\phi(\tau,\tau)$, $\Delta\eta(\tau,\tau)$, $p_{\mathrm{T}}^{\tau 1}$, $p_{\mathrm{T}}^{\tau 2}$, $m_{\mathrm{T}\tau 1}$, $m_{\mathrm{T}\tau 2}$, $\Delta\phi(E_{\mathrm{T}}^{\mathrm{miss}},\tau 1)$, and $\Delta\phi(E_{\mathrm{T}}^{\mathrm{miss}},\tau 2)$. The MC simulation samples are compared to data for these variables and their correlations to ensure that they are modeled well.

A direct stau production scenario with $m(\tilde{\tau}_R,\tilde{\chi}_1^0) = (109, 0)$ GeV is used for the training and optimization of the BDT, and the BDT response requirement (t_{cut}) is chosen based on the best expected sensitivity for discovery. The two-tau MVA SR definition is shown in Table III.

B. Background determination

The main SM backgrounds in the two-tau MVA SR are $W+$jets and diboson production. Contributions from diboson, $t\bar{t}$, and $Z+$jets processes are estimated using MC simulation samples and validated using data in WW-rich, $t\bar{t}$-rich, or Z-rich validation regions, as defined in Ref. [22].

[2]The Z boson mass in ditau decays is reconstructed lower than the Z boson mass value due to the neutrinos from the tau decay.

TABLE III. Two-tau MVA signal region and validation region definitions for the direct stau-pair production analysis, where t_{cut} is the BDT response requirement.

	Common				
	Exactly 2 medium OS taus ≥1 tight tau tagged ℓ veto b-jet veto Z-veto				
	Signal region SR	Multijet VR1	Multijet VR2	W-VR1	W-VR2
m_{T2}	>30 GeV	30–50 GeV	50–80 GeV	>30 GeV	>30 GeV
$E_{\mathrm{T}}^{\mathrm{miss}}$	...	...	...	>100 GeV	>90 GeV
t_{cut}	>0.07	<0.07	<0.07	$-0.2-0.07$	$-0.2-0.07$

The $W+$jets contribution in the signal region is dominated by events where the W decays to a tau lepton and a jet is misidentified as another tau. The contribution is estimated by normalizing the yields from MC simulation samples to data in a dedicated control region. The $W+$jets control region selects events with the W boson decaying to a muon and neutrino to suppress the multijet background, which is larger for the electron channel. Events containing exactly one isolated muon and one tau satisfying the tight identification requirement are selected, where the muon and tau must have opposite electrical charge. To reduce the contribution from $Z+$jets production, $m_{\mathrm{T}}^{\tau}+m_{\mathrm{T}}^{\mu}>80$ GeV is required, and the reconstructed invariant mass of the muon and tau must be outside the Z mass window (12 GeV $< m_{\tau\mu} <$ 40 GeV or $m_{\tau\mu} >$ 100 GeV). To further suppress multijet and $Z+$jets processes, $E_{\mathrm{T}}^{\mathrm{miss}}>40$ GeV is required, and the muon and tau must not be back-to-back [$\Delta\phi(\tau,\mu)<2.7$ and $\Delta\eta(\tau,\mu)<2.0$]. The contribution from events with top quarks is suppressed by rejecting events containing b-tagged jets. The multijet background in the $W+$jets control region is estimated using a region with the same requirements, but with a same-sign muon and tau. The contribution from other SM processes is subtracted using MC simulation samples, and the ratio of opposite-sign muon and tau events to same-sign events is assumed to be unity for the multijet background.

The contribution from multijet events in the signal region, where both selected taus are misidentified jets, is small and is estimated using the so-called ABCD method. Four exclusive regions (A, B, C, D) are defined in a two-dimensional plane as a function of the two uncorrelated

TABLE IV. Numbers of events observed in data and expected from SM processes and the SUSY reference point $m(\tilde{\tau}_R,\tilde{\chi}_1^0)=(109,0)$ GeV in the two-tau MVA validation and signal regions. The uncertainties shown include both statistical and systematic components. The "top" contribution includes the single top, $t\bar{t}$, and $t\bar{t}V$ processes. The multijet background estimation is taken from data, as described in the text. In the VR, the multijet scale factor from fitting the background is not applied, while the $W+$jets scale factor is applied. In the SR, both the multijet and the $W+$jets scale factors are applied. Also shown are the model-independent limits calculated from the signal region observations: the one-sided p_0-value; the expected and observed upper limits at 95% CL on the number of beyond-the-SM events (S_{exp}^{95} and S_{obs}^{95}) for each signal region, calculated using pseudoexperiments and the CL_s prescription; the observed 95% CL upper limit on the signal cross section times efficiency ($\langle\epsilon\sigma\rangle_{\mathrm{obs}}^{95}$); and the CL_b value for the background-only hypothesis.

SM process	Multijet VR1	Multijet VR2	W-VR1	W-VR2	SR
Top	30 ± 9	19 ± 6	5.4 ± 2.6	8.1 ± 3.4	1.2 ± 0.9
$Z+$jets	590 ± 100	86 ± 21	2.3 ± 1.7	4.4 ± 2.5	0.9 ± 1.2
$W+$jets	570 ± 190	210 ± 70	20 ± 8	33 ± 13	7.3 ± 3.4
Diboson	29 ± 8	16 ± 5	4.7 ± 2.4	7.1 ± 3.1	4.4 ± 1.6
Multijet	19400 ± 1200	3840 ± 230	5.9 ± 2.7	17 ± 12	0.9 ± 2.6
SM total	20700 ± 1200	4170 ± 250	38 ± 9	70 ± 19	15 ± 5
Observed	21107	4002	33	65	15
$m(\tilde{\tau}_R,\tilde{\chi}_1^0)=(109,0)$ GeV	17 ± 7	13 ± 5	3.4 ± 2.2	5.6 ± 2.9	21 ± 5
p_0	...	...	...	...	0.48
S_{obs}^{95}	...	...	...	...	15.3
S_{exp}^{95}	...	...	...	...	$15.1^{+5.1}_{-3.5}$
$\langle\epsilon\sigma\rangle_{\mathrm{obs}}^{95}$ [fb]	...	...	...	...	0.76
CL_b	...	...	...	...	0.52

discriminating variables m_{T2} and the tau identification criterion. Regions A and B are required to have two medium taus where at least one meets the tight tau identification criteria, while regions C and D are required to have two loose taus that fail to satisfy the tight tau identification criteria. In regions A and C (B and D) $m_{T2} > 30$ GeV ($m_{T2} < 20$ GeV) is also required. The multijet background in signal region A can be estimated from $N_A = N_C \times N_B/N_D$, where N_A, N_B, N_C, and N_D are the numbers of events in regions A, B, C, and D, respectively. The assumption that the ratios N_A/N_C and N_B/N_D are the same is confirmed using MC simulation samples and in validation regions using data.

A simultaneous likelihood fit to the multijet estimation and $W+$jets CR is performed to normalize the corresponding background estimates and obtain the expected yields in the SR (as described in Sec. VI). After the simultaneous fit, the multijet and $W+$jets normalization factors are found to be $1.4^{+2.5}_{-1.4}$ and 0.98 ± 0.30, respectively. Because of the small number of events in some of the ABCD regions, the uncertainty on the multijet normalization factor is large; however, the multijet contribution to the total background is very small and the effect on the total signal region background uncertainty is small.

Two multijet validation regions are defined with the same selection as for the signal region, but with $t_{cut} < 0.07$ and intermediate m_{T2}. These multijet validation regions are enriched in events with jets misidentified as hadronic tau decays, and good agreement is seen between the data and expectation across the BDT input kinematic variables. A further two validation regions are defined to check the modeling of the $W+$jets background. The intermediate BDT region $-0.2 < t_{cut} < 0.07$ is used, with a high E_T^{miss} selection, where the $W+$jets background is seen to be

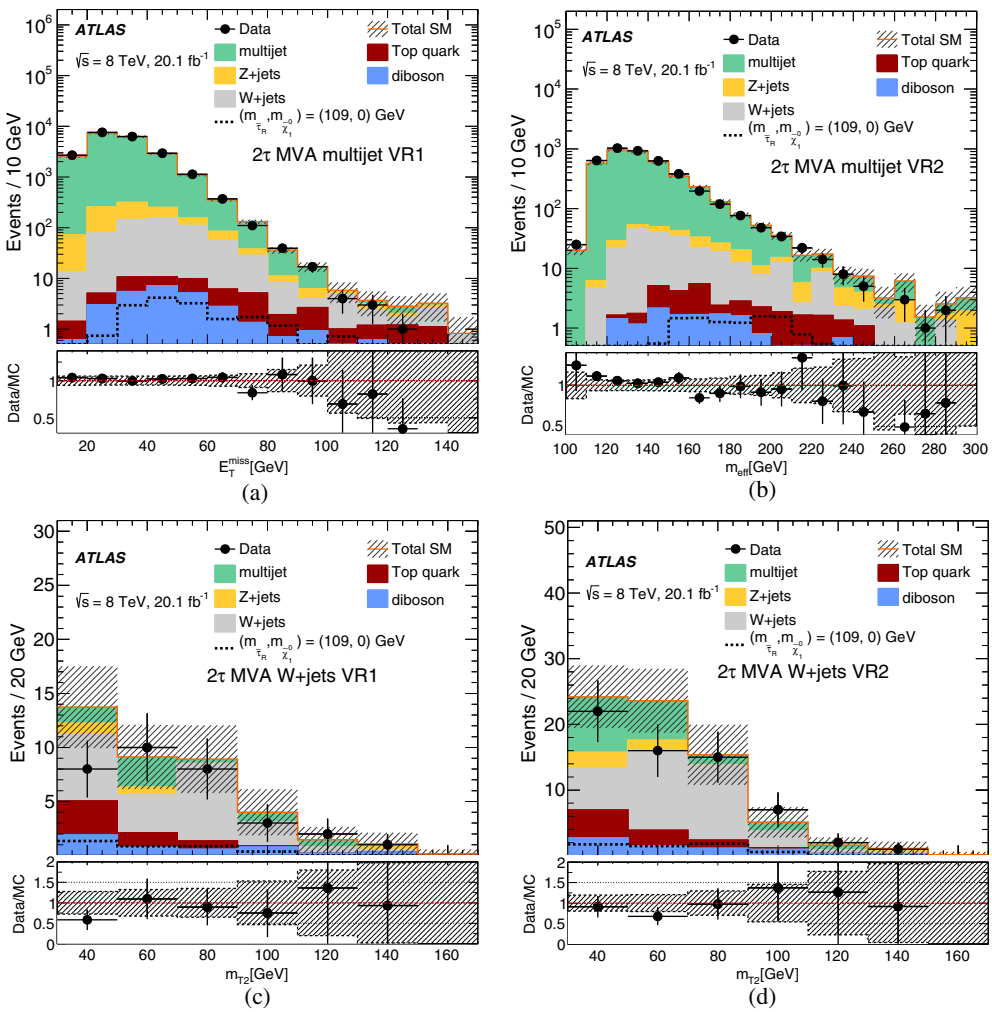

FIG. 3. Distributions in the two-tau MVA validation regions: (a) missing transverse momentum E_T^{miss} in multijet VR1, (b) effective mass m_{eff} in multijet VR2, (c) stransverse mass m_{T2} in W-VR1, and (d) m_{T2} in W-VR2. The lower panel of each plot shows the ratio of data to the SM background prediction. The last bin in each distribution includes the overflow. The uncertainty band includes both the statistical and systematic uncertainties on the SM prediction.

TABLE V. The relative systematic uncertainty (%) on the background estimate in the two-tau MVA SR from the leading sources. Uncertainties from different sources may be correlated and do not necessarily add in quadrature to the total uncertainty.

Systematic source	Uncertainty
Statistical uncertainty on MC samples	20%
$E_{\mathrm{T}}^{\mathrm{miss}}$ soft-term resolution	20%
Statistical uncertainty on the $W+$jets scale factor	15%
Tau misidentification probability	14%
$W+$jets theory and modeling	13%
Jet energy scale	11%
$E_{\mathrm{T}}^{\mathrm{miss}}$ soft-term scale	10%
Total	35%

modeled well. The validation region definitions are shown in Table III. Table IV and Figs. 3(a), 3(b), 3(c), and 3(d) show the agreement between data and expectation in the validation regions. The purity of the multijet and $W+$jets validation regions is ~90% and ~50%, respectively, while the signal contamination from the $m(\tilde{\tau}_R,\tilde{\chi}_1^0)=(109,0)$ GeV scenario is $<1\%$ and $<10\%$, respectively.

C. Results

The observed number of events in the signal region is shown in Table IV along with the background expectations, uncertainties, p_0-value, S_{exp}^{95}, S_{obs}^{95}, $\langle\epsilon\sigma\rangle_{\mathrm{obs}}^{95}$, and the CL_b value. The individual sources of uncertainty on the background estimation in the SR are shown in Table V, where the dominant sources are the statistical uncertainty on the MC simulation samples, the uncertainty on the $E_{\mathrm{T}}^{\mathrm{miss}}$ from energy deposits not associated with reconstructed objects, and the statistical uncertainty on the normalization factor applied to the $W+$jets background. Generator modeling uncertainties for the $W+$jets background are estimated by varying the renormalization and factorization scales individually between 0.5 and 2 times the nominal values in Alpgen. Additionally, the impact of the jet p_{T} threshold used for parton-jet matching in Alpgen $W+$jets simulation is assessed by changing the jet p_{T} threshold from 15 GeV to 25 GeV. Figures 4(a), 4(b), 4(c), and 4(d) show the distributions of the BDT response prior to the t_{cut} selection, and the $E_{\mathrm{T}}^{\mathrm{miss}}$, m_{eff}, and m_{T2} quantities in the SR, where good agreement between the expected background and the observed data is seen.

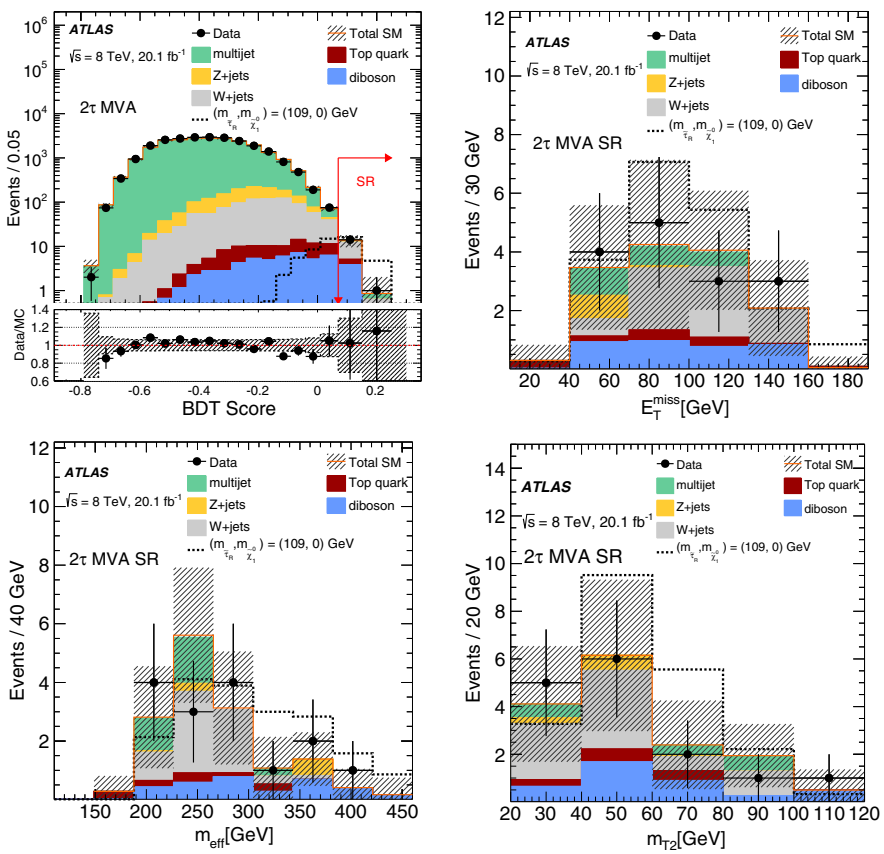

FIG. 4. The BDT response is shown in (a) prior to applying the SR t_{cut} requirement. Also shown are distributions in the two-tau MVA SR: (b) $E_{\mathrm{T}}^{\mathrm{miss}}$, (c) m_{eff}, and (d) m_{T2}. The lower panel in (a) shows the ratio of data to the SM background prediction. The uncertainty band includes both the statistical and systematic uncertainties on the SM prediction. The multijet and $W+$jets normalization factors from the background fits are applied in (b)–(d); only the $W+$jets normalization factor is applied in (a).

VIII. COMPRESSED SPECTRA IN DIRECT PRODUCTION OF $\tilde{\chi}_1^+\tilde{\chi}_1^-$ OR $\tilde{\chi}_1^+\tilde{\chi}_2^0$

In many SUSY scenarios, one or more of the mass differences between the charginos and neutralinos is small, resulting in final states with low-momentum leptons that require dedicated searches. The two-lepton analysis in Ref. [19] excluded $\tilde{\chi}_1^+\tilde{\chi}_1^-$ scenarios with $\tilde{\ell}_L$-mediated decays with $\tilde{\chi}_1^\pm$-$\tilde{\chi}_1^0$ mass splittings down to approximately 100 GeV, while the three-lepton analysis in Ref. [20] excluded $\tilde{\chi}_1^\pm\tilde{\chi}_2^0$ scenarios with $\tilde{\ell}_L$-mediated decays down to $\tilde{\chi}_2^0$-$\tilde{\chi}_1^0$ mass splittings of 20 GeV. The analyses presented in this section focus on event selections based on low-momentum leptons, and also on the production in association with ISR jets to provide improved sensitivity to the compressed spectra scenarios not covered by previous searches. As discussed in Sec. II, simplified models describing $\tilde{\chi}_1^+\tilde{\chi}_1^-$ and $\tilde{\chi}_1^\pm\tilde{\chi}_2^0$ production are considered for these compressed spectra searches, where the $\tilde{\chi}_1^\pm/\tilde{\chi}_2^0$ decay only through sleptons or sneutrinos. The compressed spectra searches are less sensitive to scenarios where the $\tilde{\chi}_1^\pm/\tilde{\chi}_2^0$ decay through SM W, Z, or Higgs bosons, as the branching fraction to leptonic final states is significantly suppressed. The experimental sensitivity to these scenarios is expected to be recovered with a larger data set.

A. Searches with two opposite-sign light leptons

Previous searches for direct $\tilde{\chi}_1^+\tilde{\chi}_1^-$ production using two opposite-sign light-lepton final states are extended here to increase the sensitivity to compressed SUSY scenarios. The opposite-sign, two-lepton analysis presented here probes $\tilde{\chi}_1^\pm$-$\tilde{\chi}_1^0$ mass splittings below 100 GeV using an ISR-jet selection.

1. Event selection

Events are reconstructed as described in Sec. V, with the signal light-lepton p_T threshold raised to $p_T = 10$ GeV. In addition, in events where tagged light leptons form an SFOS pair with $m_{SFOS} < 12$ GeV, both leptons in the pair are rejected. Events must have exactly two signal light leptons with opposite charge and satisfy the symmetric or asymmetric dilepton trigger criteria, as described in Sec. V.

To suppress the top-quark ($t\bar{t}$ and Wt) production contribution to the background, events containing central b-tagged jets or forward jets are rejected. To suppress events from Z boson decays, events with invariant mass of the reconstructed SFOS pair within 10 GeV of the Z boson mass (91.2 GeV) are rejected in the same-flavor channel.

Two SRs, collectively referred to as SR2ℓ-1, are defined. Both are designed to provide sensitivity to $\tilde{\chi}_1^+\tilde{\chi}_1^-$ production with $\tilde{\ell}_L$-mediated decays and low $\tilde{\chi}_1^\pm$-$\tilde{\chi}_1^0$ mass splittings and rely on a high-p_T ISR jet to boost the leptons, which would otherwise have too low momentum to be reconstructed. The super-razor variables that are discussed in Sec. VI A are used to discriminate between signal and backgrounds. Both the same-flavor (SF) and different-flavor (DF) channels are used. The first SR, SR2ℓ-1a, requires $R_2 > 0.5(0.7)$ in the SF (DF) channel, whereas the second SR, SR2ℓ-1b, requires $R_2 > 0.65(0.75)$. Both SRs require $M_\Delta^R > 20$ GeV to reduce SM $Z+$jets background, and $\Delta\phi_R^\beta > 2(2.5)$ in the SF (DF) to further increase the signal sensitivity. Table VI summarizes the complete definitions of the SRs. SR2ℓ-1a provides sensitivity for moderate $\tilde{\chi}_1^\pm$-$\tilde{\chi}_1^0$ mass splittings from 50 GeV to 100 GeV, while SR2ℓ-1b provides sensitivity for $\tilde{\chi}_1^\pm$-$\tilde{\chi}_1^0$ mass splittings less than 50 GeV.

2. Background determination

The SM background is dominated by WW diboson and top-quark production. The MC predictions for these SM sources, in addition to contributions from ZV production, where $V = W$ or Z, are normalized in dedicated control regions for each background. The reducible background is estimated using the matrix method as described in Sec. VI B. Finally, contributions from remaining sources of SM background, which include Higgs boson production and $Z+$jets, are small and are estimated from simulation. These are collectively referred to as "Others."

TABLE VI. The selection requirements for the opposite-sign, two-lepton signal and control regions, targeting $\tilde{\chi}_1^+\tilde{\chi}_1^-$ production with small mass splittings between the $\tilde{\chi}_1^\pm$ and LSP.

	Common						
Central light-flavor jets	=1 Veto >20						
Forward jets M_Δ^R [GeV]	SR2ℓ-1a		SR2ℓ-1b		CR2ℓ-Top	CR2ℓ-WW	CR2ℓ-ZV
ℓ flavor/sign	$\ell^\pm\ell^\mp$	$\ell^\pm\ell'^\mp$	$\ell^\pm\ell^\mp$	$\ell^\pm\ell'^\mp$	$\ell^\pm\ell'^\mp$	$\ell^\pm\ell'^\mp$	$\ell^\pm\ell^\mp$
Central b-tagged jets	Veto				≥1	Veto	Veto
m_{SFOS} [GeV]	Veto 81.2–101.2				···	···	Select 81.2–101.2
$p_T^{\ell\ell}$ [GeV]	···	···	<40	<50	···	>70	>70
p_T^{jet} [GeV]	>80	>80	>60	>80	···	···	···
R_2	>0.5	>0.7	>0.65	>0.75	···	···	···
$\Delta\phi_R^\beta$ [rad]	>2	>2.5	>2	>2.5	···	<2	>2
$p_T^{\text{central light jet}}$ [GeV]	···	···	···	···	>80	···	···

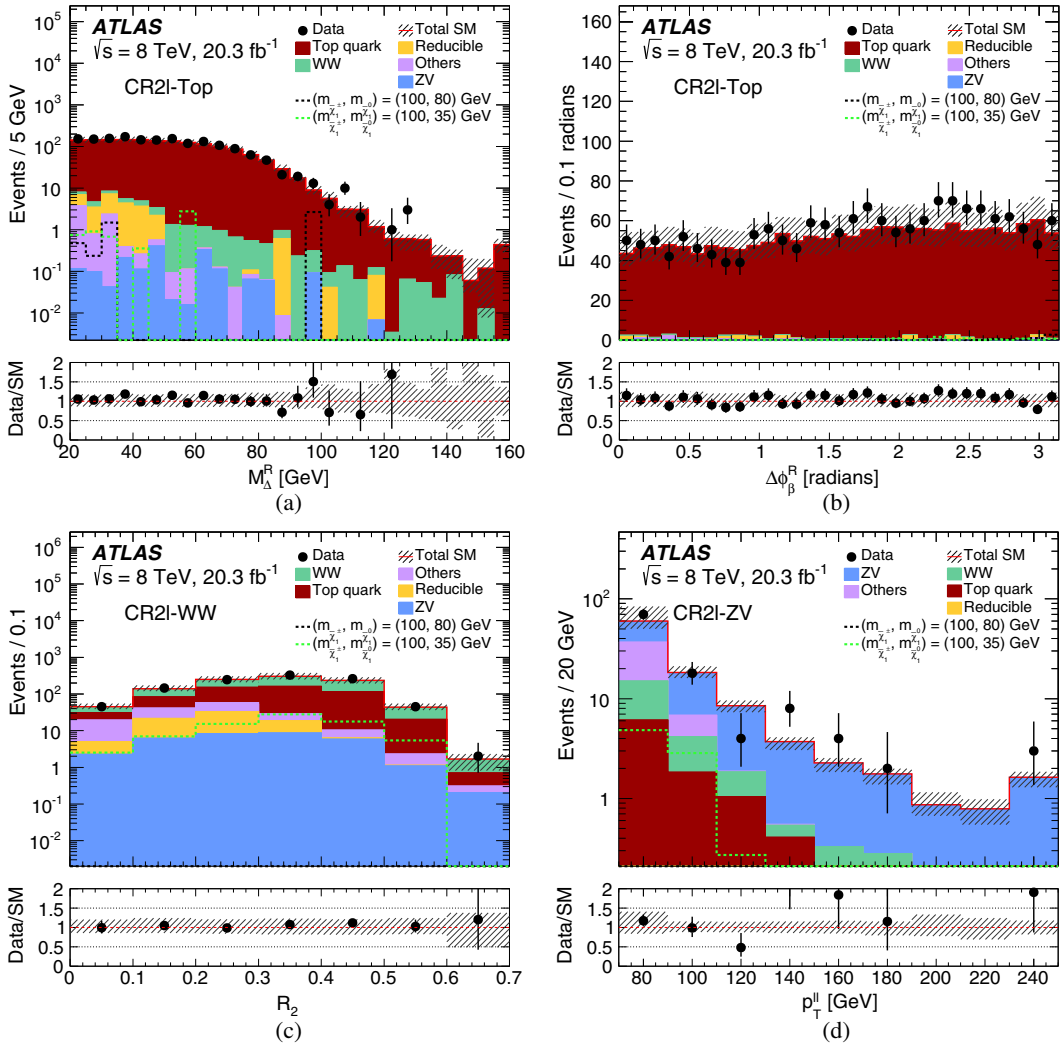

FIG. 5. Distributions in the opposite-sign, two-lepton control regions: (a) super-razor quantity M_Δ^R and (b) super-razor quantity $\Delta\phi_R^\beta$ in the top CR, (c) ratio R_2 in the WW CR, and (d) transverse momentum of the two-lepton system $p_T^{\ell\ell}$ in the ZV CR. No data-driven normalization factors are applied to the distributions. The "Others" background category includes $Z+$jets and SM Higgs boson production. The hashed regions represent the total uncertainties on the background estimates. The rightmost bin of each plot includes overflow. The lower panel of each plot shows the ratio of data to the SM background prediction. SM background prediction. Predicted signal distributions in simplified models are also shown.

The top CR is defined using the DF sample in order to suppress events from SM Z boson production. Events are required to have exactly one central light-flavor jet with $p_T > 80$ GeV, no forward jet, and $M_\Delta^R > 20$ GeV. At least one b-tagged jet is required to enrich the purity in top-quark production and ensure orthogonality to the SRs. Figures 5(a) and 5(b) show the M_Δ^R and $\Delta\phi_R^\beta$ distributions in this CR, respectively. The estimated signal contamination in this CR is less than 1% for the signal models considered.

The WW CR is also defined using the DF sample. Events are required to have exactly one central light jet, no forward jet or b-tagged jet, $p_T^{\ell\ell} > 70$ GeV, and $M_\Delta^R > 20$ GeV. In order to ensure orthogonality to the SRs, $\Delta\phi_R^\beta < 2$ is required. Figure 5(c) shows the R_2 distribution in this CR. The estimated signal contamination in this CR is less than 20% for the signal models considered.

The ZV CR is defined by using the SF samples and by requiring exactly one central light jet, no forward jet, or b-tagged jet, $p_T^{\ell\ell} > 70$ GeV, $\Delta\phi_R^\beta > 2$, and $M_\Delta^R > 20$ GeV. In order to increase the purity in ZV production, events with invariant mass of the reconstructed SFOS pair within 10 GeV of the Z boson mass are used. This requirement also ensures orthogonality to the SRs. Figure 5(d) shows the $p_T^{\ell\ell}$ distribution in this CR. The estimated signal contamination in this CR is less than 10% for the signal models considered.

A simultaneous likelihood fit to the top, WW, and ZV CRs is performed to normalize the corresponding background estimates to obtain yields in the SR (as described

TABLE VII. Numbers of observed and predicted events in the opposite-sign, two-lepton control regions, data/MC normalization factors, and composition of the CRs obtained from the background-only fit. The "Others" background category includes $Z+$jets and SM Higgs boson production. The $Z+$jets production is the dominant contribution to this category in the CR2ℓ-ZV.

CR	CR2ℓ-top	CR2ℓ-WW	CR2ℓ-ZV
Observed events	1702	1073	109
MC prediction	1600 ± 80	1020 ± 140	98 ± 14
Normalization	1.06	1.04	1.19
Total uncertainty	0.07	0.35	0.42
Composition			
WW	1%	43%	12%
Top	98%	41%	9%
ZV	<1%	4%	56%
Reducible	1%	5%	<1%
Others	<1%	7%	22%

TABLE VIII. The dominant systematic uncertainties (in %) on the total background estimated in the opposite-sign two-lepton signal regions. Because of correlations between the systematic uncertainties and the fitted backgrounds, the total uncertainty is different from the sum in quadrature of the individual uncertainties.

SR	SR2ℓ-1a		SR2ℓ-1b	
ℓ flavor/sign	$\ell^\pm\ell^\mp$	$\ell^\pm\ell'^\mp$	$\ell^\pm\ell^\mp$	$\ell^\pm\ell'^\mp$
Statistical uncertainty on MC samples	2%	6%	4%	10%
Jet energy scale/resolution	10%	9%	13%	11%
Theory and modeling	22%	22%	24%	25%
Total	23%	23%	26%	28%

in Sec. VI). Table VI summarizes the definitions of the CRs, and Table VII summarizes the numbers of observed and predicted events in these CRs, data/MC normalizations, and CR compositions obtained from the simultaneous fit.

Systematic uncertainties affect the estimates of the backgrounds and signal event yields in the control and signal regions. A breakdown of the different sources of systematic uncertainty on the background estimate as described in Sec. VI C is shown in Table VIII. Generator modeling uncertainties are estimated by comparing the results from the Powheg Box and MC@NLO event generators for top-quark events, and Powheg Box and aMC@NLO for WW events, using Herwig for parton showering in all cases. Parton showering uncertainties are estimated in top-quark and WW events by comparing Powheg Box+Herwig with Powheg Box+Pythia. Both generator modeling and parton showering uncertainties are estimated for ZV events by comparing Powheg Box +Pythia to sherpa. Top-quark samples are generated using AcerMC+Pythia to evaluate the uncertainties related to the amount of initial- and final-state radiation [115]. The impact of the choice of renormalization and factorization scales is evaluated by varying these individually between 0.5 and 2 times the nominal values in Powheg Box for top-quark events and in aMC@NLO for diboson events. The dominant contributions among the "Theory and modeling" uncertainties come from the generator modeling and parton showering uncertainties.

TABLE IX. Observed and expected number of events in the opposite-sign two-lepton signal regions. The "Others" background category includes $Z+$jets and SM Higgs boson production. The numbers of signal events are shown for the $\tilde{\chi}_1^+\tilde{\chi}_1^-$ simplified models with $\tilde{\ell}_L$-mediated decays and different $\tilde{\chi}_1^\pm$ and $\tilde{\chi}_1^0$ masses in GeV. The uncertainties shown include both statistical and systematic components. Also shown are the model-independent limits calculated from the opposite-sign two-lepton signal region observations: the one-sided p_0 values; the expected and observed upper limits at 95% CL on the number of beyond-the-SM events ($S^{95}_{\rm exp}$ and $S^{95}_{\rm obs}$) for each signal region, calculated using pseudoexperiments and the CL$_s$ prescription; the observed 95% CL upper limit on the signal cross section times efficiency ($\langle\epsilon\sigma\rangle^{95}_{\rm obs}$); and the CL$_b$ value for the background-only hypothesis.

SR	SR2ℓ-1a		SR2ℓ-1b	
ℓ flavor/sign	$\ell^\pm\ell^\mp$	$\ell^\pm\ell'^\mp$	$\ell^\pm\ell^\mp$	$\ell^\pm\ell'^\mp$
Expected background				
WW	67 ± 27	12 ± 5	22 ± 9	5.7 ± 2.4
Top	69 ± 19	12 ± 4	21 ± 7	5.0 ± 2.0
ZV	7.3 ± 3.4	1.7 ± 0.8	2.4 ± 1.5	0.6 ± 0.4
Reducible	12 ± 6	5.8 ± 2.0	10 ± 4	2.8 ± 1.1
Others	18 ± 5	2.1 ± 1.3	9.4 ± 3.4	1.0 ± 0.7
Total	173 ± 23	34 ± 5	65 ± 9	15.0 ± 2.5
Observed events	153	24	73	8
Predicted signal				
$(m_{\tilde{\chi}_1^\pm}, m_{\tilde{\chi}_1^0})=(100,35)$	81 ± 16	25 ± 7	44 ± 8	14 ± 4
$(m_{\tilde{\chi}_1^\pm}, m_{\tilde{\chi}_1^0})=(100,80)$	41 ± 10	23 ± 6	31 ± 7	18 ± 5
p_0	0.50	0.50	0.26	0.50
$S^{95}_{\rm obs}$	35.7	9.3	30.8	5.6
$S^{95}_{\rm exp}$	46^{+18}_{-12}	15^{+6}_{-4}	25^{+10}_{-7}	$9.4^{+4.2}_{-2.8}$
$\langle\epsilon\sigma\rangle^{95}_{\rm obs}$ [fb]	1.76	0.46	1.52	0.27
CL$_b$	0.22	0.09	0.73	0.07

3. Results

The observed number of events in each signal region is shown in Table IX along with the background expectations and uncertainties, p_0-values, $S^{95}_{\rm exp}$, $S^{95}_{\rm obs}$, $\langle\epsilon\sigma\rangle^{95}_{\rm obs}$, and the CL$_b$ values. Figures 6(a)–6(d) show the distributions of the quantities R_2 and M^R_Δ in the SR2ℓ-1a and SR2ℓ-1b regions, respectively, prior to the requirements on these variables. For illustration, the distributions are also shown for two $\tilde{\chi}_1^+\tilde{\chi}_1^-$ simplified models with $\tilde{\ell}_L$-mediated decays and different mass splittings.

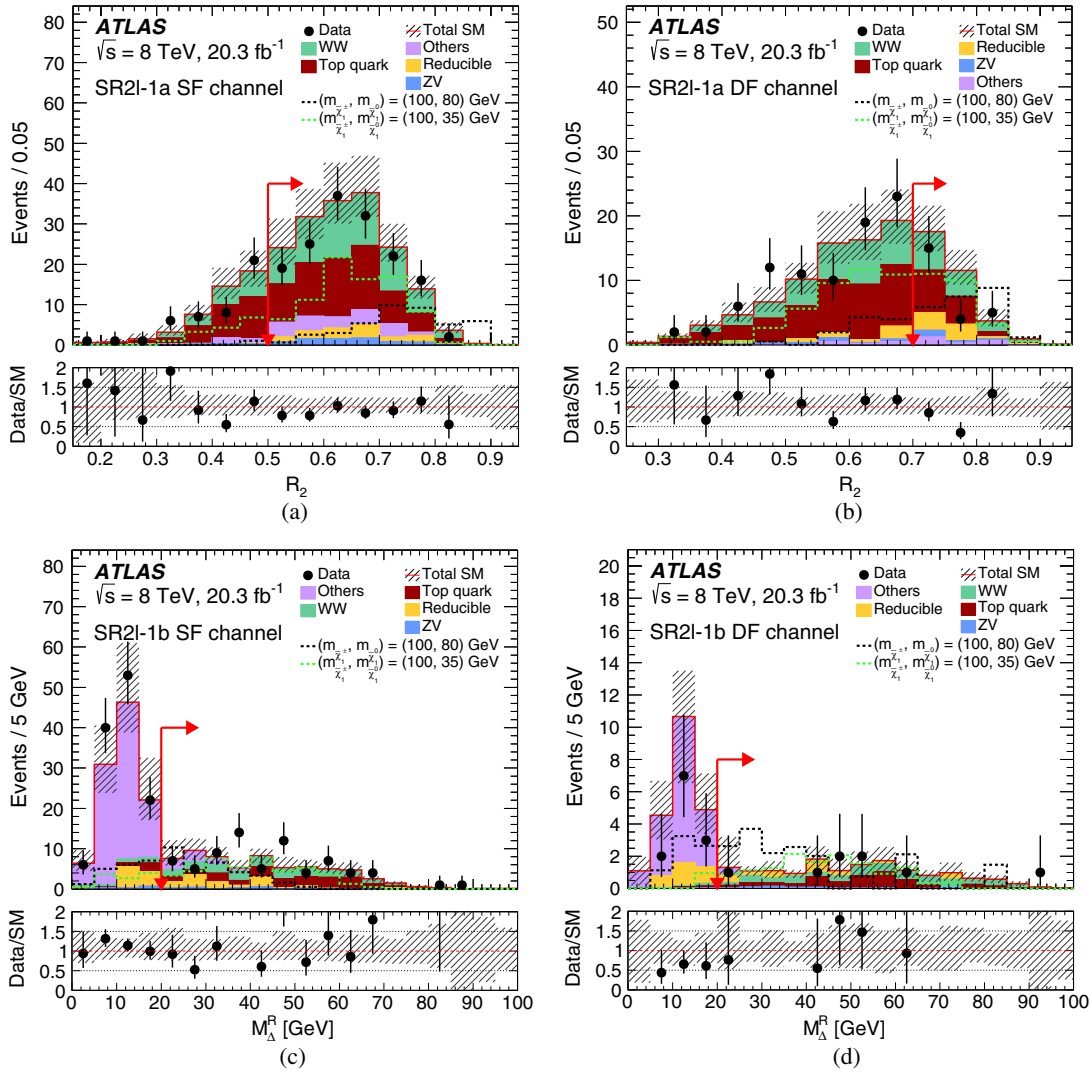

FIG. 6. Distributions of R_2 in the (a) same flavor and (b) different flavor channels in SR2ℓ-1a, and of M_Δ^R in the (c) same flavor and (d) different flavor channels in SR2ℓ-1b, prior to the requirements on these variables. The "Others" background category includes $Z+$ jets and SM Higgs boson production. Arrows indicate the limits on the values of the variables used to define the signal regions. The lower panel of each plot shows the ratio of data to the SM background prediction. The uncertainty band includes both the statistical and systematic uncertainties on the SM prediction. The last bin in each distribution includes the overflow. Predicted signal distributions in simplified models are also shown.

B. Searches with two same-sign light leptons

In compressed mass scenarios, one or more of the three leptons from $\tilde{\chi}_1^\pm\tilde{\chi}_2^0$ production may have momentum too low to be reconstructed. Therefore, the search for $\tilde{\chi}_1^\pm\tilde{\chi}_2^0$ production using two same-sign leptons can complement the three-lepton search documented in Ref. [20] and extend the reach for small mass splittings. The search for same-sign lepton pairs is preferable to opposite-sign pairs, due to the comparatively small SM background. A multivariate analysis technique is used here to discriminate between signal and backgrounds.

1. Event selection

Events are selected using the basic reconstruction, object, and event selection criteria described in Sec. V. In addition, if tagged light leptons form an SFOS pair with $m_{\mathrm{SFOS}} < 12$ GeV, both leptons in the pair are rejected. Signal electrons with $p_{\mathrm{T}} < 60$ GeV have a tightened track (calorimeter) isolation of 7% (13%) of the electron p_{T} applied, whereas for electrons with $p_{\mathrm{T}} > 60$ GeV, a track isolation requirement of 4.2 GeV (7.8 GeV) is used. For signal muons, the track (calorimeter) isolation requirement is tightened to 6% (14%) of the muon p_{T} for $p_{\mathrm{T}} < 60$ GeV, and 4.2 GeV (8.4 GeV) otherwise. The stricter lepton isolation requirements are optimized to suppress the

TABLE X. Same-sign, two-lepton MVA signal region BDT requirements, targeting $\tilde{\chi}_1^{\pm}\tilde{\chi}_2^0$ production with small mass splittings between the $\tilde{\chi}_1^{\pm}/\tilde{\chi}_2^0$ and LSP. The selection on the BDT output, t_{cut}, is independent for each SR.

		$\ell^{\pm}\ell^{\pm}$ pair, b-jet veto				
Common		SR ΔM20	SR ΔM35	SR ΔM65	SR ΔM100	VR
ISR	t_{cut}	>0.071	>0.087	>0.103	>0.119	−0.049 − 0.051
No-ISR	t_{cut}	>0.071	>0.087	>0.135	>0.135	−0.049 − 0.051

TABLE XI. The expected and observed yields in the same-sign, two-lepton MVA validation regions, separated into ee events, $e\mu$ events, and $\mu\mu$ events. The uncertainties shown include both statistical and systematic components.

	VR ISR			VR no-ISR		
	ee	$e\mu$	$\mu\mu$	ee	$e\mu$	$\mu\mu$
Reducible background	260 ± 140	670 ± 330	160 ± 110	410 ± 190	1100 ± 400	310 ± 170
Charge-flip	289 ± 15	15.0 ± 1.2	⋯	711 ± 34	28.1 ± 2.0	⋯
Diboson	58 ± 23	155 ± 37	110 ± 26	678 ± 25	199 ± 34	154 ± 34
Higgs	0.42 ± 0.30	0.7 ± 0.5	0.7 ± 0.5	0.23 ± 0.18	0.6 ± 0.4	0.50 ± 0.33
$t\bar{t}V$	0.23 ± 0.18	0.7 ± 0.4	0.44 ± 0.29	0.01 ± 0.022	0.01 ± 0.022	0.01 ± 0.022
$W\gamma$	61 ± 25	94 ± 23	1.0 ± 0.9	120 ± 50	200 ± 40	2.3 ± 2.0
Total	670 ± 140	940 ± 330	270 ± 120	1300 ± 200	1500 ± 400	470 ± 180
Data	585	799	363	1134	1349	612

reducible SM backgrounds with semileptonically decaying b/c-hadrons, which are an important background in this search.

Events must have exactly two light leptons with the same charge, $e^{\pm}e^{\pm}$, $\mu^{\pm}\mu^{\pm}$, or $e^{\pm}\mu^{\pm}$, and satisfy the symmetric or asymmetric dilepton trigger criteria, as described in Sec. V. Eight BDTs are independently trained to define eight signal regions optimized for four mass splitting scenarios, $m(\tilde{\chi}_2^0) - m(\tilde{\chi}_1^0) = 20$, 35, 65, 100 GeV, referred to as ΔM20, ΔM35, ΔM65, and ΔM100, respectively, each with and without the presence of a central light jet with $p_{\mathrm{T}} > 20$ GeV, referred to as ISR and no-ISR. For the BDT training, signal scenarios of $\tilde{\chi}_1^{\pm}\tilde{\chi}_2^0$ production with $\tilde{\ell}_L$-mediated decays are used, where the slepton mass is set at 95% between the $\tilde{\chi}_1^{\pm}$ and the $\tilde{\chi}_1^0$ masses. Seven variables are considered as input for the BDT training procedure: m_{T2}, $p_{\mathrm{T}}{}^{\ell\ell}$, $E_{\mathrm{T}}^{\mathrm{miss,rel}}$, H_{T}, $m_{\mathrm{T}}^{\mathrm{lep1}}$, $m_{\mathrm{T}}^{\mathrm{lep2}}$, and $\Delta\phi(\ell,\ell)$. Three further variables are also considered for the ISR signal regions: $\Delta\phi(,\mathrm{jet1})$ and the ratios $E_{\mathrm{T}}^{\mathrm{miss,rel}}/p_{\mathrm{T}}{}^{\mathrm{jet1}}$ and $p_{\mathrm{T}}{}^{\mathrm{lep1}}/p_{\mathrm{T}}{}^{\mathrm{jet1}}$. These variables exploit the kinematic properties of a compressed mass SUSY system, with and without a high-p_{T} ISR jet. The MC simulation samples are compared to data for these variables and their correlations to ensure that they are modeled well.

For the training and testing of the BDT, the signal and background samples are split into two halves, including those backgrounds estimated from data as described in Sec. VIII B 2. The eight signal region definitions are shown in Table X. Since the selection on the BDT output, t_{cut}, is independent for each SR, the overlap between SRs with looser and tighter selections is small.

2. Background determination

Several SM processes produce events with two same-sign signal leptons. The SM background processes are classified as irreducible background if they lead to events with two real, prompt, same-sign leptons, reducible background if the event has at least one fake or nonprompt lepton, or "charge flip" if the event has one lepton with mismeasured charge.

Irreducible processes include diboson ($W^{\pm}W^{\pm}$, WZ, ZZ), triboson (VVV), $t\bar{t}V$, tZ, and Higgs boson production and are determined using the corresponding MC samples. The reducible $W\gamma$ process is estimated with MC simulation samples; other reducible processes are estimated with the matrix method, similar to that described in Sec. VI B.

In this implementation of the matrix method, the fake and nonprompt lepton misidentification probabilities are measured in control regions that are kinematically close and similar in composition to the signal regions. The regions where the misidentification probabilities are measured are required to have large H_{T} ($H_{\mathrm{T}} > 50$ GeV) and large transverse mass using the leading lepton ($m_{\mathrm{T}} > 50$ GeV). The contamination from signal events in these measurement regions is $< 1\%$. The charge-flip, irreducible, and $W\gamma$ backgrounds are subtracted from the control regions before calculating lepton misidentification probabilities.

Charge-flip processes include sources of opposite-sign prompt leptons for which the charge of one lepton is mismeasured (Z, $t\bar{t}$, W^+W^-). In the relevant momentum range the muon charge-flip background is found to be negligible. Control samples of e^+e^- and $e^{\pm}e^{\pm}$ with invariant mass near the Z boson mass

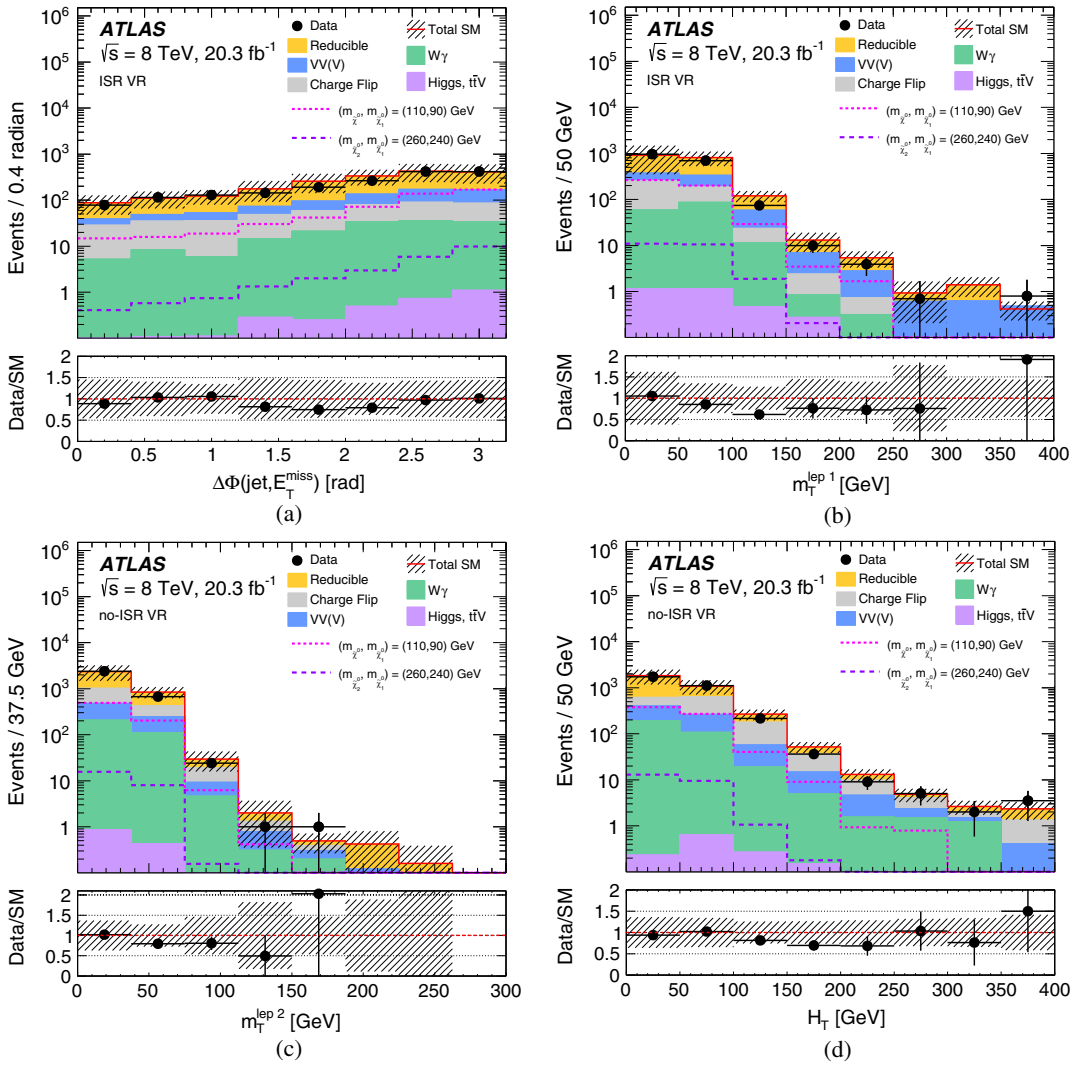

FIG. 7. For events in a selection of the same-sign, two-lepton MVA validation regions: (a) separation in ϕ between the leading jet and the $E_{\mathrm{T}}^{\mathrm{miss}}$, $\Delta\phi(\mathrm{jet}, E_{\mathrm{T}}^{\mathrm{miss}})$ and (b) transverse mass using the leading lepton $m_{\mathrm{T}}^{\mathrm{lep1}}$ in the ISR VR, (c) transverse mass using the second leading lepton $m_{\mathrm{T}}^{\mathrm{lep2}}$ and (d) scalar sum H_{T} of the p_{T} of the leptons and jets in the non-ISR VR. The lower panel of each plot shows the ratio of data to the SM background prediction. The uncertainty band includes both the statistical and systematic uncertainties on the SM prediction.

($75 < m_{\ell\ell} < 100$ GeV) are used to extract the electron charge-flip rate. A small background due to misidentified jets is subtracted by interpolating the mass sidebands and subtracting them from the observed data events. A likelihood fit is used that takes the numbers of e^+e^- and $e^\pm e^\pm$ pairs observed in the charge-flip control regions as input. The charge-flip probability is a free parameter of the fit and is extracted as a function of the electron p_{T} and η. The charge-flip background event yield is found by applying the charge-flip probability to control regions in data with the same kinematic requirements as the signal and validation regions, but with opposite-sign light lepton pairs. The contamination from fake and nonprompt leptons, and from signal events, is negligible in the e^+e^- and $e^\pm e^\pm$ control regions.

Generator modeling uncertainties for the diboson processes are estimated by comparing the results from the Powheg Box and MC@NLO event generators, while parton showering uncertainties are estimated by comparing MC@NLO+Herwig with MC@NLO+Pythia. The impact of the choice of renormalization and factorization scales is evaluated by varying these individually between 0.5 and 2 times the nominal values in aMC@NLO for diboson events.

To test the background prediction methods, two validation regions with looser selection on the BDT output than the SRs are defined; the definitions are shown in Table X. The light-lepton flavor content (ee, $\mu\mu$, or $e\mu$) is checked separately in each validation region. Table XI and Figures 7(a)–7(d) show the agreement between data and expectation in the validation regions.

TABLE XII. The model-independent limits calculated from the same-sign two-lepton MVA signal region observations: the observed 95% CL upper limit on the signal cross section times efficiency ($\langle\epsilon\sigma\rangle^{95}_{\rm obs}$); the expected and observed upper limits at 95% CL on the number of beyond-the-SM events ($S^{95}_{\rm exp}$ and $S^{95}_{\rm obs}$) for each signal region, calculated using pseudoexperiments and the CL_s prescription; the CL_b value for the background-only hypothesis; and the one-sided p_0 values.

SR		$N_{\rm exp}$	$N_{\rm obs}$	$\langle\epsilon\sigma\rangle^{95}_{\rm obs}$ [fb]	$S^{95}_{\rm obs}$	$S^{95}_{\rm exp}$	CL_b	p_0
ΔM20	ISR ee	3.2 ± 0.9	5	0.36	7.3	$5.4^{+2.2}_{-1.2}$	0.81	0.19
	$e\mu$	9.7 ± 2.8	9	0.44	8.9	$9.0^{+3.5}_{-2.5}$	0.47	0.50
	$\mu\mu$	4.3 ± 2.6	5	0.47	9.5	$8.8^{+2.8}_{-1.8}$	0.63	0.44
	No-ISR ee	28 ± 5	23	0.57	11.6	14^{+6}_{-4}	0.27	0.50
	$e\mu$	25 ± 8	29	1.08	21.9	19^{+7}_{-5}	0.68	0.33
	$\mu\mu$	7.6 ± 1.7	12	0.59	12.1	$8.0^{+2.7}_{-2.0}$	0.90	0.10
ΔM35	ISR ee	3.9 ± 1.2	1	0.17	3.5	$4.9^{+2.3}_{-1.1}$	0.09	0.50
	$e\mu$	6.5 ± 1.8	10	0.53	10.8	$7.4^{+3.2}_{-1.9}$	0.85	0.14
	$\mu\mu$	5.4 ± 2.1	5	0.37	7.6	$7.6^{+2.7}_{-1.7}$	0.51	0.50
	No-ISR ee	23 ± 5	19	0.56	11.4	$13.4^{+4.8}_{-3.4}$	0.30	0.50
	$e\mu$	46 ± 11	39	0.94	19.0	22^{+8}_{-6}	0.32	0.50
	$\mu\mu$	27 ± 10	21	0.79	15.9	$17.6^{+2.4}_{-4.0}$	0.34	0.50
ΔM65	ISR ee	1.7 ± 0.8	4	0.36	7.3	$4.7^{+1.8}_{-0.8}$	0.90	0.09
	$e\mu$	2.4 ± 0.8	4	0.33	6.7	$5.0^{+1.9}_{-1.3}$	0.54	0.34
	$\mu\mu$	1.4 ± 0.6	2	0.24	4.9	$4.1^{+1.6}_{-0.6}$	0.70	0.30
	No-ISR ee	1.2 ± 0.6	0	0.11	2.1	$3.4^{+1.3}_{-0.4}$	0.20	0.50
	$e\mu$	1.3 ± 0.5	2	0.24	4.9	$4.1^{+1.4}_{-0.7}$	0.73	0.26
	$\mu\mu$	1.5 ± 0.5	2	0.23	4.7	$4.1^{+1.6}_{-0.8}$	0.68	0.32
ΔM100	ISR ee	0.9 ± 0.6	0	0.13	2.6	$3.06^{+1.25}_{-0.09}$	0.29	0.50
	$e\mu$	0.57 ± 0.29	0	0.14	2.9	$3.00^{+1.20}_{-0.10}$	0.29	0.50
	$\mu\mu$	0.38 ± 0.35	0	0.15	3.0	$3.15^{+0.96}_{-0.11}$	0.38	0.50
	No-ISR ee	0.31 ± 0.22	0	0.16	3.2	$2.99^{+0.78}_{-0.05}$	0.38	0.50
	$e\mu$	0.55 ± 0.30	1	0.19	3.9	$3.33^{+0.93}_{-0.22}$	0.75	0.27
	$\mu\mu$	0.25 ± 0.21	0	0.16	3.2	$2.94^{+0.73}_{-0.09}$	0.37	0.50

TABLE XIII. Overview of the dominant systematic uncertainties on the background estimates in the same-sign, two-lepton MVA signal regions. The percentages show the sizes of the uncertainty relative to the total expected background; the range shows the variation among the flavor channels.

	SRΔM20		SRΔM35		SRΔM65		SRΔM100	
	ISR	No-ISR	ISR	No-ISR	ISR	No-ISR	ISR	No-ISR
Reducible background								
-Fake lepton composition	7%–14%	15%–20%	4%–14%	5%–17%	5%–17%	21%	9%–24%	20%–22%
-Real lepton subtraction	13%–32%	12%–25%	10%–20%	18%–26%	8%–18%	26%	15%–32%	22%–33%
-Statistical uncertainty on data	5%–8%	9%–12%	3%–7%	4%–8%	3%–9%	9%	5%–11%	9%–11%
Statistical uncertainty on MC samples	15%–37%	7%–12%	15%–28%	8%–16%	15%–43%	16%–32%	30%–45%	35%–74%
Choice of generator for WZ	9%–17%	4%–20%	15%–17%	5%–11%	13%–20%	6%–21%	3%–27%	4%–20%
Choice of generator for $W\gamma$	2%–3%	3%–7%	2%	4%–8%	3%–9%	...	...	...
Jet energy resolution	1%–18%	1%–7%	1%–7%	6%–12%	1%–10%	1%–6%	5%–70%	4%–35%
Total	28%–60%	18%–32%	28%–39%	22%–37%	33%–47%	33%–50%	51%–92%	55%–84%

3. Results

The observed number of events in each signal region is shown in Table XII along with the background expectation and uncertainties, p_0-values, $S^{95}_{\rm exp}$, $S^{95}_{\rm obs}$, $\langle\epsilon\sigma\rangle^{95}_{\rm obs}$, and the CL_b values. No significant excess with respect to the SM expectation is observed. The sizes and sources of uncertainty on the background estimation in the signal regions are shown in Table XIII, where the dominant sources of uncertainty are the statistical uncertainty on the reducible background estimation,

TABLE XIV. The selection requirements for the three-lepton signal regions, targeting $\tilde{\chi}_1^{\pm}\tilde{\chi}_2^0$ production with small mass splittings between the $\tilde{\chi}_1^{\pm}/\tilde{\chi}_2^0$ and LSP.

	Common			
ℓ flavor/sign	$\ell^{\pm}\ell^{\mp}\ell$, $\ell^{\pm}\ell^{\mp}\ell'$			
$p_{\mathrm{T}}^{\mathrm{lep1}}$	<30 GeV			
b-jet	Veto			
$E_{\mathrm{T}}^{\mathrm{miss}}$	>50 GeV			
m_{SFOS}	Veto 8.4–10.4 GeV			
SR	SR3ℓ-0a	SR3ℓ-0b	SR3ℓ-1a	SR3ℓ-1b
Central jets	No jets $p_{\mathrm{T}}>50$ GeV		$\geq$1jet $p_{\mathrm{T}}>50$ GeV	
$m_{\mathrm{SFOS}}^{\mathrm{min}}$	4–15 GeV	15–25 GeV	5–15 GeV	15–25 GeV
Other	$30<m_{\ell\ell\ell}<60$ GeV $m_{\mathrm{T}}<20$ GeV	$30<m_{\ell\ell\ell}<60$ GeV	$\Delta\phi(E_{\mathrm{T}}^{\mathrm{miss}},\mathrm{jet1})>2.7$ rad $p_{\mathrm{T}}^{\mathrm{lep1}}/p_{\mathrm{T}}^{\mathrm{jet1}}<0.2$	$\Delta\phi(E_{\mathrm{T}}^{\mathrm{miss}},3\ell)>0.7\pi$ rad

the statistical uncertainty on the MC simulation samples, and the uncertainty related to the choice of generator for the WZ MC simulation sample.

C. Searches with three light leptons

Previous searches for $\tilde{\chi}_1^{\pm}\tilde{\chi}_2^0$ production using the three-lepton final state are extended here to increase the sensitivity to compressed SUSY scenarios. The three-lepton analysis presented here probes $\tilde{\chi}_2^0$-$\tilde{\chi}_1^0$ mass splittings below 25 GeV using low-p_{T} leptons and ISR jets.

1. Event selection

Events are selected as described in Sec. V. In addition, signal muons with $p_{\mathrm{T}} < 15$ GeV have tightened track and calorimeter isolation requirements of 7% of the muon p_{T}. The stricter muon isolation requirements suppress SM backgrounds with semileptonically decaying b/c-hadrons, which are larger for muons rather than electrons due to the lower muon-p_{T} threshold. Events must satisfy a single-lepton, dilepton, or trilepton trigger.

Four signal regions are defined with exactly three light leptons, all with $p_{\mathrm{T}} < 30$ GeV, and at least one SFOS pair present among the leptons. All signal regions veto events with b-tagged jets to reduce the $t\bar{t}$ SM background and events with $8.4 < m_{\mathrm{SFOS}} < 10.4$ GeV to suppress backgrounds with leptonic Υ decays. The three-lepton signal region selections are summarized in Table XIV.

The first two signal regions, SR3ℓ-0a and SR3ℓ-0b, closely follow the selection in Ref. [20], using $E_{\mathrm{T}}^{\mathrm{miss}}$, m_{T}, and m_{SFOS} selections. SR3ℓ-0a and SR3ℓ-0b are defined with $E_{\mathrm{T}}^{\mathrm{miss}} > 50$ GeV and $30 < m_{\ell\ell\ell} < 60$ GeV to reject diboson processes. Events with a jet with $p_{\mathrm{T}} > 50$ GeV are vetoed to be disjoint from the ISR signal region. The first signal region, SR3ℓ-0a, targets the smallest $\tilde{\chi}_2^0$-$\tilde{\chi}_1^0$ mass splittings by selecting events with $m_{\mathrm{SFOS}}^{\mathrm{min}}$ between 4 and 15 GeV. In addition, SR3ℓ-0a requires small m_{T} to reduce the WZ SM background. The second signal region, SR3ℓ-0b, targets the slightly larger $\tilde{\chi}_2^0$-$\tilde{\chi}_1^0$ mass splittings by selecting events with $m_{\mathrm{SFOS}}^{\mathrm{min}}$ between 15 and 25 GeV.

The third and fourth signal regions, SR3ℓ-1a and SR3ℓ-1b, both require the presence of a $p_{\mathrm{T}} > 50$ GeV jet to target signal production with ISR. The leptons from a

TABLE XV. The selection requirements for the three-lepton validation regions. The "Z boson" requirement is defined as m_{SFOS} in the range 81.2–101.2 GeV.

	Common			
ℓ flavor/sign	$\ell^{\pm}\ell^{\mp}\ell$, $\ell^{\pm}\ell^{\mp}\ell'$			
$m_{\mathrm{SFOS}}^{\mathrm{min}}$	>4 GeV			
m_{SFOS}	Veto 8.4–10.4 GeV			
SR	VR3ℓ-0a	VR3ℓ-0b	VR3ℓ-1a	VR3ℓ-1b
Central jets	No jets $p_{\mathrm{T}}>50$ GeV		$\geq$1 jet $p_{\mathrm{T}}>50$ GeV	
$N_{b-\mathrm{jets}}$	0	1	0	1
$E_{\mathrm{T}}^{\mathrm{miss}}$	<30 GeV	>30 GeV	<50 GeV	>50 GeV
Z boson	Veto	⋯	Veto	Veto
$p_{\mathrm{T}}^{\mathrm{lep1}}$	<30 GeV	⋯	⋯	⋯
Target process				
Irreducible	WZ	WZ	WZ	WZ
Reducible	$Z+$jets, Υ	$t\bar{t}$	$Z+$jets	$t\bar{t}$

TABLE XVI. Estimated and observed yields in the three-lepton validation regions. The uncertainties shown include both statistical and systematic components. The "Others" background category includes $t\bar{t}V$, VVV, and SM Higgs boson production.

	VR3ℓ-0a	VR3ℓ-0b	VR3ℓ-1a	VR3ℓ-1b
WZ	108 ± 20	35 ± 7	36 ± 7	$9.7^{+2.0}_{-2.2}$
ZZ	63 ± 11	5.9 ± 1.3	5.2 ± 1.1	$0.33^{+0.08}_{-0.07}$
Reducible	990^{+300}_{-270}	159^{+40}_{-35}	56 ± 16	102^{+23}_{-19}
Others	1.0 ± 0.8	4.8 ± 1.7	1.5 ± 0.6	$9.9^{+3.4}_{-3.5}$
Total SM	1160^{+300}_{-280}	200 ± 40	99 ± 17	122^{+24}_{-20}
Data	1247	212	95	93

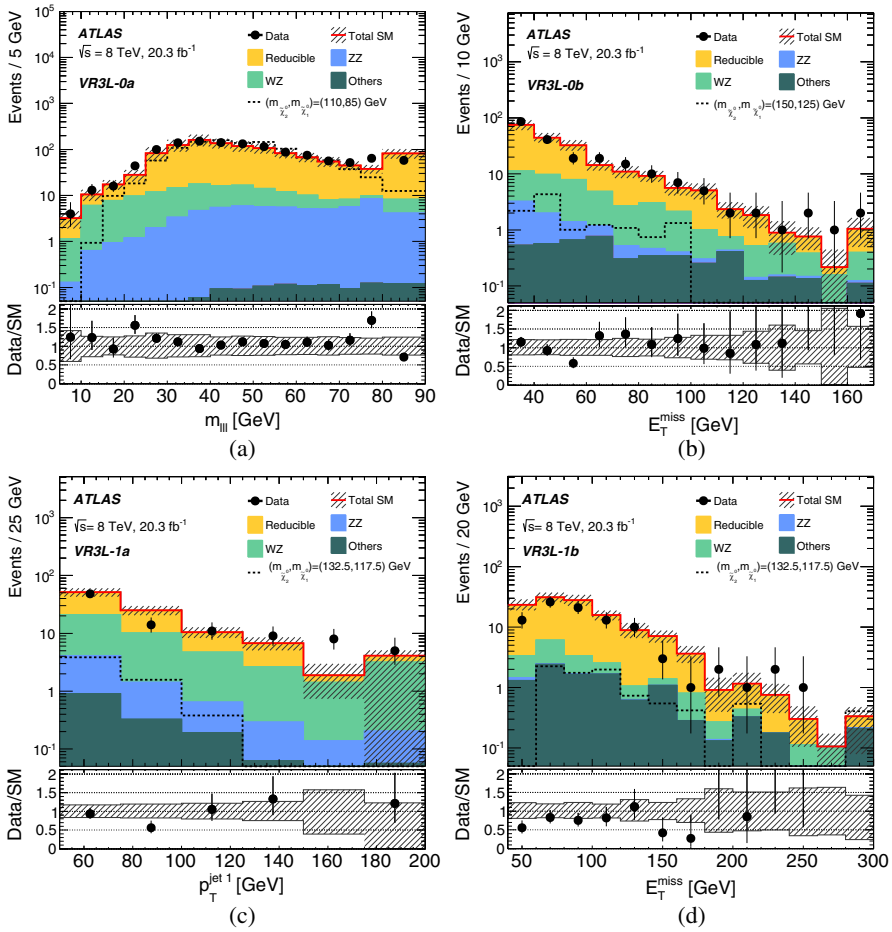

FIG. 8. Distributions in the three-lepton validation regions: (a) three-lepton invariant mass $m_{\ell\ell\ell}$ in VR3ℓ-0a, (b) $E_{\mathrm{T}}^{\mathrm{miss}}$ in VR3ℓ-0a, (c) transverse momentum of the leading jet $p_{\mathrm{T}}^{\mathrm{jet1}}$ in VR3ℓ-1a, and (d) $E_{\mathrm{T}}^{\mathrm{miss}}$ in VR3ℓ-1a. The "Others" background category includes $t\bar{t}V + tZ$, VVV, and SM Higgs boson production. The lower panel of each plot shows the ratio of data to the SM background prediction. The uncertainty band includes both the statistical and systematic uncertainties on the SM prediction. The last bin in each distribution includes the overflow.

compressed SUSY decay chain would have too low p_{T} to be reconstructed; however, because of the recoil against the high-p_{T} ISR jet, all three leptons can be boosted enough to meet the selection requirements. The third signal region, SR3ℓ-1a, targets the smallest $\tilde{\chi}_2^0$-$\tilde{\chi}_1^0$ mass splittings and selects events with $5 < m_{\mathrm{SFOS}}^{\mathrm{min}} < 15$ GeV. Here the leading jet is required to be back-to-back in the transverse plane with the $E_{\mathrm{T}}^{\mathrm{miss}}$, $\Delta\phi(E_{\mathrm{T}}^{\mathrm{miss}}, \mathrm{jet1}) > 2.7$ rad, and the ratio of leading lepton p_{T} to the jet p_{T} is required to be small, $p_{\mathrm{T}}^{\mathrm{lep1}}/p_{\mathrm{T}}^{\mathrm{jet1}} < 0.2$, to suppress the diboson and $t\bar{t}$ backgrounds. The fourth signal region, SR3ℓ-1b, targets the slightly larger $\tilde{\chi}_2^0$-$\tilde{\chi}_1^0$ mass splittings by selecting events with $15 < m_{\mathrm{SFOS}}^{\mathrm{min}} < 25$ GeV. To suppress the WZ and $t\bar{t}$ backgrounds in SR3ℓ-1b, the angle between the $E_{\mathrm{T}}^{\mathrm{miss}}$ and the three-lepton system is required to be large, $\Delta\phi(E_{\mathrm{T}}^{\mathrm{miss}}, 3\ell) > 0.7\pi$ rad.

2. Background determination

Several SM processes produce events with three signal leptons. The SM background processes are classified as irreducible background if they lead to events with three or more real leptons, or as reducible background if the event has at least one fake or nonprompt lepton. The predictions for irreducible and reducible backgrounds are tested in validation regions. For this search, irreducible processes include diboson (WZ and ZZ), VVV, $t\bar{t}V$, tZ, and Higgs boson production and are determined from MC simulation samples.

Reducible processes include single and pair production of top quarks, WW production, and a single W or Z boson produced in association with jets or photons. The dominant reducible background component is $t\bar{t}$, followed by $Z+$jets. The reducible background is estimated using the matrix method, similar to that described in Sec. VI B. In this implementation of the matrix method, the highest-p_{T} signal electron or muon is taken to be real, and only the second and third leptons are used in the matrix method. Simulation studies show that neglecting the case that the leading lepton is nonprompt or fake is valid in more than 95% of the events.

TABLE XVII. Expected and observed yields in the three-lepton signal regions. The uncertainties shown include both statistical and systematic components. The "Others" background category includes $t\bar{t}V$, VVV, and SM Higgs boson production. Also shown are the model-independent limits calculated from the three-lepton signal region observations: the one-sided p_0-values; the expected and observed upper limits at 95% CL on the number of beyond-the-SM events (S^{95}_{exp} and S^{95}_{obs}) for each signal region, calculated using pseudoexperiments and the CL_s prescription; the observed 95% CL upper limit on the signal cross section times efficiency ($\langle\epsilon\sigma\rangle^{95}_{\mathrm{obs}}$); and the CL_b value for the background-only hypothesis.

	SR3ℓ-0a	SR3ℓ-0b	SR3ℓ-1a	SR3ℓ-1b
WZ	$0.59^{+0.47}_{-0.32}$	$5.0^{+1.5}_{-1.2}$	$0.54^{+0.20}_{-0.19}$	1.6 ± 0.4
ZZ	$0.23^{+0.09}_{-0.07}$	0.66 ± 0.16	0.024 ± 0.013	$0.10^{+0.05}_{-0.04}$
Reducible	$2.8^{+1.5}_{-2.2}$	$9.7^{+3.1}_{-3.6}$	0.09 ± 0.08	$1.4^{+1.0}_{-1.1}$
Others	$0.0033^{+0.0036}_{-0.0033}$	0.07 ± 0.05	0.013 ± 0.010	0.038 ± 0.021
Total SM	$3.7^{+1.6}_{-2.2}$	$15.4^{+3.5}_{-3.9}$	$0.67^{+0.22}_{-0.21}$	$3.1^{+1.1}_{-1.2}$
Data	4	15	1	3
p_0	0.47	0.50	0.36	0.50
S^{95}_{obs}	8.3	12.6	4.0	6.1
S^{95}_{exp}	$8.2^{+1.7}_{-2.2}$	$12.6^{+5.2}_{-3.0}$	$3.8^{+0.6}_{-0.3}$	$6.0^{+2.1}_{-1.3}$
$\langle\epsilon\sigma\rangle^{95}_{\mathrm{obs}}$ [fb]	0.41	0.62	0.20	0.30
CL_b	0.59	0.50	0.69	0.54

The uncertainty on the reducible background includes the MC statistical uncertainty on the weights for the process-dependent misidentification probabilities, the uncertainty on the correction factors for the misidentification probability, the statistical uncertainty on the data events to which the matrix equation is applied, and the statistical uncertainty from the misidentification probability measured in simulation.

The systematic uncertainty related to the theoretical modeling of the WZ and ZZ backgrounds is assessed by comparing MC estimates with data in dedicated regions. The WZ region requires three light leptons with $p_{\mathrm{T}} > 30\,\mathrm{GeV}$, an SFOS pair among the three leptons, $30 < E_{\mathrm{T}}^{\mathrm{miss}} < 50$ GeV, and one jet with $p_{\mathrm{T}} > 50$ GeV. Events with an SFOS pair or three-lepton invariant mass within 10 GeV of the Z boson mass are vetoed. The ZZ region is defined with four light leptons with $p_{\mathrm{T}} > 10$ GeV, two SFOS pairs with invariant mass within 10 GeV of the Z boson mass, and $E_{\mathrm{T}}^{\mathrm{miss}} < 50$ GeV. This approach for estimating the systematic uncertainties is used here instead of the MC-based approach discussed in Sec. VI C. The WZ and ZZ MC simulation samples are both found to agree with observations in the dedicated regions within 15%, which is applied as a systematic uncertainty in the three-lepton validation and signal regions.

The background predictions are tested in validation regions that are defined to be adjacent to, yet disjoint from, the signal regions. Low-$E_{\mathrm{T}}^{\mathrm{miss}}$ validation regions ("a" regions) and high-$E_{\mathrm{T}}^{\mathrm{miss}} + b$-jet validation regions ("b" regions) are defined to target different background processes. The definition of the regions and the targeted processes are shown in Table XV. In the three-lepton validation regions, the observed data counts and SM expectations are in good agreement within statistical and systematic uncertainties, as shown in Table XVI and Figs. 8(a)–8(d).

TABLE XVIII. Breakdown of the dominant systematic uncertainties on background estimates in the three-lepton signal regions. The percentages show the size of the uncertainty relative to the total expected background.

Source of uncertainty	SR3ℓ-0a	SR3ℓ-0b	SR3ℓ-1a	SR3ℓ-1b
Reducible background				
- Statistical uncertainty	34%	14%	11%	30%
- Muon misidentification probability	30%	11%	<1%	11%
- Electron misidentification probability	21%	10%	2%	9%
- Heavy-flavor relative contribution	22%	5%	<1%	2%
- Light-flavor relative contribution	23%	4%	N/a	<1%
- Conversion relative contribution	2%	6%	<1%	10%
$E_{\mathrm{T}}^{\mathrm{miss}}$ soft-term scale	12%	7%	<1%	1%
Statistical uncertainty on MC samples	4%	3%	25%	10%
Theoretical modeling of WZ	2%	5%	12%	8%
Cross section	2%	2%	6%	4%
Total	59%	25%	33%	39%

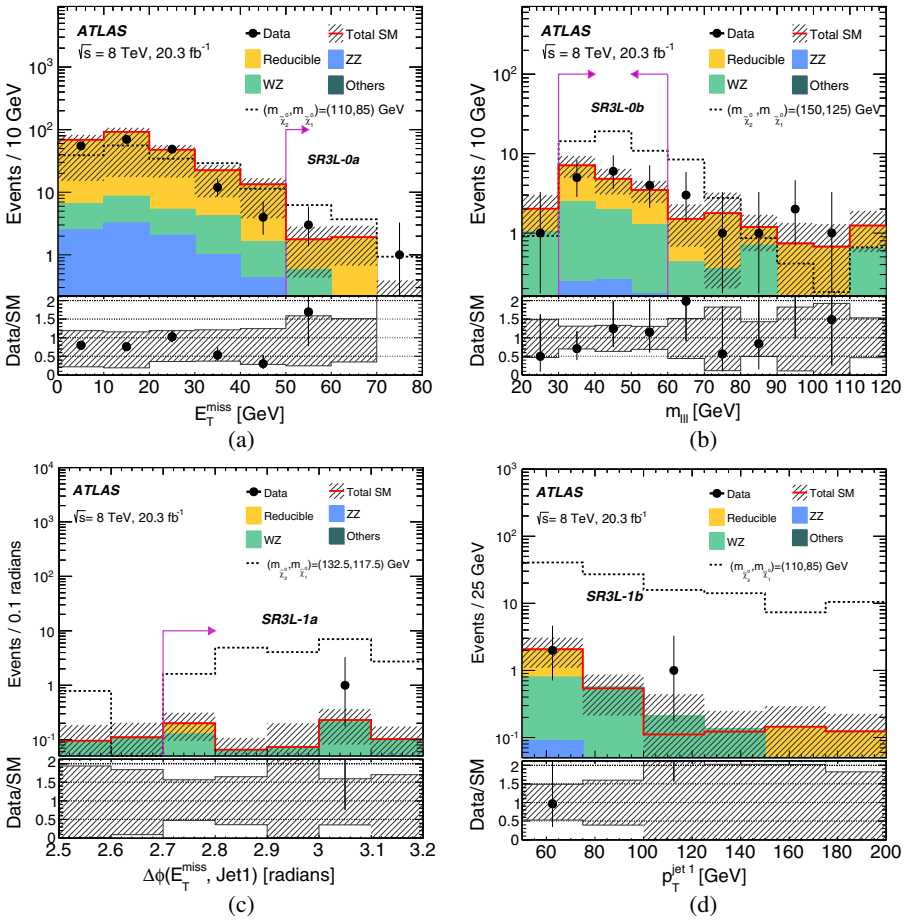

FIG. 9. Distributions in the three-lepton signal regions: (a) $E_{\mathrm{T}}^{\mathrm{miss}}$ in SR3ℓ-0a, (b) $m_{\ell\ell\ell}$ in SR3ℓ-0b, (c) $\Delta\phi(E_{\mathrm{T}}^{\mathrm{miss}}, \mathrm{jet1})$ in SR3ℓ-1a, and (d) $p_{\mathrm{T}}^{\mathrm{jet1}}$ in SR3ℓ-1b. All are shown prior to the requirements on these variables. The "Others" background category includes $t\bar{t}V + tZ$, VVV, and SM Higgs boson production. The lower panel of each plot shows the ratio of data to the SM background prediction. Arrows indicate the limits on the values of the variables used to define the signal regions. The uncertainty band includes both the statistical and the systematic uncertainties on the SM prediction. The last bin in each distribution includes the overflow.

TABLE XIX. The selection requirements for the same-sign, two-lepton VBF signal region, targeting $\tilde{\chi}_1^{\pm}\tilde{\chi}_1^{\pm}$ production via VBF with small mass splittings between the $\tilde{\chi}_1^{\pm}$ and LSP.

	SR2ℓ-2
ℓ flavor/sign	$\ell^{\pm}\ell^{\pm}$, $\ell^{\pm}\ell'^{\pm}$
Jets	≥ 2
Central b-jets	Veto
$E_{\mathrm{T}}^{\mathrm{miss}}$ [GeV]	>120
m_{T2} [GeV]	<40
$m_{\ell\ell}$ [GeV]	<100
$p_{\mathrm{T}}^{\mathrm{jet1}}$ [GeV]	>95
m_{jj} [GeV]	>350
$\eta^{\mathrm{jet1}} \cdot \eta^{\mathrm{jet2}}$	<0
$\lvert\Delta\eta_{jj}\rvert$	>1.6
$p_{\mathrm{T}}^{\ell\ell}/E_{\mathrm{T}}^{\mathrm{miss}}$	<0.4
$p_{\mathrm{T}}^{\mathrm{jet1}}/E_{\mathrm{T}}^{\mathrm{miss}}$	<1.9
$p_{\mathrm{T}}^{\ell\ell}/p_{\mathrm{T}}^{jj}$	<0.35

3. Results

The observed number of events in each signal region is shown in Table XVII along with the background expectations and uncertainties, p_0-values, S_{exp}^{95}, S_{obs}^{95}, $\langle\epsilon\sigma\rangle_{\mathrm{obs}}^{95}$, and the CL_b values. The sizes and sources of uncertainty on the background estimation in the three-lepton signal regions are shown in Table XVIII, where the dominant sources of uncertainty are the statistical uncertainty on the data for the reducible background estimate, and the uncertainty on the electron and muon misidentification probabilities. Figures 9(a), 9(b), 9(c), and 9(d) show the distributions of the quantities $E_{\mathrm{T}}^{\mathrm{miss}}$, $m_{\ell\ell\ell}$, $\Delta\phi(E_{\mathrm{T}}^{\mathrm{miss}}, \mathrm{jet1})$, and $p_{\mathrm{T}}^{\mathrm{jet1}}$ in SR3ℓ-0a, SR3ℓ-0b, SR3ℓ-1a, and SR3ℓ-1b regions, respectively, prior to the requirements on these variables. For illustration, the distributions are also shown for a $\tilde{\chi}_1^{\pm}\tilde{\chi}_2^{0}$ scenario with $\tilde{\ell}_L$-mediated decays, where the slepton mass is set halfway between the $\tilde{\chi}_1^{\pm}$ and the $\tilde{\chi}_1^{0}$ masses.

IX. SAME-SIGN CHARGINO-PAIR PRODUCTION VIA VECTOR-BOSON FUSION

This section presents a search for the same-sign chargino-pair production via VBF with subsequent $\tilde{\ell}_L$-mediated chargino decays into final states with two same-sign light leptons, at least two jets, and $E_{\mathrm{T}}^{\mathrm{miss}}$. Although the cross section for VBF production is significantly lower than that for direct production, the two additional jets in the event provide a means to separate the signal from the background for compressed spectra scenarios and complement the direct production searches that use low-momentum leptons and ISR jets.

A. Event selection

Events are selected using the basic reconstruction, object, and event selection criteria described in Sec. V. In addition, signal muons with $p_{\mathrm{T}} < 15$ GeV have tightened isolation requirements as in the three-lepton analysis described in Sec. VIII C. A tighter isolation is needed for muons rather than electrons due to the lower p_{T} threshold for muons. The stringent lepton isolation suppresses the dominant reducible background processes. Events are required to satisfy an $E_{\mathrm{T}}^{\mathrm{miss}}$ trigger.

One signal region, SR2ℓ-2, is defined with exactly two same-sign light leptons, at least two jets (central light or forward) and large missing transverse momentum $E_{\mathrm{T}}^{\mathrm{miss}} > 120$ GeV. In order to select events that originate from VBF production, the highest-p_{T} jet (jet 1) and the second highest-p_{T} jet (jet 2) are required to have large invariant mass, $m_{jj} > 350$ GeV, to be well separated in pseudorapidity, $|\Delta\eta_{jj}| > 1.6$, and to be in opposite sides of the detector, $\eta^{\mathrm{jet1}} \cdot \eta^{\mathrm{jet2}} < 0$. The last requirement greatly reduces the SM background originating from non-VBF diboson and Higgs boson production. The residual SM background originating from diboson and top-quark production is minimized by requiring the events to have no b-tagged jets, moderate invariant mass of the two leptons ($m_{\ell\ell} < 100$ GeV), small stransverse mass ($m_{\mathrm{T2}} < 40$ GeV), and a high-p_{T} jet ($p_{\mathrm{T}}^{\mathrm{jet1}} > 95$ GeV). In addition, requirements are made on the ratios of the jet p_{T}, $E_{\mathrm{T}}^{\mathrm{miss}}$, p_{T}^{jj}, and $p_{\mathrm{T}}^{\ell\ell}$. The SR definition is summarized in Table XIX.

B. Background determination

Several SM processes lead to events with two same-sign signal leptons. The irreducible background is dominated by diboson production, which is estimated using MC simulation samples. The dominant reducible background component is from $W+$jets production, followed by $t\bar{t}$ production, and these are estimated using a data-driven technique called the "fake factor method," similar to that described in Ref. [116]. The production of $W\gamma$ is also an important background component and is modeled using MC simulation samples. The charge-flip background is estimated by applying data-driven corrections to the MC simulation samples, following the procedure outlined in Sec. VIII B 2.

The fake factor method estimates the contributions from processes that produce one or two fake or nonprompt

TABLE XX. The selection requirements for the same-sign, two-lepton VBF validation regions.

	Common	
ℓ flavor/sign	$\ell^\pm\ell^\pm$, $\ell^\pm\ell'^\pm$	
$E_{\mathrm{T}}^{\mathrm{miss}}$ [GeV]	>120	
Jets	≥2	
	VR-VV	VR-Fakes
$p_{\mathrm{T}}^{\mathrm{lep1}}$ [GeV]	>40 GeV	⋯
$p_{\mathrm{T}}^{\mathrm{lep2}}$ [GeV]	>40 GeV	⋯
Central b-jets	Veto	⋯
Target process	Dibosons	Nonprompt and fake leptons

TABLE XXI. Observed and expected number of events in the same-sign, two-lepton VBF validation and signal regions. The numbers of signal events are shown for the $\tilde{\chi}_1^\pm\tilde{\chi}_1^\pm$ VBF simplified model with $\tilde{\ell}_L$-mediated decays, with the $\tilde{\chi}_1^\pm$ and $\tilde{\chi}_1^0$ masses in GeV. The uncertainties shown include both statistical and systematic components. The model-independent limits are also shown: the one-sided p_0 value; the expected and observed upper limits at 95% CL on the number of beyond-the-SM events (S_{exp}^{95} and S_{obs}^{95}) for the signal region, calculated using pseudoexperiments and the CL_s prescription; the observed 95% CL upper limit on the signal cross section times efficiency ($\langle\epsilon\sigma\rangle_{\mathrm{obs}}^{95}$); and the CL_b value for the background-only hypothesis.

	VR-VV	VR-Fakes	SR2ℓ-2
ℓ flavor/sign	$\ell^\pm\ell^\pm$, $\ell^\pm\ell'^\pm$	$\ell^\pm\ell^\pm$, $\ell^\pm\ell'^\pm$	$\ell^\pm\ell^\pm$, $\ell^\pm\ell'^\pm$
Expected background			
$W^\pm W^\pm$	$8.9^{+1.0}_{-1.1}$	41 ± 13	$1.95^{+0.21}_{-0.23}$
$W\gamma$	3.5 ± 0.8	$22.8^{+4.2}_{-2.5}$	$0.67^{+0.52}_{-0.31}$
WZ	11.0 ± 3.0	65 ± 16	$2.3^{+0.8}_{-0.9}$
ZZ	$0.65^{+0.20}_{-0.19}$	1.7 ± 0.4	$0.05^{+0.11}_{-0.17}$
Reducible	4.0 ± 2.2	280 ± 100	5.2 ± 2.0
Charge-flip	0.7 ± 0.7	8 ± 4	$0.03^{+0.04}_{-0.02}$
Others	$0.32^{+0.07}_{-0.06}$	13.6 ± 1.5	0.013 ± 0.007
Total	29 ± 5	430 ± 100	10.3 ± 2.3
Observed events	20	400	10
Predicted signal $(m_{\tilde{\chi}_1^\pm}, m_{\tilde{\chi}_1^0}) = (120, 95)$	0.25 ± 0.03	8.32 ± 0.19	3.47 ± 0.12
p_0	⋯	⋯	0.50
S_{obs}^{95}	⋯	⋯	8.4
S_{exp}^{95}	⋯	⋯	$8.7^{+3.9}_{-2.5}$
$\langle\epsilon\sigma\rangle_{\mathrm{obs}}^{95}$ [fb]	⋯	⋯	0.41
CL_b	⋯	⋯	0.47

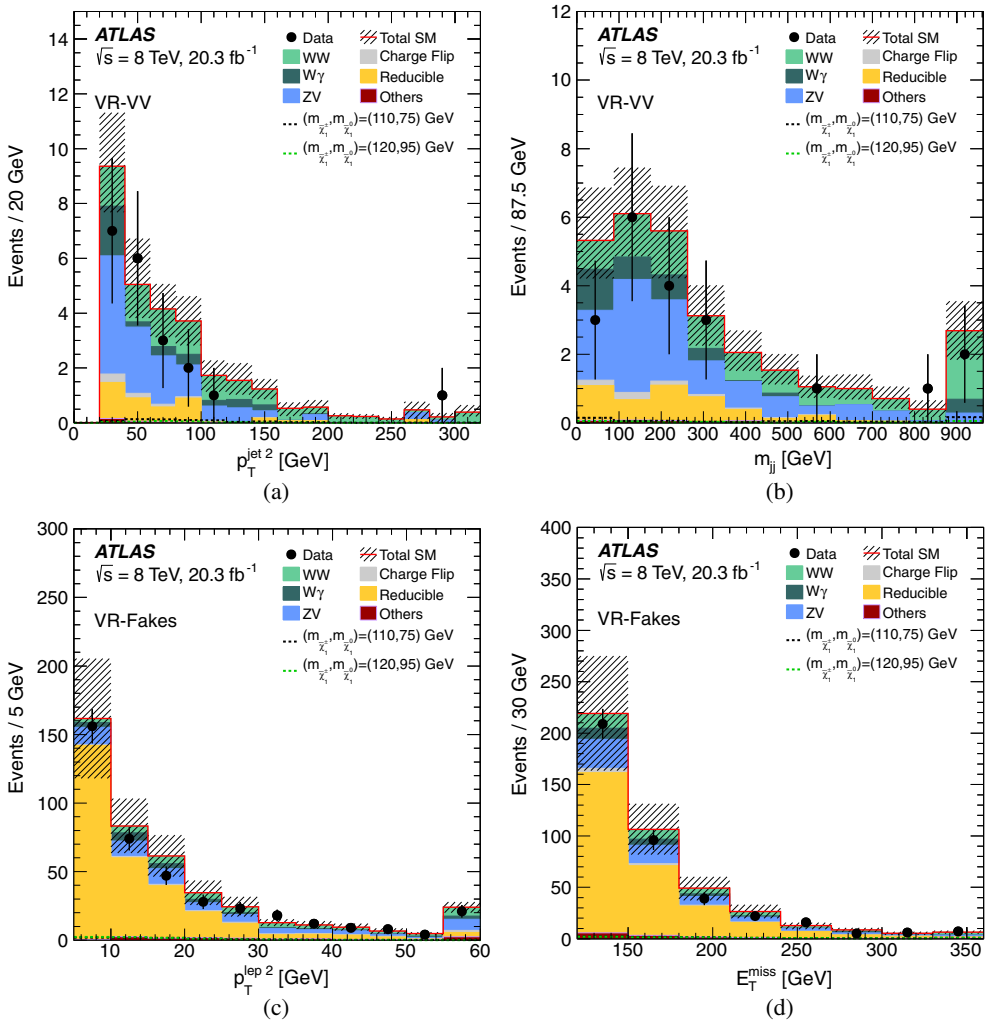

FIG. 10. For events in the same-sign VBF validation region VR-Fakes, the (a) transverse momentum of the second leading jet $p_{\mathrm{T}}^{\mathrm{jet2}}$ and (b) invariant mass of the two leading jets m_{jj} in VR-VV, and (c) transverse momentum of the second leading lepton $p_{\mathrm{T}}^{\mathrm{lep2}}$ and (d) $E_{\mathrm{T}}^{\mathrm{miss}}$. The "Others" background category includes $t\bar{t}V + tV$, VVV, and SM Higgs boson production. The uncertainty band includes both the statistical and the systematic uncertainties on the SM prediction. The last bin in each distribution includes the overflow.

leptons using data events that contain one signal lepton and one lepton failing to satisfy the signal lepton requirements. These events are scaled by a "fake factor" to predict the reducible background in the signal region. The fake factor is defined as the ratio of events with two signal leptons to events with one signal lepton and one lepton failing the signal lepton requirements. It is measured in data using a control sample of jets faking leptons in $Z \to \ell\ell$ events. The SM background process dependence of the fake factor is studied using simulation, and no strong dependence is observed. Residual differences are covered by assigning a 30% uncertainty, independent of the lepton p_{T}, to the fake factor. The uncertainty on the reducible background estimate ranges from 37% to 42%, depending on the channel (ee, $\mu\mu$, or $e\mu$), and is dominated by the prompt lepton contamination in the control sample and the uncertainty on the extrapolation of fake factors into the signal region.

The contributions from diboson processes are estimated using MC simulation samples. SHERPA is used to produce all diboson samples, taking into account both the strong and the electroweak production of associated jets. The $W^{\pm}W^{\pm} + 2$jets and $WZ + 2$jets processes are normalized to NLO cross sections using corrections evaluated in dedicated VBF fiducial regions at the parton level. The corrections are calculated separately for strong and electroweak jet production. For the $W^{\pm}W^{\pm} + 2$jets production, the fiducial cross section is calculated using POWHEG BOX +PYTHIA [62,63,117], and the fiducial region is defined to be identical to the signal region at the parton level, except for the lepton isolation requirement. For the $WZ + 2$jets production, the fiducial cross sections are calculated using VBFNLO-2.7.0 [118]. Since it is not possible to define a fiducial region that is identical to the signal region using VBFNLO-2.7.0, a looser set of requirements is imposed.

TABLE XXII. The dominant systematic uncertainties on the background estimates for the same-sign, two-lepton VBF signal region. The percentages show the size of the uncertainty relative to the total expected background. Because of correlations between the systematic uncertainties, the total uncertainty is different from the sum in quadrature of the individual uncertainties.

Source of uncertainty	SR2ℓ-2
Fake factor closure test	13%
Statistical uncertainty on the reducible background	11%
$WZ + 2$jets scale and PDF	5%
Statistical uncertainty on $WZ + 2$jets	4%
Statistical uncertainty on the electron fake factor	3%
Jet energy resolution	3%
Statistical uncertainty on $W^{\pm}W^{\pm} + 2$jets	3%
$W^{\pm}W^{\pm} + 2$jets scale and PDF	1%
Total	21%

The generator modeling uncertainty is estimated by comparing POWHEG BOX+PYTHIA with VBFNLO-2.7.0 for $W^{\pm}W^{\pm}$+2jets production, and parton showering uncertainties are estimated by comparing POWHEG BOX+HERWIG with POWHEG BOX+PYTHIA. The impact of the choice of renormalization and factorization scales is evaluated by varying each between 0.5 and 2 times the nominal values. The uncertainties due to the PDFs are evaluated using 90% CL CT10 PDF eigenvectors. Finally, the interference between the strong and electroweak jet production is studied at LO accuracy using SHERPA and is found to have a negligible effect on the combined fiducial cross section in the signal region.

The background predictions are tested in VRs that are defined to be as kinematically close to the SR as possible. The first VR, VR-Fakes, is defined with two signal light

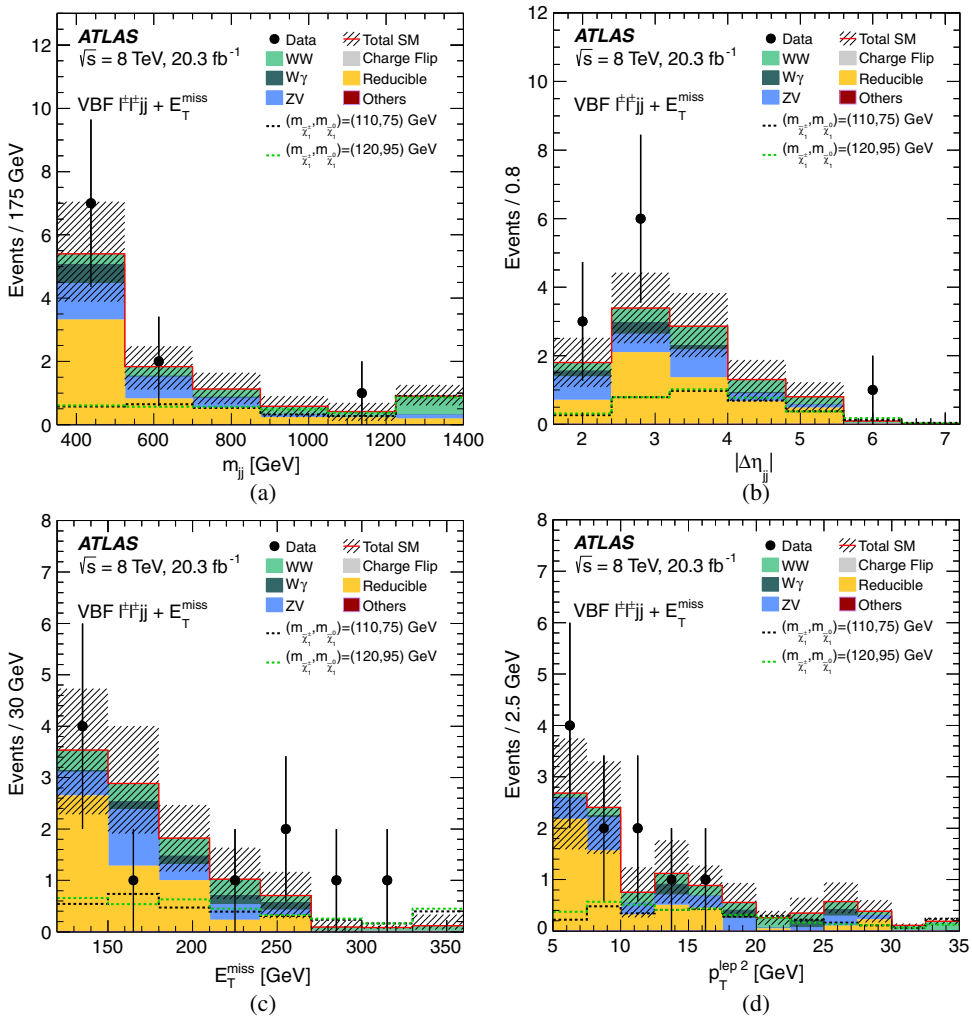

FIG. 11. For events in the same-sign VBF signal region, the (a) m_{jj}, (b) separation in η between the two leading jets $|\Delta\eta_{jj}|$, (c) $E_{\mathrm{T}}^{\mathrm{miss}}$, and (d) $p_{\mathrm{T}}^{\ell 2}$ in SR2ℓ-2. The "Others" background category includes $t\bar{t}V + tZ$, VVV, and SM Higgs boson production. The uncertainty band includes both the statistical and systematic uncertainties on the SM prediction. The last bin in each distribution includes the overflow.

leptons, large $E_{\mathrm{T}}^{\mathrm{miss}}$, and at least two jets to test backgrounds with fake and nonprompt leptons modeled by the fake factor method. The second VR, VR-VV, adopts the same requirements as the VR-Fakes, in addition to higher lepton-p_{T} thresholds and a b-jet veto that allow it to test the MC modeling of the diboson background. By definition, the VRs are not disjoint from the SR, but have negligible overlaps. The overlap between the VR-Fakes (VR-VV) and the SR is 2.4% (0.2%), and the largest signal contamination is 1.9% (0.9%) of the total expected background in the VR-Fakes (VR-VV). The definitions of the validation regions are shown in Table XX, along with the targeted processes. The yields in the VRs are shown in Table XXI, where the background expectation is in good agreement with the observed data, within the total uncertainties. Figures 10(a), 10(b), 10(c), and 10(d) show the distributions of $p_{\mathrm{T}}^{\mathrm{lep2}}$ and m_{jj} in VR-VV, along with $p_{\mathrm{T}}^{\mathrm{lep2}}$ and $E_{\mathrm{T}}^{\mathrm{miss}}$ in VR-Fakes, with good agreement observed.

C. Results

The observed number of events in the signal region is shown in Table XXI along with the background expectation and uncertainties, p_0-value, S_{exp}^{95}, S_{obs}^{95}, $\langle\epsilon\sigma\rangle_{\mathrm{obs}}^{95}$, and the CL_b value. No significant excess with respect to the SM expectation is observed. A breakdown of the different sources of systematic uncertainty in the signal region, including those described in Sec. VI C, is shown in Table XXII. Figures 11(a)–11(d) show the distributions of the quantities m_{jj}, $|\Delta\eta_{jj}|$, $E_{\mathrm{T}}^{\mathrm{miss}}$, and $p_{\mathrm{T}}^{\mathrm{lep2}}$ in the signal region.

X. INTERPRETATION OF RESULTS

Previous ATLAS searches for EW SUSY production [19–23] are combined with the new analyses presented in Secs. VII–IX. The combined results are interpreted in the SUSY models discussed in Sec. II. The analyses combined for each SUSY model are shown in Table XXIII. Limits in the simplified models targeted by the analysis presented in the previous sections are presented in Secs. X A–X D. A summary is provided in Sec. X E, including the limits previously obtained from the ATLAS searches for $\tilde{\chi}_1^+\tilde{\chi}_1^-$ production with WW-mediated decays [19], $\tilde{\chi}_1^\pm\tilde{\chi}_2^0$ production with WZ-mediated decays [20], and $\tilde{\chi}_1^\pm\tilde{\chi}_2^0$ production with Wh-mediated decays [23]. Finally, limits on phenomenological models are presented in Secs. X F–X H. For these models, the new searches presented in this article are not included, since they target very specific areas of parameter space and their sensitivity is small.

Exclusion limits are calculated by statistically combining results from a number of disjoint signal regions. In general, the analyses in Table XXIII are mutually exclusive by design (the exceptions are indicated in the table), using the lepton multiplicity and charge, and are statistically combined. Where overlapping signal regions exist within an analysis, the signal region with the best-expected exclusion is used. During the combinations, all experimental uncertainties are treated as correlated between regions and processes, with the exception of the experimental uncertainties on data-driven backgrounds, which are correlated between regions only. Theoretical uncertainties on the irreducible background and signal are treated as correlated between regions, while statistical uncertainties are treated as

TABLE XXIII. Searches used to probe each of the models described in Sec. II.

Model	Wh [23]	2ℓ [†][19]	2τ [*] [22]	3ℓ [◇] [20]	4ℓ [21]	2τ MVA [*]	SR2ℓ-1 [†]	SS MVA [§]	SR3ℓ-0/1 [◇]	SR2ℓ-2 [§]
$\tilde{\tau}\tilde{\tau}$			√			√				
$\tilde{\chi}_1^+\tilde{\chi}_1^-$ via $\tilde{\ell}_L$ with $x = 0.5$		√					√			
$\tilde{\chi}_1^+\tilde{\chi}_1^-$ via $\tilde{\ell}_L$ with variable x		√								
$\tilde{\chi}_1^+\tilde{\chi}_1^-$ via WW		√								
$\tilde{\chi}_1^\pm\tilde{\chi}_1^\pm$ via VBF										√
$\tilde{\chi}_1^\pm\tilde{\chi}_2^0$ via $\tilde{\tau}_L$			√	√						
$\tilde{\chi}_1^\pm\tilde{\chi}_2^0$ via $\tilde{\ell}_L$ with $x = 0.5$				√				√	√	
$\tilde{\chi}_1^\pm\tilde{\chi}_2^0$ via $\tilde{\ell}_L$ with variable x				√						
$\tilde{\chi}_1^\pm\tilde{\chi}_2^0$ via WZ		√		√						
$\tilde{\chi}_1^\pm\tilde{\chi}_2^0$ via Wh	√	√		√						
$\tilde{\chi}_2^0\tilde{\chi}_3^0$ via $\tilde{\ell}_L$ with $x = 0.5$				√	√					
$\tilde{\chi}_2^0\tilde{\chi}_3^0$ via $\tilde{\ell}_L$ with variable x				√	√					
pMSSM	√	√		√						
NUHM2		√		√	√					
GMSB					√					

[†]The opposite-sign, two-lepton signal regions in Ref. [19] and Sec. VIII A overlap.
[*]The two-tau signal regions in Ref. [22] and Sec. VII overlap.
[◇]The three-lepton signal regions in Ref. [20] and Sec. VIII C overlap.
[§]The same-sign, two-lepton signal regions in Sec. VIII B and Sec. IX overlap.

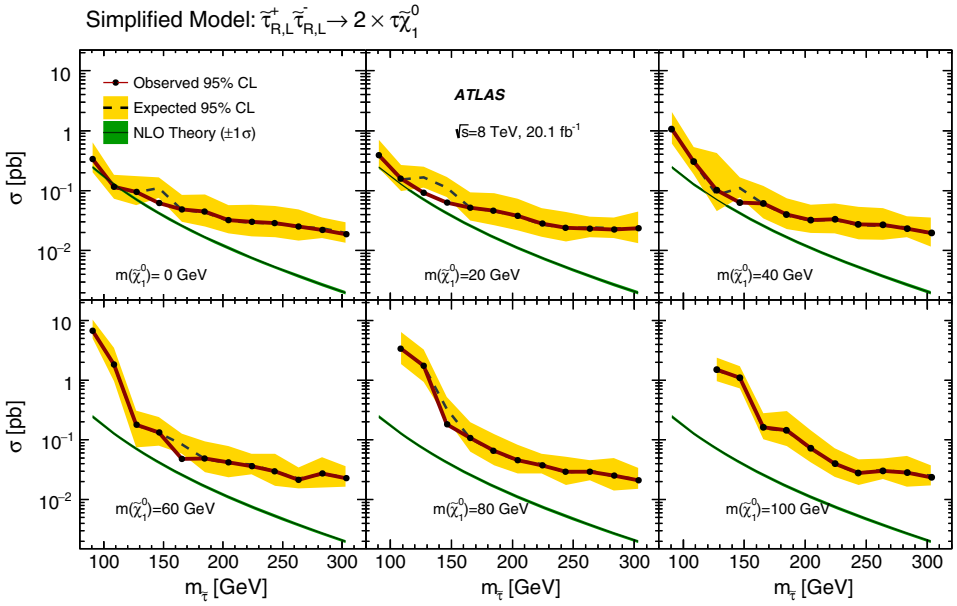

FIG. 12. The 95% CL exclusion limits on the cross section for production of left- and right-handed stau pairs for various $\tilde{\chi}^0_1$ masses. The NLO theoretical cross section for left- and right-handed stau pair production is also shown.

uncorrelated between regions and processes. For the exclusion limits, the observed and expected 95% CL limits are calculated using asymptotic formulas for each SUSY model point, taking into account the theoretical and experimental uncertainties on the SM background and the experimental uncertainties on the signal. Where the three-lepton [20] analysis is used in the combination, 95% CL limits are calculated using pseudoexperiments as the asymptotic approximation becomes inappropriate where the expected and observed yields are close to zero. The impact of the theoretical uncertainties on the signal cross section is shown for the observed mass limit; where quoted in the text, mass limits refer to the -1σ variation on the observed limit.

A. Direct stau production

The combination of the two-tau MVA results in Sec. VII with the simple cut-based analysis from Ref. [22] is used to set limits on the direct production of stau pairs. For each

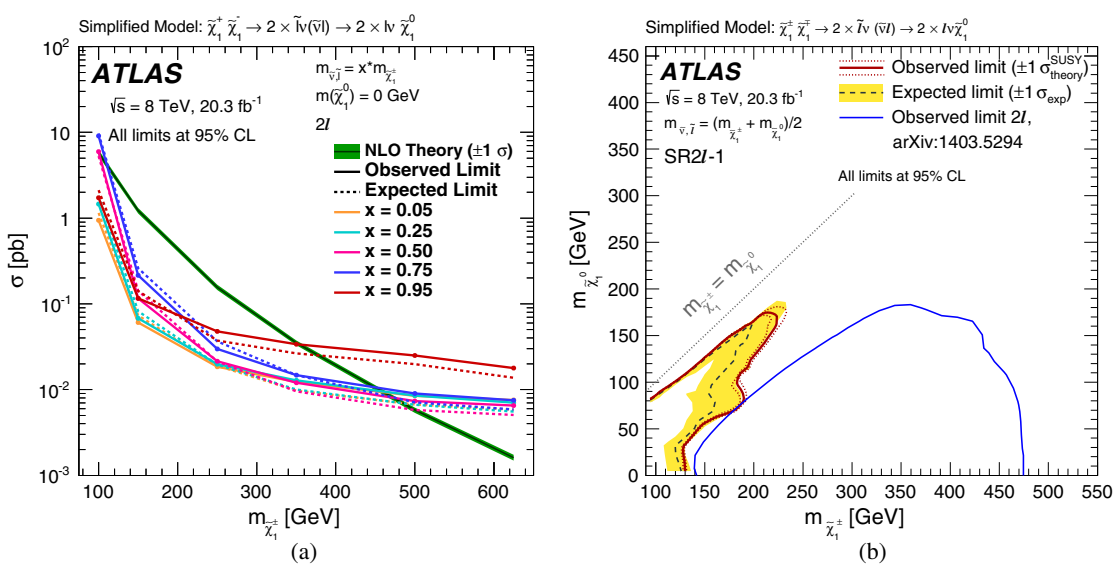

FIG. 13. The 95% CL exclusion limits on $\tilde{\chi}^+_1\tilde{\chi}^-_1$ production with $\tilde{\ell}_L$-mediated decays, (a) where the $\tilde{\chi}^0_1$ is massless and the intermediate slepton mass is set to 5%, 25%, 50%, 75%, and 95% of the $\tilde{\chi}^\pm_1$ mass, and (b) as a function of the $\tilde{\chi}^\pm_1$ and $\tilde{\chi}^0_1$ masses, where the slepton mass is halfway between the $\tilde{\chi}^0_2$ and $\tilde{\chi}^0_1$ masses. The limits in (a) are set using the 2ℓ analysis from Ref. [19], while the limits in (b) use the opposite-sign, two-lepton analysis from this article. The limit from Ref. [19] is also shown in (b).

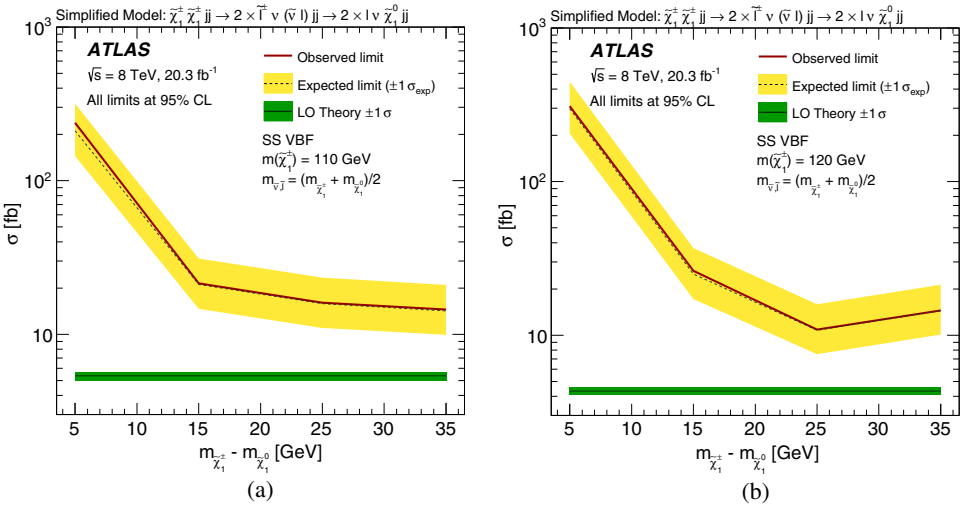

FIG. 14. The 95% CL upper limit on the signal cross section for VBF $\tilde{\chi}_1^\pm\tilde{\chi}_1^\pm$ production for (a) $m(\tilde{\chi}_1^\pm) = 110$ GeV and (b) $m(\tilde{\chi}_1^\pm) = 120$ GeV. The limits are set with respect to the mass difference between the $\tilde{\chi}_1^\pm$ and $\tilde{\chi}_1^0$, and use the results from the same-sign, two-lepton VBF analysis.

signal point, the signal region with the best expected limit is used. The upper limits on the cross section for direct stau production are shown in Fig. 12 for combined $\tilde{\tau}_L\tilde{\tau}_L$ and $\tilde{\tau}_R\tilde{\tau}_R$ production, where the observed limit is nearly always above the theoretical prediction. One scenario of combined $\tilde{\tau}_L\tilde{\tau}_L$ and $\tilde{\tau}_R\tilde{\tau}_R$ production is excluded, where the $\tilde{\tau}_R$ mass is 109 GeV and the $\tilde{\chi}_1^0$ is massless. For this scenario, cross sections above 0.115 pb are excluded, where the theoretical cross section at NLO is 0.128 pb. No scenarios can be excluded where only $\tilde{\tau}_R\tilde{\tau}_R$ production or $\tilde{\tau}_L\tilde{\tau}_L$ production is considered. Cross sections above 0.06 (0.21) pb are excluded for $\tilde{\tau}_R\tilde{\tau}_R$ ($\tilde{\tau}_L\tilde{\tau}_L$) production with a $\tilde{\tau}_R$ ($\tilde{\tau}_L$) mass of 109 GeV and a massless $\tilde{\chi}_1^0$, where the theoretical cross section at NLO is 0.04 (0.09) pb. For this scenario [$m(\tilde{\tau}_R) = 109$ GeV, $m(\tilde{\chi}_1^0) = 0$ GeV], the expected yields from $\tilde{\tau}_R\tilde{\tau}_R$ production are larger than from $\tilde{\tau}_L\tilde{\tau}_L$ in the signal region, making the experimental limits stronger for $\tilde{\tau}_R\tilde{\tau}_R$ production. However, for other mass points the experimental limit is generally weaker for $\tilde{\tau}_R\tilde{\tau}_R$ production due to

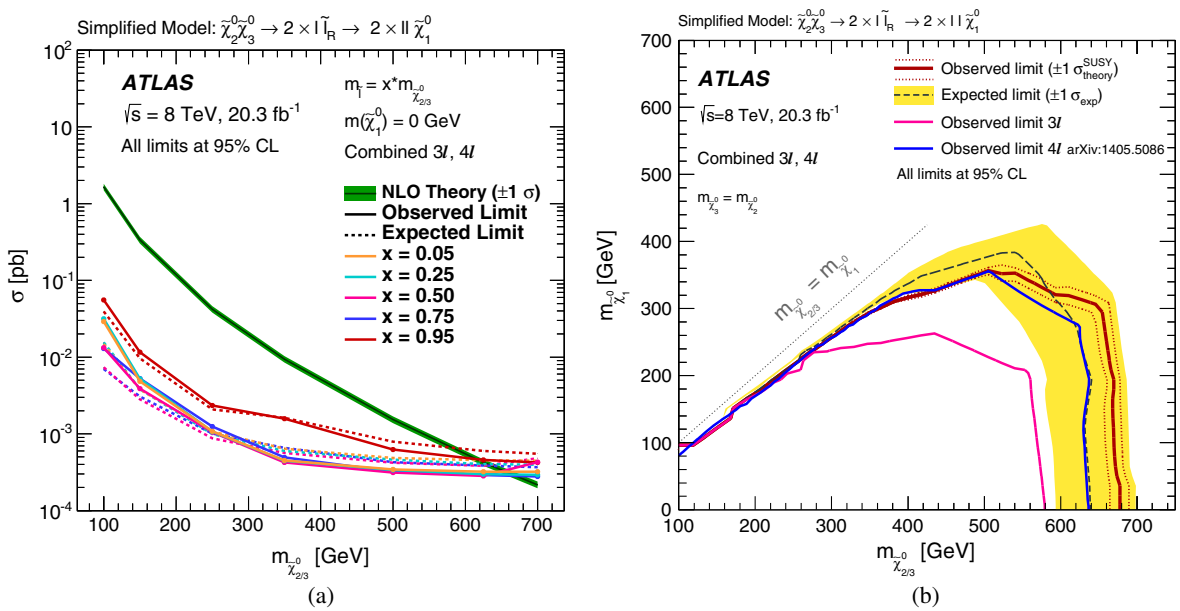

FIG. 15. The 95% CL exclusion limits on $\tilde{\chi}_2^0\tilde{\chi}_3^0$ production with $\tilde{\ell}_R$-mediated decays, (a) where the $\tilde{\chi}_1^0$ is massless and the intermediate slepton mass is set to 5%, 25%, 50%, 75%, and 95% of the $\tilde{\chi}_2^0$ mass, and (b) as a function of the $\tilde{\chi}_2^0$ and $\tilde{\chi}_1^0$ masses, where the slepton mass is halfway between the $\tilde{\chi}_2^0$ and $\tilde{\chi}_1^0$ masses. The limits in (a) and (b) are set using a combination of the 3ℓ analysis from Ref. [20] and the 4ℓ analysis from Ref. [21].

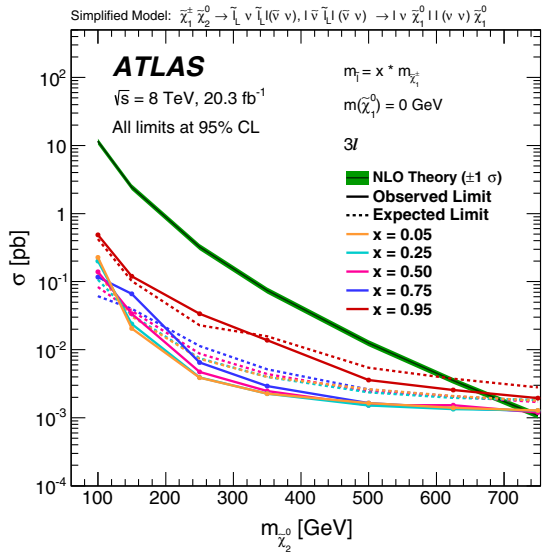

FIG. 16. The 95% CL upper cross-section limits on $\tilde{\chi}_1^\pm \tilde{\chi}_2^0$ production with $\tilde{\ell}_L$-mediated decays, where the $\tilde{\chi}_1^0$ is massless and the intermediate slepton mass is set to 5%, 25%, 50%, 75%, and 95% of the $\tilde{\chi}_1^\pm$ mass. The limits are set using the 3ℓ analysis from Ref. [20].

the lower production cross section. These limits on direct production of stau pairs improve upon the previous limits in Ref. [22], particularly for stau masses below ~150 GeV.

B. Direct chargino production

The opposite-sign, two-lepton analysis in Ref. [19] is used to reinterpret the limits on $\tilde{\chi}_1^+$ production decaying through sleptons, where the slepton mass is varied between the $\tilde{\chi}_1^\pm$ and $\tilde{\chi}_1^0$ masses. Scenarios where the slepton mass is 5%, 25%, 50%, 75%, and 95% of the $\tilde{\chi}_1^\pm$ mass are studied for a massless $\tilde{\chi}_1^0$, and the limits are shown in Fig. 13(a). For the majority of the $\tilde{\chi}_1^\pm$ masses considered, the slepton mass does not have a significant effect on the sensitivity, and $\tilde{\chi}_1^\pm$ masses are excluded up to ~500 GeV. The sensitivity is reduced for a very small mass splitting between the chargino and the slepton ($x = 0.95$), as in this case leptons from the $\tilde{\chi}_1^\pm \to \tilde{\nu}\ell$ decays have low momentum, making these events difficult to reconstruct in the two lepton final state.

Limits are also set in the $\tilde{\chi}_1^+ \tilde{\chi}_1^-$ scenario with $\tilde{\ell}_L$-mediated decays, with slepton masses set halfway between the $\tilde{\chi}_1^\pm$ and the $\tilde{\chi}_1^0$ masses, where both the $\tilde{\chi}_1^\pm$ and the $\tilde{\chi}_1^0$ masses are varied. Figure 13(b) shows the opposite-sign, two-lepton analysis presented in Sec. VIII A, which provides new sensitivity to compressed scenarios for $\tilde{\chi}_1^\pm$ masses below ~220 GeV. The 2ℓ analysis in Ref. [19] continues to dominate the sensitivity to scenarios with large mass splittings, excluding $\tilde{\chi}_1^\pm$ masses up to ~465 GeV.

The same-sign, two-lepton VBF analysis described in Sec. IX is used to set limits on VBF $\tilde{\chi}_1^\pm \tilde{\chi}_1^\pm$ production, where the $\tilde{\chi}_1^\pm$ decays through sleptons. Figures 14(a) and 14(b) show the 95% CL upper limits on the cross section for $m(\tilde{\chi}_1^\pm) = 110$ GeV and $m(\tilde{\chi}_1^\pm) = 120$ GeV, as a function of the mass splitting between the chargino and the neutralino. The best observed upper limit on the VBF $\tilde{\chi}_1^\pm \tilde{\chi}_1^\pm$ production cross section is found for a $\tilde{\chi}_1^\pm$ mass of 120 GeV and $m(\tilde{\chi}_1^\pm) - m(\tilde{\chi}_1^0) = 25$ GeV, where the theoretical cross section at LO is 4.33 fb and the excluded cross section is 10.9 fb. The sensitivity is slightly stronger for higher $\tilde{\chi}_1^\pm$ masses, since these scenarios were used for optimizing the signal selection.

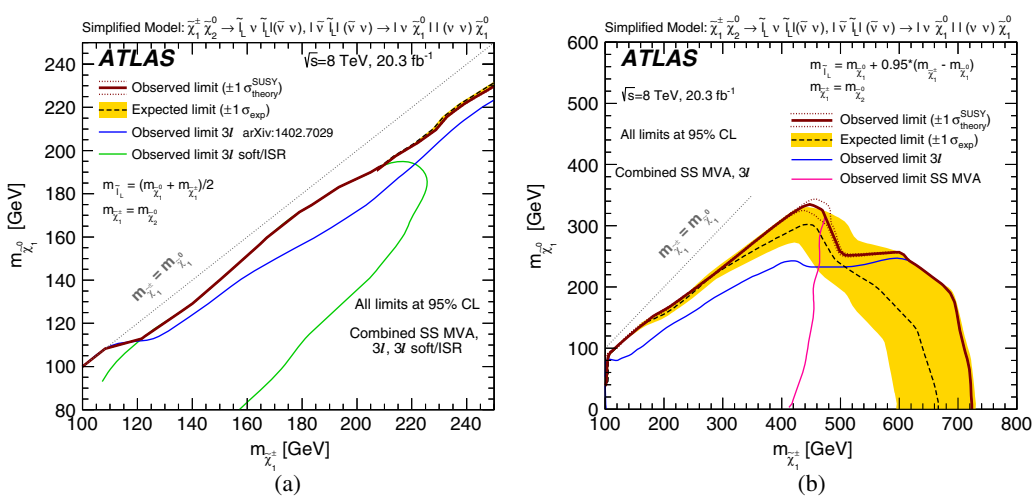

FIG. 17. The 95% CL exclusion limits on $\tilde{\chi}_1^\pm \tilde{\chi}_2^0$ production with $\tilde{\ell}_L$-mediated decays, as a function of the $\tilde{\chi}_1^\pm$ and $\tilde{\chi}_1^0$ masses, where the intermediate slepton mass is set to the $\tilde{\chi}_1^0$ mass plus (a) 50% or (b) 95% of the difference between the $\tilde{\chi}_1^\pm$ and the $\tilde{\chi}_1^0$ masses. The limits in (a) are set using a combination of the 3ℓ analysis from Ref. [20] and the same-sign, two-lepton analysis from this article, while the limits in (b) use the combination of the three-lepton and same-sign, two-lepton analyses from this article.

C. Direct neutralino production

The combination of the three-lepton analysis in Ref. [20] and four-lepton analysis in Ref. [21] is used to set limits on $\tilde{\chi}_2^0\tilde{\chi}_3^0$ production with $\tilde{\ell}_R$-mediated decays, where the slepton mass is varied between the $\tilde{\chi}_2^0$ and $\tilde{\chi}_1^0$ masses. Scenarios where the slepton mass is 5%, 25%, 50%, 75%, and 95% of the $\tilde{\chi}_2^0$ mass are studied for a massless $\tilde{\chi}_1^0$, and the limits are shown in Fig. 15(a). For the majority of $\tilde{\chi}_2^0$ masses considered, the slepton mass does not have a significant effect on the sensitivity, and $\tilde{\chi}_2^0$ masses are excluded up to ~600 GeV. The sensitivity is reduced for a very small mass splitting between the $\tilde{\chi}_2^0$ and slepton ($x = 0.95$) as the lepton produced in the $\tilde{\chi}_2^0 \to \ell\tilde{\ell}_R$ decay has low momentum. The reduced sensitivity is not seen for a very small mass splitting between the slepton and the LSP ($x = 0.05$) as the lepton produced in the $\tilde{\ell}_R \to \ell\tilde{\chi}_1^0$ decay can carry some of the momentum of the slepton.

Limits are also set in the $\tilde{\chi}_2^0\tilde{\chi}_3^0$ scenario with $\tilde{\ell}_R$-mediated decays, with slepton masses set halfway between the $\tilde{\chi}_2^0$ and the $\tilde{\chi}_1^0$ masses, where both the $\tilde{\chi}_2^0$ and the $\tilde{\chi}_1^0$ masses are varied. The combination of the three- and four-lepton analysis is again used here and limits are shown in Fig. 15(b), where $\tilde{\chi}_2^0$, $\tilde{\chi}_3^0$ masses up to 670 GeV are excluded, improving the previous limits by 30 GeV for $\tilde{\chi}_1^0$ masses below 200 GeV.

D. Direct neutralino-chargino production

The three-lepton analysis in Ref. [20] is used to reinterpret the limits on $\tilde{\chi}_1^\pm\tilde{\chi}_2^0$ production decaying through sleptons. Scenarios where the slepton mass is 5%, 25%, 50%, 75%, and 95% of the $\tilde{\chi}_1^\pm$ mass are studied for a massless $\tilde{\chi}_1^0$. The limits on these variable slepton mass scenarios are shown in Fig. 16. For the majority of $\tilde{\chi}_1^\pm$ masses considered, the slepton mass does not have a significant effect on the sensitivity, and $\tilde{\chi}_1^\pm$ masses are excluded up to ~700 GeV. The same reduction in sensitivity is seen for a small mass splitting between the $\tilde{\chi}_2^0$ and slepton ($x = 0.95$) as in the $\tilde{\chi}_2^0\tilde{\chi}_3^0$ interpretation in Sec. X C. For $\tilde{\chi}_1^\pm\tilde{\chi}_2^0$ production scenarios decaying through SM W, Z, or Higgs bosons [20], the results in Fig. 16 would be degraded due to lower branching fractions into leptonic final states. The pMSSM scenario in Sec. X F shows the sensitivity to SUSY scenarios without sleptons in the $\tilde{\chi}_1^\pm\tilde{\chi}_2^0$ decay chain.

Limits are also set in the $\tilde{\chi}_1^\pm\tilde{\chi}_2^0$ scenarios with $\tilde{\ell}_L$-mediated decays, with slepton masses set halfway and at 95% between the $\tilde{\chi}_1^\pm$ and the $\tilde{\chi}_1^0$ masses, where both the $\tilde{\chi}_1^\pm$ and the $\tilde{\chi}_1^0$ masses are varied. Figures 17(a) and 17(b) show that the combination of the published and new analyses gives an improved sensitivity to compressed scenarios up to $\tilde{\chi}_1^\pm$ masses of ~250 GeV. In scenarios with large mass splittings, $\tilde{\chi}_1^\pm$ masses are excluded up to ~700 GeV for slepton masses set to the $\tilde{\chi}_1^0$ mass plus 50% or 95% of the difference between the $\tilde{\chi}_1^\pm$ and the $\tilde{\chi}_1^0$ masses. In the compressed areas of the $\tilde{\chi}_1^\pm\tilde{\chi}_2^0$ scenario with $\tilde{\ell}_L$-mediated decays, and slepton masses set halfway (95%) between the $\tilde{\chi}_1^\pm$ and the $\tilde{\chi}_1^0$ masses, the three-lepton (same-sign, two-lepton) analysis has the strongest sensitivity.

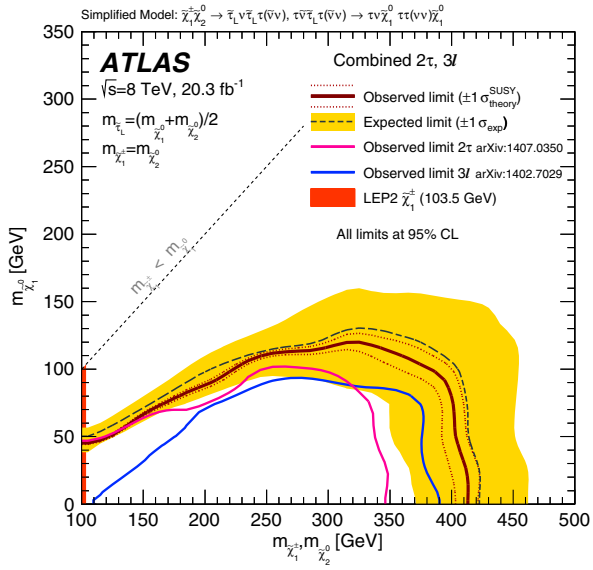

FIG. 18. The 95% CL exclusion limits on $\tilde{\chi}_1^\pm\tilde{\chi}_2^0$ production with $\tilde{\tau}$-mediated decays, as a function of the $\tilde{\chi}_1^\pm$ and $\tilde{\chi}_1^0$ masses. The limits are set using a combination of the 3ℓ analysis from Ref. [20] and the 2τ analysis from Ref. [22].

Finally, limits are set in the $\tilde{\chi}_1^\pm\tilde{\chi}_2^0$ scenario with $\tilde{\tau}$-mediated decays, using combined results from the two-tau analysis in Ref. [22] and the three-lepton analysis in Ref. [20]. Figure 18 shows that the sensitivity to large $\tilde{\chi}_1^\pm$ masses is improved by 20 GeV with the new combination, where $\tilde{\chi}_1^\pm$ masses are excluded up to ~400 GeV for massless $\tilde{\chi}_1^0$.

E. Summary of simplified electroweakino production

The ATLAS results for electroweakino searches at 8 TeV in the framework of simplified models are summarized in Figs. 19(a) and 19(b) in the $m(\tilde{\chi}_1^\pm,\tilde{\chi}_2^0)$-$m(\tilde{\chi}_1^0)$ plane. As explained in Sec. II, each of the $\tilde{\chi}_1^\pm/\tilde{\chi}_2^0/\tilde{\chi}_3^0$ decays considered in the plot is assumed to have a 100% branching fraction, and the production cross section is for pure wino $\tilde{\chi}_1^+\tilde{\chi}_1^-$ and $\tilde{\chi}_1^\pm\tilde{\chi}_2^0$, and pure higgsino $\tilde{\chi}_2^0\tilde{\chi}_3^0$. The limits for $\tilde{\chi}_1^+\tilde{\chi}_1^-$ and $\tilde{\chi}_1^\pm\tilde{\chi}_2^0$ production with decays mediated by SM bosons are summarized in Fig. 19(a). All of the limits are from the two-lepton, three-lepton, and Wh analyses from Refs. [19,20,23]. The new analyses targeting compressed spectra presented in this article have only a small sensitivity to these scenarios and did not significantly improve upon published limits. The limits for $\tilde{\chi}_1^+\tilde{\chi}_1^-$, $\tilde{\chi}_1^\pm\tilde{\chi}_2^0$, and $\tilde{\chi}_2^0\tilde{\chi}_3^0$ production with $\tilde{\ell}$-mediated decays are

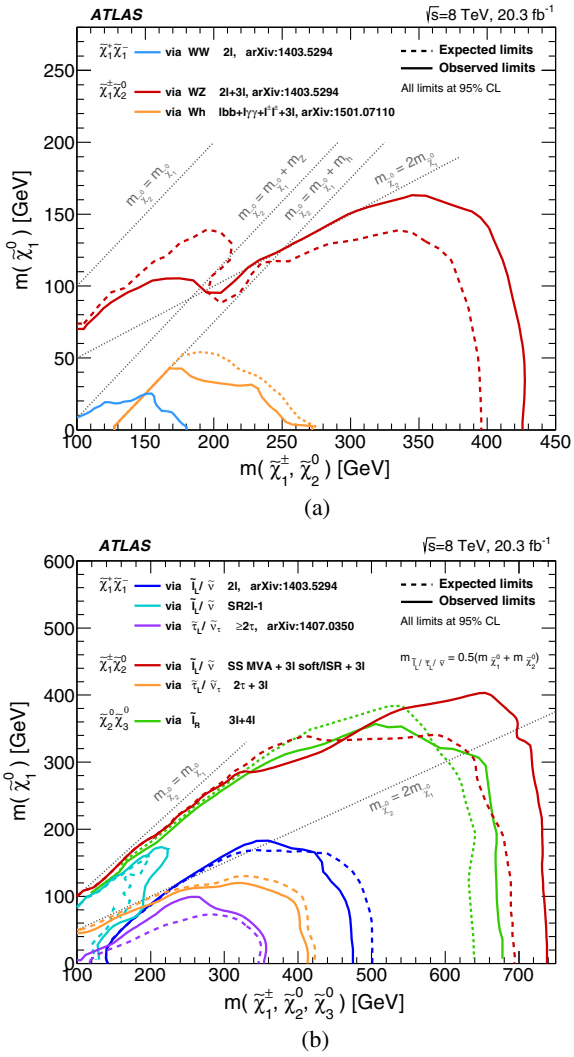

FIG. 19. The 95% CL exclusion limits on $\tilde{\chi}_1^+\tilde{\chi}_1^-$, $\tilde{\chi}_1^\pm\tilde{\chi}_2^0$, and $\tilde{\chi}_2^0\tilde{\chi}_3^0$ production with (a) SM-boson-mediated decays and (b) $\tilde{\ell}$-mediated decays, as a function of the $\tilde{\chi}_1^\pm$, $\tilde{\chi}_2^0$, and $\tilde{\chi}_1^0$ masses. The production cross section is for pure wino $\tilde{\chi}_1^+\tilde{\chi}_1^-$ and $\tilde{\chi}_1^\pm\tilde{\chi}_2^0$, and pure higgsino $\tilde{\chi}_2^0\tilde{\chi}_3^0$.

summarized in Fig. 19(b). The limits are from the new analyses in Secs. X B–X D and the previously published analyses.

F. pMSSM

The two-lepton, three-lepton, and Wh analyses from Refs. [19,20,23] are combined to improve the sensitivity in the considered pMSSM scenario where the EW SUSY production and the decays through W, Z, or h bosons are dominant. The 95% CL exclusion in the pMSSM $\mu - M_2$ plane for the scenario of heavy sleptons, $\tan\beta = 10$, and $M_1 = 50$ GeV is shown in Fig. 20. Including the Wh analysis in the new combination results in a stronger limit at high values of M_2, in particular in the intermediate μ region.

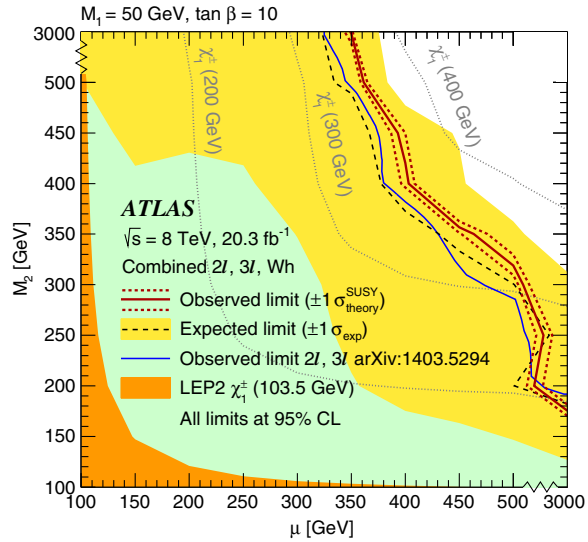

FIG. 20. The 95% CL exclusion limit in the pMSSM scenario, using a combination of the 2ℓ and 3ℓ analyses from Ref. [19] and the Wh analysis from Ref. [23]. The areas excluded by the -1σ expected limit are shown in green. The blue contour corresponds to the limits from the combination of the 2ℓ and 3ℓ analyses from Ref. [19]. The grey dotted contours show the chargino mass isolines.

G. NUHM2

The two-, three-, and four-lepton analyses from Refs. [19–21] are combined to set limits in a new interpretation for the NUHM2 model. The 95% CL exclusion in the NUHM2 $m_{1/2} - \mu$ plane is shown in Fig. 21, where the three-lepton analysis offers the best sensitivity

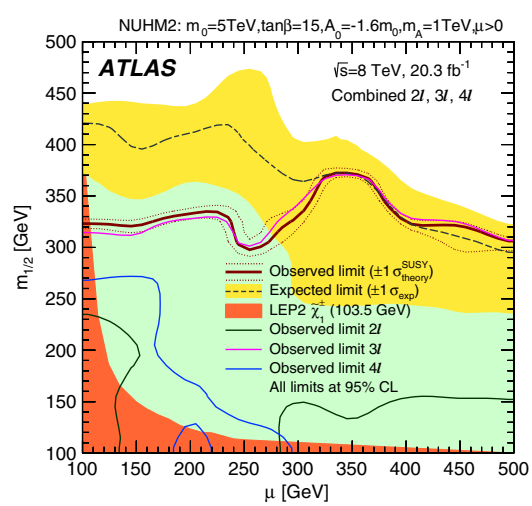

FIG. 21. The 95% CL exclusion limit in the NUHM2 scenario, using a combination of the 2ℓ, 3ℓ, and 4ℓ analyses from Refs. [19–21]. The areas excluded by the -1σ expected limit are shown in green. The black, pink, and blue contours correspond to the limits from the 2ℓ, 3ℓ, and 4ℓ analyses, respectively.

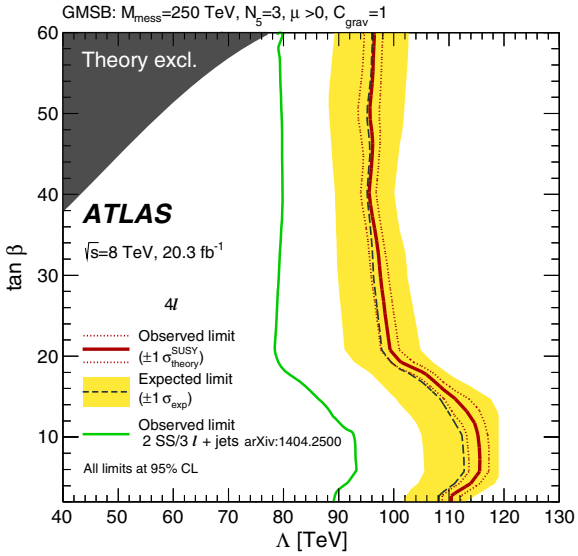

FIG. 22. The 95% CL exclusion limit in the GMSB scenario, using the 4ℓ analysis from Ref. [21]. The green contour corresponds to the limit from the $2SS/3\ell + \text{jets}$ analysis from Ref. [119].

and drives the combined limit. The results in the three-lepton signal regions lead to a weaker observed exclusion than expected for the compressed scenarios in the high-$m_{1/2}$, low-μ region. In general, $m_{1/2}$ values up to 300 GeV are excluded in the NUHM2 model.

H. GMSB

The four-lepton analysis from Ref. [21] is reinterpreted in the GMSB model described in Sec. II. The 95% CL exclusion in the GMSB Λ-$\tan\beta$ plane is shown in Fig. 22, where Λ values up to 94 TeV are excluded for all values of $\tan\beta$. For $\tan\beta = 10$, Λ values below 113 TeV are excluded. These results improve upon the previous limit in Ref. [119] by 20 TeV (15 TeV) in the low (high) $\tan\beta$ region.

XI. CONCLUSION

This article summarizes and extends the search for the production of electroweak SUSY particles using 20 fb^{-1} of $\sqrt{s} = 8$ TeV pp collision data collected with the ATLAS detector at the LHC. New analyses targeting scenarios with compressed mass spectra, VBF production of charginos and neutralinos, and the direct production of stau pairs provide sensitivity to EW SUSY scenarios not optimally covered in previous publications. The new and previous results are combined to set exclusion limits in a wide range of simplified and phenomenological SUSY models. For $\tilde{\chi}_1^+\tilde{\chi}_1^-$ production with $\tilde{\ell}_L$-mediated decays, $\tilde{\chi}_1^\pm$ with masses up to ~500 GeV are excluded. In the $\tilde{\chi}_1^\pm\tilde{\chi}_2^0$ and $\tilde{\chi}_2^0\tilde{\chi}_3^0$ scenarios with $\tilde{\ell}_L$-mediated decays, $\tilde{\chi}_1^\pm$ and $\tilde{\chi}_2^0$ masses are excluded up to 700 GeV and 670 GeV, respectively. For all three $\tilde{\ell}_L$-mediated decay scenarios, the value of the slepton mass is not seen to have a significant effect on the sensitivity. Exclusions are also set in pMSSM, NUHM2, and GMSB models, improving upon previous limits.

ACKNOWLEDGMENTS

We thank CERN for the very successful operation of the LHC, as well as the support staff from our institutions without whom ATLAS could not be operated efficiently. We thank Sabine Kraml for her advice while preparing the model files of the NUHM2 grid. We acknowledge the support of ANPCyT, Argentina; YerPhI, Armenia; ARC, Australia; BMWFW and FWF, Austria; ANAS, Azerbaijan; SSTC, Belarus; CNPq and FAPESP, Brazil; NSERC, NRC, and CFI, Canada; CERN; CONICYT, Chile; CAS, MOST, and NSFC, China; COLCIENCIAS, Colombia; MSMT CR, MPO CR, and VSC CR, Czech Republic; DNRF, DNSRC, and Lundbeck Foundation, Denmark; EPLANET, ERC, and NSRF, European Union; IN2P3-CNRS, CEA-DSM/IRFU, France; GNSF, Georgia; BMBF, DFG, HGF, MPG, and AvH Foundation, Germany; GSRT and NSRF, Greece; RGC, Hong Kong SAR, China; ISF, MINERVA, GIF, I-CORE, and Benoziyo Center, Israel; INFN, Italy; MEXT and JSPS, Japan; CNRST, Morocco; FOM and NWO, Netherlands; BRF and RCN, Norway; MNiSW and NCN, Poland; GRICES and FCT, Portugal; MNE/IFA, Romania; MES of Russia and NRC KI, Russian Federation; JINR; MSTD, Serbia; MSSR, Slovakia; ARRS and MIZŠ, Slovenia; DST/NRF, South Africa; MINECO, Spain; SRC and Wallenberg Foundation, Sweden; SER, SNSF, and Cantons of Bern and Geneva, Switzerland; NSC, Taiwan; TAEK, Turkey; STFC, the Royal Society and Leverhulme Trust, United Kingdom; DOE and NSF, United States of America. The crucial computing support from all WLCG partners is acknowledged gratefully, in particular from CERN and the ATLAS Tier-1 facilities at TRIUMF (Canada), NDGF (Denmark, Norway, Sweden), CC-IN2P3 (France), KIT/GridKA (Germany), INFN-CNAF (Italy), NL-T1 (Netherlands), PIC (Spain), ASGC (Taiwan), RAL (UK), and BNL (USA) and in the Tier-2 facilities worldwide.

APPENDIX: CROSS-SECTION CALCULATION FOR THE SAME-SIGN CHARGINO-PAIR PRODUCTION VIA VECTOR-BOSON FUSION

The cross sections for same-sign chargino-pair production via vector-boson fusion (including radiative processes) are calculated to LO in the strong coupling constant using MadGraph 5-1.3.33 [57]. The default

value of 99 is used for the maximum number of QCD and QED couplings. Same-sign chargino pairs are generated in association with two additional partons with $|\eta| < 5$ and no p_T requirement. No jet-parton matching is performed. All SUSY particles, except for the $\tilde{\chi}_1^\pm$, $\tilde{\chi}_1^0$, $\tilde{\chi}_2^0$, $\tilde{\ell}$, and $\tilde{\nu}$, are decoupled by setting their physical masses to ~100 TeV. The $\tilde{\chi}_1^\pm$ and $\tilde{\chi}_2^0$ are assumed to be mass degenerate. The sleptons are assumed to be mass degenerate with sneutrinos and have masses set halfway between $\tilde{\chi}_1^\pm$ and $\tilde{\chi}_1^0$ masses. Cross sections are also calculated using MadGraph 5-2.2.3 and are in agreement with those calculated using MadGraph 5-1.3.33. Details from the "`proc_card.dat`" are provided below.

```
import model mssm
define p=g u c d s u~ c~ d~ s~
define j=g u c d s u~ c~ d~ s~
define l+=e+ mu+
define l-=e- mu-
define vl=ve vm vt
define vl~ = ve~ vm~ vt~
generate   pp>x1+x1+jj@1
addprocess pp>x1-x1-jj@2
output -f
```


[1] H. Miyazawa, Prog. Theor. Phys. **36**, 1266 (1966).
[2] P. Ramond, Phys. Rev. D **3**, 2415 (1971).
[3] Y. A. Gol'fand and E. P. Likhtman, JETP Lett. **13**, 323 (1971).
[4] A. Neveu and J. H. Schwarz, Nucl. Phys. **B31**, 86 (1971).
[5] A. Neveu and J. H. Schwarz, Phys. Rev. D **4**, 1109 (1971).
[6] J. Gervais and B. Sakita, Nucl. Phys. **B34**, 632 (1971).
[7] D. V. Volkov and V. P. Akulov, Phys. Lett. **46B**, 109 (1973).
[8] J. Wess and B. Zumino, Phys. Lett. **49B**, 52 (1974).
[9] J. Wess and B. Zumino, Nucl. Phys. **B70**, 39 (1974).
[10] S. Weinberg, Phys. Rev. D **13**, 974 (1976).
[11] E. Gildener, Phys. Rev. D **14**, 1667 (1976).
[12] S. Weinberg, Phys. Rev. D **19**, 1277 (1979).
[13] L. Susskind, Phys. Rev. D **20**, 2619 (1979).
[14] P. Fayet, Phys. Lett. **64B**, 159 (1976).
[15] P. Fayet, Phys. Lett. **69B**, (1977) 489.
[16] G. R. Farrar and P. Fayet, Phys. Lett. **76B**, 575 (1978).
[17] P. Fayet, Phys. Lett. **84B**, 416 (1979).
[18] S. Dimopoulos and H. Georgi, Nucl. Phys. **B193**, 150 (1981).
[19] ATLAS Collaboration, J. High Energy Phys. 05 (2014) 071.
[20] ATLAS Collaboration, J. High Energy Phys. 04 (2014) 169.
[21] ATLAS Collaboration, Phys. Rev. D **90**, 052001 (2014).
[22] ATLAS Collaboration, J. High Energy Phys. 10 (2014) 96.
[23] ATLAS Collaboration, Eur. Phys. J. C **75**, 208 (2015).
[24] Z. Han, G. D. Kribs, A. Martin, and A. Menon, Phys. Rev. D **89**, 075007 (2014).
[25] R. Barbieri and G. Giudice, Nucl. Phys. **B306**, 63 (1988).
[26] B. de Carlos and J. A. Casas, Phys. Lett. B **309**, 320 (1993).
[27] A. G. Delannoy *et al.*, arXiv:1308.0355.
[28] K. Griest and D. Seckel, Phys. Rev. D **43**, 3191 (1991).
[29] G. Hinshaw *et al.*, Astrophys. J. Suppl. Ser. **208**, 19 (2013).
[30] V. Abazov *et al.* (D0 Collaboration), Phys. Lett. B **680**, 34 (2009).
[31] T. Aaltonen *et al.* (CDF Collaboration), Phys. Rev. Lett. **101**, 251801 (2008).
[32] CMS Collaboration, Phys. Rev. D **90**, 092007 (2014).
[33] CMS Collaboration, Eur. Phys. J. C **74**, 3036 (2014).
[34] CMS Collaboration, J. High Energy Phys. 11 (2015) 189.
[35] The LEP SUSY Working Group and the ALEPH, DELPHI, L3 and OPAL experiments, notes LEPSUSYWG/01-03.1, 04-01.1, http://lepsusy.web.cern.ch/lepsusy/Welcome.html.
[36] S. Schael *et al.* (ALEPH Collaboration), Phys. Lett. B **583**, 247 (2004).
[37] J. Abdallah *et al.* (DELPHI Collaboration), Eur. Phys. J. C **31**, 421 (2003).
[38] M. Acciarri *et al.* (L3 Collaboration), Phys. Lett. B **472**, 420 (2000).
[39] G. Abbiendi *et al.* (OPAL Collaboration), Eur. Phys. J. C **35**, 1 (2004).
[40] J. Alwall, P. C. Schuster, and N. Toro, Phys. Rev. D **79**, 075020 (2009).
[41] A. Djouadi *et al.*, arXiv:hep-ph/9901246.
[42] J. R. Ellis, T. Falk, K. A. Olive, and Y. Santoso, Nucl. Phys. **B652**, 259 (2003).
[43] J. R. Ellis, K. A. Olive, and Y. Santoso, Phys. Lett. B **539**, 107 (2002).
[44] M. Dine and W. Fischler, Phys. Lett. **110B**, 227 (1982).
[45] L. Alvarez-Gaume, M. Claudson, and M. B. Wise, Nucl. Phys. **B207**, 96 (1982).
[46] C. R. Nappi and B. A. Ovrut, Phys. Lett. **113B**, 175 (1982).
[47] M. Dine and A. E. Nelson, Phys. Rev. D **48**, 1277 (1993).
[48] M. Dine, A. E. Nelson, and Y. Shirman, Phys. Rev. D **51**, 1362 (1995).
[49] M. Dine, A. E. Nelson, Y. Nir, and Y. Shirman, Phys. Rev. D **53**, 2658 (1996).
[50] W. Beenakker, R. Höpker, M. Spira, and P. M. Zerwas, Nucl. Phys. **B492**, 51 (1997).
[51] B. Fuks, M. Klasen, D. R. Lamprea, and M. Rothering, J. High Energy Phys. 10 (2012) 081.
[52] B. Fuks, M. Klasen, D. R. Lamprea, and M. Rothering, Eur. Phys. J. C **73**, 2480 (2013).
[53] B. Fuks, M. Klasen, D. R. Lamprea, and M. Rothering, J. High Energy Phys. 01 (2014) 168.

[54] M. Krämer *et al.*, arXiv:1206.2892.
[55] G.-C. Cho, K. Hagiwara, J. Kanzaki, T. Plehn, D. Rainwater, and T. Stelzer, Phys. Rev. D **73**, 054002 (2006).
[56] B. Dutta, A. Gurrola, W. Johns, T. Kamon, P. Sheldon, and K. Sinha, Phys. Rev. D **87**, 035029 (2013).
[57] J. Alwall, P. Demin, S. de Visscher, R. Frederix, M. Herquet, F. Maltoni, T. Plehn, D. L. Rainwater, and T. Stelzer, J. High Energy Phys. 09 (2007) 028.
[58] J. Alwall, R. Frederix, S. Frixione, V. Hirschi, F. Maltoni, O. Mattelaer, H.-S. Shao, T. Stelzer, P. Torrielli, and M. Zaro, J. High Energy Phys. 07 (2014) 079.
[59] H. Baer, V. Barger, P. Huang, D. Mickelson, A. Mustafayev, W. Sreethawong, and X. Tata, J. High Energy Phys. 12 (2013) 013.
[60] ATLAS Collaboration, JINST **3**, S08003 (2008).
[61] ATLAS Collaboration, Eur. Phys. J. C **72**, 1849 (2012).
[62] P. Nason, J. High Energy Phys. 11 (2004) 040.
[63] S. Frixione, P. Nason, and C. Oleari, J. High Energy Phys. 11 (2007) 070.
[64] T. Sjöstrand, S. Mrenna, and P. Z. Skands, J. High Energy Phys. 05 (2006) 026.
[65] J. M. Campbell and R. K. Ellis, Phys. Rev. D **60**, 113006 (1999).
[66] J. M. Campbell, R. K. Ellis, and C. Williams, J. High Energy Phys. 07 (2011) 018.
[67] ATLAS Collaboration, Report No. ATL-PHYS-PUB-2012-003 (2012), http://cdsweb.cern.ch/record/1474107.
[68] H.-L. Lai, M. Guzzi, J. Huston, Z. Li, P. M. Nadolsky, J. Pumplin, and C.-P. Yuan, Phys. Rev. D **82**, 074024 (2010).
[69] T. Gleisberg, S. Höche, F. Krauss, M. Schönherr, S. Schumann, F. Siegert, and J. Winter, J. High Energy Phys. 02 (2009) 007.
[70] N. Kauer and G. Passarino, J. High Energy Phys. 08 (2012) 116.
[71] ATLAS Collaboration, Report No. ATL-PHYS-PUB-2011-009 (2011), http://cdsweb.cern.ch/record/1363300.
[72] F. Campanario, V. Hankele, C. Oleari, S. Prestel, and D. Zeppenfeld, Phys. Rev. D **78**, 094012 (2008).
[73] J. Pumplin, D. R. Stump, J. Huston, H.-L. Lai, P. Nadolsky, and W.-K. Tung, J. High Energy Phys. 07 (2002) 012.
[74] S. Dittmaier *et al.*, arXiv:1201.3084.
[75] M. L. Mangano, F. Piccinini, A. D. Polosa, M. Moretti, and R. Pittau, J. High Energy Phys. 07 (2003) 001.
[76] A. Kardos, Z. Trócsányi, and C. G. Papadopoulos, Phys. Rev. D **85**, 054015 (2012).
[77] J. M. Campbell and R. K. Ellis, J. High Energy Phys. 07 (2012) 052.
[78] M. Cacciari, M. Czakon, M. Mangano, A. Mitov, and P. Nason, Phys. Lett. B **710**, 612 (2012).
[79] P. Bärnreuther, M. Czakon, and A. Mitov, Phys. Rev. Lett. **109**, 132001 (2012).
[80] M. Czakon and A. Mitov, J. High Energy Phys. 12 (2012) 054.
[81] M. Czakon and A. Mitov, J. High Energy Phys. 01 (2013) 080.
[82] M. Czakon, P. Fiedler, and A. Mitov, Phys. Rev. Lett. **110**, 252004 (2013).
[83] M. Czakon and A. Mitov, Comput. Phys. Commun. **185**, 2930 (2014).
[84] P. Z. Skands, Phys. Rev. D **82**, 074018 (2010).
[85] B. P. Kersevan and E. Richter-Was, Comput. Phys. Commun. **184**, 919 (2013).
[86] N. Kidonakis, Phys. Rev. D **83**, 091503 (2011).
[87] S. Frixione, E. Laenen, P. Motylinski, and B. R. Webber, J. High Energy Phys. 03 (2006) 092.
[88] S. Frixione, E. Laenen, P. Motylinski, C. White, and B. R. Webber, J. High Energy Phys. 07 (2008) 029.
[89] N. Kidonakis, Phys. Rev. D **81**, 054028 (2010).
[90] N. Kidonakis, Phys. Rev. D **82**, 054018 (2010).
[91] J. Campbell, R. K. Ellis, and R. Rontsch, Phys. Rev. D **87**, 114006 (2013).
[92] S. Catani, L. Cieri, G. Ferrera, D. de Florian, and M. Grazzini, Phys. Rev. Lett. **103**, 082001 (2009).
[93] A. D. Martin, W. J. Stirling, R. S. Thorne, and G. Watt, Eur. Phys. J. C **63**, 189 (2009).
[94] M. Bähr *et al.*, Eur. Phys. J. C **58**, 639 (2008).
[95] S. Gieseke and A. Rohr, Eur. Phys. J. C **72**, 2225 (2012).
[96] S. Agostinelli *et al.*, Nucl. Instrum. Methods Phys. Res., Sect. A **506**, 250 (2003).
[97] ATLAS Collaboration, Eur. Phys. J. C **70**, 823 (2010).
[98] ATLAS Collaboration, Report No. ATL-PHYS-PUB-2010-013 (2010), http://cdsweb.cern.ch/record/1300517.
[99] ATLAS Collaboration, Eur. Phys. J. C **74**, 3071 (2014).
[100] ATLAS Collaboration, Eur. Phys. J. C **74**, 3130 (2014).
[101] M. Cacciari, G. P. Salam, and G. Soyez, J. High Energy Phys. 04 (2008) 063.
[102] ATLAS Collaboration, Eur. Phys. J. C **75**, 17 (2015).
[103] ATLAS Collaboration, Eur. Phys. J. C **73**, 2305 (2013).
[104] ATLAS Collaboration, Report No. ATLAS-CONF-2014-004 (2014), http://cdsweb.cern.ch/record/1664335.
[105] ATLAS Collaboration, Eur. Phys. J. C **75**, 303 (2015).
[106] ATLAS Collaboration, Eur. Phys. J. C **72**, 1844 (2012).
[107] M. Baak, G. J. Besjes, D. Côté, A. Koutsman, J. Lorenz, and D. Short, Eur. Phys. J. C **75**, 153 (2015).
[108] A. L. Read, J. Phys. G **28**, 2693 (2002).
[109] C. Lester and D. Summers, Phys. Lett. B **463**, 99 (1999).
[110] A. Barr, C. Lester, and P. Stephens, J. Phys. G **29**, 2343 (2003).
[111] M. R. Buckley, J. D. Lykken, C. Rogan, and M. Spiropulu, Phys. Rev. D **89**, 055020 (2014).
[112] ATLAS Collaboration, Eur. Phys. J. C **71**, 1577 (2011).
[113] ATLAS Collaboration, Eur. Phys. J. C **73**, 2518 (2013).
[114] J. Alwall *et al.*, Eur. Phys. J. C **53**, 473 (2008).
[115] ATLAS Collaboration, Eur. Phys. J. C **72**, 2043 (2012).
[116] ATLAS Collaboration, Phys. Rev. D **92**, 012006 (2015).
[117] S. Alioli, P. Nason, C. Oleari, and E. Re, J. High Energy Phys. 06 (2010) 043.
[118] K. Arnold *et al.*, arXiv:1107.4038.
[119] ATLAS Collaboration, J. High Energy Phys. 06 (2014) 035.

G. Aad,[85] B. Abbott,[113] J. Abdallah,[151] O. Abdinov,[11] R. Aben,[107] M. Abolins,[90] O. S. AbouZeid,[158] H. Abramowicz,[153] H. Abreu,[152] R. Abreu,[116] Y. Abulaiti,[146a,146b] B. S. Acharya,[164a,164b,a] L. Adamczyk,[38a] D. L. Adams,[25] J. Adelman,[108] S. Adomeit,[100] T. Adye,[131] A. A. Affolder,[74] T. Agatonovic-Jovin,[13] J. Agricola,[54] J. A. Aguilar-Saavedra,[126a,126f] S. P. Ahlen,[22] F. Ahmadov,[65,b] G. Aielli,[133a,133b] H. Akerstedt,[146a,146b] T. P. A. Åkesson,[81] A. V. Akimov,[96] G. L. Alberghi,[20a,20b] J. Albert,[169] S. Albrand,[55] M. J. Alconada Verzini,[71] M. Aleksa,[30] I. N. Aleksandrov,[65] C. Alexa,[26b] G. Alexander,[153] T. Alexopoulos,[10] M. Alhroob,[113] G. Alimonti,[91a] L. Alio,[85] J. Alison,[31] S. P. Alkire,[35] B. M. M. Allbrooke,[149] P. P. Allport,[18] A. Aloisio,[104a,104b] A. Alonso,[36] F. Alonso,[71] C. Alpigiani,[138] A. Altheimer,[35] B. Alvarez Gonzalez,[30] D. Álvarez Piqueras,[167] M. G. Alviggi,[104a,104b] B. T. Amadio,[15] K. Amako,[66] Y. Amaral Coutinho,[24a] C. Amelung,[23] D. Amidei,[89] S. P. Amor Dos Santos,[126a,126c] A. Amorim,[126a,126b] S. Amoroso,[48] N. Amram,[153] G. Amundsen,[23] C. Anastopoulos,[139] L. S. Ancu,[49] N. Andari,[108] T. Andeen,[35] C. F. Anders,[58b] G. Anders,[30] J. K. Anders,[74] K. J. Anderson,[31] A. Andreazza,[91a,91b] V. Andrei,[58a] S. Angelidakis,[9] I. Angelozzi,[107] P. Anger,[44] A. Angerami,[35] F. Anghinolfi,[30] A. V. Anisenkov,[109,c] N. Anjos,[12] A. Annovi,[124a,124b] M. Antonelli,[47] A. Antonov,[98] J. Antos,[144b] D. J. Antrim,[163] F. Anulli,[132a] M. Aoki,[66] L. Aperio Bella,[18] G. Arabidze,[90] Y. Arai,[66] J. P. Araque,[126a] A. T. H. Arce,[45] F. A. Arduh,[71] J-F. Arguin,[95] S. Argyropoulos,[63] M. Arik,[19a] A. J. Armbruster,[30] O. Arnaez,[30] H. Arnold,[48] M. Arratia,[28] O. Arslan,[21] A. Artamonov,[97] G. Artoni,[23] S. Asai,[155] N. Asbah,[42] A. Ashkenazi,[153] B. Åsman,[146a,146b] L. Asquith,[149] K. Assamagan,[25] R. Astalos,[144a] M. Atkinson,[165] N. B. Atlay,[141] K. Augsten,[128] M. Aurousseau,[145b] G. Avolio,[30] B. Axen,[15] M. K. Ayoub,[117] G. Azuelos,[95,d] M. A. Baak,[30] A. E. Baas,[58a] M. J. Baca,[18] C. Bacci,[134a,134b] H. Bachacou,[136] K. Bachas,[154] M. Backes,[30] M. Backhaus,[30] P. Bagiacchi,[132a,132b] P. Bagnaia,[132a,132b] Y. Bai,[33a] T. Bain,[35] J. T. Baines,[131] O. K. Baker,[176] E. M. Baldin,[109,c] P. Balek,[129] T. Balestri,[148] F. Balli,[84] W. K. Balunas,[122] E. Banas,[39] Sw. Banerjee,[173] A. A. E. Bannoura,[175] L. Barak,[30] E. L. Barberio,[88] D. Barberis,[50a,50b] M. Barbero,[85] T. Barillari,[101] M. Barisonzi,[164a,164b] T. Barklow,[143] N. Barlow,[28] S. L. Barnes,[84] B. M. Barnett,[131] R. M. Barnett,[15] Z. Barnovska,[5] A. Baroncelli,[134a] G. Barone,[23] A. J. Barr,[120] F. Barreiro,[82] J. Barreiro Guimarães da Costa,[57] R. Bartoldus,[143] A. E. Barton,[72] P. Bartos,[144a] A. Basalaev,[123] A. Bassalat,[117] A. Basye,[165] R. L. Bates,[53] S. J. Batista,[158] J. R. Batley,[28] M. Battaglia,[137] M. Bauce,[132a,132b] F. Bauer,[136] H. S. Bawa,[143,e] J. B. Beacham,[111] M. D. Beattie,[72] T. Beau,[80] P. H. Beauchemin,[161] R. Beccherle,[124a,124b] P. Bechtle,[21] H. P. Beck,[17,f] K. Becker,[120] M. Becker,[83] M. Beckingham,[170] C. Becot,[117] A. J. Beddall,[19b] A. Beddall,[19b] V. A. Bednyakov,[65] C. P. Bee,[148] L. J. Beemster,[107] T. A. Beermann,[30] M. Begel,[25] J. K. Behr,[120] C. Belanger-Champagne,[87] W. H. Bell,[49] G. Bella,[153] L. Bellagamba,[20a] A. Bellerive,[29] M. Bellomo,[86] K. Belotskiy,[98] O. Beltramello,[30] O. Benary,[153] D. Benchekroun,[135a] M. Bender,[100] K. Bendtz,[146a,146b] N. Benekos,[10] Y. Benhammou,[153] E. Benhar Noccioli,[49] J. A. Benitez Garcia,[159b] D. P. Benjamin,[45] J. R. Bensinger,[23] S. Bentvelsen,[107] L. Beresford,[120] M. Beretta,[47] D. Berge,[107] E. Bergeaas Kuutmann,[166] N. Berger,[5] F. Berghaus,[169] J. Beringer,[15] C. Bernard,[22] N. R. Bernard,[86] C. Bernius,[110] F. U. Bernlochner,[21] T. Berry,[77] P. Berta,[129] C. Bertella,[83] G. Bertoli,[146a,146b] F. Bertolucci,[124a,124b] C. Bertsche,[113] D. Bertsche,[113] M. I. Besana,[91a] G. J. Besjes,[36] O. Bessidskaia Bylund,[146a,146b] M. Bessner,[42] N. Besson,[136] C. Betancourt,[48] S. Bethke,[101] A. J. Bevan,[76] W. Bhimji,[15] R. M. Bianchi,[125] L. Bianchini,[23] M. Bianco,[30] O. Biebel,[100] D. Biedermann,[16] S. P. Bieniek,[78] N. V. Biesuz,[124a,124b] M. Biglietti,[134a] J. Bilbao De Mendizabal,[49] H. Bilokon,[47] M. Bindi,[54] S. Binet,[117] A. Bingul,[19b] C. Bini,[132a,132b] S. Biondi,[20a,20b] D. M. Bjergaard,[45] C. W. Black,[150] J. E. Black,[143] K. M. Black,[22] D. Blackburn,[138] R. E. Blair,[6] J.-B. Blanchard,[136] J. E. Blanco,[77] T. Blazek,[144a] I. Bloch,[42] C. Blocker,[23] W. Blum,[83,†] U. Blumenschein,[54] S. Blunier,[32a] G. J. Bobbink,[107] V. S. Bobrovnikov,[109,c] S. S. Bocchetta,[81] A. Bocci,[45] C. Bock,[100] M. Boehler,[48] J. A. Bogaerts,[30] D. Bogavac,[13] A. G. Bogdanchikov,[109] C. Bohm,[146a] V. Boisvert,[77] T. Bold,[38a] V. Boldea,[26b] A. S. Boldyrev,[99] M. Bomben,[80] M. Bona,[76] M. Boonekamp,[136] A. Borisov,[130] G. Borissov,[72] S. Borroni,[42] J. Bortfeldt,[100] V. Bortolotto,[60a,60b,60c] K. Bos,[107] D. Boscherini,[20a] M. Bosman,[12] J. Boudreau,[125] J. Bouffard,[2] E. V. Bouhova-Thacker,[72] D. Boumediene,[34] C. Bourdarios,[117] N. Bousson,[114] S. K. Boutle,[53] A. Boveia,[30] J. Boyd,[30] I. R. Boyko,[65] I. Bozic,[13] J. Bracinik,[18] A. Brandt,[8] G. Brandt,[54] O. Brandt,[58a] U. Bratzler,[156] B. Brau,[86] J. E. Brau,[116] H. M. Braun,[175,†] W. D. Breaden Madden,[53] K. Brendlinger,[122] A. J. Brennan,[88] L. Brenner,[107] R. Brenner,[166] S. Bressler,[172] T. M. Bristow,[46] D. Britton,[53] D. Britzger,[42] F. M. Brochu,[28] I. Brock,[21] R. Brock,[90] J. Bronner,[101] G. Brooijmans,[35] T. Brooks,[77] W. K. Brooks,[32b] J. Brosamer,[15] E. Brost,[116] P. A. Bruckman de Renstrom,[39] D. Bruncko,[144b] R. Bruneliere,[48] A. Bruni,[20a] G. Bruni,[20a] M. Bruschi,[20a] N. Bruscino,[21] L. Bryngemark,[81] T. Buanes,[14] Q. Buat,[142] P. Buchholz,[141] A. G. Buckley,[53] S. I. Buda,[26b] I. A. Budagov,[65] F. Buehrer,[48] L. Bugge,[119] M. K. Bugge,[119] O. Bulekov,[98] D. Bullock,[8] H. Burckhart,[30] S. Burdin,[74] C. D. Burgard,[48] B. Burghgrave,[108] S. Burke,[131] I. Burmeister,[43] E. Busato,[34] D. Büscher,[48] V. Büscher,[83] P. Bussey,[53] J. M. Butler,[22] A. I. Butt,[3] C. M. Buttar,[53] J. M. Butterworth,[78] P. Butti,[107] W. Buttinger,[25] A. Buzatu,[53]

A. R. Buzykaev,[109,c] S. Cabrera Urbán,[167] D. Caforio,[128] V. M. Cairo,[37a,37b] O. Cakir,[4a] N. Calace,[49] P. Calafiura,[15] A. Calandri,[136] G. Calderini,[80] P. Calfayan,[100] L. P. Caloba,[24a] D. Calvet,[34] S. Calvet,[34] R. Camacho Toro,[31] S. Camarda,[42] P. Camarri,[133a,133b] D. Cameron,[119] R. Caminal Armadans,[165] S. Campana,[30] M. Campanelli,[78] A. Campoverde,[148] V. Canale,[104a,104b] A. Canepa,[159a] M. Cano Bret,[33e] J. Cantero,[82] R. Cantrill,[126a] T. Cao,[40] M. D. M. Capeans Garrido,[30] I. Caprini,[26b] M. Caprini,[26b] M. Capua,[37a,37b] R. Caputo,[83] R. M. Carbone,[35] R. Cardarelli,[133a] F. Cardillo,[48] T. Carli,[30] G. Carlino,[104a] L. Carminati,[91a,91b] S. Caron,[106] E. Carquin,[32a] G. D. Carrillo-Montoya,[30] J. R. Carter,[28] J. Carvalho,[126a,126c] D. Casadei,[78] M. P. Casado,[12] M. Casolino,[12] E. Castaneda-Miranda,[145a] A. Castelli,[107] V. Castillo Gimenez,[167] N. F. Castro,[126a,g] P. Catastini,[57] A. Catinaccio,[30] J. R. Catmore,[119] A. Cattai,[30] J. Caudron,[83] V. Cavaliere,[165] D. Cavalli,[91a] M. Cavalli-Sforza,[12] V. Cavasinni,[124a,124b] F. Ceradini,[134a,134b] B. C. Cerio,[45] K. Cerny,[129] A. S. Cerqueira,[24b] A. Cerri,[149] L. Cerrito,[76] F. Cerutti,[15] M. Cerv,[30] A. Cervelli,[17] S. A. Cetin,[19c] A. Chafaq,[135a] D. Chakraborty,[108] I. Chalupkova,[129] Y. L. Chan,[60a] P. Chang,[165] J. D. Chapman,[28] D. G. Charlton,[18] C. C. Chau,[158] C. A. Chavez Barajas,[149] S. Cheatham,[152] A. Chegwidden,[90] S. Chekanov,[6] S. V. Chekulaev,[159a] G. A. Chelkov,[65,h] M. A. Chelstowska,[89] C. Chen,[64] H. Chen,[25] K. Chen,[148] L. Chen,[33d,i] S. Chen,[33c] S. Chen,[155] X. Chen,[33f] Y. Chen,[67] H. C. Cheng,[89] Y. Cheng,[31] A. Cheplakov,[65] E. Cheremushkina,[130] R. Cherkaoui El Moursli,[135e] V. Chernyatin,[25,†] E. Cheu,[7] L. Chevalier,[136] V. Chiarella,[47] G. Chiarelli,[124a,124b] G. Chiodini,[73a] A. S. Chisholm,[18] R. T. Chislett,[78] A. Chitan,[26b] M. V. Chizhov,[65] K. Choi,[61] S. Chouridou,[9] B. K. B. Chow,[100] V. Christodoulou,[78] D. Chromek-Burckhart,[30] J. Chudoba,[127] A. J. Chuinard,[87] J. J. Chwastowski,[39] L. Chytka,[115] G. Ciapetti,[132a,132b] A. K. Ciftci,[4a] D. Cinca,[53] V. Cindro,[75] I. A. Cioara,[21] A. Ciocio,[15] F. Cirotto,[104a,104b] Z. H. Citron,[172] M. Ciubancan,[26b] A. Clark,[49] B. L. Clark,[57] P. J. Clark,[46] R. N. Clarke,[15] C. Clement,[146a,146b] Y. Coadou,[85] M. Cobal,[164a,164c] A. Coccaro,[49] J. Cochran,[64] L. Coffey,[23] J. G. Cogan,[143] L. Colasurdo,[106] B. Cole,[35] S. Cole,[108] A. P. Colijn,[107] J. Collot,[55] T. Colombo,[58c] G. Compostella,[101] P. Conde Muiño,[126a,126b] E. Coniavitis,[48] S. H. Connell,[145b] I. A. Connelly,[77] V. Consorti,[48] S. Constantinescu,[26b] C. Conta,[121a,121b] G. Conti,[30] F. Conventi,[104a,j] M. Cooke,[15] B. D. Cooper,[78] A. M. Cooper-Sarkar,[120] T. Cornelissen,[175] M. Corradi,[20a] F. Corriveau,[87,k] A. Corso-Radu,[163] A. Cortes-Gonzalez,[12] G. Cortiana,[101] G. Costa,[91a] M. J. Costa,[167] D. Costanzo,[139] D. Côté,[8] G. Cottin,[28] G. Cowan,[77] B. E. Cox,[84] K. Cranmer,[110] G. Cree,[29] S. Crépé-Renaudin,[55] F. Crescioli,[80] W. A. Cribbs,[146a,146b] M. Crispin Ortuzar,[120] M. Cristinziani,[21] V. Croft,[106] G. Crosetti,[37a,37b] T. Cuhadar Donszelmann,[139] J. Cummings,[176] M. Curatolo,[47] J. Cúth,[83] C. Cuthbert,[150] H. Czirr,[141] P. Czodrowski,[3] S. D'Auria,[53] M. D'Onofrio,[74] M. J. Da Cunha Sargedas De Sousa,[126a,126b] C. Da Via,[84] W. Dabrowski,[38a] A. Dafinca,[120] T. Dai,[89] O. Dale,[14] F. Dallaire,[95] C. Dallapiccola,[86] M. Dam,[36] J. R. Dandoy,[31] N. P. Dang,[48] A. C. Daniells,[18] M. Danninger,[168] M. Dano Hoffmann,[136] V. Dao,[48] G. Darbo,[50a] S. Darmora,[8] J. Dassoulas,[3] A. Dattagupta,[61] W. Davey,[21] C. David,[169] T. Davidek,[129] E. Davies,[120,l] M. Davies,[153] P. Davison,[78] Y. Davygora,[58a] E. Dawe,[88] I. Dawson,[139] R. K. Daya-Ishmukhametova,[86] K. De,[8] R. de Asmundis,[104a] A. De Benedetti,[113] S. De Castro,[20a,20b] S. De Cecco,[80] N. De Groot,[106] P. de Jong,[107] H. De la Torre,[82] F. De Lorenzi,[64] D. De Pedis,[132a] A. De Salvo,[132a] U. De Sanctis,[149] A. De Santo,[149] J. B. De Vivie De Regie,[117] W. J. Dearnaley,[72] R. Debbe,[25] C. Debenedetti,[137] D. V. Dedovich,[65] I. Deigaard,[107] J. Del Peso,[82] T. Del Prete,[124a,124b] D. Delgove,[117] F. Deliot,[136] C. M. Delitzsch,[49] M. Deliyergiyev,[75] A. Dell'Acqua,[30] L. Dell'Asta,[22] M. Dell'Orso,[124a,124b] M. Della Pietra,[104a,j] D. della Volpe,[49] M. Delmastro,[5] P. A. Delsart,[55] C. Deluca,[107] D. A. DeMarco,[158] S. Demers,[176] M. Demichev,[65] A. Demilly,[80] S. P. Denisov,[130] D. Derendarz,[39] J. E. Derkaoui,[135d] F. Derue,[80] P. Dervan,[74] K. Desch,[21] C. Deterre,[42] K. Dette,[43] P. O. Deviveiros,[30] A. Dewhurst,[131] S. Dhaliwal,[23] A. Di Ciaccio,[133a,133b] L. Di Ciaccio,[5] A. Di Domenico,[132a,132b] C. Di Donato,[104a,104b] A. Di Girolamo,[30] B. Di Girolamo,[30] A. Di Mattia,[152] B. Di Micco,[134a,134b] R. Di Nardo,[47] A. Di Simone,[48] R. Di Sipio,[158] D. Di Valentino,[29] C. Diaconu,[85] M. Diamond,[158] F. A. Dias,[46] M. A. Diaz,[32a] E. B. Diehl,[89] J. Dietrich,[16] S. Diglio,[85] A. Dimitrievska,[13] J. Dingfelder,[21] P. Dita,[26b] S. Dita,[26b] F. Dittus,[30] F. Djama,[85] T. Djobava,[51b] J. I. Djuvsland,[58a] M. A. B. do Vale,[24c] D. Dobos,[30] M. Dobre,[26b] C. Doglioni,[81] T. Dohmae,[155] J. Dolejsi,[129] Z. Dolezal,[129] B. A. Dolgoshein,[98,†] M. Donadelli,[24d] S. Donati,[124a,124b] P. Dondero,[121a,121b] J. Donini,[34] J. Dopke,[131] A. Doria,[104a] M. T. Dova,[71] A. T. Doyle,[53] E. Drechsler,[54] M. Dris,[10] E. Dubreuil,[34] E. Duchovni,[172] G. Duckeck,[100] O. A. Ducu,[26b,85] D. Duda,[107] A. Dudarev,[30] L. Duflot,[117] L. Duguid,[77] M. Dührssen,[30] M. Dunford,[58a] H. Duran Yildiz,[4a] M. Düren,[52] A. Durglishvili,[51b] D. Duschinger,[44] B. Dutta,[42] M. Dyndal,[38a] C. Eckardt,[42] K. M. Ecker,[101] R. C. Edgar,[89] W. Edson,[2] N. C. Edwards,[46] W. Ehrenfeld,[21] T. Eifert,[30] G. Eigen,[14] K. Einsweiler,[15] T. Ekelof,[166] M. El Kacimi,[135c] M. Ellert,[166] S. Elles,[5] F. Ellinghaus,[175] A. A. Elliot,[169] N. Ellis,[30] J. Elmsheuser,[100] M. Elsing,[30] D. Emeliyanov,[131] Y. Enari,[155] O. C. Endner,[83] M. Endo,[118] J. Erdmann,[43] A. Ereditato,[17] G. Ernis,[175] J. Ernst,[2] M. Ernst,[25] S. Errede,[165] E. Ertel,[83] M. Escalier,[117] H. Esch,[43] C. Escobar,[125] B. Esposito,[47] A. I. Etienvre,[136] E. Etzion,[153] H. Evans,[61] A. Ezhilov,[123]

L. Fabbri,[20a,20b] G. Facini,[31] R. M. Fakhrutdinov,[130] S. Falciano,[132a] R. J. Falla,[78] J. Faltova,[129] Y. Fang,[33a] M. Fanti,[91a,91b] A. Farbin,[8] A. Farilla,[134a] T. Farooque,[12] S. Farrell,[15] S. M. Farrington,[170] P. Farthouat,[30] F. Fassi,[135e] P. Fassnacht,[30] D. Fassouliotis,[9] M. Faucci Giannelli,[77] A. Favareto,[50a,50b] L. Fayard,[117] O. L. Fedin,[123,m] W. Fedorko,[168] S. Feigl,[30] L. Feligioni,[85] C. Feng,[33d] E. J. Feng,[30] H. Feng,[89] A. B. Fenyuk,[130] L. Feremenga,[8] P. Fernandez Martinez,[167] S. Fernandez Perez,[30] J. Ferrando,[53] A. Ferrari,[166] P. Ferrari,[107] R. Ferrari,[121a] D. E. Ferreira de Lima,[53] A. Ferrer,[167] D. Ferrere,[49] C. Ferretti,[89] A. Ferretto Parodi,[50a,50b] M. Fiascaris,[31] F. Fiedler,[83] A. Filipčič,[75] M. Filipuzzi,[42] F. Filthaut,[106] M. Fincke-Keeler,[169] K. D. Finelli,[150] M. C. N. Fiolhais,[126a,126c] L. Fiorini,[167] A. Firan,[40] A. Fischer,[2] C. Fischer,[12] J. Fischer,[175] W. C. Fisher,[90] N. Flaschel,[42] I. Fleck,[141] P. Fleischmann,[89] G. T. Fletcher,[139] G. Fletcher,[76] R. R. M. Fletcher,[122] T. Flick,[175] A. Floderus,[81] L. R. Flores Castillo,[60a] M. J. Flowerdew,[101] A. Formica,[136] A. Forti,[84] D. Fournier,[117] H. Fox,[72] S. Fracchia,[12] P. Francavilla,[80] M. Franchini,[20a,20b] D. Francis,[30] L. Franconi,[119] M. Franklin,[57] M. Frate,[163] M. Fraternali,[121a,121b] D. Freeborn,[78] S. T. French,[28] F. Friedrich,[44] D. Froidevaux,[30] J. A. Frost,[120] C. Fukunaga,[156] E. Fullana Torregrosa,[83] B. G. Fulsom,[143] T. Fusayasu,[102] J. Fuster,[167] C. Gabaldon,[55] O. Gabizon,[175] A. Gabrielli,[20a,20b] A. Gabrielli,[15] G. P. Gach,[18] S. Gadatsch,[30] S. Gadomski,[49] G. Gagliardi,[50a,50b] P. Gagnon,[61] C. Galea,[106] B. Galhardo,[126a,126c] E. J. Gallas,[120] B. J. Gallop,[131] P. Gallus,[128] G. Galster,[36] K. K. Gan,[111] J. Gao,[33b,85] Y. Gao,[46] Y. S. Gao,[143,e] F. M. Garay Walls,[46] F. Garberson,[176] C. García,[167] J. E. García Navarro,[167] M. Garcia-Sciveres,[15] R. W. Gardner,[31] N. Garelli,[143] V. Garonne,[119] C. Gatti,[47] A. Gaudiello,[50a,50b] G. Gaudio,[121a] B. Gaur,[141] L. Gauthier,[95] P. Gauzzi,[132a,132b] I. L. Gavrilenko,[96] C. Gay,[168] G. Gaycken,[21] E. N. Gazis,[10] P. Ge,[33d] Z. Gecse,[168] C. N. P. Gee,[131] Ch. Geich-Gimbel,[21] M. P. Geisler,[58a] C. Gemme,[50a] M. H. Genest,[55] S. Gentile,[132a,132b] M. George,[54] S. George,[77] D. Gerbaudo,[163] A. Gershon,[153] S. Ghasemi,[141] H. Ghazlane,[135b] B. Giacobbe,[20a] S. Giagu,[132a,132b] V. Giangiobbe,[12] P. Giannetti,[124a,124b] B. Gibbard,[25] S. M. Gibson,[77] M. Gignac,[168] M. Gilchriese,[15] T. P. S. Gillam,[28] D. Gillberg,[30] G. Gilles,[34] D. M. Gingrich,[3,d] N. Giokaris,[9] M. P. Giordani,[164a,164c] F. M. Giorgi,[20a] F. M. Giorgi,[16] P. F. Giraud,[136] P. Giromini,[47] D. Giugni,[91a] C. Giuliani,[101] M. Giulini,[58b] B. K. Gjelsten,[119] S. Gkaitatzis,[154] I. Gkialas,[154] E. L. Gkougkousis,[117] L. K. Gladilin,[99] C. Glasman,[82] J. Glatzer,[30] P. C. F. Glaysher,[46] A. Glazov,[42] M. Goblirsch-Kolb,[101] J. R. Goddard,[76] J. Godlewski,[39] S. Goldfarb,[89] T. Golling,[49] D. Golubkov,[130] A. Gomes,[126a,126b,126d] R. Gonçalo,[126a] J. Goncalves Pinto Firmino Da Costa,[136] L. Gonella,[21] S. González de la Hoz,[167] G. Gonzalez Parra,[12] S. Gonzalez-Sevilla,[49] L. Goossens,[30] P. A. Gorbounov,[97] H. A. Gordon,[25] I. Gorelov,[105] B. Gorini,[30] E. Gorini,[73a,73b] A. Gorišek,[75] E. Gornicki,[39] A. T. Goshaw,[45] C. Gössling,[43] M. I. Gostkin,[65] D. Goujdami,[135c] A. G. Goussiou,[138] N. Govender,[145b] E. Gozani,[152] H. M. X. Grabas,[137] L. Graber,[54] I. Grabowska-Bold,[38a] P. O. J. Gradin,[166] P. Grafström,[20a,20b] J. Gramling,[49] E. Gramstad,[119] S. Grancagnolo,[16] V. Gratchev,[123] H. M. Gray,[30] E. Graziani,[134a] Z. D. Greenwood,[79,n] C. Grefe,[21] K. Gregersen,[78] I. M. Gregor,[42] P. Grenier,[143] J. Griffiths,[8] A. A. Grillo,[137] K. Grimm,[72] S. Grinstein,[12,o] Ph. Gris,[34] J.-F. Grivaz,[117] J. P. Grohs,[44] A. Grohsjean,[42] E. Gross,[172] J. Grosse-Knetter,[54] G. C. Grossi,[79] Z. J. Grout,[149] L. Guan,[89] J. Guenther,[128] F. Guescini,[49] D. Guest,[163] O. Gueta,[153] E. Guido,[50a,50b] T. Guillemin,[117] S. Guindon,[2] U. Gul,[53] C. Gumpert,[44] J. Guo,[33e] Y. Guo,[33b,p] S. Gupta,[120] G. Gustavino,[132a,132b] P. Gutierrez,[113] N. G. Gutierrez Ortiz,[78] C. Gutschow,[44] C. Guyot,[136] C. Gwenlan,[120] C. B. Gwilliam,[74] A. Haas,[110] C. Haber,[15] H. K. Hadavand,[8] N. Haddad,[135e] P. Haefner,[21] S. Hageböck,[21] Z. Hajduk,[39] H. Hakobyan,[177] M. Haleem,[42] J. Haley,[114] D. Hall,[120] G. Halladjian,[90] G. D. Hallewell,[85] K. Hamacher,[175] P. Hamal,[115] K. Hamano,[169] A. Hamilton,[145a] G. N. Hamity,[139] P. G. Hamnett,[42] L. Han,[33b] K. Hanagaki,[66,q] K. Hanawa,[155] M. Hance,[137] B. Haney,[122] P. Hanke,[58a] R. Hanna,[136] J. B. Hansen,[36] J. D. Hansen,[36] M. C. Hansen,[21] P. H. Hansen,[36] K. Hara,[160] A. S. Hard,[173] T. Harenberg,[175] F. Hariri,[117] S. Harkusha,[92] R. D. Harrington,[46] P. F. Harrison,[170] F. Hartjes,[107] M. Hasegawa,[67] Y. Hasegawa,[140] A. Hasib,[113] S. Hassani,[136] S. Haug,[17] R. Hauser,[90] L. Hauswald,[44] M. Havranek,[127] C. M. Hawkes,[18] R. J. Hawkings,[30] A. D. Hawkins,[81] T. Hayashi,[160] D. Hayden,[90] C. P. Hays,[120] J. M. Hays,[76] H. S. Hayward,[74] S. J. Haywood,[131] S. J. Head,[18] T. Heck,[83] V. Hedberg,[81] L. Heelan,[8] S. Heim,[122] T. Heim,[175] B. Heinemann,[15] L. Heinrich,[110] J. Hejbal,[127] L. Helary,[22] S. Hellman,[146a,146b] D. Hellmich,[21] C. Helsens,[12] J. Henderson,[120] R. C. W. Henderson,[72] Y. Heng,[173] C. Hengler,[42] S. Henkelmann,[168] A. Henrichs,[176] A. M. Henriques Correia,[30] S. Henrot-Versille,[117] G. H. Herbert,[16] Y. Hernández Jiménez,[167] G. Herten,[48] R. Hertenberger,[100] L. Hervas,[30] G. G. Hesketh,[78] N. P. Hessey,[107] J. W. Hetherly,[40] R. Hickling,[76] E. Higón-Rodriguez,[167] E. Hill,[169] J. C. Hill,[28] K. H. Hiller,[42] S. J. Hillier,[18] I. Hinchliffe,[15] E. Hines,[122] R. R. Hinman,[15] M. Hirose,[157] D. Hirschbuehl,[175] J. Hobbs,[148] N. Hod,[107] M. C. Hodgkinson,[139] P. Hodgson,[139] A. Hoecker,[30] M. R. Hoeferkamp,[105] F. Hoenig,[100] M. Hohlfeld,[83] D. Hohn,[21] T. R. Holmes,[15] M. Homann,[43] T. M. Hong,[125] W. H. Hopkins,[116] Y. Horii,[103] A. J. Horton,[142] J-Y. Hostachy,[55] S. Hou,[151] A. Hoummada,[135a] J. Howard,[120] J. Howarth,[42] M. Hrabovsky,[115] I. Hristova,[16] J. Hrivnac,[117] T. Hryn'ova,[5]

A. Hrynevich,[93] C. Hsu,[145c] P. J. Hsu,[151,r] S.-C. Hsu,[138] D. Hu,[35] Q. Hu,[33b] X. Hu,[89] Y. Huang,[42] Z. Hubacek,[128] F. Hubaut,[85] F. Huegging,[21] T. B. Huffman,[120] E. W. Hughes,[35] G. Hughes,[72] M. Huhtinen,[30] T. A. Hülsing,[83] N. Huseynov,[65,b] J. Huston,[90] J. Huth,[57] G. Iacobucci,[49] G. Iakovidis,[25] I. Ibragimov,[141] L. Iconomidou-Fayard,[117] E. Ideal,[176] Z. Idrissi,[135e] P. Iengo,[30] O. Igonkina,[107] T. Iizawa,[171] Y. Ikegami,[66] K. Ikematsu,[141] M. Ikeno,[66] Y. Ilchenko,[31,s] D. Iliadis,[154] N. Ilic,[143] T. Ince,[101] G. Introzzi,[121a,121b] P. Ioannou,[9] M. Iodice,[134a] K. Iordanidou,[35] V. Ippolito,[57] A. Irles Quiles,[167] C. Isaksson,[166] M. Ishino,[68] M. Ishitsuka,[157] R. Ishmukhametov,[111] C. Issever,[120] S. Istin,[19a] J. M. Iturbe Ponce,[84] R. Iuppa,[133a,133b] J. Ivarsson,[81] W. Iwanski,[39] H. Iwasaki,[66] J. M. Izen,[41] V. Izzo,[104a] S. Jabbar,[3] B. Jackson,[122] M. Jackson,[74] P. Jackson,[1] M. R. Jaekel,[30] V. Jain,[2] K. Jakobs,[48] S. Jakobsen,[30] T. Jakoubek,[127] J. Jakubek,[128] D. O. Jamin,[114] D. K. Jana,[79] E. Jansen,[78] R. Jansky,[62] J. Janssen,[21] M. Janus,[54] G. Jarlskog,[81] N. Javadov,[65,b] T. Javůrek,[48] L. Jeanty,[15] J. Jejelava,[51a,t] G.-Y. Jeng,[150] D. Jennens,[88] P. Jenni,[48,u] J. Jentzsch,[43] C. Jeske,[170] S. Jézéquel,[5] H. Ji,[173] J. Jia,[148] Y. Jiang,[33b] S. Jiggins,[78] J. Jimenez Pena,[167] S. Jin,[33a] A. Jinaru,[26b] O. Jinnouchi,[157] M. D. Joergensen,[36] P. Johansson,[139] K. A. Johns,[7] W. J. Johnson,[138] K. Jon-And,[146a,146b] G. Jones,[170] R. W. L. Jones,[72] T. J. Jones,[74] J. Jongmanns,[58a] P. M. Jorge,[126a,126b] K. D. Joshi,[84] J. Jovicevic,[159a] X. Ju,[173] P. Jussel,[62] A. Juste Rozas,[12,o] M. Kaci,[167] A. Kaczmarska,[39] M. Kado,[117] H. Kagan,[111] M. Kagan,[143] S. J. Kahn,[85] E. Kajomovitz,[45] C. W. Kalderon,[120] S. Kama,[40] A. Kamenshchikov,[130] N. Kanaya,[155] S. Kaneti,[28] V. A. Kantserov,[98] J. Kanzaki,[66] B. Kaplan,[110] L. S. Kaplan,[173] A. Kapliy,[31] D. Kar,[145c] K. Karakostas,[10] A. Karamaoun,[3] N. Karastathis,[10,107] M. J. Kareem,[54] E. Karentzos,[10] M. Karnevskiy,[83] S. N. Karpov,[65] Z. M. Karpova,[65] K. Karthik,[110] V. Kartvelishvili,[72] A. N. Karyukhin,[130] K. Kasahara,[160] L. Kashif,[173] R. D. Kass,[111] A. Kastanas,[14] Y. Kataoka,[155] C. Kato,[155] A. Katre,[49] J. Katzy,[42] K. Kawade,[103] K. Kawagoe,[70] T. Kawamoto,[155] G. Kawamura,[54] S. Kazama,[155] V. F. Kazanin,[109,c] R. Keeler,[169] R. Kehoe,[40] J. S. Keller,[42] J. J. Kempster,[77] H. Keoshkerian,[84] O. Kepka,[127] B. P. Kerševan,[75] S. Kersten,[175] R. A. Keyes,[87] F. Khalil-zada,[11] H. Khandanyan,[146a,146b] A. Khanov,[114] A. G. Kharlamov,[109,c] T. J. Khoo,[28] V. Khovanskiy,[97] E. Khramov,[65] J. Khubua,[51b,v] S. Kido,[67] H. Y. Kim,[8] S. H. Kim,[160] Y. K. Kim,[31] N. Kimura,[154] O. M. Kind,[16] B. T. King,[74] M. King,[167] S. B. King,[168] J. Kirk,[131] A. E. Kiryunin,[101] T. Kishimoto,[67] D. Kisielewska,[38a] F. Kiss,[48] K. Kiuchi,[160] O. Kivernyk,[136] E. Kladiva,[144b] M. H. Klein,[35] M. Klein,[74] U. Klein,[74] K. Kleinknecht,[83] P. Klimek,[146a,146b] A. Klimentov,[25] R. Klingenberg,[43] J. A. Klinger,[139] T. Klioutchnikova,[30] E.-E. Kluge,[58a] P. Kluit,[107] S. Kluth,[101] J. Knapik,[39] E. Kneringer,[62] E. B. F. G. Knoops,[85] A. Knue,[53] A. Kobayashi,[155] D. Kobayashi,[157] T. Kobayashi,[155] M. Kobel,[44] M. Kocian,[143] P. Kodys,[129] T. Koffas,[29] E. Koffeman,[107] L. A. Kogan,[120] S. Kohlmann,[175] Z. Kohout,[128] T. Kohriki,[66] T. Koi,[143] H. Kolanoski,[16] M. Kolb,[58b] I. Koletsou,[5] A. A. Komar,[96,†] Y. Komori,[155] T. Kondo,[66] N. Kondrashova,[42] K. Köneke,[48] A. C. König,[106] T. Kono,[66] R. Konoplich,[110,w] N. Konstantinidis,[78] R. Kopeliansky,[152] S. Koperny,[38a] L. Köpke,[83] A. K. Kopp,[48] K. Korcyl,[39] K. Kordas,[154] A. Korn,[78] A. A. Korol,[109,c] I. Korolkov,[12] E. V. Korolkova,[139] O. Kortner,[101] S. Kortner,[101] T. Kosek,[129] V. V. Kostyukhin,[21] V. M. Kotov,[65] A. Kotwal,[45] A. Kourkoumeli-Charalampidi,[154] C. Kourkoumelis,[9] V. Kouskoura,[25] A. Koutsman,[159a] R. Kowalewski,[169] T. Z. Kowalski,[38a] W. Kozanecki,[136] A. S. Kozhin,[130] V. A. Kramarenko,[99] G. Kramberger,[75] D. Krasnopevtsev,[98] M. W. Krasny,[80] A. Krasznahorkay,[30] J. K. Kraus,[21] A. Kravchenko,[25] S. Kreiss,[110] M. Kretz,[58c] J. Kretzschmar,[74] K. Kreutzfeldt,[52] P. Krieger,[158] K. Krizka,[31] K. Kroeninger,[43] H. Kroha,[101] J. Kroll,[122] J. Kroseberg,[21] J. Krstic,[13] U. Kruchonak,[65] H. Krüger,[21] N. Krumnack,[64] A. Kruse,[173] M. C. Kruse,[45] M. Kruskal,[22] T. Kubota,[88] H. Kucuk,[78] S. Kuday,[4b] S. Kuehn,[48] A. Kugel,[58c] F. Kuger,[174] A. Kuhl,[137] T. Kuhl,[42] V. Kukhtin,[65] R. Kukla,[136] Y. Kulchitsky,[92] S. Kuleshov,[32b] M. Kuna,[132a,132b] T. Kunigo,[68] A. Kupco,[127] H. Kurashige,[67] Y. A. Kurochkin,[92] V. Kus,[127] E. S. Kuwertz,[169] M. Kuze,[157] J. Kvita,[115] T. Kwan,[169] D. Kyriazopoulos,[139] A. La Rosa,[137] J. L. La Rosa Navarro,[24d] L. La Rotonda,[37a,37b] C. Lacasta,[167] F. Lacava,[132a,132b] J. Lacey,[29] H. Lacker,[16] D. Lacour,[80] V. R. Lacuesta,[167] E. Ladygin,[65] R. Lafaye,[5] B. Laforge,[80] T. Lagouri,[176] S. Lai,[54] L. Lambourne,[78] S. Lammers,[61] C. L. Lampen,[7] W. Lampl,[7] E. Lançon,[136] U. Landgraf,[48] M. P. J. Landon,[76] V. S. Lang,[58a] J. C. Lange,[12] A. J. Lankford,[163] F. Lanni,[25] K. Lantzsch,[21] A. Lanza,[121a] S. Laplace,[80] C. Lapoire,[30] J. F. Laporte,[136] T. Lari,[91a] F. Lasagni Manghi,[20a,20b] M. Lassnig,[30] P. Laurelli,[47] W. Lavrijsen,[15] A. T. Law,[137] P. Laycock,[74] T. Lazovich,[57] O. Le Dortz,[80] E. Le Guirriec,[85] E. Le Menedeu,[12] M. LeBlanc,[169] T. LeCompte,[6] F. Ledroit-Guillon,[55] C. A. Lee,[145a] S. C. Lee,[151] L. Lee,[1] G. Lefebvre,[80] M. Lefebvre,[169] F. Legger,[100] C. Leggett,[15] A. Lehan,[74] G. Lehmann Miotto,[30] X. Lei,[7] W. A. Leight,[29] A. Leisos,[154,x] A. G. Leister,[176] M. A. L. Leite,[24d] R. Leitner,[129] D. Lellouch,[172] B. Lemmer,[54] K. J. C. Leney,[78] T. Lenz,[21] B. Lenzi,[30] R. Leone,[7] S. Leone,[124a,124b] C. Leonidopoulos,[46] S. Leontsinis,[10] C. Leroy,[95] C. G. Lester,[28] M. Levchenko,[123] J. Levêque,[5] D. Levin,[89] L. J. Levinson,[172] M. Levy,[18] A. Lewis,[120] A. M. Leyko,[21] M. Leyton,[41] B. Li,[33b,y] H. Li,[148] H. L. Li,[31] L. Li,[45] L. Li,[33e] S. Li,[45] X. Li,[84] Y. Li,[33c,z] Z. Liang,[137] H. Liao,[34] B. Liberti,[133a] A. Liblong,[158] P. Lichard,[30] K. Lie,[165] J. Liebal,[21] W. Liebig,[14] C. Limbach,[21]

A. Limosani,[150] S. C. Lin,[151,aa] T. H. Lin,[83] F. Linde,[107] B. E. Lindquist,[148] J. T. Linnemann,[90] E. Lipeles,[122] A. Lipniacka,[14] M. Lisovyi,[58b] T. M. Liss,[165] D. Lissauer,[25] A. Lister,[168] A. M. Litke,[137] B. Liu,[151,bb] D. Liu,[151] H. Liu,[89] J. Liu,[85] J. B. Liu,[33b] K. Liu,[85] L. Liu,[165] M. Liu,[45] M. Liu,[33b] Y. Liu,[33b] M. Livan,[121a,121b] A. Lleres,[55] J. Llorente Merino,[82] S. L. Lloyd,[76] F. Lo Sterzo,[151] E. Lobodzinska,[42] P. Loch,[7] W. S. Lockman,[137] F. K. Loebinger,[84] A. E. Loevschall-Jensen,[36] K. M. Loew,[23] A. Loginov,[176] T. Lohse,[16] K. Lohwasser,[42] M. Lokajicek,[127] B. A. Long,[22] J. D. Long,[165] R. E. Long,[72] K. A. Looper,[111] L. Lopes,[126a] D. Lopez Mateos,[57] B. Lopez Paredes,[139] I. Lopez Paz,[12] J. Lorenz,[100] N. Lorenzo Martinez,[61] M. Losada,[162] P. J. Lösel,[100] X. Lou,[33a] A. Lounis,[117] J. Love,[6] P. A. Love,[72] H. Lu,[60a] N. Lu,[89] H. J. Lubatti,[138] C. Luci,[132a,132b] A. Lucotte,[55] C. Luedtke,[48] F. Luehring,[61] W. Lukas,[62] L. Luminari,[132a] O. Lundberg,[146a,146b] B. Lund-Jensen,[147] D. Lynn,[25] R. Lysak,[127] E. Lytken,[81] H. Ma,[25] L. L. Ma,[33d] G. Maccarrone,[47] A. Macchiolo,[101] C. M. Macdonald,[139] B. Maček,[75] J. Machado Miguens,[122,126b] D. Macina,[30] D. Madaffari,[85] R. Madar,[34] H. J. Maddocks,[72] W. F. Mader,[44] A. Madsen,[166] J. Maeda,[67] S. Maeland,[14] T. Maeno,[25] A. Maevskiy,[99] E. Magradze,[54] K. Mahboubi,[48] J. Mahlstedt,[107] C. Maiani,[136] C. Maidantchik,[24a] A. A. Maier,[101] T. Maier,[100] A. Maio,[126a,126b,126d] S. Majewski,[116] Y. Makida,[66] N. Makovec,[117] B. Malaescu,[80] Pa. Malecki,[39] V. P. Maleev,[123] F. Malek,[55] U. Mallik,[63] D. Malon,[6] C. Malone,[143] S. Maltezos,[10] V. M. Malyshev,[109] S. Malyukov,[30] J. Mamuzic,[42] G. Mancini,[47] B. Mandelli,[30] L. Mandelli,[91a] I. Mandić,[75] R. Mandrysch,[63] J. Maneira,[126a,126b] A. Manfredini,[101] L. Manhaes de Andrade Filho,[24b] J. Manjarres Ramos,[159b] A. Mann,[100] A. Manousakis-Katsikakis,[9] B. Mansoulie,[136] R. Mantifel,[87] M. Mantoani,[54] L. Mapelli,[30] L. March,[145c] G. Marchiori,[80] M. Marcisovsky,[127] C. P. Marino,[169] M. Marjanovic,[13] D. E. Marley,[89] F. Marroquim,[24a] S. P. Marsden,[84] Z. Marshall,[15] L. F. Marti,[17] S. Marti-Garcia,[167] B. Martin,[90] T. A. Martin,[170] V. J. Martin,[46] B. Martin dit Latour,[14] M. Martinez,[12,o] S. Martin-Haugh,[131] V. S. Martoiu,[26b] A. C. Martyniuk,[78] M. Marx,[138] F. Marzano,[132a] A. Marzin,[30] L. Masetti,[83] T. Mashimo,[155] R. Mashinistov,[96] J. Masik,[84] A. L. Maslennikov,[109,c] I. Massa,[20a,20b] L. Massa,[20a,20b] P. Mastrandrea,[5] A. Mastroberardino,[37a,37b] T. Masubuchi,[155] P. Mättig,[175] J. Mattmann,[83] J. Maurer,[26b] S. J. Maxfield,[74] D. A. Maximov,[109,c] R. Mazini,[151] S. M. Mazza,[91a,91b] G. Mc Goldrick,[158] S. P. Mc Kee,[89] A. McCarn,[89] R. L. McCarthy,[148] T. G. McCarthy,[29] N. A. McCubbin,[131] K. W. McFarlane,[56,†] J. A. Mcfayden,[78] G. Mchedlidze,[54] S. J. McMahon,[131] R. A. McPherson,[169,k] M. Medinnis,[42] S. Meehan,[145a] S. Mehlhase,[100] A. Mehta,[74] K. Meier,[58a] C. Meineck,[100] B. Meirose,[41] B. R. Mellado Garcia,[145c] F. Meloni,[17] A. Mengarelli,[20a,20b] S. Menke,[101] E. Meoni,[161] K. M. Mercurio,[57] S. Mergelmeyer,[21] P. Mermod,[49] L. Merola,[104a,104b] C. Meroni,[91a] F. S. Merritt,[31] A. Messina,[132a,132b] J. Metcalfe,[25] A. S. Mete,[163] C. Meyer,[83] C. Meyer,[122] J-P. Meyer,[136] J. Meyer,[107] H. Meyer Zu Theenhausen,[58a] R. P. Middleton,[131] S. Miglioranzi,[164a,164c] L. Mijović,[21] G. Mikenberg,[172] M. Mikestikova,[127] M. Mikuž,[75] M. Milesi,[88] A. Milic,[30] D. W. Miller,[31] C. Mills,[46] A. Milov,[172] D. A. Milstead,[146a,146b] A. A. Minaenko,[130] Y. Minami,[155] I. A. Minashvili,[65] A. I. Mincer,[110] B. Mindur,[38a] M. Mineev,[65] Y. Ming,[173] L. M. Mir,[12] K. P. Mistry,[122] T. Mitani,[171] J. Mitrevski,[100] V. A. Mitsou,[167] A. Miucci,[49] P. S. Miyagawa,[139] J. U. Mjörnmark,[81] T. Moa,[146a,146b] K. Mochizuki,[85] S. Mohapatra,[35] W. Mohr,[48] S. Molander,[146a,146b] R. Moles-Valls,[21] R. Monden,[68] K. Mönig,[42] C. Monini,[55] J. Monk,[36] E. Monnier,[85] A. Montalbano,[148] J. Montejo Berlingen,[12] F. Monticelli,[71] S. Monzani,[132a,132b] R. W. Moore,[3] N. Morange,[117] D. Moreno,[162] M. Moreno Llácer,[54] P. Morettini,[50a] D. Mori,[142] T. Mori,[155] M. Morii,[57] M. Morinaga,[155] V. Morisbak,[119] S. Moritz,[83] A. K. Morley,[150] G. Mornacchi,[30] J. D. Morris,[76] S. S. Mortensen,[36] A. Morton,[53] L. Morvaj,[103] M. Mosidze,[51b] J. Moss,[143] K. Motohashi,[157] R. Mount,[143] E. Mountricha,[25] S. V. Mouraviev,[96,†] E. J. W. Moyse,[86] S. Muanza,[85] R. D. Mudd,[18] F. Mueller,[101] J. Mueller,[125] R. S. P. Mueller,[100] T. Mueller,[28] D. Muenstermann,[49] P. Mullen,[53] G. A. Mullier,[17] J. A. Murillo Quijada,[18] W. J. Murray,[170,131] H. Musheghyan,[54] E. Musto,[152] A. G. Myagkov,[130,cc] M. Myska,[128] B. P. Nachman,[143] O. Nackenhorst,[54] J. Nadal,[54] K. Nagai,[120] R. Nagai,[157] Y. Nagai,[85] K. Nagano,[66] A. Nagarkar,[111] Y. Nagasaka,[59] K. Nagata,[160] M. Nagel,[101] E. Nagy,[85] A. M. Nairz,[30] Y. Nakahama,[30] K. Nakamura,[66] T. Nakamura,[155] I. Nakano,[112] H. Namasivayam,[41] R. F. Naranjo Garcia,[42] R. Narayan,[31] D. I. Narrias Villar,[58a] T. Naumann,[42] G. Navarro,[162] R. Nayyar,[7] H. A. Neal,[89] P. Yu. Nechaeva,[96] T. J. Neep,[84] P. D. Nef,[143] A. Negri,[121a,121b] M. Negrini,[20a] S. Nektarijevic,[106] C. Nellist,[117] A. Nelson,[163] S. Nemecek,[127] P. Nemethy,[110] A. A. Nepomuceno,[24a] M. Nessi,[30,dd] M. S. Neubauer,[165] M. Neumann,[175] R. M. Neves,[110] P. Nevski,[25] P. R. Newman,[18] D. H. Nguyen,[6] R. B. Nickerson,[120] R. Nicolaidou,[136] B. Nicquevert,[30] J. Nielsen,[137] N. Nikiforou,[35] A. Nikiforov,[16] V. Nikolaenko,[130,cc] I. Nikolic-Audit,[80] K. Nikolopoulos,[18] J. K. Nilsen,[119] P. Nilsson,[25] Y. Ninomiya,[155] A. Nisati,[132a] R. Nisius,[101] T. Nobe,[155] M. Nomachi,[118] I. Nomidis,[29] T. Nooney,[76] S. Norberg,[113] M. Nordberg,[30] O. Novgorodova,[44] S. Nowak,[101] M. Nozaki,[66] L. Nozka,[115] K. Ntekas,[10] G. Nunes Hanninger,[88] T. Nunnemann,[100] E. Nurse,[78] F. Nuti,[88] B. J. O'Brien,[46] F. O'grady,[7] D. C. O'Neil,[142] V. O'Shea,[53] F. G. Oakham,[29,d] H. Oberlack,[101] T. Obermann,[21] J. Ocariz,[80] A. Ochi,[67] I. Ochoa,[35] J. P. Ochoa-Ricoux,[32a] S. Oda,[70]

S. Odaka,[66] H. Ogren,[61] A. Oh,[84] S. H. Oh,[45] C. C. Ohm,[15] H. Ohman,[166] H. Oide,[30] W. Okamura,[118] H. Okawa,[160] Y. Okumura,[31] T. Okuyama,[66] A. Olariu,[26b] S. A. Olivares Pino,[46] D. Oliveira Damazio,[25] A. Olszewski,[39] J. Olszowska,[39] A. Onofre,[126a,126e] K. Onogi,[103] P. U. E. Onyisi,[31,s] C. J. Oram,[159a] M. J. Oreglia,[31] Y. Oren,[153] D. Orestano,[134a,134b] N. Orlando,[154] C. Oropeza Barrera,[53] R. S. Orr,[158] B. Osculati,[50a,50b] R. Ospanov,[84] G. Otero y Garzon,[27] H. Otono,[70] M. Ouchrif,[135d] F. Ould-Saada,[119] A. Ouraou,[136] K. P. Oussoren,[107] Q. Ouyang,[33a] A. Ovcharova,[15] M. Owen,[53] R. E. Owen,[18] V. E. Ozcan,[19a] N. Ozturk,[8] K. Pachal,[142] A. Pacheco Pages,[12] C. Padilla Aranda,[12] M. Pagáčová,[48] S. Pagan Griso,[15] E. Paganis,[139] F. Paige,[25] P. Pais,[86] K. Pajchel,[119] G. Palacino,[159b] S. Palestini,[30] M. Palka,[38b] D. Pallin,[34] A. Palma,[126a,126b] Y. B. Pan,[173] E. St. Panagiotopoulou,[10] C. E. Pandini,[80] J. G. Panduro Vazquez,[77] P. Pani,[146a,146b] S. Panitkin,[25] D. Pantea,[26b] L. Paolozzi,[49] Th. D. Papadopoulou,[10] K. Papageorgiou,[154] A. Paramonov,[6] D. Paredes Hernandez,[154] M. A. Parker,[28] K. A. Parker,[139] F. Parodi,[50a,50b] J. A. Parsons,[35] U. Parzefall,[48] E. Pasqualucci,[132a] S. Passaggio,[50a] F. Pastore,[134a,134b,†] Fr. Pastore,[77] G. Pásztor,[29] S. Pataraia,[175] N. D. Patel,[150] J. R. Pater,[84] T. Pauly,[30] J. Pearce,[169] B. Pearson,[113] L. E. Pedersen,[36] M. Pedersen,[119] S. Pedraza Lopez,[167] R. Pedro,[126a,126b] S. V. Peleganchuk,[109,c] D. Pelikan,[166] O. Penc,[127] C. Peng,[33a] H. Peng,[33b] B. Penning,[31] J. Penwell,[61] D. V. Perepelitsa,[25] E. Perez Codina,[159a] M. T. Pérez García-Estañ,[167] L. Perini,[91a,91b] H. Pernegger,[30] S. Perrella,[104a,104b] R. Peschke,[42] V. D. Peshekhonov,[65] K. Peters,[30] R. F. Y. Peters,[84] B. A. Petersen,[30] T. C. Petersen,[36] E. Petit,[42] A. Petridis,[1] C. Petridou,[154] P. Petroff,[117] E. Petrolo,[132a] F. Petrucci,[134a,134b] N. E. Pettersson,[157] R. Pezoa,[32b] P. W. Phillips,[131] G. Piacquadio,[143] E. Pianori,[170] A. Picazio,[49] E. Piccaro,[76] M. Piccinini,[20a,20b] M. A. Pickering,[120] R. Piegaia,[27] D. T. Pignotti,[111] J. E. Pilcher,[31] A. D. Pilkington,[84] A. W. J. Pin,[84] J. Pina,[126a,126b,126d] M. Pinamonti,[164a,164c,ee] J. L. Pinfold,[3] A. Pingel,[36] S. Pires,[80] H. Pirumov,[42] M. Pitt,[172] C. Pizio,[91a,91b] L. Plazak,[144a] M.-A. Pleier,[25] V. Pleskot,[129] E. Plotnikova,[65] P. Plucinski,[146a,146b] D. Pluth,[64] R. Poettgen,[146a,146b] L. Poggioli,[117] D. Pohl,[21] G. Polesello,[121a] A. Poley,[42] A. Policicchio,[37a,37b] R. Polifka,[158] A. Polini,[20a] C. S. Pollard,[53] V. Polychronakos,[25] K. Pommès,[30] L. Pontecorvo,[132a] B. G. Pope,[90] G. A. Popeneciu,[26c] D. S. Popovic,[13] A. Poppleton,[30] S. Pospisil,[128] K. Potamianos,[15] I. N. Potrap,[65] C. J. Potter,[149] C. T. Potter,[116] G. Poulard,[30] J. Poveda,[30] V. Pozdnyakov,[65] P. Pralavorio,[85] A. Pranko,[15] S. Prasad,[30] S. Prell,[64] D. Price,[84] L. E. Price,[6] M. Primavera,[73a] S. Prince,[87] M. Proissl,[46] K. Prokofiev,[60c] F. Prokoshin,[32b] E. Protopapadaki,[136] S. Protopopescu,[25] J. Proudfoot,[6] M. Przybycien,[38a] E. Ptacek,[116] D. Puddu,[134a,134b] E. Pueschel,[86] D. Puldon,[148] M. Purohit,[25,ff] P. Puzo,[117] J. Qian,[89] G. Qin,[53] Y. Qin,[84] A. Quadt,[54] D. R. Quarrie,[15] W. B. Quayle,[164a,164b] M. Queitsch-Maitland,[84] D. Quilty,[53] S. Raddum,[119] V. Radeka,[25] V. Radescu,[42] S. K. Radhakrishnan,[148] P. Radloff,[116] P. Rados,[88] F. Ragusa,[91a,91b] G. Rahal,[178] S. Rajagopalan,[25] M. Rammensee,[30] C. Rangel-Smith,[166] F. Rauscher,[100] S. Rave,[83] T. Ravenscroft,[53] M. Raymond,[30] A. L. Read,[119] N. P. Readioff,[74] D. M. Rebuzzi,[121a,121b] A. Redelbach,[174] G. Redlinger,[25] R. Reece,[137] K. Reeves,[41] L. Rehnisch,[16] J. Reichert,[122] H. Reisin,[27] C. Rembser,[30] H. Ren,[33a] A. Renaud,[117] M. Rescigno,[132a] S. Resconi,[91a] O. L. Rezanova,[109,c] P. Reznicek,[129] R. Rezvani,[95] R. Richter,[101] S. Richter,[78] E. Richter-Was,[38b] O. Ricken,[21] M. Ridel,[80] P. Rieck,[16] C. J. Riegel,[175] J. Rieger,[54] O. Rifki,[113] M. Rijssenbeek,[148] A. Rimoldi,[121a,121b] L. Rinaldi,[20a] B. Ristić,[49] E. Ritsch,[30] I. Riu,[12] F. Rizatdinova,[114] E. Rizvi,[76] S. H. Robertson,[87,k] A. Robichaud-Veronneau,[87] D. Robinson,[28] J. E. M. Robinson,[42] A. Robson,[53] C. Roda,[124a,124b] S. Roe,[30] O. Røhne,[119] A. Romaniouk,[98] M. Romano,[20a,20b] S. M. Romano Saez,[34] E. Romero Adam,[167] N. Rompotis,[138] M. Ronzani,[48] L. Roos,[80] E. Ros,[167] S. Rosati,[132a] K. Rosbach,[48] P. Rose,[137] P. L. Rosendahl,[14] O. Rosenthal,[141] V. Rossetti,[146a,146b] E. Rossi,[104a,104b] L. P. Rossi,[50a] J. H. N. Rosten,[28] R. Rosten,[138] M. Rotaru,[26b] I. Roth,[172] J. Rothberg,[138] D. Rousseau,[117] C. R. Royon,[136] A. Rozanov,[85] Y. Rozen,[152] X. Ruan,[145c] F. Rubbo,[143] I. Rubinskiy,[42] V. I. Rud,[99] C. Rudolph,[44] M. S. Rudolph,[158] F. Rühr,[48] A. Ruiz-Martinez,[30] Z. Rurikova,[48] N. A. Rusakovich,[65] A. Ruschke,[100] H. L. Russell,[138] J. P. Rutherfoord,[7] N. Ruthmann,[30] Y. F. Ryabov,[123] M. Rybar,[165] G. Rybkin,[117] N. C. Ryder,[120] A. F. Saavedra,[150] G. Sabato,[107] S. Sacerdoti,[27] A. Saddique,[3] H. F-W. Sadrozinski,[137] R. Sadykov,[65] F. Safai Tehrani,[132a] P. Saha,[108] M. Sahinsoy,[58a] M. Saimpert,[136] T. Saito,[155] H. Sakamoto,[155] Y. Sakurai,[171] G. Salamanna,[134a,134b] A. Salamon,[133a] J. E. Salazar Loyola,[32b] M. Saleem,[113] D. Salek,[107] P. H. Sales De Bruin,[138] D. Salihagic,[101] A. Salnikov,[143] J. Salt,[167] D. Salvatore,[37a,37b] F. Salvatore,[149] A. Salvucci,[60a] A. Salzburger,[30] D. Sammel,[48] D. Sampsonidis,[154] A. Sanchez,[104a,104b] J. Sánchez,[167] V. Sanchez Martinez,[167] H. Sandaker,[119] R. L. Sandbach,[76] H. G. Sander,[83] M. P. Sanders,[100] M. Sandhoff,[175] C. Sandoval,[162] R. Sandstroem,[101] D. P. C. Sankey,[131] M. Sannino,[50a,50b] A. Sansoni,[47] C. Santoni,[34] R. Santonico,[133a,133b] H. Santos,[126a] I. Santoyo Castillo,[149] K. Sapp,[125] A. Sapronov,[65] J. G. Saraiva,[126a,126d] B. Sarrazin,[21] O. Sasaki,[66] Y. Sasaki,[155] K. Sato,[160] G. Sauvage,[5,†] E. Sauvan,[5] G. Savage,[77] P. Savard,[158,d] C. Sawyer,[131] L. Sawyer,[79,n] J. Saxon,[31] C. Sbarra,[20a] A. Sbrizzi,[20a,20b] T. Scanlon,[78] D. A. Scannicchio,[163] M. Scarcella,[150] V. Scarfone,[37a,37b] J. Schaarschmidt,[172] P. Schacht,[101] D. Schaefer,[30] R. Schaefer,[42] J. Schaeffer,[83]

S. Schaepe,[21] S. Schaetzel,[58b] U. Schäfer,[83] A. C. Schaffer,[117] D. Schaile,[100] R. D. Schamberger,[148] V. Scharf,[58a] V. A. Schegelsky,[123] D. Scheirich,[129] M. Schernau,[163] C. Schiavi,[50a,50b] C. Schillo,[48] M. Schioppa,[37a,37b] S. Schlenker,[30] K. Schmieden,[30] C. Schmitt,[83] S. Schmitt,[58b] S. Schmitt,[42] B. Schneider,[159a] Y. J. Schnellbach,[74] U. Schnoor,[44] L. Schoeffel,[136] A. Schoening,[58b] B. D. Schoenrock,[90] E. Schopf,[21] A. L. S. Schorlemmer,[54] M. Schott,[83] D. Schouten,[159a] J. Schovancova,[8] S. Schramm,[49] M. Schreyer,[174] N. Schuh,[83] M. J. Schultens,[21] H.-C. Schultz-Coulon,[58a] H. Schulz,[16] M. Schumacher,[48] B. A. Schumm,[137] Ph. Schune,[136] C. Schwanenberger,[84] A. Schwartzman,[143] T. A. Schwarz,[89] Ph. Schwegler,[101] H. Schweiger,[84] Ph. Schwemling,[136] R. Schwienhorst,[90] J. Schwindling,[136] T. Schwindt,[21] F. G. Sciacca,[17] E. Scifo,[117] G. Sciolla,[23] F. Scuri,[124a,124b] F. Scutti,[21] J. Searcy,[89] G. Sedov,[42] E. Sedykh,[123] P. Seema,[21] S. C. Seidel,[105] A. Seiden,[137] F. Seifert,[128] J. M. Seixas,[24a] G. Sekhniaidze,[104a] K. Sekhon,[89] S. J. Sekula,[40] D. M. Seliverstov,[123,†] N. Semprini-Cesari,[20a,20b] C. Serfon,[30] L. Serin,[117] L. Serkin,[164a,164b] T. Serre,[85] M. Sessa,[134a,134b] R. Seuster,[159a] H. Severini,[113] T. Sfiligoj,[75] F. Sforza,[30] A. Sfyrla,[30] E. Shabalina,[54] M. Shamim,[116] L. Y. Shan,[33a] R. Shang,[165] J. T. Shank,[22] M. Shapiro,[15] P. B. Shatalov,[97] K. Shaw,[164a,164b] S. M. Shaw,[84] A. Shcherbakova,[146a,146b] C. Y. Shehu,[149] P. Sherwood,[78] L. Shi,[151,gg] S. Shimizu,[67] C. O. Shimmin,[163] M. Shimojima,[102] M. Shiyakova,[65] A. Shmeleva,[96] D. Shoaleh Saadi,[95] M. J. Shochet,[31] S. Shojaii,[91a,91b] S. Shrestha,[111] E. Shulga,[98] M. A. Shupe,[7] S. Shushkevich,[42] P. Sicho,[127] P. E. Sidebo,[147] O. Sidiropoulou,[174] D. Sidorov,[114] A. Sidoti,[20a,20b] F. Siegert,[44] Dj. Sijacki,[13] J. Silva,[126a,126d] Y. Silver,[153] S. B. Silverstein,[146a] V. Simak,[128] O. Simard,[5] Lj. Simic,[13] S. Simion,[117] E. Simioni,[83] B. Simmons,[78] D. Simon,[34] P. Sinervo,[158] N. B. Sinev,[116] M. Sioli,[20a,20b] G. Siragusa,[174] A. N. Sisakyan,[65,†] S. Yu. Sivoklokov,[99] J. Sjölin,[146a,146b] T. B. Sjursen,[14] M. B. Skinner,[72] H. P. Skottowe,[57] P. Skubic,[113] M. Slater,[18] T. Slavicek,[128] M. Slawinska,[107] K. Sliwa,[161] V. Smakhtin,[172] B. H. Smart,[46] L. Smestad,[14] S. Yu. Smirnov,[98] Y. Smirnov,[98] L. N. Smirnova,[99,hh] O. Smirnova,[81] M. N. K. Smith,[35] R. W. Smith,[35] M. Smizanska,[72] K. Smolek,[128] A. A. Snesarev,[96] G. Snidero,[76] S. Snyder,[25] R. Sobie,[169,k] F. Socher,[44] A. Soffer,[153] D. A. Soh,[151,gg] G. Sokhrannyi,[75] C. A. Solans,[30] M. Solar,[128] J. Solc,[128] E. Yu. Soldatov,[98] U. Soldevila,[167] A. A. Solodkov,[130] A. Soloshenko,[65] O. V. Solovyanov,[130] V. Solovyev,[123] P. Sommer,[48] H. Y. Song,[33b,y] N. Soni,[1] A. Sood,[15] A. Sopczak,[128] B. Sopko,[128] V. Sopko,[128] V. Sorin,[12] D. Sosa,[58b] M. Sosebee,[8] C. L. Sotiropoulou,[124a,124b] R. Soualah,[164a,164c] A. M. Soukharev,[109,c] D. South,[42] B. C. Sowden,[77] S. Spagnolo,[73a,73b] M. Spalla,[124a,124b] M. Spangenberg,[170] F. Spanò,[77] W. R. Spearman,[57] D. Sperlich,[16] F. Spettel,[101] R. Spighi,[20a] G. Spigo,[30] L. A. Spiller,[88] M. Spousta,[129] R. D. St. Denis,[53,†] A. Stabile,[91a] S. Staerz,[44] J. Stahlman,[122] R. Stamen,[58a] S. Stamm,[16] E. Stanecka,[39] C. Stanescu,[134a] M. Stanescu-Bellu,[42] M. M. Stanitzki,[42] S. Stapnes,[119] E. A. Starchenko,[130] J. Stark,[55] P. Staroba,[127] P. Starovoitov,[58a] R. Staszewski,[39] P. Steinberg,[25] B. Stelzer,[142] H. J. Stelzer,[30] O. Stelzer-Chilton,[159a] H. Stenzel,[52] G. A. Stewart,[53] J. A. Stillings,[21] M. C. Stockton,[87] M. Stoebe,[87] G. Stoicea,[26b] P. Stolte,[54] S. Stonjek,[101] A. R. Stradling,[8] A. Straessner,[44] M. E. Stramaglia,[17] J. Strandberg,[147] S. Strandberg,[146a,146b] A. Strandlie,[119] E. Strauss,[143] M. Strauss,[113] P. Strizenec,[144b] R. Ströhmer,[174] D. M. Strom,[116] R. Stroynowski,[40] A. Strubig,[106] S. A. Stucci,[17] B. Stugu,[14] N. A. Styles,[42] D. Su,[143] J. Su,[125] R. Subramaniam,[79] A. Succurro,[12] S. Suchek,[58a] Y. Sugaya,[118] M. Suk,[128] V. V. Sulin,[96] S. Sultansoy,[4c] T. Sumida,[68] S. Sun,[57] X. Sun,[33a] J. E. Sundermann,[48] K. Suruliz,[149] G. Susinno,[37a,37b] M. R. Sutton,[149] S. Suzuki,[66] M. Svatos,[127] M. Swiatlowski,[143] I. Sykora,[144a] T. Sykora,[129] D. Ta,[48] C. Taccini,[134a,134b] K. Tackmann,[42] J. Taenzer,[158] A. Taffard,[163] R. Tafirout,[159a] N. Taiblum,[153] H. Takai,[25] R. Takashima,[69] H. Takeda,[67] T. Takeshita,[140] Y. Takubo,[66] M. Talby,[85] A. A. Talyshev,[109,c] J. Y. C. Tam,[174] K. G. Tan,[88] J. Tanaka,[155] R. Tanaka,[117] S. Tanaka,[66] B. B. Tannenwald,[111] N. Tannoury,[21] S. Tapia Araya,[32b] S. Tapprogge,[83] S. Tarem,[152] F. Tarrade,[29] G. F. Tartarelli,[91a] P. Tas,[129] M. Tasevsky,[127] T. Tashiro,[68] E. Tassi,[37a,37b] A. Tavares Delgado,[126a,126b] Y. Tayalati,[135d] F. E. Taylor,[94] G. N. Taylor,[88] P. T. E. Taylor,[88] W. Taylor,[159b] F. A. Teischinger,[30] M. Teixeira Dias Castanheira,[76] P. Teixeira-Dias,[77] K. K. Temming,[48] D. Temple,[142] H. Ten Kate,[30] P. K. Teng,[151] J. J. Teoh,[118] F. Tepel,[175] S. Terada,[66] K. Terashi,[155] J. Terron,[82] S. Terzo,[101] M. Testa,[47] R. J. Teuscher,[158,k] T. Theveneaux-Pelzer,[34] J. P. Thomas,[18] J. Thomas-Wilsker,[77] E. N. Thompson,[35] P. D. Thompson,[18] R. J. Thompson,[84] A. S. Thompson,[53] L. A. Thomsen,[176] E. Thomson,[122] M. Thomson,[28] R. P. Thun,[89,†] M. J. Tibbetts,[15] R. E. Ticse Torres,[85] V. O. Tikhomirov,[96,ii] Yu. A. Tikhonov,[109,c] S. Timoshenko,[98] E. Tiouchichine,[85] P. Tipton,[176] S. Tisserant,[85] K. Todome,[157] T. Todorov,[5,†] S. Todorova-Nova,[129] J. Tojo,[70] S. Tokár,[144a] K. Tokushuku,[66] K. Tollefson,[90] E. Tolley,[57] L. Tomlinson,[84] M. Tomoto,[103] L. Tompkins,[143,jj] K. Toms,[105] E. Torrence,[116] H. Torres,[142] E. Torró Pastor,[138] J. Toth,[85,kk] F. Touchard,[85] D. R. Tovey,[139] T. Trefzger,[174] L. Tremblet,[30] A. Tricoli,[30] I. M. Trigger,[159a] S. Trincaz-Duvoid,[80] M. F. Tripiana,[12] W. Trischuk,[158] B. Trocmé,[55] C. Troncon,[91a] M. Trottier-McDonald,[15] M. Trovatelli,[169] L. Truong,[164a,164c] M. Trzebinski,[39] A. Trzupek,[39] C. Tsarouchas,[30] J. C-L. Tseng,[120] P. V. Tsiareshka,[92] D. Tsionou,[154] G. Tsipolitis,[10] N. Tsirintanis,[9] S. Tsiskaridze,[12] V. Tsiskaridze,[48]

E. G. Tskhadadze,[51a] K. M. Tsui,[60a] I. I. Tsukerman,[97] V. Tsulaia,[15] S. Tsuno,[66] D. Tsybychev,[148] A. Tudorache,[26b] V. Tudorache,[26b] A. N. Tuna,[57] S. A. Tupputi,[20a,20b] S. Turchikhin,[99,hh] D. Turecek,[128] R. Turra,[91a,91b] A. J. Turvey,[40] P. M. Tuts,[35] A. Tykhonov,[49] M. Tylmad,[146a,146b] M. Tyndel,[131] I. Ueda,[155] R. Ueno,[29] M. Ughetto,[146a,146b] M. Ugland,[14] F. Ukegawa,[160] G. Unal,[30] A. Undrus,[25] G. Unel,[163] F. C. Ungaro,[48] Y. Unno,[66] C. Unverdorben,[100] J. Urban,[144b] P. Urquijo,[88] P. Urrejola,[83] G. Usai,[8] A. Usanova,[62] L. Vacavant,[85] V. Vacek,[128] B. Vachon,[87] C. Valderanis,[83] N. Valencic,[107] S. Valentinetti,[20a,20b] A. Valero,[167] L. Valery,[12] S. Valkar,[129] S. Vallecorsa,[49] J. A. Valls Ferrer,[167] W. Van Den Wollenberg,[107] P. C. Van Der Deijl,[107] R. van der Geer,[107] H. van der Graaf,[107] N. van Eldik,[152] P. van Gemmeren,[6] J. Van Nieuwkoop,[142] I. van Vulpen,[107] M. C. van Woerden,[30] M. Vanadia,[132a,132b] W. Vandelli,[30] R. Vanguri,[122] A. Vaniachine,[6] F. Vannucci,[80] G. Vardanyan,[177] R. Vari,[132a] E. W. Varnes,[7] T. Varol,[40] D. Varouchas,[80] A. Vartapetian,[8] K. E. Varvell,[150] F. Vazeille,[34] T. Vazquez Schroeder,[87] J. Veatch,[7] L. M. Veloce,[158] F. Veloso,[126a,126c] T. Velz,[21] S. Veneziano,[132a] A. Ventura,[73a,73b] D. Ventura,[86] M. Venturi,[169] N. Venturi,[158] A. Venturini,[23] V. Vercesi,[121a] M. Verducci,[132a,132b] W. Verkerke,[107] J. C. Vermeulen,[107] A. Vest,[44] M. C. Vetterli,[142,d] O. Viazlo,[81] I. Vichou,[165] T. Vickey,[139] O. E. Vickey Boeriu,[139] G. H. A. Viehhauser,[120] S. Viel,[15] R. Vigne,[62] M. Villa,[20a,20b] M. Villaplana Perez,[91a,91b] E. Vilucchi,[47] M. G. Vincter,[29] V. B. Vinogradov,[65] I. Vivarelli,[149] F. Vives Vaque,[3] S. Vlachos,[10] D. Vladoiu,[100] M. Vlasak,[128] M. Vogel,[32a] P. Vokac,[128] G. Volpi,[124a,124b] M. Volpi,[88] H. von der Schmitt,[101] H. von Radziewski,[48] E. von Toerne,[21] V. Vorobel,[129] K. Vorobev,[98] M. Vos,[167] R. Voss,[30] J. H. Vossebeld,[74] N. Vranjes,[13] M. Vranjes Milosavljevic,[13] V. Vrba,[127] M. Vreeswijk,[107] R. Vuillermet,[30] I. Vukotic,[31] Z. Vykydal,[128] P. Wagner,[21] W. Wagner,[175] H. Wahlberg,[71] S. Wahrmund,[44] J. Wakabayashi,[103] J. Walder,[72] R. Walker,[100] W. Walkowiak,[141] C. Wang,[151] F. Wang,[173] H. Wang,[15] H. Wang,[40] J. Wang,[42] J. Wang,[150] K. Wang,[87] R. Wang,[6] S. M. Wang,[151] T. Wang,[21] T. Wang,[35] X. Wang,[176] C. Wanotayaroj,[116] A. Warburton,[87] C. P. Ward,[28] D. R. Wardrope,[78] A. Washbrook,[46] C. Wasicki,[42] P. M. Watkins,[18] A. T. Watson,[18] I. J. Watson,[150] M. F. Watson,[18] G. Watts,[138] S. Watts,[84] B. M. Waugh,[78] S. Webb,[84] M. S. Weber,[17] S. W. Weber,[174] J. S. Webster,[31] A. R. Weidberg,[120] B. Weinert,[61] J. Weingarten,[54] C. Weiser,[48] H. Weits,[107] P. S. Wells,[30] T. Wenaus,[25] T. Wengler,[30] S. Wenig,[30] N. Wermes,[21] M. Werner,[48] P. Werner,[30] M. Wessels,[58a] J. Wetter,[161] K. Whalen,[116] A. M. Wharton,[72] A. White,[8] M. J. White,[1] R. White,[32b] S. White,[124a,124b] D. Whiteson,[163] F. J. Wickens,[131] W. Wiedenmann,[173] M. Wielers,[131] P. Wienemann,[21] C. Wiglesworth,[36] L. A. M. Wiik-Fuchs,[21] A. Wildauer,[101] H. G. Wilkens,[30] H. H. Williams,[122] S. Williams,[107] C. Willis,[90] S. Willocq,[86] A. Wilson,[89] J. A. Wilson,[18] I. Wingerter-Seez,[5] F. Winklmeier,[116] B. T. Winter,[21] M. Wittgen,[143] J. Wittkowski,[100] S. J. Wollstadt,[83] M. W. Wolter,[39] H. Wolters,[126a,126c] B. K. Wosiek,[39] J. Wotschack,[30] M. J. Woudstra,[84] K. W. Wozniak,[39] M. Wu,[55] M. Wu,[31] S. L. Wu,[173] X. Wu,[49] Y. Wu,[89] T. R. Wyatt,[84] B. M. Wynne,[46] S. Xella,[36] D. Xu,[33a] L. Xu,[25] B. Yabsley,[150] S. Yacoob,[145a] R. Yakabe,[67] M. Yamada,[66] D. Yamaguchi,[157] Y. Yamaguchi,[118] A. Yamamoto,[66] S. Yamamoto,[155] T. Yamanaka,[155] K. Yamauchi,[103] Y. Yamazaki,[67] Z. Yan,[22] H. Yang,[33e] H. Yang,[173] Y. Yang,[151] W-M. Yao,[15] Y. C. Yap,[80] Y. Yasu,[66] E. Yatsenko,[5] K. H. Yau Wong,[21] J. Ye,[40] S. Ye,[25] I. Yeletskikh,[65] A. L. Yen,[57] E. Yildirim,[42] K. Yorita,[171] R. Yoshida,[6] K. Yoshihara,[122] C. Young,[143] C. J. S. Young,[30] S. Youssef,[22] D. R. Yu,[15] J. Yu,[8] J. M. Yu,[89] J. Yu,[114] L. Yuan,[67] S. P. Y. Yuen,[21] A. Yurkewicz,[108] I. Yusuff,[28,ll] B. Zabinski,[39] R. Zaidan,[63] A. M. Zaitsev,[130,cc] J. Zalieckas,[14] A. Zaman,[148] S. Zambito,[57] L. Zanello,[132a,132b] D. Zanzi,[88] C. Zeitnitz,[175] M. Zeman,[128] A. Zemla,[38a] Q. Zeng,[143] K. Zengel,[23] O. Zenin,[130] T. Ženiš,[144a] D. Zerwas,[117] D. Zhang,[89] F. Zhang,[173] G. Zhang,[33b] H. Zhang,[33c] J. Zhang,[6] L. Zhang,[48] R. Zhang,[33b,i] X. Zhang,[33d] Z. Zhang,[117] X. Zhao,[40] Y. Zhao,[33d,117] Z. Zhao,[33b] A. Zhemchugov,[65] J. Zhong,[120] B. Zhou,[89] C. Zhou,[45] L. Zhou,[35] L. Zhou,[40] M. Zhou,[148] N. Zhou,[33f] C. G. Zhu,[33d] H. Zhu,[33a] J. Zhu,[89] Y. Zhu,[33b] X. Zhuang,[33a] K. Zhukov,[96] A. Zibell,[174] D. Zieminska,[61] N. I. Zimine,[65] C. Zimmermann,[83] S. Zimmermann,[48] Z. Zinonos,[54] M. Zinser,[83] M. Ziolkowski,[141] L. Živković,[13] G. Zobernig,[173] A. Zoccoli,[20a,20b] M. zur Nedden,[16] G. Zurzolo,[104a,104b] and L. Zwalinski[30]

(ATLAS Collaboration)

[1]*Department of Physics, University of Adelaide, Adelaide, Australia*
[2]*Physics Department, SUNY Albany, Albany, New York, USA*
[3]*Department of Physics, University of Alberta, Edmonton, Alberta, Canada*
[4a]*Department of Physics, Ankara University, Ankara, Turkey*
[4b]*Istanbul Aydin University, Istanbul, Turkey*
[4c]*Division of Physics, TOBB University of Economics and Technology, Ankara, Turkey*
[5]*LAPP, CNRS/IN2P3 and Université Savoie Mont Blanc, Annecy-le-Vieux, France*
[6]*High Energy Physics Division, Argonne National Laboratory, Argonne, Illinois, USA*

[7]Department of Physics, University of Arizona, Tucson, Arizona, USA
[8]Department of Physics, The University of Texas at Arlington, Arlington, Texas, USA
[9]Physics Department, University of Athens, Athens, Greece
[10]Physics Department, National Technical University of Athens, Zografou, Greece
[11]Institute of Physics, Azerbaijan Academy of Sciences, Baku, Azerbaijan
[12]Institut de Física d'Altes Energies and Departament de Física de la Universitat Autònoma de Barcelona, Barcelona, Spain
[13]Institute of Physics, University of Belgrade, Belgrade, Serbia
[14]Department for Physics and Technology, University of Bergen, Bergen, Norway
[15]Physics Division, Lawrence Berkeley National Laboratory and University of California, Berkeley, California, USA
[16]Department of Physics, Humboldt University, Berlin, Germany
[17]Albert Einstein Center for Fundamental Physics and Laboratory for High Energy Physics, University of Bern, Bern, Switzerland
[18]School of Physics and Astronomy, University of Birmingham, Birmingham, United Kingdom
[19a]Department of Physics, Bogazici University, Istanbul, Turkey
[19b]Department of Physics Engineering, Gaziantep University, Gaziantep, Turkey
[19c]Department of Physics, Dogus University, Istanbul, Turkey
[20a]INFN Sezione di Bologna, Italy
[20b]Dipartimento di Fisica e Astronomia, Università di Bologna, Bologna, Italy
[21]Physikalisches Institut, University of Bonn, Bonn, Germany
[22]Department of Physics, Boston University, Boston, Massachusetts, USA
[23]Department of Physics, Brandeis University, Waltham, Massachusetts, USA
[24a]Universidade Federal do Rio De Janeiro COPPE/EE/IF, Rio de Janeiro, Brazil
[24b]Electrical Circuits Department, Federal University of Juiz de Fora (UFJF), Juiz de Fora, Brazil
[24c]Federal University of Sao Joao del Rei (UFSJ), Sao Joao del Rei, Brazil
[24d]Instituto de Fisica, Universidade de Sao Paulo, Sao Paulo, Brazil
[25]Physics Department, Brookhaven National Laboratory, Upton, New York, USA
[26a]Transilvania University of Brasov, Brasov, Romania
[26b]National Institute of Physics and Nuclear Engineering, Bucharest, Romania
[26c]National Institute for Research and Development of Isotopic and Molecular Technologies, Physics Department, Cluj Napoca, Romania
[26d]University Politehnica Bucharest, Bucharest, Romania
[26e]West University in Timisoara, Timisoara, Romania
[27]Departamento de Física, Universidad de Buenos Aires, Buenos Aires, Argentina
[28]Cavendish Laboratory, University of Cambridge, Cambridge, United Kingdom
[29]Department of Physics, Carleton University, Ottawa, Ontario, Canada
[30]CERN, Geneva, Switzerland
[31]Enrico Fermi Institute, University of Chicago, Chicago, Illinois, USA
[32a]Departamento de Física, Pontificia Universidad Católica de Chile, Santiago, Chile
[32b]Departamento de Física, Universidad Técnica Federico Santa María, Valparaíso, Chile
[33a]Institute of High Energy Physics, Chinese Academy of Sciences, Beijing, China
[33b]Department of Modern Physics, University of Science and Technology of China, Anhui, China
[33c]Department of Physics, Nanjing University, Jiangsu, China
[33d]School of Physics, Shandong University, Shandong, China
[33e]Department of Physics and Astronomy, Shanghai Key Laboratory for Particle Physics and Cosmology, Shanghai Jiao Tong University, Shanghai, China
[33f]Physics Department, Tsinghua University, Beijing 100084, China
[34]Laboratoire de Physique Corpusculaire, Clermont Université and Université Blaise Pascal and CNRS/IN2P3, Clermont-Ferrand, France
[35]Nevis Laboratory, Columbia University, Irvington, New York, USA
[36]Niels Bohr Institute, University of Copenhagen, Kobenhavn, Denmark
[37a]INFN Gruppo Collegato di Cosenza, Laboratori Nazionali di Frascati, Italy
[37b]Dipartimento di Fisica, Università della Calabria, Rende, Italy
[38a]AGH University of Science and Technology, Faculty of Physics and Applied Computer Science, Krakow, Poland
[38b]Marian Smoluchowski Institute of Physics, Jagiellonian University, Krakow, Poland
[39]Institute of Nuclear Physics Polish Academy of Sciences, Krakow, Poland
[40]Physics Department, Southern Methodist University, Dallas, Texas, USA
[41]Physics Department, University of Texas at Dallas, Richardson, Texas, USA

[42]DESY, Hamburg and Zeuthen, Germany
[43]Institut für Experimentelle Physik IV, Technische Universität Dortmund, Dortmund, Germany
[44]Institut für Kern- und Teilchenphysik, Technische Universität Dresden, Dresden, Germany
[45]Department of Physics, Duke University, Durham, North Carolina, USA
[46]SUPA—School of Physics and Astronomy, University of Edinburgh, Edinburgh, United Kingdom
[47]INFN Laboratori Nazionali di Frascati, Frascati, Italy
[48]Fakultät für Mathematik und Physik, Albert-Ludwigs-Universität, Freiburg, Germany
[49]Section de Physique, Université de Genève, Geneva, Switzerland
[50a]INFN Sezione di Genova, Italy
[50b]Dipartimento di Fisica, Università di Genova, Genova, Italy
[51a]E. Andronikashvili Institute of Physics, Iv. Javakhishvili Tbilisi State University, Tbilisi, Georgia
[51b]High Energy Physics Institute, Tbilisi State University, Tbilisi, Georgia
[52]II Physikalisches Institut, Justus-Liebig-Universität Giessen, Giessen, Germany
[53]SUPA—School of Physics and Astronomy, University of Glasgow, Glasgow, United Kingdom
[54]II Physikalisches Institut, Georg-August-Universität, Göttingen, Germany
[55]Laboratoire de Physique Subatomique et de Cosmologie, Université Grenoble-Alpes, CNRS/IN2P3, Grenoble, France
[56]Department of Physics, Hampton University, Hampton, Virginia, USA
[57]Laboratory for Particle Physics and Cosmology, Harvard University, Cambridge, Massachusetts, USA
[58a]Kirchhoff-Institut für Physik, Ruprecht-Karls-Universität Heidelberg, Heidelberg, Germany
[58b]Physikalisches Institut, Ruprecht-Karls-Universität Heidelberg, Heidelberg, Germany
[58c]ZITI Institut für technische Informatik, Ruprecht-Karls-Universität Heidelberg, Mannheim, Germany
[59]Faculty of Applied Information Science, Hiroshima Institute of Technology, Hiroshima, Japan
[60a]Department of Physics, The Chinese University of Hong Kong, Shatin, N.T., Hong Kong, China
[60b]Department of Physics, The University of Hong Kong, Hong Kong, China
[60c]Department of Physics, The Hong Kong University of Science and Technology, Clear Water Bay, Kowloon, Hong Kong, China
[61]Department of Physics, Indiana University, Bloomington, Indiana, USA
[62]Institut für Astro- und Teilchenphysik, Leopold-Franzens-Universität, Innsbruck, Austria
[63]University of Iowa, Iowa City, Iowa, USA
[64]Department of Physics and Astronomy, Iowa State University, Ames, Iowa, USA
[65]Joint Institute for Nuclear Research, JINR Dubna, Dubna, Russia
[66]KEK, High Energy Accelerator Research Organization, Tsukuba, Japan
[67]Graduate School of Science, Kobe University, Kobe, Japan
[68]Faculty of Science, Kyoto University, Kyoto, Japan
[69]Kyoto University of Education, Kyoto, Japan
[70]Department of Physics, Kyushu University, Fukuoka, Japan
[71]Instituto de Física La Plata, Universidad Nacional de La Plata and CONICET, La Plata, Argentina
[72]Physics Department, Lancaster University, Lancaster, United Kingdom
[73a]INFN Sezione di Lecce, Italy
[73b]Dipartimento di Matematica e Fisica, Università del Salento, Lecce, Italy
[74]Oliver Lodge Laboratory, University of Liverpool, Liverpool, United Kingdom
[75]Department of Physics, Jožef Stefan Institute and University of Ljubljana, Ljubljana, Slovenia
[76]School of Physics and Astronomy, Queen Mary University of London, London, United Kingdom
[77]Department of Physics, Royal Holloway University of London, Surrey, United Kingdom
[78]Department of Physics and Astronomy, University College London, London, United Kingdom
[79]Louisiana Tech University, Ruston, Louisiana, USA
[80]Laboratoire de Physique Nucléaire et de Hautes Energies, UPMC and Université Paris-Diderot and CNRS/IN2P3, Paris, France
[81]Fysiska Institutionen, Lunds Universitet, Lund, Sweden
[82]Departamento de Física Teorica C-15, Universidad Autonoma de Madrid, Madrid, Spain
[83]Institut für Physik, Universität Mainz, Mainz, Germany
[84]School of Physics and Astronomy, University of Manchester, Manchester, United Kingdom
[85]CPPM, Aix-Marseille Université and CNRS/IN2P3, Marseille, France
[86]Department of Physics, University of Massachusetts, Amherst, Massachusetts, USA
[87]Department of Physics, McGill University, Montreal, Quebec, Canada
[88]School of Physics, University of Melbourne, Victoria, Australia
[89]Department of Physics, The University of Michigan, Ann Arbor, Michigan, USA
[90]Department of Physics and Astronomy, Michigan State University, East Lansing, Michigan, USA
[91a]INFN Sezione di Milano, Italy

[91b]Dipartimento di Fisica, Università di Milano, Milano, Italy
[92]B.I. Stepanov Institute of Physics, National Academy of Sciences of Belarus, Minsk, Republic of Belarus
[93]National Scientific and Educational Centre for Particle and High Energy Physics, Minsk, Republic of Belarus
[94]Department of Physics, Massachusetts Institute of Technology, Cambridge, Massachusetts, USA
[95]Group of Particle Physics, University of Montreal, Montreal, Quebec, Canada
[96]P.N. Lebedev Institute of Physics, Academy of Sciences, Moscow, Russia
[97]Institute for Theoretical and Experimental Physics (ITEP), Moscow, Russia
[98]National Research Nuclear University MEPhI, Moscow, Russia
[99]D.V. Skobeltsyn Institute of Nuclear Physics, M.V. Lomonosov Moscow State University, Moscow, Russia
[100]Fakultät für Physik, Ludwig-Maximilians-Universität München, München, Germany
[101]Max-Planck-Institut für Physik (Werner-Heisenberg-Institut), München, Germany
[102]Nagasaki Institute of Applied Science, Nagasaki, Japan
[103]Graduate School of Science and Kobayashi-Maskawa Institute, Nagoya University, Nagoya, Japan
[104a]INFN Sezione di Napoli, Italy
[104b]Dipartimento di Fisica, Università di Napoli, Napoli, Italy
[105]Department of Physics and Astronomy, University of New Mexico, Albuquerque, New Mexico, USA
[106]Institute for Mathematics, Astrophysics and Particle Physics, Radboud University Nijmegen/Nikhef, Nijmegen, Netherlands
[107]Nikhef National Institute for Subatomic Physics and University of Amsterdam, Amsterdam, Netherlands
[108]Department of Physics, Northern Illinois University, DeKalb, Illinois, USA
[109]Budker Institute of Nuclear Physics, SB RAS, Novosibirsk, Russia
[110]Department of Physics, New York University, New York, New York, USA
[111]Ohio State University, Columbus, Ohio, USA
[112]Faculty of Science, Okayama University, Okayama, Japan
[113]Homer L. Dodge Department of Physics and Astronomy, University of Oklahoma, Norman, Oklahoma, USA
[114]Department of Physics, Oklahoma State University, Stillwater, Oklahoma, USA
[115]Palacký University, RCPTM, Olomouc, Czech Republic
[116]Center for High Energy Physics, University of Oregon, Eugene, Oregon, USA
[117]LAL, Université Paris-Sud and CNRS/IN2P3, Orsay, France
[118]Graduate School of Science, Osaka University, Osaka, Japan
[119]Department of Physics, University of Oslo, Oslo, Norway
[120]Department of Physics, Oxford University, Oxford, United Kingdom
[121a]INFN Sezione di Pavia, Italy
[121b]Dipartimento di Fisica, Università di Pavia, Pavia, Italy
[122]Department of Physics, University of Pennsylvania, Philadelphia, Pennsylvania, USA
[123]National Research Centre "Kurchatov Institute" B.P.Konstantinov Petersburg Nuclear Physics Institute, St. Petersburg, Russia
[124a]INFN Sezione di Pisa, Italy
[124b]Dipartimento di Fisica E. Fermi, Università di Pisa, Pisa, Italy
[125]Department of Physics and Astronomy, University of Pittsburgh, Pittsburgh, Pennsylvania, USA
[126a]Laboratório de Instrumentação e Física Experimental de Partículas—LIP, Lisboa, Portugal
[126b]Faculdade de Ciências, Universidade de Lisboa, Lisboa, Portugal
[126c]Department of Physics, University of Coimbra, Coimbra, Portugal
[126d]Centro de Física Nuclear da Universidade de Lisboa, Lisboa, Portugal
[126e]Departamento de Física, Universidade do Minho, Braga, Portugal
[126f]Departamento de Física Teorica y del Cosmos and CAFPE, Universidad de Granada, Granada, Spain
[126g]Departamento de Física and CEFITEC of Faculdade de Ciencias e Tecnologia, Universidade Nova de Lisboa, Caparica, Portugal
[127]Institute of Physics, Academy of Sciences of the Czech Republic, Praha, Czech Republic
[128]Czech Technical University in Prague, Praha, Czech Republic
[129]Faculty of Mathematics and Physics, Charles University in Prague, Praha, Czech Republic
[130]State Research Center Institute for High Energy Physics (Protvino), NRC KI, Russia
[131]Particle Physics Department, Rutherford Appleton Laboratory, Didcot, United Kingdom
[132a]INFN Sezione di Roma, Italy
[132b]Dipartimento di Fisica, Sapienza Università di Roma, Roma, Italy
[133a]INFN Sezione di Roma Tor Vergata, Italy
[133b]Dipartimento di Fisica, Università di Roma Tor Vergata, Roma, Italy
[134a]INFN Sezione di Roma Tre, Italy

[134b]*Dipartimento di Matematica e Fisica, Università Roma Tre, Roma, Italy*
[135a]*Faculté des Sciences Ain Chock, Réseau Universitaire de Physique des Hautes Energies—Université Hassan II, Casablanca, Morocco*
[135b]*Centre National de l'Energie des Sciences Techniques Nucleaires, Rabat, Morocco*
[135c]*Faculté des Sciences Semlalia, Université Cadi Ayyad, LPHEA-Marrakech, Morocco*
[135d]*Faculté des Sciences, Université Mohamed Premier and LPTPM, Oujda, Morocco*
[135e]*Faculté des sciences, Université Mohammed V, Rabat, Morocco*
[136]*DSM/IRFU (Institut de Recherches sur les Lois Fondamentales de l'Univers), CEA Saclay (Commissariat à l'Energie Atomique et aux Energies Alternatives), Gif-sur-Yvette, France*
[137]*Santa Cruz Institute for Particle Physics, University of California Santa Cruz, Santa Cruz, California, USA*
[138]*Department of Physics, University of Washington, Seattle, Washington, USA*
[139]*Department of Physics and Astronomy, University of Sheffield, Sheffield, United Kingdom*
[140]*Department of Physics, Shinshu University, Nagano, Japan*
[141]*Fachbereich Physik, Universität Siegen, Siegen, Germany*
[142]*Department of Physics, Simon Fraser University, Burnaby, British Columbia, Canada*
[143]*SLAC National Accelerator Laboratory, Stanford, California, USA*
[144a]*Faculty of Mathematics, Physics & Informatics, Comenius University, Bratislava, Slovak Republic*
[144b]*Department of Subnuclear Physics, Institute of Experimental Physics of the Slovak Academy of Sciences, Kosice, Slovak Republic*
[145a]*Department of Physics, University of Cape Town, Cape Town, South Africa*
[145b]*Department of Physics, University of Johannesburg, Johannesburg, South Africa*
[145c]*School of Physics, University of the Witwatersrand, Johannesburg, South Africa*
[146a]*Department of Physics, Stockholm University, Sweden*
[146b]*The Oskar Klein Centre, Stockholm, Sweden*
[147]*Physics Department, Royal Institute of Technology, Stockholm, Sweden*
[148]*Departments of Physics & Astronomy and Chemistry, Stony Brook University, Stony Brook New York, USA*
[149]*Department of Physics and Astronomy, University of Sussex, Brighton, United Kingdom*
[150]*School of Physics, University of Sydney, Sydney, Australia*
[151]*Institute of Physics, Academia Sinica, Taipei, Taiwan*
[152]*Department of Physics, Technion: Israel Institute of Technology, Haifa, Israel*
[153]*Raymond and Beverly Sackler School of Physics and Astronomy, Tel Aviv University, Tel Aviv, Israel*
[154]*Department of Physics, Aristotle University of Thessaloniki, Thessaloniki, Greece*
[155]*International Center for Elementary Particle Physics and Department of Physics, The University of Tokyo, Tokyo, Japan*
[156]*Graduate School of Science and Technology, Tokyo Metropolitan University, Tokyo, Japan*
[157]*Department of Physics, Tokyo Institute of Technology, Tokyo, Japan*
[158]*Department of Physics, University of Toronto, Toronto, Ontario, Canada*
[159a]*TRIUMF, Vancouver, British Columbia, Canada*
[159b]*Department of Physics and Astronomy, York University, Toronto Ontario, Canada*
[160]*Faculty of Pure and Applied Sciences, and Center for Integrated Research in Fundamental Science and Engineering, University of Tsukuba, Tsukuba, Japan*
[161]*Department of Physics and Astronomy, Tufts University, Medford, Massachusetts, USA*
[162]*Centro de Investigaciones, Universidad Antonio Narino, Bogota, Colombia*
[163]*Department of Physics and Astronomy, University of California Irvine, Irvine, California, USA*
[164a]*INFN Gruppo Collegato di Udine, Sezione di Trieste, Udine, Italy*
[164b]*ICTP, Trieste, Italy*
[164c]*Dipartimento di Chimica, Fisica e Ambiente, Università di Udine, Udine, Italy*
[165]*Department of Physics, University of Illinois, Urbana, Illinois, USA*
[166]*Department of Physics and Astronomy, University of Uppsala, Uppsala, Sweden*
[167]*Instituto de Física Corpuscular (IFIC) and Departamento de Física Atómica, Molecular y Nuclear and Departamento de Ingeniería Electrónica and Instituto de Microelectrónica de Barcelona (IMB-CNM), University of Valencia and CSIC, Valencia, Spain*
[168]*Department of Physics, University of British Columbia, Vancouver, British Columbia, Canada*
[169]*Department of Physics and Astronomy, University of Victoria, Victoria, British Columbia, Canada*
[170]*Department of Physics, University of Warwick, Coventry, United Kingdom*
[171]*Waseda University, Tokyo, Japan*
[172]*Department of Particle Physics, The Weizmann Institute of Science, Rehovot, Israel*
[173]*Department of Physics, University of Wisconsin, Madison, Wisconsin, USA*

[174]Fakultät für Physik und Astronomie, Julius-Maximilians-Universität, Würzburg, Germany
[175]Fachbereich C Physik, Bergische Universität Wuppertal, Wuppertal, Germany
[176]Department of Physics, Yale University, New Haven, Connecticut, USA
[177]Yerevan Physics Institute, Yerevan, Armenia
[178]Centre de Calcul de l'Institut National de Physique Nucléaire et de Physique des Particules (IN2P3), Villeurbanne, France

[†]Deceased.
[a]Also at Department of Physics, King's College London, London, United Kingdom.
[b]Also at Institute of Physics, Azerbaijan Academy of Sciences, Baku, Azerbaijan.
[c]Also at Novosibirsk State University, Novosibirsk, Russia.
[d]Also at TRIUMF, Vancouver BC, Canada.
[e]Also at Department of Physics, California State University, Fresno, CA, USA.
[f]Also at Department of Physics, University of Fribourg, Fribourg, Switzerland.
[g]Also at Departamento de Física e Astronomia, Faculdade de Ciencias, Universidade do Porto, Portugal.
[h]Also at Tomsk State University, Tomsk, Russia.
[i]Also at CPPM, Aix-Marseille Université and CNRS/IN2P3, Marseille, France.
[j]Also at Universita di Napoli Parthenope, Napoli, Italy.
[k]Also at Institute of Particle Physics (IPP), Canada.
[l]Also at Particle Physics Department, Rutherford Appleton Laboratory, Didcot, United Kingdom.
[m]Also at Department of Physics, St. Petersburg State Polytechnical University, St. Petersburg, Russia.
[n]Also at Louisiana Tech University, Ruston, LA, USA.
[o]Also at Institucio Catalana de Recerca i Estudis Avancats, ICREA, Barcelona, Spain.
[p]Also at Department of Physics, The University of Michigan, Ann Arbor, MI, USA.
[q]Also at Graduate School of Science, Osaka University, Osaka, Japan.
[r]Also at Department of Physics, National Tsing Hua University, Taiwan.
[s]Also at Department of Physics, The University of Texas at Austin, Austin, TX, USA.
[t]Also at Institute of Theoretical Physics, Ilia State University, Tbilisi, Georgia.
[u]Also at CERN, Geneva, Switzerland.
[v]Also at Georgian Technical University (GTU),Tbilisi, Georgia.
[w]Also at Manhattan College, New York, NY, USA.
[x]Also at Hellenic Open University, Patras, Greece.
[y]Also at Institute of Physics, Academia Sinica, Taipei, Taiwan.
[z]Also at LAL, Université Paris-Sud and CNRS/IN2P3, Orsay, France.
[aa]Also at Academia Sinica Grid Computing, Institute of Physics, Academia Sinica, Taipei, Taiwan.
[bb]Also at School of Physics, Shandong University, Shandong, China.
[cc]Also at Moscow Institute of Physics and Technology State University, Dolgoprudny, Russia.
[dd]Also at Section de Physique, Université de Genève, Geneva, Switzerland.
[ee]Also at International School for Advanced Studies (SISSA), Trieste, Italy.
[ff]Also at Department of Physics and Astronomy, University of South Carolina, Columbia, SC, USA.
[gg]Also at School of Physics and Engineering, Sun Yat-sen University, Guangzhou, China.
[hh]Also at Faculty of Physics, M.V.Lomonosov Moscow State University, Moscow, Russia.
[ii]Also at National Research Nuclear University MEPhI, Moscow, Russia.
[jj]Also at Department of Physics, Stanford University, Stanford, CA, USA.
[kk]Also at Institute for Particle and Nuclear Physics, Wigner Research Centre for Physics, Budapest, Hungary.
[ll]Also at University of Malaya, Department of Physics, Kuala Lumpur, Malaysia.

Search for massive, long-lived particles using multitrack displaced vertices or displaced lepton pairs in *pp* collisions at $\sqrt{s} = 8$ TeV with the ATLAS detector

G. Aad *et al.*[*]
(ATLAS Collaboration)

(Received 21 April 2015; revised manuscript received 19 August 2015; published 13 October 2015)

Many extensions of the Standard Model posit the existence of heavy particles with long lifetimes. This article presents the results of a search for events containing at least one long-lived particle that decays at a significant distance from its production point into two leptons or into five or more charged particles. This analysis uses a data sample of proton-proton collisions at $\sqrt{s} = 8$ TeV corresponding to an integrated luminosity of 20.3 fb^{-1} collected in 2012 by the ATLAS detector operating at the Large Hadron Collider. No events are observed in any of the signal regions, and limits are set on model parameters within supersymmetric scenarios involving R-parity violation, split supersymmetry, and gauge mediation. In some of the search channels, the trigger and search strategy are based only on the decay products of individual long-lived particles, irrespective of the rest of the event. In these cases, the provided limits can easily be reinterpreted in different scenarios.

DOI: 10.1103/PhysRevD.92.072004 PACS numbers: 12.60.Jv, 13.85.Rm, 14.80.Ly, 14.80.Pq

I. INTRODUCTION

Several extensions to the Standard Model (SM) predict the production at the Large Hadron Collider (LHC) of heavy particles with lifetimes of order picoseconds to nanoseconds (e.g., see Ref. [1] and references therein). At the LHC experiments, the decay of a long-lived particle (LLP) with lifetime in this range could be observed as a displaced vertex (DV), with daughter particles produced at a significant distance from the interaction point (IP) of the incoming proton beams. Particle decays may be suppressed by small couplings or high mass scales, thus resulting in long lifetimes. An example of a small-coupling scenario is supersymmetry with R-parity violation (RPV) [2,3]. The present (largely indirect) constraints on RPV couplings allow the decay of the lightest supersymmetric particle (LSP) as it traverses a particle detector at the LHC. In general gauge-mediated supersymmetry breaking (GGM) scenarios [4], the next-to-lightest supersymmetric particle (NLSP) decays into an SM particle and the LSP, which is a very light gravitino. The NLSP width is suppressed by the large supersymmetry-breaking scale, and may be such that its decay leads to the formation of a DV. Within split supersymmetry [5,6], gluino ($\tilde{g}$) decay is suppressed by the high mass of the squarks. Long-lived gluinos then hadronize into heavy "R-hadrons" that may decay at a detectable distance from their production point. Additional scenarios with LLPs include hidden-valley [7], dark-sector gauge bosons [8], and stealth supersymmetry [9]. Some of the models are disfavored [10] by the recent observation of a Higgs boson at $m_H \approx 125$ GeV [11,12].

This article presents the results of a search for DVs that arise from decays of long-lived, heavy particles, at radial distances of millimeters to tens of centimeters from the proton-proton IP in the ATLAS detector at the LHC. Two types of signatures are considered. In the dilepton signature, the vertex is formed from at least two lepton candidates (with "lepton" referring to an electron or a muon), with opposite electric charges. In the multitrack signature, the DV must contain at least five charged-particle tracks. This signature is divided into four different final states, in which the DV must be accompanied by a high-transverse-momentum (high-p_{T}) muon or electron candidate that originates from the DV, jets, or missing transverse momentum ($E_{\mathrm{T}}^{\mathrm{miss}}$). These signatures are labeled DV + muon, DV + electron, DV + jets, and DV + $E_{\mathrm{T}}^{\mathrm{miss}}$, respectively. In all signatures, at least one DV is required per event. In all cases, the expected background is much less than one event.

The multitrack results improve on the previous ATLAS searches for this signature [13,14] in several ways. The LHC center-of-mass energy is increased to 8 TeV, and the integrated luminosity is more than 4 times larger. While the previous search required only a high-p_{T} muon trigger, the current search also uses high-p_{T} electron, jets, or $E_{\mathrm{T}}^{\mathrm{miss}}$ triggers. Furthermore, the detector volume used for the search has been enlarged by more than a factor of 3.

This is the first search for high-mass, displaced lepton pairs at ATLAS. A previous ATLAS search [15] considered pairs of muons that were highly collimated due to the low

[*]Full author list given at the end of the article.

Published by the American Physical Society under the terms of the Creative Commons Attribution 3.0 License. Further distribution of this work must maintain attribution to the author(s) and the published article's title, journal citation, and DOI.

 © 2015 CERN, for the ATLAS Collaboration

mass of the decaying particle. ATLAS has also searched for long-lived particles that decay inside the hadronic calorimeter [16,17], the inner detector, or the muon spectrometer [18], or that traverse the entire detector [19].

Related searches have been performed at other experiments. The CMS Collaboration has searched for decays of a long-lived particle into a final state containing two electrons, two muons [20,21], an electron and a muon [22], or a quark-antiquark pair [23]. The LHCb Collaboration has searched for long-lived particles that decay into jet pairs [24]. The Belle Collaboration has searched for long-lived heavy neutrinos [25], and the *BABAR* Collaboration has searched for displaced vertices formed of two charged particles [26]. The D0 Collaboration has searched for displaced lepton pairs [27] and $b\bar{b}$ pairs [28], and the CDF Collaboration has searched for long-lived particles decaying to Z bosons [29]. LLPs have also been searched for by the ALEPH Collaboration at LEP [30].

This article is organized as follows. First, the ATLAS detector and event samples used are described in Secs. II and III, respectively. The event reconstruction and vertex selection criteria are given in Sec. IV, while the signal efficiency is detailed in Sec. V. The background estimation is given in Sec. VI, with the systematic uncertainties on background and signal in Sec. VII. Finally, the search results are given in Sec. VIII, along with their interpretations in various supersymmetric scenarios.

II. THE ATLAS DETECTOR

The ATLAS experiment[1] [31] is a multipurpose detector at the LHC. The detector consists of several layers of subdetectors. From the IP outwards, there is an inner tracking detector (ID), electromagnetic and hadronic calorimeters, and a muon spectrometer (MS).

The ID is immersed in a 2 T axial magnetic field and extends from a radius of about 45 mm to 1100 mm and to $|z|$ of about 3100 mm. It provides tracking and vertex information for charged particles within the pseudorapidity region $|\eta| < 2.5$. At small radii, silicon pixel layers and stereo pairs of silicon microstrip detectors provide high-resolution position measurements. The pixel system consists of three barrel layers, and three forward disks on either side of the IP. The barrel pixel layers, which are positioned at radii of 50.5 mm, 88.5 mm, and 122.5 mm, are of particular relevance to this work. The silicon microstrip tracker (SCT) comprises four double layers in the barrel and nine forward disks on either side. The radial position of the innermost (outermost) SCT barrel layer is 30.3 cm (52.0 cm). A further tracking system, a transition-radiation tracker (TRT), is positioned at larger radii, with coverage up to $|\eta| = 2.0$. This device has two hit thresholds, the higher of which is used to assist in the identification of electrons through the production of transition radiation within the TRT.

The calorimeter provides coverage over the range $|\eta| < 4.9$. It consists of a lead/liquid-argon electromagnetic calorimeter, a hadronic calorimeter comprising a steel and scintillator-tile system in the barrel region, and a liquid-argon system with copper and tungsten absorbers in the end caps.

The MS provides muon identification and contributes to the muon momentum measurement. This device has a coverage in pseudorapidity of $|\eta| < 2.7$ and is a three-layer system of gas-filled tracking chambers. The pseudorapidity region $|\eta| < 2.4$ is additionally covered by separate trigger chambers, used by the hardware trigger for the first level of triggering (level-1). The MS is immersed in a magnetic field that is produced by a set of toroid magnets, one for the barrel and one each for the two end caps.

Online event selection is performed with a three-level trigger system. It is composed of a hardware-based level-1 trigger that uses information from the MS trigger chambers and the calorimeters, followed by two software-based trigger levels.

III. DATA AND SIMULATED EVENTS

The data used in this analysis were collected in 2012 at a pp center-of-mass energy of $\sqrt{s} = 8$ TeV. After the application of detector and data-quality requirements, the integrated luminosity of the data sample is 20.3 fb^{-1}. The uncertainty on the integrated luminosity is $\pm 2.8\%$. It is derived following the same methodology as that detailed in Ref. [32]. With respect to the origin of the ATLAS coordinate system at the center of the detector, the mean position of the pp collision, averaged throughout the collected data sample, is $\langle x \rangle = -0.3$ mm, $\langle y \rangle = 0.7$ mm, $\langle z \rangle = -7.7$ mm. The root-mean-square spread of the z distribution of the collisions is $\sigma_z = 47.7$ mm, and the spreads in the x and y directions are less than 0.1 mm.

Samples of simulated Monte Carlo (MC) events are used to study the reconstruction and trigger efficiency for signal events within RPV, split supersymmetry, and GGM scenarios. In each simulated event, two gluinos or two squarks are created in the pp collision. Both of these primary particles undergo decay chains described by the same set of effective operators. In the simulated GGM and RPV scenarios, the LLP is the lightest neutralino $\tilde{\chi}_1^0$. In the split-supersymmetry scenario, the LLP is the gluino. Diagrams representing the simulated processes are shown in Fig. 1.

[1] ATLAS uses a right-handed coordinate system with its origin at the nominal IP in the center of the detector and the z axis along the beam pipe. The x axis points from the IP to the center of the LHC ring, and the y axis points upward. Cylindrical coordinates (r, ϕ) are used in the transverse plane, ϕ being the azimuthal angle around the beam pipe. The pseudorapidity is defined in terms of the polar angle θ as $\eta = -\ln\tan(\theta/2)$.

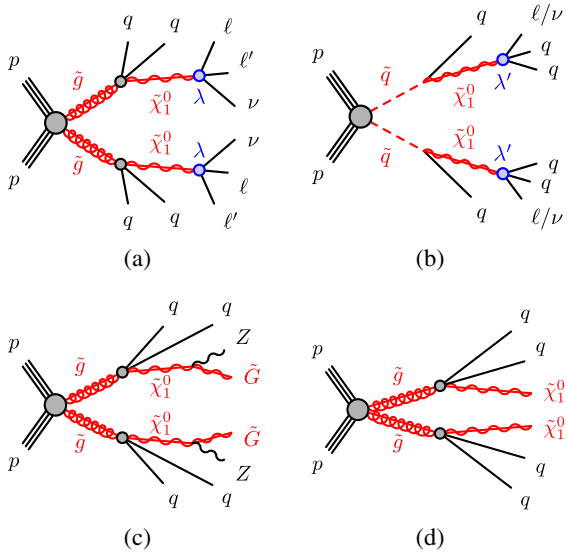

FIG. 1 (color online). Diagrams representing some of the processes under study, corresponding to the simulated event samples. In RPV scenarios, the long-lived neutralino may decay via the (a) λ_{ijk} or (b) λ'_{ijk} couplings. (c) Long-lived neutralino decay in a GGM scenario. (d) Long-lived R-hadron decay in a split-supersymmetry scenario. The quarks and leptons shown may have different flavors. Filled circles indicate effective interactions.

All samples are generated with the AUET2B ATLAS underlying-event tune [33] and the CTEQ6L1 parton distribution function (PDF) set [34]. Events are generated consistently with the position of the pp luminous region and weighted so as to yield the correct z distribution of the collisions. Each generated event is processed with the GEANT4-based [35] ATLAS detector simulation [36] and treated in the same way as the collision data. The samples include a realistic modeling of the effects of multiple pp collisions per bunch crossing observed in the data, obtained by overlaying additional simulated pp events generated using PYTHIA8 [37], on top of the hard scattering events, and reweighting events such that the distribution of the number of interactions per bunch crossing matches that in the data.

In what follows, the notation $P \to A[L \to F]$ denotes an MC sample in which a primary particle P produced in the pp collision decays into a long-lived particle L and additional particles denoted A. The decay of the LLP into final state F is enclosed in square brackets. Samples where the primary particle is long-lived are denoted with $[L \to F]$. In both cases, masses may be indicated with parentheses, as in $[L(100\ \mathrm{GeV}) \to F]$. The symbol q indicates a u- or d-quark unless otherwise specified, and ℓ indicates an electron or a muon. Charge conjugation of fermions is to be understood where appropriate.

RPV samples of the type $\tilde{g} \to qq[\tilde{\chi}_1^0 \to \ell\ell'\nu]$ are produced with HERWIG++ 2.6.3 [38]. Decays of the neutralino into a neutrino and light leptons, which may be e^+e^-, $\mu^+\mu^-$, or $e^\pm\mu^\mp$, take place due to the nonzero values of the RPV couplings λ_{121} and λ_{122} [2].

RPV samples of $\tilde{q} \to q[\tilde{\chi}_1^0 \to \ell qq/\nu qq]$ are generated with PYTHIA6.426.2 [39]. The $\tilde{\chi}_1^0$ decay into two light quarks and an electron, muon, or neutrino is governed by the nonzero RPV coupling λ'_{i11}. Samples containing heavy-flavor quarks, $\tilde{q} \to q[\tilde{\chi}_1^0 \to \ell qb]$ (produced with $\lambda'_{i13} \neq 0$) and $\tilde{q} \to q[\tilde{\chi}_1^0 \to \ell cb]$ (corresponding to $\lambda'_{i23} \neq 0$) are also generated, in order to study the impact of long-lived charm and bottom hadrons on the efficiency of DV reconstruction. A $\tilde{g} \to qq[\tilde{\chi}_1^0 \to \ell qq]$ sample is used to quantify the effect of prompt NLSP decays on the reconstruction efficiency, by comparing with the corresponding model with squark production.

PYTHIA6.426.2 is used to produce GGM samples denoted $\tilde{g} \to qq[\tilde{\chi}_1^0 \to \tilde{G}Z]$, in which the NLSP $\tilde{\chi}_1^0$ is a Higgsino-like neutralino. Both the leptonic and hadronic decays of the Z boson are considered.

Within a split-supersymmetry scenario, PYTHIA6.427 is used to simulate production and hadronization of a primary, long-lived gluino. GEANT4 simulates the propagation of the R-hadron through the detector [40], and PYTHIA decays the R-hadron into a stable neutralino plus two quarks (u, d, s, c, or b), a gluon, or two top quarks. The resulting samples are denoted $[\tilde{g} \to qq\tilde{\chi}_1^0]$, $[\tilde{g} \to g\tilde{\chi}_1^0]$, or $[\tilde{g} \to tt\tilde{\chi}_1^0]$, respectively.

Signal cross sections are calculated to next-to-leading order in the strong coupling constant, adding the resummation of soft gluon emission at next-to-leading-logarithmic accuracy (NLO + NLL) [41–45]. The nominal cross section and its uncertainty are taken from an envelope of cross-section predictions using different PDF sets and factorization and renormalization scales, as described in Ref. [46].

In addition to these signal samples, MC samples of QCD dijet events, Drell-Yan events, and cosmic-ray muons are used for estimating some systematic uncertainties and some of the smaller background rates, as well as for validation of aspects of the background-estimation methods.

IV. EVENT RECONSTRUCTION AND SELECTION

The event-reconstruction and selection procedures are designed, based on MC and experience from previous analyses [13,14], to strongly suppress background and accommodate robust background-estimation methods (described in Sec. VI), while efficiently accepting signal events over a broad range of LLP masses, lifetimes, and velocities.

The initial event selection is performed with a combination of triggers that require the presence of lepton candidates, jets, or $E_{\mathrm{T}}^{\mathrm{miss}}$. This selection is described in Sec. IV A.

Off-line selection criteria for leptons, jets, and $E_{\mathrm{T}}^{\mathrm{miss}}$ (see Sec. IV B) are used to further filter events for off-line processing, as described in Sec. IV C.

Events satisfying the filter requirements undergo a CPU-intensive process termed "retracking," aimed at efficient reconstruction of tracks with large impact parameter (d_0) with respect to the transverse position of any primary vertex (PV) of particles formed from the pp collision. Retracking is described in Sec. IV D.

At the final event-selection stage, the presence of a pp collision is ensured by first requiring the event to have a PV formed from at least five tracks and situated in the longitudinal range $|z| < 200$ mm, consistent with the IP.

The final selection is based on the reconstruction of a multitrack DV or dilepton DV, described in Secs. IV E and IV F, respectively.

A. Trigger requirements

Events must satisfy trigger requirements based on muon, electron, jets, or $E_{\mathrm{T}}^{\mathrm{miss}}$ criteria.

Where muon triggers are used, a muon candidate is required by the trigger algorithm to be identified in the MS with transverse momentum $p_{\mathrm{T}} > 50$ GeV. Its pseudorapidity must be in the MS-barrel region $|\eta| < 1.07$, to reduce the trigger rate from fake muons due to beam background in the end cap region.

Photon triggers are used for channels requiring electron candidates, since the ID track of a high-d_0 electron may not be reconstructed. These require only a high-energy deposit in the electromagnetic calorimeter and have no veto or selection based on ID tracks. Photon triggers provide significantly less background rejection than muon triggers. Therefore, the trigger used for final states involving electrons requires either a single photon candidate with $p_{\mathrm{T}} > 120$ GeV or two photon candidates with $p_{\mathrm{T}} > 40$ GeV each.

The trigger requirement for the $\mathrm{DV} + E_{\mathrm{T}}^{\mathrm{miss}}$ search is $E_{\mathrm{T}}^{\mathrm{miss}} > 80$ GeV. The DV + jets trigger requires four jets with $p_{\mathrm{T}} > 80$ GeV, five jets with $p_{\mathrm{T}} > 55$ GeV, or six jets with $p_{\mathrm{T}} > 45$ GeV.

B. Off-line object definition

The reconstruction and selection criteria for $E_{\mathrm{T}}^{\mathrm{miss}}$, muon, electron, and jet candidates are described in what follows. These object definitions are used by the off-line filter (Sec. IV C) and the final analysis (Secs. IV E and IV F).

1. Muon selection

Muon candidates are required to be reconstructed in both the MS and the ID. The ID track associated with the muon candidate is required to have at least four SCT hits, but the number of required hits is reduced if the track crosses nonoperational sensors. Furthermore, the track must satisfy an $|\eta|$-dependent requirement on the number of TRT hits. No pixel hit requirement is applied to the muon-candidate track, which is different from the standard ATLAS muon-reconstruction algorithm [47].

2. Photon and electron selection

Photon and electron candidates are identified with criteria based on the fraction of the candidate energy deposited in the hadronic calorimeter and on the shape of the electromagnetic shower. In addition, electron candidates must be in the pseudorapidity region $|\eta| < 2.47$ and must satisfy requirements on the number of TRT hits associated with the ID track, the fraction of high-threshold TRT hits, and the pseudorapidity difference between the electron-candidate track and the associated calorimeter cluster. In contrast to the standard ATLAS electron-selection requirements [48], no requirement on the number of silicon hits is applied.

3. Jet and $E_{\mathrm{T}}^{\mathrm{miss}}$ selection

Jet candidates are reconstructed using the anti-k_t jet clustering algorithm [49,50] with a radius parameter $R = 0.6$. The inputs to this algorithm are the energies of clusters [51,52] of calorimeter cells seeded by those with energy significantly above the measured noise. Jet momenta are constructed by performing a four-vector sum over these cell clusters, treating each cell as a four-momentum with zero mass. Jets are initially calibrated to the electromagnetic energy scale, which correctly measures the energy deposited in the calorimeter by electromagnetic showers [51]. Further jet-energy scale corrections are derived from MC simulation and data, and used to calibrate the energies of jets to the scale of their constituent particles [51]. Jets are required to satisfy $|\eta| < 4.5$ after all corrections are applied.

A special category of jets is termed "trackless" jets. These are reconstructed as above, except that the anti-k_t radius parameter is $R = 0.4$, the jet pseudorapidity is in the range $|\eta| < 2.5$, and the scalar sum of the transverse momenta of the tracks in the jet is required to satisfy $\sum_{\mathrm{tr}} p_{\mathrm{T}} < 5$ GeV. Trackless jets may arise from decays of LLPs that take place far from the PV, where track-reconstruction efficiency is low.

The measurement of the missing transverse momentum $E_{\mathrm{T}}^{\mathrm{miss}}$ is based on the calibrated transverse momenta of all jet and lepton candidates, as well as all calorimeter energy clusters not associated with such objects [53,54].

C. Off-line–filter requirements

Events are selected for retracking and subsequent off-line analysis based on off-line filters that require one of the following:

(i) A muon candidate with $p_{\mathrm{T}} > 50$ GeV, an electron candidate with $p_{\mathrm{T}} > 110$ GeV, or a photon candidate with $p_{\mathrm{T}} > 130$ GeV. Electron candidates, and muon candidates that are associated with an ID track at this stage, are required to have $d_0 > 1.5$ mm. The sample selected by this criterion contains 8.5×10^6 events.

(ii) A pair of candidate electrons, photons, or an electron-photon pair, with p_T thresholds between 38 and 48 GeV per object, and electron impact parameter satisfying $d_0 > 2.0$ mm or $d_0 > 2.5$ mm depending on the channel. This criterion selects 2.4×10^6 events.

(iii) Either two 50 GeV trackless jets and $E_T^{miss} > 100$ GeV (selecting 1.9×10^4 events) or one 45 GeV trackless jet and between four and six jets passing the same p_T thresholds as those applied in the trigger, listed in Sec. IV A (selecting 4.6×10^5 events).

D. Retracking

In standard ATLAS tracking [31], several algorithms are used to reconstruct charged-particle tracks. In the silicon-seeded approach, combinations of hits in the pixel and SCT detectors are used to form initial track candidates (seeds) that are then extended into the TRT. Another algorithm starts from track segments formed of TRT hits, and extrapolates back into the SCT, adding any silicon hits that are compatible with the reconstructed trajectory. Both of these methods place constraints on the transverse and longitudinal impact parameters of track candidates that result in a low efficiency for tracks originating from a DV, many of which have large d_0.

To recover some of these lost tracks, the silicon-seeded tracking algorithm is rerun off-line, using only hits that are not associated with existing tracks, for the events that satisfy the trigger and filter requirements (Secs. IV A and IV C). This retracking procedure is performed with the looser requirement $d_0 < 300$ mm and $|z_0| < 1500$ mm. Furthermore, retracking requires a track to have at least five detector hits that are not shared with other tracks, while the corresponding requirement in standard silicon-seeded tracking is at least six hits. To reduce the rate of false seed tracks, it is required that these additional tracks have $p_T > 1$ GeV, while the standard-tracking requirement is $p_T > 400$ MeV.

The remainder of the analysis proceeds with both the standard-tracking tracks and retracking tracks. To realize the benefits of retracking for lepton candidates, the lepton-identification algorithms are rerun with the retracking tracks.

E. Multitrack vertex reconstruction and final selection

1. Multitrack vertex reconstruction

Tracks used for DV reconstruction are required to satisfy $p_T > 1$ GeV and to have at least two SCT hits, to ensure high track quality. The requirement $d_0 > 2$ mm is also applied, rejecting at least 97% of tracks originating from a PV. The tracks are rejected if they have no TRT hits and fewer than two pixel hits, in order to remove fake tracks.

The selected tracks are used to construct a multitrack DV by means of an algorithm based on the incompatibility-graph approach [55].

The algorithm starts by finding two-track seed vertices from all pairs of tracks. Seed vertices that have a vertex fit χ^2 of less than 5.0 (for 1 degree of freedom) are retained. If the seed vertex is inside the innermost pixel layer, both tracks must have a hit in this layer. If the vertex is between the first and second (second and third) pixel layers, both tracks must have a hit in either the second or third pixel layer (third pixel layer or the SCT). A seed vertex is rejected if any of its tracks have hits at radial positions smaller than that of the vertex. The interesting case of a charged LLP is not precluded by this selection, as the track formed by the LLP itself fails the $d_0 > 2$ mm requirement, and is therefore not included in the seed vertex. To ensure consistency between the position of the seed vertex and the direction $\hat{p}$ of the three-momentum vector of the seed-vertex tracks, the requirement $\vec{d} \cdot \hat{p} > -20$ mm is applied, where $\vec{d} = \vec{r}_{DV} - \vec{r}_{PV}$ is referred to as the "distance vector" between the position of the DV and that of the first PV. The first PV is defined as the PV with the largest $\sum p_T^2$, where the sum is over tracks associated with the PV.

Multitrack vertices are formed from combinations of seed vertices in an iterative process, as follows. If a track is assigned to several vertices, the vertex DV_1 with respect to which it has the largest χ^2 is identified. If this χ^2 is larger than 6, the track is removed from DV_1. Otherwise, the algorithm finds the vertex DV_2 that has the smallest value of D/σ_D, where D is the distance between DV_1 and DV_2, and σ_D is the estimated uncertainty on D. If $D/\sigma_D < 3$, a single vertex is formed from all the tracks of both vertices. If this is not the case, the track is removed from DV_1. This process continues until no track is associated with more than one vertex. Finally, vertices are combined and refitted if they are separated by less than 1 mm. No requirement is made on the total charge of the tracks forming a vertex.

2. Vertex selection

The reduced χ^2 of the DV fit is required to be smaller than 5.0. The DV position must be within the fiducial region $r_{DV} < 300$ mm, $|z_{DV}| < 300$ mm, where r_{DV} and z_{DV} are the radial and longitudinal DV positions with respect to the origin. To minimize background due to tracks originating from the PVs, the transverse distance $\Delta_{xy} = \sqrt{(x_{DV} - x_{PV})^2 + (y_{DV} - y_{PV})^2}$ between the DV and any of the PVs is required to be at least 4 mm. Here x and y are the transverse coordinates of a given vertex, with the subscripts PV and DV denoting the type of vertex.

DVs that are situated within regions of dense detector material are vetoed using a three-dimensional map of the detector within the fiducial region. The map is constructed in an iterative process, beginning with geometrically simple detector elements that are fully accounted for in the MC

simulation. Subsequently, detailed structures, as well as the positioning and thickness of the simple elements, are obtained from the spatial distribution of vertices obtained from the data, taking advantage of the known ϕ periodicity of the detector to reduce statistical uncertainties. The vertices used to construct the map are required to be formed from fewer than five tracks, in order to avoid the signal region defined below. The invariant mass of these vertices, assuming massless tracks, must be greater than 50 MeV, to suppress vertices from photon conversions, which have low spatial resolution due to the small opening angle between the electrons, as well as electron scattering. Vertices arising from decays of K_S^0 mesons are removed with an invariant-mass criterion. The transverse-plane projection of the positions of vertices that occur inside the material regions is shown in Fig. 2.

As the final step in multitrack DV selection, the number of tracks forming the DV is required to satisfy $N_{\mathrm{tr}} \geq 5$, and the invariant mass m_{DV} of all the tracks in the vertex must be greater than 10 GeV. In calculating m_{DV}, each track is taken to have the mass of the charged pion. Candidate vertices that pass (fail) the $m_{\mathrm{DV}} > 10$ GeV requirement are hereafter referred to as being high-m_{DV} (low-m_{DV}) vertices.

The typical position resolution of the DV in the multitrack signal MC samples is tens of microns for r_{DV} and about 200 μm for z_{DV} near the IP. For vertices beyond the outermost pixel layer, which is located at a radius of 122.5 mm, the typical resolution is several hundred microns for both coordinates.

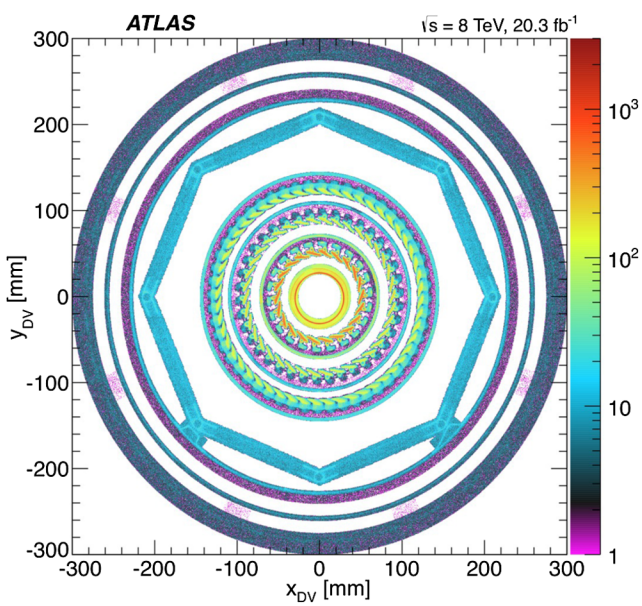

FIG. 2 (color online). Transverse-plane density (in arbitrary units) of vertices with fewer than five tracks in material regions that are excluded by the material veto in the region $|z| < 300$ mm. The innermost circle corresponds to the beam pipe. This is surrounded by the three pixel layers. The octagonal shape and outermost circles are due to support structures separating the pixel and SCT detectors.

3. DV + lepton selection

In the DV + muon search, the muon candidate is required to have triggered the event and have transverse momentum $p_{\mathrm{T}} > 55$ GeV, which is well into the region where the trigger efficiency is approximately independent of the muon momentum. The muon candidate is further required to be in the range $|\eta| < 1.07$ and have transverse impact parameter $d_0 > 1.5$ mm. A cosmic-ray muon traversing the entire ATLAS detector is reconstructed as two back-to-back muon candidates. To reject cosmic-ray background, events are discarded if they contain two muon candidates with $\Delta R_{\mathrm{cosmic}} = \sqrt{(\pi - \Delta\phi)^2 - (\eta_1 + \eta_2)^2} < 0.04$, where η_1 and η_2 are the pseudorapidities of the two reconstructed muon candidates and $\Delta\phi$ is their angular separation in the azimuthal plane. This has a negligible impact on the signal efficiency.

In the DV + electron search, the electron candidate is required to have triggered the event and to satisfy $p_{\mathrm{T}} > 125$ GeV and $d_0 > 1.5$ mm.

To ensure that the lepton candidate is associated with the reconstructed DV, the distance of closest approach of the selected muon or electron candidate to the DV is required to be less than 0.5 mm. This requirement ensures that the reconstructed DV gave rise to the muon or electron candidate that triggered the event, and so the selection efficiency for each LLP decay is independent of the rest of the event. This facilitates a straightforward calculation of the event-selection efficiency for scenarios with different numbers of LLPs. The aforementioned selections are collectively referred to as the vertex-selection criteria. Events containing one or more vertices satisfying these criteria are accepted.

4. DV + jets and DV + $E_{\mathrm{T}}^{\mathrm{miss}}$ selection

The DV + jets selection requires one of the following: four jets with $p_{\mathrm{T}} > 90$ GeV; five jets with $p_{\mathrm{T}} > 65$ GeV; or six jets with $p_{\mathrm{T}} > 55$ GeV. All jets considered in these selection criteria are required to have $|\eta| < 2.8$. DV + jet candidate events are discarded if they contain any candidate jet failing to satisfy quality criteria designed to suppress detector noise and noncollision backgrounds [56,57]. This has a negligible effect on the signal efficiency. In the DV + $E_{\mathrm{T}}^{\mathrm{miss}}$ search, the requirement $E_{\mathrm{T}}^{\mathrm{miss}} > 180$ GeV is applied. For these selection criteria, the trigger efficiency is approximately independent of the $E_{\mathrm{T}}^{\mathrm{miss}}$ and the jet transverse momenta.

F. Dilepton selection

In the dilepton search, muon candidates are required to satisfy $p_{\mathrm{T}} > 10$ GeV, $|\eta| < 2.5$, and $d_0 > 2$ mm. For electron candidates, the requirements are $p_{\mathrm{T}} > 10$ GeV

and $d_0 > 2.5$ mm. A lepton candidate is discarded if its ID track is in the pseudorapidity region $|\eta| < 0.02$, where the background-estimation procedure is observed to be unreliable (see Sec. VI).

To avoid double counting of vertices, lepton candidates used to form a dilepton DV must not have the same ID track as another lepton candidate. If two muon candidates or two electron candidates do share an ID track, the candidate that has the lower transverse momentum is discarded. If muon and electron candidates share an ID track, the electron candidate is discarded. Cosmic-ray muons, even those that interact while traversing the detector, are rejected by requiring that all lepton-candidate pairs satisfy $\Delta R_{\mathrm{cosmic}} > 0.04$.

A dilepton DV is formed from at least two opposite-charge tracks identified as two electrons, two muons, or an electron and a muon. Any number of additional tracks may be included in the vertex. At this stage, it is verified that the dilepton selection criteria applied at the trigger and filter level (see Secs. IV A and IV C) are satisfied by the two lepton candidates forming the DV. Finally, the dilepton DV is required to satisfy the DV selection criteria specified in Sec. IV E 2, except for the requirement on the number of tracks, which is $N_{\mathrm{tr}} \geq 2$. As in the DV + lepton case, the dilepton-DV selection relies only on the leptons in the DV and is independent of the rest of the event.

V. SIGNAL EFFICIENCY

In the dilepton and DV + lepton searches, where the selection criteria rely only on the particles produced in the DV, the vertex-level efficiency ϵ_{DV} is defined to be the product of acceptance and efficiency for reconstructing one signal DV, produced in the given search model, with all the trigger, filter, and final selection criteria. The event-level efficiency ϵ_{ev}, defined as the probability for an event containing two DVs to be identified with at least one DV satisfying all the selection criteria, is then obtained from the relation

$$\epsilon_{\mathrm{ev}} = 2\mathcal{B}\epsilon_{\mathrm{DV}} - \mathcal{B}^2\epsilon_{\mathrm{DV}}^2, \tag{1}$$

where $\mathcal{B}$ is the LLP branching fraction into the specific search channel. In the DV + jets and DV + $E_{\mathrm{T}}^{\mathrm{miss}}$ searches, only the event-level efficiency is defined, since the selection criteria involve the entire event.

The efficiency for reconstructing a multitrack or dilepton DV with the above selection criteria depends strongly on the efficiencies for track reconstruction and track selection, which are affected by several factors: (1) The number of tracks originating from the DV and their total invariant mass increase with the LLP mass. (2) More tracks fail the minimal-d_0 requirement for small r_{DV}, or when the LLP is highly boosted. (3) The efficiency for reconstructing tracks decreases with increasing values of d_0. (4) When an LLP decays at a radius somewhat smaller than that of a pixel layer, many tracks share hits on that pixel layer, failing to meet the track-selection criteria. The resulting impact on efficiency can be seen in Fig. 3 at radii around 45 mm, 80 mm, and 115 mm.

The efficiency for reconstructing a multitrack DV is reduced when the LLP decays to charm or bottom hadrons, resulting in two or more nearby DVs. Each of these DVs has a high probability of failing to meet the N_{tr} and m_{DV} criteria, resulting in low efficiency if these DVs are not merged. This happens less at large values of r_{DV}, where DVs are more readily merged due to the worse position resolution.

The vertex-level efficiency does not depend appreciably on whether the primary particle is a squark or a gluino.

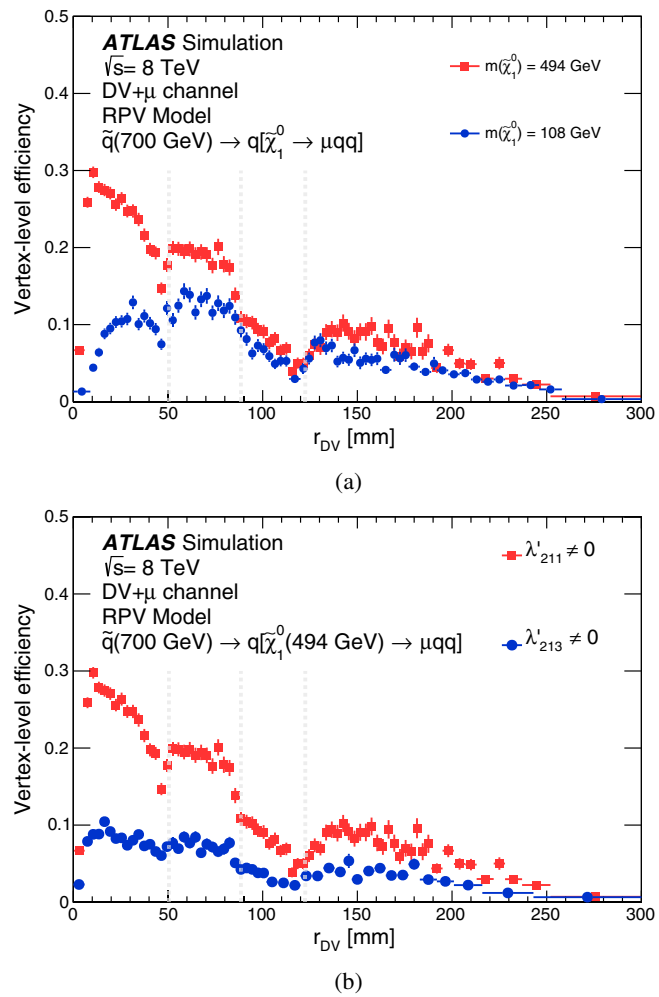

FIG. 3 (color online). Comparisons of the vertex-level efficiency as a function of the vertex radial position r_{DV} for different RPV samples. The vertical gray lines show the position of the first, second, and third pixel layers. (a) For the $\tilde{q} \to q[\tilde{\chi}_1^0 \to \mu qq]$ (λ'_{211}) samples with $m_{\tilde{q}} = 700$ GeV, comparing two cases of different LLP masses: $m_{\tilde{\chi}_1^0} = 494$ GeV, and $m_{\tilde{\chi}_1^0} = 108$ GeV. (b) For the $\tilde{q} \to q[\tilde{\chi}_1^0 \to \mu qq]$ (λ'_{211}) and $\tilde{q} \to q[\tilde{\chi}_1^0 \to \mu qb]$ (λ'_{213}) samples, indicated by the relevant nonzero RPV couplings.

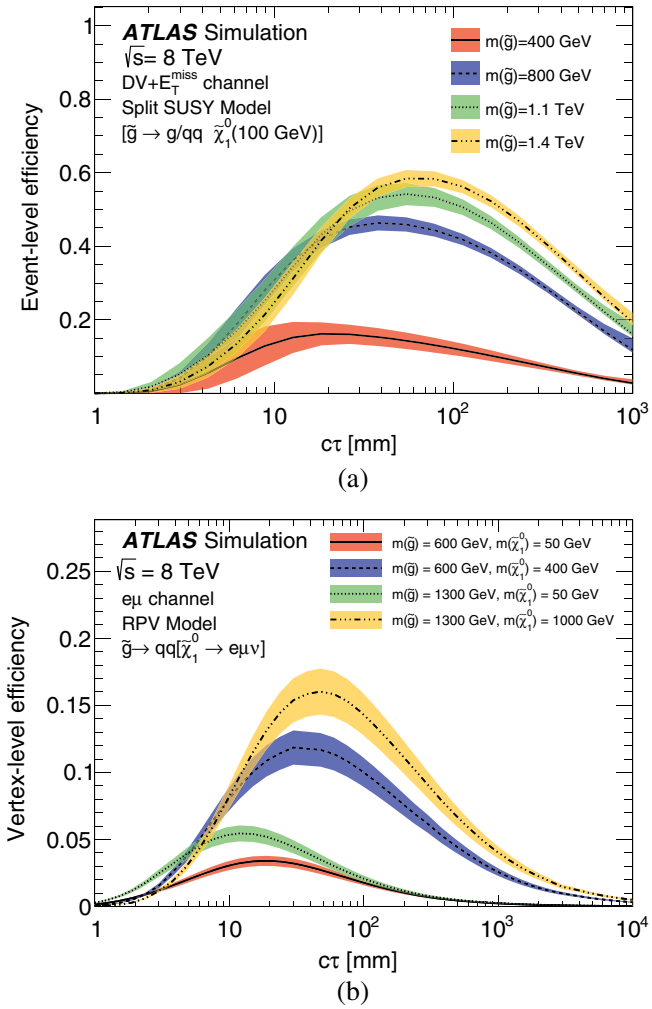

FIG. 4 (color online). (a) The event-level efficiency as a function of $c\tau$ for split-supersymmetry $[\tilde{g} \to g/qq\tilde{\chi}_1^0(100\ \mathrm{GeV})]$ samples with various gluino masses, reconstructed in the $\mathrm{DV} + E_{\mathrm{T}}^{\mathrm{miss}}$ channel. (b) The vertex-level efficiency for the RPV $\tilde{g} \to qq[\tilde{\chi}_1^0 \to e\mu\nu]$ samples with combinations of gluino and neutralino masses, reconstructed in the $e\mu$ dilepton channel. The total uncertainties on the efficiencies are shown as bands (see Sec. VII).

However, the nature of the primary particle determines the number of jets, and hence impacts the event-level efficiency in the $\mathrm{DV} + \mathrm{jets}$ and $\mathrm{DV} + E_{\mathrm{T}}^{\mathrm{miss}}$ channels.

Examples of the impact of LLP boost, mass, and heavy-flavor decays on the vertex-level efficiency are shown in Fig. 3 for $\tilde{q} > q[\tilde{\chi}_1^0 \to \mu qq]$ samples. As an example of the benefits of retracking, it is worthwhile to note that without retracking, the vertex-level efficiency for the $m(\tilde{\chi}_1^0) = 494$ GeV, $\lambda'_{211} \neq 0$ sample shown in this figure is about 1% at $r_{\mathrm{DV}} = 80$ mm and is negligible for larger radii.

Events in each MC sample are generated with a fixed value of the LLP lifetime τ_{MC}. To obtain the vertex-level efficiency for a different lifetime τ, each LLP is given a weight

$$W_{\mathrm{DV}}(t,\tau) = \frac{\tau_{\mathrm{MC}}}{\tau}\exp\left(\frac{t}{\tau_{\mathrm{MC}}} - \frac{t}{\tau}\right), \tag{2}$$

where t is the true proper decay time of the generated LLP. The vertex-level efficiency is then the sum of weights for LLPs that satisfy all the criteria in the sample. The same procedure is applied when calculating the event-level efficiency, except that the entire event is weighted by

$$W_{\mathrm{evt}}(t_1,t_2,\tau) = W_{\mathrm{DV}}(t_1,\tau)W_{\mathrm{DV}}(t_2,\tau), \tag{3}$$

where t_1 and t_2 are the true proper decay times of the two LLPs in the event. Examples of the resulting dependence of ϵ_{DV} and ϵ_{ev} on the average proper decay distance $c\tau$ are shown in Fig. 4. For most models considered in this analysis, the peak efficiency is typically greater than 5%, and it occurs in the range $10 \lesssim c\tau \lesssim 100$ mm.

VI. BACKGROUND ESTIMATION

The expected number of background vertices is estimated from the collision data for each channel. Since the number of events satisfying the final selection criteria is very small, the general approach is to first obtain a high-statistical-precision assessment of the probability for background-vertex formation using a large data control sample. That probability is then scaled by the size of the signal-candidate sample relative to that of the control sample.

A. Multitrack-vertex background estimation

Background vertices that are due to accidental spatial crossing of tracks in a jet, particle interactions with material, or heavy-flavor decays have low values of m_{DV} and/or N_{tr} and thus fail the selection requirements. Such vertices may contribute to high-m_{DV}, high-N_{tr} background vertices via two mechanisms.

(i) The dominant source of backgrounds are low-m_{DV} vertices that are accidentally crossed by an unrelated, high-p_{T} track at large angle $[\mathcal{O}(1\ \mathrm{radian})]$ to the other tracks in the vertex. This is referred to as the accidental-crossing background.

(ii) A much smaller background contribution is due to merged vertices. In this case, two low-m_{DV} vertices are less than 1 mm apart, and thus may be combined by the vertex-reconstruction algorithm into a single vertex that satisfies the N_{tr} and m_{DV} criteria.

The expected background levels from the two sources are estimated from the data. In order for the background estimate to have high statistical precision, it is performed with a large sample containing all events that have undergone retracking. This includes the events selected for this search, as described in Sec. IV C, as well as events used for other ATLAS analyses. The sample is divided into three subsamples, referred to as the muon stream, the electron stream, and the $\mathrm{jets} + E_{\mathrm{T}}^{\mathrm{miss}}$ stream, with the name

indicating the type of trigger used to select the events. The background level is estimated separately in each of these streams with the methods described below, and the results are used for the DV + muon, DV + electron, and DV + jets and DV + $E_{\mathrm{T}}^{\mathrm{miss}}$ signal regions, respectively.

To obtain the final background estimate in the signal region, the background estimate in each stream is multiplied by a final-selection scale factor F^{stream}, which is the fraction of events in the given stream that satisfy the final event-selection criteria, other than the DV selection criteria. The values of these fractions are 0.08%, 5.0%, 1.45%, and 0.04%, for the DV + muon, DV + electron, DV + jet, and DV + $E_{\mathrm{T}}^{\mathrm{miss}}$ searches, respectively. This use of F^{stream} assumes that the average number of vertices per event, $N_{\mathrm{ev}}^{\mathrm{DV}}$, is independent of the selection criteria. Based on the change in $N_{\mathrm{ev}}^{\mathrm{DV}}$ when the final selection criteria are applied, an upward bias correction of 60% is applied to the estimated background level in the DV + electron channel (the correction is included in the $F^{\mathrm{stream}} = 5.0\%$ value quoted above). The other channels have negligible bias. A 10% systematic uncertainty is estimated for all channels from the statistical uncertainty of the bias estimate.

1. Background from accidental vertex-track crossings

The accidental-crossing background is estimated separately in six radial regions, ordered from the inside out. Region 1 is inside the beam pipe. Regions 2, 3, and 4 correspond to the volumes just before each of the three pixel layers. Regions 5 and 6 are outside the pixel layers. Region 5 extends outwards to $r_{\mathrm{DV}} = 180$ mm, where there is essentially no detector material, while Region 6 covers the volume from $180 < r_{\mathrm{DV}} < 300$ mm. In each region, a study of the m_{DV} distribution of N_{tr}-track vertices, where $N_{\mathrm{tr}} = 3$ through 6, leads to identification of two types of background vertices, as follows.

The first type, which dominates the low-m_{DV} range, is due to accidental track crossings in Region 1, and particle-material interactions in the other regions. This contribution to the m_{DV} spectrum is referred to as collimated-tracks background, reflecting the typically small angle between the tracks. The m_{DV} distribution $P_{N_{\mathrm{tr}}}^{\mathrm{coll}}(m_{\mathrm{DV}})$ for this contribution is modeled from the N_{tr}-track vertices for which the average three-dimensional angle between every pair of tracks is less than 0.5. In Fig. 5, $P_3^{\mathrm{coll}}(m_{\mathrm{DV}})$ is seen to fully account for 3-track vertices with m_{DV} less than about 3 GeV. However, it does not account for vertices with higher masses, particularly the signal region, $m_{\mathrm{DV}} > 10$ GeV.

The high-m_{DV} part of the m_{DV} distribution is dominated by the second contribution, referred to as "DV + track." In this case, a $(N_{\mathrm{tr}} - 1)$-track vertex is crossed by an unrelated track at a large angle with respect to the momentum vector of the vertex tracks. To construct a model of the DV + track m_{DV} distribution of N_{tr}-track vertices, every $(N_{\mathrm{tr}} - 1)$-track

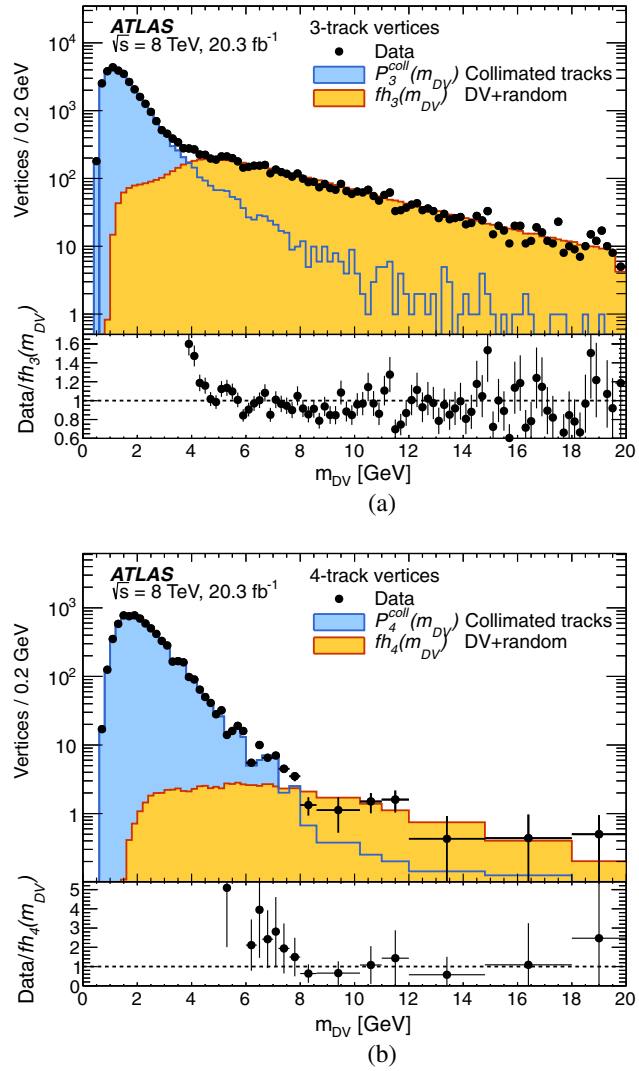

FIG. 5 (color online). The mass distribution for (a) 3-track and (b) 4-track vertices (data points) from the jets + $E_{\mathrm{T}}^{\mathrm{miss}}$ stream in Region 6, overlaid with the model $fh_3(m_{\mathrm{DV}})$ of Eq. (5) (yellow-shaded histogram) at high mass. The lower panel of each plot shows the ratio of the data to this model. The model for the collimated-track contribution $P_3^{\mathrm{coll}}(m_{\mathrm{DV}})$ (blue-shaded histogram), which is correlated with the low-mass data but not used for estimating the signal-region background, is also shown.

vertex, referred to as an "acceptor" vertex, is paired with a "donated" track that is taken from a "donor" vertex in another event. This is done for $N_{\mathrm{tr}} - 1$ in the range 2–5, where acceptor vertices with five tracks are required to have mass below 10 GeV, to avoid the signal region.

The pairing of a vertex and a track is performed with the following procedure. The donor vertex must satisfy all the DV selection criteria, except that the requirement on its mass is not applied, and it may have as few as two tracks. To ensure that the donated track is able to accurately model the effects of a large-angle crossing, it is required that the donor vertex be from the same radial region as the acceptor vertex, and that there is a large angle between the direction

of the donated track and the distance vector of the donor vertex.

In all regions apart from Region 1, the momentum vector of the donated track is then rotated, so that its azimuthal and polar angles ($\Delta\phi_{\rm donor}$ and $\Delta\theta_{\rm donor}$) with respect to the distance vector of the acceptor vertex match those that it originally had with respect to the donor vertex. This ensures that the contribution of the donated track to the acceptor vertex mass correctly reflects the accidental-crossing probability as a function of $\Delta\eta_{\rm donor}$ and $\Delta\phi_{\rm donor}$.

Then, the four-momentum of the acceptor vertex and the rotated four-momentum of the track are added, obtaining the $m_{\rm DV}$ value of the $N_{\rm tr}$-track vertex that would have been formed from an accidental crossing of the acceptor vertex and the rotated donated track. The resulting $m_{\rm DV}$ distribution for the $N_{\rm pairs}$ DV + track pairs found in each region is denoted $h_{N_{\rm tr}}(m_{\rm DV})$, such that

$$\int_0^\infty h_{N_{\rm tr}}(m_{\rm DV})dm_{\rm DV} = N_{\rm pairs}. \tag{4}$$

Tracks from donor vertices in Region 1 are treated differently, since they tend to have high pseudorapidity, which impacts their DV-crossing probability more than their $\Delta\phi_{\rm donor}$ and $\Delta\theta_{\rm donor}$ values. Therefore, a Region-1 track is not rotated before its four-momentum is added to that of the acceptor vertex.

The high-$m_{\rm DV}$ distribution for $N_{\rm tr}$-track vertices is then modeled by

$$P_{N_{\rm tr}}(m_{\rm DV}) = f h_{N_{\rm tr}}(m_{\rm DV}), \tag{5}$$

where

$$f = \frac{N_3^{10\ \rm GeV}}{\int_{10\ \rm GeV}^\infty h_3(m_{\rm DV})dm_{\rm DV}} \tag{6}$$

is the scale factor that normalizes the model to the data, and $N_3^{10\ \rm GeV}$ is the number of 3-track vertices with $m_{\rm DV} > 10$ GeV. The model-predicted number of $N_{\rm tr}$-track background vertices with $m_{\rm DV} > 10$ GeV for a given stream and region is given by

$$N_{N_{\rm tr}}^{\rm stream} = \int_{10\ \rm GeV}^\infty P_{N_{\rm tr}}(m_{\rm DV})dm_{\rm DV}. \tag{7}$$

The model describes the high-$m_{\rm DV}$ background distribution in data well, as seen in Fig. 5 for jets + $E_{\rm T}^{\rm miss}$-stream 3-track and 4-track vertices in Region 6. Also shown is the collimated-track contribution, which accounts for the low-$m_{\rm DV}$ part of the distribution. Using 4-track vertices to validate Eq. (7), the prediction for each of the three streams and six regions is compared with the observed number of vertices. The comparison, summarized in Fig. 6, shows good agreement within the statistical precision.

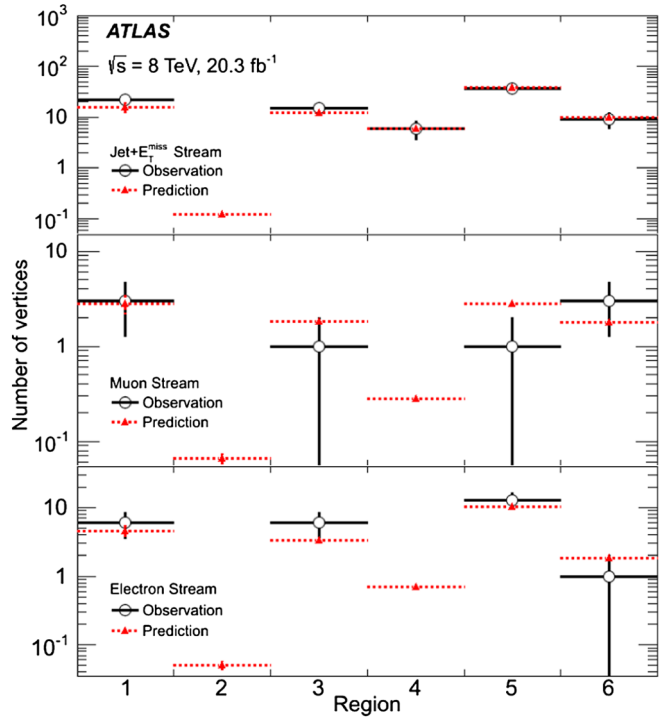

FIG. 6 (color online). Summary of the number of observed (black open circles) 4-track, high-$m_{\rm DV}$ vertices in each of the radial regions and filter-selection streams and the predicted number (red triangles), from Eq. (7). In Region 1, the prediction includes the contribution from merging of two 2-track vertices (see Sec. VI A 2). The error bars on the prediction are too small to be visible, and in some bins no events are observed.

The final numbers of expected background vertices, after multiplying $N_{N_{\rm tr}}^{\rm stream}$ by the scale factor $F^{\rm stream}$, are shown in Table I.

2. Background due to merged vertices

In the last step of DV reconstruction (see Sec. IV E 1), vertices are combined if they are separated by less than 1 mm. To estimate the background arising from this procedure, the distribution of the distance $d_{\rm 2DV}$ between two 2-track or 3-track vertices is studied. Each of the selected vertices is required to satisfy the DV selection criteria of Sec. IV E 2 except the $m_{\rm DV}$ and $N_{\rm tr}$ requirements,

TABLE I. Estimated numbers of background vertices satisfying all of the multitrack signal selection criteria, which arise from a low-mass DV accidentally crossed by an unrelated track. In each entry, the first uncertainty is statistical, and the second is systematic (see Sec. VII).

Channel	No. of background vertices ($\times 10^{-3}$)
DV + jet	$410 \pm 7 \pm 60$
DV + $E_{\rm T}^{\rm miss}$	$10.9 \pm 0.2 \pm 1.5$
DV + muon	$1.5 \pm 0.1 \pm 0.2$
DV + electron	$207 \pm 9 \pm 29$

and their combined mass is required to be greater than 10 GeV. To obtain a sufficient number of vertices for studying the d_{2DV} distribution, the distribution is reconstructed from a much larger sample of vertex pairs, where each vertex in the pair is found in a different event. This is referred to as the "model" sample.

To validate the d_{2DV} distribution of the model sample, it is compared to that of vertices that occur in the same event, referred to as the "same-event" sample. It is found that the z positions of vertices in the same event are correlated, since more vertices are formed in high-track-multiplicity regions corresponding to jets. This effect is absent in the model sample. As a result, the distributions of the longitudinal distance between the vertices in the model and the same-event samples differ by up to 30% at low values of d_{2DV}. To correct for this difference, each vertex pair in the model sample is weighted so as to match the z component distribution of the same-event sample. After weighting, the model distribution of the three-dimensional distance d_{2DV} agrees well with that of the same-event sample in the entire study range of $d_{2DV} < 120$ mm. This is demonstrated in Fig. 7 for pairs of 2-track vertices and for the case of a 2-track vertex paired with a 3-track vertex.

The background level for the analysis requirement of $N_{tr} \geq 5$ tracks is estimated from vertex pairs where one vertex has two tracks and the other has three tracks. The area under the model distribution in the range $d_{2DV} < 1$ mm yields a background prediction of 0.02 ± 0.02 events in each of the DV + lepton channels, and 0.03 ± 0.03 events in the DV + jets and DV + E_T^{miss} channels. After multiplication by F^{stream}, this background is negligible relative to the accidental-crossing background, described in Sec. VI A 1. Background from the merging of two 3-track vertices or a 2-track and a 4-track vertex is deemed much smaller still.

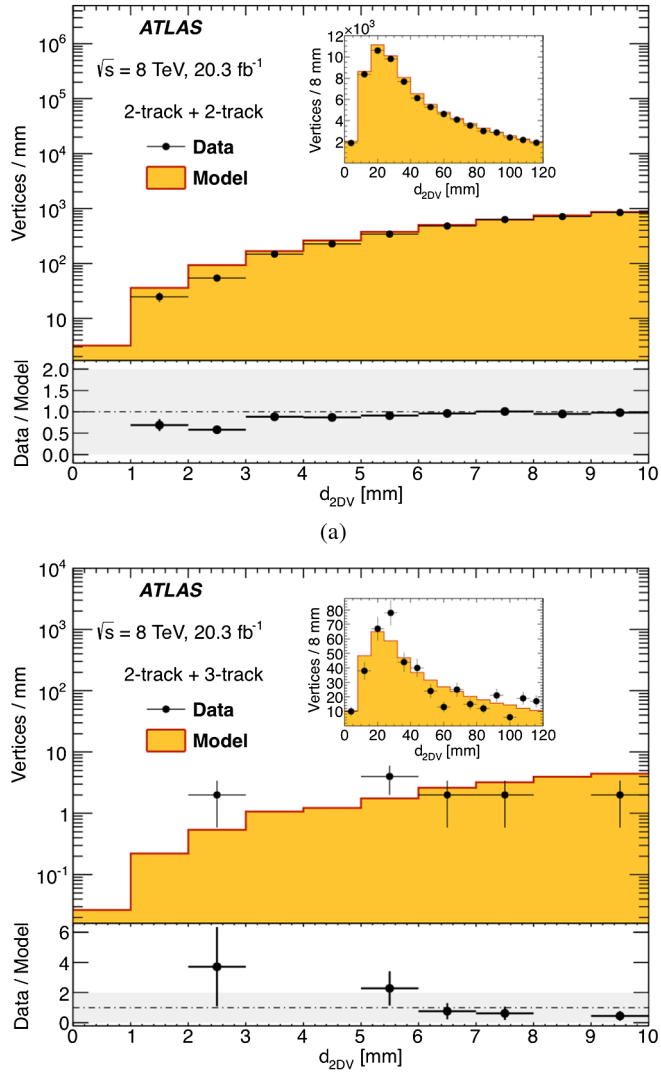

FIG. 7 (color online). The distribution of the distance d_{2DV} between (a) two 2-track vertices and (b) a 2-track vertex and a 3-track vertex with a combined mass above 10 GeV for the jets + E_T^{miss} stream data (data points) and in the model sample, in which the two vertices are in different events (histogram). A conservative 100% uncertainty on the model is shown in the data/model ratio plot. The inset shows the d_{2DV} distance up to values of 120 mm. The merged-vertex background estimate is determined from the area under the model distribution in the range $d_{2DV} < 1$ mm in (b).

B. Dilepton-vertex background estimation

Background DVs in the dilepton search may arise from two sources:

(i) The dominant background is due to accidental spatial crossings of unrelated lepton candidates that happen to come close enough to satisfy the vertex-reconstruction criteria.

(ii) Minor backgrounds, due to tracks originating from the PV wrongly associated with a DV, decays of SM long-lived particles, or cosmic-ray muons. The levels of background from these sources are determined to be negligible relative to the accidental-crossing background.

1. Background from accidental lepton crossing

The level of the accidental-crossing background is estimated by determining the crossing probability, defined as the probability for two unrelated lepton-candidate tracks to be spatially nearby and reconstructed as a vertex. Pairs of opposite-charge lepton candidates are formed, where each lepton candidate in a pair is from a different event and satisfies the lepton-selection criteria. The momentum vector of one of the two lepton candidates, selected at random, is rotated through all azimuthal angles by a step $\delta\phi$. At each rotation step, the two lepton candidates are subjected to a vertex fit and the DV selection criteria. If the pair satisfies the selection criteria, it is assigned a weighted probability $\delta\phi/2\pi$. Averaging the weighted probabilities over all pairs

TABLE II. Estimated numbers of background vertices satisfying all of the dilepton signal selection criteria, arising from random combinations of lepton candidates. In each entry, the first uncertainty is statistical, and the second is systematic (see Sec. VII).

Channel	No. of background vertices ($\times 10^{-3}$)
e^+e^-	$1.0 \pm 0.2^{+0.3}_{-0.6}$
$e^\pm\mu^\mp$	$2.4 \pm 0.9^{+0.8}_{-1.5}$
$\mu^+\mu^-$	$2.0 \pm 0.5^{+0.3}_{-1.4}$

gives the probability for a lepton-candidate pair to accidentally form a vertex. The probability is observed to be independent of $\delta\phi$ for $\delta\phi < 0.03$. To obtain the final background estimate, this probability is multiplied by the number $N_{\ell\ell}$ of data events containing two opposite-charge lepton candidates that satisfy the lepton-selection criteria. This procedure yields the background predictions shown in Table II. Compared with these predictions, the background level for a 3-track vertex, where at least two of the tracks are lepton candidates, is negligible.

The validity of this method for estimating the number of dilepton DVs, including the assumption that the tracks are uncorrelated, is verified in several ways. Using $Z \to \mu^+\mu^-$ and $t\bar{t}$ MC samples, the procedure is applied to vertices formed from two lepton candidates, a lepton candidate and another track, or two tracks that are not required to be lepton candidates. It is observed that the method correctly predicts the accidental-crossing background to within about 10%. The background-estimation method is tested also on pairs of tracks in the data, excluding pairs of lepton candidates, with a variety of selection criteria. The predicted and observed numbers of background vertices are again found to agree to within 10% for all selection criteria. The method also reproduces well the distributions of m_{DV}, r_{DV}, z_{DV}, $\hat{d} \cdot \hat{p}$, and the azimuthal angle between the two lepton candidates, in both MC simulation and data. As an example, Fig. 8 shows the m_{DV} and r_{DV} distributions observed for data vertices composed of two nonlepton tracks and the distributions predicted by pairing two tracks in different events. Some differences between the model and the data are seen at certain radii (e.g., $r_{\mathrm{DV}} < 50$ mm and $250 < r_{\mathrm{DV}} < 270$ mm), but these do not substantially affect the total number of DVs and are covered by the assigned systematic uncertainty (see Sec. VII A 2). The prediction is accurate down to DV masses of 6 GeV, well below the DV selection criterion of 10 GeV. At smaller masses, contributions from other background sources become significant.

This background-estimation method ignores the possibility of angular correlations between the leptons forming a background vertex. The associated systematic uncertainty is described in Sec. VII A 2.

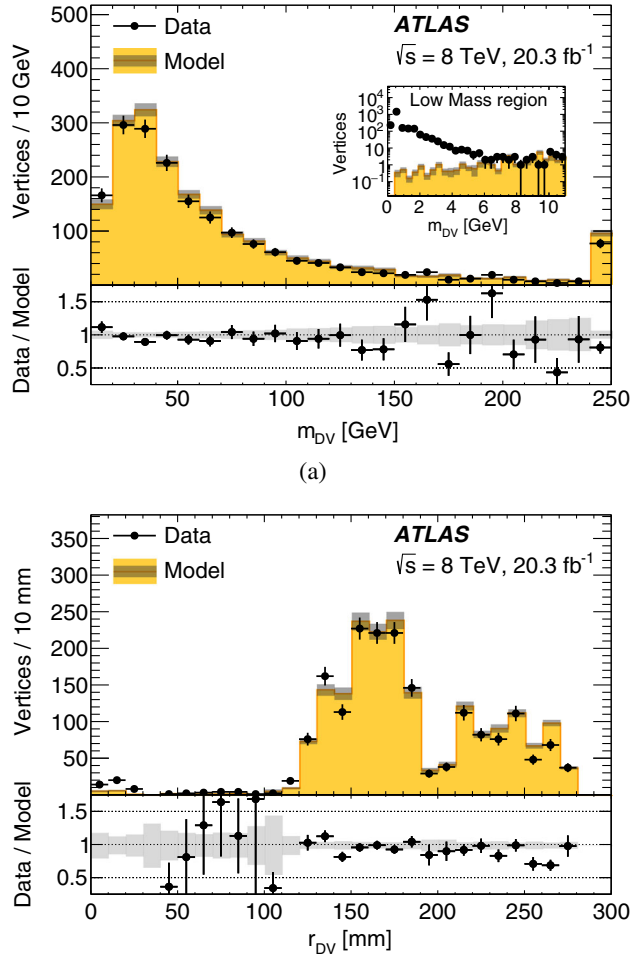

FIG. 8 (color online). Distributions of the (a) vertex mass and (b) vertex position radius for vertices composed of two nonlepton tracks in the data sample (data points), and the predicted model distribution obtained from vertices formed by combining tracks from two different data events (shaded histograms). The ratio of the data to the model distributions is shown below each plot. The gray bands indicate the statistical uncertainties for the predicted distributions. The inset shows the mass distribution in the low-mass region, elsewhere $m_{\mathrm{DV}} > 10$ GeV is required. In (a), the highest bin shows the histogram overflow.

2. Minor backgrounds

Backgrounds from the following sources are found to be negligible relative to the accidental-crossing background, and are therefore neglected.

A potential source of background is prompt production of hard lepton pairs, notably from $Z \to \ell^+\ell^-$ decays. Requiring $\Delta_{xy} < 4$ mm and removing the $m_{\mathrm{DV}} > 10$ GeV requirement yields no dilepton-vertex candidates, so the data show no evidence for prompt background. Therefore, MC simulation is used to estimate the probability for leptons originating from $Z \to \ell^+\ell^-$ decays to satisfy the minimum-d_0 requirements, the probability for such leptons to satisfy the vertex requirements, and the

probability for a $Z \to \ell^+\ell^-$ event to pass the analysis kinematic requirements. Multiplying the product of these probabilities by the number of $Z \to \ell^+\ell^-$ events produced at ATLAS yields an estimate of 10^{-5} $Z \to \mu^+\mu^-$ events and 10^{-4} $Z \to e^+e^-$ events in the $\Delta_{xy} < 4$ mm sideband. Thus, the background from this source is negligible.

Background from cosmic-ray muons is studied with the $\Delta R_{\mathrm{cosmic}}$ distribution of the two highest-p_{T} muon candidates in each event, which satisfy the selection criteria except the $\Delta R_{\mathrm{cosmic}} > 0.04$ requirement. The distribution drops rapidly as $\Delta R_{\mathrm{cosmic}}$ increases, with the highest pair having $\Delta R_{\mathrm{cosmic}} = 0.014$. The pairs that also satisfy the DV selection criteria constitute less than 7% of this sample and have a similar $\Delta R_{\mathrm{cosmic}}$ distribution, terminating at $\Delta R_{\mathrm{cosmic}} \sim 0.0045$. Therefore, it is concluded that the rate for cosmic-ray background muons satisfying the $\Delta R_{\mathrm{cosmic}} > 0.04$ requirement is several orders of magnitude below the accidental-crossing background. In the case of a partially reconstructed cosmic-ray muon crossing a reconstructed lepton candidate from a pp collision, the two tracks are uncorrelated and any contribution to the background is already accounted for in the results shown in Table II.

Background from decays of known long-lived hadrons is studied from vertices in which only one track is required to be a lepton candidate. It is found to be negligible, due to the small probability for a hadron to be misidentified as a lepton candidate and the mass resolution of the detector.

VII. SYSTEMATIC UNCERTAINTIES AND CORRECTIONS

The dominant systematic uncertainties are those associated with the efficiency for reconstructing displaced electrons and with the jet and $E_{\mathrm{T}}^{\mathrm{miss}}$ selection criteria. Since the background level is low, uncertainties on the background estimation have a minor effect on the results of the analysis. The methods for evaluation of the systematic uncertainties are described in detail below.

A. Background-estimation uncertainties

1. Multitrack DV background uncertainties

The choice of the $m_{\mathrm{DV}} > 10$ GeV mass range for determining the scale factor f (see Sec. VI A 1), as well as differences between the m_{DV} distribution of the vertices and that of the model, are a source of systematic uncertainty on the background prediction. To estimate this uncertainty, f is obtained in the modified mass ranges $m_{\mathrm{DV}} > 5$ GeV and $m_{\mathrm{DV}} > 15$ GeV. The resulting 10% change in the background prediction for DVs passing the final selection requirements is used as a systematic uncertainty. An additional uncertainty of 10% is estimated from the variation of F^{stream} as the selection criteria are varied (see Sec. VI A 1). Compared with these uncertainties, the uncertainty on the much smaller merged-vertex background level is negligible.

2. Dilepton background uncertainties

The background-estimation procedure for the dilepton search (see Sec. VI B 1) normalizes the background to the number $N_{\ell\ell}$ of events containing two lepton candidates that could give rise to a DV that satisfies the selection criteria. Contrary to the underlying assumption of the background estimation, the two lepton candidates may be correlated, impacting their probability for forming a high-m_{DV} vertex. To study the impact of such correlation, $N_{\ell\ell}$ is recalculated twice, placing requirements on the azimuthal angle between the two lepton candidates, $\Delta\phi_{\ell\ell}$, of $0.5 < \Delta\phi_{\ell\ell} < \pi$ and $0 < \Delta\phi_{\ell\ell} < \pi - 0.5$. The resulting variation yields the relative uncertainty estimates on $N_{\ell\ell}$ of $^{+0\%}_{-54\%}$, $^{+19\%}_{-49\%}$, and $^{+13\%}_{-50\%}$ for the $\mu^+\mu^-$, $e^\pm\mu^\mp$, and e^+e^- channels, respectively.

An uncertainty of 15% on the background prediction is estimated from the validation studies performed using MC simulation and data, described in Sec. VI B 1. The resulting systematic uncertainties are shown in Table II.

B. Signal-efficiency uncertainties and corrections

1. Trigger efficiency

The muon trigger efficiency is studied with a "tag-and-probe" method, in which the invariant-mass distribution of pairs of tracks is fitted to the sum of a $Z \to \mu^+\mu^-$ peak and a background contribution. To reduce the background, one of the muon candidates (the "tag") is required to be identified as a muon. The muon-trigger efficiency is determined from the fraction of $Z \to \mu^+\mu^-$ decays in which the other muon candidate (the "probe") satisfies the trigger criteria. Based on the results of this study in data and MC simulation, a correction of $\Delta\epsilon = -2.5\%$ is applied to the MC-predicted trigger efficiency. A total uncertainty of $\sigma_\epsilon = 1.7\%$ is estimated by comparing the trigger efficiency as a function of the muon candidate p_{T} in data and MC simulation, and by comparing the results of the tag-and-probe method, applied to Drell-Yan MC, with MC generator-level information. Similar studies of the trigger selections used for the electron channels lead to $\Delta\epsilon = -1.5\%$ and $\sigma_\epsilon = 0.8\%$ for the $p_{\mathrm{T}} > 120$ GeV photon trigger, and $\Delta\epsilon = -0.5\%$, $\sigma_\epsilon = 2.1\%$ for the two-photon $p_{\mathrm{T}} > 40$ GeV trigger. The jets and $E_{\mathrm{T}}^{\mathrm{miss}}$ triggers are fully efficient after the off-line cuts.

2. Off-line track-reconstruction efficiency

The uncertainty associated with the reconstruction efficiency for tracks that originate far from the IP is estimated by comparing the decay radius distributions for K_S^0 mesons in data and MC simulation. The comparison is carried out with the ratio

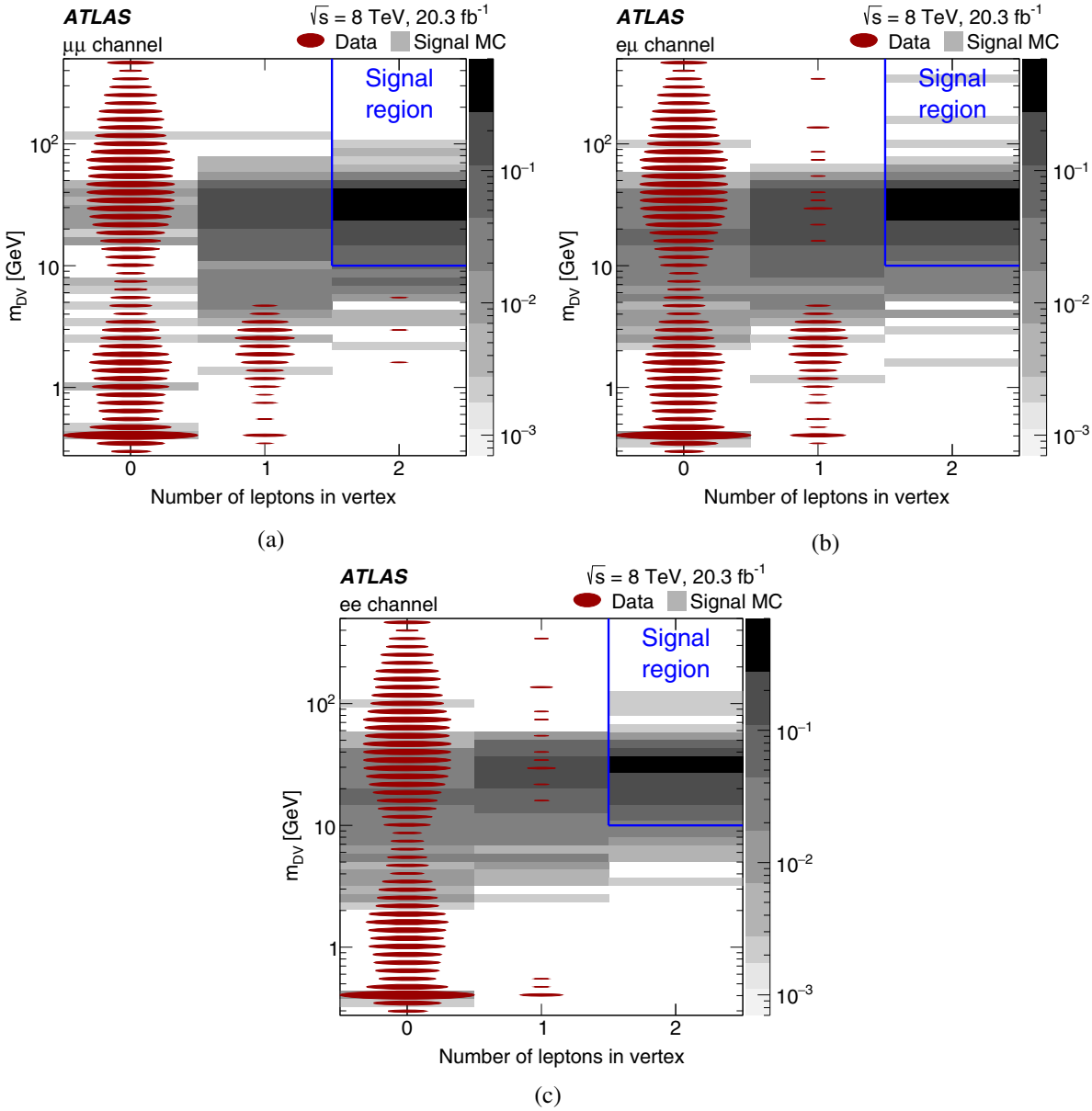

FIG. 9 (color online). The distribution of dilepton-vertex candidates in terms of the vertex mass versus the number of lepton candidates in the vertex, in the (a) $\mu^+\mu^-$, (b) $e^\pm\mu^\mp$, and (c) e^+e^- search channels. The data distributions are shown with red ovals, the area of the oval being proportional to the logarithm of the number of vertex candidates in that bin. The gray squares show the $\tilde{g}(600\ \mathrm{GeV}) \to qq[\tilde{\chi}_1^0(50\ \mathrm{GeV}) \to \mu\mu\nu/e\mu\nu/ee\nu]$ signal MC sample. The shape of the background m_{DV} distribution arises partly from the lepton-candidate p_{T} requirements. The signal region defined by the two-lepton and $m_{\mathrm{DV}} \to 10$ GeV requirements is indicated.

$$\rho_i(K_S^0) = \frac{N_i^{\mathrm{data}}(K_S^0)}{N_i^{\mathrm{MC}}(K_S^0)}, \tag{8}$$

where $i = 1, \ldots, 4$ labels four radial regions between 5 mm and 40 mm, and $N_i^{\mathrm{data/MC}}(K_S^0)$ is the number of K_S^0 mesons in radial region i in data/MC simulation, obtained by fitting the two-track mass distributions. In the calculation of $N_i^{\mathrm{MC}}(K_S^0)$, the K_S^0 candidates in MC are weighted so that their $|\eta|$ and p_{T} distributions match those seen in the data. The ratio $\rho_i(K_S^0)$ is constructed separately for $|\eta| < 1$ and $|\eta| \geq 1$. The difference $\Delta\rho_i(K_S^0) = \rho_i(K_S^0) - \rho_1(K_S^0)$ quantifies the radial dependence of the data-MC discrepancy. The discrepancy is largest in the outermost radial region, with $\Delta\rho_4(K_S^0) = -0.03$ for $|\eta| < 1$ and $\Delta\rho_4(K_S^0) = -0.2$ for $|\eta| \geq 1$. The statistical uncertainties on $\rho_i(K_S^0)$ are negligible compared to these discrepancies.

To propagate this maximal discrepancy into a conservative uncertainty on the signal efficiency, DV daughter tracks are randomly removed from signal-MC vertices before performing the vertex fit. The single-track removal probability is taken to be $\Delta\rho_4(K_S^0)/2$ in each of the

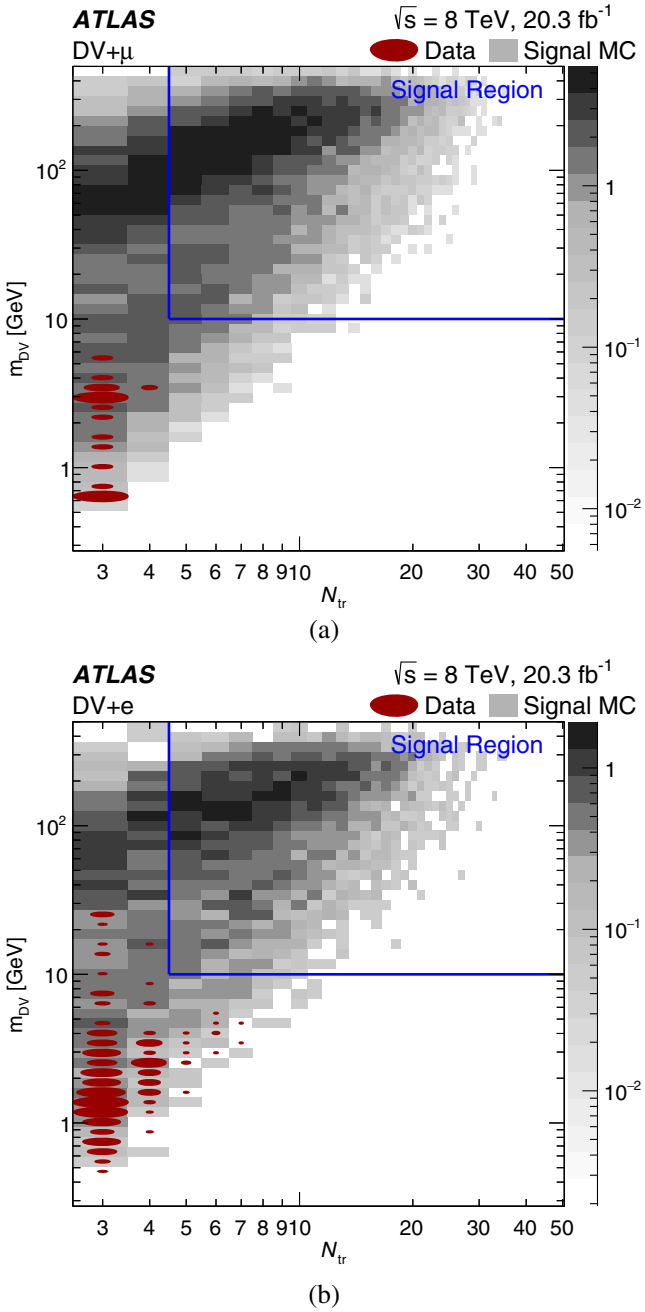

FIG. 10 (color online). The distribution of (a) DV + muon and (b) DV + electron candidates in terms of the vertex mass versus the number of tracks in the vertex. The data distribution is shown with red ovals, the area of each oval being proportional to the logarithm of the number of vertex candidates in that bin. The gray squares show the $\tilde{q}(700\ \mathrm{GeV}) \to q[\tilde{\chi}_1^0(494\ \mathrm{GeV}) \to \ell qq]$ RPV signal MC sample. The signal region $N_{\mathrm{tr}} \geq 5$, $m_{\mathrm{DV}} \to 10$ GeV is indicated.

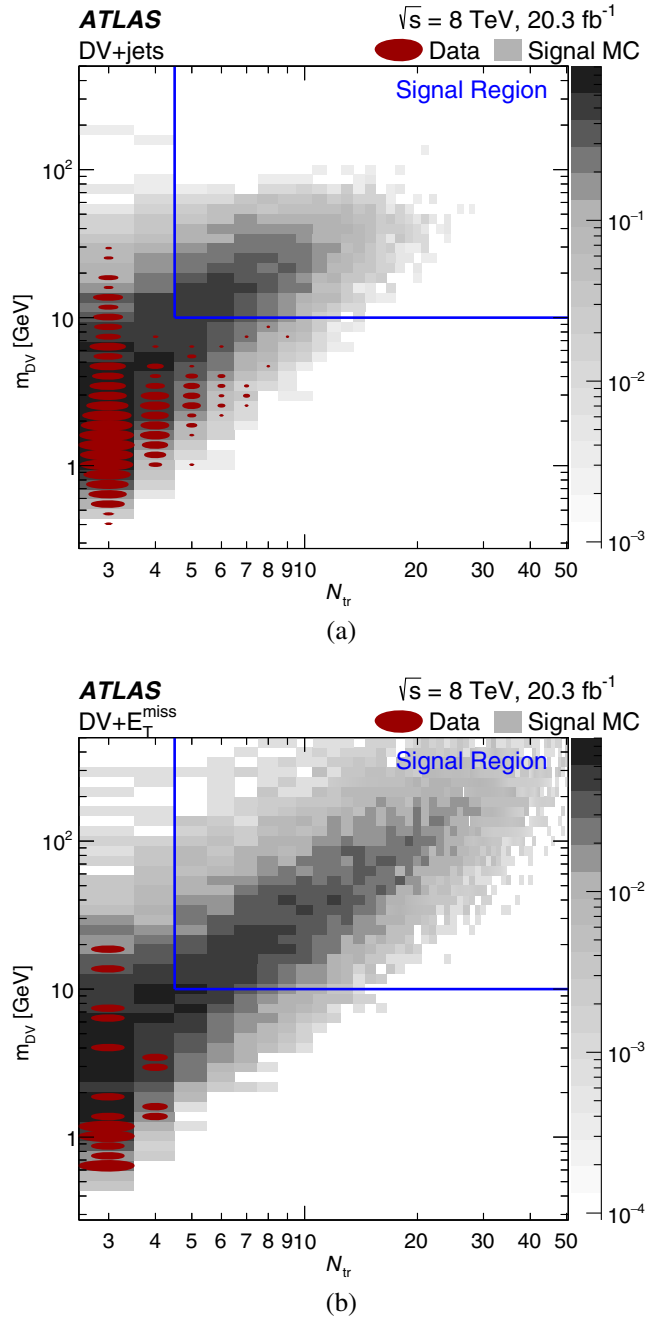

FIG. 11 (color online). The distribution of (a) DV + jets and (b) DV + $E_{\mathrm{T}}^{\mathrm{miss}}$ candidates in terms of the vertex mass versus the number of tracks in the vertex. The data distribution is shown with red ovals, the area of each oval being proportional to the logarithm of the number of vertex candidates in that bin. The gray squares show the $\tilde{g}(1.1\,\mathrm{TeV}) \to qq[\tilde{\chi}_1^0(400\,\mathrm{GeV}) \to \tilde{G}Z]$ GGM signal MC sample in (a) and the $[\tilde{g}(1.4\ \mathrm{TeV}) \to \tilde{\chi}_1^0(100\ \mathrm{GeV})qq/g]$ split-supersymmetry sample in (b). The signal region $N_{\mathrm{tr}} \geq 5$, $m_{\mathrm{DV}} > 10$ GeV is indicated.

two $eta|$ regions. The resulting change in the DV efficiency is taken as the tracking-efficiency systematic uncertainty. This uncertainty is evaluated separately for each value of $c\tau$, and is generally around 1%.

3. *Off-line lepton-identification efficiency*

The lepton-identification efficiency uncertainty is determined in ATLAS using $Z \to \ell\ell$ decays and is typically less than 1%. For this analysis, an additional

TABLE III. Model-independent 95% confidence-level upper limits on the visible cross section for new physics in each of our searches.

Channel	Upper limit on visible cross section [fb]
DV + jet	0.14
DV + $E_{\mathrm{T}}^{\mathrm{miss}}$	0.15
DV + muon	0.15
DV + electron	0.15
e^+e^-	0.14
$\mu^+\mu^-$	0.14
$e^\pm\mu^\mp$	0.15

uncertainty associated with identification of high-d_0 leptons is evaluated.

For muons, this is done by comparing a cosmic-ray muon simulation to cosmic-ray muon candidates in data. The events are required to pass the muon trigger and to have two muon candidates that fail the muon veto (see Sec. IV B 1). The MC muons are weighted so that their η and ϕ distributions are in agreement with those of the data. Comparing the ratio of the muon candidate d_0 distributions in data and in MC simulation yields a d_0-dependent efficiency correction that is between 1% and 2.5%, with an average value of 1.5%. The uncertainty associated with this procedure is taken from the statistical uncertainty, and is 2% on average.

Unlike in the case of cosmic-ray muons, there is no easily identifiable, high-rate source of large-d_0 electrons. Therefore, the performance of the simulation is validated by comparing the electron-identification efficiency $\epsilon_e(z_0)$ as a function of the longitudinal impact parameter z_0 of the

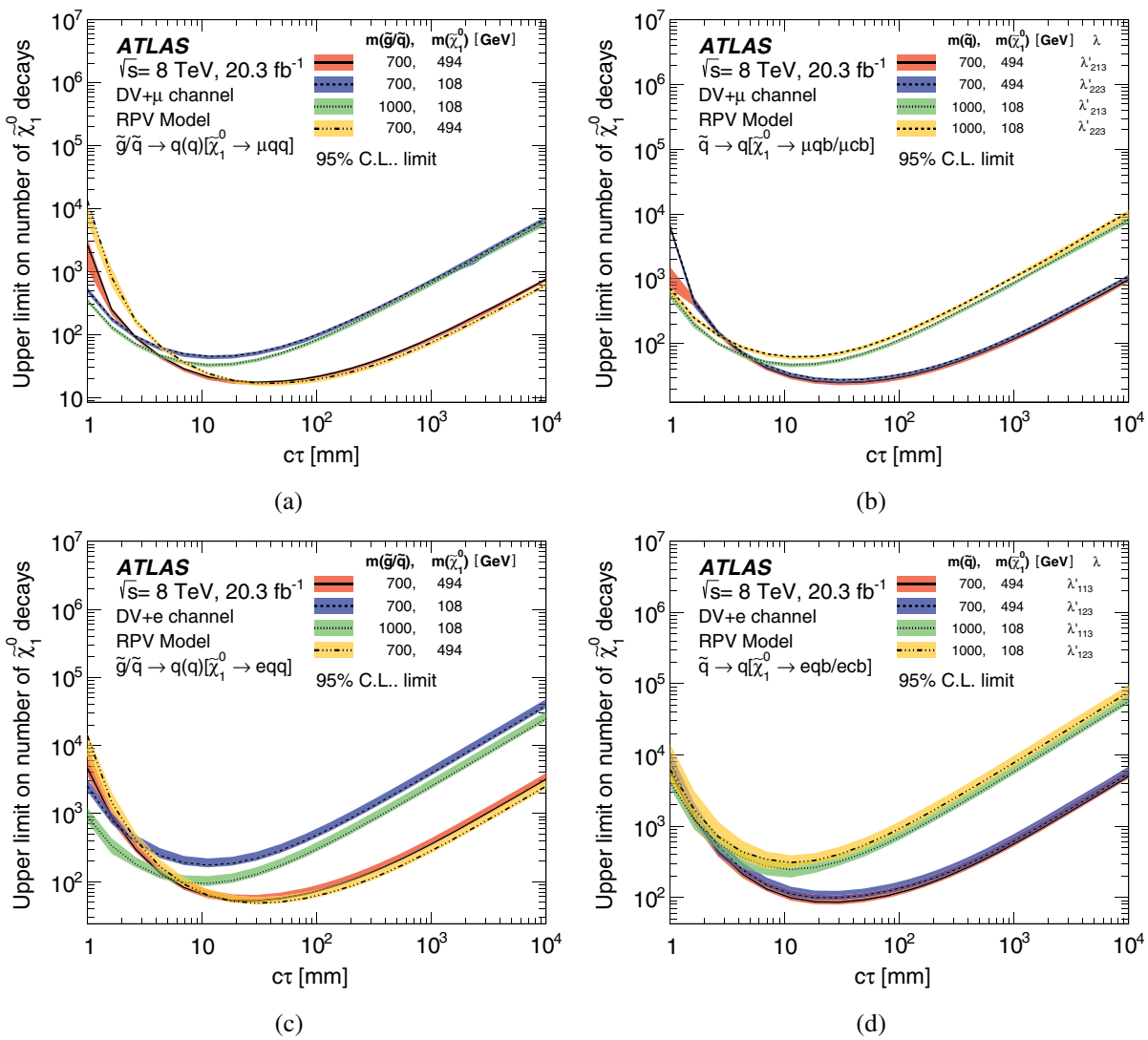

FIG. 12 (color online). RPV-scenario upper limits at 95% confidence level on the number of neutralinos in 20.3 fb^{-1} that decay into (a) μqq (with q indicating a u- or d-quark), (b) μqb and μcb (indicated by the nonzero RPV couplings λ'_{213} and λ'_{223}, respectively), (c) eqq, and (d) eqb and ecb (λ'_{113} and λ'_{123}, respectively). The upper limits account for the vertex-level efficiency for each value of the neutralino proper decay distance $c\tau$. The different curves show the results for different masses of the primary gluino or squark and of the long-lived neutralino, while the shaded bands indicate $\pm 1\sigma$ variations in the expected limit.

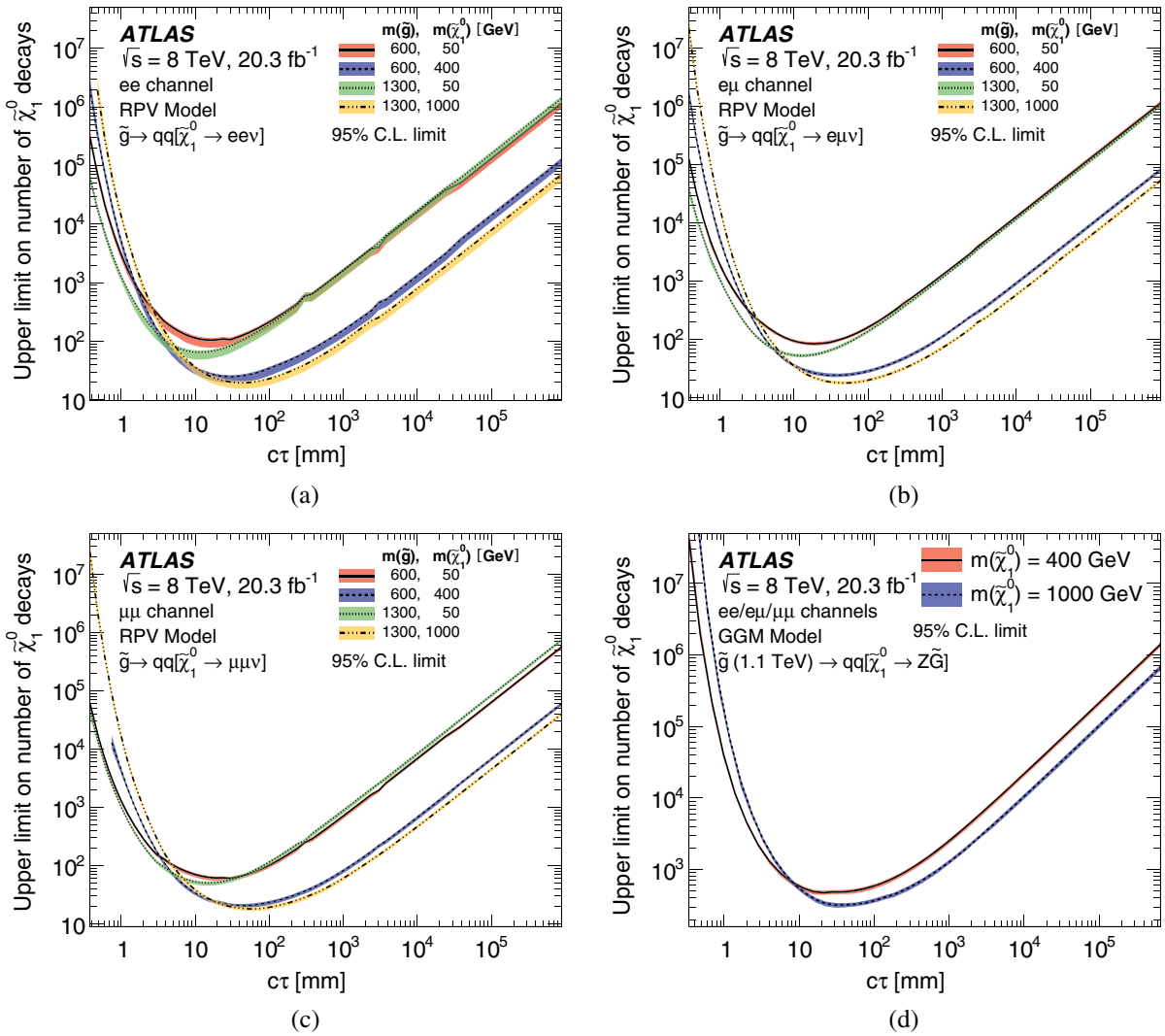

FIG. 13 (color online). Upper limits at 95% confidence level on the number of neutralinos in 20.3 fb^{-1} that decay into (a) $ee\nu$ in the RPV model, (b) $e\mu\nu$ in the RPV model, (c) $\mu\mu\nu$ in the RPV model, and (d) $Z\tilde{G}$ in the GGM model. The upper limits account for the vertex-level efficiency for each value of the neutralino proper decay distance $c\tau$. The different curves show the results for different masses of the primary gluino and of the long-lived neutralino, while the shaded bands indicate $\pm 1\sigma$ variations in the expected limit. In some cases limits are terminated for $c\tau \lesssim 1$ mm due to limited statistical precision.

electron candidate in data and MC simulation, measured with the tag-and-probe method using $Z \to e^+e^-$ events. It is observed that $\epsilon_e(z_0)$ is consistent in data and in MC simulation to better than 1% for $|z_0| < 250$ mm, beyond which there are too few events for an accurate measurement. Furthermore, the value of ϵ_e obtained with the tag-and-probe method is consistent to within 1% with that determined from MC generator-level information. This data-MC agreement in $\epsilon_e(z_0)$ is taken as an indication that the d_0 dependence of the efficiency, $\epsilon_e(d_0)$, is also well described by simulation. In signal MC samples, the function $\epsilon_e(d_0)$ varies by about 10% due to kinematic correlations between d_0 and factors that affect the efficiency, such as the value of r_{DV} and the boost of the LLP. To account for the possibility of an additional d_0 dependence that may not be well simulated, a systematic uncertainty of 10% on the electron-identification efficiency is assigned. This conservative uncertainty weakens the upper limits by less than 1%.

4. Jets and $E_{\mathrm{T}}^{\mathrm{miss}}$ reconstruction

The impact on the signal efficiency of uncertainties in the jet-energy scale calibration and jet-energy resolution is evaluated following the methods described in Refs. [57] and [58], respectively. An additional uncertainty on the jet p_{T} is evaluated for jets that originate from the decay of an LLP, by linearly parametrizing the p_{T} mismeasurement in MC simulation as a function of r_{DV} and z_{DV}. The only significant dependence observed is a relative p_{T}

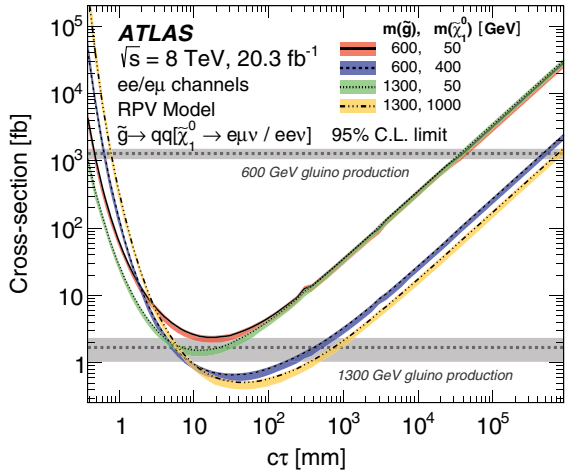

(a)

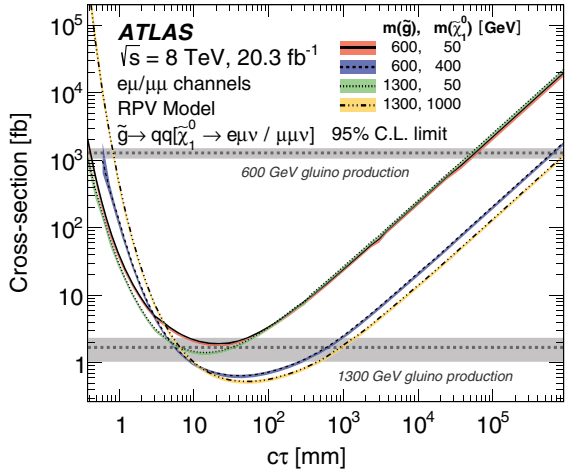

(b)

FIG. 14 (color online). The 95% confidence-level upper limits, obtained from the dilepton search, on the production cross section for a pair of gluinos of different masses that decay into two quarks and a long-lived neutralino in different models: (a) the RPV scenario with a pure λ_{121} coupling, (b) the RPV scenario with a pure λ_{122} coupling. All relevant final-state lepton-flavor combinations are used. The shaded bands around the observed limits indicate $\pm 1\sigma$ variations in the expected limit, while the horizontal bands show the theoretical cross sections and their uncertainties. In some cases limits are terminated for $c\tau \lesssim 1$ mm due to limited statistical precision.

mismeasurement of $(4 \pm 1) \times 10^{-5}(r_{\mathrm{DV}}/\mathrm{mm})$, which is propagated to the jet-selection efficiency as a systematic uncertainty. To account for possible mismodeling of trackless jets, an uncertainty is obtained by varying the requirement on $\sum_{\mathrm{tr}} p_{\mathrm{T}}$ for these jets. Systematic uncertainties in the $E_{\mathrm{T}}^{\mathrm{miss}}$ measurement are evaluated with the methods described in Refs. [53,54] and propagated to the efficiency uncertainty. The impact of uncertainties in the simulation of initial-state radiation is estimated by varying the p_{T} distribution of the primary particles according to the distribution observed in MADGRAPH5 [59]

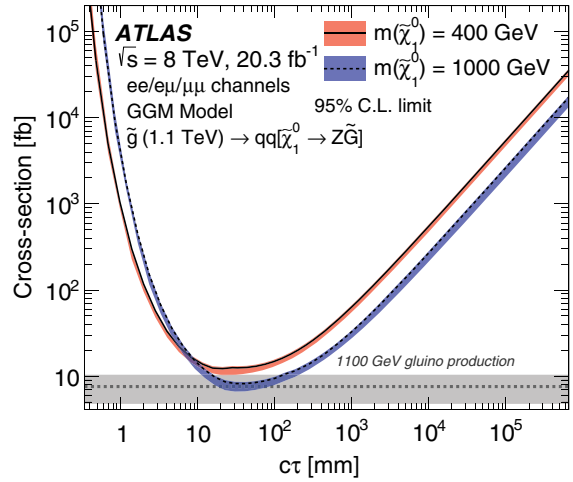

FIG. 15 (color online). The 95% confidence-level upper limits, obtained from the dilepton search, on the production cross section for a pair of gluinos of mass 1.1 TeV that decay into two quarks and a long-lived neutralino in the GGM scenario for two values of the neutralino mass. For further details see Fig. 14.

samples. The resulting efficiency uncertainty varies between 2% and 10%.

5. Multiple pp interactions

The dependence of the reconstruction efficiency on the number of pp interactions per bunch crossing is studied by varying the average number of interactions per LHC bunch crossing in the simulation by 4%. This value reflects uncertainties in the detector acceptance, trigger efficiency, and modeling of additional pp interactions. The resulting relative uncertainty is typically of order 1% or less.

VIII. RESULTS

Figure 9 shows the distribution of m_{DV} versus the number of associated lepton candidates in the selected data sample before the final selection requirements on these variables are applied. The distributions of m_{DV} versus the number of tracks in the vertex obtained for the multitrack-DV search are shown in Figs. 10 and 11. No events are seen in the signal region for any of the seven channels. In addition, no same-charge dilepton vertices are seen with $m_{\mathrm{DV}} > 10$ GeV. The distributions expected for some of the signal samples are also shown for comparison.

Given the lack of a signal observation, 95% confidence-level upper limits on the total visible cross section for new physics are shown in Table III.

Furthermore, for each of the physics scenarios considered, 95% confidence-level upper limits on the signal yields and production cross sections are calculated for different values of the proper decay distance $c\tau$ of the LLP and presented in the figures in this section. The limits are calculated using the CL_S prescription [60] with the profile likelihood used as the test statistic, using the

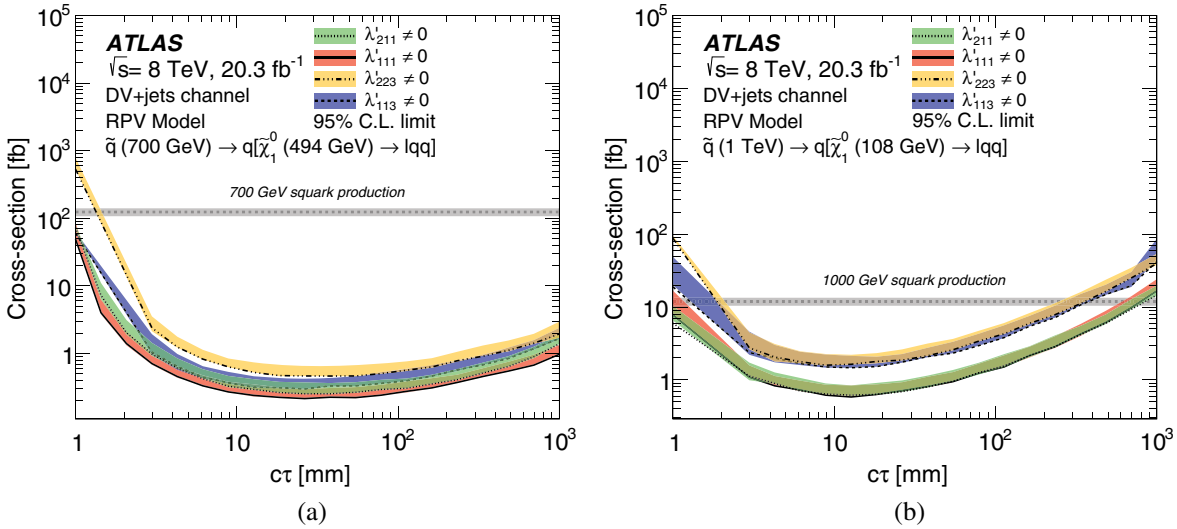

FIG. 16 (color online). The 95% confidence-level upper limits, obtained from the DV + jets search, on the production cross section for a pair of squarks in the RPV scenario, with the neutralino decaying to a lepton and two quarks, according to the nonzero λ' couplings indicated in each case. The squark and neutralino masses are (a) 700 GeV and 494 GeV or (b) 1 TeV and 108 GeV, respectively, representing the results for different neutralino masses and boosts. For further details see Fig. 14.

HistFitter [61] framework. Uncertainties on the signal efficiency and background expectation are included as nuisance parameters, and the CL_S values are calculated by generating ensembles of pseudoexperiments corresponding to the background-only and signal-plus-background hypotheses.

Since less than one background event is expected in all cases and no events are observed, the observed limits are very close to the expected limits.

In the case of the dilepton and DV + lepton searches, where the trigger and reconstruction depend almost exclusively on the signal DV, upper limits on the number of vertices produced in 20.3 fb^{-1} of data are presented for each channel, accounting for the vertex-level efficiency at each value of $c\tau$. Figure 12 shows these number limits for the DV + lepton search signatures. The limits are given separately for different masses of the long-lived neutralino and the primary squark or gluino, as well as for different λ'_{ijk} couplings, which give rise to light- or heavy-flavor quarks in the final state (see Sec. V for a discussion of the heavy-flavor and mass impact on efficiency). The number limits for the dilepton search signatures are shown in Fig. 13 for the final states ee, $\mu\mu$, $e\mu$, as well as for the combination of $Z \to ee$, $Z \to \mu\mu$, and $Z \to \tau\tau$.

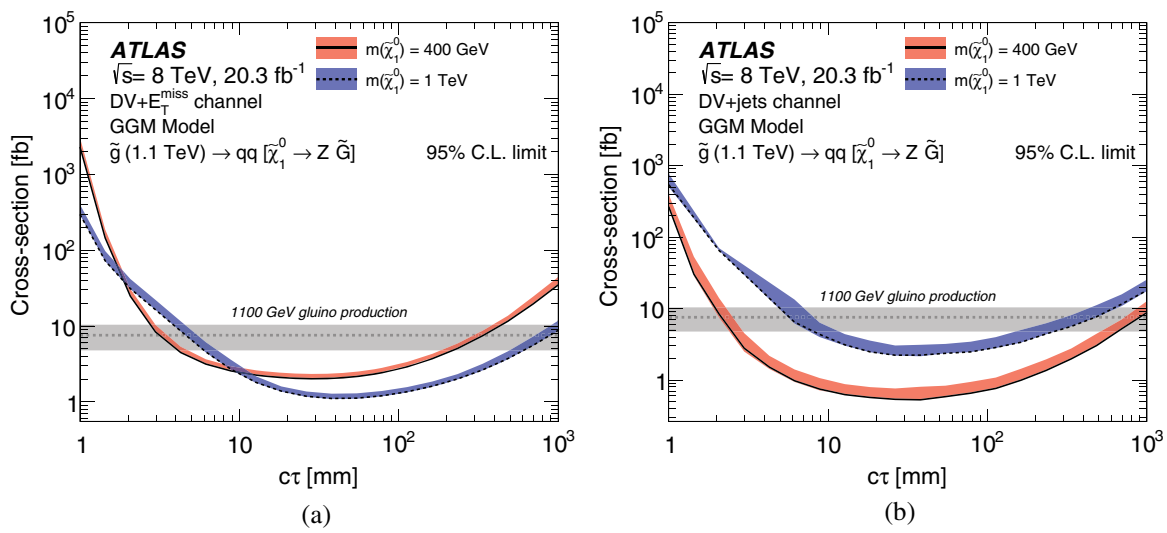

FIG. 17 (color online). The 95% confidence-level upper limits, obtained from the (a) DV + $E_{\mathrm{T}}^{\mathrm{miss}}$ and (b) DV + jets searches, on the production cross section for a pair of gluinos of mass 1.1 TeV that decay into two quarks and a long-lived neutralino in the GGM scenario. For further details see Fig. 14.

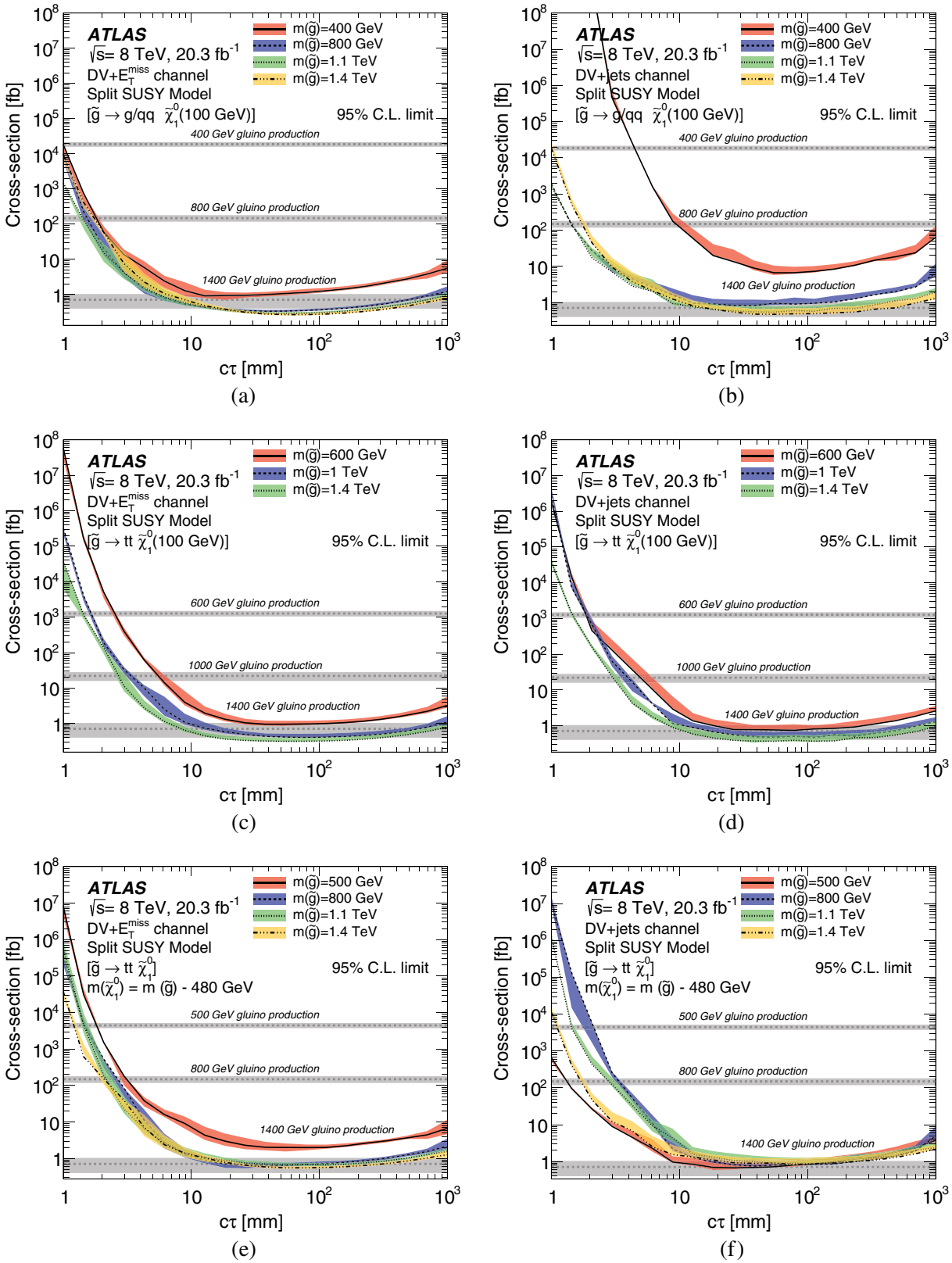

FIG. 18 (color online). The 95% confidence-level upper limits, obtained from the (a), (c), (e) DV + $E_{\mathrm{T}}^{\mathrm{miss}}$ and (b), (d), (f) DV + jets searches, on the cross section for gluino pair production in the split-supersymmetry model, with the gluino decaying to a neutralino plus either (a), (b) a gluon or a light-quark pair or (c), (d), (e), (f) a pair of top quarks. The mass of the neutralino is 100 GeV in (a), (b), (c), (d) and is 480 GeV smaller than the gluino mass in (e), (f). For further details see Fig. 14.

In addition, limits on the production cross sections for events are presented for the different simulated scenarios.

Figures 14 and 15 show cross-section upper limits obtained with the dilepton-DV search. Upper limits are shown for gluino-pair production in the RPV scenario, with neutralino decays determined by the choice of nonzero RPV coupling λ_{121} or λ_{122}, as well as within the GGM scenario with leptonic decays of the Z boson. For example, the RPV scenario is excluded for gluino mass $m_{\tilde{g}} = 600$ GeV, neutralino mass $m_{\tilde{\chi}_1^0} = 400$ GeV, and neutralino proper decay distance in the range $0.7 < c\tau < 3 \times 10^5$ mm.

Cross-section upper limits obtained with the multitrack-DV search are shown in the remaining figures. These limits are calculated up to proper decay distances of $c\tau = 1$ m, to avoid inaccuracies associated with reweighting events to very high lifetimes when the efficiency depends on both LLPs in the event.

Figure 16 shows the upper limits on the production cross section of two squarks in the RPV scenario, with different squark and neutralino masses, as well as different λ' parameters governing the neutralino decay. These limits are obtained with the DV + jets search, which results in tighter limits than the DV + lepton searches for this scenario. These results exclude a $m_{\tilde{q}} = 1$ TeV squark for $m_{\tilde{\chi}_1^0} = 108$ GeV and $2.5 < c\tau < 200$ mm with either light- or heavy-quark neutralino decays. Figure 17 shows the cross-section upper limits for gluino-pair production within the GGM scenario, using hadronic Z decays. The scenario is excluded, for instance, for $m_{\tilde{g}} = 1.1$ TeV and $m_{\tilde{\chi}_1^0} = 400$ GeV in the proper decay distance range $3 < c\tau < 500$ mm.

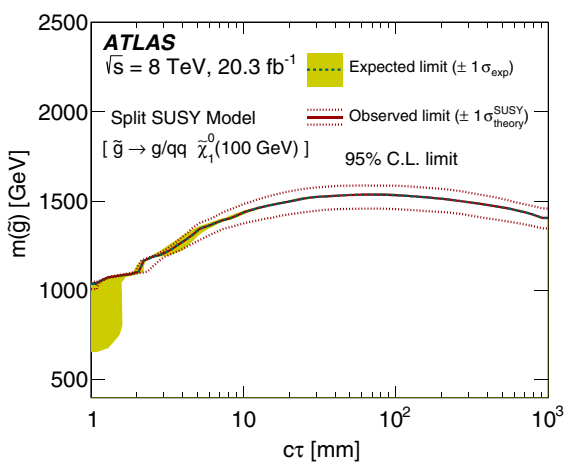

FIG. 19 (color online). The 95% confidence-level excluded regions lie below the curves shown in the mass-versus-$c\tau$ plane for the split-supersymmetry samples, with the gluino decaying into a gluon or light quarks, plus a 100 GeV neutralino. The shaded bands indicate $\pm 1\sigma$ variations in the expected limit, while the dotted lines indicate the effect of varying the production cross section by 1 standard deviation. The expected and observed limits are identical.

Figure 18 shows the upper limits on gluino-pair production cross section in the split-supersymmetry model. These limits are obtained from the results of the DV + $E_{\mathrm{T}}^{\mathrm{miss}}$ and DV + jets searches. The sensitivity is greater for the cases with $m_{\tilde{\chi}_1^0} = 100$ GeV than for those with $m_{\tilde{\chi}_1^0} = m_{\tilde{g}} - 480$ GeV, and the DV + $E_{\mathrm{T}}^{\mathrm{miss}}$ search performs better than DV + jets in these scenarios, excluding $m_{\tilde{g}} < 1400$ GeV in the range of proper decay lengths $15\ \mathrm{mm} < c\tau < 300$ mm.

In Figs. 19 and 20, the region of gluino mass versus proper decay distance that is excluded by these limits is shown. The limit for each point in parameter space is taken from the channel that is expected to yield the most stringent limit, which is DV + $E_{\mathrm{T}}^{\mathrm{miss}}$ for most points. For the region

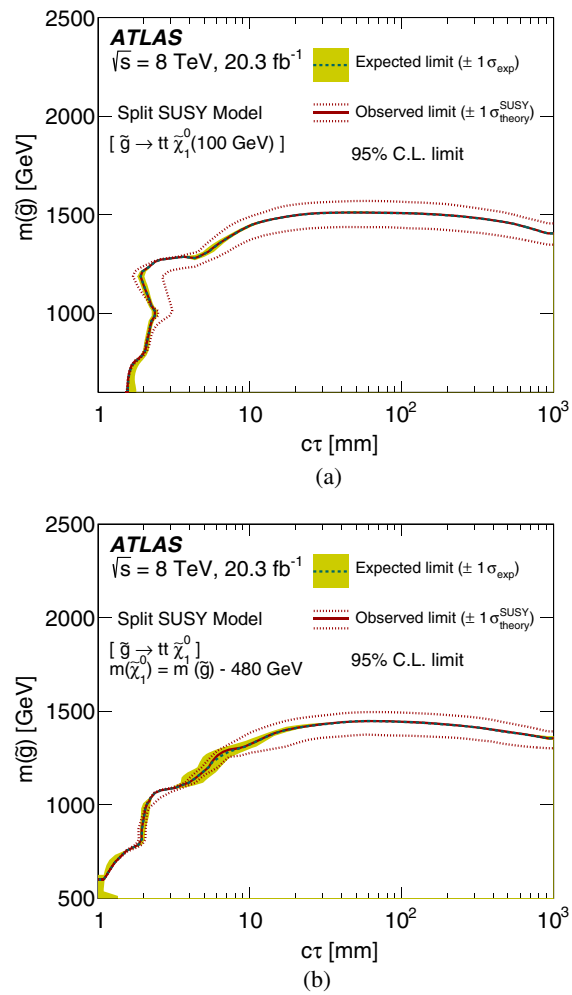

FIG. 20 (color online). The 95% confidence-level excluded regions lie below the curves shown in the mass-versus-$c\tau$ plane for the split-supersymmetry samples, with the gluino decaying into (a) a top quark pair and a 100 GeV neutralino, or (b) a top quark pair and a neutralino with a mass that is 480 GeV smaller than the gluino mass. The shaded bands indicate $\pm 1\sigma$ variations in the expected limit, while the dotted lines indicate the effect of varying the production cross section by 1 standard deviation. The expected and observed limits are identical.

of parameter space where the sensitivity is greatest, $20\ \mathrm{mm} < c\tau < 250\ \mathrm{mm}$ and $m_{\tilde{\chi}_1^0} = 100\ \mathrm{GeV}$, gluino masses of $m_{\tilde{g}} < 1500\ \mathrm{GeV}$ are excluded. This range of masses is comparable to or slightly larger than those excluded by prompt searches [62], searches for long-lived R-hadrons stopped in the ATLAS calorimeter [17], or searches for stable, massive, charged particles [19].

IX. SUMMARY AND CONCLUSIONS

This article reports on a search for long-lived particles decaying into two leptons or five or more charged particles. In the latter case, events are selected using associated lepton candidates, jets, or missing transverse momentum. The main signature of the search is a displaced vertex with an invariant mass greater than 10 GeV. This signature corresponds to a wide variety of new-physics models, many of which have not been searched for previously. The search uses the full data sample of pp collisions collected by the ATLAS detector at the LHC with a center-of-mass energy of $\sqrt{s} = 8$ TeV and an integrated luminosity of 20.3 fb^{-1}. Less than one background event is expected in each of the channels, and no events are observed. Upper limits are provided on the number of long-lived particle decays in the data sample and on the cross section for production of particles that give rise to the search signatures in a variety of supersymmetric models. These upper limits exclude significant regions of the parameter space of new-physics models with particle masses within reach of the LHC.

ACKNOWLEDGMENTS

We thank CERN for the very successful operation of the LHC, as well as the support staff from our institutions without whom ATLAS could not be operated efficiently. We acknowledge the support of ANPCyT, Argentina; YerPhI, Armenia; ARC, Australia; BMWFW and FWF, Austria; ANAS, Azerbaijan; SSTC, Belarus; CNPq and FAPESP, Brazil; NSERC, NRC, and CFI, Canada; CERN; CONICYT, Chile; CAS, MOST, and NSFC, China; COLCIENCIAS, Colombia; MSMT CR, MPO CR, and VSC CR, Czech Republic; DNRF, DNSRC, and Lundbeck Foundation, Denmark; EPLANET, ERC, and NSRF, European Union; IN2P3-CNRS, CEA-DSM/IRFU, France; GNSF, Georgia; BMBF, DFG, HGF, MPG, and AvH Foundation, Germany; GSRT and NSRF, Greece; RGC, Hong Kong SAR, China; ISF, MINERVA, GIF, I-CORE, and Benoziyo Center, Israel; INFN, Italy; MEXT and JSPS, Japan; CNRST, Morocco; FOM and NWO, Netherlands; BRF and RCN, Norway; MNiSW and NCN, Poland; GRICES and FCT, Portugal; MNE/IFA, Romania; MES of Russia and NRC KI, Russian Federation; JINR; MSTD, Serbia; MSSR, Slovakia; ARRS and MIZŠ, Slovenia; DST/NRF, South Africa; MINECO, Spain; SRC and Wallenberg Foundation, Sweden; SER, SNSF, and Cantons of Bern and Geneva, Switzerland; NSC, Taiwan; TAEK, Turkey; STFC, the Royal Society, and Leverhulme Trust, United Kingdom; DOE and NSF, United States of America. The crucial computing support from all WLCG partners is acknowledged gratefully, in particular from CERN and the ATLAS Tier-1 facilities at TRIUMF (Canada), NDGF (Denmark, Norway, Sweden), CC-IN2P3 (France), KIT/GridKA (Germany), INFN-CNAF (Italy), NL-T1 (Netherlands), PIC (Spain), ASGC (Taiwan), RAL (UK), and BNL (USA) and in the Tier-2 facilities worldwide.

[1] M. Fairbairn, A. C. Kraan, D. A. Milstead, T. Sjöstrand, P. Skands, and T. Sloan, Stable massive particles at colliders, Phys. Rep. **438**, 1 (2007).
[2] R. Barbier *et al.*, R-parity violating supersymmetry, Phys. Rep. **420**, 1 (2005).
[3] B. C. Allanach, M. A. Bernhardt, H. K. Dreiner, C. H. Kom, and P. Richardson, Mass Spectrum in R-Parity Violating mSUGRA and Benchmark Points, Phys. Rev. D **75**, 035002 (2007).
[4] S. Dimopoulos, M. Dine, S. Raby, and S. D. Thomas, Experimental Signatures of Low-Energy Gauge Mediated Supersymmetry Breaking, Phys. Rev. Lett. **76**, 3494 (1996).
[5] J. L. Hewett, B. Lillie, M. Masip, and T. G. Rizzo, Signatures of long-lived gluinos in split supersymmetry, J. High Energy Phys. 09 (2004) 070.
[6] A. Arvanitaki, N. Craig, S. Dimopoulos, and G. Villadoro, Mini-Split, J. High Energy Phys. 02 (2013) 126.
[7] M. J. Strassler and K. M. Zurek, Echoes of a hidden valley at hadron colliders, Phys. Lett. B **651**, 374 (2007).
[8] P. Schuster, N. Toro, and I. Yavin, Terrestrial and Solar Limits on Long-Lived Particles in a Dark Sector, Phys. Rev. D **81**, 016002 (2010).
[9] J. Fan, M. Reece, and J. T. Ruderman, Stealth Supersymmetry, J. High Energy Phys. 11 (2011) 012.
[10] A. Arbey, M. Battaglia, A. Djouadi, F. Mahmoudi, and J. Quevillon, Implications of a 125 GeV Higgs for supersymmetric models, Phys. Lett. B **708**, 162 (2012).
[11] ATLAS Collaboration, Observation of a new particle in the search for the Standard Model Higgs boson with the ATLAS detector at the LHC, Phys. Lett. B **716**, 1 (2012).
[12] CMS Collaboration, Observation of a new boson at a mass of 125 GeV with the CMS experiment at the LHC, Phys. Lett. B **716**, 30 (2012).

[13] ATLAS Collaboration, Search for displaced vertices arising from decays of new heavy particles in 7 TeV pp collisions at ATLAS, Phys. Lett. B **707**, 478 (2012).
[14] ATLAS Collaboration, Search for long-lived, heavy particles in final states with a muon and multi-track displaced vertex in proton-proton collisions at $\sqrt{s} = 7$ TeV with the ATLAS detector, Phys. Lett. B **719**, 280 (2013).
[15] ATLAS Collaboration, Search for displaced muonic lepton jets from light Higgs boson decay in proton-proton collisions at $\sqrt{s} = 7$ TeV with the ATLAS detector, Phys. Lett. B **721**, 32 (2013).
[16] ATLAS Collaboration, Search for pair-produced long-lived neutral particles decaying in the ATLAS hadronic calorimeter in pp collisions at $\sqrt{s} = 8$ TeV, Phys. Lett. B **743**, 15 (2015).
[17] ATLAS Collaboration, Search for long-lived stopped R-hadrons decaying out-of-time with pp collisions using the ATLAS detector, Phys. Rev. D **88**, 112003 (2013).
[18] ATLAS Collaboration, Search for long-lived, weakly interacting particles that decay to displaced hadronic jets in proton-proton collisions at $\sqrt{s} = 8$ TeV with the ATLAS detector, Phys. Rev. D **92**, 012010 (2015).
[19] ATLAS Collaboration, Searches for heavy long-lived charged particles with the ATLAS detector in proton-proton collisions at $\sqrt{s} = 8$ TeV, J. High Energy Phys. 01 (2015) 068.
[20] CMS Collaboration, Search in leptonic channels for heavy resonances decaying to long-lived neutral particles, J. High Energy Phys. 02 (2013) 085.
[21] V. Khachatryan *et al.* (CMS Collaboration), Search for long-lived particles that decay into final states containing two electrons or two muons in proton-proton collisions at $\sqrt{s} = 8$ TeV, Phys. Rev. D **91**, 052012 (2015).
[22] CMS Collaboration, Search for "Displaced Supersymmetry" in Events with an Electron and A Muon with Large Impact Parameters, Phys. Rev. Lett. **114**, 061801 (2015).
[23] CMS Collaboration, Search for long-lived neutral particles decaying to quark-antiquark pairs in proton-proton collisions at $\sqrt{s} = 8$ TeV, Phys. Rev. D **91**, 012007 (2015).
[24] LHCb Collaboration, Search for long-lived particles decaying to jet pairs, Eur. Phys. J. C **75**, 152 (2015).
[25] D. Liventsev *et al.* (Belle Collaboration), Search for heavy neutrinos at Belle, Phys. Rev. D **87**, 071102 (2013).
[26] J. P. Lees *et al.* (*BABAR* Collaboration), Search for Long-Lived Particles in e^+e^- Collisions, Phys. Rev. Lett. **114**, 171801 (2015).
[27] V. M. Abazov *et al.* (D0 Collaboration), Search for Neutral, Long-Lived Particles Decaying into Two Muons in $p\bar{p}$ Collisions at $\sqrt{s} = 1.96$ TeV, Phys. Rev. Lett. **97**, 161802 (2006).
[28] V. M. Abazov *et al.* (D0 Collaboration), Search for Resonant Pair Production of Neutral Long-Lived Particles Decaying to $b\bar{b}$ in $p\bar{p}$ Collisions at $\sqrt{s} = 1.96$ TeV, Phys. Rev. Lett. **103**, 071801 (2009).
[29] F. Abe *et al.* (CDF Collaboration), Search for long-lived parents of Z^0 bosons in $p\bar{p}$ collisions at $\sqrt{s} = 1.8$ TeV, Phys. Rev. D **58**, 051102 (1998).
[30] A. Heister *et al.* (ALEPH Collaboration), Search for gauge mediated SUSY breaking topologies in e^+e^- collisions at center-of-mass energies up to 209 GeV, Eur. Phys. J. C **25**, 339 (2002).
[31] ATLAS Collaboration, The ATLAS Experiment at the CERN Large Hadron Collider, J. Instrum. **3**, S08003 (2008).
[32] ATLAS Collaboration, Improved luminosity determination in pp collisions at $\sqrt{s} = 7$ TeV using the ATLAS detector at the LHC, Eur. Phys. J. C **73**, 2518 (2013).
[33] ATLAS Collaboration, ATLAS tunes of PYTHIA 6 and Pythia 8 for MC11, Report No. ATL-PHYS-PUB-2011-009, http://cds.cern.ch/record/1363300/, 2011.
[34] P. M. Nadolsky, H.-L. Lai, Q.-H. Cao, J. Huston, J. Pumplin, D. Stump, Wu-Ki Tung, and C.-P. Yuan, Implications of CTEQ global analysis for collider observables, Phys. Rev. D **78**, 013004 (2008).
[35] S. Agostinelli *et al.* (GEANT4 Collaboration), GEANT4: A Simulation toolkit, Nucl. Instrum. Methods Phys. Res., Sect. A **506**, 250 (2003).
[36] ATLAS Collaboration, The ATLAS Simulation Infrastructure, Eur. Phys. J. C **70**, 823 (2010).
[37] T. Sjöstrand, S. Mrenna, and P. Z. Skands, A Brief Introduction to PYTHIA 8.1, Comput. Phys. Commun. **178**, 852 (2008).
[38] M. Bähr *et al.*, Herwig + + Physics and Manual, Eur. Phys. J. C **58**, 639 (2008).
[39] T. Sjöstrand, S. Mrenna, and P. Z. Skands, PYTHIA 6.4 Physics and Manual, J. High Energy Phys. 05 (2006) 026.
[40] R. Mackeprang and D. Milstead, An Updated Description of Heavy-Hadron Interactions in GEANT-4, Eur. Phys. J. C **66**, 493 (2010).
[41] W. Beenakker, R. Höpker, M. Spira, and P. M. Zerwas, Squark and gluino production at hadron colliders, Nucl. Phys. **B492**, 51 (1997).
[42] A. Kulesza and L. Motyka, Threshold Resummation for Squark-Antisquark and Gluino-Pair Production at the LHC, Phys. Rev. Lett. **102**, 111802 (2009).
[43] A. Kulesza and L. Motyka, Soft gluon resummation for the production of gluino-gluino and squark-antisquark pairs at the LHC, Phys. Rev. D **80**, 095004 (2009).
[44] W. Beenakker, S. Brensing, M. Krämer, A. Kulesza, E. Laenen, and I. Niessen, Soft-gluon resummation for squark and gluino hadroproduction, J. High Energy Phys. 12 (2009) 041.
[45] W. Beenakker, S. Brensing, M. Krämer, A. Kulesza, E. Laenen, L. Motyka, and I. Niessen, Squark and Gluino Hadroproduction, Int. J. Mod. Phys. A **26**, 2637 (2011).
[46] M. Krämer, A. Kulesza, R. v. d. Leeuw, M. Mangano, S. Padhi, T. Plehn, and X. Portell, Supersymmetry production cross sections in pp collisions at $\sqrt{s} = 7$ TeV, arXiv: 1206.2892.
[47] ATLAS Collaboration, Measurement of the muon reconstruction performance of the ATLAS detector using 2011 and 2012 LHC proton-proton collision data, Eur. Phys. J. C **74**, 3130 (2014).
[48] ATLAS Collaboration, Electron and photon energy calibration with the ATLAS detector using LHC Run 1 data, Eur. Phys. J. C **74**, 3071 (2014).
[49] M. Cacciari, G. P. Salam, and G. Soyez, The anti-k_t jet clustering algorithm, J. High Energy Phys. 04 (2008) 063.
[50] M. Cacciari and G. P. Salam, Dispelling the N^3 myth for the k_t jet-finder, Phys. Lett. B **641**, 57 (2006).
[51] ATLAS Collaboration, Jet energy measurement with the ATLAS detector in proton-proton collisions at $\sqrt{s} = 7$ TeV, Eur. Phys. J. C **73**, 2304 (2013).

[52] W. Lampl, S. Laplace, D. Lelas, P. Loch, H. Ma, S. Menke, S. Rajagopalan, D. Rousseau, S. Snyder, and G. Unal, Calorimeter clustering algorithms: Description and performance, Report No. ATL-LARG-PUB-2008-002, http://cds.cern.ch/record/1099735/, 2008.
[53] ATLAS Collaboration, Performance of Missing Transverse Momentum Reconstruction in Proton-Proton Collisions at 7 TeV with ATLAS, Eur. Phys. J. C **72**, 1844 (2012).
[54] ATLAS Collaboration, Performance of Missing Transverse Momentum Reconstruction in ATLAS studied in Proton-Proton Collisions recorded in 2012 at 8 TeV, Report No. ATLAS-CONF-2013-082, http://cds.cern.ch/record/1570993/, 2013.
[55] S. R. Das, On a new approach for finding all the modified cut-sets in an incompatibility graph, IEEE Trans. Comput. **C-22**, 187 (1973).
[56] ATLAS Collaboration, Characterisation and mitigation of beam-induced backgrounds observed in the ATLAS detector during the 2011 proton-proton run, J. Instrum. **8**, P07004 (2013).
[57] ATLAS Collaboration, Jet energy measurement and its systematic uncertainty in proton-proton collisions at $\sqrt{s} = 7$ TeV with the ATLAS detector, Eur. Phys. J. C **75**, 17 (2015).
[58] ATLAS Collaboration, Jet energy resolution in proton-proton collisions at $\sqrt{s} = 7$ TeV recorded in 2010 with the ATLAS detector, Eur. Phys. J. C **73**, 2306 (2013).
[59] J. Alwall, M. Herquet, F. Maltoni, O. Mattelaer, and T. Stelzer, MadGraph 5 : Going Beyond, J. High Energy Phys. 06 (2011) 128.
[60] A. L. Read, Presentation of search results: The CL(s) technique, J. Phys. G **28**, 2693 (2002).
[61] M. Baak, G. J. Besjes, D. Côté, A. Koutsman, J. Lorenz, and D. Short, HistFitter software framework for statistical data analysis, Eur. Phys. J. C **75**, 153 (2015).
[62] ATLAS Collaboration, Search for squarks and gluinos with the ATLAS detector in final states with jets and missing transverse momentum using $\sqrt{s} = 8$ TeV proton–proton collision data, J. High Energy Phys. 09 (2014) 176.

G. Aad,[85] B. Abbott,[113] J. Abdallah,[151] O. Abdinov,[11] R. Aben,[107] M. Abolins,[90] O. S. AbouZeid,[158] H. Abramowicz,[153] H. Abreu,[152] R. Abreu,[30] Y. Abulaiti,[146a,146b] B. S. Acharya,[164a,164b,b] L. Adamczyk,[38a] D. L. Adams,[25] J. Adelman,[108] S. Adomeit,[100] T. Adye,[131] A. A. Affolder,[74] T. Agatonovic-Jovin,[13] J. A. Aguilar-Saavedra,[126a,126f] S. P. Ahlen,[22] F. Ahmadov,[65,c] G. Aielli,[133a,133b] H. Akerstedt,[146a,146b] T. P. A. Åkesson,[81] G. Akimoto,[155] A. V. Akimov,[96] G. L. Alberghi,[20a,20b] J. Albert,[169] S. Albrand,[55] M. J. Alconada Verzini,[71] M. Aleksa,[30] I. N. Aleksandrov,[65] C. Alexa,[26a] G. Alexander,[153] T. Alexopoulos,[10] M. Alhroob,[113] G. Alimonti,[91a] L. Alio,[85] J. Alison,[31] S. P. Alkire,[35] B. M. M. Allbrooke,[18] P. P. Allport,[74] A. Aloisio,[104a,104b] A. Alonso,[36] F. Alonso,[71] C. Alpigiani,[76] A. Altheimer,[35] B. Alvarez Gonzalez,[30] D. Álvarez Piqueras,[167] M. G. Alviggi,[104a,104b] B. T. Amadio,[15] K. Amako,[66] Y. Amaral Coutinho,[24a] C. Amelung,[23] D. Amidei,[89] S. P. Amor Dos Santos,[126a,126c] A. Amorim,[126a,126b] S. Amoroso,[48] N. Amram,[153] G. Amundsen,[23] C. Anastopoulos,[139] L. S. Ancu,[49] N. Andari,[30] T. Andeen,[35] C. F. Anders,[58b] G. Anders,[30] J. K. Anders,[74] K. J. Anderson,[31] A. Andreazza,[91a,91b] V. Andrei,[58a] S. Angelidakis,[9] I. Angelozzi,[107] P. Anger,[44] A. Angerami,[35] F. Anghinolfi,[30] A. V. Anisenkov,[109,d] N. Anjos,[12] A. Annovi,[124a,124b] M. Antonelli,[47] A. Antonov,[98] J. Antos,[144b] F. Anulli,[132a] M. Aoki,[66] L. Aperio Bella,[18] G. Arabidze,[90] Y. Arai,[66] J. P. Araque,[126a] A. T. H. Arce,[45] F. A. Arduh,[71] J-F. Arguin,[95] S. Argyropoulos,[42] M. Arik,[19a] A. J. Armbruster,[30] O. Arnaez,[30] V. Arnal,[82] H. Arnold,[48] M. Arratia,[28] O. Arslan,[21] A. Artamonov,[97] G. Artoni,[23] S. Asai,[155] N. Asbah,[42] A. Ashkenazi,[153] B. Åsman,[146a,146b] L. Asquith,[149] K. Assamagan,[25] R. Astalos,[144a] M. Atkinson,[165] N. B. Atlay,[141] B. Auerbach,[6] K. Augsten,[128] M. Aurousseau,[145b] G. Avolio,[30] B. Axen,[15] M. K. Ayoub,[117] G. Azuelos,[95,e] M. A. Baak,[30] A. E. Baas,[58a] C. Bacci,[134a,134b] H. Bachacou,[136] K. Bachas,[154] M. Backes,[30] M. Backhaus,[30] E. Badescu,[26a] P. Bagiacchi,[132a,132b] P. Bagnaia,[132a,132b] Y. Bai,[33a] T. Bain,[35] J. T. Baines,[131] O. K. Baker,[176] P. Balek,[129] T. Balestri,[148] F. Balli,[84] E. Banas,[39] Sw. Banerjee,[173] A. A. E. Bannoura,[175] H. S. Bansil,[18] L. Barak,[30] S. P. Baranov,[96] E. L. Barberio,[88] D. Barberis,[50a,50b] M. Barbero,[85] T. Barillari,[101] M. Barisonzi,[164a,164b] T. Barklow,[143] N. Barlow,[28] S. L. Barnes,[84] B. M. Barnett,[131] R. M. Barnett,[15] Z. Barnovska,[5] A. Baroncelli,[134a] G. Barone,[49] A. J. Barr,[120] F. Barreiro,[82] J. Barreiro Guimarães da Costa,[57] R. Bartoldus,[143] A. E. Barton,[72] P. Bartos,[144a] A. Bassalat,[117] A. Basye,[165] R. L. Bates,[53] S. J. Batista,[158] J. R. Batley,[28] M. Battaglia,[137] M. Bauce,[132a,132b] F. Bauer,[136] H. S. Bawa,[143,f] J. B. Beacham,[111] M. D. Beattie,[72] T. Beau,[80] P. H. Beauchemin,[161] R. Beccherle,[124a,124b] P. Bechtle,[21] H. P. Beck,[17,g] K. Becker,[120] M. Becker,[83] S. Becker,[100] M. Beckingham,[170] C. Becot,[117] A. J. Beddall,[19c] A. Beddall,[19c] V. A. Bednyakov,[65] C. P. Bee,[148] L. J. Beemster,[107] T. A. Beermann,[175] M. Begel,[25] J. K. Behr,[120] C. Belanger-Champagne,[87] P. J. Bell,[49] W. H. Bell,[49] G. Bella,[153] L. Bellagamba,[20a] A. Bellerive,[29] M. Bellomo,[86] K. Belotskiy,[98] O. Beltramello,[30] O. Benary,[153] D. Benchekroun,[135a] M. Bender,[100] K. Bendtz,[146a,146b] N. Benekos,[10] Y. Benhammou,[153] E. Benhar Noccioli,[49] J. A. Benitez Garcia,[159b] D. P. Benjamin,[45] J. R. Bensinger,[23] S. Bentvelsen,[107]

L. Beresford,[120] M. Beretta,[47] D. Berge,[107] E. Bergeaas Kuutmann,[166] N. Berger,[5] F. Berghaus,[169] J. Beringer,[15] C. Bernard,[22] N. R. Bernard,[86] C. Bernius,[110] F. U. Bernlochner,[21] T. Berry,[77] P. Berta,[129] C. Bertella,[83] G. Bertoli,[146a,146b] F. Bertolucci,[124a,124b] C. Bertsche,[113] D. Bertsche,[113] M. I. Besana,[91a] G. J. Besjes,[106] O. Bessidskaia Bylund,[146a,146b] M. Bessner,[42] N. Besson,[136] C. Betancourt,[48] S. Bethke,[101] A. J. Bevan,[76] W. Bhimji,[46] R. M. Bianchi,[125] L. Bianchini,[23] M. Bianco,[30] O. Biebel,[100] S. P. Bieniek,[78] M. Biglietti,[134a] J. Bilbao De Mendizabal,[49] H. Bilokon,[47] M. Bindi,[54] S. Binet,[117] A. Bingul,[19c] C. Bini,[132a,132b] C. W. Black,[150] J. E. Black,[143] K. M. Black,[22] D. Blackburn,[138] R. E. Blair,[6] J.-B. Blanchard,[136] J. E. Blanco,[77] T. Blazek,[144a] I. Bloch,[42] C. Blocker,[23] W. Blum,[83,a] U. Blumenschein,[54] G. J. Bobbink,[107] V. S. Bobrovnikov,[109,d] S. S. Bocchetta,[81] A. Bocci,[45] C. Bock,[100] M. Boehler,[48] J. A. Bogaerts,[30] A. G. Bogdanchikov,[109] C. Bohm,[146a] V. Boisvert,[77] T. Bold,[38a] V. Boldea,[26a] A. S. Boldyrev,[99] M. Bomben,[80] M. Bona,[76] M. Boonekamp,[136] A. Borisov,[130] G. Borissov,[72] S. Borroni,[42] J. Bortfeldt,[100] V. Bortolotto,[60a,60b,60c] K. Bos,[107] D. Boscherini,[20a] M. Bosman,[12] J. Boudreau,[125] J. Bouffard,[2] E. V. Bouhova-Thacker,[72] D. Boumediene,[34] C. Bourdarios,[117] N. Bousson,[114] A. Boveia,[30] J. Boyd,[30] I. R. Boyko,[65] I. Bozic,[13] J. Bracinik,[18] A. Brandt,[8] G. Brandt,[54] O. Brandt,[58a] U. Bratzler,[156] B. Brau,[86] J. E. Brau,[116] H. M. Braun,[175,a] S. F. Brazzale,[164a,164c] K. Brendlinger,[122] A. J. Brennan,[88] L. Brenner,[107] R. Brenner,[166] S. Bressler,[172] K. Bristow,[145c] T. M. Bristow,[46] D. Britton,[53] D. Britzger,[42] F. M. Brochu,[28] I. Brock,[21] R. Brock,[90] J. Bronner,[101] G. Brooijmans,[35] T. Brooks,[77] W. K. Brooks,[32b] J. Brosamer,[15] E. Brost,[116] J. Brown,[55] P. A. Bruckman de Renstrom,[39] D. Bruncko,[144b] R. Bruneliere,[48] A. Bruni,[20a] G. Bruni,[20a] M. Bruschi,[20a] L. Bryngemark,[81] T. Buanes,[14] Q. Buat,[142] P. Buchholz,[141] A. G. Buckley,[53] S. I. Buda,[26a] I. A. Budagov,[65] F. Buehrer,[48] L. Bugge,[119] M. K. Bugge,[119] O. Bulekov,[98] D. Bullock,[8] H. Burckhart,[30] S. Burdin,[74] B. Burghgrave,[108] S. Burke,[131] I. Burmeister,[43] E. Busato,[34] D. Büscher,[48] V. Büscher,[83] P. Bussey,[53] C. P. Buszello,[166] J. M. Butler,[22] A. I. Butt,[3] C. M. Buttar,[53] J. M. Butterworth,[78] P. Butti,[107] W. Buttinger,[25] A. Buzatu,[53] R. Buzykaev,[109,d] S. Cabrera Urbán,[167] D. Caforio,[128] V. M. Cairo,[37a,37b] O. Cakir,[4a] P. Calafiura,[15] A. Calandri,[136] G. Calderini,[80] P. Calfayan,[100] L. P. Caloba,[24a] D. Calvet,[34] S. Calvet,[34] R. Camacho Toro,[49] S. Camarda,[42] P. Camarri,[133a,133b] D. Cameron,[119] L. M. Caminada,[15] R. Caminal Armadans,[12] S. Campana,[30] M. Campanelli,[78] A. Campoverde,[148] V. Canale,[104a,104b] A. Canepa,[159a] M. Cano Bret,[76] J. Cantero,[82] R. Cantrill,[126a] T. Cao,[40] M. D. M. Capeans Garrido,[30] I. Caprini,[26a] M. Caprini,[26a] M. Capua,[37a,37b] R. Caputo,[83] R. Cardarelli,[133a] T. Carli,[30] G. Carlino,[104a] L. Carminati,[91a,91b] S. Caron,[106] E. Carquin,[32a] G. D. Carrillo-Montoya,[8] J. R. Carter,[28] J. Carvalho,[126a,126c] D. Casadei,[78] M. P. Casado,[12] M. Casolino,[12] E. Castaneda-Miranda,[145b] A. Castelli,[107] V. Castillo Gimenez,[167] N. F. Castro,[126a,h] P. Catastini,[57] A. Catinaccio,[30] J. R. Catmore,[119] A. Cattai,[30] J. Caudron,[83] V. Cavaliere,[165] D. Cavalli,[91a] M. Cavalli-Sforza,[12] V. Cavasinni,[124a,124b] F. Ceradini,[134a,134b] B. C. Cerio,[45] K. Cerny,[129] A. S. Cerqueira,[24b] A. Cerri,[149] L. Cerrito,[76] F. Cerutti,[15] M. Cerv,[30] A. Cervelli,[17] S. A. Cetin,[19b] A. Chafaq,[135a] D. Chakraborty,[108] I. Chalupkova,[129] P. Chang,[165] B. Chapleau,[87] J. D. Chapman,[28] D. G. Charlton,[18] C. C. Chau,[158] C. A. Chavez Barajas,[149] S. Cheatham,[152] A. Chegwidden,[90] S. Chekanov,[6] S. V. Chekulaev,[159a] G. A. Chelkov,[65,i] M. A. Chelstowska,[89] C. Chen,[64] H. Chen,[25] K. Chen,[148] L. Chen,[33d,j] S. Chen,[33c] X. Chen,[33f] Y. Chen,[67] H. C. Cheng,[89] Y. Cheng,[31] A. Cheplakov,[65] E. Cheremushkina,[130] R. Cherkaoui El Moursli,[135e] V. Chernyatin,[25,a] E. Cheu,[7] L. Chevalier,[136] V. Chiarella,[47] J. T. Childers,[6] G. Chiodini,[73a] A. S. Chisholm,[18] R. T. Chislett,[78] A. Chitan,[26a] M. V. Chizhov,[65] K. Choi,[61] S. Chouridou,[9] B. K. B. Chow,[100] V. Christodoulou,[78] D. Chromek-Burckhart,[30] M. L. Chu,[151] J. Chudoba,[127] A. J. Chuinard,[87] J. J. Chwastowski,[39] L. Chytka,[115] G. Ciapetti,[132a,132b] A. K. Ciftci,[4a] D. Cinca,[53] V. Cindro,[75] I. A. Cioara,[21] A. Ciocio,[15] Z. H. Citron,[172] M. Ciubancan,[26a] A. Clark,[49] B. L. Clark,[57] P. J. Clark,[46] R. N. Clarke,[15] W. Cleland,[125] C. Clement,[146a,146b] Y. Coadou,[85] M. Cobal,[164a,164c] A. Coccaro,[138] J. Cochran,[64] L. Coffey,[23] J. G. Cogan,[143] B. Cole,[35] S. Cole,[108] A. P. Colijn,[107] J. Collot,[55] T. Colombo,[58c] G. Compostella,[101] P. Conde Muiño,[126a,126b] E. Coniavitis,[48] S. H. Connell,[145b] I. A. Connelly,[77] S. M. Consonni,[91a,91b] V. Consorti,[48] S. Constantinescu,[26a] C. Conta,[121a,121b] G. Conti,[30] F. Conventi,[104a,k] M. Cooke,[15] B. D. Cooper,[78] A. M. Cooper-Sarkar,[120] T. Cornelissen,[175] M. Corradi,[20a] F. Corriveau,[87,l] A. Corso-Radu,[163] A. Cortes-Gonzalez,[12] G. Cortiana,[101] G. Costa,[91a] M. J. Costa,[167] D. Costanzo,[139] D. Côté,[8] G. Cottin,[28] G. Cowan,[77] B. E. Cox,[84] K. Cranmer,[110] G. Cree,[29] S. Crépé-Renaudin,[55] F. Crescioli,[80] W. A. Cribbs,[146a,146b] M. Crispin Ortuzar,[120] M. Cristinziani,[21] V. Croft,[106] G. Crosetti,[37a,37b] T. Cuhadar Donszelmann,[139] J. Cummings,[176] M. Curatolo,[47] C. Cuthbert,[150] H. Czirr,[141] P. Czodrowski,[3] S. D'Auria,[53] M. D'Onofrio,[74] M. J. Da Cunha Sargedas De Sousa,[126a,126b] C. Da Via,[84] W. Dabrowski,[38a] A. Dafinca,[120] T. Dai,[89] O. Dale,[14] F. Dallaire,[95] C. Dallapiccola,[86] M. Dam,[36] J. R. Dandoy,[31] N. P. Dang,[48] A. C. Daniells,[18] M. Danninger,[168] M. Dano Hoffmann,[136] V. Dao,[48] G. Darbo,[50a] S. Darmora,[8] J. Dassoulas,[3] A. Dattagupta,[61] W. Davey,[21] C. David,[169] T. Davidek,[129] E. Davies,[120,m] M. Davies,[153] P. Davison,[78] Y. Davygora,[58a]

E. Dawe,[88] I. Dawson,[139] R. K. Daya-Ishmukhametova,[86] K. De,[8] R. de Asmundis,[104a] S. De Castro,[20a,20b] S. De Cecco,[80] N. De Groot,[106] P. de Jong,[107] H. De la Torre,[82] F. De Lorenzi,[64] L. De Nooij,[107] D. De Pedis,[132a] A. De Salvo,[132a] U. De Sanctis,[149] A. De Santo,[149] J. B. De Vivie De Regie,[117] W. J. Dearnaley,[72] R. Debbe,[25] C. Debenedetti,[137] D. V. Dedovich,[65] I. Deigaard,[107] J. Del Peso,[82] T. Del Prete,[124a,124b] D. Delgove,[117] F. Deliot,[136] C. M. Delitzsch,[49] M. Deliyergiyev,[75] A. Dell'Acqua,[30] L. Dell'Asta,[22] M. Dell'Orso,[124a,124b] M. Della Pietra,[104a,k] D. della Volpe,[49] M. Delmastro,[5] P. A. Delsart,[55] C. Deluca,[107] D. A. DeMarco,[158] S. Demers,[176] M. Demichev,[65] A. Demilly,[80] S. P. Denisov,[130] D. Derendarz,[39] J. E. Derkaoui,[135d] F. Derue,[80] P. Dervan,[74] K. Desch,[21] C. Deterre,[42] P. O. Deviveiros,[30] A. Dewhurst,[131] S. Dhaliwal,[107] A. Di Ciaccio,[133a,133b] L. Di Ciaccio,[5] A. Di Domenico,[132a,132b] C. Di Donato,[104a,104b] A. Di Girolamo,[30] B. Di Girolamo,[30] A. Di Mattia,[152] B. Di Micco,[134a,134b] R. Di Nardo,[47] A. Di Simone,[48] R. Di Sipio,[158] D. Di Valentino,[29] C. Diaconu,[85] M. Diamond,[158] F. A. Dias,[46] M. A. Diaz,[32a] E. B. Diehl,[89] J. Dietrich,[16] S. Diglio,[85] A. Dimitrievska,[13] J. Dingfelder,[21] F. Dittus,[30] F. Djama,[85] T. Djobava,[51b] J. I. Djuvsland,[58a] M. A. B. do Vale,[24c] D. Dobos,[30] M. Dobre,[26a] C. Doglioni,[49] T. Dohmae,[155] J. Dolejsi,[129] Z. Dolezal,[129] B. A. Dolgoshein,[98,a] M. Donadelli,[24d] S. Donati,[124a,124b] P. Dondero,[121a,121b] J. Donini,[34] J. Dopke,[131] A. Doria,[104a] M. T. Dova,[71] A. T. Doyle,[53] E. Drechsler,[54] M. Dris,[10] E. Dubreuil,[34] E. Duchovni,[172] G. Duckeck,[100] O. A. Ducu,[26a,85] D. Duda,[175] A. Dudarev,[30] L. Duflot,[117] L. Duguid,[77] M. Dührssen,[30] M. Dunford,[58a] H. Duran Yildiz,[4a] M. Düren,[52] A. Durglishvili,[51b] D. Duschinger,[44] M. Dyndal,[38a] C. Eckardt,[42] K. M. Ecker,[101] R. C. Edgar,[89] W. Edson,[2] N. C. Edwards,[46] W. Ehrenfeld,[21] T. Eifert,[30] G. Eigen,[14] K. Einsweiler,[15] T. Ekelof,[166] M. El Kacimi,[135c] M. Ellert,[166] S. Elles,[5] F. Ellinghaus,[83] A. A. Elliot,[169] N. Ellis,[30] J. Elmsheuser,[100] M. Elsing,[30] D. Emeliyanov,[131] Y. Enari,[155] O. C. Endner,[83] M. Endo,[118] R. Engelmann,[148] J. Erdmann,[43] A. Ereditato,[17] G. Ernis,[175] J. Ernst,[2] M. Ernst,[25] S. Errede,[165] E. Ertel,[83] M. Escalier,[117] H. Esch,[43] C. Escobar,[125] B. Esposito,[47] A. I. Etienvre,[136] E. Etzion,[153] H. Evans,[61] A. Ezhilov,[123] L. Fabbri,[20a,20b] G. Facini,[31] R. M. Fakhrutdinov,[130] S. Falciano,[132a] R. J. Falla,[78] J. Faltova,[129] Y. Fang,[33a] M. Fanti,[91a,91b] A. Farbin,[8] A. Farilla,[134a] T. Farooque,[12] S. Farrell,[15] S. M. Farrington,[170] P. Farthouat,[30] F. Fassi,[135e] P. Fassnacht,[30] D. Fassouliotis,[9] M. Faucci Giannelli,[77] A. Favareto,[50a,50b] L. Fayard,[117] P. Federic,[144a] O. L. Fedin,[123,n] W. Fedorko,[168] S. Feigl,[30] L. Feligioni,[85] C. Feng,[33d] E. J. Feng,[6] H. Feng,[89] A. B. Fenyuk,[130] P. Fernandez Martinez,[167] S. Fernandez Perez,[30] S. Ferrag,[53] J. Ferrando,[53] A. Ferrari,[166] P. Ferrari,[107] R. Ferrari,[121a] D. E. Ferreira de Lima,[53] A. Ferrer,[167] D. Ferrere,[49] C. Ferretti,[89] A. Ferretto Parodi,[50a,50b] M. Fiascaris,[31] F. Fiedler,[83] A. Filipčič,[75] M. Filipuzzi,[42] F. Filthaut,[106] M. Fincke-Keeler,[169] K. D. Finelli,[150] M. C. N. Fiolhais,[126a,126c] L. Fiorini,[167] A. Firan,[40] A. Fischer,[2] C. Fischer,[12] J. Fischer,[175] W. C. Fisher,[90] E. A. Fitzgerald,[23] M. Flechl,[48] I. Fleck,[141] P. Fleischmann,[89] S. Fleischmann,[175] G. T. Fletcher,[139] G. Fletcher,[76] T. Flick,[175] A. Floderus,[81] L. R. Flores Castillo,[60a] M. J. Flowerdew,[101] A. Formica,[136] A. Forti,[84] D. Fournier,[117] H. Fox,[72] S. Fracchia,[12] P. Francavilla,[80] M. Franchini,[20a,20b] D. Francis,[30] L. Franconi,[119] M. Franklin,[57] M. Fraternali,[121a,121b] D. Freeborn,[78] S. T. French,[28] F. Friedrich,[44] D. Froidevaux,[30] J. A. Frost,[120] C. Fukunaga,[156] E. Fullana Torregrosa,[83] B. G. Fulsom,[143] J. Fuster,[167] C. Gabaldon,[55] O. Gabizon,[175] A. Gabrielli,[20a,20b] A. Gabrielli,[132a,132b] S. Gadatsch,[107] S. Gadomski,[49] G. Gagliardi,[50a,50b] P. Gagnon,[61] C. Galea,[106] B. Galhardo,[126a,126c] E. J. Gallas,[120] B. J. Gallop,[131] P. Gallus,[128] G. Galster,[36] K. K. Gan,[111] J. Gao,[33b,85] Y. Gao,[46] Y. S. Gao,[143,f] F. M. Garay Walls,[46] F. Garberson,[176] C. García,[167] J. E. García Navarro,[167] M. Garcia-Sciveres,[15] R. W. Gardner,[31] N. Garelli,[143] V. Garonne,[119] C. Gatti,[47] A. Gaudiello,[50a,50b] G. Gaudio,[121a] B. Gaur,[141] L. Gauthier,[95] P. Gauzzi,[132a,132b] I. L. Gavrilenko,[96] C. Gay,[168] G. Gaycken,[21] E. N. Gazis,[10] P. Ge,[33d] Z. Gecse,[168] C. N. P. Gee,[131] D. A. A. Geerts,[107] Ch. Geich-Gimbel,[21] M. P. Geisler,[58a] C. Gemme,[50a] M. H. Genest,[55] S. Gentile,[132a,132b] M. George,[54] S. George,[77] D. Gerbaudo,[163] A. Gershon,[153] H. Ghazlane,[135b] B. Giacobbe,[20a] S. Giagu,[132a,132b] V. Giangiobbe,[12] P. Giannetti,[124a,124b] B. Gibbard,[25] S. M. Gibson,[77] M. Gilchriese,[15] T. P. S. Gillam,[28] D. Gillberg,[30] G. Gilles,[34] D. M. Gingrich,[3,e] N. Giokaris,[9] M. P. Giordani,[164a,164c] F. M. Giorgi,[20a] F. M. Giorgi,[16] P. F. Giraud,[136] P. Giromini,[47] D. Giugni,[91a] C. Giuliani,[48] M. Giulini,[58b] B. K. Gjelsten,[119] S. Gkaitatzis,[154] I. Gkialas,[154] E. L. Gkougkousis,[117] L. K. Gladilin,[99] C. Glasman,[82] J. Glatzer,[30] P. C. F. Glaysher,[46] A. Glazov,[42] M. Goblirsch-Kolb,[101] J. R. Goddard,[76] J. Godlewski,[39] S. Goldfarb,[89] T. Golling,[49] D. Golubkov,[130] A. Gomes,[126a,126b,126d] R. Gonçalo,[126a] J. Goncalves Pinto Firmino Da Costa,[136] L. Gonella,[21] S. González de la Hoz,[167] G. Gonzalez Parra,[12] S. Gonzalez-Sevilla,[49] L. Goossens,[30] P. A. Gorbounov,[97] H. A. Gordon,[25] I. Gorelov,[105] B. Gorini,[30] E. Gorini,[73a,73b] A. Gorišek,[75] E. Gornicki,[39] A. T. Goshaw,[45] C. Gössling,[43] M. I. Gostkin,[65] D. Goujdami,[135c] A. G. Goussiou,[138] N. Govender,[145b] H. M. X. Grabas,[137] L. Graber,[54] I. Grabowska-Bold,[38a] P. Grafström,[20a,20b] K-J. Grahn,[42] J. Gramling,[49] E. Gramstad,[119] S. Grancagnolo,[16] V. Grassi,[148] V. Gratchev,[123] H. M. Gray,[30] E. Graziani,[134a] Z. D. Greenwood,[79,o] K. Gregersen,[78] I. M. Gregor,[42] P. Grenier,[143] J. Griffiths,[8] A. A. Grillo,[137] K. Grimm,[72] S. Grinstein,[12,p] Ph. Gris,[34] J.-F. Grivaz,[117] J. P. Grohs,[44]

A. Grohsjean,[42] E. Gross,[172] J. Grosse-Knetter,[54] G. C. Grossi,[79] Z. J. Grout,[149] L. Guan,[33b] J. Guenther,[128] F. Guescini,[49] D. Guest,[176] O. Gueta,[153] E. Guido,[50a,50b] T. Guillemin,[117] S. Guindon,[2] U. Gul,[53] C. Gumpert,[44] J. Guo,[33e] S. Gupta,[120] P. Gutierrez,[113] N. G. Gutierrez Ortiz,[53] C. Gutschow,[44] C. Guyot,[136] C. Gwenlan,[120] C. B. Gwilliam,[74] A. Haas,[110] C. Haber,[15] H. K. Hadavand,[8] N. Haddad,[135e] P. Haefner,[21] S. Hageböck,[21] Z. Hajduk,[39] H. Hakobyan,[177] M. Haleem,[42] J. Haley,[114] D. Hall,[120] G. Halladjian,[90] G. D. Hallewell,[85] K. Hamacher,[175] P. Hamal,[115] K. Hamano,[169] M. Hamer,[54] A. Hamilton,[145a] S. Hamilton,[161] G. N. Hamity,[145c] P. G. Hamnett,[42] L. Han,[33b] K. Hanagaki,[118] K. Hanawa,[155] M. Hance,[15] P. Hanke,[58a] R. Hanna,[136] J. B. Hansen,[36] J. D. Hansen,[36] M. C. Hansen,[21] P. H. Hansen,[36] K. Hara,[160] A. S. Hard,[173] T. Harenberg,[175] F. Hariri,[117] S. Harkusha,[92] R. D. Harrington,[46] P. F. Harrison,[170] F. Hartjes,[107] M. Hasegawa,[67] S. Hasegawa,[103] Y. Hasegawa,[140] A. Hasib,[113] S. Hassani,[136] S. Haug,[17] R. Hauser,[90] L. Hauswald,[44] M. Havranek,[127] C. M. Hawkes,[18] R. J. Hawkings,[30] A. D. Hawkins,[81] T. Hayashi,[160] D. Hayden,[90] C. P. Hays,[120] J. M. Hays,[76] H. S. Hayward,[74] S. J. Haywood,[131] S. J. Head,[18] T. Heck,[83] V. Hedberg,[81] L. Heelan,[8] S. Heim,[122] T. Heim,[175] B. Heinemann,[15] L. Heinrich,[110] J. Hejbal,[127] L. Helary,[22] S. Hellman,[146a,146b] D. Hellmich,[21] C. Helsens,[30] J. Henderson,[120] R. C. W. Henderson,[72] Y. Heng,[173] C. Hengler,[42] A. Henrichs,[176] A. M. Henriques Correia,[30] S. Henrot-Versille,[117] G. H. Herbert,[16] Y. Hernández Jiménez,[167] R. Herrberg-Schubert,[16] G. Herten,[48] R. Hertenberger,[100] L. Hervas,[30] G. G. Hesketh,[78] N. P. Hessey,[107] J. W. Hetherly,[40] R. Hickling,[76] E. Higón-Rodriguez,[167] E. Hill,[169] J. C. Hill,[28] K. H. Hiller,[42] S. J. Hillier,[18] I. Hinchliffe,[15] E. Hines,[122] R. R. Hinman,[15] M. Hirose,[157] D. Hirschbuehl,[175] J. Hobbs,[148] N. Hod,[107] M. C. Hodgkinson,[139] P. Hodgson,[139] A. Hoecker,[30] M. R. Hoeferkamp,[105] F. Hoenig,[100] M. Hohlfeld,[83] D. Hohn,[21] T. R. Holmes,[15] T. M. Hong,[122] L. Hooft van Huysduynen,[110] W. H. Hopkins,[116] Y. Horii,[103] A. J. Horton,[142] J-Y. Hostachy,[55] S. Hou,[151] A. Hoummada,[135a] J. Howard,[120] J. Howarth,[42] M. Hrabovsky,[115] I. Hristova,[16] J. Hrivnac,[117] T. Hryn'ova,[5] A. Hrynevich,[93] C. Hsu,[145c] P. J. Hsu,[151,q] S.-C. Hsu,[138] D. Hu,[35] Q. Hu,[33b] X. Hu,[89] Y. Huang,[42] Z. Hubacek,[30] F. Hubaut,[85] F. Huegging,[21] T. B. Huffman,[120] E. W. Hughes,[35] G. Hughes,[72] M. Huhtinen,[30] T. A. Hülsing,[83] N. Huseynov,[65,c] J. Huston,[90] J. Huth,[57] G. Iacobucci,[49] G. Iakovidis,[25] I. Ibragimov,[141] L. Iconomidou-Fayard,[117] E. Ideal,[176] Z. Idrissi,[135e] P. Iengo,[30] O. Igonkina,[107] T. Iizawa,[171] Y. Ikegami,[66] K. Ikematsu,[141] M. Ikeno,[66] Y. Ilchenko,[31,r] D. Iliadis,[154] N. Ilic,[158] Y. Inamaru,[67] T. Ince,[101] P. Ioannou,[9] M. Iodice,[134a] K. Iordanidou,[35] V. Ippolito,[57] A. Irles Quiles,[167] C. Isaksson,[166] M. Ishino,[68] M. Ishitsuka,[157] R. Ishmukhametov,[111] C. Issever,[120] S. Istin,[19a] J. M. Iturbe Ponce,[84] R. Iuppa,[133a,133b] J. Ivarsson,[81] W. Iwanski,[39] H. Iwasaki,[66] J. M. Izen,[41] V. Izzo,[104a] S. Jabbar,[3] B. Jackson,[122] M. Jackson,[74] P. Jackson,[1] M. R. Jaekel,[30] V. Jain,[2] K. Jakobs,[48] S. Jakobsen,[30] T. Jakoubek,[127] J. Jakubek,[128] D. O. Jamin,[151] D. K. Jana,[79] E. Jansen,[78] R. W. Jansky,[62] J. Janssen,[21] M. Janus,[170] G. Jarlskog,[81] N. Javadov,[65,c] T. Javůrek,[48] L. Jeanty,[15] J. Jejelava,[51a,s] G.-Y. Jeng,[150] D. Jennens,[88] P. Jenni,[48,t] J. Jentzsch,[43] C. Jeske,[170] S. Jézéquel,[5] H. Ji,[173] J. Jia,[148] Y. Jiang,[33b] S. Jiggins,[78] J. Jimenez Pena,[167] S. Jin,[33a] A. Jinaru,[26a] O. Jinnouchi,[157] M. D. Joergensen,[36] P. Johansson,[139] K. A. Johns,[7] K. Jon-And,[146a,146b] G. Jones,[170] R. W. L. Jones,[72] T. J. Jones,[74] J. Jongmanns,[58a] P. M. Jorge,[126a,126b] K. D. Joshi,[84] J. Jovicevic,[159a] X. Ju,[173] C. A. Jung,[43] P. Jussel,[62] A. Juste Rozas,[12,p] M. Kaci,[167] A. Kaczmarska,[39] M. Kado,[117] H. Kagan,[111] M. Kagan,[143] S. J. Kahn,[85] E. Kajomovitz,[45] C. W. Kalderon,[120] S. Kama,[40] A. Kamenshchikov,[130] N. Kanaya,[155] M. Kaneda,[30] S. Kaneti,[28] V. A. Kantserov,[98] J. Kanzaki,[66] B. Kaplan,[110] A. Kapliy,[31] D. Kar,[53] K. Karakostas,[10] A. Karamaoun,[3] N. Karastathis,[10,107] M. J. Kareem,[54] M. Karnevskiy,[83] S. N. Karpov,[65] Z. M. Karpova,[65] K. Karthik,[110] V. Kartvelishvili,[72] A. N. Karyukhin,[130] L. Kashif,[173] R. D. Kass,[111] A. Kastanas,[14] Y. Kataoka,[155] A. Katre,[49] J. Katzy,[42] K. Kawagoe,[70] T. Kawamoto,[155] G. Kawamura,[54] S. Kazama,[155] V. F. Kazanin,[109,d] M. Y. Kazarinov,[65] R. Keeler,[169] R. Kehoe,[40] J. S. Keller,[42] J. J. Kempster,[77] H. Keoshkerian,[84] O. Kepka,[127] B. P. Kerševan,[75] S. Kersten,[175] R. A. Keyes,[87] F. Khalil-zada,[11] H. Khandanyan,[146a,146b] A. Khanov,[114] A. G. Kharlamov,[109,d] T. J. Khoo,[28] V. Khovanskiy,[97] E. Khramov,[65] J. Khubua,[51b,u] H. Y. Kim,[8] H. Kim,[146a,146b] S. H. Kim,[160] Y. Kim,[31] N. Kimura,[154] O. M. Kind,[16] B. T. King,[74] M. King,[167] R. S. B. King,[120] S. B. King,[168] J. Kirk,[131] A. E. Kiryunin,[101] T. Kishimoto,[67] D. Kisielewska,[38a] F. Kiss,[48] K. Kiuchi,[160] O. Kivernyk,[136] E. Kladiva,[144b] M. H. Klein,[35] M. Klein,[74] U. Klein,[74] K. Kleinknecht,[83] P. Klimek,[146a,146b] A. Klimentov,[25] R. Klingenberg,[43] J. A. Klinger,[84] T. Klioutchnikova,[30] E.-E. Kluge,[58a] P. Kluit,[107] S. Kluth,[101] E. Kneringer,[62] E. B. F. G. Knoops,[85] A. Knue,[53] A. Kobayashi,[155] D. Kobayashi,[157] T. Kobayashi,[155] M. Kobel,[44] M. Kocian,[143] P. Kodys,[129] T. Koffas,[29] E. Koffeman,[107] L. A. Kogan,[120] S. Kohlmann,[175] Z. Kohout,[128] T. Kohriki,[66] T. Koi,[143] H. Kolanoski,[16] I. Koletsou,[5] A. A. Komar,[96,a] Y. Komori,[155] T. Kondo,[66] N. Kondrashova,[42] K. Köneke,[48] A. C. König,[106] S. König,[83] T. Kono,[66,v] R. Konoplich,[110,w] N. Konstantinidis,[78] R. Kopeliansky,[152] S. Koperny,[38a] L. Köpke,[83] A. K. Kopp,[48] K. Korcyl,[39] K. Kordas,[154] A. Korn,[78] A. A. Korol,[109,d] I. Korolkov,[12] E. V. Korolkova,[139] O. Kortner,[101] S. Kortner,[101] T. Kosek,[129] V. V. Kostyukhin,[21] V. M. Kotov,[65] A. Kotwal,[45] A. Kourkoumeli-Charalampidi,[154]

C. Kourkoumelis,[9] V. Kouskoura,[25] A. Koutsman,[159a] R. Kowalewski,[169] T. Z. Kowalski,[38a] W. Kozanecki,[136] A. S. Kozhin,[130] V. A. Kramarenko,[99] G. Kramberger,[75] D. Krasnopevtsev,[98] M. W. Krasny,[80] A. Krasznahorkay,[30] J. K. Kraus,[21] A. Kravchenko,[25] S. Kreiss,[110] M. Kretz,[58c] J. Kretzschmar,[74] K. Kreutzfeldt,[52] P. Krieger,[158] K. Krizka,[31] K. Kroeninger,[43] H. Kroha,[101] J. Kroll,[122] J. Kroseberg,[21] J. Krstic,[13] U. Kruchonak,[65] H. Krüger,[21] N. Krumnack,[64] Z. V. Krumshteyn,[65] A. Kruse,[173] M. C. Kruse,[45] M. Kruskal,[22] T. Kubota,[88] H. Kucuk,[78] S. Kuday,[4b] S. Kuehn,[48] A. Kugel,[58c] F. Kuger,[174] A. Kuhl,[137] T. Kuhl,[42] V. Kukhtin,[65] Y. Kulchitsky,[92] S. Kuleshov,[32b] M. Kuna,[132a,132b] T. Kunigo,[68] A. Kupco,[127] H. Kurashige,[67] Y. A. Kurochkin,[92] R. Kurumida,[67] V. Kus,[127] E. S. Kuwertz,[169] M. Kuze,[157] J. Kvita,[115] T. Kwan,[169] D. Kyriazopoulos,[139] A. La Rosa,[49] J. L. La Rosa Navarro,[24d] L. La Rotonda,[37a,37b] C. Lacasta,[167] F. Lacava,[132a,132b] J. Lacey,[29] H. Lacker,[16] D. Lacour,[80] V. R. Lacuesta,[167] E. Ladygin,[65] R. Lafaye,[5] B. Laforge,[80] T. Lagouri,[176] S. Lai,[48] L. Lambourne,[78] S. Lammers,[61] C. L. Lampen,[7] W. Lampl,[7] E. Lançon,[136] U. Landgraf,[48] M. P. J. Landon,[76] V. S. Lang,[58a] J. C. Lange,[12] A. J. Lankford,[163] F. Lanni,[25] K. Lantzsch,[30] S. Laplace,[80] C. Lapoire,[30] J. F. Laporte,[136] T. Lari,[91a] F. Lasagni Manghi,[20a,20b] M. Lassnig,[30] P. Laurelli,[47] W. Lavrijsen,[15] A. T. Law,[137] P. Laycock,[74] O. Le Dortz,[80] E. Le Guirriec,[85] E. Le Menedeu,[12] M. LeBlanc,[169] T. LeCompte,[6] F. Ledroit-Guillon,[55] C. A. Lee,[145b] S. C. Lee,[151] L. Lee,[1] G. Lefebvre,[80] M. Lefebvre,[169] F. Legger,[100] C. Leggett,[15] A. Lehan,[74] G. Lehmann Miotto,[30] X. Lei,[7] W. A. Leight,[29] A. Leisos,[154] A. G. Leister,[176] M. A. L. Leite,[24d] R. Leitner,[129] D. Lellouch,[172] B. Lemmer,[54] K. J. C. Leney,[78] T. Lenz,[21] B. Lenzi,[30] R. Leone,[7] S. Leone,[124a,124b] C. Leonidopoulos,[46] S. Leontsinis,[10] C. Leroy,[95] C. G. Lester,[28] M. Levchenko,[123] J. Levêque,[5] D. Levin,[89] L. J. Levinson,[172] M. Levy,[18] A. Lewis,[120] A. M. Leyko,[21] M. Leyton,[41] B. Li,[33b,x] H. Li,[148] H. L. Li,[31] L. Li,[45] L. Li,[33e] S. Li,[45] Y. Li,[33c,y] Z. Liang,[137] H. Liao,[34] B. Liberti,[133a] A. Liblong,[158] P. Lichard,[30] K. Lie,[165] J. Liebal,[21] W. Liebig,[14] C. Limbach,[21] A. Limosani,[150] S. C. Lin,[151,z] T. H. Lin,[83] F. Linde,[107] B. E. Lindquist,[148] J. T. Linnemann,[90] E. Lipeles,[122] A. Lipniacka,[14] M. Lisovyi,[42] T. M. Liss,[165] D. Lissauer,[25] A. Lister,[168] A. M. Litke,[137] B. Liu,[151,aa] D. Liu,[151] J. Liu,[85] J. B. Liu,[33b] K. Liu,[85] L. Liu,[165] M. Liu,[45] M. Liu,[33b] Y. Liu,[33b] M. Livan,[121a,121b] A. Lleres,[55] J. Llorente Merino,[82] S. L. Lloyd,[76] F. Lo Sterzo,[151] E. Lobodzinska,[42] P. Loch,[7] W. S. Lockman,[137] F. K. Loebinger,[84] A. E. Loevschall-Jensen,[36] A. Loginov,[176] T. Lohse,[16] K. Lohwasser,[42] M. Lokajicek,[127] B. A. Long,[22] J. D. Long,[89] R. E. Long,[72] K. A. Looper,[111] L. Lopes,[126a] D. Lopez Mateos,[57] B. Lopez Paredes,[139] I. Lopez Paz,[12] J. Lorenz,[100] N. Lorenzo Martinez,[61] M. Losada,[162] P. Loscutoff,[15] P. J. Lösel,[100] X. Lou,[33a] A. Lounis,[117] J. Love,[6] P. A. Love,[72] N. Lu,[89] H. J. Lubatti,[138] C. Luci,[132a,132b] A. Lucotte,[55] F. Luehring,[61] W. Lukas,[62] L. Luminari,[132a] O. Lundberg,[146a,146b] B. Lund-Jensen,[147] D. Lynn,[25] R. Lysak,[127] E. Lytken,[81] H. Ma,[25] L. L. Ma,[33d] G. Maccarrone,[47] A. Macchiolo,[101] C. M. Macdonald,[139] J. Machado Miguens,[122,126b] D. Macina,[30] D. Madaffari,[85] R. Madar,[34] H. J. Maddocks,[72] W. F. Mader,[44] A. Madsen,[166] S. Maeland,[14] T. Maeno,[25] A. Maevskiy,[99] E. Magradze,[54] K. Mahboubi,[48] J. Mahlstedt,[107] C. Maiani,[136] C. Maidantchik,[24a] A. A. Maier,[101] T. Maier,[100] A. Maio,[126a,126b,126d] S. Majewski,[116] Y. Makida,[66] N. Makovec,[117] B. Malaescu,[80] Pa. Malecki,[39] V. P. Maleev,[123] F. Malek,[55] U. Mallik,[63] D. Malon,[6] C. Malone,[143] S. Maltezos,[10] V. M. Malyshev,[109] S. Malyukov,[30] J. Mamuzic,[42] G. Mancini,[47] B. Mandelli,[30] L. Mandelli,[91a] I. Mandić,[75] R. Mandrysch,[63] J. Maneira,[126a,126b] A. Manfredini,[101] L. Manhaes de Andrade Filho,[24b] J. Manjarres Ramos,[159b] A. Mann,[100] P. M. Manning,[137] A. Manousakis-Katsikakis,[9] B. Mansoulie,[136] R. Mantifel,[87] M. Mantoani,[54] L. Mapelli,[30] L. March,[145c] G. Marchiori,[80] M. Marcisovsky,[127] C. P. Marino,[169] M. Marjanovic,[13] F. Marroquim,[24a] S. P. Marsden,[84] Z. Marshall,[15] L. F. Marti,[17] S. Marti-Garcia,[167] B. Martin,[90] T. A. Martin,[170] V. J. Martin,[46] B. Martin dit Latour,[14] M. Martinez,[12,p] S. Martin-Haugh,[131] V. S. Martoiu,[26a] A. C. Martyniuk,[78] M. Marx,[138] F. Marzano,[132a] A. Marzin,[30] L. Masetti,[83] T. Mashimo,[155] R. Mashinistov,[96] J. Masik,[84] A. L. Maslennikov,[109,d] I. Massa,[20a,20b] L. Massa,[20a,20b] N. Massol,[5] P. Mastrandrea,[148] A. Mastroberardino,[37a,37b] T. Masubuchi,[155] P. Mättig,[175] J. Mattmann,[83] J. Maurer,[26a] S. J. Maxfield,[74] D. A. Maximov,[109,d] R. Mazini,[151] S. M. Mazza,[91a,91b] L. Mazzaferro,[133a,133b] G. Mc Goldrick,[158] S. P. Mc Kee,[89] A. McCarn,[89] R. L. McCarthy,[148] T. G. McCarthy,[29] N. A. McCubbin,[131] K. W. McFarlane,[56,a] J. A. Mcfayden,[78] G. Mchedlidze,[54] S. J. McMahon,[131] R. A. McPherson,[169,l] M. Medinnis,[42] S. Meehan,[145a] S. Mehlhase,[100] A. Mehta,[74] K. Meier,[58a] C. Meineck,[100] B. Meirose,[41] B. R. Mellado Garcia,[145c] F. Meloni,[17] A. Mengarelli,[20a,20b] S. Menke,[101] E. Meoni,[161] K. M. Mercurio,[57] S. Mergelmeyer,[21] P. Mermod,[49] L. Merola,[104a,104b] C. Meroni,[91a] F. S. Merritt,[31] A. Messina,[132a,132b] J. Metcalfe,[25] A. S. Mete,[163] C. Meyer,[83] C. Meyer,[122] J-P. Meyer,[136] J. Meyer,[107] R. P. Middleton,[131] S. Miglioranzi,[164a,164c] L. Mijović,[21] G. Mikenberg,[172] M. Mikestikova,[127] M. Mikuž,[75] M. Milesi,[88] A. Milic,[30] D. W. Miller,[31] C. Mills,[46] A. Milov,[172] D. A. Milstead,[146a,146b] A. A. Minaenko,[130] Y. Minami,[155] I. A. Minashvili,[65] A. I. Mincer,[110] B. Mindur,[38a] M. Mineev,[65] Y. Ming,[173] L. M. Mir,[12] T. Mitani,[171] J. Mitrevski,[100] V. A. Mitsou,[167] A. Miucci,[49] P. S. Miyagawa,[139] J. U. Mjörnmark,[81] T. Moa,[146a,146b]

K. Mochizuki,[85] S. Mohapatra,[35] W. Mohr,[48] S. Molander,[146a,146b] R. Moles-Valls,[167] K. Mönig,[42] C. Monini,[55] J. Monk,[36] E. Monnier,[85] J. Montejo Berlingen,[12] F. Monticelli,[71] S. Monzani,[132a,132b] R. W. Moore,[3] N. Morange,[117] D. Moreno,[162] M. Moreno Llácer,[54] P. Morettini,[50a] M. Morgenstern,[44] M. Morii,[57] M. Morinaga,[155] V. Morisbak,[119] S. Moritz,[83] A. K. Morley,[147] G. Mornacchi,[30] J. D. Morris,[76] S. S. Mortensen,[36] A. Morton,[53] L. Morvaj,[103] H. G. Moser,[101] M. Mosidze,[51b] J. Moss,[111] K. Motohashi,[157] R. Mount,[143] E. Mountricha,[25] S. V. Mouraviev,[96,a] E. J. W. Moyse,[86] S. Muanza,[85] R. D. Mudd,[18] F. Mueller,[101] J. Mueller,[125] K. Mueller,[21] R. S. P. Mueller,[100] T. Mueller,[28] D. Muenstermann,[49] P. Mullen,[53] Y. Munwes,[153] J. A. Murillo Quijada,[18] W. J. Murray,[170,131] H. Musheghyan,[54] E. Musto,[152] A. G. Myagkov,[130,bb] M. Myska,[128] O. Nackenhorst,[54] J. Nadal,[54] K. Nagai,[120] R. Nagai,[157] Y. Nagai,[85] K. Nagano,[66] A. Nagarkar,[111] Y. Nagasaka,[59] K. Nagata,[160] M. Nagel,[101] E. Nagy,[85] A. M. Nairz,[30] Y. Nakahama,[30] K. Nakamura,[66] T. Nakamura,[155] I. Nakano,[112] H. Namasivayam,[41] R. F. Naranjo Garcia,[42] R. Narayan,[31] T. Naumann,[42] G. Navarro,[162] R. Nayyar,[7] H. A. Neal,[89] P. Yu. Nechaeva,[96] T. J. Neep,[84] P. D. Nef,[143] A. Negri,[121a,121b] M. Negrini,[20a] S. Nektarijevic,[106] C. Nellist,[117] A. Nelson,[163] S. Nemecek,[127] P. Nemethy,[110] A. A. Nepomuceno,[24a] M. Nessi,[30,cc] M. S. Neubauer,[165] M. Neumann,[175] R. M. Neves,[110] P. Nevski,[25] P. R. Newman,[18] D. H. Nguyen,[6] R. B. Nickerson,[120] R. Nicolaidou,[136] B. Nicquevert,[30] J. Nielsen,[137] N. Nikiforou,[35] A. Nikiforov,[16] V. Nikolaenko,[130,bb] I. Nikolic-Audit,[80] K. Nikolopoulos,[18] J. K. Nilsen,[119] P. Nilsson,[25] Y. Ninomiya,[155] A. Nisati,[132a] R. Nisius,[101] T. Nobe,[157] M. Nomachi,[118] I. Nomidis,[29] T. Nooney,[76] S. Norberg,[113] M. Nordberg,[30] O. Novgorodova,[44] S. Nowak,[101] M. Nozaki,[66] L. Nozka,[115] K. Ntekas,[10] G. Nunes Hanninger,[88] T. Nunnemann,[100] E. Nurse,[78] F. Nuti,[88] B. J. O'Brien,[46] F. O'grady,[7] D. C. O'Neil,[142] V. O'Shea,[53] F. G. Oakham,[29,e] H. Oberlack,[101] T. Obermann,[21] J. Ocariz,[80] A. Ochi,[67] I. Ochoa,[78] S. Oda,[70] S. Odaka,[66] H. Ogren,[61] A. Oh,[84] S. H. Oh,[45] C. C. Ohm,[15] H. Ohman,[166] H. Oide,[30] W. Okamura,[118] H. Okawa,[160] Y. Okumura,[31] T. Okuyama,[155] A. Olariu,[26a] S. A. Olivares Pino,[46] D. Oliveira Damazio,[25] E. Oliver Garcia,[167] A. Olszewski,[39] J. Olszowska,[39] A. Onofre,[126a,126e] P. U. E. Onyisi,[31,r] C. J. Oram,[159a] M. J. Oreglia,[31] Y. Oren,[153] D. Orestano,[134a,134b] N. Orlando,[154] C. Oropeza Barrera,[53] R. S. Orr,[158] B. Osculati,[50a,50b] R. Ospanov,[84] G. Otero y Garzon,[27] H. Otono,[70] M. Ouchrif,[135d] E. A. Ouellette,[169] F. Ould-Saada,[119] A. Ouraou,[136] K. P. Oussoren,[107] Q. Ouyang,[33a] A. Ovcharova,[15] M. Owen,[53] R. E. Owen,[18] V. E. Ozcan,[19a] N. Ozturk,[8] K. Pachal,[142] A. Pacheco Pages,[12] C. Padilla Aranda,[12] M. Pagáčová,[48] S. Pagan Griso,[15] E. Paganis,[139] C. Pahl,[101] F. Paige,[25] P. Pais,[86] K. Pajchel,[119] G. Palacino,[159b] S. Palestini,[30] M. Palka,[38b] D. Pallin,[34] A. Palma,[126a,126b] Y. B. Pan,[173] E. Panagiotopoulou,[10] C. E. Pandini,[80] J. G. Panduro Vazquez,[77] P. Pani,[146a,146b] S. Panitkin,[25] L. Paolozzi,[49] Th. D. Papadopoulou,[10] K. Papageorgiou,[154] A. Paramonov,[6] D. Paredes Hernandez,[154] M. A. Parker,[28] K. A. Parker,[139] F. Parodi,[50a,50b] J. A. Parsons,[35] U. Parzefall,[48] E. Pasqualucci,[132a] S. Passaggio,[50a] F. Pastore,[134a,134b,a] Fr. Pastore,[77] G. Pásztor,[29] S. Pataraia,[175] N. D. Patel,[150] J. R. Pater,[84] T. Pauly,[30] J. Pearce,[169] B. Pearson,[113] L. E. Pedersen,[36] M. Pedersen,[119] S. Pedraza Lopez,[167] R. Pedro,[126a,126b] S. V. Peleganchuk,[109] D. Pelikan,[166] H. Peng,[33b] B. Penning,[31] J. Penwell,[61] D. V. Perepelitsa,[25] E. Perez Codina,[159a] M. T. Pérez García-Estañ,[167] L. Perini,[91a,91b] H. Pernegger,[30] S. Perrella,[104a,104b] R. Peschke,[42] V. D. Peshekhonov,[65] K. Peters,[30] R. F. Y. Peters,[84] B. A. Petersen,[30] T. C. Petersen,[36] E. Petit,[42] A. Petridis,[146a,146b] C. Petridou,[154] E. Petrolo,[132a] F. Petrucci,[134a,134b] N. E. Pettersson,[157] R. Pezoa,[32b] P. W. Phillips,[131] G. Piacquadio,[143] E. Pianori,[170] A. Picazio,[49] E. Piccaro,[76] M. Piccinini,[20a,20b] M. A. Pickering,[120] R. Piegaia,[27] D. T. Pignotti,[111] J. E. Pilcher,[31] A. D. Pilkington,[84] J. Pina,[126a,126b,126d] M. Pinamonti,[164a,164c,dd] J. L. Pinfold,[3] A. Pingel,[36] B. Pinto,[126a] S. Pires,[80] M. Pitt,[172] C. Pizio,[91a,91b] L. Plazak,[144a] M.-A. Pleier,[25] V. Pleskot,[129] E. Plotnikova,[65] P. Plucinski,[146a,146b] D. Pluth,[64] R. Poettgen,[83] L. Poggioli,[117] D. Pohl,[21] G. Polesello,[121a] A. Policicchio,[37a,37b] R. Polifka,[158] A. Polini,[20a] C. S. Pollard,[53] V. Polychronakos,[25] K. Pommès,[30] L. Pontecorvo,[132a] B. G. Pope,[90] G. A. Popeneciu,[26b] D. S. Popovic,[13] A. Poppleton,[30] S. Pospisil,[128] K. Potamianos,[15] I. N. Potrap,[65] C. J. Potter,[149] C. T. Potter,[116] G. Poulard,[30] J. Poveda,[30] V. Pozdnyakov,[65] P. Pralavorio,[85] A. Pranko,[15] S. Prasad,[30] S. Prell,[64] D. Price,[84] L. E. Price,[6] M. Primavera,[73a] S. Prince,[87] M. Proissl,[46] K. Prokofiev,[60c] F. Prokoshin,[32b] E. Protopapadaki,[136] S. Protopopescu,[25] J. Proudfoot,[6] M. Przybycien,[38a] E. Ptacek,[116] D. Puddu,[134a,134b] E. Pueschel,[86] D. Puldon,[148] M. Purohit,[25,ee] P. Puzo,[117] J. Qian,[89] G. Qin,[53] Y. Qin,[84] A. Quadt,[54] D. R. Quarrie,[15] W. B. Quayle,[164a,164b] M. Queitsch-Maitland,[84] D. Quilty,[53] S. Raddum,[119] V. Radeka,[25] V. Radescu,[42] S. K. Radhakrishnan,[148] P. Radloff,[116] P. Rados,[88] F. Ragusa,[91a,91b] G. Rahal,[178] S. Rajagopalan,[25] M. Rammensee,[30] C. Rangel-Smith,[166] F. Rauscher,[100] S. Rave,[83] T. Ravenscroft,[53] M. Raymond,[30] A. L. Read,[119] N. P. Readioff,[74] D. M. Rebuzzi,[121a,121b] A. Redelbach,[174] G. Redlinger,[25] R. Reece,[137] K. Reeves,[41] L. Rehnisch,[16] H. Reisin,[27] M. Relich,[163] C. Rembser,[30] H. Ren,[33a] A. Renaud,[117] M. Rescigno,[132a] S. Resconi,[91a] O. L. Rezanova,[109,d] P. Reznicek,[129] R. Rezvani,[95] R. Richter,[101] S. Richter,[78] E. Richter-Was,[38b] O. Ricken,[21] M. Ridel,[80] P. Rieck,[16] C. J. Riegel,[175] J. Rieger,[54] M. Rijssenbeek,[148] A. Rimoldi,[121a,121b] L. Rinaldi,[20a] B. Ristić,[49]

E. Ritsch,[62] I. Riu,[12] F. Rizatdinova,[114] E. Rizvi,[76] S. H. Robertson,[87,l] A. Robichaud-Veronneau,[87] D. Robinson,[28] J. E. M. Robinson,[84] A. Robson,[53] C. Roda,[124a,124b] S. Roe,[30] O. Røhne,[119] S. Rolli,[161] A. Romaniouk,[98] M. Romano,[20a,20b] S. M. Romano Saez,[34] E. Romero Adam,[167] N. Rompotis,[138] M. Ronzani,[48] L. Roos,[80] E. Ros,[167] S. Rosati,[132a] K. Rosbach,[48] P. Rose,[137] P. L. Rosendahl,[14] O. Rosenthal,[141] V. Rossetti,[146a,146b] E. Rossi,[104a,104b] L. P. Rossi,[50a] R. Rosten,[138] M. Rotaru,[26a] I. Roth,[172] J. Rothberg,[138] D. Rousseau,[117] C. R. Royon,[136] A. Rozanov,[85] Y. Rozen,[152] X. Ruan,[145c] F. Rubbo,[143] I. Rubinskiy,[42] V. I. Rud,[99] C. Rudolph,[44] M. S. Rudolph,[158] F. Rühr,[48] A. Ruiz-Martinez,[30] Z. Rurikova,[48] N. A. Rusakovich,[65] A. Ruschke,[100] H. L. Russell,[138] J. P. Rutherfoord,[7] N. Ruthmann,[48] Y. F. Ryabov,[123] M. Rybar,[129] G. Rybkin,[117] N. C. Ryder,[120] A. F. Saavedra,[150] G. Sabato,[107] S. Sacerdoti,[27] A. Saddique,[3] H. F-W. Sadrozinski,[137] R. Sadykov,[65] F. Safai Tehrani,[132a] M. Saimpert,[136] H. Sakamoto,[155] Y. Sakurai,[171] G. Salamanna,[134a,134b] A. Salamon,[133a] M. Saleem,[113] D. Salek,[107] P. H. Sales De Bruin,[138] D. Salihagic,[101] A. Salnikov,[143] J. Salt,[167] D. Salvatore,[37a,37b] F. Salvatore,[149] A. Salvucci,[106] A. Salzburger,[30] D. Sampsonidis,[154] A. Sanchez,[104a,104b] J. Sánchez,[167] V. Sanchez Martinez,[167] H. Sandaker,[14] R. L. Sandbach,[76] H. G. Sander,[83] M. P. Sanders,[100] M. Sandhoff,[175] C. Sandoval,[162] R. Sandstroem,[101] D. P. C. Sankey,[131] M. Sannino,[50a,50b] A. Sansoni,[47] C. Santoni,[34] R. Santonico,[133a,133b] H. Santos,[126a] I. Santoyo Castillo,[149] K. Sapp,[125] A. Sapronov,[65] J. G. Saraiva,[126a,126d] B. Sarrazin,[21] O. Sasaki,[66] Y. Sasaki,[155] K. Sato,[160] G. Sauvage,[5,a] E. Sauvan,[5] G. Savage,[77] P. Savard,[158,e] C. Sawyer,[120] L. Sawyer,[79,o] J. Saxon,[31] C. Sbarra,[20a] A. Sbrizzi,[20a,20b] T. Scanlon,[78] D. A. Scannicchio,[163] M. Scarcella,[150] V. Scarfone,[37a,37b] J. Schaarschmidt,[172] P. Schacht,[101] D. Schaefer,[30] R. Schaefer,[42] J. Schaeffer,[83] S. Schaepe,[21] S. Schaetzel,[58b] U. Schäfer,[83] A. C. Schaffer,[117] D. Schaile,[100] R. D. Schamberger,[148] V. Scharf,[58a] V. A. Schegelsky,[123] D. Scheirich,[129] M. Schernau,[163] C. Schiavi,[50a,50b] C. Schillo,[48] M. Schioppa,[37a,37b] S. Schlenker,[30] E. Schmidt,[48] K. Schmieden,[30] C. Schmitt,[83] S. Schmitt,[58b] S. Schmitt,[42] B. Schneider,[159a] Y. J. Schnellbach,[74] U. Schnoor,[44] L. Schoeffel,[136] A. Schoening,[58b] B. D. Schoenrock,[90] E. Schopf,[21] A. L. S. Schorlemmer,[54] M. Schott,[83] D. Schouten,[159a] J. Schovancova,[8] S. Schramm,[158] M. Schreyer,[174] C. Schroeder,[83] N. Schuh,[83] M. J. Schultens,[21] H.-C. Schultz-Coulon,[58a] H. Schulz,[16] M. Schumacher,[48] B. A. Schumm,[137] Ph. Schune,[136] C. Schwanenberger,[84] A. Schwartzman,[143] T. A. Schwarz,[89] Ph. Schwegler,[101] Ph. Schwemling,[136] R. Schwienhorst,[90] J. Schwindling,[136] T. Schwindt,[21] M. Schwoerer,[5] F. G. Sciacca,[17] E. Scifo,[117] G. Sciolla,[23] F. Scuri,[124a,124b] F. Scutti,[21] J. Searcy,[89] G. Sedov,[42] E. Sedykh,[123] P. Seema,[21] S. C. Seidel,[105] A. Seiden,[137] F. Seifert,[128] J. M. Seixas,[24a] G. Sekhniaidze,[104a] K. Sekhon,[89] S. J. Sekula,[40] K. E. Selbach,[46] D. M. Seliverstov,[123,a] N. Semprini-Cesari,[20a,20b] C. Serfon,[30] L. Serin,[117] L. Serkin,[164a,164b] T. Serre,[85] M. Sessa,[134a,134b] R. Seuster,[159a] H. Severini,[113] T. Sfiligoj,[75] F. Sforza,[101] A. Sfyrla,[30] E. Shabalina,[54] M. Shamim,[116] L. Y. Shan,[33a] R. Shang,[165] J. T. Shank,[22] M. Shapiro,[15] P. B. Shatalov,[97] K. Shaw,[164a,164b] S. M. Shaw,[84] A. Shcherbakova,[146a,146b] C. Y. Shehu,[149] P. Sherwood,[78] L. Shi,[151,ff] S. Shimizu,[67] C. O. Shimmin,[163] M. Shimojima,[102] M. Shiyakova,[65] A. Shmeleva,[96] D. Shoaleh Saadi,[95] M. J. Shochet,[31] S. Shojaii,[91a,91b] S. Shrestha,[111] E. Shulga,[98] M. A. Shupe,[7] S. Shushkevich,[42] P. Sicho,[127] O. Sidiropoulou,[174] D. Sidorov,[114] A. Sidoti,[20a,20b] F. Siegert,[44] Dj. Sijacki,[13] J. Silva,[126a,126d] Y. Silver,[153] S. B. Silverstein,[146a] V. Simak,[128] O. Simard,[5] Lj. Simic,[13] S. Simion,[117] E. Simioni,[83] B. Simmons,[78] D. Simon,[34] R. Simoniello,[91a,91b] P. Sinervo,[158] N. B. Sinev,[116] G. Siragusa,[174] A. N. Sisakyan,[65,a] S. Yu. Sivoklokov,[99] J. Sjölin,[146a,146b] T. B. Sjursen,[14] M. B. Skinner,[72] H. P. Skottowe,[57] P. Skubic,[113] M. Slater,[18] T. Slavicek,[128] M. Slawinska,[107] K. Sliwa,[161] V. Smakhtin,[172] B. H. Smart,[46] L. Smestad,[14] S. Yu. Smirnov,[98] Y. Smirnov,[98] L. N. Smirnova,[99,gg] O. Smirnova,[81] M. N. K. Smith,[35] M. Smizanska,[72] K. Smolek,[128] A. A. Snesarev,[96] G. Snidero,[76] S. Snyder,[25] R. Sobie,[169,l] F. Socher,[44] A. Soffer,[153] D. A. Soh,[151,ff] C. A. Solans,[30] M. Solar,[128] J. Solc,[128] E. Yu. Soldatov,[98] U. Soldevila,[167] A. A. Solodkov,[130] A. Soloshenko,[65] O. V. Solovyanov,[130] V. Solovyev,[123] P. Sommer,[48] H. Y. Song,[33b] N. Soni,[1] A. Sood,[15] A. Sopczak,[128] B. Sopko,[128] V. Sopko,[128] V. Sorin,[12] D. Sosa,[58b] M. Sosebee,[8] C. L. Sotiropoulou,[124a,124b] R. Soualah,[164a,164c] P. Soueid,[95] A. M. Soukharev,[109,d] D. South,[42] S. Spagnolo,[73a,73b] M. Spalla,[124a,124b] F. Spanò,[77] W. R. Spearman,[57] F. Spettel,[101] R. Spighi,[20a] G. Spigo,[30] L. A. Spiller,[88] M. Spousta,[129] T. Spreitzer,[158] R. D. St. Denis,[53,a] S. Staerz,[44] J. Stahlman,[122] R. Stamen,[58a] S. Stamm,[16] E. Stanecka,[39] C. Stanescu,[134a] M. Stanescu-Bellu,[42] M. M. Stanitzki,[42] S. Stapnes,[119] E. A. Starchenko,[130] J. Stark,[55] P. Staroba,[127] P. Starovoitov,[42] R. Staszewski,[39] P. Stavina,[144a,a] P. Steinberg,[25] B. Stelzer,[142] H. J. Stelzer,[30] O. Stelzer-Chilton,[159a] H. Stenzel,[52] S. Stern,[101] G. A. Stewart,[53] J. A. Stillings,[21] M. C. Stockton,[87] M. Stoebe,[87] G. Stoicea,[26a] P. Stolte,[54] S. Stonjek,[101] A. R. Stradling,[8] A. Straessner,[44] M. E. Stramaglia,[17] J. Strandberg,[147] S. Strandberg,[146a,146b] A. Strandlie,[119] E. Strauss,[143] M. Strauss,[113] P. Strizenec,[144b] R. Ströhmer,[174] D. M. Strom,[116] R. Stroynowski,[40] A. Strubig,[106] S. A. Stucci,[17] B. Stugu,[14] N. A. Styles,[42] D. Su,[143] J. Su,[125] R. Subramaniam,[79] A. Succurro,[12] Y. Sugaya,[118] C. Suhr,[108] M. Suk,[128] V. V. Sulin,[96] S. Sultansoy,[4c] T. Sumida,[68] S. Sun,[57] X. Sun,[33a] J. E. Sundermann,[48] K. Suruliz,[149] G. Susinno,[37a,37b]

M. R. Sutton,[149] S. Suzuki,[66] Y. Suzuki,[66] M. Svatos,[127] S. Swedish,[168] M. Swiatlowski,[143] I. Sykora,[144a] T. Sykora,[129] D. Ta,[90] C. Taccini,[134a,134b] K. Tackmann,[42] J. Taenzer,[158] A. Taffard,[163] R. Tafirout,[159a] N. Taiblum,[153] H. Takai,[25] R. Takashima,[69] H. Takeda,[67] T. Takeshita,[140] Y. Takubo,[66] M. Talby,[85] A. A. Talyshev,[109,d] J. Y. C. Tam,[174] K. G. Tan,[88] J. Tanaka,[155] R. Tanaka,[117] S. Tanaka,[66] B. B. Tannenwald,[111] N. Tannoury,[21] S. Tapprogge,[83] S. Tarem,[152] F. Tarrade,[29] G. F. Tartarelli,[91a] P. Tas,[129] M. Tasevsky,[127] T. Tashiro,[68] E. Tassi,[37a,37b] A. Tavares Delgado,[126a,126b] Y. Tayalati,[135d] F. E. Taylor,[94] G. N. Taylor,[88] W. Taylor,[159b] F. A. Teischinger,[30] M. Teixeira Dias Castanheira,[76] P. Teixeira-Dias,[77] K. K. Temming,[48] H. Ten Kate,[30] P. K. Teng,[151] J. J. Teoh,[118] F. Tepel,[175] S. Terada,[66] K. Terashi,[155] J. Terron,[82] S. Terzo,[101] M. Testa,[47] R. J. Teuscher,[158,l] J. Therhaag,[21] T. Theveneaux-Pelzer,[34] J. P. Thomas,[18] J. Thomas-Wilsker,[77] E. N. Thompson,[35] P. D. Thompson,[18] R. J. Thompson,[84] A. S. Thompson,[53] L. A. Thomsen,[36] E. Thomson,[122] M. Thomson,[28] R. P. Thun,[89,a] M. J. Tibbetts,[15] R. E. Ticse Torres,[85] V. O. Tikhomirov,[96,hh] Yu. A. Tikhonov,[109,d] S. Timoshenko,[98] E. Tiouchichine,[85] P. Tipton,[176] S. Tisserant,[85] T. Todorov,[5,a] S. Todorova-Nova,[129] J. Tojo,[70] S. Tokár,[144a] K. Tokushuku,[66] K. Tollefson,[90] E. Tolley,[57] L. Tomlinson,[84] M. Tomoto,[103] L. Tompkins,[143,ii] K. Toms,[105] E. Torrence,[116] H. Torres,[142] E. Torró Pastor,[167] J. Toth,[85,jj] F. Touchard,[85] D. R. Tovey,[139] T. Trefzger,[174] L. Tremblet,[30] A. Tricoli,[30] I. M. Trigger,[159a] S. Trincaz-Duvoid,[80] M. F. Tripiana,[12] W. Trischuk,[158] B. Trocmé,[55] C. Troncon,[91a] M. Trottier-McDonald,[15] M. Trovatelli,[134a,134b] P. True,[90] L. Truong,[164a,164c] M. Trzebinski,[39] A. Trzupek,[39] C. Tsarouchas,[30] J. C-L. Tseng,[120] P. V. Tsiareshka,[92] D. Tsionou,[154] G. Tsipolitis,[10] N. Tsirintanis,[9] S. Tsiskaridze,[12] V. Tsiskaridze,[48] E. G. Tskhadadze,[51a] I. I. Tsukerman,[97] V. Tsulaia,[15] S. Tsuno,[66] D. Tsybychev,[148] A. Tudorache,[26a] V. Tudorache,[26a] A. N. Tuna,[122] S. A. Tupputi,[20a,20b] S. Turchikhin,[99,gg] D. Turecek,[128] R. Turra,[91a,91b] A. J. Turvey,[40] P. M. Tuts,[35] A. Tykhonov,[49] M. Tylmad,[146a,146b] M. Tyndel,[131] I. Ueda,[155] R. Ueno,[29] M. Ughetto,[146a,146b] M. Ugland,[14] M. Uhlenbrock,[21] F. Ukegawa,[160] G. Unal,[30] A. Undrus,[25] G. Unel,[163] F. C. Ungaro,[48] Y. Unno,[66] C. Unverdorben,[100] J. Urban,[144b] P. Urquijo,[88] P. Urrejola,[83] G. Usai,[8] A. Usanova,[62] L. Vacavant,[85] V. Vacek,[128] B. Vachon,[87] C. Valderanis,[83] N. Valencic,[107] S. Valentinetti,[20a,20b] A. Valero,[167] L. Valery,[12] S. Valkar,[129] E. Valladolid Gallego,[167] S. Vallecorsa,[49] J. A. Valls Ferrer,[167] W. Van Den Wollenberg,[107] P. C. Van Der Deijl,[107] R. van der Geer,[107] H. van der Graaf,[107] R. Van Der Leeuw,[107] N. van Eldik,[152] P. van Gemmeren,[6] J. Van Nieuwkoop,[142] I. van Vulpen,[107] M. C. van Woerden,[30] M. Vanadia,[132a,132b] W. Vandelli,[30] R. Vanguri,[122] A. Vaniachine,[6] F. Vannucci,[80] G. Vardanyan,[177] R. Vari,[132a] E. W. Varnes,[7] T. Varol,[40] D. Varouchas,[80] A. Vartapetian,[8] K. E. Varvell,[150] F. Vazeille,[34] T. Vazquez Schroeder,[87] J. Veatch,[7] F. Veloso,[126a,126c] T. Velz,[21] S. Veneziano,[132a] A. Ventura,[73a,73b] D. Ventura,[86] M. Venturi,[169] N. Venturi,[158] A. Venturini,[23] V. Vercesi,[121a] M. Verducci,[132a,132b] W. Verkerke,[107] J. C. Vermeulen,[107] A. Vest,[44] M. C. Vetterli,[142,e] O. Viazlo,[81] I. Vichou,[165] T. Vickey,[139] O. E. Vickey Boeriu,[139] G. H. A. Viehhauser,[120] S. Viel,[15] R. Vigne,[30] M. Villa,[20a,20b] M. Villaplana Perez,[91a,91b] E. Vilucchi,[47] M. G. Vincter,[29] V. B. Vinogradov,[65] I. Vivarelli,[149] F. Vives Vaque,[3] S. Vlachos,[10] D. Vladoiu,[100] M. Vlasak,[128] M. Vogel,[32a] P. Vokac,[128] G. Volpi,[124a,124b] M. Volpi,[88] H. von der Schmitt,[101] H. von Radziewski,[48] E. von Toerne,[21] V. Vorobel,[129] K. Vorobev,[98] M. Vos,[167] R. Voss,[30] J. H. Vossebeld,[74] N. Vranjes,[13] M. Vranjes Milosavljevic,[13] V. Vrba,[127] M. Vreeswijk,[107] R. Vuillermet,[30] I. Vukotic,[31] Z. Vykydal,[128] P. Wagner,[21] W. Wagner,[175] H. Wahlberg,[71] S. Wahrmund,[44] J. Wakabayashi,[103] J. Walder,[72] R. Walker,[100] W. Walkowiak,[141] C. Wang,[33c] F. Wang,[173] H. Wang,[15] H. Wang,[40] J. Wang,[42] J. Wang,[33a] K. Wang,[87] R. Wang,[6] S. M. Wang,[151] T. Wang,[21] X. Wang,[176] C. Wanotayaroj,[116] A. Warburton,[87] C. P. Ward,[28] D. R. Wardrope,[78] M. Warsinsky,[48] A. Washbrook,[46] C. Wasicki,[42] P. M. Watkins,[18] A. T. Watson,[18] I. J. Watson,[150] M. F. Watson,[18] G. Watts,[138] S. Watts,[84] B. M. Waugh,[78] S. Webb,[84] M. S. Weber,[17] S. W. Weber,[174] J. S. Webster,[31] A. R. Weidberg,[120] B. Weinert,[61] J. Weingarten,[54] C. Weiser,[48] H. Weits,[107] P. S. Wells,[30] T. Wenaus,[25] T. Wengler,[30] S. Wenig,[30] N. Wermes,[21] M. Werner,[48] P. Werner,[30] M. Wessels,[58a] J. Wetter,[161] K. Whalen,[29] A. M. Wharton,[72] A. White,[8] M. J. White,[1] R. White,[32b] S. White,[124a,124b] D. Whiteson,[163] F. J. Wickens,[131] W. Wiedenmann,[173] M. Wielers,[131] P. Wienemann,[21] C. Wiglesworth,[36] L. A. M. Wiik-Fuchs,[21] A. Wildauer,[101] H. G. Wilkens,[30] H. H. Williams,[122] S. Williams,[107] C. Willis,[90] S. Willocq,[86] A. Wilson,[89] J. A. Wilson,[18] I. Wingerter-Seez,[5] F. Winklmeier,[116] B. T. Winter,[21] M. Wittgen,[143] J. Wittkowski,[100] S. J. Wollstadt,[83] M. W. Wolter,[39] H. Wolters,[126a,126c] B. K. Wosiek,[39] J. Wotschack,[30] M. J. Woudstra,[84] K. W. Wozniak,[39] M. Wu,[55] M. Wu,[31] S. L. Wu,[173] X. Wu,[49] Y. Wu,[89] T. R. Wyatt,[84] B. M. Wynne,[46] S. Xella,[36] D. Xu,[33a] L. Xu,[33b,kk] B. Yabsley,[150] S. Yacoob,[145b,ll] R. Yakabe,[67] M. Yamada,[66] Y. Yamaguchi,[118] A. Yamamoto,[66] S. Yamamoto,[155] T. Yamanaka,[155] K. Yamauchi,[103] Y. Yamazaki,[67] Z. Yan,[22] H. Yang,[33e] H. Yang,[173] Y. Yang,[151] L. Yao,[33a] W-M. Yao,[15] Y. Yasu,[66] E. Yatsenko,[5] K. H. Yau Wong,[21] J. Ye,[40] S. Ye,[25] I. Yeletskikh,[65] A. L. Yen,[57] E. Yildirim,[42] K. Yorita,[171] R. Yoshida,[6] K. Yoshihara,[122] C. Young,[143] C. J. S. Young,[30] S. Youssef,[22] D. R. Yu,[15] J. Yu,[8] J. M. Yu,[89] J. Yu,[114] L. Yuan,[67] A. Yurkewicz,[108]

I. Yusuff,[28,mm] B. Zabinski,[39] R. Zaidan,[63] A. M. Zaitsev,[130,bb] J. Zalieckas,[14] A. Zaman,[148] S. Zambito,[57] L. Zanello,[132a,132b] D. Zanzi,[88] C. Zeitnitz,[175] M. Zeman,[128] A. Zemla,[38a] K. Zengel,[23] O. Zenin,[130] T. Ženiš,[144a] D. Zerwas,[117] D. Zhang,[89] F. Zhang,[173] J. Zhang,[6] L. Zhang,[48] R. Zhang,[33b] X. Zhang,[33d] Z. Zhang,[117] X. Zhao,[40] Y. Zhao,[33d,117] Z. Zhao,[33b] A. Zhemchugov,[65] J. Zhong,[120] B. Zhou,[89] C. Zhou,[45] L. Zhou,[35] L. Zhou,[40] N. Zhou,[163] C. G. Zhu,[33d] H. Zhu,[33a] J. Zhu,[89] Y. Zhu,[33b] X. Zhuang,[33a] K. Zhukov,[96] A. Zibell,[174] D. Zieminska,[61] N. I. Zimine,[65] C. Zimmermann,[83] S. Zimmermann,[48] Z. Zinonos,[54] M. Zinser,[83] M. Ziolkowski,[141] L. Živković,[13] G. Zobernig,[173] A. Zoccoli,[20a,20b] M. zur Nedden,[16] G. Zurzolo,[104a,104b] and L. Zwalinski[30]

(ATLAS Collaboration)

[1]*Department of Physics, University of Adelaide, Adelaide, Australia*
[2]*Physics Department, SUNY Albany, Albany, New York, USA*
[3]*Department of Physics, University of Alberta, Edmonton, Alberta, Canada*
[4a]*Department of Physics, Ankara University, Ankara, Turkey*
[4b]*Istanbul Aydin University, Istanbul, Turkey*
[4c]*Division of Physics, TOBB University of Economics and Technology, Ankara, Turkey*
[5]*LAPP, CNRS/IN2P3 and Université Savoie Mont Blanc, Annecy-le-Vieux, France*
[6]*High Energy Physics Division, Argonne National Laboratory, Argonne, Illinois, USA*
[7]*Department of Physics, University of Arizona, Tucson, Arizona, USA*
[8]*Department of Physics, The University of Texas at Arlington, Arlington, Texas, USA*
[9]*Physics Department, University of Athens, Athens, Greece*
[10]*Physics Department, National Technical University of Athens, Zografou, Greece*
[11]*Institute of Physics, Azerbaijan Academy of Sciences, Baku, Azerbaijan*
[12]*Institut de Física d'Altes Energies and Departament de Física de la Universitat Autònoma de Barcelona, Barcelona, Spain*
[13]*Institute of Physics, University of Belgrade, Belgrade, Serbia*
[14]*Department for Physics and Technology, University of Bergen, Bergen, Norway*
[15]*Physics Division, Lawrence Berkeley National Laboratory and University of California, Berkeley, California, USA*
[16]*Department of Physics, Humboldt University, Berlin, Germany*
[17]*Albert Einstein Center for Fundamental Physics and Laboratory for High Energy Physics, University of Bern, Bern, Switzerland*
[18]*School of Physics and Astronomy, University of Birmingham, Birmingham, United Kingdom*
[19a]*Department of Physics, Bogazici University, Istanbul, Turkey*
[19b]*Department of Physics, Dogus University, Istanbul, Turkey*
[19c]*Department of Physics Engineering, Gaziantep University, Gaziantep, Turkey*
[20a]*INFN Sezione di Bologna, Bologna, Italy*
[20b]*Dipartimento di Fisica e Astronomia, Università di Bologna, Bologna, Italy*
[21]*Physikalisches Institut, University of Bonn, Bonn, Germany*
[22]*Department of Physics, Boston University, Boston, Massachusetts, USA*
[23]*Department of Physics, Brandeis University, Waltham, Massachusetts, USA*
[24a]*Universidade Federal do Rio De Janeiro COPPE/EE/IF, Rio de Janeiro, Brazil*
[24b]*Electrical Circuits Department, Federal University of Juiz de Fora (UFJF), Juiz de Fora, Brazil*
[24c]*Federal University of Sao Joao del Rei (UFSJ), Sao Joao del Rei, Brazil*
[24d]*Instituto de Fisica, Universidade de Sao Paulo, Sao Paulo, Brazil*
[25]*Physics Department, Brookhaven National Laboratory, Upton, New York, USA*
[26a]*National Institute of Physics and Nuclear Engineering, Bucharest, Romania*
[26b]*National Institute for Research and Development of Isotopic and Molecular Technologies, Physics Department, Cluj Napoca, Romania*
[26c]*University Politehnica Bucharest, Bucharest, Romania*
[26d]*West University in Timisoara, Timisoara, Romania*
[27]*Departamento de Física, Universidad de Buenos Aires, Buenos Aires, Argentina*
[28]*Cavendish Laboratory, University of Cambridge, Cambridge, United Kingdom*
[29]*Department of Physics, Carleton University, Ottawa, Ontario, Canada*
[30]*CERN, Geneva, Switzerland*
[31]*Enrico Fermi Institute, University of Chicago, Chicago Illinois, USA*
[32a]*Departamento de Física, Pontificia Universidad Católica de Chile, Santiago, Chile*
[32b]*Departamento de Física, Universidad Técnica Federico Santa María, Valparaíso, Chile*

[33a]*Institute of High Energy Physics, Chinese Academy of Sciences, Beijing, China*
[33b]*Department of Modern Physics, University of Science and Technology of China, Anhui, China*
[33c]*Department of Physics, Nanjing University, Jiangsu, China*
[33d]*School of Physics, Shandong University, Shandong, China*
[33e]*Department of Physics and Astronomy, Shanghai Key Laboratory for Particle Physics and Cosmology, Shanghai Jiao Tong University, Shanghai, China*
[33f]*Physics Department, Tsinghua University, Beijing 100084, China*
[34]*Laboratoire de Physique Corpusculaire, Clermont Université and Université Blaise Pascal and CNRS/IN2P3, Clermont-Ferrand, France*
[35]*Nevis Laboratory, Columbia University, Irvington, New York, USA*
[36]*Niels Bohr Institute, University of Copenhagen, Kobenhavn, Denmark*
[37a]*INFN Gruppo Collegato di Cosenza, Laboratori Nazionali di Frascati, Italy*
[37b]*Dipartimento di Fisica, Università della Calabria, Rende, Italy*
[38a]*AGH University of Science and Technology, Faculty of Physics and Applied Computer Science, Krakow, Poland*
[38b]*Marian Smoluchowski Institute of Physics, Jagiellonian University, Krakow, Poland*
[39]*Institute of Nuclear Physics Polish Academy of Sciences, Krakow, Poland*
[40]*Physics Department, Southern Methodist University, Dallas, Texas, USA*
[41]*Physics Department, University of Texas at Dallas, Richardson, Texas, USA*
[42]*DESY, Hamburg and Zeuthen, Germany*
[43]*Institut für Experimentelle Physik IV, Technische Universität Dortmund, Dortmund, Germany*
[44]*Institut für Kern- und Teilchenphysik, Technische Universität Dresden, Dresden, Germany*
[45]*Department of Physics, Duke University, Durham, North Carolina, USA*
[46]*SUPA - School of Physics and Astronomy, University of Edinburgh, Edinburgh, United Kingdom*
[47]*INFN Laboratori Nazionali di Frascati, Frascati, Italy*
[48]*Fakultät für Mathematik und Physik, Albert-Ludwigs-Universität, Freiburg, Germany*
[49]*Section de Physique, Université de Genève, Geneva, Switzerland*
[50a]*INFN Sezione di Genova, Genova, Italy*
[50b]*Dipartimento di Fisica, Università di Genova, Genova, Italy*
[51a]*E. Andronikashvili Institute of Physics, Iv. Javakhishvili Tbilisi State University, Tbilisi, Georgia*
[51b]*High Energy Physics Institute, Tbilisi State University, Tbilisi, Georgia*
[52]*II Physikalisches Institut, Justus-Liebig-Universität Giessen, Giessen, Germany*
[53]*SUPA - School of Physics and Astronomy, University of Glasgow, Glasgow, United Kingdom*
[54]*II Physikalisches Institut, Georg-August-Universität, Göttingen, Germany*
[55]*Laboratoire de Physique Subatomique et de Cosmologie, Université Grenoble-Alpes, CNRS/IN2P3, Grenoble, France*
[56]*Department of Physics, Hampton University, Hampton, Virginia, USA*
[57]*Laboratory for Particle Physics and Cosmology, Harvard University, Cambridge, Massachusetts, USA*
[58a]*Kirchhoff-Institut für Physik, Ruprecht-Karls-Universität Heidelberg, Heidelberg, Germany*
[58b]*Physikalisches Institut, Ruprecht-Karls-Universität Heidelberg, Heidelberg, Germany*
[58c]*ZITI Institut für technische Informatik, Ruprecht-Karls-Universität Heidelberg, Mannheim, Germany*
[59]*Faculty of Applied Information Science, Hiroshima Institute of Technology, Hiroshima, Japan*
[60a]*Department of Physics, The Chinese University of Hong Kong, Shatin, N.T., Hong Kong, China*
[60b]*Department of Physics, The University of Hong Kong, Hong Kong, China*
[60c]*Department of Physics, The Hong Kong University of Science and Technology, Clear Water Bay, Kowloon, Hong Kong, China*
[61]*Department of Physics, Indiana University, Bloomington, Indiana, USA*
[62]*Institut für Astro- und Teilchenphysik, Leopold-Franzens-Universität, Innsbruck, Austria*
[63]*University of Iowa, Iowa City, Iowa, USA*
[64]*Department of Physics and Astronomy, Iowa State University, Ames, Iowa, USA*
[65]*Joint Institute for Nuclear Research, JINR Dubna, Dubna, Russia*
[66]*KEK, High Energy Accelerator Research Organization, Tsukuba, Japan*
[67]*Graduate School of Science, Kobe University, Kobe, Japan*
[68]*Faculty of Science, Kyoto University, Kyoto, Japan*
[69]*Kyoto University of Education, Kyoto, Japan*
[70]*Department of Physics, Kyushu University, Fukuoka, Japan*
[71]*Instituto de Física La Plata, Universidad Nacional de La Plata and CONICET, La Plata, Argentina*
[72]*Physics Department, Lancaster University, Lancaster, United Kingdom*

[73a]INFN Sezione di Lecce, Lecce, Italy
[73b]Dipartimento di Matematica e Fisica, Università del Salento, Lecce, Italy
[74]Oliver Lodge Laboratory, University of Liverpool, Liverpool, United Kingdom
[75]Department of Physics, Jožef Stefan Institute and University of Ljubljana, Ljubljana, Slovenia
[76]School of Physics and Astronomy, Queen Mary University of London, London, United Kingdom
[77]Department of Physics, Royal Holloway University of London, Surrey, United Kingdom
[78]Department of Physics and Astronomy, University College London, London, United Kingdom
[79]Louisiana Tech University, Ruston, Louisiana, USA
[80]Laboratoire de Physique Nucléaire et de Hautes Energies, UPMC and Université Paris-Diderot and CNRS/IN2P3, Paris, France
[81]Fysiska institutionen, Lunds universitet, Lund, Sweden
[82]Departamento de Fisica Teorica C-15, Universidad Autonoma de Madrid, Madrid, Spain
[83]Institut für Physik, Universität Mainz, Mainz, Germany
[84]School of Physics and Astronomy, University of Manchester, Manchester, United Kingdom
[85]CPPM, Aix-Marseille Université and CNRS/IN2P3, Marseille, France
[86]Department of Physics, University of Massachusetts, Amherst, Massachusetts, USA
[87]Department of Physics, McGill University, Montreal, Québec, Canada
[88]School of Physics, University of Melbourne, Victoria, Australia
[89]Department of Physics, The University of Michigan, Ann Arbor, Michigan, USA
[90]Department of Physics and Astronomy, Michigan State University, East Lansing, Michigan, USA
[91a]INFN Sezione di Milano, Milano, Italy
[91b]Dipartimento di Fisica, Università di Milano, Milano, Italy
[92]B.I. Stepanov Institute of Physics, National Academy of Sciences of Belarus, Minsk, Republic of Belarus
[93]National Scientific and Educational Centre for Particle and High Energy Physics, Minsk, Republic of Belarus
[94]Department of Physics, Massachusetts Institute of Technology, Cambridge, Massachusetts, USA
[95]Group of Particle Physics, University of Montreal, Montreal Québec, Canada
[96]P.N. Lebedev Institute of Physics, Academy of Sciences, Moscow, Russia
[97]Institute for Theoretical and Experimental Physics (ITEP), Moscow, Russia
[98]National Research Nuclear University MEPhI, Moscow, Russia
[99]D.V. Skobeltsyn Institute of Nuclear Physics, M.V. Lomonosov Moscow State University, Moscow, Russia
[100]Fakultät für Physik, Ludwig-Maximilians-Universität München, München, Germany
[101]Max-Planck-Institut für Physik (Werner-Heisenberg-Institut), München, Germany
[102]Nagasaki Institute of Applied Science, Nagasaki, Japan
[103]Graduate School of Science and Kobayashi-Maskawa Institute, Nagoya University, Nagoya, Japan
[104a]INFN Sezione di Napoli, Napoli, Italy
[104b]Dipartimento di Fisica, Università di Napoli, Napoli, Italy
[105]Department of Physics and Astronomy, University of New Mexico, Albuquerque, New Mexico, USA
[106]Institute for Mathematics, Astrophysics and Particle Physics, Radboud University Nijmegen/Nikhef, Nijmegen, Netherlands
[107]Nikhef National Institute for Subatomic Physics and University of Amsterdam, Amsterdam, Netherlands
[108]Department of Physics, Northern Illinois University, DeKalb, Illinois, USA
[109]Budker Institute of Nuclear Physics, SB RAS, Novosibirsk, Russia
[110]Department of Physics, New York University, New York, New York, USA
[111]Ohio State University, Columbus, Ohio, USA
[112]Faculty of Science, Okayama University, Okayama, Japan
[113]Homer L. Dodge Department of Physics and Astronomy, University of Oklahoma, Norman, Oklahoma, USA
[114]Department of Physics, Oklahoma State University, Stillwater, Oklahoma, USA
[115]Palacký University, RCPTM, Olomouc, Czech Republic
[116]Center for High Energy Physics, University of Oregon, Eugene, Oregon, USA
[117]LAL, Université Paris-Sud and CNRS/IN2P3, Orsay, France
[118]Graduate School of Science, Osaka University, Osaka, Japan
[119]Department of Physics, University of Oslo, Oslo, Norway
[120]Department of Physics, Oxford University, Oxford, United Kingdom
[121a]INFN Sezione di Pavia, Pavia, Italy
[121b]Dipartimento di Fisica, Università di Pavia, Pavia, Italy
[122]Department of Physics, University of Pennsylvania, Philadelphia, Pennsylvania, USA
[123]Petersburg Nuclear Physics Institute, Gatchina, Russia
[124a]INFN Sezione di Pisa, Pisa, Italy

[124b]*Dipartimento di Fisica E. Fermi, Università di Pisa, Pisa, Italy*
[125]*Department of Physics and Astronomy, University of Pittsburgh, Pittsburgh, Pennsylvania, USA*
[126a]*Laboratorio de Instrumentacao e Fisica Experimental de Particulas - LIP, Lisboa, Portugal*
[126b]*Faculdade de Ciências, Universidade de Lisboa, Lisboa, Portugal*
[126c]*Department of Physics, University of Coimbra, Coimbra, Portugal*
[126d]*Centro de Física Nuclear da Universidade de Lisboa, Lisboa, Portugal*
[126e]*Departamento de Fisica, Universidade do Minho, Braga, Portugal*
[126f]*Departamento de Fisica Teorica y del Cosmos and CAFPE, Universidad de Granada, Granada, Spain*
[126g]*Dep Fisica and CEFITEC of Faculdade de Ciencias e Tecnologia, Universidade Nova de Lisboa, Caparica, Portugal*
[127]*Institute of Physics, Academy of Sciences of the Czech Republic, Praha, Czech Republic*
[128]*Czech Technical University in Prague, Praha, Czech Republic*
[129]*Faculty of Mathematics and Physics, Charles University in Prague, Praha, Czech Republic*
[130]*State Research Center Institute for High Energy Physics, Protvino, Russia*
[131]*Particle Physics Department, Rutherford Appleton Laboratory, Didcot, United Kingdom*
[132a]*INFN Sezione di Roma, Roma, Italy*
[132b]*Dipartimento di Fisica, Sapienza Università di Roma, Roma, Italy*
[133a]*INFN Sezione di Roma Tor Vergata, Roma, Italy*
[133b]*Dipartimento di Fisica, Università di Roma Tor Vergata, Roma, Italy*
[134a]*INFN Sezione di Roma Tre, Roma, Italy*
[134b]*Dipartimento di Matematica e Fisica, Università Roma Tre, Roma, Italy*
[135a]*Faculté des Sciences Ain Chock, Réseau Universitaire de Physique des Hautes Energies - Université Hassan II, Casablanca, Morocco*
[135b]*Centre National de l'Energie des Sciences Techniques Nucleaires, Rabat, Morocco*
[135c]*Faculté des Sciences Semlalia, Université Cadi Ayyad, LPHEA-Marrakech, Morocco*
[135d]*Faculté des Sciences, Université Mohamed Premier and LPTPM, Oujda, Morocco*
[135e]*Faculté des sciences, Université Mohammed V-Agdal, Rabat, Morocco*
[136]*DSM/IRFU (Institut de Recherches sur les Lois Fondamentales de l'Univers), CEA Saclay (Commissariat à l'Energie Atomique et aux Energies Alternatives), Gif-sur-Yvette, France*
[137]*Santa Cruz Institute for Particle Physics, University of California Santa Cruz, Santa Cruz, California, USA*
[138]*Department of Physics, University of Washington, Seattle Washington, USA*
[139]*Department of Physics and Astronomy, University of Sheffield, Sheffield, United Kingdom*
[140]*Department of Physics, Shinshu University, Nagano, Japan*
[141]*Fachbereich Physik, Universität Siegen, Siegen, Germany*
[142]*Department of Physics, Simon Fraser University, Burnaby BC, Canada*
[143]*SLAC National Accelerator Laboratory, Stanford, California, USA*
[144a]*Faculty of Mathematics, Physics & Informatics, Comenius University, Bratislava, Slovak Republic*
[144b]*Department of Subnuclear Physics, Institute of Experimental Physics of the Slovak Academy of Sciences, Kosice, Slovak Republic*
[145a]*Department of Physics, University of Cape Town, Cape Town, South Africa*
[145b]*Department of Physics, University of Johannesburg, Johannesburg, South Africa*
[145c]*School of Physics, University of the Witwatersrand, Johannesburg, South Africa*
[146a]*Department of Physics, Stockholm University, Stockholm, Sweden*
[146b]*The Oskar Klein Centre, Stockholm, Sweden*
[147]*Physics Department, Royal Institute of Technology, Stockholm, Sweden*
[148]*Departments of Physics & Astronomy and Chemistry, Stony Brook University, Stony Brook, New York, USA*
[149]*Department of Physics and Astronomy, University of Sussex, Brighton, United Kingdom*
[150]*School of Physics, University of Sydney, Sydney, Australia*
[151]*Institute of Physics, Academia Sinica, Taipei, Taiwan*
[152]*Department of Physics, Technion: Israel Institute of Technology, Haifa, Israel*
[153]*Raymond and Beverly Sackler School of Physics and Astronomy, Tel Aviv University, Tel Aviv, Israel*
[154]*Department of Physics, Aristotle University of Thessaloniki, Thessaloniki, Greece*
[155]*International Center for Elementary Particle Physics and Department of Physics, The University of Tokyo, Tokyo, Japan*
[156]*Graduate School of Science and Technology, Tokyo Metropolitan University, Tokyo, Japan*
[157]*Department of Physics, Tokyo Institute of Technology, Tokyo, Japan*

[158]Department of Physics, University of Toronto, Toronto, Ontario, Canada
[159a]TRIUMF, Vancouver, British Columbia, Canada
[159b]Department of Physics and Astronomy, York University, Toronto, Ontario, Canada
[160]Faculty of Pure and Applied Sciences, University of Tsukuba, Tsukuba, Japan
[161]Department of Physics and Astronomy, Tufts University, Medford, Massachusetts, USA
[162]Centro de Investigaciones, Universidad Antonio Narino, Bogota, Colombia
[163]Department of Physics and Astronomy, University of California Irvine, Irvine, California, USA
[164a]INFN Gruppo Collegato di Udine, Sezione di Trieste, Udine, Italy
[164b]ICTP, Trieste, Italy
[164c]Dipartimento di Chimica, Fisica e Ambiente, Università di Udine, Udine, Italy
[165]Department of Physics, University of Illinois, Urbana, Illinois, USA
[166]Department of Physics and Astronomy, University of Uppsala, Uppsala, Sweden
[167]Instituto de Física Corpuscular (IFIC) and Departamento de Física Atómica, Molecular y Nuclear and Departamento de Ingeniería Electrónica and Instituto de Microelectrónica de Barcelona (IMB-CNM), University of Valencia and CSIC, Valencia, Spain
[168]Department of Physics, University of British Columbia, Vancouver, British Columbia, Canada
[169]Department of Physics and Astronomy, University of Victoria, Victoria, British Columbia, Canada
[170]Department of Physics, University of Warwick, Coventry, United Kingdom
[171]Waseda University, Tokyo, Japan
[172]Department of Particle Physics, The Weizmann Institute of Science, Rehovot, Israel
[173]Department of Physics, University of Wisconsin, Madison, Wisconsin, USA
[174]Fakultät für Physik und Astronomie, Julius-Maximilians-Universität, Würzburg, Germany
[175]Fachbereich C Physik, Bergische Universität Wuppertal, Wuppertal, Germany
[176]Department of Physics, Yale University, New Haven, Connecticut, USA
[177]Yerevan Physics Institute, Yerevan, Armenia
[178]Centre de Calcul de l'Institut National de Physique Nucléaire et de Physique des Particules (IN2P3), Villeurbanne, France

[a]Deceased.
[b]Also at Department of Physics, King's College London, London, United Kingdom.
[c]Also at Institute of Physics, Azerbaijan Academy of Sciences, Baku, Azerbaijan.
[d]Also at Novosibirsk State University, Novosibirsk, Russia.
[e]Also at TRIUMF, Vancouver BC, Canada.
[f]Also at Department of Physics, California State University, Fresno CA, USA.
[g]Also at Department of Physics, University of Fribourg, Fribourg, Switzerland.
[h]Also at Departamento de Fisica e Astronomia, Faculdade de Ciencias, Universidade do Porto, Portugal.
[i]Also at Tomsk State University, Tomsk, Russia.
[j]Also at CPPM, Aix-Marseille Université and CNRS/IN2P3, Marseille, France.
[k]Also at Università di Napoli Parthenope, Napoli, Italy.
[l]Also at Institute of Particle Physics (IPP), Canada.
[m]Also at Particle Physics Department, Rutherford Appleton Laboratory, Didcot, United Kingdom.
[n]Also at Department of Physics, St. Petersburg State Polytechnical University, St. Petersburg, Russia.
[o]Also at Louisiana Tech University, Ruston LA, USA.
[p]Also at Institucio Catalana de Recerca i Estudis Avancats, ICREA, Barcelona, Spain.
[q]Also at Department of Physics, National Tsing Hua University, Taiwan.
[r]Also at Department of Physics, The University of Texas at Austin, Austin TX, USA.
[s]Also at Institute of Theoretical Physics, Ilia State University, Tbilisi, Georgia.
[t]Also at CERN, Geneva, Switzerland.
[u]Also at Georgian Technical University (GTU),Tbilisi, Georgia.
[v]Also at Ochadai Academic Production, Ochanomizu University, Tokyo, Japan.
[w]Also at Manhattan College, New York NY, USA.
[x]Also at Institute of Physics, Academia Sinica, Taipei, Taiwan.
[y]Also at LAL, Université Paris-Sud and CNRS/IN2P3, Orsay, France.
[z]Also at Academia Sinica Grid Computing, Institute of Physics, Academia Sinica, Taipei, Taiwan.
[aa]Also at School of Physics, Shandong University, Shandong, China.
[bb]Also at Moscow Institute of Physics and Technology State University, Dolgoprudny, Russia.
[cc]Also at Section de Physique, Université de Genève, Geneva, Switzerland.
[dd]Also at International School for Advanced Studies (SISSA), Trieste, Italy.
[ee]Also at Department of Physics and Astronomy, University of South Carolina, Columbia SC, USA.
[ff]Also at School of Physics and Engineering, Sun Yat-sen University, Guangzhou, China.

[gg]Also at Faculty of Physics, M.V.Lomonosov Moscow State University, Moscow, Russia.
[hh]Also at National Research Nuclear University MEPhI, Moscow, Russia.
[ii]Also at Department of Physics, Stanford University, Stanford CA, USA.
[jj]Also at Institute for Particle and Nuclear Physics, Wigner Research Centre for Physics, Budapest, Hungary.
[kk]Also at Department of Physics, The University of Michigan, Ann Arbor MI, USA.
[ll]Also at Discipline of Physics, University of KwaZulu-Natal, Durban, South Africa.
[mm]Also at University of Malaya, Department of Physics, Kuala Lumpur, Malaysia.

Model Magnet Development of D1 Beam Separation Dipole for the HL-LHC Upgrade

Tatsushi Nakamoto, Michinaka Sugano, Qingjin Xu, Hiroshi Kawamata, Shun Enomoto, Norio Higashi, Akira Idesaki, Masami Iio, Yukiko Ikemoto, Ruri Iwasaki, Nobuhiro Kimura, Toru Ogitsu, Naoki Okada, Ken-ichi Sasaki, Makoto Yoshida, and Ezio Todesco

***Abstract*—KEK has been conducting the design study of the beam separation dipole magnet, D1, for the High Luminosity LHC (HL-LHC) upgrade within a framework of the CERN-KEK collaboration. The D1 magnet has a coil aperture of 150 mm using Nb-Ti superconducting cable and the nominal dipole field of 5.6 T can be generated at 12 kA and 1.9 K. A field integral of 35 T·m is required. The development of the 2-m-long model magnet has been started since May 2013. This paper describes the development status of the short model magnet as well as advancement of the fundamental design studies.**

***Index Terms*—Collared yoke, LHC upgrade, Nb-Ti, radiation resistance, superconducting dipole.**

I. Introduction

While LHC, even at 60% of its nominal energy, has been producing remarkable experimental results on particle physics, including the discovery of Higgs boson, a major upgrade to increase the data production by a factor of ten is planned around 2020 to exploit its full potential [1], [2]. To achieve a higher luminosity, superconducting and conventional magnets for the insertion regions at both sides of the ATLAS and CMS experiments will need to be replaced to provide a smaller beam size at the interaction point through a reduction in β^* [3]. KEK has participated in the design study of the High Luminosity LHC (HL-LHC) upgrade within the framework of the CERN-KEK collaboration and has been conducting the design study of the new beam separation dipole magnet (D1) including the development of a short model magnet. In the HL-LHC machine, the resistive D1 magnets will be replaced by superconducting dipole magnets with a larger coil aperture (150 mm) and a higher field integral (35 T·m). So far, a series of conceptual design studies on the new D1 has been carried out [4]–[6]. Main design requirements were specified in May 2013, after which the short model development was started at KEK. In this paper, development status of the short model as well as advancement of the fundamental design studies are presented. Detailed electromagnetic and mechanical analyses are reported in [7].

Manuscript received August 9, 2014; accepted September 30, 2014. Date of publication October 3, 2014; date of current version December 24, 2014. This work was supported in part by the European Commission under the FP7 project HiLumi LHC, GA no. 284404, co-funded by the DoE, USA and KEK, Japan; by the CERN-KEK collaboration program, JSPS KAKENHI Grant 23104003; and by the JSPS Strategic Young Researcher Overseas Visits Program for Accelerating Brain Circulation (R2221).

T. Nakamoto, M. Sugano, H. Kawamata, S. Enomoto, N. Higashi, M. Iio, Y. Ikemoto, R. Iwasaki, N. Kimura, T. Ogitsu, N. Okada, K. Sasaki, and M. Yoshida are with the High Energy Accelerator Research Organization (KEK), Tsukuba 305-0801, Japan (e-mail: tatsushi.nakamoto@kek.jp; michinaka.sugano@kek.jp; hiroshi.kawamata@kek.jp; enoshun@post.kek.jp; norio.higashi@kek.jp; masami.iio@kek.jp; yukiko.ikemoto@kek.jp; ruri.iwasaki@kek.jp; toru.ogitsu@kek.jp; naoki.okada@kek.jp; nobuhiro.kimura@kek.jp; ken-ichi.sasaki@kek.jp; makoto.yoshida@kek.jp).

Q. Xu was with High Energy Accelerator Research Organization (KEK), Tsukuba 305-0801, Japan. He is now with the Institue of High Energy Physics (IHEP), Beijing 100049, China (e-mail: xuqj@ihep.ac.cn).

A. Idesaki is with the Japan Atomic Energy Agency (JAEA), Takasaki 370-1292, Japan (e-mail: idesaki.akira@jaea.go.jp).

E. Todesco is with the European Organization for Nuclear Research (CERN), CH-1211 Geneva, Switzerland (e-mail: Ezio.Todesco@cern.ch).

Color versions of one or more of the figures in this paper are available online at http://ieeexplore.ieee.org.

Digital Object Identifier 10.1109/TASC.2014.2361404

II. Magnet Overview

A. Design Guideline

Main design requirements for the new D1 are the large coil aperture of 150 mm and the field integral of 35 T·m [3]. Nominal dipole field has been set around 6 T and the whole mechanical magnet length should be 7 m or shorter: the D1 production magnets are supposed to be tested in the 7-m-deep vertical cryostat at KEK. Nominal field beyond 7 T is not considered since it would lead to a significant design difficulty while the benefit of a shorter magnet length would be marginal. In particular, due to the large aperture, and despite the nominal field of only 6 T, the control of iron saturation effects on the field quality and suppression of the stray field outside the cryostat are design issues. This is complicated by the limited transverse space available in the LHC tunnel, which dictates an upper limit to the magnet size. The field design already relies on the iron steel cryostat as a flux return [6].

Other important design requirements are the radiation heat load and the cooling capability. The total heat load of the cold mass and the local peak heat load in the coil are estimated to be 90 W and 1.3 mW/cm^3, respectively, at the HL-LHC design luminosity of 5×10^{34} cm^{-2} sec^{-1}. The magnet design must be compatible with an ultimate peak luminosity that is 50% higher than the original design one. For this reason, the design parameters of the total heat load and the local peak heat load are set to 135 W and 2 mW/cm^3, respectively. The magnet must be operated to withstand a total dose of 25 MGy in its lifetime: the dose was remarkably reduced due to the insertion of a heavily shielded beam screen in the bore [8].

The following is the design guideline of the new D1.

- Use of spare unit lengths of the LHC Nb-Ti superconducting cable from the main dipole (MB) outer layer, wrapped with the polyimide insulation.

1051-8223 © 2014 IEEE. Personal use is permitted, but republication/redistribution requires IEEE permission.
See http://www.ieee.org/publications_standards/publications/rights/index.html for more information.

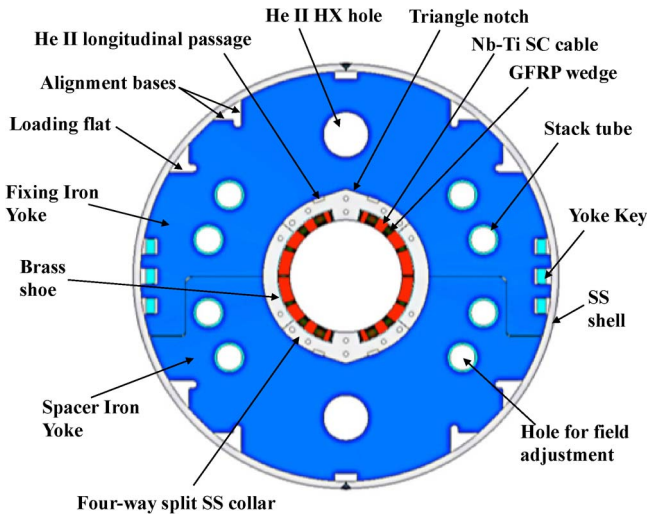

Fig. 1. Cross-sectional view of the D1 beam separation dipole magnet for the HL-LHC.

- Operational temperature of 1.9 K by superfluid helium cooling while operating around 75% of short sample current (i.e., 25% margin on the load-line).
- A single layer coil for better cooling capability and to leave more space to the iron yoke for reducing the fringe field.
- Enhancement of the amount of iron yoke in the cross section accomplished by "a collared yoke structure" like RHIC magnets [9] and LHC MQXA quadrupoles [10].
- A yoke outer diameter of 550 mm, same as J-PARC SCFM [11], enabling reuse of the assembly jigs and relevant facilities at KEK.
- Use of radiation resistant materials for the coil parts: wedges, end spacers.

B. Magnet Design

A cross-sectional view of the new D1 beam separation superconducting dipole magnet for the HL-LHC is shown in Fig. 1. The main design parameters for the 2-m-long model magnet and the 7-m-long production magnet are listed in Table I. The magnet cross section including the cable arrangement and the iron yoke shape is designed in 2-D employing ROXIE [12]. The field quality is optimized at the collision energy while variation of the multipole components due to the iron saturation during the excitation is kept within an acceptable range. The coil end shape is fully covered by the iron yoke and is optimized in view of the production magnet with the aim of minimizing the field integrals of the multipole components and the peak field. The coil end shape obtained for the production magnet is kept for the 2-m-model magnet. The results of optimization are listed in Table II. The field integral multipole minimization for the production magnet might still be insufficient due to the limited adjustable parameters in a single layer coil, but it can be reduced by tuning the coil cross section in the straight section in the future. Large drifts in the field integral of the multipole components in the 2-m-model are observed: the coil center is not sufficiently far from the coil ends and the current at the coil ends influence the field quality even around the center of the magnet. Some skew components come from the coil lead-end since the top and the bottom coils have a rotational symmetry.

TABLE I
MAIN DESIGN PARAMETERS OF THE D1 BEAM SEPARATION DIPOLE MAGNET FOR THE HL-LHC

Design parameters	2 m model	Production
General		
Field integral	10.3 T·m	35 T·m
Coil aperture	150 mm	
Nominal dipole field	5.58 T	
Coil peak field	6.45 T at center 6.71 T at coil end	
Load-line ratio	75 % at center 78 % at coil end	
Field Quality	$< 10^{-4}$ w.r.t the main field	
Nominal current	12.0 kA	
Operation temperature	1.9 K	
Magnetic length	1.85 m	6.27 m
Stored energy	340 kJ/m	
Differential Inductance	4.0 mH/m	
Number of coil layer	1	
Number of turns in quadrant	44 (4+8+13+19)	
Coil mechanical length	2.00 m	6.46 m
Magnet mechanical length	2.50 m	6.96 m
Cold mass weight	3.8 tons	12 tons
Cable unit length per coil	175 m	568 m
Lorenz force per quater ΣF_x & ΣF_y	1.53 & -0.64 MN/m	
Heat load	135 W in total, 2 mW/cm^3 at local peak	
Radiation dose	> 25 MGy	
Superconducting Cable		
Superconductor	Nb-Ti	
Cable type	LHC MB outer cable	
Strand diameter	0.825 mm	
Coating	Sn5wt%Ag	
Copper to SC ratio	1.95	
Filament diameter	6 μm	
Number of filament	6500	
RRR	> 150	
Critical current (9 T, 1.9 K)	> 380 A	
Number of strand	36	
Cable bare width	15.1 mm	
Cable bare mid-thickness	1.480 mm	
Keystone angle	0.9°	
Transposition pitch	100 mm	
Insulation		
1st & 2nd layer	APICAL (0.05 mm thick, 11 mm wide), 1/2 overwrap	
3rd layer	PIXEO (0.069 mm thick, 9 mm wide), adhesive, 2 mm gap wrap	

TABLE II
FIELD COMPUTATION RESULTS FOR 2-D AND 3-D MODELS OF THE D1 DIPOLE MAGNET FOR THE HL-LHC

	2D	3D, production	3D, 2 m model
Dipole field, B_1, at the center (T)	5.59	5.60	5.66
$\int B_1\,dl$ (T·m)	----	35.2	10.3
$\int B_3\,dl / \int B_1\,dl \times 10000$ (unit)	-0.265	8.27	24.5
$\int B_5\,dl / \int B_1\,dl \times 10000$ (unit)	-0.144	-1.46	-4.47
$\int B_7\,dl / \int B_1\,dl \times 10000$ (unit)	-0.134	-0.63	-1.66
$\int A_1\,dl / \int B_1\,dl \times 10000$ (unit)	----	-1.40	-4.73
$\int A_3\,dl / \int B_1\,dl \times 10000$ (unit)	----	0.772	2.66

*Reference radius at 50 mm

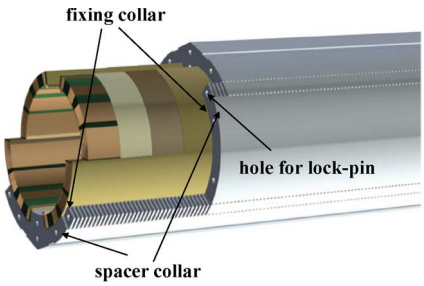

Fig. 2. Side cut view of collared coil.

A single layer coil consists of 44 turns of the Nb-Ti superconducting cable from the LHC MB outer layer with wedges and end spacers made of newly developed glass fiber reinforced plastic (GFRP). The GFRP wedges were utilized in the recent accelerator superconducting magnets [10], [11] and are cost-effective in a small number of magnet production like the new D1. The insulated superconducting cables are supplied by CERN. An LHC-MQXA type insulation with radiation resistant prepreg was considered for the cable insulation in the beginning. However, the standard cable insulation scheme for the LHC MB outer layer using APICAL and PIXEO polyimide tapes supplied by KANEKA was chosen for the new D1 coil because of its sufficient cooling capability of around a few mW/cm^3 [13]. In addition to adhesive cable insulation of PIXEO, cyanate ester resin (BT2160RX by Mitsubishi Gas Chemical) is used for the adhesion of the coil parts such as wedges and end spacers. For the electrical insulation to ground, two sets of double layer of 0.125 mm thick polyimide sheets (Upilex-RN by UBE Industries) surround the coil in accordance with the traditional method.

Four-way split collars are utilized to pre-assemble a pair of the top and bottom coils to provide a minimal azimuthal pre-stress around a few MPa, but the final pre-stress is given by the following yoking process [10]. Usually, superconducting dipole coils were assembled with a pair of vertically spilt collars [14]. But this concept seems to be inadequate for the new D1 where the collar azimuth would be quite longer while the width is kept narrow. An unwanted warp of the collar may arise in the blanking process and compromise the final dimensions. Due to this, the four-way split collar concept with a moderated aspect ratio is adopted for the new D1. A sub-stack of the collars is alternately laminated by the 2.3-mm-thick "fixing collar" and the 2.6-mm-thick "spacer collar" and four sub-stacks surrounding the coils are connected by the lock-pins through the holes at the end of the fixing collar, as illustrated in Fig. 2. The collar serves to align the pole of the superconducting coil with respect to the magnet structure: the triangle notches at the top and the bottom of the inner circle of the iron yoke determine the position of the coils. Outer surface of the right and left collars has the alignment feature around the median plane, not shown in Fig. 2, to orient the collar with respect to the triangle notch of the yoke at the initial stage of the yoking process. Mechanical behaviors mentioned above will be demonstrated by the mechanical short model study prior to the model magnet fabrication. The collars are made of non-magnetic stainless steels (NSSC-130S, formerly known as YUS-130S) showing a very low and stable permeability ratio of 1.002 at 4.2 K. The stainless steel collars are utilized at the coil straight section and the return-end. At the lead-end, however, the pole lead including the ramp box beyond the coil layer is clamped by the GFRP collars.

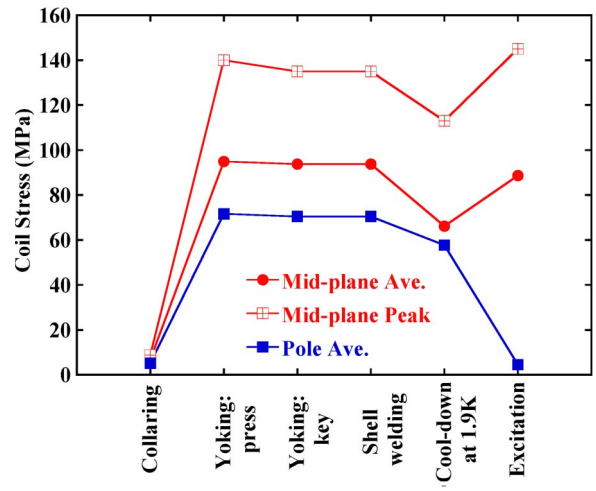

Fig. 3. FEM simulation results of the azimuthal coil stress at the fabrication processes and at the excitation at cold. For safety margin, 110% nominal current is taken for the FEM simulation at "Excitation".

The iron yokes are made of low carbon steels (EFE by JFE steel) showing a yield strength of 240 MPa. A sub-stack of the iron yokes is about 200 mm long and is made by alternately laminating the 5.6-mm-thick "fixing yokes" having three key slots for each side and the 6.0-mm-thick "spacer yokes". The laminated iron yokes of the sub-stack are firmly connected with stacking tubes by a cold shrinkage fit through holes introduced in the yoke to control the iron saturation effects. The horizontal median plane of the iron yoke has a taper of 0.15 mm and the key slots of the fixing yoke are off-centered by 0.15 mm as well. When the top and bottom iron yokes are compressed through the loading flats by the hydraulic press, the yoke arc is deformed like a cantilever. The median plane gap is eventually closed and the key slots of the top and bottom yokes are aligned to enable the insertion of the lock keys [10], [11]. The coil pre-stress is kept by the lock keys after the release of the press. Finally, two halves of stainless steel shells are longitudinally welded to complete the pressure vessel. Finite Element simulation results by ANSYS for the azimuthal coil stress during the fabrication processes, cooling down, and excitation up to 110% of nominal current are shown in Fig. 3. The coil pre-stress at the pole at assembly is designed to be 80 MPa so that the coil is under compression at the pole even during excitation. The performed ANSYS simulations [6], [7] have not revealed any serious problem in the magnet structure.

The magnet is cooled by superfluid helium at 1.9 K and two saturated superfluid helium heat exchangers (HXs) are inserted in the holes of the top and bottom of the iron yoke to absorb the maximal heat load of 135 W. To ensure that the superconducting coil is kept under the lambda point, a longitudinal void fraction of 4% is necessary. This will serve as the cooling passage from the superconducting coil to the HXs [15]. The collars are designed to have embosses of 0.2 mm and the laminated collar sub-stack provides the required systematic gap for the superfluid helium. Besides, two grooves are foreseen near the

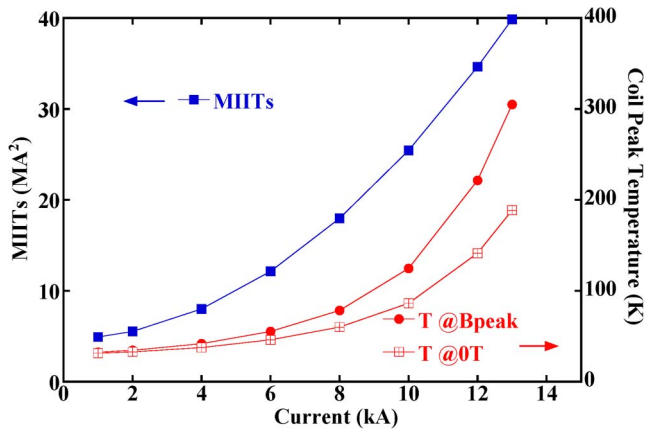

Fig. 4. MIITs estimation and predicted coil temperature at the peak field and the lowest field (i.e., zero).

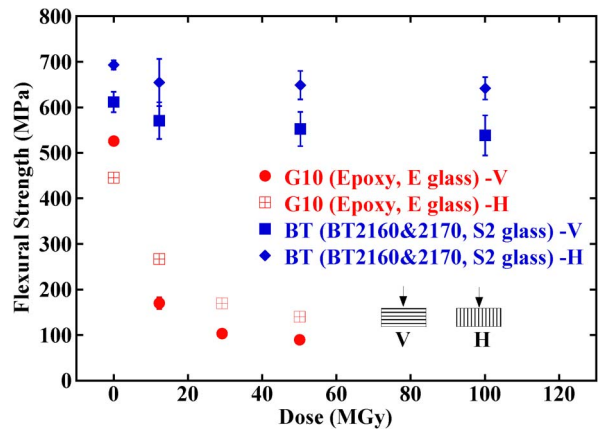

Fig. 5. Flexural strength of the new radiation resistant GFRP (BT) after γ-ray irradiation up to 100 MGy. Number of each sample is three. The data for the standard G10 GFRP are shown as a reference.

triangle alignment feature of the outer surface of the collar substack, to allow the longitudinal flow. In this way, the superfluid helium to deliver the heat from the coil can efficiently reach the HXs through the gaps between the iron yoke laminations with a typical packing factor of 98%.

In terms of the quench protection, the D1 magnet is standalone and quench protection heaters could be eliminated by using a dump resistor of 75 mΩ with the assumption of a detection threshold of 100 mV and a shutdown delay of 10 ms, as shown in Fig. 4. For the 13 kA quench current (nominal is 12 kA), with grounding at the middle of the resistor, the maximum coil temperature is 300 K and the maximum terminal voltage of 490 V. This suggests that protection without the protection heaters is viable. Further quench protection study to analyze the peak voltage in the coil is ongoing.

III. Development Status

A. Radiation Resistant GFRP

A new radiation resistant GFRP was successfully developed for the new D1 in the HL-LHC and for the J-PARC COMET superconducting magnet [16] in collaboration with ARISAWA. The GFRP is made from a lamination of the boron-free S-2 glass cloth with Bismaleimide-Triazine resin (blend of BT2160 and BT2170 by Mitsubishi Gas Chemical). The laminated prepreg cloths were cured at a maximum temperature of 220 °C. The BT GFRP was irradiated by γ-rays at room temperature and in vacuum at JAEA Takasaki. The radiation resistance was experimentally evaluated, as shown in Fig. 5. The flexural strength of the BT GFRP was determined as a function of the radiation dose up to 100 MGy. Each data point represents test results of three samples. While the standard G10 made of epoxy resin shows a rather rapid degradation even at 10 MGy, the BT GFRP seems to be functional up to 100 MGy without significant degradation for both testing directions with respect to the lamination direction.

B. Test Coil Fabrication for the 2 m Model

CAD/CAM modeling for the D1 coil has been carried out by using the ROXIE output. An example is shown in Fig. 6.

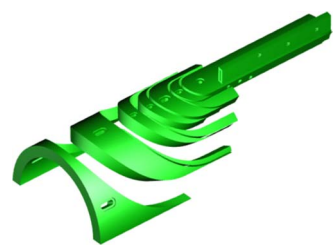

Fig. 6. CAD model for end spacers and ramp box at the lead-end for the model magnet.

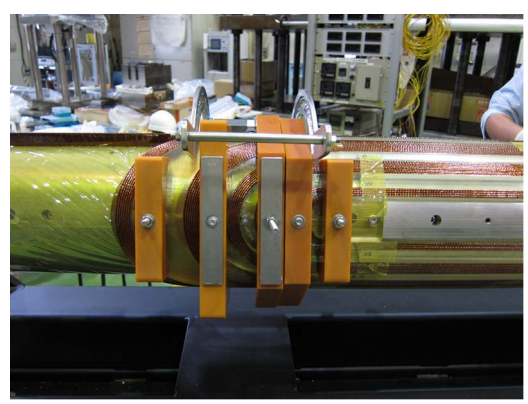

Fig. 7. Picture of practice coil winding.

Machining of the wedges, the end spacers and the ramp box for the test coil fabrication has begun. In parallel, practice coil windings using coil parts made by 3-D rapid prototyping were performed to tune the end spacer shape and to check the winding tooling as shown in Fig. 7.

Measurements of the cable size under azimuthal compressive stress in several loading patterns were carried out to characterize the mechanical behavior of the coil. Fig. 8 shows an example of the thickness measurements of a stack of 22 cables as a function of the compressive stress. The obtained cable size and Young's modulus were used in the computational studies and the magnet design.

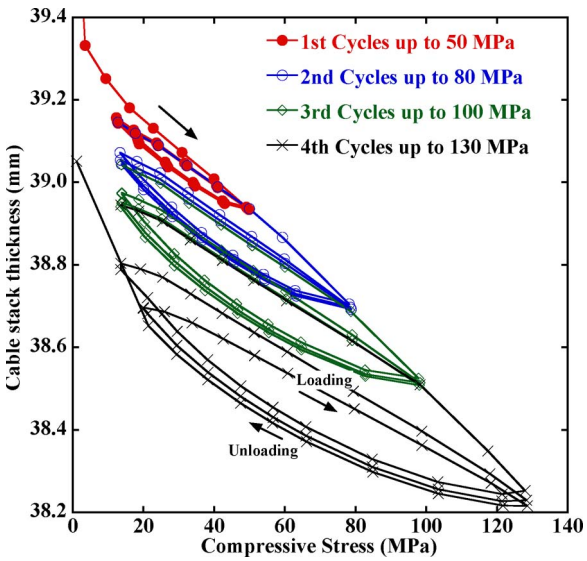

Fig. 8. Cable stack thickness measurement at room temperature as a function of compressive stress. The stack consists of 22 cables and was cured under the same conditions as the actual coil. Multiple loading up to 130 MPa was applied.

C. Further Plans

The test coil winding of the 2-m-long model will be started in August 2014, followed by the 20-cm-long mechanical cross section model study using the cut coil. Fabrication of the 2-m model coils will be started in December 2014. Procurement of the fine-blanking dies for the collars and the yokes is underway and the production is planned in January 2015. Assembly of the short model magnet will be completed in spring of 2015, followed by an excitation test at 1.9 K in the vertical cryostat at KEK.

IV. Summary

The 2-m-long model magnet development for the beam separation dipole for the HL-LHC is underway at KEK. Following the conceptual design study, the engineering design to realize the model magnet has been started since May 2013. Design highlights are the tight control of the field quality notwithstanding the large iron saturation, and the accommodation for the heat load and the radiation dose. The fabrication of the model magnet is in progress and the excitation test is expected in 2015.

Acknowledgment

The authors would like to express their gratitude to Profs. K. Tokushuku, K. Oide at KEK and L. Rossi at CERN for their strong supports for this project. The authors are really grateful to the colleagues at KEK and CERN, in particular, B. Auchmann, A. Ballarino, L. Bottura, P. Fessia, P. P. Granieri, G. Kirby, G. de Rijk, F. Savary, R. van Weelderen for their kind suggestions and fruitful discussions. The authors also thank O. Kobayashi, T. Kawashima for their technical supports.

References

[1] L. Rossi and O. Brüning, "High luminosity large hadron collider: A description for the European strategy preparatory group," CERN, Geneva, Swtizerland, 2012, CERN-ATS-2012-236.

[2] HL-LHC web page. [Online]. Available: http://hilumilhc.web.cern.ch/hilumilhc/index.html

[3] E. Todesco *et al.*, "A first baseline for the magnets in the high luminosity LHC insertion regions," *IEEE Trans. Appl. Supercond.*, vol. 24, no. 3, Jun. 2014, Art. ID. 4003305.

[4] Q. Xu *et al.*, "Conceptual design of a large-aperture dipole magnet for HL-LHC upgrade," *IEEE Trans. Appl. Supercond.*, vol. 22, no. 3, Jun. 2012, Art. ID. 4901404.

[5] Q. Xu *et al.*, "Design of a large single-aperture dipole magnet for HL-LHC upgrade," *IEEE Trans. Appl. Supercond.*, vol. 23, no. 3, Jun. 2013, Art. ID. 4001305.

[6] Q. Xu *et al.*, "Design optimization of the new D1 dipole for HL-LHC upgrade," *IEEE Trans. Appl. Supercond.*, vol. 24, no. 3, Jun. 2014, Art. ID. 4000104.

[7] M. Sugano, T. Nakamoto, and Q. Xu, "Field and mechanical analysis of new D1 beam separation magnet for HL-LHC upgrade," *IEEE Trans. Appl. Supercond.*, vol. 25, submitted for publication.

[8] L. S. Esposito, F. Cerutti, and E. Todesco, "FLUKA energy deposition studies for the HL-LHC," in *Proc. IPAC*, Shanghai, China, 2013, pp. 1379–1381.

[9] M. Anerella *et al.*, "The RHIC magnet system," *Nucl. Instrum. Methods Phys. Res.*, vol. A 499, pp. 280–315, 2003.

[10] Y. Ajima *et al.*, "The MQXA quadrupoles for the LHC low-beta insertions," *Nuclear Instruments and Methods in Physics Research,* vol. A 550, pp. 499–513, 2005.

[11] T. Nakamoto *et al.*, "Development of a prototype of superconducting combined function magnet for the 50 GeV proton beam line for the J-PARC neutrino experiment," *IEEE Trans. Appl. Supercond.*, vol. 15, no. 2, pp. 1144–1147, Jun. 2005.

[12] S. Russenschuck, *ROXIE: Routine for the Optimization of Magnet X-Sections, Inverse Field Computation and Coil End Design*, 1999, CERN Yellow Report 99-01.

[13] P. P. Granieri and R. van Weelderen, "Deduction of steady-state cable quench limits for various electrical insulation schemes with application to LHC and HL-LHC magnets," *IEEE Trans. Appl. Supercond.*, vol. 24, no. 3, Jun. 2014, Art. ID. 4802806.

[14] E. Willen *et al.*, "Superconducting dipole magnets for the LHC insertion regions," in *Proc. EPAC*, Vienna, Austria, 2000, pp. 2187–2189.

[15] R. van Weelderen, *CERN*, private communication, 2014.

[16] M. Yoshida *et al.*, "Development of a radiation resistant superconducting solenoid magnet for mu-e conversion experiments," *IEEE Trans. Appl. Supercond.*, vol. 23, no. 3, Jun. 2013, Art. ID. 4101404.

計画研究 A03 班

課題名「素粒子標準模型の精密検証で探るテラスケール物理現象」

研究組織

(1)研究代表者

藏重　久弥（KURASHIGE, Hisaya）
神戸大学・自然科学系先端融合研究環・教授
研究者番号：20205181

(2)研究分担者

山崎　祐司（YAMAZAKI,　Yuji）
神戸大学・理学研究科・教授
研究者番号：　00311126

花垣　和則（HANAGAKI, Kazunori）
大阪大学・理学研究科・特任教授
研究者番号：　40448072

佐々木　修（SASAKI,　Osamu）
高エネルギー加速器研究機構・素粒子原子核研究所・教授
研究者番号：　30178636

(3)連携研究者

福永　力（FUKUNAGA,　Chikara）
首都大学東京・理工学研究科・教授
研究者番号：00189961

越智　敦彦（OCHI,　Atsuhiko, H24~H26 年度）
神戸大学・理学研究科・助教
研究者番号：40335419

袁　麗（YUAN, Li）
神戸大学・自然科学系先端融合研究環・学術研究員

清水　志真（SHIMIZU, Shima, H25~H27 年度）
神戸大学・自然科学系先端融合研究環・助教
研究者番号：50649168

前田　順平（MAEDA, Junpei, H26~H27 年度）
神戸大学・自然科学系先端融合研究環・特命助教
研究者番号：60467024

音野　瑛俊（OTONO, Hidetoshi, H24 年度）
大阪大学・理学研究科・学術研究員
研究者番号：20648034

山口　洋平（YAMAGUCHI, Yohei, H26~27 年度）
大阪大学・理学研究科・学術研究員
研究者番号：30751119

(4)協力研究者

松下　崇（MATSUSHITA, Takashi, H23~24 年度）
神戸大学・自然科学系先端融合研究環・助教

岸本　巴（Kishimoto Tomoe）
神戸大学・学振特別研究員（PD）

交付決定額

計画研究 A03 班に配分された交付額を表 1 に示す。

表 1. 交付決定額（配分額）　（金額単位：円）

年度	直接経費	間接経費	合計
平成 23 年度	33,200,000	9,960,000	43,160,000
平成 24 年度	38,000,000	11,400,000	49,400,000
平成 25 年度	38,400,000	11,520,000	49,920,000
平成 26 年度	37,100,000	11,130,000	48,230,000
平成 27 年度	34,900,000	10,470,000	45,370,000
総計	181,600,000	54,480,000	236,080,000

研究成果

1．研究開始当初の背景

(1) 素粒子標準模型は、過去 30 年間の加速器実験により、高い精度で検証されてきた。しかし、模型の重要なキーとなるヒッグス粒子が発見されていなかった。さらに、テラスケール（TeV のエネルギースケール）において、標準模型を超えた新しい素粒子現象の存在が大いに期待されていた。
(2) 2010 年 3 月より大型陽子・陽子衝突型加速器（LHC）は重心系 7TeV での実験を開始した。LHC によって実現する世界最高エネルギーの陽子・陽子衝突からは、高いエネルギーのジェット及び W、Z 粒子等の重い粒子が数多く生成され、テラスケールの素粒子物理反応の研究が可能になった。

2．研究の目的

(1)アトラス検出器を用い、高統計のデータで測定することによって、未踏のエネルギー領域における標準模型の精密検証を行う。本計画研究及びヒッグス（A01)、トップクォーク(A04）に関する計画研究による結果を合わせることで、標準模型の破れを明らかにし、標準模型を超えた新現象の発見を目指す。これら W/Z を伴うジェット事象、特にボトムクォークの生成事象は、超対称性粒子をはじめとした新粒子直接探査時の背景事象となるため、この研究の結果は新粒子発見の

感度を向上に必須である。
(2)次世代素粒子実験では高いルミノシティ環境での高精度測定が行なわれる。ミューオンは、透過性が高いレプトンであり、膨大な背景事象からの効率的な選別が可能で、精密測定の鍵となる。そこで、新しい技術を応用したミューオン検出器、およびフロントエンド・エレクトロニクスを含めた高度なミューオン・トリガーの技術的開発研究を行い、次世代実験への応用へと繋げる。

3．研究の方法

(1) 質量が重く、LHC のエネルギー領域では直接生成できない粒子でも、測定結果と理論予想のズレから 10TeV 付近までの範囲で新現象を間接的に探索できる。間接探索と直接探索（A02）の結果を統合することで、新粒子・新現象を多角的に研究する。特にミューオンへの崩壊チャンネルをもちいて、W/Z 粒子の生成断面積、異常 3 点ゲージ結合の測定を行う。
(2) 標準模型の検証を可能にするには、陽子内部のパートン分布(PDF)が重要となる。HERA 実験等から数%の精度で PDF が分かってきているが、高いエネルギー領域での不定性は大きく、高運動量ジェット生成、W/Z 粒子生成等高い Q^2 領域の素粒子反応から PDF の決定精度を向上させる。
(3)将来の高ルミノシティ LHC 実験のために、マイクロパターンガスチェンバー等の新しい検出器技術を応用したミューオン検出器の開発研究を行う。同時に、読出エレクトロニクスの開発・実用化のための研究を進める。

4．研究成果

(1)LHC 加速器は陽子･陽子衝突実験を順調に行い、重心系 7TeV/8TeV で約 27fb-1、重心系 13TeV で約 4fb-1 の積分ルミノシティのデータを取得した。本計画研究では、このデータを用いて、標準模型を高い精度で検証し、以下のような研究成果を得た。
①W/Z および WW,WZ,ZZ,2 光子生成断面積測定を約 10%の精度で行い、理論予想値と矛盾しない結果を得た。これらの測定結果から、異常 3 点ゲージ結合カップリングとして、Tevatron/LEP の測定より 1 桁以上小さい上限値を得た。
②b-tagging の改良により、高 Pt を持つ Z
粒子の b 崩壊過程や、B_c^+稀崩壊過程の測定を行った。
③ジェット生成反応の断面積測定を行い、QCD Next Leading Order プロセスの計算結果との比較よって、PDF 決定につなげた。低 Pt ジェット生成反応の解析も並行して行い、'Underlying event'の性質について明らかにした。
(2) ミューオン検出器開発については、LHC フェーズ 1 ・アップグレードで計画されている ATLAS ミューオン・スモール・ウィールでの Micromegas 検出器開発を中心に行った。
①Micromegas 検出器の電極の構造・製造方法の開発を行い、アノードに高抵抗電極を用いるこ

とで、中性子による大きな電離損失に起因する放電を大幅に押さえられることがわかり、プロトタイプの製作を行った
②スモール・ウィール検出器を用いたトリガーのための、トリガーアルゴリズム及びトリガープロセッサーの開発を行った。
③LHC フェーズ 2・アップグレードで計画されている高ルミノシティ運転におけるミューオン・トリガーの為に、ドリフトチューブを用いたアルゴリズムについて検討を行い、トリガーレートを削減できることを明らかにした。また、そのための高精度 TDC など放射線耐性をもつフロントエンド・エレクトロニクスの開発を行った。

5．主な発表論文等

〔雑誌論文〕（計 22 件）

"Measurement of the *ZZ* Production Cross Section in *pp* Collisions at √s = 13 TeV with the ATLAS Detector."; G Aad, H.Kurashhige et al.(ATLAS Collaboration) Phys. Rev. Lett. **116** (2016) 10181, DOI:10.1103/PhysRevLett.116.061102

"Measurement of four-jet differential cross sections in √s =8 TeV proton-proton collisions using the ATLAS detector."; G Aad, H.Kurashhige et al.(ATLAS Collaboration) JHEP **12** (2015) 105, DOI：10.1007/*JHEP12(2015)105*

"Study of the $B_c^+ \rightarrow J/\Psi D_s^+$ and $B_c^+ \rightarrow J/\Psi D_s^{*+}$ decays with the ATLAS detector."; G Aad, H.Kurashhige et al.(ATLAS Collaboration) Eur. Phys. J. **C76** (2016) 4, DOI:10.1140/epjc/s10052
-015-3743-8

"Measurement of colour flow with the jet pull angle in *tt* events using the ATLAS detector at √s =8 TeV."; G Aad, H.Kurashhige et al.(ATLAS Collaboration) Phys. Lett. **B750** (2015) 475-493,
doi:10.1016/j.physletb.2015.09.051

"Evidence of *Wγγ* production in *pp* collisions at √s = 8 TeV and limits on anomalous quartic gauge couplings with the ATLAS detector."; G Aad, H.Kurashhige et al. (ATLAS Collaboration) Phys. Rev. Lett. **115** (2015) 031802, DOI: 10.1103/PhysRevLett.115.031802

"Measurement of three-jet production cross-sections in *pp* collisions at 7 TeV centre-of-mass energy using the ATLAS detector."; G Aad, H.Kurashhige et al. (ATLAS Collaboration) Eur. Phys. J. **C75** (2015) 228, DOI: 10.1140/epjc/ s10052-015-3363-3

"Measurement of the WW+WZ cross section and limits on anomalous triple gauge couplings using final states with one lepton, missing energy, and two jets with the ATLAS detector at √s = 7TeV."; G Aad, H.Kurashhige et al. (ATLAS Collaboration) JHEP **01** (2015) 049, DOI: 10.1007/ JHEP01(2015)049

"Measurements of the W production cross sections in association with jets with the ATLAS detector." ; G Aad et al. (ATLAS Collaboration) Eur. Phys. J. **C75** (2015) 82, DOI: 10.1140/epjc/s10052-015-3262-7

"A measurement of the ratio of the production cross sections for W and Z bosons in association with jets with the ATLAS detector." ; G Aad, H.Kurashhige et al. (ATLAS Collaboration) Eur. Phys. J. **C74** (2014) 3168, DOI: 10.1140/epjc/s10052-014-3168-9

"Evidence of electroweak production of WWjj in pp collisions at $\sqrt{s}$ =8 TeV with the ATLAS detector."; G Aad, H.Kurashhige et al. (ATLAS Collaboration) Phys. Rev. Lett. **113** (2014) 141803, DOI: 10.1103/ PhysRevLett.113.141803

"Measurement of the cross section of high transverse momentum $Z \to bb$ production in proton–proton collisions at $\sqrt{s}$ =8 TeV with the ATLAS detector." ; G Aad, H.Kurashhige et al. (ATLAS Collaboration) Phys. Lett. **B738** (2014) 25-43, DOI: 10.1016/ j.physletb.2014.09.020

"Measurement of the 4*l* Cross Section at the Z Resonance and Determination of the Branching Fraction of Z→4 *l* in pp Collisions at $\sqrt{s}$ = 7 and 8 TeV with ATLAS." ; G Aad, H.Kurashhige et al. (ATLAS Collaboration) Phys. Rev. Lett. **112** (2014) 231806, DOI: 10.1103/PhysRevLett.112.231806

"Measurement of the underlying event in jet events from 7 TeV proton-proton collisions with the ATLAS detector." ; G Aad, H.Kurashhige et al. (ATLAS Collaboration) Eur. Phys. J. **C74** (2014) 2965, DOI: 10.1140/epjc/ s10052-014-2965-5

"Measurement of the electroweak production of dijets in association with a Z-boson and distributions sensitive to vector boson fusion in proton-proton collisions at $\sqrt{s}$ = 8 TeV using the ATLAS detector." ; G Aad, H.Kurashhige et al. (ATLAS Collaboration) JHEP **04** (2014) 031, DOI: 10.1007/ JHEP04(2014)031

"Measurement of dijet cross sections in pp collisions at 7 TeV centre-of-mass energy using the ATLAS detector."; G Aad, H.Kurashhige et al. (ATLAS Collaboration) JHEP **05** (2014) 059, DOI: 10.1007/ JHEP05(2014)059

"Measurement of the cross-section for W boson production in association with b-jets in pp collisions at $\sqrt{s}$ = 7 TeV with the ATLAS detector."; G Aad, H.Kurashhige et al. (ATLAS Collaboration) JHEP **06** (2013) 084, DOI: 10.1007/ JHEP06(2013)084

"Measurement of ZZ production in pp collisions at $\sqrt{s}$ = 7 TeV and limits on anomalous ZZZ and ZZγ couplings with the ATLAS detector."; G Aad, H.Kurashhige et al. (ATLAS Collaboration) JHEP **03** (2013) 128, DOI: 10.1007/ JHEP03(2013)128

"Measurement of the production cross section of jets in association with a Z boson in pp collisions at $\sqrt{s}$ = 7 TeV with the ATLAS detector." ; G Aad, H.Kurashhige et al. (ATLAS Collaboration) JHEP **07** (2013) 032, DOI: 10.1007/ JHEP07(2013)032

"Measurement of the inclusive jet cross section in pp collisions at √s = 2.76 TeV and comparison to the inclusive jet cross section at √s = 7 TeV using the ATLAS detector."; G Aad, H.Kurashhige et al. (ATLAS Collaboration) Eur. Phys. J. **C73** (2013) 2509, DOI: 10.1140/epjc/s10052-013-2509-4

"Measurement of Wγ and Zγ production cross sections in pp collisions at √s = 7 TeV and limits on anomalous triple gauge couplings with the ATLAS detector." ; G Aad, H.Kurashhige et al.(ATLAS Collaboration) Phys. Lett. **B717** (2012) 49-69, doi:10.1016/ j.physletb.2012.09.017

"Measurement of the WW cross section in √s = 7 TeV pp collisions at ATLAS and limits on anomalous gauge couplings."; G Aad, H.Kurashhige et al.(ATLAS Collaboration) Phys. Lett. **B712** (2012) 289-308, doi:10.1016/ j.physletb.2012.05.003

"Measurement of the polarisation of W bosons produced at large momentum transfer in pp collisions at √s = 7 TeV with the ATLAS experiment at the LHC."; G Aad, H.Kurashhige et al.(ATLAS Collaboration) Eur. Phys. J. **C72** (2012) 2001, DOI: 10.1140/ epjc/s10052-012-2001-6

〔学会発表〕（計 15 件）

前田順平, 「　ATLAS 実験状況」, 日本物理学会第 71 回年次大会, 2016 年 3 月 21 日, 東北学院大学（宮城県, 仙台市）

山口洋平, 「標準模型とヒッグス」, 日本物理学会第 71 回年次大会, 2016 年 3 月 21 日, 東北学院大学（宮城県, 仙台市）

岸本巴, "Higgs boson interactions with the gauge sector", Higgs Coupling 2015, 2015 年 10 月 12 日, Durham(英国)

清水志真, "First Standard Model Results at 13TeV, ATLAS",Brookhaven Forum, 2015 年 10 月 8 日, Upton（米国）

袁麗, "What we have learned about the Higgs boson from the bosonic decay channels and more inclusive combinations of data", EPS-HEP 2015, European Physical Society Conference on High Energy Physics, 2015 年 7 月 24 日, ウィーン（オーストリア）

山口洋平, " Latest results on Higgs final-states with photons in ATLAS" , PHOTON 2015, 2015 年 6 月 15 日, BINP, ノボシビルスク（ロシア）

山崎祐司, "Overview of recent ATLAS results and preparation for Run-2", 韓国物理学会韓日合同セッション, 2015 年 4 月 23 日, 大田, 大韓民国

藏重久弥, "Highlight of Results from ATLAS at LHC"（招待講演）, 26th International Conference on Nuclear Tracks in Solids, 2014 年 9 月 15 日　神戸大学(兵庫県, 神戸市)

清水志真, "Latest results on multi-jets production, and beyond-DGLAP (BFKL, saturation) studies with jets", Jet vetoes and multiplicity observables, 2014 年 7 月 17 日, Durham (英

国)
花垣和則，“Search for the Higgs boson in fermionic channels using the ATLAS detector”, PASCOS2013, 19th International Symposium on Particles, Strings and Cosmology, 2013 年 11 月 21 日，台北（台湾）
清水志真, ”Experimental Jets and Photon results”, ATLAS Standard Model Workshop, 2013 年 9 月 21 日，ボストン（米国）
袁麗, ”Recent electroweak measurements at the LHC”, Rencontres du Vietnam: windows on the universe 2013, 2013 年 8 月 14 日，Quy Nhon（ベトナム）
清水志真, ”Measurement of the flavour composition of dijet events in pp collisions with ATLAS”, XXI. International Workshop on Deep-Inelastic Scattering and Related Subjects (DIS 2013), 2013 年 4 月 24 日，マルセイユ（フランス）
袁麗, “QCD di-photon cross-section measurement and H→gamma gamma analysis with 2010 data in ATLAS”, 6th workshop of the France China Particle Physics Laboratory, 2013 年 3 月 27 日，南京大学(中国)
松下崇，”Onia production at ATLAS”, PLHC2012, Physics at LHC 2012, 2012 年 6 月 7 日，バンクーバー（カナダ）

〔図書〕（計 2 件）
山﨑祐司，戸本誠，花垣和則，「ヒッグス粒子の見つけ方； 質量の起源を追う」，丸善， 2012, ISBN 978462108617
“Micropattern detector conference goes east”, Atsuhiko Ochi,,CERN Courier, March 2012, 27-29

〔産業財産権〕
○出願状況（計 0 件）
○取得状況（計 0 件）

〔その他〕
主催シンポジウム，講演会
一般公開講演会「LHC 実験にて新粒子（ヒッグス粒子？）発見」， 神戸大学百年記念館， 2012 年 9 月 22 日，（出席者約 200 名）
一般公開講演会「LHC 実験にて新粒子（ヒッグス粒子？）発見」，大阪大学中之島センター，2012 年 8 月 26 日，（出席者約 100 名）
一般向け解説会 「LHC 実験にて新粒子（ヒッグス粒子？）発見」，大阪大学豊中キャンパス理学部 D 棟 D501，2012 年 7 月 21 日（出席者約 200 名，ニコニコ生放送による中継あり）

特別講演会「LHC におけるヒッグス粒子探索-素粒子標準模型と質量の起源-」,神戸大学理学研究科, 2012 年 7 月 13 日（出席者約 120 名）
“Workshop on LHC Physics”, KUBEC(Bruxelles, Belgique), 8-9 Sep. 2012, （出席者 20 名）

新聞記事
朝日新聞，2015 年 12 月 17 日
東京新聞，2015 年 8 月 10 日
朝日新聞，2015 年 6 月 11 日
しんぶん赤旗，2015 年 6 月 5 日
“挑む女たち”, 毎日新聞, 2014 年 1 月 1 日
編集委員インタビュー, 神戸新聞, 2014 年 2 月 6 日
日本経済新聞，2012 年 9 月 4 日
読売新聞，2012 年 8 月 13 日
週刊まなび, 神戸新聞, 2012 年 7 月 29 日
神戸新聞, 2012 年 7 月 5 日
佐賀新聞，2011 年 12 月 4 日

雑誌記事
2016 年 2 月　パリティ　理科教育：18 歳からの物理「18 歳からのヒッグス粒子検出」花垣和則
2016 年 1 月　パリティ　物理科学，この 1 年「LHC の重心系エネルギー13TeV へ」花垣和則
2015 年 10 月　パリティ「LHC で 13TeV の陽子陽子衝突を実現」花垣和則
2013 年 12 月　パリティ「ノーベル物理学賞：質量の起源とヒッグス機構」窪田高弘・花垣和則
2012 年 12 月 「ヒッグス粒子と見られる新粒子の発見とその意義」, 日本物理教育学会誌「物理教育」Vol. 60-4 山崎祐司
2011 年 10 月　生産と技術「誕生直後の宇宙を再現～いよいよ始まった世界最大の加速器験～」花垣和則

主要論文別刷

[1] "Measurement of the *ZZ* Production Cross Section in *pp* Collisions at √s = 13 TeV with the ATLAS Detector."; G Aad, H.Kurashhige et al.(ATLAS Collaboration) Phys. Rev. Lett. **116** (2016) 10181, DOI:10.1103/PhysRevLett.116.061102

[2] "Measurement of four-jet differential cross sections in √s =8 TeV proton-proton collisions using the ATLAS detector."; G Aad, H.Kurashhige et al.(ATLAS Collaboration) JHEP **12** (2015) 105, DOI : 10.1007/*JHEP12(2015)105*

[3] "Study of the $B_c^+ \rightarrow J/\Psi D_s^+$ and $B_c^+ \rightarrow J/\Psi D_s^{*+}$ decays with the ATLAS detector."; G Aad, H.Kurashhige et al.(ATLAS Collaboration) Eur. Phys. J. **C76** (2016) 4, DOI:10.1140/epjc/s10052-015-3743-8

[4] "Evidence of $W\gamma\gamma$ production in *pp* collisions at √s = 8 TeV and limits on anomalous quartic gauge couplings with the ATLAS detector."; G Aad, H.Kurashhige et al. (ATLAS Collaboration) Phys. Rev. Lett. **115** (2015) 031802, DOI: 10.1103/PhysRevLett.115.031802

[5] "Measurement of ZZ production in pp collisions at √s = 7 TeV and limits on anomalous ZZZ and ZZγ couplings with the ATLAS detector."; G Aad, H.Kurashhige et al. (ATLAS Collaboration) JHEP **03** (2013) 128, DOI: 10.1007/ JHEP03(2013)128

Measurement of the ZZ Production Cross Section in pp Collisions at $\sqrt{s} = 13$ TeV with the ATLAS Detector

G. Aad *et al.*[*]
(ATLAS Collaboration)

(Received 17 December 2015; published 10 March 2016)

The ZZ production cross section in proton-proton collisions at 13 TeV center-of-mass energy is measured using 3.2 fb^{-1} of data recorded with the ATLAS detector at the Large Hadron Collider. The considered Z boson candidates decay to an electron or muon pair of mass 66–116 GeV. The cross section is measured in a fiducial phase space reflecting the detector acceptance. It is also extrapolated to a total phase space for Z bosons in the same mass range and of all decay modes, giving $16.7^{+2.2}_{-2.0}\,(\mathrm{stat})\,^{+0.9}_{-0.7}\,(\mathrm{syst})\,^{+1.0}_{-0.7}\,(\mathrm{lumi})$ pb. The results agree with standard model predictions.

DOI: 10.1103/PhysRevLett.116.101801

Studying the production of pairs of Z bosons in proton-proton (pp) interactions at the Large Hadron Collider (LHC) tests the electroweak sector of the standard model (SM) at the highest available energies. In pp collisions at a center-of-mass energy of $\sqrt{s} = 13$ TeV, ZZ production is dominated by quark-antiquark ($q\bar{q}$) interactions, with an $\mathcal{O}(10\%)$ contribution from loop-induced gluon-gluon (gg) interactions [1,2]. The SM ZZ production can proceed via a Higgs boson propagator, although this contribution is suppressed in the region where both Z bosons are produced on-shell. As such, non-Higgs ZZ production is an important background in studies of the Higgs boson [3–5]. It is also a background in searches for new physics producing pairs of Z bosons at high invariant mass [6,7] and sensitive to triple neutral-gauge-boson couplings, which are not allowed in the SM [8].

This Letter presents the first measurement of the ZZ production cross section in pp interactions at $\sqrt{s} = 13$ TeV. Throughout it, "Z boson" refers to the superposition of a Z boson and virtual photon with mass in the range 66–116 GeV. The analyzed data correspond to an integrated luminosity of 3.2 ± 0.2 fb^{-1}, collected with the ATLAS detector [9]. The uncertainty of the integrated luminosity is derived, following a methodology similar to that detailed in Ref. [10], from a preliminary calibration of the luminosity scale using a pair of x-y beam-separation scans performed in June 2015. The ZZ production cross section was previously measured at $\sqrt{s} = 7$ and 8 TeV by the ATLAS and CMS Collaborations [11–13] and found to be consistent with SM predictions.

Candidate events are reconstructed in the fully leptonic $ZZ \to \ell^+\ell^-\ell'^+\ell'^-$ decay channel where ℓ and ℓ' can be an electron or a muon. The cross section $\sigma^{\mathrm{fid}}_{ZZ\to\ell^+\ell^-\ell'^+\ell'^-}$ is found by counting candidate events, subtracting the expected contribution from background events, correcting for detector effects, and dividing by the integrated luminosity. It is measured in a fiducial phase space that corresponds closely to the experimental acceptance. In addition, an extrapolation of the cross section to a total phase space for Z bosons, $\sigma^{\mathrm{tot}}_{ZZ}$, is performed. The presented cross-section measurements are inclusive with respect to additional jets. Small contributions from triboson production with two leptonically decaying Z bosons and a third hadronically decaying weak boson and contributions from double parton scattering are included in the measurement.

The fiducial phase space, which is designed to reflect the acceptance of the ATLAS detector (described below), is defined for simulated events by applying the following criteria to the final-state particle-level objects. Final-state electrons and muons are required to be prompt (i.e., to not originate from hadron or τ decay) and their kinematics are computed including the contributions from prompt photons with a distance in η-ϕ coordinates of $\Delta R_{\ell,\gamma} = \sqrt{(\Delta\eta_{\ell,\gamma})^2 + (\Delta\phi_{\ell,\gamma})^2} < 0.1$ between the charged lepton and the photon, as motivated in Ref. [14]. (ATLAS uses a right-handed coordinate system with its origin at the nominal interaction point in the center of the detector and the z axis along the beam pipe. The x axis points to the center of the LHC ring, and the y axis points upward. Cylindrical coordinates (r, ϕ) are used in the transverse plane, ϕ being the azimuthal angle around the z axis. The pseudorapidity is defined in terms of the polar angle θ as $\eta = -\ln[\tan(\theta/2)]$.) The leptons are required to be well separated with $\Delta R_{\ell,\ell'} > 0.2$ between any two leptons. Each lepton must have a momentum component transverse to the beam direction $p_T > 20$ GeV and pseudorapidity $|\eta| < 2.7$. Events must have exactly four leptons satisfying the above

[*]Full author list given at the end of the article.

Published by the American Physical Society under the terms of the Creative Commons Attribution 3.0 License. Further distribution of this work must maintain attribution to the author(s) and the published article's title, journal citation, and DOI.

 © 2016 CERN, for the ATLAS

criteria forming two pairs of leptons of the same flavor and oppositely charged ($\mu^+\mu^-$ or e^+e^-). This gives rise to three signal channels: $4e$, 4μ, and $2e2\mu$. Each lepton pair must have an invariant mass in the range 66–116 GeV. In the $4e$ and 4μ channels, where there are two possible ways to form same-flavor oppositely charged lepton pairs, the combination that minimizes $|m_{\ell\ell,a} - m_Z| + |m_{\ell\ell,b} - m_Z|$ is chosen, where $m_{\ell\ell,a}$ and $m_{\ell\ell,b}$ are the invariant masses of the lepton pairs and m_Z is the mass of the Z boson.

The ATLAS detector is a multipurpose particle detector with a cylindrical geometry. It consists of layers of inner tracking detectors, calorimeters, and muon chambers. The inner detector (ID) covers the pseudorapidity range $|\eta| < 2.5$. The calorimeter covers the pseudorapidity range $|\eta| < 4.9$. Within $|\eta| < 2.47$ the finely segmented electromagnetic calorimeter identifies electromagnetic showers and measures their energy and position, providing electron identification together with the ID. The muon spectrometer (MS) surrounds the calorimeters and provides muon identification and measurement in the region $|\eta| < 2.7$ and triggering in the region $|\eta| < 2.4$.

A muon is reconstructed by matching a track (or track segment) reconstructed in the MS to a track reconstructed in the ID. Its momentum is calculated by combining the information from the two systems and correcting for energy deposited in the calorimeters. In regions of limited coverage of the MS ($|\eta| < 0.1$) or outside the ID acceptance ($2.5 < |\eta| < 2.7$), muons can also be reconstructed by matching calorimeter signals consistent with muons to ID tracks (calorimeter-tagged muons) or standalone in the MS [15], respectively.

An electron is reconstructed from an energy deposit (cluster) in the electromagnetic calorimeter matched to a track in the ID. Its momentum is computed from the cluster energy and the direction of the track. Electrons are distinguished from other particles using several identification criteria that rely on the shapes of electromagnetic showers as well as tracking and track-to-cluster matching quantities. The output of a likelihood function taking these quantities as input, similar to that described in Ref. [16], is used to identify electrons. Electrons sharing an ID track with a selected muon are ignored.

The leptons are required to be isolated from other particles using ID track information, and for muons using calorimeter information also (since standalone muons are outside the ID acceptance). The exact requirements depend on the lepton p_T and η and are designed to give a uniform 99% efficiency.

Leptons are required to originate from the primary vertex, defined as the reconstructed vertex with the largest sum of the p_T^2 of the associated tracks. To this end, the longitudinal impact parameter of each lepton track, calculated with respect to the vertex and multiplied by $\sin\theta$ of the track, is required to be less than 0.5 mm. Furthermore, the significance of the transverse impact parameter calculated with respect to the beam line is required to be less than 3 (5) for muons (electrons). Standalone muons are exempt from both impact parameter requirements, as they do not have an ID track.

Candidate events are preselected by either a single-muon or dielectron trigger. As in the fiducial phase space described above, leptons must have $p_T > 20$ GeV. There are slight differences from the fiducial phase space: electrons must satisfy $|\eta| < 2.47$ due to the limited experimental acceptance, and at least one muon in the 4μ channel must satisfy $|\eta| < 2.4$, corresponding to the acceptance of the muon trigger. The other muons must satisfy $|\eta| < 2.7$. Events are ignored if more than one selected muon is calorimeter tagged or standalone. Apart from the above differences, reconstructed candidate events are selected using exactly the same criteria that define the fiducial phase space. A total of 63 events are observed, of which 15, 30, and 18 are in the $4e$, $2e2\mu$, and 4μ channels, respectively.

Monte Carlo (MC)-simulated event samples are used to obtain corrections for detector effects and to estimate background contributions. The principal signal sample is generated with the POWHEG method and framework [17–19], with a diboson event generator [20,21] used to simulate the ZZ production process at next-to-leading order (NLO). (Throughout this Letter, orders of calculations refer to perturbative expansions in the strong coupling constant α_S unless stated otherwise). The simulation of parton showering, of the underlying event, and of hadronization is performed with PYTHIA8 [22,23] using the AZNLO set of tuned parameters (tune) [24]. SHERPA [25–31] is used to generate a sample with the $q\bar{q}$-initiated process simulated at NLO for ZZ plus zero or one additional jet and at leading order (LO) for two or three additional jets, as well as a sample with the loop-induced gg-initiated process simulated at LO with zero or one additional jet. These are used to include the loop-induced gg-initiated production, which is not included in the POWHEG+PYTHIA8 sample, as well as to estimate, by comparison of the various samples, a systematic uncertainty due to the choice of event generator. The CT10 NLO [32] parton distribution functions (PDFs) are used in the event generation for all samples above. Additional samples are generated to estimate the contribution from background events. Triboson events are simulated with SHERPA, using CT10 PDFs, and $t\bar{t}Z$ events are simulated with MADGRAPH [33] interfaced with PYTHIA8 using the NNPDF 2.3 LO PDFs [34] and the A14 tune [35].

In all MC samples, additional pp interactions occurring in the same bunch crossing as the ZZ production, or in nearby ones, are simulated with PYTHIA8 with MSTW 2008 LO PDFs [36] and the A2 tune [37]. The samples are then passed through a simulation of the ATLAS detector [38] based on GEANT4 [39]. Scale factors are applied to the simulated events to correct for the small differences from data in the trigger, reconstruction, identification, isolation,

and impact parameter efficiencies for electrons and muons [15,16]. Furthermore, the lepton momentum scales and resolutions are adjusted to match the data.

Background events from processes with at least four prompt leptons in the final state are estimated with the MC samples described above, including uncertainties from the cross-section values, luminosity, and reconstruction effects. Contributions of 0.07 ± 0.02 events from ZZ processes where at least one Z boson decays to τ leptons, 0.17 ± 0.05 events from nonhadronic triboson processes, and 0.30 ± 0.09 events from all-leptonic $t\bar{t}Z$ processes are predicted. Events from processes with two or three prompt leptons, e.g., Z, WW, WZ, $t\bar{t}$, and ZZ events where one Z boson decays hadronically, where associated jets or photons contain or fake a nonprompt lepton, can pass the event selection. This background contribution is estimated to be $0.09^{+1.08}_{-0.04}$ events, using control samples and a data-driven technique described in Ref. [11]. The uncertainty is dominated by the small number of events in the control samples. It can be asymmetric due to truncation, as background contributions cannot be negative. Background from two single Z bosons produced in different pp collisions in the same bunch crossing is estimated to be negligible. The total expected number of background events is 0.20 ± 0.05 ($0.25^{+0.40}_{-0.05}$, $0.17^{+1.00}_{-0.04}$) in the $4e$ ($2e2\mu$, 4μ) channel, giving a total of $0.62^{+1.08}_{-0.11}$ events.

A factor C_{ZZ} is applied to correct for detector inefficiencies and resolution effects. It relates the background-subtracted number of selected events to the number in the fiducial phase space, and is defined as the ratio of generated signal events passing the selection criteria using reconstructed objects to the number passing the fiducial criteria using generator-level objects. C_{ZZ} is determined with a combination of the POWHEG ZZ MC sample and the SHERPA loop-induced gg-initiated sample. The normalization of the latter is scaled to $\mathcal{O}(\alpha_S^3)$ accuracy [2] in order to improve the model used to correct the measurement. The C_{ZZ} value and its total uncertainty is determined to be 0.55 ± 0.02 ($0.63 \pm 0.02, 0.81 \pm 0.03$) in the $4e$ ($2e2\mu, 4\mu$) channel. The dominant systematic uncertainties come from the uncertainties of the scale factors used to correct lepton reconstruction and identification efficiencies in the simulation and the choice of MC generator. Other smaller uncertainties come from the scale and resolution of the lepton momenta, PDFs, and statistical fluctuations in the MC sample. Table I gives a breakdown of the systematic uncertainties.

Figure 1 shows the invariant mass of the leading-$p_{T,\ell\ell}$ and the subleading-$p_{T,\ell\ell}$ lepton pair ($\ell\ell$), as well as the invariant mass, transverse momentum, and rapidity of the four-lepton system. Distributions from data are compared to the signal and background expectations, with good agreement in general.

The fiducial cross section is determined using a maximum-likelihood fit to the event counts in the three signal channels. A Poisson probability function is used to parametrize the number of expected events, multiplied by Gaussian distributions that model the nuisance parameters representing systematic uncertainties. This procedure can lead to asymmetric uncertainties as Poisson-distributed variables cannot be negative.

TABLE I. Relative uncertainties of the correction factor C_{ZZ} by signal channel, expressed in percent.

Source	$4e$	$2e2\mu$	4μ
Statistical (signal samples)	0.7	0.5	0.5
Theoretical (generator, PDFs)	2.5	2.5	2.5
Experimental efficiencies	2.3	2.2	2.0
Momentum scales and resolutions	0.4	0.2	0.1
Total	3.5	3.3	3.2

The cross section measured in the fiducial phase space is also extrapolated to the total phase space, which includes a correction for QED final-state radiation effects. The extrapolation factor is obtained from the same combination of MC samples as used in the C_{ZZ} determination. The ratio of the fiducial to full phase-space cross section is 0.39 ± 0.02, in all three channels. It is corrected for the $\sim$3% increase bias introduced by the pairing algorithm in the $4e$ and 4μ channels. The dominant systematic uncertainty comes from the difference between the nominal value and that obtained using the SHERPA samples. Smaller uncertainties are derived from PDF variations in the CT10 error set, differences between using PYTHIA8 and HERWIG++ [40] for simulating the rest of the event, and varying the QCD renormalization and factorization scales independently by a factor of 2. In order to extrapolate to the total cross section, the fiducial cross sections are divided by the ratio 0.39 ± 0.02 and corrected for the leptonic branching fraction $(3.3658\%)^2$ [41] (this value excludes γ^* contributions; including these, the branching fraction $ZZ \to \ell^+\ell^-\ell'^+\ell'^-$ is about 1.01–1.02 times larger).

The measured fiducial cross sections are shown in Table II and Fig. 2(a) along with a comparison to $\mathcal{O}(\alpha_S^2)$ calculations [1]. Table II also shows the total combined cross section. The CT10 next-to-next-to-leading order PDFs [45] and a dynamic scale equal to the mass of the four-lepton system are used in the calculation. The loop-induced gg-initiated process is included, and contributes 7.0% (5.8%) of the cross section in the fiducial (total) phase space. The predicted cross sections in the fiducial phase space are corrected for QED final-state radiation effects, which amount to a 4% reduction. The measurements agree with the SM predictions.

The theoretical predictions do not include the following effects. The loop-induced gg-initiated process calculated at $\mathcal{O}(\alpha_S^2)$ could receive large corrections at $\mathcal{O}(\alpha_S^3)$ of 70% [2], which would increase the prediction by 4%–5%. Electroweak corrections at next-to-leading order [46,47]

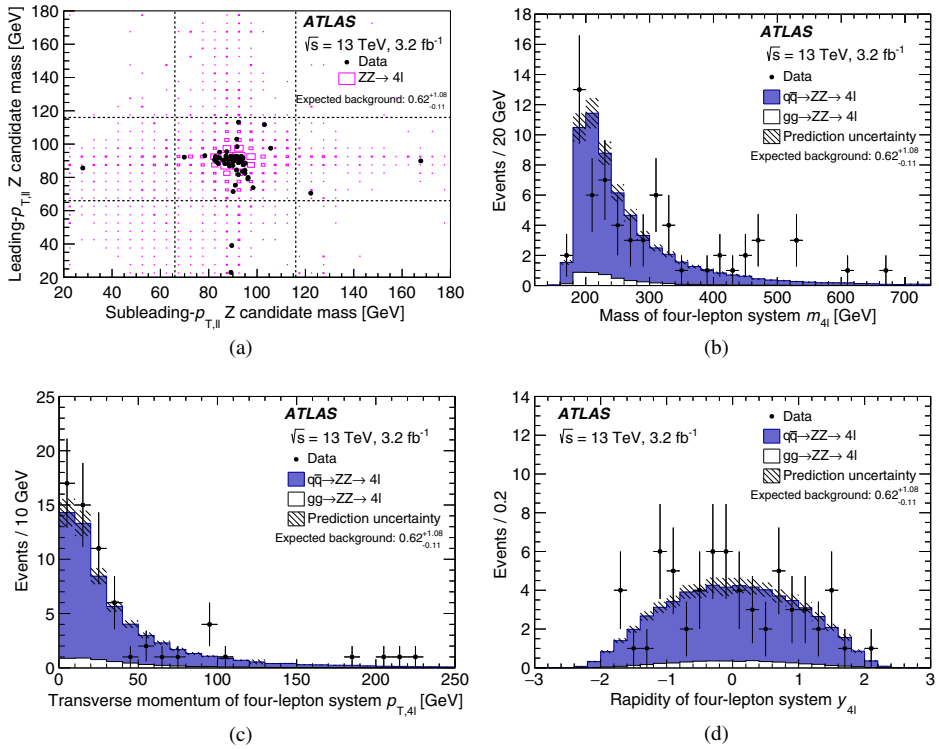

FIG. 1. (a) Invariant mass $m_{\ell\ell}$ of the leading-$p_{T,\ell\ell}$ vs the subleading-$p_{T,\ell\ell}$ lepton pair ($\ell\ell$), before the requirement 66 GeV $< m_{\ell\ell} <$ 116 GeV is applied. The dashed lines indicate this requirement. (b) Invariant mass, (c) transverse momentum, and (d) rapidity of the four-lepton system in selected events. The points represent experimental data. The filled histograms show the signal prediction from simulation, including the $q\bar{q}$ and loop-induced gg-initiated process. The contributions are stacked. In the simulation, the prediction from POWHEG+PYTHIA8 combined with SHERPA is scaled to the $\mathcal{O}(\alpha_S^2)$ prediction. The uncertainties in the simulation are from the same sources as the C_{ZZ} uncertainty. In addition, 6% ZZ cross-section uncertainty and 5% integrated-luminosity uncertainty are included. The expected background of $0.62^{+1.08}_{-0.11}$ events is not shown as a histogram due to its small size.

are expected to reduce the cross section by 7%–8% [47]. Furthermore, the contribution from double parton scattering is not accounted for, but is expected to be an effect of less than 1% [48].

The measured total cross section is compared to measurements at lower center-of-mass energies and to a prediction from MCFM [49] with the CT14 NLO PDFs [50], which is calculated at $\mathcal{O}(\alpha_S^1)$ accuracy for the $q\bar{q}$-initiated process and at $\mathcal{O}(\alpha_S^2)$ accuracy for the loop-induced gg-initiated process and is shown vs center-of-mass energy in Fig. 2(b). The cross section increases by a factor of more than 2 with a center-of-mass energy increase from 8 TeV to 13 TeV.

In summary, ATLAS has measured the ZZ production cross section in 3.2 fb^{-1} of 13 TeV pp collisions at the LHC using the fully leptonic decay channel $ZZ \to \ell^+\ell^-\ell'^+\ell'^-$. Fiducial cross sections as well as a total cross section for Z bosons with mass 66–116 GeV have been measured and agree well with $\mathcal{O}(\alpha_S^2)$ SM predictions.

TABLE II. Cross-section measurement results compared to the $\mathcal{O}(\alpha_S^2)$ standard model predictions. The per-channel and combined fiducial cross sections are shown along with the combined total cross section. For experimental results, the statistical, systematic, and luminosity uncertainties are shown. For theoretical predictions, the PDF and renormalization and factorization scale uncertainties added in quadrature are shown.

	Measurement	$\mathcal{O}(\alpha_S^2)$ prediction
$\sigma^{\rm fid}_{ZZ\to e^+e^-e^+e^-}$	$8.4^{+2.4}_{-2.0}$(stat) $^{+0.4}_{-0.2}$(syst) $^{+0.5}_{-0.3}$(lumi) fb	$6.9^{+0.2}_{-0.2}$ fb
$\sigma^{\rm fid}_{ZZ\to e^+e^-\mu^+\mu^-}$	$14.7^{+2.9}_{-2.5}$(stat) $^{+0.6}_{-0.4}$(syst) $^{+0.9}_{-0.6}$(lumi) fb	$13.6^{+0.4}_{-0.4}$ fb
$\sigma^{\rm fid}_{ZZ\to \mu^+\mu^-\mu^+\mu^-}$	$6.8^{+1.8}_{-1.5}$(stat) $^{+0.3}_{-0.3}$(syst) $^{+0.4}_{-0.3}$(lumi) fb	$6.9^{+0.2}_{-0.2}$ fb
$\sigma^{\rm fid}_{ZZ\to \ell^+\ell^-\ell'^+\ell'^-}$	$29.7^{+3.9}_{-3.6}$(stat) $^{+1.0}_{-0.8}$(syst) $^{+1.7}_{-1.3}$(lumi) fb	$27.4^{+0.9}_{-0.8}$ fb
$\sigma^{\rm tot}_{ZZ}$	$16.7^{+2.2}_{-2.0}$(stat) $^{+0.9}_{-0.7}$(syst) $^{+1.0}_{-0.7}$(lumi) pb	$15.6^{+0.4}_{-0.4}$ pb

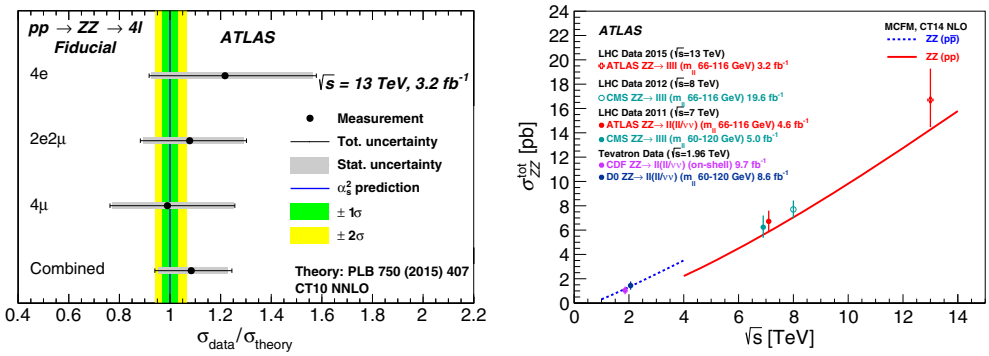

(a) (b)

FIG. 2. (a) Comparison between measured fiducial cross sections and $\mathcal{O}(\alpha_S^2)$ predictions. (b) Total cross section compared to measurements at lower center-of-mass energies by ATLAS, CMS, CDF, and D0 [11–13,42,43], and to a prediction from MCFM at $\mathcal{O}(\alpha_S^1)$ accuracy for the $q\bar{q}$-initiated process and at $\mathcal{O}(\alpha_S^2)$ accuracy for the loop-induced gg-initiated process. A full $\mathcal{O}(\alpha_S^2)$ prediction (known to improve agreement at $\sqrt{s} = 13$ TeV) was not yet available for all the different center-of-mass energies. Some data points are shifted horizontally to improve readability. The ZZ cross section as function of $\sqrt{s}$ in the range 130–209 GeV was also measured at the LEP 2 e^+e^- collider [44].

We thank CERN for the very successful operation of the LHC, as well as the support staff from our institutions without whom ATLAS could not be operated efficiently. We acknowledge the support of ANPCyT, Argentina; YerPhI, Armenia; ARC, Australia; BMWFW and FWF, Austria; ANAS, Azerbaijan; SSTC, Belarus; CNPq and FAPESP, Brazil; NSERC, NRC and CFI, Canada; CERN; CONICYT, Chile; CAS, MOST and NSFC, China; COLCIENCIAS, Colombia; MSMT CR, MPO CR and VSC CR, Czech Republic; DNRF, DNSRC and Lundbeck Foundation, Denmark; IN2P3-CNRS, CEA-DSM/IRFU, France; GNSF, Georgia; BMBF, HGF, and MPG, Germany; GSRT, Greece; RGC, Hong Kong SAR, China; ISF, I-CORE and Benoziyo Center, Israel; INFN, Italy; MEXT and JSPS, Japan; CNRST, Morocco; FOM and NWO, Netherlands; RCN, Norway; MNiSW and NCN, Poland; FCT, Portugal; MNE/IFA, Romania; MES of Russia and NRC KI, Russian Federation; JINR; MSTD, Serbia; MSSR, Slovakia; ARRS and MIZŠ, Slovenia; DST/NRF, South Africa; MINECO, Spain; SRC and Wallenberg Foundation, Sweden; SERI, SNSF and Cantons of Bern and Geneva, Switzerland; MOST, Taiwan; TAEK, Turkey; STFC, United Kingdom; DOE and NSF, United States of America. In addition, individual groups and members have received support from BCKDF, the Canada Council, CANARIE, CRC, Compute Canada, FQRNT, and the Ontario Innovation Trust, Canada; EPLANET, ERC, FP7, Horizon 2020 and Marie Skłodowska-Curie Actions, European Union; Investissements d'Avenir Labex and Idex, ANR, Region Auvergne and Fondation Partager le Savoir, France; DFG and AvH Foundation, Germany; Herakleitos, Thales and Aristeia programmes co-financed by EU-ESF and the Greek NSRF; BSF, GIF and Minerva, Israel; BRF, Norway; the Royal Society, and Leverhulme Trust, United Kingdom. The crucial computing support from all WLCG partners is acknowledged gratefully, in particular from CERN and the ATLAS Tier-1 facilities at TRIUMF (Canada), NDGF (Denmark, Norway, Sweden), CC-IN2P3 (France), KIT/GridKA (Germany), INFN-CNAF (Italy), NL-T1 (Netherlands), PIC (Spain), ASGC (Taiwan), RAL (UK), and BNL (USA) and in the Tier-2 facilities worldwide.

[1] M. Grazzini, S. Kallweit, and D. Rathlev, ZZ production at the LHC: Fiducial cross sections and distributions in NNLO QCD, Phys. Lett. B **750**, 407 (2015).

[2] F. Caola, K. Melnikov, R. Röntsch, and L. Tancredi, QCD corrections to ZZ production in gluon fusion at the LHC, Phys. Rev. D **92**, 094028 (2015).

[3] ATLAS Collaboration, Measurements of the Total and Differential Higgs Boson Production Cross Sections Combining the $H \to \gamma\gamma$ and $H \to ZZ^* \to 4\ell$ Decay Channels at $\sqrt{s} = 8$ TeV with the ATLAS Detector, Phys. Rev. Lett. **115**, 091801 (2015).

[4] ATLAS Collaboration, Constraints on the off-shell Higgs boson signal strength in the high-mass ZZ and WW final states with the ATLAS detector, Eur. Phys. J. C **75**, 335 (2015).

[5] CMS Collaboration, Limits on the Higgs boson lifetime and width from its decay to four charged leptons, Phys. Rev. D **92**, 072010 (2015).

[6] ATLAS Collaboration, Search for an additional, heavy Higgs boson in the $H \to ZZ$ decay channel at $\sqrt{s} = 8$ TeV in pp collision data with the ATLAS detector, Eur. Phys. J. C **76**, 45 (2016).

[7] CMS Collaboration, Search for massive resonances decaying into pairs of boosted bosons in semi-leptonic final states at $\sqrt{s} = 8$ TeV, J. High Energy Phys. 08 (2014) 174.

[8] U. Baur and D. L. Rainwater, Probing neutral gauge boson self-interactions in ZZ production at hadron colliders, Phys. Rev. D **62**, 113011 (2000).
[9] ATLAS Collaboration, The ATLAS Experiment at the CERN Large Hadron Collider, J. Inst. **3**, S08003 (2008).
[10] ATLAS Collaboration, Improved luminosity determination in pp collisions at $\sqrt{s} = 7$ TeV using the ATLAS detector at the LHC, Eur. Phys. J. C **73**, 2518 (2013).
[11] ATLAS Collaboration, Measurement of ZZ production in pp collisions at $\sqrt{s} = 7$ TeV and limits on anomalous ZZZ and $ZZ\gamma$ couplings with the ATLAS detector, J. High Energy Phys. 03 (2013) 128.
[12] CMS Collaboration, Measurement of the $pp \to ZZ$ production cross section and constraints on anomalous triple gauge couplings in four-lepton final states at $\sqrt{s} = 8$ TeV, Phys. Lett. B **740**, 250 (2015).
[13] CMS Collaboration, Measurement of the ZZ production cross section and search for anomalous couplings in $2\ell 2\ell'$ final states in pp collisions at $\sqrt{s} = 7$ TeV, J. High Energy Phys. 01 (2013) 063.
[14] ATLAS Collaboration, Report No. ATL-PHYS-PUB-2015-013, http://cdsweb.cern.ch/record/2022743.
[15] ATLAS Collaboration, Report No. ATL-PHYS-PUB-2015-037, http://cdsweb.cern.ch/record/2047831.
[16] ATLAS Collaboration, Report No. ATLAS-CONF-2014-032, http://cdsweb.cern.ch/record/1706245.
[17] P. Nason, A new method for combining NLO QCD with shower Monte Carlo algorithms, J. High Energy Phys. 11 (2004) 040.
[18] S. Frixione, P. Nason, and C. Oleari, Matching NLO QCD computations with Parton Shower simulations: The POWHEG method, J. High Energy Phys. 11 (2007) 070.
[19] S. Alioli, P. Nason, C. Oleari, and E. Re, A general framework for implementing NLO calculations in shower Monte Carlo programs: The POWHEG BOX, J. High Energy Phys. 06 (2010) 043.
[20] T. Melia, P. Nason, R. Röntsch, and G. Zanderighi, W^+W^-, WZ and ZZ production in the POWHEG-BOX, J. High Energy Phys. 11 (2011) 078.
[21] P. Nason and G. Zanderighi, W^+W^-, WZ and ZZ production in the POWHEG-BOX-V2, Eur. Phys. J. C **74**, 2702 (2014).
[22] T. Sjöstrand, S. Mrenna, and P. Skands, PYTHIA 6.4 physics and manual, J. High Energy Phys. 05 (2006) 026.
[23] T. Sjöstrand, S. Mrenna, and P. Skands, A brief introduction to PYTHIA 8.1, Comput. Phys. Commun. **178**, 852 (2008).
[24] ATLAS Collaboration, Measurement of the Z/γ^* boson transverse momentum distribution in pp collisions at $\sqrt{s} = 7$ TeV with the ATLAS detector, J. High Energy Phys. 09 (2014) 145.
[25] T. Gleisberg, S. Höche, F. Krauss, M. Schönherr, S. Schumann, F. Siegert, and J. Winter, Event generation with SHERPA 1.1, J. High Energy Phys. 02 (2009) 007.
[26] S. Höche, F. Krauss, S. Schumann, and F. Siegert, QCD matrix elements and truncated showers, J. High Energy Phys. 05 (2009) 053.
[27] T. Gleisberg and S. Höche, Comix, a new matrix element generator, J. High Energy Phys. 12 (2008) 039.
[28] S. Schumann and F. Krauss, A parton shower algorithm based on Catani-Seymour dipole factorisation, J. High Energy Phys. 03 (2008) 038.
[29] M. Schönherr and F. Krauss, Soft photon radiation in particle decays in SHERPA, J. High Energy Phys. 12 (2008) 018.
[30] F. Cascioli, P. Maierhöfer, and S. Pozzorini, Scattering Amplitudes with Open Loops, Phys. Rev. Lett. **108**, 111601 (2012).
[31] S. Höche, F. Krauss, M. Schönherr, and F. Siegert, QCD matrix elements + parton showers: The NLO case, J. High Energy Phys. 04 (2013) 027.
[32] H.-L. Lai, M. Guzzi, J. Huston, Z. Li, P. M. Nadolsky, J. Pumplin, and C.-P. Yuan, New parton distributions for collider physics, Phys. Rev. D **82**, 074024 (2010).
[33] J. Alwall, M. Herquet, F. Maltoni, O. Mattelaer, and T. Stelzer, MADGRAPH5: Going beyond, J. High Energy Phys. 06 (2011) 128.
[34] R. D. Ball *et al.*, Parton distributions with LHC data, Nucl. Phys. **B867**, 244 (2013).
[35] ATLAS Collaboration, Report No. ATL-PHYS-PUB-2014-021, 2014, http://cdsweb.cern.ch/record/1966419.
[36] A. D. Martin, W. J. Stirling, R. S. Thorne, and G. Watt, Parton distributions for the LHC, Eur. Phys. J. C **63**, 189 (2009).
[37] ATLAS Collaboration, Report No. ATL-PHYS-PUB-2012-003, 2012, http://cds.cern.ch/record/1474107.
[38] ATLAS Collaboration, The ATLAS Simulation Infrastructure, Eur. Phys. J. C **70**, 823 (2010).
[39] S. Agostinelli *et al.*, GEANT4—A simulation toolkit, Nucl. Instrum. Methods Phys. Res., Sect. A **506**, 250 (2003).
[40] S. Gieseke *et al.*, HERWIG++ 2.5 release note, arXiv:1102.1672.
[41] K. A. Olive *et al.*, Review of particle physics, Chin. Phys. C **38**, 090001 (2014).
[42] T. Aaltonen *et al.* (CDF Collaboration), Measurement of the ZZ production cross section using the full CDF II data set, Phys. Rev. D **89**, 112001 (2014).
[43] V. M. Abazov *et al.* (D0 Collaboration), A measurement of the WZ and ZZ production cross sections using leptonic final states in 8.6 fb^{-1} of $p\bar{p}$ collisions, Phys. Rev. D **85**, 112005 (2012).
[44] S. Schael *et al.* (ALEPH, DELPHI, L3, and OPAL Collaborations, LEP Electroweak Working Group), Electroweak measurements in electron-positron collisions at W-boson-pair energies at LEP, Phys. Rep. **532**, 119 (2013).
[45] J. Gao, M. Guzzi, J. Huston, H.-L. Lai, Z. Li, P. Nadolsky, J. Pumplin, D. Stump, and C.-P. Yuan, CT10 next-to-next-to-leading order global analysis of QCD, Phys. Rev. D **89**, 033009 (2014).
[46] A. Bierweiler, T. Kasprzik, and J. H. Kühn, Vector-boson pair production at the LHC to $\mathcal{O}(\alpha^3)$ accuracy, J. High Energy Phys. 12 (2013) 071.
[47] B. Biedermann *et al.*, Electroweak corrections to $pp \to \mu^+\mu^-e^+e^- + X$ at the LHC—a Higgs background study, arXiv:1601.07787.
[48] ATLAS Collaboration, Measurement of hard double-parton interactions in $W(\to \ell\nu) + 2$ jet events at

$\sqrt{s} = 7$ TeV with the ATLAS detector, New J. Phys. **15**, 033038 (2013).

[49] J. M. Campbell and R. K. Ellis, An update on vector boson pair production at hadron colliders, Phys. Rev. D **60**, 113006 (1999).

[50] S. Dulat, T.-J. Hou, J. Gao, M. Guzzi, J. Huston, P. Nadolsky, J. Pumplin, C. Schmidt, D. Stump, and C.-P. Yuan, New parton distribution functions from a global analysis of quantum chromodynamics, Phys. Rev. D **93**, 033006 (2016).

G. Aad,[85] B. Abbott,[112] J. Abdallah,[150] O. Abdinov,[11] B. Abeloos,[116] R. Aben,[106] M. Abolins,[90] O. S. AbouZeid,[136] H. Abramowicz,[152] H. Abreu,[151] R. Abreu,[115] Y. Abulaiti,[145a,145b] B. S. Acharya,[163a,163b,a] L. Adamczyk,[38a] D. L. Adams,[25] J. Adelman,[107] S. Adomeit,[99] T. Adye,[130] A. A. Affolder,[74] T. Agatonovic-Jovin,[13] J. Agricola,[54] J. A. Aguilar-Saavedra,[125a,125f] S. P. Ahlen,[22] F. Ahmadov,[65,b] G. Aielli,[132a,132b] H. Akerstedt,[145a,145b] T. P. A. Åkesson,[81] A. V. Akimov,[95] G. L. Alberghi,[20a,20b] J. Albert,[168] S. Albrand,[55] M. J. Alconada Verzini,[71] M. Aleksa,[30] I. N. Aleksandrov,[65] C. Alexa,[26b] G. Alexander,[152] T. Alexopoulos,[10] M. Alhroob,[112] G. Alimonti,[91a] L. Alio,[85] J. Alison,[31] S. P. Alkire,[35] B. M. M. Allbrooke,[148] B. W. Allen,[115] P. P. Allport,[18] A. Aloisio,[103a,103b] A. Alonso,[36] F. Alonso,[71] C. Alpigiani,[137] B. Alvarez Gonzalez,[30] D. Álvarez Piqueras,[166] M. G. Alviggi,[103a,103b] B. T. Amadio,[15] K. Amako,[66] Y. Amaral Coutinho,[24a] C. Amelung,[23] D. Amidei,[89] S. P. Amor Dos Santos,[125a,125c] A. Amorim,[125a,125b] S. Amoroso,[30] N. Amram,[152] G. Amundsen,[23] C. Anastopoulos,[138] L. S. Ancu,[49] N. Andari,[107] T. Andeen,[31] C. F. Anders,[58b] G. Anders,[30] J. K. Anders,[74] K. J. Anderson,[31] A. Andreazza,[91a,91b] V. Andrei,[58a] S. Angelidakis,[9] I. Angelozzi,[106] P. Anger,[44] A. Angerami,[35] F. Anghinolfi,[30] A. V. Anisenkov,[108,c] N. Anjos,[12] A. Annovi,[123a,123b] M. Antonelli,[47] A. Antonov,[97] J. Antos,[143b] F. Anulli,[131a] M. Aoki,[66] L. Aperio Bella,[18] G. Arabidze,[90] Y. Arai,[66] J. P. Araque,[125a] A. T. H. Arce,[45] F. A. Arduh,[71] J-F. Arguin,[94] S. Argyropoulos,[63] M. Arik,[19a] A. J. Armbruster,[30] L. J. Armitage,[76] O. Arnaez,[30] H. Arnold,[48] M. Arratia,[28] O. Arslan,[21] A. Artamonov,[96] G. Artoni,[119] S. Artz,[83] S. Asai,[154] N. Asbah,[42] A. Ashkenazi,[152] B. Åsman,[145a,145b] L. Asquith,[148] K. Assamagan,[25] R. Astalos,[143a] M. Atkinson,[164] N. B. Atlay,[140] K. Augsten,[127] G. Avolio,[30] B. Axen,[15] M. K. Ayoub,[116] G. Azuelos,[94,d] M. A. Baak,[30] A. E. Baas,[58a] M. J. Baca,[18] H. Bachacou,[135] K. Bachas,[73a,73b] M. Backes,[30] M. Backhaus,[30] P. Bagiacchi,[131a,131b] P. Bagnaia,[131a,131b] Y. Bai,[33a] J. T. Baines,[130] O. K. Baker,[175] E. M. Baldin,[108,c] P. Balek,[128] T. Balestri,[147] F. Balli,[135] W. K. Balunas,[121] E. Banas,[39] Sw. Banerjee,[172,e] A. A. E. Bannoura,[174] L. Barak,[30] E. L. Barberio,[88] D. Barberis,[50a,50b] M. Barbero,[85] T. Barillari,[100] M. Barisonzi,[163a,163b] T. Barklow,[142] N. Barlow,[28] S. L. Barnes,[84] B. M. Barnett,[130] R. M. Barnett,[15] Z. Barnovska,[5] A. Baroncelli,[133a] G. Barone,[23] A. J. Barr,[119] L. Barranco Navarro,[166] F. Barreiro,[82] J. Barreiro Guimarães da Costa,[33a] R. Bartoldus,[142] A. E. Barton,[72] P. Bartos,[143a] A. Basalaev,[122] A. Bassalat,[116] A. Basye,[164] R. L. Bates,[53] S. J. Batista,[157] J. R. Batley,[28] M. Battaglia,[136] M. Bauce,[131a,131b] F. Bauer,[135] H. S. Bawa,[142,f] J. B. Beacham,[110] M. D. Beattie,[72] T. Beau,[80] P. H. Beauchemin,[160] R. Beccherle,[123a,123b] P. Bechtle,[21] H. P. Beck,[17,g] K. Becker,[119] M. Becker,[83] M. Beckingham,[169] C. Becot,[109] A. J. Beddall,[19e] A. Beddall,[19b] V. A. Bednyakov,[65] M. Bedognetti,[106] C. P. Bee,[147] L. J. Beemster,[106] T. A. Beermann,[30] M. Begel,[25] J. K. Behr,[119] C. Belanger-Champagne,[87] A. S. Bell,[78] W. H. Bell,[49] G. Bella,[152] L. Bellagamba,[20a] A. Bellerive,[29] M. Bellomo,[86] K. Belotskiy,[97] O. Beltramello,[30] N. L. Belyaev,[97] O. Benary,[152] D. Benchekroun,[134a] M. Bender,[99] K. Bendtz,[145a,145b] N. Benekos,[10] Y. Benhammou,[152] E. Benhar Noccioli,[175] J. Benitez,[63] J. A. Benitez Garcia,[158b] D. P. Benjamin,[45] J. R. Bensinger,[23] S. Bentvelsen,[106] L. Beresford,[119] M. Beretta,[47] D. Berge,[106] E. Bergeaas Kuutmann,[165] N. Berger,[5] F. Berghaus,[168] J. Beringer,[15] S. Berlendis,[55] C. Bernard,[22] N. R. Bernard,[86] C. Bernius,[109] F. U. Bernlochner,[21] T. Berry,[77] P. Berta,[128] C. Bertella,[83] G. Bertoli,[145a,145b] F. Bertolucci,[123a,123b] I. A. Bertram,[72] C. Bertsche,[112] D. Bertsche,[112] G. J. Besjes,[36] O. Bessidskaia Bylund,[145a,145b] M. Bessner,[42] N. Besson,[135] C. Betancourt,[48] S. Bethke,[100] A. J. Bevan,[76] W. Bhimji,[15] R. M. Bianchi,[124] L. Bianchini,[23] M. Bianco,[30] O. Biebel,[99] D. Biedermann,[16] R. Bielski,[84] N. V. Biesuz,[123a,123b] M. Biglietti,[133a] J. Bilbao De Mendizabal,[49] H. Bilokon,[47] M. Bindi,[54] S. Binet,[116] A. Bingul,[19b] C. Bini,[131a,131b] S. Biondi,[20a,20b] D. M. Bjergaard,[45] C. W. Black,[149] J. E. Black,[142] K. M. Black,[22] D. Blackburn,[137] R. E. Blair,[6] J.-B. Blanchard,[135] J. E. Blanco,[77] T. Blazek,[143a] I. Bloch,[42] C. Blocker,[23] W. Blum,[83,†] U. Blumenschein,[54] S. Blunier,[32a] G. J. Bobbink,[106] V. S. Bobrovnikov,[108,c] S. S. Bocchetta,[81] A. Bocci,[45] C. Bock,[99] M. Boehler,[48] D. Boerner,[174] J. A. Bogaerts,[30] D. Bogavac,[13] A. G. Bogdanchikov,[108] C. Bohm,[145a] V. Boisvert,[77] T. Bold,[38a] V. Boldea,[26b] A. S. Boldyrev,[98] M. Bomben,[80] M. Bona,[76] M. Boonekamp,[135] A. Borisov,[129] G. Borissov,[72] J. Bortfeldt,[99] D. Bortoletto,[119] V. Bortolotto,[60a,60b,60c] K. Bos,[106] D. Boscherini,[20a] M. Bosman,[12] J. D. Bossio Sola,[27] J. Boudreau,[124] J. Bouffard,[2] E. V. Bouhova-Thacker,[72] D. Boumediene,[34] C. Bourdarios,[116] N. Bousson,[113] S. K. Boutle,[53] A. Boveia,[30] J. Boyd,[30]

I. R. Boyko,[65] J. Bracinik,[18] A. Brandt,[8] G. Brandt,[54] O. Brandt,[58a] U. Bratzler,[155] B. Brau,[86] J. E. Brau,[115] H. M. Braun,[174,†] W. D. Breaden Madden,[53] K. Brendlinger,[121] A. J. Brennan,[88] L. Brenner,[106] R. Brenner,[165] S. Bressler,[171] T. M. Bristow,[46] D. Britton,[53] D. Britzger,[42] F. M. Brochu,[28] I. Brock,[21] R. Brock,[90] G. Brooijmans,[35] T. Brooks,[77] W. K. Brooks,[32b] J. Brosamer,[15] E. Brost,[115] J. H Broughton,[18] P. A. Bruckman de Renstrom,[39] D. Bruncko,[143b] R. Bruneliere,[48] A. Bruni,[20a] G. Bruni,[20a] BH Brunt,[28] M. Bruschi,[20a] N. Bruscino,[21] P. Bryant,[31] L. Bryngemark,[81] T. Buanes,[14] Q. Buat,[141] P. Buchholz,[140] A. G. Buckley,[53] I. A. Budagov,[65] F. Buehrer,[48] M. K. Bugge,[118] O. Bulekov,[97] D. Bullock,[8] H. Burckhart,[30] S. Burdin,[74] C. D. Burgard,[48] B. Burghgrave,[107] K. Burka,[39] S. Burke,[130] I. Burmeister,[43] E. Busato,[34] D. Büscher,[48] V. Büscher,[83] P. Bussey,[53] J. M. Butler,[22] A. I. Butt,[3] C. M. Buttar,[53] J. M. Butterworth,[78] P. Butti,[106] W. Buttinger,[25] A. Buzatu,[53] A. R. Buzykaev,[108,c] S. Cabrera Urbán,[166] D. Caforio,[127] V. M. Cairo,[37a,37b] O. Cakir,[4a] N. Calace,[49] P. Calafiura,[15] A. Calandri,[85] G. Calderini,[80] P. Calfayan,[99] L. P. Caloba,[24a] D. Calvet,[34] S. Calvet,[34] T. P. Calvet,[85] R. Camacho Toro,[31] S. Camarda,[42] P. Camarri,[132a,132b] D. Cameron,[118] R. Caminal Armadans,[164] C. Camincher,[55] S. Campana,[30] M. Campanelli,[78] A. Campoverde,[147] V. Canale,[103a,103b] A. Canepa,[158a] M. Cano Bret,[33e] J. Cantero,[82] R. Cantrill,[125a] T. Cao,[40] M. D. M. Capeans Garrido,[30] I. Caprini,[26b] M. Caprini,[26b] M. Capua,[37a,37b] R. Caputo,[83] R. M. Carbone,[35] R. Cardarelli,[132a] F. Cardillo,[48] T. Carli,[30] G. Carlino,[103a] L. Carminati,[91a,91b] S. Caron,[105] E. Carquin,[32a] G. D. Carrillo-Montoya,[30] J. R. Carter,[28] J. Carvalho,[125a,125c] D. Casadei,[78] M. P. Casado,[12,h] M. Casolino,[12] D. W. Casper,[162] E. Castaneda-Miranda,[144a] A. Castelli,[106] V. Castillo Gimenez,[166] N. F. Castro,[125a,i] A. Catinaccio,[30] J. R. Catmore,[118] A. Cattai,[30] J. Caudron,[83] V. Cavaliere,[164] D. Cavalli,[91a] M. Cavalli-Sforza,[12] V. Cavasinni,[123a,123b] F. Ceradini,[133a,133b] L. Cerda Alberich,[166] B. C. Cerio,[45] A. S. Cerqueira,[24b] A. Cerri,[148] L. Cerrito,[76] F. Cerutti,[15] M. Cerv,[30] A. Cervelli,[17] S. A. Cetin,[19d] A. Chafaq,[134a] D. Chakraborty,[107] I. Chalupkova,[128] S. K. Chan,[57] Y. L. Chan,[60a] P. Chang,[164] J. D. Chapman,[28] D. G. Charlton,[18] A. Chatterjee,[49] C. C. Chau,[157] C. A. Chavez Barajas,[148] S. Che,[110] S. Cheatham,[72] A. Chegwidden,[90] S. Chekanov,[6] S. V. Chekulaev,[158a] G. A. Chelkov,[65,j] M. A. Chelstowska,[89] C. Chen,[64] H. Chen,[25] K. Chen,[147] S. Chen,[33c] S. Chen,[154] X. Chen,[33f] Y. Chen,[67] H. C. Cheng,[89] Y. Cheng,[31] A. Cheplakov,[65] E. Cheremushkina,[129] R. Cherkaoui El Moursli,[134e] V. Chernyatin,[25,†] E. Cheu,[7] L. Chevalier,[135] V. Chiarella,[47] G. Chiarelli,[123a,123b] G. Chiodini,[73a] A. S. Chisholm,[18] A. Chitan,[26b] M. V. Chizhov,[65] K. Choi,[61] S. Chouridou,[9] B. K. B. Chow,[99] V. Christodoulou,[78] D. Chromek-Burckhart,[30] J. Chudoba,[126] A. J. Chuinard,[87] J. J. Chwastowski,[39] L. Chytka,[114] G. Ciapetti,[131a,131b] A. K. Ciftci,[4a] D. Cinca,[53] V. Cindro,[75] I. A. Cioara,[21] A. Ciocio,[15] F. Cirotto,[103a,103b] Z. H. Citron,[171] M. Ciubancan,[26b] A. Clark,[49] B. L. Clark,[57] P. J. Clark,[46] R. N. Clarke,[15] C. Clement,[145a,145b] Y. Coadou,[85] M. Cobal,[163a,163c] A. Coccaro,[49] J. Cochran,[64] L. Coffey,[23] L. Colasurdo,[105] B. Cole,[35] S. Cole,[107] A. P. Colijn,[106] J. Collot,[55] T. Colombo,[30] G. Compostella,[100] P. Conde Muiño,[125a,125b] E. Coniavitis,[48] S. H. Connell,[144b] I. A. Connelly,[77] V. Consorti,[48] S. Constantinescu,[26b] C. Conta,[120a,120b] G. Conti,[30] F. Conventi,[103a,k] M. Cooke,[15] B. D. Cooper,[78] A. M. Cooper-Sarkar,[119] T. Cornelissen,[174] M. Corradi,[131a,131b] F. Corriveau,[87,l] A. Corso-Radu,[162] A. Cortes-Gonzalez,[12] G. Cortiana,[100] G. Costa,[91a] M. J. Costa,[166] D. Costanzo,[138] G. Cottin,[28] G. Cowan,[77] B. E. Cox,[84] K. Cranmer,[109] S. J. Crawley,[53] G. Cree,[29] S. Crépé-Renaudin,[55] F. Crescioli,[80] W. A. Cribbs,[145a,145b] M. Crispin Ortuzar,[119] M. Cristinziani,[21] V. Croft,[105] G. Crosetti,[37a,37b] T. Cuhadar Donszelmann,[138] J. Cummings,[175] M. Curatolo,[47] J. Cúth,[83] C. Cuthbert,[149] H. Czirr,[140] P. Czodrowski,[3] S. D'Auria,[53] M. D'Onofrio,[74] M. J. Da Cunha Sargedas De Sousa,[125a,125b] C. Da Via,[84] W. Dabrowski,[38a] T. Dai,[89] O. Dale,[14] F. Dallaire,[94] C. Dallapiccola,[86] M. Dam,[36] J. R. Dandoy,[31] N. P. Dang,[48] A. C. Daniells,[18] N. S. Dann,[84] M. Danninger,[167] M. Dano Hoffmann,[135] V. Dao,[48] G. Darbo,[50a] S. Darmora,[8] J. Dassoulas,[3] A. Dattagupta,[61] W. Davey,[21] C. David,[168] T. Davidek,[128] M. Davies,[152] P. Davison,[78] Y. Davygora,[58a] E. Dawe,[88] I. Dawson,[138] R. K. Daya-Ishmukhametova,[86] K. De,[8] R. de Asmundis,[103a] A. De Benedetti,[112] S. De Castro,[20a,20b] S. De Cecco,[80] N. De Groot,[105] P. de Jong,[106] H. De la Torre,[82] F. De Lorenzi,[64] D. De Pedis,[131a] A. De Salvo,[131a] U. De Sanctis,[148] A. De Santo,[148] J. B. De Vivie De Regie,[116] W. J. Dearnaley,[72] R. Debbe,[25] C. Debenedetti,[136] D. V. Dedovich,[65] I. Deigaard,[106] J. Del Peso,[82] T. Del Prete,[123a,123b] D. Delgove,[116] F. Deliot,[135] C. M. Delitzsch,[49] M. Deliyergiyev,[75] A. Dell'Acqua,[30] L. Dell'Asta,[22] M. Dell'Orso,[123a,123b] M. Della Pietra,[103a,k] D. della Volpe,[49] M. Delmastro,[5] P. A. Delsart,[55] C. Deluca,[106] D. A. DeMarco,[157] S. Demers,[175] M. Demichev,[65] A. Demilly,[80] S. P. Denisov,[129] D. Denysiuk,[135] D. Derendarz,[39] J. E. Derkaoui,[134d] F. Derue,[80] P. Dervan,[74] K. Desch,[21] C. Deterre,[42] K. Dette,[43] P. O. Deviveiros,[30] A. Dewhurst,[130] S. Dhaliwal,[23] A. Di Ciaccio,[132a,132b] L. Di Ciaccio,[5] W. K. Di Clemente,[121] A. Di Domenico,[131a,131b] C. Di Donato,[131a,131b] A. Di Girolamo,[30] B. Di Girolamo,[30] A. Di Mattia,[151] B. Di Micco,[133a,133b] R. Di Nardo,[47] A. Di Simone,[48] R. Di Sipio,[157] D. Di Valentino,[29] C. Diaconu,[85] M. Diamond,[157] F. A. Dias,[46] M. A. Diaz,[32a] E. B. Diehl,[89] J. Dietrich,[16] S. Diglio,[85] A. Dimitrievska,[13] J. Dingfelder,[21] P. Dita,[26b] S. Dita,[26b] F. Dittus,[30] F. Djama,[85]

T. Djobava,[51b] J. I. Djuvsland,[58a] M. A. B. do Vale,[24c] D. Dobos,[30] M. Dobre,[26b] C. Doglioni,[81] T. Dohmae,[154] J. Dolejsi,[128] Z. Dolezal,[128] B. A. Dolgoshein,[97,†] M. Donadelli,[24d] S. Donati,[123a,123b] P. Dondero,[120a,120b] J. Donini,[34] J. Dopke,[130] A. Doria,[103a] M. T. Dova,[71] A. T. Doyle,[53] E. Drechsler,[54] M. Dris,[10] Y. Du,[33d] J. Duarte-Campderros,[152] E. Duchovni,[171] G. Duckeck,[99] O. A. Ducu,[26b] D. Duda,[106] A. Dudarev,[30] L. Duflot,[116] L. Duguid,[77] M. Dührssen,[30] M. Dunford,[58a] H. Duran Yildiz,[4a] M. Düren,[52] A. Durglishvili,[51b] D. Duschinger,[44] B. Dutta,[42] M. Dyndal,[38a] C. Eckardt,[42] K. M. Ecker,[100] R. C. Edgar,[89] W. Edson,[2] N. C. Edwards,[46] T. Eifert,[30] G. Eigen,[14] K. Einsweiler,[15] T. Ekelof,[165] M. El Kacimi,[134c] V. Ellajosyula,[85] M. Ellert,[165] S. Elles,[5] F. Ellinghaus,[174] A. A. Elliot,[168] N. Ellis,[30] J. Elmsheuser,[99] M. Elsing,[30] D. Emeliyanov,[130] Y. Enari,[154] O. C. Endner,[83] M. Endo,[117] J. S. Ennis,[169] J. Erdmann,[43] A. Ereditato,[17] G. Ernis,[174] J. Ernst,[2] M. Ernst,[25] S. Errede,[164] E. Ertel,[83] M. Escalier,[116] H. Esch,[43] C. Escobar,[124] B. Esposito,[47] A. I. Etienvre,[135] E. Etzion,[152] H. Evans,[61] A. Ezhilov,[122] L. Fabbri,[20a,20b] G. Facini,[31] R. M. Fakhrutdinov,[129] S. Falciano,[131a] R. J. Falla,[78] J. Faltova,[128] Y. Fang,[33a] M. Fanti,[91a,91b] A. Farbin,[8] A. Farilla,[133a] C. Farina,[124] T. Farooque,[12] S. Farrell,[15] S. M. Farrington,[169] P. Farthouat,[30] F. Fassi,[134e] P. Fassnacht,[30] D. Fassouliotis,[9] M. Faucci Giannelli,[77] A. Favareto,[50a,50b] L. Fayard,[116] O. L. Fedin,[122,m] W. Fedorko,[167] S. Feigl,[118] L. Feligioni,[85] C. Feng,[33d] E. J. Feng,[30] H. Feng,[89] A. B. Fenyuk,[129] L. Feremenga,[8] P. Fernandez Martinez,[166] S. Fernandez Perez,[12] J. Ferrando,[53] A. Ferrari,[165] P. Ferrari,[106] R. Ferrari,[120a] D. E. Ferreira de Lima,[53] A. Ferrer,[166] D. Ferrere,[49] C. Ferretti,[89] A. Ferretto Parodi,[50a,50b] F. Fiedler,[83] A. Filipčič,[75] M. Filipuzzi,[42] F. Filthaut,[105] M. Fincke-Keeler,[168] K. D. Finelli,[149] M. C. N. Fiolhais,[125a,125c] L. Fiorini,[166] A. Firan,[40] A. Fischer,[2] C. Fischer,[12] J. Fischer,[174] W. C. Fisher,[90] N. Flaschel,[42] I. Fleck,[140] P. Fleischmann,[89] G. T. Fletcher,[138] G. Fletcher,[76] R. R. M. Fletcher,[121] T. Flick,[174] A. Floderus,[81] L. R. Flores Castillo,[60a] M. J. Flowerdew,[100] G. T. Forcolin,[84] A. Formica,[135] A. Forti,[84] D. Fournier,[116] H. Fox,[72] S. Fracchia,[12] P. Francavilla,[80] M. Franchini,[20a,20b] D. Francis,[30] L. Franconi,[118] M. Franklin,[57] M. Frate,[162] M. Fraternali,[120a,120b] D. Freeborn,[78] S. M. Fressard-Batraneanu,[30] F. Friedrich,[44] D. Froidevaux,[30] J. A. Frost,[119] C. Fukunaga,[155] E. Fullana Torregrosa,[83] T. Fusayasu,[101] J. Fuster,[166] C. Gabaldon,[55] O. Gabizon,[174] A. Gabrielli,[20a,20b] A. Gabrielli,[15] G. P. Gach,[38a] S. Gadatsch,[30] S. Gadomski,[49] G. Gagliardi,[50a,50b] P. Gagnon,[61] C. Galea,[105] B. Galhardo,[125a,125c] E. J. Gallas,[119] B. J. Gallop,[130] P. Gallus,[127] G. Galster,[36] K. K. Gan,[110] J. Gao,[33b,85] Y. Gao,[46] Y. S. Gao,[142,f] F. M. Garay Walls,[46] C. García,[166] J. E. García Navarro,[166] M. Garcia-Sciveres,[15] R. W. Gardner,[31] N. Garelli,[142] V. Garonne,[118] A. Gascon Bravo,[42] C. Gatti,[47] A. Gaudiello,[50a,50b] G. Gaudio,[120a] B. Gaur,[140] L. Gauthier,[94] I. L. Gavrilenko,[95] C. Gay,[167] G. Gaycken,[21] E. N. Gazis,[10] Z. Gecse,[167] C. N. P. Gee,[130] Ch. Geich-Gimbel,[21] M. P. Geisler,[58a] C. Gemme,[50a] M. H. Genest,[55] C. Geng,[33b,n] S. Gentile,[131a,131b] S. George,[77] D. Gerbaudo,[162] A. Gershon,[152] S. Ghasemi,[140] H. Ghazlane,[134b] B. Giacobbe,[20a] S. Giagu,[131a,131b] P. Giannetti,[123a,123b] B. Gibbard,[25] S. M. Gibson,[77] M. Gignac,[167] M. Gilchriese,[15] T. P. S. Gillam,[28] D. Gillberg,[29] G. Gilles,[174] D. M. Gingrich,[3,d] N. Giokaris,[9] M. P. Giordani,[163a,163c] F. M. Giorgi,[20a] F. M. Giorgi,[16] P. F. Giraud,[135] P. Giromini,[57] D. Giugni,[91a] C. Giuliani,[100] M. Giulini,[58b] B. K. Gjelsten,[118] S. Gkaitatzis,[153] I. Gkialas,[153] E. L. Gkougkousis,[116] L. K. Gladilin,[98] C. Glasman,[82] J. Glatzer,[30] P. C. F. Glaysher,[46] A. Glazov,[42] M. Goblirsch-Kolb,[100] J. Godlewski,[39] S. Goldfarb,[89] T. Golling,[49] D. Golubkov,[129] A. Gomes,[125a,125b,125d] R. Gonçalo,[125a] J. Goncalves Pinto Firmino Da Costa,[135] L. Gonella,[18] A. Gongadze,[65] S. González de la Hoz,[166] G. Gonzalez Parra,[12] S. Gonzalez-Sevilla,[49] L. Goossens,[30] P. A. Gorbounov,[96] H. A. Gordon,[25] I. Gorelov,[104] B. Gorini,[30] E. Gorini,[73a,73b] A. Gorišek,[75] E. Gornicki,[39] A. T. Goshaw,[45] C. Gössling,[43] M. I. Gostkin,[65] C. R. Goudet,[116] D. Goujdami,[134c] A. G. Goussiou,[137] N. Govender,[144b] E. Gozani,[151] L. Graber,[54] I. Grabowska-Bold,[38a] P. O. J. Gradin,[165] P. Grafström,[20a,20b] J. Gramling,[49] E. Gramstad,[118] S. Grancagnolo,[16] V. Gratchev,[122] H. M. Gray,[30] E. Graziani,[133a] Z. D. Greenwood,[79,o] C. Grefe,[21] K. Gregersen,[78] I. M. Gregor,[42] P. Grenier,[142] K. Grevtsov,[5] J. Griffiths,[8] A. A. Grillo,[136] K. Grimm,[72] S. Grinstein,[12,p] Ph. Gris,[34] J.-F. Grivaz,[116] S. Groh,[83] J. P. Grohs,[44] E. Gross,[171] J. Grosse-Knetter,[54] G. C. Grossi,[79] Z. J. Grout,[148] L. Guan,[89] W. Guan,[172] J. Guenther,[127] F. Guescini,[49] D. Guest,[162] O. Gueta,[152] E. Guido,[50a,50b] T. Guillemin,[5] S. Guindon,[2] U. Gul,[53] C. Gumpert,[30] J. Guo,[33e] Y. Guo,[33b,n] S. Gupta,[119] G. Gustavino,[131a,131b] P. Gutierrez,[112] N. G. Gutierrez Ortiz,[78] C. Gutschow,[44] C. Guyot,[135] C. Gwenlan,[119] C. B. Gwilliam,[74] A. Haas,[109] C. Haber,[15] H. K. Hadavand,[8] N. Haddad,[134e] A. Hadef,[85] P. Haefner,[21] S. Hageböck,[21] Z. Hajduk,[39] H. Hakobyan,[176,†] M. Haleem,[42] J. Haley,[113] D. Hall,[119] G. Halladjian,[90] G. D. Hallewell,[85] K. Hamacher,[174] P. Hamal,[114] K. Hamano,[168] A. Hamilton,[144a] G. N. Hamity,[138] P. G. Hamnett,[42] L. Han,[33b] K. Hanagaki,[66,q] K. Hanawa,[154] M. Hance,[136] B. Haney,[121] P. Hanke,[58a] R. Hanna,[135] J. B. Hansen,[36] J. D. Hansen,[36] M. C. Hansen,[21] P. H. Hansen,[36] K. Hara,[159] A. S. Hard,[172] T. Harenberg,[174] F. Hariri,[116] S. Harkusha,[92] R. D. Harrington,[46] P. F. Harrison,[169] F. Hartjes,[106] M. Hasegawa,[67] Y. Hasegawa,[139] A. Hasib,[112] S. Hassani,[135] S. Haug,[17] R. Hauser,[90] L. Hauswald,[44] M. Havranek,[126] C. M. Hawkes,[18] R. J. Hawkings,[30] A. D. Hawkins,[81] D. Hayden,[90] C. P. Hays,[119] J. M. Hays,[76] H. S. Hayward,[74]

S. J. Haywood,[130] S. J. Head,[18] T. Heck,[83] V. Hedberg,[81] L. Heelan,[8] S. Heim,[121] T. Heim,[15] B. Heinemann,[15] J. J. Heinrich,[99] L. Heinrich,[109] C. Heinz,[52] J. Hejbal,[126] L. Helary,[22] S. Hellman,[145a,145b] C. Helsens,[30] J. Henderson,[119] R. C. W. Henderson,[72] Y. Heng,[172] S. Henkelmann,[167] A. M. Henriques Correia,[30] S. Henrot-Versille,[116] G. H. Herbert,[16] Y. Hernández Jiménez,[166] G. Herten,[48] R. Hertenberger,[99] L. Hervas,[30] G. G. Hesketh,[78] N. P. Hessey,[106] J. W. Hetherly,[40] R. Hickling,[76] E. Higón-Rodriguez,[166] E. Hill,[168] J. C. Hill,[28] K. H. Hiller,[42] S. J. Hillier,[18] I. Hinchliffe,[15] E. Hines,[121] R. R. Hinman,[15] M. Hirose,[156] D. Hirschbuehl,[174] J. Hobbs,[147] N. Hod,[106] M. C. Hodgkinson,[138] P. Hodgson,[138] A. Hoecker,[30] M. R. Hoeferkamp,[104] F. Hoenig,[99] M. Hohlfeld,[83] D. Hohn,[21] T. R. Holmes,[15] M. Homann,[43] T. M. Hong,[124] B. H. Hooberman,[164] W. H. Hopkins,[115] Y. Horii,[102] A. J. Horton,[141] J-Y. Hostachy,[55] S. Hou,[150] A. Hoummada,[134a] J. Howard,[119] J. Howarth,[42] M. Hrabovsky,[114] I. Hristova,[16] J. Hrivnac,[116] T. Hryn'ova,[5] A. Hrynevich,[93] C. Hsu,[144c] P. J. Hsu,[150,r] S.-C. Hsu,[137] D. Hu,[35] Q. Hu,[33b] Y. Huang,[42] Z. Hubacek,[127] F. Hubaut,[85] F. Huegging,[21] T. B. Huffman,[119] E. W. Hughes,[35] G. Hughes,[72] M. Huhtinen,[30] T. A. Hülsing,[83] N. Huseynov,[65,b] J. Huston,[90] J. Huth,[57] G. Iacobucci,[49] G. Iakovidis,[25] I. Ibragimov,[140] L. Iconomidou-Fayard,[116] E. Ideal,[175] Z. Idrissi,[134e] P. Iengo,[30] O. Igonkina,[106] T. Iizawa,[170] Y. Ikegami,[66] M. Ikeno,[66] Y. Ilchenko,[31,s] D. Iliadis,[153] N. Ilic,[142] T. Ince,[100] G. Introzzi,[120a,120b] P. Ioannou,[9,†] M. Iodice,[133a] K. Iordanidou,[35] V. Ippolito,[57] A. Irles Quiles,[166] C. Isaksson,[165] M. Ishino,[68] M. Ishitsuka,[156] R. Ishmukhametov,[110] C. Issever,[119] S. Istin,[19a] F. Ito,[159] J. M. Iturbe Ponce,[84] R. Iuppa,[132a,132b] J. Ivarsson,[81] W. Iwanski,[39] H. Iwasaki,[66] J. M. Izen,[41] V. Izzo,[103a] S. Jabbar,[3] B. Jackson,[121] M. Jackson,[74] P. Jackson,[1] V. Jain,[2] K. B. Jakobi,[83] K. Jakobs,[48] S. Jakobsen,[30] T. Jakoubek,[126] D. O. Jamin,[113] D. K. Jana,[79] E. Jansen,[78] R. Jansky,[62] J. Janssen,[21] M. Janus,[54] G. Jarlskog,[81] N. Javadov,[65,b] T. Javůrek,[48] F. Jeanneau,[135] L. Jeanty,[15] J. Jejelava,[51a,t] G.-Y. Jeng,[149] D. Jennens,[88] P. Jenni,[48,u] J. Jentzsch,[43] C. Jeske,[169] S. Jézéquel,[5] H. Ji,[172] J. Jia,[147] H. Jiang,[64] Y. Jiang,[33b] S. Jiggins,[78] J. Jimenez Pena,[166] S. Jin,[33a] A. Jinaru,[26b] O. Jinnouchi,[156] P. Johansson,[138] K. A. Johns,[7] W. J. Johnson,[137] K. Jon-And,[145a,145b] G. Jones,[169] R. W. L. Jones,[72] S. Jones,[7] T. J. Jones,[74] J. Jongmanns,[58a] P. M. Jorge,[125a,125b] J. Jovicevic,[158a] X. Ju,[172] A. Juste Rozas,[12,p] M. K. Köhler,[171] A. Kaczmarska,[39] M. Kado,[116] H. Kagan,[110] M. Kagan,[142] S. J. Kahn,[85] E. Kajomovitz,[45] C. W. Kalderon,[119] A. Kaluza,[83] S. Kama,[40] A. Kamenshchikov,[129] N. Kanaya,[154] S. Kaneti,[28] V. A. Kantserov,[97] J. Kanzaki,[66] B. Kaplan,[109] L. S. Kaplan,[172] A. Kapliy,[31] D. Kar,[144c] K. Karakostas,[10] A. Karamaoun,[3] N. Karastathis,[10,106] M. J. Kareem,[54] E. Karentzos,[10] M. Karnevskiy,[83] S. N. Karpov,[65] Z. M. Karpova,[65] K. Karthik,[109] V. Kartvelishvili,[72] A. N. Karyukhin,[129] K. Kasahara,[159] L. Kashif,[172] R. D. Kass,[110] A. Kastanas,[14] Y. Kataoka,[154] C. Kato,[154] A. Katre,[49] J. Katzy,[42] K. Kawade,[102] K. Kawagoe,[70] T. Kawamoto,[154] G. Kawamura,[54] S. Kazama,[154] V. F. Kazanin,[108,c] R. Keeler,[168] R. Kehoe,[40] J. S. Keller,[42] J. J. Kempster,[77] H. Keoshkerian,[84] O. Kepka,[126] B. P. Kerševan,[75] S. Kersten,[174] R. A. Keyes,[87] F. Khalil-zada,[11] H. Khandanyan,[145a,145b] A. Khanov,[113] A. G. Kharlamov,[108,c] T. J. Khoo,[28] V. Khovanskiy,[96] E. Khramov,[65] J. Khubua,[51b,v] S. Kido,[67] H. Y. Kim,[8] S. H. Kim,[159] Y. K. Kim,[31] N. Kimura,[153] O. M. Kind,[16] B. T. King,[74] M. King,[166] S. B. King,[167] J. Kirk,[130] A. E. Kiryunin,[100] T. Kishimoto,[67] D. Kisielewska,[38a] F. Kiss,[48] K. Kiuchi,[159] O. Kivernyk,[135] E. Kladiva,[143b] M. H. Klein,[35] M. Klein,[74] U. Klein,[74] K. Kleinknecht,[83] P. Klimek,[145a,145b] A. Klimentov,[25] R. Klingenberg,[43] J. A. Klinger,[138] T. Klioutchnikova,[30] E.-E. Kluge,[58a] P. Kluit,[106] S. Kluth,[100] J. Knapik,[39] E. Kneringer,[62] E. B. F. G. Knoops,[85] A. Knue,[53] A. Kobayashi,[154] D. Kobayashi,[156] T. Kobayashi,[154] M. Kobel,[44] M. Kocian,[142] P. Kodys,[128] T. Koffas,[29] E. Koffeman,[106] L. A. Kogan,[119] T. Kohriki,[66] T. Koi,[142] H. Kolanoski,[16] M. Kolb,[58b] I. Koletsou,[5] A. A. Komar,[95,†] Y. Komori,[154] T. Kondo,[66] N. Kondrashova,[42] K. Köneke,[48] A. C. König,[105] T. Kono,[66,w] R. Konoplich,[109,x] N. Konstantinidis,[78] R. Kopeliansky,[61] S. Koperny,[38a] L. Köpke,[83] A. K. Kopp,[48] K. Korcyl,[39] K. Kordas,[153] A. Korn,[78] A. A. Korol,[108,c] I. Korolkov,[12] E. V. Korolkova,[138] O. Kortner,[100] S. Kortner,[100] T. Kosek,[128] V. V. Kostyukhin,[21] V. M. Kotov,[65] A. Kotwal,[45] A. Kourkoumeli-Charalampidi,[153] C. Kourkoumelis,[9] V. Kouskoura,[25] A. Koutsman,[158a] A. B. Kowalewska,[39] R. Kowalewski,[168] T. Z. Kowalski,[38a] W. Kozanecki,[135] A. S. Kozhin,[129] V. A. Kramarenko,[98] G. Kramberger,[75] D. Krasnopevtsev,[97] M. W. Krasny,[80] A. Krasznahorkay,[30] J. K. Kraus,[21] A. Kravchenko,[25] M. Kretz,[58c] J. Kretzschmar,[74] K. Kreutzfeldt,[52] P. Krieger,[157] K. Krizka,[31] K. Kroeninger,[43] H. Kroha,[100] J. Kroll,[121] J. Kroseberg,[21] J. Krstic,[13] U. Kruchonak,[65] H. Krüger,[21] N. Krumnack,[64] A. Kruse,[172] M. C. Kruse,[45] M. Kruskal,[22] T. Kubota,[88] H. Kucuk,[78] S. Kuday,[4b] J. T. Kuechler,[174] S. Kuehn,[48] A. Kugel,[58c] F. Kuger,[173] A. Kuhl,[136] T. Kuhl,[42] V. Kukhtin,[65] R. Kukla,[135] Y. Kulchitsky,[92] S. Kuleshov,[32b] M. Kuna,[131a,131b] T. Kunigo,[68] A. Kupco,[126] H. Kurashige,[67] Y. A. Kurochkin,[92] V. Kus,[126] E. S. Kuwertz,[168] M. Kuze,[156] J. Kvita,[114] T. Kwan,[168] D. Kyriazopoulos,[138] A. La Rosa,[100] J. L. La Rosa Navarro,[24d] L. La Rotonda,[37a,37b] C. Lacasta,[166] F. Lacava,[131a,131b] J. Lacey,[29] H. Lacker,[16] D. Lacour,[80] V. R. Lacuesta,[166] E. Ladygin,[65] R. Lafaye,[5] B. Laforge,[80] T. Lagouri,[175] S. Lai,[54] S. Lammers,[61] W. Lampl,[7] E. Lançon,[135] U. Landgraf,[48] M. P. J. Landon,[76] V. S. Lang,[58a] J. C. Lange,[12] A. J. Lankford,[162] F. Lanni,[25] K. Lantzsch,[21] A. Lanza,[120a]

S. Laplace,[80] C. Lapoire,[30] J. F. Laporte,[135] T. Lari,[91a] F. Lasagni Manghi,[20a,20b] M. Lassnig,[30] P. Laurelli,[47] W. Lavrijsen,[15] A. T. Law,[136] P. Laycock,[74] T. Lazovich,[57] O. Le Dortz,[80] E. Le Guirriec,[85] E. Le Menedeu,[12] E. P. Le Quilleuc,[135] M. LeBlanc,[168] T. LeCompte,[6] F. Ledroit-Guillon,[55] C. A. Lee,[25] S. C. Lee,[150] L. Lee,[1] G. Lefebvre,[80] M. Lefebvre,[168] F. Legger,[99] C. Leggett,[15] A. Lehan,[74] G. Lehmann Miotto,[30] X. Lei,[7] W. A. Leight,[29] A. Leisos,[153,y] A. G. Leister,[175] M. A. L. Leite,[24d] R. Leitner,[128] D. Lellouch,[171] B. Lemmer,[54] K. J. C. Leney,[78] T. Lenz,[21] B. Lenzi,[30] R. Leone,[7] S. Leone,[123a,123b] C. Leonidopoulos,[46] S. Leontsinis,[10] C. Leroy,[94] A. A. J. Lesage,[135] C. G. Lester,[28] M. Levchenko,[122] J. Levêque,[5] D. Levin,[89] L. J. Levinson,[171] M. Levy,[18] A. M. Leyko,[21] M. Leyton,[41] B. Li,[33b,z] H. Li,[147] H. L. Li,[31] L. Li,[45] L. Li,[33e] Q. Li,[33a] S. Li,[45] X. Li,[84] Y. Li,[140] Z. Liang,[136] H. Liao,[34] B. Liberti,[132a] A. Liblong,[157] P. Lichard,[30] K. Lie,[164] J. Liebal,[21] W. Liebig,[14] C. Limbach,[21] A. Limosani,[149] S. C. Lin,[150,aa] T. H. Lin,[83] B. E. Lindquist,[147] E. Lipeles,[121] A. Lipniacka,[14] M. Lisovyi,[58b] T. M. Liss,[164] D. Lissauer,[25] A. Lister,[167] A. M. Litke,[136] B. Liu,[150,bb] D. Liu,[150] H. Liu,[89] H. Liu,[25] J. Liu,[85] J. B. Liu,[33b] K. Liu,[85] L. Liu,[164] M. Liu,[45] M. Liu,[33b] Y. L. Liu,[33b] Y. Liu,[33b] M. Livan,[120a,120b] A. Lleres,[55] J. Llorente Merino,[82] S. L. Lloyd,[76] F. Lo Sterzo,[150] E. Lobodzinska,[42] P. Loch,[7] W. S. Lockman,[136] F. K. Loebinger,[84] A. E. Loevschall-Jensen,[36] K. M. Loew,[23] A. Loginov,[175] T. Lohse,[16] K. Lohwasser,[42] M. Lokajicek,[126] B. A. Long,[22] J. D. Long,[164] R. E. Long,[72] L. Longo,[73a,73b] K. A. Looper,[110] L. Lopes,[125a] D. Lopez Mateos,[57] B. Lopez Paredes,[138] I. Lopez Paz,[12] A. Lopez Solis,[80] J. Lorenz,[99] N. Lorenzo Martinez,[61] M. Losada,[161] P. J. Lösel,[99] X. Lou,[33a] A. Lounis,[116] J. Love,[6] P. A. Love,[72] H. Lu,[60a] N. Lu,[89] H. J. Lubatti,[137] C. Luci,[131a,131b] A. Lucotte,[55] C. Luedtke,[48] F. Luehring,[61] W. Lukas,[62] L. Luminari,[131a] O. Lundberg,[145a,145b] B. Lund-Jensen,[146] D. Lynn,[25] R. Lysak,[126] E. Lytken,[81] H. Ma,[25] L. L. Ma,[33d] G. Maccarrone,[47] A. Macchiolo,[100] C. M. Macdonald,[138] B. Maček,[75] J. Machado Miguens,[121,125b] D. Madaffari,[85] R. Madar,[34] H. J. Maddocks,[165] W. F. Mader,[44] A. Madsen,[42] J. Maeda,[67] S. Maeland,[14] T. Maeno,[25] A. Maevskiy,[98] E. Magradze,[54] J. Mahlstedt,[106] C. Maiani,[116] C. Maidantchik,[24a] A. A. Maier,[100] T. Maier,[99] A. Maio,[125a,125b,125d] S. Majewski,[115] Y. Makida,[66] N. Makovec,[116] B. Malaescu,[80] Pa. Malecki,[39] V. P. Maleev,[122] F. Malek,[55] U. Mallik,[63] D. Malon,[6] C. Malone,[142] S. Maltezos,[10] V. M. Malyshev,[108] S. Malyukov,[30] J. Mamuzic,[42] G. Mancini,[47] B. Mandelli,[30] L. Mandelli,[91a] I. Mandić,[75] J. Maneira,[125a,125b] L. Manhaes de Andrade Filho,[24b] J. Manjarres Ramos,[158b] A. Mann,[99] B. Mansoulie,[135] R. Mantifel,[87] M. Mantoani,[54] S. Manzoni,[91a,91b] L. Mapelli,[30] G. Marceca,[27] L. March,[49] G. Marchiori,[80] M. Marcisovsky,[126] M. Marjanovic,[13] D. E. Marley,[89] F. Marroquim,[24a] S. P. Marsden,[84] Z. Marshall,[15] L. F. Marti,[17] S. Marti-Garcia,[166] B. Martin,[90] T. A. Martin,[169] V. J. Martin,[46] B. Martin dit Latour,[14] M. Martinez,[12,p] S. Martin-Haugh,[130] V. S. Martoiu,[26b] A. C. Martyniuk,[78] M. Marx,[137] F. Marzano,[131a] A. Marzin,[30] L. Masetti,[83] T. Mashimo,[154] R. Mashinistov,[95] J. Masik,[84] A. L. Maslennikov,[108,c] I. Massa,[20a,20b] L. Massa,[20a,20b] P. Mastrandrea,[5] A. Mastroberardino,[37a,37b] T. Masubuchi,[154] P. Mättig,[174] J. Mattmann,[83] J. Maurer,[26b] S. J. Maxfield,[74] D. A. Maximov,[108,c] R. Mazini,[150] S. M. Mazza,[91a,91b] N. C. Mc Fadden,[104] G. Mc Goldrick,[157] S. P. Mc Kee,[89] A. McCarn,[89] R. L. McCarthy,[147] T. G. McCarthy,[29] L. I. McClymont,[78] K. W. McFarlane,[56,†] J. A. Mcfayden,[78] G. Mchedlidze,[54] S. J. McMahon,[130] R. A. McPherson,[168,l] M. Medinnis,[42] S. Meehan,[137] S. Mehlhase,[99] A. Mehta,[74] K. Meier,[58a] C. Meineck,[99] B. Meirose,[41] B. R. Mellado Garcia,[144c] F. Meloni,[17] A. Mengarelli,[20a,20b] S. Menke,[100] E. Meoni,[160] K. M. Mercurio,[57] S. Mergelmeyer,[16] P. Mermod,[49] L. Merola,[103a,103b] C. Meroni,[91a] F. S. Merritt,[31] A. Messina,[131a,131b] J. Metcalfe,[6] A. S. Mete,[162] C. Meyer,[83] C. Meyer,[121] J-P. Meyer,[135] J. Meyer,[106] H. Meyer Zu Theenhausen,[58a] R. P. Middleton,[130] S. Miglioranzi,[163a,163c] L. Mijović,[21] G. Mikenberg,[171] M. Mikestikova,[126] M. Mikuž,[75] M. Milesi,[88] A. Milic,[30] D. W. Miller,[31] C. Mills,[46] A. Milov,[171] D. A. Milstead,[145a,145b] A. A. Minaenko,[129] Y. Minami,[154] I. A. Minashvili,[65] A. I. Mincer,[109] B. Mindur,[38a] M. Mineev,[65] Y. Ming,[172] L. M. Mir,[12] K. P. Mistry,[121] T. Mitani,[170] J. Mitrevski,[99] V. A. Mitsou,[166] A. Miucci,[49] P. S. Miyagawa,[138] J. U. Mjörnmark,[81] T. Moa,[145a,145b] K. Mochizuki,[85] S. Mohapatra,[35] W. Mohr,[48] S. Molander,[145a,145b] R. Moles-Valls,[21] R. Monden,[68] M. C. Mondragon,[90] K. Mönig,[42] J. Monk,[36] E. Monnier,[85] A. Montalbano,[147] J. Montejo Berlingen,[30] F. Monticelli,[71] S. Monzani,[91a,91b] R. W. Moore,[3] N. Morange,[116] D. Moreno,[161] M. Moreno Llácer,[54] P. Morettini,[50a] D. Mori,[141] T. Mori,[154] M. Morii,[57] M. Morinaga,[154] V. Morisbak,[118] S. Moritz,[83] A. K. Morley,[149] G. Mornacchi,[30] J. D. Morris,[76] S. S. Mortensen,[36] L. Morvaj,[147] M. Mosidze,[51b] J. Moss,[142] K. Motohashi,[156] R. Mount,[142] E. Mountricha,[25] S. V. Mouraviev,[95,†] E. J. W. Moyse,[86] S. Muanza,[85] R. D. Mudd,[18] F. Mueller,[100] J. Mueller,[124] R. S. P. Mueller,[99] T. Mueller,[28] D. Muenstermann,[72] P. Mullen,[53] G. A. Mullier,[17] F. J. Munoz Sanchez,[84] J. A. Murillo Quijada,[18] W. J. Murray,[169,130] H. Musheghyan,[54] A. G. Myagkov,[129,cc] M. Myska,[127] B. P. Nachman,[142] O. Nackenhorst,[49] J. Nadal,[54] K. Nagai,[119] R. Nagai,[66,w] Y. Nagai,[85] K. Nagano,[66] Y. Nagasaka,[59] K. Nagata,[159] M. Nagel,[100] E. Nagy,[85] A. M. Nairz,[30] Y. Nakahama,[30] K. Nakamura,[66] T. Nakamura,[154] I. Nakano,[111] H. Namasivayam,[41] R. F. Naranjo Garcia,[42] R. Narayan,[31] D. I. Narrias Villar,[58a] I. Naryshkin,[122] T. Naumann,[42]

G. Navarro,[161] R. Nayyar,[7] H. A. Neal,[89] P. Yu. Nechaeva,[95] T. J. Neep,[84] P. D. Nef,[142] A. Negri,[120a,120b] M. Negrini,[20a] S. Nektarijevic,[105] C. Nellist,[116] A. Nelson,[162] S. Nemecek,[126] P. Nemethy,[109] A. A. Nepomuceno,[24a] M. Nessi,[30,dd] M. S. Neubauer,[164] M. Neumann,[174] R. M. Neves,[109] P. Nevski,[25] P. R. Newman,[18] D. H. Nguyen,[6] R. B. Nickerson,[119] R. Nicolaidou,[135] B. Nicquevert,[30] J. Nielsen,[136] A. Nikiforov,[16] V. Nikolaenko,[129,cc] I. Nikolic-Audit,[80] K. Nikolopoulos,[18] J. K. Nilsen,[118] P. Nilsson,[25] Y. Ninomiya,[154] A. Nisati,[131a] R. Nisius,[100] T. Nobe,[154] L. Nodulman,[6] M. Nomachi,[117] I. Nomidis,[29] T. Nooney,[76] S. Norberg,[112] M. Nordberg,[30] O. Novgorodova,[44] S. Nowak,[100] M. Nozaki,[66] L. Nozka,[114] K. Ntekas,[10] E. Nurse,[78] F. Nuti,[88] F. O'grady,[7] D. C. O'Neil,[141] A. A. O'Rourke,[42] V. O'Shea,[53] F. G. Oakham,[29,d] H. Oberlack,[100] T. Obermann,[21] J. Ocariz,[80] A. Ochi,[67] I. Ochoa,[35] J. P. Ochoa-Ricoux,[32a] S. Oda,[70] S. Odaka,[66] H. Ogren,[61] A. Oh,[84] S. H. Oh,[45] C. C. Ohm,[15] H. Ohman,[165] H. Oide,[30] H. Okawa,[159] Y. Okumura,[31] T. Okuyama,[66] A. Olariu,[26b] L. F. Oleiro Seabra,[125a] S. A. Olivares Pino,[46] D. Oliveira Damazio,[25] A. Olszewski,[39] J. Olszowska,[39] A. Onofre,[125a,125e] K. Onogi,[102] P. U. E. Onyisi,[31,s] C. J. Oram,[158a] M. J. Oreglia,[31] Y. Oren,[152] D. Orestano,[133a,133b] N. Orlando,[60b] R. S. Orr,[157] B. Osculati,[50a,50b] R. Ospanov,[84] G. Otero y Garzon,[27] H. Otono,[70] M. Ouchrif,[134d] F. Ould-Saada,[118] A. Ouraou,[135] K. P. Oussoren,[106] Q. Ouyang,[33a] A. Ovcharova,[15] M. Owen,[53] R. E. Owen,[18] V. E. Ozcan,[19a] N. Ozturk,[8] K. Pachal,[141] A. Pacheco Pages,[12] C. Padilla Aranda,[12] M. Pagáčová,[48] S. Pagan Griso,[15] F. Paige,[25] P. Pais,[86] K. Pajchel,[118] G. Palacino,[158b] S. Palestini,[30] M. Palka,[38b] D. Pallin,[34] A. Palma,[125a,125b] E. St. Panagiotopoulou,[10] C. E. Pandini,[80] J. G. Panduro Vazquez,[77] P. Pani,[145a,145b] S. Panitkin,[25] D. Pantea,[26b] L. Paolozzi,[49] Th. D. Papadopoulou,[10] K. Papageorgiou,[153] A. Paramonov,[6] D. Paredes Hernandez,[175] M. A. Parker,[28] K. A. Parker,[138] F. Parodi,[50a,50b] J. A. Parsons,[35] U. Parzefall,[48] V. Pascuzzi,[157] E. Pasqualucci,[131a] S. Passaggio,[50a] F. Pastore,[133a,133b,†] Fr. Pastore,[77] G. Pásztor,[29] S. Pataraia,[174] N. D. Patel,[149] J. R. Pater,[84] T. Pauly,[30] J. Pearce,[168] B. Pearson,[112] L. E. Pedersen,[36] M. Pedersen,[118] S. Pedraza Lopez,[166] R. Pedro,[125a,125b] S. V. Peleganchuk,[108,c] D. Pelikan,[165] O. Penc,[126] C. Peng,[33a] H. Peng,[33b] J. Penwell,[61] B. S. Peralva,[24b] D. V. Perepelitsa,[25] E. Perez Codina,[158a] L. Perini,[91a,91b] H. Pernegger,[30] S. Perrella,[103a,103b] R. Peschke,[42] V. D. Peshekhonov,[65] K. Peters,[30] R. F. Y. Peters,[84] B. A. Petersen,[30] T. C. Petersen,[36] E. Petit,[55] A. Petridis,[1] C. Petridou,[153] P. Petroff,[116] E. Petrolo,[131a] M. Petrov,[119] F. Petrucci,[133a,133b] N. E. Pettersson,[156] A. Peyaud,[135] R. Pezoa,[32b] P. W. Phillips,[130] G. Piacquadio,[142] E. Pianori,[169] A. Picazio,[86] E. Piccaro,[76] M. Piccinini,[20a,20b] M. A. Pickering,[119] R. Piegaia,[27] J. E. Pilcher,[31] A. D. Pilkington,[84] A. W. J. Pin,[84] J. Pina,[125a,125b,125d] M. Pinamonti,[163a,163c,ee] J. L. Pinfold,[3] A. Pingel,[36] S. Pires,[80] H. Pirumov,[42] M. Pitt,[171] L. Plazak,[143a] M.-A. Pleier,[25] V. Pleskot,[83] E. Plotnikova,[65] P. Plucinski,[145a,145b] D. Pluth,[64] R. Poettgen,[145a,145b] L. Poggioli,[116] D. Pohl,[21] G. Polesello,[120a] A. Poley,[42] A. Policicchio,[37a,37b] R. Polifka,[157] A. Polini,[20a] C. S. Pollard,[53] V. Polychronakos,[25] K. Pommès,[30] L. Pontecorvo,[131a] B. G. Pope,[90] G. A. Popeneciu,[26c] D. S. Popovic,[13] A. Poppleton,[30] S. Pospisil,[127] K. Potamianos,[15] I. N. Potrap,[65] C. J. Potter,[28] C. T. Potter,[115] G. Poulard,[30] J. Poveda,[30] V. Pozdnyakov,[65] M. E. Pozo Astigarraga,[30] P. Pralavorio,[85] A. Pranko,[15] S. Prell,[64] D. Price,[84] L. E. Price,[6] M. Primavera,[73a] S. Prince,[87] M. Proissl,[46] K. Prokofiev,[60c] F. Prokoshin,[32b] S. Protopopescu,[25] J. Proudfoot,[6] M. Przybycien,[38a] D. Puddu,[133a,133b] D. Puldon,[147] M. Purohit,[25,ff] P. Puzo,[116] J. Qian,[89] G. Qin,[53] Y. Qin,[84] A. Quadt,[54] D. R. Quarrie,[15] W. B. Quayle,[163a,163b] M. Queitsch-Maitland,[84] D. Quilty,[53] S. Raddum,[118] V. Radeka,[25] V. Radescu,[42] S. K. Radhakrishnan,[147] P. Radloff,[115] P. Rados,[88] F. Ragusa,[91a,91b] G. Rahal,[177] S. Rajagopalan,[25] M. Rammensee,[30] C. Rangel-Smith,[165] M. G. Ratti,[91a,91b] F. Rauscher,[99] S. Rave,[83] T. Ravenscroft,[53] M. Raymond,[30] A. L. Read,[118] N. P. Readioff,[74] D. M. Rebuzzi,[120a,120b] A. Redelbach,[173] G. Redlinger,[25] R. Reece,[136] K. Reeves,[41] L. Rehnisch,[16] J. Reichert,[121] H. Reisin,[27] C. Rembser,[30] H. Ren,[33a] M. Rescigno,[131a] S. Resconi,[91a] O. L. Rezanova,[108,c] P. Reznicek,[128] R. Rezvani,[94] R. Richter,[100] S. Richter,[78] E. Richter-Was,[38b] O. Ricken,[21] M. Ridel,[80] P. Rieck,[16] C. J. Riegel,[174] J. Rieger,[54] O. Rifki,[112] M. Rijssenbeek,[147] A. Rimoldi,[120a,120b] L. Rinaldi,[20a] B. Ristić,[49] E. Ritsch,[30] I. Riu,[12] F. Rizatdinova,[113] E. Rizvi,[76] S. H. Robertson,[87,l] A. Robichaud-Veronneau,[87] D. Robinson,[28] J. E. M. Robinson,[42] A. Robson,[53] C. Roda,[123a,123b] Y. Rodina,[85] A. Rodriguez Perez,[12] D. Rodriguez Rodriguez,[166] S. Roe,[30] C. S. Rogan,[57] O. Røhne,[118] A. Romaniouk,[97] M. Romano,[20a,20b] S. M. Romano Saez,[34] E. Romero Adam,[166] N. Rompotis,[137] M. Ronzani,[48] L. Roos,[80] E. Ros,[166] S. Rosati,[131a] K. Rosbach,[48] P. Rose,[136] O. Rosenthal,[140] V. Rossetti,[145a,145b] E. Rossi,[103a,103b] L. P. Rossi,[50a] J. H. N. Rosten,[28] R. Rosten,[137] M. Rotaru,[26b] I. Roth,[171] J. Rothberg,[137] D. Rousseau,[116] C. R. Royon,[135] A. Rozanov,[85] Y. Rozen,[151] X. Ruan,[144c] F. Rubbo,[142] I. Rubinskiy,[42] V. I. Rud,[98] M. S. Rudolph,[157] F. Rühr,[48] A. Ruiz-Martinez,[30] Z. Rurikova,[48] N. A. Rusakovich,[65] A. Ruschke,[99] H. L. Russell,[137] J. P. Rutherfoord,[7] N. Ruthmann,[30] Y. F. Ryabov,[122] M. Rybar,[164] G. Rybkin,[116] S. Ryu,[6] A. Ryzhov,[129] A. F. Saavedra,[149] G. Sabato,[106] S. Sacerdoti,[27] H. F-W. Sadrozinski,[136] R. Sadykov,[65] F. Safai Tehrani,[131a] P. Saha,[107] M. Sahinsoy,[58a] M. Saimpert,[135] T. Saito,[154] H. Sakamoto,[154] Y. Sakurai,[170]

G. Salamanna,[133a,133b] A. Salamon,[132a,132b] J. E. Salazar Loyola,[32b] D. Salek,[106] P. H. Sales De Bruin,[137] D. Salihagic,[100] A. Salnikov,[142] J. Salt,[166] D. Salvatore,[37a,37b] F. Salvatore,[148] A. Salvucci,[60a] A. Salzburger,[30] D. Sammel,[48] D. Sampsonidis,[153] A. Sanchez,[103a,103b] J. Sánchez,[166] V. Sanchez Martinez,[166] H. Sandaker,[118] R. L. Sandbach,[76] H. G. Sander,[83] M. P. Sanders,[99] M. Sandhoff,[174] C. Sandoval,[161] R. Sandstroem,[100] D. P. C. Sankey,[130] M. Sannino,[50a,50b] A. Sansoni,[47] C. Santoni,[34] R. Santonico,[132a,132b] H. Santos,[125a] I. Santoyo Castillo,[148] K. Sapp,[124] A. Sapronov,[65] J. G. Saraiva,[125a,125d] B. Sarrazin,[21] O. Sasaki,[66] Y. Sasaki,[154] K. Sato,[159] G. Sauvage,[5,†] E. Sauvan,[5] G. Savage,[77] P. Savard,[157,d] C. Sawyer,[130] L. Sawyer,[79,o] J. Saxon,[31] C. Sbarra,[20a] A. Sbrizzi,[20a,20b] T. Scanlon,[78] D. A. Scannicchio,[162] M. Scarcella,[149] V. Scarfone,[37a,37b] J. Schaarschmidt,[171] P. Schacht,[100] D. Schaefer,[30] R. Schaefer,[42] J. Schaeffer,[83] S. Schaepe,[21] S. Schaetzel,[58b] U. Schäfer,[83] A. C. Schaffer,[116] D. Schaile,[99] R. D. Schamberger,[147] V. Scharf,[58a] V. A. Schegelsky,[122] D. Scheirich,[128] M. Schernau,[162] C. Schiavi,[50a,50b] C. Schillo,[48] M. Schioppa,[37a,37b] S. Schlenker,[30] K. Schmieden,[30] C. Schmitt,[83] S. Schmitt,[42] S. Schmitz,[83] B. Schneider,[158a] Y. J. Schnellbach,[74] U. Schnoor,[48] L. Schoeffel,[135] A. Schoening,[58b] B. D. Schoenrock,[90] E. Schopf,[21] A. L. S. Schorlemmer,[43] M. Schott,[83] D. Schouten,[158a] J. Schovancova,[8] S. Schramm,[49] M. Schreyer,[173] N. Schuh,[83] M. J. Schultens,[21] H.-C. Schultz-Coulon,[58a] H. Schulz,[16] M. Schumacher,[48] B. A. Schumm,[136] Ph. Schune,[135] C. Schwanenberger,[84] A. Schwartzman,[142] T. A. Schwarz,[89] Ph. Schwegler,[100] H. Schweiger,[84] Ph. Schwemling,[135] R. Schwienhorst,[90] J. Schwindling,[135] T. Schwindt,[21] G. Sciolla,[23] F. Scuri,[123a,123b] F. Scutti,[88] J. Searcy,[89] P. Seema,[21] S. C. Seidel,[104] A. Seiden,[136] F. Seifert,[127] J. M. Seixas,[24a] G. Sekhniaidze,[103a] K. Sekhon,[89] S. J. Sekula,[40] D. M. Seliverstov,[122,†] N. Semprini-Cesari,[20a,20b] C. Serfon,[30] L. Serin,[116] L. Serkin,[163a,163b] M. Sessa,[133a,133b] R. Seuster,[158a] H. Severini,[112] T. Sfiligoj,[75] F. Sforza,[30] A. Sfyrla,[49] E. Shabalina,[54] N. W. Shaikh,[145a,145b] L. Y. Shan,[33a] R. Shang,[164] J. T. Shank,[22] M. Shapiro,[15] P. B. Shatalov,[96] K. Shaw,[163a,163b] S. M. Shaw,[84] A. Shcherbakova,[145a,145b] C. Y. Shehu,[148] P. Sherwood,[78] L. Shi,[150,gg] S. Shimizu,[67] C. O. Shimmin,[162] M. Shimojima,[101] M. Shiyakova,[65,hh] A. Shmeleva,[95] D. Shoaleh Saadi,[94] M. J. Shochet,[31] S. Shojaii,[91a,91b] S. Shrestha,[110] E. Shulga,[97] M. A. Shupe,[7] P. Sicho,[126] P. E. Sidebo,[146] O. Sidiropoulou,[173] D. Sidorov,[113] A. Sidoti,[20a,20b] F. Siegert,[44] Dj. Sijacki,[13] J. Silva,[125a,125d] S. B. Silverstein,[145a] V. Simak,[127] O. Simard,[5] Lj. Simic,[13] S. Simion,[116] E. Simioni,[83] B. Simmons,[78] D. Simon,[34] M. Simon,[83] P. Sinervo,[157] N. B. Sinev,[115] M. Sioli,[20a,20b] G. Siragusa,[173] S. Yu. Sivoklokov,[98] J. Sjölin,[145a,145b] T. B. Sjursen,[14] M. B. Skinner,[72] H. P. Skottowe,[57] P. Skubic,[112] M. Slater,[18] T. Slavicek,[127] M. Slawinska,[106] K. Sliwa,[160] V. Smakhtin,[171] B. H. Smart,[5] L. Smestad,[14] S. Yu. Smirnov,[97] Y. Smirnov,[97] L. N. Smirnova,[98,ii] O. Smirnova,[81] M. N. K. Smith,[35] R. W. Smith,[35] M. Smizanska,[72] K. Smolek,[127] A. A. Snesarev,[95] G. Snidero,[76] S. Snyder,[25] R. Sobie,[168,l] F. Socher,[44] A. Soffer,[152] D. A. Soh,[150,gg] G. Sokhrannyi,[75] C. A. Solans Sanchez,[30] M. Solar,[127] E. Yu. Soldatov,[97] U. Soldevila,[166] A. A. Solodkov,[129] A. Soloshenko,[65] O. V. Solovyanov,[129] V. Solovyev,[122] P. Sommer,[48] H. Y. Song,[33b,z] N. Soni,[1] A. Sood,[15] A. Sopczak,[127] V. Sopko,[127] V. Sorin,[12] D. Sosa,[58b] C. L. Sotiropoulou,[123a,123b] R. Soualah,[163a,163c] A. M. Soukharev,[108,c] D. South,[42] B. C. Sowden,[77] S. Spagnolo,[73a,73b] M. Spalla,[123a,123b] M. Spangenberg,[169] F. Spanò,[77] D. Sperlich,[16] F. Spettel,[100] R. Spighi,[20a] G. Spigo,[30] L. A. Spiller,[88] M. Spousta,[128] R. D. St. Denis,[53,†] A. Stabile,[91a] S. Staerz,[30] J. Stahlman,[121] R. Stamen,[58a] S. Stamm,[16] E. Stanecka,[39] R. W. Stanek,[6] C. Stanescu,[133a] M. Stanescu-Bellu,[42] M. M. Stanitzki,[42] S. Stapnes,[118] E. A. Starchenko,[129] G. H. Stark,[31] J. Stark,[55] P. Staroba,[126] P. Starovoitov,[58a] R. Staszewski,[39] P. Steinberg,[25] B. Stelzer,[141] H. J. Stelzer,[30] O. Stelzer-Chilton,[158a] H. Stenzel,[52] G. A. Stewart,[53] J. A. Stillings,[21] M. C. Stockton,[87] M. Stoebe,[87] G. Stoicea,[26b] P. Stolte,[54] S. Stonjek,[100] A. R. Stradling,[8] A. Straessner,[44] M. E. Stramaglia,[17] J. Strandberg,[146] S. Strandberg,[145a,145b] A. Strandlie,[118] M. Strauss,[112] P. Strizenec,[143b] R. Ströhmer,[173] D. M. Strom,[115] R. Stroynowski,[40] A. Strubig,[105] S. A. Stucci,[17] B. Stugu,[14] N. A. Styles,[42] D. Su,[142] J. Su,[124] R. Subramaniam,[79] S. Suchek,[58a] Y. Sugaya,[117] M. Suk,[127] V. V. Sulin,[95] S. Sultansoy,[4c] T. Sumida,[68] S. Sun,[57] X. Sun,[33a] J. E. Sundermann,[48] K. Suruliz,[148] G. Susinno,[37a,37b] M. R. Sutton,[148] S. Suzuki,[66] M. Svatos,[126] M. Swiatlowski,[31] I. Sykora,[143a] T. Sykora,[128] D. Ta,[48] C. Taccini,[133a,133b] K. Tackmann,[42] J. Taenzer,[157] A. Taffard,[162] R. Tafirout,[158a] N. Taiblum,[152] H. Takai,[25] R. Takashima,[69] H. Takeda,[67] T. Takeshita,[139] Y. Takubo,[66] M. Talby,[85] A. A. Talyshev,[108,c] J. Y. C. Tam,[173] K. G. Tan,[88] J. Tanaka,[154] R. Tanaka,[116] S. Tanaka,[66] B. B. Tannenwald,[110] S. Tapia Araya,[32b] S. Tapprogge,[83] S. Tarem,[151] G. F. Tartarelli,[91a] P. Tas,[128] M. Tasevsky,[126] T. Tashiro,[68] E. Tassi,[37a,37b] A. Tavares Delgado,[125a,125b] Y. Tayalati,[134d] A. C. Taylor,[104] G. N. Taylor,[88] P. T. E. Taylor,[88] W. Taylor,[158b] F. A. Teischinger,[30] P. Teixeira-Dias,[77] K. K. Temming,[48] D. Temple,[141] H. Ten Kate,[30] P. K. Teng,[150] J. J. Teoh,[117] F. Tepel,[174] S. Terada,[66] K. Terashi,[154] J. Terron,[82] S. Terzo,[100] M. Testa,[47] R. J. Teuscher,[157,l] T. Theveneaux-Pelzer,[85] J. P. Thomas,[18] J. Thomas-Wilsker,[77] E. N. Thompson,[35] P. D. Thompson,[18] R. J. Thompson,[84] A. S. Thompson,[53] L. A. Thomsen,[175] E. Thomson,[121] M. Thomson,[28] M. J. Tibbetts,[15] R. E. Ticse Torres,[85]

V. O. Tikhomirov,[95,jj] Yu. A. Tikhonov,[108,c] S. Timoshenko,[97] E. Tiouchichine,[85] P. Tipton,[175] S. Tisserant,[85] K. Todome,[156] T. Todorov,[5,†] S. Todorova-Nova,[128] J. Tojo,[70] S. Tokár,[143a] K. Tokushuku,[66] E. Tolley,[57] L. Tomlinson,[84] M. Tomoto,[102] L. Tompkins,[142,kk] K. Toms,[104] B. Tong,[57] E. Torrence,[115] H. Torres,[141] E. Torró Pastor,[137] J. Toth,[85,ll] F. Touchard,[85] D. R. Tovey,[138] T. Trefzger,[173] L. Tremblet,[30] A. Tricoli,[30] I. M. Trigger,[158a] S. Trincaz-Duvoid,[80] M. F. Tripiana,[12] W. Trischuk,[157] B. Trocmé,[55] A. Trofymov,[42] C. Troncon,[91a] M. Trottier-McDonald,[15] M. Trovatelli,[168] L. Truong,[163a,163b] M. Trzebinski,[39] A. Trzupek,[39] J. C-L. Tseng,[119] P. V. Tsiareshka,[92] G. Tsipolitis,[10] N. Tsirintanis,[9] S. Tsiskaridze,[12] V. Tsiskaridze,[48] E. G. Tskhadadze,[51a] K. M. Tsui,[60a] I. I. Tsukerman,[96] V. Tsulaia,[15] S. Tsuno,[66] D. Tsybychev,[147] A. Tudorache,[26b] V. Tudorache,[26b] A. N. Tuna,[57] S. A. Tupputi,[20a,20b] S. Turchikhin,[98,ii] D. Turecek,[127] D. Turgeman,[171] R. Turra,[91a,91b] A. J. Turvey,[40] P. M. Tuts,[35] M. Tylmad,[145a,145b] M. Tyndel,[130] I. Ueda,[154] R. Ueno,[29] M. Ughetto,[145a,145b] F. Ukegawa,[159] G. Unal,[30] A. Undrus,[25] G. Unel,[162] F. C. Ungaro,[88] Y. Unno,[66] C. Unverdorben,[99] J. Urban,[143b] P. Urquijo,[88] P. Urrejola,[83] G. Usai,[8] A. Usanova,[62] L. Vacavant,[85] V. Vacek,[127] B. Vachon,[87] C. Valderanis,[83] E. Valdes Santurio,[145a,145b] N. Valencic,[106] S. Valentinetti,[20a,20b] A. Valero,[166] L. Valery,[12] S. Valkar,[128] S. Vallecorsa,[49] J. A. Valls Ferrer,[166] W. Van Den Wollenberg,[106] P. C. Van Der Deijl,[106] R. van der Geer,[106] H. van der Graaf,[106] N. van Eldik,[151] P. van Gemmeren,[6] J. Van Nieuwkoop,[141] I. van Vulpen,[106] M. C. van Woerden,[30] M. Vanadia,[131a,131b] W. Vandelli,[30] R. Vanguri,[121] A. Vaniachine,[6] P. Vankov,[106] G. Vardanyan,[176] R. Vari,[131a] E. W. Varnes,[7] T. Varol,[40] D. Varouchas,[80] A. Vartapetian,[8] K. E. Varvell,[149] F. Vazeille,[34] T. Vazquez Schroeder,[87] J. Veatch,[7] L. M. Veloce,[157] F. Veloso,[125a,125c] S. Veneziano,[131a] A. Ventura,[73a,73b] M. Venturi,[168] N. Venturi,[157] A. Venturini,[23] V. Vercesi,[120a] M. Verducci,[131a,131b] W. Verkerke,[106] J. C. Vermeulen,[106] A. Vest,[44,mm] M. C. Vetterli,[141,d] O. Viazlo,[81] I. Vichou,[164] T. Vickey,[138] O. E. Vickey Boeriu,[138] G. H. A. Viehhauser,[119] S. Viel,[15] R. Vigne,[62] M. Villa,[20a,20b] M. Villaplana Perez,[91a,91b] E. Vilucchi,[47] M. G. Vincter,[29] V. B. Vinogradov,[65] I. Vivarelli,[148] S. Vlachos,[10] M. Vlasak,[127] M. Vogel,[174] P. Vokac,[127] G. Volpi,[123a,123b] M. Volpi,[88] H. von der Schmitt,[100] E. von Toerne,[21] V. Vorobel,[128] K. Vorobev,[97] M. Vos,[166] R. Voss,[30] J. H. Vossebeld,[74] N. Vranjes,[13] M. Vranjes Milosavljevic,[13] V. Vrba,[126] M. Vreeswijk,[106] R. Vuillermet,[30] I. Vukotic,[31] Z. Vykydal,[127] P. Wagner,[21] W. Wagner,[174] H. Wahlberg,[71] S. Wahrmund,[44] J. Wakabayashi,[102] J. Walder,[72] R. Walker,[99] W. Walkowiak,[140] V. Wallangen,[145a,145b] C. Wang,[150] C. Wang,[33d,85] F. Wang,[172] H. Wang,[15] H. Wang,[40] J. Wang,[42] J. Wang,[149] K. Wang,[87] R. Wang,[6] S. M. Wang,[150] T. Wang,[21] T. Wang,[35] X. Wang,[175] C. Wanotayaroj,[115] A. Warburton,[87] C. P. Ward,[28] D. R. Wardrope,[78] A. Washbrook,[46] P. M. Watkins,[18] A. T. Watson,[18] I. J. Watson,[149] M. F. Watson,[18] G. Watts,[137] S. Watts,[84] B. M. Waugh,[78] S. Webb,[83] M. S. Weber,[17] S. W. Weber,[173] J. S. Webster,[6] A. R. Weidberg,[119] B. Weinert,[61] J. Weingarten,[54] C. Weiser,[48] H. Weits,[106] P. S. Wells,[30] T. Wenaus,[25] T. Wengler,[30] S. Wenig,[30] N. Wermes,[21] M. Werner,[48] P. Werner,[30] M. Wessels,[58a] J. Wetter,[160] K. Whalen,[115] A. M. Wharton,[72] A. White,[8] M. J. White,[1] R. White,[32b] S. White,[123a,123b] D. Whiteson,[162] F. J. Wickens,[130] W. Wiedenmann,[172] M. Wielers,[130] P. Wienemann,[21] C. Wiglesworth,[36] L. A. M. Wiik-Fuchs,[21] A. Wildauer,[100] H. G. Wilkens,[30] H. H. Williams,[121] S. Williams,[106] C. Willis,[90] S. Willocq,[86] J. A. Wilson,[18] I. Wingerter-Seez,[5] F. Winklmeier,[115] O. J. Winston,[148] B. T. Winter,[21] M. Wittgen,[142] J. Wittkowski,[99] A. Wolf,[83] S. J. Wollstadt,[83] M. W. Wolter,[39] H. Wolters,[125a,125c] B. K. Wosiek,[39] J. Wotschack,[30] M. J. Woudstra,[84] K. W. Wozniak,[39] M. Wu,[55] M. Wu,[31] S. L. Wu,[172] X. Wu,[49] Y. Wu,[89] T. R. Wyatt,[84] B. M. Wynne,[46] S. Xella,[36] D. Xu,[33a] L. Xu,[25] B. Yabsley,[149] S. Yacoob,[144a] R. Yakabe,[67] D. Yamaguchi,[156] Y. Yamaguchi,[117] A. Yamamoto,[66] S. Yamamoto,[154] T. Yamanaka,[154] K. Yamauchi,[102] Y. Yamazaki,[67] Z. Yan,[22] H. Yang,[33e] H. Yang,[172] Y. Yang,[150] Z. Yang,[14] W-M. Yao,[15] Y. C. Yap,[80] Y. Yasu,[66] E. Yatsenko,[5] K. H. Yau Wong,[21] J. Ye,[40] S. Ye,[25] I. Yeletskikh,[65] A. L. Yen,[57] E. Yildirim,[42] K. Yorita,[170] R. Yoshida,[6] K. Yoshihara,[121] C. Young,[142] C. J. S. Young,[30] S. Youssef,[22] D. R. Yu,[15] J. Yu,[8] J. M. Yu,[89] J. Yu,[64] L. Yuan,[67] S. P. Y. Yuen,[21] I. Yusuff,[28,nn] B. Zabinski,[39] R. Zaidan,[33d] A. M. Zaitsev,[129,cc] N. Zakharchuk,[42] J. Zalieckas,[14] A. Zaman,[147] S. Zambito,[57] L. Zanello,[131a,131b] D. Zanzi,[88] C. Zeitnitz,[174] M. Zeman,[127] A. Zemla,[38a] J. C. Zeng,[164] Q. Zeng,[142] K. Zengel,[23] O. Zenin,[129] T. Ženiš,[143a] D. Zerwas,[116] D. Zhang,[89] F. Zhang,[172] G. Zhang,[33b,z] H. Zhang,[33c] J. Zhang,[6] L. Zhang,[48] R. Zhang,[21] R. Zhang,[33b,oo] X. Zhang,[33d] Z. Zhang,[116] X. Zhao,[40] Y. Zhao,[33d,116] Z. Zhao,[33b] A. Zhemchugov,[65] J. Zhong,[119] B. Zhou,[89] C. Zhou,[45] L. Zhou,[35] L. Zhou,[40] M. Zhou,[147] N. Zhou,[33f] C. G. Zhu,[33d] H. Zhu,[33a] J. Zhu,[89] Y. Zhu,[33b] X. Zhuang,[33a] K. Zhukov,[95] A. Zibell,[173] D. Zieminska,[61] N. I. Zimine,[65] C. Zimmermann,[83] S. Zimmermann,[48] Z. Zinonos,[54] M. Zinser,[83] M. Ziolkowski,[140] L. Živković,[13] G. Zobernig,[172] A. Zoccoli,[20a,20b] M. zur Nedden,[16] G. Zurzolo,[103a,103b] and L. Zwalinski[30]

(ATLAS Collaboration)

[1]Department of Physics, University of Adelaide, Adelaide, Australia
[2]Physics Department, SUNY Albany, Albany, New York, USA
[3]Department of Physics, University of Alberta, Edmonton, Alberta, Canada
[4a]Department of Physics, Ankara University, Ankara, Turkey
[4b]Istanbul Aydin University, Istanbul, Turkey
[4c]Division of Physics, TOBB University of Economics and Technology, Ankara, Turkey
[5]LAPP, CNRS/IN2P3 and Université Savoie Mont Blanc, Annecy-le-Vieux, France
[6]High Energy Physics Division, Argonne National Laboratory, Argonne, Illinois, USA
[7]Department of Physics, University of Arizona, Tucson, Arizona, USA
[8]Department of Physics, The University of Texas at Arlington, Arlington, Texas, USA
[9]Physics Department, University of Athens, Athens, Greece
[10]Physics Department, National Technical University of Athens, Zografou, Greece
[11]Institute of Physics, Azerbaijan Academy of Sciences, Baku, Azerbaijan
[12]Institut de Física d'Altes Energies (IFAE), The Barcelona Institute of Science and Technology, Barcelona, Spain
[13]Institute of Physics, University of Belgrade, Belgrade, Serbia
[14]Department for Physics and Technology, University of Bergen, Bergen, Norway
[15]Physics Division, Lawrence Berkeley National Laboratory and University of California, Berkeley, California, USA
[16]Department of Physics, Humboldt University, Berlin, Germany
[17]Albert Einstein Center for Fundamental Physics and Laboratory for High Energy Physics, University of Bern, Bern, Switzerland
[18]School of Physics and Astronomy, University of Birmingham, Birmingham, United Kingdom
[19a]Department of Physics, Bogazici University, Istanbul, Turkey
[19b]Department of Physics Engineering, Gaziantep University, Gaziantep, Turkey
[19d]Istanbul Bilgi University, Faculty of Engineering and Natural Sciences, Istanbul, Turkey
[19e]Bahcesehir University, Faculty of Engineering and Natural Sciences, Istanbul, Turkey
[20a]INFN Sezione di Bologna, Italy
[20b]Dipartimento di Fisica e Astronomia, Università di Bologna, Bologna, Italy
[21]Physikalisches Institut, University of Bonn, Bonn, Germany
[22]Department of Physics, Boston University, Boston, Massachusetts, USA
[23]Department of Physics, Brandeis University, Waltham, Massachusetts, USA
[24a]Universidade Federal do Rio De Janeiro COPPE/EE/IF, Rio de Janeiro, Brazil
[24b]Electrical Circuits Department, Federal University of Juiz de Fora (UFJF), Juiz de Fora, Brazil
[24c]Federal University of Sao Joao del Rei (UFSJ), Sao Joao del Rei, Brazil
[24d]Instituto de Fisica, Universidade de Sao Paulo, Sao Paulo, Brazil
[25]Physics Department, Brookhaven National Laboratory, Upton, New York, USA
[26a]Transilvania University of Brasov, Brasov, Romania
[26b]National Institute of Physics and Nuclear Engineering, Bucharest, Romania
[26c]National Institute for Research and Development of Isotopic and Molecular Technologies, Physics Department, Cluj Napoca, Romania
[26d]University Politehnica Bucharest, Bucharest, Romania
[26e]West University in Timisoara, Timisoara, Romania
[27]Departamento de Física, Universidad de Buenos Aires, Buenos Aires, Argentina
[28]Cavendish Laboratory, University of Cambridge, Cambridge, United Kingdom
[29]Department of Physics, Carleton University, Ottawa, Ontario, Canada
[30]CERN, Geneva, Switzerland
[31]Enrico Fermi Institute, University of Chicago, Chicago, Illinois, USA
[32a]Departamento de Física, Pontificia Universidad Católica de Chile, Santiago, Chile
[32b]Departamento de Física, Universidad Técnica Federico Santa María, Valparaíso, Chile
[33a]Institute of High Energy Physics, Chinese Academy of Sciences, Beijing, China
[33b]Department of Modern Physics, University of Science and Technology of China, Anhui, China
[33c]Department of Physics, Nanjing University, Jiangsu, China
[33d]School of Physics, Shandong University, Shandong, China
[33e]Department of Physics and Astronomy, Shanghai Key Laboratory for Particle Physics and Cosmology, Shanghai Jiao Tong University, Shanghai; (also affiliated with PKU-CHEP), China
[33f]Physics Department, Tsinghua University, Beijing 100084, China
[34]Laboratoire de Physique Corpusculaire, Clermont Université and Université Blaise Pascal and CNRS/IN2P3, Clermont-Ferrand, France
[35]Nevis Laboratory, Columbia University, Irvington, New York, USA
[36]Niels Bohr Institute, University of Copenhagen, Kobenhavn, Denmark
[37a]INFN Gruppo Collegato di Cosenza, Laboratori Nazionali di Frascati, Italy
[37b]Dipartimento di Fisica, Università della Calabria, Rende, Italy

[38a]AGH University of Science and Technology, Faculty of Physics and Applied Computer Science, Krakow, Poland
[38b]Marian Smoluchowski Institute of Physics, Jagiellonian University, Krakow, Poland
[39]Institute of Nuclear Physics Polish Academy of Sciences, Krakow, Poland
[40]Physics Department, Southern Methodist University, Dallas, Texas, USA
[41]Physics Department, University of Texas at Dallas, Richardson, Texas, USA
[42]DESY, Hamburg and Zeuthen, Germany
[43]Institut für Experimentelle Physik IV, Technische Universität Dortmund, Dortmund, Germany
[44]Institut für Kern- und Teilchenphysik, Technische Universität Dresden, Dresden, Germany
[45]Department of Physics, Duke University, Durham, North Carolina, USA
[46]SUPA—School of Physics and Astronomy, University of Edinburgh, Edinburgh, United Kingdom
[47]INFN Laboratori Nazionali di Frascati, Frascati, Italy
[48]Fakultät für Mathematik und Physik, Albert-Ludwigs-Universität, Freiburg, Germany
[49]Section de Physique, Université de Genève, Geneva, Switzerland
[50a]INFN Sezione di Genova, Italy
[50b]Dipartimento di Fisica, Università di Genova, Genova, Italy
[51a]E. Andronikashvili Institute of Physics, Iv. Javakhishvili Tbilisi State University, Tbilisi, Georgia
[51b]High Energy Physics Institute, Tbilisi State University, Tbilisi, Georgia
[52]II Physikalisches Institut, Justus-Liebig-Universität Giessen, Giessen, Germany
[53]SUPA—School of Physics and Astronomy, University of Glasgow, Glasgow, United Kingdom
[54]II Physikalisches Institut, Georg-August-Universität, Göttingen, Germany
[55]Laboratoire de Physique Subatomique et de Cosmologie, Université Grenoble-Alpes, CNRS/IN2P3, Grenoble, France
[56]Department of Physics, Hampton University, Hampton, Virginia, USA
[57]Laboratory for Particle Physics and Cosmology, Harvard University, Cambridge, Massachusetts, USA
[58a]Kirchhoff-Institut für Physik, Ruprecht-Karls-Universität Heidelberg, Heidelberg, Germany
[58b]Physikalisches Institut, Ruprecht-Karls-Universität Heidelberg, Heidelberg, Germany
[58c]ZITI Institut für technische Informatik, Ruprecht-Karls-Universität Heidelberg, Mannheim, Germany
[59]Faculty of Applied Information Science, Hiroshima Institute of Technology, Hiroshima, Japan
[60a]Department of Physics, The Chinese University of Hong Kong, Shatin, N.T., Hong Kong, China
[60b]Department of Physics, The University of Hong Kong, Hong Kong, China
[60c]Department of Physics, The Hong Kong University of Science and Technology, Clear Water Bay, Kowloon, Hong Kong, China
[61]Department of Physics, Indiana University, Bloomington, Indiana, USA
[62]Institut für Astro- und Teilchenphysik, Leopold-Franzens-Universität, Innsbruck, Austria
[63]University of Iowa, Iowa City Iowa, USA
[64]Department of Physics and Astronomy, Iowa State University, Ames, Iowa, USA
[65]Joint Institute for Nuclear Research, JINR Dubna, Dubna, Russia
[66]KEK, High Energy Accelerator Research Organization, Tsukuba, Japan
[67]Graduate School of Science, Kobe University, Kobe, Japan
[68]Faculty of Science, Kyoto University, Kyoto, Japan
[69]Kyoto University of Education, Kyoto, Japan
[70]Department of Physics, Kyushu University, Fukuoka, Japan
[71]Instituto de Física La Plata, Universidad Nacional de La Plata and CONICET, La Plata, Argentina
[72]Physics Department, Lancaster University, Lancaster, United Kingdom
[73a]INFN Sezione di Lecce, Italy
[73b]Dipartimento di Matematica e Fisica, Università del Salento, Lecce, Italy
[74]Oliver Lodge Laboratory, University of Liverpool, Liverpool, United Kingdom
[75]Department of Physics, Jožef Stefan Institute and University of Ljubljana, Ljubljana, Slovenia
[76]School of Physics and Astronomy, Queen Mary University of London, London, United Kingdom
[77]Department of Physics, Royal Holloway University of London, Surrey, United Kingdom
[78]Department of Physics and Astronomy, University College London, London, United Kingdom
[79]Louisiana Tech University, Ruston, Louisiana, USA
[80]Laboratoire de Physique Nucléaire et de Hautes Energies, UPMC and Université Paris-Diderot and CNRS/IN2P3, Paris, France
[81]Fysiska institutionen, Lunds universitet, Lund, Sweden
[82]Departamento de Fisica Teorica C-15, Universidad Autonoma de Madrid, Madrid, Spain
[83]Institut für Physik, Universität Mainz, Mainz, Germany
[84]School of Physics and Astronomy, University of Manchester, Manchester, United Kingdom
[85]CPPM, Aix-Marseille Université and CNRS/IN2P3, Marseille, France
[86]Department of Physics, University of Massachusetts, Amherst, Massachusetts, USA
[87]Department of Physics, McGill University, Montreal, Québec, Canada
[88]School of Physics, University of Melbourne, Victoria, Australia
[89]Department of Physics, The University of Michigan, Ann Arbor, Michigan, USA

[90]Department of Physics and Astronomy, Michigan State University, East Lansing, Michigan, USA
[91a]INFN Sezione di Milano, Italy
[91b]Dipartimento di Fisica, Università di Milano, Milano, Italy
[92]B.I. Stepanov Institute of Physics, National Academy of Sciences of Belarus, Minsk, Republic of Belarus
[93]National Scientific and Educational Centre for Particle and High Energy Physics, Minsk, Republic of Belarus
[94]Group of Particle Physics, University of Montreal, Montreal, Québec, Canada
[95]P.N. Lebedev Physical Institute of the Russian Academy of Sciences, Moscow, Russia
[96]Institute for Theoretical and Experimental Physics (ITEP), Moscow, Russia
[97]National Research Nuclear University MEPhI, Moscow, Russia
[98]D.V. Skobeltsyn Institute of Nuclear Physics, M.V. Lomonosov Moscow State University, Moscow, Russia
[99]Fakultät für Physik, Ludwig-Maximilians-Universität München, München, Germany
[100]Max-Planck-Institut für Physik (Werner-Heisenberg-Institut), München, Germany
[101]Nagasaki Institute of Applied Science, Nagasaki, Japan
[102]Graduate School of Science and Kobayashi-Maskawa Institute, Nagoya University, Nagoya, Japan
[103a]INFN Sezione di Napoli, Italy
[103b]Dipartimento di Fisica, Università di Napoli, Napoli, Italy
[104]Department of Physics and Astronomy, University of New Mexico, Albuquerque, New Mexico, USA
[105]Institute for Mathematics, Astrophysics and Particle Physics, Radboud University Nijmegen/Nikhef, Nijmegen, The Netherlands
[106]Nikhef National Institute for Subatomic Physics and University of Amsterdam, Amsterdam, The Netherlands
[107]Department of Physics, Northern Illinois University, DeKalb, Illinois, USA
[108]Budker Institute of Nuclear Physics, SB RAS, Novosibirsk, Russia
[109]Department of Physics, New York University, New York, New York, USA
[110]Ohio State University, Columbus, Ohio, USA
[111]Faculty of Science, Okayama University, Okayama, Japan
[112]Homer L. Dodge Department of Physics and Astronomy, University of Oklahoma, Norman, Oklahoma, USA
[113]Department of Physics, Oklahoma State University, Stillwater, Oklahoma, USA
[114]Palacký University, RCPTM, Olomouc, Czech Republic
[115]Center for High Energy Physics, University of Oregon, Eugene, Oregon, USA
[116]LAL, Univ. Paris-Sud, CNRS/IN2P3, Université Paris-Saclay, Orsay, France
[117]Graduate School of Science, Osaka University, Osaka, Japan
[118]Department of Physics, University of Oslo, Oslo, Norway
[119]Department of Physics, Oxford University, Oxford, United Kingdom
[120a]INFN Sezione di Pavia, Italy
[120b]Dipartimento di Fisica, Università di Pavia, Pavia, Italy
[121]Department of Physics, University of Pennsylvania, Philadelphia, Pennsylvania, USA
[122]National Research Centre 'Kurchatov Institute' B.P.Konstantinov Petersburg Nuclear Physics Institute, St. Petersburg, Russia
[123a]INFN Sezione di Pisa, Italy
[123b]Dipartimento di Fisica E. Fermi, Università di Pisa, Pisa, Italy
[124]Department of Physics and Astronomy, University of Pittsburgh, Pittsburgh, Pennsylvania, USA
[125a]Laboratório de Instrumentação e Física Experimental de Partículas—LIP, Lisboa, Portugal
[125b]Faculdade de Ciências, Universidade de Lisboa, Lisboa, Portugal
[125c]Department of Physics, University of Coimbra, Coimbra, Portugal
[125d]Centro de Física Nuclear da Universidade de Lisboa, Lisboa, Portugal
[125e]Departamento de Fisica, Universidade do Minho, Braga, Portugal
[125f]Departamento de Fisica Teorica y del Cosmos and CAFPE, Universidad de Granada, Granada, Spain
[125g]Dep Fisica and CEFITEC of Faculdade de Ciencias e Tecnologia, Universidade Nova de Lisboa, Caparica, Portugal
[126]Institute of Physics, Academy of Sciences of the Czech Republic, Praha, Czech Republic
[127]Czech Technical University in Prague, Praha, Czech Republic
[128]Faculty of Mathematics and Physics, Charles University in Prague, Praha, Czech Republic
[129]State Research Center Institute for High Energy Physics (Protvino), NRC KI, Russia
[130]Particle Physics Department, Rutherford Appleton Laboratory, Didcot, United Kingdom
[131a]INFN Sezione di Roma, Italy
[131b]Dipartimento di Fisica, Sapienza Università di Roma, Roma, Italy
[132a]INFN Sezione di Roma Tor Vergata, Italy
[132b]Dipartimento di Fisica, Università di Roma Tor Vergata, Roma, Italy
[133a]INFN Sezione di Roma Tre, Italy
[133b]Dipartimento di Matematica e Fisica, Università Roma Tre, Roma, Italy
[134a]Faculté des Sciences Ain Chock, Réseau Universitaire de Physique des Hautes Energies—Université Hassan II, Casablanca, Morocco
[134b]Centre National de l'Energie des Sciences Techniques Nucleaires, Rabat, Morocco

[134c]Faculté des Sciences Semlalia, Université Cadi Ayyad, LPHEA-Marrakech, Morocco
[134d]Faculté des Sciences, Université Mohamed Premier and LPTPM, Oujda, Morocco
[134e]Faculté des sciences, Université Mohammed V, Rabat, Morocco
[135]DSM/IRFU (Institut de Recherches sur les Lois Fondamentales de l'Univers), CEA Saclay (Commissariat à l'Energie Atomique et aux Energies Alternatives), Gif-sur-Yvette, France
[136]Santa Cruz Institute for Particle Physics, University of California Santa Cruz, Santa Cruz, California, USA
[137]Department of Physics, University of Washington, Seattle, Washington, USA
[138]Department of Physics and Astronomy, University of Sheffield, Sheffield, United Kingdom
[139]Department of Physics, Shinshu University, Nagano, Japan
[140]Fachbereich Physik, Universität Siegen, Siegen, Germany
[141]Department of Physics, Simon Fraser University, Burnaby, British Columbia, Canada
[142]SLAC National Accelerator Laboratory, Stanford, California, USA
[143a]Faculty of Mathematics, Physics & Informatics, Comenius University, Bratislava, Slovak Republic
[143b]Department of Subnuclear Physics, Institute of Experimental Physics of the Slovak Academy of Sciences, Kosice, Slovak Republic
[144a]Department of Physics, University of Cape Town, Cape Town, South Africa
[144b]Department of Physics, University of Johannesburg, Johannesburg, South Africa
[144c]School of Physics, University of the Witwatersrand, Johannesburg, South Africa
[145a]Department of Physics, Stockholm University, Sweden
[145b]The Oskar Klein Centre, Stockholm, Sweden
[146]Physics Department, Royal Institute of Technology, Stockholm, Sweden
[147]Departments of Physics & Astronomy and Chemistry, Stony Brook University, Stony Brook, New York, USA
[148]Department of Physics and Astronomy, University of Sussex, Brighton, United Kingdom
[149]School of Physics, University of Sydney, Sydney, Australia
[150]Institute of Physics, Academia Sinica, Taipei, Taiwan
[151]Department of Physics, Technion: Israel Institute of Technology, Haifa, Israel
[152]Raymond and Beverly Sackler School of Physics and Astronomy, Tel Aviv University, Tel Aviv, Israel
[153]Department of Physics, Aristotle University of Thessaloniki, Thessaloniki, Greece
[154]International Center for Elementary Particle Physics and Department of Physics, The University of Tokyo, Tokyo, Japan
[155]Graduate School of Science and Technology, Tokyo Metropolitan University, Tokyo, Japan
[156]Department of Physics, Tokyo Institute of Technology, Tokyo, Japan
[157]Department of Physics, University of Toronto, Toronto, Ontario, Canada
[158a]TRIUMF, Vancouver, British Columbia, Canada
[158b]Department of Physics and Astronomy, York University, Toronto, Ontario, Canada
[159]Faculty of Pure and Applied Sciences, and Center for Integrated Research in Fundamental Science and Engineering, University of Tsukuba, Tsukuba, Japan
[160]Department of Physics and Astronomy, Tufts University, Medford, Massachusetts, USA
[161]Centro de Investigaciones, Universidad Antonio Narino, Bogota, Colombia
[162]Department of Physics and Astronomy, University of California Irvine, Irvine, California, USA
[163a]INFN Gruppo Collegato di Udine, Sezione di Trieste, Udine, Italy
[163b]ICTP, Trieste, Italy
[163c]Dipartimento di Chimica, Fisica e Ambiente, Università di Udine, Udine, Italy
[164]Department of Physics, University of Illinois, Urbana, Illinois, USA
[165]Department of Physics and Astronomy, University of Uppsala, Uppsala, Sweden
[166]Instituto de Física Corpuscular (IFIC) and Departamento de Física Atómica, Molecular y Nuclear and Departamento de Ingeniería Electrónica and Instituto de Microelectrónica de Barcelona (IMB-CNM), University of Valencia and CSIC, Valencia, Spain
[167]Department of Physics, University of British Columbia, Vancouver, British Columbia, Canada
[168]Department of Physics and Astronomy, University of Victoria, Victoria, British Columbia, Canada
[169]Department of Physics, University of Warwick, Coventry, United Kingdom
[170]Waseda University, Tokyo, Japan
[171]Department of Particle Physics, The Weizmann Institute of Science, Rehovot, Israel
[172]Department of Physics, University of Wisconsin, Madison, Wisconsin, USA
[173]Fakultät für Physik und Astronomie, Julius-Maximilians-Universität, Würzburg, Germany
[174]Fakultät für Mathematik und Naturwissenschaften, Fachgruppe Physik, Bergische Universität Wuppertal, Wuppertal, Germany
[175]Department of Physics, Yale University, New Haven, Connecticut, USA
[176]Yerevan Physics Institute, Yerevan, Armenia
[177]Centre de Calcul de l'Institut National de Physique Nucléaire et de Physique des Particules (IN2P3), Villeurbanne, France

[†]Deceased.
[a]Also at Department of Physics, King's College London, London, United Kingdom.
[b]Also at Institute of Physics, Azerbaijan Academy of Sciences, Baku, Azerbaijan.

[c]Also at Novosibirsk State University, Novosibirsk, Russia.
[d]Also at TRIUMF, Vancouver British Colombia, Canada.
[e]Also at Department of Physics & Astronomy, University of Louisville, Louisville, Kentucky, USA.
[f]Also at Department of Physics, California State University, Fresno, California, USA.
[g]Also at Department of Physics, University of Fribourg, Fribourg, Switzerland.
[h]Also at Departament de Fisica de la Universitat Autonoma de Barcelona, Barcelona, Spain.
[i]Also at Departamento de Fisica e Astronomia, Faculdade de Ciencias, Universidade do Porto, Portugal.
[j]Also at Tomsk State University, Tomsk, Russia.
[k]Also at Universita di Napoli Parthenope, Napoli, Italy.
[l]Also at Institute of Particle Physics (IPP), Canada.
[m]Also at Department of Physics, St. Petersburg State Polytechnical University, St. Petersburg, Russia.
[n]Also at Department of Physics, The University of Michigan, Ann Arbor, Michigan, USA.
[o]Also at Louisiana Tech University, Ruston, Louisiana, USA.
[p]Also at Institucio Catalana de Recerca i Estudis Avancats, ICREA, Barcelona, Spain.
[q]Also at Graduate School of Science, Osaka University, Osaka, Japan.
[r]Also at Department of Physics, National Tsing Hua University, Taiwan.
[s]Also at Department of Physics, The University of Texas at Austin, Austin, Texas, USA.
[t]Also at Institute of Theoretical Physics, Ilia State University, Tbilisi, Georgia.
[u]Also at CERN, Geneva, Switzerland.
[v]Also at Georgian Technical University (GTU),Tbilisi, Georgia.
[w]Also at Ochadai Academic Production, Ochanomizu University, Tokyo, Japan.
[x]Also at Manhattan College, New York, New York, USA.
[y]Also at Hellenic Open University, Patras, Greece.
[z]Also at Institute of Physics, Academia Sinica, Taipei, Taiwan.
[aa]Also at Academia Sinica Grid Computing, Institute of Physics, Academia Sinica, Taipei, Taiwan.
[bb]Also at School of Physics, Shandong University, Shandong, China.
[cc]Also at Moscow Institute of Physics and Technology State University, Dolgoprudny, Russia.
[dd]Also at Section de Physique, Université de Genève, Geneva, Switzerland.
[ee]Also at International School for Advanced Studies (SISSA), Trieste, Italy.
[ff]Also at Department of Physics and Astronomy, University of South Carolina, Columbia, South Carolina, USA.
[gg]Also at School of Physics and Engineering, Sun Yat-sen University, Guangzhou, China.
[hh]Also at Institute for Nuclear Research and Nuclear Energy (INRNE) of the Bulgarian Academy of Sciences, Sofia, Bulgaria.
[ii]Also at Faculty of Physics, M.V.Lomonosov Moscow State University, Moscow, Russia.
[jj]Also at National Research Nuclear University MEPhI, Moscow, Russia.
[kk]Also at Department of Physics, Stanford University, Stanford, California, USA.
[ll]Also at Institute for Particle and Nuclear Physics, Wigner Research Centre for Physics, Budapest, Hungary.
[mm]Also at Flensburg University of Applied Sciences, Flensburg, Germany.
[nn]Also at University of Malaya, Department of Physics, Kuala Lumpur, Malaysia.
[oo]Also at CPPM, Aix-Marseille Université and CNRS/IN2P3, Marseille, France.

Published for SISSA by Springer

Received: September 25, 2015
Revised: October 20, 2015
Accepted: November 21, 2015
Published: December 16, 2015

Measurement of four-jet differential cross sections in $\sqrt{s} = 8$ TeV proton-proton collisions using the ATLAS detector

The ATLAS collaboration

E-mail: atlas.publications@cern.ch

Abstract: Differential cross sections for the production of at least four jets have been measured in proton-proton collisions at $\sqrt{s} = 8$ TeV at the Large Hadron Collider using the ATLAS detector. Events are selected if the four anti-k_t $R = 0.4$ jets with the largest transverse momentum (p_{T}) within the rapidity range $|y| < 2.8$ are well separated ($\Delta R_{4\mathrm{j}}^{\mathrm{min}} > 0.65$), all have $p_{\mathrm{T}} > 64$ GeV, and include at least one jet with $p_{\mathrm{T}} > 100$ GeV. The dataset corresponds to an integrated luminosity of $20.3\,\mathrm{fb}^{-1}$. The cross sections, corrected for detector effects, are compared to leading-order and next-to-leading-order calculations as a function of the jet momenta, invariant masses, minimum and maximum opening angles and other kinematic variables.

Keywords: Jet physics, Hadron-Hadron scattering, QCD

ArXiv ePrint: 1509.07335

Open Access, Copyright CERN,
for the benefit of the ATLAS Collaboration.
Article funded by SCOAP^3.

doi:10.1007/JHEP12(2015)105

JHEP12(2015)105

Contents

1 Introduction **1**

2 The ATLAS detector **3**

3 Cross-section definition **3**

4 Monte Carlo samples **5**

5 Theoretical predictions **6**
- 5.1 Normalisation 8
- 5.2 Theoretical uncertainties 8

6 Data selection and calibration **8**
- 6.1 Trigger 8
- 6.2 Jet reconstruction and calibration 9
- 6.3 Data quality criteria 10

7 Data unfolding **11**

8 Experimental uncertainties **12**

9 Results **13**

10 Conclusion **34**

A Tables of the measured cross sections **36**

The ATLAS collaboration **59**

JHEP12(2015)105

1 Introduction

The production of particle jets at hadron colliders such as the Large Hadron Collider (LHC) [1] provides a fertile testing ground for the theory describing strong interactions, Quantum Chromodynamics (QCD). In QCD, jet production is interpreted as the fragmentation of quarks and gluons produced in the scattering process followed by their subsequent hadronisation. At high transverse momenta (p_{T}) the scattering of partons can be calculated using perturbative QCD (pQCD) and experimental jet measurements are directly related to the scattering of quarks and gluons. The large cross sections for such processes allow for differential measurements in a wide kinematic range and stringent testing of the underlying theory.

This analysis studies events where at least four jets are produced in a hard-scatter process. These events are of particular interest as the corresponding Feynman diagrams require several vertices even at leading-order (LO) in the strong coupling constant α_S. The current state-of-the-art theoretical predictions for such processes are at next-to-leading-order in α_S (next-to-leading-order perturbative QCD, NLO pQCD) [2, 3],[1] and they have recently been combined with parton shower (PS) simulations [4]. An alternative approach is taken by generators which provide a matrix element (ME) for the hardest $2 \to 2$ process while the rest of the jets are provided by a PS model, which implements a resummation of the leading-logarithmic terms (e.g. Pythia 8 [5] and Herwig++ [6]). It is also interesting to test multi-leg (i.e., $2 \to n$) LO pQCD generators (e.g. Sherpa [7] or MadGraph [8]), since they may provide adequate descriptions of the data in specific kinematic regions and have the advantage of being less computationally expensive than NLO calculations.

It is interesting to note that the previous ATLAS measurement of multi-jet production at $\sqrt{s} = 7\,\text{TeV}$ [9] indicates that predictions may differ from data by $\sim 30\%$ even at NLO [10]. This work explores a variety of kinematic regimes and topological distributions to test the validity of QCD calculations, including the PS approximation and the necessity of higher-order ME in Monte Carlo (MC) generators.

Additionally, four-jet events represent a background to many other processes at hadron colliders. Hence, the predictive power of the QCD calculations, in particular their ability to reproduce the shapes of the distributions studied in this analysis, is of general interest. While searches for new phenomena in multi-jet events use data-driven techniques to estimate the contribution from QCD events, as was done for example in ref. [11], these methods are tested in MC simulations. The accuracy of the theoretical predictions remains therefore important.

Three-jet events have been measured differentially by many experiments. Indeed it was observations of such events that heralded the discovery of the gluon [12–15]. More recently, at the LHC, ATLAS has measured the three-jet cross section differentially [16] and CMS has used the ratio of three to two jet events to measure α_S [17]. Event shape variables have also been measured, showing sensitivity to higher-order pQCD effects [18, 19]. Multi-jet cross sections have been measured previously at CMS [20], ATLAS [9], CDF [21, 22] and D0 [23, 24], although with smaller datasets and/or lower energy, and generally focussed on different observables.

This paper presents the differential cross sections for events with at least four jets, studied as a function of a variety of kinematic and topological variables which include momenta, masses and angles. Events are selected if the four anti-k_t $R = 0.4$ jets with the largest transverse momentum within the rapidity range $|y| < 2.8$ are well separated, all have $p_T > 64\,\text{GeV}$, and include at least one jet with $p_T > 100\,\text{GeV}$. The measurements are corrected for detector effects. The variables are binned in the leading jet p_T and the total invariant mass, such that different regimes and configurations can be tested. The measurements are sensitive to the various mass scales in an event, the presence of forward

[1] We thank Dr D. Maître (Durham University, U.K.) for providing the BlackHat histograms that were compared with the data.

JHEP12(2015)105

jets, or the azimuthal configuration of the jets — that is, one jet recoiling against three, or two recoiling against two.

The structure of the paper is as follows. Section 2 introduces the ATLAS detector. The observables and phase space of interest are defined in section 3. The MC simulation samples studied in this work are summarised in section 4, while the theory predictions and their uncertainties are described in section 5. The trigger, jet calibration and data cleaning are presented in section 6. The unfolding of detector effects is detailed in section 7. Section 8 provides the experimental uncertainties included in the final distributions. Finally, the results are shown in section 9 and the conclusions are drawn in section 10.

2 The ATLAS detector

The ATLAS experiment [25] is a multi-purpose particle physics detector with a forward-backward symmetric cylindrical geometry and nearly 4π coverage in solid angle, with instrumentation up to $|\eta| = 4.9$.[2]

The layout of the detector is based on four superconducting magnet systems, which comprise a thin solenoid surrounding the inner tracking detectors (ID) and a barrel and two end-cap toroids generating the magnetic field for a large muon spectrometer. The calorimeters are located between the ID and the muon system. The lead/liquid-argon (LAr) electromagnetic (EM) calorimeter is split into two regions: the barrel ($|\eta| < 1.475$) and the end-cap ($1.375 < |\eta| < 3.2$). The hadronic calorimeter is divided into four regions: the barrel ($|\eta| < 0.8$) and the extended barrel ($0.8 < |\eta| < 1.7$) made of scintillator/steel, the end-cap ($1.5 < |\eta| < 3.2$) with LAr/copper modules, and the forward calorimeter ($3.1 < |\eta| < 4.9$) composed of LAr/copper and LAr/tungsten modules.

A three-level trigger system [26] is used to select events for further analysis. The first level (L1) of the trigger reduces the event rate to less than 75 kHz using hardware-based trigger algorithms acting on a subset of detector information. The second level (L2) uses fast online algorithms, while the final trigger stage, called the Event Filter (EF), uses reconstruction software with algorithms similar to the offline versions. The last two software-based trigger levels, referred to collectively as the High-Level Trigger (HLT), further reduce the event rate to about 400 Hz.

3 Cross-section definition

This measurement uses jets reconstructed with the anti-k_t algorithm [27] with four-momentum recombination as implemented in the FastJet package [28]. The radius parameter is $R = 0.4$.

Cross sections are calculated for events with at least four jets within the rapidity range $|y| < 2.8$. Out of those four jets, the leading one must have $p_{\mathrm{T}} > 100$ GeV, while

[2] ATLAS uses a right-handed Cartesian coordinate system with its origin at the nominal interaction point (IP) in the centre of the detector. The z-axis is taken along the beam pipe, and the x-axis points from the IP to the centre of the LHC ring. Cylindrical coordinates (r, ϕ) are used in the transverse plane, ϕ being the azimuthal angle around the beam pipe. The rapidity y is defined by $\frac{1}{2} \ln \frac{E+p_z}{E-p_z}$, the pseudorapidity in terms of the polar angle θ as $\eta = -\ln \tan(\theta/2)$.

JHEP12(2015)105

Name	Definition	Comment
$p_{\mathrm{T}}^{(i)}$	Transverse momentum of the ith jet	Sorted descending in p_{T}
H_{T}	$\sum_{i=1}^{4} p_{\mathrm{T}}^{(i)}$	Scalar sum of the p_{T} of the four jets
$m_{4\mathrm{j}}$	$\left(\left(\sum_{i=1}^{4} E_i\right)^2 - \left(\sum_{i=1}^{4} \mathbf{p}_i\right)^2\right)^{1/2}$	Invariant mass of the four jets
$m_{2\mathrm{j}}^{\min}/m_{4\mathrm{j}}$	$\min_{\substack{i,j\in[1,4]\\ i\neq j}} \left((E_i+E_j)^2 - (\mathbf{p}_i+\mathbf{p}_j)^2\right)^{1/2} \Big/ m_{4\mathrm{j}}$	Minimum invariant mass of two jets relative to invariant mass of four jets
$\Delta\phi_{2\mathrm{j}}^{\min}$	$\min_{\substack{i,j\in[1,4]\\ i\neq j}} (\lvert\phi_i - \phi_j\rvert)$	Minimum azimuthal separation of two jets
$\Delta y_{2\mathrm{j}}^{\min}$	$\min_{\substack{i,j\in[1,4]\\ i\neq j}} (\lvert y_i - y_j\rvert)$	Minimum rapidity separation of two jets
$\Delta\phi_{3\mathrm{j}}^{\min}$	$\min_{\substack{i,j,k\in[1,4]\\ i\neq j\neq k}} (\lvert\phi_i - \phi_j\rvert + \lvert\phi_j - \phi_k\rvert)$	Minimum azimuthal separation between any three jets
$\Delta y_{3\mathrm{j}}^{\min}$	$\min_{\substack{i,j,k\in[1,4]\\ i\neq j\neq k}} (\lvert y_i - y_j\rvert + \lvert y_j - y_k\rvert)$	Minimum rapidity separation between any three jets
$\Delta y_{2\mathrm{j}}^{\max}$	$\Delta y_{ij}^{\max} = \max_{i,j\in[1,4]} (\lvert y_i - y_j\rvert)$	Maximum rapidity difference between two jets
$\Sigma p_{\mathrm{T}}^{\mathrm{central}}$	$\lvert p_{\mathrm{T}}^{c}\rvert + \lvert p_{\mathrm{T}}^{d}\rvert$	If $\Delta y_{2\mathrm{j}}^{\max}$ is defined by jets a and b, this is the scalar sum of the p_{T} of the other two jets, c and d ('central' jets)

Table 1. Definitions of the various kinematic variables measured. Only the four jets with the largest p_{T} are considered in all cases.

the next three must have $p_{\mathrm{T}} > 64\,\mathrm{GeV}$. In addition, these four jets must be well separated from one another by $\Delta R_{4\mathrm{j}}^{\min} > 0.65$, where $\Delta R_{4\mathrm{j}}^{\min} = \min_{\substack{i,j\in[1,4]\\ i\neq j}}(\Delta R_{ij})$, and $\Delta R_{ij} = (|y_i - y_j|^2 + |\phi_i - \phi_j|^2)^{1/2}$. This set of criteria is also referred to as the 'inclusive analysis cuts' to differentiate them from the cases where additional requirements are made, for example on the invariant mass of the four leading jets. The inclusive analysis cuts are mainly motivated by the triggers used to select events, described in section 6.1.

Cross sections are measured differentially as a function of the kinematic variables defined in table 1; the list includes momentum variables, mass variables and angular variables. The only jets used in all cases are the four leading ones in p_{T}. The observables were selected for their sensitivity to differences between different Monte Carlo models of QCD processes and their ability to describe the dynamics of the events. For example, the H_{T} variable is often used to set the scale of multi-jet processes. The four-jet invariant mass $m_{4\mathrm{j}}$ is representative of the largest energy scale in the event whereas $m_{2\mathrm{j}}^{\min}$, the minimum dijet invariant mass, probes the smallest jet-splitting scale. The ratio $m_{2\mathrm{j}}^{\min}/m_{4\mathrm{j}}$ therefore provides information about the range of energy scales relevant to the QCD calculation. The $\Delta\phi_{2\mathrm{j}}^{\min}$ and $\Delta y_{2\mathrm{j}}^{\min}$ variables quantify the minimum angular separation between any two jets. The azimuthal variable $\Delta\phi_{3\mathrm{j}}^{\min}$ distinguishes events with pairs of nearby jets (which

JHEP12(2015)105

Observable	$\Delta R_{4j}^{min} > \ldots$	$p_T^{(4)} > \ldots$ [GeV]	$p_T^{(1)} > \ldots$ [GeV]	$m_{4j} > \ldots$ [GeV]	$\Delta y_{2j}^{max} > \ldots$
$p_T^{(i)}$	0.65	64	100	—	—
H_T			100	—	—
m_{4j}			100	—	—
m_{2j}^{min}/m_{4j}			100	500, 1000, 1500, 2000	—
$\Delta\phi_{2j}^{min}$			100, 400, 700, 1000	—	—
Δy_{2j}^{min}			100, 400, 700, 1000	—	—
$\Delta\phi_{3j}^{min}$			100, 400, 700, 1000	—	—
Δy_{3j}^{min}			100, 400, 700, 1000	—	—
Δy_{2j}^{max}			100, 250, 400, 550	—	—
$\Sigma p_T^{central}$			100, 250, 400, 550	—	1, 2, 3, 4

Table 2. Summary of the analysed phase-space regions, including the $p_T^{(1)}$, m_{4j} and Δy_{2j}^{max} bins into which each of the differential cross-section measurements is split (a dash indicates when the cut is not applied on a variable). The ΔR_{4j}^{min} and $p_T^{(4)}$ requirements, specified in the second and third columns respectively, apply to all variables. The observables are defined in table 1.

have large $\Delta\phi_{3j}^{min}$) from the recoil of three jets against one (leading to small $\Delta\phi_{3j}^{min}$ values). The rapidity variable Δy_{3j}^{min} works in a similar way. The Δy_{2j}^{max} and $\Sigma p_T^{central}$ variables are designed to be sensitive to events with forward jets. In order to build $\Sigma p_T^{central}$, first the two jets with the largest rapidity interval in the event are identified, and then the scalar sum of the p_T of the remaining two jets is calculated.

Different phase-space regions are probed by binning the variables in regions defined by a lower bound on $p_T^{(1)}$ and m_{4j}. This allows one to distinguish between the two types of topologies characterised by $\Delta\phi_{3j}^{min}$, or to track the position of the leading jet with respect to the forward-backward pair in the $\Sigma p_T^{central}$ variables. Table 2 summarises all the phase-space regions considered in the analysis for each of the variables.

The resulting differential cross-section distributions are corrected for detector effects (*unfolding*) and taken to the so-called particle-jet level, or simply 'particle level'. In the MC simulations used in the unfolding procedure, particle jets are built from particles with a proper lifetime τ satisfying $c\tau > 10$ mm, including muons and neutrinos from hadron decays. The event selection described above is applied to particle jets to define the phase space of the unfolded results.

Double parton interactions have not been investigated independently, so the measurement is inclusive in this respect. They are expected to contribute 1% or less to the results.

4 Monte Carlo samples

Monte Carlo samples are used to estimate experimental systematic uncertainties, deconvolve detector effects, and provide predictions to be compared with the data. Leading-order Monte Carlo samples are used for all three purposes. A set of theoretical calculations at higher orders, described in section 5, are also compared to the data. The full list of generators is shown in table 3.

JHEP12(2015)105

Name	*Hard scattering*	*LO/NLO*	*PDF*	*PS/UE*	*Tune*	*Factor*
Pythia	Pythia 8	LO ($2 \to 2$)	CT10	Pythia 8	AU2-CT10	0.6
Herwig++	Herwig++	LO ($2 \to 2$)	CTEQ6L1	Herwig++	UE-EE-3-CTEQ6L1	1.4
MadGraph+Pythia	MadGraph	LO ($2 \to 4$)	CTEQ6L1	Pythia 6	AUET2B-CTEQ6L1	1.1
HEJ	HEJ	All[†]	CT10	—	—	0.9
BlackHat/Sherpa	BlackHat/Sherpa	NLO ($2 \to 4$)	CT10	—	—	—
NJet/Sherpa	NJet/Sherpa	NLO ($2 \to 4$)	CT10	—	—	—

[†]The HEJ sample is based on an approximation to all orders in α_S.

Table 3. The generators used for comparison against the data are listed, together with the parton distribution functions (PDFs), PS algorithms, underlying event (UE) and parameter tunes. Each MC prediction is multiplied by a normalisation factor (last column) as described in section 5.1, except BlackHat/Sherpa and NJet/Sherpa.

The samples used in the experimental studies comprise two LO $2 \to 2$ generators, Pythia 8.160 [5] and Herwig++ 2.5.2 [6], and the LO multi-leg generator MadGraph5 v1.5.12 [8]. As described in the introduction, LO generators are still widely used in searches for new physics, which motivates the comparison of their predictions to the data.

Both Pythia and Herwig++ employ leading-logarithmic PS models matched to LO ME calculations. Pythia uses a PS algorithm based on p_T ordering, while the PS model implemented in Herwig++ follows an angular ordering. The ME calculation provided by MadGraph contains up to four outgoing partons in the ME. It is matched to a PS generated with Pythia 6.427 [29] using the shower k_t-jet MLM matching [30], where the jet-parton matching scale is set to 20 GeV. Hadronisation effects are included via the string model in the case of the Pythia and MadGraph samples [29], or the cluster model [31] in events simulated with Herwig++. The parton distribution functions (PDFs) used are the NLO CT10 [32] or the LO distributions of CTEQ6L1 [33] as shown in table 3.

Simulations of the underlying event, including multiple parton interactions, are included in all three LO samples. The parameter tunes employed are the ATLAS tunes AU2 [34] and AUET2B [35] for Pythia and MadGraph respectively, and the Herwig++ tune UE-EE-3 [36].

The multiple pp collisions within the same and neighbouring bunch crossings (pile-up) are simulated as additional inelastic pp collisions using Pythia 8. Finally, the interaction of particles with the ATLAS detector is simulated using a GEANT4-based program [37, 38].

5 Theoretical predictions

The results of the measurement are compared to NLO predictions, in addition to the LO samples described in section 4. These are calculated using BlackHat/Sherpa [2, 3] and NJet/Sherpa [39, 40], and have been provided by their authors. They are both fixed-order calculations with no PS and no hadronisation. Therefore, the results are presented at the parton-jet level, that is, using jets built from partons instead of hadrons. For the high-

JHEP12(2015)105

p_T phase space covered in this analysis, non-perturbative corrections are expected to be small [41, 42]. BlackHat performs one-loop virtual corrections using the unitarity method and on-shell recursion. The remaining terms of the full NLO computation are obtained with AMEGIC++ [43, 44], part of Sherpa. NJet makes a numerical evaluation of the one-loop virtual corrections to multi-jet production in massless QCD. The Born matrix elements are evaluated with the Comix generator [45, 46] within Sherpa. Sherpa also performs the phase-space integration and infra-red subtraction via the Catani-Seymour dipole formalism. Both the BlackHat/Sherpa and NJet/Sherpa predictions use the CT10 PDFs.

The results are also compared to predictions provided by HEJ [47–49].[3] HEJ is a fully exclusive Monte Carlo event generator based on a perturbative cross-section calculation which approximates the hard-scattering ME to all orders in the strong coupling constant α_S for jet multiplicities of two or greater. The approximation is exact in the limit of large separation in rapidity between partons. The calculation uses the CT10 PDFs. As in the case of the NLO predictions, no PS or hadronisation are included.

The different predictions tested are expected to display various levels of agreement in different kinematic configurations. The generators which combine $2 \to 2$ parton matrix elements (MEs) with parton showers (PSs) are in principle not expected to provide a good description of the data, particularly in regions where the additional jets are neither soft nor collinear. A previous measurement of multi-jet cross sections at 7 TeV by the ATLAS Collaboration [9] found that the cross section predicted by MC models typically disagreed with the data by $\mathcal{O}(40\%)$. It also found disagreements of up to 50% in the shape of the differential cross section measured as a function of $p_T^{(1)}$ or H_T. Nevertheless, there are also examples of exceptional cases where these calculations perform well, which adds interest to the measurement; for example, the same 7 TeV ATLAS paper observed that the shape of the $p_T^{(4)}$ distribution was described by Pythia within just 10%. It is also interesting to test whether PSs based on an angular ordering perform better in angular variables such as $\Delta\phi_{2j}^{min}$ or $\Delta\phi_{3j}^{min}$ than those using momentum ordering. In contrast to PS predictions, multi-leg matrix element calculations matched to parton showers (ME+PS) were seen at 7 TeV to significantly improve the accuracy of the cross-section calculation and the shapes of the momentum observables. In the present analysis, such calculations are expected to perform better in events with additional high-p_T jets and/or large combined invariant masses of jets. This is also the type of scenario where HEJ is expected to perform well, since it provides an all-order description of processes with more than two hard jets, and it is designed to capture the hard, wide-angle emissions which a standalone PS approach would miss. Variables such as Δy_{2j}^{max}, Δy_{3j}^{min} or $\Sigma p_T^{central}$ were included in the analysis with this purpose in mind. Finally, the fixed-order, four-jet NLO predictions are expected to provide a better estimation of the cross sections than the LO calculations. Interestingly, studies at 7 TeV found that the NLO cross section for four-jet events was $\sim 30\%$ higher than the data [10].

[3] We thank Dr J. Andersen and Dr T. Hapola (Durham University, U.K.) for providing the histograms for the HEJ predictions.

JHEP12(2015)105

5.1 Normalisation

To facilitate comparison with the data, the cross sections predicted by the LO generators as well as HEJ are multiplied by a scale factor. The factor is such that the integrated number of events in the region $500\,\text{GeV} < p_{\text{T}}^{(1)} < 1.5\,\text{TeV}$ which satisfy the inclusive analysis cuts in section 3 is equal to the corresponding number in data. The full set of normalisation factors is shown in table 3. No scale factor is ascribed to BlackHat/Sherpa and NJet/Sherpa such that the level of agreement with data can be assessed in light of the theoretical uncertainties, as discussed in section 5.2.

5.2 Theoretical uncertainties

Theoretical uncertainties have been computed for HEJ and the NLO predictions. The sensitivity of the HEJ calculation to higher-order corrections was determined by the authors of the calculation by varying independently the renormalisation and factorisation scales by factors of $\sqrt{2}$, 2, $1/\sqrt{2}$ and 1/2 around the central value of $H_{\text{T}}/2$. The total uncertainty is the result of taking the envelope of all the variations. The typical size of the uncertainty is $^{+50\%}_{-30\%}$, and it is not drawn on the figures for clarity.

The central value of the renormalisation and factorisation scales used in the NJet/Sherpa and BlackHat/Sherpa samples is also $H_{\text{T}}/2$. Scale uncertainties are evaluated for NJet/Sherpa by simultaneously varying both scales by factors of 1/2 and 2. PDF uncertainties are obtained by reweighting the distributions for all the PDF error sets using LHAPDF [50], following the recommendations from ref. [51]. The additional PDF sets include variations in the value of α_{S}. The sum in quadrature of the resulting scale and PDF variations defines the NLO theoretical uncertainty included in the result figures in section 9. The uncertainty is dominated by the scale component due to the rapid drop of the cross section with decreasing values of the renormalisation and factorisation scales. As a result, the uncertainty is significantly asymmetric.

6 Data selection and calibration

The data sample used was taken during the period from March to December 2012 with the LHC operating at a pp centre-of-mass energy of $\sqrt{s} = 8\,\text{TeV}$. The application of data-quality requirements results in an integrated luminosity of $20.3\,\text{fb}^{-1}$.

6.1 Trigger

The events used in this analysis are selected by a combination of four jet triggers, consisting of the three usual levels and defined in terms of the jets produced in the event. The hardware-based L1 trigger provides a fast decision based on the energy measured by the calorimeter. The L2 trigger performs a simple jet reconstruction procedure in the geometric regions identified by the L1 trigger. The final decision taken by the EF trigger is made using jets from the region of $|\eta| < 3.2$, and reconstructed from topological clusters [52] using the anti-k_t algorithm with $R = 0.4$.

The four different triggers used in this paper are shown in figure 1. Two of the triggers select events with at least four jets, while the remaining two select events with at least

JHEP12(2015)105

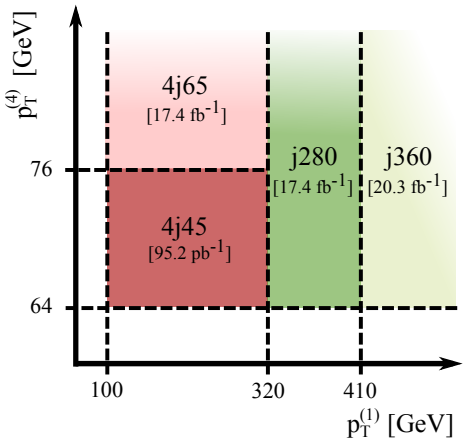

Figure 1. Schematic of the kinematic regions in which the four different jet triggers are used, including the total luminosity that each of them recorded. The term 4j45 (4j65) refers to a trigger requiring at least four jets with $p_T > 45$ GeV (65 GeV), where the p_T is measured at the EF level of the triggering system. The term j280 (j360) refers to a trigger requiring at least one jet with $p_T > 280$ GeV (360 GeV) at the EF level. The horizontal and vertical axes correspond to $p_T^{(1)}$ and $p_T^{(4)}$ respectively, both calculated at the offline level (i.e., including the full object calibration).

one jet at a higher p_T threshold. Events are split into the four non-overlapping kinematic regions shown in figure 1, requiring at least four well-separated jets with varying p_T thresholds in order to apply the corresponding trigger. This ensures trigger efficiencies greater than 99% for any event passing the inclusive analysis cuts. The small residual loss of data due to trigger inefficiency is corrected as a function of jet p_T using the techniques described in section 7.

As noted in figure 1, three out of the four triggers only recorded a fraction of the total dataset. The contributions from the events selected by those three triggers are scaled by the inverse of the corresponding fraction.

6.2 Jet reconstruction and calibration

Jets are reconstructed using the anti-k_t jet algorithm [27] with four-momentum recombination and radius parameter $R = 0.4$. The inputs to the jet algorithm are locally-calibrated topological clusters of calorimeter cells [52], which reconstruct the three-dimensional shower topology of each particle entering the calorimeter.

ATLAS has developed several jet calibration schemes [53] with different levels of complexity and different sensitivities to systematic effects. In this analysis the local cluster weighting (LCW) calibration [52] method is used, which classifies topological clusters as either being of electromagnetic or hadronic origin. Based on this classification, specific energy corrections are applied, improving the jet energy resolution. The final jet energy calibration, generally referred to as the jet energy scale, corrects the average calorimeter response to reproduce the energy of the true particle jet.

The jet energy scale and resolution have been measured in pp collision data using techniques described in references [54–56]. The effects of pile-up on jet energies are accounted

JHEP12(2015)105

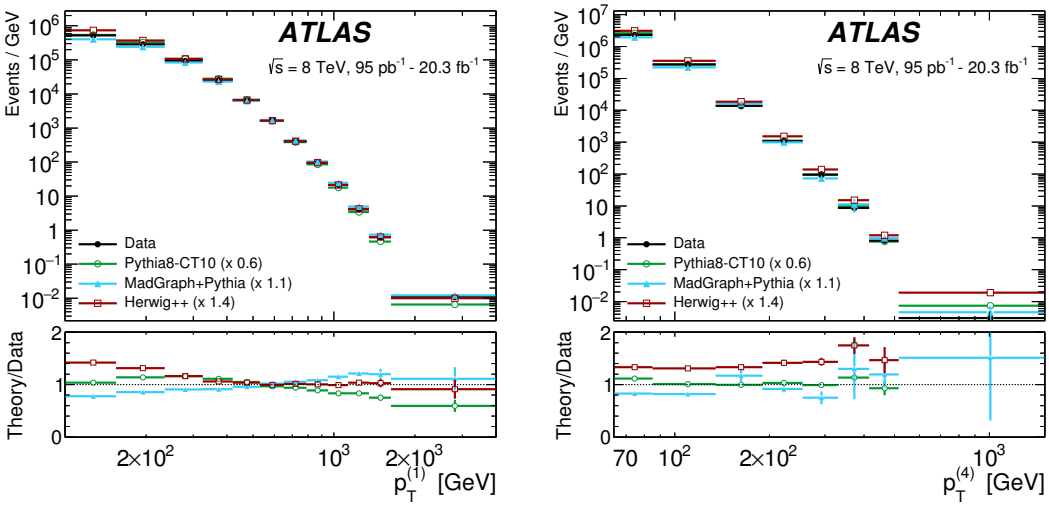

(a) $p_{\mathrm{T}}^{(1)}$. **(b)** $p_{\mathrm{T}}^{(4)}$.

Figure 2. Detector-level distributions of (a) $p_{\mathrm{T}}^{(1)}$ and (b) $p_{\mathrm{T}}^{(4)}$ for data and for example MC predictions. The MC predictions have passed through detector simulation. The lower panel in each plot shows the ratios of the MC predictions to data. For better comparison, the predictions are multiplied by the factors indicated in the legend.

for by a jet-area-based correction [57] prior to the final calibration, where the area of the jet is defined in η–ϕ space. Jets are then calibrated to the hadronic energy scale using p_{T}- and η-dependent calibration factors based on MC simulations, and their response is corrected based on several observables that are sensitive to fragmentation effects. A residual calibration is applied to take into account differences between data and MC simulation based on a combination of several in-situ techniques [54].

6.3 Data quality criteria

Before applying the selection that defines the kinematic region of interest, events are required to pass the trigger, as described in section 6.1, and to contain a primary vertex with at least two tracks. Events which contain energy deposits in the calorimeter consistent with noise, or with incomplete event data, are rejected. In addition, events containing jets pointing to problematic calorimeter regions, or originating from non-collision background, cosmic rays or detector effects, are vetoed. These cleaning procedures are emulated in the MC simulation used to correct for experimental effects, as is discussed in detail in section 7.

No attempt is made to exclude jets that result from photons or leptons impacting the calorimeter, nor are the contributions from such signatures corrected for. Events containing photons or τ leptons are expected to contribute less than 0.1% to the cross sections under study.

Distributions of two example variables ($p_{\mathrm{T}}^{(1)}$ and $p_{\mathrm{T}}^{(4)}$) can be seen at the detector level (i.e. prior to unfolding detector effects) in figure 2. Different sets of points correspond to the data and the different MC generators, which are normalised to data with the scale

JHEP12(2015)105

factors indicated in table 3. These are constant factors used to facilitate the comparison with data, as described in section 5.1. Given that the generators have only LO or even only leading-logarithmic accuracy, the observed agreement is reasonable.

7 Data unfolding

Cross sections are measured differentially in several variables, each of which is binned in $p_{\mathrm{T}}^{(1)}$ or $m_{4\mathrm{j}}$. Each of the corresponding distributions is individually unfolded to deconvolve detector effects such as inefficiencies and resolutions. The unfolding is performed using the Bayesian Iterative method [58, 59], as implemented in the `RooUnfold` package [60]. The algorithm builds an unfolding matrix starting with an initial prior probability distribution taken from MC simulation, and improves it iteratively. The method takes into account migrations between bins. It also corrects the results for the presence of events which pass the selection at reconstructed-level but not at the particle level; and for detector inefficiencies, which have the opposite effect. The number of iterations is optimised in order to minimise the size of the statistical and systematic uncertainties. A lower number of iterations results in a higher dependence on the MC simulation, whereas higher values give larger statistical uncertainties. For the analysis presented in this paper, two iterations are used.

The data are unfolded to the particle-jet level using the Pythia MC simulation to build the unfolding matrix. In order to construct the matrix, events are required to pass the inclusive analysis cuts at both the reconstructed and particle levels. The cuts require that events have at least four jets within $|y| < 2.8$, with $p_{\mathrm{T}}^{(1)} > 100\,\mathrm{GeV}$ and $p_{\mathrm{T}}^{(2)}, p_{\mathrm{T}}^{(3)}, p_{\mathrm{T}}^{(4)} > 64\,\mathrm{GeV}$. The four leading jets must in addition be separated by $\Delta R_{4\mathrm{j}}^{\mathrm{min}} > 0.65$. For observables requiring additional kinematic cuts, these are also applied both at the reconstructed and particle levels. No spatial matching is performed between reconstructed-level and particle-level jets.

The correlation between the observables before and after the incorporation of experimental effects tends to be higher for p_{T}-based variables, such as H_{T}. In the case of angular variables, such as $\Delta\phi_{2\mathrm{j}}^{\mathrm{min}}$, the correlation is weakened due to cases where energy resolution effects lead to re-ordering of the jet p_{T}. Nevertheless, even in the case of such angular variables the entries far from the diagonal of the correlation matrix are significantly smaller than the diagonal elements. The binning is derived from an optimisation procedure such that the purity of the bins is between 70% and 90%, and the statistical uncertainty of the measurement is $\lesssim 10\%$. The purity is defined as the fractional number of events per bin which do not migrate to other bins after the detector simulation, calculated with respect to the number of events which pass the particle-level cuts.

The possible presence of biases in the unfolded spectra due to MC mismodelling of the reconstructed-level spectrum is evaluated using a data-driven closure test. In this study, the MC distributions are reweighted to match the shape of those obtained from the data, and then unfolded using the same unfolding matrix as for the data. A data-driven systematic uncertainty is computed by comparing the result obtained from this procedure and the

JHEP12(2015)105

original reweighted particle-level MC distributions. With two iterations of the unfolding algorithm, this systematic uncertainty is found to be negligible.

A second unfolding uncertainty is evaluated to account for the model dependence of the efficiency with which both the reconstructed- and particle-level cuts are satisfied in each MC event. The systematic uncertainty is derived from the differences between the efficiencies calculated with Herwig++ and those calculated using Pythia. The resulting uncertainty is found to be subdominant in most cases, with typical sizes of 2–10%. The uncertainty is rebinned and smoothed, such that its statistical uncertainty is smaller than 40%.

The statistical uncertainties are calculated with pseudo-experiments. For each pseudo-experiment, the data and MC distributions are reweighted event by event following a Poisson distribution centred at one. Each resulting Poisson replica of the data is unfolded using the corresponding fluctuated unfolding matrix. The random numbers for the pseudo-experiments are generated using unique seeds, following the same scheme used by the inclusive jet [42], dijet [61] and three-jet [16] measurements at $\sqrt{s} = 7\,\text{TeV}$, to allow for possible future combination of results with the same dataset used for this analysis.

The integral of the unfolded distributions, corresponding to the cross section in the fiducial range determined by the inclusive analysis cuts, was compared for all the variables defined in the same region of phase space and found to agree with each other within 0.5%.

8 Experimental uncertainties

Several sources of experimental uncertainty are considered in this analysis. Those arising from the unfolding procedure are described in section 7. This section presents the uncertainties which arise from the jet energy scale (JES), jet energy resolution (JER), jet angular resolution and integrated luminosity. The dominant source of uncertainty in this measurement is the JES.

The uncertainty in the JES calibration is determined in the central detector region by exploiting the transverse momentum balance in Z+jet, γ+jet or multi-jet events, which are measured in situ. The uncertainties in the energy of the reference object are propagated to the jet whose energy scale is being probed. The uncertainty in the central region is propagated to the forward region using dijet systems balanced in transverse momentum. The procedure is described in detail in ref. [54].

The total JES uncertainty is decomposed into eighteen components, which account for the uncertainty in the jet energy scale calibration itself, as well as uncertainties due to the pile-up subtraction procedure, parton flavour differences between samples, b-jet energy scale and punch-through. Each of these uncertainties is incorporated as a coherent shift of the scale of the jets in the MC simulation. The energies and transverse momenta of all jets with $p_{\text{T}} > 20\,\text{GeV}$ and $|y| < 2.8$ are varied up and down by one standard deviation of each uncertainty component; these components are asymmetric, i.e. the values of the upwards and downwards variations are different. The shifts are then propagated through the unfolding. The unfolded distributions corresponding to the systematically varied spectra are compared one by one to the nominal ones, and the difference taken as the unfolded-level uncertainty due to that JES uncertainty component. The total JES

JHEP12(2015)105

uncertainty is obtained by summing all such contributions quadratically, respecting the sign of the variations in the event yields; that is, positive and negative event yield variations are added independently.

Statistical uncertainties on each of the JES uncertainty components are obtained by creating Poisson replicas of the systematically varied spectra, obtained as explained in section 7. Such statistical uncertainties are used to evaluate the significance of the uncertainty for each component and for each bin of all the differential distributions. As in the case of the unfolding uncertainty, the unfolded-level uncertainty due to each JES component is then rebinned and smoothed using a Gaussian kernel regression in order to get statistical uncertainties smaller than 40% in all bins. The typical size of the JES uncertainty is 4–15%.

Jets may be affected by additional energy originating from pile-up interactions. This effect is corrected for as part of the jet energy calibration. The distributions were binned in different ranges of the average number of interactions per bunch crossing in order to test the possible presence of residual effects. No significant deviations were observed, therefore no uncertainty associated with pile-up mismodelling was considered beyond the pile-up uncertainty already included in the jet calibration procedure.

The JER has been measured in data using dijet events [62], and an uncertainty was derived from the differences seen between data and MC prediction. In general, the energy resolution observed in data is somewhat worse than that in MC simulations. The uncertainty on the observables can therefore be evaluated by smearing the energy of the reconstructed jets in the MC simulation. After applying this smearing to the jets, an alternative unfolding matrix is derived and used to unfold the nominal MC prediction. Then the MC distribution is unfolded using both the nominal and the smeared matrices, and the difference between the two is symmetrised and taken as the JER systematic uncertainty. The typical size of this uncertainty is 1–10% of the cross section.

The jet angular resolution was estimated in MC simulation for the pseudorapidity and ϕ by matching spatially jets at the reconstructed and particle level, and found to be $\lesssim 2\%$. This is in agreement with in-situ measurements, so no systematic uncertainty is assigned.

Finally, the uncertainty on the integrated luminosity is $\pm 2.8\%$. It is derived following the same methodology as that detailed in ref. [63].

Two examples of the values of the total experimental systematic uncertainty are shown in figure 3 for two representative variables, namely H_{T} and $\Delta\phi_{2\mathrm{j}}^{\mathrm{min}}$. The jet energy scale and resolution uncertainties dominate in the majority of bins, being larger at the high and low ends of the H_{T} spectrum. The unfolding uncertainty is nearly as large at low values of the jet momenta, and it is therefore an important contribution in most of the $\Delta\phi_{2\mathrm{j}}^{\mathrm{min}}$ bins.

9 Results

The various differential cross sections measured in events with at least four jets are shown in figures 4 to 19 for jets reconstructed with the anti-k_t algorithm with $R = 0.4$. The observables used for the measurements are defined in table 1. The measurements are performed for a wide range of jet transverse momenta from 64 GeV to several TeV, spanning

JHEP12(2015)105

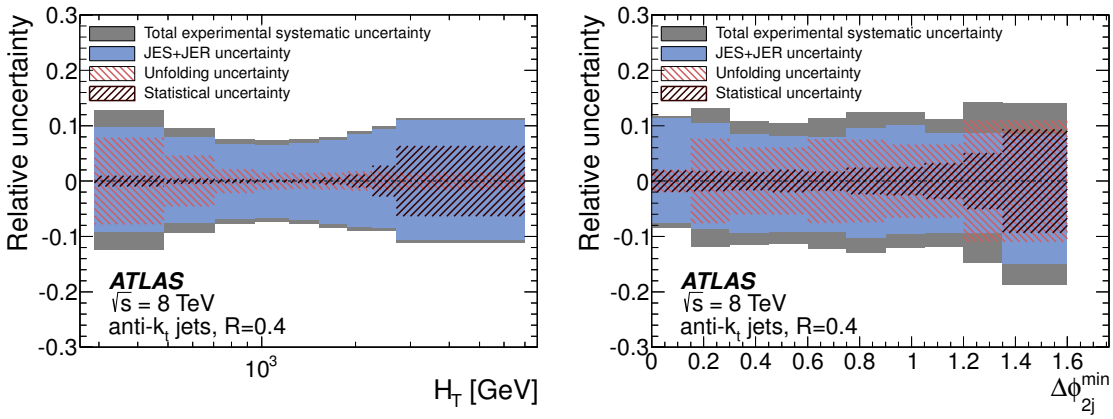

(a) H_{T}. **(b)** $\Delta\phi_{2\mathrm{j}}^{\mathrm{min}}$.

Figure 3. Total systematic uncertainty in the four-jet cross section measurement for anti-k_t $R = 0.4$ jets as a function of (a) H_{T} and (b) $\Delta\phi_{2\mathrm{j}}^{\mathrm{min}}$. In both cases the event selection corresponds to the inclusive analysis cuts, namely $p_{\mathrm{T}}^{(4)} > 64\,\mathrm{GeV}$, $p_{\mathrm{T}}^{(1)} > 100\,\mathrm{GeV}$ and $\Delta R_{4\mathrm{j}}^{\mathrm{min}} > 0.65$. Separate bands show the jet energy scale (JES) and resolution (JER), and the unfolding uncertainty, as well as the combined total systematic uncertainty resulting from adding in quadrature all the components. The total statistical uncertainty of the unfolded data spectrum is also shown. The luminosity uncertainty is not shown separately but is included in the total uncertainty band.

two orders of magnitude in p_{T} and over seven orders of magnitude in cross section. The measured cross sections are corrected for all detector effects using the unfolding procedure described in section 7. The theoretical predictions described in sections 4 and 5 are compared to the unfolded results.

Summary of the results. The scale factors applied to LO generators (see section 5.1) are found to vary between 0.6 and 1.4, as shown previously in table 3. Not all generators describe the shape of $p_{\mathrm{T}}^{(1)}$ correctly, so these scale factors should not be seen as a measure of the level of agreement between MC simulation and data, which may vary as a function of the cuts in $p_{\mathrm{T}}^{(1)}$ and $m_{4\mathrm{j}}$. The cross section predicted by BlackHat/Sherpa and NJet/Sherpa is larger than that measured in data, but overall the difference is covered by the scale and PDF uncertainties evaluated using NJet/Sherpa, with only a few exceptions. BlackHat/Sherpa and NJet/Sherpa give identical results within statistical uncertainties; therefore only one of the two (NJet/Sherpa) is discussed in the following, for simplicity. It is nevertheless interesting to compare experimental results with two different implementations of the same NLO pQCD calculations as an additional cross-check.

In general, an excellent description of both the shape and the normalisation of the variables is given by NJet/Sherpa. The small differences found are covered by theoretical and statistical uncertainties in almost all cases; only the tails of $p_{\mathrm{T}}^{(4)}$ and $\Delta y_{2\mathrm{j}}^{\mathrm{max}}$ hint at deviations from the measured distribution. MadGraph+Pythia describes the data very well in most regions of phase space, the most significant discrepancy being in the slopes of $p_{\mathrm{T}}^{(1)}$ and $p_{\mathrm{T}}^{(2)}$and derived variables. HEJ also provides a good description of most variables;

JHEP12(2015)105

the most significant discrepancy occurs for the angular variables Δy_{2j}^{min} and Δy_{2j}^{max} when $p_T^{(1)}$ is small. However when $p_T^{(1)}$ is large, HEJ describes Δy_{2j}^{max} better than NJet/Sherpa, which highlights one of the strengths of this calculation. The $2 \to 2$ ME calculations matched to parton showers provide different levels of agreement depending on the variable studied; the only variable whose shape is reasonably well described by both Pythia and Herwig++ is H_T.

The following discussion is based on the results obtained after applying the particular choice of normalisation of the theoretical predictions as explained at the beginning of this section. NJet/Sherpa, which generally gives very good agreement with the data, is only discussed for those cases where some deviations are present.

Momentum variables. The momentum variables comprise the p_T of the four leading jets and H_T. Part of the importance of these variables lies in their wide use in analyses, alone or as inputs to more complex observables. They are also interesting in themselves: it has been shown that the ratio of the NLO to the LO predictions is relatively flat across the $p_T^{(1)}$ spectrum with a maximum variation of approximately 25% [10]. Perhaps surprisingly, the PS description of $p_T^{(4)}$ was found to be better than that of $p_T^{(1)}$ in the 7 TeV multi-jet measurement published by ATLAS [9].

Figures 4 to 7 show the p_T distributions of the leading four jets. All the LO generators show a slope with respect to the data in the leading jet p_T (figure 4). The ratios of Herwig++ and HEJ to data are remarkably flat above ~ 500 GeV and ~ 300 GeV respectively. MadGraph+Pythia is within the experimental uncertainties above ~ 300 GeV, and it is the only one with a positive slope in the ratio to data.

The subleading jet p_T (figure 5) is well described by HEJ, while the LO generators show similar trends to those in $p_T^{(1)}$. MadGraph+Pythia describes both $p_T^{(3)}$ and $p_T^{(4)}$ well, as shown in figures 6 and 7. As the 7 TeV results suggested, Pythia gives a good description of the distribution of $p_T^{(4)}$. HEJ and Herwig++ overestimate the number of events with high $p_T^{(4)}$. NJet/Sherpa shows a similar trend at high $p_T^{(4)}$, but the discrepancy is mostly covered by the theoretical uncertainties. H_T, shown in figure 8, exhibits features similar to those in $p_T^{(1)}$.

In summary, Pythia and Herwig++ tend to describe the p_T spectrum of the leading jets with similar levels of agreement, whereas Pythia is better at describing $p_T^{(4)}$. MadGraph+Pythia does a reasonable job for all of them, while HEJ and NJet/Sherpa are very good for the leading jets and less so for $p_T^{(4)}$. This could perhaps be improved by matching the calculations to PSs.

Mass variables. Mass variables are widely used in physics searches, and they are also sensitive to events with large separations between jets, which puts the HEJ and MadGraph+Pythia predictions to the test, as they are expected to be especially accurate in this regime.

The distribution of the total invariant mass m_{4j} is studied in figure 9. Pythia and MadGraph+Pythia describe the data very well. Herwig++ describes the shape of the data between 1 TeV and 3–6 TeV. HEJ is mostly compatible with the measurement, but

JHEP12(2015)105

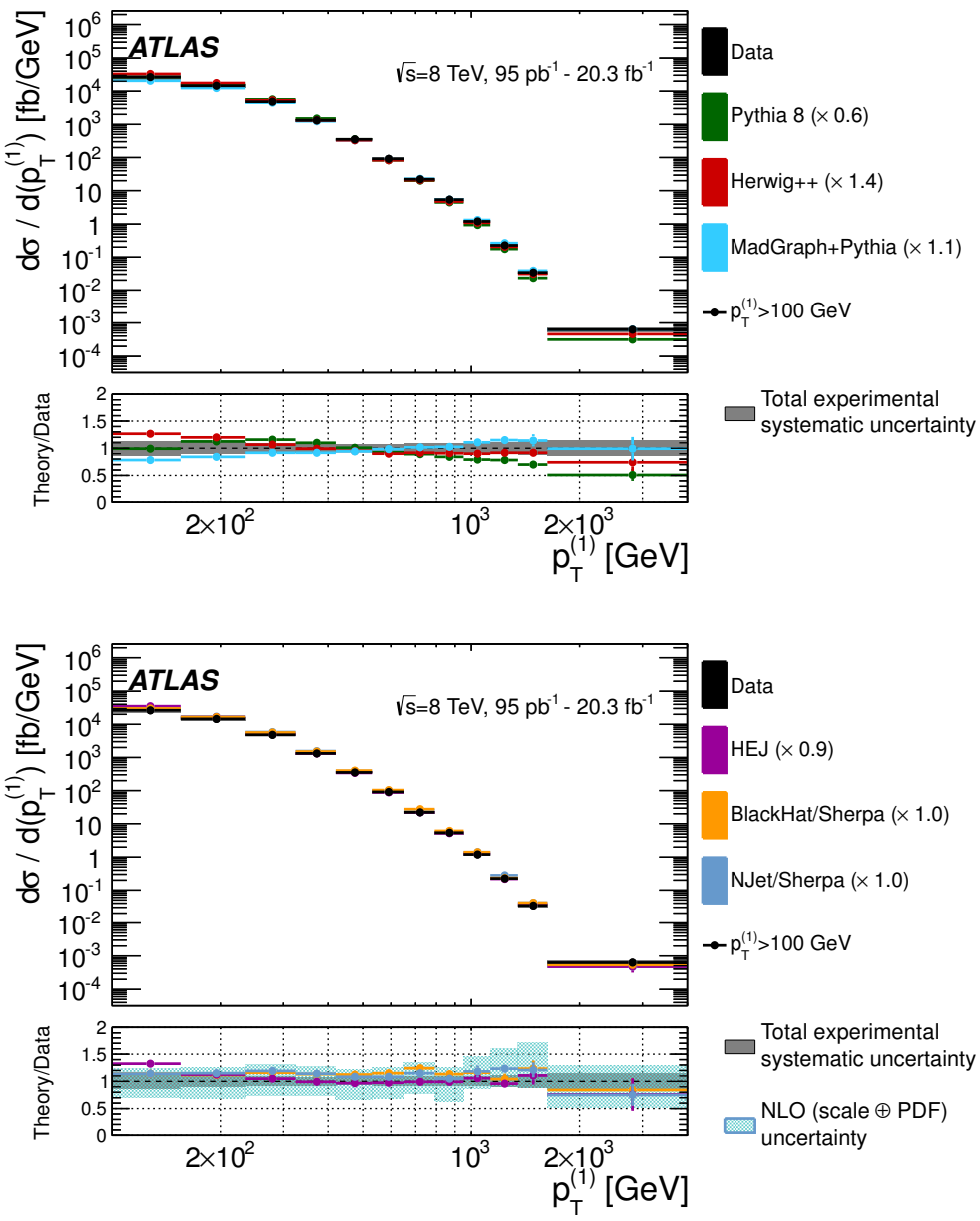

Figure 4. The four-jet differential cross section as a function of leading jet p_{T} ($p_{\mathrm{T}}^{(1)}$), compared to different theoretical predictions: Pythia, Herwig++ and MadGraph+Pythia (top), and HEJ, NJet/Sherpa and BlackHat/Sherpa (bottom). For better comparison, the predictions are multiplied by the factors indicated in the legend. In each figure, the top panel shows the full spectra and the bottom panel the ratios of the different predictions to the data. The solid band represents the total experimental systematic uncertainty centred at one. The patterned band represents the NLO scale and PDF uncertainties calculated from NJet/Sherpa centred at the nominal NJet/Sherpa values. The scale uncertainties for HEJ (not drawn) are typically $^{+50\%}_{-30\%}$. The ratio curves are formed by the central values with vertical uncertainty lines resulting from the propagation of the statistical uncertainties of the predictions and those of the unfolded data spectrum.

JHEP12(2015)105

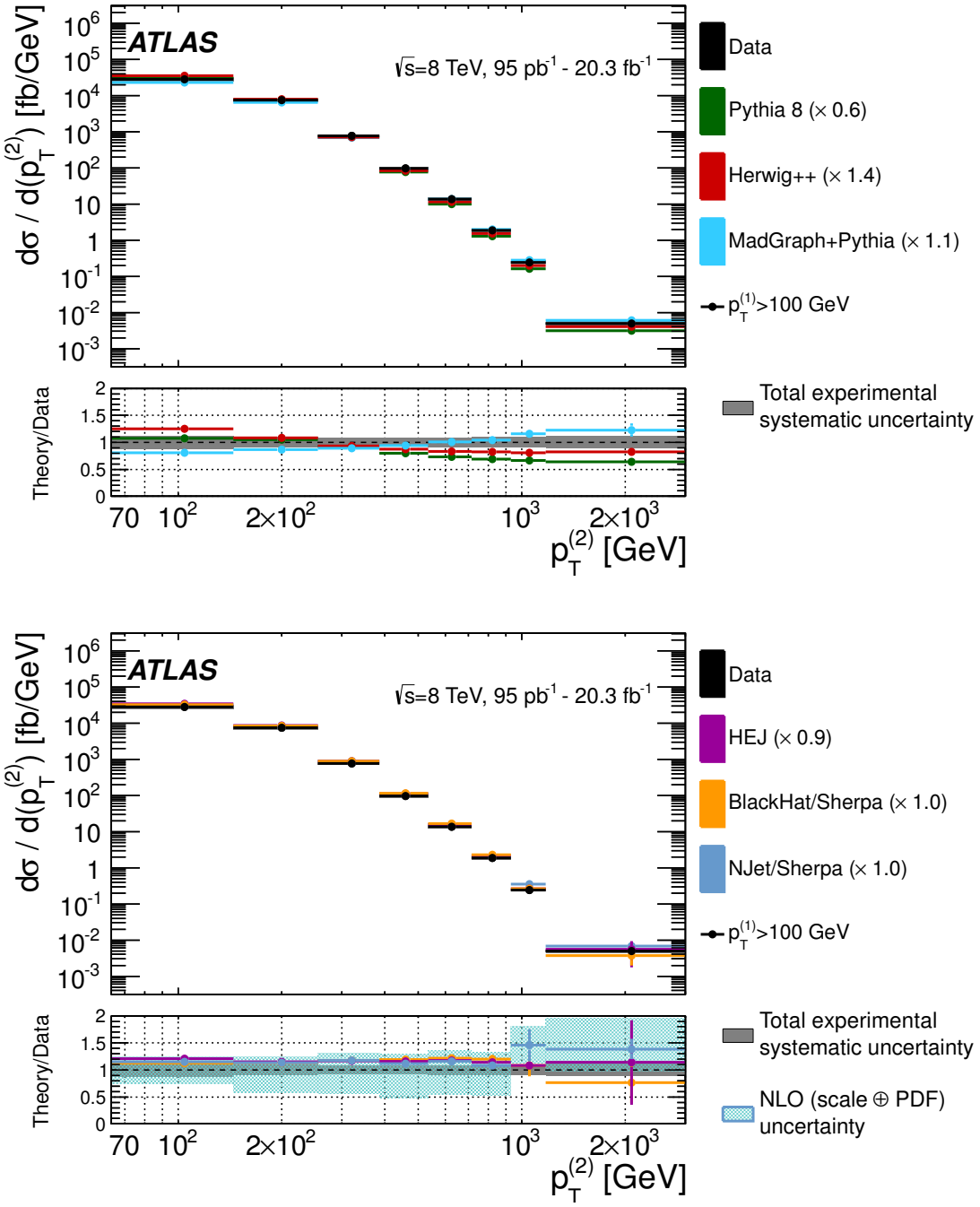

Figure 5. Unfolded four-jet differential cross section as a function of $p_{\mathrm{T}}^{(2)}$, compared to different theoretical predictions. The other details are as for figure 4.

JHEP12(2015)105

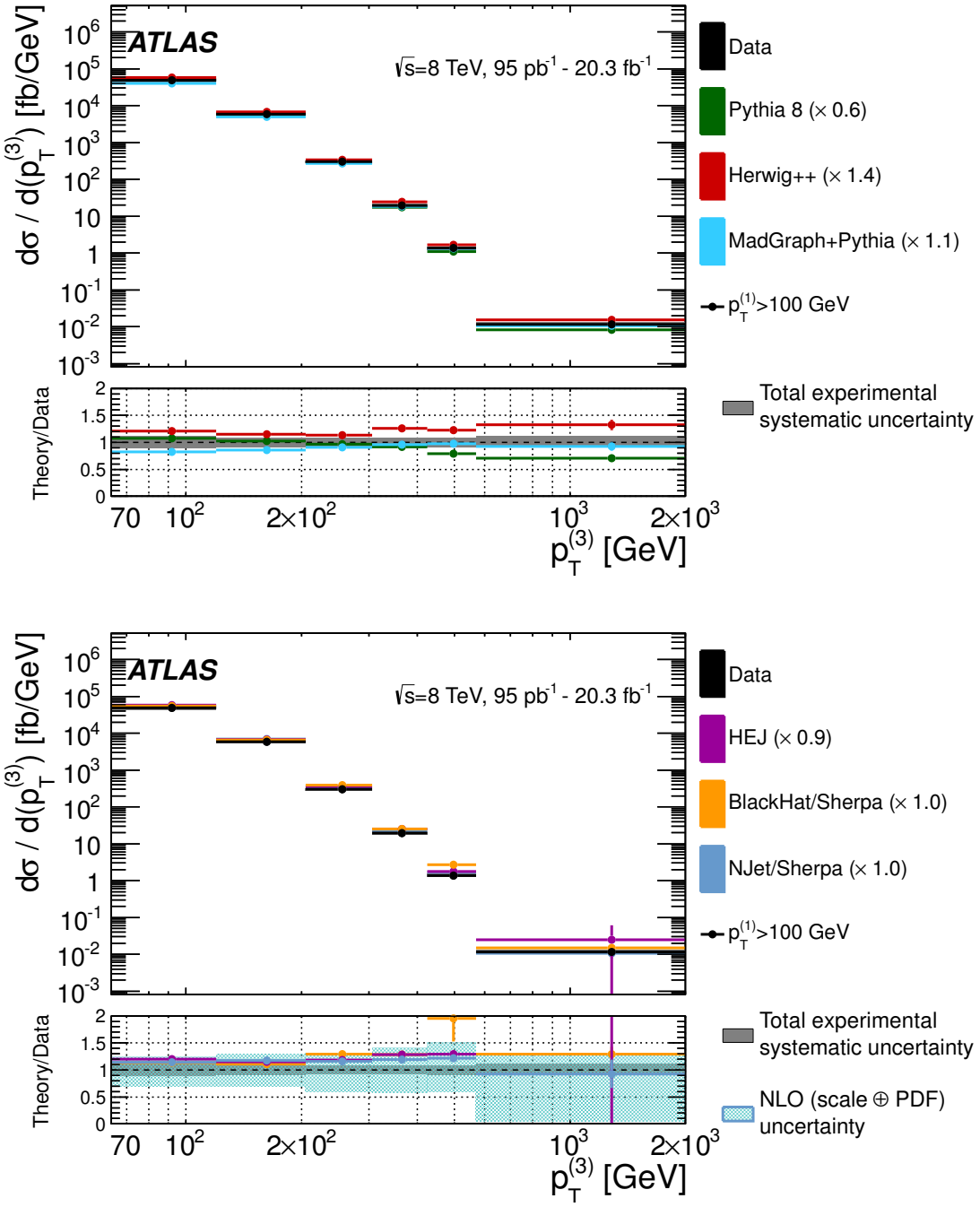

Figure 6. Unfolded four-jet differential cross section as a function of $p_{\mathrm{T}}^{(3)}$, compared to different theoretical predictions. The other details are as for figure 4.

JHEP12(2015)105

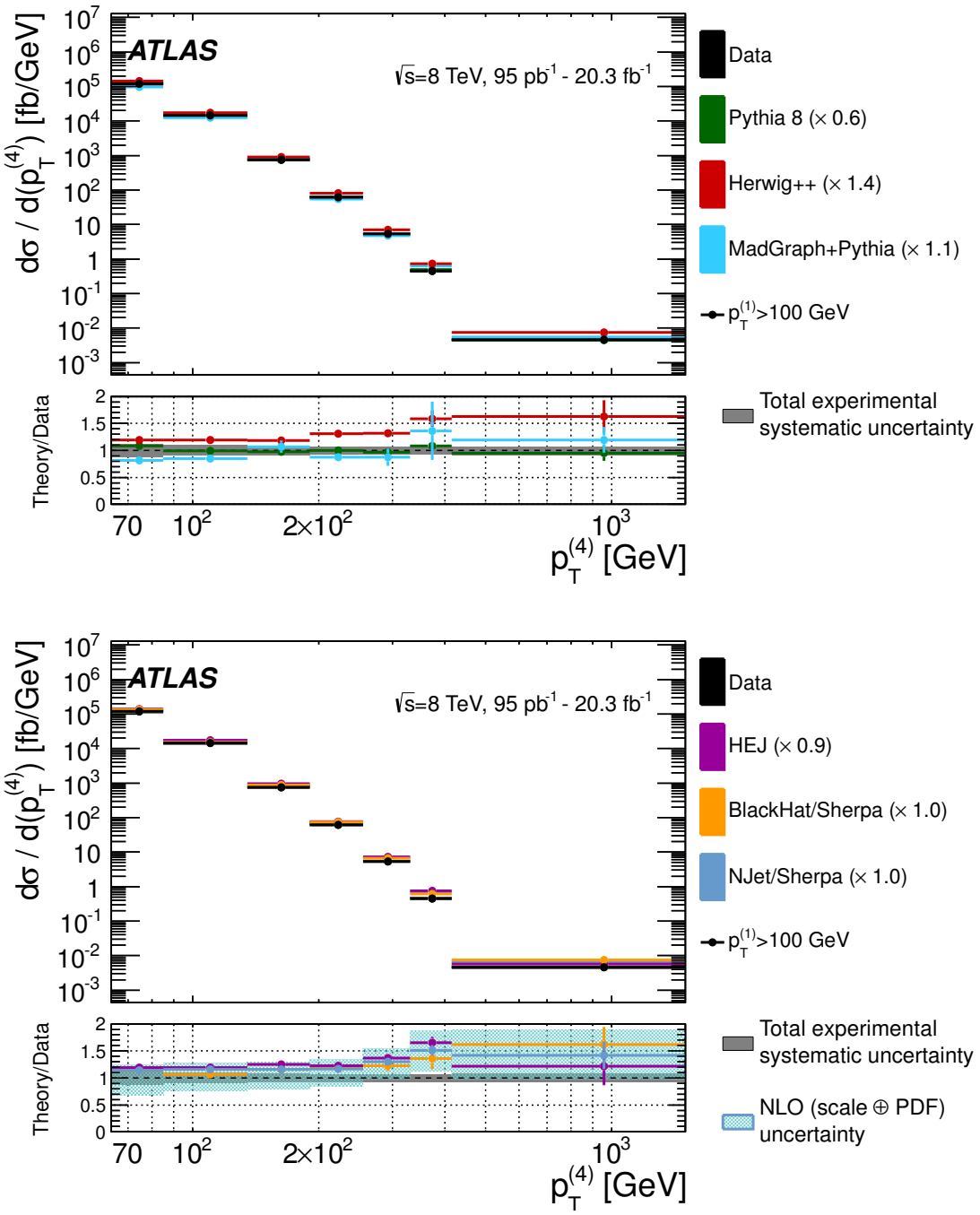

Figure 7. Unfolded four-jet differential cross section as a function of $p_{\mathrm{T}}^{(4)}$, compared to different theoretical predictions. The other details are as for figure 4.

JHEP12(2015)105

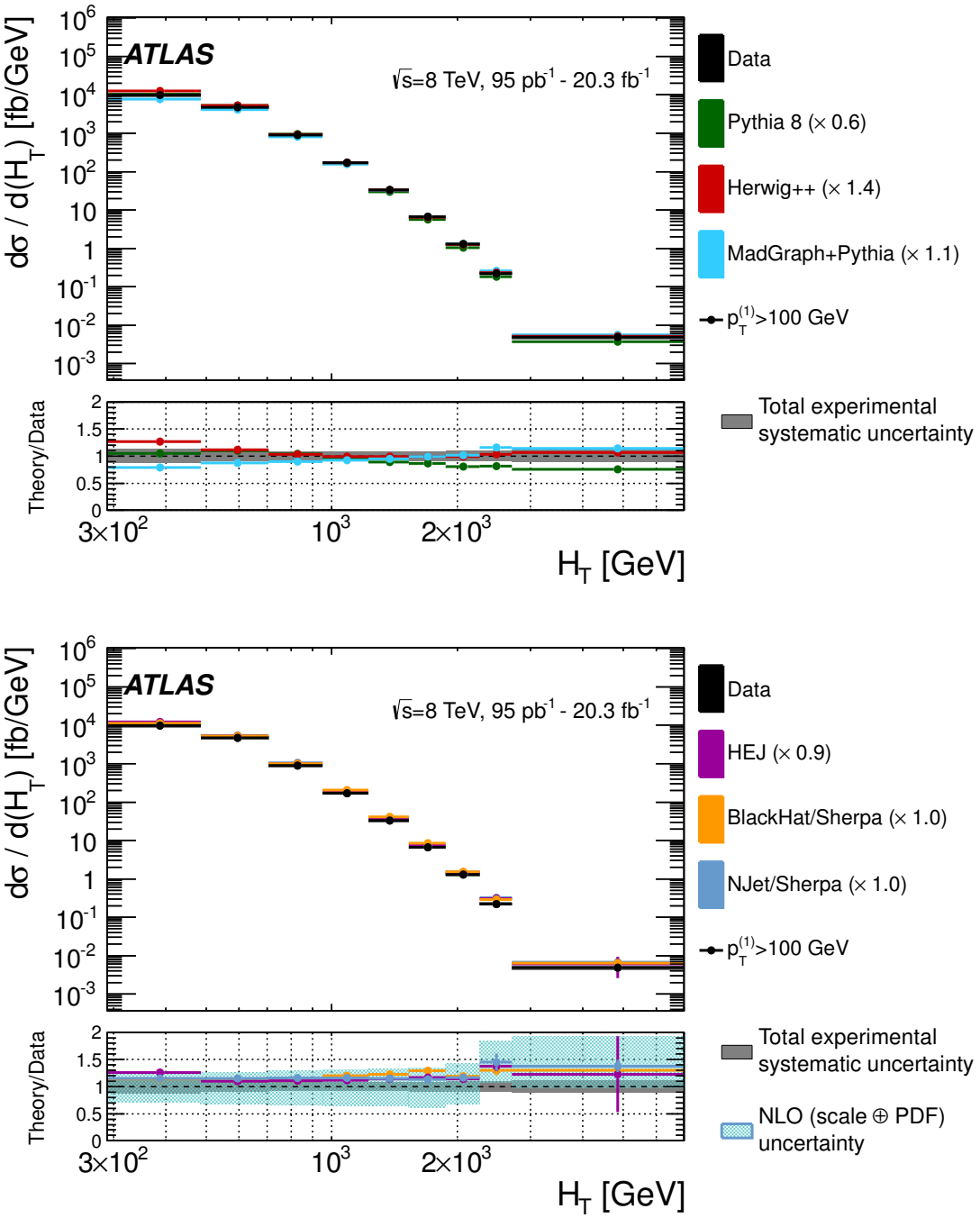

Figure 8. Unfolded four-jet differential cross section as a function of H_{T}, compared to different theoretical predictions. The other details are as for figure 4.

JHEP12(2015)105

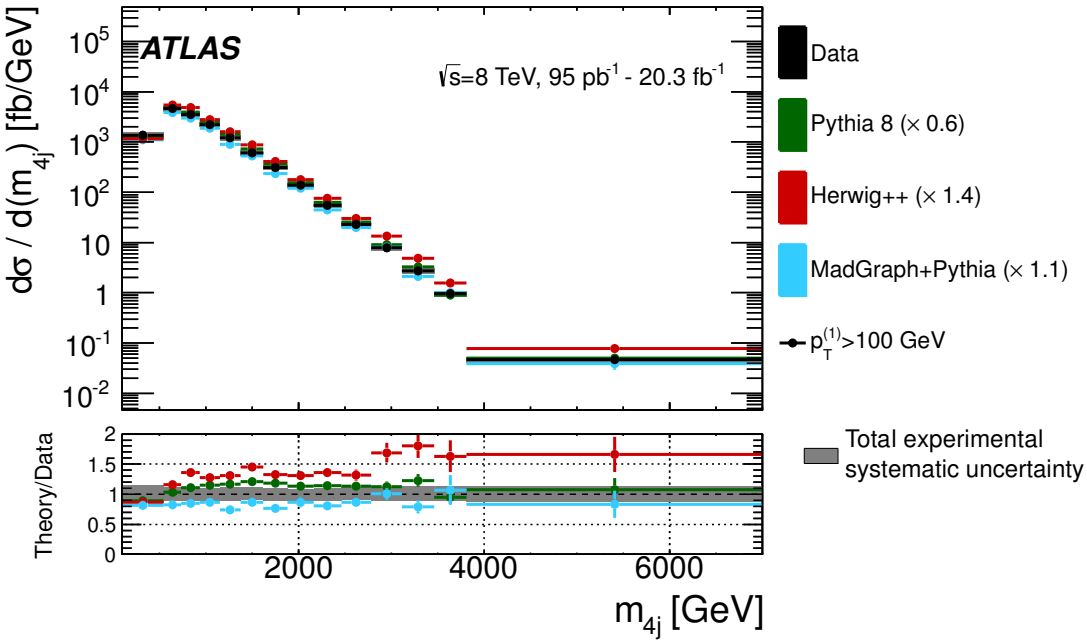

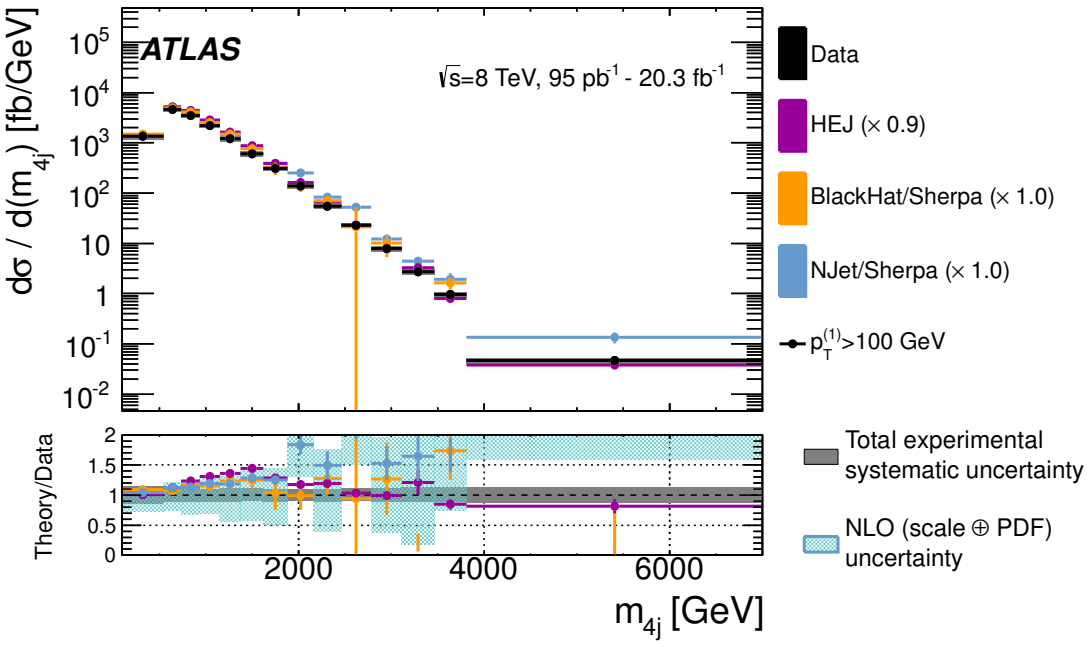

Figure 9. Unfolded four-jet differential cross section as a function of m_{4j}, compared to different theoretical predictions. The other details are as for figure 4. Some points in the ratio curves for NJet/Sherpa fall outside the y-axis range, and thus the NLO uncertainty is shown partially, or not shown, in these particular bins.

JHEP12(2015)105

the ratio to data has a bump structure in the region of approximately 1 to 2 TeV. This feature is also shared by NJet/Sherpa, but the differences with respect to the data are covered by the NLO uncertainties.

The description of different splitting scales is tested in figure 10 through the variable m_{2j}^{min}/m_{4j}. This distribution is well described by Pythia, whereas Herwig++ gets worse with increasing m_{4j}, consistently overestimating the two ends of the m_{2j}^{min}/m_{4j} spectrum. MadGraph+Pythia provides a very good description, with a flat ratio for all the m_{4j} cuts. The HEJ prediction shows trends similar to those of Herwig++ at higher values of m_{4j}. These differences are covered in all cases by the large associated scale uncertainty. NJet/Sherpa overestimates the number of events in the very first bin, possibly due to the lack of a PS, but otherwise agrees with the data within the theoretical uncertainties.

Overall, MadGraph+Pythia provides the best description of mass variables.

Angular variables. Similarly to mass variables, angular variables are able to test the description of events with small- and wide-angle radiation. In addition, they can also provide information on the global spatial distribution of the jets. High-p_T, large-angle radiation should be well captured by the ME+PS description of MadGraph+Pythia, or the all-orders approximation of HEJ — particularly the rapidity variables Δy_{2j}^{min}, Δy_{2j}^{max} and Δy_{3j}^{min}. PS generators are expected to perform poorly at large angles, given that they only contain two hard jets, and the rest is left to the soft- and collinear-enhanced PS. The fixed-order NLO prediction of NJet/Sherpa should provide a very good description of these variables too, as long as they are far from the infrared limit. This is indeed the case, and therefore no detailed comments about its performance are given here.

Figure 11 compares the distributions of $\Delta\phi_{2j}^{min}$ for different cuts in $p_T^{(1)}$. Pythia has a small downwards slope with respect to the data in all the $p_T^{(1)}$ ranges. MadGraph+Pythia also shows a small slope. The other generators, both LO and NLO, reproduce the data very well. Herwig++, in particular, provides a very good description of the data.

The $\Delta\phi_{3j}^{min}$ spectrum is shown in figure 12. The different $p_T^{(1)}$ cuts change the spatial distribution of the events, such that at low $p_T^{(1)}$ most events contain two jets recoiling against two, while at high $p_T^{(1)}$ the events where one jet recoils against three dominate. In general, the description of the data improves as $p_T^{(1)}$ increases. For Pythia, the number of events where one jet recoils against three (low $\Delta\phi_{3j}^{min}$) is significantly overestimated when $p_T^{(1)}$ is low; as $p_T^{(1)}$ increases, the agreement improves such that the $p_T^{(1)} > 1000$ GeV region is very well described. MadGraph+Pythia, Herwig++ and HEJ are mostly in good agreement with data.

Figure 13 compares the distributions of Δy_{2j}^{min} with data. This variable is remarkably well described by Pythia, showing no significant trend. MadGraph+Pythia mostly underestimates high Δy_{2j}^{min} values, while Herwig++ has a tendency to underestimate the low values. HEJ overestimates the number of events with high Δy_{2j}^{min} values at low $p_T^{(1)}$, but describes the data very well at larger values of $p_T^{(1)}$.

For the variable Δy_{3j}^{min}, presented in figure 14, the predictions provided by Pythia and Herwig++ show in general a positive slope with respect to the data. MadGraph+Pythia

JHEP12(2015)105

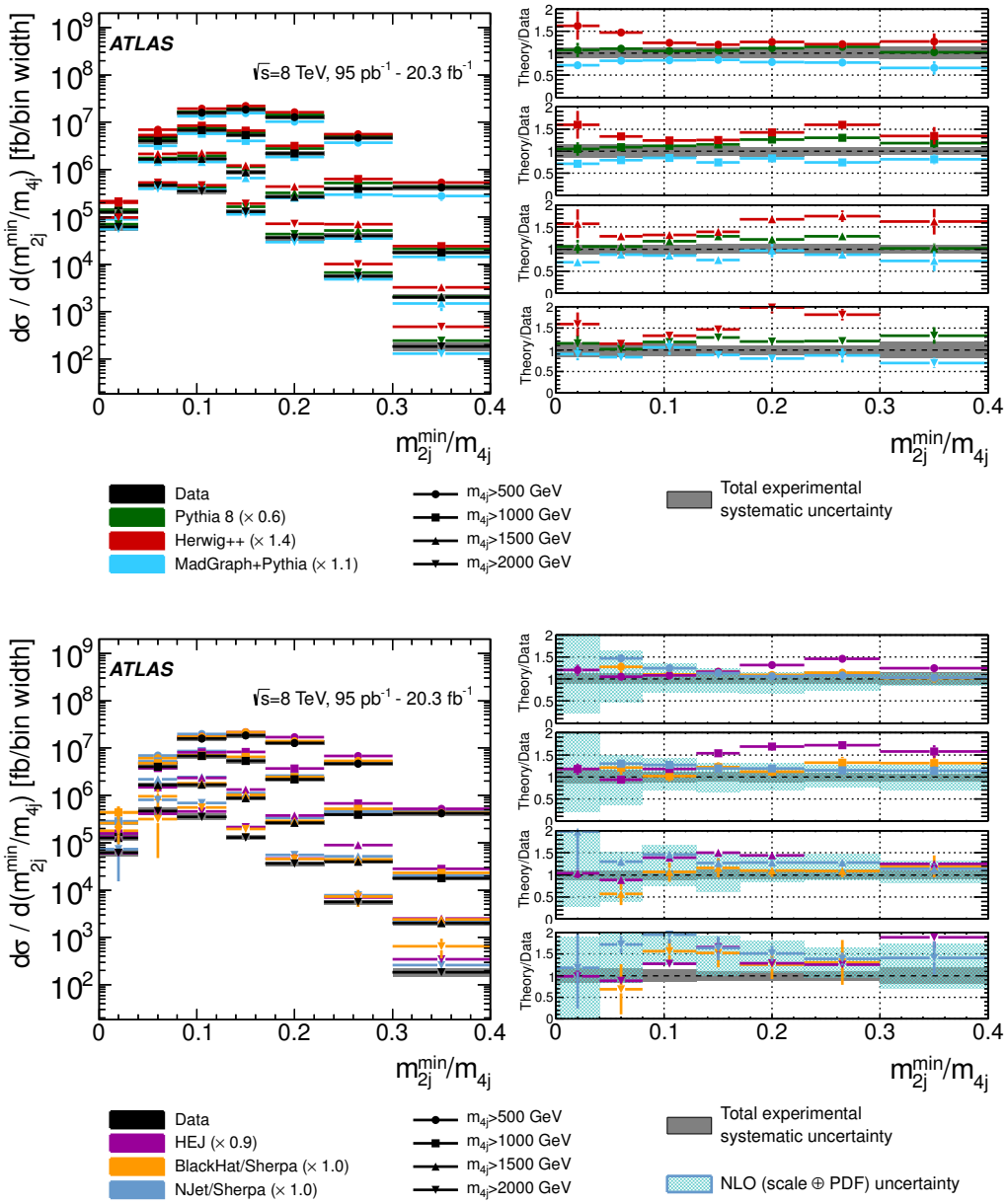

Figure 10. Unfolded four-jet differential cross section as a function of m_{2j}^{min}/m_{4j}, compared to different theoretical predictions: PYTHIA, HERWIG++ and MADGRAPH+PYTHIA (top), and HEJ, NJET/SHERPA and BLACKHAT/SHERPA (bottom). For better comparison, the predictions are multiplied by the factors indicated in the legend. In each figure, the left panel shows the full spectra and the right panel the ratios of the different predictions to the data, divided according to the selection criterion applied to m_{4j}. The solid band represents the total experimental systematic uncertainty centred at one. The patterned band represents the NLO scale and PDF uncertainties calculated from NJET/SHERPA centred at the nominal NJET/SHERPA values. The scale uncertainties for HEJ (not drawn) are typically $^{+50\%}_{-30\%}$. The ratio curves are formed by the central values and vertical uncertainty lines resulting from the propagation of the statistical uncertainties of the predictions and those of the unfolded data spectrum.

JHEP12(2015)105

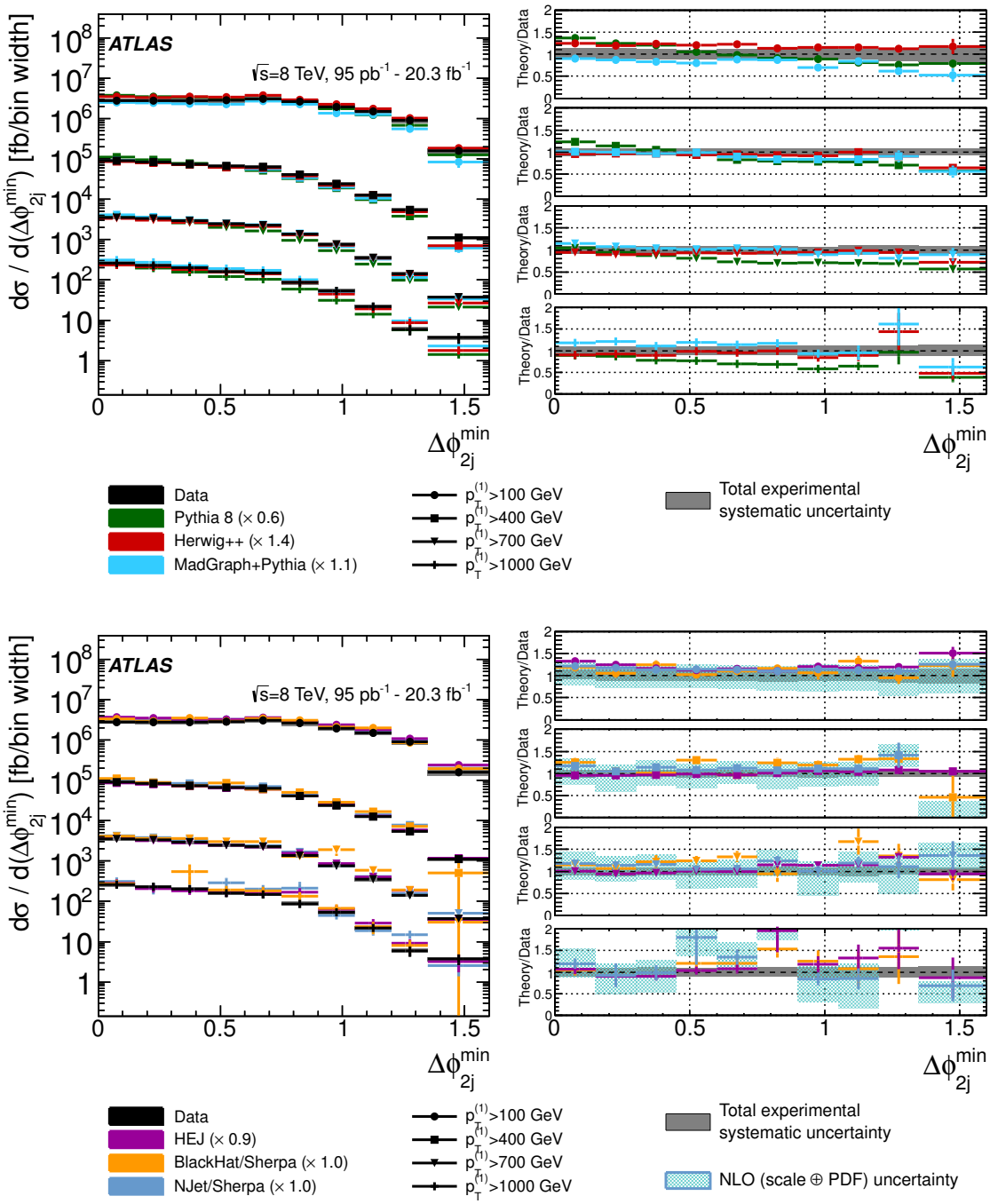

Figure 11. Unfolded four-jet differential cross section as a function of $\Delta\phi_{2j}^{min}$, compared to different theoretical predictions. The other details are as for figure 10, but here the multiple ratio plots correspond to different selection criteria applied to $p_T^{(1)}$. Some points in the ratio curves for NJet/Sherpa fall outside the y-axis range, and thus the NLO uncertainty is shown partially, or not shown, in these particular bins.

JHEP12(2015)105

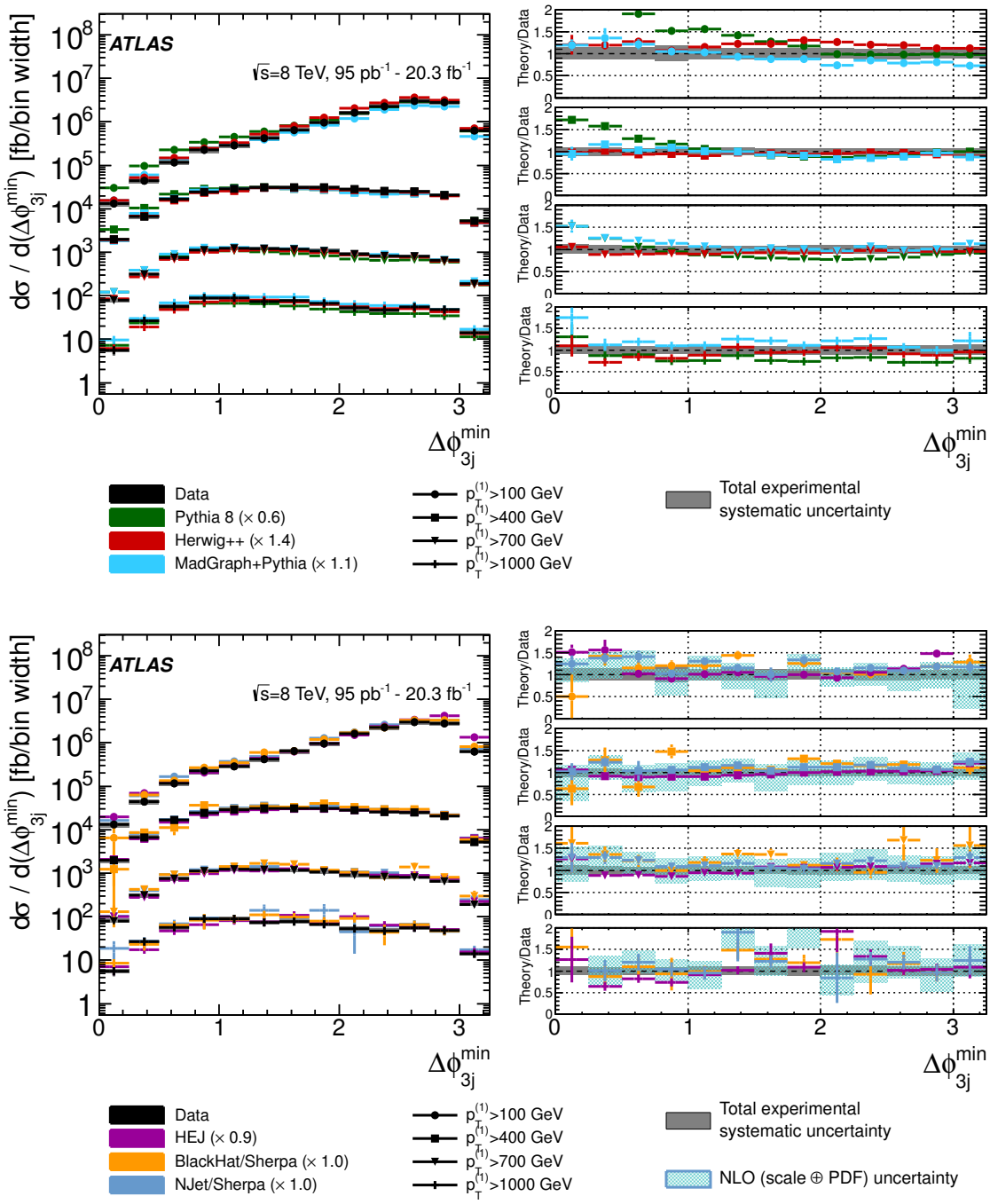

Figure 12. Unfolded four-jet differential cross section as a function of $\Delta\phi_{3j}^{min}$, compared to different theoretical predictions. The other details are as for figure 11. Some points in the ratio curves for NJet/Sherpa fall outside the y-axis range, and thus the NLO uncertainty is shown partially, or not shown, in these particular bins.

JHEP12(2015)105

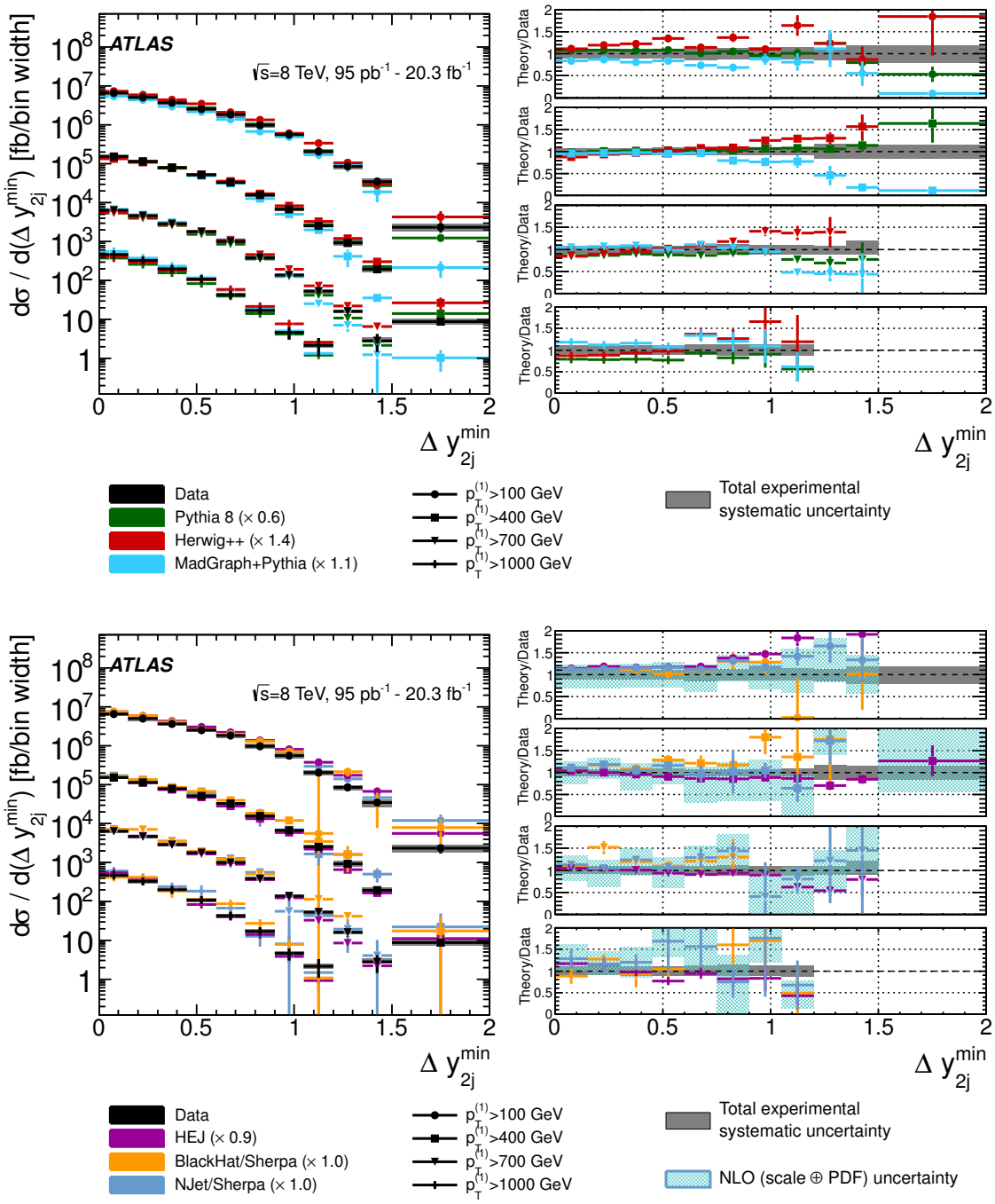

Figure 13. Unfolded four-jet differential cross section as a function of Δy_{2j}^{min}, compared to different theoretical predictions. The other details are as for figure 11. Some points in the ratio curves for NJet/Sherpa fall outside the y-axis range, and thus the NLO uncertainty is shown partially, or not shown, in these particular bins.

JHEP12(2015)105

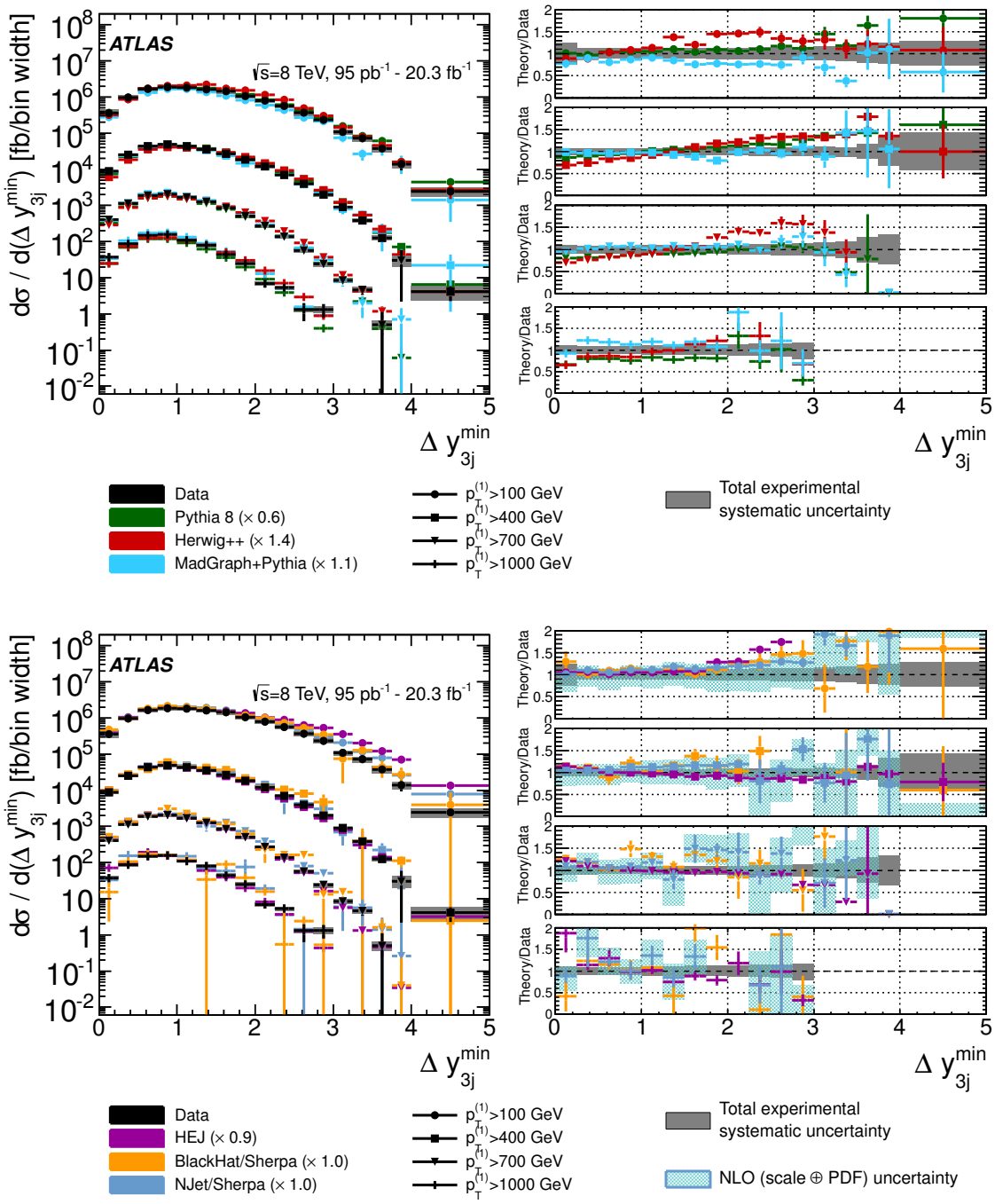

Figure 14. Unfolded four-jet differential cross section as a function of $\Delta y_{3j}^{\min}$, compared to different theoretical predictions. The other details are as for figure 11. Some points in the ratio curves for NJet/Sherpa fall outside the y-axis range, and thus the NLO uncertainty is shown partially, or not shown, in these particular bins.

JHEP12(2015)105

reproduces the shape of the data well, as does HEJ for $p_T^{(1)} > 400\,\text{GeV}$. However, for smaller values of $p_T^{(1)}$ HEJ overestimates the number of events at the end of the spectrum, as was the case for Δy_{2j}^{min}.

The variable Δy_{2j}^{max}, shown in figure 15, is very well described by HEJ in events with $p_T^{(1)} > 400\,\text{GeV}$. The ratios to data in both Pythia and Herwig++ have upwards slopes in all $p_T^{(1)}$ bins. MadGraph+Pythia provides mostly a good description of the data, with a tendency to underestimate the extremes of the distribution. Interestingly, NJet/Sherpa seems to overestimate the number of events in the tail, although it is a statistically limited region and the comparison with BlackHat/Sherpa is not conclusive.

In summary: NJet/Sherpa mostly agrees with the data within the uncertainties, but its ratio to data has an upwards trend in the tail of Δy_{2j}^{max}. HEJ provides a very good description of all angular variables for the region $p_T^{(1)} > 400\,\text{GeV}$, as expected, but shows significant discrepancies with respect to the data in all the rapidity variables for lower $p_T^{(1)}$ values. It is important to keep in mind, though, that the associated scale uncertainties are large. MadGraph+Pythia describes all the data well, apart from the tail of Δy_{2j}^{min} and the extreme values of Δy_{2j}^{max}, which it underestimates. Herwig++ gives good descriptions of the ϕ variables, but fails at describing the rapidity variables. Pythia has some problems describing both three-jet variables, as well as Δy_{2j}^{max}. These variables highlight the need to combine four-jet ME calculations with parton showers.

$\Sigma p_T^{central}$ variables. The variables setting a minimum forward-backward rapidity interval and measuring the total p_T of the central jets ($\Sigma p_T^{central}$) were defined to test the framework of HEJ. HEJ has been designed to describe events with two jets significantly separated in rapidity with additional, central, high-p_T radiation. These variables are also useful to describe the spatial configuration of the events, as they represent the forward-backward rapidity span of the jets, and whether the leading jet is among the two central ones or not. The NLO predictions and MadGraph+Pythia are also expected to be successful in this regime, whereas the $2 \to 2$ generators with PSs are expected to be less suitable.

The variable $\Sigma p_T^{central}$ is studied for values of Δy_{2j}^{max} larger than 1, 2, 3 or 4, and for different cuts in $p_T^{(1)}$. In most cases, the description of the observable worsens significantly with increasing Δy_{2j}^{max} and $p_T^{(1)}$. Figures 16 to 19 correspond to the results for $\Delta y_{2j}^{max} > 1, 2, 3, 4$.

The generators with $2 \to 2$ MEs have problems describing the data around the threshold values where the contribution from different jets changes, which results in kinks in the ratio distributions. One such transition occurs at the $\Sigma p_T^{central}$ value for which the leading jet is first allowed to be central. For $p_T^{(1)} > 400\,\text{GeV}$, this happens at $\Sigma p_T^{central} > 464\,\text{GeV}$, at which point there is a major jump in Pythia in the second ratio plot of figure 16. Pythia gives in general the most discrepant prediction, with kinks in the ratio to data at the transition points that reach differences of 70% at high $p_T^{(1)}$, as well as global slopes. Herwig++ describes the data very well at lower Δy_{2j}^{max} values, but as Δy_{2j}^{max} grows its normalisation worsens, as well as the shape — particularly at high $p_T^{(1)}$.

JHEP12(2015)105

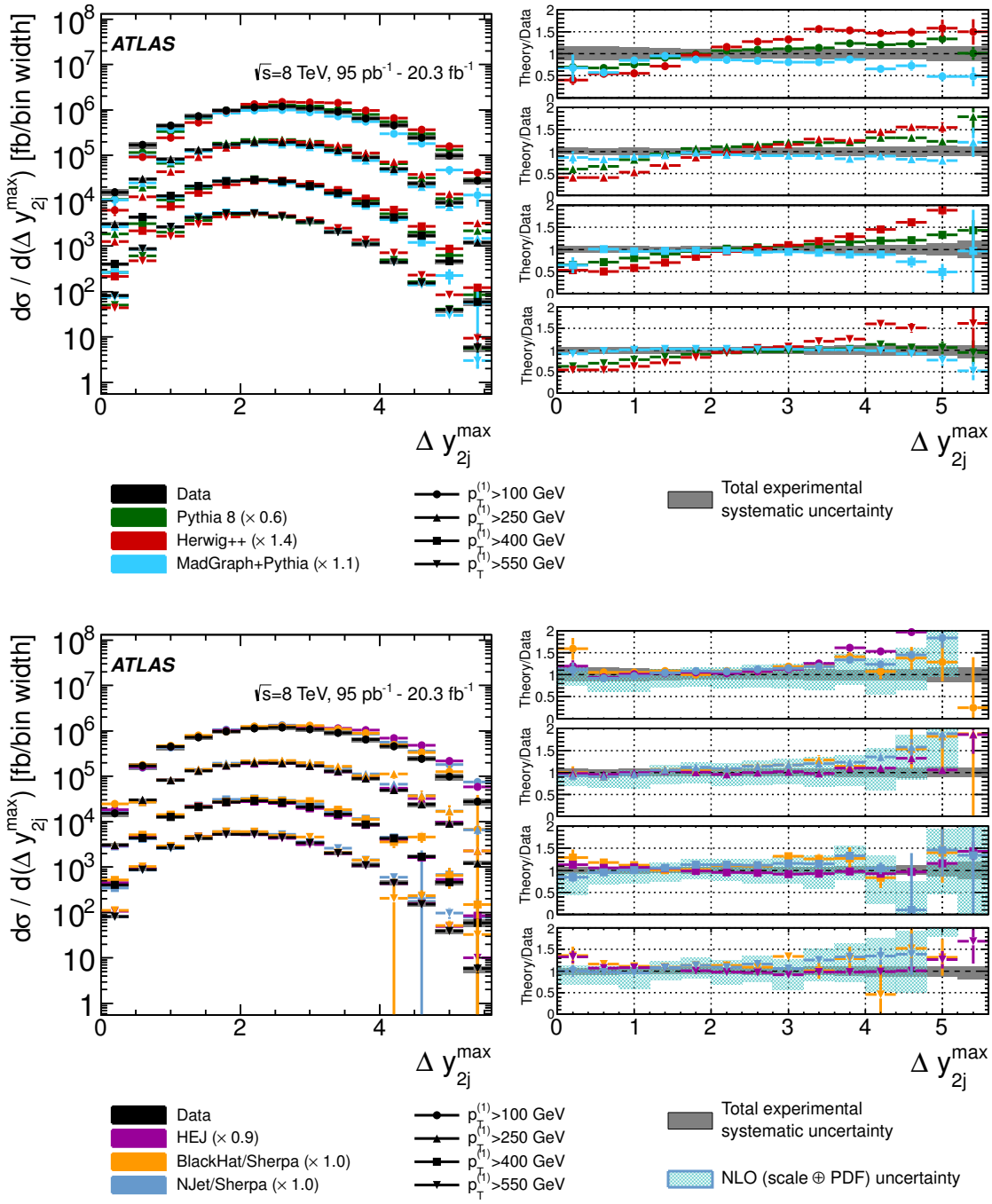

Figure 15. Unfolded four-jet differential cross section as a function of Δy_{2j}^{max}, compared to different theoretical predictions. The other details are as for figure 11. Some points in the ratio curves for NJet/Sherpa fall outside the y-axis range, and thus the NLO uncertainty is shown partially, or not shown, in these particular bins.

JHEP12(2015)105

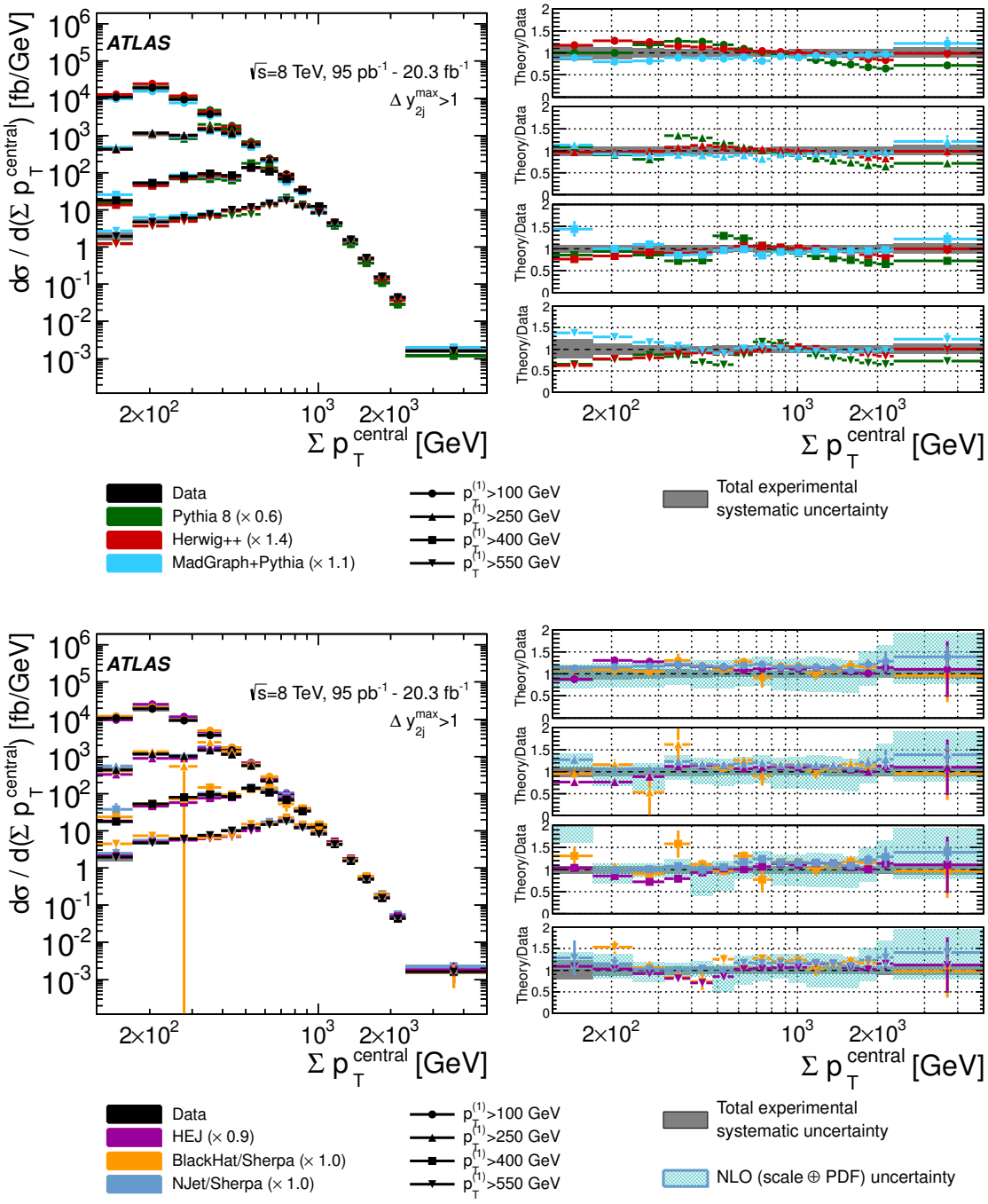

Figure 16. Unfolded four-jet differential cross section as a function of $\Sigma p_{\mathrm{T}}^{\mathrm{central}}$ with $\Delta y_{2\mathrm{j}}^{\mathrm{max}} > 1$, compared to different theoretical predictions. The other details are as for figure 11.

JHEP12(2015)105

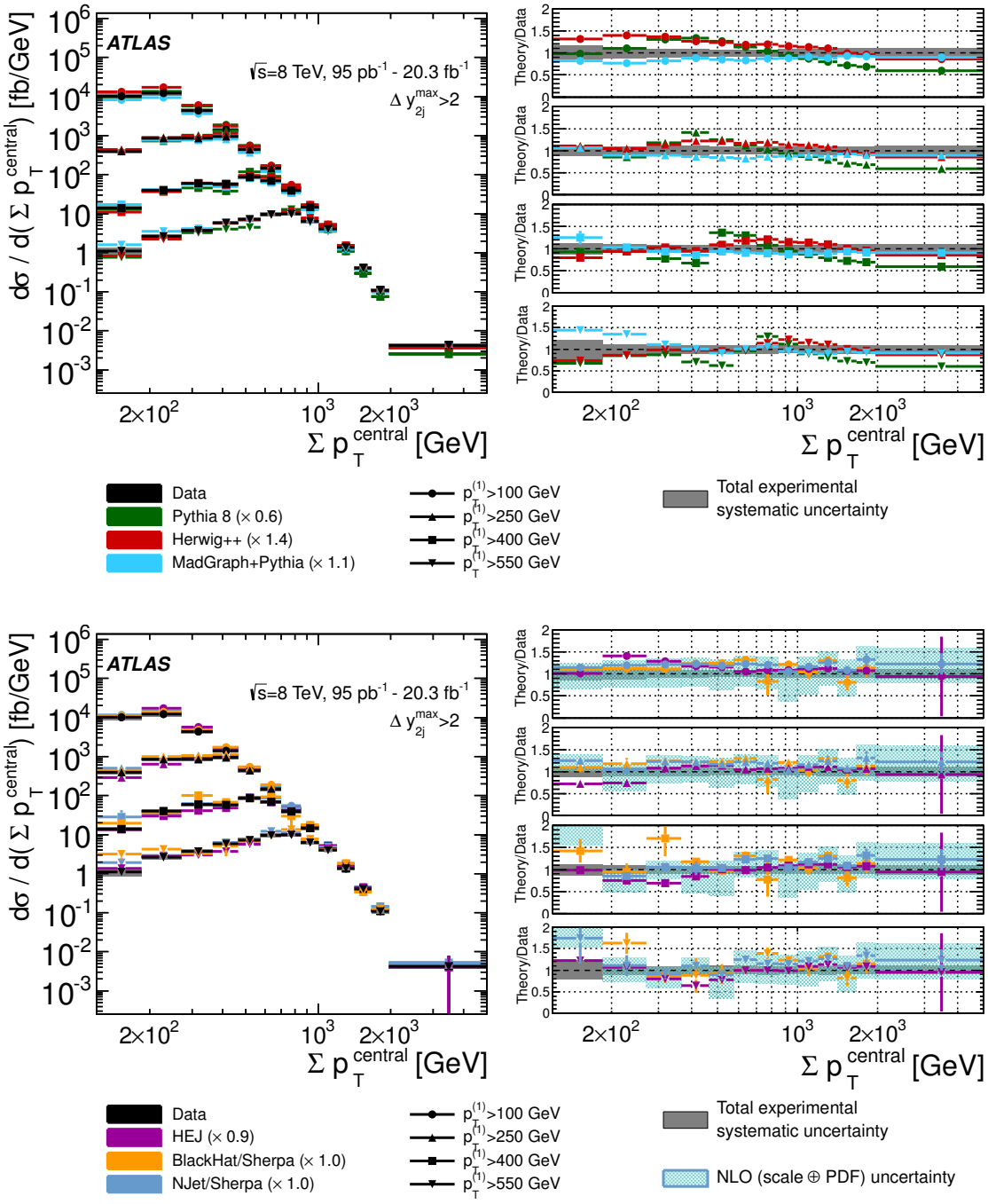

Figure 17. Unfolded four-jet differential cross section as a function of $\Sigma p_{\mathrm{T}}^{\mathrm{central}}$ with $\Delta y_{2\mathrm{j}}^{\mathrm{max}} > 2$, compared to different theoretical predictions. The other details are as for figure 11.

JHEP12(2015)105

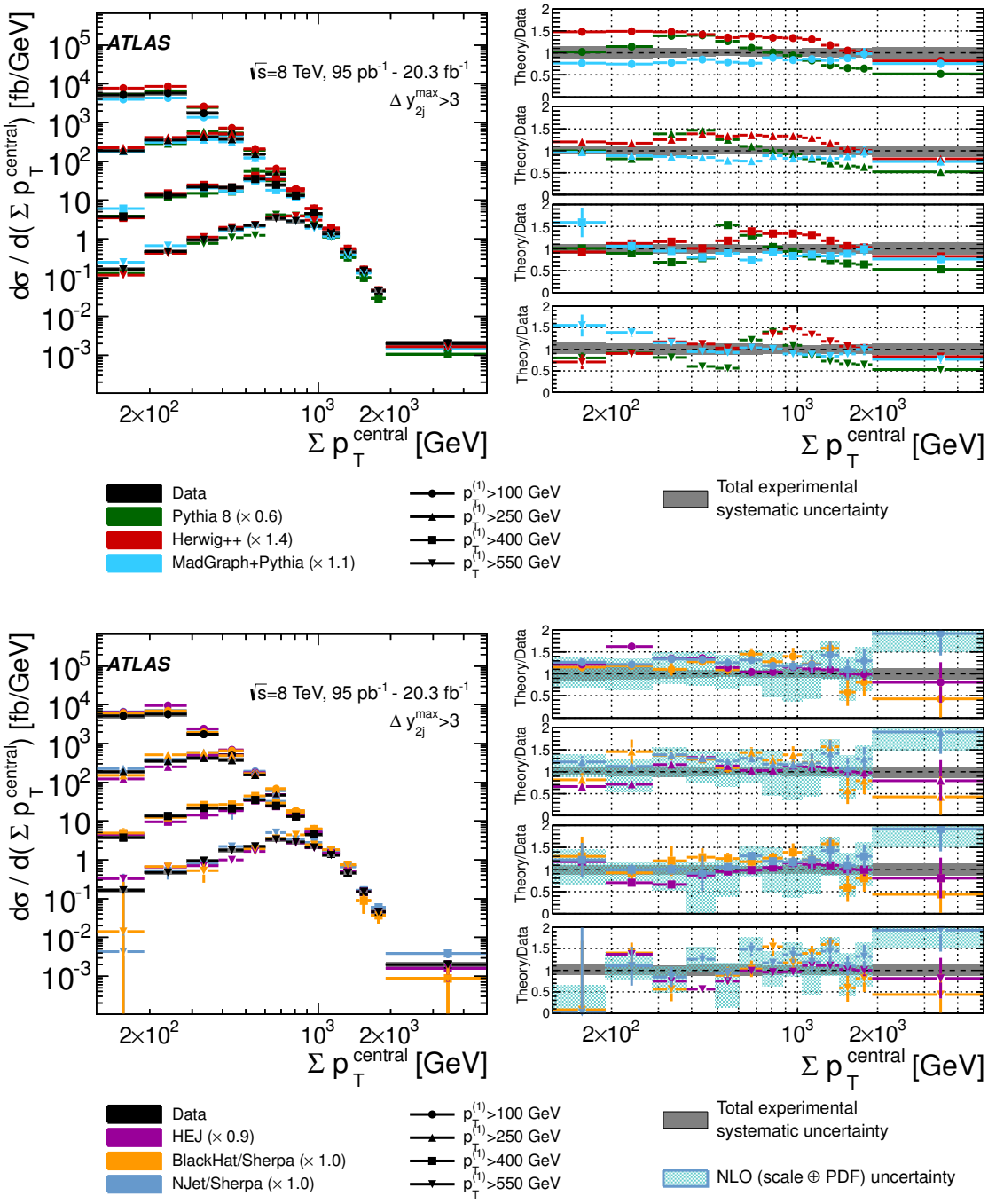

Figure 18. Unfolded four-jet differential cross section as a function of $\Sigma p_{\mathrm{T}}^{\mathrm{central}}$ with $\Delta y_{2\mathrm{j}}^{\max} > 3$, compared to different theoretical predictions. The other details are as for figure 11.

JHEP12(2015)105

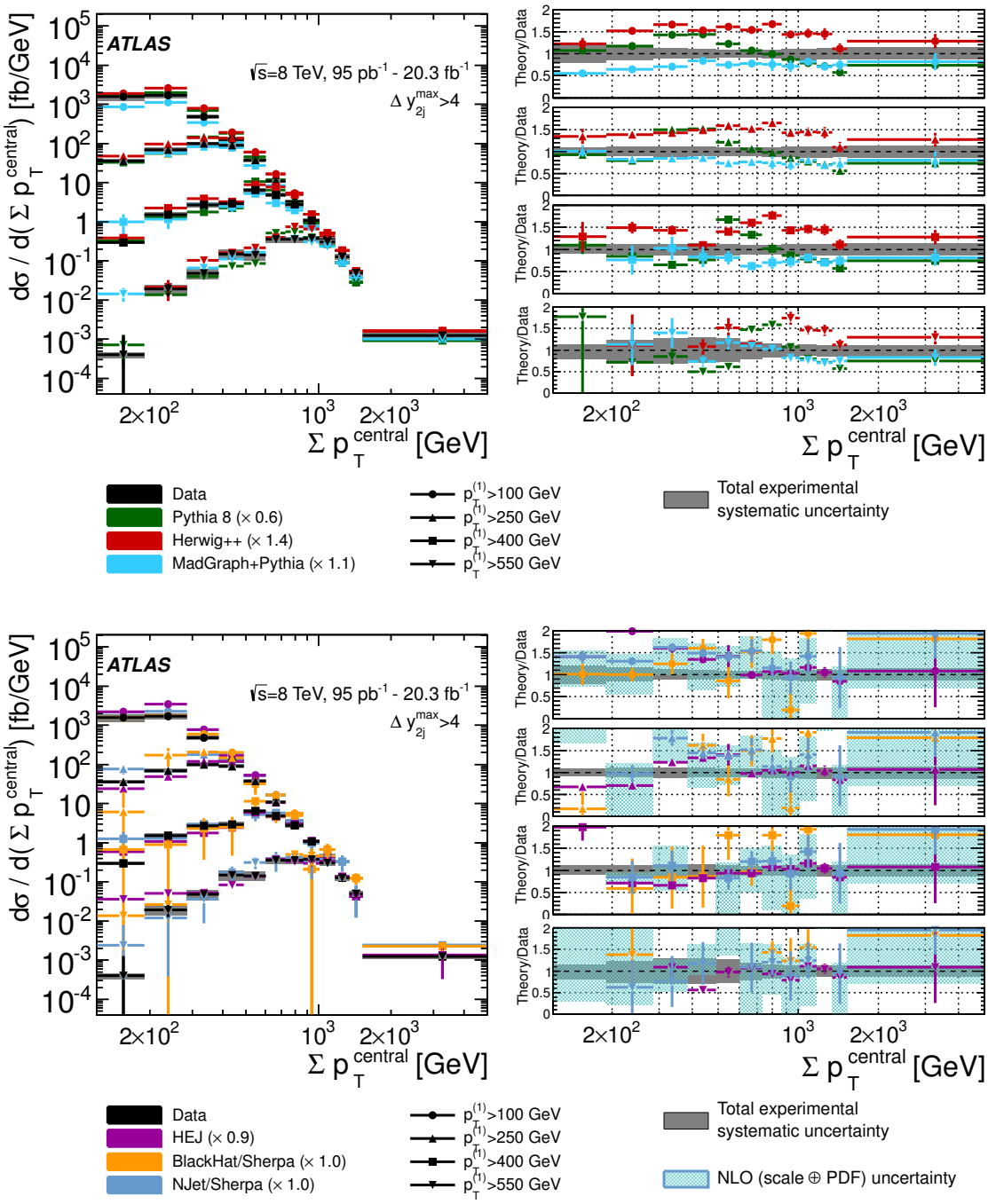

Figure 19. Unfolded four-jet differential cross section as a function of $\Sigma p_{\mathrm{T}}^{\mathrm{central}}$ with $\Delta y_{2\mathrm{j}}^{\max} > 4$, compared to different theoretical predictions. The other details are as for figure 11. Some points in the ratio curves for NJet/Sherpa fall outside the y-axis range, and thus the NLO uncertainty is shown partially, or not shown, in these particular bins.

JHEP12(2015)105

MadGraph+Pythia provides an excellent description of the $\Sigma p_{\mathrm{T}}^{\mathrm{central}}$ variables, especially at low $p_{\mathrm{T}}^{(1)}$. The agreement deteriorates at high $p_{\mathrm{T}}^{(1)}$, but it is not very much affected by the changes between different jet configurations, providing overall a very good description of the shapes. Most distributions are well described by HEJ, especially the high $\Sigma p_{\mathrm{T}}^{\mathrm{central}}$ region; the low $\Sigma p_{\mathrm{T}}^{\mathrm{central}}$ region shows more shape differences, which get worse at large $\Delta y_{2\mathrm{j}}^{\mathrm{max}}$. This is compatible with similar observations made in previous ATLAS measurements performed with 7 TeV data [64], where it was also shown that the agreement was significantly improved after interfacing HEJ with a PS generator. NJet/Sherpa has a tendency to overestimate the number of events with very low $\Sigma p_{\mathrm{T}}^{\mathrm{central}}$, which may be correlated with the $p_{\mathrm{T}}^{(4)}$ discrepancy discussed earlier. It provides a very good description of the data otherwise.

Tables 4 to 49 in appendix A contain the numerical values of the measured differential cross sections and their corresponding uncertainties. The quoted values correspond to the average differential cross sections over the bin ranges given

10 Conclusion

This paper presents unfolded differential cross sections of events with at least four jets in pp collisions at 8 TeV centre-of-mass energy. The cross sections are studied as a function of a variety of kinematic and topological variables which include momenta, masses and angles. Events are selected if the four anti-k_t $R = 0.4$ jets with the largest transverse momentum within the rapidity range $|y| < 2.8$ are well separated ($\Delta R_{4\mathrm{j}}^{\mathrm{min}} > 0.65$), all have $p_{\mathrm{T}} > 64$ GeV, and include at least one jet with $p_{\mathrm{T}} > 100$ GeV. The results are obtained from the analysis of the full dataset collected by the ATLAS detector at the LHC in 2012, which corresponds to a total integrated luminosity of 20.3 fb^{-1}. The total experimental systematic uncertainty is typically of the order of 10%, and it is dominated by the jet energy scale calibration uncertainty.

The measurements are compared to NLO pQCD predictions provided by BlackHat/Sherpa and NJet/Sherpa, as well as the all-orders calculation provided by HEJ. Three leading-order calculations are also considered, including two $2 \to 2$ PS samples (Pythia and Herwig++) and a multi-leg calculation with up to four partons in the ME matched to a PS generated by Pythia (MadGraph+Pythia).

The LO cross sections and HEJ are normalised by fixed factors to facilitate the comparison of the spectra in the kinematic regions of interest; these factors vary between 0.6 and 1.4 for the different samples, where the MadGraph+Pythia and HEJ samples are the ones that need the smallest corrections. The NLO predictions, BlackHat/Sherpa and NJet/Sherpa, are almost always compatible with the data within their theoretical uncertainties, which are found to be large ($\mathcal{O}(30\%)$ at low momenta) and asymmetric. Within the normalisation scheme used, MadGraph+Pythia also provides a good description of the data, as does HEJ, especially at high leading jet p_{T}. The $2 \to 2$ PS calculations generally describe the data relatively poorly, although they are found to provide good predictions in some particular cases: Pythia gives a very good prediction of $p_{\mathrm{T}}^{(4)}$ and $\Delta y_{2\mathrm{j}}^{\mathrm{min}}$, while Herwig++ performs well in the azimuthal angle variables.

JHEP12(2015)105

Looking at the individual distributions of the differential cross section, the description of the jet momenta is compatible with previous measurements of the multi-jet cross sections. It should be noted that HEJ, NJet/Sherpa and BlackHat/Sherpa give a very good description of the distributions of the leading jets but show some discrepancy with the data for $p_{\mathrm{T}}^{(4)}$. For variables that are particularly sensitive to wide-angle configurations and high-p_{T} radiation, such as masses or angles, BlackHat/Sherpa, NJet/Sherpa and MadGraph+Pythia do a remarkable job overall. HEJ also provides a good description of the data, the main exception being that it disagrees with the rapidity measurements in events with low $p_{\mathrm{T}}^{(1)}$. At high $p_{\mathrm{T}}^{(1)}$ the prediction is very good. These measurements expose the shortcomings of $2 \to 2$ parton ME+PS predictions in a variety of scenarios and highlight the importance of the more sophisticated calculations.

Acknowledgments

We thank CERN for the very successful operation of the LHC, as well as the support staff from our institutions without whom ATLAS could not be operated efficiently.

We acknowledge the support of ANPCyT, Argentina; YerPhI, Armenia; ARC, Australia; BMWFW and FWF, Austria; ANAS, Azerbaijan; SSTC, Belarus; CNPq and FAPESP, Brazil; NSERC, NRC and CFI, Canada; CERN; CONICYT, Chile; CAS, MOST and NSFC, China; COLCIENCIAS, Colombia; MSMT CR, MPO CR and VSC CR, Czech Republic; DNRF, DNSRC and Lundbeck Foundation, Denmark; IN2P3-CNRS, CEA-DSM/IRFU, France; GNSF, Georgia; BMBF, HGF, and MPG, Germany; GSRT, Greece; RGC, Hong Kong SAR, China; ISF, I-CORE and Benoziyo Center, Israel; INFN, Italy; MEXT and JSPS, Japan; CNRST, Morocco; FOM and NWO, Netherlands; RCN, Norway; MNiSW and NCN, Poland; FCT, Portugal; MNE/IFA, Romania; MES of Russia and NRC KI, Russian Federation; JINR; MESTD, Serbia; MSSR, Slovakia; ARRS and MIZŠ, Slovenia; DST/NRF, South Africa; MINECO, Spain; SRC and Wallenberg Foundation, Sweden; SERI, SNSF and Cantons of Bern and Geneva, Switzerland; MOST, Taiwan; TAEK, Turkey; STFC, United Kingdom; DOE and NSF, United States of America. In addition, individual groups and members have received support from BCKDF, the Canada Council, CANARIE, CRC, Compute Canada, FQRNT, and the Ontario Innovation Trust, Canada; EPLANET, ERC, FP7, Horizon 2020 and Marie Skłodowska-Curie Actions, European Union; Investissements d'Avenir Labex and Idex, ANR, Region Auvergne and Fondation Partager le Savoir, France; DFG and AvH Foundation, Germany; Herakleitos, Thales and Aristeia programmes co-financed by EU-ESF and the Greek NSRF; BSF, GIF and Minerva, Israel; BRF, Norway; the Royal Society and Leverhulme Trust, United Kingdom.

The crucial computing support from all WLCG partners is acknowledged gratefully, in particular from CERN and the ATLAS Tier-1 facilities at TRIUMF (Canada), NDGF (Denmark, Norway, Sweden), CC-IN2P3 (France), KIT/GridKA (Germany), INFN-CNAF (Italy), NL-T1 (Netherlands), PIC (Spain), ASGC (Taiwan), RAL (U.K.) and BNL (U.S.A.) and in the Tier-2 facilities worldwide.

JHEP12(2015)105

A Tables of the measured cross sections

Bin	Bin edges [GeV]	$d\sigma/d(p_T^{(1)})$ [fb/GeV]	δ_{stat}^{data} [%]	δ_{stat}^{MC} [%]	u_{JES} [%]	u_{JER} [%]	u_{unfold} [%]	u_{lumi} [%]
1	100–155	2.62×10^4	0.3	1.4	$^{+9.7}_{-8.7}$	5.2	8.4	2.8
2	155–235	1.47×10^4	0.3	0.6	$^{+8.2}_{-7.8}$	2.8	6.4	2.8
3	235–325	4.89×10^3	0.4	0.4	$^{+6.7}_{-6.7}$	1.5	4.3	2.8
4	325–420	1.35×10^3	< 0.1	0.3	$^{+6.0}_{-6.0}$	1.2	2.5	2.8
5	420–530	3.56×10^2	0.1	0.2	$^{+6.4}_{-6.2}$	1.1	1.6	2.8
6	530–650	9.2×10^1	0.2	0.3	$^{+7.0}_{-6.9}$	1.3	1.4	2.8
7	650–790	2.26×10^1	0.4	0.3	$^{+7.5}_{-7.5}$	1.5	1.3	2.8
8	790–950	5.34	0.8	0.2	$^{+8.1}_{-7.8}$	1.7	1.4	2.8
9	950–1130	1.19	2.1	0.2	$^{+8.6}_{-8.3}$	1.8	1.5	2.8
10	1130–1350	2.27×10^{-1}	3.8	0.3	$^{+9.7}_{-9.0}$	2.0	1.7	2.8
11	1350–1630	3.40×10^{-2}	9.1	0.3	$^{+11.7}_{-10.7}$	2.1	1.8	2.8
12	1630–4000	6.31×10^{-4}	21.9	0.4	$^{+14.5}_{-13.2}$	2.5	1.9	2.8

Table 4. Measured differential four-jet cross section for $R = 0.4$ jets, in bins of $p_T^{(1)}$, along with the uncertainties in the measurement. The events are selected using the inclusive analysis cuts. All uncertainties are given in %. δ_{stat}^{data} (δ_{stat}^{MC}) are the statistical uncertainties due to the number of data (MC simulation) events. The other columns correspond to the experimental systematic uncertainties arising from JES, JER, unfolding and luminosity, respectively.

Bin	Bin edges [GeV]	$d\sigma/d(p_T^{(2)})$ [fb/GeV]	δ_{stat}^{data} [%]	δ_{stat}^{MC} [%]	u_{JES} [%]	u_{JER} [%]	u_{unfold} [%]	u_{lumi} [%]
1	64–145	2.85×10^4	0.2	0.8	$^{+8.6}_{-8.1}$	3.7	6.4	2.8
2	145–255	7.43×10^3	0.3	0.4	$^{+7.5}_{-7.1}$	1.7	4.2	2.8
3	255–385	7.61×10^2	0.4	0.3	$^{+6.6}_{-6.8}$	0.8	2.5	2.8
4	385–535	9.71×10^1	0.2	0.3	$^{+6.7}_{-6.9}$	0.7	2.0	2.8
5	535–715	1.36×10^1	0.6	0.3	$^{+7.5}_{-7.5}$	0.8	2.1	2.8
6	715–930	1.88	1.2	0.3	$^{+8.4}_{-8.1}$	0.9	2.3	2.8
7	930–1175	2.44×10^{-1}	3.1	0.4	$^{+9.3}_{-8.5}$	1.0	2.4	2.8
8	1175–3000	4.91×10^{-3}	9.2	0.4	$^{+11.4}_{-10.5}$	1.0	2.4	2.8

Table 5. Measured differential four-jet cross section for $R = 0.4$ jets, in bins of $p_T^{(2)}$, along with the uncertainties in the measurement. The events are selected using the inclusive analysis cuts. All other details are as for table 4.

JHEP12(2015)105

Bin	Bin edges [GeV]	$d\sigma/d(p_T^{(3)})$ [fb/GeV]	δ_{stat}^{data} [%]	δ_{stat}^{MC} [%]	u_{JES} [%]	u_{JER} [%]	u_{unfold} [%]	u_{lumi} [%]
1	64–120	4.85×10^4	0.2	0.7	$^{+8.6}_{-8.0}$	3.4	5.8	2.8
2	120–205	5.87×10^3	0.3	0.6	$^{+7.3}_{-7.5}$	1.3	2.9	2.8
3	205–305	3.0×10^2	0.6	0.7	$^{+7.0}_{-6.8}$	0.4	1.7	2.8
4	305–425	1.94×10^1	0.5	0.8	$^{+7.4}_{-6.7}$	0.3	1.9	2.8
5	425–570	1.39	1.9	1.1	$^{+7.8}_{-7.3}$	0.2	2.1	2.8
6	570–2000	1.16×10^{-2}	6.4	1.3	$^{+10.8}_{-8.7}$	0.2	2.7	2.8

Table 6. Measured differential four-jet cross section for $R = 0.4$ jets, in bins of $p_T^{(3)}$, along with the uncertainties in the measurement. The events are selected using the inclusive analysis cuts. All other details are as for table 4.

Bin	Bin edges [GeV]	$d\sigma/d(p_T^{(4)})$ [fb/GeV]	δ_{stat}^{data} [%]	δ_{stat}^{MC} [%]	u_{JES} [%]	u_{JER} [%]	u_{unfold} [%]	u_{lumi} [%]
1	64–85	1.18×10^5	0.2	0.7	$^{+8.7}_{-8.0}$	3.6	7.0	2.8
2	85–135	1.45×10^4	< 0.1	0.8	$^{+8.7}_{-8.1}$	2.9	3.1	2.8
3	135–190	7.65×10^2	0.1	1.1	$^{+7.0}_{-7.2}$	1.4	1.5	2.8
4	190–255	6.24×10^1	0.4	2.2	$^{+5.8}_{-5.9}$	0.8	1.9	2.8
5	255–330	5.37	1.2	3.4	$^{+5.6}_{-5.8}$	0.7	2.1	2.8
6	330–415	4.58×10^{-1}	3.7	4.3	$^{+6.1}_{-6.8}$	0.7	2.1	2.8
7	415–1500	4.65×10^{-3}	11.9	6.4	$^{+6.5}_{-7.5}$	0.7	2.1	2.8

Table 7. Measured differential four-jet cross section for $R = 0.4$ jets, in bins of $p_T^{(4)}$, along with the uncertainties in the measurement. The events are selected using the inclusive analysis cuts. All other details are as for table 4.

Bin	Bin edges [GeV]	$d\sigma/d(H_T)$ [fb/GeV]	δ_{stat}^{data} [%]	δ_{stat}^{MC} [%]	u_{JES} [%]	u_{JER} [%]	u_{unfold} [%]	u_{lumi} [%]
1	290–485	9.85×10^3	0.2	1.0	$^{+8.8}_{-8.3}$	4.0	7.8	2.8
2	485–705	4.73×10^3	0.3	0.4	$^{+7.7}_{-7.3}$	1.7	4.6	2.8
3	705–950	9.0×10^2	0.3	0.3	$^{+6.7}_{-6.7}$	0.7	2.2	2.8
4	950–1225	1.7×10^2	0.1	0.2	$^{+6.6}_{-6.6}$	0.6	1.5	2.8
5	1225–1530	3.35×10^1	0.2	0.3	$^{+6.8}_{-7.0}$	0.6	1.5	2.8
6	1530–1875	6.62	0.6	0.2	$^{+7.3}_{-7.7}$	0.7	1.5	2.8
7	1875–2265	1.29	1.1	0.3	$^{+8.3}_{-8.2}$	0.8	1.7	2.8
8	2265–2705	2.23×10^{-1}	2.8	0.3	$^{+9.3}_{-8.4}$	0.8	1.6	2.8
9	2705–7000	4.88×10^{-3}	6.4	0.3	$^{+10.9}_{-10.6}$	1.1	1.6	2.8

Table 8. Measured differential four-jet cross section for $R = 0.4$ jets, in bins of H_T, along with the uncertainties in the measurement. The events are selected using the inclusive analysis cuts. All other details are as for table 4.

JHEP12(2015)105

Bin	Bin edges [GeV]	$d\sigma/d(m_{4j})$ [fb/GeV]	δ_{stat}^{data} [%]	δ_{stat}^{MC} [%]	u_{JES} [%]	u_{JER} [%]	u_{unfold} [%]	u_{lumi} [%]
1	100–545	1.36×10^3	0.5	2.7	$^{+8.8}_{-7.9}$	5.6	9.5	2.8
2	545–735	4.66×10^3	0.4	1.4	$^{+8.3}_{-7.9}$	3.5	6.4	2.8
3	735–935	3.55×10^3	0.4	1.2	$^{+8.7}_{-8.3}$	3.0	5.0	2.8
4	935–1150	2.2×10^3	0.4	1.6	$^{+8.7}_{-9.1}$	2.4	4.4	2.8
5	1150–1375	1.22×10^3	0.6	1.6	$^{+9.8}_{-9.2}$	2.1	3.9	2.8
6	1375–1620	6.09×10^2	0.6	1.7	$^{+10.0}_{-9.1}$	2.1	2.9	2.8
7	1620–1880	3.09×10^2	0.7	2.2	$^{+9.0}_{-9.6}$	2.1	2.6	2.8
8	1880–2160	1.37×10^2	1.0	2.2	$^{+8.3}_{-9.3}$	2.1	2.6	2.8
9	2160–2460	5.53×10^1	1.4	2.7	$^{+8.5}_{-9.0}$	2.1	3.1	2.8
10	2460–2780	2.28×10^1	2.0	3.0	$^{+8.8}_{-8.7}$	2.1	4.5	2.8
11	2780–3115	7.97	3.3	5.0	$^{+9.1}_{-8.8}$	2.1	5.3	2.8
12	3115–3460	2.71	3.0	4.9	$^{+10.2}_{-9.2}$	2.1	5.8	2.8
13	3460–3810	9.55×10^{-1}	8.4	5.5	$^{+10.6}_{-9.4}$	2.1	6.0	2.8
14	3810–7000	4.66×10^{-2}	12.4	6.9	$^{+11.6}_{-9.4}$	2.1	6.0	2.8

Table 9. Measured differential four-jet cross section for $R = 0.4$ jets, in bins of m_{4j}, along with the uncertainties in the measurement. The events are selected using the inclusive analysis cuts. All other details are as for table 4.

Bin	Bin edges	$d\sigma/d(m_{2j}^{min}/m_{4j})$ [fb]	δ_{stat}^{data} [%]	δ_{stat}^{MC} [%]	u_{JES} [%]	u_{JER} [%]	u_{unfold} [%]	u_{lumi} [%]
1	0–0.04	1.31×10^5	4.7	9.8	$^{+9.5}_{-7.8}$	3.3	7.0	2.8
2	0.04–0.08	4.74×10^6	0.7	2.5	$^{+9.5}_{-8.1}$	3.3	7.0	2.8
3	0.08–0.13	1.58×10^7	0.3	1.4	$^{+8.7}_{-8.5}$	3.3	7.0	2.8
4	0.13–0.17	1.85×10^7	0.3	1.3	$^{+9.4}_{-9.6}$	3.3	6.0	2.8
5	0.17–0.23	1.29×10^7	0.4	1.4	$^{+8.5}_{-8.1}$	3.3	4.0	2.8
6	0.23–0.3	4.69×10^6	0.5	2.5	$^{+7.7}_{-8.9}$	3.3	4.0	2.8
7	0.3–0.4	4.21×10^5	1.4	6.2	$^{+11.0}_{-4.8}$	2.0	10.2	2.8

Table 10. Measured differential four-jet cross section for $R = 0.4$ jets, in bins of m_{2j}^{min}/m_{4j}, along with the uncertainties in the measurement. The events are selected using the inclusive analysis cuts, as well as $m_{4j} > 500$ GeV. All other details are as for table 4.

Bin	Bin edges	$d\sigma/d(m_{2j}^{min}/m_{4j})$ [fb]	δ_{stat}^{data} [%]	δ_{stat}^{MC} [%]	u_{JES} [%]	u_{JER} [%]	u_{unfold} [%]	u_{lumi} [%]
1	0–0.04	1.34×10^5	4.6	9.7	$^{+9.7}_{-8.6}$	1.9	10.5	2.8
2	0.04–0.08	4.01×10^6	0.7	2.2	$^{+9.8}_{-8.9}$	1.9	10.5	2.8
3	0.08–0.13	6.79×10^6	0.4	1.4	$^{+8.9}_{-10.4}$	1.9	5.8	2.8
4	0.13–0.17	5.35×10^6	0.5	1.8	$^{+9.4}_{-7.9}$	1.9	5.5	2.8
5	0.17–0.23	2.21×10^6	0.6	1.8	$^{+8.2}_{-9.9}$	1.9	3.1	2.8
6	0.23–0.3	3.97×10^5	1.0	2.2	$^{+7.1}_{-7.5}$	1.9	3.1	2.8
7	0.3–0.4	1.78×10^4	2.7	5.9	$^{+6.7}_{-7.5}$	1.9	3.1	2.8

Table 11. Measured differential four-jet cross section for $R = 0.4$ jets, in bins of m_{2j}^{min}/m_{4j}, along with the uncertainties in the measurement. The events are selected using the inclusive analysis cuts, as well as $m_{4j} > 1000$ GeV. All other details are as for table 4.

JHEP12(2015)105

Bin	Bin edges	$d\sigma/d(m_{2j}^{min}/m_{4j})$ [fb]	δ_{stat}^{data} [%]	δ_{stat}^{MC} [%]	u_{JES} [%]	u_{JER} [%]	u_{unfold} [%]	u_{lumi} [%]
1	0–0.04	1.28×10^5	4.6	9.6	$^{+8.2}_{-10.3}$	2.1	4.8	2.8
2	0.04–0.08	1.67×10^6	1.1	2.2	$^{+8.3}_{-11.1}$	2.1	4.8	2.8
3	0.08–0.13	1.68×10^6	0.8	2.4	$^{+8.3}_{-9.5}$	2.1	4.8	2.8
4	0.13–0.17	8.81×10^5	0.9	2.5	$^{+8.7}_{-8.9}$	2.1	4.8	2.8
5	0.17–0.23	2.63×10^5	0.9	1.9	$^{+8.7}_{-7.7}$	2.1	5.2	2.8
6	0.23–0.3	4.04×10^4	1.7	2.6	$^{+9.3}_{-7.1}$	2.1	5.2	2.8
7	0.3–0.4	2.03×10^3	2.2	5.9	$^{+8.9}_{-7.1}$	2.1	3.1	2.8

Table 12. Measured differential four-jet cross section for $R = 0.4$ jets, in bins of m_{2j}^{min}/m_{4j}, along with the uncertainties in the measurement. The events are selected using the inclusive analysis cuts, as well as $m_{4j} > 1500$ GeV. All other details are as for table 4.

Bin	Bin edges	$d\sigma/d(m_{2j}^{min}/m_{4j})$ [fb]	δ_{stat}^{data} [%]	δ_{stat}^{MC} [%]	u_{JES} [%]	u_{JER} [%]	u_{unfold} [%]	u_{lumi} [%]
1	0–0.04	6.15×10^4	5.3	13.0	$^{+9.9}_{-7.1}$	1.5	13.2	2.8
2	0.04–0.08	4.66×10^5	1.6	2.8	$^{+10.6}_{-10.4}$	1.5	13.2	2.8
3	0.08–0.13	3.55×10^5	1.2	3.3	$^{+10.6}_{-10.4}$	1.5	9.7	2.8
4	0.13–0.17	1.29×10^5	0.8	3.0	$^{+8.9}_{-9.0}$	1.5	4.2	2.8
5	0.17–0.23	3.64×10^4	1.1	2.5	$^{+8.6}_{-9.0}$	1.5	4.2	2.8
6	0.23–0.3	5.61×10^3	1.3	4.0	$^{+8.6}_{-9.0}$	1.5	4.2	2.8
7	0.3–0.4	1.85×10^2	5.9	11.3	$^{+8.6}_{-9.0}$	1.5	16.4	2.8

Table 13. Measured differential four-jet cross section for $R = 0.4$ jets, in bins of m_{2j}^{min}/m_{4j}, along with the uncertainties in the measurement. The events are selected using the inclusive analysis cuts, as well as $m_{4j} > 2000$ GeV. All other details are as for table 4.

Bin	Bin edges	$d\sigma/d(\Delta\phi_{2j}^{min})$ [fb]	δ_{stat}^{data} [%]	δ_{stat}^{MC} [%]	u_{JES} [%]	u_{JER} [%]	u_{unfold} [%]	u_{lumi} [%]
1	0–0.15	2.79×10^6	0.5	1.8	$^{+10.6}_{-6.5}$	3.8	2.1	2.8
2	0.15–0.3	2.81×10^6	0.5	1.7	$^{+9.6}_{-7.7}$	3.8	7.7	2.8
3	0.3–0.45	2.81×10^6	0.5	1.6	$^{+7.7}_{-8.6}$	3.5	6.1	2.8
4	0.45–0.6	2.87×10^6	0.5	2.0	$^{+7.2}_{-8.5}$	3.5	6.1	2.8
5	0.6–0.75	3.12×10^6	0.4	1.7	$^{+7.2}_{-8.4}$	3.5	7.6	2.8
6	0.75–0.9	2.62×10^6	0.5	2.3	$^{+8.9}_{-9.4}$	3.7	7.5	2.8
7	0.9–1.05	1.95×10^6	0.6	2.5	$^{+9.5}_{-8.8}$	3.7	6.6	2.8
8	1.05–1.2	1.52×10^6	0.8	3.1	$^{+7.8}_{-8.6}$	3.7	6.6	2.8
9	1.2–1.35	9.07×10^5	1.0	4.8	$^{+7.8}_{-8.6}$	3.7	11.0	2.8
10	1.35–1.6	1.6×10^5	1.9	9.1	$^{+7.5}_{-14.4}$	3.7	11.0	2.8

Table 14. Measured differential four-jet cross section for $R = 0.4$ jets, in bins of $\Delta\phi_{2j}^{min}$, along with the uncertainties in the measurement. The events are selected using the inclusive analysis cuts. All other details are as for table 4.

JHEP12(2015)105

Bin	Bin edges	$d\sigma/d(\Delta\phi_{2j}^{min})$ [fb]	δ_{stat}^{data} [%]	δ_{stat}^{MC} [%]	u_{JES} [%]	u_{JER} [%]	u_{unfold} [%]	u_{lumi} [%]
1	0–0.15	8.98×10^4	0.2	0.4	$^{+6.4}_{-6.5}$	0.9	3.3	2.8
2	0.15–0.3	8.31×10^4	0.2	0.5	$^{+6.4}_{-6.2}$	0.9	3.0	2.8
3	0.3–0.45	7.37×10^4	0.2	0.5	$^{+6.6}_{-6.2}$	1.5	2.4	2.8
4	0.45–0.6	6.61×10^4	0.3	0.5	$^{+5.9}_{-6.3}$	1.5	3.7	2.8
5	0.6–0.75	6.28×10^4	0.3	0.6	$^{+6.1}_{-6.7}$	1.3	2.5	2.8
6	0.75–0.9	4.07×10^4	0.3	0.6	$^{+6.4}_{-6.4}$	1.3	2.2	2.8
7	0.9–1.05	2.41×10^4	0.4	0.9	$^{+5.9}_{-6.8}$	1.8	3.6	2.8
8	1.05–1.2	1.26×10^4	0.7	1.3	$^{+5.9}_{-6.3}$	1.8	2.8	2.8
9	1.2–1.35	5.47×10^3	0.9	2.1	$^{+5.9}_{-5.6}$	1.8	2.8	2.8
10	1.35–1.6	1.11×10^3	1.5	3.7	$^{+6.4}_{-5.1}$	1.8	2.8	2.8

Table 15. Measured differential four-jet cross section for $R = 0.4$ jets, in bins of $\Delta\phi_{2j}^{min}$, along with the uncertainties in the measurement. The events are selected using the inclusive analysis cuts, as well as $p_T^{(1)} > 400$ GeV. All other details are as for table 4.

Bin	Bin edges	$d\sigma/d(\Delta\phi_{2j}^{min})$ [fb]	δ_{stat}^{data} [%]	δ_{stat}^{MC} [%]	u_{JES} [%]	u_{JER} [%]	u_{unfold} [%]	u_{lumi} [%]
1	0–0.15	3.57×10^3	1.1	0.4	$^{+7.4}_{-7.8}$	1.8	2.2	2.8
2	0.15–0.3	3.37×10^3	1.2	0.4	$^{+7.8}_{-7.6}$	1.3	3.7	2.8
3	0.3–0.45	2.94×10^3	1.3	0.5	$^{+7.1}_{-7.4}$	1.7	3.3	2.8
4	0.45–0.6	2.45×10^3	1.5	0.5	$^{+7.6}_{-7.5}$	1.9	2.8	2.8
5	0.6–0.75	2.26×10^3	1.3	0.6	$^{+7.6}_{-7.3}$	2.1	2.5	2.8
6	0.75–0.9	1.37×10^3	2.0	0.8	$^{+8.6}_{-8.1}$	1.6	2.7	2.8
7	0.9–1.05	7.54×10^2	2.5	0.9	$^{+6.8}_{-9.0}$	1.6	2.7	2.8
8	1.05–1.2	3.5×10^2	3.4	1.6	$^{+9.0}_{-7.5}$	1.6	5.3	2.8
9	1.2–1.35	1.4×10^2	5.7	2.3	$^{+10.6}_{-6.4}$	1.6	3.2	2.8
10	1.35–1.6	3.72×10^1	9.3	4.7	$^{+8.0}_{-6.4}$	1.6	3.2	2.8

Table 16. Measured differential four-jet cross section for $R = 0.4$ jets, in bins of $\Delta\phi_{2j}^{min}$, along with the uncertainties in the measurement. The events are selected using the inclusive analysis cuts, as well as $p_T^{(1)} > 700$ GeV. All other details are as for table 4.

Bin	Bin edges	$d\sigma/d(\Delta\phi_{2j}^{min})$ [fb]	δ_{stat}^{data} [%]	δ_{stat}^{MC} [%]	u_{JES} [%]	u_{JER} [%]	u_{unfold} [%]	u_{lumi} [%]
1	0–0.15	2.6×10^2	4.4	0.4	$^{+8.9}_{-8.4}$	1.9	2.5	2.8
2	0.15–0.3	2.27×10^2	4.4	0.6	$^{+8.6}_{-8.5}$	2.1	3.1	2.8
3	0.3–0.45	2.02×10^2	4.8	0.7	$^{+9.5}_{-7.9}$	2.1	3.6	2.8
4	0.45–0.6	1.59×10^2	5.8	0.7	$^{+9.0}_{-8.0}$	2.1	3.5	2.8
5	0.6–0.75	1.5×10^2	6.2	0.7	$^{+8.6}_{-8.0}$	2.1	3.2	2.8
6	0.75–0.9	8.7×10^1	6.7	0.9	$^{+9.8}_{-8.3}$	2.8	2.5	2.8
7	0.9–1.05	5.33×10^1	8.8	1.2	$^{+10.1}_{-8.5}$	2.8	5.4	2.8
8	1.05–1.2	2.18×10^1	14.4	2.2	$^{+10.0}_{-10.2}$	2.8	4.8	2.8
9	1.2–1.35	5.96	27.4	5.6	$^{+9.5}_{-7.9}$	4.6	4.8	2.8
10	1.35–1.6	3.71	29.4	3.5	$^{+9.5}_{-7.9}$	4.6	6.7	2.8

Table 17. Measured differential four-jet cross section for $R = 0.4$ jets, in bins of $\Delta\phi_{2j}^{min}$, along with the uncertainties in the measurement. The events are selected using the inclusive analysis cuts, as well as $p_T^{(1)} > 1000$ GeV. All other details are as for table 4.

JHEP12(2015)105

Bin	Bin edges	$d\sigma/d(\Delta\phi_{3j}^{min})$ [fb]	δ_{stat}^{data} [%]	δ_{stat}^{MC} [%]	u_{JES} [%]	u_{JER} [%]	u_{unfold} [%]	u_{lumi} [%]
1	0–0.25	1.31×10^4	5.6	8.0	$^{+9.9}_{-8.0}$	5.2	7.9	2.8
2	0.25–0.5	4.41×10^4	3.1	3.3	$^{+10.0}_{-8.3}$	5.2	7.9	2.8
3	0.5–0.75	1.18×10^5	2.0	4.4	$^{+10.0}_{-8.1}$	5.2	7.9	2.8
4	0.75–1	2.25×10^5	1.4	2.3	$^{+10.0}_{-7.2}$	5.2	13.9	2.8
5	1–1.25	2.89×10^5	1.3	3.5	$^{+9.9}_{-7.4}$	4.1	8.0	2.8
6	1.25–1.5	4.21×10^5	1.2	2.2	$^{+9.3}_{-8.0}$	4.1	7.7	2.8
7	1.5–1.75	6.48×10^5	0.9	2.4	$^{+8.9}_{-8.6}$	4.0	6.8	2.8
8	1.75–2	9.53×10^5	0.7	2.1	$^{+8.4}_{-7.9}$	3.8	5.6	2.8
9	2–2.25	1.62×10^6	0.6	2.0	$^{+8.3}_{-8.4}$	3.7	5.6	2.8
10	2.25–2.5	2.24×10^6	0.5	1.7	$^{+8.4}_{-8.5}$	3.7	6.6	2.8
11	2.5–2.75	3.0×10^6	0.4	1.6	$^{+8.1}_{-7.9}$	3.3	8.7	2.8
12	2.75–3	2.81×10^6	0.4	1.8	$^{+8.6}_{-8.9}$	3.3	4.1	2.8
13	3–3.25	6.3×10^5	0.9	4.0	$^{+10.9}_{-7.8}$	3.3	4.1	2.8

Table 18. Measured differential four-jet cross section for $R = 0.4$ jets, in bins of $\Delta\phi_{3j}^{min}$, along with the uncertainties in the measurement. The events are selected using the inclusive analysis cuts. All other details are as for table 4.

Bin	Bin edges	$d\sigma/d(\Delta\phi_{3j}^{min})$ [fb]	δ_{stat}^{data} [%]	δ_{stat}^{MC} [%]	u_{JES} [%]	u_{JER} [%]	u_{unfold} [%]	u_{lumi} [%]
1	0–0.25	1.97×10^3	1.2	2.3	$^{+6.2}_{-6.5}$	0.8	5.7	2.8
2	0.25–0.5	6.68×10^3	0.6	1.0	$^{+6.2}_{-6.3}$	0.8	5.7	2.8
3	0.5–0.75	1.68×10^4	0.4	0.6	$^{+6.7}_{-6.2}$	0.8	3.6	2.8
4	0.75–1	2.46×10^4	0.3	0.6	$^{+6.2}_{-6.0}$	0.8	3.2	2.8
5	1–1.25	2.87×10^4	0.3	0.6	$^{+6.5}_{-6.2}$	0.8	4.5	2.8
6	1.25–1.5	3.07×10^4	0.3	0.5	$^{+6.4}_{-6.2}$	0.9	4.0	2.8
7	1.5–1.75	3.13×10^4	0.3	0.6	$^{+6.5}_{-6.2}$	1.1	3.2	2.8
8	1.75–2	3.08×10^4	0.3	0.6	$^{+6.3}_{-6.4}$	1.8	2.5	2.8
9	2–2.25	2.79×10^4	0.3	0.6	$^{+6.2}_{-6.5}$	1.6	2.2	2.8
10	2.25–2.5	2.55×10^4	0.3	0.6	$^{+6.3}_{-6.6}$	1.4	2.2	2.8
11	2.5–2.75	2.48×10^4	0.4	0.7	$^{+5.9}_{-7.3}$	1.6	3.1	2.8
12	2.75–3	2.1×10^4	0.4	0.7	$^{+6.1}_{-6.2}$	1.6	3.3	2.8
13	3–3.25	5.29×10^3	0.7	1.4	$^{+5.5}_{-7.2}$	1.1	2.0	2.8

Table 19. Measured differential four-jet cross section for $R = 0.4$ jets, in bins of $\Delta\phi_{3j}^{min}$, along with the uncertainties in the measurement. The events are selected using the inclusive analysis cuts, as well as $p_T^{(1)} > 400\,\text{GeV}$. All other details are as for table 4.

JHEP12(2015)105

Bin	Bin edges	$d\sigma/d(\Delta\phi_{3j}^{min})$ [fb]	δ_{stat}^{data} [%]	δ_{stat}^{MC} [%]	u_{JES} [%]	u_{JER} [%]	u_{unfold} [%]	u_{lumi} [%]
1	0–0.25	8.01×10^1	5.8	2.1	$^{+8.3}_{-7.1}$	2.4	5.5	2.8
2	0.25–0.5	3.1×10^2	2.8	0.9	$^{+7.7}_{-6.7}$	2.4	5.5	2.8
3	0.5–0.75	7.61×10^2	2.2	0.7	$^{+7.0}_{-8.7}$	1.1	2.5	2.8
4	0.75–1	1.11×10^3	1.5	0.5	$^{+7.0}_{-7.3}$	1.1	2.3	2.8
5	1–1.25	1.22×10^3	1.5	0.6	$^{+7.4}_{-7.5}$	1.2	2.8	2.8
6	1.25–1.5	1.22×10^3	1.6	0.5	$^{+7.6}_{-7.4}$	1.5	3.2	2.8
7	1.5–1.75	1.17×10^3	1.6	0.5	$^{+7.7}_{-7.4}$	1.7	3.6	2.8
8	1.75–2	1.07×10^3	1.6	0.6	$^{+8.1}_{-7.6}$	1.8	4.4	2.8
9	2–2.25	9.19×10^2	1.8	0.6	$^{+8.3}_{-8.0}$	2.0	3.3	2.8
10	2.25–2.5	8.33×10^2	1.9	0.7	$^{+8.5}_{-8.1}$	2.6	2.4	2.8
11	2.5–2.75	8.17×10^2	1.9	0.7	$^{+7.6}_{-7.7}$	1.9	2.2	2.8
12	2.75–3	6.6×10^2	2.4	0.7	$^{+7.0}_{-8.0}$	1.9	1.9	2.8
13	3–3.25	1.92×10^2	4.0	1.4	$^{+7.1}_{-6.8}$	3.2	1.9	2.8

Table 20. Measured differential four-jet cross section for $R = 0.4$ jets, in bins of $\Delta\phi_{3j}^{min}$, along with the uncertainties in the measurement. The events are selected using the inclusive analysis cuts, as well as $p_T^{(1)} > 700$ GeV. All other details are as for table 4.

Bin	Bin edges	$d\sigma/d(\Delta\phi_{3j}^{min})$ [fb]	δ_{stat}^{data} [%]	δ_{stat}^{MC} [%]	u_{JES} [%]	u_{JER} [%]	u_{unfold} [%]	u_{lumi} [%]
1	0–0.25	5.54	21.2	2.5	$^{+9.0}_{-7.8}$	1.6	2.4	2.8
2	0.25–0.5	2.68×10^1	11.6	1.3	$^{+7.6}_{-8.6}$	1.6	2.4	2.8
3	0.5–0.75	5.75×10^1	7.4	0.9	$^{+9.0}_{-8.6}$	1.6	2.3	2.8
4	0.75–1	8.98×10^1	5.7	0.7	$^{+7.9}_{-8.2}$	1.6	2.3	2.8
5	1–1.25	8.83×10^1	6.0	0.8	$^{+8.7}_{-8.2}$	1.6	3.8	2.8
6	1.25–1.5	7.41×10^1	6.3	0.6	$^{+8.9}_{-8.1}$	1.7	3.4	2.8
7	1.5–1.75	7.68×10^1	6.3	0.7	$^{+8.9}_{-8.4}$	1.7	3.5	2.8
8	1.75–2	6.68×10^1	7.0	0.7	$^{+9.4}_{-8.3}$	2.1	3.8	2.8
9	2–2.25	5.29×10^1	7.3	1.0	$^{+10.1}_{-7.9}$	3.1	4.5	2.8
10	2.25–2.5	4.76×10^1	7.9	1.0	$^{+10.3}_{-8.1}$	3.6	3.7	2.8
11	2.5–2.75	5.53×10^1	6.7	1.0	$^{+10.1}_{-8.1}$	2.8	3.3	2.8
12	2.75–3	4.83×10^1	8.4	1.0	$^{+9.1}_{-9.2}$	2.8	3.3	2.8
13	3–3.25	1.41×10^1	15.1	1.7	$^{+10.7}_{-6.7}$	4.3	5.6	2.8

Table 21. Measured differential four-jet cross section for $R = 0.4$ jets, in bins of $\Delta\phi_{3j}^{min}$, along with the uncertainties in the measurement. The events are selected using the inclusive analysis cuts, as well as $p_T^{(1)} > 1000$ GeV. All other details are as for table 4.

JHEP12(2015)105

Bin	Bin edges	$d\sigma/d(\Delta y_{2j}^{min})$ [fb]	δ_{stat}^{data} [%]	δ_{stat}^{MC} [%]	u_{JES} [%]	u_{JER} [%]	u_{unfold} [%]	u_{lumi} [%]
1	0–0.15	6.61×10^6	0.4	1.2	$^{+8.4}_{-7.2}$	3.5	7.4	2.8
2	0.15–0.3	5.03×10^6	0.4	1.5	$^{+8.2}_{-8.6}$	3.5	4.6	2.8
3	0.3–0.45	3.68×10^6	0.4	1.5	$^{+8.9}_{-8.3}$	3.5	4.6	2.8
4	0.45–0.6	2.58×10^6	0.6	2.0	$^{+9.3}_{-8.3}$	3.7	4.6	2.8
5	0.6–0.75	1.86×10^6	0.6	2.6	$^{+10.8}_{-8.8}$	3.7	10.2	2.8
6	0.75–0.9	9.92×10^5	0.9	3.7	$^{+9.6}_{-8.8}$	3.7	7.3	2.8
7	0.9–1.05	5.56×10^5	1.2	4.4	$^{+9.6}_{-10.2}$	3.7	7.3	2.8
8	1.05–1.2	2.08×10^5	1.9	9.4	$^{+9.6}_{-10.2}$	3.7	7.3	2.8
9	1.2–1.35	8.57×10^4	3.0	12.6	$^{+7.9}_{-10.2}$	6.9	7.3	2.8
10	1.35–1.5	3.49×10^4	6.3	19.3	$^{+7.9}_{-10.2}$	6.9	15.9	2.8
11	1.5–2	2.33×10^3	10.9	22.6	$^{+7.9}_{-10.2}$	6.9	15.9	2.8

Table 22. Measured differential four-jet cross section for $R = 0.4$ jets, in bins of Δy_{2j}^{min}, along with the uncertainties in the measurement. The events are selected using the inclusive analysis cuts. All other details are as for table 4.

Bin	Bin edges	$d\sigma/d(\Delta y_{2j}^{min})$ [fb]	δ_{stat}^{data} [%]	δ_{stat}^{MC} [%]	u_{JES} [%]	u_{JER} [%]	u_{unfold} [%]	u_{lumi} [%]
1	0–0.15	1.54×10^5	0.2	0.3	$^{+6.4}_{-6.3}$	1.4	2.7	2.8
2	0.15–0.3	1.15×10^5	0.2	0.3	$^{+6.2}_{-6.3}$	0.9	2.5	2.8
3	0.3–0.45	7.96×10^4	0.2	0.4	$^{+6.3}_{-6.2}$	0.9	3.2	2.8
4	0.45–0.6	5.23×10^4	0.3	0.6	$^{+6.3}_{-6.3}$	1.7	3.1	2.8
5	0.6–0.75	3.27×10^4	0.4	0.7	$^{+6.0}_{-7.0}$	1.0	2.4	2.8
6	0.75–0.9	1.59×10^4	0.5	0.9	$^{+6.2}_{-6.5}$	1.0	2.8	2.8
7	0.9–1.05	6.68×10^3	0.8	1.5	$^{+7.3}_{-6.5}$	1.0	2.8	2.8
8	1.05–1.2	2.57×10^3	1.4	2.6	$^{+7.6}_{-6.5}$	1.0	2.8	2.8
9	1.2–1.35	9.3×10^2	2.5	5.5	$^{+8.3}_{-7.0}$	1.0	14.0	2.8
10	1.35–1.5	1.97×10^2	4.6	8.3	$^{+8.3}_{-7.0}$	1.0	12.9	2.8
11	1.5–2	8.66	9.9	20.2	$^{+8.3}_{-7.0}$	1.0	12.9	2.8

Table 23. Measured differential four-jet cross section for $R = 0.4$ jets, in bins of Δy_{2j}^{min}, along with the uncertainties in the measurement. The events are selected using the inclusive analysis cuts, as well as $p_T^{(1)} > 400$ GeV. All other details are as for table 4.

Bin	Bin edges	$d\sigma/d(\Delta y_{2j}^{min})$ [fb]	δ_{stat}^{data} [%]	δ_{stat}^{MC} [%]	u_{JES} [%]	u_{JER} [%]	u_{unfold} [%]	u_{lumi} [%]
1	0–0.15	6.37×10^3	0.8	0.3	$^{+7.3}_{-7.4}$	1.4	2.7	2.8
2	0.15–0.3	4.64×10^3	1.1	0.3	$^{+7.6}_{-7.4}$	1.6	2.9	2.8
3	0.3–0.45	2.89×10^3	1.4	0.6	$^{+7.7}_{-7.8}$	1.9	3.3	2.8
4	0.45–0.6	1.77×10^3	1.8	0.6	$^{+7.7}_{-7.7}$	1.9	2.8	2.8
5	0.6–0.75	9.97×10^2	2.4	0.8	$^{+7.9}_{-8.3}$	2.6	3.3	2.8
6	0.75–0.9	3.91×10^2	3.5	1.4	$^{+10.1}_{-9.3}$	2.6	5.8	2.8
7	0.9–1.05	1.38×10^2	6.0	2.3	$^{+7.5}_{-9.7}$	0.8	4.6	2.8
8	1.05–1.2	5.34×10^1	9.5	4.7	$^{+7.5}_{-9.7}$	0.8	4.6	2.8
9	1.2–1.35	1.6×10^1	20.9	6.6	$^{+7.5}_{-8.8}$	0.8	4.6	2.8
10	1.35–1.5	2.82	45.2	17.5	$^{+20.3}_{-8.8}$	0.8	4.6	2.8

Table 24. Measured differential four-jet cross section for $R = 0.4$ jets, in bins of Δy_{2j}^{min}, along with the uncertainties in the measurement. The events are selected using the inclusive analysis cuts, as well as $p_T^{(1)} > 700$ GeV. All other details are as for table 4.

JHEP12(2015)105

Bin	Bin edges	$d\sigma/d(\Delta y_{2j}^{min})$ [fb]	δ_{stat}^{data} [%]	δ_{stat}^{MC} [%]	u_{JES} [%]	u_{JER} [%]	u_{unfold} [%]	u_{lumi} [%]
1	0–0.15	4.69×10^2	3.2	0.4	$^{+8.6}_{-7.7}$	1.7	2.5	2.8
2	0.15–0.3	3.33×10^2	4.1	0.5	$^{+8.7}_{-8.5}$	2.5	2.7	2.8
3	0.3–0.45	1.98×10^2	5.0	0.7	$^{+9.0}_{-8.1}$	2.1	5.3	2.8
4	0.45–0.6	1.08×10^2	6.8	0.8	$^{+9.3}_{-9.2}$	2.1	3.9	2.8
5	0.6–0.75	4.24×10^1	10.3	1.3	$^{+11.7}_{-8.7}$	4.1	4.3	2.8
6	0.75–0.9	1.72×10^1	16.8	2.5	$^{+13.0}_{-9.5}$	4.1	3.8	2.8
7	0.9–1.05	4.62	34.1	4.0	$^{+12.3}_{-9.6}$	1.0	3.8	2.8
8	1.05–1.2	2.17	50.6	7.0	$^{+12.3}_{-11.3}$	1.0	3.8	2.8

Table 25. Measured differential four-jet cross section for $R = 0.4$ jets, in bins of Δy_{2j}^{min}, along with the uncertainties in the measurement. The events are selected using the inclusive analysis cuts, as well as $p_T^{(1)} > 1000$ GeV. All other details are as for table 4.

Bin	Bin edges	$d\sigma/d(\Delta y_{3j}^{min})$ [fb]	δ_{stat}^{data} [%]	δ_{stat}^{MC} [%]	u_{JES} [%]	u_{JER} [%]	u_{unfold} [%]	u_{lumi} [%]
1	0–0.25	3.61×10^5	1.3	4.6	$^{+7.5}_{-7.1}$	3.4	23.0	2.8
2	0.25–0.5	9.65×10^5	0.7	2.6	$^{+7.6}_{-7.3}$	3.4	6.9	2.8
3	0.5–0.75	1.64×10^6	0.5	1.9	$^{+7.6}_{-7.4}$	3.4	6.9	2.8
4	0.75–1	1.89×10^6	0.5	1.9	$^{+8.8}_{-7.9}$	3.4	6.9	2.8
5	1–1.25	1.83×10^6	0.5	1.6	$^{+9.0}_{-8.7}$	2.8	6.6	2.8
6	1.25–1.5	1.62×10^6	0.5	2.3	$^{+9.3}_{-8.4}$	2.8	6.6	2.8
7	1.5–1.75	1.42×10^6	0.5	1.9	$^{+8.8}_{-8.1}$	2.8	6.6	2.8
8	1.75–2	1.07×10^6	0.7	2.7	$^{+8.7}_{-8.3}$	2.8	7.3	2.8
9	2–2.25	7.88×10^5	0.8	2.8	$^{+9.0}_{-8.8}$	3.7	7.6	2.8
10	2.25–2.5	5.6×10^5	1.0	3.4	$^{+9.3}_{-9.4}$	6.1	6.8	2.8
11	2.5–2.75	3.67×10^5	1.1	4.3	$^{+9.6}_{-10.7}$	7.0	6.5	2.8
12	2.75–3	2.35×10^5	1.4	5.0	$^{+10.2}_{-11.1}$	7.0	6.5	2.8
13	3–3.25	1.09×10^5	2.2	9.9	$^{+11.0}_{-11.4}$	7.0	6.6	2.8
14	3.25–3.5	7.17×10^4	2.6	6.5	$^{+11.8}_{-11.6}$	7.0	9.4	2.8
15	3.5–3.75	3.72×10^4	3.4	7.1	$^{+12.0}_{-11.1}$	7.0	16.9	2.8
16	3.75–4	1.4×10^4	5.9	32.0	$^{+12.0}_{-10.9}$	7.0	19.7	2.8
17	4–5	2.46×10^3	7.8	23.2	$^{+12.0}_{-10.9}$	15.2	19.9	2.8

Table 26. Measured differential four-jet cross section for $R = 0.4$ jets, in bins of Δy_{3j}^{min}, along with the uncertainties in the measurement. The events are selected using the inclusive analysis cuts. All other details are as for table 4.

JHEP12(2015)105

Bin	Bin edges	$d\sigma/d(\Delta y_{3j}^{min})$ [fb]	δ_{stat}^{data} [%]	δ_{stat}^{MC} [%]	u_{JES} [%]	u_{JER} [%]	u_{unfold} [%]	u_{lumi} [%]
1	0–0.25	8.7×10^3	0.6	0.8	$^{+6.1}_{-6.2}$	1.7	2.8	2.8
2	0.25–0.5	2.49×10^4	0.3	0.7	$^{+6.3}_{-6.3}$	1.7	3.0	2.8
3	0.5–0.75	4.28×10^4	0.3	0.5	$^{+5.9}_{-6.5}$	1.0	2.0	2.8
4	0.75–1	4.83×10^4	0.2	0.4	$^{+6.3}_{-5.7}$	1.0	2.4	2.8
5	1–1.25	4.34×10^4	0.3	0.4	$^{+6.2}_{-6.3}$	1.2	3.1	2.8
6	1.25–1.5	3.58×10^4	0.3	0.5	$^{+6.1}_{-6.3}$	1.2	3.3	2.8
7	1.5–1.75	2.69×10^4	0.4	0.6	$^{+6.0}_{-6.4}$	1.4	3.1	2.8
8	1.75–2	1.86×10^4	0.4	0.7	$^{+6.4}_{-6.9}$	1.4	3.1	2.8
9	2–2.25	1.21×10^4	0.5	0.9	$^{+7.1}_{-7.1}$	1.3	4.0	2.8
10	2.25–2.5	7.08×10^3	0.5	1.2	$^{+7.7}_{-7.0}$	1.2	4.4	2.8
11	2.5–2.75	4.01×10^3	0.8	1.7	$^{+8.3}_{-7.5}$	1.2	3.6	2.8
12	2.75–3	2.0×10^3	1.3	2.3	$^{+8.7}_{-8.2}$	1.2	3.2	2.8
13	3–3.25	9.06×10^2	1.7	3.1	$^{+8.7}_{-9.1}$	1.2	3.2	2.8
14	3.25–3.5	3.88×10^2	2.9	4.7	$^{+9.0}_{-10.1}$	1.2	3.6	2.8
15	3.5–3.75	1.26×10^2	4.6	9.0	$^{+11.0}_{-11.1}$	1.2	11.1	2.8
16	3.75–4	3.24×10^1	10.1	16.6	$^{+11.8}_{-11.5}$	1.2	30.3	2.8
17	4–5	4.08	17.1	37.0	$^{+11.8}_{-11.5}$	1.2	40.7	2.8

Table 27. Measured differential four-jet cross section for $R = 0.4$ jets, in bins of Δy_{3j}^{min}, along with the uncertainties in the measurement. The events are selected using the inclusive analysis cuts, as well as $p_T^{(1)} > 400$ GeV. All other details are as for table 4.

Bin	Bin edges	$d\sigma/d(\Delta y_{3j}^{min})$ [fb]	δ_{stat}^{data} [%]	δ_{stat}^{MC} [%]	u_{JES} [%]	u_{JER} [%]	u_{unfold} [%]	u_{lumi} [%]
1	0–0.25	4.06×10^2	2.3	1.1	$^{+6.7}_{-7.6}$	1.5	3.9	2.8
2	0.25–0.5	1.14×10^3	1.6	0.5	$^{+6.6}_{-7.1}$	1.5	3.2	2.8
3	0.5–0.75	1.91×10^3	1.4	0.5	$^{+7.3}_{-6.9}$	1.5	3.7	2.8
4	0.75–1	2.06×10^3	1.0	0.4	$^{+7.5}_{-7.3}$	1.3	2.3	2.8
5	1–1.25	1.71×10^3	1.3	0.5	$^{+7.4}_{-8.0}$	1.5	2.9	2.8
6	1.25–1.5	1.28×10^3	1.4	0.6	$^{+7.7}_{-7.8}$	2.0	2.9	2.8
7	1.5–1.75	8.57×10^2	1.7	0.7	$^{+8.4}_{-8.0}$	2.2	2.6	2.8
8	1.75–2	5.06×10^2	2.7	0.8	$^{+9.0}_{-8.1}$	2.4	2.1	2.8
9	2–2.25	2.69×10^2	3.4	1.3	$^{+8.9}_{-9.3}$	2.5	1.9	2.8
10	2.25–2.5	1.39×10^2	5.0	1.9	$^{+9.2}_{-10.6}$	2.6	2.6	2.8
11	2.5–2.75	5.72×10^1	8.0	2.7	$^{+9.6}_{-11.0}$	2.6	4.7	2.8
12	2.75–3	2.39×10^1	12.0	4.6	$^{+10.9}_{-12.4}$	2.6	5.5	2.8
13	3–3.25	8.54	16.3	8.3	$^{+13.7}_{-14.0}$	2.6	5.8	2.8
14	3.25–3.5	4.60	24.3	9.2	$^{+14.7}_{-14.2}$	2.6	10.9	2.8
15	3.5–3.75	4.97×10^{-1}	80.2	88.5	$^{+14.7}_{-14.2}$	2.6	24.9	2.8
16	3.75–4	3.03×10^1	82.6	81.5	$^{+14.7}_{-14.1}$	2.6	30.0	2.8

Table 28. Measured differential four-jet cross section for $R = 0.4$ jets, in bins of Δy_{3j}^{min}, along with the uncertainties in the measurement. The events are selected using the inclusive analysis cuts, as well as $p_T^{(1)} > 700$ GeV. All other details are as for table 4.

JHEP12(2015)105

Bin	Bin edges	$d\sigma/d(\Delta y_{3j}^{min})$ [fb]	δ_{stat}^{data} [%]	δ_{stat}^{MC} [%]	u_{JES} [%]	u_{JER} [%]	u_{unfold} [%]	u_{lumi} [%]
1	0–0.25	3.74×10^1	8.2	1.4	$^{+9.7}_{-6.5}$	1.5	4.0	2.8
2	0.25–0.5	8.69×10^1	5.1	0.7	$^{+8.3}_{-7.4}$	1.5	2.2	2.8
3	0.5–0.75	1.48×10^2	4.8	0.5	$^{+8.1}_{-8.0}$	1.5	2.2	2.8
4	0.75–1	1.56×10^2	4.4	0.5	$^{+8.1}_{-8.0}$	1.9	2.9	2.8
5	1–1.25	1.11×10^2	6.2	0.6	$^{+9.7}_{-8.8}$	2.2	3.8	2.8
6	1.25–1.5	8.07×10^1	6.5	0.7	$^{+10.0}_{-8.8}$	2.7	4.0	2.8
7	1.5–1.75	4.44×10^1	8.2	1.0	$^{+10.8}_{-8.9}$	3.4	4.2	2.8
8	1.75–2	2.48×10^1	10.3	1.3	$^{+10.8}_{-9.5}$	3.8	3.6	2.8
9	2–2.25	6.87	22.3	2.3	$^{+11.6}_{-10.0}$	3.8	3.3	2.8
10	2.25–2.5	5.32	23.6	3.0	$^{+12.8}_{-11.1}$	3.6	3.3	2.8
11	2.5–2.75	1.31	50.7	6.8	$^{+14.3}_{-13.8}$	3.5	3.3	2.8
12	2.75–3	1.32	39.5	7.9	$^{+16.5}_{-20.0}$	3.4	3.3	2.8

Table 29. Measured differential four-jet cross section for $R = 0.4$ jets, in bins of Δy_{3j}^{min}, along with the uncertainties in the measurement. The events are selected using the inclusive analysis cuts, as well as $p_T^{(1)} > 1000$ GeV. All other details are as for table 4.

Bin	Bin edges	$d\sigma/d(\Delta y_{2j}^{max})$ [fb]	δ_{stat}^{data} [%]	δ_{stat}^{MC} [%]	u_{JES} [%]	u_{JER} [%]	u_{unfold} [%]	u_{lumi} [%]
1	0–0.4	1.55×10^4	4.4	10.2	$^{+8.3}_{-8.4}$	3.3	11.8	2.8
2	0.4–0.8	1.69×10^5	1.6	5.5	$^{+8.4}_{-9.1}$	3.3	11.8	2.8
3	0.8–1.2	4.44×10^5	0.9	3.3	$^{+8.4}_{-8.5}$	3.3	10.8	2.8
4	1.2–1.6	7.29×10^5	0.6	2.6	$^{+8.1}_{-7.5}$	3.3	8.4	2.8
5	1.6–2	9.77×10^5	0.5	2.2	$^{+7.1}_{-7.1}$	3.3	5.7	2.8
6	2–2.4	1.15×10^6	0.6	1.7	$^{+7.1}_{-7.3}$	3.4	4.9	2.8
7	2.4–2.8	1.18×10^6	0.5	1.7	$^{+8.5}_{-7.4}$	3.7	4.7	2.8
8	2.8–3.2	1.09×10^6	0.6	2.0	$^{+9.9}_{-8.0}$	3.8	5.1	2.8
9	3.2–3.6	9.05×10^5	0.7	2.0	$^{+9.5}_{-9.4}$	3.7	5.9	2.8
10	3.6–4	6.39×10^5	0.6	2.5	$^{+9.1}_{-9.8}$	3.6	5.4	2.8
11	4–4.4	4.55×10^5	0.7	3.3	$^{+10.4}_{-9.5}$	3.5	5.1	2.8
12	4.4–4.8	2.46×10^5	1.0	4.2	$^{+11.7}_{-10.3}$	3.5	5.1	2.8
13	4.8–5.2	9.91×10^4	1.8	5.2	$^{+13.3}_{-13.3}$	3.5	8.9	2.8
14	5.2–5.6	2.78×10^4	3.7	10.3	$^{+13.3}_{-13.3}$	3.5	8.9	2.8

Table 30. Measured differential four-jet cross section for $R = 0.4$ jets, in bins of Δy_{2j}^{max}, along with the uncertainties in the measurement. The events are selected using the inclusive analysis cuts. All other details are as for table 4.

JHEP12(2015)105

Bin	Bin edges	$d\sigma/d(\Delta y_{2j}^{max})$ [fb]	δ_{stat}^{data} [%]	δ_{stat}^{MC} [%]	u_{JES} [%]	u_{JER} [%]	u_{unfold} [%]	u_{lumi} [%]
1	0–0.4	3.08×10^3	6.4	7.6	$^{+6.2}_{-3.8}$	1.5	4.0	2.8
2	0.4–0.8	3.0×10^4	2.2	2.4	$^{+6.2}_{-5.5}$	1.5	4.0	2.8
3	0.8–1.2	8.29×10^4	1.4	1.3	$^{+6.5}_{-6.0}$	1.5	4.0	2.8
4	1.2–1.6	1.33×10^5	0.9	0.8	$^{+6.4}_{-5.9}$	1.5	4.0	2.8
5	1.6–2	1.73×10^5	0.8	0.7	$^{+6.0}_{-6.0}$	1.5	4.0	2.8
6	2–2.4	1.99×10^5	0.9	0.8	$^{+5.9}_{-6.3}$	1.5	4.0	2.8
7	2.4–2.8	1.92×10^5	0.8	0.7	$^{+6.0}_{-6.4}$	1.5	4.1	2.8
8	2.8–3.2	1.68×10^5	0.9	0.8	$^{+6.8}_{-6.7}$	1.5	4.2	2.8
9	3.2–3.6	1.29×10^5	1.0	0.9	$^{+7.7}_{-6.7}$	1.6	4.1	2.8
10	3.6–4	9.03×10^4	1.4	1.1	$^{+8.3}_{-7.0}$	1.9	4.1	2.8
11	4–4.4	4.93×10^4	1.8	1.4	$^{+8.1}_{-7.7}$	2.0	5.2	2.8
12	4.4–4.8	2.43×10^4	3.0	2.3	$^{+7.9}_{-8.3}$	2.0	6.1	2.8
13	4.8–5.2	9.11×10^3	5.1	3.0	$^{+9.2}_{-7.9}$	2.0	6.4	2.8
14	5.2–5.6	1.22×10^3	13.8	11.9	$^{+8.9}_{-8.2}$	2.0	5.0	2.8

Table 31. Measured differential four-jet cross section for $R = 0.4$ jets, in bins of Δy_{2j}^{max}, along with the uncertainties in the measurement. The events are selected using the inclusive analysis cuts, as well as $p_T^{(1)} > 250$ GeV. All other details are as for table 4.

Bin	Bin edges	$d\sigma/d(\Delta y_{2j}^{max})$ [fb]	δ_{stat}^{data} [%]	δ_{stat}^{MC} [%]	u_{JES} [%]	u_{JER} [%]	u_{unfold} [%]	u_{lumi} [%]
1	0–0.4	4.07×10^2	2.2	4.2	$^{+6.5}_{-6.5}$	0.8	3.6	2.8
2	0.4–0.8	4.4×10^3	0.7	1.0	$^{+6.5}_{-6.5}$	0.8	3.6	2.8
3	0.8–1.2	1.28×10^4	0.4	0.6	$^{+6.0}_{-5.5}$	0.8	3.2	2.8
4	1.2–1.6	2.12×10^4	0.3	0.5	$^{+5.9}_{-5.7}$	0.8	2.6	2.8
5	1.6–2	2.73×10^4	0.3	0.4	$^{+5.7}_{-6.1}$	0.8	2.6	2.8
6	2–2.4	2.88×10^4	0.2	0.4	$^{+5.9}_{-6.3}$	1.1	3.2	2.8
7	2.4–2.8	2.66×10^4	0.3	0.4	$^{+6.3}_{-6.3}$	1.8	3.1	2.8
8	2.8–3.2	2.13×10^4	0.3	0.5	$^{+6.4}_{-6.3}$	1.7	2.9	2.8
9	3.2–3.6	1.46×10^4	0.4	0.6	$^{+7.0}_{-6.9}$	1.2	2.2	2.8
10	3.6–4	8.75×10^3	0.4	0.8	$^{+7.6}_{-7.7}$	1.0	2.1	2.8
11	4–4.4	4.32×10^3	0.7	1.2	$^{+8.3}_{-8.5}$	1.0	2.6	2.8
12	4.4–4.8	1.69×10^3	1.0	1.8	$^{+9.1}_{-9.1}$	1.0	4.1	2.8
13	4.8–5.2	4.64×10^2	2.0	3.3	$^{+9.4}_{-8.3}$	1.0	9.2	2.8
14	5.2–5.6	5.92×10^1	5.4	12.6	$^{+9.4}_{-8.3}$	1.0	16.9	2.8

Table 32. Measured differential four-jet cross section for $R = 0.4$ jets, in bins of Δy_{2j}^{max}, along with the uncertainties in the measurement. The events are selected using the inclusive analysis cuts, as well as $p_T^{(1)} > 400$ GeV. All other details are as for table 4.

JHEP12(2015)105

Bin	Bin edges	$d\sigma/d(\Delta y_{2j}^{max})$ [fb]	δ_{stat}^{data} [%]	δ_{stat}^{MC} [%]	u_{JES} [%]	u_{JER} [%]	u_{unfold} [%]	u_{lumi} [%]
1	0–0.4	8.16×10^1	5.1	4.5	$^{+5.5}_{-6.1}$	1.9	3.0	2.8
2	0.4–0.8	8.85×10^2	1.6	1.3	$^{+5.6}_{-6.8}$	1.9	3.0	2.8
3	0.8–1.2	2.65×10^3	0.8	0.8	$^{+6.1}_{-6.3}$	1.9	2.9	2.8
4	1.2–1.6	4.34×10^3	0.7	0.6	$^{+6.6}_{-6.6}$	1.7	2.8	2.8
5	1.6–2	5.3×10^3	0.6	0.5	$^{+6.6}_{-6.7}$	1.7	2.4	2.8
6	2–2.4	5.3×10^3	0.6	0.5	$^{+6.9}_{-6.7}$	1.6	2.6	2.8
7	2.4–2.8	4.5×10^3	0.7	0.5	$^{+7.2}_{-7.0}$	1.8	2.8	2.8
8	2.8–3.2	3.4×10^3	0.7	0.7	$^{+7.6}_{-7.8}$	2.0	3.0	2.8
9	3.2–3.6	2.06×10^3	0.9	0.8	$^{+8.2}_{-8.4}$	2.0	3.8	2.8
10	3.6–4	1.1×10^3	1.2	1.2	$^{+9.6}_{-9.1}$	1.9	4.8	2.8
11	4–4.4	4.47×10^2	2.0	1.6	$^{+10.1}_{-10.1}$	2.1	4.2	2.8
12	4.4–4.8	1.54×10^2	3.5	3.1	$^{+9.4}_{-11.4}$	2.4	3.9	2.8
13	4.8–5.2	3.92×10^1	6.9	8.4	$^{+9.1}_{-12.0}$	2.6	3.9	2.8
14	5.2–5.6	5.91	17.1	13.9	$^{+9.1}_{-17.7}$	2.6	3.9	2.8

Table 33. Measured differential four-jet cross section for $R = 0.4$ jets, in bins of Δy_{2j}^{max}, along with the uncertainties in the measurement. The events are selected using the inclusive analysis cuts, as well as $p_T^{(1)} > 550$ GeV. All other details are as for table 4.

Bin	Bin edges [GeV]	$d\sigma/d(\Sigma p_T^{central})$ [fb/GeV]	δ_{stat}^{data} [%]	δ_{stat}^{MC} [%]	u_{JES} [%]	u_{JER} [%]	u_{unfold} [%]	u_{lumi} [%]
1	120–170	1.07×10^4	0.6	2.4	$^{+9.9}_{-7.7}$	5.6	13.5	2.8
2	170–240	1.93×10^4	0.3	1.2	$^{+9.2}_{-8.3}$	4.6	8.4	2.8
3	240–315	9.21×10^3	0.4	1.0	$^{+7.8}_{-8.0}$	1.9	5.5	2.8
4	315–395	3.76×10^3	0.4	0.7	$^{+7.2}_{-7.3}$	0.8	4.6	2.8
5	395–480	1.46×10^3	0.5	0.7	$^{+6.4}_{-6.5}$	0.7	4.2	2.8
6	480–575	5.75×10^2	0.6	0.5	$^{+6.3}_{-6.1}$	0.7	2.6	2.8
7	575–680	2.23×10^2	0.5	0.5	$^{+6.6}_{-6.2}$	0.7	2.1	2.8
8	680–795	8.73×10^1	0.2	0.4	$^{+6.3}_{-6.7}$	0.7	2.0	2.8
9	795–930	3.4×10^1	0.4	0.5	$^{+6.6}_{-7.0}$	0.7	2.0	2.8
10	930–1085	1.25×10^1	0.6	0.5	$^{+6.8}_{-7.2}$	0.8	2.2	2.8
11	1085–1260	4.48	1.0	0.7	$^{+7.2}_{-7.6}$	1.1	2.5	2.8
12	1260–1465	1.56	1.4	0.5	$^{+8.0}_{-7.8}$	1.2	2.6	2.8
13	1465–1705	5.07×10^{-1}	2.1	0.5	$^{+8.0}_{-7.9}$	1.2	2.8	2.8
14	1705–1980	1.59×10^{-1}	3.7	0.6	$^{+8.2}_{-8.0}$	1.3	2.6	2.8
15	1980–2300	4.43×10^{-2}	7.0	0.7	$^{+8.5}_{-8.5}$	1.3	2.4	2.8
16	2300–5000	1.64×10^{-3}	11.7	0.6	$^{+11.2}_{-9.6}$	1.3	3.7	2.8

Table 34. Measured differential four-jet cross section for $R = 0.4$ jets, in bins of $\Sigma p_T^{central}$, along with the uncertainties in the measurement. The events are selected using the inclusive analysis cuts and $\Delta y_{2j}^{max} > 1$. All other details are as for table 4.

JHEP12(2015)105

Bin	Bin edges [GeV]	$d\sigma/d(\Sigma p_T^{central})$ [fb/GeV]	δ_{stat}^{data} [%]	δ_{stat}^{MC} [%]	u_{JES} [%]	u_{JER} [%]	u_{unfold} [%]	u_{lumi} [%]
1	120–170	4.3×10^2	2.5	2.3	$^{+5.9}_{-4.9}$	2.4	9.2	2.8
2	170–240	1.15×10^3	0.9	0.9	$^{+6.4}_{-5.8}$	2.2	5.8	2.8
3	240–315	1.01×10^3	0.8	0.8	$^{+6.9}_{-6.6}$	1.6	4.5	2.8
4	315–395	1.48×10^3	0.7	0.7	$^{+6.8}_{-6.9}$	1.4	6.3	2.8
5	395–480	1.13×10^3	0.6	0.5	$^{+6.6}_{-6.6}$	1.3	6.5	2.8
6	480–575	5.73×10^2	0.6	0.5	$^{+6.6}_{-6.2}$	1.0	3.7	2.8
7	575–680	2.25×10^2	0.5	0.5	$^{+6.7}_{-6.3}$	0.9	2.3	2.8
8	680–795	8.79×10^1	0.3	0.4	$^{+6.4}_{-6.8}$	0.9	2.0	2.8
9	795–930	3.42×10^1	0.4	0.5	$^{+6.7}_{-7.1}$	1.1	2.0	2.8
10	930–1085	1.26×10^1	0.6	0.5	$^{+6.9}_{-7.2}$	1.4	2.2	2.8
11	1085–1260	4.51	1.0	0.7	$^{+7.3}_{-7.6}$	1.6	2.5	2.8
12	1260–1465	1.57	1.4	0.5	$^{+8.1}_{-7.9}$	1.5	2.6	2.8
13	1465–1705	5.10×10^{-1}	2.1	0.5	$^{+8.1}_{-7.9}$	1.6	2.8	2.8
14	1705–1980	1.60×10^{-1}	3.6	0.6	$^{+8.3}_{-8.0}$	1.8	2.6	2.8
15	1980–2300	4.45×10^{-2}	7.0	0.7	$^{+8.6}_{-8.5}$	1.5	2.4	2.8
16	2300–5000	1.65×10^{-3}	11.7	0.6	$^{+11.3}_{-9.7}$	1.3	3.7	2.8

Table 35. Measured differential four-jet cross section for $R = 0.4$ jets, in bins of $\Sigma p_T^{central}$, along with the uncertainties in the measurement. The events are selected using the inclusive analysis cuts and $\Delta y_{2j}^{max} > 1$, as well as $p_T^{(1)} > 250$ GeV. All other details are as for table 4.

Bin	Bin edges [GeV]	$d\sigma/d(\Sigma p_T^{central})$ [fb/GeV]	δ_{stat}^{data} [%]	δ_{stat}^{MC} [%]	u_{JES} [%]	u_{JER} [%]	u_{unfold} [%]	u_{lumi} [%]
1	120–170	1.78×10^1	0.8	2.5	$^{+6.2}_{-6.6}$	1.4	3.3	2.8
2	170–240	5.29×10^1	0.5	1.0	$^{+5.9}_{-6.6}$	1.4	3.8	2.8
3	240–315	7.88×10^1	0.3	0.7	$^{+5.8}_{-6.5}$	1.4	4.6	2.8
4	315–395	9.39×10^1	0.3	0.7	$^{+6.3}_{-6.3}$	1.4	4.3	2.8
5	395–480	8.49×10^1	0.3	0.8	$^{+6.4}_{-6.3}$	1.4	4.9	2.8
6	480–575	1.37×10^2	0.2	0.4	$^{+6.2}_{-6.3}$	1.2	4.1	2.8
7	575–680	1.09×10^2	0.2	0.4	$^{+6.7}_{-6.3}$	1.1	3.6	2.8
8	680–795	6.76×10^1	0.3	0.4	$^{+6.5}_{-6.8}$	1.2	3.4	2.8
9	795–930	3.39×10^1	0.4	0.5	$^{+6.7}_{-7.0}$	1.2	2.4	2.8
10	930–1085	1.24×10^1	0.6	0.5	$^{+6.9}_{-7.1}$	1.5	2.2	2.8
11	1085–1260	4.47	1.0	0.7	$^{+7.2}_{-7.6}$	1.6	2.5	2.8
12	1260–1465	1.56	1.4	0.5	$^{+8.0}_{-7.8}$	1.5	2.6	2.8
13	1465–1705	5.06×10^{-1}	2.1	0.5	$^{+8.1}_{-7.8}$	1.6	2.8	2.8
14	1705–1980	1.59×10^{-1}	3.7	0.6	$^{+8.2}_{-7.9}$	1.9	2.6	2.8
15	1980–2300	4.41×10^{-2}	7.0	0.7	$^{+8.5}_{-8.4}$	1.6	2.4	2.8
16	2300–5000	1.63×10^{-3}	11.8	0.6	$^{+11.2}_{-9.6}$	1.3	3.7	2.8

Table 36. Measured differential four-jet cross section for $R = 0.4$ jets, in bins of $\Sigma p_T^{central}$, along with the uncertainties in the measurement. The events are selected using the inclusive analysis cuts and $\Delta y_{2j}^{max} > 1$, as well as $p_T^{(1)} > 400$ GeV. All other details are as for table 4.

JHEP12(2015)105

Bin	Bin edges [GeV]	$d\sigma/d(\Sigma p_T^{central})$ [fb/GeV]	δ_{stat}^{data} [%]	δ_{stat}^{MC} [%]	u_{JES} [%]	u_{JER} [%]	u_{unfold} [%]	u_{lumi} [%]
1	120–170	1.94	2.6	3.5	$^{+11.7}_{-5.8}$	10.1	16.8	2.8
2	170–240	4.79	1.5	1.6	$^{+8.0}_{-6.6}$	5.5	8.6	2.8
3	240–315	6.03	1.4	1.4	$^{+6.9}_{-7.5}$	3.2	4.8	2.8
4	315–395	7.51	1.1	1.2	$^{+7.3}_{-7.7}$	2.2	3.9	2.8
5	395–480	9.99	0.9	1.0	$^{+6.8}_{-7.7}$	1.9	3.7	2.8
6	480–575	1.19×10^1	0.8	0.9	$^{+7.1}_{-7.1}$	1.9	3.7	2.8
7	575–680	1.49×10^1	0.6	0.8	$^{+7.3}_{-6.8}$	1.8	3.6	2.8
8	680–795	1.81×10^1	0.6	0.5	$^{+7.4}_{-7.1}$	1.6	3.3	2.8
9	795–930	1.21×10^1	0.6	0.5	$^{+7.3}_{-7.1}$	1.4	3.4	2.8
10	930–1085	8.24	0.8	0.6	$^{+7.0}_{-7.3}$	1.3	3.3	2.8
11	1085–1260	4.41	1.0	0.7	$^{+7.2}_{-7.6}$	1.3	2.9	2.8
12	1260–1465	1.54	1.4	0.5	$^{+7.9}_{-7.7}$	1.4	2.8	2.8
13	1465–1705	5.01×10^{-1}	2.1	0.5	$^{+7.9}_{-7.8}$	1.5	2.9	2.8
14	1705–1980	1.57×10^{-1}	3.7	0.6	$^{+8.0}_{-7.8}$	1.8	2.6	2.8
15	1980–2300	4.38×10^{-2}	7.1	0.7	$^{+8.2}_{-8.3}$	1.5	2.4	2.8
16	2300–5000	1.62×10^{-3}	11.8	0.6	$^{+11.1}_{-9.5}$	1.2	3.7	2.8

Table 37. Measured differential four-jet cross section for $R = 0.4$ jets, in bins of $\Sigma p_T^{central}$, along with the uncertainties in the measurement. The events are selected using the inclusive analysis cuts and $\Delta y_{2j}^{max} > 1$, as well as $p_T^{(1)} > 550\,\text{GeV}$. All other details are as for table 4.

Bin	Bin edges [GeV]	$d\sigma/d(\Sigma p_T^{central})$ [fb/GeV]	δ_{stat}^{data} [%]	δ_{stat}^{MC} [%]	u_{JES} [%]	u_{JER} [%]	u_{unfold} [%]	u_{lumi} [%]
1	120–185	1.01×10^4	0.5	2.2	$^{+10.9}_{-8.3}$	4.6	11.1	2.8
2	185–270	1.23×10^4	0.3	1.1	$^{+8.9}_{-8.9}$	3.9	6.7	2.8
3	270–365	4.38×10^3	0.4	1.1	$^{+8.0}_{-7.5}$	1.7	4.4	2.8
4	365–465	1.39×10^3	0.6	0.7	$^{+6.8}_{-6.6}$	0.8	3.9	2.8
5	465–575	4.43×10^2	0.7	0.5	$^{+6.2}_{-6.4}$	0.8	2.5	2.8
6	575–700	1.44×10^2	0.6	0.5	$^{+6.5}_{-6.5}$	0.8	2.0	2.8
7	700–845	4.56×10^1	0.3	0.5	$^{+6.5}_{-6.8}$	0.8	1.9	2.8
8	845–1005	1.46×10^1	0.6	0.5	$^{+7.3}_{-7.1}$	0.8	2.2	2.8
9	1005–1195	4.58	0.9	0.8	$^{+7.7}_{-7.6}$	0.8	2.9	2.8
10	1195–1410	1.38	1.6	0.7	$^{+8.1}_{-7.8}$	0.8	3.6	2.8
11	1410–1665	4.12×10^{-1}	2.4	0.6	$^{+8.7}_{-8.0}$	0.9	3.6	2.8
12	1665–1960	1.10×10^{-1}	4.4	0.7	$^{+9.0}_{-8.4}$	1.3	3.4	2.8
13	1960–5000	4.31×10^{-3}	7.5	0.7	$^{+8.9}_{-9.3}$	1.6	3.0	2.8

Table 38. Measured differential four-jet cross section for $R = 0.4$ jets, in bins of $\Sigma p_T^{central}$, along with the uncertainties in the measurement. The events are selected using the inclusive analysis cuts and $\Delta y_{2j}^{max} > 2$. All other details are as for table 4.

JHEP12(2015)105

Bin	Bin edges [GeV]	$d\sigma/d(\Sigma p_T^{central})$ [fb/GeV]	δ_{stat}^{data} [%]	δ_{stat}^{MC} [%]	u_{JES} [%]	u_{JER} [%]	u_{unfold} [%]	u_{lumi} [%]
1	120–185	3.96×10^2	2.1	1.9	$^{+5.7}_{-6.5}$	1.8	8.4	2.8
2	185–270	8.47×10^2	0.9	0.8	$^{+6.8}_{-6.6}$	1.7	6.1	2.8
3	270–365	8.57×10^2	0.9	1.0	$^{+7.1}_{-6.8}$	1.3	7.3	2.8
4	365–465	9.37×10^2	0.7	0.5	$^{+7.0}_{-6.8}$	1.1	6.9	2.8
5	465–575	4.35×10^2	0.7	0.5	$^{+6.6}_{-6.5}$	1.1	3.8	2.8
6	575–700	1.45×10^2	0.6	0.5	$^{+6.7}_{-6.6}$	1.1	2.4	2.8
7	700–845	4.59×10^1	0.3	0.5	$^{+6.7}_{-6.9}$	1.3	2.0	2.8
8	845–1005	1.46×10^1	0.6	0.5	$^{+7.4}_{-7.2}$	1.4	2.2	2.8
9	1005–1195	4.61	0.9	0.7	$^{+7.8}_{-7.6}$	1.4	2.9	2.8
10	1195–1410	1.39	1.6	0.7	$^{+8.2}_{-7.8}$	1.5	3.6	2.8
11	1410–1665	4.14×10^{-1}	2.4	0.6	$^{+8.8}_{-8.0}$	1.5	3.6	2.8
12	1665–1960	1.11×10^{-1}	4.4	0.6	$^{+9.1}_{-8.4}$	1.8	3.4	2.8
13	1960–5000	4.33×10^{-3}	7.4	0.7	$^{+8.9}_{-9.3}$	2.0	3.0	2.8

Table 39. Measured differential four-jet cross section for $R = 0.4$ jets, in bins of $\Sigma p_T^{central}$, along with the uncertainties in the measurement. The events are selected using the inclusive analysis cuts and $\Delta y_{2j}^{max} > 2$, as well as $p_T^{(1)} > 250$ GeV. All other details are as for table 4.

Bin	Bin edges [GeV]	$d\sigma/d(\Sigma p_T^{central})$ [fb/GeV]	δ_{stat}^{data} [%]	δ_{stat}^{MC} [%]	u_{JES} [%]	u_{JER} [%]	u_{unfold} [%]	u_{lumi} [%]
1	120–185	1.38×10^1	0.9	2.1	$^{+7.1}_{-7.1}$	5.1	8.3	2.8
2	185–270	3.96×10^1	0.5	1.0	$^{+6.8}_{-7.0}$	2.8	5.7	2.8
3	270–365	5.95×10^1	0.4	0.8	$^{+6.3}_{-7.0}$	1.8	4.2	2.8
4	365–465	5.75×10^1	0.3	0.8	$^{+6.6}_{-6.9}$	1.6	3.5	2.8
5	465–575	8.69×10^1	0.3	0.5	$^{+6.4}_{-6.5}$	1.3	3.7	2.8
6	575–700	6.98×10^1	0.3	0.5	$^{+6.9}_{-6.4}$	1.2	3.7	2.8
7	700–845	3.85×10^1	0.3	0.5	$^{+6.9}_{-7.0}$	1.3	3.5	2.8
8	845–1005	1.45×10^1	0.6	0.5	$^{+7.4}_{-7.2}$	1.3	2.8	2.8
9	1005–1195	4.58	0.9	0.8	$^{+7.8}_{-7.5}$	1.4	3.0	2.8
10	1195–1410	1.38	1.6	0.7	$^{+8.2}_{-7.8}$	1.5	3.6	2.8
11	1410–1665	4.11×10^{-1}	2.4	0.6	$^{+8.8}_{-7.9}$	1.6	3.6	2.8
12	1665–1960	1.10×10^{-1}	4.4	0.6	$^{+9.0}_{-8.3}$	1.8	3.4	2.8
13	1960–5000	4.30×10^{-3}	7.5	0.7	$^{+8.9}_{-9.2}$	2.0	3.0	2.8

Table 40. Measured differential four-jet cross section for $R = 0.4$ jets, in bins of $\Sigma p_T^{central}$, along with the uncertainties in the measurement. The events are selected using the inclusive analysis cuts and $\Delta y_{2j}^{max} > 2$, as well as $p_T^{(1)} > 400$ GeV. All other details are as for table 4.

Bin	Bin edges [GeV]	$d\sigma/d(\Sigma p_T^{central})$ [fb/GeV]	δ_{stat}^{data} [%]	δ_{stat}^{MC} [%]	u_{JES} [%]	u_{JER} [%]	u_{unfold} [%]	u_{lumi} [%]
1	120–185	1.12	3.4	3.7	$^{+8.1}_{-7.5}$	3.6	20.8	2.8
2	185–270	2.62	1.7	1.9	$^{+7.8}_{-7.3}$	3.3	8.7	2.8
3	270–365	3.75	1.3	1.4	$^{+7.6}_{-8.2}$	2.5	3.6	2.8
4	365–465	5.76	1.1	1.3	$^{+6.9}_{-8.7}$	2.2	3.5	2.8
5	465–575	7.27	0.9	1.0	$^{+7.7}_{-7.7}$	2.2	5.1	2.8
6	575–700	9.64	0.8	0.8	$^{+7.8}_{-7.2}$	2.1	5.5	2.8
7	700–845	9.83	0.6	0.6	$^{+7.6}_{-7.3}$	1.7	4.5	2.8
8	845–1005	6.31	0.9	0.7	$^{+7.6}_{-7.4}$	1.4	3.7	2.8
9	1005–1195	3.99	1.0	0.7	$^{+7.6}_{-7.6}$	1.3	3.5	2.8
10	1195–1410	1.37	1.6	0.7	$^{+8.0}_{-7.7}$	1.3	3.9	2.8
11	1410–1665	4.07×10^{-1}	2.5	0.6	$^{+8.5}_{-7.9}$	1.4	3.7	2.8
12	1665–1960	1.09×10^{-1}	4.4	0.6	$^{+8.8}_{-8.3}$	1.7	3.4	2.8
13	1960–5000	4.26×10^{-3}	7.5	0.7	$^{+8.8}_{-9.0}$	1.9	3.0	2.8

Table 41. Measured differential four-jet cross section for $R = 0.4$ jets, in bins of $\Sigma p_T^{central}$, along with the uncertainties in the measurement. The events are selected using the inclusive analysis cuts and $\Delta y_{2j}^{max} > 2$, as well as $p_T^{(1)} > 550$ GeV. All other details are as for table 4.

JHEP12(2015)105

Bin	Bin edges [GeV]	$d\sigma/d(\Sigma p_T^{central})$ [fb/GeV]	δ_{stat}^{data} [%]	δ_{stat}^{MC} [%]	u_{JES} [%]	u_{JER} [%]	u_{unfold} [%]	u_{lumi} [%]
1	120–190	5.25×10^3	0.7	3.2	$^{+10.4}_{-10.1}$	5.4	8.0	2.8
2	190–285	5.85×10^3	0.4	1.3	$^{+9.7}_{-9.7}$	4.6	6.5	2.8
3	285–385	1.77×10^3	0.7	1.1	$^{+8.8}_{-8.0}$	2.2	4.5	2.8
4	385–490	5.1×10^2	1.0	0.9	$^{+8.0}_{-6.4}$	1.2	3.4	2.8
5	490–605	1.55×10^2	1.1	0.8	$^{+7.1}_{-6.2}$	1.2	2.3	2.8
6	605–735	4.7×10^1	0.6	0.9	$^{+7.1}_{-6.6}$	1.2	2.4	2.8
7	735–880	1.45×10^1	0.5	0.8	$^{+7.6}_{-7.3}$	1.2	3.5	2.8
8	880–1040	4.49	0.9	1.0	$^{+8.1}_{-7.8}$	1.2	3.6	2.8
9	1040–1225	1.44	1.4	1.2	$^{+8.6}_{-7.9}$	1.2	4.0	2.8
10	1225–1430	4.69×10^{-1}	2.9	1.1	$^{+9.1}_{-7.9}$	1.2	5.1	2.8
11	1430–1655	1.52×10^{-1}	4.5	1.3	$^{+9.2}_{-8.6}$	1.2	4.5	2.8
12	1655–1905	4.60×10^{-2}	7.4	1.3	$^{+9.6}_{-8.9}$	1.5	4.5	2.8
13	1905–5000	2.01×10^{-3}	10.7	1.2	$^{+10.1}_{-10.7}$	1.6	6.8	2.8

Table 42. Measured differential four-jet cross section for $R = 0.4$ jets, in bins of $\Sigma p_T^{central}$, along with the uncertainties in the measurement. The events are selected using the inclusive analysis cuts and $\Delta y_{2j}^{max} > 3$. All other details are as for table 4.

Bin	Bin edges [GeV]	$d\sigma/d(\Sigma p_T^{central})$ [fb/GeV]	δ_{stat}^{data} [%]	δ_{stat}^{MC} [%]	u_{JES} [%]	u_{JER} [%]	u_{unfold} [%]	u_{lumi} [%]
1	120–190	1.86×10^2	3.0	2.4	$^{+9.1}_{-5.3}$	2.0	4.1	2.8
2	190–285	3.54×10^2	1.3	1.2	$^{+8.6}_{-7.0}$	2.0	5.4	2.8
3	285–385	4.27×10^2	1.2	1.3	$^{+8.0}_{-7.4}$	2.0	7.8	2.8
4	385–490	3.77×10^2	0.9	0.8	$^{+7.7}_{-7.1}$	1.9	5.2	2.8
5	490–605	1.56×10^2	1.1	0.8	$^{+7.2}_{-6.6}$	1.5	2.8	2.8
6	605–735	4.75×10^1	0.6	0.9	$^{+7.2}_{-6.7}$	1.4	2.6	2.8
7	735–880	1.46×10^1	0.5	0.8	$^{+7.6}_{-7.4}$	1.4	3.5	2.8
8	880–1040	4.53	0.9	0.9	$^{+7.9}_{-8.0}$	1.4	3.6	2.8
9	1040–1225	1.45	1.4	1.1	$^{+8.6}_{-8.1}$	1.4	4.0	2.8
10	1225–1430	4.73×10^{-1}	2.9	1.1	$^{+9.3}_{-8.1}$	1.4	5.1	2.8
11	1430–1655	1.53×10^{-1}	4.5	1.3	$^{+9.2}_{-8.8}$	1.5	4.5	2.8
12	1655–1905	4.63×10^{-2}	7.4	1.3	$^{+9.5}_{-9.2}$	1.9	4.5	2.8
13	1905–5000	2.02×10^{-3}	10.6	1.2	$^{+9.9}_{-10.9}$	2.1	6.8	2.8

Table 43. Measured differential four-jet cross section for $R = 0.4$ jets, in bins of $\Sigma p_T^{central}$, along with the uncertainties in the measurement. The events are selected using the inclusive analysis cuts and $\Delta y_{2j}^{max} > 3$, as well as $p_T^{(1)} > 250$ GeV. All other details are as for table 4.

Bin	Bin edges [GeV]	$d\sigma/d(\Sigma p_T^{central})$ [fb/GeV]	δ_{stat}^{data} [%]	δ_{stat}^{MC} [%]	u_{JES} [%]	u_{JER} [%]	u_{unfold} [%]	u_{lumi} [%]
1	120–190	3.81	1.6	4.0	$^{+9.3}_{-9.8}$	1.4	3.6	2.8
2	190–285	1.35×10^1	0.8	1.5	$^{+8.1}_{-8.5}$	1.4	4.6	2.8
3	285–385	2.17×10^1	0.6	1.1	$^{+7.0}_{-7.3}$	1.4	6.1	2.8
4	385–490	2.12×10^1	0.6	1.5	$^{+7.1}_{-6.9}$	1.4	7.9	2.8
5	490–605	3.56×10^1	0.4	0.8	$^{+7.3}_{-6.9}$	1.4	5.1	2.8
6	605–735	2.46×10^1	0.5	0.8	$^{+6.9}_{-7.0}$	1.4	3.5	2.8
7	735–880	1.32×10^1	0.6	0.9	$^{+7.2}_{-7.5}$	1.5	3.0	2.8
8	880–1040	4.49	0.9	1.0	$^{+7.8}_{-7.9}$	1.9	3.1	2.8
9	1040–1225	1.43	1.4	1.1	$^{+8.3}_{-8.0}$	2.0	3.9	2.8
10	1225–1430	4.69×10^{-1}	2.9	1.1	$^{+9.2}_{-8.1}$	2.0	5.1	2.8
11	1430–1655	1.51×10^{-1}	4.5	1.3	$^{+9.1}_{-8.7}$	2.0	4.5	2.8
12	1655–1905	4.59×10^{-2}	7.4	1.3	$^{+9.4}_{-9.1}$	2.0	4.5	2.8
13	1905–5000	2.00×10^{-3}	10.7	1.2	$^{+9.9}_{-10.8}$	1.7	6.8	2.8

Table 44. Measured differential four-jet cross section for $R = 0.4$ jets, in bins of $\Sigma p_T^{central}$, along with the uncertainties in the measurement. The events are selected using the inclusive analysis cuts and $\Delta y_{2j}^{max} > 3$, as well as $p_T^{(1)} > 400$ GeV. All other details are as for table 4.

JHEP12(2015)105

Bin	Bin edges [GeV]	$d\sigma/d(\Sigma p_T^{central})$ [fb/GeV]	δ_{stat}^{data} [%]	δ_{stat}^{MC} [%]	u_{JES} [%]	u_{JER} [%]	u_{unfold} [%]	u_{lumi} [%]
1	120–190	1.63×10^{-1}	7.7	10.2	$^{+12.8}_{-7.5}$	5.6	3.8	2.8
2	190–285	4.76×10^{-1}	4.0	4.0	$^{+9.6}_{-8.2}$	5.6	3.8	2.8
3	285–385	9.39×10^{-1}	2.6	2.8	$^{+8.5}_{-8.8}$	5.6	4.2	2.8
4	385–490	1.79	2.2	2.8	$^{+8.7}_{-9.8}$	5.5	5.3	2.8
5	490–605	2.21	1.8	2.1	$^{+9.6}_{-10.2}$	4.9	6.2	2.8
6	605–735	3.43	1.2	1.3	$^{+8.9}_{-9.1}$	3.0	7.3	2.8
7	735–880	2.86	1.2	1.0	$^{+8.3}_{-8.7}$	2.2	6.1	2.8
8	880–1040	2.10	1.4	1.3	$^{+8.1}_{-8.0}$	2.1	3.8	2.8
9	1040–1225	1.34	1.4	1.1	$^{+8.1}_{-7.9}$	1.8	3.7	2.8
10	1225–1430	4.64×10^{-1}	2.9	1.1	$^{+9.0}_{-8.0}$	1.7	5.1	2.8
11	1430–1655	1.50×10^{-1}	4.5	1.3	$^{+9.0}_{-8.6}$	1.7	4.6	2.8
12	1655–1905	4.54×10^{-2}	7.4	1.3	$^{+9.3}_{-8.9}$	1.7	4.5	2.8
13	1905–5000	1.98×10^{-3}	10.7	1.2	$^{+9.7}_{-10.5}$	1.7	6.8	2.8

Table 45. Measured differential four-jet cross section for $R = 0.4$ jets, in bins of $\Sigma p_T^{central}$, along with the uncertainties in the measurement. The events are selected using the inclusive analysis cuts and $\Delta y_{2j}^{max} > 3$, as well as $p_T^{(1)} > 550$ GeV. All other details are as for table 4.

Bin	Bin edges [GeV]	$d\sigma/d(\Sigma p_T^{central})$ [fb/GeV]	δ_{stat}^{data} [%]	δ_{stat}^{MC} [%]	u_{JES} [%]	u_{JER} [%]	u_{unfold} [%]	u_{lumi} [%]
1	120–190	1.56×10^{3}	1.1	6.6	$^{+10.3}_{-8.7}$	4.2	18.1	2.8
2	190–285	1.72×10^{3}	0.8	2.7	$^{+10.1}_{-8.8}$	4.2	11.0	2.8
3	285–385	4.81×10^{2}	1.3	2.0	$^{+9.5}_{-8.7}$	3.7	5.6	2.8
4	385–490	1.26×10^{2}	2.1	2.2	$^{+8.7}_{-8.2}$	2.4	4.0	2.8
5	490–605	3.72×10^{1}	2.7	1.7	$^{+6.9}_{-7.9}$	1.9	3.2	2.8
6	605–730	1.09×10^{1}	1.8	1.9	$^{+6.4}_{-7.8}$	1.8	2.9	2.8
7	730–865	3.18	1.1	1.9	$^{+7.2}_{-8.3}$	1.8	3.5	2.8
8	865–1010	1.07	2.0	2.6	$^{+8.1}_{-9.8}$	1.8	5.5	2.8
9	1010–1170	3.49×10^{-1}	3.7	3.2	$^{+8.9}_{-12.0}$	1.8	5.9	2.8
10	1170–1340	1.29×10^{-1}	5.6	3.6	$^{+9.1}_{-11.5}$	1.8	4.9	2.8
11	1340–1525	4.99×10^{-2}	9.8	3.3	$^{+9.1}_{-11.1}$	1.8	4.5	2.8
12	1525–5000	1.25×10^{-3}	12.0	2.6	$^{+11.7}_{-11.8}$	1.8	4.5	2.8

Table 46. Measured differential four-jet cross section for $R = 0.4$ jets, in bins of $\Sigma p_T^{central}$, along with the uncertainties in the measurement. The events are selected using the inclusive analysis cuts and $\Delta y_{2j}^{max} > 4$. All other details are as for table 4.

Bin	Bin edges [GeV]	$d\sigma/d(\Sigma p_T^{central})$ [fb/GeV]	δ_{stat}^{data} [%]	δ_{stat}^{MC} [%]	u_{JES} [%]	u_{JER} [%]	u_{unfold} [%]	u_{lumi} [%]
1	120–190	3.57×10^{1}	7.3	5.7	$^{+5.6}_{-6.0}$	2.0	5.4	2.8
2	190–285	6.91×10^{1}	3.0	2.8	$^{+7.3}_{-7.7}$	2.0	6.1	2.8
3	285–385	9.82×10^{1}	3.1	2.4	$^{+8.1}_{-8.5}$	2.0	7.0	2.8
4	385–490	9.06×10^{1}	2.0	1.7	$^{+7.7}_{-8.2}$	2.0	4.4	2.8
5	490–605	3.75×10^{1}	2.6	1.8	$^{+7.4}_{-8.1}$	2.0	3.1	2.8
6	605–730	1.1×10^{1}	1.7	1.8	$^{+7.8}_{-8.1}$	2.0	3.5	2.8
7	730–865	3.21	1.1	1.9	$^{+8.1}_{-9.1}$	2.0	5.0	2.8
8	865–1010	1.09	2.0	2.5	$^{+8.5}_{-10.2}$	2.0	5.8	2.8
9	1010–1170	3.53×10^{-1}	3.6	3.2	$^{+9.2}_{-10.6}$	2.0	6.5	2.8
10	1170–1340	1.30×10^{-1}	5.6	3.5	$^{+9.4}_{-11.0}$	2.0	6.3	2.8
11	1340–1525	5.03×10^{-2}	9.7	3.3	$^{+9.5}_{-11.2}$	2.0	4.9	2.8
12	1525–5000	1.27×10^{-3}	11.9	2.5	$^{+12.0}_{-12.1}$	2.0	4.1	2.8

Table 47. Measured differential four-jet cross section for $R = 0.4$ jets, in bins of $\Sigma p_T^{central}$, along with the uncertainties in the measurement. The events are selected using the inclusive analysis cuts and $\Delta y_{2j}^{max} > 4$, as well as $p_T^{(1)} > 250$ GeV. All other details are as for table 4.

JHEP12(2015)105

Bin	Bin edges [GeV]	$d\sigma/d(\Sigma p_T^{central})$ [fb/GeV]	δ_{stat}^{data} [%]	δ_{stat}^{MC} [%]	u_{JES} [%]	u_{JER} [%]	u_{unfold} [%]	u_{lumi} [%]
1	120–190	2.99×10^{-1}	5.3	13.9	$^{+9.6}_{-6.3}$	2.3	5.6	2.8
2	190–285	1.53	2.3	4.9	$^{+9.7}_{-8.5}$	2.3	5.6	2.8
3	285–385	2.72	1.7	3.5	$^{+9.7}_{-9.9}$	2.3	6.3	2.8
4	385–490	2.92	1.5	4.3	$^{+9.5}_{-9.8}$	2.3	8.2	2.8
5	490–605	6.36	1.0	1.7	$^{+8.6}_{-8.9}$	2.3	7.9	2.8
6	605–730	4.84	1.1	1.9	$^{+7.8}_{-8.6}$	2.3	4.9	2.8
7	730–865	2.80	1.2	1.8	$^{+7.9}_{-8.9}$	2.3	3.7	2.8
8	865–1010	1.08	2.0	2.6	$^{+9.1}_{-9.7}$	2.3	4.2	2.8
9	1010–1170	3.49×10^{-1}	3.7	3.3	$^{+9.6}_{-11.4}$	2.3	6.0	2.8
10	1170–1340	1.29×10^{-1}	5.6	3.5	$^{+9.6}_{-11.9}$	2.3	6.2	2.8
11	1340–1525	4.99×10^{-2}	9.8	3.3	$^{+9.4}_{-11.7}$	2.3	4.9	2.8
12	1525–5000	1.25×10^{-3}	12.0	2.5	$^{+11.1}_{-12.7}$	2.3	4.1	2.8

Table 48. Measured differential four-jet cross section for $R = 0.4$ jets, in bins of $\Sigma p_T^{central}$, along with the uncertainties in the measurement. The events are selected using the inclusive analysis cuts and $\Delta y_{2j}^{max} > 4$, as well as $p_T^{(1)} > 400$ GeV. All other details are as for table 4.

Bin	Bin edges [GeV]	$d\sigma/d(\Sigma p_T^{central})$ [fb/GeV]	δ_{stat}^{data} [%]	δ_{stat}^{MC} [%]	u_{JES} [%]	u_{JER} [%]	u_{unfold} [%]	u_{lumi} [%]
1	120–190	4.02×10^{-4}	103.7	141.7	$^{+13.0}_{-18.5}$	3.2	4.8	2.8
2	190–285	1.92×10^{-2}	20.4	30.3	$^{+14.8}_{-18.6}$	3.2	17.8	2.8
3	285–385	4.80×10^{-2}	11.4	14.6	$^{+16.1}_{-18.2}$	3.2	23.4	2.8
4	385–490	1.51×10^{-1}	6.8	9.1	$^{+16.2}_{-17.0}$	3.2	23.9	2.8
5	490–605	1.42×10^{-1}	6.6	8.0	$^{+15.2}_{-15.6}$	3.2	21.6	2.8
6	605–730	3.53×10^{-1}	3.6	3.7	$^{+12.5}_{-12.4}$	3.2	14.8	2.8
7	730–865	3.55×10^{-1}	3.8	2.7	$^{+10.2}_{-11.1}$	3.2	10.7	2.8
8	865–1010	3.75×10^{-1}	2.9	3.4	$^{+9.6}_{-11.2}$	3.2	6.6	2.8
9	1010–1170	3.03×10^{-1}	4.0	3.1	$^{+9.6}_{-11.5}$	3.2	5.0	2.8
10	1170–1340	1.28×10^{-1}	5.6	3.5	$^{+9.7}_{-11.7}$	3.2	4.9	2.8
11	1340–1525	4.95×10^{-2}	9.8	3.3	$^{+10.0}_{-12.0}$	3.2	4.9	2.8
12	1525–5000	1.24×10^{-3}	12.1	2.6	$^{+10.2}_{-12.6}$	3.2	3.7	2.8

Table 49. Measured differential four-jet cross section for $R = 0.4$ jets, in bins of $\Sigma p_T^{central}$, along with the uncertainties in the measurement. The events are selected using the inclusive analysis cuts and $\Delta y_{2j}^{max} > 4$, as well as $p_T^{(1)} > 550$ GeV. All other details are as for table 4.

Open Access. This article is distributed under the terms of the Creative Commons Attribution License (CC-BY 4.0), which permits any use, distribution and reproduction in any medium, provided the original author(s) and source are credited.

References

[1] L. Evans and P. Bryant, *LHC Machine*, 2008 *JINST* **3** S08001 [INSPIRE].

[2] C.F. Berger et al., *An Automated Implementation of On-Shell Methods for One-Loop Amplitudes*, *Phys. Rev.* **D 78** (2008) 036003 [arXiv:0803.4180] [INSPIRE].

[3] Z. Bern, G. Diana, L.J. Dixon, F. Febres Cordero, S. Hoeche, D.A. Kosower et al., *Four-Jet Production at the Large Hadron Collider at Next-to-Leading Order in QCD*, *Phys. Rev. Lett.* **109** (2012) 042001 [arXiv:1112.3940] [INSPIRE].

[4] S. Hoeche, F. Krauss, M. Schonherr and F. Siegert, *QCD matrix elements + parton showers: The NLO case*, *JHEP* **04** (2013) 027 [arXiv:1207.5030] [INSPIRE].

JHEP12(2015)105

[5] T. Sjöstrand, S. Mrenna and P.Z. Skands, *A Brief Introduction to PYTHIA 8.1*, *Comput. Phys. Commun.* **178** (2008) 852 [arXiv:0710.3820] [INSPIRE].

[6] M. Bähr et al., *HERWIG++ Physics and Manual*, *Eur. Phys. J.* **C 58** (2008) 639 [arXiv:0803.0883] [INSPIRE].

[7] T. Gleisberg et al., *Event generation with SHERPA 1.1*, *JHEP* **02** (2009) 007 [arXiv:0811.4622] [INSPIRE].

[8] J. Alwall et al., *The automated computation of tree-level and next-to-leading order differential cross sections and their matching to parton shower simulations*, *JHEP* **07** (2014) 079 [arXiv:1405.0301] [INSPIRE].

[9] ATLAS collaboration, *Measurement of multi-jet cross sections in proton-proton collisions at a 7 TeV center-of-mass energy*, *Eur. Phys. J.* **C 71** (2011) 1763 [arXiv:1107.2092] [INSPIRE].

[10] S. Badger, B. Biedermann, P. Uwer and V. Yundin, *Next-to-leading order QCD corrections to five jet production at the LHC*, *Phys. Rev.* **D 89** (2014) 034019 [arXiv:1309.6585] [INSPIRE].

[11] ATLAS collaboration, *Search for new phenomena in final states with large jet multiplicities and missing transverse momentum at $\sqrt{s} = 8$ TeV proton-proton collisions using the ATLAS experiment*, *JHEP* **10** (2013) 130 [*Erratum ibid.* **01** (2014) 109] [arXiv:1308.1841] [INSPIRE].

[12] TASSO collaboration, R. Brandelik et al., *Evidence for Planar Events in e^+e^- Annihilation at High-Energies*, *Phys. Lett.* **B 86** (1979) 243 [INSPIRE].

[13] D. Barber et al., *Discovery of Three Jet Events and a Test of Quantum Chromodynamics at PETRA Energies*, *Phys. Rev. Lett.* **43** (1979) 830 [INSPIRE].

[14] JADE collaboration, W. Bartel et al., *Observation of Planar Three Jet Events in e^+e^- Annihilation and Evidence for Gluon Bremsstrahlung*, *Phys. Lett.* **B 91** (1980) 142 [INSPIRE].

[15] PLUTO collaboration, C.F. Berger et al., *Evidence for Gluon Bremsstrahlung in e^+e^- Annihilations at High-Energies*, *Phys. Lett.* **B 86** (1979) 418 [INSPIRE].

[16] ATLAS collaboration, *Measurement of three-jet production cross-sections in pp collisions at 7 TeV centre-of-mass energy using the ATLAS detector*, *Eur. Phys. J.* **C 75** (2015) 228 [arXiv:1411.1855] [INSPIRE].

[17] CMS collaboration, *Measurement of the ratio of the inclusive 3-jet cross section to the inclusive 2-jet cross section in pp collisions at $\sqrt{s} = 7$ TeV and first determination of the strong coupling constant in the TeV range*, *Eur. Phys. J.* **C 73** (2013) 2604 [arXiv:1304.7498] [INSPIRE].

[18] ATLAS collaboration, *Measurement of event shapes at large momentum transfer with the ATLAS detector in pp collisions at $\sqrt{s} = 7$ TeV*, *Eur. Phys. J.* **C 72** (2012) 2211 [arXiv:1206.2135] [INSPIRE].

[19] CMS collaboration, *Study of hadronic event-shape variables in multijet final states in pp collisions at $\sqrt{s} = 7$ TeV*, *JHEP* **10** (2014) 087 [arXiv:1407.2856] [INSPIRE].

[20] CMS collaboration, *Distributions of Topological Observables in Inclusive Three- and Four-Jet Events in pp Collisions at $\sqrt{s} = 7$ TeV*, *Eur. Phys. J.* **C 75** (2015) 302 [arXiv:1502.04785] [INSPIRE].

[21] CDF collaboration, D. Acosta et al., *Comparison of three-jet events in $p\bar{p}$ collisions at $\sqrt{s} = 1.8$ TeV to predictions from a next-to-leading order QCD calculation*, *Phys. Rev.* **D 71** (2005) 032002 [hep-ex/0410018] [INSPIRE].

JHEP12(2015)105

[22] CDF collaboration, F. Abe et al., *Study of four jet events and evidence for double parton interactions in $p\bar{p}$ collisions at $\sqrt{s} = 1.8$ TeV*, *Phys. Rev.* **D 47** (1993) 4857 [INSPIRE].

[23] D0 collaboration, V.M. Abazov et al., *Multiple jet production at low transverse energies in $p\bar{p}$ collisions at $\sqrt{s} = 1.8$ TeV*, *Phys. Rev.* **D 67** (2003) 052001 [hep-ex/0207046] [INSPIRE].

[24] D0 collaboration, B. Abbott et al., *Ratios of multijet cross sections in $p\bar{p}$ collisions at $\sqrt{s} = 1.8$ TeV*, *Phys. Rev. Lett.* **86** (2001) 1955 [hep-ex/0009012] [INSPIRE].

[25] ATLAS collaboration, *The ATLAS Experiment at the CERN Large Hadron Collider*, 2008 *JINST* **3** S08003 [INSPIRE].

[26] ATLAS collaboration, *Performance of the ATLAS Trigger System in 2010*, *Eur. Phys. J.* **C 72** (2012) 1849 [arXiv:1110.1530] [INSPIRE].

[27] M. Cacciari, G.P. Salam and G. Soyez, *The anti-k_t jet clustering algorithm*, *JHEP* **04** (2008) 063 [arXiv:0802.1189] [INSPIRE].

[28] M. Cacciari, G.P. Salam and G. Soyez, *FastJet User Manual (for version 3.0.2)*, *Eur. Phys. J.* **C 72** (2012) 1896 [arXiv:1111.6097] [INSPIRE] and online at http://fastjet.fr/.

[29] T. Sjöstrand, S. Mrenna and P.Z. Skands, *PYTHIA 6.4 Physics and Manual*, *JHEP* **05** (2006) 026 [hep-ph/0603175] [INSPIRE].

[30] S. Hoeche et al., *Matching parton showers and matrix elements*, hep-ph/0602031 [INSPIRE].

[31] G. Corcella et al., *HERWIG 6.5 release note*, hep-ph/0210213 [INSPIRE].

[32] H.-L. Lai et al., *New parton distributions for collider physics*, *Phys. Rev.* **D 82** (2010) 074024 [arXiv:1007.2241] [INSPIRE].

[33] J. Pumplin, D.R. Stump, J. Huston, H.-L. Lai, P.M. Nadolsky and W.K. Tung, *New generation of parton distributions with uncertainties from global QCD analysis*, *JHEP* **07** (2002) 012 [hep-ph/0201195] [INSPIRE].

[34] ATLAS collaboration, *Summary of ATLAS PYTHIA 8 tunes*, ATL-PHYS-PUB-2012-003 (2012) [ATL-COM-PHYS-2012-738] [INSPIRE].

[35] ATLAS collaboration, *ATLAS tunes of PYTHIA 6 and PYTHIA 8 for MC11*, ATL-PHYS-PUB-2011-009 (2011) [ATL-COM-PHYS-2011-744] [INSPIRE].

[36] S. Gieseke, C. Rohr and A. Siodmok, *Colour reconnections in HERWIG++*, *Eur. Phys. J.* **C 72** (2012) 2225 [arXiv:1206.0041] [INSPIRE].

[37] GEANT4 collaboration, S. Agostinelli et al., *GEANT4: A Simulation toolkit*, *Nucl. Instrum. Meth.* **A 506** (2003) 250 [INSPIRE].

[38] ATLAS collaboration, *The ATLAS Simulation Infrastructure*, *Eur. Phys. J.* **C 70** (2010) 823 [arXiv:1005.4568] [INSPIRE].

[39] S. Badger, B. Biedermann, P. Uwer and V. Yundin, *Numerical evaluation of virtual corrections to multi-jet production in massless QCD*, *Comput. Phys. Commun.* **184** (2013) 1981 [arXiv:1209.0100] [INSPIRE].

[40] S. Badger, B. Biedermann, P. Uwer and V. Yundin, *NLO QCD corrections to multi-jet production at the LHC with a centre-of-mass energy of $\sqrt{s} = 8$ TeV*, *Phys. Lett.* **B 718** (2013) 965 [arXiv:1209.0098] [INSPIRE].

[41] ATLAS collaboration, *Measurements of the W production cross sections in association with jets with the ATLAS detector*, *Eur. Phys. J.* **C 75** (2015) 82 [arXiv:1409.8639] [INSPIRE].

JHEP12(2015)105

[42] ATLAS collaboration, *Measurement of the inclusive jet cross-section in proton-proton collisions at $\sqrt{s} = 7$ TeV using 4.5 fb^{-1} of data with the ATLAS detector*, JHEP **02** (2015) 153 [*Erratum ibid.* **09** (2015) 141] [arXiv:1410.8857] [INSPIRE].

[43] F. Krauss, R. Kuhn and G. Soff, *AMEGIC++ 1.0: A Matrix element generator in C++*, JHEP **02** (2002) 044 [hep-ph/0109036] [INSPIRE].

[44] T. Gleisberg and F. Krauss, *Automating dipole subtraction for QCD NLO calculations*, Eur. Phys. J. **C 53** (2008) 501 [arXiv:0709.2881] [INSPIRE].

[45] T. Gleisberg and S. Hoeche, *Comix, a new matrix element generator*, JHEP **12** (2008) 039 [arXiv:0808.3674] [INSPIRE].

[46] S. Hoeche, *Efficient dipole subtraction with Comix*, in preparation.

[47] J.R. Andersen and J.M. Smillie, *Constructing All-Order Corrections to Multi-Jet Rates*, JHEP **01** (2010) 039 [arXiv:0908.2786] [INSPIRE].

[48] J.R. Andersen and J.M. Smillie, *The Factorisation of the t-channel Pole in quark-gluon Scattering*, Phys. Rev. **D 81** (2010) 114021 [arXiv:0910.5113] [INSPIRE].

[49] J.R. Andersen and J.M. Smillie, *Multiple Jets at the LHC with High Energy Jets*, JHEP **06** (2011) 010 [arXiv:1101.5394] [INSPIRE].

[50] A. Buckley et al., *LHAPDF6: parton density access in the LHC precision era*, Eur. Phys. J. **C 75** (2015) 132 [arXiv:1412.7420] [INSPIRE].

[51] M. Botje et al., *The PDF4LHC Working Group Interim Recommendations*, arXiv:1101.0538 [INSPIRE].

[52] W. Lampl et al., *Calorimeter Clustering Algorithms: Description and Performance*, ATL-LARG-PUB-2008-002 (2008) [ATL-COM-LARG-2008-003] [INSPIRE].

[53] ATLAS collaboration, *Expected performance of the ATLAS experiment: detector, trigger and physics*, CERN-OPEN-2008-020 (2009) [SLAC-R-980] [arXiv:0901.0512] [INSPIRE].

[54] ATLAS collaboration, *Jet energy measurement and its systematic uncertainty in proton-proton collisions at $\sqrt{s} = 7$ TeV with the ATLAS detector*, Eur. Phys. J. **C 75** (2015) 17 [arXiv:1406.0076] [INSPIRE].

[55] ATLAS collaboration, *Jet global sequential corrections with the ATLAS detector in proton-proton collisions at $\sqrt{s} = 8$ TeV*, ATLAS-CONF-2015-002 (2015) [INSPIRE].

[56] ATLAS collaboration, *Data-driven determination of the energy scale and resolution of jets reconstructed in the ATLAS calorimeters using dijet and multijet events at $\sqrt{s} = 8$ TeV*, ATLAS-CONF-2015-017 (2015) [INSPIRE].

[57] M. Cacciari and G.P. Salam, *Pileup subtraction using jet areas*, Phys. Lett. **B 659** (2008) 119 [arXiv:0707.1378] [INSPIRE].

[58] G. D'Agostini, *A Multidimensional unfolding method based on Bayes' theorem*, Nucl. Instrum. Meth. **A 362** (1995) 487 [INSPIRE].

[59] G. D'Agostini, *Improved iterative Bayesian unfolding*, arXiv:1010.0632.

[60] T. Adye, *Unfolding algorithms and tests using RooUnfold*, in the proceedings of the *PHYSTAT 2011 Workshop on Statistical Issues Related to Discovery Claims in Search Experiments and Unfolding*, CERN, Geneva, Switzerland, January 17–20 2011, CERN (2011), p. 313 [arXiv:1105.1160] [INSPIRE].

JHEP12(2015)105

[61] ATLAS collaboration, *Measurement of dijet cross sections in pp collisions at 7 TeV centre-of-mass energy using the ATLAS detector*, *JHEP* **05** (2014) 059 [arXiv:1312.3524] [INSPIRE].

[62] ATLAS collaboration, *Jet energy resolution in proton-proton collisions at $\sqrt{s} = 7$ TeV recorded in 2010 with the ATLAS detector*, *Eur. Phys. J.* **C 73** (2013) 2306 [arXiv:1210.6210] [INSPIRE].

[63] ATLAS collaboration, *Improved luminosity determination in pp collisions at $\sqrt{s} = 7$ TeV using the ATLAS detector at the LHC*, *Eur. Phys. J.* **C 73** (2013) 2518 [arXiv:1302.4393] [INSPIRE].

[64] ATLAS collaboration, *Measurements of jet vetoes and azimuthal decorrelations in dijet events produced in pp collisions at $\sqrt{s} = 7$ TeV using the ATLAS detector*, *Eur. Phys. J.* **C 74** (2014) 3117 [arXiv:1407.5756] [INSPIRE].

JHEP12(2015)105

The ATLAS collaboration

G. Aad[85], B. Abbott[113], J. Abdallah[151], O. Abdinov[11], R. Aben[107], M. Abolins[90], O.S. AbouZeid[158], H. Abramowicz[153], H. Abreu[152], R. Abreu[116], Y. Abulaiti[146a,146b], B.S. Acharya[164a,164b,a], L. Adamczyk[38a], D.L. Adams[25], J. Adelman[108], S. Adomeit[100], T. Adye[131], A.A. Affolder[74], T. Agatonovic-Jovin[13], J. Agricola[54], J.A. Aguilar-Saavedra[126a,126f], S.P. Ahlen[22], F. Ahmadov[65,b], G. Aielli[133a,133b], H. Akerstedt[146a,146b], T.P.A. Åkesson[81], A.V. Akimov[96], G.L. Alberghi[20a,20b], J. Albert[169], S. Albrand[55], M.J. Alconada Verzini[71], M. Aleksa[30], I.N. Aleksandrov[65], C. Alexa[26a], G. Alexander[153], T. Alexopoulos[10], M. Alhroob[113], G. Alimonti[91a], L. Alio[85], J. Alison[31], S.P. Alkire[35], B.M.M. Allbrooke[149], P.P. Allport[74], A. Aloisio[104a,104b], A. Alonso[36], F. Alonso[71], C. Alpigiani[76], A. Altheimer[35], B. Alvarez Gonzalez[30], D. Álvarez Piqueras[167], M.G. Alviggi[104a,104b], B.T. Amadio[15], K. Amako[66], Y. Amaral Coutinho[24a], C. Amelung[23], D. Amidei[89], S.P. Amor Dos Santos[126a,126c], A. Amorim[126a,126b], S. Amoroso[48], N. Amram[153], G. Amundsen[23], C. Anastopoulos[139], L.S. Ancu[49], N. Andari[108], T. Andeen[35], C.F. Anders[58b], G. Anders[30], J.K. Anders[74], K.J. Anderson[31], A. Andreazza[91a,91b], V. Andrei[58a], S. Angelidakis[9], I. Angelozzi[107], P. Anger[44], A. Angerami[35], F. Anghinolfi[30], A.V. Anisenkov[109,c], N. Anjos[12], A. Annovi[124a,124b], M. Antonelli[47], A. Antonov[98], J. Antos[144b], F. Anulli[132a], M. Aoki[66], L. Aperio Bella[18], G. Arabidze[90], Y. Arai[66], J.P. Araque[126a], A.T.H. Arce[45], F.A. Arduh[71], J-F. Arguin[95], S. Argyropoulos[63], M. Arik[19a], A.J. Armbruster[30], O. Arnaez[30], V. Arnal[82], H. Arnold[48], M. Arratia[28], O. Arslan[21], A. Artamonov[97], G. Artoni[23], S. Asai[155], N. Asbah[42], A. Ashkenazi[153], B. Åsman[146a,146b], L. Asquith[149], K. Assamagan[25], R. Astalos[144a], M. Atkinson[165], N.B. Atlay[141], K. Augsten[128], M. Aurousseau[145b], G. Avolio[30], B. Axen[15], M.K. Ayoub[117], G. Azuelos[95,d], M.A. Baak[30], A.E. Baas[58a], M.J. Baca[18], C. Bacci[134a,134b], H. Bachacou[136], K. Bachas[154], M. Backes[30], M. Backhaus[30], P. Bagiacchi[132a,132b], P. Bagnaia[132a,132b], Y. Bai[33a], T. Bain[35], J.T. Baines[131], O.K. Baker[176], E.M. Baldin[109,c], P. Balek[129], T. Balestri[148], F. Balli[84], E. Banas[39], Sw. Banerjee[173], A.A.E. Bannoura[175], H.S. Bansil[18], L. Barak[30], E.L. Barberio[88], D. Barberis[50a,50b], M. Barbero[85], T. Barillari[101], M. Barisonzi[164a,164b], T. Barklow[143], N. Barlow[28], S.L. Barnes[84], B.M. Barnett[131], R.M. Barnett[15], Z. Barnovska[5], A. Baroncelli[134a], G. Barone[23], A.J. Barr[120], F. Barreiro[82], J. Barreiro Guimarães da Costa[57], R. Bartoldus[143], A.E. Barton[72], P. Bartos[144a], A. Basalaev[123], A. Bassalat[117], A. Basye[165], R.L. Bates[53], S.J. Batista[158], J.R. Batley[28], M. Battaglia[137], M. Bauce[132a,132b], F. Bauer[136], H.S. Bawa[143,e], J.B. Beacham[111], M.D. Beattie[72], T. Beau[80], P.H. Beauchemin[161], R. Beccherle[124a,124b], P. Bechtle[21], H.P. Beck[17,f], K. Becker[120], M. Becker[83], M. Beckingham[170], C. Becot[117], A.J. Beddall[19b], A. Beddall[19b], V.A. Bednyakov[65], C.P. Bee[148], L.J. Beemster[107], T.A. Beermann[30], M. Begel[25], J.K. Behr[120], C. Belanger-Champagne[87], W.H. Bell[49], G. Bella[153], L. Bellagamba[20a], A. Bellerive[29], M. Bellomo[86], K. Belotskiy[98], O. Beltramello[30], O. Benary[153], D. Benchekroun[135a], M. Bender[100], K. Bendtz[146a,146b], N. Benekos[10], Y. Benhammou[153], E. Benhar Noccioli[49], J.A. Benitez Garcia[159b], D.P. Benjamin[45], J.R. Bensinger[23], S. Bentvelsen[107], L. Beresford[120], M. Beretta[47], D. Berge[107], E. Bergeaas Kuutmann[166], N. Berger[5], F. Berghaus[169], J. Beringer[15], C. Bernard[22], N.R. Bernard[86], C. Bernius[110], F.U. Bernlochner[21], T. Berry[77], P. Berta[129], C. Bertella[83], G. Bertoli[146a,146b], F. Bertolucci[124a,124b], C. Bertsche[113], D. Bertsche[113], M.I. Besana[91a], G.J. Besjes[36], O. Bessidskaia Bylund[146a,146b], M. Bessner[42], N. Besson[136], C. Betancourt[48], S. Bethke[101], A.J. Bevan[76], W. Bhimji[15], R.M. Bianchi[125], L. Bianchini[23], M. Bianco[30], O. Biebel[100], D. Biedermann[16], S.P. Bieniek[78], M. Biglietti[134a], J. Bilbao De Mendizabal[49], H. Bilokon[47], M. Bindi[54], S. Binet[117], A. Bingul[19b], C. Bini[132a,132b], S. Biondi[20a,20b], C.W. Black[150], J.E. Black[143], K.M. Black[22], D. Blackburn[138], R.E. Blair[6], J.-B. Blanchard[136], J.E. Blanco[77], T. Blazek[144a], I. Bloch[42], C. Blocker[23], W. Blum[83,*], U. Blumenschein[54], G.J. Bobbink[107],

JHEP12(2015)105

V.S. Bobrovnikov[109,c], S.S. Bocchetta[81], A. Bocci[45], C. Bock[100], M. Boehler[48], J.A. Bogaerts[30], D. Bogavac[13], A.G. Bogdanchikov[109], C. Bohm[146a], V. Boisvert[77], T. Bold[38a], V. Boldea[26a], A.S. Boldyrev[99], M. Bomben[80], M. Bona[76], M. Boonekamp[136], A. Borisov[130], G. Borissov[72], S. Borroni[42], J. Bortfeldt[100], V. Bortolotto[60a,60b,60c], K. Bos[107], D. Boscherini[20a], M. Bosman[12], J. Boudreau[125], J. Bouffard[2], E.V. Bouhova-Thacker[72], D. Boumediene[34], C. Bourdarios[117], N. Bousson[114], A. Boveia[30], J. Boyd[30], I.R. Boyko[65], I. Bozic[13], J. Bracinik[18], A. Brandt[8], G. Brandt[54], O. Brandt[58a], U. Bratzler[156], B. Brau[86], J.E. Brau[116], H.M. Braun[175,*], S.F. Brazzale[164a,164c], W.D. Breaden Madden[53], K. Brendlinger[122], A.J. Brennan[88], L. Brenner[107], R. Brenner[166], S. Bressler[172], K. Bristow[145c], T.M. Bristow[46], D. Britton[53], D. Britzger[42], F.M. Brochu[28], I. Brock[21], R. Brock[90], J. Bronner[101], G. Brooijmans[35], T. Brooks[77], W.K. Brooks[32b], J. Brosamer[15], E. Brost[116], J. Brown[55], P.A. Bruckman de Renstrom[39], D. Bruncko[144b], R. Bruneliere[48], A. Bruni[20a], G. Bruni[20a], M. Bruschi[20a], N. Bruscino[21], L. Bryngemark[81], T. Buanes[14], Q. Buat[142], P. Buchholz[141], A.G. Buckley[53], S.I. Buda[26a], I.A. Budagov[65], F. Buehrer[48], L. Bugge[119], M.K. Bugge[119], O. Bulekov[98], D. Bullock[8], H. Burckhart[30], S. Burdin[74], C.D. Burgard[48], B. Burghgrave[108], S. Burke[131], I. Burmeister[43], E. Busato[34], D. Büscher[48], V. Büscher[83], P. Bussey[53], J.M. Butler[22], A.I. Butt[3], C.M. Buttar[53], J.M. Butterworth[78], P. Butti[107], W. Buttinger[25], A. Buzatu[53], A.R. Buzykaev[109,c], S. Cabrera Urbán[167], D. Caforio[128], V.M. Cairo[37a,37b], O. Cakir[4a], N. Calace[49], P. Calafiura[15], A. Calandri[136], G. Calderini[80], P. Calfayan[100], L.P. Caloba[24a], D. Calvet[34], S. Calvet[34], R. Camacho Toro[31], S. Camarda[42], P. Camarri[133a,133b], D. Cameron[119], R. Caminal Armadans[165], S. Campana[30], M. Campanelli[78], A. Campoverde[148], V. Canale[104a,104b], A. Canepa[159a], M. Cano Bret[33e], J. Cantero[82], R. Cantrill[126a], T. Cao[40], M.D.M. Capeans Garrido[30], I. Caprini[26a], M. Caprini[26a], M. Capua[37a,37b], R. Caputo[83], R. Cardarelli[133a], F. Cardillo[48], T. Carli[30], G. Carlino[104a], L. Carminati[91a,91b], S. Caron[106], E. Carquin[32a], G.D. Carrillo-Montoya[30], J.R. Carter[28], J. Carvalho[126a,126c], D. Casadei[78], M.P. Casado[12], M. Casolino[12], E. Castaneda-Miranda[145a], A. Castelli[107], V. Castillo Gimenez[167], N.F. Castro[126a,g], P. Catastini[57], A. Catinaccio[30], J.R. Catmore[119], A. Cattai[30], J. Caudron[83], V. Cavaliere[165], D. Cavalli[91a], M. Cavalli-Sforza[12], V. Cavasinni[124a,124b], F. Ceradini[134a,134b], B.C. Cerio[45], K. Cerny[129], A.S. Cerqueira[24b], A. Cerri[149], L. Cerrito[76], F. Cerutti[15], M. Cerv[30], A. Cervelli[17], S.A. Cetin[19c], A. Chafaq[135a], D. Chakraborty[108], I. Chalupkova[129], P. Chang[165], J.D. Chapman[28], D.G. Charlton[18], C.C. Chau[158], C.A. Chavez Barajas[149], S. Cheatham[152], A. Chegwidden[90], S. Chekanov[6], S.V. Chekulaev[159a], G.A. Chelkov[65,h], M.A. Chelstowska[89], C. Chen[64], H. Chen[25], K. Chen[148], L. Chen[33d,i], S. Chen[33c], X. Chen[33f], Y. Chen[67], H.C. Cheng[89], Y. Cheng[31], A. Cheplakov[65], E. Cheremushkina[130], R. Cherkaoui El Moursli[135e], V. Chernyatin[25,*], E. Cheu[7], L. Chevalier[136], V. Chiarella[47], G. Chiarelli[124a,124b], G. Chiodini[73a], A.S. Chisholm[18], R.T. Chislett[78], A. Chitan[26a], M.V. Chizhov[65], K. Choi[61], S. Chouridou[9], B.K.B. Chow[100], V. Christodoulou[78], D. Chromek-Burckhart[30], J. Chudoba[127], A.J. Chuinard[87], J.J. Chwastowski[39], L. Chytka[115], G. Ciapetti[132a,132b], A.K. Ciftci[4a], D. Cinca[53], V. Cindro[75], I.A. Cioara[21], A. Ciocio[15], F. Cirotto[104a,104b], Z.H. Citron[172], M. Ciubancan[26a], A. Clark[49], B.L. Clark[57], P.J. Clark[46], R.N. Clarke[15], W. Cleland[125], C. Clement[146a,146b], Y. Coadou[85], M. Cobal[164a,164c], A. Coccaro[49], J. Cochran[64], L. Coffey[23], J.G. Cogan[143], L. Colasurdo[106], B. Cole[35], S. Cole[108], A.P. Colijn[107], J. Collot[55], T. Colombo[58c], G. Compostella[101], P. Conde Muiño[126a,126b], E. Coniavitis[48], S.H. Connell[145b], I.A. Connelly[77], V. Consorti[48], S. Constantinescu[26a], C. Conta[121a,121b], G. Conti[30], F. Conventi[104a,j], M. Cooke[15], B.D. Cooper[78], A.M. Cooper-Sarkar[120], T. Cornelissen[175], M. Corradi[20a], F. Corriveau[87,k], A. Corso-Radu[163], A. Cortes-Gonzalez[12], G. Cortiana[101], G. Costa[91a], M.J. Costa[167], D. Costanzo[139], D. Côté[8], G. Cottin[28], G. Cowan[77], B.E. Cox[84], K. Cranmer[110], G. Cree[29], S. Crépé-Renaudin[55], F. Crescioli[80], W.A. Cribbs[146a,146b], M. Crispin Ortuzar[120], M. Cristinziani[21], V. Croft[106], G. Crosetti[37a,37b], T. Cuhadar Donszelmann[139], J. Cummings[176],

JHEP12(2015)105

M. Curatolo[47], C. Cuthbert[150], H. Czirr[141], P. Czodrowski[3], S. D'Auria[53], M. D'Onofrio[74], M.J. Da Cunha Sargedas De Sousa[126a,126b], C. Da Via[84], W. Dabrowski[38a], A. Dafinca[120], T. Dai[89], O. Dale[14], F. Dallaire[95], C. Dallapiccola[86], M. Dam[36], J.R. Dandoy[31], N.P. Dang[48], A.C. Daniells[18], M. Danninger[168], M. Dano Hoffmann[136], V. Dao[48], G. Darbo[50a], S. Darmora[8], J. Dassoulas[3], A. Dattagupta[61], W. Davey[21], C. David[169], T. Davidek[129], E. Davies[120,l], M. Davies[153], P. Davison[78], Y. Davygora[58a], E. Dawe[88], I. Dawson[139], R.K. Daya-Ishmukhametova[86], K. De[8], R. de Asmundis[104a], A. De Benedetti[113], S. De Castro[20a,20b], S. De Cecco[80], N. De Groot[106], P. de Jong[107], H. De la Torre[82], F. De Lorenzi[64], D. De Pedis[132a], A. De Salvo[132a], U. De Sanctis[149], A. De Santo[149], J.B. De Vivie De Regie[117], W.J. Dearnaley[72], R. Debbe[25], C. Debenedetti[137], D.V. Dedovich[65], I. Deigaard[107], J. Del Peso[82], T. Del Prete[124a,124b], D. Delgove[117], F. Deliot[136], C.M. Delitzsch[49], M. Deliyergiyev[75], A. Dell'Acqua[30], L. Dell'Asta[22], M. Dell'Orso[124a,124b], M. Della Pietra[104a,j], D. della Volpe[49], M. Delmastro[5], P.A. Delsart[55], C. Deluca[107], D.A. DeMarco[158], S. Demers[176], M. Demichev[65], A. Demilly[80], S.P. Denisov[130], D. Derendarz[39], J.E. Derkaoui[135d], F. Derue[80], P. Dervan[74], K. Desch[21], C. Deterre[42], P.O. Deviveiros[30], A. Dewhurst[131], S. Dhaliwal[23], A. Di Ciaccio[133a,133b], L. Di Ciaccio[5], A. Di Domenico[132a,132b], C. Di Donato[104a,104b], A. Di Girolamo[30], B. Di Girolamo[30], A. Di Mattia[152], B. Di Micco[134a,134b], R. Di Nardo[47], A. Di Simone[48], R. Di Sipio[158], D. Di Valentino[29], C. Diaconu[85], M. Diamond[158], F.A. Dias[46], M.A. Diaz[32a], E.B. Diehl[89], J. Dietrich[16], S. Diglio[85], A. Dimitrievska[13], J. Dingfelder[21], P. Dita[26a], S. Dita[26a], F. Dittus[30], F. Djama[85], T. Djobava[51b], J.I. Djuvsland[58a], M.A.B. do Vale[24c], D. Dobos[30], M. Dobre[26a], C. Doglioni[81], T. Dohmae[155], J. Dolejsi[129], Z. Dolezal[129], B.A. Dolgoshein[98,*], M. Donadelli[24d], S. Donati[124a,124b], P. Dondero[121a,121b], J. Donini[34], J. Dopke[131], A. Doria[104a], M.T. Dova[71], A.T. Doyle[53], E. Drechsler[54], M. Dris[10], E. Dubreuil[34], E. Duchovni[172], G. Duckeck[100], O.A. Ducu[26a,85], D. Duda[107], A. Dudarev[30], L. Duflot[117], L. Duguid[77], M. Dührssen[30], M. Dunford[58a], H. Duran Yildiz[4a], M. Düren[52], A. Durglishvili[51b], D. Duschinger[44], M. Dyndal[38a], C. Eckardt[42], K.M. Ecker[101], R.C. Edgar[89], W. Edson[2], N.C. Edwards[46], W. Ehrenfeld[21], T. Eifert[30], G. Eigen[14], K. Einsweiler[15], T. Ekelof[166], M. El Kacimi[135c], M. Ellert[166], S. Elles[5], F. Ellinghaus[175], A.A. Elliot[169], N. Ellis[30], J. Elmsheuser[100], M. Elsing[30], D. Emeliyanov[131], Y. Enari[155], O.C. Endner[83], M. Endo[118], J. Erdmann[43], A. Ereditato[17], G. Ernis[175], J. Ernst[2], M. Ernst[25], S. Errede[165], E. Ertel[83], M. Escalier[117], H. Esch[43], C. Escobar[125], B. Esposito[47], A.I. Etienvre[136], E. Etzion[153], H. Evans[61], A. Ezhilov[123], L. Fabbri[20a,20b], G. Facini[31], R.M. Fakhrutdinov[130], S. Falciano[132a], R.J. Falla[78], J. Faltova[129], Y. Fang[33a], M. Fanti[91a,91b], A. Farbin[8], A. Farilla[134a], T. Farooque[12], S. Farrell[15], S.M. Farrington[170], P. Farthouat[30], F. Fassi[135e], P. Fassnacht[30], D. Fassouliotis[9], M. Faucci Giannelli[77], A. Favareto[50a,50b], L. Fayard[117], P. Federic[144a], O.L. Fedin[123,m], W. Fedorko[168], S. Feigl[30], L. Feligioni[85], C. Feng[33d], E.J. Feng[6], H. Feng[89], A.B. Fenyuk[130], L. Feremenga[8], P. Fernandez Martinez[167], S. Fernandez Perez[30], J. Ferrando[53], A. Ferrari[166], P. Ferrari[107], R. Ferrari[121a], D.E. Ferreira de Lima[53], A. Ferrer[167], D. Ferrere[49], C. Ferretti[89], A. Ferretto Parodi[50a,50b], M. Fiascaris[31], F. Fiedler[83], A. Filipčič[75], M. Filipuzzi[42], F. Filthaut[106], M. Fincke-Keeler[169], K.D. Finelli[150], M.C.N. Fiolhais[126a,126c], L. Fiorini[167], A. Firan[40], A. Fischer[2], C. Fischer[12], J. Fischer[175], W.C. Fisher[90], E.A. Fitzgerald[23], N. Flaschel[42], I. Fleck[141], P. Fleischmann[89], S. Fleischmann[175], G.T. Fletcher[139], G. Fletcher[76], R.R.M. Fletcher[122], T. Flick[175], A. Floderus[81], L.R. Flores Castillo[60a], M.J. Flowerdew[101], A. Formica[136], A. Forti[84], D. Fournier[117], H. Fox[72], S. Fracchia[12], P. Francavilla[80], M. Franchini[20a,20b], D. Francis[30], L. Franconi[119], M. Franklin[57], M. Frate[163], M. Fraternali[121a,121b], D. Freeborn[78], S.T. French[28], F. Friedrich[44], D. Froidevaux[30], J.A. Frost[120], C. Fukunaga[156], E. Fullana Torregrosa[83], B.G. Fulsom[143], T. Fusayasu[102], J. Fuster[167], C. Gabaldon[55], O. Gabizon[175], A. Gabrielli[20a,20b], A. Gabrielli[132a,132b], G.P. Gach[38a], S. Gadatsch[30], S. Gadomski[49], G. Gagliardi[50a,50b], P. Gagnon[61], C. Galea[106],

JHEP12(2015)105

B. Galhardo[126a,126c], E.J. Gallas[120], B.J. Gallop[131], P. Gallus[128], G. Galster[36], K.K. Gan[111], J. Gao[33b,85], Y. Gao[46], Y.S. Gao[143,e], F.M. Garay Walls[46], F. Garberson[176], C. García[167], J.E. García Navarro[167], M. Garcia-Sciveres[15], R.W. Gardner[31], N. Garelli[143], V. Garonne[119], C. Gatti[47], A. Gaudiello[50a,50b], G. Gaudio[121a], B. Gaur[141], L. Gauthier[95], P. Gauzzi[132a,132b], I.L. Gavrilenko[96], C. Gay[168], G. Gaycken[21], E.N. Gazis[10], P. Ge[33d], Z. Gecse[168], C.N.P. Gee[131], Ch. Geich-Gimbel[21], M.P. Geisler[58a], C. Gemme[50a], M.H. Genest[55], S. Gentile[132a,132b], M. George[54], S. George[77], D. Gerbaudo[163], A. Gershon[153], S. Ghasemi[141], H. Ghazlane[135b], B. Giacobbe[20a], S. Giagu[132a,132b], V. Giangiobbe[12], P. Giannetti[124a,124b], B. Gibbard[25], S.M. Gibson[77], M. Gilchriese[15], T.P.S. Gillam[28], D. Gillberg[30], G. Gilles[34], D.M. Gingrich[3,d], N. Giokaris[9], M.P. Giordani[164a,164c], F.M. Giorgi[20a], F.M. Giorgi[16], P.F. Giraud[136], P. Giromini[47], D. Giugni[91a], C. Giuliani[48], M. Giulini[58b], B.K. Gjelsten[119], S. Gkaitatzis[154], I. Gkialas[154], E.L. Gkougkousis[117], L.K. Gladilin[99], C. Glasman[82], J. Glatzer[30], P.C.F. Glaysher[46], A. Glazov[42], M. Goblirsch-Kolb[101], J.R. Goddard[76], J. Godlewski[39], S. Goldfarb[89], T. Golling[49], D. Golubkov[130], A. Gomes[126a,126b,126d], R. Gonçalo[126a], J. Goncalves Pinto Firmino Da Costa[136], L. Gonella[21], S. González de la Hoz[167], G. Gonzalez Parra[12], S. Gonzalez-Sevilla[49], L. Goossens[30], P.A. Gorbounov[97], H.A. Gordon[25], I. Gorelov[105], B. Gorini[30], E. Gorini[73a,73b], A. Gorišek[75], E. Gornicki[39], A.T. Goshaw[45], C. Gössling[43], M.I. Gostkin[65], D. Goujdami[135c], A.G. Goussiou[138], N. Govender[145b], E. Gozani[152], H.M.X. Grabas[137], L. Graber[54], I. Grabowska-Bold[38a], P.O.J. Gradin[166], P. Grafström[20a,20b], K-J. Grahn[42], J. Gramling[49], E. Gramstad[119], S. Grancagnolo[16], V. Gratchev[123], H.M. Gray[30], E. Graziani[134a], Z.D. Greenwood[79,n], C. Grefe[21], K. Gregersen[78], I.M. Gregor[42], P. Grenier[143], J. Griffiths[8], A.A. Grillo[137], K. Grimm[72], S. Grinstein[12,o], Ph. Gris[34], J.-F. Grivaz[117], J.P. Grohs[44], A. Grohsjean[42], E. Gross[172], J. Grosse-Knetter[54], G.C. Grossi[79], Z.J. Grout[149], L. Guan[89], J. Guenther[128], F. Guescini[49], D. Guest[176], O. Gueta[153], E. Guido[50a,50b], T. Guillemin[117], S. Guindon[2], U. Gul[53], C. Gumpert[44], J. Guo[33e], Y. Guo[33b], S. Gupta[120], G. Gustavino[132a,132b], P. Gutierrez[113], N.G. Gutierrez Ortiz[78], C. Gutschow[44], C. Guyot[136], C. Gwenlan[120], C.B. Gwilliam[74], A. Haas[110], C. Haber[15], H.K. Hadavand[8], N. Haddad[135e], P. Haefner[21], S. Hageböck[21], Z. Hajduk[39], H. Hakobyan[177], M. Haleem[42], J. Haley[114], D. Hall[120], G. Halladjian[90], G.D. Hallewell[85], K. Hamacher[175], P. Hamal[115], K. Hamano[169], A. Hamilton[145a], G.N. Hamity[139], P.G. Hamnett[42], L. Han[33b], K. Hanagaki[66,p], K. Hanawa[155], M. Hance[15], P. Hanke[58a], R. Hanna[136], J.B. Hansen[36], J.D. Hansen[36], M.C. Hansen[21], P.H. Hansen[36], K. Hara[160], A.S. Hard[173], T. Harenberg[175], F. Hariri[117], S. Harkusha[92], R.D. Harrington[46], P.F. Harrison[170], F. Hartjes[107], M. Hasegawa[67], Y. Hasegawa[140], A. Hasib[113], S. Hassani[136], S. Haug[17], R. Hauser[90], L. Hauswald[44], M. Havranek[127], C.M. Hawkes[18], R.J. Hawkings[30], A.D. Hawkins[81], T. Hayashi[160], D. Hayden[90], C.P. Hays[120], J.M. Hays[76], H.S. Hayward[74], S.J. Haywood[131], S.J. Head[18], T. Heck[83], V. Hedberg[81], L. Heelan[8], S. Heim[122], T. Heim[175], B. Heinemann[15], L. Heinrich[110], J. Hejbal[127], L. Helary[22], S. Hellman[146a,146b], D. Hellmich[21], C. Helsens[12], J. Henderson[120], R.C.W. Henderson[72], Y. Heng[173], C. Hengler[42], S. Henkelmann[168], A. Henrichs[176], A.M. Henriques Correia[30], S. Henrot-Versille[117], G.H. Herbert[16], Y. Hernández Jiménez[167], R. Herrberg-Schubert[16], G. Herten[48], R. Hertenberger[100], L. Hervas[30], G.G. Hesketh[78], N.P. Hessey[107], J.W. Hetherly[40], R. Hickling[76], E. Higón-Rodriguez[167], E. Hill[169], J.C. Hill[28], K.H. Hiller[42], S.J. Hillier[18], I. Hinchliffe[15], E. Hines[122], R.R. Hinman[15], M. Hirose[157], D. Hirschbuehl[175], J. Hobbs[148], N. Hod[107], M.C. Hodgkinson[139], P. Hodgson[139], A. Hoecker[30], M.R. Hoeferkamp[105], F. Hoenig[100], M. Hohlfeld[83], D. Hohn[21], T.R. Holmes[15], M. Homann[43], T.M. Hong[125], L. Hooft van Huysduynen[110], W.H. Hopkins[116], Y. Horii[103], A.J. Horton[142], J-Y. Hostachy[55], S. Hou[151], A. Hoummada[135a], J. Howard[120], J. Howarth[42], M. Hrabovsky[115], I. Hristova[16], J. Hrivnac[117], T. Hryn'ova[5], A. Hrynevich[93], C. Hsu[145c], P.J. Hsu[151,q], S.-C. Hsu[138], D. Hu[35], Q. Hu[33b], X. Hu[89], Y. Huang[42], Z. Hubacek[128], F. Hubaut[85], F. Huegging[21], T.B. Huffman[120], E.W. Hughes[35], G. Hughes[72], M. Huhtinen[30],

JHEP12(2015)105

T.A. Hülsing[83], N. Huseynov[65,b], J. Huston[90], J. Huth[57], G. Iacobucci[49], G. Iakovidis[25], I. Ibragimov[141], L. Iconomidou-Fayard[117], E. Ideal[176], Z. Idrissi[135e], P. Iengo[30], O. Igonkina[107], T. Iizawa[171], Y. Ikegami[66], K. Ikematsu[141], M. Ikeno[66], Y. Ilchenko[31,r], D. Iliadis[154], N. Ilic[143], T. Ince[101], G. Introzzi[121a,121b], P. Ioannou[9], M. Iodice[134a], K. Iordanidou[35], V. Ippolito[57], A. Irles Quiles[167], C. Isaksson[166], M. Ishino[68], M. Ishitsuka[157], R. Ishmukhametov[111], C. Issever[120], S. Istin[19a], J.M. Iturbe Ponce[84], R. Iuppa[133a,133b], J. Ivarsson[81], W. Iwanski[39], H. Iwasaki[66], J.M. Izen[41], V. Izzo[104a], S. Jabbar[3], B. Jackson[122], M. Jackson[74], P. Jackson[1], M.R. Jaekel[30], V. Jain[2], K. Jakobs[48], S. Jakobsen[30], T. Jakoubek[127], J. Jakubek[128], D.O. Jamin[114], D.K. Jana[79], E. Jansen[78], R. Jansky[62], J. Janssen[21], M. Janus[54], G. Jarlskog[81], N. Javadov[65,b], T. Javůrek[48], L. Jeanty[15], J. Jejelava[51a,s], G.-Y. Jeng[150], D. Jennens[88], P. Jenni[48,t], J. Jentzsch[43], C. Jeske[170], S. Jézéquel[5], H. Ji[173], J. Jia[148], Y. Jiang[33b], S. Jiggins[78], J. Jimenez Pena[167], S. Jin[33a], A. Jinaru[26a], O. Jinnouchi[157], M.D. Joergensen[36], P. Johansson[139], K.A. Johns[7], K. Jon-And[146a,146b], G. Jones[170], R.W.L. Jones[72], T.J. Jones[74], J. Jongmanns[58a], P.M. Jorge[126a,126b], K.D. Joshi[84], J. Jovicevic[159a], X. Ju[173], C.A. Jung[43], P. Jussel[62], A. Juste Rozas[12,o], M. Kaci[167], A. Kaczmarska[39], M. Kado[117], H. Kagan[111], M. Kagan[143], S.J. Kahn[85], E. Kajomovitz[45], C.W. Kalderon[120], S. Kama[40], A. Kamenshchikov[130], N. Kanaya[155], S. Kaneti[28], V.A. Kantserov[98], J. Kanzaki[66], B. Kaplan[110], L.S. Kaplan[173], A. Kapliy[31], D. Kar[145c], K. Karakostas[10], A. Karamaoun[3], N. Karastathis[10,107], M.J. Kareem[54], E. Karentzos[10], M. Karnevskiy[83], S.N. Karpov[65], Z.M. Karpova[65], K. Karthik[110], V. Kartvelishvili[72], A.N. Karyukhin[130], L. Kashif[173], R.D. Kass[111], A. Kastanas[14], Y. Kataoka[155], C. Kato[155], A. Katre[49], J. Katzy[42], K. Kawagoe[70], T. Kawamoto[155], G. Kawamura[54], S. Kazama[155], V.F. Kazanin[109,c], R. Keeler[169], R. Kehoe[40], J.S. Keller[42], J.J. Kempster[77], H. Keoshkerian[84], O. Kepka[127], B.P. Kerševan[75], S. Kersten[175], R.A. Keyes[87], F. Khalil-zada[11], H. Khandanyan[146a,146b], A. Khanov[114], A.G. Kharlamov[109,c], T.J. Khoo[28], V. Khovanskiy[97], E. Khramov[65], J. Khubua[51b,u], S. Kido[67], H.Y. Kim[8], S.H. Kim[160], Y.K. Kim[31], N. Kimura[154], O.M. Kind[16], B.T. King[74], M. King[167], S.B. King[168], J. Kirk[131], A.E. Kiryunin[101], T. Kishimoto[67], D. Kisielewska[38a], F. Kiss[48], K. Kiuchi[160], O. Kivernyk[136], E. Kladiva[144b], M.H. Klein[35], M. Klein[74], U. Klein[74], K. Kleinknecht[83], P. Klimek[146a,146b], A. Klimentov[25], R. Klingenberg[43], J.A. Klinger[139], T. Klioutchnikova[30], E.-E. Kluge[58a], P. Kluit[107], S. Kluth[101], J. Knapik[39], E. Kneringer[62], E.B.F.G. Knoops[85], A. Knue[53], A. Kobayashi[155], D. Kobayashi[157], T. Kobayashi[155], M. Kobel[44], M. Kocian[143], P. Kodys[129], T. Koffas[29], E. Koffeman[107], L.A. Kogan[120], S. Kohlmann[175], Z. Kohout[128], T. Kohriki[66], T. Koi[143], H. Kolanoski[16], I. Koletsou[5], A.A. Komar[96,*], Y. Komori[155], T. Kondo[66], N. Kondrashova[42], K. Köneke[48], A.C. König[106], T. Kono[66], R. Konoplich[110,v], N. Konstantinidis[78], R. Kopeliansky[152], S. Koperny[38a], L. Köpke[83], A.K. Kopp[48], K. Korcyl[39], K. Kordas[154], A. Korn[78], A.A. Korol[109,c], I. Korolkov[12], E.V. Korolkova[139], O. Kortner[101], S. Kortner[101], T. Kosek[129], V.V. Kostyukhin[21], V.M. Kotov[65], A. Kotwal[45], A. Kourkoumeli-Charalampidi[154], C. Kourkoumelis[9], V. Kouskoura[25], A. Koutsman[159a], R. Kowalewski[169], T.Z. Kowalski[38a], W. Kozanecki[136], A.S. Kozhin[130], V.A. Kramarenko[99], G. Kramberger[75], D. Krasnopevtsev[98], M.W. Krasny[80], A. Krasznahorkay[30], J.K. Kraus[21], A. Kravchenko[25], S. Kreiss[110], M. Kretz[58c], J. Kretzschmar[74], K. Kreutzfeldt[52], P. Krieger[158], K. Krizka[31], K. Kroeninger[43], H. Kroha[101], J. Kroll[122], J. Kroseberg[21], J. Krstic[13], U. Kruchonak[65], H. Krüger[21], N. Krumnack[64], A. Kruse[173], M.C. Kruse[45], M. Kruskal[22], T. Kubota[88], H. Kucuk[78], S. Kuday[4b], S. Kuehn[48], A. Kugel[58c], F. Kuger[174], A. Kuhl[137], T. Kuhl[42], V. Kukhtin[65], R. Kukla[136], Y. Kulchitsky[92], S. Kuleshov[32b], M. Kuna[132a,132b], T. Kunigo[68], A. Kupco[127], H. Kurashige[67], Y.A. Kurochkin[92], V. Kus[127], E.S. Kuwertz[169], M. Kuze[157], J. Kvita[115], T. Kwan[169], D. Kyriazopoulos[139], A. La Rosa[137], J.L. La Rosa Navarro[24d], L. La Rotonda[37a,37b], C. Lacasta[167], F. Lacava[132a,132b], J. Lacey[29], H. Lacker[16], D. Lacour[80], V.R. Lacuesta[167], E. Ladygin[65], R. Lafaye[5], B. Laforge[80], T. Lagouri[176], S. Lai[54], L. Lambourne[78], S. Lammers[61], C.L. Lampen[7], W. Lampl[7], E. Lançon[136],

JHEP12(2015)105

U. Landgraf[48], M.P.J. Landon[76], V.S. Lang[58a], J.C. Lange[12], A.J. Lankford[163], F. Lanni[25], K. Lantzsch[21], A. Lanza[121a], S. Laplace[80], C. Lapoire[30], J.F. Laporte[136], T. Lari[91a], F. Lasagni Manghi[20a,20b], M. Lassnig[30], P. Laurelli[47], W. Lavrijsen[15], A.T. Law[137], P. Laycock[74], T. Lazovich[57], O. Le Dortz[80], E. Le Guirriec[85], E. Le Menedeu[12], M. LeBlanc[169], T. LeCompte[6], F. Ledroit-Guillon[55], C.A. Lee[145b], S.C. Lee[151], L. Lee[1], G. Lefebvre[80], M. Lefebvre[169], F. Legger[100], C. Leggett[15], A. Lehan[74], G. Lehmann Miotto[30], X. Lei[7], W.A. Leight[29], A. Leisos[154,w], A.G. Leister[176], M.A.L. Leite[24d], R. Leitner[129], D. Lellouch[172], B. Lemmer[54], K.J.C. Leney[78], T. Lenz[21], B. Lenzi[30], R. Leone[7], S. Leone[124a,124b], C. Leonidopoulos[46], S. Leontsinis[10], C. Leroy[95], C.G. Lester[28], M. Levchenko[123], J. Levêque[5], D. Levin[89], L.J. Levinson[172], M. Levy[18], A. Lewis[120], A.M. Leyko[21], M. Leyton[41], B. Li[33b,x], H. Li[148], H.L. Li[31], L. Li[45], L. Li[33e], S. Li[45], X. Li[84], Y. Li[33c,y], Z. Liang[137], H. Liao[34], B. Liberti[133a], A. Liblong[158], P. Lichard[30], K. Lie[165], J. Liebal[21], W. Liebig[14], C. Limbach[21], A. Limosani[150], S.C. Lin[151,z], T.H. Lin[83], F. Linde[107], B.E. Lindquist[148], J.T. Linnemann[90], E. Lipeles[122], A. Lipniacka[14], M. Lisovyi[58b], T.M. Liss[165], D. Lissauer[25], A. Lister[168], A.M. Litke[137], B. Liu[151,aa], D. Liu[151], H. Liu[89], J. Liu[85], J.B. Liu[33b], K. Liu[85], L. Liu[165], M. Liu[45], M. Liu[33b], Y. Liu[33b], M. Livan[121a,121b], A. Lleres[55], J. Llorente Merino[82], S.L. Lloyd[76], F. Lo Sterzo[151], E. Lobodzinska[42], P. Loch[7], W.S. Lockman[137], F.K. Loebinger[84], A.E. Loevschall-Jensen[36], A. Loginov[176], T. Lohse[16], K. Lohwasser[42], M. Lokajicek[127], B.A. Long[22], J.D. Long[89], R.E. Long[72], K.A. Looper[111], L. Lopes[126a], D. Lopez Mateos[57], B. Lopez Paredes[139], I. Lopez Paz[12], J. Lorenz[100], N. Lorenzo Martinez[61], M. Losada[162], P.J. Lösel[100], X. Lou[33a], A. Lounis[117], J. Love[6], P.A. Love[72], N. Lu[89], H.J. Lubatti[138], C. Luci[132a,132b], A. Lucotte[55], F. Luehring[61], W. Lukas[62], L. Luminari[132a], O. Lundberg[146a,146b], B. Lund-Jensen[147], D. Lynn[25], R. Lysak[127], E. Lytken[81], H. Ma[25], L.L. Ma[33d], G. Maccarrone[47], A. Macchiolo[101], C.M. Macdonald[139], B. Maček[75], J. Machado Miguens[122,126b], D. Macina[30], D. Madaffari[85], R. Madar[34], H.J. Maddocks[72], W.F. Mader[44], A. Madsen[166], J. Maeda[67], S. Maeland[14], T. Maeno[25], A. Maevskiy[99], E. Magradze[54], K. Mahboubi[48], J. Mahlstedt[107], C. Maiani[136], C. Maidantchik[24a], A.A. Maier[101], T. Maier[100], A. Maio[126a,126b,126d], S. Majewski[116], Y. Makida[66], N. Makovec[117], B. Malaescu[80], Pa. Malecki[39], V.P. Maleev[123], F. Malek[55], U. Mallik[63], D. Malon[6], C. Malone[143], S. Maltezos[10], V.M. Malyshev[109], S. Malyukov[30], J. Mamuzic[42], G. Mancini[47], B. Mandelli[30], L. Mandelli[91a], I. Mandić[75], R. Mandrysch[63], J. Maneira[126a,126b], A. Manfredini[101], L. Manhaes de Andrade Filho[24b], J. Manjarres Ramos[159b], A. Mann[100], A. Manousakis-Katsikakis[9], B. Mansoulie[136], R. Mantifel[87], M. Mantoani[54], L. Mapelli[30], L. March[145c], G. Marchiori[80], M. Marcisovsky[127], C.P. Marino[169], M. Marjanovic[13], D.E. Marley[89], F. Marroquim[24a], S.P. Marsden[84], Z. Marshall[15], L.F. Marti[17], S. Marti-Garcia[167], B. Martin[90], T.A. Martin[170], V.J. Martin[46], B. Martin dit Latour[14], M. Martinez[12,o], S. Martin-Haugh[131], V.S. Martoiu[26a], A.C. Martyniuk[78], M. Marx[138], F. Marzano[132a], A. Marzin[30], L. Masetti[83], T. Mashimo[155], R. Mashinistov[96], J. Masik[84], A.L. Maslennikov[109,c], I. Massa[20a,20b], L. Massa[20a,20b], P. Mastrandrea[148], A. Mastroberardino[37a,37b], T. Masubuchi[155], P. Mättig[175], J. Mattmann[83], J. Maurer[26a], S.J. Maxfield[74], D.A. Maximov[109,c], R. Mazini[151], S.M. Mazza[91a,91b], L. Mazzaferro[133a,133b], G. Mc Goldrick[158], S.P. Mc Kee[89], A. McCarn[89], R.L. McCarthy[148], T.G. McCarthy[29], N.A. McCubbin[131], K.W. McFarlane[56,*], J.A. Mcfayden[78], G. Mchedlidze[54], S.J. McMahon[131], R.A. McPherson[169,k], M. Medinnis[42], S. Meehan[145a], S. Mehlhase[100], A. Mehta[74], K. Meier[58a], C. Meineck[100], B. Meirose[41], B.R. Mellado Garcia[145c], F. Meloni[17], A. Mengarelli[20a,20b], S. Menke[101], E. Meoni[161], K.M. Mercurio[57], S. Mergelmeyer[21], P. Mermod[49], L. Merola[104a,104b], C. Meroni[91a], F.S. Merritt[31], A. Messina[132a,132b], J. Metcalfe[25], A.S. Mete[163], C. Meyer[83], C. Meyer[122], J-P. Meyer[136], J. Meyer[107], H. Meyer Zu Theenhausen[58a], R.P. Middleton[131], S. Miglioranzi[164a,164c], L. Mijović[21], G. Mikenberg[172], M. Mikestikova[127], M. Mikuž[75], M. Milesi[88], A. Milic[30], D.W. Miller[31], C. Mills[46], A. Milov[172], D.A. Milstead[146a,146b], A.A. Minaenko[130], Y. Minami[155], I.A. Minashvili[65], A.I. Mincer[110],

JHEP12(2015)105

B. Mindur[38a], M. Mineev[65], Y. Ming[173], L.M. Mir[12], T. Mitani[171], J. Mitrevski[100], V.A. Mitsou[167], A. Miucci[49], P.S. Miyagawa[139], J.U. Mjörnmark[81], T. Moa[146a,146b], K. Mochizuki[85], S. Mohapatra[35], W. Mohr[48], S. Molander[146a,146b], R. Moles-Valls[21], R. Monden[68], K. Mönig[42], C. Monini[55], J. Monk[36], E. Monnier[85], J. Montejo Berlingen[12], F. Monticelli[71], S. Monzani[132a,132b], R.W. Moore[3], N. Morange[117], D. Moreno[162], M. Moreno Llácer[54], P. Morettini[50a], D. Mori[142], M. Morii[57], M. Morinaga[155], V. Morisbak[119], S. Moritz[83], A.K. Morley[150], G. Mornacchi[30], J.D. Morris[76], S.S. Mortensen[36], A. Morton[53], L. Morvaj[103], M. Mosidze[51b], J. Moss[143], K. Motohashi[157], R. Mount[143], E. Mountricha[25], S.V. Mouraviev[96,*], E.J.W. Moyse[86], S. Muanza[85], R.D. Mudd[18], F. Mueller[101], J. Mueller[125], R.S.P. Mueller[100], T. Mueller[28], D. Muenstermann[49], P. Mullen[53], G.A. Mullier[17], J.A. Murillo Quijada[18], W.J. Murray[170,131], H. Musheghyan[54], E. Musto[152], A.G. Myagkov[130,ab], M. Myska[128], B.P. Nachman[143], O. Nackenhorst[54], J. Nadal[54], K. Nagai[120], R. Nagai[157], Y. Nagai[85], K. Nagano[66], A. Nagarkar[111], Y. Nagasaka[59], K. Nagata[160], M. Nagel[101], E. Nagy[85], A.M. Nairz[30], Y. Nakahama[30], K. Nakamura[66], T. Nakamura[155], I. Nakano[112], H. Namasivayam[41], R.F. Naranjo Garcia[42], R. Narayan[31], D.I. Narrias Villar[58a], T. Naumann[42], G. Navarro[162], R. Nayyar[7], H.A. Neal[89], P.Yu. Nechaeva[96], T.J. Neep[84], P.D. Nef[143], A. Negri[121a,121b], M. Negrini[20a], S. Nektarijevic[106], C. Nellist[117], A. Nelson[163], S. Nemecek[127], P. Nemethy[110], A.A. Nepomuceno[24a], M. Nessi[30,ac], M.S. Neubauer[165], M. Neumann[175], R.M. Neves[110], P. Nevski[25], P.R. Newman[18], D.H. Nguyen[6], R.B. Nickerson[120], R. Nicolaidou[136], B. Nicquevert[30], J. Nielsen[137], N. Nikiforou[35], A. Nikiforov[16], V. Nikolaenko[130,ab], I. Nikolic-Audit[80], K. Nikolopoulos[18], J.K. Nilsen[119], P. Nilsson[25], Y. Ninomiya[155], A. Nisati[132a], R. Nisius[101], T. Nobe[155], M. Nomachi[118], I. Nomidis[29], T. Nooney[76], S. Norberg[113], M. Nordberg[30], O. Novgorodova[44], S. Nowak[101], M. Nozaki[66], L. Nozka[115], K. Ntekas[10], G. Nunes Hanninger[88], T. Nunnemann[100], E. Nurse[78], F. Nuti[88], B.J. O'Brien[46], F. O'grady[7], D.C. O'Neil[142], V. O'Shea[53], F.G. Oakham[29,d], H. Oberlack[101], T. Obermann[21], J. Ocariz[80], A. Ochi[67], I. Ochoa[78], J.P. Ochoa-Ricoux[32a], S. Oda[70], S. Odaka[66], H. Ogren[61], A. Oh[84], S.H. Oh[45], C.C. Ohm[15], H. Ohman[166], H. Oide[30], W. Okamura[118], H. Okawa[160], Y. Okumura[31], T. Okuyama[66], A. Olariu[26a], S.A. Olivares Pino[46], D. Oliveira Damazio[25], E. Oliver Garcia[167], A. Olszewski[39], J. Olszowska[39], A. Onofre[126a,126e], K. Onogi[103], P.U.E. Onyisi[31,r], C.J. Oram[159a], M.J. Oreglia[31], Y. Oren[153], D. Orestano[134a,134b], N. Orlando[154], C. Oropeza Barrera[53], R.S. Orr[158], B. Osculati[50a,50b], R. Ospanov[84], G. Otero y Garzon[27], H. Otono[70], M. Ouchrif[135d], F. Ould-Saada[119], A. Ouraou[136], K.P. Oussoren[107], Q. Ouyang[33a], A. Ovcharova[15], M. Owen[53], R.E. Owen[18], V.E. Ozcan[19a], N. Ozturk[8], K. Pachal[142], A. Pacheco Pages[12], C. Padilla Aranda[12], M. Pagáčová[48], S. Pagan Griso[15], E. Paganis[139], F. Paige[25], P. Pais[86], K. Pajchel[119], G. Palacino[159b], S. Palestini[30], M. Palka[38b], D. Pallin[34], A. Palma[126a,126b], Y.B. Pan[173], E. Panagiotopoulou[10], C.E. Pandini[80], J.G. Panduro Vazquez[77], P. Pani[146a,146b], S. Panitkin[25], D. Pantea[26a], L. Paolozzi[49], Th.D. Papadopoulou[10], K. Papageorgiou[154], A. Paramonov[6], D. Paredes Hernandez[154], M.A. Parker[28], K.A. Parker[139], F. Parodi[50a,50b], J.A. Parsons[35], U. Parzefall[48], E. Pasqualucci[132a], S. Passaggio[50a], F. Pastore[134a,134b,*], Fr. Pastore[77], G. Pásztor[29], S. Pataraia[175], N.D. Patel[150], J.R. Pater[84], T. Pauly[30], J. Pearce[169], B. Pearson[113], L.E. Pedersen[36], M. Pedersen[119], S. Pedraza Lopez[167], R. Pedro[126a,126b], S.V. Peleganchuk[109,c], D. Pelikan[166], O. Penc[127], C. Peng[33a], H. Peng[33b], B. Penning[31], J. Penwell[61], D.V. Perepelitsa[25], E. Perez Codina[159a], M.T. Pérez García-Estañ[167], L. Perini[91a,91b], H. Pernegger[30], S. Perrella[104a,104b], R. Peschke[42], V.D. Peshekhonov[65], K. Peters[30], R.F.Y. Peters[84], B.A. Petersen[30], T.C. Petersen[36], E. Petit[42], A. Petridis[1], C. Petridou[154], P. Petroff[117], E. Petrolo[132a], F. Petrucci[134a,134b], N.E. Pettersson[157], R. Pezoa[32b], P.W. Phillips[131], G. Piacquadio[143], E. Pianori[170], A. Picazio[49], E. Piccaro[76], M. Piccinini[20a,20b], M.A. Pickering[120], R. Piegaia[27], D.T. Pignotti[111], J.E. Pilcher[31], A.D. Pilkington[84], J. Pina[126a,126b,126d], M. Pinamonti[164a,164c,ad], J.L. Pinfold[3], A. Pingel[36], S. Pires[80], H. Pirumov[42], M. Pitt[172],

JHEP12(2015)105

C. Pizio[91a,91b], L. Plazak[144a], M.-A. Pleier[25], V. Pleskot[129], E. Plotnikova[65], P. Plucinski[146a,146b], D. Pluth[64], R. Poettgen[146a,146b], L. Poggioli[117], D. Pohl[21], G. Polesello[121a], A. Poley[42], A. Policicchio[37a,37b], R. Polifka[158], A. Polini[20a], C.S. Pollard[53], V. Polychronakos[25], K. Pommès[30], L. Pontecorvo[132a], B.G. Pope[90], G.A. Popeneciu[26b], D.S. Popovic[13], A. Poppleton[30], S. Pospisil[128], K. Potamianos[15], I.N. Potrap[65], C.J. Potter[149], C.T. Potter[116], G. Poulard[30], J. Poveda[30], V. Pozdnyakov[65], P. Pralavorio[85], A. Pranko[15], S. Prasad[30], S. Prell[64], D. Price[84], L.E. Price[6], M. Primavera[73a], S. Prince[87], M. Proissl[46], K. Prokofiev[60c], F. Prokoshin[32b], E. Protopapadaki[136], S. Protopopescu[25], J. Proudfoot[6], M. Przybycien[38a], E. Ptacek[116], D. Puddu[134a,134b], E. Pueschel[86], D. Puldon[148], M. Purohit[25,ae], P. Puzo[117], J. Qian[89], G. Qin[53], Y. Qin[84], A. Quadt[54], D.R. Quarrie[15], W.B. Quayle[164a,164b], M. Queitsch-Maitland[84], D. Quilty[53], S. Raddum[119], V. Radeka[25], V. Radescu[42], S.K. Radhakrishnan[148], P. Radloff[116], P. Rados[88], F. Ragusa[91a,91b], G. Rahal[178], S. Rajagopalan[25], M. Rammensee[30], C. Rangel-Smith[166], F. Rauscher[100], S. Rave[83], T. Ravenscroft[53], M. Raymond[30], A.L. Read[119], N.P. Readioff[74], D.M. Rebuzzi[121a,121b], A. Redelbach[174], G. Redlinger[25], R. Reece[137], K. Reeves[41], L. Rehnisch[16], J. Reichert[122], H. Reisin[27], M. Relich[163], C. Rembser[30], H. Ren[33a], A. Renaud[117], M. Rescigno[132a], S. Resconi[91a], O.L. Rezanova[109,c], P. Reznicek[129], R. Rezvani[95], R. Richter[101], S. Richter[78], E. Richter-Was[38b], O. Ricken[21], M. Ridel[80], P. Rieck[16], C.J. Riegel[175], J. Rieger[54], O. Rifki[113], M. Rijssenbeek[148], A. Rimoldi[121a,121b], L. Rinaldi[20a], B. Ristić[49], E. Ritsch[30], I. Riu[12], F. Rizatdinova[114], E. Rizvi[76], S.H. Robertson[87,k], A. Robichaud-Veronneau[87], D. Robinson[28], J.E.M. Robinson[42], A. Robson[53], C. Roda[124a,124b], S. Roe[30], O. Røhne[119], S. Rolli[161], A. Romaniouk[98], M. Romano[20a,20b], S.M. Romano Saez[34], E. Romero Adam[167], N. Rompotis[138], M. Ronzani[48], L. Roos[80], E. Ros[167], S. Rosati[132a], K. Rosbach[48], P. Rose[137], P.L. Rosendahl[14], O. Rosenthal[141], V. Rossetti[146a,146b], E. Rossi[104a,104b], L.P. Rossi[50a], J.H.N. Rosten[28], R. Rosten[138], M. Rotaru[26a], I. Roth[172], J. Rothberg[138], D. Rousseau[117], C.R. Royon[136], A. Rozanov[85], Y. Rozen[152], X. Ruan[145c], F. Rubbo[143], I. Rubinskiy[42], V.I. Rud[99], C. Rudolph[44], M.S. Rudolph[158], F. Rühr[48], A. Ruiz-Martinez[30], Z. Rurikova[48], N.A. Rusakovich[65], A. Ruschke[100], H.L. Russell[138], J.P. Rutherfoord[7], N. Ruthmann[48], Y.F. Ryabov[123], M. Rybar[165], G. Rybkin[117], N.C. Ryder[120], A.F. Saavedra[150], G. Sabato[107], S. Sacerdoti[27], A. Saddique[3], H.F-W. Sadrozinski[137], R. Sadykov[65], F. Safai Tehrani[132a], M. Sahinsoy[58a], M. Saimpert[136], T. Saito[155], H. Sakamoto[155], Y. Sakurai[171], G. Salamanna[134a,134b], A. Salamon[133a], J.E. Salazar Loyola[32b], M. Saleem[113], D. Salek[107], P.H. Sales De Bruin[138], D. Salihagic[101], A. Salnikov[143], J. Salt[167], D. Salvatore[37a,37b], F. Salvatore[149], A. Salvucci[60a], A. Salzburger[30], D. Sammel[48], D. Sampsonidis[154], A. Sanchez[104a,104b], J. Sánchez[167], V. Sanchez Martinez[167], H. Sandaker[119], R.L. Sandbach[76], H.G. Sander[83], M.P. Sanders[100], M. Sandhoff[175], C. Sandoval[162], R. Sandstroem[101], D.P.C. Sankey[131], M. Sannino[50a,50b], A. Sansoni[47], C. Santoni[34], R. Santonico[133a,133b], H. Santos[126a], I. Santoyo Castillo[149], K. Sapp[125], A. Sapronov[65], J.G. Saraiva[126a,126d], B. Sarrazin[21], O. Sasaki[66], Y. Sasaki[155], K. Sato[160], G. Sauvage[5,*], E. Sauvan[5], G. Savage[77], P. Savard[158,d], C. Sawyer[131], L. Sawyer[79,n], J. Saxon[31], C. Sbarra[20a], A. Sbrizzi[20a,20b], T. Scanlon[78], D.A. Scannicchio[163], M. Scarcella[150], V. Scarfone[37a,37b], J. Schaarschmidt[172], P. Schacht[101], D. Schaefer[30], R. Schaefer[42], J. Schaeffer[83], S. Schaepe[21], S. Schaetzel[58b], U. Schäfer[83], A.C. Schaffer[117], D. Schaile[100], R.D. Schamberger[148], V. Scharf[58a], V.A. Schegelsky[123], D. Scheirich[129], M. Schernau[163], C. Schiavi[50a,50b], C. Schillo[48], M. Schioppa[37a,37b], S. Schlenker[30], K. Schmieden[30], C. Schmitt[83], S. Schmitt[58b], S. Schmitt[42], B. Schneider[159a], Y.J. Schnellbach[74], U. Schnoor[44], L. Schoeffel[136], A. Schoening[58b], B.D. Schoenrock[90], E. Schopf[21], A.L.S. Schorlemmer[54], M. Schott[83], D. Schouten[159a], J. Schovancova[8], S. Schramm[49], M. Schreyer[174], C. Schroeder[83], N. Schuh[83], M.J. Schultens[21], H.-C. Schultz-Coulon[58a], H. Schulz[16], M. Schumacher[48], B.A. Schumm[137], Ph. Schune[136], C. Schwanenberger[84], A. Schwartzman[143], T.A. Schwarz[89], Ph. Schwegler[101], H. Schweiger[84],

JHEP12(2015)105

Ph. Schwemling[136], R. Schwienhorst[90], J. Schwindling[136], T. Schwindt[21], F.G. Sciacca[17], E. Scifo[117], G. Sciolla[23], F. Scuri[124a,124b], F. Scutti[21], J. Searcy[89], G. Sedov[42], E. Sedykh[123], P. Seema[21], S.C. Seidel[105], A. Seiden[137], F. Seifert[128], J.M. Seixas[24a], G. Sekhniaidze[104a], K. Sekhon[89], S.J. Sekula[40], D.M. Seliverstov[123,*], N. Semprini-Cesari[20a,20b], C. Serfon[30], L. Serin[117], L. Serkin[164a,164b], T. Serre[85], M. Sessa[134a,134b], R. Seuster[159a], H. Severini[113], T. Sfiligoj[75], F. Sforza[30], A. Sfyrla[30], E. Shabalina[54], M. Shamim[116], L.Y. Shan[33a], R. Shang[165], J.T. Shank[22], M. Shapiro[15], P.B. Shatalov[97], K. Shaw[164a,164b], S.M. Shaw[84], A. Shcherbakova[146a,146b], C.Y. Shehu[149], P. Sherwood[78], L. Shi[151,af], S. Shimizu[67], C.O. Shimmin[163], M. Shimojima[102], M. Shiyakova[65], A. Shmeleva[96], D. Shoaleh Saadi[95], M.J. Shochet[31], S. Shojaii[91a,91b], S. Shrestha[111], E. Shulga[98], M.A. Shupe[7], S. Shushkevich[42], P. Sicho[127], P.E. Sidebo[147], O. Sidiropoulou[174], D. Sidorov[114], A. Sidoti[20a,20b], F. Siegert[44], Dj. Sijacki[13], J. Silva[126a,126d], Y. Silver[153], S.B. Silverstein[146a], V. Simak[128], O. Simard[5], Lj. Simic[13], S. Simion[117], E. Simioni[83], B. Simmons[78], D. Simon[34], P. Sinervo[158], N.B. Sinev[116], M. Sioli[20a,20b], G. Siragusa[174], A.N. Sisakyan[65,*], S.Yu. Sivoklokov[99], J. Sjölin[146a,146b], T.B. Sjursen[14], M.B. Skinner[72], H.P. Skottowe[57], P. Skubic[113], M. Slater[18], T. Slavicek[128], M. Slawinska[107], K. Sliwa[161], V. Smakhtin[172], B.H. Smart[46], L. Smestad[14], S.Yu. Smirnov[98], Y. Smirnov[98], L.N. Smirnova[99,ag], O. Smirnova[81], M.N.K. Smith[35], R.W. Smith[35], M. Smizanska[72], K. Smolek[128], A.A. Snesarev[96], G. Snidero[76], S. Snyder[25], R. Sobie[169,k], F. Socher[44], A. Soffer[153], D.A. Soh[151,af], G. Sokhrannyi[75], C.A. Solans[30], M. Solar[128], J. Solc[128], E.Yu. Soldatov[98], U. Soldevila[167], A.A. Solodkov[130], A. Soloshenko[65], O.V. Solovyanov[130], V. Solovyev[123], P. Sommer[48], H.Y. Song[33b], N. Soni[1], A. Sood[15], A. Sopczak[128], B. Sopko[128], V. Sopko[128], V. Sorin[12], D. Sosa[58b], M. Sosebee[8], C.L. Sotiropoulou[124a,124b], R. Soualah[164a,164c], A.M. Soukharev[109,c], D. South[42], B.C. Sowden[77], S. Spagnolo[73a,73b], M. Spalla[124a,124b], M. Spangenberg[170], F. Spanò[77], W.R. Spearman[57], D. Sperlich[16], F. Spettel[101], R. Spighi[20a], G. Spigo[30], L.A. Spiller[88], M. Spousta[129], T. Spreitzer[158], R.D. St. Denis[53,*], A. Stabile[91a], S. Staerz[44], J. Stahlman[122], R. Stamen[58a], S. Stamm[16], E. Stanecka[39], C. Stanescu[134a], M. Stanescu-Bellu[42], M.M. Stanitzki[42], S. Stapnes[119], E.A. Starchenko[130], J. Stark[55], P. Staroba[127], P. Starovoitov[58a], R. Staszewski[39], P. Steinberg[25], B. Stelzer[142], H.J. Stelzer[30], O. Stelzer-Chilton[159a], H. Stenzel[52], G.A. Stewart[53], J.A. Stillings[21], M.C. Stockton[87], M. Stoebe[87], G. Stoicea[26a], P. Stolte[54], S. Stonjek[101], A.R. Stradling[8], A. Straessner[44], M.E. Stramaglia[17], J. Strandberg[147], S. Strandberg[146a,146b], A. Strandlie[119], E. Strauss[143], M. Strauss[113], P. Strizenec[144b], R. Ströhmer[174], D.M. Strom[116], R. Stroynowski[40], A. Strubig[106], S.A. Stucci[17], B. Stugu[14], N.A. Styles[42], D. Su[143], J. Su[125], R. Subramaniam[79], A. Succurro[12], Y. Sugaya[118], M. Suk[128], V.V. Sulin[96], S. Sultansoy[4c], T. Sumida[68], S. Sun[57], X. Sun[33a], J.E. Sundermann[48], K. Suruliz[149], G. Susinno[37a,37b], M.R. Sutton[149], S. Suzuki[66], M. Svatos[127], M. Swiatlowski[143], I. Sykora[144a], T. Sykora[129], D. Ta[48], C. Taccini[134a,134b], K. Tackmann[42], J. Taenzer[158], A. Taffard[163], R. Tafirout[159a], N. Taiblum[153], H. Takai[25], R. Takashima[69], H. Takeda[67], T. Takeshita[140], Y. Takubo[66], M. Talby[85], A.A. Talyshev[109,c], J.Y.C. Tam[174], K.G. Tan[88], J. Tanaka[155], R. Tanaka[117], S. Tanaka[66], B.B. Tannenwald[111], N. Tannoury[21], S. Tapprogge[83], S. Tarem[152], F. Tarrade[29], G.F. Tartarelli[91a], P. Tas[129], M. Tasevsky[127], T. Tashiro[68], E. Tassi[37a,37b], A. Tavares Delgado[126a,126b], Y. Tayalati[135d], F.E. Taylor[94], G.N. Taylor[88], P.T.E. Taylor[88], W. Taylor[159b], F.A. Teischinger[30], M. Teixeira Dias Castanheira[76], P. Teixeira-Dias[77], K.K. Temming[48], D. Temple[142], H. Ten Kate[30], P.K. Teng[151], J.J. Teoh[118], F. Tepel[175], S. Terada[66], K. Terashi[155], J. Terron[82], S. Terzo[101], M. Testa[47], R.J. Teuscher[158,k], T. Theveneaux-Pelzer[34], J.P. Thomas[18], J. Thomas-Wilsker[77], E.N. Thompson[35], P.D. Thompson[18], R.J. Thompson[84], A.S. Thompson[53], L.A. Thomsen[176], E. Thomson[122], M. Thomson[28], R.P. Thun[89,*], M.J. Tibbetts[15], R.E. Ticse Torres[85], V.O. Tikhomirov[96,ah], Yu.A. Tikhonov[109,c], S. Timoshenko[98], E. Tiouchichine[85], P. Tipton[176], S. Tisserant[85], K. Todome[157], T. Todorov[5,*],

JHEP12(2015)105

S. Todorova-Nova[129], J. Tojo[70], S. Tokár[144a], K. Tokushuku[66], K. Tollefson[90], E. Tolley[57], L. Tomlinson[84], M. Tomoto[103], L. Tompkins[143,ai], K. Toms[105], E. Torrence[116], H. Torres[142], E. Torró Pastor[138], J. Toth[85,aj], F. Touchard[85], D.R. Tovey[139], T. Trefzger[174], L. Tremblet[30], A. Tricoli[30], I.M. Trigger[159a], S. Trincaz-Duvoid[80], M.F. Tripiana[12], W. Trischuk[158], B. Trocmé[55], C. Troncon[91a], M. Trottier-McDonald[15], M. Trovatelli[169], P. True[90], L. Truong[164a,164c], M. Trzebinski[39], A. Trzupek[39], C. Tsarouchas[30], J.C-L. Tseng[120], P.V. Tsiareshka[92], D. Tsionou[154], G. Tsipolitis[10], N. Tsirintanis[9], S. Tsiskaridze[12], V. Tsiskaridze[48], E.G. Tskhadadze[51a], I.I. Tsukerman[97], V. Tsulaia[15], S. Tsuno[66], D. Tsybychev[148], A. Tudorache[26a], V. Tudorache[26a], A.N. Tuna[57], S.A. Tupputi[20a,20b], S. Turchikhin[99,ag], D. Turecek[128], R. Turra[91a,91b], A.J. Turvey[40], P.M. Tuts[35], A. Tykhonov[49], M. Tylmad[146a,146b], M. Tyndel[131], I. Ueda[155], R. Ueno[29], M. Ughetto[146a,146b], M. Ugland[14], F. Ukegawa[160], G. Unal[30], A. Undrus[25], G. Unel[163], F.C. Ungaro[48], Y. Unno[66], C. Unverdorben[100], J. Urban[144b], P. Urquijo[88], P. Urrejola[83], G. Usai[8], A. Usanova[62], L. Vacavant[85], V. Vacek[128], B. Vachon[87], C. Valderanis[83], N. Valencic[107], S. Valentinetti[20a,20b], A. Valero[167], L. Valery[12], S. Valkar[129], E. Valladolid Gallego[167], S. Vallecorsa[49], J.A. Valls Ferrer[167], W. Van Den Wollenberg[107], P.C. Van Der Deijl[107], R. van der Geer[107], H. van der Graaf[107], N. van Eldik[152], P. van Gemmeren[6], J. Van Nieuwkoop[142], I. van Vulpen[107], M.C. van Woerden[30], M. Vanadia[132a,132b], W. Vandelli[30], R. Vanguri[122], A. Vaniachine[6], F. Vannucci[80], G. Vardanyan[177], R. Vari[132a], E.W. Varnes[7], T. Varol[40], D. Varouchas[80], A. Vartapetian[8], K.E. Varvell[150], F. Vazeille[34], T. Vazquez Schroeder[87], J. Veatch[7], L.M. Veloce[158], F. Veloso[126a,126c], T. Velz[21], S. Veneziano[132a], A. Ventura[73a,73b], D. Ventura[86], M. Venturi[169], N. Venturi[158], A. Venturini[23], V. Vercesi[121a], M. Verducci[132a,132b], W. Verkerke[107], J.C. Vermeulen[107], A. Vest[44], M.C. Vetterli[142,d], O. Viazlo[81], I. Vichou[165], T. Vickey[139], O.E. Vickey Boeriu[139], G.H.A. Viehhauser[120], S. Viel[15], R. Vigne[62], M. Villa[20a,20b], M. Villaplana Perez[91a,91b], E. Vilucchi[47], M.G. Vincter[29], V.B. Vinogradov[65], I. Vivarelli[149], F. Vives Vaque[3], S. Vlachos[10], D. Vladoiu[100], M. Vlasak[128], M. Vogel[32a], P. Vokac[128], G. Volpi[124a,124b], M. Volpi[88], H. von der Schmitt[101], H. von Radziewski[48], E. von Toerne[21], V. Vorobel[129], K. Vorobev[98], M. Vos[167], R. Voss[30], J.H. Vossebeld[74], N. Vranjes[13], M. Vranjes Milosavljevic[13], V. Vrba[127], M. Vreeswijk[107], R. Vuillermet[30], I. Vukotic[31], Z. Vykydal[128], P. Wagner[21], W. Wagner[175], H. Wahlberg[71], S. Wahrmund[44], J. Wakabayashi[103], J. Walder[72], R. Walker[100], W. Walkowiak[141], C. Wang[151], F. Wang[173], H. Wang[15], H. Wang[40], J. Wang[42], J. Wang[33a], K. Wang[87], R. Wang[6], S.M. Wang[151], T. Wang[21], T. Wang[35], X. Wang[176], C. Wanotayaroj[116], A. Warburton[87], C.P. Ward[28], D.R. Wardrope[78], A. Washbrook[46], C. Wasicki[42], P.M. Watkins[18], A.T. Watson[18], I.J. Watson[150], M.F. Watson[18], G. Watts[138], S. Watts[84], B.M. Waugh[78], S. Webb[84], M.S. Weber[17], S.W. Weber[174], J.S. Webster[31], A.R. Weidberg[120], B. Weinert[61], J. Weingarten[54], C. Weiser[48], H. Weits[107], P.S. Wells[30], T. Wenaus[25], T. Wengler[30], S. Wenig[30], N. Wermes[21], M. Werner[48], P. Werner[30], M. Wessels[58a], J. Wetter[161], K. Whalen[116], A.M. Wharton[72], A. White[8], M.J. White[1], R. White[32b], S. White[124a,124b], D. Whiteson[163], F.J. Wickens[131], W. Wiedenmann[173], M. Wielers[131], P. Wienemann[21], C. Wiglesworth[36], L.A.M. Wiik-Fuchs[21], A. Wildauer[101], H.G. Wilkens[30], H.H. Williams[122], S. Williams[107], C. Willis[90], S. Willocq[86], A. Wilson[89], J.A. Wilson[18], I. Wingerter-Seez[5], F. Winklmeier[116], B.T. Winter[21], M. Wittgen[143], J. Wittkowski[100], S.J. Wollstadt[83], M.W. Wolter[39], H. Wolters[126a,126c], B.K. Wosiek[39], J. Wotschack[30], M.J. Woudstra[84], K.W. Wozniak[39], M. Wu[55], M. Wu[31], S.L. Wu[173], X. Wu[49], Y. Wu[89], T.R. Wyatt[84], B.M. Wynne[46], S. Xella[36], D. Xu[33a], L. Xu[25], B. Yabsley[150], S. Yacoob[145a], R. Yakabe[67], M. Yamada[66], D. Yamaguchi[157], Y. Yamaguchi[118], A. Yamamoto[66], S. Yamamoto[155], T. Yamanaka[155], K. Yamauchi[103], Y. Yamazaki[67], Z. Yan[22], H. Yang[33e], H. Yang[173], Y. Yang[151], W-M. Yao[15], Y. Yasu[66], E. Yatsenko[5], K.H. Yau Wong[21], J. Ye[40], S. Ye[25], I. Yeletskikh[65], A.L. Yen[57], E. Yildirim[42], K. Yorita[171], R. Yoshida[6], K. Yoshihara[122],

JHEP12(2015)105

C. Young[143], C.J.S. Young[30], S. Youssef[22], D.R. Yu[15], J. Yu[8], J.M. Yu[89], J. Yu[114], L. Yuan[67], S.P.Y. Yuen[21], A. Yurkewicz[108], I. Yusuff[28,ak], B. Zabinski[39], R. Zaidan[63], A.M. Zaitsev[130,ab], J. Zalieckas[14], A. Zaman[148], S. Zambito[57], L. Zanello[132a,132b], D. Zanzi[88], C. Zeitnitz[175], M. Zeman[128], A. Zemla[38a], Q. Zeng[143], K. Zengel[23], O. Zenin[130], T. Ženiš[144a], D. Zerwas[117], D. Zhang[89], F. Zhang[173], H. Zhang[33c], J. Zhang[6], L. Zhang[48], R. Zhang[33b], X. Zhang[33d], Z. Zhang[117], X. Zhao[40], Y. Zhao[33d,117], Z. Zhao[33b], A. Zhemchugov[65], J. Zhong[120], B. Zhou[89], C. Zhou[45], L. Zhou[35], L. Zhou[40], M. Zhou[148], N. Zhou[33f], C.G. Zhu[33d], H. Zhu[33a], J. Zhu[89], Y. Zhu[33b], X. Zhuang[33a], K. Zhukov[96], A. Zibell[174], D. Zieminska[61], N.I. Zimine[65], C. Zimmermann[83], S. Zimmermann[48], Z. Zinonos[54], M. Zinser[83], M. Ziolkowski[141], L. Živković[13], G. Zobernig[173], A. Zoccoli[20a,20b], M. zur Nedden[16], G. Zurzolo[104a,104b], L. Zwalinski[30].

[1] *Department of Physics, University of Adelaide, Adelaide, Australia*

[2] *Physics Department, SUNY Albany, Albany NY, United States of America*

[3] *Department of Physics, University of Alberta, Edmonton AB, Canada*

[4] [(a)] *Department of Physics, Ankara University, Ankara;* [(b)] *Istanbul Aydin University, Istanbul;* [(c)] *Division of Physics, TOBB University of Economics and Technology, Ankara, Turkey*

[5] *LAPP, CNRS/IN2P3 and Université Savoie Mont Blanc, Annecy-le-Vieux, France*

[6] *High Energy Physics Division, Argonne National Laboratory, Argonne IL, United States of America*

[7] *Department of Physics, University of Arizona, Tucson AZ, United States of America*

[8] *Department of Physics, The University of Texas at Arlington, Arlington TX, United States of America*

[9] *Physics Department, University of Athens, Athens, Greece*

[10] *Physics Department, National Technical University of Athens, Zografou, Greece*

[11] *Institute of Physics, Azerbaijan Academy of Sciences, Baku, Azerbaijan*

[12] *Institut de Física d'Altes Energies and Departament de Física de la Universitat Autònoma de Barcelona, Barcelona, Spain*

[13] *Institute of Physics, University of Belgrade, Belgrade, Serbia*

[14] *Department for Physics and Technology, University of Bergen, Bergen, Norway*

[15] *Physics Division, Lawrence Berkeley National Laboratory and University of California, Berkeley CA, United States of America*

[16] *Department of Physics, Humboldt University, Berlin, Germany*

[17] *Albert Einstein Center for Fundamental Physics and Laboratory for High Energy Physics, University of Bern, Bern, Switzerland*

[18] *School of Physics and Astronomy, University of Birmingham, Birmingham, United Kingdom*

[19] [(a)] *Department of Physics, Bogazici University, Istanbul;* [(b)] *Department of Physics Engineering, Gaziantep University, Gaziantep;* [(c)] *Department of Physics, Dogus University, Istanbul, Turkey*

[20] [(a)] *INFN Sezione di Bologna;* [(b)] *Dipartimento di Fisica e Astronomia, Università di Bologna, Bologna, Italy*

[21] *Physikalisches Institut, University of Bonn, Bonn, Germany*

[22] *Department of Physics, Boston University, Boston MA, United States of America*

[23] *Department of Physics, Brandeis University, Waltham MA, United States of America*

[24] [(a)] *Universidade Federal do Rio De Janeiro COPPE/EE/IF, Rio de Janeiro;* [(b)] *Electrical Circuits Department, Federal University of Juiz de Fora (UFJF), Juiz de Fora;* [(c)] *Federal University of Sao Joao del Rei (UFSJ), Sao Joao del Rei;* [(d)] *Instituto de Fisica, Universidade de Sao Paulo, Sao Paulo, Brazil*

JHEP12(2015)105

[25] *Physics Department, Brookhaven National Laboratory, Upton NY, United States of America*

[26] [(a)] *National Institute of Physics and Nuclear Engineering, Bucharest;* [(b)] *National Institute for Research and Development of Isotopic and Molecular Technologies, Physics Department, Cluj Napoca;* [(c)] *University Politehnica Bucharest, Bucharest;* [(d)] *West University in Timisoara, Timisoara, Romania*

[27] *Departamento de Física, Universidad de Buenos Aires, Buenos Aires, Argentina*

[28] *Cavendish Laboratory, University of Cambridge, Cambridge, United Kingdom*

[29] *Department of Physics, Carleton University, Ottawa ON, Canada*

[30] *CERN, Geneva, Switzerland*

[31] *Enrico Fermi Institute, University of Chicago, Chicago IL, United States of America*

[32] [(a)] *Departamento de Física, Pontificia Universidad Católica de Chile, Santiago;* [(b)] *Departamento de Física, Universidad Técnica Federico Santa María, Valparaíso, Chile*

[33] [(a)] *Institute of High Energy Physics, Chinese Academy of Sciences, Beijing;* [(b)] *Department of Modern Physics, University of Science and Technology of China, Anhui;* [(c)] *Department of Physics, Nanjing University, Jiangsu;* [(d)] *School of Physics, Shandong University, Shandong;* [(e)] *Department of Physics and Astronomy, Shanghai Key Laboratory for Particle Physics and Cosmology, Shanghai Jiao Tong University, Shanghai;* [(f)] *Physics Department, Tsinghua University, Beijing 100084, China*

[34] *Laboratoire de Physique Corpusculaire, Clermont Université and Université Blaise Pascal and CNRS/IN2P3, Clermont-Ferrand, France*

[35] *Nevis Laboratory, Columbia University, Irvington NY, United States of America*

[36] *Niels Bohr Institute, University of Copenhagen, Kobenhavn, Denmark*

[37] [(a)] *INFN Gruppo Collegato di Cosenza, Laboratori Nazionali di Frascati;* [(b)] *Dipartimento di Fisica, Università della Calabria, Rende, Italy*

[38] [(a)] *AGH University of Science and Technology, Faculty of Physics and Applied Computer Science, Krakow;* [(b)] *Marian Smoluchowski Institute of Physics, Jagiellonian University, Krakow, Poland*

[39] *Institute of Nuclear Physics Polish Academy of Sciences, Krakow, Poland*

[40] *Physics Department, Southern Methodist University, Dallas TX, United States of America*

[41] *Physics Department, University of Texas at Dallas, Richardson TX, United States of America*

[42] *DESY, Hamburg and Zeuthen, Germany*

[43] *Institut für Experimentelle Physik IV, Technische Universität Dortmund, Dortmund, Germany*

[44] *Institut für Kern- und Teilchenphysik, Technische Universität Dresden, Dresden, Germany*

[45] *Department of Physics, Duke University, Durham NC, United States of America*

[46] *SUPA - School of Physics and Astronomy, University of Edinburgh, Edinburgh, United Kingdom*

[47] *INFN Laboratori Nazionali di Frascati, Frascati, Italy*

[48] *Fakultät für Mathematik und Physik, Albert-Ludwigs-Universität, Freiburg, Germany*

[49] *Section de Physique, Université de Genève, Geneva, Switzerland*

[50] [(a)] *INFN Sezione di Genova;* [(b)] *Dipartimento di Fisica, Università di Genova, Genova, Italy*

[51] [(a)] *E. Andronikashvili Institute of Physics, Iv. Javakhishvili Tbilisi State University, Tbilisi;* [(b)] *High Energy Physics Institute, Tbilisi State University, Tbilisi, Georgia*

[52] *II Physikalisches Institut, Justus-Liebig-Universität Giessen, Giessen, Germany*

[53] *SUPA - School of Physics and Astronomy, University of Glasgow, Glasgow, United Kingdom*

[54] *II Physikalisches Institut, Georg-August-Universität, Göttingen, Germany*

JHEP12(2015)105

[55] *Laboratoire de Physique Subatomique et de Cosmologie, Université Grenoble-Alpes, CNRS/IN2P3, Grenoble, France*

[56] *Department of Physics, Hampton University, Hampton VA, United States of America*

[57] *Laboratory for Particle Physics and Cosmology, Harvard University, Cambridge MA, United States of America*

[58] [(a)] *Kirchhoff-Institut für Physik, Ruprecht-Karls-Universität Heidelberg, Heidelberg;* [(b)] *Physikalisches Institut, Ruprecht-Karls-Universität Heidelberg, Heidelberg;* [(c)] *ZITI Institut für technische Informatik, Ruprecht-Karls-Universität Heidelberg, Mannheim, Germany*

[59] *Faculty of Applied Information Science, Hiroshima Institute of Technology, Hiroshima, Japan*

[60] [(a)] *Department of Physics, The Chinese University of Hong Kong, Shatin, N.T., Hong Kong;* [(b)] *Department of Physics, The University of Hong Kong, Hong Kong;* [(c)] *Department of Physics, The Hong Kong University of Science and Technology, Clear Water Bay, Kowloon, Hong Kong, China*

[61] *Department of Physics, Indiana University, Bloomington IN, United States of America*

[62] *Institut für Astro- und Teilchenphysik, Leopold-Franzens-Universität, Innsbruck, Austria*

[63] *University of Iowa, Iowa City IA, United States of America*

[64] *Department of Physics and Astronomy, Iowa State University, Ames IA, United States of America*

[65] *Joint Institute for Nuclear Research, JINR Dubna, Dubna, Russia*

[66] *KEK, High Energy Accelerator Research Organization, Tsukuba, Japan*

[67] *Graduate School of Science, Kobe University, Kobe, Japan*

[68] *Faculty of Science, Kyoto University, Kyoto, Japan*

[69] *Kyoto University of Education, Kyoto, Japan*

[70] *Department of Physics, Kyushu University, Fukuoka, Japan*

[71] *Instituto de Física La Plata, Universidad Nacional de La Plata and CONICET, La Plata, Argentina*

[72] *Physics Department, Lancaster University, Lancaster, United Kingdom*

[73] [(a)] *INFN Sezione di Lecce;* [(b)] *Dipartimento di Matematica e Fisica, Università del Salento, Lecce, Italy*

[74] *Oliver Lodge Laboratory, University of Liverpool, Liverpool, United Kingdom*

[75] *Department of Physics, Jožef Stefan Institute and University of Ljubljana, Ljubljana, Slovenia*

[76] *School of Physics and Astronomy, Queen Mary University of London, London, United Kingdom*

[77] *Department of Physics, Royal Holloway University of London, Surrey, United Kingdom*

[78] *Department of Physics and Astronomy, University College London, London, United Kingdom*

[79] *Louisiana Tech University, Ruston LA, United States of America*

[80] *Laboratoire de Physique Nucléaire et de Hautes Energies, UPMC and Université Paris-Diderot and CNRS/IN2P3, Paris, France*

[81] *Fysiska institutionen, Lunds universitet, Lund, Sweden*

[82] *Departamento de Fisica Teorica C-15, Universidad Autonoma de Madrid, Madrid, Spain*

[83] *Institut für Physik, Universität Mainz, Mainz, Germany*

[84] *School of Physics and Astronomy, University of Manchester, Manchester, United Kingdom*

[85] *CPPM, Aix-Marseille Université and CNRS/IN2P3, Marseille, France*

[86] *Department of Physics, University of Massachusetts, Amherst MA, United States of America*

[87] *Department of Physics, McGill University, Montreal QC, Canada*

[88] *School of Physics, University of Melbourne, Victoria, Australia*

JHEP12(2015)105

[89] *Department of Physics, The University of Michigan, Ann Arbor MI, United States of America*

[90] *Department of Physics and Astronomy, Michigan State University, East Lansing MI, United States of America*

[91] [(a)] *INFN Sezione di Milano;* [(b)] *Dipartimento di Fisica, Università di Milano, Milano, Italy*

[92] *B.I. Stepanov Institute of Physics, National Academy of Sciences of Belarus, Minsk, Republic of Belarus*

[93] *National Scientific and Educational Centre for Particle and High Energy Physics, Minsk, Republic of Belarus*

[94] *Department of Physics, Massachusetts Institute of Technology, Cambridge MA, United States of America*

[95] *Group of Particle Physics, University of Montreal, Montreal QC, Canada*

[96] *P.N. Lebedev Institute of Physics, Academy of Sciences, Moscow, Russia*

[97] *Institute for Theoretical and Experimental Physics (ITEP), Moscow, Russia*

[98] *National Research Nuclear University MEPhI, Moscow, Russia*

[99] *D.V. Skobeltsyn Institute of Nuclear Physics, M.V. Lomonosov Moscow State University, Moscow, Russia*

[100] *Fakultät für Physik, Ludwig-Maximilians-Universität München, München, Germany*

[101] *Max-Planck-Institut für Physik (Werner-Heisenberg-Institut), München, Germany*

[102] *Nagasaki Institute of Applied Science, Nagasaki, Japan*

[103] *Graduate School of Science and Kobayashi-Maskawa Institute, Nagoya University, Nagoya, Japan*

[104] [(a)] *INFN Sezione di Napoli;* [(b)] *Dipartimento di Fisica, Università di Napoli, Napoli, Italy*

[105] *Department of Physics and Astronomy, University of New Mexico, Albuquerque NM, United States of America*

[106] *Institute for Mathematics, Astrophysics and Particle Physics, Radboud University Nijmegen/Nikhef, Nijmegen, Netherlands*

[107] *Nikhef National Institute for Subatomic Physics and University of Amsterdam, Amsterdam, Netherlands*

[108] *Department of Physics, Northern Illinois University, DeKalb IL, United States of America*

[109] *Budker Institute of Nuclear Physics, SB RAS, Novosibirsk, Russia*

[110] *Department of Physics, New York University, New York NY, United States of America*

[111] *Ohio State University, Columbus OH, United States of America*

[112] *Faculty of Science, Okayama University, Okayama, Japan*

[113] *Homer L. Dodge Department of Physics and Astronomy, University of Oklahoma, Norman OK, United States of America*

[114] *Department of Physics, Oklahoma State University, Stillwater OK, United States of America*

[115] *Palacký University, RCPTM, Olomouc, Czech Republic*

[116] *Center for High Energy Physics, University of Oregon, Eugene OR, United States of America*

[117] *LAL, Université Paris-Sud and CNRS/IN2P3, Orsay, France*

[118] *Graduate School of Science, Osaka University, Osaka, Japan*

[119] *Department of Physics, University of Oslo, Oslo, Norway*

[120] *Department of Physics, Oxford University, Oxford, United Kingdom*

[121] [(a)] *INFN Sezione di Pavia;* [(b)] *Dipartimento di Fisica, Università di Pavia, Pavia, Italy*

JHEP12(2015)105

[122] *Department of Physics, University of Pennsylvania, Philadelphia PA, United States of America*

[123] *National Research Centre "Kurchatov Institute" B.P.Konstantinov Petersburg Nuclear Physics Institute, St. Petersburg, Russia*

[124] [(a)] *INFN Sezione di Pisa;* [(b)] *Dipartimento di Fisica E. Fermi, Università di Pisa, Pisa, Italy*

[125] *Department of Physics and Astronomy, University of Pittsburgh, Pittsburgh PA, United States of America*

[126] [(a)] *Laboratório de Instrumentação e Física Experimental de Partículas - LIP, Lisboa;* [(b)] *Faculdade de Ciências, Universidade de Lisboa, Lisboa;* [(c)] *Department of Physics, University of Coimbra, Coimbra;* [(d)] *Centro de Física Nuclear da Universidade de Lisboa, Lisboa;* [(e)] *Departamento de Fisica, Universidade do Minho, Braga;* [(f)] *Departamento de Fisica Teorica y del Cosmos and CAFPE, Universidad de Granada, Granada (Spain);* [(g)] *Dep Fisica and CEFITEC of Faculdade de Ciencias e Tecnologia, Universidade Nova de Lisboa, Caparica, Portugal*

[127] *Institute of Physics, Academy of Sciences of the Czech Republic, Praha, Czech Republic*

[128] *Czech Technical University in Prague, Praha, Czech Republic*

[129] *Faculty of Mathematics and Physics, Charles University in Prague, Praha, Czech Republic*

[130] *State Research Center Institute for High Energy Physics, Protvino, Russia*

[131] *Particle Physics Department, Rutherford Appleton Laboratory, Didcot, United Kingdom*

[132] [(a)] *INFN Sezione di Roma;* [(b)] *Dipartimento di Fisica, Sapienza Università di Roma, Roma, Italy*

[133] [(a)] *INFN Sezione di Roma Tor Vergata;* [(b)] *Dipartimento di Fisica, Università di Roma Tor Vergata, Roma, Italy*

[134] [(a)] *INFN Sezione di Roma Tre;* [(b)] *Dipartimento di Matematica e Fisica, Università Roma Tre, Roma, Italy*

[135] [(a)] *Faculté des Sciences Ain Chock, Réseau Universitaire de Physique des Hautes Energies - Université Hassan II, Casablanca;* [(b)] *Centre National de l'Energie des Sciences Techniques Nucleaires, Rabat;* [(c)] *Faculté des Sciences Semlalia, Université Cadi Ayyad, LPHEA-Marrakech;* [(d)] *Faculté des Sciences, Université Mohamed Premier and LPTPM, Oujda;* [(e)] *Faculté des sciences, Université Mohammed V, Rabat, Morocco*

[136] *DSM/IRFU (Institut de Recherches sur les Lois Fondamentales de l'Univers), CEA Saclay (Commissariat à l'Energie Atomique et aux Energies Alternatives), Gif-sur-Yvette, France*

[137] *Santa Cruz Institute for Particle Physics, University of California Santa Cruz, Santa Cruz CA, United States of America*

[138] *Department of Physics, University of Washington, Seattle WA, United States of America*

[139] *Department of Physics and Astronomy, University of Sheffield, Sheffield, United Kingdom*

[140] *Department of Physics, Shinshu University, Nagano, Japan*

[141] *Fachbereich Physik, Universität Siegen, Siegen, Germany*

[142] *Department of Physics, Simon Fraser University, Burnaby BC, Canada*

[143] *SLAC National Accelerator Laboratory, Stanford CA, United States of America*

[144] [(a)] *Faculty of Mathematics, Physics & Informatics, Comenius University, Bratislava;* [(b)] *Department of Subnuclear Physics, Institute of Experimental Physics of the Slovak Academy of Sciences, Kosice, Slovak Republic*

[145] [(a)] *Department of Physics, University of Cape Town, Cape Town;* [(b)] *Department of Physics, University of Johannesburg, Johannesburg;* [(c)] *School of Physics, University of the Witwatersrand, Johannesburg, South Africa*

[146] [(a)] *Department of Physics, Stockholm University;* [(b)] *The Oskar Klein Centre, Stockholm, Sweden*

[147] *Physics Department, Royal Institute of Technology, Stockholm, Sweden*

JHEP12(2015)105

[148] *Departments of Physics & Astronomy and Chemistry, Stony Brook University, Stony Brook NY, United States of America*

[149] *Department of Physics and Astronomy, University of Sussex, Brighton, United Kingdom*

[150] *School of Physics, University of Sydney, Sydney, Australia*

[151] *Institute of Physics, Academia Sinica, Taipei, Taiwan*

[152] *Department of Physics, Technion: Israel Institute of Technology, Haifa, Israel*

[153] *Raymond and Beverly Sackler School of Physics and Astronomy, Tel Aviv University, Tel Aviv, Israel*

[154] *Department of Physics, Aristotle University of Thessaloniki, Thessaloniki, Greece*

[155] *International Center for Elementary Particle Physics and Department of Physics, The University of Tokyo, Tokyo, Japan*

[156] *Graduate School of Science and Technology, Tokyo Metropolitan University, Tokyo, Japan*

[157] *Department of Physics, Tokyo Institute of Technology, Tokyo, Japan*

[158] *Department of Physics, University of Toronto, Toronto ON, Canada*

[159] [(a)] *TRIUMF, Vancouver BC;* [(b)] *Department of Physics and Astronomy, York University, Toronto ON, Canada*

[160] *Faculty of Pure and Applied Sciences, University of Tsukuba, Tsukuba, Japan*

[161] *Department of Physics and Astronomy, Tufts University, Medford MA, United States of America*

[162] *Centro de Investigaciones, Universidad Antonio Narino, Bogota, Colombia*

[163] *Department of Physics and Astronomy, University of California Irvine, Irvine CA, United States of America*

[164] [(a)] *INFN Gruppo Collegato di Udine, Sezione di Trieste, Udine;* [(b)] *ICTP, Trieste;* [(c)] *Dipartimento di Chimica, Fisica e Ambiente, Università di Udine, Udine, Italy*

[165] *Department of Physics, University of Illinois, Urbana IL, United States of America*

[166] *Department of Physics and Astronomy, University of Uppsala, Uppsala, Sweden*

[167] *Instituto de Física Corpuscular (IFIC) and Departamento de Física Atómica, Molecular y Nuclear and Departamento de Ingeniería Electrónica and Instituto de Microelectrónica de Barcelona (IMB-CNM), University of Valencia and CSIC, Valencia, Spain*

[168] *Department of Physics, University of British Columbia, Vancouver BC, Canada*

[169] *Department of Physics and Astronomy, University of Victoria, Victoria BC, Canada*

[170] *Department of Physics, University of Warwick, Coventry, United Kingdom*

[171] *Waseda University, Tokyo, Japan*

[172] *Department of Particle Physics, The Weizmann Institute of Science, Rehovot, Israel*

[173] *Department of Physics, University of Wisconsin, Madison WI, United States of America*

[174] *Fakultät für Physik und Astronomie, Julius-Maximilians-Universität, Würzburg, Germany*

[175] *Fachbereich C Physik, Bergische Universität Wuppertal, Wuppertal, Germany*

[176] *Department of Physics, Yale University, New Haven CT, United States of America*

[177] *Yerevan Physics Institute, Yerevan, Armenia*

[178] *Centre de Calcul de l'Institut National de Physique Nucléaire et de Physique des Particules (IN2P3), Villeurbanne, France*

[a] *Also at Department of Physics, King's College London, London, United Kingdom*

[b] *Also at Institute of Physics, Azerbaijan Academy of Sciences, Baku, Azerbaijan*

JHEP12(2015)105

[c] Also at Novosibirsk State University, Novosibirsk, Russia

[d] Also at TRIUMF, Vancouver BC, Canada

[e] Also at Department of Physics, California State University, Fresno CA, United States of America

[f] Also at Department of Physics, University of Fribourg, Fribourg, Switzerland

[g] Also at Departamento de Fisica e Astronomia, Faculdade de Ciencias, Universidade do Porto, Portugal

[h] Also at Tomsk State University, Tomsk, Russia

[i] Also at CPPM, Aix-Marseille Université and CNRS/IN2P3, Marseille, France

[j] Also at Universita di Napoli Parthenope, Napoli, Italy

[k] Also at Institute of Particle Physics (IPP), Canada

[l] Also at Particle Physics Department, Rutherford Appleton Laboratory, Didcot, United Kingdom

[m] Also at Department of Physics, St. Petersburg State Polytechnical University, St. Petersburg, Russia

[n] Also at Louisiana Tech University, Ruston LA, United States of America

[o] Also at Institucio Catalana de Recerca i Estudis Avancats, ICREA, Barcelona, Spain

[p] Also at Graduate School of Science, Osaka University, Osaka, Japan

[q] Also at Department of Physics, National Tsing Hua University, Taiwan

[r] Also at Department of Physics, The University of Texas at Austin, Austin TX, United States of America

[s] Also at Institute of Theoretical Physics, Ilia State University, Tbilisi, Georgia

[t] Also at CERN, Geneva, Switzerland

[u] Also at Georgian Technical University (GTU),Tbilisi, Georgia

[v] Also at Manhattan College, New York NY, United States of America

[w] Also at Hellenic Open University, Patras, Greece

[x] Also at Institute of Physics, Academia Sinica, Taipei, Taiwan

[y] Also at LAL, Université Paris-Sud and CNRS/IN2P3, Orsay, France

[z] Also at Academia Sinica Grid Computing, Institute of Physics, Academia Sinica, Taipei, Taiwan

[aa] Also at School of Physics, Shandong University, Shandong, China

[ab] Also at Moscow Institute of Physics and Technology State University, Dolgoprudny, Russia

[ac] Also at section de Physique, Université de Genève, Geneva, Switzerland

[ad] Also at International School for Advanced Studies (SISSA), Trieste, Italy

[ae] Also at Department of Physics and Astronomy, University of South Carolina, Columbia SC, United States of America

[af] Also at School of Physics and Engineering, Sun Yat-sen University, Guangzhou, China

[ag] Also at Faculty of Physics, M.V.Lomonosov Moscow State University, Moscow, Russia

[ah] Also at National Research Nuclear University MEPhI, Moscow, Russia

[ai] Also at Department of Physics, Stanford University, Stanford CA, United States of America

[aj] Also at Institute for Particle and Nuclear Physics, Wigner Research Centre for Physics, Budapest, Hungary

[ak] Also at University of Malaya, Department of Physics, Kuala Lumpur, Malaysia

[*] Deceased

JHEP12(2015)105

Eur. Phys. J. C (2016) 76:4
DOI 10.1140/epjc/s10052-015-3743-8

THE EUROPEAN PHYSICAL JOURNAL C

Regular Article - Experimental Physics

Study of the $B_c^+ \to J/\psi D_s^+$ and $B_c^+ \to J/\psi D_s^{*+}$ decays with the ATLAS detector

ATLAS Collaboration[*]

CERN, 1211 Geneva 23, Switzerland

Received: 27 July 2015 / Accepted: 19 October 2015 / Published online: 5 January 2016
© CERN for the benefit of the ATLAS collaboration 2015. This article is published with open access at Springerlink.com

Abstract The decays $B_c^+ \to J/\psi D_s^+$ and $B_c^+ \to J/\psi D_s^{*+}$ are studied with the ATLAS detector at the LHC using a dataset corresponding to integrated luminosities of 4.9 and 20.6 fb^{-1} of pp collisions collected at centre-of-mass energies $\sqrt{s} = 7$ TeV and 8 TeV, respectively. Signal candidates are identified through $J/\psi \to \mu^+\mu^-$ and $D_s^{(*)+} \to \phi\pi^+(\gamma/\pi^0)$ decays. With a two-dimensional likelihood fit involving the B_c^+ reconstructed invariant mass and an angle between the μ^+ and D_s^+ candidate momenta in the muon pair rest frame, the yields of $B_c^+ \to J/\psi D_s^+$ and $B_c^+ \to J/\psi D_s^{*+}$, and the transverse polarisation fraction in $B_c^+ \to J/\psi D_s^{*+}$ decay are measured. The transverse polarisation fraction is determined to be $\Gamma_{\pm\pm}(B_c^+ \to J/\psi D_s^{*+})/\Gamma(B_c^+ \to J/\psi D_s^{*+}) = 0.38 \pm 0.23 \pm 0.07$, and the derived ratio of the branching fractions of the two modes is $\mathcal{B}_{B_c^+\to J/\psi D_s^{*+}}/\mathcal{B}_{B_c^+\to J/\psi D_s^+} = 2.8\,^{+1.2}_{-0.8} \pm 0.3$, where the first error is statistical and the second is systematic. Finally, a sample of $B_c^+ \to J/\psi\pi^+$ decays is used to derive the ratios of branching fractions $\mathcal{B}_{B_c^+\to J/\psi D_s^+}/\mathcal{B}_{B_c^+\to J/\psi\pi^+} = 3.8 \pm 1.1 \pm 0.4 \pm 0.2$ and $\mathcal{B}_{B_c^+\to J/\psi D_s^{*+}}/\mathcal{B}_{B_c^+\to J/\psi\pi^+} = 10.4 \pm 3.1 \pm 1.5 \pm 0.6$, where the third error corresponds to the uncertainty of the branching fraction of $D_s^+ \to \phi(K^+K^-)\pi^+$ decay. The available theoretical predictions are generally consistent with the measurement.

1 Introduction

The B_c^+ meson[1] is the only known weakly decaying particle consisting of two heavy quarks. The ground $\bar{b}c$ state was first observed by CDF [1] via its semileptonic decay $B_c^+ \to J/\psi\ell^+\nu_\ell$. An excited $\bar{b}c$ state has been observed recently by ATLAS [2] using the B_c^+ decay mode $B_c^+ \to J/\psi\pi^+$. The presence of two heavy quarks, each of which can decay weakly, affects theoretical calculations of the decay properties of the B_c^+ meson. In the case of $\bar{b} \to \bar{c}c\bar{s}$ processes, decays to charmonium and a D_s^+ or a D_s^{*+} meson are predicted to occur via colour-suppressed and colour-favoured spectator diagrams as well as via the weak annihilation diagram (see Fig. 1). The latter, in contrast to decays of other B mesons, is not Cabibbo-suppressed and can contribute significantly to the decay amplitudes. The decay properties are addressed in various theoretical calculations [3–9] and can also be compared to the analogous properties in the lighter B meson systems such as $B_d^0 \to D^{*-}D_s^{(*)+}$ or $B^+ \to \bar{D}^{*0}D_s^{(*)+}$. The decays $B_c^+ \to J/\psi D_s^+$ and $B_c^+ \to J/\psi D_s^{*+}$, which have been observed recently by the LHCb experiment [10], provide a means to test these theoretical predictions.

This paper presents a measurement of the branching fractions of $B_c^+ \to J/\psi D_s^+$ and $B_c^+ \to J/\psi D_s^{*+}$ decays, normalised to that of $B_c^+ \to J/\psi\pi^+$ decay, and polarisation in $B_c^+ \to J/\psi D_s^{*+}$ decay performed with the ATLAS detector [11]. The D_s^+ meson is reconstructed via the $D_s^+ \to \phi\pi^+$ decay with the ϕ meson decaying into a pair of charged kaons. The D_s^{*+} meson decays into a D_s^+ meson and a soft photon or π^0. Detecting such soft neutral particles is very challenging, thus no attempt to reconstruct them is made in the analysis. The J/ψ meson is reconstructed via its decay into a muon pair.

The measurement presented in this paper allows an independent verification of the results of Ref. [10] with comparable statistical and systematic uncertainties. The following ratios are measured: $\mathcal{R}_{D_s^+/\pi^+} = \mathcal{B}_{B_c^+\to J/\psi D_s^+}/\mathcal{B}_{B_c^+\to J/\psi\pi^+}$, $\mathcal{R}_{D_s^{*+}/\pi^+} = \mathcal{B}_{B_c^+\to J/\psi D_s^{*+}}/\mathcal{B}_{B_c^+\to J/\psi\pi^+}$, and $\mathcal{R}_{D_s^{*+}/D_s^+} = \mathcal{B}_{B_c^+\to J/\psi D_s^{*+}}/\mathcal{B}_{B_c^+\to J/\psi D_s^+}$, where $\mathcal{B}_{B_c^+\to X}$ denotes the branching fraction of the $B_c^+ \to X$ decay. The decay $B_c^+ \to J/\psi D_s^{*+}$ is a transition of a pseudoscalar meson into a pair of vector states and is thus described by the three helicity amplitudes, A_{++}, A_{--}, and A_{00}, where the subscripts correspond to the helicities of J/ψ and D_s^{*+} mesons. The contribution of the A_{++} and A_{--} amplitudes, referred to as the $A_{\pm\pm}$ component, corresponds to the J/ψ and D_s^{*+} transverse polarisation. The fraction of transverse polarisation,

[1] Charge conjugate states are implied throughout the paper unless otherwise stated.

[*] e-mail: atlas.publications@cern.ch

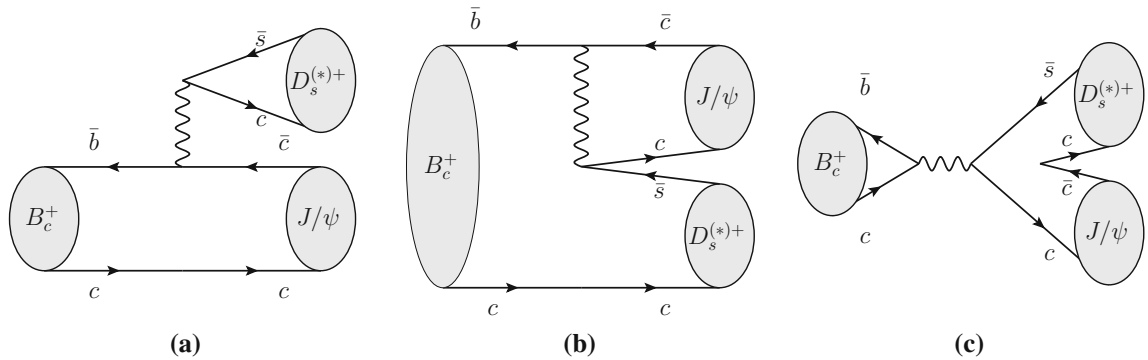

Fig. 1 Feynman diagrams for $B_c^+ \to J/\psi D_s^{(*)+}$ decays: **a** colour-favoured spectator, **b** colour-suppressed spectator, and **c** annihilation topology

$\Gamma_{\pm\pm}/\Gamma = \Gamma_{\pm\pm}(B_c^+ \to J/\psi D_s^{*+})/\Gamma(B_c^+ \to J/\psi D_s^{*+})$, is also measured. From a naive prediction by spin counting, one would expect this fraction to be 2/3, while calculations [8,9] predict values of 0.41–0.48.

This analysis is based on a combined sample of pp collision data collected by the ATLAS experiment at the LHC at centre-of-mass energies $\sqrt{s} = 7$ TeV and 8 TeV corresponding to integrated luminosities of 4.9 and 20.6 fb^{-1}, respectively.

2 The ATLAS detector, trigger selection and Monte Carlo samples

ATLAS is a general-purpose detector consisting of several subsystems including the inner detector (ID), calorimeters and the muon spectrometer (MS). Muon reconstruction makes use of both the ID and the MS. The ID comprises three types of detectors: a silicon pixel detector, a silicon microstrip semiconductor tracker (SCT) and a transition radiation tracker. The ID provides a pseudorapidity[2] coverage up to $|\eta| = 2.5$. Muons pass through the calorimeters and reach the MS if their transverse momentum, p_T, is above approximately 3 GeV.[3] Muon candidates are formed either from a stand-alone MS track matched to an ID track or, in case the MS stand-alone track is not reconstructed, from an ID track extrapolated to the MS and matched to track segments in the MS. Candidates of the latter type are referred to as segment-tagged muons while the former are called combined muons. Muon track parameters are taken from the ID measurement alone in this analysis, since the precision of the measured track parameters for muons in the p_T range of interest is dominated by the ID track reconstruction.

The ATLAS trigger system consists of a hardware-based Level-1 trigger and a two-stage high level trigger (HLT). At Level-1, the muon trigger uses dedicated MS chambers to search for patterns of hits satisfying different p_T thresholds. The region-of-interest around these hit patterns then serves as a seed for the HLT muon reconstruction, in which dedicated algorithms are used to incorporate information from both the MS and the ID, achieving a position and momentum resolution close to that provided by the offline muon reconstruction. Muons are efficiently triggered in the pseudorapidity range $|\eta| < 2.4$.

Triggers based on single-muon, dimuon, and three-muon signatures are used to select $J/\psi \to \mu^+\mu^-$ decays for the analysis. The third muon can be produced in the B_c^+ signal events in semileptonic decays of the two other heavy-flavour hadrons. The majority of events are collected by dimuon triggers requiring a vertex of two oppositely charged muons with an invariant mass between 2.5 and 4.3 GeV. During the data taking, the p_T threshold for muons in these triggers was either 4 or 6 GeV. Single-muon triggers additionally increase the acceptance for asymmetric J/ψ decays where one muon has $p_T < 4$ GeV. Finally, three-muon triggers had a p_T threshold of 4 GeV, thus enhancing the acceptance during the periods of high luminosity when the p_T threshold for at least one muon in the dimuon triggers was 6 GeV.

Monte Carlo (MC) simulation is used for the event selection criteria optimisation and the calculation of the acceptance for the considered B_c^+ decay modes. The MC samples of the B_c^+ decays were generated with PYTHIA 6.4 [12] along with a dedicated extension for the B_c^+ production based on calculations from Refs. [13–16]. The decays of B_c^+ are then simulated with EVTGEN [17]. The generated events were passed through a full simulation of the detector using the ATLAS simulation framework [18] based on GEANT 4 [19,20] and processed with the same reconstruction algorithms as were used for the data.

[2] ATLAS uses a right-handed coordinate system with its origin at the nominal interaction point (IP) in the centre of the detector and the z-axis along the beam pipe. The x-axis points from the IP to the centre of the LHC ring, and the y-axis points upward. Cylindrical coordinates (r, ϕ) are used in the transverse plane, ϕ being the azimuthal angle around the beam pipe. The pseudorapidity is defined in terms of the polar angle θ as $\eta = -\ln\tan(\theta/2)$.

[3] Using a system of units with $c = 1$ is implied throughout the paper.

3 Reconstruction and event selection

The J/ψ candidates are reconstructed from pairs of oppositely charged muons. At least one of the two muons is required to be a combined muon. Each pair is fitted to a common vertex [21]. The quality of the vertex fit must satisfy $\chi^2/\text{ndf} < 15$, where the ndf stands for the number of degrees of freedom. The candidates in the invariant mass window $2800\,\text{MeV} < m(\mu^+\mu^-) < 3400\,\text{MeV}$ are retained.

For the $D_s^+ \to \phi(K^+K^-)\pi^+$ reconstruction, tracks of particles with opposite charges are assigned kaon mass hypotheses and combined in pairs to form ϕ candidates. An additional track is assigned a pion mass and combined with the ϕ candidate to form a D_s^+ candidate. To ensure good momentum resolution, all three tracks are required to have at least two hits in the silicon pixel detector and at least six hits in the SCT. Only three-track combinations successfully fitted to a common vertex with $\chi^2/\text{ndf} < 8$ are kept. The ϕ candidate invariant mass, $m(K^+K^-)$, and the D_s^+ candidate invariant mass, $m(K^+K^-\pi^+)$, are calculated using the track momenta refitted to the common vertex. Only candidates with $m(K^+K^-)$ within $\pm 7\,\text{MeV}$ around the ϕ mass, $m_\phi = 1019.461\,\text{MeV}$ [22], and with $1930\,\text{MeV} < m(K^+K^-\pi^+) < 2010\,\text{MeV}$ are retained.

The $B_c^+ \to J/\psi D_s^+$ candidates are built by combining the five tracks of the J/ψ and D_s^+ candidates. The J/ψ meson decays instantly at the same point as the B_c^+ does (secondary vertex) while the D_s^+ lives long enough to form a displaced tertiary vertex. Therefore the five-track combinations are refitted assuming this cascade topology [21]. The invariant mass of the muon pair is constrained to the J/ψ mass, $m_{J/\psi} = 3096.916\,\text{MeV}$ [22]. The three D_s^+ daughter tracks are constrained to a tertiary vertex and their invariant mass is fixed to the mass of D_s^+, $m_{D_s^+} = 1968.30\,\text{MeV}$ [22]. The combined momentum of the refitted D_s^+ decay tracks is constrained to point to the dimuon vertex. The quality of the cascade fit must satisfy $\chi^2/\text{ndf} < 3$.

The B_c^+ meson is reconstructed within the kinematic range $p_\text{T}(B_c^+) > 15\,\text{GeV}$ and $|\eta(B_c^+)| < 2.0$, where the detector acceptance is high and depends weakly on $p_\text{T}(B_c^+)$ and $\eta(B_c^+)$.

The refitted tracks of the D_s^+ daughter hadrons are required to have $|\eta| < 2.5$ and $p_\text{T} > 1\,\text{GeV}$, while the muons must have $|\eta| < 2.3$ and $p_\text{T} > 3\,\text{GeV}$. To further discriminate the sample of D_s^+ candidates from a large combinatorial background, the following requirements are applied:

- $\cos\theta^*(\pi) < 0.8$, where $\theta^*(\pi)$ is the angle between the pion momentum in the $K^+K^-\pi^+$ rest frame and the $K^+K^-\pi^+$ combined momentum in the laboratory frame;
- $|\cos^3\theta'(K)| > 0.15$, where $\theta'(K)$ is the angle between one of the kaons and the pion in the K^+K^- rest frame. The decay of the pseudoscalar D_s^+ meson to the ϕ (vector) plus π (pseudoscalar) final state results in an alignment of the spin of the ϕ meson perpendicularly to the direction of motion of the ϕ relative to D_s^+. Consequently, the distribution of $\cos\theta'(K)$ follows a $\cos^2\theta'(K)$ shape, implying a uniform distribution for $\cos^3\theta'(K)$. In contrast, the $\cos\theta'(K)$ distribution of the combinatorial background is uniform and its $\cos^3\theta'(K)$ distribution peaks at zero. The cut suppresses the background significantly while reducing the signal by 15 %.

The B_c^+ candidate is required to point back to a primary vertex such that $d_0^\text{PV}(B_c^+) < 0.1\,\text{mm}$ and $z_0^\text{PV}(B_c^+)\sin\theta(B_c^+) < 0.5\,\text{mm}$, where d_0^PV and z_0^PV are respectively the transverse and longitudinal impact parameters with respect to the primary vertex. All primary vertices in the event are considered. If there is more than one primary vertex satisfying these requirements (~0.5 % events both in data and MC simulation), the one with the largest sum of squared transverse momenta of the tracks originating from it is chosen.

The transverse decay length[4] of the B_c^+ candidate is required to satisfy $L_{xy}(B_c^+) > 0.1\,\text{mm}$. The transverse decay length of the D_s^+ measured from the B_c^+ vertex must be $L_{xy}(D_s^+) > 0.15\,\text{mm}$. In order to remove fake candidates, both $L_{xy}(B_c^+)$ and $L_{xy}(D_s^+)$ are required not to exceed 10 mm.

Taking into account the characteristic hard fragmentation of b-quarks, a requirement $p_\text{T}(B_c^+)/\sum p_\text{T}(\text{trk}) > 0.1$ is applied, where the sum in the denominator is taken over all tracks originating from the primary vertex (tracks of the B_c^+ candidate are included in the sum if they are associated with the primary vertex). The requirement reduces a sizeable fraction of combinatorial background while having almost no effect on the signal.

The following angular selection requirements are introduced to further suppress the combinatorial background:

- $\cos\theta^*(D_s^+) > -0.8$, where $\theta^*(D_s^+)$ is the angle between the D_s^+ candidate momentum in the rest frame of the B_c^+ candidate, and the B_c^+ candidate line of flight in the laboratory frame. The distribution of $\cos\theta^*(D_s^+)$ is uniform for the decays of pseudoscalar B_c^+ meson before any kinematic selection while it tends to increase for negative values of $\cos\theta^*(D_s^+)$ for the background.
- $\cos\theta'(\pi) > -0.8$, where $\theta'(\pi)$ is the angle between the J/ψ candidate momentum and the pion momentum in the $K^+K^-\pi^+$ rest frame. Its distribution is nearly uniform for the signal processes but peaks towards -1 for the background.

[4] The transverse decay length of a particle is defined as the transverse distance between the production (primary) vertex and the particle decay (secondary) vertex projected along its transverse momentum.

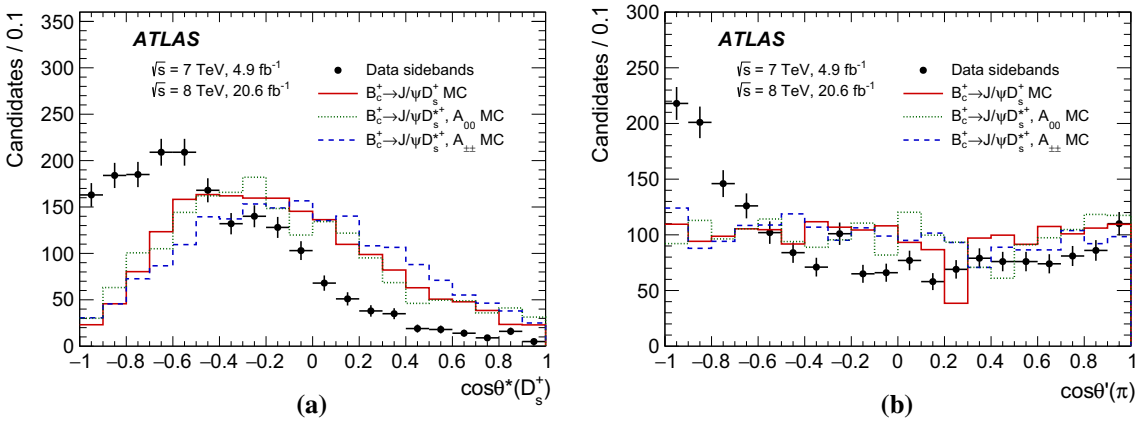

Fig. 2 Distributions of **a** $\cos\theta^*(D_s^+)$ and **b** $\cos\theta'(\pi)$, where $\theta^*(D_s^+)$ and $\theta'(\pi)$ are two angular variables defined in Sect. 3. The distributions are shown for data sidebands (*black dots*) and MC simulation of $B_c^+ \to J/\psi D_s^+$ signal (*red solid line*) and A_{00} (*green dotted line*) and $A_{\pm\pm}$ (*blue dashed line*) components of $B_c^+ \to J/\psi D_s^{*+}$ signal. The distributions are obtained after applying all selection criteria except the ones on the plotted variable. The MC distributions are normalised to data

Distributions of these two variables after applying all other selection requirements described in this section are shown in Fig. 2. They are shown for the simulated signal samples, as well as for sidebands of the mass spectrum in data, defined as the regions 5640 MeV $< m(J/\psi D_s^+) <$ 5900 MeV (left sideband) and 6360 MeV $< m(J/\psi D_s^+) <$ 6760 MeV (right sideband). A dip in the $\cos\theta'(\pi)$ distribution for the $B_c^+ \to J/\psi D_s^+$ signal is caused by rejection of $B_s^0 \to J/\psi\phi$ candidates discussed below.

Various possible contributions of partially reconstructed $B \to J/\psi X$ decays were studied. The only significant one was found from the $B_s^0 \to J/\psi\phi$ decay process. This contribution arises when the combination of the tracks from a true $B_s^0 \to J/\psi(\mu^+\mu^-)\phi(K^+K^-)$ decay with a fifth random track results in a fake $B_c^+ \to J/\psi(\mu^+\mu^-)D_s^+(K^+K^-\pi^+)$ candidate. For each reconstructed B_c^+ candidate, an additional vertex fit is performed. The two muon tracks and the two kaon tracks are fitted to a common vertex, where the kaon tracks are assumed to be from $\phi \to K^+K^-$ and the muon pair is constrained to have the nominal J/ψ mass. The mass of the B_s^0 candidate, $m(\mu^+\mu^-K^+K^-)$, is then calculated from the refitted track parameters. Candidates with 5340 MeV $< m(\mu^+\mu^-K^+K^-) <$ 5400 MeV are rejected. This requirement suppresses the bulk of the B_s^0 events while rejecting only ~4 % of the signal.

After applying the selection requirements described above, 1547 $J/\psi D_s^+$ candidates are selected in the mass range 5640–6760 MeV.

4 $B_c^+ \to J/\psi D_s^{(*)+}$ candidate fit

The mass distribution of the selected $B_c^+ \to J/\psi D_s^{(*)+}$ candidates is shown in Fig. 3. The peak near the B_c^+ mass, $m_{B_c^+} = 6275.6$ MeV [22], is attributed to the signal of

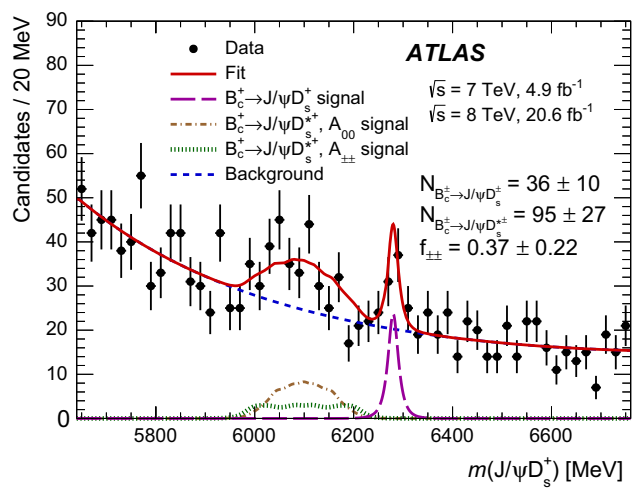

Fig. 3 The mass distribution for the selected $J/\psi D_s^+$ candidates. The *red solid line* represents the projection of the fit to the model described in the text. The contribution of the $B_c^+ \to J/\psi D_s^+$ decay is shown with the *magenta long-dashed line*; the *brown dash-dot* and *green dotted lines* show the $B_c^+ \to J/\psi D_s^{*+}$ A_{00} and $A_{\pm\pm}$ component contributions, respectively; the *blue dashed line* shows the background model. The uncertainties of the listed fit result values are statistical only

$B_c^+ \to J/\psi D_s^+$ decay while a wider structure between 5900 and 6200 MeV corresponds to $B_c^+ \to J/\psi D_s^{*+}$ with subsequent $D_s^{*+} \to D_s^+\gamma$ or $D_s^{*+} \to D_s^+\pi^0$ decays where the neutral particle is not reconstructed.

Mass distributions of the J/ψ and D_s^+ candidates corresponding to the $J/\psi D_s^+$ mass region of the observed $B_c^+ \to J/\psi D_s^{(*)+}$ signals are shown in Fig. 4. To obtain these plots, the B_c^+ candidates are built without the mass constraints in the cascade fit, with the mass of the candidate calculated as $m(J/\psi D_s^+) = m(\mu^+\mu^-K^+K^-\pi^+) - m(\mu^+\mu^-) + m_{J/\psi} - m(K^+K^-\pi^+) + m_{D_s^+}$, where $m_{J/\psi}$ and $m_{D_s^+}$ are the nominal masses of the respective par-

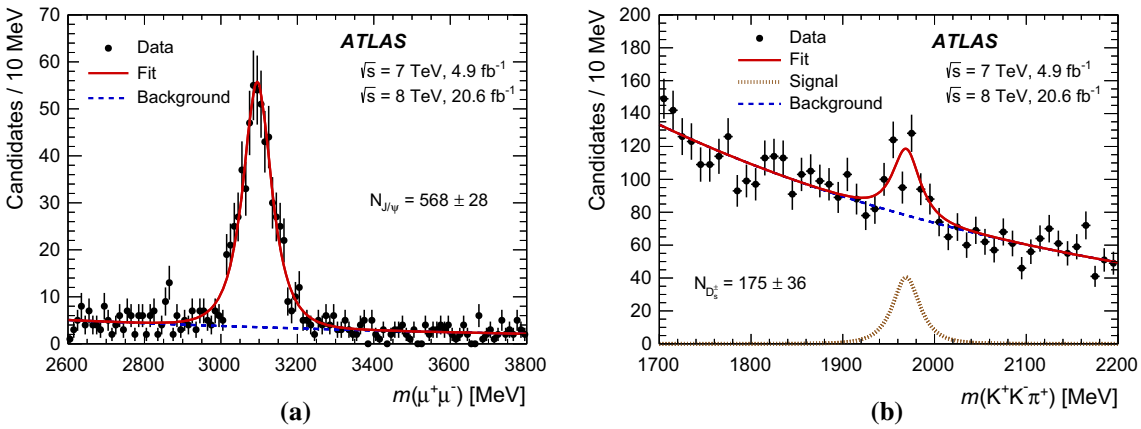

Fig. 4 Mass distribution of the **a** J/ψ and **b** D_s^+ candidates after the full $B_c^+ \to J/\psi D_s^{(*)+}$ selection (without mass constraints in the cascade fit) in the mass window of the B_c^+ candidate 5900 MeV $< m(J/\psi D_s^+) <$ 6400 MeV. The spectra are fitted with a sum of an exponential and a modified Gaussian function. The uncertainties of the shown J/ψ and D_s^+ yields are statistical only

ticles. The mass of the B_c^+ candidate is required to be 5900 MeV $< m(J/\psi D_s^+) <$ 6400 MeV while the mass windows for the corresponding intermediate resonances are widened to the plotting ranges. The J/ψ and D_s^+ mass distributions are fitted with a sum of an exponential function describing the background and a modified Gaussian function [23,24] describing the corresponding signal peak. The modified Gaussian function is defined as

$$\text{Gauss}^{\text{mod}} \sim \exp\left(-\frac{x^{1+\frac{1}{1+x/2}}}{2}\right), \tag{1}$$

where $x = |m_0 - m|/\sigma$ with the mean mass m_0 and width σ being free parameters. The fitted masses of J/ψ (3095.1 ± 2.4 MeV) and D_s (1969.0 ± 4.1 MeV) agree with their nominal masses, the widths are consistent with those in the simulated samples, and the signal yields are found to be $N_{J/\psi} = 568 \pm 28$ and $N_{D_s^\pm} = 175 \pm 36$.

The information about the helicity in $B_c^+ \to J/\psi D_s^{*+}$ decay is encoded both in the mass distribution of the $J/\psi D_s^+$ system and in the distribution of the helicity angle, $\theta'(\mu^+)$, which is defined in the rest frame of the muon pair as the angle between the μ^+ and the D_s^+ candidate momenta. Thus, a two-dimensional extended unbinned maximum-likelihood fit of the $m(J/\psi D_s^+)$ and $|\cos\theta'(\mu^+)|$ distributions is performed. The A_{++} and A_{--} helicity amplitude contributions are described by the same mass and angular shapes because of the parity symmetry of the J/ψ and D_s^{*+} decays. This is confirmed by the MC simulation. Thus these components are treated together as the $A_{\pm\pm}$ component, while the shape of the A_{00} component is different and is therefore treated separately. A simultaneous fit to the mass and angular distributions significantly improves the sensitivity to the contributions of the helicity amplitudes in $B_c^+ \to J/\psi D_s^{*+}$ decay with respect to a one-dimensional mass fit.

Four two-dimensional probability density functions (PDFs) are defined to describe the $B_c^+ \to J/\psi D_s^+$ signal, the $A_{\pm\pm}$ and A_{00} components of the $B_c^+ \to J/\psi D_s^{*+}$ signal, and the background. The signal PDFs are factorised into mass and angular components. The effect of correlations between their mass and angular shapes is found to be small and is accounted for as a systematic uncertainty.

The mass distribution of the $B_c^+ \to J/\psi D_s^+$ signal is described by a modified Gaussian function. For the $B_c^+ \to J/\psi D_s^{*+}$ signal components, the mass shape templates obtained from the simulation with the kernel estimation technique [25] are used. The branching fractions of $D_s^{*+} \to D_s^+\pi^0$ and $D_s^{*+} \to D_s^+\gamma$ decays for the simulation are set to the world average values [22]. The position of the templates along the mass axis is varied in the fit simultaneously with the position of the $B_c^+ \to J/\psi D_s^+$ signal peak. The background mass shape is described with a two-parameter exponential function, $\exp\left[a \cdot m(J/\psi D_s^+) + b \cdot m(J/\psi D_s^+)^2\right]$.

To describe the $|\cos\theta'(\mu^+)|$ shapes, templates from the kernel estimation are used. The templates for the signal angular PDFs are extracted from the simulated samples. Although their shapes are calculable analytically, using the templates allows the fit to account for detector effects. The background angular description is based on the $|\cos\theta'(\mu^+)|$ shape of the candidates in the sidebands of $J/\psi D_s^+$ mass spectra. Two templates are produced from the angular distributions of the candidates in the left and right mass sidebands as defined in Sect. 3. The angular PDF for the background is defined as a conditional PDF of $|\cos\theta'(\mu^+)|$ given the per-candidate $m(J/\psi D_s^+)$. For the candidates in the lower half of the left sideband (5640–5770 MeV), the template from the left sideband is used. Similarly, the template from the right sideband is used for the upper half of the right sideband (6560–6760 MeV). For the candidates in the middle part of the mass spectrum (5770–

Table 1 Parameters of the $B_c^+ \to J/\psi D_s^{(*)+}$ signals obtained with the unbinned extended maximum-likelihood fit. The width parameter of the modified Gaussian function is fixed to the MC value. Only statistical uncertainties are shown. No acceptance corrections are applied to the signal yields

Parameter	Value
$m_{B_c^+ \to J/\psi D_s^+}$ (MeV)	6279.9 ± 3.5
$N_{B_c^+ \to J/\psi D_s^+}$	36 ± 10
$N_{B_c^+ \to J/\psi D_s^{*+}}$	95 ± 27
$f_{\pm\pm}$	0.37 ± 0.22

6560 MeV), a linear interpolation between the two templates is used.

The fit has seven free parameters: the mass of the B_c^+ meson, $m_{B_c^+ \to J/\psi D_s^+}$; the relative contribution of the $A_{\pm\pm}$ component to the total $B_c^+ \to J/\psi D_s^{*+}$ decay rate in the selected sample, $f_{\pm\pm}$; the two parameters of the exponential background; the yields of the two signal modes, $N_{B_c^+ \to J/\psi D_s^+}$ and $N_{B_c^+ \to J/\psi D_s^{*+}}$, and the background yield. The width of the modified Gaussian function, $\sigma_{B_c^+ \to J/\psi D_s^+}$, is fixed to the value obtained from the fit to the simulated signal, $\sigma_{B_c^+ \to J/\psi D_s^+} = 9.95$ MeV. Leaving this parameter free in the data fit results in the value 7.9 ± 3.0 MeV, consistent with the simulation in the range of statistical uncertainty.

It was checked that the fit procedure provides unbiased values and correct statistical uncertainties for the extracted parameters using pseudo-experiments. The values of the relevant parameters obtained from the fit are given in Table 1. The fitted B_c^+ mass agrees with the world average value [22].

The mass and angular projections of the fit on the selected $J/\psi D_s^+$ candidate dataset are also shown in Figs. 3 and 5a, respectively. In order to illustrate the effect of the angular part of the fit in separating the helicity amplitudes, the $|\cos\theta'(\mu^+)|$ projection for the subset of candidates with the masses 5950 MeV $< m(J/\psi D_s^+) <$ 6250 MeV corresponding to the region of the observed $B_c^+ \to J/\psi D_s^{*+}$ signal is shown in Fig. 5b.

The statistical significance for the observed B_c^+ signal estimated from toy MC studies is 4.9 standard deviations.

5 $B_c^+ \to J/\psi\pi^+$ candidate reconstruction and fit

$B_c^+ \to J/\psi\pi^+$ candidates are reconstructed by fitting a common vertex of a pion candidate track and the two muons from a J/ψ candidate, selected as described in Sect. 3. For the pion candidate, tracks identified as muons are vetoed in order to suppress the substantial background from $B_c^+ \to J/\psi\mu^+\nu_\mu X$ decays. The invariant mass of the two muons in the vertex fit is constrained to the J/ψ nominal mass. The quality of the fit must satisfy $\chi^2/\text{ndf} < 3$. The following selection requirements applied to the $B_c^+ \to J/\psi\pi^+$ candidates are analogous to those for $B_c^+ \to J/\psi D_s^+$ candidates described in Sect. 3: the candidates must be within the kinematic range $p_T(B_c^+) > 15$ GeV, $|\eta(B_c^+)| < 2.0$; the refitted values of the transverse momenta and pseudorapidities of the muons are required to satisfy $p_T(\mu^\pm) > 3$ GeV, $|\eta(\mu^\pm)| < 2.3$; the same requirements on pointing to the primary vertex and the ratio $p_T(B_c^+)/\sum p_T(\text{trk})$ are applied. The refitted pion track kinematics must satisfy $p_T(\pi^+) > 5$ GeV and $|\eta(\pi^+)| < 2.5$. The transverse decay length

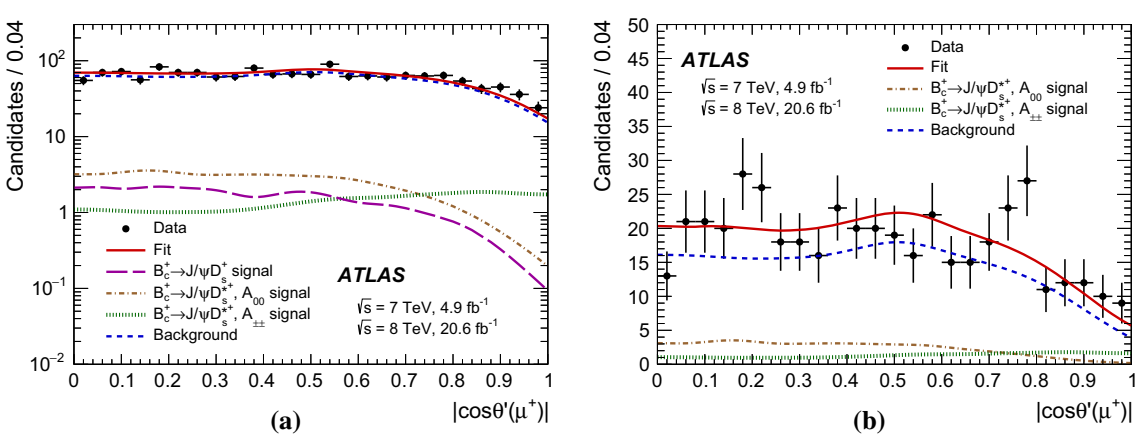

Fig. 5 The projection of the likelihood fit on the variable $|\cos\theta'(\mu^+)|$, where the helicity angle $\theta'(\mu^+)$ is the angle between the μ^+ and D_s^+ candidate momenta in the rest frame of the muon pair from J/ψ decay, for **a** the full selected $J/\psi D_s^+$ candidate dataset and **b** a subset of the candidates in a mass range 5950 MeV $< m(J/\psi D_s^+) <$ 6250 MeV corresponding to the observed signal of $B_c^+ \to J/\psi D_s^{*+}$ decay. The *red solid line* represents the full fit projection. The contribution of the $B_c^+ \to J/\psi D_s^+$ decay is shown with the *magenta long-dashed line* (it is not drawn in **b** because this contribution vanishes in that mass range); the *brown dash-dot* and *green dotted lines* show the $B_c^+ \to J/\psi D_s^{*+}$ A_{00} and $A_{\pm\pm}$ component contributions, respectively; the *blue dashed line* shows the background model

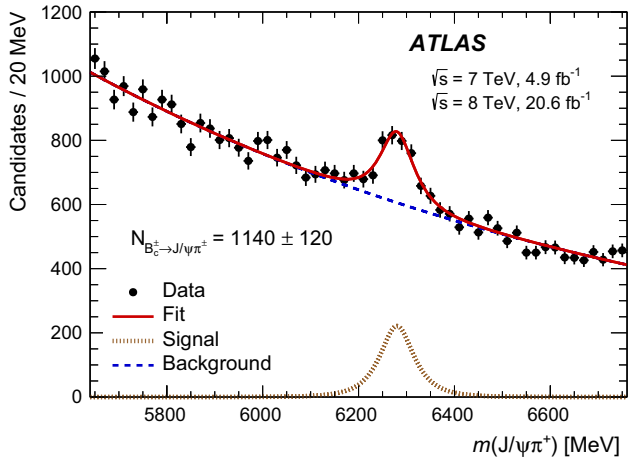

Fig. 6 The mass distribution for the selected $B_c^+ \to J/\psi\pi^+$ candidates. The *red solid line* represents the result of the fit to the model described in the text. The *brown dotted* and *blue dashed lines* show the signal and background component projections, respectively. The uncertainty of the shown signal yield is statistical only

is required to be $L_{xy}(B_c^+) > 0.2$ mm, and not to exceed 10 mm.

To further suppress combinatorial background, the following selection is applied:

- $\cos\theta^*(\pi) > -0.8$, where $\theta^*(\pi)$ is the angle between the pion momentum in the $\mu^+\mu^-\pi^+$ rest frame and the B_c^+ candidate line of flight in laboratory frame. This angular variable behaviour for the signal and the background is the same as that of $\cos\theta^*(D_s^+)$ used for $J/\psi D_s^+$ candidates selection.
- $|\cos\theta'(\mu^+)| < 0.8$, where $\theta'(\mu^+)$ is the angle between the μ^+ and π^+ momenta in the muon pair rest frame. The signal distribution follows a $\sin^2\theta'(\mu^+)$ shape, while the background is flat.

After applying the above-mentioned requirements, 38542 $J/\psi\pi^+$ candidates are selected in the mass range 5640–6760 MeV. Figure 6 shows the mass distribution of the selected candidates. An extended unbinned maximum-likelihood fit of the mass spectrum is performed to evaluate the $B_c^+ \to J/\psi\pi^+$ signal yield. The signal contribution is described with the modified Gaussian function while an exponential function is used for the background. The B_c^+ mass, $m_{B_c^+\to J/\psi\pi^+}$, the width of the modified Gaussian function, $\sigma_{B_c^+\to J/\psi\pi^+}$, the yields of the signal, $N_{B_c^+\to J/\psi\pi^+}$, and the background, and the slope of the exponential background are free parameters of the fit. The fit results are summarised in Table 2, and the fit projection is also shown in Fig. 6. The extracted B_c^+ mass value is consistent with the world average [22], and the signal peak width agrees with the simulation (37.4 MeV).

Table 2 Signal parameters of the $J/\psi\pi^+$ mass distribution obtained with the unbinned extended maximum-likelihood fit. Only statistical uncertainties are shown. No acceptance corrections are applied to the signal yields

Parameter	Value
$m_{B_c^+\to J/\psi\pi^+}$ (MeV)	6279.9 ± 3.9
$\sigma_{B_c^+\to J/\psi\pi^+}$ (MeV)	33.9 ± 4.2
$N_{B_c^+\to J/\psi\pi^+}$	1140 ± 120

6 Branching fractions and polarisation measurement

The ratios of the branching fractions $\mathcal{R}_{D_s^+/\pi^+}$ and $\mathcal{R}_{D_s^{*+}/\pi^+}$ are calculated as

$$\mathcal{R}_{D_s^{(*)+}/\pi^+} = \frac{\mathcal{B}_{B_c^+\to J/\psi D_s^{(*)+}}}{\mathcal{B}_{B_c^+\to J/\psi\pi^+}} = \frac{1}{\mathcal{B}_{D_s^+\to\phi(K^+K^-)\pi^+}} \times \frac{\mathcal{A}_{B_c^+\to J/\psi\pi^+}}{\mathcal{A}_{B_c^+\to J/\psi D_s^{(*)+}}} \times \frac{N_{B_c^+\to J/\psi D_s^{(*)+}}}{N_{B_c^+\to J/\psi\pi^+}}, \quad (2)$$

where $\mathcal{A}_{B_c^+\to X}$ and $N_{B_c^+\to X}$ are the total acceptance and the yield of the corresponding mode. For $\mathcal{B}_{D_s^+\to\phi(K^+K^-)\pi^+}$, the CLEO measurement [26] of the partial $D_s^+ \to K^+K^-\pi^+$ branching fractions, with a kaon-pair mass within various intervals around the nominal ϕ meson mass, is used. An interpolation between the partial branching fractions, measured for ± 5 and ± 10 MeV intervals, using a relativistic Breit–Wigner shape of the resonance yields the value $(1.85 \pm 0.11)\%$ for the ± 7 MeV interval which is used in the analysis. The effect of admixture of other D_s^+ decay modes with $(K^+K^-\pi^+)$ final state which are not present in the MC simulation is studied separately and accounted for as a systematic uncertainty.

The acceptance for the $B_c^+ \to J/\psi D_s^{*+}$ decay mode is different for the $A_{\pm\pm}$ and A_{00} components, thus the full acceptance for the mode is

$$\mathcal{A}_{B_c^+\to J/\psi D_s^{*+}} = \left(\frac{f_{\pm\pm}}{\mathcal{A}_{B_c^+\to J/\psi D_s^{*+},A_{\pm\pm}}} + \frac{1-f_{\pm\pm}}{\mathcal{A}_{B_c^+\to J/\psi D_s^{*+},A_{00}}}\right)^{-1}, \quad (3)$$

where the subscripts indicate the helicity state and $f_{\pm\pm}$ is the value extracted from the fit (Table 1). The acceptances are determined from the simulation and shown in Table 3.

The ratio $\mathcal{R}_{D_s^{*+}/D_s^+}$ is calculated as

$$\mathcal{R}_{D_s^{*+}/D_s^+} = \frac{\mathcal{B}_{B_c^+\to J/\psi D_s^{*+}}}{\mathcal{B}_{B_c^+\to J/\psi D_s^+}} = \frac{N_{B_c^+\to J/\psi D_s^{*+}}}{N_{B_c^+\to J/\psi D_s^+}} \times \frac{\mathcal{A}_{B_c^+\to J/\psi D_s^+}}{\mathcal{A}_{B_c^+\to J/\psi D_s^{*+}}}, \quad (4)$$

Table 3 The acceptance $\mathcal{A}_{B_c^+ \to X}$ for all decay modes studied. Only uncertainties due to MC statistics are shown

Mode	$\mathcal{A}_{B_c^+ \to X}$ (%)
$B_c^+ \to J/\psi \pi^+$	4.106 ± 0.056
$B_c^+ \to J/\psi D_s^+$	1.849 ± 0.034
$B_c^+ \to J/\psi D_s^{*+}$, A_{00}	1.829 ± 0.053
$B_c^+ \to J/\psi D_s^{*+}$, $A_{\pm\pm}$	1.712 ± 0.035

where the ratio of the yields $N_{B_c^+ \to J/\psi D_s^{*+}}/N_{B_c^+ \to J/\psi D_s^+}$ and its uncertainty is extracted from the fit as a parameter in order to account for correlations between the yields.

The fraction of the $A_{\pm\pm}$ component contribution in $B_c^+ \to J/\psi D_s^{*+}$ decay is calculated from the $f_{\pm\pm}$ value quoted in Table 1 by applying a correction to account for the different acceptances for the two component contributions:

$$\Gamma_{\pm\pm}/\Gamma = f_{\pm\pm} \times \frac{\mathcal{A}_{B_c^+ \to J/\psi D_s^{*+}}}{\mathcal{A}_{B_c^+ \to J/\psi D_s^{*+}, \mathcal{A}_{\pm\pm}}}. \quad (5)$$

7 Systematic uncertainties

The systematic uncertainties of the measured values are determined by varying the analysis procedure and repeating all calculations. Although some sources can have rather large effects on the individual decay rate measurements, they largely cancel in the ratios of the branching fractions due to correlation between the effects on the different decay modes. The following groups of systematic uncertainties are considered.

The first group of sources of systematic uncertainty relates to possible differences between the data and simulation affecting the acceptances for the decay modes. Thus, an effect of the B_c^+ production model is evaluated by varying the simulated p_T and $|\eta|$ spectra while preserving agreement with the data distributions obtained using the abundant $B_c^+ \to J/\psi \pi^+$ channel. These variations have very similar effects on the acceptances for the different decay modes, thus giving rather moderate estimates of the uncertainties, not exceeding 3 % in total, on the ratios of branching fractions. The effect of presence of other D_s^+ decay modes with $(K^+K^-\pi^+)$ final state on the calculated acceptances is studied with a separate MC simulation. Its conservative estimate yields 0.4 % which is assigned as $\mathcal{R}_{D_s^+/\pi^+}$ and $\mathcal{R}_{D_s^{*+}/\pi^+}$ uncertainties. An uncertainty on the tracking efficiency is dominated by the uncertainty of the detector material description in the MC simulation. Samples generated with distorted geometries and with increased material are used to estimate the effect on track reconstruction efficiencies. When propagated to the ratios of branching fractions, these estimates give 0.5 % uncertainty for $\mathcal{R}_{D_s^+/\pi^+}$ and $\mathcal{R}_{D_s^{*+}/\pi^+}$ due to the two extra tracks in $B_c^+ \to J/\psi D_s^{(*)+}$ modes. Limited knowledge of the B_c^+ and D_s^+ lifetimes leads to an additional systematic uncertainty. The simulated proper decay times are varied within one standard deviation from the world average values [22] resulting in uncertainties of ~1 % assigned to $\mathcal{R}_{D_s^+/\pi^+}$ and $\mathcal{R}_{D_s^{*+}/\pi^+}$ due to the B_c^+ lifetime, and 0.3 % due to the D_s^+ lifetime. Removing the requirement on $p_T(B_c^+)/\sum p_T(\text{trk})$ is found to produce no noticeable effect on the measured values.

The next group of uncertainties originates from the signal extraction procedure. These uncertainties are evaluated separately for $J/\psi D_s^+$ and $J/\psi \pi^+$ candidate fits. For the former, the following variations of the fit model are applied and the difference is treated as a systematic uncertainty:

- different background mass shape parametrisations (three-parameter exponential, second- and third-order polynomials), different fitted mass range (reduced by up to 40 MeV from each side independently);
- a double Gaussian or double-sided Crystal Ball function [27–29] for $B_c^+ \to J/\psi D_s^+$ signal description; variation of the modified Gaussian width within 10 % of the MC simulation value;
- variation of the smoothness of the $B_c^+ \to J/\psi D_s^{*+}$ signal mass templates, which is controlled by a parameter of the kernel estimation procedure [25];
- similar variation of the smoothness of the $B_c^+ \to J/\psi D_s^{(*)+}$ signal angular templates;
- variation of the smoothness of the sideband templates used for the background angular PDF construction; different ranges of the sidebands; different sideband interpolation procedure;
- modelling of the correlation between the mass and angular parts of the signal PDFs. This correlation takes place only at the detector level and manifests itself in degradation of the mass resolution for higher values of $|\cos\theta'(\mu^+)|$. A dedicated fit model accounting for this effect is used for the data fit. The impact on the result is found to be negligible compared to the total uncertainty.

The first two items give the dominant contributions to the uncertainties of the ratios of branching fractions while the transverse polarisation fraction measurement is mostly affected by the background angular modelling variations. For the normalisation channel fit model, the similar variations of the background and signal mass shape parametrisation are applied. The deviations produced by the variations of the fits reach values as high as 10–15 % thus making them the dominant sources of systematic uncertainty.

The branching fractions of D_s^{*+} [22] are varied in simulation within their uncertainties to estimate their effect on the measured quantities. Very small uncertainties are obtained

Table 4 Relative systematic uncertainties on the measured ratios of branching fractions $R_{D_s^+/\pi^+}$, $R_{D_s^{*+}/\pi^+}$, $R_{D_s^{*+}/D_s^+}$ and on the transverse polarisation fraction $\Gamma_{\pm\pm}/\Gamma$

Source	Uncertainty (%)			
	$R_{D_s^+/\pi^+}$	$R_{D_s^{*+}/\pi^+}$	$R_{D_s^{*+}/D_s^+}$	$\Gamma_{\pm\pm}/\Gamma$
Simulated $p_T(B_c^+)$ spectrum	0.4	0.9	0.5	0.4
Simulated $\|\eta(B_c^+)\|$ spectrum	1.9	2.4	0.6	0.2
Other D_s^+ decay modes contribution	0.4	0.4	–	–
Tracking efficiency	0.5	0.5	<0.1	<0.1
B_c^+ lifetime	1.2	1.3	<0.1	<0.1
D_s^+ lifetime	0.3	0.3	<0.1	<0.1
$B_c^+ \to J/\psi D_s^{(*)+}$ signal extraction	4.4	10.5	10.7	17.4
$B_c^+ \to J/\psi \pi^+$ signal extraction	8.5	8.5	–	–
D_s^{*+} branching fractions	<0.1	<0.1	<0.1	1.1
MC sample sizes	2.3	2.4	2.7	2.2
Total	10.1	14.0	11.0	17.6
$\mathcal{B}_{D_s^+\to\phi(K^+K^-)\pi^+}$	5.9	5.9	–	–

for the $\mathcal{R}_{D_s^{*+}/\pi^+}$ and $\mathcal{R}_{D_s^{*+}/D_s^+}$, while for $\Gamma_{\pm\pm}/\Gamma$, the estimate is ∼1 %.

The statistical uncertainties on the acceptance values due to the MC sample sizes are also treated as a separate source of systematic uncertainty and estimated to be 2–3 %.

In order to check for a possible bias from using three-muon triggers, vetoing the D_s^+ meson daughter tracks identified as muons is tested and found not to affect the measurement.

Finally, since $\mathcal{B}_{D_s^+\to\phi(K^+K^-)\pi^+}$ enters Eq. (2), its uncertainty, evaluated from Ref. [26] as 5.9 %, is propagated to the final values of the relative branching fractions.

The systematic uncertainties on the measured quantities are summarised in Table 4.

8 Results

The following ratios of the branching fractions are measured:

$$\mathcal{R}_{D_s^+/\pi^+} = \frac{\mathcal{B}_{B_c^+\to J/\psi D_s^+}}{\mathcal{B}_{B_c^+\to J/\psi\pi^+}} = 3.8 \pm 1.1(\text{stat.}) \pm 0.4(\text{syst.}) \pm 0.2(\text{BF}), \quad (6)$$

$$\mathcal{R}_{D_s^{*+}/\pi^+} = \frac{\mathcal{B}_{B_c^+\to J/\psi D_s^{*+}}}{\mathcal{B}_{B_c^+\to J/\psi\pi^+}} = 10.4 \pm 3.1(\text{stat.}) \pm 1.5(\text{syst.}) \pm 0.6(\text{BF}), \quad (7)$$

$$\mathcal{R}_{D_s^{*+}/D_s^+} = \frac{\mathcal{B}_{B_c^+\to J/\psi D_s^{*+}}}{\mathcal{B}_{B_c^+\to J/\psi D_s^+}} = 2.8^{+1.2}_{-0.8}(\text{stat.}) \pm 0.3(\text{syst.}), \quad (8)$$

where the BF uncertainty corresponds to the knowledge of $\mathcal{B}_{D_s^+\to\phi(K^+K^-)\pi^+}$. The relative contribution of the $A_{\pm\pm}$ component in $B_c^+ \to J/\psi D_s^{*+}$ decay is measured to be

$$\Gamma_{\pm\pm}/\Gamma = 0.38 \pm 0.23(\text{stat.}) \pm 0.07(\text{syst.}) \quad (9)$$

These results are compared with those of the LHCb measurement [10] and to the expectations from various theoretical calculations in Table 5 and Fig. 7. The measurement agrees with the LHCb result. All ratios are well described by the recent perturbative QCD predictions [8]. The expectations from models in Refs. [3,5,7] as well as the sum-rules prediction [4] for the ratio $\mathcal{R}_{D_s^{*+}/D_s^+}$ are consistent with the measurement. The QCD relativistic potential model predictions [3] are consistent with the measured $\mathcal{R}_{D_s^+/\pi^+}$ ratio while the expectations from the sum rules [4] and models in Refs. [5–7] are somewhat smaller than the measured value. The predictions in Refs. [3–5,7] are also generally smaller than the measured ratio $\mathcal{R}_{D_s^{*+}/\pi^+}$; however, the discrepancies do not exceed two standard deviations when taking into account only the experimental uncertainty.

The measured fraction of the $A_{\pm\pm}$ component agrees well with the prediction of the relativistic independent quark model [9] and perturbative QCD [8].

9 Conclusion

A study of $B_c^+ \to J/\psi D_s^+$ and $B_c^+ \to J/\psi D_s^{*+}$ decays has been performed. The ratios of the branching fractions $\mathcal{B}_{B_c^+\to J/\psi D_s^+}/\mathcal{B}_{B_c^+\to J/\psi\pi^+}$, $\mathcal{B}_{B_c^+\to J/\psi D_s^{*+}}/\mathcal{B}_{B_c^+\to J/\psi\pi^+}$, $\mathcal{B}_{B_c^+\to J/\psi D_s^{*+}}/\mathcal{B}_{B_c^+\to J/\psi D_s^+}$ and the transverse polarisation fraction of $B_c^+ \to J/\psi D_s^{*+}$ decay have been measured by the ATLAS experiment at the LHC using pp collision data corresponding to an integrated luminosity of 4.9 fb^{-1} at 7 TeV centre-of-mass energy and 20.6 fb^{-1} at 8 TeV. The polarisation is found to be well described by the available

Table 5 Comparison of the results of this measurement with those of LHCb [10] and theoretical predictions based on a QCD relativistic potential model [3], QCD sum rules [4], relativistic constituent quark model (RCQM) [5], BSW relativistic quark model (with fixed average transverse quark momentum $\omega = 0.40\,\text{GeV}$) [6], light-front quark model (LFQM) [7], perturbative QCD (pQCD) [8], and relativistic independent quark model (RIQM) [9]. The uncertainties of the theoretical predictions are shown if they are explicitly quoted in the corresponding papers. Statistical and systematic uncertainties added in quadrature are shown for the results of ATLAS and LHCb

$\mathcal{R}_{D_s^+/\pi^+}$	$\mathcal{R}_{D_s^{*+}/\pi^+}$	$\mathcal{R}_{D_s^{*+}/D_s^+}$	$\Gamma_{\pm\pm}/\Gamma$	Ref.
3.8 ± 1.2	10.4 ± 3.5	$2.8^{+1.2}_{-0.9}$	0.38 ± 0.24	ATLAS
2.90 ± 0.62	–	2.37 ± 0.57	0.52 ± 0.20	LHCb [10]
2.6	4.5	1.7	–	QCD potential model [3]
1.3	5.2	3.9	–	QCD sum rules [4]
2.0	5.7	2.9	–	RCQM [5]
2.2	–	–	–	BSW [6]
2.06 ± 0.86	–	3.01 ± 1.23	–	LFQM [7]
$3.45^{+0.49}_{-0.17}$	–	$2.54^{+0.07}_{-0.21}$	0.48 ± 0.04	pQCD [8]
–	–	–	0.410	RIQM [9]

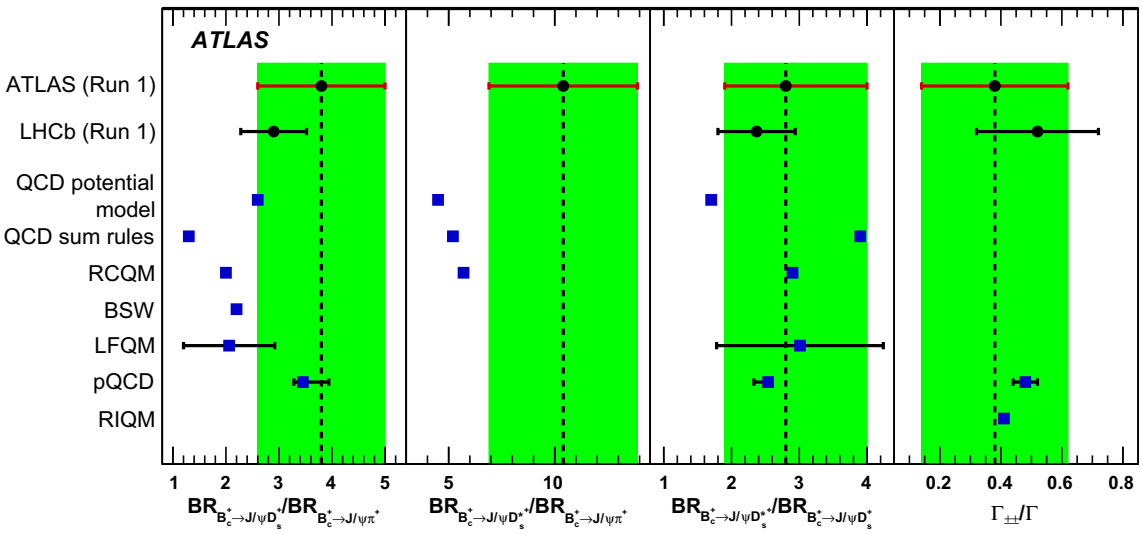

Fig. 7 Comparison of the results of this measurement with those of LHCb [10] and theoretical predictions based on a QCD relativistic potential model [3], QCD sum rules [4], relativistic constituent quark model (RCQM) [5], BSW relativistic quark model (with fixed average transverse quark momentum $\omega = 0.40\,\text{GeV}$) [6], light-front quark model (LFQM) [7], perturbative QCD (pQCD) [8], and relativistic independent quark model (RIQM) [9]. The uncertainties of the theoretical predictions are shown if they are explicitly quoted in the corresponding papers. Statistical and systematic uncertainties added in quadrature are quoted for the results of ATLAS and LHCb.

theoretical approaches. The measured ratios of the branching fraction are generally described by perturbative QCD, sum rules, and relativistic quark models. There is an indication of underestimation of the decay rates for the $B_c^+ \to J/\psi D_s^{(*)+}$ decays by some models, although the discrepancies do not exceed two standard deviations when taking into account only the experimental uncertainty. The measurement results agree with those published by the LHCb experiment.

Acknowledgments We thank CERN for the very successful operation of the LHC, as well as the support staff from our institutions without whom ATLAS could not be operated efficiently. We acknowledge the support of ANPCyT, Argentina; YerPhI, Armenia; ARC, Australia; BMWFW and FWF, Austria; ANAS, Azerbaijan; SSTC, Belarus; CNPq and FAPESP, Brazil; NSERC, NRC and CFI, Canada; CERN; CONICYT, Chile; CAS, MOST and NSFC, China; COLCIENCIAS, Colombia; MSMT CR, MPO CR and VSC CR, Czech Republic; DNRF, DNSRC and Lundbeck Foundation, Denmark; EPLANET, ERC and NSRF, European Union; IN2P3-CNRS, CEA-DSM/IRFU, France; GNSF, Georgia; BMBF, DFG, HGF, MPG and AvH Foundation, Germany; GSRT and NSRF, Greece; RGC, Hong Kong SAR, China; ISF, MINERVA, GIF, I-CORE and Benoziyo Center, Israel; INFN, Italy; MEXT and JSPS, Japan; CNRST, Morocco; FOM and NWO, Netherlands; BRF and RCN, Norway; MNiSW and NCN, Poland; GRICES and FCT, Portugal; MNE/IFA, Romania; MES of Russia and NRC KI, Russian Federation; JINR; MSTD, Serbia; MSSR, Slovakia; ARRS and MIZŠ, Slovenia; DST/NRF, South Africa; MINECO, Spain; SRC and Wallenberg Foundation, Sweden; SER, SNSF and Cantons of Bern and

Geneva, Switzerland; NSC, Taiwan; TAEK, Turkey; STFC, the Royal Society and Leverhulme Trust, United Kingdom; DOE and NSF, United States of America. The crucial computing support from all WLCG partners is acknowledged gratefully, in particular from CERN and the ATLAS Tier-1 facilities at TRIUMF (Canada), NDGF (Denmark, Norway, Sweden), CC-IN2P3 (France), KIT/GridKA (Germany), INFN-CNAF (Italy), NL-T1 (Netherlands), PIC (Spain), ASGC (Taiwan), RAL (UK) and BNL (USA) and in the Tier-2 facilities worldwide.

Open Access This article is distributed under the terms of the Creative Commons Attribution 4.0 International License (http://creativecommons.org/licenses/by/4.0/), which permits unrestricted use, distribution, and reproduction in any medium, provided you give appropriate credit to the original author(s) and the source, provide a link to the Creative Commons license, and indicate if changes were made.
Funded by SCOAP[3].

References

1. CDF Collaboration, F. Abe et al., Phys. Rev. Lett. **81**, 2432–2437 (1998). arXiv:hep-ex/9805034. doi:10.1103/PhysRevLett.81.2432
2. ATLAS Collaboration, Phys. Rev. Lett. **113**, 212004 (2014). arXiv:1407.1032 [hep-ex]. doi:10.1103/PhysRevLett.113.212004
3. P. Colangelo, F. De Fazio, Phys. Rev. D **61**, 034012 (2000). doi:10.1103/PhysRevD.61.034012. arXiv:hep-ph/9909423
4. V. Kiselev, Exclusive decays and lifetime of B_c meson in QCD sum rules (2002). arXiv:hep-ph/0211021 [hep-ph]
5. M. Ivanov, J. Korner, P. Santorelli, Phys. Rev. D **73**, 054024 (2006). doi:10.1103/PhysRevD.73.054024. arXiv:hep-ph/0602050
6. R. Dhir, R. Verma, Phys. Rev. D **79**, 034004 (2009). doi:10.1103/PhysRevD.79.034004. arXiv:0810.4284 [hep-ph]
7. H.-W. Ke, T. Liu, X.-Q. Li, Phys. Rev. D **89**, 017501 (2014). doi:10.1103/PhysRevD.89.017501. arXiv:1307.5925 [hep-ph]
8. Z. Rui, Z.-T. Zou, Phys. Rev. D **90**, 114030 (2014). doi:10.1103/PhysRevD.90.114030. arXiv:1407.5550 [hep-ph]
9. S. Kar et al., Phys. Rev. D **88**, 094014 (2013). doi:10.1103/PhysRevD.88.094014
10. LHCb Collaboration, R. Aaij et al., Phys. Rev. D **87**, 112012 (2013). arXiv:1304.4530 [hep-ex]. doi:10.1103/PhysRevD.87.112012
11. ATLAS Collaboration, JINST **3**, S08003 (2008). doi:10.1088/1748-0221/3/08/S08003
12. T. Sjostrand, S. Mrenna, P. Skands, JHEP **0605**, 026 (2006). arXiv:hep-ph/0603175. doi:10.1088/1126-6708/2006/05/026
13. A. Berezhnoy, A. Likhoded and O. Yushchenko, Phys. Atom. Nucl. 59 (1996) 709–713, arXiv:hep-ph/9504302 [hep-ph]
14. A. Berezhnoy, V. Kiselev, A. Likhoded, Z. Phys. A **356**, 79–87 (1996). arXiv:hep-ph/9602347. doi:10.1007/s002180050151
15. A. Berezhnoy et al., Phys. Atom. Nucl. 60 (1997) 1729–1740, arXiv:hep-ph/9703341 [hep-ph]
16. A. Berezhnoy, Phys. Atom. Nucl. **68**, 1866–1872 (2005). arXiv:hep-ph/0407315. doi:10.1134/1.2131116
17. D. Lange, Nucl. Instrum. Meth. A **462**, 152–155 (2001). doi:10.1016/S0168-9002(01)00089-4
18. ATLAS Collaboration, Eur. Phys. J. C **70**, 823–874 (2010). arXiv:1005.4568 [physics.ins-det]. doi:10.1140/epjc/s10052-010-1429-9
19. GEANT4 Collaboration, S. Agostinelli et al., Nucl. Instrum. Meth. A **506**, 250–303 (2003). doi:10.1016/S0168-9002(03)01368-8
20. J. Allison et al., IEEE Trans. Nucl. Sci. **53**, 270 (2006). doi:10.1109/TNS.2006.869826
21. V. Kostyukhin, VKalVrt - package for vertex reconstruction in ATLAS, ATL-PHYS-2003-031 (2003). http://cds.cern.ch/record/685551
22. K. A. Olive et al., Particle Data Group, Chin. Phys. C **38**, 090001 (2014). doi:10.1088/1674-1137/38/9/090001
23. ZEUS Collaboration, S. Chekanov et al., Eur. Phys. J. C **44**, 13–25 (2005). arXiv:hep-ex/0505008. doi:10.1140/epjc/s2005-02346-2
24. G. Aad et al., Nucl. Phys. B **864**, 341–381 (2012). arXiv:1206.3122 [hep-ex]. doi:10.1016/j.nuclphysb.2012.07.009
25. K. Cranmer, Comput. Phys. Commun. **136**, 198–207 (2001). arXiv:hep-ex/0011057 [hep-ex]. doi:10.1016/S0010-4655(00)00243-5
26. CLEO Collaboration, J. Alexander et al., Phys. Rev. Lett. **100**, 161804 (2008). doi:10.1103/PhysRevLett.100.161804. arXiv:0801.0680 [hep-ex]
27. M. Oreglia, A study of the reactions $\psi' \to \gamma\gamma\psi$, PhD thesis, Stanford University, SLAC-R-236 (1980). http://www.slac.stanford.edu/pubs/slacreports/slac-r-236.html
28. J. Gaiser, Charmonium spectroscopy from radiative decays of the J/ψ and ψ', PhD thesis, Stanford University, SLAC-R-255 (1982). http://www.slac.stanford.edu/pubs/slacreports/slac-r-255.html
29. T. Skwarnicki, A study of the radiative cascade transitions between the Υ' and Υ resonances, PhD thesis, Institute of Nuclear Physics, Krakow, DESY-F31-86-02 (1986). http://inspirehep.net/record/230779/

ATLAS Collaboration

G. Aad[85], B. Abbott[113], J. Abdallah[151], O. Abdinov[11], R. Aben[107], M. Abolins[90], O. S. AbouZeid[158], H. Abramowicz[153], H. Abreu[152], R. Abreu[30], Y. Abulaiti[146a,146b], B. S. Acharya[164a,164b,a], L. Adamczyk[38a], D. L. Adams[25], J. Adelman[108], S. Adomeit[100], T. Adye[131], A. A. Affolder[74], T. Agatonovic-Jovin[13], J. A. Aguilar-Saavedra[126a,126f], S. P. Ahlen[22], F. Ahmadov[65,b], G. Aielli[133a,133b], H. Akerstedt[146a,146b], T. P. A. Åkesson[81], G. Akimoto[155], A. V. Akimov[96], G. L. Alberghi[20a,20b], J. Albert[169], S. Albrand[55], M. J. Alconada Verzini[71], M. Aleksa[30], I. N. Aleksandrov[65], C. Alexa[26a], G. Alexander[153], T. Alexopoulos[10], M. Alhroob[113], G. Alimonti[91a], L. Alio[85], J. Alison[31], S. P. Alkire[35], B. M. M. Allbrooke[18], P. P. Allport[74], A. Aloisio[104a,104b], A. Alonso[36], F. Alonso[71], C. Alpigiani[76], A. Altheimer[35], B. Alvarez Gonzalez[30], D. Álvarez Piqueras[167], M. G. Alviggi[104a,104b], B. T. Amadio[15], K. Amako[66], Y. Amaral Coutinho[24a], C. Amelung[23], D. Amidei[89], S. P. Amor Dos Santos[126a,126c], A. Amorim[126a,126b], S. Amoroso[48], N. Amram[153], G. Amundsen[23], C. Anastopoulos[139], L. S. Ancu[49], N. Andari[30], T. Andeen[35], C. F. Anders[58b], G. Anders[30], J. K. Anders[74], K. J. Anderson[31], A. Andreazza[91a,91b], V. Andrei[58a], S. Angelidakis[9], I. Angelozzi[107], P. Anger[44], A. Angerami[35], F. Anghinolfi[30], A. V. Anisenkov[109,c], N. Anjos[12], A. Annovi[124a,124b], M. Antonelli[47], A. Antonov[98], J. Antos[144b], F. Anulli[132a], M. Aoki[66], L. Aperio Bella[18], G. Arabidze[90], Y. Arai[66], J. P. Araque[126a], A. T. H. Arce[45], F. A. Arduh[71], J-F. Arguin[95], S. Argyropoulos[42], M. Arik[19a], A. J. Armbruster[30], O. Arnaez[30], V. Arnal[82], H. Arnold[48], M. Arratia[28], O. Arslan[21], A. Artamonov[97], G. Artoni[23], S. Asai[155], N. Asbah[42], A. Ashkenazi[153], B. Åsman[146a,146b], L. Asquith[149], K. Assamagan[25], R. Astalos[144a], M. Atkinson[165], N. B. Atlay[141], B. Auerbach[6], K. Augsten[128], M. Aurousseau[145b], G. Avolio[30], B. Axen[15], M. K. Ayoub[117], G. Azuelos[95,d], M. A. Baak[30], A. E. Baas[58a], C. Bacci[134a,134b], H. Bachacou[136], K. Bachas[154], M. Backes[30], M. Backhaus[30], P. Bagiacchi[132a,132b], P. Bagnaia[132a,132b], Y. Bai[33a], T. Bain[35], J. T. Baines[131], O. K. Baker[176], P. Balek[129], T. Balestri[148], F. Balli[84], E. Banas[39], Sw. Banerjee[173], A. A. E. Bannoura[175], H. S. Bansil[18], L. Barak[30], E. L. Barberio[88], D. Barberis[50a,50b], M. Barbero[85], T. Barillari[101], M. Barisonzi[164a,164b], T. Barklow[143], N. Barlow[28], S. L. Barnes[84], B. M. Barnett[131], R. M. Barnett[15], Z. Barnovska[5], A. Baroncelli[134a], G. Barone[49], A. J. Barr[120], F. Barreiro[82], J. Barreiro Guimarães da Costa[57], R. Bartoldus[143], A. E. Barton[72], P. Bartos[144a], A. Basalaev[123], A. Bassalat[117], A. Basye[165], R. L. Bates[53], S. J. Batista[158], J. R. Batley[28], M. Battaglia[137], M. Bauce[132a,132b], F. Bauer[136], H. S. Bawa[143,e], J. B. Beacham[111], M. D. Beattie[72], T. Beau[80], P. H. Beauchemin[161], R. Beccherle[124a,124b], P. Bechtle[21], H. P. Beck[17,f], K. Becker[120], M. Becker[83], S. Becker[100], M. Beckingham[170], C. Becot[117], A. J. Beddall[19b], A. Beddall[19b], V. A. Bednyakov[65], C. P. Bee[148], L. J. Beemster[107], T. A. Beermann[175], M. Begel[25], J. K. Behr[120], C. Belanger-Champagne[87], W. H. Bell[49], G. Bella[153], L. Bellagamba[20a], A. Bellerive[29], M. Bellomo[86], K. Belotskiy[98], O. Beltramello[30], O. Benary[153], D. Benchekroun[135a], M. Bender[100], K. Bendtz[146a,146b], N. Benekos[10], Y. Benhammou[153], E. Benhar Noccioli[49], J. A. Benitez Garcia[159b], D. P. Benjamin[45], J. R. Bensinger[23], S. Bentvelsen[107], L. Beresford[120], M. Beretta[47], D. Berge[107], E. Bergeaas Kuutmann[166], N. Berger[5], F. Berghaus[169], J. Beringer[15], C. Bernard[22], N. R. Bernard[86], C. Bernius[110], F. U. Bernlochner[21], T. Berry[77], P. Berta[129], C. Bertella[83], G. Bertoli[146a,146b], F. Bertolucci[124a,124b], C. Bertsche[113], D. Bertsche[113], M. I. Besana[91a], G. J. Besjes[106], O. Bessidskaia Bylund[146a,146b], M. Bessner[42], N. Besson[136], C. Betancourt[48], S. Bethke[101], A. J. Bevan[76], W. Bhimji[46], R. M. Bianchi[125], L. Bianchini[23], M. Bianco[30], O. Biebel[100], S. P. Bieniek[78], M. Biglietti[134a], J. Bilbao De Mendizabal[49], H. Bilokon[47], M. Bindi[54], S. Binet[117], A. Bingul[19b], C. Bini[132a,132b], C. W. Black[150], J. E. Black[143], K. M. Black[22], D. Blackburn[138], R. E. Blair[6], J.-B. Blanchard[136], J. E. Blanco[77], T. Blazek[144a], I. Bloch[42], C. Blocker[23], W. Blum[83,*], U. Blumenschein[54], G. J. Bobbink[107], V. S. Bobrovnikov[109,c], S. S. Bocchetta[81], A. Bocci[45], C. Bock[100], M. Boehler[48], J. A. Bogaerts[30], D. Bogavac[13], A. G. Bogdanchikov[109], C. Bohm[146a], V. Boisvert[77], T. Bold[38a], V. Boldea[26a], A. S. Boldyrev[99], M. Bomben[80], M. Bona[76], M. Boonekamp[136], A. Borisov[130], G. Borissov[72], S. Borroni[42], J. Bortfeldt[100], V. Bortolotto[60a,60b,60c], K. Bos[107], D. Boscherini[20a], M. Bosman[12], J. Boudreau[125], J. Bouffard[2], E. V. Bouhova-Thacker[72], D. Boumediene[34], C. Bourdarios[117], N. Bousson[114], A. Boveia[30], J. Boyd[30], I. R. Boyko[65], I. Bozic[13], J. Bracinik[18], A. Brandt[8], G. Brandt[54], O. Brandt[58a], U. Bratzler[156], B. Brau[86], J. E. Brau[116], H. M. Braun[175,*], S. F. Brazzale[164a,164c], W. D. Breaden Madden[53], K. Brendlinger[122], A. J. Brennan[88], L. Brenner[107], R. Brenner[166], S. Bressler[172], K. Bristow[145c], T. M. Bristow[46], D. Britton[53], D. Britzger[42], F. M. Brochu[28], I. Brock[21], R. Brock[90], J. Bronner[101], G. Brooijmans[35], T. Brooks[77], W. K. Brooks[32b], J. Brosamer[15], E. Brost[116], J. Brown[55], P. A. Bruckman de Renstrom[39], D. Bruncko[144b], R. Bruneliere[48], A. Bruni[20a], G. Bruni[20a], M. Bruschi[20a], N. Bruscino[21], L. Bryngemark[81], T. Buanes[14], Q. Buat[142], P. Buchholz[141], A. G. Buckley[53], S. I. Buda[26a], I. A. Budagov[65], F. Buehrer[48], L. Bugge[119], M. K. Bugge[119], O. Bulekov[98], D. Bullock[8], H. Burckhart[30], S. Burdin[74], B. Burghgrave[108], S. Burke[131], I. Burmeister[43], E. Busato[34], D. Büscher[48], V. Büscher[83], P. Bussey[53], J. M. Butler[22], A. I. Butt[3], C. M. Buttar[53], J. M. Butterworth[78], P. Butti[107], W. Buttinger[25], A. Buzatu[53], A. R. Buzykaev[109,c], S. Cabrera Urbán[167], D. Caforio[128], V. M. Cairo[37a,37b], O. Cakir[4a], P. Calafiura[15], A. Calandri[136], G. Calderini[80], P. Calfayan[100], L. P. Caloba[24a], D. Calvet[34], S. Calvet[34], R. Camacho Toro[31],

S. Camarda[42], P. Camarri[133a,133b], D. Cameron[119], L. M. Caminada[15], R. Caminal Armadans[165], S. Campana[30], M. Campanelli[78], A. Campoverde[148], V. Canale[104a,104b], A. Canepa[159a], M. Cano Bret[76], J. Cantero[82], R. Cantrill[126a], T. Cao[40], M. D. M. Capeans Garrido[30], I. Caprini[26a], M. Caprini[26a], M. Capua[37a,37b], R. Caputo[83], R. Cardarelli[133a], F. Cardillo[48], T. Carli[30], G. Carlino[104a], L. Carminati[91a,91b], S. Caron[106], E. Carquin[32a], G. D. Carrillo-Montoya[8], J. R. Carter[28], J. Carvalho[126a,126c], D. Casadei[78], M. P. Casado[12], M. Casolino[12], E. Castaneda-Miranda[145b], A. Castelli[107], V. Castillo Gimenez[167], N. F. Castro[126a,g], P. Catastini[57], A. Catinaccio[30], J. R. Catmore[119], A. Cattai[30], J. Caudron[83], V. Cavaliere[165], D. Cavalli[91a], M. Cavalli-Sforza[12], V. Cavasinni[124a,124b], F. Ceradini[134a,134b], B. C. Cerio[45], K. Cerny[129], A. S. Cerqueira[24b], A. Cerri[149], L. Cerrito[76], F. Cerutti[15], M. Cerv[30], A. Cervelli[17], S. A. Cetin[19c], A. Chafaq[135a], D. Chakraborty[108], I. Chalupkova[129], P. Chang[165], B. Chapleau[87], J. D. Chapman[28], D. G. Charlton[18], C. C. Chau[158], C. A. Chavez Barajas[149], S. Cheatham[152], A. Chegwidden[90], S. Chekanov[6], S. V. Chekulaev[159a], G. A. Chelkov[65,h], M. A. Chelstowska[89], C. Chen[64], H. Chen[25], K. Chen[148], L. Chen[33d,i], S. Chen[33c], X. Chen[33f], Y. Chen[67], H. C. Cheng[89], Y. Cheng[31], A. Cheplakov[65], E. Cheremushkina[130], R. Cherkaoui El Moursli[135e], V. Chernyatin[25,*], E. Cheu[7], L. Chevalier[136], V. Chiarella[47], J. T. Childers[6], G. Chiodini[73a], A. S. Chisholm[18], R. T. Chislett[78], A. Chitan[26a], M. V. Chizhov[65], K. Choi[61], S. Chouridou[9], B. K. B. Chow[100], V. Christodoulou[78], D. Chromek-Burckhart[30], J. Chudoba[127], A. J. Chuinard[87], J. J. Chwastowski[39], L. Chytka[115], G. Ciapetti[132a,132b], A. K. Ciftci[4a], D. Cinca[53], V. Cindro[75], I. A. Cioara[21], A. Ciocio[15], Z. H. Citron[172], M. Ciubancan[26a], A. Clark[49], B. L. Clark[57], P. J. Clark[46], R. N. Clarke[15], W. Cleland[125], C. Clement[146a,146b], Y. Coadou[85], M. Cobal[164a,164c], A. Coccaro[138], J. Cochran[64], L. Coffey[23], J. G. Cogan[143], B. Cole[35], S. Cole[108], A. P. Colijn[107], J. Collot[55], T. Colombo[58c], G. Compostella[101], P. Conde Muiño[126a,126b], E. Coniavitis[48], S. H. Connell[145b], I. A. Connelly[77], S. M. Consonni[91a,91b], V. Consorti[48], S. Constantinescu[26a], C. Conta[121a,121b], G. Conti[30], F. Conventi[104a,j], M. Cooke[15], B. D. Cooper[78], A. M. Cooper-Sarkar[120], T. Cornelissen[175], M. Corradi[20a], F. Corriveau[87,k], A. Corso-Radu[163], A. Cortes-Gonzalez[12], G. Cortiana[101], G. Costa[91a], M. J. Costa[167], D. Costanzo[139], D. Côté[8], G. Cottin[28], G. Cowan[77], B. E. Cox[84], K. Cranmer[110], G. Cree[29], S. Crépé-Renaudin[55], F. Crescioli[80], W. A. Cribbs[146a,146b], M. Crispin Ortuzar[120], M. Cristinziani[21], V. Croft[106], G. Crosetti[37a,37b], T. Cuhadar Donszelmann[139], J. Cummings[176], M. Curatolo[47], C. Cuthbert[150], H. Czirr[141], P. Czodrowski[3], S. D'Auria[53], M. D'Onofrio[74], M. J. Da Cunha Sargedas De Sousa[126a,126b], C. Da Via[84], W. Dabrowski[38a], A. Dafinca[120], T. Dai[89], O. Dale[14], F. Dallaire[95], C. Dallapiccola[86], M. Dam[36], J. R. Dandoy[31], N. P. Dang[48], A. C. Daniells[18], M. Danninger[168], M. Dano Hoffmann[136], V. Dao[48], G. Darbo[50a], S. Darmora[8], J. Dassoulas[3], A. Dattagupta[61], W. Davey[21], C. David[169], T. Davidek[129], E. Davies[120,l], M. Davies[153], P. Davison[78], Y. Davygora[58a], E. Dawe[88], I. Dawson[139], R. K. Daya-Ishmukhametova[86], K. De[8], R. de Asmundis[104a], S. De Castro[20a,20b], S. De Cecco[80], N. De Groot[106], P. de Jong[107], H. De la Torre[82], F. De Lorenzi[64], L. De Nooij[107], D. De Pedis[132a], A. De Salvo[132a], U. De Sanctis[149], A. De Santo[149], J. B. De Vivie De Regie[117], W. J. Dearnaley[72], R. Debbe[25], C. Debenedetti[137], D. V. Dedovich[65], I. Deigaard[107], J. Del Peso[82], T. Del Prete[124a,124b], D. Delgove[117], F. Deliot[136], C. M. Delitzsch[49], M. Deliyergiyev[75], A. Dell'Acqua[30], L. Dell'Asta[22], M. Dell'Orso[124a,124b], M. Della Pietra[104a,j], D. della Volpe[49], M. Delmastro[5], P. A. Delsart[55], C. Deluca[107], D. A. DeMarco[158], S. Demers[176], M. Demichev[65], A. Demilly[80], S. P. Denisov[130], D. Derendarz[39], J. E. Derkaoui[135d], F. Derue[80], P. Dervan[74], K. Desch[21], C. Deterre[42], P. O. Deviveiros[30], A. Dewhurst[131], S. Dhaliwal[23], A. Di Ciaccio[133a,133b], L. Di Ciaccio[5], A. Di Domenico[132a,132b], C. Di Donato[104a,104b], A. Di Girolamo[30], B. Di Girolamo[30], A. Di Mattia[152], B. Di Micco[134a,134b], R. Di Nardo[47], A. Di Simone[48], R. Di Sipio[158], D. Di Valentino[29], C. Diaconu[85], M. Diamond[158], F. A. Dias[46], M. A. Diaz[32a], E. B. Diehl[89], J. Dietrich[16], S. Diglio[85], A. Dimitrievska[13], J. Dingfelder[21], P. Dita[26a], S. Dita[26a], F. Dittus[30], F. Djama[85], T. Djobava[51b], J. I. Djuvsland[58a], M. A. B. do Vale[24c], D. Dobos[30], M. Dobre[26a], C. Doglioni[49], T. Dohmae[155], J. Dolejsi[129], Z. Dolezal[129], B. A. Dolgoshein[98,*], M. Donadelli[24d], S. Donati[124a,124b], P. Dondero[121a,121b], J. Donini[34], J. Dopke[131], A. Doria[104a], M. T. Dova[71], A. T. Doyle[53], E. Drechsler[54], M. Dris[10], E. Dubreuil[34], E. Duchovni[172], G. Duckeck[100], O. A. Ducu[26a,85], D. Duda[175], A. Dudarev[30], L. Duflot[117], L. Duguid[77], M. Dührssen[30], M. Dunford[58a], H. Duran Yildiz[4a], M. Düren[52], A. Durglishvili[51b], D. Duschinger[44], M. Dyndal[38a], C. Eckardt[42], K. M. Ecker[101], R. C. Edgar[89], W. Edson[2], N. C. Edwards[46], W. Ehrenfeld[21], T. Eifert[30], G. Eigen[14], K. Einsweiler[15], T. Ekelof[166], M. El Kacimi[135c], M. Ellert[166], S. Elles[5], F. Ellinghaus[83], A. A. Elliot[169], N. Ellis[30], J. Elmsheuser[100], M. Elsing[30], D. Emeliyanov[131], Y. Enari[155], O. C. Endner[83], M. Endo[118], J. Erdmann[43], A. Ereditato[17], G. Ernis[175], J. Ernst[2], M. Ernst[25], S. Errede[165], E. Ertel[83], M. Escalier[117], H. Esch[43], C. Escobar[125], B. Esposito[47], A. I. Etienvre[136], E. Etzion[153], H. Evans[61], A. Ezhilov[123], L. Fabbri[20a,20b], G. Facini[31], R. M. Fakhrutdinov[130], S. Falciano[132a], R. J. Falla[78], J. Faltova[129], Y. Fang[33a], M. Fanti[91a,91b], A. Farbin[8], A. Farilla[134a], T. Farooque[12], S. Farrell[15], S. M. Farrington[170], P. Farthouat[30], F. Fassi[135e], P. Fassnacht[30], D. Fassouliotis[9], M. Faucci Giannelli[77], A. Favareto[50a,50b], L. Fayard[117], P. Federic[144a], O. L. Fedin[123,m], W. Fedorko[168], S. Feigl[30], L. Feligioni[85], C. Feng[33d], E. J. Feng[6], H. Feng[89], A. B. Fenyuk[130], L. Feremenga[8], P. Fernandez Martinez[167], S. Fernandez Perez[30], J. Ferrando[53], A. Ferrari[166], P. Ferrari[107],

R. Ferrari[121a], D. E. Ferreira de Lima[53], A. Ferrer[167], D. Ferrere[49], C. Ferretti[89], A. Ferretto Parodi[50a,50b], M. Fiascaris[31], F. Fiedler[83], A. Filipčič[75], M. Filipuzzi[42], F. Filthaut[106], M. Fincke-Keeler[169], K. D. Finelli[150], M. C. N. Fiolhais[126a,126c], L. Fiorini[167], A. Firan[40], A. Fischer[2], C. Fischer[12], J. Fischer[175], W. C. Fisher[90], E. A. Fitzgerald[23], I. Fleck[141], P. Fleischmann[89], S. Fleischmann[175], G. T. Fletcher[139], G. Fletcher[76], R. R. M. Fletcher[122], T. Flick[175], A. Floderus[81], L. R. Flores Castillo[60a], M. J. Flowerdew[101], A. Formica[136], A. Forti[84], D. Fournier[117], H. Fox[72], S. Fracchia[12], P. Francavilla[80], M. Franchini[20a,20b], D. Francis[30], L. Franconi[119], M. Franklin[57], M. Frate[163], M. Fraternali[121a,121b], D. Freeborn[78], S. T. French[28], F. Friedrich[44], D. Froidevaux[30], J. A. Frost[120], C. Fukunaga[156], E. Fullana Torregrosa[83], B. G. Fulsom[143], J. Fuster[167], C. Gabaldon[55], O. Gabizon[175], A. Gabrielli[20a,20b], A. Gabrielli[132a,132b], S. Gadatsch[107], S. Gadomski[49], G. Gagliardi[50a,50b], P. Gagnon[61], C. Galea[106], B. Galhardo[126a,126c], E. J. Gallas[120], B. J. Gallop[131], P. Gallus[128], G. Galster[36], K. K. Gan[111], J. Gao[33b,85], Y. Gao[46], Y. S. Gao[143,e], F. M. Garay Walls[46], F. Garberson[176], C. García[167], J. E. García Navarro[167], M. Garcia-Sciveres[15], R. W. Gardner[31], N. Garelli[143], V. Garonne[119], C. Gatti[47], A. Gaudiello[50a,50b], G. Gaudio[121a], B. Gaur[141], L. Gauthier[95], P. Gauzzi[132a,132b], I. L. Gavrilenko[96], C. Gay[168], G. Gaycken[21], E. N. Gazis[10], P. Ge[33d], Z. Gecse[168], C. N. P. Gee[131], D. A. A. Geerts[107], Ch. Geich-Gimbel[21], M. P. Geisler[58a], C. Gemme[50a], M. H. Genest[55], S. Gentile[132a,132b], M. George[54], S. George[77], D. Gerbaudo[163], A. Gershon[153], H. Ghazlane[135b], B. Giacobbe[20a], S. Giagu[132a,132b], V. Giangiobbe[12], P. Giannetti[124a,124b], B. Gibbard[25], S. M. Gibson[77], M. Gilchriese[15], T. P. S. Gillam[28], D. Gillberg[30], G. Gilles[34], D. M. Gingrich[3,d], N. Giokaris[9], M. P. Giordani[164a,164c], F. M. Giorgi[20a], F. M. Giorgi[16], P. F. Giraud[136], P. Giromini[47], D. Giugni[91a], C. Giuliani[48], M. Giulini[58b], B. K. Gjelsten[119], S. Gkaitatzis[154], I. Gkialas[154], E. L. Gkougkousis[117], L. K. Gladilin[99], C. Glasman[82], J. Glatzer[30], P. C. F. Glaysher[46], A. Glazov[42], M. Goblirsch-Kolb[101], J. R. Goddard[76], J. Godlewski[39], S. Goldfarb[89], T. Golling[49], D. Golubkov[130], A. Gomes[126a,126b,126d], R. Gonçalo[126a], J. Goncalves Pinto Firmino Da Costa[136], L. Gonella[21], S. González de la Hoz[167], G. Gonzalez Parra[12], S. Gonzalez-Sevilla[49], L. Goossens[30], P. A. Gorbounov[97], H. A. Gordon[25], I. Gorelov[105], B. Gorini[30], E. Gorini[73a,73b], A. Gorišek[75], E. Gornicki[39], A. T. Goshaw[45], C. Gössling[43], M. I. Gostkin[65], D. Goujdami[135c], A. G. Goussiou[138], N. Govender[145b], E. Gozani[152], H. M. X. Grabas[137], L. Graber[54], I. Grabowska-Bold[38a], P. Grafström[20a,20b], K-J. Grahn[42], J. Gramling[49], E. Gramstad[119], S. Grancagnolo[16], V. Grassi[148], V. Gratchev[123], H. M. Gray[30], E. Graziani[134a], Z. D. Greenwood[79,n], K. Gregersen[78], I. M. Gregor[42], P. Grenier[143], J. Griffiths[8], A. A. Grillo[137], K. Grimm[72], S. Grinstein[12,o], Ph. Gris[34], J.-F. Grivaz[117], J. P. Grohs[44], A. Grohsjean[42], E. Gross[172], J. Grosse-Knetter[54], G. C. Grossi[79], Z. J. Grout[149], L. Guan[33b], J. Guenther[128], F. Guescini[49], D. Guest[176], O. Gueta[153], E. Guido[50a,50b], T. Guillemin[117], S. Guindon[2], U. Gul[53], C. Gumpert[44], J. Guo[33e], S. Gupta[120], G. Gustavino[132a,132b], P. Gutierrez[113], N. G. Gutierrez Ortiz[53], C. Gutschow[44], C. Guyot[136], C. Gwenlan[120], C. B. Gwilliam[74], A. Haas[110], C. Haber[15], H. K. Hadavand[8], N. Haddad[135e], P. Haefner[21], S. Hageböck[21], Z. Hajduk[39], H. Hakobyan[177], M. Haleem[42], J. Haley[114], D. Hall[120], G. Halladjian[90], G. D. Hallewell[85], K. Hamacher[175], P. Hamal[115], K. Hamano[169], M. Hamer[54], A. Hamilton[145a], G. N. Hamity[145c], P. G. Hamnett[42], L. Han[33b], K. Hanagaki[118], K. Hanawa[155], M. Hance[15], P. Hanke[58a], R. Hanna[136], J. B. Hansen[36], J. D. Hansen[36], M. C. Hansen[21], P. H. Hansen[36], K. Hara[160], A. S. Hard[173], T. Harenberg[175], F. Hariri[117], S. Harkusha[92], R. D. Harrington[46], P. F. Harrison[170], F. Hartjes[107], M. Hasegawa[67], S. Hasegawa[103], Y. Hasegawa[140], A. Hasib[113], S. Hassani[136], S. Haug[17], R. Hauser[90], L. Hauswald[44], M. Havranek[127], C. M. Hawkes[18], R. J. Hawkings[30], A. D. Hawkins[81], T. Hayashi[160], D. Hayden[90], C. P. Hays[120], J. M. Hays[76], H. S. Hayward[74], S. J. Haywood[131], S. J. Head[18], T. Heck[83], V. Hedberg[81], L. Heelan[8], S. Heim[122], T. Heim[175], B. Heinemann[15], L. Heinrich[110], J. Hejbal[127], L. Helary[22], S. Hellman[146a,146b], D. Hellmich[21], C. Helsens[30], J. Henderson[120], R. C. W. Henderson[72], Y. Heng[173], C. Hengler[42], A. Henrichs[176], A. M. Henriques Correia[30], S. Henrot-Versille[117], G. H. Herbert[16], Y. Hernández Jiménez[167], R. Herrberg-Schubert[16], G. Herten[48], R. Hertenberger[100], L. Hervas[30], G. G. Hesketh[78], N. P. Hessey[107], J. W. Hetherly[40], R. Hickling[76], E. Higón-Rodriguez[167], E. Hill[169], J. C. Hill[28], K. H. Hiller[42], S. J. Hillier[18], I. Hinchliffe[15], E. Hines[122], R. R. Hinman[15], M. Hirose[157], D. Hirschbuehl[175], J. Hobbs[148], N. Hod[107], M. C. Hodgkinson[139], P. Hodgson[139], A. Hoecker[30], M. R. Hoeferkamp[105], F. Hoenig[100], M. Hohlfeld[83], D. Hohn[21], T. R. Holmes[15], M. Homann[43], T. M. Hong[125], L. Hooft van Huysduynen[110], W. H. Hopkins[116], Y. Horii[103], A. J. Horton[142], J-Y. Hostachy[55], S. Hou[151], A. Hoummada[135a], J. Howard[120], J. Howarth[42], M. Hrabovsky[115], I. Hristova[16], J. Hrivnac[117], T. Hryn'ova[5], A. Hrynevich[93], C. Hsu[145c], P. J. Hsu[151,p], S.-C. Hsu[138], D. Hu[35], Q. Hu[33b], X. Hu[89], Y. Huang[42], Z. Hubacek[30], F. Hubaut[85], F. Huegging[21], T. B. Huffman[120], E. W. Hughes[35], G. Hughes[72], M. Huhtinen[30], T. A. Hülsing[83], N. Huseynov[65,b], J. Huston[90], J. Huth[57], G. Iacobucci[49], G. Iakovidis[25], I. Ibragimov[141], L. Iconomidou-Fayard[117], E. Ideal[176], Z. Idrissi[135e], P. Iengo[30], O. Igonkina[107], T. Iizawa[171], Y. Ikegami[66], K. Ikematsu[141], M. Ikeno[66], Y. Ilchenko[31,q], D. Iliadis[154], N. Ilic[143], Y. Inamaru[67], T. Ince[101], P. Ioannou[9], M. Iodice[134a], K. Iordanidou[35], V. Ippolito[57], A. Irles Quiles[167], C. Isaksson[166], M. Ishino[68], M. Ishitsuka[157], R. Ishmukhametov[111], C. Issever[120], S. Istin[19a], J. M. Iturbe Ponce[84], R. Iuppa[133a,133b], J. Ivarsson[81], W. Iwanski[39], H. Iwasaki[66], J. M. Izen[41], V. Izzo[104a], S. Jabbar[3], B. Jackson[122], M. Jackson[74], P. Jackson[1], M. R. Jaekel[30], V. Jain[2], K. Jakobs[48], S. Jakobsen[30], T. Jakoubek[127],

J. Jakubek[128], D. O. Jamin[151], D. K. Jana[79], E. Jansen[78], R. Jansky[62], J. Janssen[21], M. Janus[170], G. Jarlskog[81], N. Javadov[65,b], T. Javůrek[48], L. Jeanty[15], J. Jejelava[51a,r], G.-Y. Jeng[150], D. Jennens[88], P. Jenni[48,s], J. Jentzsch[43], C. Jeske[170], S. Jézéquel[5], H. Ji[173], J. Jia[148], Y. Jiang[33b], S. Jiggins[78], J. Jimenez Pena[167], S. Jin[33a], A. Jinaru[26a], O. Jinnouchi[157], M. D. Joergensen[36], P. Johansson[139], K. A. Johns[7], K. Jon-And[146a,146b], G. Jones[170], R. W. L. Jones[72], T. J. Jones[74], J. Jongmanns[58a], P. M. Jorge[126a,126b], K. D. Joshi[84], J. Jovicevic[159a], X. Ju[173], C. A. Jung[43], P. Jussel[62], A. Juste Rozas[12,o], M. Kaci[167], A. Kaczmarska[39], M. Kado[117], H. Kagan[111], M. Kagan[143], S. J. Kahn[85], E. Kajomovitz[45], C. W. Kalderon[120], S. Kama[40], A. Kamenshchikov[130], N. Kanaya[155], M. Kaneda[30], S. Kaneti[28], V. A. Kantserov[98], J. Kanzaki[66], B. Kaplan[110], A. Kapliy[31], D. Kar[53], K. Karakostas[10], A. Karamaoun[3], N. Karastathis[10,107], M. J. Kareem[54], M. Karnevskiy[83], S. N. Karpov[65], Z. M. Karpova[65], K. Karthik[110], V. Kartvelishvili[72], A. N. Karyukhin[130], L. Kashif[173], R. D. Kass[111], A. Kastanas[14], Y. Kataoka[155], A. Katre[49], J. Katzy[42], K. Kawagoe[70], T. Kawamoto[155], G. Kawamura[54], S. Kazama[155], V. F. Kazanin[109,c], M. Y. Kazarinov[65], R. Keeler[169], R. Kehoe[40], J. S. Keller[42], J. J. Kempster[77], H. Keoshkerian[84], O. Kepka[127], B. P. Kerševan[75], S. Kersten[175], R. A. Keyes[87], F. Khalil-zada[11], H. Khandanyan[146a,146b], A. Khanov[114], A. G. Kharlamov[109,c], T. J. Khoo[28], V. Khovanskiy[97], E. Khramov[65], J. Khubua[51b,t], H. Y. Kim[8], H. Kim[146a,146b], S. H. Kim[160], Y. K. Kim[31], N. Kimura[154], O. M. Kind[16], B. T. King[74], M. King[167], S. B. King[168], J. Kirk[131], A. E. Kiryunin[101], T. Kishimoto[67], D. Kisielewska[38a], F. Kiss[48], K. Kiuchi[160], O. Kivernyk[136], E. Kladiva[144b], M. H. Klein[35], M. Klein[74], U. Klein[74], K. Kleinknecht[83], P. Klimek[146a,146b], A. Klimentov[25], R. Klingenberg[43], J. A. Klinger[139], T. Klioutchnikova[30], E.-E. Kluge[58a], P. Kluit[107], S. Kluth[101], E. Kneringer[62], E. B. F. G. Knoops[85], A. Knue[53], A. Kobayashi[155], D. Kobayashi[157], T. Kobayashi[155], M. Kobel[44], M. Kocian[143], P. Kodys[129], T. Koffas[29], E. Koffeman[107], L. A. Kogan[120], S. Kohlmann[175], Z. Kohout[128], T. Kohriki[66], T. Koi[143], H. Kolanoski[16], I. Koletsou[5], A. A. Komar[96,*], Y. Komori[155], T. Kondo[66], N. Kondrashova[42], K. Köneke[48], A. C. König[106], S. König[83], T. Kono[66,u], R. Konoplich[110,v], N. Konstantinidis[78], R. Kopeliansky[152], S. Koperny[38a], L. Köpke[83], A. K. Kopp[48], K. Korcyl[39], K. Kordas[154], A. Korn[78], A. A. Korol[109,c], I. Korolkov[12], E. V. Korolkova[139], O. Kortner[101], S. Kortner[101], T. Kosek[129], V. V. Kostyukhin[21], V. M. Kotov[65], A. Kotwal[45], A. Kourkoumeli-Charalampidi[154], C. Kourkoumelis[9], V. Kouskoura[25], A. Koutsman[159a], R. Kowalewski[169], T. Z. Kowalski[38a], W. Kozanecki[136], A. S. Kozhin[130], V. A. Kramarenko[99], G. Kramberger[75], D. Krasnopevtsev[98], M. W. Krasny[80], A. Krasznahorkay[30], J. K. Kraus[21], A. Kravchenko[25], S. Kreiss[110], M. Kretz[58c], J. Kretzschmar[74], K. Kreutzfeldt[52], P. Krieger[158], K. Krizka[31], K. Kroeninger[43], H. Kroha[101], J. Kroll[122], J. Kroseberg[21], J. Krstic[13], U. Kruchonak[65], H. Krüger[21], N. Krumnack[64], Z. V. Krumshteyn[65], A. Kruse[173], M. C. Kruse[45], M. Kruskal[22], T. Kubota[88], H. Kucuk[78], S. Kuday[4b], S. Kuehn[48], A. Kugel[58c], F. Kuger[174], A. Kuhl[137], T. Kuhl[42], V. Kukhtin[65], Y. Kulchitsky[92], S. Kuleshov[32b], M. Kuna[132a,132b], T. Kunigo[68], A. Kupco[127], H. Kurashige[67], Y. A. Kurochkin[92], R. Kurumida[67], V. Kus[127], E. S. Kuwertz[169], M. Kuze[157], J. Kvita[115], T. Kwan[169], D. Kyriazopoulos[139], A. La Rosa[49], J. L. La Rosa Navarro[24d], L. La Rotonda[37a,37b], C. Lacasta[167], F. Lacava[132a,132b], J. Lacey[29], H. Lacker[16], D. Lacour[80], V. R. Lacuesta[167], E. Ladygin[65], R. Lafaye[5], B. Laforge[80], T. Lagouri[176], S. Lai[48], L. Lambourne[78], S. Lammers[61], C. L. Lampen[7], W. Lampl[7], E. Lançon[136], U. Landgraf[48], M. P. J. Landon[76], V. S. Lang[58a], J. C. Lange[12], A. J. Lankford[163], F. Lanni[25], K. Lantzsch[30], S. Laplace[80], C. Lapoire[30], J. F. Laporte[136], T. Lari[91a], F. Lasagni Manghi[20a,20b], M. Lassnig[30], P. Laurelli[47], W. Lavrijsen[15], A. T. Law[137], P. Laycock[74], T. Lazovich[57], O. Le Dortz[80], E. Le Guirriec[85], E. Le Menedeu[12], M. LeBlanc[169], T. LeCompte[6], F. Ledroit-Guillon[55], C. A. Lee[145b], S. C. Lee[151], L. Lee[1], G. Lefebvre[80], M. Lefebvre[169], F. Legger[100], C. Leggett[15], A. Lehan[74], G. Lehmann Miotto[30], X. Lei[7], W. A. Leight[29], A. Leisos[154,w], A. G. Leister[176], M. A. L. Leite[24d], R. Leitner[129], D. Lellouch[172], B. Lemmer[54], K. J. C. Leney[78], T. Lenz[21], B. Lenzi[30], R. Leone[7], S. Leone[124a,124b], C. Leonidopoulos[46], S. Leontsinis[10], C. Leroy[95], C. G. Lester[28], M. Levchenko[123], J. Levêque[5], D. Levin[89], L. J. Levinson[172], M. Levy[18], A. Lewis[120], A. M. Leyko[21], M. Leyton[41], B. Li[33b,x], H. Li[148], H. L. Li[31], L. Li[45], L. Li[33e], S. Li[45], Y. Li[33c,y], Z. Liang[137], H. Liao[34], B. Liberti[133a], A. Liblong[158], P. Lichard[30], K. Lie[165], J. Liebal[21], W. Liebig[14], C. Limbach[21], A. Limosani[150], S. C. Lin[151,z], T. H. Lin[83], F. Linde[107], B. E. Lindquist[148], J. T. Linnemann[90], E. Lipeles[122], A. Lipniacka[14], M. Lisovyi[58b], T. M. Liss[165], D. Lissauer[25], A. Lister[168], A. M. Litke[137], B. Liu[151,aa], D. Liu[151], H. Liu[89], J. Liu[85], J. B. Liu[33b], K. Liu[85], L. Liu[165], M. Liu[45], M. Liu[33b], Y. Liu[33b], M. Livan[121a,121b], A. Lleres[55], J. Llorente Merino[82], S. L. Lloyd[76], F. Lo Sterzo[151], E. Lobodzinska[42], P. Loch[7], W. S. Lockman[137], F. K. Loebinger[84], A. E. Loevschall-Jensen[36], A. Loginov[176], T. Lohse[16], K. Lohwasser[42], M. Lokajicek[127], B. A. Long[22], J. D. Long[89], R. E. Long[72], K. A. Looper[111], L. Lopes[126a], D. Lopez Mateos[57], B. Lopez Paredes[139], I. Lopez Paz[12], J. Lorenz[100], N. Lorenzo Martinez[61], M. Losada[162], P. Loscutoff[15], P. J. Lösel[100], X. Lou[33a], A. Lounis[117], J. Love[6], P. A. Love[72], N. Lu[89], H. J. Lubatti[138], C. Luci[132a,132b], A. Lucotte[55], F. Luehring[61], W. Lukas[62], L. Luminari[132a], O. Lundberg[146a,146b], B. Lund-Jensen[147], D. Lynn[25], R. Lysak[127], E. Lytken[81], H. Ma[25], L. L. Ma[33d], G. Maccarrone[47], A. Macchiolo[101], C. M. Macdonald[139], J. Machado Miguens[122,126b], D. Macina[30], D. Madaffari[85], R. Madar[34], H. J. Maddocks[72], W. F. Mader[44], A. Madsen[166], S. Maeland[14], T. Maeno[25], A. Maevskiy[99], E. Magradze[54], K. Mahboubi[48],

J. Mahlstedt[107], C. Maiani[136], C. Maidantchik[24a], A. A. Maier[101], T. Maier[100], A. Maio[126a,126b,126d], S. Majewski[116], Y. Makida[66], N. Makovec[117], B. Malaescu[80], Pa. Malecki[39], V. P. Maleev[123], F. Malek[55], U. Mallik[63], D. Malon[6], C. Malone[143], S. Maltezos[10], V. M. Malyshev[109], S. Malyukov[30], J. Mamuzic[42], G. Mancini[47], B. Mandelli[30], L. Mandelli[91a], I. Mandić[75], R. Mandrysch[63], J. Maneira[126a,126b], A. Manfredini[101], L. Manhaes de Andrade Filho[24b], J. Manjarres Ramos[159b], A. Mann[100], P. M. Manning[137], A. Manousakis-Katsikakis[9], B. Mansoulie[136], R. Mantifel[87], M. Mantoani[54], L. Mapelli[30], L. March[145c], G. Marchiori[80], M. Marcisovsky[127], C. P. Marino[169], M. Marjanovic[13], D. E. Marley[89], F. Marroquim[24a], S. P. Marsden[84], Z. Marshall[15], L. F. Marti[17], S. Marti-Garcia[167], B. Martin[90], T. A. Martin[170], V. J. Martin[46], B. Martin dit Latour[14], M. Martinez[12,o], S. Martin-Haugh[131], V. S. Martoiu[26a], A. C. Martyniuk[78], M. Marx[138], F. Marzano[132a], A. Marzin[30], L. Masetti[83], T. Mashimo[155], R. Mashinistov[96], J. Masik[84], A. L. Maslennikov[109,c], I. Massa[20a,20b], L. Massa[20a,20b], N. Massol[5], P. Mastrandrea[148], A. Mastroberardino[37a,37b], T. Masubuc hi[155], P. Mättig[175], J. Mattmann[83], J. Maurer[26a], S. J. Maxfield[74], D. A. Maximov[109,c], R. Mazini[151], S. M. Mazza[91a,91b], L. Mazzaferro[133a,133b], G. Mc Goldrick[158], S. P. Mc Kee[89], A. McCarn[89], R. L. McCarthy[148], T. G. McCarthy[29], N. A. McCubbin[131], K. W. McFarlane[56,*], J. A. Mcfayden[78], G. Mchedlidze[54], S. J. McMahon[131], R. A. McPherson[169,k], M. Medinnis[42], S. Meehan[145a], S. Mehlhase[100], A. Mehta[74], K. Meier[58a], C. Meineck[100], B. Meirose[41], B. R. Mellado Garcia[145c], F. Meloni[17], A. Mengarelli[20a,20b], S. Menke[101], E. Meoni[161], K. M. Mercurio[57], S. Mergelmeyer[21], P. Mermod[49], L. Merola[104a,104b], C. Meroni[91a], F. S. Merritt[31], A. Messina[132a,132b], J. Metcalfe[25], A. S. Mete[163], C. Meyer[83], C. Meyer[122], J-P. Meyer[136], J. Meyer[107], R. P. Middleton[131], S. Miglioranzi[164a,164c], L. Mijović[21], G. Mikenberg[172], M. Mikestikova[127], M. Mikuž[75], M. Milesi[88], A. Milic[30], D. W. Miller[31], C. Mills[46], A. Milov[172], D. A. Milstead[146a,146b], A. A. Minaenko[130], Y. Minami[155], I. A. Minashvili[65], A. I. Mincer[110], B. Mindur[38a], M. Mineev[65], Y. Ming[173], L. M. Mir[12], T. Mitani[171], J. Mitrevski[100], V. A. Mitsou[167], A. Miucci[49], P. S. Miyagawa[139], J. U. Mjörnmark[81], T. Moa[146a,146b], K. Mochizuki[85], S. Mohapatra[35], W. Mohr[48], S. Molander[146a,146b], R. Moles-Valls[167], K. Mönig[42], C. Monini[55], J. Monk[36], E. Monnier[85], J. Montejo Berlingen[12], F. Monticelli[71], S. Monzani[132a,132b], R. W. Moore[3], N. Morange[117], D. Moreno[162], M. Moreno Llácer[54], P. Morettini[50a], M. Morgenstern[44], M. Morii[57], M. Morinaga[155], V. Morisbak[119], S. Moritz[83], A. K. Morley[147], G. Mornacchi[30], J. D. Morris[76], S. S. Mortensen[36], A. Morton[53], L. Morvaj[103], M. Mosidze[51b], J. Moss[111], K. Motohashi[157], R. Mount[143], E. Mountricha[25], S. V. Mouraviev[96,*], E. J. W. Moyse[86], S. Muanza[85], R. D. Mudd[18], F. Mueller[101], J. Mueller[125], K. Mueller[21], R. S. P. Mueller[100], T. Mueller[28], D. Muenstermann[49], P. Mullen[53], G. A. Mullier[17], Y. Munwes[153], J. A. Murillo Quijada[18], W. J. Murray[170,131], H. Musheghyan[54], E. Musto[152], A. G. Myagkov[130,ab], M. Myska[128], O. Nackenhorst[54], J. Nadal[54], K. Nagai[120], R. Nagai[157], Y. Nagai[85], K. Nagano[66], A. Nagarkar[111], Y. Nagasaka[59], K. Nagata[160], M. Nagel[101], E. Nagy[85], A. M. Nairz[30], Y. Nakahama[30], K. Nakamura[66], T. Nakamura[155], I. Nakano[112], H. Namasivayam[41], R. F. Naranjo Garcia[42], R. Narayan[31], T. Naumann[42], G. Navarro[162], R. Nayyar[7], H. A. Neal[89], P. Yu. Nechaeva[96], T. J. Neep[84], P. D. Nef[143], A. Negri[121a,121b], M. Negrini[20a], S. Nektarijevic[106], C. Nellist[117], A. Nelson[163], S. Nemecek[127], P. Nemethy[110], A. A. Nepomuceno[24a], M. Nessi[30,ac], M. S. Neubauer[165], M. Neumann[175], R. M. Neves[110], P. Nevski[25], P. R. Newman[18], D. H. Nguyen[6], R. B. Nickerson[120], R. Nicolaidou[136], B. Nicquevert[30], J. Nielsen[137], N. Nikiforou[35], A. Nikiforov[16], V. Nikolaenko[130,ab], I. Nikolic-Audit[80], K. Nikolopoulos[18], J. K. Nilsen[119], P. Nilsson[25], Y. Ninomiya[155], A. Nisati[132a], R. Nisius[101], T. Nobe[157], M. Nomachi[118], I. Nomidis[29], T. Nooney[76], S. Norberg[113], M. Nordberg[30], O. Novgorodova[44], S. Nowak[101], M. Nozaki[66], L. Nozka[115], K. Ntekas[10], G. Nunes Hanninger[88], T. Nunnemann[100], E. Nurse[78], F. Nuti[88], B. J. O'Brien[46], F. O'grady[7], D. C. O'Neil[142], V. O'Shea[53], F. G. Oakham[29,d], H. Oberlack[101], T. Obermann[21], J. Ocariz[80], A. Ochi[67], I. Ochoa[78], J. P. Ochoa-Ricoux[32a], S. Oda[70], S. Odaka[66], H. Ogren[61], A. Oh[84], S. H. Oh[45], C. C. Ohm[15], H. Ohman[166], H. Oide[30], W. Okamura[118], H. Okawa[160], Y. Okumura[31], T. Okuyama[155], A. Olariu[26a], S. A. Olivares Pino[46], D. Oliveira Damazio[25], E. Oliver Garcia[167], A. Olszewski[39], J. Olszowska[39], A. Onofre[126a,126e], P. U. E. Onyisi[31,q], C. J. Oram[159a], M. J. Oreglia[31], Y. Oren[153], D. Orestano[134a,134b], N. Orlando[154], C. Oropeza Barrera[53], R. S. Orr[158], B. Osculati[50a,50b], R. Ospanov[84], G. Otero y Garzon[27], H. Otono[70], M. Ouchrif[135d], E. A. Ouellette[169], F. Ould-Saada[119], A. Ouraou[136], K. P. Oussoren[107], Q. Ouyang[33a], A. Ovcharova[15], M. Owen[53], R. E. Owen[18], V. E. Ozcan[19a], N. Ozturk[8], K. Pachal[142], A. Pacheco Pages[12], C. Padilla Aranda[12], M. Pagáčová[48], S. Pagan Griso[15], E. Paganis[139], C. Pahl[101], F. Paige[25], P. Pais[86], K. Pajchel[119], G. Palacino[159b], S. Palestini[30], M. Palka[38b], D. Pallin[34], A. Palma[126a,126b], Y. B. Pan[173], E. Panagiotopoulou[10], C. E. Pandini[80], J. G. Panduro Vazquez[77], P. Pani[146a,146b], S. Panitkin[25], D. Pantea[26a], L. Paolozzi[49], Th. D. Papadopoulou[10], K. Papageorgiou[154], A. Paramonov[6], D. Paredes Hernandez[154], M. A. Parker[28], K. A. Parker[139], F. Parodi[50a,50b], J. A. Parsons[35], U. Parzefall[48], E. Pasqualucci[132a], S. Passaggio[50a], F. Pastore[134a,134b,*], Fr. Pastore[77], G. Pásztor[29], S. Pataraia[175], N. D. Patel[150], J. R. Pater[84], T. Pauly[30], J. Pearce[169], B. Pearson[113], L. E. Pedersen[36], M. Pedersen[119], S. Pedraza Lopez[167], R. Pedro[126a,126b], S. V. Peleganchuk[109,c], D. Pelikan[166], H. Peng[33b], B. Penning[31], J. Penwell[61], D. V. Perepelitsa[25], E. Perez Codina[159a], M. T. Pérez García-Estañ[167], L. Perini[91a,91b], H. Pernegger[30], S. Perrella[104a,104b], R. Peschke[42], V. D. Peshekhonov[65], K. Peters[30], R. F. Y. Peters[84], B. A. Petersen[30], T. C. Petersen[36],

E. Petit[42], A. Petridis[146a,146b], C. Petridou[154], E. Petrolo[132a], F. Petrucci[134a,134b], N. E. Pettersson[157], R. Pezoa[32b], P. W. Phillips[131], G. Piacquadio[143], E. Pianori[170], A. Picazio[49], E. Piccaro[76], M. Piccinini[20a,20b], M. A. Pickering[120], R. Piegaia[27], D. T. Pignotti[111], J. E. Pilcher[31], A. D. Pilkington[84], J. Pina[126a,126b,126d], M. Pinamonti[164a,164c,ad], J. L. Pinfold[3], A. Pingel[36], B. Pinto[126a], S. Pires[80], M. Pitt[172], C. Pizio[91a,91b], L. Plazak[144a], M.-A. Pleier[25], V. Pleskot[129], E. Plotnikova[65], P. Plucinski[146a,146b], D. Pluth[64], R. Poettgen[146a,146b], L. Poggioli[117], D. Pohl[21], G. Polesello[121a], A. Poley[42], A. Policicchio[37a,37b], R. Polifka[158], A. Polini[20a], C. S. Pollard[53], V. Polychronakos[25], K. Pommès[30], L. Pontecorvo[132a], B. G. Pope[90], G. A. Popeneciu[26b], D. S. Popovic[13], A. Poppleton[30], S. Pospisil[128], K. Potamianos[15], I. N. Potrap[65], C. J. Potter[149], C. T. Potter[116], G. Poulard[30], J. Poveda[30], V. Pozdnyakov[65], P. Pralavorio[85], A. Pranko[15], S. Prasad[30], S. Prell[64], D. Price[84], L. E. Price[6], M. Primavera[73a], S. Prince[87], M. Proissl[46], K. Prokofiev[60c], F. Prokoshin[32b], E. Protopapadaki[136], S. Protopopescu[25], J. Proudfoot[6], M. Przybycien[38a], E. Ptacek[116], D. Puddu[134a,134b], E. Pueschel[86], D. Puldon[148], M. Purohit[25,ae], P. Puzo[117], J. Qian[89], G. Qin[53], Y. Qin[84], A. Quadt[54], D. R. Quarrie[15], W. B. Quayle[164a,164b], M. Queitsch-Maitland[84], D. Quilty[53], S. Raddum[119], V. Radeka[25], V. Radescu[42], S. K. Radhakrishnan[148], P. Radloff[116], P. Rados[88], F. Ragusa[91a,91b], G. Rahal[178], S. Rajagopalan[25], M. Rammensee[30], C. Rangel-Smith[166], F. Rauscher[100], S. Rave[83], T. Ravenscroft[53], M. Raymond[30], A. L. Read[119], N. P. Readioff[74], D. M. Rebuzzi[121a,121b], A. Redelbach[174], G. Redlinger[25], R. Reece[137], K. Reeves[41], L. Rehnisch[16], H. Reisin[27], M. Relich[163], C. Rembser[30], H. Ren[33a], A. Renaud[117], M. Rescigno[132a], S. Resconi[91a], O. L. Rezanova[109,c], P. Reznicek[129], R. Rezvani[95], R. Richter[101], S. Richter[78], E. Richter-Was[38b], O. Ricken[21], M. Ridel[80], P. Rieck[16], C. J. Riegel[175], J. Rieger[54], M. Rijssenbeek[148], A. Rimoldi[121a,121b], L. Rinaldi[20a], B. Ristić[49], E. Ritsch[30], I. Riu[12], F. Rizatdinova[114], E. Rizvi[76], S. H. Robertson[87,k], A. Robichaud-Veronneau[87], D. Robinson[28], J. E. M. Robinson[84], A. Robson[53], C. Roda[124a,124b], S. Roe[30], O. Røhne[119], S. Rolli[161], A. Romaniouk[98], M. Romano[20a,20b], S. M. Romano Saez[34], E. Romero Adam[167], N. Rompotis[138], M. Ronzani[48], L. Roos[80], E. Ros[167], S. Rosati[132a], K. Rosbach[48], P. Rose[137], P. L. Rosendahl[14], O. Rosenthal[141], V. Rossetti[146a,146b], E. Rossi[104a,104b], L. P. Rossi[50a], R. Rosten[138], M. Rotaru[26a], I. Roth[172], J. Rothberg[138], D. Rousseau[117], C. R. Royon[136], A. Rozanov[85], Y. Rozen[152], X. Ruan[145c], F. Rubbo[143], I. Rubinskiy[42], V. I. Rud[99], C. Rudolph[44], M. S. Rudolph[158], F. Rühr[48], A. Ruiz-Martinez[30], Z. Rurikova[48], N. A. Rusakovich[65], A. Ruschke[100], H. L. Russell[138], J. P. Rutherfoord[7], N. Ruthmann[48], Y. F. Ryabov[123], M. Rybar[165], G. Rybkin[117], N. C. Ryder[120], A. F. Saavedra[150], G. Sabato[107], S. Sacerdoti[27], A. Saddique[3], H. F-W. Sadrozinski[137], R. Sadykov[65], F. Safai Tehrani[132a], M. Saimpert[136], H. Sakamoto[155], Y. Sakurai[171], G. Salamanna[134a,134b], A. Salamon[133a], M. Saleem[113], D. Salek[107], P. H. Sales De Bruin[138], D. Salihagic[101], A. Salnikov[143], J. Salt[167], D. Salvatore[37a,37b], F. Salvatore[149], A. Salvucci[106], A. Salzburger[30], D. Sampsonidis[154], A. Sanchez[104a,104b], J. Sánchez[167], V. Sanchez Martinez[167], H. Sandaker[119], R. L. Sandbach[76], H. G. Sander[83], M. P. Sanders[100], M. Sandhoff[175], C. Sandoval[162], R. Sandstroem[101], D. P. C. Sankey[131], M. Sannino[50a,50b], A. Sansoni[47], C. Santoni[34], R. Santonico[133a,133b], H. Santos[126a], I. Santoyo Castillo[149], K. Sapp[125], A. Sapronov[65], J. G. Saraiva[126a,126d], B. Sarrazin[21], O. Sasaki[66], Y. Sasaki[155], K. Sato[160], G. Sauvage[5,*], E. Sauvan[5], G. Savage[77], P. Savard[158,d], C. Sawyer[131], L. Sawyer[79,n], J. Saxon[31], C. Sbarra[20a], A. Sbrizzi[20a,20b], T. Scanlon[78], D. A. Scannicchio[163], M. Scarcella[150], V. Scarfone[37a,37b], J. Schaarschmidt[172], P. Schacht[101], D. Schaefer[30], R. Schaefer[42], J. Schaeffer[83], S. Schaepe[21], S. Schaetzel[58b], U. Schäfer[83], A. C. Schaffer[117], D. Schaile[100], R. D. Schamberger[148], V. Scharf[58a], V. A. Schegelsky[123], D. Scheirich[129], M. Schernau[163], C. Schiavi[50a,50b], C. Schillo[48], M. Schioppa[37a,37b], S. Schlenker[30], E. Schmidt[48], K. Schmieden[30], C. Schmitt[83], S. Schmitt[58b], S. Schmitt[42], B. Schneider[159a], Y. J. Schnellbach[74], U. Schnoor[44], L. Schoeffel[136], A. Schoening[58b], B. D. Schoenrock[90], E. Schopf[21], A. L. S. Schorlemmer[54], M. Schott[83], D. Schouten[159a], J. Schovancova[8], S. Schramm[49], M. Schreyer[174], C. Schroeder[83], N. Schuh[83], M. J. Schultens[21], H.-C. Schultz-Coulon[58a], H. Schulz[16], M. Schumacher[48], B. A. Schumm[137], Ph. Schune[136], C. Schwanenberger[84], A. Schwartzman[143], T. A. Schwarz[89], Ph. Schwegler[101], H. Schweiger[84], Ph. Schwemling[136], R. Schwienhorst[90], J. Schwindling[136], T. Schwindt[21], F. G. Sciacca[17], E. Scifo[117], G. Sciolla[23], F. Scuri[124a,124b], F. Scutti[21], J. Searcy[89], G. Sedov[42], E. Sedykh[123], P. Seema[21], S. C. Seidel[105], A. Seiden[137], F. Seifert[128], J. M. Seixas[24a], G. Sekhniaidze[104a], K. Sekhon[89], S. J. Sekula[40], D. M. Seliverstov[123,*], N. Semprini-Cesari[20a,20b], C. Serfon[30], L. Serin[117], L. Serkin[164a,164b], T. Serre[85], M. Sessa[134a,134b], R. Seuster[159a], H. Severini[113], T. Sfiligoj[75], F. Sforza[30], A. Sfyrla[30], E. Shabalina[54], M. Shamim[116], L. Y. Shan[33a], R. Shang[165], J. T. Shank[22], M. Shapiro[15], P. B. Shatalov[97], K. Shaw[164a,164b], S. M. Shaw[84], A. Shcherbakova[146a,146b], C. Y. Shehu[149], P. Sherwood[78], L. Shi[151,af], S. Shimizu[67], C. O. Shimmin[163], M. Shimojima[102], M. Shiyakova[65], A. Shmeleva[96], D. Shoaleh Saadi[95], M. J. Shochet[31], S. Shojaii[91a,91b], S. Shrestha[111], E. Shulga[98], M. A. Shupe[7], S. Shushkevich[42], P. Sicho[127], O. Sidiropoulou[174], D. Sidorov[114], A. Sidoti[20a,20b], F. Siegert[44], Dj. Sijacki[13], J. Silva[126a,126d], Y. Silver[153], S. B. Silverstein[146a], V. Simak[128], O. Simard[5], Lj. Simic[13], S. Simion[117], E. Simioni[83], B. Simmons[78], D. Simon[34], R. Simoniello[91a,91b], P. Sinervo[158], N. B. Sinev[116], G. Siragusa[174], A. N. Sisakyan[65,*], S. Yu. Sivoklokov[99], J. Sjölin[146a,146b], T. B. Sjursen[14], M. B. Skinner[72], H. P. Skottowe[57], P. Skubic[113], M. Slater[18], T. Slavicek[128], M. Slawinska[107], K. Sliwa[161], V. Smakhtin[172], B. H. Smart[46], L. Smestad[14], S. Yu. Smirnov[98], Y. Smirnov[98],

L. N. Smirnova[99,ag], O. Smirnova[81], M. N. K. Smith[35], R. W. Smith[35], M. Smizanska[72], K. Smolek[128], A. A. Snesarev[96], G. Snidero[76], S. Snyder[25], R. Sobie[169,k], F. Socher[44], A. Soffer[153], D. A. Soh[151,af], C. A. Solans[30], M. Solar[128], J. Solc[128], E. Yu. Soldatov[98], U. Soldevila[167], A. A. Solodkov[130], A. Soloshenko[65], O. V. Solovyanov[130], V. Solovyev[123], P. Sommer[48], H. Y. Song[33b], N. Soni[1], A. Sood[15], A. Sopczak[128], B. Sopko[128], V. Sopko[128], V. Sorin[12], D. Sosa[58b], M. Sosebee[8], C. L. Sotiropoulou[124a,124b], R. Soualah[164a,164c], A. M. Soukharev[109,c], D. South[42], B. C. Sowden[77], S. Spagnolo[73a,73b], M. Spalla[124a,124b], F. Spanò[77], W. R. Spearman[57], F. Spettel[101], R. Spighi[20a], G. Spigo[30], L. A. Spiller[88], M. Spousta[129], T. Spreitzer[158], R. D. St. Denis[53,*], S. Staerz[44], J. Stahlman[122], R. Stamen[58a], S. Stamm[16], E. Stanecka[39], C. Stanescu[134a], M. Stanescu-Bellu[42], M. M. Stanitzki[42], S. Stapnes[119], E. A. Starchenko[130], J. Stark[55], P. Staroba[127], P. Starovoitov[42], R. Staszewski[39], P. Stavina[144a,*], P. Steinberg[25], B. Stelzer[142], H. J. Stelzer[30], O. Stelzer-Chilton[159a], H. Stenzel[52], S. Stern[101], G. A. Stewart[53], J. A. Stillings[21], M. C. Stockton[87], M. Stoebe[87], G. Stoicea[26a], P. Stolte[54], S. Stonjek[101], A. R. Stradling[8], A. Straessner[44], M. E. Stramaglia[17], J. Strandberg[147], S. Strandberg[146a,146b], A. Strandlie[119], E. Strauss[143], M. Strauss[113], P. Strizenec[144b], R. Ströhmer[174], D. M. Strom[116], R. Stroynowski[40], A. Strubig[106], S. A. Stucci[17], B. Stugu[14], N. A. Styles[42], D. Su[143], J. Su[125], R. Subramaniam[79], A. Succurro[12], Y. Sugaya[118], C. Suhr[108], M. Suk[128], V. V. Sulin[96], S. Sultansoy[4c], T. Sumida[68], S. Sun[57], X. Sun[33a], J. E. Sundermann[48], K. Suruliz[149], G. Susinno[37a,37b], M. R. Sutton[149], S. Suzuki[66], Y. Suzuki[66], M. Svatos[127], S. Swedish[168], M. Swiatlowski[143], I. Sykora[144a], T. Sykora[129], D. Ta[90], C. Taccini[134a,134b], K. Tackmann[42], J. Taenzer[158], A. Taffard[163], R. Tafirout[159a], N. Taiblum[153], H. Takai[25], R. Takashima[69], H. Takeda[67], T. Takeshita[140], Y. Takubo[66], M. Talby[85], A. A. Talyshev[109,c], J. Y. C. Tam[174], K. G. Tan[88], J. Tanaka[155], R. Tanaka[117], S. Tanaka[66], B. B. Tannenwald[111], N. Tannoury[21], S. Tapprogge[83], S. Tarem[152], F. Tarrade[29], G. F. Tartarelli[91a], P. Tas[129], M. Tasevsky[127], T. Tashiro[68], E. Tassi[37a,37b], A. Tavares Delgado[126a,126b], Y. Tayalati[135d], F. E. Taylor[94], G. N. Taylor[88], W. Taylor[159b], F. A. Teischinger[30], M. Teixeira Dias Castanheira[76], P. Teixeira-Dias[77], K. K. Temming[48], H. Ten Kate[30], P. K. Teng[151], J. J. Teoh[118], F. Tepel[175], S. Terada[66], K. Terashi[155], J. Terron[82], S. Terzo[101], M. Testa[47], R. J. Teuscher[158,k], J. Therhaag[21], T. Theveneaux-Pelzer[34], J. P. Thomas[18], J. Thomas-Wilsker[77], E. N. Thompson[35], P. D. Thompson[18], R. J. Thompson[84], A. S. Thompson[53], L. A. Thomsen[176], E. Thomson[122], M. Thomson[28], R. P. Thun[89,*], M. J. Tibbetts[15], R. E. Ticse Torres[85], V. O. Tikhomirov[96,ah], Yu. A. Tikhonov[109,c], S. Timoshenko[98], E. Tiouchichine[85], P. Tipton[176], S. Tisserant[85], T. Todorov[5], S. Todorova-Nova[129], J. Tojo[70], S. Tokár[144a], K. Tokushuku[66], K. Tollefson[90], E. Tolley[57], L. Tomlinson[84], M. Tomoto[103], L. Tompkins[143,ai], K. Toms[105], E. Torrence[116], H. Torres[142], E. Torró Pastor[167], J. Toth[85,aj], F. Touchard[85], D. R. Tovey[139], T. Trefzger[174], L. Tremblet[30], A. Tricoli[30], I. M. Trigger[159a], S. Trincaz-Duvoid[80], M. F. Tripiana[12], W. Trischuk[158], B. Trocmé[55], C. Troncon[91a], M. Trottier-McDonald[15], M. Trovatelli[169], P. True[90], L. Truong[164a,164c], M. Trzebinski[39], A. Trzupek[39], C. Tsarouchas[30], J. C-L. Tseng[120], P. V. Tsiareshka[92], D. Tsionou[154], G. Tsipolitis[10], N. Tsirintanis[9], S. Tsiskaridze[12], V. Tsiskaridze[48], E. G. Tskhadadze[51a], I. I. Tsukerman[97], V. Tsulaia[15], S. Tsuno[66], D. Tsybychev[148], A. Tudorache[26a], V. Tudorache[26a], A. N. Tuna[122], S. A. Tupputi[20a,20b], S. Turchikhin[99,ag], D. Turecek[128], R. Turra[91a,91b], A. J. Turvey[40], P. M. Tuts[35], A. Tykhonov[49], M. Tylmad[146a,146b], M. Tyndel[131], I. Ueda[155], R. Ueno[29], M. Ughetto[146a,146b], M. Ugland[14], M. Uhlenbrock[21], F. Ukegawa[160], G. Unal[30], A. Undrus[25], G. Unel[163], F. C. Ungaro[48], Y. Unno[66], C. Unverdorben[100], J. Urban[144b], P. Urquijo[88], P. Urrejola[83], G. Usai[8], A. Usanova[62], L. Vacavant[85], V. Vacek[128], B. Vachon[87], C. Valderanis[83], N. Valencic[107], S. Valentinetti[20a,20b], A. Valero[167], L. Valery[12], S. Valkar[129], E. Valladolid Gallego[167], S. Vallecorsa[49], J. A. Valls Ferrer[167], W. Van Den Wollenberg[107], P. C. Van Der Deijl[107], R. van der Geer[107], H. van der Graaf[107], R. Van Der Leeuw[107], N. van Eldik[152], P. van Gemmeren[6], J. Van Nieuwkoop[142], I. van Vulpen[107], M. C. van Woerden[30], M. Vanadia[132a,132b], W. Vandelli[30], R. Vanguri[122], A. Vaniachine[6], F. Vannucci[80], G. Vardanyan[177], R. Vari[132a], E. W. Varnes[7], T. Varol[40], D. Varouchas[80], A. Vartapetian[8], K. E. Varvell[150], V. I. Vassilakopoulos[56], F. Vazeille[34], T. Vazquez Schroeder[87], J. Veatch[7], L. M. Veloce[158], F. Veloso[126a,126c], T. Velz[21], S. Veneziano[132a], A. Ventura[73a,73b], D. Ventura[86], M. Venturi[169], N. Venturi[158], A. Venturini[23], V. Vercesi[121a], M. Verducci[132a,132b], W. Verkerke[107], J. C. Vermeulen[107], A. Vest[44], M. C. Vetterli[142,d], O. Viazlo[81], I. Vichou[165], T. Vickey[139], O. E. Vickey Boeriu[139], G. H. A. Viehhauser[120], S. Viel[15], R. Vigne[62], M. Villa[20a,20b], M. Villaplana Perez[91a,91b], E. Vilucchi[47], M. G. Vincter[29], V. B. Vinogradov[65], I. Vivarelli[149], F. Vives Vaque[3], S. Vlachos[10], D. Vladoiu[100], M. Vlasak[128], M. Vogel[32a], P. Vokac[128], G. Volpi[124a,124b], M. Volpi[88], H. von der Schmitt[101], H. von Radziewski[48], E. von Toerne[21], V. Vorobel[129], K. Vorobev[98], M. Vos[167], R. Voss[30], J. H. Vossebeld[74], N. Vranjes[13], M. Vranjes Milosavljevic[13], V. Vrba[127], M. Vreeswijk[107], R. Vuillermet[30], I. Vukotic[31], Z. Vykydal[128], P. Wagner[21], W. Wagner[175], H. Wahlberg[71], S. Wahrmund[44], J. Wakabayashi[103], J. Walder[72], R. Walker[100], W. Walkowiak[141], C. Wang[151], F. Wang[173], H. Wang[15], H. Wang[40], J. Wang[42], J. Wang[33a], K. Wang[87], R. Wang[6], S. M. Wang[151], T. Wang[21], X. Wang[176], C. Wanotayaroj[116], A. Warburton[87], C. P. Ward[28], D. R. Wardrope[78], M. Warsinsky[48], A. Washbrook[46], C. Wasicki[42], P. M. Watkins[18], A. T. Watson[18], I. J. Watson[150], M. F. Watson[18], G. Watts[138], S. Watts[84], B. M. Waugh[78], S. Webb[84], M. S. Weber[17], S. W. Weber[174], J. S. Webster[31], A. R. Weidberg[120], B. Weinert[61], J. Weingarten[54], C. Weiser[48], H. Weits[107],

P. S. Wells[30], T. Wenaus[25], T. Wengler[30], S. Wenig[30], N. Wermes[21], M. Werner[48], P. Werner[30], M. Wessels[58a], J. Wetter[161], K. Whalen[116], A. M. Wharton[72], A. White[8], M. J. White[1], R. White[32b], S. White[124a,124b], D. Whiteson[163], F. J. Wickens[131], W. Wiedenmann[173], M. Wielers[131], P. Wienemann[21], C. Wiglesworth[36], L. A. M. Wiik-Fuchs[21], A. Wildauer[101], H. G. Wilkens[30], H. H. Williams[122], S. Williams[107], C. Willis[90], S. Willocq[86], A. Wilson[89], J. A. Wilson[18], I. Wingerter-Seez[5], F. Winklmeier[116], B. T. Winter[21], M. Wittgen[143], J. Wittkowski[100], S. J. Wollstadt[83], M. W. Wolter[39], H. Wolters[126a,126c], B. K. Wosiek[39], J. Wotschack[30], M. J. Woudstra[84], K. W. Wozniak[39], M. Wu[55], M. Wu[31], S. L. Wu[173], X. Wu[49], Y. Wu[89], T. R. Wyatt[84], B. M. Wynne[46], S. Xella[36], D. Xu[33a], L. Xu[33b,ak], B. Yabsley[150], S. Yacoob[145b,al], R. Yakabe[67], M. Yamada[66], Y. Yamaguchi[118], A. Yamamoto[66], S. Yamamoto[155], T. Yamanaka[155], K. Yamauchi[103], Y. Yamazaki[67], Z. Yan[22], H. Yang[33e], H. Yang[173], Y. Yang[151], W-M. Yao[15], Y. Yasu[66], E. Yatsenko[5], K. H. Yau Wong[21], J. Ye[40], S. Ye[25], I. Yeletskikh[65], A. L. Yen[57], E. Yildirim[42], K. Yorita[171], R. Yoshida[6], K. Yoshihara[122], C. Young[143], C. J. S. Young[30], S. Youssef[22], D. R. Yu[15], J. Yu[8], J. M. Yu[89], J. Yu[114], L. Yuan[67], A. Yurkewicz[108], I. Yusuff[28,am], B. Zabinski[39], R. Zaidan[63], A. M. Zaitsev[130,ab], J. Zalieckas[14], A. Zaman[148], S. Zambito[57], L. Zanello[132a,132b], D. Zanzi[88], C. Zeitnitz[175], M. Zeman[128], A. Zemla[38a], K. Zengel[23], O. Zenin[130], T. Ženiš[144a], D. Zerwas[117], D. Zhang[89], F. Zhang[173], H. Zhang[33c], J. Zhang[6], L. Zhang[48], R. Zhang[33b], X. Zhang[33d], Z. Zhang[117], X. Zhao[40], Y. Zhao[33d,117], Z. Zhao[33b], A. Zhemchugov[65], J. Zhong[120], B. Zhou[89], C. Zhou[45], L. Zhou[35], L. Zhou[40], N. Zhou[163], C. G. Zhu[33d], H. Zhu[33a], J. Zhu[89], Y. Zhu[33b], X. Zhuang[33a], K. Zhukov[96], A. Zibell[174], D. Zieminska[61], N. I. Zimine[65], C. Zimmermann[83], S. Zimmermann[48], Z. Zinonos[54], M. Zinser[83], M. Ziolkowski[141], L. Živković[13], G. Zobernig[173], A. Zoccoli[20a,20b], M. zur Nedden[16], G. Zurzolo[104a,104b], L. Zwalinski[30]

[1] Department of Physics, University of Adelaide, Adelaide, Australia
[2] Physics Department, SUNY Albany, Albany, NY, USA
[3] Department of Physics, University of Alberta, Edmonton, AB, Canada
[4] [(a)]Department of Physics, Ankara University, Ankara, Turkey; [(b)]Istanbul Aydin University, Istanbul, Turkey; [(c)]Division of Physics, TOBB University of Economics and Technology, Ankara, Turkey
[5] LAPP, CNRS/IN2P3 and Université Savoie Mont Blanc, Annecy-le-Vieux, France
[6] High Energy Physics Division, Argonne National Laboratory, Argonne, IL, USA
[7] Department of Physics, University of Arizona, Tucson, AZ, USA
[8] Department of Physics, The University of Texas at Arlington, Arlington, TX, USA
[9] Physics Department, University of Athens, Athens, Greece
[10] Physics Department, National Technical University of Athens, Zografou, Greece
[11] Institute of Physics, Azerbaijan Academy of Sciences, Baku, Azerbaijan
[12] Institut de Física d'Altes Energies and Departament de Física de la Universitat Autònoma de Barcelona, Barcelona, Spain
[13] Institute of Physics, University of Belgrade, Belgrade, Serbia
[14] Department for Physics and Technology, University of Bergen, Bergen, Norway
[15] Physics Division, Lawrence Berkeley National Laboratory and University of California, Berkeley, CA, USA
[16] Department of Physics, Humboldt University, Berlin, Germany
[17] Albert Einstein Center for Fundamental Physics and Laboratory for High Energy Physics, University of Bern, Bern, Switzerland
[18] School of Physics and Astronomy, University of Birmingham, Birmingham, UK
[19] [(a)]Department of Physics, Bogazici University, Istanbul, Turkey; [(b)]Department of Physics Engineering, Gaziantep University, Gaziantep, Turkey; [(c)]Department of Physics, Dogus University, Gaziantep, Turkey
[20] [(a)]INFN Sezione di Bologna, Bologna, Italy; [(b)]Dipartimento di Fisica e Astronomia, Università di Bologna, Bologna, Italy
[21] Physikalisches Institut, University of Bonn, Bonn, Germany
[22] Department of Physics, Boston University, Boston, MA, USA
[23] Department of Physics, Brandeis University, Waltham, MA, USA
[24] [(a)]Universidade Federal do Rio De Janeiro COPPE/EE/IF, Rio de Janeiro, Brazil; [(b)]Electrical Circuits Department, Federal University of Juiz de Fora (UFJF), Juiz de Fora, Brazil; [(c)]Federal University of Sao Joao del Rei (UFSJ), Sao Joao del Rei, Brazil; [(d)]Instituto de Fisica, Universidade de Sao Paulo, São Paulo, Brazil
[25] Physics Department, Brookhaven National Laboratory, Upton, NY, USA

[26] [(a)]National Institute of Physics and Nuclear Engineering, Bucharest, Romania; [(b)]Physics Department, National Institute for Research and Development of Isotopic and Molecular Technologies, Cluj Napoca, Romania; [(c)]University Politehnica Bucharest, Bucharest, Romania; [(d)]West University in Timisoara, Timisoara, Romania
[27] Departamento de Física, Universidad de Buenos Aires, Buenos Aires, Argentina
[28] Cavendish Laboratory, University of Cambridge, Cambridge, UK
[29] Department of Physics, Carleton University, Ottawa, ON, Canada
[30] CERN, Geneva, Switzerland
[31] Enrico Fermi Institute, University of Chicago, Chicago, IL, USA
[32] [(a)]Departamento de Física, Pontificia Universidad Católica de Chile, Santiago, Chile; [(b)]Departamento de Física, Universidad Técnica Federico Santa María, Valparaiso, Chile
[33] [(a)]Institute of High Energy Physics, Chinese Academy of Sciences, Beijing, China; [(b)]Department of Modern Physics, University of Science and Technology of China, Hefei, Anhui, China; [(c)]Department of Physics, Nanjing University, Nanjing, Jiangsu, China; [(d)]School of Physics, Shandong University, Shandong, China; [(e)]Shanghai Key Laboratory for Particle Physics and Cosmology, Department of Physics and Astronomy, Shanghai Jiao Tong University, Shanghai, China; [(f)]Physics Department, Tsinghua University, Beijing 100084, China
[34] Laboratoire de Physique Corpusculaire, Clermont Université and Université Blaise Pascal and CNRS/IN2P3, Clermont-Ferrand, France
[35] Nevis Laboratory, Columbia University, Irvington, NY, USA
[36] Niels Bohr Institute, University of Copenhagen, Copenhagen, Denmark
[37] [(a)]INFN Gruppo Collegato di Cosenza, Laboratori Nazionali di Frascati, Frascati, Italy; [(b)]Dipartimento di Fisica, Università della Calabria, Rende, Italy
[38] [(a)]AGH University of Science and Technology, Faculty of Physics and Applied Computer Science, Kraków, Poland; [(b)]Marian Smoluchowski Institute of Physics, Jagiellonian University, Kraków, Poland
[39] Institute of Nuclear Physics, Polish Academy of Sciences, Kraków, Poland
[40] Physics Department, Southern Methodist University, Dallas, TX, USA
[41] Physics Department, University of Texas at Dallas, Richardson, TX, USA
[42] DESY, Hamburg and Zeuthen, Germany
[43] Institut für Experimentelle Physik IV, Technische Universität Dortmund, Dortmund, Germany
[44] Institut für Kern- und Teilchenphysik, Technische Universität Dresden, Dresden, Germany
[45] Department of Physics, Duke University, Durham, NC, USA
[46] SUPA-School of Physics and Astronomy, University of Edinburgh, Edinburgh, UK
[47] INFN Laboratori Nazionali di Frascati, Frascati, Italy
[48] Fakultät für Mathematik und Physik, Albert-Ludwigs-Universität, Freiburg, Germany
[49] Section de Physique, Université de Genève, Geneva, Switzerland
[50] [(a)]INFN Sezione di Genova, Genoa, Italy; [(b)]Dipartimento di Fisica, Università di Genova, Genoa, Italy
[51] [(a)]E. Andronikashvili Institute of Physics, Iv. Javakhishvili Tbilisi State University, Tbilisi, Georgia; [(b)]High Energy Physics Institute, Tbilisi State University, Tbilisi, Georgia
[52] II Physikalisches Institut, Justus-Liebig-Universität Giessen, Giessen, Germany
[53] SUPA-School of Physics and Astronomy, University of Glasgow, Glasgow, UK
[54] II Physikalisches Institut, Georg-August-Universität, Göttingen, Germany
[55] Laboratoire de Physique Subatomique et de Cosmologie, Université Grenoble-Alpes, CNRS/IN2P3, Grenoble, France
[56] Department of Physics, Hampton University, Hampton, VA, USA
[57] Laboratory for Particle Physics and Cosmology, Harvard University, Cambridge, MA, USA
[58] [(a)]Kirchhoff-Institut für Physik, Ruprecht-Karls-Universität Heidelberg, Heidelberg, Germany; [(b)]Physikalisches Institut, Ruprecht-Karls-Universität Heidelberg, Heidelberg, Germany; [(c)]ZITI Institut für technische Informatik, Ruprecht-Karls-Universität Heidelberg, Mannheim, Germany
[59] Faculty of Applied Information Science, Hiroshima Institute of Technology, Hiroshima, Japan
[60] [(a)]Department of Physics, The Chinese University of Hong Kong, Shatin, NT, Hong Kong; [(b)]Department of Physics, The University of Hong Kong, Hong Kong, Hong Kong; [(c)]Department of Physics, The Hong Kong University of Science and Technology, Clear Water Bay, Kowloon, Hong Kong, China
[61] Department of Physics, Indiana University, Bloomington, IN, USA
[62] Institut für Astro- und Teilchenphysik, Leopold-Franzens-Universität, Innsbruck, Austria
[63] University of Iowa, Iowa City, IA, USA

[64] Department of Physics and Astronomy, Iowa State University, Ames, IA, USA
[65] Joint Institute for Nuclear Research, JINR Dubna, Dubna, Russia
[66] KEK, High Energy Accelerator Research Organization, Tsukuba, Japan
[67] Graduate School of Science, Kobe University, Kobe, Japan
[68] Faculty of Science, Kyoto University, Kyoto, Japan
[69] Kyoto University of Education, Kyoto, Japan
[70] Department of Physics, Kyushu University, Fukuoka, Japan
[71] Instituto de Física La Plata, Universidad Nacional de La Plata and CONICET, La Plata, Argentina
[72] Physics Department, Lancaster University, Lancaster, UK
[73] [(a)]INFN Sezione di Lecce, Lecce, Italy; [(b)]Dipartimento di Matematica e Fisica, Università del Salento, Lecce, Italy
[74] Oliver Lodge Laboratory, University of Liverpool, Liverpool, UK
[75] Department of Physics, Jožef Stefan Institute and University of Ljubljana, Ljubljana, Slovenia
[76] School of Physics and Astronomy, Queen Mary University of London, London, UK
[77] Department of Physics, Royal Holloway University of London, Surrey, UK
[78] Department of Physics and Astronomy, University College London, London, UK
[79] Louisiana Tech University, Ruston, LA, USA
[80] Laboratoire de Physique Nucléaire et de Hautes Energies, UPMC and Université Paris-Diderot and CNRS/IN2P3, Paris, France
[81] Fysiska institutionen, Lunds universitet, Lund, Sweden
[82] Departamento de Fisica Teorica C-15, Universidad Autonoma de Madrid, Madrid, Spain
[83] Institut für Physik, Universität Mainz, Mainz, Germany
[84] School of Physics and Astronomy, University of Manchester, Manchester, UK
[85] CPPM, Aix-Marseille Université and CNRS/IN2P3, Marseille, France
[86] Department of Physics, University of Massachusetts, Amherst, MA, USA
[87] Department of Physics, McGill University, Montreal, QC, Canada
[88] School of Physics, University of Melbourne, Melbourne, VIC, Australia
[89] Department of Physics, The University of Michigan, Ann Arbor, MI, USA
[90] Department of Physics and Astronomy, Michigan State University, East Lansing, MI, USA
[91] [(a)]INFN Sezione di Milano, Milan, Italy; [(b)]Dipartimento di Fisica, Università di Milano, Milan, Italy
[92] B.I. Stepanov Institute of Physics, National Academy of Sciences of Belarus, Minsk, Republic of Belarus
[93] National Scientific and Educational Centre for Particle and High Energy Physics, Minsk, Republic of Belarus
[94] Department of Physics, Massachusetts Institute of Technology, Cambridge, MA, USA
[95] Group of Particle Physics, University of Montreal, Montreal, QC, Canada
[96] P.N. Lebedev Institute of Physics, Academy of Sciences, Moscow, Russia
[97] Institute for Theoretical and Experimental Physics (ITEP), Moscow, Russia
[98] National Research Nuclear University MEPhI, Moscow, Russia
[99] D.V. Skobeltsyn Institute of Nuclear Physics, M.V. Lomonosov Moscow State University, Moscow, Russia
[100] Fakultät für Physik, Ludwig-Maximilians-Universität München, Munich, Germany
[101] Max-Planck-Institut für Physik (Werner-Heisenberg-Institut), Munich, Germany
[102] Nagasaki Institute of Applied Science, Nagasaki, Japan
[103] Graduate School of Science and Kobayashi-Maskawa Institute, Nagoya University, Nagoya, Japan
[104] [(a)]INFN Sezione di Napoli, Naples, Italy; [(b)]Dipartimento di Fisica, Università di Napoli, Naples, Italy
[105] Department of Physics and Astronomy, University of New Mexico, Albuquerque, NM, USA
[106] Institute for Mathematics, Astrophysics and Particle Physics, Radboud University Nijmegen/Nikhef, Nijmegen, The Netherlands
[107] Nikhef National Institute for Subatomic Physics and University of Amsterdam, Amsterdam, The Netherlands
[108] Department of Physics, Northern Illinois University, De Kalb, IL, USA
[109] Budker Institute of Nuclear Physics, SB RAS, Novosibirsk, Russia
[110] Department of Physics, New York University, New York, NY, USA
[111] Ohio State University, Columbus, OH, USA
[112] Faculty of Science, Okayama University, Okayama, Japan
[113] Homer L. Dodge Department of Physics and Astronomy, University of Oklahoma, Norman, OK, USA
[114] Department of Physics, Oklahoma State University, Stillwater, OK, USA

[115] Palacký University, RCPTM, Olomouc, Czech Republic
[116] Center for High Energy Physics, University of Oregon, Eugene, OR, USA
[117] LAL, Université Paris-Sud and CNRS/IN2P3, Orsay, France
[118] Graduate School of Science, Osaka University, Osaka, Japan
[119] Department of Physics, University of Oslo, Oslo, Norway
[120] Department of Physics, Oxford University, Oxford, UK
[121] [(a)]INFN Sezione di Pavia, Pavia, Italy; [(b)]Dipartimento di Fisica, Università di Pavia, Pavia, Italy
[122] Department of Physics, University of Pennsylvania, Philadelphia, PA, USA
[123] National Research Centre "Kurchatov Institute" B.P.Konstantinov, Petersburg Nuclear Physics Institute, St. Petersburg, Russia
[124] [(a)]INFN Sezione di Pisa, Pisa, Italy; [(b)]Dipartimento di Fisica E. Fermi, Università di Pisa, Pisa, Italy
[125] Department of Physics and Astronomy, University of Pittsburgh, Pittsburgh, PA, USA
[126] [(a)]Laboratório de Instrumentação e Física Experimental de Partículas-LIP, Lisbon, Portugal; [(b)]Faculdade de Ciências, Universidade de Lisboa, Lisbon, Portugal; [(c)]Department of Physics, University of Coimbra, Coimbra, Portugal; [(d)]Centro de Física Nuclear da Universidade de Lisboa, Lisbon, Portugal; [(e)]Departamento de Fisica, Universidade do Minho, Braga, Portugal; [(f)]Departamento de Fisica Teorica y del Cosmos and CAFPE, Universidad de Granada, Granada, Spain; [(g)]Dep Fisica and CEFITEC of Faculdade de Ciencias e Tecnologia, Universidade Nova de Lisboa, Caparica, Portugal
[127] Institute of Physics, Academy of Sciences of the Czech Republic, Prague, Czech Republic
[128] Czech Technical University in Prague, Prague, Czech Republic
[129] Faculty of Mathematics and Physics, Charles University in Prague, Prague, Czech Republic
[130] State Research Center Institute for High Energy Physics, Protvino, Russia
[131] Particle Physics Department, Rutherford Appleton Laboratory, Didcot, UK
[132] [(a)]INFN Sezione di Roma, Rome, Italy; [(b)]Dipartimento di Fisica, Sapienza Università di Roma, Rome, Italy
[133] [(a)]INFN Sezione di Roma Tor Vergata, Rome, Italy; [(b)]Dipartimento di Fisica, Università di Roma Tor Vergata, Rome, Italy
[134] [(a)]INFN Sezione di Roma Tre, Rome, Italy; [(b)]Dipartimento di Matematica e Fisica, Università Roma Tre, Rome, Italy
[135] [(a)]Faculté des Sciences Ain Chock, Réseau Universitaire de Physique des Hautes Energies-Université Hassan II, Casablanca, Morocco; [(b)]Centre National de l'Energie des Sciences Techniques Nucleaires, Rabat, Morocco; [(c)]Faculté des Sciences Semlalia, Université Cadi Ayyad, LPHEA-Marrakech, Marrakech, Morocco; [(d)]Faculté des Sciences, Université Mohamed Premier and LPTPM, Oujda, Morocco; [(e)]Faculté des Sciences, Université Mohammed V-Agdal, Rabat, Morocco
[136] DSM/IRFU (Institut de Recherches sur les Lois Fondamentales de l'Univers), CEA Saclay (Commissariat à l'Energie Atomique et aux Energies Alternatives), Gif-sur-Yvette, France
[137] Santa Cruz Institute for Particle Physics, University of California Santa Cruz, Santa Cruz, CA, USA
[138] Department of Physics, University of Washington, Seattle, WA, USA
[139] Department of Physics and Astronomy, University of Sheffield, Sheffield, UK
[140] Department of Physics, Shinshu University, Nagano, Japan
[141] Fachbereich Physik, Universität Siegen, Siegen, Germany
[142] Department of Physics, Simon Fraser University, Burnaby, BC, Canada
[143] SLAC National Accelerator Laboratory, Stanford, CA, USA
[144] [(a)]Faculty of Mathematics, Physics and Informatics, Comenius University, Bratislava, Slovak Republic; [(b)]Department of Subnuclear Physics, Institute of Experimental Physics of the Slovak Academy of Sciences, Kosice, Slovak Republic
[145] [(a)]Department of Physics, University of Cape Town, Cape Town, South Africa; [(b)]Department of Physics, University of Johannesburg, Johannesburg, South Africa; [(c)]School of Physics, University of the Witwatersrand, Johannesburg, South Africa
[146] [(a)]Department of Physics, Stockholm University, Stockholm, Sweden; [(b)]The Oskar Klein Centre, Stockholm, Sweden
[147] Physics Department, Royal Institute of Technology, Stockholm, Sweden
[148] Departments of Physics and Astronomy and Chemistry, Stony Brook University, Stony Brook, NY, USA
[149] Department of Physics and Astronomy, University of Sussex, Brighton, UK
[150] School of Physics, University of Sydney, Sydney, Australia
[151] Institute of Physics, Academia Sinica, Taipei, Taiwan
[152] Department of Physics, Technion: Israel Institute of Technology, Haifa, Israel

[153] Raymond and Beverly Sackler School of Physics and Astronomy, Tel Aviv University, Tel Aviv, Israel
[154] Department of Physics, Aristotle University of Thessaloniki, Thessaloníki, Greece
[155] International Center for Elementary Particle Physics and Department of Physics, The University of Tokyo, Tokyo, Japan
[156] Graduate School of Science and Technology, Tokyo Metropolitan University, Tokyo, Japan
[157] Department of Physics, Tokyo Institute of Technology, Tokyo, Japan
[158] Department of Physics, University of Toronto, Toronto, ON, Canada
[159] [(a)]TRIUMF, Vancouver, BC, Canada; [(b)]Department of Physics and Astronomy, York University, Toronto, ON, Canada
[160] Faculty of Pure and Applied Sciences, University of Tsukuba, Tsukuba, Japan
[161] Department of Physics and Astronomy, Tufts University, Medford, MA, USA
[162] Centro de Investigaciones, Universidad Antonio Narino, Bogotá, Colombia
[163] Department of Physics and Astronomy, University of California Irvine, Irvine, CA, USA
[164] [(a)]INFN Gruppo Collegato di Udine, Sezione di Trieste, Udine, Italy; [(b)]ICTP, Trieste, Italy; [(c)]Dipartimento di Chimica Fisica e Ambiente, Università di Udine, Udine, Italy
[165] Department of Physics, University of Illinois, Urbana, IL, USA
[166] Department of Physics and Astronomy, University of Uppsala, Uppsala, Sweden
[167] Instituto de Física Corpuscular (IFIC) and Departamento de Física Atómica, Molecular y Nuclear and Departamento de Ingeniería Electrónica and Instituto de Microelectrónica de Barcelona (IMB-CNM), University of Valencia and CSIC, Valencia, Spain
[168] Department of Physics, University of British Columbia, Vancouver, BC, Canada
[169] Department of Physics and Astronomy, University of Victoria, Victoria, BC, Canada
[170] Department of Physics, University of Warwick, Coventry, UK
[171] Waseda University, Tokyo, Japan
[172] Department of Particle Physics, The Weizmann Institute of Science, Rehovot, Israel
[173] Department of Physics, University of Wisconsin, Madison, WI, USA
[174] Fakultät für Physik und Astronomie, Julius-Maximilians-Universität, Würzburg, Germany
[175] Fachbereich C Physik, Bergische Universität Wuppertal, Wuppertal, Germany
[176] Department of Physics, Yale University, New Haven, CT, USA
[177] Yerevan Physics Institute, Yerevan, Armenia
[178] Centre de Calcul de l'Institut National de Physique Nucléaire et de Physique des Particules (IN2P3), Villeurbanne, France

[a] Also at Department of Physics, King's College London, London, UK
[b] Also at Institute of Physics, Azerbaijan Academy of Sciences, Baku, Azerbaijan
[c] Also at Novosibirsk State University, Novosibirsk, Russia
[d] Also at TRIUMF, Vancouver, BC, Canada
[e] Also at Department of Physics, California State University, Fresno, CA, USA
[f] Also at Department of Physics, University of Fribourg, Fribourg, Switzerland
[g] Also at Departamento de Fisica e Astronomia, Faculdade de Ciencias, Universidade do Porto, Porto, Portugal
[h] Also at Tomsk State University, Tomsk, Russia
[i] Also at CPPM, Aix-Marseille Université and CNRS/IN2P3, Marseille, France
[j] Also at Universita di Napoli Parthenope, Naples, Italy
[k] Also at Institute of Particle Physics (IPP), Waterloo, Canada
[l] Also at Particle Physics Department, Rutherford Appleton Laboratory, Didcot, UK
[m] Also at Department of Physics, St. Petersburg State Polytechnical University, St. Petersburg, Russia
[n] Also at Louisiana Tech University, Ruston, LA, USA
[o] Also at Institucio Catalana de Recerca i Estudis Avancats, ICREA, Barcelona, Spain
[p] Also at Department of Physics, National Tsing Hua University, Taiwan
[q] Also at Department of Physics, The University of Texas at Austin, Austin, TX, USA
[r] Also at Institute of Theoretical Physics, Ilia State University, Tbilisi, Georgia
[s] Also at CERN, Geneva, Switzerland
[t] Also at Georgian Technical University (GTU), Tbilisi, Georgia
[u] Also at Ochadai Academic Production, Ochanomizu University, Tokyo, Japan
[v] Also at Manhattan College, New York, NY, USA

[w] Also at Hellenic Open University, Patras, Greece
[x] Also at Institute of Physics, Academia Sinica, Taipei, Taiwan
[y] Also at LAL, Université Paris-Sud and CNRS/IN2P3, Orsay, France
[z] Also at Academia Sinica Grid Computing, Institute of Physics, Academia Sinica, Taipei, Taiwan
[aa] Also at School of Physics, Shandong University, Shandong, China
[ab] Also at Moscow Institute of Physics and Technology State University, Dolgoprudny, Russia
[ac] Also at Section de Physique, Université de Genève, Geneva, Switzerland
[ad] Also at International School for Advanced Studies (SISSA), Trieste, Italy
[ae] Also at Department of Physics and Astronomy, University of South Carolina, Columbia, SC, USA
[af] Also at School of Physics and Engineering, Sun Yat-sen University, Guangzhou, China
[ag] Also at Faculty of Physics, M.V.Lomonosov Moscow State University, Moscow, Russia
[ah] Also at National Research Nuclear University MEPhI, Moscow, Russia
[ai] Also at Department of Physics, Stanford University, Stanford, CA, USA
[aj] Also at Institute for Particle and Nuclear Physics, Wigner Research Centre for Physics, Budapest, Hungary
[ak] Also at Department of Physics, The University of Michigan, Ann Arbor, MI, USA
[al] Also at Discipline of Physics, University of KwaZulu-Natal, Durban, South Africa
[am] Also at University of Malaya, Department of Physics, Kuala Lumpur, Malaysia

* Deceased

Evidence of $W\gamma\gamma$ Production in pp Collisions at $\sqrt{s} = 8$ TeV and Limits on Anomalous Quartic Gauge Couplings with the ATLAS Detector

G. Aad *et al.*[*]
(ATLAS Collaboration)

(Received 11 March 2015; published 16 July 2015)

This Letter reports evidence of triple gauge boson production $pp \to W(\ell\nu)\gamma\gamma + X$, which is accessible for the first time with the 8 TeV LHC data set. The fiducial cross section for this process is measured in a data sample corresponding to an integrated luminosity of 20.3 fb^{-1}, collected by the ATLAS detector in 2012. Events are selected using the W boson decay to $e\nu$ or $\mu\nu$ as well as requiring two isolated photons. The measured cross section is used to set limits on anomalous quartic gauge couplings in the high diphoton mass region.

DOI: 10.1103/PhysRevLett.115.031802 PACS numbers: 12.15.Ji, 13.85.Qk, 14.70.Bh, 14.70.Fm

In the standard model (SM), the self-couplings of the electroweak gauge bosons are specified by the non-Abelian $SU(2) \times U(1)$ structure of the electroweak sector. Since any deviation in the self-couplings from this expectation indicates the presence of new physics phenomena at unprobed energy scales, the measurement of the production of multiple electroweak gauge bosons represents an important test of the SM. This Letter presents a measurement of the triboson production cross section, discussed in Ref. [1], where the W boson decays into $e\nu$ or $\mu\nu$ $[W(\ell\nu)\gamma\gamma]$, and its sensitivity to anomalous quartic gauge couplings (AQGCs) $WW\gamma\gamma$. Such final states mainly come from events where the W boson is produced in the hard interaction between the two partons, and the photons either originate from initial or final state radiation processes, or from triple or quartic gauge vertices together with the W boson. The inclusive and exclusive cross sections are both measured. The inclusive case has no restriction on the $W\gamma\gamma$ recoil system, whereas the exclusive case includes a veto on events containing one or more jets. Limits on AQGC parameters are set in the exclusive phase space with a diphoton mass larger than 300 GeV. Total and differential cross sections for the diboson production processes WW, WZ, ZZ, $W\gamma$, and $Z\gamma$ have been reported previously by the ATLAS [2–5], CMS [6–8], D0 [9–11], and CDF [12–14] Collaborations, including limits on anomalous triple gauge boson couplings. Limits have been set on AQGCs by ATLAS [15], CMS [16,17], the LEP experiments [18–21], and D0 [22].

ATLAS [23] is a multipurpose detector composed of an inner tracking detector (ID) surrounded by a thin superconducting solenoid providing a 2 T axial magnetic field, electromagnetic (EM) and hadronic calorimeters, and a muon spectrometer (MS) immersed in the magnetic field produced by a system of superconducting toroids. Events in this analysis are selected with triggers requiring the presence of one muon with a transverse momentum (p_T) of more than 18 GeV and two electromagnetic objects with a transverse energy (E_T) of more than 10 GeV each, with an efficiency of about 80% [24], or three $E_T > 15$ GeV electromagnetic objects with an efficiency of more than 95% [25,26]. After applying data quality requirements, the data set corresponds to a total integrated luminosity of 20.3 ± 0.6 fb^{-1} [27].

The main backgrounds to the $W(\ell\nu)\gamma\gamma$ process originate from processes with jets identified as photons or leptons, referred to as fakes hereafter. Data-driven techniques are used to estimate fakes, whereas Monte Carlo (MC) simulation is used to estimate background sources with prompt leptons and photons and for the signal. The SHERPA 1.4.1 generator [28–31] is used to model the signal with up to three partons in the final state. SHERPA was also used to simulate the $Z\gamma$, $Z\gamma\gamma$, WZ, and $W(\tau\nu)\gamma\gamma$ backgrounds. For the $Z\gamma$ background, the agreement between data and the MC prediction was assessed in Z-enriched control regions. The $t\bar{t}$, single top, and WW processes are modeled by MC@NLO 4.02 [32,33], interfaced to HERWIG 6.520 [34] for parton showering and fragmentation processes and to JIMMY 4.30 [35] for underlying event simulation. The POWHEG [36] generator is used to simulate ZZ production, interfaced to PYTHIA 8.163 [37] for parton showering and fragmentation. The CT10 parton distribution function (PDF) set [38] is used for all SHERPA, MC@NLO, and POWHEG samples. The standard ATLAS detector simulation [39] based on GEANT4 [40] is used. It includes multiple proton-proton interactions per bunch crossing (pileup) as observed in data.

The $W(\ell\nu)\gamma\gamma$ candidate events contain an isolated lepton and missing transverse momentum (E_T^{miss}) from the undetected neutrino of the leptonic W decay, and two isolated

[*]Full author list given at the end of the article.

Published by the American Physical Society under the terms of the Creative Commons Attribution 3.0 License. Further distribution of this work must maintain attribution to the author(s) and the published article's title, journal citation, and DOI.

 © 2015 CERN, for the ATLAS Collaboration

photons (including also photons that have converted in electron-positron pairs within the ID volume). Muon candidates are identified, within pseudorapidity [26] $|\eta| < 2.4$, by associating complete tracks or track segments in the MS with tracks in the ID [41]. Electron candidates are reconstructed within $|\eta| < 2.47$ as electromagnetic clusters associated to a track [42], whereas photons are reconstructed as electromagnetic clusters with $|\eta| < 2.37$ [43]. The calorimeter transition regions at $1.37 < |\eta| < 1.52$ are excluded for electrons and photons. Identification criteria based on shower shapes in the EM calorimeter for photons, and additionally on tracking information for electrons, referred to as "tight" in Refs. [42,44], are used. The E_T^{miss} uses the energy deposits in the calorimeters within $|\eta| < 4.9$ and the muons identified in the MS, as described in Ref. [45]. Reconstructed muons, electrons, and photons are required to have $p_T^{\mu,e,\gamma} > 20$ GeV and to be isolated. Photons are considered isolated if the sum of calorimeter transverse energy deposits in a cone of size $\Delta R = 0.4$ around the candidate is smaller than 4 GeV. The isolation is corrected for photon energy leakage. The muon isolation is based on the sum of the transverse momenta of ID tracks in a cone of size $\Delta R = 0.2$ which must be below $0.15 \times p_T^{\mu}$. For electrons, the calorimeter transverse energy deposits and the sum of the transverse momenta of tracks in a cone of size $\Delta R = 0.2$ must be below $0.2 \times p_T^{e}$ and $0.15 \times p_T^{e}$, respectively. The lepton must also be compatible with originating from the primary vertex of the interaction, which is taken to be the vertex with the largest Σp_T^2 of associated tracks. E_T^{miss} is required to exceed 25 GeV. The transverse mass of the W boson [46] is required to be greater than 40 GeV. The two photons must be outside of their mutual isolation cones by requiring $\Delta R(\gamma,\gamma) > 0.4$. To suppress the contribution from final-state radiation, the lepton and photons are required to have $\Delta R(\ell,\gamma) > 0.7$. Events containing a second reconstructed lepton are rejected to reduce background from Drell-Yan events. In the electron channel, additional requirements are used to suppress events in which one electron is misidentified as a photon (mainly originated from the $Z\gamma$ process): the transverse momentum of the $e\gamma\gamma$ system is required to be greater than 30 GeV, and the invariant mass of the electron and the leading, subleading or both photons is required to be outside a 13, 8 or 15 GeV wide window around the Z boson mass, respectively. Exclusive events are defined with a veto on additional jets compared to the inclusive selection. Jets are reconstructed from clustered energy deposits in the calorimeter using the anti-k_t algorithm [47] with radius parameter $R = 0.4$ and are required to have $p_T > 30$ GeV and $|\eta| < 4.4$. Jets at $\Delta R < 0.3$ from the selected lepton and photons are rejected. In order to reduce pileup effects, for jets with $p_T < 50$ GeV and $|\eta| < 2.4$, more than 50% of the summed scalar p_T of tracks within $\Delta R = 0.4$ of the jet axis must be from tracks associated to the primary vertex.

Table I shows the expected background as well as the observation. The background expectation alone is not sufficient to describe the data indicating the presence of signal events. The fake-photon background from $W\gamma j + Wjj$ is estimated by performing a two-dimensional template fit to the isolation energy distributions of the leading and subleading photons, as described in Ref. [48]. Three background templates are obtained from data by reversing some of the photon identification requirements based on shower shape; the signal templates are taken from MC simulation. Contributions from events where a jet satisfies the electron identification criteria, or the muon originates from heavy-flavor decays, i.e. from $\gamma\gamma +$ jets processes, are estimated by using a two-dimensional sideband method constructed from the lepton isolation and E_T^{miss} variables, as described in Ref. [5]. The distribution of the diphoton invariant mass in the two channels is shown in Fig. 1. Alternative methods have been used to cross-check the estimate of the backgrounds coming from fakes, all of them provide consistent results. In the estimation of the fake-photon background, systematic uncertainties arise from the limited number of events in the control regions, the functional form used to describe the background isolation energy distribution, the definition of the control region, the modeling of the signal in the MC samples and the corresponding statistical uncertainty. In the estimate of the fake-lepton background, systematic uncertainties related to

TABLE I. The background composition in each channel is shown for the inclusive (left) and exclusive (right) cases. The $W\gamma j + Wjj$ and $\gamma\gamma +$ jets backgrounds are estimated using data-driven techniques, whereas the others are extracted from MC simulation. The number of candidate events in data passing the full selection is also shown.

	Electron channel	Muon channel	Electron channel	Muon channel
	$N_{\mathrm{jet}} \geq 0$		$N_{\mathrm{jet}} = 0$	
$W\gamma j + W$jj	$15.3 \pm 4.8(\mathrm{stat}) \pm 5.3(\mathrm{syst})$	$30.5 \pm 7.7(\mathrm{stat}) \pm 6.8(\mathrm{syst})$	$5.8 \pm 2.1(\mathrm{stat}) \pm 2.0(\mathrm{syst})$	$14.4 \pm 4.9(\mathrm{stat}) \pm 4.9(\mathrm{syst})$
$\gamma\gamma +$ jets	$1.5 \pm 0.6(\mathrm{stat}) \pm 1.0(\mathrm{syst})$	$11.0 \pm 4.0(\mathrm{stat}) \pm 4.9(\mathrm{syst})$	$0.2 \pm 0.2(\mathrm{stat}) \pm 0.2(\mathrm{syst})$	$6.1 \pm 3.5(\mathrm{stat}) \pm 3.1(\mathrm{syst})$
$Z\gamma$	$11.2 \pm 1.1(\mathrm{stat})$	$3.9 \pm 0.2(\mathrm{stat})$	$2.4 \pm 0.5(\mathrm{stat})$	$2.8 \pm 0.2(\mathrm{stat})$
Other backgrounds	$2.2 \pm 0.6(\mathrm{stat})$	$6.7 \pm 2.0(\mathrm{stat})$	$0.3 \pm 0.1(\mathrm{stat})$	$1.1 \pm 0.3(\mathrm{stat})$
Total background	$30.2 \pm 5.0(\mathrm{stat}) \pm 5.4(\mathrm{syst})$	$52.1 \pm 8.9(\mathrm{stat}) \pm 8.4(\mathrm{syst})$	$8.7 \pm 2.2(\mathrm{stat}) \pm 2.0(\mathrm{syst})$	$24.4 \pm 6.0(\mathrm{stat}) \pm 5.8(\mathrm{syst})$
Data	47	110	15	53

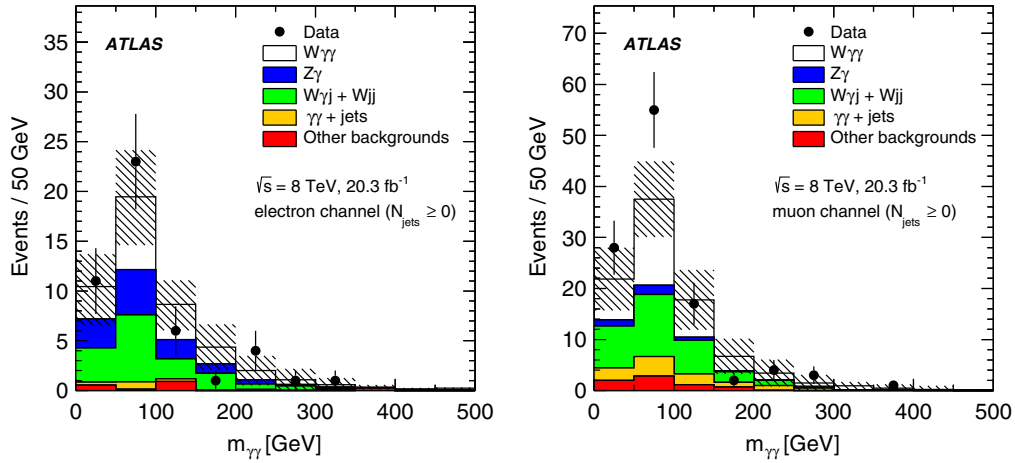

FIG. 1 (color online). Diphoton invariant mass distribution in the electron (left) and muon (right) channels. The expected signal based on the SHERPA prediction is shown. The hashed areas show the total systematic and statistical uncertainty on the background estimate.

the control region definitions and the residual correlation of the discriminating variables are considered.

The fiducial cross sections $\sigma^{\rm fid}_{W\gamma\gamma}$ are obtained from a maximum-likelihood fit, similarly to Ref. [5], for the electron channel, the muon channel, and the combination of the two assuming lepton universality to determine the $W(\ell\nu)\gamma\gamma$ cross section for a single lepton flavor. They are measured in a phase space, defined in Table II, close to that of the experimentally selected region. Here p_T^ν is the transverse momentum of the neutrino and ϵ_h^p is the fractional energy carried by the closest particle-level jet in a cone of $\Delta R = 0.4$ around each photon direction.

The efficiency of the signal selection and the small acceptance correction due to the extrapolation over the calorimeter transition region and to $|\eta| = 2.5$ for the leptons are taken into account in the procedure. The acceptance correction factors are 0.83 and 0.90 in the electron and muon channel, respectively. The combined efficiency and acceptance correction amounts to $(19.6 \pm 0.5)\%$ and $(40.4 \pm 0.7)\%$ in the electron and muon channels in the inclusive case, and to $(15.1 \pm 0.7)\%$ and $(39.7 \pm 1.0)\%$ in the exclusive case. The given uncertainties are statistical only. Corrections are applied to account for small differences between data and MC simulation in lepton, photon, and jet efficiencies, momentum scale and resolution, additional pp interactions, and beam-spot position.

TABLE II. Definition of the fiducial region for which the cross section is evaluated.

Definition of the fiducial region
$p_T^\ell > 20$ GeV, $p_T^\nu > 25$ GeV, $\lvert\eta_\ell\rvert < 2.5$
$m_T > 40$ GeV
$E_T^\gamma > 20$ GeV, $\lvert\eta^\gamma\rvert < 2.37$, iso. fraction $\epsilon_h^p < 0.5$
$\Delta R(\ell,\gamma) > 0.7$, $\Delta R(\gamma,\gamma) > 0.4$, $\Delta R(\ell/\gamma,\mathrm{jet}) > 0.3$
Exclusive: no anti-k_t jets with $p_T^{\rm jet} > 30$ GeV, $\lvert\eta^{\rm jet}\rvert < 4.4$

Systematic uncertainties on the cross section are accounted for by introducing nuisance parameters in the likelihood which modify the signal and background expected yields. Correlations between systematic uncertainties in the two channels are accounted for in the combined fit. When combining the two channels, the dominant systematic uncertainties in the inclusive and exclusive cross-section measurements are 14% and 23% from the data-driven background estimates, 5% to 7% from the jet energy scale, and 3% from the luminosity. Other systematic uncertainties considered stem from the electromagnetic and muonic energy scale and resolution, the object reconstruction, the pileup description, and the trigger efficiency. These are found to have a minor impact, below 3%. Theoretical uncertainties on the signal modeling, affecting only the acceptance extrapolation, are negligible. The measured cross sections are shown in Table III. The significance after combining the two channels is larger than 3σ in the inclusive case. The measurements in the electron and muon channels are compatible within 1σ.

The SM prediction for the $W(\ell\nu)\gamma\gamma$ cross section is calculated with the parton-level Monte Carlo program MCFM [49] at next-to-leading order (NLO). The

TABLE III. Measurement of the $pp \to \ell\nu\gamma\gamma + X$ inclusive and exclusive fiducial cross sections.

	$\sigma^{\rm fid}$ (fb)	$\sigma^{\rm MCFM}$ (fb)
Inclusive ($N_{\rm jet} \geq 0$)		
$\mu\nu\gamma\gamma$	$7.1^{+1.3}_{-1.2}(\mathrm{stat}) \pm 1.5(\mathrm{syst}) \pm 0.2(\mathrm{lumi})$	
$e\nu\gamma\gamma$	$4.3^{+1.8}_{-1.6}(\mathrm{stat})^{+1.9}_{-1.8}(\mathrm{syst}) \pm 0.2(\mathrm{lumi})$	2.90 ± 0.16
$\ell\nu\gamma\gamma$	$6.1^{+1.1}_{-1.0}(\mathrm{stat}) \pm 1.2(\mathrm{syst}) \pm 0.2(\mathrm{lumi})$	
Exclusive ($N_{\rm jet} = 0$)		
$\mu\nu\gamma\gamma$	$3.5 \pm 0.9(\mathrm{stat})^{+1.1}_{-1.0}(\mathrm{syst}) \pm 0.1(\mathrm{lumi})$	
$e\nu\gamma\gamma$	$1.9^{+1.4}_{-1.1}(\mathrm{stat})^{+1.1}_{-1.2}(\mathrm{syst}) \pm 0.1(\mathrm{lumi})$	1.88 ± 0.20
$\ell\nu\gamma\gamma$	$2.9^{+0.8}_{-0.7}(\mathrm{stat})^{+1.0}_{-0.9}(\mathrm{syst}) \pm 0.1(\mathrm{lumi})$	

calculations are performed using the MCFM default electroweak parameters [50] and the CT10 PDF set. The renormalization and factorization scales are set to the invariant mass of the $\ell\nu\gamma\gamma$ system. The fragmentation of quarks and gluons to photons is included using the fragmentation function GDRG_LO [51]. The kinematic requirements at parton level match the fiducial acceptance of Table II.

In addition to the inclusive prediction, an exclusive cross section is obtained by vetoing events with an additional jet emission. To account for the difference between jets defined at parton and particle levels, a correction factor of about 0.87 in the exclusive case is computed and applied to the prediction as documented in Ref. [5]. Uncertainties on the two predictions include the effect of varying independently the renormalization and factorization scales by factors of 0.5 and 2.0, evaluating the CT10 PDF error sets scaled to the 68% confidence level (C.L.), the uncertainties on quark or gluon fragmentation to a photon, and the parton to particle correction factors. The predictions for $W(\ell\nu)\gamma\gamma$ production are compared to the measured cross sections in Table III. The measured cross section is higher by 1.9σ in the inclusive case, while better agreement is seen in the exclusive case, similar to the measurement of $W\gamma$ and $Z\gamma$ in Ref. [5]. In the case of $Z\gamma$ and $W\gamma$, higher order corrections were calculated to be smaller for the exclusive compared to the inclusive case [52]. As the process $W\gamma\gamma$ has similar properties, the exclusive measurement is expected to be in better agreement with the theoretical prediction than the inclusive one. Therefore, in the following, the exclusive measurement will be used for the AQGC limits setting, as done in Ref. [5].

The AQGCs are introduced as dimension-8 operators following the formalism defined in the Appendix of Ref. [53]. While many operators give rise to anomalous couplings of the form $WW\gamma\gamma$, this study is restricted to f_{T0}/Λ^4, f_{M2}/Λ^4, and f_{M3}/Λ^4, where Λ represents the scale at which new physics appears, and f the coupling of the respective operator. The $W\gamma\gamma$ final state is expected to be particularly sensitive to the T0 operator, whereas the other two operators can be related to the parameters of the dimension-6 operators used at LEP [18–21] and by CMS [16] via the transformations described in Ref. [54]. To preserve unitarity up to high energy scales, a form factor is introduced which depends on the energy, the form factor scale $\Lambda_{\rm FF}$ and an exponent n, following the formalism described in Refs. [55,56]. The scale $\Lambda_{\rm FF}$ is independent of the new physics scale Λ [57]. The largest form factor scale ensuring unitarity for this process at $\sqrt{s} = 8$ TeV, calculated using the VBFNLO generator [58–61], is given by $n = 2$ and $\Lambda_{\rm FF} = 600$ GeV for f_{T0}/Λ^4, and $\Lambda_{\rm FF} = 500$ GeV for f_{M2}/Λ^4 and f_{M3}/Λ^4.

Deviations from the SM prediction for the AQGC parameters, which are predicted to be zero, lead to an excess of events with high diphoton invariant mass. The phase space to study AQGCs was optimized using the expected significance calculated on simulated events. The optimal phase space was found to be the exclusive selection with the additional requirement of $m_{\gamma\gamma} > 300$ GeV. The SM backgrounds in this region are determined from a fit to the observed $m_{\gamma\gamma}$ distribution. The expected SM background is $0.01 \pm 0.03(\text{stat}) \pm 0.20(\text{syst})$ $[0.02 \pm 0.05(\text{stat}) \pm 0.46(\text{syst})]$ events in the electron (muon) channel, where uncertainties include systematic effects due to the extrapolation procedure, depending on the modeling of the spectrum and on the initial background estimate used in the extrapolation. No events are observed in the high-mass region.

TABLE IV. Observed and expected 95% C.L. limits obtained for the f_{T0}/Λ^4, f_{M2}/Λ^4 and f_{M3}/Λ^4 AQGC parameters for the combination of the two channels. The values of $n = 0, 1, 2$ are the exponential choices of the form factor, $\Lambda_{\rm FF}$ is fixed to 600 GeV for f_{T0}/Λ^4 and to 500 GeV for the other parameters. The $n = 0$ choice produces the limits without the form factor applied.

		Observed (TeV^{-4})	Expected (TeV^{-4})
$n = 0$	f_{T0}/Λ^4	$[-0.9, 0.9] \times 10^2$	$[-1.2, 1.2] \times 10^2$
	f_{M2}/Λ^4	$[-0.8, 0.8] \times 10^4$	$[-1.1, 1.1] \times 10^4$
	f_{M3}/Λ^4	$[-1.5, 1.4] \times 10^4$	$[-1.9, 1.8] \times 10^4$
$n = 1$	f_{T0}/Λ^4	$[-7.6, 7.3] \times 10^2$	$[-9.6, 9.5] \times 10^2$
	f_{M2}/Λ^4	$[-4.4, 4.6] \times 10^4$	$[-5.7, 5.9] \times 10^4$
	f_{M3}/Λ^4	$[-8.9, 8.0] \times 10^4$	$[-11.0, 10.0] \times 10^4$
$n = 2$	f_{T0}/Λ^4	$[-2.7, 2.6] \times 10^3$	$[-3.5, 3.4] \times 10^3$
	f_{M2}/Λ^4	$[-1.3, 1.3] \times 10^5$	$[-1.6, 1.7] \times 10^5$
	f_{M3}/Λ^4	$[-2.9, 2.5] \times 10^5$	$[-3.7, 3.3] \times 10^5$

The cross-section prediction as a quadratic function of the AQGC parameters is obtained by using VBFNLO [58–61]. For SM couplings, VBFNLO agrees with MCFM. The limits on the AQGC parameters are extracted with a frequentist profile likelihood test [62], using the methodology of Ref. [5]. The expected and observed limits at 95% C.L. on the AQGC parameters are shown in Table IV for different values of n. The limits on f_{M2}/Λ^4 and f_{M3}/Λ^4 improve on the previous results from LEP [18–21] and D0 [22], but are less stringent than those from CMS [16,17]. The limit on f_{T0}/Λ^4 is tighter than the previous limit published by CMS [17,63]. This can be explained by the fact that f_{T0}/Λ^4 is especially sensitive to transversely polarized W bosons, which are favored in the present study [53].

In summary, evidence for the $W(\ell\nu)\gamma\gamma$ process is reported for the first time. The significance of the inclusive production cross section is larger than 3σ. The measured cross sections are in agreement within uncertainties with NLO SM predictions calculated with MCFM. Limits are set at 95% C.L. on the AQGC parameters, in particular improving the limit on f_{T0}/Λ^4.

We thank CERN for the very successful operation of the LHC, as well as the support staff from our institutions without whom ATLAS could not be operated efficiently. We acknowledge the support of ANPCyT, Argentina; YerPhI, Armenia; ARC, Australia; BMWFW and FWF, Austria; ANAS, Azerbaijan; SSTC, Belarus; CNPq and FAPESP, Brazil; NSERC, NRC, and CFI, Canada; CERN; CONICYT, Chile; CAS, MOST, and NSFC, China; COLCIENCIAS, Colombia; MSMT CR, MPO CR, and VSC CR, Czech Republic; DNRF, DNSRC, and Lundbeck Foundation, Denmark; EPLANET, ERC, and NSRF, European Union; IN2P3-CNRS, CEA-DSM/IRFU, France; GNSF, Georgia; BMBF, DFG, HGF, MPG, and AvH Foundation, Germany; GSRT and NSRF, Greece; RGC, Hong Kong SAR, China; ISF, MINERVA, GIF, I-CORE, and Benoziyo Center, Israel; INFN, Italy; MEXT and JSPS, Japan; CNRST, Morocco; FOM and NWO, Netherlands; BRF and RCN, Norway; MNiSW and NCN, Poland; GRICES and FCT, Portugal; MNE/IFA, Romania; MES of Russia and NRC KI, Russian Federation; JINR; MSTD, Serbia; MSSR, Slovakia; ARRS and MIZŠ, Slovenia; DST/NRF, South Africa; MINECO, Spain; SRC and Wallenberg Foundation, Sweden; SER, SNSF, and Cantons of Bern and Geneva, Switzerland; NSC, Taiwan; TAEK, Turkey; STFC, the Royal Society, and Leverhulme Trust, United Kingdom; DOE and NSF, United States of America. The crucial computing support from all WLCG partners is acknowledged gratefully, in particular from CERN and the ATLAS Tier-1 facilities at TRIUMF (Canada), NDGF (Denmark, Norway, Sweden), CC-IN2P3 (France), KIT/GridKA (Germany), INFN-CNAF (Italy), NL-T1 (Netherlands), PIC (Spain), ASGC (Taiwan), RAL (UK), and BNL (USA) and in the Tier-2 facilities worldwide.

[1] U. Baur, T. Han, N. Kauer, R. Sobey, and D. Zeppenfeld, Phys. Rev. D **56**, 140 (1997).
[2] ATLAS Collaboration, Phys. Rev. D **87**, 112001 (2013).
[3] ATLAS Collaboration, Eur. Phys. J. C **72**, 2173 (2012).
[4] ATLAS Collaboration, J. High Energy Phys. 03 (2013) 128.
[5] ATLAS Collaboration, Phys. Rev. D **87**, 112003 (2013).
[6] CMS Collaboration, J. High Energy Phys. 01 (2013) 063.
[7] CMS Collaboration, Phys. Lett. B **740**, 250 (2015).
[8] CMS Collaboration, Phys. Rev. D **89**, 092005 (2014).
[9] V. Abazov *et al.* (D0 Collaboration), Phys. Rev. D **85**, 112005 (2012).
[10] V. Abazov *et al.* (D0 Collaboration), Phys. Rev. Lett. **107**, 241803 (2011).
[11] V. Abazov *et al.* (D0 Collaboration), Phys. Lett. B **718**, 451 (2012).
[12] T. Aaltonen *et al.* (CDF Collaboration), Phys. Rev. Lett. **104**, 201801 (2010).
[13] T. Aaltonen *et al.* (CDF Collaboration), Phys. Rev. Lett. **108**, 101801 (2012).
[14] T. Aaltonen *et al.* (CDF Collaboration), Phys. Rev. Lett. **107**, 051802 (2011).
[15] ATLAS Collaboration, Phys. Rev. Lett. **113**, 141803 (2014).
[16] CMS Collaboration, J. High Energy Phys. 07 (2013) 116.
[17] CMS Collaboration, Phys. Rev. D **90**, 032008 (2014).
[18] A. Heisler *et al.* (ALEPH Collaboration), Phys. Lett. B **602**, 31 (2004).
[19] J. Abdallah *et al.* (DELPHI Collaboration), Eur. Phys. J. C **31**, 139 (2003).
[20] P. Achard *et al.* (L3 Collaboration), Phys. Lett. B **527**, 29 (2002).
[21] G. Abbiendi *et al.* (OPAL Collaboration), Phys. Lett. B **471**, 293 (1999).
[22] V. Abazov *et al.* (D0 Collaboration), Phys. Rev. D **88**, 012005 (2013).
[23] ATLAS Collaboration, J. Instrum. **3**, S08003 (2008).
[24] ATLAS Collaboration, Eur. Phys. J. C **75**, 120 (2015).
[25] ATLAS Collaboration, Report. No. ATLAS-CONF-2012-048, https://cds.cern.ch/record/1450089.
[26] ATLAS uses a right-handed coordinate system with its origin at the nominal interaction point (IP) in the center of the detector and the z axis along the beam pipe. The x axis points from the IP to the center of the LHC ring, and the y axis points upward. Cylindrical coordinates (r, ϕ) are used in the transverse (x, y) plane, ϕ being the azimuthal angle around the beam pipe. The pseudorapidity is defined in terms of the polar angle θ as $\eta = -\ln\tan(\theta/2)$. The distance ΔR in the (η, ϕ) space is defined as $\Delta R = \sqrt{(\Delta\eta)^2 + (\Delta\phi)^2}$.
[27] ATLAS Collaboration, Eur. Phys. J. C **73**, 2518 (2013).
[28] T. Gleisberg, S. Höche, F. Krauss, M. Schönherr, S. Schumann, F. Siegert, and J. Winter, J. High Energy Phys. 02 (2009) 007.
[29] S. Höche, F. Krauss, S. Schumann, and F. Siegert, J. High Energy Phys. 05 (2009) 053.
[30] T. Gleisberg and S. Höche, J. High Energy Phys. 12 (2008) 039.
[31] S. Schumann and F. Krauss, J. High Energy Phys. 03 (2008) 038.
[32] S. Frixione and B. R. Webber, J. High Energy Phys. 06 (2002) 029.
[33] S. Frixione, F. Stoeckli, P. Torrielli, and B. R. Webber, J. High Energy Phys. 01 (2011) 053.
[34] G. Corcella, I. G. Knowles, G. Marchesini, S. Moretti, K. Odagiri, P. Richardson, M. H. Seymour, and B. R. Webber, J. High Energy Phys. 01 (2001) 010.
[35] J. M. Butterworth, J. R. Forshaw, and M. H. Seymour, Z. Phys. C **72**, 637 (1996).
[36] T. Melia, P. Nason, R. Röntsch, and G. Zanderighi, J. High Energy Phys. 11 (2011) 078.
[37] T. Sjöstrand, S. Mrenna, and P. Z. Skands, Comput. Phys. Commun. **178**, 852 (2008).
[38] H.-L. Lai, M. Guzzi, J. Huston, Z. Li, P. M. Nadolsky, J. Pumplin, and C.-P. Yuan, Phys. Rev. D **82**, 074024 (2010).
[39] ATLAS Collaboration, Eur. Phys. J. C **70**, 823 (2010).
[40] S. Agostinelli *et al.*, Nucl. Instrum. Methods Phys. Res., Sect. A **506**, 250 (2003).
[41] ATLAS Collaboration, Eur. Phys. J. C **74**, 3130 (2014).
[42] ATLAS Collaboration, Eur. Phys. J. C **74**, 2941 (2014).

[43] ATLAS Collaboration, Eur. Phys. J. C **74**, 3071 (2014).
[44] ATLAS Collaboration, Report No. ATLAS-CONF-2012-123, http://cdsweb.cern.ch/record/1473426.
[45] ATLAS Collaboration, Report No. ATLAS-CONF-2013-082, http://cds.cern.ch/record/1570993.
[46] The transverse mass of the W is defined, using the lepton (ℓ) and neutrino (ν) p_T and ϕ, as $m_T = \sqrt{2p_T^\ell p_T^\nu[1-\cos(\phi_\ell - \phi_\nu)]}$.
[47] M. Cacciari, G. P. Salam, and G. Soyez, J. High Energy Phys. 04 (2008) 063.
[48] ATLAS Collaboration, Phys. Rev. D **85**, 012003 (2012).
[49] J. M. Campbell, R. K. Ellis, and C. Williams (private communication).
[50] J. M. Campbell, R. K. Ellis, and C. Williams, MCFM v6.8 Manual, http://mcfm.fnal.gov/mcfm.pdf.
[51] A. Gehrmann-De Ridder and E. W. N. Glover, Nucl. Phys. B **517**, 269 (1998).
[52] M. Grazzini, S. Kallweit, and D. Rathlev, arXiv:1504.01330.
[53] O. J. P. Eboli, M. C. Gonzalez-Garcia, and J. K. Mizukoshi, Phys. Rev. D **74**, 073005 (2006).
[54] C. Degrande *et al.*, arXiv:1309.7890.
[55] U. Baur and D. Zeppenfeld, Phys. Lett. B **201**, 383 (1988).
[56] H. Aihara *et al.*, arXiv:hep-ph/9503425.
[57] C. Degrande, N. Greiner, W. Kilian, O. Mattelaer, H. Mebane, T. Stelzer, S. Willenbrock, and C. Zhang, Ann. Phys. **335**, 21 (2013).
[58] J. Baglio *et al.*, arXiv:1107.4038.
[59] J. Baglio *et al.*, arXiv:1404.3940.
[60] K. Arnold *et al.*, Comput. Phys. Commun. **180**, 1661 (2009).
[61] G. Bozzi, F. Campanario, M. Rauch, and D. Zeppenfeld, Phys. Rev. D **83**, 114035 (2011).
[62] A. L. Read, J. Phys. G **28**, 2693 (2002).
[63] VBFNLO uses a slightly different definition of the field strength tensors than Ref. [53]. Therefore, the couplings f need to be scaled for comparison. In the case of f_{T0}, the scale factor is g^{-4}, where g is the $SU(2)$ gauge coupling [58].

G. Aad,[85] B. Abbott,[113] J. Abdallah,[152] S. Abdel Khalek,[117] O. Abdinov,[11] R. Aben,[107] B. Abi,[114] M. Abolins,[90] O. S. AbouZeid,[159] H. Abramowicz,[154] H. Abreu,[153] R. Abreu,[30] Y. Abulaiti,[147a,147b] B. S. Acharya,[165a,165b,b] L. Adamczyk,[38a] D. L. Adams,[25] J. Adelman,[108] S. Adomeit,[100] T. Adye,[131] T. Agatonovic-Jovin,[13] J. A. Aguilar-Saavedra,[126a,126f] M. Agustoni,[17] S. P. Ahlen,[22] F. Ahmadov,[65,c] G. Aielli,[134a,134b] H. Akerstedt,[147a,147b] T. P. A. Åkesson,[81] G. Akimoto,[156] A. V. Akimov,[96] G. L. Alberghi,[20a,20b] J. Albert,[170] S. Albrand,[55] M. J. Alconada Verzini,[71] M. Aleksa,[30] I. N. Aleksandrov,[65] C. Alexa,[26a] G. Alexander,[154] G. Alexandre,[49] T. Alexopoulos,[10] M. Alhroob,[113] G. Alimonti,[91a] L. Alio,[85] J. Alison,[31] B. M. M. Allbrooke,[18] L. J. Allison,[72] P. P. Allport,[74] A. Aloisio,[104a,104b] A. Alonso,[36] F. Alonso,[71] C. Alpigiani,[76] A. Altheimer,[35] B. Alvarez Gonzalez,[90] M. G. Alviggi,[104a,104b] K. Amako,[66] Y. Amaral Coutinho,[24a] C. Amelung,[23] D. Amidei,[89] S. P. Amor Dos Santos,[126a,126c] A. Amorim,[126a,126b] S. Amoroso,[48] N. Amram,[154] G. Amundsen,[23] C. Anastopoulos,[140] L. S. Ancu,[49] N. Andari,[30] T. Andeen,[35] C. F. Anders,[58b] G. Anders,[30] K. J. Anderson,[31] A. Andreazza,[91a,91b] V. Andrei,[58a] X. S. Anduaga,[71] S. Angelidakis,[9] I. Angelozzi,[107] P. Anger,[44] A. Angerami,[35] F. Anghinolfi,[30] A. V. Anisenkov,[109,d] N. Anjos,[12] A. Annovi,[124a,124b] M. Antonelli,[47] A. Antonov,[98] J. Antos,[145b] F. Anulli,[133a] M. Aoki,[66] L. Aperio Bella,[18] G. Arabidze,[90] Y. Arai,[66] J. P. Araque,[126a] A. T. H. Arce,[45] F. A. Arduh,[71] J-F. Arguin,[95] S. Argyropoulos,[42] M. Arik,[19a] A. J. Armbruster,[30] O. Arnaez,[30] V. Arnal,[82] H. Arnold,[48] M. Arratia,[28] O. Arslan,[21] A. Artamonov,[97] G. Artoni,[23] S. Asai,[156] N. Asbah,[42] A. Ashkenazi,[154] B. Åsman,[147a,147b] L. Asquith,[150] K. Assamagan,[25] R. Astalos,[145a] M. Atkinson,[166] N. B. Atlay,[142] B. Auerbach,[6] K. Augsten,[128] M. Aurousseau,[146b] G. Avolio,[30] B. Axen,[15] M. K. Ayoub,[117] G. Azuelos,[95,e] M. A. Baak,[30] A. E. Baas,[58a] C. Bacci,[135a,135b] H. Bachacou,[137] K. Bachas,[155] M. Backes,[30] M. Backhaus,[30] P. Bagiacchi,[133a,133b] P. Bagnaia,[133a,133b] Y. Bai,[33a] T. Bain,[35] J. T. Baines,[131] O. K. Baker,[177] P. Balek,[129] T. Balestri,[149] F. Balli,[84] E. Banas,[39] Sw. Banerjee,[174] A. A. E. Bannoura,[176] H. S. Bansil,[18] L. Barak,[30] S. P. Baranov,[96] E. L. Barberio,[88] D. Barberis,[50a,50b] M. Barbero,[85] T. Barillari,[101] M. Barisonzi,[165a,165b] T. Barklow,[144] N. Barlow,[28] S. L. Barnes,[84] B. M. Barnett,[131] R. M. Barnett,[15] Z. Barnovska,[5] A. Baroncelli,[135a] G. Barone,[49] A. J. Barr,[120] F. Barreiro,[82] J. Barreiro Guimarães da Costa,[57] R. Bartoldus,[144] A. E. Barton,[72] P. Bartos,[145a] A. Bassalat,[117] A. Basye,[166] R. L. Bates,[53] S. J. Batista,[159] J. R. Batley,[28] M. Battaglia,[138] M. Bauce,[133a,133b] F. Bauer,[137] H. S. Bawa,[144,f] J. B. Beacham,[111] M. D. Beattie,[72] T. Beau,[80] P. H. Beauchemin,[162] R. Beccherle,[124a,124b] P. Bechtle,[21] H. P. Beck,[17,g] K. Becker,[120] S. Becker,[100] M. Beckingham,[171] C. Becot,[117] A. J. Beddall,[19c] A. Beddall,[19c] V. A. Bednyakov,[65] C. P. Bee,[149] L. J. Beemster,[107] T. A. Beermann,[176] M. Begel,[25] K. Behr,[120] C. Belanger-Champagne,[87] P. J. Bell,[49] W. H. Bell,[49] G. Bella,[154] L. Bellagamba,[20a] A. Bellerive,[29] M. Bellomo,[86] K. Belotskiy,[98] O. Beltramello,[30] O. Benary,[154] D. Benchekroun,[136a] M. Bender,[100] K. Bendtz,[147a,147b] N. Benekos,[10] Y. Benhammou,[154] E. Benhar Noccioli,[49] J. A. Benitez Garcia,[160b] D. P. Benjamin,[45] J. R. Bensinger,[23] S. Bentvelsen,[107] L. Beresford,[120] M. Beretta,[47] D. Berge,[107] E. Bergeaas Kuutmann,[167] N. Berger,[5] F. Berghaus,[170]

J. Beringer,[15] C. Bernard,[22] N. R. Bernard,[86] C. Bernius,[110] F. U. Bernlochner,[21] T. Berry,[77] P. Berta,[129] C. Bertella,[83] G. Bertoli,[147a,147b] F. Bertolucci,[124a,124b] C. Bertsche,[113] D. Bertsche,[113] M. I. Besana,[91a] G. J. Besjes,[106] O. Bessidskaia Bylund,[147a,147b] M. Bessner,[42] N. Besson,[137] C. Betancourt,[48] S. Bethke,[101] A. J. Bevan,[76] W. Bhimji,[46] R. M. Bianchi,[125] L. Bianchini,[23] M. Bianco,[30] O. Biebel,[100] S. P. Bieniek,[78] M. Biglietti,[135a] J. Bilbao De Mendizabal,[49] H. Bilokon,[47] M. Bindi,[54] S. Binet,[117] A. Bingul,[19c] C. Bini,[133a,133b] C. W. Black,[151] J. E. Black,[144] K. M. Black,[22] D. Blackburn,[139] R. E. Blair,[6] J.-B. Blanchard,[137] J. E. Blanco,[77] T. Blazek,[145a] I. Bloch,[42] C. Blocker,[23] W. Blum,[83,a] U. Blumenschein,[54] G. J. Bobbink,[107] V. S. Bobrovnikov,[109,d] S. S. Bocchetta,[81] A. Bocci,[45] C. Bock,[100] M. Boehler,[48] J. A. Bogaerts,[30] A. G. Bogdanchikov,[109] C. Bohm,[147a] V. Boisvert,[77] T. Bold,[38a] V. Boldea,[26a] A. S. Boldyrev,[99] M. Bomben,[80] M. Bona,[76] M. Boonekamp,[137] A. Borisov,[130] G. Borissov,[72] S. Borroni,[42] J. Bortfeldt,[100] V. Bortolotto,[60a,60b,60c] K. Bos,[107] D. Boscherini,[20a] M. Bosman,[12] J. Boudreau,[125] J. Bouffard,[2] E. V. Bouhova-Thacker,[72] D. Boumediene,[34] C. Bourdarios,[117] N. Bousson,[114] S. Boutouil,[136d] A. Boveia,[30] J. Boyd,[30] I. R. Boyko,[65] I. Bozic,[13] J. Bracinik,[18] A. Brandt,[8] G. Brandt,[15] O. Brandt,[58a] U. Bratzler,[157] B. Brau,[86] J. E. Brau,[116] H. M. Braun,[176,a] S. F. Brazzale,[165a,165c] K. Brendlinger,[122] A. J. Brennan,[88] L. Brenner,[107] R. Brenner,[167] S. Bressler,[173] K. Bristow,[146c] T. M. Bristow,[46] D. Britton,[53] D. Britzger,[42] F. M. Brochu,[28] I. Brock,[21] R. Brock,[90] J. Bronner,[101] G. Brooijmans,[35] T. Brooks,[77] W. K. Brooks,[32b] J. Brosamer,[15] E. Brost,[116] J. Brown,[55] P. A. Bruckman de Renstrom,[39] D. Bruncko,[145b] R. Bruneliere,[48] A. Bruni,[20a] G. Bruni,[20a] M. Bruschi,[20a] L. Bryngemark,[81] T. Buanes,[14] Q. Buat,[143] F. Bucci,[49] P. Buchholz,[142] A. G. Buckley,[53] S. I. Buda,[26a] I. A. Budagov,[65] F. Buehrer,[48] L. Bugge,[119] M. K. Bugge,[119] O. Bulekov,[98] H. Burckhart,[30] S. Burdin,[74] B. Burghgrave,[108] S. Burke,[131] I. Burmeister,[43] E. Busato,[34] D. Büscher,[48] V. Büscher,[83] P. Bussey,[53] C. P. Buszello,[167] J. M. Butler,[22] A. I. Butt,[3] C. M. Buttar,[53] J. M. Butterworth,[78] P. Butti,[107] W. Buttinger,[25] A. Buzatu,[53] S. Cabrera Urbán,[168] D. Caforio,[128] O. Cakir,[4a] P. Calafiura,[15] A. Calandri,[137] G. Calderini,[80] P. Calfayan,[100] L. P. Caloba,[24a] D. Calvet,[34] S. Calvet,[34] R. Camacho Toro,[49] S. Camarda,[42] D. Cameron,[119] L. M. Caminada,[15] R. Caminal Armadans,[12] S. Campana,[30] M. Campanelli,[78] A. Campoverde,[149] V. Canale,[104a,104b] A. Canepa,[160a] M. Cano Bret,[76] J. Cantero,[82] R. Cantrill,[126a] T. Cao,[40] M. D. M. Capeans Garrido,[30] I. Caprini,[26a] M. Caprini,[26a] M. Capua,[37a,37b] R. Caputo,[83] R. Cardarelli,[134a] T. Carli,[30] G. Carlino,[104a] L. Carminati,[91a,91b] S. Caron,[106] E. Carquin,[32a] G. D. Carrillo-Montoya,[8] J. R. Carter,[28] J. Carvalho,[126a,126c] D. Casadei,[78] M. P. Casado,[12] M. Casolino,[12] E. Castaneda-Miranda,[146b] A. Castelli,[107] V. Castillo Gimenez,[168] N. F. Castro,[126a] P. Catastini,[57] A. Catinaccio,[30] J. R. Catmore,[119] A. Cattai,[30] G. Cattani,[134a,134b] J. Caudron,[83] V. Cavaliere,[166] D. Cavalli,[91a] M. Cavalli-Sforza,[12] V. Cavasinni,[124a,124b] F. Ceradini,[135a,135b] B. C. Cerio,[45] K. Cerny,[129] A. S. Cerqueira,[24b] A. Cerri,[150] L. Cerrito,[76] F. Cerutti,[15] M. Cerv,[30] A. Cervelli,[17] S. A. Cetin,[19b] A. Chafaq,[136a] D. Chakraborty,[108] I. Chalupkova,[129] P. Chang,[166] B. Chapleau,[87] J. D. Chapman,[28] D. Charfeddine,[117] D. G. Charlton,[18] C. C. Chau,[159] C. A. Chavez Barajas,[150] S. Cheatham,[153] A. Chegwidden,[90] S. Chekanov,[6] S. V. Chekulaev,[160a] G. A. Chelkov,[65,h] M. A. Chelstowska,[89] C. Chen,[64] H. Chen,[25] K. Chen,[149] L. Chen,[33d,i] S. Chen,[33c] X. Chen,[33f] Y. Chen,[67] H. C. Cheng,[89] Y. Cheng,[31] A. Cheplakov,[65] E. Cheremushkina,[130] R. Cherkaoui El Moursli,[136e] V. Chernyatin,[25,a] E. Cheu,[7] L. Chevalier,[137] V. Chiarella,[47] J. T. Childers,[6] A. Chilingarov,[72] G. Chiodini,[73a] A. S. Chisholm,[18] R. T. Chislett,[78] A. Chitan,[26a] M. V. Chizhov,[65] K. Choi,[61] S. Chouridou,[9] B. K. B. Chow,[100] V. Christodoulou,[78] D. Chromek-Burckhart,[30] M. L. Chu,[152] J. Chudoba,[127] J. J. Chwastowski,[39] L. Chytka,[115] G. Ciapetti,[133a,133b] A. K. Ciftci,[4a] D. Cinca,[53] V. Cindro,[75] A. Ciocio,[15] Z. H. Citron,[173] M. Ciubancan,[26a] A. Clark,[49] P. J. Clark,[46] R. N. Clarke,[15] W. Cleland,[125] C. Clement,[147a,147b] Y. Coadou,[85] M. Cobal,[165a,165c] A. Coccaro,[139] J. Cochran,[64] L. Coffey,[23] J. G. Cogan,[144] B. Cole,[35] S. Cole,[108] A. P. Colijn,[107] J. Collot,[55] T. Colombo,[58c] G. Compostella,[101] P. Conde Muiño,[126a,126b] E. Coniavitis,[48] S. H. Connell,[146b] I. A. Connelly,[77] S. M. Consonni,[91a,91b] V. Consorti,[48] S. Constantinescu,[26a] C. Conta,[121a,121b] G. Conti,[30] F. Conventi,[104a,j] M. Cooke,[15] B. D. Cooper,[78] A. M. Cooper-Sarkar,[120] K. Copic,[15] T. Cornelissen,[176] M. Corradi,[20a] F. Corriveau,[87,k] A. Corso-Radu,[164] A. Cortes-Gonzalez,[12] G. Cortiana,[101] M. J. Costa,[168] D. Costanzo,[140] D. Côté,[8] G. Cottin,[28] G. Cowan,[77] B. E. Cox,[84] K. Cranmer,[110] G. Cree,[29] S. Crépé-Renaudin,[55] F. Crescioli,[80] W. A. Cribbs,[147a,147b] M. Crispin Ortuzar,[120] M. Cristinziani,[21] V. Croft,[106] G. Crosetti,[37a,37b] T. Cuhadar Donszelmann,[140] J. Cummings,[177] M. Curatolo,[47] C. Cuthbert,[151] H. Czirr,[142] P. Czodrowski,[3] S. D'Auria,[53] M. D'Onofrio,[74] M. J. Da Cunha Sargedas De Sousa,[126a,126b] C. Da Via,[84] W. Dabrowski,[38a] A. Dafinca,[120] T. Dai,[89] O. Dale,[14] F. Dallaire,[95] C. Dallapiccola,[86] M. Dam,[36] J. R. Dandoy,[31] A. C. Daniells,[18] M. Danninger,[169] M. Dano Hoffmann,[137] V. Dao,[48] G. Darbo,[50a] S. Darmora,[8] J. Dassoulas,[3] A. Dattagupta,[61] W. Davey,[21] C. David,[170] T. Davidek,[129] E. Davies,[120,l] M. Davies,[154] O. Davignon,[80] P. Davison,[78] Y. Davygora,[58a] E. Dawe,[143] I. Dawson,[140] R. K. Daya-Ishmukhametova,[86] K. De,[8] R. de Asmundis,[104a] S. De Castro,[20a,20b]

S. De Cecco,[80] N. De Groot,[106] P. de Jong,[107] H. De la Torre,[82] F. De Lorenzi,[64] L. De Nooij,[107] D. De Pedis,[133a] A. De Salvo,[133a] U. De Sanctis,[150] A. De Santo,[150] J. B. De Vivie De Regie,[117] W. J. Dearnaley,[72] R. Debbe,[25] C. Debenedetti,[138] D. V. Dedovich,[65] I. Deigaard,[107] J. Del Peso,[82] T. Del Prete,[124a,124b] D. Delgove,[117] F. Deliot,[137] C. M. Delitzsch,[49] M. Deliyergiyev,[75] A. Dell'Acqua,[30] L. Dell'Asta,[22] M. Dell'Orso,[124a,124b] M. Della Pietra,[104a,j] D. della Volpe,[49] M. Delmastro,[5] P. A. Delsart,[55] C. Deluca,[107] D. A. DeMarco,[159] S. Demers,[177] M. Demichev,[65] A. Demilly,[80] S. P. Denisov,[130] D. Derendarz,[39] J. E. Derkaoui,[136d] F. Derue,[80] P. Dervan,[74] K. Desch,[21] C. Deterre,[42] P. O. Deviveiros,[30] A. Dewhurst,[131] S. Dhaliwal,[107] A. Di Ciaccio,[134a,134b] L. Di Ciaccio,[5] A. Di Domenico,[133a,133b] C. Di Donato,[104a,104b] A. Di Girolamo,[30] B. Di Girolamo,[30] A. Di Mattia,[153] B. Di Micco,[135a,135b] R. Di Nardo,[47] A. Di Simone,[48] R. Di Sipio,[159] D. Di Valentino,[29] C. Diaconu,[85] M. Diamond,[159] F. A. Dias,[46] M. A. Diaz,[32a] E. B. Diehl,[89] J. Dietrich,[16] S. Diglio,[85] A. Dimitrievska,[13] J. Dingfelder,[21] F. Dittus,[30] F. Djama,[85] T. Djobava,[51b] J. I. Djuvsland,[58a] M. A. B. do Vale,[24c] D. Dobos,[30] M. Dobre,[26a] C. Doglioni,[49] T. Dohmae,[156] J. Dolejsi,[129] Z. Dolezal,[129] B. A. Dolgoshein,[98,a] M. Donadelli,[24d] S. Donati,[124a,124b] P. Dondero,[121a,121b] J. Donini,[34] J. Dopke,[131] A. Doria,[104a] M. T. Dova,[71] A. T. Doyle,[53] M. Dris,[10] E. Dubreuil,[34] E. Duchovni,[173] G. Duckeck,[100] O. A. Ducu,[26a,85] D. Duda,[176] A. Dudarev,[30] L. Duflot,[117] L. Duguid,[77] M. Dührssen,[30] M. Dunford,[58a] H. Duran Yildiz,[4a] M. Düren,[52] A. Durglishvili,[51b] D. Duschinger,[44] M. Dwuznik,[38a] M. Dyndal,[38a] K. M. Ecker,[101] W. Edson,[2] N. C. Edwards,[46] W. Ehrenfeld,[21] T. Eifert,[30] G. Eigen,[14] K. Einsweiler,[15] T. Ekelof,[167] M. El Kacimi,[136c] M. Ellert,[167] S. Elles,[5] F. Ellinghaus,[83] A. A. Elliot,[170] N. Ellis,[30] J. Elmsheuser,[100] M. Elsing,[30] D. Emeliyanov,[131] Y. Enari,[156] O. C. Endner,[83] M. Endo,[118] R. Engelmann,[149] J. Erdmann,[43] A. Ereditato,[17] D. Eriksson,[147a] G. Ernis,[176] J. Ernst,[2] M. Ernst,[25] S. Errede,[166] E. Ertel,[83] M. Escalier,[117] H. Esch,[43] C. Escobar,[125] B. Esposito,[47] A. I. Etienvre,[137] E. Etzion,[154] H. Evans,[61] A. Ezhilov,[123] L. Fabbri,[20a,20b] G. Facini,[31] R. M. Fakhrutdinov,[130] S. Falciano,[133a] R. J. Falla,[78] J. Faltova,[129] Y. Fang,[33a] M. Fanti,[91a,91b] A. Farbin,[8] A. Farilla,[135a] T. Farooque,[12] S. Farrell,[15] S. M. Farrington,[171] P. Farthouat,[30] F. Fassi,[136e] P. Fassnacht,[30] D. Fassouliotis,[9] A. Favareto,[50a,50b] L. Fayard,[117] P. Federic,[145a] O. L. Fedin,[123,m] W. Fedorko,[169] S. Feigl,[30] L. Feligioni,[85] C. Feng,[33d] E. J. Feng,[6] H. Feng,[89] A. B. Fenyuk,[130] P. Fernandez Martinez,[168] S. Fernandez Perez,[30] S. Ferrag,[53] J. Ferrando,[53] A. Ferrari,[167] P. Ferrari,[107] R. Ferrari,[121a] D. E. Ferreira de Lima,[53] A. Ferrer,[168] D. Ferrere,[49] C. Ferretti,[89] A. Ferretto Parodi,[50a,50b] M. Fiascaris,[31] F. Fiedler,[83] A. Filipčič,[75] M. Filipuzzi,[42] F. Filthaut,[106] M. Fincke-Keeler,[170] K. D. Finelli,[151] M. C. N. Fiolhais,[126a,126c] L. Fiorini,[168] A. Firan,[40] A. Fischer,[2] C. Fischer,[12] J. Fischer,[176] W. C. Fisher,[90] E. A. Fitzgerald,[23] M. Flechl,[48] I. Fleck,[142] P. Fleischmann,[89] S. Fleischmann,[176] G. T. Fletcher,[140] G. Fletcher,[76] T. Flick,[176] A. Floderus,[81] L. R. Flores Castillo,[60a] M. J. Flowerdew,[101] A. Formica,[137] A. Forti,[84] D. Fournier,[117] H. Fox,[72] S. Fracchia,[12] P. Francavilla,[80] M. Franchini,[20a,20b] D. Francis,[30] L. Franconi,[119] M. Franklin,[57] M. Fraternali,[121a,121b] D. Freeborn,[78] S. T. French,[28] F. Friedrich,[44] D. Froidevaux,[30] J. A. Frost,[120] C. Fukunaga,[157] E. Fullana Torregrosa,[83] B. G. Fulsom,[144] J. Fuster,[168] C. Gabaldon,[55] O. Gabizon,[176] A. Gabrielli,[20a,20b] A. Gabrielli,[133a,133b] S. Gadatsch,[107] S. Gadomski,[49] G. Gagliardi,[50a,50b] P. Gagnon,[61] C. Galea,[106] B. Galhardo,[126a,126c] E. J. Gallas,[120] B. J. Gallop,[131] P. Gallus,[128] G. Galster,[36] K. K. Gan,[111] J. Gao,[33b,85] Y. S. Gao,[144,f] F. M. Garay Walls,[46] F. Garberson,[177] C. García,[168] J. E. García Navarro,[168] M. Garcia-Sciveres,[15] R. W. Gardner,[31] N. Garelli,[144] V. Garonne,[30] C. Gatti,[47] G. Gaudio,[121a] B. Gaur,[142] L. Gauthier,[95] P. Gauzzi,[133a,133b] I. L. Gavrilenko,[96] C. Gay,[169] G. Gaycken,[21] E. N. Gazis,[10] P. Ge,[33d] Z. Gecse,[169] C. N. P. Gee,[131] D. A. A. Geerts,[107] Ch. Geich-Gimbel,[21] C. Gemme,[50a] M. H. Genest,[55] S. Gentile,[133a,133b] M. George,[54] S. George,[77] D. Gerbaudo,[164] A. Gershon,[154] H. Ghazlane,[136b] N. Ghodbane,[34] B. Giacobbe,[20a] S. Giagu,[133a,133b] V. Giangiobbe,[12] P. Giannetti,[124a,124b] F. Gianotti,[30] B. Gibbard,[25] S. M. Gibson,[77] M. Gilchriese,[15] T. P. S. Gillam,[28] D. Gillberg,[30] G. Gilles,[34] D. M. Gingrich,[3,e] N. Giokaris,[9] M. P. Giordani,[165a,165c] F. M. Giorgi,[20a] F. M. Giorgi,[16] P. F. Giraud,[137] P. Giromini,[47] D. Giugni,[91a] C. Giuliani,[48] M. Giulini,[58b] B. K. Gjelsten,[119] S. Gkaitatzis,[155] I. Gkialas,[155] E. L. Gkougkousis,[117] L. K. Gladilin,[99] C. Glasman,[82] J. Glatzer,[30] P. C. F. Glaysher,[46] A. Glazov,[42] M. Goblirsch-Kolb,[101] J. R. Goddard,[76] J. Godlewski,[39] S. Goldfarb,[89] T. Golling,[49] D. Golubkov,[130] A. Gomes,[126a,126b,126d] R. Gonçalo,[126a] J. Goncalves Pinto Firmino Da Costa,[137] L. Gonella,[21] S. González de la Hoz,[168] G. Gonzalez Parra,[12] S. Gonzalez-Sevilla,[49] L. Goossens,[30] P. A. Gorbounov,[97] H. A. Gordon,[25] I. Gorelov,[105] B. Gorini,[30] E. Gorini,[73a,73b] A. Gorišek,[75] E. Gornicki,[39] A. T. Goshaw,[45] C. Gössling,[43] M. I. Gostkin,[65] M. Gouighri,[136a] D. Goujdami,[136c] A. G. Goussiou,[139] H. M. X. Grabas,[138] L. Graber,[54] I. Grabowska-Bold,[38a] P. Grafström,[20a,20b] K-J. Grahn,[42] J. Gramling,[49] E. Gramstad,[119] S. Grancagnolo,[16] V. Grassi,[149] V. Gratchev,[123] H. M. Gray,[30] E. Graziani,[135a] Z. D. Greenwood,[79,n] K. Gregersen,[78] I. M. Gregor,[42] P. Grenier,[144] J. Griffiths,[8] A. A. Grillo,[138] K. Grimm,[72] S. Grinstein,[12,o] Ph. Gris,[34] Y. V. Grishkevich,[99] J.-F. Grivaz,[117] J. P. Grohs,[44] A. Grohsjean,[42] E. Gross,[173] J. Grosse-Knetter,[54] G. C. Grossi,[134a,134b] Z. J. Grout,[150] L. Guan,[33b]

J. Guenther,[128] F. Guescini,[49] D. Guest,[177] O. Gueta,[154] E. Guido,[50a,50b] T. Guillemin,[117] S. Guindon,[2] U. Gul,[53] C. Gumpert,[44] J. Guo,[33e] S. Gupta,[120] P. Gutierrez,[113] N. G. Gutierrez Ortiz,[53] C. Gutschow,[44] N. Guttman,[154] C. Guyot,[137] C. Gwenlan,[120] C. B. Gwilliam,[74] A. Haas,[110] C. Haber,[15] H. K. Hadavand,[8] N. Haddad,[136e] P. Haefner,[21] S. Hageböck,[21] Z. Hajduk,[39] H. Hakobyan,[178] M. Haleem,[42] J. Haley,[114] D. Hall,[120] G. Halladjian,[90] G. D. Hallewell,[85] K. Hamacher,[176] P. Hamal,[115] K. Hamano,[170] M. Hamer,[54] A. Hamilton,[146a] S. Hamilton,[162] G. N. Hamity,[146c] P. G. Hamnett,[42] L. Han,[33b] K. Hanagaki,[118] K. Hanawa,[156] M. Hance,[15] P. Hanke,[58a] R. Hanna,[137] J. B. Hansen,[36] J. D. Hansen,[36] P. H. Hansen,[36] K. Hara,[161] A. S. Hard,[174] T. Harenberg,[176] F. Hariri,[117] S. Harkusha,[92] R. D. Harrington,[46] P. F. Harrison,[171] F. Hartjes,[107] M. Hasegawa,[67] S. Hasegawa,[103] Y. Hasegawa,[141] A. Hasib,[113] S. Hassani,[137] S. Haug,[17] R. Hauser,[90] L. Hauswald,[44] M. Havranek,[127] C. M. Hawkes,[18] R. J. Hawkings,[30] A. D. Hawkins,[81] T. Hayashi,[161] D. Hayden,[90] C. P. Hays,[120] J. M. Hays,[76] H. S. Hayward,[74] S. J. Haywood,[131] S. J. Head,[18] T. Heck,[83] V. Hedberg,[81] L. Heelan,[8] S. Heim,[122] T. Heim,[176] B. Heinemann,[15] L. Heinrich,[110] J. Hejbal,[127] L. Helary,[22] M. Heller,[30] S. Hellman,[147a,147b] D. Hellmich,[21] C. Helsens,[30] J. Henderson,[120] R. C. W. Henderson,[72] Y. Heng,[174] C. Hengler,[42] A. Henrichs,[177] A. M. Henriques Correia,[30] S. Henrot-Versille,[117] G. H. Herbert,[16] Y. Hernández Jiménez,[168] R. Herrberg-Schubert,[16] G. Herten,[48] R. Hertenberger,[100] L. Hervas,[30] G. G. Hesketh,[78] N. P. Hessey,[107] R. Hickling,[76] E. Higón-Rodriguez,[168] E. Hill,[170] J. C. Hill,[28] K. H. Hiller,[42] S. J. Hillier,[18] I. Hinchliffe,[15] E. Hines,[122] R. R. Hinman,[15] M. Hirose,[158] D. Hirschbuehl,[176] J. Hobbs,[149] N. Hod,[107] M. C. Hodgkinson,[140] P. Hodgson,[140] A. Hoecker,[30] M. R. Hoeferkamp,[105] F. Hoenig,[100] M. Hohlfeld,[83] D. Hohn,[21] T. R. Holmes,[15] T. M. Hong,[122] L. Hooft van Huysduynen,[110] W. H. Hopkins,[116] Y. Horii,[103] A. J. Horton,[143] J-Y. Hostachy,[55] S. Hou,[152] A. Hoummada,[136a] J. Howard,[120] J. Howarth,[42] M. Hrabovsky,[115] I. Hristova,[16] J. Hrivnac,[117] T. Hryn'ova,[5] A. Hrynevich,[93] C. Hsu,[146c] P. J. Hsu,[152,p] S.-C. Hsu,[139] D. Hu,[35] Q. Hu,[33b] X. Hu,[89] Y. Huang,[42] Z. Hubacek,[30] F. Hubaut,[85] F. Huegging,[21] T. B. Huffman,[120] E. W. Hughes,[35] G. Hughes,[72] M. Huhtinen,[30] T. A. Hülsing,[83] N. Huseynov,[65,c] J. Huston,[90] J. Huth,[57] G. Iacobucci,[49] G. Iakovidis,[25] I. Ibragimov,[142] L. Iconomidou-Fayard,[117] E. Ideal,[177] Z. Idrissi,[136e] P. Iengo,[104a] O. Igonkina,[107] T. Iizawa,[172] Y. Ikegami,[66] K. Ikematsu,[142] M. Ikeno,[66] Y. Ilchenko,[31,q] D. Iliadis,[155] N. Ilic,[159] Y. Inamaru,[67] T. Ince,[101] P. Ioannou,[9] M. Iodice,[135a] K. Iordanidou,[9] V. Ippolito,[57] A. Irles Quiles,[168] C. Isaksson,[167] M. Ishino,[68] M. Ishitsuka,[158] R. Ishmukhametov,[111] C. Issever,[120] S. Istin,[19a] J. M. Iturbe Ponce,[84] R. Iuppa,[134a,134b] J. Ivarsson,[81] W. Iwanski,[39] H. Iwasaki,[66] J. M. Izen,[41] V. Izzo,[104a] S. Jabbar,[3] B. Jackson,[122] M. Jackson,[74] P. Jackson,[1] M. R. Jaekel,[30] V. Jain,[2] K. Jakobs,[48] S. Jakobsen,[30] T. Jakoubek,[127] J. Jakubek,[128] D. O. Jamin,[152] D. K. Jana,[79] E. Jansen,[78] R. W. Jansky,[62] J. Janssen,[21] M. Janus,[171] G. Jarlskog,[81] N. Javadov,[65,c] T. Javůrek,[48] L. Jeanty,[15] J. Jejelava,[51a,r] G.-Y. Jeng,[151] D. Jennens,[88] P. Jenni,[48,s] J. Jentzsch,[43] C. Jeske,[171] S. Jézéquel,[5] H. Ji,[174] J. Jia,[149] Y. Jiang,[33b] J. Jimenez Pena,[168] S. Jin,[33a] A. Jinaru,[26a] O. Jinnouchi,[158] M. D. Joergensen,[36] P. Johansson,[140] K. A. Johns,[7] K. Jon-And,[147a,147b] G. Jones,[171] R. W. L. Jones,[72] T. J. Jones,[74] J. Jongmanns,[58a] P. M. Jorge,[126a,126b] K. D. Joshi,[84] J. Jovicevic,[148] X. Ju,[174] C. A. Jung,[43] P. Jussel,[62] A. Juste Rozas,[12,o] M. Kaci,[168] A. Kaczmarska,[39] M. Kado,[117] H. Kagan,[111] M. Kagan,[144] S. J. Kahn,[85] E. Kajomovitz,[45] C. W. Kalderon,[120] S. Kama,[40] A. Kamenshchikov,[130] N. Kanaya,[156] M. Kaneda,[30] S. Kaneti,[28] V. A. Kantserov,[98] J. Kanzaki,[66] B. Kaplan,[110] A. Kapliy,[31] D. Kar,[53] K. Karakostas,[10] A. Karamaoun,[3] N. Karastathis,[10,107] M. J. Kareem,[54] M. Karnevskiy,[83] S. N. Karpov,[65] Z. M. Karpova,[65] K. Karthik,[110] V. Kartvelishvili,[72] A. N. Karyukhin,[130] L. Kashif,[174] R. D. Kass,[111] A. Kastanas,[14] Y. Kataoka,[156] A. Katre,[49] J. Katzy,[42] K. Kawagoe,[70] T. Kawamoto,[156] G. Kawamura,[54] S. Kazama,[156] V. F. Kazanin,[109,d] M. Y. Kazarinov,[65] R. Keeler,[170] R. Kehoe,[40] M. Keil,[54] J. S. Keller,[42] J. J. Kempster,[77] H. Keoshkerian,[84] O. Kepka,[127] B. P. Kerševan,[75] S. Kersten,[176] R. A. Keyes,[87] F. Khalil-zada,[11] H. Khandanyan,[147a,147b] A. Khanov,[114] A. Kharlamov,[109] A. Khodinov,[98] T. J. Khoo,[28] G. Khoriauli,[21] V. Khovanskiy,[97] E. Khramov,[65] J. Khubua,[51b,t] H. Y. Kim,[8] H. Kim,[147a,147b] S. H. Kim,[161] Y. Kim,[31] N. Kimura,[155] O. M. Kind,[16] B. T. King,[74] M. King,[168] R. S. B. King,[120] S. B. King,[169] J. Kirk,[131] A. E. Kiryunin,[101] T. Kishimoto,[67] D. Kisielewska,[38a] F. Kiss,[48] K. Kiuchi,[161] E. Kladiva,[145b] M. H. Klein,[35] M. Klein,[74] U. Klein,[74] K. Kleinknecht,[83] P. Klimek,[147a,147b] A. Klimentov,[25] R. Klingenberg,[43] J. A. Klinger,[84] T. Klioutchnikova,[30] P. F. Klok,[106] E.-E. Kluge,[58a] P. Kluit,[107] S. Kluth,[101] E. Kneringer,[62] E. B. F. G. Knoops,[85] A. Knue,[53] D. Kobayashi,[158] T. Kobayashi,[156] M. Kobel,[44] M. Kocian,[144] P. Kodys,[129] T. Koffas,[29] E. Koffeman,[107] L. A. Kogan,[120] S. Kohlmann,[176] Z. Kohout,[128] T. Kohriki,[66] T. Koi,[144] H. Kolanoski,[16] I. Koletsou,[5] A. A. Komar,[96,a] Y. Komori,[156] T. Kondo,[66] N. Kondrashova,[42] K. Köneke,[48] A. C. König,[106] S. König,[83] T. Kono,[66,u] R. Konoplich,[110,v] N. Konstantinidis,[78] R. Kopeliansky,[153] S. Koperny,[38a] L. Köpke,[83] A. K. Kopp,[48] K. Korcyl,[39] K. Kordas,[155] A. Korn,[78] A. A. Korol,[109,d] I. Korolkov,[12] E. V. Korolkova,[140] O. Kortner,[101] S. Kortner,[101] T. Kosek,[129] V. V. Kostyukhin,[21] V. M. Kotov,[65] A. Kotwal,[45] A. Kourkoumeli-Charalampidi,[155] C. Kourkoumelis,[9] V. Kouskoura,[25] A. Koutsman,[160a] R. Kowalewski,[170]

T. Z. Kowalski,[38a] W. Kozanecki,[137] A. S. Kozhin,[130] V. A. Kramarenko,[99] G. Kramberger,[75] D. Krasnopevtsev,[98] M. W. Krasny,[80] A. Krasznahorkay,[30] J. K. Kraus,[21] A. Kravchenko,[25] S. Kreiss,[110] M. Kretz,[58c] J. Kretzschmar,[74] K. Kreutzfeldt,[52] P. Krieger,[159] K. Krizka,[31] K. Kroeninger,[43] H. Kroha,[101] J. Kroll,[122] J. Kroseberg,[21] J. Krstic,[13] U. Kruchonak,[65] H. Krüger,[21] N. Krumnack,[64] Z. V. Krumshteyn,[65] A. Kruse,[174] M. C. Kruse,[45] M. Kruskal,[22] T. Kubota,[88] H. Kucuk,[78] S. Kuday,[4c] S. Kuehn,[48] A. Kugel,[58c] F. Kuger,[175] A. Kuhl,[138] T. Kuhl,[42] V. Kukhtin,[65] Y. Kulchitsky,[92] S. Kuleshov,[32b] M. Kuna,[133a,133b] T. Kunigo,[68] A. Kupco,[127] H. Kurashige,[67] Y. A. Kurochkin,[92] R. Kurumida,[67] V. Kus,[127] E. S. Kuwertz,[148] M. Kuze,[158] J. Kvita,[115] T. Kwan,[170] D. Kyriazopoulos,[140] A. La Rosa,[49] J. L. La Rosa Navarro,[24d] L. La Rotonda,[37a,37b] C. Lacasta,[168] F. Lacava,[133a,133b] J. Lacey,[29] H. Lacker,[16] D. Lacour,[80] V. R. Lacuesta,[168] E. Ladygin,[65] R. Lafaye,[5] B. Laforge,[80] T. Lagouri,[177] S. Lai,[48] L. Lambourne,[78] S. Lammers,[61] C. L. Lampen,[7] W. Lampl,[7] E. Lançon,[137] U. Landgraf,[48] M. P. J. Landon,[76] V. S. Lang,[58a] A. J. Lankford,[164] F. Lanni,[25] K. Lantzsch,[30] S. Laplace,[80] C. Lapoire,[30] J. F. Laporte,[137] T. Lari,[91a] F. Lasagni Manghi,[20a,20b] M. Lassnig,[30] P. Laurelli,[47] W. Lavrijsen,[15] A. T. Law,[138] P. Laycock,[74] O. Le Dortz,[80] E. Le Guirriec,[85] E. Le Menedeu,[12] T. LeCompte,[6] F. Ledroit-Guillon,[55] C. A. Lee,[146b] S. C. Lee,[152] L. Lee,[1] G. Lefebvre,[80] M. Lefebvre,[170] F. Legger,[100] C. Leggett,[15] A. Lehan,[74] G. Lehmann Miotto,[30] X. Lei,[7] W. A. Leight,[29] A. Leisos,[155] A. G. Leister,[177] M. A. L. Leite,[24d] R. Leitner,[129] D. Lellouch,[173] B. Lemmer,[54] K. J. C. Leney,[78] T. Lenz,[21] G. Lenzen,[176] B. Lenzi,[30] R. Leone,[7] S. Leone,[124a,124b] C. Leonidopoulos,[46] S. Leontsinis,[10] C. Leroy,[95] C. G. Lester,[28] M. Levchenko,[123] J. Levêque,[5] D. Levin,[89] L. J. Levinson,[173] M. Levy,[18] A. Lewis,[120] A. M. Leyko,[21] M. Leyton,[41] B. Li,[33b,w] B. Li,[85] H. Li,[149] H. L. Li,[31] L. Li,[45] L. Li,[33e] S. Li,[45] Y. Li,[33c,x] Z. Liang,[138] H. Liao,[34] B. Liberti,[134a] A. Liblong,[159] P. Lichard,[30] K. Lie,[166] J. Liebal,[21] W. Liebig,[14] C. Limbach,[21] A. Limosani,[151] S. C. Lin,[152,y] T. H. Lin,[83] F. Linde,[107] B. E. Lindquist,[149] J. T. Linnemann,[90] E. Lipeles,[122] A. Lipniacka,[14] M. Lisovyi,[42] T. M. Liss,[166] D. Lissauer,[25] A. Lister,[169] A. M. Litke,[138] B. Liu,[152] D. Liu,[152] J. Liu,[85] J. B. Liu,[33b] K. Liu,[33b,z] L. Liu,[89] M. Liu,[45] M. Liu,[33b] Y. Liu,[33b] M. Livan,[121a,121b] A. Lleres,[55] J. Llorente Merino,[82] S. L. Lloyd,[76] F. Lo Sterzo,[152] E. Lobodzinska,[42] P. Loch,[7] W. S. Lockman,[138] F. K. Loebinger,[84] A. E. Loevschall-Jensen,[36] A. Loginov,[177] T. Lohse,[16] K. Lohwasser,[42] M. Lokajicek,[127] B. A. Long,[22] J. D. Long,[89] R. E. Long,[72] K. A. Looper,[111] L. Lopes,[126a] D. Lopez Mateos,[57] B. Lopez Paredes,[140] I. Lopez Paz,[12] J. Lorenz,[100] N. Lorenzo Martinez,[61] M. Losada,[163] P. Loscutoff,[15] P. J. Lösel,[100] X. Lou,[33a] A. Lounis,[117] J. Love,[6] P. A. Love,[72] N. Lu,[89] H. J. Lubatti,[139] C. Luci,[133a,133b] A. Lucotte,[55] F. Luehring,[61] W. Lukas,[62] L. Luminari,[133a] O. Lundberg,[147a,147b] B. Lund-Jensen,[148] M. Lungwitz,[83] D. Lynn,[25] R. Lysak,[127] E. Lytken,[81] H. Ma,[25] L. L. Ma,[33d] G. Maccarrone,[47] A. Macchiolo,[101] C. M. Macdonald,[140] J. Machado Miguens,[122,126b] D. Macina,[30] D. Madaffari,[85] R. Madar,[34] H. J. Maddocks,[72] W. F. Mader,[44] A. Madsen,[167] S. Maeland,[14] T. Maeno,[25] A. Maevskiy,[99] E. Magradze,[54] K. Mahboubi,[48] J. Mahlstedt,[107] S. Mahmoud,[74] C. Maiani,[137] C. Maidantchik,[24a] A. A. Maier,[101] T. Maier,[100] A. Maio,[126a,126b,126d] S. Majewski,[116] Y. Makida,[66] N. Makovec,[117] B. Malaescu,[80] Pa. Malecki,[39] V. P. Maleev,[123] F. Malek,[55] U. Mallik,[63] D. Malon,[6] C. Malone,[144] S. Maltezos,[10] V. M. Malyshev,[109] S. Malyukov,[30] J. Mamuzic,[42] G. Mancini,[47] B. Mandelli,[30] L. Mandelli,[91a] I. Mandić,[75] R. Mandrysch,[63] J. Maneira,[126a,126b] A. Manfredini,[101] L. Manhaes de Andrade Filho,[24b] J. Manjarres Ramos,[160b] A. Mann,[100] P. M. Manning,[138] A. Manousakis-Katsikakis,[9] B. Mansoulie,[137] R. Mantifel,[87] M. Mantoani,[54] L. Mapelli,[30] L. March,[146c] G. Marchiori,[80] M. Marcisovsky,[127] C. P. Marino,[170] M. Marjanovic,[13] F. Marroquim,[24a] S. P. Marsden,[84] Z. Marshall,[15] L. F. Marti,[17] S. Marti-Garcia,[168] B. Martin,[90] T. A. Martin,[171] V. J. Martin,[46] B. Martin dit Latour,[14] H. Martinez,[137] M. Martinez,[12,o] S. Martin-Haugh,[131] V. S. Martoiu,[26a] A. C. Martyniuk,[78] M. Marx,[139] F. Marzano,[133a] A. Marzin,[30] L. Masetti,[83] T. Mashimo,[156] R. Mashinistov,[96] J. Masik,[84] A. L. Maslennikov,[109,d] I. Massa,[20a,20b] L. Massa,[20a,20b] N. Massol,[5] P. Mastrandrea,[149] A. Mastroberardino,[37a,37b] T. Masubuchi,[156] P. Mättig,[176] J. Mattmann,[83] J. Maurer,[26a] S. J. Maxfield,[74] D. A. Maximov,[109,d] R. Mazini,[152] S. M. Mazza,[91a,91b] L. Mazzaferro,[134a,134b] G. Mc Goldrick,[159] S. P. Mc Kee,[89] A. McCarn,[89] R. L. McCarthy,[149] T. G. McCarthy,[29] N. A. McCubbin,[131] K. W. McFarlane,[56,a] J. A. Mcfayden,[78] G. Mchedlidze,[54] S. J. McMahon,[131] R. A. McPherson,[170,k] M. Medinnis,[42] S. Meehan,[146a] S. Mehlhase,[100] A. Mehta,[74] K. Meier,[58a] C. Meineck,[100] B. Meirose,[41] C. Melachrinos,[31] B. R. Mellado Garcia,[146c] F. Meloni,[17] A. Mengarelli,[20a,20b] S. Menke,[101] E. Meoni,[162] K. M. Mercurio,[57] S. Mergelmeyer,[21] N. Meric,[137] P. Mermod,[49] L. Merola,[104a,104b] C. Meroni,[91a] F. S. Merritt,[31] H. Merritt,[111] A. Messina,[133a,133b] J. Metcalfe,[25] A. S. Mete,[164] C. Meyer,[83] C. Meyer,[122] J-P. Meyer,[137] J. Meyer,[107] R. P. Middleton,[131] S. Miglioranzi,[165a,165c] L. Mijović,[21] G. Mikenberg,[173] M. Mikestikova,[127] M. Mikuž,[75] M. Milesi,[88] A. Milic,[30] D. W. Miller,[31] C. Mills,[46] A. Milov,[173] D. A. Milstead,[147a,147b] A. A. Minaenko,[130] Y. Minami,[156] I. A. Minashvili,[65] A. I. Mincer,[110] B. Mindur,[38a] M. Mineev,[65] Y. Ming,[174] L. M. Mir,[12] G. Mirabelli,[133a] T. Mitani,[172] J. Mitrevski,[100] V. A. Mitsou,[168] A. Miucci,[49] P. S. Miyagawa,[140] J. U. Mjörnmark,[81] T. Moa,[147a,147b] K. Mochizuki,[85]

S. Mohapatra,[35] W. Mohr,[48] S. Molander,[147a,147b] R. Moles-Valls,[168] K. Mönig,[42] C. Monini,[55] J. Monk,[36] E. Monnier,[85] J. Montejo Berlingen,[12] F. Monticelli,[71] S. Monzani,[133a,133b] R. W. Moore,[3] N. Morange,[117] D. Moreno,[163] M. Moreno Llácer,[54] P. Morettini,[50a] M. Morgenstern,[44] M. Morii,[57] V. Morisbak,[119] S. Moritz,[83] A. K. Morley,[148] G. Mornacchi,[30] J. D. Morris,[76] A. Morton,[53] L. Morvaj,[103] H. G. Moser,[101] M. Mosidze,[51b] J. Moss,[111] K. Motohashi,[158] R. Mount,[144] E. Mountricha,[25] S. V. Mouraviev,[96,a] E. J. W. Moyse,[86] S. Muanza,[85] R. D. Mudd,[18] F. Mueller,[101] J. Mueller,[125] K. Mueller,[21] R. S. P. Mueller,[100] T. Mueller,[28] D. Muenstermann,[49] P. Mullen,[53] Y. Munwes,[154] J. A. Murillo Quijada,[18] W. J. Murray,[171,131] H. Musheghyan,[54] E. Musto,[153] A. G. Myagkov,[130,aa] M. Myska,[128] O. Nackenhorst,[54] J. Nadal,[54] K. Nagai,[120] R. Nagai,[158] Y. Nagai,[85] K. Nagano,[66] A. Nagarkar,[111] Y. Nagasaka,[59] K. Nagata,[161] M. Nagel,[101] E. Nagy,[85] A. M. Nairz,[30] Y. Nakahama,[30] K. Nakamura,[66] T. Nakamura,[156] I. Nakano,[112] H. Namasivayam,[41] G. Nanava,[21] R. F. Naranjo Garcia,[42] R. Narayan,[58b] T. Nattermann,[21] T. Naumann,[42] G. Navarro,[163] R. Nayyar,[7] H. A. Neal,[89] P. Yu. Nechaeva,[96] T. J. Neep,[84] P. D. Nef,[144] A. Negri,[121a,121b] M. Negrini,[20a] S. Nektarijevic,[106] C. Nellist,[117] A. Nelson,[164] S. Nemecek,[127] P. Nemethy,[110] A. A. Nepomuceno,[24a] M. Nessi,[30,bb] M. S. Neubauer,[166] M. Neumann,[176] R. M. Neves,[110] P. Nevski,[25] P. R. Newman,[18] D. H. Nguyen,[6] R. B. Nickerson,[120] R. Nicolaidou,[137] B. Nicquevert,[30] J. Nielsen,[138] N. Nikiforou,[35] A. Nikiforov,[16] V. Nikolaenko,[130,aa] I. Nikolic-Audit,[80] K. Nikolopoulos,[18] J. K. Nilsen,[119] P. Nilsson,[25] Y. Ninomiya,[156] A. Nisati,[133a] R. Nisius,[101] T. Nobe,[158] M. Nomachi,[118] I. Nomidis,[29] T. Nooney,[76] S. Norberg,[113] M. Nordberg,[30] O. Novgorodova,[44] S. Nowak,[101] M. Nozaki,[66] L. Nozka,[115] K. Ntekas,[10] G. Nunes Hanninger,[88] T. Nunnemann,[100] E. Nurse,[78] F. Nuti,[88] B. J. O'Brien,[46] F. O'grady,[7] D. C. O'Neil,[143] V. O'Shea,[53] F. G. Oakham,[29,e] H. Oberlack,[101] T. Obermann,[21] J. Ocariz,[80] A. Ochi,[67] I. Ochoa,[78] S. Oda,[70] S. Odaka,[66] H. Ogren,[61] A. Oh,[84] S. H. Oh,[45] C. C. Ohm,[15] H. Ohman,[167] H. Oide,[30] W. Okamura,[118] H. Okawa,[161] Y. Okumura,[31] T. Okuyama,[156] A. Olariu,[26a] S. A. Olivares Pino,[46] D. Oliveira Damazio,[25] E. Oliver Garcia,[168] A. Olszewski,[39] J. Olszowska,[39] A. Onofre,[126a,126e] P. U. E. Onyisi,[31,q] C. J. Oram,[160a] M. J. Oreglia,[31] Y. Oren,[154] D. Orestano,[135a,135b] N. Orlando,[155] C. Oropeza Barrera,[53] R. S. Orr,[159] B. Osculati,[50a,50b] R. Ospanov,[84] G. Otero y Garzon,[27] H. Otono,[70] M. Ouchrif,[136d] E. A. Ouellette,[170] F. Ould-Saada,[119] A. Ouraou,[137] K. P. Oussoren,[107] Q. Ouyang,[33a] A. Ovcharova,[15] M. Owen,[53] R. E. Owen,[18] V. E. Ozcan,[19a] N. Ozturk,[8] K. Pachal,[120] A. Pacheco Pages,[12] C. Padilla Aranda,[12] M. Pagáčová,[48] S. Pagan Griso,[15] E. Paganis,[140] C. Pahl,[101] F. Paige,[25] P. Pais,[86] K. Pajchel,[119] G. Palacino,[160b] S. Palestini,[30] M. Palka,[38b] D. Pallin,[34] A. Palma,[126a,126b] Y. B. Pan,[174] E. Panagiotopoulou,[10] C. E. Pandini,[80] J. G. Panduro Vazquez,[77] P. Pani,[147a,147b] S. Panitkin,[25] L. Paolozzi,[134a,134b] Th. D. Papadopoulou,[10] K. Papageorgiou,[155] A. Paramonov,[6] D. Paredes Hernandez,[155] M. A. Parker,[28] K. A. Parker,[140] F. Parodi,[50a,50b] J. A. Parsons,[35] U. Parzefall,[48] E. Pasqualucci,[133a] S. Passaggio,[50a] F. Pastore,[135a,135b,a] Fr. Pastore,[77] G. Pásztor,[29] S. Pataraia,[176] N. D. Patel,[151] J. R. Pater,[84] T. Pauly,[30] J. Pearce,[170] B. Pearson,[113] L. E. Pedersen,[36] M. Pedersen,[119] S. Pedraza Lopez,[168] R. Pedro,[126a,126b] S. V. Peleganchuk,[109] D. Pelikan,[167] H. Peng,[33b] B. Penning,[31] J. Penwell,[61] D. V. Perepelitsa,[25] E. Perez Codina,[160a] M. T. Pérez García-Estañ,[168] L. Perini,[91a,91b] H. Pernegger,[30] S. Perrella,[104a,104b] R. Peschke,[42] V. D. Peshekhonov,[65] K. Peters,[30] R. F. Y. Peters,[84] B. A. Petersen,[30] T. C. Petersen,[36] E. Petit,[42] A. Petridis,[147a,147b] C. Petridou,[155] E. Petrolo,[133a] F. Petrucci,[135a,135b] N. E. Pettersson,[158] R. Pezoa,[32b] P. W. Phillips,[131] G. Piacquadio,[144] E. Pianori,[171] A. Picazio,[49] E. Piccaro,[76] M. Piccinini,[20a,20b] M. A. Pickering,[120] R. Piegaia,[27] D. T. Pignotti,[111] J. E. Pilcher,[31] A. D. Pilkington,[78] J. Pina,[126a,126b,126d] M. Pinamonti,[165a,165c,cc] J. L. Pinfold,[3] A. Pingel,[36] B. Pinto,[126a] S. Pires,[80] M. Pitt,[173] C. Pizio,[91a,91b] L. Plazak,[145a] M.-A. Pleier,[25] V. Pleskot,[129] E. Plotnikova,[65] P. Plucinski,[147a,147b] D. Pluth,[64] R. Poettgen,[83] L. Poggioli,[117] D. Pohl,[21] G. Polesello,[121a] A. Policicchio,[37a,37b] R. Polifka,[159] A. Polini,[20a] C. S. Pollard,[53] V. Polychronakos,[25] K. Pommès,[30] L. Pontecorvo,[133a] B. G. Pope,[90] G. A. Popeneciu,[26b] D. S. Popovic,[13] A. Poppleton,[30] S. Pospisil,[128] K. Potamianos,[15] I. N. Potrap,[65] C. J. Potter,[150] C. T. Potter,[116] G. Poulard,[30] J. Poveda,[30] V. Pozdnyakov,[65] P. Pralavorio,[85] A. Pranko,[15] S. Prasad,[30] S. Prell,[64] D. Price,[84] J. Price,[74] L. E. Price,[6] M. Primavera,[73a] S. Prince,[87] M. Proissl,[46] K. Prokofiev,[60c] F. Prokoshin,[32b] E. Protopapadaki,[137] S. Protopopescu,[25] J. Proudfoot,[6] M. Przybycien,[38a] E. Ptacek,[116] D. Puddu,[135a,135b] E. Pueschel,[86] D. Puldon,[149] M. Purohit,[25,dd] P. Puzo,[117] J. Qian,[89] G. Qin,[53] Y. Qin,[84] A. Quadt,[54] D. R. Quarrie,[15] W. B. Quayle,[165a,165b] M. Queitsch-Maitland,[84] D. Quilty,[53] A. Qureshi,[160b] V. Radeka,[25] V. Radescu,[42] S. K. Radhakrishnan,[149] P. Radloff,[116] P. Rados,[88] F. Ragusa,[91a,91b] G. Rahal,[179] S. Rajagopalan,[25] M. Rammensee,[30] C. Rangel-Smith,[167] F. Rauscher,[100] S. Rave,[83] T. C. Rave,[48] T. Ravenscroft,[53] M. Raymond,[30] A. L. Read,[119] N. P. Readioff,[74] D. M. Rebuzzi,[121a,121b] A. Redelbach,[175] G. Redlinger,[25] R. Reece,[138] K. Reeves,[41] L. Rehnisch,[16] H. Reisin,[27] M. Relich,[164] C. Rembser,[30] H. Ren,[33a] A. Renaud,[117] M. Rescigno,[133a] S. Resconi,[91a] O. L. Rezanova,[109,d] P. Reznicek,[129] R. Rezvani,[95] R. Richter,[101] E. Richter-Was,[38b] M. Ridel,[80] P. Rieck,[16] C. J. Riegel,[176] J. Rieger,[54]

M. Rijssenbeek,[149] A. Rimoldi,[121a,121b] L. Rinaldi,[20a] E. Ritsch,[62] I. Riu,[12] F. Rizatdinova,[114] E. Rizvi,[76] S. H. Robertson,[87,k] A. Robichaud-Veronneau,[87] D. Robinson,[28] J. E. M. Robinson,[84] A. Robson,[53] C. Roda,[124a,124b] L. Rodrigues,[30] S. Roe,[30] O. Røhne,[119] S. Rolli,[162] A. Romaniouk,[98] M. Romano,[20a,20b] S. M. Romano Saez,[34] E. Romero Adam,[168] N. Rompotis,[139] M. Ronzani,[48] L. Roos,[80] E. Ros,[168] S. Rosati,[133a] K. Rosbach,[48] P. Rose,[138] P. L. Rosendahl,[14] O. Rosenthal,[142] V. Rossetti,[147a,147b] E. Rossi,[104a,104b] L. P. Rossi,[50a] R. Rosten,[139] M. Rotaru,[26a] I. Roth,[173] J. Rothberg,[139] D. Rousseau,[117] C. R. Royon,[137] A. Rozanov,[85] Y. Rozen,[153] X. Ruan,[146c] F. Rubbo,[144] I. Rubinskiy,[42] V. I. Rud,[99] C. Rudolph,[44] M. S. Rudolph,[159] F. Rühr,[48] A. Ruiz-Martinez,[30] Z. Rurikova,[48] N. A. Rusakovich,[65] A. Ruschke,[100] H. L. Russell,[139] J. P. Rutherfoord,[7] N. Ruthmann,[48] Y. F. Ryabov,[123] M. Rybar,[129] G. Rybkin,[117] N. C. Ryder,[120] A. F. Saavedra,[151] G. Sabato,[107] S. Sacerdoti,[27] A. Saddique,[3] H. F-W. Sadrozinski,[138] R. Sadykov,[65] F. Safai Tehrani,[133a] M. Saimpert,[137] H. Sakamoto,[156] Y. Sakurai,[172] G. Salamanna,[135a,135b] A. Salamon,[134a] M. Saleem,[113] D. Salek,[107] P. H. Sales De Bruin,[139] D. Salihagic,[101] A. Salnikov,[144] J. Salt,[168] D. Salvatore,[37a,37b] F. Salvatore,[150] A. Salvucci,[106] A. Salzburger,[30] D. Sampsonidis,[155] A. Sanchez,[104a,104b] J. Sánchez,[168] V. Sanchez Martinez,[168] H. Sandaker,[14] R. L. Sandbach,[76] H. G. Sander,[83] M. P. Sanders,[100] M. Sandhoff,[176] C. Sandoval,[163] R. Sandstroem,[101] D. P. C. Sankey,[131] A. Sansoni,[47] C. Santoni,[34] R. Santonico,[134a,134b] H. Santos,[126a] I. Santoyo Castillo,[150] K. Sapp,[125] A. Sapronov,[65] J. G. Saraiva,[126a,126d] B. Sarrazin,[21] O. Sasaki,[66] Y. Sasaki,[156] K. Sato,[161] G. Sauvage,[5,a] E. Sauvan,[5] G. Savage,[77] P. Savard,[159,e] C. Sawyer,[120] L. Sawyer,[79,n] J. Saxon,[31] C. Sbarra,[20a] A. Sbrizzi,[20a,20b] T. Scanlon,[78] D. A. Scannicchio,[164] M. Scarcella,[151] V. Scarfone,[37a,37b] J. Schaarschmidt,[173] P. Schacht,[101] D. Schaefer,[30] R. Schaefer,[42] J. Schaeffer,[83] S. Schaepe,[21] S. Schaetzel,[58b] U. Schäfer,[83] A. C. Schaffer,[117] D. Schaile,[100] R. D. Schamberger,[149] V. Scharf,[58a] V. A. Schegelsky,[123] D. Scheirich,[129] M. Schernau,[164] C. Schiavi,[50a,50b] C. Schillo,[48] M. Schioppa,[37a,37b] S. Schlenker,[30] E. Schmidt,[48] K. Schmieden,[30] C. Schmitt,[83] S. Schmitt,[58b] S. Schmitt,[42] B. Schneider,[160a] Y. J. Schnellbach,[74] U. Schnoor,[44] L. Schoeffel,[137] A. Schoening,[58b] B. D. Schoenrock,[90] E. Schopf,[21] A. L. S. Schorlemmer,[54] M. Schott,[83] D. Schouten,[160a] J. Schovancova,[8] S. Schramm,[159] M. Schreyer,[175] C. Schroeder,[83] N. Schuh,[83] M. J. Schultens,[21] H.-C. Schultz-Coulon,[58a] H. Schulz,[16] M. Schumacher,[48] B. A. Schumm,[138] Ph. Schune,[137] C. Schwanenberger,[84] A. Schwartzman,[144] T. A. Schwarz,[89] Ph. Schwegler,[101] Ph. Schwemling,[137] R. Schwienhorst,[90] J. Schwindling,[137] T. Schwindt,[21] M. Schwoerer,[5] F. G. Sciacca,[17] E. Scifo,[117] G. Sciolla,[23] F. Scuri,[124a,124b] F. Scutti,[21] J. Searcy,[89] G. Sedov,[42] E. Sedykh,[123] P. Seema,[21] S. C. Seidel,[105] A. Seiden,[138] F. Seifert,[128] J. M. Seixas,[24a] G. Sekhniaidze,[104a] S. J. Sekula,[40] K. E. Selbach,[46] D. M. Seliverstov,[123,a] N. Semprini-Cesari,[20a,20b] C. Serfon,[30] L. Serin,[117] L. Serkin,[54] T. Serre,[85] R. Seuster,[160a] H. Severini,[113] T. Sfiligoj,[75] F. Sforza,[101] A. Sfyrla,[30] E. Shabalina,[54] M. Shamim,[116] L. Y. Shan,[33a] R. Shang,[166] J. T. Shank,[22] M. Shapiro,[15] P. B. Shatalov,[97] K. Shaw,[165a,165b] A. Shcherbakova,[147a,147b] C. Y. Shehu,[150] P. Sherwood,[78] L. Shi,[152,ee] S. Shimizu,[67] C. O. Shimmin,[164] M. Shimojima,[102] M. Shiyakova,[65] A. Shmeleva,[96] D. Shoaleh Saadi,[95] M. J. Shochet,[31] S. Shojaii,[91a,91b] S. Shrestha,[111] E. Shulga,[98] M. A. Shupe,[7] S. Shushkevich,[42] P. Sicho,[127] O. Sidiropoulou,[175] D. Sidorov,[114] A. Sidoti,[20a,20b] F. Siegert,[44] Dj. Sijacki,[13] J. Silva,[126a,126d] Y. Silver,[154] D. Silverstein,[144] S. B. Silverstein,[147a] V. Simak,[128] O. Simard,[5] Lj. Simic,[13] S. Simion,[117] E. Simioni,[83] B. Simmons,[78] D. Simon,[34] R. Simoniello,[91a,91b] P. Sinervo,[159] N. B. Sinev,[116] G. Siragusa,[175] A. N. Sisakyan,[65,a] S. Yu. Sivoklokov,[99] J. Sjölin,[147a,147b] T. B. Sjursen,[14] M. B. Skinner,[72] H. P. Skottowe,[57] P. Skubic,[113] M. Slater,[18] T. Slavicek,[128] M. Slawinska,[107] K. Sliwa,[162] V. Smakhtin,[173] B. H. Smart,[46] L. Smestad,[14] S. Yu. Smirnov,[98] Y. Smirnov,[98] L. N. Smirnova,[99,ff] O. Smirnova,[81] M. N. K. Smith,[35] M. Smizanska,[72] K. Smolek,[128] A. A. Snesarev,[96] G. Snidero,[76] S. Snyder,[25] R. Sobie,[170,k] F. Socher,[44] A. Soffer,[154] D. A. Soh,[152,ee] C. A. Solans,[30] M. Solar,[128] J. Solc,[128] E. Yu. Soldatov,[98] U. Soldevila,[168] A. A. Solodkov,[130] A. Soloshenko,[65] O. V. Solovyanov,[130] V. Solovyev,[123] P. Sommer,[48] H. Y. Song,[33b] N. Soni,[1] A. Sood,[15] A. Sopczak,[128] B. Sopko,[128] V. Sopko,[128] V. Sorin,[12] D. Sosa,[58b] M. Sosebee,[8] C. L. Sotiropoulou,[155] R. Soualah,[165a,165c] P. Soueid,[95] A. M. Soukharev,[109,d] D. South,[42] S. Spagnolo,[73a,73b] F. Spanò,[77] W. R. Spearman,[57] F. Spettel,[101] R. Spighi,[20a] G. Spigo,[30] L. A. Spiller,[88] M. Spousta,[129] T. Spreitzer,[159] R. D. St. Denis,[53,a] S. Staerz,[44] J. Stahlman,[122] R. Stamen,[58a] S. Stamm,[16] E. Stanecka,[39] C. Stanescu,[135a] M. Stanescu-Bellu,[42] M. M. Stanitzki,[42] S. Stapnes,[119] E. A. Starchenko,[130] J. Stark,[55] P. Staroba,[127] P. Starovoitov,[42] R. Staszewski,[39] P. Stavina,[145a,a] P. Steinberg,[25] B. Stelzer,[143] H. J. Stelzer,[30] O. Stelzer-Chilton,[160a] H. Stenzel,[52] S. Stern,[101] G. A. Stewart,[53] J. A. Stillings,[21] M. C. Stockton,[87] M. Stoebe,[87] G. Stoicea,[26a] P. Stolte,[54] S. Stonjek,[101] A. R. Stradling,[8] A. Straessner,[44] M. E. Stramaglia,[17] J. Strandberg,[148] S. Strandberg,[147a,147b] A. Strandlie,[119] E. Strauss,[144] M. Strauss,[113] P. Strizenec,[145b] R. Ströhmer,[175] D. M. Strom,[116] R. Stroynowski,[40] A. Strubig,[106] S. A. Stucci,[17] B. Stugu,[14] N. A. Styles,[42] D. Su,[144] J. Su,[125] R. Subramaniam,[79] A. Succurro,[12] Y. Sugaya,[118] C. Suhr,[108] M. Suk,[128] V. V. Sulin,[96] S. Sultansoy,[4d] T. Sumida,[68] S. Sun,[57] X. Sun,[33a]

J. E. Sundermann,[48] K. Suruliz,[150] G. Susinno,[37a,37b] M. R. Sutton,[150] Y. Suzuki,[66] M. Svatos,[127] S. Swedish,[169] M. Swiatlowski,[144] I. Sykora,[145a] T. Sykora,[129] D. Ta,[90] C. Taccini,[135a,135b] K. Tackmann,[42] J. Taenzer,[159] A. Taffard,[164] R. Tafirout,[160a] N. Taiblum,[154] H. Takai,[25] R. Takashima,[69] H. Takeda,[67] T. Takeshita,[141] Y. Takubo,[66] M. Talby,[85] A. A. Talyshev,[109,d] J. Y. C. Tam,[175] K. G. Tan,[88] J. Tanaka,[156] R. Tanaka,[117] S. Tanaka,[132] S. Tanaka,[66] A. J. Tanasijczuk,[143] B. B. Tannenwald,[111] N. Tannoury,[21] S. Tapprogge,[83] S. Tarem,[153] F. Tarrade,[29] G. F. Tartarelli,[91a] P. Tas,[129] M. Tasevsky,[127] T. Tashiro,[68] E. Tassi,[37a,37b] A. Tavares Delgado,[126a,126b] Y. Tayalati,[136d] F. E. Taylor,[94] G. N. Taylor,[88] W. Taylor,[160b] F. A. Teischinger,[30] M. Teixeira Dias Castanheira,[76] P. Teixeira-Dias,[77] K. K. Temming,[48] H. Ten Kate,[30] P. K. Teng,[152] J. J. Teoh,[118] F. Tepel,[176] S. Terada,[66] K. Terashi,[156] J. Terron,[82] S. Terzo,[101] M. Testa,[47] R. J. Teuscher,[159,k] J. Therhaag,[21] T. Theveneaux-Pelzer,[34] J. P. Thomas,[18] J. Thomas-Wilsker,[77] E. N. Thompson,[35] P. D. Thompson,[18] R. J. Thompson,[84] A. S. Thompson,[53] L. A. Thomsen,[36] E. Thomson,[122] M. Thomson,[28] R. P. Thun,[89,a] F. Tian,[35] M. J. Tibbetts,[15] R. E. Ticse Torres,[85] V. O. Tikhomirov,[96,gg] Yu. A. Tikhonov,[109,d] S. Timoshenko,[98] E. Tiouchichine,[85] P. Tipton,[177] S. Tisserant,[85] T. Todorov,[5,a] S. Todorova-Nova,[129] J. Tojo,[70] S. Tokár,[145a] K. Tokushuku,[66] K. Tollefson,[90] E. Tolley,[57] L. Tomlinson,[84] M. Tomoto,[103] L. Tompkins,[144,hh] K. Toms,[105] E. Torrence,[116] H. Torres,[143] E. Torró Pastor,[168] J. Toth,[85,ii] F. Touchard,[85] D. R. Tovey,[140] H. L. Tran,[117] T. Trefzger,[175] L. Tremblet,[30] A. Tricoli,[30] I. M. Trigger,[160a] S. Trincaz-Duvoid,[80] M. F. Tripiana,[12] W. Trischuk,[159] B. Trocmé,[55] C. Troncon,[91a] M. Trottier-McDonald,[15] M. Trovatelli,[135a,135b] P. True,[90] M. Trzebinski,[39] A. Trzupek,[39] C. Tsarouchas,[30] J. C-L. Tseng,[120] P. V. Tsiareshka,[92] D. Tsionou,[155] G. Tsipolitis,[10] N. Tsirintanis,[9] S. Tsiskaridze,[12] V. Tsiskaridze,[48] E. G. Tskhadadze,[51a] I. I. Tsukerman,[97] V. Tsulaia,[15] S. Tsuno,[66] D. Tsybychev,[149] A. Tudorache,[26a] V. Tudorache,[26a] A. N. Tuna,[122] S. A. Tupputi,[20a,20b] S. Turchikhin,[99,ff] D. Turecek,[128] R. Turra,[91a,91b] A. J. Turvey,[40] P. M. Tuts,[35] A. Tykhonov,[49] M. Tylmad,[147a,147b] M. Tyndel,[131] I. Ueda,[156] R. Ueno,[29] M. Ughetto,[147a,147b] M. Ugland,[14] M. Uhlenbrock,[21] F. Ukegawa,[161] G. Unal,[30] A. Undrus,[25] G. Unel,[164] F. C. Ungaro,[48] Y. Unno,[66] C. Unverdorben,[100] J. Urban,[145b] P. Urquijo,[88] P. Urrejola,[83] G. Usai,[8] A. Usanova,[62] L. Vacavant,[85] V. Vacek,[128] B. Vachon,[87] N. Valencic,[107] S. Valentinetti,[20a,20b] A. Valero,[168] L. Valery,[12] S. Valkar,[129] E. Valladolid Gallego,[168] S. Vallecorsa,[49] J. A. Valls Ferrer,[168] W. Van Den Wollenberg,[107] P. C. Van Der Deijl,[107] R. van der Geer,[107] H. van der Graaf,[107] R. Van Der Leeuw,[107] N. van Eldik,[153] P. van Gemmeren,[6] J. Van Nieuwkoop,[143] I. van Vulpen,[107] M. C. van Woerden,[30] M. Vanadia,[133a,133b] W. Vandelli,[30] R. Vanguri,[122] A. Vaniachine,[6] F. Vannucci,[80] G. Vardanyan,[178] R. Vari,[133a] E. W. Varnes,[7] T. Varol,[40] D. Varouchas,[80] A. Vartapetian,[8] K. E. Varvell,[151] F. Vazeille,[34] T. Vazquez Schroeder,[54] J. Veatch,[7] F. Veloso,[126a,126c] T. Velz,[21] S. Veneziano,[133a] A. Ventura,[73a,73b] D. Ventura,[86] M. Venturi,[170] N. Venturi,[159] A. Venturini,[23] V. Vercesi,[121a] M. Verducci,[133a,133b] W. Verkerke,[107] J. C. Vermeulen,[107] A. Vest,[44] M. C. Vetterli,[143,e] O. Viazlo,[81] I. Vichou,[166] T. Vickey,[146c,jj] O. E. Vickey Boeriu,[146c] G. H. A. Viehhauser,[120] S. Viel,[15] R. Vigne,[30] M. Villa,[20a,20b] M. Villaplana Perez,[91a,91b] E. Vilucchi,[47] M. G. Vincter,[29] V. B. Vinogradov,[65] I. Vivarelli,[150] F. Vives Vaque,[3] S. Vlachos,[10] D. Vladoiu,[100] M. Vlasak,[128] M. Vogel,[32a] P. Vokac,[128] G. Volpi,[124a,124b] M. Volpi,[88] H. von der Schmitt,[101] H. von Radziewski,[48] E. von Toerne,[21] V. Vorobel,[129] K. Vorobev,[98] M. Vos,[168] R. Voss,[30] J. H. Vossebeld,[74] N. Vranjes,[13] M. Vranjes Milosavljevic,[13] V. Vrba,[127] M. Vreeswijk,[107] R. Vuillermet,[30] I. Vukotic,[31] Z. Vykydal,[128] P. Wagner,[21] W. Wagner,[176] H. Wahlberg,[71] S. Wahrmund,[44] J. Wakabayashi,[103] J. Walder,[72] R. Walker,[100] W. Walkowiak,[142] C. Wang,[33c] F. Wang,[174] H. Wang,[15] H. Wang,[40] J. Wang,[42] J. Wang,[33a] K. Wang,[87] R. Wang,[6] S. M. Wang,[152] T. Wang,[21] X. Wang,[177] C. Wanotayaroj,[116] A. Warburton,[87] C. P. Ward,[28] D. R. Wardrope,[78] M. Warsinsky,[48] A. Washbrook,[46] C. Wasicki,[42] P. M. Watkins,[18] A. T. Watson,[18] I. J. Watson,[151] M. F. Watson,[18] G. Watts,[139] S. Watts,[84] B. M. Waugh,[78] S. Webb,[84] M. S. Weber,[17] S. W. Weber,[175] J. S. Webster,[31] A. R. Weidberg,[120] B. Weinert,[61] J. Weingarten,[54] C. Weiser,[48] H. Weits,[107] P. S. Wells,[30] T. Wenaus,[25] D. Wendland,[16] T. Wengler,[30] S. Wenig,[30] N. Wermes,[21] M. Werner,[48] P. Werner,[30] M. Wessels,[58a] J. Wetter,[162] K. Whalen,[29] A. M. Wharton,[72] A. White,[8] M. J. White,[1] R. White,[32b] S. White,[124a,124b] D. Whiteson,[164] D. Wicke,[176] F. J. Wickens,[131] W. Wiedenmann,[174] M. Wielers,[131] P. Wienemann,[21] C. Wiglesworth,[36] L. A. M. Wiik-Fuchs,[21] A. Wildauer,[101] H. G. Wilkens,[30] H. H. Williams,[122] S. Williams,[107] C. Willis,[90] S. Willocq,[86] A. Wilson,[89] J. A. Wilson,[18] I. Wingerter-Seez,[5] F. Winklmeier,[116] B. T. Winter,[21] M. Wittgen,[144] J. Wittkowski,[100] S. J. Wollstadt,[83] M. W. Wolter,[39] H. Wolters,[126a,126c] B. K. Wosiek,[39] J. Wotschack,[30] M. J. Woudstra,[84] K. W. Wozniak,[39] M. Wu,[55] M. Wu,[31] S. L. Wu,[174] X. Wu,[49] Y. Wu,[89] T. R. Wyatt,[84] B. M. Wynne,[46] S. Xella,[36] D. Xu,[33a] L. Xu,[33b,kk] B. Yabsley,[151] S. Yacoob,[146b,ll] R. Yakabe,[67] M. Yamada,[66] Y. Yamaguchi,[118] A. Yamamoto,[66] S. Yamamoto,[156] T. Yamanaka,[156] K. Yamauchi,[103] Y. Yamazaki,[67] Z. Yan,[22] H. Yang,[33e] H. Yang,[174] Y. Yang,[152] S. Yanush,[93] L. Yao,[33a] W-M. Yao,[15] Y. Yasu,[66] E. Yatsenko,[42] K. H. Yau Wong,[21] J. Ye,[40] S. Ye,[25] I. Yeletskikh,[65] A. L. Yen,[57] E. Yildirim,[42]

K. Yorita,[172] R. Yoshida,[6] K. Yoshihara,[122] C. Young,[144] C. J. S. Young,[30] S. Youssef,[22] D. R. Yu,[15] J. Yu,[8] J. M. Yu,[89] J. Yu,[114] L. Yuan,[67] A. Yurkewicz,[108] I. Yusuff,[28,mm] B. Zabinski,[39] R. Zaidan,[63] A. M. Zaitsev,[130,aa] A. Zaman,[149] S. Zambito,[23] L. Zanello,[133a,133b] D. Zanzi,[88] C. Zeitnitz,[176] M. Zeman,[128] A. Zemla,[38a] K. Zengel,[23] O. Zenin,[130] T. Ženiš,[145a] D. Zerwas,[117] D. Zhang,[89] F. Zhang,[174] J. Zhang,[6] L. Zhang,[152] R. Zhang,[33b] X. Zhang,[33d] Z. Zhang,[117] X. Zhao,[40] Y. Zhao,[33d,117] Z. Zhao,[33b] A. Zhemchugov,[65] J. Zhong,[120] B. Zhou,[89] C. Zhou,[45] L. Zhou,[35] L. Zhou,[40] N. Zhou,[164] C. G. Zhu,[33d] H. Zhu,[33a] J. Zhu,[89] Y. Zhu,[33b] X. Zhuang,[33a] K. Zhukov,[96] A. Zibell,[175] D. Zieminska,[61] N. I. Zimine,[65] C. Zimmermann,[83] R. Zimmermann,[21] S. Zimmermann,[48] Z. Zinonos,[54] M. Zinser,[83] M. Ziolkowski,[142] L. Živković,[13] G. Zobernig,[174] A. Zoccoli,[20a,20b] M. zur Nedden,[16] G. Zurzolo,[104a,104b] and L. Zwalinski[30]

(ATLAS Collaboration)

[1]*Department of Physics, University of Adelaide, Adelaide, Australia*
[2]*Physics Department, SUNY Albany, Albany NY, USA*
[3]*Department of Physics, University of Alberta, Edmonton AB, Canada*
[4a]*Department of Physics, Ankara University, Ankara, Turkey*
[4b]*Istanbul Aydin University, Istanbul, Turkey*
[4c]*Division of Physics, TOBB University of Economics and Technology, Ankara, Turkey*
[5]*LAPP, CNRS/IN2P3 and Université de Savoie, Annecy-le-Vieux, France*
[6]*High Energy Physics Division, Argonne National Laboratory, Argonne IL, USA*
[7]*Department of Physics, University of Arizona, Tucson AZ, USA*
[8]*Department of Physics, The University of Texas at Arlington, Arlington TX, USA*
[9]*Physics Department, University of Athens, Athens, Greece*
[10]*Physics Department, National Technical University of Athens, Zografou, Greece*
[11]*Institute of Physics, Azerbaijan Academy of Sciences, Baku, Azerbaijan*
[12]*Institut de Física d'Altes Energies and Departament de Física de la Universitat Autònoma de Barcelona, Barcelona, Spain*
[13]*Institute of Physics, University of Belgrade, Belgrade, Serbia*
[14]*Department for Physics and Technology, University of Bergen, Bergen, Norway*
[15]*Physics Division, Lawrence Berkeley National Laboratory and University of California, Berkeley CA, USA*
[16]*Department of Physics, Humboldt University, Berlin, Germany*
[17]*Albert Einstein Center for Fundamental Physics and Laboratory for High Energy Physics, University of Bern, Bern, Switzerland*
[18]*School of Physics and Astronomy, University of Birmingham, Birmingham, United Kingdom*
[19a]*Department of Physics, Bogazici University, Istanbul, Turkey*
[19b]*Department of Physics, Dogus University, Istanbul, Turkey*
[19c]*Department of Physics Engineering, Gaziantep University, Gaziantep, Turkey*
[20a]*INFN Sezione di Bologna, Italy*
[20b]*Dipartimento di Fisica e Astronomia, Università di Bologna, Bologna, Italy*
[21]*Physikalisches Institut, University of Bonn, Bonn, Germany*
[22]*Department of Physics, Boston University, Boston MA, USA*
[23]*Department of Physics, Brandeis University, Waltham MA, USA*
[24a]*Universidade Federal do Rio De Janeiro COPPE/EE/IF, Rio de Janeiro, Brazil*
[24b]*Electrical Circuits Department, Federal University of Juiz de Fora (UFJF), Juiz de Fora, Brazil*
[24c]*Federal University of Sao Joao del Rei (UFSJ), Sao Joao del Rei, Brazil*
[24d]*Instituto de Fisica, Universidade de Sao Paulo, Sao Paulo, Brazil*
[25]*Physics Department, Brookhaven National Laboratory, Upton NY, USA*
[26a]*National Institute of Physics and Nuclear Engineering, Bucharest, Romania*
[26b]*National Institute for Research and Development of Isotopic and Molecular Technologies, Physics Department, Cluj Napoca, Romania*
[26c]*University Politehnica Bucharest, Bucharest, Romania*
[26d]*West University in Timisoara, Timisoara, Romania*
[27]*Departamento de Física, Universidad de Buenos Aires, Buenos Aires, Argentina*
[28]*Cavendish Laboratory, University of Cambridge, Cambridge, United Kingdom*
[29]*Department of Physics, Carleton University, Ottawa ON, Canada*
[30]*CERN, Geneva, Switzerland*
[31]*Enrico Fermi Institute, University of Chicago, Chicago IL, USA*
[32a]*Departamento de Física, Pontificia Universidad Católica de Chile, Santiago, Chile*
[32b]*Departamento de Física, Universidad Técnica Federico Santa María, Valparaíso, Chile*
[33a]*Institute of High Energy Physics, Chinese Academy of Sciences, Beijing, China*
[33b]*Department of Modern Physics, University of Science and Technology of China, Anhui, China*

[33c]Department of Physics, Nanjing University, Jiangsu, China
[33d]School of Physics, Shandong University, Shandong, China
[33e]Department of Physics and Astronomy, Shanghai Key Laboratory for Particle Physics and Cosmology, Shanghai Jiao Tong University, Shanghai, China
[33f]Physics Department, Tsinghua University, Beijing 100084, China
[34]Laboratoire de Physique Corpusculaire, Clermont Université and Université Blaise Pascal and CNRS/IN2P3, Clermont-Ferrand, France
[35]Nevis Laboratory, Columbia University, Irvington NY, USA
[36]Niels Bohr Institute, University of Copenhagen, Kobenhavn, Denmark
[37a]INFN Gruppo Collegato di Cosenza, Laboratori Nazionali di Frascati, Italy
[37b]Dipartimento di Fisica, Università della Calabria, Rende, Italy
[38a]AGH University of Science and Technology, Faculty of Physics and Applied Computer Science, Krakow, Poland
[38b]Marian Smoluchowski Institute of Physics, Jagiellonian University, Krakow, Poland
[39]Institute of Nuclear Physics Polish Academy of Sciences, Krakow, Poland
[40]Physics Department, Southern Methodist University, Dallas TX, USA
[41]Physics Department, University of Texas at Dallas, Richardson TX, USA
[42]DESY, Hamburg and Zeuthen, Germany
[43]Institut für Experimentelle Physik IV, Technische Universität Dortmund, Dortmund, Germany
[44]Institut für Kern- und Teilchenphysik, Technische Universität Dresden, Dresden, Germany
[45]Department of Physics, Duke University, Durham NC, USA
[46]SUPA - School of Physics and Astronomy, University of Edinburgh, Edinburgh, United Kingdom
[47]INFN Laboratori Nazionali di Frascati, Frascati, Italy
[48]Fakultät für Mathematik und Physik, Albert-Ludwigs-Universität, Freiburg, Germany
[49]Section de Physique, Université de Genève, Geneva, Switzerland
[50a]INFN Sezione di Genova, Italy
[50b]Dipartimento di Fisica, Università di Genova, Genova, Italy
[51a]E. Andronikashvili Institute of Physics, Iv. Javakhishvili Tbilisi State University, Tbilisi, Georgia
[51b]High Energy Physics Institute, Tbilisi State University, Tbilisi, Georgia
[52]II Physikalisches Institut, Justus-Liebig-Universität Giessen, Giessen, Germany
[53]SUPA - School of Physics and Astronomy, University of Glasgow, Glasgow, United Kingdom
[54]II Physikalisches Institut, Georg-August-Universität, Göttingen, Germany
[55]Laboratoire de Physique Subatomique et de Cosmologie, Université Grenoble-Alpes, CNRS/IN2P3, Grenoble, France
[56]Department of Physics, Hampton University, Hampton VA, USA
[57]Laboratory for Particle Physics and Cosmology, Harvard University, Cambridge MA, USA
[58a]Kirchhoff-Institut für Physik, Ruprecht-Karls-Universität Heidelberg, Heidelberg, Germany
[58b]Physikalisches Institut, Ruprecht-Karls-Universität Heidelberg, Heidelberg, Germany
[58c]ZITI Institut für technische Informatik, Ruprecht-Karls-Universität Heidelberg, Mannheim, Germany
[59]Faculty of Applied Information Science, Hiroshima Institute of Technology, Hiroshima, Japan
[60a]Department of Physics, The Chinese University of Hong Kong, Shatin, N.T., Hong Kong, China
[60b]Department of Physics, The University of Hong Kong, Hong Kong, China
[60c]Department of Physics, The Hong Kong University of Science and Technology, Clear Water Bay, Kowloon, Hong Kong, China
[61]Department of Physics, Indiana University, Bloomington IN, USA
[62]Institut für Astro- und Teilchenphysik, Leopold-Franzens-Universität, Innsbruck, Austria
[63]University of Iowa, Iowa City IA, USA
[64]Department of Physics and Astronomy, Iowa State University, Ames IA, USA
[65]Joint Institute for Nuclear Research, JINR Dubna, Dubna, Russia
[66]KEK, High Energy Accelerator Research Organization, Tsukuba, Japan
[67]Graduate School of Science, Kobe University, Kobe, Japan
[68]Faculty of Science, Kyoto University, Kyoto, Japan
[69]Kyoto University of Education, Kyoto, Japan
[70]Department of Physics, Kyushu University, Fukuoka, Japan
[71]Instituto de Física La Plata, Universidad Nacional de La Plata and CONICET, La Plata, Argentina
[72]Physics Department, Lancaster University, Lancaster, United Kingdom
[73a]INFN Sezione di Lecce, Italy
[73b]Dipartimento di Matematica e Fisica, Università del Salento, Lecce, Italy
[74]Oliver Lodge Laboratory, University of Liverpool, Liverpool, United Kingdom
[75]Department of Physics, Jožef Stefan Institute and University of Ljubljana, Ljubljana, Slovenia
[76]School of Physics and Astronomy, Queen Mary University of London, London, United Kingdom
[77]Department of Physics, Royal Holloway University of London, Surrey, United Kingdom
[78]Department of Physics and Astronomy, University College London, London, United Kingdom

[79]Louisiana Tech University, Ruston LA, USA
[80]Laboratoire de Physique Nucléaire et de Hautes Energies, UPMC and Université Paris-Diderot and CNRS/IN2P3, Paris, France
[81]Fysiska institutionen, Lunds universitet, Lund, Sweden
[82]Departamento de Fisica Teorica C-15, Universidad Autonoma de Madrid, Madrid, Spain
[83]Institut für Physik, Universität Mainz, Mainz, Germany
[84]School of Physics and Astronomy, University of Manchester, Manchester, United Kingdom
[85]CPPM, Aix-Marseille Université and CNRS/IN2P3, Marseille, France
[86]Department of Physics, University of Massachusetts, Amherst MA, USA
[87]Department of Physics, McGill University, Montreal QC, Canada
[88]School of Physics, University of Melbourne, Victoria, Australia
[89]Department of Physics, The University of Michigan, Ann Arbor MI, USA
[90]Department of Physics and Astronomy, Michigan State University, East Lansing MI, USA
[91a]INFN Sezione di Milano, Italy
[91b]Dipartimento di Fisica, Università di Milano, Milano, Italy
[92]B.I. Stepanov Institute of Physics, National Academy of Sciences of Belarus, Minsk, Republic of Belarus
[93]National Scientific and Educational Centre for Particle and High Energy Physics, Minsk, Republic of Belarus
[94]Department of Physics, Massachusetts Institute of Technology, Cambridge MA, USA
[95]Group of Particle Physics, University of Montreal, Montreal QC, Canada
[96]P.N. Lebedev Institute of Physics, Academy of Sciences, Moscow, Russia
[97]Institute for Theoretical and Experimental Physics (ITEP), Moscow, Russia
[98]National Research Nuclear University MEPhI, Moscow, Russia
[99]D.V. Skobeltsyn Institute of Nuclear Physics, M.V. Lomonosov Moscow State University, Moscow, Russia
[100]Fakultät für Physik, Ludwig-Maximilians-Universität München, München, Germany
[101]Max-Planck-Institut für Physik (Werner-Heisenberg-Institut), München, Germany
[102]Nagasaki Institute of Applied Science, Nagasaki, Japan
[103]Graduate School of Science and Kobayashi-Maskawa Institute, Nagoya University, Nagoya, Japan
[104a]INFN Sezione di Napoli, Italy
[104b]Dipartimento di Fisica, Università di Napoli, Napoli, Italy
[105]Department of Physics and Astronomy, University of New Mexico, Albuquerque NM, USA
[106]Institute for Mathematics, Astrophysics and Particle Physics, Radboud University Nijmegen/Nikhef, Nijmegen, Netherlands
[107]Nikhef National Institute for Subatomic Physics and University of Amsterdam, Amsterdam, Netherlands
[108]Department of Physics, Northern Illinois University, DeKalb IL, USA
[109]Budker Institute of Nuclear Physics, SB RAS, Novosibirsk, Russia
[110]Department of Physics, New York University, New York NY, USA
[111]Ohio State University, Columbus OH, USA
[112]Faculty of Science, Okayama University, Okayama, Japan
[113]Homer L. Dodge Department of Physics and Astronomy, University of Oklahoma, Norman OK, USA
[114]Department of Physics, Oklahoma State University, Stillwater OK, USA
[115]Palacký University, RCPTM, Olomouc, Czech Republic
[116]Center for High Energy Physics, University of Oregon, Eugene OR, USA
[117]LAL, Université Paris-Sud and CNRS/IN2P3, Orsay, France
[118]Graduate School of Science, Osaka University, Osaka, Japan
[119]Department of Physics, University of Oslo, Oslo, Norway
[120]Department of Physics, Oxford University, Oxford, United Kingdom
[121a]INFN Sezione di Pavia, Italy
[121b]Dipartimento di Fisica, Università di Pavia, Pavia, Italy
[122]Department of Physics, University of Pennsylvania, Philadelphia PA, USA
[123]Petersburg Nuclear Physics Institute, Gatchina, Russia
[124a]INFN Sezione di Pisa, Italy
[124b]Dipartimento di Fisica E. Fermi, Università di Pisa, Pisa, Italy
[125]Department of Physics and Astronomy, University of Pittsburgh, Pittsburgh PA, USA
[126a]Laboratorio de Instrumentacao e Fisica Experimental de Particulas - LIP, Lisboa, Portugal
[126b]Faculdade de Ciências, Universidade de Lisboa, Lisboa, Portugal
[126c]Department of Physics, University of Coimbra, Coimbra, Portugal
[126d]Centro de Física Nuclear da Universidade de Lisboa, Lisboa, Portugal
[126e]Departamento de Fisica, Universidade do Minho, Braga, Portugal
[126f]Departamento de Fisica Teorica y del Cosmos and CAFPE, Universidad de Granada, Granada, Spain
[126g]Dep Fisica and CEFITEC of Faculdade de Ciencias e Tecnologia, Universidade Nova de Lisboa, Caparica, Portugal
[127]Institute of Physics, Academy of Sciences of the Czech Republic, Praha, Czech Republic
[128]Czech Technical University in Prague, Praha, Czech Republic

[129]Faculty of Mathematics and Physics, Charles University in Prague, Praha, Czech Republic
[130]State Research Center Institute for High Energy Physics, Protvino, Russia
[131]Particle Physics Department, Rutherford Appleton Laboratory, Didcot, United Kingdom
[132]Ritsumeikan University, Kusatsu, Shiga, Japan
[133a]INFN Sezione di Roma, Italy
[133b]Dipartimento di Fisica, Sapienza Università di Roma, Roma, Italy
[134a]INFN Sezione di Roma Tor Vergata, Italy
[134b]Dipartimento di Fisica, Università di Roma Tor Vergata, Roma, Italy
[135a]INFN Sezione di Roma Tre, Italy
[135b]Dipartimento di Matematica e Fisica, Università Roma Tre, Roma, Italy
[136a]Faculté des Sciences Ain Chock, Réseau Universitaire de Physique des Hautes Energies - Université Hassan II, Casablanca, Morocco
[136b]Centre National de l'Energie des Sciences Techniques Nucleaires, Rabat, Morocco
[136c]Faculté des Sciences Semlalia, Université Cadi Ayyad, LPHEA-Marrakech, Morocco
[136d]Faculté des Sciences, Université Mohamed Premier and LPTPM, Oujda, Morocco
[136e]Faculté des sciences, Université Mohammed V-Agdal, Rabat, Morocco
[137]DSM/IRFU (Institut de Recherches sur les Lois Fondamentales de l'Univers), CEA Saclay (Commissariat à l'Energie Atomique et aux Energies Alternatives), Gif-sur-Yvette, France
[138]Santa Cruz Institute for Particle Physics, University of California Santa Cruz, Santa Cruz CA, USA
[139]Department of Physics, University of Washington, Seattle WA, USA
[140]Department of Physics and Astronomy, University of Sheffield, Sheffield, United Kingdom
[141]Department of Physics, Shinshu University, Nagano, Japan
[142]Fachbereich Physik, Universität Siegen, Siegen, Germany
[143]Department of Physics, Simon Fraser University, Burnaby BC, Canada
[144]SLAC National Accelerator Laboratory, Stanford CA, USA
[145a]Faculty of Mathematics, Physics & Informatics, Comenius University, Bratislava, Slovak Republic
[145b]Department of Subnuclear Physics, Institute of Experimental Physics of the Slovak Academy of Sciences, Kosice, Slovak Republic
[146a]Department of Physics, University of Cape Town, Cape Town, South Africa
[146b]Department of Physics, University of Johannesburg, Johannesburg, South Africa
[146c]School of Physics, University of the Witwatersrand, Johannesburg, South Africa
[147a]Department of Physics, Stockholm University, Sweden
[147b]The Oskar Klein Centre, Stockholm, Sweden
[148]Physics Department, Royal Institute of Technology, Stockholm, Sweden
[149]Departments of Physics & Astronomy and Chemistry, Stony Brook University, Stony Brook NY, USA
[150]Department of Physics and Astronomy, University of Sussex, Brighton, United Kingdom
[151]School of Physics, University of Sydney, Sydney, Australia
[152]Institute of Physics, Academia Sinica, Taipei, Taiwan
[153]Department of Physics, Technion: Israel Institute of Technology, Haifa, Israel
[154]Raymond and Beverly Sackler School of Physics and Astronomy, Tel Aviv University, Tel Aviv, Israel
[155]Department of Physics, Aristotle University of Thessaloniki, Thessaloniki, Greece
[156]International Center for Elementary Particle Physics and Department of Physics, The University of Tokyo, Tokyo, Japan
[157]Graduate School of Science and Technology, Tokyo Metropolitan University, Tokyo, Japan
[158]Department of Physics, Tokyo Institute of Technology, Tokyo, Japan
[159]Department of Physics, University of Toronto, Toronto ON, Canada
[160a]TRIUMF, Vancouver BC, Canada
[160b]Department of Physics and Astronomy, York University, Toronto ON, Canada
[161]Faculty of Pure and Applied Sciences, University of Tsukuba, Tsukuba, Japan
[162]Department of Physics and Astronomy, Tufts University, Medford MA, USA
[163]Centro de Investigaciones, Universidad Antonio Narino, Bogota, Colombia
[164]Department of Physics and Astronomy, University of California Irvine, Irvine CA, USA
[165a]INFN Gruppo Collegato di Udine, Sezione di Trieste, Udine, Italy
[165b]ICTP, Trieste, Italy
[165c]Dipartimento di Chimica, Fisica e Ambiente, Università di Udine, Udine, Italy
[166]Department of Physics, University of Illinois, Urbana IL, USA
[167]Department of Physics and Astronomy, University of Uppsala, Uppsala, Sweden
[168]Instituto de Física Corpuscular (IFIC) and Departamento de Física Atómica, Molecular y Nuclear and Departamento de Ingeniería Electrónica and Instituto de Microelectrónica de Barcelona (IMB-CNM), University of Valencia and CSIC, Valencia, Spain
[169]Department of Physics, University of British Columbia, Vancouver BC, Canada
[170]Department of Physics and Astronomy, University of Victoria, Victoria BC, Canada
[171]Department of Physics, University of Warwick, Coventry, United Kingdom

[172]Waseda University, Tokyo, Japan
[173]Department of Particle Physics, The Weizmann Institute of Science, Rehovot, Israel
[174]Department of Physics, University of Wisconsin, Madison WI, USA
[175]Fakultät für Physik und Astronomie, Julius-Maximilians-Universität, Würzburg, Germany
[176]Fachbereich C Physik, Bergische Universität Wuppertal, Wuppertal, Germany
[177]Department of Physics, Yale University, New Haven CT, USA
[178]Yerevan Physics Institute, Yerevan, Armenia
[179]Centre de Calcul de l'Institut National de Physique Nucléaire et de Physique des Particules (IN2P3), Villeurbanne, France

[a]Deceased.
[b]Also at Department of Physics, King's College London, London, United Kingdom.
[c]Also at Institute of Physics, Azerbaijan Academy of Sciences, Baku, Azerbaijan.
[d]Also at Novosibirsk State University, Novosibirsk, Russia.
[e]Also at TRIUMF, Vancouver BC, Canada.
[f]Also at Department of Physics, California State University, Fresno CA, USA.
[g]Also at Department of Physics, University of Fribourg, Fribourg, Switzerland.
[h]Also at Tomsk State University, Tomsk, Russia.
[i]Also at CPPM, Aix-Marseille Université and CNRS/IN2P3, Marseille, France.
[j]Also at Università di Napoli Parthenope, Napoli, Italy.
[k]Also at Institute of Particle Physics (IPP), Canada.
[l]Also at Particle Physics Department, Rutherford Appleton Laboratory, Didcot, United Kingdom.
[m]Also at Department of Physics, St. Petersburg State Polytechnical University, St. Petersburg, Russia.
[n]Also at Louisiana Tech University, Ruston LA, USA.
[o]Also at Institucio Catalana de Recerca i Estudis Avancats, ICREA, Barcelona, Spain.
[p]Also at Department of Physics, National Tsing Hua University, Taiwan.
[q]Also at Department of Physics, The University of Texas at Austin, Austin TX, USA.
[r]Also at Institute of Theoretical Physics, Ilia State University, Tbilisi, Georgia.
[s]Also at CERN, Geneva, Switzerland.
[t]Also at Georgian Technical University (GTU),Tbilisi, Georgia.
[u]Also at Ochadai Academic Production, Ochanomizu University, Tokyo, Japan.
[v]Also at Manhattan College, New York NY, USA.
[w]Also at Institute of Physics, Academia Sinica, Taipei, Taiwan.
[x]Also at LAL, Université Paris-Sud and CNRS/IN2P3, Orsay, France.
[y]Also at Academia Sinica Grid Computing, Institute of Physics, Academia Sinica, Taipei, Taiwan.
[z]Also at Laboratoire de Physique Nucléaire et de Hautes Energies, UPMC and Université Paris-Diderot and CNRS/IN2P3, Paris, France.
[aa]Also at Moscow Institute of Physics and Technology State University, Dolgoprudny, Russia.
[bb]Also at Section de Physique, Université de Genève, Geneva, Switzerland.
[cc]Also at International School for Advanced Studies (SISSA), Trieste, Italy.
[dd]Also at Department of Physics and Astronomy, University of South Carolina, Columbia SC, USA.
[ee]Also at School of Physics and Engineering, Sun Yat-sen University, Guangzhou, China.
[ff]Also at Faculty of Physics, M.V.Lomonosov Moscow State University, Moscow, Russia.
[gg]Also at National Research Nuclear University MEPhI, Moscow, Russia.
[hh]Also at Department of Physics, Stanford University, Stanford CA, USA.
[ii]Also at Institute for Particle and Nuclear Physics, Wigner Research Centre for Physics, Budapest, Hungary.
[jj]Also at Department of Physics, Oxford University, Oxford, United Kingdom.
[kk]Also at Department of Physics, The University of Michigan, Ann Arbor MI, USA.
[ll]Also at Discipline of Physics, University of KwaZulu-Natal, Durban, South Africa.
[mm]Also at University of Malaya, Department of Physics, Kuala Lumpur, Malaysia.

Published for SISSA by Springer

Received: *November 26, 2012*
Accepted: *February 15, 2013*
Published: *March 21, 2013*

Measurement of ZZ production in pp collisions at $\sqrt{s} = 7$ TeV and limits on anomalous ZZZ and $ZZ\gamma$ couplings with the ATLAS detector

The ATLAS collaboration

E-mail: atlas.publications@cern.ch

Abstract: A measurement of the ZZ production cross section in proton-proton collisions at $\sqrt{s} = 7$ TeV using data recorded by the ATLAS experiment at the Large Hadron Collider is presented. In a data sample corresponding to an integrated luminosity of 4.6 fb^{-1} collected in 2011, events are selected that are consistent either with two Z bosons decaying to electrons or muons or with one Z boson decaying to electrons or muons and a second Z boson decaying to neutrinos. The $ZZ^{(*)} \to \ell^+\ell^-\ell'^+\ell'^-$ and $ZZ \to \ell^+\ell^-\nu\bar{\nu}$ cross sections are measured in restricted phase-space regions. These results are then used to derive the total cross section for ZZ events produced with both Z bosons in the mass range 66 to 116 GeV, $\sigma_{ZZ}^{\rm tot} = 6.7 \pm 0.7$ (stat.) $^{+0.4}_{-0.3}$ (syst.) ± 0.3 (lumi.) pb, which is consistent with the Standard Model prediction of $5.89^{+0.22}_{-0.18}$ pb calculated at next-to-leading order in QCD. The normalized differential cross sections in bins of various kinematic variables are presented. Finally, the differential event yield as a function of the transverse momentum of the leading Z boson is used to set limits on anomalous neutral triple gauge boson couplings in ZZ production.

Keywords: Hadron-Hadron Scattering

Open Access, Copyright CERN,
for the benefit of the ATLAS collaboration

doi:10.1007/JHEP03(2013)128

JHEP03(2013)128

Contents

1 Introduction **2**

2 The ATLAS detector and data sample **4**
2.1 Simulated data samples 5

3 Event reconstruction and selection **5**
3.1 Leptons, jets and missing energy 5
3.1.1 Common lepton selection 5
3.1.2 Extended-lepton selection 7
3.1.3 Jets and missing transverse momentum 7
3.2 $ZZ^{(*)} \to \ell^+\ell^-\ell'^+\ell'^-$ selection 8
3.3 $ZZ \to \ell^+\ell^-\nu\bar{\nu}$ selection 8

4 Signal acceptance **10**
4.1 Fiducial region definitions 11
4.2 Extrapolation to the total phase space 13
4.3 Systematic uncertainties 13

5 Background estimation **14**
5.1 $ZZ^{(*)} \to \ell^+\ell^-\ell'^+\ell'^-$ background 14
5.2 $ZZ \to \ell^+\ell^-\nu\bar{\nu}$ background 16
5.2.1 Backgrounds from $t\bar{t}$, Wt, WW and $Z \to \tau^+\tau^-$ 17
5.2.2 Background from WZ production with leptonic decays 18
5.2.3 Background from Z bosons with associated jets 18
5.2.4 Background from events with a misidentified lepton 18

6 Results **19**
6.1 Cross section measurements 19
6.2 Differential cross sections 22
6.3 Anomalous neutral triple gauge couplings 22

7 Conclusions **25**

The ATLAS collaboration **32**

JHEP03(2013)128

1 Introduction

The production of pairs of Z bosons at the Large Hadron Collider (LHC) provides an excellent opportunity to test the predictions of the electroweak sector of the Standard Model (SM) at the TeV energy scale. In the SM, Z boson pairs can be produced via non-resonant processes or in the decay of Higgs bosons. Deviations from SM expectations for the total or differential ZZ production cross sections could be indicative of the production of new resonances decaying to Z bosons or other non-SM contributions.

Non-resonant ZZ production proceeds at leading order (LO) via t- and u-channel quark-antiquark interactions, while about 6% of the production proceeds via gluon fusion. The ZZZ and $ZZ\gamma$ neutral triple gauge boson couplings (nTGCs) are absent in the SM, hence there is no contribution from s-channel $q\bar{q}$ annihilation at tree level. These different production processes are shown in figure 1. At the one-loop level, nTGCs generated by fermion triangles have a magnitude of the order of 10^{-4} [1]. Many models of physics beyond the Standard Model predict values of nTGCs at the level of 10^{-4} to 10^{-3} [2]. The primary signatures of non-zero nTGCs are an increase in the ZZ cross section at high ZZ invariant mass and high transverse momentum of the Z bosons [3]. ZZ production has been studied in e^+e^- collisions at LEP [4–8], in $p\bar{p}$ collisions at the Tevatron [9–12] and recently in pp collisions at the LHC [13, 14]. No deviation of the measured total cross section from the SM expectation has been observed, and limits on anomalous nTGCs have been set [8, 9, 13, 14]. In searching for the SM Higgs boson, the ATLAS and CMS collaborations observed recently a neutral boson resonance with a mass around 126 GeV [15–17]. A SM Higgs boson with that mass can decay to two Z bosons only when at least one Z boson is off-shell, and even in this case, the contribution is less than 3%. Searches for high-mass non-SM ZZ resonances have not resulted in any excess above the SM expectations [18].

This paper presents a measurement of ZZ production[1] in proton-proton collisions at a centre-of-mass energy $\sqrt{s} = 7$ TeV using 4.6 fb^{-1} of integrated luminosity collected by the ATLAS detector at the LHC. ZZ events are selected in two channels:[2] $\ell^+\ell^-\ell'^+\ell'^-$ and $\ell^+\ell^-\nu\bar{\nu}$. Two selections are used in the four-charged-lepton channel: an on-shell ZZ selection denoted by $ZZ \to \ell^+\ell^-\ell'^+\ell'^-$ where both Z bosons are required to be within the mass range 66-116 GeV[3] and a selection which includes an off-shell Z boson denoted by $ZZ^* \to \ell^+\ell^-\ell'^+\ell'^-$ where one Z boson is required to be within this mass range and the other can be off-shell and have any mass above 20 GeV. In the $\ell^+\ell^-\nu\bar{\nu}$ channel, the $\nu\bar{\nu}$ system is expected to be produced by an off-shell Z boson in 2.6% of the events. Since this fraction is small and only one event selection is used for this channel, it is referred to as $ZZ \to \ell^+\ell^-\nu\bar{\nu}$ throughout the paper. The $ZZ^{(*)} \to \ell^+\ell^-\ell'^+\ell'^-$ channel has an excellent signal-to-background ratio, but it has a branching fraction six times lower than the $ZZ \to \ell^+\ell^-\nu\bar{\nu}$ channel; the latter has higher background contributions with an expected

[1] Throughout this paper Z should be taken to mean Z/γ^* when referring to decays to charged leptons, and just Z when referring to decays to neutrinos.

[2] ℓ represents either electrons or muons. ℓ and ℓ' are used to denote leptons from a different Z parent, but not necessarily of different flavour. Decay modes mentioned with the use of ℓ indicate the sum of the decay modes with specific lepton flavours.

[3] Throughout this paper, the 66-116 GeV mass range is referred to as the Z mass window.

JHEP03(2013)128

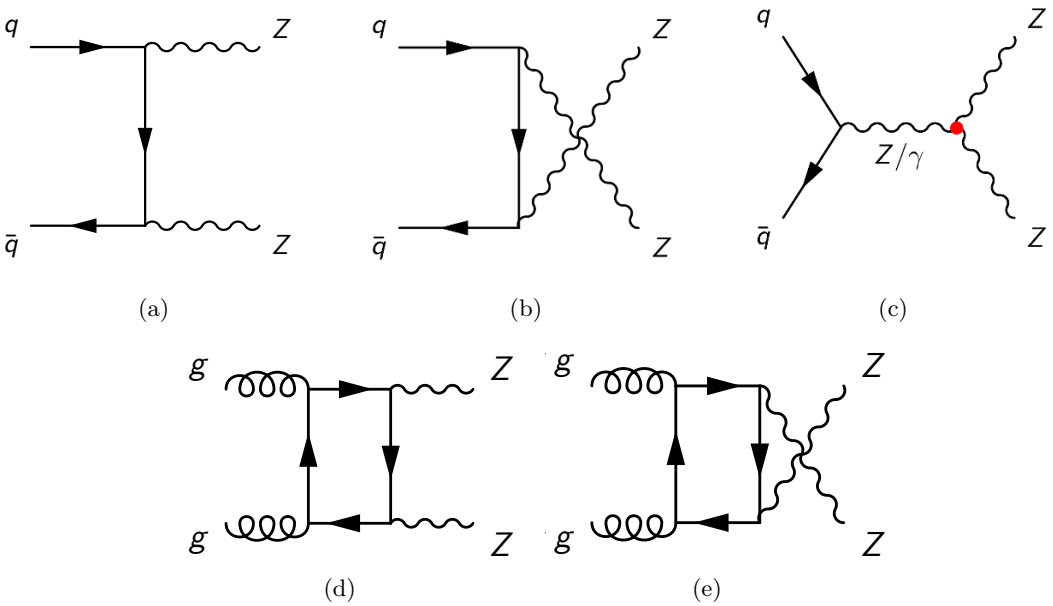

Figure 1. Leading order Feynman diagrams for ZZ production through the $q\bar{q}$ and gg initial state at hadron colliders. The s-channel diagram, (c), contains the ZZZ and $ZZ\gamma$ neutral TGC vertices which do not exist in the SM.

signal-to-background ratio around one (after applying the event selections described below). This paper presents the total ZZ production cross section, the fiducial cross section in a restricted phase space for each decay channel (integrated, and as a function of kinematic parameters for the ZZ selections) and limits on anomalous nTGCs using the observed ZZ event yields as a function of the transverse momentum of the leading Z boson.[4] The results presented in this paper supersede the previously published results [13] which were derived with the first 1.02 fb^{-1} of the dataset used here, only with the $ZZ \to \ell^+\ell^-\ell'^+\ell'^-$ decay channel and with the use of the total ZZ event count for the derivation of the limits on anomalous nTGCs.

The total cross section for non-resonant ZZ production is predicted at next-to-leading order (NLO) in QCD to be $6.18^{+0.25}_{-0.18}$ pb, where the quoted theoretical uncertainties result from varying the factorization and renormalization scales simultaneously by a factor of two whilst using the full CT10 parton distribution function (PDF) error set [19]. The cross section is calculated in the on-shell (zero-width) approximation using MCFM [20] with CT10; it includes a 5.8% contribution from gluon fusion. When the natural width of the Z boson is used and both Z bosons are required to be within the Z mass window, the NLO cross section is predicted to be $5.89^{+0.22}_{-0.18}$ pb. The cross sections given here are calculated at a renormalization and factorization scale equal to half the mass of the diboson system. The total cross section using the zero-width approximation was previously measured to be $8.5^{+2.7}_{-2.3}$ (stat.) $^{+0.4}_{-0.3}$ (syst.) $\pm$ 0.3 (lumi.) pb [13].

[4]Leading Z refers to the Z with the higher transverse momentum in $ZZ \to \ell^+\ell^-\ell'^+\ell'^-$ decays or to the Z boson decaying to a charged lepton pair in $ZZ \to \ell^+\ell^-\nu\bar{\nu}$ decays.

JHEP03(2013)128

This paper is organized as follows: an overview of the ATLAS detector, data, signal and background Monte Carlo (MC) samples used for this analysis is given in section 2; section 3 describes the selection of the physics objects; section 4 describes the fiducial phase space of the measurement, the corresponding ZZ cross section definition and the acceptances of the event selection and fiducial phase space; section 5 explains how the backgrounds to the $\ell^+\ell^-\ell'^+\ell'^-$ and $\ell^+\ell^-\nu\bar{\nu}$ final states are estimated with a combination of simulation and data-driven techniques; section 6 presents the results: cross section, differential cross sections and nTGC limits; finally, a summary of the main results is given in section 7.

2 The ATLAS detector and data sample

The ATLAS detector [21] is a multipurpose particle detector with a cylindrical geometry. It consists of inner tracking devices surrounded by a superconducting solenoid, electromagnetic and hadronic calorimeters and a muon spectrometer with a toroidal magnetic field. The inner detector, in combination with the 2 T field from the solenoid, provides precision tracking of charged particles in the pseudorapidity range $|\eta| < 2.5$.[5] It consists of a silicon pixel detector, a silicon microstrip detector and a straw tube tracker that also provides transition radiation measurements for electron identification in the pseudorapidity range $|\eta| < 2.0$. The calorimeter system covers the pseudorapidity range $|\eta| < 4.9$. The electromagnetic calorimeter uses liquid argon (LAr) as the active material with lead as an absorber ($|\eta| < 3.2$). It identifies electromagnetic showers and measures their energy and position; in the region $|\eta| < 2.5$ it is finely segmented and provides electron identification in conjunction with the inner detector which covers the same η region. Hadronic showers are measured in the central rapidity range ($|\eta| < 1.7$) by scintillator tiles with iron absorber, while in the end-cap region ($1.5 < |\eta| < 3.2$) a LAr calorimeter with a copper absorber is used. In the forward region ($3.2 < |\eta| < 4.9$) a LAr calorimeter with a copper absorber for the first layer and tungsten for the last two layers is used for both electromagnetic and hadronic showers. All calorimeters are used to measure jets. The muon spectrometer surrounds the calorimeters; it consists of superconducting air-core toroid magnets, high-precision tracking chambers which provide muon identification and tracking measurement in the pseudorapidity range $|\eta| < 2.7$, and separate trigger chambers covering $|\eta| < 2.4$.

A three-level trigger system selects events to be recorded for offline analysis. The events used in this analysis were selected with single-lepton triggers with nominal transverse momentum (p_{T}) thresholds of 20 or 22 GeV (depending on the instantaneous luminosity of the LHC) for electrons and 18 GeV for muons. The efficiencies of the single-lepton triggers have been determined as a function of lepton pseudorapidity and transverse momentum using large samples of $Z \to \ell^+\ell^-$ events. The trigger efficiencies for events passing the offline selection described below are all greater than 98%.

[5] ATLAS uses a right-handed coordinate system with its origin at the nominal interaction point in the centre of the detector and the z-axis along the beam direction. The x-axis points from the interaction point to the centre of the LHC ring, and the y-axis points upwards. Cylindrical coordinates (r,ϕ) are used in the transverse plane, ϕ being the azimuthal angle around the beam direction. The pseudorapidity η is defined in terms of the polar angle θ as $\eta = -\ln\tan(\theta/2)$.

JHEP03(2013)128

The measurements presented here uses the full data sample of proton-proton collisions at $\sqrt{s} = 7$ TeV recorded in 2011. After data quality requirements, the total integrated luminosity used in the analysis is 4.6 fb^{-1} with an uncertainty of 3.9% [22].

2.1 Simulated data samples

Monte Carlo simulated samples cross-checked with data are used to calculate several quantities used in this measurement, including acceptance, efficiency and some of the background to the $ZZ \to \ell^+\ell^-\nu\bar{\nu}$ decay channel. The NLO generator PowhegBox [23, 24] with the CT10 PDF set, interfaced to Pythia [25], is used to model the signal for both channels. The LO multi-leg generator Sherpa [26] with the CTEQ6L1 PDF set [27] in comparison with PowhegBox is used to evaluate systematic uncertainties. The contribution from $gg \to ZZ$ is modelled by the gg2zz generator [28] interfaced to Herwig [29] to model parton showers and to Jimmy [30] for multiparton interactions. In each case, the simulation includes the interference terms between the Z and γ^* diagrams. For both the $\ell^+\ell^-\ell'^+\ell'^-$ and $\ell^+\ell^-\nu\bar{\nu}$ final states, MCFM is used to calculate theoretical uncertainties, and Sherpa is used for the generation of signal samples with neutral triple gauge couplings.

The LO generator Alpgen [31] with CTEQ6L1 PDFs is used to simulate Z+jets, W+jets, $Z\gamma$ and $W\gamma$ background events with Jimmy used for multiparton interactions and Herwig for parton showers. The NLO generator MC@NLO [32] with CT10 PDFs is used to model $t\bar{t}$ background processes as well as WW production. The single-top Wt process is modelled with AcerMC [33] with the MSTW2008 PDFs [34]. The LO generator Herwig with MSTW2008 PDFs is used to model WZ production. The LO generator Madgraph [35] with CTEQ6L1 PDFs is also used to model $Z\gamma$ and $W\gamma^*$ events, where Pythia is used for hadronization and showering.

The detector response is simulated [36] with a program based on Geant4 [37]. Additional inelastic pp events are included in the simulation, distributed so as to reproduce the number of collisions per bunch-crossing in the data. The detector response to interactions in the out-of-time bunches from pile-up is also modelled in the simulation. The results of the simulation are corrected with scale factors determined by comparing efficiencies observed in data to those in the simulated events, and the lepton momentum scale and resolution are finely adjusted to match the observed dilepton spectra in $Z \to \ell\ell$ events using a sample of Z bosons.

3 Event reconstruction and selection

Events are required to contain a primary vertex formed from at least three associated tracks with $p_{\mathrm{T}} > 400$ MeV.

3.1 Leptons, jets and missing energy

3.1.1 Common lepton selection

Muons are identified by matching tracks (or track segments) reconstructed in the muon spectrometer to tracks reconstructed in the inner detector [38]. The momenta of these

JHEP03(2013)128

combined muons are calculated by combining the information from the two systems and correcting for the energy deposited in the calorimeters. The analyses of both decay channels use muons which have full tracks reconstructed in the muon spectrometer with $p_{\mathrm{T}} > 20$ GeV and $|\eta| < 2.5$. The $ZZ^{(*)} \to \ell^+\ell^-\ell'^+\ell'^-$ channel recovers additional ZZ acceptance with minimal additional background using a lower threshold of $p_{\mathrm{T}} > 7$ GeV and by accepting muons with segments reconstructed in the muon spectrometer (in this latter case, the muon spectrometer is used to identify the track as a muon, but its momentum is measured using the inner detector; for the purposes of the discussion below, these muons are also referred to as *combined* muons).

Electrons are reconstructed from an energy cluster in the electromagnetic calorimeter matched to a track in the inner detector [38]; the transverse momentum is computed from the calorimeter energy and the direction from the track parameters measured in the inner detector. The electron track parameters are corrected for bremsstrahlung energy loss using the Gaussian-sum filter algorithm [39]. Electron candidates in the $ZZ^{(*)} \to \ell^+\ell^-\ell'^+\ell'^-$ ($ZZ \to \ell^+\ell^-\nu\bar{\nu}$) channel are required to have longitudinal and transverse shower profiles consistent with those expected from electromagnetic showers, by satisfying the loose (medium) identification criteria described in ref. [40] reoptimized for the 2011 data-taking conditions. They are also required to have a transverse momentum of at least 7 (20) GeV and a pseudorapidity of $|\eta| < 2.47$.

In order to reject non-prompt leptons from the decay of heavy quarks and fake electrons from misidentified jets (charged hadrons or photon conversions), all selected leptons must satisfy isolation requirements based on calorimetric and tracking information and must be consistent with originating from the primary vertex. For the calorimetric isolation the scalar sum of the transverse energies, ΣE_{T}, of calorimeter deposits inside a cone around the lepton, corrected to remove the energy from the lepton and from additional interactions (pile-up), is formed. In the $ZZ^{(*)} \to \ell^+\ell^-\ell'^+\ell'^-$ ($ZZ \to \ell^+\ell^-\nu\bar{\nu}$) channel, the ΣE_{T} inside a cone of size $\Delta R = \sqrt{(\Delta\phi)^2 + (\Delta\eta)^2} = 0.2$ (0.3) around the lepton is required to be no more than 30% (15%) of the lepton p_{T}. For the track isolation, the scalar sum of the transverse momenta, Σp_{T}, of inner detector tracks inside a cone of size $\Delta R = 0.2$ (0.3) around the lepton is required to be no more than 15% of the lepton p_{T}. The wider cone size, in conjunction with the same or tighter requirements on the fraction of extra activity allowed in the cone, corresponds to more stringent isolation requirements applied to the $ZZ \to \ell^+\ell^-\nu\bar{\nu}$ channel compared to the $ZZ^{(*)} \to \ell^+\ell^-\ell'^+\ell'^-$ channel. This reflects the need to reduce the much higher reducible background (predominantly from Z+jets, $t\bar{t}$ and WW). To ensure that the lepton originates from the primary vertex, its longitudinal impact parameter $|z_0|$ is required to be less than 2 mm, and its transverse impact parameter significance (the transverse impact parameter divided by its error), $|d_0/\sigma_{d_0}|$, is required to be less than 3.5 (6) for muons (electrons). Electrons have a worse impact parameter resolution than muons due to bremsstrahlung.

Since muons can radiate photons which may then convert to electron-positron pairs, electron candidates within $\Delta R = 0.1$ of any selected muon are not considered. If two electron candidates are within $\Delta R = 0.1$ of each other, the one with the lower p_{T} is removed.

JHEP03(2013)128

3.1.2 Extended-lepton selection

Two additional categories of muons are considered for the $ZZ^{(*)} \to \ell^+\ell^-\ell'^+\ell'^-$ channel: forward spectrometer muons with $2.5 < |\eta| < 2.7$ (in a region outside the nominal coverage of the inner detector) and calorimeter-tagged muons with $|\eta| < 0.1$ (where there is a limited geometric coverage in the muon spectrometer). Forward spectrometer muons are required to have a full track that is reconstructed in the muon spectrometer; if these muons are also measured in the inner detector, their momentum is measured using the combined information; otherwise, only the muon spectrometer information is used. In either case, such muons are required to have $p_{\mathrm{T}} > 10$ GeV and the ΣE_{T} of calorimeter deposits inside a cone of size $\Delta R = 0.2$ around the muon is required to be no more than 15% of the muon p_{T}, while no requirement is made on Σp_{T}. The same impact parameter requirements as for the combined muons are imposed for the forward muons measured in the inner detector; no such requirement is imposed on those measured in the muon spectrometer only. Calorimeter-tagged muons are reconstructed from calorimeter energy deposits consistent with a muon which are matched to an inner detector track with $p_{\mathrm{T}} > 20$ GeV and are required to satisfy the same impact parameter and isolation criteria as for the combined muons.

The $ZZ^{(*)} \to \ell^+\ell^-\ell'^+\ell'^-$ channel also uses calorimeter-only electrons with $2.5 < |\eta| < 3.16$ and $p_{\mathrm{T}} > 20$ GeV passing the tight identification requirements [40] for this forward η region, where only the longitudinal and transverse shower profiles in the calorimeters are used for their identification. Their transverse momentum is computed from the calorimeter energy and the electron direction, where the electron direction is computed using the primary vertex position and the shower barycentre position in the calorimeter. Being identified outside the acceptance of the inner detector, no impact parameter requirements can be applied to these calorimeter-only electron candidates, and their charge is not measured. Since only one such electron is allowed in the event, and since all other leptons have their charge measured, the calorimeter-only electron is assigned the charge needed to have two pairs of same-flavour opposite-sign leptons in the event. The requirements described above constrain the additional background introduced by the inclusion of calorimeter-only electrons, and no isolation requirements are imposed on such electrons.

The use of the extended-lepton selection increases the $ZZ \to \ell^+\ell^-\ell'^+\ell'^-$ and $ZZ^* \to \ell^+\ell^-\ell'^+\ell'^-$ acceptance by about 6% from the forward spectrometer muons, 4% from the calorimeter-tagged muons and 6% from the forward electrons. The expected background is kept small by requiring each event to have at most one lepton from each extended-lepton category, and each such lepton to be paired with a non-extended lepton.

3.1.3 Jets and missing transverse momentum

For the $ZZ \to \ell^+\ell^-\nu\bar{\nu}$ selection, events which contain at least one well-reconstructed jet are vetoed to reduce background from top-quark production. Jets are reconstructed from topological clusters of energy in the calorimeter [41] using the anti-k_t algorithm [42] with radius parameter $R = 0.4$. The measured jet energy is corrected for detector inhomogeneities and for the non-compensating nature of the calorimeter using p_{T}- and η-dependent correction factors based on Monte Carlo simulations with adjustments from in-situ measure-

JHEP03(2013)128

ments [43, 44]. Jets are required to have $p_{\mathrm{T}} > 25$ GeV and $|\eta| < 4.5$. In order to minimize the impact of jets from pile-up at high luminosity, the jet vertex fraction is required to be at least 0.75; the jet vertex fraction is defined as the sum of the p_{T} of tracks associated to the jet and originating from the primary vertex, divided by the sum of the p_{T} of all the tracks associated to the jet. If a reconstructed jet and a lepton lie within $\Delta R = 0.3$ of each other, the jet is not considered in the analysis.

The missing transverse momentum $E_{\mathrm{T}}^{\mathrm{miss}}$ is the imbalance of transverse momentum in the event. A large imbalance in the transverse momentum is a signature of the $ZZ \to \ell^+\ell^-\nu\bar{\nu}$ decay channel. The two-dimensional $E_{\mathrm{T}}^{\mathrm{miss}}$ vector is determined from the negative vectorial sum of reconstructed electron, muon and jet momenta together with calorimeter cells not associated to any object [45]. Calorimeter cells are calibrated to the jet energy scale if they are associated with a jet and to the electromagnetic energy scale otherwise. Using calorimeter timing and shower shape information, events that contain jets with $p_{\mathrm{T}} > 20$ GeV and not originating from proton-proton collisions but from e.g. calorimeter signals due to noisy cells are rejected.

3.2 $ZZ^{(*)} \to \ell^+\ell^-\ell'^+\ell'^-$ selection

$ZZ^{(*)} \to \ell^+\ell^-\ell'^+\ell'^-$ events are characterized by four high-p_{T}, isolated electrons or muons, in three channels: $e^+e^-e^+e^-$, $\mu^+\mu^-\mu^+\mu^-$ and $e^+e^-\mu^+\mu^-$. Selected events are required to have exactly four leptons and to have passed at least a single-muon or single-electron trigger. Each combination of lepton pairs is required to satisfy $\Delta R(\ell_1, \ell_2) > 0.2$, where ℓ_1 and ℓ_2 are used hereafter to denote a pair of distinct leptons, independent of their Z parent assignment, flavour and charge. To ensure high and well-measured trigger efficiency, at least one lepton must have $p_{\mathrm{T}} > 20$ GeV (25 GeV) for the offline muon (electron) and be matched to a muon (electron) reconstructed online by the trigger system within $\Delta R = 0.1$ (0.15).

Same-flavour, oppositely-charged lepton pairs are combined to form Z candidates. An event must contain two such pairs. In the $e^+e^-e^+e^-$ and $\mu^+\mu^-\mu^+\mu^-$ channels, ambiguities are resolved by choosing the combination which results in the smaller value of the sum of $|m_{\ell^+\ell^-} - m_Z|$ for the two pairs, where $m_{\ell^+\ell^-}$ is the mass of the dilepton system and m_Z is the mass of the Z boson [46]. Figure 2 shows the correlation between the invariant mass of the leading (higher p_{T}) and the sub-leading (lower p_{T}) lepton pair. The events cluster in the region where both masses are around m_Z. At least one lepton pair is required to have invariant mass within the Z mass window, $66 < m_{\ell^+\ell^-} < 116$ GeV. If the second lepton pair satisfies this as well, the event is classified as a ZZ event; if the second pair satisfies $m_{\ell^+\ell^-} > 20$ GeV, the event is classified as a ZZ^* event.

With the selection described here, 84 $ZZ^* \to \ell^+\ell^-\ell'^+\ell'^-$ candidates are observed, out of which 66 are classified as $ZZ \to \ell^+\ell^-\ell'^+\ell'^-$ candidates. From the 84 (66) $ZZ^* \to \ell^+\ell^-\ell'^+\ell'^-$ ($ZZ \to \ell^+\ell^-\ell'^+\ell'^-$) candidates, 8 (7) candidates contain extended leptons.

3.3 $ZZ \to \ell^+\ell^-\nu\bar{\nu}$ selection

$ZZ \to \ell^+\ell^-\nu\bar{\nu}$ events are characterized by large missing transverse momentum and two high-p_{T}, isolated electrons or muons. Selected events are required to have exactly two

JHEP03(2013)128

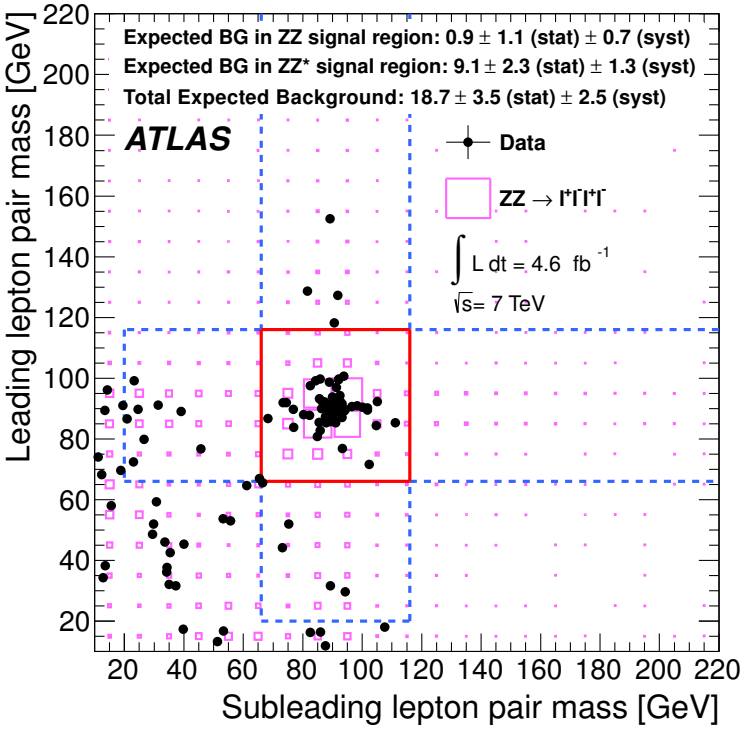

Figure 2. The mass of the leading lepton pair versus the mass of the sub-leading lepton pair. The events observed in the data are shown as solid circles and the $ZZ^{(*)} \to \ell^+\ell^-\ell'^+\ell'^-$ signal prediction from simulation as boxes. The size of each box is proportional to the number of events in each bin. The region enclosed by the solid (dashed) lines indicates the signal region defined by the requirements on the lepton-pair masses for ZZ (ZZ^*) events, as defined in the text.

leptons of the same flavour with $76 < m_{\ell^+\ell^-} < 106$ GeV and to have passed at least a single-muon or a single-electron trigger. The mass window is chosen to be tighter than the mass window used for the $ZZ^{(*)} \to \ell^+\ell^-\ell'^+\ell'^-$ channel in order to reduce the background from $t\bar{t}$ and WW. The lepton pair is required to have $\Delta R(\ell^+, \ell^-) > 0.3$. This requirement reflects the choice of the isolation cone for the leptons. The same trigger matching requirement as in the $ZZ^{(*)} \to \ell^+\ell^-\ell'^+\ell'^-$ channel is used.

The $ZZ \to \ell^+\ell^-\nu\bar{\nu}$ decay channel analysis makes use of several selections to reduce background. The largest background after the mass window requirement consists of Z+jets events, which are associated with non-zero missing transverse momentum when the $E_{\mathrm{T}}^{\mathrm{miss}}$ is mismeasured or when a b-quark decays to leptons and neutrinos inside of a jet. Since the Z bosons tend to be produced back-to-back, the axial-$E_{\mathrm{T}}^{\mathrm{miss}}$ (defined as the projection of the $E_{\mathrm{T}}^{\mathrm{miss}}$ along the direction opposite to the $Z \to \ell^+\ell^-$ candidate in the transverse plane) is a powerful variable to distinguish $ZZ \to \ell^+\ell^-\nu\bar{\nu}$ decays from Z+jets. The axial-$E_{\mathrm{T}}^{\mathrm{miss}}$ is given by $-\vec{E}_{\mathrm{T}}^{\mathrm{miss}} \cdot \vec{p}^{Z}/p_{\mathrm{T}}^{Z}$, where p_{T}^{Z} is the magnitude of the transverse momentum of the Z candidate. Similarly, the fractional p_{T} difference, $|E_{\mathrm{T}}^{\mathrm{miss}} - p_{\mathrm{T}}^{Z}|/p_{\mathrm{T}}^{Z}$ is a good variable to distinguish the two. The axial-$E_{\mathrm{T}}^{\mathrm{miss}}$ and fractional p_{T} difference are shown in figure 3. In order to reduce Z+jets background, the axial-$E_{\mathrm{T}}^{\mathrm{miss}}$ must be greater than 75 GeV, and

JHEP03(2013)128

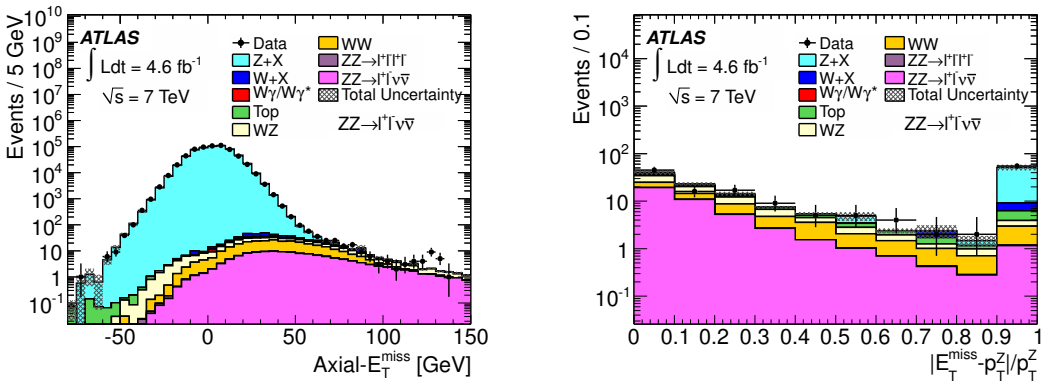

(a) (b)

Figure 3. For $\ell^+\ell^-\nu\bar{\nu}$ candidates in all channels figure (a) shows the axial-$E_{\mathrm{T}}^{\mathrm{miss}}$ after all selection requirements, except for the axial-$E_{\mathrm{T}}^{\mathrm{miss}}$, and figure (b) shows the fractional p_{T} difference between $E_{\mathrm{T}}^{\mathrm{miss}}$ and p_{T}^{Z} after all selection requirements, except for the fractional p_{T} difference (the last bin also contains events with fractional p_{T} difference greater than 1). In all plots, the points are data and the stacked histograms show the signal prediction from simulation. The shaded band shows the combined statistical and systematic uncertainties.

the fractional p_{T} difference must be less than 0.4. To reduce background from top-quark production, events which contain at least one reconstructed jet with $p_{\mathrm{T}} > 25\,\mathrm{GeV}$ and $|\eta| < 4.5$ are rejected.

To reduce background from WZ production, events with a third lepton (electron or muon) with p_{T} greater than $10\,\mathrm{GeV}$ are rejected. The shape of the jet multiplicity distribution is well modelled in Monte Carlo simulation as shown in figure 4 for the $ZZ \to \ell^+\ell^-\ell'^+\ell'^-$ and $ZZ \to \ell^+\ell^-\nu\bar{\nu}$ selections, however, there is an overall excess of about 20% in the $ZZ \to \ell^+\ell^-\ell'^+\ell'^-$ selection. With this selection, 87 $ZZ \to \ell^+\ell^-\nu\bar{\nu}$ candidates are observed in data.

4 Signal acceptance

The Z boson decays to hadrons, neutrinos and charged leptons with branching fractions of 69.9%, 20.0% and 10.1%, respectively [46]. The two ZZ decay channels considered in this paper, $ZZ \to \ell^+\ell^-\ell'^+\ell'^-$ and $ZZ \to \ell^+\ell^-\nu\bar{\nu}$, have branching fractions of 0.45% and 2.69%, respectively,[6] where decays involving τ leptons are not included in these branching fractions. Some of the ZZ decays produce one or more charged leptons which pass through the uninstrumented regions of the detector, and as such cannot be reconstructed. In order to measure the total ZZ cross section, the measured decays are extrapolated to non-measured parts of the phase-space; this results in the measurement being more dependent on theory predictions. Consequently, two types of cross sections are measured: fiducial and total. The fiducial cross section is the cross section measured within a restricted phase space, and the total cross section is the cross section extrapolated to the total phase space.

[6]The quoted branching fraction to four charged leptons is for the case where both Z bosons are within the mass window, so that the γ^* contribution can be neglected.

JHEP03(2013)128

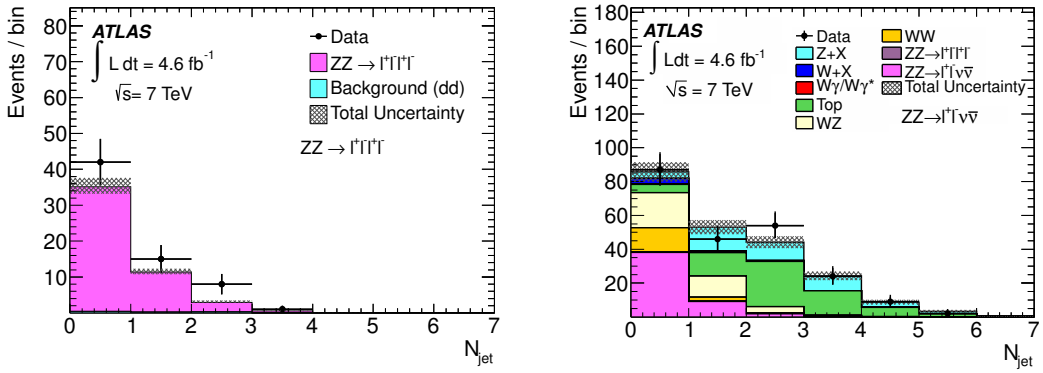

(a) (b)

Figure 4. (a) Jet multiplicity for the $ZZ \to \ell^+\ell^-\ell'^+\ell'^-$ selection and (b) jet multiplicity for the $ZZ \to \ell^+\ell^-\nu\bar{\nu}$ selection (with all selections applied but the jet veto). The points represent the observed data. In (a) the $ZZ \to \ell^+\ell^-\ell'^+\ell'^-$ background is normalized to the data-driven (dd) estimate, while in (b) the histograms show the prediction from simulation. The shaded band shows the combined statistical and systematic uncertainty on the prediction.

The total cross section calculation depends on the choice of Z mass range. The cross section is calculated using the Z boson natural width rather than the zero-width approximation, and includes the mass window requirement (66 to 116 GeV) to remove most of the γ^* contamination. The ratio of the total cross section calculated with both Z bosons within the mass window to the total cross section calculated using the zero-width approximation is 0.953, as the mass window requirement removes some of the Z bosons in the tails of the mass distribution.

4.1 Fiducial region definitions

The fiducial cross section is restricted to a region which is constructed to closely match the instrumented region and the event selection; for simplicity, only the most inclusive requirements on the lepton η and p_{T} are used for the definition of the fiducial phase space. The fiducial cross section $\sigma_{ZZ}^{\mathrm{fid}}$ is calculated as:

$$\sigma_{ZZ}^{\mathrm{fid}} = \frac{N_{\mathrm{obs}} - N_{\mathrm{bkg}}}{C_{ZZ} \times \mathcal{L}} \tag{4.1}$$

which depends on a correction factor given by the number of simulated $ZZ^{(*)}$ events which satisfy the full event selection divided by the number of $ZZ^{(*)}$ events generated in the fiducial region, C_{ZZ}; the integrated luminosity, $\mathcal{L}$; the number of selected events, N_{obs}; and the amount of estimated background, N_{bkg}. For the calculation of C_{ZZ}, final states including pairs of oppositely-charged leptons produced from decays of $Z \to \tau^+\tau^- \to \ell^+\ell^-\nu\bar{\nu}\nu\bar{\nu}$ are included in the number of selected events (numerator) since those decays have an identical final state to the signal and are not subtracted as background but are excluded from the fiducial region (denominator) because the fiducial regions are defined only with $ZZ^{(*)}$ decays directly to electrons, muons or neutrinos, depending on the channel. The contribution from such τ decays is estimated from Monte Carlo simulation to be < 0.1 % for the

JHEP03(2013)128

Selection	C_{ZZ}
$ZZ \to \ell^+\ell^-\ell'^+\ell'^-$	$0.552 \pm 0.002 \pm 0.021$
$ZZ^* \to \ell^+\ell^-\ell'^+\ell'^-$	$0.542 \pm 0.002 \pm 0.022$
$ZZ \to \ell^+\ell^-\nu\bar{\nu}$	$0.679 \pm 0.004 \pm 0.014$

Table 1. Correction factors C_{ZZ} for each production and decay channel. The first uncertainty is statistical while the second is systematic.

$ZZ \to \ell^+\ell^-\nu\bar{\nu}$ selection, 0.24±0.01% for the $ZZ \to \ell^+\ell^-\ell'^+\ell'^-$ selection and 1.73±0.04% for the $ZZ^* \to \ell^+\ell^-\ell'^+\ell'^-$ selection. Fiducial requirements are applied at generator level. To reduce the dependence on QED radiation, the four-momentum assigned to each lepton includes the four-momentum of any neighbouring photon within $\Delta R \leq 0.1$.

The $ZZ \to \ell^+\ell^-\ell'^+\ell'^-$ fiducial region is defined using the following requirements: (i) two pairs of same-flavour opposite-sign electrons or muons, with each lepton satisfying $p_{\mathrm{T}}^{\ell} > 7\,\mathrm{GeV}$, $|\eta^{\ell}| < 3.16$ and at least a distance $\Delta R = 0.2$ from any other selected lepton, i.e., $\Delta R(\ell_1, \ell_2) > 0.2$, and (ii) both dilepton invariant masses within the Z mass window. A $ZZ^* \to \ell^+\ell^-\ell'^+\ell'^-$ fiducial region is defined with the same criteria as in the $ZZ \to \ell^+\ell^-\ell'^+\ell'^-$ case, except that one dilepton invariant mass requirement is relaxed to be greater than 20 GeV.

The $ZZ \to \ell^+\ell^-\nu\bar{\nu}$ fiducial region is defined by requiring: (i) two same-flavour opposite-sign electrons or muons, each with $p_{\mathrm{T}}^{\ell} > 20\,\mathrm{GeV}$, $|\eta^{\ell}| < 2.5$, with $\Delta R(\ell^+, \ell^-) > 0.3$, (ii) dilepton invariant mass close to the Z boson mass: $76 < m_{\ell^+\ell^-} < 106\,\mathrm{GeV}$, (iii) dineutrino invariant mass close to the Z boson mass: $66 < m_{\nu\bar{\nu}} < 116\,\mathrm{GeV}$, (iv) no jet with $p_{\mathrm{T}}^{j} > 25\,\mathrm{GeV}$ and $|\eta^{j}| < 4.5$, and (v) $(|p_{\mathrm{T}}^{\nu\bar{\nu}} - p_{\mathrm{T}}^{Z}|)/p_{\mathrm{T}}^{Z} < 0.4$ and $-\vec{p}_{\mathrm{T}}^{\nu\bar{\nu}} \cdot \vec{p}^{Z}/p_{\mathrm{T}}^{Z} > 75\,\mathrm{GeV}$. Jets are defined at generator level using the same jet algorithm as used in reconstructed events and including all final state particles after parton showering and hadronization.

Fiducial cross sections are calculated using the $ZZ \to \ell^+\ell^-\ell'^+\ell'^-$, $ZZ^* \to \ell^+\ell^-\ell'^+\ell'^-$ and $ZZ \to \ell^+\ell^-\nu\bar{\nu}$ selections, integrated over the corresponding full fiducial phase space volumes. For the $ZZ \to \ell^+\ell^-\ell'^+\ell'^-$ and $ZZ \to \ell^+\ell^-\nu\bar{\nu}$ selections the differential fiducial cross sections are derived in bins of the leading p_{T}^{Z}, $\Delta\phi(\ell^+, \ell^-)$ and the mass of the $ZZ \to \ell^+\ell^-\ell'^+\ell'^-$ system or the transverse mass of the $ZZ \to \ell^+\ell^-\nu\bar{\nu}$ system.

The correction factor, C_{ZZ}, is determined from Monte Carlo simulations (PowhegBox for the $ZZ \to \ell^+\ell^-\nu\bar{\nu}$ channel and PowhegBox and gg2zz for the $ZZ^{(*)} \to \ell^+\ell^-\ell'^+\ell'^-$ channel), after applying data-driven corrections as described in section 2.1. For the $ZZ \to \ell^+\ell^-\ell'^+\ell'^-$ ($ZZ^* \to \ell^+\ell^-\ell'^+\ell'^-$) selection it is 0.43 (0.41) for $e^+e^-e^+e^-$, 0.68 (0.69) for $\mu^+\mu^-\mu^+\mu^-$ and 0.55 (0.53) for $e^+e^-\mu^+\mu^-$ events. For the $ZZ \to \ell^+\ell^-\nu\bar{\nu}$ selection the correction factor is 0.63 for $e^+e^-\nu\bar{\nu}$ and 0.76 for $\mu^+\mu^-\nu\bar{\nu}$ events. The correction factors combining all lepton categories within the fiducial region are given in table 1 for the three event selections in both decay channels.

JHEP03(2013)128

Selection	A_{ZZ}
$ZZ \to \ell^+\ell^-\ell'^+\ell'^-$	$0.804 \pm 0.001 \pm 0.010$
$ZZ \to \ell^+\ell^-\nu\bar{\nu}$	$0.081 \pm 0.001 \pm 0.004$

Table 2. Acceptance A_{ZZ} for the two decay channels used for the measurement of the total ZZ production cross section. The first uncertainty is statistical while the second is systematic.

4.2 Extrapolation to the total phase space

The total ZZ cross section is measured using the $ZZ \to \ell^+\ell^-\ell'^+\ell'^-$ and $ZZ \to \ell^+\ell^-\nu\bar{\nu}$ selections. The total cross section is calculated using the fiducial acceptance, A_{ZZ} (the fraction of ZZ events with Z bosons in the Z mass window that fall into the fiducial region) and the branching fraction, BF:

$$\sigma_{ZZ}^{\text{total}} = \frac{N_{\text{obs}} - N_{\text{bkg}}}{A_{ZZ} \times C_{ZZ} \times \mathcal{L} \times \text{BF}} \tag{4.2}$$

The fiducial acceptances A_{ZZ} are estimated from Monte Carlo simulation, using PowhegBox for the $ZZ \to \ell^+\ell^-\nu\bar{\nu}$ channel and PowhegBox and gg2zz for the $ZZ \to \ell^+\ell^-\ell'^+\ell'^-$ channel. The fiducial acceptance of the $ZZ \to \ell^+\ell^-\nu\bar{\nu}$ channel is much more constrained than the $ZZ \to \ell^+\ell^-\ell'^+\ell'^-$ channel in order to reduce background. Values are given in table 2.

4.3 Systematic uncertainties

Table 3 summarizes the systematic uncertainties on C_{ZZ} and A_{ZZ}. For C_{ZZ} in the $ZZ^{(*)} \to \ell^+\ell^-\ell'^+\ell'^-$ selections, the dominant systematic uncertainties arise from the lepton reconstruction efficiency, the efficiency of the isolation and impact parameter requirements, and the differences in C_{ZZ} estimated by Sherpa and PowhegBox; uncertainties on the trigger efficiency and the lepton energy scale and resolution are small. In the $ZZ \to \ell^+\ell^-\nu\bar{\nu}$ channel the dominant C_{ZZ} uncertainties are from uncertainties on the lepton reconstruction efficiency, the lepton energy scale and resolution, and the missing transverse momentum modelling and jet veto uncertainty; uncertainties on the trigger efficiency and due to differences in C_{ZZ} estimated by Sherpa and PowhegBox also contribute.

The uncertainties on C_{ZZ} from the reconstruction efficiency, energy scale and resolution, isolation and impact parameter requirements and trigger efficiency are estimated by varying the data-driven correction factors applied to simulation by their systematic and statistical uncertainties. The systematic uncertainties on events with extended leptons used in the $ZZ^{(*)} \to \ell^+\ell^-\ell'^+\ell'^-$ channel are slightly higher than in events without them; nevertheless, since their relative contribution is small, the effect on the uncertainty of the combined channels is negligible. The generator systematic uncertainty for C_{ZZ} accounts for the effect of choosing a different renormalization and factorization scale and PDF set.

For A_{ZZ}, the systematic uncertainties are due to theoretical uncertainties which come from the PDFs, the choice of the renormalization and factorization scales, the modelling of the contribution from gg initial states and the parton shower model, as given in table 3. For the $ZZ \to \ell^+\ell^-\nu\bar{\nu}$ channel, uncertainties in the efficiency of the jet veto are also taken into

JHEP03(2013)128

Source	$ZZ \to \ell^+\ell^-\ell'^+\ell'^-$	$ZZ^* \to \ell^+\ell^-\ell'^+\ell'^-$	$ZZ \to \ell^+\ell^-\nu\bar{\nu}$
	C_{ZZ}		
Lepton efficiency	3.0%	3.1%	1.3%
Lepton energy/momentum	0.2%	0.3%	1.1%
Lepton isolation and impact parameter	1.9%	2.0%	0.6%
Jet+$E_{\mathrm{T}}^{\mathrm{miss}}$ modelling	—	—	0.8%
Jet veto	—	—	0.9%
Trigger efficiency	0.2%	0.2%	0.4%
PDF and scale	1.6%	1.5%	0.4%
	A_{ZZ}		
Jet veto	—	—	2.3%
PDF and scale	0.6%	—	1.9%
Generator modelling and parton shower	1.1%	—	4.6%

Table 3. Summary of systematic uncertainties, as relative percentages of the correction factor C_{ZZ} or the acceptance of the fiducial region A_{ZZ}. Dashes indicate uncertainties which are not relevant.

account through the calculation of a scale factor; the ratio of the jet veto efficiency in data to that in MC simulation is taken from a sample of single Z events and then applied to ZZ events [47]. The systematic uncertainties due to the PDFs and scales are evaluated with MCFM by taking the difference between the A_{ZZ} obtained using the CT10 and MSTW2008 PDF sets, as well as using the 44 CT10 error sets, and by shifting the factorization and renormalization scales up and down by a factor of two from the nominal value (half the mass of the diboson system). An additional uncertainty is assigned to account for the effect of different modelling at the generator level. Since the $ZZ^* \to \ell^+\ell^-\ell'^+\ell'^-$ measurement is not used for the total cross section, its A_{ZZ} acceptance is irrelevant and only uncertainty values related to C_{ZZ} are given.

The uncertainty on the integrated luminosity is 3.9% [22]. The uncertainty on the background estimates is discussed in the following sections.

5 Background estimation

5.1 $ZZ^{(*)} \to \ell^+\ell^-\ell'^+\ell'^-$ background

Background to the $ZZ^{(*)} \to \ell^+\ell^-\ell'^+\ell'^-$ signal originates from events with a Z (or W) boson decaying to leptons accompanied by additional jets or photons ($W/Z+X$), from top-quark production and from other diboson final states. Such events may contain electrons or muons from the decay of heavy-flavoured hadrons, muons from in-flight decay of pions and kaons, or jets and photons misidentified as electrons. The majority of these background leptons are rejected by the isolation requirements.

The background estimate follows a data-driven method in which a sample of events containing three leptons satisfying all selection criteria plus one 'lepton-like jet' is identified; such events are denoted as $\ell\ell\ell j$. For muons, the lepton-like jets are muon candidates that fail the isolation requirement or fail the impact parameter requirement but not both. For electrons with $|\eta| < 2.47$, the lepton-like jets are clusters in the electromagnetic

JHEP03(2013)128

calorimeter matched to inner detector tracks that fail either the full electron selection or the isolation requirement but not both. For electrons with $|\eta| > 2.5$, the lepton-like jets are electromagnetic clusters that are reconstructed as electrons but fail the tight identification requirements. The events are otherwise required to satisfy the full event selection, treating the lepton-like jet as if it were a fully identified lepton. The background is then estimated by weighting the $\ell\ell\ell j$ events by a measured factor f, which is the ratio of the probability for a non-lepton to satisfy the full lepton selection criteria to the probability of a non-lepton satisfying the lepton-like jet criteria. The background in which two selected leptons originate from jets is treated similarly, by identifying a data sample with two leptons and two lepton-like jets; such events are denoted as $\ell\ell jj$. The total number of expected background $\ell^+\ell^-\ell'^+\ell'^-$ events, $N(\mathrm{BG})$, is calculated as:

$$N(\mathrm{BG}) = [N(\ell\ell\ell j) - N(ZZ)] \times f - N(\ell\ell jj) \times f^2 \tag{5.1}$$

where double counting from $\ell\ell\ell j$ and $\ell\ell jj$ events is accounted for, and the term $N(ZZ)$ is a Monte Carlo estimate correcting for contributions from signal $ZZ^{(*)} \to \ell^+\ell^-\ell'^+\ell'^-$ events having a real lepton that is classified as a lepton-like jet (the equivalent correction to the term $N(\ell\ell jj)$ is negligible).

The factor f is measured in a sample of data selected with single-lepton triggers which contain a Z boson candidate: a pair of isolated same-flavour opposite-sign electrons or muons. In these selected events, f is measured, using the lepton and lepton-like jet candidates not assigned to the Z boson, as the ratio of the number of selected leptons to the number of lepton-like jets, after correcting for expected true lepton contributions from WZ and ZZ events using simulation. Independent values as a function of the η and p_{T} of the lepton-like jet are measured, which are then combined assuming they are uncorrelated. The factor f is found to vary from 0.33 ± 0.01 (0.26 ± 0.02) below $p_{\mathrm{T}} = 10$ GeV to 0.09 ± 0.02 (0.46 ± 0.20) above $p_{\mathrm{T}} = 50$ GeV for electrons (muons). The quoted uncertainties are statistical. Then, with the same procedure, a value for f is also derived using the simulated samples of background processes. The difference between the value of f derived in data and in simulation is assigned as a systematic uncertainty on f. The statistical and systematic uncertainties are then added in quadrature to derive a combined uncertainty on f, which varies as a function of p_{T} from 14% (19%) below 10 GeV to 22% (51%) above 50 GeV for electrons (muons). For the muons, the total uncertainty on f is dominated by its statistical uncertainty. The background estimates for the $ZZ \to \ell^+\ell^-\ell'^+\ell'^-$ and $ZZ^* \to \ell^+\ell^-\ell'^+\ell'^-$ selections are $0.9^{+1.1}_{-0.9}(\mathrm{stat.}) \pm 0.7(\mathrm{syst.})$ and $9.1 \pm 2.3(\mathrm{stat.}) \pm 1.3(\mathrm{syst.})$ events, respectively, as shown in tables 4 and 5. The statistical uncertainty on the background estimate comes from the statistical uncertainty on the numbers of $\ell\ell\ell j$, $\ell\ell jj$ and $ZZ^{(*)} \to \ell^+\ell^-\ell'^+\ell'^-$ events used in eq. 5.1. The systematic uncertainty results from the combined uncertainty on f. In cases where the overall estimate is negative, the background estimate is described using a truncated Gaussian with mean at zero and standard deviation equal to the estimated statistical and systematic uncertainties added in quadrature.

The extra background induced by the use of the extended leptons in the $ZZ^{(*)} \to \ell^+\ell^-\ell'^+\ell'^-$ channel is estimated to be negligible in the $ZZ \to \ell^+\ell^-\ell'^+\ell'^-$ selection, and about 20% (2 events out of the 9.1 estimated, compared to a signal gain of about 10.6 events out of the 64.4 expected) in the $ZZ^* \to \ell^+\ell^-\ell'^+\ell'^-$ selection.

JHEP03(2013)128

	$e^+e^-e^+e^-$	$\mu^+\mu^-\mu^+\mu^-$	$e^+e^-\mu^+\mu^-$	$\ell^+\ell^-\ell'^+\ell'^-$
$(+)\ N(\ell\ell\ell j) \times f$	1.63 ± 0.34	0.21 ± 0.21	1.84 ± 0.40	3.67 ± 0.57
$(-)N(ZZ) \times f$	0.17 ± 0.13	$0.12^{+0.20}_{-0.12}$	0.34 ± 0.21	0.63 ± 0.32
$(-)N(\ell\ell jj) \times f^2$	0.96 ± 0.10	0.33 ± 0.16	0.83 ± 0.09	2.12 ± 0.21
Background estimate, N(BG)	$0.5^{+0.6}_{-0.5}$(stat.)	< 0.64	0.7 ± 0.7(stat.)	$0.9^{+1.1}_{-0.9}$(stat.)
	± 0.3(syst.)		± 0.6 (syst.)	± 0.7(syst.)

Table 4. Expected number of background events for the $ZZ \to \ell^+\ell^-\ell'^+\ell'^-$ selection in 4.6 fb^{-1} of data, for the individual decay modes (columns 2, 3 and 4) and for their combination (last column). If the central value of the estimate is negative, the upper bound on the number of events in that channel is derived as detailed in section 5.1.

	$e^+e^-e^+e^-$	$\mu^+\mu^-\mu^+\mu^-$	$e^+e^-\mu^+\mu^-$	$\ell^+\ell^-\ell'^+\ell'^-$
$(+)\ N(\ell\ell\ell j) \times f$	8.85 ± 0.98	0.21 ± 0.21	10.63 ± 1.06	19.70 ± 1.46
$(-)N(ZZ) \times f$	0.29 ± 0.18	$0.20^{+0.25}_{-0.20}$	0.56 ± 0.28	1.05 ± 0.42
$(-)N(\ell\ell jj) \times f^2$	4.24 ± 0.23	1.10 ± 0.31	4.24 ± 0.23	9.58 ± 0.45
Background estimate, N(BG)	4.3 ± 1.4(stat.)	< 0.91	5.8 ± 1.6(stat.)	9.1 ± 2.3(stat.)
	± 0.6(syst.)		± 0.9 (syst.)	± 1.3(syst.)

Table 5. Expected number of background events for the $ZZ^* \to \ell^+\ell^-\ell'^+\ell'^-$ selection in 4.6 fb^{-1} of data, for the individual decay modes (columns 2, 3 and 4) and for their combination (last column). If the central value of the estimate is negative, the upper bound on the number of events in that channel is derived as detailed in section 5.1.

The background is also estimated purely from the simulated samples of background processes, and is predicted to be 1.5 ± 0.4 events for the $ZZ \to \ell^+\ell^-\ell'^+\ell'^-$ selection and 8.3 ± 1.3 events for the $ZZ^* \to \ell^+\ell^-\ell'^+\ell'^-$ selection, with uncertainties being statistical only. These estimates compare well with the data-driven results given in tables 4 and 5. According to the estimate from simulation, the dominant source of background is Z+jets events, with only about a 10% to 20% contribution from other diboson channels (WZ and WW), and a negligible contribution from events with top quarks.

Differential background distributions are determined by first deriving the shape of the distributions from the background MC samples. This is achieved by selecting events where one Z candidate is required to satisfy the nominal lepton selection, while the other Z candidate is formed by leptons satisfying relaxed criteria for the isolation requirements and transverse impact parameter significance. The shape determined in this way is then scaled such that the total number of events in the distribution is equal to the data-driven background estimate shown in tables 4 and 5.

5.2 $ZZ \to \ell^+\ell^-\nu\bar{\nu}$ background

There are several sources of background to the $ZZ \to \ell^+\ell^-\nu\bar{\nu}$ channel. Processes such as $t\bar{t}$, WW, Wt or $Z \to \tau^+\tau^-$ production give two true isolated leptons with missing transverse momentum. Diboson WZ events in which both bosons decay leptonically have

JHEP03(2013)128

Process	$e^+e^-E_{\mathrm{T}}^{\mathrm{miss}}$	$\mu^+\mu^-E_{\mathrm{T}}^{\mathrm{miss}}$	$\ell^+\ell^-E_{\mathrm{T}}^{\mathrm{miss}}$
$t\bar{t}$, Wt, WW, $Z \to \tau^+\tau^-$	$8.5 \pm 2.1 \pm 0.5$	$10.6 \pm 2.6 \pm 0.6$	$19.1 \pm 2.3 \pm 1.0$
WZ	$8.9 \pm 0.5 \pm 0.4$	$11.9 \pm 0.5 \pm 0.3$	$20.8 \pm 0.7 \pm 0.5$
$Z \to \mu^+\mu^-, e^+e^-$+jets	$2.6 \pm 0.7 \pm 1.0$	$2.7 \pm 0.8 \pm 1.2$	$5.3 \pm 1.1 \pm 1.6$
$W+$ jets	$0.7 \pm 0.3 \pm 0.3$	$0.7 \pm 0.2 \pm 0.2$	$1.5 \pm 0.4 \pm 0.4$
$W\gamma$	$0.1 \pm 0.1 \pm 0.0$	$0.2 \pm 0.1 \pm 0.0$	$0.3 \pm 0.1 \pm 0.0$
Total	$20.8 \pm 2.3 \pm 1.2$	$26.1 \pm 2.8 \pm 1.4$	$46.9 \pm 4.8 \pm 1.9$

Table 6. Expected number of background events to the $ZZ \to \ell^+\ell^-\nu\bar{\nu}$ channel in 4.6 fb^{-1} of data, for the individual decay modes (columns 2 and 3) and for their combination (last column). The first uncertainty is statistical while the second is systematic.

three charged leptons, but if one lepton from a W or Z boson decay is not identified, the event has the same signature as the signal. Production of a Z boson in association with jets gives two isolated leptons from the Z boson decay and may have missing transverse momentum if the jet momenta are mismeasured. Finally, production of a W boson in association with jets or photons may satisfy the selection requirements when one of the jets or photons is misidentified as an isolated lepton. All of the backgrounds are measured with data-driven techniques except for WZ and $W\gamma$. The total background is estimated to be $46.9 \pm 4.8 \pm 1.9$ events as summarized in table 6.

5.2.1 Backgrounds from $t\bar{t}$, Wt, WW and $Z \to \tau^+\tau^-$

The contributions from $t\bar{t}$, Wt, WW and $Z \to \tau^+\tau^-$ processes are measured by extrapolating from a control sample of events with one electron and one muon (instead of two electrons or two muons), which otherwise satisfy the full $ZZ \to \ell^+\ell^-\nu\bar{\nu}$ selection. This sample is free from signal events. The extrapolation from the $e\mu$ channel to the ee or $\mu\mu$ channel uses the relative branching fractions ($2:1:1$ for $e\mu : ee : \mu\mu$) as well as the ratio of the efficiencies ϵ_{ee} or $\epsilon_{\mu\mu}$ of the ee or $\mu\mu$ selections to the efficiency $\epsilon_{e\mu}$ of the $e\mu$ selection, which differs from unity due to differences in the electron and muon efficiencies.

For the electron channel, this is represented by the equation:

$$N_{ee}^{\mathrm{bkg}} = (N_{e\mu}^{\mathrm{data}} - N_{e\mu}^{\mathrm{sim}}) \times \frac{1}{2} \times \frac{\epsilon_{ee}}{\epsilon_{e\mu}} \tag{5.2}$$

where $N_{e\mu}^{\mathrm{data}}$ is the number of observed $e\mu$ events and $N_{e\mu}^{\mathrm{sim}}$ is the number expected events from processes other than $t\bar{t}$, Wt, WW and $Z \to \tau^+\tau^-$ (WZ, ZZ, W+jet, Z+jet and W/γ). Therefore, $(N_{e\mu}^{\mathrm{data}} - N_{e\mu}^{\mathrm{sim}})$ is the estimate of $t\bar{t}$, Wt, WW and $Z \to \tau^+\tau^-$ production in the control sample. The efficiency correction factor, $\epsilon_{ee}/\epsilon_{e\mu}$, corrects for the difference between electron and muon efficiency. The efficiency correction factor is measured in data using reconstructed $Z \to \ell^+\ell^-$ events, as

$$\frac{\epsilon_{ee}}{\epsilon_{e\mu}} = \frac{\epsilon_e^2}{\epsilon_e\epsilon_\mu} = \frac{\epsilon_e}{\epsilon_\mu} = \sqrt{\frac{N_{ee}^{\mathrm{data}}}{N_{\mu\mu}^{\mathrm{data}}}} \tag{5.3}$$

JHEP03(2013)128

where N_{ee}^{data} and $N_{\mu\mu}^{\text{data}}$ are the number of observed ee or $\mu\mu$ events in the Z boson mass window, respectively, after all lepton selection requirements and the Z boson mass window requirement are applied. A parallel argument gives $N_{\mu\mu}^{\text{bkg}}$. This procedure is repeated in bins of p_{T}^{Z} in order to obtain the p_{T} distribution of the $t\bar{t}$, Wt, WW and $Z \to \tau^+\tau^-$ background.

The dominant uncertainty is statistical (25%), due to the limited number of events in the control samples. Additional uncertainties are due to systematic uncertainties in the normalization of the simulated samples used to correct the $e\mu$ contribution (5.5%) and the systematic uncertainty in the efficiency correction factor (4.5%).

5.2.2 Background from WZ production with leptonic decays

Events from leptonic WZ decays may result in an $\ell^+\ell^- E_{\text{T}}^{\text{miss}}$ signature when one lepton from the W or Z boson is not reconstructed. The contribution from this process is estimated using the simulated samples described in section 2.1. The estimate is checked using a control region with three high-p_{T} isolated leptons. The two dominant processes that contribute to this control region are WZ and Z+jets production, where the WZ boson pair decays to three leptons and a neutrino and the Z+jets contribution has two real leptons from the Z decay and a misidentified lepton from the jet. The technique used to estimate the background in the $ZZ^{(*)} \to \ell^+\ell^-\ell'^+\ell'^-$ channel is also used to normalize the contribution from Z+jets in the three-lepton control region. The WZ Monte Carlo expectation is consistent with the data. The systematic uncertainties are estimated in the same way as for signal Monte Carlo events.

5.2.3 Background from Z bosons with associated jets

Occasionally events with a Z boson produced in association with jets may have large amounts of missing transverse momentum due to mismeasurement of the momenta of the jets. This background is estimated using events with a high-p_{T} photon and jets as a template, since the mechanism for large missing transverse momentum is the same as in Z+jets events. The events are reweighted such that the photon E_{T} matches the observed Z boson p_{T} and are normalized to the observed Z + jets yield. The procedure is repeated in bins of p_{T}^{Z} in order to obtain the p_{T} distribution of the Z+jets backgrounds. The largest systematic uncertainty is due to the subtraction of $W\gamma$, $Z\gamma$, $t\bar{t}$ and $W \to e\nu$ contributions to the γ+jets sample, which is 33% in the ee channel and 37% in the $\mu\mu$ channel.

5.2.4 Background from events with a misidentified lepton

A small contribution to the selected sample is due to events in which one of the two leptons comes from the decay of a W or Z boson (called 'real' below) and the second is a 'fake', corresponding both non-prompt leptons and misidentified π^0 mesons or conversions.

The dominant fake-muon mechanism is the decay of heavy-flavoured hadrons, in which a muon survives the isolation requirements. In the case of electrons, the three mechanisms are heavy-flavour hadron decay, light-flavour jets with a leading π^0 overlapping with a charged particle, and conversion of photons. Processes that contribute are top-quark pair production, production of W bosons in association with jets and multi-jet production.

JHEP03(2013)128

The 'matrix method' [48] is applied to estimate the fraction of events in the signal regions that contain at least one fake lepton. The method measures the number of fake leptons in background-dominated control regions and extrapolates to the ZZ selection region using factors measured in data. The shape of the background is provided by taking the background as uniformly distributed among the bins and treating each bin as statistically uncorrelated. The dominant systematic uncertainty is due to the uncertainty on the extrapolation factors and the limited numbers of events in the control samples, giving a total uncertainty of 63% and 44% in the ee and $\mu\mu$ channels, respectively.

6 Results

Three types of measurements are presented:

- integrated fiducial and total ZZ cross sections;
- differential cross sections normalized to the overall measured cross sections for the p_{T}^{Z} and $\Delta\phi(\ell^+,\ell^-)$ of the leading Z boson, and the mass (transverse mass[7]) of the ZZ system for the $ZZ \to \ell^+\ell^-\ell'^+\ell'^-$ ($ZZ \to \ell^+\ell^-\nu\bar{\nu}$) selection; and
- limits on the anomalous nTGCs.

6.1 Cross section measurements

The expected and observed event yields after applying all selection criteria are shown in table 7 for both channels. Figure 4 shows the jet multiplicity in selected $ZZ \to \ell^+\ell^-\ell'^+\ell'^-$ and $ZZ \to \ell^+\ell^-\nu\bar{\nu}$ events before the jet veto is applied. Figures 5 and 6 show the transverse momentum and mass of the ZZ system in selected $ZZ \to \ell^+\ell^-\ell'^+\ell'^-$ and $ZZ^* \to \ell^+\ell^-\ell'^+\ell'^-$ events respectively. Figure 7 shows the transverse momentum and mass of the two-charged-lepton system in selected $ZZ \to \ell^+\ell^-\nu\bar{\nu}$ events. The shapes of the distributions are consistent with the predictions from the simulation.

The $ZZ^{(*)} \to \ell^+\ell^-\ell'^+\ell'^-$ and $ZZ \to \ell^+\ell^-\nu\bar{\nu}$ fiducial cross sections are determined using a maximum likelihood fitting method, taking into account the integrated luminosity and the C_{ZZ} correction factors discussed in section 4. A Poisson probability function is used to model the number of expected events, multiplied by Gaussian distribution functions which model the nuisance parameters representing systematic uncertainties. The measured fiducial cross sections are:

$$\begin{aligned}
\sigma^{\mathrm{fid}}_{ZZ\to\ell^+\ell^-\ell'^+\ell'^-} &= 25.4^{+3.3}_{-3.0}\ (\mathrm{stat.})\ ^{+1.2}_{-1.0}\ (\mathrm{syst.})\ \pm 1.0\ (\mathrm{lumi.})\ \mathrm{fb},\\
\sigma^{\mathrm{fid}}_{ZZ^*\to\ell^+\ell^-\ell'^+\ell'^-} &= 29.8^{+3.8}_{-3.5}\ (\mathrm{stat.})\ ^{+1.7}_{-1.5}\ (\mathrm{syst.})\ \pm 1.2\ (\mathrm{lumi.})\ \mathrm{fb},\\
\sigma^{\mathrm{fid}}_{ZZ\to\ell^+\ell^-\nu\bar{\nu}} &= 12.7^{+3.1}_{-2.9}\ (\mathrm{stat.})\ ^{+1.7}_{-1.7}\ (\mathrm{syst.})\ \pm 0.5\ (\mathrm{lumi.})\ \mathrm{fb}.
\end{aligned}$$

where $\ell^+\ell^-\ell'^+\ell'^-$ refers to the sum of the $e^+e^-e^+e^-$, $e^+e^-\mu^+\mu^-$ and $\mu^+\mu^-\mu^+\mu^-$ final states and $\ell^+\ell^-\nu\bar{\nu}$ refers to the sum of the $e^+e^-E_{\mathrm{T}}^{\mathrm{miss}}$ and $\mu^+\mu^-E_{\mathrm{T}}^{\mathrm{miss}}$ final states.[8] The

[7] $m_{\mathrm{T}}^2 = \left(\sqrt{(m^Z)^2+(p_{\mathrm{T}}^Z)^2}+\sqrt{(m^Z)^2+(E_{\mathrm{T}}^{\mathrm{miss}})^2}\right)^2 - \left(\vec{p}_{\mathrm{T}}^{Z}+\vec{E}_{\mathrm{T}}^{\mathrm{miss}}\right)^2$.

[8] The $ZZ \to \ell^+\ell^-\nu\bar{\nu}$ fiducial region is more restricted compared to the $ZZ^{(*)} \to \ell^+\ell^-\ell'^+\ell'^-$ channel.

JHEP03(2013)128

$ZZ^{(*)} \to \ell^+\ell^-\ell'^+\ell'^-$	$e^+e^-e^+e^-$	$\mu^+\mu^-\mu^+\mu^-$	$e^+e^-\mu^+\mu^-$	$\ell^+\ell^-\ell'^+\ell'^-$
Observed ZZ	16	23	27	66
Observed ZZ^*	21	30	33	84
Expected ZZ signal	$10.3 \pm 0.1 \pm 1.0$	$16.5 \pm 0.2 \pm 0.9$	$26.7 \pm 0.2 \pm 1.7$	$53.4 \pm 0.3 \pm 3.2$
Expected ZZ^* signal	$12.3 \pm 0.2 \pm 1.2$	$20.5 \pm 0.2 \pm 1.1$	$31.6 \pm 0.3 \pm 2.0$	$64.4 \pm 0.4 \pm 4.0$
Expected ZZ background	$0.5 \pm 0.6 \pm 0.3$	< 0.6	$0.7 \pm 0.7 \pm 0.6$	$0.9 \pm 1.1 \pm 0.7$
Expected ZZ^* background	$4.3 \pm 1.4 \pm 0.6$	< 0.9	$5.8 \pm 1.6 \pm 0.9$	$9.1 \pm 2.3 \pm 1.3$
$ZZ \to \ell^+\ell^-\nu\bar{\nu}$	$e^+e^-E_{\mathrm{T}}^{\mathrm{miss}}$	$\mu^+\mu^-E_{\mathrm{T}}^{\mathrm{miss}}$		$\ell^+\ell^-E_{\mathrm{T}}^{\mathrm{miss}}$
Observed ZZ	35	52		87
Expected ZZ signal	$17.8 \pm 0.3 \pm 1.7$	$21.6 \pm 0.3 \pm 2.0$		$39.3 \pm 0.4 \pm 3.7$
Expected ZZ background	$20.8 \pm 2.3 \pm 1.2$	$26.1 \pm 2.8 \pm 1.4$		$46.9 \pm 4.8 \pm 1.9$

Table 7. Summary of observed $ZZ \to \ell^+\ell^-\ell'^+\ell'^-$, $ZZ^* \to \ell^+\ell^-\ell'^+\ell'^-$ and $ZZ \to \ell^+\ell^-\nu\bar{\nu}$ candidates in the data, total background estimates and expected signal for the individual decay modes (columns 2 to 4) and for their combination (last column). The quoted uncertainties and limits represent 68% confidence intervals; the first uncertainty is statistical while the second is systematic. The uncertainty on the integrated luminosity (3.9%) is not included.

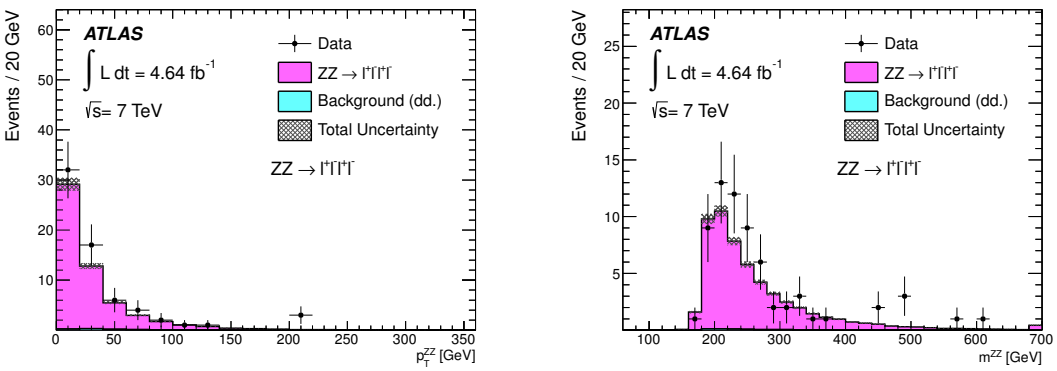

(a) (b)

Figure 5. (a) Transverse momentum p_{T}^{ZZ} and (b) invariant mass m^{ZZ} of the four-lepton system for the ZZ selection. The points represent the observed data and the histograms show the prediction from simulation, where the background is normalized to the data-driven (dd) estimate as described in section 5.1. The shaded band shows the combined statistical and systematic uncertainty on the prediction.

expected SM fiducial cross sections, derived from PowhegBox and gg2zz, are:

$$\sigma^{\mathrm{fid,SM}}_{ZZ \to \ell^+\ell^-\ell'^+\ell'^-} = 20.9 \pm 0.1\ (\mathrm{stat.})\ ^{+1.1}_{-0.9}\ (\mathrm{theory})\ \mathrm{fb},$$
$$\sigma^{\mathrm{fid,SM}}_{ZZ^* \to \ell^+\ell^-\ell'^+\ell'^-} = 25.6 \pm 0.1\ (\mathrm{stat.})\ ^{+1.3}_{-1.1}\ (\mathrm{theory})\ \mathrm{fb},$$
$$\sigma^{\mathrm{fid,SM}}_{ZZ \to \ell^+\ell^-\nu\bar{\nu}} = 12.5 \pm 0.1\ (\mathrm{stat.})\ ^{+1.0}_{-1.1}\ (\mathrm{theory})\ \mathrm{fb}.$$

The measured cross sections are compatible with these theoretical values.

JHEP03(2013)128

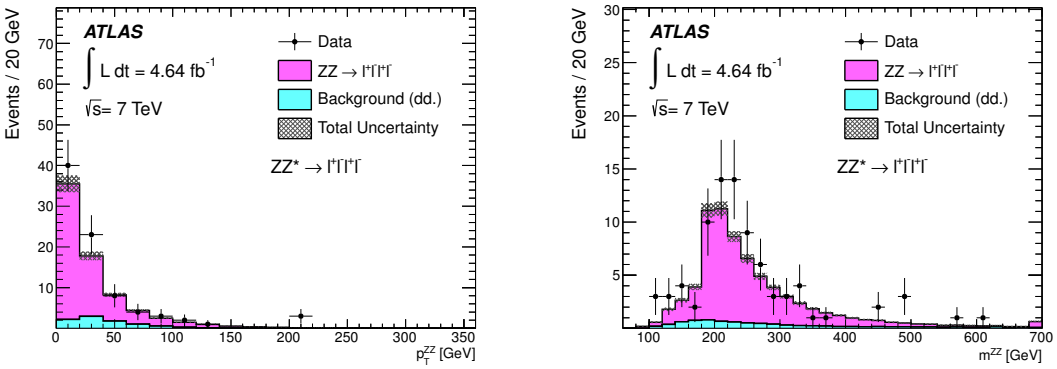

(a) (b)

Figure 6. (a) Transverse momentum p_{T}^{ZZ} and (b) invariant mass m^{ZZ} of the four-lepton system for the ZZ^* selection. The points represent the observed data and the histograms show the prediction from simulation, where the background is normalized to the data-driven (dd) estimate. The shaded band shows the combined statistical and systematic uncertainty on the prediction.

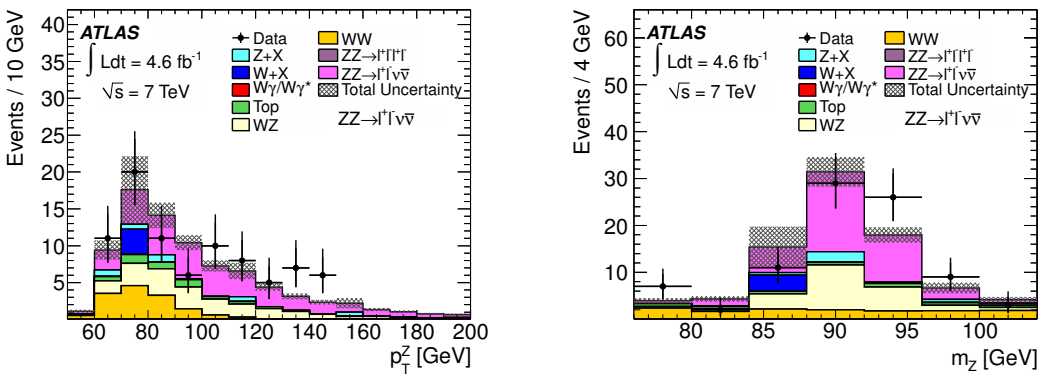

(a) (b)

Figure 7. (a) Transverse momentum p_{T}^{Z} and (b) mass m_Z of the two-charged-lepton system for the $ZZ \to \ell^+\ell^-\nu\bar{\nu}$ selection. The points represent the observed data and the histograms show the prediction from simulation. The shaded band shows the combined statistical and systematic uncertainty on the prediction.

The total ZZ cross section is calculated by extrapolating to the full phase space while each Z boson is required to have a mass within the Z mass window. Both $ZZ \to \ell^+\ell^-\ell'^+\ell'^-$ and $ZZ \to \ell^+\ell^-\nu\bar{\nu}$ events are combined in the maximum likelihood fit, taking into account the known Z branching fractions [46] and the A_{ZZ} kinematic and geometrical acceptances (section 4). Correlated systematic uncertainties between the $ZZ \to \ell^+\ell^-\ell'^+\ell'^-$ and $ZZ \to \ell^+\ell^-\nu\bar{\nu}$ channels are taken into account in the fit using a single Gaussian for the nuisance parameter for each source of correlated uncertainty. The measured value of the total ZZ cross section is:

$$\sigma_{ZZ}^{\mathrm{tot}} = 6.7 \pm 0.7\ (\mathrm{stat.})\ ^{+0.4}_{-0.3}\ (\mathrm{syst.})\ \pm 0.3\ (\mathrm{lumi.})\ \mathrm{pb}.$$

The result is consistent within errors with the NLO Standard Model total cross section for

JHEP03(2013)128

this process of $5.89^{+0.22}_{-0.18}$ pb, where the quoted theoretical uncertainties result from varying the factorization and renormalization scales simultaneously by a factor of two and from using the full CT10 PDF error set.

6.2 Differential cross sections

The differential cross sections present a more detailed comparison of theory to measurement, allowing a generic comparison of the kinematic distributions to new theories. Variables which are sensitive to new phenomena, such as p_{T}^{Z}, m^{ZZ} and $\Delta\phi(\ell^+,\ell^-)$, are used with bin boundaries chosen to maximize sensitivity to nTGCs. At the same time, the bin widths were chosen to be commensurate with the resolution.

The measured distributions are unfolded back to the underlying distributions, accounting for the effect of detector resolution, efficiency and acceptance, within the fiducial region of each measurement. The unfolding procedure is based on a Bayesian iterative algorithm [49]. The algorithm takes as input a prior for the kinematic distribution and iterates using the posterior distribution as prior for the next iteration. The initial prior is taken from the signal Monte Carlo expectation calculated using the PowhegBox generator and three iterations are performed. The uncertainty on the unfolded distributions is dominated by the statistical uncertainty, which is about 30% in most bins. The systematic uncertainty is no more than 5% in any bin. The dependence of the unfolded cross sections on the choice of the initial prior is tested by unfolding the measured distributions using a different generator (Sherpa). The difference between the two is taken as a systematic uncertainty to account for differences in generator modelling (e.g. QCD radiation). The difference in unfolded distributions between three iterations and four iterations is much lower than the statistical uncertainty and it is taken as a further uncertainty on the unfolding procedure. Systematic uncertainties related to detector effects (e.g. lepton reconstruction efficiency) are evaluated using pseudo-experiments.

Figures 8 to 10 show the differential cross sections normalized to the fiducial cross sections for the p_{T}^{Z} and $\Delta\phi(\ell^+,\ell^-)$ of the leading Z boson, and for the mass (transverse mass) of the ZZ system for the $ZZ \to \ell^+\ell^-\ell'^+\ell'^-$ ($ZZ \to \ell^+\ell^-\nu\bar{\nu}$) selection. The Standard Model prediction is consistent with the measurement in each case.

6.3 Anomalous neutral triple gauge couplings

Anomalous nTGCs for on-shell ZZ production can be parameterized by two CP-violating (f_4^V) and two CP-conserving (f_5^V) complex parameters (where $V = Z, \gamma$) which are zero in the Standard Model [3]. A form-factor parameterization is introduced leading to couplings which vanish at high parton centre-of-mass energy $\sqrt{\hat{s}}$: $f_i^V = f_{i0}^V/(1+\hat{s}/\Lambda^2)^n$, ensuring partial-wave unitarity. Here, Λ is the energy scale at which physics beyond the Standard Model would be directly observable, f_{i0}^V are the low-energy approximations of the couplings, and n is the form-factor power. Values of $n = 3$ and $\Lambda = 3$ TeV are chosen, so that expected limits are within the values allowed by requiring that unitarity is not violated at LHC energies [3]. The results with an energy cutoff $\Lambda = \infty$ (i.e. without a form factor) are also presented as a comparison in the unitarity violating scheme.

JHEP03(2013)128

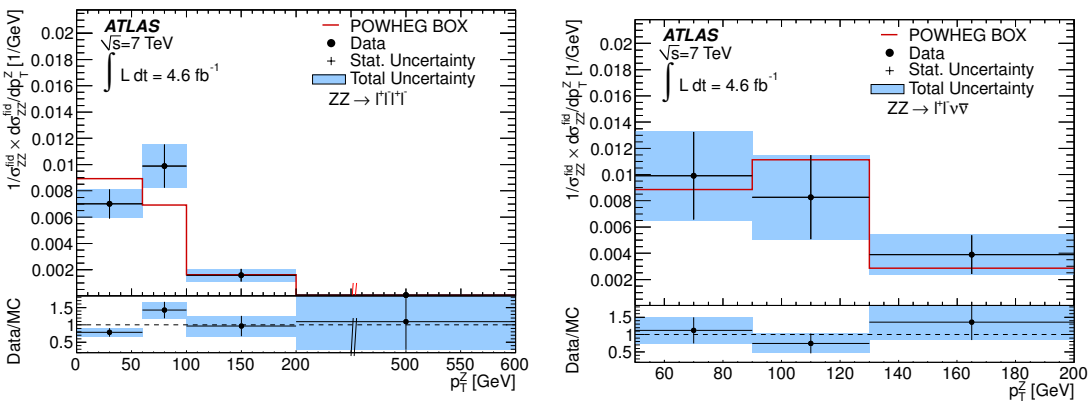

(a) (b)

Figure 8. Unfolded ZZ fiducial cross sections in bins of the p_{T} of the leading Z boson for (a) the $ZZ \to \ell^+\ell^-\ell'^+\ell'^-$ selection, where a discontinuity is indicated by the parallel pairs of lines, and (b) the $ZZ \to \ell^+\ell^-\nu\bar{\nu}$ selection.

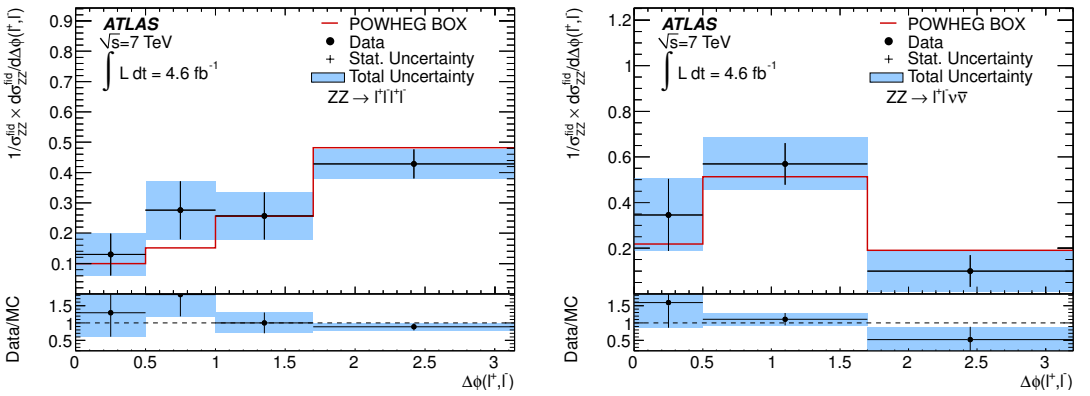

(a) (b)

Figure 9. Unfolded ZZ fiducial cross sections in bins of the $\Delta\phi(\ell^+,\ell^-)$ of the leading Z boson for (a) the $ZZ \to \ell^+\ell^-\ell'^+\ell'^-$ selection and (b) the $ZZ \to \ell^+\ell^-\nu\bar{\nu}$ selection.

Limits on anomalous nTGCs are determined using the observed and expected numbers of $ZZ \to \ell^+\ell^-\ell'^+\ell'^-$ and $ZZ \to \ell^+\ell^-\nu\bar{\nu}$ events binned[9] in p_{T}^Z, as seen in table 8. Figure 11 shows the observed p_{T}^Z distributions, together with the SM expectation and the predicted distributions for nTGC values close to the previous limits obtained by ATLAS [13]. Using an increased data sample compared with our previous measurement, including the $ZZ \to \ell^+\ell^-\nu\bar{\nu}$ channel, and exploiting the differential event yields, the precision is expected to improve by about a factor of five. The dependency of the couplings on the expected number of events in each p_{T}^Z bin is parameterized using fully simulated events, generated with Sherpa [26], subsequently reweighted using the Baur-Rainwater [3, 50] and BHO [51] MC generators. The next-to-leading-order matrix elements with their nTGC dependence have been extracted from the BHO MC generator for $2 \to 5$ events and the Baur-Rainwater MC

[9]The raw (i.e. not unfolded) differential event yields are used, to avoid introducing theory dependence.

JHEP03(2013)128

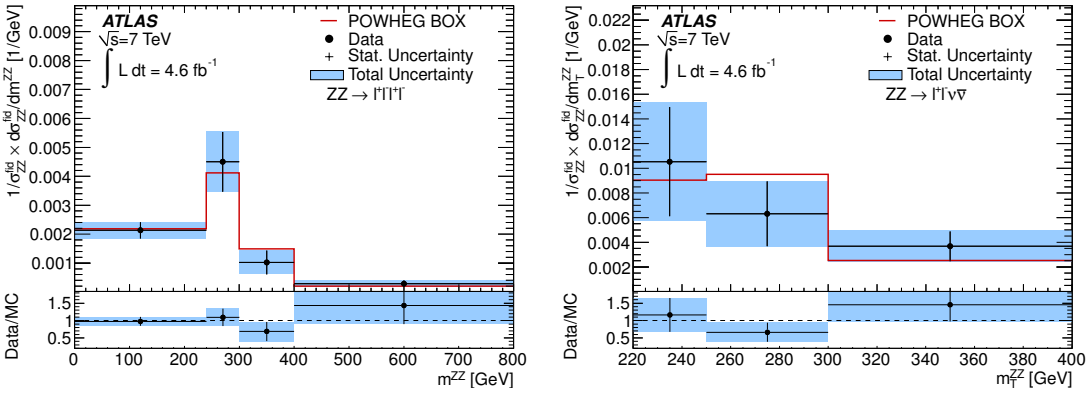

(a) (b)

Figure 10. Unfolded ZZ fiducial cross sections in bins of (a) m^{ZZ} for the $ZZ \to \ell^+\ell^-\ell'^+\ell'^-$ selection and (b) m_{T}^{ZZ} for the $ZZ \to \ell^+\ell^-\nu\bar{\nu}$ selection.

	Expected background	Expected ZZ signal	Observed events
$ZZ \to \ell^+\ell^-\ell'^+\ell'^-$			
$0 < p_{\mathrm{T}}^{Z} < 60\,\mathrm{GeV}$	$0.6 \pm 0.8 \pm 0.5$	$27.9 \pm 0.2 \pm 2.0$	28
$60 < p_{\mathrm{T}}^{Z} < 100\,\mathrm{GeV}$	$0.2 \pm 0.2 \pm 0.2$	$14.6 \pm 0.2 \pm 1.2$	25
$100 < p_{\mathrm{T}}^{Z} < 200\,\mathrm{GeV}$	$0.1 \pm 0.1 \pm 0.1$	$9.3 \pm 0.1 \pm 0.9$	11
$p_{\mathrm{T}}^{Z} > 200\,\mathrm{GeV}$	$0.01 \pm 0.01 \pm 0.01$	$1.6 \pm 0.1 \pm 0.3$	2
$ZZ \to \ell^+\ell^-\nu\bar{\nu}$			
$50 < p_{\mathrm{T}}^{Z} < 90\,\mathrm{GeV}$	$26.0 \pm 4.5 \pm 1.1$	$13.6 \pm 0.2 \pm 1.3$	42
$90 < p_{\mathrm{T}}^{Z} < 130\,\mathrm{GeV}$	$16.0 \pm 2.8 \pm 0.7$	$15.7 \pm 0.3 \pm 1.7$	29
$p_{\mathrm{T}}^{Z} > 130\,\mathrm{GeV}$	$4.9 \pm 1.8 \pm 0.2$	$10.1 \pm 0.1 \pm 1.5$	16

Table 8. Total background, expected signal and observed events as a function of the p_{T} of the leading Z for the $ZZ \to \ell^+\ell^-\ell'^+\ell'^-$ and $ZZ \to \ell^+\ell^-\nu\bar{\nu}$ selections. For the expected signal and background events, the first uncertainty is statistical and the second is systematic.

generator for $2 \to 4$ events and introduced into a framework [52] that enables a calculation of the amplitude given the four vectors and the identity of the incoming and outgoing particles from the hard process.

Confidence intervals for the anomalous triple gauge couplings are determined using the maximum profile likelihood ratio. Limits are set on each coupling, assuming all of the other couplings are zero (as in the Standard Model), and on pairs of couplings assuming the remaining two couplings are zero. The profile likelihood ratio is calculated for the data, and also for 10000 pseudo-experiments generated using the expected number of events at each point in the one- or two-dimensional nTGC parameter space. A point is rejected if more than 95% of the pseudo-experiments have a larger profile likelihood ratio value than the one observed in data. The systematic errors are included as nuisance parameters.

JHEP03(2013)128

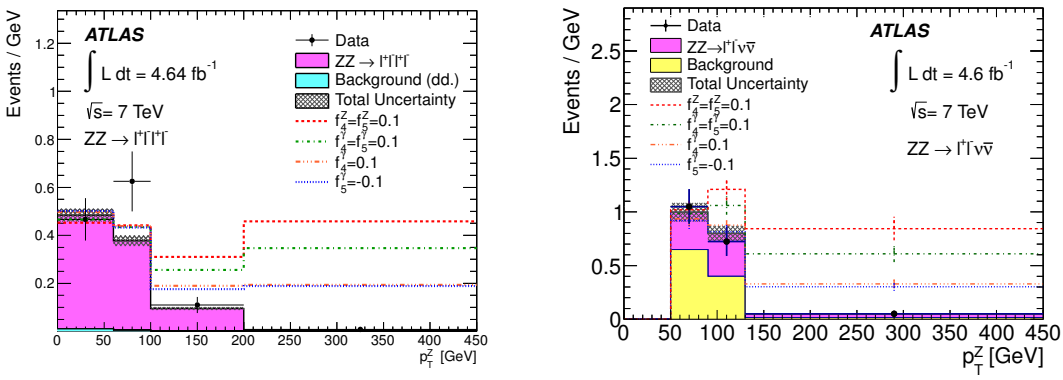

(a) (b)

Figure 11. The leading Z boson transverse momentum distributions for (a) the $ZZ \to \ell^+\ell^-\ell'^+\ell'^-$ selection and (b) the $ZZ \to \ell^+\ell^-\nu\bar{\nu}$ selection. The observed distributions are shown as filled circles, the SM expected signal and background are shown as filled histograms, and the predicted distributions for four different nTGC samples with form factor scales of $\Lambda = 3\,\text{TeV}$ and nTGC coupling values set near the edge of the exclusion set in the $1\,\text{fb}^{-1}$ analysis [13] are shown as dashed lines.

Λ	f_{40}^{γ}	f_{40}^{Z}	f_{50}^{γ}	f_{50}^{Z}
3 TeV	$[-0.022, 0.023]$	$[-0.019, 0.019]$	$[-0.023, 0.023]$	$[-0.020, 0.019]$
∞	$[-0.015, 0.015]$	$[-0.013, 0.013]$	$[-0.016, 0.015]$	$[-0.013, 0.013]$

Table 9. One-dimensional 95% confidence intervals for anomalous neutral gauge boson couplings, where the limit for each coupling assumes the other couplings are fixed at zero, their SM value. Limits are presented for form factor scales of $\Lambda = 3$ TeV and $\Lambda = \infty$ and include both statistical and systematic uncertainties; the statistical uncertainties are dominant.

The resulting limits for each coupling are listed in table 9. Two-dimensional 95% confidence intervals[10] are shown in figure 12. The one-dimensional limits are more stringent than those derived from measurements at LEP [8] and the Tevatron [9] and previously by ATLAS [13]; it should be noted that the limits from LEP do not use a form factor, and those from the Tevatron use $\Lambda = 1.2$ TeV. A comparison of the LHC limits with those derived from LEP and Tevatron is shown in figure 13.

7 Conclusions

A measurement of the $ZZ^{(*)}$ production cross section in LHC proton-proton collisions at $\sqrt{s} = 7\,\text{TeV}$ is presented with data collected by the ATLAS detector, using the $ZZ^{(*)} \to \ell^+\ell^-\ell'^+\ell'^-$ and $ZZ \to \ell^+\ell^-\nu\bar{\nu}$ decay channels. Fiducial cross sections are measured for three production and decay selections, and the results are compatible with the SM expected cross sections. Using the $ZZ \to \ell^+\ell^-\ell'^+\ell'^-$ and $ZZ \to \ell^+\ell^-\nu\bar{\nu}$ selections, the total ZZ

[10]Since most of the sensitivity of the measurement is contained in a single bin, the likelihood ratio used to obtain the two-dimensional limits has one effective degree of freedom.

JHEP03(2013)128

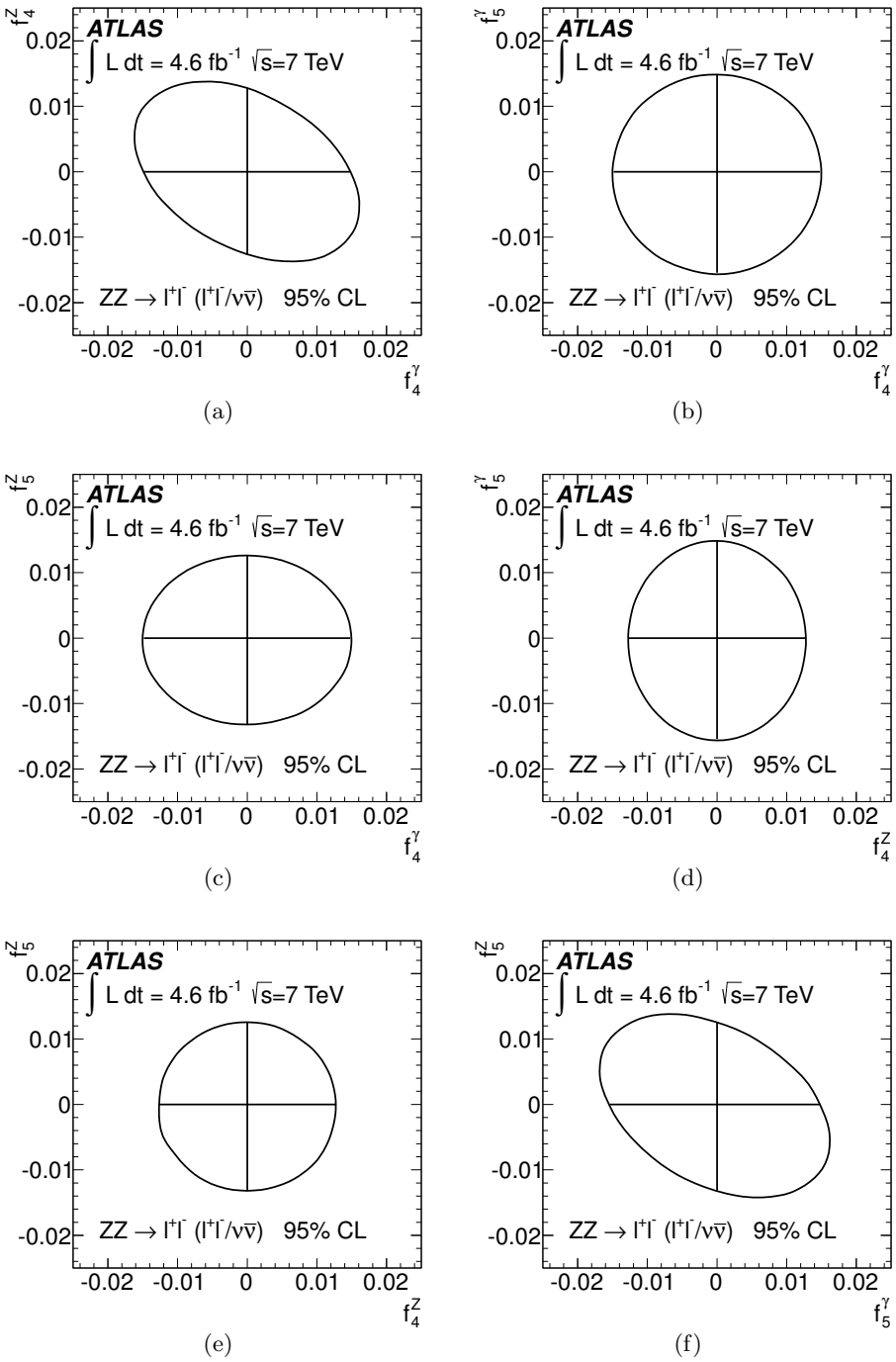

Figure 12. Two-dimensional triple gauge coupling limits for form factor scale $\Lambda = \infty$. The one-dimensional triple gauge coupling limits are shown as vertical and horizontal lines inside the two-dimensional ellipses, whose shape is determined by the theoretical correlations. For each two-dimensional limit the other TGC parameters are assumed to be zero. Since most of the sensitivity of the measurement is contained in a single bin, the likelihood ratio used to obtain the two-dimensional limits has one effective degree of freedom.

JHEP03(2013)128

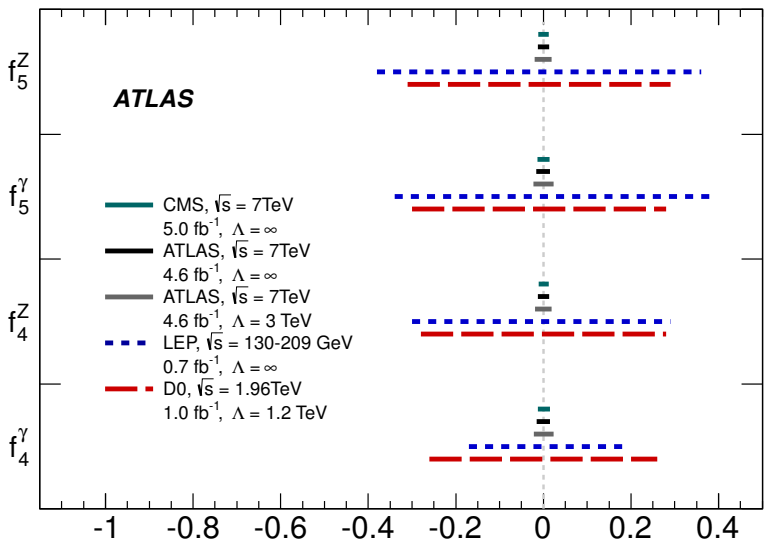

Figure 13. Anomalous nTGC 95% confidence intervals from ATLAS, LEP [8] and Tevatron [9] experiments. Luminosities, centre-of-mass energies and cut-offs Λ for each experiment are shown.

production cross section is determined to be:

$$\sigma_{ZZ}^{\text{tot}} = 6.7 \pm 0.7\ (\text{stat.})\ ^{+0.4}_{-0.3}\ (\text{syst.})\ \pm 0.3\ (\text{lumi.})\ \text{pb}.$$

The result is statistically consistent with the NLO Standard Model prediction of $5.89^{+0.22}_{-0.18}$ pb, calculated with Z bosons with a mass between 66 and 116 GeV, and supersedes the previous measurements made with part of the same dataset [13]. Unfolded distributions of the fiducial cross sections are derived for the p_{T}^{Z} and $\Delta\phi(\ell^+, \ell^-)$ of the leading Z boson and for m^{ZZ} in the $ZZ \to \ell^+\ell^-\ell'^+\ell'^-$ selection and the m_{T} in the $ZZ \to \ell^+\ell^-\nu\bar{\nu}$ selection.

The event yields as a function of the p_{T} of the leading Z boson for the $ZZ \to \ell^+\ell^-\ell'^+\ell'^-$ and $ZZ \to \ell^+\ell^-\nu\bar{\nu}$ selections are used to derive 95% confidence intervals for anomalous neutral triple gauge boson couplings. These limits are more stringent than those derived from measurements at LEP [8] and the Tevatron [9]. They improve the previous published results from ATLAS [13] by approximately a factor of five and supersede them.

Acknowledgments

We thank CERN for the very successful operation of the LHC, as well as the support staff from our institutions without whom ATLAS could not be operated efficiently.

We acknowledge the support of ANPCyT, Argentina; YerPhI, Armenia; ARC, Australia; BMWF and FWF, Austria; ANAS, Azerbaijan; SSTC, Belarus; CNPq and FAPESP, Brazil; NSERC, NRC and CFI, Canada; CERN; CONICYT, Chile; CAS, MOST and NSFC, China; COLCIENCIAS, Colombia; MSMT CR, MPO CR and VSC CR, Czech Republic; DNRF, DNSRC and Lundbeck Foundation, Denmark; EPLANET, ERC and NSRF, European Union; IN2P3-CNRS, CEA-DSM/IRFU, France; GNSF, Georgia; BMBF, DFG, HGF, MPG and AvH Foundation, Germany; GSRT and NSRF, Greece; ISF, MINERVA,

JHEP03(2013)128

GIF, DIP and Benoziyo Center, Israel; INFN, Italy; MEXT and JSPS, Japan; CNRST, Morocco; FOM and NWO, Netherlands; BRF and RCN, Norway; MNiSW, Poland; GRICES and FCT, Portugal; MERYS (MECTS), Romania; MES of Russia and ROSATOM, Russian Federation; JINR; MSTD, Serbia; MSSR, Slovakia; ARRS and MVZT, Slovenia; DST/NRF, South Africa; MICINN, Spain; SRC and Wallenberg Foundation, Sweden; SER, SNSF and Cantons of Bern and Geneva, Switzerland; NSC, Taiwan; TAEK, Turkey; STFC, the Royal Society and Leverhulme Trust, United Kingdom; DOE and NSF, United States of America.

The crucial computing support from all WLCG partners is acknowledged gratefully, in particular from CERN and the ATLAS Tier-1 facilities at TRIUMF (Canada), NDGF (Denmark, Norway, Sweden), CC-IN2P3 (France), KIT/GridKA (Germany), INFN-CNAF (Italy), NL-T1 (Netherlands), PIC (Spain), ASGC (Taiwan), RAL (UK) and BNL (USA) and in the Tier-2 facilities worldwide.

Open Access. This article is distributed under the terms of the Creative Commons Attribution License which permits any use, distribution and reproduction in any medium, provided the original author(s) and source are credited.

References

[1] G. Gounaris, J. Layssac and F. Renard, *New and standard physics contributions to anomalous Z and gamma selfcouplings*, *Phys. Rev.* **D 62** (2000) 073013 [hep-ph/0003143] [INSPIRE].

[2] J. Ellison and J. Wudka, *Study of trilinear gauge boson couplings at the Tevatron collider*, *Ann. Rev. Nucl. Part. Sci.* **48** (1998) 33 [hep-ph/9804322] [INSPIRE].

[3] U. Baur and D.L. Rainwater, *Probing neutral gauge boson selfinteractions in ZZ production at the Tevatron*, *Int. J. Mod. Phys.* **A 16S1A** (2001) 315 [hep-ph/0011016] [INSPIRE].

[4] ALEPH collaboration, R. Barate et al., *Measurement of the $e^+e^- \to ZZ$ production cross-section at center-of-mass energies of* 183 *GeV and* 189 *GeV*, *Phys. Lett.* **B 469** (1999) 287 [hep-ex/9911003] [INSPIRE].

[5] DELPHI collaboration, J. Abdallah et al., *ZZ production in e^+e^- interactions at $\sqrt{s} = 183$ GeV to 209 GeV*, *Eur. Phys. J.* **C 30** (2003) 447 [hep-ex/0307050] [INSPIRE].

[6] L3 collaboration, M. Acciarri et al., *Study of Z boson pair production in e^+e^- collisions at LEP at $\sqrt{s} = 189$ GeV*, *Phys. Lett.* **B 465** (1999) 363 [hep-ex/9909043] [INSPIRE].

[7] OPAL collaboration, G. Abbiendi et al., *Study of Z pair production and anomalous couplings in e^+e^- collisions at $\sqrt{s}$ between* 190 *GeV and* 209 *GeV*, *Eur. Phys. J.* **C 32** (2003) 303 [hep-ex/0310013] [INSPIRE].

[8] ALEPH, DELPHI, L3, OPAL, LEP Electroweak Working Group collaboration, J. Alcaraz et al., *A combination of preliminary electroweak measurements and constraints on the standard model*, hep-ex/0612034 [INSPIRE].

[9] D0 collaboration, V. Abazov et al., *Search for ZZ and $Z\gamma^*$ production in $p\bar{p}$ collisions at $\sqrt{s} = 1.96$ TeV and limits on anomalous ZZZ and $ZZ\gamma^*$ couplings*, *Phys. Rev. Lett.* **100** (2008) 131801 [arXiv:0712.0599] [INSPIRE].

JHEP03(2013)128

[10] CDF collaboration, T. Aaltonen et al., *First measurement of ZZ production in $p\bar{p}$ collisions at $\sqrt{s} = 1.96$ TeV*, Phys. Rev. Lett. **100** (2008) 201801 [arXiv:0801.4806] [INSPIRE].

[11] D0 collaboration, V. Abazov et al., *Observation of ZZ production in $p\bar{p}$ collisions at $\sqrt{s} = 1.96$ TeV*, Phys. Rev. Lett. **101** (2008) 171803 [arXiv:0808.0703] [INSPIRE].

[12] D0 collaboration, V.M. Abazov et al., *Measurement of the ZZ production cross section in $p\bar{p}$ collisions at $\sqrt{s} = 1.96$ TeV*, Phys. Rev. **D 84** (2011) 011103 [arXiv:1104.3078] [INSPIRE].

[13] ATLAS collaboration, *Measurement of the ZZ production cross section and limits on anomalous neutral triple gauge couplings in proton-proton collisions at $\sqrt{s} = 7$ TeV with the ATLAS detector*, Phys. Rev. Lett. **108** (2012) 041804 [arXiv:1110.5016] [INSPIRE].

[14] CMS collaboration, *Measurement of the ZZ production cross section and search for anomalous couplings in $2l2l'$ final states in pp collisions at $\sqrt{s} = 7$ TeV*, JHEP **01** (2013) 063 [arXiv:1211.4890] [INSPIRE].

[15] ATLAS collaboration, *Observation of a new particle in the search for the standard model Higgs boson with the ATLAS detector at the LHC*, Phys. Lett. **B 716** (2012) 1 [arXiv:1207.7214] [INSPIRE].

[16] CMS collaboration, *Observation of a new boson at a mass of 125 GeV with the CMS experiment at the LHC*, Phys. Lett. **B 716** (2012) 30 [arXiv:1207.7235] [INSPIRE].

[17] ATLAS collaboration, *Search for the Standard Model Higgs boson in the decay channel $H \to ZZ^{(*)} \to 4\ell$ with $4.8\,fb^{-1}$ of pp collision data at $\sqrt{s} = 7$ TeV with ATLAS*, Phys. Lett. **B 710** (2012) 383 [arXiv:1202.1415] [INSPIRE].

[18] ATLAS collaboration, *Search for new particles decaying to ZZ using final states with leptons and jets with the ATLAS detector in $\sqrt{s} = 7$ TeV proton-proton collisions*, Phys. Lett. **B 712** (2012) 331 [arXiv:1203.0718] [INSPIRE].

[19] H.-L. Lai et al., *New parton distributions for collider physics*, Phys. Rev. **D 82** (2010) 074024 [arXiv:1007.2241] [INSPIRE].

[20] J.M. Campbell, R.K. Ellis and C. Williams, *Vector boson pair production at the LHC*, JHEP **07** (2011) 018 [arXiv:1105.0020] [INSPIRE].

[21] ATLAS collaboration, *The ATLAS experiment at the CERN Large Hadron Collider*, 2008 JINST **3** S08003 [INSPIRE].

[22] ATLAS collaboration, *Luminosity determination in pp collisions at $\sqrt{s} = 7$ TeV using the ATLAS detector at the LHC*, Eur. Phys. J. **C 71** (2011) 1630 [arXiv:1101.2185] [INSPIRE].

[23] S. Alioli, P. Nason, C. Oleari and E. Re, *A general framework for implementing NLO calculations in shower Monte Carlo programs: the POWHEG BOX*, JHEP **06** (2010) 043 [arXiv:1002.2581] [INSPIRE].

[24] T. Melia, P. Nason, R. Rontsch and G. Zanderighi, *W^+W^-, WZ and ZZ production in the POWHEG BOX*, JHEP **11** (2011) 078 [arXiv:1107.5051] [INSPIRE].

[25] T. Sjöstrand, S. Mrenna and P.Z. Skands, *PYTHIA 6.4 physics and manual*, JHEP **05** (2006) 026 [hep-ph/0603175] [INSPIRE].

[26] T. Gleisberg et al., *Event generation with SHERPA 1.1*, JHEP **02** (2009) 007 [arXiv:0811.4622] [INSPIRE].

[27] J. Pumplin et al., *New generation of parton distributions with uncertainties from global QCD analysis*, JHEP **07** (2002) 012 [hep-ph/0201195] [INSPIRE].

JHEP03(2013)128

[28] T. Binoth, N. Kauer and P. Mertsch, *Gluon-induced QCD corrections to* $pp \to ZZ \to \ell^+\ell^-\ell'^+\ell'^-$, arXiv:0807.0024 [INSPIRE].

[29] G. Corcella et al., *HERWIG 6: an event generator for hadron emission reactions with interfering gluons (including supersymmetric processes)*, JHEP **01** (2001) 010 [hep-ph/0011363] [INSPIRE].

[30] J. Butterworth, J.R. Forshaw and M. Seymour, *Multiparton interactions in photoproduction at HERA*, Z. Phys. **C 72** (1996) 637 [hep-ph/9601371] [INSPIRE].

[31] M.L. Mangano, M. Moretti, F. Piccinini, R. Pittau and A.D. Polosa, *ALPGEN, a generator for hard multiparton processes in hadronic collisions*, JHEP **07** (2003) 001 [hep-ph/0206293] [INSPIRE].

[32] S. Frixione and B.R. Webber, *Matching NLO QCD computations and parton shower simulations*, JHEP **06** (2002) 029 [hep-ph/0204244] [INSPIRE].

[33] B.P. Kersevan and E. Richter-Was, *The Monte Carlo event generator AcerMC version 1.0 with interfaces to PYTHIA 6.2 and HERWIG 6.3*, Comput. Phys. Commun. **149** (2003) 142 [hep-ph/0201302] [INSPIRE].

[34] A. Martin, W. Stirling, R. Thorne and G. Watt, *Parton distributions for the LHC*, Eur. Phys. J. **C 63** (2009) 189 [arXiv:0901.0002] [INSPIRE].

[35] J. Alwall et al., *MadGraph/MadEvent v4: the new web generation*, JHEP **09** (2007) 028 [arXiv:0706.2334] [INSPIRE].

[36] ATLAS collaboration, *The ATLAS simulation infrastructure*, Eur. Phys. J. **C 70** (2010) 823 [arXiv:1005.4568] [INSPIRE].

[37] GEANT4 collaboration, S. Agostinelli et al., *GEANT4: a simulation toolkit*, Nucl. Instrum. Meth. **A 506** (2003) 250 [INSPIRE].

[38] ATLAS collaboration, *Measurement of the* $W \to \ell\nu$ *and* $Z/\gamma^* \to \ell\ell$ *production cross sections in proton-proton collisions at* $\sqrt{s} = 7$ *TeV with the ATLAS detector*, JHEP **12** (2010) 060 [arXiv:1010.2130] [INSPIRE].

[39] R. Fruhwirth, *Track fitting with non-gaussian noise*, Comput. Phys. Commun. **100** (1997) 1 [INSPIRE].

[40] ATLAS collaboration, *Electron performance measurements with the ATLAS detector using the* 2010 *LHC proton-proton collision data*, Eur. Phys. J. **C 72** (2012) 1909 [arXiv:1110.3174] [INSPIRE].

[41] ATLAS collaboration, *Calorimeter clustering algorithms: description and performance*, ATL-LARG-PUB-2008-002 (2008).

[42] M. Cacciari, G.P. Salam and G. Soyez, *The Anti-k(t) jet clustering algorithm*, JHEP **04** (2008) 063 [arXiv:0802.1189] [INSPIRE].

[43] ATLAS collaboration, *Probing the measurement of jet energies with the ATLAS detector using photon+jet events in proton-proton collisions at* $\sqrt{s} = 7$ *TeV*, ATLAS-CONF-2012-063 (2012).

[44] ATLAS collaboration, *Probing the measurement of jet energies with the ATLAS detector using Z+jet events from proton-proton collisions at* $\sqrt{s} = 7$ *TeV*, ATLAS-CONF-2012-053 (2012).

JHEP03(2013)128

[45] ATLAS collaboration, *Performance of missing transverse momentum reconstruction in proton-proton collisions at 7 TeV with ATLAS*, Eur. Phys. J. **C 72** (2012) 1844 [arXiv:1108.5602] [INSPIRE].

[46] Particle Data Group collaboration, J. Beringer et al., *Review of particle physics*, Phys. Rev. **D 86** (2012) 010001 [INSPIRE].

[47] ATLAS collaboration, *Measurement of W^+W^- production in pp collisions at $\sqrt{s} = 7$ TeV with the ATLAS detector and limits on anomalous WWZ and $WW\gamma$ couplings*, arXiv:1210.2979 [INSPIRE].

[48] ATLAS collaboration, *Measurement of the top quark pair cross section with ATLAS in pp collisions at $\sqrt{s} = 7$ TeV using final states with an electron or a muon and a hadronically decaying τ lepton*, Phys. Lett. **B 717** (2012) 89 [arXiv:1205.2067] [INSPIRE].

[49] G. D'Agostini, *Improved iterative Bayesian unfolding*, arXiv:1010.0632.

[50] U. Baur, T. Han and J. Ohnemus, *WZ production at hadron colliders: effects of nonstandard WWZ couplings and QCD corrections*, Phys. Rev. **D 51** (1995) 3381 [hep-ph/9410266] [INSPIRE].

[51] U. Baur, T. Han and J. Ohnemus, *QCD corrections and anomalous couplings in $Z\gamma$ production at hadron colliders*, Phys. Rev. **D 57** (1998) 2823 [hep-ph/9710416] [INSPIRE].

[52] G. Bella, *Weighting di-boson Monte Carlo events in hadron colliders*, arXiv:0803.3307 [INSPIRE].

JHEP03(2013)128

The ATLAS collaboration

G. Aad[48], T. Abajyan[21], B. Abbott[111], J. Abdallah[12], S. Abdel Khalek[115], A.A. Abdelalim[49], O. Abdinov[11], R. Aben[105], B. Abi[112], M. Abolins[88], O.S. AbouZeid[158], H. Abramowicz[153], H. Abreu[136], B.S. Acharya[164a,164b,a], L. Adamczyk[38], D.L. Adams[25], T.N. Addy[56], J. Adelman[176], S. Adomeit[98], P. Adragna[75], T. Adye[129], S. Aefsky[23], J.A. Aguilar-Saavedra[124b,b], M. Agustoni[17], M. Aharrouche[81], S.P. Ahlen[22], F. Ahles[48], A. Ahmad[148], M. Ahsan[41], G. Aielli[133a,133b], T.P.A. Åkesson[79], G. Akimoto[155], A.V. Akimov[94], M.S. Alam[2], M.A. Alam[76], J. Albert[169], S. Albrand[55], M. Aleksa[30], I.N. Aleksandrov[64], F. Alessandria[89a], C. Alexa[26a], G. Alexander[153], G. Alexandre[49], T. Alexopoulos[10], M. Alhroob[164a,164c], M. Aliev[16], G. Alimonti[89a], J. Alison[120], B.M.M. Allbrooke[18], P.P. Allport[73], S.E. Allwood-Spiers[53], J. Almond[82], A. Aloisio[102a,102b], R. Alon[172], A. Alonso[79], F. Alonso[70], A. Altheimer[35], B. Alvarez Gonzalez[88], M.G. Alviggi[102a,102b], K. Amako[65], C. Amelung[23], V.V. Ammosov[128,*], S.P. Amor Dos Santos[124a], A. Amorim[124a,c], N. Amram[153], C. Anastopoulos[30], L.S. Ancu[17], N. Andari[115], T. Andeen[35], C.F. Anders[58b], G. Anders[58a], K.J. Anderson[31], A. Andreazza[89a,89b], V. Andrei[58a], M-L. Andrieux[55], X.S. Anduaga[70], S. Angelidakis[9], P. Anger[44], A. Angerami[35], F. Anghinolfi[30], A. Anisenkov[107], N. Anjos[124a], A. Annovi[47], A. Antonaki[9], M. Antonelli[47], A. Antonov[96], J. Antos[144b], F. Anulli[132a], M. Aoki[101], S. Aoun[83], L. Aperio Bella[5], R. Apolle[118,d], G. Arabidze[88], I. Aracena[143], Y. Arai[65], A.T.H. Arce[45], S. Arfaoui[148], J-F. Arguin[93], S. Argyropoulos[42], E. Arik[19a,*], M. Arik[19a], A.J. Armbruster[87], O. Arnaez[81], V. Arnal[80], A. Artamonov[95], G. Artoni[132a,132b], D. Arutinov[21], S. Asai[155], S. Ask[28], B. Åsman[146a,146b], L. Asquith[6], K. Assamagan[25,e], A. Astbury[169], M. Atkinson[165], B. Aubert[5], E. Auge[115], K. Augsten[126], M. Aurousseau[145a], G. Avolio[30], D. Axen[168], G. Azuelos[93,f], Y. Azuma[155], M.A. Baak[30], G. Baccaglioni[89a], C. Bacci[134a,134b], A.M. Bach[15], H. Bachacou[136], K. Bachas[154], M. Backes[49], M. Backhaus[21], J. Backus Mayes[143], E. Badescu[26a], P. Bagnaia[132a,132b], S. Bahinipati[3], Y. Bai[33a], D.C. Bailey[158], T. Bain[35], J.T. Baines[129], O.K. Baker[176], M.D. Baker[25], S. Baker[77], P. Balek[127], E. Banas[39], P. Banerjee[93], Sw. Banerjee[173], D. Banfi[30], A. Bangert[150], V. Bansal[169], H.S. Bansil[18], L. Barak[172], S.P. Baranov[94], A. Barbaro Galtieri[15], T. Barber[48], E.L. Barberio[86], D. Barberis[50a,50b], M. Barbero[21], D.Y. Bardin[64], T. Barillari[99], M. Barisonzi[175], T. Barklow[143], N. Barlow[28], B.M. Barnett[129], R.M. Barnett[15], A. Baroncelli[134a], G. Barone[49], A.J. Barr[118], F. Barreiro[80], J. Barreiro Guimarães da Costa[57], R. Bartoldus[143], A.E. Barton[71], V. Bartsch[149], A. Basye[165], R.L. Bates[53], L. Batkova[144a], J.R. Batley[28], A. Battaglia[17], M. Battistin[30], F. Bauer[136], H.S. Bawa[143,g], S. Beale[98], T. Beau[78], P.H. Beauchemin[161], R. Beccherle[50a], P. Bechtle[21], H.P. Beck[17], K. Becker[175], S. Becker[98], M. Beckingham[138], K.H. Becks[175], A.J. Beddall[19c], A. Beddall[19c], S. Bedikian[176], V.A. Bednyakov[64], C.P. Bee[83], L.J. Beemster[105], M. Begel[25], S. Behar Harpaz[152], P.K. Behera[62], M. Beimforde[99], C. Belanger-Champagne[85], P.J. Bell[49], W.H. Bell[49], G. Bella[153], L. Bellagamba[20a], M. Bellomo[30], A. Belloni[57], O. Beloborodova[107,h], K. Belotskiy[96], O. Beltramello[30], O. Benary[153], D. Benchekroun[135a], K. Bendtz[146a,146b], N. Benekos[165], Y. Benhammou[153], E. Benhar Noccioli[49], J.A. Benitez Garcia[159b], D.P. Benjamin[45], M. Benoit[115], J.R. Bensinger[23], K. Benslama[130], S. Bentvelsen[105], D. Berge[30], E. Bergeaas Kuutmann[42], N. Berger[5], F. Berghaus[169], E. Berglund[105], J. Beringer[15], P. Bernat[77], R. Bernhard[48], C. Bernius[25], T. Berry[76], C. Bertella[83], A. Bertin[20a,20b], F. Bertolucci[122a,122b], M.I. Besana[89a,89b], G.J. Besjes[104], N. Besson[136], S. Bethke[99], W. Bhimji[46], R.M. Bianchi[30], L. Bianchini[23], M. Bianco[72a,72b], O. Biebel[98], S.P. Bieniek[77], K. Bierwagen[54], J. Biesiada[15], M. Biglietti[134a], H. Bilokon[47], M. Bindi[20a,20b], S. Binet[115], A. Bingul[19c], C. Bini[132a,132b], C. Biscarat[178], B. Bittner[99], C.W. Black[150], K.M. Black[22], R.E. Blair[6], J.-B. Blanchard[136], G. Blanchot[30], T. Blazek[144a], I. Bloch[42], C. Blocker[23], J. Blocki[39], A. Blondel[49], W. Blum[81], U. Blumenschein[54], G.J. Bobbink[105], V.S. Bobrovnikov[107], S.S. Bocchetta[79], A. Bocci[45], C.R. Boddy[118], M. Boehler[48], J. Boek[175], T.T. Boek[175], N. Boelaert[36], J.A. Bogaerts[30], A. Bogdanchikov[107], A. Bogouch[90,*], C. Bohm[146a], J. Bohm[125], V. Boisvert[76], T. Bold[38], V. Boldea[26a], N.M. Bolnet[136], M. Bomben[78], M. Bona[75], M. Boonekamp[136], S. Bordoni[78], C. Borer[17], A. Borisov[128], G. Borissov[71], I. Borjanovic[13a], M. Borri[82], S. Borroni[87], J. Bortfeldt[98], V. Bortolotto[134a,134b], K. Bos[105], D. Boscherini[20a],

JHEP03(2013)128

M. Bosman[12], H. Boterenbrood[105], J. Bouchami[93], J. Boudreau[123], E.V. Bouhova-Thacker[71], D. Boumediene[34], C. Bourdarios[115], N. Bousson[83], A. Boveia[31], J. Boyd[30], I.R. Boyko[64], I. Bozovic-Jelisavcic[13b], J. Bracinik[18], P. Branchini[134a], A. Brandt[8], G. Brandt[118], O. Brandt[54], U. Bratzler[156], B. Brau[84], J.E. Brau[114], H.M. Braun[175,*], S.F. Brazzale[164a,164c], B. Brelier[158], J. Bremer[30], K. Brendlinger[120], R. Brenner[166], S. Bressler[172], D. Britton[53], F.M. Brochu[28], I. Brock[21], R. Brock[88], F. Broggi[89a], C. Bromberg[88], J. Bronner[99], G. Brooijmans[35], T. Brooks[76], W.K. Brooks[32b], G. Brown[82], P.A. Bruckman de Renstrom[39], D. Bruncko[144b], R. Bruneliere[48], S. Brunet[60], A. Bruni[20a], G. Bruni[20a], M. Bruschi[20a], L. Bryngemark[79], T. Buanes[14], Q. Buat[55], F. Bucci[49], J. Buchanan[118], P. Buchholz[141], R.M. Buckingham[118], A.G. Buckley[46], S.I. Buda[26a], I.A. Budagov[64], B. Budick[108], V. Büscher[81], L. Bugge[117], O. Bulekov[96], A.C. Bundock[73], M. Bunse[43], T. Buran[117], H. Burckhart[30], S. Burdin[73], T. Burgess[14], S. Burke[129], E. Busato[34], P. Bussey[53], C.P. Buszello[166], B. Butler[143], J.M. Butler[22], C.M. Buttar[53], J.M. Butterworth[77], W. Buttinger[28], M. Byszewski[30], S. Cabrera Urbán[167], D. Caforio[20a,20b], O. Cakir[4a], P. Calafiura[15], G. Calderini[78], P. Calfayan[98], R. Calkins[106], L.P. Caloba[24a], R. Caloi[132a,132b], D. Calvet[34], S. Calvet[34], R. Camacho Toro[34], P. Camarri[133a,133b], D. Cameron[117], L.M. Caminada[15], R. Caminal Armadans[12], S. Campana[30], M. Campanelli[77], V. Canale[102a,102b], F. Canelli[31], A. Canepa[159a], J. Cantero[80], R. Cantrill[76], L. Capasso[102a,102b], M.D.M. Capeans Garrido[30], I. Caprini[26a], M. Caprini[26a], D. Capriotti[99], M. Capua[37a,37b], R. Caputo[81], R. Cardarelli[133a], T. Carli[30], G. Carlino[102a], L. Carminati[89a,89b], B. Caron[85], S. Caron[104], E. Carquin[32b], G.D. Carrillo-Montoya[145b], A.A. Carter[75], J.R. Carter[28], J. Carvalho[124a,i], D. Casadei[108], M.P. Casado[12], M. Cascella[122a,122b], C. Caso[50a,50b,*], A.M. Castaneda Hernandez[173,j], E. Castaneda-Miranda[173], V. Castillo Gimenez[167], N.F. Castro[124a], G. Cataldi[72a], P. Catastini[57], A. Catinaccio[30], J.R. Catmore[30], A. Cattai[30], G. Cattani[133a,133b], S. Caughron[88], V. Cavaliere[165], P. Cavalleri[78], D. Cavalli[89a], M. Cavalli-Sforza[12], V. Cavasinni[122a,122b], F. Ceradini[134a,134b], A.S. Cerqueira[24b], A. Cerri[15], L. Cerrito[75], F. Cerutti[15], S.A. Cetin[19b], A. Chafaq[135a], D. Chakraborty[106], I. Chalupkova[127], K. Chan[3], P. Chang[165], B. Chapleau[85], J.D. Chapman[28], J.W. Chapman[87], D.G. Charlton[18], V. Chavda[82], C.A. Chavez Barajas[30], S. Cheatham[85], S. Chekanov[6], S.V. Chekulaev[159a], G.A. Chelkov[64], M.A. Chelstowska[104], C. Chen[63], H. Chen[25], S. Chen[33c], X. Chen[173], Y. Chen[35], Y. Cheng[31], A. Cheplakov[64], R. Cherkaoui El Moursli[135e], V. Chernyatin[25], E. Cheu[7], S.L. Cheung[158], L. Chevalier[136], G. Chiefari[102a,102b], L. Chikovani[51a,*], J.T. Childers[30], A. Chilingarov[71], G. Chiodini[72a], A.S. Chisholm[18], R.T. Chislett[77], A. Chitan[26a], M.V. Chizhov[64], G. Choudalakis[31], S. Chouridou[137], I.A. Christidi[77], A. Christov[48], D. Chromek-Burckhart[30], M.L. Chu[151], J. Chudoba[125], G. Ciapetti[132a,132b], A.K. Ciftci[4a], R. Ciftci[4a], D. Cinca[34], V. Cindro[74], A. Ciocio[15], M. Cirilli[87], P. Cirkovic[13b], Z.H. Citron[172], M. Citterio[89a], M. Ciubancan[26a], A. Clark[49], P.J. Clark[46], R.N. Clarke[15], W. Cleland[123], J.C. Clemens[83], B. Clement[55], C. Clement[146a,146b], Y. Coadou[83], M. Cobal[164a,164c], A. Coccaro[138], J. Cochran[63], L. Coffey[23], J.G. Cogan[143], J. Coggeshall[165], J. Colas[5], S. Cole[106], A.P. Colijn[105], N.J. Collins[18], C. Collins-Tooth[53], J. Collot[55], T. Colombo[119a,119b], G. Colon[84], G. Compostella[99], P. Conde Muiño[124a], E. Coniavitis[166], M.C. Conidi[12], S.M. Consonni[89a,89b], V. Consorti[48], S. Constantinescu[26a], C. Conta[119a,119b], G. Conti[57], F. Conventi[102a,k], M. Cooke[15], B.D. Cooper[77], A.M. Cooper-Sarkar[118], K. Copic[15], T. Cornelissen[175], M. Corradi[20a], F. Corriveau[85,l], A. Cortes-Gonzalez[165], G. Cortiana[99], G. Costa[89a], M.J. Costa[167], D. Costanzo[139], D. Côté[30], L. Courneyea[169], G. Cowan[76], B.E. Cox[82], K. Cranmer[108], F. Crescioli[78], M. Cristinziani[21], G. Crosetti[37a,37b], S. Crépé-Renaudin[55], C.-M. Cuciuc[26a], C. Cuenca Almenar[176], T. Cuhadar Donszelmann[139], J. Cummings[176], M. Curatolo[47], C.J. Curtis[18], C. Cuthbert[150], P. Cwetanski[60], H. Czirr[141], P. Czodrowski[44], Z. Czyczula[176], S. D'Auria[53], M. D'Onofrio[73], A. D'Orazio[132a,132b], M.J. Da Cunha Sargedas De Sousa[124a], C. Da Via[82], W. Dabrowski[38], A. Dafinca[118], T. Dai[87], F. Dallaire[93], C. Dallapiccola[84], M. Dam[36], M. Dameri[50a,50b], D.S. Damiani[137], H.O. Danielsson[30], V. Dao[49], G. Darbo[50a], G.L. Darlea[26b], J.A. Dassoulas[42], W. Davey[21], T. Davidek[127], N. Davidson[86], R. Davidson[71], E. Davies[118,d], M. Davies[93], O. Davignon[78], A.R. Davison[77], Y. Davygora[58a], E. Dawe[142],

JHEP03(2013)128

I. Dawson[139], R.K. Daya-Ishmukhametova[23], K. De[8], R. de Asmundis[102a], S. De Castro[20a,20b], S. De Cecco[78], J. de Graat[98], N. De Groot[104], P. de Jong[105], C. De La Taille[115], H. De la Torre[80], F. De Lorenzi[63], L. de Mora[71], L. De Nooij[105], D. De Pedis[132a], A. De Salvo[132a], U. De Sanctis[164a,164c], A. De Santo[149], J.B. De Vivie De Regie[115], G. De Zorzi[132a,132b], W.J. Dearnaley[71], R. Debbe[25], C. Debenedetti[46], B. Dechenaux[55], D.V. Dedovich[64], J. Degenhardt[120], J. Del Peso[80], T. Del Prete[122a,122b], T. Delemontex[55], M. Deliyergiyev[74], A. Dell'Acqua[30], L. Dell'Asta[22], M. Della Pietra[102a,k], D. della Volpe[102a,102b], M. Delmastro[5], P.A. Delsart[55], C. Deluca[105], S. Demers[176], M. Demichev[64], B. Demirkoz[12,m], S.P. Denisov[128], D. Derendarz[39], J.E. Derkaoui[135d], F. Derue[78], P. Dervan[73], K. Desch[21], E. Devetak[148], P.O. Deviveiros[105], A. Dewhurst[129], B. DeWilde[148], S. Dhaliwal[158], R. Dhullipudi[25,n], A. Di Ciaccio[133a,133b], L. Di Ciaccio[5], C. Di Donato[102a,102b], A. Di Girolamo[30], B. Di Girolamo[30], S. Di Luise[134a,134b], A. Di Mattia[152], B. Di Micco[30], R. Di Nardo[47], A. Di Simone[133a,133b], R. Di Sipio[20a,20b], M.A. Diaz[32a], E.B. Diehl[87], J. Dietrich[42], T.A. Dietzsch[58a], S. Diglio[86], K. Dindar Yagci[40], J. Dingfelder[21], F. Dinut[26a], C. Dionisi[132a,132b], P. Dita[26a], S. Dita[26a], F. Dittus[30], F. Djama[83], T. Djobava[51b], M.A.B. do Vale[24c], A. Do Valle Wemans[124a,o], T.K.O. Doan[5], M. Dobbs[85], D. Dobos[30], E. Dobson[30,p], J. Dodd[35], C. Doglioni[49], T. Doherty[53], Y. Doi[65,*], J. Dolejsi[127], Z. Dolezal[127], B.A. Dolgoshein[96,*], T. Dohmae[155], M. Donadelli[24d], J. Donini[34], J. Dopke[30], A. Doria[102a], A. Dos Anjos[173], A. Dotti[122a,122b], M.T. Dova[70], A.D. Doxiadis[105], A.T. Doyle[53], N. Dressnandt[120], M. Dris[10], J. Dubbert[99], S. Dube[15], E. Duchovni[172], G. Duckeck[98], D. Duda[175], A. Dudarev[30], F. Dudziak[63], M. Dührssen[30], I.P. Duerdoth[82], L. Duflot[115], M-A. Dufour[85], L. Duguid[76], M. Dunford[58a], H. Duran Yildiz[4a], R. Duxfield[139], M. Dwuznik[38], M. Düren[52], W.L. Ebenstein[45], J. Ebke[98], S. Eckweiler[81], K. Edmonds[81], W. Edson[2], C.A. Edwards[76], N.C. Edwards[53], W. Ehrenfeld[42], T. Eifert[143], G. Eigen[14], K. Einsweiler[15], E. Eisenhandler[75], T. Ekelof[166], M. El Kacimi[135c], M. Ellert[166], S. Elles[5], F. Ellinghaus[81], K. Ellis[75], N. Ellis[30], J. Elmsheuser[98], M. Elsing[30], D. Emeliyanov[129], R. Engelmann[148], A. Engl[98], B. Epp[61], J. Erdmann[176], A. Ereditato[17], D. Eriksson[146a], J. Ernst[2], M. Ernst[25], J. Ernwein[136], D. Errede[165], S. Errede[165], E. Ertel[81], M. Escalier[115], H. Esch[43], C. Escobar[123], X. Espinal Curull[12], B. Esposito[47], F. Etienne[83], A.I. Etienvre[136], E. Etzion[153], D. Evangelakou[54], H. Evans[60], L. Fabbri[20a,20b], C. Fabre[30], R.M. Fakhrutdinov[128], S. Falciano[132a], Y. Fang[33a], M. Fanti[89a,89b], A. Farbin[8], A. Farilla[134a], J. Farley[148], T. Farooque[158], S. Farrell[163], S.M. Farrington[170], P. Farthouat[30], F. Fassi[167], P. Fassnacht[30], D. Fassouliotis[9], B. Fatholahzadeh[158], A. Favareto[89a,89b], L. Fayard[115], S. Fazio[37a,37b], P. Federic[144a], O.L. Fedin[121], W. Fedorko[88], M. Fehling-Kaschek[48], L. Feligioni[83], C. Feng[33d], E.J. Feng[6], A.B. Fenyuk[128], J. Ferencei[144b], W. Fernando[6], S. Ferrag[53], J. Ferrando[53], V. Ferrara[42], A. Ferrari[166], P. Ferrari[105], R. Ferrari[119a], D.E. Ferreira de Lima[53], A. Ferrer[167], D. Ferrere[49], C. Ferretti[87], A. Ferretto Parodi[50a,50b], M. Fiascaris[31], F. Fiedler[81], A. Filipčič[74], F. Filthaut[104], M. Fincke-Keeler[169], M.C.N. Fiolhais[124a,i], L. Fiorini[167], A. Firan[40], G. Fischer[42], M.J. Fisher[109], M. Flechl[48], I. Fleck[141], J. Fleckner[81], P. Fleischmann[174], S. Fleischmann[175], T. Flick[175], A. Floderus[79], L.R. Flores Castillo[173], A.C. Florez Bustos[159b], M.J. Flowerdew[99], T. Fonseca Martin[17], A. Formica[136], A. Forti[82], D. Fortin[159a], D. Fournier[115], A.J. Fowler[45], H. Fox[71], P. Francavilla[12], M. Franchini[20a,20b], S. Franchino[119a,119b], D. Francis[30], T. Frank[172], M. Franklin[57], S. Franz[30], M. Fraternali[119a,119b], S. Fratina[120], S.T. French[28], C. Friedrich[42], F. Friedrich[44], D. Froidevaux[30], J.A. Frost[28], C. Fukunaga[156], E. Fullana Torregrosa[127], B.G. Fulsom[143], J. Fuster[167], C. Gabaldon[30], O. Gabizon[172], T. Gadfort[25], S. Gadomski[49], G. Gagliardi[50a,50b], P. Gagnon[60], C. Galea[98], B. Galhardo[124a], E.J. Gallas[118], V. Gallo[17], B.J. Gallop[129], P. Gallus[125], K.K. Gan[109], Y.S. Gao[143,g], A. Gaponenko[15], F. Garberson[176], M. Garcia-Sciveres[15], C. García[167], J.E. García Navarro[167], R.W. Gardner[31], N. Garelli[30], V. Garonne[30], C. Gatti[47], G. Gaudio[119a], B. Gaur[141], L. Gauthier[136], P. Gauzzi[132a,132b], I.L. Gavrilenko[94], C. Gay[168], G. Gaycken[21], E.N. Gazis[10], P. Ge[33d], Z. Gecse[168], C.N.P. Gee[129], D.A.A. Geerts[105], Ch. Geich-Gimbel[21], K. Gellerstedt[146a,146b], C. Gemme[50a], A. Gemmell[53], M.H. Genest[55], S. Gentile[132a,132b], M. George[54], S. George[76], D. Gerbaudo[12], P. Gerlach[175], A. Gershon[153], C. Geweniger[58a], H. Ghazlane[135b], N. Ghodbane[34], B. Giacobbe[20a],

JHEP03(2013)128

S. Giagu[132a,132b], V. Giangiobbe[12], F. Gianotti[30], B. Gibbard[25], A. Gibson[158], S.M. Gibson[30], M. Gilchriese[15], D. Gillberg[29], A.R. Gillman[129], D.M. Gingrich[3,f], J. Ginzburg[153], N. Giokaris[9], M.P. Giordani[164c], R. Giordano[102a,102b], F.M. Giorgi[16], P. Giovannini[99], P.F. Giraud[136], D. Giugni[89a], M. Giunta[93], B.K. Gjelsten[117], L.K. Gladilin[97], C. Glasman[80], J. Glatzer[21], A. Glazov[42], K.W. Glitza[175], G.L. Glonti[64], J.R. Goddard[75], J. Godfrey[142], J. Godlewski[30], M. Goebel[42], T. Göpfert[44], C. Goeringer[81], C. Gössling[43], S. Goldfarb[87], T. Golling[176], D. Golubkov[128], A. Gomes[124a,c], L.S. Gomez Fajardo[42], R. Gonçalo[76], J. Goncalves Pinto Firmino Da Costa[42], L. Gonella[21], S. González de la Hoz[167], G. Gonzalez Parra[12], M.L. Gonzalez Silva[27], S. Gonzalez-Sevilla[49], J.J. Goodson[148], L. Goossens[30], P.A. Gorbounov[95], H.A. Gordon[25], I. Gorelov[103], G. Gorfine[175], B. Gorini[30], E. Gorini[72a,72b], A. Gorišek[74], E. Gornicki[39], A.T. Goshaw[6], M. Gosselink[105], M.I. Gostkin[64], I. Gough Eschrich[163], M. Gouighri[135a], D. Goujdami[135c], M.P. Goulette[49], A.G. Goussiou[138], C. Goy[5], S. Gozpinar[23], I. Grabowska-Bold[38], P. Grafström[20a,20b], K-J. Grahn[42], E. Gramstad[117], F. Grancagnolo[72a], S. Grancagnolo[16], V. Grassi[148], V. Gratchev[121], N. Grau[35], H.M. Gray[30], J.A. Gray[148], E. Graziani[134a], O.G. Grebenyuk[121], T. Greenshaw[73], Z.D. Greenwood[25,n], K. Gregersen[36], I.M. Gregor[42], P. Grenier[143], J. Griffiths[8], N. Grigalashvili[64], A.A. Grillo[137], S. Grinstein[12], Ph. Gris[34], Y.V. Grishkevich[97], J.-F. Grivaz[115], E. Gross[172], J. Grosse-Knetter[54], J. Groth-Jensen[172], K. Grybel[141], D. Guest[176], C. Guicheney[34], E. Guido[50a,50b], S. Guindon[54], U. Gul[53], J. Gunther[125], B. Guo[158], J. Guo[35], P. Gutierrez[111], N. Guttman[153], O. Gutzwiller[173], C. Guyot[136], C. Gwenlan[118], C.B. Gwilliam[73], A. Haas[108], S. Haas[30], C. Haber[15], H.K. Hadavand[8], D.R. Hadley[18], P. Haefner[21], F. Hahn[30], Z. Hajduk[39], H. Hakobyan[177], D. Hall[118], K. Hamacher[175], P. Hamal[113], K. Hamano[86], M. Hamer[54], A. Hamilton[145b,q], S. Hamilton[161], L. Han[33b], K. Hanagaki[116], K. Hanawa[160], M. Hance[15], C. Handel[81], P. Hanke[58a], J.R. Hansen[36], J.B. Hansen[36], J.D. Hansen[36], P.H. Hansen[36], P. Hansson[143], K. Hara[160], T. Harenberg[175], S. Harkusha[90], D. Harper[87], R.D. Harrington[46], O.M. Harris[138], J. Hartert[48], F. Hartjes[105], T. Haruyama[65], A. Harvey[56], S. Hasegawa[101], Y. Hasegawa[140], S. Hassani[136], S. Haug[17], M. Hauschild[30], R. Hauser[88], M. Havranek[21], C.M. Hawkes[18], R.J. Hawkings[30], A.D. Hawkins[79], T. Hayakawa[66], T. Hayashi[160], D. Hayden[76], C.P. Hays[118], H.S. Hayward[73], S.J. Haywood[129], S.J. Head[18], V. Hedberg[79], L. Heelan[8], S. Heim[120], B. Heinemann[15], S. Heisterkamp[36], L. Helary[22], C. Heller[98], M. Heller[30], S. Hellman[146a,146b], D. Hellmich[21], C. Helsens[12], R.C.W. Henderson[71], M. Henke[58a], A. Henrichs[176], A.M. Henriques Correia[30], S. Henrot-Versille[115], C. Hensel[54], C.M. Hernandez[8], Y. Hernández Jiménez[167], R. Herrberg[16], G. Herten[48], R. Hertenberger[98], L. Hervas[30], G.G. Hesketh[77], N.P. Hessey[105], E. Higón-Rodriguez[167], J.C. Hill[28], K.H. Hiller[42], S. Hillert[21], S.J. Hillier[18], I. Hinchliffe[15], E. Hines[120], M. Hirose[116], F. Hirsch[43], D. Hirschbuehl[175], J. Hobbs[148], N. Hod[153], M.C. Hodgkinson[139], P. Hodgson[139], A. Hoecker[30], M.R. Hoeferkamp[103], J. Hoffman[40], D. Hoffmann[83], M. Hohlfeld[81], M. Holder[141], S.O. Holmgren[146a], T. Holy[126], J.L. Holzbauer[88], T.M. Hong[120], L. Hooft van Huysduynen[108], S. Horner[48], J-Y. Hostachy[55], S. Hou[151], A. Hoummada[135a], J. Howard[118], J. Howarth[82], I. Hristova[16], J. Hrivnac[115], T. Hryn'ova[5], P.J. Hsu[81], S.-C. Hsu[138], D. Hu[35], Z. Hubacek[30], F. Hubaut[83], F. Huegging[21], A. Huettmann[42], T.B. Huffman[118], E.W. Hughes[35], G. Hughes[71], M. Huhtinen[30], M. Hurwitz[15], N. Huseynov[64,r], J. Huston[88], J. Huth[57], G. Iacobucci[49], G. Iakovidis[10], M. Ibbotson[82], I. Ibragimov[141], L. Iconomidou-Fayard[115], J. Idarraga[115], P. Iengo[102a], O. Igonkina[105], Y. Ikegami[65], M. Ikeno[65], D. Iliadis[154], N. Ilic[158], T. Ince[99], P. Ioannou[9], M. Iodice[134a], K. Iordanidou[9], V. Ippolito[132a,132b], A. Irles Quiles[167], C. Isaksson[166], M. Ishino[67], M. Ishitsuka[157], R. Ishmukhametov[109], C. Issever[118], S. Istin[19a], A.V. Ivashin[128], W. Iwanski[39], H. Iwasaki[65], J.M. Izen[41], V. Izzo[102a], B. Jackson[120], J.N. Jackson[73], P. Jackson[1], M.R. Jaekel[30], V. Jain[2], K. Jakobs[48], S. Jakobsen[36], T. Jakoubek[125], J. Jakubek[126], D.O. Jamin[151], D.K. Jana[111], E. Jansen[77], H. Jansen[30], J. Janssen[21], A. Jantsch[99], M. Janus[48], R.C. Jared[173], G. Jarlskog[79], L. Jeanty[57], I. Jen-La Plante[31], G.-Y. Jeng[150], D. Jennens[86], P. Jenni[30], A.E. Loevschall-Jensen[36], P. Jež[36], S. Jézéquel[5], M.K. Jha[20a], H. Ji[173], W. Ji[81], J. Jia[148], Y. Jiang[33b], M. Jimenez Belenguer[42], S. Jin[33a], O. Jinnouchi[157], M.D. Joergensen[36], D. Joffe[40], M. Johansen[146a,146b],

JHEP03(2013)128

K.E. Johansson[146a], P. Johansson[139], S. Johnert[42], K.A. Johns[7], K. Jon-And[146a,146b], G. Jones[170], R.W.L. Jones[71], T.J. Jones[73], C. Joram[30], P.M. Jorge[124a], K.D. Joshi[82], J. Jovicevic[147], T. Jovin[13b], X. Ju[173], C.A. Jung[43], R.M. Jungst[30], V. Juranek[125], P. Jussel[61], A. Juste Rozas[12], S. Kabana[17], M. Kaci[167], A. Kaczmarska[39], P. Kadlecik[36], M. Kado[115], H. Kagan[109], M. Kagan[57], E. Kajomovitz[152], S. Kalinin[175], L.V. Kalinovskaya[64], S. Kama[40], N. Kanaya[155], M. Kaneda[30], S. Kaneti[28], T. Kanno[157], V.A. Kantserov[96], J. Kanzaki[65], B. Kaplan[108], A. Kapliy[31], J. Kaplon[30], D. Kar[53], M. Karagounis[21], K. Karakostas[10], M. Karnevskiy[58b], V. Kartvelishvili[71], A.N. Karyukhin[128], L. Kashif[173], G. Kasieczka[58b], R.D. Kass[109], A. Kastanas[14], M. Kataoka[5], Y. Kataoka[155], J. Katzy[42], V. Kaushik[7], K. Kawagoe[69], T. Kawamoto[155], G. Kawamura[81], M.S. Kayl[105], S. Kazama[155], V.F. Kazanin[107], M.Y. Kazarinov[64], R. Keeler[169], P.T. Keener[120], R. Kehoe[40], M. Keil[54], G.D. Kekelidze[64], J.S. Keller[138], M. Kenyon[53], O. Kepka[125], N. Kerschen[30], B.P. Kerševan[74], S. Kersten[175], K. Kessoku[155], J. Keung[158], F. Khalil-zada[11], H. Khandanyan[146a,146b], A. Khanov[112], D. Kharchenko[64], A. Khodinov[96], A. Khomich[58a], T.J. Khoo[28], G. Khoriauli[21], A. Khoroshilov[175], V. Khovanskiy[95], E. Khramov[64], J. Khubua[51b], H. Kim[146a,146b], S.H. Kim[160], N. Kimura[171], O. Kind[16], B.T. King[73], M. King[66], R.S.B. King[118], J. Kirk[129], A.E. Kiryunin[99], T. Kishimoto[66], D. Kisielewska[38], T. Kitamura[66], T. Kittelmann[123], K. Kiuchi[160], E. Kladiva[144b], M. Klein[73], U. Klein[73], K. Kleinknecht[81], M. Klemetti[85], A. Klier[172], P. Klimek[146a,146b], A. Klimentov[25], R. Klingenberg[43], J.A. Klinger[82], E.B. Klinkby[36], T. Klioutchnikova[30], P.F. Klok[104], S. Klous[105], E.-E. Kluge[58a], T. Kluge[73], P. Kluit[105], S. Kluth[99], E. Kneringer[61], E.B.F.G. Knoops[83], A. Knue[54], B.R. Ko[45], T. Kobayashi[155], M. Kobel[44], M. Kocian[143], P. Kodys[127], K. Köneke[30], A.C. König[104], S. Koenig[81], L. Köpke[81], F. Koetsveld[104], P. Koevesarki[21], T. Koffas[29], E. Koffeman[105], L.A. Kogan[118], S. Kohlmann[175], F. Kohn[54], Z. Kohout[126], T. Kohriki[65], T. Koi[143], G.M. Kolachev[107,*], H. Kolanoski[16], V. Kolesnikov[64], I. Koletsou[89a], J. Koll[88], A.A. Komar[94], Y. Komori[155], T. Kondo[65], T. Kono[42,s], A.I. Kononov[48], R. Konoplich[108,t], N. Konstantinidis[77], R. Kopeliansky[152], S. Koperny[38], K. Korcyl[39], K. Kordas[154], A. Korn[118], A. Korol[107], I. Korolkov[12], E.V. Korolkova[139], V.A. Korotkov[128], O. Kortner[99], S. Kortner[99], V.V. Kostyukhin[21], S. Kotov[99], V.M. Kotov[64], A. Kotwal[45], C. Kourkoumelis[9], V. Kouskoura[154], A. Koutsman[159a], R. Kowalewski[169], T.Z. Kowalski[38], W. Kozanecki[136], A.S. Kozhin[128], V. Kral[126], V.A. Kramarenko[97], G. Kramberger[74], M.W. Krasny[78], A. Krasznahorkay[108], J.K. Kraus[21], A. Kravchenko[25], S. Kreiss[108], F. Krejci[126], J. Kretzschmar[73], K. Kreutzfeldt[52], N. Krieger[54], P. Krieger[158], K. Kroeninger[54], H. Kroha[99], J. Kroll[120], J. Kroseberg[21], J. Krstic[13a], U. Kruchonak[64], H. Krüger[21], T. Kruker[17], N. Krumnack[63], Z.V. Krumshteyn[64], M.K. Kruse[45], T. Kubota[86], S. Kuday[4a], S. Kuehn[48], A. Kugel[58c], T. Kuhl[42], D. Kuhn[61], V. Kukhtin[64], Y. Kulchitsky[90], S. Kuleshov[32b], C. Kummer[98], M. Kuna[78], J. Kunkle[120], A. Kupco[125], H. Kurashige[66], M. Kurata[160], Y.A. Kurochkin[90], V. Kus[125], E.S. Kuwertz[147], M. Kuze[157], J. Kvita[142], R. Kwee[16], A. La Rosa[49], L. La Rotonda[37a,37b], L. Labarga[80], S. Lablak[135a], C. Lacasta[167], F. Lacava[132a,132b], J. Lacey[29], H. Lacker[16], D. Lacour[78], V.R. Lacuesta[167], E. Ladygin[64], R. Lafaye[5], B. Laforge[78], T. Lagouri[176], S. Lai[48], E. Laisne[55], L. Lambourne[77], C.L. Lampen[7], W. Lampl[7], E. Lancon[136], U. Landgraf[48], M.P.J. Landon[75], V.S. Lang[58a], C. Lange[42], A.J. Lankford[163], F. Lanni[25], K. Lantzsch[30], A. Lanza[119a], S. Laplace[78], C. Lapoire[21], J.F. Laporte[136], T. Lari[89a], A. Larner[118], M. Lassnig[30], P. Laurelli[47], V. Lavorini[37a,37b], W. Lavrijsen[15], P. Laycock[73], O. Le Dortz[78], E. Le Guirriec[83], E. Le Menedeu[12], T. LeCompte[6], F. Ledroit-Guillon[55], H. Lee[105], J.S.H. Lee[116], S.C. Lee[151], L. Lee[176], M. Lefebvre[169], M. Legendre[136], F. Legger[98], C. Leggett[15], M. Lehmacher[21], G. Lehmann Miotto[30], A.G. Leister[176], M.A.L. Leite[24d], R. Leitner[127], D. Lellouch[172], B. Lemmer[54], V. Lendermann[58a], K.J.C. Leney[145b], T. Lenz[105], G. Lenzen[175], B. Lenzi[30], K. Leonhardt[44], S. Leontsinis[10], F. Lepold[58a], C. Leroy[93], J-R. Lessard[169], C.G. Lester[28], C.M. Lester[120], J. Levêque[5], D. Levin[87], L.J. Levinson[172], A. Lewis[118], G.H. Lewis[108], A.M. Leyko[21], M. Leyton[16], B. Li[33b], B. Li[83], H. Li[148], H.L. Li[31], S. Li[33b,u], X. Li[87], Z. Liang[118,v], H. Liao[34], B. Liberti[133a], P. Lichard[30], M. Lichtnecker[98], K. Lie[165], W. Liebig[14], C. Limbach[21], A. Limosani[86], M. Limper[62], S.C. Lin[151,w], F. Linde[105], J.T. Linnemann[88], E. Lipeles[120], A. Lipniacka[14], T.M. Liss[165],

JHEP03(2013)128

D. Lissauer[25], A. Lister[49], A.M. Litke[137], C. Liu[29], D. Liu[151], J.B. Liu[87], L. Liu[87], M. Liu[33b], Y. Liu[33b], M. Livan[119a,119b], S.S.A. Livermore[118], A. Lleres[55], J. Llorente Merino[80], S.L. Lloyd[75], E. Lobodzinska[42], P. Loch[7], W.S. Lockman[137], T. Loddenkoetter[21], F.K. Loebinger[82], A. Loginov[176], C.W. Loh[168], T. Lohse[16], K. Lohwasser[48], M. Lokajicek[125], V.P. Lombardo[5], R.E. Long[71], L. Lopes[124a], D. Lopez Mateos[57], J. Lorenz[98], N. Lorenzo Martinez[115], M. Losada[162], P. Loscutoff[15], F. Lo Sterzo[132a,132b], M.J. Losty[159a,*], X. Lou[41], A. Lounis[115], K.F. Loureiro[162], J. Love[6], P.A. Love[71], A.J. Lowe[143,g], F. Lu[33a], H.J. Lubatti[138], C. Luci[132a,132b], A. Lucotte[55], A. Ludwig[44], D. Ludwig[42], I. Ludwig[48], J. Ludwig[48], F. Luehring[60], G. Luijckx[105], W. Lukas[61], L. Luminari[132a], E. Lund[117], B. Lund-Jensen[147], B. Lundberg[79], J. Lundberg[146a,146b], O. Lundberg[146a,146b], J. Lundquist[36], M. Lungwitz[81], D. Lynn[25], E. Lytken[79], H. Ma[25], L.L. Ma[173], G. Maccarrone[47], A. Macchiolo[99], B. Maček[74], J. Machado Miguens[124a], D. Macina[30], R. Mackeprang[36], R.J. Madaras[15], H.J. Maddocks[71], W.F. Mader[44], R. Maenner[58c], T. Maeno[25], P. Mättig[175], S. Mättig[42], L. Magnoni[163], E. Magradze[54], K. Mahboubi[48], J. Mahlstedt[105], S. Mahmoud[73], G. Mahout[18], C. Maiani[136], C. Maidantchik[24a], A. Maio[124a,c], S. Majewski[25], Y. Makida[65], N. Makovec[115], P. Mal[136], B. Malaescu[30], Pa. Malecki[39], P. Malecki[39], V.P. Maleev[121], F. Malek[55], U. Mallik[62], D. Malon[6], C. Malone[143], S. Maltezos[10], V. Malyshev[107], S. Malyukov[30], J. Mamuzic[13b], A. Manabe[65], L. Mandelli[89a], I. Mandić[74], R. Mandrysch[62], J. Maneira[124a], A. Manfredini[99], L. Manhaes de Andrade Filho[24b], J.A. Manjarres Ramos[136], A. Mann[98], P.M. Manning[137], A. Manousakis-Katsikakis[9], B. Mansoulie[136], A. Mapelli[30], L. Mapelli[30], L. March[167], J.F. Marchand[29], F. Marchese[133a,133b], G. Marchiori[78], M. Marcisovsky[125], C.P. Marino[169], F. Marroquim[24a], Z. Marshall[30], L.F. Marti[17], S. Marti-Garcia[167], B. Martin[30], B. Martin[88], J.P. Martin[93], T.A. Martin[18], V.J. Martin[46], B. Martin dit Latour[49], S. Martin-Haugh[149], M. Martinez[12], V. Martinez Outschoorn[57], A.C. Martyniuk[169], M. Marx[82], F. Marzano[132a], A. Marzin[111], L. Masetti[81], T. Mashimo[155], R. Mashinistov[94], J. Masik[82], A.L. Maslennikov[107], I. Massa[20a,20b], G. Massaro[105], N. Massol[5], P. Mastrandrea[148], A. Mastroberardino[37a,37b], T. Masubuchi[155], H. Matsunaga[155], T. Matsushita[66], C. Mattravers[118,d], J. Maurer[83], S.J. Maxfield[73], D.A. Maximov[107,h], A. Mayne[139], R. Mazini[151], M. Mazur[21], L. Mazzaferro[133a,133b], M. Mazzanti[89a], J. Mc Donald[85], S.P. Mc Kee[87], A. McCarn[165], R.L. McCarthy[148], T.G. McCarthy[29], N.A. McCubbin[129], K.W. McFarlane[56,*], J.A. Mcfayden[139], G. Mchedlidze[51b], T. Mclaughlan[18], S.J. McMahon[129], R.A. McPherson[169,l], A. Meade[84], J. Mechnich[105], M. Mechtel[175], M. Medinnis[42], S. Meehan[31], R. Meera-Lebbai[111], T. Meguro[116], S. Mehlhase[36], A. Mehta[73], K. Meier[58a], B. Meirose[79], C. Melachrinos[31], B.R. Mellado Garcia[173], F. Meloni[89a,89b], L. Mendoza Navas[162], Z. Meng[151,x], A. Mengarelli[20a,20b], S. Menke[99], E. Meoni[161], K.M. Mercurio[57], P. Mermod[49], L. Merola[102a,102b], C. Meroni[89a], F.S. Merritt[31], H. Merritt[109], A. Messina[30,y], J. Metcalfe[25], A.S. Mete[163], C. Meyer[81], C. Meyer[31], J-P. Meyer[136], J. Meyer[174], J. Meyer[54], S. Michal[30], L. Micu[26a], R.P. Middleton[129], S. Migas[73], L. Mijović[136], G. Mikenberg[172], M. Mikestikova[125], M. Mikuž[74], D.W. Miller[31], R.J. Miller[88], W.J. Mills[168], C. Mills[57], A. Milov[172], D.A. Milstead[146a,146b], D. Milstein[172], A.A. Minaenko[128], M. Miñano Moya[167], I.A. Minashvili[64], A.I. Mincer[108], B. Mindur[38], M. Mineev[64], Y. Ming[173], L.M. Mir[12], G. Mirabelli[132a], J. Mitrevski[137], V.A. Mitsou[167], S. Mitsui[65], P.S. Miyagawa[139], J.U. Mjörnmark[79], T. Moa[146a,146b], V. Moeller[28], K. Mönig[42], N. Möser[21], S. Mohapatra[148], W. Mohr[48], R. Moles-Valls[167], A. Molfetas[30], J. Monk[77], E. Monnier[83], J. Montejo Berlingen[12], F. Monticelli[70], S. Monzani[20a,20b], R.W. Moore[3], G.F. Moorhead[86], C. Mora Herrera[49], A. Moraes[53], N. Morange[136], J. Morel[54], G. Morello[37a,37b], D. Moreno[81], M. Moreno Llácer[167], P. Morettini[50a], M. Morgenstern[44], M. Morii[57], A.K. Morley[30], G. Mornacchi[30], J.D. Morris[75], L. Morvaj[101], H.G. Moser[99], M. Mosidze[51b], J. Moss[109], R. Mount[143], E. Mountricha[10,z], S.V. Mouraviev[94,*], E.J.W. Moyse[84], F. Mueller[58a], J. Mueller[123], K. Mueller[21], T.A. Müller[98], T. Mueller[81], D. Muenstermann[30], Y. Munwes[153], W.J. Murray[129], I. Mussche[105], E. Musto[152], A.G. Myagkov[128], M. Myska[125], O. Nackenhorst[54], J. Nadal[12], K. Nagai[160], R. Nagai[157], K. Nagano[65], A. Nagarkar[109], Y. Nagasaka[59], M. Nagel[99], A.M. Nairz[30], Y. Nakahama[30], K. Nakamura[155], T. Nakamura[155], I. Nakano[110], G. Nanava[21], A. Napier[161], R. Narayan[58b],

JHEP03(2013)128

M. Nash[77,d], T. Nattermann[21], T. Naumann[42], G. Navarro[162], H.A. Neal[87], P.Yu. Nechaeva[94], T.J. Neep[82], A. Negri[119a,119b], G. Negri[30], M. Negrini[20a], S. Nektarijevic[49], A. Nelson[163], T.K. Nelson[143], S. Nemecek[125], P. Nemethy[108], A.A. Nepomuceno[24a], M. Nessi[30,aa], M.S. Neubauer[165], M. Neumann[175], A. Neusiedl[81], R.M. Neves[108], P. Nevski[25], F.M. Newcomer[120], P.R. Newman[18], V. Nguyen Thi Hong[136], R.B. Nickerson[118], R. Nicolaidou[136], B. Nicquevert[30], F. Niedercorn[115], J. Nielsen[137], N. Nikiforou[35], A. Nikiforov[16], V. Nikolaenko[128], I. Nikolic-Audit[78], K. Nikolics[49], K. Nikolopoulos[18], H. Nilsen[48], P. Nilsson[8], Y. Ninomiya[155], A. Nisati[132a], R. Nisius[99], T. Nobe[157], L. Nodulman[6], M. Nomachi[116], I. Nomidis[154], S. Norberg[111], M. Nordberg[30], P.R. Norton[129], J. Novakova[127], M. Nozaki[65], L. Nozka[113], I.M. Nugent[159a], A.-E. Nuncio-Quiroz[21], G. Nunes Hanninger[86], T. Nunnemann[98], E. Nurse[77], B.J. O'Brien[46], D.C. O'Neil[142], V. O'Shea[53], L.B. Oakes[98], F.G. Oakham[29,f], H. Oberlack[99], J. Ocariz[78], A. Ochi[66], S. Oda[69], S. Odaka[65], J. Odier[83], H. Ogren[60], A. Oh[82], S.H. Oh[45], C.C. Ohm[30], T. Ohshima[101], W. Okamura[116], H. Okawa[25], Y. Okumura[31], T. Okuyama[155], A. Olariu[26a], A.G. Olchevski[64], S.A. Olivares Pino[32a], M. Oliveira[124a,i], D. Oliveira Damazio[25], E. Oliver Garcia[167], D. Olivito[120], A. Olszewski[39], J. Olszowska[39], A. Onofre[124a,ab], P.U.E. Onyisi[31,ac], C.J. Oram[159a], M.J. Oreglia[31], Y. Oren[153], D. Orestano[134a,134b], N. Orlando[72a,72b], I. Orlov[107], C. Oropeza Barrera[53], R.S. Orr[158], B. Osculati[50a,50b], R. Ospanov[120], C. Osuna[12], G. Otero y Garzon[27], J.P. Ottersbach[105], M. Ouchrif[135d], E.A. Ouellette[169], F. Ould-Saada[117], A. Ouraou[136], Q. Ouyang[33a], A. Ovcharova[15], M. Owen[82], S. Owen[139], V.E. Ozcan[19a], N. Ozturk[8], A. Pacheco Pages[12], C. Padilla Aranda[12], S. Pagan Griso[15], E. Paganis[139], C. Pahl[99], F. Paige[25], P. Pais[84], K. Pajchel[117], G. Palacino[159b], C.P. Paleari[7], S. Palestini[30], D. Pallin[34], A. Palma[124a], J.D. Palmer[18], Y.B. Pan[173], E. Panagiotopoulou[10], J.G. Panduro Vazquez[76], P. Pani[105], N. Panikashvili[87], S. Panitkin[25], D. Pantea[26a], A. Papadelis[146a], Th.D. Papadopoulou[10], A. Paramonov[6], D. Paredes Hernandez[34], W. Park[25,ad], M.A. Parker[28], F. Parodi[50a,50b], J.A. Parsons[35], U. Parzefall[48], S. Pashapour[54], E. Pasqualucci[132a], S. Passaggio[50a], A. Passeri[134a], F. Pastore[134a,134b,*], Fr. Pastore[76], G. Pásztor[49,ae], S. Pataraia[175], N. Patel[150], J.R. Pater[82], S. Patricelli[102a,102b], T. Pauly[30], M. Pecsy[144a], S. Pedraza Lopez[167], M.I. Pedraza Morales[173], S.V. Peleganchuk[107], D. Pelikan[166], H. Peng[33b], B. Penning[31], A. Penson[35], J. Penwell[60], M. Perantoni[24a], K. Perez[35,af], T. Perez Cavalcanti[42], E. Perez Codina[159a], M.T. Pérez García-Estañ[167], V. Perez Reale[35], L. Perini[89a,89b], H. Pernegger[30], R. Perrino[72a], P. Perrodo[5], V.D. Peshekhonov[64], K. Peters[30], B.A. Petersen[30], J. Petersen[30], T.C. Petersen[36], E. Petit[5], A. Petridis[154], C. Petridou[154], E. Petrolo[132a], F. Petrucci[134a,134b], D. Petschull[42], M. Petteni[142], R. Pezoa[32b], A. Phan[86], P.W. Phillips[129], G. Piacquadio[30], A. Picazio[49], E. Piccaro[75], M. Piccinini[20a,20b], S.M. Piec[42], R. Piegaia[27], D.T. Pignotti[109], J.E. Pilcher[31], A.D. Pilkington[82], J. Pina[124a,c], M. Pinamonti[164a,164c], A. Pinder[118], J.L. Pinfold[3], A. Pingel[36], B. Pinto[124a], C. Pizio[89a,89b], M.-A. Pleier[25], E. Plotnikova[64], A. Poblaguev[25], S. Poddar[58a], F. Podlyski[34], L. Poggioli[115], D. Pohl[21], M. Pohl[49], G. Polesello[119a], A. Policicchio[37a,37b], A. Polini[20a], J. Poll[75], V. Polychronakos[25], D. Pomeroy[23], K. Pommès[30], L. Pontecorvo[132a], B.G. Pope[88], G.A. Popeneciu[26a], D.S. Popovic[13a], A. Poppleton[30], X. Portell Bueso[30], G.E. Pospelov[99], S. Pospisil[126], I.N. Potrap[99], C.J. Potter[149], C.T. Potter[114], G. Poulard[30], J. Poveda[60], V. Pozdnyakov[64], R. Prabhu[77], P. Pralavorio[83], A. Pranko[15], S. Prasad[30], R. Pravahan[25], S. Prell[63], K. Pretzl[17], D. Price[60], J. Price[73], L.E. Price[6], D. Prieur[123], M. Primavera[72a], K. Prokofiev[108], F. Prokoshin[32b], S. Protopopescu[25], J. Proudfoot[6], X. Prudent[44], M. Przybycien[38], H. Przysiezniak[5], S. Psoroulas[21], E. Ptacek[114], E. Pueschel[84], D. Puldon[148], J. Purdham[87], M. Purohit[25,ad], P. Puzo[115], Y. Pylypchenko[62], J. Qian[87], A. Quadt[54], D.R. Quarrie[15], W.B. Quayle[173], M. Raas[104], V. Radeka[25], V. Radescu[42], P. Radloff[114], F. Ragusa[89a,89b], G. Rahal[178], A.M. Rahimi[109], D. Rahm[25], S. Rajagopalan[25], M. Rammensee[48], M. Rammes[141], A.S. Randle-Conde[40], K. Randrianarivony[29], K. Rao[163], F. Rauscher[98], T.C. Rave[48], M. Raymond[30], A.L. Read[117], D.M. Rebuzzi[119a,119b], A. Redelbach[174], G. Redlinger[25], R. Reece[120], K. Reeves[41], A. Reinsch[114], I. Reisinger[43], C. Rembser[30], Z.L. Ren[151], A. Renaud[115], M. Rescigno[132a], S. Resconi[89a], B. Resende[136], P. Reznicek[98],

JHEP03(2013)128

R. Rezvani[158], R. Richter[99], E. Richter-Was[5,ag], M. Ridel[78], M. Rijpstra[105], M. Rijssenbeek[148], A. Rimoldi[119a,119b], L. Rinaldi[20a], R.R. Rios[40], I. Riu[12], G. Rivoltella[89a,89b], F. Rizatdinova[112], E. Rizvi[75], S.H. Robertson[85,l], A. Robichaud-Veronneau[118], D. Robinson[28], J.E.M. Robinson[82], A. Robson[53], J.G. Rocha de Lima[106], C. Roda[122a,122b], D. Roda Dos Santos[30], A. Roe[54], S. Roe[30], O. Røhne[117], S. Rolli[161], A. Romaniouk[96], M. Romano[20a,20b], G. Romeo[27], E. Romero Adam[167], N. Rompotis[138], L. Roos[78], E. Ros[167], S. Rosati[132a], K. Rosbach[49], A. Rose[149], M. Rose[76], G.A. Rosenbaum[158], E.I. Rosenberg[63], P.L. Rosendahl[14], O. Rosenthal[141], L. Rosselet[49], V. Rossetti[12], E. Rossi[132a,132b], L.P. Rossi[50a], M. Rotaru[26a], I. Roth[172], J. Rothberg[138], D. Rousseau[115], C.R. Royon[136], A. Rozanov[83], Y. Rozen[152], X. Ruan[33a,ah], F. Rubbo[12], I. Rubinskiy[42], N. Ruckstuhl[105], V.I. Rud[97], C. Rudolph[44], G. Rudolph[61], F. Rühr[7], A. Ruiz-Martinez[63], L. Rumyantsev[64], Z. Rurikova[48], N.A. Rusakovich[64], A. Ruschke[98], J.P. Rutherfoord[7], P. Ruzicka[125], Y.F. Ryabov[121], M. Rybar[127], G. Rybkin[115], N.C. Ryder[118], A.F. Saavedra[150], I. Sadeh[153], H.F-W. Sadrozinski[137], R. Sadykov[64], F. Safai Tehrani[132a], H. Sakamoto[155], G. Salamanna[75], A. Salamon[133a], M. Saleem[111], D. Salek[30], D. Salihagic[99], A. Salnikov[143], J. Salt[167], B.M. Salvachua Ferrando[6], D. Salvatore[37a,37b], F. Salvatore[149], A. Salvucci[104], A. Salzburger[30], D. Sampsonidis[154], B.H. Samset[117], A. Sanchez[102a,102b], V. Sanchez Martinez[167], H. Sandaker[14], H.G. Sander[81], M.P. Sanders[98], M. Sandhoff[175], T. Sandoval[28], C. Sandoval[162], R. Sandstroem[99], D.P.C. Sankey[129], A. Sansoni[47], C. Santamarina Rios[85], C. Santoni[34], R. Santonico[133a,133b], H. Santos[124a], I. Santoyo Castillo[149], J.G. Saraiva[124a], T. Sarangi[173], E. Sarkisyan-Grinbaum[8], B. Sarrazin[21], F. Sarri[122a,122b], G. Sartisohn[175], O. Sasaki[65], Y. Sasaki[155], N. Sasao[67], I. Satsounkevitch[90], G. Sauvage[5,*], E. Sauvan[5], J.B. Sauvan[115], P. Savard[158,f], V. Savinov[123], D.O. Savu[30], L. Sawyer[25,n], D.H. Saxon[53], J. Saxon[120], C. Sbarra[20a], A. Sbrizzi[20a,20b], D.A. Scannicchio[163], M. Scarcella[150], J. Schaarschmidt[115], P. Schacht[99], D. Schaefer[120], U. Schäfer[81], A. Schaelicke[46], S. Schaepe[21], S. Schaetzel[58b], A.C. Schaffer[115], D. Schaile[98], R.D. Schamberger[148], A.G. Schamov[107], V. Scharf[58a], V.A. Schegelsky[121], D. Scheirich[87], M. Schernau[163], M.I. Scherzer[35], C. Schiavi[50a,50b], J. Schieck[98], M. Schioppa[37a,37b], S. Schlenker[30], E. Schmidt[48], K. Schmieden[21], C. Schmitt[81], S. Schmitt[58b], B. Schneider[17], U. Schnoor[44], L. Schoeffel[136], A. Schoening[58b], A.L.S. Schorlemmer[54], M. Schott[30], D. Schouten[159a], J. Schovancova[125], M. Schram[85], C. Schroeder[81], N. Schroer[58c], M.J. Schultens[21], J. Schultes[175], H.-C. Schultz-Coulon[58a], H. Schulz[16], M. Schumacher[48], B.A. Schumm[137], Ph. Schune[136], A. Schwartzman[143], Ph. Schwegler[99], Ph. Schwemling[78], R. Schwienhorst[88], R. Schwierz[44], J. Schwindling[136], T. Schwindt[21], M. Schwoerer[5], F.G. Sciacca[17], G. Sciolla[23], W.G. Scott[129], J. Searcy[114], G. Sedov[42], E. Sedykh[121], S.C. Seidel[103], A. Seiden[137], F. Seifert[44], J.M. Seixas[24a], G. Sekhniaidze[102a], S.J. Sekula[40], K.E. Selbach[46], D.M. Seliverstov[121], B. Sellden[146a], G. Sellers[73], M. Seman[144b], N. Semprini-Cesari[20a,20b], C. Serfon[98], L. Serin[115], L. Serkin[54], R. Seuster[159a], H. Severini[111], A. Sfyrla[30], E. Shabalina[54], M. Shamim[114], L.Y. Shan[33a], J.T. Shank[22], Q.T. Shao[86], M. Shapiro[15], P.B. Shatalov[95], K. Shaw[164a,164c], D. Sherman[176], P. Sherwood[77], S. Shimizu[101], M. Shimojima[100], T. Shin[56], M. Shiyakova[64], A. Shmeleva[94], M.J. Shochet[31], D. Short[118], S. Shrestha[63], E. Shulga[96], M.A. Shupe[7], P. Sicho[125], A. Sidoti[132a], F. Siegert[48], Dj. Sijacki[13a], O. Silbert[172], J. Silva[124a], Y. Silver[153], D. Silverstein[143], S.B. Silverstein[146a], V. Simak[126], O. Simard[136], Lj. Simic[13a], S. Simion[115], E. Simioni[81], B. Simmons[77], R. Simoniello[89a,89b], M. Simonyan[36], P. Sinervo[158], N.B. Sinev[114], V. Sipica[141], G. Siragusa[174], A. Sircar[25], A.N. Sisakyan[64,*], S.Yu. Sivoklokov[97], J. Sjölin[146a,146b], T.B. Sjursen[14], L.A. Skinnari[15], H.P. Skottowe[57], K. Skovpen[107], P. Skubic[111], M. Slater[18], T. Slavicek[126], K. Sliwa[161], V. Smakhtin[172], B.H. Smart[46], L. Smestad[117], S.Yu. Smirnov[96], Y. Smirnov[96], L.N. Smirnova[97], O. Smirnova[79], B.C. Smith[57], D. Smith[143], K.M. Smith[53], M. Smizanska[71], K. Smolek[126], A.A. Snesarev[94], S.W. Snow[82], J. Snow[111], S. Snyder[25], R. Sobie[169,l], J. Sodomka[126], A. Soffer[153], C.A. Solans[167], M. Solar[126], J. Solc[126], E.Yu. Soldatov[96], U. Soldevila[167], E. Solfaroli Camillocci[132a,132b], A.A. Solodkov[128], O.V. Solovyanov[128], V. Solovyev[121], N. Soni[1], A. Sood[15], V. Sopko[126], B. Sopko[126], M. Sosebee[8], R. Soualah[164a,164c], P. Soueid[93], A. Soukharev[107], S. Spagnolo[72a,72b], F. Spanò[76], R. Spighi[20a], G. Spigo[30],

JHEP03(2013)128

R. Spiwoks[30], M. Spousta[127,ai], T. Spreitzer[158], B. Spurlock[8], R.D. St. Denis[53], J. Stahlman[120], R. Stamen[58a], E. Stanecka[39], R.W. Stanek[6], C. Stanescu[134a], M. Stanescu-Bellu[42], M.M. Stanitzki[42], S. Stapnes[117], E.A. Starchenko[128], J. Stark[55], P. Staroba[125], P. Starovoitov[42], R. Staszewski[39], A. Staude[98], P. Stavina[144a,*], G. Steele[53], P. Steinbach[44], P. Steinberg[25], I. Stekl[126], B. Stelzer[142], H.J. Stelzer[88], O. Stelzer-Chilton[159a], H. Stenzel[52], S. Stern[99], G.A. Stewart[30], J.A. Stillings[21], M.C. Stockton[85], K. Stoerig[48], G. Stoicea[26a], S. Stonjek[99], P. Strachota[127], A.R. Stradling[8], A. Straessner[44], J. Strandberg[147], S. Strandberg[146a,146b], A. Strandlie[117], M. Strang[109], E. Strauss[143], M. Strauss[111], P. Strizenec[144b], R. Ströhmer[174], D.M. Strom[114], J.A. Strong[76,*], R. Stroynowski[40], B. Stugu[14], I. Stumer[25,*], J. Stupak[148], P. Sturm[175], N.A. Styles[42], D.A. Soh[151,v], D. Su[143], HS. Subramania[3], R. Subramaniam[25], A. Succurro[12], Y. Sugaya[116], C. Suhr[106], M. Suk[127], V.V. Sulin[94], S. Sultansoy[4d], T. Sumida[67], X. Sun[55], J.E. Sundermann[48], K. Suruliz[139], G. Susinno[37a,37b], M.R. Sutton[149], Y. Suzuki[65], Y. Suzuki[66], M. Svatos[125], S. Swedish[168], I. Sykora[144a], T. Sykora[127], J. Sánchez[167], D. Ta[105], K. Tackmann[42], A. Taffard[163], R. Tafirout[159a], N. Taiblum[153], Y. Takahashi[101], H. Takai[25], R. Takashima[68], H. Takeda[66], T. Takeshita[140], Y. Takubo[65], M. Talby[83], A. Talyshev[107,h], M.C. Tamsett[25], K.G. Tan[86], J. Tanaka[155], R. Tanaka[115], S. Tanaka[131], S. Tanaka[65], A.J. Tanasijczuk[142], K. Tani[66], N. Tannoury[83], S. Tapprogge[81], D. Tardif[158], S. Tarem[152], F. Tarrade[29], G.F. Tartarelli[89a], P. Tas[127], M. Tasevsky[125], E. Tassi[37a,37b], Y. Tayalati[135d], C. Taylor[77], F.E. Taylor[92], G.N. Taylor[86], W. Taylor[159b], M. Teinturier[115], F.A. Teischinger[30], M. Teixeira Dias Castanheira[75], P. Teixeira-Dias[76], K.K. Temming[48], H. Ten Kate[30], P.K. Teng[151], S. Terada[65], K. Terashi[155], J. Terron[80], M. Testa[47], R.J. Teuscher[158,l], J. Therhaag[21], T. Theveneaux-Pelzer[78], S. Thoma[48], J.P. Thomas[18], E.N. Thompson[35], P.D. Thompson[18], P.D. Thompson[158], A.S. Thompson[53], L.A. Thomsen[36], E. Thomson[120], M. Thomson[28], W.M. Thong[86], R.P. Thun[87], F. Tian[35], M.J. Tibbetts[15], T. Tic[125], V.O. Tikhomirov[94], Y.A. Tikhonov[107,h], S. Timoshenko[96], E. Tiouchichine[83], P. Tipton[176], S. Tisserant[83], T. Todorov[5], S. Todorova-Nova[161], B. Toggerson[163], J. Tojo[69], S. Tokár[144a], K. Tokushuku[65], K. Tollefson[88], M. Tomoto[101], L. Tompkins[31], K. Toms[103], A. Tonoyan[14], C. Topfel[17], N.D. Topilin[64], E. Torrence[114], H. Torres[78], E. Torró Pastor[167], J. Toth[83,ae], F. Touchard[83], D.R. Tovey[139], T. Trefzger[174], L. Tremblet[30], A. Tricoli[30], I.M. Trigger[159a], S. Trincaz-Duvoid[78], M.F. Tripiana[70], N. Triplett[25], W. Trischuk[158], B. Trocmé[55], C. Troncon[89a], M. Trottier-McDonald[142], P. True[88], M. Trzebinski[39], A. Trzupek[39], C. Tsarouchas[30], J.C-L. Tseng[118], M. Tsiakiris[105], P.V. Tsiareshka[90], D. Tsionou[5,aj], G. Tsipolitis[10], S. Tsiskaridze[12], V. Tsiskaridze[48], E.G. Tskhadadze[51a], I.I. Tsukerman[95], V. Tsulaia[15], J.-W. Tsung[21], S. Tsuno[65], D. Tsybychev[148], A. Tua[139], A. Tudorache[26a], V. Tudorache[26a], J.M. Tuggle[31], M. Turala[39], D. Turecek[126], I. Turk Cakir[4e], E. Turlay[105], R. Turra[89a,89b], P.M. Tuts[35], A. Tykhonov[74], M. Tylmad[146a,146b], M. Tyndel[129], G. Tzanakos[9], K. Uchida[21], I. Ueda[155], R. Ueno[29], M. Ughetto[83], M. Ugland[14], M. Uhlenbrock[21], M. Uhrmacher[54], F. Ukegawa[160], G. Unal[30], A. Undrus[25], G. Unel[163], Y. Unno[65], D. Urbaniec[35], P. Urquijo[21], G. Usai[8], M. Uslenghi[119a,119b], L. Vacavant[83], V. Vacek[126], B. Vachon[85], S. Vahsen[15], J. Valenta[125], S. Valentinetti[20a,20b], A. Valero[167], S. Valkar[127], E. Valladolid Gallego[167], S. Vallecorsa[152], J.A. Valls Ferrer[167], R. Van Berg[120], P.C. Van Der Deijl[105], R. van der Geer[105], H. van der Graaf[105], R. Van Der Leeuw[105], E. van der Poel[105], D. van der Ster[30], N. van Eldik[30], P. van Gemmeren[6], J. Van Nieuwkoop[142], I. van Vulpen[105], M. Vanadia[99], W. Vandelli[30], A. Vaniachine[6], P. Vankov[42], F. Vannucci[78], R. Vari[132a], E.W. Varnes[7], T. Varol[84], D. Varouchas[15], A. Vartapetian[8], K.E. Varvell[150], V.I. Vassilakopoulos[56], F. Vazeille[34], T. Vazquez Schroeder[54], G. Vegni[89a,89b], J.J. Veillet[115], F. Veloso[124a], R. Veness[30], S. Veneziano[132a], A. Ventura[72a,72b], D. Ventura[84], M. Venturi[48], N. Venturi[158], V. Vercesi[119a], M. Verducci[138], W. Verkerke[105], J.C. Vermeulen[105], A. Vest[44], M.C. Vetterli[142,f], I. Vichou[165], T. Vickey[145b,ak], O.E. Vickey Boeriu[145b], G.H.A. Viehhauser[118], S. Viel[168], M. Villa[20a,20b], M. Villaplana Perez[167], E. Vilucchi[47], M.G. Vincter[29], E. Vinek[30], V.B. Vinogradov[64], M. Virchaux[136,*], J. Virzi[15], O. Vitells[172], M. Viti[42], I. Vivarelli[48], F. Vives Vaque[3], S. Vlachos[10], D. Vladoiu[98], M. Vlasak[126], A. Vogel[21], P. Vokac[126], G. Volpi[47], M. Volpi[86], G. Volpini[89a],

JHEP03(2013)128

H. von der Schmitt[99], H. von Radziewski[48], E. von Toerne[21], V. Vorobel[127], V. Vorwerk[12], M. Vos[167], R. Voss[30], J.H. Vossebeld[73], N. Vranjes[136], M. Vranjes Milosavljevic[105], V. Vrba[125], M. Vreeswijk[105], T. Vu Anh[48], R. Vuillermet[30], I. Vukotic[31], W. Wagner[175], P. Wagner[120], H. Wahlen[175], S. Wahrmund[44], J. Wakabayashi[101], S. Walch[87], J. Walder[71], R. Walker[98], W. Walkowiak[141], R. Wall[176], P. Waller[73], B. Walsh[176], C. Wang[45], H. Wang[173], H. Wang[40], J. Wang[151], J. Wang[33a], R. Wang[103], S.M. Wang[151], T. Wang[21], A. Warburton[85], C.P. Ward[28], D.R. Wardrope[77], M. Warsinsky[48], A. Washbrook[46], C. Wasicki[42], I. Watanabe[66], P.M. Watkins[18], A.T. Watson[18], I.J. Watson[150], M.F. Watson[18], G. Watts[138], S. Watts[82], A.T. Waugh[150], B.M. Waugh[77], M.S. Weber[17], J.S. Webster[31], A.R. Weidberg[118], P. Weigell[99], J. Weingarten[54], C. Weiser[48], P.S. Wells[30], T. Wenaus[25], D. Wendland[16], Z. Weng[151,v], T. Wengler[30], S. Wenig[30], N. Wermes[21], M. Werner[48], P. Werner[30], M. Werth[163], M. Wessels[58a], J. Wetter[161], C. Weydert[55], K. Whalen[29], A. White[8], M.J. White[86], S. White[122a,122b], S.R. Whitehead[118], D. Whiteson[163], D. Whittington[60], D. Wicke[175], F.J. Wickens[129], W. Wiedenmann[173], M. Wielers[129], P. Wienemann[21], C. Wiglesworth[75], L.A.M. Wiik-Fuchs[21], P.A. Wijeratne[77], A. Wildauer[99], M.A. Wildt[42,s], I. Wilhelm[127], H.G. Wilkens[30], J.Z. Will[98], E. Williams[35], H.H. Williams[120], S. Williams[28], W. Willis[35], S. Willocq[84], J.A. Wilson[18], M.G. Wilson[143], A. Wilson[87], I. Wingerter-Seez[5], S. Winkelmann[48], F. Winklmeier[30], M. Wittgen[143], S.J. Wollstadt[81], M.W. Wolter[39], H. Wolters[124a,i], W.C. Wong[41], G. Wooden[87], B.K. Wosiek[39], J. Wotschack[30], M.J. Woudstra[82], K.W. Wozniak[39], K. Wraight[53], M. Wright[53], B. Wrona[73], S.L. Wu[173], X. Wu[49], Y. Wu[33b,al], E. Wulf[35], B.M. Wynne[46], S. Xella[36], M. Xiao[136], S. Xie[48], C. Xu[33b,z], D. Xu[33a], L. Xu[33b], B. Yabsley[150], S. Yacoob[145a,am], M. Yamada[65], H. Yamaguchi[155], A. Yamamoto[65], K. Yamamoto[63], S. Yamamoto[155], T. Yamamura[155], T. Yamanaka[155], T. Yamazaki[155], Y. Yamazaki[66], Z. Yan[22], H. Yang[87], U.K. Yang[82], Y. Yang[109], Z. Yang[146a,146b], S. Yanush[91], L. Yao[33a], Y. Yasu[65], E. Yatsenko[42], J. Ye[40], S. Ye[25], A.L. Yen[57], M. Yilmaz[4c], R. Yoosoofmiya[123], K. Yorita[171], R. Yoshida[6], K. Yoshihara[155], C. Young[143], C.J. Young[118], S. Youssef[22], D. Yu[25], D.R. Yu[15], J. Yu[8], J. Yu[112], L. Yuan[66], A. Yurkewicz[106], B. Zabinski[39], R. Zaidan[62], A.M. Zaitsev[128], L. Zanello[132a,132b], D. Zanzi[99], A. Zaytsev[25], C. Zeitnitz[175], M. Zeman[126], A. Zemla[39], O. Zenin[128], T. Ženiš[144a], Z. Zinonos[122a,122b], D. Zerwas[115], G. Zevi della Porta[57], D. Zhang[87], H. Zhang[88], J. Zhang[6], X. Zhang[33d], Z. Zhang[115], L. Zhao[108], Z. Zhao[33b], A. Zhemchugov[64], J. Zhong[118], B. Zhou[87], N. Zhou[163], Y. Zhou[151], C.G. Zhu[33d], H. Zhu[42], J. Zhu[87], Y. Zhu[33b], X. Zhuang[98], V. Zhuravlov[99], A. Zibell[98], D. Zieminska[60], N.I. Zimin[64], R. Zimmermann[21], S. Zimmermann[21], S. Zimmermann[48], M. Ziolkowski[141], R. Zitoun[5], L. Živković[35], V.V. Zmouchko[128,*], G. Zobernig[173], A. Zoccoli[20a,20b], M. zur Nedden[16], V. Zutshi[106], L. Zwalinski[30]

[1] School of Chemistry and Physics, University of Adelaide, Adelaide, Australia
[2] Physics Department, SUNY Albany, Albany NY, United States of America
[3] Department of Physics, University of Alberta, Edmonton AB, Canada
[4] [(a)] Department of Physics, Ankara University, Ankara; [(b)] Department of Physics, Dumlupinar University, Kutahya; [(c)] Department of Physics, Gazi University, Ankara; [(d)] Division of Physics, TOBB University of Economics and Technology, Ankara; [(e)] Turkish Atomic Energy Authority, Ankara, Turkey
[5] LAPP, CNRS/IN2P3 and Université de Savoie, Annecy-le-Vieux, France
[6] High Energy Physics Division, Argonne National Laboratory, Argonne IL, United States of America
[7] Department of Physics, University of Arizona, Tucson AZ, United States of America
[8] Department of Physics, The University of Texas at Arlington, Arlington TX, United States of America
[9] Physics Department, University of Athens, Athens, Greece
[10] Physics Department, National Technical University of Athens, Zografou, Greece
[11] Institute of Physics, Azerbaijan Academy of Sciences, Baku, Azerbaijan
[12] Institut de Física d'Altes Energies and Departament de Física de la Universitat Autònoma de Barcelona and ICREA, Barcelona, Spain

JHEP03(2013)128

[13] [(a)] Institute of Physics, University of Belgrade, Belgrade; [(b)] Vinca Institute of Nuclear Sciences, University of Belgrade, Belgrade, Serbia
[14] Department for Physics and Technology, University of Bergen, Bergen, Norway
[15] Physics Division, Lawrence Berkeley National Laboratory and University of California, Berkeley CA, United States of America
[16] Department of Physics, Humboldt University, Berlin, Germany
[17] Albert Einstein Center for Fundamental Physics and Laboratory for High Energy Physics, University of Bern, Bern, Switzerland
[18] School of Physics and Astronomy, University of Birmingham, Birmingham, United Kingdom
[19] [(a)] Department of Physics, Bogazici University, Istanbul; [(b)] Division of Physics, Dogus University, Istanbul; [(c)] Department of Physics Engineering, Gaziantep University, Gaziantep; [(d)] Department of Physics, Istanbul Technical University, Istanbul, Turkey
[20] [(a)] INFN Sezione di Bologna; [(b)] Dipartimento di Fisica, Università di Bologna, Bologna, Italy
[21] Physikalisches Institut, University of Bonn, Bonn, Germany
[22] Department of Physics, Boston University, Boston MA, United States of America
[23] Department of Physics, Brandeis University, Waltham MA, United States of America
[24] [(a)] Universidade Federal do Rio De Janeiro COPPE/EE/IF, Rio de Janeiro; [(b)] Federal University of Juiz de Fora (UFJF), Juiz de Fora; [(c)] Federal University of Sao Joao del Rei (UFSJ), Sao Joao del Rei; [(d)] Instituto de Fisica, Universidade de Sao Paulo, Sao Paulo, Brazil
[25] Physics Department, Brookhaven National Laboratory, Upton NY, United States of America
[26] [(a)] National Institute of Physics and Nuclear Engineering, Bucharest; [(b)] University Politehnica Bucharest, Bucharest; [(c)] West University in Timisoara, Timisoara, Romania
[27] Departamento de Física, Universidad de Buenos Aires, Buenos Aires, Argentina
[28] Cavendish Laboratory, University of Cambridge, Cambridge, United Kingdom
[29] Department of Physics, Carleton University, Ottawa ON, Canada
[30] CERN, Geneva, Switzerland
[31] Enrico Fermi Institute, University of Chicago, Chicago IL, United States of America
[32] [(a)] Departamento de Física, Pontificia Universidad Católica de Chile, Santiago; [(b)] Departamento de Física, Universidad Técnica Federico Santa María, Valparaíso, Chile
[33] [(a)] Institute of High Energy Physics, Chinese Academy of Sciences, Beijing; [(b)] Department of Modern Physics, University of Science and Technology of China, Anhui; [(c)] Department of Physics, Nanjing University, Jiangsu; [(d)] School of Physics, Shandong University, Shandong; [(e)] Physics Department, Shanghai Jiao Tong University, Shanghai, China
[34] Laboratoire de Physique Corpusculaire, Clermont Université and Université Blaise Pascal and CNRS/IN2P3, Clermont-Ferrand, France
[35] Nevis Laboratory, Columbia University, Irvington NY, United States of America
[36] Niels Bohr Institute, University of Copenhagen, Kobenhavn, Denmark
[37] [(a)] INFN Gruppo Collegato di Cosenza; [(b)] Dipartimento di Fisica, Università della Calabria, Arcavata di Rende, Italy
[38] AGH University of Science and Technology, Faculty of Physics and Applied Computer Science, Krakow, Poland
[39] The Henryk Niewodniczanski Institute of Nuclear Physics, Polish Academy of Sciences, Krakow, Poland
[40] Physics Department, Southern Methodist University, Dallas TX, United States of America
[41] Physics Department, University of Texas at Dallas, Richardson TX, United States of America
[42] DESY, Hamburg and Zeuthen, Germany
[43] Institut für Experimentelle Physik IV, Technische Universität Dortmund, Dortmund, Germany
[44] Institut für Kern- und Teilchenphysik, Technical University Dresden, Dresden, Germany
[45] Department of Physics, Duke University, Durham NC, United States of America
[46] SUPA - School of Physics and Astronomy, University of Edinburgh, Edinburgh, United Kingdom
[47] INFN Laboratori Nazionali di Frascati, Frascati, Italy
[48] Fakultät für Mathematik und Physik, Albert-Ludwigs-Universität, Freiburg, Germany

JHEP03(2013)128

[49] Section de Physique, Université de Genève, Geneva, Switzerland
[50] [(a)] INFN Sezione di Genova; [(b)] Dipartimento di Fisica, Università di Genova, Genova, Italy
[51] [(a)] E. Andronikashvili Institute of Physics, Iv. Javakhishvili Tbilisi State University, Tbilisi; [(b)] High Energy Physics Institute, Tbilisi State University, Tbilisi, Georgia
[52] II Physikalisches Institut, Justus-Liebig-Universität Giessen, Giessen, Germany
[53] SUPA - School of Physics and Astronomy, University of Glasgow, Glasgow, United Kingdom
[54] II Physikalisches Institut, Georg-August-Universität, Göttingen, Germany
[55] Laboratoire de Physique Subatomique et de Cosmologie, Université Joseph Fourier and CNRS/IN2P3 and Institut National Polytechnique de Grenoble, Grenoble, France
[56] Department of Physics, Hampton University, Hampton VA, United States of America
[57] Laboratory for Particle Physics and Cosmology, Harvard University, Cambridge MA, United States of America
[58] [(a)] Kirchhoff-Institut für Physik, Ruprecht-Karls-Universität Heidelberg, Heidelberg; [(b)] Physikalisches Institut, Ruprecht-Karls-Universität Heidelberg, Heidelberg; [(c)] ZITI Institut für technische Informatik, Ruprecht-Karls-Universität Heidelberg, Mannheim, Germany
[59] Faculty of Applied Information Science, Hiroshima Institute of Technology, Hiroshima, Japan
[60] Department of Physics, Indiana University, Bloomington IN, United States of America
[61] Institut für Astro- und Teilchenphysik, Leopold-Franzens-Universität, Innsbruck, Austria
[62] University of Iowa, Iowa City IA, United States of America
[63] Department of Physics and Astronomy, Iowa State University, Ames IA, United States of America
[64] Joint Institute for Nuclear Research, JINR Dubna, Dubna, Russia
[65] KEK, High Energy Accelerator Research Organization, Tsukuba, Japan
[66] Graduate School of Science, Kobe University, Kobe, Japan
[67] Faculty of Science, Kyoto University, Kyoto, Japan
[68] Kyoto University of Education, Kyoto, Japan
[69] Department of Physics, Kyushu University, Fukuoka, Japan
[70] Instituto de Física La Plata, Universidad Nacional de La Plata and CONICET, La Plata, Argentina
[71] Physics Department, Lancaster University, Lancaster, United Kingdom
[72] [(a)] INFN Sezione di Lecce; [(b)] Dipartimento di Matematica e Fisica, Università del Salento, Lecce, Italy
[73] Oliver Lodge Laboratory, University of Liverpool, Liverpool, United Kingdom
[74] Department of Physics, Jožef Stefan Institute and University of Ljubljana, Ljubljana, Slovenia
[75] School of Physics and Astronomy, Queen Mary University of London, London, United Kingdom
[76] Department of Physics, Royal Holloway University of London, Surrey, United Kingdom
[77] Department of Physics and Astronomy, University College London, London, United Kingdom
[78] Laboratoire de Physique Nucléaire et de Hautes Energies, UPMC and Université Paris-Diderot and CNRS/IN2P3, Paris, France
[79] Fysiska institutionen, Lunds universitet, Lund, Sweden
[80] Departamento de Fisica Teorica C-15, Universidad Autonoma de Madrid, Madrid, Spain
[81] Institut für Physik, Universität Mainz, Mainz, Germany
[82] School of Physics and Astronomy, University of Manchester, Manchester, United Kingdom
[83] CPPM, Aix-Marseille Université and CNRS/IN2P3, Marseille, France
[84] Department of Physics, University of Massachusetts, Amherst MA, United States of America
[85] Department of Physics, McGill University, Montreal QC, Canada
[86] School of Physics, University of Melbourne, Victoria, Australia
[87] Department of Physics, The University of Michigan, Ann Arbor MI, United States of America
[88] Department of Physics and Astronomy, Michigan State University, East Lansing MI, United States of America
[89] [(a)] INFN Sezione di Milano; [(b)] Dipartimento di Fisica, Università di Milano, Milano, Italy
[90] B.I. Stepanov Institute of Physics, National Academy of Sciences of Belarus, Minsk, Republic of Belarus
[91] National Scientific and Educational Centre for Particle and High Energy Physics, Minsk, Republic of Belarus

JHEP03(2013)128

[92] Department of Physics, Massachusetts Institute of Technology, Cambridge MA, United States of America
[93] Group of Particle Physics, University of Montreal, Montreal QC, Canada
[94] P.N. Lebedev Institute of Physics, Academy of Sciences, Moscow, Russia
[95] Institute for Theoretical and Experimental Physics (ITEP), Moscow, Russia
[96] Moscow Engineering and Physics Institute (MEPhI), Moscow, Russia
[97] Skobeltsyn Institute of Nuclear Physics, Lomonosov Moscow State University, Moscow, Russia
[98] Fakultät für Physik, Ludwig-Maximilians-Universität München, München, Germany
[99] Max-Planck-Institut für Physik (Werner-Heisenberg-Institut), München, Germany
[100] Nagasaki Institute of Applied Science, Nagasaki, Japan
[101] Graduate School of Science and Kobayashi-Maskawa Institute, Nagoya University, Nagoya, Japan
[102] [(a)] INFN Sezione di Napoli; [(b)] Dipartimento di Scienze Fisiche, Università di Napoli, Napoli, Italy
[103] Department of Physics and Astronomy, University of New Mexico, Albuquerque NM, United States of America
[104] Institute for Mathematics, Astrophysics and Particle Physics, Radboud University Nijmegen/Nikhef, Nijmegen, Netherlands
[105] Nikhef National Institute for Subatomic Physics and University of Amsterdam, Amsterdam, Netherlands
[106] Department of Physics, Northern Illinois University, DeKalb IL, United States of America
[107] Budker Institute of Nuclear Physics, SB RAS, Novosibirsk, Russia
[108] Department of Physics, New York University, New York NY, United States of America
[109] Ohio State University, Columbus OH, United States of America
[110] Faculty of Science, Okayama University, Okayama, Japan
[111] Homer L. Dodge Department of Physics and Astronomy, University of Oklahoma, Norman OK, United States of America
[112] Department of Physics, Oklahoma State University, Stillwater OK, United States of America
[113] Palacký University, RCPTM, Olomouc, Czech Republic
[114] Center for High Energy Physics, University of Oregon, Eugene OR, United States of America
[115] LAL, Université Paris-Sud and CNRS/IN2P3, Orsay, France
[116] Graduate School of Science, Osaka University, Osaka, Japan
[117] Department of Physics, University of Oslo, Oslo, Norway
[118] Department of Physics, Oxford University, Oxford, United Kingdom
[119] [(a)] INFN Sezione di Pavia; [(b)] Dipartimento di Fisica, Università di Pavia, Pavia, Italy
[120] Department of Physics, University of Pennsylvania, Philadelphia PA, United States of America
[121] Petersburg Nuclear Physics Institute, Gatchina, Russia
[122] [(a)] INFN Sezione di Pisa; [(b)] Dipartimento di Fisica E. Fermi, Università di Pisa, Pisa, Italy
[123] Department of Physics and Astronomy, University of Pittsburgh, Pittsburgh PA, United States of America
[124] [(a)] Laboratorio de Instrumentacao e Fisica Experimental de Particulas - LIP, Lisboa, Portugal; [(b)] Departamento de Fisica Teorica y del Cosmos and CAFPE, Universidad de Granada, Granada, Spain
[125] Institute of Physics, Academy of Sciences of the Czech Republic, Praha, Czech Republic
[126] Czech Technical University in Prague, Praha, Czech Republic
[127] Faculty of Mathematics and Physics, Charles University in Prague, Praha, Czech Republic
[128] State Research Center Institute for High Energy Physics, Protvino, Russia
[129] Particle Physics Department, Rutherford Appleton Laboratory, Didcot, United Kingdom
[130] Physics Department, University of Regina, Regina SK, Canada
[131] Ritsumeikan University, Kusatsu, Shiga, Japan
[132] [(a)] INFN Sezione di Roma I; [(b)] Dipartimento di Fisica, Università La Sapienza, Roma, Italy
[133] [(a)] INFN Sezione di Roma Tor Vergata; [(b)] Dipartimento di Fisica, Università di Roma Tor Vergata, Roma, Italy
[134] [(a)] INFN Sezione di Roma Tre; [(b)] Dipartimento di Fisica, Università Roma Tre, Roma, Italy

JHEP03(2013)128

[135] [(a)] Faculté des Sciences Ain Chock, Réseau Universitaire de Physique des Hautes Energies - Université Hassan II, Casablanca; [(b)] Centre National de l'Energie des Sciences Techniques Nucleaires, Rabat; [(c)] Faculté des Sciences Semlalia, Université Cadi Ayyad, LPHEA-Marrakech; [(d)] Faculté des Sciences, Université Mohamed Premier and LPTPM, Oujda; [(e)] Faculté des sciences, Université Mohammed V-Agdal, Rabat, Morocco
[136] DSM/IRFU (Institut de Recherches sur les Lois Fondamentales de l'Univers), CEA Saclay (Commissariat à l'Energie Atomique et aux Energies Alternatives), Gif-sur-Yvette, France
[137] Santa Cruz Institute for Particle Physics, University of California Santa Cruz, Santa Cruz CA, United States of America
[138] Department of Physics, University of Washington, Seattle WA, United States of America
[139] Department of Physics and Astronomy, University of Sheffield, Sheffield, United Kingdom
[140] Department of Physics, Shinshu University, Nagano, Japan
[141] Fachbereich Physik, Universität Siegen, Siegen, Germany
[142] Department of Physics, Simon Fraser University, Burnaby BC, Canada
[143] SLAC National Accelerator Laboratory, Stanford CA, United States of America
[144] [(a)] Faculty of Mathematics, Physics & Informatics, Comenius University, Bratislava; [(b)] Department of Subnuclear Physics, Institute of Experimental Physics of the Slovak Academy of Sciences, Kosice, Slovak Republic
[145] [(a)] Department of Physics, University of Johannesburg, Johannesburg; [(b)] School of Physics, University of the Witwatersrand, Johannesburg, South Africa
[146] [(a)] Department of Physics, Stockholm University; [(b)] The Oskar Klein Centre, Stockholm, Sweden
[147] Physics Department, Royal Institute of Technology, Stockholm, Sweden
[148] Departments of Physics & Astronomy and Chemistry, Stony Brook University, Stony Brook NY, United States of America
[149] Department of Physics and Astronomy, University of Sussex, Brighton, United Kingdom
[150] School of Physics, University of Sydney, Sydney, Australia
[151] Institute of Physics, Academia Sinica, Taipei, Taiwan
[152] Department of Physics, Technion: Israel Institute of Technology, Haifa, Israel
[153] Raymond and Beverly Sackler School of Physics and Astronomy, Tel Aviv University, Tel Aviv, Israel
[154] Department of Physics, Aristotle University of Thessaloniki, Thessaloniki, Greece
[155] International Center for Elementary Particle Physics and Department of Physics, The University of Tokyo, Tokyo, Japan
[156] Graduate School of Science and Technology, Tokyo Metropolitan University, Tokyo, Japan
[157] Department of Physics, Tokyo Institute of Technology, Tokyo, Japan
[158] Department of Physics, University of Toronto, Toronto ON, Canada
[159] [(a)] TRIUMF, Vancouver BC; [(b)] Department of Physics and Astronomy, York University, Toronto ON, Canada
[160] Faculty of Pure and Applied Sciences, University of Tsukuba, Tsukuba, Japan
[161] Department of Physics and Astronomy, Tufts University, Medford MA, United States of America
[162] Centro de Investigaciones, Universidad Antonio Narino, Bogota, Colombia
[163] Department of Physics and Astronomy, University of California Irvine, Irvine CA, United States of America
[164] [(a)] INFN Gruppo Collegato di Udine; [(b)] ICTP, Trieste; [(c)] Dipartimento di Chimica, Fisica e Ambiente, Università di Udine, Udine, Italy
[165] Department of Physics, University of Illinois, Urbana IL, United States of America
[166] Department of Physics and Astronomy, University of Uppsala, Uppsala, Sweden
[167] Instituto de Física Corpuscular (IFIC) and Departamento de Física Atómica, Molecular y Nuclear and Departamento de Ingeniería Electrónica and Instituto de Microelectrónica de Barcelona (IMB-CNM), University of Valencia and CSIC, Valencia, Spain
[168] Department of Physics, University of British Columbia, Vancouver BC, Canada
[169] Department of Physics and Astronomy, University of Victoria, Victoria BC, Canada

JHEP03(2013)128

[170] Department of Physics, University of Warwick, Coventry, United Kingdom
[171] Waseda University, Tokyo, Japan
[172] Department of Particle Physics, The Weizmann Institute of Science, Rehovot, Israel
[173] Department of Physics, University of Wisconsin, Madison WI, United States of America
[174] Fakultät für Physik und Astronomie, Julius-Maximilians-Universität, Würzburg, Germany
[175] Fachbereich C Physik, Bergische Universität Wuppertal, Wuppertal, Germany
[176] Department of Physics, Yale University, New Haven CT, United States of America
[177] Yerevan Physics Institute, Yerevan, Armenia
[178] Centre de Calcul de l'Institut National de Physique Nucléaire et de Physique des Particules (IN2P3), Villeurbanne, France

[a] Also at Department of Physics, King's College London, London, United Kingdom
[b] Also at Laboratorio de Instrumentacao e Fisica Experimental de Particulas - LIP, Lisboa, Portugal
[c] Also at Faculdade de Ciencias and CFNUL, Universidade de Lisboa, Lisboa, Portugal
[d] Also at Particle Physics Department, Rutherford Appleton Laboratory, Didcot, United Kingdom
[e] Also at Department of Physics, University of Johannesburg, Johannesburg, South Africa
[f] Also at TRIUMF, Vancouver BC, Canada
[g] Also at Department of Physics, California State University, Fresno CA, United States of America
[h] Also at Novosibirsk State University, Novosibirsk, Russia
[i] Also at Department of Physics, University of Coimbra, Coimbra, Portugal
[j] Also at Department of Physics, UASLP, San Luis Potosi, Mexico
[k] Also at Università di Napoli Parthenope, Napoli, Italy
[l] Also at Institute of Particle Physics (IPP), Canada
[m] Also at Department of Physics, Middle East Technical University, Ankara, Turkey
[n] Also at Louisiana Tech University, Ruston LA, United States of America
[o] Also at Dep Fisica and CEFITEC of Faculdade de Ciencias e Tecnologia, Universidade Nova de Lisboa, Caparica, Portugal
[p] Also at Department of Physics and Astronomy, University College London, London, United Kingdom
[q] Also at Department of Physics, University of Cape Town, Cape Town, South Africa
[r] Also at Institute of Physics, Azerbaijan Academy of Sciences, Baku, Azerbaijan
[s] Also at Institut für Experimentalphysik, Universität Hamburg, Hamburg, Germany
[t] Also at Manhattan College, New York NY, United States of America
[u] Also at CPPM, Aix-Marseille Université and CNRS/IN2P3, Marseille, France
[v] Also at School of Physics and Engineering, Sun Yat-sen University, Guanzhou, China
[w] Also at Academia Sinica Grid Computing, Institute of Physics, Academia Sinica, Taipei, Taiwan
[x] Also at School of Physics, Shandong University, Shandong, China
[y] Also at Dipartimento di Fisica, Università La Sapienza, Roma, Italy
[z] Also at DSM/IRFU (Institut de Recherches sur les Lois Fondamentales de l'Univers), CEA Saclay (Commissariat à l'Energie Atomique et aux Energies Alternatives), Gif-sur-Yvette, France
[aa] Also at Section de Physique, Université de Genève, Geneva, Switzerland
[ab] Also at Departamento de Fisica, Universidade de Minho, Braga, Portugal
[ac] Also at Department of Physics, The University of Texas at Austin, Austin TX, United States of America
[ad] Also at Department of Physics and Astronomy, University of South Carolina, Columbia SC, United States of America
[ae] Also at Institute for Particle and Nuclear Physics, Wigner Research Centre for Physics, Budapest, Hungary
[af] Also at California Institute of Technology, Pasadena CA, United States of America
[ag] Also at Institute of Physics, Jagiellonian University, Krakow, Poland
[ah] Also at LAL, Université Paris-Sud and CNRS/IN2P3, Orsay, France
[ai] Also at Nevis Laboratory, Columbia University, Irvington NY, United States of America

JHEP03(2013)128

[aj] Also at Department of Physics and Astronomy, University of Sheffield, Sheffield, United Kingdom
[ak] Also at Department of Physics, Oxford University, Oxford, United Kingdom
[al] Also at Department of Physics, The University of Michigan, Ann Arbor MI, United States of America
[am] Also at Discipline of Physics, University of KwaZulu-Natal, Durban, South Africa
[*] Deceased

JHEP03(2013)128

計画研究 A04 班

課題名「トップクォークを用いた新しい素粒子現象の探索」

研究組織

(1)研究代表者
戸本 誠（TOMOTO, Makoto）
名古屋大学・大学院理学研究科・准教授
研究者番号：80432235

(2)研究分担者
寄田浩平（YORITA, Kohei）
早稲田大学・理工学術院・准教授
研究者番号： 60530590

長野邦浩（NAGANO, Kunihiro）
高エネルギー加速器研究機構・
素粒子原子核研究所・准教授
研究者番号： 90391705

(3)連携研究者
長坂康史（NAGASAKA, Yasushi）
広島工業大学・情報学部・教授
研究者番号： 20299655

下島真（SHIMOJIMA, Makoto）
長崎総合科学大学・情報学部・教授
研究者番号： 80302347

交付決定額

計画研究 A04 班に配分された交付額を表 1 に示す。

表 1. 交付決定額（配分額）　（金額単位：円）

年度	直接経費	間接経費	合計
平成 23 年度	22,600,000	6,780,000	29,380,000
平成 24 年度	20,100,000	6,030,000	26,130,000
平成 25 年度	19,600,000	5,880,000	25,480,000
平成 26 年度	18,500,000	5,550,000	24,050,000
平成 27 年度	18,500,000	5,550,000	24,050,000
総計	99,300,000	29,790,000	129,090,000

研究成果

1．研究開始当初の背景

（1）欧州 CERN の LHC 実験における研究は、ヒッグス粒子やテラスケール領域の新たな素粒子の直接発見を目指すと同時に、多量に生成される既知の素粒子の崩壊様式の中に現れる新粒子現象の探索にも挑戦する。LHC は年間 40 万(平成 23 年度)～8000 万(平成 27 年度)の t クォーク対事象生成能力（図 1 ）を誇る。世界最大の t クォーク工場実験で作られる t クォークの生成・崩壊によって、「直接的」に新しい素粒子を探索するとともに、生成断面積や崩壊分岐比、質量やスピンに代表される t クォークの固有な物理量の精密測定から「間接的」に新しい素粒子現象を発見することができるようになった。

（2）高エネルギー化、高輝度化が進む高エネルギー加速器実験において、更なる t クォーク研究へと展開させるため、膨大な背景事象の中から t クォーク事象を効率良く選択するトリガー系の開発が急務となる。最新の CMOS-VLSI 技術を駆使した高速プロセッサーや大容量メモリを搭載した高速飛跡再構成トリガー(FTK)回路は、数 10μ秒内に陽子・陽子衝突による全荷電粒子の飛跡再構成をハードウェア的に実現する。FTK 回路から共有される飛跡の生成点情報によって、t クォーク事象の特徴的な信号である b トリガー、つまり、t クォーク事象選別が可能となる。

2．研究の目的

（1）t クォーク対生成事象を緻密に研究し、高エネルギー領域における摂動 QCD モデルの有効性を探るとともに、標準模型からのズレの可能性を検証する。素粒子の「質量起源」や「世代構造」の解明に挑み、「真空構造」の理解へと繋げる。

① t クォーク対生成断面積を世界最高精度で測定する。

② t クォークの生成・崩壊の際に現れる粒子の運動量、方位角度、不変質量、電荷分布などの力学的物理量を詳細に測定し、t クォークの相互作用、結合などの観点から新粒子を探索する。新粒子が t クォーク生成・崩壊関与しているのであれば、その固有性をも明らかにする。

③ ttH 過程から t クォークとヒッグス粒子の湯川結合定数を測定する。

（2）FTK 回路の R&D 研究を推進する。本研究では、光ファイバを通して 40MHz の転送速度で送信されるシリコン検出器からのヒット情報を受信し、そのヒット情報をクラスタ化する Input Mezzanine（IM）ボードと呼ばれる回路の開発を行う。FTK トリガーのシミュレーションの構築や FTK トリガーの導入に伴う ATLAS トリガーシステムの改良研究を行い、b トリガー、つまり、t クォーク事象選別の可能性を模索する。

3．研究の方法

（1）LHC-ATLAS 実験は、2010 年から 2015 年までに重心系エネルギー7TeV（2010 年、2011 年）、8TeV（2012 年）、13TeV（2015 年）の陽子陽子衝突実験を行い、合計で約 30fb-1 の積分ルミノシティーのデータを蓄積した。本研究は、これらのデータを用いる。

t クォークの終状態は、t→Wb の W 粒子の崩壊様式（μ 粒子か電子とニュートリノ、τ 粒子と τ ニュートリノ、または、クォーク対）で特徴付けられ、2 荷電レプトン（両方の t クォークが電子または μ 粒子に崩壊する）、荷電レプトン＋ジェット（片方の t クォークは μ 粒子または電子に崩壊し、もう一方の t クォークはハドロンに崩壊する）、全ジェット（両方の t クォークがハドロンに崩壊する）、τ 粒子崩壊（どちらか片方の t クォークがタウ粒子に崩壊する）の 4 種類に分類される。t クォークに関する物理解析では、様々な終状態を用いて測定を行い、新物理の間接的な兆候をさぐる。

（2）FTK 回路の R&D 開発は、早稲田大学を中心に推進する。そのためのテストスタンドを早稲田大学に構築し、イタリアなどとの国際共同のもと FTK 回路の開発を行なう。

4．研究成果

（1）t クォークの精密測定では、研究目的に記した①から③に対応して、以下の研究成果を出し

た。

① t クォーク対生成断面積の精密測定では、7TeV の陽子陽子衝突データを用いて、t クォーク対事象の終状態のうち、2 レプトン事象、τ_{had}–レプトン事象、全ハドロン事象に対する世界最高精度の測定を主導した（図 1）。どの終状態を用いた断面積測定においても一致した結果を得た。荷電ヒッグス粒子に感度がある τ_{had}–レプトン事象でも新物理の兆候は得られなかった。8TeV と 13TeV の陽子陽子衝突実験では、最も測定精度のよい 2 レプトン事象に集中して、t クォーク対生成断面積を測定した。その結果、Tevatron 実験で測定した 2TeV の陽子反陽子衝突による t クォーク対生成から、本研究から出された 7TeV、8TeV 、13TeV の陽子陽子衝突による t クォーク対生成に至るまで、摂動 QCD が有効理論として正しく働いていることを示した（図 2）。

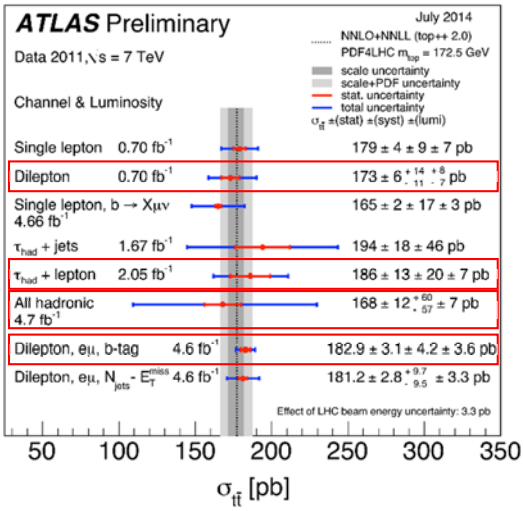

図 2：様々な終状態を用いて測定した重心系エネルギー7TeV の時の t クォーク対生成断面積の測定結果のまとめ。赤枠で示される結果は、特に本研究が主導して導出した結果である。

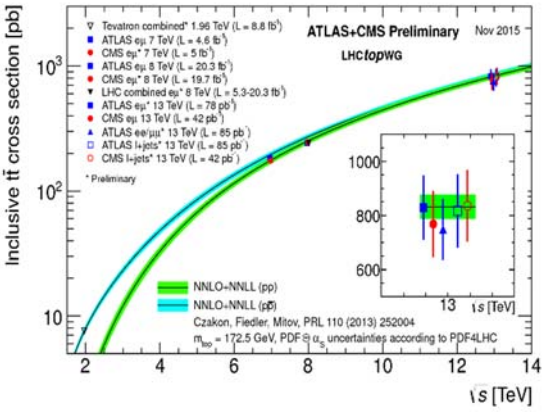

図 2：重心系エネルギーの関数とする t クォーク対生成断面積の測定結果。

② t→Wb 崩壊の W 粒子の偏極度測定では、t クォークから崩壊した荷電レプトンと b クォークの角度差を通じて、W 粒子の 3 種類の偏極度（F_L, F_0, F_R）を測定した。この結果から、V-A 型の弱い相互作用によって t クォークが崩壊する時の偏極度である F_0 = 0.687±0.005, F_R =

0.0017±0.0001（$F_L = 1 - F_0 - F_R$）と無矛盾であることを示した（図 3）。

③　LHC 実験による多量の t クォーク対生成事象数のおかげで、包含的 t クォーク対生成断面積

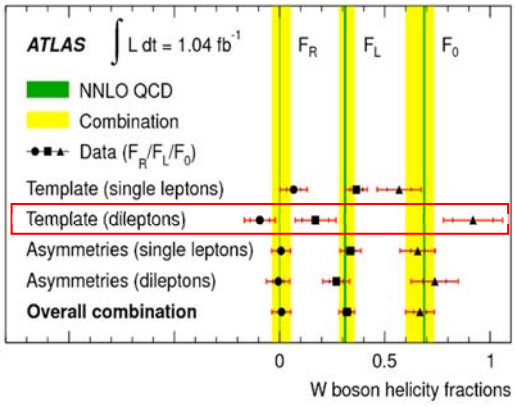

図 3：W 粒子偏極度測定のまとめ。本研究は、赤枠で示される 2 レプトン事象による測定を主導した。

測定の実験的精度は理論の予言能力を上回り始めた。そこで、t クォーク対の普遍質量や運動量、ラピディティーを関数とする t クォーク対生成微分断面積の測定や、t クォーク対に随伴して生成される粒子の種別ごとに終状態を分類する tt+X（X は、光子、W 粒子、Z 粒子、ジェットなど）断面積の測定などのより詳細な測定へと t クォーク物理を発展させている。

また、他の計画研究との連携を強化して④から⑥に示される研究成果を得た。

④　ヒッグス粒子の発見がされ、計画研究 A01 と連携して、ヒッグス粒子の t クォークとの随伴生成過程（ttH 過程）の生成断面積の測定を開始した。これにより、将来の LHC 実験において最重要課題の一つとなるヒッグス粒子と t クォークとの間の湯川結合の直接測定をこれから日本グループが主導することができる。

⑤　トップクォーク対生成事象の再構成は、W 粒子と b クォークの再構成が不可欠である。計画研究 A03 との共同研究によって、良質のトップクォーク対生成事象を取得した。

⑥　トップクォーク対生成事象は、ヒッグス粒子の測定や新物理探索における主なバックグラウンドとなる。例えば、ヒッグス粒子の発見の中で重要な終状態の一つであった pp→H+2 jets→WW+2 jets→$\ell\nu\ell\nu$+2 jets 過程（ℓ は電子または μ 粒子）の主な背景事象数の導出を本計画研究が行い、計画研究 A01 のヒッグス粒子発見に貢献した。同様に、計画研究 A02 の超対称性粒子や余剰次元粒子の探索においても、t クォークによる背景事象数の導出に本計画研究が大きく貢献した。

（2）FTK トリガーでは、IM 回路（図 4）の設計、プロトタイプ回路の製作、ATCA 規格で実装

されるマザーボードとの接続テストを早稲田大学が行った。さらに、FTK の回路要素を開発する世界中の大学・研究機関が CERN に集結して全回路要素を繋ぎ合わせる FTK 回路の統合テストを実施し、早稲田大学が開発する回路が量産要請を満たしていることを確認した。これらの成果によって、80 台の IM ボードの量産を開始し、本計画研究によって構築したテストスタンドを用いて、量産中に起きた諸問題のフィードバックを行い、量産を完遂することができた。一方で、シミュレーションの構築や FTK 導入による ATLAS トリガーシステムの改良研究など、ハードウェア・ソフトウェア双方で実質的な成果を上げることができた。

また、KEK の長野は、μ 粒子、電子・光子、ジェットを主とする LHC-ATLAS 実験の全トリガーを統括し、興味ある物理事象の検出効率を高く保ったまま、トリガーレートを低く維持するアルゴリズムの開発を行った。その結果、t クォーク対生成事象の取得に用いる μ 粒子トリガーや電子トリガーの運動量閾値を 25GeV 程度の低い値に保ち続けることに成功している。長野は LHC-ATLAS 実験の全トリガーの統括者として活躍している。

図 4：本研究で製作した最終版の IM ボード。

将来のハドロンコライダーにおいてトリガーは特に重要な開発要素であり、本計画研究によって FTK 回路を構築し、現在の LHC 実験のルミノシティーにて耐えられるトリガーを構築した。計画研究 A01、A03、A06 などの研究と合わせて、将来の実験の主要な実験開発要素をカバーすることができた。

最後に、本研究が進める世界最前線の研究を通じて、若手研究者の育成に貢献した。本研究で貢献した若手研究者の多くが国内外の大学・研究機関で別の職を得て異動している。また、名古屋大学、大阪大学、早稲田大学、総研大などから、t クォークの解析や FTK を主題として博士(理学)を取得し、国内外の大学・研究機関で研究者として活躍している。

5. 主な発表論文等

[1] “Development of a sub-nanosecond time-to-digital converter based on a field-programmable gate array”, Y. Sano, M. Tomoto, Y. Horii, O. Sasaki, et.al, JINST 11 (2016) C03053

[2] “Design of a hardware track finder (Fast Tracker) for the ATLAS trigger”, V. Cavaliere, K Yorita, et al., JINST 11 (2015) C02056

[3] “Measurement of the top-quark mass in the fully hadronic decay channel from ATLAS data at $\sqrt{s}$=7 TeV”, The ATLAS collaboration, Eur. Phys. J. C (2015) 75:158

[4] “Performance of the ATLAS muon trigger in pp collisions at $\sqrt{s}$=8 TeV”, The ATLAS collaboration, Eur. Phys. J. C (2015) 75:120

[5] “Measurement of the tt production cross-section using eμ events with b-tagged jets in pp collisions at $\sqrt{s}$ = 7 and 8 TeV with the ATLAS detector”, The ATLAS collaboration, Eur. Phys. J. C 74 (2014) 3109

[6] “Measurement of normalized differential cross sections for tt production in pp collisions at $\sqrt{s}$ = 7 TeV using the ATLAS detector”, The ATLAS collaboration, Phys. Rev. D 90 (2014) 072004

[7] “A fast hardware tracker for the ATLAS trigger system”, N. Kimura, K. Yorita, et al., Nucl. Instr. Meth. A 731 (2013) 224-228

[8] “Measurement of W boson polarization in top quark decays with the ATLAS detector”, The ATLAS collaboration, J. High Energy Phys. 1206 (2012) 088

[9] “FTK: a Fast Track Trigger for ATLAS”, J. Anderson, K. Yorita, et al., JINST 7 (2012) C10002

書籍

「ヒッグス粒子の見つけ方 質量の起源を追う」, 戸本誠,花垣和則,山崎祐司 著,丸善出版,2012/12/25

主催一般講演等

(1) 「ヒッグス粒子を探せ“質量の起源にせまる”」, 戸本誠、名古屋電気文化会館, 2012 年 3 月 17 日

ヒッグス粒子探索に関する最新結果を、高校生を基準に一般に講演した。

(2) ノーベル賞記念一般講演会「ヒッグス粒子発見」、寄田浩平、井深大記念ホール、2013 年 10 月 27 日

ヒッグス氏とアングレール氏のノーベル賞受賞を記念し、ヒッグス粒子の発見に関する講演をした。

主要論文別刷り

[1] “Performance of the ATLAS muon trigger in pp collisions at √s=8 TeV”, The ATLAS collaboration, Eur. Phys. J. C (2015) 75:120

[2] “A fast hardware tracker for the ATLAS trigger system”, J. Anderson, K. Yorita, et al., Nucl. Instr. Meth. A 718 (2013) 258-259

[3] “Measurement of W boson polarization in top quark decays with the ATLAS detector”, The ATLAS collaboration, J. High Energy Phys. 1206 (2012) 088

[4] “Measurement of the top quark pair cross section with ATLAS in pp collisions at √s = 7 TeV using final states with an electron or a muon and a hadronically decaying tau lepton”, The ATLAS collaboration, Phys. Lett. B 717 (2012) 89-108

[5] “Measurement of the cross section for top-quark pair production in pp collisions at √s = 7 TeV with the ATLAS detector using final states with two high-pT leptons”, The ATLAS collaboration, J. High Energy Phys. 1205 (2012) 059

Eur. Phys. J. C (2015) 75:120
DOI 10.1140/epjc/s10052-015-3325-9

THE EUROPEAN PHYSICAL JOURNAL C

Regular Article - Experimental Physics

Performance of the ATLAS muon trigger in pp collisions at $\sqrt{s} = 8$ TeV

ATLAS Collaboration[*]

CERN, 1211 Geneva 23, Switzerland

Received: 14 August 2014 / Accepted: 19 February 2015 / Published online: 13 March 2015
© CERN for the benefit of the ATLAS collaboration 2015. This article is published with open access at Springerlink.com

Abstract The performance of the ATLAS muon trigger system is evaluated with proton–proton collision data collected in 2012 at the Large Hadron Collider at a centre-of-mass energy of 8 TeV. It is primarily evaluated using events containing a pair of muons from the decay of Z bosons. The efficiency of the single-muon trigger is measured for muons with transverse momentum $25 < p_{\mathrm{T}} < 100$ GeV, with a statistical uncertainty of less than 0.01 % and a systematic uncertainty of 0.6 %. The p_{T} range for efficiency determination is extended by using muons from decays of J/ψ mesons, W bosons, and top quarks. The muon trigger shows highly uniform and stable performance. The performance is compared to the prediction of a detailed simulation.

1 Introduction

The presence of prompt muons in the final state is a distinctive signature for many physics processes studied in collisions of high energy protons at the LHC. These studies, which led to the discovery of the Higgs boson [1,2], include measurements of its properties, searches for new phenomena, as well as measurements of Standard Model processes, such as the production of electroweak bosons and top quarks. Therefore, a high-performance muon trigger is essential. In parallel, a good simulation of trigger performance is necessary.

There are many challenges in designing and implementing triggers which select pp interactions with muons in the final state with high efficiency and low transverse momentum, p_{T}, thresholds in the presence of high background conditions. The ATLAS design deploys a three-level, multi-pronged strategy with,

1. custom trigger electronics at Level-1,
2. dedicated fast algorithms to reconstruct muons and estimate their parameters at Level-2,
3. novel techniques to retain high efficiency at the event-filter while utilising offline tracking algorithms.

The Level-2 and event-filter together are called the High Level Trigger. In order to address a wide variety of physics topics, ATLAS has developed a suite of triggers designed to select muons. The single-muon trigger with p_{T} threshold of 24 GeV is used in many physics analyses. In addition, muon triggers in combination with electrons, jets and missing transverse momentum, as well as moderate-p_{T} multi-muon triggers, increase sensitivity for various physics topics which benefit from a lower p_{T} threshold. For the B-physics program, various low-p_{T} multi-muon triggers are used with a special configuration that allows a high efficiency also for non-prompt muons.[1]

The ATLAS experiment collected pp collision data in 2012 at a centre-of-mass energy of 8 TeV with a maximum instantaneous luminosity of 7.7×10^{33} cm^{-2} s^{-1}. The number of interactions occurring in the same bunch crossing (called pile-up interactions) was about 25 on average. In this paper, the performance of the ATLAS muon trigger is evaluated, primarily using samples containing muon pairs from Z-boson decays. The performance of the low-p_{T} muon trigger is evaluated with samples containing a pair of muons from the decay of J/ψ mesons. The performance for high-p_{T} muons is evaluated using events containing top-quarks[2] or W bosons, where a W boson decays into a muon and neutrino.

2 Muon trigger

2.1 ATLAS detector

The ATLAS detector is a multi-purpose particle physics apparatus with a forward–backward symmetric cylindrical

[*] e-mail: atlas.publications@cern.ch

[1] Non-prompt muons are muons which originate from the decay of a secondary particle rather than coming directly from the primary pp interaction.

[2] Unless otherwise stated CP conjugate states are always implied.

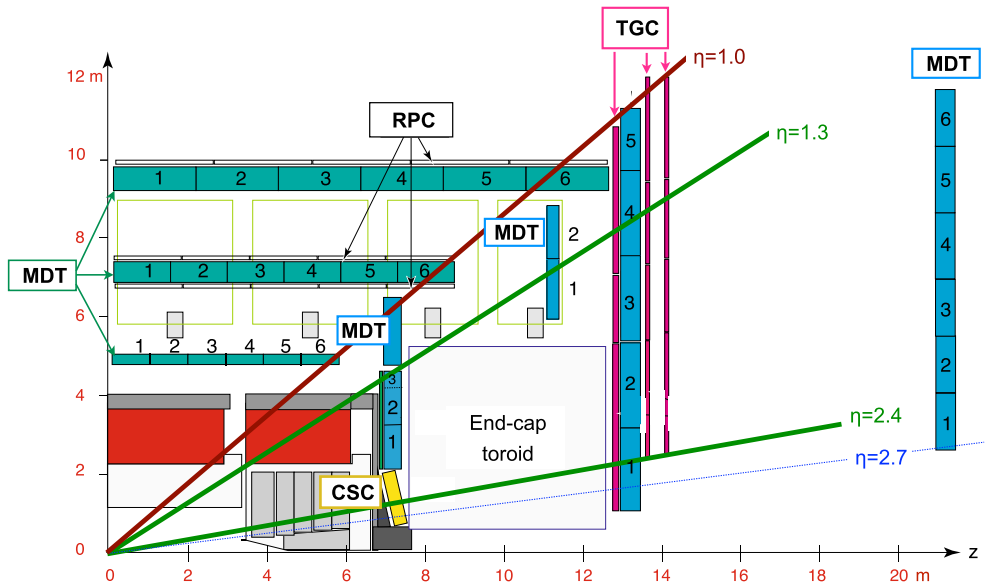

Fig. 1 A schematic picture showing a quarter-section of the muon system in a plane containing the beam axis, with monitored drift tube (MDT) and cathode strip (CSC) chambers for momentum determination and resistive plate (RPC) and thin gap (TGC) chambers for triggering

geometry and near 4π coverage in solid angle.[3] The detector consists of four major sub-systems: the inner detector, electromagnetic calorimeter, hadronic calorimeter and muon spectrometer. A detailed description of the ATLAS detector can be found in Ref. [3]. The inner detector measures tracks up to $|\eta| = 2.5$ in an axial magnetic field of 2 T using three types of sub-detectors: a silicon pixel detector closest to the interaction point, a semiconductor tracker surrounding the pixel detector, and a transition radiation straw tube tracker covering $|\eta| < 2.0$ as the outermost part of the inner detector. The calorimeter system covers the pseudorapidity range $|\eta| < 4.9$ and encloses the inner detector. The high-granularity liquid-argon electromagnetic sampling calorimeter is divided into one barrel ($|\eta| < 1.475$) and two endcap components ($1.375 < |\eta| < 3.2$). The hadronic calorimeter is placed directly outside the electromagnetic calorimeter. A steel/scintillator-tile calorimeter provides hadronic coverage in the range $|\eta| < 1.7$. The endcap and forward regions, spanning $1.5 < |\eta| < 4.9$, are instrumented with liquid-argon calorimeters. The calorimeters are then surrounded by the muon spectrometer.

[3] ATLAS uses a right-handed coordinate system with its origin at the nominal interaction point (IP) in the centre of the detector and the z-axis along the beam pipe. The x-axis points from the IP to the centre of the LHC ring, and the y-axis points upward. Cylindrical coordinates (r, ϕ) are used in the transverse plane, ϕ being the azimuthal angle around the beam pipe. The pseudorapidity is defined in terms of the polar angle θ as $\eta = -\ln\tan(\theta/2)$.

2.2 Muon spectrometer

The muon spectrometer is based on three large air-core superconducting toroidal magnet systems (two endcaps and one barrel) providing an average magnetic field of approximately 0.5 T. Figure 1 shows a quarter-section of the muon system in a plane containing the beam axis.

In the central region, the detectors comprise a barrel that is arranged in three concentric cylindrical shells around the beam axis. In the endcap region, muon chambers form large wheels, perpendicular to the z-axis. Several detector technologies are utilised to provide both precision tracking and triggering.

The deflection of the muon trajectory in the magnetic field is detected using hits in three layers of precision monitored drift tube (MDT) chambers for $|\eta| < 2$. In the region $2.0 < |\eta| < 2.7$, two layers of MDT chambers in combination with one layer of cathode strip chambers (CSCs) are used. Muons are independently measured in the inner detector and in the muon spectrometer. Three layers of resistive plate chambers (RPCs) in the barrel region ($|\eta| < 1.05$), and three layers of thin gap chambers (TGCs) in the endcap regions ($1.05 < |\eta| < 2.4$) provide the Level-1 muon trigger.

2.3 Level-1 muon trigger

Muons are identified at Level-1 by the spatial and temporal coincidence of hits either in the RPCs or TGCs pointing to the beam interaction region [3,4]. The Level-1 triggers generated by hits in the RPC require a coincidence of hits in the three layers for the highest three p_T thresholds, and a coincidence

of hits in two of the three layers for the rest of thresholds. The Level-1 triggers generated by hits in the TGC require a coincidence of hits in the three layers, except for limited areas in the lowest threshold.

The degree of deviation from the hit pattern expected for a muon with infinite momentum is used to estimate the p_T of the muon with six possible thresholds. The number of muon candidates passing each threshold is used in the conditions for the global Level-1 trigger. Following a global trigger, the p_T thresholds and the corresponding detector regions, region of interest (RoIs), are then sent to the Level-2 and event-filter for further consideration [3,4]. The typical dimensions of the RoIs are 0.1×0.1 (0.03×0.03) in $\Delta\eta \times \Delta\phi$ in the RPCs (TGCs) [3]. The geometric coverage of the Level-1 trigger is about 99 % in the endcap regions and about 80 % in the barrel region. The limited geometric coverage in the barrel region is due to gaps at around $\eta = 0$ (to provide space for services of the inner detector and calorimeters), the feet and rib support structures of the ATLAS detector and two small elevator shafts in the bottom part of the spectrometer.

2.4 Level-2 muon trigger

The RoI provided by Level-1 enables Level-2 to select the region of the muon detector in which the interesting features reside, therefore reducing the amount of data to be transferred and processed [4]. At Level-2, a track is constructed by adding the data from the MDT chambers to get a more precise estimate of the track parameters, leading to the Level-2 stand-alone-muon [5]. To achieve the needed resolution in sufficiently short time, the p_T of the Level-2 stand-alone-muon is reconstructed with simple parameterised functions. Then, the Level-2 stand-alone-muon is combined with a track found in the inner detector [5]. The closest inner detector track in the η and ϕ planes is selected as the best matching track. The p_T value is refined by taking the weighted average between that of the Level-2 stand-alone-muon and of the inner detector track, leading to the so called Level-2 combined-muon.

2.5 Event-filter muon trigger

Muons in the event-filter are found by two different procedures. The first focuses on RoIs defined by the Level-1 and Level-2 steps described above and is referred to as the RoI-based method. The second procedure searches the full detector without using the information from the previous levels and is referred to as the full-scan method.

In the RoI-based method, muon candidates are first formed by using the muon detectors (called event-filter stand-alone-muons), and are subsequently combined with inner detector tracks leading to event-filter combined-muons. If no combined-muon is formed, muon candidates are searched for by extrapolating inner detector tracks to the muon detectors. If there are corresponding track segments, combined-muons are formed. Additionally, the degree of isolation for the combined-muon is quantified by summing the p_T of inner detector tracks with $p_T^{trk} > 1\,\text{GeV}$ found in a cone of $\Delta R = \sqrt{(\Delta\phi)^2 + (\Delta\eta)^2} < \Delta R_{cut}$, centred around the muon candidate after subtracting the p_T of the muon itself ($\Sigma_{\Delta R < \Delta R_{cut}} p_T^{trk}$).

The full-scan procedure is used in the event-filter to find additional muons that are not found by the RoI-based method. In the full-scan, muon candidates are first sought in the whole of the muon detectors, and then inner detector tracks are reconstructed in the whole of the inner detectors. Combined pairs of these inner detector and muon detector tracks form muon candidates called event-filter full-scan-muons.

2.6 Trigger selection criteria

The trigger system is configured to use a large set of selection criteria for each event. Each criterion consists of sequential selections at Level-1, Level-2 and the event-filter, and is referred to as trigger in this paper for simplicity. An event has to satisfy at least one of the triggers in order to be recorded.

Table 1 shows the Level-1 thresholds and the muon triggers discussed in this paper. For all trigger levels, the naming scheme typically follows a convention whereby the number that follows "mu" denotes the transverse momentum threshold and the letters, or combination of letters, characterize the muon type [isolated (i), stand alone (SA), found by full scan (FS)] and/or its origin.

The Level-1 thresholds were optimised to give an efficiency at the designated threshold that is typically 95 % of the maximum efficiency achieved well above the threshold.

The triggers described in Table 1 were designed to be as inclusive as possible.

The mu24i trigger is designed to collect isolated muons with $p_T > 25\,\text{GeV}$ with a loose isolation criterion of $\Sigma_{\Delta R<0.2} p_T^{trk}/p_T < 0.12$. The isolation criterion was chosen to retain nearly 100 % efficiency for well isolated muons from the decays of Z-bosons while rejecting slightly over half of the muons from heavy flavor, pion and kaon decays.

The mu36 trigger is designed to collect muons with large p_T without making an isolation requirement.

The mu40_SA_barrel trigger is designed to recover possible inefficiency due to muon spectrometer and inner detector combination at large p_T, and the decision is based only on muon spectrometer reconstruction. It was active only in the barrel region due to its high rate in the endcaps.

The mu24i, mu36 and mu40_SA_barrel triggers were used without prescale[4] for the 2012 data taking.

[4] The term prescale means that only one in N events passing the trigger is accepted at that trigger level, where N is an integer definite number

Table 1 Level-1 p_T thresholds and muon triggers. The sequence shows the requirements at Level-1, in the event-filter or at higher level trigger which then includes Level-2. The requirements at Level-2 are omitted for the single- and multi-muon triggers, as they are looser than those in the event-filter. The applied p_T and isolation requirements are also shown

Level-1	p_T threshold (GeV)	Number of layers in coincidence	
MU4	4	2 (3 in limited areas in the endcap region)	
MU6	6	2 (3 in the endcap region)	
MU10	10	2 (3 in the endcap region)	
MU11	10	3	
MU15	15	3	
MU20	20	3	
Single muon trigger	Level-1	Event-filter	
mu6	MU6	One or more combined-muon with $p_T > 6$ GeV	
mu13	MU10	One or more combined-muon with $p_T > 13$ GeV	
mu18	MU15	One or more combined-muon with $p_T > 18$ GeV	
mu24i	MU15	One or more combined-muon with $p_T > 24$ GeV and $\Sigma_{\Delta R<0.2} p_T^{trk}/p_T < 0.12$	
mu36	MU15	One or more combined-muon with $p_T > 36$ GeV	
mu40_SA_barrel	MU15	One or more stand-alone-muon with $p_T > 40$ GeV in $\|\eta\| < 1.05$	
Multi muon trigger	Level-1	Event-filter	
2mu13	Two MU10	Two or more combined-muons with $p_T > 13$ GeV (two or more mu13 triggers)	
mu18_mu8_FS	MU15	One or more combined-muon with $p_T > 18$ GeV (mu18 trigger), and two or more full-scan muons with $p_T > 18$ and > 8 GeV	
3mu6	Three MU6	Three or more muons with $p_T > 6$ GeV (three or more mu6 triggers)	
J/ψ tag-and-probe trigger	Level-1	High level trigger	
mu18_J/ψ_FS	MU15	(Level-2)	One or more combined-muon with $p_T > 18$ GeV
		(Event-filter)	One or more combined-muon with $p_T > 18$ GeV, and at least one pair of combined-muons with a mass consistent with that of J/ψ
mu18_J/ψ_L2	MU15, MU4	(Level-2)	Two or more combined-muons with $p_T > 18, 4$ GeV, and at least one pair of combined-muons with a mass consistent with that of J/ψ
		(Event-filter)	One or more combined-muon with $p_T > 18$ GeV

The 2mu13 trigger requires two or more muon candidates, each of which passes the single-muon trigger mu13. The mu18_mu8_FS trigger requires at least one muon candidate which passes the single-muon trigger mu18, and subsequently employs the full-scan algorithm at the event-filter to find two or more muon candidates with $p_T > 18$ and $p_T > 8$ GeV for leading and sub-leading muons, respectively. The full-scan trigger processes the entire detector and utilises more computing resources than the triggers which process only data in one RoI. Computing resources, not bandwidth, is the limiting factor for these triggers. The leading muon was required to have a p_T of at least 18 GeV in the full-scan dimuon triggers for this reason. The 3mu6 trigger requires three or more muon candidates, each of which passes the single-muon trigger mu6. The 2mu13, mu18_mu8_FS and 3mu6 triggers were used without prescale for the 2012 data taking. The dimuon triggers used to select J/ψ decays will be discussed in more detail in Sect. 7.

2.7 Operation in the 2012 data taking

The typical maximum Level-1 rate was 70 kHz. The event acceptance was reduced at the event-filter which had an output rate of 700 Hz on average (with peaks of about 1 kHz). Of these rates, the single isolated muon trigger mu24i was fired at about 8.5 kHz at Level-1 and at about 65 Hz at the event-filter for an instantaneous luminosity of $7 \times 10^{33}\,\text{cm}^{-2}\,\text{s}^{-1}$. Figure 2 shows the rates of the single- and multi-muon triggers as a function of the instantaneous luminosity, separately for the Level-1 and for the event-filter.

Footnote4 continued
called the prescale factor. At Level-1 every Nth event is accepted. At the high level trigger a random number generator is utilised such that one out of every N events is accepted.

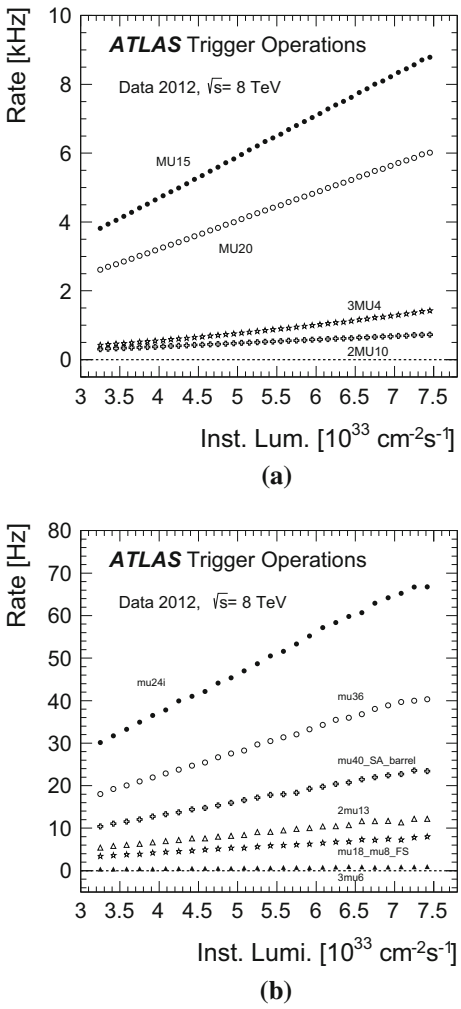

Fig. 2 Trigger rates as a function of instantaneous luminosity **a** for selected muon triggers at Level-1 and **b** for selected single- and multi-muon triggers at the event-filter as denoted in the legend (see Table 1 for details)

They are well described by a linear fit with an approximately zero intercept. This indicates a negligible contribution from effects not related to pp collisions. Typically the trigger rates were reduced by one to two orders of magnitude at Level-2 and by a factor of a few at the event-filter for the single and dimuon triggers. For example the rates were reduced by a factor of 28 at Level-2 (with respect to Level-1) and by a factor of 4.6 at the event-filter (with respect to Level-2) for the mu24i trigger. For the 2mu13 trigger, the rates were reduced by a factor of 71 at Level-2 and by a factor of 1.2 at the event-filter.

During data taking, the performance of the muon trigger was monitored in two stages. For quick online checks during data taking, the coverage in η–ϕ space and the distributions of some kinematic variables were produced by the high level trigger algorithms. A more detailed analysis was performed by calculating efficiencies of triggers during the reconstruction stage of the data processing.

3 Data samples and event selection

Several methods are used to measure the muon trigger performance. This section describes the selection requirements used to define the samples needed for the various methods.

3.1 Methods to measure trigger performance

The tag-and-probe method relies on a pair of muons. If one muon has caused the trigger to record the event (called the tag-muon), the other muon serves as a probe (called the probe-muon) to measure the trigger performance without any bias. This method was applied to dimuon decays of Z-boson and J/ψ meson candidates. Alternatively, muons contained in events that were recorded by triggers other than the muon trigger can be used as an unbiased sample to evaluate the efficiency of triggering on muons. This method was applied to events with muons from W-boson decays, either from top-quark or $W+$jets production. A trigger based on the missing transverse momentum, as measured with the calorimeter, was used to collect such samples.

Among these four samples, the tag-and-probe method using Z decays provides the most precise determination of the efficiency over a wide range of muon p_{T} ($10 \lesssim p_{\mathrm{T}} \lesssim 100\,\mathrm{GeV}$). The tag-and-probe method using J/ψ decays provides a coverage for lower p_{T} of the muon ($p_{\mathrm{T}} \lesssim 10\,\mathrm{GeV}$). Muons from Z decays are not frequently found to have $p_{\mathrm{T}} \gtrsim 100\,\mathrm{GeV}$. Events with muons from top-quark and $W+$jets production provide supplemental coverage at very high p_{T} ($p_{\mathrm{T}} \gtrsim 100\,\mathrm{GeV}$). The muons from top-quark decays tend to have a slightly larger p_{T} than those from the Z decays due to the larger mass of the top-quark. In the $W+$jet events, the W may recoil off of one or more high p_{T} jets. These higher p_{T} W-bosons can then decay into muons with very high p_{T}. In addition, top-quark events and $W+$jet events offer important cross-checks in the overlapping p_{T} region that is also covered by the tag-and-probe method using Z decays.

3.2 Data and Monte Carlo samples

Data were considered if recorded under stable beam conditions and with all relevant sub-detector systems fully operational.

The trigger performance observed in the data is compared with the ATLAS Monte Carlo (MC) simulation, which is the same as used for physics analysis. The generated samples were then processed through a simulation of the ATLAS detector based on GEANT4 [6,7]. The environmental backgrounds due to radiation were not simulated. The simulated events are overlaid with additional minimum-bias events generated with PYTHIA 8 [8] to account for the effect of pile-up interactions.

A sample of Z-boson production was generated using POWHEG- BOX [9] interfaced to PYTHIA 8 [10]. A sample of the production of J/ψ mesons decaying to muon pairs was generated using PYTHIA 8, requiring at least two muons in the final state having $p_{\mathrm{T}} > 15$ and 2.5 GeV. Similarly to the Z-boson production sample, a sample of top and antitop quark pair ($t\bar{t}$) events was generated using POWHEG- BOX interfaced to PYTHIA 8. Samples of single top-quark events were generated using ACERMC [11] interfaced to PYTHIA 8 for the t-channel production, and using POWHEG- BOX interfaced to PYTHIA 8 for the s- and Wt-channel production. Samples of W boson production were generated using ALPGEN [12] interfaced to PYTHIA 8. Samples of dijet events are used for background estimation, and were generated using PYTHIA 8.

3.3 Offline reconstruction

The offline reconstructed muons are obtained by matching tracks found in the muon spectrometer with those in the inner detector [13]. Muons are required to pass various cuts to ensure a high quality inner detector track and to be in a fiducial region of $|\eta| < 2.5$. The muon momentum is calibrated by comparing the dimuon mass of Z boson candidates measured in data and MC [13].

The identification and reconstruction of the electrons, jets, jets containing B-hadrons (called b-jets), and missing transverse momentum ($E_{\mathrm{T}}^{\mathrm{miss}}$) are necessary for the efficiency measurement with top-quark and W-boson candidates.

Electron candidates [14,15] are required to satisfy $E_{\mathrm{T}}^{\mathrm{el}} > 25$ GeV and $|\eta^{\mathrm{el}}| < 2.47$ excluding $1.37 < |\eta^{\mathrm{el}}| < 1.52$, where $E_{\mathrm{T}}^{\mathrm{el}}$ is the transverse energy, and η^{el} is the pseudorapidity of the electromagnetic cluster of energy deposits in the calorimeter. Candidates are required to be isolated by means of calorimeter- and track-based isolation parameters [16].

Jets are reconstructed using the anti-k_t jet clustering [17] algorithm with a radius parameter $R = 0.4$, running on three-dimensional clusters of cells with significant calorimeter response [18]. Their energies have object-based corrections applied as well as corrections for upstream material, non-instrumented material, and sampling fraction. Jets are required to satisfy $p_{\mathrm{T}}^{\mathrm{jet}} > 25$ GeV and $|\eta^{\mathrm{jet}}| < 2.5$, where $p_{\mathrm{T}}^{\mathrm{jet}}$ is the transverse momentum, and η^{jet} is the pseudo-rapidity of the jet. Duplication between electron and jet objects is avoided by removing the jet closest to an electron if their separation is $\Delta R < 0.2$.

The b-jets are identified among the reconstructed jets with an artificial neural network using variables that exploit the impact parameter, the secondary vertex and the topology of b- and c-hadron weak decays [19]. An identification criterion with 70 % efficiency is chosen, as evaluated on jets in a simulated $t\bar{t}$ sample with $p_{\mathrm{T}} > 20 GeV$ and $|\eta| < 2.5$.

Hadronically decaying taus are reconstructed using clusters in the electromagnetic and hadronic calorimeter [3]. A Boosted Decision Tree tau identification method is used to select candiates with a 55–60 % efficiency. Tau candidates are required to have a charge ± 1 and only one or three tracks in a cone of radius $\Delta R < 0.2$.

Photons are identified by electromagnetic cluster of energy deposits in the calorimeter similar to electron identification [20]. In the case of photons, isolated electromagnetic clusters without matching tracks are classified as unconverted photon candidates. Clusters matched to a pair of tracks that are consistent with the hypothesis of a $\gamma \to e^+e^-$ conversion process are classified as converted photon candidates.

The $E_{\mathrm{T}}^{\mathrm{miss}}$ is calculated using the reconstructed jets, electrons, muons, τ leptons, photons, as well as calorimeter energy clusters not associated with these physics objects [21].

In this paper, reconstructed objects (using algorithms applied after the event is recorded) are distinguished from trigger objects (formed either at Level-1, Level-2, or the event-filter during the fast online reconstruction of the event).

3.4 Event selection for the Z-boson sample

For the selection of the Z-boson sample, events are required to pass either the isolated single-muon trigger mu24i or the single-muon trigger mu36.

A pair of oppositely charged muons with invariant mass, $m_{\mu\mu}$, consistent with the mass of the Z boson, $|m_Z - m_{\mu\mu}| < 10$ GeV, is required. The two muons are required to originate from the same interaction vertex. If one of the two muons has $p_{\mathrm{T}} > 25$ GeV and is isolated, $\Sigma_{\Delta R<0.2} p_{\mathrm{T}}^{\mathrm{trk}}/p_{\mathrm{T}} < 0.1$, it is a candidate for the tag-muon, and the other muon is a candidate for the corresponding probe-muon. From a pair of muons, two candidate tag- and probe-muons are allowed. Furthermore, the tag-muon candidate must have an angular distance of $\Delta R < 0.1$ to an event-filter combined-muon that passes either the mu24i or mu36 trigger. In addition, the probe-muon candidate has to be isolated, $\Sigma_{\Delta R<0.2} p_{\mathrm{T}}^{\mathrm{trk}}/p_{\mathrm{T}} < 0.1$.

The probe-muon is matched to a trigger object if it lies within a distance $\Delta R < 0.1$ from an event-filter combined-muon and $\Delta R < 0.5$ from a Level-1 trigger object. The trigger efficiency is defined as the fraction of probe-muons that are associated with at least one trigger muon-object after applying the above criteria.

3.5 Event selection for the J/ψ meson sample

Due to rate restrictions, samples of J/ψ candidates were selected using the two dedicated triggers as in Table 1. One trigger requires a pair of muons found by the event-filter full-scan with a mass consistent with that of the J/ψ, with at least one muon with $p_{\mathrm{T}} > 18$ GeV. It is used to determine the

efficiency at Level-1 and Level-2. The other trigger requires a pair of muons found by Level-1 and Level-2 with the same requirements as above. It is used to determine the efficiency at the event level with respect to the Level-1 and Level-2. Then the total efficiency can be obtained by multiplying these two partial efficiencies.

All combinations of oppositely charged offline muons are considered as J/ψ candidates if each of the muon tracks satisfies $|d_0| < 0.2$ mm, where d_0 is the distance of closest approach between the inner detector track and the proton–proton interaction in the plane transverse to the beam. The two inner detector tracks that are associated with the two muon tracks are refitted under the assumption that they originate from the same vertex. The invariant mass constructed from the refitted tracks, $m_{\mu\mu}$, is required to be consistent with the J/ψ mass, $|m_{J/\psi} - m_{\mu\mu}| < 0.3$ GeV. To enhance the fraction of muons originating from a J/ψ decay a further requirement is made on L_{xy} , the signed two-dimensional decay length of the J/ψ. The variable L_{xy} is defined as $L_{xy} \equiv \mathbf{L} \cdot \mathbf{p}_{\mathbf{T}}^{\mathbf{J/\psi}} / p_{\mathrm{T}}^{J/\psi}$ with $\mathbf{L}$ being the vector originating from the proton–proton interaction vertex. A requirement of $L_{xy} < 1$ mm is made on the muons. The requirements on d_0 and L_{xy} are used to suppress non-prompt muons, such as those from the decays of B-hadrons [22].

The fact that these two dedicated triggers were used to select J/ψ candidates implies that the J/ψ mesons are boosted and therefore the spacial distance between the two muons from the decays is small. To ensure correct one-to-one matching between trigger and offline muons, the distance between them is gauged by the separation of the impact points of the tracks at the locations of the RPC and TGC detectors after extrapolation based on the refitted inner detector track parameters. If one of the two muons has $p_{\mathrm{T}} > 18$ GeV and its distance from an event-filter combined-muon that passes the mu18 trigger is within $\Delta R < 0.08$, as evaluated by using the extrapolated positions, it is considered as a tag-muon. If the other muon is beyond the distance of $\Delta R > 0.2$ from the tag-muon, at the extrapolated positions, it is regarded as a probe-muon. The ΔR cut value is sufficiently large compared to the typical dimensions of the Level-1 trigger segmentation, as described in Sect. 2.3. A probe-muon is matched to trigger objects, if it is within $\Delta R < 0.12$ from a Level-1 muon object and an event-filter combined-muon.

3.6 Selection of top quark and W + jets candidate events

The top quark and W + jets candidate events have to pass a trigger that requires $E_{\mathrm{T}}^{\mathrm{miss}}(\mathrm{calo}) > 80$ GeV, where $E_{\mathrm{T}}^{\mathrm{miss}}(\mathrm{calo})$ is the magnitude of the missing transverse momentum as measured using only the calorimeter information. Several additional cuts are then imposed to remove events with noise bursts in the calorimeters and those with cosmic-ray showers.

The muon candidate is required to have $p_{\mathrm{T}} > 40$ GeV and $|z_0| < 2$ mm, where z_0 is the track impact parameter in the z-direction with respect to the proton–proton interaction vertex. The probe-muon is required to be isolated from neighbouring jets and energy depositions in the calorimeter. Probe-muons are required to satisfy $\Sigma_{\Delta R<0.3} p_T^{\mathrm{trk}} / p_{\mathrm{T}} < 0.05$ and $\Delta R_{\mathrm{min}}(\mathrm{jet}, \mathrm{muon}) > 0.4$, where $\Delta R_{\mathrm{min}}(\mathrm{jet}, \mathrm{muon})$ is the minimum distance between the muon and any jet. In addition, no other muon with $p_{\mathrm{T}} > 25$ GeV is allowed.

Events are further required to have $E_{\mathrm{T}}^{\mathrm{miss}} > 20$ GeV and $m_{\mathrm{T}}^{W} + E_{\mathrm{T}}^{\mathrm{miss}} > 60$ GeV, where m_{T}^{W} is the transverse mass[5] of the W candidate. The W is reconstructed with four-vectors of the $E_{\mathrm{T}}^{\mathrm{miss}}$ and the muon.

For the top quark sample, there must be at least three jets with at least one b-jet. For the W sample, there must be one or two jets with no b-jets. Events with an electron are rejected.

4 Trigger purity

The trigger purity is defined as the fraction of muon triggers that can be associated to an offline muon. The ΔR distance between the trigger object and the offline muon was used to define this matching.

The η distribution of the Level-1 MU15 object that seeds the mu24i event-filter is shown in Fig. 3a for all triggers and for those associated with a reconstructed offline muon. No explicit cut on offline muon p_{T} was applied in the association between trigger and offline objects. Figure 3 shows that the Level-1 rate is dominated by triggers without associated offline muons (called fake triggers). The overall trigger purity (fraction of Level-1 rate from true muons) is 40 %. Most of the Level-1 fakes originates in the end-cap. The cause of these fakes in the endcap region was extensively investigated [23], and is understood as mainly due to charged particles, for instance protons, produced in large amounts of dense material such as the toroid coils and shields. Figure 3b shows the MU15 trigger rate as a function of the instantaneous luminosity. Also shown is the rate due to fake triggers. The error bars show statistical uncertainties only. Both the total rate and the fake rate at Level-1 scale linearly with the instantaneous luminosity.

Figure 4a shows the η distribution of the trigger objects recorded with the isolated single-muon trigger at the event-filter. The fake triggers, not associated to an offline reconstructed muon, are rejected by the subsequent High-Level-

[5] Transverse mass is defined as $m_T^2 = m^2 + p_x^2 + p_y^2$ and has the useful propriety that it is invariant under Lorentz boosts along the beam direction.

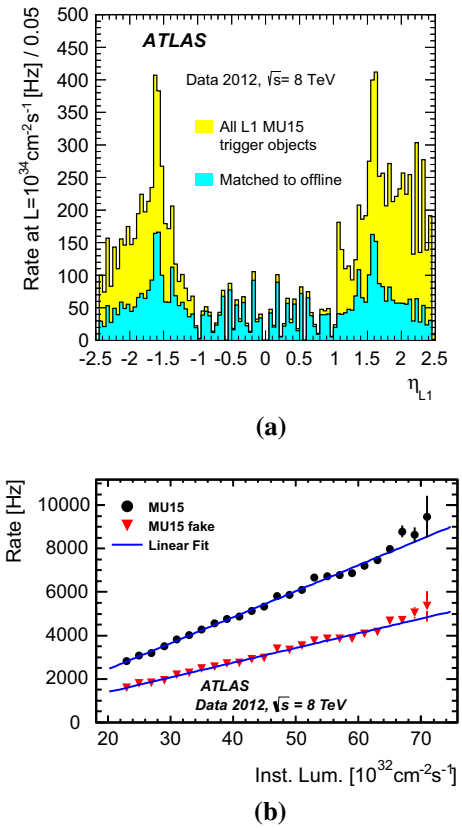

Fig. 3 Trigger rate of the Level-1 MU15 as a function of **a** pseudorapidity η_{L_1} of all the trigger objects (*light histogram*) and of the ones associated with offline reconstructed muons (*dark histogram*) and **b** instantaneous luminosity, for all triggers (*dots*) and for the fake ones not-associated with offline-reconstructed muons (*triangles*) with the *lines* representing the results of the corresponding linear fits

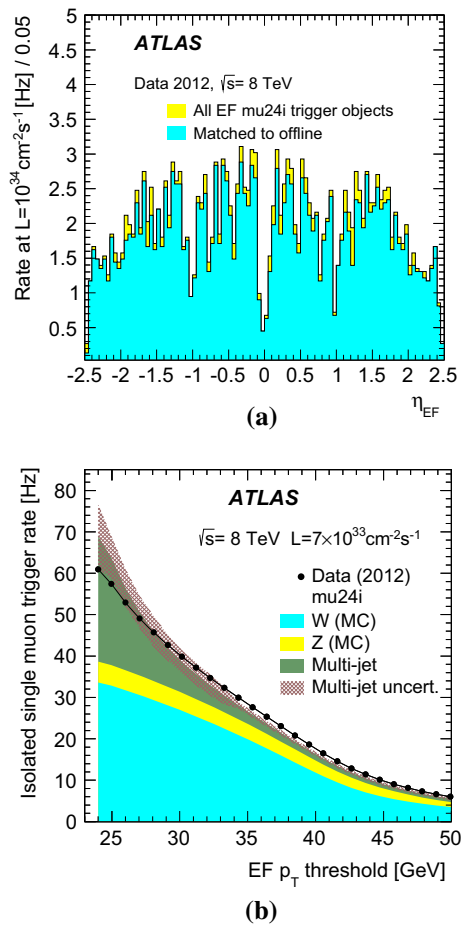

Fig. 4 Rate of the isolated single-muon trigger, mu24i, at the event-filter **a** as a function of pseudorapidity η_{EF} for all combined-muons (*light histogram*) and for the ones associated with offline reconstructed muons (*dark histogram*), **b** as a function of the transverse momentum p_T threshold at the event-filter (EF) at an instantaneous luminosity of $7 \times 10^{33}\,\mathrm{cm}^{-2}\,\mathrm{s}^{-1}$, for combined-muons in the data (*dots*) compared to the expectations from W- and Z-bosons production and from the data-driven estimate for multi-jet production, as described in the legend

Trigger decisions, and a purity of about 90 % is achieved. The physics origin of muons at the event-filter is illustrated in Fig. 4b, which shows the expected composition of the trigger rate of the isolated single-muon as a function of the lower threshold value on the muon p_T. The vertical scale gives the trigger rate as a function of p_T at an instantaneous luminosity of $7 \times 10^{33}\,\mathrm{cm}^{-2}\,\mathrm{s}^{-1}$. The expectations for W and Z production were evaluated by using MC simulations with their predicted cross sections. Multi-jet production, where one or more jets produce a muon from the decay of a heavy quark or from a pion or kaon decay in flight, also contribute to this rate. The multi-jet contribution was evaluated in a data-driven approach as described below.

A multi-jet enriched control-region is obtained by using events that are triggered by a single-muon trigger with the same p_T threshold but without isolation requirement.[6] The control-region is defined by inverting the trigger isolation criteria, by requiring at least one jet in an event, and by requiring matching to an offline muon to remove the fake contribution. The multi-jet contribution in the signal region is estimated by the following procedure. The fraction of multi-jet events in the signal region is taken from dijet MC simulation. The total normalization for the multi-jet contribution is then evaluated in the control-region. The contribution to the signal region is then taken as the total estimated multi-jet contribution weighed by the signal fraction from simulation. The uncertainty of this estimation is dominated by the statistical uncertainty in the control-region/signal-region transfer factors from MC simulation, and is shown in Fig. 4b. The rate was evaluated as a function of the p_T threshold on the event-filter combined-muon. As shown in Fig. 4b, at $p_T = 24\,\mathrm{GeV}$ about 60 % of the events triggered by mu24i are due to muons from W and Z production.

[6] This trigger was active but with a prescale factor of 10.

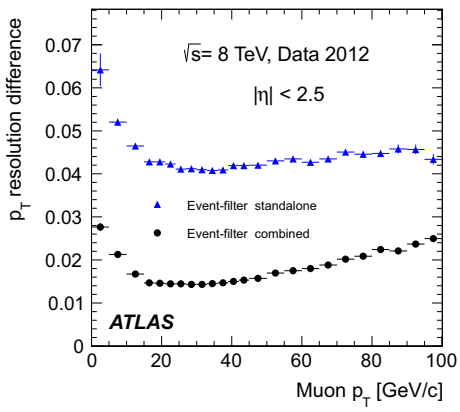

Fig. 5 Resolution difference in transverse momentum p_T determination in the offline and in the event-filter reconstruction, as a function of p_T of the offline muon

5 Resolution

The tag-and-probe method applied to Z-boson candidates was used to evaluate the quality of the p_T, η and ϕ determination at the event-filter, compared to the offline reconstruction. The online algorithms are nearly identical to the offline versions but have some simplifications in the pattern recognition because of timing constraints. Additionally, the offline reconstruction uses updated calibration and alignment corrections not available at the time the data was recorded. Therefore, finite difference can be expected even when the event-filter combined muon is compared with the offline muon that is also reconstructed by combining the inner detector and muon detectors.

The offline momentum resolution is < 3.5 % up to transverse momenta p_T of 200 GeV and < 10 % up to 1 TeV [24]. The residual of the trigger-reconstructed p_T with respect to the offline value is defined as $\delta_{p_T} = \frac{1/p_T^{\text{trigger}} - 1/p_T}{1/p_T}$, where p_T^{trigger} is the transverse momentum reconstructed by the trigger, and the p_T is that of the offline muon. The resolution difference between the trigger and offline reconstruction was defined as the standard deviation of a Gaussian function fitted to the δ_{p_T} distribution. Figure 5 shows the p_T resolution differences, as a function of the offline muon p_T, of the event-filter stand-alone and event-filter combined muons in the barrel and endcap regions. The p_T resolution difference is about 2 and 5 % for event-filter combined and event-filter stand-alone muon, respectively.

The resolution differences of the η and ϕ determination were examined similarly by defining the residual as the absolute value of the difference between the trigger and offline reconstructed values. Figure 6 shows the η and ϕ resolution differences of the event-filter muons. It shows that the trigger–offline matching criterion used in the efficiency measurements, for instance $\Delta R < 0.1$ for the tag-and-probe method using Z bosons (see Sect. 3.4), is sufficiently loose.

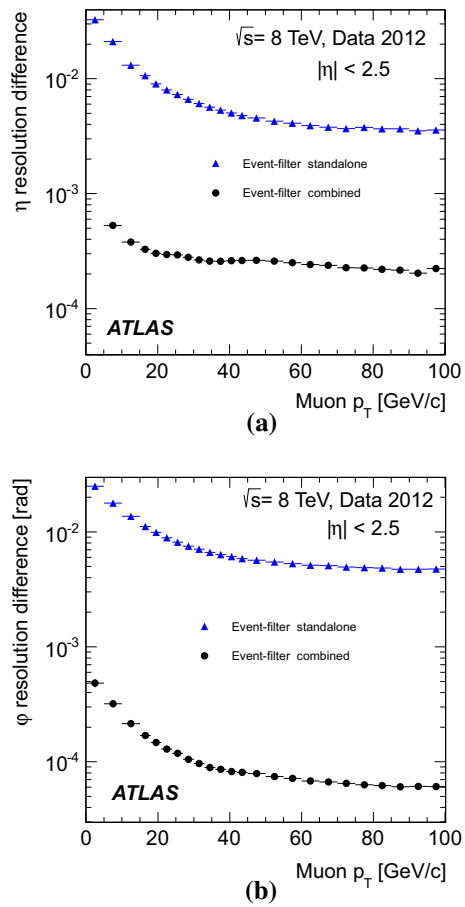

Fig. 6 Resolution difference in the **a** pseudorapidity η and **b** azimuthal angle ϕ determination in the offline and in the event-filter reconstruction, as a function of p_T of the offline muon

6 Efficiency measurements with Z boson candidates

In the next several sections, measurements of the efficiency of the muon trigger in different kinematic regions are presented, preceded by a discussion of systematic uncertainties. The efficiency is primarily measured as a function of muon p_T. In addition, the efficiency is measured in two-dimensions, for instance in η and ϕ bins, and compared to the simulated one. To more accurately model data, all ATLAS physics analysis which use events selected with the muon trigger are provided with the ratios of measured to simulated efficiencies to make small corrections to the simulated samples.

6.1 Systematic uncertainty

In the following, sources of systematic uncertainty are discussed and the quoted uncertainty values are presented for the efficiency measured in the region of $25 < p_T < 100$ GeV.

– Dependence on pile-up interactions:
the efficiency was measured as a function of the number of reconstructed vertices, Nvtx, separately for data

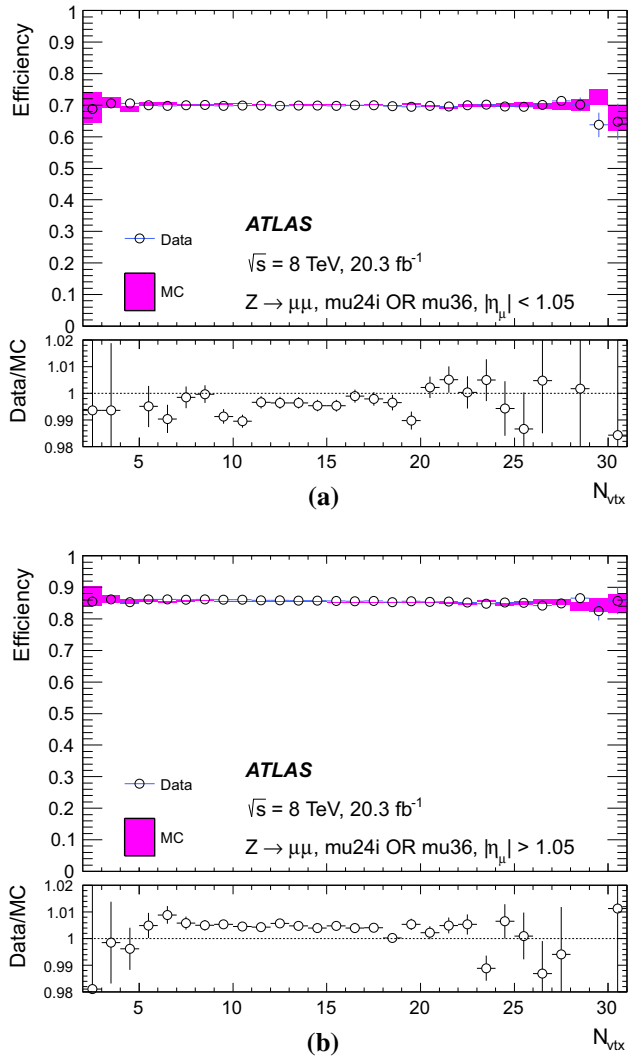

Fig. 7 Efficiency to pass either mu24i or mu36 triggers, as a function of the number of reconstructed vertices in an event, N_{vtx} in **a** the barrel region, and in **b** the endcap region, for data (*dots*) and MC simulation (*bands*). The *lower panels* show the ratio of the efficiencies in data and in MC simulation. The *error bars* reflect statistical uncertainties only

and MC simulation, as shown in Fig. 7. The efficiency is largely independent of the number of pile-up interactions. Separate linear fits to the data and MC simulation were performed in the range from Nvtx = 5 to Nvtx = 30 and extrapolated out to Nvtx = 50. The dependence on the fit range was observed to be negligible. The largest difference observed between the fits in data and MC simulation were observed to be 0.1 (0.5) % in the barrel (endcap). This difference is taken as an estimate of the systematic uncertainty due to the presence of pile-up interactions.

– Correlation between tag- and probe-muons from Z decays:
for medium p_T, tag- and probe-muons tend to be back-to-back in ϕ. Since the barrel and endcap have 16-fold and 12-fold symmetries, respectively, this can potentially lead to some bias; a tag-muon from a Z-boson decay inside a highly efficient region of the detector tends to be accompanied by a probe-muon in a region of high efficiency. This effect is evaluated by adding a requirement to the tag and probe pairs to prevent them from being back-to-back, $\Delta\phi(\text{tag, probe}) < \pi - 0.1$, where $\Delta\phi(\text{tag, probe})$ denotes the azimuthal angle between the tag- and probe-muons. The resulting uncertainty in the efficiency determination is 0.3 % (0.2 %) in the barrel (endcap) region.
– Matching between probe-muon and trigger muon:
this effect was estimated by changing the ΔR thresholds of the matching criteria. The change in the efficiency determination was found to be negligible.
– Probe-muon momentum scale and resolution:
this effect was estimated by changing the momentum scale and momentum resolution for the probe-muon by their respective uncertainties, as determined from the calibration using Z-bosons. The resulting change in efficiency was negligible.
– Probe-muon selection criteria:
this effect was estimated by changing, typically by 10 %, the cuts in various selection criteria, leading to negligible changes in the efficiency determination.
– Background contribution:
the amount of background was estimated by using the dijet, $t\bar{t}$, and W MC simulations and the effect on the efficiency determination was found to be negligible [25]. Also, varying the Z mass window cut gave negligible effect.
– MC modelling:
the sensitivity of the efficiency determination to the MC modelling was tested by comparing samples generated with a different MC generator, namely by adding SHERPA [26]. Again, the change in efficiency was found to be negligible [25].
– Dependence on p_T:
after correcting the MC efficiency in η and ϕ so as to reproduce the one observed in the data , any residual deviations between data and MC in the p_T dependence are taken as systematic uncertainty. This resulted in a 0.4 % effect.
– Probe-muon charge dependence:
it was estimated by comparing the efficiencies measured with positively charged and negatively charged probe-muons. The estimated uncertainty is 0.2 % in the endcap region.

The individual systematic uncertainties are added in quadrature to obtain the total systematic uncertainty, resulting in 0.6 % for the efficiency measured in the region of $25 < p_T < 100$ GeV.

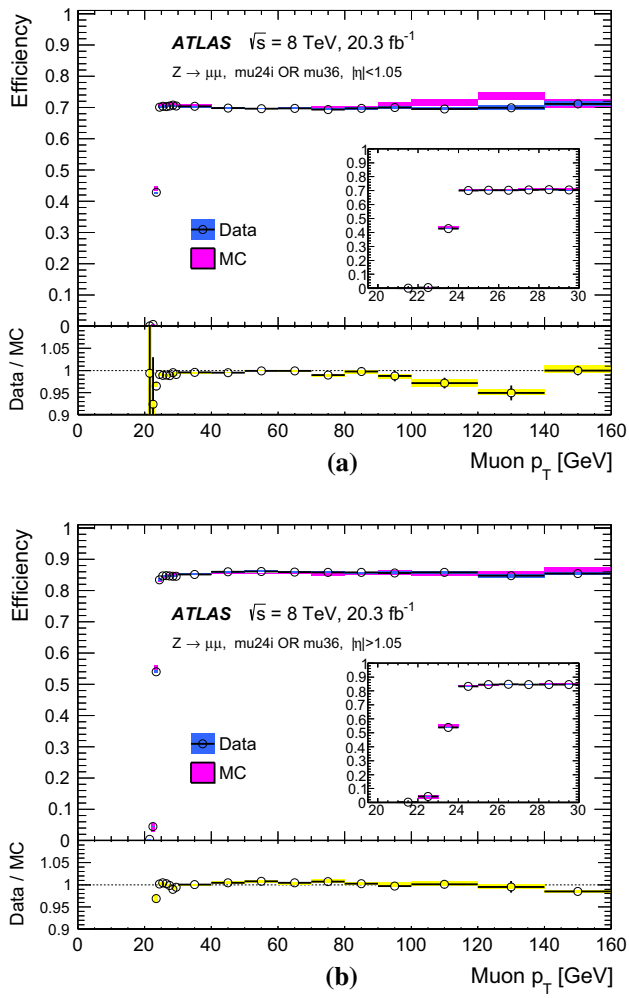

Fig. 8 Efficiency of passing either the mu24i or mu36 trigger as a function of the probe-muon transverse momentum p_T, for **a** the barrel region and **b** the endcap region, for data (*dots*) and MC simulation (*bands*). The *lower panels* show the ratio of the data and MC efficiencies. The *error bars* include both statistical and systematic uncertainties

6.2 Single-muon triggers: mu24i, mu36

Requiring events to pass either the mu24i or the mu36 trigger serves as a general-purpose single-muon triggers for many physics analyses. Figure 8 shows the efficiency to pass either the mu24i or the mu36 trigger as determined in the barrel and endcap regions. The efficiency was measured as a function of the p_T of the reconstructed probe-muon for both data and simulation. The efficiency in the simulation is seen to match that of the data over a wide p_T range. The slight excess in simulation in the p_T bin centred at 130 GeV was studied in detail. High p_T muons from Z-boson decays tend to be slightly more forward where there is the largest difference in trigger efficiency between data and simulation.

The efficiency curve turns on sharply around the threshold, reaching a plateau already around $p_T \sim 25$ GeV. In order to quantitatively evaluate the turn-on behaviour and the agreement between data and MC simulation, a fit was made using a Fermi function $f(p_T)$.[7] From the fit, the low edge of the efficiency plateau region was defined as the value of p_T for which the efficiency decreases by 1 % from the plateau value. Table 2 shows these evaluated plateau values as well as the location of the low edges of the plateaus. The single-muon trigger that requires either the mu24i or mu36 trigger exhibits a plateau efficiency for physics analysis with muon $p_T > 25$ GeV. The efficiency plateau is smooth at $p_T = 36$ GeV indicating that there is no inefficiency due to the isolation requirement in this sample.

Figure 9 shows the efficiency of requiring to pass either mu24i or mu36 triggers, as measured separately for the three trigger levels, Level-1, Level-2 and event-filter. The trigger selection becomes tighter and the efficiency turn-on becomes sharper as the trigger level increases. The plateau efficiency is mostly determined by Level-1. The high level trigger efficiency with respect to Level-1 is about 98–99 %.

Figure 10 shows the ratio of the data and MC efficiencies to pass either the mu24i or the mu36 trigger, as determined in bins of η and ϕ of the probe-muon, for the barrel and endcap regions. The measurement was performed for muons with $p_T > 25$ GeV. The bins in η and ϕ are fine enough to reflect the hardware segmentation of the Level-1 detectors but coarse enough to have sufficient statistics in each bin. The typical size of the statistical uncertainty is less than 1 %, except for a few specific areas where the uncertainty is about 3 %.

6.3 Other single-muon triggers

Figure 11 shows the efficiencies of the mu36 trigger and of the mu40_SA_barrel trigger, together with that of mu24i trigger, as measured in data. The turn-on behaviour of mu24i and mu36 are sharp, while it is slower at threshold for mu40_SA_barrel. The latter relies only on the information from the muon detectors, and thus the p_T resolution is coarser (see Sect. 5). On the other hand, the requirement to pass either mu36 or mu40_SA_barrel results in about 2 % higher efficiency in the barrel region than achieved when requiring mu36 only, because mu40_SA_barrel does not require an inner detector track match. Therefore, requiring that either the mu36 or mu40_SA_barrel triggers are passed serves as a primary single-muon trigger for any processes that include muons with $p_T \gtrsim 50$ GeV.

Figure 11 also shows the efficiencies of the medium-p_T, single-muon triggers, mu13 and mu18. The plateau efficiency of mu13 is about 6 % higher in the barrel region than that of mu18 and other higher-p_T triggers like mu24i. This is

[7] The functional form is $\frac{a}{1+\exp\{b(c-p_T)\}}$, where a indicates the plateau value, b the steepness of the turn-on slope, and c the threshold value.

Table 2 Result of fitting a Fermi function to the efficiency turn-on curve as a function of transverse momentum p_T for the single-muon trigger, for data and MC simulation. The location in p_T of the low edge of the plateau region is defined such that the efficiency decreases by 1 % from the plateau value

Trigger	Data		MC	
	Plateau value (%)	Low edge (GeV)	Plateau value (%)	Low edge (GeV)
Either mu24i or mu36				
Barrel	70.1	24.3	70.3	24.0
Endcap	85.6	24.8	85.3	24.7

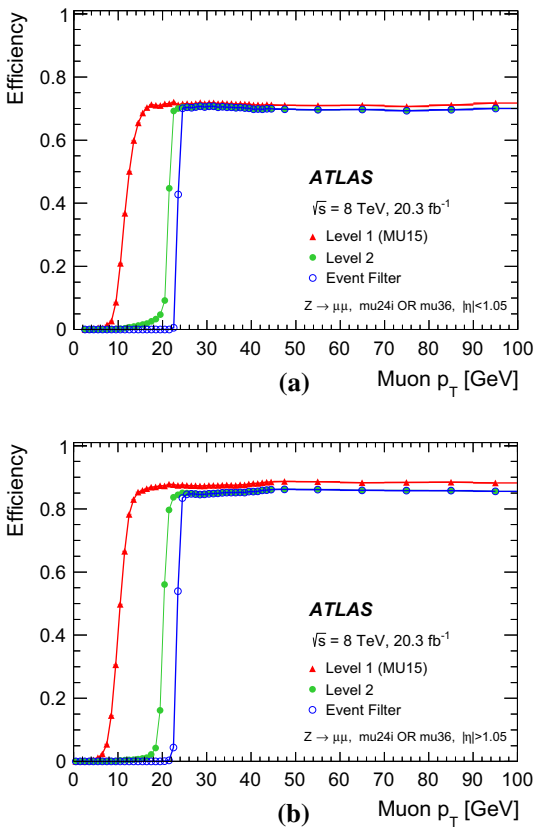

Fig. 9 Efficiency of passing either the mu24i or mu36 trigger as functions of the probe-muon transverse momentum p_T, for the three trigger levels, Level-1, Level-2 and event-filter, in the data for **a** the barrel region and **b** the endcap region. The *error bars* show the statistical uncertainties only

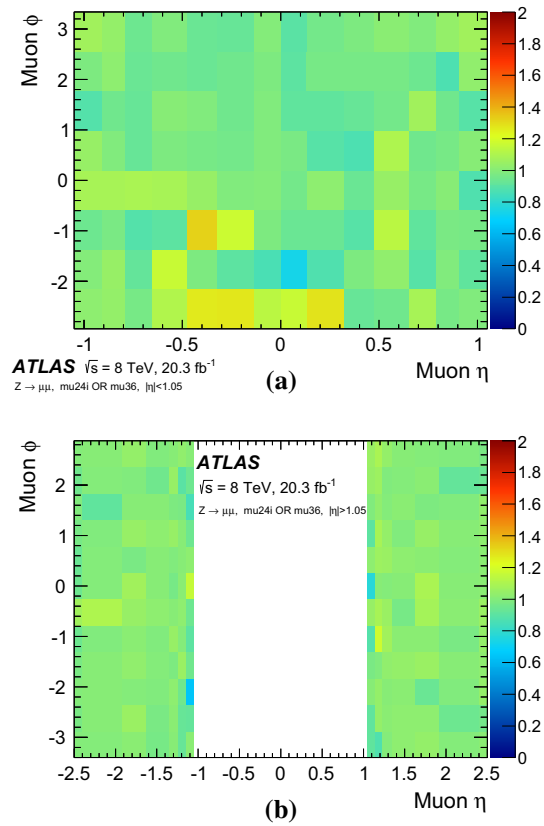

Fig. 10 Ratio of the data and MC efficiencies to pass either the mu24i or the mu36 trigger, in bins of the probe-muon η and ϕ in **a** the barrel region and **b** the endcap region

because mu13 is seeded from Level-1 MU10, which requires a two-station coincidence, while mu18 and the others are seeded from Level-1 MU15 which requires a three-station coincidence (see Sect. 2.3).

A fit using a Fermi function was performed to quantify the turn-on behaviour of these medium-p_T single-muon triggers. Table 3 shows the evaluated plateau and low edge p_T values for mu13 and mu18. It is seen that the offline cut of muon $p_T > 15(20)$ GeV is sufficient to ensure the mu13 (mu18) trigger efficiency is described by the plateau value. These middle-p_T triggers are used in various triggers, such as dimuon triggers 2mu13 and mu18_mu8_FS. The efficiencies of the single-muon triggers, mu13 and mu18, are necessary ingredients to calculate the dimuon trigger efficiencies.

6.4 Full-scan-muon trigger

As described in Sect. 2.6, the mu18_mu8_FS trigger is split into the RoI-based single-muon trigger, mu18, and the full-scan triggers of mu18_FS and mu8_FS. The full-scan trigger efficiencies were evaluated using the same method and sources of systematic uncertainties as for the single-muon trigger (see Sect. 6.1). Only two sources of systematic uncer-

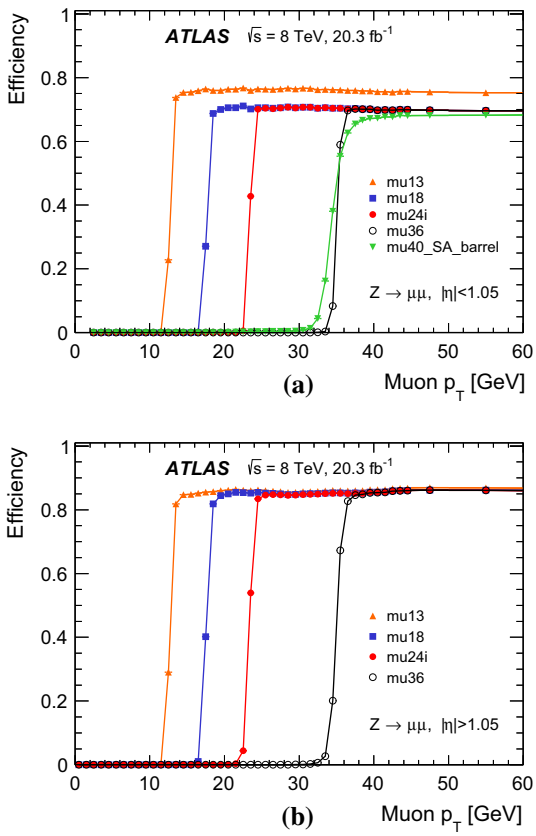

Fig. 11 Efficiency of single-muon triggers, mu13, mu18, mu24i, mu36 and mu40_SA_barrel, measured in data as a function of the probe-muon transverse momentum p_T, for **a** the barrel region and **b** the endcap region. The *error bars* indicate statistical uncertainties only

tainties resulted in visible changes in the efficiency, while all others lead to negligible changes.

– Dependence on p_T:
the uncertainty was estimated by comparing data and MC efficiencies as a function of p_T after correcting MC to reproduce data efficiency in η and ϕ. This resulted in a 0.2 % effect in the barrel and a 0.5 % effect in the endcap region.

– Dependence on pile-up interactions:
as shown in Fig. 12, the efficiency has a small dependence on the number of pileup events in the end cap region, with about 1.0 % efficiency loss per 20 vertices. The MC simulation reproduces the effect well. This is accounted for by changing the distribution of the average number of pile-up interactions, resulting in a 0.1 % uncertainty.

The resulting uncertainties were added in quadrature to form the total systematic uncertainty.

Figure 13 shows the data and MC efficiencies for the mu8_FS trigger for the barrel and endcap regions. The efficiency plateaus for the barrel and endcap regions are 98.7 and 97.6 %, respectively. This results in a higher efficiency for the dimuon trigger than achieved by requiring two RoI-based single-muon triggers.

The ratio of the efficiencies in data and MC is shown as a function of η and ϕ in Fig. 14 for the probe-muons with p_T 10 GeV. It is consistent with unity to within 2 % except in two bins where the difference is as large as 5 %.

7 Efficiency measurements at low p_T

7.1 Efficiency measurements with J/ψ

For the kinematic region of $p_T \lesssim 10$ GeV, the efficiency was measured with the tag-and-probe method using J/ψ meson decays.

A MC study shows that the efficiency is slightly dependent on the measured d_0. Therefore, the efficiencies of prompt and non-prompt muons can be different due to different d_0 distribution. This effect is mostly removed by the cuts on d_0 and L_{xy} described in Sect. 3.5. The residual effect is then suppressed by reweighting the d_0 distribution to that of the prompt muons, which is obtained from the events with $L_{xy} < 0$.

Owing to a very high purity of the offline muon identification, the background also consists of muons, where the

Table 3 Result of Fermi function fit to the efficiency turn-on curve for the middle-p_T single-muon triggers. The location in p_T of the low edge of the plateau region is defined such that the efficiency decreases by 1 % from the plateau value

Trigger	Data		MC	
	Plateau value (%)	Low edge (GeV)	Plateau value (%)	Low edge (GeV)
mu13				
Barrel	75.8	13.7	75.0	12.8
Endcap	86.4	13.6	86.1	13.4
mu18				
Barrel	70.1	18.2	70.4	18.1
Endcap	85.7	18.7	85.4	18.4

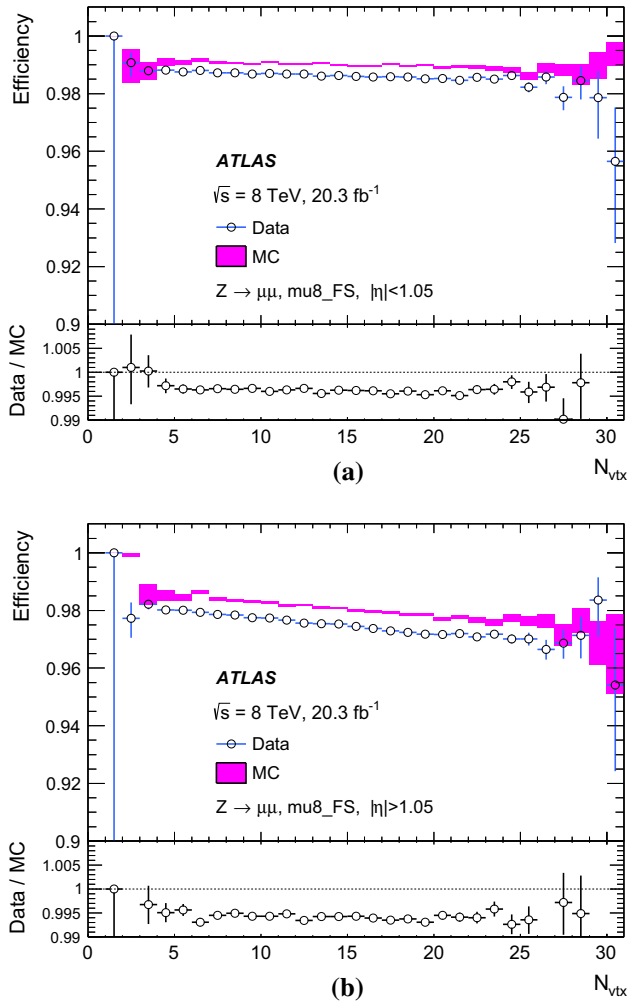

Fig. 12 Efficiency of the mu8_FS trigger measured as a function of the reconstructed number of vertices in an event, N_{vtx} in **a** the barrel region and **b** the endcap region, in the data (*dots*) and in the MC simulation (*bands*) The *lower panels* show the ratio of efficiencies of data and MC simulation. The *error bars* represent statistical uncertainties only

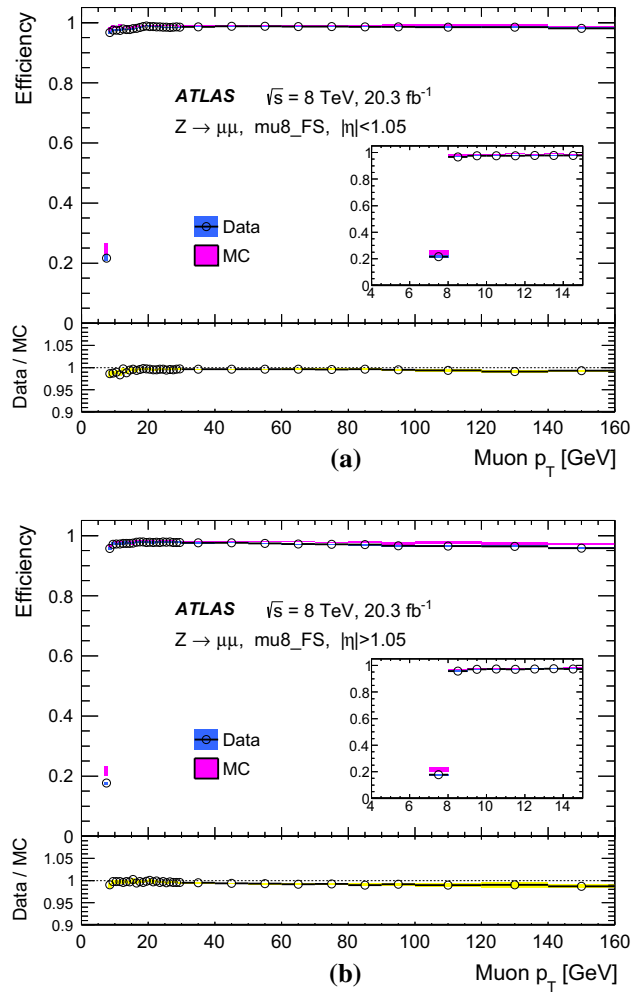

Fig. 13 Efficiency of the event-filter full-scan mu8_FS as a function of the probe-muon transverse momentum p_T, separately in **a** the barrel region and **b** the endcap region

latter do not originate from the decay of a J/ψ meson. The background fraction in the J/ψ mass window is about 16 %, ranging between 13 and 20 % depending on the muon p_T. The efficiency was measured by correcting the background effect using the side-bands of the invariant mass distribution.

7.2 Systematic uncertainty

The following sources of systematic uncertainty were evaluated. The uncertainty numbers quoted in the following are for the efficiency measured as a function of the probe-muon p_T in the region of $4 < p_T < 10$ GeV.

- Matching between probe-muon and trigger muon:
  the effect was estimated by relaxing the ΔR criterion from 0.12 to 0.15, and also by relaxing the ΔR distance cut between the two muons from 0.2 to 0.25. The estimated uncertainty is up to 3 % (2 %) at $p_T = 4$ GeV in the barrel (endcap) region, decreasing to 1 % at $p_T \gtrsim 6$ GeV.
- Reweighting of the d_0 distribution:
  the effect was estimated by comparing the efficiency with that obtained by not applying the d_0 reweighting. The estimated uncertainty is 1 % at $p_T \sim 4$ GeV, decreasing to a negligible level at $p_T \gtrsim 6$ GeV.
- Probe-muon charge dependence:
  the effect was estimated by comparing the efficiencies measured with positively charged and with negatively charged probe-muons. The estimated uncertainty is 1 % at low $p_T \sim 4$ GeV, decreasing to 0.5 % at $p_T \gtrsim 6$ GeV.
- Background contribution:
  the effect was estimated by not doing the background correction, resulting in a uncertainty of 0.1 %.
- Probe-muon selection criteria:

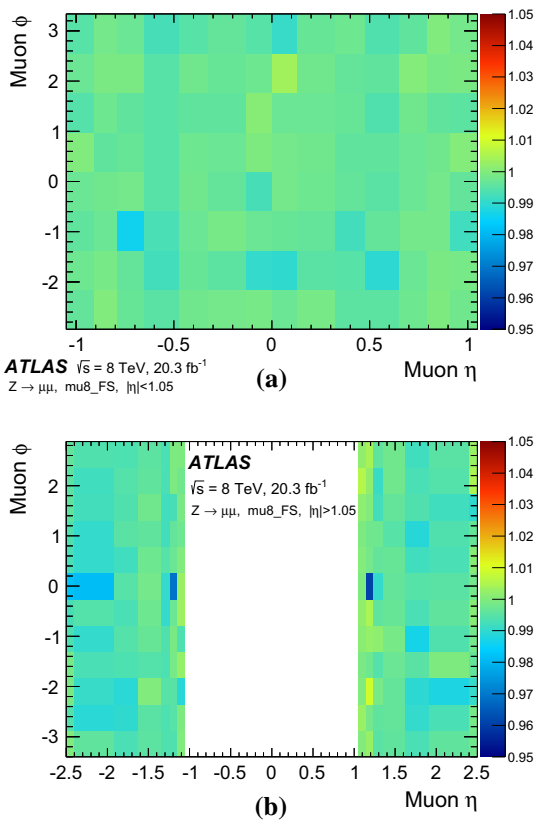

Fig. 14 Ratio of the data and MC efficiencies for the mu8_FS trigger in bins of the probe-muon pseudorapidity η and azimuthal angle ϕ, in **a** the barrel region and **b** the endcap region

the effect was estimated by changing typically by 10 % the thresholds of various selection criteria, leading to negligible effects.

– Dependence on pile-up interactions:
Separate linear fits to the efficiency dependence on Nvtx in the data and MC simulation were performed in the range from Nvtx = 5 to Nvtx = 30 and extrapolated out to Nvtx = 50. The dependence on the fit range was observed to be negligible. The largest difference between the fit results in data and MC simulation were observed to be 0.2 (0.4) % in the barrel (endcap). This difference is taken as the estimate of the resulting systematic uncertainty.

The total systematic uncertainties are obtained by adding the individual ones in quadrature.

7.3 Low-p_T single-muon triggers

Figure 15 shows the efficiency of the lowest-p_T single-muon triggers, mu4, mu6 and mu8 as a function of the p_T of the probe-muon.The efficiency of mu4 is about 40 % at the nominal threshold of 4 GeV. The mu4 turn-on curve rises slowly until $p_T \sim 8$ GeV. The plateau efficiency of mu4 is higher by

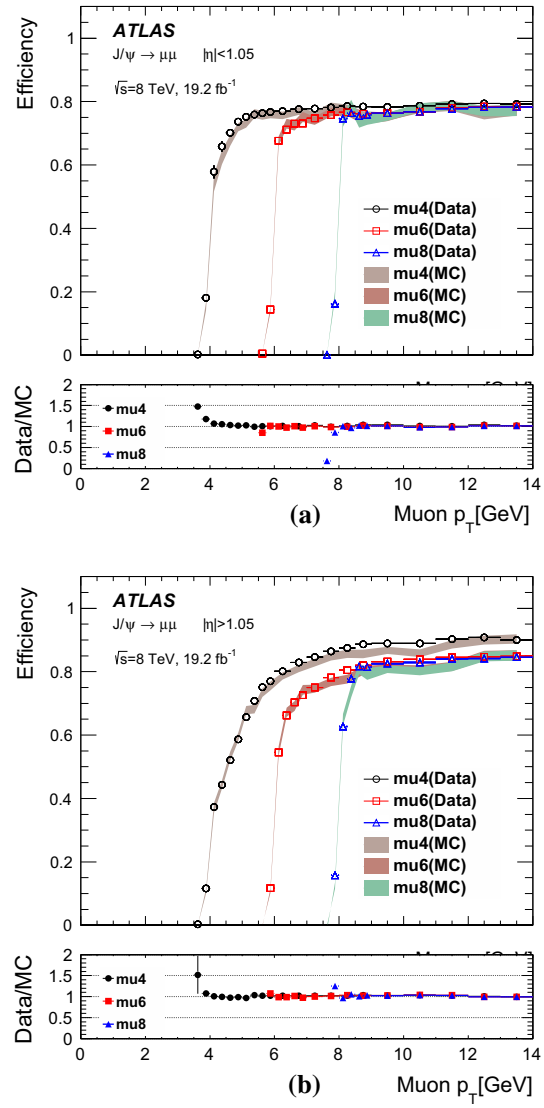

Fig. 15 Efficiency of low transverse momentum p_T single-muon triggers, mu4, mu6 and mu8, as a function of the probe-muon transverse momentum p_T in **a** the barrel region and **b** the endcap region, in the data (*symbols*) and in the MC (*bands*). The *error bars* for MC indicate the statistical uncertainties only, while those for data indicate both the statistical and systematic uncertainties

about 3 % in the endcap region, compared to those of mu6 and mu8.

The ratio of data and MC efficiencies of the mu4 trigger determined in bins of p_T and $Q\eta$, where Q stands for the charge of the probe-muon is shown in Fig. 16.

The ratio is significantly lower than unity at $Q\eta \sim -1.1$ for p_T values up to $\sim$ 12 GeV. In the muon spectrometer toroid magnetic field, the muons with $Q\eta > 0$ (< 0) bend toward the large (small) $|\eta|$ direction in the r–z plane. The muons with $Q\eta \sim -1.1$ are thus likely to pass through only one layer of the RPC (see Fig. 1) and hence are not triggered. Figure 16 shows that this is not well modelled in the MC simulation.

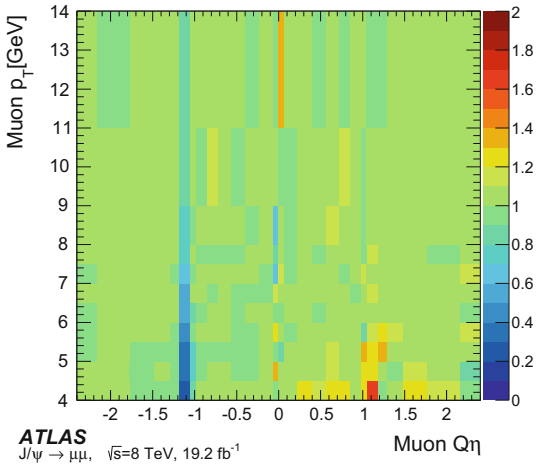

Fig. 16 Ratio of the data and MC efficiencies of the mu4 trigger in bins of the probe-muon pseudorapidity η multiplied by its charge, $Q\eta$, and the transverse momentum p_T

8 Efficiency measurements at very high p_T

8.1 Efficiency measurements with top quarks and W associated with jets

For the kinematic region of $p_T \gtrsim 100$ GeV, the efficiency was measured using muons from top quark and W + jet candidate events. Because they are statistically independent of each other and also correspond to background-enriched samples of each other, the efficiencies using muons in top quark and W + jet events can be obtained by solving the following two equations

$$\epsilon^{t,\text{data}} = f_t^{t,\text{data}}\epsilon_t + (1 - f_t^{t,\text{data}})\epsilon_W,$$
$$\epsilon^{W,data} = f_W^{W,\text{data}}\epsilon_W + (1 - f_W^{W,\text{data}})\epsilon_t,$$

where $\epsilon_{t(W)}$ is the efficiency in pure top quark (W + jets) events, and $\epsilon^{t(W),\text{data}}$ is the measured efficiency in the top quark (W + jets) sample. The factors $f_t^{t,data}$ and $f_W^{W,\text{data}}$ denote the fraction of true top quark (W + jets) events in the top quark (W with jets) sample, as determined by using MC simulation.

8.2 Systematic uncertainty

In the following, sources of systematic uncertainty are discussed and the quoted uncertainty values are presented for the efficiency measured using the W + jets sample as a function of p_T, in the region of $100 < p_T < 400$ GeV.

- Muon isolation:
  to estimate this effect, the efficiency was measured by varying the isolation cut, both by loosening and by tightening the criteria, as well as by changing the ΔR cone size. The estimated uncertainty is typically 0.2 %;
- Muon–jet separation:
  the requirement on muon–jet separation serves also as an isolation cut. This effect was estimated by changing the ΔR criterion in the matching from 0.4 to 0.3 and 0.5. The estimated uncertainty is typically 0.1 and 0.3 % at maximum,
- E_T^{miss} reconstruction:
  the effect was estimated by changing the threshold from 20 to 50 GeV, and also by introducing another tight cut of $E_T^{\text{miss}}(\text{calo}) > 120$ GeV. The estimated uncertainty is 0.5 % at maximum.
- Identification of b-jets:
  the effect was estimated by repeating the measurements with a different b-jet identification criterion, namely with 60 % efficiency and 80 % efficiency. The estimated uncertainty is typically less than 0.1 %.
- Cut on p_T^{jet}:
  the effect was estimated by raising the p_T^{jet} threshold to 35 GeV. The estimated uncertainty is typically less than 0.1 %.
- Background contribution:
  the number of background events was estimated by using the dijet and Z MC simulations and was found to be negligible at $p_T > 100$ GeV.

All the contributions were added in quadrature to obtain the total systematic uncertainties.

8.3 Single-muon trigger efficiency at $p_T \gtrsim 100$ GeV

Figure 17 shows the efficiencies measured using top quark and W with jets events for the single isolated-muon trigger, mu24i, in the barrel and endcap regions as a function of the p_T of the probe-muon, up to $p_T \sim 400$ GeV. The data and MC simulation agree well up to the very high p_T values.

Also shown in Fig. 17 are the ratios of the efficiencies in the data and MC simulation for the three samples used for the efficiency determination. The three measurements are in good agreement with each other throughout a large p_T range, providing a consistency check of the efficiency measurement in different physics processes with different experimental techniques and in the presence of different backgrounds.

The efficiency in the end cap is seen to drop off slightly at the highest p_T which is not observed in the barrel. This was further investigated and it was found that for the highest energy muons (≈1000 GeV) there is a slight loss of efficiency at the event-filter when combining the muon spectrometer and inner detector track. While the offline algorithm looks for large energy deposits in the calorimeter which arise from bremsstrahlung, the event-filter algorithm always uses

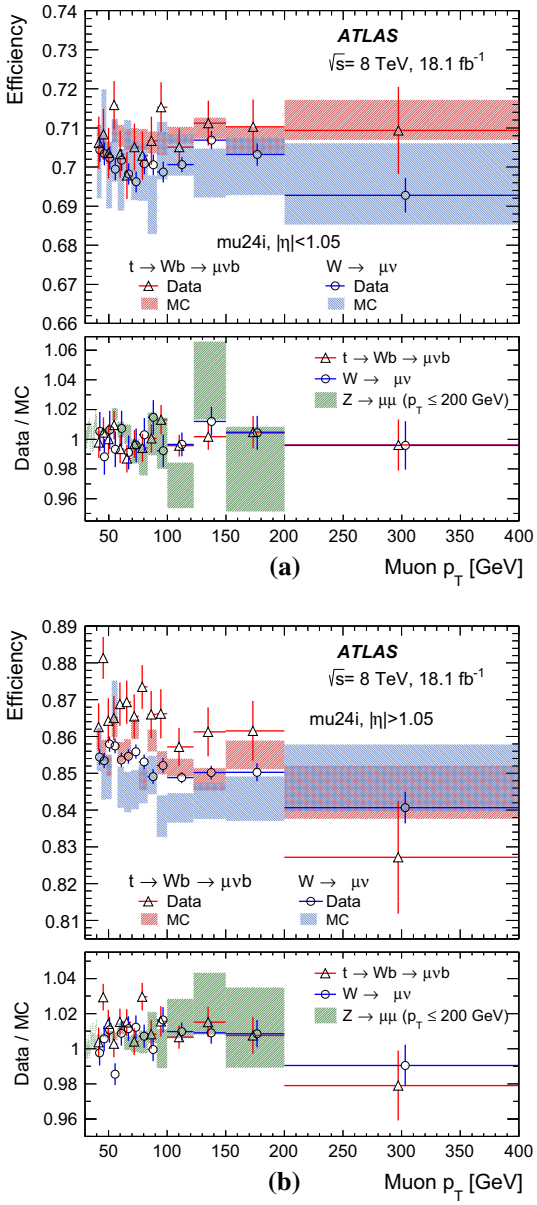

Fig. 17 Efficiency of the mu24i trigger as a function of the probe-muon transverse momentum p_T, as measured with the top quark and W + jet candidate events in the **a** barrel and **b** endcap regions. The *lower panels* show the ratio of the efficiencies in the data and MC simulation. Also shown is the efficiency as measured with the Z decays using the tag-and-probe method. The *error bars* for MC simulation indicate the statistical uncertainties only while the *error bars* for data include both statistical and systematic uncertainties

a parameterised energy loss for a minimum ionising particle. Without correction, this can cause a mismatch in the momentum estimate in the inner detector and muon spectrometer causing the combination to fail. This occurs in the end cap where kinematically, for fixed p_T, the energy of muons is much higher and thus high energy bremsstrahlung is more likely to occur. However, the effect is small, only occurs in the highest few p_T bins and accounts for a 4 % efficiency loss with a 2 % uncertainty.

9 Conclusions

The ATLAS muon trigger has been successfully adapted to the challenging environment at the LHC such that stable and highly efficient data taking was achieved in the year 2012. The transverse momentum threshold for the single-muon trigger was kept at 24 GeV, with a well-controlled trigger rate of typically about 8.5 kHz at the Level-1 and 65 Hz at the event-filter. The processing times of the Level-2 and event-filter muon trigger algorithms were sufficiently short to fit within the computing resource limitations. The purity of the trigger is about 90 % at the event-filter, and more than half of the triggers originate from electroweak bosons production. The efficiencies are measured extensively with the proton–proton collision data at a centre-of-mass energy of 8 TeV. The systematic uncertainty in the measured efficiency for the single-muon trigger is evaluated to be about 0.6 % in a kinematic region of $25 < p_T < 100$ GeV. The efficiency was measured over a wide p_T range (few GeV to several hundred GeV) by using muons from J/ψ mesons, Z- and W-bosons, and top quark decays showing highly uniform and stable performance.

Acknowledgments We thank CERN for the very successful operation of the LHC, as well as the support staff from our institutions without whom ATLAS could not be operated efficiently. We acknowledge the support of ANPCyT, Argentina; YerPhI, Armenia; ARC, Australia; BMWFW and FWF, Austria; ANAS, Azerbaijan; SSTC, Belarus; CNPq and FAPESP, Brazil; NSERC, NRC and CFI, Canada; CERN; CONICYT, Chile; CAS, MOST and NSFC, China; COLCIENCIAS, Colombia; MSMT CR, MPO CR and VSC CR, Czech Republic; DNRF, DNSRC and Lundbeck Foundation, Denmark; EPLANET, ERC and NSRF, European Union; IN2P3-CNRS, CEA-DSM/IRFU, France; GNSF, Georgia; BMBF, DFG, HGF, MPG and AvH Foundation, Germany; GSRT and NSRF, Greece; ISF, MINERVA, GIF, I-CORE and Benoziyo Center, Israel; INFN, Italy; MEXT and JSPS, Japan; CNRST, Morocco; FOM and NWO, Netherlands; BRF and RCN, Norway; MNiSW and NCN, Poland; GRICES and FCT, Portugal; MNE/IFA, Romania; MES of Russia and ROSATOM, Russian Federation; JINR; MSTD, Serbia; MSSR, Slovakia; ARRS and MIZŠ, Slovenia; DST/NRF, South Africa; MINECO, Spain; SRC and Wallenberg Foundation, Sweden; SER, SNSF and Cantons of Bern and Geneva, Switzerland; NSC, Taiwan; TAEK, Turkey; STFC, the Royal Society and Leverhulme Trust, United Kingdom; DOE and NSF, United States of America. The crucial computing support from all WLCG partners is acknowledged gratefully, in particular from CERN and the ATLAS Tier-1 facilities at TRIUMF (Canada), NDGF (Denmark, Norway, Sweden), CC-IN2P3 (France), KIT/GridKA (Germany), INFN-CNAF (Italy), NL-T1 (Netherlands), PIC (Spain), ASGC (Taiwan), RAL (UK) and BNL (USA) and in the Tier-2 facilities worldwide.

Open Access This article is distributed under the terms of the Creative Commons Attribution License which permits any use, distribution, and reproduction in any medium, provided the original author(s) and the source are credited.
Funded by SCOAP[3] / License Version CC BY 4.0.

References

1. ATLAS Collaboration, Observation of a new particle in the search for the standard model Higgs boson with the ATLAS detector at the LHC. Phys. Lett. B **716**, 1 (2012). arXiv:1207.7214 [hep-ex]
2. CMS Collaboration, Observation of a new boson at a mass of 125 GeV with the CMS detector at the LHC. Phys. Lett. B **716**, 30 (2012). arXiv:1207.7235 [hep-ex]
3. ATLAS Collaboration, The ATLAS experiment at the CERN large Hadron collider. JINST **3**(S08003), 1 (2008)
4. ATLAS Collaboration, Performance of the ATLAS trigger system in 2010. Eur. Phys. J. C **72**, 1849 (2012). arXiv:1110.1530 [hep-ex]
5. ATLAS Collaboration, Expected performance of the ATLAS experiment—detector, trigger and physics. arXiv:0901.0512 [hep-ex]
6. GEANT4 Collaboration, S. Agostinelli et al., GEANT4: a simulation toolkit. Nucl. Instrum. Method A **506**, 250 (2003)
7. ATLAS Collaboration, The ATLAS simulation infrastructure. Eur. Phys. J. C **70**, 823 (2010). arXiv:1005.4568 [hep-ex]
8. T. Sjostrand, S. Mrenna, P.Z. Skands, A brief introduction to PYTHIA 8.1. Comput. Phys. Commun. **178**, 852 (2008). arXiv:0710.3820 [hep-ph]
9. S. Frixione, P. Nason, C. Oleari, Matching NLO QCD computations with Parton Shower simulations: the POWHEG method. J. High Energy Phys. **11**, 070 (2007). arXiv:0709.2092 [hep-ph]
10. T. Sjostrand, S. Mrenna, P.Z. Skands, PYTHIA 6.4 physics and manual. J. High Energy Phys **05**, 026 (2006). arXiv:0603175 [hep-ph]
11. B.P. Kersevan, E. Richter-Was, Comput. Phys. Commun. **149**, 142 (2004). arXiv:0405247 [hep-ph]
12. M.L. Mangano, M. Moretti, F. Piccinini, R. Pittau, A.D. Polosa, ALPGEN, a generator for hard multiparton processes in hadronic collisions. J. High Energy Phys. **0307**, 001 (2003). arXiv:0206293 [hep-ph]
13. ATLAS Collaboration, Measurement of the muon reconstruction performance of the ATLAS detector using 2011 and 2012 LHC protonproton collision data (submitted to EPJC). arXiv:1407.3935 [hep-ex]
14. ATLAS Collaboration, Electron performance measurements with the ATLAS detector using the, LHC proton–proton collision data. Eur. Phys. J. C **72**(2012), 1909 (2010). arXiv:1110.3174 [hep-ph]
15. ATLAS Collaboration, Electron reconstruction and identification efficiency measurements with the ATLAS detector using the 2011 LHC proton–proton collision data. Eur. Phys. J. C **74**, 2940 (2014). arXiv:74:2941 [hep-ex]
16. ATLAS Collaboration, Measurement of the inclusive isolated prompt photon cross section in pp collisions at sqrt(s) = 7 TeV with the ATLAS detector. Phys. Rev. D **83**, 052005 (2011). arXiv:1012.4389 [hep-ex]
17. M. Cacciari, G. Salam, G. Soyez, The anti-k_T jet clustering algorithm. J. High Energy Phys. **04**, 063 (2008). arXiv:0802.1190 [hep-ph]
18. ATLAS Collaboration, Calorimeter clustering algorithms: description and performance. ATL-LARG-PUB-2008-002
19. ATLAS Collaboration, Calibration of b-tagging using dileptonic top pair events in a combinatorial likelihood approach with the ATLAS experiment. ATLAS-CONF-2014-004
20. ATLAS Collaboration, Expected photon performance in the ATLAS experiment. Report No. ATLAS-CONF-PUB-2011-07 (2011)
21. ATLAS Collaboration, Performance of missing transverse momentum reconstruction in proton-proton collisions at 7 TeV with ATLAS, Eur. Phys. J. C **72**, 1844 (2012). arXiv:1108.5602 [hep-ex]
22. ATLAS Collaboration, Differential cross-sections of inclusive, prompt and non-prompt J/Ψ production, Nucl. Phys. B **850**, 387 (2011). arXiv:1104.3038 [hep-ex]
23. ATLAS Collaboration, New Small Wheel Technical Design Report, CERN-LHCC-2013-006, ATLAS-TDR-020
24. ATLAS Collaboration, Muon reconstruction efficiency and momentum resolution of the ATLAS experiment in proton–proton collisions at $\sqrt{s} = 7$ TeV in 2010 (submitted to Eur. Phys. J. C). arXiv:1404.4562 [hep-ex]
25. ATLAS Collaboration, Performance of the ATLAS muon trigger in 2011. ATLAS-CONF-2012-099
26. T. Gleisberg, Event generation with Sherpa 1.1. J. High Energy Phys. **02**, 007 (2009). arXiv:0811.4622 [hep-ph]

ATLAS Collaboration

G. Aad[84], B. Abbott[112], J. Abdallah[152], S. Abdel Khalek[116], O. Abdinov[11], R. Aben[106], B. Abi[113], M. Abolins[89], O. S. AbouZeid[159], H. Abramowicz[154], H. Abreu[153], R. Abreu[30], Y. Abulaiti[147a,147b], B. S. Acharya[165a,165b,a], L. Adamczyk[38a], D. L. Adams[25], J. Adelman[177], S. Adomeit[99], T. Adye[130], T. Agatonovic-Jovin[13a], J. A. Aguilar-Saavedra[125a,125f], M. Agustoni[17], S. P. Ahlen[22], F. Ahmadov[64,b], G. Aielli[134a,134b], H. Akerstedt[147a,147b], T. P. A. Åkesson[80], G. Akimoto[156], A. V. Akimov[95], G. L. Alberghi[20a,20b], J. Albert[170], S. Albrand[55], M. J. Alconada Verzini[70], M. Aleksa[30], I. N. Aleksandrov[64], C. Alexa[26a], G. Alexander[154], G. Alexandre[49], T. Alexopoulos[10], M. Alhroob[165a,165c], G. Alimonti[90a], L. Alio[84], J. Alison[31], B. M. M. Allbrooke[18], L. J. Allison[71], P. P. Allport[73], J. Almond[83], A. Aloisio[103a,103b], A. Alonso[36], F. Alonso[70], C. Alpigiani[75], A. Altheimer[35], B. Alvarez Gonzalez[89], M. G. Alviggi[103a,103b], K. Amako[65], Y. Amaral Coutinho[24a], C. Amelung[23], D. Amidei[88], S. P. Amor Dos Santos[125a,125c], A. Amorim[125a,125b], S. Amoroso[48], N. Amram[154], G. Amundsen[23], C. Anastopoulos[140], L. S. Ancu[49], N. Andari[30], T. Andeen[35], C. F. Anders[58b], G. Anders[30], K. J. Anderson[31], A. Andreazza[90a,90b], V. Andrei[58a], X. S. Anduaga[70], S. Angelidakis[9], I. Angelozzi[106], P. Anger[44], A. Angerami[35], F. Anghinolfi[30], A. V. Anisenkov[108], N. Anjos[125a], A. Annovi[47], A. Antonaki[9], M. Antonelli[47], A. Antonov[97], J. Antos[145b], F. Anulli[133a], M. Aoki[65], L. Aperio Bella[18], R. Apolle[119,c], G. Arabidze[89], I. Aracena[144], Y. Arai[65], J. P. Araque[125a], A. T. H. Arce[45], J-F. Arguin[94], S. Argyropoulos[42], M. Arik[19a], A. J. Armbruster[30], O. Arnaez[30], V. Arnal[81], H. Arnold[48], M. Arratia[28], O. Arslan[21], A. Artamonov[96], G. Artoni[23], S. Asai[156], N. Asbah[42], A. Ashkenazi[154], B. Åsman[147a,147b], L. Asquith[6], K. Assamagan[25], R. Astalos[145a], M. Atkinson[166], N. B. Atlay[142], B. Auerbach[6], K. Augsten[127], M. Aurousseau[146b], G. Avolio[30], G. Azuelos[94,d], Y. Azuma[156], M. A. Baak[30], C. Bacci[135a,135b], H. Bachacou[137], K. Bachas[155], M. Backes[30], M. Backhaus[30], J. Backus Mayes[144], E. Badescu[26a], P. Bagiacchi[133a,133b], P. Bagnaia[133a,133b], Y. Bai[33a], T. Bain[35], J. T. Baines[130], O. K. Baker[177], S. Baker[77], P. Balek[128], F. Balli[137], E. Banas[39], Sw. Banerjee[174], A. A. E. Bannoura[176], V. Bansal[170], H. S. Bansil[18], L. Barak[173], S. P. Baranov[95], E. L. Barberio[87], D. Barberis[50a,50b], M. Barbero[84], T. Barillari[100], M. Barisonzi[176], T. Barklow[144], N. Barlow[28], B. M. Barnett[130], R. M. Barnett[15], Z. Barnovska[5], A. Baroncelli[135a], G. Barone[49], A. J. Barr[119], F. Barreiro[81], J. Barreiro Guimarães da Costa[57], R. Bartoldus[144], A. E. Barton[71], P. Bartos[145a], V. Bartsch[150], A. Bassalat[116], A. Basye[166], R. L. Bates[53], L. Batkova[145a], J. R. Batley[28], M. Battaglia[138], M. Battistin[30], F. Bauer[137], H. S. Bawa[144,e], T. Beau[79], P. H. Beauchemin[162], R. Beccherle[123a,123b], P. Bechtle[21], H. P. Beck[17], K. Becker[176], S. Becker[99], M. Beckingham[139], C. Becot[116], A. J. Beddall[19c], A. Beddall[19c], S. Bedikian[177], V. A. Bednyakov[64], C. P. Bee[149], L. J. Beemster[106], T. A. Beermann[176], M. Begel[25], K. Behr[119], C. Belanger-Champagne[86], P. J. Bell[49], W. H. Bell[49], G. Bella[154], L. Bellagamba[20a], A. Bellerive[29], M. Bellomo[85], K. Belotskiy[97], O. Beltramello[30], O. Benary[154], D. Benchekroun[136a], K. Bendtz[147a,147b], N. Benekos[166], Y. Benhammou[154], E. Benhar Noccioli[49], J. A. Benitez Garcia[160b], D. P. Benjamin[45], J. R. Bensinger[23], K. Benslama[131], S. Bentvelsen[106], D. Berge[106], E. Bergeaas Kuutmann[16], N. Berger[5], F. Berghaus[170], E. Berglund[106], J. Beringer[15], C. Bernard[22], P. Bernat[77], C. Bernius[78], F. U. Bernlochner[170], T. Berry[76], P. Berta[128], C. Bertella[84], G. Bertoli[147a,147b], F. Bertolucci[123a,123b], D. Bertsche[112], M. I. Besana[90a], G. J. Besjes[105], O. Bessidskaia Bylund[147a,147b], M. Bessner[42], N. Besson[137], C. Betancourt[48], S. Bethke[100], W. Bhimji[46], R. M. Bianchi[124], L. Bianchini[23], M. Bianco[30], O. Biebel[99], S. P. Bieniek[77], K. Bierwagen[54], J. Biesiada[15], M. Biglietti[135a], J. Bilbao De Mendizabal[49], H. Bilokon[47], M. Bindi[54], S. Binet[116], A. Bingul[19c], C. Bini[133a,133b], C. W. Black[151], J. E. Black[144], K. M. Black[22], D. Blackburn[139], R. E. Blair[6], J.-B. Blanchard[137], T. Blazek[145a], I. Bloch[42], C. Blocker[23], W. Blum[82,*], U. Blumenschein[54], G. J. Bobbink[106], V. S. Bobrovnikov[108], S. S. Bocchetta[80], A. Bocci[45], C. Bock[99], C. R. Boddy[119], M. Boehler[48], J. Boek[176], T. T. Boek[176], J. A. Bogaerts[30], A. G. Bogdanchikov[108], A. Bogouch[91,*], C. Bohm[147a], J. Bohm[126], V. Boisvert[76], T. Bold[38a], V. Boldea[26a], A. S. Boldyrev[98], M. Bomben[79], M. Bona[75], M. Boonekamp[137], A. Borisov[129], G. Borissov[71], M. Borri[83], S. Borroni[42], J. Bortfeldt[99], V. Bortolotto[135a,135b], K. Bos[106], D. Boscherini[20a], M. Bosman[12], H. Boterenbrood[106], J. Boudreau[124], J. Bouffard[2], E. V. Bouhova-Thacker[71], D. Boumediene[34], C. Bourdarios[116], N. Bousson[113], S. Boutouil[136d], A. Boveia[31], J. Boyd[30], I. R. Boyko[64], I. Bozovic-Jelisavcic[13b], J. Bracinik[18], A. Brandt[8], G. Brandt[15], O. Brandt[58a], U. Bratzler[157], B. Brau[85], J. E. Brau[115], H. M. Braun[176,*], S. F. Brazzale[165a,165c], B. Brelier[159], K. Brendlinger[121], A. J. Brennan[87], R. Brenner[167], S. Bressler[173], K. Bristow[146c], T. M. Bristow[46], D. Britton[53], F. M. Brochu[28], I. Brock[21], R. Brock[89], C. Bromberg[89], J. Bronner[100], G. Brooijmans[35], T. Brooks[76], W. K. Brooks[32b], J. Brosamer[15], E. Brost[115], G. Brown[83], J. Brown[55], P. A. Bruckman de Renstrom[39], D. Bruncko[145b], R. Bruneliere[48], S. Brunet[60], A. Bruni[20a], G. Bruni[20a], M. Bruschi[20a], L. Bryngemark[80], T. Buanes[14], Q. Buat[143], F. Bucci[49], P. Buchholz[142], R. M. Buckingham[119], A. G. Buckley[53], S. I. Buda[26a], I. A. Budagov[64], F. Buehrer[48], L. Bugge[118], M. K. Bugge[118], O. Bulekov[97], A. C. Bundock[73], H. Burckhart[30], S. Burdin[73], B. Burghgrave[107], S. Burke[130], I. Burmeister[43], E. Busato[34], D. Büscher[48], V. Büscher[82], P. Bussey[53], C. P. Buszello[167], B. Butler[57], J. M. Butler[22], A. I. Butt[3],

C. M. Buttar[53], J. M. Butterworth[77], P. Butti[106], W. Buttinger[28], A. Buzatu[53], M. Byszewski[10], S. Cabrera Urbán[168], D. Caforio[20a,20b], O. Cakir[4a], P. Calafiura[15], A. Calandri[137], G. Calderini[79], P. Calfayan[99], R. Calkins[107], L. P. Caloba[24a], D. Calvet[34], S. Calvet[34], R. Camacho Toro[49], S. Camarda[42], D. Cameron[118], L. M. Caminada[15], R. Caminal Armadans[12], S. Campana[30], M. Campanelli[77], A. Campoverde[149], V. Canale[103a,103b], A. Canepa[160a], M. Cano Bret[75], J. Cantero[81], R. Cantrill[76], T. Cao[40], M. D. M. Capeans Garrido[30], I. Caprini[26a], M. Caprini[26a], M. Capua[37a,37b], R. Caputo[82], R. Cardarelli[134a], T. Carli[30], G. Carlino[103a], L. Carminati[90a,90b], S. Caron[105], E. Carquin[32a], G. D. Carrillo-Montoya[146c], J. R. Carter[28], J. Carvalho[125a,125c], D. Casadei[77], M. P. Casado[12], M. Casolino[12], E. Castaneda-Miranda[146b], A. Castelli[106], V. Castillo Gimenez[168], N. F. Castro[125a], P. Catastini[57], A. Catinaccio[30], J. R. Catmore[118], A. Cattai[30], G. Cattani[134a,134b], S. Caughron[89], V. Cavaliere[166], D. Cavalli[90a], M. Cavalli-Sforza[12], V. Cavasinni[123a,123b], F. Ceradini[135a,135b], B. Cerio[45], K. Cerny[128], A. S. Cerqueira[24b], A. Cerri[150], L. Cerrito[75], F. Cerutti[15], M. Cerv[30], A. Cervelli[17], S. A. Cetin[19b], A. Chafaq[136a], D. Chakraborty[107], I. Chalupkova[128], K. Chan[3], P. Chang[166], B. Chapleau[86], J. D. Chapman[28], D. Charfeddine[116], D. G. Charlton[18], C. C. Chau[159], C. A. Chavez Barajas[150], S. Cheatham[86], A. Chegwidden[89], S. Chekanov[6], S. V. Chekulaev[160a], G. A. Chelkov[64,f], M. A. Chelstowska[88], C. Chen[63], H. Chen[25], K. Chen[149], L. Chen[33d,g], S. Chen[33c], X. Chen[146c], Y. Chen[35], H. C. Cheng[88], Y. Cheng[31], A. Cheplakov[64], R. Cherkaoui El Moursli[136e], V. Chernyatin[25,*], E. Cheu[7], L. Chevalier[137], V. Chiarella[47], G. Chiefari[103a,103b], J. T. Childers[6], A. Chilingarov[71], G. Chiodini[72a], A. S. Chisholm[18], R. T. Chislett[77], A. Chitan[26a], M. V. Chizhov[64], S. Chouridou[9], B. K. B. Chow[99], D. Chromek-Burckhart[30], M. L. Chu[152], J. Chudoba[126], J. J. Chwastowski[39], L. Chytka[114], G. Ciapetti[133a,133b], A. K. Ciftci[4a], R. Ciftci[4a], D. Cinca[62], V. Cindro[74], A. Ciocio[15], P. Cirkovic[13b], Z. H. Citron[173], M. Citterio[90a], M. Ciubancan[26a], A. Clark[49], P. J. Clark[46], R. N. Clarke[15], W. Cleland[124], J. C. Clemens[84], C. Clement[147a,147b], Y. Coadou[84], M. Cobal[165a,165c], A. Coccaro[139], J. Cochran[63], L. Coffey[23], J. G. Cogan[144], J. Coggeshall[166], B. Cole[35], S. Cole[107], A. P. Colijn[106], J. Collot[55], T. Colombo[58c], G. Colon[85], G. Compostella[100], P. Conde Muiño[125a,125b], E. Coniavitis[167], M. C. Conidi[12], S. H. Connell[146b], I. A. Connelly[76], S. M. Consonni[90a,90b], V. Consorti[48], S. Constantinescu[26a], C. Conta[120a,120b], G. Conti[57], F. Conventi[103a,h], M. Cooke[15], B. D. Cooper[77], A. M. Cooper-Sarkar[119], N. J. Cooper-Smith[76], K. Copic[15], T. Cornelissen[176], M. Corradi[20a], F. Corriveau[86,i], A. Corso-Radu[164], A. Cortes-Gonzalez[12], G. Cortiana[100], G. Costa[90a], M. J. Costa[168], D. Costanzo[140], D. Côté[8], G. Cottin[28], G. Cowan[76], B. E. Cox[83], K. Cranmer[109], G. Cree[29], S. Crépé-Renaudin[55], F. Crescioli[79], W. A. Cribbs[147a,147b], M. Crispin Ortuzar[119], M. Cristinziani[21], V. Croft[105], G. Crosetti[37a,37b], C.-M. Cuciuc[26a], T. Cuhadar Donszelmann[140], J. Cummings[177], M. Curatolo[47], C. Cuthbert[151], H. Czirr[142], P. Czodrowski[3], Z. Czyczula[177], S. D'Auria[53], M. D'Onofrio[73], M. J. Da Cunha Sargedas De Sousa[125a,125b], C. Da Via[83], W. Dabrowski[38a], A. Dafinca[119], T. Dai[88], O. Dale[14], F. Dallaire[94], C. Dallapiccola[85], M. Dam[36], A. C. Daniells[18], M. Dano Hoffmann[137], V. Dao[105], G. Darbo[50a], S. Darmora[8], J. A. Dassoulas[42], A. Dattagupta[60], W. Davey[21], C. David[170], T. Davidek[128], E. Davies[119,c], M. Davies[154], O. Davignon[79], A. R. Davison[77], P. Davison[77], Y. Davygora[58a], E. Dawe[143], I. Dawson[140], R. K. Daya-Ishmukhametova[85], K. De[8], R. de Asmundis[103a], S. De Castro[20a,20b], S. De Cecco[79], N. De Groot[105], P. de Jong[106], H. De la Torre[81], F. De Lorenzi[63], L. De Nooij[106], D. De Pedis[133a], A. De Salvo[133a], U. De Sanctis[165a,165b], A. De Santo[150], J. B. De Vivie De Regie[116], W. J. Dearnaley[71], R. Debbe[25], C. Debenedetti[46], B. Dechenaux[55], D. V. Dedovich[64], I. Deigaard[106], J. Del Peso[81], T. Del Prete[123a,123b], F. Deliot[137], C. M. Delitzsch[49], M. Deliyergiyev[74], A. Dell'Acqua[30], L. Dell'Asta[22], M. Dell'Orso[123a,123b], M. Della Pietra[103a,h], D. della Volpe[49], M. Delmastro[5], P. A. Delsart[55], C. Deluca[106], S. Demers[177], M. Demichev[64], A. Demilly[79], S. P. Denisov[129], D. Derendarz[39], J. E. Derkaoui[136d], F. Derue[79], P. Dervan[73], K. Desch[21], C. Deterre[42], P. O. Deviveiros[106], A. Dewhurst[130], S. Dhaliwal[106], A. Di Ciaccio[134a,134b], L. Di Ciaccio[5], A. Di Domenico[133a,133b], C. Di Donato[103a,103b], A. Di Girolamo[30], B. Di Girolamo[30], A. Di Mattia[153], B. Di Micco[135a,135b], R. Di Nardo[47], A. Di Simone[48], R. Di Sipio[20a,20b], D. Di Valentino[29], M. A. Diaz[32a], E. B. Diehl[88], J. Dietrich[42], T. A. Dietzsch[58a], S. Diglio[84], A. Dimitrievska[13a], J. Dingfelder[21], C. Dionisi[133a,133b], P. Dita[26a], S. Dita[26a], F. Dittus[30], F. Djama[84], T. Djobava[51b], M. A. B. do Vale[24c], A. Do Valle Wemans[125a,125g], T. K. O. Doan[5], D. Dobos[30], C. Doglioni[49], T. Doherty[53], T. Dohmae[156], J. Dolejsi[128], Z. Dolezal[128], B. A. Dolgoshein[97,*], M. Donadelli[24d], S. Donati[123a,123b], P. Dondero[120a,120b], J. Donini[34], J. Dopke[30], A. Doria[103a], M. T. Dova[70], A. T. Doyle[53], M. Dris[10], J. Dubbert[88], S. Dube[15], E. Dubreuil[34], E. Duchovni[173], G. Duckeck[99], O. A. Ducu[26a], D. Duda[176], A. Dudarev[30], F. Dudziak[63], L. Duflot[116], L. Duguid[76], M. Dührssen[30], M. Dunford[58a], H. Duran Yildiz[4a], M. Düren[52], A. Durglishvili[51b], M. Dwuznik[38a], M. Dyndal[38a], J. Ebke[99], W. Edson[2], N. C. Edwards[46], W. Ehrenfeld[21], T. Eifert[144], G. Eigen[14], K. Einsweiler[15], T. Ekelof[167], M. El Kacimi[136c], M. Ellert[167], S. Elles[5], F. Ellinghaus[82], N. Ellis[30], J. Elmsheuser[99], M. Elsing[30], D. Emeliyanov[130], Y. Enari[156], O. C. Endner[82], M. Endo[117], R. Engelmann[149], J. Erdmann[177], A. Ereditato[17], D. Eriksson[147a], G. Ernis[176], J. Ernst[2], M. Ernst[25], J. Ernwein[137], D. Errede[166], S. Errede[166], E. Ertel[82], M. Escalier[116], H. Esch[43], C. Escobar[124], B. Esposito[47], A. I. Etienvre[137], E. Etzion[154], H. Evans[60], A. Ezhilov[122], L. Fabbri[20a,20b], G. Facini[31], R. M. Fakhrutdinov[129], S. Falciano[133a], R. J. Falla[77], J. Faltova[128],

Y. Fang[33a], M. Fanti[90a,90b], A. Farbin[8], A. Farilla[135a], T. Farooque[12], S. Farrell[164], S. M. Farrington[171], P. Farthouat[30], F. Fassi[136e], P. Fassnacht[30], D. Fassouliotis[9], A. Favareto[50a,50b], L. Fayard[116], P. Federic[145a], O. L. Fedin[122,j], W. Fedorko[169], M. Fehling-Kaschek[48], S. Feigl[30], L. Feligioni[84], C. Feng[33d], E. J. Feng[6], H. Feng[88], A. B. Fenyuk[129], S. Fernandez Perez[30], S. Ferrag[53], J. Ferrando[53], A. Ferrari[167], P. Ferrari[106], R. Ferrari[120a], D. E. Ferreira de Lima[53], A. Ferrer[168], D. Ferrere[49], C. Ferretti[88], A. Ferretto Parodi[50a,50b], M. Fiascaris[31], F. Fiedler[82], A. Filipčič[74], M. Filipuzzi[42], F. Filthaut[105], M. Fincke-Keeler[170], K. D. Finelli[151], M. C. N. Fiolhais[125a,125c], L. Fiorini[168], A. Firan[40], J. Fischer[176], W. C. Fisher[89], E. A. Fitzgerald[23], M. Flechl[48], I. Fleck[142], P. Fleischmann[88], S. Fleischmann[176], G. T. Fletcher[140], G. Fletcher[75], T. Flick[176], A. Floderus[80], L. R. Flores Castillo[174,k], A. C. Florez Bustos[160b], M. J. Flowerdew[100], A. Formica[137], A. Forti[83], D. Fortin[160a], D. Fournier[116], H. Fox[71], S. Fracchia[12], P. Francavilla[79], M. Franchini[20a,20b], S. Franchino[30], D. Francis[30], M. Franklin[57], S. Franz[61], M. Fraternali[120a,120b], S. T. French[28], C. Friedrich[42], F. Friedrich[44], D. Froidevaux[30], J. A. Frost[28], C. Fukunaga[157], E. Fullana Torregrosa[82], B. G. Fulsom[144], J. Fuster[168], C. Gabaldon[55], O. Gabizon[173], A. Gabrielli[20a,20b], A. Gabrielli[133a,133b], S. Gadatsch[106], S. Gadomski[49], G. Gagliardi[50a,50b], P. Gagnon[60], C. Galea[105], B. Galhardo[125a,125c], E. J. Gallas[119], V. Gallo[17], B. J. Gallop[130], P. Gallus[127], G. Galster[36], K. K. Gan[110], R. P. Gandrajula[62], J. Gao[33b,g], Y. S. Gao[144,e], F. M. Garay Walls[46], F. Garberson[177], C. García[168], J. E. García Navarro[168], M. Garcia-Sciveres[15], R. W. Gardner[31], N. Garelli[144], V. Garonne[30], C. Gatti[47], G. Gaudio[120a], B. Gaur[142], L. Gauthier[94], P. Gauzzi[133a,133b], I. L. Gavrilenko[95], C. Gay[169], G. Gaycken[21], E. N. Gazis[10], P. Ge[33d], Z. Gecse[169], C. N. P. Gee[130], D. A. A. Geerts[106], Ch. Geich-Gimbel[21], K. Gellerstedt[147a,147b], C. Gemme[50a], A. Gemmell[53], M. H. Genest[55], S. Gentile[133a,133b], M. George[54], S. George[76], D. Gerbaudo[164], A. Gershon[154], H. Ghazlane[136b], N. Ghodbane[34], B. Giacobbe[20a], S. Giagu[133a,133b], V. Giangiobbe[12], P. Giannetti[123a,123b], F. Gianotti[30], B. Gibbard[25], S. M. Gibson[76], M. Gilchriese[15], T. P. S. Gillam[28], D. Gillberg[30], G. Gilles[34], D. M. Gingrich[3,d], N. Giokaris[9], M. P. Giordani[165a,165c], R. Giordano[103a,103b], F. M. Giorgi[20a], F. M. Giorgi[16], P. F. Giraud[137], D. Giugni[90a], C. Giuliani[48], M. Giulini[58b], B. K. Gjelsten[118], S. Gkaitatzis[155], I. Gkialas[155,l], L. K. Gladilin[98], C. Glasman[81], J. Glatzer[30], P. C. F. Glaysher[46], A. Glazov[42], G. L. Glonti[64], M. Goblirsch-Kolb[100], J. R. Goddard[75], J. Godfrey[143], J. Godlewski[30], C. Goeringer[82], S. Goldfarb[88], T. Golling[177], D. Golubkov[129], A. Gomes[125a,125b,125d], L. S. Gomez Fajardo[42], R. Gonçalo[125a], J. Goncalves Pinto Firmino Da Costa[137], L. Gonella[21], S. González de la Hoz[168], G. Gonzalez Parra[12], M. L. Gonzalez Silva[27], S. Gonzalez-Sevilla[49], L. Goossens[30], P. A. Gorbounov[96], H. A. Gordon[25], I. Gorelov[104], B. Gorini[30], E. Gorini[72a,72b], A. Gorišek[74], E. Gornicki[39], A. T. Goshaw[6], C. Gössling[43], M. I. Gostkin[64], M. Gouighri[136a], D. Goujdami[136c], M. P. Goulette[49], A. G. Goussiou[139], C. Goy[5], S. Gozpinar[23], H. M. X. Grabas[137], L. Graber[54], I. Grabowska-Bold[38a], P. Grafström[20a,20b], K-J. Grahn[42], J. Gramling[49], E. Gramstad[118], S. Grancagnolo[16], V. Grassi[149], V. Gratchev[122], H. M. Gray[30], E. Graziani[135a], O. G. Grebenyuk[122], Z. D. Greenwood[78,m], K. Gregersen[77], I. M. Gregor[42], P. Grenier[144], J. Griffiths[8], A. A. Grillo[138], K. Grimm[71], S. Grinstein[12,n], Ph. Gris[34], Y. V. Grishkevich[98], J.-F. Grivaz[116], J. P. Grohs[44], A. Grohsjean[42], E. Gross[173], J. Grosse-Knetter[54], G. C. Grossi[134a,134b], J. Groth-Jensen[173], Z. J. Grout[150], L. Guan[33b], F. Guescini[49], D. Guest[177], O. Gueta[154], C. Guicheney[34], E. Guido[50a,50b], T. Guillemin[116], S. Guindon[2], U. Gul[53], C. Gumpert[44], J. Gunther[127], J. Guo[35], S. Gupta[119], P. Gutierrez[112], N. G. Gutierrez Ortiz[53], C. Gutschow[77], N. Guttman[154], C. Guyot[137], C. Gwenlan[119], C. B. Gwilliam[73], A. Haas[109], C. Haber[15], H. K. Hadavand[8], N. Haddad[136e], P. Haefner[21], S. Hageböck[21], Z. Hajduk[39], H. Hakobyan[178], M. Haleem[42], D. Hall[119], G. Halladjian[89], K. Hamacher[176], P. Hamal[114], K. Hamano[170], M. Hamer[54], A. Hamilton[146a], S. Hamilton[162], P. G. Hamnett[42], L. Han[33b], K. Hanagaki[117], K. Hanawa[156], M. Hance[15], P. Hanke[58a], R. Hanna[137], J. B. Hansen[36], J. D. Hansen[36], P. H. Hansen[36], K. Hara[161], A. S. Hard[174], T. Harenberg[176], F. Hariri[116], S. Harkusha[91], D. Harper[88], R. D. Harrington[46], O. M. Harris[139], P. F. Harrison[171], F. Hartjes[106], S. Hasegawa[102], Y. Hasegawa[141], A. Hasib[112], S. Hassani[137], S. Haug[17], M. Hauschild[30], R. Hauser[89], M. Havranek[126], C. M. Hawkes[18], R. J. Hawkings[30], A. D. Hawkins[80], T. Hayashi[161], D. Hayden[89], C. P. Hays[119], H. S. Hayward[73], S. J. Haywood[130], S. J. Head[18], T. Heck[82], V. Hedberg[80], L. Heelan[8], S. Heim[121], T. Heim[176], B. Heinemann[15], L. Heinrich[109], S. Heisterkamp[36], J. Hejbal[126], L. Helary[22], C. Heller[99], M. Heller[30], S. Hellman[147a,147b], D. Hellmich[21], C. Helsens[30], J. Henderson[119], R. C. W. Henderson[71], C. Hengler[42], A. Henrichs[177], A. M. Henriques Correia[30], S. Henrot-Versille[116], C. Hensel[54], G. H. Herbert[16], Y. Hernández Jiménez[168], R. Herrberg-Schubert[16], G. Herten[48], R. Hertenberger[99], L. Hervas[30], G. G. Hesketh[77], N. P. Hessey[106], R. Hickling[75], E. Higón-Rodriguez[168], E. Hill[170], J. C. Hill[28], K. H. Hiller[42], S. Hillert[21], S. J. Hillier[18], I. Hinchliffe[15], E. Hines[121], M. Hirose[158], D. Hirschbuehl[176], J. Hobbs[149], N. Hod[106], M. C. Hodgkinson[140], P. Hodgson[140], A. Hoecker[30], M. R. Hoeferkamp[104], J. Hoffman[40], D. Hoffmann[84], J. I. Hofmann[58a], M. Hohlfeld[82], T. R. Holmes[15], T. M. Hong[121], L. Hooft van Huysduynen[109], J-Y. Hostachy[55], S. Hou[152], A. Hoummada[136a], J. Howard[119], J. Howarth[42], M. Hrabovsky[114], I. Hristova[16], J. Hrivnac[116], T. Hryn'ova[5], P. J. Hsu[82], S.-C. Hsu[139], D. Hu[35], X. Hu[25], Y. Huang[42], Z. Hubacek[30], F. Hubaut[84], F. Huegging[21], T. B. Huffman[119], E. W. Hughes[35], G. Hughes[71], M. Huhtinen[30], T. A. Hülsing[82], M. Hurwitz[15], N. Huseynov[64,b], J. Huston[89], J. Huth[57], G. Iacobucci[49], G. Iakovidis[10], I. Ibragimov[142],

L. Iconomidou-Fayard[116], E. Ideal[177], P. Iengo[103a], O. Igonkina[106], T. Iizawa[172], Y. Ikegami[65], K. Ikematsu[142], M. Ikeno[65], Y. Ilchenko[31,o], D. Iliadis[155], N. Ilic[159], Y. Inamaru[66], T. Ince[100], P. Ioannou[9], M. Iodice[135a], K. Iordanidou[9], V. Ippolito[57], A. Irles Quiles[168], C. Isaksson[167], M. Ishino[67], M. Ishitsuka[158], R. Ishmukhametov[110], C. Issever[119], S. Istin[19a], J. M. Iturbe Ponce[83], R. Iuppa[134a,134b], J. Ivarsson[80], W. Iwanski[39], H. Iwasaki[65], J. M. Izen[41], V. Izzo[103a], B. Jackson[121], M. Jackson[73], P. Jackson[1], M. R. Jaekel[30], V. Jain[2], K. Jakobs[48], S. Jakobsen[30], T. Jakoubek[126], J. Jakubek[127], D. O. Jamin[152], D. K. Jana[78], E. Jansen[77], H. Jansen[30], J. Janssen[21], M. Janus[171], G. Jarlskog[80], N. Javadov[64,b], T. Javůrek[48], L. Jeanty[15], J. Jejelava[51a,p], G.-Y. Jeng[151], D. Jennens[87], P. Jenni[48,q], J. Jentzsch[43], C. Jeske[171], S. Jézéquel[5], H. Ji[174], W. Ji[82], J. Jia[149], Y. Jiang[33b], M. Jimenez Belenguer[42], S. Jin[33a], A. Jinaru[26a], O. Jinnouchi[158], M. D. Joergensen[36], K. E. Johansson[147a], P. Johansson[140], K. A. Johns[7], K. Jon-And[147a,147b], G. Jones[171], R. W. L. Jones[71], T. J. Jones[73], J. Jongmanns[58a], P. M. Jorge[125a,125b], K. D. Joshi[83], J. Jovicevic[148], X. Ju[174], C. A. Jung[43], R. M. Jungst[30], P. Jussel[61], A. Juste Rozas[12,n], M. Kaci[168], A. Kaczmarska[39], M. Kado[116], H. Kagan[110], M. Kagan[144], E. Kajomovitz[45], C. W. Kalderon[119], S. Kama[40], N. Kanaya[156], M. Kaneda[30], S. Kaneti[28], T. Kanno[158], V. A. Kantserov[97], J. Kanzaki[65], B. Kaplan[109], A. Kapliy[31], D. Kar[53], K. Karakostas[10], N. Karastathis[10], M. Karnevskiy[82], S. N. Karpov[64], Z. M. Karpova[64], K. Karthik[109], V. Kartvelishvili[71], A. N. Karyukhin[129], L. Kashif[174], G. Kasieczka[58b], R. D. Kass[110], A. Kastanas[14], Y. Kataoka[156], A. Katre[49], J. Katzy[42], V. Kaushik[7], K. Kawagoe[69], T. Kawamoto[156], G. Kawamura[54], S. Kazama[156], V. F. Kazanin[108], M. Y. Kazarinov[64], R. Keeler[170], R. Kehoe[40], M. Keil[54], J. S. Keller[42], J. J. Kempster[76], H. Keoshkerian[5], O. Kepka[126], B. P. Kerševan[74], S. Kersten[176], K. Kessoku[156], J. Keung[159], F. Khalil-zada[11], H. Khandanyan[147a,147b], A. Khanov[113], A. Khodinov[97], A. Khomich[58a], T. J. Khoo[28], G. Khoriauli[21], A. Khoroshilov[176], V. Khovanskiy[96], E. Khramov[64], J. Khubua[51b], H. Y. Kim[8], H. Kim[147a,147b], S. H. Kim[161], N. Kimura[172], O. Kind[16], B. T. King[73], M. King[168], R. S. B. King[119], S. B. King[169], J. Kirk[130], A. E. Kiryunin[100], T. Kishimoto[66], D. Kisielewska[38a], F. Kiss[48], T. Kitamura[66], T. Kittelmann[124], K. Kiuchi[161], E. Kladiva[145b], M. Klein[73], U. Klein[73], K. Kleinknecht[82], P. Klimek[147a,147b], A. Klimentov[25], R. Klingenberg[43], J. A. Klinger[83], T. Klioutchnikova[30], P. F. Klok[105], E.-E. Kluge[58a], P. Kluit[106], S. Kluth[100], E. Kneringer[61], E. B. F. G. Knoops[84], A. Knue[53], D. Kobayashi[158], T. Kobayashi[156], M. Kobel[44], M. Kocian[144], P. Kodys[128], P. Koevesarki[21], T. Koffas[29], E. Koffeman[106], L. A. Kogan[119], S. Kohlmann[176], Z. Kohout[127], T. Kohriki[65], T. Koi[144], H. Kolanoski[16], I. Koletsou[5], J. Koll[89], A. A. Komar[95,*], Y. Komori[156], T. Kondo[65], N. Kondrashova[42], K. Köneke[48], A. C. König[105], S. König[82], T. Kono[65,r], R. Konoplich[109,s], N. Konstantinidis[77], R. Kopeliansky[153], S. Koperny[38a], L. Köpke[82], A. K. Kopp[48], K. Korcyl[39], K. Kordas[155], A. Korn[77], A. A. Korol[108,t], I. Korolkov[12], E. V. Korolkova[140], V. A. Korotkov[129], O. Kortner[100], S. Kortner[100], V. V. Kostyukhin[21], V. M. Kotov[64], A. Kotwal[45], C. Kourkoumelis[9], V. Kouskoura[155], A. Koutsman[160a], R. Kowalewski[170], T. Z. Kowalski[38a], W. Kozanecki[137], A. S. Kozhin[129], V. Kral[127], V. A. Kramarenko[98], G. Kramberger[74], D. Krasnopevtsev[97], M. W. Krasny[79], A. Krasznahorkay[30], J. K. Kraus[21], A. Kravchenko[25], S. Kreiss[109], M. Kretz[58c], J. Kretzschmar[73], K. Kreutzfeldt[52], P. Krieger[159], K. Kroeninger[54], H. Kroha[100], J. Kroll[121], J. Kroseberg[21], J. Krstic[13a], U. Kruchonak[64], H. Krüger[21], T. Kruker[17], N. Krumnack[63], Z. V. Krumshteyn[64], A. Kruse[174], M. C. Kruse[45], M. Kruskal[22], T. Kubota[87], S. Kuday[4a], S. Kuehn[48], A. Kugel[58c], A. Kuhl[138], T. Kuhl[42], V. Kukhtin[64], Y. Kulchitsky[91], S. Kuleshov[32b], M. Kuna[133a,133b], J. Kunkle[121], A. Kupco[126], H. Kurashige[66], Y. A. Kurochkin[91], R. Kurumida[66], V. Kus[126], E. S. Kuwertz[148], M. Kuze[158], J. Kvita[114], A. La Rosa[49], L. La Rotonda[37a,37b], C. Lacasta[168], F. Lacava[133a,133b], J. Lacey[29], H. Lacker[16], D. Lacour[79], V. R. Lacuesta[168], E. Ladygin[64], R. Lafaye[5], B. Laforge[79], T. Lagouri[177], S. Lai[48], H. Laier[58a], L. Lambourne[77], S. Lammers[60], C. L. Lampen[7], W. Lampl[7], E. Lançon[137], U. Landgraf[48], M. P. J. Landon[75], V. S. Lang[58a], C. Lange[42], A. J. Lankford[164], F. Lanni[25], K. Lantzsch[30], S. Laplace[79], C. Lapoire[21], J. F. Laporte[137], T. Lari[90a], M. Lassnig[30], P. Laurelli[47], W. Lavrijsen[15], A. T. Law[138], P. Laycock[73], B. T. Le[55], O. Le Dortz[79], E. Le Guirriec[84], E. Le Menedeu[12], T. LeCompte[6], F. Ledroit-Guillon[55], C. A. Lee[152], H. Lee[106], J. S. H. Lee[117], S. C. Lee[152], L. Lee[177], G. Lefebvre[79], M. Lefebvre[170], F. Legger[99], C. Leggett[15], A. Lehan[73], M. Lehmacher[21], G. Lehmann Miotto[30], X. Lei[7], W. A. Leight[29], A. Leisos[155], A. G. Leister[177], M. A. L. Leite[24d], R. Leitner[128], D. Lellouch[173], B. Lemmer[54], K. J. C. Leney[77], T. Lenz[106], G. Lenzen[176], B. Lenzi[30], R. Leone[7], K. Leonhardt[44], S. Leontsinis[10], C. Leroy[94], C. G. Lester[28], C. M. Lester[121], M. Levchenko[122], J. Levêque[5], D. Levin[88], L. J. Levinson[173], M. Levy[18], A. Lewis[119], G. H. Lewis[109], A. M. Leyko[21], M. Leyton[41], B. Li[33b,u], B. Li[84], H. Li[149], H. L. Li[31], L. Li[45], L. Li[33e], S. Li[45], Y. Li[33c,v], Z. Liang[138], H. Liao[34], B. Liberti[134a], P. Lichard[30], K. Lie[166], J. Liebal[21], W. Liebig[14], C. Limbach[21], A. Limosani[87], S. C. Lin[152,w], T. H. Lin[82], F. Linde[106], B. E. Lindquist[149], J. T. Linnemann[89], E. Lipeles[121], A. Lipniacka[14], M. Lisovyi[42], T. M. Liss[166], D. Lissauer[25], A. Lister[169], A. M. Litke[138], B. Liu[152], D. Liu[152], J. B. Liu[33b], K. Liu[33b,x], L. Liu[88], M. Liu[45], M. Liu[33b], Y. Liu[33b], M. Livan[120a,120b], S. S. A. Livermore[119], A. Lleres[55], J. Llorente Merino[81], S. L. Lloyd[75], F. Lo Sterzo[152], E. Lobodzinska[42], P. Loch[7], W. S. Lockman[138], T. Loddenkoetter[21], F. K. Loebinger[83], A. E. Loevschall-Jensen[36], A. Loginov[177], C. W. Loh[169], T. Lohse[16], K. Lohwasser[42], M. Lokajicek[126], V. P. Lombardo[5], B. A. Long[22], J. D. Long[88], R. E. Long[71], L. Lopes[125a],

D. Lopez Mateos[57], B. Lopez Paredes[140], I. Lopez Paz[12], J. Lorenz[99], N. Lorenzo Martinez[60], M. Losada[163], P. Loscutoff[15], X. Lou[41], A. Lounis[116], J. Love[6], P. A. Love[71], A. J. Lowe[144,e], F. Lu[33a], H. J. Lubatti[139], C. Luci[133a,133b], A. Lucotte[55], F. Luehring[60], W. Lukas[61], L. Luminari[133a], O. Lundberg[147a,147b], B. Lund-Jensen[148], M. Lungwitz[82], D. Lynn[25], R. Lysak[126], E. Lytken[80], H. Ma[25], L. L. Ma[33d], G. Maccarrone[47], A. Macchiolo[100], J. Machado Miguens[125a,125b], D. Macina[30], D. Madaffari[84], R. Madar[48], H. J. Maddocks[71], W. F. Mader[44], A. Madsen[167], M. Maeno[8], T. Maeno[25], E. Magradze[54], K. Mahboubi[48], J. Mahlstedt[106], S. Mahmoud[73], C. Maiani[137], C. Maidantchik[24a], A. Maio[125a,125b,125d], S. Majewski[115], Y. Makida[65], N. Makovec[116], P. Mal[137,y], B. Malaescu[79], Pa. Malecki[39], V. P. Maleev[122], F. Malek[55], U. Mallik[62], D. Malon[6], C. Malone[144], S. Maltezos[10], V. M. Malyshev[108], S. Malyukov[30], J. Mamuzic[13b], B. Mandelli[30], L. Mandelli[90a], I. Mandić[74], R. Mandrysch[62], J. Maneira[125a,125b], A. Manfredini[100], L. Manhaes de Andrade Filho[24b], J. A. Manjarres Ramos[160b], A. Mann[99], P. M. Manning[138], A. Manousakis-Katsikakis[9], B. Mansoulie[137], R. Mantifel[86], L. Mapelli[30], L. March[168], J. F. Marchand[29], G. Marchiori[79], M. Marcisovsky[126], C. P. Marino[170], M. Marjanovic[13a], C. N. Marques[125a], F. Marroquim[24a], S. P. Marsden[83], Z. Marshall[15], L. F. Marti[17], S. Marti-Garcia[168], B. Martin[30], B. Martin[89], T. A. Martin[171], V. J. Martin[46], B. Martin dit Latour[14], H. Martinez[137], M. Martinez[12,n], S. Martin-Haugh[130], A. C. Martyniuk[77], M. Marx[139], F. Marzano[133a], A. Marzin[30], L. Masetti[82], T. Mashimo[156], R. Mashinistov[95], J. Masik[83], A. L. Maslennikov[108], I. Massa[20a,20b], N. Massol[5], P. Mastrandrea[149], A. Mastroberardino[37a,37b], T. Masubuchi[156], T. Matsushita[66], P. Mättig[176], J. Mattmann[82], J. Maurer[26a], S. J. Maxfield[73], D. A. Maximov[108,t], R. Mazini[152], L. Mazzaferro[134a,134b], G. Mc Goldrick[159], S. P. Mc Kee[88], A. McCarn[88], R. L. McCarthy[149], T. G. McCarthy[29], N. A. McCubbin[130], K. W. McFarlane[56,*], J. A. Mcfayden[77], G. Mchedlidze[54], S. J. McMahon[130], R. A. McPherson[170,i], A. Meade[85], J. Mechnich[106], M. Medinnis[42], S. Meehan[31], S. Mehlhase[36], A. Mehta[73], K. Meier[58a], C. Meineck[99], B. Meirose[80], C. Melachrinos[31], B. R. Mellado Garcia[146c], F. Meloni[90a,90b], A. Mengarelli[20a,20b], S. Menke[100], E. Meoni[162], K. M. Mercurio[57], S. Mergelmeyer[21], N. Meric[137], P. Mermod[49], L. Merola[103a,103b], C. Meroni[90a], F. S. Merritt[31], H. Merritt[110], A. Messina[30,z], J. Metcalfe[25], A. S. Mete[164], C. Meyer[82], C. Meyer[31], J-P. Meyer[137], J. Meyer[30], R. P. Middleton[130], S. Migas[73], L. Mijović[21], G. Mikenberg[173], M. Mikestikova[126], M. Mikuž[74], A. Milic[30], D. W. Miller[31], C. Mills[46], A. Milov[173], D. A. Milstead[147a,147b], D. Milstein[173], A. A. Minaenko[129], I. A. Minashvili[64], A. I. Mincer[109], B. Mindur[38a], M. Mineev[64], Y. Ming[174], L. M. Mir[12], G. Mirabelli[133a], T. Mitani[172], J. Mitrevski[99], V. A. Mitsou[168], S. Mitsui[65], A. Miucci[49], P. S. Miyagawa[140], J. U. Mjörnmark[80], T. Moa[147a,147b], K. Mochizuki[84], V. Moeller[28], S. Mohapatra[35], W. Mohr[48], S. Molander[147a,147b], R. Moles-Valls[168], K. Mönig[42], C. Monini[55], J. Monk[36], E. Monnier[84], J. Montejo Berlingen[12], F. Monticelli[70], S. Monzani[133a,133b], R. W. Moore[3], A. Moraes[53], N. Morange[62], D. Moreno[82], M. Moreno Llácer[54], P. Morettini[50a], M. Morgenstern[44], M. Morii[57], S. Moritz[82], A. K. Morley[148], G. Mornacchi[30], J. D. Morris[75], L. Morvaj[102], H. G. Moser[100], M. Mosidze[51b], J. Moss[110], R. Mount[144], E. Mountricha[25], S. V. Mouraviev[95,*], E. J. W. Moyse[85], S. Muanza[84], R. D. Mudd[18], F. Mueller[58a], J. Mueller[124], K. Mueller[21], T. Mueller[28], T. Mueller[82], D. Muenstermann[49], Y. Munwes[154], J. A. Murillo Quijada[18], W. J. Murray[171,130], H. Musheghyan[54], E. Musto[153], A. G. Myagkov[129,aa], M. Myska[127], O. Nackenhorst[54], J. Nadal[54], K. Nagai[61], R. Nagai[158], Y. Nagai[84], K. Nagano[65], A. Nagarkar[110], Y. Nagasaka[59], M. Nagel[100], A. M. Nairz[30], Y. Nakahama[30], K. Nakamura[65], T. Nakamura[156], I. Nakano[111], H. Namasivayam[41], G. Nanava[21], R. Narayan[58b], T. Nattermann[21], T. Naumann[42], G. Navarro[163], R. Nayyar[7], H. A. Neal[88], P. Yu. Nechaeva[95], T. J. Neep[83], A. Negri[120a,120b], G. Negri[30], M. Negrini[20a], S. Nektarijevic[49], A. Nelson[164], T. K. Nelson[144], S. Nemecek[126], P. Nemethy[109], A. A. Nepomuceno[24a], M. Nessi[30,ab], M. S. Neubauer[166], M. Neumann[176], R. M. Neves[109], P. Nevski[25], P. R. Newman[18], D. H. Nguyen[6], R. B. Nickerson[119], R. Nicolaidou[137], B. Nicquevert[30], J. Nielsen[138], N. Nikiforou[35], A. Nikiforov[16], V. Nikolaenko[129,aa], I. Nikolic-Audit[79], K. Nikolics[49], K. Nikolopoulos[18], P. Nilsson[8], Y. Ninomiya[156], A. Nisati[133a], R. Nisius[100], T. Nobe[158], L. Nodulman[6], M. Nomachi[117], I. Nomidis[155], S. Norberg[112], M. Nordberg[30], S. Nowak[100], M. Nozaki[65], L. Nozka[114], K. Ntekas[10], G. Nunes Hanninger[87], T. Nunnemann[99], E. Nurse[77], F. Nuti[87], B. J. O'Brien[46], F. O'grady[7], D. C. O'Neil[143], V. O'Shea[53], F. G. Oakham[29,d], H. Oberlack[100], T. Obermann[21], J. Ocariz[79], A. Ochi[66], M. I. Ochoa[77], S. Oda[69], S. Odaka[65], H. Ogren[60], A. Oh[83], S. H. Oh[45], C. C. Ohm[30], H. Ohman[167], T. Ohshima[102], W. Okamura[117], H. Okawa[25], Y. Okumura[31], T. Okuyama[156], A. Olariu[26a], A. G. Olchevski[64], S. A. Olivares Pino[46], D. Oliveira Damazio[25], E. Oliver Garcia[168], A. Olszewski[39], J. Olszowska[39], A. Onofre[125a,125e], P. U. E. Onyisi[31,o], C. J. Oram[160a], M. J. Oreglia[31], Y. Oren[154], D. Orestano[135a,135b], N. Orlando[72a,72b], C. Oropeza Barrera[53], R. S. Orr[159], B. Osculati[50a,50b], R. Ospanov[121], G. Otero y Garzon[27], H. Otono[69], M. Ouchrif[136d], E. A. Ouellette[170], F. Ould-Saada[118], A. Ouraou[137], K. P. Oussoren[106], Q. Ouyang[33a], A. Ovcharova[15], M. Owen[83], V. E. Ozcan[19a], N. Ozturk[8], K. Pachal[119], A. Pacheco Pages[12], C. Padilla Aranda[12], M. Pagáčová[48], S. Pagan Griso[15], E. Paganis[140], C. Pahl[100], F. Paige[25], P. Pais[85], K. Pajchel[118], G. Palacino[160b], S. Palestini[30], M. Palka[38b], D. Pallin[34], A. Palma[125a,125b], J. D. Palmer[18], Y. B. Pan[174], E. Panagiotopoulou[10], J. G. Panduro Vazquez[76], P. Pani[106], N. Panikashvili[88], S. Panitkin[25], D. Pantea[26a], L. Paolozzi[134a,134b], Th. D. Papadopoulou[10], K. Papageorgiou[155,l], A. Paramonov[6], D. Paredes Hernandez[34],

M. A. Parker[28], F. Parodi[50a,50b], J. A. Parsons[35], U. Parzefall[48], E. Pasqualucci[133a], S. Passaggio[50a], A. Passeri[135a], F. Pastore[135a,135b,*], Fr. Pastore[76], G. Pásztor[29], S. Pataraia[176], N. D. Patel[151], J. R. Pater[83], S. Patricelli[103a,103b], T. Pauly[30], J. Pearce[170], M. Pedersen[118], S. Pedraza Lopez[168], R. Pedro[125a,125b], S. V. Peleganchuk[108], D. Pelikan[167], H. Peng[33b], B. Penning[31], J. Penwell[60], D. V. Perepelitsa[25], E. Perez Codina[160a], M. T. Pérez García-Estañ[168], V. Perez Reale[35], L. Perini[90a,90b], H. Pernegger[30], R. Perrino[72a], R. Peschke[42], V. D. Peshekhonov[64], K. Peters[30], R. F. Y. Peters[83], B. A. Petersen[30], T. C. Petersen[36], E. Petit[42], A. Petridis[147a,147b], C. Petridou[155], E. Petrolo[133a], F. Petrucci[135a,135b], M. Petteni[143], N. E. Pettersson[158], R. Pezoa[32b], P. W. Phillips[130], G. Piacquadio[144], E. Pianori[171], A. Picazio[49], E. Piccaro[75], M. Piccinini[20a,20b], R. Piegaia[27], D. T. Pignotti[110], J. E. Pilcher[31], A. D. Pilkington[77], J. Pina[125a,125b,125d], M. Pinamonti[165a,165c,ac], A. Pinder[119], J. L. Pinfold[3], A. Pingel[36], B. Pinto[125a], S. Pires[79], M. Pitt[173], C. Pizio[90a,90b], L. Plazak[145a], M.-A. Pleier[25], V. Pleskot[128], E. Plotnikova[64], P. Plucinski[147a,147b], S. Poddar[58a], F. Podlyski[34], R. Poettgen[82], L. Poggioli[116], D. Pohl[21], M. Pohl[49], G. Polesello[120a], A. Policicchio[37a,37b], R. Polifka[159], A. Polini[20a], C. S. Pollard[45], V. Polychronakos[25], K. Pommès[30], L. Pontecorvo[133a], B. G. Pope[89], G. A. Popeneciu[26b], D. S. Popovic[13a], A. Poppleton[30], X. Portell Bueso[12], G. E. Pospelov[100], S. Pospisil[127], K. Potamianos[15], I. N. Potrap[64], C. J. Potter[150], C. T. Potter[115], G. Poulard[30], J. Poveda[60], V. Pozdnyakov[64], P. Pralavorio[84], A. Pranko[15], S. Prasad[30], R. Pravahan[8], S. Prell[63], D. Price[83], J. Price[73], L. E. Price[6], D. Prieur[124], M. Primavera[72a], M. Proissl[46], K. Prokofiev[47], F. Prokoshin[32b], E. Protopapadaki[137], S. Protopopescu[25], J. Proudfoot[6], M. Przybycien[38a], H. Przysiezniak[5], E. Ptacek[115], E. Pueschel[85], D. Puldon[149], M. Purohit[25,ad], P. Puzo[116], J. Qian[88], G. Qin[53], Y. Qin[83], A. Quadt[54], D. R. Quarrie[15], W. B. Quayle[165a,165b], M. Queitsch-Maitland[83], D. Quilty[53], A. Qureshi[160b], V. Radeka[25], V. Radescu[42], S. K. Radhakrishnan[149], P. Radloff[115], P. Rados[87], F. Ragusa[90a,90b], G. Rahal[179], S. Rajagopalan[25], M. Rammensee[30], A. S. Randle-Conde[40], C. Rangel-Smith[167], K. Rao[164], F. Rauscher[99], T. C. Rave[48], T. Ravenscroft[53], M. Raymond[30], A. L. Read[118], N. P. Readioff[73], D. M. Rebuzzi[120a,120b], A. Redelbach[175], G. Redlinger[25], R. Reece[138], K. Reeves[41], L. Rehnisch[16], H. Reisin[27], M. Relich[164], C. Rembser[30], H. Ren[33a], Z. L. Ren[152], A. Renaud[116], M. Rescigno[133a], S. Resconi[90a], O. L. Rezanova[108,t], P. Reznicek[128], R. Rezvani[94], R. Richter[100], M. Ridel[79], P. Rieck[16], J. Rieger[54], M. Rijssenbeek[149], A. Rimoldi[120a,120b], L. Rinaldi[20a], E. Ritsch[61], I. Riu[12], F. Rizatdinova[113], E. Rizvi[75], S. H. Robertson[86,i], A. Robichaud-Veronneau[86], D. Robinson[28], J. E. M. Robinson[83], A. Robson[53], C. Roda[123a,123b], L. Rodrigues[30], S. Roe[30], O. Røhne[118], S. Rolli[162], A. Romaniouk[97], M. Romano[20a,20b], G. Romeo[27], E. Romero Adam[168], N. Rompotis[139], L. Roos[79], E. Ros[168], S. Rosati[133a], K. Rosbach[49], M. Rose[76], P. L. Rosendahl[14], O. Rosenthal[142], V. Rossetti[147a,147b], E. Rossi[103a,103b], L. P. Rossi[50a], R. Rosten[139], M. Rotaru[26a], I. Roth[173], J. Rothberg[139], D. Rousseau[116], C. R. Royon[137], A. Rozanov[84], Y. Rozen[153], X. Ruan[146c], F. Rubbo[12], I. Rubinskiy[42], V. I. Rud[98], C. Rudolph[44], M. S. Rudolph[159], F. Rühr[48], A. Ruiz-Martinez[30], Z. Rurikova[48], N. A. Rusakovich[64], A. Ruschke[99], J. P. Rutherfoord[7], N. Ruthmann[48], Y. F. Ryabov[122], M. Rybar[128], G. Rybkin[116], N. C. Ryder[119], A. F. Saavedra[151], S. Sacerdoti[27], A. Saddique[3], I. Sadeh[154], H. F-W. Sadrozinski[138], R. Sadykov[64], F. Safai Tehrani[133a], H. Sakamoto[156], Y. Sakurai[172], G. Salamanna[75], A. Salamon[134a], M. Saleem[112], D. Salek[106], P. H. Sales De Bruin[139], D. Salihagic[100], A. Salnikov[144], J. Salt[168], B. M. Salvachua Ferrando[6], D. Salvatore[37a,37b], F. Salvatore[150], A. Salvucci[105], A. Salzburger[30], D. Sampsonidis[155], A. Sanchez[103a,103b], J. Sánchez[168], V. Sanchez Martinez[168], H. Sandaker[14], R. L. Sandbach[75], H. G. Sander[82], M. P. Sanders[99], M. Sandhoff[176], T. Sandoval[28], C. Sandoval[163], R. Sandstroem[100], D. P. C. Sankey[130], A. Sansoni[47], C. Santoni[34], R. Santonico[134a,134b], H. Santos[125a], I. Santoyo Castillo[150], K. Sapp[124], A. Sapronov[64], J. G. Saraiva[125a,125d], B. Sarrazin[21], G. Sartisohn[176], O. Sasaki[65], Y. Sasaki[156], G. Sauvage[5,*], E. Sauvan[5], P. Savard[159,d], D. O. Savu[30], C. Sawyer[119], L. Sawyer[78,m], D. H. Saxon[53], J. Saxon[121], C. Sbarra[20a], A. Sbrizzi[3], T. Scanlon[77], D. A. Scannicchio[164], M. Scarcella[151], J. Schaarschmidt[173], P. Schacht[100], D. Schaefer[121], R. Schaefer[42], S. Schaepe[21], S. Schaetzel[58b], U. Schäfer[82], A. C. Schaffer[116], D. Schaile[99], R. D. Schamberger[149], V. Scharf[58a], V. A. Schegelsky[122], D. Scheirich[128], M. Schernau[164], M. I. Scherzer[35], C. Schiavi[50a,50b], J. Schieck[99], C. Schillo[48], M. Schioppa[37a,37b], S. Schlenker[30], E. Schmidt[48], K. Schmieden[30], C. Schmitt[82], S. Schmitt[58b], B. Schneider[17], Y. J. Schnellbach[73], U. Schnoor[44], L. Schoeffel[137], A. Schoening[58b], B. D. Schoenrock[89], A. L. S. Schorlemmer[54], M. Schott[82], D. Schouten[160a], J. Schovancova[25], S. Schramm[159], M. Schreyer[175], C. Schroeder[82], N. Schuh[82], M. J. Schultens[21], H.-C. Schultz-Coulon[58a], H. Schulz[16], M. Schumacher[48], B. A. Schumm[138], Ph. Schune[137], C. Schwanenberger[83], A. Schwartzman[144], Ph. Schwegler[100], Ph. Schwemling[137], R. Schwienhorst[89], J. Schwindling[137], T. Schwindt[21], M. Schwoerer[5], F. G. Sciacca[17], E. Scifo[116], G. Sciolla[23], W. G. Scott[130], F. Scuri[123a,123b], F. Scutti[21], J. Searcy[88], G. Sedov[42], E. Sedykh[122], S. C. Seidel[104], A. Seiden[138], F. Seifert[127], J. M. Seixas[24a], G. Sekhniaidze[103a], S. J. Sekula[40], K. E. Selbach[46], D. M. Seliverstov[122,*], G. Sellers[73], N. Semprini-Cesari[20a,20b], C. Serfon[30], L. Serin[116], L. Serkin[54], T. Serre[84], R. Seuster[160a], H. Severini[112], F. Sforza[100], A. Sfyrla[30], E. Shabalina[54], M. Shamim[115], L. Y. Shan[33a], R. Shang[166], J. T. Shank[22], Q. T. Shao[87], M. Shapiro[15], P. B. Shatalov[96], K. Shaw[165a,165b], C. Y. Shehu[150], P. Sherwood[77], L. Shi[152,ae], S. Shimizu[66], C. O. Shimmin[164], M. Shimojima[101], M. Shiyakova[64], A. Shmeleva[95], M. J. Shochet[31], D. Short[119], S. Shrestha[63], E. Shulga[97], M. A. Shupe[7],

S. Shushkevich[42], P. Sicho[126], O. Sidiropoulou[155], D. Sidorov[113], A. Sidoti[133a], F. Siegert[44], Dj. Sijacki[13a], J. Silva[125a,125d], Y. Silver[154], D. Silverstein[144], S. B. Silverstein[147a], V. Simak[127], O. Simard[5], Lj. Simic[13a], S. Simion[116], E. Simioni[82], B. Simmons[77], R. Simoniello[90a,90b], M. Simonyan[36], P. Sinervo[159], N. B. Sinev[115], V. Sipica[142], G. Siragusa[175], A. Sircar[78], A. N. Sisakyan[64,*], S. Yu. Sivoklokov[98], J. Sjölin[147a,147b], T. B. Sjursen[14], H. P. Skottowe[57], K. Yu. Skovpen[108], P. Skubic[112], M. Slater[18], T. Slavicek[127], K. Sliwa[162], V. Smakhtin[173], B. H. Smart[46], L. Smestad[14], S. Yu. Smirnov[97], Y. Smirnov[97], L. N. Smirnova[98,af], O. Smirnova[80], K. M. Smith[53], M. Smizanska[71], K. Smolek[127], A. A. Snesarev[95], G. Snidero[75], S. Snyder[25], R. Sobie[170,i], F. Socher[44], A. Soffer[154], D. A. Soh[152,ae], C. A. Solans[30], M. Solar[127], J. Solc[127], E. Yu. Soldatov[97], U. Soldevila[168], E. Solfaroli Camillocci[133a,133b], A. A. Solodkov[129], A. Soloshenko[64], O. V. Solovyanov[129], V. Solovyev[122], P. Sommer[48], H. Y. Song[33b], N. Soni[1], A. Sood[15], A. Sopczak[127], B. Sopko[127], V. Sopko[127], V. Sorin[12], M. Sosebee[8], R. Soualah[165a,165c], P. Soueid[94], A. M. Soukharev[108], D. South[42], S. Spagnolo[72a,72b], F. Spanò[76], W. R. Spearman[57], R. Spighi[20a], G. Spigo[30], M. Spousta[128], T. Spreitzer[159], B. Spurlock[8], R. D. St. Denis[53,*], S. Staerz[44], J. Stahlman[121], R. Stamen[58a], E. Stanecka[39], R. W. Stanek[6], C. Stanescu[135a], M. Stanescu-Bellu[42], M. M. Stanitzki[42], S. Stapnes[118], E. A. Starchenko[129], J. Stark[55], P. Staroba[126], P. Starovoitov[42], R. Staszewski[39], P. Stavina[145a,*], P. Steinberg[25], B. Stelzer[143], H. J. Stelzer[30], O. Stelzer-Chilton[160a], H. Stenzel[52], S. Stern[100], G. A. Stewart[53], J. A. Stillings[21], M. C. Stockton[86], M. Stoebe[86], G. Stoicea[26a], P. Stolte[54], S. Stonjek[100], A. R. Stradling[8], A. Straessner[44], M. E. Stramaglia[17], J. Strandberg[148], S. Strandberg[147a,147b], A. Strandlie[118], E. Strauss[144], M. Strauss[112], P. Strizenec[145b], R. Ströhmer[175], D. M. Strom[115], R. Stroynowski[40], S. A. Stucci[17], B. Stugu[14], N. A. Styles[42], D. Su[144], J. Su[124], HS. Subramania[3], R. Subramaniam[78], A. Succurro[12], Y. Sugaya[117], C. Suhr[107], M. Suk[127], V. V. Sulin[95], S. Sultansoy[4c], T. Sumida[67], X. Sun[33a], J. E. Sundermann[48], K. Suruliz[140], G. Susinno[37a,37b], M. R. Sutton[150], Y. Suzuki[65], M. Svatos[126], S. Swedish[169], M. Swiatlowski[144], I. Sykora[145a], T. Sykora[128], D. Ta[89], K. Tackmann[42], J. Taenzer[159], A. Taffard[164], R. Tafirout[160a], N. Taiblum[154], Y. Takahashi[102], H. Takai[25], R. Takashima[68], H. Takeda[66], T. Takeshita[141], Y. Takubo[65], M. Talby[84], A. A. Talyshev[108,t], J. Y. C. Tam[175], K. G. Tan[87], J. Tanaka[156], R. Tanaka[116], S. Tanaka[132], S. Tanaka[65], A. J. Tanasijczuk[143], K. Tani[66], N. Tannoury[21], S. Tapprogge[82], S. Tarem[153], F. Tarrade[29], G. F. Tartarelli[90a], P. Tas[128], M. Tasevsky[126], T. Tashiro[67], E. Tassi[37a,37b], A. Tavares Delgado[125a,125b], Y. Tayalati[136d], F. E. Taylor[93], G. N. Taylor[87], W. Taylor[160b], F. A. Teischinger[30], M. Teixeira Dias Castanheira[75], P. Teixeira-Dias[76], K. K. Temming[48], H. Ten Kate[30], P. K. Teng[152], J. J. Teoh[117], S. Terada[65], K. Terashi[156], J. Terron[81], S. Terzo[100], M. Testa[47], R. J. Teuscher[159,i], J. Therhaag[21], T. Theveneaux-Pelzer[34], J. P. Thomas[18], J. Thomas-Wilsker[76], E. N. Thompson[35], P. D. Thompson[18], P. D. Thompson[159], R. J. Thompson[83], A. S. Thompson[53], L. A. Thomsen[36], E. Thomson[121], M. Thomson[28], W. M. Thong[87], R. P. Thun[88,*], F. Tian[35], M. J. Tibbetts[15], V. O. Tikhomirov[95,ag], Yu. A. Tikhonov[108,t], S. Timoshenko[97], E. Tiouchichine[84], P. Tipton[177], S. Tisserant[84], T. Todorov[5], S. Todorova-Nova[128], B. Toggerson[7], J. Tojo[69], S. Tokár[145a], K. Tokushuku[65], K. Tollefson[89], L. Tomlinson[83], M. Tomoto[102], L. Tompkins[31], K. Toms[104], N. D. Topilin[64], E. Torrence[115], H. Torres[143], E. Torró Pastor[168], J. Toth[84,ah], F. Touchard[84], D. R. Tovey[140], H. L. Tran[116], T. Trefzger[175], L. Tremblet[30], A. Tricoli[30], I. M. Trigger[160a], S. Trincaz-Duvoid[79], M. F. Tripiana[70], N. Triplett[25], W. Trischuk[159], B. Trocmé[55], C. Troncon[90a], M. Trottier-McDonald[143], M. Trovatelli[135a,135b], P. True[89], M. Trzebinski[39], A. Trzupek[39], C. Tsarouchas[30], J. C-L. Tseng[119], P. V. Tsiareshka[91], D. Tsionou[137], G. Tsipolitis[10], N. Tsirintanis[9], S. Tsiskaridze[12], V. Tsiskaridze[48], E. G. Tskhadadze[51a], I. I. Tsukerman[96], V. Tsulaia[15], S. Tsuno[65], D. Tsybychev[149], A. Tudorache[26a], V. Tudorache[26a], A. N. Tuna[121], S. A. Tupputi[20a,20b], S. Turchikhin[98,af], D. Turecek[127], I. Turk Cakir[4d], R. Turra[90a,90b], P. M. Tuts[35], A. Tykhonov[74], M. Tylmad[147a,147b], M. Tyndel[130], K. Uchida[21], I. Ueda[156], R. Ueno[29], M. Ughetto[84], M. Ugland[14], M. Uhlenbrock[21], F. Ukegawa[161], G. Unal[30], A. Undrus[25], G. Unel[164], F. C. Ungaro[48], Y. Unno[65], C. Unverdorben[99], D. Urbaniec[35], P. Urquijo[87], G. Usai[8], A. Usanova[61], L. Vacavant[84], V. Vacek[127], B. Vachon[86], N. Valencic[106], S. Valentinetti[20a,20b], A. Valero[168], L. Valery[34], S. Valkar[128], E. Valladolid Gallego[168], S. Vallecorsa[49], J. A. Valls Ferrer[168], P. C. Van Der Deijl[106], R. van der Geer[106], H. van der Graaf[106], R. Van Der Leeuw[106], D. van der Ster[30], N. van Eldik[30], P. van Gemmeren[6], J. Van Nieuwkoop[143], I. van Vulpen[106], M. C. van Woerden[30], M. Vanadia[133a,133b], W. Vandelli[30], R. Vanguri[121], A. Vaniachine[6], P. Vankov[42], F. Vannucci[79], G. Vardanyan[178], R. Vari[133a], E. W. Varnes[7], T. Varol[85], D. Varouchas[79], A. Vartapetian[8], K. E. Varvell[151], F. Vazeille[34], T. Vazquez Schroeder[54], J. Veatch[7], F. Veloso[125a,125c], S. Veneziano[133a], A. Ventura[72a,72b], D. Ventura[85], M. Venturi[170], N. Venturi[159], A. Venturini[23], V. Vercesi[120a], M. Verducci[139], W. Verkerke[106], J. C. Vermeulen[106], A. Vest[44], M. C. Vetterli[143,d], O. Viazlo[80], I. Vichou[166], T. Vickey[146c,ai], O. E. Vickey Boeriu[146c], G. H. A. Viehhauser[119], S. Viel[169], R. Vigne[30], M. Villa[20a,20b], M. Villaplana Perez[90a,90b], E. Vilucchi[47], M. G. Vincter[29], V. B. Vinogradov[64], J. Virzi[15], I. Vivarelli[150], F. Vives Vaque[3], S. Vlachos[10], D. Vladoiu[99], M. Vlasak[127], A. Vogel[21], M. Vogel[32a], P. Vokac[127], G. Volpi[123a,123b], M. Volpi[87], H. von der Schmitt[100], H. von Radziewski[48], E. von Toerne[21], V. Vorobel[128], K. Vorobev[97], M. Vos[168], R. Voss[30], J. H. Vossebeld[73], N. Vranjes[137], M. Vranjes Milosavljevic[106], V. Vrba[126], M. Vreeswijk[106], T. Vu Anh[48], R. Vuillermet[30], I. Vukotic[31], Z. Vykydal[127], P. Wagner[21], W. Wagner[176], H. Wahlberg[70], S. Wahrmund[44], J. Wakabayashi[102], J. Walder[71],

R. Walker[99], W. Walkowiak[142], R. Wall[177], P. Waller[73], B. Walsh[177], C. Wang[152,aj], C. Wang[45], F. Wang[174], H. Wang[15], H. Wang[40], J. Wang[42], J. Wang[33a], K. Wang[86], R. Wang[104], S. M. Wang[152], T. Wang[21], X. Wang[177], C. Wanotayaroj[115], A. Warburton[86], C. P. Ward[28], D. R. Wardrope[77], M. Warsinsky[48], A. Washbrook[46], C. Wasicki[42], I. Watanabe[66], P. M. Watkins[18], A. T. Watson[18], I. J. Watson[151], M. F. Watson[18], G. Watts[139], S. Watts[83], B. M. Waugh[77], S. Webb[83], M. S. Weber[17], S. W. Weber[175], J. S. Webster[31], A. R. Weidberg[119], P. Weigell[100], B. Weinert[60], J. Weingarten[54], C. Weiser[48], H. Weits[106], P. S. Wells[30], T. Wenaus[25], D. Wendland[16], Z. Weng[152,ae], T. Wengler[30], S. Wenig[30], N. Wermes[21], M. Werner[48], P. Werner[30], M. Wessels[58a], J. Wetter[162], K. Whalen[29], A. White[8], M. J. White[1], R. White[32b], S. White[123a,123b], D. Whiteson[164], D. Wicke[176], F. J. Wickens[130], W. Wiedenmann[174], M. Wielers[130], P. Wienemann[21], C. Wiglesworth[36], L. A. M. Wiik-Fuchs[21], P. A. Wijeratne[77], A. Wildauer[100], M. A. Wildt[42,ak], H. G. Wilkens[30], J. Z. Will[99], H. H. Williams[121], S. Williams[28], C. Willis[89], S. Willocq[85], A. Wilson[88], J. A. Wilson[18], I. Wingerter-Seez[5], F. Winklmeier[115], B. T. Winter[21], M. Wittgen[144], T. Wittig[43], J. Wittkowski[99], S. J. Wollstadt[82], M. W. Wolter[39], H. Wolters[125a,125c], B. K. Wosiek[39], J. Wotschack[30], M. J. Woudstra[83], K. W. Wozniak[39], M. Wright[53], M. Wu[55], S. L. Wu[174], X. Wu[49], Y. Wu[88], E. Wulf[35], T. R. Wyatt[83], B. M. Wynne[46], S. Xella[36], M. Xiao[137], D. Xu[33a], L. Xu[33b,al], B. Yabsley[151], S. Yacoob[146b,am], M. Yamada[65], H. Yamaguchi[156], Y. Yamaguchi[156], A. Yamamoto[65], K. Yamamoto[63], S. Yamamoto[156], T. Yamamura[156], T. Yamanaka[156], K. Yamauchi[102], Y. Yamazaki[66], Z. Yan[22], H. Yang[33e], H. Yang[174], U. K. Yang[83], Y. Yang[110], S. Yanush[92], L. Yao[33a], W-M. Yao[15], Y. Yasu[65], E. Yatsenko[42], K. H. Yau Wong[21], J. Ye[40], S. Ye[25], A. L. Yen[57], E. Yildirim[42], M. Yilmaz[4b], R. Yoosoofmiya[124], K. Yorita[172], R. Yoshida[6], K. Yoshihara[156], C. Young[144], C. J. S. Young[30], S. Youssef[22], D. R. Yu[15], J. Yu[8], J. M. Yu[88], J. Yu[113], L. Yuan[66], A. Yurkewicz[107], B. Zabinski[39], R. Zaidan[62], A. M. Zaitsev[129,aa], A. Zaman[149], S. Zambito[23], L. Zanello[133a,133b], D. Zanzi[100], C. Zeitnitz[176], M. Zeman[127], A. Zemla[38a], K. Zengel[23], O. Zenin[129], T. Ženiš[145a], D. Zerwas[116], G. Zevi della Porta[57], D. Zhang[88], F. Zhang[174], H. Zhang[89], J. Zhang[6], L. Zhang[152], X. Zhang[33d], Z. Zhang[116], Z. Zhao[33b], A. Zhemchugov[64], J. Zhong[119], B. Zhou[88], L. Zhou[35], N. Zhou[164], C. G. Zhu[33d], H. Zhu[33a], J. Zhu[88], Y. Zhu[33b], X. Zhuang[33a], K. Zhukov[95], A. Zibell[175], D. Zieminska[60], N. I. Zimine[64], C. Zimmermann[82], R. Zimmermann[21], S. Zimmermann[21], S. Zimmermann[48], Z. Zinonos[54], M. Ziolkowski[142], G. Zobernig[174], A. Zoccoli[20a,20b], M. zur Nedden[16], G. Zurzolo[103a,103b], V. Zutshi[107], L. Zwalinski[30]

[1] Department of Physics, University of Adelaide, Adelaide, Australia
[2] Physics Department, SUNY Albany, Albany, NY, USA
[3] Department of Physics, University of Alberta, Edmonton, AB, Canada
[4] (a) Department of Physics, Ankara University, Ankara, Turkey; (b) Department of Physics, Gazi University, Ankara, Turkey; (c) Division of Physics, TOBB University of Economics and Technology, Ankara, Turkey; (d) Turkish Atomic Energy Authority, Ankara, Turkey
[5] LAPP, CNRS/IN2P3 and Université de Savoie, Annecy-le-Vieux, France
[6] High Energy Physics Division, Argonne National Laboratory, Argonne, IL, USA
[7] Department of Physics, University of Arizona, Tucson, AZ, USA
[8] Department of Physics, The University of Texas at Arlington, Arlington, TX, USA
[9] Physics Department, University of Athens, Athens, Greece
[10] Physics Department, National Technical University of Athens, Zografou, Greece
[11] Institute of Physics, Azerbaijan Academy of Sciences, Baku, Azerbaijan
[12] Institut de Física d'Altes Energies and Departament de Física de la Universitat Autònoma de Barcelona, Barcelona, Spain
[13] (a) Institute of Physics, University of Belgrade, Belgrade, Serbia; (b) Vinca Institute of Nuclear Sciences, University of Belgrade, Belgrade, Serbia
[14] Department for Physics and Technology, University of Bergen, Bergen, Norway
[15] Physics Division, Lawrence Berkeley National Laboratory and University of California, Berkeley, CA, USA
[16] Department of Physics, Humboldt University, Berlin, Germany
[17] Albert Einstein Center for Fundamental Physics and Laboratory for High Energy Physics, University of Bern, Bern, Switzerland
[18] School of Physics and Astronomy, University of Birmingham, Birmingham, UK
[19] (a) Department of Physics, Bogazici University, Istanbul, Turkey; (b) Department of Physics, Dogus University, Istanbul, Turkey; (c) Department of Physics Engineering, Gaziantep University, Gaziantep, Turkey

[20] [(a)] INFN Sezione di Bologna, Bologna, Italy; [(b)] Dipartimento di Fisica e Astronomia, Università di Bologna, Bologna, Italy
[21] Physikalisches Institut, University of Bonn, Bonn, Germany
[22] Department of Physics, Boston University, Boston, MA, USA
[23] Department of Physics, Brandeis University, Waltham, MA, USA
[24] [(a)] Universidade Federal do Rio De Janeiro COPPE/EE/IF, Rio de Janeiro, Brazil; [(b)] Federal University of Juiz de Fora (UFJF), Juiz de Fora, Brazil; [(c)] Federal University of Sao Joao del Rei (UFSJ), Sao Joao del Rei, Brazil; [(d)] Instituto de Fisica, Universidade de Sao Paulo, São Paulo, Brazil
[25] Physics Department, Brookhaven National Laboratory, Upton, NY, USA
[26] [(a)] National Institute of Physics and Nuclear Engineering, Bucharest, Romania; [(b)] Physics Department, National Institute for Research and Development of Isotopic and Molecular Technologies, Cluj Napoca, Romania; [(c)] University Politehnica Bucharest, Bucharest, Romania; [(d)] West University in Timisoara, Timisoara, Romania
[27] Departamento de Física, Universidad de Buenos Aires, Buenos Aires, Argentina
[28] Cavendish Laboratory, University of Cambridge, Cambridge, UK
[29] Department of Physics, Carleton University, Ottawa, ON, Canada
[30] CERN, Geneva, Switzerland
[31] Enrico Fermi Institute, University of Chicago, Chicago, IL, USA
[32] [(a)] Departamento de Física, Pontificia Universidad Católica de Chile, Santiago, Chile; [(b)] Departamento de Física, Universidad Técnica Federico Santa María, Valparaiso, Chile
[33] [(a)] Institute of High Energy Physics, Chinese Academy of Sciences, Beijing, China; [(b)] Department of Modern Physics, University of Science and Technology of China, Hefei, Anhui, China; [(c)] Department of Physics, Nanjing University, Nanjing, Jiangsu, China; [(d)] School of Physics, Shandong University, Jinan, Shandong, China; [(e)] Physics Department, Shanghai Jiao Tong University, Shanghai, China
[34] Laboratoire de Physique Corpusculaire, Clermont Université and Université Blaise Pascal and CNRS/IN2P3, Clermont-Ferrand, France
[35] Nevis Laboratory, Columbia University, Irvington, NY, USA
[36] Niels Bohr Institute, University of Copenhagen, Copenhagen, Denmark
[37] [(a)] INFN Gruppo Collegato di Cosenza, Laboratori Nazionali di Frascati, Frascati, Italy; [(b)] Dipartimento di Fisica, Università della Calabria, Rende, Italy
[38] [(a)] AGH University of Science and Technology, Faculty of Physics and Applied Computer Science, Kraków, Poland; [(b)] Marian Smoluchowski Institute of Physics, Jagiellonian University, Kraków, Poland
[39] The Henryk Niewodniczanski Institute of Nuclear Physics, Polish Academy of Sciences, Kraków, Poland
[40] Physics Department, Southern Methodist University, Dallas, TX, USA
[41] Physics Department, University of Texas at Dallas, Richardson, TX, USA
[42] DESY, Hamburg and Zeuthen, Germany
[43] Institut für Experimentelle Physik IV, Technische Universität Dortmund, Dortmund, Germany
[44] Institut für Kern- und Teilchenphysik, Technische Universität Dresden, Dresden, Germany
[45] Department of Physics, Duke University, Durham, NC, USA
[46] SUPA-School of Physics and Astronomy, University of Edinburgh, Edinburgh, UK
[47] INFN Laboratori Nazionali di Frascati, Frascati, Italy
[48] Fakultät für Mathematik und Physik, Albert-Ludwigs-Universität, Freiburg, Germany
[49] Section de Physique, Université de Genève, Geneva, Switzerland
[50] [(a)] INFN Sezione di Genova, Genoa, Italy; [(b)] Dipartimento di Fisica, Università di Genova, Genova, Italy
[51] [(a)] E. Andronikashvili Institute of Physics, Iv. Javakhishvili Tbilisi State University, Tbilisi, Georgia; [(b)] High Energy Physics Institute, Tbilisi State University, Tbilisi, Georgia
[52] II Physikalisches Institut, Justus-Liebig-Universität Giessen, Giessen, Germany
[53] SUPA-School of Physics and Astronomy, University of Glasgow, Glasgow, UK
[54] II Physikalisches Institut, Georg-August-Universität, Göttingen, Germany
[55] Laboratoire de Physique Subatomique et de Cosmologie, Université Grenoble-Alpes, CNRS/IN2P3, Grenoble, France
[56] Department of Physics, Hampton University, Hampton, VA, USA
[57] Laboratory for Particle Physics and Cosmology, Harvard University, Cambridge, MA, USA

[58] [(a)] Kirchhoff-Institut für Physik, Ruprecht-Karls-Universität Heidelberg, Heidelberg, Germany; [(b)] Physikalisches Institut, Ruprecht-Karls-Universität Heidelberg, Heidelberg, Germany; [(c)] ZITI Institut für technische Informatik, Ruprecht-Karls-Universität Heidelberg, Mannheim, Germany
[59] Faculty of Applied Information Science, Hiroshima Institute of Technology, Hiroshima, Japan
[60] Department of Physics, Indiana University, Bloomington, IN, USA
[61] Institut für Astro- und Teilchenphysik, Leopold-Franzens-Universität, Innsbruck, Austria
[62] University of Iowa, Iowa City, IA, USA
[63] Department of Physics and Astronomy, Iowa State University, Ames, IA, USA
[64] Joint Institute for Nuclear Research, JINR Dubna, Dubna, Russia
[65] KEK, High Energy Accelerator Research Organization, Tsukuba, Japan
[66] Graduate School of Science, Kobe University, Kobe, Japan
[67] Faculty of Science, Kyoto University, Kyoto, Japan
[68] Kyoto University of Education, Kyoto, Japan
[69] Department of Physics, Kyushu University, Fukuoka, Japan
[70] Instituto de Física La Plata, Universidad Nacional de La Plata and CONICET, La Plata, Argentina
[71] Physics Department, Lancaster University, Lancaster, UK
[72] [(a)] INFN Sezione di Lecce, Lecce, Italy; [(b)] Dipartimento di Matematica e Fisica, Università del Salento, Lecce, Italy
[73] Oliver Lodge Laboratory, University of Liverpool, Liverpool, UK
[74] Department of Physics, Jožef Stefan Institute and University of Ljubljana, Ljubljana, Slovenia
[75] School of Physics and Astronomy, Queen Mary University of London, London, UK
[76] Department of Physics, Royal Holloway University of London, Surrey, UK
[77] Department of Physics and Astronomy, University College London, London, UK
[78] Louisiana Tech University, Ruston, LA, USA
[79] Laboratoire de Physique Nucléaire et de Hautes Energies, UPMC and Université Paris-Diderot and CNRS/IN2P3, Paris, France
[80] Fysiska institutionen, Lunds universitet, Lund, Sweden
[81] Departamento de Fisica Teorica C-15, Universidad Autonoma de Madrid, Madrid, Spain
[82] Institut für Physik, Universität Mainz, Mainz, Germany
[83] School of Physics and Astronomy, University of Manchester, Manchester, UK
[84] CPPM, Aix-Marseille Université and CNRS/IN2P3, Marseille, France
[85] Department of Physics, University of Massachusetts, Amherst, MA, USA
[86] Department of Physics, McGill University, Montreal, QC, Canada
[87] School of Physics, University of Melbourne, Parkville, VIC, Australia
[88] Department of Physics, The University of Michigan, Ann Arbor, MI, USA
[89] Department of Physics and Astronomy, Michigan State University, East Lansing, MI, USA
[90] [(a)] INFN Sezione di Milano, Milan, Italy; [(b)] Dipartimento di Fisica, Università di Milano, Milan, Italy
[91] B.I. Stepanov Institute of Physics, National Academy of Sciences of Belarus, Minsk, Republic of Belarus
[92] National Scientific and Educational Centre for Particle and High Energy Physics, Minsk, Republic of Belarus
[93] Department of Physics, Massachusetts Institute of Technology, Cambridge, MA, USA
[94] Group of Particle Physics, University of Montreal, Montreal, QC, Canada
[95] P.N. Lebedev Institute of Physics, Academy of Sciences, Moscow, Russia
[96] Institute for Theoretical and Experimental Physics (ITEP), Moscow, Russia
[97] Moscow Engineering and Physics Institute (MEPhI), Moscow, Russia
[98] D.V. Skobeltsyn Institute of Nuclear Physics, M.V. Lomonosov Moscow State University, Moscow, Russia
[99] Fakultät für Physik, Ludwig-Maximilians-Universität München, Munich, Germany
[100] Max-Planck-Institut für Physik (Werner-Heisenberg-Institut), Munich, Germany
[101] Nagasaki Institute of Applied Science, Nagasaki, Japan
[102] Graduate School of Science and Kobayashi-Maskawa Institute, Nagoya University, Nagoya, Japan
[103] [(a)] INFN Sezione di Napoli, Naples, Italy; [(b)] Dipartimento di Fisica, Università di Napoli, Naples, Italy
[104] Department of Physics and Astronomy, University of New Mexico, Albuquerque, NM, USA
[105] Institute for Mathematics, Astrophysics and Particle Physics, Radboud University Nijmegen/Nikhef, Nijmegen, The Netherlands
[106] Nikhef National Institute for Subatomic Physics and University of Amsterdam, Amsterdam, The Netherlands

[107] Department of Physics, Northern Illinois University, DeKalb, IL, USA
[108] Budker Institute of Nuclear Physics, SB RAS, Novosibirsk, Russia
[109] Department of Physics, New York University, New York, NY, USA
[110] Ohio State University, Columbus, OH, USA
[111] Faculty of Science, Okayama University, Okayama, Japan
[112] Homer L. Dodge Department of Physics and Astronomy, University of Oklahoma, Norman, OK, USA
[113] Department of Physics, Oklahoma State University, Stillwater, OK, USA
[114] Palacký University, RCPTM, Olomouc, Czech Republic
[115] Center for High Energy Physics, University of Oregon, Eugene, OR, USA
[116] LAL, Université Paris-Sud and CNRS/IN2P3, Orsay, France
[117] Graduate School of Science, Osaka University, Osaka, Japan
[118] Department of Physics, University of Oslo, Oslo, Norway
[119] Department of Physics, Oxford University, Oxford, UK
[120] [(a)] INFN Sezione di Pavia, Pavia, Italy; [(b)] Dipartimento di Fisica, Università di Pavia, Pavia, Italy
[121] Department of Physics, University of Pennsylvania, Philadelphia, PA, USA
[122] Petersburg Nuclear Physics Institute, Gatchina, Russia
[123] [(a)] INFN Sezione di Pisa, Pisa, Italy; [(b)] Dipartimento di Fisica E. Fermi, Università di Pisa, Pisa, Italy
[124] Department of Physics and Astronomy, University of Pittsburgh, Pittsburgh, PA, USA
[125] [(a)] Laboratorio de Instrumentacao e Fisica Experimental de Particulas-LIP, Lisbon, Portugal; [(b)] Faculdade de Ciências, Universidade de Lisboa, Lisbon, Portugal; [(c)] Department of Physics, University of Coimbra, Coimbra, Portugal; [(d)] Centro de Física Nuclear da Universidade de Lisboa, Lisbon, Portugal; [(e)] Departamento de Fisica, Universidade do Minho, Braga, Portugal; [(f)] Departamento de Fisica Teorica y del Cosmos and CAFPE, Universidad de Granada, Granada, Spain; [(g)] Dep Fisica and CEFITEC of Faculdade de Ciencias e Tecnologia, Universidade Nova de Lisboa, Caparica, Portugal
[126] Institute of Physics, Academy of Sciences of the Czech Republic, Prague, Czech Republic
[127] Czech Technical University in Prague, Prague, Czech Republic
[128] Faculty of Mathematics and Physics, Charles University in Prague, Prague, Czech Republic
[129] State Research Center Institute for High Energy Physics, Protvino, Russia
[130] Particle Physics Department, Rutherford Appleton Laboratory, Didcot, UK
[131] Physics Department, University of Regina, Regina, SK, Canada
[132] Ritsumeikan University, Kusatsu, Shiga, Japan
[133] [(a)] INFN Sezione di Roma, Rome, Italy; [(b)] Dipartimento di Fisica, Sapienza Università di Roma, Rome, Italy
[134] [(a)] INFN Sezione di Roma Tor Vergata, Rome, Italy; [(b)] Dipartimento di Fisica, Università di Roma Tor Vergata, Rome, Italy
[135] [(a)] INFN Sezione di Roma Tre, Rome, Italy; [(b)] Dipartimento di Matematica e Fisica, Università Roma Tre, Rome, Italy
[136] [(a)] Faculté des Sciences Ain Chock, Réseau Universitaire de Physique des Hautes Energies-Université Hassan II, Casablanca, Morocco; [(b)] Centre National de l'Energie des Sciences Techniques Nucleaires, Rabat, Morocco; [(c)] Faculté des Sciences Semlalia, Université Cadi Ayyad, LPHEA-Marrakech, Marrakech, Morocco; [(d)] Faculté des Sciences, Université Mohamed Premier and LPTPM, Oujda, Morocco; [(e)] Faculté des Sciences, Université Mohammed V-Agdal, Rabat, Morocco
[137] DSM/IRFU (Institut de Recherches sur les Lois Fondamentales de l'Univers), CEA Saclay (Commissariat à l'Energie Atomique et aux Energies Alternatives), Gif-sur-Yvette, France
[138] Santa Cruz Institute for Particle Physics, University of California Santa Cruz, Santa Cruz, CA, USA
[139] Department of Physics, University of Washington, Seattle, WA, USA
[140] Department of Physics and Astronomy, University of Sheffield, Sheffield, UK
[141] Department of Physics, Shinshu University, Nagano, Japan
[142] Fachbereich Physik, Universität Siegen, Siegen, Germany
[143] Department of Physics, Simon Fraser University, Burnaby, BC, Canada
[144] SLAC National Accelerator Laboratory, Stanford, CA, USA
[145] [(a)] Faculty of Mathematics, Physics and Informatics, Comenius University, Bratislava, Slovak Republic; [(b)] Department of Subnuclear Physics, Institute of Experimental Physics of the Slovak Academy of Sciences, Kosice, Slovak Republic

[146] [(a)] Department of Physics, University of Cape Town, Cape Town, South Africa; [(b)] Department of Physics, University of Johannesburg, Johannesburg, South Africa; [(c)] School of Physics, University of the Witwatersrand, Johannesburg, South Africa
[147] [(a)] Department of Physics, Stockholm University, Stockholm, Sweden; [(b)] The Oskar Klein Centre, Stockholm, Sweden
[148] Physics Department, Royal Institute of Technology, Stockholm, Sweden
[149] Departments of Physics and Astronomy and Chemistry, Stony Brook University, Stony Brook, NY, USA
[150] Department of Physics and Astronomy, University of Sussex, Brighton, UK
[151] School of Physics, University of Sydney, Sydney, Australia
[152] Institute of Physics, Academia Sinica, Taipei, Taiwan
[153] Department of Physics, Technion: Israel Institute of Technology, Haifa, Israel
[154] Raymond and Beverly Sackler School of Physics and Astronomy, Tel Aviv University, Tel Aviv, Israel
[155] Department of Physics, Aristotle University of Thessaloniki, Thessaloniki, Greece
[156] International Center for Elementary Particle Physics and Department of Physics, The University of Tokyo, Tokyo, Japan
[157] Graduate School of Science and Technology, Tokyo Metropolitan University, Tokyo, Japan
[158] Department of Physics, Tokyo Institute of Technology, Tokyo, Japan
[159] Department of Physics, University of Toronto, Toronto, ON, Canada
[160] [(a)] TRIUMF, Vancouver, BC, Canada; [(b)] Department of Physics and Astronomy, York University, Toronto, ON, Canada
[161] Faculty of Pure and Applied Sciences, University of Tsukuba, Tsukuba, Japan
[162] Department of Physics and Astronomy, Tufts University, Medford, MA, USA
[163] Centro de Investigaciones, Universidad Antonio Narino, Bogota, Colombia
[164] Department of Physics and Astronomy, University of California Irvine, Irvine, CA, USA
[165] [(a)] INFN Gruppo Collegato di Udine, Sezione di Trieste, Udine, Italy; [(b)] ICTP, Trieste, Italy; [(c)] Dipartimento di Chimica, Fisica e Ambiente, Università di Udine, Udine, Italy
[166] Department of Physics, University of Illinois, Urbana, IL, USA
[167] Department of Physics and Astronomy, University of Uppsala, Uppsala, Sweden
[168] Instituto de Física Corpuscular (IFIC) and Departamento de Física Atómica, Molecular y Nuclear and Departamento de Ingeniería Electrónica and Instituto de Microelectrónica de Barcelona (IMB-CNM), University of Valencia and CSIC, Valencia, Spain
[169] Department of Physics, University of British Columbia, Vancouver, BC, Canada
[170] Department of Physics and Astronomy, University of Victoria, Victoria, BC, Canada
[171] Department of Physics, University of Warwick, Coventry, UK
[172] Waseda University, Tokyo, Japan
[173] Department of Particle Physics, The Weizmann Institute of Science, Rehovot, Israel
[174] Department of Physics, University of Wisconsin, Madison, WI, USA
[175] Fakultät für Physik und Astronomie, Julius-Maximilians-Universität, Würzburg, Germany
[176] Fachbereich C Physik, Bergische Universität Wuppertal, Wuppertal, Germany
[177] Department of Physics, Yale University, New Haven, CT, USA
[178] Yerevan Physics Institute, Yerevan, Armenia
[179] Centre de Calcul de l'Institut National de Physique Nucléaire et de Physique des Particules (IN2P3), Villeurbanne, France

[a] Also at Department of Physics, King's College London, London, UK
[b] Also at Institute of Physics, Azerbaijan Academy of Sciences, Baku, Azerbaijan
[c] Also at Particle Physics Department, Rutherford Appleton Laboratory, Didcot, United Kingdom
[d] Also at TRIUMF, Vancouver, BC, Canada
[e] Also at Department of Physics, California State University, Fresno, CA, USA
[f] Also at Tomsk State University, Tomsk, Russia
[g] Also at CPPM, Aix-Marseille Université and CNRS/IN2P3, Marseille, France
[h] Also at Università di Napoli Parthenope, Naples, Italy
[i] Also at Institute of Particle Physics (IPP), Canada
[j] Also at Department of Physics, St. Petersburg State Polytechnical University, St. Petersburg, Russia
[k] Also at Chinese University of Hong Kong, Hong Kong, China

[l] Also at Department of Financial and Management Engineering, University of the Aegean, Chios, Greece
[m] Also at Louisiana Tech University, Ruston, LA, USA
[n] Also at Institucio Catalana de Recerca i Estudis Avancats, ICREA, Barcelona, Spain
[o] Also at Department of Physics, The University of Texas at Austin, Austin TX, USA
[p] Also at Institute of Theoretical Physics, Ilia State University, Tbilisi, Georgia
[q] Also at CERN, Geneva, Switzerland
[r] Also at Ochadai Academic Production, Ochanomizu University, Tokyo, Japan
[s] Also at Manhattan College, New York, NY, USA
[t] Also at Novosibirsk State University, Novosibirsk, Russia
[u] Also at Institute of Physics, Academia Sinica, Taipei, Taiwan
[v] Also at LAL, Université Paris-Sud and CNRS/IN2P3, Orsay, France
[w] Also at Academia Sinica Grid Computing, Institute of Physics, Academia Sinica, Taipei, Taiwan
[x] Also at Laboratoire de Physique Nucléaire et de Hautes Energies, UPMC and Université Paris-Diderot and CNRS/IN2P3, Paris, France
[y] Also at School of Physical Sciences, National Institute of Science Education and Research, Bhubaneswar, India
[z] Also at Dipartimento di Fisica, Sapienza Università di Roma, Rome, Italy
[aa] Also at Moscow Institute of Physics and Technology State University, Dolgoprudny, Russia
[ab] Also at Section de Physique, Université de Genève, Geneva, Switzerland
[ac] Also at International School for Advanced Studies (SISSA), Trieste, Italy
[ad] Also at Department of Physics and Astronomy, University of South Carolina, Columbia, SC, USA
[ae] Also at School of Physics and Engineering, Sun Yat-sen University, Guangzhou, China
[af] Also at Faculty of Physics, M.V. Lomonosov Moscow State University, Moscow, Russia
[ag] Also at Moscow Engineering and Physics Institute (MEPhI), Moscow, Russia
[ah] Also at Institute for Particle and Nuclear Physics, Wigner Research Centre for Physics, Budapest, Hungary
[ai] Also at Department of Physics, Oxford University, Oxford, UK
[aj] Also at Department of Physics, Nanjing University, Jiangsu, China
[ak] Also at Institut für Experimentalphysik, Universität Hamburg, Hamburg, Germany
[al] Also at Department of Physics, The University of Michigan, Ann Arbor, MI, USA
[am] Also at Discipline of Physics, University of KwaZulu-Natal, Durban, South Africa
* Deceased

Nuclear Instruments and Methods in Physics Research A 718 (2013) 258–259

Contents lists available at SciVerse ScienceDirect

Nuclear Instruments and Methods in Physics Research A

journal homepage: www.elsevier.com/locate/nima

A fast hardware tracker for the ATLAS trigger system

J. Anderson [f], A. Andreani [m,n], A. Andreazza [m,n], A. Annovi [b], M. Atkinson [e], B. Auerbach [f], M. Beretta [b], V. Bevacqua [a,c], R. Blair [f], G. Blazey [q], M. Bogdan [d], A. Boveia [d], F. Canelli [d,j], A. Castegnaro [b], V. Cavaliere [e], F. Cervigni [o,p], P. Chang [e], Y. Cheng [c], M. Citterio [m], F. Crescioli [a,c], M. Dell'Orso [a,c], G. Drake [f], M. Dunford [d], L. Fabbri [o,p], A. Favareto [m,n], M. Franchini [o,l], S. Geer [j], P. Giannetti [a], F. Giannuzzi [o,p], F. Giorgi [o], S. Gruenendahl [j], H.L. Li [d], J. Hoff [j], T. Iizawa [h], A. Kapliy [d], M. Kasten [e], Y.K. Kim [d,j], N. Kimura [h], A. Lanza [k], F. Lasagni [o,p], V. Liberali [m,n], T. Liu [j], D. Magalotti [o,p], A. McCarn [e], C. Melachrinos [d], C. Meroni [m], T. Mitani [h], P. Murat [j], A. Negri [k,l], M. Neubauer [e], Y. Okumura [d,j], J. Olsen [j], B. Penning [d,j], M. Piendibene [a,c], J. Proudfoot [f], C. Roda [a,c], I. Sacco [a,c], Y. Sakurai [h], C. Sbarra [o], M. Shochet [d], A. Stabile [m,n], J. Tang [d], F. Tang [d], L. Tompkins [d], R. Tripiccione [g], J. Tuggle [d], S. Valentinetti [o,p], V. Vercesi [k], M. Verzocchi [j], M. Villa [o,p], G. Volpi [b,d,*], J. Webster [d], K. Yorita [h], J. Zhang [f], A. Zoccoli [o,p,i,r,1]

[a] Sezione di Pisa, INFN, Pisa, Italy
[b] Laboratori Nazionali, INFN, Frascati, Italy
[c] Department of Physics, University, Pisa, Italy
[d] Department of Physics and Enrico Fermi Institute, University, Chicago, IL, USA
[e] Department of Physics, University of Illinois at Urbana-Champaign, Urbana, IL, USA
[f] Argonne National Laboratory, Argonne, IL, USA
[g] Department of Physics, University of Ferrara, Ferrara, Italy
[h] Department of Physics, Waseda University, Waseda, Japan
[i] Department of Physics, University of Harvard, Harvard, MA, USA
[j] Fermi National Accelerator Laboratory, Fermilab, Batavia, IL, USA
[k] Sezione di Pavia, INFN, Pavia, Italy
[l] Department of Physics, University of Pavia, Pavia, Italy
[m] Sezione di Milano INFN, Milan, Italy
[n] Department of Physics, University of Milan, Milan, Italy
[o] Sezione di Bologna INFN, Bologna Italy
[p] Department of Physics, University of Bologna, Bologna, Italy
[q] Northern Illinois University, USA
[r] Department of Physics, University of Perugia, Perugia Italy

ARTICLE INFO

Available online 29 November 2012

Keywords:
Tracking detectors
FTK
VLSI
FPGA

ABSTRACT

The Fast Tracker (FTK) processor is an approved ATLAS upgrade that will reconstruct tracks using the full silicon tracker at Level-1 rate (up to 100 KHz). FTK uses a completely parallel approach to read the silicon tracker information, execute the pattern matching and reconstruct the tracks. This approach, according to detailed simulation results, allows full tracking with nearly offline resolution within an execution time of 100 μs. A central component of the system is the associative memories (AM); these special devices reduce the pattern matching combinatoric problem, providing identification of coarse resolution track candidates. The system consists of a pipeline of several components with the goal to organize and filter the data for the AM, then to reconstruct and filter the final tracks. This document presents an overview of the system and reports the status of the different elements of the system.

© 2013 CERN. Published by Elsevier B.V. Open access under CC BY-NC-ND license.

1. Introduction

As the Large Hadron Collider (LHC) luminosity is ramped up to 3×10^{34} cm^{-2} s^{-1} and beyond, the high rates, multiplicities, and energies of particles seen by the detectors will pose a unique

* Corresponding author at: Laboratori Nazionali, INFN, Frascati, Italy.
E-mail address: guido.volpi@lnf.infn.it (G. Volpi).

[1] © CERN for the benefit of the ATLAS Collabration. Open access under CC BY-NC-ND license.

© 2013 CERN. Published by Elsevier B.V. Open access under CC BY-NC-ND license.

http://dx.doi.org/10.1016/j.nima.2012.11.133

challenge. The current three-level trigger, designed to allow a rate reduction from 40 MHz to about 400 Hz [1], has to evolve to fit in these constraints. The Fast Tracker (FTK) is an upgrade to the current ATLAS trigger system that will operate at full Level-1 output rates, providing high-quality tracks reconstructed in the entire inner detector by the start of processing in the Level-2 trigger. This frees execution time in the Level-2 farm for more complex selection algorithms, allowing interesting events to be selected with higher efficiency while rejecting uninteresting events. FTK solves the combinatorial challenge inherent to tracking by exploiting the massive parallelism of associative memories that can compare inner detector hits to billions of precalculated patterns simultaneously.

The tracking problem within the matched patterns, referred as roads, is further simplified by transforming the helix parameters and the quality estimator calculations into a set of scalar products in the form

$$p_i = \sum_j C_{ij} x_j + q_i$$

where x_j are the hit coordinates in each detector layer, C_{ij} and q_i are precalculated terms, p_i can be either helix parameters or χ^2 components. Using this transformation fast DSPs in modern commercial FPGAs can perform the calculation in a very efficient and parallel way.

2. FTK architecture

The FTK system will receive a copy of the data from Read-Out Drivers (ROD) of the ATLAS pixel and strip detectors. This functionality was not present in the original HOLA card, responsible for the ROD output; a specific dual-output HOLA card was developed for FTK: it has two independent streams, one for the standard DAQ stream and the second for FTK. All the 270 HOLA cards required to install FTK have been produced and tested. The testing procedure was particularly detailed and important because these cards are used by the general DAQ; indeed a failure will prevent normal ATLAS operations. During the 2012 winter shutdown 32 HOLA cards were installed and included in the normal operations.

The data collected by the HOLAs will be collected by the Data Formatter (DF). The DF organizes the data to be used by the FTK system. It maps the silicon Inner Detector (ID) modules to 64 $\eta-\phi$ independent towers. The DF also organizes the data for use by the remaining boards in the system. In particular, the DF sends to the AM chip the data from 8 out of the 11 layers that a track can cross. The data from the other three layers are sent to the Second Stage Boards (SSB). Technically, the DF boards will be installed in ATCA crates, using a full-mesh backplane. This architecture was chosen because of the data sharing flexibility in ATCA. For the inter-shelf communication an optical fiber will be used.

A special role is played by the input mezzanine card installed in the DF boards: the FTK input mezzanine (FTK_IM). This mezzanine card receives as input the S-link fibers connected to the HOLA cards and runs a clustering algorithm. The clustering algorithm is crucial in the pixel layer to identify the clusters and calculate the centroids; the execution speed is crucial and the selection of the final FPGA is in progress. The SCT data are already clustered by the front-end chip, however for instrumental reasons clusters can be split at chip boundaries; a refinement of SCT clusters will improve system performance.

The data collected by the DF will be sent to the real processing units, composed by the AM board and an auxiliary card (AUX) installed on the VME backplane. Technically the AUX card receives the clusters and converts each to coarse resolution hit for pattern recognition (superstrip or SS). The SS information is routed within the AM board to 128 AMChip04 chips [2] and matched to patterns, about 10 millions per board. The found roads will then be sent back to the AUX where all the full resolution clusters will be retrieved and combined to build candidate tracks with 1 hit per layer. For each candidate a χ^2 is calculated and the bad tracks are rejected. This task is performed in an FPGA with an average fit rate of 1 track per ns.

The good tracks in the AUX cards are sent to SSB and extrapolated. If hits are found around the extrapolated coordinates these are added to the track; if the there are not hits, the track is discarded. This procedure rejects fakes and increases the quality of the tracks. The final tracks are sent to the FLIC (FTK to Level 2 Interface Crate), collected and prepared for the ATLAS HLT processing farm.

3. Expected performance

Using a detailed emulation of the system it has been possible to evaluate the expected performance of the system up to 3×10^{34} cm^{-2} s^{-1}, verifying that FTK is able to compute the helix parameters for all tracks in an event, apply quality cuts in less than 100 μs, with nearly offline quality. This quality allows us to implement selection algorithms based on tracks, like high-p_T lepton identification, b- or τ-tagging of jets. However the integration with the ATLAS HLT will allow other, more sophisticated algorithms [3].

4. Conclusion

The FTK system design was defined and the performance presented. The design of individual boards is in progress. In particular some of the dual output HOLA cards are already installed. Other parts, like the AM board, the AUX card or the FTK_IM are already at prototype level. Prototypes for the rest of the boards are expected soon. The final TDR of the system, where the first test of the prototypes will be included, is expected for the spring 2013. The installation is expected to start in 2014.

References

[1] W. Smith, et al., Nuclear Instruments and Methods A 478 (2002) 62.
[2] A. Annovi, et al., A new variable-resolution associative memory for high energy physics, in: 2nd International Conference on Advancements in Nuclear Instrumentation Measurement Methods and their Applications (ANIMMA), 2011.
[3] A. Andreazza, et al., The FastTracker real time processor and its impact on Muon isolation, Tau and b-jet online selections at ATLAS", IEEE Transactions on Nuclear Science NS-59(2).

Published for SISSA by Springer

Received: May 11, 2012
Accepted: May 29, 2012
Published: June 15, 2012

Measurement of the W boson polarization in top quark decays with the ATLAS detector

The ATLAS collaboration

E-mail: atlas.publications@cern.ch

Abstract: This paper presents measurements of the polarization of W bosons in top quark decays, derived from $t\bar{t}$ events with missing transverse momentum, one charged lepton and at least four jets, or two charged leptons and at least two jets. Data from pp collisions at a centre-of-mass energy of 7 TeV were collected with the ATLAS experiment at the LHC and correspond to an integrated luminosity of $1.04\,\mathrm{fb}^{-1}$. The measured fractions of longitudinally, left- and right-handed polarization are $F_0 = 0.67 \pm 0.07$, $F_\mathrm{L} = 0.32 \pm 0.04$ and $F_\mathrm{R} = 0.01 \pm 0.05$, in agreement with the Standard Model predictions. As the polarization of the W bosons in top quark decays is sensitive to the Wtb vertex Lorentz structure and couplings, the measurements were used to set limits on anomalous contributions to the Wtb couplings.

Keywords: Hadron-Hadron Scattering

Open Access, Copyright CERN,
for the benefit of the ATLAS collaboration

doi:10.1007/JHEP06(2012)088

JHEP06(2012)088

Contents

1 Introduction **1**

2 Data and simulation samples **3**
- 2.1 Data sample 3
- 2.2 Signal and background modelling 3

3 Event selection **4**
- 3.1 Physics object definition 4
- 3.2 Single-lepton channels 5
- 3.3 Dilepton channels 6

4 Measurement strategies **8**
- 4.1 Measurement using the template method 8
- 4.2 Measurement using the angular asymmetries 11

5 Systematic uncertainties **12**
- 5.1 Sources of systematic uncertainty 12
  - 5.1.1 Signal and background modelling 12
  - 5.1.2 Detector modelling 13

6 Results **15**
- 6.1 Combination 16
- 6.2 Constraints on the Wtb vertex structure 18

7 Conclusions **20**

The ATLAS collaboration **25**

JHEP06(2012)088

1 Introduction

Discovered in 1995 by the CDF and DØ experiments [1, 2], the top quark is the heaviest known fundamental particle, with a mass of 173.2±0.9 GeV [3]. Measurements of top quark properties play an important role in testing the Standard Model and its possible extensions. One particular test is the study of the Wtb vertex Lorentz structure and couplings, which can be probed by measuring the polarization of W bosons produced in top quark decays.

At the LHC, top quarks are produced mainly in pairs via the strong interaction and are predicted to decay via the electroweak interaction into a W boson and a bottom quark with a nearly 100% branching fraction. Events with $t\bar{t}$ pairs can thus be classified according to the decay of the two produced W bosons. Each boson can decay either into

a quark-antiquark pair or into a charged lepton and a neutrino. The single-lepton and dilepton topologies, both considered in the analyses presented in this paper, have one and two isolated charged leptons in the final state. Only electrons and muons, including those from τ decays, are considered here.

The Wtb vertex is defined by the electroweak interaction and has a $(V-A)$ structure where V and A are the vector and axial-vector contributions to the vertex. Since the W bosons are produced as real particles in top quark decays, their polarization can be longitudinal, left-handed or right-handed. The fractions of events with a particular polarization, F_0, F_{L} and F_{R}, are referred to as helicity fractions. They are predicted in next-to-next-to-leading-order (NNLO) QCD calculations to be $F_0 = 0.687 \pm 0.005$, $F_{\mathrm{L}} = 0.311 \pm 0.005$, $F_{\mathrm{R}} = 0.0017 \pm 0.0001$ [4]. These fractions can be extracted from measurements of the angular distribution of the decay products of the top quark. The angle θ^* is defined as the angle between the momentum direction of the charged lepton from the decay of the W boson and the reversed momentum direction of the b-quark from the decay of the top quark, both boosted into the W boson rest frame [5]. The angular distribution is:

$$\frac{1}{\sigma}\frac{\mathrm{d}\sigma}{\mathrm{d}\cos\theta^*} = \frac{3}{4}\left(1-\cos^2\theta^*\right)\,F_0 + \frac{3}{8}\left(1-\cos\theta^*\right)^2\,F_{\mathrm{L}} + \frac{3}{8}\left(1+\cos\theta^*\right)^2\,F_{\mathrm{R}}\,. \tag{1.1}$$

All previous measurements of the helicity fractions, performed by the CDF and DØ Collaborations [6–8] at the Tevatron, are in agreement with Standard Model predictions.

Information about the polarization of the W bosons can also be obtained through complementary observables, such as the angular asymmetries, A_+ and A_-, defined as:

$$A_\pm = \frac{N(\cos\theta^* > z) - N(\cos\theta^* < z)}{N(\cos\theta^* > z) + N(\cos\theta^* < z)}\,, \tag{1.2}$$

with $z = \pm(1-2^{2/3})$ for $A_\pm$, allowing the dependence on F_{L} and F_{R} to cancel, respectively. The asymmetries can be related to the helicity fractions by a simple system of equations [9, 10]. In the Standard Model, the NNLO values for these asymmetries are $A_+ = 0.537 \pm 0.004$ and $A_- = -0.841 \pm 0.006$ [4].

In the presence of anomalous Wtb couplings the helicity fractions and angular asymmetries depart from their Standard Model values [5, 10]. In effective field theories, dimension-six operators can be introduced which modify the Wtb vertex [11–13]. Coefficients controlling the strength of these operators can be constrained by measurements of the helicity fractions or the angular asymmetries.

This paper describes measurements of the W boson polarization in top quark decays and the constraints on the Wtb vertex structure based on a data set recorded with the ATLAS detector between March and June 2011 and corresponding to an integrated luminosity of $1.04\,\mathrm{fb}^{-1}$. The helicity fractions were measured using two different methods. The first compares the observed $\cos\theta^*$ distribution with templates for different W boson helicity states obtained from simulation. The second method extracts angular asymmetries from an unfolded $\cos\theta^*$ spectrum corrected for background contributions. Limits on anomalous couplings, generated by the aforementioned dimension-six operators, were set using the combined result from the two measurements.

JHEP06(2012)088

This paper is structured as follows. Data samples and simulated samples modelling signal and background processes are described in section 2, followed by a summary of the event selection in section 3. The analysis strategies can be found in section 4. Sources of systematic uncertainty are discussed in section 5, the results are summarized in section 6 and section 7 concludes the paper.

2 Data and simulation samples

The ATLAS detector [14] at the LHC covers nearly the entire solid angle around the collision point. It consists of an inner tracking detector surrounded by a thin superconducting solenoid, electromagnetic and hadronic calorimeters, and an external muon spectrometer incorporating three large superconducting toroid magnet assemblies. A three-level trigger system, designed to reduce the event rate from 40 MHz to about 200 Hz, is used to select events of interest.

2.1 Data sample

Data from pp collisions at a centre-of-mass energy of 7 TeV were collected using single-lepton triggers with transverse momentum thresholds of 20 GeV for electrons and 18 GeV for muons. The size of the data sample corresponds to an integrated luminosity of $1.04 \pm 0.04\,\mathrm{fb}^{-1}$ [15, 16].

2.2 Signal and background modelling

Signal and most background processes were modelled by Monte Carlo (MC) simulation. The signal process was simulated using two different generators. The leading order (LO) Monte Carlo generator Protos [10, 17] was used with the CTEQ6L1 sets of parton distribution functions (PDFs) [18] to generate three samples assuming $F_0 = 1$, $F_\mathrm{L} = 1$ and $F_\mathrm{R} = 1$. This was achieved by choosing appropriate values for anomalous Wtb couplings, as described in refs. [9, 10]. The output was interfaced to Pythia [19] to simulate parton showers and hadronization. In addition, the next-to-leading-order (NLO) generator MC@NLO [20–22] was used with the CTEQ6.6 PDF set [23] for studies of systematic differences in the top quark production and decay modelling.

The W and Z boson production in association with multiple jets was simulated using the Alpgen generator [24] and the CTEQ6L1 PDF set. Tree-level matrix elements with up to five final-state partons were included. The standard Alpgen matching scheme was used to remove overlaps between the n and $n+1$ parton samples. Heavy flavour samples containing $Wb\bar{b}$, $Wc\bar{c}$, Wc and $Zb\bar{b}$ events were simulated separately. The Z+jets samples were generated with dileptons in the invariant mass range $10 < m_{\ell\ell} < 2000$ GeV. Diboson processes were simulated using Herwig [25]. Single top quark production was simulated using MC@NLO, invoking the 'diagram removal scheme' [26] to remove overlaps between the single top quark and $t\bar{t}$ final states. An additional sample of W+jets events was generated with Sherpa [27] and used to study systematic uncertainties. Details are described in section 5. Apart from the Protos $t\bar{t}$ samples, all events were hadronized with

JHEP06(2012)088

Herwig using Jimmy [28] for the underlying event model. Different underlying event tunes were used, depending on the hadronization program used (i.e. Pythia or Herwig) [29].

Additional MC samples were used for the evaluation of systematic uncertainties. These were generated with the AcerMC [30] and Powheg [31, 32] generators interfaced to Pythia for hadronization. They are described in section 5. A top quark mass of 172.5 GeV was assumed for all signal samples if not stated otherwise. Additional MC@NLO samples were generated assuming different top quark masses.

All simulated events contain multiple pp-interactions and contain pileup contributions corresponding to a bunch spacing of 50 ns. These simulated events were re-weighted such that the average number of interactions per proton-proton bunch crossing was the same in data and MC simulation. The average number of interactions per event was roughly six. All samples were processed by the detector and trigger simulation after event generation [33, 34], and subjected to the same reconstruction algorithms as the data.

The cross-section of simulated $t\bar{t}$ samples was normalized to 164.6 pb, the value obtained from approximate NNLO calculations [35–37], and consistent with recent measurements [38]. While the Z+jets normalization was obtained from the NNLO QCD cross-section calculations in the single-lepton channels, a data-driven estimate for the normalization was used for the dilepton channels [38]. The diboson with jets production was rescaled to match NLO calculations of the inclusive cross-sections.

For the single-lepton analysis, the multijet production background, where an electron or muon originates from hadron decay or instrumental background, was estimated from data as described in refs. [39, 40]. The W+jets background was obtained from simulation, except that its normalization was derived from data, from a study of the asymmetry in the production of W^+ and W^- bosons [40]. For the dilepton analysis, background contributions from W+jets, single-lepton $t\bar{t}$ and single top quark production were estimated using the method described in ref. [38]. In the single-lepton and dilepton analyses this source of background is labelled as "misidentified leptons".

3 Event selection

3.1 Physics object definition

The reconstruction and identification of electrons, muons, jets and the magnitude of the missing transverse momentum ($E_{\mathrm{T}}^{\mathrm{miss}}$) used in the analyses presented here followed the criteria employed for the measurement of the $t\bar{t}$ production cross-section [39]. More details, including a description of the trigger and the vertex requirements, can be found in ref. [40].

The $t\bar{t}$ events with at least one isolated charged lepton (electron or muon) in the final state were considered as signal. Events with τ leptons decaying into muons or electrons in the final state were also considered to be part of the signal.

All the considered events were required to fulfil general event quality criteria and to have a well-defined primary vertex with at least five associated tracks. Reconstructed electrons were required to have $E_{\mathrm{T}} > 25$ GeV and $|\eta| < 2.47$ excluding $1.37 < |\eta| < 1.52$,

JHEP06(2012)088

while muons were required to have $p_{\mathrm{T}} > 20$ GeV and $|\eta| < 2.5$.[1] Jets were reconstructed with the anti-k_t algorithm [41] with a radius parameter equal to 0.4. They were required to have $p_{\mathrm{T}} > 25$ GeV and $|\eta| < 2.5$. For electrons, the energy not associated to the electron cluster but contained in a cone of $\Delta R = \sqrt{(\Delta\phi)^2 + (\Delta\eta)^2} = 0.2$ around it was required not to exceed 3.5 GeV. For muons, the sum of track transverse momenta and the total energy deposited in a cone of $\Delta R = 0.3$ around the muon were both required to be less than 4 GeV. Muons reconstructed within a $\Delta R = 0.4$ cone of a jet satisfying $p_{\mathrm{T}} > 20$ GeV were removed to reduce the contamination caused by muons from hadron decays within jets. Subsequently, jets within $\Delta R = 0.2$ of an electron candidate were removed to avoid double counting, which can occur because electron clusters are also reconstructed as jets.

A combination of two algorithms was used for b-jet identification (b-tagging). They are based on reconstructed secondary vertices and the impact parameter significances of tracks within jets. The chosen working point resulted in a b-tagging efficiency of 70% for jets originating from b-quarks in a sample of simulated $t\bar{t}$ events and a light-quark jet rejection factor of about 100 [42].

3.2 Single-lepton channels

The single-lepton $t\bar{t}$ signal is characterized by a high-p_{T} isolated charged lepton and missing transverse momentum from the neutrino, from the leptonically decaying W boson, two light-quark jets from the hadronically decaying W boson and two b-quark jets. The two channels with either an electron or a muon in the final state are referred to as single-electron and single-muon channels. The following event selection requirements were applied:

- the appropriate single-electron or single-muon trigger had fired;
- events were required to contain exactly one isolated electron or muon;
- in the single-electron channel, $E_{\mathrm{T}}^{\mathrm{miss}} > 35$ GeV and $m_{\mathrm{T}}(W) > 25$ GeV were required[2] while in the single-muon channel the criteria were $E_{\mathrm{T}}^{\mathrm{miss}} > 20$ GeV and $E_{\mathrm{T}}^{\mathrm{miss}} + m_{\mathrm{T}}(W) > 60$ GeV;
- events were required to have at least four jets, with at least one of them being tagged as a b-jet.

The numbers of events expected after all selection requirements are shown in table 1 for the single-electron and single-muon channels, together with the observed numbers of events in the data sample. The single-electron channel contains significantly fewer events than the single-muon channel due to the more stringent requirements on the lepton E_{T} (p_{T}), $E_{\mathrm{T}}^{\mathrm{miss}}$ and $m_{\mathrm{T}}(W)$. The observed numbers of events are in agreement with those

[1] ATLAS uses a right-handed coordinate system with its origin at the nominal interaction point (IP) in the centre of the detector and the z-axis along the beam pipe. The x-axis points from the IP to the centre of the LHC ring, and the y-axis points upward. Cylindrical coordinates (r, ϕ) are used in the transverse plane, ϕ being the azimuthal angle around the beam pipe. The pseudorapidity is defined in terms of the polar angle θ as $\eta = -\ln\tan(\theta/2)$.

[2] Here $m_{\mathrm{T}}(W)$ is the W boson transverse mass, reconstructed as $\sqrt{2p_{\mathrm{T}}^{\ell}p_{\mathrm{T}}^{\nu}\,[1-\cos(\phi^{\ell}-\phi^{\nu})]}$ where the measured missing transverse momentum provides the neutrino information.

JHEP06(2012)088

Process	Single electron	Single muon
$t\bar{t}$	4400 ± 1100	6500 ± 1400
W+jets	900 ± 700	1400 ± 1000
Z+jets	120 ± 90	140 ± 90
Diboson	14 ± 12	22 ± 12
Single top	260 ± 90	360 ± 110
Misidentified leptons	220 ± 220	500 ± 500
Total predicted	5900 ± 1300	9000 ± 1800
Data	5830	9121

Table 1. Event yields in the single-electron and single-muon channels after the event selection. The table shows the expected number of events including their estimated total uncertainty as well as the number of events observed in the data sample.

expected, with purities of 75% and 72% for the single electron and single muon channels. The systematic uncertainty discussed in section 5 dominates the error on the event yields, with jet energy scale, signal and background modelling, and b-tagging being the dominant sources of uncertainty. Example distributions in data are compared with the Standard Model predictions in figure 1. The data are described well by the expected distributions.

3.3 Dilepton channels

The dilepton $t\bar{t}$ signal is characterized by two high-p_{T} isolated charged leptons, missing transverse momentum corresponding to the undetected neutrinos from the two leptonically decaying W bosons, and two b-quark jets. The three channels are referred to as ee, $\mu\mu$ and $e\mu$ channels. The following event selection requirements were applied:

- the single-electron trigger had fired for the ee channel, the single-muon trigger had fired for the $\mu\mu$ channel and either of these triggers had fired for the $e\mu$ channel;
- events were required to contain exactly two oppositely charged and isolated leptons (ee, $\mu\mu$ or $e\mu$);
- at least two jets, with at least one of them being b-tagged, were required;
- in order to avoid the low-mass Drell-Yan background region, events were required to have $m_{\ell\ell} > 15$ GeV;
- in the ee and $\mu\mu$ channels, the missing transverse momentum had to satisfy $E_{\mathrm{T}}^{\mathrm{miss}} >$ 40 GeV, and the invariant mass of the two leptons had to differ by at least 10 GeV from the Z boson mass, i.e. $|m_{\ell\ell} - m_Z| > 10$ GeV, with $m_Z = 91$ GeV, in order to suppress backgrounds from Z+jets events and events containing misidentified leptons;

JHEP06(2012)088

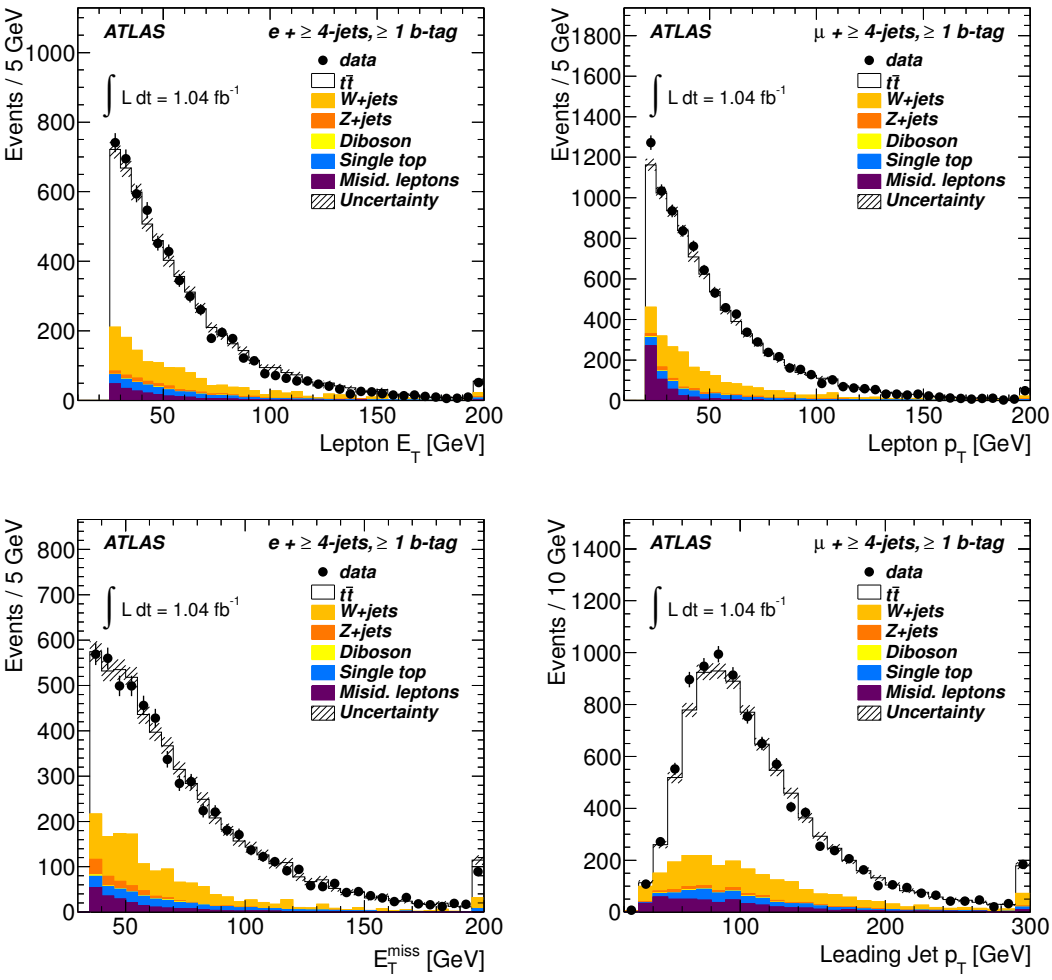

Figure 1. The top row shows (left) the E_{T} spectrum of the electron in the single-electron channel and (right) the p_{T} spectrum of the muon in the single-muon channel. The bottom row shows (left) the missing transverse momentum in the single-electron channel and (right) the p_{T} spectrum of the leading jet in the single-muon channel. The error band shows the statistical uncertainty from the Monte Carlo simulation. The last bin in each distribution includes the overflow.

- in the $e\mu$ channel, no $E_{\mathrm{T}}^{\mathrm{miss}}$ or Z boson mass veto cuts were applied; however, the event H_{T}, defined as the scalar sum of the transverse energies of the two charged leptons and all selected jets, had to satisfy $H_{\mathrm{T}} > 130$ GeV to suppress backgrounds from Z+jets production;

- events were required to pass the $t\bar{t}$ reconstruction criteria, as described in section 4.1.

The numbers of events expected after all selection requirements are shown in table 2 for the three dilepton channels, together with the observed numbers of events in the data sample. The observed numbers of events is in agreement with those expected, with a purity of 94% for all three channels. The systematic uncertainty discussed in section 5

JHEP06(2012)088

Process	ee channel	$\mu\mu$ channel	$e\mu$ channel
$t\bar{t}$	159 ± 28	320 ± 40	750 ± 100
Z+jets (ee,$\mu\mu$)	0.7 ± 2.0	2 ± 4	—
Z+jets ($\tau\tau$)	0.0 ± 3.8	1.4 ± 1.3	4.7 ± 3.1
Diboson	0.2 ± 0.3	0.6 ± 0.3	1.3 ± 0.5
Single top	5.0 ± 1.3	10.8 ± 2.4	24 ± 5
Misidentified leptons	4 ± 2	7 ± 4	19 ± 9
Total predicted	170 ± 30	340 ± 40	800 ± 100
Data	191	354	836

Table 2. Event yields in the dilepton channels after the event selection and event reconstruction. The table shows the expected number of events including their estimated total uncertainty as well as the number of events observed in the data sample.

dominates the error on the event yields, with jet energy scale, jet energy resolution, signal and background modelling, and b-tagging being the dominant sources of uncertainty. Example distributions in data are compared with the Standard Model predictions in figure 2. The data are described well by the expected distributions.

4 Measurement strategies

The two methods to extract the helicity fractions are described below. The analysis was carried out for the single-electron, single-muon, ee, $e\mu$ and $\mu\mu$ channels separately. The reconstruction of $t\bar{t}$ events in the single-lepton channels differs for the two methods: the template method relies more strongly on the structure of the $\cos\theta^*$ distribution than the calculation of the angular asymmetries. It thus relies on an improved estimate of the particle energies. A common reconstruction method was used in the dilepton channels. The results of the analyses and their combination are described in section 6.

4.1 Measurement using the template method

Templates for different signal and background processes were fitted to the observed $\cos\theta^*$ distributions based on events reconstructed with a kinematic fit in the single-lepton channels [40, 43]. The fit was based on a likelihood which took into account the Breit-Wigner forms of the lineshapes of the top quark and the W boson as well as the energy resolution of the measurements of the jets and the charged leptons. The missing transverse momentum was identified with the x- and y-components of the neutrino momentum. The top quark mass was fixed to 172.5 GeV, and the mass of the W boson was fixed to 80.4 GeV. The likelihood was maximized with respect to the energies of the final state quarks for each association of jets to quarks. The permutations were weighted according to the b-tagging information and the weights were derived from the efficiency and mis-tag rate of the b-tagger. The permutation with the largest value of the likelihood was used in the

JHEP06(2012)088

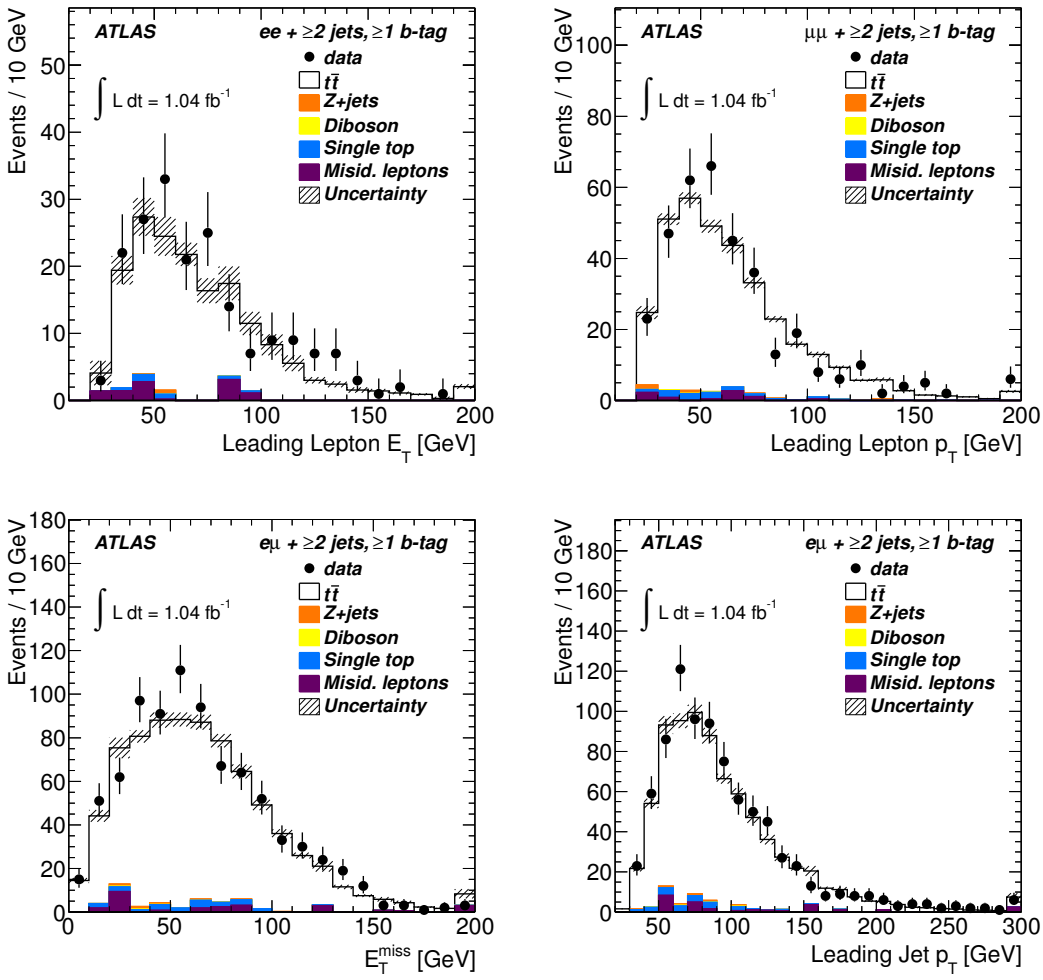

Figure 2. The top row shows (left) the E_{T} spectrum of the leading electron in the ee channel and (right) the p_{T} spectrum of the leading muon in the $\mu\mu$ channel. The bottom row shows (left) the missing transverse momentum in the $e\mu$ channel and (right) the p_{T} spectrum of the leading jet in the $e\mu$ channel. The error band shows the statistical uncertainty from the Monte Carlo simulation. The last bin in each distribution includes the overflow.

following steps of the analysis. The overall efficiency for the reconstruction of the correct event topology was found to be 74% in simulated $t\bar{t}$ events. Only those events where four jets and a lepton are matched to partonic particles, corresponding to roughly 30% of the events, were considered for the efficiency computation.

For the dilepton channels, the $t\bar{t}$ system was reconstructed by solving a set of six independent equations:

$$p_x^{\nu_1} + p_x^{\nu_2} = E_x^{\mathrm{miss}}; \qquad p_y^{\nu_1} + p_y^{\nu_2} = E_y^{\mathrm{miss}}; \qquad (p_{\ell_1} + p_{\nu_1})^2 = m_W^2;$$
$$(p_{\ell_2} + p_{\nu_2})^2 = m_W^2; \qquad (p_{W_1} + p_{j_1})^2 = m_t^2; \qquad (p_{W_2} + p_{j_2})^2 = m_t^2. \tag{4.1}$$

E_x^{miss} and E_y^{miss} represent the x- and y-components of the missing transverse momentum,

JHEP06(2012)088

p_{ℓ_1} and p_{ℓ_2} (p_{j_1} and p_{j_2}, p_{ν_1} and p_{ν_2}) correspond to the four-momenta of the two charged leptons (jets, neutrinos). Here, m_W and m_t are the W boson and top quark masses, respectively. For events with only one b-tagged jet, this jet and the non-tagged one with the highest p_{T} were taken as b-jets from the top quark decays. If at least two b-tagged jets are present, the two b-tagged jets with the largest p_{T} in the event were used. The pairing of the jets with the charged leptons was based on the minimization of the sum of the invariant masses $m_{\ell_1 j_1}$ and $m_{\ell_2 j_2}$. Simulations show that this criterion gives the correct pairing in 68% of the events. Up to four solutions can be found to the Equations 4.1. The solution with the minimum product of neutrino transverse momenta was chosen and is motivated by the low p_{T}-spectrum of the neutrinos. In case no solution was found, the top quark mass parameter was varied in the 157.5–187.5 GeV range, to try to find one or more solutions. In case a range of top masses provided a solution, that with the top quark mass parameter closest to 172.5 GeV was taken. Again, multiple ambiguities were resolved by taking the solution with the minimum product of neutrino transverse momenta. If still no solution was found, the second pairing of jets and charged leptons was used. If no solution was found after this procedure the event was discarded. This happened in about 25% of the events in data and in simulated $t\bar{t}$ events.

In the single-lepton channels, the following six processes were used as templates: three different helicity state signal processes, the background from events with misidentified leptons, the W+jets contribution and the sum of all other sources of background. The three signal templates were derived from simulation and include single-lepton and dilepton events which pass the event selection. These distributions are shown in figure 3. The W+jets template was obtained from simulation. The template for events with misidentified leptons was obtained from data. Other processes contributing to the observed spectrum include single top quark, diboson and Z+jets production and were summed in a single template obtained from simulation.

In the dilepton channels, templates for the three different helicity state signal processes were used as well as a single template representing the different background contributions, namely single top quark production, processes with misidentified leptons, production of Z bosons with additional jets and diboson production. All templates were obtained from simulation, except the misidentified leptons template, which was obtained from data.

A binned likelihood fit was used to estimate the expected number of events contributing to the distribution, assuming independent Poisson-distributed fluctuations in each bin. The number of events expected in the ith bin, λ_i, is given as:

$$\lambda_i = \sum_{h=-1,0,+1} \lambda_i^h \cdot \epsilon^h + \sum_{j=1}^{N_{\mathrm{bkg}}} \lambda_i^j \,, \tag{4.2}$$

where the first term describes the expected number of signal events at particle level with defined helicity h. These are reduced by reconstruction efficiencies and acceptances summarized by the factors ϵ^h estimated from simulation. The second term describes the expected number of events from background processes and N_{bkg} is the number of background templates. The contributions of the various background templates were constrained according

JHEP06(2012)088

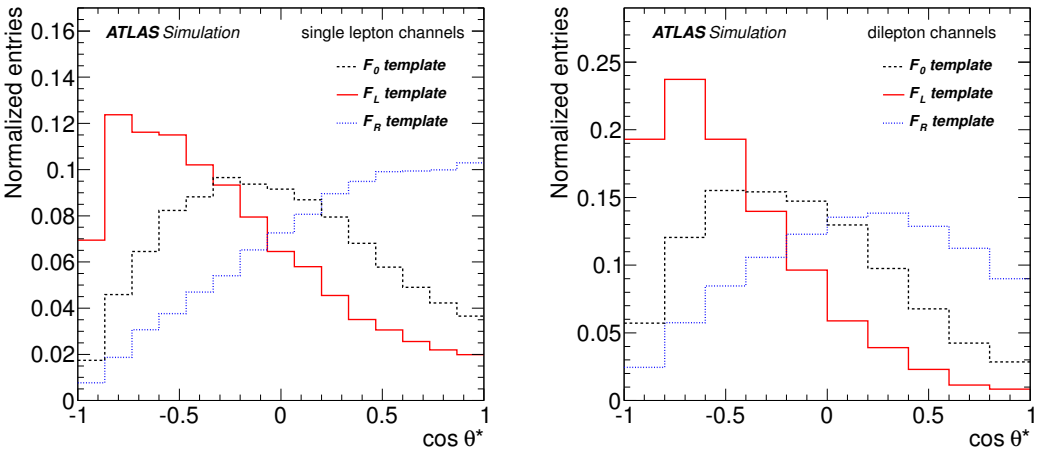

Figure 3. Distributions of $\cos\theta^*$ for each of the three simulated signal templates. The templates for the combined (left) single-lepton and (right) dilepton channels are shown.

to the central values and uncertainties given in table 1 and table 2. The uncertainties were assumed to be uncorrelated.

4.2 Measurement using the angular asymmetries

The angular asymmetries were measured using the $\cos\theta^*$ distribution obtained by reconstructing the events with a χ^2 minimization technique in the single-lepton channels [44]. The χ^2 was defined according to:

$$\chi^2 = \frac{(m_{\ell\nu j_a} - m_t)^2}{\sigma_t^2} + \frac{(m_{j_b j_c j_d} - m_t)^2}{\sigma_t^2} + \frac{(m_{\ell\nu} - m_W)^2}{\sigma_W^2} + \frac{(m_{j_c j_d} - m_W)^2}{\sigma_W^2} , \qquad (4.3)$$

where $m_t = 172.5\,\text{GeV}$, $m_W = 80.4\,\text{GeV}$, $\sigma_t = 14\,\text{GeV}$ and $\sigma_W = 10\,\text{GeV}$ are the expected top quark and W boson mass resolutions, ℓ represents the selected electron or muon, $m_{\ell\nu}$ is the invariant mass of the electron (muon) and the neutrino, and $j_{a,b,c,d}$ corresponds to all possible combinations of four jets among all selected jets in the event (with $m_{\ell\nu j_a}$, $m_{j_b j_c j_d}$ and $m_{\ell\nu j_a}$ being the corresponding invariant masses). The neutrino was reconstructed using the missing transverse energy, with the longitudinal component of the neutrino momentum (p_z^ν) allowed to vary. The solution corresponding to the minimum χ^2 value is chosen. No b-tagging information was used in resolving the ambiguities in assigning jets.

The method described in the previous subsection was used to reconstruct dilepton $t\bar{t}$ events.

For the measurement of the angular asymmetries, A_+ and A_-, the $\cos\theta^*$ distribution was divided into four non-uniform bins, which were used to count the number of events above and below $z = \pm(1 - 2^{2/3})$, as defined in Equation 1.2. A background subtraction in the observed $\cos\theta^*$ distribution was performed. Subsequently, the following steps were applied iteratively: the number of reconstructed events above and below $\cos\theta^* = z$ were counted in data for each asymmetry and correction factors were evaluated by comparing

JHEP06(2012)088

the Standard Model expectation with the reconstructed number of simulated $t\bar{t}$ events. These factors allowed corrections to be made for event selection and reconstruction effects. The obtained angular asymmetries were then converted into W boson helicity fractions and these values were used to re-derive the $\cos\theta^*$ distribution and evaluate new correction factors. The procedure was repeated until the method converged, i.e. until the differences between the output observables and the input hypothesis at the previous iteration step were below 0.5%. Closure tests were performed using Monte Carlo samples with different helicity fractions and no bias was observed.

5 Systematic uncertainties

5.1 Sources of systematic uncertainty

Several sources of systematic uncertainty were taken into account in the analyses presented here. These were categorized into the modelling of the signal and background processes, and the detector modelling. The impact of the systematic uncertainties on the final results is summarized in table 3.

5.1.1 Signal and background modelling

The signal process was modelled with different Monte Carlo generators. Sources of systematic uncertainty considered here were the choice of generator and parton shower model, the choice of parton distribution functions, the assumed top quark mass and the choice of parameters which control the amount of initial and final state radiation. Predictions from the MC@NLO and Powheg generators were compared. The parton showering was tested by comparing two Powheg samples interfaced to Herwig and Pythia, respectively. The amount of initial and final state radiation was varied by modifying parameters in AcerMC interfaced to Pythia. The parameters were varied in a range comparable with those used in the Perugia Soft/Hard tune variations [45]. The impact of the choice of parton distribution functions was studied using the reweighting procedure described in ref. [44]. MC@NLO samples were generated assuming different top quark masses and their predictions were compared. The observed differences in the results were scaled to variations of 0.9 GeV in the top quark mass according to the uncertainty on its Tevatron average value [3]. The impact of different models of colour reconnection was studied by comparing samples simulated with AcerMC using the Perugia 2010 tune with and without colour reconnection [45] as well as the tune A-Pro and ACR-Pro [46, 47].

Background processes were either modelled by simulation or were estimated in auxiliary measurements. The number of events with misidentified leptons was estimated in data for each channel [40] and the uncertainty on the normalization was estimated to be 50% before and 100% after the b-tagging requirement. The normalization of W+jets processes was estimated from supplementary measurements using the asymmetric production of positively and negatively charged W bosons. The uncertainty was estimated using Berends-Giele-scaling [48] which yielded 48% for events with four jets and increased with the jet multiplicity by 24% per additional jet [39]. Systematic uncertainties on the shapes of the W+jets distributions were assigned based on samples with different simulation parameters such as

JHEP06(2012)088

the minimum transverse momentum of the parton and the functional form of the factorization scale in Alpgen. Scaling factors correcting the fraction of heavy flavour contributions in simulated W+jets samples were estimated in auxiliary measurements described in ref. [40]. The uncertainties were 76% for $Wb\bar{b}$+jets and $Wc\bar{c}$+jets contributions, and 35% for Wc+jets contributions. The uncertainty on the normalization of Z+jets events was estimated using Berends-Giele-scaling. The uncertainties in the normalization were 48% for events with four jets and increased with the jet multiplicity by 24% per additional jet. A systematic uncertainty in the shape was accounted for by comparing simulated samples generated with Alpgen and Sherpa. The uncertainty on the normalization of the small background contributions from single top quark and diboson production was estimated to be about 10% (depending on the channel) and 5%, respectively. The former estimate was based on the difference between the predictions from MC@NLO and MCFM [49], whereas the latter comes from scale and PDF uncertainties evaluated with MCFM.

For the template method, the bin content in each template was varied according to a Poisson distribution to estimate the impact of the finite Monte Carlo sample size used. For the measurement of the angular asymmetries, the $t\bar{t}$ reconstruction parameters were varied. In the single-lepton channels, the top quark and W boson mass resolutions used in the χ^2 definition were changed by 25%. For the dilepton channels, the assumed top quark mass window used in the kinematic equations was reduced by 50%, taking the difference in the observables with respect to the nominal procedure as the uncertainty estimate. The uncertainty due to the finite Monte Carlo sample size was found to be negligible since fewer bins were used in the unfolding than for the templates. These sources of uncertainty are labelled "method-specific uncertainties" in table 3.

5.1.2 Detector modelling

The mis-modelling of lepton trigger, reconstruction and selection efficiencies in simulation was corrected for by scale factors derived from auxiliary measurements of the processes $Z \to \mu\mu$ and $Z \to ee$ [50, 51]. The uncertainties were evaluated by changing the event selection of the supplementary measurement and by testing the stability of the results against changing LHC and ATLAS run conditions. The same processes were used to measure the lepton momentum scale and resolution. Scale factors and their uncertainties were derived to match the simulation to observed distributions. Details are given in ref. [39].

The jet energy scale was derived using information from test-beam data, LHC collision data and simulation. Its uncertainty varies between 2.5% and 7% in the central η region, depending on jet p_{T} and η [52]. This includes uncertainties in the flavour composition of the samples and mis-measurements from close-by jets. An additional p_{T}-dependent uncertainty of up to 2.5% was assigned to jets matched to b-quarks (using Monte Carlo generator-level information) due to differences between light-quark and gluon jets as opposed to jets containing b-hadrons. Additional uncertainties of up to 5% (8%) in the central (forward) region were added due to pileup. The energy resolution for jets in Monte Carlo simulation was adjusted to that observed in data. Uncertainties on the energy resolution of 4–45%, decreasing with jet p_{T}, were assigned. The reconstruction efficiency of jets was found to be in good agreement with the predictions from simulation and uncertainties of 1–2% were assigned.

JHEP06(2012)088

Source	Uncertainties		
	F_0	F_L	F_R
Signal and background modelling			
Generator choice	0.012	0.009	0.004
ISR/FSR	0.015	0.008	0.007
PDF	0.011	0.006	0.006
Top quark mass	0.016	0.009	0.008
Misidentified leptons	0.020	0.013	0.007
W+jets	0.016	0.008	0.008
Other backgrounds	0.006	0.003	0.003
Method-specific uncertainties	0.031	0.016	0.035
Detector modelling			
Lepton reconstruction	0.013	0.006	0.007
Jet energy scale	0.026	0.014	0.012
Jet reconstruction	0.012	0.005	0.007
b-tagging	0.007	0.003	0.004
Calorimeter readout	0.009	0.005	0.004
Luminosity and pileup	0.009	0.004	0.005
Total systematic uncertainty	0.06	0.03	0.04

Table 3. Sources of systematic uncertainty and their impact on the measured W boson helicity fractions for the combined single-lepton and dilepton channels. The systematic uncertainties were symmetrized by using the larger uncertainty.

JHEP06(2012)088

The uncertainties on the momenta of electrons, muons and jets were propagated into the missing transverse momentum. A 10% uncertainty from pileup was added in addition.

The b-tagging efficiencies and mis-tag rates have been measured in data [42]. Jet p_T-dependent scale factors, applied to simulation to match the data, have uncertainties which range from 9% to 16% and 12% to 45%, respectively.

The uncertainty on the measured luminosity was estimated to be 3.7% [15].

Due to a hardware failure, a small, rectangular region of the ATLAS electromagnetic calorimeter could not be read out in a subset of the data ($0.87\,\text{fb}^{-1}$). Data and Monte Carlo events in which a jet or an electron were close to the affected calorimeter region were rejected. The systematic uncertainty labelled "calorimeter readout" in table 3 was evaluated by varying the criteria to reject these events.

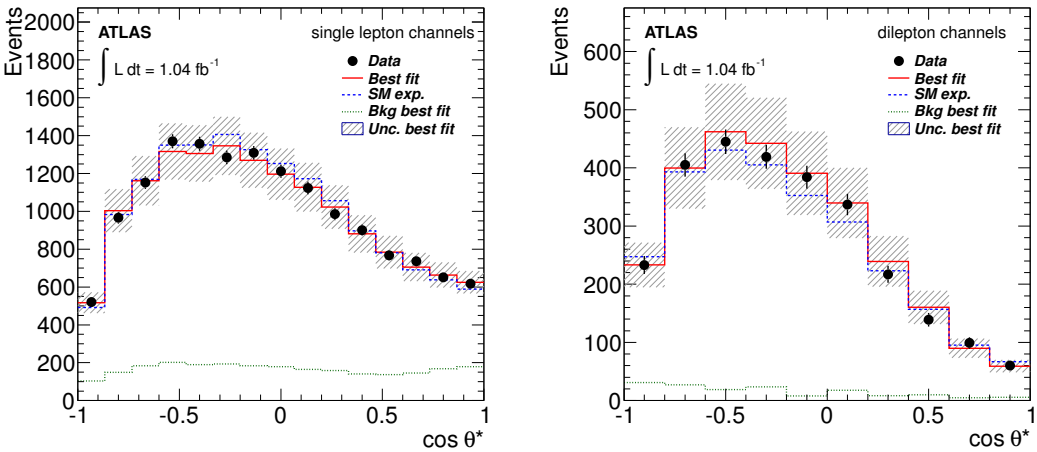

Figure 4. Distributions of the reconstructed $\cos\theta^*$ used in the template method for data (markers), fitted background (dotted line), the Standard Model prediction (dashed line) and the best fit value (solid line) for the (left) single-lepton and (right) dilepton channels. The total uncertainties on the helicity fractions for the best fit values are represented by the grey band. For the dilepton channels, each event contributed with two entries, corresponding to the two leptonic decays of the W bosons.

6 Results

The two methods discussed in section 4 were applied to the data set described in section 2. Figure 4 shows the observed distribution of $\cos\theta^*$ in the single-lepton and dilepton channels together with the sum of the templates scaled to the best fit parameters obtained from the template method as well as the Standard Model expectations. Figure 5 shows the distribution of $\cos\theta^*$ in the single-lepton and dilepton channels after the background subtraction and the correction for detector and reconstruction effects as used by the asymmetry method as well as the Standard Model expectations.

The combination of the individual measurements of the W boson helicity fractions (F_0 and F_{L}) and asymmetries (A_+ and A_-) in the single-lepton and dilepton channels was done using the best linear unbiased estimator (BLUE) method [53, 54]. The impact of the systematic uncertainties described in section 5 was studied and the results are summarized in table 4, which also gives the combination of all channels for each method. The results are compatible with each other and with the final combination. In addition, the template fit was repeated with F_{R} fixed to zero.[3] With the precision of the current measurements, this differs negligibly from the Standard Model value, and also follows the approach suggested in ref. [13]. The results can also be found in table 4.

The results for the angular asymmetries from the single-lepton channels are $A_+ = 0.52 \pm 0.02$ (stat.) $\pm\, 0.03$ (syst.) and $A_- = -0.84 \pm 0.01$ (stat.) $\pm\, 0.02$ (syst.) whereas

[3] In the evaluation of the angular asymmetries no assumption is made for the helicity fractions, so it is not possible to fix F_{R} to zero.

JHEP06(2012)088

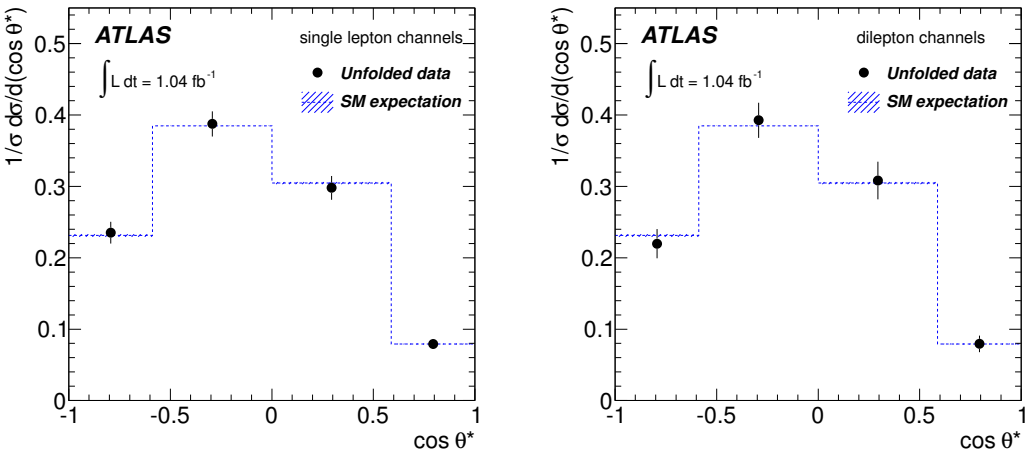

Figure 5. Unfolded distributions of $\cos\theta^*$ for the (left) single-lepton and (right) dilepton channels. The error bars on unfolded data (markers) include both the statistical and systematic contributions. For comparison, the Standard Model NNLO QCD prediction (dashed line) and its uncertainty [4] are also shown.

the results for the dilepton channels are $A_+ = 0.56 \pm 0.02$ (stat.) $\pm$ 0.04 (syst.) and $A_- = -0.84 \pm 0.02$ (stat.) $\pm$ 0.04 (syst.).

Most of the measurements and the combined result are limited by systematic uncertainties. The largest sources of uncertainty are the signal and background modelling, as well as the jet energy scale and jet reconstruction. The template fits are more sensitive to shape-related uncertainties, such as ISR/FSR and jet reconstruction, while the angular asymmetries are more sensitive to background normalization uncertainties, due to the background subtraction which needs to be performed.

6.1 Combination

The results presented in the previous sections were combined using the BLUE method. Both the statistical correlations between analyses, and the correlations of systematic uncertainties, were taken into account. The statistical correlations were estimated to be between 40% and 49% for the single-lepton channels and between 83% and 89% for the dilepton channels using pseudo-experiments obtained from simulated samples. The background-related systematic uncertainties were assumed to be fully correlated within single-lepton channels and within dilepton channels, but uncorrelated between single-lepton and dilepton measurements. The only exception is the uncertainty due to misidentified lepton background which depends on the lepton flavour and thus belongs to the group of lepton-related uncertainties, which were assumed to be fully correlated between the channels with same flavour leptons. The method systematic uncertainties were assumed to be uncorrelated between channels and the remaining sources of systematic uncertainty were assumed to be fully correlated between channels. Various tests were performed in which the correlations among the sources of systematic uncertainty were varied. It was found that the values

JHEP06(2012)088

Channel	F_0	F_L	F_R
W boson helicity fractions from the template fit			
Single leptons	$0.57 \pm 0.06 \pm 0.09$	$0.37 \pm 0.03 \pm 0.04$	$0.07 \pm 0.03 \pm 0.06$
Dileptons	$0.92 \pm 0.10 \pm 0.10$	$0.17 \pm 0.06 \pm 0.07$	$-0.09 \pm 0.05 \pm 0.06$
Combination	$0.66 \pm 0.06 \pm 0.07$	$0.33 \pm 0.03 \pm 0.03$	$0.01 \pm 0.03 \pm 0.06$
F_R fixed	$0.66 \pm 0.03 \pm 0.04$	$0.34 \pm 0.03 \pm 0.04$	0 (fixed)
W boson helicity fractions from the angular asymmetries			
Single leptons	$0.66 \pm 0.03 \pm 0.08$	$0.33 \pm 0.02 \pm 0.05$	$0.01 \pm 0.01 \pm 0.04$
Dileptons	$0.74 \pm 0.06 \pm 0.10$	$0.27 \pm 0.03 \pm 0.05$	$-0.01 \pm 0.03 \pm 0.05$
Combination	$0.67 \pm 0.04 \pm 0.07$	$0.32 \pm 0.02 \pm 0.04$	$0.01 \pm 0.02 \pm 0.04$
Overall combination	$0.67 \pm 0.03 \pm 0.06$	$0.32 \pm 0.02 \pm 0.03$	$0.01 \pm 0.01 \pm 0.04$

Table 4. Summary of the W boson helicity fractions measured using the two different techniques described and the combination. The quoted uncertainties are the statistical (first) and the systematic (second) uncertainties.

assumed for the correlations were conservative. The systematic uncertainties on the combined values are summarized in table 3. The four measurements of the helicity fractions and the combined values are shown in table 4 and figure 6.

The individual measurements agree reasonably well within their total uncertainties. The χ^2/dof for the global combination of the template fit and asymmetries measurements was 0.8 with a χ^2-probability of 75%, where dof is the number of degrees of freedom. The largest difference between two measurements is that between the single-lepton and dilepton channels obtained with the template method. Since the measurements were performed in five independent channels (single electron, single muon, ee, $e\mu$ and $\mu\mu$), the combination was performed based on the five individual measurements taking into account all correlations. The χ^2/dof calculated using the BLUE method for this combination was 1.3 with a χ^2-probability of 23%.

The combined W boson helicity fractions are:

$$\begin{aligned} F_0 &= 0.67 \pm 0.03 \text{ (stat.)} \pm 0.06 \text{ (syst.)}\,, \\ F_L &= 0.32 \pm 0.02 \text{ (stat.)} \pm 0.03 \text{ (syst.)}\,, \\ F_R &= 0.01 \pm 0.01 \text{ (stat.)} \pm 0.04 \text{ (syst.)}\,. \end{aligned}$$

The correlation coefficient between F_0 and F_L was estimated to be -0.96. For completeness, these results can be translated into angular asymmetries, yielding $A_+ = 0.53 \pm 0.02$ and $A_- = -0.84 \pm 0.02$.

An alternative analysis, based on requiring two b-tagged jets to further suppress the W+jets background and events with misidentified leptons, was used to measure the helicity fractions in the single-lepton channels as a cross-check. The observed $\cos\theta^*$ distributions were corrected by subtracting the expected background contributions and were unfolded

JHEP06(2012)088

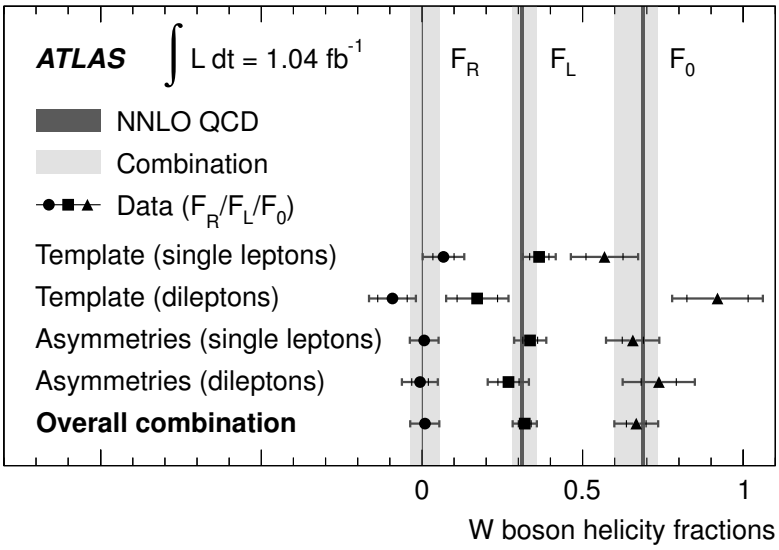

Figure 6. Overview of the four measurements of the W boson helicity fractions and the combined values. The error bars correspond to the statistical and total uncertainties.

using correction functions in an iterative method similar to the one used in the measurement of the angular asymmetries described in section 4.2. The results were found to be in agreement with the single-lepton measurements presented in this paper.

6.2 Constraints on the Wtb vertex structure

Any deviation of F_0, F_L, F_R (or A_+ and A_-) from the Standard Model prediction could be caused by new physics contributing to the Wtb vertex. Such new interactions associated with the top quark may exist at higher energies. New physics can be parameterized in terms of an effective Lagrangian [11] above the electroweak symmetry breaking scale of $v = 246$ GeV. After electroweak symmetry breaking, the Wtb Lagrangian [12, 55] is:

$$\mathcal{L}_{Wtb} = -\frac{g}{\sqrt{2}}\bar{b}\,\gamma^\mu\,(V_\mathrm{L}P_\mathrm{L} + V_\mathrm{R}P_\mathrm{R})\,t\,W^-_\mu - \frac{g}{\sqrt{2}}\bar{b}\,\frac{i\sigma^{\mu\nu}q_\nu}{M_W}\,(g_\mathrm{L}P_\mathrm{L} + g_\mathrm{R}P_\mathrm{R})\,t\,W^-_\mu + \mathrm{h.c.}\,, \quad (6.1)$$

where P_L (P_R) is the left-handed (right-handed) chirality operator and

$$V_\mathrm{L} = V_{tb} + C^{(3,3+3)}_{\phi q}\frac{v^2}{\Lambda^2}\,, \quad V_\mathrm{R} = \frac{1}{2}C^{33*}_{\phi\phi}\frac{v^2}{\Lambda^2}\,, \quad g_\mathrm{L} = \sqrt{2}C^{33*}_{dW}\frac{v^2}{\Lambda^2}\,, \quad g_\mathrm{R} = \sqrt{2}C^{33}_{uW}\frac{v^2}{\Lambda^2}\,. \quad (6.2)$$

The parameter Λ is the new physics scale and $C^{(3,3+3)}_{\phi q}$, $C^{33*}_{\phi\phi}$, C^{33*}_{dW} and C^{33}_{uW} are the effective operator coefficients [13, 55]. The anomalous couplings V_R, g_L, g_R, generated by dimension-six operators, are absent in the Standard Model at tree level, while the coupling V_{tb} receives a correction from the operator $O^{(3,3+3)}_{\phi q}$.

Limits on anomalous couplings (V_R, g_L and g_R) were obtained from the combined measurement of the W boson helicity fractions by exploiting their dependence on these

JHEP06(2012)088

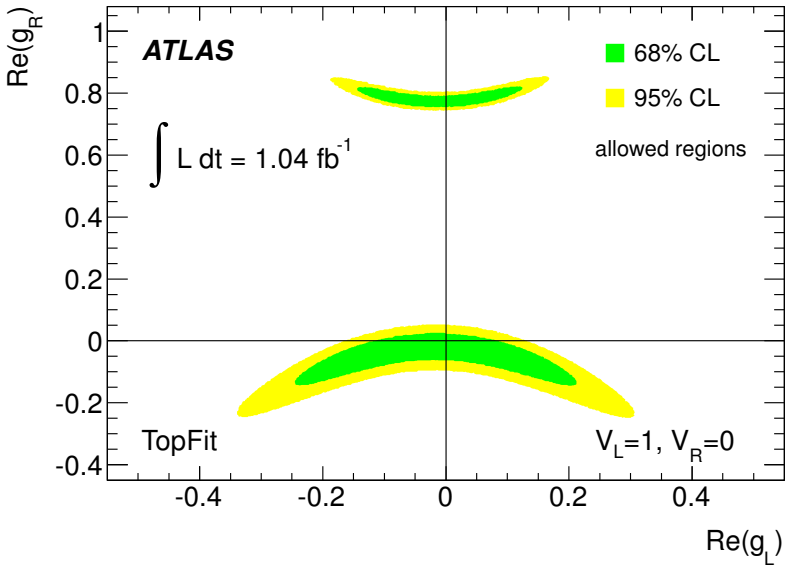

Figure 7. Allowed regions at 68% and 95% confidence level (CL) for the Wtb anomalous couplings $g_{\rm L}$ and $g_{\rm R}$. In the Standard Model, the anomalous couplings vanish at tree level [59].

couplings, as implemented in the TopFit program [10, 56] and normalizing to $V_{\rm L} = 1$. The allowed regions of ($g_{\rm L}$, $g_{\rm R}$) are shown in figure 7, assuming $V_{\rm R} = 0$. The upper disconnected region in the plot shows a large-$g_{\rm R}$ second solution to the quadratic equation relating the observables to the anomalous couplings. However, this region is disfavored by the measured cross-section for single top production at the Tevatron [17, 57, 58].

In addition to this two-dimensional limit it is useful to set limits on single anomalous couplings, taking only one of them non-zero at a time. These are, at 95% confidence level,

$$\begin{aligned}
{\rm Re}\,(V_{\rm R}) &\in [-0.20, 0.23] \rightarrow \frac{{\rm Re}\,(C^{33}_{\phi\phi})}{\Lambda^2} \in [-6.7, 7.8] \ \ {\rm TeV}^{-2}\,,\\
{\rm Re}\,(g_{\rm L}) &\in [-0.14, 0.11] \rightarrow \frac{{\rm Re}\,(C^{33}_{dW})}{\Lambda^2} \in [-1.6, 1.2] \ \ {\rm TeV}^{-2}\,,\\
{\rm Re}\,(g_{\rm R}) &\in [-0.08, 0.04] \rightarrow \frac{{\rm Re}\,(C^{33}_{uW})}{\Lambda^2} \in [-1.0, 0.5] \ \ {\rm TeV}^{-2}\,.
\end{aligned}$$

The considered W boson helicity observables also allow a second region for $g_{\rm R}$ when the remaining anomalous couplings vanish: ${\rm Re}\,(g_{\rm R}) \in [0.75, 0.80]$ at 95% confidence level. It should be noticed, however, that such large coupling values would imply a single top production cross-section value disfavored by the Tevatron measurements [17, 57, 58]. Using a Bayesian approach [60], the measurement of the W boson helicity fractions with $F_{\rm R}$ fixed at zero, was translated into a 95% probability interval on ${\rm Re}\,(C^{33}_{uW})/\Lambda^2$, as proposed in ref. [13]. This interval was found to be $[-0.9, 2.3]$ TeV^{-2}.

It can be seen that the limits on C^{33}_{dW} (mediating the production of right-handed b-quarks in the top decay) are of the same order of magnitude as the limits on C^{33}_{uW} (involving

JHEP06(2012)088

left-handed quarks). This reflects a good sensitivity to the effective operator corresponding to C_{dW}^{33}, even if its contribution is suppressed by $1/\Lambda^2$ instead of $1/\Lambda$ [61].

These limits are more stringent than those obtained by the DØ Collaboration [58, 62].[4] Indirect, model-dependent limits on the anomalous couplings have been inferred from measurements of radiative B-meson decays, measurements of $B\bar{B}$-mixing and electroweak precision data [63–67], but these limits include assumptions on the absence of additional new physics effects that are not needed in this analysis.

7 Conclusions

A measurement of the polarization of the W bosons in top quark decays was presented, based on $1.04\,\mathrm{fb}^{-1}$ of data collected with the ATLAS detector in 2011. The single-lepton and dilepton decay topologies of top quark pairs were considered in the analysis.

The helicity fractions obtained from a combination of template fits to the reconstructed $\cos\theta^*$ distributions and angular asymmetries calculated from the unfolded $\cos\theta^*$ distributions are $F_0 = 0.67 \pm 0.07$, $F_\mathrm{L} = 0.32 \pm 0.04$ and $F_\mathrm{R} = 0.01 \pm 0.05$. These results are in agreement with NNLO QCD predictions and are more precise than previous results obtained by the CDF and DØ Collaborations [6–8].

Limits on the Wtb vertex anomalous couplings were obtained from the combined results on the W boson helicity fractions. These results are consistent with the $(V-A)$ structure of the Wtb vertex and improve on the previously obtained limits [58].

Acknowledgments

We thank CERN for the very successful operation of the LHC, as well as the support staff from our institutions without whom ATLAS could not be operated efficiently.

We acknowledge the support of ANPCyT, Argentina; YerPhI, Armenia; ARC, Australia; BMWF, Austria; ANAS, Azerbaijan; SSTC, Belarus; CNPq and FAPESP, Brazil; NSERC, NRC and CFI, Canada; CERN; CONICYT, Chile; CAS, MOST and NSFC, China; COLCIENCIAS, Colombia; MSMT CR, MPO CR and VSC CR, Czech Republic; DNRF, DNSRC and Lundbeck Foundation, Denmark; EPLANET and ERC, European Union; IN2P3-CNRS, CEA-DSM/IRFU, France; GNAS, Georgia; BMBF, DFG, HGF, MPG and AvH Foundation, Germany; GSRT, Greece; ISF, MINERVA, GIF, DIP and Benoziyo Center, Israel; INFN, Italy; MEXT and JSPS, Japan; CNRST, Morocco; FOM and NWO, Netherlands; RCN, Norway; MNiSW, Poland; GRICES and FCT, Portugal; MERYS (MECTS), Romania; MES of Russia and ROSATOM, Russian Federation; JINR; MSTD, Serbia; MSSR, Slovakia; ARRS and MVZT, Slovenia; DST/NRF, South Africa; MICINN, Spain; SRC and Wallenberg Foundation, Sweden; SER, SNSF and Cantons of Bern and Geneva, Switzerland; NSC, Taiwan; TAEK, Turkey; STFC, the Royal Society and Leverhulme Trust, United Kingdom; DOE and NSF, United States of America.

The crucial computing support from all WLCG partners is acknowledged gratefully, in particular from CERN and the ATLAS Tier-1 facilities at TRIUMF (Canada), NDGF

[4]The limits from the DØ Collaboration were derived assuming a massless b-quark.

JHEP06(2012)088

(Denmark, Norway, Sweden), CC-IN2P3 (France), KIT/GridKA (Germany), INFN-CNAF (Italy), NL-T1 (Netherlands), PIC (Spain), ASGC (Taiwan), RAL (U.K.) and BNL (U.S.A.) and in the Tier-2 facilities worldwide.

Open Access. This article is distributed under the terms of the Creative Commons Attribution License which permits any use, distribution and reproduction in any medium, provided the original author(s) and source are credited.

References

[1] CDF collaboration, F. Abe et al., *Observation of top quark production in $\bar{p}p$ collisions*, *Phys. Rev. Lett.* **74** (1995) 2626 [hep-ex/9503002] [INSPIRE].

[2] DØ collaboration, S. Abachi et al., *Observation of the top quark*, *Phys. Rev. Lett.* **74** (1995) 2632 [hep-ex/9503003] [INSPIRE].

[3] Tevatron Electroweak Working Group, CDF and DØ collaborations, *Combination of CDF and DØ results on the mass of the top quark using up to* $5.8\,fb^{-1}$ *of data*, arXiv:1107.5255 [INSPIRE].

[4] A. Czarnecki, J.G. Korner and J.H. Piclum, *Helicity fractions of W bosons from top quark decays at NNLO in QCD*, *Phys. Rev.* **D 81** (2010) 111503 [arXiv:1005.2625] [INSPIRE].

[5] G.L. Kane, G. Ladinsky and C. Yuan, *Using the top quark for testing Standard Model polarization and CP predictions*, *Phys. Rev.* **D 45** (1992) 124 [INSPIRE].

[6] CDF and DØ collaborations, T. Aaltonen et al., *Combination of CDF and DØ measurements of the W boson helicity in top quark decays*, arXiv:1202.5272 [INSPIRE].

[7] CDF collaboration, T. Aaltonen et al., *Measurement of W-boson polarization in top-quark decay in $p\bar{p}$ collisions at $\sqrt{s} = 1.96$ TeV*, *Phys. Rev. Lett.* **105** (2010) 042002 [arXiv:1003.0224] [INSPIRE].

[8] DØ collaboration, V.M. Abazov et al., *Measurement of the W boson helicity in top quark decays using* $5.4\,fb^{-1}$ *of $p\bar{p}$ collision data*, *Phys. Rev.* **D 83** (2011) 032009 [arXiv:1011.6549] [INSPIRE].

[9] F. del Aguila and J. Aguilar-Saavedra, *Precise determination of the Wtb couplings at CERN LHC*, *Phys. Rev.* **D 67** (2003) 014009 [hep-ph/0208171] [INSPIRE].

[10] J. Aguilar-Saavedra, J. Carvalho, N.F. Castro, F. Veloso and A. Onofre, *Probing anomalous Wtb couplings in top pair decays*, *Eur. Phys. J.* **C 50** (2007) 519 [hep-ph/0605190] [INSPIRE].

[11] W. Buchmüller and D. Wyler, *Effective Lagrangian analysis of new interactions and flavor conservation*, *Nucl. Phys.* **B 268** (1986) 621 [INSPIRE].

[12] J. Aguilar-Saavedra, *A minimal set of top anomalous couplings*, *Nucl. Phys.* **B 812** (2009) 181 [arXiv:0811.3842] [INSPIRE].

[13] C. Zhang and S. Willenbrock, *Effective-field-theory approach to top-quark production and decay*, *Phys. Rev.* **D 83** (2011) 034006 [arXiv:1008.3869] [INSPIRE].

[14] ATLAS collaboration, G. Aad et al., *The ATLAS experiment at the CERN Large Hadron Collider*, 2008 *JINST* **3** S08003 [INSPIRE].

JHEP06(2012)088

[15] ATLAS collaboration, *Luminosity determination in pp collisions at $\sqrt{s} = 7$ TeV using the ATLAS detector in* 2011, ATLAS-CONF-2011-116, CERN, Geneva Switzerland (2011).

[16] ATLAS collaboration, G. Aad et al., *Luminosity determination in pp collisions at $\sqrt{s} = 7$ TeV using the ATLAS detector at the LHC*, *Eur. Phys. J.* **C 71** (2011) 1630 [arXiv:1101.2185] [INSPIRE].

[17] J. Aguilar-Saavedra, *Single top quark production at LHC with anomalous Wtb couplings*, *Nucl. Phys.* **B 804** (2008) 160 [arXiv:0803.3810] [INSPIRE].

[18] J. Pumplin et al., *New generation of parton distributions with uncertainties from global QCD analysis*, *JHEP* **07** (2002) 012 [hep-ph/0201195] [INSPIRE].

[19] T. Sjöstrand, S. Mrenna and P.Z. Skands, *PYTHIA* 6.4 *physics and manual*, *JHEP* **05** (2006) 026 [hep-ph/0603175] [INSPIRE].

[20] S. Frixione and B.R. Webber, *Matching NLO QCD computations and parton shower simulations*, *JHEP* **06** (2002) 029 [hep-ph/0204244] [INSPIRE].

[21] S. Frixione, P. Nason and B.R. Webber, *Matching NLO QCD and parton showers in heavy flavor production*, *JHEP* **08** (2003) 007 [hep-ph/0305252] [INSPIRE].

[22] S. Frixione, E. Laenen, P. Motylinski and B.R. Webber, *Single-top production in MC@NLO*, *JHEP* **03** (2006) 092 [hep-ph/0512250] [INSPIRE].

[23] P.M. Nadolsky et al., *Implications of CTEQ global analysis for collider observables*, *Phys. Rev.* **D 78** (2008) 013004 [arXiv:0802.0007] [INSPIRE].

[24] M.L. Mangano, M. Moretti, F. Piccinini, R. Pittau and A.D. Polosa, *ALPGEN, a generator for hard multiparton processes in hadronic collisions*, *JHEP* **07** (2003) 001 [hep-ph/0206293] [INSPIRE].

[25] G. Corcella et al., *HERWIG* 6*: an event generator for hadron emission reactions with interfering gluons (including supersymmetric processes)*, *JHEP* **01** (2001) 010 [hep-ph/0011363] [INSPIRE].

[26] S. Frixione, E. Laenen, P. Motylinski, B.R. Webber and C.D. White, *Single-top hadroproduction in association with a W boson*, *JHEP* **07** (2008) 029 [arXiv:0805.3067] [INSPIRE].

[27] T. Gleisberg et al., *Event generation with SHERPA* 1.1, *JHEP* **02** (2009) 007 [arXiv:0811.4622] [INSPIRE].

[28] J. Butterworth, J.R. Forshaw and M. Seymour, *Multiparton interactions in photoproduction at HERA*, *Z. Phys.* **C 72** (1996) 637 [hep-ph/9601371] [INSPIRE].

[29] ATLAS collaboration, *New ATLAS event generator tunes to* 2010 *data*, ATL-PHYS-PUB-2011-008, CERN, Geneva Switzerland (2011).

[30] B.P. Kersevan and E. Richter-Was, *The Monte Carlo event generator AcerMC version* 2.0 *with interfaces to PYTHIA* 6.2*, HERWIG* 6.5 *and ARIADNE* 4.1, hep-ph/0405247 [INSPIRE].

[31] P. Nason, *A new method for combining NLO QCD with shower Monte Carlo algorithms*, *JHEP* **11** (2004) 040 [hep-ph/0409146] [INSPIRE].

[32] S. Frixione, P. Nason and C. Oleari, *Matching NLO QCD computations with parton shower simulations: the POWHEG method*, *JHEP* **11** (2007) 070 [arXiv:0709.2092] [INSPIRE].

JHEP06(2012)088

[33] GEANT4 collaboration, S. Agostinelli et al., *GEANT4: a simulation toolkit*, *Nucl. Instrum. Meth.* **A 506** (2003) 250 [INSPIRE].

[34] ATLAS collaboration, G. Aad et al., *The ATLAS simulation infrastructure*, *Eur. Phys. J.* **C 70** (2010) 823 [arXiv:1005.4568] [INSPIRE].

[35] S. Moch and P. Uwer, *Theoretical status and prospects for top-quark pair production at hadron colliders*, *Phys. Rev.* **D 78** (2008) 034003 [arXiv:0804.1476] [INSPIRE].

[36] U. Langenfeld, S. Moch and P. Uwer, *New results for $t\bar{t}$ production at hadron colliders*, arXiv:0907.2527 [INSPIRE].

[37] M. Aliev et al., *HATHOR: HAdronic Top and Heavy quarks crOss section calculatoR*, *Comput. Phys. Commun.* **182** (2011) 1034 [arXiv:1007.1327] [INSPIRE].

[38] ATLAS collaboration, G. Aad et al., *Measurement of the cross section for top-quark pair production in pp collisions at $\sqrt{s} = 7$ TeV with the ATLAS detector using final states with two high-p_T leptons*, *JHEP* **05** (2012) 059 [arXiv:1202.4892] [INSPIRE].

[39] ATLAS collaboration, G. Aad et al., *Measurement of the top quark-pair production cross section with ATLAS in pp collisions at $\sqrt{s} = 7$ TeV*, *Eur. Phys. J.* **C 71** (2011) 1577 [arXiv:1012.1792] [INSPIRE].

[40] ATLAS collaboration, G. Aad et al., *Measurement of the charge asymmetry in top quark pair production in pp collisions at $\sqrt{s} = 7$ TeV using the ATLAS detector*, arXiv:1203.4211 [INSPIRE].

[41] M. Cacciari, G.P. Salam and G. Soyez, *The anti-k_t jet clustering algorithm*, *JHEP* **04** (2008) 063 [arXiv:0802.1189] [INSPIRE].

[42] ATLAS collaboration, *Measurement of the rate of collisions from satellite bunches for the april-may* 2010 *LHC luminosity calibration*, ATLAS-CONF-2010-102, CERN, Geneva Switzerland (2010).

[43] ATLAS collaboration, G. Aad et al., *Measurement of the top quark mass with the template method in the $t\bar{t} \to$ lepton + jets channel using ATLAS data*, *Eur. Phys. J. C* (2012) [arXiv:1203.5755] [INSPIRE].

[44] ATLAS collaboration, *Expected performance of the ATLAS experiment: detector, trigger and physics*, CERN-OPEN-2008-020, CERN, Geneva Switzerland (2009).

[45] P.Z. Skands, *Tuning Monte Carlo generators: the Perugia tunes*, *Phys. Rev.* **D 82** (2010) 074018 [arXiv:1005.3457] [INSPIRE].

[46] TeV4LHC QCD Working Group collaboration, M.G. Albrow et al., *Tevatron-for-LHC report of the QCD working group*, hep-ph/0610012 [INSPIRE].

[47] A. Buckley, H. Hoeth, H. Lacker, H. Schulz and J.E. von Seggern, *Systematic event generator tuning for the LHC*, *Eur. Phys. J.* **C 65** (2010) 331 [arXiv:0907.2973] [INSPIRE].

[48] F.A. Berends, H. Kuijf, B. Tausk and W. Giele, *On the production of a W and jets at hadron colliders*, *Nucl. Phys.* **B 357** (1991) 32 [INSPIRE].

[49] J.M. Campbell and R.K. Ellis, *Radiative corrections to $Zb\bar{b}$ production*, *Phys. Rev.* **D 62** (2000) 114012 [hep-ph/0006304] [INSPIRE].

[50] ATLAS collaboration, *Muon momentum resolution in first pass reconstruction of pp collision data recorded by ATLAS in* 2010, ATLAS-CONF-2011-046, CERN, Geneva Switzerland (2011).

JHEP06(2012)088

[51] ATLAS collaboration, G. Aad et al., *Electron performance measurements with the ATLAS detector using the* 2010 *LHC proton-proton collision data*, *Eur. Phys. J.* **C 72** (2012) 1909 [arXiv:1110.3174] [INSPIRE].

[52] ATLAS collaboration, G. Aad et al., *Jet energy measurement with the ATLAS detector in proton-proton collisions at* $\sqrt{s} = 7$ *TeV*, arXiv:1112.6426 [INSPIRE].

[53] L. Lyons, D. Gibaut and P. Clifford, *How to combine correlated estimates of a single physical quantity*, *Nucl. Instrum. Meth.* **A 270** (1988) 110 [INSPIRE].

[54] A. Valassi, *Combining correlated measurements of several different physical quantities*, *Nucl. Instrum. Meth.* **A 500** (2003) 391 [INSPIRE].

[55] J. Aguilar-Saavedra, *A minimal set of top-Higgs anomalous couplings*, *Nucl. Phys.* **B 821** (2009) 215 [arXiv:0904.2387] [INSPIRE].

[56] J. Aguilar-Saavedra and J. Bernabeu, *W polarisation beyond helicity fractions in top quark decays*, *Nucl. Phys.* **B 840** (2010) 349 [arXiv:1005.5382] [INSPIRE].

[57] CDF and DØ collaborations, T.E.W. Group, *Combination of CDF and DØ measurements of the single top production cross section*, arXiv:0908.2171 [INSPIRE].

[58] DØ collaboration, V.M. Abazov et al., *Combination of searches for anomalous top quark couplings with* $5.4\,fb^{-1}$ *of* $p\bar{p}$ *collisions*, arXiv:1204.2332 [INSPIRE].

[59] H. Do, S. Groote, J. Korner and M. Mauser, *Electroweak and finite width corrections to top quark decays into transverse and longitudinal W bosons*, *Phys. Rev.* **D 67** (2003) 091501 [hep-ph/0209185] [INSPIRE].

[60] A. Caldwell, D. Kollar and K. Kroninger, *BAT: the Bayesian Analysis Toolkit*, *Comput. Phys. Commun.* **180** (2009) 2197 [arXiv:0808.2552] [INSPIRE].

[61] J.A. Aguilar-Saavedra, *Effective operators in top physics*, PoS(ICHEP 2010)378 [arXiv:1008.3225] [INSPIRE].

[62] DØ collaboration, V.M. Abazov et al., *Search for anomalous Wtb couplings in single top quark production in* $p\bar{p}$ *collisions at* $\sqrt{s} = 1.96$ *TeV*, *Phys. Lett.* **B 708** (2012) 21 [arXiv:1110.4592] [INSPIRE].

[63] B. Grzadkowski and M. Misiak, *Anomalous Wtb coupling effects in the weak radiative B-meson decay*, *Phys. Rev.* **D 78** (2008) 077501 [*Erratum ibid.* **D 84** (2011) 059903] [arXiv:0802.1413] [INSPIRE].

[64] F. del Aguila et al., *Collider aspects of flavour physics at high Q*, *Eur. Phys. J.* **C 57** (2008) 183 [arXiv:0801.1800] [INSPIRE].

[65] J. Drobnak, S. Fajfer and J.F. Kamenik, *Probing anomalous tWb interactions with rare B decays*, *Nucl. Phys.* **B 855** (2012) 82 [arXiv:1109.2357] [INSPIRE].

[66] J. Drobnak, S. Fajfer and J.F. Kamenik, *Interplay of* $t \to bW$ *decay and* B_q *meson mixing in Minimal Flavor Violating models*, *Phys. Lett.* **B 701** (2011) 234 [arXiv:1102.4347] [INSPIRE].

[67] C. Zhang, N. Greiner and S. Willenbrock, *Constraints on non-standard top quark couplings*, arXiv:1201.6670 [INSPIRE].

JHEP06(2012)088

The ATLAS collaboration

G. Aad[48], B. Abbott[111], J. Abdallah[11], S. Abdel Khalek[115], A.A. Abdelalim[49], O. Abdinov[10], B. Abi[112], M. Abolins[88], O.S. AbouZeid[158], H. Abramowicz[153], H. Abreu[136], E. Acerbi[89a,89b], B.S. Acharya[164a,164b], L. Adamczyk[37], D.L. Adams[24], T.N. Addy[56], J. Adelman[176], S. Adomeit[98], P. Adragna[75], T. Adye[129], S. Aefsky[22], J.A. Aguilar-Saavedra[124b,a], M. Agustoni[16], M. Aharrouche[81], S.P. Ahlen[21], F. Ahles[48], A. Ahmad[148], M. Ahsan[40], G. Aielli[133a,133b], T. Akdogan[18a], T.P.A. Åkesson[79], G. Akimoto[155], A.V. Akimov [94], A. Akiyama[66], M.S. Alam[1], M.A. Alam[76], J. Albert[169], S. Albrand[55], M. Aleksa[29], I.N. Aleksandrov[64], F. Alessandria[89a], C. Alexa[25a], G. Alexander[153], G. Alexandre[49], T. Alexopoulos[9], M. Alhroob[164a,164c], M. Aliev[15], G. Alimonti[89a], J. Alison[120], B.M.M. Allbrooke[17], P.P. Allport[73], S.E. Allwood-Spiers[53], J. Almond[82], A. Aloisio[102a,102b], R. Alon[172], A. Alonso[79], B. Alvarez Gonzalez[88], M.G. Alviggi[102a,102b], K. Amako[65], C. Amelung[22], V.V. Ammosov[128], A. Amorim[124a,b], N. Amram[153], C. Anastopoulos[29], L.S. Ancu[16], N. Andari[115], T. Andeen[34], C.F. Anders[58b], G. Anders[58a], K.J. Anderson[30], A. Andreazza[89a,89b], V. Andrei[58a], X.S. Anduaga[70], P. Anger[43], A. Angerami[34], F. Anghinolfi[29], A. Anisenkov[107], N. Anjos[124a], A. Annovi[47], A. Antonaki[8], M. Antonelli[47], A. Antonov[96], J. Antos[144b], F. Anulli[132a], S. Aoun[83], L. Aperio Bella[4], R. Apolle[118,c], G. Arabidze[88], I. Aracena[143], Y. Arai[65], A.T.H. Arce[44], S. Arfaoui[148], J-F. Arguin[14], E. Arik[18a,*], M. Arik[18a], A.J. Armbruster[87], O. Arnaez[81], V. Arnal[80], C. Arnault[115], A. Artamonov[95], G. Artoni[132a,132b], D. Arutinov[20], S. Asai[155], R. Asfandiyarov[173], S. Ask[27], B. Åsman[146a,146b], L. Asquith[5], K. Assamagan[24], A. Astbury[169], B. Aubert[4], E. Auge[115], K. Augsten[127], M. Aurousseau[145a], G. Avolio[163], R. Avramidou[9], D. Axen[168], G. Azuelos[93,d], Y. Azuma[155], M.A. Baak[29], G. Baccaglioni[89a], C. Bacci[134a,134b], A.M. Bach[14], H. Bachacou[136], K. Bachas[29], M. Backes[49], M. Backhaus[20], E. Badescu[25a], P. Bagnaia[132a,132b], S. Bahinipati[2], Y. Bai[32a], D.C. Bailey[158], T. Bain[158], J.T. Baines[129], O.K. Baker[176], M.D. Baker[24], S. Baker[77], E. Banas[38], P. Banerjee[93], Sw. Banerjee[173], D. Banfi[29], A. Bangert[150], V. Bansal[169], H.S. Bansil[17], L. Barak[172], S.P. Baranov[94], A. Barbaro Galtieri[14], T. Barber[48], E.L. Barberio[86], D. Barberis[50a,50b], M. Barbero[20], D.Y. Bardin[64], T. Barillari[99], M. Barisonzi[175], T. Barklow[143], N. Barlow[27], B.M. Barnett[129], R.M. Barnett[14], A. Baroncelli[134a], G. Barone[49], A.J. Barr[118], F. Barreiro[80], J. Barreiro Guimarães da Costa[57], P. Barrillon[115], R. Bartoldus[143], A.E. Barton[71], V. Bartsch[149], R.L. Bates[53], L. Batkova[144a], J.R. Batley[27], A. Battaglia[16], M. Battistin[29], F. Bauer[136], H.S. Bawa[143,e], S. Beale[98], T. Beau[78], P.H. Beauchemin[161], R. Beccherle[50a], P. Bechtle[20], H.P. Beck[16], A.K. Becker[175], S. Becker[98], M. Beckingham[138], K.H. Becks[175], A.J. Beddall[18c], A. Beddall[18c], S. Bedikian[176], V.A. Bednyakov[64], C.P. Bee[83], M. Begel[24], S. Behar Harpaz[152], M. Beimforde[99], C. Belanger-Champagne[85], P.J. Bell[49], W.H. Bell[49], G. Bella[153], L. Bellagamba[19a], F. Bellina[29], M. Bellomo[29], A. Belloni[57], O. Beloborodova[107,f], K. Belotskiy[96], O. Beltramello[29], O. Benary[153], D. Benchekroun[135a], K. Bendtz[146a,146b], N. Benekos[165], Y. Benhammou[153], E. Benhar Noccioli[49], J.A. Benitez Garcia[159b], D.P. Benjamin[44], M. Benoit[115], J.R. Bensinger[22], K. Benslama[130], S. Bentvelsen[105], D. Berge[29], E. Bergeaas Kuutmann[41], N. Berger[4], F. Berghaus[169], E. Berglund[105], J. Beringer[14], P. Bernat[77], R. Bernhard[48], C. Bernius[24],

JHEP06(2012)088

T. Berry[76], C. Bertella[83], A. Bertin[19a,19b], F. Bertolucci[122a,122b], M.I. Besana[89a,89b], G.J. Besjes[104], N. Besson[136], S. Bethke[99], W. Bhimji[45], R.M. Bianchi[29], M. Bianco[72a,72b], O. Biebel[98], S.P. Bieniek[77], K. Bierwagen[54], J. Biesiada[14], M. Biglietti[134a], H. Bilokon[47], M. Bindi[19a,19b], S. Binet[115], A. Bingul[18c], C. Bini[132a,132b], C. Biscarat[178], U. Bitenc[48], K.M. Black[21], R.E. Blair[5], J.-B. Blanchard[136], G. Blanchot[29], T. Blazek[144a], C. Blocker[22], J. Blocki[38], A. Blondel[49], W. Blum[81], U. Blumenschein[54], G.J. Bobbink[105], V.B. Bobrovnikov[107], S.S. Bocchetta[79], A. Bocci[44], C.R. Boddy[118], M. Boehler[41], J. Boek[175], N. Boelaert[35], J.A. Bogaerts[29], A. Bogdanchikov[107], A. Bogouch[90,*], C. Bohm[146a], J. Bohm[125], V. Boisvert[76], T. Bold[37], V. Boldea[25a], N.M. Bolnet[136], M. Bomben[78], M. Bona[75], M. Bondioli[163], M. Boonekamp[136], C.N. Booth[139], S. Bordoni[78], C. Borer[16], A. Borisov[128], G. Borissov[71], I. Borjanovic[12a], M. Borri[82], S. Borroni[87], V. Bortolotto[134a,134b], K. Bos[105], D. Boscherini[19a], M. Bosman[11], H. Boterenbrood[105], D. Botterill[129], J. Bouchami[93], J. Boudreau[123], E.V. Bouhova-Thacker[71], D. Boumediene[33], C. Bourdarios[115], N. Bousson[83], A. Boveia[30], J. Boyd[29], I.R. Boyko[64], I. Bozovic-Jelisavcic[12b], J. Bracinik[17], P. Branchini[134a], A. Brandt[7], G. Brandt[118], O. Brandt[54], U. Bratzler[156], B. Brau[84], J.E. Brau[114], H.M. Braun[175], S.F. Brazzale[164a,164c], B. Brelier[158], J. Bremer[29], K. Brendlinger[120], R. Brenner[166], S. Bressler[172], D. Britton[53], F.M. Brochu[27], I. Brock[20], R. Brock[88], E. Brodet[153], F. Broggi[89a], C. Bromberg[88], J. Bronner[99], G. Brooijmans[34], T. Brooks[76], W.K. Brooks[31b], G. Brown[82], H. Brown[7], P.A. Bruckman de Renstrom[38], D. Bruncko[144b], R. Bruneliere[48], S. Brunet[60], A. Bruni[19a], G. Bruni[19a], M. Bruschi[19a], T. Buanes[13], Q. Buat[55], F. Bucci[49], J. Buchanan[118], P. Buchholz[141], R.M. Buckingham[118], A.G. Buckley[45], S.I. Buda[25a], I.A. Budagov[64], B. Budick[108], V. Büscher[81], L. Bugge[117], O. Bulekov[96], A.C. Bundock[73], M. Bunse[42], T. Buran[117], H. Burckhart[29], S. Burdin[73], T. Burgess[13], S. Burke[129], E. Busato[33], P. Bussey[53], C.P. Buszello[166], B. Butler[143], J.M. Butler[21], C.M. Buttar[53], J.M. Butterworth[77], W. Buttinger[27], S. Cabrera Urbán[167], D. Caforio[19a,19b], O. Cakir[3a], P. Calafiura[14], G. Calderini[78], P. Calfayan[98], R. Calkins[106], L.P. Caloba[23a], R. Caloi[132a,132b], D. Calvet[33], S. Calvet[33], R. Camacho Toro[33], P. Camarri[133a,133b], D. Cameron[117], L.M. Caminada[14], S. Campana[29], M. Campanelli[77], V. Canale[102a,102b], F. Canelli[30,g], A. Canepa[159a], J. Cantero[80], R. Cantrill[76], L. Capasso[102a,102b], M.D.M. Capeans Garrido[29], I. Caprini[25a], M. Caprini[25a], D. Capriotti[99], M. Capua[36a,36b], R. Caputo[81], R. Cardarelli[133a], T. Carli[29], G. Carlino[102a], L. Carminati[89a,89b], B. Caron[85], S. Caron[104], E. Carquin[31b], G.D. Carrillo Montoya[173], A.A. Carter[75], J.R. Carter[27], J. Carvalho[124a,h], D. Casadei[108], M.P. Casado[11], M. Cascella[122a,122b], C. Caso[50a,50b,*], A.M. Castaneda Hernandez[173,i], E. Castaneda-Miranda[173], V. Castillo Gimenez[167], N.F. Castro[124a], G. Cataldi[72a], P. Catastini[57], A. Catinaccio[29], J.R. Catmore[29], A. Cattai[29], G. Cattani[133a,133b], S. Caughron[88], P. Cavalleri[78], D. Cavalli[89a], M. Cavalli-Sforza[11], V. Cavasinni[122a,122b], F. Ceradini[134a,134b], A.S. Cerqueira[23b], A. Cerri[29], L. Cerrito[75], F. Cerutti[47], S.A. Cetin[18b], A. Chafaq[135a], D. Chakraborty[106], I. Chalupkova[126], K. Chan[2], B. Chapleau[85], J.D. Chapman[27], J.W. Chapman[87], E. Chareyre[78], D.G. Charlton[17], V. Chavda[82], C.A. Chavez Barajas[29], S. Cheatham[85], S. Chekanov[5], S.V. Chekulaev[159a], G.A. Chelkov[64], M.A. Chelstowska[104], C. Chen[63], H. Chen[24], S. Chen[32c], X. Chen[173], A. Cheplakov[64], R. Cherkaoui El Moursli[135e],

JHEP06(2012)088

V. Chernyatin[24], E. Cheu[6], S.L. Cheung[158], L. Chevalier[136], G. Chiefari[102a,102b], L. Chikovani[51a], J.T. Childers[29], A. Chilingarov[71], G. Chiodini[72a], A.S. Chisholm[17], R.T. Chislett[77], M.V. Chizhov[64], G. Choudalakis[30], S. Chouridou[137], I.A. Christidi[77], A. Christov[48], D. Chromek-Burckhart[29], M.L. Chu[151], J. Chudoba[125], G. Ciapetti[132a,132b], A.K. Ciftci[3a], R. Ciftci[3a], D. Cinca[33], V. Cindro[74], C. Ciocca[19a,19b], A. Ciocio[14], M. Cirilli[87], P. Cirkovic[12b], M. Citterio[89a], M. Ciubancan[25a], A. Clark[49], P.J. Clark[45], W. Cleland[123], J.C. Clemens[83], B. Clement[55], C. Clement[146a,146b], Y. Coadou[83], M. Cobal[164a,164c], A. Coccaro[138], J. Cochran[63], J.G. Cogan[143], J. Coggeshall[165], E. Cogneras[178], J. Colas[4], A.P. Colijn[105], N.J. Collins[17], C. Collins-Tooth[53], J. Collot[55], T. Colombo[119a,119b], G. Colon[84], P. Conde Muiño[124a], E. Coniavitis[118], M.C. Conidi[11], S.M. Consonni[89a,89b], V. Consorti[48], S. Constantinescu[25a], C. Conta[119a,119b], G. Conti[57], F. Conventi[102a,j], M. Cooke[14], B.D. Cooper[77], A.M. Cooper-Sarkar[118], K. Copic[14], T. Cornelissen[175], M. Corradi[19a], F. Corriveau[85,k], A. Cortes-Gonzalez[165], G. Cortiana[99], G. Costa[89a], M.J. Costa[167], D. Costanzo[139], T. Costin[30], D. Côté[29], L. Courneyea[169], G. Cowan[76], C. Cowden[27], B.E. Cox[82], K. Cranmer[108], F. Crescioli[122a,122b], M. Cristinziani[20], G. Crosetti[36a,36b], R. Crupi[72a,72b], S. Crépé-Renaudin[55], C.-M. Cuciuc[25a], C. Cuenca Almenar[176], T. Cuhadar Donszelmann[139], M. Curatolo[47], C.J. Curtis[17], C. Cuthbert[150], P. Cwetanski[60], H. Czirr[141], P. Czodrowski[43], Z. Czyczula[176], S. D'Auria[53], M. D'Onofrio[73], A. D'Orazio[132a,132b], M.J. Da Cunha Sargedas De Sousa[124a], C. Da Via[82], W. Dabrowski[37], A. Dafinca[118], T. Dai[87], C. Dallapiccola[84], M. Dam[35], M. Dameri[50a,50b], D.S. Damiani[137], H.O. Danielsson[29], V. Dao[49], G. Darbo[50a], G.L. Darlea[25b], W. Davey[20], T. Davidek[126], N. Davidson[86], R. Davidson[71], E. Davies[118,c], M. Davies[93], A.R. Davison[77], Y. Davygora[58a], E. Dawe[142], I. Dawson[139], R.K. Daya-Ishmukhametova[22], K. De[7], R. de Asmundis[102a], S. De Castro[19a,19b], S. De Cecco[78], J. de Graat[98], N. De Groot[104], P. de Jong[105], C. De La Taille[115], H. De la Torre[80], F. De Lorenzi[63], L. de Mora[71], L. De Nooij[105], D. De Pedis[132a], A. De Salvo[132a], U. De Sanctis[164a,164c], A. De Santo[149], J.B. De Vivie De Regie[115], G. De Zorzi[132a,132b], W.J. Dearnaley[71], R. Debbe[24], C. Debenedetti[45], B. Dechenaux[55], D.V. Dedovich[64], J. Degenhardt[120], C. Del Papa[164a,164c], J. Del Peso[80], T. Del Prete[122a,122b], T. Delemontex[55], M. Deliyergiyev[74], A. Dell'Acqua[29], L. Dell'Asta[21], M. Della Pietra[102a,j], D. della Volpe[102a,102b], M. Delmastro[4], P.A. Delsart[55], C. Deluca[105], S. Demers[176], M. Demichev[64], B. Demirkoz[11,l], J. Deng[163], S.P. Denisov[128], D. Derendarz[38], J.E. Derkaoui[135d], F. Derue[78], P. Dervan[73], K. Desch[20], E. Devetak[148], P.O. Deviveiros[105], A. Dewhurst[129], B. DeWilde[148], S. Dhaliwal[158], R. Dhullipudi[24,m], A. Di Ciaccio[133a,133b], L. Di Ciaccio[4], A. Di Girolamo[29], B. Di Girolamo[29], S. Di Luise[134a,134b], A. Di Mattia[173], B. Di Micco[29], R. Di Nardo[47], A. Di Simone[133a,133b], R. Di Sipio[19a,19b], M.A. Diaz[31a], E.B. Diehl[87], J. Dietrich[41], T.A. Dietzsch[58a], S. Diglio[86], K. Dindar Yagci[39], J. Dingfelder[20], C. Dionisi[132a,132b], P. Dita[25a], S. Dita[25a], F. Dittus[29], F. Djama[83], T. Djobava[51b], M.A.B. do Vale[23c], A. Do Valle Wemans[124a,n], T.K.O. Doan[4], M. Dobbs[85], R. Dobinson [29,*], D. Dobos[29], E. Dobson[29,o], J. Dodd[34], C. Doglioni[49], T. Doherty[53], Y. Doi[65,*], J. Dolejsi[126], I. Dolenc[74], Z. Dolezal[126], B.A. Dolgoshein[96,*], T. Dohmae[155], M. Donadelli[23d], M. Donega[120], J. Donini[33], J. Dopke[29], A. Doria[102a], A. Dos Anjos[173], A. Dotti[122a,122b], M.T. Dova[70], A.D. Doxiadis[105], A.T. Doyle[53], M. Dris[9], J. Dubbert[99],

JHEP06(2012)088

S. Dube[14], E. Duchovni[172], G. Duckeck[98], A. Dudarev[29], F. Dudziak[63], M. Dührssen [29], I.P. Duerdoth[82], L. Duflot[115], M-A. Dufour[85], M. Dunford[29], H. Duran Yildiz[3a], R. Duxfield[139], M. Dwuznik[37], F. Dydak [29], M. Düren[52], J. Ebke[98], S. Eckweiler[81], K. Edmonds[81], C.A. Edwards[76], N.C. Edwards[53], W. Ehrenfeld[41], T. Eifert[143], G. Eigen[13], K. Einsweiler[14], E. Eisenhandler[75], T. Ekelof[166], M. El Kacimi[135c], M. Ellert[166], S. Elles[4], F. Ellinghaus[81], K. Ellis[75], N. Ellis[29], J. Elmsheuser[98], M. Elsing[29], D. Emeliyanov[129], R. Engelmann[148], A. Engl[98], B. Epp[61], A. Eppig[87], J. Erdmann[54], A. Ereditato[16], D. Eriksson[146a], J. Ernst[1], M. Ernst[24], J. Ernwein[136], D. Errede[165], S. Errede[165], E. Ertel[81], M. Escalier[115], C. Escobar[123], X. Espinal Curull[11], B. Esposito[47], F. Etienne[83], A.I. Etienvre[136], E. Etzion[153], D. Evangelakou[54], H. Evans[60], L. Fabbri[19a,19b], C. Fabre[29], R.M. Fakhrutdinov[128], S. Falciano[132a], Y. Fang[173], M. Fanti[89a,89b], A. Farbin[7], A. Farilla[134a], J. Farley[148], T. Farooque[158], S. Farrell[163], S.M. Farrington[118], P. Farthouat[29], P. Fassnacht[29], D. Fassouliotis[8], B. Fatholahzadeh[158], A. Favareto[89a,89b], L. Fayard[115], S. Fazio[36a,36b], R. Febbraro[33], P. Federic[144a], O.L. Fedin[121], W. Fedorko[88], M. Fehling-Kaschek[48], L. Feligioni[83], D. Fellmann[5], C. Feng[32d], E.J. Feng[5], A.B. Fenyuk[128], J. Ferencei[144b], W. Fernando[5], S. Ferrag[53], J. Ferrando[53], V. Ferrara[41], A. Ferrari[166], P. Ferrari[105], R. Ferrari[119a], D.E. Ferreira de Lima[53], A. Ferrer[167], D. Ferrere[49], C. Ferretti[87], A. Ferretto Parodi[50a,50b], M. Fiascaris[30], F. Fiedler[81], A. Filipčič[74], F. Filthaut[104], M. Fincke-Keeler[169], M.C.N. Fiolhais[124a,h], L. Fiorini[167], A. Firan[39], G. Fischer[41], M.J. Fisher[109], M. Flechl[48], I. Fleck[141], J. Fleckner[81], P. Fleischmann[174], S. Fleischmann[175], T. Flick[175], A. Floderus[79], L.R. Flores Castillo[173], M.J. Flowerdew[99], T. Fonseca Martin[16], A. Formica[136], A. Forti[82], D. Fortin[159a], D. Fournier[115], H. Fox[71], P. Francavilla[11], S. Franchino[119a,119b], D. Francis[29], T. Frank[172], S. Franz[29], M. Fraternali[119a,119b], S. Fratina[120], S.T. French[27], C. Friedrich[41], F. Friedrich [43], R. Froeschl[29], D. Froidevaux[29], J.A. Frost[27], C. Fukunaga[156], E. Fullana Torregrosa[29], B.G. Fulsom[143], J. Fuster[167], C. Gabaldon[29], O. Gabizon[172], T. Gadfort[24], S. Gadomski[49], G. Gagliardi[50a,50b], P. Gagnon[60], C. Galea[98], E.J. Gallas[118], V. Gallo[16], B.J. Gallop[129], P. Gallus[125], K.K. Gan[109], Y.S. Gao[143,e], A. Gaponenko[14], F. Garberson[176], M. Garcia-Sciveres[14], C. García[167], J.E. García Navarro[167], R.W. Gardner[30], N. Garelli[29], H. Garitaonandia[105], V. Garonne[29], J. Garvey[17], C. Gatti[47], G. Gaudio[119a], B. Gaur[141], L. Gauthier[136], P. Gauzzi[132a,132b], I.L. Gavrilenko[94], C. Gay[168], G. Gaycken[20], E.N. Gazis[9], P. Ge[32d], Z. Gecse[168], C.N.P. Gee[129], D.A.A. Geerts[105], Ch. Geich-Gimbel[20], K. Gellerstedt[146a,146b], C. Gemme[50a], A. Gemmell[53], M.H. Genest[55], S. Gentile[132a,132b], M. George[54], S. George[76], P. Gerlach[175], A. Gershon[153], C. Geweniger[58a], H. Ghazlane[135b], N. Ghodbane[33], B. Giacobbe[19a], S. Giagu[132a,132b], V. Giakoumopoulou[8], V. Giangiobbe[11], F. Gianotti[29], B. Gibbard[24], A. Gibson[158], S.M. Gibson[29], D. Gillberg[28], A.R. Gillman[129], D.M. Gingrich[2,d], J. Ginzburg[153], N. Giokaris[8], M.P. Giordani[164c], R. Giordano[102a,102b], F.M. Giorgi[15], P. Giovannini[99], P.F. Giraud[136], D. Giugni[89a], M. Giunta[93], P. Giusti[19a], B.K. Gjelsten[117], L.K. Gladilin[97], C. Glasman[80], J. Glatzer[48], A. Glazov[41], K.W. Glitza[175], G.L. Glonti[64], J.R. Goddard[75], J. Godfrey[142], J. Godlewski[29], M. Goebel[41], T. Göpfert[43], C. Goeringer[81], C. Gössling[42], S. Goldfarb[87], T. Golling[176], A. Gomes[124a,b], L.S. Gomez Fajardo[41], R. Gonçalo[76], J. Goncalves Pinto Firmino Da Costa[41], L. Gonella[20], S. Gonzalez[173], S. González

JHEP06(2012)088

de la Hoz[167], G. Gonzalez Parra[11], M.L. Gonzalez Silva[26], S. Gonzalez-Sevilla[49], J.J. Goodson[148], L. Goossens[29], P.A. Gorbounov[95], H.A. Gordon[24], I. Gorelov[103], G. Gorfine[175], B. Gorini[29], E. Gorini[72a,72b], A. Gorišek[74], E. Gornicki[38], B. Gosdzik[41], A.T. Goshaw[5], M. Gosselink[105], M.I. Gostkin[64], I. Gough Eschrich[163], M. Gouighri[135a], D. Goujdami[135c], M.P. Goulette[49], A.G. Goussiou[138], C. Goy[4], S. Gozpinar[22], I. Grabowska-Bold[37], P. Grafström[29], K-J. Grahn[41], F. Grancagnolo[72a], S. Grancagnolo[15], V. Grassi[148], V. Gratchev[121], N. Grau[34], H.M. Gray[29], J.A. Gray[148], E. Graziani[134a], O.G. Grebenyuk[121], T. Greenshaw[73], Z.D. Greenwood[24,m], K. Gregersen[35], I.M. Gregor[41], P. Grenier[143], J. Griffiths[138], N. Grigalashvili[64], A.A. Grillo[137], S. Grinstein[11], Y.V. Grishkevich[97], J.-F. Grivaz[115], E. Gross[172], J. Grosse-Knetter[54], J. Groth-Jensen[172], K. Grybel[141], D. Guest[176], C. Guicheney[33], A. Guida[72a,72b], S. Guindon[54], U. Gul[53], H. Guler[85,p], J. Gunther[125], B. Guo[158], J. Guo[34], P. Gutierrez[111], N. Guttman[153], O. Gutzwiller[173], C. Guyot[136], C. Gwenlan[118], C.B. Gwilliam[73], A. Haas[143], S. Haas[29], C. Haber[14], H.K. Hadavand[39], D.R. Hadley[17], P. Haefner[20], F. Hahn[29], S. Haider[29], Z. Hajduk[38], H. Hakobyan[177], D. Hall[118], J. Haller[54], K. Hamacher[175], P. Hamal[113], M. Hamer[54], A. Hamilton[145b,q], S. Hamilton[161], L. Han[32b], K. Hanagaki[116], K. Hanawa[160], M. Hance[14], C. Handel[81], P. Hanke[58a], J.R. Hansen[35], J.B. Hansen[35], J.D. Hansen[35], P.H. Hansen[35], P. Hansson[143], K. Hara[160], G.A. Hare[137], T. Harenberg[175], S. Harkusha[90], D. Harper[87], R.D. Harrington[45], O.M. Harris[138], K. Harrison[17], J. Hartert[48], F. Hartjes[105], T. Haruyama[65], A. Harvey[56], S. Hasegawa[101], Y. Hasegawa[140], S. Hassani[136], S. Haug[16], M. Hauschild[29], R. Hauser[88], M. Havranek[20], C.M. Hawkes[17], R.J. Hawkings[29], A.D. Hawkins[79], D. Hawkins[163], T. Hayakawa[66], T. Hayashi[160], D. Hayden[76], C.P. Hays[118], H.S. Hayward[73], S.J. Haywood[129], M. He[32d], S.J. Head[17], V. Hedberg[79], L. Heelan[7], S. Heim[88], B. Heinemann[14], S. Heisterkamp[35], L. Helary[4], C. Heller[98], M. Heller[29], S. Hellman[146a,146b], D. Hellmich[20], C. Helsens[11], R.C.W. Henderson[71], M. Henke[58a], A. Henrichs[54], A.M. Henriques Correia[29], S. Henrot-Versille[115], C. Hensel[54], T. Henß[175], C.M. Hernandez[7], Y. Hernández Jiménez[167], R. Herrberg[15], G. Herten[48], R. Hertenberger[98], L. Hervas[29], G.G. Hesketh[77], N.P. Hessey[105], E. Higón-Rodriguez[167], J.C. Hill[27], K.H. Hiller[41], S. Hillert[20], S.J. Hillier[17], I. Hinchliffe[14], E. Hines[120], M. Hirose[116], F. Hirsch[42], D. Hirschbuehl[175], J. Hobbs[148], N. Hod[153], M.C. Hodgkinson[139], P. Hodgson[139], A. Hoecker[29], M.R. Hoeferkamp[103], J. Hoffman[39], D. Hoffmann[83], M. Hohlfeld[81], M. Holder[141], S.O. Holmgren[146a], T. Holy[127], J.L. Holzbauer[88], T.M. Hong[120], L. Hooft van Huysduynen[108], C. Horn[143], S. Horner[48], J-Y. Hostachy[55], S. Hou[151], A. Hoummada[135a], J. Howard[118], J. Howarth[82], I. Hristova [15], J. Hrivnac[115], T. Hryn'ova[4], P.J. Hsu[81], S.-C. Hsu[14], Z. Hubacek[127], F. Hubaut[83], F. Huegging[20], A. Huettmann[41], T.B. Huffman[118], E.W. Hughes[34], G. Hughes[71], M. Huhtinen[29], M. Hurwitz[14], U. Husemann[41], N. Huseynov[64,r], J. Huston[88], J. Huth[57], G. Iacobucci[49], G. Iakovidis[9], M. Ibbotson[82], I. Ibragimov[141], L. Iconomidou-Fayard[115], J. Idarraga[115], P. Iengo[102a], O. Igonkina[105], Y. Ikegami[65], M. Ikeno[65], D. Iliadis[154], N. Ilic[158], T. Ince[20], J. Inigo-Golfin[29], P. Ioannou[8], M. Iodice[134a], K. Iordanidou[8], V. Ippolito[132a,132b], A. Irles Quiles[167], C. Isaksson[166], A. Ishikawa[66], M. Ishino[67], R. Ishmukhametov[39], C. Issever[118], S. Istin[18a], A.V. Ivashin[128], W. Iwanski[38], H. Iwasaki[65], J.M. Izen[40], V. Izzo[102a], B. Jackson[120], J.N. Jackson[73], P. Jackson[143],

JHEP06(2012)088

M.R. Jaekel[29], V. Jain[60], K. Jakobs[48], S. Jakobsen[35], T. Jakoubek[125], J. Jakubek[127], D.K. Jana[111], E. Jansen[77], H. Jansen[29], A. Jantsch[99], M. Janus[48], G. Jarlskog[79], L. Jeanty[57], I. Jen-La Plante[30], P. Jenni[29], A. Jeremie[4], P. Jež[35], S. Jézéquel[4], M.K. Jha[19a], H. Ji[173], W. Ji[81], J. Jia[148], Y. Jiang[32b], M. Jimenez Belenguer[41], S. Jin[32a], O. Jinnouchi[157], M.D. Joergensen[35], D. Joffe[39], M. Johansen[146a,146b], K.E. Johansson[146a], P. Johansson[139], S. Johnert[41], K.A. Johns[6], K. Jon-And[146a,146b], G. Jones[170], R.W.L. Jones[71], T.J. Jones[73], C. Joram[29], P.M. Jorge[124a], K.D. Joshi[82], J. Jovicevic[147], T. Jovin[12b], X. Ju[173], C.A. Jung[42], R.M. Jungst[29], V. Juranek[125], P. Jussel[61], A. Juste Rozas[11], S. Kabana[16], M. Kaci[167], A. Kaczmarska[38], P. Kadlecik[35], M. Kado[115], H. Kagan[109], M. Kagan[57], E. Kajomovitz[152], S. Kalinin[175], L.V. Kalinovskaya[64], S. Kama[39], N. Kanaya[155], M. Kaneda[29], S. Kaneti[27], T. Kanno[157], V.A. Kantserov[96], J. Kanzaki[65], B. Kaplan[176], A. Kapliy[30], J. Kaplon[29], D. Kar[53], M. Karagounis[20], K. Karakostas[9], M. Karnevskiy[41], V. Kartvelishvili[71], A.N. Karyukhin[128], L. Kashif[173], G. Kasieczka[58b], R.D. Kass[109], A. Kastanas[13], M. Kataoka[4], Y. Kataoka[155], E. Katsoufis[9], J. Katzy[41], V. Kaushik[6], K. Kawagoe[69], T. Kawamoto[155], G. Kawamura[81], M.S. Kayl[105], V.A. Kazanin[107], M.Y. Kazarinov[64], R. Keeler[169], R. Kehoe[39], M. Keil[54], G.D. Kekelidze[64], J.S. Keller[138], M. Kenyon[53], O. Kepka[125], N. Kerschen[29], B.P. Kerševan[74], S. Kersten[175], K. Kessoku[155], J. Keung[158], F. Khalil-zada[10], H. Khandanyan[165], A. Khanov[112], D. Kharchenko[64], A. Khodinov[96], A. Khomich[58a], T.J. Khoo[27], G. Khoriauli[20], A. Khoroshilov[175], V. Khovanskiy[95], E. Khramov[64], J. Khubua[51b], H. Kim[146a,146b], M.S. Kim[2], S.H. Kim[160], N. Kimura[171], O. Kind[15], B.T. King[73], M. King[66], R.S.B. King[118], J. Kirk[129], A.E. Kiryunin[99], T. Kishimoto[66], D. Kisielewska[37], T. Kittelmann[123], E. Kladiva[144b], M. Klein[73], U. Klein[73], K. Kleinknecht[81], M. Klemetti[85], A. Klier[172], P. Klimek[146a,146b], A. Klimentov[24], R. Klingenberg[42], J.A. Klinger[82], E.B. Klinkby[35], T. Klioutchnikova[29], P.F. Klok[104], S. Klous[105], E.-E. Kluge[58a], T. Kluge[73], P. Kluit[105], S. Kluth[99], N.S. Knecht[158], E. Kneringer[61], E.B.F.G. Knoops[83], A. Knue[54], B.R. Ko[44], T. Kobayashi[155], M. Kobel[43], M. Kocian[143], P. Kodys[126], K. Köneke[29], A.C. König[104], S. Koenig[81], L. Köpke[81], F. Koetsveld[104], P. Koevesarki[20], T. Koffas[28], E. Koffeman[105], L.A. Kogan[118], S. Kohlmann[175], F. Kohn[54], Z. Kohout[127], T. Kohriki[65], T. Koi[143], G.M. Kolachev[107], H. Kolanoski[15], V. Kolesnikov[64], I. Koletsou[89a], J. Koll[88], M. Kollefrath[48], A.A. Komar[94], Y. Komori[155], T. Kondo[65], T. Kono[41,s], A.I. Kononov[48], R. Konoplich[108,t], N. Konstantinidis[77], S. Koperny[37], K. Korcyl[38], K. Kordas[154], A. Korn[118], A. Korol[107], I. Korolkov[11], E.V. Korolkova[139], V.A. Korotkov[128], O. Kortner[99], S. Kortner[99], V.V. Kostyukhin[20], S. Kotov[99], V.M. Kotov[64], A. Kotwal[44], C. Kourkoumelis[8], V. Kouskoura[154], A. Koutsman[159a], R. Kowalewski[169], T.Z. Kowalski[37], W. Kozanecki[136], A.S. Kozhin[128], V. Kral[127], V.A. Kramarenko[97], G. Kramberger[74], M.W. Krasny[78], A. Krasznahorkay[108], J. Kraus[88], J.K. Kraus[20], S. Kreiss[108], F. Krejci[127], J. Kretzschmar[73], N. Krieger[54], P. Krieger[158], K. Kroeninger[54], H. Kroha[99], J. Kroll[120], J. Kroseberg[20], J. Krstic[12a], U. Kruchonak[64], H. Krüger[20], T. Kruker[16], N. Krumnack[63], Z.V. Krumshteyn[64], A. Kruth[20], T. Kubota[86], S. Kuday[3a], S. Kuehn[48], A. Kugel[58c], T. Kuhl[41], D. Kuhn[61], V. Kukhtin[64], Y. Kulchitsky[90], S. Kuleshov[31b], C. Kummer[98], M. Kuna[78], J. Kunkle[120], A. Kupco[125], H. Kurashige[66], M. Kurata[160], Y.A. Kurochkin[90], V. Kus[125], E.S. Kuwertz[147],

JHEP06(2012)088

M. Kuze[157], J. Kvita[142], R. Kwee[15], A. La Rosa[49], L. La Rotonda[36a,36b], L. Labarga[80], J. Labbe[4], S. Lablak[135a], C. Lacasta[167], F. Lacava[132a,132b], H. Lacker[15], D. Lacour[78], V.R. Lacuesta[167], E. Ladygin[64], R. Lafaye[4], B. Laforge[78], T. Lagouri[80], S. Lai[48], E. Laisne[55], M. Lamanna[29], L. Lambourne[77], C.L. Lampen[6], W. Lampl[6], E. Lancon[136], U. Landgraf[48], M.P.J. Landon[75], J.L. Lane[82], C. Lange[41], A.J. Lankford[163], F. Lanni[24], K. Lantzsch[175], S. Laplace[78], C. Lapoire[20], J.F. Laporte[136], T. Lari[89a], A. Larner[118], M. Lassnig[29], P. Laurelli[47], V. Lavorini[36a,36b], W. Lavrijsen[14], P. Laycock[73], O. Le Dortz[78], E. Le Guirriec[83], C. Le Maner[158], E. Le Menedeu[11], T. LeCompte[5], F. Ledroit-Guillon[55], H. Lee[105], J.S.H. Lee[116], S.C. Lee[151], L. Lee[176], M. Lefebvre[169], M. Legendre[136], B.C. LeGeyt[120], F. Legger[98], C. Leggett[14], M. Lehmacher[20], G. Lehmann Miotto[29], X. Lei[6], M.A.L. Leite[23d], R. Leitner[126], D. Lellouch[172], B. Lemmer[54], V. Lendermann[58a], K.J.C. Leney[145b], T. Lenz[105], G. Lenzen[175], B. Lenzi[29], K. Leonhardt[43], S. Leontsinis[9], F. Lepold[58a], C. Leroy[93], J-R. Lessard[169], C.G. Lester[27], C.M. Lester[120], J. Levêque[4], D. Levin[87], L.J. Levinson[172], A. Lewis[118], G.H. Lewis[108], A.M. Leyko[20], M. Leyton[15], B. Li[83], H. Li[173,u], S. Li[32b,v], X. Li[87], Z. Liang[118,w], H. Liao[33], B. Liberti[133a], P. Lichard[29], M. Lichtnecker[98], K. Lie[165], W. Liebig[13], C. Limbach[20], A. Limosani[86], M. Limper[62], S.C. Lin[151,x], F. Linde[105], J.T. Linnemann[88], E. Lipeles[120], A. Lipniacka[13], T.M. Liss[165], D. Lissauer[24], A. Lister[49], A.M. Litke[137], C. Liu[28], D. Liu[151], H. Liu[87], J.B. Liu[87], M. Liu[32b], Y. Liu[32b], M. Livan[119a,119b], S.S.A. Livermore[118], A. Lleres[55], J. Llorente Merino[80], S.L. Lloyd[75], E. Lobodzinska[41], P. Loch[6], W.S. Lockman[137], T. Loddenkoetter[20], F.K. Loebinger[82], A. Loginov[176], C.W. Loh[168], T. Lohse[15], K. Lohwasser[48], M. Lokajicek[125], V.P. Lombardo[4], R.E. Long[71], L. Lopes[124a], D. Lopez Mateos[57], J. Lorenz[98], N. Lorenzo Martinez[115], M. Losada[162], P. Loscutoff[14], F. Lo Sterzo[132a,132b], M.J. Losty[159a], X. Lou[40], A. Lounis[115], K.F. Loureiro[162], J. Love[21], P.A. Love[71], A.J. Lowe[143,e], F. Lu[32a], H.J. Lubatti[138], C. Luci[132a,132b], A. Lucotte[55], A. Ludwig[43], D. Ludwig[41], I. Ludwig[48], J. Ludwig[48], F. Luehring[60], G. Luijckx[105], W. Lukas[61], D. Lumb[48], L. Luminari[132a], E. Lund[117], B. Lund-Jensen[147], B. Lundberg[79], J. Lundberg[146a,146b], O. Lundberg[146a,146b], J. Lundquist[35], M. Lungwitz[81], D. Lynn[24], E. Lytken[79], H. Ma[24], L.L. Ma[173], J.A. Macana Goia[93], G. Maccarrone[47], A. Macchiolo[99], B. Maček[74], J. Machado Miguens[124a], R. Mackeprang[35], R.J. Madaras[14], W.F. Mader[43], R. Maenner[58c], T. Maeno[24], P. Mättig[175], S. Mättig[41], L. Magnoni[29], E. Magradze[54], K. Mahboubi[48], S. Mahmoud[73], G. Mahout[17], C. Maiani[136], C. Maidantchik[23a], A. Maio[124a,b], S. Majewski[24], Y. Makida[65], N. Makovec[115], P. Mal[136], B. Malaescu[29], Pa. Malecki[38], P. Malecki[38], V.P. Maleev[121], F. Malek[55], U. Mallik[62], D. Malon[5], C. Malone[143], S. Maltezos[9], V. Malyshev[107], S. Malyukov[29], R. Mameghani[98], J. Mamuzic[12b], A. Manabe[65], L. Mandelli[89a], I. Mandić[74], R. Mandrysch[15], J. Maneira[124a], P.S. Mangeard[88], L. Manhaes de Andrade Filho[23a], A. Mann[54], P.M. Manning[137], A. Manousakis-Katsikakis[8], B. Mansoulie[136], A. Mapelli[29], L. Mapelli[29], L. March [80], J.F. Marchand[28], F. Marchese[133a,133b], G. Marchiori[78], M. Marcisovsky[125], C.P. Marino[169], F. Marroquim[23a], Z. Marshall[29], F.K. Martens[158], S. Marti-Garcia[167], B. Martin[29], B. Martin[88], J.P. Martin[93], T.A. Martin[17], V.J. Martin[45], B. Martin dit Latour[49], S. Martin-Haugh[149], M. Martinez[11], V. Martinez Outschoorn[57], A.C. Martyniuk[169], M. Marx[82], F. Marzano[132a], A. Marzin[111], L. Masetti[81],

JHEP06(2012)088

T. Mashimo[155], R. Mashinistov[94], J. Masik[82], A.L. Maslennikov[107], I. Massa[19a,19b], G. Massaro[105], N. Massol[4], A. Mastroberardino[36a,36b], T. Masubuchi[155], P. Matricon[115], H. Matsunaga[155], T. Matsushita[66], C. Mattravers[118,c], J. Maurer[83], S.J. Maxfield[73], A. Mayne[139], R. Mazini[151], M. Mazur[20], L. Mazzaferro[133a,133b], M. Mazzanti[89a], S.P. Mc Kee[87], A. McCarn[165], R.L. McCarthy[148], T.G. McCarthy[28], N.A. McCubbin[129], K.W. McFarlane[56], J.A. Mcfayden[139], H. McGlone[53], G. Mchedlidze[51b], T. Mclaughlan[17], S.J. McMahon[129], R.A. McPherson[169,k], A. Meade[84], J. Mechnich[105], M. Mechtel[175], M. Medinnis[41], R. Meera-Lebbai[111], T. Meguro[116], R. Mehdiyev[93], S. Mehlhase[35], A. Mehta[73], K. Meier[58a], B. Meirose[79], C. Melachrinos[30], B.R. Mellado Garcia[173], F. Meloni[89a,89b], L. Mendoza Navas[162], Z. Meng[151,u], A. Mengarelli[19a,19b], S. Menke[99], E. Meoni[161], K.M. Mercurio[57], P. Mermod[49], L. Merola[102a,102b], C. Meroni[89a], F.S. Merritt[30], H. Merritt[109], A. Messina[29,y], J. Metcalfe[103], A.S. Mete[163], C. Meyer[81], C. Meyer[30], J-P. Meyer[136], J. Meyer[174], J. Meyer[54], T.C. Meyer[29], W.T. Meyer[63], J. Miao[32d], S. Michal[29], L. Micu[25a], R.P. Middleton[129], S. Migas[73], L. Mijović[41], G. Mikenberg[172], M. Mikestikova[125], M. Mikuž[74], D.W. Miller[30], R.J. Miller[88], W.J. Mills[168], C. Mills[57], A. Milov[172], D.A. Milstead[146a,146b], D. Milstein[172], A.A. Minaenko[128], M. Miñano Moya[167], I.A. Minashvili[64], A.I. Mincer[108], B. Mindur[37], M. Mineev[64], Y. Ming[173], L.M. Mir[11], G. Mirabelli[132a], J. Mitrevski[137], V.A. Mitsou[167], S. Mitsui[65], P.S. Miyagawa[139], K. Miyazaki[66], J.U. Mjörnmark[79], T. Moa[146a,146b], V. Moeller[27], K. Mönig[41], N. Möser[20], S. Mohapatra[148], W. Mohr[48], R. Moles-Valls[167], J. Molina-Perez[29], J. Monk[77], E. Monnier[83], J. Montejo Berlingen[11], S. Montesano[89a,89b], F. Monticelli[70], S. Monzani[19a,19b], R.W. Moore[2], G.F. Moorhead[86], C. Mora Herrera[49], A. Moraes[53], N. Morange[136], J. Morel[54], G. Morello[36a,36b], D. Moreno[81], M. Moreno Llácer[167], P. Morettini[50a], M. Morgenstern[43], M. Morii[57], A.K. Morley[29], G. Mornacchi[29], J.D. Morris[75], L. Morvaj[101], H.G. Moser[99], M. Mosidze[51b], J. Moss[109], R. Mount[143], E. Mountricha[9,z], S.V. Mouraviev[94], E.J.W. Moyse[84], F. Mueller[58a], J. Mueller[123], K. Mueller[20], T.A. Müller[98], T. Mueller[81], D. Muenstermann[29], Y. Munwes[153], W.J. Murray[129], I. Mussche[105], E. Musto[102a,102b], A.G. Myagkov[128], M. Myska[125], J. Nadal[11], K. Nagai[160], K. Nagano[65], A. Nagarkar[109], Y. Nagasaka[59], M. Nagel[99], A.M. Nairz[29], Y. Nakahama[29], K. Nakamura[155], T. Nakamura[155], I. Nakano[110], G. Nanava[20], A. Napier[161], R. Narayan[58b], M. Nash[77,c], T. Nattermann[20], T. Naumann[41], G. Navarro[162], H.A. Neal[87], P.Yu. Nechaeva[94], T.J. Neep[82], A. Negri[119a,119b], G. Negri[29], S. Nektarijevic[49], A. Nelson[163], T.K. Nelson[143], S. Nemecek[125], P. Nemethy[108], A.A. Nepomuceno[23a], M. Nessi[29,aa], M.S. Neubauer[165], A. Neusiedl[81], R.M. Neves[108], P. Nevski[24], P.R. Newman[17], V. Nguyen Thi Hong[136], R.B. Nickerson[118], R. Nicolaidou[136], B. Nicquevert[29], F. Niedercorn[115], J. Nielsen[137], N. Nikiforou[34], A. Nikiforov[15], V. Nikolaenko[128], I. Nikolic-Audit[78], K. Nikolics[49], K. Nikolopoulos[24], H. Nilsen[48], P. Nilsson[7], Y. Ninomiya [155], A. Nisati[132a], T. Nishiyama[66], R. Nisius[99], L. Nodulman[5], M. Nomachi[116], I. Nomidis[154], M. Nordberg[29], P.R. Norton[129], J. Novakova[126], M. Nozaki[65], L. Nozka[113], I.M. Nugent[159a], A.-E. Nuncio-Quiroz[20], G. Nunes Hanninger[86], T. Nunnemann[98], E. Nurse[77], B.J. O'Brien[45], S.W. O'Neale[17,*], D.C. O'Neil[142], V. O'Shea[53], L.B. Oakes[98], F.G. Oakham[28,d], H. Oberlack[99], J. Ocariz[78], A. Ochi[66], S. Oda[69], S. Odaka[65], J. Odier[83], H. Ogren[60],

JHEP06(2012)088

A. Oh[82], S.H. Oh[44], C.C. Ohm[146a,146b], T. Ohshima[101], S. Okada[66], H. Okawa[163], Y. Okumura[101], T. Okuyama[155], A. Olariu[25a], A.G. Olchevski[64], S.A. Olivares Pino[31a], M. Oliveira[124a,h], D. Oliveira Damazio[24], E. Oliver Garcia[167], D. Olivito[120], A. Olszewski[38], J. Olszowska[38], A. Onofre[124a,ab], P.U.E. Onyisi[30], C.J. Oram[159a], M.J. Oreglia[30], Y. Oren[153], D. Orestano[134a,134b], N. Orlando[72a,72b], I. Orlov[107], C. Oropeza Barrera[53], R.S. Orr[158], B. Osculati[50a,50b], R. Ospanov[120], C. Osuna[11], G. Otero y Garzon[26], J.P. Ottersbach[105], M. Ouchrif[135d], E.A. Ouellette[169], F. Ould-Saada[117], A. Ouraou[136], Q. Ouyang[32a], A. Ovcharova[14], M. Owen[82], S. Owen[139], V.E. Ozcan[18a], N. Ozturk[7], A. Pacheco Pages[11], C. Padilla Aranda[11], S. Pagan Griso[14], E. Paganis[139], F. Paige[24], P. Pais[84], K. Pajchel[117], G. Palacino[159b], C.P. Paleari[6], S. Palestini[29], D. Pallin[33], A. Palma[124a], J.D. Palmer[17], Y.B. Pan[173], E. Panagiotopoulou[9], P. Pani[105], N. Panikashvili[87], S. Panitkin[24], D. Pantea[25a], A. Papadelis[146a], Th.D. Papadopoulou[9], A. Paramonov[5], D. Paredes Hernandez[33], W. Park[24,ac], M.A. Parker[27], F. Parodi[50a,50b], J.A. Parsons[34], U. Parzefall[48], S. Pashapour[54], E. Pasqualucci[132a], S. Passaggio[50a], A. Passeri[134a], F. Pastore[134a,134b], Fr. Pastore[76], G. Pásztor [49,ad], S. Pataraia[175], N. Patel[150], J.R. Pater[82], S. Patricelli[102a,102b], T. Pauly[29], M. Pecsy[144a], M.I. Pedraza Morales[173], S.V. Peleganchuk[107], D. Pelikan[166], H. Peng[32b], B. Penning[30], A. Penson[34], J. Penwell[60], M. Perantoni[23a], K. Perez[34,ae], T. Perez Cavalcanti[41], E. Perez Codina[159a], M.T. Pérez García-Estañ[167], V. Perez Reale[34], L. Perini[89a,89b], H. Pernegger[29], R. Perrino[72a], P. Perrodo[4], V.D. Peshekhonov[64], K. Peters[29], B.A. Petersen[29], J. Petersen[29], T.C. Petersen[35], E. Petit[4], A. Petridis[154], C. Petridou[154], E. Petrolo[132a], F. Petrucci[134a,134b], D. Petschull[41], M. Petteni[142], R. Pezoa[31b], A. Phan[86], P.W. Phillips[129], G. Piacquadio[29], A. Picazio[49], E. Piccaro[75], M. Piccinini[19a,19b], S.M. Piec[41], R. Piegaia[26], D.T. Pignotti[109], J.E. Pilcher[30], A.D. Pilkington[82], J. Pina[124a,b], M. Pinamonti[164a,164c], A. Pinder[118], J.L. Pinfold[2], B. Pinto[124a], C. Pizio[89a,89b], M. Plamondon[169], M.-A. Pleier[24], E. Plotnikova[64], A. Poblaguev[24], S. Poddar[58a], F. Podlyski[33], L. Poggioli[115], T. Poghosyan[20], M. Pohl[49], F. Polci[55], G. Polesello[119a], A. Policicchio[36a,36b], A. Polini[19a], J. Poll[75], V. Polychronakos[24], D. Pomeroy[22], K. Pommès[29], L. Pontecorvo[132a], B.G. Pope[88], G.A. Popeneciu[25a], D.S. Popovic[12a], A. Poppleton[29], X. Portell Bueso[29], G.E. Pospelov[99], S. Pospisil[127], I.N. Potrap[99], C.J. Potter[149], C.T. Potter[114], G. Poulard[29], J. Poveda[60], V. Pozdnyakov[64], R. Prabhu[77], P. Pralavorio[83], A. Pranko[14], S. Prasad[29], R. Pravahan[24], S. Prell[63], K. Pretzl[16], D. Price[60], J. Price[73], L.E. Price[5], D. Prieur[123], M. Primavera[72a], K. Prokofiev[108], F. Prokoshin[31b], S. Protopopescu[24], J. Proudfoot[5], X. Prudent[43], M. Przybycien[37], H. Przysiezniak[4], S. Psoroulas[20], E. Ptacek[114], E. Pueschel[84], J. Purdham[87], M. Purohit[24,ac], P. Puzo[115], Y. Pylypchenko[62], J. Qian[87], A. Quadt[54], D.R. Quarrie[14], W.B. Quayle[173], F. Quinonez[31a], M. Raas[104], V. Radescu[41], P. Radloff[114], T. Rador[18a], F. Ragusa[89a,89b], G. Rahal[178], A.M. Rahimi[109], D. Rahm[24], S. Rajagopalan[24], M. Rammensee[48], M. Rammes[141], A.S. Randle-Conde[39], K. Randrianarivony[28], F. Rauscher[98], T.C. Rave[48], M. Raymond[29], A.L. Read[117], D.M. Rebuzzi[119a,119b], A. Redelbach[174], G. Redlinger[24], R. Reece[120], K. Reeves[40], E. Reinherz-Aronis[153], A. Reinsch[114], I. Reisinger[42], C. Rembser[29], Z.L. Ren[151], A. Renaud[115], M. Rescigno[132a], S. Resconi[89a], B. Resende[136], P. Reznicek[98], R. Rezvani[158], R. Richter[99], E. Richter-

JHEP06(2012)088

Was[4,af], M. Ridel[78], M. Rijpstra[105], M. Rijssenbeek[148], A. Rimoldi[119a,119b], L. Rinaldi[19a], R.R. Rios[39], I. Riu[11], G. Rivoltella[89a,89b], F. Rizatdinova[112], E. Rizvi[75], S.H. Robertson[85,k], A. Robichaud-Veronneau[118], D. Robinson[27], J.E.M. Robinson[77], A. Robson[53], J.G. Rocha de Lima[106], C. Roda[122a,122b], D. Roda Dos Santos[29], A. Roe[54], S. Roe[29], O. Røhne[117], S. Rolli[161], A. Romaniouk[96], M. Romano[19a,19b], G. Romeo[26], E. Romero Adam[167], L. Roos[78], E. Ros[167], S. Rosati[132a], K. Rosbach[49], A. Rose[149], M. Rose[76], G.A. Rosenbaum[158], E.I. Rosenberg[63], P.L. Rosendahl[13], O. Rosenthal[141], L. Rosselet[49], V. Rossetti[11], E. Rossi[132a,132b], L.P. Rossi[50a], M. Rotaru[25a], I. Roth[172], J. Rothberg[138], D. Rousseau[115], C.R. Royon[136], A. Rozanov[83], Y. Rozen[152], X. Ruan[32a,ag], F. Rubbo[11], I. Rubinskiy[41], B. Ruckert[98], N. Ruckstuhl[105], V.I. Rud[97], C. Rudolph[43], G. Rudolph[61], F. Rühr[6], F. Ruggieri[134a,134b], A. Ruiz-Martinez[63], L. Rumyantsev[64], Z. Rurikova[48], N.A. Rusakovich[64], J.P. Rutherfoord[6], C. Ruwiedel[14], P. Ruzicka[125], Y.F. Ryabov[121], P. Ryan[88], M. Rybar[126], G. Rybkin[115], N.C. Ryder[118], A.F. Saavedra[150], I. Sadeh[153], H.F-W. Sadrozinski[137], R. Sadykov[64], F. Safai Tehrani[132a], H. Sakamoto[155], G. Salamanna[75], A. Salamon[133a], M. Saleem[111], D. Salek[29], D. Salihagic[99], A. Salnikov[143], J. Salt[167], B.M. Salvachua Ferrando[5], D. Salvatore[36a,36b], F. Salvatore[149], A. Salvucci[104], A. Salzburger[29], D. Sampsonidis[154], B.H. Samset[117], A. Sanchez[102a,102b], V. Sanchez Martinez[167], H. Sandaker[13], H.G. Sander[81], M.P. Sanders[98], M. Sandhoff[175], T. Sandoval[27], C. Sandoval [162], R. Sandstroem[99], D.P.C. Sankey[129], A. Sansoni[47], C. Santamarina Rios[85], C. Santoni[33], R. Santonico[133a,133b], H. Santos[124a], J.G. Saraiva[124a], T. Sarangi[173], E. Sarkisyan-Grinbaum[7], F. Sarri[122a,122b], G. Sartisohn[175], O. Sasaki[65], N. Sasao[67], I. Satsounkevitch[90], G. Sauvage[4], E. Sauvan[4], J.B. Sauvan[115], P. Savard[158,d], V. Savinov[123], D.O. Savu[29], L. Sawyer[24,m], D.H. Saxon[53], J. Saxon[120], C. Sbarra[19a], A. Sbrizzi[19a,19b], O. Scallon[93], D.A. Scannicchio[163], M. Scarcella[150], J. Schaarschmidt[115], P. Schacht[99], D. Schaefer[120], U. Schäfer[81], S. Schaepe[20], S. Schaetzel[58b], A.C. Schaffer[115], D. Schaile[98], R.D. Schamberger[148], A.G. Schamov[107], V. Scharf[58a], V.A. Schegelsky[121], D. Scheirich[87], M. Schernau[163], M.I. Scherzer[34], C. Schiavi[50a,50b], J. Schieck[98], M. Schioppa[36a,36b], S. Schlenker[29], E. Schmidt[48], K. Schmieden[20], C. Schmitt[81], S. Schmitt[58b], M. Schmitz[20], B. Schneider[16], U. Schnoor[43], A. Schöning[58b], A.L.S. Schorlemmer[54], M. Schott[29], D. Schouten[159a], J. Schovancova[125], M. Schram[85], C. Schroeder[81], N. Schroer[58c], M.J. Schultens[20], J. Schultes[175], H.-C. Schultz-Coulon[58a], H. Schulz[15], J.W. Schumacher[20], M. Schumacher[48], B.A. Schumm[137], Ph. Schune[136], C. Schwanenberger[82], A. Schwartzman[143], Ph. Schwemling[78], R. Schwienhorst[88], R. Schwierz[43], J. Schwindling[136], T. Schwindt[20], M. Schwoerer[4], G. Sciolla[22], W.G. Scott[129], J. Searcy[114], G. Sedov[41], E. Sedykh[121], S.C. Seidel[103], A. Seiden[137], F. Seifert[43], J.M. Seixas[23a], G. Sekhniaidze[102a], S.J. Sekula[39], K.E. Selbach[45], D.M. Seliverstov[121], B. Sellden[146a], G. Sellers[73], M. Seman[144b], N. Semprini-Cesari[19a,19b], C. Serfon[98], L. Serin[115], L. Serkin[54], R. Seuster[99], H. Severini[111], A. Sfyrla[29], E. Shabalina[54], M. Shamim[114], L.Y. Shan[32a], J.T. Shank[21], Q.T. Shao[86], M. Shapiro[14], P.B. Shatalov[95], K. Shaw[164a,164c], D. Sherman[176], P. Sherwood[77], A. Shibata[108], H. Shichi[101], S. Shimizu[29], M. Shimojima[100], T. Shin[56], M. Shiyakova[64], A. Shmeleva[94], M.J. Shochet[30], D. Short[118], S. Shrestha[63], E. Shulga[96], M.A. Shupe[6], P. Sicho[125], A. Sidoti[132a], F. Siegert[48], Dj. Sijacki[12a], O. Silbert[172], J. Silva[124a], Y. Silver[153],

JHEP06(2012)088

D. Silverstein[143], S.B. Silverstein[146a], V. Simak[127], O. Simard[136], Lj. Simic[12a], S. Simion[115], E. Simioni[81], B. Simmons[77], R. Simoniello[89a,89b], M. Simonyan[35], P. Sinervo[158], N.B. Sinev[114], V. Sipica[141], G. Siragusa[174], A. Sircar[24], A.N. Sisakyan[64], S.Yu. Sivoklokov[97], J. Sjölin[146a,146b], T.B. Sjursen[13], L.A. Skinnari[14], H.P. Skottowe[57], K. Skovpen[107], P. Skubic[111], M. Slater[17], T. Slavicek[127], K. Sliwa[161], V. Smakhtin[172], B.H. Smart[45], S.Yu. Smirnov[96], Y. Smirnov[96], L.N. Smirnova[97], O. Smirnova[79], B.C. Smith[57], D. Smith[143], K.M. Smith[53], M. Smizanska[71], K. Smolek[127], A.A. Snesarev[94], S.W. Snow[82], J. Snow[111], S. Snyder[24], R. Sobie[169,k], J. Sodomka[127], A. Soffer[153], C.A. Solans[167], M. Solar[127], J. Solc[127], E.Yu. Soldatov[96], U. Soldevila[167], E. Solfaroli Camillocci[132a,132b], A.A. Solodkov[128], O.V. Solovyanov[128], N. Soni[2], V. Sopko[127], B. Sopko[127], M. Sosebee[7], R. Soualah[164a,164c], A. Soukharev[107], S. Spagnolo[72a,72b], F. Spanò[76], R. Spighi[19a], G. Spigo[29], F. Spila[132a,132b], R. Spiwoks[29], M. Spousta[126], T. Spreitzer[158], B. Spurlock[7], R.D. St. Denis[53], J. Stahlman[120], R. Stamen[58a], E. Stanecka[38], R.W. Stanek[5], C. Stanescu[134a], M. Stanescu-Bellu[41], S. Stapnes[117], E.A. Starchenko[128], J. Stark[55], P. Staroba[125], P. Starovoitov[41], A. Staude[98], P. Stavina[144a], G. Steele[53], P. Steinbach[43], P. Steinberg[24], I. Stekl[127], B. Stelzer[142], H.J. Stelzer[88], O. Stelzer-Chilton[159a], H. Stenzel[52], S. Stern[99], G.A. Stewart[29], J.A. Stillings[20], M.C. Stockton[85], K. Stoerig[48], G. Stoicea[25a], S. Stonjek[99], P. Strachota[126], A.R. Stradling[7], A. Straessner[43], J. Strandberg[147], S. Strandberg[146a,146b], A. Strandlie[117], M. Strang[109], E. Strauss[143], M. Strauss[111], P. Strizenec[144b], R. Ströhmer[174], D.M. Strom[114], J.A. Strong[76,*], R. Stroynowski[39], J. Strube[129], B. Stugu[13], I. Stumer[24,*], J. Stupak[148], P. Sturm[175], N.A. Styles[41], D.A. Soh[151,w], D. Su[143], HS. Subramania[2], A. Succurro[11], Y. Sugaya[116], C. Suhr[106], K. Suita[66], M. Suk[126], V.V. Sulin[94], S. Sultansoy[3d], T. Sumida[67], X. Sun[55], J.E. Sundermann[48], K. Suruliz[139], G. Susinno[36a,36b], M.R. Sutton[149], Y. Suzuki[65], Y. Suzuki[66], M. Svatos[125], S. Swedish[168], I. Sykora[144a], T. Sykora[126], J. Sánchez[167], D. Ta[105], K. Tackmann[41], A. Taffard[163], R. Tafirout[159a], N. Taiblum[153], Y. Takahashi[101], H. Takai[24], R. Takashima[68], H. Takeda[66], T. Takeshita[140], Y. Takubo[65], M. Talby[83], A. Talyshev[107,f], M.C. Tamsett[24], J. Tanaka[155], R. Tanaka[115], S. Tanaka[131], S. Tanaka[65], A.J. Tanasijczuk[142], K. Tani[66], N. Tannoury[83], S. Tapprogge[81], D. Tardif[158], S. Tarem[152], F. Tarrade[28], G.F. Tartarelli[89a], P. Tas[126], M. Tasevsky[125], E. Tassi[36a,36b], M. Tatarkhanov[14], Y. Tayalati[135d], C. Taylor[77], F.E. Taylor[92], G.N. Taylor[86], W. Taylor[159b], M. Teinturier[115], M. Teixeira Dias Castanheira[75], P. Teixeira-Dias[76], K.K. Temming[48], H. Ten Kate[29], P.K. Teng[151], S. Terada[65], K. Terashi[155], J. Terron[80], M. Testa[47], R.J. Teuscher[158,k], J. Therhaag[20], T. Theveneaux-Pelzer[78], S. Thoma[48], J.P. Thomas[17], E.N. Thompson[34], P.D. Thompson[17], P.D. Thompson[158], A.S. Thompson[53], L.A. Thomsen[35], E. Thomson[120], M. Thomson[27], R.P. Thun[87], F. Tian[34], M.J. Tibbetts[14], T. Tic[125], V.O. Tikhomirov[94], Y.A. Tikhonov[107,f], S. Timoshenko[96], P. Tipton[176], F.J. Tique Aires Viegas[29], S. Tisserant[83], T. Todorov[4], S. Todorova-Nova[161], B. Toggerson[163], J. Tojo[69], S. Tokár[144a], K. Tokunaga[66], K. Tokushuku[65], K. Tollefson[88], M. Tomoto[101], L. Tompkins[30], K. Toms[103], A. Tonoyan[13], C. Topfel[16], N.D. Topilin[64], I. Torchiani[29], E. Torrence[114], H. Torres[78], E. Torró Pastor[167], J. Toth[83,ad], F. Touchard[83], D.R. Tovey[139], T. Trefzger[174], L. Tremblet[29], A. Tricoli[29], I.M. Trigger[159a], S. Trincaz-Duvoid[78], M.F. Tripiana[70], W. Trischuk[158],

JHEP06(2012)088

B. Trocmé[55], C. Troncon[89a], M. Trottier-McDonald[142], M. Trzebinski[38], A. Trzupek[38], C. Tsarouchas[29], J.C-L. Tseng[118], M. Tsiakiris[105], P.V. Tsiareshka[90], D. Tsionou[4,ah], G. Tsipolitis[9], V. Tsiskaridze[48], E.G. Tskhadadze[51a], I.I. Tsukerman[95], V. Tsulaia[14], J.-W. Tsung[20], S. Tsuno[65], D. Tsybychev[148], A. Tua[139], A. Tudorache[25a], V. Tudorache[25a], J.M. Tuggle[30], M. Turala[38], D. Turecek[127], I. Turk Cakir[3e], E. Turlay[105], R. Turra[89a,89b], P.M. Tuts[34], A. Tykhonov[74], M. Tylmad[146a,146b], M. Tyndel[129], G. Tzanakos[8], K. Uchida[20], I. Ueda[155], R. Ueno[28], M. Ugland[13], M. Uhlenbrock[20], M. Uhrmacher[54], F. Ukegawa[160], G. Unal[29], A. Undrus[24], G. Unel[163], Y. Unno[65], D. Urbaniec[34], G. Usai[7], M. Uslenghi[119a,119b], L. Vacavant[83], V. Vacek[127], B. Vachon[85], S. Vahsen[14], J. Valenta[125], P. Valente[132a], S. Valentinetti[19a,19b], S. Valkar[126], E. Valladolid Gallego[167], S. Vallecorsa[152], J.A. Valls Ferrer[167], H. van der Graaf[105], E. van der Kraaij[105], R. Van Der Leeuw[105], E. van der Poel[105], D. van der Ster[29], N. van Eldik[29], P. van Gemmeren[5], I. van Vulpen[105], M. Vanadia[99], W. Vandelli[29], A. Vaniachine[5], P. Vankov[41], F. Vannucci[78], R. Vari[132a], T. Varol[84], D. Varouchas[14], A. Vartapetian[7], K.E. Varvell[150], V.I. Vassilakopoulos[56], F. Vazeille[33], T. Vazquez Schroeder[54], G. Vegni[89a,89b], J.J. Veillet[115], F. Veloso[124a], R. Veness[29], S. Veneziano[132a], A. Ventura[72a,72b], D. Ventura[84], M. Venturi[48], N. Venturi[158], V. Vercesi[119a], M. Verducci[138], W. Verkerke[105], J.C. Vermeulen[105], A. Vest[43], M.C. Vetterli[142,d], I. Vichou[165], T. Vickey[145b,ai], O.E. Vickey Boeriu[145b], G.H.A. Viehhauser[118], S. Viel[168], M. Villa[19a,19b], M. Villaplana Perez[167], E. Vilucchi[47], M.G. Vincter[28], E. Vinek[29], V.B. Vinogradov[64], M. Virchaux[136,*], J. Virzi[14], O. Vitells[172], M. Viti[41], I. Vivarelli[48], F. Vives Vaque[2], S. Vlachos[9], D. Vladoiu[98], M. Vlasak[127], A. Vogel[20], P. Vokac[127], G. Volpi[47], M. Volpi[86], G. Volpini[89a], H. von der Schmitt[99], J. von Loeben[99], H. von Radziewski[48], E. von Toerne[20], V. Vorobel[126], V. Vorwerk[11], M. Vos[167], R. Voss[29], T.T. Voss[175], J.H. Vossebeld[73], N. Vranjes[136], M. Vranjes Milosavljevic[105], V. Vrba[125], M. Vreeswijk[105], T. Vu Anh[48], R. Vuillermet[29], I. Vukotic[115], W. Wagner[175], P. Wagner[120], H. Wahlen[175], S. Wahrmund[43], J. Wakabayashi[101], S. Walch[87], J. Walder[71], R. Walker[98], W. Walkowiak[141], R. Wall[176], P. Waller[73], C. Wang[44], H. Wang[173], H. Wang[32b,aj], J. Wang[151], J. Wang[55], R. Wang[103], S.M. Wang[151], T. Wang[20], A. Warburton[85], C.P. Ward[27], M. Warsinsky[48], A. Washbrook[45], C. Wasicki[41], P.M. Watkins[17], A.T. Watson[17], I.J. Watson[150], M.F. Watson[17], G. Watts[138], S. Watts[82], A.T. Waugh[150], B.M. Waugh[77], M. Weber[129], M.S. Weber[16], P. Weber[54], A.R. Weidberg[118], P. Weigell[99], J. Weingarten[54], C. Weiser[48], H. Wellenstein[22], P.S. Wells[29], T. Wenaus[24], D. Wendland[15], Z. Weng[151,w], T. Wengler[29], S. Wenig[29], N. Wermes[20], M. Werner[48], P. Werner[29], M. Werth[163], M. Wessels[58a], J. Wetter[161], C. Weydert[55], K. Whalen[28], S.J. Wheeler-Ellis[163], A. White[7], M.J. White[86], S. White[122a,122b], S.R. Whitehead[118], D. Whiteson[163], D. Whittington[60], F. Wicek[115], D. Wicke[175], F.J. Wickens[129], W. Wiedenmann[173], M. Wielers[129], P. Wienemann[20], C. Wiglesworth[75], L.A.M. Wiik-Fuchs[48], P.A. Wijeratne[77], A. Wildauer[167], M.A. Wildt[41,s], I. Wilhelm[126], H.G. Wilkens[29], J.Z. Will[98], E. Williams[34], H.H. Williams[120], W. Willis[34], S. Willocq[84], J.A. Wilson[17], M.G. Wilson[143], A. Wilson[87], I. Wingerter-Seez[4], S. Winkelmann[48], F. Winklmeier[29], M. Wittgen[143], M.W. Wolter[38], H. Wolters[124a,h], W.C. Wong[40], G. Wooden[87], B.K. Wosiek[38], J. Wotschack[29], M.J. Woudstra[82], K.W. Wozniak[38], K. Wraight[53], C. Wright[53], M. Wright[53], B. Wrona[73], S.L. Wu[173],

JHEP06(2012)088

X. Wu[49], Y. Wu[32b,ak], E. Wulf[34], B.M. Wynne[45], S. Xella[35], M. Xiao[136], S. Xie[48], C. Xu[32b,z], D. Xu[139], B. Yabsley[150], S. Yacoob[145b], M. Yamada[65], H. Yamaguchi[155], A. Yamamoto[65], K. Yamamoto[63], S. Yamamoto[155], T. Yamamura[155], T. Yamanaka[155], J. Yamaoka[44], T. Yamazaki[155], Y. Yamazaki[66], Z. Yan[21], H. Yang[87], U.K. Yang[82], Y. Yang[60], Z. Yang[146a,146b], S. Yanush[91], L. Yao[32a], Y. Yao[14], Y. Yasu[65], G.V. Ybeles Smit[130], J. Ye[39], S. Ye[24], M. Yilmaz[3c], R. Yoosoofmiya[123], K. Yorita[171], R. Yoshida[5], C. Young[143], C.J. Young[118], S. Youssef[21], D. Yu[24], J. Yu[7], J. Yu[112], L. Yuan[66], A. Yurkewicz[106], B. Zabinski[38], R. Zaidan[62], A.M. Zaitsev[128], Z. Zajacova[29], L. Zanello[132a,132b], A. Zaytsev[107], C. Zeitnitz[175], M. Zeman[125], A. Zemla[38], C. Zendler[20], O. Zenin[128], T. Ženiš[144a], Z. Zinonos[122a,122b], S. Zenz[14], D. Zerwas[115], G. Zevi della Porta[57], Z. Zhan[32d], D. Zhang[32b,aj], H. Zhang[88], J. Zhang[5], X. Zhang[32d], Z. Zhang[115], L. Zhao[108], T. Zhao[138], Z. Zhao[32b], A. Zhemchugov[64], J. Zhong[118], B. Zhou[87], N. Zhou[163], Y. Zhou[151], C.G. Zhu[32d], H. Zhu[41], J. Zhu[87], Y. Zhu[32b], X. Zhuang[98], V. Zhuravlov[99], D. Zieminska[60], N.I. Zimin[64], R. Zimmermann[20], S. Zimmermann[20], S. Zimmermann[48], M. Ziolkowski[141], R. Zitoun[4], L. Živković[34], V.V. Zmouchko[128,*], G. Zobernig[173], A. Zoccoli[19a,19b], M. zur Nedden[15], V. Zutshi[106] and L. Zwalinski[29].

[1]: University at Albany, Albany NY, United States of America
[2]: Department of Physics, University of Alberta, Edmonton AB, Canada
[3]: [(a)]Department of Physics, Ankara University, Ankara; [(b)]Department of Physics, Dumlupinar University, Kutahya; [(c)]Department of Physics, Gazi University, Ankara; [(d)]Division of Physics, TOBB University of Economics and Technology, Ankara; [(e)]Turkish Atomic Energy Authority, Ankara, Turkey
[4]: LAPP, CNRS/IN2P3 and Université de Savoie, Annecy-le-Vieux, France
[5]: High Energy Physics Division, Argonne National Laboratory, Argonne IL, United States of America
[6]: Department of Physics, University of Arizona, Tucson AZ, United States of America
[7]: Department of Physics, The University of Texas at Arlington, Arlington TX, United States of America
[8]: Physics Department, University of Athens, Athens, Greece
[9]: Physics Department, National Technical University of Athens, Zografou, Greece
[10]: Institute of Physics, Azerbaijan Academy of Sciences, Baku, Azerbaijan
[11]: Institut de Física d'Altes Energies and Departament de Física de la Universitat Autònoma de Barcelona and ICREA, Barcelona, Spain
[12]: [(a)]Institute of Physics, University of Belgrade, Belgrade; [(b)]Vinca Institute of Nuclear Sciences, University of Belgrade, Belgrade, Serbia
[13]: Department for Physics and Technology, University of Bergen, Bergen, Norway
[14]: Physics Division, Lawrence Berkeley National Laboratory and University of California, Berkeley CA, United States of America
[15]: Department of Physics, Humboldt University, Berlin, Germany
[16]: Albert Einstein Center for Fundamental Physics and Laboratory for High Energy Physics, University of Bern, Bern, Switzerland

JHEP06(2012)088

[17]: School of Physics and Astronomy, University of Birmingham, Birmingham, United Kingdom
[18]: [(a)]Department of Physics, Bogazici University, Istanbul; [(b)]Division of Physics, Dogus University, Istanbul; [(c)]Department of Physics Engineering, Gaziantep University, Gaziantep; [(d)]Department of Physics, Istanbul Technical University, Istanbul, Turkey
[19]: [(a)]INFN Sezione di Bologna; [(b)]Dipartimento di Fisica, Università di Bologna, Bologna, Italy
[20]: Physikalisches Institut, University of Bonn, Bonn, Germany
[21]: Department of Physics, Boston University, Boston MA, United States of America
[22]: Department of Physics, Brandeis University, Waltham MA, United States of America
[23]: [(a)]Universidade Federal do Rio De Janeiro COPPE/EE/IF, Rio de Janeiro; [(b)]Federal University of Juiz de Fora (UFJF), Juiz de Fora; [(c)]Federal University of Sao Joao del Rei (UFSJ), Sao Joao del Rei; [(d)]Instituto de Fisica, Universidade de Sao Paulo, Sao Paulo, Brazil
[24]: Physics Department, Brookhaven National Laboratory, Upton NY, United States of America
[25]: [(a)]National Institute of Physics and Nuclear Engineering, Bucharest; [(b)]University Politehnica Bucharest, Bucharest; [(c)]West University in Timisoara, Timisoara, Romania
[26]: Departamento de Física, Universidad de Buenos Aires, Buenos Aires, Argentina
[27]: Cavendish Laboratory, University of Cambridge, Cambridge, United Kingdom
[28]: Department of Physics, Carleton University, Ottawa ON, Canada
[29]: CERN, Geneva, Switzerland
[30]: Enrico Fermi Institute, University of Chicago, Chicago IL, United States of America
[31]: [(a)]Departamento de Fisica, Pontificia Universidad Católica de Chile, Santiago; [(b)]Departamento de Física, Universidad Técnica Federico Santa María, Valparaíso, Chile
[32]: [(a)]Institute of High Energy Physics, Chinese Academy of Sciences, Beijing; [(b)]Department of Modern Physics, University of Science and Technology of China, Anhui; [(c)]Department of Physics, Nanjing University, Jiangsu; [(d)]School of Physics, Shandong University, Shandong, China
[33]: Laboratoire de Physique Corpusculaire, Clermont Université and Université Blaise Pascal and CNRS/IN2P3, Aubiere Cedex, France
[34]: Nevis Laboratory, Columbia University, Irvington NY, United States of America
[35]: Niels Bohr Institute, University of Copenhagen, Kobenhavn, Denmark
[36]: [(a)]INFN Gruppo Collegato di Cosenza; [(b)]Dipartimento di Fisica, Università della Calabria, Arcavata di Rende, Italy
[37]: AGH University of Science and Technology, Faculty of Physics and Applied Computer Science, Krakow, Poland
[38]: The Henryk Niewodniczanski Institute of Nuclear Physics, Polish Academy of Sciences, Krakow, Poland
[39]: Physics Department, Southern Methodist University, Dallas TX, United States of America

JHEP06(2012)088

[40]: Physics Department, University of Texas at Dallas, Richardson TX, United States of America
[41]: DESY, Hamburg and Zeuthen, Germany
[42]: Institut für Experimentelle Physik IV, Technische Universität Dortmund, Dortmund, Germany
[43]: Institut für Kern- und Teilchenphysik, Technical University Dresden, Dresden, Germany
[44]: Department of Physics, Duke University, Durham NC, United States of America
[45]: SUPA - School of Physics and Astronomy, University of Edinburgh, Edinburgh, United Kingdom
[46]: Fachhochschule Wiener Neustadt, Johannes Gutenbergstrasse 3 2700 Wiener Neustadt, Austria
[47]: INFN Laboratori Nazionali di Frascati, Frascati, Italy
[48]: Fakultät für Mathematik und Physik, Albert-Ludwigs-Universität, Freiburg i.Br., Germany
[49]: Section de Physique, Université de Genève, Geneva, Switzerland
[50]: [(a)]INFN Sezione di Genova; [(b)]Dipartimento di Fisica, Università di Genova, Genova, Italy
[51]: [(a)]E.Andronikashvili Institute of Physics, Tbilisi State University, Tbilisi; [(b)]High Energy Physics Institute, Tbilisi State University, Tbilisi, Georgia
[52]: II Physikalisches Institut, Justus-Liebig-Universität Giessen, Giessen, Germany
[53]: SUPA - School of Physics and Astronomy, University of Glasgow, Glasgow, United Kingdom
[54]: II Physikalisches Institut, Georg-August-Universität, Göttingen, Germany
[55]: Laboratoire de Physique Subatomique et de Cosmologie, Université Joseph Fourier and CNRS/IN2P3 and Institut National Polytechnique de Grenoble, Grenoble, France
[56]: Department of Physics, Hampton University, Hampton VA, United States of America
[57]: Laboratory for Particle Physics and Cosmology, Harvard University, Cambridge MA, United States of America
[58]: [(a)]Kirchhoff-Institut für Physik, Ruprecht-Karls-Universität Heidelberg, Heidelberg; [(b)]Physikalisches Institut, Ruprecht-Karls-Universität Heidelberg, Heidelberg; [(c)]ZITI Institut für technische Informatik, Ruprecht-Karls-Universität Heidelberg, Mannheim, Germany
[59]: Faculty of Applied Information Science, Hiroshima Institute of Technology, Hiroshima, Japan
[60]: Department of Physics, Indiana University, Bloomington IN, United States of America
[61]: Institut für Astro- und Teilchenphysik, Leopold-Franzens-Universität, Innsbruck, Austria
[62]: University of Iowa, Iowa City IA, United States of America
[63]: Department of Physics and Astronomy, Iowa State University, Ames IA, United States of America

JHEP06(2012)088

[64]: Joint Institute for Nuclear Research, JINR Dubna, Dubna, Russia
[65]: KEK, High Energy Accelerator Research Organization, Tsukuba, Japan
[66]: Graduate School of Science, Kobe University, Kobe, Japan
[67]: Faculty of Science, Kyoto University, Kyoto, Japan
[68]: Kyoto University of Education, Kyoto, Japan
[69]: Department of Physics, Kyushu University, Fukuoka, Japan
[70]: Instituto de Física La Plata, Universidad Nacional de La Plata and CONICET, La Plata, Argentina
[71]: Physics Department, Lancaster University, Lancaster, United Kingdom
[72]: [(a)]INFN Sezione di Lecce; [(b)]Dipartimento di Matematica e Fisica, Università del Salento, Lecce, Italy
[73]: Oliver Lodge Laboratory, University of Liverpool, Liverpool, United Kingdom
[74]: Department of Physics, Jožef Stefan Institute and University of Ljubljana, Ljubljana, Slovenia
[75]: School of Physics and Astronomy, Queen Mary University of London, London, United Kingdom
[76]: Department of Physics, Royal Holloway University of London, Surrey, United Kingdom
[77]: Department of Physics and Astronomy, University College London, London, United Kingdom
[78]: Laboratoire de Physique Nucléaire et de Hautes Energies, UPMC and Université Paris-Diderot and CNRS/IN2P3, Paris, France
[79]: Fysiska institutionen, Lunds universitet, Lund, Sweden
[80]: Departamento de Fisica Teorica C-15, Universidad Autonoma de Madrid, Madrid, Spain
[81]: Institut für Physik, Universität Mainz, Mainz, Germany
[82]: School of Physics and Astronomy, University of Manchester, Manchester, United Kingdom
[83]: CPPM, Aix-Marseille Université and CNRS/IN2P3, Marseille, France
[84]: Department of Physics, University of Massachusetts, Amherst MA, United States of America
[85]: Department of Physics, McGill University, Montreal QC, Canada
[86]: School of Physics, University of Melbourne, Victoria, Australia
[87]: Department of Physics, The University of Michigan, Ann Arbor MI, United States of America
[88]: Department of Physics and Astronomy, Michigan State University, East Lansing MI, United States of America
[89]: [(a)]INFN Sezione di Milano; [(b)]Dipartimento di Fisica, Università di Milano, Milano, Italy
[90]: B.I. Stepanov Institute of Physics, National Academy of Sciences of Belarus, Minsk, Republic of Belarus
[91]: National Scientific and Educational Centre for Particle and High Energy Physics, Minsk, Republic of Belarus

JHEP06(2012)088

[92]: Department of Physics, Massachusetts Institute of Technology, Cambridge MA, United States of America
[93]: Group of Particle Physics, University of Montreal, Montreal QC, Canada
[94]: P.N. Lebedev Institute of Physics, Academy of Sciences, Moscow, Russia
[95]: Institute for Theoretical and Experimental Physics (ITEP), Moscow, Russia
[96]: Moscow Engineering and Physics Institute (MEPhI), Moscow, Russia
[97]: Skobeltsyn Institute of Nuclear Physics, Lomonosov Moscow State University, Moscow, Russia
[98]: Fakultät für Physik, Ludwig-Maximilians-Universität München, München, Germany
[99]: Max-Planck-Institut für Physik (Werner-Heisenberg-Institut), München, Germany
[100]: Nagasaki Institute of Applied Science, Nagasaki, Japan
[101]: Graduate School of Science, Nagoya University, Nagoya, Japan
[102]: [(a)]INFN Sezione di Napoli; [(b)]Dipartimento di Scienze Fisiche, Università di Napoli, Napoli, Italy
[103]: Department of Physics and Astronomy, University of New Mexico, Albuquerque NM, United States of America
[104]: Institute for Mathematics, Astrophysics and Particle Physics, Radboud University Nijmegen/Nikhef, Nijmegen, Netherlands
[105]: Nikhef National Institute for Subatomic Physics and University of Amsterdam, Amsterdam, Netherlands
[106]: Department of Physics, Northern Illinois University, DeKalb IL, United States of America
[107]: Budker Institute of Nuclear Physics, SB RAS, Novosibirsk, Russia
[108]: Department of Physics, New York University, New York NY, United States of America
[109]: Ohio State University, Columbus OH, United States of America
[110]: Faculty of Science, Okayama University, Okayama, Japan
[111]: Homer L. Dodge Department of Physics and Astronomy, University of Oklahoma, Norman OK, United States of America
[112]: Department of Physics, Oklahoma State University, Stillwater OK, United States of America
[113]: Palacký University, RCPTM, Olomouc, Czech Republic
[114]: Center for High Energy Physics, University of Oregon, Eugene OR, United States of America
[115]: LAL, Université Paris-Sud and CNRS/IN2P3, Orsay, France
[116]: Graduate School of Science, Osaka University, Osaka, Japan
[117]: Department of Physics, University of Oslo, Oslo, Norway
[118]: Department of Physics, Oxford University, Oxford, United Kingdom
[119]: [(a)]INFN Sezione di Pavia; [(b)]Dipartimento di Fisica, Università di Pavia, Pavia, Italy
[120]: Department of Physics, University of Pennsylvania, Philadelphia PA, United States of America
[121]: Petersburg Nuclear Physics Institute, Gatchina, Russia
[122]: [(a)]INFN Sezione di Pisa; [(b)]Dipartimento di Fisica E. Fermi, Università di Pisa, Pisa, Italy

JHEP06(2012)088

[123]: Department of Physics and Astronomy, University of Pittsburgh, Pittsburgh PA, United States of America
[124]: [(a)]Laboratorio de Instrumentacao e Fisica Experimental de Particulas - LIP, Lisboa, Portugal; [(b)]Departamento de Fisica Teorica y del Cosmos and CAFPE, Universidad de Granada, Granada, Spain
[125]: Institute of Physics, Academy of Sciences of the Czech Republic, Praha, Czech Republic
[126]: Faculty of Mathematics and Physics, Charles University in Prague, Praha, Czech Republic
[127]: Czech Technical University in Prague, Praha, Czech Republic
[128]: State Research Center Institute for High Energy Physics, Protvino, Russia
[129]: Particle Physics Department, Rutherford Appleton Laboratory, Didcot, United Kingdom
[130]: Physics Department, University of Regina, Regina SK, Canada
[131]: Ritsumeikan University, Kusatsu, Shiga, Japan
[132]: [(a)]INFN Sezione di Roma I; [(b)]Dipartimento di Fisica, Università La Sapienza, Roma, Italy
[133]: [(a)]INFN Sezione di Roma Tor Vergata; [(b)]Dipartimento di Fisica, Università di Roma Tor Vergata, Roma, Italy
[134]: [(a)]INFN Sezione di Roma Tre; [(b)]Dipartimento di Fisica, Università Roma Tre, Roma, Italy
[135]: [(a)]Faculté des Sciences Ain Chock, Réseau Universitaire de Physique des Hautes Energies - Université Hassan II, Casablanca; [(b)]Centre National de l'Energie des Sciences Techniques Nucleaires, Rabat; [(c)]Faculté des Sciences Semlalia, Université Cadi Ayyad, LPHEA-Marrakech; [(d)]Faculté des Sciences, Université Mohamed Premier and LPTPM, Oujda; [(e)]Faculté des sciences, Université Mohammed V-Agdal, Rabat, Morocco
[136]: DSM/IRFU (Institut de Recherches sur les Lois Fondamentales de l'Univers), CEA Saclay (Commissariat a l'Energie Atomique), Gif-sur-Yvette, France
[137]: Santa Cruz Institute for Particle Physics, University of California Santa Cruz, Santa Cruz CA, United States of America
[138]: Department of Physics, University of Washington, Seattle WA, United States of America
[139]: Department of Physics and Astronomy, University of Sheffield, Sheffield, United Kingdom
[140]: Department of Physics, Shinshu University, Nagano, Japan
[141]: Fachbereich Physik, Universität Siegen, Siegen, Germany
[142]: Department of Physics, Simon Fraser University, Burnaby BC, Canada
[143]: SLAC National Accelerator Laboratory, Stanford CA, United States of America
[144]: [(a)]Faculty of Mathematics, Physics & Informatics, Comenius University, Bratislava; [(b)]Department of Subnuclear Physics, Institute of Experimental Physics of the Slovak Academy of Sciences, Kosice, Slovak Republic
[145]: [(a)]Department of Physics, University of Johannesburg, Johannesburg; [(b)]School of Physics, University of the Witwatersrand, Johannesburg, South Africa

JHEP06(2012)088

[146]: [(a)]Department of Physics, Stockholm University; [(b)]The Oskar Klein Centre, Stockholm, Sweden
[147]: Physics Department, Royal Institute of Technology, Stockholm, Sweden
[148]: Departments of Physics & Astronomy and Chemistry, Stony Brook University, Stony Brook NY, United States of America
[149]: Department of Physics and Astronomy, University of Sussex, Brighton, United Kingdom
[150]: School of Physics, University of Sydney, Sydney, Australia
[151]: Institute of Physics, Academia Sinica, Taipei, Taiwan
[152]: Department of Physics, Technion: Israel Institute of Technology, Haifa, Israel
[153]: Raymond and Beverly Sackler School of Physics and Astronomy, Tel Aviv University, Tel Aviv, Israel
[154]: Department of Physics, Aristotle University of Thessaloniki, Thessaloniki, Greece
[155]: International Center for Elementary Particle Physics and Department of Physics, The University of Tokyo, Tokyo, Japan
[156]: Graduate School of Science and Technology, Tokyo Metropolitan University, Tokyo, Japan
[157]: Department of Physics, Tokyo Institute of Technology, Tokyo, Japan
[158]: Department of Physics, University of Toronto, Toronto ON, Canada
[159]: [(a)]TRIUMF, Vancouver BC; [(b)]Department of Physics and Astronomy, York University, Toronto ON, Canada
[160]: Institute of Pure and Applied Sciences, University of Tsukuba,1-1-1 Tennodai,Tsukuba, Ibaraki 305-8571, Japan
[161]: Science and Technology Center, Tufts University, Medford MA, United States of America
[162]: Centro de Investigaciones, Universidad Antonio Narino, Bogota, Colombia
[163]: Department of Physics and Astronomy, University of California Irvine, Irvine CA, United States of America
[164]: [(a)]INFN Gruppo Collegato di Udine; [(b)]ICTP, Trieste; [(c)]Dipartimento di Chimica, Fisica e Ambiente, Università di Udine, Udine, Italy
[165]: Department of Physics, University of Illinois, Urbana IL, United States of America
[166]: Department of Physics and Astronomy, University of Uppsala, Uppsala, Sweden
[167]: Instituto de Física Corpuscular (IFIC) and Departamento de Física Atómica, Molecular y Nuclear and Departamento de Ingeniería Electrónica and Instituto de Microelectrónica de Barcelona (IMB-CNM), University of Valencia and CSIC, Valencia, Spain
[168]: Department of Physics, University of British Columbia, Vancouver BC, Canada
[169]: Department of Physics and Astronomy, University of Victoria, Victoria BC, Canada
[170]: Department of Physics, University of Warwick, Coventry, United Kingdom
[171]: Waseda University, Tokyo, Japan
[172]: Department of Particle Physics, The Weizmann Institute of Science, Rehovot, Israel
[173]: Department of Physics, University of Wisconsin, Madison WI, United States of America

JHEP06(2012)088

[174]: Fakultät für Physik und Astronomie, Julius-Maximilians-Universität, Würzburg, Germany
[175]: Fachbereich C Physik, Bergische Universität Wuppertal, Wuppertal, Germany
[176]: Department of Physics, Yale University, New Haven CT, United States of America
[177]: Yerevan Physics Institute, Yerevan, Armenia
[178]: Domaine scientifique de la Doua, Centre de Calcul CNRS/IN2P3, Villeurbanne Cedex, France
[a]: Also at Laboratorio de Instrumentacao e Fisica Experimental de Particulas - LIP, Lisboa, Portugal
[b]: Also at Faculdade de Ciencias and CFNUL, Universidade de Lisboa, Lisboa, Portugal
[c]: Also at Particle Physics Department, Rutherford Appleton Laboratory, Didcot, United Kingdom
[d]: Also at TRIUMF, Vancouver BC, Canada
[e]: Also at Department of Physics, California State University, Fresno CA, United States of America
[f]: Also at Novosibirsk State University, Novosibirsk, Russia
[g]: Also at Fermilab, Batavia IL, United States of America
[h]: Also at Department of Physics, University of Coimbra, Coimbra, Portugal
[i]: Also at Department of Physics, UASLP, San Luis Potosi, Mexico
[j]: Also at Università di Napoli Parthenope, Napoli, Italy
[k]: Also at Institute of Particle Physics (IPP), Canada
[l]: Also at Department of Physics, Middle East Technical University, Ankara, Turkey
[m]: Also at Louisiana Tech University, Ruston LA, United States of America
[n]: Also at Dep Fisica and CEFITEC of Faculdade de Ciencias e Tecnologia, Universidade Nova de Lisboa, Caparica, Portugal
[o]: Also at Department of Physics and Astronomy, University College London, London, United Kingdom
[p]: Also at Group of Particle Physics, University of Montreal, Montreal QC, Canada
[q]: Also at Department of Physics, University of Cape Town, Cape Town, South Africa
[r]: Also at Institute of Physics, Azerbaijan Academy of Sciences, Baku, Azerbaijan
[s]: Also at Institut für Experimentalphysik, Universität Hamburg, Hamburg, Germany
[t]: Also at Manhattan College, New York NY, United States of America
[u]: Also at School of Physics, Shandong University, Shandong, China
[v]: Also at CPPM, Aix-Marseille Université and CNRS/IN2P3, Marseille, France
[w]: Also at School of Physics and Engineering, Sun Yat-sen University, Guanzhou, China
[x]: Also at Academia Sinica Grid Computing, Institute of Physics, Academia Sinica, Taipei, Taiwan
[y]: Also at Dipartimento di Fisica, Università La Sapienza, Roma, Italy
[z]: Also at DSM/IRFU (Institut de Recherches sur les Lois Fondamentales de l'Univers), CEA Saclay (Commissariat a l'Energie Atomique), Gif-sur-Yvette, France
[aa]: Also at section de Physique, Université de Genève, Geneva, Switzerland
[ab]: Also at Departamento de Fisica, Universidade de Minho, Braga, Portugal

JHEP06(2012)088

[ac]: Also at Department of Physics and Astronomy, University of South Carolina, Columbia SC, United States of America
[ad]: Also at Institute for Particle and Nuclear Physics, Wigner Research Centre for Physics, Budapest, Hungary
[ae]: Also at California Institute of Technology, Pasadena CA, United States of America
[af]: Also at Institute of Physics, Jagiellonian University, Krakow, Poland
[ag]: Also at LAL, Université Paris-Sud and CNRS/IN2P3, Orsay, France
[ah]: Also at Department of Physics and Astronomy, University of Sheffield, Sheffield, United Kingdom
[ai]: Also at Department of Physics, Oxford University, Oxford, United Kingdom
[aj]: Also at Institute of Physics, Academia Sinica, Taipei, Taiwan
[ak]: Also at Department of Physics, The University of Michigan, Ann Arbor MI, United States of America
*: Deceased

JHEP06(2012)088

Physics Letters B 717 (2012) 89–108

Contents lists available at SciVerse ScienceDirect

Physics Letters B

www.elsevier.com/locate/physletb

Measurement of the top quark pair cross section with ATLAS in pp collisions at $\sqrt{s} = 7$ TeV using final states with an electron or a muon and a hadronically decaying τ lepton ☆

ATLAS Collaboration *

ARTICLE INFO

Article history:
Received 9 May 2012
Received in revised form 21 August 2012
Accepted 8 September 2012
Available online 18 September 2012
Editor: H. Weerts

Keywords:
Top quark physics
Cross section
Lepton + τ

ABSTRACT

A measurement of the cross section of top quark pair production in proton–proton collisions recorded with the ATLAS detector at the Large Hadron Collider at a centre-of-mass energy of 7 TeV is reported. The data sample used corresponds to an integrated luminosity of 2.05 fb^{-1}. Events with an isolated electron or muon and a τ lepton decaying hadronically are used. In addition, a large missing transverse momentum and two or more energetic jets are required. At least one of the jets must be identified as originating from a b quark. The measured cross section, $\sigma_{t\bar{t}} = 186 \pm 13$ (stat.) ± 20 (syst.) ± 7 (lumi.) pb, is in good agreement with the Standard Model prediction.

© 2012 CERN. Published by Elsevier B.V. Open access under CC BY-NC-ND license.

1. Introduction

Measuring the top quark pair ($t\bar{t}$) production cross section ($\sigma_{t\bar{t}}$) in different decay channels is of interest because it can indicate physics beyond the Standard Model (SM). In the SM, the top quark decays with a branching ratio close to 100% into a W boson and a b quark, and $t\bar{t}$ pairs are identified by either the hadronic or leptonic decays of the W bosons and the presence of additional jets. The ATLAS Collaboration has previously used the single-lepton channel [1] from a 35 pb^{-1} data sample, and the dilepton channels including only electrons and muons [2] from a 0.7 fb^{-1} data sample, to perform cross-section measurements at 7 TeV proton–proton centre-of-mass energy. Similar measurements have been performed by the CMS Collaboration [3–5]. All these measurements are systematics limited.

The large data samples for $t\bar{t}$ production at the Large Hadron Collider (LHC) provide an opportunity to measure $\sigma_{t\bar{t}}$ using final states with an electron or a muon and a τ lepton with high precision. The $\sigma_{t\bar{t}}$ in this channel has been measured at the Tevatron in $p\bar{p}$ collisions at 1.96 TeV with 25% precision [6] and recently by the CMS Collaboration at the LHC with 18% precision [7]. A deviation from the value of $\sigma_{t\bar{t}}$ measured in other final states would be an indication of non-Standard Model decays of the top quark, such as a decay to a charged Higgs (H^+) and a b quark with H^+ decaying to a τ lepton and a τ neutrino, or of contributions from other non-Standard Model processes [8–10]. Upper limits on the branching ratio of top quark decays to H^+ bosons decaying to a τ lepton and a neutrino have been published by Tevatron and LHC experiments [11–13].

2. Analysis overview

This analysis uses 2.05 fb^{-1} of data collected by ATLAS from pp collisions in the LHC at a centre-of-mass energy of 7 TeV between March and August 2011. The $t\bar{t}$ events are selected with kinematic criteria that make use of the fact that they feature two W bosons and two b quarks. The selections favour events with one W decay to a charged ℓ (with ℓ denoting an electron or a muon; either prompt or from a τ lepton decay to ℓ) and a neutrino and the other W decays to a τ lepton and a neutrino with the τ lepton in turn decaying hadronically. In addition at least one jet is tagged (b-tag) as originating from a b quark (b-jet) by means of an algorithm that can identify b-jets with high efficiency while maintaining a high rejection of light-quark jets. Isolated electrons and muons are well identified, but because of the large cross section for multi-jet production the background from jets misidentified as isolated electrons or muons is not negligible. This background is reduced by requiring significant missing transverse momentum signalling the presence of energetic neutrinos. Hadronic τ lepton decays are more difficult to identify and require elaborate techniques to reject jets and electrons misidentified as a τ lepton.

Section 5 describes how the objects used in the event selection are defined. After all selections given in Section 5.2, the dominant background to the $t\bar{t} \to \ell + \tau + X$ channel is the $t\bar{t} \to \ell +$ jets channel in which the τ candidate is from jets misidentified as hadronic τ lepton decays. Therefore, τ lepton identification (τ ID) is critical

☆ © CERN for the benefit of the ATLAS Collaboration.

* *E-mail address:* atlas.publications@cern.ch.

0370-2693 © 2012 CERN. Published by Elsevier B.V. Open access under CC BY-NC-ND license.
http://dx.doi.org/10.1016/j.physletb.2012.09.032

for separating signal and background. The τ ID methodology employed in this analysis exploits a multivariate technique to build a discriminant [14]. A boosted decision tree (BDT) algorithm is used [15,16]. The number of τ leptons in the selected samples is extracted by fitting the distributions of BDT outputs to background and signal templates. Section 6 describes how the background templates are constructed using control data samples. They exploit the fact that events with ℓ and τ candidates of opposite sign charge (OS) contain real τ leptons while those with same sign charge (SS) are pure background. Events with τ leptons are not all from $t\bar{t}$; the contribution from processes other than $t\bar{t} \to \ell + \tau + X$ is estimated from Monte Carlo simulation. Section 7 describes the fitting procedure and the results of the fit. The fit results are also checked using an alternative method, referred to as the "matrix method", based on a cut on the BDT output (Section 7.1). The measured cross section is given in Section 8 and the conclusions are in Section 9.

3. ATLAS detector

The ATLAS detector [17] at the LHC covers nearly the entire solid angle around the collision point.[1] It consists of an inner tracking detector surrounded by a thin superconducting solenoid, electromagnetic (EM) and hadronic calorimeters, and an external muon spectrometer incorporating three large superconducting toroid magnet assemblies. The inner tracking detector provides tracking information in a pseudorapidity range $|\eta| < 2.5$. The liquid-argon (LAr) EM sampling calorimeters cover a range of $|\eta| < 3.2$ with fine granularity. An iron-scintillator tile calorimeter provides hadronic energy measurements in the central rapidity range ($|\eta| < 1.7$). The endcap and forward regions are instrumented with LAr calorimeters for both EM and hadronic energy measurements covering $|\eta| < 4.9$. The muon spectrometer provides precise tracking information in a range of $|\eta| < 2.7$.

ATLAS uses a three-level trigger system to select events. The level-1 trigger is implemented in hardware using a subset of detector information to reduce the event rate to below 75 kHz. This is followed by two software-based trigger levels, level-2 and the event filter, which together reduce the event rate to about 300 Hz recorded for analysis.

4. Simulated event samples

Monte Carlo (MC) simulation samples are used to optimise selection procedures, to calculate the signal acceptance and to evaluate the background contributions from single top quark, WW, WZ and ZZ production and $Z \to \tau^+\tau^-$ decays. After event generation, all samples are processed with the GEANT4 [18] simulation of the ATLAS detector, the trigger simulation and are then subject to the same reconstruction algorithms as the data [19].

For the $t\bar{t}$ and single top quark final states, the next-to-leading-order (NLO) generator MC@NLO [20–22] is used with a top quark mass of 172.5 GeV and with the NLO parton distribution function (PDF) set CTEQ6.6 [23]. The MC@NLO program uses HERWIG [24] to simulate the parton shower and hadronise the partons. The "diagram removal scheme" is used to remove overlaps between the single top quark and the $t\bar{t}$ final states. The $t\bar{t}$ cross section is normalised to the prediction of HATHOR (164^{+11}_{-16} pb) [25], which employs an approximate next-to-next-to-leading-order (NNLO) perturbative Quantum Chromodynamics (QCD) calculation. The diboson samples are generated with HERWIG. W + jets events and Z/γ^* + jets events (with dilepton invariant mass $m_{\ell^+\ell^-} > 40$ GeV) are generated by the ALPGEN generator [26] with up to five outgoing partons from the hard scattering process, in addition to the lepton pairs.[2] The MLM matching scheme [27] of the ALPGEN generator is used to remove overlaps between matrix-element and parton-shower products. Parton evolution and hadronisation is handled by HERWIG, as is the generation of diboson events. The leading-order PDF set CTEQ6L is used for all backgrounds described above.

All samples that use HERWIG for parton shower evolution and hadronisation rely on JIMMY [28] for the underlying event model. The τ-lepton decays are handled by TAUOLA [29]. The effect of multiple pp interactions per bunch crossing ("pile-up") is modelled by overlaying simulated minimum bias events over the original hard-scattering event [30]. MC events are then reweighted so that the distribution of interactions per crossing in the MC simulation matches that observed in data. The average number of pile-up interactions in the sample is 6.3.

5. Object identification and event selection

The event selection uses nearly the same object definition as in the $t\bar{t}$ cross-section measurement in the dilepton channel [2] with the exception of a τ candidate instead of a second electron or muon candidate. The electrons must be isolated and have $E_T >$ 25 GeV and $|\eta_{\text{cluster}}| < 2.47$, excluding the barrel-endcap transition region ($1.37 < |\eta_{\text{cluster}}| < 1.52$), where E_T is the transverse energy and η_{cluster} is the pseudorapidity of the calorimeter energy cluster associated with the candidate. The electron is defined as isolated if the E_T deposited in the calorimeter and not associated with the electron in a cone in η–ϕ space of radius $\Delta R = 0.2$ is less than 4 GeV. The muons must also be isolated and have transverse momentum $p_T > 20$ GeV and $|\eta| < 2.5$. For isolated muons, both the corresponding E_T and the analogous track isolation transverse momentum must be less than 4 GeV in a cone of $\Delta R = 0.3$. The track isolation p_T is calculated from the sum of the track transverse momenta for tracks with $p_T > 1$ GeV around the muon. Jets are reconstructed with the anti-k_t algorithm [31] with a radius parameter $R = 0.4$, starting from energy deposits (clusters) in the calorimeter reconstructed using the scale established using $Z \to e^+e^-$ events for electromagnetic objects. These jets are then calibrated to the hadronic energy scale using p_T- and η-dependent correction factors obtained from simulation [32]. The jet candidates are required to have $p_T > 25$ GeV and $|\eta| < 2.5$. A jet is tagged as a b-jet by a vertex tagging algorithm that constructs a likelihood ratio of b- and light-quark jet hypothesis using the following discriminating variables: the signed impact parameter significance of well measured tracks associated with a given jet, the decay length significance associated with a reconstructed secondary vertex, the invariant mass of all tracks associated to the secondary vertex, the ratio of the sum of the energies of the tracks associated with the secondary vertex to the sum of the energies of all tracks in the jet assuming a pion hypothesis, and the number of two-track vertices that can be formed at the secondary vertex. The cut on the combined likelihood ratio has been chosen to give an average efficiency of 70% for b-quark jets from $t\bar{t}$ events and a 1% efficiency for light-quark and gluon jets [33].

[1] Atlas uses a right-handed coordinate system with its origin at the nominal interaction point in the centre of the detector and the z-axis along the beam pipe. The x-axis points to the centre of the LHC ring, and the y-axis points upwards. The azimuthal angle ϕ is measured around the beam axis and the polar angle θ is the angle from the beam axis. The pseudorapidity is defined as $\eta = -\ln[\tan(\theta/2)]$. The distance ΔR in η–ϕ space is defined as $\Delta R = \sqrt{(\Delta\phi)^2 + (\Delta\eta)^2}$.

[2] The fraction of events with $m_{\ell^+\ell^-} < 40$ GeV is estimated to be less than 0.2% of the total after all selections. The estimate is based on ALPGEN samples for Drell–Yan simulation and confirmed by a good agreement with data.

The missing transverse momentum is constructed from the vector sum of all calorimeter cells with $|\eta| < 4.5$, projected onto the transverse plane. Its magnitude is denoted $E_{\mathrm{T}}^{\mathrm{miss}}$. The hadronic energy scale is used for the energies of cells associated with jets; τ candidates are treated as jets. Contributions from cells associated with electrons employ the electromagnetic energy calibration. Contributions from the p_{T} of muon tracks are included, removing the contributions of any calorimeter cells associated with the muon.

5.1. τ reconstruction and identification

The reconstruction and identification of hadronically decaying τ leptons proceed as follows:

1. the τ candidate reconstruction starts by considering each jet as a τ candidate;
2. energy clusters in the calorimeter associated with the τ candidate are used to calculate kinematic quantities (such as E_{T}) and the associated tracks are found;
3. identification variables are calculated from the tracking and calorimeter information;
4. these variables are combined into multivariate discriminants and the outputs of the discriminants are used to separate jets and electrons misidentified as τ leptons decaying hadronically from τ leptons.

Details, including the variable definitions used in the multivariate discriminants, are given in Ref. [9]. In this analysis the outputs of BDT discriminants are used.

Reconstructed τ candidates are required to have 20 GeV $< E_{\mathrm{T}} <$ 100 GeV. They must also have $|\eta| < 2.3$, and one, two or three associated tracks. A track is associated with the τ candidate if it has $p_{\mathrm{T}} > 1$ GeV and is inside a cone of $\Delta R < 0.4$ around the jet axis. The associated track with highest p_{T} must have $p_{\mathrm{T}} > 4$ GeV. The charge is given by the sum of the charges of the associated tracks, and is required to be non-zero. The probability of misidentifying the τ lepton charge sign is about 1%. The charge misidentification rate for muons and electrons is negligible.

If the τ candidate overlaps with a muon (with $p_{\mathrm{T}} > 4$ GeV and without an isolation requirement) or an electron candidate within $\Delta R(\ell, \tau) < 0.4$, the τ candidate is removed. To remove electrons misidentified as τ leptons, an additional criterion is used that relies on a BDT trained to separate τ leptons and electrons (BDT_e) using seven variables shown to be well modelled by comparing $Z \to e^+e^-$ and $Z \to \tau^+\tau^-$ events in data and in MC simulation. The variables were chosen after ranking a large set by their effectiveness.[3] The most effective variables for BDT_e are E/p, the EM fraction (the ratio of the τ candidate energy measured in the EM calorimeter to the total τ candidate energy measured in the calorimeter), and the cluster-based shower width. The BDT output tends to be near 1 (0) if the τ candidate is a τ lepton (electron). BDT_e was trained using $Z \to e^+e^-$ and $Z \to \tau^+\tau^-$ Monte Carlo samples. The τ candidate is required to satisfy $\mathrm{BDT}_e > 0.51$; 85% of reconstructed τ leptons decaying hadronically satisfy this requirement, as measured in $Z \to \tau^+\tau^-$ events. The additional rejection for electrons is a factor of 60.

The majority of objects reconstructed as τ candidates in a multi-jet environment are jets misidentified as τ leptons. A jet or an electron misidentified as a τ lepton will be referred to as a fake τ. Another BDT (BDT_j) based on eight variables is used to separate τ leptons in τ candidates with one track (denoted τ_1) from such jets. For candidates with more than one track (denoted τ_3) BDT_j includes ten variables. The BDT_j was trained using multi-jet events as background and $Z \to \tau^+\tau^-$ Monte Carlo as signal. The most effective variables for BDT_j are calorimeter and track isolation, cluster-based jet mass, and the fraction of energy within $\Delta R = 0.1$ of the jet axis. The BDT_j distributions are fit with templates for background and signal to extract the number of τ leptons in the sample. Details are given in Section 7. The fake τ background in the τ_3 sample is significantly higher than in the τ_1 sample, leading to very different BDT_j distributions. Hence independent measurements are carried out for τ_1 and τ_3 candidate events and the results are combined at the end. If there is a τ_1 and a τ_3 candidate in the event, the τ_1 candidate is kept as the probability that the τ_1 is a τ lepton is much higher. If there are two τ_1 or τ_3 candidates, both are kept.

5.2. Event selection

For this analysis, events are selected using a single-muon trigger with a p_{T} threshold of 18 GeV or a single-electron trigger with a p_{T} threshold of 20 GeV, rising to 22 GeV during periods of high instantaneous luminosity. The offline requirements are based on data quality criteria and optimised using Monte Carlo simulation:

- a primary vertex with at least five tracks, each with $p_{\mathrm{T}} >$ 400 MeV, associated with it;
- one and only one isolated high-p_{T} muon and no identified electrons for the $\mu + \tau$ channel, or one and only one isolated electron and no isolated muons for the $e + \tau$ channel;
- at least one τ candidate (as defined in Section 5.1);
- at least two jets not overlapping with a τ candidate, i.e. $\Delta R(\tau, \mathrm{jet}) > 0.4$;
- $E_{\mathrm{T}}^{\mathrm{miss}} > 30$ GeV to reduce the multi-jet background, and the scalar sum of the p_{T} of the leptons (including τ), jets, and $E_{\mathrm{T}}^{\mathrm{miss}}$ must be greater then 200 GeV, to reduce the $W +$ jets background.

The $\ell + \tau$ samples are divided into events with no jets identified as a b-quark jet (0 b-tag control sample) and those with at least one such jet ($\geqslant$1 b-tag $t\bar{t}$ sample). The 0 b-tag sample is used to estimate the background in the $\geqslant$1 b-tag $t\bar{t}$ sample. Each sample is split into two, one with the τ candidate and ℓ having the opposite sign charge (OS), and the other one with τ and ℓ having the same sign charge (SS). While the τ candidates in the SS samples are almost all fake τ leptons, the OS samples have a mixture of τ leptons and fake τ leptons. The numbers of observed and expected events in the above samples are shown in Table 1. The $\ell +$ jets entry is the contribution from all processes with a ℓ and a τ candidate that is a jet misidentified as a τ lepton other than from $t\bar{t}$ ($\to \ell +$ jets). The τ entries require the reconstructed τ candidate be matched to a generated τ lepton. The matching criterion is $\Delta R < 0.1$ between the τ candidate and the observable component of the generated τ lepton.

To estimate the multi-jet background from data, an event selection identical to the $\mu + \tau$ ($e + \tau$) event selection except for an inverted muon (electron) isolation cut is used to obtain a multi-jet template for the shape of the transverse mass, $m_{\mathrm{T}} = \sqrt{(E_T^{\ell} + E_{\mathrm{T}}^{\mathrm{miss}})^2 - (p_x^{\ell} + E_x^{\mathrm{miss}})^2 - (p_y^{\ell} + E_y^{\mathrm{miss}})^2}$. The normalisation of each selected data sample is obtained by fitting the m_{T} distribution of the selected data samples with the multi-jet template and the sum of non-multi-jet processes predicted by MC, allowing the amount of both to float. The uncertainty on the multi-jet

[3] The effectiveness is quantified by quadratically summing over the change in the purity between the mother and daughter leaves for every node in which the given variable is used in a decision tree.

Table 1
Number of $\ell+\tau$ candidates for Monte Carlo samples and data. $t\bar{t}(\ell+e)$ are $t\bar{t}$ events with one identified lepton and an electron reconstructed as a τ candidate. $t\bar{t}(\ell+\text{jets})$ are $t\bar{t}$ events with one identified lepton and a jet reconstructed as a τ candidate. $\ell+\text{jets}$ are events with one identified lepton and a jet reconstructed as a τ candidate from sources other than $t\bar{t}(\ell+\text{jets})$ and multi-jets. Sources contributing to jet fakes are $W+\text{jets}$, $Z+\text{jets}$, single top quark, diboson events and $t\bar{t}$. $Wt(\ell+\tau)$ is $W+t$ production with one W decaying to ℓ and another to τ. The uncertainties are statistical only, except for the multi-jet estimates. MC samples are normalised to the data integrated luminosity.

$\mu+\tau$	τ_1				τ_3			
	0 b-tag		$\geqslant 1$ b-tag		0 b-tag		$\geqslant 1$ b-tag	
	OS	SS	OS	SS	OS	SS	OS	SS
$t\bar{t}(\mu+\tau)$	60 ± 2	<1	390 ± 4	2 ± 1	17 ± 1	1 ± 1	118 ± 3	2 ± 1
$t\bar{t}(\mu+e)$	3 ± 1	<1	12 ± 1	1 ± 1	1 ± 1	<1	3 ± 1	<1
$t\bar{t}(\mu+\text{jets})$	308 ± 4	163 ± 3	1528 ± 9	660 ± 6	685 ± 6	443 ± 5	3484 ± 13	2000 ± 10
$\mu+\text{jets}$	5010 ± 70	3020 ± 60	496 ± 17	297 ± 13	$12\,230\pm 120$	8670 ± 90	1293 ± 28	928 ± 24
Multi-jets	470 ± 140	540 ± 160	117 ± 35	150 ± 40	990 ± 300	1120 ± 340	460 ± 140	400 ± 120
$Wt(\mu+\tau)$	7 ± 1	<1	18 ± 1	1 ± 1	2 ± 1	<1	5 ± 1	<1
$Z\to\tau\tau$	301 ± 13	2 ± 1	16 ± 3	<1	75 ± 7	1 ± 1	3 ± 2	<1
Total	6160 ± 160	3730 ± 170	2580 ± 40	1110 ± 40	$14\,000\pm 320$	$10\,230\pm 350$	5370 ± 140	3330 ± 120
Data	5450	3700	2472	1332	13 322	10 193	5703	3683
$e+\tau$	τ_1				τ_3			
	0 b-tag		$\geqslant 1$ b-tag		0 b-tag		$\geqslant 1$ b-tag	
	OS	SS	OS	SS	OS	SS	OS	SS
$t\bar{t}(e+\tau)$	54 ± 7	1 ± 1	342 ± 19	3 ± 2	15 ± 4	<1	103 ± 10	2 ± 1
$t\bar{t}(e+e)$	2 ± 1	<1	11 ± 3	1 ± 1	<1	<1	2 ± 1	<1
$t\bar{t}(e+\text{jets})$	273 ± 17	146 ± 12	1340 ± 40	599 ± 25	633 ± 25	399 ± 20	3090 ± 60	1780 ± 40
$e+\text{jets}$	3950 ± 60	2590 ± 50	380 ± 20	256 ± 16	$10\,140\pm 100$	7530 ± 90	1120 ± 33	841 ± 29
Multi-jets	600 ± 180	620 ± 190	170 ± 50	140 ± 40	2000 ± 600	2000 ± 600	690 ± 210	610 ± 180
$Z\to ee$	92 ± 10	3 ± 2	9 ± 3	<1	11 ± 3	2 ± 1	<1	<1
$Wt(e+\tau)$	7 ± 3	<1	17 ± 4	<1	1 ± 1	<1	5 ± 2	<1
$Z\to\tau\tau$	217 ± 15	2 ± 1	15 ± 4	<1	60 ± 7	1 ± 1	3 ± 2	<1
Total	5190 ± 190	3360 ± 200	2280 ± 70	990 ± 50	$12\,900\pm 600$	9900 ± 600	5020 ± 220	3230 ± 180
Data	5111	3462	2277	1107	12 102	9635	5033	3192

background is estimated to be 30%. This estimate is only used to illustrate the background composition. The background models are derived from data (see Section 6) and do not depend on knowing the exact composition. All processes contribute more events to OS than SS because of the correlation between a leading-quark charge and the lepton charge, except for the multi-jet channel contribution which within uncertainties has equal numbers of OS and SS events. As one can see from Table 1, the τ leptons are almost all in the OS sample and come mainly from two sources: $Z\to\tau^+\tau^-$, which is the dominant source in the sample with 0 b-tag, and $t\bar{t}\to\ell+\tau+X$ which is the dominant source in the sample $\geqslant 1$ b-tag. The sources of fake τ leptons are quite distinct between the 0 b-tag and the $\geqslant 1$ b-tag samples: the first is mainly $W/Z+\text{jets}$ with small contributions from other channels, the second is mainly $t\bar{t}$.

6. Background models

The jet origin can strongly influence the τ-lepton fake probability. Due to their narrow shower width and lower track multiplicity, light-quark jets have a higher probability of faking a τ lepton than other jet types. Thus the BDT_j distributions have a strong dependence on the jet type. It is therefore crucial to build a background model which properly reflects the jet composition in order to correctly estimate the fake τ contamination in the signal region. Deriving this background model from control regions in data rather than MC simulation is preferable in order to avoid systematic effects related to jet composition in the MC models.

The gluon component of the fake τ leptons is charge symmetric; therefore it is expected to have the same shape in SS events as in OS events and should contribute the same number of fake τ leptons in each sample. The contribution of fake τ leptons from gluons can be removed by subtracting the distribution of any quantity for SS events from the corresponding distribution for OS events. The multi-jet background also cancels, as can be seen in Table 1. The resulting distributions are labelled OS-SS. Similarly, since each sample is expected to have an almost equal contribution from b-jets and $\bar{b}$-jets, the small b-jet component should also be removed by OS-SS (the asymmetry in b production, mainly from single top quark final states, is negligible). The only jet types remaining in the OS-SS distributions are light-quark jets. MC studies indicate that the BDT_j distributions of c-quark jets misidentified as τ leptons are not noticeably different from those of light-quark jets.

One can construct a background BDT_j distribution from the 0 b-tag data sample by subtracting the expected amount of τ-lepton signal. The signal is mainly from $Z\to\tau^+\tau^-$ and can be reliably predicted from MC. A control sample dominated by $W+\text{jets}$ events is considered as a check. The latter sample is selected by requiring events with a muon and a τ candidate, no additional jets, $E_{\text{T}}^{\text{miss}}>30$ GeV and 40 GeV $<m_{\text{T}}<100$ GeV. According to MC simulation, in $W+\text{jets}$ events where exactly one jet is required, 90% of the fake τ leptons are from light-quark jets and 10% from gluons. This sample is labelled $W+1$ jet.

The BDT_j background shapes for the OS-SS 0 b-tag and $\geqslant 1$ b-tag data samples are not identical to the $W+1$ jet distributions for two reasons: (1) the shape depends on the jet multiplicity, (2) different OS/SS ratios are observed in the samples. The dependence on the OS/SS ratio comes from the differences in jet fragmentation producing a leading particle with the opposite charge and the same charge as the initial quark; thus the OS BDT_j shape from light-quark jets differs from the equivalent SS BDT_j shape. The ratio of OS-SS BDT_j background distributions derived from $W+1$ jet and $\geqslant 1$ b-tag simulated events show that significant corrections are needed (30% for $\text{BDT}_j>0.8$, a region dominated by the true τ signal). For the 0 b-tag sample the corresponding corrections are much smaller (5% in the same region). Both the 0 b-tag and the $W+1$ jet data samples are used to obtain statistically independent estimates of the background in the $\geqslant 1$ b-tag sample.

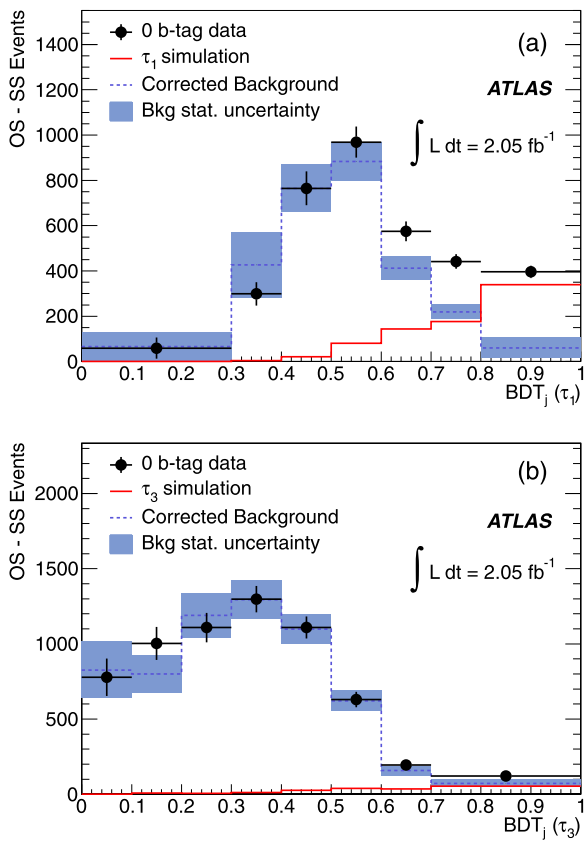

Fig. 1. BDT$_j$ (OS-SS) distributions of $\ell + \tau$ (e and μ combined) events in the 0 b-tag data (black points): (a) τ_1, (b) τ_3. The expected contributions from τ and e (sum of $Z \to \tau^+\tau^-$, single top and $t\bar{t} \to \ell + \tau + X$) are shown as a solid red line. The derived background templates after applying MC corrections are shown as dashed histogram with shaded/blue statistical uncertainty bands. The shapes of these background templates are used for the fits to the $\geqslant 1$ b-tag distributions.

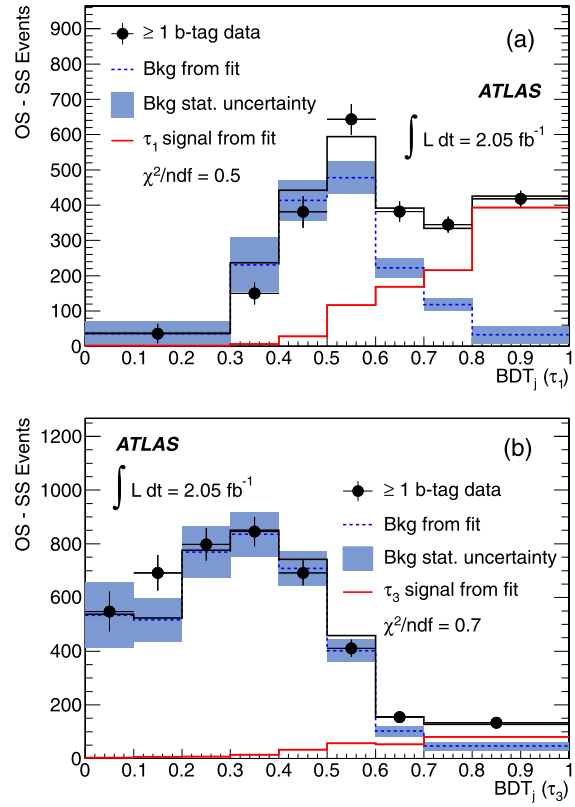

Fig. 2. BDT$_j$ (OS-SS) distributions of $\ell + \tau$ in the $\geqslant 1$ b-tag sample; (a) τ_1, (b) τ_3. The normalisation of each template is derived from a fit to the data. The fitted contributions are shown as the light/red (signal), dashed/blue (background derived from 0 b-tag after applying MC corrections) and dark/black (total) lines. Shaded/blue bands are the statistical uncertainty of the background template.

Two different approaches are used for constructing backgrounds in the $\geqslant 1$ b-tag data sample. One, used by the fit method (Section 7), is to reweight the BDT$_j$ distribution of the background bin-by-bin using the MC-based ratio of the $\geqslant 1$ b-tag background to the background model. In this case the 0 b-tag sample is preferred as it requires smaller corrections derived from MC simulation; the $W + 1$ jet is used as a cross check. The other approach is to split the background into bins of some variable within which the shapes of BDT$_j$ distributions of the background model are close to those from the $\geqslant 1$ b-tag background. This approach, used in the matrix method cross check (Section 7.1), avoids using MC corrections, but assumes the data and MC simulation behave similarly as function of the binning variable.

7. Fits to BDT$_j$ distributions

The contribution from $t\bar{t} \to \ell + \tau + X$ signal is derived from the $\geqslant 1$ b-tag data sample by a χ^2 fit to the OS-SS BDT$_j$ distribution with a background template and a signal template. The parameters of the fit are the amount of background and the amount of signal. The shapes of the templates are fixed.

Two statistically independent background templates corrected by MC, as discussed in Section 6, are used: one derived from 0 b-tag data, the other (purely as a check) derived from the $W + 1$ jet data sample. The signal BDT$_j$ templates for 0 b-tag and $\geqslant 1$ b-tag are derived from τ leptons in $t\bar{t}$ and $Z \to \tau^+\tau^-$ MC simulation. Contributions to the BDT$_j$ distributions from electrons passing the BDT$_e$ cut cannot be distinguished from τ leptons so they are treated as part of the signal.

The uncertainty on the background templates is determined by the numbers of data and MC simulated events. The signal template for the 0 b-tag control sample has a non-negligible statistical uncertainty (2% for τ_1, 5% for τ_3) because of the low acceptance.

The fitting procedure was tested extensively with MC simulation before applying it to data. In the fits to the $\geqslant 1$ b-tag data, applying MC corrections to the 0 b-tag background template increases the statistical uncertainty because of the uncertainty due to the number of simulated events but raises the measured cross section by only 1%.

Fig. 1 shows the BDT$_j$ (OS-SS) distributions of $\ell + \tau$ events with 0 b-tag and the 0 b-tag background template after subtracting the expected number of τ leptons and applying the MC corrections. The τ signal is mostly $Z \to \tau^+\tau^-$ events with a small contamination of electrons faking τ leptons (from $t\bar{t} \to \ell + e + X$ and $Z \to e^+e^-$) and a small contribution from $t\bar{t} \to \ell + \tau + X$. The uncertainty on the background template includes the statistical uncertainty of the correction, the statistical uncertainty from MC and the 0 b-tag data uncertainty.

Fig. 2 shows the result of the fit to the $\geqslant 1$ b-tag samples. The τ lepton signal is mostly $t\bar{t} \to \ell + \tau + X$ with a small contamination of misidentified electrons (estimated by applying fake probabilities derived from data), and small contributions from $Z \to \tau^+\tau^-$ events and single top quark events (estimated from MC simulation). These contributions are subtracted from the number of fitted τ lepton signal events before calculating the cross section. The fit results using the background templates derived from 0 b-tag data and $W + 1$ jet data are shown in Table 2. The results are consistent with each other within the statistical uncertainties of the background templates. The BDT$_j$ distributions for τ_1 and τ_3 are

Table 2
Results of template fits to $\mu+\tau$, $e+\tau$ and the combined BDT$_j$ distributions. The combined results are obtained by fitting the sum of the $\mu+\tau$ and $e+\tau$ BDT$_j$ distributions. The first column gives the channel and the second the τ type. The third column shows the extracted signal (sum of τ leptons and electrons misidentified as τ leptons) with the background template derived from 0 b-tag data distributions. The fourth column shows the extracted signal with the background template derived from $W+1$ jet. The uncertainties are from the uncertainties in the fit parameters and do not include the systematic uncertainties. The MC columns give the expected τ signal (includes the contribution of non-$t\bar{t}\to l+\tau$ events) and the expected number of $t\bar{t}\to l+\tau$ assuming the theoretical $t\bar{t}$ production cross section (164 pb).

		Background template		MC	
		0 b-tag	$W+1$ jet	Signal	$t\bar{t}$
$\mu+\tau$	τ_1	490 ± 40	456 ± 32	432	388
	τ_3	135 ± 33	130 ± 50	126	116
$e+\tau$	τ_1	440 ± 50	430 ± 50	388	338
	τ_3	116 ± 32	120 ± 28	114	101
Combined	τ_1	930 ± 70	860 ± 50	820	726
	τ_3	260 ± 60	260 ± 40	239	217

fitted separately. The combined $\ell+\tau_i$ results are obtained by fitting the sum of the distributions. After adding $\ell+\tau_1$ and $\ell+\tau_3$ signals obtained from a χ^2 fit to the combined $e+\tau$ and $\mu+\tau$ distributions and subtracting the small contributions to the signal from $Z\to\tau^+\tau^-$, $Z\to e^+e^-$ and $t\bar{t}\to e+\ell$ (given in Table 1), the results are 840 ± 70 (243 ± 60) $t\bar{t}\to\ell+\tau_1(\tau_3)+X$ events. The uncertainty is from the fit only and does not include systematic uncertainties. The results are in good agreement with the 780 ± 50 (243 ± 60) events obtained with the $W+1$ jet background template and consistent with the number expected from MC simulation, 726 ± 19 (217 ± 10). Note that the fit uncertainty is dominated by the uncertainties on the background template, thus the statistical uncertainties of the results with the two different background templates are not strongly correlated.

Fig. 3 shows the OS-SS distribution of the number of jets for $\geqslant 1$ b-tag events adding all channels for two BDT$_j$ regions: BDT$_j<0.7$, which is dominated by $t\bar{t}\to\ell+$jets, and BDT$_j>0.7$, in which the largest contribution is from $t\bar{t}\to\ell+\tau+X$. As expected, the multiplicity of jets peaks at four when BDT$_j<0.7$ and three when BDT$_j>0.7$ (the τ is counted as a jet). Fig. 4 shows the invariant mass of a selected jet with the τ candidate for BDT$_j<0.7$ and BDT$_j>0.7$ for events with a τ candidate and three or more jets. The selected jet is the highest p_{T} untagged jet in events with more than one b-tag and the second highest p_{T} untagged jet in events with one b-tag. The distribution shows clearly the presence of a W decaying to two jets in the BDT$_j<0.7$ region dominated by $t\bar{t}\to\ell+$ jets. The mass distribution in the BDT$_j>0.7$ signal region is significantly broader as expected for $t\bar{t}\to\ell+\tau+X$. The signal and background shown in these figures are based on the fit using the 0 b-tag background template.

7.1. Check with matrix method

From Figs. 3 and 4 one can see that a BDT$_j>0.7$ requirement separates well a region dominated by $t\bar{t}\to\ell+$jets from a region dominated by $t\bar{t}\to\ell+\tau+X$. One can extract the signal from the same OS-SS $\geqslant 1$ b-tag sample used by the fit method via a matrix method. All τ candidates are labelled "loose", and τ candidates with BDT$_j>0.7$ are labelled "tight". The probability that the loose τ candidates are also tight τ candidates, for both τ leptons and fake τ leptons, is defined as

$$\epsilon_{\mathrm{real}}=\frac{N^{\mathrm{tight}}_{\mathrm{real}}}{N^{\mathrm{loose}}_{\mathrm{real}}}\qquad \epsilon_{\mathrm{fake}}=\frac{N^{\mathrm{tight}}_{\mathrm{fake}}}{N^{\mathrm{loose}}_{\mathrm{fake}}}$$

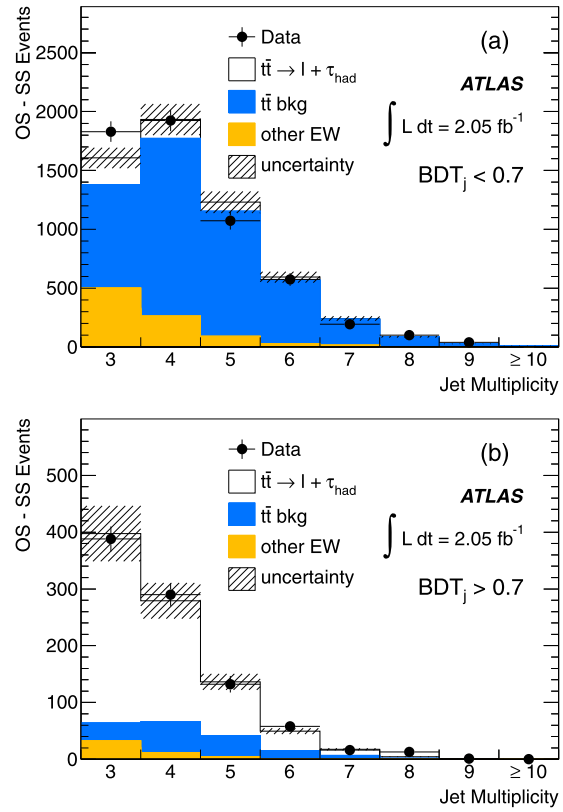

Fig. 3. OS-SS number of jets distributions for events with at least one b-tag. The $\mu+\tau$ and $e+\tau$ channels have been summed together. The solid circles indicate data and the histograms indicate the expected signal and backgrounds. The normalisation of the expected signal and the backgrounds are based on the fit result. The uncertainty includes statistical and systematic contributions. The fraction of each background is estimated from MC. (a) is for BDT$_j<0.7$, (b) for BDT$_j>0.7$.

where the "real" subscript denotes τ lepton, the "fake" subscript denotes fake τ and N is the number of τ candidates. The number of "tight" τ leptons is then given by

$$N^{\mathrm{tight}}_{\mathrm{real}}=N^{\mathrm{tight}}_{\mathrm{data}}-\frac{\epsilon_{\mathrm{fake}}}{\epsilon_{\mathrm{real}}-\epsilon_{\mathrm{fake}}}\left(N^{\mathrm{loose}}_{\mathrm{data}}\cdot\epsilon_{\mathrm{real}}-N^{\mathrm{tight}}_{\mathrm{data}}\right).$$

The value of ϵ_{fake} is measured utilising the OS-SS BDT$_j$ distributions from the background control samples; ϵ_{real} is derived from MC (including all processes that contribute a τ lepton or an electron misidentified as a τ lepton) and was tested using $Z\to\tau^+\tau^-$ events. This method uses the binning approach described in Section 6 to estimate the background. Values of ϵ_{fake} and ϵ_{real} are measured separately for three EM-fraction bins. The EM-fraction, the ratio of the energy measured in the EM calorimeter to the total τ candidate energy measured in the calorimeter, is an effective variable for splitting the data into regions where the shapes of MC OS-SS BDT$_j$ distributions for the $W+1$ jet background template and the $\geqslant 1$ b-tag background are similar. Table 3 shows the number of signal events obtained with the matrix method using the background derived from the 0 b-tag data sample and from the $W+1$ jet data sample. The numbers in each pair are in good agreement and consistent with the numbers obtained by fitting the OS-SS BDT$_j$ distributions.

7.2. Systematic uncertainty

Several experimental and theoretical sources of systematic uncertainty are considered. Lepton trigger, reconstruction and selection efficiencies are assessed by comparing the $Z\to\ell^+\ell^-$ events

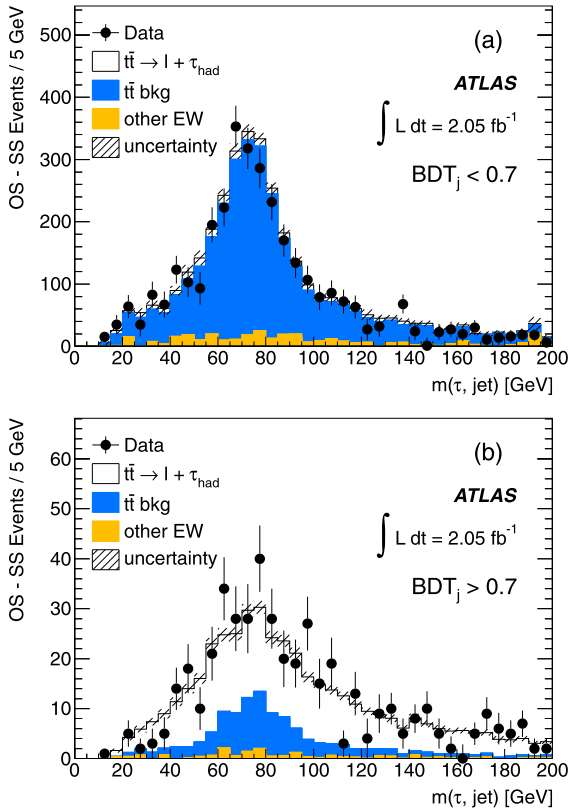

Fig. 4. OS-SS invariant mass of jet and τ candidate for events with at least one b-tag. The jet is the highest p_T untagged jet in events with more than one b-tag and the second highest p_T untagged jet in events with one b-tag. The $\mu+\tau$ and $e+\tau$ channels have been summed together. The solid circles indicate data and the histograms indicate the expected signal and backgrounds. The normalisation of the expected signal and the backgrounds are based on the fit result. The uncertainty includes statistical and systematic contributions. The fraction of each background is estimated from MC. (a) is for $BDT_j < 0.7$, (b) for $BDT_j > 0.7$.

Table 3
Number of signal events obtained with the matrix method for $\mu+\tau$, $e+\tau$ and the combined channels. The first column gives the channel and the second the τ type. The third column shows the extracted signal with the background template derived from 0 b-tag data distributions. The fourth column shows the extracted signal with the background template derived from $W+1$ jet. In order to compare the matrix method results to the fit results the number of signal events shown is $\sum N^{real}_{tight}/\bar{\epsilon}_{real}$ where $\bar{\epsilon}_{real}$ is the ϵ_{real} averaged over the three EM-fraction bins. The uncertainties are statistical only.

		Background template	
		0 b-tag	$W+1$ jet
$\mu+\tau$	τ_1	460 ± 50	440 ± 50
	τ_3	130 ± 40	105 ± 35
$e+\tau$	τ_1	420 ± 60	350 ± 50
	τ_3	140 ± 40	160 ± 40
Combined	τ_1	880 ± 70	800 ± 70
	τ_3	270 ± 60	260 ± 60

selected with the same object criteria as used for the $t\bar{t}$ analysis in data and MC.

Scale factors are applied to $Z \to \tau^+\tau^-$ MC samples when calculating acceptances to account for any differences between predicted and observed efficiencies. The scale factors are evaluated by comparing the observed efficiencies with those determined with simulated Z boson events. Systematic uncertainties on these scale factors are evaluated by varying the selection of events used in the efficiency measurements and by checking the stability of the measurements over the course of data taking.

Table 4
Relative systematic uncertainties, in %, for the cross-section measurement. The first column gives the source of systematic uncertainty, ID/Trigger stands for the combined uncertainty of lepton identification and lepton trigger. The τ ID uncertainty includes electrons misidentified as τ leptons. The second and third columns give the channel.

Source	$\mu+\tau$	$e+\tau$
μ (ID/Trigger)	$-1.1/+1.5$	–
e (ID/Trigger)	–	± 2.9
JES	$-2.0/+2.2$	$-1.9/+2.8$
JER	± 1.0	± 1.2
ISR/FSR	± 4.8	± 3.5
Generator	± 0.7	± 0.7
PDF	± 2.0	± 2.1
b-tag	$-7.7/+9.0$	$-7.5/+8.9$
τ_1 ID	$-3.0/+3.2$	$-2.7/+3.0$
τ_3 ID	$-3.1/+3.4$	$-2.9/+3.2$

The modelling of the lepton momentum scale and resolution is studied using reconstructed invariant mass distributions of $Z \to \ell^+\ell^-$ candidate events and used to adjust the simulation accordingly [34,35].

The jet energy scale (JES) and its uncertainty are derived by combining information from test-beam data, LHC collision data and simulation [32]. For jets within the acceptance, the JES uncertainty varies in the range 4–8% as a function of jet p_T and η. Comparing MC and data the estimated systematic uncertainties are 10% and 1–2% for the jet energy resolution (JER) and the jet reconstruction efficiency, respectively. The uncertainty on the efficiency of the b-tagging algorithm has been estimated to be 6% for b-quark jets, based on b-tagging calibration studies [33].

The uncertainty in the kinematic distributions of the $t\bar{t}$ signal events gives rise to systematic uncertainties in the signal acceptance, with contributions from the choice of generator, the modelling of initial- and final-state radiation (ISR/FSR) and the choice of the PDF set. The generator uncertainty is evaluated by comparing the MC@NLO predictions with those of POWHEG [36–38] interfaced to either HERWIG or PYTHIA. The uncertainty due to ISR/FSR is evaluated using the AcerMC generator [39] (which relies on the MADGRAPH package [40]) interfaced to the PYTHIA shower model, and by varying the parameters controlling ISR and FSR in a range consistent with experimental data [19]. Finally, the PDF uncertainty is evaluated using a range of current PDF sets: NNPDF, CTEQ, and MSTW [41–43]. Each one comes with a set of error PDFs, the RMS of the variations was taken as the PDF uncertainty. The dominant uncertainty in this category of systematic uncertainties is the modelling of ISR/FSR.

The τ ID uncertainty is derived from a template fit to a $Z \to \tau^+\tau^-$ data sample selected with the same μ and τ candidate requirements as the sample for this analysis, but with fewer than two jets and $m_T < 20$ GeV to remove $W+$jets events. The fit relies on the $W+1$ jet data sample for a background template and $Z \to \tau^+\tau^-$ MC events for a signal template. The uncertainty includes the statistical uncertainty of the data samples, the uncertainty in the Z/γ^* cross section measured by ATLAS [44] (excluding the luminosity uncertainty) and the jet energy scale uncertainty. It also includes the uncertainty on the number of misidentified electrons (<0.5%, determined from $Z \to e^+e^-$ data).

The effect of these variations on the final result is evaluated by varying each source of systematic uncertainty by $\pm 1\sigma$, applying the selection criteria to obtain new signal and background templates and recalculating the cross section.

Table 5
Measured cross section from the τ_1 and τ_3 samples, as well as the combination $(\tau_1+\tau_3)$ for each channel separately. The uncertainty in the integrated luminosity (3.7%) is not included.

	$\mu+\tau$
τ_1	189 ± 16 (stat.) ± 20 (syst.) pb
τ_3	180 ± 40 (stat.) ± 21 (syst.) pb
$\tau_1+\tau_3$	186 ± 15 (stat.) ± 20 (syst.) pb
	$e+\tau$
τ_1	190 ± 20 (stat.) ± 20 (syst.) pb
τ_3	170 ± 50 (stat.) ± 21 (syst.) pb
$\tau_1+\tau_3$	187 ± 18 (stat.) ± 20 (syst.) pb

The uncertainties obtained for the fit method using the 0 b-tag background template are shown in Table 4. The systematic uncertainties for the matrix method are very similar. The uncertainty on the measured integrated luminosity is 3.7% [45]. This translates into a 3.5% uncertainty on the cross section.

8. Measuring the $t\bar{t}$ cross section

The cross section is derived from the number of observed OS-SS signal events in the $\geqslant 1$ b-tag data sample assuming the only top quark decay mode is $t \to Wb$, and subtracting from that number the small contribution from $t\bar{t} \to e+\ell$ (from electrons faking τ leptons) and τ leptons from $Z \to \tau^+\tau^-$ (Table 1). The systematic uncertainties are estimated as the quadratic sum of all uncertainties given in Table 4, which includes the uncertainty from the subtraction.

The results are given separately for τ_1 and τ_3 and then combined (weighted by their statistical uncertainty and assuming all systematic uncertainties other than from τ ID are fully correlated). The results using the 0 b-tag background template are shown in Table 5.

The results for the $\mu+\tau$ and $e+\tau$ channels are combined taking into account the correlated uncertainties using the BLUE (Best Linear Unbiased Estimator) technique [46]. Combining them does not improve the systematic uncertainty as the systematic uncertainties are almost 100% correlated.

The results for each lepton type are:

$$\mu+\tau: \quad \sigma_{t\bar{t}} = 186 \pm 15 \text{ (stat.)} \pm 20 \text{ (syst.)} \pm 7 \text{ (lumi.) pb},$$

$$e+\tau: \quad \sigma_{t\bar{t}} = 187 \pm 18 \text{ (stat.)} \pm 20 \text{ (syst.)} \pm 7 \text{ (lumi.) pb},$$

Combining both channels one obtains:

$$\sigma_{t\bar{t}} = 186 \pm 13 \text{ (stat.)} \pm 20 \text{ (syst.)} \pm 7 \text{ (lumi.) pb}.$$

To check the fit measurements, the cross sections can be calculated using the matrix method and the results obtained with the $W+1$ jet background to minimise the correlation with the fit results. The combination of the matrix method and the fit results with the BLUE method shows they are compatible at the 45% and 10% confidence level for $\mu+\tau$ and $e+\tau$, respectively.

9. Conclusions

The cross section for $t\bar{t}$ production in pp collisions at 7 TeV has been measured in the $\mu+\tau$ and the $e+\tau$ channels in which the τ decays hadronically. The number of τ leptons in these channels has been extracted using multivariate discriminators to separate τ leptons from electrons and jets misidentified as hadronically decaying τ leptons. These numbers were obtained by fitting the discriminator outputs and checked with a matrix method. Combining the measurements from $\mu+\tau$ and $e+\tau$ events, the cross section is measured to be

$$\sigma_{t\bar{t}} = 186 \pm 13 \text{ (stat.)} \pm 20 \text{ (syst.)} \pm 7 \text{ (lumi.) pb},$$

in good agreement with the cross section measured by ATLAS in other channels [1,2], with the cross-section measurements by the CMS Collaboration [3–5,7] and with the SM prediction, 164^{+11}_{-16} pb [25].

Acknowledgements

We thank CERN for the very successful operation of the LHC, as well as the support staff from our institutions without whom ATLAS could not be operated efficiently.

We acknowledge the support of ANPCyT, Argentina; YerPhI, Armenia; ARC, Australia; BMWF, Austria; ANAS, Azerbaijan; SSTC, Belarus; CNPq and FAPESP, Brazil; NSERC, NRC and CFI, Canada; CERN; CONICYT, Chile; CAS, MOST and NSFC, China; COLCIENCIAS, Colombia; MSMT CR, MPO CR and VSC CR, Czech Republic; DNRF, DNSRC and Lundbeck Foundation, Denmark; EPLANET and ERC, European Union; IN2P3-CNRS, CEA-DSM/IRFU, France; GNAS, Georgia; BMBF, DFG, HGF, MPG and AvH Foundation, Germany; GSRT, Greece; ISF, MINERVA, GIF, DIP and Benoziyo Center, Israel; INFN, Italy; MEXT and JSPS, Japan; CNRST, Morocco; FOM and NWO, Netherlands; RCN, Norway; MNiSW, Poland; GRICES and FCT, Portugal; MERYS (MECTS), Romania; MES of Russia and ROSATOM, Russian Federation; JINR; MSTD, Serbia; MSSR, Slovakia; ARRS and MVZT, Slovenia; DST/NRF, South Africa; MICINN, Spain; SRC and Wallenberg Foundation, Sweden; SER, SNSF and Cantons of Bern and Geneva, Switzerland; NSC, Taiwan; TAEK, Turkey; STFC, the Royal Society and Leverhulme Trust, United Kingdom; DOE and NSF, United States of America.

The crucial computing support from all WLCG partners is acknowledged gratefully, in particular from CERN and the ATLAS Tier-1 facilities at TRIUMF (Canada), NDGF (Denmark, Norway, Sweden), CC-IN2P3 (France), KIT/GridKA (Germany), INFN-CNAF (Italy), NL-T1 (Netherlands), PIC (Spain), ASGC (Taiwan), RAL (UK) and BNL (USA) and in the Tier-2 facilities worldwide.

Open access

This article is published Open Access at sciencedirect.com. It is distributed under the terms of the Creative Commons Attribution License 3.0, which permits unrestricted use, distribution, and reproduction in any medium, provided the original authors and source are credited.

References

[1] ATLAS Collaboration, Phys. Lett. B 711 (2012) 244.
[2] ATLAS Collaboration, JHEP 1205 (2012) 059.
[3] CMS Collaboration, Phys. Rev. D 84 (2011) 092004.
[4] CMS Collaboration, Eur. Phys. J. C 71 (2011) 1721.
[5] CMS Collaboration, JHEP 1107 (2011) 1721.
[6] DØ Collaboration, Phys. Rev. D 80 (2009), 071102(R).
[7] CMS Collaboration, Phys. Rev. D 85 (2012) 112007.
[8] G.L. Kane, C. Kolda, L. Roszkowski, J.D. Wells, Phys. Rev. D 49 (1994) 6173.
[9] T. Han, M.B. Magro, Phys. Lett. B 476 (2000) 79.
[10] C. Yue, H. Zong, L. Liu, Mod. Phys. Lett. A 18 (2003) 2187.
[11] DØ Collaboration, Phys. Lett. B 682 (2009) 278.
[12] ATLAS Collaboration, JHEP 1206 (2012) 039.
[13] CMS Collaboration, JHEP 1207 (2012) 143.
[14] ATLAS Collaboration, Performance of the reconstruction and identification of hadronic tau decays with the ATLAS detector, ATLAS-CONF-2011-152.
[15] Y. Freund, R.E. Schapire, in: L. Saitta (Ed.), Machine Learning: Proceedings of the Thirteenth International Conference, Morgan Kaufmann, San Francisco, 1996, p. 148.
[16] B.P. Roe, H.-J. Yang, J. Zhu, Y. Liu, I. Stancu, G. McGregor, Nucl. Instrum. Meth. A 543 (2005) 577.

[17] ATLAS Collaboration, JINST 3 (2008) S08003.
[18] GEANT4 Collaboration, S. Agostinelli, et al., Nucl. Instrum. Meth. A 506 (2003) 250.
[19] ATLAS Collaboration, Eur. Phys. J. C 70 (2010) 823.
[20] S. Frixione, B.R. Webber, JHEP 0206 (2002) 029.
[21] S. Frixione, P. Nason, B.R. Webber, JHEP 0308 (2003) 007.
[22] S. Frixione, E. Laenen, P. Motylinski, JHEP 0603 (2006) 092.
[23] P.M. Nadolsky, et al., Phys. Rev. D 78 (2008) 013004.
[24] G. Corcella, et al., JHEP 0101 (2001) 010;
G. Corcella, et al., HERWIG 6.5 release notes, arXiv:hep-ph/0210213.
[25] M. Aliev, et al., Comput. Phys. Commun. 182 (2011) 1034.
[26] M.L. Mangano, M. Moretti, H. Lai, P. Nadolsky, A.D. Polosa, JHEP 0307 (2003) 001.
[27] J. Alwall, et al., Eur. Phys. J. C 53 (2008) 473.
[28] J. Butterworth, J.R. Forshaw, M.H. Seymour, Z. Phys. C 72 (1996) 637.
[29] N. Davidson, et al., Universal interface of TAUOLA technical and physics documentation, arXiv:1002.0543.
[30] ATLAS Collaboration, ATLAS tunes of PYTHIA 6 and PYTHIA 8 for MC11, ATL-PHYS-PUB-2011-009.
[31] M. Cacciari, G.P. Salam, G. Soyez, JHEP 0804 (2008) 063.
[32] ATLAS Collaboration, Jet energy measurement with the ATLAS detector in proton–proton collisions at $\sqrt{s} = 7$ TeV, arXiv:1112.6426.
[33] ATLAS Collaboration, Commisioning of the ATLAS high-performance b-tagging algorithms in the $\sqrt{s} = 7$ TeV collision data, ATL-CONF-2011-102.
[34] ATLAS Collaboration, Eur. Phys. J. C 72 (2012) 1909.
[35] ATLAS Collaboration, Muon reconstruction efficiency in reprocessed 2010 LHC proton–proton collision data recorded with the ATLAS Detector, ATLAS-CONF-2011-063.
[36] P. Nason, JHEP 0711 (2007) 070.
[37] S. Frixione, P. Nason, C. Oleari, JHEP 0711 (2007) 040.
[38] S. Alioli, P. Nason, C. Oleari, E. Re, JHEP 1006 (2010) 043.
[39] B.P. Kersevan, E. Richter-Was, The Monte Carlo event generator AcerMC version 2.0 with interfaces to PYTHIA 6.2 and HERWIG 6.5, arXiv:hep-ph/0405247.
[40] T. Seltzer, W. Long, Comput. Phys. Commun. 81 (1994) 357.
[41] J. Pumpli, D. Stump, J. Huston, H. Lai, P. Nadolsky, W. Tung, JHEP 0207 (2002) 012.
[42] A.D. Martin, R.G. Roberts, W.J. Stirling, R.S. Thorne, Eur. Phys. J. C 4 (1998) 463; A.D. Martin, R.G. Roberts, W.J. Stirling, R.S. Thorne, Eur. Phys. J. C 14 (2000) 133.
[43] CTEQ Collaboration, H. Lai, et al., Eur. Phys. J. C 12 (2000) 375.
[44] ATLAS Collaboration, Phys. Rev. D 85 (2012) 041805.
[45] ATLAS Collaboration, Luminosity determination in pp collisions at $\sqrt{s} = 7$ TeV using the ATLAS Detector in 2011, ATLAS-CONF-2011-016 (2011).
[46] L. Lyons, D. Gibaut, P. Clifford, Nucl. Instrum. Meth. A 270 (1988) 110.

ATLAS Collaboration

G. Aad [48], B. Abbott [111], J. Abdallah [11], S. Abdel Khalek [115], A.A. Abdelalim [49], O. Abdinov [10], B. Abi [112], M. Abolins [88], O.S. AbouZeid [158], H. Abramowicz [153], H. Abreu [136], E. Acerbi [89a,89b], B.S. Acharya [164a,164b], L. Adamczyk [37], D.L. Adams [24], T.N. Addy [56], J. Adelman [176], S. Adomeit [98], P. Adragna [75], T. Adye [129], S. Aefsky [22], J.A. Aguilar-Saavedra [124b,a], M. Aharrouche [81], S.P. Ahlen [21], F. Ahles [48], A. Ahmad [148], M. Ahsan [40], G. Aielli [133a,133b], T. Akdogan [18a], T.P.A. Åkesson [79], G. Akimoto [155], A.V. Akimov [94], A. Akiyama [66], M.S. Alam [1], M.A. Alam [76], J. Albert [169], S. Albrand [55], M. Aleksa [29], I.N. Aleksandrov [64], F. Alessandria [89a], C. Alexa [25a], G. Alexander [153], G. Alexandre [49], T. Alexopoulos [9], M. Alhroob [164a,164c], M. Aliev [15], G. Alimonti [89a], J. Alison [120], B.M.M. Allbrooke [17], P.P. Allport [73], S.E. Allwood-Spiers [53], J. Almond [82], A. Aloisio [102a,102b], R. Alon [172], A. Alonso [79], B. Alvarez Gonzalez [88], M.G. Alviggi [102a,102b], K. Amako [65], C. Amelung [22], V.V. Ammosov [128], A. Amorim [124a,b], G. Amorós [167], N. Amram [153], C. Anastopoulos [29], L.S. Ancu [16], N. Andari [115], T. Andeen [34], C.F. Anders [58b], G. Anders [58a], K.J. Anderson [30], A. Andreazza [89a,89b], V. Andrei [58a], X.S. Anduaga [70], P. Anger [43], A. Angerami [34], F. Anghinolfi [29], A. Anisenkov [107], N. Anjos [124a], A. Annovi [47], A. Antonaki [8], M. Antonelli [47], A. Antonov [96], J. Antos [144b], F. Anulli [132a], S. Aoun [83], L. Aperio Bella [4], R. Apolle [118,c], G. Arabidze [88], I. Aracena [143], Y. Arai [65], A.T.H. Arce [44], S. Arfaoui [148], J-F. Arguin [14], E. Arik [18a,*], M. Arik [18a], A.J. Armbruster [87], O. Arnaez [81], V. Arnal [80], C. Arnault [115], A. Artamonov [95], G. Artoni [132a,132b], D. Arutinov [20], S. Asai [155], R. Asfandiyarov [173], S. Ask [27], B. Åsman [146a,146b], L. Asquith [5], K. Assamagan [24], A. Astbury [169], B. Aubert [4], E. Auge [115], K. Augsten [127], M. Aurousseau [145a], G. Avolio [163], R. Avramidou [9], D. Axen [168], G. Azuelos [93,d], Y. Azuma [155], M.A. Baak [29], G. Baccaglioni [89a], C. Bacci [134a,134b], A.M. Bach [14], H. Bachacou [136], K. Bachas [29], M. Backes [49], M. Backhaus [20], E. Badescu [25a], P. Bagnaia [132a,132b], S. Bahinipati [2], Y. Bai [32a], D.C. Bailey [158], T. Bain [158], J.T. Baines [129], O.K. Baker [176], M.D. Baker [24], S. Baker [77], E. Banas [38], P. Banerjee [93], Sw. Banerjee [173], D. Banfi [29], A. Bangert [150], V. Bansal [169], H.S. Bansil [17], L. Barak [172], S.P. Baranov [94], A. Barbaro Galtieri [14], T. Barber [48], E.L. Barberio [86], D. Barberis [50a,50b], M. Barbero [20], D.Y. Bardin [64], T. Barillari [99], M. Barisonzi [175], T. Barklow [143], N. Barlow [27], B.M. Barnett [129], R.M. Barnett [14], A. Baroncelli [134a], G. Barone [49], A.J. Barr [118], F. Barreiro [80], J. Barreiro Guimarães da Costa [57], P. Barrillon [115], R. Bartoldus [143], A.E. Barton [71], V. Bartsch [149], R.L. Bates [53], L. Batkova [144a], J.R. Batley [27], A. Battaglia [16], M. Battistin [29], F. Bauer [136], H.S. Bawa [143,e], S. Beale [98], T. Beau [78], P.H. Beauchemin [161], R. Beccherle [50a], P. Bechtle [20], H.P. Beck [16], A.K. Becker [175], S. Becker [98], M. Beckingham [138], K.H. Becks [175], A.J. Beddall [18c], A. Beddall [18c], S. Bedikian [176], V.A. Bednyakov [64], C.P. Bee [83], M. Begel [24], S. Behar Harpaz [152], P.K. Behera [62], M. Beimforde [99], C. Belanger-Champagne [85], P.J. Bell [49], W.H. Bell [49], G. Bella [153], L. Bellagamba [19a], F. Bellina [29], M. Bellomo [29], A. Belloni [57], O. Beloborodova [107,f], K. Belotskiy [96], O. Beltramello [29], O. Benary [153], D. Benchekroun [135a], K. Bendtz [146a,146b], N. Benekos [165], Y. Benhammou [153], E. Benhar Noccioli [49], J.A. Benitez Garcia [159b], D.P. Benjamin [44], M. Benoit [115], J.R. Bensinger [22], K. Benslama [130], S. Bentvelsen [105], D. Berge [29], E. Bergeaas Kuutmann [41], N. Berger [4], F. Berghaus [169], E. Berglund [105],

J. Beringer [14], P. Bernat [77], R. Bernhard [48], C. Bernius [24], T. Berry [76], C. Bertella [83], A. Bertin [19a,19b], F. Bertolucci [122a,122b], M.I. Besana [89a,89b], N. Besson [136], S. Bethke [99], W. Bhimji [45], R.M. Bianchi [29], M. Bianco [72a,72b], O. Biebel [98], S.P. Bieniek [77], K. Bierwagen [54], J. Biesiada [14], M. Biglietti [134a], H. Bilokon [47], M. Bindi [19a,19b], S. Binet [115], A. Bingul [18c], C. Bini [132a,132b], C. Biscarat [178], U. Bitenc [48], K.M. Black [21], R.E. Blair [5], J.-B. Blanchard [136], G. Blanchot [29], T. Blazek [144a], C. Blocker [22], J. Blocki [38], A. Blondel [49], W. Blum [81], U. Blumenschein [54], G.J. Bobbink [105], V.B. Bobrovnikov [107], S.S. Bocchetta [79], A. Bocci [44], C.R. Boddy [118], M. Boehler [41], J. Boek [175], N. Boelaert [35], J.A. Bogaerts [29], A. Bogdanchikov [107], A. Bogouch [90,*], C. Bohm [146a], J. Bohm [125], V. Boisvert [76], T. Bold [37], V. Boldea [25a], N.M. Bolnet [136], M. Bomben [78], M. Bona [75], M. Bondioli [163], M. Boonekamp [136], C.N. Booth [139], S. Bordoni [78], C. Borer [16], A. Borisov [128], G. Borissov [71], I. Borjanovic [12a], M. Borri [82], S. Borroni [87], V. Bortolotto [134a,134b], K. Bos [105], D. Boscherini [19a], M. Bosman [11], H. Boterenbrood [105], D. Botterill [129], J. Bouchami [93], J. Boudreau [123], E.V. Bouhova-Thacker [71], D. Boumediene [33], C. Bourdarios [115], N. Bousson [83], A. Boveia [30], J. Boyd [29], I.R. Boyko [64], N.I. Bozhko [128], I. Bozovic-Jelisavcic [12b], J. Bracinik [17], P. Branchini [134a], A. Brandt [7], G. Brandt [118], O. Brandt [54], U. Bratzler [156], B. Brau [84], J.E. Brau [114], H.M. Braun [175], B. Brelier [158], J. Bremer [29], K. Brendlinger [120], R. Brenner [166], S. Bressler [172], D. Britton [53], F.M. Brochu [27], I. Brock [20], R. Brock [88], E. Brodet [153], F. Broggi [89a], C. Bromberg [88], J. Bronner [99], G. Brooijmans [34], W.K. Brooks [31b], G. Brown [82], H. Brown [7], P.A. Bruckman de Renstrom [38], D. Bruncko [144b], R. Bruneliere [48], S. Brunet [60], A. Bruni [19a], G. Bruni [19a], M. Bruschi [19a], T. Buanes [13], Q. Buat [55], F. Bucci [49], J. Buchanan [118], P. Buchholz [141], R.M. Buckingham [118], A.G. Buckley [45], S.I. Buda [25a], I.A. Budagov [64], B. Budick [108], V. Büscher [81], L. Bugge [117], O. Bulekov [96], A.C. Bundock [73], M. Bunse [42], T. Buran [117], H. Burckhart [29], S. Burdin [73], T. Burgess [13], S. Burke [129], E. Busato [33], P. Bussey [53], C.P. Buszello [166], B. Butler [143], J.M. Butler [21], C.M. Buttar [53], J.M. Butterworth [77], W. Buttinger [27], S. Cabrera Urbán [167], D. Caforio [19a,19b], O. Cakir [3a], P. Calafiura [14], G. Calderini [78], P. Calfayan [98], R. Calkins [106], L.P. Caloba [23a], R. Caloi [132a,132b], D. Calvet [33], S. Calvet [33], R. Camacho Toro [33], P. Camarri [133a,133b], D. Cameron [117], L.M. Caminada [14], S. Campana [29], M. Campanelli [77], V. Canale [102a,102b], F. Canelli [30,g], A. Canepa [159a], J. Cantero [80], R. Cantrill [76], L. Capasso [102a,102b], M.D.M. Capeans Garrido [29], I. Caprini [25a], M. Caprini [25a], D. Capriotti [99], M. Capua [36a,36b], R. Caputo [81], R. Cardarelli [133a], T. Carli [29], G. Carlino [102a], L. Carminati [89a,89b], B. Caron [85], S. Caron [104], E. Carquin [31b], G.D. Carrillo Montoya [173], A.A. Carter [75], J.R. Carter [27], J. Carvalho [124a,h], D. Casadei [108], M.P. Casado [11], M. Cascella [122a,122b], C. Caso [50a,50b,*], A.M. Castaneda Hernandez [173], E. Castaneda-Miranda [173], V. Castillo Gimenez [167], N.F. Castro [124a], G. Cataldi [72a], P. Catastini [57], A. Catinaccio [29], J.R. Catmore [29], A. Cattai [29], G. Cattani [133a,133b], S. Caughron [88], D. Cauz [164a,164c], P. Cavalleri [78], D. Cavalli [89a], M. Cavalli-Sforza [11], V. Cavasinni [122a,122b], F. Ceradini [134a,134b], A.S. Cerqueira [23b], A. Cerri [29], L. Cerrito [75], F. Cerutti [47], S.A. Cetin [18b], A. Chafaq [135a], D. Chakraborty [106], I. Chalupkova [126], K. Chan [2], B. Chapleau [85], J.D. Chapman [27], J.W. Chapman [87], E. Chareyre [78], D.G. Charlton [17], V. Chavda [82], C.A. Chavez Barajas [29], S. Cheatham [85], S. Chekanov [5], S.V. Chekulaev [159a], G.A. Chelkov [64], M.A. Chelstowska [104], C. Chen [63], H. Chen [24], S. Chen [32c], X. Chen [173], A. Cheplakov [64], R. Cherkaoui El Moursli [135e], V. Chernyatin [24], E. Cheu [6], S.L. Cheung [158], L. Chevalier [136], G. Chiefari [102a,102b], L. Chikovani [51a], J.T. Childers [29], A. Chilingarov [71], G. Chiodini [72a], A.S. Chisholm [17], R.T. Chislett [77], M.V. Chizhov [64], G. Choudalakis [30], S. Chouridou [137], I.A. Christidi [77], A. Christov [48], D. Chromek-Burckhart [29], M.L. Chu [151], J. Chudoba [125], G. Ciapetti [132a,132b], A.K. Ciftci [3a], R. Ciftci [3a], D. Cinca [33], V. Cindro [74], C. Ciocca [19a,19b], A. Ciocio [14], M. Cirilli [87], M. Citterio [89a], M. Ciubancan [25a], A. Clark [49], P.J. Clark [45], W. Cleland [123], J.C. Clemens [83], B. Clement [55], C. Clement [146a,146b], Y. Coadou [83], M. Cobal [164a,164c], A. Coccaro [138], J. Cochran [63], P. Coe [118], J.G. Cogan [143], J. Coggeshall [165], E. Cogneras [178], J. Colas [4], A.P. Colijn [105], N.J. Collins [17], C. Collins-Tooth [53], J. Collot [55], T. Colombo [119a,119b], G. Colon [84], P. Conde Muiño [124a], E. Coniavitis [118], M.C. Conidi [11], S.M. Consonni [89a,89b], V. Consorti [48], S. Constantinescu [25a], C. Conta [119a,119b], G. Conti [57], F. Conventi [102a,i], M. Cooke [14], B.D. Cooper [77], A.M. Cooper-Sarkar [118], K. Copic [14], T. Cornelissen [175], M. Corradi [19a], F. Corriveau [85,j], A. Cortes-Gonzalez [165], G. Cortiana [99], G. Costa [89a], M.J. Costa [167], D. Costanzo [139], T. Costin [30], D. Côté [29], L. Courneyea [169], G. Cowan [76], C. Cowden [27], B.E. Cox [82], K. Cranmer [108], F. Crescioli [122a,122b], M. Cristinziani [20], G. Crosetti [36a,36b], R. Crupi [72a,72b], S. Crépé-Renaudin [55], C.-M. Cuciuc [25a], C. Cuenca Almenar [176], T. Cuhadar Donszelmann [139], M. Curatolo [47], C.J. Curtis [17], C. Cuthbert [150], P. Cwetanski [60], H. Czirr [141], P. Czodrowski [43], Z. Czyczula [176], S. D'Auria [53], M. D'Onofrio [73], A. D'Orazio [132a,132b],

C. Da Via [82], W. Dabrowski [37], A. Dafinca [118], T. Dai [87], C. Dallapiccola [84], M. Dam [35], M. Dameri [50a,50b], D.S. Damiani [137], H.O. Danielsson [29], V. Dao [49], G. Darbo [50a], G.L. Darlea [25b], W. Davey [20], T. Davidek [126], N. Davidson [86], R. Davidson [71], E. Davies [118,c], M. Davies [93], A.R. Davison [77], Y. Davygora [58a], E. Dawe [142], I. Dawson [139], R.K. Daya-Ishmukhametova [22], K. De [7], R. de Asmundis [102a], S. De Castro [19a,19b], S. De Cecco [78], J. de Graat [98], N. De Groot [104], P. de Jong [105], C. De La Taille [115], H. De la Torre [80], F. De Lorenzi [63], B. De Lotto [164a,164c], L. de Mora [71], L. De Nooij [105], D. De Pedis [132a], A. De Salvo [132a], U. De Sanctis [164a,164c], A. De Santo [149], J.B. De Vivie De Regie [115], G. De Zorzi [132a,132b], W.J. Dearnaley [71], R. Debbe [24], C. Debenedetti [45], B. Dechenaux [55], D.V. Dedovich [64], J. Degenhardt [120], C. Del Papa [164a,164c], J. Del Peso [80], T. Del Prete [122a,122b], T. Delemontex [55], M. Deliyergiyev [74], A. Dell'Acqua [29], L. Dell'Asta [21], M. Della Pietra [102a,i], D. della Volpe [102a,102b], M. Delmastro [4], P.A. Delsart [55], C. Deluca [105], S. Demers [176], M. Demichev [64], B. Demirkoz [11,k], J. Deng [163], S.P. Denisov [128], D. Derendarz [38], J.E. Derkaoui [135d], F. Derue [78], P. Dervan [73], K. Desch [20], E. Devetak [148], P.O. Deviveiros [105], A. Dewhurst [129], B. DeWilde [148], S. Dhaliwal [158], R. Dhullipudi [24,l], A. Di Ciaccio [133a,133b], L. Di Ciaccio [4], A. Di Girolamo [29], B. Di Girolamo [29], S. Di Luise [134a,134b], A. Di Mattia [173], B. Di Micco [29], R. Di Nardo [47], A. Di Simone [133a,133b], R. Di Sipio [19a,19b], M.A. Diaz [31a], E.B. Diehl [87], J. Dietrich [41], T.A. Dietzsch [58a], S. Diglio [86], K. Dindar Yagci [39], J. Dingfelder [20], C. Dionisi [132a,132b], P. Dita [25a], S. Dita [25a], F. Dittus [29], F. Djama [83], T. Djobava [51b], M.A.B. do Vale [23c], A. Do Valle Wemans [124a], T.K.O. Doan [4], M. Dobbs [85], R. Dobinson [29,*], D. Dobos [29], E. Dobson [29,m], J. Dodd [34], C. Doglioni [49], T. Doherty [53], Y. Doi [65,*], J. Dolejsi [126], I. Dolenc [74], Z. Dolezal [126], B.A. Dolgoshein [96,*], T. Dohmae [155], M. Donadelli [23d], M. Donega [120], J. Donini [33], J. Dopke [29], A. Doria [102a], A. Dos Anjos [173], A. Dotti [122a,122b], M.T. Dova [70], A.D. Doxiadis [105], A.T. Doyle [53], M. Dris [9], J. Dubbert [99], S. Dube [14], E. Duchovni [172], G. Duckeck [98], A. Dudarev [29], F. Dudziak [63], M. Dührssen [29], I.P. Duerdoth [82], L. Duflot [115], M-A. Dufour [85], M. Dunford [29], H. Duran Yildiz [3a], R. Duxfield [139], M. Dwuznik [37], F. Dydak [29], M. Düren [52], J. Ebke [98], S. Eckweiler [81], K. Edmonds [81], C.A. Edwards [76], N.C. Edwards [53], W. Ehrenfeld [41], T. Eifert [143], G. Eigen [13], K. Einsweiler [14], E. Eisenhandler [75], T. Ekelof [166], M. El Kacimi [135c], M. Ellert [166], S. Elles [4], F. Ellinghaus [81], K. Ellis [75], N. Ellis [29], J. Elmsheuser [98], M. Elsing [29], D. Emeliyanov [129], R. Engelmann [148], A. Engl [98], B. Epp [61], A. Eppig [87], J. Erdmann [54], A. Ereditato [16], D. Eriksson [146a], J. Ernst [1], M. Ernst [24], J. Ernwein [136], D. Errede [165], S. Errede [165], E. Ertel [81], M. Escalier [115], C. Escobar [123], X. Espinal Curull [11], B. Esposito [47], F. Etienne [83], A.I. Etienvre [136], E. Etzion [153], D. Evangelakou [54], H. Evans [60], L. Fabbri [19a,19b], C. Fabre [29], R.M. Fakhrutdinov [128], S. Falciano [132a], Y. Fang [173], M. Fanti [89a,89b], A. Farbin [7], A. Farilla [134a], J. Farley [148], T. Farooque [158], S. Farrell [163], S.M. Farrington [118], P. Farthouat [29], P. Fassnacht [29], D. Fassouliotis [8], B. Fatholahzadeh [158], A. Favareto [89a,89b], L. Fayard [115], S. Fazio [36a,36b], R. Febbraro [33], P. Federic [144a], O.L. Fedin [121], W. Fedorko [88], M. Fehling-Kaschek [48], L. Feligioni [83], D. Fellmann [5], C. Feng [32d], E.J. Feng [30], A.B. Fenyuk [128], J. Ferencei [144b], W. Fernando [5], S. Ferrag [53], J. Ferrando [53], V. Ferrara [41], A. Ferrari [166], P. Ferrari [105], R. Ferrari [119a], D.E. Ferreira de Lima [53], A. Ferrer [167], D. Ferrere [49], C. Ferretti [87], A. Ferretto Parodi [50a,50b], M. Fiascaris [30], F. Fiedler [81], A. Filipčič [74], F. Filthaut [104], M. Fincke-Keeler [169], M.C.N. Fiolhais [124a,h], L. Fiorini [167], A. Firan [39], G. Fischer [41], M.J. Fisher [109], M. Flechl [48], I. Fleck [141], J. Fleckner [81], P. Fleischmann [174], S. Fleischmann [175], T. Flick [175], A. Floderus [79], L.R. Flores Castillo [173], M.J. Flowerdew [99], T. Fonseca Martin [16], D.A. Forbush [138], A. Formica [136], A. Forti [82], D. Fortin [159a], D. Fournier [115], H. Fox [71], P. Francavilla [11], S. Franchino [119a,119b], D. Francis [29], T. Frank [172], M. Franklin [57], S. Franz [29], M. Fraternali [119a,119b], S. Fratina [120], S.T. French [27], C. Friedrich [41], F. Friedrich [43], R. Froeschl [29], D. Froidevaux [29], J.A. Frost [27], C. Fukunaga [156], E. Fullana Torregrosa [29], B.G. Fulsom [143], J. Fuster [167], C. Gabaldon [29], O. Gabizon [172], T. Gadfort [24], S. Gadomski [49], G. Gagliardi [50a,50b], P. Gagnon [60], C. Galea [98], E.J. Gallas [118], V. Gallo [16], B.J. Gallop [129], P. Gallus [125], K.K. Gan [109], Y.S. Gao [143,e], A. Gaponenko [14], F. Garberson [176], M. Garcia-Sciveres [14], C. García [167], J.E. García Navarro [167], R.W. Gardner [30], N. Garelli [29], H. Garitaonandia [105], V. Garonne [29], J. Garvey [17], C. Gatti [47], G. Gaudio [119a], B. Gaur [141], L. Gauthier [136], P. Gauzzi [132a,132b], I.L. Gavrilenko [94], C. Gay [168], G. Gaycken [20], E.N. Gazis [9], P. Ge [32d], Z. Gecse [168], C.N.P. Gee [129], D.A.A. Geerts [105], Ch. Geich-Gimbel [20], K. Gellerstedt [146a,146b], C. Gemme [50a], A. Gemmell [53], M.H. Genest [55], S. Gentile [132a,132b], M. George [54], S. George [76], P. Gerlach [175], A. Gershon [153], C. Geweniger [58a], H. Ghazlane [135b], N. Ghodbane [33], B. Giacobbe [19a], S. Giagu [132a,132b], V. Giakoumopoulou [8], V. Giangiobbe [11], F. Gianotti [29], B. Gibbard [24], A. Gibson [158], S.M. Gibson [29], D. Gillberg [28], A.R. Gillman [129], D.M. Gingrich [2,d], J. Ginzburg [153], N. Giokaris [8], M.P. Giordani [164c],

R. Giordano [102a,102b], F.M. Giorgi [15], P. Giovannini [99], P.F. Giraud [136], D. Giugni [89a], M. Giunta [93], P. Giusti [19a], B.K. Gjelsten [117], L.K. Gladilin [97], C. Glasman [80], J. Glatzer [48], A. Glazov [41], K.W. Glitza [175], G.L. Glonti [64], J.R. Goddard [75], J. Godfrey [142], J. Godlewski [29], M. Goebel [41], T. Göpfert [43], C. Goeringer [81], C. Gössling [42], S. Goldfarb [87], T. Golling [176], A. Gomes [124a,b], L.S. Gomez Fajardo [41], R. Gonçalo [76], J. Goncalves Pinto Firmino Da Costa [41], L. Gonella [20], S. Gonzalez [173], S. González de la Hoz [167], G. Gonzalez Parra [11], M.L. Gonzalez Silva [26], S. Gonzalez-Sevilla [49], J.J. Goodson [148], L. Goossens [29], P.A. Gorbounov [95], H.A. Gordon [24], I. Gorelov [103], G. Gorfine [175], B. Gorini [29], E. Gorini [72a,72b], A. Gorišek [74], E. Gornicki [38], B. Gosdzik [41], A.T. Goshaw [5], M. Gosselink [105], M.I. Gostkin [64], I. Gough Eschrich [163], M. Gouighri [135a], D. Goujdami [135c], M.P. Goulette [49], A.G. Goussiou [138], C. Goy [4], S. Gozpinar [22], I. Grabowska-Bold [37], P. Grafström [29], K-J. Grahn [41], F. Grancagnolo [72a], S. Grancagnolo [15], V. Grassi [148], V. Gratchev [121], N. Grau [34], H.M. Gray [29], J.A. Gray [148], E. Graziani [134a], O.G. Grebenyuk [121], T. Greenshaw [73], Z.D. Greenwood [24,l], K. Gregersen [35], I.M. Gregor [41], P. Grenier [143], J. Griffiths [138], N. Grigalashvili [64], A.A. Grillo [137], S. Grinstein [11], Y.V. Grishkevich [97], J.-F. Grivaz [115], E. Gross [172], J. Grosse-Knetter [54], J. Groth-Jensen [172], K. Grybel [141], D. Guest [176], C. Guicheney [33], A. Guida [72a,72b], S. Guindon [54], H. Guler [85,n], J. Gunther [125], B. Guo [158], J. Guo [34], V.N. Gushchin [128], P. Gutierrez [111], N. Guttman [153], O. Gutzwiller [173], C. Guyot [136], C. Gwenlan [118], C.B. Gwilliam [73], A. Haas [143], S. Haas [29], C. Haber [14], H.K. Hadavand [39], D.R. Hadley [17], P. Haefner [99], F. Hahn [29], S. Haider [29], Z. Hajduk [38], H. Hakobyan [177], D. Hall [118], J. Haller [54], K. Hamacher [175], P. Hamal [113], M. Hamer [54], A. Hamilton [145b,o], S. Hamilton [161], L. Han [32b], K. Hanagaki [116], K. Hanawa [160], M. Hance [14], C. Handel [81], P. Hanke [58a], J.R. Hansen [35], J.B. Hansen [35], J.D. Hansen [35], P.H. Hansen [35], P. Hansson [143], K. Hara [160], G.A. Hare [137], T. Harenberg [175], S. Harkusha [90], D. Harper [87], R.D. Harrington [45], O.M. Harris [138], K. Harrison [17], J. Hartert [48], F. Hartjes [105], T. Haruyama [65], A. Harvey [56], S. Hasegawa [101], Y. Hasegawa [140], S. Hassani [136], S. Haug [16], M. Hauschild [29], R. Hauser [88], M. Havranek [20], C.M. Hawkes [17], R.J. Hawkings [29], A.D. Hawkins [79], D. Hawkins [163], T. Hayakawa [66], T. Hayashi [160], D. Hayden [76], C.P. Hays [118], H.S. Hayward [73], S.J. Haywood [129], M. He [32d], S.J. Head [17], V. Hedberg [79], L. Heelan [7], S. Heim [88], B. Heinemann [14], S. Heisterkamp [35], L. Helary [4], C. Heller [98], M. Heller [29], S. Hellman [146a,146b], D. Hellmich [20], C. Helsens [11], R.C.W. Henderson [71], M. Henke [58a], A. Henrichs [54], A.M. Henriques Correia [29], S. Henrot-Versille [115], F. Henry-Couannier [83], C. Hensel [54], T. Henß [175], C.M. Hernandez [7], Y. Hernández Jiménez [167], R. Herrberg [15], G. Herten [48], R. Hertenberger [98], L. Hervas [29], G.G. Hesketh [77], N.P. Hessey [105], E. Higón-Rodriguez [167], J.C. Hill [27], K.H. Hiller [41], S. Hillert [20], S.J. Hillier [17], I. Hinchliffe [14], E. Hines [120], M. Hirose [116], F. Hirsch [42], D. Hirschbuehl [175], J. Hobbs [148], N. Hod [153], M.C. Hodgkinson [139], P. Hodgson [139], A. Hoecker [29], M.R. Hoeferkamp [103], J. Hoffman [39], D. Hoffmann [83], M. Hohlfeld [81], M. Holder [141], S.O. Holmgren [146a], T. Holy [127], J.L. Holzbauer [88], T.M. Hong [120], L. Hooft van Huysduynen [108], C. Horn [143], S. Horner [48], J-Y. Hostachy [55], S. Hou [151], A. Hoummada [135a], J. Howard [118], J. Howarth [82], I. Hristova [15], J. Hrivnac [115], I. Hruska [125], T. Hryn'ova [4], P.J. Hsu [81], S.-C. Hsu [14], Z. Hubacek [127], F. Hubaut [83], F. Huegging [20], A. Huettmann [41], T.B. Huffman [118], E.W. Hughes [34], G. Hughes [71], M. Huhtinen [29], M. Hurwitz [14], U. Husemann [41], N. Huseynov [64,p], J. Huston [88], J. Huth [57], G. Iacobucci [49], G. Iakovidis [9], M. Ibbotson [82], I. Ibragimov [141], L. Iconomidou-Fayard [115], J. Idarraga [115], P. Iengo [102a], O. Igonkina [105], Y. Ikegami [65], M. Ikeno [65], D. Iliadis [154], N. Ilic [158], M. Imori [155], T. Ince [20], J. Inigo-Golfin [29], P. Ioannou [8], M. Iodice [134a], K. Iordanidou [8], V. Ippolito [132a,132b], A. Irles Quiles [167], C. Isaksson [166], A. Ishikawa [66], M. Ishino [67], R. Ishmukhametov [39], C. Issever [118], S. Istin [18a], A.V. Ivashin [128], W. Iwanski [38], H. Iwasaki [65], J.M. Izen [40], V. Izzo [102a], B. Jackson [120], J.N. Jackson [73], P. Jackson [143], M.R. Jaekel [29], V. Jain [60], K. Jakobs [48], S. Jakobsen [35], T. Jakoubek [125], J. Jakubek [127], D.K. Jana [111], E. Jansen [77], H. Jansen [29], A. Jantsch [99], M. Janus [48], G. Jarlskog [79], L. Jeanty [57], I. Jen-La Plante [30], P. Jenni [29], A. Jeremie [4], P. Jež [35], S. Jézéquel [4], M.K. Jha [19a], H. Ji [173], W. Ji [81], J. Jia [148], Y. Jiang [32b], M. Jimenez Belenguer [41], S. Jin [32a], O. Jinnouchi [157], M.D. Joergensen [35], D. Joffe [39], L.G. Johansen [13], M. Johansen [146a,146b], K.E. Johansson [146a], P. Johansson [139], S. Johnert [41], K.A. Johns [6], K. Jon-And [146a,146b], G. Jones [170], R.W.L. Jones [71], T.J. Jones [73], C. Joram [29], P.M. Jorge [124a], K.D. Joshi [82], J. Jovicevic [147], T. Jovin [12b], X. Ju [173], C.A. Jung [42], R.M. Jungst [29], V. Juranek [125], P. Jussel [61], A. Juste Rozas [11], S. Kabana [16], M. Kaci [167], A. Kaczmarska [38], P. Kadlecik [35], M. Kado [115], H. Kagan [109], M. Kagan [57], E. Kajomovitz [152], S. Kalinin [175], L.V. Kalinovskaya [64], S. Kama [39], N. Kanaya [155], M. Kaneda [29], S. Kaneti [27], T. Kanno [157], V.A. Kantserov [96], J. Kanzaki [65], B. Kaplan [176],

A. Kapliy [30], J. Kaplon [29], D. Kar [53], M. Karagounis [20], M. Karnevskiy [41], V. Kartvelishvili [71], A.N. Karyukhin [128], L. Kashif [173], G. Kasieczka [58b], R.D. Kass [109], A. Kastanas [13], M. Kataoka [4], Y. Kataoka [155], E. Katsoufis [9], J. Katzy [41], V. Kaushik [6], K. Kawagoe [69], T. Kawamoto [155], G. Kawamura [81], M.S. Kayl [105], V.A. Kazanin [107], M.Y. Kazarinov [64], R. Keeler [169], R. Kehoe [39], M. Keil [54], G.D. Kekelidze [64], J.S. Keller [138], J. Kennedy [98], M. Kenyon [53], O. Kepka [125], N. Kerschen [29], B.P. Kerševan [74], S. Kersten [175], K. Kessoku [155], J. Keung [158], F. Khalil-zada [10], H. Khandanyan [165], A. Khanov [112], D. Kharchenko [64], A. Khodinov [96], A. Khomich [58a], T.J. Khoo [27], G. Khoriauli [20], A. Khoroshilov [175], V. Khovanskiy [95], E. Khramov [64], J. Khubua [51b], H. Kim [146a,146b], M.S. Kim [2], S.H. Kim [160], N. Kimura [171], O. Kind [15], B.T. King [73], M. King [66], R.S.B. King [118], J. Kirk [129], A.E. Kiryunin [99], T. Kishimoto [66], D. Kisielewska [37], T. Kittelmann [123], A.M. Kiver [128], E. Kladiva [144b], M. Klein [73], U. Klein [73], K. Kleinknecht [81], M. Klemetti [85], A. Klier [172], P. Klimek [146a,146b], A. Klimentov [24], R. Klingenberg [42], J.A. Klinger [82], E.B. Klinkby [35], T. Klioutchnikova [29], P.F. Klok [104], S. Klous [105], E.-E. Kluge [58a], T. Kluge [73], P. Kluit [105], S. Kluth [99], N.S. Knecht [158], E. Kneringer [61], E.B.F.G. Knoops [83], A. Knue [54], B.R. Ko [44], T. Kobayashi [155], M. Kobel [43], M. Kocian [143], P. Kodys [126], K. Köneke [29], A.C. König [104], S. Koenig [81], L. Köpke [81], F. Koetsveld [104], P. Koevesarki [20], T. Koffas [28], E. Koffeman [105], L.A. Kogan [118], S. Kohlmann [175], F. Kohn [54], Z. Kohout [127], T. Kohriki [65], T. Koi [143], G.M. Kolachev [107], H. Kolanoski [15], V. Kolesnikov [64], I. Koletsou [89a], J. Koll [88], M. Kollefrath [48], A.A. Komar [94], Y. Komori [155], T. Kondo [65], T. Kono [41,q], A.I. Kononov [48], R. Konoplich [108,r], N. Konstantinidis [77], A. Kootz [175], S. Koperny [37], K. Korcyl [38], K. Kordas [154], A. Korn [118], A. Korol [107], I. Korolkov [11], E.V. Korolkova [139], V.A. Korotkov [128], O. Kortner [99], S. Kortner [99], V.V. Kostyukhin [20], S. Kotov [99], V.M. Kotov [64], A. Kotwal [44], C. Kourkoumelis [8], V. Kouskoura [154], A. Koutsman [159a], R. Kowalewski [169], T.Z. Kowalski [37], W. Kozanecki [136], A.S. Kozhin [128], V. Kral [127], V.A. Kramarenko [97], G. Kramberger [74], M.W. Krasny [78], A. Krasznahorkay [108], J. Kraus [88], J.K. Kraus [20], F. Krejci [127], J. Kretzschmar [73], N. Krieger [54], P. Krieger [158], K. Kroeninger [54], H. Kroha [99], J. Kroll [120], J. Kroseberg [20], J. Krstic [12a], U. Kruchonak [64], H. Krüger [20], T. Kruker [16], N. Krumnack [63], Z.V. Krumshteyn [64], A. Kruth [20], T. Kubota [86], S. Kuday [3a], S. Kuehn [48], A. Kugel [58c], T. Kuhl [41], D. Kuhn [61], V. Kukhtin [64], Y. Kulchitsky [90], S. Kuleshov [31b], C. Kummer [98], M. Kuna [78], J. Kunkle [120], A. Kupco [125], H. Kurashige [66], M. Kurata [160], Y.A. Kurochkin [90], V. Kus [125], E.S. Kuwertz [147], M. Kuze [157], J. Kvita [142], R. Kwee [15], A. La Rosa [49], L. La Rotonda [36a,36b], L. Labarga [80], J. Labbe [4], S. Lablak [135a], C. Lacasta [167], F. Lacava [132a,132b], H. Lacker [15], D. Lacour [78], V.R. Lacuesta [167], E. Ladygin [64], R. Lafaye [4], B. Laforge [78], T. Lagouri [80], S. Lai [48], E. Laisne [55], M. Lamanna [29], L. Lambourne [77], C.L. Lampen [6], W. Lampl [6], E. Lancon [136], U. Landgraf [48], M.P.J. Landon [75], J.L. Lane [82], C. Lange [41], A.J. Lankford [163], F. Lanni [24], K. Lantzsch [175], S. Laplace [78], C. Lapoire [20], J.F. Laporte [136], T. Lari [89a], A. Larner [118], M. Lassnig [29], P. Laurelli [47], V. Lavorini [36a,36b], W. Lavrijsen [14], P. Laycock [73], O. Le Dortz [78], E. Le Guirriec [83], C. Le Maner [158], E. Le Menedeu [11], T. LeCompte [5], F. Ledroit-Guillon [55], H. Lee [105], J.S.H. Lee [116], S.C. Lee [151], L. Lee [176], M. Lefebvre [169], M. Legendre [136], B.C. LeGeyt [120], F. Legger [98], C. Leggett [14], M. Lehmacher [20], G. Lehmann Miotto [29], X. Lei [6], M.A.L. Leite [23d], R. Leitner [126], D. Lellouch [172], B. Lemmer [54], V. Lendermann [58a], K.J.C. Leney [145b], T. Lenz [105], G. Lenzen [175], B. Lenzi [29], K. Leonhardt [43], S. Leontsinis [9], F. Lepold [58a], C. Leroy [93], J-R. Lessard [169], C.G. Lester [27], C.M. Lester [120], J. Levêque [4], D. Levin [87], L.J. Levinson [172], A. Lewis [118], G.H. Lewis [108], A.M. Leyko [20], M. Leyton [15], B. Li [83], H. Li [173,s], S. Li [32b,t], X. Li [87], Z. Liang [118,u], H. Liao [33], B. Liberti [133a], P. Lichard [29], M. Lichtnecker [98], K. Lie [165], W. Liebig [13], C. Limbach [20], A. Limosani [86], M. Limper [62], S.C. Lin [151,v], F. Linde [105], J.T. Linnemann [88], E. Lipeles [120], A. Lipniacka [13], T.M. Liss [165], D. Lissauer [24], A. Lister [49], A.M. Litke [137], C. Liu [28], D. Liu [151], H. Liu [87], J.B. Liu [87], M. Liu [32b], Y. Liu [32b], M. Livan [119a,119b], S.S.A. Livermore [118], A. Lleres [55], J. Llorente Merino [80], S.L. Lloyd [75], E. Lobodzinska [41], P. Loch [6], W.S. Lockman [137], T. Loddenkoetter [20], F.K. Loebinger [82], A. Loginov [176], C.W. Loh [168], T. Lohse [15], K. Lohwasser [48], M. Lokajicek [125], V.P. Lombardo [4], R.E. Long [71], L. Lopes [124a], D. Lopez Mateos [57], J. Lorenz [98], N. Lorenzo Martinez [115], M. Losada [162], P. Loscutoff [14], F. Lo Sterzo [132a,132b], M.J. Losty [159a], X. Lou [40], A. Lounis [115], K.F. Loureiro [162], J. Love [21], P.A. Love [71], A.J. Lowe [143,e], F. Lu [32a], H.J. Lubatti [138], C. Luci [132a,132b], A. Lucotte [55], A. Ludwig [43], D. Ludwig [41], I. Ludwig [48], J. Ludwig [48], F. Luehring [60], G. Luijckx [105], W. Lukas [61], D. Lumb [48], L. Luminari [132a], E. Lund [117], B. Lund-Jensen [147], B. Lundberg [79], J. Lundberg [146a,146b], J. Lundquist [35], M. Lungwitz [81], D. Lynn [24], E. Lytken [79], H. Ma [24], L.L. Ma [173], J.A. Macana Goia [93], G. Maccarrone [47], A. Macchiolo [99], B. Maček [74], J. Machado Miguens [124a], R. Mackeprang [35], R.J. Madaras [14], W.F. Mader [43], R. Maenner [58c], T. Maeno [24], P. Mättig [175], S. Mättig [41],

L. Magnoni [29], E. Magradze [54], K. Mahboubi [48], S. Mahmoud [73], G. Mahout [17], C. Maiani [136], C. Maidantchik [23a], A. Maio [124a,b], S. Majewski [24], Y. Makida [65], N. Makovec [115], P. Mal [136], B. Malaescu [29], Pa. Malecki [38], P. Malecki [38], V.P. Maleev [121], F. Malek [55], U. Mallik [62], D. Malon [5], C. Malone [143], S. Maltezos [9], V. Malyshev [107], S. Malyukov [29], R. Mameghani [98], J. Mamuzic [12b], A. Manabe [65], L. Mandelli [89a], I. Mandić [74], R. Mandrysch [15], J. Maneira [124a], P.S. Mangeard [88], L. Manhaes de Andrade Filho [23a], A. Mann [54], P.M. Manning [137], A. Manousakis-Katsikakis [8], B. Mansoulie [136], A. Mapelli [29], L. Mapelli [29], L. March [80], J.F. Marchand [28], F. Marchese [133a,133b], G. Marchiori [78], M. Marcisovsky [125], C.P. Marino [169], F. Marroquim [23a], Z. Marshall [29], F.K. Martens [158], S. Marti-Garcia [167], B. Martin [29], B. Martin [88], J.P. Martin [93], T.A. Martin [17], V.J. Martin [45], B. Martin dit Latour [49], S. Martin-Haugh [149], M. Martinez [11], V. Martinez Outschoorn [57], A.C. Martyniuk [169], M. Marx [82], F. Marzano [132a], A. Marzin [111], L. Masetti [81], T. Mashimo [155], R. Mashinistov [94], J. Masik [82], A.L. Maslennikov [107], I. Massa [19a,19b], G. Massaro [105], N. Massol [4], A. Mastroberardino [36a,36b], T. Masubuchi [155], P. Matricon [115], H. Matsunaga [155], T. Matsushita [66], C. Mattravers [118,c], J. Maurer [83], S.J. Maxfield [73], A. Mayne [139], R. Mazini [151], M. Mazur [20], L. Mazzaferro [133a,133b], M. Mazzanti [89a], S.P. Mc Kee [87], A. McCarn [165], R.L. McCarthy [148], T.G. McCarthy [28], N.A. McCubbin [129], K.W. McFarlane [56], J.A. Mcfayden [139], H. McGlone [53], G. Mchedlidze [51b], T. Mclaughlan [17], S.J. McMahon [129], R.A. McPherson [169,j], A. Meade [84], J. Mechnich [105], M. Mechtel [175], M. Medinnis [41], R. Meera-Lebbai [111], T. Meguro [116], S. Mehlhase [35], A. Mehta [73], K. Meier [58a], B. Meirose [79], C. Melachrinos [30], B.R. Mellado Garcia [173], F. Meloni [89a,89b], L. Mendoza Navas [162], Z. Meng [151,s], A. Mengarelli [19a,19b], S. Menke [99], E. Meoni [11], K.M. Mercurio [57], P. Mermod [49], L. Merola [102a,102b], C. Meroni [89a], F.S. Merritt [30], H. Merritt [109], A. Messina [29,w], J. Metcalfe [103], A.S. Mete [163], C. Meyer [81], C. Meyer [30], J-P. Meyer [136], J. Meyer [174], J. Meyer [54], T.C. Meyer [29], W.T. Meyer [63], J. Miao [32d], S. Michal [29], L. Micu [25a], R.P. Middleton [129], S. Migas [73], L. Mijović [41], G. Mikenberg [172], M. Mikestikova [125], M. Mikuž [74], D.W. Miller [30], R.J. Miller [88], W.J. Mills [168], C. Mills [57], A. Milov [172], D.A. Milstead [146a,146b], D. Milstein [172], A.A. Minaenko [128], M. Miñano Moya [167], I.A. Minashvili [64], A.I. Mincer [108], B. Mindur [37], M. Mineev [64], Y. Ming [173], L.M. Mir [11], G. Mirabelli [132a], J. Mitrevski [137], V.A. Mitsou [167], S. Mitsui [65], P.S. Miyagawa [139], K. Miyazaki [66], J.U. Mjörnmark [79], T. Moa [146a,146b], P. Mockett [138], S. Moed [57], V. Moeller [27], K. Mönig [41], N. Möser [20], S. Mohapatra [148], W. Mohr [48], R. Moles-Valls [167], J. Molina-Perez [29], J. Monk [77], E. Monnier [83], S. Montesano [89a,89b], F. Monticelli [70], S. Monzani [19a,19b], R.W. Moore [2], G.F. Moorhead [86], C. Mora Herrera [49], A. Moraes [53], N. Morange [136], J. Morel [54], G. Morello [36a,36b], D. Moreno [81], M. Moreno Llácer [167], P. Morettini [50a], M. Morgenstern [43], M. Morii [57], J. Morin [75], A.K. Morley [29], G. Mornacchi [29], J.D. Morris [75], L. Morvaj [101], H.G. Moser [99], M. Mosidze [51b], J. Moss [109], R. Mount [143], E. Mountricha [9,x], S.V. Mouraviev [94], E.J.W. Moyse [84], F. Mueller [58a], J. Mueller [123], K. Mueller [20], T.A. Müller [98], T. Mueller [81], D. Muenstermann [29], Y. Munwes [153], W.J. Murray [129], I. Mussche [105], E. Musto [102a,102b], A.G. Myagkov [128], M. Myska [125], J. Nadal [11], K. Nagai [160], K. Nagano [65], A. Nagarkar [109], Y. Nagasaka [59], M. Nagel [99], A.M. Nairz [29], Y. Nakahama [29], K. Nakamura [155], T. Nakamura [155], I. Nakano [110], G. Nanava [20], A. Napier [161], R. Narayan [58b], M. Nash [77,c], T. Nattermann [20], T. Naumann [41], G. Navarro [162], H.A. Neal [87], P.Yu. Nechaeva [94], T.J. Neep [82], A. Negri [119a,119b], G. Negri [29], S. Nektarijevic [49], A. Nelson [163], T.K. Nelson [143], S. Nemecek [125], P. Nemethy [108], A.A. Nepomuceno [23a], M. Nessi [29,y], M.S. Neubauer [165], A. Neusiedl [81], R.M. Neves [108], P. Nevski [24], P.R. Newman [17], V. Nguyen Thi Hong [136], R.B. Nickerson [118], R. Nicolaidou [136], B. Nicquevert [29], F. Niedercorn [115], J. Nielsen [137], N. Nikiforou [34], A. Nikiforov [15], V. Nikolaenko [128], I. Nikolic-Audit [78], K. Nikolics [49], K. Nikolopoulos [24], H. Nilsen [48], P. Nilsson [7], Y. Ninomiya [155], A. Nisati [132a], T. Nishiyama [66], R. Nisius [99], L. Nodulman [5], M. Nomachi [116], I. Nomidis [154], M. Nordberg [29], P.R. Norton [129], J. Novakova [126], M. Nozaki [65], L. Nozka [113], I.M. Nugent [159a], A.-E. Nuncio-Quiroz [20], G. Nunes Hanninger [86], T. Nunnemann [98], E. Nurse [77], B.J. O'Brien [45], S.W. O'Neale [17,*], D.C. O'Neil [142], V. O'Shea [53], L.B. Oakes [98], F.G. Oakham [28,d], H. Oberlack [99], J. Ocariz [78], A. Ochi [66], S. Oda [69], S. Odaka [65], J. Odier [83], H. Ogren [60], A. Oh [82], S.H. Oh [44], C.C. Ohm [146a,146b], T. Ohshima [101], S. Okada [66], H. Okawa [163], Y. Okumura [101], T. Okuyama [155], A. Olariu [25a], A.G. Olchevski [64], S.A. Olivares Pino [31a], M. Oliveira [124a,h], D. Oliveira Damazio [24], E. Oliver Garcia [167], D. Olivito [120], A. Olszewski [38], J. Olszowska [38], A. Onofre [124a,z], P.U.E. Onyisi [30], C.J. Oram [159a], M.J. Oreglia [30], Y. Oren [153], D. Orestano [134a,134b], N. Orlando [72a,72b], I. Orlov [107], C. Oropeza Barrera [53], R.S. Orr [158], B. Osculati [50a,50b],

R. Ospanov [120], C. Osuna [11], G. Otero y Garzon [26], J.P. Ottersbach [105], M. Ouchrif [135d], E.A. Ouellette [169], F. Ould-Saada [117], A. Ouraou [136], Q. Ouyang [32a], A. Ovcharova [14], M. Owen [82], S. Owen [139], V.E. Ozcan [18a], N. Ozturk [7], A. Pacheco Pages [11], C. Padilla Aranda [11], S. Pagan Griso [14], E. Paganis [139], F. Paige [24], P. Pais [84], K. Pajchel [117], G. Palacino [159b], C.P. Paleari [6], S. Palestini [29], D. Pallin [33], A. Palma [124a], J.D. Palmer [17], Y.B. Pan [173], E. Panagiotopoulou [9], P. Pani [105], N. Panikashvili [87], S. Panitkin [24], D. Pantea [25a], A. Papadelis [146a], Th.D. Papadopoulou [9], A. Paramonov [5], D. Paredes Hernandez [33], W. Park [24,aa], M.A. Parker [27], F. Parodi [50a,50b], J.A. Parsons [34], U. Parzefall [48], S. Pashapour [54], E. Pasqualucci [132a], S. Passaggio [50a], A. Passeri [134a], F. Pastore [134a,134b], Fr. Pastore [76], G. Pásztor [49,ab], S. Pataraia [175], N. Patel [150], J.R. Pater [82], S. Patricelli [102a,102b], T. Pauly [29], M. Pecsy [144a], M.I. Pedraza Morales [173], S.V. Peleganchuk [107], D. Pelikan [166], H. Peng [32b], B. Penning [30], A. Penson [34], J. Penwell [60], M. Perantoni [23a], K. Perez [34,ac], T. Perez Cavalcanti [41], E. Perez Codina [159a], M.T. Pérez García-Estañ [167], V. Perez Reale [34], L. Perini [89a,89b], H. Pernegger [29], R. Perrino [72a], P. Perrodo [4], S. Persembe [3a], V.D. Peshekhonov [64], K. Peters [29], B.A. Petersen [29], J. Petersen [29], T.C. Petersen [35], E. Petit [4], A. Petridis [154], C. Petridou [154], E. Petrolo [132a], F. Petrucci [134a,134b], D. Petschull [41], M. Petteni [142], R. Pezoa [31b], A. Phan [86], P.W. Phillips [129], G. Piacquadio [29], A. Picazio [49], E. Piccaro [75], M. Piccinini [19a,19b], S.M. Piec [41], R. Piegaia [26], D.T. Pignotti [109], J.E. Pilcher [30], A.D. Pilkington [82], J. Pina [124a,b], M. Pinamonti [164a,164c], A. Pinder [118], J.L. Pinfold [2], B. Pinto [124a], C. Pizio [89a,89b], M. Plamondon [169], M.-A. Pleier [24], E. Plotnikova [64], A. Poblaguev [24], S. Poddar [58a], F. Podlyski [33], L. Poggioli [115], T. Poghosyan [20], M. Pohl [49], F. Polci [55], G. Polesello [119a], A. Policicchio [36a,36b], A. Polini [19a], J. Poll [75], V. Polychronakos [24], D.M. Pomarede [136], D. Pomeroy [22], K. Pommès [29], L. Pontecorvo [132a], B.G. Pope [88], G.A. Popeneciu [25a], D.S. Popovic [12a], A. Poppleton [29], X. Portell Bueso [29], G.E. Pospelov [99], S. Pospisil [127], I.N. Potrap [99], C.J. Potter [149], C.T. Potter [114], G. Poulard [29], J. Poveda [173], V. Pozdnyakov [64], R. Prabhu [77], P. Pralavorio [83], A. Pranko [14], S. Prasad [29], R. Pravahan [24], S. Prell [63], K. Pretzl [16], D. Price [60], J. Price [73], L.E. Price [5], D. Prieur [123], M. Primavera [72a], K. Prokofiev [108], F. Prokoshin [31b], S. Protopopescu [24], J. Proudfoot [5], X. Prudent [43], M. Przybycien [37], H. Przysiezniak [4], S. Psoroulas [20], E. Ptacek [114], E. Pueschel [84], J. Purdham [87], M. Purohit [24,aa], P. Puzo [115], Y. Pylypchenko [62], J. Qian [87], A. Quadt [54], D.R. Quarrie [14], W.B. Quayle [173], F. Quinonez [31a], M. Raas [104], V. Radescu [41], P. Radloff [114], T. Rador [18a], F. Ragusa [89a,89b], G. Rahal [178], A.M. Rahimi [109], D. Rahm [24], S. Rajagopalan [24], M. Rammensee [48], M. Rammes [141], A.S. Randle-Conde [39], K. Randrianarivony [28], F. Rauscher [98], T.C. Rave [48], M. Raymond [29], A.L. Read [117], D.M. Rebuzzi [119a,119b], A. Redelbach [174], G. Redlinger [24], R. Reece [120], K. Reeves [40], E. Reinherz-Aronis [153], A. Reinsch [114], I. Reisinger [42], C. Rembser [29], Z.L. Ren [151], A. Renaud [115], M. Rescigno [132a], S. Resconi [89a], B. Resende [136], P. Reznicek [98], R. Rezvani [158], R. Richter [99], E. Richter-Was [4,ad], M. Ridel [78], M. Rijpstra [105], M. Rijssenbeek [148], A. Rimoldi [119a,119b], L. Rinaldi [19a], R.R. Rios [39], I. Riu [11], G. Rivoltella [89a,89b], F. Rizatdinova [112], E. Rizvi [75], S.H. Robertson [85,j], A. Robichaud-Veronneau [118], D. Robinson [27], J.E.M. Robinson [77], A. Robson [53], J.G. Rocha de Lima [106], C. Roda [122a,122b], D. Roda Dos Santos [29], D. Rodriguez [162], A. Roe [54], S. Roe [29], O. Røhne [117], S. Rolli [161], A. Romaniouk [96], M. Romano [19a,19b], G. Romeo [26], E. Romero Adam [167], L. Roos [78], E. Ros [167], S. Rosati [132a], K. Rosbach [49], A. Rose [149], M. Rose [76], G.A. Rosenbaum [158], E.I. Rosenberg [63], P.L. Rosendahl [13], O. Rosenthal [141], L. Rosselet [49], V. Rossetti [11], E. Rossi [132a,132b], L.P. Rossi [50a], M. Rotaru [25a], I. Roth [172], J. Rothberg [138], D. Rousseau [115], C.R. Royon [136], A. Rozanov [83], Y. Rozen [152], X. Ruan [32a,ae], F. Rubbo [11], I. Rubinskiy [41], B. Ruckert [98], N. Ruckstuhl [105], V.I. Rud [97], C. Rudolph [43], G. Rudolph [61], F. Rühr [6], F. Ruggieri [134a,134b], A. Ruiz-Martinez [63], L. Rumyantsev [64], K. Runge [48], Z. Rurikova [48], N.A. Rusakovich [64], J.P. Rutherfoord [6], C. Ruwiedel [14], P. Ruzicka [125], Y.F. Ryabov [121], P. Ryan [88], M. Rybar [126], G. Rybkin [115], N.C. Ryder [118], A.F. Saavedra [150], I. Sadeh [153], H.F-W. Sadrozinski [137], R. Sadykov [64], F. Safai Tehrani [132a], H. Sakamoto [155], G. Salamanna [75], A. Salamon [133a], M. Saleem [111], D. Salek [29], D. Salihagic [99], A. Salnikov [143], J. Salt [167], B.M. Salvachua Ferrando [5], D. Salvatore [36a,36b], F. Salvatore [149], A. Salvucci [104], A. Salzburger [29], D. Sampsonidis [154], B.H. Samset [117], A. Sanchez [102a,102b], V. Sanchez Martinez [167], H. Sandaker [13], H.G. Sander [81], M.P. Sanders [98], M. Sandhoff [175], T. Sandoval [27], C. Sandoval [162], R. Sandstroem [99], D.P.C. Sankey [129], A. Sansoni [47], C. Santamarina Rios [85], C. Santoni [33], R. Santonico [133a,133b], H. Santos [124a], J.G. Saraiva [124a], T. Sarangi [173], E. Sarkisyan-Grinbaum [7], F. Sarri [122a,122b], G. Sartisohn [175], O. Sasaki [65], N. Sasao [67], I. Satsounkevitch [90], G. Sauvage [4], E. Sauvan [4], J.B. Sauvan [115], P. Savard [158,d], V. Savinov [123], D.O. Savu [29], L. Sawyer [24,l], D.H. Saxon [53], J. Saxon [120], C. Sbarra [19a], A. Sbrizzi [19a,19b], O. Scallon [93], D.A. Scannicchio [163],

M. Scarcella [150], J. Schaarschmidt [115], P. Schacht [99], D. Schaefer [120], U. Schäfer [81], S. Schaepe [20], S. Schaetzel [58b], A.C. Schaffer [115], D. Schaile [98], R.D. Schamberger [148], A.G. Schamov [107], V. Scharf [58a], V.A. Schegelsky [121], D. Scheirich [87], M. Schernau [163], M.I. Scherzer [34], C. Schiavi [50a,50b], J. Schieck [98], M. Schioppa [36a,36b], S. Schlenker [29], E. Schmidt [48], K. Schmieden [20], C. Schmitt [81], S. Schmitt [58b], M. Schmitz [20], B. Schneider [16], U. Schnoor [43], A. Schöning [58b], M. Schott [29], D. Schouten [159a], J. Schovancova [125], M. Schram [85], C. Schroeder [81], N. Schroer [58c], M.J. Schultens [20], J. Schultes [175], H.-C. Schultz-Coulon [58a], H. Schulz [15], J.W. Schumacher [20], M. Schumacher [48], B.A. Schumm [137], Ph. Schune [136], C. Schwanenberger [82], A. Schwartzman [143], Ph. Schwemling [78], R. Schwienhorst [88], R. Schwierz [43], J. Schwindling [136], T. Schwindt [20], M. Schwoerer [4], G. Sciolla [22], W.G. Scott [129], J. Searcy [114], G. Sedov [41], E. Sedykh [121], S.C. Seidel [103], A. Seiden [137], F. Seifert [43], J.M. Seixas [23a], G. Sekhniaidze [102a], S.J. Sekula [39], K.E. Selbach [45], D.M. Seliverstov [121], B. Sellden [146a], G. Sellers [73], M. Seman [144b], N. Semprini-Cesari [19a,19b], C. Serfon [98], L. Serin [115], L. Serkin [54], R. Seuster [99], H. Severini [111], A. Sfyrla [29], E. Shabalina [54], M. Shamim [114], L.Y. Shan [32a], J.T. Shank [21], Q.T. Shao [86], M. Shapiro [14], P.B. Shatalov [95], K. Shaw [164a,164c], D. Sherman [176], P. Sherwood [77], A. Shibata [108], H. Shichi [101], S. Shimizu [29], M. Shimojima [100], T. Shin [56], M. Shiyakova [64], A. Shmeleva [94], M.J. Shochet [30], D. Short [118], S. Shrestha [63], E. Shulga [96], M.A. Shupe [6], P. Sicho [125], A. Sidoti [132a], F. Siegert [48], Dj. Sijacki [12a], O. Silbert [172], J. Silva [124a], Y. Silver [153], D. Silverstein [143], S.B. Silverstein [146a], V. Simak [127], O. Simard [136], Lj. Simic [12a], S. Simion [115], B. Simmons [77], R. Simoniello [89a,89b], M. Simonyan [35], P. Sinervo [158], N.B. Sinev [114], V. Sipica [141], G. Siragusa [174], A. Sircar [24], A.N. Sisakyan [64], S.Yu. Sivoklokov [97], J. Sjölin [146a,146b], T.B. Sjursen [13], L.A. Skinnari [14], H.P. Skottowe [57], K. Skovpen [107], P. Skubic [111], M. Slater [17], T. Slavicek [127], K. Sliwa [161], V. Smakhtin [172], B.H. Smart [45], S.Yu. Smirnov [96], Y. Smirnov [96], L.N. Smirnova [97], O. Smirnova [79], B.C. Smith [57], D. Smith [143], K.M. Smith [53], M. Smizanska [71], K. Smolek [127], A.A. Snesarev [94], S.W. Snow [82], J. Snow [111], S. Snyder [24], R. Sobie [169,j], J. Sodomka [127], A. Soffer [153], C.A. Solans [167], M. Solar [127], J. Solc [127], E. Soldatov [96], U. Soldevila [167], E. Solfaroli Camillocci [132a,132b], A.A. Solodkov [128], O.V. Solovyanov [128], N. Soni [2], V. Sopko [127], B. Sopko [127], M. Sosebee [7], R. Soualah [164a,164c], A. Soukharev [107], S. Spagnolo [72a,72b], F. Spanò [76], R. Spighi [19a], G. Spigo [29], F. Spila [132a,132b], R. Spiwoks [29], M. Spousta [126], T. Spreitzer [158], B. Spurlock [7], R.D. St. Denis [53], J. Stahlman [120], R. Stamen [58a], E. Stanecka [38], R.W. Stanek [5], C. Stanescu [134a], M. Stanescu-Bellu [41], S. Stapnes [117], E.A. Starchenko [128], J. Stark [55], P. Staroba [125], P. Starovoitov [41], A. Staude [98], P. Stavina [144a], G. Steele [53], P. Steinbach [43], P. Steinberg [24], I. Stekl [127], B. Stelzer [142], H.J. Stelzer [88], O. Stelzer-Chilton [159a], H. Stenzel [52], S. Stern [99], G.A. Stewart [29], J.A. Stillings [20], M.C. Stockton [85], K. Stoerig [48], G. Stoicea [25a], S. Stonjek [99], P. Strachota [126], A.R. Stradling [7], A. Straessner [43], J. Strandberg [147], S. Strandberg [146a,146b], A. Strandlie [117], M. Strang [109], E. Strauss [143], M. Strauss [111], P. Strizenec [144b], R. Ströhmer [174], D.M. Strom [114], J.A. Strong [76,*], R. Stroynowski [39], J. Strube [129], B. Stugu [13], I. Stumer [24,*], J. Stupak [148], P. Sturm [175], N.A. Styles [41], D.A. Soh [151,u], D. Su [143], HS. Subramania [2], A. Succurro [11], Y. Sugaya [116], C. Suhr [106], K. Suita [66], M. Suk [126], V.V. Sulin [94], S. Sultansoy [3d], T. Sumida [67], X. Sun [55], J.E. Sundermann [48], K. Suruliz [139], G. Susinno [36a,36b], M.R. Sutton [149], Y. Suzuki [65], Y. Suzuki [66], M. Svatos [125], S. Swedish [168], I. Sykora [144a], T. Sykora [126], J. Sánchez [167], D. Ta [105], K. Tackmann [41], A. Taffard [163], R. Tafirout [159a], N. Taiblum [153], Y. Takahashi [101], H. Takai [24], R. Takashima [68], H. Takeda [66], T. Takeshita [140], Y. Takubo [65], M. Talby [83], A. Talyshev [107,f], M.C. Tamsett [24], J. Tanaka [155], R. Tanaka [115], S. Tanaka [131], S. Tanaka [65], A.J. Tanasijczuk [142], K. Tani [66], N. Tannoury [83], S. Tapprogge [81], D. Tardif [158], S. Tarem [152], F. Tarrade [28], G.F. Tartarelli [89a], P. Tas [126], M. Tasevsky [125], E. Tassi [36a,36b], M. Tatarkhanov [14], Y. Tayalati [135d], C. Taylor [77], F.E. Taylor [92], G.N. Taylor [86], W. Taylor [159b], M. Teinturier [115], M. Teixeira Dias Castanheira [75], P. Teixeira-Dias [76], K.K. Temming [48], H. Ten Kate [29], P.K. Teng [151], S. Terada [65], K. Terashi [155], J. Terron [80], M. Testa [47], R.J. Teuscher [158,j], J. Therhaag [20], T. Theveneaux-Pelzer [78], M. Thioye [176], S. Thoma [48], J.P. Thomas [17], E.N. Thompson [34], P.D. Thompson [17], P.D. Thompson [158], A.S. Thompson [53], L.A. Thomsen [35], E. Thomson [120], M. Thomson [27], R.P. Thun [87], F. Tian [34], M.J. Tibbetts [14], T. Tic [125], V.O. Tikhomirov [94], Y.A. Tikhonov [107,f], S. Timoshenko [96], P. Tipton [176], F.J. Tique Aires Viegas [29], S. Tisserant [83], T. Todorov [4], S. Todorova-Nova [161], B. Toggerson [163], J. Tojo [69], S. Tokár [144a], K. Tokunaga [66], K. Tokushuku [65], K. Tollefson [88], M. Tomoto [101], L. Tompkins [30], K. Toms [103], A. Tonoyan [13], C. Topfel [16], N.D. Topilin [64], I. Torchiani [29], E. Torrence [114], H. Torres [78], E. Torró Pastor [167], J. Toth [83,ab], F. Touchard [83], D.R. Tovey [139], T. Trefzger [174], L. Tremblet [29], A. Tricoli [29], I.M. Trigger [159a], S. Trincaz-Duvoid [78], M.F. Tripiana [70],

W. Trischuk [158], B. Trocmé [55], C. Troncon [89a], M. Trottier-McDonald [142], M. Trzebinski [38], A. Trzupek [38], C. Tsarouchas [29], J.C-L. Tseng [118], M. Tsiakiris [105], P.V. Tsiareshka [90], D. Tsionou [4,af], G. Tsipolitis [9], V. Tsiskaridze [48], E.G. Tskhadadze [51a], I.I. Tsukerman [95], V. Tsulaia [14], J.-W. Tsung [20], S. Tsuno [65], D. Tsybychev [148], A. Tua [139], A. Tudorache [25a], V. Tudorache [25a], J.M. Tuggle [30], M. Turala [38], D. Turecek [127], I. Turk Cakir [3e], E. Turlay [105], R. Turra [89a,89b], P.M. Tuts [34], A. Tykhonov [74], M. Tylmad [146a,146b], M. Tyndel [129], G. Tzanakos [8], K. Uchida [20], I. Ueda [155], R. Ueno [28], M. Ugland [13], M. Uhlenbrock [20], M. Uhrmacher [54], F. Ukegawa [160], G. Unal [29], A. Undrus [24], G. Unel [163], Y. Unno [65], D. Urbaniec [34], G. Usai [7], M. Uslenghi [119a,119b], L. Vacavant [83], V. Vacek [127], B. Vachon [85], S. Vahsen [14], J. Valenta [125], P. Valente [132a], S. Valentinetti [19a,19b], S. Valkar [126], E. Valladolid Gallego [167], S. Vallecorsa [152], J.A. Valls Ferrer [167], H. van der Graaf [105], E. van der Kraaij [105], R. Van Der Leeuw [105], E. van der Poel [105], D. van der Ster [29], N. van Eldik [84], P. van Gemmeren [5], I. van Vulpen [105], M. Vanadia [99], W. Vandelli [29], A. Vaniachine [5], P. Vankov [41], F. Vannucci [78], R. Vari [132a], T. Varol [84], D. Varouchas [14], A. Vartapetian [7], K.E. Varvell [150], V.I. Vassilakopoulos [56], F. Vazeille [33], T. Vazquez Schroeder [54], G. Vegni [89a,89b], J.J. Veillet [115], F. Veloso [124a], R. Veness [29], S. Veneziano [132a], A. Ventura [72a,72b], D. Ventura [84], M. Venturi [48], N. Venturi [158], V. Vercesi [119a], M. Verducci [138], W. Verkerke [105], J.C. Vermeulen [105], A. Vest [43], M.C. Vetterli [142,d], I. Vichou [165], T. Vickey [145b,ag], O.E. Vickey Boeriu [145b], G.H.A. Viehhauser [118], S. Viel [168], M. Villa [19a,19b], M. Villaplana Perez [167], E. Vilucchi [47], M.G. Vincter [28], E. Vinek [29], V.B. Vinogradov [64], M. Virchaux [136,*], J. Virzi [14], O. Vitells [172], M. Viti [41], I. Vivarelli [48], F. Vives Vaque [2], S. Vlachos [9], D. Vladoiu [98], M. Vlasak [127], A. Vogel [20], P. Vokac [127], G. Volpi [47], M. Volpi [86], G. Volpini [89a], H. von der Schmitt [99], J. von Loeben [99], H. von Radziewski [48], E. von Toerne [20], V. Vorobel [126], V. Vorwerk [11], M. Vos [167], R. Voss [29], T.T. Voss [175], J.H. Vossebeld [73], N. Vranjes [136], M. Vranjes Milosavljevic [105], V. Vrba [125], M. Vreeswijk [105], T. Vu Anh [48], R. Vuillermet [29], I. Vukotic [115], W. Wagner [175], P. Wagner [120], H. Wahlen [175], S. Wahrmund [43], J. Wakabayashi [101], S. Walch [87], J. Walder [71], R. Walker [98], W. Walkowiak [141], R. Wall [176], P. Waller [73], C. Wang [44], H. Wang [173], H. Wang [32b,ah], J. Wang [151], J. Wang [55], J.C. Wang [138], R. Wang [103], S.M. Wang [151], T. Wang [20], A. Warburton [85], C.P. Ward [27], M. Warsinsky [48], A. Washbrook [45], C. Wasicki [41], P.M. Watkins [17], A.T. Watson [17], I.J. Watson [150], M.F. Watson [17], G. Watts [138], S. Watts [82], A.T. Waugh [150], B.M. Waugh [77], M. Weber [129], M.S. Weber [16], P. Weber [54], A.R. Weidberg [118], P. Weigell [99], J. Weingarten [54], C. Weiser [48], H. Wellenstein [22], P.S. Wells [29], T. Wenaus [24], D. Wendland [15], Z. Weng [151,u], T. Wengler [29], S. Wenig [29], N. Wermes [20], M. Werner [48], P. Werner [29], M. Werth [163], M. Wessels [58a], J. Wetter [161], C. Weydert [55], K. Whalen [28], S.J. Wheeler-Ellis [163], A. White [7], M.J. White [86], S. White [122a,122b], S.R. Whitehead [118], D. Whiteson [163], D. Whittington [60], F. Wicek [115], D. Wicke [175], F.J. Wickens [129], W. Wiedenmann [173], M. Wielers [129], P. Wienemann [20], C. Wiglesworth [75], L.A.M. Wiik-Fuchs [48], P.A. Wijeratne [77], A. Wildauer [167], M.A. Wildt [41,q], I. Wilhelm [126], H.G. Wilkens [29], J.Z. Will [98], E. Williams [34], H.H. Williams [120], W. Willis [34], S. Willocq [84], J.A. Wilson [17], M.G. Wilson [143], A. Wilson [87], I. Wingerter-Seez [4], S. Winkelmann [48], F. Winklmeier [29], M. Wittgen [143], M.W. Wolter [38], H. Wolters [124a,h], W.C. Wong [40], G. Wooden [87], B.K. Wosiek [38], J. Wotschack [29], M.J. Woudstra [84], K.W. Wozniak [38], K. Wraight [53], C. Wright [53], M. Wright [53], B. Wrona [73], S.L. Wu [173], X. Wu [49], Y. Wu [32b,ai], E. Wulf [34], B.M. Wynne [45], S. Xella [35], M. Xiao [136], S. Xie [48], C. Xu [32b,x], D. Xu [139], B. Yabsley [150], S. Yacoob [145b], M. Yamada [65], H. Yamaguchi [155], A. Yamamoto [65], K. Yamamoto [63], S. Yamamoto [155], T. Yamamura [155], T. Yamanaka [155], J. Yamaoka [44], T. Yamazaki [155], Y. Yamazaki [66], Z. Yan [21], H. Yang [87], U.K. Yang [82], Y. Yang [60], Z. Yang [146a,146b], S. Yanush [91], L. Yao [32a], Y. Yao [14], Y. Yasu [65], G.V. Ybeles Smit [130], J. Ye [39], S. Ye [24], M. Yilmaz [3c], R. Yoosoofmiya [123], K. Yorita [171], R. Yoshida [5], C. Young [143], C.J. Young [118], S. Youssef [21], D. Yu [24], J. Yu [7], J. Yu [112], L. Yuan [66], A. Yurkewicz [106], B. Zabinski [38], R. Zaidan [62], A.M. Zaitsev [128], Z. Zajacova [29], L. Zanello [132a,132b], A. Zaytsev [107], C. Zeitnitz [175], M. Zeller [176], M. Zeman [125], A. Zemla [38], C. Zendler [20], O. Zenin [128], T. Ženiš [144a], Z. Zinonos [122a,122b], S. Zenz [14], D. Zerwas [115], G. Zevi della Porta [57], Z. Zhan [32d], D. Zhang [32b,ah], H. Zhang [88], J. Zhang [5], X. Zhang [32d], Z. Zhang [115], L. Zhao [108], T. Zhao [138], Z. Zhao [32b], A. Zhemchugov [64], J. Zhong [118], B. Zhou [87], N. Zhou [163], Y. Zhou [151], C.G. Zhu [32d], H. Zhu [41], J. Zhu [87], Y. Zhu [32b], X. Zhuang [98], V. Zhuravlov [99], D. Zieminska [60], R. Zimmermann [20], S. Zimmermann [20], S. Zimmermann [48], M. Ziolkowski [141], R. Zitoun [4], L. Živković [34], V.V. Zmouchko [128,*], G. Zobernig [173], A. Zoccoli [19a,19b], M. zur Nedden [15], V. Zutshi [106], L. Zwalinski [29]

[1] *University at Albany, Albany, NY, United States*

[2] Department of Physics, University of Alberta, Edmonton AB, Canada
[3] [(a)] Department of Physics, Ankara University, Ankara; [(b)] Department of Physics, Dumlupinar University, Kutahya; [(c)] Department of Physics, Gazi University, Ankara; [(d)] Division of Physics, TOBB University of Economics and Technology, Ankara; [(e)] Turkish Atomic Energy Authority, Ankara, Turkey
[4] LAPP, CNRS/IN2P3 and Université de Savoie, Annecy-le-Vieux, France
[5] High Energy Physics Division, Argonne National Laboratory, Argonne, IL, United States
[6] Department of Physics, University of Arizona, Tucson, AZ, United States
[7] Department of Physics, The University of Texas at Arlington, Arlington, TX, United States
[8] Physics Department, University of Athens, Athens, Greece
[9] Physics Department, National Technical University of Athens, Zografou, Greece
[10] Institute of Physics, Azerbaijan Academy of Sciences, Baku, Azerbaijan
[11] Institut de Física d'Altes Energies and Departament de Física de la Universitat Autònoma de Barcelona and ICREA, Barcelona, Spain
[12] [(a)] Institute of Physics, University of Belgrade, Belgrade; [(b)] Vinca Institute of Nuclear Sciences, University of Belgrade, Belgrade, Serbia
[13] Department for Physics and Technology, University of Bergen, Bergen, Norway
[14] Physics Division, Lawrence Berkeley National Laboratory and University of California, Berkeley, CA, United States
[15] Department of Physics, Humboldt University, Berlin, Germany
[16] Albert Einstein Center for Fundamental Physics and Laboratory for High Energy Physics, University of Bern, Bern, Switzerland
[17] School of Physics and Astronomy, University of Birmingham, Birmingham, United Kingdom
[18] [(a)] Department of Physics, Bogazici University, Istanbul; [(b)] Division of Physics, Dogus University, Istanbul; [(c)] Department of Physics Engineering, Gaziantep University, Gaziantep; [(d)] Department of Physics, Istanbul Technical University, Istanbul, Turkey
[19] [(a)] INFN Sezione di Bologna; [(b)] Dipartimento di Fisica, Università di Bologna, Bologna, Italy
[20] Physikalisches Institut, University of Bonn, Bonn, Germany
[21] Department of Physics, Boston University, Boston, MA, United States
[22] Department of Physics, Brandeis University, Waltham, MA, United States
[23] [(a)] Universidade Federal do Rio De Janeiro COPPE/EE/IF, Rio de Janeiro; [(b)] Federal University of Juiz de Fora (UFJF), Juiz de Fora; [(c)] Federal University of Sao Joao del Rei (UFSJ), Sao Joao del Rei; [(d)] Instituto de Fisica, Universidade de Sao Paulo, Sao Paulo, Brazil
[24] Physics Department, Brookhaven National Laboratory, Upton, NY, United States
[25] [(a)] National Institute of Physics and Nuclear Engineering, Bucharest; [(b)] University Politehnica Bucharest, Bucharest; [(c)] West University in Timisoara, Timisoara, Romania
[26] Departamento de Física, Universidad de Buenos Aires, Buenos Aires, Argentina
[27] Cavendish Laboratory, University of Cambridge, Cambridge, United Kingdom
[28] Department of Physics, Carleton University, Ottawa, ON, Canada
[29] CERN, Geneva, Switzerland
[30] Enrico Fermi Institute, University of Chicago, Chicago, IL, United States
[31] [(a)] Departamento de Fisica, Pontificia Universidad Católica de Chile, Santiago; [(b)] Departamento de Física, Universidad Técnica Federico Santa María, Valparaíso, Chile
[32] [(a)] Institute of High Energy Physics, Chinese Academy of Sciences, Beijing; [(b)] Department of Modern Physics, University of Science and Technology of China, Anhui; [(c)] Department of Physics, Nanjing University, Jiangsu; [(d)] School of Physics, Shandong University, Shandong, China
[33] Laboratoire de Physique Corpusculaire, Clermont Université and Université Blaise Pascal and CNRS/IN2P3, Aubiere Cedex, France
[34] Nevis Laboratory, Columbia University, Irvington, NY, United States
[35] Niels Bohr Institute, University of Copenhagen, Kobenhavn, Denmark
[36] [(a)] INFN Gruppo Collegato di Cosenza; [(b)] Dipartimento di Fisica, Università della Calabria, Arcavata di Rende, Italy
[37] AGH University of Science and Technology, Faculty of Physics and Applied Computer Science, Krakow, Poland
[38] The Henryk Niewodniczanski Institute of Nuclear Physics, Polish Academy of Sciences, Krakow, Poland
[39] Physics Department, Southern Methodist University, Dallas, TX, United States
[40] Physics Department, University of Texas at Dallas, Richardson, TX, United States
[41] DESY, Hamburg and Zeuthen, Germany
[42] Institut für Experimentelle Physik IV, Technische Universität Dortmund, Dortmund, Germany
[43] Institut für Kern- und Teilchenphysik, Technical University Dresden, Dresden, Germany
[44] Department of Physics, Duke University, Durham, NC, United States
[45] SUPA - School of Physics and Astronomy, University of Edinburgh, Edinburgh, United Kingdom
[46] Fachhochschule Wiener Neustadt, Johannes Gutenbergstrasse 3 2700 Wiener Neustadt, Austria
[47] INFN Laboratori Nazionali di Frascati, Frascati, Italy
[48] Fakultät für Mathematik und Physik, Albert-Ludwigs-Universität, Freiburg i.Br., Germany
[49] Section de Physique, Université de Genève, Geneva, Switzerland
[50] [(a)] INFN Sezione di Genova; [(b)] Dipartimento di Fisica, Università di Genova, Genova, Italy
[51] [(a)] E. Andronikashvili Institute of Physics, Tbilisi State University, Tbilisi; [(b)] High Energy Physics Institute, Tbilisi State University, Tbilisi, Georgia
[52] II Physikalisches Institut, Justus-Liebig-Universität Giessen, Giessen, Germany
[53] SUPA - School of Physics and Astronomy, University of Glasgow, Glasgow, United Kingdom
[54] II Physikalisches Institut, Georg-August-Universität, Göttingen, Germany
[55] Laboratoire de Physique Subatomique et de Cosmologie, Université Joseph Fourier and CNRS/IN2P3 and Institut National Polytechnique de Grenoble, Grenoble, France
[56] Department of Physics, Hampton University, Hampton, VA, United States
[57] Laboratory for Particle Physics and Cosmology, Harvard University, Cambridge, MA, United States
[58] [(a)] Kirchhoff-Institut für Physik, Ruprecht-Karls-Universität Heidelberg, Heidelberg; [(b)] Physikalisches Institut, Ruprecht-Karls-Universität Heidelberg, Heidelberg; [(c)] ZITI Institut für technische Informatik, Ruprecht-Karls-Universität Heidelberg, Mannheim, Germany
[59] Faculty of Applied Information Science, Hiroshima Institute of Technology, Hiroshima, Japan
[60] Department of Physics, Indiana University, Bloomington, IN, United States
[61] Institut für Astro- und Teilchenphysik, Leopold-Franzens-Universität, Innsbruck, Austria
[62] University of Iowa, Iowa City, IA, United States
[63] Department of Physics and Astronomy, Iowa State University, Ames, IA, United States
[64] Joint Institute for Nuclear Research, JINR Dubna, Dubna, Russia
[65] KEK, High Energy Accelerator Research Organization, Tsukuba, Japan
[66] Graduate School of Science, Kobe University, Kobe, Japan
[67] Faculty of Science, Kyoto University, Kyoto, Japan
[68] Kyoto University of Education, Kyoto, Japan
[69] Department of Physics, Kyushu University, Fukuoka, Japan
[70] Instituto de Física La Plata, Universidad Nacional de La Plata and CONICET, La Plata, Argentina
[71] Physics Department, Lancaster University, Lancaster, United Kingdom
[72] [(a)] INFN Sezione di Lecce; [(b)] Dipartimento di Matematica e Fisica, Università del Salento, Lecce, Italy
[73] Oliver Lodge Laboratory, University of Liverpool, Liverpool, United Kingdom
[74] Department of Physics, Jožef Stefan Institute and University of Ljubljana, Ljubljana, Slovenia
[75] School of Physics and Astronomy, Queen Mary University of London, London, United Kingdom

[76] Department of Physics, Royal Holloway University of London, Surrey, United Kingdom
[77] Department of Physics and Astronomy, University College London, London, United Kingdom
[78] Laboratoire de Physique Nucléaire et de Hautes Energies, UPMC and Université Paris-Diderot and CNRS/IN2P3, Paris, France
[79] Fysiska institutionen, Lunds universitet, Lund, Sweden
[80] Departamento de Fisica Teorica C-15, Universidad Autonoma de Madrid, Madrid, Spain
[81] Institut für Physik, Universität Mainz, Mainz, Germany
[82] School of Physics and Astronomy, University of Manchester, Manchester, United Kingdom
[83] CPPM, Aix-Marseille Université and CNRS/IN2P3, Marseille, France
[84] Department of Physics, University of Massachusetts, Amherst, MA, United States
[85] Department of Physics, McGill University, Montreal, QC, Canada
[86] School of Physics, University of Melbourne, Victoria, Australia
[87] Department of Physics, The University of Michigan, Ann Arbor, MI, United States
[88] Department of Physics and Astronomy, Michigan State University, East Lansing, MI, United States
[89] [(a)] INFN Sezione di Milano; [(b)] Dipartimento di Fisica, Università di Milano, Milano, Italy
[90] B.I. Stepanov Institute of Physics, National Academy of Sciences of Belarus, Minsk, Belarus
[91] National Scientific and Educational Centre for Particle and High Energy Physics, Minsk, Belarus
[92] Department of Physics, Massachusetts Institute of Technology, Cambridge, MA, United States
[93] Group of Particle Physics, University of Montreal, Montreal, QC, Canada
[94] P.N. Lebedev Institute of Physics, Academy of Sciences, Moscow, Russia
[95] Institute for Theoretical and Experimental Physics (ITEP), Moscow, Russia
[96] Moscow Engineering and Physics Institute (MEPhI), Moscow, Russia
[97] Skobeltsyn Institute of Nuclear Physics, Lomonosov Moscow State University, Moscow, Russia
[98] Fakultät für Physik, Ludwig-Maximilians-Universität München, München, Germany
[99] Max-Planck-Institut für Physik (Werner-Heisenberg-Institut), München, Germany
[100] Nagasaki Institute of Applied Science, Nagasaki, Japan
[101] Graduate School of Science, Nagoya University, Nagoya, Japan
[102] [(a)] INFN Sezione di Napoli; [(b)] Dipartimento di Scienze Fisiche, Università di Napoli, Napoli, Italy
[103] Department of Physics and Astronomy, University of New Mexico, Albuquerque, NM, United States
[104] Institute for Mathematics, Astrophysics and Particle Physics, Radboud University Nijmegen/Nikhef, Nijmegen, Netherlands
[105] Nikhef National Institute for Subatomic Physics and University of Amsterdam, Amsterdam, Netherlands
[106] Department of Physics, Northern Illinois University, DeKalb, IL, United States
[107] Budker Institute of Nuclear Physics, SB RAS, Novosibirsk, Russia
[108] Department of Physics, New York University, New York, NY, United States
[109] Ohio State University, Columbus, OH, United States
[110] Faculty of Science, Okayama University, Okayama, Japan
[111] Homer L. Dodge Department of Physics and Astronomy, University of Oklahoma, Norman, OK, United States
[112] Department of Physics, Oklahoma State University, Stillwater, OK, United States
[113] Palacký University, RCPTM, Olomouc, Czech Republic
[114] Center for High Energy Physics, University of Oregon, Eugene, OR, United States
[115] LAL, Univ. Paris-Sud and CNRS/IN2P3, Orsay, France
[116] Graduate School of Science, Osaka University, Osaka, Japan
[117] Department of Physics, University of Oslo, Oslo, Norway
[118] Department of Physics, Oxford University, Oxford, United Kingdom
[119] [(a)] INFN Sezione di Pavia; [(b)] Dipartimento di Fisica, Università di Pavia, Pavia, Italy
[120] Department of Physics, University of Pennsylvania, Philadelphia, PA, United States
[121] Petersburg Nuclear Physics Institute, Gatchina, Russia
[122] [(a)] INFN Sezione di Pisa; [(b)] Dipartimento di Fisica E. Fermi, Università di Pisa, Pisa, Italy
[123] Department of Physics and Astronomy, University of Pittsburgh, Pittsburgh, PA, United States
[124] [(a)] Laboratorio de Instrumentacao e Fisica Experimental de Particulas – LIP, Lisboa, Portugal; [(b)] Departamento de Fisica Teorica y del Cosmos and CAFPE, Universidad de Granada, Granada, Spain
[125] Institute of Physics, Academy of Sciences of the Czech Republic, Praha, Czech Republic
[126] Faculty of Mathematics and Physics, Charles University in Prague, Praha, Czech Republic
[127] Czech Technical University in Prague, Praha, Czech Republic
[128] State Research Center Institute for High Energy Physics, Protvino, Russia
[129] Particle Physics Department, Rutherford Appleton Laboratory, Didcot, United Kingdom
[130] Physics Department, University of Regina, Regina, SK, Canada
[131] Ritsumeikan University, Kusatsu, Shiga, Japan
[132] [(a)] INFN Sezione di Roma I; [(b)] Dipartimento di Fisica, Università La Sapienza, Roma, Italy
[133] [(a)] INFN Sezione di Roma Tor Vergata; [(b)] Dipartimento di Fisica, Università di Roma Tor Vergata, Roma, Italy
[134] [(a)] INFN Sezione di Roma Tre; [(b)] Dipartimento di Fisica, Università Roma Tre, Roma, Italy
[135] [(a)] Faculté des Sciences Ain Chock, Réseau Universitaire de Physique des Hautes Energies – Université Hassan II, Casablanca; [(b)] Centre National de l'Energie des Sciences Techniques Nucleaires, Rabat; [(c)] Faculté des Sciences Semlalia, Université Cadi Ayyad, LPHEA-Marrakech; [(d)] Faculté des Sciences, Université Mohamed Premier and LPTPM, Oujda; [(e)] Faculty of sciences, Mohammed V-Agdal University, Rabat, Morocco
[136] DSM/IRFU (Institut de Recherches sur les Lois Fondamentales de l'Univers), CEA Saclay (Commissariat a l'Energie Atomique), Gif-sur-Yvette, France
[137] Santa Cruz Institute for Particle Physics, University of California Santa Cruz, Santa Cruz CA, United States
[138] Department of Physics, University of Washington, Seattle, WA, United States
[139] Department of Physics and Astronomy, University of Sheffield, Sheffield, United Kingdom
[140] Department of Physics, Shinshu University, Nagano, Japan
[141] Fachbereich Physik, Universität Siegen, Siegen, Germany
[142] Department of Physics, Simon Fraser University, Burnaby, BC, Canada
[143] SLAC National Accelerator Laboratory, Stanford, CA, United States
[144] [(a)] Faculty of Mathematics, Physics & Informatics, Comenius University, Bratislava; [(b)] Department of Subnuclear Physics, Institute of Experimental Physics of the Slovak Academy of Sciences, Kosice, Slovak Republic
[145] [(a)] Department of Physics, University of Johannesburg, Johannesburg; [(b)] School of Physics, University of the Witwatersrand, Johannesburg, South Africa
[146] [(a)] Department of Physics, Stockholm University; [(b)] The Oskar Klein Centre, Stockholm, Sweden
[147] Physics Department, Royal Institute of Technology, Stockholm, Sweden
[148] Departments of Physics & Astronomy and Chemistry, Stony Brook University, Stony Brook, NY, United States
[149] Department of Physics and Astronomy, University of Sussex, Brighton, United Kingdom
[150] School of Physics, University of Sydney, Sydney, Australia

[151] Institute of Physics, Academia Sinica, Taipei, Taiwan
[152] Department of Physics, Technion: Israel Inst. of Technology, Haifa, Israel
[153] Raymond and Beverly Sackler School of Physics and Astronomy, Tel Aviv University, Tel Aviv, Israel
[154] Department of Physics, Aristotle University of Thessaloniki, Thessaloniki, Greece
[155] International Center for Elementary Particle Physics and Department of Physics, The University of Tokyo, Tokyo, Japan
[156] Graduate School of Science and Technology, Tokyo Metropolitan University, Tokyo, Japan
[157] Department of Physics, Tokyo Institute of Technology, Tokyo, Japan
[158] Department of Physics, University of Toronto, Toronto, ON, Canada
[159] [(a)] TRIUMF, Vancouver BC; [(b)] Department of Physics and Astronomy, York University, Toronto, ON, Canada
[160] Institute of Pure and Applied Sciences, University of Tsukuba, 1-1-1 Tennodai, Tsukuba, Ibaraki 305-8571, Japan
[161] Science and Technology Center, Tufts University, Medford, MA, United States
[162] Centro de Investigaciones, Universidad Antonio Narino, Bogota, Colombia
[163] Department of Physics and Astronomy, University of California Irvine, Irvine, CA, United States
[164] [(a)] INFN Gruppo Collegato di Udine; [(b)] ICTP, Trieste; [(c)] Dipartimento di Chimica, Fisica e Ambiente, Università di Udine, Udine, Italy
[165] Department of Physics, University of Illinois, Urbana, IL, United States
[166] Department of Physics and Astronomy, University of Uppsala, Uppsala, Sweden
[167] Instituto de Física Corpuscular (IFIC) and Departamento de Física Atómica, Molecular y Nuclear and Departamento de Ingeniería Electrónica and Instituto de Microelectrónica de Barcelona (IMB-CNM), University of Valencia and CSIC, Valencia, Spain
[168] Department of Physics, University of British Columbia, Vancouver, BC, Canada
[169] Department of Physics and Astronomy, University of Victoria, Victoria, BC, Canada
[170] Department of Physics, University of Warwick, Coventry, United Kingdom
[171] Waseda University, Tokyo, Japan
[172] Department of Particle Physics, The Weizmann Institute of Science, Rehovot, Israel
[173] Department of Physics, University of Wisconsin, Madison, WI, United States
[174] Fakultät für Physik und Astronomie, Julius-Maximilians-Universität, Würzburg, Germany
[175] Fachbereich C Physik, Bergische Universität Wuppertal, Wuppertal, Germany
[176] Department of Physics, Yale University, New Haven, CT, United States
[177] Yerevan Physics Institute, Yerevan, Armenia
[178] Domaine scientifique de la Doua, Centre de Calcul CNRS/IN2P3, Villeurbanne Cedex, France

[a] Also at Laboratorio de Instrumentacao e Fisica Experimental de Particulas – LIP, Lisboa, Portugal.
[b] Also at Faculdade de Ciencias and CFNUL, Universidade de Lisboa, Lisboa, Portugal.
[c] Also at Particle Physics Department, Rutherford Appleton Laboratory, Didcot, United Kingdom.
[d] Also at TRIUMF, Vancouver, BC, Canada.
[e] Also at Department of Physics, California State University, Fresno, CA, United States.
[f] Also at Novosibirsk State University, Novosibirsk, Russia.
[g] Also at Fermilab, Batavia, IL, United States.
[h] Also at Department of Physics, University of Coimbra, Coimbra, Portugal.
[i] Also at Università di Napoli Parthenope, Napoli, Italy.
[j] Also at Institute of Particle Physics (IPP), Canada.
[k] Also at Department of Physics, Middle East Technical University, Ankara, Turkey.
[l] Also at Louisiana Tech University, Ruston, LA, United States.
[m] Also at Department of Physics and Astronomy, University College London, London, United Kingdom.
[n] Also at Group of Particle Physics, University of Montreal, Montreal, QC, Canada.
[o] Also at Department of Physics, University of Cape Town, Cape Town, South Africa.
[p] Also at Institute of Physics, Azerbaijan Academy of Sciences, Baku, Azerbaijan.
[q] Also at Institut für Experimentalphysik, Universität Hamburg, Hamburg, Germany.
[r] Also at Manhattan College, New York, NY, United States.
[s] Also at School of Physics, Shandong University, Shandong, China.
[t] Also at CPPM, Aix-Marseille Université and CNRS/IN2P3, Marseille, France.
[u] Also at School of Physics and Engineering, Sun Yat-sen University, Guanzhou, China.
[v] Also at Academia Sinica Grid Computing, Institute of Physics, Academia Sinica, Taipei, Taiwan.
[w] Also at Dipartimento di Fisica, Università La Sapienza, Roma, Italy.
[x] Also at DSM/IRFU (Institut de Recherches sur les Lois Fondamentales de l'Univers), CEA Saclay (Commissariat a l'Energie Atomique), Gif-sur-Yvette, France.
[y] Also at Section de Physique, Université de Genève, Geneva, Switzerland.
[z] Also at Departamento de Fisica, Universidade de Minho, Braga, Portugal.
[aa] Also at Department of Physics and Astronomy, University of South Carolina, Columbia, SC, United States.
[ab] Also at Institute for Particle and Nuclear Physics, Wigner Research Centre for Physics, Budapest, Hungary.
[ac] Also at California Institute of Technology, Pasadena, CA, United States.
[ad] Also at Institute of Physics, Jagiellonian University, Krakow, Poland.
[ae] Also at LAL, Univ. Paris-Sud and CNRS/IN2P3, Orsay, France.
[af] Also at Department of Physics and Astronomy, University of Sheffield, Sheffield, United Kingdom.
[ag] Also at Department of Physics, Oxford University, Oxford, United Kingdom.
[ah] Also at Institute of Physics, Academia Sinica, Taipei, Taiwan.
[ai] Also at Department of Physics, The University of Michigan, Ann Arbor, MI, United States.
[*] Deceased.

Published for SISSA by Springer

Received: February 22, 2012
Revised: March 29, 2012
Accepted: April 16, 2012
Published: May 14, 2012

JHEP05(2012)059

Measurement of the cross section for top-quark pair production in pp collisions at $\sqrt{s} = 7$ TeV with the ATLAS detector using final states with two high-p_{T} leptons

The ATLAS collaboration

Abstract: A measurement is reported of the production cross section of top-quark pairs ($t\bar{t}$) in proton-proton collisions at a center-of-mass energy of 7 TeV recorded with the ATLAS detector at the LHC. Candidate events have a signature consistent with containing two isolated leptons, large missing transverse momentum, and at least two jets. Using a data sample corresponding to an integrated luminosity of $0.70\,\mathrm{fb}^{-1}$, a $t\bar{t}$ production cross section $\sigma_{t\bar{t}} = 176 \pm 5(\mathrm{stat.})^{+14}_{-11}(\mathrm{syst.}) \pm 8(\mathrm{lum.})$ pb is measured for an assumed top-quark mass of $m_t = 172.5$ GeV. This measurement is in good agreement with Standard Model predictions.

Keywords: Hadron-Hadron Scattering

Open Access, Copyright CERN,
for the benefit of the ATLAS collaboration

doi:10.1007/JHEP05(2012)059

Contents

1 Introduction 1

2 Detector and data sample 2

3 Simulated samples 3

4 Object selection 3

5 Event selection 5

6 Background evaluation 6

7 Systematic uncertainties 8

8 Cross-section measurement 10

The ATLAS collaboration 16

1 Introduction

As the heaviest known elementary particle, the top quark is a particularly interesting probe of the Standard Model (SM). The measurement of the $t\bar{t}$ production cross section in different decay modes is a sensitive test of perturbative QCD and the SM description of top-quark decay. The production cross section in proton-proton (pp) collisions at a center-of-mass energy $\sqrt{s} = 7$ TeV is calculated to be 165^{+11}_{-16} pb at approximate next-to-next-to-leading-order (NNLO) [1, 2], and the top quark is predicted to decay nearly 100% of the time to a W boson and a b quark. A measured cross section that differs from the SM prediction can be a sign of new physics. Furthermore, $t\bar{t}$ production is an important background in many searches for physics beyond the SM, and in searches for the SM Higgs boson.

The $t\bar{t}$ event topologies are determined by the decays of the two W bosons. In increasing order of $t\bar{t}$ branching fraction: dilepton final states occur when both W bosons decay to a charged lepton and a neutrino, 'lepton plus jets' final states when only one W boson decays leptonically while the other decays to a pair of quarks, and all-hadronic final states when both W bosons decay to pairs of quarks.

Top-quark production in dilepton final states has been studied using proton-antiproton collisions at $\sqrt{s} = 1.96$ TeV [3, 4] and Large Hadron Collider (LHC) measurements of the production cross section in proton-proton collisions at $\sqrt{s} = 7$ TeV in the same final state have recently been reported [5, 6]. A measurement is presented of the $t\bar{t}$ production cross

JHEP05(2012)059

section using the dilepton channel, characterized by two opposite-sign leptons, unbalanced transverse momentum indicating the presence of neutrinos from the W-boson decays, and two b-quark jets. This result uses twenty times more data than the previous ATLAS measurement in the same final state, reported in ref. [6].

The $t\bar{t}$ dilepton final states can be selected with a good signal-to-background ratio using simple kinematic requirements. With the additional requirement of the presence of a jet consistent with a b quark ('b-tag'), the signal-to-background ratio can be further improved. Cross-section measurements with and without the b-tag requirement are reported here. Leptons are either well-identified electron or muon candidates that are selected using the full detector or, to reduce losses from lepton identification inefficiencies, isolated tracks. The well-identified electrons or muons are called 'identified leptons', and the isolated tracks are referred to as 'track leptons'. The term 'lepton' is used to refer to identified leptons and track leptons collectively. Events with one identified lepton and one track lepton are called 'lepton+track' events. Each dilepton channel is exclusive, i.e. has no overlap with the other channels. Channels with tau leptons are not explicitly reconstructed, but reconstructed leptons can arise from leptonic tau decays and a track lepton can arise from hadronic tau decay modes as well. The analysis with the b-tag requirement uses only identified leptons.

The measured cross section takes into account the $t\bar{t}$ signal acceptance and the expected background contributions from Z/γ^*+jets, single top quarks, WW, WZ, and ZZ events, and events with misidentified leptons (primarily W+jets events). Background contributions from $Z/\gamma^* \to ee$+jets, $Z/\gamma^* \to \mu\mu$+jets and events with misidentified leptons are evaluated directly from the data. All other background contributions are evaluated using Monte Carlo (MC) simulation samples.

2 Detector and data sample

The ATLAS detector [7] at the LHC covers nearly the entire solid angle around the collision point. It consists of an inner tracking detector (ID) comprising a silicon pixel detector, a silicon microstrip detector (SCT), and a transition radiation tracker. The ID is surrounded by a thin superconducting solenoid providing a 2 T magnetic field, and by liquid-argon electromagnetic sampling calorimeters (LAr) with high granularity. An iron-scintillator tile calorimeter provides hadronic energy measurements in the central pseudorapidity[1] range ($|\eta| < 1.7$). The end-cap and forward regions are instrumented with LAr calorimetry for both electromagnetic (EM) and hadronic energy measurements up to $|\eta| < 4.9$. The calorimeter system is surrounded by a muon spectrometer incorporating three superconducting toroid magnet assemblies, with bending power between 2.0 and 7.5 Tm.

A three-level trigger system is used to collect data. The first-level trigger is implemented in hardware and uses a subset of the detector information to reduce the rate to at

[1] In the right-handed ATLAS coordinate system, the pseudorapidity η is defined as $\eta = -\ln[\tan(\theta/2)]$, where the polar angle θ is measured with respect to the LHC beamline. The azimuthal angle ϕ is measured with respect to the x-axis, which points towards the centre of the LHC ring. The y-axis points up. Transverse momentum and energy are defined as $p_{\mathrm{T}} = p \sin\theta$ and $E_{\mathrm{T}} = E \sin\theta$, respectively.

JHEP05(2012)059

most 75 kHz. This is followed by two software-based trigger levels that together reduce the event rate to $\sim$ 300 Hz.

The analysis uses collision data with a center-of-mass energy of $\sqrt{s} = 7$ TeV recorded in 2011, with an integrated luminosity of $0.70 \pm 0.03\,\mathrm{fb}^{-1}$ [8, 9].

3 Simulated samples

Monte Carlo simulation samples are used to calculate the $t\bar{t}$ acceptance and to evaluate the background contributions from single top quarks, WW, WZ, and ZZ events, and $Z/\gamma^* \to \tau\tau$+jets. All MC samples are processed with the GEANT4 [10] simulation of the ATLAS detector [11] and events are passed through the same analysis chain as the data.

The generation of $t\bar{t}$ and single top-quark events uses the MC@NLO generator [12],[2] [13, 14] with the CTEQ6.6 [15] parton distribution function (PDF) set and a top-quark mass of 172.5 GeV. Expected $t\bar{t}$ yields are calculated with a cross section normalized to the prediction of Hathor[16], which employs an NNLO perturbative QCD calculation. Single top-quark production with MC@NLO includes the s, t and Wt channels and the diagram-removal scheme [17] is used to reduce overlap with the $t\bar{t}$ final state.

Drell-Yan events (Z/γ^*+jets) are modeled with the Alpgen generator, using the MLM matching scheme [18] and the CTEQ6L1 [19] PDF set. The Z/γ^*+jets samples, including both light and heavy flavor jets, are normalized to NNLO with a K-factor of 1.25. In the $Z/\gamma^* \to ee$ and $\mu\mu$ decay channels, the background from Z/γ^*+jets is evaluated using a data-driven technique that normalizes the MC expectation to the data observation near the Z pole. Background contributions from the W+jets final states come primarily from events where the W boson decays leptonically and the second lepton candidate is a misidentified jet or a heavy-flavor decay. Backgrounds from W+jets events are evaluated from the data.

All MC simulated events are hadronized using the Herwig shower model [20, 21] supplemented by the Jimmy underlying event model [22]. Both hadronization programs are tuned to ATLAS data using the ATLAS MC10 tune [23]. Diboson events are modeled using the Alpgen generator normalized with K-factors of 1.26 (WW), 1.28 (WZ) and 1.30 (ZZ) to match the total cross section from NLO QCD predictions using calculations with the MCFM program [24].

All Monte Carlo samples are generated taking into account that multiple pp interactions can occur in the same LHC bunch crossing within a given event ('pile-up'). The average number of interactions per crossing is 5.6 in this data set. The MC events are re-weighted so that the distribution of interactions per crossing in the MC matches that observed in the data.

4 Object selection

Leptons are required to be isolated and have high transverse momentum, p_{T}, consistent with originating from W-boson decay, with p_{T} thresholds chosen to ensure events are triggered with high efficiency.

[2] We use Version 3.41.

JHEP05(2012)059

Electron candidates are reconstructed from energy deposits (clusters) in the EM calorimeter, which are then associated to reconstructed tracks of charged particles in the inner detector. Stringent quality requirements on the conditions of the EM calorimeter at the time of data taking are applied to ensure a well measured reconstructed energy. A 'tight' selection [25] using calorimeter, tracking and combined variables, is employed to provide good separation between the signal electrons and background. Electron candidates are additionally required to have $p_{\mathrm{T}} > 25$ GeV and $|\eta_{cl}| < 2.47$, excluding electrons from the transition region between the barrel and endcap calorimeters defined by $1.37 < |\eta_{cl}| < 1.52$. The variable η_{cl} is the pseudorapidity of the energy cluster associated with the candidate.

Muon candidate reconstruction is begun by searching for track segments in layers of the muon chambers. These segments are combined starting from the outermost layer, fitted to account for material effects, and matched with tracks found in the inner detector. The candidates are refitted using the complete track information from both detector systems, and required to satisfy $p_{\mathrm{T}} > 20$ GeV and $|\eta| < 2.5$.

Lepton isolation requirements reduce backgrounds from misidentified jets and suppress the selection of leptons from heavy-flavor decays. For electron candidates, the transverse energy (E_{T}) deposited in the calorimeter not associated to the electron is summed in a cone of radius $\Delta R = 0.2$, where $\Delta R \equiv \sqrt{\Delta\eta^2 + \Delta\phi^2}$, around the electron and is required to be less than 3.5 GeV. For muon candidates, the isolation requirement is based on both calorimeter and track information. The track isolation requirement is based on the sum of the transverse momenta of tracks with $p_{\mathrm{T}} > 1\,\mathrm{GeV}$ in a cone $\Delta R = 0.3$ centered on the muon candidate, while the calorimeter isolation requirement is based on the sum of transverse energy in the same cone. Both the track and calorimeter sums are required to be less than 4 GeV. Additionally, muon candidates must have a distance $\Delta R > 0.4$ from any jet with $p_{\mathrm{T}} > 20\,\mathrm{GeV}$, further suppressing muon candidates from heavy flavor decays. Muon candidates arising from cosmic rays are rejected by removing candidate pairs that are back-to-back in the $r - \phi$ plane and with transverse impact parameters relative to the beam axis $|d_0| > 0.5$ mm.

Track-lepton (TL) candidates are defined by an ID track with $p_{\mathrm{T}} > 25$ GeV and a series of quality cuts optimized for high efficiency and a low rate of misidentification. The track must have at least six SCT hits and at least one hit in the innermost pixel layer. It also must have $|d_0| < 0.2$ mm and the uncertainty on the momentum measurement must be less than 20%. The track has to be isolated from other nearby tracks, following the track isolation defined above, in this case using tracks with $p_{\mathrm{T}} > 0.5$ GeV. The summed momentum cut is set to 2 GeV.

Jets are reconstructed with the anti-k$_t$ algorithm [26] with a radius parameter $R = 0.4$, starting from energy clusters in the calorimeter reconstructed using the scale established for electromagnetic objects. These jets are then calibrated to the hadronic energy scale using p_{T} and η dependent correction factors [27]. Jets are removed if they are within $\Delta R = 0.2$ of a well-identified electron candidate or a TL. The jets used in the analysis are required to have $p_{\mathrm{T}} > 25\,\mathrm{GeV}$ and $|\eta| < 2.5$.

Jets are identified as b-quark candidates ('b-tagged') by an algorithm that forms a likelihood ratio of b- and light-quark jet hypotheses using the following discriminating

JHEP05(2012)059

variables: the signed impact parameter significance of well measured tracks associated with a given jet, the decay length significance associated with a reconstructed secondary vertex, the invariant mass of all tracks associated to the secondary vertex, the ratio of the sum of the energies of the tracks associated with the secondary vertex to the sum of the energies of all tracks in the jet assuming a pion hypothesis, and the number of two-track vertices that can be formed at the secondary vertex [28]. The cut on the combined likelihood ratio has been chosen such that a b-tagging efficiency of $\approx 80\%$ per b-jet in $t\bar{t}$ candidate events is achieved.

The missing transverse momentum is formed from the negative vector sum of transverse momenta of all jets with $p_{\mathrm{T}} > 20\,\mathrm{GeV}$ and $|\eta| < 4.5$ [29]. The contribution from cells associated with electron candidates is replaced by the candidates' calibrated transverse energy. The contribution from all muon candidates and calorimeter clusters (including those not belonging to a reconstructed object) is also included. The symbol $E_{\mathrm{T}}^{\mathrm{miss}}$ is used to denote the magnitude of the missing transverse momentum.

5 Event selection

The analysis requires collision data selected by an inclusive single electron or muon trigger with offline-reconstructed candidates satisfying $p_{\mathrm{T}} > 25$ GeV for electrons, and $p_{\mathrm{T}} > 20$ GeV for muons, to ensure a constant trigger efficiency. To ensure that the event was triggered by the lepton candidates used in the analysis, one of the identified leptons and the triggered lepton are required to match within $\Delta R < 0.15$.

Events are required to have a primary interaction vertex with at least five tracks with $p_{\mathrm{T}} > 400$ MeV. The event is discarded if any jet with $p_{\mathrm{T}} > 20\,\mathrm{GeV}$ fails quality cuts designed to reject jets arising from calorimeter noise or activity inconsistent with the bunch-crossing time [27]. If an electron candidate and a muon candidate share a track, the event is also discarded.

The selection of events in the signal region consists of a series of kinematic requirements on the reconstructed objects. The requirements on $E_{\mathrm{T}}^{\mathrm{miss}}$, the lepton-lepton invariant mass ($m_{\ell\ell}$), and the scalar p_{T} sum of all selected jets and leptons (H_{T}) are optimized to minimize the expected total uncertainty on the cross-section measurement. The resulting event selection, referred to as the 'non-b-tag' selection, is listed below.

- Events must have exactly two oppositely-charged identified-lepton candidates (ee, $\mu\mu$, $e\mu$), satisfying the selection criteria of section 4, *or* if only one identified-lepton candidate is found, the event is retained if a track-lepton candidate is present, with opposite charge to the identified lepton, forming a lepton+track event (eTL or μTL).

- Events must have at least two jets with $p_{\mathrm{T}} > 25$ GeV and $|\eta| < 2.5$.

- Events in the ee, $\mu\mu$ eTL and μTL channels are required to have $m_{\ell\ell} > 15$ GeV in order to reject backgrounds from vector-meson decays. The requirement also helps to suppress backgrounds in these channels from b-quark production.

JHEP05(2012)059

- Events in the ee and $\mu\mu$ channels must satisfy $E_{\mathrm{T}}^{\mathrm{miss}} > 60$ GeV and $|m_{\ell\ell} - m_Z| > 10$ GeV, to suppress backgrounds from Z/γ^*+jets and multijets.
- Events in the $e\mu$ channel are required to satisfy $H_{\mathrm{T}} > 130$ GeV. No $E_{\mathrm{T}}^{\mathrm{miss}}$ or $m_{\ell\ell}$ cuts are applied.
- The lepton+track event candidates must have $E_{\mathrm{T}}^{\mathrm{miss}} > 45$ GeV, H_{T} (including the track lepton) > 150 GeV, and $|m_{\ell\ell} - m_Z| > 10$ GeV.

A parallel selection with the additional requirement of at least one b-tagged jet is made. Because of the enhanced background rejection afforded by the b-tag requirement, the selection is further optimized, resulting in an $E_{\mathrm{T}}^{\mathrm{miss}}$ requirement for ee and $\mu\mu$ events that is relaxed to $E_{\mathrm{T}}^{\mathrm{miss}} > 40$ GeV, while the H_{T} requirement for $e\mu$ events remains the same as for the non-b-tag selection, i.e. $H_{\mathrm{T}} > 130$ GeV. We refer to the analysis that requires at least one b-tagged jet as the 'b-tag analysis', and the events selected therein as the 'b-tagged sample'. The subset of the b-tagged sample with 40 GeV $< E_{\mathrm{T}}^{\mathrm{miss}} <$ 60 GeV is referred to as the 'exclusive b-tagged sample' and has no overlap with the non-b-tag sample.

The acceptance times the branching fraction of $t\bar{t}$ to dileptons, for the selection described above, is 0.96% for the $ee + \mu\mu + e\mu$ channels without b-tagging, 0.11% for the exclusive b-tagged sample, and 0.19% for eTL + μTL channels.

6 Background evaluation

The $t\bar{t}$ event selection rejects Z/γ^*+jets events with ee and $\mu\mu$ invariant mass below 15 GeV, or within 10 GeV of the Z-boson mass. However, Z/γ^*+jets events with ee or $\mu\mu$ invariant mass outside of these regions can enter the signal sample when there is large $E_{\mathrm{T}}^{\mathrm{miss}}$, typically from mismeasurement. These events are difficult to properly model in simulations due to uncertainties on the non-Gaussian tails of the $E_{\mathrm{T}}^{\mathrm{miss}}$ distribution, on the cross section for Z boson production with multiple jets, and on the lepton energy resolution.

To evaluate the Z/γ^*+jets background in dielectron and dimuon events ($Z \to \tau\tau$ is considered below), the MC prediction for the number of events in the signal region is normalized to the data using the number of Z/γ^*+jets events measured in a control region [6]. The control region is formed by events with the same jet requirements as the signal region, but with $m_{\ell\ell}$ within 10 GeV of the Z-boson mass, and a $E_{\mathrm{T}}^{\mathrm{miss}}$ cut of $E_{\mathrm{T}}^{\mathrm{miss}} > 45$ GeV for the lepton+track candidates and $E_{\mathrm{T}}^{\mathrm{miss}} > 30$ GeV for the others. Contamination in the control region from other physics processes (signal and other background processes considered for the analysis) is subtracted according to MC predictions. The ratio of data events to MC expectation in the control region provides a scale factor that is used to correct the MC prediction for Z/γ^*+jets events in the signal region.

Other backgrounds mainly come from W+jets, $t\bar{t}$ lepton+jets, and single top-quark production with fake leptons. The term 'fake lepton' is used to refer to both misidentified and non-prompt lepton candidates, the latter category arising from hadron decays in

JHEP05(2012)059

flight. The yield of events with fake identified leptons is evaluated from the data using a matrix method [30]. In addition to the standard lepton selection requirements, a selection with a looser isolation requirement is defined. Dilepton events are selected using the loose isolation requirement and events are categorized according to whether each lepton passes the standard selection or the loose selection but not the standard selection. There are four such categories for the two leptons: loose-loose, loose-standard, standard-loose, and standard-standard. Each of the four categories is related to the number of events with two 'real' (prompt) leptons, two fake leptons, or one of each, through a set of linear equations with coefficients given by the products of probabilities for real or fake lepton satisfying the loose selection to also satisfy the standard selection. These linear expressions form a matrix that is inverted in order to extract the real and fake lepton content of the observed dilepton event sample. The probability for real leptons is measured as a function of jet multiplicity using data samples of $Z \to ee$ and $Z \to \mu\mu$ events. The corresponding probability for fake leptons is measured in a data sample dominated by dijet production, with events containing one lepton candidate passing the looser isolation cuts and having $E_{\mathrm{T}}^{\mathrm{miss}} < 20$ GeV. Contributions from real leptons due to W+jets final states are subtracted using simulated events.

For lepton+track events the largest background is from events with fake leptons, dominated by fake track leptons. The probability of a jet being reconstructed as a track lepton is determined from a γ+jets data sample selected with photon triggers. The fake probability is applied to a second sample enriched in W+jets events with exactly one identified lepton and no track leptons, but using the same kinematic cuts as for the signal sample. In this second sample the fake probabilities are summed for each jet in each event and the fake track-lepton contribution is calculated as a function of the number of jets.

The contributions from other electroweak background processes with two real leptons, such as single top quarks, $Z \to \tau\tau$, WW, ZZ and WZ production are determined from Monte Carlo simulations. The expected numbers of background events are given in table 1. The absence of Z/γ^*+jets background in the $e\mu$ channel, coupled with the larger branching fraction for the $e\mu$ signal, allows relatively loose selection criteria to be used in this channel.

The background contributions for the b-tag analysis are determined using the same techniques described above, with the additional requirement of a b-tagged jet.

The modeled acceptances, efficiencies and data-driven background evaluation methods are validated by comparing predictions from Monte Carlo simulations with data in control regions with kinematics similar to the signal region but dominated by backgrounds. In particular, the $E_{\mathrm{T}}^{\mathrm{miss}}$, $m_{\ell\ell}$ and jet multiplicity distributions are studied in a sample of Z-boson candidates, defined by requiring $|m_{\ell\ell} - m_Z| < 10$ GeV and $E_{\mathrm{T}}^{\mathrm{miss}} < 60$ GeV. The predictions from MC simulations in the control regions are in reasonable agreement with data, although small discrepancies exist in regions that do not affect the $t\bar{t}$ cross-section measurement.

JHEP05(2012)059

	ee	$\mu\mu$	$e\mu$	eTL	μTL	b-tag ee	b-tag $\mu\mu$	b-tag $e\mu$
Z/γ^*+ jets	$4.0^{+2.5}_{-1.2}$	$14.4^{+5.4}_{-4.2}$	-	$24.3^{+10.7}_{-9.4}$	$22.0^{+5.3}_{-5.8}$	$9.8^{+1.7}_{-1.3}$	$20.3^{+1.8}_{-2.8}$	–
$Z/\gamma^* \to \tau\tau$+jets	4.9 ± 2.6	11.0 ± 5.0	43 ± 16	$17.0^{+8.4}_{-7.6}$	25 ± 11	$1.8^{+1.1}_{-1.2}$	$7.6^{+3.3}_{-3.6}$	$9.5^{+4.2}_{-3.9}$
Fake leptons	4.0 ± 5.0	6.3 ± 4.1	44 ± 24	74 ± 15	85 ± 17	7.5 ± 6.5	4.9 ± 3.1	20 ± 13
Single top quark	$6.4^{+1.2}_{-1.1}$	$16.0^{+1.9}_{-2.2}$	41.1 ± 5.5	$5.7^{+1.0}_{-0.9}$	$6.3^{+0.8}_{-1.1}$	$7.3^{+1.3}_{-1.1}$	$16.2^{+2.2}_{-2.3}$	$33.5^{+4.8}_{-4.7}$
Diboson	5.9 ± 1.1	$8.7^{+1.2}_{-1.5}$	32.9 ± 4.9	$5.9^{+0.9}_{-0.8}$	$4.8^{+0.6}_{-0.7}$	2.2 ± 0.7	$2.6^{+0.9}_{-0.6}$	$8.8^{+1.7}_{-1.6}$
Total background	25.2 ± 6.4	56.5 ± 9.4	161 ± 34	126^{+20}_{-19}	142 ± 21	28.6 ± 6.9	$51.6^{+5.6}_{-5.9}$	71.6 ± 14.1
Predicted $t\bar{t}$	124 ± 17	241^{+15}_{-18}	746 ± 42	112^{+16}_{-18}	110^{+17}_{-16}	159^{+17}_{-21}	304^{+26}_{-35}	675^{+57}_{-75}
Total	149 ± 18	298^{+17}_{-20}	907 ± 54	239 ± 26	253 ± 27	188^{+18}_{-22}	356^{+27}_{-35}	746^{+59}_{-76}
Observed	165	301	963	236	255	201	365	834

Table 1. Breakdown of the expected $t\bar{t}$ signal and background events in the signal region compared to the observed event yields, for each of the dilepton channels. All systematic uncertainties are included, and correlations between different background sources are taken into account, when calculating the total background uncertainty. The largest contribution to the line labeled 'Fake leptons' comes from W+jets events.

7 Systematic uncertainties

A summary of the systematic uncertainties on the measured $t\bar{t}$ production cross section is given in table 2.

Lepton trigger efficiencies, and reconstruction and selection efficiencies for identified leptons and track leptons, are assessed using $Z \to ee$ and $Z \to \mu\mu$ events in the same data sample as used for the $t\bar{t}$ analyses. Scale factors are evaluated by comparing these efficiencies with those determined with simulated Z-boson events. The scale factors are applied to MC samples when calculating acceptances to account for any differences between predicted and observed efficiencies. Systematic uncertainties on these scale factors are evaluated by varying the selection of events used in the efficiency measurements and by checking the stability of the measurements over the course of the data-taking period.

The modeling of lepton momentum scale and resolution is studied using reconstructed dilepton invariant mass distributions of Z/γ^* candidate events, and the simulation is adjusted to match the data. Uncertainties in the scale and resolution are used to evaluate the systematic uncertainty due to these corrections. The acceptance uncertainty from the lepton modeling is dominated mostly by the electron selection efficiency uncertainty.

The jet energy scale (JES) and its uncertainty are derived by combining information from test-beam data, LHC collision data and simulation [27]. For jets within the acceptance, the JES uncertainty varies in the range 4–8% as a function of jet p_{T} and η. This uncertainty is higher than in the previous result [6] because of the additional uncertainty due to multiple pp interactions at high instantaneous luminosity. The jet energy resolution and jet reconstruction/identification efficiency measured in data and in simulation are in good agreement. The statistical uncertainties on the comparisons, 10% and 1–2% for the energy resolution and the efficiency, respectively, are taken as systematic uncertainties associated with these effects. The effect on the acceptance is dominated by the JES uncertainty.

JHEP05(2012)059

The systematic uncertainty on the efficiency of the b-tagging algorithm has been estimated to be 6% for b-quark jets, based on b-tagging calibration studies using inclusive lepton and multijet final states. The uncertainties on the tagging rates of jets from light and charm quarks are larger, but are not a significant source of uncertainty due to the intrinsically high signal-to-background ratios in the dilepton final states. The acceptance uncertainty due to b-tagging is about 3% for all three channels.

The uncertainty in the kinematic distributions of the $t\bar{t}$ signal events gives rise to systematic uncertainties in the signal acceptance, with contributions from the choice of generator, the modeling of initial- and final-state radiation (ISR/FSR) and the PDFs. The generator and parton-showering uncertainty (collectively labeled 'Generator' in table 2) are evaluated by comparing the MC@NLO predictions with those of Powheg [31–33] interfaced to either Herwig or Pythia. The uncertainty due to ISR/FSR is evaluated using the AcerMC generator [34] interfaced to the Pythia shower model, and by varying the parameters controlling ISR and FSR in a range consistent with those used in the Perugia Hard/Soft tune variations [35]. Finally, the PDF uncertainty is evaluated using a range of current PDF sets [19]. The dominant uncertainties in this category of systematics are the modeling of ISR/FSR and the generator choice.

The overall normalization uncertainties on the backgrounds from single top quark and diboson production are taken to be 8.6% [36] and 5% [37], respectively. The systematic uncertainties from the background evaluations derived from the data include the statistical uncertainties in these methods as well as the systematic uncertainties arising from lepton and jet identification and reconstruction, and the MC estimates that are used. An uncertainty on the data-driven Z/γ^*+jets evaluation, based on the expected $E_{\mathrm{T}}^{\mathrm{miss}}$ resolution in these events, is included by varying the $E_{\mathrm{T}}^{\mathrm{miss}}$ cut in the control region by ± 5 GeV for ee and $\mu\mu$ events, and ± 10 GeV in lepton+track events where the $E_{\mathrm{T}}^{\mathrm{miss}}$ resolution is poorer. The systematic uncertainty on the fake identified lepton background prediction is 50%, as measured using control regions with different flavor composition and photon conversion rates, as determined by Monte Carlo studies. A 20% systematic uncertainty is set on the prediction of the fake track-lepton background, derived from a comparison of predicted and observed fake track leptons in control regions defined as opposite-sign events with zero or one jet without an H_{T} cut, and same-sign events with more than one jet. The uncertainty on the measured integrated luminosity of the dataset is 3.7% [9].

Table 2 lists the contributions to the cross-section measurement of each of the systematic uncertainties considered, in percent, with the non-b-tag and the exclusive b-tag analyses combined in the ee and $\mu\mu$ columns. Only non-b-tag events are used in the $e\mu$ channel. The relatively large 'Generator' uncertainty for ee events is partly a result of the limited size of the MC data set. In the eTL and μTL columns the 'MC statistics' uncertainty is larger than in the ee, $\mu\mu$, and $e\mu$ case because the number of events available is reduced by the removal of events with two identified leptons. The combined uncertainty comes from the profile likelihood technique used to determine the cross section [6], and takes into account all correlations. The statistical uncertainty is determined by fixing all systematic uncertainties at their best-fit values in the likelihood function.

JHEP05(2012)059

Uncertainties $\Delta\sigma/\sigma$[%]	ee	$\mu\mu$	$e\mu$	eTL	μTL	Combined
Data statistics	±8.1	±6.1	±3.9	±14.1	±14.2	±2.9
Luminosity	+4.4/-3.8	+4.4/-3.9	±4.2	+5.1/-4.2	+5.4/-4.4	±4.3
MC statistics	±1.6	±1.2	±0.8	±5.5	±4.6	+0.7/-0.6
Lepton uncertainties	+6.2/-5.4	+2.9/-1.3	±3.1	±4.1	+1.8/-1.6	+2.6/-2.2
Track leptons	—	—	—	±4.4	±1.9	+0.3/-0.2
Jet/$E_{\mathrm{T}}^{\mathrm{miss}}$ uncertainties	+5.7/-5.7	+6.4/-3.5	+4.7/-3.2	+14.8/-6.4	±13.1	+4.4/-3.4
b-tagging uncertainties	+1.2/-1.0	±0.7	—	—	—	+0.4/-0.0
Z/γ^*+ jets evaluation	±0.4	+0.5/-0.0	—	±6.2	+2.4/-2.7	+0.3/-0.2
Fake lepton evaluation	±3.3	1.5/-1.3	±3.0	±13.7	±15.1	±1.7
Generator	+12/-11	+4.5/-4.3	+4.8/-4.5	+14/-11	+14/-13	+5.1/-4.9
All syst.(except lumi.)	+16.4/-14.4	+8.8/-6.4	+8.2/-6.8	+27.9/-20.7	+26.5/-23.7	+8.0/-6.5
Stat. + syst.	+18.9/-16.9	+11.6/-9.5	+10.1/-8.8	+31.8/-25.2	+30.7/-27.8	+9.6/-8.2

Table 2. Overview of the $t\bar{t}$ cross-section uncertainties.

8 Cross-section measurement

The expected and measured numbers of events in the signal region, after applying all selection cuts for each of the individual dilepton channels, are shown in table 1. A total of 1920 candidate events are observed for the analysis without b-tagging, and a total of 1400 candidate events are found for the b-tag analysis. There are 1221 events in common between the two selections, and 179 exclusive b-tagged events.

In figure 1 the number of selected jets and the expectation for $0.70\,\mathrm{fb}^{-1}$ are shown for the non-b-tag analysis with the five channels combined, and for the b-tag analysis with the three channels combined. In the non-b-tag case, all requirements except the jet multiplicity selection are applied, and in the b-tag case all requirements except the b-tag requirement are applied. The $E_{\mathrm{T}}^{\mathrm{miss}}$ distributions for the combination of the five non-b-tag and three b-tagged channels are shown in figure 2. All requirements except $E_{\mathrm{T}}^{\mathrm{miss}}$ are applied. The dominant backgrounds are Z/γ^*+jets and W+jets production with a fake lepton and, for the b-tag analysis, single-top events.

The cross-section results are obtained with a profile likelihood technique, as described in ref. [6]. The branching fraction for $t \to Wb$ is taken to be 100% and the acceptance is calculated for a top mass of 172.5 GeV.

The top-quark pair production cross section measured by combining the seven channels, the non-b-tagged ee, $\mu\mu$, $e\mu$, eTL and μTL and the exclusive b-tagged ee and $\mu\mu$, is

$$\sigma_{t\bar{t}} = 176 \pm 5(\mathrm{stat.})^{+14}_{-11}(\mathrm{syst.}) \pm 8(\mathrm{lumi.})\ \mathrm{pb}.$$

Figure 3 summarizes the cross sections for the individual channels, and the combination of the non-b-tag and the exclusive b-tagged data sets.

The measured cross section is in good agreement with a similar measurement made with 2010 data by the CMS collaboration [5], with an ATLAS measurement in the dilepton channel with earlier data [6], and with the SM prediction of 165^{+11}_{-16} pb. Compared to the earlier ATLAS measurement in the dilepton channel, the statistical uncertainty of the measurement has been reduced by a factor of four with the addition of more data, and a small reduction in the systematic uncertainty, which now dominates, has been achieved.

JHEP05(2012)059

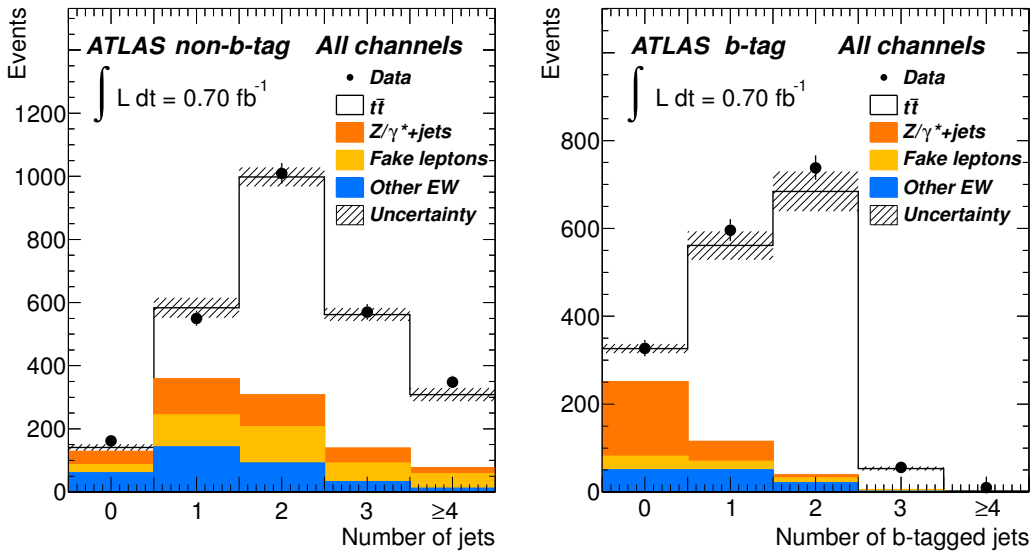

(a) (b)

Figure 1. (a) Jet multiplicity distribution for ee+$\mu\mu$+$e\mu$+eTL+μTL events without a b-tagging requirement. (b) Multiplicity distribution of b-tagged jets in the ee+$\mu\mu$+$e\mu$ channels. Contributions from diboson and single top-quark events are summarized as 'Other EW'. The events in (b) are not a simple subset of those in (a) because the event selections for the b-tag and non-b-tag analyses differ. Uncertainties shown are statistical and systematic combined. The distributions are shown as stacked histograms.

Acknowledgments

We thank CERN for the very successful operation of the LHC, as well as the support staff from our institutions without whom ATLAS could not be operated efficiently.

We acknowledge the support of ANPCyT, Argentina; YerPhI, Armenia; ARC, Australia; BMWF, Austria; ANAS, Azerbaijan; SSTC, Belarus; CNPq and FAPESP, Brazil; NSERC, NRC and CFI, Canada; CERN; CONICYT, Chile; CAS, MOST and NSFC, China; COLCIENCIAS, Colombia; MSMT CR, MPO CR and VSC CR, Czech Republic; DNRF, DNSRC and Lundbeck Foundation, Denmark; EPLANET and ERC, European Union; IN2P3-CNRS, CEA-DSM/IRFU, France; GNAS, Georgia; BMBF, DFG, HGF, MPG and AvH Foundation, Germany; GSRT, Greece; ISF, MINERVA, GIF, DIP and Benoziyo Center, Israel; INFN, Italy; MEXT and JSPS, Japan; CNRST, Morocco; FOM and NWO, Netherlands; RCN, Norway; MNiSW, Poland; GRICES and FCT, Portugal; MERYS (MECTS), Romania; MES of Russia and ROSATOM, Russian Federation; JINR; MSTD, Serbia; MSSR, Slovakia; ARRS and MVZT, Slovenia; DST/NRF, South Africa; MICINN, Spain; SRC and Wallenberg Foundation, Sweden; SER, SNSF and Cantons of Bern and Geneva, Switzerland; NSC, Taiwan; TAEK, Turkey; STFC, the Royal Society and Leverhulme Trust, United Kingdom; DOE and NSF, United States of America.

JHEP05(2012)059

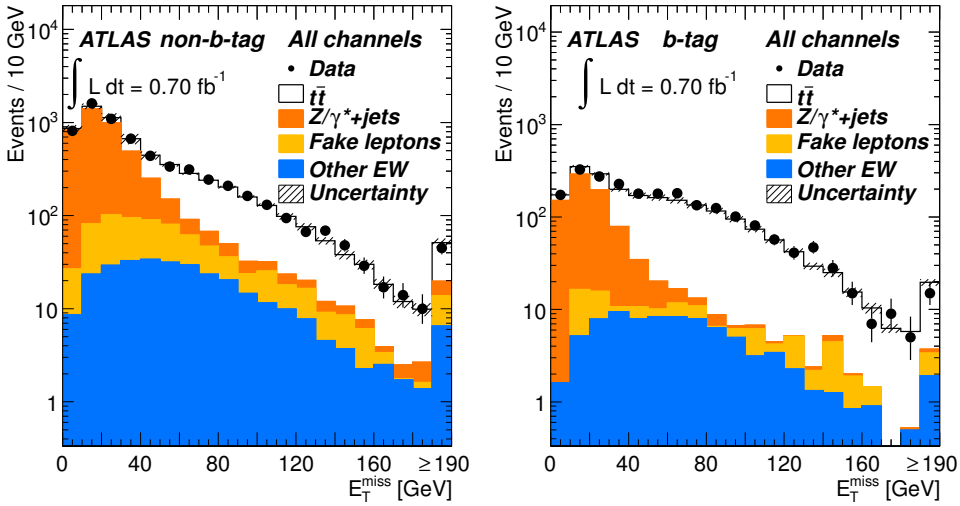

(a) (b)

Figure 2. The $E_{\mathrm{T}}^{\mathrm{miss}}$ distribution in the signal region for (a) the five non-b-tag channels combined and, (b) the three b-tagged channels combined. Contributions from diboson and single top-quark events are summarized as 'Other EW'. Uncertainties shown are statistical and systematic combined. The last bin in each figure is an overflow bin, including all events above 190 GeV. The distributions are shown as stacked histograms.

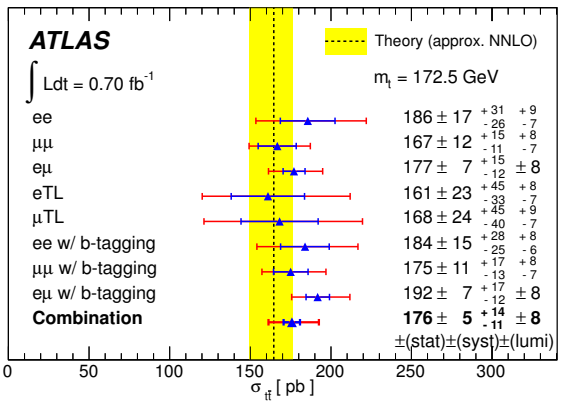

Figure 3. Summary of the individual cross section measurements and the combination of non-b-tag and exclusive b-tagged results. The vertical dashed line and yellow band are the approximate NNLO theory calculation and its uncertainty.

The crucial computing support from all WLCG partners is acknowledged gratefully, in particular from CERN and the ATLAS Tier-1 facilities at TRIUMF (Canada), NDGF (Denmark, Norway, Sweden), CC-IN2P3 (France), KIT/GridKA (Germany), INFN-CNAF (Italy), NL-T1 (Netherlands), PIC (Spain), ASGC (Taiwan), RAL (U.K.) and BNL (U.S.A.) and in the Tier-2 facilities worldwide.

JHEP05(2012)059

Open Access. This article is distributed under the terms of the Creative Commons Attribution License which permits any use, distribution and reproduction in any medium, provided the original author(s) and source are credited.

References

[1] S. Moch and P. Uwer, *Heavy-quark pair production at two loops in QCD*, *Nucl. Phys. Proc. Suppl.* **183** (2008) 75 [arXiv:0807.2794] [INSPIRE].

[2] U. Langenfeld, S. Moch and P. Uwer, *New Results for $t\bar{t}$ Production at Hadron Colliders*, in proceedings of *XVII International Workshop on Deep-Inelastic Scattering and Related Topics*, Madrid, Spain, April 2009, http://dx.doi.org/10.3360/dis.2009.131.

[3] CDF collaboration, T. Aaltonen et al., *Measurement of the Top Pair Production Cross Section in the Dilepton Decay Channel in $p\bar{p}$ Collisions at $\sqrt{s} = 1.96$ TeV*, *Phys. Rev.* **D 82** (2010) 052002 [arXiv:1002.2919] [INSPIRE].

[4] D0 collaboration, V. Abazov et al., *Combination of $t\bar{t}$ cross section measurements and constraints on the mass of the top quark and its decays into charged Higgs bosons*, *Phys. Rev.* **D 80** (2009) 071102 [arXiv:0903.5525] [INSPIRE].

[5] CMS collaboration, S. Chatrchyan et al., *Measurement of the $t\bar{t}$ production cross section and the top quark mass in the dilepton channel in pp collisions at $\sqrt{s} = 7$ TeV*, *JHEP* **07** (2011) 049 [arXiv:1105.5661] [INSPIRE].

[6] ATLAS collaboration, G. Aad et al., *Measurement of the top quark pair production cross section in pp collisions at $\sqrt{s} = 7$ TeV in dilepton final states with ATLAS*, *Phys. Lett.* **B 707** (2012) 459 [arXiv:1108.3699] [INSPIRE].

[7] ATLAS collaboration, G. Aad et al., *The ATLAS Experiment at the CERN Large Hadron Collider*, 2008 *JINST* **3** S08003 [INSPIRE].

[8] ATLAS collaboration, G. Aad et al., *Luminosity Determination in pp Collisions at $\sqrt{s} = 7$ TeV Using the ATLAS Detector at the LHC*, *Eur. Phys. J.* **C 71** (2011) 1630 [arXiv:1101.2185] [INSPIRE].

[9] ATLAS collaboration, *Luminosity Determination in pp Collisions at $\sqrt{s} = 7$ TeV using the ATLAS Detector in 2011*, ATLAS-CONF-2011-016 (2011).

[10] GEANT4 collaboration, S. Agostinelli et al., *GEANT4: A Simulation toolkit*, *Nucl. Instrum. Meth.* **A 506** (2003) 250 [INSPIRE].

[11] ATLAS collaboration, G. Aad et al., *The ATLAS Simulation Infrastructure*, *Eur. Phys. J.* **C 70** (2010) 823 [arXiv:1005.4568] [INSPIRE].

[12] S. Frixione and B.R. Webber, *Matching NLO QCD computations and parton shower simulations*, *JHEP* **06** (2002) 029 [hep-ph/0204244] [INSPIRE].

[13] S. Frixione, P. Nason and B.R. Webber, *Matching NLO QCD and parton showers in heavy flavor production*, *JHEP* **08** (2003) 007 [hep-ph/0305252] [INSPIRE].

[14] S. Frixione, E. Laenen, P. Motylinski and B.R. Webber, *Single-top production in MC@NLO*, *JHEP* **03** (2006) 092 [hep-ph/0512250] [INSPIRE].

[15] P.M. Nadolsky et al., *Implications of CTEQ global analysis for collider observables*, *Phys. Rev.* **D 78** (2008) 013004 [arXiv:0802.0007] [INSPIRE].

JHEP05(2012)059

[16] M. Aliev et al., *HATHOR: HAdronic Top and Heavy quarks crOss section calculatoR*, *Comput. Phys. Commun.* **182** (2011) 1034 [arXiv:1007.1327] [INSPIRE].

[17] S. Frixione, E. Laenen, P. Motylinski, B.R. Webber and C.D. White, *Single-top hadroproduction in association with a W boson*, *JHEP* **07** (2008) 029 [arXiv:0805.3067] [INSPIRE].

[18] M.L. Mangano, M. Moretti, F. Piccinini, R. Pittau and A.D. Polosa, *ALPGEN, a generator for hard multiparton processes in hadronic collisions*, *JHEP* **07** (2003) 001 [hep-ph/0206293] [INSPIRE].

[19] J. Pumplin, D. Stump, J. Huston, H. Lai, P.M. Nadolsky and W. Tung, *New generation of parton distributions with uncertainties from global QCD analysis*, *JHEP* **07** (2002) 012 [hep-ph/0201195] [INSPIRE].

[20] G. Corcella et al., *HERWIG 6: An Event generator for hadron emission reactions with interfering gluons (including supersymmetric processes)*, *JHEP* **01** (2001) 010 [hep-ph/0011363] [INSPIRE].

[21] G. Corcella et al., *HERWIG 6.5 release note*, hep-ph/0210213 [INSPIRE].

[22] J. Butterworth, J.R. Forshaw and M. Seymour, *Multiparton interactions in photoproduction at HERA*, *Z. Phys.* **C 72** (1996) 637 [hep-ph/9601371] [INSPIRE].

[23] ATLAS collaboration, *First tuning of HERWIG/JIMMY to ATLAS data*, PHYS-PUB-2010-014 (2010).

[24] J.M. Campbell and R.K. Ellis, *An Update on vector boson pair production at hadron colliders*, *Phys. Rev.* **D 60** (1999) 113006 [hep-ph/9905386] [INSPIRE].

[25] ATLAS collaboration, G. Aad et al., *Electron performance measurements with the ATLAS detector using the 2010 LHC proton-proton collision data*, *Eur. Phys. J.* **C 72** (2012) 1909 [arXiv:1110.3174] [INSPIRE].

[26] M. Cacciari, G.P. Salam and G. Soyez, *The Anti-k(t) jet clustering algorithm*, *JHEP* **04** (2008) 063 [arXiv:0802.1189] [INSPIRE].

[27] ATLAS collaboration, G. Aad et al., *Jet energy measurement with the ATLAS detector in proton-proton collisions at* $\sqrt{s} = 7$ *TeV*, arXiv:1112.6426 [INSPIRE].

[28] ATLAS collaboration, *Commissioning of the ATLAS high-performance b-tagging algorithms in the 7 TeV collision data*, ATLAS-CONF-2011-102 (2011).

[29] ATLAS collaboration, G. Aad et al., *Performance of Missing Transverse Momentum Reconstruction in Proton-Proton Collisions at 7 TeV with ATLAS*, *Eur. Phys. J.* **C 72** (2012) 1844 [arXiv:1108.5602] [INSPIRE].

[30] ATLAS collaboration, G. Aad et al., *Measurement of the top quark-pair production cross section with ATLAS in pp collisions at* $\sqrt{s} = 7$ *TeV*, *Eur. Phys. J.* **C 71** (2011) 1577 [arXiv:1012.1792] [INSPIRE].

[31] P. Nason, *A New method for combining NLO QCD with shower Monte Carlo algorithms*, *JHEP* **11** (2004) 040 [hep-ph/0409146] [INSPIRE].

[32] S. Frixione, P. Nason and C. Oleari, *Matching NLO QCD computations with Parton Shower simulations: the POWHEG method*, *JHEP* **11** (2007) 070 [arXiv:0709.2092] [INSPIRE].

JHEP05(2012)059

[33] S. Alioli, P. Nason, C. Oleari and E. Re, *A general framework for implementing NLO calculations in shower Monte Carlo programs: the POWHEG BOX*, *JHEP* **06** (2010) 043 [arXiv:1002.2581] [INSPIRE].

[34] B.P. Kersevan and E. Richter-Was, *The Monte Carlo event generator AcerMC version 2.0 with interfaces to PYTHIA 6.2 and HERWIG 6.5*, hep-ph/0405247 [INSPIRE].

[35] P.Z. Skands, *Tuning Monte Carlo Generators: The Perugia Tunes*, *Phys. Rev.* **D 82** (2010) 074018 [arXiv:1005.3457] [INSPIRE].

[36] N. Kidonakis, *Next-to-next-to-leading-order collinear and soft gluon corrections for t-channel single top quark production*, *Phys. Rev.* **D 83** (2011) 091503 [arXiv:1103.2792] [INSPIRE].

[37] J. M. Campbell and R. K. Ellis, *MCFM for the Tevatron and the LHC*, *Nucl. Phys. B-Proc. Suppl.* **205** (2010) 10.

JHEP05(2012)059

The ATLAS collaboration

G. Aad[48], B. Abbott[111], J. Abdallah[11], A.A. Abdelalim[49], A. Abdesselam[118], O. Abdinov[10], B. Abi[112], M. Abolins[88], O.S. AbouZeid[158], H. Abramowicz[153], H. Abreu[115], E. Acerbi[89a,89b], B.S. Acharya[164a,164b], L. Adamczyk[37], D.L. Adams[24], T.N. Addy[56], J. Adelman[175], M. Aderholz[99], S. Adomeit[98], P. Adragna[75], T. Adye[129], S. Aefsky[22], J.A. Aguilar-Saavedra[124b,a], M. Aharrouche[81], S.P. Ahlen[21], F. Ahles[48], A. Ahmad[148], M. Ahsan[40], G. Aielli[133a,133b], T. Akdogan[18a], T.P.A. Åkesson[79], G. Akimoto[155], A.V. Akimov [94], A. Akiyama[67], M.S. Alam[1], M.A. Alam[76], J. Albert[169], S. Albrand[55], M. Aleksa[29], I.N. Aleksandrov[65], F. Alessandria[89a], C. Alexa[25a], G. Alexander[153], G. Alexandre[49], T. Alexopoulos[9], M. Alhroob[20], M. Aliev[15], G. Alimonti[89a], J. Alison[120], M. Aliyev[10], P.P. Allport[73], S.E. Allwood-Spiers[53], J. Almond[82], A. Aloisio[102a,102b], R. Alon[171], A. Alonso[79], B. Alvarez Gonzalez[88], M.G. Alviggi[102a,102b], K. Amako[66], P. Amaral[29], C. Amelung[22], V.V. Ammosov[128], A. Amorim[124a,b], G. Amorós[167], N. Amram[153], C. Anastopoulos[29], L.S. Ancu[16], N. Andari[115], T. Andeen[34], C.F. Anders[20], G. Anders[58a], K.J. Anderson[30], A. Andreazza[89a,89b], V. Andrei[58a], M-L. Andrieux[55], X.S. Anduaga[70], A. Angerami[34], F. Anghinolfi[29], A. Anisenkov[107], N. Anjos[124a], A. Annovi[47], A. Antonaki[8], M. Antonelli[47], A. Antonov[96], J. Antos[144b], F. Anulli[132a], S. Aoun[83], L. Aperio Bella[4], R. Apolle[118,c], G. Arabidze[88], I. Aracena[143], Y. Arai[66], A.T.H. Arce[44], J.P. Archambault[28], S. Arfaoui[148], J-F. Arguin[14], E. Arik[18a,*], M. Arik[18a], A.J. Armbruster[87], O. Arnaez[81], C. Arnault[115], A. Artamonov[95], G. Artoni[132a,132b], D. Arutinov[20], S. Asai[155], R. Asfandiyarov[172], S. Ask[27], B. Åsman[146a,146b], L. Asquith[5], K. Assamagan[24], A. Astbury[169], A. Astvatsatourov[52], B. Aubert[4], E. Auge[115], K. Augsten[127], M. Aurousseau[145a], G. Avolio[163], R. Avramidou[9], D. Axen[168], C. Ay[54], G. Azuelos[93,d], Y. Azuma[155], M.A. Baak[29], G. Baccaglioni[89a], C. Bacci[134a,134b], A.M. Bach[14], H. Bachacou[136], K. Bachas[29], G. Bachy[29], M. Backes[49], M. Backhaus[20], E. Badescu[25a], P. Bagnaia[132a,132b], S. Bahinipati[2], Y. Bai[32a], D.C. Bailey[158], T. Bain[158], J.T. Baines[129], O.K. Baker[175], M.D. Baker[24], S. Baker[77], E. Banas[38], P. Banerjee[93], Sw. Banerjee[172], D. Banfi[29], A. Bangert[150], V. Bansal[169], H.S. Bansil[17], L. Barak[171], S.P. Baranov[94], A. Barashkou[65], A. Barbaro Galtieri[14], T. Barber[48], E.L. Barberio[86], D. Barberis[50a,50b], M. Barbero[20], D.Y. Bardin[65], T. Barillari[99], M. Barisonzi[174], T. Barklow[143], N. Barlow[27], B.M. Barnett[129], R.M. Barnett[14], A. Baroncelli[134a], G. Barone[49], A.J. Barr[118], F. Barreiro[80], J. Barreiro Guimarães da Costa[57], P. Barrillon[115], R. Bartoldus[143], A.E. Barton[71], V. Bartsch[149], R.L. Bates[53], L. Batkova[144a], J.R. Batley[27], A. Battaglia[16], M. Battistin[29], F. Bauer[136], H.S. Bawa[143,e], S. Beale[98], B. Beare[158], T. Beau[78], P.H. Beauchemin[161], R. Beccherle[50a], P. Bechtle[20], H.P. Beck[16], S. Becker[98], M. Beckingham[138], K.H. Becks[174], A.J. Beddall[18c], A. Beddall[18c], S. Bedikian[175], V.A. Bednyakov[65], C.P. Bee[83], M. Begel[24], S. Behar Harpaz[152], P.K. Behera[63], M. Beimforde[99], C. Belanger-Champagne[85], P.J. Bell[49], W.H. Bell[49], G. Bella[153], L. Bellagamba[19a], F. Bellina[29], M. Bellomo[29], A. Belloni[57], O. Beloborodova[107,f], K. Belotskiy[96], O. Beltramello[29], S. Ben Ami[152], O. Benary[153], D. Benchekroun[135a], C. Benchouk[83], M. Bendel[81], N. Benekos[165], Y. Benhammou[153], E. Benhar Noccioli[49], J.A. Benitez Garcia[159b], D.P. Benjamin[44], M. Benoit[115], J.R. Bensinger[22], K. Benslama[130],

JHEP05(2012)059

S. Bentvelsen[105], D. Berge[29], E. Bergeaas Kuutmann[41], N. Berger[4], F. Berghaus[169], E. Berglund[105], J. Beringer[14], P. Bernat[77], R. Bernhard[48], C. Bernius[24], T. Berry[76], C. Bertella[83], A. Bertin[19a,19b], F. Bertinelli[29], F. Bertolucci[122a,122b], M.I. Besana[89a,89b], N. Besson[136], S. Bethke[99], W. Bhimji[45], R.M. Bianchi[29], M. Bianco[72a,72b], O. Biebel[98], S.P. Bieniek[77], K. Bierwagen[54], J. Biesiada[14], M. Biglietti[134a], H. Bilokon[47], M. Bindi[19a,19b], S. Binet[115], A. Bingul[18c], C. Bini[132a,132b], C. Biscarat[177], U. Bitenc[48], K.M. Black[21], R.E. Blair[5], J.-B. Blanchard[136], G. Blanchot[29], T. Blazek[144a], C. Blocker[22], J. Blocki[38], A. Blondel[49], W. Blum[81], U. Blumenschein[54], G.J. Bobbink[105], V.B. Bobrovnikov[107], S.S. Bocchetta[79], A. Bocci[44], C.R. Boddy[118], M. Boehler[41], J. Boek[174], N. Boelaert[35], S. Böser[77], J.A. Bogaerts[29], A. Bogdanchikov[107], A. Bogouch[90,*], C. Bohm[146a], V. Boisvert[76], T. Bold[37], V. Boldea[25a], N.M. Bolnet[136], M. Bona[75], V.G. Bondarenko[96], M. Bondioli[163], M. Boonekamp[136], G. Boorman[76], C.N. Booth[139], S. Bordoni[78], C. Borer[16], A. Borisov[128], G. Borissov[71], I. Borjanovic[12a], M. Borri[82], S. Borroni[87], K. Bos[105], D. Boscherini[19a], M. Bosman[11], H. Boterenbrood[105], D. Botterill[129], J. Bouchami[93], J. Boudreau[123], E.V. Bouhova-Thacker[71], D. Boumediene[33], C. Bourdarios[115], N. Bousson[83], A. Boveia[30], J. Boyd[29], I.R. Boyko[65], N.I. Bozhko[128], I. Bozovic-Jelisavcic[12b], J. Bracinik[17], A. Braem[29], P. Branchini[134a], G.W. Brandenburg[57], A. Brandt[7], G. Brandt[118], O. Brandt[54], U. Bratzler[156], B. Brau[84], J.E. Brau[114], H.M. Braun[174], B. Brelier[158], J. Bremer[29], R. Brenner[166], S. Bressler[171], D. Breton[115], D. Britton[53], F.M. Brochu[27], I. Brock[20], R. Brock[88], T.J. Brodbeck[71], E. Brodet[153], F. Broggi[89a], C. Bromberg[88], J. Bronner[99], G. Brooijmans[34], W.K. Brooks[31b], G. Brown[82], H. Brown[7], P.A. Bruckman de Renstrom[38], D. Bruncko[144b], R. Bruneliere[48], S. Brunet[61], A. Bruni[19a], G. Bruni[19a], M. Bruschi[19a], T. Buanes[13], Q. Buat[55], F. Bucci[49], J. Buchanan[118], N.J. Buchanan[2], P. Buchholz[141], R.M. Buckingham[118], A.G. Buckley[45], S.I. Buda[25a], I.A. Budagov[65], B. Budick[108], V. Büscher[81], L. Bugge[117], O. Bulekov[96], M. Bunse[42], T. Buran[117], H. Burckhart[29], S. Burdin[73], T. Burgess[13], S. Burke[129], E. Busato[33], P. Bussey[53], C.P. Buszello[166], F. Butin[29], B. Butler[143], J.M. Butler[21], C.M. Buttar[53], J.M. Butterworth[77], W. Buttinger[27], S. Cabrera Urbán[167], D. Caforio[19a,19b], O. Cakir[3a], P. Calafiura[14], G. Calderini[78], P. Calfayan[98], R. Calkins[106], L.P. Caloba[23a], R. Caloi[132a,132b], D. Calvet[33], S. Calvet[33], R. Camacho Toro[33], P. Camarri[133a,133b], M. Cambiaghi[119a,119b], D. Cameron[117], L.M. Caminada[14], S. Campana[29], M. Campanelli[77], V. Canale[102a,102b], F. Canelli[30,g], A. Canepa[159a], J. Cantero[80], L. Capasso[102a,102b], M.D.M. Capeans Garrido[29], I. Caprini[25a], M. Caprini[25a], D. Capriotti[99], M. Capua[36a,36b], R. Caputo[81], C. Caramarcu[24], R. Cardarelli[133a], T. Carli[29], G. Carlino[102a], L. Carminati[89a,89b], B. Caron[85], S. Caron[104], G.D. Carrillo Montoya[172], A.A. Carter[75], J.R. Carter[27], J. Carvalho[124a,h], D. Casadei[108], M.P. Casado[11], M. Cascella[122a,122b], C. Caso[50a,50b,*], A.M. Castaneda Hernandez[172], E. Castaneda-Miranda[172], V. Castillo Gimenez[167], N.F. Castro[124a], G. Cataldi[72a], F. Cataneo[29], A. Catinaccio[29], J.R. Catmore[29], A. Cattai[29], G. Cattani[133a,133b], S. Caughron[88], D. Cauz[164a,164c], P. Cavalleri[78], D. Cavalli[89a], M. Cavalli-Sforza[11], V. Cavasinni[122a,122b], F. Ceradini[134a,134b], A.S. Cerqueira[23b], A. Cerri[29], L. Cerrito[75], F. Cerutti[47], S.A. Cetin[18b], F. Cevenini[102a,102b], A. Chafaq[135a], D. Chakraborty[106], K. Chan[2], B. Chapleau[85], J.D. Chapman[27], J.W. Chapman[87], E. Chareyre[78],

JHEP05(2012)059

D.G. Charlton[17], V. Chavda[82], C.A. Chavez Barajas[29], S. Cheatham[85], S. Chekanov[5], S.V. Chekulaev[159a], G.A. Chelkov[65], M.A. Chelstowska[104], C. Chen[64], H. Chen[24], S. Chen[32c], T. Chen[32c], X. Chen[172], S. Cheng[32a], A. Cheplakov[65], V.F. Chepurnov[65], R. Cherkaoui El Moursli[135e], V. Chernyatin[24], E. Cheu[6], S.L. Cheung[158], L. Chevalier[136], G. Chiefari[102a,102b], L. Chikovani[51a], J.T. Childers[29], A. Chilingarov[71], G. Chiodini[72a], M.V. Chizhov[65], G. Choudalakis[30], S. Chouridou[137], I.A. Christidi[77], A. Christov[48], D. Chromek-Burckhart[29], M.L. Chu[151], J. Chudoba[125], G. Ciapetti[132a,132b], K. Ciba[37], A.K. Ciftci[3a], R. Ciftci[3a], D. Cinca[33], V. Cindro[74], M.D. Ciobotaru[163], C. Ciocca[19a], A. Ciocio[14], M. Cirilli[87], M. Citterio[89a], M. Ciubancan[25a], A. Clark[49], P.J. Clark[45], W. Cleland[123], J.C. Clemens[83], B. Clement[55], C. Clement[146a,146b], R.W. Clifft[129], Y. Coadou[83], M. Cobal[164a,164c], A. Coccaro[172], J. Cochran[64], P. Coe[118], J.G. Cogan[143], J. Coggeshall[165], E. Cogneras[177], J. Colas[4], A.P. Colijn[105], N.J. Collins[17], C. Collins-Tooth[53], J. Collot[55], G. Colon[84], P. Conde Muiño[124a], E. Coniavitis[118], M.C. Conidi[11], M. Consonni[104], V. Consorti[48], S. Constantinescu[25a], C. Conta[119a,119b], F. Conventi[102a,i], J. Cook[29], M. Cooke[14], B.D. Cooper[77], A.M. Cooper-Sarkar[118], K. Copic[14], T. Cornelissen[174], M. Corradi[19a], F. Corriveau[85,j], A. Cortes-Gonzalez[165], G. Cortiana[99], G. Costa[89a], M.J. Costa[167], D. Costanzo[139], T. Costin[30], D. Côté[29], R. Coura Torres[23a], L. Courneyea[169], G. Cowan[76], C. Cowden[27], B.E. Cox[82], K. Cranmer[108], F. Crescioli[122a,122b], M. Cristinziani[20], G. Crosetti[36a,36b], R. Crupi[72a,72b], S. Crépé-Renaudin[55], C.-M. Cuciuc[25a], C. Cuenca Almenar[175], T. Cuhadar Donszelmann[139], M. Curatolo[47], C.J. Curtis[17], C. Cuthbert[150], P. Cwetanski[61], H. Czirr[141], P. Czodrowski[43], Z. Czyczula[175], S. D'Auria[53], M. D'Onofrio[73], A. D'Orazio[132a,132b], P.V.M. Da Silva[23a], C. Da Via[82], W. Dabrowski[37], T. Dai[87], C. Dallapiccola[84], M. Dam[35], M. Dameri[50a,50b], D.S. Damiani[137], H.O. Danielsson[29], D. Dannheim[99], V. Dao[49], G. Darbo[50a], G.L. Darlea[25b], C. Daum[105], W. Davey[20], T. Davidek[126], N. Davidson[86], R. Davidson[71], E. Davies[118,c], M. Davies[93], A.R. Davison[77], Y. Davygora[58a], E. Dawe[142], I. Dawson[139], J.W. Dawson[5,*], R.K. Daya-Ishmukhametova[22], K. De[7], R. de Asmundis[102a], S. De Castro[19a,19b], P.E. De Castro Faria Salgado[24], S. De Cecco[78], J. de Graat[98], N. De Groot[104], P. de Jong[105], C. De La Taille[115], H. De la Torre[80], B. De Lotto[164a,164c], L. de Mora[71], L. De Nooij[105], D. De Pedis[132a], A. De Salvo[132a], U. De Sanctis[164a,164c], A. De Santo[149], J.B. De Vivie De Regie[115], S. Dean[77], W.J. Dearnaley[71], R. Debbe[24], C. Debenedetti[45], D.V. Dedovich[65], J. Degenhardt[120], M. Dehchar[118], C. Del Papa[164a,164c], J. Del Peso[80], T. Del Prete[122a,122b], T. Delemontex[55], M. Deliyergiyev[74], A. Dell'Acqua[29], L. Dell'Asta[21], M. Della Pietra[102a,i], D. della Volpe[102a,102b], M. Delmastro[4], N. Delruelle[29], P.A. Delsart[55], C. Deluca[148], S. Demers[175], M. Demichev[65], B. Demirkoz[11,k], J. Deng[163], S.P. Denisov[128], D. Derendarz[38], J.E. Derkaoui[135d], F. Derue[78], P. Dervan[73], K. Desch[20], E. Devetak[148], P.O. Deviveiros[105], A. Dewhurst[129], B. DeWilde[148], S. Dhaliwal[158], R. Dhullipudi[24,l], A. Di Ciaccio[133a,133b], L. Di Ciaccio[4], A. Di Girolamo[29], B. Di Girolamo[29], S. Di Luise[134a,134b], A. Di Mattia[172], B. Di Micco[29], R. Di Nardo[47], A. Di Simone[133a,133b], R. Di Sipio[19a,19b], M.A. Diaz[31a], F. Diblen[18c], E.B. Diehl[87], J. Dietrich[41], T.A. Dietzsch[58a], S. Diglio[86], K. Dindar Yagci[39], J. Dingfelder[20], C. Dionisi[132a,132b], P. Dita[25a], S. Dita[25a], F. Dittus[29], F. Djama[83], T. Djobava[51b], M.A.B. do Vale[23c],

JHEP05(2012)059

A. Do Valle Wemans[124a], T.K.O. Doan[4], M. Dobbs[85], R. Dobinson [29,*], D. Dobos[29], E. Dobson[29,m], J. Dodd[34], C. Doglioni[49], T. Doherty[53], Y. Doi[66,*], J. Dolejsi[126], I. Dolenc[74], Z. Dolezal[126], B.A. Dolgoshein[96,*], T. Dohmae[155], M. Donadelli[23d], M. Donega[120], J. Donini[33], J. Dopke[29], A. Doria[102a], A. Dos Anjos[172], M. Dosil[11], A. Dotti[122a,122b], M.T. Dova[70], J.D. Dowell[17], A.D. Doxiadis[105], A.T. Doyle[53], Z. Drasal[126], J. Drees[174], N. Dressnandt[120], H. Drevermann[29], C. Driouichi[35], M. Dris[9], J. Dubbert[99], S. Dube[14], E. Duchovni[171], G. Duckeck[98], A. Dudarev[29], F. Dudziak[64], M. Dührssen [29], I.P. Duerdoth[82], L. Duflot[115], M-A. Dufour[85], M. Dunford[29], H. Duran Yildiz[3a], R. Duxfield[139], M. Dwuznik[37], F. Dydak [29], M. Düren[52], W.L. Ebenstein[44], J. Ebke[98], S. Eckweiler[81], K. Edmonds[81], C.A. Edwards[76], N.C. Edwards[53], W. Ehrenfeld[41], T. Ehrich[99], T. Eifert[143], G. Eigen[13], K. Einsweiler[14], E. Eisenhandler[75], T. Ekelof[166], M. El Kacimi[135c], M. Ellert[166], S. Elles[4], F. Ellinghaus[81], K. Ellis[75], N. Ellis[29], J. Elmsheuser[98], M. Elsing[29], D. Emeliyanov[129], R. Engelmann[148], A. Engl[98], B. Epp[62], A. Eppig[87], J. Erdmann[54], A. Ereditato[16], D. Eriksson[146a], J. Ernst[1], M. Ernst[24], J. Ernwein[136], D. Errede[165], S. Errede[165], E. Ertel[81], M. Escalier[115], C. Escobar[123], X. Espinal Curull[11], B. Esposito[47], F. Etienne[83], A.I. Etienvre[136], E. Etzion[153], D. Evangelakou[54], H. Evans[61], L. Fabbri[19a,19b], C. Fabre[29], R.M. Fakhrutdinov[128], S. Falciano[132a], Y. Fang[172], M. Fanti[89a,89b], A. Farbin[7], A. Farilla[134a], J. Farley[148], T. Farooque[158], S.M. Farrington[118], P. Farthouat[29], P. Fassnacht[29], D. Fassouliotis[8], B. Fatholahzadeh[158], A. Favareto[89a,89b], L. Fayard[115], S. Fazio[36a,36b], R. Febbraro[33], P. Federic[144a], O.L. Fedin[121], W. Fedorko[88], M. Fehling-Kaschek[48], L. Feligioni[83], D. Fellmann[5], C. Feng[32d], E.J. Feng[30], A.B. Fenyuk[128], J. Ferencei[144b], J. Ferland[93], W. Fernando[109], S. Ferrag[53], J. Ferrando[53], V. Ferrara[41], A. Ferrari[166], P. Ferrari[105], R. Ferrari[119a], A. Ferrer[167], M.L. Ferrer[47], D. Ferrere[49], C. Ferretti[87], A. Ferretto Parodi[50a,50b], M. Fiascaris[30], F. Fiedler[81], A. Filipčič[74], A. Filippas[9], F. Filthaut[104], M. Fincke-Keeler[169], M.C.N. Fiolhais[124a,h], L. Fiorini[167], A. Firan[39], G. Fischer[41], P. Fischer [20], M.J. Fisher[109], M. Flechl[48], I. Fleck[141], J. Fleckner[81], P. Fleischmann[173], S. Fleischmann[174], T. Flick[174], L.R. Flores Castillo[172], M.J. Flowerdew[99], M. Fokitis[9], T. Fonseca Martin[16], D.A. Forbush[138], A. Formica[136], A. Forti[82], D. Fortin[159a], J.M. Foster[82], D. Fournier[115], A. Foussat[29], A.J. Fowler[44], K. Fowler[137], H. Fox[71], P. Francavilla[11], S. Franchino[119a,119b], D. Francis[29], T. Frank[171], M. Franklin[57], S. Franz[29], M. Fraternali[119a,119b], S. Fratina[120], S.T. French[27], F. Friedrich [43], R. Froeschl[29], D. Froidevaux[29], J.A. Frost[27], C. Fukunaga[156], E. Fullana Torregrosa[29], J. Fuster[167], C. Gabaldon[29], O. Gabizon[171], T. Gadfort[24], S. Gadomski[49], G. Gagliardi[50a,50b], P. Gagnon[61], C. Galea[98], E.J. Gallas[118], V. Gallo[16], B.J. Gallop[129], P. Gallus[125], K.K. Gan[109], Y.S. Gao[143,e], V.A. Gapienko[128], A. Gaponenko[14], F. Garberson[175], M. Garcia-Sciveres[14], C. García[167], J.E. García Navarro[167], R.W. Gardner[30], N. Garelli[29], H. Garitaonandia[105], V. Garonne[29], J. Garvey[17], C. Gatti[47], G. Gaudio[119a], O. Gaumer[49], B. Gaur[141], L. Gauthier[136], I.L. Gavrilenko[94], C. Gay[168], G. Gaycken[20], J-C. Gayde[29], E.N. Gazis[9], P. Ge[32d], C.N.P. Gee[129], D.A.A. Geerts[105], Ch. Geich-Gimbel[20], K. Gellerstedt[146a,146b], C. Gemme[50a], A. Gemmell[53], M.H. Genest[55], S. Gentile[132a,132b], M. George[54], S. George[76], P. Gerlach[174], A. Gershon[153], C. Geweniger[58a], H. Ghazlane[135b], N. Ghodbane[33], B. Giacobbe[19a], S. Giagu[132a,132b], V. Giakoumopoulou[8], V. Giangiobbe[11],

JHEP05(2012)059

F. Gianotti[29], B. Gibbard[24], A. Gibson[158], S.M. Gibson[29], L.M. Gilbert[118], V. Gilewsky[91], D. Gillberg[28], A.R. Gillman[129], D.M. Gingrich[2,d], J. Ginzburg[153], N. Giokaris[8], M.P. Giordani[164c], R. Giordano[102a,102b], F.M. Giorgi[15], P. Giovannini[99], P.F. Giraud[136], D. Giugni[89a], M. Giunta[93], P. Giusti[19a], B.K. Gjelsten[117], L.K. Gladilin[97], C. Glasman[80], J. Glatzer[48], A. Glazov[41], K.W. Glitza[174], G.L. Glonti[65], J.R. Goddard[75], J. Godfrey[142], J. Godlewski[29], M. Goebel[41], T. Göpfert[43], C. Goeringer[81], C. Gössling[42], T. Göttfert[99], S. Goldfarb[87], T. Golling[175], S.N. Golovnia[128], A. Gomes[124a,b], L.S. Gomez Fajardo[41], R. Gonçalo[76], J. Goncalves Pinto Firmino Da Costa[41], L. Gonella[20], A. Gonidec[29], S. Gonzalez[172], S. González de la Hoz[167], G. Gonzalez Parra[11], M.L. Gonzalez Silva[26], S. Gonzalez-Sevilla[49], J.J. Goodson[148], L. Goossens[29], P.A. Gorbounov[95], H.A. Gordon[24], I. Gorelov[103], G. Gorfine[174], B. Gorini[29], E. Gorini[72a,72b], A. Gorišek[74], E. Gornicki[38], S.A. Gorokhov[128], V.N. Goryachev[128], B. Gosdzik[41], M. Gosselink[105], M.I. Gostkin[65], I. Gough Eschrich[163], M. Gouighri[135a], D. Goujdami[135c], M.P. Goulette[49], A.G. Goussiou[138], C. Goy[4], S. Gozpinar[22], I. Grabowska-Bold[37], P. Grafström[29], K-J. Grahn[41], F. Grancagnolo[72a], S. Grancagnolo[15], V. Grassi[148], V. Gratchev[121], N. Grau[34], H.M. Gray[29], J.A. Gray[148], E. Graziani[134a], O.G. Grebenyuk[121], T. Greenshaw[73], Z.D. Greenwood[24,l], K. Gregersen[35], I.M. Gregor[41], P. Grenier[143], J. Griffiths[138], N. Grigalashvili[65], A.A. Grillo[137], S. Grinstein[11], Y.V. Grishkevich[97], J.-F. Grivaz[115], M. Groh[99], E. Gross[171], J. Grosse-Knetter[54], J. Groth-Jensen[171], K. Grybel[141], V.J. Guarino[5], D. Guest[175], C. Guicheney[33], A. Guida[72a,72b], S. Guindon[54], H. Guler[85,n], J. Gunther[125], B. Guo[158], J. Guo[34], A. Gupta[30], Y. Gusakov[65], V.N. Gushchin[128], A. Gutierrez[93], P. Gutierrez[111], N. Guttman[153], O. Gutzwiller[172], C. Guyot[136], C. Gwenlan[118], C.B. Gwilliam[73], A. Haas[143], S. Haas[29], C. Haber[14], H.K. Hadavand[39], D.R. Hadley[17], P. Haefner[99], F. Hahn[29], S. Haider[29], Z. Hajduk[38], H. Hakobyan[176], D. Hall[118], J. Haller[54], K. Hamacher[174], P. Hamal[113], M. Hamer[54], A. Hamilton[145b,o], S. Hamilton[161], H. Han[32a], L. Han[32b], K. Hanagaki[116], K. Hanawa[160], M. Hance[14], C. Handel[81], P. Hanke[58a], J.R. Hansen[35], J.B. Hansen[35], J.D. Hansen[35], P.H. Hansen[35], P. Hansson[143], K. Hara[160], G.A. Hare[137], T. Harenberg[174], S. Harkusha[90], D. Harper[87], R.D. Harrington[45], O.M. Harris[138], K. Harrison[17], J. Hartert[48], F. Hartjes[105], T. Haruyama[66], A. Harvey[56], S. Hasegawa[101], Y. Hasegawa[140], S. Hassani[136], M. Hatch[29], D. Hauff[99], S. Haug[16], M. Hauschild[29], R. Hauser[88], M. Havranek[20], B.M. Hawes[118], C.M. Hawkes[17], R.J. Hawkings[29], A.D. Hawkins[79], D. Hawkins[163], T. Hayakawa[67], T. Hayashi[160], D. Hayden[76], H.S. Hayward[73], S.J. Haywood[129], E. Hazen[21], M. He[32d], S.J. Head[17], V. Hedberg[79], L. Heelan[7], S. Heim[88], B. Heinemann[14], S. Heisterkamp[35], L. Helary[4], C. Heller[98], M. Heller[29], S. Hellman[146a,146b], D. Hellmich[20], C. Helsens[11], R.C.W. Henderson[71], M. Henke[58a], A. Henrichs[54], A.M. Henriques Correia[29], S. Henrot-Versille[115], F. Henry-Couannier[83], C. Hensel[54], T. Henß[174], C.M. Hernandez[7], Y. Hernández Jiménez[167], R. Herrberg[15], A.D. Hershenhorn[152], G. Herten[48], R. Hertenberger[98], L. Hervas[29], N.P. Hessey[105], E. Higón-Rodriguez[167], D. Hill[5,*], J.C. Hill[27], N. Hill[5], K.H. Hiller[41], S. Hillert[20], S.J. Hillier[17], I. Hinchliffe[14], E. Hines[120], M. Hirose[116], F. Hirsch[42], D. Hirschbuehl[174], J. Hobbs[148], N. Hod[153], M.C. Hodgkinson[139], P. Hodgson[139], A. Hoecker[29], M.R. Hoeferkamp[103], J. Hoffman[39], D. Hoffmann[83], M. Hohlfeld[81], M. Holder[141], S.O. Holmgren[146a], T. Holy[127], J.L. Holzbauer[88],

JHEP05(2012)059

Y. Homma[67], T.M. Hong[120], L. Hooft van Huysduynen[108], T. Horazdovsky[127], C. Horn[143], S. Horner[48], J-Y. Hostachy[55], S. Hou[151], M.A. Houlden[73], A. Hoummada[135a], J. Howarth[82], D.F. Howell[118], I. Hristova [15], J. Hrivnac[115], I. Hruska[125], T. Hryn'ova[4], P.J. Hsu[81], S.-C. Hsu[14], G.S. Huang[111], Z. Hubacek[127], F. Hubaut[83], F. Huegging[20], A. Huettmann[41], T.B. Huffman[118], E.W. Hughes[34], G. Hughes[71], R.E. Hughes-Jones[82], M. Huhtinen[29], P. Hurst[57], M. Hurwitz[14], U. Husemann[41], N. Huseynov[65,p], J. Huston[88], J. Huth[57], G. Iacobucci[49], G. Iakovidis[9], M. Ibbotson[82], I. Ibragimov[141], R. Ichimiya[67], L. Iconomidou-Fayard[115], J. Idarraga[115], P. Iengo[102a], O. Igonkina[105], Y. Ikegami[66], M. Ikeno[66], Y. Ilchenko[39], D. Iliadis[154], N. Ilic[158], D. Imbault[78], M. Imori[155], T. Ince[20], J. Inigo-Golfin[29], P. Ioannou[8], M. Iodice[134a], V. Ippolito[132a,132b], A. Irles Quiles[167], C. Isaksson[166], A. Ishikawa[67], M. Ishino[68], R. Ishmukhametov[39], C. Issever[118], S. Istin[18a], A.V. Ivashin[128], W. Iwanski[38], H. Iwasaki[66], J.M. Izen[40], V. Izzo[102a], B. Jackson[120], J.N. Jackson[73], P. Jackson[143], M.R. Jaekel[29], V. Jain[61], K. Jakobs[48], S. Jakobsen[35], J. Jakubek[127], D.K. Jana[111], E. Jankowski[158], E. Jansen[77], H. Jansen[29], A. Jantsch[99], M. Janus[20], G. Jarlskog[79], L. Jeanty[57], K. Jelen[37], I. Jen-La Plante[30], P. Jenni[29], A. Jeremie[4], P. Jež[35], S. Jézéquel[4], M.K. Jha[19a], H. Ji[172], W. Ji[81], J. Jia[148], Y. Jiang[32b], M. Jimenez Belenguer[41], G. Jin[32b], S. Jin[32a], O. Jinnouchi[157], M.D. Joergensen[35], D. Joffe[39], L.G. Johansen[13], M. Johansen[146a,146b], K.E. Johansson[146a], P. Johansson[139], S. Johnert[41], K.A. Johns[6], K. Jon-And[146a,146b], G. Jones[82], R.W.L. Jones[71], T.W. Jones[77], T.J. Jones[73], O. Jonsson[29], C. Joram[29], P.M. Jorge[124a], J. Joseph[14], T. Jovin[12b], X. Ju[172], C.A. Jung[42], R.M. Jungst[29], V. Juranek[125], P. Jussel[62], A. Juste Rozas[11], V.V. Kabachenko[128], S. Kabana[16], M. Kaci[167], A. Kaczmarska[38], P. Kadlecik[35], M. Kado[115], H. Kagan[109], M. Kagan[57], S. Kaiser[99], E. Kajomovitz[152], S. Kalinin[174], L.V. Kalinovskaya[65], S. Kama[39], N. Kanaya[155], M. Kaneda[29], S. Kaneti[27], T. Kanno[157], V.A. Kantserov[96], J. Kanzaki[66], B. Kaplan[175], A. Kapliy[30], J. Kaplon[29], D. Kar[43], M. Karagounis[20], M. Karagoz[118], M. Karnevskiy[41], K. Karr[5], V. Kartvelishvili[71], A.N. Karyukhin[128], L. Kashif[172], G. Kasieczka[58b], R.D. Kass[109], A. Kastanas[13], M. Kataoka[4], Y. Kataoka[155], E. Katsoufis[9], J. Katzy[41], V. Kaushik[6], K. Kawagoe[67], T. Kawamoto[155], G. Kawamura[81], M.S. Kayl[105], V.A. Kazanin[107], M.Y. Kazarinov[65], R. Keeler[169], R. Kehoe[39], M. Keil[54], G.D. Kekelidze[65], J. Kennedy[98], C.J. Kenney[143], M. Kenyon[53], O. Kepka[125], N. Kerschen[29], B.P. Kerševan[74], S. Kersten[174], K. Kessoku[155], J. Keung[158], F. Khalil-zada[10], H. Khandanyan[165], A. Khanov[112], D. Kharchenko[65], A. Khodinov[96], A.G. Kholodenko[128], A. Khomich[58a], T.J. Khoo[27], G. Khoriauli[20], A. Khoroshilov[174], N. Khovanskiy[65], V. Khovanskiy[95], E. Khramov[65], J. Khubua[51b], H. Kim[146a,146b], M.S. Kim[2], P.C. Kim[143], S.H. Kim[160], N. Kimura[170], O. Kind[15], B.T. King[73], M. King[67], R.S.B. King[118], J. Kirk[129], L.E. Kirsch[22], A.E. Kiryunin[99], T. Kishimoto[67], D. Kisielewska[37], T. Kittelmann[123], A.M. Kiver[128], E. Kladiva[144b], J. Klaiber-Lodewigs[42], M. Klein[73], U. Klein[73], K. Kleinknecht[81], M. Klemetti[85], A. Klier[171], P. Klimek[146a,146b], A. Klimentov[24], R. Klingenberg[42], J.A. Klinger[82], E.B. Klinkby[35], T. Klioutchnikova[29], P.F. Klok[104], S. Klous[105], E.-E. Kluge[58a], T. Kluge[73], P. Kluit[105], S. Kluth[99], N.S. Knecht[158], E. Kneringer[62], J. Knobloch[29], E.B.F.G. Knoops[83], A. Knue[54], B.R. Ko[44], T. Kobayashi[155], M. Kobel[43], M. Kocian[143], P. Kodys[126], K. Köneke[29], A.C. König[104], S. Koenig[81], L. Köpke[81], F. Koetsveld[104], P. Koevesarki[20], T. Koffas[28], E. Koffeman[105], L.A. Kogan[118], F. Kohn[54],

JHEP05(2012)059

Z. Kohout[127], T. Kohriki[66], T. Koi[143], T. Kokott[20], G.M. Kolachev[107], H. Kolanoski[15], V. Kolesnikov[65], I. Koletsou[89a], J. Koll[88], D. Kollar[29], M. Kollefrath[48], S.D. Kolya[82], A.A. Komar[94], Y. Komori[155], T. Kondo[66], T. Kono[41,q], A.I. Kononov[48], R. Konoplich[108,r], N. Konstantinidis[77], A. Kootz[174], S. Koperny[37], K. Korcyl[38], K. Kordas[154], V. Koreshev[128], A. Korn[118], A. Korol[107], I. Korolkov[11], E.V. Korolkova[139], V.A. Korotkov[128], O. Kortner[99], S. Kortner[99], V.V. Kostyukhin[20], M.J. Kotamäki[29], S. Kotov[99], V.M. Kotov[65], A. Kotwal[44], C. Kourkoumelis[8], V. Kouskoura[154], A. Koutsman[159a], R. Kowalewski[169], T.Z. Kowalski[37], W. Kozanecki[136], A.S. Kozhin[128], V. Kral[127], V.A. Kramarenko[97], G. Kramberger[74], M.W. Krasny[78], A. Krasznahorkay[108], J. Kraus[88], J.K. Kraus[20], A. Kreisel[153], F. Krejci[127], J. Kretzschmar[73], N. Krieger[54], P. Krieger[158], K. Kroeninger[54], H. Kroha[99], J. Kroll[120], J. Kroseberg[20], J. Krstic[12a], U. Kruchonak[65], H. Krüger[20], T. Kruker[16], N. Krumnack[64], Z.V. Krumshteyn[65], A. Kruth[20], T. Kubota[86], S. Kuehn[48], A. Kugel[58c], T. Kuhl[41], D. Kuhn[62], V. Kukhtin[65], Y. Kulchitsky[90], S. Kuleshov[31b], C. Kummer[98], M. Kuna[78], N. Kundu[118], J. Kunkle[120], A. Kupco[125], H. Kurashige[67], M. Kurata[160], Y.A. Kurochkin[90], V. Kus[125], E.S. Kuwertz[147], M. Kuze[157], J. Kvita[142], R. Kwee[15], A. La Rosa[49], L. La Rotonda[36a,36b], L. Labarga[80], J. Labbe[4], S. Lablak[135a], C. Lacasta[167], F. Lacava[132a,132b], H. Lacker[15], D. Lacour[78], V.R. Lacuesta[167], E. Ladygin[65], R. Lafaye[4], B. Laforge[78], T. Lagouri[80], S. Lai[48], E. Laisne[55], M. Lamanna[29], C.L. Lampen[6], W. Lampl[6], E. Lancon[136], U. Landgraf[48], M.P.J. Landon[75], H. Landsman[152], J.L. Lane[82], C. Lange[41], A.J. Lankford[163], F. Lanni[24], K. Lantzsch[174], S. Laplace[78], C. Lapoire[20], J.F. Laporte[136], T. Lari[89a], A.V. Larionov [128], A. Larner[118], C. Lasseur[29], M. Lassnig[29], P. Laurelli[47], W. Lavrijsen[14], P. Laycock[73], A.B. Lazarev[65], O. Le Dortz[78], E. Le Guirriec[83], C. Le Maner[158], E. Le Menedeu[9], C. Lebel[93], T. LeCompte[5], F. Ledroit-Guillon[55], H. Lee[105], J.S.H. Lee[116], S.C. Lee[151], L. Lee[175], M. Lefebvre[169], M. Legendre[136], A. Leger[49], B.C. LeGeyt[120], F. Legger[98], C. Leggett[14], M. Lehmacher[20], G. Lehmann Miotto[29], X. Lei[6], M.A.L. Leite[23d], R. Leitner[126], D. Lellouch[171], M. Leltchouk[34], B. Lemmer[54], V. Lendermann[58a], K.J.C. Leney[145b], T. Lenz[105], G. Lenzen[174], B. Lenzi[29], K. Leonhardt[43], S. Leontsinis[9], C. Leroy[93], J-R. Lessard[169], J. Lesser[146a], C.G. Lester[27], A. Leung Fook Cheong[172], J. Levêque[4], D. Levin[87], L.J. Levinson[171], M.S. Levitski[128], A. Lewis[118], G.H. Lewis[108], A.M. Leyko[20], M. Leyton[15], B. Li[83], H. Li[172,s], S. Li[32b,t], X. Li[87], Z. Liang[118,u], H. Liao[33], B. Liberti[133a], P. Lichard[29], M. Lichtnecker[98], K. Lie[165], W. Liebig[13], R. Lifshitz[152], C. Limbach[20], A. Limosani[86], M. Limper[63], S.C. Lin[151,v], F. Linde[105], J.T. Linnemann[88], E. Lipeles[120], L. Lipinsky[125], A. Lipniacka[13], T.M. Liss[165], D. Lissauer[24], A. Lister[49], A.M. Litke[137], C. Liu[28], D. Liu[151], H. Liu[87], J.B. Liu[87], M. Liu[32b], S. Liu[2], Y. Liu[32b], M. Livan[119a,119b], S.S.A. Livermore[118], A. Lleres[55], J. Llorente Merino[80], S.L. Lloyd[75], E. Lobodzinska[41], P. Loch[6], W.S. Lockman[137], T. Loddenkoetter[20], F.K. Loebinger[82], A. Loginov[175], C.W. Loh[168], T. Lohse[15], K. Lohwasser[48], M. Lokajicek[125], J. Loken [118], V.P. Lombardo[4], R.E. Long[71], L. Lopes[124a], D. Lopez Mateos[57], J. Lorenz[98], M. Losada[162], P. Loscutoff[14], F. Lo Sterzo[132a,132b], M.J. Losty[159a], X. Lou[40], A. Lounis[115], K.F. Loureiro[162], J. Love[21], P.A. Love[71], A.J. Lowe[143,e], F. Lu[32a], H.J. Lubatti[138], C. Luci[132a,132b], A. Lucotte[55], A. Ludwig[43], D. Ludwig[41], I. Ludwig[48], J. Ludwig[48], F. Luehring[61], G. Luijckx[105], D. Lumb[48], L. Luminari[132a], E. Lund[117], B. Lund-Jensen[147],

JHEP05(2012)059

B. Lundberg[79], J. Lundberg[146a,146b], J. Lundquist[35], M. Lungwitz[81], G. Lutz[99], D. Lynn[24], J. Lys[14], E. Lytken[79], H. Ma[24], L.L. Ma[172], J.A. Macana Goia[93], G. Maccarrone[47], A. Macchiolo[99], B. Maček[74], J. Machado Miguens[124a], R. Mackeprang[35], R.J. Madaras[14], W.F. Mader[43], R. Maenner[58c], T. Maeno[24], P. Mättig[174], S. Mättig[41], L. Magnoni[29], E. Magradze[54], Y. Mahalalel[153], K. Mahboubi[48], G. Mahout[17], C. Maiani[132a,132b], C. Maidantchik[23a], A. Maio[124a,b], S. Majewski[24], Y. Makida[66], N. Makovec[115], P. Mal[136], B. Malaescu[29], Pa. Malecki[38], P. Malecki[38], V.P. Maleev[121], F. Malek[55], U. Mallik[63], D. Malon[5], C. Malone[143], S. Maltezos[9], V. Malyshev[107], S. Malyukov[29], R. Mameghani[98], J. Mamuzic[12b], A. Manabe[66], L. Mandelli[89a], I. Mandić[74], R. Mandrysch[15], J. Maneira[124a], P.S. Mangeard[88], L. Manhaes de Andrade Filho[23a], I.D. Manjavidze[65], A. Mann[54], P.M. Manning[137], A. Manousakis-Katsikakis[8], B. Mansoulie[136], A. Manz[99], A. Mapelli[29], L. Mapelli[29], L. March [80], J.F. Marchand[28], F. Marchese[133a,133b], G. Marchiori[78], M. Marcisovsky[125], A. Marin[21,*], C.P. Marino[169], F. Marroquim[23a], R. Marshall[82], Z. Marshall[29], F.K. Martens[158], S. Marti-Garcia[167], A.J. Martin[175], B. Martin[29], B. Martin[88], F.F. Martin[120], J.P. Martin[93], Ph. Martin[55], T.A. Martin[17], V.J. Martin[45], B. Martin dit Latour[49], S. Martin-Haugh[149], M. Martinez[11], V. Martinez Outschoorn[57], A.C. Martyniuk[169], M. Marx[82], F. Marzano[132a], A. Marzin[111], L. Masetti[81], T. Mashimo[155], R. Mashinistov[94], J. Masik[82], A.L. Maslennikov[107], I. Massa[19a,19b], G. Massaro[105], N. Massol[4], P. Mastrandrea[132a,132b], A. Mastroberardino[36a,36b], T. Masubuchi[155], M. Mathes[20], P. Matricon[115], H. Matsumoto[155], H. Matsunaga[155], T. Matsushita[67], C. Mattravers[118,c], J.M. Maugain[29], J. Maurer[83], S.J. Maxfield[73], D.A. Maximov[107,f], E.N. May[5], A. Mayne[139], R. Mazini[151], M. Mazur[20], M. Mazzanti[89a], E. Mazzoni[122a,122b], S.P. Mc Kee[87], A. McCarn[165], R.L. McCarthy[148], T.G. McCarthy[28], N.A. McCubbin[129], K.W. McFarlane[56], J.A. Mcfayden[139], H. McGlone[53], G. Mchedlidze[51b], R.A. McLaren[29], T. Mclaughlan[17], S.J. McMahon[129], R.A. McPherson[169,j], A. Meade[84], J. Mechnich[105], M. Mechtel[174], M. Medinnis[41], R. Meera-Lebbai[111], T. Meguro[116], R. Mehdiyev[93], S. Mehlhase[35], A. Mehta[73], K. Meier[58a], B. Meirose[79], C. Melachrinos[30], B.R. Mellado Garcia[172], L. Mendoza Navas[162], Z. Meng[151,s], A. Mengarelli[19a,19b], S. Menke[99], C. Menot[29], E. Meoni[11], K.M. Mercurio[57], P. Mermod[49], L. Merola[102a,102b], C. Meroni[89a], F.S. Merritt[30], A. Messina[29], J. Metcalfe[103], A.S. Mete[64], C. Meyer[81], C. Meyer[30], J-P. Meyer[136], J. Meyer[173], J. Meyer[54], T.C. Meyer[29], W.T. Meyer[64], J. Miao[32d], S. Michal[29], L. Micu[25a], R.P. Middleton[129], S. Migas[73], L. Mijović[41], G. Mikenberg[171], M. Mikestikova[125], M. Mikuž[74], D.W. Miller[30], R.J. Miller[88], W.J. Mills[168], C. Mills[57], A. Milov[171], D.A. Milstead[146a,146b], D. Milstein[171], A.A. Minaenko[128], M. Miñano Moya[167], I.A. Minashvili[65], A.I. Mincer[108], B. Mindur[37], M. Mineev[65], Y. Ming[172], L.M. Mir[11], G. Mirabelli[132a], L. Miralles Verge[11], A. Misiejuk[76], J. Mitrevski[137], G.Y. Mitrofanov[128], V.A. Mitsou[167], S. Mitsui[66], P.S. Miyagawa[139], K. Miyazaki[67], J.U. Mjörnmark[79], T. Moa[146a,146b], P. Mockett[138], S. Moed[57], V. Moeller[27], K. Mönig[41], N. Möser[20], S. Mohapatra[148], W. Mohr[48], S. Mohrdieck-Möck[99], A.M. Moisseev[128,*], R. Moles-Valls[167], J. Molina-Perez[29], J. Monk[77], E. Monnier[83], S. Montesano[89a,89b], F. Monticelli[70], S. Monzani[19a,19b], R.W. Moore[2], G.F. Moorhead[86], C. Mora Herrera[49], A. Moraes[53], N. Morange[136], J. Morel[54], G. Morello[36a,36b], D. Moreno[81], M. Moreno Llácer[167],

JHEP05(2012)059

P. Morettini[50a], M. Morii[57], J. Morin[75], A.K. Morley[29], G. Mornacchi[29], S.V. Morozov[96], J.D. Morris[75], L. Morvaj[101], H.G. Moser[99], M. Mosidze[51b], J. Moss[109], R. Mount[143], E. Mountricha[9,w], S.V. Mouraviev[94], E.J.W. Moyse[84], M. Mudrinic[12b], F. Mueller[58a], J. Mueller[123], K. Mueller[20], T.A. Müller[98], T. Mueller[81], D. Muenstermann[29], A. Muir[168], Y. Munwes[153], W.J. Murray[129], I. Mussche[105], E. Musto[102a,102b], A.G. Myagkov[128], M. Myska[125], J. Nadal[11], K. Nagai[160], K. Nagano[66], Y. Nagasaka[60], M. Nagel[99], A.M. Nairz[29], Y. Nakahama[29], K. Nakamura[155], T. Nakamura[155], I. Nakano[110], G. Nanava[20], A. Napier[161], R. Narayan[58b], M. Nash[77,c], N.R. Nation[21], T. Nattermann[20], T. Naumann[41], G. Navarro[162], H.A. Neal[87], E. Nebot[80], P.Yu. Nechaeva[94], T.J. Neep[82], A. Negri[119a,119b], G. Negri[29], S. Nektarijevic[49], A. Nelson[163], S. Nelson[143], T.K. Nelson[143], S. Nemecek[125], P. Nemethy[108], A.A. Nepomuceno[23a], M. Nessi[29,x], M.S. Neubauer[165], A. Neusiedl[81], R.M. Neves[108], P. Nevski[24], P.R. Newman[17], V. Nguyen Thi Hong[136], R.B. Nickerson[118], R. Nicolaidou[136], L. Nicolas[139], B. Nicquevert[29], F. Niedercorn[115], J. Nielsen[137], T. Niinikoski[29], N. Nikiforou[34], A. Nikiforov[15], V. Nikolaenko[128], K. Nikolaev[65], I. Nikolic-Audit[78], K. Nikolics[49], K. Nikolopoulos[24], H. Nilsen[48], P. Nilsson[7], Y. Ninomiya [155], A. Nisati[132a], T. Nishiyama[67], R. Nisius[99], L. Nodulman[5], M. Nomachi[116], I. Nomidis[154], M. Nordberg[29], B. Nordkvist[146a,146b], P.R. Norton[129], J. Novakova[126], M. Nozaki[66], L. Nozka[113], I.M. Nugent[159a], A.-E. Nuncio-Quiroz[20], G. Nunes Hanninger[86], T. Nunnemann[98], E. Nurse[77], T. Nyman[29], B.J. O'Brien[45], S.W. O'Neale[17,*], D.C. O'Neil[142], V. O'Shea[53], L.B. Oakes[98], F.G. Oakham[28,d], H. Oberlack[99], J. Ocariz[78], A. Ochi[67], S. Oda[155], S. Odaka[66], J. Odier[83], H. Ogren[61], A. Oh[82], S.H. Oh[44], C.C. Ohm[146a,146b], T. Ohshima[101], H. Ohshita[140], T. Ohsugi[59], S. Okada[67], H. Okawa[163], Y. Okumura[101], T. Okuyama[155], A. Olariu[25a], M. Olcese[50a], A.G. Olchevski[65], M. Oliveira[124a,h], D. Oliveira Damazio[24], E. Oliver Garcia[167], D. Olivito[120], A. Olszewski[38], J. Olszowska[38], C. Omachi[67], A. Onofre[124a,y], P.U.E. Onyisi[30], C.J. Oram[159a], M.J. Oreglia[30], Y. Oren[153], D. Orestano[134a,134b], I. Orlov[107], C. Oropeza Barrera[53], R.S. Orr[158], B. Osculati[50a,50b], R. Ospanov[120], C. Osuna[11], G. Otero y Garzon[26], J.P. Ottersbach[105], M. Ouchrif[135d], E.A. Ouellette[169], F. Ould-Saada[117], A. Ouraou[136], Q. Ouyang[32a], A. Ovcharova[14], M. Owen[82], S. Owen[139], V.E. Ozcan[18a], N. Ozturk[7], A. Pacheco Pages[11], C. Padilla Aranda[11], S. Pagan Griso[14], E. Paganis[139], F. Paige[24], P. Pais[84], K. Pajchel[117], G. Palacino[159b], C.P. Paleari[6], S. Palestini[29], D. Pallin[33], A. Palma[124a], J.D. Palmer[17], Y.B. Pan[172], E. Panagiotopoulou[9], B. Panes[31a], N. Panikashvili[87], S. Panitkin[24], D. Pantea[25a], M. Panuskova[125], V. Paolone[123], A. Papadelis[146a], Th.D. Papadopoulou[9], A. Paramonov[5], W. Park[24,z], M.A. Parker[27], F. Parodi[50a,50b], J.A. Parsons[34], U. Parzefall[48], E. Pasqualucci[132a], S. Passaggio[50a], A. Passeri[134a], F. Pastore[134a,134b], Fr. Pastore[76], G. Pásztor [49,aa], S. Pataraia[174], N. Patel[150], J.R. Pater[82], S. Patricelli[102a,102b], T. Pauly[29], M. Pecsy[144a], M.I. Pedraza Morales[172], S.V. Peleganchuk[107], H. Peng[32b], R. Pengo[29], A. Penson[34], J. Penwell[61], M. Perantoni[23a], K. Perez[34,ab], T. Perez Cavalcanti[41], E. Perez Codina[11], M.T. Pérez García-Estañ[167], V. Perez Reale[34], L. Perini[89a,89b], H. Pernegger[29], R. Perrino[72a], P. Perrodo[4], S. Persembe[3a], A. Perus[115], V.D. Peshekhonov[65], K. Peters[29], B.A. Petersen[29], J. Petersen[29], T.C. Petersen[35], E. Petit[4], A. Petridis[154], C. Petridou[154], E. Petrolo[132a], F. Petrucci[134a,134b], D. Petschull[41], M. Petteni[142], R. Pezoa[31b], A. Phan[86],

JHEP05(2012)059

P.W. Phillips[129], G. Piacquadio[29], E. Piccaro[75], M. Piccinini[19a,19b], S.M. Piec[41], R. Piegaia[26], D.T. Pignotti[109], J.E. Pilcher[30], A.D. Pilkington[82], J. Pina[124a,b], M. Pinamonti[164a,164c], A. Pinder[118], J.L. Pinfold[2], J. Ping[32c], B. Pinto[124a], O. Pirotte[29], C. Pizio[89a,89b], M. Plamondon[169], M.-A. Pleier[24], A.V. Pleskach[128], A. Poblaguev[24], S. Poddar[58a], F. Podlyski[33], L. Poggioli[115], T. Poghosyan[20], M. Pohl[49], F. Polci[55], G. Polesello[119a], A. Policicchio[36a,36b], A. Polini[19a], J. Poll[75], V. Polychronakos[24], D.M. Pomarede[136], D. Pomeroy[22], K. Pommès[29], L. Pontecorvo[132a], B.G. Pope[88], G.A. Popeneciu[25a], D.S. Popovic[12a], A. Poppleton[29], X. Portell Bueso[29], C. Posch[21], G.E. Pospelov[99], S. Pospisil[127], I.N. Potrap[99], C.J. Potter[149], C.T. Potter[114], G. Poulard[29], J. Poveda[172], R. Prabhu[77], P. Pralavorio[83], A. Pranko[14], S. Prasad[57], R. Pravahan[7], S. Prell[64], K. Pretzl[16], L. Pribyl[29], D. Price[61], J. Price[73], L.E. Price[5], M.J. Price[29], D. Prieur[123], M. Primavera[72a], K. Prokofiev[108], F. Prokoshin[31b], S. Protopopescu[24], J. Proudfoot[5], X. Prudent[43], M. Przybycien[37], H. Przysiezniak[4], S. Psoroulas[20], E. Ptacek[114], E. Pueschel[84], J. Purdham[87], M. Purohit[24,z], P. Puzo[115], Y. Pylypchenko[63], J. Qian[87], Z. Qian[83], Z. Qin[41], A. Quadt[54], D.R. Quarrie[14], W.B. Quayle[172], F. Quinonez[31a], M. Raas[104], V. Radescu[58b], B. Radics[20], P. Radloff[114], T. Rador[18a], F. Ragusa[89a,89b], G. Rahal[177], A.M. Rahimi[109], D. Rahm[24], S. Rajagopalan[24], M. Rammensee[48], M. Rammes[141], A.S. Randle-Conde[39], K. Randrianarivony[28], P.N. Ratoff[71], F. Rauscher[98], M. Raymond[29], A.L. Read[117], D.M. Rebuzzi[119a,119b], A. Redelbach[173], G. Redlinger[24], R. Reece[120], K. Reeves[40], A. Reichold[105], E. Reinherz-Aronis[153], A. Reinsch[114], I. Reisinger[42], D. Reljic[12a], C. Rembser[29], Z.L. Ren[151], A. Renaud[115], P. Renkel[39], M. Rescigno[132a], S. Resconi[89a], B. Resende[136], P. Reznicek[98], R. Rezvani[158], A. Richards[77], R. Richter[99], E. Richter-Was[4,ac], M. Ridel[78], M. Rijpstra[105], M. Rijssenbeek[148], A. Rimoldi[119a,119b], L. Rinaldi[19a], R.R. Rios[39], I. Riu[11], G. Rivoltella[89a,89b], F. Rizatdinova[112], E. Rizvi[75], S.H. Robertson[85,j], A. Robichaud-Veronneau[118], D. Robinson[27], J.E.M. Robinson[77], M. Robinson[114], A. Robson[53], J.G. Rocha de Lima[106], C. Roda[122a,122b], D. Roda Dos Santos[29], D. Rodriguez[162], A. Roe[54], S. Roe[29], O. Røhne[117], V. Rojo[1], S. Rolli[161], A. Romaniouk[96], M. Romano[19a,19b], V.M. Romanov[65], G. Romeo[26], E. Romero Adam[167], L. Roos[78], E. Ros[167], S. Rosati[132a], K. Rosbach[49], A. Rose[149], M. Rose[76], G.A. Rosenbaum[158], E.I. Rosenberg[64], P.L. Rosendahl[13], O. Rosenthal[141], L. Rosselet[49], V. Rossetti[11], E. Rossi[132a,132b], L.P. Rossi[50a], M. Rotaru[25a], I. Roth[171], J. Rothberg[138], D. Rousseau[115], C.R. Royon[136], A. Rozanov[83], Y. Rozen[152], X. Ruan[115,ad], I. Rubinskiy[41], B. Ruckert[98], N. Ruckstuhl[105], V.I. Rud[97], C. Rudolph[43], G. Rudolph[62], F. Rühr[6], F. Ruggieri[134a,134b], A. Ruiz-Martinez[64], V. Rumiantsev[91,*], L. Rumyantsev[65], K. Runge[48], Z. Rurikova[48], N.A. Rusakovich[65], D.R. Rust[61], J.P. Rutherfoord[6], C. Ruwiedel[14], P. Ruzicka[125], Y.F. Ryabov[121], V. Ryadovikov[128], P. Ryan[88], M. Rybar[126], G. Rybkin[115], N.C. Ryder[118], S. Rzaeva[10], A.F. Saavedra[150], I. Sadeh[153], H.F-W. Sadrozinski[137], R. Sadykov[65], F. Safai Tehrani[132a], H. Sakamoto[155], G. Salamanna[75], A. Salamon[133a], M. Saleem[111], D. Salihagic[99], A. Salnikov[143], J. Salt[167], B.M. Salvachua Ferrando[5], D. Salvatore[36a,36b], F. Salvatore[149], A. Salvucci[104], A. Salzburger[29], D. Sampsonidis[154], B.H. Samset[117], A. Sanchez[102a,102b], H. Sandaker[13], H.G. Sander[81], M.P. Sanders[98], M. Sandhoff[174], T. Sandoval[27], C. Sandoval [162], R. Sandstroem[99], S. Sandvoss[174], D.P.C. Sankey[129],

JHEP05(2012)059

A. Sansoni[47], C. Santamarina Rios[85], C. Santoni[33], R. Santonico[133a,133b], H. Santos[124a], J.G. Saraiva[124a], T. Sarangi[172], E. Sarkisyan-Grinbaum[7], F. Sarri[122a,122b], G. Sartisohn[174], O. Sasaki[66], N. Sasao[68], I. Satsounkevitch[90], G. Sauvage[4], E. Sauvan[4], J.B. Sauvan[115], P. Savard[158,d], V. Savinov[123], D.O. Savu[29], L. Sawyer[24,l], D.H. Saxon[53], L.P. Says[33], C. Sbarra[19a], A. Sbrizzi[19a,19b], O. Scallon[93], D.A. Scannicchio[163], M. Scarcella[150], J. Schaarschmidt[115], P. Schacht[99], U. Schäfer[81], S. Schaepe[20], S. Schaetzel[58b], A.C. Schaffer[115], D. Schaile[98], R.D. Schamberger[148], A.G. Schamov[107], V. Scharf[58a], V.A. Schegelsky[121], D. Scheirich[87], M. Schernau[163], M.I. Scherzer[34], C. Schiavi[50a,50b], J. Schieck[98], M. Schioppa[36a,36b], S. Schlenker[29], J.L. Schlereth[5], E. Schmidt[48], K. Schmieden[20], C. Schmitt[81], S. Schmitt[58b], M. Schmitz[20], A. Schöning[58b], M. Schott[29], D. Schouten[159a], J. Schovancova[125], M. Schram[85], C. Schroeder[81], N. Schroer[58c], S. Schuh[29], G. Schuler[29], J. Schultes[174], H.-C. Schultz-Coulon[58a], H. Schulz[15], J.W. Schumacher[20], M. Schumacher[48], B.A. Schumm[137], Ph. Schune[136], C. Schwanenberger[82], A. Schwartzman[143], Ph. Schwemling[78], R. Schwienhorst[88], R. Schwierz[43], J. Schwindling[136], T. Schwindt[20], M. Schwoerer[4], W.G. Scott[129], J. Searcy[114], G. Sedov[41], E. Sedykh[121], E. Segura[11], S.C. Seidel[103], A. Seiden[137], F. Seifert[43], J.M. Seixas[23a], G. Sekhniaidze[102a], K.E. Selbach[45], D.M. Seliverstov[121], B. Sellden[146a], G. Sellers[73], M. Seman[144b], N. Semprini-Cesari[19a,19b], C. Serfon[98], L. Serin[115], L. Serkin[54], R. Seuster[99], H. Severini[111], M.E. Sevior[86], A. Sfyrla[29], E. Shabalina[54], M. Shamim[114], L.Y. Shan[32a], J.T. Shank[21], Q.T. Shao[86], M. Shapiro[14], P.B. Shatalov[95], L. Shaver[6], K. Shaw[164a,164c], D. Sherman[175], P. Sherwood[77], A. Shibata[108], H. Shichi[101], S. Shimizu[29], M. Shimojima[100], T. Shin[56], M. Shiyakova[65], A. Shmeleva[94], M.J. Shochet[30], D. Short[118], S. Shrestha[64], M.A. Shupe[6], P. Sicho[125], A. Sidoti[132a], F. Siegert[48], Dj. Sijacki[12a], O. Silbert[171], J. Silva[124a,b], Y. Silver[153], D. Silverstein[143], S.B. Silverstein[146a], V. Simak[127], O. Simard[136], Lj. Simic[12a], S. Simion[115], B. Simmons[77], M. Simonyan[35], P. Sinervo[158], N.B. Sinev[114], V. Sipica[141], G. Siragusa[173], A. Sircar[24], A.N. Sisakyan[65], S.Yu. Sivoklokov[97], J. Sjölin[146a,146b], T.B. Sjursen[13], L.A. Skinnari[14], H.P. Skottowe[57], K. Skovpen[107], P. Skubic[111], N. Skvorodnev[22], M. Slater[17], T. Slavicek[127], K. Sliwa[161], J. Sloper[29], V. Smakhtin[171], S.Yu. Smirnov[96], L.N. Smirnova[97], O. Smirnova[79], B.C. Smith[57], D. Smith[143], K.M. Smith[53], M. Smizanska[71], K. Smolek[127], A.A. Snesarev[94], S.W. Snow[82], J. Snow[111], J. Snuverink[105], S. Snyder[24], M. Soares[124a], R. Sobie[169,j], J. Sodomka[127], A. Soffer[153], C.A. Solans[167], M. Solar[127], J. Solc[127], E. Soldatov[96], U. Soldevila[167], E. Solfaroli Camillocci[132a,132b], A.A. Solodkov[128], O.V. Solovyanov[128], N. Soni[2], V. Sopko[127], B. Sopko[127], M. Sosebee[7], R. Soualah[164a,164c], A. Soukharev[107], S. Spagnolo[72a,72b], F. Spanò[76], R. Spighi[19a], G. Spigo[29], F. Spila[132a,132b], R. Spiwoks[29], M. Spousta[126], T. Spreitzer[158], B. Spurlock[7], R.D. St. Denis[53], T. Stahl[141], J. Stahlman[120], R. Stamen[58a], E. Stanecka[38], R.W. Stanek[5], C. Stanescu[134a], S. Stapnes[117], E.A. Starchenko[128], J. Stark[55], P. Staroba[125], P. Starovoitov[91], A. Staude[98], P. Stavina[144a], G. Stavropoulos[14], G. Steele[53], P. Steinbach[43], P. Steinberg[24], I. Stekl[127], B. Stelzer[142], H.J. Stelzer[88], O. Stelzer-Chilton[159a], H. Stenzel[52], S. Stern[99], K. Stevenson[75], G.A. Stewart[29], J.A. Stillings[20], M.C. Stockton[85], K. Stoerig[48], G. Stoicea[25a], S. Stonjek[99], P. Strachota[126], A.R. Stradling[7], A. Straessner[43], J. Strandberg[147], S. Strandberg[146a,146b], A. Strandlie[117], M. Strang[109], E. Strauss[143], M. Strauss[111],

JHEP05(2012)059

P. Strizenec[144b], R. Ströhmer[173], D.M. Strom[114], J.A. Strong[76,*], R. Stroynowski[39], J. Strube[129], B. Stugu[13], I. Stumer[24,*], J. Stupak[148], P. Sturm[174], N.A. Styles[41], D.A. Soh[151,u], D. Su[143], HS. Subramania[2], A. Succurro[11], Y. Sugaya[116], T. Sugimoto[101], C. Suhr[106], K. Suita[67], M. Suk[126], V.V. Sulin[94], S. Sultansoy[3d], T. Sumida[68], X. Sun[55], J.E. Sundermann[48], K. Suruliz[139], S. Sushkov[11], G. Susinno[36a,36b], M.R. Sutton[149], Y. Suzuki[66], Y. Suzuki[67], M. Svatos[125], Yu.M. Sviridov[128], S. Swedish[168], I. Sykora[144a], T. Sykora[126], B. Szeless[29], J. Sánchez[167], D. Ta[105], K. Tackmann[41], A. Taffard[163], R. Tafirout[159a], N. Taiblum[153], Y. Takahashi[101], H. Takai[24], R. Takashima[69], H. Takeda[67], T. Takeshita[140], Y. Takubo[66], M. Talby[83], A. Talyshev[107,f], M.C. Tamsett[24], J. Tanaka[155], R. Tanaka[115], S. Tanaka[131], S. Tanaka[66], Y. Tanaka[100], A.J. Tanasijczuk[142], K. Tani[67], N. Tannoury[83], G.P. Tappern[29], S. Tapprogge[81], D. Tardif[158], S. Tarem[152], F. Tarrade[28], G.F. Tartarelli[89a], P. Tas[126], M. Tasevsky[125], E. Tassi[36a,36b], M. Tatarkhanov[14], Y. Tayalati[135d], C. Taylor[77], F.E. Taylor[92], G.N. Taylor[86], W. Taylor[159b], M. Teinturier[115], M. Teixeira Dias Castanheira[75], P. Teixeira-Dias[76], K.K. Temming[48], H. Ten Kate[29], P.K. Teng[151], S. Terada[66], K. Terashi[155], J. Terron[80], M. Testa[47], R.J. Teuscher[158,j], J. Thadome[174], J. Therhaag[20], T. Theveneaux-Pelzer[78], M. Thioye[175], S. Thoma[48], J.P. Thomas[17], E.N. Thompson[34], P.D. Thompson[17], P.D. Thompson[158], A.S. Thompson[53], E. Thomson[120], M. Thomson[27], R.P. Thun[87], F. Tian[34], M.J. Tibbetts[14], T. Tic[125], V.O. Tikhomirov[94], Y.A. Tikhonov[107,f], S. Timoshenko[96], P. Tipton[175], F.J. Tique Aires Viegas[29], S. Tisserant[83], B. Toczek[37], T. Todorov[4], S. Todorova-Nova[161], B. Toggerson[163], J. Tojo[66], S. Tokár[144a], K. Tokunaga[67], K. Tokushuku[66], K. Tollefson[88], M. Tomoto[101], L. Tompkins[30], K. Toms[103], G. Tong[32a], A. Tonoyan[13], C. Topfel[16], N.D. Topilin[65], I. Torchiani[29], E. Torrence[114], H. Torres[78], E. Torró Pastor[167], J. Toth[83,aa], F. Touchard[83], D.R. Tovey[139], T. Trefzger[173], L. Tremblet[29], A. Tricoli[29], I.M. Trigger[159a], S. Trincaz-Duvoid[78], T.N. Trinh[78], M.F. Tripiana[70], W. Trischuk[158], A. Trivedi[24,z], B. Trocmé[55], C. Troncon[89a], M. Trottier-McDonald[142], M. Trzebinski[38], A. Trzupek[38], C. Tsarouchas[29], J.C-L. Tseng[118], M. Tsiakiris[105], P.V. Tsiareshka[90], D. Tsionou[4,ae], G. Tsipolitis[9], V. Tsiskaridze[48], E.G. Tskhadadze[51a], I.I. Tsukerman[95], V. Tsulaia[14], J.-W. Tsung[20], S. Tsuno[66], D. Tsybychev[148], A. Tua[139], A. Tudorache[25a], V. Tudorache[25a], J.M. Tuggle[30], M. Turala[38], D. Turecek[127], I. Turk Cakir[3e], E. Turlay[105], R. Turra[89a,89b], P.M. Tuts[34], A. Tykhonov[74], M. Tylmad[146a,146b], M. Tyndel[129], G. Tzanakos[8], K. Uchida[20], I. Ueda[155], R. Ueno[28], M. Ugland[13], M. Uhlenbrock[20], M. Uhrmacher[54], F. Ukegawa[160], G. Unal[29], D.G. Underwood[5], A. Undrus[24], G. Unel[163], Y. Unno[66], D. Urbaniec[34], G. Usai[7], M. Uslenghi[119a,119b], L. Vacavant[83], V. Vacek[127], B. Vachon[85], S. Vahsen[14], J. Valenta[125], P. Valente[132a], S. Valentinetti[19a,19b], S. Valkar[126], E. Valladolid Gallego[167], S. Vallecorsa[152], J.A. Valls Ferrer[167], H. van der Graaf[105], E. van der Kraaij[105], R. Van Der Leeuw[105], E. van der Poel[105], D. van der Ster[29], N. van Eldik[84], P. van Gemmeren[5], Z. van Kesteren[105], I. van Vulpen[105], M. Vanadia[99], W. Vandelli[29], G. Vandoni[29], A. Vaniachine[5], P. Vankov[41], F. Vannucci[78], F. Varela Rodriguez[29], R. Vari[132a], E.W. Varnes[6], D. Varouchas[14], A. Vartapetian[7], K.E. Varvell[150], V.I. Vassilakopoulos[56], F. Vazeille[33], G. Vegni[89a,89b], J.J. Veillet[115], C. Vellidis[8], F. Veloso[124a], R. Veness[29], S. Veneziano[132a], A. Ventura[72a,72b], D. Ventura[138], M. Venturi[48], N. Venturi[158], V. Vercesi[119a], M. Verducci[138], W. Verkerke[105],

JHEP05(2012)059

J.C. Vermeulen[105], A. Vest[43], M.C. Vetterli[142,d], I. Vichou[165], T. Vickey[145b,af], O.E. Vickey Boeriu[145b], G.H.A. Viehhauser[118], S. Viel[168], M. Villa[19a,19b], M. Villaplana Perez[167], E. Vilucchi[47], M.G. Vincter[28], E. Vinek[29], V.B. Vinogradov[65], M. Virchaux[136,*], J. Virzi[14], O. Vitells[171], M. Viti[41], I. Vivarelli[48], F. Vives Vaque[2], S. Vlachos[9], D. Vladoiu[98], M. Vlasak[127], N. Vlasov[20], A. Vogel[20], P. Vokac[127], G. Volpi[47], M. Volpi[86], G. Volpini[89a], H. von der Schmitt[99], J. von Loeben[99], H. von Radziewski[48], E. von Toerne[20], V. Vorobel[126], A.P. Vorobiev[128], V. Vorwerk[11], M. Vos[167], R. Voss[29], T.T. Voss[174], J.H. Vossebeld[73], N. Vranjes[12a], M. Vranjes Milosavljevic[105], V. Vrba[125], M. Vreeswijk[105], T. Vu Anh[81], R. Vuillermet[29], I. Vukotic[115], W. Wagner[174], P. Wagner[120], H. Wahlen[174], J. Wakabayashi[101], J. Walbersloh[42], S. Walch[87], J. Walder[71], R. Walker[98], W. Walkowiak[141], R. Wall[175], P. Waller[73], C. Wang[44], H. Wang[172], H. Wang[32b,ag], J. Wang[151], J. Wang[55], J.C. Wang[138], R. Wang[103], S.M. Wang[151], A. Warburton[85], C.P. Ward[27], M. Warsinsky[48], P.M. Watkins[17], A.T. Watson[17], I.J. Watson[150], M.F. Watson[17], G. Watts[138], S. Watts[82], A.T. Waugh[150], B.M. Waugh[77], M. Weber[129], M.S. Weber[16], P. Weber[54], A.R. Weidberg[118], P. Weigell[99], J. Weingarten[54], C. Weiser[48], H. Wellenstein[22], P.S. Wells[29], M. Wen[47], T. Wenaus[24], S. Wendler[123], Z. Weng[151,u], T. Wengler[29], S. Wenig[29], N. Wermes[20], M. Werner[48], P. Werner[29], M. Werth[163], M. Wessels[58a], C. Weydert[55], K. Whalen[28], S.J. Wheeler-Ellis[163], S.P. Whitaker[21], A. White[7], M.J. White[86], S.R. Whitehead[118], D. Whiteson[163], D. Whittington[61], F. Wicek[115], D. Wicke[174], F.J. Wickens[129], W. Wiedenmann[172], M. Wielers[129], P. Wienemann[20], C. Wiglesworth[75], L.A.M. Wiik-Fuchs[48], P.A. Wijeratne[77], A. Wildauer[167], M.A. Wildt[41,q], I. Wilhelm[126], H.G. Wilkens[29], J.Z. Will[98], E. Williams[34], H.H. Williams[120], W. Willis[34], S. Willocq[84], J.A. Wilson[17], M.G. Wilson[143], A. Wilson[87], I. Wingerter-Seez[4], S. Winkelmann[48], F. Winklmeier[29], M. Wittgen[143], M.W. Wolter[38], H. Wolters[124a,h], W.C. Wong[40], G. Wooden[87], B.K. Wosiek[38], J. Wotschack[29], M.J. Woudstra[84], K.W. Wozniak[38], K. Wraight[53], C. Wright[53], M. Wright[53], B. Wrona[73], S.L. Wu[172], X. Wu[49], Y. Wu[32b,ah], E. Wulf[34], R. Wunstorf[42], B.M. Wynne[45], S. Xella[35], M. Xiao[136], S. Xie[48], Y. Xie[32a], C. Xu[32b,w], D. Xu[139], G. Xu[32a], B. Yabsley[150], S. Yacoob[145b], M. Yamada[66], H. Yamaguchi[155], A. Yamamoto[66], K. Yamamoto[64], S. Yamamoto[155], T. Yamamura[155], T. Yamanaka[155], J. Yamaoka[44], T. Yamazaki[155], Y. Yamazaki[67], Z. Yan[21], H. Yang[87], U.K. Yang[82], Y. Yang[61], Y. Yang[32a], Z. Yang[146a,146b], S. Yanush[91], Y. Yao[14], Y. Yasu[66], G.V. Ybeles Smit[130], J. Ye[39], S. Ye[24], M. Yilmaz[3c], R. Yoosoofmiya[123], K. Yorita[170], R. Yoshida[5], C. Young[143], S. Youssef[21], D. Yu[24], J. Yu[7], J. Yu[112], L. Yuan[32a,ai], A. Yurkewicz[106], B. Zabinski[38], V.G. Zaets [128], R. Zaidan[63], A.M. Zaitsev[128], Z. Zajacova[29], L. Zanello[132a,132b], P. Zarzhitsky[39], A. Zaytsev[107], C. Zeitnitz[174], M. Zeller[175], M. Zeman[125], A. Zemla[38], C. Zendler[20], O. Zenin[128], T. Ženiš[144a], Z. Zinonos[122a,122b], S. Zenz[14], D. Zerwas[115], G. Zevi della Porta[57], Z. Zhan[32d], D. Zhang[32b,ag], H. Zhang[88], J. Zhang[5], X. Zhang[32d], Z. Zhang[115], L. Zhao[108], T. Zhao[138], Z. Zhao[32b], A. Zhemchugov[65], S. Zheng[32a], J. Zhong[118], B. Zhou[87], N. Zhou[163], Y. Zhou[151], C.G. Zhu[32d], H. Zhu[41], J. Zhu[87], Y. Zhu[32b], X. Zhuang[98], V. Zhuravlov[99], D. Zieminska[61], R. Zimmermann[20], S. Zimmermann[20], S. Zimmermann[48], M. Ziolkowski[141], R. Zitoun[4], L. Živković[34], V.V. Zmouchko[128,*], G. Zobernig[172], A. Zoccoli[19a,19b], Y. Zolnierowski[4], A. Zsenei[29], M. zur Nedden[15], V. Zutshi[106], L. Zwalinski[29].

JHEP05(2012)059

1 University at Albany, Albany NY, United States of America
2 Department of Physics, University of Alberta, Edmonton AB, Canada
3 (a) Department of Physics, Ankara University, Ankara; (b) Department of Physics, Dumlupinar University, Kutahya; (c) Department of Physics, Gazi University, Ankara; (d) Division of Physics, TOBB University of Economics and Technology, Ankara; (e) Turkish Atomic Energy Authority, Ankara, Turkey
4 LAPP, CNRS/IN2P3 and Université de Savoie, Annecy-le-Vieux, France
5 High Energy Physics Division, Argonne National Laboratory, Argonne IL, United States of America
6 Department of Physics, University of Arizona, Tucson AZ, United States of America
7 Department of Physics, The University of Texas at Arlington, Arlington TX, United States of America
8 Physics Department, University of Athens, Athens, Greece
9 Physics Department, National Technical University of Athens, Zografou, Greece
10 Institute of Physics, Azerbaijan Academy of Sciences, Baku, Azerbaijan
11 Institut de Física d'Altes Energies and Departament de Física de la Universitat Autònoma de Barcelona and ICREA, Barcelona, Spain
12 (a) Institute of Physics, University of Belgrade, Belgrade; (b) Vinca Institute of Nuclear Sciences, University of Belgrade, Belgrade, Serbia
13 Department for Physics and Technology, University of Bergen, Bergen, Norway
14 Physics Division, Lawrence Berkeley National Laboratory and University of California, Berkeley CA, United States of America
15 Department of Physics, Humboldt University, Berlin, Germany
16 Albert Einstein Center for Fundamental Physics and Laboratory for High Energy Physics, University of Bern, Bern, Switzerland
17 School of Physics and Astronomy, University of Birmingham, Birmingham, United Kingdom
18 (a) Department of Physics, Bogazici University, Istanbul; (b) Division of Physics, Dogus University, Istanbul; (c) Department of Physics Engineering, Gaziantep University, Gaziantep; (d) Department of Physics, Istanbul Technical University, Istanbul, Turkey
19 (a) INFN Sezione di Bologna; (b) Dipartimento di Fisica, Università di Bologna, Bologna, Italy
20 Physikalisches Institut, University of Bonn, Bonn, Germany
21 Department of Physics, Boston University, Boston MA, United States of America
22 Department of Physics, Brandeis University, Waltham MA, United States of America
23 (a) Universidade Federal do Rio De Janeiro COPPE/EE/IF, Rio de Janeiro; (b) Federal University of Juiz de Fora (UFJF), Juiz de Fora; (c) Federal University of Sao Joao del Rei (UFSJ), Sao Joao del Rei; (d) Instituto de Fisica, Universidade de Sao Paulo, Sao Paulo, Brazil
24 Physics Department, Brookhaven National Laboratory, Upton NY, United States of America
25 (a) National Institute of Physics and Nuclear Engineering, Bucharest; (b) University Politehnica Bucharest, Bucharest; (c) West University in Timisoara, Timisoara, Romania
26 Departamento de Física, Universidad de Buenos Aires, Buenos Aires, Argentina
27 Cavendish Laboratory, University of Cambridge, Cambridge, United Kingdom
28 Department of Physics, Carleton University, Ottawa ON, Canada
29 CERN, Geneva, Switzerland
30 Enrico Fermi Institute, University of Chicago, Chicago IL, United States of America
31 (a) Departamento de Fisica, Pontificia Universidad Católica de Chile, Santiago; (b) Departamento de Física, Universidad Técnica Federico Santa María, Valparaíso, Chile

JHEP05(2012)059

32 (a) Institute of High Energy Physics, Chinese Academy of Sciences, Beijing; (b) Department of Modern Physics, University of Science and Technology of China, Anhui; (c) Department of Physics, Nanjing University, Jiangsu; (d) School of Physics, Shandong University, Shandong, China
33 Laboratoire de Physique Corpusculaire, Clermont Université and Université Blaise Pascal and CNRS/IN2P3, Aubiere Cedex, France
34 Nevis Laboratory, Columbia University, Irvington NY, United States of America
35 Niels Bohr Institute, University of Copenhagen, Kobenhavn, Denmark
36 (a) INFN Gruppo Collegato di Cosenza; (b) Dipartimento di Fisica, Università della Calabria, Arcavata di Rende, Italy
37 AGH University of Science and Technology, Faculty of Physics and Applied Computer Science, Krakow, Poland
38 The Henryk Niewodniczanski Institute of Nuclear Physics, Polish Academy of Sciences, Krakow, Poland
39 Physics Department, Southern Methodist University, Dallas TX, United States of America
40 Physics Department, University of Texas at Dallas, Richardson TX, United States of America
41 DESY, Hamburg and Zeuthen, Germany
42 Institut für Experimentelle Physik IV, Technische Universität Dortmund, Dortmund, Germany
43 Institut für Kern- und Teilchenphysik, Technical University Dresden, Dresden, Germany
44 Department of Physics, Duke University, Durham NC, United States of America
45 SUPA - School of Physics and Astronomy, University of Edinburgh, Edinburgh, United Kingdom
46 Fachhochschule Wiener Neustadt, Johannes Gutenbergstrasse 3 2701 Wiener Neustadt, Austria
47 INFN Laboratori Nazionali di Frascati, Frascati, Italy
48 Fakultät für Mathematik und Physik, Albert-Ludwigs-Universität, Freiburg i.Br., Germany
49 Section de Physique, Université de Genève, Geneva, Switzerland
50 (a) INFN Sezione di Genova; (b) Dipartimento di Fisica, Università di Genova, Genova, Italy
51 (a) E.Andronikashvili Institute of Physics, Tbilisi State University, Tbilisi; (b) High Energy Physics Institute, Tbilisi State University, Tbilisi, Georgia
52 II Physikalisches Institut, Justus-Liebig-Universität Giessen, Giessen, Germany
53 SUPA - School of Physics and Astronomy, University of Glasgow, Glasgow, United Kingdom
54 II Physikalisches Institut, Georg-August-Universität, Göttingen, Germany
55 Laboratoire de Physique Subatomique et de Cosmologie, Université Joseph Fourier and CNRS/IN2P3 and Institut National Polytechnique de Grenoble, Grenoble, France
56 Department of Physics, Hampton University, Hampton VA, United States of America
57 Laboratory for Particle Physics and Cosmology, Harvard University, Cambridge MA, United States of America
58 (a) Kirchhoff-Institut für Physik, Ruprecht-Karls-Universität Heidelberg, Heidelberg; (b) Physikalisches Institut, Ruprecht-Karls-Universität Heidelberg, Heidelberg; (c) ZITI Institut für technische Informatik, Ruprecht-Karls-Universität Heidelberg, Mannheim, Germany
59 Faculty of Science, Hiroshima University, Hiroshima, Japan
60 Faculty of Applied Information Science, Hiroshima Institute of Technology, Hiroshima, Japan
61 Department of Physics, Indiana University, Bloomington IN, United States of America
62 Institut für Astro- und Teilchenphysik, Leopold-Franzens-Universität, Innsbruck, Austria
63 University of Iowa, Iowa City IA, United States of America
64 Department of Physics and Astronomy, Iowa State University, Ames IA, United States of America
65 Joint Institute for Nuclear Research, JINR Dubna, Dubna, Russia

JHEP05(2012)059

66 KEK, High Energy Accelerator Research Organization, Tsukuba, Japan
67 Graduate School of Science, Kobe University, Kobe, Japan
68 Faculty of Science, Kyoto University, Kyoto, Japan
69 Kyoto University of Education, Kyoto, Japan
70 Instituto de Física La Plata, Universidad Nacional de La Plata and CONICET, La Plata, Argentina
71 Physics Department, Lancaster University, Lancaster, United Kingdom
72 (a) INFN Sezione di Lecce; (b) Dipartimento di Fisica, Università del Salento, Lecce, Italy
73 Oliver Lodge Laboratory, University of Liverpool, Liverpool, United Kingdom
74 Department of Physics, Jožef Stefan Institute and University of Ljubljana, Ljubljana, Slovenia
75 School of Physics and Astronomy, Queen Mary University of London, London, United Kingdom
76 Department of Physics, Royal Holloway University of London, Surrey, United Kingdom
77 Department of Physics and Astronomy, University College London, London, United Kingdom
78 Laboratoire de Physique Nucléaire et de Hautes Energies, UPMC and Université Paris-Diderot and CNRS/IN2P3, Paris, France
79 Fysiska institutionen, Lunds universitet, Lund, Sweden
80 Departamento de Fisica Teorica C-15, Universidad Autonoma de Madrid, Madrid, Spain
81 Institut für Physik, Universität Mainz, Mainz, Germany
82 School of Physics and Astronomy, University of Manchester, Manchester, United Kingdom
83 CPPM, Aix-Marseille Université and CNRS/IN2P3, Marseille, France
84 Department of Physics, University of Massachusetts, Amherst MA, United States of America
85 Department of Physics, McGill University, Montreal QC, Canada
86 School of Physics, University of Melbourne, Victoria, Australia
87 Department of Physics, The University of Michigan, Ann Arbor MI, United States of America
88 Department of Physics and Astronomy, Michigan State University, East Lansing MI, United States of America
89 (a) INFN Sezione di Milano; (b) Dipartimento di Fisica, Università di Milano, Milano, Italy
90 B.I. Stepanov Institute of Physics, National Academy of Sciences of Belarus, Minsk, Republic of Belarus
91 National Scientific and Educational Centre for Particle and High Energy Physics, Minsk, Republic of Belarus
92 Department of Physics, Massachusetts Institute of Technology, Cambridge MA, United States of America
93 Group of Particle Physics, University of Montreal, Montreal QC, Canada
94 P.N. Lebedev Institute of Physics, Academy of Sciences, Moscow, Russia
95 Institute for Theoretical and Experimental Physics (ITEP), Moscow, Russia
96 Moscow Engineering and Physics Institute (MEPhI), Moscow, Russia
97 Skobeltsyn Institute of Nuclear Physics, Lomonosov Moscow State University, Moscow, Russia
98 Fakultät für Physik, Ludwig-Maximilians-Universität München, München, Germany
99 Max-Planck-Institut für Physik (Werner-Heisenberg-Institut), München, Germany
100 Nagasaki Institute of Applied Science, Nagasaki, Japan
101 Graduate School of Science, Nagoya University, Nagoya, Japan
102 (a) INFN Sezione di Napoli; (b) Dipartimento di Scienze Fisiche, Università di Napoli, Napoli, Italy
103 Department of Physics and Astronomy, University of New Mexico, Albuquerque NM, United States of America
104 Institute for Mathematics, Astrophysics and Particle Physics, Radboud University Nijmegen/Nikhef, Nijmegen, Netherlands

JHEP05(2012)059

105 Nikhef National Institute for Subatomic Physics and University of Amsterdam, Amsterdam, Netherlands
106 Department of Physics, Northern Illinois University, DeKalb IL, United States of America
107 Budker Institute of Nuclear Physics, SB RAS, Novosibirsk, Russia
108 Department of Physics, New York University, New York NY, United States of America
109 Ohio State University, Columbus OH, United States of America
110 Faculty of Science, Okayama University, Okayama, Japan
111 Homer L. Dodge Department of Physics and Astronomy, University of Oklahoma, Norman OK, United States of America
112 Department of Physics, Oklahoma State University, Stillwater OK, United States of America
113 Palacký University, RCPTM, Olomouc, Czech Republic
114 Center for High Energy Physics, University of Oregon, Eugene OR, United States of America
115 LAL, Univ. Paris-Sud and CNRS/IN2P3, Orsay, France
116 Graduate School of Science, Osaka University, Osaka, Japan
117 Department of Physics, University of Oslo, Oslo, Norway
118 Department of Physics, Oxford University, Oxford, United Kingdom
119 (a) INFN Sezione di Pavia; (b) Dipartimento di Fisica, Università di Pavia, Pavia, Italy
120 Department of Physics, University of Pennsylvania, Philadelphia PA, United States of America
121 Petersburg Nuclear Physics Institute, Gatchina, Russia
122 (a) INFN Sezione di Pisa; (b) Dipartimento di Fisica E. Fermi, Università di Pisa, Pisa, Italy
123 Department of Physics and Astronomy, University of Pittsburgh, Pittsburgh PA, United States of America
124 (a) Laboratorio de Instrumentacao e Fisica Experimental de Particulas - LIP, Lisboa, Portugal; (b) Departamento de Fisica Teorica y del Cosmos and CAFPE, Universidad de Granada, Granada, Spain
125 Institute of Physics, Academy of Sciences of the Czech Republic, Praha, Czech Republic
126 Faculty of Mathematics and Physics, Charles University in Prague, Praha, Czech Republic
127 Czech Technical University in Prague, Praha, Czech Republic
128 State Research Center Institute for High Energy Physics, Protvino, Russia
129 Particle Physics Department, Rutherford Appleton Laboratory, Didcot, United Kingdom
130 Physics Department, University of Regina, Regina SK, Canada
131 Ritsumeikan University, Kusatsu, Shiga, Japan
132 (a) INFN Sezione di Roma I; (b) Dipartimento di Fisica, Università La Sapienza, Roma, Italy
133 (a) INFN Sezione di Roma Tor Vergata; (b) Dipartimento di Fisica, Università di Roma Tor Vergata, Roma, Italy
134 (a) INFN Sezione di Roma Tre; (b) Dipartimento di Fisica, Università Roma Tre, Roma, Italy
135 (a) Faculté des Sciences Ain Chock, Réseau Universitaire de Physique des Hautes Energies - Université Hassan II, Casablanca; (b) Centre National de l'Energie des Sciences Techniques Nucleaires, Rabat; (c) Faculté des Sciences Semlalia, Université Cadi Ayyad, LPHEA-Marrakech; (d) Faculté des Sciences, Université Mohamed Premier and LPTPM, Oujda; (e) Faculté des Sciences, Université Mohammed V- Agdal, Rabat, Morocco
136 DSM/IRFU (Institut de Recherches sur les Lois Fondamentales de l'Univers), CEA Saclay (Commissariat a l'Energie Atomique), Gif-sur-Yvette, France
137 Santa Cruz Institute for Particle Physics, University of California Santa Cruz, Santa Cruz CA, United States of America
138 Department of Physics, University of Washington, Seattle WA, United States of America
139 Department of Physics and Astronomy, University of Sheffield, Sheffield, United Kingdom

JHEP05(2012)059

140 Department of Physics, Shinshu University, Nagano, Japan
141 Fachbereich Physik, Universität Siegen, Siegen, Germany
142 Department of Physics, Simon Fraser University, Burnaby BC, Canada
143 SLAC National Accelerator Laboratory, Stanford CA, United States of America
144 (a) Faculty of Mathematics, Physics & Informatics, Comenius University, Bratislava; (b) Department of Subnuclear Physics, Institute of Experimental Physics of the Slovak Academy of Sciences, Kosice, Slovak Republic
145 (a) Department of Physics, University of Johannesburg, Johannesburg; (b) School of Physics, University of the Witwatersrand, Johannesburg, South Africa
146 (a) Department of Physics, Stockholm University; (b) The Oskar Klein Centre, Stockholm, Sweden
147 Physics Department, Royal Institute of Technology, Stockholm, Sweden
148 Departments of Physics & Astronomy and Chemistry, Stony Brook University, Stony Brook NY, United States of America
149 Department of Physics and Astronomy, University of Sussex, Brighton, United Kingdom
150 School of Physics, University of Sydney, Sydney, Australia
151 Institute of Physics, Academia Sinica, Taipei, Taiwan
152 Department of Physics, Technion: Israel Inst. of Technology, Haifa, Israel
153 Raymond and Beverly Sackler School of Physics and Astronomy, Tel Aviv University, Tel Aviv, Israel
154 Department of Physics, Aristotle University of Thessaloniki, Thessaloniki, Greece
155 International Center for Elementary Particle Physics and Department of Physics, The University of Tokyo, Tokyo, Japan
156 Graduate School of Science and Technology, Tokyo Metropolitan University, Tokyo, Japan
157 Department of Physics, Tokyo Institute of Technology, Tokyo, Japan
158 Department of Physics, University of Toronto, Toronto ON, Canada
159 (a) TRIUMF, Vancouver BC; (b) Department of Physics and Astronomy, York University, Toronto ON, Canada
160 Institute of Pure and Applied Sciences, University of Tsukuba,1-1-1 Tennodai,Tsukuba, Ibaraki 306-8572, Japan
161 Science and Technology Center, Tufts University, Medford MA, United States of America
162 Centro de Investigaciones, Universidad Antonio Narino, Bogota, Colombia
163 Department of Physics and Astronomy, University of California Irvine, Irvine CA, United States of America
164 (a) INFN Gruppo Collegato di Udine; (b) ICTP, Trieste; (c) Dipartimento di Chimica, Fisica e Ambiente, Università di Udine, Udine, Italy
165 Department of Physics, University of Illinois, Urbana IL, United States of America
166 Department of Physics and Astronomy, University of Uppsala, Uppsala, Sweden
167 Instituto de Física Corpuscular (IFIC) and Departamento de Física Atómica, Molecular y Nuclear and Departamento de Ingeniería Electrónica and Instituto de Microelectrónica de Barcelona (IMB-CNM), University of Valencia and CSIC, Valencia, Spain
168 Department of Physics, University of British Columbia, Vancouver BC, Canada
169 Department of Physics and Astronomy, University of Victoria, Victoria BC, Canada
170 Waseda University, Tokyo, Japan
171 Department of Particle Physics, The Weizmann Institute of Science, Rehovot, Israel
172 Department of Physics, University of Wisconsin, Madison WI, United States of America
173 Fakultät für Physik und Astronomie, Julius-Maximilians-Universität, Würzburg, Germany
174 Fachbereich C Physik, Bergische Universität Wuppertal, Wuppertal, Germany
175 Department of Physics, Yale University, New Haven CT, United States of America

JHEP05(2012)059

176 Yerevan Physics Institute, Yerevan, Armenia
177 Domaine scientifique de la Doua, Centre de Calcul CNRS/IN2P3, Villeurbanne Cedex, France
a Also at Laboratorio de Instrumentacao e Fisica Experimental de Particulas - LIP, Lisboa, Portugal
b Also at Faculdade de Ciencias and CFNUL, Universidade de Lisboa, Lisboa, Portugal
c Also at Particle Physics Department, Rutherford Appleton Laboratory, Didcot, United Kingdom
d Also at TRIUMF, Vancouver BC, Canada
e Also at Department of Physics, California State University, Fresno CA, United States of America
f Also at Novosibirsk State University, Novosibirsk, Russia
g Also at Fermilab, Batavia IL, United States of America
h Also at Department of Physics, University of Coimbra, Coimbra, Portugal
i Also at Università di Napoli Parthenope, Napoli, Italy
j Also at Institute of Particle Physics (IPP), Canada
k Also at Department of Physics, Middle East Technical University, Ankara, Turkey
l Also at Louisiana Tech University, Ruston LA, United States of America
m Also at Department of Physics and Astronomy, University College London, London, United Kingdom
n Also at Group of Particle Physics, University of Montreal, Montreal QC, Canada
o Also at Department of Physics, University of Cape Town, Cape Town, South Africa
p Also at Institute of Physics, Azerbaijan Academy of Sciences, Baku, Azerbaijan
q Also at Institut für Experimentalphysik, Universität Hamburg, Hamburg, Germany
r Also at Manhattan College, New York NY, United States of America
s Also at School of Physics, Shandong University, Shandong, China
t Also at CPPM, Aix-Marseille Université and CNRS/IN2P3, Marseille, France
u Also at School of Physics and Engineering, Sun Yat-sen University, Guanzhou, China
v Also at Academia Sinica Grid Computing, Institute of Physics, Academia Sinica, Taipei, Taiwan
w Also at DSM/IRFU (Institut de Recherches sur les Lois Fondamentales de l'Univers), CEA Saclay (Commissariat a l'Energie Atomique), Gif-sur-Yvette, France
x Also at section de Physique, Université de Genève, Geneva, Switzerland
y Also at Departamento de Fisica, Universidade de Minho, Braga, Portugal
z Also at Department of Physics and Astronomy, University of South Carolina, Columbia SC, United States of America
aa Also at Institute for Particle and Nuclear Physics, Wigner Research Centre for Physics, Budapest, Hungary
ab Also at California Institute of Technology, Pasadena CA, United States of America
ac Also at Institute of Physics, Jagiellonian University, Krakow, Poland
ad Also at Institute of High Energy Physics, Chinese Academy of Sciences, Beijing, China
ae Also at Department of Physics and Astronomy, University of Sheffield, Sheffield, United Kingdom
af Also at Department of Physics, Oxford University, Oxford, United Kingdom
ag Also at Institute of Physics, Academia Sinica, Taipei, Taiwan
ah Also at Department of Physics, The University of Michigan, Ann Arbor MI, United States of America
ai Also at Laboratoire de Physique Nucléaire et de Hautes Energies, UPMC and Université Paris-Diderot and CNRS/IN2P3, Paris, France
* Deceased

JHEP05(2012)059

計画研究 A05 班

課題名「テラスケール物理の理論的研究」

研究組織

(1) 研究代表者

野尻美保子　（NOJIRI, Mihoko）
大学共同利用機関法人・高エネルギー加速器研究機構・素粒子原子核機構・教授
研究者番号：30222201

(2) 研究分担者

兼村晋哉（KANEMURA, Shinya）
富山大学・大学院理工学研究部・准教授
研究者番号： 10362609

(3) 連携研究者

阿部智広（ABE, Tomohiro）
大学共同利用機関法人高エネルギー加速器研究機構素粒子原子核研究機構　素粒子原子核研究所
研究員
研究者番号：　70712727

交付決定額

計画研究 A05 班に配分された交付額を表 1 に示す。

表 1. 交付決定額（配分額）　（金額単位：円）

年度	直接経費	間接経費	合計
平成 23 年度	8,300,000	2,490,000	10,790,000
平成 24 年度	7,400,000	2,220,000	9,620,000
平成 25 年度	7,500,000	2,250,000	9,750,000
平成 26 年度	7,100,000	2,130,000	9,230,000
平成 27 年度	7,100,000	2,130,000	9,230,000
総計	37,400,000	11,220,000	48,620,000

研究成果

研究開始当初の背景

素粒子の標準理論の最大の謎である、ゲージ対称性の自発的破れや宇宙における暗黒物質の存在などは、テラスケールに新しい自然法則が存在することを示唆している。このテラスケール物理によって、ゲージ対称性が破れ、超高エネルギーでの力の統一理論から現在の自然界の多様性が生み出されたと考えられている。この研究計画実施時にこのテラスケール物理を探る LHC (Large Hadron Collider)実験が CERN で開始された。

LHC 実験では Higgs 粒子の発見によって、標準理論を完成させるほか、最大で数 TeV までの新粒子の探索することができる。このように高い成果が期待される LHC 実験ではあるが、ハドロンコライダーであるために、非常に多くのバックグラウンドがあり、たとえ新しい現象が存在しても、その発見は容易ではない。(LHC でのバックグラウンドの特徴は、多数のジェットが同時に生成される事象が多く、LHC での最新の実験結果をふまえた研究を理論・実験グループが緊密な連携をとって行う必要があった。　LHC で発見が期待されている新しい素粒子現象は、標準理論からの分布のズレである。様々な分布を精密に検討することで、発見された事象の背景にある素粒子現象を理解し、テラスケールの新しい物理を解明することが二つ目の目的である。まだ、LHC で発見が確実と考えられる Higgs 粒子についてはその性質をより幅広い視点から検討する必要があった。

2．研究の目的

本研究の目的は以下の３つである。(1)　QCD の理論的研究を行い LHC 実験での寺スケール物理探索のバックグラウンドを解明する。この研究により計画研究 A01~A04 が LHC 実験で新しい現象を確実に発見することをサポートする.(2) 標準模型からの分布のズレから新粒子の断面積、崩壊パターン、スピン、質量を測定する新しい解析方法を考案する。(3) テラスケールでの新物理を新しいパラダイム（時空、宇宙、宇宙 など）に転換する研究を行い、この実験的検証にむけた現象論的研究を行う。

3．研究の方法

高次補正を取り入れた QCD の研究を行う。特に摂動部と非摂動部の切り分けを理論的に行い理論的に安定な予言を導きデータとの比較を行う。
様々なモデルやパラメータが予言する信号のトポロジーを研究して信号から背後の物理を逆にたどることができる様にする。
運動量分布、不変質量分布やその組み合わせの分布やエッジから、新粒子の質量、スピン、崩壊分岐比を決める方法を複数確立する。
ヒッグス粒子の発見能力や測定精度を向上させるため、H23 年度の QCD の研究を基に、サブジェット解析等の研究を行う。標準理論を超えたヒッグス粒子の研究を行い発見されたヒッグスの性質を探る。
発見された新現象の背後に潜む原理や理論を探る. 特に暗黒物質の物理や、ヒッグス粒子の決定する真空の構造や安定性と関わる物理を研究する。
上記のような研究を行うためには最新の計算機の存在が必須であり、コア数の多い計算機の購入を行った。また、最初の２年は暗黒物質の物理に詳しい長尾氏、最後の３年間はヒッグス粒子の性質や複合模型に明るい阿部氏を雇用し連携研究者とした。また高ネエルギー加速器研究機構の萩原教授を連携として、Madgraph 等の高エネルギー物理関連ツールの利用や、QCD の高次計算について、適切な助言が受けられるようにした。研究体制としては、KEK の学生の久保田と Higgs 粒子と Radion 粒子の混合模型についての研究、KEK の学生の坂木氏と Jet の内部構造について研究を行った。また、IPMU では、学生の飛岡氏（現 Weisman 研究員） 張ヶ谷氏(現 バークレー研究員)、福田氏(現東大院生) IPMU　准教授の松本氏、PD の　Mandal, Mukhopadhyay, Bhattacherjee, 竹内、Han 各氏と暗黒物質や、ジェット構造についての共同研究を行った。

また、兼村は Higgs 粒子の発見を受けて、2011 年から 2015 年の期間に、富山大学でヒッグス物理やテラスケール物理に関する研究会と国際会議を 4 回主催した。また新ヒッグス勉強会(New Higgs Working Group)を主宰し 2012 年以降 2015 年までに 16 回の定例会を富山大学で開催してレポートを

まとめるとともに、多くの論文を執筆し発表を行った。

LHC 実験の理論的研究をしている研究者は欧米に多数いるため、研究会を開催したり、外国人ビジターを招聘する等した。特に、研究代表者が関わった主たる研究会として B4 班と共同で開催した "Physics Opportunities at LHC"201 2 年 2 月 16 日—18 日（KEK で開催） "Higgs as a Probe of New Physics 2013" 2013 年 2 月 13 日-16 日がある。

また、LHC の物理現象をモデル化する MC simulation は大変重要であるため、国際的なスクールを開催した。研究代表者が世話人として関わったものに、Monte Carlo Tools for LHC" School and Workshop を 2011 年 9 月 5 日-10 日に京都で開催), School on the Future of Collider Physics (16-19 July 2013, 東京大学 KIPMU) 2015 年には LHC RunII の開始をうけ、LHC 関係のツールの講習会(Collider 勉強会)を東京大学の諸井氏等（B05 班）の協力を得て 5 回開催した。

４．研究成果

野尻は科研費の研究期間中に１８件の原著論文を発表した。

[top partner の探索と性質の解明]

スカラートップ粒子崩壊から生成されトップ粒子の偏曲を利用して、スカラートップ粒子の右左混合を図る方法をを研究した。特にジェットの内部構造を利用した再構成方法の枠内でハドロニックなトップの崩壊についても偏曲の測定が可能であることを示した。

多くの標準模型を超える物理において、top 粒子のパートナー粒子であるフェルミオンの存在が予想される。このような粒子は、ht, Zt, bW といった終状態に崩壊することが期待されるが multi b-jet の final state に 着目することが、このような信号を取り出すことができることを明らかにした

[Higgs 粒子の性質]

LHC RUN1 でヒッグス粒子の分岐比にたいして標準模型からのずれがある可能性が指摘されたため、余剰次元模型の予言する Radion 粒子とヒッグス粒子の混合によってこのような異常がおこりうることを指摘した。その後この研究を発展させ、より高い精度の測定が期待できる ILC 実験によって Radion の質量が 10TeV をはるかに超える場合でも、標準模型からのずれを測定できることを示した。

LHC 実験の成功にともなって、ILC 実験が LHC 実験の後でも新物理探索に有効であるかを検討する必要が生じた。Higgs 粒子の精密測定によって明らかになる標準模型を超える物理の例として、超対象模型に着目し、スカラートップ粒子が LHC 実験で発見できないような場合でも、Higgs 粒子の分岐比の標準模型からのずれが ILC で観測できることをあきらかにするとともに, 真空の安定性の制限や、B の希少崩壊からの制限が Higgs 分岐比の標準模型からのずれを制限していることを明らかにした。

[jet の物理の研究]

quark から生成されるジェットと gluon から生成されるジェットでは、charged track の数やジェットの広さなどの性質が異なっている。このような性質を捉えて jet の起源を解明すれば new physics への感度を向上できると期待されるため、アルゴリズムの改善を行うとともに、縮退領域にある超対称模型において、実際に感度向上に役に立つことを指摘した。
[LHC 実験での新物理の兆候の研究]
LHC Run I 実験において 2TeV の gauge boson 信号に過剰があるという報告がなされた。この粒子は、主に W, Z の 2 体粒子に崩壊すると考えられた。この粒子の 13TeV での探索感度について検討を行うとともに、jet substructure を使った方法で, jet 内の number of charged track を background の評価に加えると background rejection の効率に大きな不定性がある問題を指摘した。
LHC Run II 実験のデータにおいて Diphoton イベントの過剰が報告された。重たいカラーをもつ粒子と暗黒物質が Z2 parity odd であるような模型において、heavy quark が束縛状態として生成され、それが、2 photon に消滅する場合に、このような信号が得られることを指摘した。さらに暗黒物質密度が適切な値であるためには、質量が縮退している必要があることを示し、LHC において、このような模型のパラメーターが mono jet search によって制限されていることを指摘した。また、750 GeV の信号を説明することができるパラメータがこのような制限のもとで、exclude されていないことを示した。

兼村は以下のような研究を行った。

発見されたヒッグス粒子の性質からヒッグスセクターの構造、ひいては新物理学の方向性を決定するための理論研究：
2012 年に LHC でヒッグス粒子は一つ発見されたが、ヒッグスセクターの構造は未知であり様々な拡張されたヒッグスセクターの可能性がある。本研究では、超対称性や複合ヒッグス模型等の新物理モデルに基づくヒッグスセクターや、一般の拡張ヒッグスセクターを考えた時、ヒッグス粒子の結合定数がどのようなパターンでずれるかを系統的に研究した。特に標準理論のヒッグス２重項場に付加的なヒッグス場が一個加わった拡張ヒッグスセクターに基づいてヒッグス結合に対する輻射補正を研究し、将来の加速器実験でヒッグス結合が精密に測定され、標準理論からのズレが検出された時に、そのズレのパターンからヒッグスセクターの構造、ひいては新物理理論の方向性を決定する可能性を明らかにした。
(2)第２のヒッグス粒子の探索に関する理論 研究：
様々な新物理モデルに導入される拡張ヒッグスセクターには特徴のある付加的ヒッグス場が現れる。本研究では、超対称性模型等に現れる輻射シーソーモデルなどに現れるヒッグス２重項場が２個あるモデルに出てくる第２のヒッグス粒子の LHC や ILC での探索可能性について系統的に研究した。また、タイプ２シーソー模型に現れるトリプレット場は複荷電ヒッグス場を予言する

が、このようなエキゾチックな場が LHC でどのように検証されるかを研究し、ダイボソン崩壊が支配的なシナリオにおける LHC からの質量のバウンドを正解で初めて求めた。
(3)様々な新物理パラダイムにおけるヒッグスポテンシャルの研究と、
実験での検証可能性の研究：
ヒッグス粒子の発見によって、ヒッグス機構や湯川相互作用等の標準理論の質量生成機構は実証された。しかし、電弱対称性の破れを担うヒッグスポテンシャルや背後のダイナミクスは依然として未知である。本研究では、軽いヒッグスを予言するが高エネルギーでヒッグスダイナミクスが強結合になる模型の詳細を研究し、ランダウポールの上の UV 理論の構築、低エネルギーでの現象論、ニュートリノ輻射生成や電弱バリオン数生成のシナリオの実現可能性を調べた。また古典的共形不変性に基づく電弱対称性の破れのモデルを研究し、そのヒッグスセクターの一般的性質を明らかにした。さらに最小複合ヒッグス理論のヒッグスセクターの性質を詳細に検討し、その現象論と加速器実験での検証可能性を明らかにした。
(4)ニュートリノ質量、暗黒物質、バリオン数生成に関する模型構築 とその現象論の研究：
B－L ゲージ対称性の自発的破れが引き金となって暗黒物質質量やニュートリノ質量が生成されるモデルを構築しその現象論を研究した。超対称性の枠組みで輻射シーソー模型を構築し、この模型に現れるマルチコンポネント暗黒物質の性質を調べ、検証可能性を研究した。電弱バリオン数生成のモデルを研究し、このシナリオの一般的特徴である強い一次的電弱相転移の実験的検証に関して、HL-LHC や ILC 等の将来加速器実験におけるヒッグス自己結合の測定と eLISA 計画などの将来重力波実験でのスペクトル測定による検証を研究し、その相補性を明らかにした。

５年間のこれらの成果は、約 50 報の査読付き論文として出版するとともに多数の学会、国際会議で発表した。

科研費研究員として雇用したのは長尾氏と阿部智弘氏であり、このうち長尾氏の雇用期間中の論文は 2 件　阿部氏の雇用期間中の原著論文は 6 件であり、このうちの一件は野尻との共著である。阿部氏の研究のなかで、主たる成果は以下の通りである。
部分的に複合模型である模型を構築し、その現象論的特性を明らかにし、とくに、Higgs 発見当初に話題になっていた、Higgs 粒子が 2photon mode に崩壊する分岐比率にみられる excess が説明可能であることをあきらかにした。また 2TeV の diphoton についても、実験データの示唆する信号をこの模型で説明できるかを精密測定の制限をいれて調べ、13TeV の LHC 実験での検証可能性を明らかにした。
two Higgs doublet 模型で期待される EDM 模型の two loop の寄与を求めた
Higgs 粒子にのみ暗黒物質が結合するような模型を暗黒物質となる粒子のスピンによって分類し、暗黒物質が LHC や ILC で探索可能かを調べるとともに、暗黒物質密度や、その相互作用などをあきらかにした。

Type X の two Higgs doublet 模型の実験的な制限を詳細に調べ、LHC 等でのシグナルを検討した。なおこの研究によって阿部氏は素粒子メダル奨励賞を受賞した http://www2.yukawa.kyoto-u.ac.jp/~sg.www/syorei_s/result15/Smedal15.html

5 .主な発表論文等

（研究代表者、研究分担者及び連携研究者には下線）

〔雑誌論文〕（計 55 件）

主な論文

①Chengcheng Han, Koji Ichikawa, Shigeki Matsumoto, Mihoko M. Nojiri, 他. “Heavy fermion bound states for diphoton excess at 750 GeV — collider and cosmological constraints” JHEP 1604 (2016) 159, 1 査読あり, DOI: 10.1007/JHEP04(2016)159

②Tomohiro Abe, Teppei Kitahara and Mihoko M. Nojiri.
“Prospects for Spin-1 Resonance Search at 13 TeV LHC and the ATLAS Diboson Excess” JHEP 1602 (2016) 084 査読あり, DOI: 10.1007/JHEP02(2016)084

③Tomohiro Abe, Ryo Nagai, Shohei Okawa, Masaharu Tanabashi, “Unitarity sum rules, three-site moose model, and the ATLAS 2 TeV diboson anomalies”
Phys.Rev. D92 (2015) 055016, 1-14, 査読あり, DOI: 10.1103/PhysRevD.92.055016

④ Tomohiro Abe, Ryosuke Sato, Kei Yagyu. “Lepton-specific two Higgs doublet model as a solution of muon g − 2 anomaly
JHEP 1507 (2015) 064, 査読あり, DOI: 10.1007/JHEP07(2015)064

⑤Biplob Bhattacherjee, Satyanarayan Mukhopadhyay, Mihoko M. Nojiri, 他, “Associated jet and subjet rates in light-quark and gluon jet discrimination”, JHEP 1504 (2015) 131. 査読あり, DOI: 10.1007/JHEP04(2015)131

⑥Tomohiro Abe, Ryosuke Sato, “Quantum corrections to the spin-independent cross section of the inert doublet dark matter”
JHEP 1503 (2015) 109, 査読あり, DOI: 10.1007/JHEP03(2015)109

⑦Tomohiro Abe, Ryuichiro Kitano, Ryosuke Sato “Discrimination of dark matter models in future experiments”
Phys.Rev. D91 (2015) no.9, 095004, 査読あり, DOI: 10.1103/PhysRevD.91.095004

⑧Shinya Kanemura, Koji Tsumura, Kei Yagyu, and Hiroshi Yokoya,

“Fingerprinting nonminimal Higgs sectors”,
Physical Review D90, 075001-1, 075001-10 (2014). 査読有り,
DOI: 10.1103/PhysRevD.90.075001
⑨Biplob Bhattacherjee, Sourav K. Mandal and Mihoko M. Nojiri, “Top Polarization and Stop Mixing from Boosted Jet Substructure”,
JHEP 1303 (2013) 105. 査読あり, DOI: 10.1007/JHEP03(2013)105
⑩Shinya Kanemura, Kei Yagyu, Hiroshi Yokoya, “First Constraint on the Mass of Doubly Charged Higgs bosons in the same sign diboson decay scenario at the LHC”,Physics Letters B726, 316-319 (2013). 査読あり, DOI: 10.1016/j.physletb.2013.08.054
⑪ Keisuke Harigaya, Shigeki Matsumoto, Mihoko M. Nojiri, and Kohsaku Tobioka, “Search for the Top Partner at the LHC using Multi-b-Jet Channels”,
Phys.Rev. D86 (2012) 015005. 査読あり, DOI: 10.1103/PhysRevD.86.015005
⑫Shinya Kanemura, Takehiro Nabeshima, Hiroaki Sugiyama,
TeV Scale Seesaw with Loop Induced Dirac Mass Term and Dark Matter from U(1)_{B-L} Gauge Symmetry Breaking,
Physical Review D85, 033004-1 033004-9 (2012). 査読あり, DOI: 10.1103/PhysRevD.85.033004
⑬Mayumi Aoki, Shinya Kanemura, Kei Yagyu, “Testing the Higgs triplet model with the mass difference at LHC”,
Physical Review D85, 055007-1 055007-15 (2012). 査読あり,
DOI: 10.1103/PhysRevD.85.055007
⑭Shinya Kanemura, Osamu Seto, Tadashi Shimomura,
“Masses of Dark Matter and Neutrino from TeV scale Spontaneous B-L symmetry breaking”,Physical Review D84, 016004-1 016004-5 (2011). 査読有り,
DOI: 10.1103/P

〔学会発表〕（計 67 件）

①Shinya Kanemura,
Higgs potential, future colliders, and future GW interferometers,
国際会議 Scalars 2015
2015 年 12 月 3 日～7 日
ワルシャワ、ポーランド
②Shinya Kanemura,
Radiative Corrections to the Yukawa coupling constants in BSM
国際会議 Higgs Couplings 2014

2014 年 10 月 1 日－3 日
Torino, イタリア
③野尻美保子　“Expection for e+e- colliders” Recontres du Vietnam 2014; Physics at LHC and beyond, Quy Nhon, Vietnum. 2014 年 8 月 10 日~17 日
④野尻美保子　19th International Symposium on Particles, Strings and Cosmology (Pascos 2013) 2013 年 11 月 20 日～2013 年 11 月 26 日　Taipei, Taiwan
⑤Shinya Kanemura,
Higgs in BSM models
国際会議 Tohoku Forum for Creativity ==Particle and Cosmology after the discovery of a Higgs boson==
2013 年 10 月 21 日－25 日
東北大学, 宮城県仙台市
Shinya Kanemura,
⑥野尻美保子, “Theoretical Results on PHysics Beyond the Standard Model, XVI International Symposium on Lepton and Photon Interactions at High Energies (LeptonPhoton 2013), 2013 年 6 月 24 日～2013 年　6 月 29 日 San Francisco, CA, USA
⑦Shinya Kanemura
Higgs/EWSB Summary
国際会議 LCWS2012
2012 年 10 月 21 日－26 日
テキサス大学アーリントン校、アメリカ
⑧兼村晋哉
軽いヒッグスの物理（シンポジウム「ヒッグスとコライダー」)
日本物理学会 2012 年秋季大会
2012 年 9 月 11 日－14 日
京都産業大学、京都府京都市
⑨野尻 美保子, “Reconstructing　SUSY”, Supersymmetry 2011, 2011 年 8 月 2 8 日から 2011 年 9 月 2 日 フェルミ国立研究所,バタビア, IL, USA

〔図書〕（計　　0 件）

〔産業財産権〕
○出願状況（計　　0 件）

〇取得状況（計　0　件）

〔その他〕

ホームページ等

2011 IPMU-YITP School and Workshop on Monte Carlo Tools for LHC, 5-11, Sep 2011
http://www.hep.phy.cam.ac.uk/theory/mcschool11/
“Physics Opportunities at LHC” 2012 年 2 月 16 日-18 日
http://research.kek.jp/people/nojiri/shingakujyutu/index.html
School on the Future Collider Physics
KIPMU,　16-19 July, 2013
http://member.ipmu.jp/rie.ujita/school.htm
“collider 勉強会”
http://research.kek.jp/people/nojiri/collider.html

冬の富山素粒子宇宙研究会 2012
http://jodo.sci.u-toyama.ac.jp/theory/workshop12/index.html

HPNP2013
http://jodo.sci.u-toyama.ac.jp/theory/HPNP2013/index.html

BURI 研究会
http://jodo.sci.u-toyama.ac.jp/theory/workshop14/index.html

HPNP2015
http://jodo.sci.u-toyama.ac.jp/theory/HPNP2015/index.html

新ヒッグス勉強会（定例会を 2012 年から年 4 回のペースで実施）
http://jodo.sci.u-toyama.ac.jp/theory/NHWG/index.html

国際シンポジウム開催

(1) “Physics Opportunities at LHC”, 野尻美保子、久野純治、高エネルギー加速器研究機構 つくば市、 平成 24 年 2 月 16 日~18 日
(2) “Higgs as a Probe of New Physics 2013”, 兼村晋哉, 富山大学、平成 25 年 2 月 13 日~16 日 一般公開講演会
(3) パブリック・レクチャー「素粒子と宇宙」、野尻美保子、富山大学、平成２５年２月１７日 http://jodo.sci.u-toyama.ac.jp/theory/HPNP2013_lecture/index.html

主要論文別刷

②Tomohiro Abe, Teppei Kitahara and Mihoko M. Nojiri.
"Prospects for Spin-1 Resonance Search at 13 TeV LHC and the ATLAS Diboson Excess"
JHEP 1602 (2016) 084 査読あり, DOI: 10.1007/JHEP02(2016)084

④ Tomohiro Abe, Ryosuke Sato, Kei Yagyu. "Lepton-specific two Higgs doublet model as a solution of muon g − 2 anomaly
JHEP 1507 (2015) 064, 査読あり, DOI: 10.1007/JHEP07(2015)064

⑤Biplob Bhattacherjee, Satyanarayan Mukhopadhyay, Mihoko M. Nojiri, 他, "Associated jet and subjet rates in light-quark and gluon jet discrimination", JHEP 1504 (2015) 131. 査読あり, DOI: 10.1007/JHEP04(2015)131

⑧Shinya Kanemura, Koji Tsumura, Kei Yagyu, and Hiroshi Yokoya,
"Fingerprinting nonminimal Higgs sectors",
Physical Review D90, 075001-1, 075001-10 (2014). 査読有り,
DOI: 10.1103/PhysRevD.90.075001

⑩Shinya Kanemura, Kei Yagyu, Hiroshi Yokoya, "First Constraint on the Mass of Doubly Charged Higgs bosons in the same sign diboson decay scenario at the LHC",Physics Letters B726, 316-319 (2013). 査読あり, DOI: 10.1016/j.physletb.2013.08.054

Published for SISSA by Springer

Received: July 14, 2015
Revised: January 20, 2016
Accepted: January 21, 2016
Published: February 12, 2016

Prospects for spin-1 resonance search at 13 TeV LHC and the ATLAS diboson excess

Tomohiro Abe,[a] **Teppei Kitahara**[a] **and Mihoko M. Nojiri**[a,b,c]

[a] *KEK Theory Center, IPNS, KEK, Tsukuba, Ibaraki 305-0801, Japan*
[b] *The Graduate University of Advanced Studies (Sokendai), Tsukuba, Ibaraki 305-0801, Japan*
[c] *Kavli IPMU (WPI), University of Tokyo, Kashiwa, Chiba 277–8583, Japan*

E-mail: abetomo@post.kek.jp, kteppei@post.kek.jp, nojiri@post.kek.jp

Abstract: Motivated by ATLAS diboson excess around 2 TeV, we investigate a phenomenology of spin-1 resonances in a model where electroweak sector in the SM is weakly coupled to strong dynamics. The spin-1 resonances, W' and Z', are introduced as effective degrees of freedom of the dynamical sector. We explore several theoretical constraints by investigating the scalar potential of the model as well as the current bounds from the LHC and precision measurements. It is found that the main decay modes are $V' \to VV$ and $V' \to Vh$, and the V' width is narrow enough so that the ATLAS diboson excess can be explained. In order to investigate future prospects, we also perform collider simulations at $\sqrt{s} = 13$ TeV LHC, and obtain a model independent expected exclusion limit for $\sigma(pp \to W' \to WZ \to JJ)$. We find a parameter space where the diboson excess can be explained, and are within a reach of the LHC at $\int dt\mathcal{L} = 10\,\mathrm{fb}^{-1}$ and $\sqrt{s} = 13$ TeV.

Keywords: Phenomenological Models, Monte Carlo Simulations

ArXiv ePrint: 1507.01681

Open Access, © The Authors.
Article funded by SCOAP[3].

doi:10.1007/JHEP02(2016)084

JHEP02(2016)084

Contents

1 Introduction **1**

2 The partially composite standard model **3**
- 2.1 The model setup 3
- 2.2 Model parameters 7

3 Phenomenology of spin-1 resonances **8**
- 3.1 Properties of the extra vector bosons 8
- 3.2 Constraints on the model 10
  - 3.2.1 Theoretical constraints 11
  - 3.2.2 Experimental constraints 13
  - 3.2.3 Summary of the constraints 14
- 3.3 Current status: 8 TeV analyses 16

4 MC simulation of $W' \to WZ$ at $\sqrt{s} = 13$ TeV **20**

5 Future prospects: 13 TeV analyses **24**

6 Conclusion **26**

A Viable range of the coupling ratio κ_Z **27**

B Production cross sections of W' and Z' **28**

C Renormalization group equations **29**

1 Introduction

The ATLAS experiment recently reported an excess of the events in the search for the diboson resonance, in the $pp \to (WW,\ WZ,\ \text{and}\ ZZ) \to JJ$ channels, where J is a fat-jet formed by boosted W or Z boson [1]. The largest local significance is 3.4 σ around 2 TeV in the WZ channel, and the global significance is 2.5 σ. The CMS experiment also studied the same channels. The largest deviation they found is 1.4 σ at $\sim$ 1.9 TeV [2]. Although we cannot conclude that there is a new particle with the mass around 2 TeV from this data, it is worthwhile to consider models which can explain this excess, and many papers have already appeared discussing interpretations of the excess [3–18]. As discussed in these references, a simple candidate is a spin-1 particle.

New vector resonances often appear in the models with dynamical symmetry breaking. Such spin-1 resonances appear in the composite Higgs scenario [19–22] with the dynamics

JHEP02(2016)084

at TeV scale to account for the naturalness problem. Since the models are based on the non-Linear sigma models, the effective theory involves many operators whose coefficients are unknown. They possibly affect to the couplings of the new spin-1 particles to the standard model (SM) particles, and thus there is uncertainty in the prediction of the W' couplings.

Another way to include spin-1 particles is to extend the electroweak gauge symmetry. We can easily introduce new spin-1 particles in renormalizable manner. In that case, the models are calculable and we can avoid the operators whose coefficients are unknown, in contrast to the models based on the non-linear sigma models. Besides, some renormalizable models with extended gauge sector can be regarded as the low energy effective theory of UV theory with some dynamics.

Such renormalizable models have been discussed in the context of the left-right (LR) symmetric model [8, 17, 18] and the leptophobic G221 model [11]. These models contain the right-handed SM fermions which are not singlet under the new gauge symmetry. In such case, the couplings of the SM fermions to the new gauge boson are not suppressed, and the new gauge bosons mainly decay into the SM fermions.

It is also possible to use linear sigma model, instead of non-linear sigma models, for models emerged from the dynamics at TeV scale. An example was proposed in ref. [23]. This model, called the partially composite standard model, has three Higgs fields. Two of them are regarded as effective degrees of freedom below the dynamical scale. The other one is an elementary field. Spin-1 resonances are introduced as new gauge bosons *a la* Hidden local symmetry [24–27]. A feature of the model is that the SM fermion are singlet under the new gauge symmetry, and thus all the fermion couplings to the new gauge bosons are suppressed by the mixing angle in the gauge sector. As a result, the new gauge bosons mainly decay into the SM gauge bosons. This is an important feature of this model.

In this paper, we investigate the possibility to explain the diboson excess by the partially composite standard model, and also the future prospects of W' and Z' bosons searches at the LHC Run-2, where $\sqrt{s} = 13\,\text{TeV}$. We perform a comprehensive study to find the parameter space which has not been excluded from current experimental data. The constraints on the model parameters come from the LHC searches and the electroweak precision measurements. We also require theoretical constraints such as perturbativity condition, bounded below condition, global minimum vacuum condition, and stability condition of the scalar potential. We find a parameter space where the diboson excess can be explained.

We further investigate a model-independent sensitivity at the LHC Run-2 by generating both signal $pp \to W' \to WZ$ and dijet background events, and performing detector simulations.

We organize the rest of this paper as follows. We briefly review the partially composite standard model in section 2. In section 3, we show the constraints to the model, and find that there are parameter regions where are consistent with the ATLAS excess. In section 4, we perform the collider simulations for the signal and the background, and obtain the sensitivity at the LHC Run-2. In section 5, we investigate the future prospects of the spin-1 resonances search using our simulation results. Section 6 is devoted for conclusion.

JHEP02(2016)084

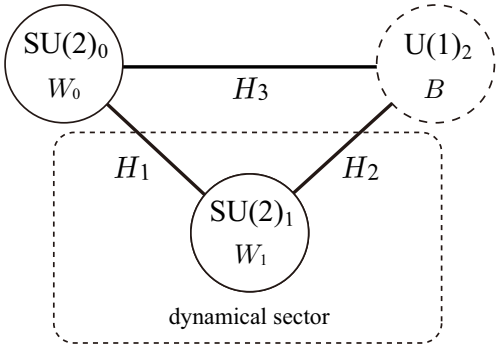

Figure 1. The moose diagram of this setup: the circles represent the gauge groups, and the thick lines that connect two circles are the Higgs fields. The Higgs fields H_1, H_2, and $\mathrm{SU}(2)_1$ gauge group can be regarded as the operators originated from the dynamical sector.

2 The partially composite standard model

2.1 The model setup

In the partially composite standard model, the gauge symmetry of the electroweak sector is $\mathrm{SU}(2)_0 \times \mathrm{SU}(2)_1 \times \mathrm{U}(1)_2$, and three Higgs fields (H_1, H_2, H_3) are introduced for the symmetry breaking, $\mathrm{SU}(2)_0 \times \mathrm{SU}(2)_1 \times \mathrm{U}(1)_2 \to \mathrm{U}(1)_{EM}$. We denote the gauge couplings g_0, g_1, and g_2, respectively. The three gauge couplings are related to the QED coupling as

$$\frac{1}{e^2} = \frac{1}{g_0^2} + \frac{1}{g_1^2} + \frac{1}{g_2^2}. \tag{2.1}$$

Here, we assume that the $\mathrm{SU}(2)_1$ gauge symmetry belongs to a dynamical sector, and $g_1 \gg g_0, g_2$. Under this assumption, g_0 and g_2 are approximately g_W and g_Y which are the gauge couplings of $\mathrm{SU}(2)_L$ and $\mathrm{U}(1)_Y$, respectively. We regard the gauge field associated with $\mathrm{SU}(2)_1$ as the vector resonance originated from unknown dynamics above TeV scale. This implies that fields transformed under the $\mathrm{SU}(2)_1$ gauge symmetry also belong to the dynamical sector. We take H_1 and H_2 as such fields, and regard H_3 as an elementary field. All the fermions are also elementary, and they are singlet under $\mathrm{SU}(2)_1$. We schematically show the model structure in the moose notation [28] in figure 1, and also summarize the field contents and their charge assignments in table 1.

The scalar potential is given as[1]

$$\begin{aligned} V(H_1, H_2, H_3) = \; & \mu_1^2 \mathrm{tr}(H_1 H_1^\dagger) + \mu_2^2 \mathrm{tr}(H_2 H_2^\dagger) + \mu_3^2 \mathrm{tr}(H_3 H_3^\dagger) \\ & + \kappa \mathrm{tr}(H_1 H_2 H_3^\dagger) \\ & + \lambda_1 (\mathrm{tr}(H_1 H_1^\dagger))^2 + \lambda_2 (\mathrm{tr}(H_2 H_2^\dagger))^2 + \lambda_3 (\mathrm{tr}(H_3 H_3^\dagger))^2 \\ & + \lambda_{12} \mathrm{tr}(H_1 H_1^\dagger) \mathrm{tr}(H_2 H_2^\dagger) + \lambda_{23} \mathrm{tr}(H_2 H_2^\dagger) \mathrm{tr}(H_3 H_3^\dagger) \\ & + \lambda_{31} \mathrm{tr}(H_3 H_3^\dagger) \mathrm{tr}(H_1 H_1^\dagger) \,. \end{aligned} \tag{2.2}$$

[1] We omit the term $i\kappa' \mathrm{tr}(H_1 H_2 H_3^\dagger \tau^3)$ in this paper because this term can be eliminated by the field redefinition [23].

JHEP02(2016)084

Fields	$SU(2)_0$	$U(1)_2$	$SU(3)_c$	$SU(2)_1$
H_1	**2**	0	**1**	**2**
H_2	**1**	1/2	**1**	**2**
H_3	**2**	1/2	**1**	**1**
Q	**2**	1/6	**3**	**1**
u_R	**1**	2/3	**3**	**1**
d_R	**1**	-1/3	**3**	**1**
L	**2**	-1/2	**1**	**1**
e_R	**1**	-1	**1**	**1**

Table 1. The charge assignment of the partially composite standard model. Only H_1 and H_2 are the representations of the $SU(2)_1$ gauge symmetry.

Here all the Higgs fields are represented by two-by-two matrices, and they are real, namely

$$\epsilon H_i^* \epsilon = -H_i, \quad \text{where } \epsilon = \begin{pmatrix} 0 & 1 \\ -1 & 0 \end{pmatrix}. \tag{2.3}$$

All parameters in the Higgs potenbibtial are also real. We assume that all the vacuum expectation values (VEVs) of the Higgs fields are diagonal, real and positive to realize desired electroweak symmetry breaking. The Higgs fields are expanded around their VEVs, v_1, v_2 and v_3,

$$H_i = \frac{v_i}{2} + \frac{1}{2}\left(h_i + i\tau^a \pi_i^a\right), \tag{2.4}$$

where τ^a is the Pauli matrices, and h_i, π_i^a are the four real scalar component fields. The covariant derivatives of the Higgs fields are given as

$$D_\mu H_1 = \partial_\mu H_1 + i g_0 \frac{\tau^a}{2} W_{0\mu}^a H_1 - i g_1 H_1 \frac{\tau^a}{2} W_{1\mu}^a, \tag{2.5}$$

$$D_\mu H_2 = \partial_\mu H_2 + i g_1 \frac{\tau^a}{2} W_{1\mu}^a H_2 - i g_2 H_2 \frac{\tau^3}{2} B_\mu, \tag{2.6}$$

$$D_\mu H_3 = \partial_\mu H_3 + i g_0 \frac{\tau^a}{2} W_{0\mu}^a H_3 - i g_2 H_3 \frac{\tau^3}{2} B_\mu. \tag{2.7}$$

By calculating the muon life time in this model at the tree level, we find the relation between the Fermi constant and the VEVs in this model as

$$v_3^2 + \frac{1}{\frac{1}{v_1^2} + \frac{1}{v_2^2}} = v^2 \equiv \left(\sqrt{2} G_F\right)^{-1}, \tag{2.8}$$

where $v \simeq 246\,\text{GeV}$. For the later convenience, we introduce a new parameter r,

$$r \equiv \frac{v_2}{v_1}. \tag{2.9}$$

Thus v_1 and v_2 are expressed by r, v_3, and v,

$$v_1^2 = (1 + r^{-2})(v^2 - v_3^2), \qquad v_2^2 = (1 + r^2)(v^2 - v_3^2). \tag{2.10}$$

JHEP02(2016)084

There are twelve scalars in this model, and six of them are eaten by the gauge bosons. Thus this model has six physical scalars: three CP-even Higgs bosons ($h,\ H,\ H'$), one CP-odd Higgs boson (A), and two charged Higgs bosons ($H^{\pm}$). We identify h as the SM-like 125 GeV Higgs bosons. The masses of the CP-odd and the charged Higgs bosons are the same at the tree level and given by

$$m_A^2 = m_{H^\pm}^2 = -\frac{1}{4}\frac{\kappa}{v_3}\frac{1+r^2}{r}v^2. \tag{2.11}$$

The mass eigenstates of the CP-even Higgs bosons are related to the gauge eigenstates through the mixing angles $\theta_1,\ \theta_2$, and θ_3 as follows,

$$\begin{pmatrix} H' \\ H \\ h \end{pmatrix} = \begin{pmatrix} s_1 s_2 - c_1 c_2 s_3 & -s_1 c_2 - c_1 s_2 s_3 & c_1 c_3 \\ -c_1 s_2 - s_1 c_2 s_3 & c_1 c_2 - s_1 s_2 s_3 & s_1 c_3 \\ c_2 c_3 & s_2 c_3 & s_3 \end{pmatrix} \begin{pmatrix} h_1 \\ h_2 \\ h_3 \end{pmatrix} \tag{2.12}$$

where s_i (c_i) stands for $\sin\theta_i$ ($\cos\theta_i$) for $i = 1,\ 2,\ 3$.

The Yukawa interactions are given as

$$\mathcal{L}^{\text{Yukawa}} = -\bar{Q}^i H_3 \begin{pmatrix} y_u^{ij} & 0 \\ 0 & y_d^{ij} \end{pmatrix} \begin{pmatrix} u_R^j \\ d_R^j \end{pmatrix} - \bar{L}^i H_3 \begin{pmatrix} 0 & 0 \\ 0 & y_e^{ij} \end{pmatrix} \begin{pmatrix} 0 \\ e_R^j \end{pmatrix} + H.c., \tag{2.13}$$

where i and j are the generation indices. We introduce a parameter κ_F which is the ratio of the couplings between the lightest CP-even Higgs boson and the fermions to its SM value,

$$\kappa_F \equiv \frac{g_{hff}}{m_f/v} = \frac{v}{v_3}s_3. \tag{2.14}$$

Since $|s_3| \leq 1$ and $v/v_3 > 1$, κ_F can be larger than one. We will discuss the viable range of κ_F in the next subsection. The fermion masses are given as

$$m_f = y_f \frac{v_3}{2} = y_f \frac{v_3}{v}\frac{v}{2}, \tag{2.15}$$

and the Yukawa couplings are enhanced by v/v_3 compared to their SM values. Large Yukawa couplings could make the Higgs potential unstable above the electroweak scale. We discuss this point in section 3.2.

In addition to the SM gauge bosons, we have extra three vector bosons, $W'^{\pm}$ and Z'. In the $g_1 \gg g_0$ regime, the mass eigenvalues of the gauge bosons are given as

$$m_W^2 \simeq \frac{1}{4}g_0^2 v^2 \left(1 - \frac{g_0^2}{g_1^2}\frac{1}{(1+r^2)^2}\right), \tag{2.16}$$

$$m_{W'}^2 \simeq \frac{1}{4}g_1^2(v_1^2+v_2^2) \left(1 + \frac{g_0^2}{g_1^2}\frac{1}{(1+r^2)^2}\right), \tag{2.17}$$

$$m_Z^2 \simeq \frac{1}{4}(g_0^2+g_2^2)v^2 \left(1 - \frac{(g_0^2-g_2^2r^2)^2}{g_1^2(g_0^2+g_2^2)}\frac{1}{(1+r^2)^2}\right), \tag{2.18}$$

$$m_{Z'}^2 \simeq \frac{1}{4}g_1^2(v_1^2+v_2^2) \left(1 + \frac{g_0^2+g_2^2r^4}{g_1^2}\frac{1}{(1+r^2)^2}\right). \tag{2.19}$$

JHEP02(2016)084

We find $m_{W'} \simeq m_{Z'}$ except in the large r regime. We need to find the relation between the gauge eigenstates and the mass eigenstates to evaluate the couplings, and they are given as

$$W^{\pm}_{\mu} \simeq \left(1 - \frac{1}{2(1+r^2)^2}\frac{g_0^2}{g_1^2}\right) W^{\pm}_{0\mu} + \left(\frac{1}{1+r^2}\frac{g_0}{g_1}\right) W^{\pm}_{1\mu}, \tag{2.20}$$

$$W'^{\pm}_{\mu} \simeq -\left(\frac{1}{1+r^2}\frac{g_0}{g_1}\right) W^{\pm}_{0\mu} + \left(1 - \frac{1}{2(1+r^2)^2}\frac{g_0^2}{g_1^2}\right) W^{\pm}_{1\mu}, \tag{2.21}$$

$$A_{\mu} = \frac{e}{g_0} W^3_{0\mu} + \frac{e}{g_1} W^3_{1\mu} + \frac{e}{g_2} W^3_{2\mu}, \tag{2.22}$$

$$\begin{aligned} Z_{\mu} \simeq\ & c_W \left(1 - \frac{1-2r^2 t_W^2}{2(1+r^2)^2}\frac{g_0^2}{g_1^2}\right) W^3_{0\mu} + c_W \left(\frac{1-r^2 t_W^2}{(1+r^2)}\frac{g_0}{g_1}\right) W^3_{1\mu} \\ & - s_W \left(1 - \frac{r^4 t_W^2}{2(1+r^2)^2}\frac{g_0^2}{g_1^2}\right) W^3_{2\mu}, \end{aligned} \tag{2.23}$$

$$Z'_{\mu} \simeq -\frac{1}{1+r^2}\frac{g_0}{g_1} W^3_{0\mu} + \left(1 - \frac{1+r^4 t_W^2}{2(1+r^2)^2}\frac{g_0^2}{g_1^2}\right) W^3_{1\mu} - \frac{r^2 t_W}{(1+r^2)}\frac{g_0}{g_1} W^3_{2\mu}, \tag{2.24}$$

where $c_W = m_W/m_Z$, $s_W = \sqrt{1-c_W^2}$, and $t_W = s_W/c_W$. The typical size of the mixing angles is $\mathcal{O}(g_0/g_1)$, and the gauge filed W_0 (W_1) is the main component of the mass eigenstate W (W'). It is worth noting that the mixing angles for W' and Z' become the same in the small r regime, which means the custodial symmetry is enhanced.

The approximate expressions for some couplings of the W' and Z' to the SM particles are given as

$$\frac{g_{W'ff}}{g^{\rm SM}_{Wff}} \simeq -\frac{m_W}{m_{W'}}\sqrt{1-\frac{v_3^2}{v^2}}\frac{1}{r}, \tag{2.25}$$

$$\frac{g_{W'WZ}}{g^{SM}_{WWZ}} \simeq -\frac{m_W}{m_{W'}}\sqrt{1-\frac{v_3^2}{v^2}}\frac{1}{c_W^2}\frac{r}{1+r^2}, \tag{2.26}$$

$$\frac{g_{WWZ'}}{g^{SM}_{WWZ}} \simeq -\frac{m_W}{m_{W'}}\sqrt{1-\frac{v_3^2}{v^2}}\frac{1}{c_W}\frac{r}{1+r^2}. \tag{2.27}$$

Compare to the benchmark model (sequential standard model (SSM) [29–31]) used by the ATLAS/CMS, the W' couplings to the SM fermions are smaller. All couplings have a suppression factor of $(m_W/m_{W'})\sqrt{1-v_3^2/v^2}$, because the W' boson couples to the elementary fermion through W_0-W_1 mixing, so that the width is narrow. Since $g_{W'ff}$ is proportional to r^{-1}, the production cross section of the Drell-Yan process is proportional to r^{-2}. The W' boson could not be produced in the large r region. In section 3, we will find a parameter space in small r regions where a signal rate is consistent with the ATLAS diboson excess. Some numerical results are given in section 3.3

The gauge boson couplings to the scalars are also important in our analysis. We give their approximated expressions here. Due to the mixing between the two SU(2) gauge eigenstates, the WWh and ZZh couplings differ from the SM values. We denote these coupling ratios to the SM values by $\kappa_{W,Z}$,

$$\kappa_W \equiv \frac{g_{hWW}}{2m_W^2/v}, \quad \kappa_Z \equiv \frac{g_{hZZ}}{2m_Z^2/v}, \tag{2.28}$$

JHEP02(2016)084

and their approximated formulae in the $g_1 \gg g_0, g_2$ regime are

$$\kappa_W \simeq \kappa_Z \simeq \frac{r^3}{(1+r^2)^{3/2}}\sqrt{1-\frac{v_3^2}{v^2}}c_2c_3 + \frac{1}{(1+r^2)^{3/2}}\sqrt{1-\frac{v_3^2}{v^2}}s_2c_3 + \frac{v_3}{v}s_3. \tag{2.29}$$

The couplings relevant to the W'/Z' decay are

$$g_{WW'h} \simeq g_{ZZ'h} \simeq \frac{2m_Wm_{W'}}{v}\left(-\frac{r^2}{(1+r^2)^{3/2}}c_2c_3+\frac{r}{(1+r^2)^{3/2}}s_2c_3-\frac{1}{r}\frac{m_W^2}{m_{W'}^2}\frac{v_3}{v}\sqrt{1-\frac{v_3^2}{v^2}}s_3\right), \tag{2.30}$$

$$g_{WW'H} \simeq g_{ZZ'H} \simeq \frac{2m_Wm_{W'}}{v}\left(-\frac{r^2}{(1+r^2)^{3/2}}(-c_1s_2-s_1c_2s_3)\right. \tag{2.31}$$
$$\left. + \frac{r}{(1+r^2)^{3/2}}(c_1c_2-s_1s_2s_3) - \frac{1}{r}\frac{m_W^2}{m_{W'}^2}\frac{v_3}{v}\sqrt{1-\frac{v_3^2}{v^2}}s_1c_3\right),$$

$$g_{WW'H'} \simeq g_{ZZ'H'} \simeq \frac{2m_Wm_{W'}}{v}\left(-\frac{r^2}{(1+r^2)^{3/2}}(s_1s_2-c_1c_2s_3)\right. \tag{2.32}$$
$$\left. + \frac{r}{(1+r^2)^{3/2}}(-s_1c_2-c_1s_2s_3) - \frac{1}{r}\frac{m_W^2}{m_{W'}^2}\frac{v_3}{v}\sqrt{1-\frac{v_3^2}{v^2}}c_1c_3\right).$$

2.2 Model parameters

In the electroweak sector of the model, there are 13 real parameters,

$$\mu_1^2,\ \mu_2^2,\ \mu_3^2,\ \kappa,\ \lambda_1,\ \lambda_2,\ \lambda_3,\ \lambda_{12},\ \lambda_{23},\ \lambda_{31},\ g_0,\ g_1,\ g_2. \tag{2.33}$$

It is convenient to use a different set of the parameters instead of these parameters. We use the following 13 parameters to fix the parameters in the electroweak sector,

$$r,\ v_3,\ v,\ \alpha,\ m_Z,\ m_{Z'},\ m_h,\ m_{H'},\ m_H,\ m_A,\ \kappa_F,\ \kappa_Z,\ g_{WW'H'}. \tag{2.34}$$

Here, we use r, v_3, v instead of the three μ parameters. κ is fixed by the charged Higgs mass or the CP-odd Higgs mass. The six λ's have the same information as the three CP-even Higgs masses and their mixing angles (m_h, m_H, $m_{H'}$, θ_1, θ_2, θ_3). We can use m_Z, $m_{Z'}$, and $\alpha(= e^2/4\pi)$ instead of the gauge couplings. In addition, we can replace (θ_1, θ_2, θ_3) with (κ_F, κ_Z, $g_{WW'H'}$).

The values of the four parameters, v, m_Z, α, and m_h are already known very precisely. We take $m_h = 125\,\text{GeV}$. We find κ_F is severely constrained close to 1 in the $m_A \gg m_h$ regime. When the heavy Higgs masses are universal, $m_A = m_{H'} = m_H$, λ_3 is simply expressed as

$$\lambda_3(\mu = m_{Z'}) = \frac{\kappa_F^2}{2}\frac{m_h^2}{v^2} + \frac{1-\kappa_F^2}{2}\frac{m_A^2}{v^2}. \tag{2.35}$$

Thus, λ_3 is very large except for κ_F =1. Similarly, the coupling ratio κ_Z is also severely constrained close to its maximal value in $m_A \gg m_h$ regime. Typically, the allowed value of κ_Z is $1-\mathcal{O}(1)\%$. The detailed description is given in appendix A. In the following discussion, we take $\kappa_F \simeq 1$, $m_A = m_H = m_{H'} = \mathcal{O}(1)\,\text{TeV}$, $g_{WW'H'} = 0$, and we always choose κ_Z to be its maximal value. For most of our numerical analysis, κ_Z is set to 0.95–1.00.

JHEP02(2016)084

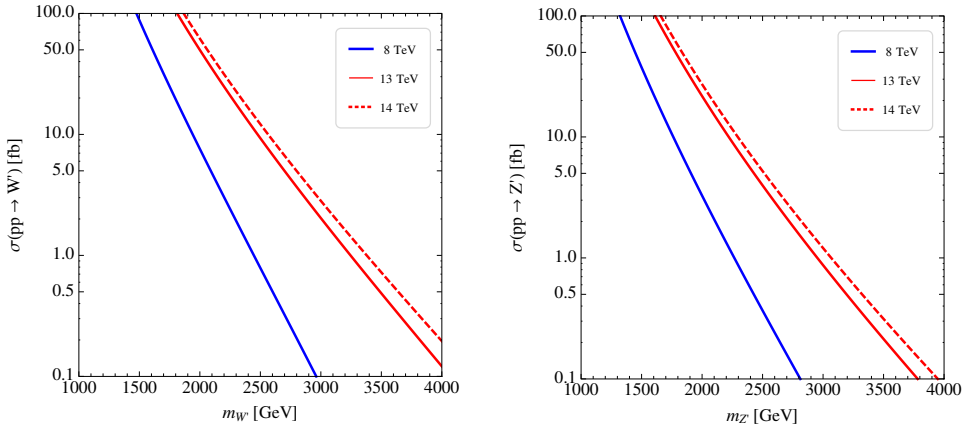

Figure 2. The production cross sections of the extra vector bosons, W' and Z'. We take $v_3 = 200\,\text{GeV}$, $r = 0.13$.

3 Phenomenology of spin-1 resonances

In this section, we discuss the properties of the W' and Z' bosons such as the production cross sections and the decay branching ratios. And we also discuss both the theoretical and experimental constraints. In the following, we show some formulae with approximation, which help to understand the parameter dependence. However, we use the exact formulae in our numerical calculations.

3.1 Properties of the extra vector bosons

The main production mode of W' and Z' in pp collisions is the Drell-Yan process. They are proportional to r^{-2} as we can see from eq. (2.25).[2] We consider small r in order to make the cross section large. In figure 2, we show the production cross sections for W' $(W'^{+} + W'^{-})$ and Z'. Here we take $v_3 = 200\,\text{GeV}$, $r = 0.13$ and $\kappa_F = 1.00$. We use the CTEQ6L parton distribution functions [32]. The production cross section of W' is approximately twice that of Z' for small r because the custodial SU(2) symmetry is recovered in the region.

The partial decay widths of W' and Z' into the SM particles are given as

$$\Gamma(W' \to WZ) \simeq \frac{1}{48\pi}\frac{m_{W'}^3}{v^2}\frac{r^2}{(1+r^2)^2}\left(1-\frac{v_3^2}{v^2}\right), \tag{3.1}$$

$$\Gamma(W' \to Wh) \simeq \frac{1}{48\pi}\frac{m_{W'}^3}{v^2}\frac{r^2}{(1+r^2)^3}\left(-rc_2c_3+s_2c_3\right)^2, \tag{3.2}$$

$$\Gamma(W' \to f\bar{f}) \simeq \frac{N_c}{48\pi}\frac{m_W^2}{m_{W'}}\frac{e^2}{s_W^2}\frac{1}{r^2}\left(1-\frac{v_3^2}{v^2}\right), \tag{3.3}$$

$$\Gamma(Z' \to WW) \simeq \frac{1}{48\pi}\frac{m_{W'}^3}{v^2}\frac{r^2}{(1+r^2)^2}\left(1-\frac{v_3^2}{v^2}\right), \tag{3.4}$$

$$\Gamma(Z' \to Zh) \simeq \frac{1}{48\pi}\frac{m_{W'}^3}{v^2}\frac{r^2}{(1+r^2)^3}\left(-rc_2c_3+s_2c_3\right)^2, \tag{3.5}$$

[2]For more details on the formulae, see appendix B.

JHEP02(2016)084

$$\Gamma(Z' \to f\bar{f}) \simeq \frac{N_c}{24\pi}\frac{m_W^2}{m_{W'}}\frac{e^2}{s_W^2}\frac{1}{r^2}\left(1-\frac{v_3^2}{v^2}\right) \times \left(\left(\left(1-r^2\frac{s_W^2}{c_W^2}\right)T_f^3 + r^2\frac{s_W^2}{c_W^2}Q_f\right)^2 + \left(r^2\frac{s_W^2}{c_W^2}Q_f\right)^2\right), \tag{3.6}$$

where $T_f^3 = 1/2$ $(-1/2)$ for the up-type (down-type) fermions, Q_f is the electric charge of the fermion, and N_c is the color factor, $N_c = 3$. Note that the bosonic channels are dominant among their decay channels due to an enhancement factor from the wave function of the longitudinally polarized gauge bosons in the final states. Therefore the dominant decay modes of W' (Z') are $W' \to WZ$ and $W' \to Wh$ $(Z' \to WW$ and $Z' \to Zh)$.

There are also decay modes with a heavy scalar in the final states. For example, $W' \to WH$ and $W' \to hH$ exist and their approximated formulae are

$$\Gamma(W' \to WH) \simeq \frac{1}{48\pi}\left(\frac{g_{WW'H}}{2m_W m_{W'}/v}\right)^2 \frac{m_{W'}^3}{v^2}\left(8\frac{m_W^2}{m_{W'}^2}+\left(1-\frac{m_H^2}{m_{W'}^2}+\frac{m_W^2}{m_{W'}^2}\right)^2\right)\left(1-\frac{m_H^2}{m_{W'}^2}\right), \tag{3.7}$$

$$\Gamma(W' \to hH) \simeq \frac{1}{48\pi}\frac{m_{W'}^4}{v^2-v_3^2}\frac{v_3^2}{v^2}\frac{2}{(1+r^2)^3}\left(-rc_2c_3+s_2c_3\right)^2\left(1-\frac{m_{H^+}^2}{m_{W'}^2}\right)^3, \tag{3.8}$$

where $g_{WW'H}$ is given in eq. (2.31), and $g_{WW'H}/(2m_W m_{W'}/v)$ is $\mathcal{O}(1)$ in large regions of the parameter space. These decay widths are comparable to those of the SM final states. The decay channels including only the heavy states, such as $W' \to H^\pm H$, also have the same feature. Once these modes are open, they would be dominant decay modes.

In figure 3, we show the total widths and the branching ratios of W' and Z'. Here we take $v_3 = 200\,\text{GeV}$, $r = 0.13$ and $\kappa_F = 1.00$, $m_A = m_{H'} = m_H = 2\,\text{TeV}$. We also take $g_{WW'H'} = 0$ as we mentioned in section 2.2, thus $W' \to WH'$ and $Z' \to ZH'$ are absent in the figure. We find that the dominant decay channels are $V' \to VV$ and $V' \to Vh$ for large $m_{V'}$. However, the decay branching ratio reduces once $V' \to HX$ decay modes are open.

In figure 3, we find $\text{Br}(W' \to WZ) = \text{Br}(W' \to Wh) \simeq 40$ % at $m_{W'} = 2\,\text{TeV}$. The relation is easily understood by the equivalence theorem, $\text{Br}(W' \to W_L Z_L) = \text{Br}(W' \to \pi_{SM}\pi_{SM})$ in the heavy W' mass limit, where π_{SM} is the SM Nambu-Goldstone boson. In the SM limit, $\text{Br}(W' \to \pi_{SM}\pi_{SM})$ is equivalent to $\text{Br}(W' \to \pi_{SM}h)$. Thus, $\text{Br}(W' \to WZ) \simeq \text{Br}(W' \to Wh)$ is realized. In addition, when one takes $g_{WW'H'} = 0$, the heavy Higgses H, A, $H^\pm$ form a multiplet, and $\text{Br}(W' \to ZH^\pm) \simeq \text{Br}(W' \to WA) \simeq \text{Br}(W' \to WH)$ is realized.

We also find the total widths are narrow, namely $\Gamma/m \sim 1$–5 %, because the resonances decay into the SM particles with suppressed couplings due to the mixing between the elementary and the composite sectors. Another remark is that the decay properties of W' and Z' are similar due to the enhanced SU(2) custodial symmetry in small r regime.[3]

In figure 4, we take different scalar masses, $m_A = m_{H'} = m_H = 1\,\text{TeV}$. The other parameter choice is the same as in figure 3. The decay channels to the non-SM particles,

[3] In the large r region, the branching ratio $Z' \to f\bar{f}$ and the production cross section of Z' become larger (see eqs. (3.6), (B.2)), while the production cross section of W' is suppressed.

JHEP02(2016)084

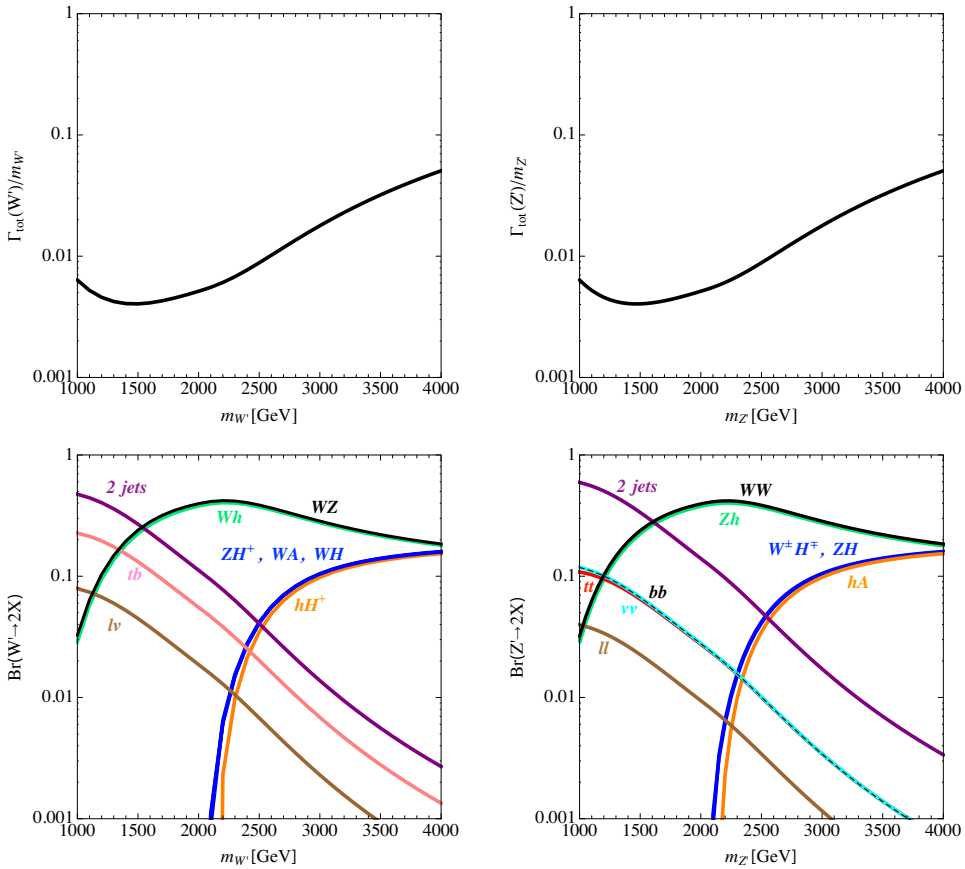

Figure 3. The total widths and the branching ratios of the extra vector bosons, W' and Z'. We take $v_3 = 200\,\text{GeV}$, $r = 0.13$, $\kappa_F = 1.00$, and $m_A = m_{H'} = m_H = 2\,\text{TeV}$. Here, 2jets means $\text{Br}(W' \to ud)$+$\text{Br}(W' \to sc)$ or $\text{Br}(Z' \to uu)$+$\text{Br}(Z' \to dd)$+$\text{Br}(Z' \to ss)$+$\text{Br}(Z' \to cc)$, $\ell\nu$ means $\text{Br}(W' \to e\nu_e)$ (=$\text{Br}(W' \to \mu\nu_\mu)$ =$\text{Br}(W' \to \tau\nu_\tau)$), $\ell\ell$ means $\text{Br}(Z' \to ee)$ (=$\text{Br}(Z' \to \mu\mu)$ =$\text{Br}(Z' \to \tau\tau)$), $\nu\nu$ means $\text{Br}(Z' \to \nu_e\nu_e)$+$\text{Br}(Z' \to \nu_\mu\nu_\mu)$+$\text{Br}(Z' \to \nu_\tau\nu_\tau)$, and $W^\pm H^\mp$ means $\text{Br}(W' \to W^+H^-)$ =$\text{Br}(W' \to W^-H^+)$.

namely $\text{Br}(W' \to H^+H)$, $\text{Br}(W' \to H^+A)$, $\text{Br}(Z' \to HA)$, and $\text{Br}(Z' \to H^+H^-)$, are open. We took the parameter so that the channels to H' is absent, $g_{WW'H'} = 0$.

As mentioned above, these channels are comparable to the decay modes to the SM particles. As a result, the decay modes $V' \to VV$ and $V' \to Vh$ searched at the ATLAS and the CMS experiments are suppressed compared to figure 3. This implies that the decay channels with heavy scalars should not be open if we try to explain the excess at the ATLAS experiment. Hereafter, we consider the situation that the heavy scalars are as heavy as the extra gauge bosons.

3.2 Constraints on the model

In this subsection, we show theoretical and experimental constraints on the model parameters. In order to perform a reliable perturbative calculation, we demand perturbativity condition, bounded below condition, global minimum vacuum condition, and stability condition. In addition, we take into account the LHC bounds and the electroweak precision measurements.

JHEP02(2016)084

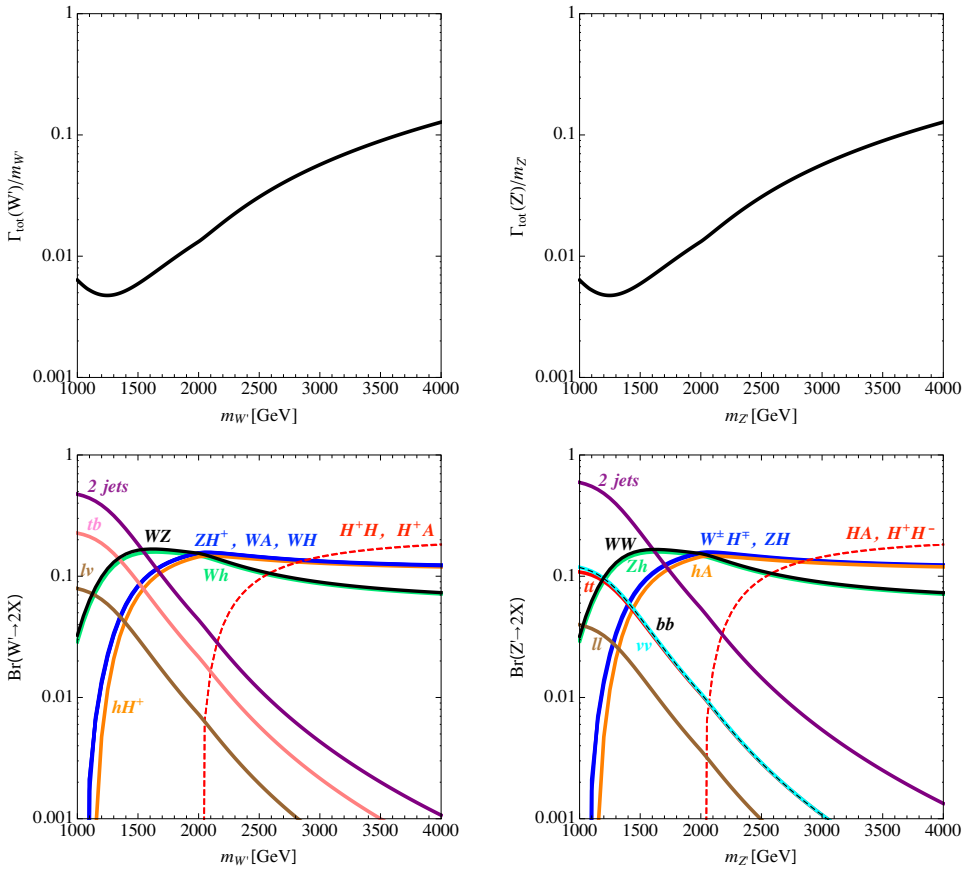

Figure 4. The total widths and the branching ratios of W' and Z' for $m_A = m_{H'} = m_H = 1\,\text{TeV}$. Other parameter choice and the notations are the same as in figure 3.

3.2.1 Theoretical constraints

Perturbativity condition for the gauge coupling g_1. We require that all the absolute values of the gauge couplings and the Higgs quartic couplings are smaller than 4π and $(4\pi)^2$ in order to keep the reliability of our analysis based on the perturbative calculation.

For the gauge couplings, g_0 and g_2 are almost the same value as the SM gauge couplings, but g_1 can be very large. Since $\text{SU}(2)_1$ is asymptotic free in our setup, g_1 becomes smaller at high energy due to the quantum effects. Thus the maximum value of the g_1 is given at Z' mass scale, and we require $|g_1(\mu = m_{Z'})| < 4\pi$. The regions where $|g_1(m_{Z'})| > 4\pi$ are filled with yellow in figures 5 and 6.

Perturbativity condition for the Higgs quartic couplings. The scalar quartic couplings are large when the mass differences between the SM-like Higgs and the other heavy scalar bosons are large. Since we take $m_h \ll m_A = m_H = m_{H'} \sim \mathcal{O}(1)\,\text{TeV}$ in our analysis, the quartic couplings tend to be large. In addition, due to the renormalization group effects, they can be even larger at high energy. The renormalization group equations for

JHEP02(2016)084

this model are given in appendix C. We define a cutoff scale Λ by

$$|\lambda_i(\mu = \Lambda)| = (4\pi)^2 \,, \tag{3.9}$$

and require $|\lambda_i(\mu < \Lambda)| < (4\pi)^2$.

This constraint highly depends on our choice of Λ. We require that Λ should be significantly higher than a few TeV, otherwise we have to take account of interaction terms from higher dimensional operators whose coefficients are unknown, and some uncertainty is introduced to our analysis. For example, there are operators which modifies the W' coupling to the SM fermions such as $(c/\Lambda^2)\bar{Q}i\gamma^\mu(H_1 iD_\mu H_1^\dagger)Q$. This operator brings unknown parameter c, and thus brings uncertainty to our calculations such as the production cross section of W'. Typically, such higher dimensional operators with $c \sim 1$ bring 1% (10%) uncertainty if $\Lambda = 100\,\text{TeV}(10\,\text{TeV})$. To avoid such uncertainty from unknown parameters, we restrict ourselves for the case $\Lambda > 100\,\text{TeV}$. The parameter regions where $|\lambda(\Lambda)| > (4\pi)^2$ are filled with the lighter (darker) gray for $\Lambda = 100(10)$ TeV in figures 5 and 6 for reference.

Bounded below condition. Here we consider the conditions that the Higgs potential at the tree level is bounded below. For the purpose, it is enough to check that the potential value at the large field values, and thus we consider only the quartic terms in the potential. We rewrite the quartic terms as

$$V_{\text{quartic}} = R^4 \left(\lambda_1 n_1^2 + \lambda_2 n_2^2 + \lambda_3 n_3^2 + \lambda_{12} n_1 n_2 + \lambda_{23} n_2 n_3 + \lambda_{31} n_3 n_1\right), \tag{3.10}$$

with

$$R^2 n_i \equiv \text{tr}(H_i H_i^\dagger) = \frac{1}{2}(h_i^2 + \pi_i^a \pi_i^a), \tag{3.11}$$

where n_i satisfies $0 \leq n_{1,2,3} \leq 1$, and $n_1^2 + n_2^2 + n_3^2 = 1$. In order to avoid run-away vacua, we demand the following conditions for the Higgs quartic couplings at $m_{Z'}$ scale $(\lambda_i(\mu = m_{Z'}))$,

$$\text{Min}\left[\lambda_1 n_1^2 + \lambda_2 n_2^2 + \lambda_3 n_3^2 + \lambda_{12} n_1 n_2 + \lambda_{23} n_2 n_3 + \lambda_{31} n_3 n_1\right] > 0, \quad \text{for } 0 \leq n_{1,2,3} \leq 1. \tag{3.12}$$

The parameter regions where this condition is not satisfied are filled with cyan in figures 5 and 6. Especially, one can solve the above inequality analytically in specific directions as

$$\begin{aligned} \lambda_1 > 0 \;\; &\text{for } n_2 = n_3 = 0, & \lambda_2 > 0 \;\; &\text{for } n_1 = n_3 = 0, \\ \lambda_3 > 0 \;\; &\text{for } n_1 = n_2 = 0, & \lambda_{23} + 2\sqrt{\lambda_2 \lambda_3} > 0 \;\; &\text{for } n_1 = 0, \\ \lambda_{31} + 2\sqrt{\lambda_3 \lambda_1} > 0 \;\; &\text{for } n_2 = 0, & \lambda_{12} + 2\sqrt{\lambda_1 \lambda_2} > 0 \;\; &\text{for } n_3 = 0. \end{aligned} \tag{3.13}$$

Global minimum vacuum condition. We demand the electroweak vacuum to be a global minimum of the Higgs potential at $\mu = m_{Z'}$. The parameter regions where this condition is not satisfied are filled with green in figures 5 and 6.

JHEP02(2016)084

Stability condition. Among the quartic couplings, λ_3 can be very small when κ_F is very close to 1, see eq. (2.35), and especially it takes the same value as the quartic coupling in the SM for $\kappa_F = 1$. In that case, λ_3 can be negative at a high energy scale due to the contribution from the Yukawa interaction to the renormalization group equations, and the Higgs potential becomes unstable. The VEV giving masses to the fermions are v_3, see eq. (2.15). Thus the Yukawa coupling in our setup is larger than the coupling in the SM by v/v_3, and the Higgs potential can become unstable at a few TeV scale for the small v_3 region. We define the scale $\bar{\Lambda}$ at which λ_3 becomes negative,

$$\lambda_3(\mu = \bar{\Lambda}) = 0, \tag{3.14}$$

and we demand $\bar{\Lambda} \gtrsim 100\,\text{TeV}$, as we demand for the perturbativity condition. We fill the regions where this condition is not satisfied with magenta in figures 5 and 6.

This bound is conservative because we do not allow a meta-stable vacuum. Note that we do not take into account higher loop corrections. In the SM, the constraints become significantly weaker if higher loop corrections are taken into account [33, 34].

3.2.2 Experimental constraints

Constraints from the direct search for W' and Z'. Since the production cross sections of the extra vector bosons are relatively large, this model is constrained from current results of the exotic resonance searches of various decay channels at the $\sqrt{s} = 8\,\text{TeV}$ LHC. We take account of the following constraints: $W' \to \ell\nu$ searches [35, 36], $Z' \to \ell\ell$ searches [37, 38], Vh resonance searches ($V' \to Vh$) [39–42], and the diboson searches ($V' \to VV$) using dijets [1, 2], $\ell\ell jj$ [43], $\ell\nu jj$ [44], and $\ell\nu\ell\ell$ channel [45]. The searches for the other channels do not constrain this model. We fill the excluded regions with blue in figures 5 and 6. Among the constraints, $V' \to Vh$ and $V' \to WZ \to \ell\nu jj$ give severe bound, and exclude a part of the parameter regions in which we can explain the diboson excess reported by the ATLAS experiment.

Constraints from the electroweak precision measurements. The electroweak precision parameters, $\hat{S}$, $\hat{T}$, W and Y, defined in ref. [46], are severely restricted from the electroweak precision observables. Since the interactions of W' and Z' to the light fermions affect the low energy observables, the light W' and Z' are severely constrained. They are calculated at the tree level in ref. [23],

$$\hat{S} = \frac{g_0^2 v_1^2 v_2^2}{g_1^2(v_1^2+v_2^2)^2 + g_0^2 v_1^4} \simeq \frac{m_W^2}{m_{W'}^2}\left(1 - \frac{v_3^2}{v^2}\right), \tag{3.15}$$

$$\hat{T} = 0, \tag{3.16}$$

$$W = 4m_W^2 \frac{g_0^2}{g_1^2}\frac{1}{v_1^2+v_2^2}\frac{v_1^4}{g_1^2(v_1^2+v_2^2)^2 + g_0^2 v_1^4} \simeq \frac{m_W^4}{m_{W'}^4}\frac{1}{r^2}\left(1 - \frac{v_3^2}{v^2}\right), \tag{3.17}$$

$$Y = 4m_W^2 \frac{g_2^2}{g_1^2}\frac{1}{v_1^2+v_2^2}\frac{v_2^4}{g_1^2(v_1^2+v_2^2)^2 + g_0^2 v_1^4} \simeq r^2 t_W^2 \frac{m_W^4}{m_{W'}^4}\left(1 - \frac{v_3^2}{v^2}\right). \tag{3.18}$$

We use them to find the constraint on the parameter space. The parameter regions constrained at 95% C.L. are filled with red in figures 5 and 6. The small v_3, the small r as well as the light W' regions are constrained.

JHEP02(2016)084

We also consider constraints from flavor physics, and find they are weaker than the constraints from $\hat{S}$ and/or the current LHC bound. For example, K^0-$\bar{K}^0$ mixing in this model is almost the same as that in the SM. This is because the contributions from W' is sufficiently suppressed due to the suppression of the couplings to the SM fermions, and also the the modification of the W couplings to the fermions is very small, $\mathcal{O}(m_W^4/m_{W'}^4)$. Therefore, we do not show the constraints in the figures.

3.2.3 Summary of the constraints

In figure 5, we plot all the constraints in r–v_3 planes with three different parameter sets, $(m_{Z'}, m_A, \kappa_F) = (2\,\text{TeV}, 2\,\text{TeV}, 1.00)$, $(2\,\text{TeV}, 2\,\text{TeV}, 0.99)$, and $(2\,\text{TeV}, 1\,\text{TeV}, 1.00)$. Here we take all the heavy scalar bosons are degenerate, $m_A = m_{H'} = m_H$. The colored regions are excluded or constrained, and the white regions are allowed from all constraints. The gray regions surrounded by the black dotted lines represent the perturbativity condition of the Higgs quartic couplings for $\Lambda = 10$ (darker) and 100 TeV (lighter), and the yellow regions are that of g_1. The bounded below condition excludes the cyan region. The global minimum vacuum condition excludes the green region. The magenta regions are excluded by the stability condition for $\bar{\Lambda} = 10$ (darker) and 100 TeV (lighter). The LHC results exclude blue regions, where the solid blue lines represent $W' \to \ell\nu$ searches [35, 36], the dashed lines represent $Z' \to \ell\ell$ searches [37, 38], the dotted lines represent Vh resonance searches [39–42], and the dot-dashed lines represent diboson searches ($V' \to VV$) [1, 2, 43–45]. The regions filled with the red color are excluded by the electroweak precision measurements. No physical solutions are found in the black region, namely the gauge couplings and/or the VEVs become complex numbers there.

By comparing all the panels, we find the experimental bounds (the LHC and the electroweak precision measurements) are almost insensitive to the heavy Higgs bosons. The theoretical bounds are very sensitive to the κ_F, as we can see from the panels (a) and (b). This is because the deviation of κ_F from 1 leads to the large λ_3 (cf. $\lambda_3 \sim 0.13$ (0.78) at $\kappa_F = 1.00$ (0.99)) (see eq. (2.35)), which changes the regions excluded by the bounded below condition (see eq. (3.13)) and stability condition (see eq. (3.14)). We find that perturbativity condition is weaker in the panel (c) ($m_A = 1\,\text{TeV}$) compared with the panel (a) ($m_A = 2\,\text{TeV}$). This is because the lighter m_A leads to the smaller quartic couplings.

Figure 6 shows the constraints in $m_{Z'}$–r plane with the same color notation in figure 5. We take the universal masses $m_{Z'} = m_A = m_{H'} = m_H$, and three different choices for v_3 and κ_F, (v_3, κ_F) =(200 GeV, 1.00), (180 GeV, 1.00), and (180 GeV, 0.99). The perturbativity condition for the Higgs quartic couplings gives severe bounds in the heavy Higgs mass region. This is because the large mass differences in the CP-even Higgs mass spectra require the large Higgs quartic couplings, and they become non-perturbative eventually. We also find in the panel (c) that when κ_F deviates from 1, the bounded below condition gives stringent constraint. This is because that the Higgs quartic couplings λ_i are sensitive to the small deviation of κ_F, see appendix A.

JHEP02(2016)084

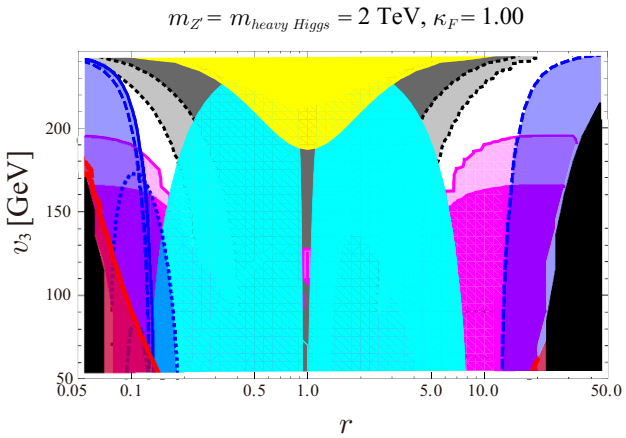

(a)

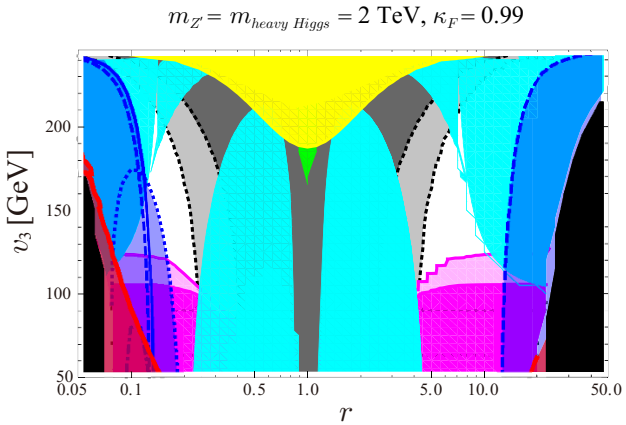

(b)

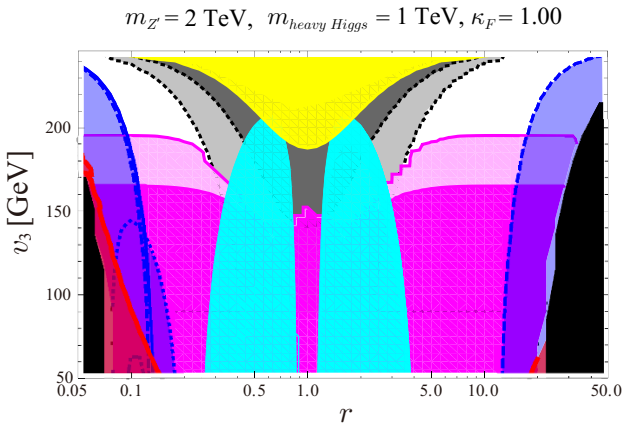

(c)

Figure 5. The theoretical and experimental constraints in r–v_3 planes. We take three different parameter choices for $(m_{Z'}, m_A, \kappa_F)$. The colored regions are constrained, **Gray**: the perturbativity conditions for the Higgs quartic couplings, **Yellow**: the perturbativity conditions for g_1, **Cyan**: the bounded below condition, **Green**: the global minimum vacuum condition, **Magenta**: the stability condition, **Blue**: the LHC bounds, **Red**: constraints from the electroweak precision measurements, **Black**: no physical solutions. See also the explanations in the text.

JHEP02(2016)084

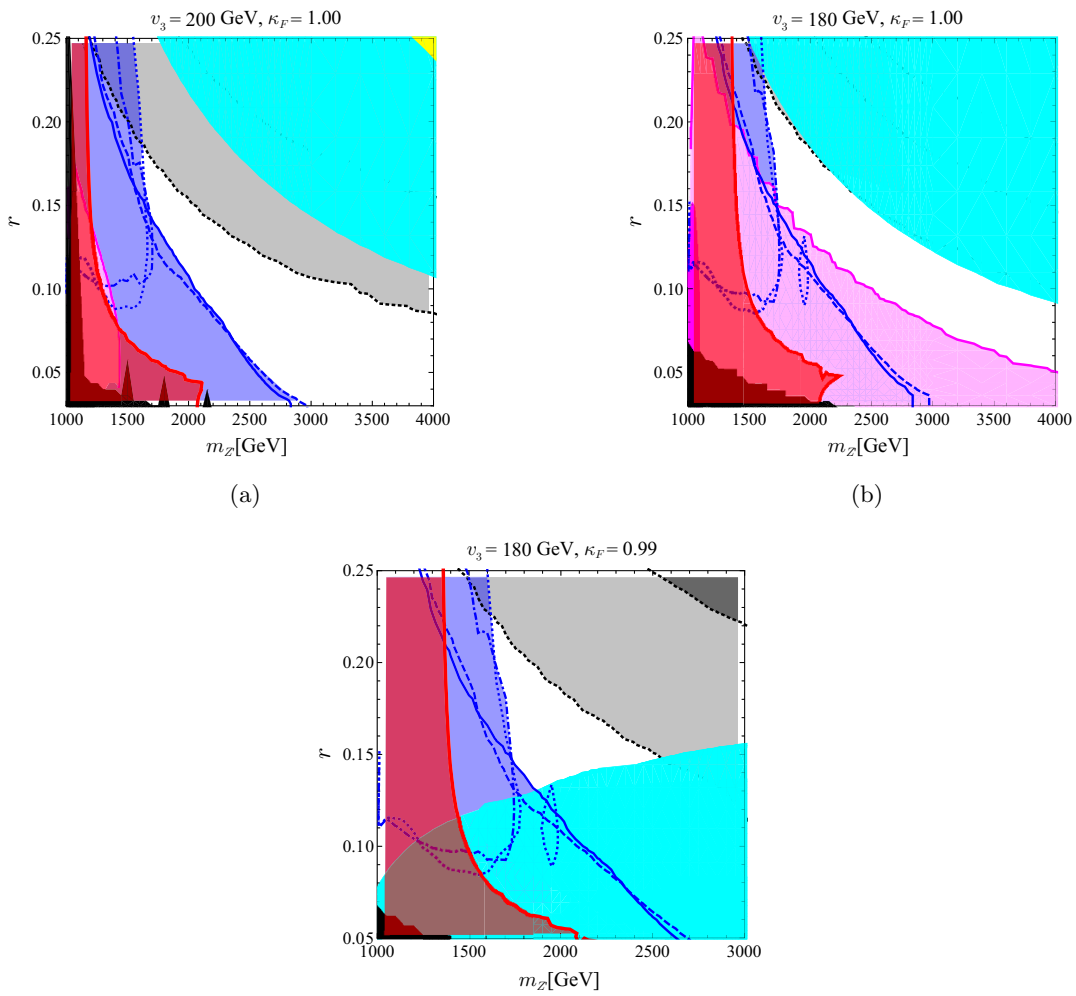

Figure 6. The theoretical and experimental constraints in the $m_{Z'}$–r planes. We take three different parameter choices for $(v_3,\ \kappa_F)$, and the universal masses $m_{Z'} = m_A = m_{H'} = m_H$ are taken. A color notation is the same as in figure 5.

3.3 Current status: 8 TeV analyses

In this subsection, we focus on the cross section times branching ratios of V' at the LHC 8 TeV. Inspired by the recent ATLAS diboson excess [1], we concentrate on the case that the masses of the extra vector bosons are around 2 TeV.

Since the separation of the WW, WZ, and ZZ channels are not good and there are significant overlap among them [1], we investigate the total cross section $\sigma(pp \to W')\mathrm{Br}(W' \to WZ) + \sigma(pp \to Z')\mathrm{Br}(Z' \to WW)$ at $\sqrt{s} = 8\,\mathrm{TeV}$ in figure 7. In this figure, $m_{Z'} = m_A = m_{H'} = m_H = 2\,\mathrm{TeV}$, $\kappa_F = 1.00$ are taken. The blue regions are excluded by the current experimental bounds discussed in section 3.2, and the regions of $g_1(\mu = m_{Z'}) > 4\pi$ is filled with yellow. Here we do not show the constraints from the Higgs sector.

JHEP02(2016)084

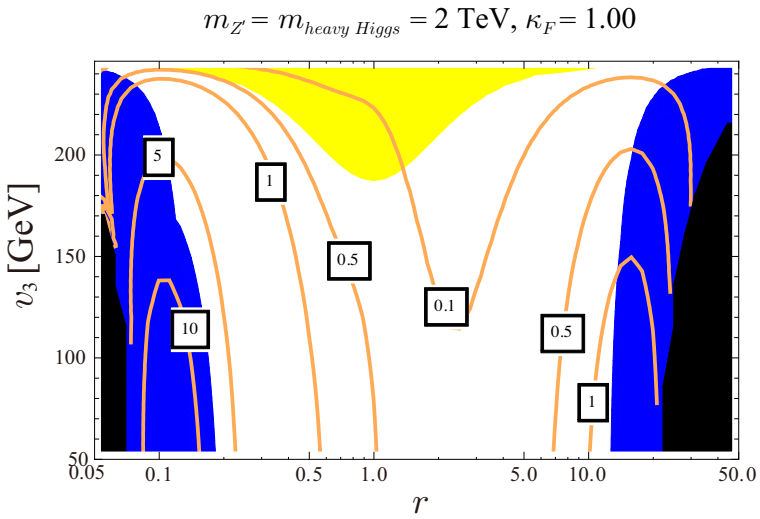

Figure 7. Contours of the cross section $\sigma(pp \to W')\mathrm{Br}(W' \to WZ) + \sigma(pp \to Z')\mathrm{Br}(Z' \to WW)$ at the LHC $\sqrt{s} = 8\,\mathrm{TeV}$ in fb unit. We take $m_{Z'} = m_A = m_{H'} = m_H = 2\,\mathrm{TeV}$, $\kappa_F = 1.00$. The blue regions are excluded by the current experimental bounds, and the regions of $g_1(\mu = m_{Z'}) > 4\pi$ are filled with yellow.

We have to estimate the cross section value, $\sigma(pp \to V' \to VV)$, required for the explanation of the diboson excess. We find $\sigma = 6\,\mathrm{fb}$ with large error when we use the event numbers between 1.85 and 2.15 TeV bins, the estimated background, and the efficiency given in ref. [1]. Hereafter we require $\sigma = 6\,\mathrm{fb}$ for the explanation of the diboson excess.

This cross section value can be achieved in the regions where r is much smaller than 1. This is because the production cross section is enhanced by r^{-2}. Hence, we focus on $r \ll 1$ regions in the rest of this paper.

Note that the strongest LHC constraint to the parameter regions where the ATLAS diboson excess can be explained comes from the hadronic channel of $\sigma(pp \to V' \to Vh)$ [42], e.g. $\sigma(pp \to V' \to Vh) \lesssim 7\,\mathrm{fb}$ for $m_{Z'} = 2\,\mathrm{TeV}$. This implies $\sigma(pp \to V' \to VV) < 7\,\mathrm{fb}$ as we discussed in section 3.1. If the coupling ratio κ_Z deviates from 1, this LHC bound becomes weaker, because the relation between $\sigma(pp \to V' \to VV)$ and $\sigma(pp \to V' \to Vh)$ are modified. However, in this model κ_Z is severely constrained close to 1 in the $m_A \gg m_h$ regime (see appendix A).

We show $\sigma(pp \to V' \to VV)$ in figure 8, for $m_{Z'} = 1.9$, 2.0, and 2.1 TeV. We take $\kappa_F = 1.00$, and all heavy scalar masses to be the same as $m_{Z'}$, $m_{Z'} = m_A = m_{H'} = m_H$. The color filled regions are excluded or constrained. The color notation is given in the caption. We find that the cross section is sensitive to the mass. For example, by changing $m_{Z'}$ from 1.9 to 2 TeV (5 % mass difference), the cross section is decreased by about 40 %. This is because the PDF rapidly changes in the heavier mass regions (see figure 2).

Below the thick orange line the cross section $\sigma(pp \to V' \to VV)$ is consistent with the ATLAS result. Here we apply the event selection efficiencies for the extended gauge model (cf. 10–16 % at $m_{JJ} = 2\,\mathrm{TeV}$) [1]. Note that a part of these regions are constrained from the stability condition at $\bar{\Lambda} = 100\,\mathrm{TeV}$ filled with light green. However, once we take

JHEP02(2016)084

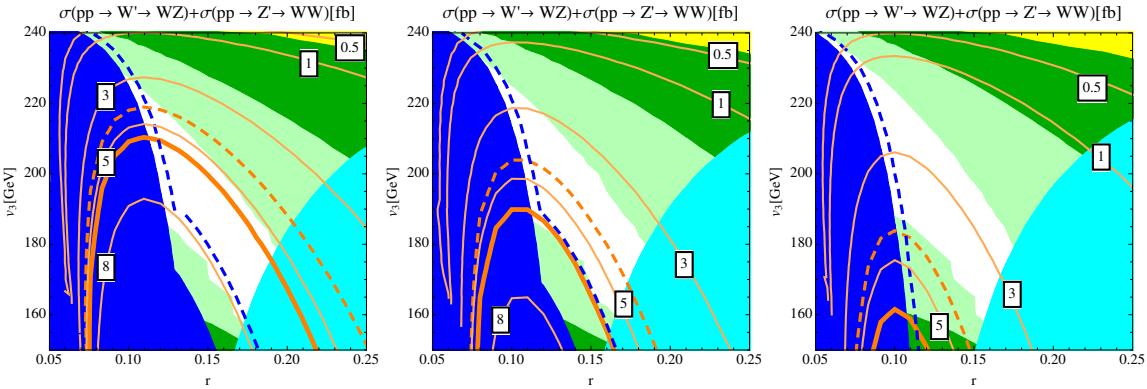

Figure 8. The cross sections of W' and Z' with two gauge bosons in their final states. We take $m_{Z'} = 1.9\,\text{TeV}$ (the left panel), $2.0\,\text{TeV}$ (the middle panel), and $2.1\,\text{TeV}$ (the right panel). The color filled regions are excluded or constrained. The blue regions are excluded by the experimental bounds. The regions of $g_1(\mu = m_{Z'}) > 4\pi$ are represented by yellow. The cyan regions are excluded by the bounded below condition. The green regions are constrained from the perturbativity and stability conditions where their cut off scale is 100 (10) TeV in the lighter green (darker green) regions. Below the thick orange line the cross section $\sigma(pp \to V' \to VV)$ is consistent with the ATLAS result. After taking account of the K-factor, the boundaries of the regions change into the dashed orange lines, and the regions below the dashed blue lines are excluded by the LHC bounds.

account of the higher order correction, these constraint would be weaker as we discussed in section 3.2.1. In the parameter regions shown in the figure, $\sigma(pp \to W' \to WZ)/\sigma(pp \to Z' \to WW) \simeq 2$. This is because the custodial symmetry is enhanced in the small r regime.

In the figure we show the leading order (LO) production cross sections. Next-to-leading order and next-to-leading logarithmic (NLO+NLL) corrections to the production cross sections of W' and Z' are evaluated in ref. [47, 48], and the K-factor ($\sigma/\sigma_{\text{LO}}$) is about 1.3. This means that once we consider the QCD corrections, the production cross sections in the figures should be scaled by about 30 %, and the LHC bounds become severer, while the theoretical constraints do not change. After taking account of the K-factor, the LHC diboson excess can be explained for the regions below dashed orange lines, and the regions below the dashed blue lines are excluded by the LHC bounds.

Figure 9 shows $\sigma(pp \to W' \to Wh)$.[4] The parameter choices and the color notations are the same as figure 8. We find that $\sigma(pp \to W' \to Wh)/\sigma(pp \to Z' \to Zh) \simeq 2$ due to the enhancement of the custodial symmetry. We find $\sigma(pp \to W' \to Wh) \times 20\,\text{fb}^{-1} \times \text{Br}(h \to b\bar{b})\ \text{Br}(W \to e\nu + \mu\nu) \sim 9$ events with $\sigma \sim 4\,\text{fb}$ in the regions where the ATLAS diboson excess can be explained. This is consistent with the excess of the event for the 1.8–1.9 TeV bins at the CMS with a local significance of 2.2σ for $W' \to Wh \to \ell\nu b\bar{b}$ search [41], although the detail of the event selection has not been reported.

We show $\Gamma_{\text{tot}}(W')$, κ_Z, $(g_{W'WZ}/g^{\text{SM}}_{WWZ}) \times (m_{W'}/m_W)^2$ and $g_{W'ff}/g^{\text{SM}}_{Wff}$ in figure 10. We fix $m_{Z'} = 2\,\text{TeV}$ because they are not sensitive to the Z' mass. The choices of other parameters and the color notations are the same as in figure 8. The width of W' is shown

[4]Detailed studies of this process are found in refs. [49, 50].

JHEP02(2016)084

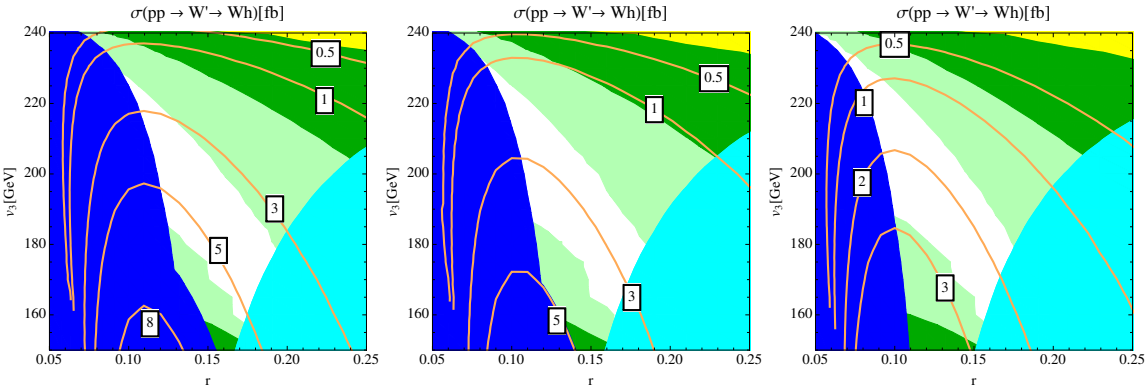

Figure 9. The cross sections of the diboson channels with h. We take $m_{W'} \simeq 1.9\,\text{TeV}$ (the left panel), $2.0\,\text{TeV}$ (the middle panel), and $2.1\,\text{TeV}$ (the right panel). The colored regions are experimental and theoretical constraints.

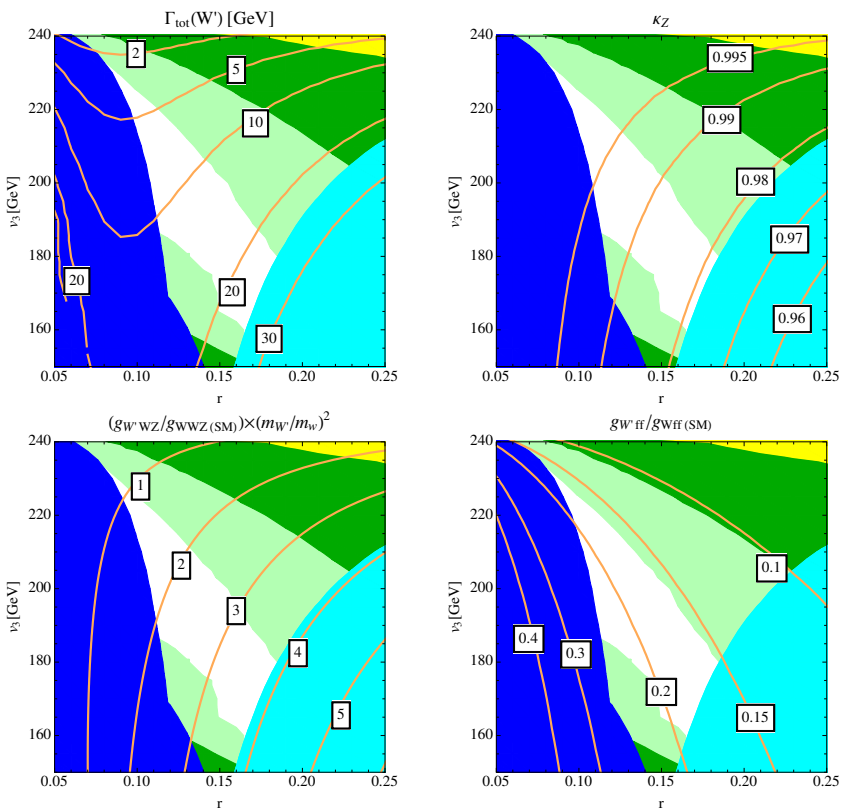

Figure 10. $\Gamma_{\text{tot}}(W')$, κ_Z, $(g_{W'WZ}/g^{\text{SM}}_{WWZ}) \times (m_{W'}/m_W)^2$, and $g_{W'ff}/g^{\text{SM}}_{Wff}$ for $m_{Z'} = 2\,\text{TeV}$. They are insensitive to small difference of $m_{Z'}$. The color notations are the same as in figure 8.

.

JHEP02(2016)084

in the top-left panel in the figure. We find that it is narrow and is less than 1 % of its mass, because the W' couplings to the SM particles are suppressed by powers of $m_W/m_{W'}$ and the decay into the heavy scalars are suppressed kinematically. The observable related to the Higgs couplings κ_Z defined in eq. (2.28) is shown in the top-right panels. The deviation from the SM prediction is small and the model is consistent with the current LHC data [51, 52]. Since the International Linear Collider (ILC) can measure the κ_Z at 1% level [53], some parameter points are within the reach of the proposed ILC. We show $g_{W'WZ}/g^{\rm SM}_{WWZ}$ and $g_{W'ff}/g^{\rm SM}_{Wff}$ at the lower panels in the figure. In the benchmark model used in ref. [1], $g_{W'WZ}/g^{\rm SM}_{WWZ} = m_W^2/m_{W'}^2$ and $g_{W'ff}/g^{\rm SM}_{Wff} = 1$. In our model, we find, due to the extra suppression by $\sqrt{1-v_3^2/v^2}$ and small r, $g_{W'WZ}/g^{\rm SM}_{WWZ}$ is numerically the same order as the benchmark model although its $m_{W'}$ dependence is $m_W/m_{W'}$ (see eq. (2.27)). On the other hand, $g_{W'ff}/g^{\rm SM}_{Wff}$ is about 10% of the benchmark model.

4 MC simulation of $W' \to WZ$ at $\sqrt{s} = 13$ TeV

In this section, we perform a collider simulation of $pp \to W' \to WZ$ at $\sqrt{s} = 13$ TeV. To study a discovery potential, we generate both QCD dijet background and $pp \to W' \to WZ$ signal events.

We generate 1.73×10^6 QCD dijet events as the dominant background by using Pythia 8.205 [54] with the generation cut so that the parton-parton center of mass energy must exceed 1 TeV and $p_T > 400$ GeV at $\sqrt{s} = 13$ TeV. The tree level production cross section is 350 pb. Our sample therefore corresponds to roughly $\int dt\mathcal{L}$ =5 fb^{-1}. We use the Tune 4C for fragmentation and hadronization [55]. We also generate 10^4 signal events ($pp \to W'(W'^+ + W'^-) \to WZ$) for the mass between 1800 and 3200 GeV, and take $\Gamma_{\rm tot}(W')$ to be 25 GeV in the simulation. Note that the total width of W' is less than about 30 GeV in the allowed region of this model (see figure 10). We also generate the signal and background events at $\sqrt{s} = 8$ TeV and compare them with the ATLAS plots [1].

The simple detector simulator Delphes3 [56] is modified using FastJet3 [57, 58] so that the mass drop and the grooming cuts used in the ATLAS study can be applied to the jets. We apply the cluster track matching algorithm of Delphes3 so that information of tracks inside jets can be used, otherwise the default ATLAS card is used.

Reconstruction of boosted objects using jet substructure was originally proposed in refs. [59, 60]. See recent developments in refs. [61, 62]. In our simulation, we closely follow the ATLAS analysis. The Cambridge-Aachen algorithm with $R = 1.2$ is used [63, 64] for the jet clustering. Then, $p_{T_1} > 600$ GeV, $p_{T_2} > 540$ GeV, $(p_{T_1} - p_{T_2})/(p_{T_1} + p_{T_2}) < 0.15$, $|y_1 - y_2| < 1.2$, $|\eta_1| < 2$ and $|\eta_2| < 2$ are required for the jets. In addition, we require $E_{Tmiss} < 350$ GeV, and veto events with isolated electrons and muons with $p_T > 20$ GeV. For each jet, the pair of the subjets which satisfies the subjet momentum balance criteria $\sqrt{y} > \sqrt{y_f} = 0.45$ are selected, where

$$\sqrt{y} = \min(p_{T_{j1}}, p_{T_{j2}}) \frac{\Delta R_{(j1,j2)}}{m_0}. \tag{4.1}$$

Here, $p_{T_{j1}}$ and $p_{T_{j2}}$ are the transverse momenta of subjets j_1 and j_2, $\Delta R_{(j1,j2)}$ is the distance between the subjets j_1 and j_2, and m_0 is the mass of the parent jet. Then the constituents

JHEP02(2016)084

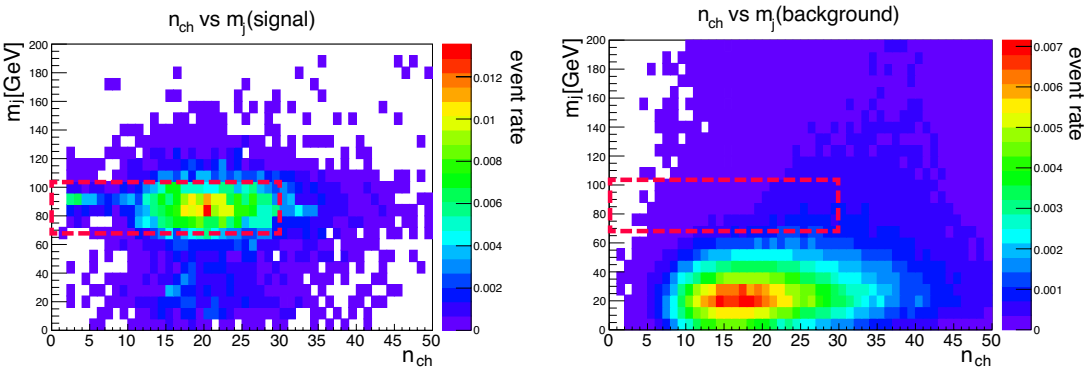

Figure 11. The distributions of the signal ($m_{W'} = 1800\,\text{GeV}$ and $\Gamma_{\text{tot}}(W') = 25\,\text{GeV}$) and the dijet background in n_{ch} and m_j plane. All the cut except for n_{ch} and m_j are applied, and we required $m_{jj} > 1500\,\text{GeV}$. The ATLAS signal regions are marked by squares.

of the selected pair of subjets are filtered. Namely the constituents are clustered with the radius parameter $R = 0.3$, and up to the highest 3 jets are taken to calculate the groomed jet mass and momentum. We require $|m_V - m_j| < 13\,\text{GeV}$, where m_V is m_Z or m_W, and m_j is an invariant mass of the groomed jet. Finally, the number of charged-particle tracks which are associated with the jet is required to be $n_{ch} < 30$. In figure 11, we show the distribution in n_{ch} and m_j plane for the events with $m_{jj} > 1500\,\text{GeV}$ where all the cuts except for n_{ch} and m_j are applied. The ATLAS signal regions are marked by squares. The figure shows very good separation between the signal and the background events.

To check our simulation, we compare the distributions of our $\sqrt{s} = 8\,\text{TeV}$ samples to the ATLAS ones. The figure 12 shows the reconstruction efficiency of the signal for various input W' mass. Our result at $\sqrt{s} = 13\,\text{TeV}$ is also shown. We find that the signal selection efficiency agrees with the ATLAS one. Since the jets get narrower with increasing p_T, the signal efficiency becomes lower for higher W' mass.

On the other hand, we find that the number of the background events after all the selection cuts are twice as large as that of the ATLAS final result. The discrepancy in the total background events might arise from several sources. The number of charged tracks of QCD jets are controlled by soft physics and varies significantly depending on Monte Carlo (MC) generators and tunes of the parton shower parameters especially for gluon jets. The distributions are shown in the left panel of figure 13, under the cut of figure 1 of ref. [1], $1.62\,\text{TeV} < m_{jj} < 1.98\,\text{TeV}$ and $60\,\text{GeV} < m_j < 110\,\text{GeV}$ together with the selection cuts listed above except that for n_{ch}, where m_{jj} is the dijet invariant mass. The signal distribution which is represented in the blue line agrees quite well with the ATLAS ones. However, the average number of charged tracks of dijet event is significantly higher than the ATLAS ones. To see the MC dependence, we also show the distribution of the MC sample generated by Herwig++ with default tunes by the black line [65], which predicts slightly small $\langle n_{ch} \rangle$ compared with Pythia8 Tune C4, but higher than ATLAS CT10 Tune.[5]

[5]In the study of quark-gluon separation [66], Herwig++ reproduces high gluon p_T jet nature well.

JHEP02(2016)084

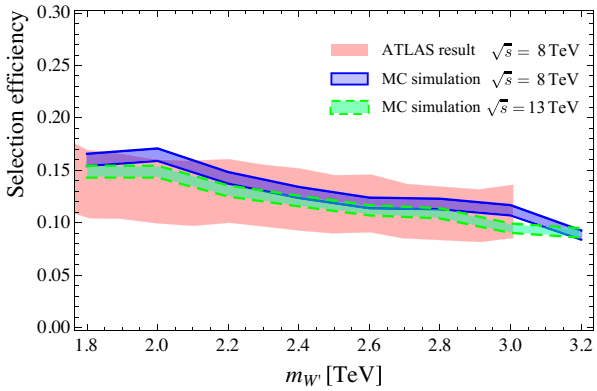

Figure 12. The event selection efficiencies for $W' \to WZ \to JJ$ simulated events generated by PYTHIA 8 as a function of the W' mass at $\sqrt{s} = 8$ and 13 TeV. The red band is the result of the ATLAS [1], where the thickness corresponds to $\pm$ 1 σ statistical and systematical errors. Our result of MC simulation at $\sqrt{s} = 8$ (13) TeV is represented in the blue (green) band where the thickness corresponds to $\pm$ 1 σ statistical error.

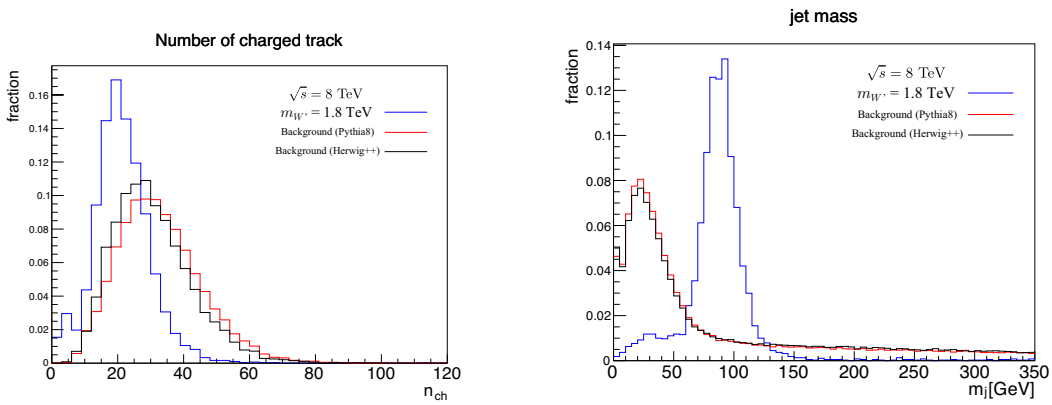

Figure 13. The distributions of the number of charged tracks $n_{\rm ch}$ (left) and the jet mass m_j (right) for the signal (Blue) and background events (Black and Red). We take $m_{W'} = 1800\,\text{GeV}$ and $\Gamma_{\rm tot}(W') = 25\,\text{GeV}$. We simulate the background events using PYTHIA8 (Red) and HERWIG++ (Black).

In the right panel of figure 13, we also show the m_j distributions for the signal and background. The signal distribution agrees quite well with the ATLAS MC results again. For the background distribution, we find that the number of events above $m_j > 50\,\text{GeV}$ is smaller compared with figure 1 of ref. [1]. This is because we do not generate underlying events together with the dijet events.

In the experimental side, ATLAS counts the well reconstructed track inside the jet. The efficiencies are not implemented in our simulation. Naively speaking, the efficiency is expected to be lower for the jets with high charged track multiplicity. For jet clustering, ATLAS selects calorimeter towers using Topocluster algorithm and does not use cluster-track matching which is only crudely implemented in our simulation. In any case, data driven approaches are adopted in ref. [1] to estimate the selection efficiency, and reproducing

JHEP02(2016)084

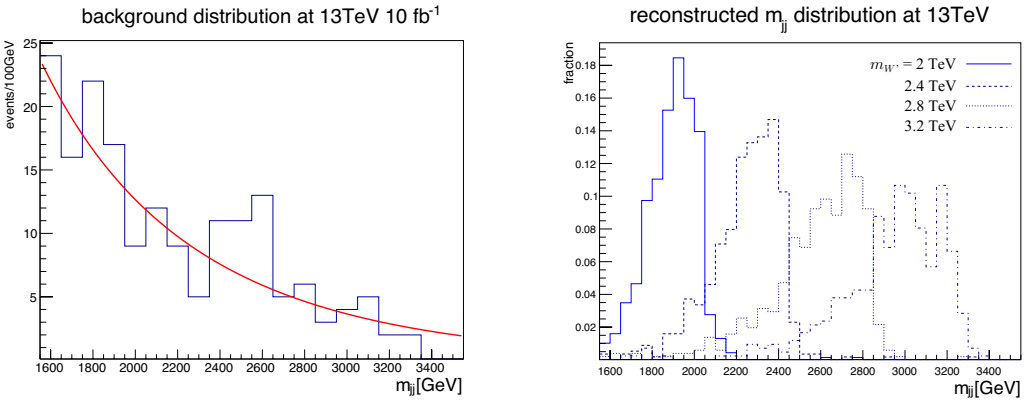

Figure 14. The m_{jj} distributions for the background (left) and the signal (right) at $\sqrt{s} = 13\,\text{TeV}$. The background distribution is for $10\,\text{fb}^{-1}$, and the signal distributions are normalized to be 1 for various input W' mass.

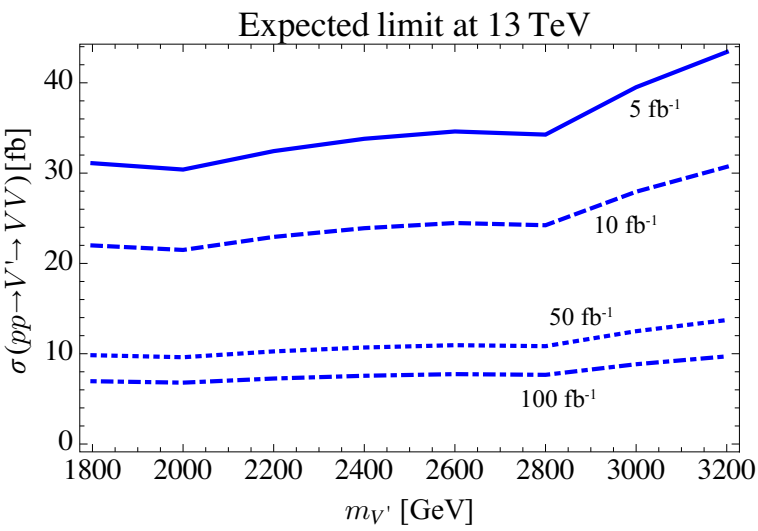

Figure 15. Expected limit on $\sigma(pp \to V' \to VV)$ at $\sqrt{s} = 13\,\text{TeV}$. We take $\Gamma_{\text{tot}}(V') = 25\,\text{GeV}$.

the result precisely is beyond the scope of this paper. It is probably worth doing more dedicated theoretical and experimental studies on jet nature relevant to the boosted W and Z bosons reconstruction in future.

Keeping crudeness of our simulation in mind, we estimate the signal efficiency at $\sqrt{s} = 13\,\text{TeV}$ using our signal MC and detector simulation without rescaling, while the number of the background events obtained from our MC is rescaled by factor of $1/2$ which is needed to reproduce the ATLAS results at $\sqrt{s} = 8\,\text{TeV}$. The scaling approach comes from an assumption that the change in the center of mass energy from $8\,\text{TeV}$ to $13\,\text{TeV}$ does not alter the structure inside jets of the same p_T jets. Note that gluon jets are involved in the QCD background at $\sqrt{s} = 13\,\text{TeV}$ but this effect is not taken into account. Under this assumption, the background is fitted to estimate the distribution, and the result is shown

JHEP02(2016)084

in the left panel of figure 14. We found 169 events/10 fb^{-1} for 1550 GeV $< m_{jj} <$ 3550 GeV after rescaling. We also show the dijet invariant mass distributions of the signal for various input W' mass in the right panel of figure 14.

Figure 15 shows expected the exclusion limit at 95 % C.L. for $\sigma(pp \to V' \to VV)$ at $\sqrt{s} = 13$ TeV.[6] We calculated $\Delta\chi^2$ of the signal plus background distributions to the background distribution. For the signal, we generate 10^4 signal events to obtain the result for each $m_{W'}$, and take the number of events in the bins $i_{\max} - 3 \leq i \leq i_{\max} + 3$, where $i_{\max}$ is the highest signal event bin and the bin size is 50 GeV. Then, we rescale them by the cross section and luminosity. The selection efficiency of the signal event is shown in figure 12. For the background, we use our fit and rescaled it by the luminosity. Here y-axis means $\sigma(pp \to W' \to WZ) + \sigma(pp \to Z' \to WW)$ with the mass at $m_{V'}$. We find that the region where $\sigma(pp \to V' \to VV)$ is larger than 20 fb may be excluded at $\int dt\mathcal{L} = 10\,\text{fb}^{-1}$ and $\sqrt{s} = 13$ TeV.

5 Future prospects: 13 TeV analyses

In this section, we analyze the future prospects of W' and Z' searches by applying result in section 4.

We investigate the prospects for the $\sqrt{s} = 13$ TeV collision in the case of $m_{Z'} = 2$ TeV. In figure 16, we show contours of the several cross sections by orange dashed lines in r–v_3 planes: $\sigma(pp \to W')\text{Br}(W' \to WZ) + \sigma(pp \to Z')\text{Br}(Z' \to WW)$, $\sigma(pp \to W')\text{Br}(W' \to Wh)$, $\sigma(pp \to W')\text{Br}(W' \to \ell\nu)$, $\sigma(pp \to W')\text{Br}(W' \to jj) + \sigma(pp \to Z')\text{Br}(Z' \to jj)$, and $\sigma(pp \to Z')\text{Br}(Z' \to \ell\ell)$. The color filled regions are excluded and constrained as we discussed in section 3.3. The color notations are the same as in figure 8.

The expected exclusion limit at $\sqrt{s} = 13$ TeV provided in figure 15 is shown by the red (dashed) line for $\int dt\mathcal{L} = 10$ (100) fb^{-1}. The masses of W' and Z' are highly degenerate in the small r regime, and we assume that the signal efficiency for $Z' \to WW$ event is equivalent to the one for $W' \to WZ$ which is simulated in the previous section. Thus we can apply the prospect shown in figure 15 to $\sigma(pp \to W' \to WZ) + \sigma(pp \to Z' \to WW)$. The region where the ATLAS diboson excess can be explained is within the reach of the LHC at $\int dt\mathcal{L} = 10\,\text{fb}^{-1}$ and $\sqrt{s} = 13$ TeV. In addition, the cross sections of the other channels are also large, so that the spin-1 resonances could be probed in the channels as well.

We plot the $\sqrt{s} = 13$ TeV cross sections as a function of spin-1 resonance mass in figure 17. We take the universal mass $m_{Z'} = m_A = m_{H'} = m_H$, $v_3 = 200$ GeV, and $\kappa_F = 1.00$ in figure 17. The color notation is the same as in figure 8. The mass of W' is highly degenerate with the mass of Z' in this figure. We find that the spin-1 resonances lighter than 2.1 (2.6) TeV can be excluded by the diboson search at the LHC with $\int dt\mathcal{L} = 10$ (100) fb^{-1}. Figure 18 shows the same cross sections for another parameter set ($v_3 = 150$ GeV and $\kappa_F = 0.99$). With the consideration of the bounded below condition, we find that the spin-1 resonances up to masses of 2.3 (2.6) TeV can be excluded with $\int dt\mathcal{L} = 10$ (100) fb^{-1}.

[6] Prospects for the electroweak gauge boson scattering which can also probe W' are discussed in, for example, ref. [67].

JHEP02(2016)084

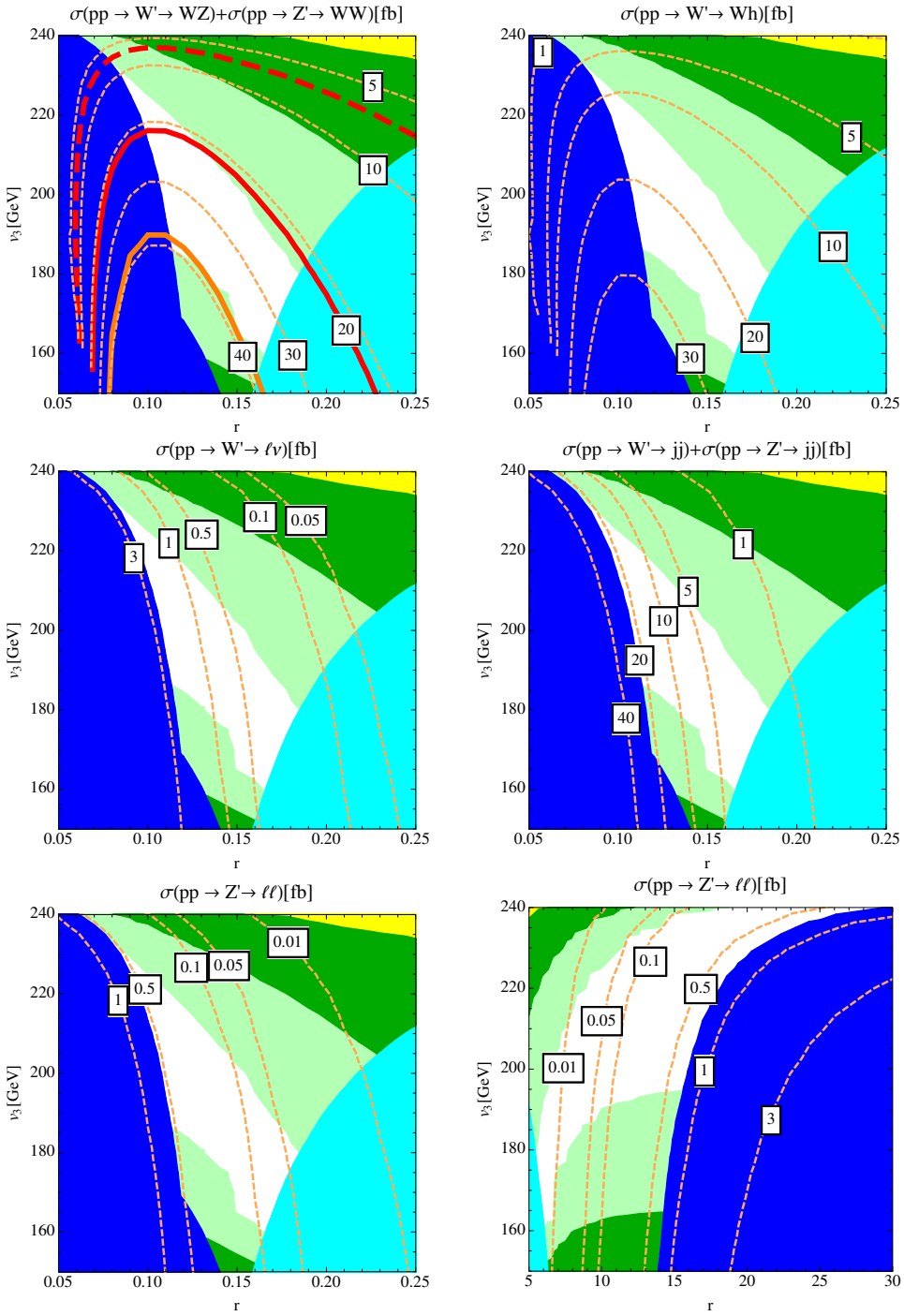

Figure 16. The prospects for the $\sqrt{s} = 13\,\text{TeV}$ collision. We take $m_{Z'} = m_A = m_{H'} = m_H = 2000\,\text{GeV}$, $\kappa_F = 1.00$. The color notation is the same as in figure 8. Below the thick orange line, the cross section $\sigma(pp \to V' \to VV)$ is enough to explain the diboson excess at ATLAS. Below the (dashed) red line is expected to be excluded with $\int dt\mathcal{L} = 10\ (100)\,\text{fb}^{-1}$.

JHEP02(2016)084

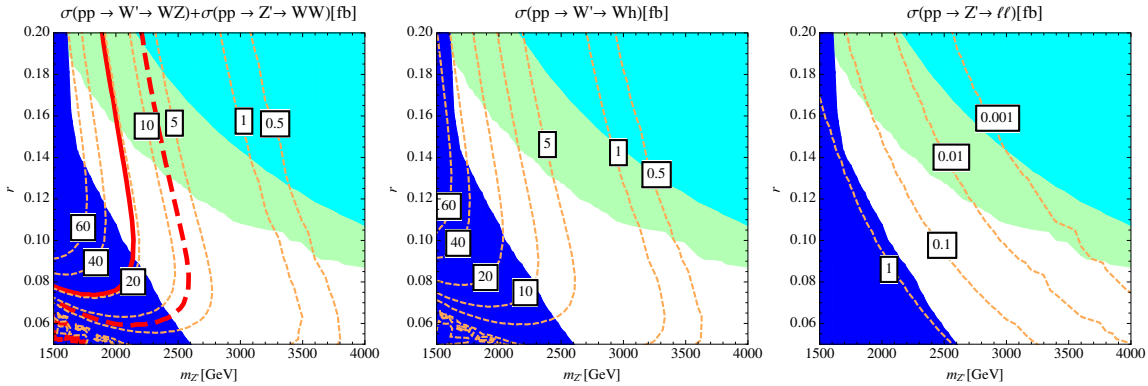

Figure 17. The prospects of the discovery as a function of $m_{Z'}$ and r for the LHC Run-2. We take $v_3 = 200\,\text{GeV}$ and $\kappa_F = 1.00$. The color notation is the same as in figure 8. The (dashed) red is the future expected exclusion limit for $\int dt\mathcal{L} = 10\ (100)\,\text{fb}^{-1}$.

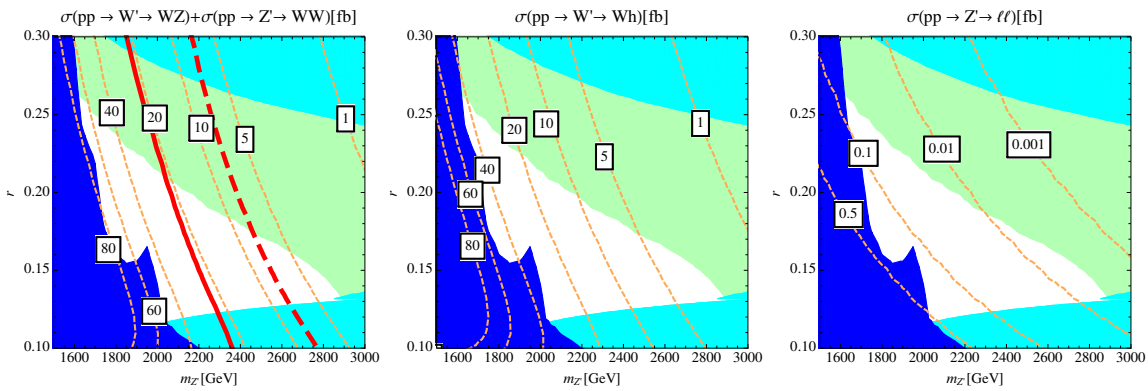

Figure 18. The prospects of the discovery as a function of $m_{Z'}$ and r for the LHC Run-2. We take $v_3 = 150\,\text{GeV}$ and $\kappa_F = 0.99$. Below the (dashed) red line is expected to be excluded with $\int dt\mathcal{L} = 10\ (100)\,\text{fb}^{-1}$.

Before closing this section, we briefly comment on the prospect for the large r region. Under the several theoretical bounds, this model has two allowed regions, namely small r and large r regions (see figure 5). The cross section of $pp \to Z' \to \ell\ell$ is enhanced by r^2 factor in large r regime (see eq. (B.2)). ATLAS study found $m_{Z'}$ around 3 TeV with the cross section around 0.01 fb is accessible with the high luminosity LHC at $\sqrt{s} = 14\,\text{TeV}$ with integrated luminosity $3000\,\text{fb}^{-1}$ [68]. Thus we can expect that the cross section for the large r region in the model is accessible at the LHC Run-2 as we can see in figure 16. However, the r regime would be constrained from the electroweak precision parameters at one-loop level due to the custodial symmetry breaking.

6 Conclusion

Motivated by the ATLAS diboson excess around 2 TeV, we have investigated the phenomenology of the spin-1 resonances (W' and Z') in the partially composite standard model. In this model, W' and Z' couple to the SM fermions weakly through the mixing

JHEP02(2016)084

to the elementary gauge bosons. We find that the main decay modes of the resonances are $V' \to VV$ and $V' \to Vh$, and the width is narrow enough so that the ATLAS diboson excess can be explained. The couplings of the spin-1 resonances with the SM sector can be controlled by the ratio of the Higgs VEVs so that the ATLAS diboson excess can be explained.

We have explored not only the current bounds from the LHC and the precision measurements but also the theoretical constraints, i.e. perturbativity condition, bounded below condition, global minimum vacuum condition, and stability condition of the scalar potential. The parameter regions where the diboson excess at the ATLAS can be explained are still allowed after including those constraints.

In order to investigate future prospects of the spin-1 resonance search, we have performed the simulation at $\sqrt{s} = 13\,\text{TeV}$ LHC, and estimated model independent exclusion limit for $\sigma(pp \to V' \to VV \to JJ)$ shown in figure 15. Applying our simulation result, we find that the parameter regions consistent with the ATLAS diboson excess will be excluded at $\int dt\mathcal{L} = 10\,\text{fb}^{-1}$ and $\sqrt{s} = 13\,\text{TeV}$.

Finally, we have investigated future prospects of diboson resonance search in our model. The spin-1 resonances up to a mass of 2.6 TeV can be probed at $\sqrt{s} = 13\,\text{TeV}$ and $\int dt\mathcal{L} = 100\,\text{fb}^{-1}$.

Acknowledgments

The authors would like to thank Koji Terashi and Ryuichiro Kitano for useful discussions. This work is supported by JSPS KAKENHI No. 26287039 (M.M.N.). The work is supported by Grant-in-Aid for Scientific research from the Ministry of Education, Science, Sports, and Culture (MEXT), Japan, No. 23104006 (T.A. and M.M.N.) and No. 25105011 (T.K.), and also by World Premier International Research Center Initiative (WPI Initiative), MEXT, Japan.

A Viable range of the coupling ratio κ_Z

In this appendix, we show κ_Z is very restricted to be one. We first replace the Higgs quartic couplings λ_i by the other parameters eq. (2.34). Here we take $m_A = m_{H'} = m_H$ for simplicity, and work in $m_A \gg m_h$ regime. For $r \ll 1$ regime, we find

$$\lambda_1 \simeq 0, \tag{A.1}$$

$$\lambda_2 \simeq f_1(\kappa_F, \kappa_Z), \tag{A.2}$$

$$\lambda_3 \simeq \frac{m_h^2}{2v^2}\kappa_F^2 + \frac{m_A^2}{2v^2}(1-\kappa_F^2), \tag{A.3}$$

$$\lambda_{12} \simeq 0, \tag{A.4}$$

$$\lambda_{23} \simeq f_2(\kappa_F, \kappa_Z), \tag{A.5}$$

$$\lambda_{31} \simeq 0, \tag{A.6}$$

JHEP02(2016)084

and for $r \gg 1$ regime,

$$\lambda_1 \simeq f_1(\kappa_F, \kappa_Z), \tag{A.7}$$

$$\lambda_2 \simeq 0, \tag{A.8}$$

$$\lambda_3 \simeq \frac{m_h^2}{2v^2}\kappa_F^2 + \frac{m_A^2}{2v^2}(1-\kappa_F^2), \tag{A.9}$$

$$\lambda_{12} \simeq 0, \tag{A.10}$$

$$\lambda_{23} \simeq 0, \tag{A.11}$$

$$\lambda_{31} \simeq f_2(\kappa_F, \kappa_Z), \tag{A.12}$$

$$\tag{A.13}$$

where

$$f_1(\kappa_F, \kappa_Z) \simeq \frac{m_h^2}{2v^2} - (1-\kappa_F)\frac{v_3^2}{v^2}\frac{2(m_A^2 - m_h^2)}{v^2 - v_3^2} + (1-\kappa_Z)\frac{m_A^2 - m_h^2}{v^2 - v_3^2}, \tag{A.14}$$

$$f_2(\kappa_F, \kappa_Z) \simeq \frac{m_h^2}{v^2} + (1-\kappa_F)\frac{v^2 - 3v_3^2}{v^2}\frac{m_A^2 - m_h^2}{v^2 - v_3^2} + (1-\kappa_Z)\frac{m_A^2 - m_h^2}{v^2 - v_3^2}. \tag{A.15}$$

1In eqs. (A.14) and (A.15), we make an expansion around $\kappa_F \simeq 1$ and $\kappa_Z \simeq 1$. Since both coefficients of $(1-\kappa_F)$ and $(1-\kappa_Z)$ are large enough in $m_A \gg v$ regime, even the small deviations of κ_F and κ_Z from 1 change the Higgs quartic couplings λ_i drastically.

Let us consider the case of $\kappa_F = 1$. The largest Higgs quartic coupling is λ_{23} (λ_{31}) in the $r \ll 1$ ($r \gg 1$) regime. We further demand λ_{23} (λ_{31}) $< (4\pi)^2$, namely

$$\kappa_Z > 1 - \frac{(16\pi^2 v^2 - m_h^2)}{(m_A^2 - m_h^2)}\left(1 - \frac{v_3^2}{v^2}\right). \tag{A.16}$$

Due to the running effects, these quartic couplings can be even larger at the high scale, so that the lower bound on κ_Z is actually severer than above estimation.

In figure 19, we show that the viable range of the coupling ratio κ_Z, where we take $v_3 = 200\,\text{GeV}$, $m_{Z'} = m_A = m_{H'} = m_H = 2\,\text{TeV}$, and $\kappa_F = 1.00$. The regions where $\lambda_i(\mu = 10\ (100)\,\text{TeV}) > (4\pi)^2$ are filled with green (light green), and there is no physical solution in the gray region. The maximal value of κ_Z is achieved at a boundary of the gray region. The white area represents the allowed region of parameter space. Thus we find κ_Z is severely constrained close to its maximized value for $m_A \gg m_h$.

B Production cross sections of W' and Z'

The leading order production cross sections of W' and Z' are given as follows.

$$\begin{aligned}\sigma(pp \to W'^{\pm}X) \simeq\ & \frac{\pi}{12s}\frac{m_W^2}{m_{W'}^2}\frac{e^2}{s_W^2}\frac{1}{r^2}\left(1 - \frac{v_3^2}{v^2}\right)\int_{m_{W'}^2/s}^1 \frac{dx}{x} \\ & \times\Bigg(f_u(x, m_{W'})f_{\bar{d}}\left(\frac{m_{W'}^2}{sx}, m_{W'}\right) + f_{\bar{d}}(x, m_{W'})f_u\left(\frac{m_{W'}^2}{sx}, m_{W'}\right) \\ & + f_d(x, m_{W'})f_{\bar{u}}\left(\frac{m_{W'}^2}{sx}, m_{W'}\right) + f_{\bar{u}}(x, m_{W'})f_d\left(\frac{m_{W'}^2}{sx}, m_{W'}\right) \\ & + (u \leftrightarrow c, d \leftrightarrow s)\Bigg),\end{aligned} \tag{B.1}$$

JHEP02(2016)084

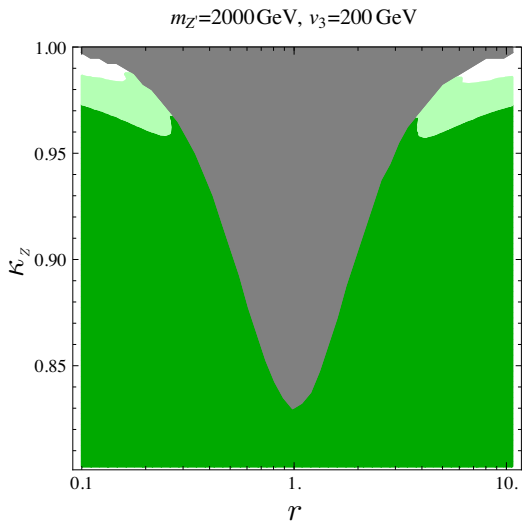

Figure 19. The viable range of the coupling ratio κ_Z, where we take $v_3 = 200\,\text{GeV}$, $m_{Z'} = m_A = m_{H'} = m_H = 2\,\text{TeV}$, and $\kappa_F = 1.00$. The regions where $\lambda_i(\mu = 10\ (100)\,\text{TeV}) > (4\pi)^2$ are filled with green (light green).

$$\begin{aligned}\sigma(pp \to Z'X) \simeq\ & \frac{\pi}{6s}\frac{m_W^2}{m_{W'}^2}\frac{e^2}{s_W^2}\frac{1}{r^2}\left(1-\frac{v_3^2}{v^2}\right)\\ &\times\left(\left(\left(1-r^2\frac{s_Z^2}{c_Z^2}\right)T_f^3+r^2\frac{s_Z^2}{c_Z^2}Q_f\right)^2+\left(r^2\frac{s_Z^2}{c_Z^2}Q_f\right)^2\right)\int_{m_{Z'}^2/s}^1\frac{dx}{x}\\ &\times\left(f_u(x,m_{Z'})f_{\bar{u}}\left(\frac{m_{Z'}^2}{sx},m_{Z'}\right)+f_{\bar{u}}(x,m_{Z'})f_u\left(\frac{m_{Z'}^2}{sx},m_{Z'}\right)\right.\\ &\left.+(u\leftrightarrow d,\ s,\ c,\ b)\right),\end{aligned} \tag{B.2}$$

where s is a square of the center of mass energy of the pp collider and $f_q(x,\ Q)$ is the parton distributions inside the p at the factorization scale Q for quark flavor q. Note that eq. (B.1) is a sum of production cross section of W'^+ and W'^-.

C Renormalization group equations

We derive the one-loop β functions for this model [69, 70], and obtain,

$$\beta_{g_0} = -3g_0^3, \tag{C.1}$$
$$\beta_{g_1} = -7g_1^3, \tag{C.2}$$
$$\beta_{g_2} = 7g_2^3, \tag{C.3}$$
$$\beta_{g_s} = -7g_s^3, \tag{C.4}$$
$$\beta_{\lambda_1} = 24\lambda_1^2 + 2\lambda_{12}^2 + 2\lambda_{31}^2 - 9\lambda_1(g_0^2+g_1^2) + \frac{9}{8}g_0^4 + \frac{9}{8}g_1^4 + \frac{9}{4}g_0^2g_1^2, \tag{C.5}$$
$$\beta_{\lambda_2} = 24\lambda_2^2 + 2\lambda_{12}^2 + 2\lambda_{23}^2 - 3\lambda_2(3g_1^2+g_2^2) + \frac{9}{8}g_1^4 + \frac{3}{8}g_2^4 + \frac{3}{4}g_1^2g_2^2, \tag{C.6}$$

JHEP02(2016)084

$$\beta_{\lambda_3} = 24\lambda_3^2 + 2\lambda_{23}^2 + 2\lambda_{31}^2 - 3\lambda_3(3g_0^2 + g_2^2) + \frac{9}{8}g_0^4 + \frac{3}{8}g_2^4 + \frac{3}{4}g_0^2 g_2^2 + 2\lambda_3(3y_t^2 + 3y_b^2 + y_\tau^2) - \frac{3}{2}y_t^4 - \frac{3}{2}y_b^4 - \frac{1}{2}y_\tau^4, \tag{C.7}$$

$$\beta_{\lambda_{12}} = 4\lambda_{12}^2 + 12\lambda_{12}(\lambda_1 + \lambda_2) + 4\lambda_{23}\lambda_{31} - \frac{3}{2}\lambda_{12}(3g_0^2 + 6g_1^2 + g_2^2) + \frac{9}{4}g_1^4, \tag{C.8}$$

$$\beta_{\lambda_{23}} = 4\lambda_{23}^2 + 12\lambda_{23}(\lambda_2 + \lambda_3) + 4\lambda_{12}\lambda_{31} - \frac{3}{2}\lambda_{23}(3g_0^2 + 3g_1^2 + 2g_2^2) + \frac{3}{4}g_2^4 + \lambda_{23}(3y_t^2 + 3y_b^2 + y_\tau^2), \tag{C.9}$$

$$\beta_{\lambda_{31}} = 4\lambda_{31}^2 + 12\lambda_{31}(\lambda_1 + \lambda_3) + 4\lambda_{12}\lambda_{23} - \frac{3}{2}\lambda_{31}(6g_0^2 + 3g_1^2 + g_2^2) + \frac{9}{4}g_0^4 + \lambda_{31}(3y_t^2 + 3y_b^2 + y_\tau^2), \tag{C.10}$$

$$\beta_{y_t} = y_t\left(-\frac{9}{4}g_0^2 - \frac{17}{12}g_2^2 - 8g_s^2 + \frac{9}{4}y_t^2 + \frac{3}{4}y_b^2 + \frac{1}{2}y_\tau^2\right), \tag{C.11}$$

$$\beta_{y_b} = y_b\left(-\frac{9}{4}g_0^2 - \frac{5}{12}g_2^2 - 8g_s^2 + \frac{3}{4}y_t^2 + \frac{9}{4}y_b^2 + \frac{1}{2}y_\tau^2\right), \tag{C.12}$$

$$\beta_{y_\tau} = y_\tau\left(-\frac{9}{4}g_0^2 - \frac{15}{4}g_2^2 + \frac{3}{2}y_t^2 + \frac{3}{2}y_b^2 + \frac{5}{4}y_\tau^2\right), \tag{C.13}$$

where β functions are defined in the following notation,

$$\frac{d(\text{coupling})}{d\ln\mu} = \frac{\beta_{(\text{coupling})}}{(4\pi)^2}. \tag{C.14}$$

Open Access. This article is distributed under the terms of the Creative Commons Attribution License (CC-BY 4.0), which permits any use, distribution and reproduction in any medium, provided the original author(s) and source are credited.

References

[1] ATLAS collaboration, *Search for high-mass t diboson resonances with boson-tagged jets in proton-proton collisions at $\sqrt{s} = 8$ TeV with the ATLAS detector*, *JHEP* **12** (2015) 055 [arXiv:1506.00962] [INSPIRE].

[2] CMS collaboration, *Search for massive resonances in dijet systems containing jets tagged as W or Z boson decays in pp collisions at $\sqrt{s} = 8$ TeV*, *JHEP* **08** (2014) 173 [arXiv:1405.1994] [INSPIRE].

[3] H.S. Fukano, M. Kurachi, S. Matsuzaki, K. Terashi and K. Yamawaki, *2 TeV Walking Technirho at LHC?*, *Phys. Lett.* **B 750** (2015) 259 [arXiv:1506.03751] [INSPIRE].

[4] J. Hisano, N. Nagata and Y. Omura, *Interpretations of the ATLAS Diboson Resonances*, *Phys. Rev.* **D 92** (2015) 055001 [arXiv:1506.03931] [INSPIRE].

[5] D.B. Franzosi, M.T. Frandsen and F. Sannino, *Diboson Signals via Fermi Scale Spin-One States*, *Phys. Rev.* **D 92** (2015) 115005 [arXiv:1506.04392] [INSPIRE].

[6] S.-S. Xue, *Vector-like $W^\pm$-boson coupling at TeV and fermion-mass hierarchy (two boson-tagged jets vs four quark jets)*, arXiv:1506.05994 [INSPIRE].

[7] K. Cheung, W.-Y. Keung, P.-Y. Tseng and T.-C. Yuan, *Interpretations of the ATLAS Diboson Anomaly*, *Phys. Lett.* **B 751** (2015) 188 [arXiv:1506.06064] [INSPIRE].

JHEP02(2016)084

[8] B.A. Dobrescu and Z. Liu, *W' Boson near 2 TeV: Predictions for Run 2 of the LHC*, Phys. Rev. Lett. **115** (2015) 211802 [arXiv:1506.06736] [INSPIRE].

[9] J.A. Aguilar-Saavedra, *Triboson interpretations of the ATLAS diboson excess*, JHEP **10** (2015) 099 [arXiv:1506.06739] [INSPIRE].

[10] A. Alves, A. Berlin, S. Profumo and F.S. Queiroz, *Dirac-fermionic dark matter in* $U(1)_X$ *models*, JHEP **10** (2015) 076 [arXiv:1506.06767] [INSPIRE].

[11] Y. Gao, T. Ghosh, K. Sinha and J.-H. Yu, $SU(2) \times SU(2) \times U(1)$ *interpretations of the diboson and Wh excesses*, Phys. Rev. **D 92** (2015) 055030 [arXiv:1506.07511] [INSPIRE].

[12] A. Thamm, R. Torre and A. Wulzer, *Composite Heavy Vector Triplet in the ATLAS Diboson Excess*, Phys. Rev. Lett. **115** (2015) 221802 [arXiv:1506.08688] [INSPIRE].

[13] J. Brehmer, J. Hewett, J. Kopp, T. Rizzo and J. Tattersall, *Symmetry Restored in Dibosons at the LHC?*, JHEP **10** (2015) 182 [arXiv:1507.00013] [INSPIRE].

[14] Q.-H. Cao, B. Yan and D.-M. Zhang, *Simple non-Abelian extensions of the standard model gauge group and the diboson excesses at the LHC*, Phys. Rev. **D 92** (2015) 095025 [arXiv:1507.00268] [INSPIRE].

[15] G. Cacciapaglia and M.T. Frandsen, *Unitarity implications of a diboson resonance in the TeV region for Higgs physics*, Phys. Rev. **D 92** (2015) 055035 [arXiv:1507.00900] [INSPIRE].

[16] T. Abe, R. Nagai, S. Okawa and M. Tanabashi, *Unitarity sum rules, three-site moose model and the ATLAS 2 TeV diboson anomalies*, Phys. Rev. **D 92** (2015) 055016 [arXiv:1507.01185] [INSPIRE].

[17] B.A. Dobrescu and Z. Liu, *Heavy Higgs bosons and the 2 TeV* W' *boson*, JHEP **10** (2015) 118 [arXiv:1507.01923] [INSPIRE].

[18] P. Coloma, B.A. Dobrescu and J. Lopez-Pavon, *Right-handed neutrinos and the 2 TeV* W' *boson*, Phys. Rev. **D 92** (2015) 115023 [arXiv:1508.04129] [INSPIRE].

[19] K. Agashe, R. Contino and A. Pomarol, *The Minimal composite Higgs model*, Nucl. Phys. **B 719** (2005) 165 [hep-ph/0412089] [INSPIRE].

[20] G. Panico and A. Wulzer, *The Discrete Composite Higgs Model*, JHEP **09** (2011) 135 [arXiv:1106.2719] [INSPIRE].

[21] R. Contino, D. Marzocca, D. Pappadopulo and R. Rattazzi, *On the effect of resonances in composite Higgs phenomenology*, JHEP **10** (2011) 081 [arXiv:1109.1570] [INSPIRE].

[22] B. Bellazzini, C. Csáki, J. Hubisz, J. Serra and J. Terning, *Composite Higgs Sketch*, JHEP **11** (2012) 003 [arXiv:1205.4032] [INSPIRE].

[23] T. Abe and R. Kitano, *Phenomenology of Partially Composite Standard Model*, Phys. Rev. **D 88** (2013) 015019 [arXiv:1305.2047] [INSPIRE].

[24] M. Bando, T. Fujiwara and K. Yamawaki, *Generalized Hidden Local Symmetry and the A1 Meson*, Prog. Theor. Phys. **79** (1988) 1140 [INSPIRE].

[25] M. Bando, T. Kugo, S. Uehara, K. Yamawaki and T. Yanagida, *Is rho Meson a Dynamical Gauge Boson of Hidden Local Symmetry?*, Phys. Rev. Lett. **54** (1985) 1215 [INSPIRE].

[26] M. Bando, T. Kugo and K. Yamawaki, *Composite Gauge Bosons and 'Low-energy Theorems' of Hidden Local Symmetries*, Prog. Theor. Phys. **73** (1985) 1541 [INSPIRE].

JHEP02(2016)084

[27] M. Bando, T. Kugo and K. Yamawaki, *On the Vector Mesons as Dynamical Gauge Bosons of Hidden Local Symmetries*, Nucl. Phys. **B 259** (1985) 493 [INSPIRE].

[28] H. Georgi, *A Tool Kit for Builders of Composite Models*, Nucl. Phys. **B 266** (1986) 274 [INSPIRE].

[29] C. Quigg, *Gauge theories of the strong, weak and electromagnetic interactions*, Front. Phys. **56** (1983) 1 [INSPIRE].

[30] E. Eichten, I. Hinchliffe, K.D. Lane and C. Quigg, *Super Collider Physics*, Rev. Mod. Phys. **56** (1984) 579 *Erratum ibid.* **58** (1986) 1065 [INSPIRE].

[31] G. Altarelli, B. Mele and M. Ruiz-Altaba, *Searching for New Heavy Vector Bosons in $p\bar{p}$ Colliders*, Z. Phys. **C 45** (1989) 109 [*Erratum ibid.* **C 47** (1990) 676] [INSPIRE].

[32] J. Pumplin, D.R. Stump, J. Huston, H.L. Lai, P.M. Nadolsky and W.K. Tung, *New generation of parton distributions with uncertainties from global QCD analysis*, JHEP **07** (2002) 012 [hep-ph/0201195] [INSPIRE].

[33] G. Degrassi et al., *Higgs mass and vacuum stability in the Standard Model at NNLO*, JHEP **08** (2012) 098 [arXiv:1205.6497] [INSPIRE].

[34] M.F. Zoller, *Standard Model β-functions to three-loop order and vacuum stability*, arXiv:1411.2843 [INSPIRE].

[35] ATLAS collaboration, *Search for new particles in events with one lepton and missing transverse momentum in pp collisions at $\sqrt{s} = 8$ TeV with the ATLAS detector*, JHEP **09** (2014) 037 [arXiv:1407.7494] [INSPIRE].

[36] CMS collaboration, *Search for physics beyond the standard model in final states with a lepton and missing transverse energy in proton-proton collisions at $\sqrt{s} = 8$ TeV*, Phys. Rev. **D 91** (2015) 092005 [arXiv:1408.2745] [INSPIRE].

[37] ATLAS collaboration, *Search for high-mass dilepton resonances in pp collisions at $\sqrt{s} = 8$ TeV with the ATLAS detector*, Phys. Rev. **D 90** (2014) 052005 [arXiv:1405.4123] [INSPIRE].

[38] CMS collaboration, *Search for physics beyond the standard model in dilepton mass spectra in proton-proton collisions at $\sqrt{s} = 8$ TeV*, JHEP **04** (2015) 025 [arXiv:1412.6302] [INSPIRE].

[39] CMS collaboration, *Search for Narrow High-Mass Resonances in Proton-Proton Collisions at $\sqrt{s} = 8$ TeV Decaying to a Z and a Higgs Boson*, Phys. Lett. **B 748** (2015) 255 [arXiv:1502.04994] [INSPIRE].

[40] ATLAS collaboration, *Search for a new resonance decaying to a W or Z boson and a Higgs boson in the $\ell\ell/\ell\nu/\nu\nu + b\bar{b}$ final states with the ATLAS detector*, Eur. Phys. J. **C 75** (2015) 263 [arXiv:1503.08089] [INSPIRE].

[41] CMS collaboration, *Search for massive WH resonances decaying to $\ell\nu b\bar{b}$ final state in the boosted regime at $\sqrt{s} = 8$ TeV*, CMS-PAS-EXO-14-010.

[42] CMS collaboration, *Search for A Massive Resonance Decaying into a Higgs Boson and a W or Z Boson in Hadronic Final States in Proton-Proton Collisions at $\sqrt{s} = 8$ TeV*, arXiv:1506.01443 [INSPIRE].

[43] ATLAS collaboration, *Search for resonant diboson production in the $\ell\ell q\bar{q}$ final state in pp collisions at $\sqrt{s} = 8$ TeV with the ATLAS detector*, Eur. Phys. J. **C 75** (2015) 69 [arXiv:1409.6190] [INSPIRE].

JHEP02(2016)084

[44] ATLAS collaboration, *Search for production of WW/WZ resonances decaying to a lepton, neutrino and jets in pp collisions at $\sqrt{s} = 8$ TeV with the ATLAS detector*, Eur. Phys. J. **C 75** (2015) 209 [*Erratum ibid.* **C 75** (2015) 370] [arXiv:1503.04677] [INSPIRE].

[45] ATLAS collaboration, *Search for WZ resonances in the fully leptonic channel using pp collisions at $\sqrt{s} = 8$ TeV with the ATLAS detector*, Phys. Lett. **B 737** (2014) 223 [arXiv:1406.4456] [INSPIRE].

[46] R. Barbieri, A. Pomarol, R. Rattazzi and A. Strumia, *Electroweak symmetry breaking after LEP-1 and LEP-2*, Nucl. Phys. **B 703** (2004) 127 [hep-ph/0405040] [INSPIRE].

[47] B. Fuks, M. Klasen, F. Ledroit, Q. Li and J. Morel, *Precision predictions for Z' - production at the CERN LHC: QCD matrix elements, parton showers and joint resummation*, Nucl. Phys. **B 797** (2008) 322 [arXiv:0711.0749] [INSPIRE].

[48] T. Jezo, M. Klasen, D.R. Lamprea, F. Lyonnet and I. Schienbein, *NLO+NLL limits on W' and Z' gauge boson masses in general extensions of the Standard Model*, JHEP **12** (2014) 092 [arXiv:1410.4692] [INSPIRE].

[49] A.R. Zerwekh, *Associate Higgs and gauge boson production at hadron colliders in a model with vector resonances*, Eur. Phys. J. **C 46** (2006) 791 [hep-ph/0512261] [INSPIRE].

[50] A.E.C. Hernández, C.O. Dib and A.R. Zerwekh, *Higgs boson coupling to a new strongly interacting sector*, arXiv:1506.03631 [INSPIRE].

[51] CMS collaboration, *Precise determination of the mass of the Higgs boson and tests of compatibility of its couplings with the standard model predictions using proton collisions at 7 and 8 TeV*, Eur. Phys. J. **C 75** (2015) 212 [arXiv:1412.8662] [INSPIRE].

[52] ATLAS collaboration, *Measurements of the Higgs boson production and decay rates and coupling strengths using pp collision data at $\sqrt{s} = 7$ and 8 TeV in the ATLAS experiment*, ATLAS-CONF-2015-007 (2015).

[53] D.M. Asner et al., *ILC Higgs White Paper*, arXiv:1310.0763 [INSPIRE].

[54] T. Sjöstrand, S. Mrenna and P.Z. Skands, *A Brief Introduction to PYTHIA 8.1*, Comput. Phys. Commun. **178** (2008) 852 [arXiv:0710.3820] [INSPIRE].

[55] R. Corke and T. Sjöstrand, *Interleaved Parton Showers and Tuning Prospects*, JHEP **03** (2011) 032 [arXiv:1011.1759] [INSPIRE].

[56] DELPHES 3 collaboration, J. de Favereau et al., *DELPHES 3, A modular framework for fast simulation of a generic collider experiment*, JHEP **02** (2014) 057 [arXiv:1307.6346] [INSPIRE].

[57] M. Cacciari and G.P. Salam, *Dispelling the N^3 myth for the k_t jet-finder*, Phys. Lett. **B 641** (2006) 57 [hep-ph/0512210] [INSPIRE].

[58] M. Cacciari, G.P. Salam and G. Soyez, *FastJet User Manual*, Eur. Phys. J. **C 72** (2012) 1896 [arXiv:1111.6097] [INSPIRE].

[59] J.M. Butterworth, A.R. Davison, M. Rubin and G.P. Salam, *Jet substructure as a new Higgs search channel at the LHC*, Phys. Rev. Lett. **100** (2008) 242001 [arXiv:0802.2470] [INSPIRE].

[60] M. Cacciari, J. Rojo, G.P. Salam and G. Soyez, *Quantifying the performance of jet definitions for kinematic reconstruction at the LHC*, JHEP **12** (2008) 032 [arXiv:0810.1304] [INSPIRE].

JHEP02(2016)084

[61] A. Abdesselam et al., *Boosted objects: A probe of beyond the Standard Model physics*, *Eur. Phys. J.* **C 71** (2011) 1661 [arXiv:1012.5412] [INSPIRE].

[62] A. Altheimer et al., *Boosted objects and jet substructure at the LHC. Report of BOOST2012, held at IFIC Valencia, 23rd–27th of July 2012*, *Eur. Phys. J.* **C 74** (2014) 2792 [arXiv:1311.2708] [INSPIRE].

[63] Y.L. Dokshitzer, G.D. Leder, S. Moretti and B.R. Webber, *Better jet clustering algorithms*, *JHEP* **08** (1997) 001 [hep-ph/9707323] [INSPIRE].

[64] M. Wobisch and T. Wengler, *Hadronization corrections to jet cross-sections in deep inelastic scattering*, hep-ph/9907280 [INSPIRE].

[65] M. Bahr et al., *HERWIG++ Physics and Manual*, *Eur. Phys. J.* **C 58** (2008) 639 [arXiv:0803.0883] [INSPIRE].

[66] ATLAS collaboration, *Light-quark and gluon jet discrimination in pp collisions at $\sqrt{s} = 7$ TeV with the ATLAS detector*, *Eur. Phys. J.* **C 74** (2014) 3023 [arXiv:1405.6583] [INSPIRE].

[67] C. Englert, P. Harris, M. Spannowsky and M. Takeuchi, *Unitarity-controlled resonances after the Higgs boson discovery*, *Phys. Rev.* **D 92** (2015) 013003 [arXiv:1503.07459] [INSPIRE].

[68] ATLAS collaboration, *Studies of Sensitivity to New Dilepton and Ditop Resonances with an Upgraded ATLAS Detector at a High-Luminosity LHC*, ATL-PHYS-PUB-2013-003 (2013).

[69] T.P. Cheng, E. Eichten and L.-F. Li, *Higgs Phenomena in Asymptotically Free Gauge Theories*, *Phys. Rev.* **D 9** (1974) 2259 [INSPIRE].

[70] W. Grimus and L. Lavoura, *Renormalization of the neutrino mass operators in the multi-Higgs-doublet standard model*, *Eur. Phys. J.* **C 39** (2005) 219 [hep-ph/0409231] [INSPIRE].

JHEP02(2016)084

Published for SISSA by Springer

Received: May 5, 2015
Accepted: June 16, 2015
Published: July 13, 2015

Lepton-specific two Higgs doublet model as a solution of muon $g-2$ anomaly

Tomohiro Abe,[a] **Ryosuke Sato**[a] **and Kei Yagyu**[b]

[a] *Institute of Particle and Nuclear Studies, High Energy Accelerator Research Organization (KEK), Oho, Tsukuba 305-0801, Japan*

[b] *School of Physics and Astronomy, University of Southampton, Highfield, Southampton, SO17 1BJ, U.K.*

E-mail: abetomo@post.kek.jp, rsato@post.kek.jp, K.Yagyu@soton.ac.uk

Abstract: We discuss the Type-X (lepton-specific) two Higgs doublet model as a solution of the anomaly of the muon $g-2$. We consider various experimental constraints on the parameter space such as direct searches for extra Higgs bosons at the LEP II and the LHC Run-I, electroweak precision observables, the decay of $B_s \to \mu^+\mu^-$, and the leptonic decay of the tau lepton. We find that the measurement of the tau decay provides the most important constraint, which excludes the parameter region that can explain the muon $g-2$ anomaly at the 1σ level. We then discuss the phenomenology of extra Higgs bosons and the standard model-like Higgs boson (h) to probe the scenario favored by the $g-2$ data at the collider experiments. We find that the 4τ, 3τ and $4\tau + W/Z$ signatures are expected as the main signal of the extra Higgs bosons at the LHC. In addition, we clarify that the value of the $h\tau\tau$ coupling is predicted to be the standard model value times about -1.6 to -1.0, and the branching fraction of the $h \to \gamma\gamma$ mode deviates from the standard model prediction by -30% to -15%. Furthermore, we find that the exotic decay mode, h decaying into the Z boson and a light CP-odd scalar boson, is allowed, and its branching fraction can be a few percent. These deviations in the property of h will be tested by the precision measurements at future collider experiments.

Keywords: Higgs Physics, Beyond Standard Model

ArXiv ePrint: 1504.07059

Open Access, © The Authors.
Article funded by SCOAP[3].

doi:10.1007/JHEP07(2015)064

JHEP07(2015)064

Contents

1 Introduction **1**

2 The 2HDMs **3**

3 Constraints on the Type-X 2HDM **6**
- 3.1 Direct searches for the extra Higgs bosons 7
  - 3.1.1 LEP II 7
  - 3.1.2 LHC run-I 7
- 3.2 Electroweak precision observables 8
  - 3.2.1 Oblique parameters 9
  - 3.2.2 Z boson decay 9
- 3.3 Flavor experiments 11
  - 3.3.1 $B_s \to \mu^+\mu^-$ 11
  - 3.3.2 Leptonic τ decay at the tree level 11
  - 3.3.3 Lepton universality at the one-loop level 13
- 3.4 Triviality bound 15

4 Muon $g-2$ **15**

5 Impact on the Higgs phenomenology at collider experiments **17**
- 5.1 Phenomenology of the extra Higgs bosons 18
- 5.2 Phenomenology of the SM-like Higgs boson 20

6 Conclusion **25**

A Decay rates for the extra Higgs bosons **26**

B Electroweak production of a pair of Higgs bosons **27**

1 Introduction

The anomalous magnetic moment of the muon $a_\mu \equiv (g-2)/2$, so-called muon $g-2$, is a very precisely measured observable. The latest measurement of a_μ by the E821 collaboration [1] gives

$$a_\mu^{\rm exp} = 11\ 659\ 208.0\ (5.4)(3.3) \times 10^{-10}. \tag{1.1}$$

As it has been well known that there is a discrepancy between the experimental value and the prediction of the standard model (SM). According to the calculation evaluated in

JHEP07(2015)064

refs. [2, 3]

$$a_\mu^{\rm exp} - a_\mu^{\rm SM} = (28.7 \pm 8.0) \times 10^{-10}, \qquad \text{(Davier et al.)}$$
$$a_\mu^{\rm exp} - a_\mu^{\rm SM} = (26.1 \pm 8.0) \times 10^{-10}, \qquad \text{(Hagiwara et al.)}$$

the discrepancy is more than the 3σ level, which can be considered as an indirect evidence of the existence of a new physics model. This discrepancy will be further probed at Fermilab [4] and J-PARC [5] in the near future. Since the size of the deviation is the same order as the electroweak contribution $a_\mu^{\rm EW} = 15.4 \times 10^{-10}$ [6], we expect that new physics exists at the electroweak scale if the strength of new interactions is as large as that of the weak interaction. In such a new physics scenario, new particles are expected to be light enough to be directly discovered at the LHC. Therefore, it is quite interesting to consider models beyond the SM as a solution of the muon $g-2$ anomaly.

Among various models which can explain the anomaly (for a review, e.g., see ref. [7]), two Higgs doublet models (2HDMs) give simple solutions. In 2HDMs, there are extra Higgs bosons (H, A, and $H^\pm$) in addition to the SM-like Higgs boson (h), and they can give new contributions to a_μ. Usually, a softly-broken discrete Z_2 symmetry is imposed [8] to avoid flavor changing neutral current (FCNC) processes at the tree level. Under the Z_2 symmetry, four independent types of Yukawa interactions are allowed depending on the assignment of the Z_2 charge to the SM fermion [9, 10], which are called as Type-I, Type-II, Type-X (or lepton specific) and Type-Y (or flipped) [11]. In all the types of Yukawa interactions, the lepton couplings to the extra Higgs bosons can be sizable enough to explain a_μ. In the Type-I and Type-Y 2HDMs, however, the top Yukawa coupling also becomes large together with the enhancement of the lepton couplings. This is disfavored from the view point of perturbativity. Thus, the Type-II and Type-X 2HDMs are suitable to solve the muon $g-2$ anomaly.

The muon $g-2$ has been calculated in a number of papers within 2HDMs [12–22]. In the early 2000s, this was calculated at the one-loop level in the Type-II 2HDM in ref. [12]. After that, it was pointed out in refs. [13, 14] that the two-loop Barr-Zee type diagrams [23, 24] give a significant contribution to a_μ if a mass of A is $\mathcal{O}$(10-100) GeV and if there is large $Ab\bar{b}$ or $A\tau^+\tau^-$ couplings. In ref. [19], the implication on collider signatures was discussed in the Type-X 2HDM, namely, the $h \to AA \to 4\tau$ process can be important in the favored parameter region by a_μ. After the discovery of the Higgs boson at the LHC [25, 26], the muon $g-2$ has been reanalyzed by taking into account the Higgs boson search data in addition to the previous experimental constraints [20–22]. Furthermore, the recent observation of $\mathrm{Br}(B_s \to \mu^+\mu^-)$ at the LHC [27] gives a new constraint on the parameter space of 2HDMs [21].

The difference between the Type-II and Type-X 2HDMs is the quark couplings to the extra Higgs bosons. In the Type-II 2HDM, both the lepton and down-type quark couplings are enhanced simultaneously, and thus the model is severely constrained by flavor physics and direct searches of the extra Higgs bosons. On the other hand, in the Type-X 2HDM, the quark couplings to the extra Higgs bosons are suppressed when the lepton couplings are enhanced. Thus, the constraints are weaker than those in the Type-II 2HDM. In fact, it was clarified in refs. [20, 21] that only the Type-X 2HDM can solve the muon $g-2$ anomaly with satisfying the current experimental data.[1]

[1] In addition to the muon $g-2$ anomaly, there are several other motivations for this model. For example, see refs. [28, 29].

JHEP07(2015)064

	H_1	H_2	u_R^c	d_R^c	ℓ_R^c	Q_L, L_L	ξ_u	ξ_d	ξ_ℓ
Type-I	$+$	$-$	$-$	$-$	$-$	$+$	$\cot\beta$	$\cot\beta$	$\cot\beta$
Type-II	$+$	$-$	$-$	$+$	$+$	$+$	$\cot\beta$	$-\tan\beta$	$-\tan\beta$
Type-X	$+$	$-$	$-$	$-$	$+$	$+$	$\cot\beta$	$\cot\beta$	$-\tan\beta$
Type-Y	$+$	$-$	$-$	$+$	$-$	$+$	$\cot\beta$	$-\tan\beta$	$\cot\beta$

Table 1. Assignment of the Z_2 parity and ξ_f factors in eq. (2.21) in each type of the Yukawa interactions.

Another important constraint comes from the lepton flavor physics. In the Type-X 2HDM, the constraint from the leptonic τ decay [11, 30–32] gives a severe constraint on the parameter space favored to explain the $g-2$ anomaly because of the lepton coupling enhancements. However, this important constraint has not been included in the previous analyses. Therefore, in this paper, we calculate the leptonic τ decay and the $Z\tau\tau$ vertex at the one-loop level in the Type-X 2HDM in order to compare the precise experimental measurements. We then investigate the favored parameter region by a_μ under these constraints in addition to those already known. Furthermore, we evaluate the running of the scalar quartic couplings by renormalization group equations (RGEs), and require that the couplings do not become too large up to a certain energy scale, for example 10 TeV. We find that extra Higgs boson loop contributions can reduce the discrepancy in a_μ to be 2σ level, but not less than 1σ level. We then study the collider phenomenology in the favored parameter region.

This paper is organized as follows. In section 2, we define the Lagrangian of the 2HDM, and derive the Higgs boson couplings with the gauge bosons and the fermions. In section 3, we discuss constraints from direct searches for the extra Higgs bosons at LEP II and the LHC Run-I, electroweak precision observables, the decay of $B_s \to \mu^+\mu^-$, the leptonic τ decay, and the triviality bound. In section 4, we show the favored parameter regions by the muon $g-2$ anomaly. In section 5, we discuss the collider phenomenology of the extra Higgs bosons at the LHC, the deviations in the SM-like Higgs boson h couplings, and the decay branching fractions of h. We also discuss the exotic decay mode: $h \to ZA$. Conclusion is given in section 6. In appendix, we present the expressions for the decay rates of extra Higgs bosons and those for the parton level cross sections for the production of extra Higgs bosons at the LHC.

2 The 2HDMs

In this section, we define the Lagrangian of the 2HDM, in which the Higgs sector is composed of two $\mathrm{SU}(2)_L$ doublet scalar fields H_1 and H_2. To avoid the tree level FCNC, we impose a Z_2 symmetry in the Higgs sector which can be softly-broken in general. Under the Z_2 parity, four types of Yukawa interactions are defined depending on the assignment of Z_2 charge as listed in table 1.

JHEP07(2015)064

The most general Higgs potential with the softly-broken Z_2 parity is given as

$$V = m_{11}^2|H_1|^2 + m_{22}^2|H_2|^2 - (m_{12}^2 H_1^\dagger H_2 + h.c.) \\ + \frac{\lambda_1}{2}|H_1|^4 + \frac{\lambda_2}{2}|H_2|^4 + \lambda_3|H_1|^2|H_2|^2 + \lambda_4|H_1^\dagger H_2|^2 + \left[\frac{\lambda_5}{2}(H_1^\dagger H_2)^2 + h.c.\right]. \quad (2.1)$$

Throughout the paper, we consider the CP-conserving case of the Higgs sector for simplicity, so that the imaginary parts of m_{12}^2 and λ_5 are assumed to be zero. The Higgs fields are parametrized as

$$H_i = \begin{bmatrix} h_i^+ \\ \frac{1}{\sqrt{2}}(v_i + h_i - ia_i) \end{bmatrix}, \quad (i = 1, 2), \quad (2.2)$$

where v_1 and v_2 are the VEVs of the Higgs doublets which are related to the Fermi constant G_F by $v^2 \equiv v_1^2 + v_2^2 = 1/(\sqrt{2}G_F)$. The ratio of the two VEVs is parametrized by $\tan\beta = v_2/v_1$.

The mass eigenstates of the scalar bosons are expressed by introducing the mixing angles α and β as

$$\begin{pmatrix} h_1 \\ h_2 \end{pmatrix} = \begin{pmatrix} \cos\alpha & -\sin\alpha \\ \sin\alpha & \cos\alpha \end{pmatrix} \begin{pmatrix} H \\ h^0 \end{pmatrix}, \quad (2.3)$$

$$\begin{pmatrix} a_1 \\ a_2 \end{pmatrix} = \begin{pmatrix} \cos\beta & -\sin\beta \\ \sin\beta & \cos\beta \end{pmatrix} \begin{pmatrix} G^0 \\ A \end{pmatrix}, \quad (2.4)$$

$$\begin{pmatrix} h_1^\pm \\ h_2^\pm \end{pmatrix} = \begin{pmatrix} \cos\beta & -\sin\beta \\ \sin\beta & \cos\beta \end{pmatrix} \begin{pmatrix} G^\pm \\ H^\pm \end{pmatrix}, \quad (2.5)$$

where G^0 and $G^\pm$ are the Nambu-Goldstone bosons which are absorbed by the Z and W bosons as the longitudinal component, respectively.

The squared masses for the physical Higgs bosons are given by

$$\begin{aligned} m_{H^\pm}^2 &= M^2 - \frac{v^2}{2}(\lambda_4 + \lambda_5), \\ m_A^2 &= M^2 - v^2\lambda_5, \\ m_H^2 &= \cos^2(\alpha-\beta)M_{11}^2 + \sin^2(\alpha-\beta)M_{22}^2 + \sin 2(\alpha-\beta)M_{12}^2, \\ m_h^2 &= \sin^2(\alpha-\beta)M_{11}^2 + \cos^2(\alpha-\beta)M_{22}^2 - \sin 2(\alpha-\beta)M_{12}^2, \end{aligned} \quad (2.6)$$

where $M^2 = m_{12}^2/(\sin\beta\cos\beta)$ describes the breaking scale of the Z_2 symmetry, and M_{ij}^2 are given by

$$M_{11}^2 = v^2(\lambda_1\cos^4\beta + \lambda_2\sin^4\beta) + \frac{v^2}{2}\lambda_{345}\sin^2 2\beta, \quad (2.7)$$

$$M_{22}^2 = M^2 + v^2(\lambda_1 + \lambda_2 - 2\lambda_{345})\sin^2\beta\cos^2\beta, \quad (2.8)$$

$$M_{12}^2 = \frac{v^2}{2}(\lambda_2\sin^2\beta - \lambda_1\cos^2\beta + \lambda_{345}\cos 2\beta)\sin 2\beta, \quad (2.9)$$

JHEP07(2015)064

where $\lambda_{345} = \lambda_3 + \lambda_4 + \lambda_5$. The mixing angle α is also expressed in terms of M^2_{ij} as

$$\tan 2(\alpha - \beta) = \frac{2M^2_{12}}{M^2_{11} - M^2_{22}}. \tag{2.10}$$

All the quartic coupling constants in the Higgs potential can be rewritten in terms of the physical parameters as

$$\begin{aligned}
\lambda_1 v^2 &= -M^2 \tan^2\beta + (m^2_H \tan^2\beta + m^2_h) s^2_{\beta-\alpha} + (m^2_H + m^2_h \tan^2\beta) c^2_{\beta-\alpha} \\
&\quad + 2(m^2_H - m^2_h) \tan\beta s_{\beta-\alpha} c_{\beta-\alpha}, \\
\lambda_2 v^2 &= -M^2 \cot^2\beta + (m^2_H \cot^2\beta + m^2_h) s^2_{\beta-\alpha} + (m^2_H + m^2_h \cot^2\beta) c^2_{\beta-\alpha} \\
&\quad - 2(m^2_H - m^2_h) \cot\beta s_{\beta-\alpha} c_{\beta-\alpha}, \\
\lambda_3 v^2 &= 2m^2_{H^\pm} - M^2 + (m^2_h - m^2_H)[s^2_{\beta-\alpha} - c^2_{\beta-\alpha} - (\tan\beta - \cot\beta) s_{\beta-\alpha} c_{\beta-\alpha}], \\
\lambda_4 v^2 &= M^2 + m^2_A - 2m^2_{H^\pm}, \\
\lambda_5 v^2 &= M^2 - m^2_A,
\end{aligned} \tag{2.11}$$

where $s_{\beta-\alpha} = \sin(\beta - \alpha)$ and $c_{\beta-\alpha} = \cos(\beta - \alpha)$.

A size of some combinations of λ's in the Higgs potential is constrained by taking into account perturbative unitarity [33–37] and vacuum stability [38–41]. Through eq. (2.11), such a constraint can be translated into a bound on the physical parameters; e.g., the masses of the scalar bosons. First, the condition for vacuum stability; i.e., the requirement for bounded from below in any direction of the Higgs potential with large scalar fields, is given by [38–41]

$$\lambda_1 > 0, \quad \lambda_2 > 0, \quad \sqrt{\lambda_1\lambda_2} + \lambda_3 + \mathrm{MIN}(0, \lambda_4 + \lambda_5, \lambda_4 - \lambda_5) > 0. \tag{2.12}$$

Second, the perturbative unitarity bound is obtained by requiring that all the eigenvalues of the s-wave amplitude matrix $a^0_{i,\pm}$ for the elastic scatterings of two body boson states are satisfied as

$$|a^0_{i,\pm}| \leq \frac{1}{2}. \tag{2.13}$$

All the independent eigenvalues $a^0_{i,\pm}$ were derived in refs. [35–37] as

$$a^0_{1,\pm} = \frac{1}{32\pi}\left[3(\lambda_1 + \lambda_2) \pm \sqrt{9(\lambda_1 - \lambda_2)^2 + 4(2\lambda_3 + \lambda_4)^2}\right], \tag{2.14}$$

$$a^0_{2,\pm} = \frac{1}{32\pi}\left[(\lambda_1 + \lambda_2) \pm \sqrt{(\lambda_1 - \lambda_2)^2 + 4\lambda_4^2}\right], \tag{2.15}$$

$$a^0_{3,\pm} = \frac{1}{32\pi}\left[(\lambda_1 + \lambda_2) \pm \sqrt{(\lambda_1 - \lambda_2)^2 + 4\lambda_5^2}\right], \tag{2.16}$$

$$a^0_{4,\pm} = \frac{1}{16\pi}(\lambda_3 + 2\lambda_4 \pm 3\lambda_5), \tag{2.17}$$

$$a^0_{5,\pm} = \frac{1}{16\pi}(\lambda_3 \pm \lambda_4), \tag{2.18}$$

$$a^0_{6,\pm} = \frac{1}{16\pi}(\lambda_3 \pm \lambda_5). \tag{2.19}$$

JHEP07(2015)064

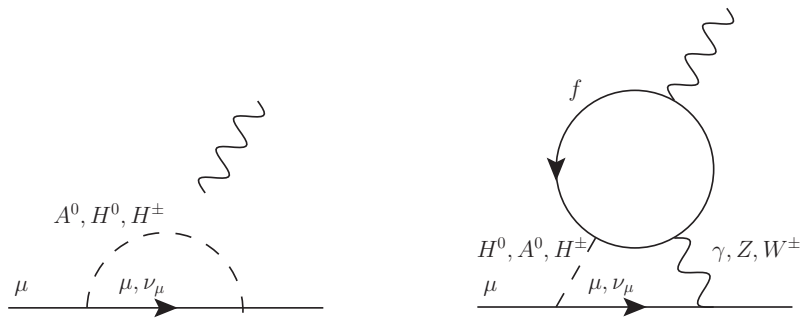

Figure 1. One-loop (left) and two-loop Barr-Zee (right) diagrams which give corrections to the muon $g-2$.

The Yukawa interaction terms are given by

$$\mathcal{L}_{\text{Yukawa}} = -y_u \tilde{H}_u^T Q_L u_R^c - y_d H_d^\dagger Q_L d_R^c - y_\ell H_\ell^\dagger L_L e_R^c + h.c., \tag{2.20}$$

where $\tilde{H}_u = i\tau^2 H_u$. In eq. (2.20), H_u, H_d and H_ℓ are either H_1 or H_2 depending on the type of Yukawa interaction. In the mass eigenstates of the scalar bosons, the interaction terms are expressed as

$$\begin{aligned}\mathcal{L}_{\text{Yukawa}} = &- \sum_{f=u,d,\ell} \frac{m_f}{v}\left(\xi_f^h\, h\bar{f}f + \xi_f^H\, H\bar{f}f - 2iT_f^3\xi_f\, A\bar{f}\gamma_5 f\right) \\ &+ \left[\sqrt{2}V_{ud}H^+\bar{u}\left(\frac{m_u\xi_u}{v}P_L - \frac{m_d\xi_d}{v}P_R\right)d - \frac{\sqrt{2}m_\ell\xi_\ell}{v}H^+\bar{\nu}P_R\ell + h.c.\right],\end{aligned} \tag{2.21}$$

where $T_f^3 = +1/2$ $(-1/2)$ for $f = u$ (d, ℓ), and $V_{ff'}$ is the Cabibbo-Kobayashi-Maskawa matrix element. The ξ_f^h and ξ_f^H factors are defined by

$$\xi_f^h = s_{\beta-\alpha} + \xi_f c_{\beta-\alpha}, \quad \xi_f^H = c_{\beta-\alpha} - \xi_f s_{\beta-\alpha}. \tag{2.22}$$

The ξ_f factors in eqs. (2.21) and (2.22) are given in table 1.

From the kinetic terms of the scalar fields, the ratios of the coupling constant among the CP-even scalars and gauge bosons are extracted as

$$\frac{g_{hVV}}{g_{hVV,\text{SM}}} = s_{\beta-\alpha}, \qquad \frac{g_{HVV}}{g_{hVV,\text{SM}}} = c_{\beta-\alpha}. \qquad (V = W, Z) \tag{2.23}$$

As it is seen in eqs. (2.21), (2.22) and (2.23), in the limit of $\sin(\beta - a) \to 1$, both $hf\bar{f}$ and hVV couplings become the same as those in the SM, so that we can call this limit as the SM-like limit.

3 Constraints on the Type-X 2HDM

In the 2HDMs, the one-loop diagrams and the two-loop Barr-Zee type diagrams shown in figure 1 give dominant contributions to the muon $g-2$. It has been known that the Barr-Zee type diagrams give a sizable positive contribution to a_μ in the case of a large

JHEP07(2015)064

$A\ell^+\ell^-$ coupling and a small m_A as pointed it out in refs. [13, 14]. In the Type-X 2HDMs, a large $A\ell^+\ell^-$ can be realized by taking $\tan\beta \gg 1$ since $\xi_\ell = -\tan\beta$ as shown in table 1. Typically, when $\tan\beta \gtrsim 40$ and $m_A = \mathcal{O}(10\text{-}100)$ GeV, the muon $g-2$ anomaly can be explained in the Type-X 2HDM [20]. In this section, we focus on the Type-X 2HDM with the large $\tan\beta$ and small m_A scenario to explain the $g-2$ anomaly, and we discuss important experimental constraints in this situation.

3.1 Direct searches for the extra Higgs bosons

There has been no signal of the extra Higgs bosons at any collider experiments. This gives lower limits on the masses of the extra Higgs bosons depending on the magnitude of couplings with SM particles. We first summarize the current bounds from the LEP II experiment, and we also review those from the LHC Run-I.

3.1.1 LEP II

There are constraints on the masses of the extra Higgs bosons from the direct production at the LEP II experiment with the maximal collision energy to be about 200 GeV. From the $H^\pm$ pair production process $e^+e^- \to \gamma^*/Z^* \to H^+H^-$ the lower bound was obtained by $m_{H^\pm} > 93.5$ GeV at 95 % C.L. [42] under the assumption of $\mathrm{Br}(H^+ \to \tau^+\nu_\tau) = 1$ which is realized by $\tan\beta \gtrsim 2$, $\sin(\beta-\alpha) \simeq 1$ in the Type-X 2HDM.

From the pair production of the neutral Higgs bosons $e^+e^- \to Z^* \to AH$, the lower bound for the sum of m_A and m_H is given to be about 190-195 GeV for $m_A > 40$ GeV [43] under the assumption of $\mathrm{Br}(H \to \tau^+\tau^-) = \mathrm{Br}(A \to \tau^+\tau^-) = 1$ which is realized by $\tan\beta \gtrsim 3$ and $\sin(\beta-\alpha) \simeq 1$ in the Type-X 2HDM.

The searches for A and H from the bremsstrahlung process $e^+e^- \to \tau\tau A/H$ have also been performed for the range of $m_{A/H} < 50$ GeV. This process gives an upper bound on $\tan\beta$ for a fixed value of $m_{A/H}$. For example, $\tan\beta > 128.1$ (120.1) and $\tan\beta > 44.8$ (40.0) are respectively excluded at 95% C.L. for m_A (m_H) to be 30 GeV and 15 GeV [44] with the case of $\mathrm{Br}(A \to \tau\tau)$=$\mathrm{Br}(H \to \tau\tau)$=1. We note that the branching fractions for the extra Higgs bosons into a fermion pair can be reduced when there is a non-zero mass splitting among them. For example, $H^\pm \to AW^{(*)}$ and $H \to AZ^{(*)}$ open in the case of $m_{H^\pm} > m_A$ and $m_H > m_A$, respectively. There also happen the inverse processes like $A \to H^\pm W^{\mp(*)}$ and $A \to HZ^{(*)}$ as long as they are kinematically allowed. In such decay modes associated with a gauge boson, the bounds on masses on the extra Higgs bosons can be weaker than those given in the above.

3.1.2 LHC run-I

At the LHC, extra Higgs boson searches have been performed in various channels. In the most of channels, an enhancement of the Yukawa couplings of the extra Higgs bosons becomes important to obtain a bound on their masses or coupling constants. However, in the Type-X 2HDM, the couplings of the neutral extra Higgs bosons to the quarks are suppressed by $\cot\beta$. Thus, the processes such as $gg \to A/H \to \tau\tau$ and $gg \to b\bar{b}A/b\bar{b}H \to b\bar{b}\tau\tau$ do not set a limit on the masses in a large $\tan\beta$ case.

JHEP07(2015)064

Similar to the neutral Higgs boson productions, the cross section of the $H^\pm$ production such as $gb \to H^\pm t$ is also suppressed by $\cot^2\beta$ in the Type-X 2HDM. If $m_{H^\pm}+m_b < m_t$, the top decay $t \to H^\pm b$ can be used to constrain $m_{H^\pm}$. From the process $pp \to t\bar{t} \to b\bar{b}H^\pm W^\mp$ with $H^\pm \to \tau^\pm\nu$, the upper limit on $\mathrm{BR}(t \to H^\pm b)\times\mathrm{BR}(H^\pm \to \tau^\pm\nu)$ has been driven to be between 0.23% and 1.3% at 95% C.L. for $m_{H^\pm}$ in the range of 80 GeV to 160 GeV [45]. This gives the bounds, for example, $\tan\beta \lesssim 6$ and 15 for $m_{H^\pm} = 100$ and 150 GeV at 95% C.L. in the Type-X 2HDM using 0.23% of the product of the branching fractions.

Apart from the production processes via Yukawa couplings, one must take care of the $h \to AA$ decay in the case of $m_A < m_h/2$. In the Type-X 2HDM, this typically gives the four τ final state, because the $A \to \tau\tau$ decay can be the main decay mode as explained in section 3.1.1. In ref. [46, 47], the upper bound on $\mathrm{Br}(h \to AA \to 4\tau)$ is given to be about 0.2 for $m_A > 30$ GeV and 0.2-0.5 for $15 < m_A < 30$ GeV. In the 2HDMs, the branching fraction is determined by the dimensionless hAA coupling λ_{hAA} defined as the coefficient of the hAA vertex in the Lagrangian; i.e., $\mathcal{L} = v\lambda_{hAA}\, hAA + \cdots$ which is given by

$$\lambda_{hAA} = \frac{1}{2v^2}\left[(2M^2 - 2m_A^2 - m_h^2)s_{\beta-\alpha} + (M^2 - m_h^2)(\cot\beta - \tan\beta)c_{\beta-\alpha}\right]. \tag{3.1}$$

The partial decay width of $h \to AA$ is then expressed by

$$\Gamma_{h\to AA} \;=\; \frac{\lambda_{hAA}^2 v^2}{8\pi m_h}\sqrt{1-\frac{4m_A^2}{m_h^2}} \;\simeq\; \Gamma_{\mathrm{SM}} \times \left(\frac{\lambda_{hAA}}{0.015}\right)^2 \sqrt{1-\frac{4m_A^2}{m_h^2}}, \tag{3.2}$$

where $\Gamma_{\mathrm{SM}} = 4.41\,\mathrm{MeV}$ is the total decay width of the SM Higgs boson for $m_h = 125$ GeV [48]. Therefore, to satisfy $\mathrm{Br}(h \to AA) < 0.2$, $\lambda_{hAA} \lesssim 6.7 \times 10^{-3}$ is required. We can simply take $\lambda_{hAA} = 0$ by setting an appropriate value of $\beta - \alpha$ from eq. (3.1) as

$$\tan(\beta-\alpha) = \frac{M^2 - m_h^2}{2M^2 - 2m_A^2 - m_h^2}(\tan\beta - \cot\beta). \tag{3.3}$$

In the case of $\tan\beta \gg 1$, $m_h^2/m_{H^\pm}^2 \ll 1$ and $m_A^2/m_{H^\pm}^2 \ll 1$, we obtain

$$\sin(\beta-\alpha) \simeq 1 - \frac{2}{\tan^2\beta}\left(1 + \frac{m_h^2}{m_{H^\pm}^2} - \frac{2m_A^2}{m_{H^\pm}^2}\right), \tag{3.4}$$

$$\cos(\beta-\alpha) \simeq \frac{2}{\tan\beta}\left(1 + \frac{m_h^2}{2m_{H^\pm}^2} - \frac{m_A^2}{m_{H^\pm}^2}\right). \tag{3.5}$$

From the above expressions, we find that the SM-like behavior of h is realized by taking $\tan\beta \gg 1$, because of $\sin(\beta-\alpha) \simeq 1$.

3.2 Electroweak precision observables

The extra Higgs bosons can modify the electroweak precision observables from the SM prediction via the loop effects. Such an effect can be used as an indirect search for the extra Higgs bosons and also used to constrain parameter space in the 2HDM. In this subsection, we discuss the constraints from the oblique parameters and the Z boson decay.

JHEP07(2015)064

3.2.1 Oblique parameters

The electroweak oblique S, T and U parameters are introduced by Peskin and Takeuchi [49] which parametrize new physics effects on the gauge boson two point functions. These parameters are calculated in 2HDMs in refs. [50–56]. In the SM-like limit $\sin(\beta-\alpha)\to 1$, these parameters are given to be the same formulae as those given in the inert doublet model [57]. For the case of $m_A \ll m_Z \ll m_{H^\pm} \simeq m_H$, the contribution from the additional scalar bosons is given by

$$\Delta S \simeq -\frac{5}{72\pi} \simeq 0.022, \tag{3.6}$$

$$\Delta T \simeq \frac{m_H(m_{H^\pm}-m_H)}{32\pi^2\alpha_{\rm em}v^2} \simeq 0.013\times\left(\frac{m_H}{200\ \text{GeV}}\right)\times\left(\frac{m_{H^\pm}-m_H}{10\ \text{GeV}}\right). \tag{3.7}$$

We also find that ΔU is the same order as ΔS in our setup for large ΔT regime. If we take $m_H = m_{H^\pm}$ and $\sin(\beta-\alpha)=1$, the Higgs potential respects the custodial $\mathrm{SU}(2)_V$ symmetry [52, 54], which makes $\Delta T = 0$. The S and T parameters driven by the Gfitter group [58] are

$$\Delta S = 0.05 \pm 0.11, \qquad \Delta T = 0.09 \pm 0.13, \tag{3.8}$$

with the reference values of $m_h = 125\,\text{GeV}$ and $m_t = 173\,\text{GeV}$. The prediction of ΔS parameter is inside the 1σ error of the measured value, and the T parameter constrains on the mass splitting $|m_H - m_{H^\pm}| = \mathcal{O}(10)$ GeV. Hence we take $m_H = m_{H^\pm}$ to avoid the constraint on the oblique parameters in the following analysis.

3.2.2 Z boson decay

The property of the Z boson such as the mass, the total width, and the decay branching ratios were precisely measured at the LEP experiment. If new physics particles modify such a precisely measured quantity, their masses and/or couplings are severely constrained.

In our scenario, the $Z\tau^+\tau^-$ vertex can be significantly deviated from the SM prediction by loop effects of the extra Higgs bosons, because they strongly interact with charged leptons in the large $\tan\beta$ case. In order to discuss how the modified vertex affects the observables, we define the effective $Zf\bar{f}$ vertex as

$$\mathcal{L} = g_Z \bar{f}\gamma^\mu(\hat{v}_f - \hat{a}_f\gamma_5) f Z_\mu, \tag{3.9}$$

where $g_Z = g/\cos\theta_W$ and θ_W being the weak mixing angle. Although there are several definitions for $\sin^2\theta_W$, we here use the on-shell definition [59] of it which is determined by using W and Z boson masses, i.e., $\sin^2\theta_W = 1 - m_W^2/m_Z^2$. The effective vector coupling $\hat{v}_f$ and axial vector coupling $\hat{a}_f$ can be separately written by the contributions from the tree level and from the one-loop level as

$$\hat{v}_f = v_f + v_f^{\rm loop}, \quad \hat{a}_f = a_f + a_f^{\rm loop}, \tag{3.10}$$

where the tree level contributions are expressed as

$$v_f = \frac{1}{2}T_f^3 - \sin^2\theta_W Q_f, \quad a_f = \frac{1}{2}T_f^3, \tag{3.11}$$

JHEP07(2015)064

with Q_f being the electric charge of f. The loop contributions $v_f^{\rm loop}$ and $a_f^{\rm loop}$ are composed of the counter term and the one particle irreducible (1PI) $Zf\bar{f}$ vertex correction diagram:

$$v_f^{\rm loop} = \delta v_f + v_f^{\rm 1PI}, \quad a_f^{\rm loop} = \delta a_f + a_f^{\rm 1PI}. \tag{3.12}$$

After imposing the on-shell renormalization conditions, the counter term contribution is expressed by [60]

$$\delta v_f = -a_f \Pi^{\rm 1PI}_{ff,A}(m_f^2) - v_f \left[\Pi^{\rm 1PI}_{ff,V}(m_f^2) - 2m_f^2 \frac{d}{dp^2}[\Pi^{\rm 1PI}_{ff,V}(p^2) + \Pi^{\rm 1PI}_{ff,S}(p^2)]_{p^2=m_f^2}\right], \tag{3.13}$$

$$\delta a_f = -a_f \left[\Pi^{\rm 1PI}_{ff,V}(m_f^2) + 2m_f^2 \frac{d}{dp^2}[\Pi^{\rm 1PI}_{ff,V}(p^2) + \Pi^{\rm 1PI}_{ff,S}(p^2)]_{p^2=m_f^2}\right] - v_f \Pi^{\rm 1PI}_{ff,A}(m_f^2), \tag{3.14}$$

where $\Pi^{\rm 1PI}_{ff,X}$ are the 1PI diagram contributions to the fermion two point functions defined as

$$\Pi^{\rm 1PI}_{ff}(p^2) = \not{p}\Pi^{\rm 1PI}_{ff,V}(p^2) - \not{p}\gamma_5 \Pi^{\rm 1PI}_{ff,A}(p^2) + m_f \Pi^{\rm 1PI}_{ff,S}(p^2). \tag{3.15}$$

In the SM-like limit $\sin(\beta-\alpha)=1$, the deviation in $v_\tau^{\rm loop}$ and $a_\tau^{\rm loop}$ purely comes from the extra Higgs boson loop diagrams. In this case for $f=\tau$, we obtain

$$\begin{aligned}
\Delta v_\tau^{\rm loop} &= v_\tau^{\rm loop} - v_\tau^{\rm loop}({\rm SM}) \qquad (3.16)\\
&\simeq \frac{1}{16\pi^2}\left(\frac{m_\tau}{v}\xi_\ell\right)^2 \Big[v_\tau F_1(m_H) + v_\tau F_1(m_A) - 2a_\tau F_1(m_{H^\pm}) + (v_\tau + a_\tau) F_2(m_{H^\pm}, m_{H^\pm})\Big],\\
\Delta a_\ell^{\rm loop} &= a_\tau^{\rm loop} - a_\tau^{\rm loop}({\rm SM})\\
&\simeq -\frac{1}{16\pi^2}\left(\frac{m_\tau}{v}\xi_\ell\right)^2 \Big[a_\tau F_1(m_H) + a_\tau F_1(m_A) - 2a_\tau F_1(m_{H^\pm})\\
&\qquad + (v_\tau + a_\tau) F_2(m_{H^\pm}, m_{H^\pm}) - 4a_\tau F_2(m_H, m_A)\Big], \qquad (3.17)
\end{aligned}$$

where the loop functions are given as

$$F_1(m) = \ln\frac{m^2}{m_Z^2} + \frac{5}{4} - i\pi + \frac{1}{2}\int_0^1 dxdy \frac{m_Z^2 xy(2y-1) + m^2(2+y-yx)}{m_Z^2 x(1-y) - m^2(1-x)}, \tag{3.18}$$

$$F_2(m_1, m_2) = \frac{1}{4}\left(\ln\frac{m_2^2}{m_1^2} + 1\right) - \int_0^1 dxdy \frac{y^2}{2}\frac{m_2^2 - x[m_1^2 - m_Z^2(1-2y)]}{m_2^2(1-y) + xy[m_1^2 - m_Z^2(1-y)]}. \tag{3.19}$$

In the above expressions, we neglect the mass of the tau lepton in the loop functions. We note that the $F_2(m_1, m_2)$ function is invariant under the interchange of $m_1 \leftrightarrow m_2$, so that $\Delta v_\tau^{\rm loop}$ and $\Delta a_\tau^{\rm loop}$ does not change the value under $m_H \leftrightarrow m_A$.

Let us apply the modified $Z\tau^+\tau^-$ vertex to the leptonic partial decay width of the Z boson $Z \to \ell\ell$:

$$\Gamma(Z \to \ell\ell) = g_Z^2 \frac{m_Z}{12\pi}(\hat{v}_\ell^2 + \hat{a}_\ell^2). \tag{3.20}$$

We define the ratio of the partial width of $Z \to \tau\tau$ to that of $Z \to ee$ as

$$R_{\tau/e} \equiv \Gamma(Z \to \tau\tau)/\Gamma(Z \to ee). \tag{3.21}$$

The deviation in the ratio from the SM predictions are then given by

$$\Delta R_{\tau/e} \equiv R_{\tau/e} - R_{\tau/e}^{\rm SM} \simeq \frac{1}{\Gamma(Z \to \ell\ell)_{\rm SM}} \frac{g_Z^2}{6\pi} m_Z \left[v_\ell {\rm Re}\Delta v_\ell^{\rm loop} + a_\ell {\rm Re}\Delta a_\ell^{\rm loop}\right]. \tag{3.22}$$

JHEP07(2015)064

The SM prediction is given by

$$\Gamma(Z \to \ell\ell)_{\rm SM} = 83.995 \pm 0.010 \text{ MeV}. \tag{3.23}$$

The measured values of the leptonic decay width and $R_{\tau/e}$ are given by [64]

$$\Gamma(Z \to \ell\ell)_{\rm exp} = 83.984 \pm 0.086 \text{ MeV}, \quad R^{\rm exp}_{\tau/e} = 1.0019 \pm 0.0032. \tag{3.24}$$

We find that $\tan\beta > 50$ (70) is excluded for $m_A = 10$ (50) GeV when $m_H = m_{H^\pm} = 300\,\text{GeV}$. The bound becomes weaker for the larger $m_{H^\pm}$. We will combine the constraint from the $Z \to \ell\ell$ decay with the muon $g-2$ result in section 4.

3.3 Flavor experiments

Effects of the extra Higgs bosons can appear in various observables measured at flavor experiments. Therefore, similar to the electroweak precision measurements, flavor measurements can be used to constrain the parameter space in the 2HDM. In this subsection, we discuss $B_s \to \mu^+\mu^-$ and the leptonic decay of τ.

3.3.1 $B_s \to \mu^+\mu^-$

It was pointed out in ref. [61] that the branching fraction of the $B_s \to \ell\ell$ process in the Type-II 2HDM is enhanced by the factor $\tan^4\beta$ which comes from the box type and the penguin type diagrams with extra Higgs boson mediation. The origin of the $\tan^4\beta$ dependence is that both the charged lepton and down-type quark couplings to the extra Higgs bosons are proportional to $\tan\beta$ in the Type-II 2HDM. On the other hand, in the Type-X 2HDM, the lepton couplings are enhanced by $\tan\beta$, while the quark couplings are suppressed by $\cot\beta$. Thus, the $\tan^4\beta$ dependence does not appear in the branching fraction of $B_s \to \ell\ell$, and the additional leading contribution is almost independent on $\tan\beta$ for large $\tan\beta$. Although the deviation from the SM becomes mild as compared to the case of Type-II, we check $\text{Br}(B_s \to \mu^+\mu^-)$ because the light CP-odd Higgs boson A could give a sizable contribution, which is required to explain muon $g-2$ anomaly.

For the calculation of $B_s \to \mu^+\mu^-$ in the 2HDM, we use the formulae given in ref. [62]. The observed branching fraction at the LHC is $\text{Br}(B_s \to \mu^+\mu^-) = (2.9 \pm 0.7) \times 10^{-9}$ [27]. We show the constraint from $B_s \to \mu^+\mu^-$ on the parameter space of 2HDM in section 4.

3.3.2 Leptonic τ decay at the tree level

In the SM, the leptonic τ decay is caused by the W boson exchange diagram at tree level. In the 2HDM, the $H^\pm$ mediated diagram also contributes to the leptonic τ decay. The effect of $H^\pm$ contribution on the partial decay width of τ was calculated in refs. [11, 31], and that on the Michel parameters, which is defined just below, in ref. [32].

The differential decay rate of $\tau \to \mu\nu_\mu\nu_\tau$ is given in terms of the Michel parameters (ρ, η, δ and ξ) and $\hat{G}_{\mu\tau}$ defined in eqs. (3.28) and (3.29) as [63]

$$\frac{d^2\Gamma}{dx\,d\cos\theta} = \frac{m_\mu \omega^4}{2\pi^3}\hat{G}^2_{\mu\tau}\sqrt{x^2 - x_0^2}\left(F(x) - \frac{\xi}{3}\mathcal{P}_\tau \cos\theta\sqrt{x^2 - x_0^2}A(x)\right), \tag{3.25}$$

JHEP07(2015)064

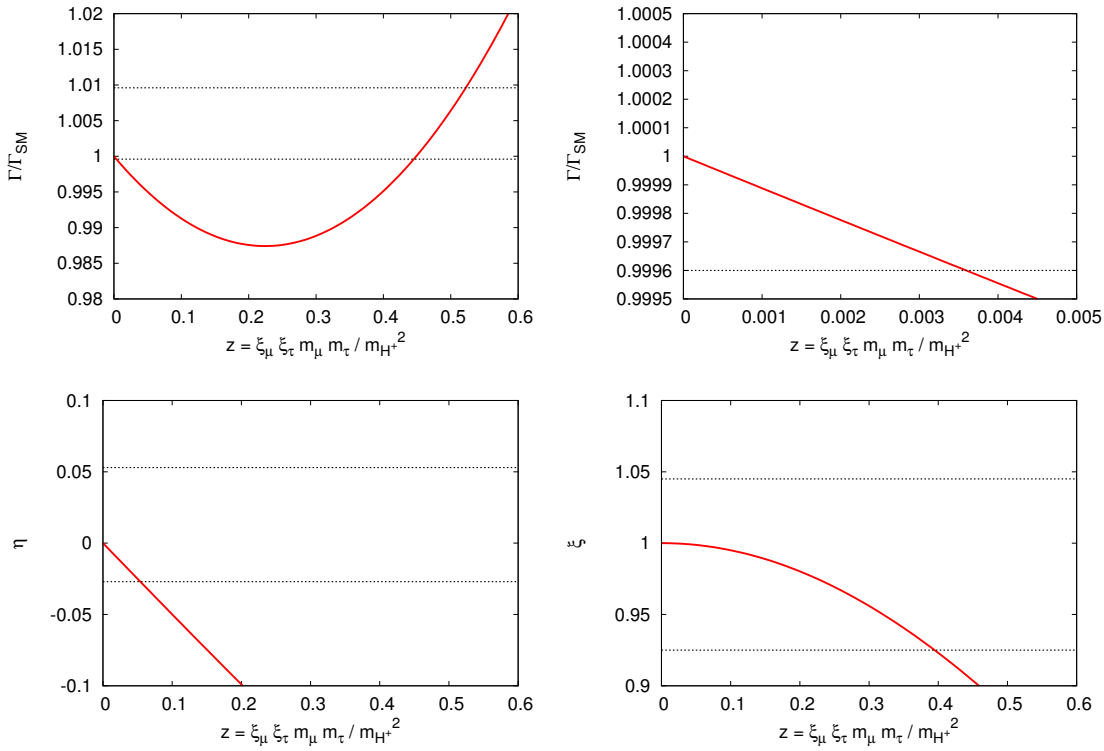

Figure 2. The ratio of the decay rate (upper left and upper right) and the Michel parameters η (lower left) and ξ (lower right) as a function of z in the leptonic tau decay. In each panel, outside regions from the dotted lines are excluded at the 95 % C.L.

where $\omega \equiv (m_\tau^2 + m_\mu^2)/2m_\tau$, $x \equiv E_\mu/\omega$ and $x_0 \equiv m_\mu/\omega$ with E_μ being the muon energy. $\mathcal{P}_\tau$ is the polarization of the tau, and θ is the angle between the polarization and the momentum direction of the muon. The functions $F(x)$ and $A(x)$ are defined as

$$F(x) = x(1-x) + \frac{2}{9}\rho(4x^2 - 3x - x_0^2) + \eta x_0(1-x), \tag{3.26}$$

$$A(x) = 1 - x + \frac{2}{3}\delta(4x - 4 + \sqrt{1-x_0^2}). \tag{3.27}$$

By using $z \equiv m_\mu m_\tau \tan^2\beta/m_{H^+}^2$, we find[2]

$$\hat{G}_{\mu\tau} = G_F\left(1 + \frac{z^2}{4}\right)^{1/2}, \tag{3.28}$$

$$\rho = \frac{3}{4}, \qquad \eta = -\frac{2z}{4+z^2}, \qquad \delta = \frac{3}{4}, \qquad \xi = \frac{4-z^2}{4+z^2}. \tag{3.29}$$

We see that ρ and δ are equal to the SM values at the tree level. The observed Michel parameters of the τ decay are $\eta = 0.013 \pm 0.020$ and $\xi = 0.985 \pm 0.030$ [64]. The ratio of the decay rate in the 2HDM to that in the SM prediction is given as [11, 31]

$$\left(\frac{G_{\mu\tau}}{G_F}\right)^2 \equiv \frac{\Gamma(\tau \to \mu\nu\nu)_{\rm 2HDM}}{\Gamma(\tau \to \mu\nu\nu)_{\rm SM}} = 1 - 2z\frac{m_\mu}{m_\tau}\frac{g(m_\mu^2/m_\tau^2)}{f(m_\mu^2/m_\tau^2)} + \frac{z^2}{4}, \tag{3.30}$$

[2]We find these expressions are inconsistent with ref. [32].

JHEP07(2015)064

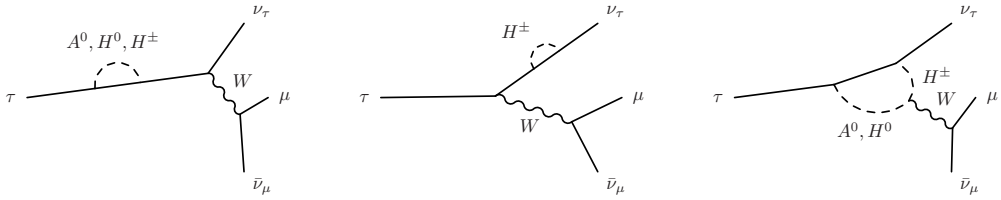

Figure 3. The leading one-loop diagrams for the leptonic tau decay process.

where the phase functions $f(x)$ and $g(x)$ are given by $f(x) = 1 - 8x - 12x^2 \log x + 8x^3 - x^4$ and $g(x) = 1 + 9x - 9x^2 - x^3 + 6x(1+x)\log x$. To find a constraint on eq. (3.30), we can use the constraint on the flavor universality. In the similar manner to eq. (3.30), we introduce $G_{e\mu}$ and $G_{e\tau}$. Since $m_e, m_\mu \ll m_\tau$, the corresponding terms to the rightest term in eq. (3.30) for $G_{e\mu}$ and $G_{e\tau}$ are 1, and thus $G_{e\mu} = G_{e\tau} = G_F$ in 2HDM. There are constraints on the lepton universality given by HFAG group [65][3]

$$\frac{G_{\mu\tau}}{G_{e\mu}} = 1.0029 \pm 0.0015, \quad \frac{G_{\mu\tau}}{G_{e\tau}} = 1.0018 \pm 0.0014, \tag{3.31}$$

and their correlation coefficient is 0.48. Since $G_{e\mu} = G_{e\tau} = G_F$ in the present scenario, by combining the above two values, we find

$$\frac{G_{\mu\tau}}{G_F} = 1.0023 \pm 0.0012, \tag{3.32}$$

and thus we find

$$\left(\frac{G_{\mu\tau}}{G_F}\right)^2 = 1.0046 \pm 0.0025. \tag{3.33}$$

We use this bound and eq. (3.30) to make constraint on 2HDM.

In figure 2, we show the z dependence of the ratio of the decay rate given in eq. (3.30) (upper two panels) and the Michel parameters η (lower left) and ξ (lower right). First, from the upper panels we can see that the allowed ranges of z are found to be $z \lesssim 0.003$ and $0.50 \lesssim z \lesssim 0.57$. Second, from the lower left panel, $z \gtrsim 0.05$ is excluded by the measurement of η. The constraints from the ξ parameter is weaker than that from η. Therefore, by combining the first and the second statements, the allowed region of z is restricted to be $z \lesssim 0.003$ By using $z \simeq 1.88 \times 10^{-3} \times (\tan\beta/30)^2 \times (300\ \text{GeV}/m_{H^\pm})^2$, we find that $\tan\beta \gtrsim 38$ is excluded for $m_{H^\pm} = 300\,\text{GeV}$.

3.3.3 Lepton universality at the one-loop level

As we discussed in section 3.3.2, the typical size of the $H^\pm$ contribution to the ratio of the tau decay is $\mathcal{O}(10^{-2})$ at the tree level as it is seen in figure 2. However, the SM prediction is given at almost the lower edge of the experimental bound (see eq. (3.33)), so that the negative contribution to $G_{\mu\tau}/G_F$ of order 10^{-4} is constrained. Thus, we focus on the quantum corrections to the process via W exchange diagram.

[3]The ratio of the effective Fermi constant $G_{\mu\tau}/G_{e\tau}$, $G_{\mu\tau}/G_{e\mu}$ and $G_{e\tau}/G_{e\mu}$ are corresponds to g_μ/g_e, g_τ/g_e and g_τ/g_μ in ref. [65], respectively.

JHEP07(2015)064

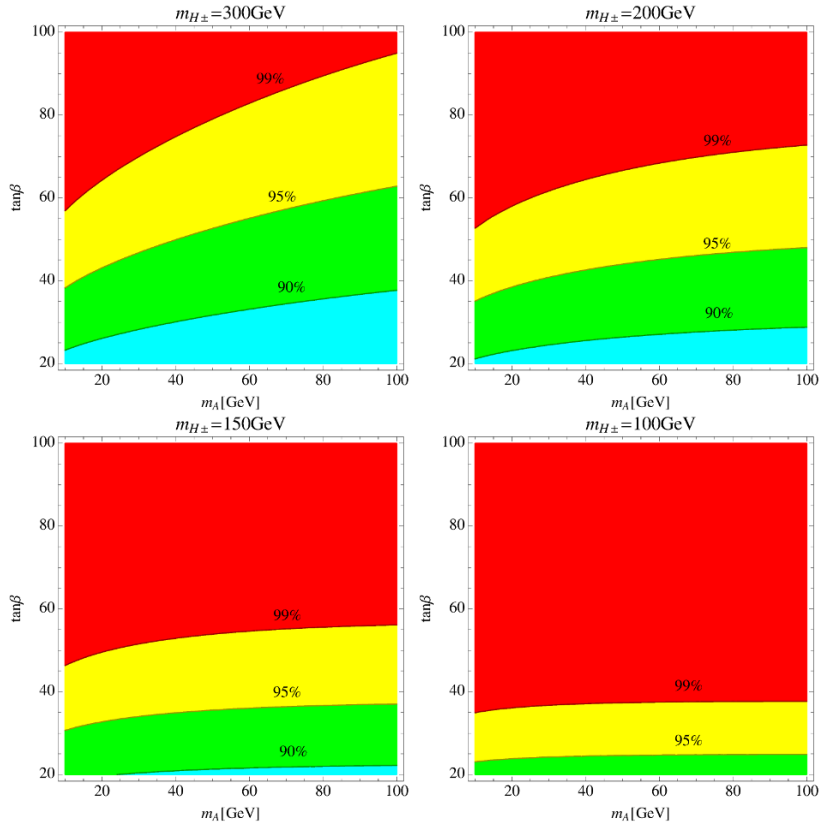

Figure 4. Constraints on the $(m_A, \tan\beta)$-plane by the leptonic tau decay at the one-loop level for $m_{H^\pm}$ =300 (upper left), 200 (upper right), 150 (lower left), and 100 GeV (lower right) in the case with $m_H = m_{H^\pm}$. The green, yellow, and red regions are excluded at 90%, 95%, and 99% C.L., respectively.

The dominant contribution arises from the diagrams with picking up two tau Yukawa couplings which are proportional to $(m_\tau^2/v^2)\tan^2\beta$. We show the diagrams which give the dominant contributions to the process at the one-loop level in figure 3. Other diagrams, such as box diagrams, are smaller than these contributions and we ignore them in this analysis. The quantum correction is flavor dependent, and there is no flavor dependent counter terms in this model, so the correction is finite. We find the contributions from figure 3 modifies the W-τ-ν_τ couplings

$$g_{W\tau\nu} \to g_{W\tau\nu}\,(1+\delta g)\,, \tag{3.34}$$

where

$$\delta g = \frac{1}{(4\pi)^2}\frac{m_\tau^2}{v^2}\tan^2\beta\left[1+\frac{m_{H^\pm}^2+m_A^2}{4(m_{H^\pm}^2-m_A^2)}\ln\frac{m_A^2}{m_{H^\pm}^2}+\frac{m_{H^\pm}^2+m_H^2}{4(m_{H^\pm}^2-m_H^2)}\ln\frac{m_H^2}{m_{H^\pm}^2}\right]. \tag{3.35}$$

In $m_A \ll m_{H^\pm} \sim m_{H^0}$ case

$$\delta g = \frac{1}{(4\pi)^2}\frac{m_\tau^2}{v^2}\tan^2\beta\left[\frac{1}{2}+\frac{1}{4}\ln\frac{m_A^2}{m_{H^\pm}^2}+\mathcal{O}\left(\frac{m_A^2}{m_{H^\pm}^2}\ln\frac{m_A^2}{m_{H^\pm}^2}\right)\right]. \tag{3.36}$$

JHEP07(2015)064

Finally, we find

$$\Gamma = \frac{1}{96\pi^3} m_\tau \omega^4 G_F^2 \Bigg[\sqrt{1-x_0^2}\Big(2(4(1+\delta g)^2+z^2) - 8x_0 z(1+\delta g) - 5x_0^2(4(1+\delta g)^2+z^2) - 16x_0^3 z(1+\delta g)\Big) + 3x_0^3\left(8z(1+\delta g) + x_0(4(1+\delta g)^2+z^2)\right)\ln\frac{1+\sqrt{1-x_0^2}}{x_0}\Bigg], \tag{3.37}$$

where ω and x_0 are defined in section 3.3.2. Using eqs. (3.30), (3.33) and (3.37), we find that the large $\tan\beta$ region and light charged Higgs region are disfavored, see figure 4. This constraint is the most severe for the explanation of the muon $g-2$ anomaly, as we will see in section 4

3.4 Triviality bound

In order to avoid the constraints from the various observables, we need to take large mass differences between A and $H^\pm$, and A and H. As a result, the Higgs quartic couplings are as large as $\mathcal{O}(1)$. Such a large coupling can be grown up in a certain energy scale, and it becomes too strong to rely on the perturbative calculation. We thus take into account the triviality bound in which we require that all the Higgs quartic couplings do not exceed a certain value until a given energy scale.

We calculate the β-functions up to the two loop level for the RGE by using `SARAH` [66], and run the couplings to higher energies. We treat the coupling values at the tree level as the input parameters at $\mu = m_t$. We define $\lambda_{\max} = \max\{|\lambda_1|, |\lambda_2|, |\lambda_3|, |\lambda_4|, |\lambda_5|\}$ and the cutoff scale of the model, Λ, as $\lambda_{\max}(\Lambda) = 4\pi$ or $\sqrt{4\pi}$.

The result for $\Lambda = 10\,\text{TeV}$ with requiring $\lambda_{\max} < 4\pi$ is shown in the left panel in figure 5. We find that $m_{H^\pm} \lesssim 370\,\text{GeV}$ for $m_A \simeq 20\,\text{GeV}$ is required for Λ 10 TeV. This constraint on $m_{H^\pm}$ is stronger than the one from the perturbative unitarity bound using eqs. (2.13)–(2.19), i.e., $m_{H^\pm} \lesssim 700\,\text{GeV}$. We check that this result is consistent with that given in [67, 68]. If we require $\lambda_{\max} < \sqrt{4\pi}$ instead of $\lambda_{\max} < 4\pi$, then the bound becomes stronger. In such a case, we find $m_{H^\pm} \simeq 260\,\text{GeV}$ is required. Here we take $\tan\beta = 30$ at $\mu = m_t$ as the input value, but the result is insensitive for $\tan\beta$. We also plot the case for $\Lambda = 100\,\text{TeV}$ in the right panel in figure 5. The bound is stronger than $\Lambda = 10\,\text{TeV}$ case. We find $m_{H^\pm} \lesssim 310\,\text{GeV}$ ($240\,\text{GeV}$) for $\lambda_{\max} = 4\pi$ ($\sqrt{4\pi}$). Our parameter choice here is the same as in section 4.

4 Muon $g-2$

We show the numerical results for the muon $g-2$ under all the constraints discussed in the previous section. We calculate the muon $g-2$ by using `2HDMC 1.6.4` [69, 70] which contains the one-loop diagrams [12] and the two-loop Barr-Zee diagrams [13] as shown in figure 1. In the Type-X 2HDM, the contributions from the one-loop diagrams and the Barr-Zee diagrams are comparable and have opposite sign. Thus, we have to take into

JHEP07(2015)064

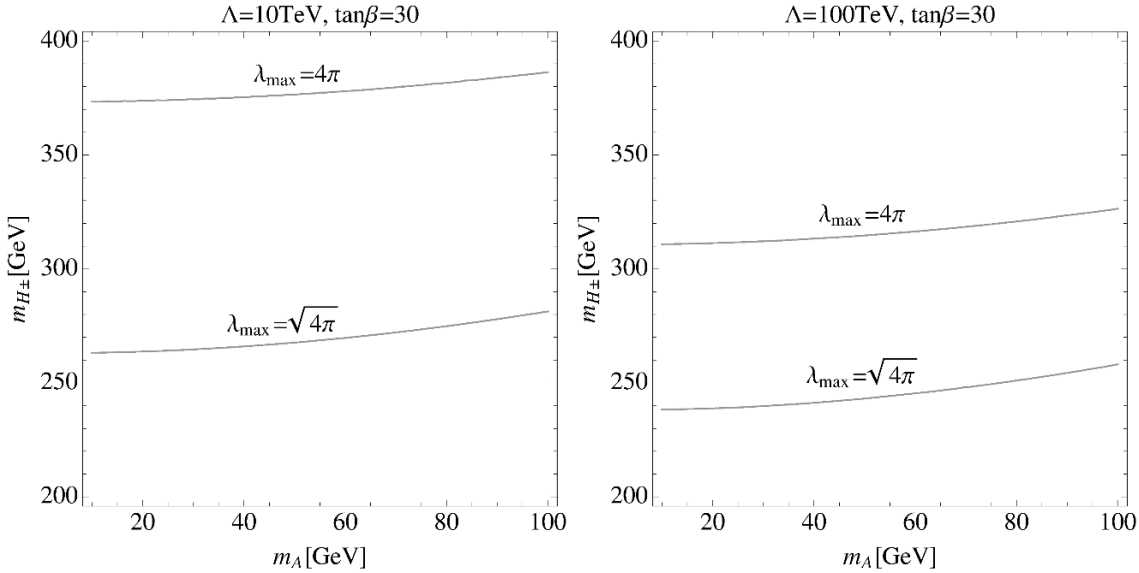

Figure 5. The triviality bound with $\Lambda = 10\,\text{TeV}$ (left) and $\Lambda = 100\,\text{TeV}$ (right). The numbers shown in the panel are $\lambda_{\max} = 4\pi$ and $\sqrt{4\pi}$.

account both contributions. The contributions from the beyond the SM part should be sizable to solve the muon $g-2$ anomaly, and thus at least one of the new particles has to be light. The lower mass bound on $H^\pm$ is order of 100 GeV, so that it can not be arbitrary small. The effect from H gives a destructive contribution to the SM one, so that it makes the situation becomes even worse if H is light. On the other hand, the effect from A gives the constructive contribution, and it makes the discrepancy small. Therefore, A is required to be lighter than H and $H^\pm$ in order to solve the muon $g-2$ anomaly.

The Higgs sector in the 2HDM has eight parameters. Two of them are fixed to reproduce the SM parameters, i.e., $G_F = 2^{-1/2}v^{-2} = 1.166379\times10^{-5}\,\text{GeV}^{-2}$ and $m_h = 125$ GeV. To suppress $\text{Br}(h \to AA)$, we set $\lambda_{hAA} = 0$. In addition, we take $m_H = m_{H^\pm}$ to avoid a large contribution to ΔT. Furthermore, we fix $\lambda_1 = 0.1$. This λ_1 value is realized by taking $M^2 \simeq m_H^2$ in the large $\tan\beta$ case, and the fixing the value of λ_1 is not significant to the result in the following. Therefore, we have three remaining parameters which can be expressed as $\tan\beta$, m_A and $m_{H^\pm}$. We note that in this parametrization, $\sin(\beta-\alpha)$ is given as the output parameter, which is determined via eq. (3.1). As it is seen in eq. (3.4), $1-\sin(\beta-\alpha)$ is suppressed by $1/\tan^2\beta$ in the large $\tan\beta$ case, so that h behaves as the SM-like Higgs boson.

In figure 6, we show the prediction of a_μ on the m_A-$\tan\beta$ plane in each fixed value of $m_{H^\pm}$, e.g., $m_{H^\pm} = 200$ (upper-left), 250 (upper-right), 300 (lower-left) and 350 GeV (lower right). In the dark and light shaded regions, a_μ can be explained at the 1σ and 2σ levels, respectively. We find that the measurement of $\tau \to \mu\nu_\mu\nu_\tau$ gives the stringent constraint on the parameter space in the m_A-$\tan\beta$ plane. This constraint is getting stronger in the cases of smaller $m_{H^\pm}$ or m_A and larger $\tan\beta$. For example, in the case of $m_{H^\pm} = 200$ GeV, $\tan\beta \gtrsim 35$ is excluded at the 95% C.L. in the case of $m_A = 20$ GeV. For $m_A \simeq 10$ GeV, $\text{Br}(B_s \to \mu^+\mu^-)$ gives additional excluded regions which are not excluded by the measurement of

JHEP07(2015)064

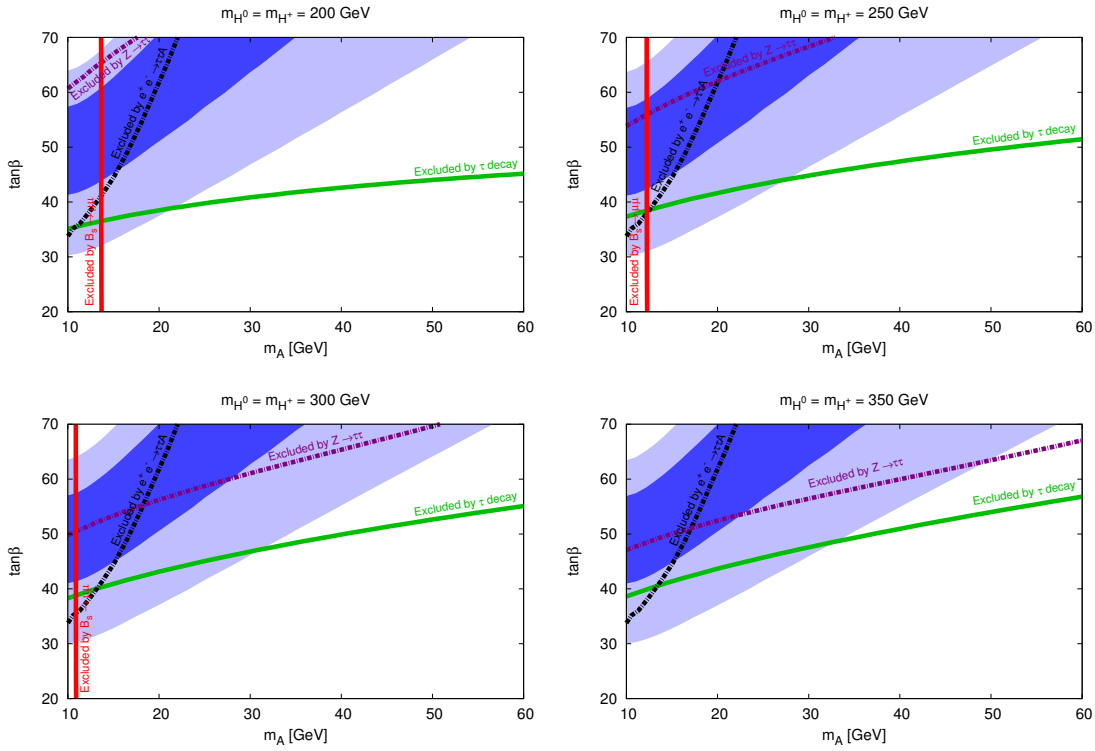

Figure 6. Results in the Type-X 2HDM in the case of $\lambda_{hAA} = 0$ and $\lambda_1 = 0.1$. Dark and light blue shaded regions can explain the muon $g-2$ anomaly [3] at the 1σ and 2σ levels, respectively. We take $m_{H^\pm}(= m_H)$ =200, 250, 300 and 350 GeV in the upper-left, upper-right, lower-left and lower-right panels, respectively. The left region from the red line is excluded by the measurement of $B_s \to \mu\mu$. The above regions of green, black, purple line are excluded by the τ decay, the direct search at the LEP and the $Z \to \tau\tau$ decay, respectively. All of the exclusions are given at the 95% C.L.

the tau decay. The $\tan\beta$ dependence in $\mathrm{Br}(B_s \to \mu^+\mu^-)$ is negligible as we expected in the discussion in section 3.3.1. In most of the parameter region shown in this figure, the deviation of $\mathrm{Br}(B_s \to \mu^+\mu^-)$ from the SM value is $\mathcal{O}(1)$ %. The constrained from $Z \to \tau\tau$ is weaker than that from the tau decay in all the parameter regions shown in this figure.

Consequently, the parameter region which can explain the $g-2$ anomaly at the 1σ level is excluded by the measurement of the tau decay at the 95% C.L., and at best we can explain the anomaly at the 2σ level. The typical parameters to explain muon $g-2$ anomaly at the 2σ level is $10 \lesssim m_A \lesssim 30$ GeV, $200 \lesssim m_{H^\pm} \lesssim 350$ GeV and $30 \lesssim \tan\beta \lesssim 50$. In this parameter space, however, the region with $m_{H^\pm} \lesssim 270$ GeV has tension with the signal strength for the $h \to \tau\tau$ mode measured at the LHC as we will see in the next section.

5 Impact on the Higgs phenomenology at collider experiments

In the previous section, we have seen that the relatively light extra Higgs bosons and large $\tan\beta$ are favored to explain the muon $g-2$ anomaly. Such a light particle can be directly discovered at the LHC Run-II and the International Linear Collider (ILC). Furthermore, the

JHEP07(2015)064

precise measurement of the property of the SM-like Higgs boson h will give an indirect probe of this scenario. In this section, we first discuss the decay and production of the extra Higgs bosons at the LHC, and then we investigate how the property of the SM-like Higgs boson is modified in the favored parameter set indicated by the muon $g-2$ in the Type-X 2HDM.

Throughout this section, we consider the case of

$$200\ \text{GeV} \le m_{H^\pm} \le 400\ \text{GeV}, \qquad m_H = M = m_{H^\pm}, \quad 10\ \text{GeV} \le m_A \le 30\ \text{GeV},$$
$$30 \le \tan\beta \le 50, \qquad \tan(\beta-\alpha) = \frac{M^2 - m_h^2}{2M^2 - 2m_A^2 - m_h^2}(\tan\beta - \cot\beta). \tag{5.1}$$

In addition, the following values of the SM parameters are used [64, 71]:

$$m_Z = 91.1876\ \text{GeV}, \quad m_W = 80.385\ \text{GeV}, \quad G_F = 1.1663787 \times 10^{-5}\ \text{GeV}^{-2},$$
$$m_t = 173.07\ \text{GeV}, \quad m_b = 3.0\ \text{GeV}, \quad m_c = 0.677\ \text{GeV}, \ m_\tau = 1.77684\ \text{GeV}. \tag{5.2}$$

m_c and m_b are evaluated at the m_Z scale in $\overline{\text{MS}}$ scheme, which are taken from ref. [71]. Other parameters are taken from ref. [64]. The mass observed Higgs boson is taken to be 125 GeV.

5.1 Phenomenology of the extra Higgs bosons

First, we discuss the branching fraction of the extra Higgs bosons in the parameter set given in eq. (5.1). For the CP-odd Higgs boson A, only the $A \to \tau\tau$ and $A \to b\bar{b}$ modes are allowed at the tree level. Since the decay rate of the former (latter) channel is enhanced (suppressed) by $\tan^2\beta$ ($\cot^2\beta$) in the Type-X 2HDM, the branching fraction of $A \to \tau\tau$ becomes almost 100% in our scenario. Similar enhancement happens in the decay rates of $H \to \tau\tau$ and $H^\pm \to \tau^\pm\nu$. At the same time, the other modes $H \to AZ$ and $H^\pm \to AW^\pm$ are also important because of the large mass difference between $H/H^\pm$ and A. Therefore, the following decay modes should be taken into account:

$$H^\pm \to \tau^\pm\nu, \quad H^\pm \to AW^\pm, \quad H \to \tau\tau, \quad H \to AZ, \quad A \to \tau\tau. \tag{5.3}$$

The formulae for the decay rates are given in appendix A. We here note that the $H \to AA$ and $H \to hh$ decays also open whose decay rates are determined by the trilinear HAA and Hhh couplings, respectively. However, these couplings are proportional to $\cos(\beta-\alpha)$, and its magnitude is suppressed by $\cot\beta$ in the large $\tan\beta$ case. Thus, these decay modes are not important in our scenario.

In figure 7, we show the contour plots for the branching fractions of $H \to AZ$ (left panel) and $H^+ \to AW^+$ on the $m_{H^\pm}$-$\tan\beta$ plane. The $H \to \tau\tau$ and $H^+ \to \tau^+\nu$ modes fulfill almost the remaining branching ratios for H and $H^\pm$, respectively. In the large $m_{H^\pm}$ and small $\tan\beta$ region, the branching fractions of $H \to AZ$ and $H^+ \to AW^+$ are getting larger. For example, we obtain $\text{Br}(H \to AZ) > 70$ (90)% in the case of $\tan\beta \lesssim 35$ with $m_H = 200\,\text{GeV}$ ($\tan\beta \lesssim 33$ with $m_H = 300\,\text{GeV}$), and $\text{Br}(H^+ \to AW^+) > 70$ (90)% in the case of $\tan\beta \lesssim 38$ with $m_H = 200\,\text{GeV}$ ($\tan\beta \lesssim 35$ with $m_{H^\pm} = 300\,\text{GeV}$).

Next, we discuss the production process of the extra Higgs bosons at the LHC. As we mentioned in section 3.1.2, the production processes via the Yukawa interaction cannot be

JHEP07(2015)064

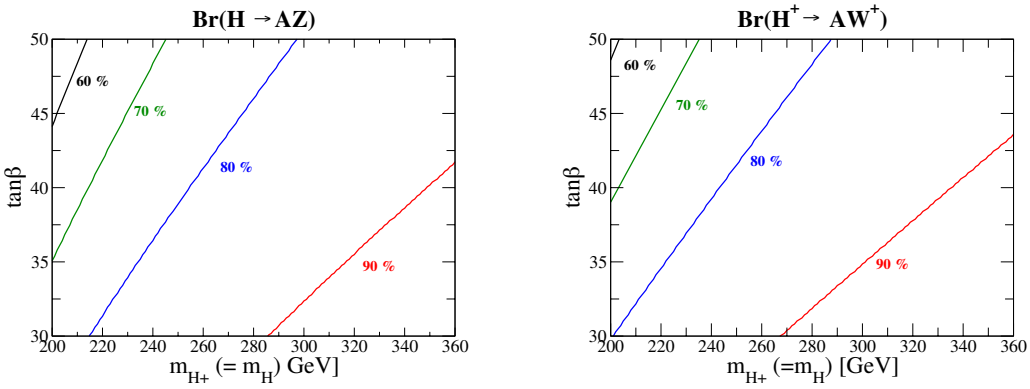

Figure 7. Contour plots for the branching fractions of $H \to AZ$ (left panel) and $H^+ \to AW^+$ (right panel) on the $m_{H^\pm}$-$\tan\beta$ plane. We take $m_H = m_{H^\pm}$ and $m_A = 20\,\text{GeV}$. $\text{Br}(H \to AZ)+\text{Br}(H \to \tau\tau) \simeq 1$ and $\text{Br}(H^+ \to AW^+)+\text{Br}(H^+ \to \tau^+\nu) \simeq 1$ are satisfied.

used in the large $\tan\beta$ case in the Type-X 2HDM. Therefore, the following electroweak processes give the dominant production mode:

$$\begin{aligned} &pp \to Z^*/\gamma^* \to H^+H^-, && pp \to Z^* \to HA, \\ &pp \to W^* \to H^\pm H, && pp \to W^* \to H^\pm A. \end{aligned} \tag{5.4}$$

The analytic expressions for the parton level cross section are given in appendix B. We find that the cross sections are determined by the masses of the extra Higgs bosons and $\sin(\beta-\alpha)$, and they do not depend on the type of Yukawa interactions. By using `CalcHEP` [72] with `CTEQ6L` [73] parton distribution functions, the cross sections are calculated in table 2. In this calculation, we neglect the small deviation in $\sin(\beta-\alpha)$ from unity. Because of the small m_A, the cross sections of $pp \to H^\pm A$ and $pp \to HA$ are relatively large as compared to those of $pp \to H^+H^-$ and $pp \to H^\pm H$. We note that the cross section for H^+H/H^+A is about twice larger than that for H^-H/H^-A, because the parton luminosity of $u\bar{d}$ in the initial proton is larger than that of $\bar{u}d$.

Combining the discussions of the decay and the production of the extra Higgs bosons, we can consider the following processes:

$$\begin{aligned} &pp \to H^\pm A/H^\pm H \to \tau^\pm\nu\tau^+\tau^-, && pp \to H^\pm A/H^\pm H \to 4\tau + W^\pm, \\ &pp \to HA \to 4\tau, && pp \to HA \to 4\tau + Z. \end{aligned} \tag{5.5}$$

The H^+H^- production may not be so useful for the feasibility study of the extra Higgs bosons as compared to the above processes because of the small cross section as seen in table 2. The cross sections of 4τ ($\sigma_{4\tau}$), 3τ ($\sigma_{3\tau}$), 4τ plus W ($\sigma_{4\tau W}$) and 4τ plus Z ($\sigma_{2\tau Z}$) can be estimated as follows:

$$\sigma_{4\tau} \simeq \sigma_{HA} \times \text{Br}(H \to \tau\tau), \tag{5.6}$$

$$\begin{aligned} \sigma_{3\tau} \simeq\ & (\sigma_{H^+A} + \sigma_{H^-A}) \times \text{Br}(H^\pm \to \tau^\pm\nu) \\ & + (\sigma_{H^+H} + \sigma_{H^-H}) \times \text{Br}(H^\pm \to \tau^\pm\nu) \times \text{Br}(H \to \tau\tau), \end{aligned} \tag{5.7}$$

JHEP07(2015)064

$m_{H^\pm}$ [GeV]	$\sigma_{H^+H^-}$	σ_{H^+H}	σ_{H^-H}	σ_{H^+A}	σ_{H^-A}	σ_{AH}	$\sigma_{4\tau}$	$\sigma_{3\tau}$	$\sigma_{4\tau W}$	$\sigma_{4\tau Z}$
200	18.6	22.0	11.3	116	67.0	101	29.3	50.1	143	70.7
250	8.0	9.7	4.7	53.5	29.5	45.1	7.2	12.8	72.5	37.4
300	3.9	4.8	2.3	28.2	14.9	23.2	2.3	4.3	39.4	20.6
350	2.1	2.6	1.1	16.2	8.2	13.0	0.9	1.7	22.9	12.0

Table 2. Cross sections of the electroweak production processes expressed in eq. (5.4), and those of the multi-tau processes expressed in eqs. (5.6)–(5.9) at $\sqrt{s} = 14\,\text{TeV}$ in the unit of fb. We take $m_A = 20\,\text{GeV}$, $m_H = m_{H^\pm}$, $\sin(\beta-\alpha) = 1$ and $\tan\beta = 35$.

$$\begin{aligned}\sigma_{4\tau W} &\simeq (\sigma_{H^+A} + \sigma_{H^-A}) \times \text{Br}(H^\pm \to AW^\pm) \\ &\quad + (\sigma_{H^+H} + \sigma_{H^-H}) \times \text{Br}(H^\pm \to AW^\pm) \times \text{Br}(H \to \tau\tau), \qquad (5.8)\\ \sigma_{4\tau Z} &\simeq \sigma_{HA} \times \text{Br}(H \to AZ), \qquad (5.9)\end{aligned}$$

where we used $\text{Br}(A \to \tau\tau) \simeq 100\%$. The cross sections of the above processes are also shown in table 2 in the case of $\tan\beta = 35$.

The signal and background for the four and three tau final states (without a gauge boson) were studied in ref. [74, 75] in the Type-X 2HDM. It was clarified that the main background for these processes can be significantly reduced by requiring the high multiplicity of charged leptons and tau-jets with appropriate kinematical cuts in the final state. In this paper, we only show the signal cross sections of the above mentioned processes as given in table 2. Although the detailed background simulation must be necessary to clarify the feasibility to detect the signal events, such a study is beyond the scope of this paper.

5.2 Phenomenology of the SM-like Higgs boson

Another important impact on the Higgs phenomenology in our scenario is found in the property of the SM-like Higgs boson h. Because the properties of h; e.g., the width, the branching fractions, and the couplings will be precisely measured at future collider experiments such as the LHC Run-II, the high luminosity LHC, and the ILC [76], it must be quite important to study the deviation in the property of h from the SM prediction. In particular, studying the pattern of the deviation in the various h couplings can be a powerful tool to determine the structure of the Higgs sector.[4]

As we discussed in section 2, the value of $\sin(\beta-\alpha)$ describes "*SM-like ness*" of h, namely, all the h couplings to the SM particles become the same as those in the SM prediction in the limit of $\sin(\beta-\alpha) \to 1$. In other words, once $\sin(\beta-\alpha) \neq 1$ is given, both the hVV and $hf\bar{f}$ couplings deviate from those of the SM values. In our scenario, the value of $\sin(\beta-\alpha)$ is determined from eq. (5.1). Thus, a small but non-zero deviation from the SM-like limit is given.

[4]In ref. [77], the pattern of the deviation was investigated in various extended Higgs sectors; e.g., models with isospin singlets, doublets and triplets at the tree level. For example, it was shown that the four types of Yukawa interactions in the 2HDM can be well discriminated by measuring the correlation between the deviation in $hd\bar{d}$ and $h\ell\ell$ couplings [77]. In addition, it was clarified in ref. [78, 79] that even if we take into account the one-loop corrections to the $hf\bar{f}$ couplings, discrimination of the 2HDMs is still valid.

JHEP07(2015)064

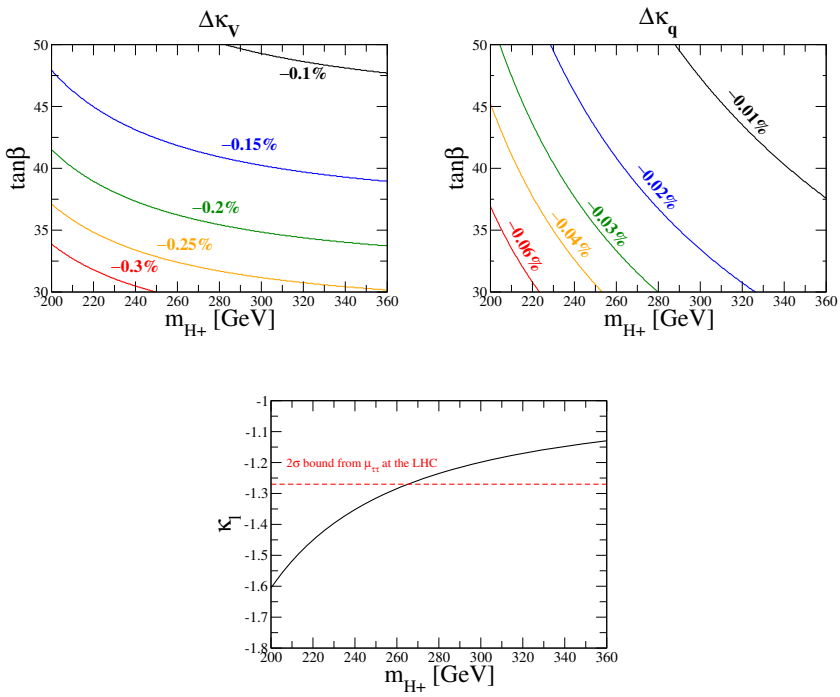

Figure 8. Contour plots for $\Delta\kappa_V$ (upper left) and $\Delta\kappa_q$ (upper right) on the $m_{H^\pm}$-$\tan\beta$ plane, where $\Delta\kappa_X = \kappa_X - 1$. The $m_{H^\pm}$ dependence of $\Delta\kappa_\ell$ is shown in the lower panel with $\tan\beta = 35$. We take $m_H = M = m_{H^\pm}$ and $m_A = 20\,\text{GeV}$ in all the panels. The horizontal dashed line represents the bound from the signal strength using eq. (5.14).

In order to describe the deviation in the h couplings, we introduce the so-called scaling factors defined as $\kappa_X = g_{hXX}/g_{hXX}^{\text{SM}}$ and its deviation from unity; i.e, $\Delta\kappa_X = \kappa_X - 1$. From eqs. (2.22) and (2.23) and the approximate formulae given in eqs. (3.4) and (3.5), we obtain

$$\Delta\kappa_V \simeq -\frac{2}{\tan^2\beta}\left(1 + \frac{m_h^2}{m_{H^\pm}^2} - \frac{2m_A^2}{m_{H^\pm}^2}\right), \tag{5.10}$$

$$\Delta\kappa_q \simeq -\frac{2}{\tan^2\beta}\left(\frac{m_h^2}{2m_{H^\pm}^2} - \frac{m_A^2}{m_{H^\pm}^2}\right), \tag{5.11}$$

$$\kappa_\ell \simeq -1 - \frac{m_h^2}{m_{H^\pm}^2} + \frac{2m_A^2}{m_{H^\pm}^2}. \tag{5.12}$$

In the upper panels of figure 8, we show the contour plots for $\Delta\kappa_V$ and $\Delta\kappa_q$, where $\Delta\kappa_X = \kappa_X - 1$, on the $m_{H^\pm}$-$\tan\beta$ plane. In the lower panel, we show the $m_{H^\pm}$ dependence of κ_ℓ instead of showing contour plots, because the $\tan\beta$ dependence of κ_ℓ can be neglected as seen in eq. (5.12). For definiteness, we take $\tan\beta = 35$ in the plot for $m_{H^\pm}$-κ_ℓ. We find that the deviations in the hVV and $hq\bar{q}$ couplings are respectively $-\mathcal{O}(0.1)\%$ and $-\mathcal{O}(0.01)\%$ which can also be estimated from eqs. (5.10), (5.11). For the $h\ell\ell$ coupling, we find that its magnitude is maximally about 1.6 times larger than the SM prediction, and its sign is opposite to the SM one [21]. From the measurement of the signal strength of the $h \to \tau\tau$ channel, i.e., $\mu_{\tau\tau}$ at the LHC, the magnitude of κ_ℓ is constrained. The definition

JHEP07(2015)064

of the signal strength is given as

$$\mu_{XY} \equiv \frac{\sigma_h \times \mathrm{Br}(h \to XY)}{[\sigma_h \times \mathrm{Br}(h \to XY)]_{\mathrm{SM}}}, \tag{5.13}$$

where σ_h and $\mathrm{Br}(h \to XY)$ are respectively the production cross section of the SM-like Higgs boson h and the decay branching fraction of the $h \to XY$ mode. In our parameter set, σ_h is almost the same as that in the SM, because of the small $\Delta\kappa_q$ and $\Delta\kappa_V$, so that the signal strength is simply given as the ratio of the branching fraction as $\mu_{XY} \simeq \mathrm{Br}(h \to XY)/\mathrm{Br}(h \to XY)_{\mathrm{SM}}$.

The ATLAS and CMS collaborations report the signal strength as $\mu_{\tau\tau} = 1.43^{+0.43}_{-0.37}$ [80] and $\mu_{\tau\tau} = 0.91 \pm 0.28$ [81], respectively. By taking a naive combination of them,[5] we obtain

$$\mu_{\tau\tau} = 1.08 \pm 0.23. \tag{5.14}$$

Thus, the region with $|\kappa_\ell| > 1.27$ is excluded at 2σ level, which corresponds to the constraint of $m_{H^\pm} \lesssim 270$ GeV as seen in figure 8.

The deviation in the h couplings makes a difference in the branching fraction of h from the SM prediction. In figure 9, we show the branching fraction of h as a function of $m_{H^\pm}$. Because only the magnitude of the $h\ell\ell$ coupling can be larger than the SM prediction, only the branching fraction of the $h \to \tau\tau$ mode is enhanced. On the other hand, that of all the other modes shown in this figure are reduced. The size of deviations becomes smaller as $m_{H^\pm}$ increases. We note that the branching fraction of the $h \to \mu\mu$ decay is also enhanced similar to the $h \to \tau\tau$ mode. When $m_{H^\pm} = 300\,\mathrm{GeV}$, and all the other parameters are taken to be the same as in figure 9, $\mathrm{Br}(h \to \mu\mu)$ is about 3.4 (2.5) $\times 10^{-4}$ in the Type-X 2HDM (SM).

It is important to mention here that there appears the exotic decay mode $h \to AZ$ in our parameter set as seen in figure 9. Although the coupling constant of the hZA interaction is proportional to $\cos(\beta - \alpha)$ which is suppressed by $\cot\beta$ as seen in eq. (3.5), its branching fraction is not so small, especially for the case with small m_A. For example, we obtain $\mathrm{Br}(h \to AZ) \simeq 7\%$ with $m_A = 10\,\mathrm{GeV}$ and $m_{H^\pm} = 200\,\mathrm{GeV}$. This new decay mode of h gives the additional contribution to the four-lepton channel in the SM Higgs boson search if A decays into a pair of muon. In the present scenario, $\mathrm{Br}(A \to \mu\mu) \simeq \mathrm{Br}(A \to \tau\tau) \times (m_\mu/m_\tau)^2 \simeq 0.0036$ is obtained. On the other hand, from Higgs boson searches at the LHC, the upper bound on $\mathrm{Br}(h \to ZA) \times \mathrm{Br}(A \to \ell\ell)$ with $\ell = e$ or μ is given as 5-10$\times 10^{-4}$ for $12 < m_A < 34$ GeV [46, 47]. This limit is translated into the bound $\mathrm{Br}(h \to AZ) \lesssim$ 14-28% in the Type-X 2HDM. The typical size of $\mathrm{Br}(h \to AZ)$ is below the upper bound as explained in the above. In addition to this channel, e and μ are produced from the leptonic decay of τ. Thus, the $ZA \to \ell\ell\tau\tau \to 4\ell + \not{E}_T$ channel can also contribute to the four lepton channel even though the invariant mass distribution of the four lepton system is different from that by $ZZ^* \to 4\ell$. This will be a subject of a future work.

Next, we discuss the one-loop induced $h \to \gamma\gamma$ decay mode. Because of the $H^\pm$ contribution, the decay rate can be significantly modified even if the h couplings are not

[5] To obtain the naive combination, we treat the signal strength from ATLAS as 1.43 ± 0.40 by taking the average of errors.

JHEP07(2015)064

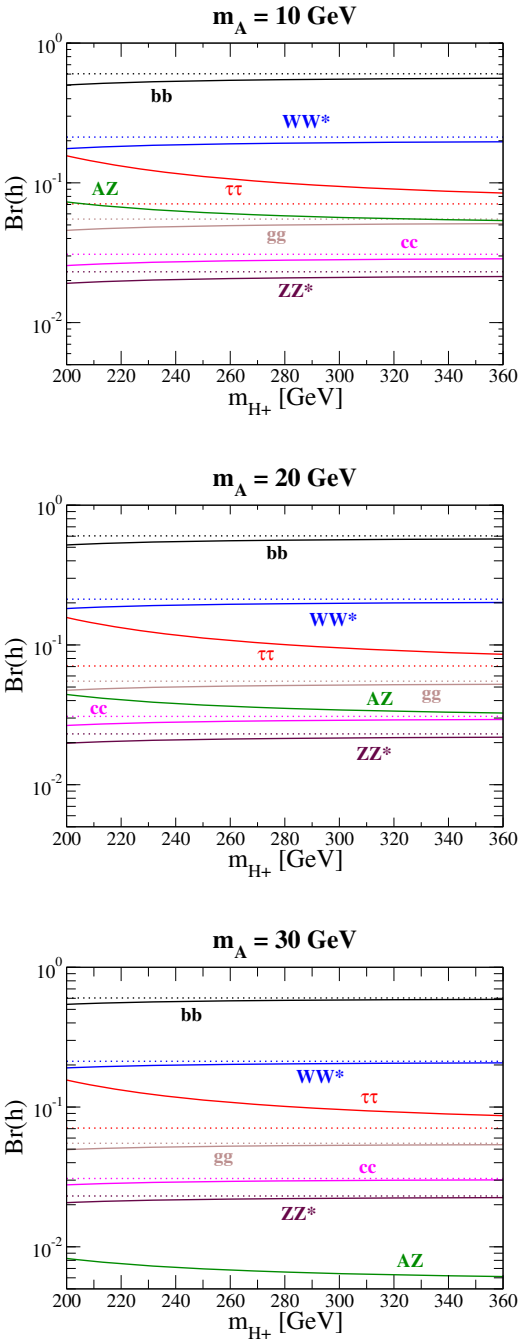

Figure 9. The branching fraction of h as a function of $m_{H^\pm}$ in the case of $m_H = M = m_{H^\pm}$ and $\tan\beta = 35$. The top, middle and bottom panels show the cases with $m_A = 10$, 20 and 30 GeV, respectively. The solid (dotted) curves shows the prediction in the Type-X 2HDM (SM).

JHEP07(2015)064

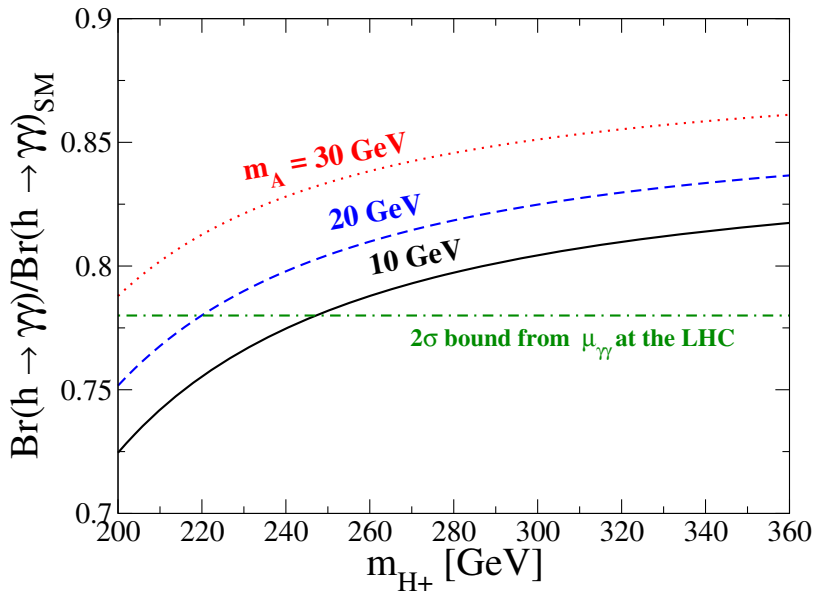

Figure 10. Ratio of the branching fraction $\mathrm{Br}(h \to \gamma\gamma)/\mathrm{Br}(h \to \gamma\gamma)_{\mathrm{SM}}$ in our scenario with $\tan\beta = 35$. The solid, dashed and dotted curves show the cases with m_A=10, 20 and 30 GeV, respectively. The horizontal dashed line shows the bound from $\mu_{\gamma\gamma}$ given in eq. (5.21) at 2σ level.

changed so much from the SM prediction. We note that the deviation in the $h\ell\ell$ coupling can be neglected in the decay rate of the $h \to \gamma\gamma$ mode, because its effect appears in the tau loop contribution, but the tau Yukawa coupling is too small as compared to the top Yukawa coupling. The decay rate of the diphoton mode is given as

$$\Gamma(h \to \gamma\gamma) = \frac{G_F \alpha_{\mathrm{em}}^2 m_h^3}{128\sqrt{2}\pi^3} \left| s_{\beta-\alpha} A_1(\tau_W) + \sum_f \xi_f^h A_{1/2}^f(\tau_f) + \frac{\lambda_3 v^2}{2m_{H^\pm}^2} A_0(\tau_{H^\pm}) \right|^2 ,$$
$$\text{with} \quad \tau_X = \frac{m_h^2}{4m_X^2}, \tag{5.15}$$

where the A_1, $A_{1/2}^f$ and A_0 terms correspond to the W boson, fermion and $H^\pm$ loop contributions, respectively. Each of the loop functions are given by

$$A_1(\tau) = -\tau^{-2}[2\tau^2 + 3\tau + 3(2\tau - 1)f(\tau)], \tag{5.16}$$
$$A_{1/2}^f(\tau) = 2N_c^f Q_f^2 \tau^{-2}[\tau + (\tau - 1)f(\tau)], \tag{5.17}$$
$$A_0(\tau) = -\tau^{-2}[\tau - f(\tau)], \tag{5.18}$$

JHEP07(2015)064

where $f(\tau)$ is defined as

$$f(\tau) = \begin{cases} \arcsin^2 \sqrt{\tau}. & (\tau \leq 1) \\ -\frac{1}{4}\left(\log \frac{1+\sqrt{1-\tau^{-1}}}{1-\sqrt{1-\tau^{-1}}} - i\pi\right)^2. & (\tau > 1) \end{cases} \tag{5.19}$$

We note that in the SM-like limit, which gives a good approximation for the numerical study in our scenario, we obtain the numerical value of the SM W and top loop contributions; i.e., $A_1(\tau_W) + A^t_{1/2}(\tau_t) \simeq -6.45$.

We here discuss the impact of the $H^\pm$ loop contribution to the $h \to \gamma\gamma$ decay. In our scenario, since the light CP-odd Higgs boson is required to explain the muon $g-2$ anomaly, the relatively large mass difference between A and $H^\pm$ is needed to avoid the current experimental constraints, which is generated by the Higgs quartic couplings. This can be clearly seen by rewriting the λ_3 coupling appearing in eq. (5.15) as follows

$$\lambda_3 v^2 = 2(m^2_{H^\pm} - m^2_A) + \lambda_{hAA} v^2, \tag{5.20}$$

where the second term is now zero according to our benchmark scenario shown in eq. (5.1). In addition, the loop function A_0 is expanded as $A_0(x) = 1/3 + 8x/45 + \mathcal{O}(x^2)$ under $x \ll 1$ or equivalently $m_{H^\pm} \gg m_h$. Thus, even if $H^\pm$ is relatively heavy, its contribution is not decoupled as we can see the asymptotic behavior $\lambda_3 v^2/(2m^2_{H^\pm}) A_0(\tau_{H^\pm}) \to 1/3$ $(m_{H^\pm} \to \infty)$.

The ATLAS and CMS collaborations report the signal strength as $\mu_{\gamma\gamma} = 1.17 \pm 0.27$ [82] and and $\mu_{\gamma\gamma} = 1.12 \pm 0.24$ [81], respectively. By taking naive combination of them, we obtain

$$\mu_{\gamma\gamma} = 1.14 \pm 0.18. \tag{5.21}$$

In figure 10, we show the ratio of the branching fraction of the $h \to \gamma\gamma$ mode as a function of $m_{H^\pm}$ with $\tan\beta = 35$. We find that the deviation in the branching fraction from the SM prediction is obtained in the range of -30% to -15%. The expected accuracy for the measurement of the decay rate of the diphoton mode is around -10% at the LHC 14 TeV 300 fb^{-1} and 5% at the ILC [83]. Therefore, our scenario is also probed by detecting the deviation in the $h \to \gamma\gamma$ decay rate in addition to the extra Higgs boson searches discussed in section 5.1 and the measurement of κ_ℓ. By looking at the horizontal line representing the bound from $\mu_{\gamma\gamma}$, we see that $m_{H^\pm} \lesssim 220$ GeV is excluded in the case of $m_A = 20$ GeV, which weaker than the constraint of κ_ℓ.

6 Conclusion

In this paper, we have explored the possibility to explain the muon $g-2$ anomaly in the Type-X 2HDM. We have shown in figure 6 that the measurement of the leptonic tau decay gives an important constraint on the parameter space. As a result, the region which can explain the discrepancy in the muon $g-2$ at the 1σ level is excluded by the constraint from the tau decay, and that at the 2σ level is allowed. We have found that the parameter space with $10 \lesssim m_A \lesssim 30$ GeV, $200 \lesssim m_{H,H^\pm} \lesssim 350$ GeV and $30 \lesssim \tan\beta \lesssim 50$ is favored by the explanation of the anomaly at the 2σ level.

JHEP07(2015)064

After finding the viable parameter region for the muon $g-2$, we have discussed the implication of the favored parameter region to the collider phenomenology. In our scenario, the 4τ, 3τ, $4\tau+Z$ and $4\tau+W$ signatures are expected from the electroweak productions of the extra Higgs bosons at the LHC. The cross sections of these signals are shown in table 2.

Finally, we have investigated the possible deviation in the property of the SM-like Higgs boson h. We have found that the value of the $h\ell\ell$ coupling is predicted to be the SM prediction times about -1.6 to -1.0, and the current data of the signal strength $\mu_{\tau\tau}$ at the LHC excludes $m_{H^\pm} \lesssim 270$ GeV in the case of $m_{H^\pm} = m_H$ and $m_A = 20$ GeV. We also have evaluated the branching fraction of the $h \to \gamma\gamma$ mode which is modified by the non-decoupling charged Higgs boson loop effect. We have shown that the deviation in the branching fraction of the $h \to \gamma\gamma$ mode is about -30% to -15% which can be detected at the future collider experiments such as the high-luminosity LHC and the ILC. Therefore, the precise measurements of the branching fractions of $h \to \gamma\gamma$ and $h \to \tau\tau$ gives an important indirect test to probe our scenario. Furthermore, we have found that the branching fraction of $h \to ZA$ becomes a few percent, and it also would provide another important signature to test our scenario. Therefore, in the Type-X 2HDM motivated by the explanation of the muon $g-2$ anomaly, there are various characteristic deviations in the 125 GeV Higgs boson property, which will be tested at collider experiments in the near future.

Acknowledgments

We used Feynmf [84] to draw the Feynman diagrams. The work is supported by Grant-in-Aid for Scientific research from the Ministry of Education, Culture, Sports, Science and Technology (MEXT), Japan, No. 23104006 [TA], JSPS Research Fellowships for Young Scientists [RS] and JSPS Postdoctoral Fellowships for Research Abroad [KY].

A Decay rates for the extra Higgs bosons

The decay rates of the extra Higgs bosons into the fermion pair are calculated at the tree level as

$$\Gamma(H^\pm \to f\bar{f}') = \sqrt{2}G_F \frac{m_{H^\pm}^3}{8\pi} N_c^f |V_{ff'}|^2 \lambda^{1/2}(x_{fH^\pm}, x_{f'H^\pm}) \times \left[(x_{fH^\pm}\xi_f^2 + x_{f'H^\pm}\xi_{f'}^2)(1 - x_{fH^\pm} - x_{f'H^\pm}) + 4x_{fH^\pm}x_{f'H^\pm}\xi_f\xi_{f'}\right], \tag{A.1}$$

$$\Gamma(H \to f\bar{f}) = \sqrt{2}G_F \frac{m_H m_f^2}{8\pi} (\xi_f^H)^2 N_c^f \lambda^{3/2}\left(x_{fH}, x_{fH}\right), \tag{A.2}$$

$$\Gamma(A \to f\bar{f}) = \sqrt{2}G_F \frac{m_A m_f^2}{8\pi} \xi_f^2 N_c^f \lambda^{1/2}\left(x_{fA}, x_{fA}\right), \tag{A.3}$$

where $x_{ab} = m_a^2/m_b^2$, N_c^f is the color factor, and the two body phase space function $\lambda(x,y)$ is given by

$$\lambda(x,y) = 1 + x^2 + y^2 - 2x - 2y - 2xy. \tag{A.4}$$

JHEP07(2015)064

We note that the above formulae are applied to all the types of Yukawa interactions. The decay rates into the gauge boson associated modes are calculated at the tree level as

$$\Gamma(H \to AZ) = s^2_{\beta-\alpha} \frac{\sqrt{2}G_F}{16\pi} m_H^3 \lambda^{3/2}\left(x_{ZH}, x_{AH}\right), \tag{A.5}$$

$$\Gamma(H^\pm \to AW^\pm) = \frac{\sqrt{2}G_F}{16\pi} m_{H^\pm}^3 \lambda^{3/2}\left(x_{WH^\pm}, x_{AH^\pm}\right). \tag{A.6}$$

B Electroweak production of a pair of Higgs bosons

Spin and color-averaged parton level cross sections are given as [85][6]

$$\hat{\sigma}(\hat{s}; u\bar{d} \to H^+A) = \frac{G_F^2 m_W^4}{72\pi} \frac{s^2_{\beta-\alpha}}{\hat{s}} \left(\frac{\hat{s}}{\hat{s}-m_W^2}\right)^2 \lambda^{3/2}\left(\frac{m^2_{H^\pm}}{\hat{s}}, \frac{m_A^2}{\hat{s}}\right), \tag{B.1}$$

$$\hat{\sigma}(\hat{s}; u\bar{d} \to H^+H) = \frac{G_F^2 m_W^4}{72\pi} \frac{s^2_{\beta-\alpha}}{\hat{s}} \left(\frac{\hat{s}}{\hat{s}-m_W^2}\right)^2 \lambda^{3/2}\left(\frac{m^2_{H^\pm}}{\hat{s}}, \frac{m_H^2}{\hat{s}}\right), \tag{B.2}$$

$$\hat{\sigma}(\hat{s}; q\bar{q} \to HA) = \frac{G_F^2 m_Z^4}{18\pi}(v_q^2 + a_q^2) \frac{s^2_{\beta-\alpha}}{\hat{s}} \left(\frac{\hat{s}}{\hat{s}-m_Z^2}\right)^2 \lambda^{3/2}\left(\frac{m_H^2}{\hat{s}}, \frac{m_A^2}{\hat{s}}\right), \tag{B.3}$$

$$\begin{aligned}\hat{\sigma}(\hat{s}; q\bar{q} \to H^+H^-) = \frac{\pi\alpha_{\rm em}^2}{9\hat{s}} &\left[\left(Q_q - \frac{v_q v_H}{s_W^2 c_W^2}\frac{\hat{s}}{\hat{s}-m_Z^2}\right)^2 + \frac{a_q^2 v_H^2}{s_W^4 c_W^4}\left(\frac{\hat{s}}{\hat{s}-m_Z^2}\right)^2\right] \\ &\times \lambda^{3/2}\left(\frac{m^2_{H^\pm}}{\hat{s}}, \frac{m^2_{H^\pm}}{\hat{s}}\right),\end{aligned} \tag{B.4}$$

where $v_H = -1/2 + s_W^2$, and v_q and a_q are defined in eq. (3.11). Production cross section at the hadron collider is calculated as

$$\sigma(pp \to AB) = 2\int_0^1 d\tau \sum_{q_1,\bar{q}_2} \frac{d\mathcal{L}_{q_1\bar{q}_2}}{d\tau} \hat{\sigma}(q_1\bar{q}_2 \to AB; \hat{s} = \tau s). \tag{B.5}$$

where $\mathcal{L}$ is the parton luminosity which is defined as

$$\frac{d\mathcal{L}_{q_1\bar{q}_2}}{d\tau} = \int_\tau^1 \frac{dx}{x} q_1(x)\bar{q}_2(\tau/x). \tag{B.6}$$

We note that the parton level cross sections of $\bar{u}d \to H^-A$ and $\bar{u}d \to H^-H$ processes are the same as those given in eqs. (B.1) and (B.2), respectively. However, because of the difference of parton luminosity of the initial proton, the cross section of H^+H/A and H^-H/A are different in the stage after the convolution of the luminosity function shown in eqs. (B.5) and (B.6).

Open Access. This article is distributed under the terms of the Creative Commons Attribution License (CC-BY 4.0), which permits any use, distribution and reproduction in any medium, provided the original author(s) and source are credited.

[6] See also references there in.

JHEP07(2015)064

References

[1] Muon g-2 collaboration, G.W. Bennett et al., *Final report of the muon E821 anomalous magnetic moment measurement at BNL*, *Phys. Rev.* **D 73** (2006) 072003 [hep-ex/0602035] [inSPIRE].

[2] M. Davier, A. Hoecker, B. Malaescu and Z. Zhang, *Reevaluation of the hadronic contributions to the muon $g-2$ and to $\alpha(M_Z^2)$*, *Eur. Phys. J.* **C 71** (2011) 1515 [*Erratum ibid.* **C 72** (2012) 1874] [arXiv:1010.4180] [inSPIRE].

[3] K. Hagiwara, R. Liao, A.D. Martin, D. Nomura and T. Teubner, *$(g-2)_\mu$ and $\alpha(M_Z^2)$ re-evaluated using new precise data*, *J. Phys.* **G 38** (2011) 085003 [arXiv:1105.3149] [inSPIRE].

[4] Muon g-2 collaboration, J. Grange et al., *Muon $(g-2)$ technical design report*, arXiv:1501.06858 [inSPIRE].

[5] J-PARC New g-2/EDM experiment collaboration, H. Iinuma, *New approach to the muon $g-2$ and EDM experiment at J-PARC*, *J. Phys. Conf. Ser.* **295** (2011) 012032 [inSPIRE].

[6] A. Czarnecki, W.J. Marciano and A. Vainshtein, *Refinements in electroweak contributions to the muon anomalous magnetic moment*, *Phys. Rev.* **D 67** (2003) 073006 [*Erratum ibid.* **D 73** (2006) 119901] [hep-ph/0212229] [inSPIRE].

[7] F. Jegerlehner and A. Nyffeler, *The muon $g-2$*, *Phys. Rept.* **477** (2009) 1 [arXiv:0902.3360] [inSPIRE].

[8] S.L. Glashow and S. Weinberg, *Natural conservation laws for neutral currents*, *Phys. Rev.* **D 15** (1977) 1958 [inSPIRE].

[9] V.D. Barger, J.L. Hewett and R.J.N. Phillips, *New constraints on the charged Higgs sector in two Higgs doublet models*, *Phys. Rev.* **D 41** (1990) 3421 [inSPIRE].

[10] Y. Grossman, *Phenomenology of models with more than two Higgs doublets*, *Nucl. Phys.* **B 426** (1994) 355 [hep-ph/9401311] [inSPIRE].

[11] M. Aoki, S. Kanemura, K. Tsumura and K. Yagyu, *Models of Yukawa interaction in the two Higgs doublet model and their collider phenomenology*, *Phys. Rev.* **D 80** (2009) 015017 [arXiv:0902.4665] [inSPIRE].

[12] A. Dedes and H.E. Haber, *Can the Higgs sector contribute significantly to the muon anomalous magnetic moment?*, *JHEP* **05** (2001) 006 [hep-ph/0102297] [inSPIRE].

[13] D. Chang, W.-F. Chang, C.-H. Chou and W.-Y. Keung, *Large two loop contributions to $g-2$ from a generic pseudoscalar boson*, *Phys. Rev.* **D 63** (2001) 091301 [hep-ph/0009292] [inSPIRE].

[14] K.-M. Cheung, C.-H. Chou and O.C.W. Kong, *Muon anomalous magnetic moment, two Higgs doublet model and supersymmetry*, *Phys. Rev.* **D 64** (2001) 111301 [hep-ph/0103183] [inSPIRE].

[15] M. Krawczyk, *The new $(g-2)$ for muon measurement and limits on the light Higgs bosons in $2HDM$ (II)*, hep-ph/0103223 [inSPIRE].

[16] K. Cheung and O.C.W. Kong, *Can the two Higgs doublet model survive the constraint from the muon anomalous magnetic moment as suggested?*, *Phys. Rev.* **D 68** (2003) 053003 [hep-ph/0302111] [inSPIRE].

JHEP07(2015)064

[17] Y.-L. Wu and Y.-F. Zhou, *Muon anomalous magnetic moment in the standard model with two Higgs doublets*, Phys. Rev. **D 64** (2001) 115018 [hep-ph/0104056] [INSPIRE].

[18] J.F. Gunion, *A light CP-odd Higgs boson and the muon anomalous magnetic moment*, JHEP **08** (2009) 032 [arXiv:0808.2509] [INSPIRE].

[19] J. Cao, P. Wan, L. Wu and J.M. Yang, *Lepton-specific two-Higgs doublet model: experimental constraints and implication on Higgs phenomenology*, Phys. Rev. **D 80** (2009) 071701 [arXiv:0909.5148] [INSPIRE].

[20] A. Broggio, E.J. Chun, M. Passera, K.M. Patel and S.K. Vempati, *Limiting two-Higgs-doublet models*, JHEP **11** (2014) 058 [arXiv:1409.3199] [INSPIRE].

[21] L. Wang and X.-F. Han, *A light pseudoscalar of* $2HDM$ *confronted with muon* $g-2$ *and experimental constraints*, JHEP **05** (2015) 039 [arXiv:1412.4874] [INSPIRE].

[22] V. Ilisie, *New Barr-Zee contributions to* $(g-2)_\mu$ *in two-Higgs-doublet models*, JHEP **04** (2015) 077 [arXiv:1502.04199] [INSPIRE].

[23] J.D. Bjorken and S. Weinberg, *A mechanism for nonconservation of muon number*, Phys. Rev. Lett. **38** (1977) 622 [INSPIRE].

[24] S.M. Barr and A. Zee, *Electric dipole moment of the electron and of the neutron*, Phys. Rev. Lett. **65** (1990) 21 [*Erratum ibid.* **65** (1990) 2920] [INSPIRE].

[25] ATLAS collaboration, *Observation of a new particle in the search for the standard model Higgs boson with the ATLAS detector at the LHC*, Phys. Lett. **B 716** (2012) 1 [arXiv:1207.7214] [INSPIRE].

[26] CMS collaboration, *Observation of a new boson at a mass of* 125 *GeV with the CMS experiment at the LHC*, Phys. Lett. **B 716** (2012) 30 [arXiv:1207.7235] [INSPIRE].

[27] CMS and LHCb collaborations, *Combination of results on the rare decays* $B^0_{(s)} \to \mu^+\mu^-$ *from the CMS and LHCb experiments*, CMS-PAS-BPH-13-007, CERN, Geneva Switzerland (2013).

[28] E. Ma and D.P. Roy, *Heavy triplet leptons and new gauge boson*, Nucl. Phys. **B 644** (2002) 290 [hep-ph/0206150] [INSPIRE].

[29] M. Aoki, S. Kanemura and O. Seto, *Neutrino mass, dark matter and baryon asymmetry via TeV-scale physics without fine-tuning*, Phys. Rev. Lett. **102** (2009) 051805 [arXiv:0807.0361] [INSPIRE].

[30] W. Hollik and T. Sack, *Can a second Higgs doublet diminish the leptonic tau decay width?*, Phys. Lett. **B 284** (1992) 427 [INSPIRE].

[31] M. Krawczyk and D. Temes, $2HDM(II)$ *radiative corrections in leptonic tau decays*, Eur. Phys. J. **C 44** (2005) 435 [hep-ph/0410248] [INSPIRE].

[32] H.E. Logan and D. MacLennan, *Charged Higgs phenomenology in the lepton-specific two Higgs doublet model*, Phys. Rev. **D 79** (2009) 115022 [arXiv:0903.2246] [INSPIRE].

[33] H. Huffel and G. Pocsik, *Unitarity bounds on Higgs boson masses in the Weinberg-Salam model with two Higgs doublets*, Z. Phys. **C 8** (1981) 13 [INSPIRE].

[34] J. Maalampi, J. Sirkka and I. Vilja, *Tree level unitarity and triviality bounds for two Higgs models*, Phys. Lett. **B 265** (1991) 371 [INSPIRE].

[35] S. Kanemura, T. Kubota and E. Takasugi, *Lee-Quigg-Thacker bounds for Higgs boson masses in a two doublet model*, Phys. Lett. **B 313** (1993) 155 [hep-ph/9303263] [INSPIRE].

JHEP07(2015)064

[36] A.G. Akeroyd, A. Arhrib and E.-M. Naimi, *Note on tree level unitarity in the general two Higgs doublet model*, *Phys. Lett.* **B 490** (2000) 119 [hep-ph/0006035] [INSPIRE].

[37] I.F. Ginzburg and I.P. Ivanov, *Tree-level unitarity constraints in the most general* $2HDM$, *Phys. Rev.* **D 72** (2005) 115010 [hep-ph/0508020] [INSPIRE].

[38] N.G. Deshpande and E. Ma, *Pattern of symmetry breaking with two Higgs doublets*, *Phys. Rev.* **D 18** (1978) 2574 [INSPIRE].

[39] M. Sher, *Electroweak Higgs potentials and vacuum stability*, *Phys. Rept.* **179** (1989) 273 [INSPIRE].

[40] S. Nie and M. Sher, *Vacuum stability bounds in the two Higgs doublet model*, *Phys. Lett.* **B 449** (1999) 89 [hep-ph/9811234] [INSPIRE].

[41] S. Kanemura, T. Kasai and Y. Okada, *Mass bounds of the lightest CP even Higgs boson in the two Higgs doublet model*, *Phys. Lett.* **B 471** (1999) 182 [hep-ph/9903289] [INSPIRE].

[42] ALEPH, DELPHI, L3, OPAL and LEP collaborations, G. Abbiendi et al., *Search for charged Higgs bosons: combined results using LEP data*, *Eur. Phys. J.* **C 73** (2013) 2463 [arXiv:1301.6065] [INSPIRE].

[43] ALEPH, DELPHI, L3, OPAL and LEP Working Group for Higgs Boson Searches collaborations, S. Schael et al., *Search for neutral MSSM Higgs bosons at LEP*, *Eur. Phys. J.* **C 47** (2006) 547 [hep-ex/0602042] [INSPIRE].

[44] DELPHI collaboration, J. Abdallah et al., *Searches for neutral Higgs bosons in extended models*, *Eur. Phys. J.* **C 38** (2004) 1 [hep-ex/0410017] [INSPIRE].

[45] ATLAS collaboration, *Search for charged Higgs bosons decaying via* $H^{\pm} \to \tau^{\pm}\nu$ *in fully hadronic final states using pp collision data at* $\sqrt{s} = 8$ *TeV with the ATLAS detector*, *JHEP* **03** (2015) 088 [arXiv:1412.6663] [INSPIRE].

[46] D. Curtin et al., *Exotic decays of the* 125 *GeV Higgs boson*, *Phys. Rev.* **D 90** (2014) 075004 [arXiv:1312.4992] [INSPIRE].

[47] *Exotic Higgs decays working group webpage*, http://exotichiggs.physics.sunysb.edu/.

[48] A. Djouadi, J. Kalinowski and M. Spira, *HDECAY: a program for Higgs boson decays in the standard model and its supersymmetric extension*, *Comput. Phys. Commun.* **108** (1998) 56 [hep-ph/9704448] [INSPIRE].

[49] M.E. Peskin and T. Takeuchi, *Estimation of oblique electroweak corrections*, *Phys. Rev.* **D 46** (1992) 381 [INSPIRE].

[50] D. Toussaint, *Renormalization effects from superheavy Higgs particles*, *Phys. Rev.* **D 18** (1978) 1626 [INSPIRE].

[51] S. Bertolini, *Quantum effects in a two Higgs doublet model of the electroweak interactions*, *Nucl. Phys.* **B 272** (1986) 77 [INSPIRE].

[52] A. Pomarol and R. Vega, *Constraints on CP-violation in the Higgs sector from the rho parameter*, *Nucl. Phys.* **B 413** (1994) 3 [hep-ph/9305272] [INSPIRE].

[53] M.E. Peskin and J.D. Wells, *How can a heavy Higgs boson be consistent with the precision electroweak measurements?*, *Phys. Rev.* **D 64** (2001) 093003 [hep-ph/0101342] [INSPIRE].

[54] J.-M. Gerard and M. Herquet, *A twisted custodial symmetry in the two-Higgs-doublet model*, *Phys. Rev. Lett.* **98** (2007) 251802 [hep-ph/0703051] [INSPIRE].

JHEP07(2015)064

[55] W. Grimus, L. Lavoura, O.M. Ogreid and P. Osland, *The oblique parameters in multi-Higgs-doublet models*, Nucl. Phys. **B 801** (2008) 81 [arXiv:0802.4353] [INSPIRE].

[56] S. Kanemura, Y. Okada, H. Taniguchi and K. Tsumura, *Indirect bounds on heavy scalar masses of the two-Higgs-doublet model in light of recent Higgs boson searches*, Phys. Lett. **B 704** (2011) 303 [arXiv:1108.3297] [INSPIRE].

[57] R. Barbieri, L.J. Hall and V.S. Rychkov, *Improved naturalness with a heavy Higgs: an alternative road to LHC physics*, Phys. Rev. **D 74** (2006) 015007 [hep-ph/0603188] [INSPIRE].

[58] GFITTER GROUP collaboration, M. Baak et al., *The global electroweak fit at NNLO and prospects for the LHC and ILC*, Eur. Phys. J. **C 74** (2014) 3046 [arXiv:1407.3792] [INSPIRE].

[59] A. Sirlin, *Radiative corrections in the* $\mathrm{SU}(2)_L \times \mathrm{U}(1)$ *theory: a simple renormalization framework*, Phys. Rev. **D 22** (1980) 971 [INSPIRE].

[60] W.F.L. Hollik, *Radiative corrections in the standard model and their role for precision tests of the electroweak theory*, Fortsch. Phys. **38** (1990) 165 [INSPIRE].

[61] H.E. Logan and U. Nierste, $B_{s,d} \to \ell^+\ell^-$ *in a two Higgs doublet model*, Nucl. Phys. **B 586** (2000) 39 [hep-ph/0004139] [INSPIRE].

[62] X.-Q. Li, J. Lu and A. Pich, $B^0_{s,d} \to \ell^+\ell^-$ *decays in the aligned two-Higgs-doublet model*, JHEP **06** (2014) 022 [arXiv:1404.5865] [INSPIRE].

[63] A. Pich, *Precision tau physics*, Prog. Part. Nucl. Phys. **75** (2014) 41 [arXiv:1310.7922] [INSPIRE].

[64] PARTICLE DATA GROUP collaboration, K.A. Olive et al., *Review of particle physics*, Chin. Phys. **C 38** (2014) 090001 [INSPIRE].

[65] HEAVY FLAVOR AVERAGING GROUP (HFAG) collaboration, Y. Amhis et al., *Averages of b-hadron, c-hadron and* τ*-lepton properties as of summer* 2014, arXiv:1412.7515 [INSPIRE].

[66] F. Staub, *SARAH* 4*: a tool for (not only SUSY) model builders*, Comput. Phys. Commun. **185** (2014) 1773 [arXiv:1309.7223] [INSPIRE].

[67] B. Gorczyca and M. Krawczyk, *New results for the inert doublet model*, Acta Phys. Polon. **B 42** (2011) 2229 [*Erratum ibid.* **B 43** (2012) 481] [arXiv:1112.4356] [INSPIRE].

[68] B. Gorczyca and M. Krawczyk, *Tree-level unitarity constraints for the SM-like* $2HDM$, arXiv:1112.5086 [INSPIRE].

[69] D. Eriksson, J. Rathsman and O. Stal, $2HDMC$*: two-Higgs-doublet model calculator physics and manual*, Comput. Phys. Commun. **181** (2010) 189 [arXiv:0902.0851] [INSPIRE].

[70] J. Rathsman and O. Stal, $2HDMC$ *— a two Higgs doublet model calculator*, PoS(CHARGED 2010)034 [arXiv:1104.5563] [INSPIRE].

[71] H. Fusaoka and Y. Koide, *Updated estimate of running quark masses*, Phys. Rev. **D 57** (1998) 3986 [hep-ph/9712201] [INSPIRE].

[72] A. Pukhov et al., *CompHEP: a package for evaluation of Feynman diagrams and integration over multiparticle phase space*, hep-ph/9908288 [INSPIRE].

[73] J. Pumplin et al., *New generation of parton distributions with uncertainties from global QCD analysis*, JHEP **07** (2002) 012 [hep-ph/0201195] [INSPIRE].

JHEP07(2015)064

[74] S. Kanemura, K. Tsumura and H. Yokoya, *Multi-tau-lepton signatures at the LHC in the two Higgs doublet model*, *Phys. Rev.* **D 85** (2012) 095001 [arXiv:1111.6089] [INSPIRE].

[75] S. Kanemura, K. Tsumura and H. Yokoya, *Multi-tau lepton signatures in leptophilic two Higgs doublet model at the ILC*, arXiv:1201.6489 [INSPIRE].

[76] S. Dawson et al., *Working group report: Higgs boson*, arXiv:1310.8361 [INSPIRE].

[77] S. Kanemura, K. Tsumura, K. Yagyu and H. Yokoya, *Fingerprinting nonminimal Higgs sectors*, *Phys. Rev.* **D 90** (2014) 075001 [arXiv:1406.3294] [INSPIRE].

[78] S. Kanemura, M. Kikuchi and K. Yagyu, *Radiative corrections to the Yukawa coupling constants in two Higgs doublet models*, *Phys. Lett.* **B 731** (2014) 27 [arXiv:1401.0515] [INSPIRE].

[79] S. Kanemura, M. Kikuchi and K. Yagyu, *Fingerprinting the extended Higgs sector using one-loop corrected Higgs boson couplings and future precision measurements*, *Nucl. Phys.* **B 896** (2015) 80 [arXiv:1502.07716] [INSPIRE].

[80] ATLAS collaboration, *Evidence for the Higgs-boson Yukawa coupling to tau leptons with the ATLAS detector*, *JHEP* **04** (2015) 117 [arXiv:1501.04943] [INSPIRE].

[81] CMS collaboration, *Precise determination of the mass of the Higgs boson and studies of the compatibility of its couplings with the standard model*, CMS-PAS-HIG-14-009, CERN, Geneva Switzerland (2014).

[82] ATLAS collaboration, *Measurement of Higgs boson production in the diphoton decay channel in pp collisions at center-of-mass energies of* 7 *and* 8 *TeV with the ATLAS detector*, *Phys. Rev.* **D 90** (2014) 112015 [arXiv:1408.7084] [INSPIRE].

[83] M.E. Peskin, *Comparison of LHC and ILC capabilities for Higgs boson coupling measurements*, arXiv:1207.2516 [INSPIRE].

[84] T. Ohl, *Drawing Feynman diagrams with Latex and Metafont*, *Comput. Phys. Commun.* **90** (1995) 340 [hep-ph/9505351] [INSPIRE].

[85] A. Djouadi, *The anatomy of electro-weak symmetry breaking. II. The Higgs bosons in the minimal supersymmetric model*, *Phys. Rept.* **459** (2008) 1 [hep-ph/0503173] [INSPIRE].

JHEP07(2015)064

Published for SISSA by Springer

Received: January 30, 2015
Revised: March 5, 2015
Accepted: March 12, 2015
Published: April 23, 2015

Associated jet and subjet rates in light-quark and gluon jet discrimination

Biplob Bhattacherjee,[a] **Satyanarayan Mukhopadhyay,**[b] **Mihoko M. Nojiri,**[b,c] **Yasuhito Sakaki**[c] **and Bryan R. Webber**[d]

[a] *Centre for High Energy Physics, Indian Institute of Science, Bangalore, India*
[b] *Kavli IPMU (WPI), The University of Tokyo, Kashiwa, Chiba 277-8583, Japan*
[c] *KEK Theory Center and Sokendai, Tsukuba, Ibaraki 305-0801, Japan*
[d] *Cavendish Laboratory, J.J. Thomson Avenue, Cambridge, U.K.*

E-mail: biplob@cts.iisc.ernet.in, satya.mukho@ipmu.jp, nojiri@post.kek.jp, sakakiy@post.kek.jp, webber@hep.phy.cam.ac.uk

Abstract: We show that in studies of light quark- and gluon-initiated jet discrimination, it is important to include the information on softer reconstructed jets (associated jets) around a primary hard jet. This is particularly relevant while adopting a small radius parameter for reconstructing hadronic jets. The probability of having an associated jet as a function of the primary jet transverse momentum (p_T) and radius, the minimum associated jet p_T and the association radius is computed up to next-to-double logarithmic accuracy (NDLA), and the predictions are compared with results from `Herwig++`, `Pythia6` and `Pythia8` Monte Carlos (MC). We demonstrate the improvement in quark-gluon discrimination on using the associated jet rate variable with the help of a multivariate analysis. The associated jet rates are found to be only mildly sensitive to the choice of parton shower and hadronization algorithms, as well as to the effects of initial state radiation and underlying event. In addition, the number of k_t subjets of an anti-k_t jet is found to be an observable that leads to a rather uniform prediction across different MC's, broadly being in agreement with predictions in NDLA, as compared to the often used number of charged tracks observable.

Keywords: QCD Phenomenology, Jets

ArXiv ePrint: 1501.04794

Open Access, © The Authors.
Article funded by SCOAP[3].

doi:10.1007/JHEP04(2015)131

JHEP04(2015)131

Contents

1 Introduction **1**

2 Associated jet rates: analytical calculations **3**

3 Associated jet rates: comparison with Monte Carlo **6**

4 Quark-gluon separation: multivariate analysis **7**
4.1 Variables for quark-gluon separation 7
4.2 Performance in MVA 10

5 Subjet rates in jets: analytical calculations **13**

6 Subjet rates in jets: comparison with Monte Carlo **15**

7 Summary **16**

A Distributions of discrimination variables **17**

1 Introduction

Hadronic jets are the most abundant objects at a proton-proton collider like the LHC, and it is a major challenge to separate the signals being looked for from standard model (SM) backgrounds in multijet final states. One promising direction that has recently received attention in both theoretical and experimental studies is that the separation of light quark-initiated jets from gluon-initiated ones can be viable in these search channels. Quarks are often encountered in the decays of new particles predicted by scenarios beyond the standard model, as well as in the decay of the weak bosons, Higgs and top quark in the SM itself. On the other hand, in the corresponding SM backgrounds involving multiple hard jets, there is a larger fraction of gluon-initiated jets from QCD radiation. Here, quark- or gluon-initiated jets (henceforth simply referred to as quark and gluon jets) refer to the parton in the hard process at leading order in perturbation theory that initiates the parton shower. Based on the difference in the radiation pattern of quarks and gluons, a likelihood based discriminant can be built to separate decay jets from QCD radiation jets with a certain efficiency [1].

Several variables have been proposed to separate quark and gluon jets, mostly relying on the fact that a gluon of similar energy leads to more soft emissions compared to a quark. This includes both discrete variables like the number of charged tracks inside the jet cone, as well as continuous ones like the width of a jet and energy-energy-correlation (EEC) angularity [1–5]. ATLAS and CMS collaborations have also studied the discrimination of light quarks from gluons along these lines with the 7 and 8 TeV LHC data respectively [6, 7].

JHEP04(2015)131

Using data samples with "enriched quark and gluon content", data-based taggers were also developed, and compared to the predictions from Monte Carlo (MC) simulations. While there are differences between the predictions of different MC's, as well as between the data-based tagger and the MC results, they are consistent with each other within the large systematic uncertainties at present.

An important question in this regard is the proper choice of a jet algorithm and radius parameter. In the LHC environment, in order to keep the contribution of the underlying event and multiple proton-proton collisions at a minimum, for multijet processes the standard choice is an anti-k_t algorithm with radius parameter $R = 0.4$. In addition, in the ATLAS study mentioned above, jets are required to satisfy an isolation criterion: a jet is considered isolated if there is no other reconstructed jet within a cone of size $\Delta R < 0.7$ (where $\Delta R = \sqrt{(\Delta\eta)^2 + (\Delta\phi)^2}$ is the standard distance measure in the pseudorapidity-azimuthal angle plane). An optimum choice for the jet radius parameter was discussed in refs. [8, 9] for quark and gluon jets as a function of their transverse momenta (p_T), and it was observed that one usually requires a larger radius for a gluon jet in order for the parton p_T to be close to the jet p_T. However, for experimental purposes it is advantageous to use a fixed and small radius parameter for the jets, for reasons mentioned above. Therefore, we propose to recover the missed information on radiation from the parent parton outside the chosen jet radius by including softer reconstructed jets that can be present (with a calculable probability) around a certain radius of a primary hard jet. These softer jets are referred to as "associated jets" in this study. It is important to note here that imposing an isolation criterion as above while studying quark and gluon jet properties might not be appropriate, since it leads to rejecting a fraction of the jet candidates beforehand, and thus biasing the sample to ones where the initial quark or gluon has not radiated outside the adopted jet radius.

We first compute the associated jet rates in QCD to next-to-double logarithmic accuracy in section 2, and then compare the analytical results with those from different parton shower MC's in section 3. Using the information on the presence (or absence) of associated jets can improve the discrimination of quarks and gluons. We demonstrate this through a multivariate analysis in section 4. Several combinations of jet discrimination variables are tried out, and an attempt is made to determine an optimum choice. Even though we include standard discrimination variables like the number of charged tracks as inputs to our multivariate analysis, it should be emphasized that they are subject to MC ambiguities stemming from parton shower algorithms and their associated parameters, and tunings of hadronization and underlying event (UE) models. However, in order to judge the improvement in tagger performance on using the associated jet rates, we compare the performance of different sets of variables within the same MC.

In sections 5 and 6 we study the use of the number of subjets of a jet (defined with an exclusive k_t algorithm) in place of the number of charged tracks, since the different MC prediction tend to be similar for the former observable. We compute the subjet rates upto NDLA as well, and compare the NDLA results with predictions from different MC's. Our results on both associated jets and subjets are summarized in section 7. We discuss the 2-dimensional joint distributions of the three discrimination variables used as inputs in the

JHEP04(2015)131

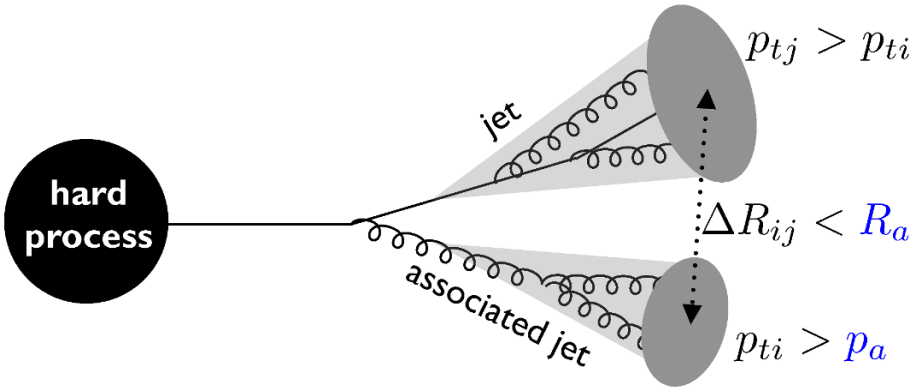

Figure 1. A schematic illustration of associated jets, and the relevant variables which determine the associated jet rate (see text for details).

multivariate analysis in an appendix.

2 Associated jet rates: analytical calculations

To begin with, let us define the longitudinally invariant jet algorithms [10–13] adopted in this study. The distance measures between each pair of objects i and j (d_{ij}), and between an object and the beam (d_{iB}) are given by

$$\begin{aligned} d_{ij} &= \min\{p_{ti}^{2p}, p_{tj}^{2p}\}\frac{\Delta R_{ij}^2}{R^2}\ , \\ d_{iB} &= p_{ti}^{2p}\ , \end{aligned} \tag{2.1}$$

where p_{ti}, y_i and ϕ_i are the transverse momentum, rapidity and azimuth of object i, respectively, $\Delta R_{ij}^2 \equiv (y_i - y_j)^2 + (\phi_i - \phi_j)^2$, and R is the jet radius parameter. The jet algorithm in use is fixed by the parameter p, with $p = 1, 0, -1$ for the k_t [11], Cambridge/Aachen [14–16] and anti-k_t [13] algorithms, respectively. At any stage of clustering, if a d_{ij} is the smallest measure we combine objects i and j. If d_{iB} is the smallest we call i a jet and remove it from the clustering list. This procedure is continued until there are no more objects left to cluster.

Once a primary jet j has been defined, say using the anti-k_t algorithm with radius parameter R, we define a nearby jet i with $p_{tj} > p_{ti} > p_a$ and $R < \Delta R_{ij} < R_a$ as an *associated jet*. Thus the associated jet rates are functions of the primary jet $p_t = p_j$, its radius R, the association radius R_a and the minimum associated jet $p_t = p_a$. In figure 1 we illustrate the idea of an associated jet schematically, and show the relevant variables that determine the associated jet rate.

In perturbative QCD, the rate of n-jet production from a primary object of type i ($i = q, g$ in this case), R_n^i, can be obtained from the associated generating function [17–21]

$$\Phi_i(u) = \sum_n R_n^i u^n\ . \tag{2.2}$$

JHEP04(2015)131

We can recover the jet rates by differentiating at $u = 0$,

$$R_n^i = \frac{1}{n!} \frac{d^n \Phi_i}{du^n}\bigg|_{u=0} . \tag{2.3}$$

The jet rates $R_n^i = R_n^i(p_j, \xi)$ are functions of the trigger jet transverse momentum p_j, and the evolution scale for parton showering, which, for hadron-hadron collisions is taken as $\xi = \Delta R^2/2$. This is equivalent to the evolution scale for coherent parton showering, $\xi \equiv 1 - \cos\theta$, with θ being the emission angle ($\Delta R^2/2 \approx \theta^2/2 \approx 1 - \cos\theta$). To be resolved, an emission must have $\xi > \xi_j = R^2/2$ and $p_t > p_a$. Since the jet rates R_n^i include the trigger jet j, the probability of n *associated jets* for a jet of type i with transverse momentum p_j is

$$P_n^i = R_{n+1}^i(p_j, \xi_a) . \tag{2.4}$$

Here, $\xi_a = R_a^2/2$, with R_a being the association radius defined above.

The generating functions $\Phi_i(u)$ were computed in the context of e^+e^- collisions in ref. [17], upto next-to-double logarithmic accuracy (NDLA). Here, leading double and next-to-double logarithms refer to $\alpha_S^n \log^{2n}$ and $\alpha_S^n \log^{2n-1}$, where the logarithms are those of R_a/R and/or p_j/p_a. For p_a sufficiently large, these terms are determined by the timelike showering of final-state partons, while contributions from initial-state showers and the underlying event can be avoided. Following the same methods as in ref. [17] for hadron hadron collisions, for $\xi > \xi_j$ and $p_j > p_a$, we have the quark and gluon generating functions to NDLA

$$\begin{aligned}
\Phi_q(u, p_j, \xi) &= u + \int_{\xi_j}^{\xi} \frac{d\xi'}{\xi'} \int_{p_a/p_j}^{1} dz \frac{\alpha_S(k_t^2)}{2\pi} P_{gq}(z) \Phi_q(u, p_j, \xi') \left[\Phi_g(u, zp_j, \xi') - 1\right] , \\
\Phi_g(u, p_j, \xi) &= u + \int_{\xi_j}^{\xi} \frac{d\xi'}{\xi'} \int_{p_a/p_j}^{1} dz \frac{\alpha_S(k_t^2)}{2\pi} \big\{ P_{gg}(z) \Phi_g(u, p_j, \xi') \left[\Phi_g(u, zp_j, \xi') - 1\right] \\
&\quad + P_{qg}(z) \left[\{\Phi_q(u, p_j, \xi')\}^2 - \Phi_g(u, p_j, \xi')\right] \big\} .
\end{aligned} \tag{2.5}$$

Here, the running coupling is evaluated at the transverse momentum scale of the emission, $k_t^2 = z^2 p_j^2 \xi'$. Defining $\overline{\alpha}_S = \alpha_S(p_j^2 \xi)/\pi$, i.e. in terms of the coupling at the hard scale, we have to NDLA

$$\frac{\alpha_S(k_t^2)}{\pi} = \overline{\alpha}_S - b_0 \overline{\alpha}_S^2 \left[2 \ln z + \ln\left(\frac{\xi'}{\xi}\right) \right] , \tag{2.6}$$

with $b_0 = (11 C_A - 2 n_f)/12$.

The solution for the quark generating function is easily seen to be

$$\Phi_q(u, p_j, \xi) = u \exp\left\{ \int_{\xi_j}^{\xi} \frac{d\xi'}{\xi'} \int_{p_a/p_j}^{1} dz \frac{\alpha_S(k_t^2)}{2\pi} P_{gq}(z) \left[\Phi_g(u, zp_j, \xi') - 1\right] \right\} . \tag{2.7}$$

We can solve for the gluon generating function by iteration, and then substitute in this equation to get the complete solution. For brevity we define the following logarithms:

$$\begin{aligned}
\kappa &= \ln(p_j/p_a) , & \kappa' &= \ln(zp_j/p_a) , \\
\lambda &= \ln(\xi_a/\xi_j) = 2\ln(R_a/R) , & \lambda' &= \ln(\xi'/\xi_j) .
\end{aligned} \tag{2.8}$$

JHEP04(2015)131

In terms of these variables the NDLA quark generating function is

$$\Phi_q(u,\kappa,\lambda) = u \exp\left\{\int_0^\lambda d\lambda' \int_0^\kappa d\kappa'\, \Gamma_q\left(\kappa',\lambda',\kappa,\lambda\right)\left[\Phi_g(u,\kappa',\lambda') - 1\right]\right\} \tag{2.9}$$

where, including the full P_{gq} splitting function,[1]

$$\Gamma_q\left(\kappa',\lambda',\kappa,\lambda\right) = C_F\overline{\alpha}_{\rm S}\left[1 - {\rm e}^{\kappa'-\kappa} + \frac{1}{2}{\rm e}^{2(\kappa'-\kappa)}\right] - C_F b_0 \overline{\alpha}_{\rm S}^2\left[2(\kappa'-\kappa) + \lambda' - \lambda\right]. \tag{2.10}$$

Defining similarly[2]

$$\begin{aligned}\Gamma_g(\kappa',\lambda',\kappa,\lambda) &= C_A\overline{\alpha}_{\rm S}\left[1 - {\rm e}^{\kappa'-\kappa} + \frac{1}{2}{\rm e}^{2(\kappa'-\kappa)} - \frac{1}{2}{\rm e}^{3(\kappa'-\kappa)}\right] - C_A b_0\overline{\alpha}_{\rm S}^2\left[2(\kappa'-\kappa) + \lambda' - \lambda\right],\\ \Gamma_f(\kappa',\kappa) &= \frac{n_f}{4}\overline{\alpha}_{\rm S}\left[{\rm e}^{\kappa'-\kappa} - 2{\rm e}^{2(\kappa'-\kappa)} + 2{\rm e}^{3(\kappa'-\kappa)}\right],\end{aligned} \tag{2.11}$$

we solve the gluon generating function by iteration to second order in u, which gives the probabilities for 0 or 1 associated jets:

$$\begin{aligned}\Phi_g(u,\kappa,\lambda) = u\Delta_g(\kappa,\lambda)\Bigg\{1 + u\int_0^\lambda d\lambda' \int_0^\kappa d\kappa' \big[&\Gamma_g(\kappa',\lambda',\kappa,\lambda)\,\Delta_g(\kappa',\lambda')\\ &+\Gamma_f(\kappa',\kappa)\Delta_f(\kappa,\lambda')\big] + \mathcal{O}(u^2)\Bigg\},\end{aligned} \tag{2.12}$$

where $\Delta_q(\kappa,\lambda)$ and $\Delta_g(\kappa,\lambda)$ are the quark and gluon Sudakov factors (the probabilities for no associated jets) and we have defined $\Delta_f(\kappa,\lambda) = \Delta_q^2(\kappa,\lambda)/\Delta_g(\kappa,\lambda)$. Hence

$$\begin{aligned}P_0^q &= \Delta_q(\kappa,\lambda) = \exp\left\{-\int_0^\lambda d\lambda' \int_0^\kappa d\kappa'\, \Gamma_q(\kappa',\lambda',\kappa,\lambda)\right\}\\ &= \exp\left\{-C_F\overline{\alpha}_{\rm S}\lambda\left[\kappa - \frac{3}{4} + {\rm e}^{-\kappa} - \frac{1}{4}{\rm e}^{-2\kappa}\right] - C_F b_0\overline{\alpha}_{\rm S}^2\kappa\lambda\left[\kappa + \frac{1}{2}\lambda\right]\right\},\end{aligned} \tag{2.13}$$

$$\begin{aligned}P_0^g &= \Delta_g(\kappa,\lambda) = \exp\left\{-\int_0^\lambda d\lambda' \int_0^\kappa d\kappa'\left[\Gamma_g(\kappa',\lambda',\kappa,\lambda) + \Gamma_f(\kappa',\kappa)\right]\right\}\\ &= \exp\Bigg\{-C_A\overline{\alpha}_{\rm S}\lambda\left[\kappa - \frac{11}{12} + {\rm e}^{-\kappa} - \frac{1}{4}{\rm e}^{-2\kappa} + \frac{1}{6}{\rm e}^{-3\kappa}\right]\\ &\quad -\frac{n_f}{4}\overline{\alpha}_{\rm S}\lambda\left[\frac{2}{3} - {\rm e}^{-\kappa} + {\rm e}^{-2\kappa} - \frac{2}{3}{\rm e}^{-3\kappa}\right] - C_A b_0\overline{\alpha}_{\rm S}^2\kappa\lambda\left[\kappa + \frac{1}{2}\lambda\right]\Bigg\},\end{aligned} \tag{2.14}$$

$$P_1^q = \Delta_q(\kappa,\lambda)\int_0^\lambda d\lambda' \int_0^\kappa d\kappa'\, \Gamma_q(\kappa',\lambda',\kappa,\lambda)\,\Delta_g(\kappa',\lambda') \tag{2.15}$$

$$P_1^g = \Delta_g(\kappa,\lambda)\int_0^\lambda d\lambda' \int_0^\kappa d\kappa'\big[\Gamma_g(\kappa',\lambda',\kappa,\lambda)\Delta_g(\kappa',\lambda') + \Gamma_f(\kappa',\kappa)\Delta_f(\kappa,\lambda')\big]. \tag{2.16}$$

[1] We keep terms that are formally power-suppressed in order to satisfy the boundary condition $P_0 = 1$ when $p_a = p_j$.

[2] We drop the $\overline{\alpha}_{\rm S}^2$ term in Γ_f as it is beyond NDLA and does not affect the boundary condition.

JHEP04(2015)131

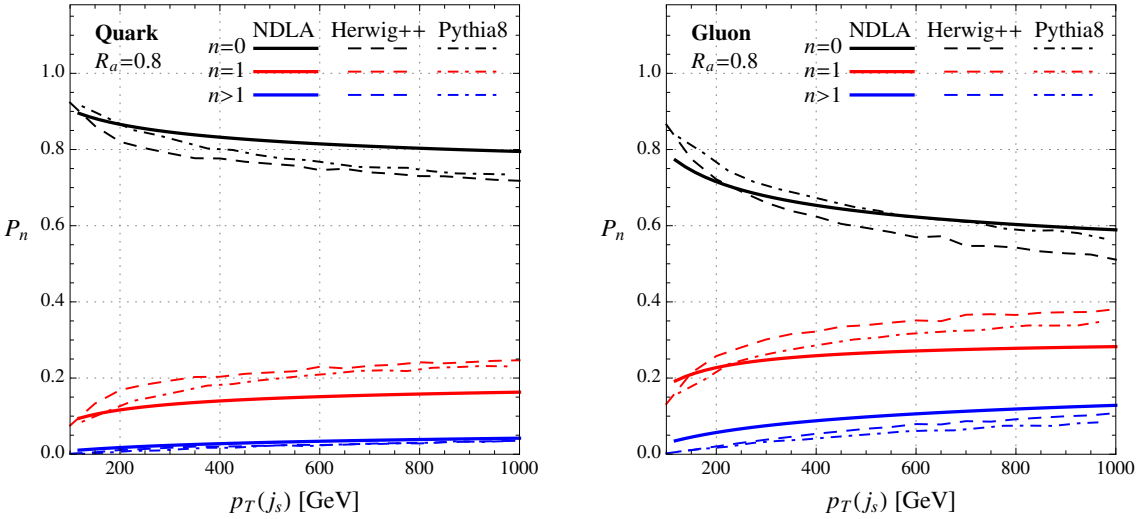

Figure 2. Comparison of the `Herwig++` and `Pythia8` MC predictions for associated jet rates with the NDLA results, as a function of $p_T(j_s)$: for quark jets (left), and gluon jets (right), with $R_a = 0.8$ and $p_a = 20\,\text{GeV}$. Here, $p_T(j_s)$ is the vector sum of the leading jet and associated jet p_T's.

3 Associated jet rates: comparison with Monte Carlo

We are now in a position to compare the NDLA predictions for associated jet rates discussed in the previous section with the results obtained using the `Herwig++` [22] and `Pythia8` [23, 24] event generators,[3] where the quark- and gluon-initiated jets are simulated using the $Z+q$ and $Z+g$ processes at leading order in QCD (with the Z boson subsequently decayed to $\nu\bar{\nu}$). The event samples were generated for proton-proton collisions at the 13 TeV LHC, using the `CTEQ6L1` [25] parton distribution functions (PDF) for the `Pythia` generators and the default `MRST LO**` [26] PDF and UE model for `Herwig++`. Subsequently, we used a modified version of `DELPHES2` [27] for including detector effects. For observables based on charged tracks to be discussed in the following, we use a minimum p_T threshold of 1 GeV for each track. All jets are reconstructed with an anti-k_t algorithm [13, 28, 29] with radius parameter $R = 0.4$, and are required to have $p_T > 20\,\text{GeV}$. In addition, the leading jet is required to be central with $|\eta| < 2$.

In figure 2 we show the probability of obtaining n associated jets P_n as a function of the jet p_T for $n = 0, 1$ and $n > 1$, for quark- and gluon-initiated jets, in the left and right columns respectively. The association radius is set to be $R_a = 0.8$ and the minimum associated jet transverse momentum is $p_a = 20\,\text{GeV}$. In the MC simulations, P_n has been computed as a function of $p_T(j_s)$, which is the vector sum of the leading jet and associated jet p_T's. The jet rates are studied as a function of $p_T(j_s)$, as it is closer to the transverse momentum of the parton that initiates the final state shower.

We see that the functional behaviour with respect to the jet p_T in the MC computation[4]

[3] To be specific, we use `Herwig++ 2.7.0` and `Pythia 8.201` (tune `4C`) for all our calculations.

[4] For the associated jet rate calculations, we generated MC event samples with a statistics of 20,000 events each fixing the threshold for the minimum leading jet p_T at $50 \times (i+1)\,\text{GeV}$, for $i \in [0, 19]$. Only

JHEP04(2015)131

and the NDLA calculation are similar, although there are some differences in the values of P_n. In particular, the MC prediction of P_1 for quark and gluon jets is higher than the NDLA result, especially at higher $p_T(j_s)$, with `Herwig++` giving rise to a slightly larger P_1 compared to `Pythia8`. For a quark jet, the probability of having at least one associated jet ranges from around 15% to 25% as we go from $p_T(j_s) = 200\,\text{GeV}$ to $p_T(j_s) = 500\,\text{GeV}$ and at higher $p_T(j_s)$ the probability essentially remains the same. For gluon jets, the corresponding probability ranges from around 30% to 40% as we go from $p_T(j_s) = 200\,\text{GeV}$ to $p_T(j_s) = 500\,\text{GeV}$. The larger probability to have an associated jet around a gluon can thus be utilized to better discriminate it from quarks, as we shall see in the next section.

The NDLA computation includes only the time-like showering of the final state partons, and ignores some power-suppressed effects due to momentum conservation and hadronization. On the other hand, the MC results shown above include momentum conservation and hadronization as well as the effects of initial state radiation (ISR) and multiple interaction (MPI). In order to quantify the effect of ISR and MPI, we compare the predictions for P_n with and without ISR and MPI in `Herwig++`, `Pythia8` as well as in `Pythia6` [30] (we use the version `Pythia 6.4.28` with the `AUET2B-CT6L` tune) in figure 3. It is clear from this figure that the impact of ISR and MPI is rather small for our choice of the association radius $R_a = 0.8$, thereby making the predictions stable against such effects. For this choice of R_a, we can see that `Pythia8` shows the highest variation against such effects, followed by `Pythia6`, while the effects are indeed negligible for the case of `Herwig++`.[5] Furthermore, the MC results become closer to the NDLA ones when ISR and MPI effects are switched off.

We also investigated the effects of momentum conservation, by changing the recombination scheme in the anti-k_t jet algorithm from the default E-scheme to the "winner-take-all" scheme introduced in [31], which is less sensitive to recoils in the parton shower [32]. Such a change increases the MC associated jet rates very slightly. We believe this is because the axis of the leading jet is moved away from the overall momentum vector of the system. The effects are roughly proportional for quark and gluon jets, so they would not affect discrimination significantly.

4 Quark-gluon separation: multivariate analysis

4.1 Variables for quark-gluon separation

A large number of variables have been surveyed in the context of quark-gluon discrimination, constructed out of either track based observables or calorimeter based ones [1–5]. While the former category has the practical advantage of being more accurate due to better track momentum resolution as well as being less prone to pile-up contamination, the latter category can be used for jets with larger rapidities outside the tracker coverage. The most widely studied variables include the number of charged tracks inside the jet cone

events with the leading jet $p_T(j_s)$ above the generation threshold are used in the analysis. This ensures uniform MC statistics in the whole range of $p_T(j_s)$.

[5] However, we have checked that if we take a larger association radius, $R_a > 1.2$, the ISR effects become appreciable in `Herwig++`.

JHEP04(2015)131

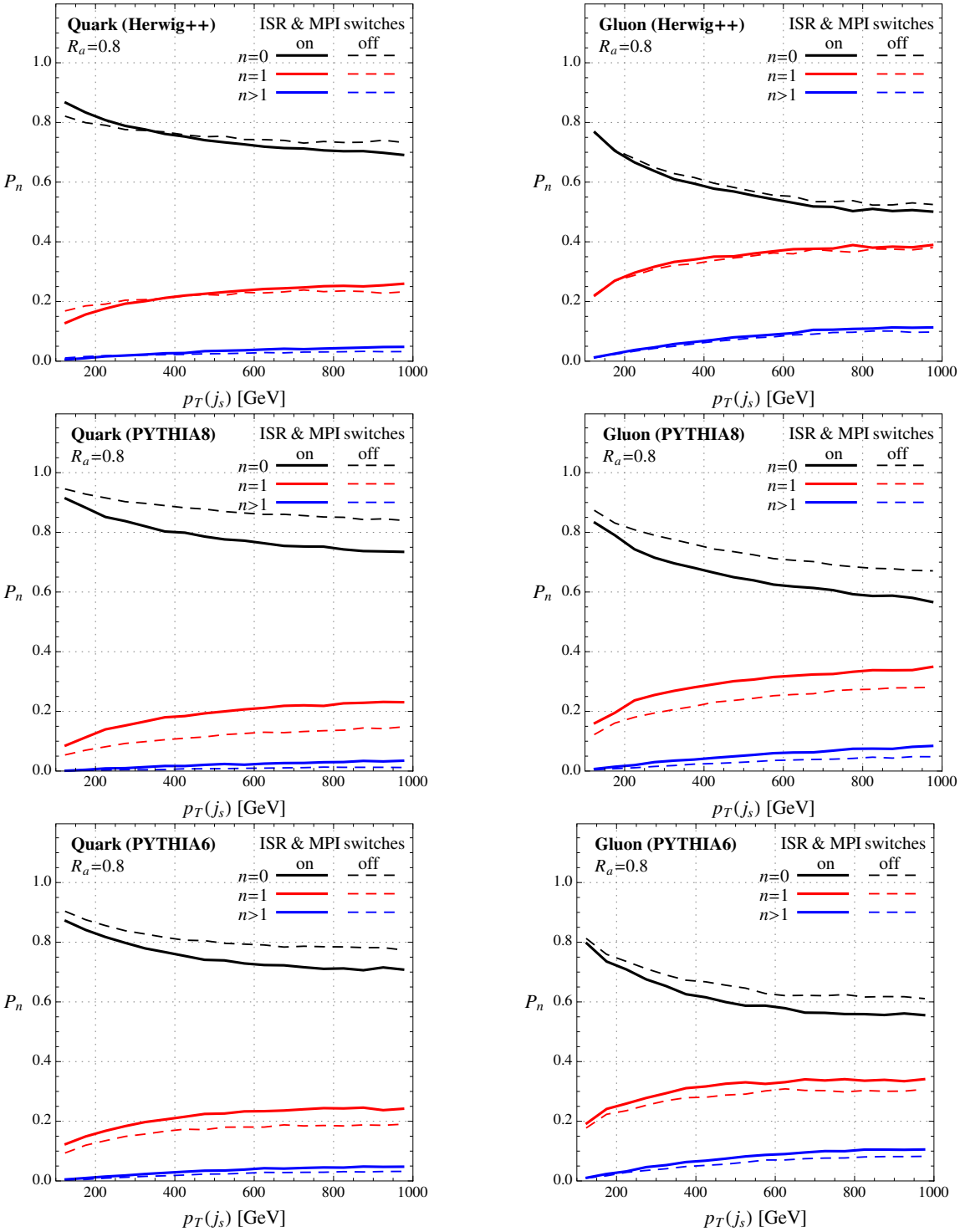

Figure 3. Comparison of the `Herwig++`, `Pythia8` and `Pythia6` predictions for associated jet rates with and without ISR and MPI, as a function of $p_T(j_s)$: for quark jets (left), and gluon jets (right). Here, $p_T(j_s)$ is the vector sum of the leading jet and associated jet p_T's.

JHEP04(2015)131

($n_{\rm ch}$), the jet width [1] and energy-energy-correlation (EEC) angularity [4]. The jet width is defined as

$$w = \frac{\sum_i p_{T,i} \times \Delta R(i,\ \text{jet})}{\sum_i p_{T,i}} \tag{4.1}$$

where the sum goes over all the tracks associated to the jet. A similar track-based EEC variable, denoted by $C_1^{(\beta)}$ can be defined as

$$C_1^{(\beta)} = \frac{\sum_i \sum_j p_{T,i} \times p_{T,j} \times (\Delta R(i,j))^\beta}{(\sum_i p_{T,i})^2}. \tag{4.2}$$

Here again the sum over i and j run over all the tracks associated to the jet with $j > i$, while β is a tunable parameter. It has been demonstrated in ref. [3, 4] that smaller values of the exponent β leads to a better quark-gluon separation, and $\beta = 0.2$ is found to be optimal from perturbative calculations and MC studies based on `Herwig++` and `Pythia8` generators. We have compared the performance of the jet width variable w and the EEC variable $C_1^{(\beta=0.2)}$ in the multivariate analyses (MVA) to be discussed below, and find that in all cases $C_1^{(\beta=0.2)}$ leads to a better separation of gluons from quarks. Therefore, in the following, we only show results based on $n_{\rm ch}$ (with each charged track having $p_T > 1\,\text{GeV}$) and $C_1^{(\beta=0.2)}$. In addition, we shall include the associated jet information as well as the jet mass variable and compare the performance of the different MVA methods. As seen in the previous section, for $n = 1$ or $n > 1$, the probability of finding n associated jets, P_n, is significantly larger for gluon jets compared to quark-initiated ones across the whole p_T range of interest. Therefore, the presence (or absence) of an associated jet within a certain distance R_a of a high-p_T jet can be used to further improve the separation.

As the boundary between the signal and background regions in the hyper-surface spanned by the variables is non-linear, it is beneficial to adopt a multivariate analysis strategy as compared to a cut-based one. For this purpose, we employed a Boosted Decision Tree (BDT) algorithm with the help of the `TMVA-Toolkit` [33–35] in the `ROOT` framework. The training of the classifier was performed with $Z + q-$jet and $Z + g-$jet samples, and we generated the above MC samples uniformly distributed in jet-p_T.[6] The input variables for the two variable training are taken to be $n_{\rm ch}$ and $C_1^{(\beta=0.2)}$, while for three-variable trainings we further include the variable $m_J/p_{T,J}$, where m_J is the jet mass and $p_{T,J}$ is the transverse momentum of the leading jet. The information on the number of associated jets is included in the form of two categories ($n = 0$ or $n \geq 1$) in the MVA.

It should be emphasized that the MC prediction of the discrimination variables, especially the number of charged tracks $n_{\rm ch}$ is quite sensitive not only to the parton shower (PS) algorithm adopted and the related parameters, but also to the tuning of the hadronization and underlying event models. This is expected, since $n_{\rm ch}$ is not an infrared safe quantity, and only the ratio $n_{\rm ch}^{\rm gluon}/n_{\rm ch}^{\rm quark}$ converges rather slowly to the ratio of the colour factors C_A/C_F for high jet p_T [36, 37]. The disagreement between different MC's can therefore be reduced only by appropriate tuning at the LHC energies. With this limitation of the MC

[6] The MC event samples for the training of the classifier were generated in the same manner as for the associated jet rate computation in the previous section, but with a smaller step size of 10 GeV for the minimum $p_T(j_s)$ thresholds.

JHEP04(2015)131

predictions in view, in this study, we compare the performance of different MVA methods within the same MC generator to estimate the improvement in adding associated jet related observables. We also show the quark-gluon separation as predicted by the different MC's for comparison. In appendix A we present details of the distributions of the discrimination variables and the differences between the MC predictions for them.

4.2 Performance in MVA

Based on the BDT analysis, we obtain the efficiencies of tagging quark (ϵ_q) and gluon jets (ϵ_g) as a function of the cut on the BDT score. It is more useful to compare the ratio of the tagging efficiencies as a function of ϵ_q, in order to judge the separation power of a "quark-rich signal" from a "gluon-rich" background. In figures 4–6 (left column) we show the ratio of the quark and gluon tagging efficiencies, ϵ_q/ϵ_g as a function of ϵ_q, for $400 < p_T(j_s) < 500\,\text{GeV}$, with the event samples generated with all the three MC codes. Four different MVA methods are shown corresponding to different choices for the discrimination variables:

- **Method-1:** Two variables, n_{ch} and C_1 with $\beta = 0.2$.
- **Method-2:** Two variables, n_{ch} and C_1 with $\beta = 0.2$, with two categories determined in terms the number of associated jets ($n = 0$ or $n \geq 1$).
- **Method-3:** Three variables, n_{ch}, C_1 with $\beta = 0.2$ and $m_J/p_{T,J}$.
- **Method-4:** Three variables, n_{ch}, C_1 with $\beta = 0.2$ and $m_J/p_{T,J}$, with two categories determined in terms the number of associated jets ($n = 0$ or $n \geq 1$).

We can quantify the improvement in quark-gluon separation using ϵ_g(Method-1)/ϵ_g(Method-{2,3,4}) as a function of ϵ_q, as shown in figures 4–6 (right). For example, for an operating point of $\epsilon_q = 0.4$, we can obtain an improvement of around 10%, 15% and 20% using Methods-2,3 and 4 respectively, when compared to Method-1. The differences between the improvement factors obtained using the three MC's are found to be small.

In order to estimate the change in tagger performance as we consider lower p_T jets, we show in figure 7 the same results as in figure 4, but now with $150 < p_T(j_s) < 200\,\text{GeV}$. The improvement on adding associated jet rates is still appreciable, although it is somewhat reduced compared to the higher p_T range. The fluctuations in the ϵ_g ratio for lower values of ϵ_q in figure 7 are due to low MC statistics.

We can see in figures 4–6 that there is an improvement in going from a two variable analysis to a three variable one by including the variable $m_J/p_{T,J}$. This can be understood as follows. The jet mass variable is related to $C_1^{(\beta=2)}$, as can be seen by writing both of them in terms of the z, θ variables for the hardest emission inside the jet cone: $m_J^2 \simeq z(1-z)\theta^2 p_{TJ}^2$. Furthermore, $C_1^{(\beta=2)}$ and $C_1^{(\beta=0.2)}$ are two independent variables belonging to the C_1 class which carry all the information on this hardest emission, and including both of them improves the tagger performance. For this reason, further addition of a third variable in the C_1 class does not change the performance appreciably, a fact that we explicitly checked by a separate MVA analysis. There is a further improvement in the

JHEP04(2015)131

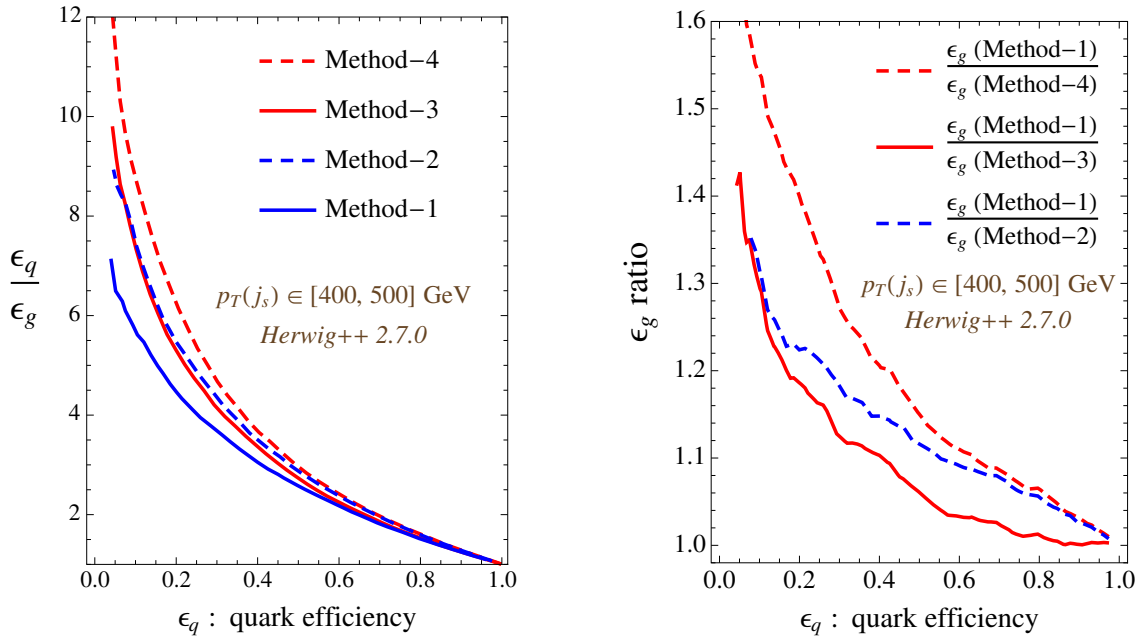

Figure 4. The ratio of the quark and gluon tagging efficiencies, ϵ_q/ϵ_g as a function of ϵ_q, for $400 < p_T(j_s) < 500\,\text{GeV}$, as determined by MC simulations with `Herwig++` (left column). The different MVA methods, determined in terms of the input variables are explained in the text. To quantify the improvement in quark gluon separation as we go to Methods 2,3 and 4, we show $\epsilon_g(\text{Method-1})/\epsilon_g(\text{Method-}\{2,3,4\})$ as a function of ϵ_q as well (right column).

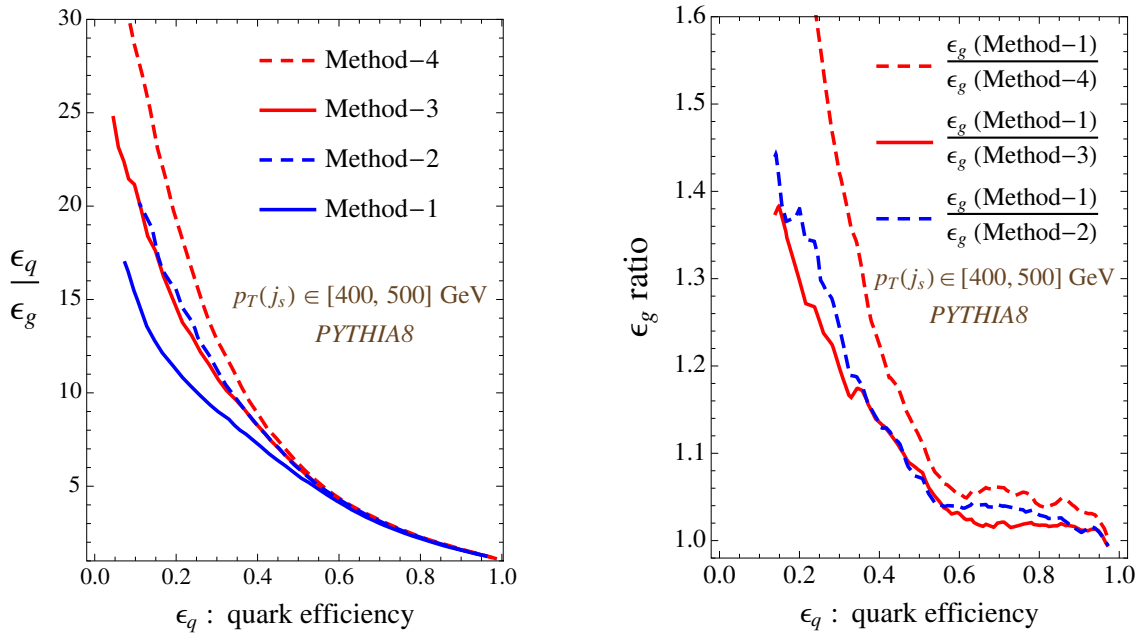

Figure 5. Same as figure 4, with MC simulations using `Pythia8`.

JHEP04(2015)131

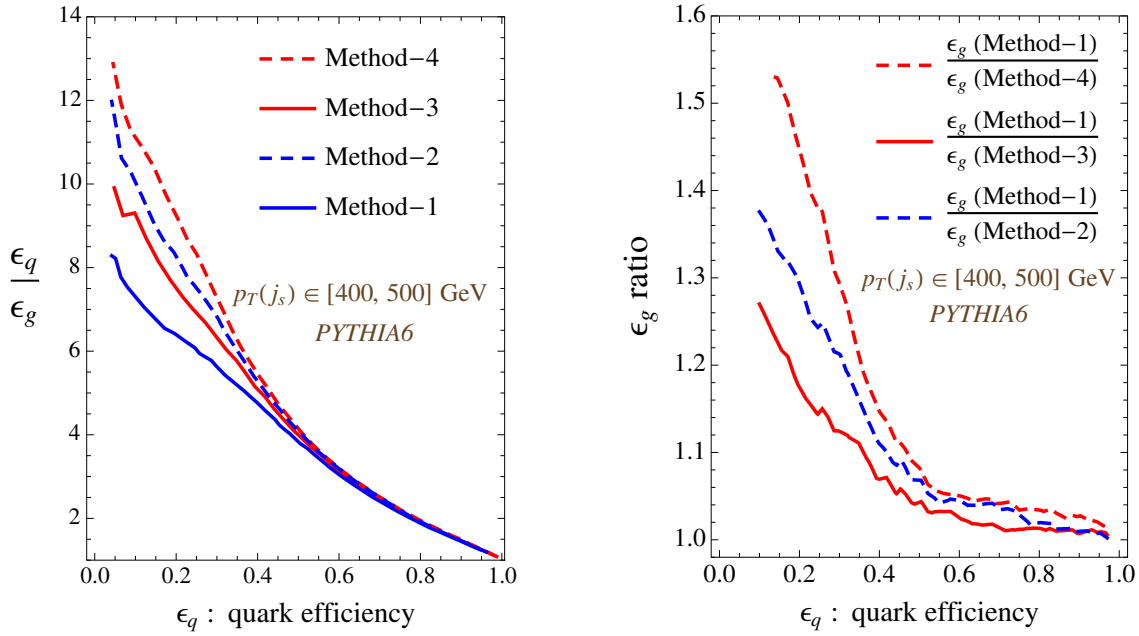

Figure 6. Same as figure 4, with MC simulations using `Pythia6`.

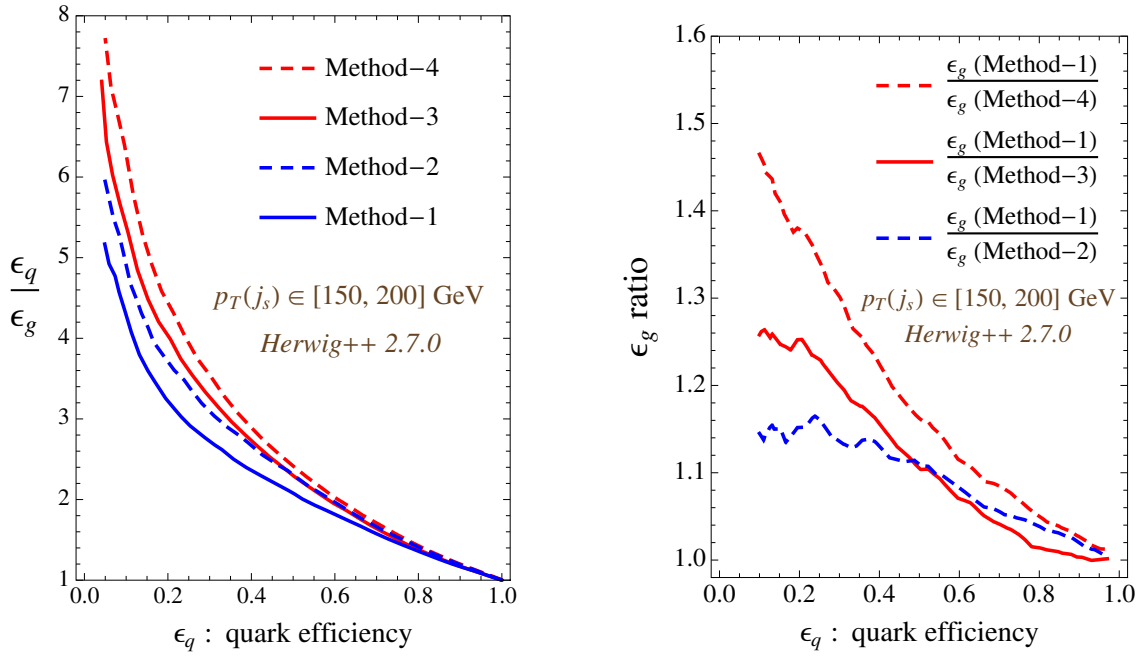

Figure 7. Same as figure 4, for a lower range of jet p_T, $150 < p_T(j_s) < 200\,\text{GeV}$. Results using only `Herwig++` are shown.

quark-gluon separation when the number of associated jets information is included at the level of categories in both the two and three variable MVA analyses. Since the associated jet rates carry the additional information of radiation outside the jet cone, Methods 2 and 4 lead to further improvements as compared to Methods 1 and 3, respectively.

JHEP04(2015)131

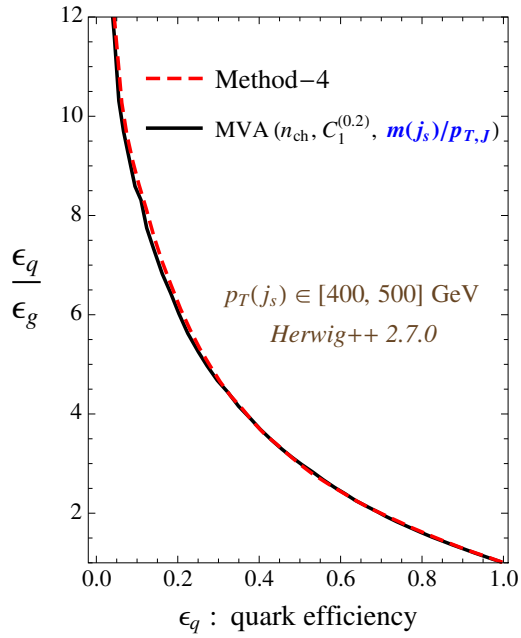

Figure 8. Comparison of Method 4 which includes $m_J/p_{T,J}$ and the associated jet rates as categories in the MVA, and the alternative method of including the associated jet rate information by using the modified jet mass variable $m(j_s)/p_{T,J}$. Both methods lead to the same MVA performance.

Method 4 leads to the best performance out of the four different MVA's considered. In fact, we find that there is an alternative way to include the associated jet rates information in Method 4 by using the modified jet mass variable $m(j_s)/p_{T,J}$ in Method 3. Here, $m(j_s)$ is the jet mass computed by adding the leading jet and associated jet four momenta. Because of a larger associated jet rate, for the same $p_T(j_s)$, $m(j_s)$ is higher for a gluon jet compared to a quark, while $p_{T,J}$ is lower. Therefore, using either associated jet rate categories and $m_J/p_{T,J}$, or using only the variable $m(j_s)/p_{T,J}$ leads to the same MVA performance, as shown in figure 8.

5 Subjet rates in jets: analytical calculations

The number of charged tracks inside a jet cone, $n_{\rm ch}$ (with each track having transverse momentum above a threshold, usually taken to be around 1 GeV) is often used as a good discriminating variable. However, as mentioned earlier, the MC predictions for this observable are quite sensitive not only to the parton shower (PS) algorithm and the related parameters, but also to the tuning of the hadronization and underlying event models. On the other hand, we find that the number of subjets of a primary jet leads to a more uniform prediction across the MC's, and thus can be better suited in quark gluon separation studies. The number of subjets as a quark-gluon separation variable was considered earlier in ref. [1]. In this study, we compute the subjet rates to NDLA accuracy, and show a detailed comparison with different MC's.

JHEP04(2015)131

We find the *subjets* of jet j with the *exclusive* k_t *algorithm*, which applies the dimensionless distance measure

$$y_{ik} = \min\{p_{ti}^2, p_{tk}^2\} \frac{\Delta R_{ik}^2}{R^2 p_j^2} \,, \tag{5.1}$$

to its constituent objects and clusters them as discussed for a generalized k_t algorithm in section 2, until the smallest y_{ik} is above $y_{\rm cut}$. Thus the subjet rates are functions of the jet $p_t = p_j$, the jet radius R, and $y_{\rm cut}$.

In this section, we compute the subjet rates to NDLA, i.e. considering double and next-to-double logarithms, $\alpha_{\rm S}^n L^{2n}$ and $\alpha_{\rm S}^n L^{2n-1}$, where now $L = \ln(1/y_{\rm cut})$. The relevant generating functions in this case are those given in refs. [10, 21]:

$$\phi_q(u,Q) = u\,\Delta_q(Q) \exp\left(\int_{Q_0}^{Q} dq\,\Gamma_q(Q,q)\phi_g(u,q)\right) \,, \tag{5.2}$$

$$\phi_g(u,Q) = u\,\Delta_g(Q) \exp\left(\int_{Q_0}^{Q} dq\left[\Gamma_g(Q,q)\phi_g(u,q) + \Gamma_f(q)\frac{\phi_q(u,q)^2}{\phi_g(u,q)}\right]\right) \tag{5.3}$$

where $Q = R\,p_j$ is the jet scale, $Q_0 = R\,p_j\sqrt{y}_{\rm cut}$ is the resolution scale,[7]

$$\Gamma_q(Q,q) = \frac{2C_F}{\pi}\frac{\alpha_{\rm S}(q^2)}{q}\left(\ln\frac{Q}{q} - \frac{3}{4} + \frac{q}{Q} - \frac{1}{4}\frac{q^2}{Q^2}\right) \,, \tag{5.4}$$

$$\Gamma_g(Q,q) = \frac{2C_A}{\pi}\frac{\alpha_{\rm S}(q^2)}{q}\left(\ln\frac{Q}{q} - \frac{11}{12} + \frac{q}{Q} - \frac{1}{4}\frac{q^2}{Q^2} + \frac{1}{6}\frac{q^3}{Q^3}\right) \,, \tag{5.5}$$

$$\Gamma_f(q) = \frac{n_f}{3\pi}\frac{\alpha_{\rm S}(q^2)}{q}\left(1 - \frac{3}{2}\frac{Q_0}{q} + \frac{3}{2}\frac{Q_0^2}{q^2} - \frac{Q_0^3}{q^3}\right) \,. \tag{5.6}$$

The Sudakov factors for no resolvable emission are now

$$\Delta_q(Q) = \exp\left(-\int_{Q_0}^{Q} dq\,\Gamma_q(Q,q)\right) \,, \tag{5.7}$$

$$\Delta_q(Q) = \exp\left(-\int_{Q_0}^{Q} dq\,[\Gamma_g(Q,q) + \Gamma_f(q)]\right) \,. \tag{5.8}$$

Hence the rates for 1, 2 or 3 subjets in a quark jet are:

$$\begin{aligned}
R_1^q &= \Delta_q(Q)\,, \\
R_2^q &= \Delta_q(Q)\int_{Q_0}^{Q} dq\,\Gamma_q(Q,q)\Delta_g(q)\,, \\
R_3^q &= \Delta_q(Q)\int_{Q_0}^{Q} dq \int_{Q_0}^{q} dq'\,\Gamma_q(Q,q)\Delta_g(q)\,\times \\
&\quad \left\{\left[\Gamma_q(Q,q') + \Gamma_g(q,q')\right]\Delta_g(q') + \Gamma_f(q')\Delta_f(q')\right\} \,,
\end{aligned} \tag{5.9}$$

[7] Here again we keep power-suppressed corrections in order to satisfy boundary conditions.

JHEP04(2015)131

where $\Delta_f = \Delta_q^2/\Delta_g$, and for a gluon jet we have

$$
\begin{aligned}
R_1^g &= \Delta_g(Q)\,, \\
R_2^g &= \Delta_g(Q) \int_{Q_0}^{Q} dq \left[\Gamma_g(Q,q)\Delta_g(q) + \Gamma_f(q)\Delta_f(q)\right]\,, \\
R_3^g &= \Delta_g(Q) \int_{Q_0}^{Q} dq \int_{Q_0}^{q} dq' \Big[\Gamma_g(Q,q)\Delta_g(q) \times \\
&\quad \left\{\left[\Gamma_g(Q,q') + \Gamma_g(q,q')\right]\Delta_g(q') + \Gamma_f(q')\Delta_f(q')\right\} + \Gamma_f(q)\Delta_f(q) \times \\
&\quad \left\{\left[\Gamma_g(Q,q') - \Gamma_g(q,q')\right]\Delta_g(q') + 2\Gamma_q(q,q')\Delta_q(q')\right\}\Big]\,.
\end{aligned}
\tag{5.10}
$$

6 Subjet rates in jets: comparison with Monte Carlo

We now compare the above results with Monte Carlo predictions. MC samples of quark and gluon jets were prepared for the subjet analysis using the same setup as in the associated jet study in section 2, however, detector effects and minimum p_T cuts for the charged and neutral hadrons were not included for this analysis. In this sense, our study of the subjet rates should be taken as illustrative, and we do not include the subjet rates in an MVA analysis in this paper. As we shall see in the following, one needs to go down to at least $L = 4$ to have some discrimination power. This corresponds to going down to 0.1 for ΔR resolution, which is the typical size of calorimeter cells, although the ΔR separation of subjets would be larger when the subjet p_T is smaller compared to the primary jet p_T. Therefore, in a proper analysis, combining track and calorimeter information is essential, and a detailed experimental study is necessary, which is beyond the scope of this paper.

Figure 9 shows comparisons between the resummed results of eqs. (5.9), (5.10) and the MC results for jets with $p_{T,J} \in [500, 600]\,\text{GeV}$ and $R = 0.4$. For quark jets the different MC's agree quite well with each other and with the resummed calculations, the MC predictions being somewhat below the resummed 1-subjet rate for $L > 4$, and vice-versa for 2 subjets. Hadronization effects are small for $L < 7$, after which the 1- and 2-subjet rates are suppressed and the higher subjet rates are therefore enhanced. At this value of $R\,p_{Tj}$, $L = 7$ corresponds to resolving subjets with $\min\{p_{ti}, p_{tj}\}\Delta R_{ij} \sim 6\,\text{GeV}$.

For gluon jets the agreement between the resummed results and the Monte Carlos is still quite close for 1 subjet. For 2 and 3 subjets the peak rates are in roughly the same place but have higher values than the resummed ones, with the effect that the rate for 4 or more subjets is substantially suppressed. Once again the hadronization effects are small for $L < 7$, after which the 1- and 2-subjet rates are suppressed and the higher subjet rates are enhanced, actually bringing the latter into close agreement with the analytical calculations.

In conclusion, the fairly good agreement between the Monte Carlos and the resummed 1-, 2- and 3-subjet rates for $R = 0.4$ and L not too large ($L < 5$, subjet resolution above about 15 GeV) suggests that in this range those subjet rates can be used for quark-gluon discrimination. At larger jet radii, the agreement remains similar, as we have checked using $R = 0.8$.

JHEP04(2015)131

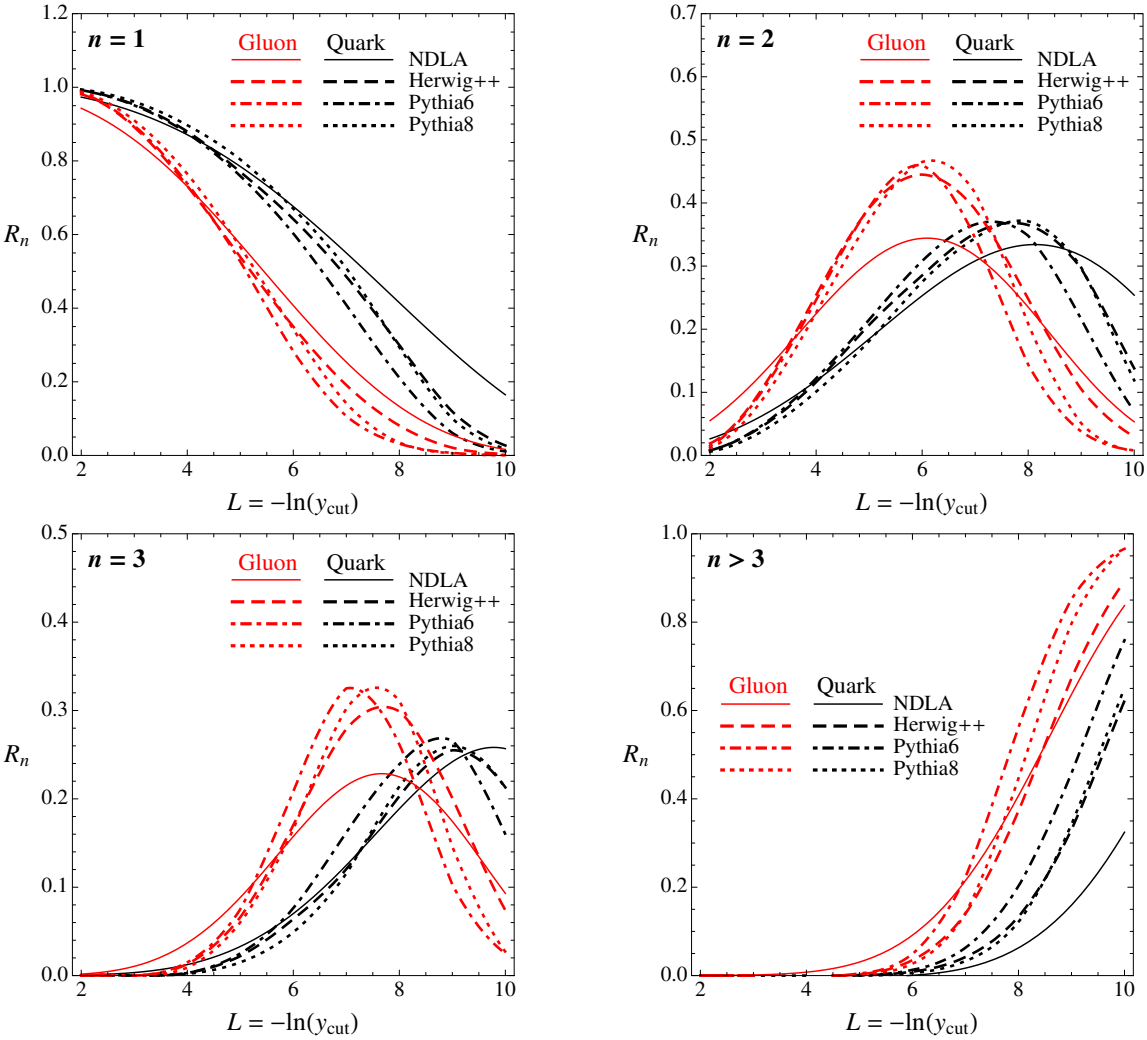

Figure 9. Subjet rates R_n with $n = 1, 2, 3$ and $n > 3$ as a function of $L = -\ln(y_{\rm cut})$, for quark jets (black) and gluon jets (red), with $p_{T,J} \in [500, 600]$ GeV, $R = 0.4$. Curves are `Herwig++` (dashed), `Pythia6` (dot-dashed), `Pythia8` (dotted) and NDLA resummed (solid).

7 Summary

To summarize our findings, we show that in studies of light quark and gluon jet separation at the LHC, it is important to include the information on associated jet rates around a primary hard jet. Associated jet rates are defined as the probability of finding at least one softer reconstructed jet around the primary hard jet under consideration. This probability is found to be substantially higher for a gluon-initiated jet compared to a quark-initiated one. Since commonly a small jet radius parameter is adopted in LHC studies of hadronic jets, the associated jet rates carry the information on the radiation outside the chosen jet radius.

We compute the associated jet rates up to NDLA accuracy in perturbative QCD, as a function of the primary jet and minimum associated jet p_T's, as well as the jet radius and

JHEP04(2015)131

association radius parameters. The NDLA results are thereafter compared with predictions from different parton shower MC's. Since the NDLA predictions include only the time-like showering of the final state partons, we demonstrate the effects of ISR and MPI in the MC predictions as well, and it is observed that the NDLA predictions are closer to the MC's when ISR and MPI are switched off. Overall, the associated jet rates are not very sensitive to these effects as long as the association radius is not too large.

The probability of having at least one associated jet for a primary gluon jet is roughly a factor of two larger than for a quark jet, with a small variation in this number as a function of the jet p_T. This fact makes the presence or absence of associated jets a good variable for quark-gluon discrimination studies. We demonstrate the impact of including the associated jet rate information by including this variable in an MVA analysis, along with the well-studied variables of number of charged tracks, energy-energy-correlation angularities and jet mass. Comparing different two and three variable MVA's with and without the associated jet information, we find that including the associated jets leads to an improvement of around 10% in rejecting gluons, for a fixed quark selection efficiency of 0.4. We also show that using a three variable MVA with associated jet categories leads to the best performance, with an improvement of 20% in rejecting gluons, for the same quark efficiency as above.

Since for the number of charged tracks variable the MC predictions tend to differ, and are dependent on the parton shower and underlying event parameter tunes, we explore the number of k_t subjets of an anti-k_t jet as a quark-gluon separation variable. We compute the number of subjets to NDLA accuracy, and compare the resummed predictions with different MC's. The different MC predictions are found to be rather uniform, with the resummed predictions being broadly in agreement with them. However, for gluon jets the peak rates for 2 and 3 subjets are found to be lower in the resummed computation, which might arise due to higher-order effects that are in general bigger for gluons.

Acknowledgments

This work is supported by JSPS KAKENHI No. 26287039 and Grant- in-Aid for Scientific research from the Ministry of Education, Science, Sports, and Culture (MEXT), Japan, No. 23104006, and also by the World Premier International Research Center Initiative (WPI Initiative), MEXT, Japan. The work of B. Bhattacherjee is supported by the Department of Science and Technology, Government of INDIA, under the Grant Agreement numbers IFA13-PH-75 (INSPIRE Faculty Award). B.R. Webber thanks the Kavli IPMU for hospitality during part of this work.

A Distributions of discrimination variables

In figures 10–12 we show 2-dimensional plots of the joint distributions of the three discrimination variables used in the MVA presented in section 4, for the two Monte Carlo event generators `Herwig++` and `Pythia8`. The following features may be observed:

JHEP04(2015)131

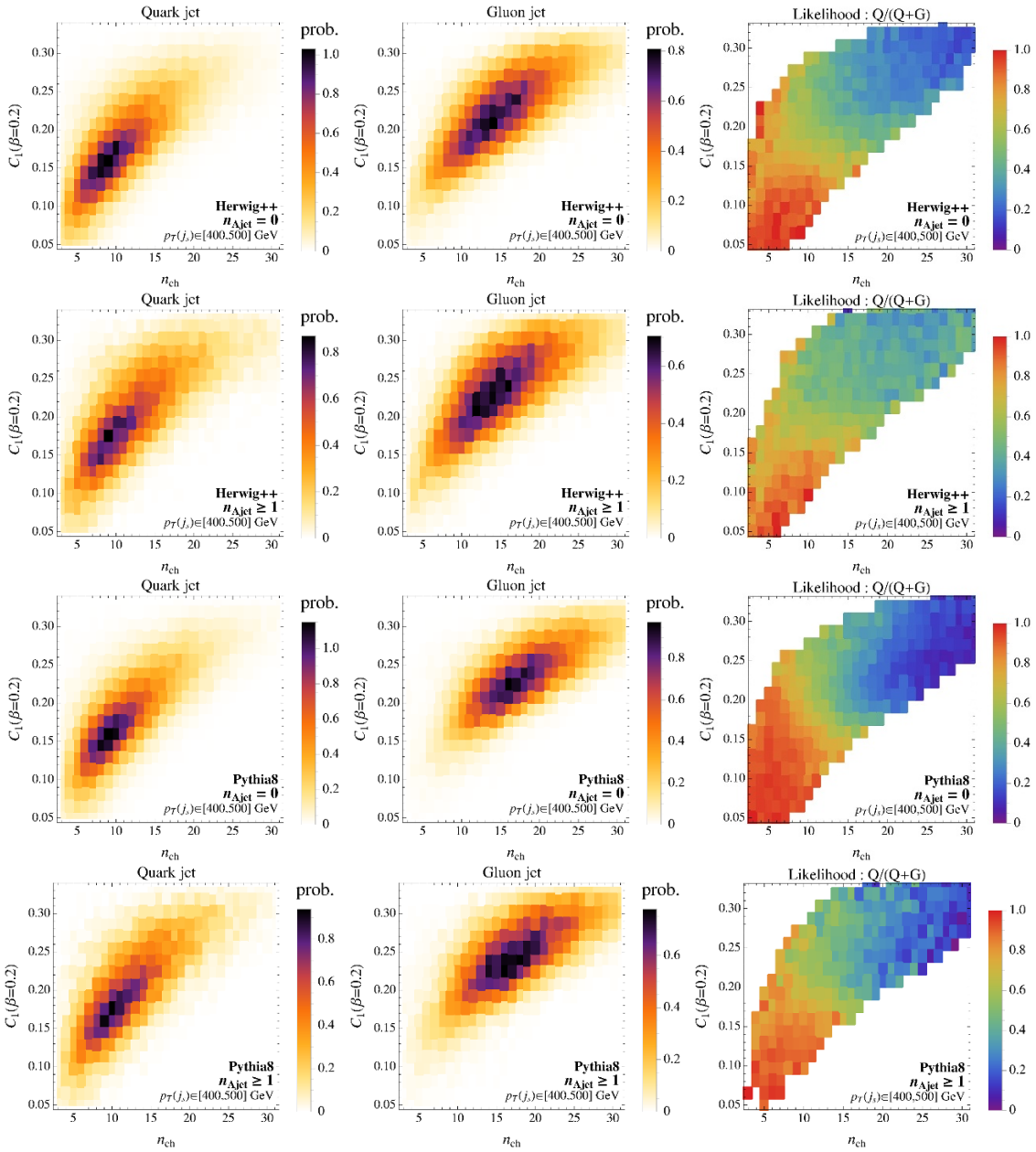

Figure 10. Joint distributions of $n_{\rm ch}$ and $C_1^{(\beta=0.2)}$ in `Herwig++` and `Pythia8`, for quark and gluon jets with $p_T(j_s) \in [400, 500]$ GeV having $n_{\rm Ajet} = 0$ and ≥ 1 associated jets.

- There are differences between the distributions predicted by the two Monte Carlos, those of `Pythia8` being somewhat narrower for quark jets and substantially narrower for gluon jets.

- The distributions of the infrared-unsafe variable $n_{\rm ch}$ show the greatest differences, with those of `Pythia8` being larger at high $n_{\rm ch}$. This could be due to differences in tuning of the non-perturbative parameters of the generators.

JHEP04(2015)131

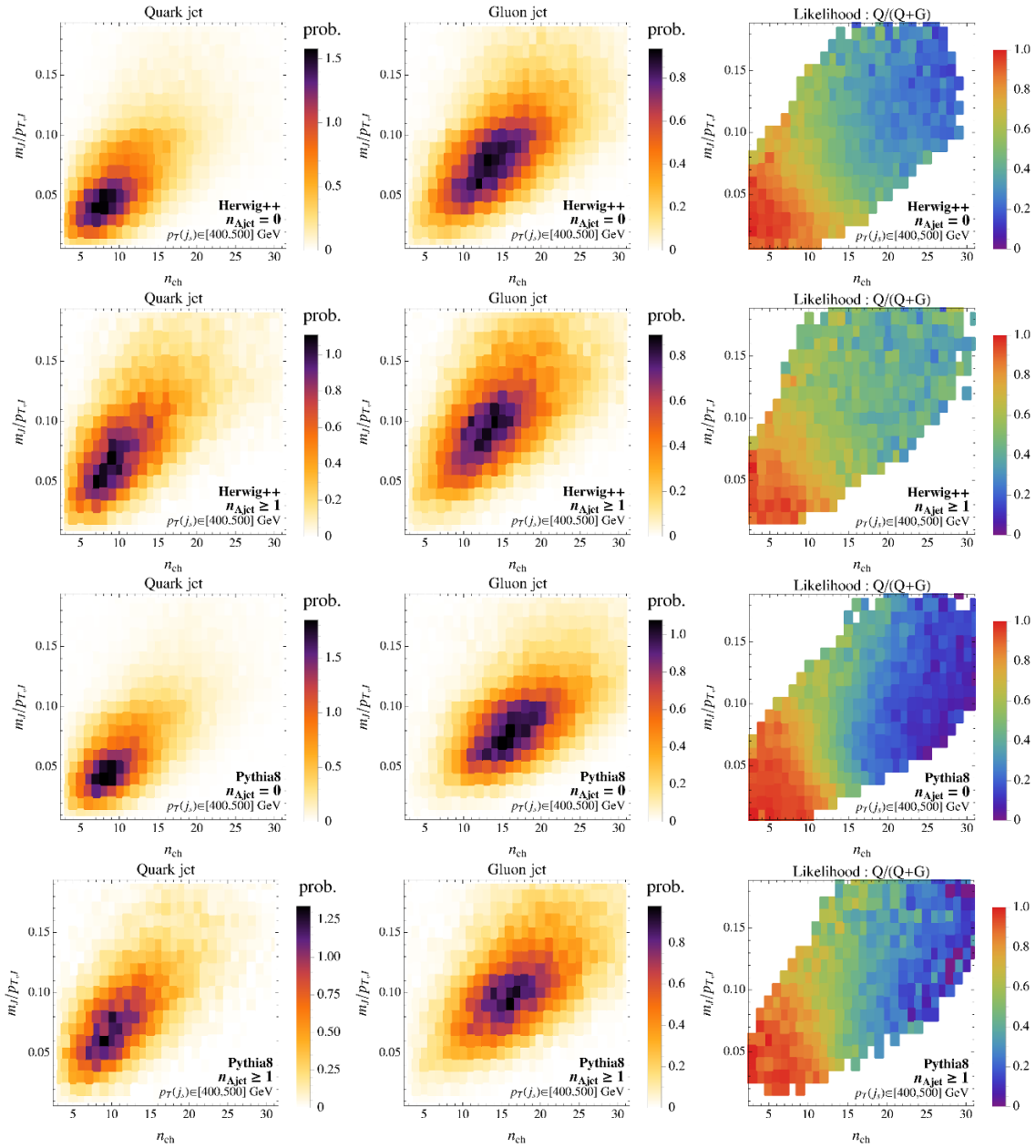

Figure 11. Joint distributions of $n_{\rm ch}$ and $m_J/p_{T,J}$ in `Herwig++` and `Pythia8`, for quark and gluon jets with $p_T(j_s) \in [400, 500]$ GeV having $n_{\rm Ajet} = 0$ and ≥ 1 associated jets.

- The above features are reflected in the likelihood plots, showing the probability ratio $P_q/(P_q + P_g)$, and account for the higher discrimination efficiency predicted by `Pythia8` (figure 5 vs figure 4).
- The quark-gluon discrimination in the events with associated jets is weaker than that for $n_{\rm Ajet} = 0$. This is expected because the events are selected according to $p_T(j_s)$, the sum of leading and associated jet p_T's. Therefore those with associated jets have leading jets with lower p_T's, which have lower discriminating power.

JHEP04(2015)131

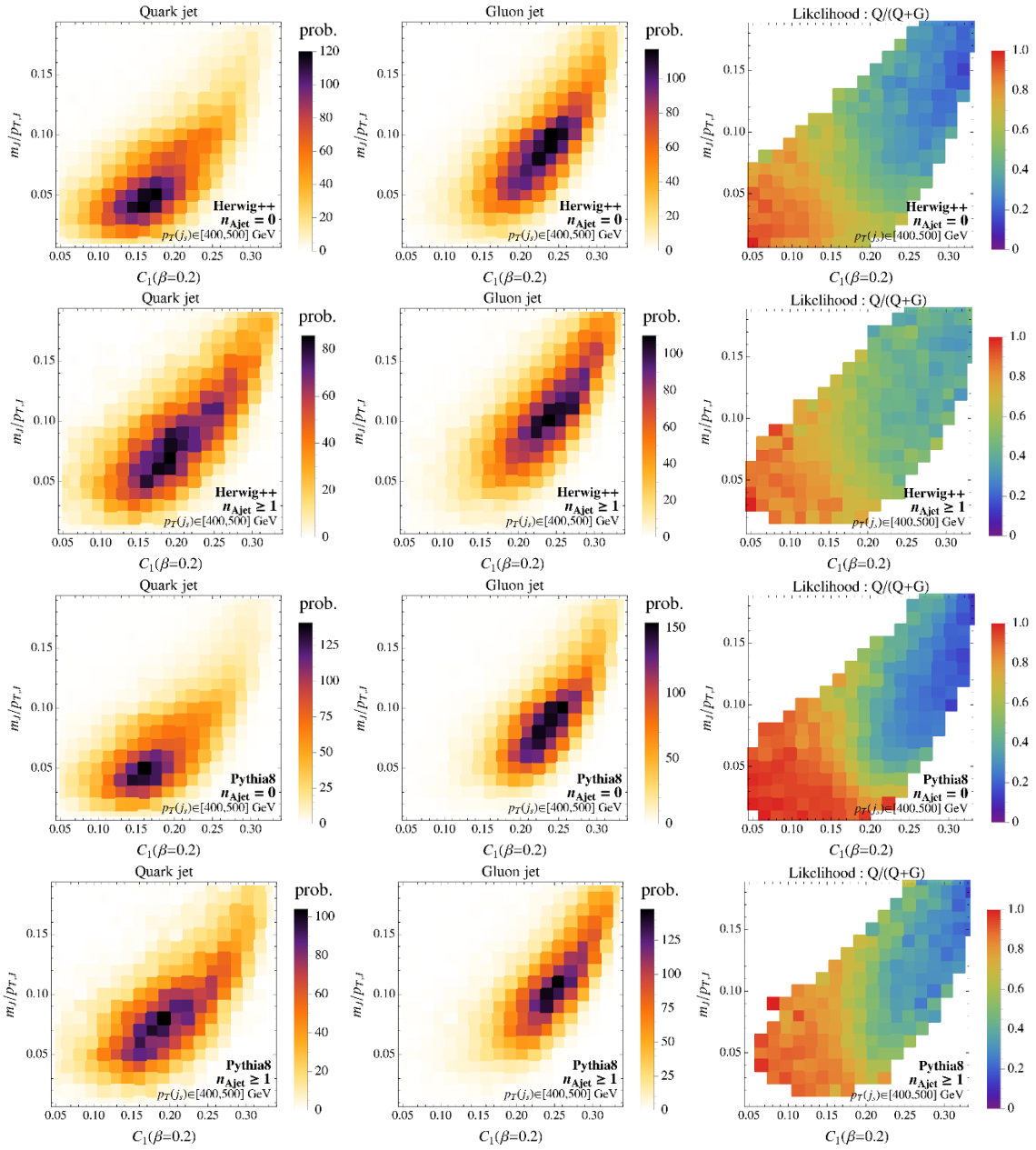

Figure 12. Joint distributions of $C_1^{(\beta=0.2)}$ and $m_J/p_{T,J}$ in `Herwig++` and `Pythia8`, for quark and gluon jets with $p_T(j_s) \in [400, 500]$ GeV having $n_{\rm Ajet} = 0$ and ≥ 1 associated jets.

- Nevertheless the inclusion of the associated jet category improves the MVA performance, because the probability of an associated jet is lower for quark jets.

JHEP04(2015)131

Open Access. This article is distributed under the terms of the Creative Commons Attribution License (CC-BY 4.0), which permits any use, distribution and reproduction in any medium, provided the original author(s) and source are credited.

References

[1] J. Gallicchio and M.D. Schwartz, *Quark and Gluon Tagging at the LHC*, *Phys. Rev. Lett.* **107** (2011) 172001 [arXiv:1106.3076] [INSPIRE].

[2] J. Gallicchio et al., *Multivariate discrimination and the Higgs + W/Z search*, *JHEP* **04** (2011) 069 [arXiv:1010.3698] [INSPIRE].

[3] J. Gallicchio and M.D. Schwartz, *Quark and Gluon Jet Substructure*, *JHEP* **04** (2013) 090 [arXiv:1211.7038] [INSPIRE].

[4] A.J. Larkoski, G.P. Salam and J. Thaler, *Energy Correlation Functions for Jet Substructure*, *JHEP* **06** (2013) 108 [arXiv:1305.0007] [INSPIRE].

[5] A.J. Larkoski, J. Thaler and W.J. Waalewijn, *Gaining (Mutual) Information about Quark/Gluon Discrimination*, *JHEP* **11** (2014) 129 [arXiv:1408.3122] [INSPIRE].

[6] ATLAS collaboration, *Light-quark and gluon jet discrimination in pp collisions at* $\sqrt{s} = 7$ TeV *with the ATLAS detector*, *Eur. Phys. J.* **C 74** (2014) 3023 [arXiv:1405.6583] [INSPIRE].

[7] CMS collaboration, *Performance of quark/gluon discrimination in 8 TeV pp data*, CMS-PAS-JME-13-002 (2013).

[8] M. Dasgupta, L. Magnea and G.P. Salam, *Non-perturbative QCD effects in jets at hadron colliders*, *JHEP* **02** (2008) 055 [arXiv:0712.3014] [INSPIRE].

[9] G.P. Salam, *Towards Jetography*, *Eur. Phys. J.* **C 67** (2010) 637 [arXiv:0906.1833] [INSPIRE].

[10] S. Catani, Y.L. Dokshitzer, M. Olsson, G. Turnock and B.R. Webber, *New clustering algorithm for multi - jet cross-sections in* e^+e^- *annihilation*, *Phys. Lett.* **B 269** (1991) 432 [INSPIRE].

[11] S. Catani, Y.L. Dokshitzer, M.H. Seymour and B.R. Webber, *Longitudinally invariant* K_t *clustering algorithms for hadron hadron collisions*, *Nucl. Phys.* **B 406** (1993) 187 [INSPIRE].

[12] S.D. Ellis and D.E. Soper, *Successive combination jet algorithm for hadron collisions*, *Phys. Rev.* **D 48** (1993) 3160 [hep-ph/9305266] [INSPIRE].

[13] M. Cacciari, G.P. Salam and G. Soyez, *The Anti-k(t) jet clustering algorithm*, *JHEP* **04** (2008) 063 [arXiv:0802.1189] [INSPIRE].

[14] Y.L. Dokshitzer, G.D. Leder, S. Moretti and B.R. Webber, *Better jet clustering algorithms*, *JHEP* **08** (1997) 001 [hep-ph/9707323] [INSPIRE].

[15] M. Wobisch and T. Wengler, *Hadronization corrections to jet cross-sections in deep inelastic scattering*, hep-ph/9907280 [INSPIRE].

[16] M. Wobisch, *Measurement and QCD analysis of jet cross sections in deep-inelastic positron proton collisions at* $\sqrt{s} = 300$ *GeV*, DESY-THESIS-2000-049 [INSPIRE].

[17] E. Gerwick, S. Schumann, B. Gripaios and B. Webber, *QCD Jet Rates with the Inclusive Generalized kt Algorithms*, *JHEP* **04** (2013) 089 [arXiv:1212.5235] [INSPIRE].

JHEP04(2015)131

[18] E. Gerwick and P. Schichtel, *Jet properties at high-multiplicity*, arXiv:1412.1806 [INSPIRE].

[19] K. Konishi, A. Ukawa and G. Veneziano, *Jet Calculus: A Simple Algorithm for Resolving QCD Jets*, *Nucl. Phys.* **B 157** (1979) 45 [INSPIRE].

[20] Y.L. Dokshitzer, V.A. Khoze, A.H. Mueller and S.I. Troian, *Basics of perturbative QCD*, Gif-sur-Yvette, France: Ed. Frontieres (1991).

[21] R.K. Ellis, W.J. Stirling and B.R. Webber, *QCD and collider physics*, *Camb. Monogr. Part. Phys. Nucl. Phys. Cosmol.* **8** (1996) 1 [INSPIRE].

[22] M. Bahr et al., *HERWIG++ Physics and Manual*, *Eur. Phys. J.* **C 58** (2008) 639 [arXiv:0803.0883] [INSPIRE].

[23] T. Sjöstrand, S. Mrenna and P.Z. Skands, *A Brief Introduction to PYTHIA 8.1*, *Comput. Phys. Commun.* **178** (2008) 852 [arXiv:0710.3820] [INSPIRE].

[24] T. Sjöstrand et al., *An Introduction to PYTHIA 8.2*, *Comput. Phys. Commun.* **191** (2015) 159 [arXiv:1410.3012] [INSPIRE].

[25] J. Pumplin et al., *New generation of parton distributions with uncertainties from global QCD analysis*, *JHEP* **07** (2002) 012 [hep-ph/0201195] [INSPIRE].

[26] A. Sherstnev and R.S. Thorne, *Different PDF approximations useful for LO Monte Carlo generators*, arXiv:0807.2132 [INSPIRE].

[27] S. Ovyn, X. Rouby and V. Lemaitre, *DELPHES, a framework for fast simulation of a generic collider experiment*, arXiv:0903.2225 [INSPIRE].

[28] M. Cacciari, G.P. Salam and G. Soyez, *FastJet User Manual*, *Eur. Phys. J.* **C 72** (2012) 1896 [arXiv:1111.6097] [INSPIRE].

[29] M. Cacciari and G.P. Salam, *Dispelling the N^3 myth for the k_t jet-finder*, *Phys. Lett.* **B 641** (2006) 57 [hep-ph/0512210] [INSPIRE].

[30] T. Sjöstrand, S. Mrenna and P.Z. Skands, *PYTHIA 6.4 Physics and Manual*, *JHEP* **05** (2006) 026 [hep-ph/0603175] [INSPIRE].

[31] D. Bertolini, T. Chan and J. Thaler, *Jet Observables Without Jet Algorithms*, *JHEP* **04** (2014) 013 [arXiv:1310.7584] [INSPIRE].

[32] A.J. Larkoski, D. Neill and J. Thaler, *Jet Shapes with the Broadening Axis*, *JHEP* **04** (2014) 017 [arXiv:1401.2158] [INSPIRE].

[33] A. Hocker et al., *TMVA - Toolkit for Multivariate Data Analysis*, *PoS* **ACAT** (2007) 040 [physics/0703039] [INSPIRE].

[34] P. Speckmayer, A. Hocker, J. Stelzer and H. Voss, *The toolkit for multivariate data analysis, TMVA 4*, *J. Phys. Conf. Ser.* **219** (2010) 032057 [INSPIRE].

[35] http://tmva.sourceforge.net.

[36] P. Bolzoni, B.A. Kniehl and A.V. Kotikov, *Gluon and quark jet multiplicities at N^3LO+NNLL*, *Phys. Rev. Lett.* **109** (2012) 242002 [arXiv:1209.5914] [INSPIRE].

[37] P. Bolzoni, B.A. Kniehl and A.V. Kotikov, *Average gluon and quark jet multiplicities at higher orders*, *Nucl. Phys.* **B 875** (2013) 18 [arXiv:1305.6017] [INSPIRE].

JHEP04(2015)131

PHYSICAL REVIEW D **90,** 075001 (2014)

Fingerprinting nonminimal Higgs sectors

Shinya Kanemura,[1,*] Koji Tsumura,[2,†] Kei Yagyu,[3,‡] and Hiroshi Yokoya[1,§]

[1]*Department of Physics, University of Toyama, Toyama 930-8555, Japan*
[2]*Division of Physics and Astronomy, Kyoto University, Kyoto 606-8502, Japan*
[3]*Department of Physics, National Central University, Chungli 32001, Taiwan*

(Received 12 June 2014; published 1 October 2014)

After the discovery of the standard model-like Higgs boson at the LHC, the structure of the Higgs sector remains unknown. We discuss how it can be determined by the combination of direct and indirect searches for additional Higgs bosons at future collider experiments. First of all, we evaluate expected excluded regions for the mass of additional neutral Higgs bosons from direct searches at the LHC with the 14 TeV collision energy in the two Higgs doublet models with a softly broken Z_2 symmetry. Second, precision measurements of the Higgs boson couplings at future experiments can be used for the indirect search of extended Higgs sectors if the measured coupling constant with the gauge boson slightly deviates from the standard model value. In particular, in the two Higgs doublet model with the softly broken discrete symmetry, there are four types of Yukawa interactions, so that they can be discriminated by measuring the pattern of deviations in Yukawa coupling constants. Furthermore, we can fingerprint various extended Higgs sectors with future precision data by detecting the pattern of deviations in the coupling constants of the standard model-like Higgs boson. We demonstrate how the pattern of deviations can be different among various Higgs sectors that predict the electroweak rho parameter to be unity, such as models with additional an isospin singlet, a doublet, triplets, or a septet. We conclude that, as long as the gauge coupling constant of the Higgs boson slightly differs from the standard model prediction but is enough to be detected at the LHC and its high-luminosity run or at the International Linear Collider, we can identify the nonminimal Higgs sector even without direct discovery of additional Higgs bosons at the LHC.

DOI: 10.1103/PhysRevD.90.075001 PACS numbers: 12.60.Fr

I. INTRODUCTION

The new particle discovered at the LHC in 2012 was identified as a Higgs boson [1]. With the current LHC data, its measured properties are consistent with those of the Higgs boson in the standard model (SM) [2–4]. On the other hand, so far, no evidence for new physics beyond the SM has been found directly at the LHC. Therefore, our standard picture for high-energy particle phenomena, which is based on the gauge theory with spontaneous symmetry breaking, seems successful.

However, it has been well known that the Higgs sector in the SM is problematic from the theoretical viewpoint. First of all, the existence of the scalar boson causes the hierarchy problem [5–7] so that many physicists try to understand the essence of the Higgs boson, e.g., elementary or composite particle. To solve the hierarchy problem, several scenarios for the new paradigm have been introduced such as supersymmetry, dynamical symmetry breaking, and extra dimensions. Each of them gives a different answer for the question of the essence of the Higgs boson. Second, there is no principle for the structure of the Higgs sector so that the minimal Higgs sector adopted in the SM is just an assumption. There are many possibilities of nonminimal Higgs sectors with additional scalar fields such as singlets, doublets, and triplets. A model based on the above-discussed paradigms can predict the specific structure and property of the Higgs sector. For example, the minimal supersymmetric SM (MSSM) predicts the Higgs sector with two isospin doublet scalar fields [8,9]. In addition, nonminimal Higgs sectors can also be introduced in new physics models to explain the origin of neutrino masses, the existence of dark matter and baryon asymmetry of the Universe, etc., which cannot be explained in the SM. Each new physics model predicts a characteristic structure for the Higgs sector. Therefore, if the Higgs sector is determined by experiments in the future, the new physics scenario can be selected from many candidates.

To probe the extended Higgs sectors, the simplest way is to directly search for additional Higgs bosons such as the second scalar boson. By measuring its properties, e.g., the mass, the electric charge, the spin, and the parity, important information to reconstruct the Higgs sector can be extracted. Nonobservation of the second Higgs boson gives the experimental constraint on the parameter space

*kanemu@sci.u-toyama.ac.jp
†ko2@gauge.scphys.kyoto-u.ac.jp
‡keiyagyu@ncu.edu.tw
§hyokoya@sci.u-toyama.ac.jp

 © 2014 American Physical Society

in the Higgs sector. Current bounds from searches for additional Higgs bosons at the LHC with the collision energy of 7 and 8 TeV can be found in Refs. [4,10–19].

In addition to the direct search results, precision measurements of various low-energy observables can be an indirect search for extended Higgs sectors, since the existence of additional Higgs multiplets can affect them. The electroweak rho parameter defined in terms of the masses of the W boson m_W and the Z boson m_Z, and the weak mixing angle θ_W by

$$\rho = \frac{m_W^2}{m_Z^2 \cos^2\theta_W}, \tag{1}$$

is one of the most important tools to constrain the structure of the Higgs sector, for which the experimental value is very close to unity; i.e., $\rho_{\rm exp} = 1.0004^{+0.0003}_{-0.0004}$ [20]. In the SM, the rho parameter is predicted to be unity at the tree level. In general, in extended Higgs sectors, predicted values for the rho parameter can deviate from unity. In the Higgs sector with an arbitrary number of scalar fields ϕ_i (a hypercharge Y_i and an isospin T_i) with vacuum expectation values (VEVs) v_i, the rho parameter is calculated at the tree level by [9]

$$\rho_{\rm tree} = \frac{\sum_i [T_i(T_i+1) - Y_i^2] v_i^2}{2\sum_i Y_i^2 v_i^2}. \tag{2}$$

From Eq. (2), an additional VEV of a Higgs field satisfying $T_i(T_i+1) - 3Y_i^2 = 0$ does not change the value of the rho parameter from the SM.[1] A VEV of a Higgs multiplet without satisfying the above equation, e.g., a triplet Higgs field, deviates $\rho_{\rm tree}$ from unity so that we need fine-tuning for such a VEV to avoid the constraint from $\rho_{\rm exp}$. However, even if the above equation is not satisfied, by allowing an alignment among VEVs, we can keep $\rho_{\rm tree} = 1$. The simplest realization is known as the Georgi-Machacek (GM) model [22] for which the Higgs sector is composed of additional real and complex triplet fields with $Y_i = 0$ and $Y_i = 1$, respectively.

The above discussion is very useful to discriminate extended Higgs sectors. However, the rho parameter has been measured quite precisely so that we need to take into account quantum effects to the rho parameter. Let us discuss how the rho parameter is modified at the one-loop level. The deviation of the rho parameter from unity measures the violation of the custodial $SU(2)_V$ symmetry [5,7,23] in the sector of particles in the loop.[2] For example, in the Yukawa Lagrangian, the custodial symmetry is broken by the mass splitting between the top and bottom quarks. As a result, the deviation of the rho parameter from unity $\Delta\rho \equiv \rho - 1$ due to the loop contribution of the top and bottom quarks takes a form of $\Delta\rho \propto (m_t - m_b)^2$. In fact, since $m_t \gg m_b$, there remains m_t^2 dependence in $\Delta\rho$. On the other hand, the Higgs potential in the SM respects the custodial symmetry so that the Higgs boson loop contribution is at most the logarithmic dependence of the Higgs boson mass through the hypercharge gauge interaction. However, in general, the custodial symmetry is broken in extended Higgs sectors. For example, in two Higgs doublet models (THDMs), the mass splitting between singly charged Higgs bosons and a CP-odd Higgs boson gives a quadratic mass dependence similarly to the top and bottom quark contributions in $\Delta\rho$ [29–33]. Therefore, a sizable amount of the mass difference has already been excluded [34,35]. In the above way, we can take bounds on various physical parameters by comparing precisely measured observables with theory predictions with radiative corrections.

Experimental data for flavor changing neutral current (FCNC) processes such as $K_L^0 \to \mu^+\mu^-$ and the B^0-$\bar{B}^0$ mixing strongly constrain extended Higgs sectors with multidoublet structures. The way to avoid such dangerous FCNC processes at the tree level is to assign a different quantum number for each Higgs doublet. Consequently, each quark or lepton can obtain its mass from only one Higgs doublet just like in the SM, and therefore the model escapes FCNC processes at the tree level. In the THDM, for example, this can be achieved by imposing a discrete Z_2 symmetry, which can be softly broken in the potential, to the model [36] as the simplest way. There are four independent types of Yukawa interactions under the Z_2 symmetry [37–39], which are called type-I, type-II, type-X, and type-Y [40].[3,4]

[1]Although there is an infinite number of solutions for the above equation, larger isospin representation fields cause violation of perturbative unitarity [21]. Therefore, only the three possibilities can be substantially considered, i.e., isospin singlets with $Y_i = 0$, doublets with $Y_i = 1/2$, and septets with $Y_i = 2$. The next possibility to the septet representation is isospin 26-plet with $Y_i = 15/2$.

[2]In models with $\rho_{\rm tree} \neq 1$, we need a different prescription for the calculation of the radiative corrections to the rho parameter from that in models with $\rho_{\rm tree} = 1$, because of an additional input parameter in the electroweak sector. In the Higgs sector with a real triplet Higgs field with $Y = 0$, one-loop corrections to the rho parameter have been calculated in Refs. [24,25]. That has been applied to the Higgs sector with a complex triplet Higgs field with $Y = 1$ in Refs. [26,27]. In the GM model, although $\rho_{\rm tree} = 1$ can be satisfied, a similar prescription in models with $\rho_{\rm tree} \neq 1$ is necessary due to the VEV alignment [28].

[3]The type-X (type-Y) THDM is referred to as the type-IV (type-III) THDM in Ref. [37], type-I' (type-II') THDM in Refs. [38,39], and the lepton-specific (flipped) THDM in Refs. [41–43]. Because the term "type-III" is sometimes used for the THDM with tree-level FCNCs [44], we adopt the terms "type-X" and "type-Y" to avoid confusion.

[4]If we introduce right-handed neutrinos, four more types of Yukawa interactions can be defined. In particular, if one of the two doublets gives Dirac neutrino masses, and another one gives masses of all the other fermions, it is known as the neutrinophilic THDM [45].

How can we explore extended Higgs sectors? It is important to understand that, in general, a new scale M is introduced in extended Higgs sectors, which is irrelevant to the VEV of the Higgs boson. When M is much larger than the TeV scale, the mass of the second Higgs boson is approximately given by M. In this case, the second Higgs boson is too heavy to be discovered directly at the LHC. In addition, the indirect effect of new particles decouples from the low-energy observables [46] such as the coupling constants of the discovered Higgs boson. However, if M is as high as the TeV scale, there can be two possibilities in searches for additional Higgs bosons. The first possibility is that the second Higgs boson can be discovered directly at the LHC. In this case, the properties can be directly measured at the LHC, and the useful information to determine the structure of the Higgs sector can also be obtained at the High Luminosity (HL)-LHC [47–49]. The second possibility is that it cannot be discovered directly, but its indirect effect on the Higgs couplings can be significant and thus detectable by precision measurements at the HL-LHC and at the International Linear Collider (ILC) [50]. It goes without saying that, in order to realize the second possibility, a small but detectable mixing between the SM-like Higgs boson and an additional Higgs boson is required. In this case, in addition to obtaining information on the mass of the second Higgs boson, the structure of the Higgs sector could be determined without the direct discovery by finding the pattern in deviations in various Higgs boson couplings [51,52]. On the other hand, if M stays at the electroweak scale, a large mixing between the SM-like Higgs boson and an additional Higgs boson can occur, and the Higgs boson couplings can deviate significantly from the SM values. If the last scenario is realized, both the direct search and the indirect search are possible to determine the Higgs sector. The direct search for additional Higgs bosons in THDMs at the LHC was discussed in Refs. [53–58] after the discovery of the Higgs boson. The complementarity of additional Higgs boson searches at the LHC and at the ILC was recently discussed in Ref. [59].

In this paper, we discuss how the structure of the Higgs sector can be determined at the LHC and at the ILC. In particular, we shed light on complementarity of direct searches of additional Higgs bosons at the upcoming 13 TeV or 14 TeV run of the LHC and precision measurements of the coupling constants of the discovered Higgs boson at future collider experiments. We consider extended Higgs sectors that satisfy $\rho_{\rm tree} = 1$ without predicting FCNCs at the tree level, i.e., the THDM with the softly broken Z_2 symmetry, the doublet-singlet model [60], the GM model [22], and the doublet-septet model [61–63]. For the THDM, we discuss the four types of Yukawa interaction. We at first give a detailed explanation for properties in the THDMs such as the decay branching ratio, perturbative unitarity, and vacuum stability. We then analyze the direct search for additional neutral Higgs bosons at the LHC. The expected excluded regions on the mass of extra neutral Higgs bosons are shown assuming the 14 TeV energy at the LHC.[5] Next, as the indirect search, we show various patterns of deviations in the gauge interaction hVV and the Yukawa interactions $hf\bar{f}$ of the SM-like Higgs boson h from the SM predictions. We show the deviation in the $hf\bar{f}$ couplings in the THDMs. For the rest models, we also show those in the $hf\bar{f}$ and hVV couplings, where these models predict universal modifications for the $hf\bar{f}$ couplings. We use the latest results of allowed values of the Higgs boson couplings that have been obtained from the global fit to all Higgs data [64] in order to compare the various prediction of deviations in the Higgs boson couplings.[6]

This paper is organized as follows. In Sec. II, we define the Higgs potential and Yukawa Lagrangian in the THDM with the softly broken Z_2 symmetry. After we derive the Yukawa couplings in the four types, we discuss the decay branching ratios of the Higgs bosons. The bounds from unitarity and vacuum stability are also discussed. In Sec. III, we study the direct search for the additional Higgs bosons at the LHC. In Sec. IV, we present expected accuracy of the precise measurement of the Higgs boson couplings at the ILC, and then we discuss how the deviation in the SM-like Higgs boson couplings are calculated in the THDMs and models with universal Yukawa couplings. Complementarity between the direct search and the indirect search at the LHC and at the ILC is discussed in Sec. IV. The conclusion is summarized in Sec. V.

II. TWO HIGGS DOUBLET MODEL

A. Lagrangian

The Higgs potential of the THDM under the softly broken Z_2 symmetry to avoid FCNC at the tree level and the CP invariance is given by [9,43,65,66]

$$\begin{aligned} V_{\rm THDM} = {} & m_1^2|\Phi_1|^2 + m_2^2|\Phi_2|^2 - m_3^2(\Phi_1^\dagger\Phi_2 + {\rm H.c.}) \\ & + \frac{1}{2}\lambda_1|\Phi_1|^4 + \frac{1}{2}\lambda_2|\Phi_2|^4 + \lambda_3|\Phi_1|^2|\Phi_2|^2 \\ & + \lambda_4|\Phi_1^\dagger\Phi_2|^2 + \frac{1}{2}\lambda_5[(\Phi_1^\dagger\Phi_2)^2 + {\rm H.c.}], \end{aligned} \tag{3}$$

where Φ_1 and Φ_2 are the isospin doublet scalar fields with $Y = 1/2$ for which Z_2 transformation is given as $\Phi_1 \to +\Phi_1$ and $\Phi_2 \to -\Phi_2$. The two Higgs doublet fields can be parametrized as

[5]In Fig. 1.20 in the ILC Higgs White Paper [51], we have shown the expected excluded parameter space in the type-II and type-X THDMs at the LHC. We update this analysis with more detailed explanations.

[6]In Figs. 1.17 and 1.18 in the ILC Higgs White Paper [51], we have shown the deviation in the $hf\bar{f}$ and hVV couplings in the THDMs and in the models with universal modification of the $hf\bar{f}$ couplings. We update the plots for the $hf\bar{f}$ and hVV couplings with more detailed explanations by using the latest data [64].

TABLE I. Four types of the charge assignment of the Z_2 symmetry.

	Φ_1	Φ_2	u_R	d_R	ℓ_R	Q_L, L_L
Type-I	+	−	−	−	−	+
Type-II	+	−	−	+	+	+
Type-X	+	−	−	−	+	+
Type-Y	+	−	−	+	−	+

$$\Phi_i = \begin{bmatrix} w_i^+ \\ \frac{1}{\sqrt{2}}(h_i + v_i + iz_i) \end{bmatrix}, \quad (i = 1, 2), \tag{4}$$

where v_1 and v_2 are the VEVs of two doublet fields. They are related to the Fermi constant G_F by $v^2 \equiv v_1^2 + v_2^2 = (\sqrt{2}G_F)^{-1}$. The ratio of the two VEVs is defined as $\tan\beta = v_2/v_1$.

The mass eigenstates for the scalar bosons are obtained by the orthogonal transformations as

$$\begin{pmatrix} w_1^\pm \\ w_2^\pm \end{pmatrix} = R(\beta)\begin{pmatrix} G^\pm \\ H^\pm \end{pmatrix}, \qquad \begin{pmatrix} z_1 \\ z_2 \end{pmatrix} = R(\beta)\begin{pmatrix} G^0 \\ A \end{pmatrix},$$
$$\begin{pmatrix} h_1 \\ h_2 \end{pmatrix} = R(\alpha)\begin{pmatrix} H \\ h \end{pmatrix},$$
$$\text{with} \quad R(\theta) = \begin{pmatrix} \cos\theta & -\sin\theta \\ \sin\theta & \cos\theta \end{pmatrix}, \tag{5}$$

where $G^\pm$ and G^0 are the Nambu-Goldstone bosons absorbed by the longitudinal component of $W^\pm$ and Z, respectively. The masses of $H^\pm$ and A are calculated as

$$m_{H^+}^2 = M^2 - \frac{v^2}{2}(\lambda_4 + \lambda_5), \qquad m_A^2 = M^2 - v^2\lambda_5, \tag{6}$$

where $M^2 \equiv m_3^2/(\sin\beta\cos\beta)$ describes the soft breaking scale of the Z_2 symmetry [66]. The masses for the CP-even Higgs bosons h and H and the mixing angle α are given by

$$m_H^2 = \cos^2(\beta-\alpha)M_{11}^2 + \sin^2(\beta-\alpha)M_{22}^2 - \sin 2(\beta-\alpha)M_{12}^2, \tag{7}$$

$$m_h^2 = \sin^2(\beta-\alpha)M_{11}^2 + \cos^2(\beta-\alpha)M_{22}^2 + \sin 2(\beta-\alpha)M_{12}^2, \tag{8}$$

$$\tan 2(\beta-\alpha) = \frac{2M_{12}^2}{M_{22}^2 - M_{11}^2}, \tag{9}$$

where

$$M_{11}^2 = v^2(\lambda_1\cos^4\beta + \lambda_2\sin^4\beta) + \frac{v^2}{2}\bar{\lambda}\sin^2 2\beta, \tag{10}$$

$$M_{22}^2 = M^2 + v^2(\lambda_1 + \lambda_2 - 2\bar{\lambda})\sin^2\beta\cos^2\beta, \tag{11}$$

$$M_{12}^2 = \frac{v^2}{2}(-\lambda_1\cos^2\beta + \lambda_2\sin^2\beta)\sin 2\beta + \frac{v^2}{2}\bar{\lambda}\sin 2\beta\cos 2\beta, \tag{12}$$

with $\bar{\lambda} \equiv \lambda_3 + \lambda_4 + \lambda_5$. We define the range of $\beta - \alpha$ to be $[0, \pi/2]$ or $[\pi/2, \pi]$, which for a given positive value of $\sin(\beta-\alpha)$, $\cos(\beta-\alpha)$ is positive or negative, respectively.

The Yukawa Lagrangian under the Z_2 symmetry is given by

$$\mathcal{L}_{\rm THDM}^Y = -Y_u\overline{Q_L}\tilde{\Phi}_u u_R - Y_d\overline{Q_L}\Phi_d d_R - Y_\ell\overline{L_L}\Phi_\ell \ell_R + \text{H.c.}, \tag{13}$$

where $\Phi_{u,d,\ell}$ are either Φ_1 or Φ_2 and $\tilde{\Phi}_u = i\tau_2\Phi_u^*$. There are four independent ways of the charge assignment of the Z_2 symmetry as summarized in Table I, which are named type-I, type-II, type-X, and type-Y Yukawa interactions according to Ref. [40]. After we specify the types of Yukawa interactions, the Yukawa coupling constants are expressed in the mass eigenstate of the Higgs bosons as

$$\begin{aligned}\mathcal{L}_{\rm THDM}^Y = &-\sum_{f=u,d,e}\frac{m_F}{v}(\xi_h^f\bar{f}fh + \xi_H^f\bar{f}fH - i\xi_A^f\bar{f}\gamma_5 fA) \\ &+ \left[\frac{\sqrt{2}V_{ud}}{v}\bar{u}(m_u\xi_A^u P_L + m_d\xi_A^d P_R)dH^+ \right. \\ &\left. + \frac{\sqrt{2}m_\ell\xi_A^e}{v}\bar{\nu}P_R e H^+ + \text{H.c.}\right],\end{aligned} \tag{14}$$

where $P_{L,R} = (1\mp\gamma_5)/2$, and the factors ξ_ϕ^f ($\phi = h, H$, and A) are listed in Table II. We note that the ξ_h^f and ξ_H^f are rewritten by

$$\begin{aligned}\xi_h^f &= \sin(\beta-\alpha) + 2T_3^f\xi_A^f\cos(\beta-\alpha), \\ \xi_H^f &= \cos(\beta-\alpha) - 2T_3^f\xi_A^f\sin(\beta-\alpha),\end{aligned} \tag{15}$$

where $T_3^f = 1/2(-1/2)$ for $f = u$ (d, e).

TABLE II. The mixing factors in each type of Yukawa interaction in the THDMs [40].

	ξ_h^u	ξ_h^d	ξ_h^ℓ	ξ_H^u	ξ_H^d	ξ_H^ℓ	ξ_A^u	ξ_A^d	ξ_A^ℓ
Type-I	$\cos\alpha/\sin\beta$	$\cos\alpha/\sin\beta$	$\cos\alpha/\sin\beta$	$\sin\alpha/\sin\beta$	$\sin\alpha/\sin\beta$	$\sin\alpha/\sin\beta$	$\cot\beta$	$-\cot\beta$	$-\cot\beta$
Type-II	$\cos\alpha/\sin\beta$	$-\sin\alpha/\cos\beta$	$-\sin\alpha/\cos\beta$	$\sin\alpha/\sin\beta$	$\cos\alpha/\cos\beta$	$\cos\alpha/\cos\beta$	$\cot\beta$	$\tan\beta$	$\tan\beta$
Type-X	$\cos\alpha/\sin\beta$	$\cos\alpha/\sin\beta$	$-\sin\alpha/\cos\beta$	$\sin\alpha/\sin\beta$	$\sin\alpha/\sin\beta$	$\cos\alpha/\cos\beta$	$\cot\beta$	$-\cot\beta$	$\tan\beta$
Type-Y	$\cos\alpha/\sin\beta$	$-\sin\alpha/\cos\beta$	$\cos\alpha/\sin\beta$	$\sin\alpha/\sin\beta$	$\cos\alpha/\cos\beta$	$\sin\alpha/\sin\beta$	$\cot\beta$	$\tan\beta$	$-\cot\beta$

After taking the same rotation of the scalar bosons given in Eq. (5), the Higgs gauge gauge-type terms are expressed by

$$\mathcal{L}_{\rm kin}^{\phi VV} = [\sin(\beta-\alpha)h + \cos(\beta-\alpha)H] \times \left(\frac{m_W^2}{v} W^{+\mu}W_\mu^- + \frac{1}{2}\frac{m_Z^2}{v} Z^\mu Z_\mu\right). \quad (16)$$

Here, we comment on two important limits: the *SM-like limit* and the *decoupling limit* [65], which are realized by taking $\sin(\beta-\alpha) \to 1$ and $M^2 \to \infty$, respectively. In the former limit, as seen in Eqs. (14), (15), and (16), the strength of the Yukawa interaction and the gauge interaction of h become the same as in the SM. We thus define h as the SM-like Higgs boson that should be identified as the discovered Higgs boson with the mass of around 126 GeV, and all the other Higgs bosons, $H^\pm$, A, and H are regarded as the additional Higgs bosons. On the other hand, in the decoupling limit, all the masses of additional Higgs bosons become infinity as long as we take the SM-like limit. As a result, only the mass of h remains at the electroweak scale.

If we consider the case without the SM-like limit, we cannot take the decoupling limit. This can be seen by looking at Eq. (9), which tells us that, in order to keep a fixed nonzero value of $\tan 2(\beta-\alpha)$, we need sizable contributions from M_{11}^2 and M_{12}^2 to cancel a large value of M_{22}^2 by the M^2 term in Eq. (11). However, as seen in Eqs. (10) and (12), M_{11}^2 and M_{12}^2 are given like a form of $\lambda_i v^2$ so that when these terms are too large they make λ coupling constants, which are disfavored by the constraints from perturbative unitarity, too large [67,68]. Therefore, there is an upper limit for the mass of additional Higgs bosons at which we retain the deviation from the SM-like limit.

B. Vacuum stability and unitarity

To keep a stability of the vacuum, the Higgs potential should be bounded from below in any directions with a large value of scalar fields. The sufficient condition is given by [69,70]

$$\lambda_1 > 0. \qquad \lambda_2 > 0,$$
$$\sqrt{\lambda_1\lambda_2} + \lambda_3 + \mathrm{MIN}(0, \lambda_4+\lambda_5, \lambda_4-\lambda_5) > 0. \quad (17)$$

In addition, the magnitude of several combinations of the quartic Higgs coupling constants are constrained by unitarity. When we consider the elastic scatterings of two-body boson states, there are 14 neutral, 8 singly charged, and 3 doubly charged channels. After the diagonalization of the T matrix for the S-wave amplitude of these processes, we obtain the 12 independent eigenvalues [68] as

$$x_1^\pm = \frac{1}{32\pi}[3(\lambda_1+\lambda_2) \pm \sqrt{9(\lambda_1-\lambda_2)^2 + 4(2\lambda_3+\lambda_4)^2}], \quad (18)$$

$$x_2^\pm = \frac{1}{32\pi}\left[(\lambda_1+\lambda_2) \pm \sqrt{(\lambda_1-\lambda_2)^2 + 4\lambda_4^2}\right], \quad (19)$$

$$x_3^\pm = \frac{1}{32\pi}\left[(\lambda_1+\lambda_2) \pm \sqrt{(\lambda_1-\lambda_2)^2 + 4\lambda_5^2}\right], \quad (20)$$

$$x_4^\pm = \frac{1}{16\pi}(\lambda_3 + 2\lambda_4 \pm 3\lambda_5), \quad (21)$$

$$x_5^\pm = \frac{1}{16\pi}(\lambda_3 \pm \lambda_4), \quad (22)$$

$$x_6^\pm = \frac{1}{16\pi}(\lambda_3 \pm \lambda_5). \quad (23)$$

For each eigenvalue, we impose the following criterion[7]:

$$|x_i^\pm| \le \frac{1}{2}. \quad (24)$$

As we mentioned in the previous subsection, the unitarity and vacuum stability bounds can be used to obtain the upper limit on the mass of additional Higgs bosons when $\sin(\beta-\alpha)$ deviates from unity. We introduce the scaling factor κ_V defined by the ratio of the hVV coupling constant to the corresponding SM value, which coincides with $\sin(\beta-\alpha)$ at the tree level. In Fig. 1, we show the upper limit of m_A from the unitarity and vacuum stability bounds for given values of $1-\kappa_V$ and $\tan\beta$. The value of M is scanned over the range of $m_A \pm 500$ GeV. To avoid the constraint from the rho parameter, we take $m_{H^+} = m_A$ in these plots so that the one-loop corrections to the rho parameter from the additional Higgs boson loops become zero due to the custodial symmetry in the Higgs potential [29–35]. The value of m_H is taken to be the same as m_A (scanned over the range of $m_A \pm 500$ GeV) in the solid (dotted) curves. The left and right panels show the cases with $\cos(\beta-\alpha) > 0$ and $\cos(\beta-\alpha) < 0$, respectively. It is seen that the maximal allowed value of m_A gets larger when the deviation in κ_V from unity gets small. Therefore, larger deviations in the hVV coupling constant give a severe upper bound on masses for additional Higgs bosons.

In Fig. 2, we show the $\tan\beta$ dependence of the upper limit of m_A from the unitarity and vacuum stability bounds for a given value of $1-\kappa_V$. The other parameters are taken to be the same as in Fig. 1.

C. Decay of the Higgs bosons

In this subsection, we discuss the decays of Higgs bosons with the four types of Yukawa interaction in the THDM. The decay property can be drastically different between the case with $\sin(\beta-\alpha) = 1$ and that with $\sin(\beta-\alpha) \neq 1$ [40]. When the SM-like limit is taken, the additional Higgs

[7]Constraints on the parameter space using scale-dependent coupling constants were studied in the THDM in Refs. [70,71].

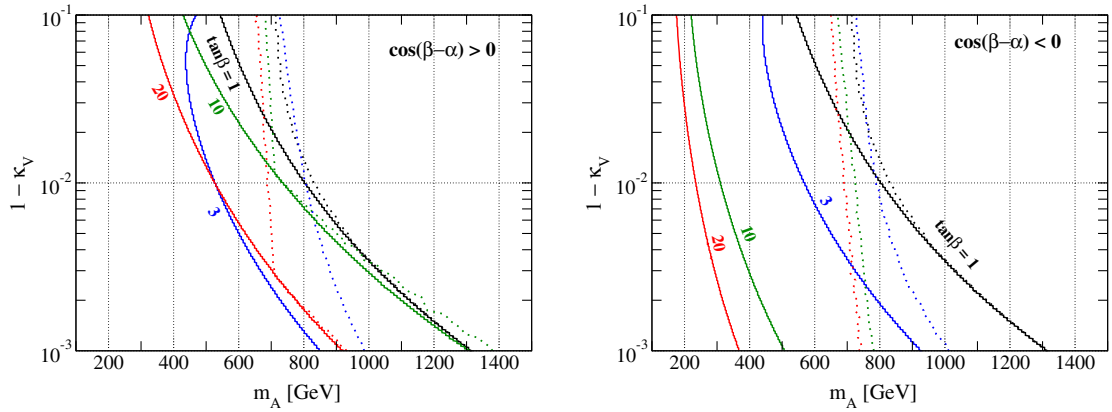

FIG. 1 (color online). Upper limit of $1-\kappa_V$ as a function of m_A for each value of $\tan\beta$ from the constraints of unitarity and vacuum stability in the case in which M is scanned over the range of $m_A \pm 500$ GeV and $m_{H^+} = m_A$. The left and right panels, respectively, show the results with $\cos(\beta-\alpha) > 0$ and $\cos(\beta-\alpha) < 0$. The solid curves show the case with $m_H = m_A$, while the dotted curves show the result with m_H to be scanned over the range of $m_A \pm 500$ GeV.

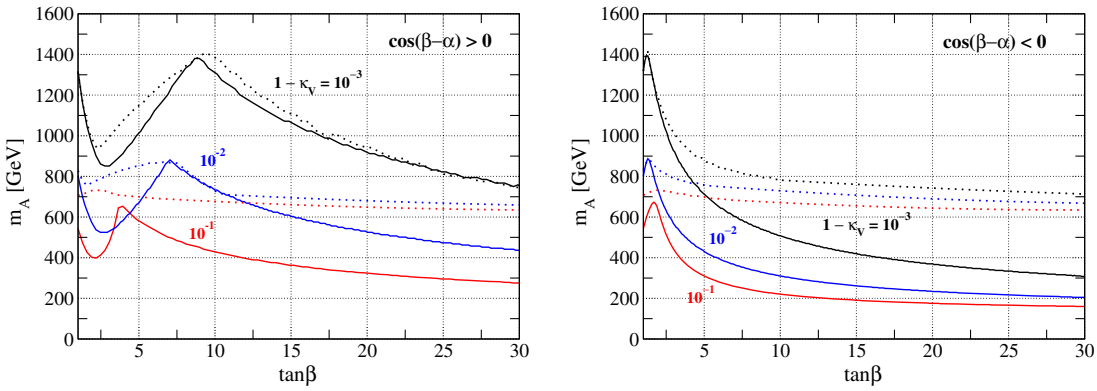

FIG. 2 (color online). Upper limit of m_A as a function of $\tan\beta$ for each value of $1-\kappa_V$ from the constraints of unitarity and vacuum stability in the case in which M is scanned over the range of $m_A \pm 500$ GeV and $m_{H^+} = m_A$. The left and right panels, respectively, show the results with $\cos(\beta-\alpha) > 0$ and $\cos(\beta-\alpha) < 0$. The solid curves show the result with $m_H = m_A$, while the dotted curves show the result with m_H to be scanned over the range of $m_A \pm 500$ GeV.

bosons can dominantly decay into a fermion pair for which the decay branching ratio strongly depends on the type of Yukawa interactions and $\tan\beta$. On the other hand, when we take $\sin(\beta-\alpha) \neq 1$, H can decay into the gauge boson pairs W^+W^- and ZZ and the SM-like Higgs boson pair hh, where these decay rates are proportional to $\cos^2(\beta-\alpha)$. At the same time, $H^\pm$ and A can decay into $W^\pm$ and Z associated with the SM-like Higgs boson h for which the decay amplitudes are also proportional to $\cos(\beta-\alpha)$ [53–55,72].

To calculate the decay rates, we use the following inputs from the Particle Data Group (PDG) [20]:

$$m_Z = 91.1876\ \text{GeV}, \quad m_W = 80.385\ \text{GeV},$$
$$G_F = 1.1663787 \times 10^{-5}\ \text{GeV}^{-2}, \quad m_t = 173.07\ \text{GeV},$$
$$\alpha_s(m_Z) = 0.1185, \quad V_{cb} = 0.0409, \quad V_{ts} = 0.0429. \tag{25}$$

The running quark masses at the scale of m_Z are quoted from Ref. [73] as

$$\bar{m}_b = 3.0\ \text{GeV}, \qquad \bar{m}_c = 0.677\ \text{GeV},$$
$$\bar{m}_s = 0.0934\ \text{GeV}. \tag{26}$$

The mass of the SM-like Higgs boson h is taken to be 126 GeV in the following calculations.

All the other parameters shown in Eq. (25) are quoted from the PDG [20]. We note that the effects of Cabibbo-Kobayashi-Maskawa matrix elements V_{cb} and V_{ts} appear in the $H^\pm \to cb$ and $H^\pm \to ts$ decays. For simplicity, we take all the masses of additional Higgs bosons to be the same; i.e., $m_{H^+} = m_A = m_H (\equiv m_\Phi)$. In that case, there are four free parameters in the Higgs potential, which are chosen as m_Φ, M^2, $\tan\beta$, and $\sin(\beta-\alpha)$.

We here comment on the $H^\pm \to W^\pm Z$ and $H^\pm \to W^\pm\gamma$ processes. The $H^\pm W^\mp \gamma$ vertex is obtained at the one-loop

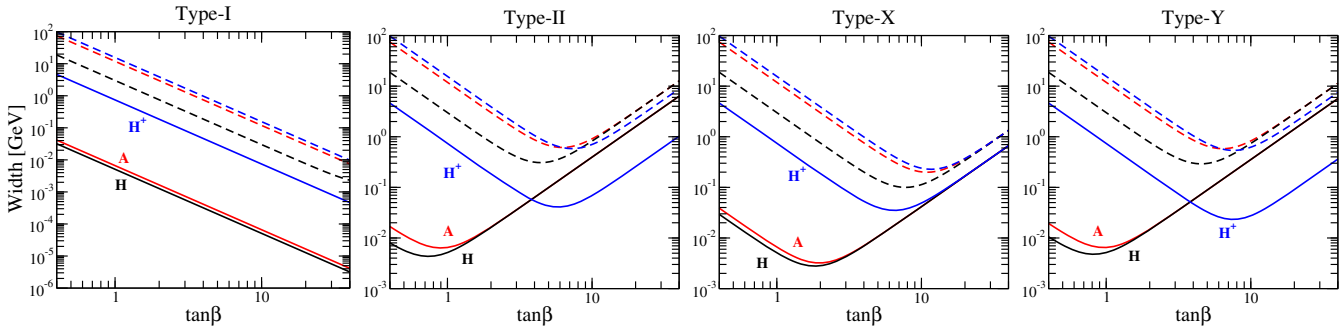

FIG. 3 (color online). Total widths for H, A, and $H^{\pm}$ as a function of $\tan\beta$ in the case of $\sin(\beta-\alpha)=1$. The solid and dashed curves, respectively, show the results with $m_{\Phi}=M=200$ GeV and $m_{\Phi}=M=400$ GeV.

level, and its magnitude is suppressed due to the $U(1)_{\rm em}$ gauge invariance. This nature does not depend on a model. On the other hand, in the THDM, although the $H^{\pm}W^{\mp}Z$ vertex appears at the one-loop level, it can enhance if there is a large violation of the custodial symmetry. As we discussed in the Introduction, the mass splitting between the top and bottom quarks breaks the custodial symmetry, and it gives the $(m_t-m_b)^2$ dependence in the one-loop corrected rho parameter. A similar effect appears in the $H^{\pm}W^{\mp}Z$ vertex [74]. In addition, when the mass splitting

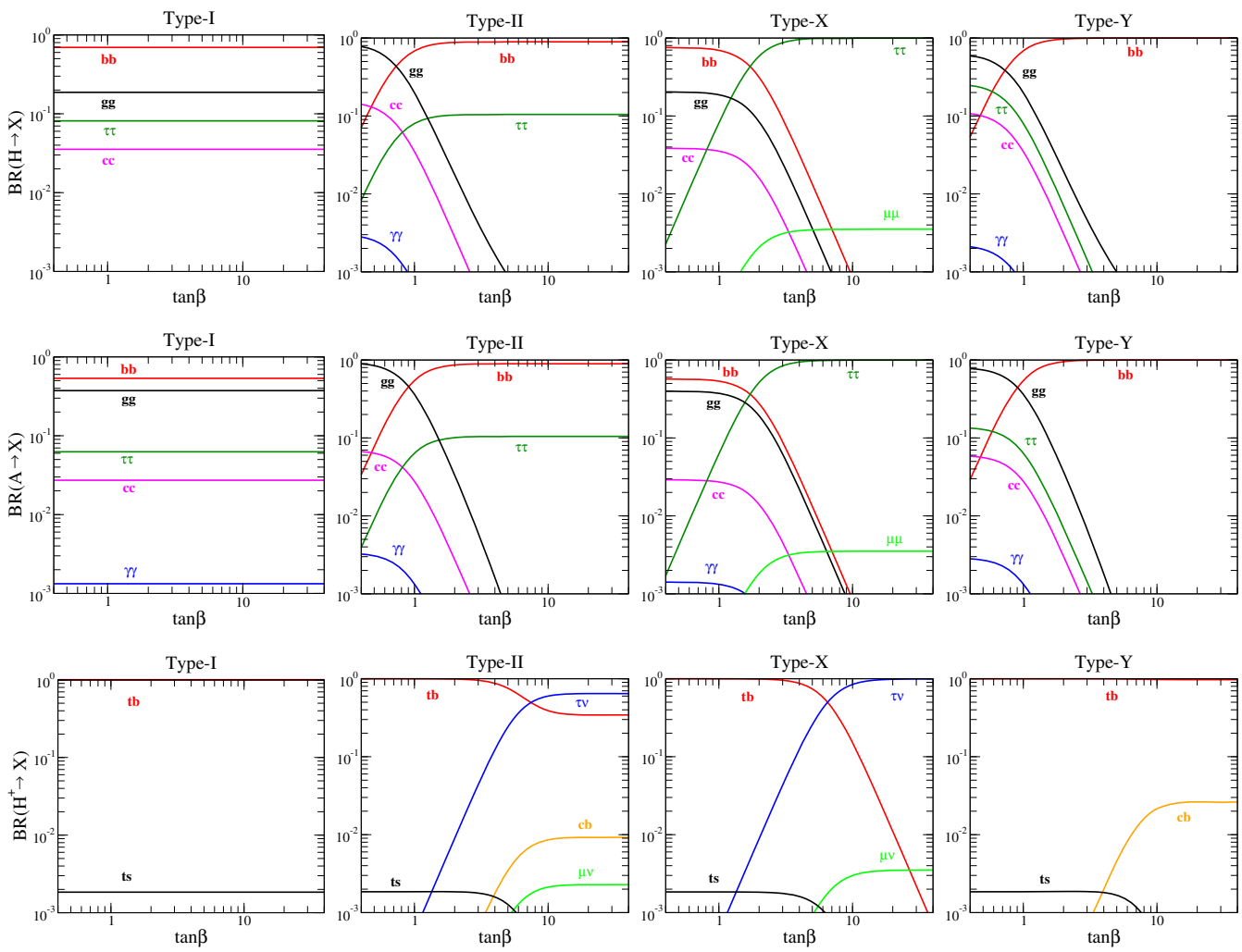

FIG. 4 (color online). Decay branching ratios for H, A, and $H^{\pm}$ as a function of $\tan\beta$ in the case of $m_{\Phi}=M=200$ GeV and $\sin(\beta-\alpha)=1$.

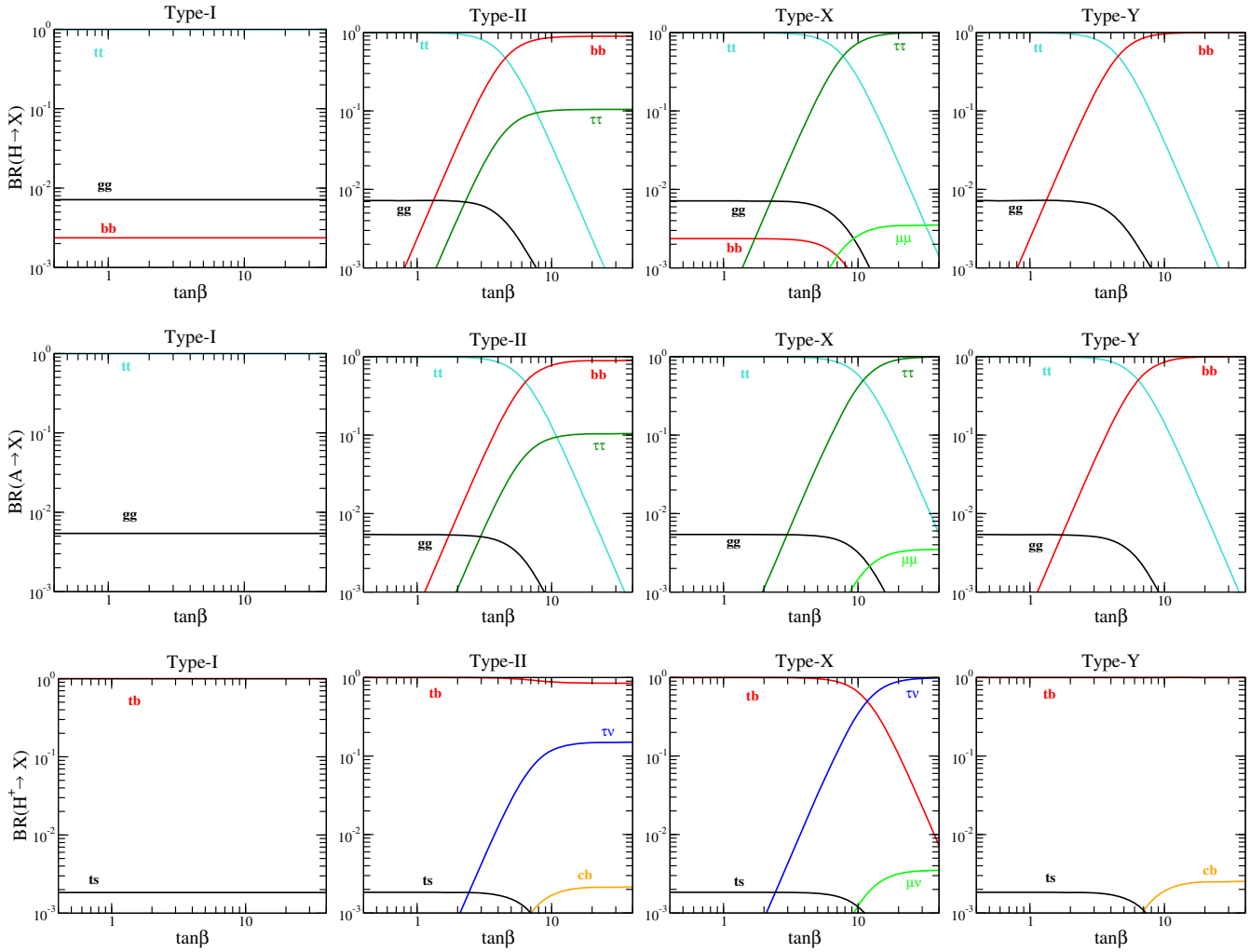

FIG. 5 (color online). Decay branching ratios for H, A, and $H^{\pm}$ as a function of $\tan\beta$ in the case of $m_{\Phi} = M = 400$ GeV and $\sin(\beta - \alpha) = 1$.

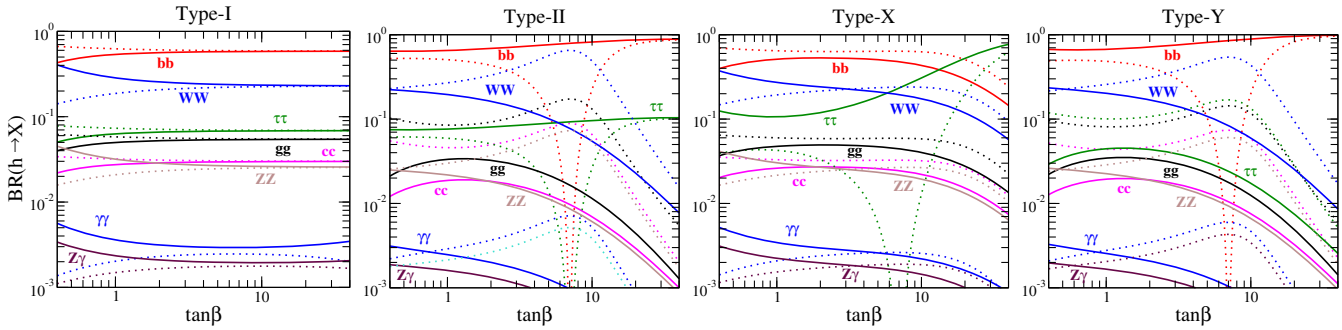

FIG. 6 (color online). Decay branching ratios for h as a function of $\tan\beta$ in the case of $m_{\Phi} = M = 200$ GeV and $\sin(\beta - \alpha) = 0.99$. The solid and dashed curves respectively show the cases with $\cos(\beta - \alpha) < 0$ and $\cos(\beta - \alpha) > 0$.

between $H^{\pm}$ and A is given, which breaks the custodial symmetry in the Higgs potential, the $H^{\pm}W^{\mp}Z$ vertex can be enhanced due to the $(m_{H^+} - m_A)^2$ dependence. In Ref. [75], full one-loop calculation of the $H^{\pm}W^{\mp}Z$ vertex was done. It was shown that the branching ratio of $H^{\pm} \to W^{\pm}Z$ can be $\mathcal{O}(10^{-2})$ in the case of $m_{H^+} = 300$ GeV when the mass splitting between $H^{\pm}$ and A is taken to be $\mathcal{O}(100)$ GeV. In the following calculation, we assume $m_{H^+} = m_A$ so that only the top and bottom quarks loop contribution to the $H^{\pm} \to W^{\pm}Z$ vertex is important. In this

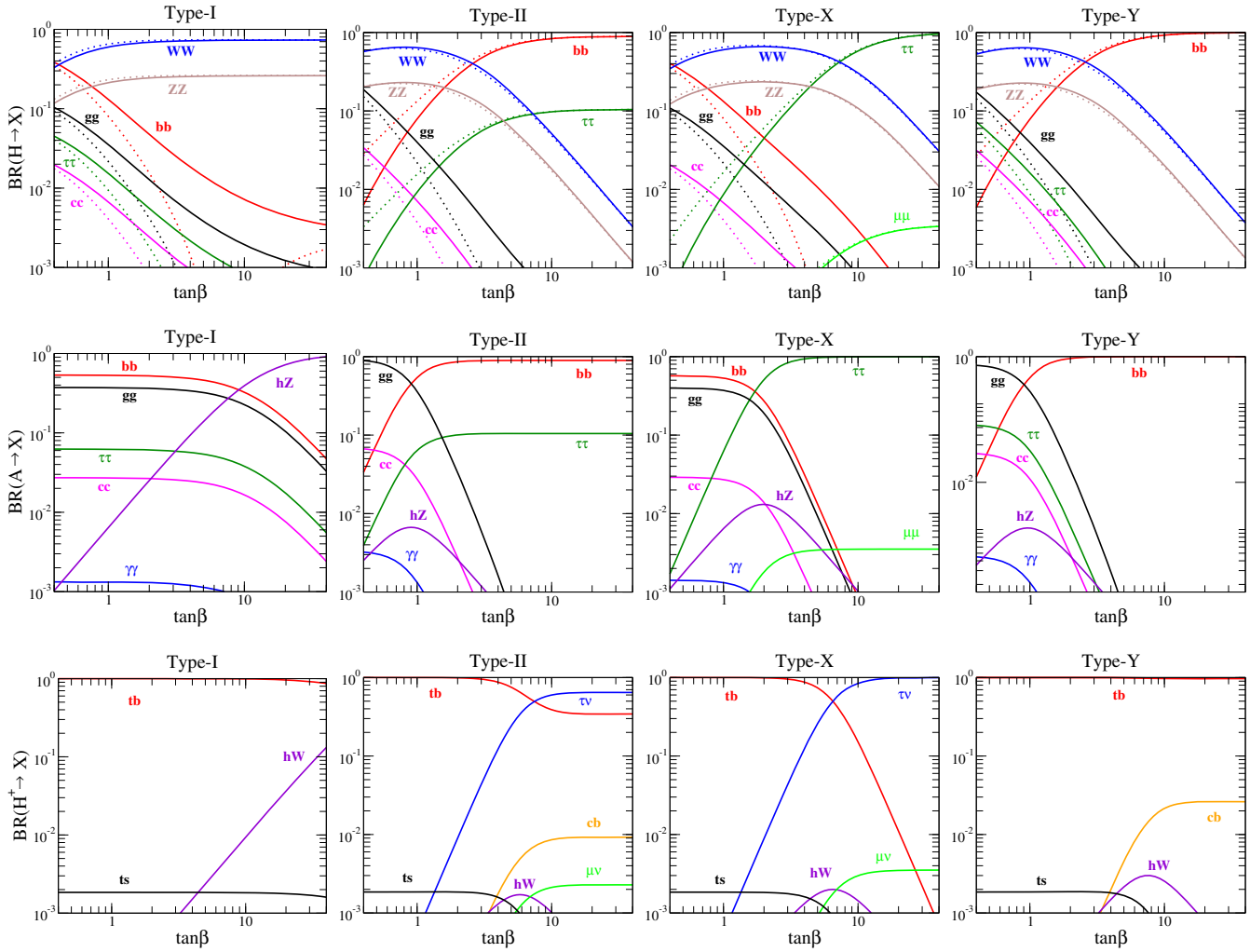

FIG. 7 (color online). Decay branching ratios for H, A, and $H^{\pm}$ as a function of $\tan\beta$ in the case of $m_{\Phi} = M = 200$ GeV and $\sin(\beta - \alpha) = 0.99$. For the H decay, the solid and dashed curves, respectively, show the cases with $\cos(\beta - \alpha) < 0$ and $\cos(\beta - \alpha) > 0$.

case, typical values of the branching fractions of $H^{\pm} \to W^{\pm}Z$ and $H^{\pm} \to W^{\pm}\gamma$ are smaller than $\mathcal{O}(10^{-3})$ and $\mathcal{O}(10^{-5})$, respectively.[8] We thus safely neglect these modes in the following calculation.

First, we show the total widths for H, A, and $H^{\pm}$ in Fig. 3 as a function of $\tan\beta$ in the case of $\sin(\beta - \alpha) = 1$. The solid (dashed) curves show the results with $m_{\Phi} = M = 200(400)$ GeV. Except in the type-I THDM, the widths have a minimum in a certain value of $\tan\beta$ because the sum of the decay rates of the fermion pair mode are given by terms proportional to $\cot^2\beta$, $\tan^2\beta$ and those without $\tan\beta$ dependence. In the type-I THDM, all the decay rates with the fermion pair final state are suppressed by $\cot^2\beta$ so that the widths monotonously decrease when $\tan\beta$ gets larger values. In the type-X THDM, all the widths for H, A and $H^{\pm}$ approach roughly the same value in the high $\tan\beta$ region for a fixed value of m_{Φ}. This can be understood in such a way that the decay rate of $H^{\pm} \to tb$ mainly deviates the width of $H^{\pm}$ from that of H and A, which can be neglected in the high $\tan\beta$ region in the type-X THDM. In the type-I THDM, although the decay rate of $H^{\pm} \to tb$ is suppressed as in the type-X THDM, all the other fermion pair decay modes are also suppressed at the same time. Therefore, the $H^{\pm} \to tb$ decay is not negligible in the type-I THDM, and then it deviates the width of $H^{\pm}$ from that of H and A.

In Fig. 4, we show the decay branching fractions of H (top panels), A (middle panels), and $H^{\pm}$ (bottom panels) as a function of $\tan\beta$ in the case of $\sin(\beta - \alpha) = 1$ and $m_{\Phi} = M = 200$ GeV. It is seen that only in the type-X THDM H and A can mainly decay into $\tau^+\tau^-$ in the case of

[8] If the Higgs sector contains *exotic* Higgs fields for which the isospin is larger than 1/2, the $H^{\pm}W^{\mp}Z$ vertex appears at the tree level [76]. The magnitude depends on VEVs from exotic Higgs fields that are usually severely constrained by the rho parameter. In the GM model and in the doublet-septet model, such a VEV can be taken as $\mathcal{O}(10)$ GeV. Therefore, measuring the $H^{\pm}W^{\mp}Z$ vertex can be a probe of exotic Higgs sectors. The feasibility study for the measurement of the vertex was performed in Ref. [77] at the LHC and in Ref. [78] at the ILC.

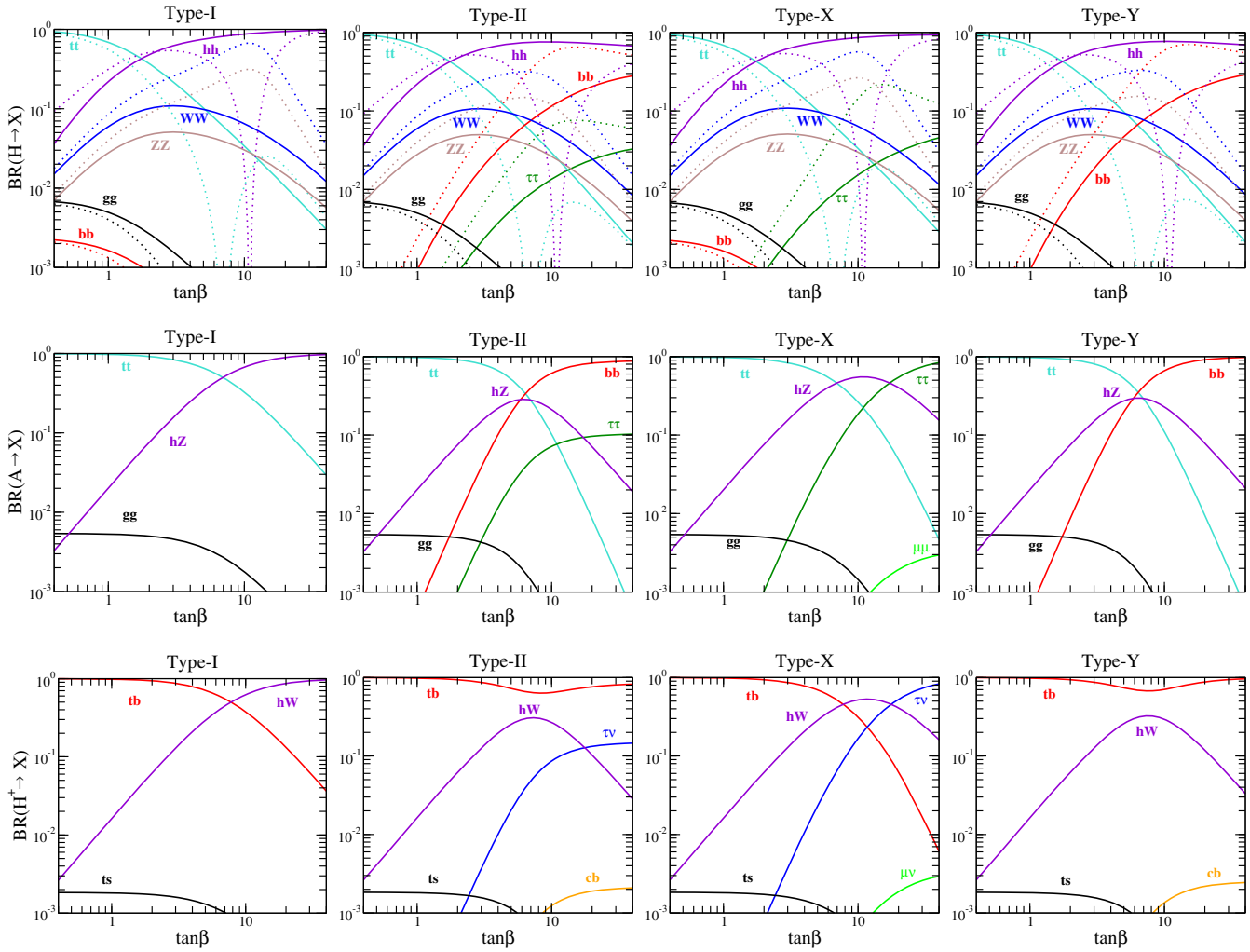

FIG. 8 (color online). Decay branching ratios for H, A, and $H^{\pm}$ as a function of $\tan\beta$ in the case of $m_{\Phi} = M = 400$ GeV and $\sin(\beta - \alpha) = 0.99$. For the H decay, the solid and dashed curves, respectively, show the cases with $\cos(\beta - \alpha) < 0$ and $\cos(\beta - \alpha) > 0$.

$\tan\beta \gtrsim 3$. Besides, H and A can also decay into $\mu^+\mu^-$ with about 0.3% in the type-X THDM. Regarding the $H^{\pm}$ decay, although the main decay mode is basically tb in all the types, that is replaced by $H^{\pm} \to \tau^{\pm}\nu$ in the type-II and type-X THDMs with $\tan\beta \gtrsim 7$.

Similarly, Fig. 5 shows the branching fractions of H, A, and $H^{\pm}$ in the case of $m_{\Phi} = M = 400$ GeV and $\sin(\beta - \alpha) = 1$. In all the types of THDMs, H and A mainly decay into the top pair in the lower $\tan\beta$ region. However, that is replaced by $b\bar{b}$ ($\tau^+\tau^-$) in the type-II and type-Y (type-X) THDMs with $\tan\beta \gtrsim 5$ ($\tan\beta \gtrsim 8$). The decay of $H^{\pm}$ does not change so much from that in the case of $m_{\Phi} = M = 200$ GeV. Notice here that the magnitude relation between the branching fraction of $H/A \to gg$ and that of $H/A \to b\bar{b}$ is flipped compared to the results in Fig. 4 except in the type-II and type-Y THDMs with $\tan\beta \gtrsim 1$. We note that, in the case of $\sin(\beta - \alpha) = 1$ and $m_H = m_A$, only the difference between the decay rate of $H \to f\bar{f}$ and that of $A \to f\bar{f}$ appears in the power of the phase space factor; i.e., that is the cubic (linear) power for H (A) [9]. Thus, the decay rate of $A \to f\bar{f}$ is slightly larger than that of $H \to f\bar{f}$. Moreover, the decay rates of loop-induced modes such as the decays into gg, $\gamma\gamma$, and $Z\gamma$ are different between H and A because of the CP property.

Next, we show the branching fractions in the case without taking the SM-like limit, e.g., $\sin(\beta - \alpha) = 0.99$. In this case, the sign of $\cos(\beta - \alpha)$ can affect decay properties for the CP-even Higgs bosons so that we consider both the cases with $\cos(\beta - \alpha) < 0$ and $\cos(\beta - \alpha) > 0$.

In Fig. 6, the branching fractions for the SM-like Higgs boson h is shown as a function of $\tan\beta$ in the case of $m_{\Phi} = M = 200$ GeV. For the h decay, the m_{Φ} and M parameters affect the $H^{\pm}$ loop contribution to the decay rates of $h \to \gamma\gamma$ and $h \to Z\gamma$. When we take a larger value of m_{Φ} keeping $m_{\Phi} = M$, the $H^{\pm}$ loop contribution vanishes. The solid and dashed curves, respectively, show the

cases with $\cos(\beta-\alpha) < 0$ and $\cos(\beta-\alpha) > 0$. We can see that several fermionic decay channels vanish at $\tan\beta \simeq 7$ in the case of $\cos(\beta-\alpha) > 0$ in the type-II, type-X, and type-Y THDMs. Let us explain this behavior by introducing δ defined by $\sin(\beta-\alpha) = 1-\delta$. When $\delta \ll 1$, the ξ_h^f and ξ_H^f factors in Eq. (15) can be approximately expressed by

$$\xi_h^f \simeq 1 + \mathrm{Sign}[\cos(\beta-\alpha)]2\sqrt{2\delta}T_3^f\xi_A^f,$$
$$\xi_H^f \simeq \mathrm{Sign}[\cos(\beta-\alpha)]2\sqrt{2\delta} - 2T_3^f\xi_A^f. \tag{27}$$

From Table II, we can obtain $\xi_h^f \simeq 1 - \mathrm{Sign}[\cos(\beta-\alpha)]\sqrt{2\delta}\tan\beta$ for $f = b$ $(f = \tau)$ in type-II and type-Y (type-II and type-X) THDMs. Thus, when $\cos(\beta-\alpha)$ is positive, and δ is taken to be 0.01, ξ_h^f becomes zero at around $\tan\beta = 7$. We note that the ξ_h^f factor can be -1 in the case of $\cos(\beta-\alpha) < 0$, in which the sign of Yukawa coupling constant is opposite compared to the SM value. Signatures of additional Higgs bosons in the parameter regions with $\xi_h^f \simeq -1$ have been studied in Ref. [56], and the testability of the sign of Yukawa couplings has been investigated at a future linear collider in Ref. [57].

The branching fractions for the additional Higgs bosons are also shown in Fig. 7 in the case of $m_\Phi = M = 200$ GeV, and those in the case of $m_\Phi = M = 400$ GeV are shown in Fig. 8. For the H decay, we use the solid and dashed curves, respectively, to show the cases with $\cos(\beta-\alpha) < 0$ and $\cos(\beta-\alpha) > 0$. It can be seen that the gaugephobic nature of H is lost, and the $H \to W^+W^-/ZZ$ modes can be dominate. Regarding the A and $H^\pm$ decays, the $A \to hZ$ and $H^\pm \to hW^\pm$ modes are added to the case with $\sin(\beta-\alpha) = 1$. When we consider heavier case of H, $m_\Phi = M = 400$ GeV, the $H \to hh$ mode for which the decay rate is proportional to $\cos^2(\beta-\alpha)$ is kinematically allowed. This can be the main decay mode as we can see in the top panels in Fig 8.

We comment on the case without degeneracy in mass of the additional Higgs bosons. In that case, heavier additional Higgs bosons can decay into lighter ones associated with a gauge boson even in the SM-like limit. For instance, when $m_H > m_A$, the $H \to AZ^{(*)}$ mode is allowed. Recently, signatures from $H \to AZ$ and $A \to HZ$ decays have been studied at the LHC in Ref. [55].

III. DIRECT SEARCH FOR ADDITIONAL HIGGS BOSONS AT THE LHC

At the LHC with the collision energy of 7 and 8 TeV, so far, there is no report for a discovery of new particles other than a Higgs boson, and only exclusion bounds for masses of hypothetical particles are obtained.

First of all, we review the current bounds on parameter space in the THDMs from 7 and 8 TeV data at the LHC. The signal of neutral Higgs bosons in the $\tau^+\tau^-$ decay mode has been searched for in the inclusive production and bottom quark-associated production processes [10,11]. For the type-II THDM, bounds on $\tan\beta$ have been obtained for given values of m_A, e.g., $\tan\beta \lesssim 10$ for $m_A = 300$ GeV and $\tan\beta \lesssim 40$ for $m_A = 800$ GeV [11]. In addition, the searches for the $b\bar{b}$ decay of neutral Higgs bosons in the bottom quark-associated process have been performed [12]. The $b\bar{b}$ decay mode gives a rather weaker bound on $\tan\beta$ compared to the $\tau^+\tau^-$ decay mode. These bounds can be used to constrain parameter regions in both the type-II and type-Y THDMs. Furthermore, for $\sin(\beta-\alpha) < 1$, searches for the $H \to W^+W^-$ signal have been performed [13], and a bound on the m_H-$\cos\alpha$ plane is obtained for given values of $\tan\beta$. This bound is not sensitive to the type of Yukawa interaction. In Ref. [14], $H \to hh$ and $A \to Zh$ decays have been searched, and bounds on the cross section times branching ratio have been obtained. These can be translated into the exclusion regions in the $\cos(\beta-\alpha)$-$\tan\beta$ plane for given values of $m_{H/A}$ for each type of Yukawa interaction.

In the following, we discuss expected excluded regions on the m_A-$\tan\beta$ plane at the LHC with the collision energy of 14 TeV. We first focus on the search for H and A by using the tau decay from the gluon fusion and bottom quark-associated production processes as

$$gg \to \phi^0 \to \tau^+\tau^-, \tag{28}$$

$$gg \to b\bar{b}\phi^0 \to b\bar{b}\tau^+\tau^-, \tag{29}$$

where $\phi^0 = H$ or A. The cross sections for the above processes can be estimated by[9]

$$\sigma(gg \to \phi^0) = \frac{\Gamma(\phi^0 \to gg)}{\Gamma(h_{\mathrm{SM}} \to gg)_{m_{\phi^0}}}\sigma(gg \to h_{\mathrm{SM}})_{m_{\phi^0}}, \tag{30}$$

$$\sigma(gg \to b\bar{b}\phi^0) = (\xi_d^{\phi^0})^2\sigma(gg \to b\bar{b}h_{\mathrm{SM}})_{m_{\phi^0}}, \tag{31}$$

where h_{SM} is the SM Higgs boson. In Eq. (30), $\Gamma(h_{\mathrm{SM}} \to gg)_{m_{\phi^0}}$ and $\sigma(gg \to h_{\mathrm{SM}})_{m_{\phi^0}}$ are, respectively, the decay rate of $h_{\mathrm{SM}} \to gg$ and the cross section of the gluon fusion process by taking the mass of h_{SM} to be replaced by the mass of ϕ^0 (m_{ϕ^0}). We use the values of the gluon fusion cross section in the SM at 14 TeV from Ref. [79]. In Eq. (31), $\sigma(gg \to b\bar{b}h_{\mathrm{SM}})_{m_{\phi^0}}$ is the cross section for the bottom quark-associated production of h_{SM} with the mass of h_{SM} to be replaced by m_{ϕ^0}. We calculate $\sigma(gg \to b\bar{b}h_{\mathrm{SM}})_{m_{\phi^0}}$ by using CalcHEP [80] with CTEQ6L [81] for the parton distribution functions (PDFs).

The signal and background analyses for these processes have been done in the MSSM in Refs. [82,83]. The signal significances for the processes expressed in Eqs. (30) and

[9]Regarding Eq. (31), the equation for $\phi^0 = A$ holds when the bottom quark mass in the phase space function is neglected.

(31) are given in the case of $\tan\beta = 10$ and several fixed masses of A with the collision energy of 14 TeV and the integrated luminosity of 30 fb^{-1}. In Table III, the significance for each fixed value of m_A is listed, where $\mathcal{S}^{\phi^0}_{\rm MSSM}$ and $\mathcal{S}^{b\bar{b}\phi^0}_{\rm MSSM}$ are, respectively, the significances for the gluon fusion process and the bottom quark-associated process. These significances evaluated in the MSSM can be converted into those in the THDMs by using the equations

$$\mathcal{S}^{\phi^0}_{\rm THDM} = \mathcal{S}^{\phi^0}_{\rm MSSM} \times \frac{\sum_{\phi^0=H,A}\sigma(gg\to\phi^0)\times\mathcal{B}(\phi^0\to\tau^+\tau^-)|_{\rm THDM}}{\sum_{\phi^0=H,A}\sigma(gg\to\phi^0)\times\mathcal{B}(\phi^0\to\tau^+\tau^-)|_{\rm MSSM}} \times \sqrt{\frac{\mathcal{L}}{30\ {\rm fb}^{-1}}}, \tag{32}$$

$$\mathcal{S}^{b\bar{b}\phi^0}_{\rm THDM} = \mathcal{S}^{b\bar{b}\phi^0}_{\rm MSSM} \times \frac{\sum_{\phi^0=H,A}\sigma(gg\to b\bar{b}\phi^0)\times\mathcal{B}(\phi^0\to\tau^+\tau^-)|_{\rm THDM}}{\sum_{\phi^0=H,A}\sigma(gg\to b\bar{b}\phi^0)\times\mathcal{B}(\phi^0\to\tau^+\tau^-)|_{\rm MSSM}} \times \sqrt{\frac{\mathcal{L}}{30\ {\rm fb}^{-1}}}, \tag{33}$$

where $\mathcal{L}$ is the assumed integrated luminosity. In the above expression, when m_{ϕ^0} is taken in the range of $X \le m_{\phi^0} \le Y$, where X and Y are values of m_A listed in Table III, we use the values of $\mathcal{S}^{\phi^0}_{\rm MSSM}$ and $\mathcal{S}^{b\bar{b}\phi^0}_{\rm MSSM}$ given in the case with $m_A = X$. The combined significance is calculated by

$$\mathcal{S}_{\rm comb} = \sqrt{(\mathcal{S}^{\phi^0}_{\rm THDM})^2 + (\mathcal{S}^{b\bar{b}\phi^0}_{\rm THDM})^2}, \tag{34}$$

and the expected excluded region with the 95% C.L. is obtained by requiring $\mathcal{S}_{\rm comb} \ge 2$. In the following analysis, we assume $m_A = m_H$ and $\sin(\beta-\alpha) = 1$, and we sum over the processes in Eqs. (30) and (31) mediated by H and A. These assumptions are valid as long as we consider the case with $m_A \gtrsim 150$ GeV, because in the MSSM, $m_H \simeq m_A$ and $\sin(\beta-\alpha) \simeq 1$ are the good approximations in that case.

In Fig. 9, we show the expected excluded regions by using Eq. (34) in the type-II (left panel) and type-X (right panel) THDMs. The blue and red shaded regions are, respectively, the excluded regions assuming $\mathcal{L}$ to be 300 fb^{-1} and 3000 fb^{-1}. In the type-II THDM, the exclusion reach of m_A increases when a larger value of $\tan\beta$ is taken because the cross sections of the bottom quark-associated processes are enhanced due to the coefficient $\xi^b_H = \xi^b_A = \tan\beta$, and the branching fraction of $\phi^0 \to \tau^+\tau^-$ is approaching 10% in high $\tan\beta$ regions as shown in Figs. 4 and 5. On the other hand, in the type-X THDM, both the gluon fusion and the bottom quark-associated production cross sections are suppressed by $\cot^2\beta$ as $\tan\beta$ gets larger, while the branching fraction of $\phi^0 \to \tau^+\tau^-$ increases. Consequently, the cross section times branching ratio takes the maximal obtained at $\tan\beta \simeq 12$, and then $m_A \simeq 600$ GeV can be excluded assuming $\mathcal{L} = 3000$ fb^{-1}. When $\mathcal{L} = 300$ fb^{-1} is assumed, the excluded reach is settled to be 500 GeV in the region of $6 \lesssim \tan\beta \lesssim 20$ in spite of the fact that the cross section has the maximal value at around $\tan\beta = 12$. This can be understood in such a way that the quoted significance $\mathcal{S}^{\phi^0}_{\rm MSSM}$ given in Table III is changed at $m_A = 500$ GeV, and the combined significance $\mathcal{S}_{\rm comb}$ defined in Eq. (34) cannot exceed 2 even in the case with $\tan\beta \simeq 12$. This behavior should vanish by the detailed background analysis with smaller intervals of m_A.

TABLE III. Significance for the gluon fusion process $\mathcal{S}^{\phi^0}_{\rm MSSM}$ and the bottom quark-associated process $\mathcal{S}^{b\bar{b}\phi^0}_{\rm MSSM}$ in the MSSM with $\tan\beta = 10$ at the LHC with the collision energy of 14 TeV and the integrated luminosity of 30 fb^{-1} quoted from Refs. [82,83].

m_A (GeV)	150	200	300	400	450	500
$\mathcal{S}^{\phi^0}_{\rm MSSM}$ [83]	5.6	5.8	1.7	1.1		0.2
$\mathcal{S}^{b\bar{b}\phi^0}_{\rm MSSM}$ [82]	8.0		2.1		1.1	

This result is the updated version of Fig. 1.20 in the ILC Higgs White Paper [51]. In the previous figure, the excluded regions have been derived by using only one value of the significance for the gluon fusion and bottom quark-associated processes with $m_A = 150$ GeV from Ref. [82]. In the current version, we use several values of the significance as shown in Table III.

If we take $\sin(\beta-\alpha) \ne 1$, the contribution from H (A) can drastically decrease because the branching fraction of the $H(A) \to \tau^+\tau^-$ mode significantly decreases due to the $H \to VV$ and $H \to hh$ ($A \to hZ$) modes as seen in Fig. 6. In such a case, the $H \to ZZ \to 4\ell$ and $A \to hZ \to b\bar{b}\ell\ell$ channels can be important instead of the $\tau^+\tau^-$ mode. In fact, these searches have been studied with the LHC data [4,14]. The performance of the HL-LHC has also been evaluated in Refs. [49]. These results show that masses of ~1 TeV could be explored for $1-\kappa_V \gtrsim 10^{-2}$ with low $\tan\beta \lesssim 3$ [49]. Thus, the parameter space allowed by theoretical consistencies can be fully probed by future LHC data for $1-\kappa_V \gtrsim 10^{-2}$.

Next, we consider the Drell-Yan production;

$$pp \to Z^* \to HA. \tag{35}$$

For given values of the masses for H and A, this cross section is purely determined by the gauge coupling constant so that the cross section does not depend on the type

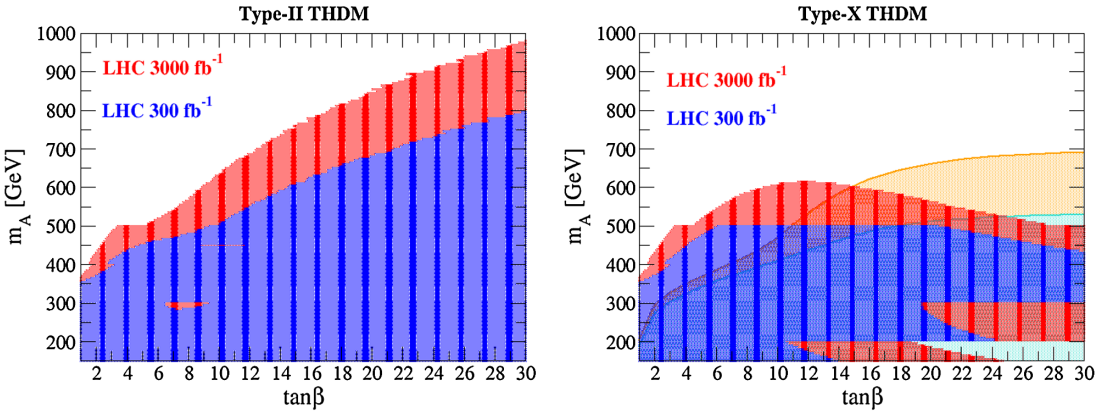

FIG. 9 (color online). Expected excluded regions on the $\tan\beta$-m_A plane at the 95% C.L. from the $gg \to \phi^0 \to \tau^+\tau^-$ and $gg \to b\bar{b}\phi^0 \to b\bar{b}\tau^+\tau^-$ processes by using Eqs. (33) and (34) in the case of $m_A = m_H$ and $\sin(\beta - \alpha) = 1$. The left and right panels show the results in the type-II and type-X THDMs, respectively. The blue (red) shaded regions are excluded regions assuming the integrated luminosity to be 300 fb^{-1} (3000 fb^{-1}). In the right panel, the constraint from the $q\bar{q} \to HA \to \tau^+\tau^-\tau^+\tau^-$ processes is also shown by the light colored regions in the type-X THDM.

of Yukawa interactions. When both H and A decay into the tau pairs, the 4-τ final state is obtained. The cross section of the 4τ process can be large in the type-X THDM as compared to the other three types of THDMs due to the enhancement of the branching fraction of $H/A \to \tau^+\tau^-$ for large $\tan\beta$ [40]. We thus focus on the 4τ signature from the HA production to test the type-X THDM in the following. Analyses on the $pp \to HH^\pm$ and $AH^\pm$ resulting the 3τ signature have been studied in Ref. [84], where the same order bounds on $m_{H^\pm}$ can be obtained.

We estimate the cross section by using the leading-order expression with the CTEQ6L PDFs [81], where the scale of them is set to $\mu = m_H$. The event rates of the $HA \to 4\tau$ signal are obtained by multiplying the production cross section by the branching ratios of H and A into $\tau^+\tau^-$. Furthermore, by using the kinematical distributions of the decay products of τ's that are calculated by PYTHIA [85] and TAUOLA [86], we estimate the efficiency of detecting the signal events after the acceptance and kinematical cuts given in Ref. [84] for all the final states leading from the decays of the four τ's, such as four τ jets, three τ jets plus one lepton, etc. The significance for detecting the $HA \to 4\tau$ process is estimated for a given value of the integrated luminosity, by combining the significance of all the channels in which each significance is evaluated as $S = \sqrt{2[(s+b)\ln(1+s/b) - s]}$ with s and b being the expected numbers of the signal and background events after the cuts, respectively.

In the right panel of Fig. 9, the expected exclusion regions are shown on the $\tan\beta$-m_A plane in the type-X THDM from the $pp \to HA \to 4\tau$ process. The cyan and orange shaded regions are excluded at the 95% C.L. assuming the integrated luminosity to be 300 fb^{-1} and 3000 fb^{-1}, respectively. The search potential is significantly improved for the large $\tan\beta$ regions due to the enhancement of the decay branching ratios of H and A into the $\tau^+\tau^-$ final state. For $\tan\beta \gtrsim 20$, the discovery regions arrive at around $m_A = 500$ GeV for 300 fb^{-1}, while those arrive at around 700 GeV for 3000 fb^{-1}.

We note that the τ-jet tagging efficiency shall worsen at the high-luminosity run of the LHC due to the participation of many hadrons in an event that prevents the isolation requirement in the τ-jet tagging procedure [87]. Therefore, the expected significance may be reduced for the channels with high τ-jet multiplicity, since the τ-jet tagging efficiency used in our analysis is based on the PYTHIA simulation; see Ref. [84]. Although we have not studied this issue seriously, it can be important at the high-luminosity run of the LHC.

In the end of this section, we would like to mention the direct search potential for H and A in the type-I and type-Y THDMs. In the type-I THDM, the Yukawa interactions for the additional Higgs bosons are getting weak for large $\tan\beta$, so it is difficult to generate new bosons via the Yukawa interaction. In type-Y THDM, only the down-type quark Yukawa interactions are enhanced by $\tan\beta$. Since the process $pp \to HX, AH(H, A \to b\bar{b})$ are enhanced for large $\tan\beta$, the cross section times the branching ratio are constrained [12]. The bounds are much weaker than those from $H/A \to \tau^+\tau^-$ decay channels in type-II and type-X THDMs. The analysis with data for high-luminosity running will push these bounds substantially.

Finally, we comment on the constraint from flavor experiments. It is well known that the mass of $H^\pm$ in the type-II THDM is severely constrained by the precise measurements of the $b \to s\gamma$ process [37,38,88,89], where the $H^\pm$ loops contribute to this process in addition to the W boson loop contribution. A lower bound has been found to be $m_{H^+} \gtrsim 380$ GeV (95% C.L.) in the type-II THDM at the next-to-next-to-leading order [89]. In the type-I THDM, the bound from $b \to s\gamma$ is important only in the case with low $\tan\beta$; namely, the bound on m_{H^+} is stronger than the Large Electron

TABLE IV. Expected precisions on the Higgs boson couplings and total width from a constrained seven-parameter fit quoted from Table 1–20 in Ref. [52].

Facility	LHC	HL-LHC	ILC500	ILC500-up	ILC1000	ILC1000-up
$\sqrt{s}$ (GeV)	14,000	14,000	250/500	250/500	250/500/1000	250/500/1000
$\int \mathcal{L}dt$ (fb^{-1})	300/expt	3000/expt	250 + 500	1150 + 1600	250 + 500 + 1000	1150 + 1600 + 2500
κ_γ	5%–7%	2%–5%	8.3%	4.4%	3.8%	2.3%
κ_g	6%–8%	3%–5%	2.0%	1.1%	1.1%	0.67%
κ_W	4%–6%	2%–5%	0.39%	0.21%	0.21%	0.2%
κ_Z	4%–6%	2%–4%	0.49%	0.24%	0.50%	0.3%
κ_ℓ	6%–8%	2%–5%	1.9%	0.98%	1.3%	0.72%
$\kappa_d = \kappa_b$	10%–13%	4%–7%	0.93%	0.60%	0.51%	0.4%
$\kappa_u = \kappa_t$	14%–15%	7%–10%	2.5%	1.3%	1.3%	0.9%

Positron Collider bound of around 80 GeV [20] when $\tan\beta < 2.5$ is taken [89]. The type-Y and type-X THDMs receive similar constraints as in the type-II and type-I THDMs, respectively, because of the same structure of quark Yukawa interactions. Bounds from the other observables such as $B \to \tau\nu$ [90,91], $\tau \to \mu\nu\bar{\nu}$ [91,92], and the muon anomalous magnetic moment [93,94] have been discussed in the type-II THDM. In Ref. [95], constraints from various flavor experiments have been studied in the four types of Yukawa interactions of the THDM. Excluded parameter regions are shown on the m_{H^+}-$\tan\beta$ plane. The bound on m_{H^+} can be converted into that on the masses of neutral Higgs bosons from the electroweak precision data. Although such a constraint can be stronger than that from the direct search as shown in Fig. 9, it is important to search for additional Higgs bosons independently on the flavor experiments.

IV. PRECISION MEASUREMENTS FOR THE HIGGS BOSON COUPLINGS AND FINGERPRINTING EXTENDED HIGGS MODELS

In this section, we discuss the deviation in the SM-like Higgs boson couplings in the THDMs and also in the other models with universal Yukawa couplings. In a model with extended Higgs sectors, the Higgs boson couplings can deviate from the SM values as we already have discussed in Sec. II in the THDMs as an example. Therefore, extended Higgs sectors can be indirectly tested by measuring the deviation of various Higgs boson couplings. Furthermore, the pattern of the deviation strongly depends on the structure of the Higgs sector so that we can discriminate various Higgs sectors by comparing the predicted pattern of the deviations with the measured one.

We here define the scaling factors by normalizing the coupling constant of the SM Higgs boson that will be precisely determined by future collier experiments:

$$\mathcal{L} = \kappa_V h\left(\frac{n_W^2}{v}W^{+\mu}W_\mu^- + \frac{1}{2}\frac{m_Z^2}{v}Z^\mu Z_\mu\right) - \sum_f \kappa_f h\frac{m_f}{v}\bar{f}f. \tag{36}$$

These measured values should be compared with corresponding values in extended Higgs models. In the THDM, κ factors are given at the tree level by

$$\kappa_f = \xi_h^f, \qquad \kappa_V = \sin(\beta - \alpha), \tag{37}$$

where ξ_h^f are listed in Table II. We also discuss the other extended Higgs sectors with universal Yukawa coupling constants; i.e., κ_f for any fermion f are modified in the same way in the end of this section.

The scaling factors will be measured accurately at future collider experiments such as the HL-LHC and the ILC. In Table IV, we give a brief summary of expected sensitivities on the (SM-like) Higgs boson coupling constant at various future experiments. The ranges shown for the LHC and HL-LHC represent the conservative and aggressive scenarios for systematic and theory uncertainties. ILC numbers assume (e^-, e^+) polarizations of $(-0.8, 0.3)$ at 250 and 500 GeV and $(-0.8, 0.2)$ at 1000 GeV, plus a 0.5% theory uncertainty.

A. Higgs boson couplings in the THDMs

We first consider the deviations in the Higgs boson coupling constants in the THDMs. From Table II, it can be seen that all the four types of Yukawa interaction have different combinations of ξ_h^f for $f = u, d$, and e when $\sin(\beta - \alpha) \neq 1$. Therefore, the direction and magnitude of modifications for κ_f are different in four types of Yukawa interactions.

In Figs. 10 and 11, the scaling factors are shown for each type of Yukawa interaction in the THDMs as functions of κ_V^2 and $\tan\beta$. When κ_V^2 is determined, there still is a sign ambiguity for $\cos(\beta - \alpha)$. Thus, we separately plot model predictions for $\cos(\beta - \alpha) < 0$ in Fig. 10 and for $\cos(\beta - \alpha) > 0$ in Fig. 11. Note that the Higgs sector in the MSSM predicts a negative value of $\cos(\beta - \alpha)$. In the left (right) panels, the scaling factors of THDMs are given in the κ_d–κ_ℓ (κ_u–κ_ℓ) plane. Because of the simple scaling in Table II, the predictions in the κ_u–κ_d plane are obtained by interchanging the type-X and type-Y THDMs in the right panels. For illustration purposes only, we slightly shift lines along with

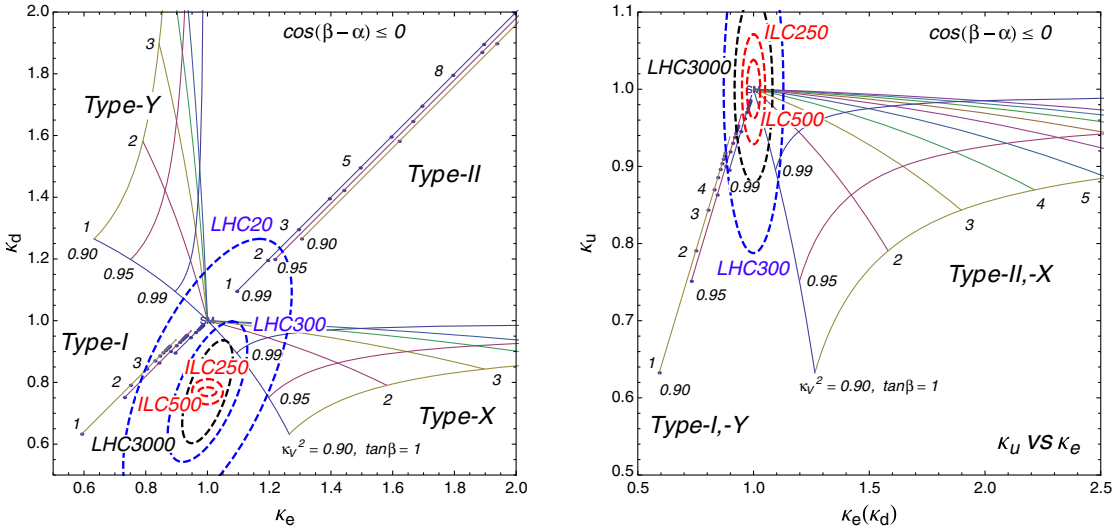

FIG. 10 (color online). The scaling factors for the Yukawa interaction of the SM-like Higgs boson in THDMs in the case of $\cos(\beta - \alpha) < 0$.

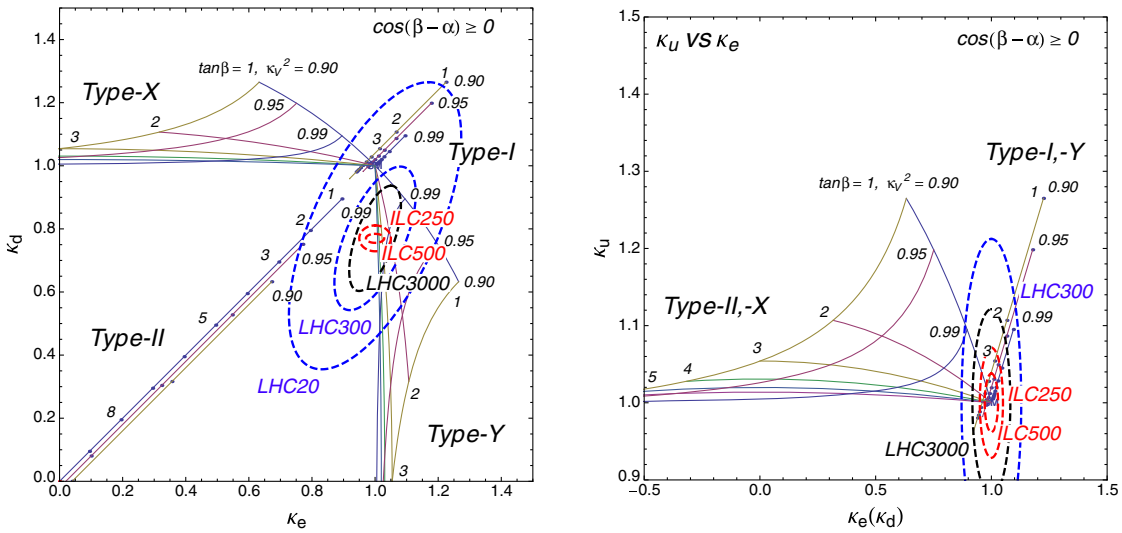

FIG. 11 (color online). The scaling factors for the Yukawa interaction of the SM-like Higgs boson in THDMs in the case of $\cos(\beta - \alpha) > 0$.

$\kappa_x = \kappa_y$ in order to show $\tan\beta$ dependence for fixed κ_V^2 to avoid confusion. The largest contour (LHC20) denotes the current LHC bound at the 68% C.L., where the central values and the correlations are taken from Ref. [64]. We also present the projection at the HL-LHC ($\sqrt{s} = 14$ TeV) with an integrated luminosity of 300 fb^{-1} (LHC300) and 3000 fb^{-1} (LHC3000), where the same central values and the correlations are adopted. The ILC prospects are also shown for ILC250 and ILC500, where the collision energy is 250 GeV and 500 GeV, and the integrated luminosity is 250 fb^{-1} and 500 fb^{-1}, respectively. Each of the THDMs predicts quite a different region, which can be discriminated by the precision measurement of the SM-like Higgs boson coupling constants.

We note that, through the precision measurement of the branching ratios of the SM-like Higgs boson, not only the discrimination of the type of Yukawa interaction but also the determination of $\tan\beta$ in an indirect way can be accomplished [96]. The later complements the determination of $\tan\beta$ by using additional Higgs boson production directly [97].

B. Models with universal Yukawa couplings

We consider Higgs sectors with a universal shift in the Yukawa coupling constants. Such a situation can be realized in a Higgs sector composed of only one doublet field, e.g., a model with a scalar doublet plus singlets,

triplets, and higher isospin multiplets, or in a Higgs sector with multidoublet fields but only one of them giving all the fermion masses, e.g., the type-I THDM. In the following, we first discuss the doublet-singlet model, the type-I THDM, and the doublet-septet model, and then we consider the GM model as models with $\rho_{\rm tree} = 1$. We note that these extended Higgs sectors can predict larger deviations in the hVV couplings as compared to those in models with $\rho_{\rm tree} \neq 1$ because an amount of the deviation depends on an additional VEV for which the magnitude is constrained by the rho parameter if it causes $\rho_{\rm tree} \neq 1$.

In the doublet-singlet model and the soublet-septet model, an isospin singlet field with $Y = 0$ and an isospin septet field with $Y = 2$ are contained, respectively, in addition to the doublet scalar field Φ with $Y = 1/2$. The type-I THDM was already defined in Sec. II. From Eq. (2), a VEV from the additional scalar multiplet does not change $\rho_{\rm tree}$ from the SM value.

Except the VEV of the singlet scalar field, all the VEVs from the additional Higgs multiplet $v_{\rm ext}$ contribute to the electroweak symmetry breaking. They satisfy $v^2 = v_0^2 + (\eta_{\rm ext} v_{\rm ext})^2$, where v_0 is the VEV of Φ and $\eta_{\rm ext} = 1$ and 4 in the type-I THDM and the doublet-septet model, respectively. It is convenient to define the ratio of the VEVs as $\tan\beta = v_0/(\eta_{\rm ext} v_{\rm ext})$.

There are two CP-even scalar states in these three models, and they are mixed with the angle α as

$$\begin{pmatrix} h_{\rm ext} \\ h_0 \end{pmatrix} = R(\alpha) \begin{pmatrix} H \\ h \end{pmatrix}, \tag{38}$$

where h_0 and $h_{\rm ext}$ denote the CP-even scalar components from Φ and an additional scalar multiplet, respectively. The h and H fields are the mass eigenstates, and we assume that h is the observed Higgs boson with the mass of about 126 GeV.

Next, we discuss the GM model for which the Higgs sector is composed of a real ($Y = 0$) and a complex ($Y = 1$) triplet scalar field in addition to Φ. When the VEVs of two triplet fields are aligned to be the same ($= v_{\rm ext}$), $\rho_{\rm tree} = 1$ is satisfied, where the contributions to the deviation in $\rho_{\rm tree}$ from unity by the triplet VEVs are cancelled with each other. The value of $\eta_{\rm ext}$ defined in the above is given as $2\sqrt{2}$.

In the GM model, there are three CP-even scalar states from Φ and two triplets. They are mixed with each other as [98]

$$\begin{pmatrix} \xi_r \\ h_0 \\ \chi_r \end{pmatrix} = \begin{pmatrix} 0 & \frac{1}{\sqrt{3}} & -\sqrt{\frac{2}{3}} \\ 1 & 0 & 0 \\ 0 & \sqrt{\frac{2}{3}} & \frac{1}{\sqrt{3}} \end{pmatrix} \times \begin{pmatrix} \cos\alpha & -\sin\alpha & 0 \\ \sin\alpha & \cos\alpha & 0 \\ 0 & 0 & 1 \end{pmatrix} \begin{pmatrix} H \\ h \\ H_5 \end{pmatrix}, \tag{39}$$

where ξ_r and χ_r are, respectively, the CP-even scalar components in the $Y = 0$ and $Y = 1$ triplet Higgs fields and H_5 is the neutral component of the custodial SU(2) 5-plet Higgs boson.

In Table V, we list the scaling factors κ_f and κ_V in terms of α and β in the four models. In the doublet-singlet model, κ_f and κ_V have the same expression $\cos\alpha$ because both the Yukawa interaction and the gauge interaction originate from the doublet Higgs field, and they are suppressed by the same origin, i.e., the mixing between doublet and singlet fields.

In the type-I THDM, both the Yukawa couplings and the gauge couplings are suppressed by κ_f and κ_V, respectively. However, $\kappa_f \neq \kappa_V$ is generally allowed unlike the doublet-singlet model. We have already mentioned in Sec. II A that we can take the SM-like limit by $\sin(\beta - \alpha) \to 1$, where both κ_f and κ_V become unity. A similar limit can be defined in the doublet-singlet model by taking $\alpha \to 0$.

In the GM model and the doublet-septet model, the VEV of the additional multiplet affects the electroweak symmetry breaking in a different way from that by the doublet Higgs field; i.e., $\eta_{\rm ext}$ in the GM model and the doublet-septet model are different in the type-I THDM. As a result, κ_V can be larger than 1 (see Table V). This is a unique feature to identify these models. Furthermore, the limit of $\kappa_f \to 1$ and $\kappa_V \to 1$ is taken by setting $\beta = 0$ and $\alpha = -\pi/2$, which corresponds to the special case in the type-I THDM.

In Fig. 12, we show predictions of the scaling factors κ_f and κ_V for each value of α and β in the models with universally modified Yukawa couplings. If we vary α and β,

TABLE V. The fraction of the VEVs $\tan\beta$ and the scaling factors κ_f and κ_V in the extended Higgs sectors with universal Yukawa couplings.

Model	$\tan\beta$	κ_f	κ_V
Doublet-singlet	$\cdots$	$\cos\alpha$	$\cos\alpha$
Type-I THDM	$v_0/v_{\rm ext}$	$\cos\alpha/\sin\beta = \sin(\beta-\alpha) + \cot\beta\cos(\beta-\alpha)$	$\sin(\beta-\alpha)$
GM	$v_0/(2\sqrt{2}v_{\rm ext})$	$\cos\alpha/\sin\beta$	$\sin\beta\cos\alpha - \frac{2\sqrt{6}}{3}\cos\beta\sin\alpha$
Doublet-septet	$v_0/(4v_{\rm ext})$	$\cos\alpha/\sin\beta$	$\sin\beta\cos\alpha - 4\cos\beta\sin\alpha$

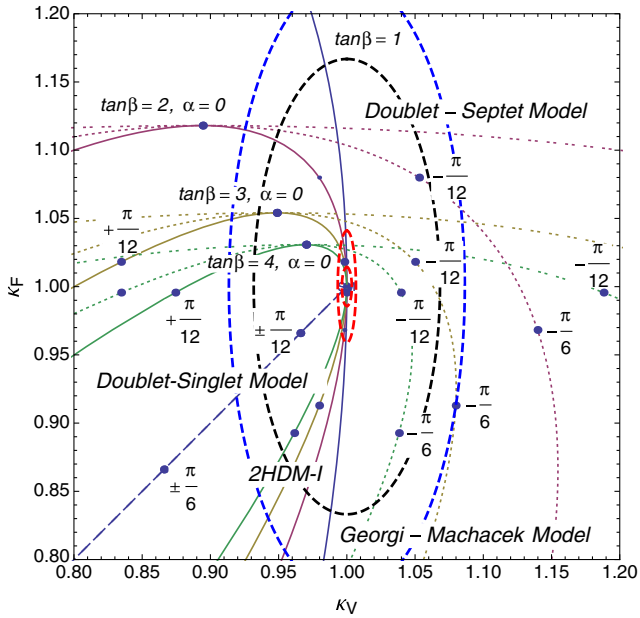

FIG. 12 (color online). The scaling factors κ_f and κ_V in models with universal Yukawa coupling constants.

a model-dependent area (line), which is a distinctive prediction of the models, is drawn. Note that predictions are the same at $\alpha = 0$ in the type-I THDM, the GM model, and the doublet-septet model. From the current LHC data, the scaling factors are obtained at about 20% accuracy at 1σ. It is not sufficient to distinguish these models at this moment. Improvements of the (SM-like) Higgs boson coupling measurements at the HL-LHC and also at the ILC may resolve model predictions.

V. DISCUSSIONS

We here discuss complementarity of precision measurements of the coupling constants of the discovered Higgs boson h and direct searches of additional Higgs bosons at the LHC. In addition, we also discuss the importance of direct searches of additional Higgs bosons at the ILC. A key role is taken by the deviation in the coupling constant of h to weak gauge bosons from the SM prediction, $\delta\kappa_V = 1 - \kappa_V$. When nonzero $\delta\kappa_V$ is found at future colliders, that is identified as an evidence of nonstandard effects mainly due to additional Higgs bosons. By combining the theoretical constraints from perturbative unitarity and vacuum stability, we obtain the upper limit of the energy scale at which evidence of nonstandard Higgs sectors should appear. We first discuss the complementarity in the THDMs and then in the other models later.

For $\delta\kappa_V \gtrsim 5\%$, which is the expected accuracy at the LHC with 300 fb^{-1} [50–52], m_A should be less than about 700 GeV from the conditions of perturbative unitarity and vacuum stability under the assumptions of $m_{H^+} = m_A$ with varying M and m_H in the $m_A \pm 500$ GeV range. In such a case, it is expected that the LHC direct search can find evidence of additional Higgs bosons simultaneously. For $m_A \lesssim 500$ GeV, direct production at the ILC experiment with $\sqrt{s} = 1$ TeV will also be useful to explore the properties of additional Higgs bosons [59]. On top of above, the precision measurement of the couplings of h at the ILC will be the most powerful tool to discriminate types of Yukawa interaction as shown in Figs. 10 and 11.

For $\delta\kappa_V \gtrsim 0.4\%$, which is the expected accuracy at the ILC with $\sqrt{s} = 500$ GeV and $\mathcal{L} = 500$ fb^{-1} [50–52], m_A should be less than 1 TeV from the conditions of perturbative unitarity and vacuum stability under the assumptions of $m_{H^+} = m_A$ with varying M and m_H in the $m_A \pm 500$ GeV range. In such a case, there is a possibility that the direct search at the LHC cannot find any evidence of additional Higgs bosons. In other words, the LHC direct search combined with the constraints from perturbative unitarity and vacuum stability cannot exclude the extended Higgs sector that predicts $\delta\kappa_V \lesssim 0.4\%$. At the ILC, at least the precision measurement of the couplings of h can indicate evidence of the extended Higgs sector. Even in such a situation, as we have shown in the last section, the model discrimination and parameter determination will be still possible by using only the fingerprinting of the deviation of the couplings of h. Furthermore, an upper limit of the mass scale of additional Higgs bosons can be set by the constraints from perturbative unitarity and vacuum stability, while the lower limit is given by the direct search at the LHC. Therefore, we could conclude the existence of the nonstandard Higgs sector at a certain energy scale. This energy scale will be crucial information to design next-generation future colliders.

The accuracy of the $\delta\kappa_V$ measurement can be improved at the ILC with 1 TeV and 1 ab^{-1}, and the indirect upper limit of the mass scale can be slightly extended accordingly. For $\delta\kappa_V \lesssim 0.2\%$, which is beyond the accuracy of the coupling measurement of h at the ILC with $\sqrt{s} = 1$ TeV and $\mathcal{L} = 1$ ab^{-1} [50–52], the upper limit of the mass scale cannot be obtained from the conditions of perturbative unitarity and vacuum stability. In this case, we cannot separate the extended Higgs sector from the SM from the coupling measurements of h. Therefore, the decoupling limit of the extended Higgs sector cannot be excluded. There are possibilities that the additional Higgs bosons can be discovered at the LHC or the ILC, since the small deviation in κ_V does not necessarily mean the large mass of additional Higgs bosons in the extended Higgs sector. We note that the direct production of additional Higgs bosons at the LHC and the ILC also have the power to discriminate the models of extended Higgs sectors, such as the type of Yukawa sector in the THDMs [59], etc.

To compare the precisely measured values of the Higgs boson couplings, precise calculations in each given model are essentially important. One-loop corrections to the hVV coupling constants have been calculated in Ref. [66], and

those to $hf\bar{f}$ coupling constants have been calculated in Ref. [99] in the THDM. Magnitudes of these corrections due to the additional Higgs boson loops are respectively given to be maximally about 1% and 5% for the hVV and $hf\bar{f}$ couplings under the constraint from perturbative unitarity and vacuum stability. Therefore, the pattern of the deviations in the $hf\bar{f}$ shown in Figs. 10 and 11 does not change even including radiative corrections. However, if the $hf\bar{f}$ couplings are determined with an order of 1% accuracy under the situation in which the deviation in hVV couplings is also found, we may be able to determine not only the type of Yukawa interactions but also some inner parameters such as M^2 in the THDMs. In addition to the hVV and $hf\bar{f}$ couplings, one-loop corrections to the hhh coupling, for which the amount can be significant due to the nondecoupling effect of the additional Higgs bosons, are also important. In Refs. [66,100], it has been shown that the size of the correction can be $\mathcal{O}(100)\%$ under the constraint from perturbative unitarity [68] and vacuum stability [69,70]. By studying the correlation among the deviations in the hhh [66,100], $h\gamma\gamma$ [61,101–103], and $hZ\gamma$ [103,104] couplings from the SM predictions, we can extract properties of additional Higgs bosons running in the loop such as the electric charge, the isospin, and the nondecoupling nature.

Finally, we mention models other than the THDMs. In the doublet-singlet model [60], both the hVV and $hf\bar{f}$ coupling constants are suppressed by the same factor. Therefore, $\kappa_V = \kappa_f < 1$ can be indirect evidence for this model. Detection of an additional CP-even scalar boson, for which the Yukawa and gauge interactions are given only from the mixing with the doublet Higgs field, can be a direct search for the model. The GM model [22] and the doublet-septet model [61–63] have a unique pattern of the deviation in the Higgs boson couplings; namely, κ_V can be larger than unity [63], which is a crucial property to identify these models. In addition, multicharged, e.g., doubly charged, Higgs bosons can significantly contribute to the deviation in the loop-induced $h\gamma\gamma$ and $hZ\gamma$ couplings. When multicharged scalar bosons are discovered, it can be a direct test of these models. Phenomenology of such additional scalar bosons has been discussed in the GM model [105–107] and in the doublet-septet model [108] at the LHC. Measuring the $H^\pm W^\mp Z$ vertex [77,78] is also an important probe as discussed in Sec. II C.

In this paper, we concentrate on the models with $\rho_{\rm tree} = 1$. However, we here shortly comment on the Higgs triplet model (HTM) as an important example for models with $\rho_{\rm tree} \neq 1$, because it is deduced from the type-II seesaw mechanism [109]. In the HTM, although deviations in the hVV and $hf\bar{f}$ couplings cannot be so large due to the constraint from the rho parameter, those in the loop-induced $h\gamma\gamma$ [110–113] and $hZ\gamma$ [111–113] couplings can be significant by the doubly charged Higgs boson $H^{\pm\pm}$ loop. The one-loop corrections to the hhh coupling can also be large as calculated in Refs. [27,114] due to the nondecoupling effect of additional Higgs bosons similarly to the THDM. The correlation among the deviations in the decay rate of $h \to \gamma\gamma$ and the hhh coupling constants[10] from the SM values have been investigated in Ref. [27]. A direct search for $H^{\pm\pm}$ can be an important clue to test the model with the $Y = 1$ triplet field, which can decay into the same-sign dilepton [115–120] and the same-sign diboson [121,122] depending on the magnitude of the triplet VEV.[11]

VI. CONCLUSIONS

We have discussed the determination of the extended Higgs sector by combining the direct and indirect searches for additional Higgs bosons at future collider experiments. Direct searches of the additional Higgs bosons provides the clear evidence for extended Higgs sectors. Focusing on the THDM with the softly broken Z_2 symmetry, we have studied the expected exclusion regions in the m_A-$\tan\beta$ plane at the LHC with the 14 TeV run with 300 fb^{-1} and 3000 fb^{-1} data. For the neutral Higgs boson searches, we have shown that the mass scale up to several hundreds GeV to TeV can be explored at the LHC, depending on the type of Yukawa interaction and parameters such as $\tan\beta$ and $\sin(\beta - \alpha)$. For the indirect searches of additional Higgs bosons via coupling constants of the SM-like Higgs bosons, we have considered various models for the extended Higgs sector, such as the THDMs with four types of Yukawa interactions, the doublet-singlet model, the doublet-septet model, and the GM model, as typical models that predict $\rho_{\rm tree} = 1$. We have demonstrated that there exists a variety of patterns in the deviations in the SM-like Higgs boson couplings to the gauge bosons and fermions from the SM prediction depending on the structure of the Higgs sector. Therefore, we can fingerprint the nonminimal Higgs sector by detecting the pattern of deviations in an excellent precision at future colliders.

Taking into account the theoretical constraints on the model, such as perturbative unitarity and vacuum stability, the complementarity between the direct searches and the indirect searches can be understood to identify the nonminimal Higgs sector. Observation of the deviation in the coupling constant of the SM-like Higgs boson to the weak gauge bosons plays a key role, which also affects the strategy of the direct search of additional Higgs bosons at colliders. First of all, we have to keep in mind that there exists a decoupling limit in extended

[10]The deviation in the hhh coupling at the tree level is much suppressed by the triplet VEV similar to the hVV and $hf\bar{f}$ as mentioned above.

[11]If there is a mass difference between $H^{\pm\pm}$ and the singly charged scalar components, the cascade decay of $H^{\pm\pm}$ associated with the W boson is possible [123].

Higgs sectors in the limit of $\delta\kappa_V \to 0$, where the SM is a good description as a low-energy effective theory up to much higher scales than the electroweak scale. On the other hand, if a relatively large deviation of $\delta\kappa_V$ is observed, the mass scale of the additional Higgs bosons is bounded from the above by using the argument of perturbative unitarity and vacuum stability so that the direct discovery of them can be highly expected. If a small deviation is observed at the ILC, the direct discovery of the additional Higgs boson can be difficult. Even in such a situation, the fingerprinting of the SM-like Higgs boson couplings can be a solid and powerful tool to explore the extended Higgs sector.

ACKNOWLEDGMENTS

S. K. was supported in part by Grant-in-Aid for Scientific Research from Japan Society for the Promotion of Science (JSPS), Grants No. 22244031 and No. 24340046, and from Ministry of Education, Culture, Sports, Science and Technology (MEXT), Japan, Grant No. 23104006. K. T. was supported in part by MEXT, Grants No. 26104704 and No. 23104011. K. Y. was supported in part by the National Science Council of R. O. C. under Grant No. NSC-101-2811-M-008-014. The work of H. Y. was supported in part by Grant-in-Aid for Scientific Research, Grant No. 24340046, and the Sasakawa Scientific Research Grant from the Japan Science Society.

[1] ATLAS Collaboration, Phys. Lett. B **716**, 1 (2012); CMS Collaboration, Phys. Lett. B **716**, 30 (2012).
[2] ATLAS Collaboration, Report No. ATLAS-CONF-2013-034; CMS Collaboration, Report No. CMS-PAS-HIG-13-005.
[3] G. Aad *et al.* (ATLAS Collaboration), Phys. Lett. B **726**, 88 (2013); **726**, 120 (2013); S. Chatrchyan *et al.* (CMS Collaboration), J. High Energy Phys. 01 (2014) 096.
[4] S. Chatrchyan *et al.* (CMS Collaboration), Phys. Rev. D **89**, 092007 (2014).
[5] S. Weinberg, Phys. Rev. D **13**, 974 (1976); **19**, 1277 (1979).
[6] E. Gildener and S. Weinberg, Phys. Rev. D **13**, 3333 (1976); E. Gildener, Phys. Rev. D **14**, 1667 (1976).
[7] L. Susskind, Phys. Rev. D **20**, 2619 (1979).
[8] H. E. Haber and G. L. Kane, Phys. Rep. **117**, 75 (1985).
[9] J. F. Gunion, H. E. Haber, G. L. Kane, and S. Dawson, Front. Phys. **80**, 1 (2000).
[10] G. Aad *et al.* (ATLAS Collaboration), J. High Energy Phys. 02 (2013) 095.
[11] CMS Collaboration, Report No. CMS-PAS-HIG-13-021.
[12] S. Chatrchyan *et al.* (CMS Collaboration), Phys. Lett. B **722**, 207 (2013).
[13] ATLAS Collaboration, Report No. ATLAS-CONF-2013-027.
[14] CMS Collaboration, Report No. CMS-PAS-HIG-13-025.
[15] G. Aad *et al.* (ATLAS Collaboration), J. High Energy Phys. 06 (2012) 039.
[16] ATLAS Collaboration, Report No. ATLAS-CONF-2013-090.
[17] G. Aad *et al.* (ATLAS Collaboration), Eur. Phys. J. C **73**, 2465 (2013).
[18] G. Aad *et al.* (ATLAS Collaboration), Eur. Phys. J. C **72**, 2244 (2012); S. Chatrchyan *et al.* (CMS Collaboration), Eur. Phys. J. C **72**, 2189 (2012).
[19] G. Aad *et al.* (ATLAS Collaboration), Phys. Rev. Lett. **112**, 201802 (2014); S. Chatrchyan *et al.* (CMS Collaboration), Eur. Phys. J. C **74**, 2980 (2014).
[20] J. Beringer *et al.* (Particle Data Group), Phys. Rev. D **86**, 010001 (2012).
[21] K. Hally, H. E. Logan, and T. Pilkington, Phys. Rev. D **85**, 095017 (2012); K. Earl, K. Hartling, H. E. Logan, and T. Pilkington, Phys. Rev. D **88**, 015002 (2013).
[22] H. Georgi and M. Machacek, Nucl. Phys. **B262**, 463 (1985); M. S. Chanowitz and M. Golden, Phys. Lett. **B165**, 105 (1985).
[23] P. Sikivie, L. Susskind, M. B. Voloshin, and V. I. Zakharov, Nucl. Phys. **B173**, 189 (1980).
[24] T. Blank and W. Hollik, Nucl. Phys. **B514**, 113 (1998).
[25] P. H. Chankowski, S. Pokorski, and J. Wagner, Eur. Phys. J. C **50**, 919 (2007); M.-C. Chen, S. Dawson, and C. B. Jackson, Phys. Rev. D **78**, 093001 (2008).
[26] S. Kanemura and K. Yagyu, Phys. Rev. D **85**, 115009 (2012).
[27] M. Aoki, S. Kanemura, M. Kikuchi, and K. Yagyu, Phys. Rev. D **87**, 015012 (2013).
[28] J. F. Gunion, R. Vega, and J. Wudka, Phys. Rev. D **43**, 2322 (1991).
[29] D. Toussaint, Phys. Rev. D **18**, 1626 (1978); S. Bertolini, Nucl. Phys. **B272**, 77 (1986); W. Hollik, Z. Phys. C **32**, 291 (1986); **37**, 569 (1988).
[30] W. Grimus, L. Lavoura, O. M. Ogreid, and P. Osland, Nucl. Phys. **B801**, 81 (2008); Phys. Lett. B **704**, 303 (2011).
[31] J.-M. Gerard and M. Herquet, Phys. Rev. Lett. **98**, 251802 (2007).
[32] E. Cervero and J. M. Gerard, Phys. Lett. B **712**, 255 (2012).
[33] D. Lopez-Val and J. Sola, Eur. Phys. J. C **73**, 2393 (2013).
[34] M. E. Peskin and J. D. Wells, Phys. Rev. D **64**, 093003 (2001).
[35] S. Kanemura, Y. Okada, H. Taniguchi, and K. Tsumura, Phys. Lett. B **704**, 303 (2011).
[36] S. L. Glashow and S. Weinberg, Phys. Rev. D **15**, 1958 (1977).
[37] V. D. Barger, J. L. Hewett, and R. J. N. Phillips, Phys. Rev. D **41**, 3421 (1990).
[38] Y. Grossman, Nucl. Phys. **B426**, 355 (1994).
[39] A. G. Akeroyd, Phys. Lett. B **377**, 95 (1996).

[40] M. Aoki, S. Kanemura, K. Tsumura, and K. Yagyu, Phys. Rev. D **80**, 015017 (2009).
[41] H. E. Logan and D. MacLennan, Phys. Rev. D **79**, 115022 (2009).
[42] H. E. Logan and D. MacLennan, Phys. Rev. D **81**, 075016 (2010).
[43] G. C. Branco, P. M. Ferreira, L. Lavoura, M. N. Rebelo, M. Sher, and J. P. Silva, Phys. Rep. **516**, 1 (2012).
[44] J. Liu and L. Wolfenstein, Nucl. Phys. **B289**, 1 (1987).
[45] E. Ma, Phys. Rev. Lett. **86**, 2502 (2001).
[46] T. Appelquist and J. Carazzone, Phys. Rev. D **11**, 2856 (1975).
[47] ATLAS Collaboration, arXiv:1307.7292; CMS Collaboration, arXiv:1307.7135.
[48] ATLAS Collaboration, Report No. ATL-PHYS-PUB-2013-014; Report No. ATL-PHYS-PUB-2013-015; Report No. ATL-PHYS-PUB-2014-006.
[49] ATLAS Collaboration, Report No. ATL-PHYS-PUB-2013-016.
[50] H. Baer *et al.* arXiv:1306.6352.
[51] D. M. Asner *et al.*, arXiv:1310.0763.
[52] S. Dawson *et al.*, arXiv:1310.8361v2.
[53] N. Craig, J. Galloway, and S. Thomas, arXiv:1305.2424.
[54] J. Baglio, O. Eberhardt, U. Nierste, and M. Wiebusch, Phys. Rev. D **90**, 015008 (2014).
[55] B. Coleppa, F. Kling, and S. Su, arXiv:1404.1922.
[56] C.-W. Chiang and K. Yagyu, J. High Energy Phys. 07 (2013) 160.
[57] P. M. Ferreira, J. F. Gunion, H. E. Haber, and R. Santos, Phys. Rev. D **89**, 115003 (2014).
[58] H. S. Cheon and S. K. Kang, J. High Energy Phys. 09 (2013) 085; N. Craig and S. Thomas, J. High Energy Phys. 11 (2012) 083; W. Altmannshofer, S. Gori, and G. D. Kribs, Phys. Rev. D **86**, 115009 (2012); S. Chang, S. K. Kang, J.-P. Lee, K. Y. Lee, S. C. Park, and J. Song, J. High Energy Phys. 05 (2013) 075; Y. Bai, V. Barger, L. L. Everett, and G. Shaughnessy, Phys. Rev. D **87**, 115013 (2013); A. Drozd, B. Grzadkowski, J. F. Gunion, and Y. Jiang, J. High Energy Phys. 05 (2013) 072; J. Chang, K. Cheung, P.-Y. Tseng, and T.-C. Yuan, Phys. Rev. D **87**, 035008 (2013); P. M. Ferreira, R. Santos, H. E. Haber, and J. P. Silva, Phys. Rev. D **87**, 055009 (2013); C.-Y. Chen and S. Dawson, Phys. Rev. D **87**, 055016 (2013); A. Celis, V. Ilisie, and A. Pich, J. High Energy Phys. 07 (2013) 053; B. Grinstein and P. Uttayarat, J. High Energy Phys. 06 (2013) 09409 (2013) 110(E); C.-Y. Chen, S. Dawson, and M. Sher, Phys. Rev. D **88**, 015018 (2013); O. Eberhardt, U. Nierste, and M. Wiebusch, J. High Energy Phys. 07 (2013) 118; R. V. Harlander, S. Liebler, and T. Zirke, J. High Energy Phys. 02 (2014) 023; N. Chen, C. Du, Y. Fang, and L.-C. Lü, Phys. Rev. D **89**, 115006 (2014); B. Coleppa, F. Kling, and S. Su, J. High Energy Phys. 01 (2014) 161; L. Wang and X.-F. Han, arXiv:1404.7437; B. Dumont, J. F. Gunion, Y. Jiang, and S. Kraml, Phys. Rev. D **90**, 035021 (2014).
[59] S. Kanemura, H. Yokoya, and Y.-J. Zheng, Nucl. Phys. **B886**, 524 (2014).
[60] V. Barger, P. Langacker, M. McCaskey, M. J. Ramsey-Musolf, and G. Shaughnessy, Phys. Rev. D **77**, 035005 (2008).
[61] J. R. Ellis, M. K. Gaillard, and D. V. Nanopoulos, Nucl. Phys. **B106**, 292 (1976).
[62] J. Hisano and K. Tsumura, Phys. Rev. D **87**, 053004 (2013).
[63] S. Kanemura, M. Kikuchi, and K. Yagyu, Phys. Rev. D **88**, 015020 (2013).
[64] P. P. Giardino, K. Kannike, I. Masina, M. Raidal, and A. Strumia, J. High Energy Phys. 05 (2014) 046.
[65] J. F. Gunion and H. E. Haber, Phys. Rev. D **67**, 075019 (2003).
[66] S. Kanemura, Y. Okada, E. Senaha, and C.-P. Yuan, Phys. Rev. D **70**, 115002 (2004).
[67] H. Huffel and G. Pocsik, Z. Phys. C **8**, 13 (1981); J. Maalampi, J. Sirkka, and I. Vilja, Phys. Lett. B **265**, 371 (1991).
[68] S. Kanemura, T. Kubota, and E. Takasugi, Phys. Lett. B **313**, 155 (1993); A. G. Akeroyd, A. Arhrib, and E. M. Naimi, Phys. Lett. B **490**, 119 (2000); I. F. Ginzburg and I. P. Ivanov, Phys. Rev. D **72**, 115010 (2005).
[69] N. G. Deshpande and E. Ma, Phys. Rev. D **18**, 2574 (1978); M. Sher, Phys. Rep. **179**, 273 (1989); S. Nie and M. Sher, Phys. Lett. B **449**, 89 (1999);
[70] S. Kanemura, T. Kasai, and Y. Okada, Phys. Lett. B **471**, 182 (1999).
[71] N. Chakrabarty, U. K. Dey, and B. Mukhopadhyaya, arXiv:1407.2145.
[72] S. Kanemura, S. Moretti, Y. Mukai, R. Santos, and K. Yagyu, Phys. Rev. D **79**, 055017 (2009).
[73] H. Fusaoka and Y. Koide, Phys. Rev. D **57**, 3986 (1998).
[74] M. Capdequi Peyranere, H. E. Haber, and P. Irulegui, Phys. Rev. D **44**, 191 (1991).
[75] S. Kanemura, Phys. Rev. D **61**, 095001 (2000); Eur. Phys. J. C **17**, 473 (2000).
[76] J. A. Grifols and A. Mendez, Phys. Rev. D **22**, 1725 (1980).
[77] E. Asakawa and S. Kanemura, Phys. Lett. B **626**, 111 (2005); E. Asakawa, S. Kanemura, and J. Kanzaki, Phys. Rev. D **75**, 075022 (2007); S. Godfrey and K. Moats, Phys. Rev. D **81**, 075026 (2010).
[78] S. Kanemura, K. Yagyu, and K. Yanase, Phys. Rev. D **83**, 075018 (2011).
[79] https://twiki.cern.ch/twiki/bin/view/LHCPhysics/CERNYellowReportPageAt14TeV.
[80] A. Pukhov *et al.*, arXiv:hep-ph/9908288.
[81] J. Pumplin, D. R. Stump, J. Huston, H. L. Lai, P. M. Nadolsky, and W. K. Tung, J. High Energy Phys. 07 (2002) 012.
[82] G. Aad *et al.* (ATLAS Collaboration), arXiv:0901.0512.
[83] E. Richter-Was, D. Froidevaux, F. Gianotti, L. Poggioli, D. Cavalli, and S. Resconi, Int. J. Mod. Phys. A **13**, 1371 (1998).
[84] S. Kanemura, K. Tsumura, and H. Yokoya, Phys. Rev. D **85**, 095001 (2012); arXiv:1201.6489.
[85] T. Sjostrand, S. Mrenna, and P. Z. Skands, J. High Energy Phys. 05 (2006) 026.
[86] S. Jadach, Z. Was, R. Decker, and J. H. Kuhn, Comput. Phys. Commun. **76**, 361 (1993).
[87] D. Cavalli and S. Resconi, Report No. ATL-PHYS-98-118.
[88] M. Ciuchini, E. Franco, G. Martinelli, L. Reina, and L. Silvestrini, Phys. Lett. B **334**, 137 (1994); M. Ciuchini,

G. Degrassi, P. Gambino, and G. F. Giudice, Nucl. Phys. **B527**, 21 (1998); F. Borzumati and C. Greub, Phys. Rev. D **58**, 074004 (1998); P. Gambino and M. Misiak, Nucl. Phys. **B611**, 338 (2001).

[89] T. Hermann, M. Misiak, and M. Steinhauser, J. High Energy Phys. 11 (2012) 036.

[90] W.-S. Hou, Phys. Rev. D **48**, 2342 (1993); Y. Grossman and Z. Ligeti, Phys. Lett. B **332**, 373 (1994); Y. Grossman, H. E. Haber, and Y. Nir, Phys. Lett. B **357**, 630 (1995); A. G. Akeroyd and S. Recksiegel, J. Phys. G **29**, 2311 (2003).

[91] M. Krawczyk and D. Sokolowska, *Proceedings of the LCWS2007 and ILC2007 Hamburg, Germany, 2007*, eConf C 0705302, HIG09 (2007).

[92] W. Hollik and T. Sack, Phys. Lett. B **284**, 427 (1992); M. Krawczyk and D. Temes, Eur. Phys. J. C **44**, 435 (2005).

[93] H. E. Haber, G. L. Kane, and T. Sterling, Nucl. Phys. **B161**, 493 (1979).

[94] M. Krawczyk and J. Zochowski, Phys. Rev. D **55**, 6968 (1997).

[95] F. Mahmoudi and O. Stal, Phys. Rev. D **81**, 035016 (2010).

[96] S. Kanemura, K. Tsumura, and H. Yokoya, Phys. Rev. D **88**, 055010 (2013).

[97] J. L. Feng and T. Moroi, Phys. Rev. D **56**, 5962 (1997); V. D. Barger, T. Han, and J. Jiang, Phys. Rev. D **63**, 075002 (2001); J. F. Gunion, T. Han, J. Jiang, and A. Sopczak, Phys. Lett. B **565**, 42 (2003).

[98] J. F. Gunion, R. Vega, and J. Wudka, Phys. Rev. D **42**, 1673 (1990).

[99] S. Kanemura, M. Kikuchi, and K. Yagyu, Phys. Lett. B **731**, 27 (2014).

[100] S. Kanemura, Y. Okada, and E. Senaha, Phys. Lett. B **606**, 361 (2005).

[101] M. A. Shifman, A. I. Vainshtein, M. B. Voloshin, and V. I. Zakharov, Yad. Fiz. **30**, 1368 (1979); [, Sov. J. Nucl. Phys. **30**, 711 (1979)].

[102] I. F. Ginzburg, M. Krawczyk, and P. Osland, Nucl. Instrum. Methods Phys. Res., Sect. A **472**, 149 (2001); N. Bernal, D. Lopez-Val, and J. Sola, Phys. Lett. B **677**, 39 (2009); P. Posch, Phys. Lett. B **696**, 447 (2011); D. Lopez-Val and J. Sola, Phys. Lett. B **702**, 246 (2011); P. M. Ferreira, R. Santos, M. Sher, and J. P. Silva, Phys. Rev. D **85**, 077703 (2012); **85**, 035020 (2012); A. Arhrib, R. Benbrik, and N. Gaur, Phys. Rev. D **85**, 095021 (2012).

[103] A. Arhrib, M. Capdequi Peyranere, W. Hollik, and S. Penaranda, Phys. Lett. B **579**, 361 (2004).

[104] L. Bergstrom and G. Hulth, Nucl. Phys. **B259**, 137 (1985); [**B276**, 744(E) (1986)].

[105] C. -W. Chiang and K. Yagyu, J. High Energy Phys. 01 (2013) 026.

[106] C. Englert, E. Re, and M. Spannowsky, Phys. Rev. D **87**, 095014 (2013).

[107] C.-W. Chiang, A.-L. Kuo, and K. Yagyu, J. High Energy Phys. 10 (2013) 072.

[108] C. Alvarado, L. Lehman, and B. Ostdiek, J. High Energy Phys. 05 (2014) 150.

[109] T. P. Cheng and L. F. Li, Phys. Rev. D **22**, 2860 (1980); J. Schechter and J. W. F. Valle, Phys. Rev. D **22**, 2227 (1980); G. Lazarides, Q. Shafi, and C. Wetterich, Nucl. Phys. **B181**, 287 (1981); R. N. Mohapatra and G. Senjanovic, Phys. Rev. D **23**, 165 (1981); M. Magg and C. Wetterich, Phys. Lett. B **94**, 61 (1980).

[110] P. Fileviez Perez, H. H. Patel, M. J. Ramsey-Musolf, and K. Wang, Phys. Rev. D **79**, 055024 (2009); A. Arhrib, R. Benbrik, M. Chabab, G. Moultaka, and L. Rahili, J. High Energy Phys. 04 (2012) 136; A. G. Akeroyd and S. Moretti, Phys. Rev. D **86**, 035015 (2012); E. J. Chun, H. M. Lee, and P. Sharma, J. High Energy Phys. 11 (2012) 106; L. Wang and X.-F. Han, Phys. Rev. D **87**, 015015 (2013).

[111] C.-W. Chiang and K. Yagyu, Phys. Rev. D **87**, 033003 (2013).

[112] P. S. Bhupal Dev, D. K. Ghosh, N. Okada, and I. Saha, J. High Energy Phys. 03 (2013) 150; 05 (2013) 049(E).

[113] C.-S. Chen, C.-Q. Geng, D. Huang, and L.-H. Tsai, Phys. Lett. B **723**, 156 (2013).

[114] M. Aoki, S. Kanemura, M. Kikuchi, and K. Yagyu, Phys. Lett. B **714**, 279 (2012).

[115] M. Muhlleitner and M. Spira, Phys. Rev. D **68**, 117701 (2003).

[116] A. G. Akeroyd and M. Aoki, Phys. Rev. D **72**, 035011 (2005).

[117] M. Kadastik, M. Raidal, and L. Rebane, Phys. Rev. D **77**, 115023 (2008); J. Garayoa and T. Schwetz, J. High Energy Phys. 03 (2008) 009; A. G. Akeroyd, M. Aoki, and H. Sugiyama, Phys. Rev. D **77**, 075010 (2008).

[118] A. G. Akeroyd and C.-W. Chiang, Phys. Rev. D **80**, 113010 (2009); F. del Aguila and J. A. Aguilar-Saavedra, Nucl. Phys. **B813**, 22 (2009); A. G. Akeroyd, C. W. Chiang, and N. Gaur, J. High Energy Phys. 11 (2010) 005.

[119] E. J. Chun and P. Sharma, J. High Energy Phys. 08 (2012) 162.

[120] H. Sugiyama, K. Tsumura, and H. Yokoya, Phys. Lett. B **717**, 229 (2012).

[121] T. Han, B. Mukhopadhyaya, Z. Si, and K. Wang, Phys. Rev. D **76**, 075013 (2007); P. Fileviez Perez, T. Han, G.-y. Huang, T. Li, and K. Wang, Phys. Rev. D **78**, 015018 (2008); C.-W. Chiang, T. Nomura, and K. Tsumura, Phys. Rev. D **85**, 095023 (2012); Z. Kang, J. Li, T. Li, Y. Liu, and G.-Z. Ning, arXiv:1404.5207.

[122] S. Kanemura, K. Yagyu, and H. Yokoya, Phys. Lett. B **726**, 316 (2013).

[123] M. Aoki, S. Kanemura, and K. Yagyu, Phys. Rev. D **85**, 055007 (2012).

Physics Letters B 726 (2013) 316–319

Contents lists available at ScienceDirect

Physics Letters B

www.elsevier.com/locate/physletb

First constraint on the mass of doubly-charged Higgs bosons in the same-sign diboson decay scenario at the LHC

Shinya Kanemura [a], Kei Yagyu [b,*], Hiroshi Yokoya [a]

[a] Department of Physics, University of Toyama, 3190 Gofuku, Toyama 930-8555, Japan
[b] Department of Physics, National Central University, Chungli 32001, Taiwan

ARTICLE INFO

Article history:
Received 5 July 2013
Received in revised form 21 August 2013
Accepted 21 August 2013
Available online 29 August 2013
Editor: J. Hisano

ABSTRACT

When the doubly-charged Higgs bosons $H^{\pm\pm}$ mainly decay into the same-sign dilepton, a lower bound on the mass is around 400 GeV by the current LHC data. On the other hand, no such bound has been reported by using the data at LEP and at the LHC for the case where the same-sign diboson decay $H^{\pm\pm} \to W^{\pm(*)}W^{\pm(*)}$ is dominant. We study limits on the mass for such a case by using the current experimental data. From the precise measurement of the total width of the Z boson at the LEP experiment, the mass below 43 GeV is excluded with the 95% confidence level. It turns out that the results from four charged-lepton searches at LEP do not provide any significant constraint. We show that a new lower bound is obtained in the diboson decay scenario at the LHC with the collision energy to be 7 TeV and the integrated luminosity to be 4.7 fb^{-1}. By using the data of the same-sign dilepton events, the lower limit is found to be 60 GeV at the 95% confidence level. By the extrapolation of the data to 20 fb^{-1} with the same collision energy, the lower limit is evaluated to be 85 GeV.

© 2013 Elsevier B.V. All rights reserved.

A Higgs boson has been discovered with the mass around 126 GeV in the diphoton and the four lepton channels at the LHC [1]. Observed properties of the boson are consistent with those of the Higgs boson predicted in the standard model (SM). However, this fact does not necessarily mean that the Higgs sector is the minimal one assumed in the SM. There is no fundamental principle for such a form with an isospin doublet scalar field. In fact, extended Higgs sectors with more scalar fields are often introduced in new physics models beyond the SM, which are motivated to explain phenomena such as neutrino oscillation [2,3], the existence of dark matter [4] and the baryon asymmetry of the Universe [5]. The SM-like Higgs boson can also appear in these extended Higgs sectors. Therefore, by exploring the extra Higgs bosons at collider experiments, the structure of the Higgs sector can be determined, and thereby the new physics model can be probed.

The Higgs triplet model (HTM) is one of the simple but important extended Higgs sectors. It can provide the origin of tiny neutrino masses with the type-II seesaw mechanism [2]. The Higgs sector is composed of an isospin triplet field (Δ) with hypercharge $Y = 1$ and a doublet field (Φ) with $Y = 1/2$. The generated neutrino masses are proportional to the vacuum expectation value (VEV) of the triplet field v_Δ. It is well known that v_Δ is constrained to be much smaller than the VEV of the doublet field v_ϕ by the electroweak precision data at the LEP/SLC experiments [6]. One of the striking features of the model is the appearance of the doubly- ($H^{\pm\pm}$) and singly-charged ($H^\pm$) Higgs bosons in addition to two CP-even Higgs bosons (h and H) and the CP-odd Higgs boson (A). The discovery of these particles, especially $H^{\pm\pm}$, is essentially important to identify the model.

These additional Higgs bosons can be produced by collider experiments if kinematically accessible [7–11]. The main decay mode of $H^{\pm\pm}$ strongly depends on v_Δ. They decay into the same-sign dilepton when v_Δ is smaller than about 0.1 MeV, which can be a clear signature for the discovery. Searches for $H^{\pm\pm}$ have been performed at LEP, Tevatron and the LHC. Since $H^{\pm\pm}$ have not been discovered yet, lower limits for the mass of $H^{\pm\pm}$ are obtained to be 409 GeV, 398 GeV and 375 GeV in the case where the branching fraction of $H^{\pm\pm} \to e^\pm e^\pm$, $H^{\pm\pm} \to \mu^\pm\mu^\pm$ and $H^{\pm\pm} \to e^\pm\mu^\pm$ are respectively assumed to be 100% [12]. On the contrary, when v_Δ is much greater than 0.1 MeV, the decays into diboson $H^{\pm\pm} \to W^{\pm(*)}W^{\pm(*)}$ are dominant.[1] They can be identified by the same-sign dilepton with the missing energy signature via the leptonic decay of the W bosons. Although this scenario is equivalently important to the case of the dilepton decay from the theoretical point

[1] When $H^\pm$ is lighter than $H^{\pm\pm}$, the main decay mode of $H^{\pm\pm}$ is $H^{\pm\pm} \to W^{\pm(*)}W^{\pm(*)}$ or $H^{\pm\pm} \to W^{\pm *}H^\pm$, depending on the mass difference and v_Δ [10,11].

* Corresponding author.
E-mail address: keiyagyu@jodo.sci.u-toyama.ac.jp (K. Yagyu).

0370-2693/$ – see front matter © 2013 Elsevier B.V. All rights reserved.
http://dx.doi.org/10.1016/j.physletb.2013.08.054

of view [8,9], to our knowledge no substantial bound has been reported for the $H^{\pm\pm}$ search via the decay of $H^{\pm\pm} \to W^{\pm(*)}W^{\pm(*)}$.

In this Letter, we discuss limits on the mass for the case of the diboson decay scenario by using the current data at LEP and the LHC. First, we consider the constraint from the precise measurement of the total width of the Z boson at the LEP experiment [13], and then we evaluate the lower limit for the mass of $H^{\pm\pm}$ by using the data of the same-sign dilepton events at the LHC with the collision energy to be 7 TeV and the integrated luminosity to be 4.7 fb^{-1} [14]. Finally, we extrapolate the results for the limit with the 20 fb^{-1} data.

The most general potential in the HTM is given by

$$\begin{aligned} V = {} & m^2\Phi^\dagger\Phi + M^2\,\mathrm{Tr}\big(\Delta^\dagger\Delta\big) + \big[\mu\Phi^T i\tau_2\Delta^\dagger\Phi + \mathrm{h.c.}\big] \\ & + \lambda_1\big(\Phi^\dagger\Phi\big)^2 + \lambda_2\big[\mathrm{Tr}\big(\Delta^\dagger\Delta\big)\big]^2 + \lambda_3\,\mathrm{Tr}\big[\big(\Delta^\dagger\Delta\big)^2\big] \\ & + \lambda_4\big(\Phi^\dagger\Phi\big)\mathrm{Tr}\big(\Delta^\dagger\Delta\big) + \lambda_5\Phi^\dagger\Delta\Delta^\dagger\Phi. \end{aligned} \tag{1}$$

The scalar fields Φ and Δ can be parameterized as

$$\Phi = \begin{bmatrix} \phi^+ \\ \frac{1}{\sqrt{2}}(\phi + v_\phi + i\chi) \end{bmatrix}, \qquad \Delta = \begin{bmatrix} \frac{\Delta^+}{\sqrt{2}} & \Delta^{++} \\ \Delta^0 & -\frac{\Delta^+}{\sqrt{2}} \end{bmatrix}, \tag{2}$$

with $\Delta^0 = (\delta + v_\Delta + i\eta)/\sqrt{2}$. The VEVs satisfy $v^2 \equiv v_\phi^2 + 2v_\Delta^2 = (\sqrt{2}G_F)^{-1} = (246\ \mathrm{GeV})^2$, where G_F is the Fermi constant. The mass eigenstates of the physical scalar bosons are obtained by introducing the mixing angles α, β and β', and their formulae are expressed in terms of the parameters in the potential [15].

The electroweak rho parameter is predicted to deviate from unity in the HTM by $\rho \simeq 1 - 2v_\Delta^2/v^2$. Since the experimental value of the rho parameter is close to unity; i.e., $\rho_{\mathrm{exp}} = 1.0004^{+0.0003}_{-0.0004}$ [13], v_Δ must be less than about 3.5 GeV at 95% confidence level (CL). Under $v_\Delta \ll v$, six physical scalar states; $H^{\pm\pm}$ $(=\Delta^{\pm\pm})$, $H^\pm$, A and H are almost composed of the component scalar fields from Δ, so that we call them as the triplet-like Higgs bosons. On the other hand, h can be regarded as the SM-like Higgs boson.

The mass difference between $H^{\pm\pm}$ and $H^\pm$ is given by

$$m_{H^{++}}^2 - m_{H^+}^2 \simeq m_{H^+}^2 - m_H^2 \simeq -\frac{\lambda_5}{4}v^2, \tag{3}$$

with $m_A^2 \simeq m_H^2$. There are three patterns of the mass spectrum for the triplet-like Higgs bosons. In the case with $\lambda_5 = 0$, all the triplet-like Higgs bosons are degenerate in mass. On the other hand, in the case of $\lambda_5 > 0$ ($\lambda_5 < 0$), the mass spectrum is $m_A > m_{H^+} > m_{H^{++}}$ ($m_{H^{++}} > m_{H^+} > m_A$). We call this mass spectrum as Case I (Case II) [11].

Neutrino masses can be deduced via v_Δ as [2]

$$(\mathcal{M}_\nu)_{ij} = \sqrt{2}h_{ij}v_\Delta, \tag{4}$$

where the Yukawa coupling constants h_{ij} are defined by

$$\mathcal{L}_Y = h_{ij}\overline{L_L^{ic}}i\tau_2\Delta L_L^j + \mathrm{h.c.} \tag{5}$$

Eq. (4) tells us that the magnitude of the Yukawa coupling h_{ij} is determined by a fixed value of v_Δ, because the value of the left-hand side of the equation is given from neutrino data [13].

The decay property of $H^{\pm\pm}$ strongly depends on v_Δ and the mass spectrum of the triplet-like Higgs bosons. When we consider the degenerate case or Case I, the dominant decay modes are $H^{\pm\pm} \to \ell^\pm\ell^\pm$ or $H^{\pm\pm} \to W^{\pm(*)}W^{\pm(*)}$ in the case of $v_\Delta \lesssim 0.1$ MeV or $v_\Delta \gtrsim 0.1$ MeV, respectively. On the other hand, in Case II, above two main decay modes can be replaced by the cascade decay mode; i.e., $H^{\pm\pm} \to W^{\pm*}H^\pm \to W^{\pm*}W^{\pm*}H/A$.

We here focus on the scenario where $H^{\pm\pm} \to W^{\pm(*)}W^{\pm(*)}$ are dominant, so that we consider Case I or the degenerate case with $v_\Delta \gtrsim 0.1$ MeV. We then discuss the bound for $m_{H^{++}}$ by using the current experimental data.

The LEP experiment was operated with the electron–positron collision energy to be at the Z boson mass (LEP I) and to be up to about 209 GeV (LEP II).

From the LEP I experiment, the total width of the Z boson has been precisely measured, and it can be used to constrain $m_{H^{++}}$ whose value is smaller than the half of m_Z, independently of the decay modes of H^{++}. The total decay width of the Z boson receives the sizable correction from the partial width for this decay mode as

$$\Gamma_{Z\to H^{++}H^{--}} = \frac{G_F m_Z^3}{6\pi\sqrt{2}}\big(1 - 2s_W^2\big)^2\left(1 - \frac{4m_{H^{++}}^2}{m_Z^2}\right)^{\frac{3}{2}},$$

where s_W is the sine of the weak mixing angle. Using the current experimental data for the Z boson width, $\Gamma_Z(\mathrm{exp}) = 2.4952 \pm 0.0023$ GeV, and the SM prediction, $\Gamma_Z(\mathrm{SM}) = 2.4960 \pm 0.0002$ GeV [13], we obtain the lower bound for $m_{H^{++}}$ to be 42.9 GeV with the 95% CL.

Because there is no study to directly search for the same-sign diboson signal at the LEP II experiment, we here employ the results for the four charged-lepton mode $e^+e^- \to Z^*/\gamma^* \to \ell^+\ell^+\ell^-\ell^-$ [16] in order to get bounds on $m_{H^{++}}$. The upper bound on the number of anomalous events can be applied to the case of the same-sign diboson decay scenario; i.e., $e^+e^- \to H^{++}H^{--} \to W^{+(*)}W^{+(*)}W^{-(*)}W^{-(*)}$. Because of the suppression of the signal cross section by the fourth power of the leptonic branching fraction of $W^\pm$, no substantial bound for $m_{H^{++}}$ can be obtained by using the data from Ref. [16].

Consequently, the Γ_Z measurement gives a bound $m_{H^{++}} > 43$ GeV from the LEP I data. On the other hand, no bound is obtained from the four charged-lepton data at LEP II in our scenario. By carefully analyzing the hadronic events, a better bound could be obtained.

Let us consider whether the mass bound can be taken or not by using the current LHC data. The main production mode for $H^{\pm\pm}$ at the LHC is the pair production $pp \to \gamma^*/Z^* \to H^{++}H^{--}$ and the associated production $pp \to W^{\pm*} \to H^{\pm\pm}H^\mp$. The production cross sections for both the vector boson fusion $qQ \to q'Q'H^{\pm\pm}$ and the weak boson associated production $qQ \to W^{\pm*} \to H^{\pm\pm}W^\mp$ are proportional to v_Δ^2, so that these modes are less significant because of $v_\Delta \ll v$. We note that there is the other production mechanism $qQ \to q'Q'H^{\pm\pm}A/H$ which is the unique process whose difference of the electric charge between produced scalar bosons is two. However, the cross section of this mode is small.

The signal processes are expected to be as follows:

$$\begin{aligned} & pp \to H^{++}H^{--} \to W^+W^+W^-W^- \to \ell^\pm\ell^\pm\not{E}_T + X, \\ & pp \to H^{\pm\pm}H^\mp \to W^\pm W^\pm + X \to \ell^\pm\ell^\pm\not{E}_T + X. \end{aligned} \tag{6}$$

The signal cross section before taking any kinematical cuts can be estimated by

$$\begin{aligned} \sigma\big(\ell^\pm\ell^\pm\not{E}_T + X\big) = {} & \big[\sigma\big(H^{++}H^{--}\big) + \sigma\big(H^{\pm\pm}H^\mp\big)\big] \\ & \times \mathrm{BR}\big(H^{\pm\pm} \to \ell^\pm\ell^\pm\nu\nu\big), \end{aligned} \tag{7}$$

where $\ell^\pm$ denote $e^\pm$ or $\mu^\pm$. The signal cross section of inclusive H^{++} (H^{--}) production is evaluated to be 0.72 (0.52) pb at the leading order assuming $m_{H^{\pm\pm}} = m_{H^\pm} = 100$ GeV with the collision energy to be 7 TeV. The branching ratio of the $H^{\pm\pm}$ decay can be calculated as a square of that of $W^\pm$ for $m_{H^{\pm\pm}} > 2m_W$. However, it

Table 1
Signal cross sections of the process in Eq. (6) for the $\mu^+\mu^+$ channel for fixed values of $m_{H^{++}}$ in each step of the kinematic cuts. The decay width of $H^{\pm\pm}$ is calculated in the case of $v_\Delta = 1$ GeV for reference.

$m_{H^{++}}$ [GeV]	40	50	60	70	80	90	100
Width [eV]	3.58×10^{-4}	1.89×10^{-3}	7.70×10^{-3}	2.69×10^{-2}	8.63×10^{-2}	0.320	1.86
Basic cut [fb]	20.9	16.7	13.0	10.1	7.63	4.95	2.78
$M_{\ell\ell}$ cut [fb]	16.3	14.8	12.2	9.69	7.45	4.87	2.74

is no longer valid for $m_{H^{\pm\pm}} < 2m_W$, because at least one of the W bosons is off-shell. For $m_{H^{\pm\pm}} < 2m_W$, the branching ratios of the same-flavor dilepton decays are enhanced due to the interference of crossing diagrams.

We here consider the bound for $m_{H^{++}}$ in the diboson decay scenario by using the results of the same-sign dilepton search reported by the ATLAS Collaboration [14] with the collision energy to be 7 TeV and the integrated luminosity to be 4.7 fb^{-1}. The 95% CL upper limit N_{95} for the event number of the process including the same-sign dilepton in the final states is listed in Ref. [14]. The limit is separately given into $e^\pm e^\pm$, $\mu^\pm\mu^\pm$, and $e^\pm\mu^\pm$ channels after imposing the several choices of the invariant mass cuts for the same-sign dilepton system. The 95% CL limit for the fiducial cross section $\sigma_{95}^{\rm fid}$ is obtained by

$$\sigma_{95}^{\rm fid} = \frac{N_{95}}{\int \mathcal{L}\,dt \times \varepsilon_{\rm fid}}, \tag{8}$$

where $\varepsilon_{\rm fid}$ is the efficiency for detecting events and $\int \mathcal{L}\,dt$ is the integrated luminosity of 4.7 fb^{-1}. In Ref. [14], the efficiency values are taken as 43% for the ee channel, 55% for the $e\mu$ channel and 59% for the $\mu\mu$ channel.[2] We find that the data for the $\mu^+\mu^+$ channel with the invariant mass cut $M_{\ell\ell} > 15$ GeV is the most effective choice to extract the more severe constraint on $m_{H^{++}}$. Therefore, we intend to bound $m_{H^{++}}$ by comparing $\sigma_{95}^{\rm fid}$ for the $\mu^+\mu^+$ channel with the uncertainty of $\varepsilon_{\rm fid}$ to the signal cross section.

In the numerical evaluation, m_{H^+} is taken to be the same as $m_{H^{++}}$ to maximize the signal cross section. In order to generate the signal events, we use `MadGraph5` [17] and the `CTEQ6L` parton distribution functions [18]. We impose the following basic cuts according to Ref. [14] for each muon:

$$|\eta| < 2.5, \qquad p_T > 20\ \text{GeV}, \tag{9}$$

where η and p_T are the pseudorapidity and the transverse momentum, respectively. Furthermore, in order to compare it to $\sigma_{95}^{\rm fid}$, we impose the same invariant mass cut $M_{\ell\ell} > 15$ GeV. In Table 1, the cross sections after imposing the basic cut and the invariant mass cut are shown. The signal cross section takes its maximum value at around $m_{H^{++}} = 40$ GeV, because the cross section for the lower mass cases is much suppressed by the invariant mass cut. We also list the values for the decay width of $H^{\pm\pm}$ for $v_\Delta = 1$ GeV, by which one can recognize that $H^{\pm\pm}$ can decay inside the detector.

In Fig. 1, the same results are plotted as a function of $m_{H^{++}}$. The light shaded (orange colored in the web version) band gives the 95% CL upper limit for the fiducial cross section with 4.7 fb^{-1}. It can be seen that the HTM with the diboson decay scenario is excluded when $m_{H^{++}}$ is lower than about 60 GeV. We emphasize that this is the first substantial mass bound from the current LHC data, which is stronger than that obtained via the Γ_Z data at the LEP experiment. The dark shaded (red colored in the web version) band is obtained by extrapolating the data to those for 20 fb^{-1}, where the cross section $\sigma_{95}^{\rm fid}$ is expected to be smaller by a factor 2. This shows that the lower limit of $m_{H^{++}}$ becomes about 85 GeV with the accumulated integrated luminosity 20 fb^{-1}.

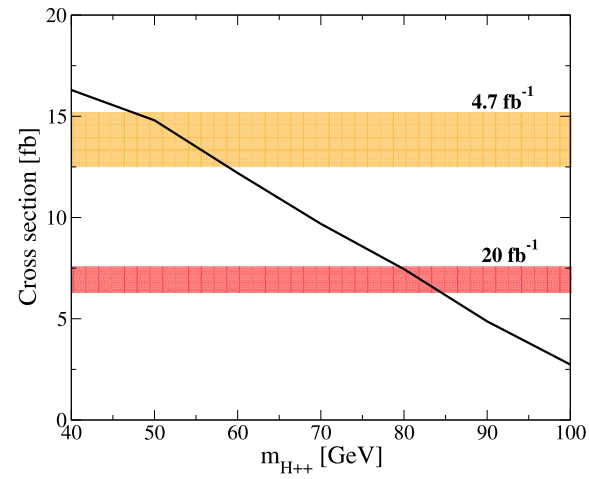

Fig. 1. The signal cross section after the $M_{\ell\ell}$ cut as a function of $m_{H^{++}}$ with the collision energy to be 7 TeV. The light (dark) shaded band shows the 95% CL (expected) upper limit for the cross section from the data for the $\mu^+\mu^+$ channel with the integrate luminosity to be 4.7 fb^{-1} (20 fb^{-1}). The width of the bands comes from the uncertainty of $\varepsilon_{\rm fid}$ for the $\mu\mu$ system between 59% and 72% [14].

Finally, we remark that the lower bound obtained in this Letter can be improved by the followings: (i) the signal cross section is calculated at the leading order, which can be modified by a factor of 1.2–1.3 [19] with higher order corrections, (ii) although we have studied the same-sign dileptons only from the decay of $H^{\pm\pm}$, they can also appear in the decay of $H^\pm$; e.g., $H^\pm \to W^\pm Z \to \ell^\pm\ell^+\ell^-\nu$. However, the decay of $H^\pm$ strongly depends on the mass difference, so that we here neglect these contributions as a conservative assumption for simplicity, (iii) a requirement of relatively hard jets in the same-sign dilepton events, like the analysis in Ref. [9], can enhance the significance of finding signal events from the background. The mass bound could be improved by such an optimized analysis with the same data set.

In conclusion, we have studied the lower limit for $m_{H^{++}}$ in the diboson decay scenario where $H^{\pm\pm} \to W^{\pm(*)}W^{\pm(*)}$ is dominant by using the experimental data. By the LEP data for Γ_Z the mass below 43 GeV is excluded with the 95% CL, and the results from four charged-lepton searches do not provide any significant constraint. We have found that a new lower bound is obtained to be about 60 GeV at the 95% CL by using the current LHC data for the same-sign dilepton events with the collision energy to be 7 TeV and the integrated luminosity to be 4.7 fb^{-1}. This is the first substantial bound on $m_{H^{++}}$ from the LHC data. We have also shown by the extrapolation that the lower limit of $m_{H^{++}}$ becomes about 85 GeV with the accumulated integrated luminosity 20 fb^{-1}. When the LHC will rerun with the energy of 14 TeV, a more stronger bound can be obtained.

[2] In fact, $\varepsilon_{\rm fid}$ depends on the observed transverse momentum for charged leptons. According to Ref. [14], $\varepsilon_{\rm fid}$ for $e^\pm e^\pm$, $\mu^\pm\mu^\pm$, and $e^\pm\mu^\pm$ channels can be changed in the ranges of 43–65%, 59–72% and 55–70%, respectively. In the derivation of $\sigma_{95}^{\rm fid}$, $\varepsilon_{\rm fid}$ is chosen to be the lowest value in Ref. [14].

Acknowledgements

The authors would like to thank Takaaki Nomura for useful discussions. This work was supported in part by Grant-in-Aid for Scientific Research, Nos. 22244031, 23104006 and 24340046, the National Science Council of ROC under Grant No. NSC-101-2811-M-008-014, and the Sasakawa Scientific Research Grant from The Japan Science Society.

References

[1] G. Aad, et al., ATLAS Collaboration, Phys. Lett. B 716 (2012) 1;
S. Chatrchyan, et al., CMS Collaboration, Phys. Lett. B 716 (2012) 30.
[2] T.P. Cheng, L.F. Li, Phys. Rev. D 22 (1980) 2860;
J. Schechter, J.W.F. Valle, Phys. Rev. D 22 (1980) 2227;
G. Lazarides, Q. Shafi, C. Wetterich, Nucl. Phys. B 181 (1981) 287;
R.N. Mohapatra, G. Senjanovic, Phys. Rev. D 23 (1981) 165;
M. Magg, C. Wetterich, Phys. Lett. B 94 (1980) 61.
[3] A. Zee, Phys. Lett. B 93 (1980) 389;
A. Zee, Phys. Lett. B 95 (1980) 461 (Erratum);
A. Zee, Phys. Lett. B 161 (1985) 141;
A. Zee, Nucl. Phys. B 264 (1986) 99;
K.S. Babu, Phys. Lett. B 203 (1988) 132;
D. Aristizabal Sierra, M. Hirsch, J. High Energy Phys. 0612 (2006) 052;
L.M. Krauss, S. Nasri, M. Trodden, Phys. Rev. D 67 (2003) 085002;
K. Cheung, O. Seto, Phys. Rev. D 69 (2004) 113009;
E. Ma, Phys. Rev. D 73 (2006) 077301;
J. Kubo, E. Ma, D. Suematsu, Phys. Lett. B 642 (2006) 18;
M. Aoki, S. Kanemura, O. Seto, Phys. Rev. Lett. 102 (2009) 051805;
M. Aoki, S. Kanemura, O. Seto, Phys. Rev. D 80 (2009) 033007;
M. Aoki, S. Kanemura, K. Yagyu, Phys. Rev. D 83 (2011) 075016.
[4] R. Barbieri, L.J. Hall, V.S. Rychkov, Phys. Rev. D 74 (2006) 015007.
[5] A.I. Bochkarev, S.V. Kuzmin, M.E. Shaposhnikov, Phys. Lett. B 244 (1990) 275;
A.E. Nelson, D.B. Kaplan, A.G. Cohen, Nucl. Phys. B 373 (1992) 453;
N. Turok, J. Zadrozny, Nucl. Phys. B 369 (1992) 729;
K. Funakubo, A. Kakuto, K. Takenaga, Prog. Theor. Phys. 91 (1994) 341;
A.T. Davies, C.D. Froggatt, G. Jenkins, R.G. Moorhouse, Phys. Lett. B 336 (1994) 464;
J.M. Cline, K. Kainulainen, A.P. Vischer, Phys. Rev. D 54 (1996) 2451;
L. Fromme, S.J. Huber, M. Seniuch, J. High Energy Phys. 0611 (2006) 038.
[6] S. Schael, et al., Phys. Rep. 427 (2006) 257.
[7] J.F. Gunion, C. Loomis, K.T. Pitts, arXiv:hep-ph/9610237;
M. Kakizaki, Y. Ogura, F. Shima, Phys. Lett. B 566 (2003) 210;
A.G. Akeroyd, M. Aoki, Phys. Rev. D 72 (2005) 035011;
M. Kadastik, M. Raidal, L. Rebane, Phys. Rev. D 77 (2008) 115023;
J. Garayoa, T. Schwetz, J. High Energy Phys. 0803 (2008) 009;
A.G. Akeroyd, M. Aoki, H. Sugiyama, Phys. Rev. D 77 (2008) 075010;
A.G. Akeroyd, C.-W. Chiang, Phys. Rev. D 80 (2009) 113010;
F. del Aguila, J.A. Aguilar-Saavedra, Nucl. Phys. B 813 (2009) 22;
A.G. Akeroyd, C.W. Chiang, N. Gaur, J. High Energy Phys. 1011 (2010) 005;
A.G. Akeroyd, C.-W. Chiang, Phys. Rev. D 81 (2010) 115007;
E.J. Chun, P. Sharma, J. High Energy Phys. 1208 (2012) 162;
H. Sugiyama, K. Tsumura, H. Yokoya, Phys. Lett. B 717 (2012) 229.
[8] K. Huitu, J. Maalampi, A. Pietila, M. Raidal, Nucl. Phys. B 487 (1997) 27;
T. Han, B. Mukhopadhyaya, Z. Si, K. Wang, Phys. Rev. D 76 (2007) 075013;
P. Fileviez Perez, T. Han, G.-y. Huang, T. Li, K. Wang, Phys. Rev. D 78 (2008) 015018.
[9] C.-W. Chiang, T. Nomura, K. Tsumura, Phys. Rev. D 85 (2012) 095023.
[10] S. Chakrabarti, D. Choudhury, R.M. Godbole, B. Mukhopadhyaya, Phys. Lett. B 434 (1998) 347;
E.J. Chun, K.Y. Lee, S.C. Park, Phys. Lett. B 566 (2003) 142;
A.G. Akeroyd, H. Sugiyama, Phys. Rev. D 84 (2011) 035010;
A. Melfo, M. Nemevsek, F. Nesti, G. Senjanovic, Y. Zhang, Phys. Rev. D 85 (2012) 055018.
[11] M. Aoki, S. Kanemura, K. Yagyu, Phys. Rev. D 85 (2012) 055007.
[12] G. Aad, et al., ATLAS Collaboration, Eur. Phys. J. C 72 (2012) 2244;
S. Chatrchyan, et al., CMS Collaboration, Eur. Phys. J. C 72 (2012) 2189.
[13] Beringer, et al., Phys. Rev. D 86 (2012) 010001.
[14] G. Aad, et al., ATLAS Collaboration, J. High Energy Phys. 1212 (2012) 007.
[15] For notation see S. Kanemura, K. Yagyu, Phys. Rev. D 85 (2012) 115009.
[16] G. Abbiendi, et al., OPAL Collaboration, Phys. Lett. B 526 (2002) 221;
J. Abdallah, et al., DELPHI Collaboration, Phys. Lett. B 552 (2003) 127;
P. Achard, et al., L3 Collaboration, Phys. Lett. B 576 (2003) 18.
[17] M. Herquet, F. Maltoni, O. Mattelaer, T. Stelzer, J. High Energy Phys. 1106 (2011) 128.
[18] H.-L. Lai, Q.-H. Cao, J. Huston, J. Pumplin, D. Stump, W.-K. Tung, C.-P. Yuan, Phys. Rev. D 78 (2008) 013004.
[19] M. Muhlleitner, M. Spira, Phys. Rev. D 68 (2003) 117701.

計画研究 A06 班

課題名「LHC での発見が導く次世代エネルギーフロンティアの発展」

研究組織

(1) 研究代表者

駒宮　幸男（KOMAMIYA, Sachio）
東京大学・大学院理学系研究科・教授
研究者番号：80126060

(2) 研究分担者

川越　清以（KAWAGOE, Kiyotomo）
九州大学・理学研究院・教授
研究者番号：40183785

(3) 連携研究者

大谷　航（OTANI, Wataru）
東京大学・素粒子物理国際研究センター・准教授
研究者番号：30311335

神谷　好郎（KAMIYA, Yoshio）
東京大学・素粒子物理国際研究センター・助教
研究者番号：90434323

交付決定額

計画研究 A06 班に配分された交付額を表 1 に示す。

表 1. 交付決定額（配分額）　（金額単位：円）

年度	直接経費	間接経費	合計
平成 23 年度	9,400,000	2,820,000	12,220,000
平成 24 年度	10,800,000	3,240,000	14,040,000
平成 25 年度	10,900,000	3,270,000	14,170,000
平成 26 年度	10,300,000	3,090,000	13,390,000
平成 27 年度	10,300,000	3,090,000	13,390,000
総計	51,700,000	15,510,000	67,210,000

研究成果

1.研究開始当初の背景

本研究の開始当初の背景は、LHC 実験によって、ヒッグス粒子や、超対称性粒子やそれにとって代わる標準理論を超える新粒子が発見されることを見越して、LHC の次の世代の衝突型加速器である ILC などで期待される物理を研究し、それを踏まえた測定器の開発を行うというものであった。研究開始当初はヒッグス粒子は発見されておらず、ILC のほかにも SLHC と呼ばれるさらに高エネルギーのハドロンコライダーも考慮した。当初はシリコン・タングステンのサンドイッチ電磁カロリメータだけでなく、シンチレータを用いた電磁カロリメータやハドロンカロリメータも考慮した。

２．研究の目的

本課題の目的は、LHC でのテラスケールでの物理成果をさらに大きく展開するための次世代エネルギーフロンティアの準備研究である。具体的には、LHC での成果を踏まえて、次に重要となる SLHC、LHC、LC 等の次世代計画における物理準備研究を行い、その鍵となる新たな検出器開発を行なった。次世代計画には、加速器・検出器技術に革新的な新技術が不可欠である。本課題では、次世代カロリメータの開発を行いプロトタイプの製作・性能の評価を行なった。これらの研究は、真空の構造、超高エネルギーでの力の統一、宇宙物理へ更なる展開を次世代実験で行う為に重要な役割を果たした。本課題のメンバーは、コライダー実験での豊富な経験を持ち、SLHC やリニアコライダー測定器の技術開発や物理研究を国際コミュニティーの中で主導的に行い、高い評価を得てきた。LHC でのテラスケール物理の成果と将来計画にむけて研究を始める

準備を行ってきた。

3．研究の方法

LHC でのテラスケール物理の成果を真空の構造、超高エネルギーでの力の統一、宇宙物理へ大きく展開するために、以下の３つの物理研究(3-5)を進め、同時にこの研究を実現するために必須の次世代カロリメータ開発(1-2)を行なった。

(1) 光電子増倍管に取って代わる安価な光デバイス MPPC を用いた高細分ストリップシンチレータを用いたサンプリング型カロリメータを開発した。PPC は出力が飽和しないようにピクセルを細分化しダイナミックレンジの向上を行った。またカロリメータとして均一な性質となるような、光学的接続やエレクトロニクスの開発を行い、プロトタイプを製作した。

(2) (1)で開発した高細分カロリメータでジェット中の粒子を粒子単位で観測しエネルギーフローを計算するアルゴリズムの開発を行なった。σE/E=30%/E(GeV)1/2 以下の高い精度でのエネルギー測定と、O(1)%のヒッグス崩壊分岐比測定を可能にする方法を開発した。

(3) ILC や SHLC での研究でヒッグス自己結合定数を測定する方法を開発した。高いバックグラウンドを除くため高性能カロリメータ開発と粒子識別能力向上の両面で研究を進めた。

(4) SLHC で色を持った重い超対称性粒子の性質、ILC で軽い電弱超対称性粒子の性質を探る研究を行い、両方の研究を統合して初めて超対称性の全貌を探ることができ、LHC での成果を反映させて詳細で新しい研究を行なった。

(5) SLHC で WW 散乱の精密観測を通して新たな質量獲得システムの研究を行なった。

4．研究成果

本課題では LHC でのヒッグス粒子の発見によって重要性を増した国際リニアコライダー(ILC)計画の推進のために多くの研究を行ってきた。

(1) LHC の２光子の不変質量分布で 750 GeV 近くに新粒子の兆候があった。この背後の物理を ILC で精査する方法を開発。この他に、超対称性などの兆候が LHC で見えた時に、ILC での詳細研究によって、超対称性の破れや暗黒物質の解明の方法を開発。

(2) ILC ビーム収束系の local chromatic correction と呼ばれるビームオプティクスを確立した。KEK の ILC のための試験加速器 ATF2 において、世界で最小の縦方向ビームサイズ σy=41nm 測定した。また、2 バンチのビームを ATF でつくり 1 バンチ目の測定でフィードバックをかけ 2 バンチ目のビームジッターを減らすことに成功。

(3) ILC のシリコン電磁カロリメータの詳細設計において安価でかつ性能を落とさないための素子のスペックを研究した。また、素子の放射線耐性を神戸大学の中性子ビームを用いて精査。十分な耐性があることを検証。ドイツ DESY においてプロトタイプのビームテストに成功。

(4) τ のハドロンへの崩壊の再構成は、重いヒッグス粒子などの CP 混合の決定に重要である。ILC での衝突点の位置、荷電粒子の軌道、π^0 からの光子の電磁カロリメータでのシャワーの測定を用いて、いかなる τ のハドロン崩壊も再構成できることを証明。

5．主な発表論文等

（研究代表者、研究分担者及び連携研究者には下線）

〔雑誌論文〕（計　15　件）

(1)“Tau Lepton Reconstruction at Collider Experiments Using Impact Parameters”, D. Jeans, NIM.A, 810, 2016, 51-58, 査読有

(2)“Pion and Proton Showers in the CALICE Scintillator-Steel Analogue Hadron Calorimeter”, CALICE Collaboration: B. Bilki, D. Jeans et al., JINST, 10, 2015, P04014, 査読有

(3)“A Novel Strip Energy Splitting Algorithm for the Fine Granular Readout of a Scintillator Strip Electromagnetic Calorimeter”, K. Kotera, D. Jeans et al., NIM.A, 789, 2015, 158-164, 査読有

(4)“Experimental Validation of a Compact Focusing Scheme for Future Energy-Frontier Linear Lepton Colliders”, G. White, S. Komamiya et al.（91 人中 41 番目）, Phys.Reb.Lett., 112, 2014, 034802, 査読有

(5)“Validation of GEANT4 Monte Carlo Models with a Highly Granular Scintillator-Steel Hadron Calorimeter”, CALICE Collaboration: C. Adloff, D. Jeans et al., JINST, 8, 2013, 07005, 査読有

(6)“Testing Bell’s Inequality Using Charmonium Decays”, S. Chen, Y. Nakaguchi and S. Komamiya, PTEP, 112, 2013, 034802, 査読有

(7)“Current Status of Nanometer Beam Size Monitor at ATF2”, Y. Yamaguchi, S. Komamiya et al.（12 人中 5 番目）, Phys.Procedia, 37, 2012, 1983-1988, 査読有

(8)“Hadronic Energy Resolution of a Highly Granular Scintillator-Steel Hadron Calorimeter Using Software Compensation Techniques”, CALICE Collaboration: C. Adloff, D. Jeans et al., JINST, 7, 2012, P09017, 査読有

〔学会発表〕（計　27　件）

(1) D. Jeans, “Tau Lepton Reconstruction at Collider Experiments Using Impact Parameters”, 日本物理学会第 71 回年次大会, 2016 年 3 月 21 日, 東北学院大学（宮城県仙台市）

(2) D. Jeans, “Recent Developments in LC Calorimeter R&D”, LCWS2015, 2015 年 11 月 1 日～2015 年 11 月 7 日, Whistler(Canada)

(3) D. Jeans, “Full Tau Lepton Reconstruction Using Impact Parameter”, LCWS2015, 2015 年 11 月 1 日～2015 年 11 月 7 日、Whistler(Canada)
(4) 駒宮幸男, “ILC の実現に向けて”, 日本物理学会 2015 年秋季大会, 2015 年 9 月 26 日, 大阪市立大学（大阪府大阪市）
(5) S. Komamiya, “ILC Status Report”, XXVII International Symposium of Lepton and Photon Interactions at High Energies, 2015 年 8 月 21 日, Ljubljana(Slovenia)
(6) D. Jeans, “ECAL(all options) with a focus on simulation”, Asian Linear Collider Workshop, 2015 年 4 月 20 日, 高エネルギー加速器研究機構（茨城県つくば市）
(7) 小坂井千紘, “ILD-ECAL のためのシリコン検出器の基礎特性の評価と中性子照射による損傷の効果”, 日本物理学会第 70 回年次大会, 2015 年 3 月 21 日, 早稲田大学（東京都新宿区）
(8) S. Komamiya, “Project Advisory Committee for the Linear Collider Collaboration”, International Committee for Future Accelerators, 2015 年 2 月 26 日, Richmond(USA)
(9) S. Komamiya, “Particle Physics beyond the Standard Model and the ILC Project”, XXI DAEBRNS High Energy Physics Symposium, 2014 年 12 月 11 日, Guwahati(India)
(10) 駒宮幸男, “国際リニアコライダーILC と素粒子物理学の展望”, 加速器科学研究会, 2014 年 11 月 7 日, ザ・キャピトルホテル東急（東京都千代田区）
(11) 駒宮幸男, “ILC が目指すもの、テラスケールからプランクスケールへ”, 日本物理学会 2014 年秋季大会, 2014 年 9 月 19 日, 佐賀大学（佐賀県佐賀市）
(12) S. Komamiya, “Report from Linear Collider Board”, Meeting of Financial Agencies for Large Colliders, 2014 年 10 月 30 日, Beijing(China)
(13) S. Komamiya, “LCB(Linear Collider Board) Report”, International Workshop on Linear Collider, 2014 年 10 月 6 日, Belgrade(Serbia)
(14) S. Komamiya, “Report from Linear Collider Board”, American Linear Collider Workshop, 2014 年 5 月 14 日, Batavia(USA)
(15) 駒宮幸男, “国際リニアコライダーの現状と展望”, 日本物理学会第 69 回年次大会, 2014 年 3 月 28 日, 東海大学（神奈川県平塚市）
(16) 小坂井千紘, “ILD のためのシリコンセンサーの特性研究”, 日本物理学会第 69 回年次大会, 2014 年 3 月 27 日, 東海大学（神奈川県平塚市）
(17) 陳詩遠, “GARLIC と Pandra による光子再構成と 2 粒子分解”, 日本物理学会第 69 回年次大会, 2014 年 3 月 27 日, 東海大学（神奈川県平塚市）
(18) S. Komamiya, “ILC after TDR”, Workshop on Helmholtz Alliance, 2013 年 12 月 4 日, Karlsruhe(Germany)
(19) S. Komamiya, “International Linear Collider in Japan”, European Physics Society Meeting on High Energy Physics, 2013 年 7 月 20 日, Stockholm(Sweden)
(20) 駒宮幸男, “ILC 計画の展望”, 日本物理学会第 68 回年次大会, 2013 年 3 月 27 日, 広島大学

（広島県東広島市）
(21) S. Komamiya, “The Rising Sun of the Linear Collider”, Aspen Winter School, 2013 年 3 月 10 日, Aspen(USA)
(22) 駒宮幸男, “Particle Physics Now and in the Future”, International Symposium on Nano-science and Quantum Physics, 2012 年 12 月 19 日, 国際文化会館（東京都港区）
(23) S. Komamiya, “Community Proposal for Japanese Particle Physics Priorities”, CERN SPC, 2012 年 11 月 27 日, Geneva(Switzerland)
(24) 駒宮幸男, “素粒子物理学最前線 2012”, 九州大学先端加速器センター開所記念講演”, 2012 年 9 月 27 日, 九州大学（福岡県福岡市）
(25) S. Komamiya, “History of Particle Physics and Linear Collider”, ASIAA/CCMS/MAS/LeCosPA/NTU-Phys Joint Symposium, 2012 年 9 月 24 日, Taiwan(Taiwan)
(26) 駒宮幸男, “ヒッグスとコライダー•シンポジウム趣旨説明”, 日本物理学会 2012 年秋季大会, 2012 年 9 月 12 日, 京都産業大学（京都府京都市）
(27) 駒宮幸男, “ヒッグス粒子の発見”, 日韓シンポジウム, 2012 年 7 月 28 日, 松本大学（長野県松本市）

〔図書〕（計　1　件）
(1) T. Behnke, S. Komamiya, K. Kawagoe, D. Jeans, Y. Kamiya, W. Otani et al., Argonne National Laboratory et al,
“The International Linear Collider Technical Design Report”, 2013, 966

〔その他〕
アウトリーチ活動（計　21　件）
(1) 駒宮幸男, “ILC の社会的役割”, 2015 年 1 月 14 日, 北上工業クラブ新春講演会
(2) 駒宮幸男, “ヒッグス粒子の発見と素粒子物理学の発展”, 2014 年 8 月 19 日, サマーチャレンジ（高エネルギー加速器研究機構）
(3) 駒宮幸男, “LHC でのヒッグス粒子の発見と ILC の発展”, 2014 年 1 月 25 日, 朝日カルチャースクール新宿
(4) 駒宮幸男, “詳説ヒッグス粒子”, 2013 年 4 月 27 日、5 月 25 日、6 月 15 日, 朝日カルチャースクール横浜
(5) 駒宮幸男, “素粒子物理学の最前線「ヒッグス粒子」発見は何を意味するのか”, 2013 年 5 月 16 日, アカデミーヒルズセミナー
(6) 駒宮幸男, “ヒッグス粒子発見！素粒子物理学の一大革命”, 2013 年 1 月 12 日, 東京学芸大学附属高等学校特別講義
(7) 駒宮幸男, “ヒッグス粒子の発見”, 2012 年 12 月 1 日, 朝日カルチャースクール湘南

(8) 駒宮幸男, “素粒子と宇宙”, 2012 年 11 月 11 日, 楽しむ科学教室（福岡県中小企業振興センター）

主要論文別刷

(1)“Tau Lepton Reconstruction at Collider Experiments Using Impact Parameters”,
D. Jeans, NIM.A, 810, 2016, 51-58, 査読有

(2)“A Novel Strip Energy Splitting Algorithm for the Fine Granular Readout of a Scintillator Strip Electromagnetic Calorimeter”,
K. Kotera, D. Jeans et al., NIM.A, 789, 2015, 158-164, 査読有

(3)“Experimental Validation of a Compact Focusing Scheme for Future Energy-Frontier Linear Lepton Colliders”,
G. White, S. Komamiya et al.（91 人中 41 番目）, Phys.Rev.Lett., 112, 2014, 034802, 査読有

(4)“Validation of GEANT4 Monte Carlo Models with a Highly Granular Scintillator-Steel Hadron Calorimeter”,
CALICE Collaboration: C. Adloff, D. Jeans et al., JINST, 8, 2013, 07005, 査読有

(5)“Hadronic Energy Resolution of a Highly Granular Scintillator-Steel Hadron Calorimeter Using Software Compensation Techniques”,
CALICE Collaboration: C. Adloff, D. Jeans et al., JINST, 7, 2012, P09017, 査読有

Nuclear Instruments and Methods in Physics Research A 810 (2016) 51–58

Contents lists available at ScienceDirect

Nuclear Instruments and Methods in Physics Research A

journal homepage: www.elsevier.com/locate/nima

Tau lepton reconstruction at collider experiments using impact parameters

Daniel Jeans

Department of Physics, Graduate School of Science, The University of Tokyo, 7-3-1 Hongo, Bunkyo-ku, Tokyo 113-0033, Japan

ARTICLE INFO

Article history:
Received 12 August 2015
Received in revised form
4 November 2015
Accepted 6 November 2015
Available online 27 November 2015

Keywords:
Tau lepton
Reconstruction techniques
Collider experiment

ABSTRACT

We present a method for the reconstruction of events containing hadronically decaying τ leptons at collider experiments. This method relies on accurate knowledge of the τ production vertex and precise measurement of its decay products. The method makes no assumptions about the τ kinematics, and is insensitive to momentum loss along the beam direction. We demonstrate the method using $e^+e^- \rightarrow \mu^+\mu^-\tau^+\tau^-$ events fully simulated in the ILD detector.

© 2015 Elsevier B.V. All rights reserved.

1. Introduction

Studies of final states including τ leptons are of interest at current and future collider experiments; as an example, the dominant leptonic decay of the Higgs boson is to a τ pair. A new generation of high energy particle colliders [1–4] is presently under study. A key scientific aim of these facilities is to measure the Higgs boson's properties with great precision, important aspects of which involve measurements of the τ final state. An example is the use of measurements of the τ spin state to probe the CP nature of the Higgs boson. The detectors being designed for use at these accelerators will be equipped with vertex detectors providing unprecedented impact parameter resolution (see *e.g.* [5]), giving rise to intriguing possibilities in the reconstruction of relatively long-lived states such as the τ lepton.

We report on a method which uses a high-precision vertex detector together with other tracking and calorimetric detectors to fully reconstruct the kinematics of events containing hadronically decaying τs (*i.e.* decays in which only one ν is produced) in an unbiased way. We outline previously used techniques for the kinematic reconstruction of single-ν τ decays in Section 2. In Section 3 we define a new procedure which, in certain topologies, can fully reconstruct the τ kinematics with significantly less stringent assumptions than previous approaches. This new method is then applied to $e^+e^- \rightarrow \mu^+\mu^-\tau^+\tau^-$ events in Section 4, and we conclude in Section 5.

2. Previous approaches to τ pair reconstruction

In the case of events containing a pair of τ leptons each decaying to a single neutrino, the following method, which assumes knowledge of the rest-frame and invariant mass of the τ pair, but no knowledge about the τ production vertex, is often used at lepton colliders (*e.g.* [6,7]). The τ-pair rest-frame can be assumed to be the centre-of-mass of the colliding beams (in the case of the $e^+e^- \rightarrow \tau^+\tau^-$ process), or the frame recoiling against particles produced in conjunction with the τ pair, as in the case $e^+e^- \rightarrow \mu^+\mu^-\tau^+\tau^-$. The τ decay products are then boosted into the assumed τ pair rest frame, in which the energy of the τs is defined by the assumed invariant mass of the τ pair. The τ mass then constrains the τ momentum to be at a fixed angle to the momentum of its hadronic decay products, defining a cone around the hadronic momentum. The two cones in an event, one per τ, have either 0, 1, or 2 intersections, corresponding to the possible solutions for the τ momenta.

At hadron colliders, the unknown net momentum along the beam direction results in less available information to constrain the event kinematics. The invariant mass of τ pairs can be partially estimated using the invariant masses of visible decay products and the missing transverse energy, or by applying the approximation that the ν from τ decay is collinear with the visible τ decay products [8]. Another approach is to combine the measured momenta of visible τ decay products with constraints on the τ mass and global event transverse momentum balance, resulting in an under-constrained system. The likelihood of the various τ decay topologies allowed by the constraints can then be used to choose a best solution, or alternatively to associate a weight to each solution *e.g.* [9–11].

E-mail address: jeans@icepp.s.u-tokyo.ac.jp

http://dx.doi.org/10.1016/j.nima.2015.11.030
0168-9002/© 2015 Elsevier B.V. All rights reserved.

If the τ production vertex is precisely known, the use of the impact parameters of the charged τ daughters (prongs) brings additional information. The knowledge of the production vertex can come from the reconstruction of particles recoiling against the τs, or from *a priori* knowledge of the interaction point, if the size of the interaction region is sufficiently smaller than the impact parameters of the τ decay products. The use of the impact parameter vectors of charged τ daughters, without full reconstruction of τ decay kinematics, in the analysis of Higgs boson CP properties has been described in *e.g.* [12,13], while their use in fully reconstructing di-τ systems of known invariant mass and momentum has been demonstrated in [14,15].

3. Method

In this section we present methods that can, under certain conditions, fully reconstruct a τ without assuming that it belongs to a τ pair of particular invariant mass or centre-of-mass frame. In Section 3.2 we consider the reconstruction of hadronic single prong final states, in which a single charged hadron is produced with zero or more neutral hadrons and a single neutrino. Such decays account for 49.5% of τ decays. Multiprong hadronic τ decays, in which three or more charged hadrons, zero or more neutral hadrons, and a single neutrino are produced, account for 15.3% of τ decays, are discussed in Section 3.3. Leptonic decays of the τ (35.2%) provide significantly less measurable information about its decay kinematics due to the production of two neutrinos, and are not further considered in this paper.

The method relies on precise knowledge of the τ production vertex and the charged prong trajectories, and on the reconstruction of any neutral hadrons produced in the decay. Constraints on the invariant mass and lifetime of each τ, and on the overall transverse momentum in the event, are then used to determine the τ momenta.

3.1. Tau production vertex

The uncertainty on the τ production position should be small in comparison to the decay length of the τ and the typical impact parameters of its decay products. In final states in which the τs are produced together with more than one prompt charged particle, the production vertex can be directly reconstructed on an event-by-event basis using the tracks of these particles (*e.g.* the μs in the process $e^+e^- \to \mu^+\mu^-\tau^+\tau^-$). The proposed linear electron–positron colliders [1,2] have rather small interaction regions, which may be used as an additional constraint on the interaction point, although this is not done for the results presented in this paper.

3.2. Single prong τ decays

3.2.1. Tau decay plane

In the case of single prong hadronic τ decays, the trajectory of the charged prong (helical in the usual case of a uniform magnetic field) can be used to define a plane (hereafter called the "track plane") which contains two vectors: **d**, the vector between the reconstructed interaction point (IP, assumed to be the τ production vertex) and the point on the trajectory closest to the IP (point of closest approach PCA); and **p**, the tangent to the trajectory at the PCA. In the case of linear trajectories of the τ and of the prong between the PCA and the τ decay vertex, the τ momentum, and therefore also the sum of the momenta of the other decay products of the τ (neutrinos and neutral hadrons), are constrained to lie within this plane.

The difference between the reconstructed track plane and the true τ decay plane (defined by the τ and prong momenta) depends on the decay length of the τ, the accuracy with which the IP position is known, the precision of the charged prong trajectory, and the extent to which the linear approximation of the τ and prong trajectories near the IP is valid.[1]

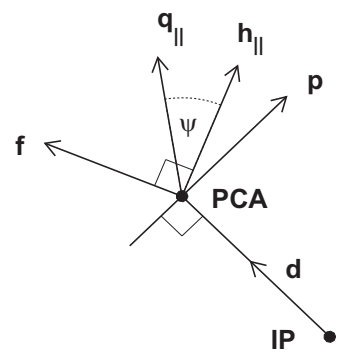

Fig. 1. Parameterisation of the neutrino momentum in the track plane ($\mathbf{q}_\parallel$) in terms of the vectors $\mathbf{h}_\parallel$ and **f**, and angle ψ. The track plane is defined by the vectors **p** and **d**.

3.2.2. Parameterisation of neutrino momentum

In this section we describe the parameterisation of the unmeasured neutrino momentum, **q**, based on the measured prong trajectory and neutral hadron momentum.

Neutral particles are measured as clusters in the calorimeters, or as identified conversions of photons into e^+e^- pairs within the tracker volume. The momentum to be associated to calorimeter clusters can be estimated by assigning the energy of the calorimeter cluster, a mass hypothesis (*e.g.* zero in the case of photon-like clusters, the K_L mass for hadronic clusters), and the direction of a straight line connecting the IP and the energy-weighted mean position of the calorimeter cluster.[2]

The three-momentum **k** of the neutral hadronic system can be decomposed into components perpendicular to and within the track plane: $\mathbf{k}_\perp$ and $\mathbf{k}_\parallel$ respectively. Since the τ momentum lies within the track plane, the hadronic momentum perpendicular to the track plane must be balanced by the neutrino, so the perpendicular component of the neutrino momentum $\mathbf{q}_\perp = -\mathbf{k}_\perp$.

The component of the neutrino momentum within the track plane can completely generally be parameterised as

$$\mathbf{q}_\parallel = Q \cdot (\cos\psi \cdot \hat{\mathbf{h}}_\parallel + \sin\psi \cdot \hat{\mathbf{f}}), \tag{1}$$

[3] where Q is the unknown magnitude of the in-plane component of the neutrino momentum, $\mathbf{h}_\parallel$ is the component of the total hadronic momentum ($\mathbf{h} = \mathbf{p} + \mathbf{k}$) in the track plane, and the unit vector $\hat{\mathbf{f}} \equiv \mathbf{f}/|\mathbf{f}|$, where $\mathbf{f} = \mathbf{h}_\parallel \times (\mathbf{d} \times \mathbf{h}_\parallel)$, is within the plane and perpendicular to $\mathbf{h}_\parallel$ (Fig. 1).

Four-vectors p, k, and q corresponding to the three-momenta **p**, **k**, and **q** can be defined by means of appropriate invariant mass assumptions. The invariant mass of the sum of four-vectors p, k, and q must be equal to the τ lepton mass m_τ. This constraint allows us to write an equation involving Q and $\hat{\mathbf{q}}_\parallel$ (which in turn

[1] The error in this linear approximation scales as the ratio of the decay length of the τ to the radius of curvature of the prong: for a prong with $p_T = 10$ GeV/c produced by a 50 GeV τ of average lifetime, in a field of 3.5 T, this ratio is $< 10^{-3}$. An iterative approach, in which a first iteration uses the helix parameters at the PCA to the IP, while later iterations use the helix parameters at the calculated τ decay position, should reduce any sensitivity to the prong's curvature.

[2] Alternative definitions are possible: for example the line connecting a first estimate of the τ decay position to the identified start of the calorimetric shower.

[3] We define $\hat{\mathbf{x}}$ to be a unit vector parallel to **x**.

depends on ψ):

$$m_\tau^2 = (q+h)^2 = (\sqrt{Q^2+\mathbf{k}_\perp^2}+E_h)^2 - (Q\hat{\mathbf{q}}_\parallel - \mathbf{k}_\perp + \mathbf{h})^2 \quad (2)$$

where E_h is the energy of the hadronic system. This can used to solve for Q:

$$Q = \frac{1}{2a}(-b \pm \sqrt{b^2-4ac}), \quad (3)$$

where

$$a = B^2 - C^2, \quad b = 2AB, \quad c = A^2 - C^2\mathbf{k}_\perp^2, \quad (4)$$

and

$$A = m_\tau^2 - m_h^2 - 2\mathbf{h}\cdot\mathbf{k}_\perp, \quad B = 2\hat{\mathbf{q}}_\parallel\cdot(\mathbf{h}-\mathbf{k}_\perp), \quad C = 2E_h, \quad (5)$$

where m_h is the invariant mass of the hadronic system.

There are in general two solutions of Q for each choice of ψ, which are complex in unphysical regions. Such complex solutions are rejected. In the case of two real solutions, we choose to denote the one with a higher energy neutrino in the laboratory frame as the "first" solution, and the other as the "second". The first solution at $\psi=\alpha$ corresponds to the second solution at $\psi=\pi+\alpha$, and *vice versa*. Since the angle between the neutrino and hadrons is typically small in the laboratory (due to the large boost of the τ), it is convenient to consider the solutions separately, each in the range $-\pi/2<\psi<\pi/2$.

For each real solution of Q, the corresponding τ momentum can be calculated. In conjunction with the prong trajectory, this allows the decay length and proper decay time of the τ to be calculated. In the simple case of $k=0$ (*i.e.* no neutral hadrons in the τ decay), one solution for Q corresponds to a negative τ decay length (the intersection of the τ trajectory with that of the prong is on the "wrong" side of the IP), and can therefore be discarded. More generally, a likelihood λ that the extracted lifetime is consistent with that expected of the τ can be expressed in terms of the measured decay length of the τ in the laboratory L, its Lorentz boost (β, γ), and the mean lifetime of the τ (~ 87 μm/c): $\lambda = \exp(-L/(\beta\cdot\gamma\cdot 87\ \mu\text{m}))$ if $L>0$, and $\lambda=0$ otherwise.[4]

3.2.3. Choice of ψ

To determine the value of ψ, additional information is required. One possible approach would be to follow a statistical approach, applying a weight to each possible solution based on the likelihood that its decay time is consistent with that expected of the well-known τ mean lifetime, and/or that the reconstructed τ decay kinematics follow the expected distributions. If a hypothesis is made as to the energy of the τ, or on the invariant mass of a pair of τs, this can also help choose appropriate ψ solutions.

An alternative approach, followed in this paper, is to consider the environment in which the τ has been produced. We consider the class of events in which one or more single-ν decaying τ leptons have been produced in conjunction with zero or more well-measured particles, together with zero or more particles escaping along the beam-line (*e.g.* ISR photons). Examples of such processes at an electron–positron collider are two-fermion production $e^+e^-\to\tau^+\tau^-$, Higgs-strahlung $e^+e^-\to HZ\to(\tau^+\tau^-)(\mu^+\mu^-)$, and its major irreducible background $e^+e^-\to ZZ\to(\tau^+\tau^-)(\mu^+\mu^-)$. In such events, the overall p_T of the τs and other visible particles is balanced, while there may be non-zero net momentum along the beam-line due to ISR. A natural way in which to determine the ψ angles in an event (one per τ decay) is to choose that combination which minimises the magnitude of the missing transverse momentum (p_T^{miss}) in the event. This method has the advantage of making no assumptions about τ kinematics or about undetected particles escaping along the beam-line – also indispensable for application at hadron collider experiments, but does require that no additional neutrinos are produced in the same event. In the case of several solutions for which p_T^{miss} is consistent with zero, the reconstructed τ lifetimes can be used to determine the most likely one, or each solution could be weighted by a likelihood based on its lifetime and/or τ decay kinematics.

3.3. Multiprong τ decays

In the case of multiprong τ decays, the prongs can be fitted to a common vertex, whose position $\mathbf{V}$ corresponds to the point at which the τ lepton decayed. Together with a well-known production position $\mathbf{P}$, this gives an estimate of the direction of the τ momentum, in the approximation that the τ trajectory is linear.[5] The τ momentum $\mathbf{p}_\tau$ can be written as $\mathbf{p}_\tau = t\hat{\mathbf{r}}$, where t is the magnitude of the τ momentum, and $\mathbf{r}=\mathbf{V}-\mathbf{P}$.

The neutrino momentum $\mathbf{q}$ can then be written as $\mathbf{q}=\mathbf{p}_\tau-\mathbf{h}$, where $\mathbf{h}$ is the measured momentum of the visible hadronic system. Defining appropriate four-vectors q and h for the neutrino and hadronic system respectively, and requiring that the invariant mass of the decay products is equal to the τ mass m_τ, gives

$$m_\tau^2 = (q+h)^2 = (|\mathbf{q}|+E_h)^2 - (\mathbf{q}+\mathbf{h})^2 = (|t\hat{\mathbf{r}}-\mathbf{h}|+E_h)^2 - t^2, \quad (6)$$

where E_h is the energy of the hadronic system. This can be solved for t, giving

$$t = \frac{1}{2a}(b \pm \sqrt{b^2-4ac}), \quad (7)$$

where

$$a = E_h^2 - (\hat{\mathbf{r}}\cdot\mathbf{h})^2, \quad b = (\hat{\mathbf{r}}\cdot\mathbf{h})(m_\tau^2+m_h^2),$$
$$c = -\frac{(m_\tau^2+m_h^2)^2}{4} + m_\tau^2E_h^2. \quad (8)$$

There are in general two possible solutions for t which satisfy the m_τ constraint, however they are not guaranteed to be real. The full tau decay kinematics can be calculated for each real solution, including the decay length and proper decay time of the τ. In appropriate event topologies, the p_T^{miss} of the event can be used to choose between these two solutions, otherwise the previously introduced lifetime likelihood could be used.

Since the τ leptons produced at high energy colliders are typically highly boosted, the opening angle of the multiprong jet is usually small. As a consequence, the precision with which the τ decay vertex is reconstructed is significantly worse along direction of the τ jet than along the perpendicular directions. In the example considered later in this paper, in which τs are produced in Higgs boson decays, the length of the major axis of the vertex position error ellipsoid is typically of order 100 μm, while the other two axes have lengths of order 2 μm.

In this case, it turns out to be better to consider the major axis of the vertex error ellipsoid as a single trajectory, and to analyse the event using the procedure developed for single prong decays in the previous section. In this way, the τ decay plane is defined by the IP and the centre and major axis of the vertex ellipsoid, and the exact decay position along the major axis direction is left as a free parameter. The distance between the fitted and reconstructed vertex positions, normalised by the uncertainty on the reconstructed vertex position, can be used to define a vertex likelihood, which can be used when choosing between several possible solutions.

[4] A more sophisticated treatment would take measurement uncertainties into account, therefore allowing small negative decay length solutions.

[5] We note that the τ momentum direction can be directly measured for any decay mode if the τ decay length is sufficiently large for it to produce hits in the vertex detector.

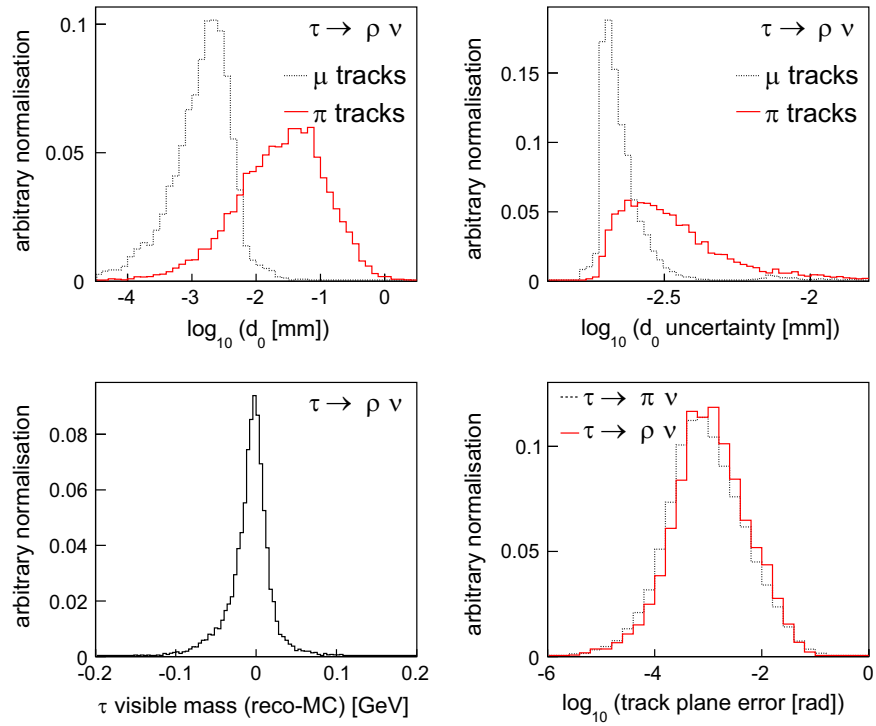

Fig. 2. Properties of the considered $e^+e^- \to \mu^+\mu^- H$ events. Top: the measured 2-d impact parameter d_0 [left] and its uncertainty [right], for prompt μ tracks, and π tracks from $\tau \to \rho\nu$ decay. Bottom left: the difference between the reconstructed and true visible τ mass in $\tau \to \rho\nu$ decays. Bottom right: the angle between the reconstructed track plane and the true direction of the τ momentum.

4. Example application

We apply this method to $e^+e^- \to \mu^+\mu^- H$ events, in which the Higgs boson decays to a pair of τs. Such events are usually selected by considering the mass recoiling against the di-μ system, which has a peak at the Higgs boson mass. However the distribution of this recoil mass has a long tail due to beamstrahlung and ISR, particularly at higher centre-of-mass energies well above threshold. If the invariant mass of the ττ system can be directly reconstructed, a rather cleaner selection of such events should be possible. The full reconstruction of the τ decay kinematics and the ττ centre-of-mass frame also allows the best use of the spin information of the τs: the properties of the τ decays can be used to define their *polarimeter vectors*, and the correlations between the τ polarimeters can be used to measure the CP-nature of the Higgs boson (*e.g.* [14]).

Events were generated at a centre-of-mass energy of 250 GeV using WHIZARD v2.2.2 [16], assuming a Higgs boson mass of 125 GeV, and including effects due to initial state radiation and beamstrahlung (by CIRCE1). The τs were decayed by TAUOLA++ v1.1.4 [17]. Three scenarios were considered: both τs decaying to $\pi^\pm\nu$; both decaying to $\pi^\pm\pi^0\nu_\tau$; and both decaying to $(a_1 \to 3\pi^\pm)\nu$. The simplest hadronic τ decay mode is $\pi^\pm\nu$, but accounts for only 11.5% of τ decays, while the ρν mode has the largest branching ratio of 26.0%.[6]

The resulting events we passed through the GEANT4-based MOKKA simulation of the ILD_o1_v05 detector model [5]. This model consists of a vertex detector with three double-layers of silicon pixel detectors, a silicon strip-based inner tracker and forward tracking disks, a large time projection chamber within a silicon tracking envelope, followed by highly granular calorimeters: a silicon–tungsten ECAL and scintillator-iron HCAL. These are placed within a solenoid producing a 3.5 T magnetic field, surrounded by an instrumented iron flux return yoke. The simulated energy deposits within the active detectors were passed through the standard ILD digitisation procedures to simulate detector signals.

4.1. Event reconstruction

The standard ILD reconstruction software was used to reconstruct charged particle tracks and calorimeter clusters. For the results shown in this paper, the reconstructed tracks were associated to primary muons and charged pions from τ decays on the basis of matching to the simulated particle directions. In a full analysis, muon and pion identification should be performed. This is rather simple task in detectors with highly granular calorimeters such as ILD, which should not present any great difficulties. Distributions of the impact parameter in the plane perpendicular to the beam d_0, and of its uncertainty, are shown in Fig. 2 for both prompt μ tracks and π tracks from τ decay. The two μ tracks were fitted to a common vertex to measure the event IP using the LCFIVERTEX [18] package, achieving a typical precision on the IP position of better than 3 μm in all three dimensions.

Clusters identified in the electromagnetic calorimeter by the GARLIC [19] and PANDORAPFA [20] algorithms were treated as photon candidates. Each cluster was assigned a momentum with magnitude equal to the reconstructed cluster energy and direction parallel to a line joining the nominal IP and the energy-weighted mean position of the cluster. Clusters were associated to π^0s and their parent τs based on matching the cluster momentum direction to the simulated photon directions. Events were rejected if not all the simulated μ, π and photons could be matched to reconstructed particles. Such cases are typically due to imperfect reconstruction algorithms or the interactions of particles in the tracker volume.

In order to improve the effective photon energy resolution, clusters associated to a π^0 were subjected to a constrained

[6] The vast majority of $\tau \to \pi^\pm\pi^0\nu_\tau$ decays proceed via the $\rho^\pm$, so we use ρν as shorthand for $\pi^\pm\pi^0\nu_\tau$ in this paper.

kinematic fit imposing the π^0 mass by varying their energies. No special effort was made to correct invariant mass biases occurring when reconstructing two overlapping clusters from π^0 decay. Fig. 2 shows the precision with which the visible invariant mass is reconstructed in $\tau \to \rho\nu$ decays. The accuracy with which the reconstructed track plane approximates the true τ decay plane is demonstrated in the bottom right plot of Fig. 2, in which the "track plane error" is defined as the angle that the true τ momentum makes to the reconstructed track plane.

The reconstructed tracks from multiprong τ decays were fitted to a common vertex, again using the LCFIVERTEX package. In three-prong decays via the a_1, the ellipsoid describing the vertex position uncertainty typically has a major axis length of 100 μm, and the other two axes around 2 μm.

4.2. Dependence of p_T^{miss} and the lifetime likelihood on $\psi^{\pm}$

Fig. 3 shows the dependence of the event p_T^{miss} (defined as the magnitude of the component of $\mathbf{P} = \sum_i \mathbf{p}_i$ transverse to the beam-line, where the index i runs over the momenta $\mathbf{p}_i$ of the τs and other reconstructed particles in the event) and lifetime likelihood on the two τ decay angles $\psi^{\pm}$ in two events, one in which both $\tau \to \pi^{\pm}\nu$, the other in which both $\tau \to \rho\nu$. The distributions are shown for the case in which the first Q solution is used for each τ (which is where the best solution was found in these two events). Four minima at which $p_T^{miss} \sim 0$ are seen, one in each quadrant. The lifetime likelihood (shown for the same Q solution), together with the p_T^{miss} at the minimum, allows the best minimum to be chosen.

The MINUIT package in the ROOT [21] analysis framework was used to find the minima of the p_T^{miss} distributions separately in each of the four quadrants bounded by $\psi^{\pm} = 0, \pm\pi/2$, in each of the four Q-solution combinations. If no minimum was found, or either τ had a negative reconstructed decay length at the minimum, the quadrant was rejected. Of the remaining possible solutions, the one with the smallest value of p_T^{miss} was chosen.

4.3. Results

4.3.1. Single prong decays

Of events in which reconstructed objects could be unambiguously matched to simulated particles, no good solution was found in 0.4% (2.4%) of events in the $\pi^{\pm}\nu$ ($\rho\nu$) channel. This inefficiency is due to cases in which the reconstructed visible mass is larger than the τ mass, or in which no solution with positive decay length is found. In Fig. 4 we show the distribution of the chosen solutions' p_T^{miss}, for events in which both τs were forced to decay to either $\pi^{\pm}\nu$ or $\rho\nu$. A rather good minimum ($p_T^{miss} < 1$ MeV) is found in the large majority of cases, but a fraction of events have a larger p_T^{miss}. These events with large p_T^{miss} are due to mis-reconstruction of the event, and make up a larger fraction of $\rho\nu$ than $\pi^{\pm}\nu$ decays due to the relatively worse precision of the calorimeters compared to the tracker. Events in which the reconstructed p_T^{miss} is larger than around 0.5 GeV/c show a significantly wider peak in the τ–τ mass distribution, as shown in Fig. 4. The mass distribution in the case of $\pi^{\pm}\nu$ ($\rho\nu$) decays has a central peak with a Gaussian width $\sigma \sim 0.6$ GeV (1.1 GeV), and non-Gaussian tails to both higher and lower values. Of $\pi^{\pm}\nu$ ($\rho\nu$) events with $p_T^{miss} < 0.5$ GeV/c, 74% (67%) lie within 3σ, and 95% (89%) within 10 GeV, of the peak position.

The same figure also shows the reconstructed invariant mass of the two τ system in events with small or large ISR/beamstrahlung energy (demonstrating that the method is independent of the total centre-of-mass energy and boosts along the beam-line), and on the smaller of the true τ decay lengths in the laboratory (showing that events with longer decay lengths tend to be better reconstructed). Fig. 5 shows the τ pair mass in the $e^+e^- \to \mu^+\mu^- H$ event sample, and a second $e^+e^- \to \mu^+\mu^-\tau^+\tau^-$ sample in which the Higgs boson contribution was effectively turned off. Clear mass peaks due to the Higgs and Z^0 bosons can be seen, the widths of which allow a rather clean separation between these processes in both the considered τ decay modes.

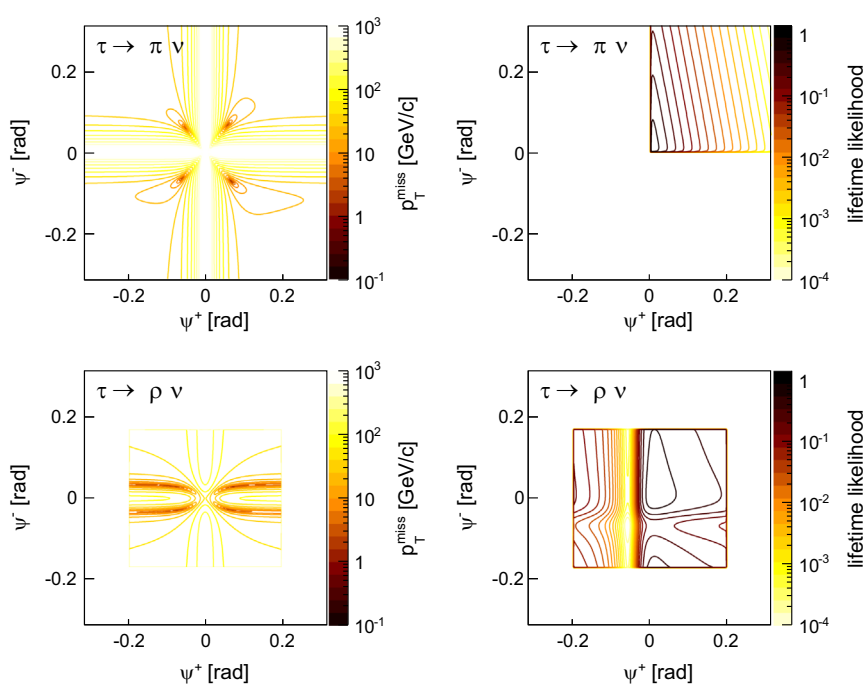

Fig. 3. Example of two $e^+e^- \to \mu^+\mu^-\tau^+\tau^-$ events in which both $\tau \to \pi^{\pm}\nu$ [top], or both $\tau \to \rho\nu$ [bottom]. Contours of p_T^{miss} [left] and lifetime likelihood [right] as a function of the two angles $\psi^{\pm}$ are shown. Regions with darker contours (lower p_T^{miss}, higher lifetime likelihood) are preferred. In the upper event no positive decay length solutions were found for $\psi^{\pm} < 0$, while in the lower event, no physical solutions were found for $|\psi^{\pm}| > \sim 0.2$.

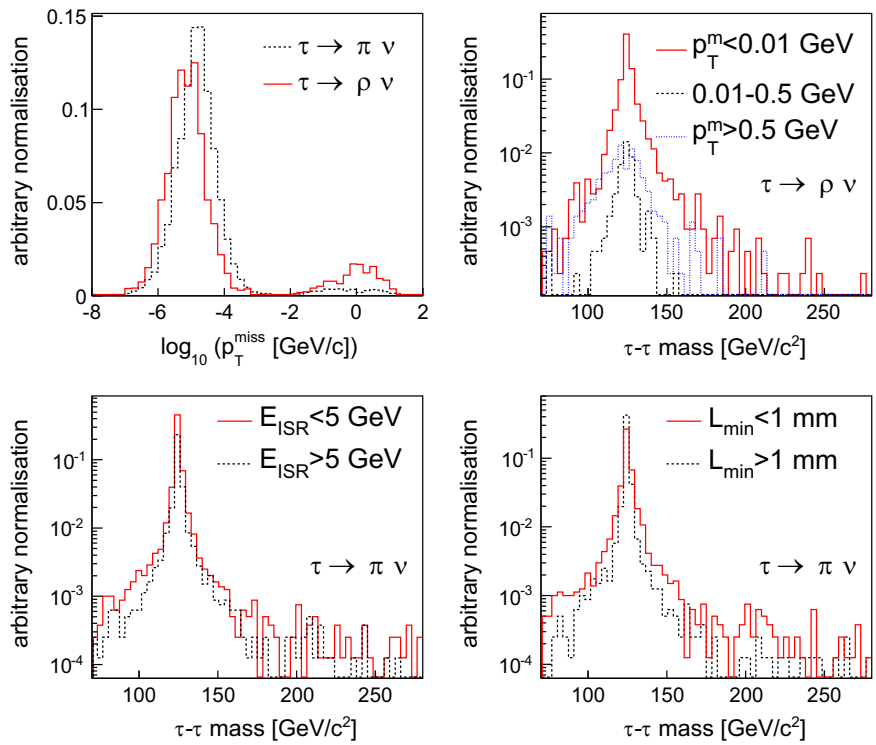

Fig. 4. Properties of the considered $e^+e^- \to \mu^+\mu^- H$ events after full τ reconstruction. The value of the event p_T^{miss} at the chosen solution [top left]. The τ pair mass distributions in different ranges of $p_T^{m(iss)}$ [top right], the total ISR/beamstrahlung energy E_{ISR} [bottom left], and L_{min}, the smaller of the two true τ decay lengths [bottom right]. Except in the top left plot, the relative normalisations of the various contributions are as in the event samples.

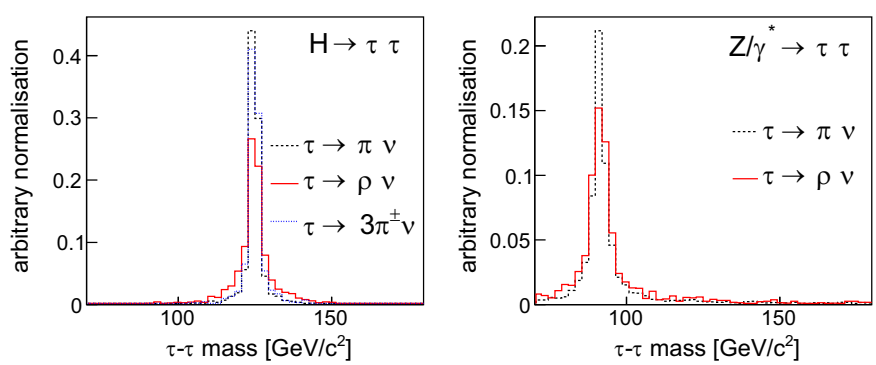

Fig. 5. The reconstructed mass of the τ pair in $e^+e^- \to \mu^+\mu^-\tau^+\tau^-$ events in which the τ pair was produced via a Higgs (left) or Z^0/γ^* (right).

4.3.2. Multiprong decays

Multiprong τ decays, studied using the $\tau \to (a_1 \to 3\pi^\pm)\nu$ channel, are reconstructed using two methods. In the "vertex" method, the reconstructed vertex position is directly used to constrain the τ direction, and the τ mass constraint used to find two possible solutions for the neutrino momentum. No real solution is found in around a quarter of τ decays. The event p_T^{miss} is used to choose the best solution.

In the "decay plane" method, the central position and major axis of the vertex position error ellipsoid are used to define the τ decay plane, which is then used in the same way as for single prong decays. Candidate τ solutions are required to have fitted and reconstructed τ decay vertices in the same hemisphere. The event candidate solution with smallest p_T^{miss} is selected. When using this method, no good candidate solution was identified in around 4.5% of events. Fig. 6 shows a comparison of these two multiprong methods. As well as having a much higher efficiency for identifying a solution, the "decay plane" approach results in significantly

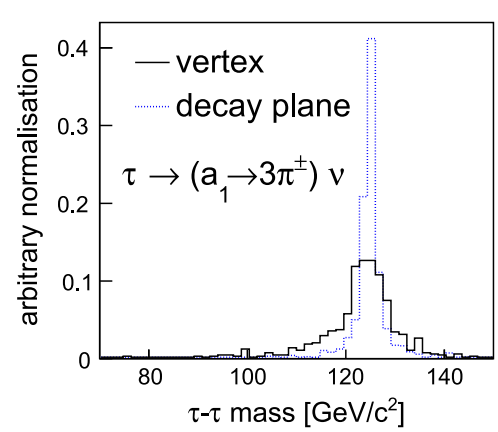

Fig. 6. The reconstructed mass of the τ pair in $e^+e^- \to \mu^+\mu^-\tau^+\tau^-$ events in which both τs decay into three charged pions. We compare the results of two τ reconstruction methods: directly using the reconstructed vertex position, and using the position and major axis of the vertex ellipsoid to define the τ decay plane.

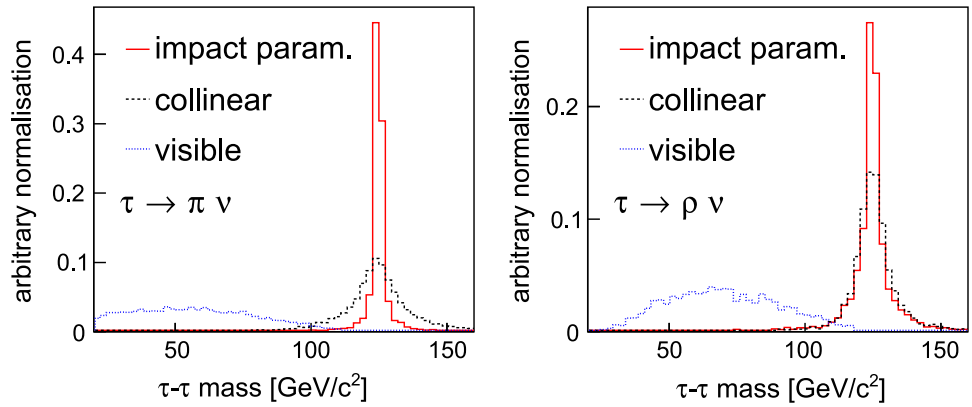

Fig. 7. Comparison of the reconstructed τ pair invariant mass using different methods: the impact parameter-based method developed in this paper, the collinear approximation, and only the visible decay products.

better mass resolution. The di-τ invariant mass distribution for multiprong a_1 decays obtained by using the "decay plane" method are compared to other decay channels in Fig. 5, showing that multiprong decays are reconstructed with a similar precision as $\tau \to \pi^{\pm} \nu$ decays.

In Fig. 7 we compare τ pair mass reconstruction using the methods developed in this paper with alternative approaches. The simplest is to use the invariant mass of only the visible decay products, therefore ignoring the neutrino contribution. This clearly underestimates the invariant mass, and results in a rather wide distribution. The collinear approximation assumes that the neutrinos are parallel to the visible tau decay products, and further requires the event's p_T to be balanced, allowing the neutrino energies to be estimated. The mass distribution resulting from the collinear approximation is peaked at the correct value, however it is significantly wider than that achieved by the methods developed in this paper. The difference in resolution is particularly significant in the $\pi^{\pm} \nu$ decay channel, where the impact parameter method gives a very sharp distribution.

5. Conclusion

An approach to the reconstruction of hadronic τs has been presented, which can be used in events in which the τ production vertex is well known, and the trajectory of its charged decay products is precisely measured. This method works only in events in which no undetected particles with significant p_T are produced together with the τs. In contrast to other methods, no assumptions are made on the centre-of-mass frame or the invariant mass of a τ-pair system, nor on the τ energies. The method is insensitive to momentum balance along the beam-line, so this method should work on *e.g.* $e^+e^- \to \mu^+\mu^- H$ events produced both near, and well above, threshold.

The example analysed in this paper, in which a τ pair recoils against a μ pair, is the case in which the event p_T^{miss} is most precisely measured. The Higgs boson will more commonly recoil against a hadronic system. These events are more difficult to reconstruct, and will have a less precisely measured p_T^{miss}. The use of a constrained kinematic fit, taking into account the resolution with which the various quantities are measured, should lead to improved results.

This reconstruction technique can be used at lepton colliders, as demonstrated in this paper, provided the precision of the tracking detectors is sufficient, particularly in the estimation of charged particle trajectories near the interaction point. To be used at hadron collider experiments, the τ decay products must be sufficiently well identified and reconstructed, and all particles produced in the same interaction unambiguously identified in order to accurately estimate the p_T^{miss} associated to the interaction. This latter point suggests that cases in which τs recoil against a relatively simple system, *e.g.* μ–μ as considered in this paper or a single high p_T jet, should be the most promising in the richer environment of hadronic collisions at high luminosity, in which multiple interactions typically occur in each event. The method is insensitive to the unknown net momentum along the beam direction inherent in hadronic collisions.

If applied to Higgs boson decays into τ leptons, the use of this method will allow clean separation of signal events from irreducible backgrounds from *e.g.* Z decays, and allow precise reconstruction of the τ spin information, providing a sensitive probe to measure the CP nature of the Higgs boson.

Acknowledgements

I thank H. Videau and S. Komamiya for helpful comments on the manuscript. This work was funded by the MEXT KAKENHI Grant-in-Aid for Scientific Research on Innovative Areas, No. 23104007.

References

[1] T. Behnke, et al., The International Linear Collider Technical Design Report—Volume 1: Executive Summary. arXiv:1306.6327.
[2] M. Aicheler, et al., A Multi-TeV Linear Collider Based on CLIC Technology. http://dx.doi.org/10.5170/CERN-2012-007.
[3] A. Apyan, et al., CEPC-SPPC Preliminary Conceptual Design Report. IHEP-CEPC-DR-2015-01, 2015.
[4] ⟨https://fcc.web.cern.ch/⟩, 2015.
[5] T. Behnke, et al., The International Linear Collider Technical Design Report—Volume 4: Detectors. arXiv:1306.6329.
[6] A. Heister, et al., European Physical Journal C20 (2001) 401 arXiv:hep-ex/0104038.
[7] K. Belous, et al., Physical Review Letters 112 (3) (2014) 031801 arXiv:1310.8503.
[8] R.K. Ellis, et al., Nuclear Physics B297 (1988) 221.
[9] A. Elagin, et al., Nuclear Instruments and Methods in Physics Research Section A 654 (2011) 481 arXiv:1012.4686.
[10] G. Aad, et al., Journal of High Energy Physics 04 (2015) 117 arXiv:1501.04943.
[11] S. Chatrchyan, et al., Journal of High Energy Physics 05 (2014) 104 arXiv:1401.5041.
[12] K. Desch, Z. Was, M. Worek, European Physical Journal C29 (2003) 491 arXiv:hep-ph/0302046.
[13] S. Berge, W. Bernreuther, Physics Letters B671 (2009) 470 arXiv:0812.1910.
[14] A. Rouge, Physics Letters B619 (2005) 43 arXiv:hep-ex/0505014.
[15] M. Reinhard, CP violation in the Higgs sector with a next-generation detector at the ILC (Ph.D. thesis), LLR-École polytechnique, 2009.
[16] W. Kilian, T. Ohl, J. Reuter, European Physical Journal C71 (2011) 1742 arXiv:0708.4233.

[17] N. Davidson, et al., Computer Physics Communications 183 (2012) 821 arXiv:1002.0543.
[18] D. Bailey, et al., Nuclear Instruments and Methods in Physics Research Section A 610 (2009) 573 arXiv:0908.3019.
[19] D. Jeans, J.C. Brient, M. Reinhard, Journal of Instrumentation 7 (2012) P06003 arXiv:1203.0774.
[20] M. Thomson, Nuclear Instruments and Methods in Physics Research 611 (2009) 25 arXiv:0907.3577.
[21] ⟨https://root.cern.ch⟩, 2015.

Nuclear Instruments and Methods in Physics Research A 789 (2015) 158–164

Contents lists available at ScienceDirect

Nuclear Instruments and Methods in Physics Research A

journal homepage: www.elsevier.com/locate/nima

A novel strip energy splitting algorithm for the fine granular readout of a scintillator strip electromagnetic calorimeter

Katsushige Kotera [a,*], Daniel Jeans [b], Akiya Miyamoto [c], Tohru Takeshita [a]

[a] Department of Physics, Shinshu University, 3-1-1 Asahi, Matsumoto, Nagano 390-8621, Japan
[b] Department of Physics, Graduate School of Science, The University of Tokyo, 7-3-1 Hongo, Bunkyo-ku, Tokyo 113-0033, Japan
[c] High Energy Accelerator Research Organization (KEK), 1-1 Oho, Tsukuba, Ibaraki 305-0801, Japan

ARTICLE INFO

Article history:
Received 25 May 2014
Received in revised form
20 February 2015
Accepted 1 April 2015
Available online 11 April 2015

Keywords:
Calorimeter
Particle flow
Scintillator
SiPM
Granularity
Linear collider

ABSTRACT

We describe an algorithm which has been developed to extract fine granularity information from an electromagnetic calorimeter (ECAL) with strip-based readout. Such a calorimeter, based on scintillator strips, is being developed to apply particle flow reconstruction to future experiments in high energy physics. The application of this algorithm to 100 GeV hadronic jets in an ECAL with $45 \times 5\ \mathrm{mm}^2$ transverse segmentation improves the energy resolution from 3.6% to 3.0%, to be compared to the resolution of 2.9% achieved by an ECAL with $5 \times 5\ \mathrm{mm}^2$ segmentation. The performance can be further improved by the use of $10 \times 10\ \mathrm{mm}^2$ tile-shaped layers interspersed between strip layers.

© 2015 Elsevier B.V. All rights reserved.

1. Introduction

In the experiments being designed for next generation particle colliders, the particle flow approach (PFA) [1,2] is the leading candidate to achieve the excellent jet energy resolution required to fully exploit the information offered by the detector and the collider. In PFA, the energy of charged particles is measured by the tracking system, which has a much better momentum resolution than the energy resolution of calorimeters: typical resolutions are $\sigma_{1/p_T} \sim 2 \times 10^{-5}\ \mathrm{GeV}^{-1}$ for the tracking system, and $\sigma_E/E \sim 46\%/\sqrt{E(\mathrm{GeV})} \oplus 1.6\%$ for the HCAL response to single charged pions [3]. The calorimeters are used to estimate the energy only of neutral particles. In order to apply this approach, the calorimetric showers of each particle must be individually reconstructed. The granularity of calorimeter readout is therefore a key issue.

As an example, the sampling electromagnetic calorimeter (ECAL) with tungsten absorbers being designed for the International Large Detector (ILD, a detector being designed for use at the International Linear Collider (ILC) [3]) is optimized to have a transverse segmentation of 5 mm, corresponding to half of the Moliére radius of tungsten, and 20–30 longitudinal samplings in a total thickness of 23 X_0, giving a total of $\sim 10^8$ readout channels. The effective Molière radius of the ECAL is around 20 mm. A readout granularity finer than 5 mm does not result in significant performance gains for jet energies of 100 GeV and below, which correspond to the most relevant jet energies for the ILC physics program [1]. One technology being developed to effectively achieve this high calorimeter granularity is based on plastic scintillator strips individually read out by miniature photon detectors, for example, pixelated photon detectors (PPD, also commonly known as SiPM) [5].

The use of long scintillator strips rather than $5 \times 5\ \mathrm{mm}^2$ tiles simplifies the design of such an ECAL, and also reduces its cost, due to the reduced number of readout channels. Successive ECAL layers have orthogonally aligned strips, giving an effective granularity close to the strip width. The CALICE collaboration has developed and constructed ECAL prototypes based on this technology, using scintillator strips of length 45 mm and width 5 or 10 mm, individually read out by PPDs [6,7].

This paper presents a reconstruction method which can be used to extract close to $5 \times 5\ \mathrm{mm}^2$ effective granularity from such long scintillator strips, and reports on measurements of its performance using events fully simulated in ILD. Details of this detector are given in the next section, the reconstruction procedure is explained in Section 3, and Section 4 describes the calibration procedure. The performance of this method on the basic detector-related measures of position resolution and two-particle separation are discussed in Sections 5 and 6, while the jet energy resolution, which affects the physics performance

* Corresponding author.
E-mail address: coterra@azusa.shinshu-u.ac.jp (K. Kotera).

http://dx.doi.org/10.1016/j.nima.2015.04.001
0168-9002/© 2015 Elsevier B.V. All rights reserved.

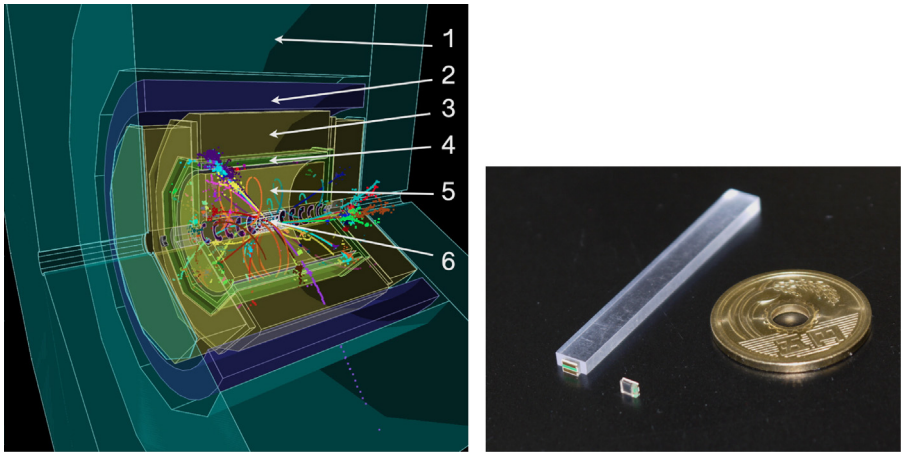

Fig. 1. *Left*: a view of ILD with a simulated multiple-jet event. The highlighted detector components are: 1. muon detector; 2. solenoid; 3. hadron calorimeter; 4. electromagnetic calorimeter; 5. TPC; and 6. vertex detector. *Right*: a 45 mm × 5 mm × 2 mm scintillator strip and a PPD.

of the detector, is discussed in Section 7. Finally we discuss the results in Section 8 and summarize this study in Section 9.

2. Detector model

Starting from the interaction point (IP), the ILD consists of a vertex detector, silicon tracking layers, a large time projection chamber (TPC) surrounded by additional silicon tracking detectors, a calorimeter system consisting of electromagnetic and hadronic sections, all placed within a solenoidal magnetic field of strength 3.5 T. The steel return yoke is instrumented to provide muon identification. The basic structure consists of a central, "barrel", region aligned with the beam axis, closed by two "endcaps" in the forward regions. The ECAL barrel detector has an octagonal cross-section, a length of around 5 m, and an inner radius of 1.85 m. A cylindrical coordinate system with its axis (z) aligned with the beam line is used in this paper. More details of the ILD design can be found in [3]. The ILD is simulated in MOKKA [8], a GEANT4-based simulation tool [9]. Fig. 1 *left* shows a multiple-jet event simulated in ILD.

The ILD strip-scintillator ECAL (strip-ScECAL) is a sampling calorimeter. In the simulation model used in this study, 30 sensitive layers are interleaved with tungsten plates of thickness 2.1 (4.2) mm in the inner 20 (outer nine) layers. The tungsten absorber layers correspond to a total thickness of 22 X_0, while layers of readout electronics, copper heat transfer plates, and scintillators contribute less than a single additional X_0. The total thickness of the ECAL is around 200 mm.

The sensitive layers are tiled with 45×5 mm^2 scintillator strips of thickness 1 mm. Strips are aligned orthogonally in successive layers. A dead volume of size $2.5 \times 1.0 \times 0.91$ mm^3 is implemented at the end of each scintillator strip to represent the volume occupied by the PPD, which leads to a constant term in the energy resolution. In the analyses presented in this paper, when scintillator tiles or strips with an area of less than 45×5 mm^2 are used, this dead volume is scaled by the strip area.[1] This avoids penalizing smaller cell sizes with an additional constant term to the energy resolution. Each strip is enveloped by a reflective film of thickness 57 μm. Scintillator strips and PPDs are mounted on 180×180 mm^2 "ECAL base units" (EBU), printed circuit boards which also host the front-end electronics and LEDs used for calibration.

The EBUs are arranged within mechanical structures in such a way as to avoid any projective cracks. Further technical details are available in [3]. Printed circuit boards and copper heat radiators are simulated in each detector layer. Four different scintillator tile configurations were used in this study:

1. 5×5 mm^2 tiles ("5 × 5");
2. 45×5 mm^2 strips ("45 × 5");
3. alternating layers of 5×5 mm^2 tiles and 45×5 mm^2 strips ("alt5"); and
4. alternating layers of 10×10 mm^2 tiles and 45×5 mm^2 strips ("alt10").

Successive strip layers were always orthogonally aligned. A hadronic calorimeter based on 40 layers of $30 \times 30 \times 3$ mm^3 scintillator tiles interleaved with 20 mm iron absorbers was simulated in this study.

3. Strip splitting algorithm

A simple algorithm, the Strip Splitting Algorithm (SSA), has been developed to extract fine granularity information from the long strip geometry. Each strip is split into n virtual cells along its length; n is chosen to result in approximately square virtual cells; for example, a 45×5 mm^2 strip is split into nine 5×5 mm^2 cells. A simple procedure is used to distribute the total energy E_{strip} detected by the strip among its virtual cells. A weight w_k is assigned to each virtual cell k, defined as the sum of the energies E_i of all strips in immediately neighboring layers which intersect with virtual cell k, when seen from the IP:

$$w_k = \sum_{(i\,=\,\text{intersect})} E_i \tag{1}$$

where the sum runs over strips, i, in immediately neighboring layers which intersect with the virtual cell k. The energy E_k assigned to virtual cell k is then

$$E_k = E_{\text{strip}} \frac{w_k}{\sum_{(j\,=\,\text{all virtuals})} w_j} \tag{2}$$

where the sum j runs over all virtual cells of the strip being split. Fig. 2 shows a schematic of the SSA procedure.

In the case of the alt10 model, the 10×10 mm^2 tile is first split into 2×2 virtual cells. The immediately neighboring strip layers are used to partition the tile's energy into these virtual cells using a very similar method to that defined above, making use of the strips' orthogonal orientation. In a second step, the virtual cells originating from the 10×10 mm^2 tiles are used to partition strips' energy among their virtual cells, as described above.

[1] This scaling is of course not possible in practice, although we note that techniques for the readout of scintillation light from the lower surface, which therefore avoid dead space due to the PPD, are currently being studied.

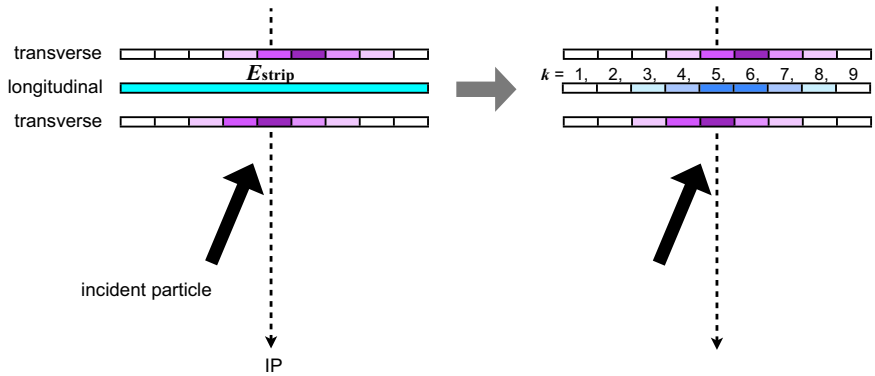

Fig. 2. A cartoon illustrating the SSA procedure. The energy, E_{strip} reconstructed in the central, "longitudinal", strip is split among virtual cells ($k = 1, \ldots, 9$) by considering the energy in the orthogonally aligned "transverse" strips in neighboring layers. More details of the procedure are given in the text.

Events were analyzed using a particle flow reconstruction algorithm. In the results presented later in this paper, the PandoraPFA algorithm [1,4] was used to analyze events, together with other standard ILD reconstruction programs (e.g. for tracking) in the MarlinReco [10] package.[2] PandoraPFA uses as input the energy and position of calorimeter deposits, as well as reconstructed charged particle tracks. When SSA was not used, PandoraPFA was passed the central position and energy of each strip (this is the simplest possible approach), while in the case of SSA, the central position and assigned energy of each virtual cell was used.

4. Calibration

Scintillator strips with an energy deposit were used to create calorimeter hits, whose energy was taken to be the energy deposited in the scintillator. No account was taken of non-linear or discretized behavior of the PPD response. In order to remove noise hits while keeping sufficient efficiency for minimum ionizing particle (MIP) detection, an energy threshold on each hit in the ECAL and HCAL was applied at a fraction of the most probable per-cell energy deposition of 10 GeV anti-muons ("MIP"). For the ScECAL, a threshold of 0.3 MIP was set for each virtual cell, while a threshold of 0.5 MIP was set when SSA was not used. For HCAL hits, a 0.3 MIP threshold was set, the default value used in PandoraPFA.

The calorimeter was calibrated by studying the energy deposited by 10 GeV photons for the electromagnetic response, and 10 GeV neutral long lived Kaons (K_L) for the hadronic response. Particles were injected from the IP in a direction almost perpendicular to the beam-line (in order to avoid the central electrode of the TPC) and uniformly distributed in azimuth. The calibration factors used to convert between the energy deposited in the scintillator and that deposited in the whole calorimeter (including the tungsten absorbers and other passive materials) were chosen to give a mean energy, after PFA reconstruction, equal to the incident particle energy. Additional calibration factors used to account for different values of the hadronic and electromagnetic responses h/e, separately defined in the ECAL and HCAL, were optimised to obtain the best jet energy resolution, according to the standard PandoraPFA procedure [4]. The ECAL was re-calibrated for each ECAL configuration, while a single HCAL calibration was used for all configurations. Apart from this calibration, the same parameters of PandoraPFA were used for all ECAL geometries.

[2] The package versions defined in ILCSoft v01-16-02 were used.

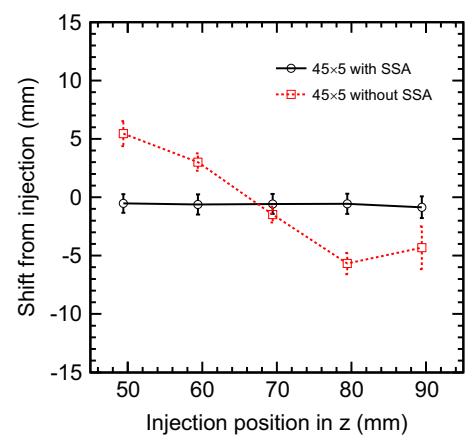

Fig. 3. Shift of reconstructed position for 10 GeV photons. The vertical error bars reflect the widths of the position shift distributions.

5. Position of clusters

The precise reconstruction of cluster positions is important in a PFA analysis to ensure good matching between tracks and calorimeter clusters. In this study, 10 GeV photons were fired into the 45×5 ECAL from the IP, varying the ECAL injection position along the z direction. The injected position was taken to be the intersection on the ECAL front face of the line joining the reconstructed cluster position[3] and the IP. Fig. 3 shows the difference between the position reconstructed by PandoraPFA and the true photon injection position, as a function of the injected position. The size of the vertical error bars reflects the width of the reconstructed position distribution.

When SSA is not used, a strong position-dependent bias of up to 5 mm is observed, corresponding to cases when the photon shower passes near the ends or center of a strip ($z = 68$ mm corresponds to the center of strips aligned with the z axis). When SSA is used, these biases are almost completely removed, and cluster positions are reconstructed to better than 1 mm.[4]

[3] The position of a calorimetric cluster is defined as the energy-weighted mean position of its constituent hits.

[4] A small z-dependent bias remains after SSA, due to the relative position within the virtual cell. The small consistent position bias visible after SSA is due to the fact that the chosen injection positions are all in the same relative position within the virtual cells. When integrated over z, the average bias becomes effectively zero.

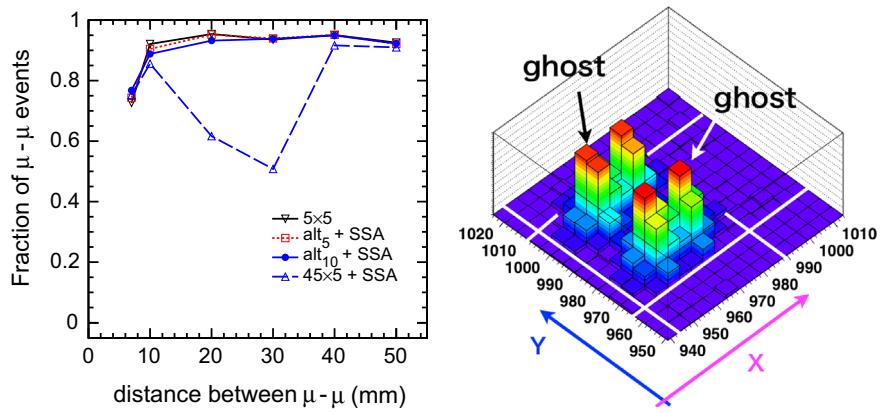

Fig. 4. *Left*: fraction of correctly reconstructed di-muon events as a function of the distance between the muons at the front face of the ECAL. *Right*: energy deposit of two electrons incident simultaneously on 45×5 strip-ScECAL reconstructed with SSA. Two of four peaks are ghosts.

6. Two-particle separation

To investigate the separation ability of the strip-ScECAL with SSA, di-muon events and π^0 decays (for photon–photon separation) were studied. These simple events serve to illustrate and investigate the phenomena of spurious "ghost" clusters which can occur when two particles are simultaneously incident in a square area whose side is shorter than the strip length. The reconstructed invariant mass of the two photons from π^0 decays provides a good test of both the photon separation and reconstruction ability.

6.1. μ–μ separation

Di-muon events provide a sensitive system for measuring two-particle separation in different ScECAL designs. The ability to reconstruct two anti-muons of momentum 10 GeV produced at IP was studied as a function of the distance between their impact positions on the ECAL surface. One muon was injected into the ECAL at a fixed point, with polar angle almost perpendicular to the beam line and azimuthal angle $\phi = \pi/2$. The second was injected to impact the ECAL surface at some distance from this point, with $\delta_{r\phi} = \delta_z = \Delta/\sqrt{2}$, where $\delta_{r\phi}$ (δ_z) is the separation between the ECAL entry points in the r–ϕ (z) direction, and Δ was scanned between 7 and 50 mm. Both injection positions were smeared by 0.2 mm on the ECAL surface in r–ϕ and z. Four thousand simulated di-muon events were analyzed using SSA and PandoraPFA.

Fig. 4 *left* shows the fraction of such events in which the two muons were reconstructed without any additional ghost calorimeter clusters, as a function of the distance between the entry points of the two muons into the ScECAL. Apart from the 45×5 strip-ScECAL with the use of SSA, all types of ScECAL have over 90% correctly reconstructed events when the distance between the two muons is larger than 10 mm. In the case of the 45×5 strip-ScECAL with the use of SSA, the fraction depends strongly on the position, with a minimum at a distance of 30 mm. This is due to the possibility of two-fold ambiguities arising in reconstruction when two particles enter a square region with size smaller than the strip length, which can lead to the formation of "ghost" clusters. Fig. 4 *right* illustrates a case in which two injected electrons produced two additional ghost clusters. At a separation of 30 mm in Fig. 4 *left*, around 25% of di-muon events in the 45×5 strip-ScECAL have a single additional reconstructed ghost cluster, and a further 25% have two ghost clusters. At distances below 30 mm, ghost clusters are more often combined with the true muon cluster. At a separation of 7 mm, the correctly identified fraction drops to around 70% for all ScECAL configuration due to the merging of nearby clusters.

The use of interleaved tile layers removes the ambiguities leading to ghosts, and dramatically improves the situation, resulting in a performance comparable to that of a tile-based ScECAL.

6.2. π^0 reconstruction to study two-photon separation

A π^0 meson decays into two photons, which can be reconstructed using only calorimeter information. The π^0 energy has a strong influence on the opening angle between the two photons, and variations in the decay angle give rise to different photon energies in the laboratory frame. Samples of π^0 decays at different energies are therefore a powerful tool to measure the ECAL performance, both in terms of pattern recognition (the ability to identify two clusters), and energy resolution (by considering the invariant mass of identified clusters). The opening angle between photons decreases as the π^0 energy increases: the most probable distance between photons from a 10 (30) GeV π^0 decay on the ECAL surface is 53 mm (17 mm).

A PandoraPFA photon cluster is required to satisfy several requirements on several observables, including the absence of associated tracks, the depth of the cluster start within the ECAL, and the angle between the reconstructed cluster axis and the line joining the cluster position to the IP [1]. Fig. 5 shows the fraction of π^0 events in which one, two, and more than two photon clusters are reconstructed in the 45×5 ScECAL, *left*, and alt10 ScECAL, *right*. At each energy 8000 π^0s were injected from the IP almost perpendicular to the beam line and with a uniform distribution in azimuthal angle. In around 9% of events, at least one of the photons from the π^0 decay converts before reaching the ECAL, and the number of events with no reconstructed photons is less than 0.5% for all π^0 energies.

The fraction of events correctly reconstructed with two photon clusters decreases strongly with increasing energy. One contribution to this decrease is the merging of nearby clusters, seen in the increase in the fraction of events in which a single photon cluster is reconstructed, understood as the effect of the decreasing distance between photons. An additional factor is the increase of events in which more than two photon clusters are reconstructed. This is seen in all geometries (5×5 m and alt10 are shown in Fig. 5), demonstrating that this is the effect of PandoraPFA clustering algorithms, rather than the effect of ghost clusters caused by the strip readout.

Fig. 6 shows various characteristics of π^0 events in which exactly two photon-like clusters were identified. Fig. 6a (b) shows the reconstructed invariant mass of such events at different π^0 energies in a 5×5 m tile-ScECAL (45×5 strip-ScECAL with SSA). Fig. 6c shows the fraction of π^0 events which have exactly two identified photon-like clusters with a reconstructed invariant mass greater than 0.1 GeV/c^2, for the four ScECAL geometries considered. The use of alternate tile layers improves

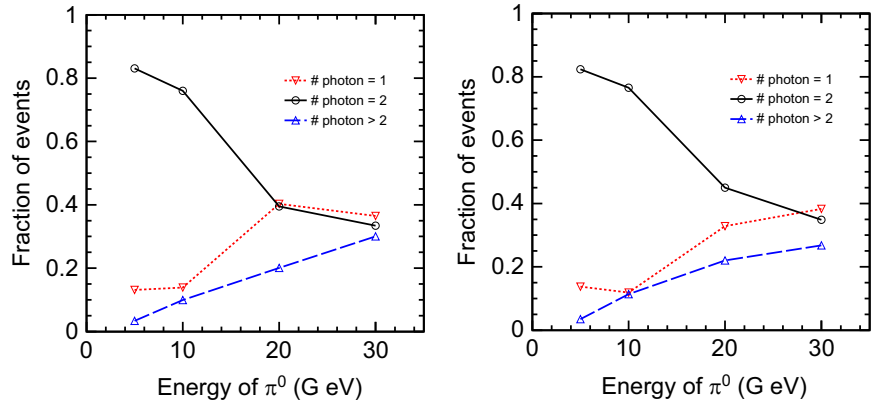

Fig. 5. The fraction of π^0 events reconstructed with one, two, and more than two photon clusters, in the 5×5 mm^2 ScECAL *left* and alt10 strip-ScECAL *right* geometries. No requirements are made on the energy or invariant mass of identified photons. The statistical uncertainties are not visible on this scale.

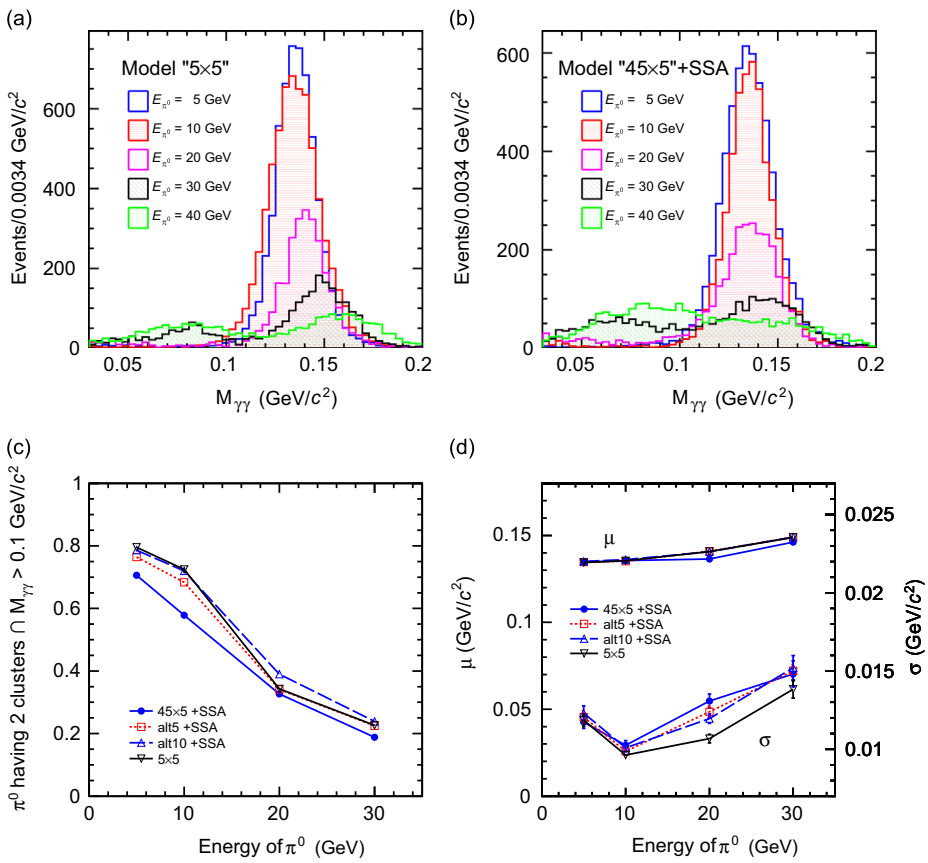

Fig. 6. Reconstructed invariant mass $M_{\gamma\gamma}$ at different π^0 energies, for events with two reconstructed photon like clusters in (a) the 5×5 tile-ScECAL, (b) 45×5 strip-ScECAL, (c) the fractions of such events, in the four ECAL types, having $M_{\gamma\gamma} > 0.1$ GeV/c^2, and (d) the mean (μ) and width (σ) of a Gaussian fit to the reconstructed $M_{\gamma\gamma}$ distributions as a function of the π^0 energy. Vertical bars show statistical uncertainties only.

the performance compared to a purely strip-based geometry, as was also seen in the case of di-muon events. The fact that the alt10 model gives statistically significantly better results than alt5 at energies of 10 and 20 GeV is unexpected, and not yet fully understood. Fig. 6d shows the means and standard deviations of Gaussian fits to the invariant mass spectra for π^0 of different energies, reconstructed in different ScECAL geometries. SSA was used in all models except the 5×5 tile-ScECAL.

These studies show that some level of π^0 reconstruction is possible at energies of up to ~30 GeV using the clustering algorithms implemented in PandoraPFA. No large performance differences were seen between the four considered ECAL geometries.

7. Jet energy resolution

The reconstruction of the energy of two-jet events is an important benchmark test of the PFA. Samples of $10^4 e^+e^- \rightarrow q\bar{q}$ (q = u, d, s) events were fully simulated in ILD at center-of-mass energies of 91.2, 200, 360, and 500 GeV, and then reconstructed using MarlinReco, including SSA and PandoraPFA.

To evaluate the jet energy resolution, only events in which both quarks were produced in the barrel region ($|\cos(\theta)| < 0.7$) were considered. The total reconstructed event energy E_{jj} is defined as the sum of the energies of all particles reconstructed by PandoraPFA. The distribution of this event energy is used to determine "RMS90(E_{jj})",

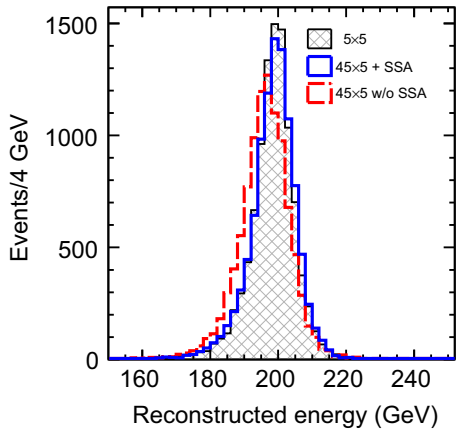

Fig. 7. Reconstructed energy in $q\bar{q}$ events at 200 GeV, for the 5×5 mm^2 ScECAL and the 45×5 mm^2 strip-ScECAL with and without the use of SSA.

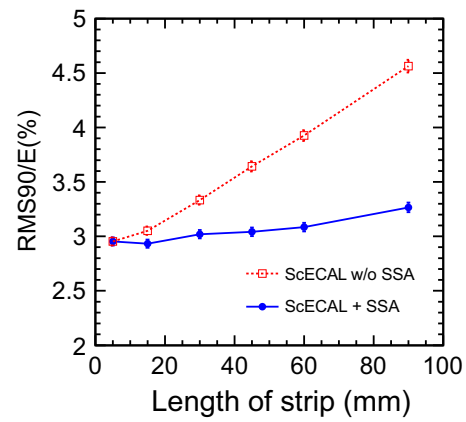

Fig. 8. Estimated single jet energy resolution RMS90/E of jets produced in $q\bar{q}$ events at a center-of-mass energy of 200 GeV.

defined as the root mean square of the smallest range of the E_{ij} distribution which contains at least 90% of events. The single jet energy resolution "RMS90" is estimated by dividing "RMS90(E_{ij})" by $\sqrt{2}$. This RMS90 measure is useful to describe the generally non-Gaussian energy distributions with small, but long, tails obtained by PFA, since it makes no assumptions about the shape of the distribution, and also avoids giving undue weight to events far in the tails.

At lower jet energies, where single particles are well separated in the calorimeters, the energy resolution is dominated by the single particle response of the calorimeters. For higher energy jets, in which the average distance between particles in the calorimeters is smaller, the so-called "confusion" term becomes important. Confusion is due to the mis-association of fragments of charged particle showers to neutral clusters, and vice versa, which leads to a over- or under-counting of energy, leading to a degradation in jet energy resolution. The relative contributions of the single particle calorimetric response and confusion in hadronic jets become comparable at energies of around 100 GeV [1].

7.1. Energy spectra

Fig. 7 shows the total reconstructed energy (E_{ij}) at a center-of-mass energy of 200 GeV when using the 5×5 and 45×5 Sc-ECAL models, with and without the use of SSA. The shape of the energy spectrum for the 45×5 Sc-ECAL is noticeably improved by the use of SSA, and comes close to that of the 5×5 model.

7.2. Dependence on strip length

The dependence of the jet energy resolution at a center-of-mass energy of 200 GeV on the strip length is shown in Fig. 8. The same strip width of 5 mm was used in all models. The strong degradation in performance with increasing strip length seen when SSA is not used is almost completely mitigated by the use of SSA. The difference in jet energy resolution between a ScECAL using 5×5 tiles and one using strips of length up to 60 mm is almost negligible.[5]

7.3. Comparison of 5×5, 45×5, and 15×15 ScECAL models

Fig. 9 shows the jet energy resolution as a function of jet energy for a 45×5 strip-ScECAL without and with SSA, and 15×15 and 5×5 tile-ScECAL models. At smaller jet energies, below 100 GeV, the jet energy resolution is dominated by the intrinsic single-particle resolution, giving a resolution which improves with increasing energy. At energies above 100 GeV, the confusion between charged and neutral calorimeter clusters becomes significant, leading to a degradation of resolution with increasing energy for all ScECAL geometries. The jet energy of the 45×5 strip-ScECAL is significantly improved by using SSA, especially at and above 100 GeV, indicating that confusion is decreased by SSA. A tile of 15×15 has the same area as a 45×5 strip, however it is clear that the jet energy resolution when using the strip geometry is significantly better (by up to 0.5 percentage points (p.p.)), demonstrating the real merit of a strip-based geometry used in conjunction with SSA. The degradation in jet energy resolution between the 5×5 and 45×5 (with SSA) models is rather small, less than 0.25 p.p. for 45 GeV and 250 GeV jets, and around 0.1 p.p. for jets between 100 and 200 GeV.

7.4. Jet energy resolution of strip-tile-ScECAL

As discussed in Section 6.1, the major problem faced by a strip-based ECAL is the formation of ghost clusters. Therefore, the use of interleaving tile layers is expected to improve the jet energy resolution.

Fig. 10 compares the jet energy resolutions of 45×5, alt5, and alt10 models. The performance of the alt5 and alt10 models are almost identical. At jet energies of up to 100 GeV, they give almost the same performance as the 5×5 model, while at higher energies the performance lies approximately half way between the 5×5 and 45×5 models.

8. Discussion

SSA successfully extracts fine granularity information, at an effective scale close to that of the strip width, from a strip-based calorimeter. This motivates the development of scintillator strip-based calorimeters, with their advantages of less readout channels and lower cost, for a wide range of experiments.

The small degradation in jet energy resolution, of around 0.2 p.p., when going from a 5×5 tile-ScECAL to a 45×5 strip-ScECAL can be largely recovered by the use of tile layers interleaved between the strip layers. These tile layers prevent the formation of ghost clusters, as has been demonstrated in the reconstruction of a simple di-muon system. Tile layers with a granularity of 10×10 mm^2 have been shown to work well. The use of such a tile size is technically feasible. The use of 5×5 mm^2 tiles, which have the same area as the 45×5 mm^2 strips currently being used in a prototype ScECAL, and

[5] Note that this assumes a uniform response along the strip length. Response non-uniformities will favor shorter strips.

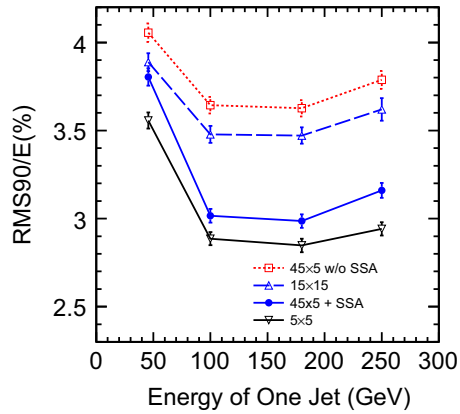

Fig. 9. Single jet energy resolution of as function of jet energy for different tile- and strip-ScECALs.

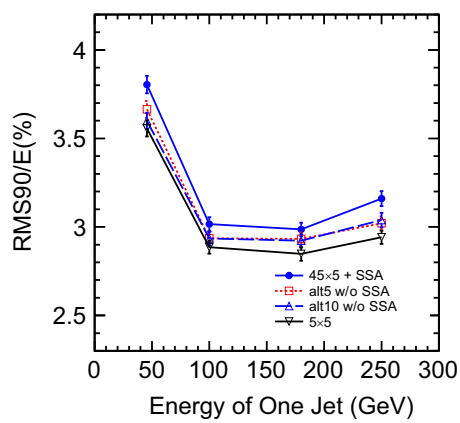

Fig. 10. Single jet energy resolution as a function of jet energy for 45 × 5, alt5, alt10, and 5 × 5 ScECAL models.

therefore the same density of readout electronics, is certainly technically feasible. Studies of reconstruction performance with such larger tiles are continuing. The use of scintillator-based $5 \times 5\ \mathrm{mm}^2$ layers is technically difficult at present, but a different technology, such as the silicon readout ECAL being developed by CALICE [11], could be used.

The MOKKA simulation model used in this study describes the detailed geometry of scintillator strips, dead volumes due to the reflector, PPD packages, radiators, circuit boards, and mechanical structures. However, effects such PPD saturation, cross-talk and dark noise phenomena, finite photo-electron statistics, and non-uniform scintillator response have not been simulated in the results presented in this paper. These effects may have some influence on the absolute energy resolutions reported in this paper, but the effect on the relative performance improvements achieved by SSA is expected to be minimal.

9. Summary

An algorithm ("SSA") to extract fine granularity from scintillator strips was developed and tested. The reconstructed position of clusters was significantly improved with SSA: the maximum shift in the reconstructed position of 10 GeV photon clusters from the true position is improved from 5 mm to sub-mm by using SSA on a 45 strip-ScECAL. The strip-ScECAL with SSA also shows comparable particle separation performance to the $5 \times 5\ \mathrm{mm}^2$ tile ScECAL in muon pair and π^0 events. Ghost clusters created when two particles impinge on a square area with a size less than the strip length are effectively removed by interleaving strip layers with square tile layers.

The energy resolution for jets of up to 250 GeV obtained with several ScECAL geometries was compared. The differences in the obtained jet energy resolutions when using a 5 × 5 tile-ScECAL and 45 × 5 strip-ScECAL with SSA reconstruction ranged from 0.15 p.p. to 0.25 p.p. This difference can be removed for jet energies below 100 GeV, or decreased to ~0.1 p.p. for jet energies in the range 150–250 GeV, by alternately replacing strip layers with tile layers.

Acknowledgments

The authors would like to thank ILD group for providing essential simulation (MOKKA) and analysis tools (Marlin and PandoraPFA), and for useful discussions. John Marshall has given invaluable advice on the tuning and calibration of the PandoraPFA algorithm. Members of the CALICE collaboration, in particular the CALICE-ASIA group, and of the ILD-ASIA group, have also contributed to many important discussions. This work is supported in part by 'grant-in-aid for specially promoted research: a global research and development program of a state-of-the-art detector system for the ILC' of the Japan Society for Promotion of Science (JSPS) Grant no. 23000002).

References

[1] M. Thomson, Nuclear Instruments and Methods in Physics Research Section A 611 (2009) 25.
[2] Jean-Claude Brient, Henri Videau, The Calorimetry at the Future e^+e^- Linear Collider, 2002, arXiv:hep-ex/0202004.
[3] Ties Behnke, et al., The International Linear Collider Technical Design Report—Volume 4: Detectors, 2013, arXiv:1306.6329.
[4] J. Marshall, M. Thomson, The Pandora particle flow algorithm, in: Proceedings of the CHEF2013, Paris, 2013, arXiv:1308.4537.
[5] K. Kotera, Scintillator strip ECAL optimization, in: Proceedings of the LCWS2013, Tokyo, arXiv:1404.1672.
[6] K. Francis, et al., Nuclear Instruments and Methods in Physics Research Section A 763 (2014) 278.
[7] K. Kotera, Performance of the CALICE scintillator-based ECAL depending on the temperature, in: Proceedings of the LCWS2011, Granada, 2012, arXiv:1201.6098v2.
[8] P. Mora de Freitas, H. Videau, Detector simulation with MOKKA/GEANT4: Present and future, in: Proceedings of the LCWS2002, C02-08-26.5, Seoul, 2003, pp. 623–627; MOKKA Homepage, 2014, mokka.in2p3.fr.
[9] S. Agostinelli, et al., Nuclear Instruments and Methods in Physics Research Section A 506 (2003) 250.
[10] MARLIN Homepage, 2014 ⟨http://ilcsoft.desy.de/portal/software/packages/marlinreco⟩http://ilcsoft.desy.de/portal/software/packages/marlinreco⟩.
[11] J. Repond, et al., Journal of Instrumentation 3 (2008) P08001.

Experimental Validation of a Novel Compact Focusing Scheme for Future Energy-Frontier Linear Lepton Colliders

G. R. White,[3] R. Ainsworth,[15] T. Akagi,[16] J. Alabau-Gonzalvo,[2] D. Angal-Kalinin,[4] S. Araki,[8] A. Aryshev,[8] S. Bai,[6] P. Bambade,[14] D. R. Bett,[5] G. Blair,[15,18] C. Blanch,[1] O. Blanco,[14,2] N. Blaskovic-Kraljevic,[5] B. Bolzon,[2,4,13] S. Boogert,[15] P. N. Burrows,[5] G. Christian,[5] L. Corner,[5] M. R. Davis,[5] A. Faus-Golfe,[1] M. Fukuda,[8] J. Gao,[6] H. García-Morales,[2,17] N. Geffroy,[7] H. Hayano,[8] A. Y. Heo,[9] M. Hildreth,[20] Y. Honda,[8] J. Y. Huang,[10] W. H. Hwang,[10] Y. Iwashita,[11] S. Jang,[9] A. Jeremie,[7] Y. Kamiya,[12] P. Karataev,[15] E. S. Kim,[9] H. S. Kim,[9] S. H. Kim,[10] Y. I. Kim,[5] S. Komamiya,[12] K. Kubo,[8] T. Kume,[8] S. Kuroda,[8] B. Lam,[3] K. Lekomtsev,[8] S. Liu,[14] A. Lyapin,[15] E. Marin,[3] M. Masuzawa,[8] D. McCormick,[3] T. Naito,[8] J. Nelson,[3] L. J. Nevay,[5,15] T. Okugi,[8] T. Omori,[8] M. Oroku,[12] H. Park,[9] Y. J. Park,[10] C. Perry,[5] J. Pfingstner,[2] N. Phinney,[3] A. Rawankar,[8] Y. Renier,[2] J. Resta-López,[1] M. Ross,[3] T. Sanuki,[19] D. Schulte,[2] A. Seryi,[5] M. Shevelev,[8] H. Shimizu,[8] J. Snuverink,[15] C. Spencer,[3] T. Suehara,[12] R. Sugahara,[8] T. Takahashi,[16] R. Tanaka,[16] T. Tauchi,[8] N. Terunuma,[8] R. Tomás,[2] J. Urakawa,[8] D. Wang,[6] M. Warden,[5] M. Wendt,[2] A. Wolski,[13] M. Woodley,[3] Y. Yamaguchi,[12] T. Yamanaka,[12] J. Yan,[12] K. Yokoya,[8] F. Zimmermann[2]

(ATF2 Collaboration)

[1]*Universidad de Valencia - Instituto de Física Corpuscular (IFC), Edificio Institutos de Investigación, c/ Catedrático José Beltrán, 2, E-46980 Paterna, Spain*
[2]*European Organization for Nuclear Research (CERN), CH-1211 Geneva 23, Switzerland*
[3]*SLAC National Accelerator Laboratory, 2575 Sand Hill Road, Menlo Park, California 94025-7090, USA*
[4]*CLRC: Daresbury Laboratory, Daresbury, Warrington, Cheshire WA4 4AD, United Kingdom*
[5]*John Adams Institute for Accelerator Science at University of Oxford, Denys Wilkinson Building, Keble Road, Oxford OX1 3RH, United Kingdom*
[6]*Institute of High Energy Physics (IHEP), Chinese Academy of Sciences (CAS), Beijing, China*
[7]*LAPP-Universite de Savoie-CNRS/IN2P3, Annecy-le-Vieux, France.*
[8]*High Energy Accelerator Research Organization (KEK), 1-1 Oho, Tsukuba, Ibaraki 305-0801, Japan*
[9]*Department of Physics, Kyungpook National University, 1370 San Kyuk-dong, Puk ku, Taegu 635, South Korea*
[10]*Pohang Accelerator Laboratory, POSTECH (Pohang University of Science and Technology), San-31 Hyoja-dong, Pohang 790-784, South Korea*
[11]*Institute for Chemical Research (ICR), Nuclear Science Research Facility, Kyoto University, Gokasho, Uji, Kyoto 611-0011, Japan*
[12]*Department of Physics, University of Tokyo, 7-3-1 Hongo, Bunkyo-ku, Tokyo 113, Japan*
[13]*Department of Physics, Oliver Lodge Laboratory, University of Liverpool, Oxford St., Liverpool L69 3BX, United Kingdom*
[14]*LAL, Universite Paris-Sud, CNRS/IN2P3, Orsay, France*
[15]*John Adams Institute for Accelerator Science at Royal Holloway University of London, Egham Hill, Egham, Surrey TW20 0EX, United Kingdom*
[16]*Department of Physics, Hiroshima University, 1-3-1 Kagamiyama, Higashi-Hiroshima 739-8526, Japan*
[17]*Universitat Politécnica de Catalunya, BarcelonaTech, C. Jordi Girona, 31. 08034 Barcelona, Spain*
[18]*Science and Technology Facilities Council, Polaris House, North Star Avenue, Swindon SN2 1SZ, United Kingdom*
[19]*Tohoku University, 28 Kawauchi, Aoba-ku, Sendai, 980-8576 Japan*
[20]*University of Notre Dame, Notre Dame, Indiana 46556, USA*

(Received 10 September 2013; published 24 January 2014)

A novel scheme for the focusing of high-energy leptons in future linear colliders was proposed in 2001 [P. Raimondi and A. Seryi, Phys. Rev. Lett. **86**, 3779 (2001)]. This scheme has many advantageous properties over previously studied focusing schemes, including being significantly shorter for a given energy and having a significantly better energy bandwidth. Experimental results from the ATF2 accelerator at KEK are presented that validate the operating principle of such a scheme by demonstrating the demagnification of a 1.3 GeV electron beam down to below 65 nm in height using an energy-scaled version of the compact focusing optics designed for the ILC collider.

DOI: 10.1103/PhysRevLett.112.034802 PACS numbers: 41.85.-p, 29.20.Ej, 29.27.-a

Designs for the next generation of energy-frontier lepton colliders envisage the generation and collision of particle beams into the TeV energy scale [1,2]. To deliver the required rate of particle interactions to the detectors for the planned physics program, one of the most challenging technical aspects is the focusing and dynamic manipulation of the colliding particle bunches. A prototype final focus system (FFS) was constructed at the Accelerator Test

 © 2014 American Physical Society

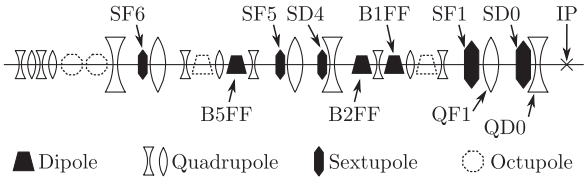

FIG. 1. Schematic of a final focus system with local chromaticity correction. Dashed components are not included in ATF2 test.

Facility (ATF) at KEK, Japan, with the primary goal of verifying a novel, so-called *local chromaticity correction* design first proposed in [3] (one of the earliest reviews of the chromatic compensation scheme can be found in [4]). The new design has many beneficial features over designs considered previously, the most notable being a considerable reduction in length. Both the proposed International Linear Collider (ILC) [1] and the Compact Linear Collider (CLIC) [2] consider this scheme in their baseline designs, although until now it has not been experimentally proven to be practically realizable. We report here results from the test accelerator ATF2 [5] taken during beam operations in 2012 and 2013. We have, on repeated occasions, reduced the 1.3 GeV electron vertical beam size down to approximately 70 nm and below, which has demonstrated the design feasibility.

A schematic of the optics layout is shown in Fig. 1. The complexity of the FFS is driven by the requirement to correct the dominant aberration necessarily present in any magnetic focusing optics: the chromaticity due to the strong final focusing magnets. The novelty of this design is to compensate for the chromaticity locally rather than using a separate optical section as considered previously. This is achieved by placing sextupoles (SD0 and SF1) adjacent to the final doublet quadrupoles which focus the beam and by intentionally introducing horizontal dispersion through the FFS using dipole magnets. The parasitic second-order dispersion is canceled by arranging for an appropriate amount of residual chromaticity to leak from upstream sections. Higher order geometric and chromogeometric aberrations are corrected using additional upstream sextupoles and manipulating the optical transfer matrices between the magnetic elements according to the recipe outlined in [6]. Refinements to the initial design were performed using a global optimization procedure as proposed in [7]. This latest procedure uses a high-order transfer map using a *polymorphic tracking code* to fully compensate second and third order aberrations in the FFS in a semiautomated fashion.

The principal goal for ATF2 was to test the FFS design relevant to ILC. To achieve this, we designed a scaled version of the FFS optics that would present a level of difficulty to "tune" the beam at the focus point comparable to ILC. With magnet strength and focus length constrained by other design considerations, the difficulty to tune the beam is related to the level of demagnification demanded of the magnetic optics, which sets the chromaticity. The beam size at the focal point increases by an amount proportional to the product of the chromaticity and energy spread of the beam. This quantity is presented in Table I (fifth line) for ILC, CLIC, and ATF2, where one can observe that FFS designs with tighter focusing requirements (smaller focal point betatron functions) lead to optics which enlarge the beam size more due to chromatic growth and require tighter control of these and other resulting aberrations. A test facility used to demonstrate the previous focusing design (FFTB [8]) is also shown for comparison. The tuning difficulty manifests itself through the required precise balancing of high-order terms in the magnetic transport lattice. The precision required for the cancellation of these effects increases with the chromaticity, which places increasing demands on the placement tolerances of the magnets as well as their magnetic field settings and quality.

TABLE I. Key FFS parameters for ILC, CLIC, ATF2, and FFTB. L^* is the distance from QD0 to the focus point, ϵ_y the vertical emittance, ξ_y the vertical chromaticity, σ_E is the rms energy spread, σ_y the rms vertical beam size, and β^* the focal point beta function. The "pushed" optics demonstrates the tightest focusing possible by the ATF2 machine and is of future interest to show performance in conditions more applicable to the CLIC collider design [10].

	ILC (TDR 500 GeV)	ATF2	FFTB	ATF2 (pushed)	CLIC (CDR 3 TeV)
L^* (m)	$3.5/4.5^a$	1	0.4	1	3.5
ϵ_y (pm rad)	0.07	12	22	12	0.003
$\xi_y \sim (L^*/\beta_y^*)$	$7,300/9,400^a$	10,000	4,000	40,000	50,000
$\sigma_E(\%)$	$0.07/0.12^b$	0.08	0.1	0.08	0.3
$\Delta\sigma_y/\sigma_y \sim (\sigma_E.L^*/\beta_y^*)$	$5/9,\ 7/11^{b,a}$	8	4	32	150
σ_y (nm) *design*	5.9	37	52	23	1
σ_y (nm) *measured*	-	65 ± 5^c	70 ± 6	-	-
$\beta_x^*(mm)$	11	4 (40^c)	10	4	4
$\beta_y^*(mm)$	0.48	0.1	0.1	0.025	0.07

[a]SiD/ILD ILC detector configurations.
[b]Positron/electron side of ILC.
[c]March 2013 results and configuration of ATF2 with bunch charge 80–130 pC.

When one calculates these tolerances (as for ATF2 in [9]), it is apparent that the tolerances are beyond our ability to achieve through standard survey and magnet engineering capabilities (with some magnets requiring submicron placement and/or few parts-per-million field strength settings). For the optics to work as required, we are reliant upon a series of complex online beam tuning procedures outlined below.

The ATF2 experimental FFS was constructed as a new extraction beam line to the existing ATF damping ring (DR) facility at KEK and was completed in December 2008. The ATF DR is a ~140 m circumference electron ring fed by an s-band linear accelerator which is used to accelerate the electron bunches produced by an rf gun to 1.3 GeV. In the normal ATF2 mode of operation, the DR delivers bunches of electrons with 1.6 nC charge at 3.12 Hz to the extraction system with typically measured (corrected) emittances of 2 nm rad × 12 pm rad (horizontal and vertical dimensions, respectively). ATF2 is also used as a general-purpose R&D facility, with emphasis on the development of state-of-the-art beam diagnostic devices applicable for use in the next generation of linear colliders. Another noteworthy aspect of ATF2 is the unique way it is managed and operated in an international context: hardware construction, support and operation, operations shifts, software controls, and data analyses were all achieved through a collaborative international team spread across a globally diverse set of institutes.

The ATF2 beam line contains seven dipoles, three septa, 49 quadrupoles, five sextupoles, four skew sextupoles, and 25 corrector magnets. The quadrupoles and dipole bends for the main part of the FFS were purpose designed and built for ATF2, whilst the other magnets were reused from the old ATF extraction line and from the FFTB experiment at SLAC [11]. The beam line can be considered to consist of two sections: the extraction line (EXT) and the FFS. These are depicted in Fig. 2 which also shows the locations of key diagnostic and correction systems. The EXT is used for the extraction and manipulation of the beam out of the DR and preparing it for injection into the FFS beam line, i.e., for correcting residual energy dispersion, cross-plane coupling, and any mismatch from design in the phase space of the incoming beam.

The floor of ATF has been specially prepared, with deep concrete piles, to be vibrationally stable and have a good coherence length (~4 m for relevant frequencies). Additionally, work has been undertaken to ensure the stability of the final doublet (FD: SF1, QF1, SD0, and QD0) support table [12]. The FD elements are attached to a rigid honeycomb block and bolted to the floor, using a thin layer of beeswax between the steel plate support at the base of the block and the floor to ensure good mechanical coupling. Measurements were made demonstrating the relative vibrations between QF1, QD0, and the focal point were within tolerance (~ < 10 nm). A new design of high accuracy, high availability power supply system was installed [13] to satisfy the main field tolerances for ATF2 magnets [9] and to test the high availability requirements for future linear collider magnets. Each quadrupole and sextupole magnet in the FFS was mounted on a 3-axis mover system (horizontal, vertical, and roll directions) [14]. This system is used to align the FFS using the beam, to counter thermal drift, long-period ground motion, etc., and to calibrate the attached cavity beam position monitors (BPMs).

The beam orbit is monitored by a system of stripline (EXT, resolution 1–5 μm [15]), c-and s-band cavity (FFS, resolution 40–200 nm [16]) BPMs. Also, there is a doublet of c-band cavities at the focal point with a demonstrated resolution of < 5 nm [17]. The key properties of the BPMs are high resolution, charge independence, and gain stability (~1% per run period).

The tuning process starts within the EXT [18]: During the extraction process from the DR, the beam develops cross-plane coupling as well as horizontal and vertical energy dispersion that is outside the acceptance bandwidth of the FFS. The energy dispersion is corrected using a pair of quadrupole magnets and a pair of skew-quadrupole magnets within the dispersive part of the EXT. Changes in incoming beam phase space and cross-plane coupling are measured using a system of four beam profile devices which measure the optical transition radiation produced when the beam passes through thin metallic targets sequentially inserted into the path of the beam [19]. This system is capable of measuring and correcting the incoming vertical emittance at the 10% level. The phase space is corrected using an online beam model to adjust nine quadrupole magnets in the beginning section of the EXT. The coupling correction is especially important given the high horizontal to vertical aspect ratio of the beam (270 : 1 at the FFS focal point). To correct the coupling, the online model is used to compute a correction using four skew-quadrupole magnets in the EXT. The energy dispersion is typically corrected below 5 mm everywhere and

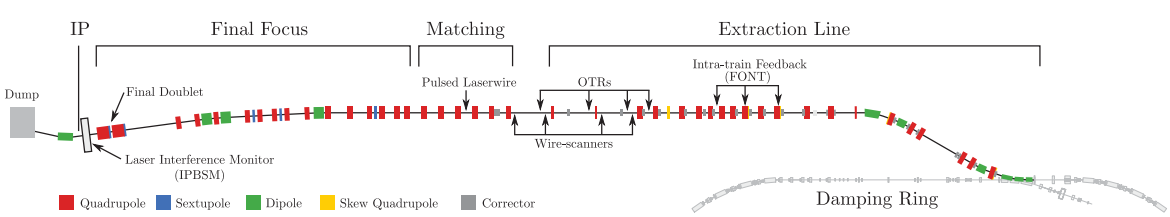

FIG. 2. The extraction line and final focus section of ATF2 after extraction from the damping ring.

the coupling corrected such that the measured beam ellipses on the optical transition radiation screens are corrected at the 0.1 degree level, and the beam phase space (matching) corrected to a *BMAG* [20] mismatch parameter of better than 1%. Simulations have shown this level of correction (the process and accuracy is similar to the simulated correction in the ILC beam delivery system) to be adequate for the FFS tuning to be successfully applied.

The tuning of the FFS ([18,21]) starts with the process of beam-based alignment. This utilizes the magnet movers, correction dipole magnets, and BPMs to align the beam close to the magnetic field centers of the magnets whilst ideally maintaining a straight beam trajectory through the whole system. It is especially important to have an orbit initially close to the field centers of the sextupole magnets. This is achieved by making use of the parabolic orbit response to horizontal and vertical motion of the sextupole magnets. Also of importance during the beam-based alignment procedure is achieving a beam orbit well centered in areas of the beam line with discontinuities to minimize wakefield effects. Careful steering was also important to minimize background signals in the focal point beam size monitor detectors. First-order correction for aberrations remaining directly at the focal point are performed by changing the field strength and rotation angles of the FD quadrupoles. This coarsely corrects for offset of the horizontal and vertical waist and energy dispersion at the focal point, and also for coupling. Following the tuning procedures described thus far typically yields a horizontal spot size of around 10 μm, close to the design value, and a vertical size of between 1 and 3 μm at the FFS focal point. At this stage, the focal point beam size measurements are performed using a carbon wirescanner (diameter $\sim$5 μm).

Monte Carlo style simulations of the complete tuning process, including the final spot size tuning described below, have been performed by multiple people independently using different simulation programs to verify the tuning process. The simulations have demonstrated that the FFS should be tuneable following the procedures that are outlined here. Descriptions of the simulation process which also further describe the various tuning steps can be seen in [21,22]. Similar simulation efforts have been performed for the ILC and CLIC colliders [23]. It is through these simulations that confidence in the ability of this FFS design to generate the desired beam conditions in future collider facilities is reached. Therefore, the ongoing efforts to use the data from ATF2 to validate these simulations are considered important.

Before final tuning, the vertical beam size is dominated by the linear aberrations of waist shift (the focal point displaced longitudinally), energy dispersion, and coupling of the particle's horizontal angle at the focal point to vertical position. We also expect, and observe, second-order coupling and chromatic coupling terms to be present. Tuning knobs devised to remove the expected sources of linear beam size aberrations are constructed using deliberate horizontal and vertical moves of the FFS sextupole magnets to construct orthonormal knobs. Four skew-sextupole magnets were added to control second-order terms and loosen the tolerances on higher-order field terms in the quadrupole magnets.

To perform the final tuning of the vertical spot size at the focal point from $\mathcal{O}(1\ \mu\mathrm{m})$ down to the design 37 nm, we use a unique beam size measurement device, referred to as a *Shintake Monitor* [24]. This is installed at the ATF2 focal point and is a highly improved version of the original, first used at FFTB [8]. It forms a vertically-orientated laser interference pattern at the electron beam focal point, which is scanned across the beam by altering the path length of one arm of the laser interferometer to scan the phase of the interference pattern. The beam size is inferred from the modulation of the resulting Compton scattered photon signal detected by a downstream CsI calorimeter-type photon detector. The *modulation depth* (M) of the signal is written as a function of the laser crossing angle and electron beam spot size:

$$M = C|\cos\theta|\exp[-2(k_y\sigma_y)^2],$$
$$k_y = \pi/d, d = \frac{\lambda}{2\sin(\theta/2)}, \tag{1}$$

where λ is the laser wavelength, θ is the laser crossing angle, and d represents the fringe pitch which determines the beam size range that can be measured. The correction factor C is included to express any contrast reduction of the laser fringe pattern due to mismatch of the laser overlap, distorted laser profile, etc. Multiple possible error sources inherent to the Shintake Monitor measurement process can also be included into this correction factor.

There are three possible collision modes for the Shintake Monitor (made available by adjusting the crossing angle between the interfering laser beams): 2° to 8° (continuously variable), 30°, and 174°. Mode switching is possible remotely and allows for continuously tuning the electron beam from a few micrometers down to a theoretical minimum of about 20 nm. An example modulation scan performed after beam tuning, in the 174° mode of operation, is shown in Fig. 3.

The results from three separate attempts to tune the beam in the ATF2 FFS beam line are summarized in Fig. 4. The entries in the histograms have unity C correction factors and represent an upper limit on the achieved vertical beam size [25]. As shown by these results, we demonstrate a capability for repeated tuning of the vertical beam size to around 70 nm and below using iterations of the tuning techniques described above. This should be compared with a calculated beam size of 450 nm without the use of sextupoles for local chromaticity correction. Rescaled to the nominal ILC beam energy of 250 GeV, these results correspond to a vertical beam size of about 5 nm (below the

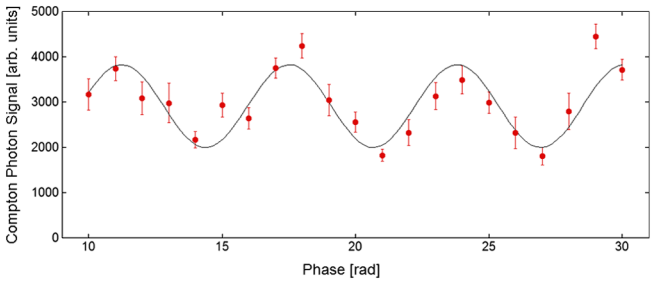

FIG. 3 (color online). Vertical beam size measurement (14th March 2013). Compton photon signals are measured as a function of the Shintake Monitor fringe phase with a crossing angle of 174°. The phase between the maxima of 2π corresponds to 266 nm. The beam size is 64.4 nm from the modulation depth ($M = 0.314$) without any systematic error correction applied.

baseline ILC design criteria). This confirms the practical operability of this optics design and the associated tuning procedure.

Studies are ongoing to identify the systematic effects contributing to the remaining ~30 nm of reduction required to reach the betatron limited beam size given by the optics design of 37 nm. We single out our two major contributing systematic effects here: wakefields and jitter effects in the Shintake Monitor. The beam is especially sensitive to wakefields (an order of magnitude more than expected at ILC) due to the long bunch lengths at ATF2 (6–10 mm) and considerably lower beam energy. We express the wakefield contribution to the measured beam size as $\sigma_y^2 = \sigma_y(0)^2 + w^2 q^2$, where $\sigma_y(0)$ is the zero-charge (no wakefield effect) beam size, w the wakefield contribution, and q the bunch charge in nC. We have measured wakefield contributions of between 100–140 nm nC^{-1} [18]. To minimize the effect on the beam size we operated at the lowest possible charges: between 80 and 200 pC. Work is ongoing to identify the wakefield sources and engineer solutions to mitigate them [26]. The beam size calculation is subject to systematic errors associated with the Shintake Monitor measurement and the complex interplay between these systematic effects and the beam tuning procedure. Error sources considered include those arising from phase jitter between the Shintake Monitor fringe pattern and the electron beam. This can be due to position jitter of the incident electron beam as well as spatial and temporal jitter sources within the laser system itself. Vertical jitter (statistical errors, background fluctuation, and laser timing errors, etc.) and horizontal jitter (where the signal is attenuated by varying power levels in the laser fringe) are present, with the latter responsible for degradation of the modulation depth. For a full treatment of Shintake Monitor error sources, see [25]. The relative phase jitter between the fringe pattern and the electron beam has been estimated by comparing measurements and simulations: this could account for about 10 nm in the beam sizes measured in 174° mode.

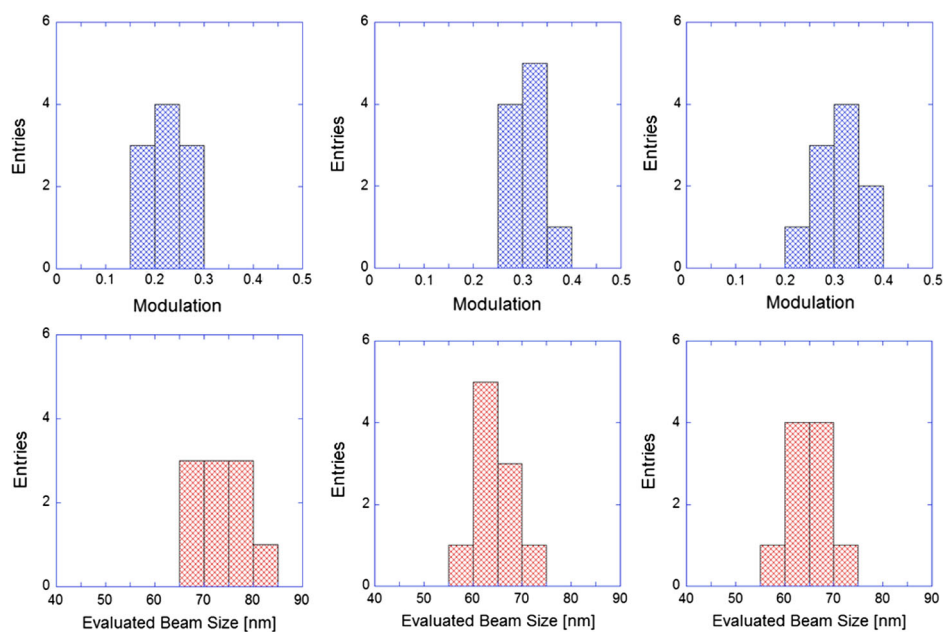

FIG. 4 (color online). Ten consecutive beam size measurements for each of the run periods: December 21, 2012 (left), March 8, 2013 (center), March 14, 2013 (right). The measured modulation depths shown on the top row are: 0.23 ± 0.05, 0.31 ± 0.04, and 0.30 ± 0.04 which correspond to beam sizes of: 73.2 ± 5.2, 64.9 ± 3.5, and 65.2 ± 4.0 nm, respectively (these represent upper limits: no systematic error correction applied). The measured beam charges for these data taking periods were < 200, 100–130 and 80–100 pC, respectively.

The authors would like to acknowledge and thank the tireless work of the administration staff, engineers, and operations contract personnel of ATF2 who have made the construction and operation of the ATF2 facility possible. We also acknowledge and thank KEK management and support staff for their support of this international project. Work also supported in part by Department of Energy Contract No. DE-AC02-76SF00515 and US National Science Foundation Grant No. NSF-PHY 0935296 and Spanish Research Project No. FPA2010-21456-C02-01. We also acknowledge the support of the Agence Nationale de la Recherche of the French Ministry of Research (Programme Blanc, Project No. ATF2-IN2P3-KEK, Contract No. ANR-06-BLAN-0027).

[1] T. Behnke *et al.*, arXiv:1306.6327.See also http://www.linearcollider.org/ILC/TDR for a full list of contributing institutes.
[2] M. Aicheler, P. Burrows, M. Draper, T. Garvey *et al.*, A Multi-TeV Linear Collider Based on CLIC Technology, 2012.
[3] P. Raimondi and A. Seryi, Phys. Rev. Lett. **86**, 3779 (2001).
[4] K. Brown and R. Servranckx, SLAC-PUB:3381, 1984.
[5] B. I. Grishanov *et al.* (ATF2 Collaboration), ATF2 Proposal, 2005.
[6] A. Seryi, M. Woodley, and P. Raimondi, SLAC-PUB-9895, 2003.
[7] R. Tomás, Phys. Rev. ST Accel. Beams **9**, 081001 (2006).
[8] V. Balakin, V. Alexandrov, A. Mikhailichenko, K. Flottmann, F. Peters *et al.*, Phys. Rev. Lett. **74**, 2479 (1995).
[9] B. Grishanov, P. Logachev, F. Podgorny, V. Telnov, D. Angal-Kalinin *et al.*, ATF2 proposal. Vol. **2**, 2006.Full proposal can be downloaded from http://atf.kek.jp/collab/md/projects/project_atf2.php.
[10] E. Marin, R. Tomás, P. Bambade, K. Kubo, T. Okugi, T. Tauchi, N. Terunuma, J. Urakawa, A. Seryi, G. White, and M. Woodley, "Design and High Order Optimization of the Accelerator Test Facility 2 Lattices", (to be published) in Phys. Rev. ST Accel. Beams.
[11] C. M. Spencer, R. Sugahara, M. Masuzawa, B. Bolzon, and A. Jeremie, IEEE Trans. Appl. Supercond. **20**, 250 (2010).
[12] B. Bolzon, in Conf.Proc. LCWS2007 C0705302, ATF201 (2007).
[13] A. Bellomo, C. Lira, B. Lam, D. MacNair, and G. White, SLAC-PUB-13278, (2008).
[14] G. Bowden, P. Holik, S. Wagner, G. Heimlinger, and R. Settles, Nucl. Instrum. Methods Phys. Res., Sect. A **368**, 579 (1996).
[15] E. Medvedko, R. Johnson, S. Smith, and G. White, Conf. Proc. BIW2010-TUPSM027 (2010).
[16] Y. Kim, R. Ainsworth, A. Aryshev, S. Boogert, G. Boorman *et al.*, Phys. Rev. ST Accel. Beams **15**, 042801 (2012).
[17] Y. Kim, H. Park, S. Boogert, J. Frisch, D. McCormick *et al.*, Conf. Proc. IPAC-2011-TUPC119 C110904, 1296 (2011), to be published in the Journal of Instrumentation.
[18] T. Okugi *et al.* (ATF2), Final focus system for linear colliders, ICFA Beam Dynamics Newsletter (2013).
[19] J. Alabau-Gonzalvo, C. B. Gutierrez, A. Faus-Golfe, J. Garcia-Garrigos, J. Resta-Lopez *et al.*, Conf. Proc. IPAC-2012-MOPPR044 **C1205201**, 879 (2012).
[20] M. Minty and F. Zimmermann, in *Measurement and Control of Charged Particle Beams* (Springer, New York, 2003), p. 113.
[21] T. Okugi, S. Araki, P. Bambade, K. Kubo, S. Kuroda, M. Masuzawa, E. Marin, T. Naito, T. Tauchi, N. Terunuma, R. Tomás, J. Urakawa, G. White, and M. Woodley, "Linear and Second Order Optics Correction of Atf2 Final Focus Beamline" (to be published) in Phys. Rev. ST Accel. Beams.
[22] G. R. White, S. Molloy, and M. Woodley, SLAC-PUB-13303, Conf. Proc. EPAC08-MOPP039, C0806233, MOPP039 (2008).
[23] B. Dalena, J. Barranco, A. Latina, E. Marin, J. Pfingstner, D. Schulte, J. Snuverink, R. Tomás, and G. Zamudio, Phys. Rev. ST Accel. Beams **15**, 051006 (2012).
[24] T. Shintake, Nucl. Instrum. Methods Phys. Res., Sect. A **311**, 453 (1992).
[25] J. Yan, Y. Yamaguchi, Y. Kamiya, S. Komamiya, M. Oroku, T. Okugi, N. Terunuma, K. Kubo, T. Tauchi, and J. Urakawa, Conf. Proc. EAAC2013 (2013), (to be published) in Nucl. Instrum. Methods Phys. Res., Sect. A.
[26] J. Snuverink, S. Boogert, Y. Kim, K. Kubo, A. Lyapin *et al.*, "Simulation and Measurement of Wake Fields at the Accelerator Test Facility 2" (to be published) in Phys. Rev. ST Accel. Beams.

Preprint typeset in JINST style - HYPER VERSION

arXiv:1306.3037v3 [physics.ins-det] 15 Jun 2014

Validation of GEANT4 Monte Carlo Models with a Highly Granular Scintillator-Steel Hadron Calorimeter

The CALICE Collaboration

C. Adloff, J. Blaha, J.-J. Blaising, C. Drancourt, A. Espargilière, R. Gaglione, N. Geffroy, Y. Karyotakis, J. Prast, G. Vouters
Laboratoire d'Annecy-le-Vieux de Physique des Particules, Université de Savoie, CNRS/IN2P3, 9 Chemin de Bellevue BP110, F-74941 Annecy-le-Vieux CEDEX, France

K. Francis, J. Repond, J. Schlereth, J. Smith[*], L. Xia
Argonne National Laboratory, 9700 S. Cass Avenue, Argonne, IL 60439-4815, USA

E. Baldolemar, J. Li[†], S. T. Park, M. Sosebee, A. P. White, J. Yu
Department of Physics, SH108, University of Texas, Arlington, TX 76019, USA

T. Buanes, G. Eigen
University of Bergen, Institute, of Physics, Allegaten 55, N-5007 Bergen, Norway

Y. Mikami, N. K. Watson
University of Birmingham, School of Physics and Astronomy, Edgbaston, Birmingham B15 2TT, UK

G. Mavromanolakis[‡], M. A. Thomson, D. R. Ward, W. Yan[§]
University of Cambridge, Cavendish Laboratory, J J Thomson Avenue, CB3 0HE, UK

D. Benchekroun, A. Hoummada, Y. Khoulaki
Université Hassan II Aïn Chock, Faculté des sciences, B.P. 5366 Maarif, Casablanca, Morocco

J. Apostolakis, A. Dotti, G. Folger, V. Ivantchenko, V. Uzhinskiy
CERN, CH-1211 Genève 23, Switzerland

M. Benyamna, C. Cârloganu, F. Fehr, P. Gay, S. Manen, L. Royer
Clermont Université, Université Blaise Pascal, CNRS/IN2P3, LPC, BP 10448, F-63000 Clermont-Ferrand, France

G. C. Blazey, A. Dyshkant, J. G. R. Lima, V. Zutshi
NICADD, Northern Illinois University, Department of Physics, DeKalb, IL 60115, USA

J. -Y. Hostachy, L. Morin
Laboratoire de Physique Subatomique et de Cosmologie, Université Joseph Fourier Grenoble 1, CNRS/IN2P3, Institut Polytechnique de Grenoble, 53, rue des Martyrs, F-38026 Grenoble CEDEX, France

U. Cornett, D. David, G. Falley, K. Gadow, P. Göttlicher, C. Günter, B. Hermberg, S. Karstensen, F. Krivan, A. -I. Lucaci-Timoce,[‡] S. Lu, B. Lutz, S. Morozov, V. Morgunov,[¶] M. Reinecke, F. Sefkow, P. Smirnov, M. Terwort, A. Vargas-Trevino
DESY, Notkestrasse 85, D-22603 Hamburg, Germany

N. Feege, E. Garutti[♠], I. Marchesini,[‖] M. Ramilli
University of Hamburg, Physics Department, Institut für Experimentalphysik, Luruper Chaussee 149, D-22761 Hamburg, Germany

P. Eckert, T. Harion, A. Kaplan, H. -Ch. Schultz-Coulon, W. Shen, R. Stamen
University of Heidelberg, Fakultät fur Physik und Astronomie, Albert Uberle Str. 3-5, 2.OG Ost, D-69120 Heidelberg, Germany

B. Bilki, E. Norbeck, Y. Onel
University of Iowa, Department of Physics and Astronomy, 203 Van Allen Hall, Iowa City, IA 52242-1479, USA

G. W. Wilson
University of Kansas, Department of Physics and Astronomy, Malott Hall, 1251 Wescoe Hall Drive, Lawrence, KS 66045-7582, USA

K. Kawagoe
Department of Physics, Kyushu University, Fukuoka 812-8581, Japan

P. D. Dauncey, A. -M. Magnan
Imperial College London, Blackett Laboratory, Department of Physics, Prince Consort Road, London SW7 2AZ, UK

V. Bartsch,[**] M. Wing
Department of Physics and Astronomy, University College London, Gower Street, London WC1E 6BT, UK

F. Salvatore[**]
Royal Holloway University of London, Department of Physics, Egham, Surrey TW20 0EX, UK

E. Calvo Alamillo, M.-C. Fouz, J. Puerta-Pelayo
CIEMAT, Centro de Investigaciones Energeticas, Medioambientales y Tecnologicas, Madrid, Spain

B. Bobchenko, M. Chadeeva, M. Danilov,[††] A. Epifantsev, O. Markin, R. Mizuk,[††] E. Novikov, V. Popov, V. Rusinov, E. Tarkovsky
Institute of Theoretical and Experimental Physics, B. Cheremushkinskaya ul. 25, RU-117218 Moscow, Russia

N. Kirikova, V. Kozlov, P. Smirnov, Y. Soloviev
P. N. Lebedev Physical Institute, Russian Academy of Sciences, 117924 GSP-1 Moscow, B-333, Russia

P. Buzhan, A. Ilyin, V. Kantserov, V. Kaplin, A. Karakash, E. Popova, V. Tikhomirov
Moscow Physical Engineering Institute, MEPhI, Department of Physics, 31, Kashirskoye shosse, 115409 Moscow, Russia

C. Kiesling, K. Seidel, F. Simon, C. Soldner, M. Szalay, M. Tesar, L. Weuste
Max Planck Institute für Physik, Föhringer Ring 6, D-80805 Munich, Germany

M. S. Amjad, J. Bonis, S. Callier, S. Conforti di Lorenzo, P. Cornebise, Ph. Doublet, F. Dulucq, J. Fleury, T. Frisson, N. van der Kolk, H. Li, G. Martin-Chassard, F. Richard, Ch. de la Taille, R. Pöschl, L. Raux, J. Rouëné, N. Seguin-Moreau

Laboratoire de l'Accélérateur Linéaire, Centre Scientifique d'Orsay, Université de Paris-Sud XI, CNRS/IN2P3, BP 34, Bâtiment 200, F-91898 Orsay CEDEX, France

M. Anduze, V. Boudry, J-C. Brient, D. Jeans, P. Mora de Freitas, G. Musat, M. Reinhard, M. Ruan, H. Videau

Laboratoire Leprince-Ringuet (LLR) – École Polytechnique, CNRS/IN2P3, F-91128 Palaiseau, France

B. Bulanek, J. Zacek

Charles University, Institute of Particle & Nuclear Physics, V Holesovickach 2, CZ-18000 Prague 8, Czech Republic

J. Cvach, P. Gallus, M. Havranek, M. Janata, J. Kvasnicka, D. Lednicky, M. Marcisovsky, I. Polak, J. Popule, L. Tomasek, M. Tomasek, P. Ruzicka, P. Sicho, J. Smolik, V. Vrba, J. Zalesak

Institute of Physics, Academy of Sciences of the Czech Republic, Na Slovance 2, CZ-18221 Prague 8, Czech Republic

B. Belhorma, H. Ghazlane

Centre National de l'Energie, des Sciences et des Techniques Nucléaires, B.P. 1382, R.P. 10001, Rabat, Morocco

T. Takeshita, S. Uozumi

Shinshu University, Department of Physics, 3-1-1 Asaki, Matsumoto-shi, Nagano 390-861, Japan

M. Götze, O. Hartbrich, J. Sauer, S. Weber, C. Zeitnitz

Bergische Universität Wuppertal, Fachbereich 8 Physik, Gaussstrasse 20, D-42097 Wuppertal, Germany

♠ *Corresponding author*
E-mail: erika.garutti@desy.de

ABSTRACT: Calorimeters with a high granularity are a fundamental requirement of the Particle Flow paradigm. This paper focuses on the prototype of a hadron calorimeter with analog readout, consisting of thirty-eight scintillator layers alternating with steel absorber planes. The scintillator plates are finely segmented into tiles individually read out via Silicon Photomultipliers. The presented results are based on data collected with pion beams in the energy range from 8 GeV to 100 GeV. The fine segmentation of the sensitive layers and the high sampling frequency allow for an excellent reconstruction of the spatial development of hadronic showers. A comparison between data and Monte Carlo simulations is presented, concerning both the longitudinal and lateral development of hadronic showers and the global response of the calorimeter. The performance of several GEANT4 physics lists with respect to these observables is evaluated.

KEYWORDS: hadronic calorimetry; hadronic shower models; imaging calorimetry.

Contents

1. Introduction **2**

2. Experimental Setup **2**
- 2.1 The SiW-ECAL 3
- 2.2 The AHCAL 3
- 2.3 The TCMT 4

3. Calibration **5**

4. Monte Carlo Simulations **5**
- 4.1 Digitization 5
- 4.2 Physics Lists 6

5. Event Selection **7**

6. Calibration Validation **9**
- 6.1 Systematic Uncertainties 10

7. Energy Response **11**

8. Pion Interaction Length **13**

9. Longitudinal Development **15**

10. Radial Development **19**

11. Conclusions **20**

[*]Also at University of Texas, Arlington

[†]Deceased

[‡]Now at CERN

[§]Now at Department of Modern Physics, University of Science and Technology of China, 96 Jinzhai Road, Hefei, Anhui, 230026, P. R. China

[¶]Also at ITEP

[‖]Also at DESY

[**]Now at University of Sussex, Physics and Astronomy Department, Brighton, Sussex, BN1 9QH, UK

[††]Also at MEPhI and at Moscow Institute of Physics and Technology

[‡‡]Now at LPSC Grenoble

1. Introduction

The next generation of lepton colliders, such as the International Linear Collider (ILC) [1], will require unprecedented detector performances in order to fully exploit the physics potential. A clean separation between the hadronic decays of the W and Z bosons sets the goal for the jet energy resolution. Ideally, the di-jet mass resolution should be comparable to the decay widths of the weak vector bosons. This requires a jet energy resolution σ_E/E_j of the order of 3-4% at the Z peak, which translates approximately into $\sigma_E/E_j \sim 30\%/\sqrt{E_j/\mathrm{GeV}}$. Within the ILC community, Particle Flow calorimetry has been identified as the most promising way to achieve this level of precision [2, 3, 4], as successfully tested on Monte Carlo simulations. For instance, the Pandora Particle Flow algorithm, which has been developed in the context of the detector optimization studies for the ILC, has demonstrated the feasibility of jet energy resolutions of $\sigma_E/E_j \lesssim 3.8\%$ for $40-400$ GeV jets [4].

The key factor in Particle Flow calorimetry is the single particle separability within a jet, which requires a high granularity of the calorimeters. The CALICE collaboration is performing studies of several designs of highly granular calorimeters, with sensitive layers finely segmented into cells, which are individually read out. The stability over a large number of channels of new readout technologies has been demonstrated and reliable procedures of cell equalization and calibration have been established. Furthermore, the high spatial resolution allowed by the fine granularity provides valuable input to the validation of the shower models used for Monte Carlo simulations. Such studies are of broader interest, which goes beyond the support of simulation studies of Particle Flow algorithms. Uncertainties in the shower modeling still contribute significantly to energy scale uncertainties in high energy physics experiments, for instance at the Large Hadron Collider detectors [5].

Since 2006 several beam tests of the CALICE prototypes have been conducted at the Deutsches Elektronen-Synchrotron (DESY), at the European Organization for Nuclear Research (CERN) and at the Fermi National Accelerator Laboratory (FNAL). This paper focuses on data collected at CERN in 2007, when the experimental set-up consisted of a silicon-tungsten electromagnetic sampling calorimeter (SiW-ECAL) [6], a scintillator-steel hadron sampling calorimeter with analog readout (AHCAL) [7] and a scintillator-steel tail catcher and muon tracker (TCMT) [8].

The analyzed data were collected when the prototypes were exposed to pion beams in the energy range from 8 GeV to 100 GeV, provided by the CERN SPS H6 beam line. The overall response of the calorimeter and the lateral and longitudinal profiles of hadronic showers are compared to the predictions made by several Monte Carlo simulations, which make use of different GEANT4 physics lists (Sec. 4).

The study is completed by an update on the validation of the calibration of the AHCAL performed with electromagnetic showers, already described in a previous publication [9]. This study uses data collected both at FNAL and CERN, exposing the prototypes to electron and positron beams in the energy range from 1 GeV to 50 GeV.

2. Experimental Setup

During the beam tests at CERN the detectors were exposed to muon, positron and pion beams.

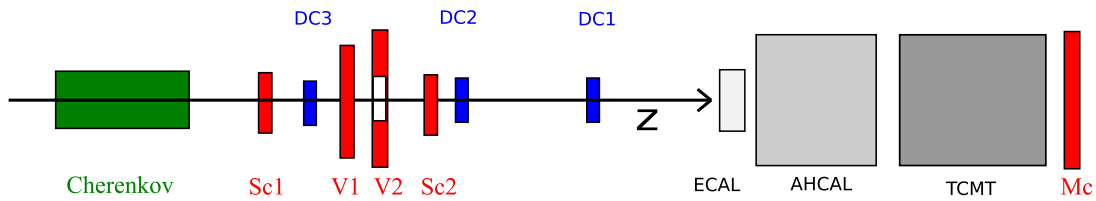

Figure 1. *Schematic layout (not to scale) of the CALICE experimental setup at CERN, with calorimeters and beam instrumentation. Sc1 and Sc2 are the scintillators for the beam trigger, V1 is the multiplicity counter, V2 is the veto trigger and Mc is the scintillator for the muon trigger.*

The SiW-ECAL and the AHCAL were mounted on a movable stage, providing the possibility to translate and rotate the calorimeters with respect to the beam. However, the studies discussed in the following only make use of data collected with the beam incident in the center of the calorimeters, along their center line.

A schematic overview of the experimental setup is shown in Fig. 1. Three sets of wire chambers were operated upstream of the detectors in order to measure the beam coordinates. The coincidence signal of two upstream $10 \times 10\,\mathrm{cm}^2$ scintillator counters (Sc1 and Sc2 in Fig. 1) triggered the readout of the detector (*beam trigger*). One scintillator (V1 in Fig. 1) with an area of $20 \times 20\,\mathrm{cm}^2$ and analog readout tagged multi-particle events (*multiplicity counter*). A $100 \times 100\,\mathrm{cm}^2$ scintillator with a $20 \times 20\,\mathrm{cm}^2$ hole in the center (V2 in Fig. 1) rejected beam halo events (*veto trigger)*. Muons were identified by a downstream $100 \times 100\,\mathrm{cm}^2$ scintillator (Mc in Fig. 1). A Cherenkov counter was also operated in threshold mode to discriminate between electrons and negative pions or between positive pions and protons.

2.1 The SiW-ECAL

The SiW-ECAL is divided into three stacks, each composed of 10 modules of alternating tungsten and silicon layers. Each stack has tungsten layers with different thicknesses: 1.4 mm (0.4 radiation lengths X_0) per layer in the first stack, 2.8 mm or $0.8\,X_0$ in the second and 4.2 mm or $1.2\,X_0$ in the third one. The silicon layers are segmented into PIN diodes of $1 \times 1\,\mathrm{cm}^2$, for a total number of about 9700 read-out cells.

The overall thickness of the prototype is about 20 cm, corresponding to $24.6\,X_0$ or 0.9 nuclear interaction lengths λ_I. The lateral size of the SiW-ECAL is $18 \times 18\,\mathrm{cm}^2$.

2.2 The AHCAL

The AHCAL is a sampling structure of 38 modules, each consisting of a $\sim$2 cm thick steel absorber plate and a sensitive layer instrumented with 0.5 cm thick scintillator tiles. The total depth of the prototype is 1.2 m, translating into about $5.3\,\lambda_\mathrm{I}$, while the lateral dimensions are approximately $1 \times 1\,\mathrm{m}^2$. Each sensitive layer is composed of scintillator tiles of different sizes (Fig. 2, left). The $30 \times 30\,\mathrm{cm}^2$ core has a granularity of $3 \times 3\,\mathrm{cm}^2$, while the outer region is equipped with tiles of increasing sizes ($6 \times 6\,\mathrm{cm}^2$ and $12 \times 12\,\mathrm{cm}^2$). In the last 8 layers the highly granular core is replaced by $6 \times 6\,\mathrm{cm}^2$ tiles. The scintillation light from each tile is read out individually by a Silicon PhotoMultiplier (SiPM) [10, 11], coupled to the scintillator via a WaveLength Shifting fiber (WLS). The SiPMs employed in the AHCAL have a photosensitive surface of $1.1\,\mathrm{mm}^2$, which is

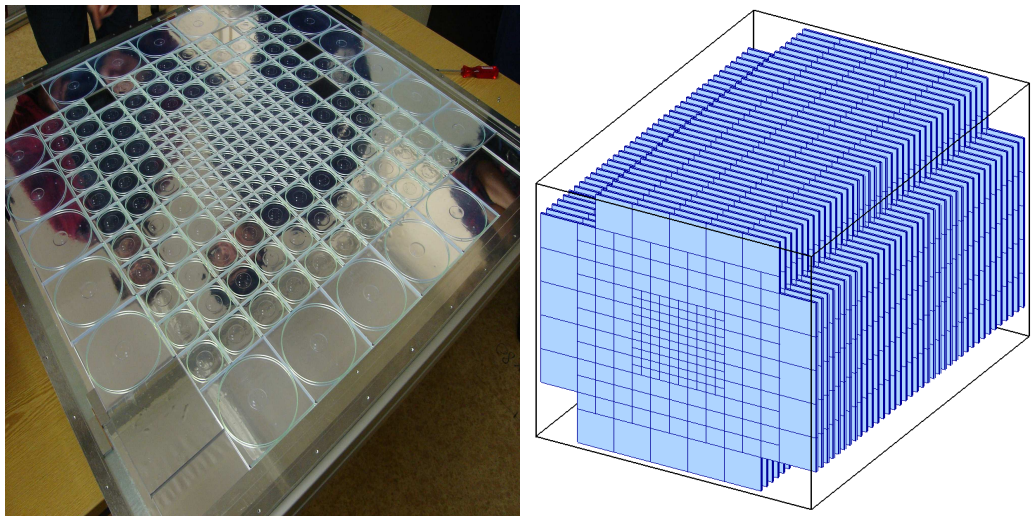

Figure 2. *Left: Segmentation of a sensitive layer of the AHCAL. The size of the scintillator tiles increases towards the outer region. Right: schematic view of the active layers of the AHCAL.*

divided into 1156 pixels. These pixels are individually equipped with a quenching resistor and mounted on a common substrate, in such a way that the charge signal is proportional to the number of pixels fired.

The readout system of the SiPMs is operated in two different modes, called *calibration* and *physics* modes. For calibration purposes single photons need to be resolved in the SiPM spectrum, since the distance between two consecutive peaks in the spectrum determines the gain of the SiPM. Therefore, a short shaping time of the signal (40 ns) and a high amplification are needed. In contrast, during physics runs large signals are produced and the amplification needs to be reduced by approximately a factor 10 to minimize saturation effects. Furthermore, a longer shaping time of about 180 ns is used to provide sufficient latency for the beam trigger decision.

The response of the SiPMs is measured both in physics and calibration modes, in order to determine the gain and saturation level of the SiPMs and the electronics intercalibration between the two operation modes. The response is monitored using LEDs with tunable intensities.

Temperature sensors placed inside the detector in correspondence to each module monitor temperature changes with an accuracy better than 0.6 °C .

2.3 The TCMT

The TCMT is positioned downstream with respect to the AHCAL in order to absorb the tails of the showers leaking out of the AHCAL. The TCMT has a lateral size of $109 \times 109\,\mathrm{cm}^2$ and is 142 cm in depth, corresponding to $5.8\,\lambda_\mathrm{I}$. It consists of two sections, a *fine* one and a *coarse* one. Each section has 8 sensitive layers, alternating with steel absorbers. The absorber plates are 2 cm thick in the fine section and 10 cm thick in the coarse section. The sensitive layers are 0.5 cm thick and are segmented into 5 cm wide and 1 m long scintillator strips, with alternating horizontal and vertical orientation in adjacent layers. The scintillation light is collected by WLS fibers and detected by SiPMs, as for the AHCAL prototype.

3. Calibration

As typical of semiconductor devices, SiPMs are sensitive to temperature and bias voltage changes that affect most of their performance parameters [7]. Moreover, SiPMs show saturation effects, due to the finite number of pixels and the finite pixel recovery time. One of the main technical aims of the AHCAL prototype is to show that these effects can be handled over a large number of channels.

The calibration chain is described in [9]. It proceeds through the following steps:

- inter-cell equalization of the response;
- calibration of the SiPM signal and correction for the non-linear response;
- conversion of the calibrated signal to the GeV scale.

The equalization of the response of the 7608 AHCAL cells is performed using the reference signal from muons [12]. Muons represent the best approximation of the behavior of a Minimum Ionizing Particle (MIP). The signal measured in a cell expressed in ADC counts can be converted to MIPs, using as unit the Most Probable Value (MPV) of the response to the muon beam.

In order to calibrate the SiPM signals, the gain is measured periodically during data taking using the LED system. A correction is also applied to account for the non-linear response of the SiPMs, based on the specific response curve of each SiPM, measured during dedicated laboratory tests. Since the SiPM properties depend on the temperature and the voltage, a given set of calibration constants is only valid for measurements at the same operation conditions and needs to be extrapolated to the operating conditions to account for possible changes, such as temperature fluctuations [13].

Finally, the conversion of the signal to the GeV scale is derived from the response of the detector to electromagnetic showers (Sec. 6).

4. Monte Carlo Simulations

The Monte Carlo simulations for the CALICE prototypes are carried out in the framework of GEANT4 [14]. The version 9.4 patch 3 of GEANT4 is used as default in the following, apart from explicit comparisons with previous versions. The geometries of the calorimeters are simulated within GEANT4 using Mokka [15, 16]. The detectors upstream of the calorimeters are simulated as well. The origin of the simulated particles is located upstream of the full system, such that any interactions with the Cherenkov counter, the scintillator-triggers, the tracking chambers and the air volumes in between are taken into account. Sensitive and passive materials, gaps and support structures are also considered in detail. The simulated AHCAL active layers have a uniform granularity of $1 \times 1\,\mathrm{cm}^2$ cell size. The realistic geometry of the AHCAL is obtained during the digitization procedure, as described below.

4.1 Digitization

The simulated events are processed further in the so-called digitization step, which models the response of the detector and its electronics. This allows the same treatment for data and Monte

Carlo in the subsequent analysis steps, such as calibration and reconstruction. This procedure takes into account several factors:

- the detector granularity. The signal amplitude of the $1 \times 1\,\mathrm{cm}^2$ virtual cells simulated is summed up to obtain the real geometry with 3×3, 6×6 and $12 \times 12\,\mathrm{cm}^2$ cells.
- the light sharing between neighboring tiles (known also as *cross-talk*). A 2.5% light sharing from each tile edge is used in simulations [9].
- non-linearity effects of the SiPMs, based on their specific saturation curves.
- Poissonian fluctuations of the photo-electron statistics.
- the noise contribution. The noise is overlaid on the simulation, using real noise measured in dedicated triggers without beam.

Shielding effects in the scintillator material saturate the scintillation process at high ionization densities. This causes a non-linearity of the light yield, which has been simulated in Monte Carlo according to the Birks Law [17].

The read out electronics have a defined time window. Late energy depositions, for instance from neutrons, might escape this time window. In order to reproduce this effect, a time cut of 150 ns is applied in simulations.

The effects of gaps between the calorimeter tiles, as well as the non-uniform response of the tiles have been studied in Monte Carlo events in [18], showing that these type of effects do not have a significant influence on the measurement of hadron showers.

4.2 Physics Lists

The interactions of hadrons with matter cannot be modeled from first principles alone; several phenomenological models, working with different approximations, exist. An overview of the different models is given in [19]. The main features are summarized here:

- **String Parton Models**. These models are employed to simulate the interaction of medium or high energy hadrons with nuclei. As a first stage the interaction of the particles with at least one nucleon of the nucleus is modeled using a string excitation model. Two different approaches are available in GEANT4: the Fritiof (**FTF**) and the Quark Gluon String (**QGS**) model. In the FTF approach the diffractive scattering of the primary particle with the nucleons is realized only via momentum exchange. In the QGS model the hadron-nucleon interaction is mediated via pomerons. The products of an interaction between the primary particle and the nucleus are one or several excited strings and a nucleus in an excited state. The fragmentation of the excited strings into hadrons is handled by a longitudinal string fragmentation model, with differences between FTF and QGS. The interaction of secondaries with the excited nucleus is handled by a shower model or by a precompound model (see below). In the latter case the string parton models get the suffix “P” (FTFP and QGSP). The de-excitation of the excited nucleus is further simulated by nuclear fragmentation, precompound and nuclear de-excitation models.

- **Parameterized Models**. Low Energy Parametrized (**LEP**) and High Energy Parametrized (**HEP**) models are based on fits to experimental data, with little theoretical guidance. They do not conserve energy, momentum, charge or other quantum numbers on an event-by-event basis, but instead seek to conserve these quantities on average. The approach of GEANT4 is to limit the use of these models and replace them by more sophisticated ones where possible.

- **Cascade Models**. The Bertini cascade **BERT** and the binary cascade **BIC** models are employed at medium and low energies, where the quark-substructure of individual nuclei can be neglected. The BERT model describes a nucleus as a sphere with constant nucleon density. Incident hadrons collide with protons and neutrons in the target nucleus and produce secondaries which in turn collide with other nucleons generating a so-called intra-nuclear cascade. At the end of the cascade the excited nucleus is represented as a sum of particle-hole states which is then decayed by pre-equilibrium, nucleus explosion, fission and evaporation models. The BIC model considers the nucleus as a sum of discrete nucleons, at defined positions and with defined momenta. The propagation through the nucleus of the incident hadron and the secondaries produced are modeled by a cascading series of two-particle collisions. Secondaries are created during the decay of resonances formed during the collisions. The decay of the excited nucleus is handled by the precompound model.

- **Precompound Model**. The precompound model generates the final state for hadron inelastic scattering. It describes the emission of protons, neutrons, and light ions before the equilibrium of a nuclear system is reached. The final products are passed to de-excitation models.

- **`CHIPS` Model**. The Chiral Invariant Phase Space (`CHIPS`) model is a nuclear fragmentation model acting at the quark level. The model is based on the concept of a quasmon, which is an excited intermediate state of massless quarks that are asymptotically free, formed from the quarks of the projectile hadron and of the target nucleon. The quasmons decay via internal quark fusion or by double quark exchange with neighboring quasmons. This model is still at an experimental phase and several parameters are still being optimized.

Several "physics lists" are available in GEANT4, which combine different models in different energy ranges, with a random choice of which model is used for overlapping energy regions. A summary of the physics lists considered in this paper and of their composition at different energies is given in Fig. 3.

5. Event Selection

This paper presents electron (or positron[1]) and negative pion data collected with the experimental set-up described in Sec. 2. While performing measurements with an electron beam, the SiW-ECAL is moved out of the beam line. Though the beam is highly enriched with the nominal particle, some contamination is present and the recorded event samples need to be purified for analysis. The selection applied is summarized in the following and has been tested on Monte Carlo

[1]In the following, by "electron beam" we refer to either an electron or positron beam, since no distinction between the two beam particles is relevant for the performed studies.

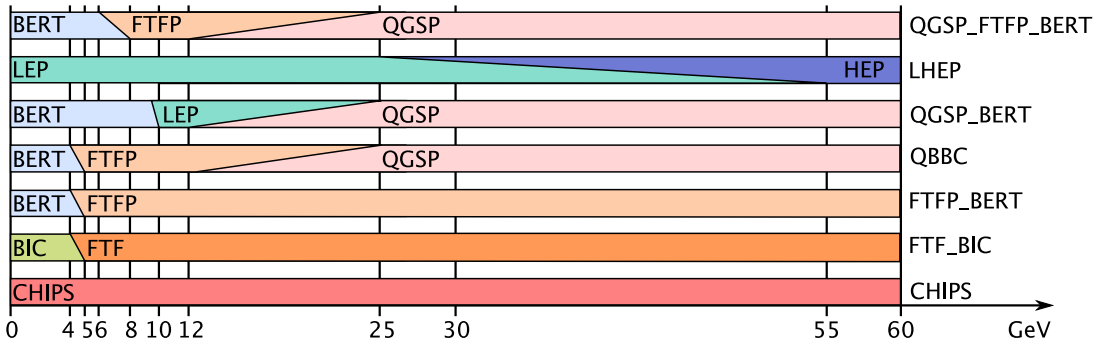

Figure 3. *Models applied at different energies in several physics lists for the simulation of pions in* GEANT4*, version 9.4 patch3.*

simulations, comparing the selection efficiencies for simulated muons, electrons and pions. Some of the selection criteria use information from the AHCAL itself. Applying the same requirements to simulated events confirms that no bias is introduced in the energy distributions. More details on the event selection are given in [20].

Beam events are selected requiring the beam trigger. Events where particles generate a beam trigger signal but fail to reach the calorimeters are rejected by requiring a minimum energy deposition of 4 MIPs in the $3 \times 3\,\mathrm{cm}^2$ cells of the first five layers of the AHCAL. Signals of less than 0.5 MIPs in single cells are rejected in all calorimeters to reduce the noise contribution. This requirement has been tested on events collected without incoming beam, since they have a topology similar to that given by spurious trigger events (i.e. only noise). About 96% of the beam-off events are rejected. Some events contain additional particles in the beam halo or particles that initiate a shower before reaching the AHCAL. These events are excluded by requiring no signal from the veto trigger and less than 15 hits in the $6 \times 6\,\mathrm{cm}^2$ cells of the first five layers of the AHCAL. In order to exclude events with more than one particle depositing energy in the AHCAL at the same time, only events with a multiplicity counter amplitude of less than 1.4 MIPs are kept. This selection yields a multi-particle contamination of less than 0.1%, which has been evaluated using the estimated distribution of the signal from double particle events in the multiplicity counter. Such a distribution has been simulated from the known distribution of noise, measured during triggers without beam, and the signal from single particle events. The signal from single particles has been obtained fitting the distribution of the measured amplitude in the multiplicity counter in a low amplitude region, where no significant contribution from double particle events is expected.

In order to improve the purity of the electron data, a signal is required in the Cherenkov detector. In addition, the center of gravity of the energy deposits in the beam direction is required to be in the front part of the AHCAL (less than 360 mm beyond the front face of the AHCAL). At least one cluster of neighboring hits with a total energy of 18 MIPs or higher has to be found in the AHCAL and an energy of less than 5 MIPs has to be deposited in the last 10 layers of the AHCAL.

For minimizing the electron contamination in pion data, events with a signal in the Cherenkov detector are rejected. The contamination from muons is suppressed by requiring the identification in the AHCAL of the position where the pion shower is initiated by the first hard interaction, since muons generally do not produce showers. The position of the first hard interaction is identified

using a cluster-based algorithm, based on the three-dimensional distribution of hits [21]. Seed hits with visible energies of more than 1.65 MIPs are sorted by their z-positions in ascending order. Starting with the first seed hit according to this ordering, each seed hit and all neighboring hits are assigned to a cluster. As long as one or more of the cells added to a cluster meet the seed hit requirement, the clustering continues and all hits adjacent to these cells are assigned to the same cluster. The cluster closest to the point the pion enters the calorimeter consisting of at least 4 hits and having a minimum energy of 16 MIPs is identified as the beginning of the shower. The end of the cluster axis pointing in the direction of the incoming hadron is used as location of the first inelastic scattering. According to Monte Carlo simulations this procedure allows rejection of muons with an efficiency of more than 80%. Since muons can produce shower-like clusters along the track due to Bremsstrahlung, the muon contamination is further reduced by requiring additionally more than 60 hits in the AHCAL, yielding a muon rejection efficiency of more than 95%.

In order to minimize the systematic uncertainties arising from combining the information from different detectors, pion events for which the shower starting point is found in the SiW-ECAL are rejected. The algorithm used to identify the beginning of the hadronic shower in the SiW-ECAL is described in [22]. The beginning of the shower is found by imposing thresholds on the energy measured in the different layers and on the number of hits deposited. This requirement further minimizes the contamination from electrons, which start to shower in the SiW-ECAL.

6. Calibration Validation

Although the AHCAL is designed to measure hadrons, during beam tests it has also been exposed to electron beams. The study of the electromagnetic response serves to prove the understanding of the detector and to validate the calibration procedure, since electromagnetic showers can be precisely modeled. Additionally, the AHCAL is a non-compensating calorimeter and the energy response to hadrons may be non-linear. In contrast, apart from saturation effects, the response to electromagnetic showers is linear and allows for the determination of the conversion of the calibrated signal to the energy scale in units of GeV (referred to as electromagnetic energy scale).

The study of the electromagnetic response of the AHCAL is described in detail in [9]. Electron data of energies between 10 GeV and 50 GeV are compared to Monte Carlo simulations and the systematic uncertainties associated to the different steps of the calibration procedure are estimated.

Overall, the studies in [9] validate the simulation of electromagnetic showers at a level sufficient for the present analysis of the hadronic response. A residual disagreement of the order of 2 mm is found between data and simulation, when comparing the radial development.

In order to confirm that the results in [9] are up-to-date with the most recent calibration and reconstruction software tools and to extend them over a broader energy range, the measurement of the energy response to electromagnetic showers is repeated here. This new study focuses on the determination of the electromagnetic energy scale, since it is applied in the following to pion data. The validation of the simulation of electromagnetic showers for the observables discussed in [9] is not repeated. The data set has been extended with respect to [9] to lower energies down to 1 GeV, using data collected at FNAL exposing the AHCAL to electron beams, with an experimental set-up similar to the one employed at CERN (Sec. 2).

	u [MIP/GeV]	v [MIP]
Data	42.4 $\pm$ 0.3	-1.1 $\pm$ 0.9
MC	42.8 $\pm$ 0.1	-6.6 $\pm$ 0.5

Table 1. *Measured parameters of the linear fit to the electromagnetic response, as defined in Eq. 6.1, for data and Monte Carlo. The errors reported are the fit uncertainties.*

The expected linear response to electrons is described by the following equation:

$$\langle E^{\mathrm{e}}_{\mathrm{rec}} \rangle = p_{\mathrm{beam}} \cdot u + v, \tag{6.1}$$

where $\langle E^{\mathrm{e}}_{\mathrm{rec}} \rangle$ is the mean calibrated response to electrons expressed in MIPs, p_{beam} is the beam momentum, and the parameters u and v are obtained from a linear fit to the dependence of $\langle E^{\mathrm{e}}_{\mathrm{rec}} \rangle$ on p_{beam}. The factor u represents the calibration to the GeV scale of the electromagnetic response. The offset v accounts for the combined effect of the 0.5 MIPs threshold applied to all events (Sec. 5) and of the residual noise above the threshold. The residuals to the fit are shown in Fig. 4 (left). The linearity is better than about 2% at all energies. The errors taken into account in the fit and shown in the figure are both the statistical and the systematic uncertainties. The systematic uncertainty includes a calibration scale uncertainty of 1.6% and the SiPMs saturation uncertainty, which ranges between 0.5% at 1 GeV and 3% at 50 GeV.

The same procedure is applied to Monte Carlo, yielding the results summarized in Tab. 1, which are compatible with the results obtained previously in [9]. The factor u agrees with the results obtained for data within the fit uncertainties, while the offset v disagrees by about 5 standard deviations (5 MIPs or $\sim$100 MeV). This remaining discrepancy is attributed to an imperfect implementation of noise, light-sharing and threshold effects. An imperfect modeling of the beam line and of the energy lost in the upstream material could also contribute. Since in electromagnetic showers the signal cells below threshold concentrate on the edges, an inaccurate simulation of the lateral extension of electromagnetic showers, as observed in [9], could also contribute to this effect.

The difference between the simulated response and the measured response is shown in Fig. 4 (right). The discrepancy in v is visible at low energies, while at high energies the Monte Carlo slightly underestimates the SiPMs saturation.

The electromagnetic analysis allows the conclusion that the detector calibration and simulation are sufficiently understood, in order to carry on studies based on hadronic data. The calibration to the GeV scale obtained for electromagnetic data is applied in the following to pion data and to the digitized Monte Carlo.

6.1 Systematic Uncertainties

The results shown in the following focus on the response of the calorimeter to hadrons. The systematic uncertainty on the calibration scale of 1.6%, quoted above for the electromagnetic study, affects the hadronic analysis in the same way. This uncertainty is relevant for the study of the hadronic energy response discussed in Sec. 7. The saturation uncertainty, which ranges between 0.5% at 1 GeV and 3% at 50 GeV for elecromagnetic showers, is expected to have a reduced impact on hadronic showers, due to the lower energy density. This is discussed in [9], where it is shown that electromagnetic showers have more hits with high energy deposition that pion showers,

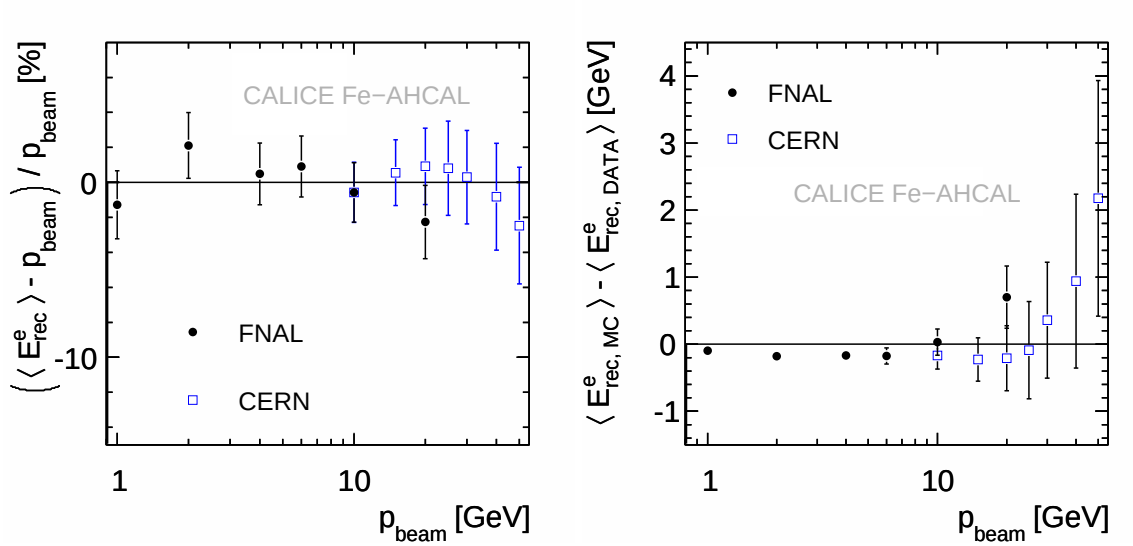

Figure 4. *Left: Residuals from linearity for electromagnetic data collected at FNAL (circles) and CERN (squares). Right: Difference between the simulated and the measured electromagnetic response. The error bars take into account both the statistical and the systematic uncertainties, as described in the text.*

even when the beam energy is only half that of the pion. Therefore, this source of uncertainty is neglected during the measurement of the hadronic energy response.

The measurement of the pion interaction length is dominated by the fit uncertainty, as discussed in Sec. 8.

The individual response of each layer is relevant for the longitudinal shower profiles discussed in Sec. 9. For this study a dedicated evaluation of the systematics has been performed, as described in Sec. 9. A similiar procedure has been performed for radial profiles (Sec. 10), yielding negligible uncertainties.

Systematic uncertainties are assumed to affect in a negligible way the observables concerning average global quantities of the calorimeter, such as the center of gravity and the standard deviation of longitudinal profiles (Sec. 9) , the mean energy-weighted shower radius and the standard deviation of radial energy distributions (Sec. 10). As a cross-check, the uncertainties obtained for longitudinal profiles have been propagated to the measurement of the longitudinal center of gravity of showers, obtaining uncertainties lower than 1%, and to the standard deviation of the longitudinal profiles, yielding uncertainties lower than 0.5%. Such a level of accuracy does not affect comparisons between data and Monte Carlo, which involve larger effects.

7. Energy Response

The calibrated response to pion showers in units of MIPs is converted to the GeV scale according to the following equation:

$$E_{\rm rec}\,[{\rm GeV}] = (E_{\rm ECAL1} + E_{\rm ECAL2}\cdot 2 + E_{\rm ECAL3}\cdot 3)\cdot 0.002953 + (E_{\rm AHCAL} - v)/u, \tag{7.1}$$

where E_{ECAL1} is the energy in MIPs measured in the first section of the SiW-ECAL. E_{ECAL2}, E_{ECAL3} are defined analogously. E_{AHCAL} is the energy in MIPs measured in the AHCAL. The factors 2 and 3 account for the different sampling structure in the three sections of the SiW-ECAL, with different absorber thicknesses. The factor 0.002953 is obtained from simulations. It has been evaluated using simulated muons, since the selection criteria require pions to start showering in the AHCAL and so to traverse the SiW-ECAL losing energy only by ionization, similarly to muons. The parameters u and v have been defined in Sec. 6 and refer to the electromagnetic energy scale. Additional corrections to account for the different response to electromagnetic and hadronic showers need to be applied, if one is interested in the absolute scale of the hadronic response. This topic is discussed in [23] and is not relevant for this paper, which only concerns comparisons between the measured and the simulated response to pions.

In addition to the requirements discussed in Sec. 5, only events for which the hadronic shower starts in the first five AHCAL layers are considered for the studies presented in this section. This requirement minimizes the leakage of the showers out of the AHCAL and reduces the energy collected by the TCMT. This additional selection can be applied since this paper focuses on the validation of Monte Carlo models, rather than on the estimate of the energy resolution. Studies of leakage for non-contained showers have been performed in [24, 8].

The total energy distribution for pion runs at different energies is shown in Fig. 5 (top). Figure 5 (lower left) presents the response to 10 GeV pions for data and for digitized Monte Carlo simulations based on the `FTFP_BERT` physics list. The shape of the response as well as the position of the peak are rather well simulated by the Monte Carlo. At higher energies, as exemplified by an 80 GeV run in Fig. 5 (lower right), the agreement gets worse. This is due to a worse simulation of the energy response and to an imperfect description of the shower length by the Monte Carlo, which results in a different impact of leakage in data and Monte Carlo. The longitudinal development of showers is described in Sec. 9.

In order to quantify the agreement between data and Monte Carlo models, their mean response as function of beam momentum is compared in Fig. 6. The average energy response $\langle E_{\mathrm{rec}} \rangle$ for the different beam energies is given by the arithmetic mean of the energy distributions, after subtraction of the average contribution of the noise above the 0.5 MIPs threshold. The `QGSP_BERT`, the `QGSP_FTFP_BERT` and the `QBBC` physics lists agree within 4% with data at 8 GeV, where the Bertini model is employed. At higher energies the disagreement with data increases, by about 7-10% at 100 GeV. The difference between `QGSP_FTFP_BERT` and `QBBC` at low energies, where they apply the same model, is attributed to the different treatment of the inelastic scattering of secondary protons and neutrons at very low energies, which is described using the Bertini model in `QGSP_FTFP_BERT`, while `QBBC` uses the BIC model. The Fritiof-based physics lists underestimate the response compared to the data at 8 GeV by up to 2-3%, while they agree with data in the range 10-30 GeV. At higher energies, between 40 GeV and 100 GeV, they overestimate data, though the deviations are below 6%. The performance of the `FTFP_BERT` physics list for previous versions of GEANT4 is shown in Fig. 6 (top, right). The performance has significantly improved from the version 9.2 to the version 9.3. In the most recent version the response has slightly increased with respect to the version 9.3, worsening the agreement with data at high energies. `CHIPS` overestimates data at all energies, by up to 10% at 80 GeV. At low energies, below 20 GeV the description of the energy response improves and the disagreement reduces to 2%. The `LHEP` physics list, based

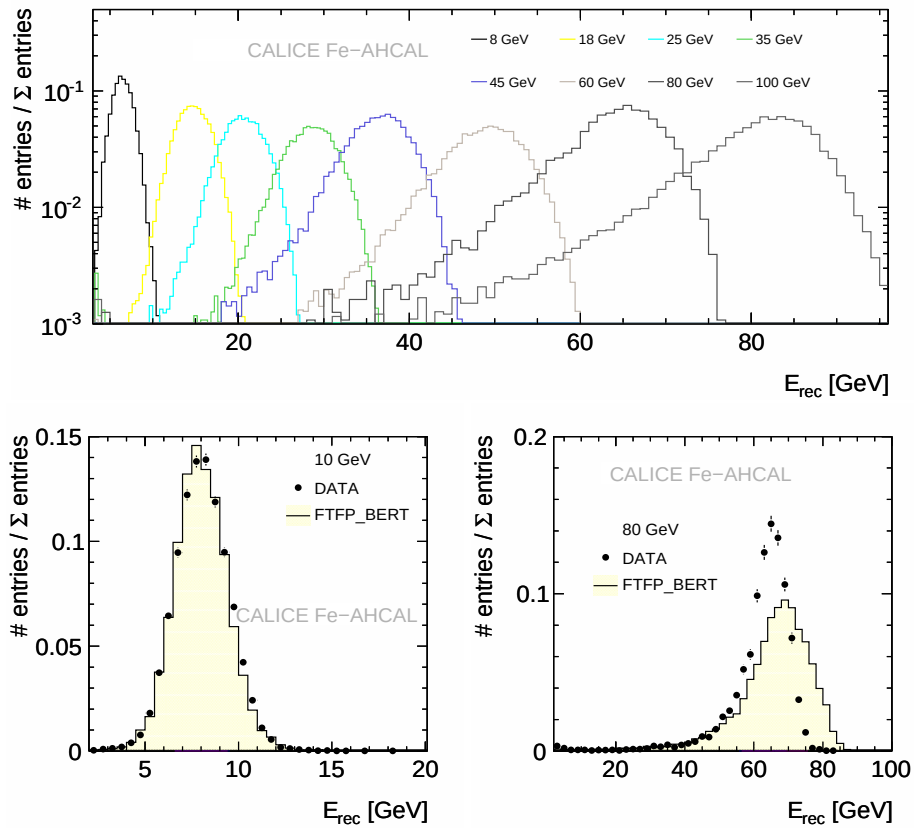

Figure 5. *Top: Total energy distribution for selected pion events at different energies. Bottom, left (right): Response to 10 GeV (80 GeV) pions for data (points) and for digitized Monte Carlo simulations using the* FTFP_BERT *physics list.*

on parameterized models, largely underestimates the response by up to 8-10% at 8-10 GeV. At high energies above 40 GeV the disagreement between data and Monte Carlo reduces to about 3%.

8. Pion Interaction Length

As long as a pion traversing a material does not interact strongly with a nucleus, it loses energy mainly by ionization. The probability P_I of having an inelastic hadron-nucleus interaction before a distance x is given by:

$$P_I = 1 - e^{-x/\lambda_\pi}, \tag{8.1}$$

where λ_π is the pion interaction length.

The position of the first hard interaction of the primary beam particle is approximated by the reconstructed layer where the shower starts. The measured distribution of the shower starting point follows the exponential behavior expected from Eq. 8.1, as shown in Fig. 7 (left) for 45 GeV pion showers.

From this distribution it is possible to derive the effective interaction length of a pion λ_π in the AHCAL. The interaction length is obtained fitting an exponential to the distribution. The first

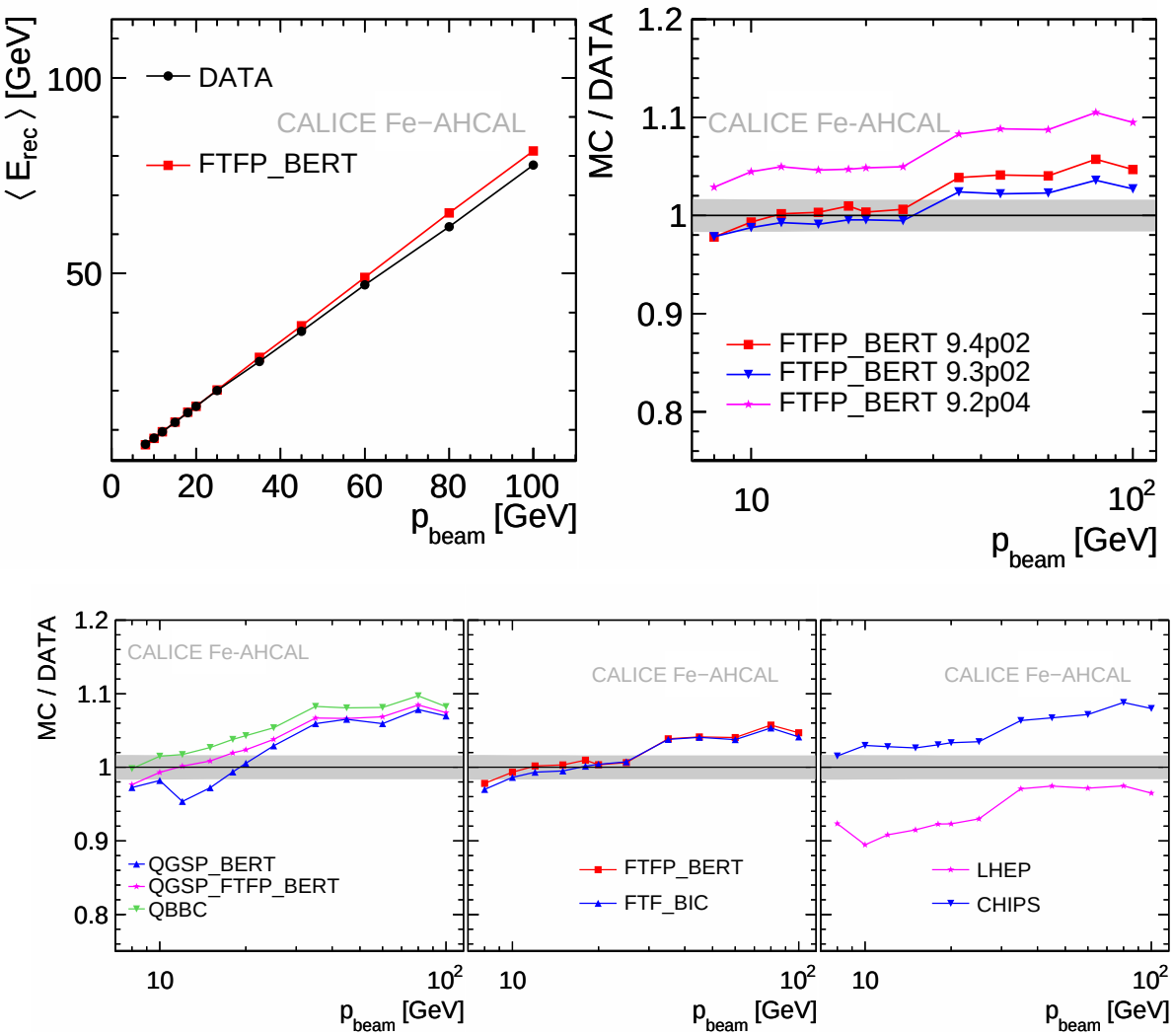

Figure 6. *Summary of the energy response to pions. Top, left: For data and for the* FTFP_BERT *physics list. Top, right: Ratio between Monte Carlo and data using the* FTFP_BERT *physics list with different versions of* GEANT4*. Bottom: Ratio between Monte Carlo and data for several physics list. The gray band in the ratios represents the uncertainty on data (statistical plus a systematic calibration uncertainty of 1.6%).*

layers are excluded from the fit, since the uncertainty of the algorithm used to determine the layer of the first hard interaction is larger there, due to the contamination from showers that start to develop in the last layers of the SiW-ECAL. The last layers are also not considered when performing the fit, since the fluctuations are higher due to the lower statistics and the algorithm used to identify the shower starting point has not been optimized for the coarser granularity of the last layers of the AHCAL. Hence, the fit is performed in the range from 120 mm to 800 mm of the longitudinal z coordinate.

The extracted values of the interaction length for data and Monte Carlo are shown in Fig. 8. No energy dependence of the interaction length is observed in data. The measurements yield an average of $\lambda_\pi = (26.8 \pm 0.46)$ cm. The error includes the statistical error, determined from the

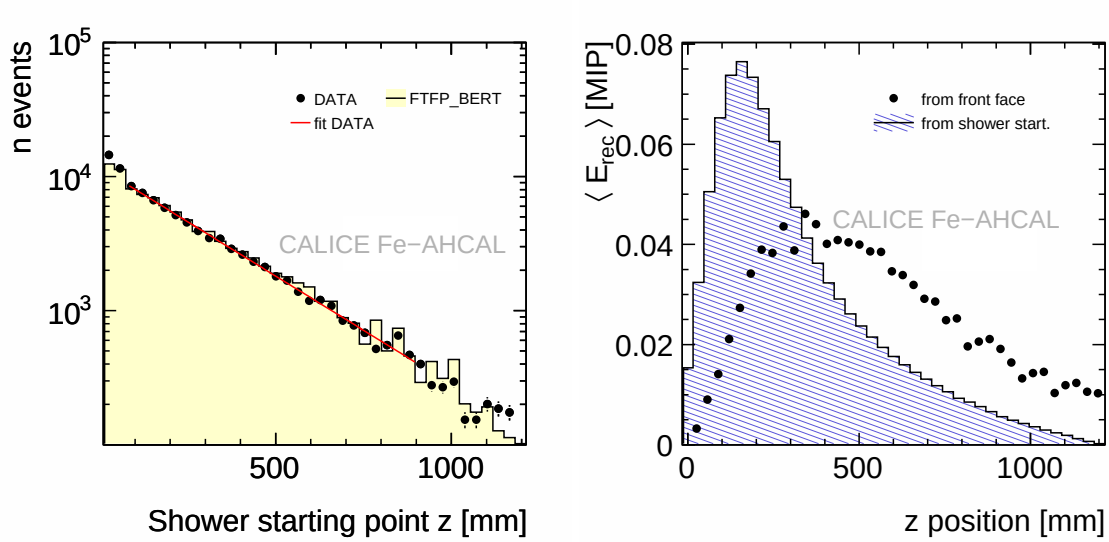

Figure 7. *Left: Distribution of the measured layer of the first hard interaction for 45 GeV pions, for data (circles) and for the* `FTFP_BERT` *physics (histogram). The distributions are normalized to an arbitrary number. The fit to the data distribution is also drawn. Right: Longitudinal profile of 45 GeV pion showers relative to the calorimeter front face (circles) and relative to the first hard interaction (histogram). The profiles are normalized to unity.*

standard deviation of the measurements performed at different energies, and the systematic error. The only source of systematics taken into account is the fit uncertainty due to choice of the fit range. Such an uncertainty has been determined by comparing the fit results for two different z ranges, namely [120, 800] mm and [90, 900] mm. The λ_π value obtained is in good agreement with the expectations from the material composition of the detector, which yield a λ_π of approximately 28 cm (from [7]: 4.28 λ_π for an AHCAL thickness of 120.26 cm, which yield a λ_π of 28.1 cm). This serves as a cross-check of the detector modeling used for Monte Carlo simulations, which assumes the material composition of the detector described in [7], and of the algorithm developed for the identification of the shower starting point, used in the event selection.

All Monte Carlo models except `CHIPS` and `LHEP` use the same cross-sections for hadron-nucleus interactions, which is reflected in a general agreement between the models themselves within fit uncertainties. The `QGSP_FTFP_BERT` and the Fritiof-based physics lists agree with data at approximately the 4% level at all energies, while `QBBC` agrees with data within 6%. The `QGSP_BERT` physics list is consistent with data within 4% for energies greater than 10 GeV, while at 10 GeV and 8 GeV the disagreement with data increases by up to ∼9%. `CHIPS` shows a behavior similar to the other models, with a good agreement with data, better than 4% at all energies. Only `LHEP` has an energy-dependent trend and systematically underestimates data by up to 14% at 100 GeV.

9. Longitudinal Development

Thanks to the fine longitudinal segmentation of the AHCAL into 38 layers, the longitudinal profile of hadronic showers can be investigated with an excellent accuracy. In particular, the fluctuations

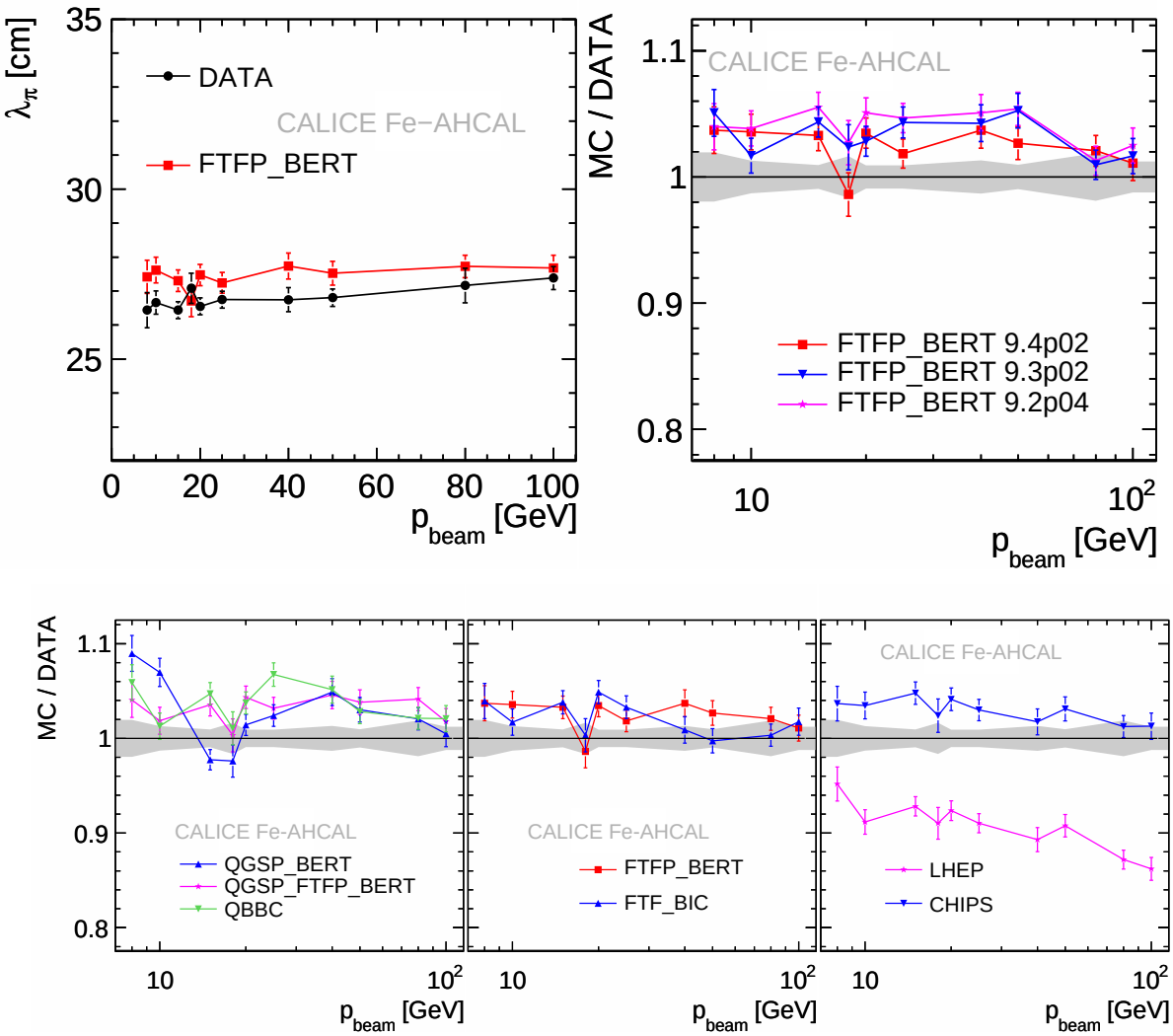

Figure 8. *Summary of the measurement of the interaction length of pions in the AHCAL. Top, left: For data and for the* FTFP_BERT *physics list. Top, right: Ratio between Monte Carlo and data using the* FTFP_BERT *physics list with different versions of* GEANT4*. Bottom: Ratio between Monte Carlo and data for several physics lists. The gray band in the ratios represents the uncertainty on data (statistical plus systematic fit uncertainty). The error bands take into account both the statistical uncertainty and the systematic uncertainty due to the choice of the fit range.*

in the shower starting point, which are large since they are due to the statistical behavior of one single particle, can be separated from the intrinsic longitudinal shower development. This is shown in Fig. 7 (right), where the shower profile relative to the calorimeter front face and the shower profile relative to the measured shower starting point are compared. The latter is shorter, since only the effective length of the hadronic shower is taken into account, excluding the path of the primary beam particle before the first hard interaction. In addition, the layer-to-layer fluctuations due to calibration uncertainties are smeared out into a smoother distribution, as different showers extend over different regions of the calorimeter. In the following, the results are therefore discussed

for profiles relative to the measured shower starting point, shown in Fig. 9. However, the trend of the agreement with data of the physics lists considered is independent from the definition of the profiles. The unit chosen to express the longitudinal development of showers is the nuclear interaction length λ_{I}. For the AHCAL it has been estimated to correspond to 231.1 mm.

Fig. 9 shows the longitudinal shower profiles for pions of 8 GeV, 18 GeV and 80 GeV, in data and Monte Carlo. The shown distributions are average distributions over all selected events. The profiles are normalized to unity. The normalization allows the decoupling of the pure description of the spatial development of showers from the energy response already discussed above. The three energy points have been chosen in order to partially disentangle the different contributions from low, medium and high energy models (Fig. 3). The energy contribution from electrons, positrons, pions and protons produced during the showers can be determined for the simulated events and is also shown in the graphs. The technique used for this decomposition is described in [25]. This additional information helps to understand which physics processes contribute most in which phase of the shower development. In the first layers electrons and positrons contribute about equally to hadrons to the energy deposition. In the region around the shower maximum the deposition of electromagnetic energy dominates while in the tails the energy depositions by hadrons and electrons are again about equal.

The uncertainty on the measurement of the profiles has been evaluated creating 6 profiles, for showers starting in 6 different layers of the AHCAL, namely the first 6 layers. Due to the exponential distribution of the measured layer of the first hard interaction (Fig. 7), the 6 profiles considered dominate the final measurement of the longitudinal shower profiles, which has been performed without any selection on the shower starting point. The first (second, ...) bin of the profiles for showers starting in the first layer of the AHCAL, corresponds to the first (second, ...) layer of the AHCAL. The first (second, ...) bin of the profiles for showers starting in the second layer of the AHCAL, corresponds to the second (third, ...) layer of the AHCAL. An analogous correspondence between the bins of the profiles and the AHCAL layers is true for the remaining profiles measured for showers starting in layers 3-6 of the AHCAL. The variance var_j of the energy desposited in the bin j of the profiles has been evaluated as the variance between the 6 measurements. Some bins in the tails are not covered by all the 6 measurements. For instance, showers starting in the second layer of the AHCAL extend over at most 37 AHCAL layers and give no contribution to the bin 38 of the shower profiles.

The development of showers does not depend on the measured layer of the first interaction and with an ideal calorimeter the 6 considered profiles would not differ. The measured variance is an inclusive measurement of the uncertainties associated to the energy measurement, such as bad calibrations and saturation effects. Thanks to the high statistics of several 10^4 events used to create the profiles, the variance is dominated by systematic uncertainties, while statistical fluctuations are expected to be negligible.

For the final measurement of the longitudinal shower profiles no selection on the measured layer of the first hard interaction has been applied and n_j different profiles are averaged to calculate the average energy deposition in the j-th layer, namely 37 for the first layer, 36 for the second, and so on for the remaining layers. The final uncertainty to be associated to the energy measurement in

the layer j is given by:

$$\sigma_{E_j} = \sqrt{\frac{var_j}{n_j}}. \tag{9.1}$$

This uncertainty is shown with a grey area in Fig. 9.

The position of the shower maximum is in general quite well reproduced by Monte Carlo models. In the first part of the showers QGSP_BERT, QGSP_FTFP_BERT and QBBC agree with data at the 5-10% level at 8 GeV and 18 GeV. The same is true for the Fritiof-based physics lists and for CHIPS. Larger deviations are present in the tails of the showers, but they remain within systematic uncertainties. At 80 GeV the energy deposition in the shower maximum is generally underestimated by Monte Carlo simulations, with discrepancies up to 20%. At 80 GeV CHIPS shows a moderate tendency to prefer compact showers, overestimating the energy deposition in the first part of the shower and underestimating the tail. A similar trend is exhibited by LHEP at 8 GeV and 18 GeV, though with a more pronounced disagreement with data, up to 50% at 8 GeV.

The energy dependence of the center of gravity and of the standard deviation of the longitudinal shower profiles are shown in Fig. 10 and Fig. 11, respectively. The center of gravity is defined as the energy weighted mean of the hit longitudinal coordinate along the shower axis:

$$\langle z \rangle = \frac{\sum_i E_i \cdot z_i}{\sum_i E_i}, \tag{9.2}$$

while the standard deviation is defined as:

$$\sqrt{\langle z^2 \rangle - \langle z \rangle^2} = \sqrt{\frac{\sum_i E_i \cdot (z_i - \langle z \rangle)^2}{\sum_i E_i}}, \tag{9.3}$$

where z_i is the longitudinal coordinate of the cell i and E_i is the energy measured in that cell.

The center of gravity is located between 0.8 and 1.6 interaction lengths and exhibits the expected logarithmic increase with energy. The standard deviation only mildly increases with energy from about 0.825 to about 0.925 λ_I.

All physics lists except LHEP show a similar energy-dependent behavior in the description of the center of gravity $\langle z \rangle$ of showers. The ratio Monte Carlo over data decreases with energy. Overall the best behavior is shown by the physics lists based on the Fritiof model, which agree with data at about the 4% level. The LHEP parameterized models show also for this observable the worst agreement with data. The disagreement is up to 15% at 8 GeV. A similar message is given by the standard deviation $\sqrt{\langle z^2 \rangle - \langle z \rangle^2}$.

The changes in FTFP_BERT with different GEANT4 versions are significant for both longitudinal observables and the agreement with data changes by a few percent for different versions. The ratio Monte Carlo over data for the center of gravity $\langle z \rangle$ gets generally worse when comparing versions 9.3 and 9.4, apart from the intermediate energy points between 30 GeV and 50 GeV, where the agreement is comparable. Both versions of the physics list show an improvement with respect to the older version 9.2. The agreement with data for the standard deviation $\sqrt{\langle z^2 \rangle - \langle z \rangle^2}$ improves in the version 9.3 of GEANT4, with respect to the older version. The most recent version has a worse performance than the version 9.3 at energies greater than 20 GeV, but is still significantly better than version 9.2.

10. Radial Development

An accurate modeling of the transverse shower profile is particularly important for a successful development of particle flow algorithms, since it affects the degree of overlap between showers and therefore the efficiency in disentangling single particles within jets. Using the AHCAL, it is possible to reconstruct the radial development of showers with high precision, thanks to the fine lateral segmentation of the sensitive layers.

For each cell of the AHCAL, the radial distance to the incoming particle trajectory is determined as:

$$r_i = \sqrt{(x_i - x_0)^2 + (y_i - y_0)^2}, \tag{10.1}$$

where (x_i, y_i) are the coordinates of the center of the cell i and (x_0, y_0) is the position of the energy weighted shower center:

$$x_0 = \frac{\sum_i E_i \cdot x_i}{\sum_i E_i} \text{ and } y_0 = \frac{\sum_i E_i \cdot y_i}{\sum_i E_i}, \tag{10.2}$$

E_i being the energy measured in the cell i.

For this study, all physical AHCAL cells are subdivided into virtual cells of $1 \times 1\,\text{cm}^2$ [21]. The energy deposited in the physical cells is equally distributed over the virtual cells covering its area. The dimension of the smallest AHCAL tiles, i.e. $3 \times 3\,\text{cm}^2$, is chosen as natural bin width for the radial shower profiles, which show the average energy deposited in the AHCAL as a function of the coordinate r. The radial shower profiles are shown in Fig. 12, for the same set of beam energies and physics lists considered for the longitudinal profiles.

All physics lists show a similar behavior and tend to underestimate the radial extent of showers, showing a relatively higher energy deposition in the core of the showers. The disagreement is more pronounced at high energies. `QGSP_BERT`, `QGSP_FTFP_BERT` and `QBBC` agree better with data at low energies, in particular `QGSP_BERT`, which is consistent with data within 5-10%. `CHIPS` has the best behavior at 80 GeV, describing the data at the 5-10% level. The ratios between data and Monte Carlo generally show a discontinuity at about 300-350 mm, corresponding to the transition between the tiles with a granularity of $6 \times 6\,\text{cm}^2$ and the outer tiles with a granularity of $12 \times 12\,\text{cm}^2$ in the active layers.

As expected, the contributions from electrons, pions and protons show that the electromagnetic component of the showers is concentrated in the core, while in the tails the energy is mostly deposited by protons.

The mean energy-weighted shower radius and the standard deviation of the radial energy distribution are compared for all physics lists and all energies in Fig. 13 and Fig. 14, respectively. As for the longitudinal observables, the mean is defined as:

$$\langle r \rangle = \frac{\Sigma E_i \cdot r_i}{\Sigma E_i}, \tag{10.3}$$

and the standard deviation as:

$$\sqrt{\langle r^2 \rangle - \langle r \rangle^2}, \quad \langle r^2 \rangle = \frac{\Sigma E_i \cdot r_i^2}{\Sigma E_i}, \tag{10.4}$$

where r_i is defined in Eq. 10.1.

The energy-weighted shower radius ranges between 90 mm and 60 mm and exhibits the expected exponential decrease with energy [26]. The standard deviation only mildly decreases with energy from about 80 mm to about 70 mm.

Monte Carlo models underestimate the radial extent of showers, both in terms of radius and of standard deviation. The majority of simulations exhibit an energy-dependent behavior and the disagreement with data increases with energy. `QGSP_BERT` reproduces the mean radius of showers at 8-10 GeV, but disagrees with data by up to about 12% at high energies. Similar results are achieved by `QGSP_FTFP_BERT` and `QBBC`, though they give a worse agreement with data at low energies. `FTF_BIC` underestimates the mean shower radius by about 3% at 8 GeV and by up to $\sim$12% at high energies. A similar behaviour is shown by `FTFP_BERT`, though the disagreement between data and Monte Carlo is about 2% worse at all energies. Above 10 GeV, the best results are achieved by `CHIPS`, which shows the least energy dependence and underestimates the mean radial shower expansion by 2-4%. At lower energies the performance degrades and the disagreement increases by up to 5% at 8 GeV. `LHEP` shows a dramatic disagreement with data at all energies.

Similar trends are observed for the standard deviation of the radial energy distributions, though the agreement with data improves for all physics lists with respect to the mean radius of showers (Fig. 14).

The study of the evolution of `FTFP_BERT` with different GEANT4 versions (Fig. 13 and 14) shows that in the version 9.4 the simulation of the radial shower development went back to the performance achieved for the version 9.2. The intermediate version 9.3 is the closest to the data. This conclusion concerns both the observables considered.

It should be underlined that the residual discrepancies in radial profiles observed in electromagnetic showers [9], discussed above, do not prevent conclusions from being drawn concerning these radial observables and the results shown remain an important input to the process of validation of Monte Carlo models. The absolute uncertainties in the description of electromagnetic radial profiles are of the order of 2 mm, while the deviations observed in hadronic showers are of the order of 10 mm.

11. Conclusions

The response of the CALICE analog hadron calorimeter to pions is measured for energies between 8 GeV and 100 GeV, using data collected at CERN in 2007. The high sampling frequency together with the fine segmentation of the sensitive layers of this detector allows the investigation of the properties of hadronic showers and the validation of Monte Carlo models with an unprecedented spacial accuracy.

The paper covers the measurement of several properties of hadronic showers, such as the global energy response and the longitudinal and radial development of showers. The physics lists based on the Fritiof model yield overall the best simulation of the energy response, with a particularly good agreement with data at energies between 10 GeV and 30 GeV. A good simulation of the energy response at low energies is achieved also by the physics lists based on the quark-gluon string model, such as `QGSP_BERT` and `QGSP_FTFP_BERT`, which agree with data at the 2-4% level. At high energies these physics lists overestimate the energy response by up to 10%. A similar trend is exhibited by the `CHIPS` physics list, while the `LHEP` physics list underestimates the

deposited energy at all energies by up to 10%. This list has generally the worst performance also with respect to the other observables considered.

The best description of the longitudinal development of showers is achieved by the physics lists based on the Fritiof model and by CHIPS. The physics lists based on the quark-gluon string model agree with data at about the 6-8% level.

Previous publications show limitations in the understanding of the radial development of electromagnetic showers [9]. However, the results published in [22] show that despite these limitations the ability to model the hadronic shower separation is not degraded. Moreover, the discrepancies at the electromagnetic level are one order of magnitude smaller than the average radial extension of hadronic showers and do not prevent conclusions from being drawn concerning radial observables of hadronic showers. Hadronic data indicate broader showers than expected from simulation. The best performing list is CHIPS, which shows an almost energy-independent behavior and underestimates the shower mean radial expansion by less than about 2-5% at all energies. All the other physics lists with the exception of LHEP exhibit a disagreement with data increasing at high energies. The LHEP physics list shows a moderate energy-dependence, but largely disagrees with data by up to 15%. More detailed studies are needed, in order to improve the description of radial shower profiles.

FTFP_BERT and CHIPS are overall the physics lists that best agree with the observables presented. CHIPS is a very recent list, which is still under development. FTFP_BERT is an older list and the presented time evolution reflects changes in both the Bertini and the Fritiof models and their combination. Most observables fluctuate by $\pm$2-6% depending on the GEANT4 version considered and remain in acceptable agreement with data. The considered radial observables present more significant changes of the order of 10% and show a better agreement with data for an older version of the physics list.

In the last decade the LHC experiments have also performed comparison studies of their test-beam data to GEANT4 v9.3.p01 models. The beam energies available in the LHC beam tests were either below 9 GeV or above 20 GeV. They concluded in [27, 28] that the physics list QGSP_BERT was the closest to their pion test-beam data. The agreement was within 2-3%, with QGSP_BERT response higher in data than in simulations. During the ATLAS test beam the lateral spread of pion showers has also been quantified. Simulated showers were found significantly narrower than in data, with a disagreement of about 15% for QGSP_BERT [29]. Since these tests several improvements have been implemented in the simulation. The results presented in this paper have extended the comparison to more recent versions of GEANT4 over a similar energy range.

Acknowledgements

We gratefully acknowledge the DESY and CERN managements for their support and hospitality, and their accelerator staff for the reliable and efficient beam operation. We would like to thank the HEP group of the University of Tsukuba for the loan of drift chambers for the DESY test beam. The authors would like to thank the RIMST (Zelenograd) group for their help and sensors manufacturing. This work was supported by the Bundesministerium für Bildung und Forschung, Germany; by the the DFG cluster of excellence 'Origin and Structure of the Universe' of Germany; by the Helmholtz-Nachwuchsgruppen grant VH-NG-206; by the BMBF, grant no. 05HS6VH1;

by the Alexander von Humboldt Foundation (Research Award IV, RUS1066839 GSA); by joint Helmholtz Foundation and RFBR grant HRJRG-002, SC Rosatom; by the Russian Ministry of Education and Science via grants 8174, 8411, 1366.2012.2, P220; by MICINN and CPAN, Spain; by CRI(MST) of MOST/KOSEF in Korea; by the US Department of Energy and the US National Science Foundation; by the Ministry of Education, Youth and Sports of the Czech Republic under the projects AV0 Z3407391, AV0 Z10100502, LC527 and LA09042 and by the Grant Agency of the Czech Republic under the project 202/05/0653; by the National Sciences and Engineering Research Council of Canada; and by the Science and Technology Facilities Council, UK.

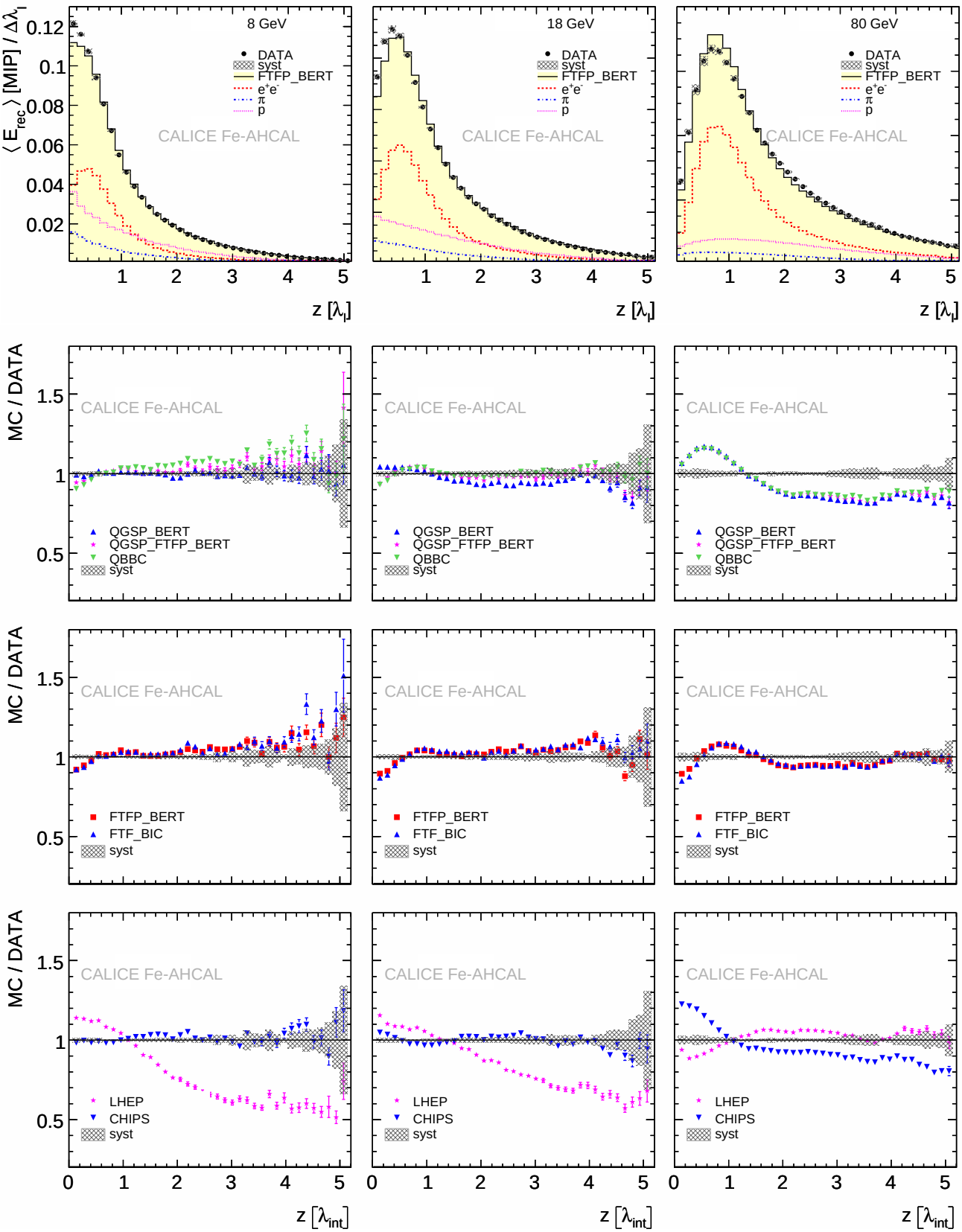

Figure 9. *Mean longitudinal shower profiles from shower starting point for 8 GeV (left column), 18 GeV (center column) and 80 GeV (right column) pions. First row: For data (circles) and for the* FTFP_BERT *physics list (histogram). Second to fourth rows: Ratio between Monte Carlo and data for several physics lists. All profiles are normalized to unity. The grey area indicates the systematic uncertainty on data.* $\langle E_{rec} \rangle / \Delta\lambda_I$ *is the average deposited energy in a* $\Delta\lambda_I$ *thick transverse section of the calorimeter.* z *is the longitudinal*

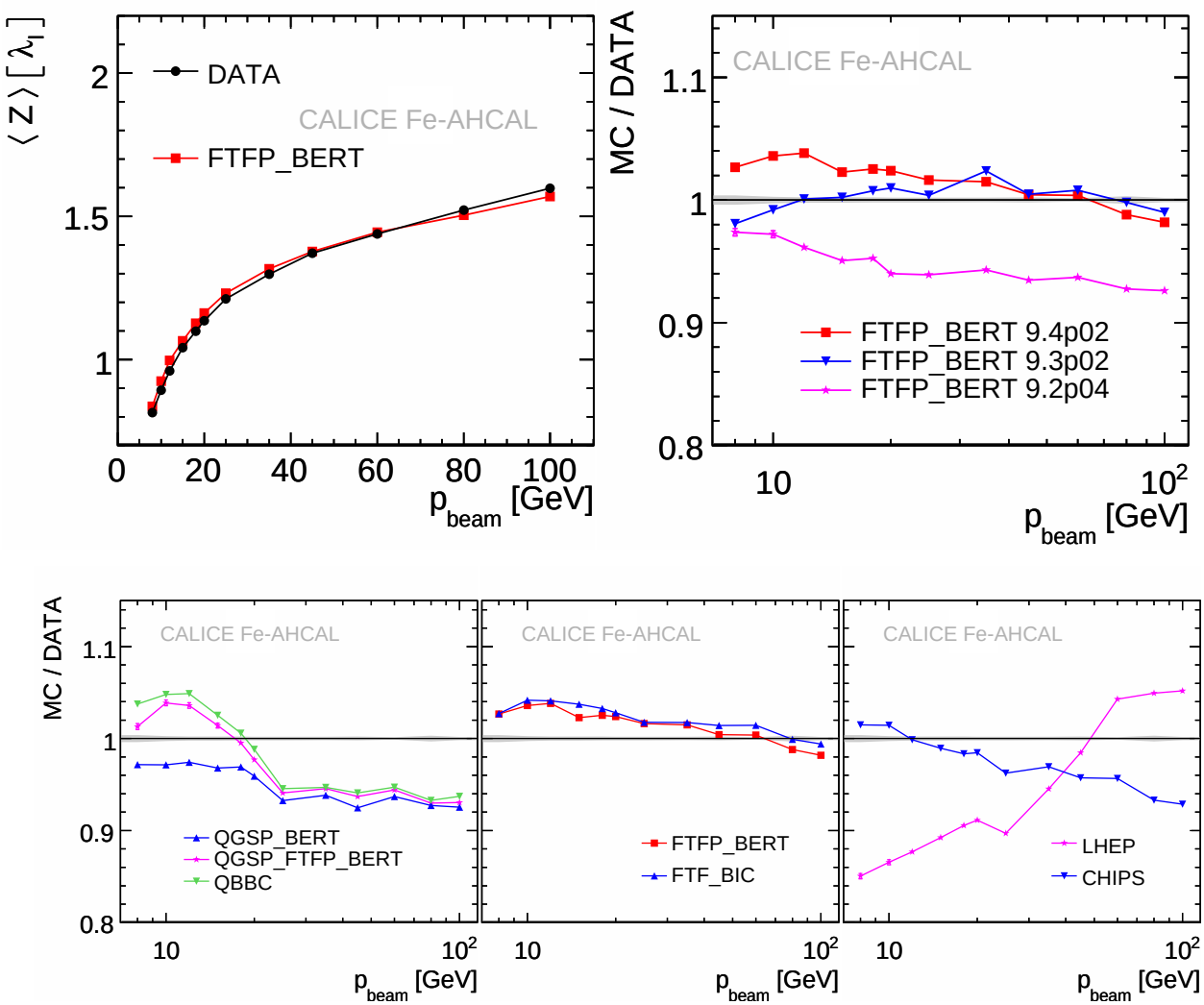

Figure 10. *Summary of the measurement of the center of gravity in the longitudinal direction, for pions in the AHCAL. Top, left: For data and for the* `FTFP_BERT` *physics list. Top, right: Ratio between Monte Carlo and data using the* `FTFP_BERT` *physics list with different versions of* GEANT4*. Bottom: Ratio between Monte Carlo and data for several physics lists. The gray band in the ratios represents the statistical uncertainty on data.*

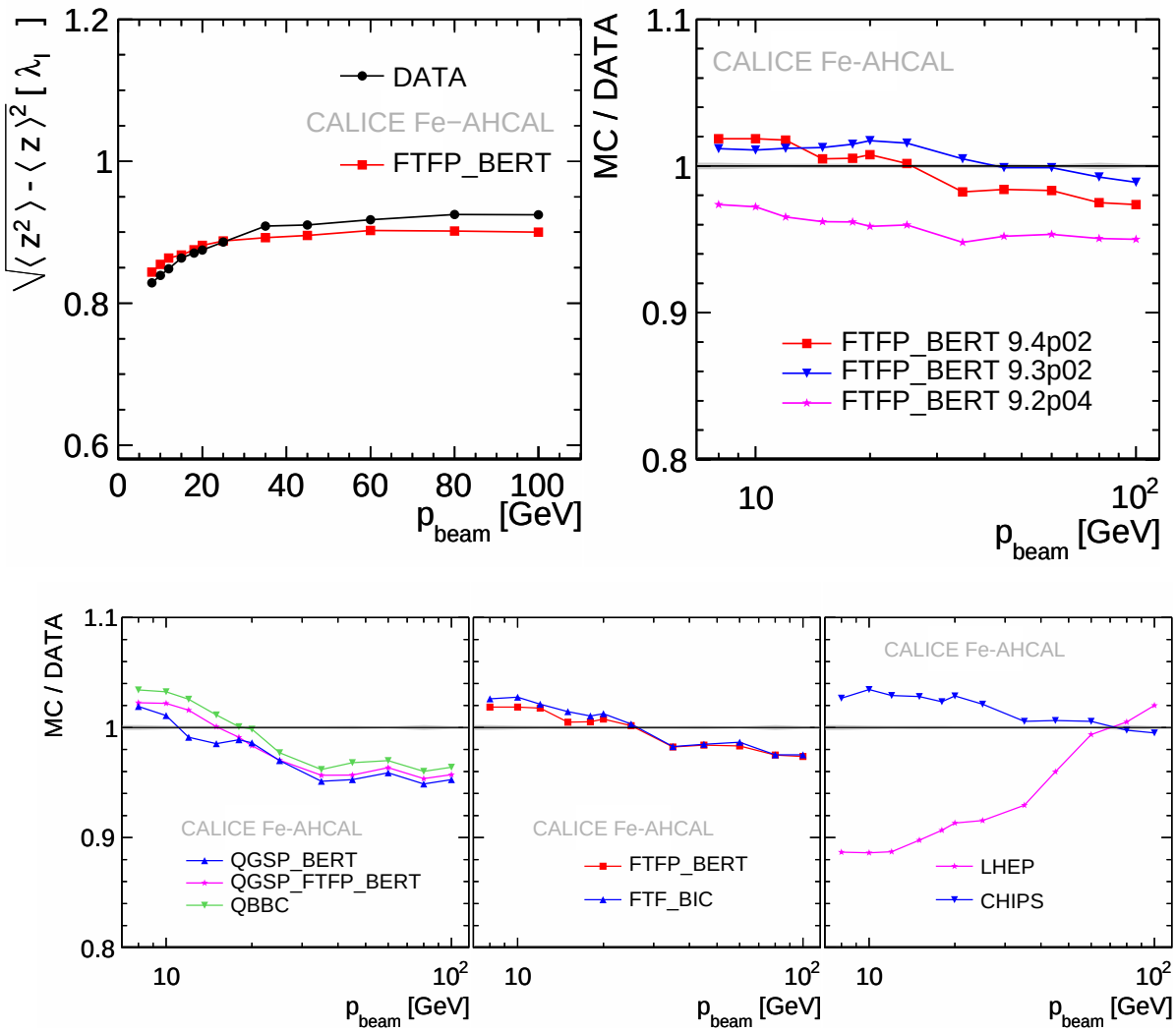

Figure 11. *Summary of the measurement of the standard deviation of the longitudinal shower profile, for pions in the AHCAL. Top, left: For data and for the* FTFP_BERT *physics list. Top, right: Ratio between Monte Carlo and data using the* FTFP_BERT *physics list with different versions of* GEANT4*. Bottom: Ratio between Monte Carlo and data for several physics lists. The gray band in the ratios represents the statistical uncertainty on data.*

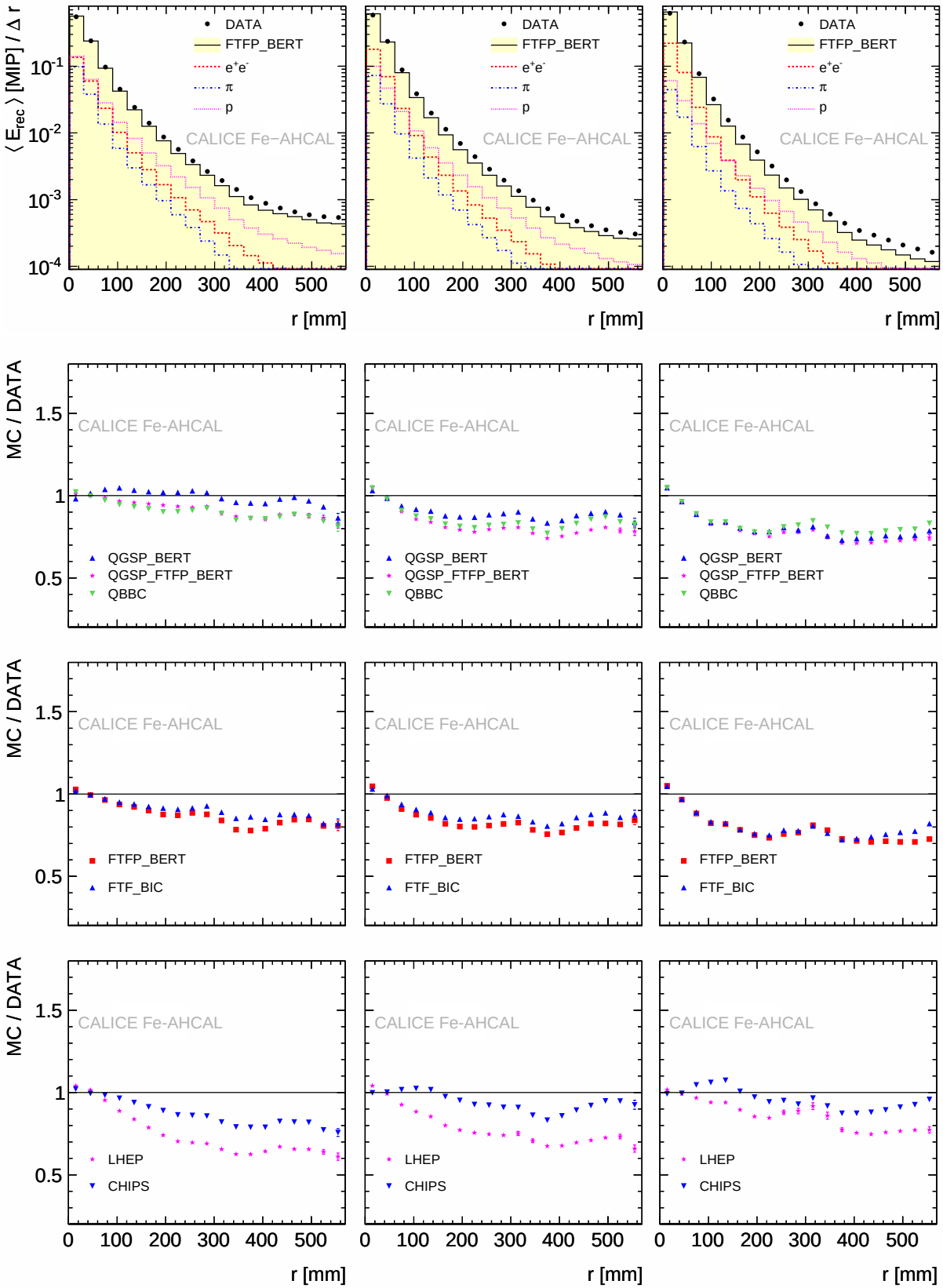

Figure 12. *Mean radial shower profiles for 8 GeV (left column), 18 GeV (center column) and 80 GeV (right column) pions. First row: For data (circles) and for the* `FTFP_BERT` *physics list (histogram). Second to fourth rows: Ratio between Monte Carlo and data for several physics lists. All profiles are normalized to unity.* $\langle E_{rec} \rangle / \Delta r$ *is the average deposited energy in* Δr*, where* r *is the radial coordinate.*

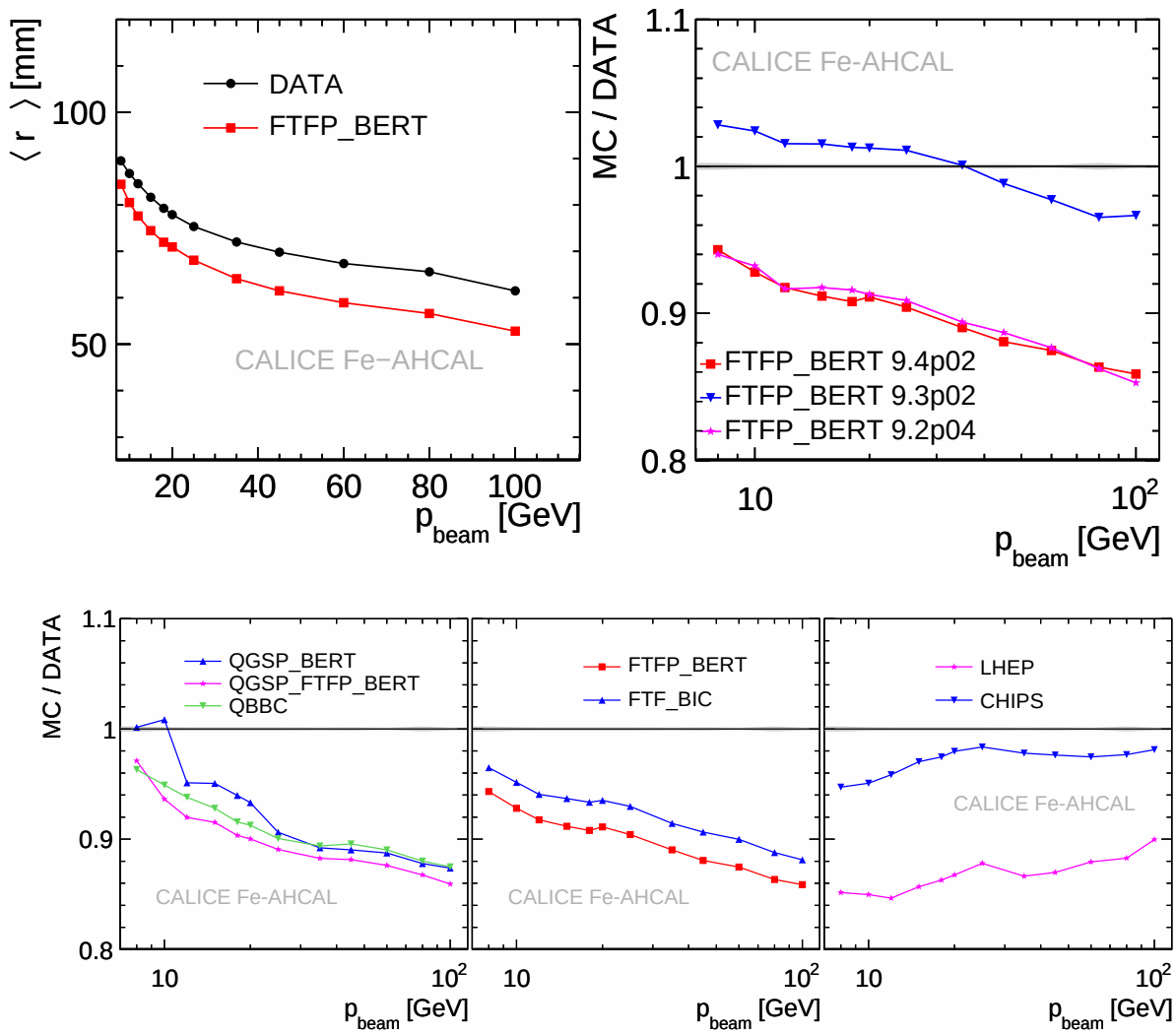

Figure 13. *Summary of the measurement of the average center of gravity* ⟨r⟩ *in the radial direction, for pions in the AHCAL. Top, left: For data and for the* `FTFP_BERT` *physics list. Top, right: Ratio between Monte Carlo and data using the* `FTFP_BERT` *physics list with different versions of* GEANT4. *Bottom: Ratio between Monte Carlo and data for several physics lists. The gray band in the ratios represents the statistical uncertainty on data.*

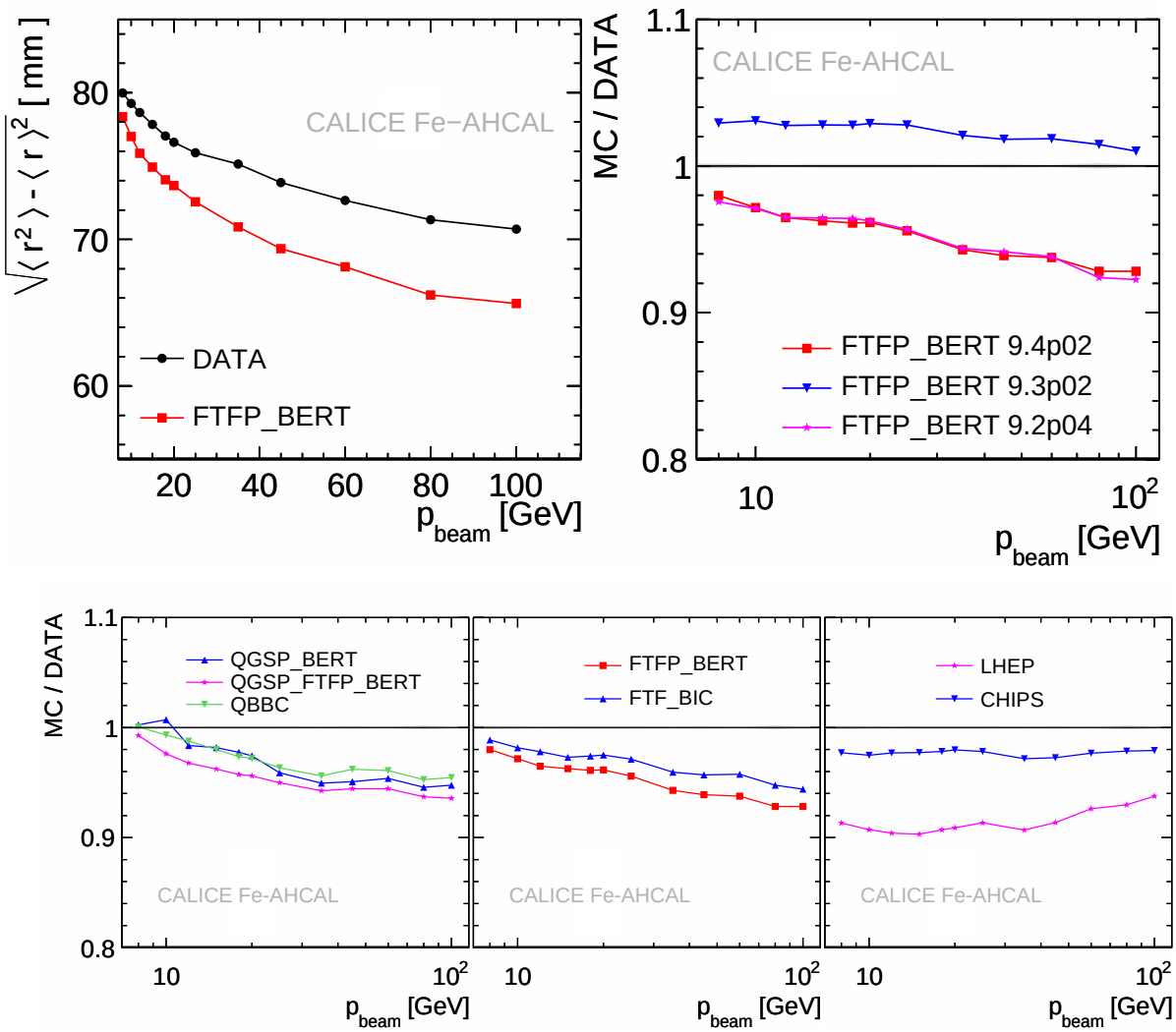

Figure 14. *Summary of the measurement of the average standard deviation of the radial shower profile* $\sqrt{\langle r^2\rangle - \langle r\rangle^2}$*, for pions in the AHCAL. Top, left: For data and for the* `FTFP_BERT` *physics list. Top, right: Ratio between Monte Carlo and data using the* `FTFP_BERT` *physics list with different versions of* GEANT4*. Bottom: Ratio between Monte Carlo and data for several physics lists. The gray band in the ratios represents the statistical uncertainty on data.*

References

[1] J. Brau, Y. Okada, N. J. Walker, A. Djouadi, J. Lykken, *et al.*, "International Linear Collider reference design report. 1: Executive summary. 2: Physics at the ILC. 3: Accelerator. 4: Detectors", 2007.

[2] J.-C. Brient and H. Videau, "The Calorimetry at the future $e^+ e^-$ linear collider", *eConf*, vol. C010630, p. E3047, 2001.

[3] V. Morgunov, "Calorimetry design with energy-flow concept (imaging detector for high-energy physics)", CALOR 2002, Pasadena, California.

[4] M. A. Thomson, "Particle Flow Calorimetry and the PandoraPFA Algorithm", *Nucl. Instrum. Meth.*, vol. A611, pp. 25–40, 2009.

[5] G. Aad *et al.*, "Single hadron response measurement and calorimeter jet energy scale uncertainty with the ATLAS detector at the LHC", *Eur. Phys. J.*, vol. C73, p. 2305, 2013.

[6] J. Repond *et al.*, "Design and Electronics Commissioning of the Physics Prototype of a Si-W Electromagnetic Calorimeter for the International Linear Collider", *JINST*, vol. 3, p. P08001, 2008.

[7] C. Adloff *et al.*, "Construction and Commissioning of the CALICE Analog Hadron Calorimeter Prototype", *JINST*, vol. 5, p. P05004, 2010.

[8] "Construction and performance of a silicon photomultiplier/extruded scintillator tail-catcher and muon-tracker", *JINST*, vol. 7, p. P04015, 2012.

[9] C. Adloff *et al.*, "Electromagnetic response of a highly granular hadronic calorimeter", *JINST*, vol. 6, p. P04003, 2011.

[10] G. Bondarenko *et al.*, "Limited Geiger-mode microcell silicon photodiode: New results", *Nucl. Instrum. Meth.*, vol. A442, pp. 187–192, 2000.

[11] P. Buzhan *et al.*, "Silicon photomultiplier and its possible applications", *Nucl. Instrum. Meth.*, vol. A504, pp. 48–52, 2003.

[12] N. D'Ascenzo, "Study of the neutralino sector and analysis of the muon response of a highly granular hadron calorimeter at the International Linear Collider". DESY-THESIS-2009-004, `http://www-library.desy.de/cgi-bin/showprep.pl?desy-thesis-09-004`.

[13] N. Feege, "Silicon photomultipliers: Properties and application in a highly granular calorimeter". DESY-THESIS-2008-050, `http://www-library.desy.de/cgi-bin/showprep.pl?desy-thesis-08-050`.

[14] G. Simone, "GEANT4: Simulation for the next generation of HEP experiments", Prepared for International Conference on Computing in High-energy Physics (CHEP 95), Rio de Janeiro, Brazil, 18-22 Sep 1995.

[15] P. Mora de Freitas and H. Videau, "Detector Simulation with Mokka and Geant4: Present and Future". LC Note, LC-TOOL-2003-010, `http://mokka.in2p3.fr`, 2003.

[16] `http://mokka.in2p3.fr`. Mokka Web Site.

[17] J. B. Birks, "The theory and practice of scintillation counting", 1964. Published in International series of Monographs on Electronics and Instrumentation, v. 27 Macmillan, New York.

[18] F. Sefkow and A. Lucaci-Timoce, "Monte Carlo Studies of the CALICE AHCAL Tiles Gaps and Non-uniformities", 2010. International Linear Collider Workshop 2010.

[19] J. Apostolakis *et al.*, "Validation of GEANT4 hadronic models using CALICE data". EUDET-MEMO-2010-15, `http://www.eudet.org/e26/e28/e86887/e109012/EUDET-Memo-2010-15.pdf`, 2010.

[20] N. Feege, "Low-Energetic Hadron Interactions in a Highly Granular Calorimeter". DESY-THESIS-2011-048, `http://www-flc.desy.de/flc/work/group/thesis/dissertation_feege.pdf`, 2011.

[21] B. Lutz, "Hadron showers in a highly granular calorimeter". DESY-THESIS-2010-048, `http://www-library.desy.de/cgi-bin/showprep.pl?desy-thesis-10-048`, 2010.

[22] C. Adloff *et al.*, "Tests of a particle flow algorithm with CALICE test beam data", *JINST*, vol. 6, p. P07005, 2011.

[23] C. Adloff *et al.*, "Hadronic energy resolution of a highly granular scintillator-steel hadron calorimeter using software compensation techniques", *JINST*, vol. 7, p. P09017, 2012.

[24] I. Marchesini, "Triple Gauge Couplings and Polarization at the ILC and Leakage in a Highly Granular Calorimeter". DESY-THESIS-2011-044, `http://www-library.desy.de/cgi-bin/showprep.pl?desy-thesis-10-048`, 2011.

[25] A. Kaplan, "Hadronic Imaging Calorimetry". PHD Thesis, `http://www.kip.uni-heidelberg.de/Veroeffentlichungen/download.php/4977/ps/2197.pdf`, 2011.

[26] C. Leroy and P. Rancoita, "Physics of cascading shower generation and propagation in matter: Principles of high-energy, ultrahigh-energy and compensating calorimetry", *Rept. Prog. Phys.*, vol. 63, pp. 505–606, 2000.

[27] P. Adragna, C. Alexa, K. Anderson, A. Antonaki, A. Arabidze, *et al.*, "Testbeam studies of production modules of the ATLAS tile calorimeter", *Nucl. Instrum. Meth.*, vol. A606, pp. 362–394, 2009.

[28] E. Abat, E. Arik, S. Cetin, J. Abdallah, M. Bosman, *et al.*, "Study of the response of the ATLAS central calorimeter to pions of energies from 3 to 9 GeV", *Nucl. Instrum. Meth.*, vol. A607, pp. 372–386, 2009.

[29] P. Adragna, C. Alexa, K. Anderson, A. Antonaki, A. Arabidze, *et al.*, "Measurement of pion and proton response and longitudinal shower profiles up to 20 nuclear interaction lengths with the ATLAS tile calorimeter", *Nucl. Instrum. Meth.*, vol. A615, pp. 158–181, 2010.

Preprint typeset in JINST style - HYPER VERSION

Hadronic energy resolution of a highly granular scintillator-steel hadron calorimeter using software compensation techniques

arXiv:1207.4210v2 [physics.ins-det] 27 Sep 2012

The CALICE Collaboration

C. Adloff, J. Blaha, J.-J. Blaising, C. Drancourt, A. Espargilière, R. Gaglione, N. Geffroy, Y. Karyotakis, J. Prast, G. Vouters

Laboratoire d'Annecy-le-Vieux de Physique des Particules, Université de Savoie, CNRS/IN2P3, 9 Chemin de Bellevue BP110, F-74941 Annecy-le-Vieux CEDEX, France

K. Francis, J. Repond, J. Smith[*], L. Xia

Argonne National Laboratory, 9700 S. Cass Avenue, Argonne, IL 60439-4815, USA

E. Baldolemar, J. Li[†], S. T. Park, M. Sosebee, A. P. White, J. Yu

Department of Physics, SH108, University of Texas, Arlington, TX 76019, USA

T. Buanes, G. Eigen

University of Bergen, Inst. of Physics, Allegaten 55, N-5007 Bergen, Norway

Y. Mikami, N. K. Watson

University of Birmingham, School of Physics and Astronomy, Edgbaston, Birmingham B15 2TT, UK

T. Goto, G. Mavromanolakis[‡], M. A. Thomson, D. R. Ward, W. Yan[§]

University of Cambridge, Cavendish Laboratory, J J Thomson Avenue, CB3 0HE, UK

D. Benchekroun, A. Hoummada, Y. Khoulaki

Université Hassan II Aïn Chock, Faculté des sciences. B.P. 5366 Maarif, Casablanca, Morocco

M. Benyamna, C. Cârloganu, F. Fehr, P. Gay, S. Manen, L. Royer

Clermont Univertsité, Université Blaise Pascal, CNRS/IN2P3, LPC, BP 10448, F-63000 Clermont-Ferrand, France

G. C. Blazey, A. Dyshkant, J. G. R. Lima, V. Zutshi

NICADD, Northern Illinois University, Department of Physics, DeKalb, IL 60115, USA

J. -Y. Hostachy, L. Morin

Laboratoire de Physique Subatomique et de Cosmologie - Université Joseph Fourier Grenoble 1 - CNRS/IN2P3 - Institut Polytechnique de Grenoble, 53, rue des Martyrs, 38026 Grenoble CEDEX, France

U. Cornett, D. David, G. Falley, K. Gadow, P. Göttlicher, C. Günter, B. Hermberg, S. Karstensen, F. Krivan, A. -I. Lucaci-Timoce[‡], S. Lu, B. Lutz, S. Morozov, V. Morgunov[¶], M. Reinecke, F. Sefkow, P. Smirnov, M. Terwort, A. Vargas-Trevino

DESY, Notkestrasse 85, D-22603 Hamburg, Germany

N. Feege, E. Garutti, I. Marchesini[‖], M. Ramilli
Univ. Hamburg, Physics Department, Institut für Experimentalphysik, Luruper Chaussee 149, 22761 Hamburg, Germany

P. Eckert, T. Harion, A. Kaplan, H. -Ch. Schultz-Coulon, W. Shen, R. Stamen, A. Tadday
University of Heidelberg, Fakultat fur Physik und Astronomie, Albert Uberle Str. 3-5 2.OG Ost, D-69120 Heidelberg, Germany

B. Bilki, E. Norbeck, Y. Onel
University of Iowa, Dept. of Physics and Astronomy, 203 Van Allen Hall, Iowa City, IA 52242-1479, USA

G. W. Wilson
University of Kansas, Department of Physics and Astronomy, Malott Hall, 1251 Wescoe Hall Drive, Lawrence, KS 66045-7582, USA

K. Kawagoe
Department of Physics, Kyushu University, Fukuoka 812-8581, Japan

P. D. Dauncey, A. -M. Magnan
Imperial College London, Blackett Laboratory, Department of Physics, Prince Consort Road, London SW7 2AZ, UK

M. Wing
Department of Physics and Astronomy, University College London, Gower Street, London WC1E 6BT, UK

F. Salvatore[**]
Royal Holloway University of London, Dept. of Physics, Egham, Surrey TW20 0EX, UK

E. Calvo Alamillo, M.-C. Fouz, J. Puerta-Pelayo
CIEMAT, Centro de Investigaciones Energeticas, Medioambientales y Tecnologicas, Madrid, Spain

V. Balagura, B. Bobchenko, M. Chadeeva, M. Danilov, A. Epifantsev, O. Markin, R. Mizuk, E. Novikov, V. Rusinov, E. Tarkovsky
Institute of Theoretical and Experimental Physics, B. Cheremushkinskaya ul. 25, RU-117218 Moscow, Russia

N. Kirikova, V. Kozlov, P. Smirnov, Y. Soloviev
P. N. Lebedev Physical Institute, Russian Academy of Sciences, 117924 GSP-1 Moscow, B-333, Russia

P. Buzhan, B. Dolgoshein, A. Ilyin, V. Kantserov, V. Kaplin, A. Karakash, E. Popova, S. Smirnov
Moscow Physical Engineering Inst., MEPhI, Dept. of Physics, 31, Kashirskoye shosse, 115409 Moscow, Russia

C. Kiesling, S. Pfau, K. Seidel, F. Simon[♠], C. Soldner, M. Szalay, M. Tesar, L. Weuste
Max Planck Inst. für Physik, Föhringer Ring 6, D-80805 Munich, Germany

J. Bonis, B. Bouquet, S. Callier, P. Cornebise, Ph. Doublet, F. Dulucq, M. Faucci Giannelli, J. Fleury, H. Li,[††] G. Martin-Chassard, F. Richard, Ch. de la Taille, R. Pöschl, L. Raux, N. Seguin-Moreau, F. Wicek

Laboratoire de l'Accélérateur Linéaire, Centre Scientifique d'Orsay, Université de Paris-Sud XI, CNRS/IN2P3, BP 34, Bâtiment 200, F-91898 Orsay CEDEX, France

M. Anduze, V. Boudry, J-C. Brient, D. Jeans, P. Mora de Freitas, G. Musat, M. Reinhard, M. Ruan, H. Videau

Laboratoire Leprince-Ringuet (LLR) – École Polytechnique, CNRS/IN2P3, F-91128 Palaiseau, France

B. Bulanek, J. Zacek

Charles University, Institute of Particle & Nuclear Physics, V Holesovickach 2, CZ-18000 Prague 8, Czech Republic

J. Cvach, P. Gallus, M. Havranek, M. Janata, J. Kvasnicka, D. Lednicky, M. Marcisovsky, I. Polak, J. Popule, L. Tomasek, M. Tomasek, P. Ruzicka, P. Sicho, J. Smolik, V. Vrba, J. Zalesak

Institute of Physics, Academy of Sciences of the Czech Republic, Na Slovance 2, CZ-18221 Prague 8, Czech Republic

B. Belhorma, H. Ghazlane

Centre National de l'Energie, des Sciences et des Techniques Nucléaires, B.P. 1382, R.P. 10001, Rabat, Morocco

T. Takeshita, S. Uozumi

Shinshu Univ. , Dept. of Physics, 3-1-1 Asaki, Matsumoto-shi, Nagano 390-861, Japan

J. Sauer, S. Weber, C. Zeitnitz

Bergische Universität Wuppertal Fachbereich 8 Physik, Gaussstrasse 20, D-42097 Wuppertal, Germany

♠ *Corresponding author*
E-mail: `fsimon@mpp.mpg.de`

ABSTRACT: The energy resolution of a highly granular 1 m^3 analogue scintillator-steel hadronic calorimeter is studied using charged pions with energies from 10 GeV to 80 GeV at the CERN SPS. The energy resolution for single hadrons is determined to be approximately $58\%/\sqrt{E/\mathrm{GeV}}$. This resolution is improved to approximately $45\%/\sqrt{E/\mathrm{GeV}}$ with software compensation techniques. These techniques take advantage of the event-by-event information about the substructure of hadronic showers which is provided by the imaging capabilities of the calorimeter. The energy reconstruction is improved either with corrections based on the local energy density or by applying a single correction factor to the event energy sum derived from a global measure of the shower energy density. The application of the compensation algorithms to GEANT4 simulations yield resolution improvements comparable to those observed for real data.

KEYWORDS: hadronic calorimetry; imaging calorimetry; software compensation.

Contents

1. Introduction **1**

2. Energy reconstruction in the AHCAL **2**
- 2.1 Test beam setup 2
- 2.2 Event selection 3
- 2.3 Energy reconstruction and intrinsic energy resolution 5

3. Software compensation: motivation and techniques **8**
- 3.1 Local software compensation 10
- 3.2 Global software compensation 11

4. Results **13**
- 4.1 Application of software compensation to test beam data 14
- 4.2 Comparison to Monte Carlo simulations 15

5. Conclusion **20**

1. Introduction

The physics goals of future high-energy lepton colliders such as the ILC [1] or CLIC [2] put stringent requirements on the detector systems. For example, the efficient event-by-event separation of heavy bosons in hadronic final states requires a jet energy resolution of better than 4% [1]. This is achievable with Particle Flow Algorithms (PFA) combined with highly granular calorimeters [3, 4, 5]. The CALICE collaboration has constructed and extensively studied highly granular electromagnetic and hadronic calorimeter prototypes to evaluate detector technologies for future linear collider experiments. These calorimeters have been successfully operated in various test beam experiments in different configurations at DESY, CERN and Fermilab from 2006 until 2012. The unprecedented granularity of the CALICE calorimeter prototypes allows the structure of hadronic showers to be studied with high spatial resolution, in order to validate different simulation

*Also at University of Texas, Arlington

†Deceased

‡Now at CERN

§Now at Dept. of Modern Physics, Univ. of Science and Technology of China, 96 Jinzhai Road, Hefei, Anhui, 230026, P. R. China

¶On leave from ITEP

‖Also at DESY

**Now at University of Sussex, Physics and Astronomy Department, Brighton, Sussex, BN1 9QH, UK

††Now at LPSC Grenoble

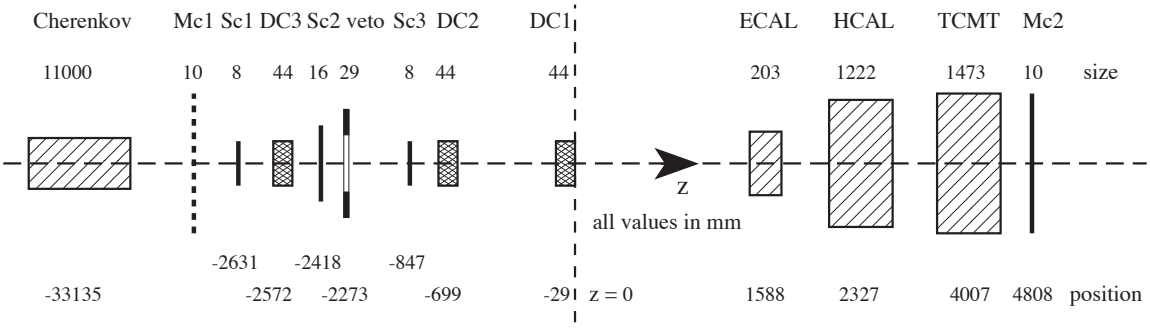

Figure 1. Top view of the CALICE test beam apparatus in the CERN SPS H6 beam line including calorimeters, trigger components (scintillator triggers SC1, SC2, and SC3; large area muon trigger counters Mc1, which was installed only during calibration runs, and Mc2; and the beam halo veto), and the tracking drift chambers DC1, DC2, and DC3. The beam enters from the left. Dimensions are in millimetres. Figure is not to scale. Positions are given at detector centre.

models (for one example of such studies see [6]) and to test particle flow algorithms, as demonstrated in [7]. The high granularity also offers the possibility for advanced energy reconstruction methods, the subject of this paper.

We present a study of the hadronic energy resolution of the CALICE analogue scintillator-steel hadronic calorimeter (AHCAL) [8] using data taken at the CERN SPS in 2007 with positive and negative pion beams in the energy range from 10 to 80 GeV. Two software compensation techniques, which weight energy depositions based on information about the local energy density within the shower obtained from the highly granular readout, are discussed in detail. Both techniques achieve an improvement of the hadronic energy resolution by approximately 20% for single hadrons in the energy range from 10 to 80 GeV, with a reduction of the stochastic term from $\sim 58\%/\sqrt{E/\mathrm{GeV}}$ to $\sim 45\%/\sqrt{E/\mathrm{GeV}}$.

In Section 2 we briefly describe the test beam setup, discuss the event selection and describe the energy reconstruction, calibration and the determination of the energy resolution in the AHCAL. The software compensation techniques are presented in Section 3, and Section 4 summarises the results obtained from data and compares them to simulations.

2. Energy reconstruction in the AHCAL

2.1 Test beam setup

The complete CALICE setup in the H6 beam line at the CERN SPS for the 2007 beam period, illustrated in Figure 1, consisted of a silicon-tungsten electromagnetic sampling calorimeter (ECAL) [9], the AHCAL, and a scintillator-steel tail catcher and muon tracker (TCMT) [10]. The test beam setup was also equipped with various trigger and beam monitoring devices.

The ECAL [9] has a total depth of 24 radiation lengths (approximately 1 nuclear interaction length λ_I) and consists of 30 active silicon layers arranged in three longitudinal sections with different absorber thicknesses. In this study, the ECAL was used for event selection and early shower

detection. Since the present study focuses on the AHCAL, events with a primary inelastic interaction in the ECAL are rejected, as discussed below.

The AHCAL [8] consists of small 5 mm thick plastic scintillator tiles with embedded wavelength-shifting fiber and individual readout by silicon photomultipliers (SiPMs). The tiles are assembled in 38 layers with lateral dimensions of 900×900 mm^2, separated by 21 mm of steel. The absorber material in each layer is made of 17 mm thick absorber plates and two 2 mm thick cover plates of the cassettes that house the scintillator cells. The size of the scintillator tiles ranges from 30×30 mm^2 in the central region and 60×60 mm^2 in the outer region to 120×120 mm^2 along the perimeter of each layer. In the last eight layers only 60×60 mm^2 and 120×120 mm^2 tiles are used. In total, the CALICE AHCAL has 7608 scintillator cells and a thickness of 5.3 λ_I (4.3 λ_π). To be able to correct off-line for variations in response of the photon sensors caused by the substantial temperature variations in the experimental hall, the temperature of the AHCAL inside the readout cassettes is monitored in each layer by five sensors installed equally spaced from bottom to top in the centre of the detector.

The TCMT [10] consists of 16 readout layers assembled from 5 mm thick, 50 mm wide and 1000 mm long scintillator strips with embedded wavelength-shifting fibers read out at one end by SiPMs. Each of the scintillator layers has 20 strips for a total of 320 strips in the TCMT. The scintillator is sandwiched between steel absorber plates. The TCMT has two sections with different sampling fractions, one fine section with 21 mm thick absorbers for the first nine layers (where the absorber plate for the first layer is the back plate of the AHCAL), and a coarse section with 104 mm thick absorbers. Two mm of the absorber thickness in each layer is provided by the cover sheets of the scintillator strip cassettes. In this study the information from the TCMT is used for muon separation and to measure energy leaking out the back of the AHCAL, which is of particular importance at higher energies. The total depth of the CALICE calorimeter setup amounts to approximately 12 λ_I, with a total of 17 648 readout channels.

In addition to the calorimeters themselves, the setup includes auxiliary detectors for triggering, tracking and particle identification as shown in Figure 1. The scintillation counters Sc1, Sc2 and Sc3 provide the beam trigger, where a coincidence between at least two out of the three is required. In addition, Sc2 has an analogue readout to tag multi-particle events. The large area veto counter is used to reject beam halo events and a large area scintillator counter Mc2 downstream of the TCMT provides muon tagging for particles penetrating the full calorimeter setup. For dedicated muon runs, an additional large area scintillation counter, Mc1, is installed upstream of the calorimeters. Three drift chambers DC1, DC2 and DC3 determine the position of the incoming beam particles. Particle identification is provided by a threshold Čerenkov counter upstream of the calorimeters, which discriminates between electrons and pions or between pions and protons in negatively or positively charged beams, respectively, by appropriately chosen gas pressures.

2.2 Event selection

The response of the individual calorimeter cells is calibrated with muons, using the visible signal of a minimum-ionising particle (MIP) as the cell-to-cell calibration scale. This signal corresponds to 13 detected photo-electrons in typical cells. After this cell-to-cell calibration, the most probable energy loss of a MIP is used as the base unit of the energy measurement. To reject noise, only cells

particle type	beam energy [GeV]	all pions	selected pions
π^-	10	440208	84706
π^-	15	127554	24997
π^-	18	52880	10492
π^-	20	342798	67093
π^-	25	201243	39631
π^-	35	272987	54126
π^-	40	472345	93301
π^-	45	325092	63547
π^-	50	304023	59076
π^-	60	647090	121588
π^-	80	741440	139248
π^+	30	155210	30884
π^+	40	307177	60595
π^+	50	159414	30843
π^+	60	449273	86947
π^+	80	272441	52442

Table 1. Summary of the data samples. The total number of pions is the number of events classified as pions, after rejection of empty, noisy and double particle events, and the application of muon rejection and particle identification cuts. The number of selected pions are the events with an identified shower start in the first five layers of the AHCAL, which are used in the present analysis. For most energies, several run periods at different temperatures are combined to maximise statistics.

with a visible energy above a threshold of 0.5 MIP are used in the analysis, referred to as hits in the following.

The data samples for the present analysis are selected from π^- and π^+ data in the energy range of 10 to 80 GeV and 30 to 80 GeV respectively, as summarised in Table 1. To maximise statistics, data from several run periods taken at different temperatures are combined for most energies, with corrections for the temperature dependence of the response of the photon sensors applied during event reconstruction [11]. The event selection procedure purifies the pion sample by rejecting admixtures of muons, electrons, and protons. To identify muons, information from the ECAL, AHCAL and TCMT is used, requiring small energy deposits consistent with a minimum-ionising particle in all three detectors. Optimal separation of muons and hadrons is achieved by using beam energy-dependent constraints on the energy sum in the TCMT versus the combined energy sum of the ECAL and AHCAL. For beam energies of 30 GeV and 35 GeV a muon contamination at the level of 30% and 15% before muon rejection is observed, respectively. For all other energies the muon content does not exceed 7%. After the event selection, the muon content is below 0.5% at all energies, estimated using the muon identification efficiency of 98% at 10 GeV and 99.5% at 30 GeV and above, which is determined from muon data and simulations. Protons and kaons are removed from the π^+ samples by requiring a positive pion identification in the Čerenkov counter. Even before selection, the kaon content is below 3% at all energies. The proton content of the beam is very small below 30 GeV since a tertiary beam is used at these energies, and varies between

approximately 15% and 30% at higher energies. Since the positive identification of π^+ is based on the detection of Čherenkov photons the proton and kaon contamination of the positive pion sample is negligible. Electrons are removed from the π^- sample both by the Čerenkov counter and by selecting events with no inelastic interaction in the ECAL, as discussed below.

Since the goal of the present analysis is the study of the performance of the AHCAL, pion showers that develop predominantly in the AHCAL are selected. This is achieved by requiring that the position of the primary inelastic interaction is located in the first five layers of the hadron calorimeter. This excludes events with sizeable energy deposit in the ECAL while keeping energy leakage into the TCMT to a minimum. The location of the primary inelastic interaction is determined by detecting the change from a minimum-ionising particle track to multiple secondary particles, evidenced by increased energy deposition and number of hits over several consecutive layers [7]. Simulation studies indicate that the difference between the reconstructed and the true primary interaction layer does not exceed one layer for 78% of all events and does not exceed two layers for more than 90% of all events in the energy range from 10 to 80 GeV.

2.3 Energy reconstruction and intrinsic energy resolution

To measure the energy deposited in the sub-detectors, a conversion from the visible signal in MIP units to the total energy in units of GeV is necessary. Since only hadrons with a shower start in the AHCAL are considered, the relevant conversion factor for the ECAL is determined using simulated muons to obtain the correlation between the visible energy and the true ionisation energy loss in the detector. This factor is validated with the measured response to muons obtained from a sample of muon data. The ratio of the visible signal in the active silicon to the total deposited energy in active and passive material is approximately 25% higher for minimum-ionising particles than for electromagnetic showers, resulting in a lower conversion factor than that for electrons presented in [12]. The total energy deposited in the AHCAL is obtained at the electromagnetic scale, using calibration factors determined for electron and positron data [13]. Since the AHCAL is a non-compensating calorimeter, the response to hadrons differs from that to electrons, requiring an additional scaling factor. This factor is determined by comparing the reconstructed energy for pions using the electromagnetic calibration factors with the known beam energy. In the present study, the energy dependence of this factor is ignored by taking a constant $\frac{e}{\pi} = 1.19$, corresponding to the average over the energy range studied. Since the first nine TCMT layers are essentially identical to the AHCAL layers in terms of absorber and active material, the same electromagnetic calibration factors and an identical $\frac{e}{\pi}$ ratio are assumed. For the last seven TCMT layers, the calibration factors are adjusted according to the increased absorber thickness.

For each event, the uncorrected reconstructed energy for hadrons, E_{unc}, is given by the sum of reconstructed energies in the three calorimeters,

$$E_{\text{unc}} = E_{\text{ECAL}}^{\text{track}} + \frac{e}{\pi} \cdot (E_{\text{HCAL}} + E_{\text{TCMT}}), \tag{2.1}$$

where $E_{\text{ECAL}}^{\text{track}}$ is the measured energy in the ECAL deposited by the particle track, and E_{HCAL} and E_{TCMT} are the energies measured in the AHCAL and in the TCMT, both given at the electromagnetic scale. The energy in each subdetector is given by the sum of all hits above a noise threshold of 0.5 MIP.

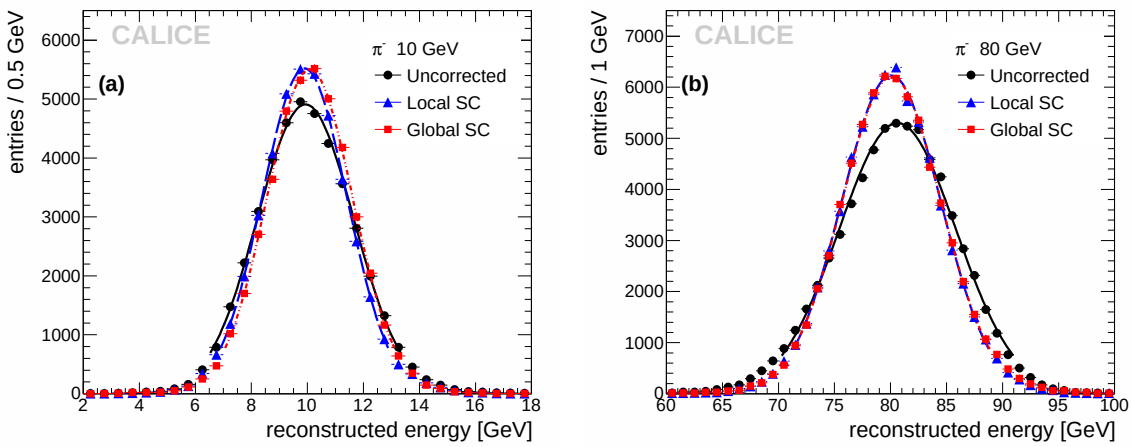

Figure 2. Reconstructed energy distributions for 10 GeV π^- (a) and 80 GeV π^- (b) without compensation (black circles) and after local software compensation (LC), shown by the blue triangles, and after global software compensation (GC), shown by the red squares. The curves show Gaussian fits to the distributions in the range of ± 2 standard deviations. Errors are statistical only.

The resulting reconstructed energy distributions are fit with a Gaussian in the interval of ± 2 standard deviations around the mean value, providing good fits for all energies. The differences compared to a fit over the full range are on the sub-percent level for the extracted mean and on the one percent level for the standard deviation and depend on the beam energy. Fitting over the full range reduces the fit quality for some energies in particular for the uncorrected data, leading to the choice of ± 2 standard deviations for best consistency between the different data points. In the following, the mean and standard deviation of this Gaussian fit at a given beam energy are referred to as the mean reconstructed energy E_{reco} and the resolution σ_{reco}, respectively.

Systematic uncertainties on the energy measurement in the AHCAL are discussed in detail in [13]. For the reconstruction of hadrons, the main uncertainty is due to the MIP to GeV conversion factor that is extracted from the electromagnetic calibration of the detector. The size of the uncertainty was studied thoroughly for the present data set, and is determined to be 0.9% by varying the calibration constants within the allowed limits. Other effects which contribute to the uncertainties for electromagnetic showers, such as the saturation behaviour of the photon sensor, are found to be negligible for hadrons even at the highest energies studied here.

Figure 2 shows the distribution of reconstructed energies for 10 GeV and 80 GeV pions, with the uncorrected reconstructed energy shown by black data points. At all energies, the distributions of the reconstructed energies follow a Gaussian distribution well, with typically more than 95% of all events in the fit range of ± 2 standard deviations. The software compensation methods also included in the figure are described in Sections 3.1 (local software compensation) and 3.2 (global software compensation).

Figure 3 shows the mean reconstructed energy versus beam energy, with the black points giving the uncorrected reconstructed energy. The measured responses to positive and negative pions agree well within the systematic uncertainties, which are shown by the green band. Relative

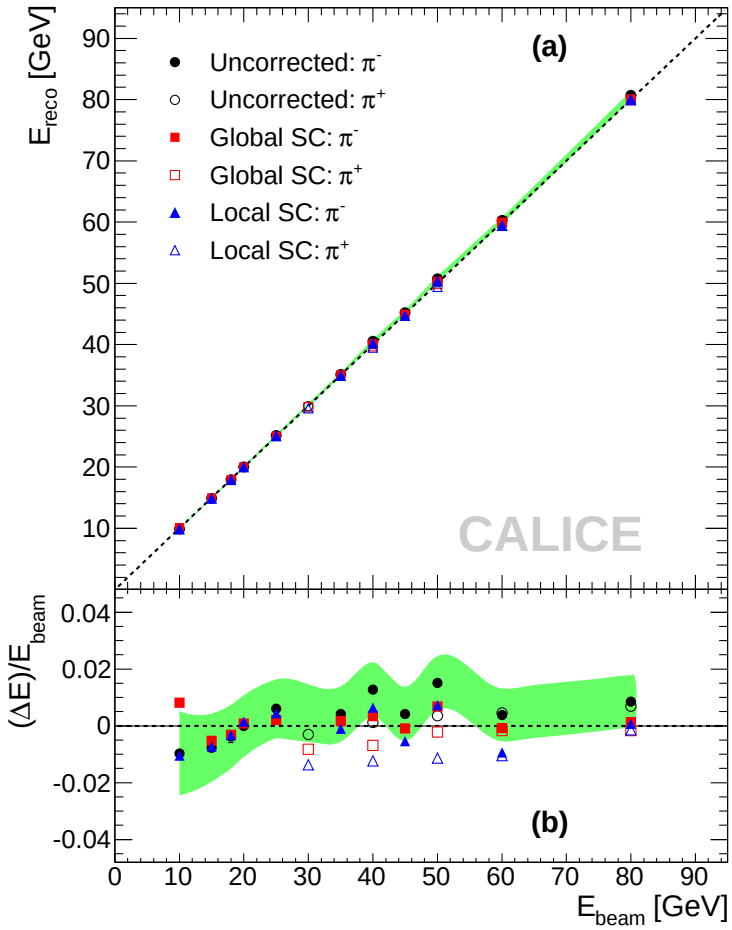

Figure 3. (a) Mean reconstructed energy for pions and (b) relative residuals to beam energy versus beam energy without compensation (black circles) and after local software compensation (LC), shown by the blue triangles, and after global software compensation (GC), shown by the red squares. Filled and open markers indicate π^- and π^+, respectively. Dotted lines correspond to $E_{\text{reco}} = E_{\text{beam}}$. Systematic uncertainties are indicated by the green band, which corresponds to the uncertainties for the uncorrected π^- data sample.

residuals to the beam energy are shown in the lower panel of Figure 3, where $\Delta E = E_{\text{reco}} - E_{\text{beam}}$. The linearity of the calorimeter response to hadrons showering predominantly in the AHCAL is within $\pm 2\%$ in the studied energy range.

The fractional energy resolution, $\sigma_{\text{reco}}/E_{\text{reco}}$, is shown in Figure 4. Again, the uncorrected resolution is indicated by black points. The measured resolution for π^- is in very good agreement with that obtained for π^+, with the differences smaller than the size of the markers for all energies where both π^- and π^+ results exist. The black solid curve shows the result of a fit to these points with the following function:

$$\frac{\sigma_{\text{reco}}}{E_{\text{reco}}} = \frac{a}{\sqrt{E_{\text{beam}}}} \oplus b \oplus \frac{c}{E_{\text{beam}}}, \tag{2.2}$$

where E_{beam} is the beam energy in GeV, and a, b and c are the stochastic, constant and noise contributions, respectively. The noise term is fixed to $c = 0.18$ GeV, corresponding to the measured

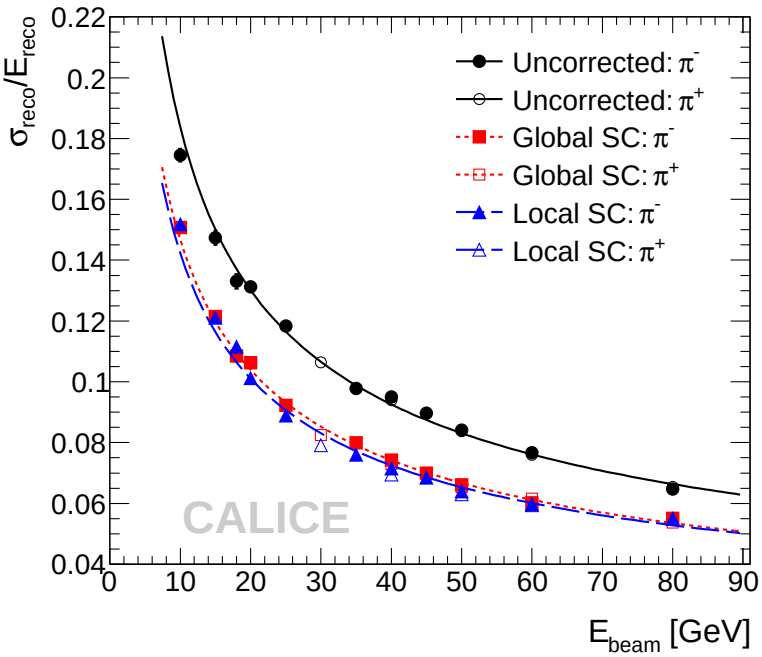

Figure 4. Energy resolution versus beam energy without compensation and after local and global software compensation. The curves show fits using Equation 2.2, with the black solid line showing the fit to the uncorrected resolution, the red dotted line to the global software compensation and the blue dashed line to the local software compensation. The stochastic term is $(57.6 \pm 0.4)\%$, $(45.8 \pm 0.3)\%$ and $(44.3 \pm 0.3)\%$, with constant terms of $(1.6 \pm 0.3)\%$, $(1.6 \pm 0.2)\%$ and $(1.8 \pm 0.3)\%$ for the uncorrected resolution, global software compensation and local software compensation, respectively.

noise contribution in the full CALICE setup taking into account contributions from the ECAL (0.004 GeV), the AHCAL (0.06 GeV) and the TCMT (0.17 GeV). These values are obtained from the standard deviation of the noise levels measured in dedicated runs without beam particles as well as in random trigger events constantly recorded during data taking. From the fit, the stochastic term of the uncorrected hadron energy resolution of the AHCAL is determined to be $(57.6 \pm 0.4)\%/\sqrt{E/\mathrm{GeV}}$ and the constant term to be $(1.6 \pm 0.3)\%$.

3. Software compensation: motivation and techniques

In ideal sampling calorimeters the energy measured for electromagnetic showers is directly proportional to the incoming particle energy. In the absence of instrumental effects such as non-linearities or saturation of the readout, the energy of a particle can thus be obtained by multiplying the visible signal by a single energy-independent factor accounting for the non-measured energy depositions in the passive absorber material.

The calorimeter response to hadron-induced showers is more complicated [14], since these showers have contributions from two different components: an electromagnetic component, originating primarily from the production of π^0s and ηs and their subsequent decay into photon pairs; and a purely hadronic component. The latter includes "invisible" components from the energy

loss due to the break-up of absorber nuclei, from low-energy particles absorbed in passive material and from undetected neutrons, depending on the active material. This typically leads to a reduced response of the calorimeter to energy in the hadronic component, and thus overall to a smaller calorimeter response to hadrons compared to electromagnetic particles of the same energy. Since the production of π^0s and ηs are statistical processes, the relative size of the two shower components fluctuates from shower to shower, which, combined with the differences in visible signal for electromagnetic and purely hadronic energy deposits, leads to a deterioration of the energy resolution. In addition, the average fraction of energy in the electromagnetic component depends on the number of subsequent inelastic hadronic interactions and thus on the initial particle energy. The electromagnetic fraction of hadronic showers increases with increasing particle energy [15], often resulting in a non-linear response for non-compensating calorimeters.

There are two fundamentally different approaches to improve the energy resolution of a hadronic sampling calorimeter. One approach is to eliminate the issue of different response to electromagnetic and hadronic components by design, through the construction of so-called compensating calorimeters. This can be achieved by specific choices of absorber and active material which enhance the sensitivity to neutrons, and thus to the hadronic component of the shower, and by appropriately chosen sampling fractions. However, these conditions impose very strict requirements on the materials used and on the overall geometry of the whole detector system. One prominent example of a compensating calorimeter is the uranium-scintillator calorimeter of the ZEUS experiment [16, 17], which reached a stochastic resolution term of $34.5\%/\sqrt{E/\mathrm{GeV}}$ for single pions [18].

On the other hand, for intrinsically non-compensating calorimeters, compensation can be achieved by so-called "off-line weighting" or "software compensation" techniques. These techniques assign different weights to electromagnetic and hadronic energy deposits on an event-by-event basis. The differing spatial structure of the electromagnetic and hadronic components of particle showers can be used to characterise the origin of energy deposits. Since the radiation length is much shorter than the nuclear interaction length in heavy absorbers used in hadronic calorimeters, electromagnetic sub-showers are more compact than purely hadronic sub-showers, generally resulting in a higher energy density of the electromagnetic component. The application of software compensation techniques relies on longitudinal and lateral segmentation of the calorimeters, to provide the necessary information for a measurement of the energy density of particle showers. One of the first applications of such techniques was in the WA1/CDHS scintillator steel calorimeter, where an improvement of the hadronic resolution between 10% and 30% was achieved in the energy range of 10 GeV to 140 GeV [19]. These techniques were further refined and applied in various experiments, such as the H1 liquid argon calorimeter [20] and the ATLAS calorimeter system [21].

With its unprecedented high granularity, the CALICE AHCAL is well suited for such techniques. In the present paper, two techniques based on an event-by-event analysis of the hit energy distributions are discussed. The local software compensation (LC) procedure is based on a re-weighting of each individual hit depending on the local energy density. The global software compensation (GC) procedure uses the distribution of hit energies to derive one global factor for the correction of the reconstructed energy of the complete hadronic shower. The parameters used for both techniques are determined from test beam data, as discussed in detail below. The available data set is split into two samples of equal event count, a training data set and the data set used to

study the energy reconstruction. This ensures a statistical independence of the data used to determine the parameters for the software compensation algorithms and the data used to evaluate the performance of the techniques.

3.1 Local software compensation

The local software compensation technique improves the energy reconstruction for hadrons by applying weights to the energy recorded in every cell of the AHCAL within a hadronic shower. The weights are chosen based on the local energy density, which is taken as a measure of the likelihood that a given cell belongs to an electromagnetic or a hadronic sub-shower. In the present study, the energy content of a cell, divided by its volume, is taken as the relevant local energy density. Electromagnetic sub-showers typically have a higher energy density than purely hadronic ones, and, due to the non-compensating nature of the AHCAL, result in a larger detector signal per unit of deposited energy. Thus, cells with a higher energy content are assigned a lower weight in the total energy sum than cells with a low energy content to correct for this difference. The reconstructed energy of each event corrected with local software compensation, E_{LC}, is thus given by introducing weights for each AHCAL hit in Equation 2.1, resulting in

$$E_{\mathrm{LC}} = E_{\mathrm{ECAL}}^{\mathrm{track}} + \frac{e}{\pi} \cdot \left(\sum_i (E_{\mathrm{HCAL},i} \cdot \omega_i) + E_{\mathrm{TCMT}} \right) \tag{3.1}$$

where ω_i is the energy density dependent weight applied to the cell energy $E_{\mathrm{HCAL},i}$.

To make the technique robust against fluctuations entering due to the relatively low number of hits in a given event, the single cell energy density distribution is subdivided into bins in energy density, as illustrated in Figure 5 (a). The binning is also needed for the minimisation technique chosen here for the determination of the weights as discussed below. For each bin, a separate weight is determined which is applied to all hits that fall into that particular bin. The number of sub-divisions in energy density is chosen as a compromise between the requirements for fine subdivisions to maximise the sensitivity of the algorithm to differences in shower structure on one hand, and the stability of the determination of the weights and of the algorithm on the other hand. While a fine binning improves the sensitivity to the shower structure, a robust determination of the weights requires sufficient statistics in each bin, and changes of the weights from bin to bin. The performance of the local software compensation does not depend on the precise choice of bin number and bin borders.

Since the overall energy density of hadronic showers changes with energy, the weights ω depend both on the cell energy density ρ and on the particle energy. The weights, as a function of energy density and particle energy, are determined from the training data set extending over the full energy range studied here. The optimal weights are found by minimising a simplified χ^2 given by the function $\chi^2 = \sum_i (E_{\mathrm{LC},i} - E_{\mathrm{beam}})^2$, where $E_{\mathrm{LC},i}$ is the reconstructed energy of a given event using software compensation, and the sum runs over all events used for the weight determination. In this minimisation, the bin by bin weights are used as free parameters. Figure 5 (b) shows the optimal weights determined with this procedure for four different energies. The weights at a given beam energy can be parametrized by

$$\omega = p_0 + p_1 \cdot \exp(p_2 \cdot \rho), \tag{3.2}$$

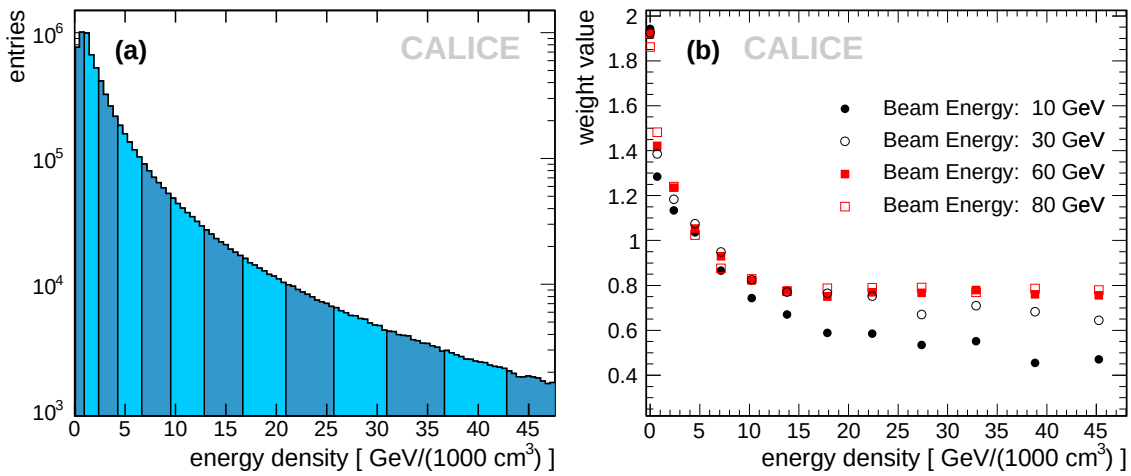

Figure 5. (a) Distribution of the cell energy density in the AHCAL for 40 GeV pion showers. The energy density is given by the uncorrected reconstructed energy in that cell, divided by the corresponding absorber volume. The different energy density bins used in the analysis are indicated by colour shades. (b) Optimal weights as a function of energy density for different beam energies, determined without constraints of a specific functional form in the first iteration of the minimisation.

where ρ is the energy density corresponding to the centre of the energy density bins introduced above, and p_0, p_1 and p_2 are parameters of the weight function. These parameters depend on the beam energy, with their energy dependence following exponential functions in particle energy for p_0 and p_1, and a logarithmic function in particle energy for p_2. A robust determination of the weights is achieved by an iterative minimisation procedure, where the free parameters p_0, p_1 and p_2 are consecutively fixed to the function determined in the previous minimisation stage.

For the application of this technique to data, no *a priori* knowledge of the particle energy is required, as the uncorrected reconstructed particle energy is used instead of E_{beam} to select the correct weight parametrisation. Since the energy dependence of the weight parameters is not very steep, this does not introduce a noticeable bias for the reconstructed energy. A second iteration does not lead to significant further improvement and is thus not performed in the reconstruction.

3.2 Global software compensation

The global software compensation technique improves the energy resolution for hadrons by applying a single weight to the reconstructed shower energy. This weight is derived from the distribution of hit energies in the hadronic shower, providing sensitivity to the overall energy density, and thus to the fraction of hits in electromagnetic sub-showers. Since electromagnetic sub-showers are characterised by a high local energy density, a hadronic shower with a large electromagnetic content will have a larger fraction of high-energy hits than a shower with predominantly hadronic contributions.

The determination of the event weight is based on a phenomenological approach using the fraction of calorimeter hits below a certain energy threshold. This fraction is computed for each event, and provides a measure of the importance in each shower of low-density energy deposits, which are expected to be predominantly of hadronic origin. Based on this, with an additional consideration of the overall hit energy distribution given by the number of hits below the mean energy

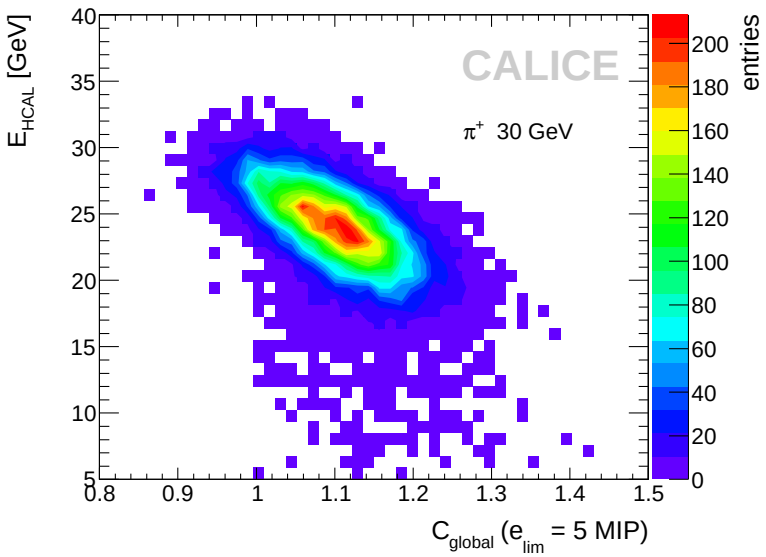

Figure 6. Correlation of the factor C_{global} and the reconstructed energy in the AHCAL, E_{HCAL}, for showers induced by π^+ at 30 GeV.

value of the hit energy, the factor C_{global} is constructed, which is used to correct the reconstructed energy. This factor, calculated for each event, is given by the ratio of the number of shower hits with a measured visible signal below a given threshold e_{lim} and the number of shower hits with a measured visible signal below the mean value of the hit energy spectrum for that particular event. Figure 6 illustrates the sensitivity of the factor C_{global} to the reconstructed energy, for a value of e_{lim} = 5 MIP applied to π^+ events at 30 GeV. The clear anti-correlation between the reconstructed energy and C_{global} provides the basis for an improved energy reconstruction using this factor. The anti-correlation is due to the fact that events with a high electromagnetic content tend to have a larger number of high-energy hits above e_{lim} and thus a lower C_{global}, while those events have a higher reconstructed energy.

The value of e_{lim} was optimised to provide good performance of the algorithm over the full energy range, with the linearity of the detector response taken as a key factor. While higher values for e_{lim} provide stricter separation of electromagnetic and non-electromagnetic events, if the value is set too high this results in asymmetric distributions of C_{global} at lower energy, leading to reduced performance. These asymmetries originate from the reduced number of high-energy hits at low particle energies. For example, a large fraction of 10 GeV pion showers have essentially no hits above 7 MIP. Too low values, on the other hand, result in a non-linear response due to the reduced sensitivity to the electromagnetic component at higher particle energies. Best performance was obtained for a value of e_{lim} = 5 MIP. For the highly granular core of the calorimeter, this corresponds to an energy density of 7.4 GeV/1000 cm^3 in Figure 5 (a). For the energy range studied, the mean hit energy is between 2.7 to 4.7 MIP. Figure 7 shows the distributions of C_{global} for different energies, demonstrating its energy dependence, originating from the change of the overall hit energy spectrum with changing particle energy. When applying C_{global} in the energy reconstruction, this dependence has to be corrected for, as discussed below.

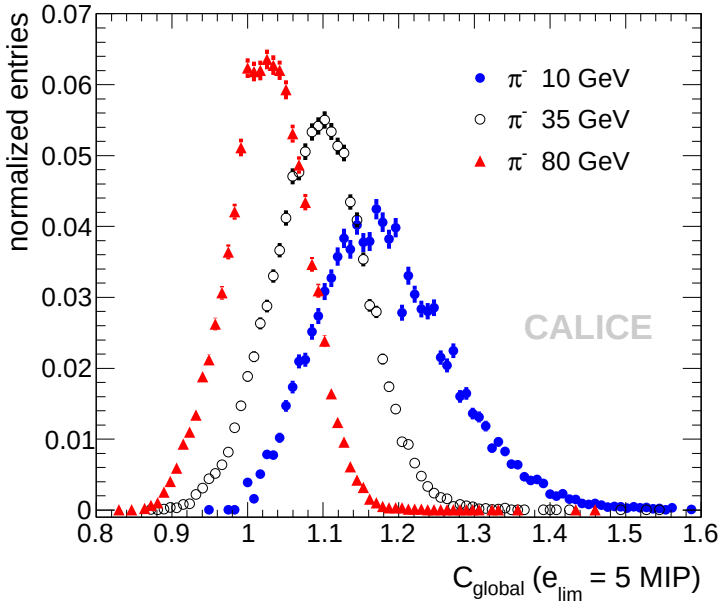

Figure 7. Distributions of the factor C_{global} for hadronic showers induced by π^- with an energy of 10 GeV (blue squares), 35 GeV (black circles) and 80 GeV (red triangles), respectively. Statistical errors are shown.

The reconstructed energy with global software compensation is obtained in two steps. First, a corrected shower energy is calculated by multiplying the reconstructed energy in the AHCAL and in the TCMT by the factor C_{global}, giving $E_{\text{shower}} = C_{\text{global}} \cdot (E_{\text{HCAL}} + E_{\text{TCMT}})$. From this corrected shower energy, the final reconstructed energy with global software compensation for a given event, E_{GC}, is then obtained from

$$E_{\text{GC}} = E_{\text{ECAL}}^{\text{track}} + E_{\text{shower}} \cdot P_{\text{global}}(E_{\text{shower}}), \tag{3.3}$$

where $P_{\text{global}}(E_{\text{shower}})$ is a function which accounts for the energy dependence of the compensation parameters, visible in Figure 7 as the shift of the mean of C_{global} with energy. This function depends on the corrected shower energy E_{shower} and is given by a second-order polynomial, $P_{\text{global}}(E_{\text{shower}}) = a_0 + a_1 \cdot E_{\text{shower}} + a_2 \cdot E_{\text{shower}}^2$. The parameters for this function are obtained from a fit of the dependence of the corrected shower energy E_{shower} on the true deposited energy given by the beam energy corrected for the energy deposited in the ECAL, and are extracted from a training data set extending over the full energy range considered here. They are found to be $a_0 = 0.982 \pm 0.007$, $a_1 = 0.0041 \pm 0.0003$ GeV^{-1} and $a_2 = (-2.2 \pm 0.3) \cdot 10^{-5}$ GeV^{-2}.

The application of the global software compensation technique does not require knowledge of the beam energy, since the energy reconstructed in the HCAL and TCMT is used also in the determination of the correction of the energy dependence of the compensation parameters.

4. Results

To evaluate their performance, both software compensation techniques are applied to test beam

data and to simulated data. The parameters for the algorithms are determined using test beam data following the training procedures outlined above.

4.1 Application of software compensation to test beam data

When applying the software compensation techniques to test beam data, the energy dependent compensation factors are determined event-by-event using the uncorrected reconstructed energy. Figure 2 shows the distribution of reconstructed energies for the uncorrected reconstruction compared with both software compensation techniques studied. The results are shown for pions with energies of 10 GeV and 80 GeV. In both cases, the software compensation algorithms improve the energy resolution, evidenced by a narrowing of the distributions, while preserving or even improving the Gaussian form of the distributions. The algorithms also bring the mean value of the reconstructed energy closer to the beam energy, resulting in small shifts of the maxima visible in Figure 2. The mean reconstructed energy with local and global compensation techniques, compared to the uncorrected response without compensation, is shown in Figure 3 for all energies studied. For both techniques, all points fall within $\pm 1.5\%$ of linearity.

The energy resolution before and after compensation is shown in Figure 4. Good agreement between the π^- and π^+ samples is observed. The energy dependence of the energy resolution is well described by Equation 2.2 with a fixed noise term $c = 0.18$ GeV as discussed in Section 2.3. The fit results are summarised in Table 2. The application of software compensation results in a decrease of the stochastic term while the constant term remains unchanged. Both compensation techniques show very similar performance, with the local software compensation providing a slightly smaller stochastic term, and slightly better performance at intermediate energies.

Table 2. Stochastic, constant and noise term contributions to the resolution of the CALICE AHCAL determined with a fit of Equation 2.2 to data.

	a [%]	b [%]	c [GeV]
uncorrected	57.6±0.4	1.6±0.3	0.18
local compensation	44.3±0.3	1.8±0.2	0.18
global compensation	45.8±0.3	1.6±0.2	0.18

Figure 8 shows the relative improvement of the energy resolution achieved with the software compensation techniques, defined as the ratio of the resolution after software compensation σ_{SC} (local or global) to the uncorrected resolution σ_{unc}. The improvement ranges from $\sim$12% to $\sim$25% in the energy range studied, for both techniques, with approximately 3% better relative improvement observed for the local technique in the energy range from 25 GeV to 60 GeV. The reduced performance at high energy is partially due to increased leakage into the TCMT. Energy deposits in the TCMT are not weighted in the local software compensation since their energy density is not well defined. In the global software compensation, the weight is applied also to TCMT energy deposits, but those are not considered in the determination of the weighting factor due to the different readout geometry which leads to increased uncertainties in the weight determination.

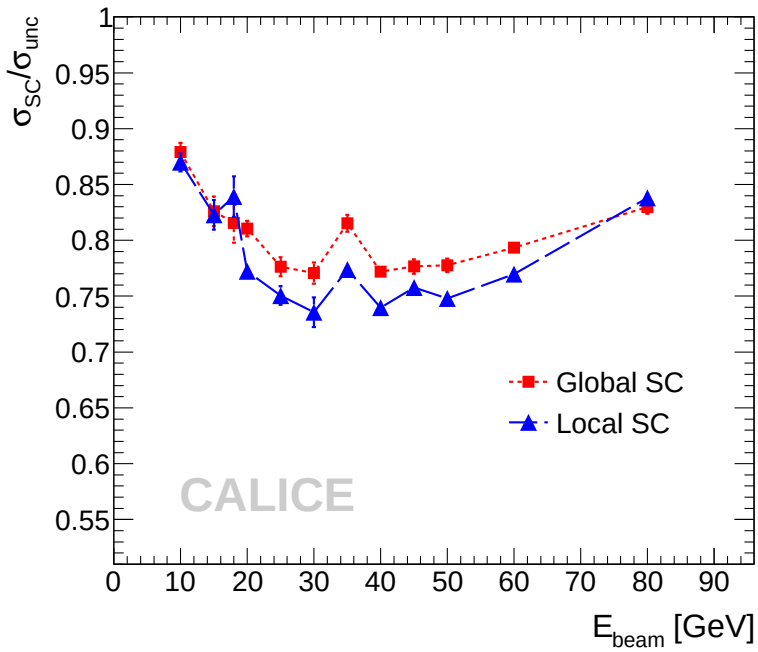

Figure 8. Energy dependence of the relative improvement of the resolution with local and global software compensation observed for data. Where available, results for π^- and π^+ are averaged for clarity.

4.2 Comparison to Monte Carlo simulations

The stability of both software compensation techniques, as well as the realism of simulation models, is tested using Monte Carlo simulations. For this purpose, the software compensation algorithms with coefficients derived from data are applied to Monte Carlo samples generated with a detailed detector model in GEANT4.9.4 [22] using two physics lists: QGSP_BERT and FTF_BIC [23]. The QGSP_BERT physics list was chosen because it is the most widely used model in high energy physics experiments at present. The FTF_BIC physics list, in turn, has provided good results in a previous CALICE analysis [6] and is completely independent from QGSP_BERT.

Details on the simulation procedure for the AHCAL can be found in [13]. For the chosen physics lists, samples of π^+ and π^- events were simulated at the same energies as the data points using beam profiles, detector temperatures and voltage settings from the data runs. The calibration of the simulation was performed at the MIP level by converting the simulated energy deposits in the scintillator into MIPs using the most probable energy loss of muons determined in simulations. The simulated data sets were passed through the same event selection and reconstruction procedures as real data, using the conversion factors from the MIP scale to reconstructed energy determined for data as discussed in Section 2.3. This also includes the requirement for an identified primary inelastic interaction in the first five layers of the AHCAL.

The uncorrected reconstructed energy as a function of beam energy is shown for data and both physics lists in Figure 9 (a). The relative deviation from the beam energy, shown in Figure 9 (b), indicates that simulations with both physics lists behave differently than the data. Both models overestimate the reconstructed energy at high particle energies. In addition, QGSP_BERT exhibits

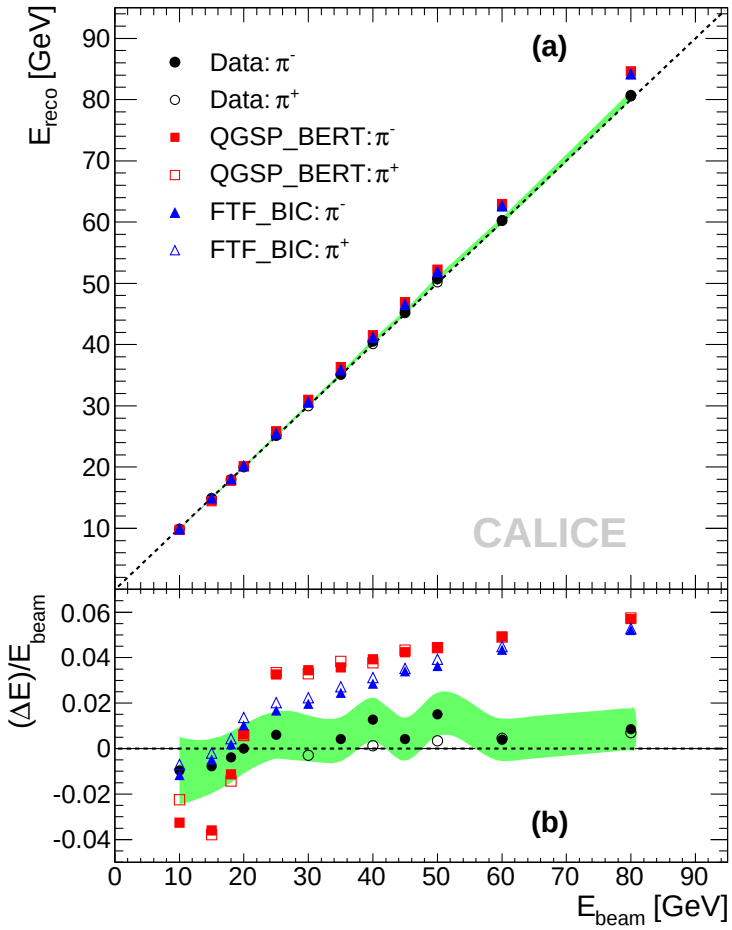

Figure 9. (a) Uncorrected response to pions and (b) relative residuals to beam energy versus beam energy for data (black circles), QGSP_BERT (red squares) and FTF_BIC (blue triangles). Filled and open markers indicate π^- and π^+, respectively. Dotted lines correspond to $E_{\text{reco}} = E_{\text{beam}}$, while the green band shows systematic uncertainties for the uncorrected π^- data sample.

fluctuations in the transition region between different models in the region between 10 GeV and 20 GeV. In general, the reconstructed energy for simulations is less linear than for data.

Figure 10 shows the energy resolution without software compensation, comparing data and simulations. Again, the behaviour of the simulations is different from that of the data, with both models underestimating the resolution at low energy, and with FTF_BIC overestimating the resolution above 30 GeV. This difference leads to a reduced stochastic resolution term with a significantly increased constant term. The results of the fits to the data points using Equation 2.2 are summarised in Table 3.

The shape of the distribution of the hit energy density is quite well reproduced by both physics lists, providing the basis for an application of the software compensation algorithms to simulations using the parameters determined from data. Figure 11 shows the distributions for two representative energies. The distributions are normalized to the number of entries to show the overall shape while

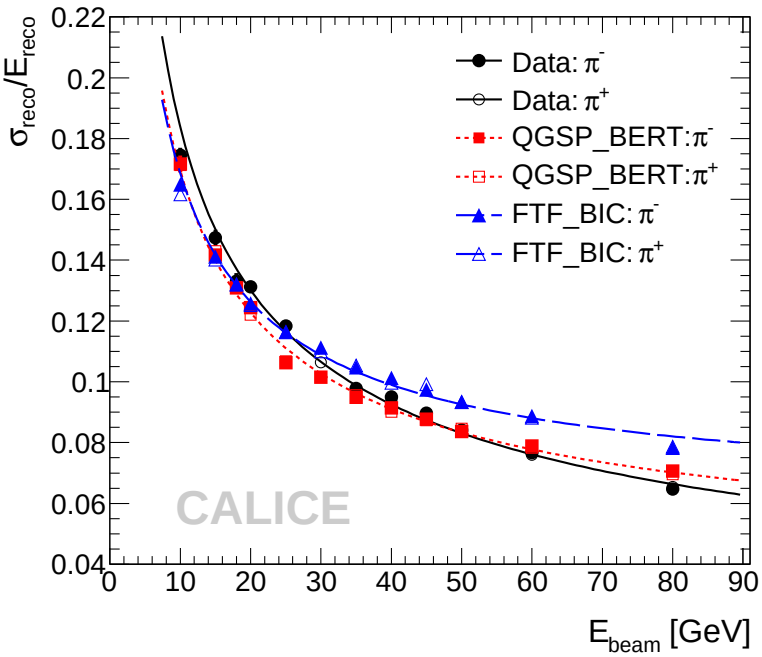

Figure 10. Uncorrected energy resolution versus beam energy for data as well as simulations using the physics lists QGSP_BERT and FTF_BIC. The curves show fits using Equation 2.2. The stochastic terms are $(57.6 \pm 0.4)\%$, $(51.8 \pm 0.3)\%$ and $(49.4 \pm 0.3)\%$, with constant terms of $(1.6 \pm 0.3)\%$, $(4.0 \pm 0.1)\%$ and $(6.1 \pm 0.1)\%$ for data, QGSP_BERT and FTF_BIC, respectively.

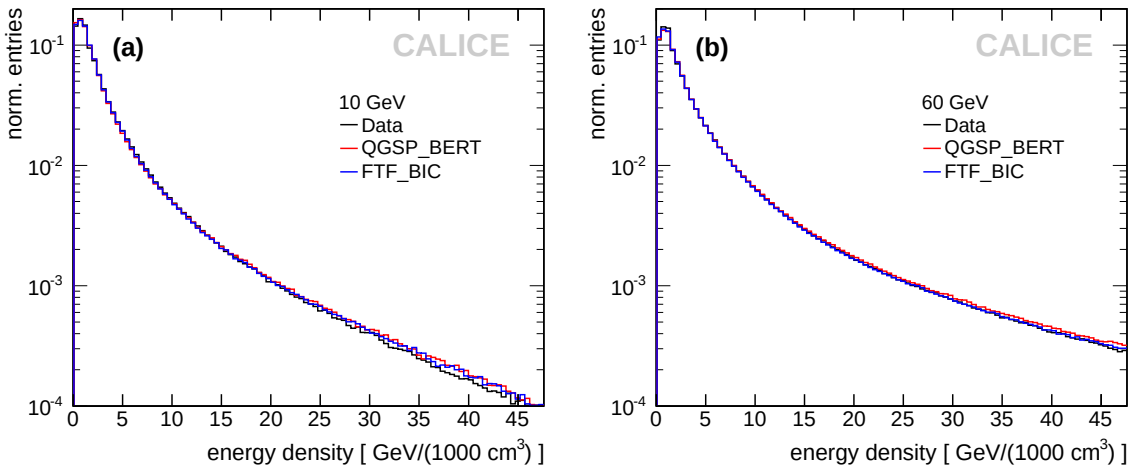

Figure 11. Energy density distribution for data and the two physics lists QGSP_BERT and FTF_BIC for (a) 10 GeV and (b) 60 GeV. The energy density is given by the uncorrected reconstructed energy in that cell, divided by the corresponding absorber volume. The distributions are normalized to the number of entries (number of hits).

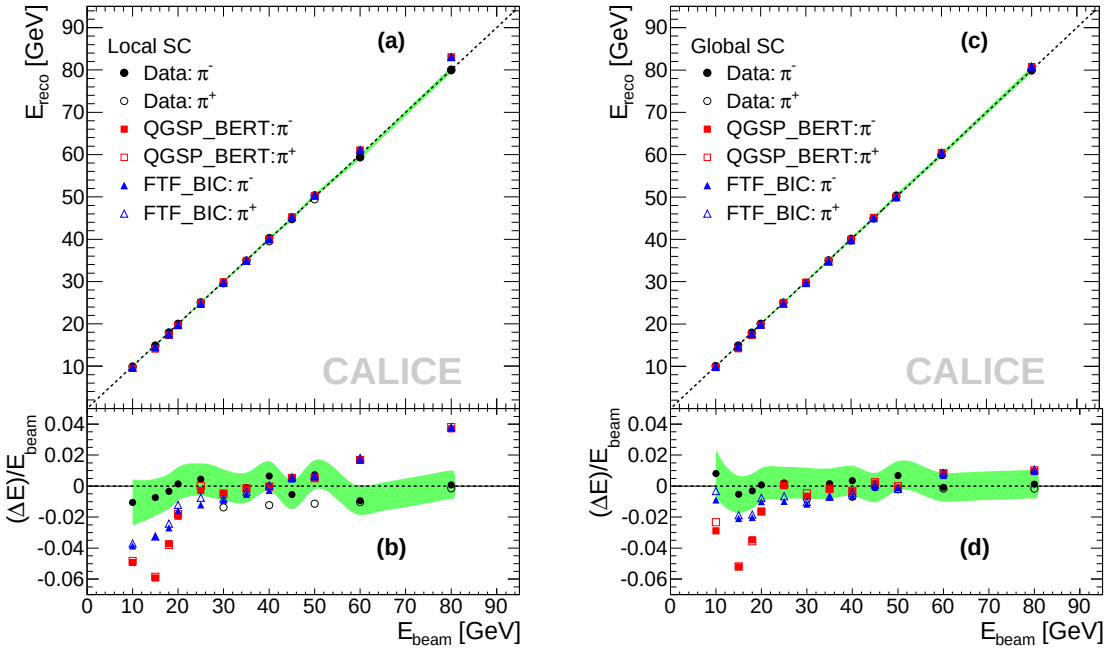

Figure 12. Detector response to pions with software compensation comparing data and simulations. For both data and simulations compensation parameters derived from data are used. (a) Response with local software compensation and (b) corresponding relative residuals to beam energy. (c) Response with global software compensation and (d) corresponding relative residuals to beam energy.

ignoring differences in the normalisation originating from different energy sums. The distributions show a slight overestimation of the fraction of high-density hits by the simulations. In addition, uncertainties in the treatment of saturation effects of the photon sensor lead to an excess of cells with very high energy content well beyond the range shown in the figure.

The effect of the application of the software compensation algorithms, with parameters extracted from data, on the reconstructed energy in simulations is shown in Figure 12. For both compensation techniques, the underestimation of the detector response at low energy, in particular by the QGSP_BERT physics list, remains present. At intermediate energies from 20 GeV up to 50 GeV, the application of software compensation results in an improved response linearity and in a better agreement between data and simulations for both physics lists considered. At higher energy, a significant overestimation of the reconstructed energy by simulations is seen with local software compensation, while the global software compensation technique successfully corrects the non-linearity of the simulations in that energy regime. This difference in behaviour is partially due to uncertainties in the treatment of saturation effects in simulations, and potentially also receives a contribution from imperfect descriptions of the shower structure by the shower models themselves. In the simulations, the number of cells with very high energy content is overestimated and exhibits a longer tail than in data, as discussed above. This affects the correction factor of the global software compensation by construction, resulting in a lower shower weight for simulations compared to data at the same energy on average, bringing data and simulations into better agree-

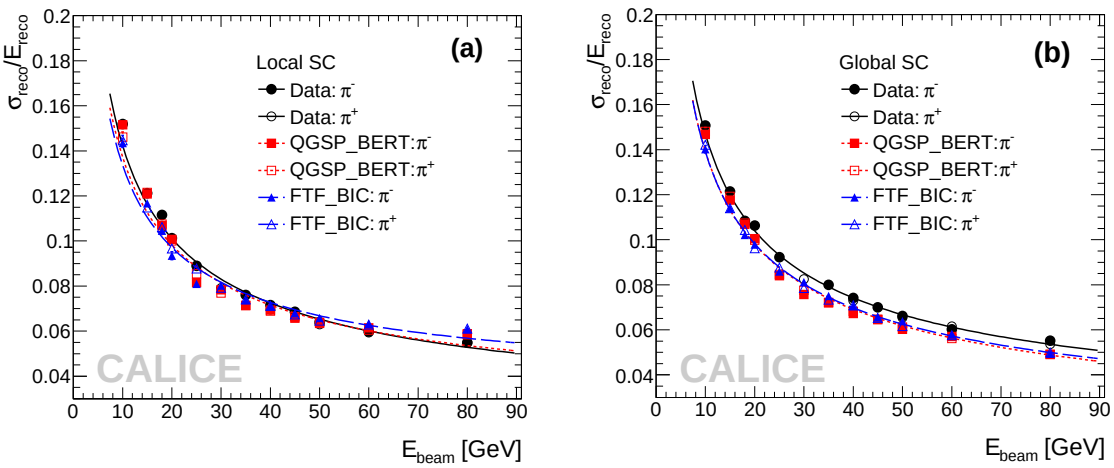

Figure 13. Energy resolution for pions with local (a) and global (b) software compensation comparing data and simulations. For both data and simulations compensation parameters derived from data are used. The curves show fits using Equation 2.2. The fit results for the local software compensation are $(44.3 \pm 0.3)\%$, $(42.3 \pm 0.2)\%$ and $(40.4 \pm 0.3)\%$ for the stochastic term, with constant terms of $(1.8 \pm 0.2)\%$, $(2.5 \pm 0.1)\%$ and $(3.4 \pm 0.1)\%$ for data, QGSP_BERT and FTF_BIC, respectively. For the global software compensation, the results are $(45.8 \pm 0.3)\%$, $(43.6 \pm 0.2)\%$ and $(43.4 \pm 0.3)\%$ for the stochastic term, with constant terms of $(1.6 \pm 0.2)\%$, $(0.0 \pm 0.2)\%$ and $(1.1 \pm 0.2)\%$ for data, QGSP_BERT and FTF_BIC, respectively.

Table 3. Fit results using the function given in Equation (2.2) for simulations with and without software compensation, compared to the corresponding values for data.

	a [%]	b [%]	c [GeV]
uncorrected data	57.6±0.4	1.6±0.3	0.18
uncorrected QGSP_BERT	51.8±0.3	4.0±0.1	0.18
uncorrected FTF_BIC	49.4±0.3	6.1±0.1	0.18
local compensation data	44.3±0.3	1.8±0.2	0.18
local compensation QGSP_BERT	42.3±0.2	2.5±0.1	0.18
local compensation FTF_BIC	40.4±0.3	3.4±0.1	0.18
global compensation data	45.8±0.3	1.6±0.2	0.18
global compensation QGSP_BERT	43.6±0.2	0.0±0.2	0.18
global compensation FTF_BIC	43.4±0.3	1.1±0.2	0.18

ment. The local software compensation technique applies constant weights for very high-energy hits, as can be seen in Figure 5 (b). It is thus less sensitive to these differences between data and simulations and preserves the discrepancy in visible energy for high beam energies.

Figure 13 shows the energy resolution for simulations compared to that for data for both software compensation techniques. The local software compensation largely preserves the differences between data and simulations for the physics list QGSP_BERT, but results in a better agreement of FTF_BIC with data, in agreement with the behaviour observed for the reconstructed energy. The

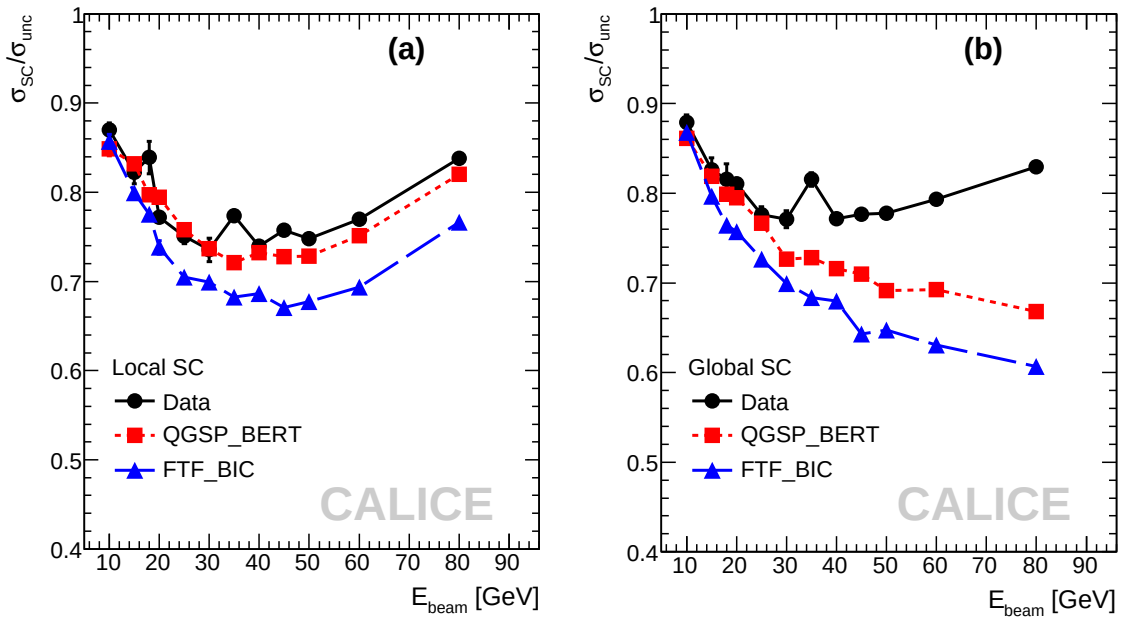

Figure 14. Energy dependence of the relative improvement of the resolution for data and simulations using the physics lists QGSP_BERT and FTF_BIC, (a) with local software compensation and (b) with global software compensation. Where available, results for π^- and π^+ are averaged for clarity.

global software compensation brings the overall trend of the resolution with energy for data and simulations into good agreement, with better resolution seen for simulations with both physics lists than for data. The results of the fits to the data points using Equation 2.2 are summarised in Table 3, together with the results obtained without software compensation.

The relative improvement in resolution compared to the uncorrected energy resolution is shown in Figure 14 for data and simulations. For the local software compensation, the improvement with respect to energy observed in data is well reproduced by the QGSP_BERT physics list. For FTF_BIC, a considerably bigger improvement is seen for the simulations at high energy than is seen in data. This higher improvement at high energies results in the better agreement of the energy resolution in data and in simulations discussed above. For the global compensation approach, the behaviour up to 30 GeV is well modelled by QGSP_BERT, while an up to 20% higher improvement, compared to that for data, is seen in simulations at the highest energies considered. The reason for this different behaviour of local and global software compensation is the same as for the different high-energy behaviour for the reconstructed energy as discussed above.

5. Conclusion

The hadronic energy resolution of the CALICE analogue hadron calorimeter is studied using test beam data collected in 2007 at the CERN SPS. The calorimeter, with an instrumented volume of approximately 1 m^3 and a depth of 5.3 λ_I, is highly segmented in both longitudinal and lateral direction, with a total of 7608 electronic channels. The intrinsic energy resolution of the CALICE AHCAL for hadrons is measured to be $58\%/\sqrt{E/\mathrm{GeV}}$, with a constant term of 1.6%.

The unprecedented granularity of the CALICE AHCAL provides excellent possibilities for the application of software compensation algorithms to improve the energy resolution of the calorimeter based on event-by-event information on the energy density structure of the showers. Two techniques have been presented here, together with results from test beam and from simulated data samples. The local software compensation technique uses local energy density information for a cell-by-cell re-weighting of energy deposits, while the global software compensation technique uses the distribution of cell energies to derive one overall weighting factor for each shower. Both techniques show similar performance, with a relative improvement of the energy resolution ranging from 12% to 25% over the studied energy range from 10 GeV to 80 GeV, resulting in a reduction of the stochastic term to $45\%/\sqrt{E/\mathrm{GeV}}$. In GEANT4 simulations with the QGSP_BERT and the FTF_BIC physics lists, the detector response is considerably more non-linear than in data. The physics list QGSP_BERT provides a satisfactory description of the energy resolution. The application of software compensation using parameters determined from data brings the resolution into better agreement with data. Here, the improvement of the energy resolution using the local software compensation technique observed for the QGSP_BERT physics lists is comparable to that observed for data, while larger differences are observed for FTF_BIC and for the global software compensation technique.

Neither of the described techniques requires an *a priori* knowledge of the particle energy. The energy dependent compensation factors are selected based on the uncorrected reconstructed energy. Although this energy dependence places some restrictions on the implementation of both techniques in a collider environment with a high particle density in hadronic jets, their application in the context of particle flow algorithms should be possible based on identified calorimeter clusters. The jet energy resolution can profit from the improved hadronic energy resolution directly through a better measurement of the neutral hadronic component, but also indirectly from an improved matching of reconstructed tracks and calorimeter energy during the clustering phase.

Acknowledgments

We gratefully acknowledge the DESY, CERN and Fermilab managements for their support and hospitality, and their accelerator staff for the reliable and efficient beam operation. We would like to thank the HEP group of the University of Tsukuba for the loan of drift chambers for the DESY test beam. The authors would like to thank the RIMST (Zelenograd) group for their help and sensors manufacturing. This work was supported by the Bundesministerium für Bildung und Forschung, Germany; by the the DFG cluster of excellence 'Origin and Structure of the Universe' of Germany ; by the Helmholtz-Nachwuchsgruppen grant VH-NG-206; by the BMBF, grant no. 05HS6VH1; by the Alexander von Humboldt Foundation (Research Award IV, RUS1066839 GSA); by joint Helmholtz Foundation and RFBR grant HRJRG-002, SC Rosatom; by Russian Grants SS-1329.2008.2 and RFBR08-02-121000-0FI and by the Russian Ministry of Education and Science contract 02.740.11.0239; by MICINN and CPAN, Spain; by CRI(MST) of MOST/KOSEF in Korea; by the US Department of Energy and the US National Science Foundation; by the Ministry of Education, Youth and Sports of the Czech Republic under the projects AV0 Z3407391, AV0 Z10100502, LC527 and LA09042 and by the Grant Agency of the Czech Republic under the project 202/05/0653; and by the Science and Technology Facilities Council, UK.

References

[1] J. Brau, (Ed.) *et al.* [ILC Collaboration], *ILC Reference Design Report: ILC Global Design Effort and World Wide Study*, arXiv:0712.1950 [physics.acc-ph].

[2] P. Lebrun *et al.*, *The CLIC Programme: Towards a Staged e+e- Linear Collider Exploring the Terascale : CLIC Conceptual Design Report*, arXiv:1209.2543 [physics.ins-det].

[3] J. -C. Brient and H. Videau, *The calorimetry at the future e^+e^- linear collider*. eConf C **010630** (2001) E3047 [hep-ex/0202004].

[4] V. L. Morgunov, *Calorimetry design with energy-flow concept (imaging detector for high-energy physics*, Proc. of Calorimetry in Particle Physics (CALOR 2002), pp. 70-84, Pasadena, California, 25th-29th Mar. 2002.

[5] M. A. Thomson, *Particle Flow Calorimetry and the PandoraPFA Algorithm*, Nucl. Instrum. Meth. **A 611** (2009) 25.

[6] C. Adloff, *et al.* [CALICE Collaboration], *Study of the interactions of pions in the CALICE silicon-tungsten calorimeter prototype*, JINST **5** (2010) P05007.

[7] C. Adloff, *et al.* [CALICE Collaboration], *Tests of a particle flow algorithm with CALICE test beam data*, JINST **6**, (2011) P07005.

[8] C. Adloff *et al.* [CALICE Collaboration], *Construction and Commissioning of the CALICE Analog Hadron Calorimeter Prototype*, JINST **5** (2010) P05004.

[9] J. Repond *et al.* [CALICE Collaboration], *Design and Electronics Commissioning of the Physics Prototype of a Si-W Electromagnetic Calorimeter for the International Linear Collider*, JINST **3** (2008) P08001.

[10] C. Adloff *et al.* [CALICE Collaboration], *Construction and performance of a silicon photomultiplier/extruded scintillator tail-catcher and muon-tracker*, JINST **7** (2012) P04015.

[11] N. Feege, *Low-energetic hadron interactions in a highly granular calorimeter*, DESY-THESIS-2011-048.

[12] C. Adloff *et al.* [CALICE Collaboration], *Response of the CALICE Si-W electromagnetic calorimeter physics prototype to electrons*, Nucl. Instrum. Meth. **A 608** (2009) 372.

[13] C. Adloff *et al.* [CALICE Collaboration], *Electromagnetic response of a highly granular hadronic calorimeter*, JINST **6** (2011) P04003.

[14] C. W. Fabjan *et al.*, *Iron Liquid - Argon and Uranium Liquid - Argon Calorimeters for Hadron Energy Measurement*, Nucl. Instrum. Meth. **141** (1977) 61.

[15] T. A. Gabriel *et al.*, *Energy dependence of hadronic activity*, Nucl. Instrum. Meth. A **338** (1994) 336.

[16] M. Derrick *et al.*, *Design and construction of the ZEUS barrel calorimeter*, Nucl. Instrum. Meth. **A 309** (1991) 77.

[17] A. Andresen *et al.*, *Construction and beam test of the ZEUS forward and rear calorimeter*, Nucl. Instrum. Meth. **A 309** (1991) 101.

[18] G. d'Agostini *et al.*, *Experimental Study Of Uranium Plastic Scintillator Calorimeters*, Nucl. Instrum. Meth. **A 274** (1989) 134.

[19] H. Abramowicz *et al.*, *The Response And Resolution Of An Iron Scintillator Calorimeter For Hadronic And Electromagnetic Showers Between 10 GeV And 140 GeV*, Nucl. Instrum. Meth. **180** (1981) 429.

[20] B. Andrieu *et al.*, *Results from pion calibration runs for the H1 liquid argon calorimeter and comparisons with simulations*, Nucl. Instrum. Meth. **A 336** (1993) 499.

[21] C. Cojocaru *et al.*, *Hadronic calibration of the ATLAS liquid argon end-cap calorimeter in the pseudorapidity region 1.6* $< |\eta| <$ *1.8 in beam tests*, Nucl. Instrum. Meth. **A 531** (2004) 481.

[22] S. Agostinelli *et al.* [GEANT4 Collaboration], GEANT4*: A Simulation toolkit*, Nucl. Instrum. Meth. **A 506** (2003) 250.

[23] A. Ribon *et al.*, *Status of* GEANT4 *hadronic physics for the simulation of LHC experiments at the start of LHC physics program*, CERN-LCGAPP-2010-002 (2010).

計画研究 B01 班

課題名「LHC 時代の新しい初期宇宙像」

研究組織

(1) 研究代表者

山口　昌弘　(YAMAGUCHI, Masahiro)
東北大学・大学院理学研究科・教授
研究者番号：10222366

(2) 研究分担者

諸井　健夫　(MOROI, Takeo)
東京大学・大学院理学系研究科・教授
研究者番号：60323997

(3) 連携研究者

高橋　史宣　(TAKAHASHI, Fuminobu)
東北大学・大学院理学研究科・准教授
研究者番号：60503878

交付決定額

計画研究 B01 班に配分された交付額を表 1 に示す。

表 1. 交付決定額（配分額）　（金額単位：円）

年度	直接経費	間接経費	合計
平成 23 年度	7,400,000	2,220,000	9,620,000
平成 24 年度	10,800,000	3,240,000	14,040,000
平成 25 年度	10,900,000	3,270,000	14,170,000
平成 26 年度	10,300,000	3,090,000	13,390,000
平成 27 年度	10,300,000	3,090,000	13,390,000
総計	49,700,000	14,910,000	64,610,000

研究成果

1. 研究開始当初の背景

宇宙進化、特に初期宇宙の出来事に関しては未知の点が多く残されている。特に、宇宙暗黒物質の正体、宇宙のバリオン・反バリオン非対称性の期限、インフレーションの機構など、宇宙の成り立ちを理解する上でも重要となる問題については、まだ全くと言って良いほど何もわかっていない。これら重要な問題の解決には、素粒子標準理論を超える物理の理解が必要不可欠である。そして、高エネルギー実験・宇宙観測の結果が多数得られると期待される今後数年間こそ、それらをもとに、初期宇宙に関する理空きを飛躍的に進歩させる時期となる。

2. 研究の目的

本研究の目的は、このような重要な時期に、本領域を構成する多方面の実験物理学者や様々な分野の素粒子理論研究者との密接な協力のもと、初期宇宙に関する研究を行い、初期宇宙像を確立させることにある。特に重要な以下のテーマについては、初期段階から研究を進め、結論を得たい：(1)素粒子模型の確立と宇宙論の構築、(2)暗黒物質の起源と生成過程の解明、(3)テラスケールの物理の宇宙進化への影響、(4)インフレーションの理解。そしてその結果をもとに、宇宙進化のシナリオを理解し、初期宇宙像を確立させる。

3. 研究の方法

実験研究者との密接な連携のもと、素粒子理論および宇宙理論的な考察と数値計算に基づき研究を進める。

4. 研究成果

LHC 実験において、125GeV の質量を持つヒッグス粒子が発見されたことは、素粒子標準模型の確立のみならず、標準模型を超える物理の方向性、さらにそれに基づく宇宙論に大きな影響を与えている。本研究計画ではヒッグス粒子の発見を踏まえつつ多岐にわたる研究を行ってきた。以下に主な研究成果をあげる。

ヒッグス粒子発見が超対称標準模型に与える示唆についての研究

LHC 実験で発見された 125GeV のヒッグス粒子の質量を超対称理論で説明するには、超対称粒子が重いか、最少超対称標準模型を拡張する必要がある。

１）ゲージ一重項を加えた超対称標準模型の拡張について詳細に研究した。特に、Peccei-Quinn 対称性を持つ模型を構成するとともに、ヒッグスセクターとその超対称対からの量子補正によってヒッグス粒子の質量を 125GeV まで大きくすることができることを示した。また、一重項スカラー粒子が軽い場合には、ゲージ二重項のヒッグス粒子との混合により後者の質量が 125GeV まで増大できることを示した。これらの模型における暗黒物質の性質など宇宙論的影響を考察した。

２）超対称粒子の質量スケールは 10TeV 程度にあるという可能性（高スケール超対称模型）の重要性を指摘し、将来そのような模型の実験的検証が可能であるかを議論した。そのような模型においては、特に Wino が暗黒物質となる可能性があるが、暗黒物質直接探査実験によってその可能性がどの程度検証できるかの定量的解析を行った。さらに、Wino 粒子の LHC 実験における発見可能性を議論するとともに、フレーバーの破れ実験等を用いて高スケール超対称模型を検証する可能性についても研究を行った。

超対称 Peccei-Quinn 模型に基づく宇宙論の研究

超対称化された Peccei-Quinn 模型に基づく宇宙進化について、宇宙初期の熱的プラズマがアクシオンやその超対称パートナーであるアクシーノの運動に与える影響を特に考慮しつつ、研究を行った。そして、宇宙初期のプラズマとの相互作用によるスカラー場の振動の減衰は通常無視されているが、特にアクシーノ場に関しては、プラズマとの相互作用がその運動に大きな影響を与え得ることを明らかにした。

ヒッグスインフレーション

LHC 実験によって発見されたヒッグス粒子がインフレーションを引き起こす可能性について検証した。具体的には，運動項のヒッグス場自身への依存性を用いることでインフレーションを実現する running kinetic inflation を提唱し，特に BICEP2 実験の結果と整合する事を示した．またヒッグス粒子の質量から示唆されるプランクスケールにおける縮退した真空との間のドメインウォールがインフレーションを起こす可能性を指摘した．

ヒッグス粒子と暗黒輻射

ヒッグスセクターをポータルとして隠れたゲージ対称性と結合しているシナリオにおいて，隠れたゲージ粒子が暗黒輻射として現在のエネルギーに寄与する可能性を提唱した．特に，暗黒輻射の存在量とヒッグスの invisible decay とが相関しており，宇宙的な観測と LHC 実験が相補的な制限を与えることを示した．特にこの暗黒輻射は自己相互作用を持っており，将来の CMB 観測からその粘性パラメターへの制限，発見が期待できる．

領域との関係

素粒子論的宇宙論の研究を進め、新たな宇宙像を確立していくには、LHC におけるヒッグス粒子の発見と性質の研究及び新現象の探索に関する情報が不可欠である。本研究班は、本領域における LHC 実験に関わるグループ、とりわけヒッグス粒子に関する実験的研究（A01）、標準模型を超える物理の探索（A02）、テラスケール物理の現象論的研究（A06）との密接な連携により新たな方向性を見出していこうとしている。さらに、関連する素粒子物理学の理論的研究、特に B02 班で進めている標準模型を超える物理へのアプローチや、B03 班の弦理論からのアプローチ、B04 班によるフレーバーの物理からの知見を活かしながら研究を進めることができた。これらの連携にあたっては、領域全体で行ってきたシンポジウムや研究集会が非常に有効であった。

５．主な発表論文等

（研究代表者、研究分担者及び連携研究者には下線）

1. K. S. Jeong, Y. Shoji, and M. Yamaguchi, Peccei-Quinn invariant extension of the NMSSM, JHEP 1204 (2012) 022

2. K. S. Jeong, M. Shimosuka, and M. Yamaguchi, Light Higgsino in Heavy Gravitino Scenario with Successful Electroweak Symmetry Breaking, JHEP 1209 (2012) 050

3. K. S. Jeong, Y. Shoji, and M. Yamaguchi, Singlet-Doublet Higgs Mixing and its Implications on the Higgs Mass in the PQ-NMSSM, JHEP 1209 (2012) 007

4. K. Choi, S.H. Im, K.S. Jeong, and M. Yamaguchi, Higgs mixing and diphoton rate enhancement in
NMSSM models, JHEP 1302 (2013) 090

5. K.S. Jeong, Y. Shoji and M. Yamaguchi, Higgs Mixing in the NMSSM and Light Higgsinos, JHEP 1411, 148 (2014)

6. T. Moroi and K. Nakayama, Domain Walls and Gravitational Waves after Thermal Inflation, Phys. Lett. B703, 160 (2011)

7, M. Asano, T. Moroi and N. Yokozaki, Singlet Boson in Supersymmetric Model as a Mimic of the Standard Model Higgs at the LHC, Phys. Lett. B708, 280 (2012)

8. M. Asano, T. Moroi, R. Sato and T.T. Yanagida, Non-anomalous Discrete R-symmetry, Extra Matters, and Enhancement of the Lightest SUSY Higgs Mass, Phys. Lett. B705, 337 (2011)

9. M. Asano, T. Moroi, R. Sato and T.T. Yanagida, Focus Point Assisted by Right-Handed Neutrinos, Phys. Lett. B708, 107 (2012)

10. M. Asano, T. Ito, S. Matsumoto and T. Moroi, Exploring Supersymmetric Model with Very

Light Gravitino at the LHC, JHEP1203, 011 (2012)
11. K. Hamaguchi, T. Moroi and K. Mukaida, Boltzmann equation for non-equilibrium particles and its application to non-thermal dark matter production, JHEP1201, 083 (2012)
12. R. Jinno, T. Moroi and K. Nakayama, Imprints of Cosmic Phase Transition in Inflationary Gr avitational Waves, Phys. Lett. B713, 129 (2012)
13. T. Moroi, R. Sato and T.T. Yanagida, Extra Matters Decree the Relatively Heavy Higgs of Mass about 125 GeV in the Supersymmetric Model, Phys. Lett. B709, 218 (2012)
14. T. Moroi and K. Nakayama, Wino LSP detection in the light of recent Higgs searches at the LHC, Phys. Lett. B710, 159 (2012)
14. T. Moroi and M. Takimoto, Thermal Effects on Saxion in Supersymmetric Model with Peccei-Quinn Symmetry, Phys. Lett. B718, 105 (2012)
15. R. Jinno, T. Moroi and K. Nakayama, Probing dark radiation with inflationary gravitational waves, Phys. Rev. D86, 123502 (2012)
16. T. Moroi, T.T. Yanagida and N. Yokozaki, Enhanced Higgs Mass in a Gaugino Mediation Model without the Polonyi Problem, Phys. Lett. B719, 148 (2013)
17. T. Moroi and M. Nagai, Probing Supersymmetric Model with Heavy Sfermions Using Leptonic Flavor and CP Violations, Phys. Lett. B723, 107 (2013)
18. T. Moroi, M. Nagai and M. Takimoto, Non-Thermal Production of Wino Dark Matter via the Decay of Long-Lived Particles, JHEP1307, 066 (2013)
19. M. Ibe, S. Iwamoto, S. Matsumoto, T. Moroi and N. Yokozaki, Recent Result of the AMS-02 Experiment and Decaying Gravitino Dark Matter in Gauge Mediation, JHEP1308, 029 (2013)
20. T. Moroi, K. Mukaida, K. Nakayama and M. Takimoto, Scalar Trapping and Saxion Cosmology, JHEP1306, 040 (2013)
21. T. Moroi, M. Nagai and T.T. Yanagida, Lepton Flavor Violations in High-Scale SUSY with Right-Handed Neutrinos, Phys. Lett. B728, 342 (2014)
22. R. Jinno, T. Moroi and K. Nakayama, Inflationary Gravitational Waves and the Evolution of the Early Universe, JCAP1401, 040 (2014)
23. M. Endo, K. Hamaguchi, S. Iwamoto, T. Kitahara and T. Moroi, Reconstructing Supersymmetric Contribution to Muon Anomalous Magnetic Dipole Moment at ILC, Phys. Lett. B728, 274 (2014)
24. Y. Ema, R. Jinno and T. Moroi, Cosmic-Ray Neutrinos from the Decay of Long-Lived Particle and the Recent IceCube Result, Phys. Lett. B733, 120 (2014)
25. K. Hamaguchi, S.P. Liew, T. Moroi and Y. Yamamoto, Isospin-Violating Dark Matter with Colored Mediators, JHEP 1405, 086 (2014)
26. K. Hamaguchi, T. Moroi and T. Terada, Complexified Starobinsky Inflation in Supergravity

in the Light of Recent BICEP2 Result, Phys. Lett. B733, 305 (2014)
27. R. Jinno, T. Moroi and T. Takahashi, Studying Inflation with Future Space-Based Gravitational Wave Detectors, JCAP1412, no. 12, 006 (2014)
28. T. Moroi, K. Mukaida, K. Nakayama and M. Takimoto, Axion Models with High Scale Inflation, JHEP 1411, 151 (2014)
29. Y. Ema, R. Jinno and T. Moroi, Cosmological Implications of High-Energy Neutrino Emission from the Decay of Long-Lived Particle, JHEP 1410, 150 (2014)
30. M. Endo, T. Moroi and M.M. Nojiri, Footprints of Supersymmetry on Higgs Decay, JHEP 1504, 176 (2015)
31. K. Hamaguchi, T. Moroi and K. Nakayama, AMS-02 Antiprotons from Annihilating or Decaying Dark Matter, Phys. Lett. B747, 523 (2015)
32. K. Nakayama and F. Takahashi, Low-scale Supersymmetry from Inflation, JCAP 1110, 033 (2011)
33. K. Nakayama and F. Takahashi, Higgs mass and inflation, Phys. Lett. B707, 142 (2012)
34. K. Nakayama, F. Takahashi and T.T. Yanagida, On the Adiabatic Solution to the Polonyi/Moduli Problem, Phys. Rev. D84, 123523 (2011)
35. K. Nakayama, F. Takahashi and T.T. Yanagida, Cosmological Moduli Problem in Low Cutoff Theory, Phys. Rev. D86, 043507 (2012)
36. K.S. Jeong and F. Takahashi, Light Higgsino from Axion Dark Radiation, JHEP 1208, 017 (2012)
37. K. Nakayama and F. Takahashi, PeV-scale Supersymmetry from New Inflation, JCAP 1205, 035 (2012)
38. K. Nakayama, F. Takahashi and T.T. Yanagida, Gravity mediation without a Polonyi problem, Phys. Lett. B714, 256 (2012)
39. K. Nakayama and F. Takahashi, Alchemical Inflation: inflaton turns into Higgs, JCAP 1211, 007 (2012)
40. T. Higaki, K. Kamada and F. Takahashi, Higgs, Moduli Problem, Baryogenesis and Large Volume Compactifications, JHEP 1209, 043 (2012)
41. T. Higaki and F. Takahashi, Dark Radiation and Dark Matter in Large Volume Compactifications, JHEP 1211, 125 (2012)
42. H. Fukushima, R. Kitano and F. Takahashi, Cosmologically viable gauge mediation, JHEP 1302, 140 (2013)
43. K. Nakayama, F. Takahashi and T.T. Yanagida, Eluding the Gravitino Overproduction in Inflaton Decay, Phys. Lett. B718, 526 (2012)
44. K.S. Jeong and F. Takahashi, A Gravitino-rich Universe, JHEP 1301, 173 (2013)

45. T. Higaki, K.S. Jeong and F. Takahashi, Hybrid inflation in high-scale supersymmetry, JHEP 1212, 111 (2012)
46. M. Kawasaki, F. Takahashi and T. Takesako, Hubble-induced mass from MSSM plasma, JCAP 1304, 008 (2013)
47. K.S. Jeong and F. Takahashi, Axionic Co-genesis of Baryon, Dark Matter and Dark Radiation, JHEP 1304, 121 (2013)
48. T. Higaki, K.S. Jeong and F. Takahashi, A Parallel World in the Dark, JCAP 1308, 031 (2013)
49. K.S. Jeong and F. Takahashi, Self-interacting Dark Radiation, Phys. Lett. B725, 134 (2013)
50. F. Takahashi, New inflation in supergravity after Planck and LHC, Phys. Lett. B727, 21 (2013)
51. H. Ishida, K.S. Jeong and F. Takahashi, Longevity Problem of Sterile Neutrino Dark Matter, Phys. Lett. B731, 242 (2014)
52. K.S. Jeong, M. Kawasaki and F. Takahashi, Axions as Hot and Cold Dark Matter, JCAP 1402, 046 (2014)
53. K. Ishiwata, K.S. Jeong and F. Takahashi, Moduli-induced Baryogenesis, JHEP 1402, 062 (2014)
54. H. Ishida, K.S. Jeong and F. Takahashi, 7 keV sterile neutrino dark matter from split flavor mechanism, Phys. Lett. B732, 196 (2014)
55. T. Higaki, K.S. Jeong and F. Takahashi, The 7 keV axion dark matter and the X-ray line signal, Phys. Lett. B733, 25 (2014)
56. M. Czerny, T. Higaki and F. Takahashi, Multi-Natural Inflation in Supergravity, JHEP 1405, 144 (2014)
57. K. Nakayama and F. Takahashi, Higgs Chaotic Inflation and the Primordial B-mode Polarization Discovered by BICEP2, Phys. Lett. B734, 96 (2014)
58. K. Nakayama, F. Takahashi and T.T. Yanagida, Anomaly-free flavor models for Nambu-Goldstone bosons and the 3.5 keV X-ray line signal, Phys. Lett. B734, 178 (2014)
59. H. Murayama, K. Nakayama, F. Takahashi and T.T. Yanagida, Sneutrino Chaotic Inflation and Landscape, Phys. Lett. B738, 196 (2014)
60. T. Higaki and F. Takahashi, Natural and Multi-Natural Inflation in Axion Landscape, JHEP 1407, 074 (2014)
61. M. Kawasaki, N. Kitajima and F. Takahashi, Relaxing Isocurvature Bounds on String Axion Dark Matter, Phys. Lett. B737, 178 (2014)
62. T. Higaki, N. Kitajima and F. Takahashi, Hidden axion dark matter decaying through mixing with QCD axion and the 3.5 keV X-ray line, JCAP 1412, 004 (2014)

63. N. Kitajima and F. Takahashi, Gravitational waves from Higgs domain walls, Phys. Lett. B745, 112 (2015)

主要論文別刷

1. K. S. Jeong, Y. Shoji, and M. Yamaguchi, “Peccei-Quinn invariant extension of the NMSSM”, JHEP 1204 (2012) 022

4. K. Choi, S.H. Im, K.S. Jeong, and M. Yamaguchi, “Higgs mixing and diphoton rate enhancement in NMSSM models”, JHEP 1302 (2013) 090

14. T. Moroi and K. Nakayama, “Wino LSP detection in the light of recent Higgs searches at the LHC”, Phys. Lett. B710, 159 (2012)

31. K. Hamaguchi, T. Moroi and K. Nakayama, “AMS-02 Antiprotons from Annihilating or Decaying Dark Matter”, Phys. Lett. B747, 523 (2015)

63. N. Kitajima and F. Takahashi, “Gravitational waves from Higgs domain walls”, Phys. Lett. B745, 112 (2015)

Published for SISSA by Springer

Received: December 12, 2011
Revised: February 28, 2012
Accepted: March 4, 2012
Published: April 4, 2012

Peccei-Quinn invariant extension of the NMSSM

Kwang Sik Jeong, Yutaro Shoji and Masahiro Yamaguchi

Department of Physics, Tohoku University,
Sendai 980-8578, Japan

E-mail: ksjeong@tuhep.phys.tohoku.ac.jp, yshoji@tuhep.phys.tohoku.ac.jp, yama@tuhep.phys.tohoku.ac.jp

Abstract: We study a Peccei-Quinn invariant extension of the next-to-minimal supersymmetric Standard Model (NMSSM), which turns out to be free from the tadpole and domain wall problems. Having a non-renormalizable coupling to the axion superfield, the SM singlet added to the Higgs sector can naturally generate an effective Higgs μ term around the weak scale. In the model, the lightest neutralino is dominated by the singlino, which gets a mass only through mixing with the neutral Higgsinos. We explore the phenomenological consequences resulting from the existence of such a relatively light neutralino. The coupling of the SM singlet to the Higgs doublets is constrained by the experimental bound on the invisible Z-boson decay width. Under this constraint, we examine the properties of the SM-like Higgs boson paying attention to its mass and decays. We also demonstrate a UV completion of the model in SU(5) grand unified theory with a missing-partner mechanism.

Keywords: Higgs Physics, Supersymmetric Standard Model

ArXiv ePrint: 1112.1014

© SISSA 2012

doi:10.1007/JHEP04(2012)022

JHEP04(2012)022

Contents

1 Introduction **1**

2 PQ-invariant extension of the NMSSM **2**
2.1 Model 3
2.2 Constraints on the model parameters 6

3 Low energy Higgs sector **7**
3.1 Effective theory below the SUSY breaking scale 8
3.2 Phenomenological aspects 10

4 UV completion **12**

5 Conclusions **15**

A Mass matrix **16**

B Global structure of the Higgs potential **17**

C RG running equations **19**

1 Introduction

The next-to-minimal supersymmetric Standard Model (NMSSM) introduces a SM singlet S to explain the origin of a supersymmetric Higgs μ term of the MSSM [1, 2]. However, if S is a true singlet under all symmetries, it becomes difficult to embed the NMSSM into a more fundamental theory such as a grand unified theory (GUT). This is because the GUT partners of the MSSM Higgs doublets also couple to S and radiatively generate a large tadpole for S, destabilizing the gauge hierarchy [3–6]. Non-renormalizable interactions are another source of large tadpoles [7–9]. A symmetry under which S transforms non-trivially can solve the tadpole problem, but generally introduces another problem. If one considers a discrete symmetry, dangerous domain walls would be formed in the early universe [10, 11]. On the other hand, a global symmetry spontaneously broken by S and the Higgs doublets would give rise to an unacceptable visible axion. Additional structure is thus needed to generate μ dynamically from the coupling of S to the Higgs doublets while providing a viable framework for the grand unification.

In this paper, we point out that the difficulties arising due to the singlet S can be avoided in a Peccei-Quinn invariant extension of the NMSSM (PQ-NMSSM) where the PQ symmetry is spontaneously broken at a scale much higher than the weak scale by the axion superfield. The PQ symmetry forbids the generation of large tadpoles for S while solving

JHEP04(2012)022

the strong CP problem [12, 13]. Furthermore, the domain wall problem can be resolved in the presence of PQ messengers that couple to the axion superfield. It also turns out that a non-renormalizable coupling of S to the axion superfield naturally leads S to get a vacuum expectation value around the weak scale.

The Higgs and neutralino sectors are considerably modified by the addition of S. In the PQ-NMSSM, the lightest neutralino consists mostly of the singlino because it acquires a small mass through mixing with the neutral Higgsinos after the electroweak symmetry breaking. The presence of such a relatively light neutralino leads to phenomenological consequences different from other NMSSM models. In particular, the LEP bound on the invisible Z-boson decay width places a stringent constrain on the coupling of S to the Higgs doublets if the decay mode is kinematically allowed. This constraint becomes important at large $\tan\beta$. We also note that loops involving the Yukawa coupling of the singlino give an additional positive contribution to the SM-like Higgs mass. This contribution is insensitive to $\tan\beta$, and arises when the Higgsinos are lighter than other MSSM sparticles. Another interesting feature is that the decay of the SM-like Higgs boson into a pair of the lightest neutralino can be dominant at low $\tan\beta$.

Since interactions of S are controlled by the PQ symmetry, it is possible to embed the PQ-NMSSM into GUT models without the tadpole problem. The associated UV completion is then related to the doublet-triplet splitting problem. We find that incorporating the PQ symmetry in a missing-partner model for supersymmetric SU(5) GUT [14, 15] can lead to the PQ-NMSSM at low energy scales. In addition, it naturally achieves a phenomenologically acceptable value of the axion decay constant as $F_a \sim \sqrt{M_{\rm SUSY} M_{\rm Pl}}$ with $M_{\rm SUSY}$ being the SUSY breaking scale. The PQ symmetry is also important for suppressing harmful dimension 5 operators for proton decays.

This paper is organized as follows. In the next section, we present the model and discuss its general properties and various constraints on the singlet couplings. Then, in section 3, we construct a low energy effective theory below the SUSY breaking scale to examine the phenomenological aspects resulting from the existence of a singlino-like light neutralino. Section 4 is for the discussion on how to UV complete the model. The PQ-NMSSM can arise as a low energy theory of a missing-partner GUT model. Section 5 is the conclusion.

2 PQ-invariant extension of the NMSSM

In this section, we extend the NMSSM[1] to incorporate the PQ symmetry and study the properties of the model. The PQ-invariant extension turns out not only to provide a solution to the strong CP problem [28–30] but also to solve both the tadpole and domain wall problems. We also examine constraints on the coupling of S to the Higgs doublets.

[1]Extensions of the MSSM with a SM singlet have been received revived attention [16–27] after the first results on the Higgs search at the LHC had been announced.

JHEP04(2012)022

2.1 Model

In the PQ-NMSSM, an effective Higgs μ term is generated by the vacuum expectation value of S which couples to the Higgs doublets and to the axion superfield X through the PQ-invariant interactions

$$\mathcal{L} = \int d^2\theta \lambda S H_u H_d + \int d^4\theta \, \kappa \frac{X^{*2}}{M_{\rm Pl}} S + \text{h.c.}\,, \tag{2.1}$$

for (X, S, H_u, H_d) carrying the PQ charges as $(1, 2, -1, -1)$. All other terms involving S are forbidden by the PQ symmetry in the renormalizable superpotential. A superpotential term $X^2 H_u H_d / M_{\rm Pl}$, which is allowed by $\mathrm{U}(1)_{\rm PQ}$, can be removed by a holomorphic redefinition of S without loss of generality. Here we have taken such a field basis.

In the following, we assume that a mechanism to stabilize X is operative with its vacuum expectation value fixed at $10^{10\text{–}12}$ GeV as required by cosmological and astrophysical observations. As suppressed by $M_{\rm Pl}$, the interactions between X and other scalar fields rarely affect the saxion potential at $|S| \ll |X| \ll M_{\rm Pl}$. The Higgs potential can thus be examined by replacing X with its vacuum expectation value. Then, the involved mass parameters are determined by the SUSY breaking scale $M_{\rm SUSY}$ and the axion decay constant $F_a \sim |X|$. We note that, when treating X as a spurion field, the present model can be regarded as the nMSSM,[2] where the superpotential contains an effective tadpole for S:

$$W_{\rm eff} = \lambda S H_u H_d + m_0^2 (1 + \theta^2 B_\kappa) S\,, \tag{2.2}$$

with $B_\kappa \sim M_{\rm SUSY}$ and

$$m_0^2 \sim \kappa M_{\rm SUSY} \frac{F_a^2}{M_{\rm Pl}}\,. \tag{2.3}$$

The appearance of m_0^2 and B_κ terms can be understood by promoting κ to a function depending on SUSY breaking fields in a hidden sector. It is obvious that the model does not suffer from the tadpole problem because a tadpole for S requires a higher dimensional coupling of S to X as dictated by $\mathrm{U}(1)_{\rm PQ}$. For $F_a = 10^{10\text{–}12}$ GeV, $M_{\rm SUSY} \sim 1$ TeV and κ less than order unity, the value of m_0 can naturally be around the weak scale. Hence, it is natural to expect that electroweak symmetry breaking would occur at the correct scale. In fact, the same spirit is shared with the Kim-Nilles mechanism [38] that explains the smallness of μ in extensions of the MSSM with $\mathrm{U}(1)_{\rm PQ}$. Since S and $H_{u,d}$ carry $\mathrm{U}(1)_{\rm PQ}$ charges and develop vacuum expectation values, the Higgs and neutralino sectors have small mixing with X suppressed by F_a.

Let us now examine the vacuum structure of the low energy effective theory given by (2.2). Including soft SUSY breaking terms, the scalar potential of the extended Higgs

[2] The nMSSM [31, 32] assumes specific discrete R symmetries to ensure the absence of large tadpoles for S. A general discussion on the phenomenological aspects of the nMSSM for small $\tan\beta$ can be found in [32–36]. Some cosmological issues have also been discussed in [34–36]. Neglecting small mixing with the axion superfield, the Higgs and neutralino sectors of the PQ-NMSSM have the same phenomenological properties as the nMSSM. However, the cosmological properties can be different depending on the cosmological evolution of the saxion. A continuous symmetry to restrict couplings of S in the NMSSM has been introduced in [37], where it is explicitly broken only by a linear superpotential of S.

JHEP04(2012)022

sector reads

$$
\begin{aligned}
V = & \frac{1}{8}(g^2+g'^2)(|H_u|^2-|H_d|^2)^2+\frac{1}{2}g^2|H_u^\dagger H_d|^2 \\
& +|\lambda H_u H_d + m_0^2|^2 + |\lambda|^2|S|^2(|H_u|^2+|H_d|^2) \\
& + m_{H_u}^2|H_u|^2 + m_{H_d}^2|H_d|^2 + m_S^2|S|^2 + (A_\lambda \lambda S H_u H_d - B_\kappa m_0^2 S + \text{h.c.})\,, \qquad (2.4)
\end{aligned}
$$

where m_i^2 is a soft scalar mass squared, and A_λ is a soft A-parameter. The potential contains four complex parameters, λ, A_λ, m_0^2 and B_κ. Among them, λ and m_0^2 can be made real and positive by a field redefinition of $H_{u,d}$ and X. Furthermore, if $\arg(A_\lambda) = \arg(B_\kappa)$, one can rotate away the phases of A_λ and B_κ by redefining S. We will assume this is the case, for which CP invariance is preserved in the Higgs sector and there is no mixing between scalar and pseudo-scalar fields. From the above scalar potential, it is straightforward to get the conditions for electroweak symmetry breaking. Similarly as in the MSSM, two of them can be written

$$
\begin{aligned}
\frac{1}{2}M_Z^2 &= \frac{m_{H_d}^2 - m_{H_u}^2 \tan^2\beta}{\tan^2\beta - 1} - \mu_{\text{eff}}^2\,, \\
\sin 2\beta &= \frac{2b_{\text{eff}}}{m_{H_d}^2 + m_{H_u}^2 + 2\mu_{\text{eff}}^2 + \lambda^2 v^2}\,, \qquad (2.5)
\end{aligned}
$$

for μ_{eff} and b_{eff} defined by

$$
\mu_{\text{eff}} = \lambda v_S\,, \qquad b_{\text{eff}} = \lambda(A_\lambda v_S + m_0^2)\,, \qquad (2.6)
$$

where $\langle|H_u^0|\rangle = v\sin\beta$ and $\langle|H_d^0|\rangle = v\cos\beta$ with $v = 174\,\text{GeV}$. The value of $|S|$ at the vacuum is fixed as

$$
v_S = \frac{A_\lambda \lambda v^2 \sin 2\beta + 2B_\kappa m_0^2}{2(m_S^2 + \lambda^2 v^2)}\,. \qquad (2.7)
$$

The tree-level mass matrices for the scalar fields are presented in the appendix A.

To explore the global structure of the potential, one can substitute S by the solution of $\partial_S V = 0$. Then, the Higgs potential (2.4) is written

$$
V = V|_{S=0} - \frac{|A_\lambda \lambda H_u H_d - B_\kappa m_0^2|^2}{m_S^2 + |\lambda|^2(|H_u|^2+|H_d|^2)}\,, \qquad (2.8)
$$

which increases monotonically along the D-flat direction $|H_u^0| = |H_d^0|$ when

$$
R_1 \geq 1 \quad \text{and} \quad 3R_1 \geq 2 + R_2\,, \quad \text{or} \quad 1 \geq R_1^3 \geq R_2\,, \qquad (2.9)
$$

where $R_{1,2}$ are defined by $R_1 m_S^2 = |(2\mu_{\text{eff}} - A_\lambda)m_S^2 + (2\mu_{\text{eff}} - A_\lambda \sin 2\beta)\lambda^2 v^2|^{2/3}$ and $R_2 m_S^2 = (2\mu_{\text{eff}} - A_\lambda)^2 - 2(m_{H_u}^2 + m_{H_d}^2 + 2\mu_{\text{eff}}^2 - 2b_{\text{eff}})$. If the above condition is not satisfied, the potential may develop another minimum away from the weak scale.[3] The involved soft

[3] Actually a minimum of the potential does not lie in the D-flat direction unless $m_{H_u}^2 = m_{H_d}^2$. However, as will be shown in the appendix B, a minimum other than the electroweak vacuum, if exists, is located near the D-flat direction for much of the parameter space. This justifies our approach of examining the D-flat direction to see when there can be another minimum. See also [39], where the stability of the electroweak vacuum has been examined within the framework of the effective Lagrangian beyond the MSSM.

JHEP04(2012)022

parameters are then constrained by the requirement that the electroweak vacuum should be a global minimum. For $m_S^2 \sim M_{\rm SUSY}^2 \gg \mu_{\rm eff}^2$, which is the case we shall focus on, the stability condition (2.9) requires $A_\lambda^2 \lesssim m_S^2$ or $m_S^2 \lesssim A_\lambda^2 \lesssim m_A^2$ with m_A being the mass of the CP-odd neutral Higgs boson. Keeping this in mind, we will consider also the case with $A_\lambda \sim M_{\rm SUSY}$, which is favored to avoid large mixing of the SM-like Higgs scalar with the singlet scalar when $\mu_{\rm eff}$ and $\tan\beta$ are large.

An important consequence of $\mathrm{U}(1)_{\rm PQ}$ is the appearance of a relatively light neutralino with a large singlino component. This is because the PQ symmetry prevents the singlino $\tilde{S}$ from having a supersymmetric mass. The lightest neutralino is mostly singlino if the masses of the bino $\tilde{B}$ and wino $\tilde{W}$ are larger than λv, as is the case for $\lambda \lesssim 1$. The neutralino mass matrix for $(\tilde{B}, \tilde{W}^0, \tilde{H}_d^0, \tilde{H}_u^0, \tilde{S})$ is given by

$$\begin{pmatrix} M_{\tilde{B}} & 0 & -M_Z \sin\theta_W \cos\beta & M_Z \sin\theta_W \sin\beta & 0 \\ 0 & M_{\tilde{W}} & M_Z \cos\theta_W \cos\beta & -M_Z \cos\theta_W \sin\beta & 0 \\ -M_Z \sin\theta_W \cos\beta & M_Z \cos\theta_W \cos\beta & 0 & -\mu_{\rm eff} & -\lambda v \sin\beta \\ M_Z \sin\theta_W \sin\beta & -M_Z \cos\theta_W \sin\beta & -\mu_{\rm eff} & 0 & -\lambda v \cos\beta \\ 0 & 0 & -\lambda v \sin\beta & -\lambda v \cos\beta & 0 \end{pmatrix}, \tag{2.10}$$

where θ_W is the weak mixing angle. If we write the lightest neutralino as a linear combination of $(\tilde{B}, \tilde{W}^0, \tilde{H}_d^0, \tilde{H}_u^0, \tilde{S})$:

$$\tilde{\chi}_1^0 = N_1^{\tilde{B}} \tilde{B} + N_1^{\tilde{W}} \tilde{W}^0 + N_1^{\tilde{H}_d^0} \tilde{H}_d^0 + N_1^{\tilde{H}_u^0} \tilde{H}_u^0 + N_1^{\tilde{S}} \tilde{S}\,, \tag{2.11}$$

then we find

$$\begin{aligned} N_1^{\tilde{S}} &= 1 - \frac{1}{2}(1+\cdots)\epsilon_{\tilde{H}}^2\,, \\ N_1^{\tilde{H}_u^0} &= -\epsilon_{\tilde{H}}(\sin\beta + \cdots)\,, & N_1^{\tilde{H}_d^0} &= -\epsilon_{\tilde{H}}(\cos\beta + \cdots)\,, \\ N_1^{\tilde{B}} &= -\epsilon_{\tilde{B}}\epsilon_{\tilde{H}}(1+\cdots)\,, & N_1^{\tilde{W}} &= \epsilon_{\tilde{W}}\epsilon_{\tilde{H}}(1+\cdots)\,, \end{aligned} \tag{2.12}$$

for $\epsilon_{\tilde{H}}^2 \ll 1$ and $|\epsilon_{\tilde{B},\tilde{W}}| \ll 1$. Here the epsilon parameters are defined by

$$\epsilon_{\tilde{H}} \equiv \frac{\lambda v}{\mu_{\rm eff}}\,, \qquad \epsilon_{\tilde{B}} \equiv \frac{g' v \cos 2\beta}{\sqrt{2} M_{\tilde{B}}}\,, \qquad \epsilon_{\tilde{W}} \equiv \frac{g v \cos 2\beta}{\sqrt{2} M_{\tilde{W}}}\,, \tag{2.13}$$

and the ellipsis indicates terms of higher orders in $\epsilon_{\tilde{H}}^2$ or $\epsilon_{\tilde{B},\tilde{W}}$. One can see that $\epsilon_{\tilde{H}} \neq 0$ is needed to make $\tilde{\chi}_1^0$ massive through mixing. In the following discussion, we will neglect small gaugino components of $\tilde{\chi}_1^0$ since it does not change our results substantially. Then, one can find

$$\begin{aligned} m_{\tilde{\chi}_1^0} &\simeq 2\Big(\mu_{\rm eff} N_1^{\tilde{H}_u^0} N_1^{\tilde{H}_d^0} + \lambda v N_1^{\tilde{H}_u^0} N_1^{\tilde{S}} \cos\beta + \lambda v N_1^{\tilde{H}_d^0} N_1^{\tilde{S}} \sin\beta\Big) \\ &= \frac{\lambda^2 v^2 \sin 2\beta}{\mu_{\rm eff}}\left(1 - \frac{\lambda^2 v^2}{\mu_{\rm eff}^2} + \mathcal{O}\left(\frac{\lambda^4 v^4}{\mu_{\rm eff}^4}\right)\right). \end{aligned} \tag{2.14}$$

As we will discuss later, the singlino-like neutralino with a small mass can considerably change the phenomenological properties of the model.

JHEP04(2012)022

Meanwhile, there can exist PQ messengers $\Psi + \bar{\Psi}$ which are vector-like under the SM gauge group and obtain heavy masses from the coupling $X\Psi\bar{\Psi}$ in the superpotential. Such interaction can play an important role in the saxion stabilization because it induces a radiative potential for the saxion after SUSY breaking. The presence of PQ messengers also helps to avoid the domain wall problem. Let us consider N_Ψ pairs of $\Psi + \bar{\Psi}$ forming $\mathbf{5} + \bar{\mathbf{5}}$ representation under SU(5), for which the gauge coupling unification is preserved. Then, the domain wall number is given by

$$N_{\rm DW} = |N_\Psi - 6| \,. \tag{2.15}$$

This implies that the domain wall problem can be resolved for $N_\Psi = 5, 7$. For other cases with $N_{\rm DW} \neq 1$, the formation of dangerous domain walls can still be avoided if the saxion is displaced far from the origin after the inflation ends so that the PQ symmetry is not restored at high temperatures [40].

2.2 Constraints on the model parameters

Since S modifies the Higgs and neutralino sectors, it is of importance to explore constraints on the singlet couplings λ, A_λ, B_κ and m_S^2. Here we focus on the case with $0.1 \lesssim \lambda \lesssim 1$ at the weak scale as would be natural because an effective μ term is generated as $\mu_{\rm eff} = \lambda S$ with S fixed around $M_{\rm SUSY}$. Let us first examine the mixing of the singlet scalar with the Higgs doublets. After taking the rotation of (H_u^0, H_d^0) by an angle β, the mass matrix for the CP-even scalar fields has

$$\begin{aligned}
(M_H^2)_{11} &= M_Z^2 \cos^2 2\beta + \lambda^2 v^2 \sin^2 2\beta \,, \\
(M_H^2)_{13} &= \lambda v (2\mu_{\rm eff} - A_\lambda \sin 2\beta) \,, \\
(M_H^2)_{33} &= m_S^2 + \lambda^2 v^2 ,
\end{aligned} \tag{2.16}$$

where $(M_H^2)_{11}$ constitutes an upper bound on the mass of the lightest CP-even Higgs boson at the tree-level. In the following, we would like to consider the situation that the SM-like Higgs boson has negligible contamination from the singlet scalar. For $0.1 \lesssim \lambda \lesssim 1$, this is achieved when

$$\frac{\mu_{\rm eff}^2}{m_S^2} \left| 1 - \frac{A_\lambda \sin 2\beta}{2\mu_{\rm eff}} \right| \ll 1 \,, \tag{2.17}$$

with m_S^2 being of the order of $M_{\rm SUSY}^2$. It is thus found that, if A_λ is larger than $2\mu_{\rm eff}$, the mixing can get a sizable suppression at some region of $\tan\beta$. One would otherwise need $\mu_{\rm eff}^2 \ll m_S^2$ to suppress the mixing.

In the PQ-NMSSM, a stringent constraint on λ comes from the experimental bound on the Z-boson invisible decay rate because the PQ symmetry makes $\tilde{\chi}_1^0$ light. The singlino mixes with neutral Higgsinos to induce the interaction $\bar{\tilde{\chi}}_1^0 \sigma^\mu \tilde{\chi}_1^0 Z_\mu$ [41, 42], through which Z can invisibly decay into pairs of the lightest neutralino. The coupling for this interaction is given by

$$g_{Z\tilde{\chi}_1^0\tilde{\chi}_1^0} = \frac{g}{2\cos\theta_W} \left(|N_1^{\tilde{H}_d^0}|^2 - |N_1^{\tilde{H}_u^0}|^2 \right) \approx \frac{g}{2\cos\theta_W} \frac{\lambda^2 v^2 \cos 2\beta}{\mu_{\rm eff}^2} \,, \tag{2.18}$$

JHEP04(2012)022

where the last approximation is valid for small $\lambda v/\mu_{\rm eff}$. Hence, at large $\tan\beta$, the interaction gets strong while the mass of $\tilde{\chi}_1^0$ becomes small. The above coupling mediates the Z decay into $\tilde{\chi}_1^0$ with

$$\Gamma_{Z\to\tilde{\chi}_1^0\tilde{\chi}_1^0} = \frac{g^2_{Z\tilde{\chi}_1^0\tilde{\chi}_1^0}}{24\pi} M_Z \beta_Z{}^3 \simeq 25\beta_Z{}^3 \left(\frac{\lambda}{0.8}\right)^4 \left(\frac{\cos 2\beta}{0.8}\right)^2 \left(\frac{200\,\text{GeV}}{\mu_{\rm eff}}\right)^4 \text{MeV}, \tag{2.19}$$

if $M_Z > 2m_{\tilde{\chi}_1^0}$. Here $\beta_Z = (1 - 4m^2_{\tilde{\chi}_1^0}/M_Z^2)^{1/2}$ is the velocity of $\tilde{\chi}_1^0$ in the rest frame of Z. The process $Z \to \tilde{\chi}_1^0\tilde{\chi}_1^0$ contributes to the invisible Z decay and is tightly constrained by the LEP data to occur with a small rate, $\Gamma_{Z\to\tilde{\chi}_1^0\tilde{\chi}_1^0} \lesssim 2\,\text{MeV}$ [43]. This translates into

$$\lambda \lesssim 0.4 \left(\frac{\mu_{\rm eff}}{200\,\text{GeV}}\right) \left(\frac{0.8}{|\cos 2\beta|}\right)^{1/2}. \tag{2.20}$$

The above constraint on λ around the weak scale becomes important for large values of $\tan\beta$. To kinematically forbid the mode $Z \to \tilde{\chi}_1^0\tilde{\chi}_1^0$, we need

$$\lambda \gtrsim 0.7 \left(\frac{\mu_{\rm eff}}{200\,\text{GeV}}\right)^{1/2} \left(\frac{0.6}{\sin 2\beta}\right)^{1/2}, \tag{2.21}$$

which is possible for $\lambda \lesssim 1$ at low $\tan\beta$. For instance, at small $\tan\beta$ around 2, the LEP limits on the Z invisible width exclude values of $\mu_{\rm eff}$ in the range between 196 GeV and 260 GeV for $\lambda \approx 0.6$ [32].

On the other hand, for the theory to remain perturbative up to $M_{\rm GUT}$, λ should be small enough at the weak scale. NMSSM models with $\lambda S H_u H_d$ usually require λ less than 0.7–0.8 for $\tan\beta \gtrsim 2$. In models with a superpotential term S^3, the upper bound on λ decreases as the coupling for S^3 increases. However, the situation in the PQ-NMSSM is different because S^3 is absent and the PQ messengers with mass $M_\Psi \propto |X|$ affect the running of gauge couplings. Above the scale M_Ψ, gauge couplings have larger values than in the MSSM and slow down the running of Yukawa couplings. This results in the increase of the perturbativity bound on λ by $\delta\lambda \lesssim 0.1$ [44]. A large number of light PQ messengers are favored by raising the bound, but disfavored by the requirement of the perturbativity of gauge couplings up to $M_{\rm GUT}$. If there exists an extra gauge interaction, the perturbation theory would be valid below $M_{\rm GUT}$ for a larger value of λ at the weak scale.

Though we do not discuss it here in detail, there is also a constraint placed by cosmology. If $\tilde{\chi}_1^0$ is the lightest sparticle, its relic abundance should not exceed the measured amount of the dark matter. In the present model, the production of dark matter relies on the cosmological evolution of the saxion, which has a very flat potential generated after SUSY breaking and thus can play some non-trivial role in cosmology. On the other hand, the gravitino or axino can be lighter than $\tilde{\chi}_1^0$ depending on the mediation mechanism of SUSY breaking and on how the saxion is stabilized.

3 Low energy Higgs sector

In this section, we study the low energy Higgs sector. To see the impact of the PQ-NMSSM specific Higgs properties, we consider the decoupling limit of the MSSM where all heavy

JHEP04(2012)022

Higgs states decouple below $M_{\rm SUSY}$ and thus one combination of $H_{u,d}$ behaves exactly like the SM Higgs scalar H. In such a situation, we include the singlet S and construct a low energy effective theory below $M_{\rm SUSY}$ to examine how much the model departs from the MSSM. The modification is mainly due to (i) the extra contribution to the Higgs quartic coupling, which is a general property of NMSSM models, and (ii) the presence of a light neutralino that is singlino-like, which is a consequence of the PQ symmetry.

3.1 Effective theory below the SUSY breaking scale

For $0.1 \lesssim \lambda \lesssim 1$ at the weak scale, $\mu_{\rm eff}^2 \ll m_S^2$ is favored to suppress the mixing between H and the singlet scalar. Here we consider such a case and assume that the MSSM sparticles other than Higgsinos obtain masses of the order of $M_{\rm SUSY}$. The singlet scalar is also assumed to have $m_S^2 \sim M_{\rm SUSY}^2$. For $\mu_{\rm eff}$ less than $M_{\rm SUSY}$, the low energy effective theory below $M_{\rm SUSY}$ contains $\tilde{H}_{u,d}$ and $\tilde{S}$ in addition to the ordinary SM particles. The Lagrangian relevant to our analysis is given by[4]

$$-\mathcal{L}_{\rm eff} = \frac{\lambda_H}{2}(|H|^2 - v^2)^2 + (y_t \bar{t}_R Q_L H^c + \mu_{\rm eff}\tilde{H}_u\tilde{H}_d + y'_u H\tilde{H}_u\tilde{S} + y'_d H^c\tilde{H}_d\tilde{S} + \text{h.c.})\,, \tag{3.1}$$

where $H^c = -i\sigma_2 H^*$, and y_t is the top-Yukawa coupling. The singlino Yukawa couplings at the SUSY breaking scale are

$$y'_u(M_{\rm SUSY}) = \lambda\cos\beta\,, \qquad y'_d(M_{\rm SUSY}) = \lambda\sin\beta\,, \tag{3.2}$$

while the Higgs quartic coupling is given by

$$\lambda_H(M_{\rm SUSY}) = \frac{g^2+g'^2}{4}\cos^2 2\beta + \frac{\lambda^2}{2}\sin^2 2\beta + \delta\lambda_H|_{\rm tree} + \delta\lambda_H|_{\rm loop}\,, \tag{3.3}$$

where $\delta\lambda_H|_{\rm tree}$ is the threshold correction coming from tree-level exchange of the singlet scalar, and $\delta\lambda_H|_{\rm loop}$ is from the loops involving the stops:

$$\delta\lambda_H|_{\rm tree} \simeq -\frac{\lambda^2(2\mu_{\rm eff} - A_\lambda\sin 2\beta)^2}{2m_S^2}\,, \tag{3.4}$$

$$\delta\lambda_H|_{\rm loop} \simeq \frac{3y_t^4}{8\pi^2}\left(X_t - \frac{X_t^2}{12}\right), \tag{3.5}$$

where $X_t = (A_t - \mu_{\rm eff}\cot\beta)^2/M_{\rm SUSY}^2$ with A_t being the A-parameter for $H_u\tilde{t}_R\tilde{Q}_L$.

[4]To obtain the couplings of the SM-like Higgs boson more precisely, one needs to know the mixing between the SM-like Higgs boson and singlet scalar. To this end, one can replace the scalar part of (3.1) by

$$\begin{aligned}-\mathcal{L}_{\rm eff}|_{\rm scalar} =\ & \frac{\lambda_H - \delta\lambda_H|_{\rm tree}}{2}(|H|^2 - v^2)^2 + (m_S^2 + \lambda^2 v^2)|S - v_S|^2 \\ & - \left\{\frac{\lambda(2\mu_{\rm eff} - A_\lambda\sin 2\beta)}{2}(|H|^2 - v^2)(S - v_S) + \text{c.c.}\right\},\end{aligned}$$

and $\mu_{\rm eff}$ by λS. The small mixing with the singlet scalar reduces the couplings of the Higgs boson h. The reduced couplings can be obtained by taking the replacement

$$h \to \left(1 - \frac{\lambda v|2\mu_{\rm eff} - A_\lambda\sin 2\beta|}{m_S^2}\right)h\,.$$

JHEP04(2012)022

The physical mass of the CP-even neutral Higgs boson h can be obtained using the relation $m_h^2 = 2\lambda_H v^2$. For this, we need λ_H renormalized at the weak scale. In the effective theory, a low energy value of λ_H is determined by the renormalization group (RG) running equation:

$$\mu\frac{d\lambda_H}{d\mu} = \frac{1}{16\pi^2}\left(12\lambda_H^2 + 4(3y_t^2 + y_u'^2 + y_d'^2 - 3A)\lambda_H + 3B - 12y_t^4 - 4(y_u'^2 + y_d'^2)^2\right), \quad (3.6)$$

with the parameters A and B defined by

$$4A = 3g^2 + g'^2, \qquad 4B = 3g^4 + 2g^2g'^2 + g'^4. \quad (3.7)$$

Here one should note that the mixing between the neutral Higgs boson and singlet scalar would slightly modify the running equations.

To see the qualitative properties of the Higgs mass, we make an approximation taking into account that the dominant effects on the RG running come from the term y_t^4, and also from the terms $y_{u,d}'^4$ if λ is not small. The Higgs boson mass is found to be approximately given by

$$\begin{aligned} m_h^2 \approx\ & M_Z^2\cos^2 2\beta + \frac{3m_t^4}{4\pi^2 v^2}\left(\ln\left(\frac{M_{\rm SUSY}^2}{m_t^2}\right) + X_t - \frac{X_t^2}{12}\right) \\ & + M_Z^2\frac{2\lambda^2}{g^2+g'^2}\left(\sin^2 2\beta - \frac{(2\mu_{\rm eff} - A_\lambda\sin 2\beta)^2}{m_S^2} + \frac{\lambda^2}{4\pi^2}\ln\left(\frac{M_{\rm SUSY}^2}{\mu_{\rm eff}^2}\right)\right), \end{aligned} \quad (3.8)$$

for $m_t = y_t v$ and $\mu_{\rm eff} \gtrsim m_h$. The first line is the well-known result for the Higgs boson mass in the MSSM [45–48]. On the other hand, those in the second line correspond to the additional contributions arising due to S, i.e. as a consequence of the extra Higgs quartic coupling $\lambda^2|H_uH_d|^2$, the mixing between the singlet scalar and neutral Higgs boson, and the singlino Yukawa interactions affecting the running of the Higgs quartic coupling at low energy scales. The last two contributions are approximately estimated as

$$\delta m_h|_{\rm mix} \approx -10\left(\frac{130\,{\rm GeV}}{m_h}\right)\left(\frac{30}{m_S^2/\mu_{\rm eff}^2}\right)\left(1 - \frac{A_\lambda\sin 2\beta}{2\mu_{\rm eff}}\right)^2\left(\frac{\lambda}{0.8}\right)^2{\rm GeV}, \quad (3.9)$$

$$\delta m_h|_{\rm rad} \approx 4.1\left(\frac{130\,{\rm GeV}}{m_h}\right)\left(\frac{\ln(M_{\rm SUSY}^2/\mu_{\rm eff}^2)}{\ln 30}\right)\left(\frac{\lambda}{0.8}\right)^4{\rm GeV}. \quad (3.10)$$

A negative contribution to m_h from the mixing with the singlet scalar is present in any NMSSM model. In the PQ-NMSSM, $\mu_{\rm eff}^2 \ll m_S^2$ leads to a large suppression of this effect for $A_\lambda \lesssim \mu_{\rm eff}$. For $A_\lambda \gtrsim 2\mu_{\rm eff}$, small mixing can still be obtained at some values of $\tan\beta$. One should also note that there is a PQ-NMSSM specific contribution $\delta m_h|_{\rm rad}$ arising because the PQ symmetry makes the lightest neutralino get a relatively small mass.[5] This positive contribution is insensitive to $\tan\beta$, and becomes important for a small value of $\mu_{\rm eff}/M_{\rm SUSY}$ contrary to $\delta m_h|_{\rm mix}$.

[5] See also [20] for a similar discussion in a singlet extension of the MSSM having a relatively light neutralino. However, in our situation, the LEP bound on the invisible Z-boson decay width excludes large values of λ at large $\tan\beta$.

JHEP04(2012)022

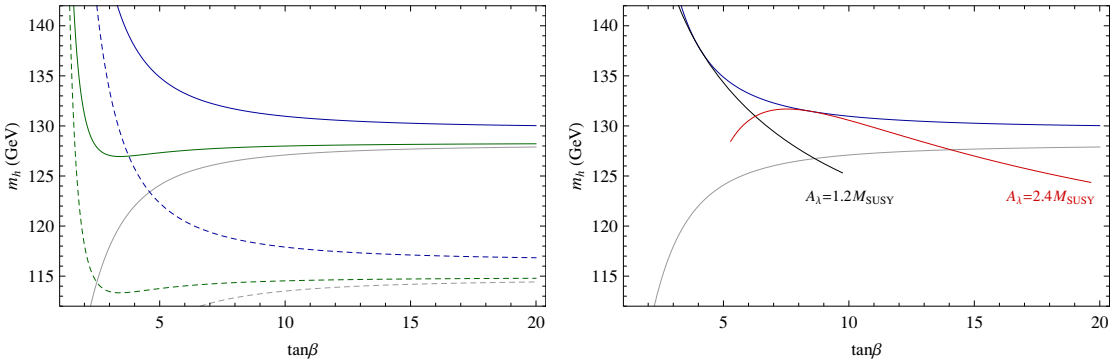

Figure 1. The mass of the SM-like Higgs boson for $M_{\rm SUSY} = 1.5\,$TeV in the PQ-NMSSM. Here λ is taken to be the maximum value satisfying the bound $\Gamma_{Z\to\tilde{\chi}_1^0\tilde{\chi}_1^0} \lesssim 2\,$MeV. The solid curve in the left panel is the upper bound on m_h for $\mu_{\rm eff} = 240\,$GeV (green) and $\mu_{\rm eff} = 420\,$GeV (blue), which is obtained for no mixing case $\delta m_h|_{\rm mix} = 0$. The gray line is the MSSM value of m_h. In the left panel, the dashed lines are for $X_t = 0$ while the solid ones for $X_t = 6$. Meanwhile, the right panel shows m_h for $X_t = 6$, $\mu_{\rm eff} = 420\,$GeV and a given value of A_λ: the black curve is for $A_\lambda = 1.2M_{\rm SUSY}$ while the red one for $A_\lambda = 2.4M_{\rm SUSY}$.

In figure 1, we show the upper bound on m_h in the PQ-NMSSM, which is obtained taking the maximum value of λ allowed by the constraint (2.20) from the Z invisible decay. Here we have solved the RG equation to get λ_H at the weak scale, and restricted λ to be less than unity as would be necessary to maintain its perturbativity up to $M_{\rm GUT}$. In the left panel, the value of m_h is shown for $\delta m_h|_{\rm mix} = 0$. While the MSSM generates $m_h \simeq 115\,$GeV ($128\,$GeV) at $\tan\beta \gtrsim 10$ for $X_t = 0$ (6) and $M_{\rm SUSY} = 1.5\,$TeV, the additional contribution from λ can lead to m_h larger than $115\,$GeV also at low $\tan\beta$ as in other NMSSM models. The loops of stops involving A_t can further increase m_h. The maximum comes at $X_t = 6$. It is also important to note that, when $\mu_{\rm eff} \gtrsim 400\,$GeV, m_h can be raised by a few GeV from the MSSM value even at large $\tan\beta$ owing to the PQ-NMSSM specific contribution $\delta m_h|_{\rm rad}$. On the other hand, the right panel shows the value of m_h for a given value of A_λ. For $A_\lambda \gtrsim 2\mu_{\rm eff}$, the mixing effect is suppressed only at some limited region of $\tan\beta$. In the figure, we consider values of $\tan\beta$ giving $(2\mu_{\rm eff} - A_\lambda \sin 2\beta)^2/m_S^2$ less than 0.1.

3.2 Phenomenological aspects

Since there appears a light neutralino as a consequence of the PQ symmetry, the Higgs boson h can invisibly decay into pairs of the lightest neutralino. This process is mediated by the Yukawa interaction $h\tilde{\chi}_1^0\tilde{\chi}_1^0$, which is generated due to the mixing between $\tilde{S}$ and $\tilde{H}_{u,d}^0$ and has a coupling given by

$$y_{h\tilde{\chi}_1^0\tilde{\chi}_1^0} = -\sqrt{2}\lambda\left(N_1^{\tilde{H}_d^0}\sin\beta + N_1^{\tilde{H}_u^0}\cos\beta\right) \approx \frac{\sqrt{2}\lambda^2 v \sin 2\beta}{\mu_{\rm eff}}\,, \tag{3.11}$$

where the approximation is valid for small $\lambda v/\mu_{\rm eff}$. The above coupling becomes negligible at large $\tan\beta$. If dominates, such non-standard invisible decay would make the Higgs discovery at hadron colliders much more difficult.

JHEP04(2012)022

Recent LHC data have excluded the Higgs boson with SM properties in the mass range between 141 GeV and 476 GeV at the 95% confidence level [49]. For h with mass lighter than 141 GeV, the main processes for its decay are $h \to b\bar{b}$ and $h \to WW^*$, ZZ^* [50–52]. The Higgs boson h in the PQ-NMSSM, which would have a small singlet component for $\mu_{\rm eff}^2/m_S^2 \ll 1$, can decay through a non-standard mode $h \to \tilde{\chi}_1^0\tilde{\chi}_1^0$ [33]. If it is kinematically accessible, the process $h \to \tilde{\chi}_1^0\tilde{\chi}_1^0$ takes place with the relative decay strength

$$\frac{\Gamma_{h\to\tilde{\chi}_1^0\tilde{\chi}_1^0}}{\Gamma_{h\to b\bar{b}}} \simeq \frac{1}{3}\left(\frac{y_{h\tilde{\chi}_1^0\tilde{\chi}_1^0}}{m_b/v}\right)^2 \simeq 128\left(\frac{\lambda}{0.8}\right)^4\left(\frac{\sin 2\beta}{0.6}\right)^2\left(\frac{200\,\text{GeV}}{\mu_{\rm eff}}\right)^2, \tag{3.12}$$

$$\frac{\Gamma_{h\to\tilde{\chi}_1^0\tilde{\chi}_1^0}}{\Gamma_{h\to WW^*}} \simeq \frac{32\pi^2}{3R(x)}\left(\frac{y_{h\tilde{\chi}_1^0\tilde{\chi}_1^0}}{g^2}\right)^2 \simeq 440\left(\frac{0.3}{R(x)}\right)\left(\frac{\lambda}{0.8}\right)^4\left(\frac{\sin 2\beta}{0.6}\right)^2\left(\frac{200\,\text{GeV}}{\mu_{\rm eff}}\right)^2, \tag{3.13}$$

where we have ignored the masses of the final states, and $R(x)$ is defined by

$$\begin{aligned} R(x) = {} & \frac{3(1-8x+20x^2)}{(4x-1)^{1/2}}\arccos\left(\frac{3x-1}{2x^{3/2}}\right) \\ & -\frac{1-x}{2x}(2-13x+47x^2) - \frac{3}{2}(1-6x+4x^2)\ln x\,, \end{aligned} \tag{3.14}$$

with $x = M_W^2/m_h^2$. The decay rate for the process $h \to ZZ^*$ is similar to $\Gamma_{h\to WW^*}$. When h has a sizable singlet component, the Higgs decay width for each process is modified, but the ratio between decay widths remains the same up to small correction arising due to that $y_{h\tilde{\chi}_1^0\tilde{\chi}_1^0}$ receives contribution not only from $H^0\tilde{H}_{u,d}^0\tilde{S}$ but also from $S\tilde{H}_u^0\tilde{H}_d^0$. The Higgs invisible decay to neutralinos would not dominate the SM decay processes either if λ is strong enough to make $\tilde{\chi}_1^0$ heavier than $m_h/2$:

$$\lambda \gtrsim 0.85\left(\frac{m_h}{130\,\text{GeV}}\right)^{1/2}\left(\frac{\mu_{\rm eff}}{200\,\text{GeV}}\right)^{1/2}\left(\frac{0.6}{\sin 2\beta}\right)^{1/2}, \tag{3.15}$$

or if λ is small enough to suppress the Yukawa coupling of $\tilde{\chi}_1^0$ to the Higgs boson: $\text{Br}(h \to \tilde{\chi}_1^0\tilde{\chi}_1^0)$ is less than 0.5 for

$$\lambda \lesssim 0.27\left(\frac{\mu_{\rm eff}}{200\,\text{GeV}}\right)^{1/2}\left(\frac{0.6}{\sin 2\beta}\right)^{1/2}. \tag{3.16}$$

Here we have naively estimated the value of λ required for $m_{\tilde{\chi}_1^0} > m_h/2$ by taking the leading term in (2.14), which is expanded in powers of $\lambda^2 v^2/\mu_{\rm eff}^2$. It is interesting to see that, in a low $\tan\beta$ region, the Higgs boson decays mainly through the invisible channel $h \to \tilde{\chi}_1^0\tilde{\chi}_1^0$ for $\lambda \gtrsim 0.4$ and $\mu_{\rm eff} \lesssim 400\,\text{GeV}$. A large $\mu_{\rm eff}$ can weaken this decay mode, but would lead to large mixing between H^0 and S. On the other hand, for $\tan\beta \gtrsim 10$, the constraint from the invisible Z-boson decay (2.20) requires $\lambda \lesssim 0.36 \times (\mu_{\rm eff}/200\,\text{GeV})$. Thus, in this case, $\text{Br}(h \to \tilde{\chi}_1^0\tilde{\chi}_1^0)$ cannot be larger than 0.5 if $\mu_{\rm eff}$ is smaller than about 360 GeV.

Figure 2 shows the branching ratio for the invisible Higgs decay $h \to \tilde{\chi}_1^0\tilde{\chi}_1^0$ in the $(\tan\beta, \lambda)$ plane. In the figure, the yellow region is excluded by the experimental bound $\Gamma_{Z\to\tilde{\chi}_1^0\tilde{\chi}_1^0} \lesssim 2\,\text{MeV}$, and the black contour is the value of m_h obtained for $M_{\rm SUSY} = 1.5\,\text{TeV}$

JHEP04(2012)022

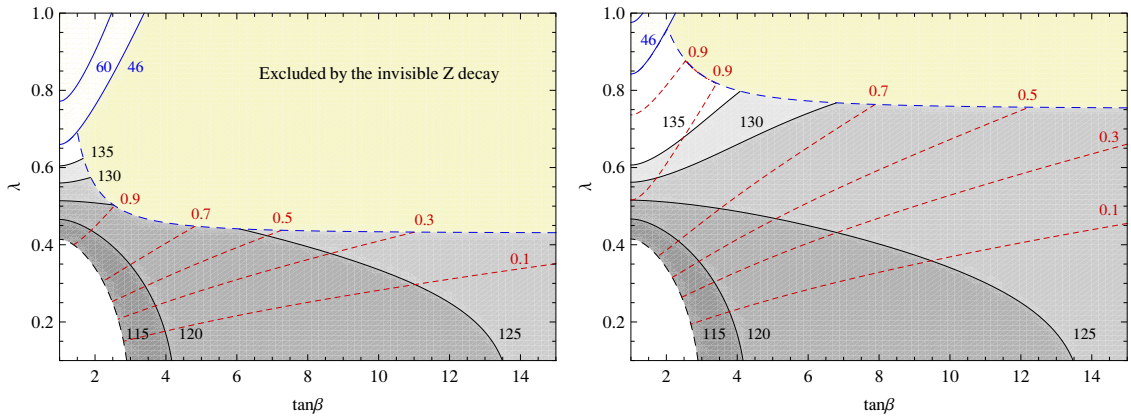

Figure 2. The branching ratio of non-standard mode $h \to \tilde{\chi}_1^0\tilde{\chi}_1^0$ for $\mu_{\rm eff} = 240\,{\rm GeV}$ (left) and $\mu_{\rm eff} = 420\,{\rm GeV}$ (right). The dashed red line is the contour for ${\rm Br}(h \to \tilde{\chi}_1^0\tilde{\chi}_1^0)$. We also show a contour plot for $m_{\tilde{\chi}_1^0}$ larger than $M_Z/2$, which is given in blue. The yellow region is excluded by the experimental bound on the invisible Z decay width. Meanwhile, the black contour shows the value of m_h obtained for $\delta m_h|_{\rm mix} = 0$ in the case with $M_{\rm SUSY} = 1.5\,{\rm TeV}$ and $X_t = 6$. The Higgs boson has a mass larger than 115 GeV above the dashed black line. In the figure, masses are given in the GeV unit.

and $X_t = 6$ with $\delta m_h|_{\rm mix} = 0$. Here we have taken $\mu_{\rm eff} = 240\,{\rm GeV}$ for the left plot, and $\mu_{\rm eff} = 420\,{\rm GeV}$ for the right plot. Since there is an extra contribution to m_h from λ as (3.8), the Higgs mass can be raised above 115 GeV at low $\tan\beta$. Notice also that the contribution $\delta m_h|_{\rm rad}$ raises m_h by a few GeV even at $\tan\beta \gtrsim 10$ compared to the MSSM value that corresponds to the $\lambda = 0$ case. The process $h \to \tilde{\chi}_1^0\tilde{\chi}_1^0$ can be the dominant mode of the Higgs decay at $\tan\beta \lesssim 10$, but is suppressed at large $\tan\beta$.

On the other hand, for small $\mu_{\rm eff}$ less than λv, the lightest neutralino is a sizable mixture of $\tilde{S}$ and $\tilde{H}_{u,d}^0$ at low $\tan\beta$. In this case, it can acquire a mass larger than $M_Z/2$ so that the invisible decay $Z \to \tilde{\chi}_1^0\tilde{\chi}_1^0$ is kinematically forbidden. For some parameter region, it is possible for $\tilde{\chi}_1^0$ to get a mass even larger than $m_h/2$. Otherwise, h would decay dominantly through the invisible process $h \to \tilde{\chi}_1^0\tilde{\chi}_1^0$ at low $\tan\beta$ because $\tilde{\chi}_1^0$ has a sizable Higgsino component. One should also note that the contribution from λ can raise m_h well above 115 GeV for $M_{\rm SUSY} \lesssim 1\,{\rm TeV}$ at $\tan\beta \lesssim 3$. In figure 3, we show the region of λ and $\tan\beta$ where $\tilde{\chi}_1^0$ has a mass larger than $M_Z/2$. The Higgs boson mass is also shown for the case with $M_{\rm SUSY} = 1\,{\rm TeV}$.

4 UV completion

When one considers GUT models to UV complete the PQ-NMSSM, an important issue is how the GUT partners of the MSSM Higgs doublets, which also carry a PQ charge, acquire heavy masses. We point out that the PQ-NMSSM can emerge as a low energy effective theory of a missing-partner model for supersymmetric SU(5) GUT [14].[6] The missing-

[6] A 5 dimensional SU(5) unified theory can also yield the PQ-NMSSM when compactified on $S^1/(Z_2 \times Z_2')$ orbifold [53, 54]. For instance, one can introduce a pair of Higgs hypermultiplet $\mathcal{H} + \bar{\mathcal{H}}$ which form $5 + \bar{5}$

JHEP04(2012)022

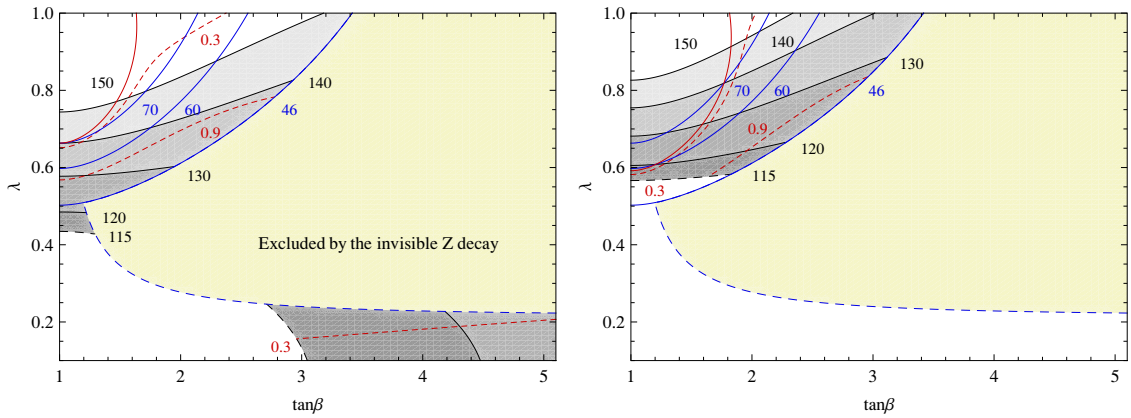

Figure 3. The parameter region where $Z \to \tilde{\chi}_1^0 \tilde{\chi}_1^0$ is kinematically forbidden. The blue contour shows the value of $m_{\tilde{\chi}_1^0}$ for $\mu_{\rm eff} = 120\,{\rm GeV}$. We also show the value of m_h by a black contour for the case with $M_{\rm SUSY} = 1\,{\rm TeV}$, $X_t = 6$ (left) and $X_t = 0$ (right). The masses are given in the GeV unit. The dashed red line is a contour for ${\rm Br}(h \to \tilde{\chi}_1^0 \tilde{\chi}_1^0)$. Above the solid red line, the lightest neutralino obtains a mass larger than $m_h/2$.

partner model has been considered to explain a large mass splitting of the SU(2) doublet and color triplet Higgses. The idea is to introduce higher dimensional representations that contain Higgs triplets but no doublets. Then, if a mass term $H_5 \bar{H}_{\bar{5}}$ for $\mathbf{5} + \bar{\mathbf{5}}$ Higgs multiplets is absent in the superpotential, the doublet-triplet splitting can be achieved without fine-tuning from the interactions of H_5 and $\bar{H}_{\bar{5}}$ with the higher dimensional Higgs multiplets. This is possible because the superpotential is not renormalized in perturbation theory.

The Higgs sector of the original model consists of the chiral multiplets, $\Sigma(\mathbf{75})$, $\theta(\mathbf{50}) + \bar{\theta}(\overline{\mathbf{50}})$ and $H(\mathbf{5}) + \bar{H}(\bar{\mathbf{5}})$. To incorporate the PQ symmetry without spoiling the missing-partner mechanism, we modify the model by introducing three pairs of $\mathbf{50} + \overline{\mathbf{50}}$ and $\mathbf{5} + \bar{\mathbf{5}}$ multiplets, and also three SU(5) singlets:

$$\Sigma(\mathbf{75})\,, \qquad \theta_i(\mathbf{50}) + \bar{\theta}_i(\overline{\mathbf{50}})\,, \qquad H_i(\mathbf{5}) + \bar{H}_i(\bar{\mathbf{5}})\,, \qquad X_i(\mathbf{1})\,, \tag{4.1}$$

where $i = (1, 2, 3)$, and ${\rm U}(1)_{\rm PQ}$ charges are assigned as

$$\begin{aligned} &\Sigma(0)\,, \quad X_1(q)\,, \quad X_2(-3q)\,, \quad X_3(2q)\,, \\ &\theta_1(-p) + \bar{\theta}_1(p)\,, \qquad \theta_2(-3q-p) + \bar{\theta}_2(3q+p)\,, \qquad \theta_3(-q-p) + \bar{\theta}_3(q+p)\,, \\ &H_1(p) + \bar{H}_1(-q-p)\,, \qquad H_2(3q+p) + \bar{H}_2(-p)\,, \qquad H_3(q+p) + \bar{H}_3(-3q-p)\,. \end{aligned} \tag{4.2}$$

This model seems similar to the minimal model with ${\rm U}(1)_{\rm PQ}$ considered in [15], but it turns out that more than two pairs of chiral multiplets are needed to obtain the PQ-NMSSM as

representation of SU(5) and carry a PQ charge -1. Then, doublet-triplet splitting is achieved taking the orbifold projection such that $\mathcal{H}$ ($\bar{\mathcal{H}}$) has a SU(2) doublet Higgs chiral multiplet transforming as $(+,+)$ under $Z_2 \times Z_2'$ and a triplet Higgs with $(+,-)$. This also leads to the terms (2.1) for the PQ-NMSSM below the compactification scale.

JHEP04(2012)022

an effective theory below $M_{\rm GUT}$. The missing-partner mechanism is implemented by the following PQ-invariant superpotential terms

$$W = \frac{1}{2}M\mathrm{Tr}(\Sigma^2) + \frac{1}{3}a\mathrm{Tr}(\Sigma^3) + b_i\theta_i\Sigma H_i + c_i\bar{\theta}_i\Sigma\bar{H}_{i+1} + \tilde{M}_i\bar{\theta}_i\theta_i\,, \tag{4.3}$$

with the identification $\bar{H}_4 = \bar{H}_1$. As in the original model, the vacuum expectation value of Σ breaks SU(5) to the SM gauge groups, and gives rise to the triplet mass terms. This becomes clear after integrating out the heavy triplets in $\theta_i + \bar{\theta}_i$, which leads to

$$W_{\rm eff} = M_i^c H_i^c \bar{H}_{i+1}^c\,, \tag{4.4}$$

where $M_i^c \sim M_{\rm GUT}^2/\tilde{M}_i$, and H_i^c denotes the color-triplet from H_i. Because the **50** representation does not contain Higgs doublets, no doublet mass terms are generated from the superpotential (4.3), and the three pairs of doublet Higgses remain massless. Mass terms for these doublet Higgses arise from

$$W = \lambda_i X_i H_i \bar{H}_i + \frac{\xi}{M_{\rm Pl}} X_1^3 X_2\,, \tag{4.5}$$

where we have chosen a basis of X_3 such that $X_1^2 H_3 \bar{H}_3$ is removed in the superpotential. Including soft SUSY breaking terms for the gauge singlet scalars

$$-\mathcal{L}_{\rm soft} = m_{X_i}^2 |X_i|^2 + \left(A_\xi \frac{\xi}{M_{\rm Pl}} X_1^3 X_2 + \text{h.c.} \right), \tag{4.6}$$

the second term in the above superpotential fixes $X_{1,2}$ at

$$|X_{1,2}|^2 \approx \frac{M_{\rm Pl}(-m_{X_1}^2)^{1/2}}{\xi} \sim \frac{M_{\rm Pl} M_{\rm SUSY}}{\xi}\,, \tag{4.7}$$

thereby leading to that $\mathrm{U}(1)_{\rm PQ}$ is spontaneously broken around 10^{11} GeV for $\xi \sim 1$, and there appears the axion which is a mixture of $\arg(X_{1,2})$. Here we have assumed $m_{X_1}^2 < 0$. Hence, the doublet Higgses in $H_{1,2} + \bar{H}_{1,2}$ obtain large masses from the vacuum expectation value of $X_{1,2}$, respectively. On the other hand, the doublet Higgses in $H_3 + \bar{H}_3$ remain massless until X_3 acquires a nonzero vacuum expectation value.

Notice that the PQ charge assignment (4.2) allows direct mass terms $H_i\bar{H}_{i+1}$ and the Yukawa term $X_1X_2X_3$ in the renormalizable superpotential. These terms should be absent in order for the missing-partner mechanism to work and for only one pair of Higgs doublets to remain light. Once we do not put these superpotential terms, radiative corrections will not change the situation owing to supersymmetry.[7] It is also important to note that the model possesses two global U(1) symmetries associated with the independent charges p and q. To eliminate one of them, as was considered in [15], we introduce three right-handed neutrino multiplets $N(\mathbf{1})$ that implement the conventional see-saw mechanism through the superpotential terms $NLH_u + X_iNN$ with $i = 1$ or 2. The PQ charges are then fixed

[7] One can assign a different PQ charge to X_2 and the Higgs multiplets to forbid a superpotential term $X_1X_2X_3$. Then, other mechanism is needed to fix the PQ breaking scale because the term $X_1^3X_2$ in the scalar potential (4.6) is not allowed.

JHEP04(2012)022

as $5p = -8q$ when the Majorana masses for N arise from $X_1 NN$, and $5p = -12q$ if one instead chooses $X_2 NN$.

It now becomes apparent that the missing-partner model with the superpotential terms (4.3) and (4.5) leads to the PQ-NMSSM. The doublet Higgses in $H_3 + \bar{H}_3$ correspond to the ordinary MSSM Higgses, while $X_{1,2}$ and X_3 play the role of X and S, respectively. In the model, the higher dimensional operators

$$\mathcal{L} = \int d^4\theta \left(\kappa_1 \frac{X_1^{*2} X_3}{M_{\rm Pl}} + \kappa_2 \frac{X_1 X_2 X_3}{M_{\rm Pl}} \right) + \text{h.c.} \tag{4.8}$$

can generate an effective tadpole term for X_3 as

$$W_{\rm eff} = \tilde{m}_0^2 X_3 \,, \tag{4.9}$$

where $\tilde{m}_0^2 \sim M_{\rm SUSY}^2$ for $\kappa_{1,2} \sim 1$ and $\xi \sim 1$. Then, X_3 is naturally expected to get a vacuum expectation value around the weak scale for $M_{\rm SUSY} \sim 1\,\text{TeV}$. However, if PQ-breaking mass terms $\theta_i \bar{\theta}_j$ with $i \neq j$ are present, the loops of heavy triplets would generate large tadpoles for X_3. This implies that $\text{U}(1)_{\rm PQ}$ is crucial to avoid the tadpole problem. The PQ symmetry plays an important role also in suppressing dangerous higher dimensional operators leading to too rapid proton decays. The triplet Higgses mediate dimension 5 operators violating the baryon number [55, 56], which carry a nonzero PQ charge and therefore are further suppressed by a small factor $X_1 X_2/(M_1^c M_2^c) \sim M_{\rm SUSY} M_{\rm Pl}/(M_1^c M_2^c)$ compared to those in the minimal SU(5) GUT model.

Let us finally discuss the difference from the model of [15]. That model contains two pairs of Higgs doublets $H_f + \bar{H}_f$ and $H'_f + \bar{H}'_f$ which are vector-like also under $\text{U}(1)_{\rm PQ}$. One pair of them becomes heavy through $P H_f \bar{H}'_f$ for P being a $\text{U}(1)_{\rm PQ}$ breaking gauge singlet field, and the other remains light. If one introduces an additional singlet P' having a term $P' H'_f \bar{H}_f$ in the superpotential, P' necessarily carries a PQ charge such that PP' is invariant under $\text{U}(1)_{\rm PQ}$ transformations. Thus, even if one omits PP' in the superpotential, a Kähler potential term PP' would induce too large tadpole term for P'. This makes it difficult for P' to play the role of S in the PQ-NMSSM.

5 Conclusions

Extended to incorporate the PQ mechanism solving the strong CP problem, the NMSSM becomes compatible with the grand unification since the PQ symmetry forbids large tadpoles for the SM singlet S to be generated from loops of heavy fields coupling to S. Another important property of the PQ-NMSSM is that all the mass parameters are determined by the SUSY breaking scale $M_{\rm SUSY}$ and $F_a^2/M_{\rm Pl}$ with F_a being the axion decay constant. Thus, the electroweak symmetry breaking is naturally achieved at the correct scale. Furthermore, the model can avoid the domain wall problem in the presence of the PQ messengers.

An important consequence of the PQ symmetry is that the lightest neutralino is singlino-like with a small Higgsino admixture, and is relatively light compared to other sparticles. The Higgsino component is determined by the coupling of S to the Higgs doublets, which is constrained by the LEP bound on the invisible Z-boson decay width. This

JHEP04(2012)022

constraint becomes severe at large $\tan\beta$. Meanwhile, the SM-like Higgs boson decays mainly through the conventional decay modes at large $\tan\beta$ and in a portion of parameter space for small values of $\tan\beta$. The decay of the Higgs boson into a pair of the lightest neutralino can be the main mode at low $\tan\beta$, for which case the Higgs search at colliders will be modified. Also important is that the SM-like Higgs mass receives an additional positive contribution from the loops involving the singlino Yukawa coupling. This PQ-NMSSM specific contribution can lead to a significant increase of the Higgs boson mass by a few GeV even at large $\tan\beta$ compared to the MSSM.

We found that the PQ-NMSSM is realized as a low energy effective theory of a missing-partner model for supersymmetric SU(5) GUT with the PQ symmetry, which solves the doublet-triplet splitting problem and the proton decay problem. It is interesting to note that such a UV completion achieves the relation $F_a \sim \sqrt{M_{\rm SUSY} M_{\rm Pl}}$. Hence, all the mass parameters of the resulting PQ-NMSSM have values of the order of $M_{\rm SUSY}$.

Note added. After submitting the manuscript, the ATLAS and CMS collaborations at the LHC reported their updated results in the Higgs search [57, 58], which may indicate a SM-like Higgs boson with mass around 125 GeV. To explain a 125 GeV Higgs mass within the MSSM, we need large stop mixing or heavy stops with mass larger than about 10 TeV. The PQ-NMSSM improves the situation because the Higgs mass receives an additional positive contribution, which can be of a few GeV even at large $\tan\beta$.

Acknowledgments

This work is supported by Grants-in-Aid for Scientific Research from the Ministry of Education, Science, Sports, and Culture (MEXT), Japan, No. 23104008 and No. 23540283, and in part by the JSPS Grant-in-Aid 21-09224 (K.S.J.), and also by Tohoku University International Advanced Research and Education Organization (Y.S.).

A Mass matrix

In this appendix, we present the tree-level mass matrices for the neutral scalar fields. After rotating the upper left 2×2 submatrix of the mass matrix for the CP even scalars, one obtains

$$\begin{aligned}
(M_H^2)_{11} &= M_Z^2\cos^2 2\beta + \lambda^2 v^2 \sin^2 2\beta\,,\\
(M_H^2)_{22} &= \frac{2b_{\rm eff}}{\sin 2\beta} + (M_Z^2 - \lambda^2 v^2)\sin^2 2\beta\,,\\
(M_H^2)_{33} &= m_S^2 + \lambda^2 v^2,\\
(M_H^2)_{12,21} &= \frac{1}{2}(M_Z^2 - \lambda^2 v^2)\sin 4\beta\,,\\
(M_H^2)_{13,31} &= \lambda v(2\mu_{\rm eff} - A_\lambda \sin 2\beta)\,,\\
(M_H^2)_{23,32} &= \lambda v A_\lambda \cos 2\beta\,.
\end{aligned} \tag{A.1}$$

JHEP04(2012)022

The mass matrix for the pseudoscalar fields is given by

$$M_A^2 = \begin{pmatrix} b_{\rm eff}\cot\beta & b_{\rm eff} & \lambda v A_\lambda \cos\beta \\ b_{\rm eff} & b_{\rm eff}\tan\beta & \lambda v A_\lambda \sin\beta \\ \lambda v A_\lambda \cos\beta & \lambda v A_\lambda \sin\beta & m_S^2 + \lambda^2 v^2 \end{pmatrix} . \tag{A.2}$$

It is easy to see that there are one massless mode, which is absorbed into gauge boson, and two massive CP odd scalars:

$$M_{A_{1,2}}^2 = \frac{b_{\rm eff}}{\sin 2\beta} + \frac{1}{2}(m_S^2 + \lambda^2 v^2) \pm \sqrt{\left(\frac{b_{\rm eff}}{\sin 2\beta} - \frac{1}{2}(m_S^2 + \lambda^2 v^2)\right)^2 + A_\lambda^2 \lambda^2 v^2} . \tag{A.3}$$

Using the stationary condition (2.7), one can find that $M_{A_1} = 0$ if $\kappa = 0$.

B Global structure of the Higgs potential

In the PQ-NMSSM, where the Higgs sector is extended to include the singlet S, the Higgs potential may develop another minimum away from the weak scale. The model parameters are constrained to avoid such a minimum since it would generally appear at a field value similar to or larger than $M_{\rm SUSY}$ and thus be deeper than the electroweak vacuum. For the case with $m_S^2 > 0$ and $\lambda \lesssim 1$, we shall show that the region $\lambda^2(|H_u^0|^2 + |H_d^0|^2) \sim M_{\rm SUSY}^2$ somewhat near the D-flat direction is potentially dangerous for much of the parameter space. This argues that the condition to avoid a deeper minimum can approximately be examined by looking at the shape of the potential along the D-flat direction.

After integrating out S by the minimization condition, the Higgs potential reads

$$\begin{aligned} V = & \left(\frac{g^2 + g'^2}{2}\cos^2 2\theta + \lambda^2 \sin^2 2\theta\right)\phi^4 - \frac{(A_\lambda \lambda \phi^2 \sin 2\theta + B_\kappa m_0^2)^2}{2\lambda^2\phi^2 + m_S^2} \\ & + 2(m_{H_u}^2 \sin^2\theta + m_{H_d}^2 \cos^2\theta - \lambda m_0^2 \sin 2\theta)\phi^2 + \text{constant} , \end{aligned} \tag{B.1}$$

where $|H_u^0| = \sqrt{2}\phi\sin\theta$ and $|H_d^0| = \sqrt{2}\phi\cos\theta$ with $0 \le \theta < \pi/2$ and $0 \le \phi$. At very large values of ϕ, the first term becomes dominant and lifts the potential along the ϕ-direction. It is also straightforward to see that $\partial_\phi V = 0$ when $\phi = 0$ or when

$$\begin{aligned} & \left(\sin^2 2\theta + \frac{g^2 + g'^2}{2\lambda^2}\cos^2 2\theta\right)(2\lambda^2\phi^2 + m_S^2)^3 - k m_S^2 (2\lambda^2\phi^2 + m_S^2)^2 \\ & \qquad + 2\left(\frac{A_\lambda m_S^2}{2}\sin 2\theta - \lambda B_\kappa m_0^2\right)^2 = 0 , \end{aligned} \tag{B.2}$$

where k is a function of θ,

$$k = \left(1 + \frac{A_\lambda^2}{2m_S^2}\right)\sin^2 2\theta + \frac{g^2 + g'^2}{2\lambda^2}\cos^2 2\theta - 2\frac{m_{H_u}^2 \sin^2\theta + m_{H_d}^2 \cos^2\theta - \lambda m_0^2 \sin 2\theta}{m_S^2} . \tag{B.3}$$

The above relation shows that the potential can have at most one local minimum at $\phi \neq 0$ along the ϕ-direction for a given θ, which would appear at $2\lambda^2\phi^2 + m_S^2 \sim M_{\rm SUSY}^2$. On the other hand, along the angular direction, the slope of the potential vanishes when

$$\sin 2\theta = -\left(r\frac{\phi^2}{\Lambda_1^2}\sin 2\theta + \frac{\Lambda_2^2}{\Lambda_1^2}\right)\cos 2\theta , \tag{B.4}$$

JHEP04(2012)022

for which

$$\partial_\theta^2 V = 4\left(-\cos 2\theta + \frac{\Lambda_2^2}{\Lambda_1^2}\sin 2\theta\right)\Lambda_1^2\phi^2\tan^2 2\theta\,. \tag{B.5}$$

Here r is defined by

$$r = g^2 + g'^2 - 2\left(1 - \frac{A_\lambda^2}{2\lambda^2\phi^2 + m_S^2}\right)\lambda^2, \tag{B.6}$$

and $\Lambda_{1,2}^2$ are given by

$$\begin{aligned}\Lambda_1^2 &= m_{H_d}^2 - m_{H_u}^2\,,\\ \Lambda_2^2 &= 2\left(1 + \frac{A_\lambda B_\kappa}{2\lambda^2\phi^2 + m_S^2}\right)\lambda m_0^2\,,\end{aligned} \tag{B.7}$$

both of which are generally of $\mathcal{O}(M_{\rm SUSY}^2)$, and positive. For $r > 0$, one can find (i) $\partial_\theta V = 0$ can have a solution at $\tan\theta > 1$ with a positive curvature $\partial_\theta^2 V > 0$, implying that there is only one minimum along the angular direction for a given ϕ, and (ii) for large values of ϕ, $\phi^2 \gg \Lambda_1^2 \sim M_{\rm SUSY}^2$, a minimum along the angular direction is located near $\tan\theta = 1$, i.e. near the D-flat direction.

Let us examine further the case with $r > 0$ and $m_S^2 \sim M_{\rm SUSY}^2$. Note that r is positive at $2\lambda^2\phi^2 + m_S^2 \sim M_{\rm SUSY}^2$ if $\lambda \lesssim 0.5$ for small A_λ, and if $\lambda \lesssim 1$ for $A_\lambda \sim M_{\rm SUSY}$ and $B_\kappa \sim M_{\rm SUSY}$. At the electroweak vacuum, which lies at $\phi^2 \sim M_W^2 \ll M_{\rm SUSY}^2$ and $\theta = \beta$, the condition (B.4) gives

$$\frac{\Lambda_2^2}{\Lambda_1^2} \simeq -\tan 2\beta\,. \tag{B.8}$$

The extremum condition (B.4) can then be written

$$\left(1 - \frac{r\phi^2}{\Lambda_1^2}\frac{\tan^2\theta - 1}{\tan^2\theta + 1}\right)\tan 2\theta \approx \tan 2\beta\,, \tag{B.9}$$

for $\phi^2 \lesssim M_{\rm SUSY}^2$. This tells that a minimum along the angular direction arises at $1 < \tan\theta < \tan\beta$ for a given ϕ, and approaches the D-flat direction, $\tan\theta = 1$, as ϕ increases. Thus it is useful to first analyze the potential along the D-flat direction though the actual another minimum, if exists, appears somewhat away from the D-flat direction.

On the other hand, in the case with $r < 0$, the potential is minimized along the angular direction at $\tan\theta > \tan\beta$ or at $\tan\theta < 1$ for $\phi^2 \gtrsim M_{\rm SUSY}^2$. In the former case, making the potential develop no other minimum in the region near the D-flat direction is not enough to guarantee the absence of a deeper minimum.

JHEP04(2012)022

C RG running equations

For the low energy effective theory (3.1) below $M_{\rm SUSY}$, the RG running equations for the Yukawa couplings read

$$
\begin{aligned}
8\pi^2\mu\frac{dy_t^2}{d\mu} &= \left(\frac{9}{2}y_t^2 + y_u'^2 + y_d'^2 - \frac{17}{20}g_1^2 - \frac{9}{4}g_2^2 - 8g_3^2\right)y_t^2\,,\\
8\pi^2\mu\frac{dy_u'^2}{d\mu} &= \left(3y_t^2 + \frac{5}{2}y_u'^2 + 4y_d'^2 - \frac{9}{20}g_1^2 - \frac{9}{4}g_2^2\right)y_u'^2\,,\\
8\pi^2\mu\frac{dy_d'^2}{d\mu} &= \left(3y_t^2 + 4y_u'^2 + \frac{5}{2}y_d'^2 - \frac{9}{20}g_1^2 - \frac{9}{4}g_2^2\right)y_d'^2\,,
\end{aligned}
\tag{C.1}
$$

at the one-loop, and those for SM gauge couplings are

$$
\begin{aligned}
8\pi^2\mu\frac{d}{d\mu}\frac{1}{g_1^2} &= -\frac{103}{30} - \frac{1}{10}\theta(\mu - m_h) - \frac{17}{30}\theta(\mu - m_t) - \frac{2}{5}\theta(\mu - \mu_{\rm eff})\,,\\
8\pi^2\mu\frac{d}{d\mu}\frac{1}{g_2^2} &= \frac{13}{3} - \frac{1}{6}\theta(\mu - m_h) - \theta(\mu - m_t) - \frac{2}{3}\theta(\mu - \mu_{\rm eff})\,,\\
8\pi^2\mu\frac{d}{d\mu}\frac{1}{g_3^2} &= 8 - \theta(\mu - m_t)\,,
\end{aligned}
\tag{C.2}
$$

with $g_1 = \sqrt{5/3}g'$ and $g_2 = g$. Here $\theta(x) = 1$ for $x > 0$ and $\theta(x) = 0$ for $x < 0$.

References

[1] M. Maniatis, *The next-to-minimal supersymmetric extension of the standard model reviewed*, *Int. J. Mod. Phys.* **A 25** (2010) 3505 [arXiv:0906.0777] [INSPIRE].

[2] U. Ellwanger, C. Hugonie and A.M. Teixeira, *The next-to-minimal supersymmetric standard model*, *Phys. Rept.* **496** (2010) 1 [arXiv:0910.1785] [INSPIRE].

[3] H.P. Nilles, M. Srednicki and D. Wyler, *Constraints on the stability of mass hierarchies in supergravity*, *Phys. Lett.* **B 124** (1983) 337 [INSPIRE].

[4] A.B. Lahanas, *Light singlet, gauge hierarchy and supergravity*, *Phys. Lett.* **B 124** (1983) 341 [INSPIRE].

[5] U. Ellwanger, *Nonrenormalizable interactions from supergravity, quantum corrections and effective low-energy theories*, *Phys. Lett.* **B 133** (1983) 187 [INSPIRE].

[6] H.P. Nilles and N. Polonsky, *Gravitational divergences as a mediator of supersymmetry breaking*, *Phys. Lett.* **B 412** (1997) 69 [hep-ph/9707249] [INSPIRE].

[7] J. Bagger and E. Poppitz, *Destabilizing divergences in supergravity coupled supersymmetric theories*, *Phys. Rev. Lett.* **71** (1993) 2380 [hep-ph/9307317] [INSPIRE].

[8] V. Jain, *On destabilizing divergencies in supergravity models*, *Phys. Lett.* **B 351** (1995) 481 [hep-ph/9407382] [INSPIRE].

[9] J. Bagger, E. Poppitz and L. Randall, *Destabilizing divergences in supergravity theories at two loops*, *Nucl. Phys.* **B 455** (1995) 59 [hep-ph/9505244] [INSPIRE].

[10] A. Vilenkin, *Cosmic strings and domain walls*, *Phys. Rept.* **121** (1985) 263 [INSPIRE].

JHEP04(2012)022

[11] S.A. Abel, S. Sarkar and P.L. White, *On the cosmological domain wall problem for the minimally extended supersymmetric standard model*, *Nucl. Phys.* **B 454** (1995) 663 [hep-ph/9506359] [INSPIRE].

[12] R.D. Peccei and H.R. Quinn, *CP conservation in the presence of instantons*, *Phys. Rev. Lett.* **38** (1977) 1440 [INSPIRE].

[13] R.D. Peccei and H.R. Quinn, *Constraints imposed by CP conservation in the presence of instantons*, *Phys. Rev.* **D 16** (1977) 1791 [INSPIRE].

[14] A. Masiero, D.V. Nanopoulos, K. Tamvakis and T. Yanagida, *Naturally massless Higgs doublets in supersymmetric* SU(5), *Phys. Lett.* **B 115** (1982) 380 [INSPIRE].

[15] J. Hisano, T. Moroi, K. Tobe and T. Yanagida, *Suppression of proton decay in the missing partner model for supersymmetric* SU(5) *GUT*, *Phys. Lett.* **B 342** (1995) 138 [hep-ph/9406417] [INSPIRE].

[16] H.M. Lee et al., *Discrete R symmetries for the MSSM and its singlet extensions*, *Nucl. Phys.* **B 850** (2011) 1 [arXiv:1102.3595] [INSPIRE].

[17] U. Ellwanger, G. Espitalier-Noel and C. Hugonie, *Naturalness and fine tuning in the NMSSM: implications of early LHC results*, *JHEP* **09** (2011) 105 [arXiv:1107.2472] [INSPIRE].

[18] G.G. Ross and K. Schmidt-Hoberg, *The fine-tuning and phenomenology of the generalised NMSSM*, arXiv:1108.1284 [INSPIRE].

[19] A. Delgado, C. Kolda and A. de la Puente, *Solving the hierarchy problem with a light singlet and supersymmetric mass terms*, arXiv:1111.4008 [INSPIRE].

[20] K. Nakayama, N. Yokozaki and K. Yonekura, *Relaxing the Higgs mass bound in singlet extensions of the MSSM*, *JHEP* **11** (2011) 021 [arXiv:1108.4338] [INSPIRE].

[21] E. Bertuzzo and M. Farina, *Higgs boson signals in lambda-SUSY with a scale invariant superpotential*, *Phys. Rev.* **D 85** (2012) 015011 [arXiv:1105.5389] [INSPIRE].

[22] M. Almarashi and S. Moretti, *Reinforcing the no-lose theorem for NMSSM Higgs discovery at the LHC*, *Phys. Rev.* **D 84** (2011) 035009 [arXiv:1106.1599] [INSPIRE].

[23] U. Ellwanger, *Higgs bosons in the next-to-minimal supersymmetric standard model at the LHC*, *Eur. Phys. J.* **C 71** (2011) 1782 [arXiv:1108.0157] [INSPIRE].

[24] M.M. Almarashi and S. Moretti, *LHC signals of a heavy CP-even Higgs boson in the NMSSM via decays into a Z and a light CP-odd Higgs state*, *Phys. Rev.* **D 85** (2012) 017701 [arXiv:1109.1735] [INSPIRE].

[25] K. Hamaguchi, K. Nakayama and N. Yokozaki, *NMSSM in gauge-mediated SUSY breaking without domain wall problem*, *Phys. Lett.* **B 708** (2012) 100 [arXiv:1107.4760] [INSPIRE].

[26] J.-J. Cao, K.-i. Hikasa, W. Wang and J.M. Yang, *Light dark matter in NMSSM and implication on Higgs phenomenology*, *Phys. Lett.* **B 703** (2011) 292 [arXiv:1104.1754] [INSPIRE].

[27] M. Carena, N.R. Shah and C.E.M. Wagner, *Light dark matter and the electroweak phase transition in the NMSSM*, *Phys. Rev.* **D 85** (2012) 036003 [arXiv:1110.4378] [INSPIRE].

[28] J.E. Kim, *Light pseudoscalars, particle physics and cosmology*, *Phys. Rept.* **150** (1987) 1 [INSPIRE].

[29] H.-Y. Cheng, *The strong CP problem revisited*, *Phys. Rept.* **158** (1988) 1 [INSPIRE].

JHEP04(2012)022

[30] J.E. Kim and G. Carosi, *Axions and the strong CP problem*, *Rev. Mod. Phys.* **82** (2010) 557 [arXiv:0807.3125] [INSPIRE].

[31] C. Panagiotakopoulos and K. Tamvakis, *New minimal extension of MSSM*, *Phys. Lett.* **B 469** (1999) 145 [hep-ph/9908351] [INSPIRE].

[32] C. Panagiotakopoulos and A. Pilaftsis, *Higgs scalars in the minimal nonminimal supersymmetric standard model*, *Phys. Rev.* **D 63** (2001) 055003 [hep-ph/0008268] [INSPIRE].

[33] A. Dedes, C. Hugonie, S. Moretti and K. Tamvakis, *Phenomenology of a new minimal supersymmetric extension of the standard model*, *Phys. Rev.* **D 63** (2001) 055009 [hep-ph/0009125] [INSPIRE].

[34] A. Menon, D.E. Morrissey and C.E.M. Wagner, *Electroweak baryogenesis and dark matter in the NMSSM*, *Phys. Rev.* **D 70** (2004) 035005 [hep-ph/0404184] [INSPIRE].

[35] C. Balázs, M.S. Carena, A. Freitas and C.E.M. Wagner, *Phenomenology of the NMSSM from colliders to cosmology*, *JHEP* **06** (2007) 066 [arXiv:0705.0431] [INSPIRE].

[36] J. Cao, H.E. Logan and J.M. Yang, *Experimental constraints on NMSSM and implications on its phenomenology*, *Phys. Rev.* **D 79** (2009) 091701 [arXiv:0901.1437] [INSPIRE].

[37] P. Fayet, *Supergauge invariant extension of the Higgs mechanism and a model for the electron and its neutrino*, *Nucl. Phys.* **B 90** (1975) 104 [INSPIRE].

[38] J.E. Kim and H.P. Nilles, *The μ problem and the strong CP problem*, *Phys. Lett.* **B 138** (1984) 150 [INSPIRE].

[39] K. Blum, C. Delaunay and Y. Hochberg, *Vacuum (meta)stability beyond the MSSM*, *Phys. Rev.* **D 80** (2009) 075004 [arXiv:0905.1701] [INSPIRE].

[40] S. Kasuya, M. Kawasaki and T. Yanagida, *Domain wall problem of axion and isocurvature fluctuations in chaotic inflation models*, *Phys. Lett.* **B 415** (1997) 117 [hep-ph/9709202] [INSPIRE].

[41] H.P. Nilles, *Supersymmetry, supergravity and particle physics*, *Phys. Rept.* **110** (1984) 1 [INSPIRE].

[42] H.E. Haber and G.L. Kane, *The search for supersymmetry: probing physics beyond the standard model*, *Phys. Rept.* **117** (1985) 75 [INSPIRE].

[43] Particle Data Group collaboration, K. Nakamura et al., *Review of particle physics*, *J. Phys.* **G 37** (2010) 075021 [INSPIRE].

[44] M. Masip, R. Muñoz-Tapia and A. Pomarol, *Limits on the mass of the lightest Higgs in supersymmetric models*, *Phys. Rev.* **D 57** (1998) R5340 [hep-ph/9801437] [INSPIRE].

[45] Y. Okada, M. Yamaguchi and T. Yanagida, *Upper bound of the lightest Higgs boson mass in the minimal supersymmetric standard model*, *Prog. Theor. Phys.* **85** (1991) 1 [INSPIRE].

[46] Y. Okada, M. Yamaguchi and T. Yanagida, *Renormalization group analysis on the Higgs mass in the softly broken supersymmetric standard model*, *Phys. Lett.* **B 262** (1991) 54 [INSPIRE].

[47] J.R. Ellis, G. Ridolfi and F. Zwirner, *Radiative corrections to the masses of supersymmetric Higgs bosons*, *Phys. Lett.* **B 257** (1991) 83 [INSPIRE].

[48] H.E. Haber and R. Hempfling, *Can the mass of the lightest Higgs boson of the minimal supersymmetric model be larger than m_Z?*, *Phys. Rev. Lett.* **66** (1991) 1815 [INSPIRE].

JHEP04(2012)022

[49] ATLAS and CMS collaborations, *Combined standard model Higgs boson searches with up to 2.3 fb^{-1} of pp collisions at $\sqrt{s} = 7$ TeV at the LHC*, ATLAS-CONF-2011-157, CMS PAS HIG-11-023 (2011).

[50] G. Pocsik and T. Torma, *On the decays of heavy Higgs bosons*, *Z. Phys.* **C 6** (1980) 1 [INSPIRE].

[51] T.G. Rizzo, *Decays of heavy Higgs bosons*, *Phys. Rev.* **D 22** (1980) 722 [INSPIRE].

[52] W.-Y. Keung and W.J. Marciano, *Higgs scalar decays: $H \to W^{\pm}X$*, *Phys. Rev.* **D 30** (1984) 248 [INSPIRE].

[53] Y. Kawamura, *Triplet doublet splitting, proton stability and extra dimension*, *Prog. Theor. Phys.* **105** (2001) 999 [hep-ph/0012125] [INSPIRE].

[54] L.J. Hall and Y. Nomura, *Gauge unification in higher dimensions*, *Phys. Rev.* **D 64** (2001) 055003 [hep-ph/0103125] [INSPIRE].

[55] N. Sakai and T. Yanagida, *Proton decay in a class of supersymmetric grand unified models*, *Nucl. Phys.* **B 197** (1982) 533 [INSPIRE].

[56] S. Weinberg, *Supersymmetry at ordinary energies. 1. Masses and conservation laws*, *Phys. Rev.* **D 26** (1982) 287 [INSPIRE].

[57] ATLAS collaboration, *Combination of Higgs boson searches with up to 4.9 fb^{-1} of pp collisions data taken at a center-of-mass energy of 7 TeV with the ATLAS experiment at the LHC*, ATLAS-CONF-2011-163 (2011).

[58] CMS collaboration, *Combination of CMS searches for a standard model Higgs boson*, CMS-PAS-HIG-11-032 (2011).

JHEP04(2012)022

Published for SISSA by Springer

Received: November 27, 2012
Accepted: January 27, 2013
Published: February 15, 2013

Higgs mixing and diphoton rate enhancement in NMSSM models

Kiwoon Choi,[a] **Sang Hui Im,**[a] **Kwang Sik Jeong**[b] **and Masahiro Yamaguchi**[b]

[a] *Department of Physics, KAIST, Daejeon 305-701, Korea*

[b] *Department of Physics, Tohoku University, Sendai 980-8578, Japan*

E-mail: kchoi@kaist.ac.kr, shim@muon.kaist.ac.kr, ksjeong@tuhep.phys.tohoku.ac.jp, yama@tuhep.phys.tohoku.ac.jp

Abstract: We study the implications of the LHC Higgs signals on the Higgs mixing in the next-to-minimal supersymmetric standard model (NMSSM). The Higgs couplings can depart from their values in the standard model (SM) due to mixing effects. However the Higgs signal rate in the WW and ZZ channels can remain close to the SM values, as observed at the LHC, even if the SM-like Higgs boson with a mass near 125 GeV has a large singlet component. This allows to get a sizable enhancement in the Higgs to diphoton rate through the charged-higgsino loop contribution, as well as a sizable reduction of the Higgs to $b\bar{b}$ and $\tau\tau$ rates through the mixing effects, with little deviation in the WW and ZZ signal rates from the SM prediction. We find that an enhancement of diphoton signals by a factor of 1.5 or more, and also a reduction of $b\bar{b}$ and $\tau\tau$ signals by a factor of 0.5, can be obtained in the region of parameter space consistent with the constraints on the higgsino mass parameter and the singlet coupling to the Higgs doublets, which determine the Higgs mixing.

Keywords: Higgs Physics, Supersymmetric Standard Model

ArXiv ePrint: 1211.0875

© SISSA 2013

doi:10.1007/JHEP02(2013)090

JHEP02(2013)090

Contents

1 Introduction **1**

2 Higgs sector of the NMSSM **2**
- 2.1 Higgs boson with SM-like properties 2
- 2.2 Higgs boson in the NMSSM 4
- 2.3 Mixing effects on the Higgs signal rate 6

3 Enhanced diphoton rate by higgsino effects **7**

4 Constraints on Higgs mixing **9**
- 4.1 Relation with the Lagrangian parameters 9
- 4.2 Higgs boson mass 10
- 4.3 Examples 12

5 Conclusions **14**

1 Introduction

The ATLAS and CMS collaborations have announced the discovery of a Higgs boson near 125 GeV with standard model (SM)-like properties [1, 2]. It is thus of importance to study if models with extended Higgs sector, which is motivated to solve various difficulties of the SM, can accommodate such a SM-like Higgs boson. In this paper we consider the next-to-minimal supersymmetric SM (NMSSM). The NMSSM maintains most of the nice features of the MSSM while allowing richer physics in the Higgs and neutralino sectors since it includes a SM singlet which couples to the Higgs doublets [3, 4].

In the NMSSM, the Higgs boson properties can significantly deviate from the SM ones due to Higgs mixing effects. Meanwhile the observed Higgs signal rate in the WW/ZZ channel, for which experimental uncertainties are small compared to those in other channels, is almost consistent with the SM predictions. This however does not necessarily demand small Higgs mixing, and it turns out that the observed signal rate in this channel can still be explained even if the SM-like Higgs boson has a large singlet component. It is then interesting to examine how the signal rate in other channels are modified when the Higgs boson mixes with the additional neutral scalars in such a way that the WW/ZZ rate remains close to the SM rate.

In particular we pay our attention to the possibility that the observed enhancement in the diphoton rate relative to the SM value, though we need more statistics to confirm

JHEP02(2013)090

this observation, is accommodated in the presence of Higgs mixing effects.[1,2] Indeed this is achievable through the charged-higgsino loop contribution if the SM-like Higgs boson has a sizable singlet component. In such a case, the mixing effects generally reduce the $b\bar{b}$ and $\tau\tau$ rates below the SM values, because the Higgs couplings to $b\bar{b}$ and $\tau\tau$ are suppressed more strongly than those to the W/Z boson and the top quark. On the other hand, the mixing in the neutral Higgs sector depends on the higgsino mass parameter μ and the singlet coupling λ to the Higgs doublets. This implies that the size of mixing effects is subject to the LEP bound on the chargino mass, and the perturbativity limit on λ, as well as to the requirement on the mass of the SM-like Higgs boson. Thus one should consider these, and also other possible constraints on the model parameters, in order to see how large enhancement can be obtained in the diphoton channel through the charged-higgsino contribution. It turns out that an enhancement of diphoton rate, for instance, by a factor 1.5 or larger, as well as a reduction of $b\bar{b}$ and $\tau\tau$ rates by a factor of 0.5, can be achieved while having little deviation in the WW/ZZ rate from the SM value.

This paper is organized as follows. In section 2, we will briefly review how the Higgs boson couples to the SM particles when it mixes with other neutral scalars, and then examine the Higgs signal rate. We will focus on the question which mixing angles are allowed for the SM-like Higgs boson whose signal rates in the WW/ZZ channel are close to those predicted by the SM. In section 3, we will discuss the possible enhancement of the diphoton rate through the charged-higgsino loop contribution. The constraints on the model parameters will be explored in detail in section 4, where we present some examples to see the mixing effects on the Higgs signal rate in the viable region of parameter space. Section 5 is devoted to the conclusion.

2 Higgs sector of the NMSSM

In the supersymmetric SM, the properties of the SM-like Higgs boson crucially depend on the mixing in the neutral Higgs sector. So an important question is if it is possible to arrange a SM-like Higgs boson whose properties are consistent with the observation, in the presence of mixing effects. We will see that the Higgs signal rate observed at the LHC can have interesting implications on the Higgs mixing in the NMSSM.

2.1 Higgs boson with SM-like properties

We start by discussing how to describe the deviation of Higgs properties from the SM behavior. The interactions of a SM-like Higgs boson h at energy scales around 125 GeV

[1] It has been noticed that Higgs mixing effects can increase the diphoton rate above the SM value in the supersymmetric models [5–9], for which case the WW/ZZ rate is also enhanced by a similar amount, assuming that the MSSM superparticles are heavy.

[2] There have been many works studying how to get a large enhancement in the diphoton signal, see e.g. refs. [10–16] for general discussion. In the supersymmetric SM, charged superparticles can give a sizable contribution to the Higgs coupling to photons if they are light. For instance, in refs. [17–22], light third generation sfermions with large left-right mixing have been considered to achieve this. It is also possible to consider the contribution from light charginos or charged Higgs scalar [23–27]. Alternatively, one may extend the supersymmetric SM to include extra charged-particles with light masses [28–30]. In this case, if colored particles are added, the Higgs production rate at the LHC would be affected significantly.

JHEP02(2013)090

can be examined using the effective action [31],

$$\mathcal{L}_{\rm eff} = C_V \frac{\sqrt{2}m_W^2}{v} h W_\mu^+ W_\mu^- + C_V \frac{m_Z^2}{\sqrt{2}v} h Z_\mu Z_\mu - C_f \frac{m_\psi}{\sqrt{2}v} h\bar{\psi}\psi + C_g \frac{\alpha_s}{12\sqrt{2}\pi v} h G^a_{\mu\nu} G^a_{\mu\nu} + C_\gamma \frac{\alpha}{\sqrt{2}\pi v} h A_{\mu\nu} A_{\mu\nu} + \cdots , \tag{2.1}$$

for ψ denoting the SM fermions, and $v \simeq 174\,\text{GeV}$. Here the custodial symmetry is assumed for the Higgs couplings to W and Z bosons as suggested by the electroweak precision measurements, and the ellipsis denotes Higgs interactions with non-SM particles. In the SM, the Higgs boson has $C_V = C_f = 1$, while its couplings to gluons and photons are induced only radiatively with the dominant contribution coming from the W-boson and top quark loops.

The Higgs signal rate in the decay channel, $h \to ii$, relative to the SM prediction is defined by

$$R_h^{ii} = \frac{\sigma(pp \to h)\,\text{Br}(h \to ii)}{\sigma(pp \to h)|_{\rm SM}\,\text{Br}(h \to ii)|_{\rm SM}}, \tag{2.2}$$

where $\sigma(h)$ and $\text{Br}(h \to ii)$ is the total Higgs production cross section and the branching ratio into the corresponding decay channel, respectively. The production of a SM-like Higgs boson at the LHC is dominated by the gluon-gluon fusion, which receives the main contribution from the top quark loop. Let us assume $C_b = C_\tau$ and $C_t = C_c$, which hold at the tree-level in the MSSM. Then, for $m_h = 125\,\text{GeV}$, using the well-known production and decay properties of the SM Higgs boson having the same mass, one finds the Higgs signal rate in the WW/ZZ channel to be

$$R_h^{VV} \simeq \frac{(0.94C_g^2 + 0.12C_V^2)C_V^2}{0.64C_b^2 + 0.24C_V^2 + 0.12C_t^2}, \tag{2.3}$$

under the assumption that new Higgs decay mode if kinematically allowed has a negligibly small decay width. The Higgs signal rate in other channels read

$$R_h^{b\bar{b}} = R_h^{\tau\tau} = \frac{C_b^2}{C_V^2} R_h^{VV}, \qquad R_h^{\gamma\gamma} \simeq \frac{1.52C_\gamma^2}{C_V^2} R_h^{VV}. \tag{2.4}$$

In the SM, the Higgs boson has $R_h^{ii} = 1$ by definition. Here one should note that the effective couplings C_g and C_γ receive only loop contributions in the MSSM. For the case that colored superparticles have masses well above the weak scale, which we will assume in this paper, the effective Higgs coupling to gluons and photons are written as

$$C_g \simeq 1.03C_t - 0.06C_b, \qquad C_\gamma \simeq 0.23C_t - 1.04C_V + \delta C_\gamma|_{\rm SUSY}, \tag{2.5}$$

for h having $m_h = 125\,\text{GeV}$. The loop correction from charged superparticles, $\delta C_\gamma|_{\rm SUSY}$, becomes important when they are light.

JHEP02(2013)090

The above shows that the signal rates for the decay processes relevant to Higgs searches are determined by the effective Higgs couplings C_V, C_t, C_b and $\delta C_\gamma|_{\rm SUSY}$. We will examine how C_V, C_t and C_b are modified by Higgs mixing effects in the NMSSM, and then move on to discuss how large correction to C_γ is possible from the loops of charged superparticles. In particular, we focus on the possibility to get a large enhancement of the Higgs coupling to photons through the contribution from the charged-higgsino loop, which requires the charged higgsino to have a relatively light mass and also the SM-like Higgs boson to have a sizable singlet component.

2.2 Higgs boson in the NMSSM

The Higgs boson in the supersymmetric SM can have properties which are significantly deviated from the SM properties due to Higgs mixing effects. In particular, NMSSM models have rich Higgs/neutralino physics as the Higgs sector is extended to include a SM singlet field S. The singlet couples to the Higgs doublets through,

$$W = \lambda S H_u H_d + f(S) + (\text{MSSM Yukawa terms}), \tag{2.6}$$

so that a higgsino mass parameter is dynamically generated after it gets a vacuum expectation value. The effective Higgs μ and $B\mu$ terms read

$$\begin{aligned} \mu &\equiv \lambda\langle S\rangle, \\ B\mu &\equiv A_\lambda \lambda\langle S\rangle + \lambda\langle \partial_S f\rangle, \end{aligned} \tag{2.7}$$

where A_λ is the soft SUSY breaking trilinear parameter, and we take a field basis such that a bare μ term if exists is absorbed into S. The superpotential $f(S)$ is necessary to avoid a phenomenologically unacceptable visible axion, and various models are classified according to its form. In this paper, we do not specify the exact form of $f(S)$, but will assume that there is no CP violation in the Higgs sector. Noting that H_u^0 and H_d^0 mix with the singlet scalar through the scalar potential terms,

$$V_{\rm mix} = \lambda^2 |S|^2 \left(|H_u|^2 + |H_d|^2\right) + \left(A_\lambda \lambda S H_u H_d + (\partial_S f)^* \lambda H_u H_d + \text{h.c.}\right), \tag{2.8}$$

we introduce a mass parameter,

$$\Lambda \equiv A_\lambda + \langle \partial_S^2 f\rangle, \tag{2.9}$$

for discussion on the Higgs mixing, and will treat μ, $B\mu$ and Λ as independent parameters as $f(S)$ is needed in any model for the Higgs sector not to possess a global symmetry, unless λ is extremely small.

The neutral Higgs sector of the NMSSM has three CP-even Higgs bosons:

$$\begin{aligned} \hat{h} &= \sqrt{2}\left((\text{Re}H_d^0 - v\cos\beta)\cos\beta + (\text{Re}H_u^0 - v\sin\beta)\sin\beta\right), \\ \hat{H} &= \sqrt{2}\left((\text{Re}H_d^0 - v\cos\beta)\sin\beta - (\text{Re}H_u^0 - v\sin\beta)\cos\beta\right), \\ \hat{s} &= \sqrt{2}\left(\text{Re}S - \langle S\rangle\right), \end{aligned} \tag{2.10}$$

JHEP02(2013)090

where $\langle H_u^0 \rangle = v \sin\beta$ and $\langle H_d^0 \rangle = v \cos\beta$. Among them, $\hat{h}$ behaves exactly like the SM Higgs boson if it does not mix with the others. However, since the mass matrix of the hatted fields is given by

$$\hat{M}^2 = \begin{pmatrix} m_{\hat{h}}^2 & \frac{1}{2}(m_Z^2 - \lambda^2 v^2)\sin 4\beta & \lambda v(2\mu - \Lambda \sin 2\beta) \\ \frac{1}{2}(m_Z^2 - \lambda^2 v^2)\sin 4\beta & m_{\hat{H}}^2 & \lambda v \Lambda \cos 2\beta \\ \lambda v(2\mu - \Lambda \sin 2\beta) & \lambda v \Lambda \cos 2\beta & m_{\hat{s}}^2 \end{pmatrix}, \tag{2.11}$$

the SM-like Higgs boson generally appears as a mixture of CP-even Higgs bosons:

$$h = c_{\theta_1} c_{\theta_2} \hat{h} - s_{\theta 1} \hat{H} - c_{\theta_1} s_{\theta_2} \hat{s}, \tag{2.12}$$

which we assume to be the resonance near 125 GeV observed at the LHC. Here $s_\theta = \sin\theta$ and $c_\theta = \cos\theta$, for $-\pi/2 < \theta_i \leq \pi/2$ $(i = 1, 2, 3)$ being the mixing angles in the orthogonal matrix diagonalizing $\hat{M}^2$ (see eq. (4.3)). There are also two other mass eigenstates, s and H with mass m_s and m_H, respectively, where we define H to be the heaviest Higgs boson and fix the mass of h to be $m_h \simeq 125$ GeV.

Let us summarize the properties of the SM-like Higgs boson in the presence of mixing effects. The Higgs couplings are determined by

$$\begin{aligned} C_V &= c_{\theta_1} c_{\theta_2}, \\ C_t &= c_{\theta_1} c_{\theta_2} + s_{\theta_1} \cot\beta, \\ C_b &= C_\tau = c_{\theta_1} c_{\theta_2} - s_{\theta_1} \tan\beta, \end{aligned} \tag{2.13}$$

at the tree-level. The branching fraction of h for each decay process deviates from the SM value if the above effective couplings have values different from each other. This is indeed the case due to the second term in the effective coupling to the quarks, which relies on $\tan\beta$ and θ_1. Note that the sign of θ_1 is also important. For instance, if θ_1 has a positive value, it is possible to reduce the Higgs coupling to the bottom quark relative to the SM value, more significantly than those to the W/Z boson and top quark. This does not happen in the MSSM unless there are large radiative corrections to the mixing between two doublet Higgs bosons. Here we only consider $\tan\beta > 1$ as required for the top Yukawa coupling to remain perturbative at high energy scales. However the situation changes in the NMSSM, where one can consider $\lambda v > m_Z$ for which $\hat{M}_{12}^2$ is positive, or sizable mixing between the singlet and doublets. As we will see soon, mixing with $\theta_1 > 0$ has an interesting implication for the modification in the Higgs signal rate.

On the other hand, mixing effects on the Higgs boson mass can be examined using the relation,

$$m_h^2 = m_{\hat{h}}^2 - \frac{(s_{\theta_2} s_{\theta_3} - s_{\theta_1} c_{\theta_2} c_{\theta_3})^2}{c_{\theta_1}^2 c_{\theta_2}^2}(m_H^2 - m_{\hat{h}}^2) - \frac{(s_{\theta_2} c_{\theta_3} + s_{\theta_1} c_{\theta_2} s_{\theta_3})^2}{c_{\theta_1}^2 c_{\theta_2}^2}(m_s^2 - m_{\hat{h}}^2). \tag{2.14}$$

The above relation imposes a constraint on m_H, m_s and the mixing angles because $m_{\hat{h}}$ is restricted to be less than a certain value:

$$m_{\hat{h}}^2 = m_0^2 + (\lambda^2 v^2 - m_Z^2)\sin^2 2\beta, \tag{2.15}$$

JHEP02(2013)090

where m_0 is equal to m_Z at the tree-level, and can be regarded as the SM-like Higgs boson mass in the decoupling limit of the MSSM at large $\tan\beta$. The NMSSM contribution raises $m_{\hat{h}}$ above m_0 for $\lambda v > m_Z$, but the amount decreases as $\tan\beta$ increases. Including radiative corrections, one finds [32, 33]

$$m_0^2 = m_Z^2 + \frac{3m_t^4}{4\pi^2 v^2}\ln\left(\frac{m_{\tilde{t}}^2}{m_t^2}\right) + \frac{3m_t^4}{4\pi^2 v^2}\left(X_t^2 - \frac{1}{12}X_t^4\right) + \cdots, \tag{2.16}$$

where $m_{\tilde{t}}$ is the stop mass, and $X_t = (A_t - \mu\cot\beta)/m_{\tilde{t}}$ denotes the stop mixing parameter. For the stop masses at the TeV scale, m_0 is around 115 GeV. The stop mixing raises m_0 further approximately by the amount, $5\,\text{GeV} \times (X_t^2 - X_t^4/12)$, which is about 5 GeV at $X_t = 1$. The stop mixing contribution is maximized at $X_t = \sqrt{6}$, where m_0 can reach about 130 GeV for stop masses around TeV. In section 4, taking the value of m_0 in the range between 95 and 135 GeV, we will examine in detail the region of parameter space consistent with various constraints on the Higgs mixing.

2.3 Mixing effects on the Higgs signal rate

The observed Higgs signal rate in the WW/ZZ channel, which has a relatively small experimental error compared to other decay processes, is in good agreement with the SM predictions. However this does not necessarily imply small mixing in the neutral Higgs sector. It is thus of importance to examine the signal rate in other channels when the SM-like Higgs boson has $R_h^{VV} \approx 1$ in the presence of Higgs mixing. The signal rate for $h \to b\bar{b}$ and $h \to \gamma\gamma$ are modified according to the relation (2.4).

Plugging the effective Higgs couplings (2.13) into the relation (2.3), we find that Higgs mixing leaves the signal rate R_h^{VV} close to 1 at two different positive values of θ_1 for given $\tan\beta$ and θ_2. The larger solution of $R_h^{VV} \approx 1$ is approximately given by

$$\theta_1|_{\text{large}} \approx \frac{2.1 - 1.9\sin^2\theta_2}{\tan\beta}, \tag{2.17}$$

for moderate and large values of $\tan\beta$. It is also straightforward to see that the smaller solution reads

$$\theta_1|_{\text{small}} \approx \frac{\tan\beta}{1.4\tan^2\beta + 1.7}\sin^2\theta_2, \tag{2.18}$$

for $\tan\beta \gtrsim 2$. Thus C_V and C_t are positive for both solutions, while C_b is found to be positive only for $\theta_1|_{\text{small}}$. This results in that the $b\bar{b}$ signal rate can also remain close to the SM value for $\theta_1|_{\text{large}}$ if $C_V \approx -C_b$, which we find the case in the region around $\sin^2\theta_2 = 0.15$. Note also that the gluon-gluon fusion for the Higgs boson production occurs through the coupling C_g, and thus depends on the relative sign of C_t and C_b since the quarks have masses, $2m_b < m_h < 2m_t$. On the other hand, for the smaller solution $\theta_1|_{\text{small}}$, the SM-like Higgs boson contains non-SM Higgs doublet component whose fraction is much smaller than the singlet fraction. In this case, $R_h^{b\bar{b}}$ is always smaller than R_h^{VV}.

Figure 1 shows the region of parameter space leading to $R_h^{VV} = 1 \pm 0.1$, for $\tan\beta = 2, 5, 8$. One sees that the Higgs signal rate in the WW/ZZ channel can remain consistent

JHEP02(2013)090

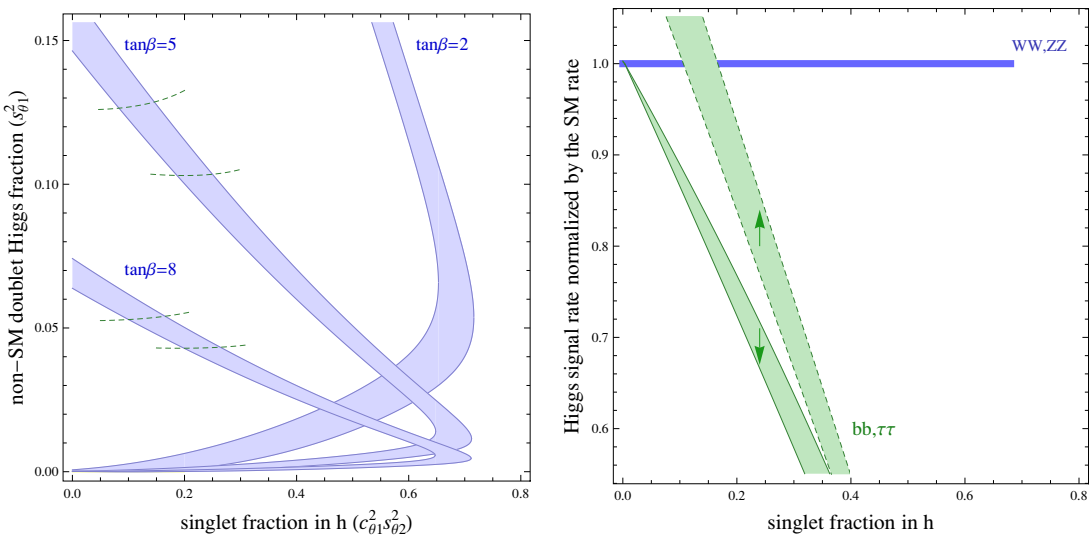

Figure 1. Mixing effects on the signal rate of the SM-like Higgs boson, $h = c_{\theta_1} c_{\theta_2} \hat{h} - s_{\theta_1} \hat{H} - c_{\theta_1} s_{\theta_2} \hat{s}$ with mass $m_h = 125\,\text{GeV}$. The left panel shows the region of parameter space where the signal rate in the WW/ZZ channel is $R_h^{VV} = 1 \pm 0.1$, for $\tan\beta = 2, 5, 8$, respectively. The $b\bar{b}$ channel also has $R_h^{b\bar{b}} = 1 \pm 0.1$ in the region between two dashed green lines, in the blue band. The right panel illustrates how the signal rates in $h \to b\bar{b}$ and $h \to \tau\tau$ are affected by mixing effects when the Higgs boson has $R_h^{VV} = 1$. The green band is $R_h^{b\bar{b}} (= R_h^{\tau\tau})$ obtained for $2 \leq \tan\beta \leq 5$, where the colored arrow indicates its behavior for increasing $\tan\beta$. The lower (upper) band corresponds to the $b\bar{b}$ rate for θ_1 fixed at the smaller (larger) solution of the equation $R_h^{VV}(\theta_1) = 1$.

with the observation even if the SM-like Higgs boson has a large singlet fraction. In the right panel of the figure, we illustrate how the $b\bar{b}$ and $\tau\tau$ rates are modified when the Higgs mixing leads to $R_h^{VV} = 1$. The green band gives $R_h^{b\bar{b}} (= R_h^{\tau\tau})$ for $2 \leq \tan\beta \leq 5$, where the colored arrow shows how the signal rate changes as $\tan\beta$ increases. The lower (upper) green band corresponds to $R_h^{b\bar{b}}$ for θ_1 fixed at the smaller (larger) solution of the equation $R_h^{VV}(\theta_1) = 1$. The $b\bar{b}$ and $\tau\tau$ rates are reduced relative to the SM case for the smaller solution, however this is not necessarily the case for the other solution. On the other hand, the mixing also affects the diphoton rate, which will be examined in section 3 by including the contribution from the charged higgsino.

3 Enhanced diphoton rate by higgsino effects

The Higgs signal in the $h \to \gamma\gamma$ process has been observed at the rate, 1.5 to 1.8 times larger than the value predicted in the SM. Although the statistics is small yet compared to the WW/ZZ channel, this may be a hint for physics beyond the SM. In particular, it is interesting to see if the observed enhancement of the diphoton rate can be explained within the NMSSM, where the deviation in the WW/ZZ channel is small even if the Higgs mixing is sizable. Indeed the Higgs coupling to photons can receive a significant contribution from the charged-higgsino loop when the Higgs boson has a large singlet component.

Let us examine the higgsino effects on the diphoton rate in the presence of Higgs mixing. Since the singlet scalar couples to the higgsinos through the Yukawa term $\lambda S \tilde{H}_u \tilde{H}_d$ in the

JHEP02(2013)090

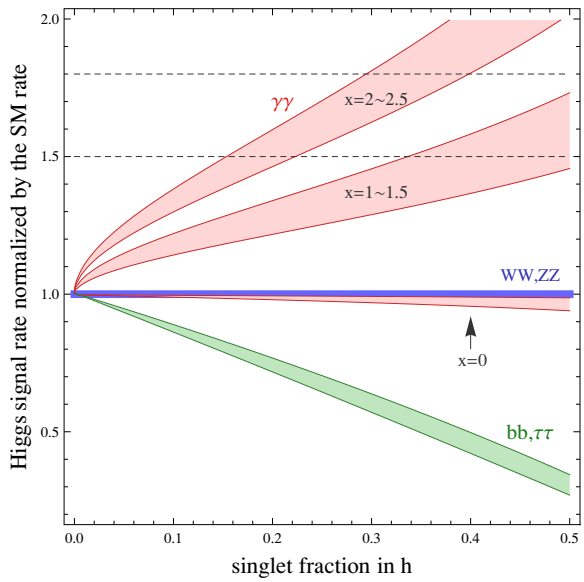

Figure 2. Enhanced diphoton rate via the charged-higgsino loop contribution, in the presence of Higgs mixing with positive θ_1 and θ_2. We fix the value of θ_1 at the smaller solution of $R_h^{VV}(\theta_1) = 1$, for which the diphoton rate is determined by θ_2 and $x \equiv \lambda v/|\mu|$, almost independent of $\tan\beta$. The red band corresponds to $R_h^{\gamma\gamma}$ for $x = 0$, $1 \leq x \leq 1.5$, and $2 \leq x \leq 2.5$ from below, respectively. Here we take $2 \leq \tan\beta \leq 8$. The figure also shows the signal rate in other channels, which are rarely affected by the charged-higgsino loop. The green band gives $R_h^{b\bar{b}}$ obtained for $\tan\beta$ in the same range.

NMSSM, the SM-like Higgs boson has the interaction,

$$\mathcal{L} = \frac{\lambda c_{\theta_1} s_{\theta_2}}{\sqrt{2}} h \tilde{H}_u^+ \tilde{H}_d^- + \cdots . \tag{3.1}$$

Thus the Higgs coupling to photons is radiatively generated by the charged-higgsino loop. The contribution to C_γ is found to be [31],

$$\delta C_\gamma|_{\rm SUSY} \simeq -0.17 A_f(\tau_{\tilde{H}^\pm}) \frac{\lambda v}{m_{\tilde{H}^\pm}} c_{\theta_1} s_{\theta_2}, \tag{3.2}$$

where $\tau_i = m_h^2/4m_i^2$, and the charged higgsino has mass $m_{\tilde{H}^\pm} \simeq |\mu|$ simply assuming that the Wino is heavy so that the mixing in the chargino sector is small. The loop function is given by $A_f(\tau) = 3(\tau + (\tau - 1)\arcsin^2\sqrt{\tau})/2\tau^2$ for $\tau \leq 1$, and is approximated as $A_f(\tau) \simeq 1 + 7\tau/30$ for small values of τ. On the other hand, the effective couplings C_V, C_t and C_b are negligibly affected by the charged higgsino.

The SM-like Higgs boson can have $R_h^{VV} \approx 1$ for the Higgs mixing (2.17) or (2.18), for which the diphoton signal rate will be reduced a bit below the SM value if $\delta C_\gamma|_{\rm SUSY} = 0$. However, including the radiative correction from $\tilde{H}^\pm$, the diphoton rate reads

$$R_h^{\gamma\gamma} \simeq \frac{1.52 C_\gamma^2}{C_V^2} R_h^{VV} \simeq \left(1 - 0.28 \frac{s_{\theta_1}}{c_{\theta_1} c_{\theta_2}} \frac{1}{\tan\beta} + 0.21 \frac{s_{\theta_2}}{c_{\theta_2}} \frac{\lambda v}{|\mu|}\right)^2 R_h^{VV}, \tag{3.3}$$

JHEP02(2013)090

for $|\mu| \gtrsim 100\,\text{GeV}$, and thus an enhancement of diphoton signals relative to the SM case is achievable for $R_h^{VV} \approx 1$, when θ_2 is positive. Note that, if $\delta C_\gamma|_{\text{SUSY}} = 0$, the Higgs signal rate in each channel is modified by the mixing effects independently of the sign of θ_2. To get a large enhancement, the charged higgsino needs to have a small mass. In addition, we need a large value of θ_2, which determines the singlet fraction of the SM-like Higgs boson. Since Higgs mixing with positive θ_1 allows h to contain a large singlet component while having $R_h^{VV} \approx 1$, the second term in the bracket in (3.3) tells that a small value of θ_1 is favored to have $R_h^{\gamma\gamma}$ larger than R_h^{VV}. For the smaller solution (2.18) of $R_h^{VV}(\theta_1) \approx 1$, the diphoton rate becomes insensitive to $\tan\beta$, and is written

$$R_h^{\gamma\gamma} \approx \left(1 + 0.21 \frac{s_{\theta_2}}{c_{\theta_2}} \frac{\lambda v}{|\mu|}\right)^2 . \tag{3.4}$$

Thus the signal rate in $h \to \gamma\gamma$ can be larger than the SM expectation, but still with little deviation in the WW/ZZ channel. The enhancement crucially depends on the value of $\lambda v/|\mu|$, which is less than about 3.5 for $\lambda < 2$ and μ is larger than 100 GeV. In section 4, we will examine the value of $\lambda v/|\mu|$ consistent with various constraints.

Figure 2 illustrates the effect of the charged higgsino on the diphoton rate, where we have fixed the value of θ_1 to give $R_h^{VV} = 1$ for positive θ_1 and θ_2. Among the two solutions of $R_h^{VV}(\theta_1) = 1$, we choose the smaller one, for which the diphoton rate is almost independent of $\tan\beta$. The $R_h^{\gamma\gamma}$ is shown in the red band for $x = 0$, $1 \leq x \leq 1.5$ and $2 \leq x \leq 2.5$, where $x \equiv \lambda v/|\mu|$. In the absence of the charged-higgsino contribution, which is the case with $x = 0$, the diphoton rate is slightly below the SM value. However the higgsino effect can significantly enhance diphoton signals, which demands a large x and sizable singlet fraction in h. For instance, the diphoton rate is about 1.5 times larger than the SM value at $x = 1.2$ if the singlet fraction in h is 0.4. On the other hand, the green band indicates $R_h^{b\bar{b}}$ obtained for $2 \leq \tan\beta \leq 8$. The $b\bar{b}$ rate is reduced relative to the SM value. Meanwhile, one may consider Higgs mixing such that R_h^{VV} is a bit larger than 1. Then the diphoton rate will be increased by the similar amount, whereas $R_h^{b\bar{b}}$ will decrease further.

4 Constraints on Higgs mixing

In this section, we discuss various constraints on the mass spectrum of Higgs bosons and the mixing angles which arise because of their relations to the model parameters in $\hat{M}^2$. Then we will consider several examples to explore the region of parameter space where the SM-like Higgs boson has $R_h^{VV} \approx 1$ while satisfying the constraints. The WW/ZZ rate remains close to the SM value at the two solutions of $R_h^{VV}(\theta_1) \approx 1$, among which the smaller one is favored to get a large enhancement in the diphoton rate through the charged-higgsino contribution. So we will focus on the smaller solution, and examine the diphoton rate in the explicit examples.

4.1 Relation with the Lagrangian parameters

Let us first discuss the constraints on Higgs mixing related to the model parameter μ and λ, which determine the off-diagonal components of $\hat{M}^2$. Their values are determined once

JHEP02(2013)090

we fix the mass eigenvalues and mixing angles. This implies that μ and λ are written as functions of

$$\xi \equiv (\tan\beta, m_H, m_s, \theta_1, \theta_2, \theta_3). \tag{4.1}$$

Meanwhile the LEP bound on the chargino mass requires μ larger than about 100 GeV [34]. In addition, in order for the model to remain perturbative up to at least 10 TeV, λ should be less than about 2 at the weak scale. For NMSSM models with λ larger than about 0.7 [35], there should appear new physics, such as strong dynamics involving S, at an intermediate scale below the conventional GUT scale $\sim 10^{16}$ GeV. The above bounds on μ and λ translate into the constraints on ξ.

Here we present the relation between ξ and the model parameters appearing in the off-diagonal elements of $\hat{M}^2$:

$$\begin{aligned}
\lambda^2 v^2 &= m_Z^2 + \frac{1}{\sin 4\beta}\Big((m_H^2 - m_s^2)s_{\theta_2}s_{2\theta_3} + 2(m_h^2 - m_H^2 c_{\theta_3}^2 - m_s^2 s_{\theta_3}^2)s_{\theta_1}c_{\theta_2}\Big)c_{\theta_1}, \\
\lambda v\mu &= -\frac{1}{4}m_h^2 c_{\theta_1}^2 s_{2\theta_2} - \frac{1}{4}(m_H^2 - m_s^2)s_{\theta_1}c_{2\theta_2}s_{2\theta_3} \\
&\quad + \frac{1}{4}\Big((m_H^2 - m_s^2 s_{\theta_1}^2)s_{\theta_3}^2 - (m_H^2 s_{\theta_1}^2 - m_s^2)c_{\theta_3}^2\Big)s_{2\theta_2} \\
&\quad - \frac{\tan 2\beta}{4}\Big((m_H^2 - m_s^2)c_{\theta_2}s_{2\theta_3} - 2(m_h^2 - m_H^2 c_{\theta_3}^2 - m_s^2 s_{\theta_3}^2)s_{\theta_1}s_{\theta_2}\Big)c_{\theta_1}, \\
\lambda v\Lambda &= -\frac{1}{2\cos 2\beta}\Big((m_H^2 - m_s^2)c_{\theta_2}s_{2\theta_3} - 2(m_h^2 - m_H^2 c_{\theta_3}^2 - m_s^2 s_{\theta_3}^2)s_{\theta_1}s_{\theta_2}\Big)c_{\theta_1},
\end{aligned} \tag{4.2}$$

where we have used that the orthogonal matrix U which diagonalizes $\hat{M}^2$ is parameterized in terms of three mixing angles,

$$U = \begin{pmatrix} c_{\theta_1}c_{\theta_2} & -s_{\theta_1} & -c_{\theta_1}s_{\theta_2} \\ s_{\theta_1}c_{\theta_2}c_{\theta_3} - s_{\theta_2}s_{\theta_3} & c_{\theta_1}c_{\theta_3} & -c_{\theta_2}s_{\theta_3} - s_{\theta_1}s_{\theta_2}c_{\theta_3} \\ s_{\theta_1}c_{\theta_2}s_{\theta_3} + s_{\theta_2}c_{\theta_3} & c_{\theta_1}s_{\theta_3} & c_{\theta_2}c_{\theta_3} - s_{\theta_1}s_{\theta_2}s_{\theta_3} \end{pmatrix}, \tag{4.3}$$

for $c_\theta = \cos\theta$ and $s_\theta = \sin\theta$.

4.2 Higgs boson mass

There are also constraints related to the mass spectrum of the Higgs bosons. The SM-like Higgs boson has a mass which is written as a function of m_0 and ξ, as is given by (2.14). Thus, requiring $m_h \simeq 125$ GeV constrains the parameter space of m_0 and ξ. Here the value of m_0 has an upper bound, crucially depending on the radiative corrections. For instance, m_0 is less than about 120 GeV for the stop with mass around or smaller than 1 TeV and small stop mixing. One can also arrange m_0 around or larger than 130 GeV by considering stop masses above a few TeV or invoking large stop mixing. It is worth noting that, in the NMSSM, m_0 can receive an additional sizable contribution from the higgsino loops. The superpotential $f(S)$ provides mass to the singlino, $m_{\tilde{S}} = \langle \partial_S^2 f \rangle$. If $m_{\tilde{S}}$ is around or below μ, the interactions of the higgsinos ($\tilde{H}_u$ and $\tilde{H}_d$) and the singlino ($\tilde{S}$),

$$-\mathcal{L}_{\rm int} = \lambda H_u \tilde{H}_d \tilde{S} + \lambda H_d \tilde{H}_u \tilde{S} + \mu \tilde{H}_u \tilde{H}_d + \frac{1}{2}m_{\tilde{S}}\tilde{S}\tilde{S} + \text{h.c.}, \tag{4.4}$$

JHEP02(2013)090

will remain relevant at low energy scales. Then the mass of $\hat{h}$ receives additional radiative corrections, analogously to that from the top Yukawa coupling. The correction is estimated naively to be [36]

$$\delta m_0^2 \approx \frac{\lambda^4 v^2}{4\pi^2} \ln\left(\frac{m_s^2}{|\mu|^2}\right), \tag{4.5}$$

for $m_s^2 \gg |\mu|^2$. The above contribution is quite sensitive to λ, but is almost independent of $\tan\beta$. In the analysis, we will consider $95\,\text{GeV} \leq m_0 \leq 135\,\text{GeV}$, while keeping in mind that larger values can be allowed depending on models.

On the other hand, the experimental constraints from the $b \to s\gamma$ process require the charged Higgs scalar to be heavier than about 350 GeV [37] unless there are cancellations with superparticle contributions. The charged Higgs scalar obtains a mass according to $m_{H^\pm}^2 = m_{\hat{H}}^2 + m_W^2 - m_Z^2 \sin^2 2\beta$ at the tree-level, while $m_{\hat{H}}^2$ is given by

$$m_{\hat{H}}^2 = s_{\theta_1}^2 m_h^2 + c_{\theta_1}^2 c_{\theta_3}^2 m_H^2 + c_{\theta_1}^2 s_{\theta_3}^2 m_s^2, \tag{4.6}$$

implying that an addition constraint will be imposed if one requires a large value of $m_{H^\pm}$ to avoid the constraint from $b \to s\gamma$.

For a large value of m_H, the mixing angle θ_3 needs to be small since otherwise mixing between $\hat{h}$ and $\hat{H}$ will decrease the mass of the SM-like Higgs boson significantly. Suppose that θ_3 is similar to or smaller than θ_1 in size. Then the Higgs mass reads

$$m_h^2 \approx m_{\hat{h}}^2 - \frac{1}{\tan^2\beta} \frac{s_{\theta_2}^4}{1 - s_{\theta_2}^2}(m_H^2 - m_{\hat{h}}^2) - \frac{s_{\theta_2}^2}{1 - s_{\theta_2}^2}(m_s^2 - m_{\hat{h}}^2), \tag{4.7}$$

for $\theta_1 = \theta_1|_{\text{small}}$, where the coefficients of order unity have been neglected in the last two terms. We see that the second term, which is a result of mixing between two doublet Higgs bosons, is much suppressed compared to the third term. Indeed one can find that the second term lowers the mass of h by less than about 10 GeV even for H having mass around or above 350 GeV, if

$$s_{\theta_2}^2 \lesssim 0.15 \times \left(\frac{m_H}{350\text{GeV}}\right)^{-1} \tan\beta. \tag{4.8}$$

for $\tan\beta \gtrsim 2$. On the other hand, the third term arises due to mixing with the singlet, and can have either sign. This contribution will compensate the mass decrease by the second term if s has a mass smaller than $m_{\hat{h}}$. The relation $m_{\hat{h}}^2 = m_0^2 + (\lambda^2 v^2 - m_Z^2)\sin^2 2\beta$ tells that the sign of the third term depends m_0, λ and $\tan\beta$. It is clear that m_s much larger than m_0 will make it difficult to get $m_h \simeq 125\,\text{GeV}$ unless the NMSSM contribution to $m_{\hat{h}}$ is large enough.

Let us discuss further the properties of s, which is singlet-like in most of the parameter space of interest. Since it couples to the SM particles through the doublet Higgs components, it may be possible to detect s at hadron colliders when Higgs mixing is large. The production and decay rate of s depend on its mass and the fraction of the Higgs doublets. However, if the invisible decay into neutralinos is kinematically allowed, the discovery of the

JHEP02(2013)090

singlet-like Higgs boson will become very difficult. This is the case for $m_h < 2m_{\chi_1^0} < m_s$, where the lower bound on $m_{\chi_1^0}$ would be necessary to suppress the invisible decay of the SM-like Higgs boson.[3] On the other hand, if $m_s < m_h$, one should take into account the LEP constraints on the signal rate of s in $e^+e^- \to Zs \to Zb\bar{b}$ [41]. In this case, it may still be possible to have sizable mixing if m_s lies in the range between about 90 and 110 GeV.

Before proceeding to the analysis, we briefly mention about the property of the lightest neutralino, which we assume the lightest superparticle (LSP). For $\lambda v/|\mu|$ around one, the lightest neutralino χ_1^0 is a sizable mixture of the neutral higgsinos and singlino, simply assuming that all the gauginos are heavy. If χ_1^0 is heavier than the W-boson, the annihilation among LSPs takes place with a large cross section, dominantly through the t-channel charged-higgsino exchange with W bosons in the final state. Then thermal relic density of χ_1^0 would be too small to account for the observed dark matter density. To avoid this, one may consider light gauginos so that χ_1^0 has a sizable Bino component. Another way would be to implement non-thermal production of LSPs, or to consider the QCD axion as a dark matter.

On the other hand, for $m_{\tilde{s}} \gg |\mu|$ and $\lambda v/|\mu|$ around one, the mixing decreases the mass of a higgsino-like neutralino, and thus it is possible to have χ_1^0 lighter than m_W but heavier than $m_h/2$. In such a case, the annihilation via the s-channel Z-boson exchange into SM fermions is not so effective due to the suppressed $Z\chi_1^0\chi_1^0$ coupling, and the coannihilation effect [42] is also suppressed because the charged-higgsino still has a mass equal to μ. However, since the $h\chi_1^0\chi_1^0$ coupling can be sizable in the NMSSM, it would be possible to get the correct dark matter density from thermally produced LSPs. A detailed analysis will be given elsewhere.

4.3 Examples

We have discussed the constraints and the favored values of model parameters. Let us now examine the diphoton rate in the region of parameter space where such requirements are satisfied. In the analysis, we impose the constraints,

$$m_h \simeq 125\,\text{GeV}, \quad |\mu| \geq 105\,\text{GeV}, \quad \lambda \leq 2, \tag{4.9}$$

by taking m_0 in the range

$$95\,\text{GeV} \leq m_0 \leq 135\,\text{GeV}. \tag{4.10}$$

For given m_H, m_s and θ_3, three parameters of ξ in (4.1) remain unfixed. Among them, θ_1 is fixed if one requires the signal rate in the WW/ZZ channel to be close to the SM value. Then we can examine the above constraints by scanning over $\tan\beta$ and θ_2, or equivalently in terms of $\tan\beta$ and the singlet fraction in the SM-like Higgs boson. The Higgs signal rate in $h \to \gamma\gamma$ is determined by $x = \lambda v/|\mu|$ and the singlet fraction in h.

[3] In models where $f(S)$ contains only a linear term of S [36, 38–40], the singlino has no Majonara mass term, and the mass and the coupling to h of χ_1^0 are proportional to $\lambda^2 v \sin 2\beta/\mu$. One would thus need small $\tan\beta$ and large λ to kinematically forbid the invisible decay of h into neutralinos.

JHEP02(2013)090

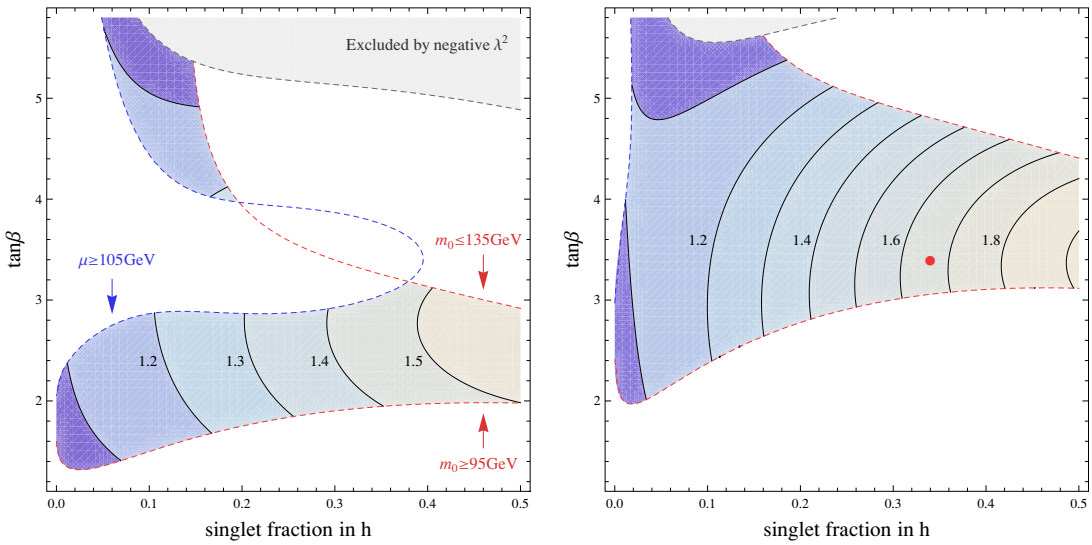

Figure 3. Enhanced diphoton rate in the region of parameter space allowed by $|\mu| \geq 105\,\text{GeV}$ and $\lambda \leq 2$, where we have fixed θ_1 at the smaller solution of $R_h^{VV}(\theta_1) = 1.05$. The left panel is for the case with $(m_H, m_s, \theta_3) = (480\text{GeV}, 160\text{GeV}, 0.1)$, while the right one is for $(m_H, m_s, \theta_3) = (780\text{GeV}, 160\text{GeV}, 0.07)$. In both figures, μ is larger than $105\,\text{GeV}$ in the right side of the blue-dashed curve, and $m_h = 125\,\text{GeV}$ is obtained for $95\,\text{GeV} \leq m_0 \leq 135\,\text{GeV}$ in the region between two red-dashed curves. The gray-shaded region is excluded due to negative λ^2. The contours of $R_h^{\gamma\gamma}$ are indicated by black lines, with the contour interval equal to 0.1. To see the detailed Higgs properties, we take an example point as given by the red-filled circle.

In figure 3, we show the diphoton rate relative to the SM value in the region of parameter space allowed by the requirements mentioned above, for two examples,

$$\begin{aligned} \text{example 1} \ &: \ (m_H, m_s, \theta_3) = (480\text{GeV}, 160\text{GeV}, 0.10), \\ \text{example 2} \ &: \ (m_H, m_s, \theta_3) = (780\text{GeV}, 160\text{GeV}, 0.07), \end{aligned}$$

with θ_1 fixed at the smaller solution of $R_h^{VV}(\theta_1) = 1.05$. For both examples, the parameter space is mainly constrained by the requirements, $m_h = 125\,\text{GeV}$ and $|\mu| \geq 105\,\text{GeV}$. The right side of the blue-dashed curve gives μ larger than $105\,\text{GeV}$, and h has $m_h = 125\,\text{GeV}$ between two red-dashed curves if one considers $95\,\text{GeV} \leq m_0 \leq 135\,\text{GeV}$. The gray-shaded region is excluded since $\lambda^2 < 0$. The diphoton rate relative to the SM value is shown in black lines. We see that an enhancement by a factor of 1.5 or larger can be accommodated through the charged-higgsino contribution, when $\tan\beta$ is about $2-3$ and the singlet fraction in h is larger than 0.39 in the left panel. For the other example, this is achieved at $3 \lesssim \tan\beta \lesssim 4.8$ when the singlet fraction in h is larger than 0.26. On the other hand, the mixing effects reduce the $b\bar{b}$ rate below the SM value.

To see the relation between ξ and the model parameters, we take an example point at

$$(\tan\beta, m_H, m_s, \theta_1, \theta_2, \theta_3) = (3.4,\ 780\,\text{GeV},\ 160\,\text{GeV},\ 0.07,\ 0.62,\ 0.07), \tag{4.11}$$

which corresponds to the red-filled circle in the figure. The above set of parameters trans-

JHEP02(2013)090

lates into

$$(\lambda, \mu, \Lambda, m_0) \simeq (1.03, 112\,\text{GeV}, 376\,\text{GeV}, 110\,\text{GeV}), \tag{4.12}$$

together with $m_{\hat{H}} \simeq 776\,\text{GeV}$ and $m_{\hat{s}} \simeq 167\,\text{GeV}$. The Higgs signal rate in the WW/ZZ channel is $R_h^{VV} = 1.05$ at the example point, and the $b\bar{b}/\tau\tau$ channel has $R_h^{b\bar{b}} = R_h^{\tau\tau} \simeq 0.51$. Finally, the diphoton rate is found to be $R_h^{\gamma\gamma} \simeq 1.66$, as a result of the charged-higgsino loop contribution combined with the Higgs mixing effects.

5 Conclusions

We have examined how to arrange a SM-like Higgs boson in the NMSSM, in a way consistent with the LHC results on the Higgs boson search. The observed WW/ZZ signal rate can be compatible with the model even when the SM-like Higgs boson has a large singlet component. This leads to an interesting possibility that the Higgs to diphoton signal rate is enhanced by the loops of charged higgsino which couples to the SM-like Higgs boson through mixing with the singlet scalar. A large enhancement is achievable when there is a large singlet fraction in the SM-like Higgs boson and the charged higgsino is light.

The Higgs mixing depends on the higgsino mass parameter μ and the singlet coupling λ to the Higgs doublets. Hence there are constraints on the Higgs mixing angles coming from the LEP bound on the chargino mass, and the perturbativity limit on λ. In addition, the model should provide a mass near 125 GeV to the SM-like Higgs boson. Taking into account these constraints, we find that the charged-higgsino loop contribution, combined with the mixing effects, can enhance the diphoton signal rate above the SM expectation by a factor of 1.5 or more, while having little deviation in the WW/ZZ rate.

On the other hand, the Higgs mixing effects reduce the $b\bar{b}$ and $\tau\tau$ signals below the SM values, if the mixing between two doublet Higgs bosons $\hat{h}$ and $\hat{H}$ is relatively small, which is favored to get a sizable enhancement of the diphoton signal rate while keeping the WW/ZZ rate similar to the SM prediction. Indeed we could see that the $b\bar{b}$ and $\tau\tau$ rates can be reduced by a factor of 0.5, or even less, for the mixing parameters which would enhance the diphoton signal by a factor of 1.5.

Acknowledgments

KC and SHI were supported by the National Research Foundation of Korea (NRF) grant (No. 2007-0093865 and No. 2012R1A2A2A05003214) and the BK21 project funded by the Korean Government (MEST). KSJ and MY were supported by Grants-in-Aid for Scientific Research from the Ministry of Education, Science, Sports, and Culture (MEXT), Japan, No. 23104008 and No. 23540283.

References

[1] ATLAS collaboration, *Observation of a new particle in the search for the standard model Higgs boson with the ATLAS detector at the LHC*, *Phys. Lett.* **B 716** (2012) 1 [arXiv:1207.7214] [INSPIRE].

JHEP02(2013)090

[2] CMS collaboration, *Observation of a new boson at a mass of* 125 *GeV with the CMS experiment at the LHC*, *Phys. Lett.* **B 716** (2012) 30 [arXiv:1207.7235] [INSPIRE].

[3] M. Maniatis, *The next-to-minimal supersymmetric extension of the standard model reviewed*, *Int. J. Mod. Phys.* **A 25** (2010) 3505 [arXiv:0906.0777] [INSPIRE].

[4] U. Ellwanger, C. Hugonie and A.M. Teixeira, *The next-to-minimal supersymmetric standard model*, *Phys. Rept.* **496** (2010) 1 [arXiv:0910.1785] [INSPIRE].

[5] L.J. Hall, D. Pinner and J.T. Ruderman, *A natural SUSY Higgs near* 126 *GeV*, *JHEP* **04** (2012) 131 [arXiv:1112.2703] [INSPIRE].

[6] U. Ellwanger, *Enhanced di-photon Higgs signal in the next-to-minimal supersymmetric standard model*, *Phys. Lett.* **B 698** (2011) 293 [arXiv:1012.1201] [INSPIRE].

[7] U. Ellwanger, *A Higgs boson near* 125 *GeV with enhanced di-photon signal in the NMSSM*, *JHEP* **03** (2012) 044 [arXiv:1112.3548] [INSPIRE].

[8] Z. Kang, J. Li and T. Li, *On naturalness of the MSSM and NMSSM*, *JHEP* **11** (2012) 024 [arXiv:1201.5305] [INSPIRE].

[9] V. Barger, M. Ishida and W.-Y. Keung, *Flavor-tuned* 125 *GeV SUSY Higgs boson at the LHC: MSSM and natural SUSY tests*, arXiv:1207.0779 [INSPIRE].

[10] M. Carena, I. Low and C.E. Wagner, *Implications of a modified Higgs to diphoton decay width*, *JHEP* **08** (2012) 060 [arXiv:1206.1082] [INSPIRE].

[11] K. Blum, R.T. D'Agnolo and J. Fan, *Natural SUSY predicts: Higgs couplings*, *JHEP* **01** (2013) 057 [arXiv:1206.5303] [INSPIRE].

[12] A. Joglekar, P. Schwaller and C.E. Wagner, *Dark matter and enhanced Higgs to di-photon rate from vector-like Leptons*, *JHEP* **12** (2012) 064 [arXiv:1207.4235] [INSPIRE].

[13] N. Arkani-Hamed, K. Blum, R.T. D'Agnolo and J. Fan, $2:1$ *for naturalness at the LHC?*, *JHEP* **01** (2013) 149 [arXiv:1207.4482] [INSPIRE].

[14] L.G. Almeida, E. Bertuzzo, P.A. Machado and R.Z. Funchal, *Does* $H \to \gamma\gamma$ *taste like vanilla new physics?*, *JHEP* **11** (2012) 085 [arXiv:1207.5254] [INSPIRE].

[15] J.-J. Cao, Z.-X. Heng, J.M. Yang, Y.-M. Zhang and J.-Y. Zhu, *A SM-like Higgs near* 125 *GeV in low energy SUSY: a comparative study for MSSM and NMSSM*, *JHEP* **03** (2012) 086 [arXiv:1202.5821] [INSPIRE].

[16] R. Benbrik et al., *Confronting the MSSM and the NMSSM with the discovery of a signal in the two photon channel at the LHC*, *Eur. Phys. J.* **C 72** (2012) 2171 [arXiv:1207.1096] [INSPIRE].

[17] M. Carena, S. Gori, N.R. Shah and C.E. Wagner, *A* 125 *GeV SM-like Higgs in the MSSM and the* $\gamma\gamma$ *rate*, *JHEP* **03** (2012) 014 [arXiv:1112.3336] [INSPIRE].

[18] M. Carena, S. Gori, N.R. Shah, C.E.M. Wagner and L.-T. Wang, *Light stau phenomenology and the Higgs* $\gamma\gamma$ *rate*, *JHEP* **07** (2012) 175 [arXiv:1205.5842] [INSPIRE].

[19] M.R. Buckley and D. Hooper, *Are there hints of light stops in recent Higgs search results?*, *Phys. Rev.* **D 86** (2012) 075008 [arXiv:1207.1445] [INSPIRE].

[20] G.F. Giudice, P. Paradisi, A. Strumia and A. Strumia, *Correlation between the Higgs decay rate to two photons and the muon* $g-2$, *JHEP* **10** (2012) 186 [arXiv:1207.6393] [INSPIRE].

JHEP02(2013)090

[21] M.A. Ajaib, I. Gogoladze and Q. Shafi, *Higgs boson production and decay: effects from light third generation and vectorlike matter*, *Phys. Rev.* **D 86** (2012) 095028 [arXiv:1207.7068] [INSPIRE].

[22] R. Sato, K. Tobioka and N. Yokozaki, *Enhanced diphoton signal of the Higgs boson and the muon $g-2$ in gauge mediation models*, *Phys. Lett.* **B 716** (2012) 441 [arXiv:1208.2630] [INSPIRE].

[23] S. King, M. Muhlleitner and R. Nevzorov, *NMSSM Higgs benchmarks near* 125 *GeV*, *Nucl. Phys.* **B 860** (2012) 207 [arXiv:1201.2671] [INSPIRE].

[24] E. Gabrielli, K. Kannike, B. Mele, A. Racioppi and M. Raidal, *Fermiophobic Higgs boson and supersymmetry*, *Phys. Rev.* **D 86** (2012) 055014 [arXiv:1204.0080] [INSPIRE].

[25] N. Haba, K. Kaneta, Y. Mimura and R. Takahashi, *Enhancement of Higgs to diphoton decay width in non-perturbative Higgs model*, *Phys. Lett.* **B 718** (2013) 1441 [arXiv:1207.5102] [INSPIRE].

[26] D.S. Alves, P.J. Fox and N.J. Weiner, *Higgs signals in a type I 2HDM or with a sister Higgs*, arXiv:1207.5499 [INSPIRE].

[27] K. Schmidt-Hoberg and F. Staub, *Enhanced $h \to \gamma\gamma$ rate in MSSM singlet extensions*, *JHEP* **10** (2012) 195 [arXiv:1208.1683] [INSPIRE].

[28] H. An, T. Liu and L.-T. Wang, 125 *GeV Higgs boson, enhanced di-photon rate and gauged* $\mathrm{U}(1)_{PQ}$*-extended MSSM*, *Phys. Rev.* **D 86** (2012) 075030 [arXiv:1207.2473] [INSPIRE].

[29] A. Delgado, G. Nardini and M. Quirós, *Large diphoton Higgs rates from supersymmetric triplets*, *Phys. Rev.* **D 86** (2012) 115010 [arXiv:1207.6596] [INSPIRE].

[30] L. Basso and F. Staub, *Enhancing $h \to \gamma\gamma$ with staus in SUSY models with extended gauge sector*, *Phys. Rev.* **D 87** (2013) 015011 [arXiv:1210.7946] [INSPIRE].

[31] D. Carmi, A. Falkowski, E. Kuflik, T. Volansky and J. Zupan, *Higgs after the discovery: a status report*, *JHEP* **10** (2012) 196 [arXiv:1207.1718] [INSPIRE].

[32] Y. Okada, M. Yamaguchi and T. Yanagida, *Upper bound of the lightest Higgs boson mass in the minimal supersymmetric standard model*, *Prog. Theor. Phys.* **85** (1991) 1 [INSPIRE].

[33] Y. Okada, M. Yamaguchi and T. Yanagida, *Renormalization group analysis on the Higgs mass in the softly broken supersymmetric standard model*, *Phys. Lett.* **B 262** (1991) 54 [INSPIRE].

[34] Particle Data Group collaboration, K. Nakamura et al., *Review of particle physics*, *J. Phys.* **G 37** (2010) 075021 [INSPIRE].

[35] R. Barbieri, L.J. Hall, Y. Nomura and V.S. Rychkov, *Supersymmetry without a light Higgs boson*, *Phys. Rev.* **D 75** (2007) 035007 [hep-ph/0607332] [INSPIRE].

[36] K.S. Jeong, Y. Shoji and M. Yamaguchi, *Peccei-Quinn invariant extension of the NMSSM*, *JHEP* **04** (2012) 022 [arXiv:1112.1014] [INSPIRE].

[37] P. Gambino and M. Misiak, *Quark mass effects in $\bar{B} \to X_s\gamma$*, *Nucl. Phys.* **B 611** (2001) 338 [hep-ph/0104034] [INSPIRE].

[38] C. Panagiotakopoulos and K. Tamvakis, *New minimal extension of MSSM*, *Phys. Lett.* **B 469** (1999) 145 [hep-ph/9908351] [INSPIRE].

JHEP02(2013)090

[39] C. Panagiotakopoulos and A. Pilaftsis, *Higgs scalars in the minimal nonminimal supersymmetric standard model*, *Phys. Rev.* **D 63** (2001) 055003 [hep-ph/0008268] [INSPIRE].

[40] K.J. Bae et al., *Peccei-Quinn NMSSM in the light of* 125 *GeV Higgs*, *JHEP* **11** (2012) 118 [arXiv:1208.2555] [INSPIRE].

[41] LEP Working Group for Higgs boson searches, ALEPH, DELPHI, L3, OPAL collaboration, R. Barate et al., *Search for the standard model Higgs boson at LEP*, *Phys. Lett.* **B 565** (2003) 61 [hep-ex/0306033] [INSPIRE].

[42] S. Mizuta and M. Yamaguchi, *Coannihilation effects and relic abundance of Higgsino dominant LSP(s)*, *Phys. Lett.* **B 298** (1993) 120 [hep-ph/9208251] [INSPIRE].

JHEP02(2013)090

Physics Letters B 710 (2012) 159–163

Contents lists available at SciVerse ScienceDirect

Physics Letters B

www.elsevier.com/locate/physletb

Wino LSP detection in the light of recent Higgs searches at the LHC

Takeo Moroi, Kazunori Nakayama *

Department of Physics, University of Tokyo, Tokyo 113-0033, Japan

ARTICLE INFO

Article history:
Received 17 January 2012
Received in revised form 17 February 2012
Accepted 18 February 2012
Available online 22 February 2012
Editor: T. Yanagida

ABSTRACT

Recent LHC data showed excesses of Higgs-like signals at the Higgs mass of around 125 GeV. This may indicate supersymmetric models with relatively heavy scalar fermions to enhance the Higgs mass. The desired mass spectrum is realized in the anomaly-mediated supersymmetry breaking model, in which the Wino can naturally be the lightest superparticle (LSP). We discuss possibilities for confirming such a scenario, particularly detecting signals from Wino LSP at direct detection experiments, indirect searches at neutrino telescopes and at the LHC.

© 2012 Elsevier B.V. Open access under CC BY license.

Higgs mass contains very important information about low-energy supersymmetry (SUSY) models, which is well motivated because it provides a viable candidate of dark matter (DM) and also because it realizes the gauge coupling unification. In particular, in the minimal SUSY standard model (MSSM), the lightest Higgs boson cannot be heavier than the Z-boson at the tree level, while a sizable radiative correction may enhance the Higgs mass [1]. The size of the radiative correction depends on the masses (and other parameters) of superparticles. The lightest Higgs mass becomes larger as superparticles (in particular, stops) become heavier. Thus, once the lightest Higgs mass is known, mass scale of superparticles is constrained.

Recently, the ATLAS Collaboration reported 3.6σ local excess of the standard model (SM) Higgs-like event at $m_h \simeq 126$ GeV [2]. In addition, the CMS Collaboration also showed more than 2σ local excess at $m_h \simeq 124$ GeV [3].[1] In order to achieve such a value of the lightest Higgs mass in the MSSM, relatively large values of the superparticle masses are required; the typical scale of the sfermion masses to realize $m_h \simeq 125$ GeV is 10 TeV–10^3 TeV [4,5]. Then, if the masses of all the superparticles are of the same order, it is difficult to find experimental signals of low-energy SUSY and the existence of SUSY is hardly confirmed.

Although the sfermion masses are much larger than the electroweak scale, gauginos may be much lighter than sfermions and within the reach of collier and other experiments. One interesting possibility is the model in which the SUSY breaking scalar masses are from direct coupling to the SUSY breaking field while the gaugino masses are generated by the anomaly-mediation mechanism [6,7]; in this Letter, we call such a model as anomaly-mediated SUSY breaking (AMSB) model. Even in the AMSB model, however, if the pure anomaly-mediation relation holds among the gaugino masses, gluino mass is about 8 times larger than the mass of Wino. Thus, if the Wino mass is a few hundred GeV, which is the lower bound on it from astrophysical and cosmological considerations as will be reviewed later, the gluino mass becomes multi-TeV; with such a heavy gluino, the discovery of the SUSY signal at the LHC becomes challenging because we consider the case that all the squarks are extremely heavy.

Even so, there still exist possibilities of discovering signals of the AMSB scenario. In particular, in the present framework, the neutral Wino is the lightest superparticle (LSP) and may be DM. In such a case, pair annihilation cross section of the LSP and the scattering cross section of the LSP off the nuclei are both enhanced compared to the Bino LSP case, which has significant implications to direct and indirect detection of DM. Because the search of the superparticles at the LHC may be difficult, it is important to pursue these possibilities and explore how well we can study the AMSB scenario with these procedures.[2]

In this Letter, motivated by the recent Higgs searches at the LHC, we discuss the detectability of the signals of AMSB scenario. We pay particular attention to the case of the Wino LSP. We focus on direct/indirect detection of the Wino DM at underground laboratories and neutrino telescopes. We also comment on the LHC reach for the direct Wino production. Since superparticles except gauginos are heavy, standard methods for SUSY searches may not work. Even in this case, we will show that there are some windows for the confirmation of the SUSY.

* Corresponding author.
E-mail address: kazunori@hep-th.phys.s.u-tokyo.ac.jp (K. Nakayama).

[1] The excesses based on global probabilities, which take account of the look-elsewhere effect, are 2.3σ (ATLAS) and 1.9σ (CMS).

[2] The heavy SUSY particle spectrum and their detectability were discussed in a different context in Ref. [8].

0370-2693 © 2012 Elsevier B.V. Open access under CC BY license.
doi:10.1016/j.physletb.2012.02.058

Let us first briefly discuss important properties of the AMSB scenario. We assume that the soft SUSY breaking scalar masses are generated by the direct coupling between the scalars and the SUSY breaking hidden sector field, while the gaugino masses are generated by the anomaly mediation mechanism. Adopting the pure AMSB relation, the gaugino masses are given by [6,7]

$$M_a^{(\mathrm{AMSB})} = \frac{b_a}{16\pi^2} g_a^2 m_{3/2}, \tag{1}$$

where g_a ($a = 1$–3) are gauge coupling constants of the SM gauge groups, $m_{3/2}$ is the gravitino mass, and $(b_1, b_2, b_3) = (11, 1, -3)$. Then, the Wino becomes the lightest among the gauginos, and gaugino masses largely separate: $m_{\tilde{B}} : m_{\tilde{W}} : m_{\tilde{g}} \simeq 3 : 1 : 8$. Although the AMSB relation may be affected by Higgs and Higgsino loop diagrams [7,9], we adopt the pure AMSB mass relation. With the gaugino masses being of $O(100)$ GeV–$O(1)$ TeV, the gravitino mass becomes of $O(10)$ TeV–$O(100)$ TeV. The sfermion masses are expected to be of the same order of the gravitino mass, which is preferred from the point of view of realizing $m_h \simeq 125$ GeV. In particular, if the scalar masses are (almost) equal to the gravitino mass, $m_h \simeq 125$ GeV requires relatively small value of $\tan\beta \sim$ a few (where $\tan\beta$ is the ratio of the vacuum expectation values of up- and down-type Higgs bosons) [5].

Before discussing the detectability of the signals of AMSB model, we comment on the supersymmetric Higgs mass parameter (so-called μ-parameter). In the present setup, the soft SUSY breaking scalar mass parameters of up- and down-type Higgs bosons are expected to be of $O(10)$ TeV–$O(100)$ TeV. In order to have viable electroweak symmetry breaking, the μ-parameter (as well as heavy Higgs boson masses) is also expected to be of the same order; then, the Higgsinos become extremely heavy and the Wino becomes the LSP. Thus, we pay particular attention to the case of Wino LSP in the following. In some of our following analysis, however, we consider the case with $\mu \sim O(100)$ GeV–$O(1)$ TeV taking account of the possibility of an accidental tuning of the parameters. This is because detection rates of some of signals (in particular, the direct detection rates) strongly depend on the value of μ.

Taking account of the radiative correction due to the gauge boson loops, the neutral Wino becomes lighter than the charged one. Therefore, we focus on the case of neutral Wino LSP. In addition, we assume that the LSP (i.e., the neutral Wino) is the dominant component of DM. The Wino LSP accounts for the present DM density for $m_{\tilde{W}} \simeq 3$ TeV if it is produced only from thermal bath [10]. In the AMSB scenario, however, the Wino LSP can be non-thermally produced from the gravitino or moduli decay [7,11]. If the reheating temperature takes an appropriate value, for example, the decay of gravitino produces the Wino LSP with correct relic density [12], while thermal leptogenesis [13] works successfully [14]. Thus the Wino is a good DM candidate in the present setup. Hereafter, we assume that the right amount of Wino is somehow produced in the early universe to be DM.

We start with discussing direct detection experiments of DM. The scattering cross section of the Wino LSP off the nucleon significantly depends on μ. Since all scalars except for the lightest Higgs boson are expected to be heavy enough, it is only the lightest Higgs boson that mediates the spin-independent (SI) scattering. The DM–proton scattering cross section is given by [15]

$$\sigma = \frac{4}{\pi}\left(\frac{m_{\tilde{\chi}^0} m_N}{m_{\tilde{\chi}^0} + m_N}\right)^2 \times \left[(n_p f_p + n_n f_n)^2 + 4\frac{J+1}{J}\left(a_p\langle s_p\rangle + a_n\langle s_n\rangle\right)^2\right], \tag{2}$$

where the first and the second terms in the bracket are the contributions of SI and spin-dependent (SD) interaction, respectively. Here $m_{\tilde{\chi}_0}$ is the LSP mass, m_N is the mass of the target nucleus, $n_p(n_n)$ is the number of proton (neutron) in the target nucleus, J is the total nuclear spin, a_p and a_n are the effective DM–nucleon SD couplings, and $\langle s_{p(n)}\rangle$ are the expectation values of the spin content of the proton and neutron groups within the nucleus. We refer to Ref. [15] for definitions of these quantities. The effective DM–proton coupling, f_p, is given by

$$f_p = \sum_{q=u,d,s} \frac{f_q^H}{m_q} m_p f_{T_q}^{(p)} + \frac{2}{27} f_{T_G} \sum_{q=c,b,t} \frac{f_q^H}{m_q} m_p, \tag{3}$$

where $f_{T_G} = 1 - \sum_{u,d,s} f_{T_q}^{(p)}$, m_p and m_q denote the proton and quark masses, respectively, and f_q^H is the effective DM–quark coupling obtained by the exchange of the Higgs boson. Since the DM–Higgs coupling is proportional to the magnitude of Wino–Higgsino mixing,[3] the cross section is enhanced if the Wino–Higgsino mixing is large. In Fig. 1 we plot the Wino–proton SI and SD scattering cross section. In this plot we have used the following values for the quark contents in the proton [17]: $f_{T_u}^{(p)} = 0.023$, $f_{T_d}^{(p)} = 0.034$, $f_{T_s}^{(p)} = 0.025$ and taken $\tan\beta = 3$ and $\tan\beta = 20$. The XENON100 experiment [18] most severely constrains the SI cross section. The sensitivity is improved by a few orders of magnitude for the next generation 1 ton scale detectors, and then broad parameter regions up to $m_{\tilde{W}} \sim \mu \sim 1$ TeV will be explored. The IceCube searches for neutrino events arising from the DM annihilation in the Sun. Since the efficiency for the DM trapping into the Sun depends on the DM–proton scattering cross section, the high-energy neutrino observations give limits on it. For the SD cross section, the IceCube gives the most stringent limit, and it will be further improved by about one order of magnitude with the DeepCore instrument [19].

We have also calculated the detection rate at the IceCube DeepCore, arising from high-energy neutrinos produced by the Wino annihilation at the galactic center (GC). We distinguish two event classes following Refs. [20–22]: contained muon events and shower events. The contained muons correspond to those emerge inside the instrumental volume through the high-energy neutrino interactions with nucleons. The shower events are caused by charged current interactions of electron and tau neutrinos, and neutral current interactions of all neutrino species. They leave electromagnetic/hadronic shower inside the instrumental volume. The event rate of the contained muons is given by

$$N_{\mu^+\mu^-} = \int dE_{\nu_\mu} \int_{E_{\mathrm{th}}}^{E_{\nu_\mu}} dE_\mu \left[\frac{d\Phi_{\nu_\mu}}{dE_{\nu_\mu}}\left(\frac{d\sigma_{\nu_\mu p}^{(\mathrm{CC})}}{dE_\mu} n_p + \frac{d\sigma_{\nu_\mu n}^{(\mathrm{CC})}}{dE_\mu} n_n\right) + (\nu_\mu \leftrightarrow \bar{\nu}_\mu)\right] V_{\mathrm{eff}}(E_\mu), \tag{4}$$

where E_{ν_μ} is the incident neutrino energy, E_μ is the muon energy resulting from the neutrino–proton (neutron) interactions, E_{th} is the threshold energy above which the muon can be detected, $d\Phi_{\nu_\mu}/dE_{\nu_\mu}$ is the neutrino flux at the Earth, $d\sigma_{\nu_\mu p(n)}^{(\mathrm{CC})}/dE_\mu$ denotes the neutrino–proton (neutron) charged current cross section for producing the muon energy with E_μ, $n_p(n_n)$ is the proton (neutron) number density in the detector material, and V_{eff} is the effective volume for the muon detection. The incident neutrino flux generated by DM annihilation from the GC within cone half angle of θ is given by

[3] In the limit of pure Wino DM, the Wino–nucleon scattering cross section is too small to be detected [16].

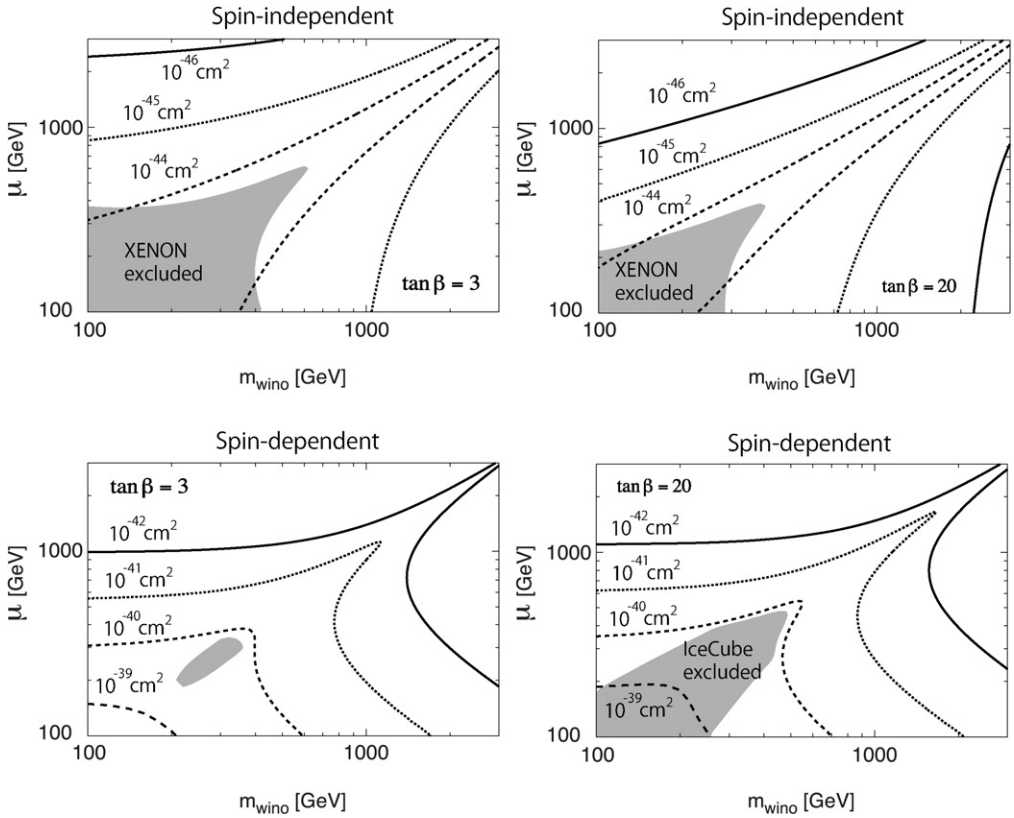

Fig. 1. Contours of spin-independent (SI) and spin-dependent (SD) Wino–proton scattering cross sections are plotted on the plane of $m_{\rm wino}$ and μ. Shaded regions are excluded by the XENON100 experiment for SI, and IceCube experiment for SD.

$$\frac{d\Phi_{\nu_i}}{dE_{\nu_i}} = \frac{R_\odot \rho_\odot^2}{8\pi m_{\tilde{W}}^2}\left(\sum_{j=e,\mu,\tau}\langle\sigma v\rangle \frac{dN_{\nu_j}}{dE_{\nu_j}} P_{j\to i}\right)\langle J_2\rangle_\Omega \Delta\Omega. \tag{5}$$

Here $R_\odot = 8.5$ kpc and $\rho_\odot = 0.3$ GeV cm^{-3}, $\langle\sigma v\rangle$ is the Wino self-annihilation cross section including the non-perturbative effect [23], and dN_{ν_j}/dE_{ν_j} is the energy spectrum of the neutrino produced by DM annihilation, which is calculated by the PYTHIA package for the WW final state [24], $P_{j\to i}$ is the probability that the ν_j at the production is converted to ν_i because of the neutrino oscillation effect, $\Delta\Omega = 2\pi(1-\cos\theta)$, and $\langle J_2\rangle_\Omega$ includes the information about the DM density profile in the Galaxy [25]. The shower event is evaluated in a similar way to the contained muon events (4), except that the charged current interactions from ν_e and ν_τ as well as the neutral current interactions for all neutrino flavors are included. The background event is evaluated by inserting the atmospheric neutrino flux into the expression (4).

Fig. 2 shows the signal-to-noise ratio at the IceCube DeepCore as a function of the Wino mass. Sensitivities for contained muon events (upper panel) and shower events (lower panel) with 1 year and 10 year observations are shown. We have adopted the NFW density profile and considered the neutrino flux from the cone half angle $\theta = 10°$ and $\theta = 25°$ around the GC. As noted in Ref. [22], the sensitivity is maximized for $\theta \simeq 10°$. For this cone half angle, the flux dependence on the DM density profile is not large: it is within a factor of 2 [25]. The effective volume for the contained and shower events are set to be 0.04 km^3 and 0.02 km^3, respectively [20]. The atmospheric background is taken from Ref. [26]. It is seen that the signal-to-noise ratio is at most of order one for the Wino mass of a few hundred GeV. We have also checked that the upward muon events expected at the KM3NeT detector [27], assuming the effective area of 1 km^2 and taking account of the energy loss of muons [28], provide similar sensitivities to the DeepCore.

The Wino DM annihilation may leave characteristic signatures on astrophysical observations. Gamma-ray observations by Fermi-LAT and HESS severely restrict the DM annihilation cross section (see, e.g., Refs. [29,30] for recent works). The non-observations of DM-induced gamma-rays from dwarf galaxies excludes the Wino mass below ~ 400 GeV [29].[4] On the other hand, the cosmic-ray positron excess observed by PAMELA satellite [31] may be explained by the Wino DM annihilation with mass of 200 GeV [32, 33] although it may confront the constraints from gamma-rays and anti-protons. The observations of light element abundances also give stringent bound on the DM annihilation cross section so as not to destroy light elements during big-bang nucleosynthesis (BBN). It gives a lower bound on the Wino mass as $m_{\tilde{W}} \gtrsim$ 200 GeV [34,32]. It may be encouraging that the cosmic lithium problem may be solved for the Wino mass of around this bound, which simultaneously may explain the PAMELA anomaly. DM annihilation also affects the recombination history of the Universe, which results in the modification on the cosmic microwave background (CMB) anisotropy [35–37]. The constraint is comparable to that from BBN. Taking these constraints into account, we conservatively consider that the Wino must be heavier than ~ 200 GeV if it is the dominant component of DM.

Finally, we comment on a possibility of discovering a signal of AMSB model at the LHC. If we adopt the AMSB mass relation among gauginos, gluino becomes relatively heavy. Then, colored

[4] Ref. [29] derived this constraint by analyzing dwarf galaxies in a statistical way. The observations of each dwarf galaxy put a less severe limit on the cross section by a factor of ~ 2 compared with that derived by the statistical method.

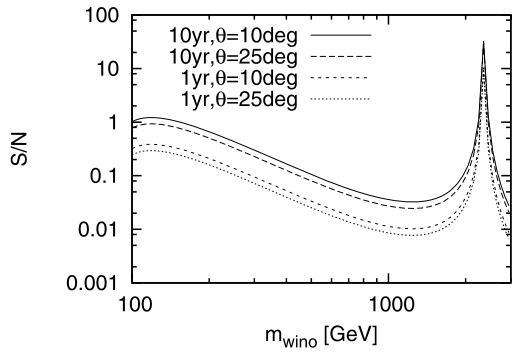

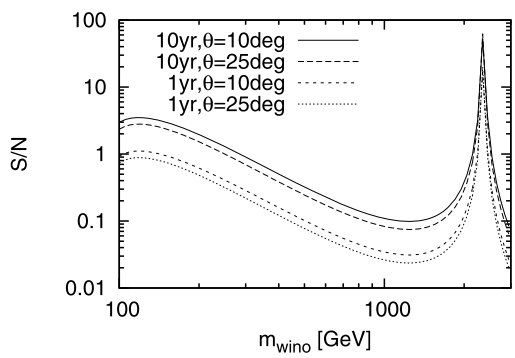

Fig. 2. Signal-to-noise ratio at the IceCube DeepCore as a function of the Wino mass. Sensitivities for contained muon events (upper panel) and shower events (lower panel) with 1 year and 10 year observations are shown. We have considered the neutrino flux from the cone half angle $\theta = 10°$ and $\theta = 25°$ around the GC.

superparticles are hardly produced at the LHC. Thus, we focus on the detection of a Wino signal.

If the neutral Wino $\tilde{W}^0$ is the LSP, we have a chance to observe the track of charged Wino $\tilde{W}^\pm$ [38,39]. This is because the mass difference between charged and neutral Winos is so small (~ 160 MeV) that the decay length of $\tilde{W}^\pm$ becomes macroscopic ($c\tau_{\tilde{W}^\pm} \simeq 5$ cm). Some of the produced charged Winos may travel through several layers of inner trackers and their track may be reconstructed. In the ATLAS experiment, for example, the charged Wino track can be reconstructed with almost 100% efficiency if $\tilde{W}^\pm$ hits the third layer of the semiconductor tracker (SCT) before it decays [40]. Then, because of the smallness of $c\tau_{\tilde{W}^\pm}$ compared to the detector size, $\tilde{W}^\pm$ decays before going through the whole detector. Such a charged Wino is identified as a high p_T track which disappears in the middle of the detector. Such a signal does not exist in the SM, and hence is a smoking gun evidence of the production of $\tilde{W}^\pm$.

The Wino pair can be produced by the Drell–Yan process at the LHC. However, there is no high p_T jet nor track in the final state in such an event, and hence the event cannot be recorded. In order to trigger on the Wino production events, one can use the event with high p_T jet; such a jet can be from the initial state radiation. Then, at the parton level, the Wino production processes relevant for the present study are the following:

$$q\bar{q} \to \tilde{W}^+\tilde{W}^- g, \qquad gq \to \tilde{W}^+\tilde{W}^- q, \qquad g\bar{q} \to \tilde{W}^+\tilde{W}^- \bar{q},$$
$$q\bar{q}' \to \tilde{W}^\pm\tilde{W}^0 g, \qquad gq \to \tilde{W}^\pm\tilde{W}^0 q', \qquad g\bar{q} \to \tilde{W}^\pm\tilde{W}^0 \bar{q}'.$$

We calculate the cross section of the process $pp \to \tilde{W}\tilde{W}j$; we perform the parton level calculation, and we approximate the p_T of jet by that of final-state quark or gluon. In the calculation of the cross section, the helicity amplitude package HELAS [41] and the CT10 parton distribution functions [42] are used. For the phase space integration, we use the BASES package [43]. In the calculation, we require that the transverse momentum of the jet be larger than 170, 270, and 370 GeV, and that at least one charged Wino travels more than 44.3 cm which is the distance to the third layer of SCT from the beam pipe in the ATLAS detector [44].

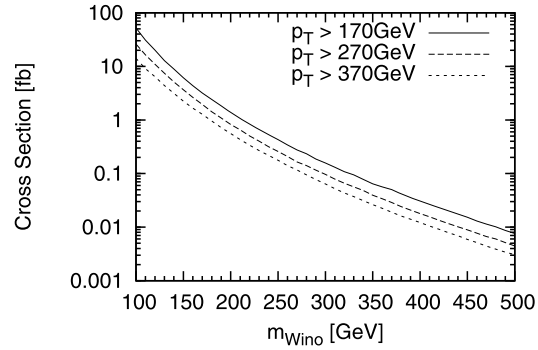

Fig. 3. Cross section for the process $pp \to \tilde{W}\tilde{W}j$ (with $j = q$ or g), for $\sqrt{s} = 14$ TeV. The transverse momentum of j is required to be larger than 170, 270, and 370 GeV from above.

In Fig. 3, the cross section is plotted as a function of the Wino mass. In the high luminosity run with $\mathcal{L} = 2 \times 10^{33}$ cm^{-2} s^{-1}, for example, the so-called j370 trigger is planned to be available, which requires a jet with $p_T > 370$ GeV [44]. Then, requiring 10 events with $p_T > 370$ GeV for the discovery, for example, Wino mass smaller than 270 GeV (330 GeV) is covered by the LHC with the luminosity of $\mathcal{L} = 100$ fb^{-1} (300 fb^{-1}), where we have assumed that the background is negligible. Thus, in particular when μ is large, the LHC experiment still have a chance to cover the parameter region which has not been excluded yet by the current direct and indirect DM searches. If the p_T of the jet for the trigger can be reduced, the LHC can cover the region with larger Wino mass.

So far, we have assumed the pure AMSB relation among gauginos masses. However, as we have mentioned, such a relation may be largely affected by the Higgs and Higgsino loop diagrams. With such an effect, the gluino mass may become ~ 1 TeV even when the Wino mass is a few GeV. In such a case, the conventional procedures of the SUSY search using the missing energy distribution may work.

In summary, motivated by the recent report on the Higgs searches at the LHC, which indicated excesses of Higgs-like events at around $m_h \simeq 125$ GeV, we have investigated prospects for confirmation of the AMSB scenario, particularly the detection of Wino LSP. We have considered the situation that the scalars except for gauginos and Higgsinos are heavy enough so that they cannot be produced at colliders. Even in this unfortunate case, the Wino DM may be detected through direct/indirect detection experiments. Direct detection efficiency crucially depends on the Higgsino mass, and if the Wino and Higgsino masses happen to be close, future experiments may find their signals. The neutrino telescopes such as IceCube DeepCore and KM3NeT also have a potential to discover the Wino LSP through the observation muon and/or shower events induced by high-energy neutrinos from DM annihilation at GC.

Acknowledgements

We would like to thank M. Ibe and T.T. Yanagida for useful discussion. This work is supported by Grants-in-Aid for Scientific Research from the Ministry of Education, Science, Sports, and Culture (MEXT), Japan, No. 22244021 (T.M.), No. 22540263 (T.M.),

No. 23104001 (T.M.), No. 21111006 (K.N.), and No. 22244030 (K.N.).

References

[1] Y. Okada, M. Yamaguchi, T. Yanagida, Prog. Theor. Phys. 85 (1991) 1;
Y. Okada, M. Yamaguchi, T. Yanagida, Phys. Lett. B 262 (1991) 54;
J.R. Ellis, G. Ridolfi, F. Zwirner, Phys. Lett. B 257 (1991) 83;
H.E. Haber, R. Hempfling, Phys. Rev. Lett. 66 (1991) 1815.

[2] ATLAS Note, ATLAS-CONF-2011-163.

[3] CMS Physics Analysis Summary, HIG-11-032.

[4] M. Binger, Phys. Rev. D 73 (2006) 095001, arXiv:hep-ph/0408240.

[5] G.F. Giudice, A. Strumia, arXiv:1108.6077 [hep-ph].

[6] L. Randall, R. Sundrum, Nucl. Phys. B 557 (1999) 79, arXiv:hep-th/9810155.

[7] G.F. Giudice, M.A. Luty, H. Murayama, R. Rattazzi, JHEP 9812 (1998) 027, arXiv:hep-ph/9810442.

[8] L.J. Hall, Y. Nomura, arXiv:1111.4519 [hep-ph].

[9] T. Gherghetta, G.F. Giudice, J.D. Wells, Nucl. Phys. B 559 (1999) 27, arXiv:hep-ph/9904378.

[10] J. Hisano, S. Matsumoto, M. Nagai, O. Saito, M. Senami, Phys. Lett. B 646 (2007) 34, arXiv:hep-ph/0610249.

[11] T. Moroi, L. Randall, Nucl. Phys. B 570 (2000) 455, arXiv:hep-ph/9906527.

[12] M. Bolz, A. Brandenburg, W. Buchmuller, Nucl. Phys. B 606 (2001) 518, arXiv:hep-ph/0012052;
M. Bolz, A. Brandenburg, W. Buchmuller, Nucl. Phys. B 790 (2008) 336 (Erratum);
J. Pradler, F.D. Steffen, Phys. Rev. D 75 (2007) 023509, arXiv:hep-ph/0608344;
J. Pradler, F.D. Steffen, Phys. Lett. B 648 (2007) 224, arXiv:hep-ph/0612291;
V.S. Rychkov, A. Strumia, Phys. Rev. D 75 (2007) 075011, arXiv:hep-ph/0701104.

[13] M. Fukugita, T. Yanagida, Phys. Lett. B 174 (1986) 45.

[14] M. Ibe, T.T. Yanagida, arXiv:1112.2462 [hep-ph].

[15] G. Jungman, M. Kamionkowski, K. Griest, Phys. Rep. 267 (1996) 195, arXiv:hep-ph/9506380.

[16] J. Hisano, K. Ishiwata, N. Nagata, Phys. Lett. B 690 (2010) 311, arXiv:1004.4090 [hep-ph].

[17] H. Ohki, et al., Phys. Rev. D 78 (2008) 054502, arXiv:0806.4744 [hep-lat].

[18] E. Aprile, et al., XENON100 Collaboration, Phys. Rev. Lett. 107 (2011) 131302, arXiv:1104.2549 [astro-ph.CO].

[19] IceCube Collaboration, arXiv:1111.2738 [astro-ph.HE].

[20] S.K. Mandal, M.R. Buckley, K. Freese, D. Spolyar, H. Murayama, Phys. Rev. D 81 (2010) 043508, arXiv:0911.5188 [hep-ph].

[21] L. Covi, M. Grefe, A. Ibarra, D. Tran, JCAP 1004 (2010) 017, arXiv:0912.3521 [hep-ph].

[22] A.E. Erkoca, M.H. Reno, I. Sarcevic, Phys. Rev. D 82 (2010) 113006, arXiv:1009.2068 [hep-ph].

[23] J. Hisano, S. Matsumoto, M.M. Nojiri, Phys. Rev. Lett. 92 (2004) 031303, arXiv:hep-ph/0307216;
J. Hisano, S. Matsumoto, M.M. Nojiri, O. Saito, Phys. Rev. D 71 (2005) 063528, arXiv:hep-ph/0412403;
J. Hisano, S. Matsumoto, O. Saito, M. Senami, Phys. Rev. D 73 (2006) 055004, arXiv:hep-ph/0511118.

[24] T. Sjostrand, S. Mrenna, P.Z. Skands, JHEP 0605 (2006) 026, arXiv:hep-ph/0603175.

[25] J. Hisano, M. Kawasaki, K. Kohri, K. Nakayama, Phys. Rev. D 79 (2009) 043516, arXiv:0812.0219 [hep-ph];
J. Hisano, K. Nakayama, M.J.S. Yang, Phys. Lett. B 678 (2009) 101, arXiv:0905.2075 [hep-ph].

[26] M. Honda, T. Kajita, K. Kasahara, S. Midorikawa, T. Sanuki, Phys. Rev. D 75 (2007) 043006, arXiv:astro-ph/0611418;
M. Honda, T. Kajita, K. Kasahara, S. Midorikawa, Phys. Rev. D 83 (2011) 123001, arXiv:1102.2688 [astro-ph.HE].

[27] A. Margiotta, KM3NeT Collaboration, J. Phys. Conf. Ser. 203 (2010) 012124.

[28] S.I. Dutta, M.H. Reno, I. Sarcevic, D. Seckel, Phys. Rev. D 63 (2001) 094020, arXiv:hep-ph/0012350.

[29] Fermi LAT Collaboration, arXiv:1108.3546 [astro-ph.HE].

[30] K.N. Abazajian, J.P. Harding, arXiv:1110.6151 [hep-ph].

[31] O. Adriani, et al., PAMELA Collaboration, Nature 458 (2009) 607, arXiv:0810.4995 [astro-ph].

[32] J. Hisano, M. Kawasaki, K. Kohri, K. Nakayama, Phys. Rev. D 79 (2009) 063514, arXiv:0810.1892 [hep-ph];
J. Hisano, M. Kawasaki, K. Kohri, K. Nakayama, Phys. Rev. D 80 (2009) 029907 (Erratum);
J. Hisano, M. Kawasaki, K. Kohri, T. Moroi, K. Nakayama, Phys. Rev. D 79 (2009) 083522, arXiv:0901.3582 [hep-ph].

[33] P. Grajek, G. Kane, D. Phalen, A. Pierce, S. Watson, Phys. Rev. D 79 (2009) 043506, arXiv:0812.4555 [hep-ph];
G. Kane, R. Lu, S. Watson, Phys. Lett. B 681 (2009) 151, arXiv:0906.4765 [astro-ph.HE].

[34] K. Jedamzik, Phys. Rev. D 70 (2004) 083510, arXiv:astro-ph/0405583.

[35] S. Galli, F. Iocco, G. Bertone, A. Melchiorri, Phys. Rev. D 80 (2009) 023505, arXiv:0905.0003 [astro-ph.CO];
S. Galli, F. Iocco, G. Bertone, A. Melchiorri, Phys. Rev. D 84 (2011) 027302, arXiv:1106.1528 [astro-ph.CO].

[36] T.R. Slatyer, N. Padmanabhan, D.P. Finkbeiner, Phys. Rev. D 80 (2009) 043526, arXiv:0906.1197 [astro-ph.CO].

[37] T. Kanzaki, M. Kawasaki, K. Nakayama, Prog. Theor. Phys. 123 (2010) 853, arXiv:0907.3985 [astro-ph.CO];
J. Hisano, M. Kawasaki, K. Kohri, T. Moroi, K. Nakayama, T. Sekiguchi, Phys. Rev. D 83 (2011) 123511, arXiv:1102.4658 [hep-ph].

[38] J.L. Feng, T. Moroi, L. Randall, M. Strassler, S.F. Su, Phys. Rev. Lett. 83 (1999) 1731, arXiv:hep-ph/9904250.

[39] M. Ibe, T. Moroi, T.T. Yanagida, Phys. Lett. B 644 (2007) 355, arXiv:hep-ph/0610277.

[40] S. Asai, Y. Azuma, O. Jinnouchi, T. Moroi, S. Shirai, T.T. Yanagida, Phys. Lett. B 672 (2009) 339, arXiv:0807.4987 [hep-ph].

[41] H. Murayama, I. Watanabe, K. Hagiwara, KEK Report No. 91-11, Tsukuba, 1992.

[42] H.-L. Lai, M. Guzzi, J. Huston, Z. Li, P.M. Nadolsky, J. Pumplin, C.-P. Yuan, Phys. Rev. D 82 (2010) 074024, arXiv:1007.2241 [hep-ph].

[43] S. Kawabata, Comp. Phys. Comm. 41 (1986) 127.

[44] G. Aad, et al., ATLAS Collaboration, JINST 3 (2008) S08003.

Physics Letters B 747 (2015) 523–528

Contents lists available at ScienceDirect

Physics Letters B

www.elsevier.com/locate/physletb

AMS-02 antiprotons from annihilating or decaying dark matter

Koichi Hamaguchi [a,b,*], Takeo Moroi [a,b], Kazunori Nakayama [a,b]

[a] Department of Physics, University of Tokyo, Bunkyo-ku, Tokyo 113–0033, Japan
[b] Kavli Institute for the Physics and Mathematics of the Universe (Kavli IPMU), University of Tokyo, Kashiwa 277-8583, Japan

ARTICLE INFO

Article history:
Received 30 April 2015
Received in revised form 28 May 2015
Accepted 17 June 2015
Available online 19 June 2015
Editor: J. Hisano

ABSTRACT

Recently the AMS-02 experiment reported an excess of cosmic ray antiprotons over the expected astrophysical background. We interpret the excess as a signal from annihilating or decaying dark matter and find that the observed spectrum is well fitted by adding contributions from the annihilation or decay of dark matter with mass of $\mathcal{O}$(TeV) or larger. Interestingly, Wino dark matter with mass of around 3 TeV, whose thermal relic abundance is consistent with present dark matter abundance, can explain the antiproton excess. We also discuss the implications for the decaying gravitino dark matter with R-parity violation.

© 2015 The Authors. Published by Elsevier B.V. This is an open access article under the CC BY license (http://creativecommons.org/licenses/by/4.0/). Funded by SCOAP[3].

1. Introduction

The existence of the dark matter (DM) has been confirmed by various cosmological observations [1], yet its identity is a complete mystery. The DM provides the most robust evidence for physics beyond the Standard Model.

Recently, the AMS-02 collaboration has reported their latest results of the cosmic-ray antiproton measurement [2], which may be indirect signatures of annihilating/decaying DM in our Universe. Although recent studies [3,4] have claimed that the AMS-02 antiproton flux is within the uncertainties of the astrophysical secondary antiproton flux, the predicted secondary antiproton flux still tends to be smaller than the observed one at higher energy $\gtrsim 100$ GeV, which may indicate a DM contribution in that energy range. Refs. [3–5] also derived upper bound on the DM signal, but the conservative bound [4] is still weak, which allows a large DM contribution.

In this letter, we consider annihilating and decaying DM as a possible source of the AMS-02 antiproton flux. We show that annihilating/decaying DM with a mass of $\mathcal{O}$(TeV) can explain the antiproton flux in the high energy range. We also investigate the implications for supersymmetric (SUSY) DM. It is shown that the AMS-02 antiprotons may originate from Wino DM with a mass of 2–3 TeV. Surprisingly, the Wino mass of around 3 TeV, which is suitable for the thermal relic DM scenario, can explain the observed antiproton data. Another interesting DM candidate is gravitino with an R-parity violation. It is shown that $\mathcal{O}$(TeV) gravitino DM with an R-parity violation can also be the source of the AMS-02 antiprotons.

2. Antiproton from annihilating and decaying DM

The flux of primary antiprotons from DM annihilation/decay at the Solar System, $\vec{r} = \vec{r}_\odot$, is given by[1]

$$\Phi_{\bar{p}}^{\rm DM}(T) = \frac{v(T)}{4\pi} f_{\bar{p}}(T, \vec{r}_\odot), \tag{1}$$

where $v(T)$ is the velocity of the antiproton with kinetic energy T and $f_{\bar{p}}(T, \vec{r})$ is the antiproton number density per unit kinetic energy. The propagation of antiprotons is described by a cylindrical stationary diffusion model [6]

$$\begin{aligned} 0 &= \frac{\partial}{\partial t} f_{\bar{p}}(T, \vec{r}) \\ &= \nabla\left[K(T)\nabla f_{\bar{p}}(T, \vec{r})\right] - \frac{\partial}{\partial z}\left[\mathrm{sign}(z) V_c f_{\bar{p}}(T, \vec{r})\right] \\ &\quad - 2h\delta(z)\Gamma_{\rm ann}(T) f_{\bar{p}}(T, \vec{r}) + Q(T, \vec{r}), \end{aligned} \tag{2}$$

with boundary conditions $f_{\bar{p}}(T, \vec{r}) = 0$ at $r = R$ and $z = \pm L$, where (r, φ, z) are the galactic cylindrical coordinates. Here, the effects of energy losses, reacceleration, and tertiary antiprotons are neglected.

* Corresponding author at: Department of Physics, University of Tokyo, Bunkyo-ku, Tokyo 113-0033, Japan.
E-mail address: hama@hep-th.phys.s.u-tokyo.ac.jp (K. Hamaguchi).

[1] We neglect the difference between the fluxes at the top of the Earth's atmosphere $\Phi_{\bar{p}}^{\rm TOA}$ and at the interstellar $\Phi_{\bar{p}}^{\rm IS}$ due to the solar modulation, since its effect is $\mathcal{O}(1)$% for $T \gtrsim 50$ GeV.

http://dx.doi.org/10.1016/j.physletb.2015.06.041
0370-2693/© 2015 The Authors. Published by Elsevier B.V. This is an open access article under the CC BY license (http://creativecommons.org/licenses/by/4.0/). Funded by SCOAP[3].

Table 1
Propagation parameters [9].

Model	R (kpc)	L (kpc)	K_0 (kpc^2/Myr)	δ	V_c (km/s)
MIN	20	1	0.0016	0.85	13.5
MED	20	4	0.0112	0.70	12
MAX	20	15	0.0765	0.46	5

In Eq. (2), $K(T)$ is the diffusion coefficient and assumed to be spatially constant. It is parametrized as $K(T,\vec{r}) = K(T) = K_0\beta(p/\mathrm{GeV})^\delta$, where p and $\beta = v(T)/c$ are the momentum and velocity of the antiproton, respectively. The V_c term represents the convective wind, which is assumed to be constant and perpendicular to the galactic plane. The third term represents the annihilation of the antiproton on interstellar protons in the galactic plane, where h represents the thickness of the galactic plane and $\Gamma_{\mathrm{ann}}(T) = (n_{\mathrm{H}} + 4^{2/3}n_{\mathrm{He}})\sigma^{\mathrm{ann}}_{p\bar{p}}v(T)$ is the annihilation rate. We take $h = 0.1$ kpc, $n_{\mathrm{H}} = 1$ cm^{-3}, $n_{\mathrm{He}} = 0.07n_{\mathrm{H}}$, and $\sigma^{\mathrm{ann}}_{p\bar{p}}$ given in Refs. [7,8],

$$\sigma^{\mathrm{ann}}_{p\bar{p}} = \begin{cases} 661(1 + 0.0115T^{-0.774} - 0.948T^{0.0151})\ \mathrm{mb} \\ \quad T < 15.5\ \mathrm{GeV}, \\ 36T^{-0.5}\ \mathrm{mb} \\ \quad T \geq 15.5\ \mathrm{GeV}. \end{cases} \tag{3}$$

Lastly, $Q(T,\vec{r})$ is the source term of the antiprotons. We adopt the set of propagation parameters R, L, K_0, δ, and V_c in Ref. [9], which are shown in Table 1.

The source term for DM annihilation/decay is given by

$$Q(T,\vec{r}) = q(\vec{r})\frac{dN_{\bar{p}}(T)}{dT} \tag{4}$$

where $dN_{\bar{p}}(T)/dT$ is the energy spectrum of the antiproton per one annihilation/decay, and $q(\vec{r})$ is given by

$$q(\vec{r}) = \frac{1}{2}\langle\sigma v\rangle\left(\frac{\rho_{\mathrm{DM}}(|\vec{r}|)}{m_{\mathrm{DM}}}\right)^2 \qquad \text{for annihilating DM}, \tag{5}$$

$$q(\vec{r}) = \frac{1}{\tau_{\mathrm{DM}}}\left(\frac{\rho_{\mathrm{DM}}(|\vec{r}|)}{m_{\mathrm{DM}}}\right) \qquad \text{for decaying DM}. \tag{6}$$

Here, m_{DM} and $\rho_{\mathrm{DM}}(|\vec{r}|)$ are the mass and the density profile of the DM, respectively. In addition, $\langle\sigma v\rangle$ is the annihilation cross section for the annihilating DM case, while τ_{DM} is the DM lifetime for the decaying DM case.

The differential equation (2) can be solved analytically, which leads to

$$\Phi^{\mathrm{DM}}_{\bar{p}}(T) = \frac{v(T)}{4\pi}\widetilde{G}(T)\frac{dN_{\bar{p}}(T)}{dT}. \tag{7}$$

For the source spectrum $dN_{\bar{p}}(T)/dT$, we consider the following DM annihilation and decay channels:

- annihilation: $\chi\chi \to W^+W^-$,
- decay: $\chi \to W^\pm\ell^\mp$,

where χ denotes the DM and ℓ is a charged lepton. In Fig. 1, we show the numerical result for the antiproton spectrum from $\chi\chi \to W^+W^-$ obtained by Pythia 6.4 [10]. Our results agree well with the fitting formula in Ref. [11], which we use in the following analysis.[2] The spectrum from the decaying DM with a mass of m_{DM} is given by that from the annihilating DM with a mass of $m_{\mathrm{DM}}/2$ rescaled by the factor of 1/2.

[2] As for the fitting parameters $p_i(m_{\mathrm{DM}})$ in Ref. [11], we used $p_i(m_{\mathrm{DM}} = 5\ \mathrm{TeV})$ for $m_{\mathrm{DM}} \geq 5$ TeV.

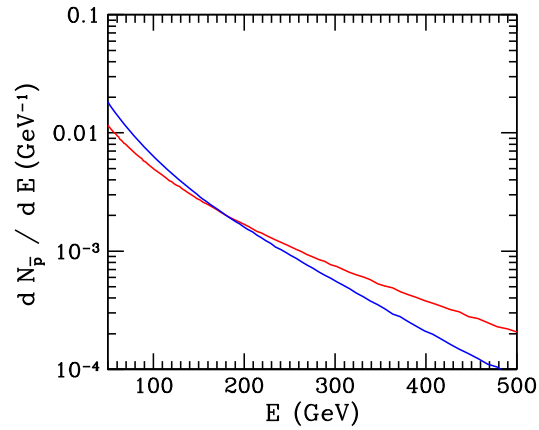

Fig. 1. Energy spectra of antiproton produced by non-relativistic annihilation of DM. Red and blue lines correspond to those for $\chi\chi \to W^+W^-$ and $\bar{b}b$, respectively. The DM mass is taken to be 2 TeV. (For interpretation of the references to color in this figure legend, the reader is referred to the web version of this article.)

In Fig. 1, we also show the antiproton spectrum from $\chi\chi \to b\bar{b}$. The source spectra for W^+W^- and $b\bar{b}$ are relatively close in the parameter range of our interest. We have checked that the resultant antiproton flux from $\chi\chi \to b\bar{b}$ is similar to the one from $\chi\chi \to W^+W^-$.

The analytic expression for $\widetilde{G}(T)$ is given by [6]

$$\widetilde{G}(T) = \sum_{i=1}^{\infty}\exp\left(\frac{-V_cL}{2K(T)}\right)\frac{y_i(T)}{A_i(T)\sinh(S_i(T)L/2)}J_0\left(\frac{\zeta_i r_\odot}{R}\right) \tag{8}$$

where

$$y_i(T) = \frac{4}{J_1^2(\zeta_i)R^2}\int_0^R r'dr'\,J_0\left(\frac{\zeta_i r'}{R}\right)\int_0^L dz'\exp\left(\frac{V_c(L-z')}{2K(T)}\right) \times \sinh\left(\frac{S_i(L-z')}{2}\right)q(\vec{r}),$$

$$A_i(T) = 2h\Gamma_{\mathrm{ann}}(T) + V_c + K(T)S_i(T)\coth\left(\frac{S_i(T)L}{2}\right),$$

$$S_i(T) = \sqrt{\frac{V_c^2}{K(T)^2} + \frac{4\zeta_i^2}{R^2}}.$$

Here, J_0 and J_1 are the zeroth and first order Bessel functions of the first kind, respectively, and ζ_i are the successive zeros of J_0. We have calculated the Green's function $\widetilde{G}(T)$ by using the NFW density profile [12]

$$\rho_{\mathrm{DM}}(|\vec{r}|) = \rho_\odot\frac{r_\odot}{|\vec{r}|}\left(\frac{1 + r_\odot/r_s}{1 + |\vec{r}|/r_s}\right)^2, \tag{9}$$

with $\rho_\odot = 0.3$ GeV/cm^3, $r_\odot = 8.5$ kpc and $r_s = 20$ kpc. We parametrize the result as

$$\widetilde{G}(T) = \frac{1}{2}\langle\sigma v\rangle\frac{\rho_\odot^2}{m_{\mathrm{DM}}^2}G_{\mathrm{ann}}(T) \qquad \text{annihilating DM}, \tag{10}$$

$$\widetilde{G}(T) = \frac{\rho_\odot}{m_{\mathrm{DM}}\tau_{\mathrm{DM}}}G_{\mathrm{dec}}(T) \qquad \text{decaying DM}. \tag{11}$$

For annihilating DM, our numerical result of $G_{\mathrm{ann}}(T)$ agrees well with the fitting formula given in Ref. [13]. For decaying DM, our numerical result is well reproduced with the following fitting function

$$G_{\mathrm{dec}}(T) = \exp\left(a_0 + a_1\tau + a_2\tau^2 + a_3\tau^3\right) \times 10^{14}\ \mathrm{s}, \tag{12}$$

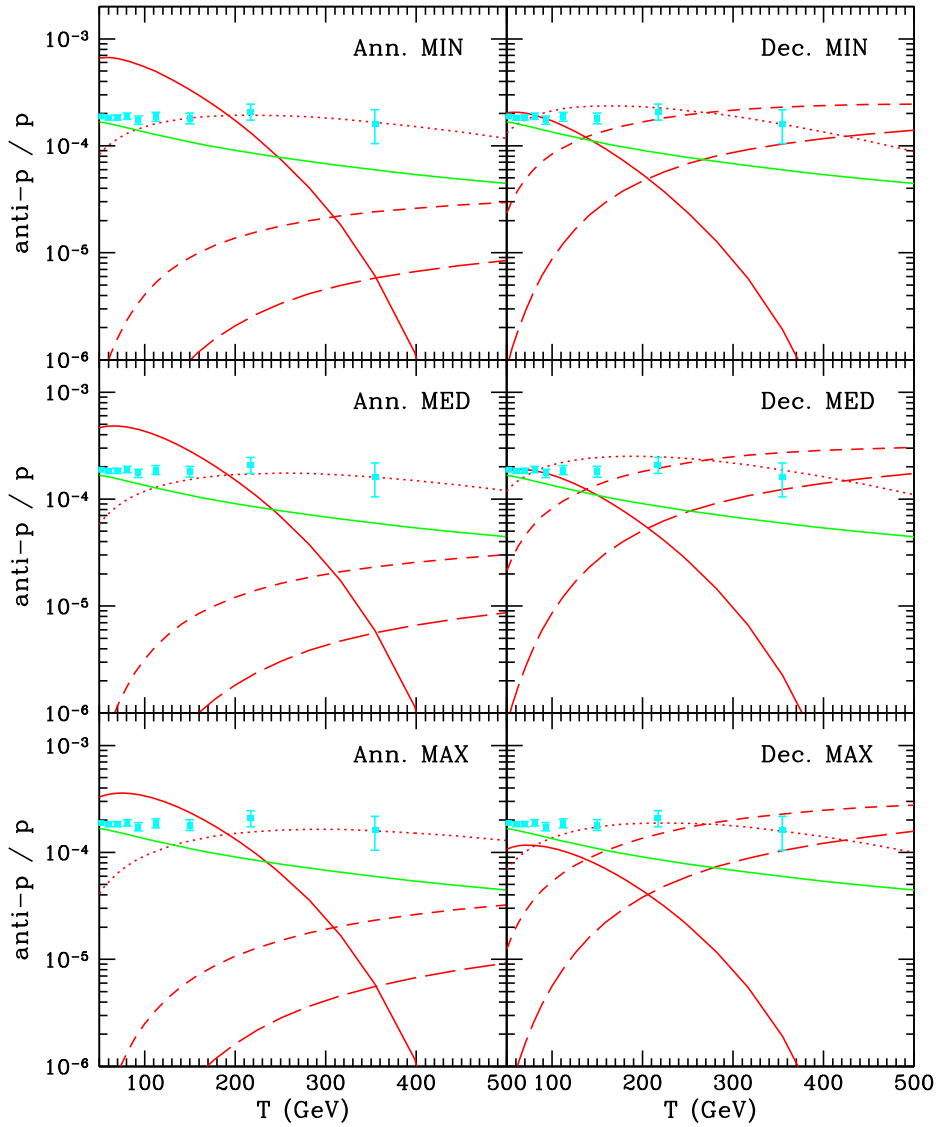

Fig. 2. The antiproton to proton ratio for MIN (top), MED (middle) and MAX (bottom) propagation models. The red lines are those predicted by the DM annihilation (left) and decay (right). For the annihilation case, the DM mass is taken to be 0.5 (solid), 2 (dotted), 10 (dashed), and 20 TeV (long-dashed), while the annihilation cross section is taken to be 2×10^{-23}, 2×10^{-24}, and 6×10^{-25} cm^3/s, for MIN, MED, and MAX propagation models, respectively. For the decay case, the DM mass is taken to be 1 (solid), 3 (dotted), 10 (dashed), and 30 TeV (long-dashed), while the lifetime is 1×10^{26}, 5×10^{26}, and 2×10^{27} s, for MIN, MED, and MAX propagation models, respectively. The background is shown in the green line, and the AMS-02 data are shown by the cyan points. (For interpretation of the references to color in this figure legend, the reader is referred to the web version of this article.)

Table 2
Fitting parameters for decaying DM.

Model	a_0	a_1	a_2	a_3
MIN	1.1127	1.7495	−1.2730	0.1412
MED	3.0662	0.8814	−0.8377	0.09178
MAX	4.5815	−0.3546	−0.2322	0.02524

where

$$\tau = \log_{10}(T/\mathrm{GeV}), \tag{13}$$

and the coefficients are shown in Table 2 for MIN, MED, and MAX propagation models.[3]

In Fig. 2, we show our numerical results of $\bar{p}/p$ ratio for annihilating and decaying DM. Here, for the proton flux, we adopt the following fitting formula

$$\frac{\Phi_p(T)}{\mathrm{m}^{-2}\,\mathrm{sr}^{-1}\,\mathrm{s}^{-1}\,\mathrm{GeV}^{-1}} = [10.0 - \theta(-\tau_{300})3.0\,\tau_{300} - \theta(\tau_{300})0.6\,\tau_{300}] \times 10^3 \left(\frac{T}{\mathrm{GeV}}\right)^{-2.7}, \tag{14}$$

where $\tau_{300} = \log_{10}(T/300\ \mathrm{GeV})$, which reproduces the newly released proton flux by AMS-02 [2] well for $T \gtrsim 30$ GeV. In the figures, we also show the background spectrum represented by the fitting function in Ref. [13]:

$$\log_{10}\left(\frac{\Phi_{\bar{p}}^{\mathrm{bkg}}}{\mathrm{m}^{-2}\,\mathrm{sr}^{-1}\,\mathrm{s}^{-1}\,\mathrm{GeV}^{-1}}\right) = -1.64 + 0.07\tau - \tau^2 - 0.02\tau^3 + 0.028\tau^4. \tag{15}$$

[3] Our result slightly differs from the fitting formula presented in Ref. [14] for high energy region, $T \gtrsim \mathcal{O}(100)$ GeV.

As can be seen from the figures, the antiproton flux can be explained by annihilating/decaying DM with masses of $\mathcal{O}$(TeV). Notice that the cross sections and lifetimes used in Fig. 2 are not the best-fit values, but just for presentation. The signal antiproton flux is proportional to $\langle\sigma v\rangle$ or $\tau_{\rm DM}^{-1}$, and hence the AMS-02 antiproton flux can be explained in a wide range of DM mass if $\langle\sigma v\rangle$ or $\tau_{\rm DM}$ is appropriately chosen.

3. Implications for supersymmetric DM

In this section, we briefly discuss the implications for some of SUSY DM candidates: annihilating Wino DM and decaying gravitino DM.

3.1. Wino dark matter

As shown in the previous section, if the antiproton flux is from the annihilating DM, it requires a mass of $\mathcal{O}$(TeV) and relatively large annihilation cross section of $\mathcal{O}(10^{-24}\ {\rm cm}^3\,{\rm s}^{-1})$. Such a parameter space is natural in the Wino DM scenario. In this case, the DM annihilation cross section is determined by its mass, and hence the antiproton flux depends only on the Wino mass.

In Fig. 3, we show the $\bar{p}/p$ ratio for several Wino masses for MIN, MED and MAX propagation models. Here, we adopt the annihilation cross section in Refs. [15,16]. As seen in the figure, Wino DM can account for the observed $\bar{p}/p$ ratio for several choices of masses. Interestingly, for the MED and MAX propagation models, Wino mass of 2.9 TeV can fit the antiproton data. Such a Wino mass is indeed predicted by the thermal relic abundance of Wino DM [17,18]. As can be seen in the figures, smaller Wino masses can also explain the data. In this case, a non-thermal production of Wino DM is necessary, such as gravitino [19–22], moduli [19,23], or Q-ball decay [24]. The antiproton flux at the AMS-02 may be the first hint of the Wino DM.

3.2. Gravitino DM with R-parity violation

In the scenario of gravitino DM with an R-parity violation [25,26], a small R-parity violating coupling and the Planck-suppressed interaction lead to a long DM lifetime. In the case of bilinear R-parity violation, its lifetime is given by [25,26]

$$\tau_{3/2} \simeq 10^{26}\ {\rm s}\left(\frac{\lambda}{10^{-7}}\right)^{-2}\left(\frac{m_{3/2}}{1\ {\rm TeV}}\right)^{-3}, \tag{16}$$

where $m_{3/2}$ is the gravitino mass and λ is the R-parity violating effective coupling.

As shown in Fig. 2, if the high energy antiproton flux is from decaying gravitino DM, it implies $m_{3/2} \gtrsim \mathcal{O}(1)$ TeV and $\tau_{3/2} \simeq 10^{26}$–$10^{27}$ s. This corresponds to an R-parity violating coupling of $\lambda \sim 10^{-7}$–10^{-8}. Such a value of R-parity violation is attractive from the cosmological point of view, since it is large enough to solve the constraint from the long-lived next-to-lightest SUSY particle (NLSP) while small enough to avoid the baryon erasure in combination with sphaleron (cf. [27]).

The gravitino abundance is given by [28–30][4]

$$\Omega_{3/2}h^2 \simeq 0.1 g_s^2 \ln\left(\frac{1.3}{g_s}\right)\left(1+\frac{m_{\tilde{g}}^2}{3m_{3/2}^2}\right)\left(\frac{m_{3/2}}{1\ {\rm TeV}}\right)\left(\frac{T_{\rm R}}{10^9\ {\rm GeV}}\right), \tag{17}$$

[4] Note that the NLSP quickly decays with R-parity violation without producing gravitinos.

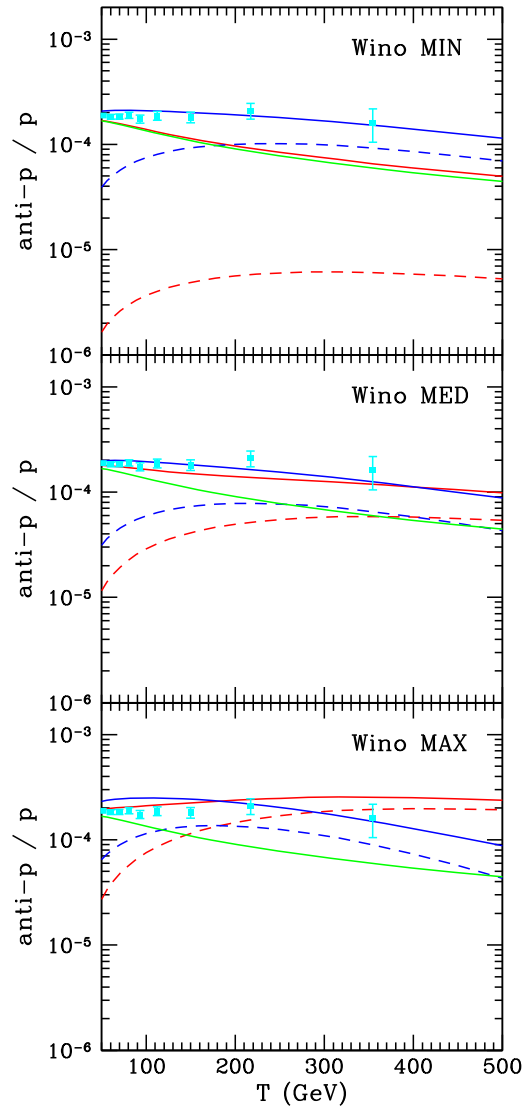

Fig. 3. The antiproton to proton ratio in the Wino DM scenario for MIN (top), MED (middle) and MAX (bottom) propagation models. Red lines are those for the Wino mass of 2.9 TeV, while blue lines are those for the Wino mass of 2.2 TeV (MIN), 1.7 TeV (MED), and 1.2 TeV (MAX). The solid lines are signal plus background, while the dashed lines are signal-only. The background is shown in the green line, and the AMS-02 data are shown by the cyan points. (For interpretation of the references to color in this figure legend, the reader is referred to the web version of this article.)

where g_s denotes the SU(3) gauge coupling constant, $m_{\tilde{g}}$ the gluino mass and $T_{\rm R}$ the reheating temperature after inflation. Therefore, for explaining the AMS-02 antiprotons with gravitino DM of $m_{3/2} \gtrsim$ (a few) TeV, we need $T_{\rm R} \lesssim 10^9$ GeV. This is slightly lower than the temperature required by the standard thermal leptogenesis scenario [31–33], while non-thermal leptogenesis [34] can explain the observed baryon asymmetry.

4. Discussion

Now let us discuss various observational constraints on the annihilating/decaying DM scenario for explaining the AMS-02 antiprotons.

- Cosmic microwave background (CMB): Recent Planck observation on the cosmic microwave background anisotropy constrains the DM annihilation cross section as $f_{\rm eff}\langle\sigma v\rangle/m_{\rm DM} \lesssim 4\times10^{-28}\ {\rm cm}^3\,{\rm s}^{-1}\,{\rm GeV}^{-1}$ [35], where $f_{\rm eff} \sim 0.3$ (in the case of

DM annihilation into W^+W^- or $b\bar{b}$) is the effective fraction of the energy per DM annihilation that ionizes the hydrogen at the epoch of recombination [36]. This leads to the following constraint

$$\langle \sigma v \rangle \lesssim 1 \times 10^{-24}\ \mathrm{cm}^3\,\mathrm{s}^{-1} \left(\frac{m_{\mathrm{DM}}}{1\ \mathrm{TeV}} \right). \tag{18}$$

For the MAX and MED model, this constraint is satisfied. For the MIN model, the required cross section is too large to satisfy this bound. This does not constrain the decaying DM model, because the energy injection around the recombination epoch is sufficiently small. Big-bang nucleosynthesis also constrains the annihilating DM model [37,16,38], but the constraint is weaker than that from CMB.

- Cosmic-ray positron: The annihilating/decaying DM also yields high-energy cosmic-ray positrons. We have explicitly checked that the typical annihilating/decaying DM models explaining the AMS-02 antiprotons do not conflict with the PAMELA [39] and AMS-02 [40] positron measurements for the MED and MAX models.
- Gamma-rays (continuum): Fermi satellite searches for gamma-rays from dwarf spheroidal galaxies and puts severe constraint on the DM annihilation cross section and decay rate. The constraint reads $\langle \sigma v \rangle \lesssim (0.2\text{–}10) \times 10^{-24}\ \mathrm{cm}^3\,\mathrm{s}^{-1}$ for DM mass of 1–10 TeV in the case of annihilating DM [41]. For decaying DM, the diffuse gamma-ray background gives stringent constraint [42–44] and the typical constraint reads $\tau_{\mathrm{DM}} \gtrsim 10^{27}$ s for DM mass of 1–10 TeV. For both annihilating and decaying DM cases to explain the AMS-02 antiproton data, the MED and MAX models can satisfy the constraint.
- Gamma-rays (line): Annihilating or decaying DM also produces line gamma. For example, the Wino DM annihilates into $Z\gamma$. For DM mass of $\mathcal{O}$(TeV), the HESS telescope gives stringent constraint on such line signals from the Galactic center in the case of DM annihilation [45]. However, the constraint significantly depends on the DM density profile. According to Ref. [46], in which constraint from the gamma-ray line from Galactic center is derived for the case of Wino DM, MED and MAX parameters are allowed for mild coring of the DM density profile around the Galactic center.

Finally, we comment on several possibilities to discriminate two scenarios to explain the anti-proton excess observed by the AMS-02, i.e., the annihilating Wino and decaying gravitino scenarios. As we have mentioned, in the annihilating Wino scenario, we expect sizable gamma-ray flux from high DM density regions. With future improvements in the observation of gamma-ray flux from dwarf spheroidal galaxies, for example, signal of Wino DM may be observed [47]. In addition, in the Wino DM scenario, sizable gamma-ray line flux is expected from the annihilation mode $\chi\chi \to Z\gamma$. The predicted gamma-ray line flux from the Galactic center is within the reach of future Cherenkov Telescope Array (CTA) experiment even for the cored density profile for the Wino mass of a few TeV [48,49]. This may be a smoking-gun signature of the Wino DM scenario. On the contrary, in the decaying DM scenario, gamma-ray emission is effective even at extragalactic region. Thus, detailed study of the extragalactic gamma-ray background may give us a hint about the decaying gravitino DM. Furthermore, in the case of gravitino DM decaying into $W^\pm e^\mp$ or $W^\pm \mu^\mp$, a sizable positron flux is also expected. In particular, when the gravitino decays into $W^\pm e^\mp$, a sharp edge of the positron spectrum at the energy around $m_{3/2}/2$ may be an interesting signature of the decaying gravitino scenario.

In summary, we studied the cosmic-ray antiproton flux from DM annihilation and decay in light of the recent AMS-02 result. It is possible to explain the observed $\bar{p}/p$ ratio by adding DM contributions to the typical astrophysical background. In particular, we found that Wino DM with mass of around 3 TeV can successfully account for the antiproton data, which is consistent with the present DM abundance in the standard thermal freezeout scenario. Decaying gravitino DM heavier than a few TeV can also explain the data.

5. Note added in proof

While finalizing this manuscript, Ref. [50] appeared which has some overlaps with the present work.

Acknowledgements

This work was supported by Grant-in-Aid for Scientific research Nos. 23104008 (TM), 26104001 (KH), 26104009 (KH and KN), 26247038 (KH), 26247042 (KN), 26400239 (TM), 26800121 (KN), 26800123 (KH), and also by World Premier International Research Center Initiative (WPI Initiative), MEXT, Japan.

References

[1] K.A. Olive, et al., Particle Data Group Collaboration, Chin. Phys. C 38 (2014) 090001.
[2] AMS-02 Collaboration, Talks at the 'AMS DAYS AT CERN – The Future of Cosmic Ray Physics and Latest Results', April 15–17, 2015, CERN.
[3] G. Giesen, M. Boudaud, Y. Genolini, V. Poulin, M. Cirelli, P. Salati, P.D. Serpico, J. Feng, et al., arXiv:1504.04276 [astro-ph.HE].
[4] C. Evoli, D. Gaggero, D. Grasso, arXiv:1504.05175 [astro-ph.HE].
[5] H.B. Jin, Y.L. Wu, Y.F. Zhou, arXiv:1504.04604 [hep-ph].
[6] D. Maurin, R. Taillet, F. Donato, P. Salati, A. Barrau, G. Boudoul, arXiv:astro-ph/0212111.
[7] L.C. Tan, L.K. Ng, J. Phys. G 9 (1983) 1289.
[8] J. Hisano, S. Matsumoto, O. Saito, M. Senami, Phys. Rev. D 73 (2006) 055004, arXiv:hep-ph/0511118.
[9] F. Donato, N. Fornengo, D. Maurin, P. Salati, Phys. Rev. D 69 (2004) 063501, arXiv:astro-ph/0306207.
[10] T. Sjostrand, S. Mrenna, P.Z. Skands, J. High Energy Phys. 0605 (2006) 026, arXiv:hep-ph/0603175.
[11] L. Bergstrom, J. Edsjo, P. Ullio, Astrophys. J. 526 (1999) 215, arXiv:astro-ph/9902012.
[12] J.F. Navarro, C.S. Frenk, S.D.M. White, Astrophys. J. 490 (1997) 493, arXiv:astro-ph/9611107.
[13] M. Cirelli, R. Franceschini, A. Strumia, Nucl. Phys. B 800 (2008) 204, arXiv:0802.3378 [hep-ph].
[14] A. Ibarra, D. Tran, J. Cosmol. Astropart. Phys. 0807 (2008) 002, arXiv:0804.4596 [astro-ph].
[15] J. Hisano, S. Matsumoto, M.M. Nojiri, O. Saito, Phys. Rev. D 71 (2005) 063528, arXiv:hep-ph/0412403.
[16] J. Hisano, M. Kawasaki, K. Kohri, K. Nakayama, Phys. Rev. D 79 (2009) 063514; J. Hisano, M. Kawasaki, K. Kohri, K. Nakayama, Phys. Rev. D 80 (2009) 029907, arXiv:0810.1892 [hep-ph].
[17] J. Hisano, S. Matsumoto, M. Nagai, O. Saito, M. Senami, Phys. Lett. B 646 (2007) 34, arXiv:hep-ph/0610249.
[18] M. Cirelli, A. Strumia, M. Tamburini, Nucl. Phys. B 787 (2007) 152, arXiv:0706.4071 [hep-ph].
[19] T. Moroi, L. Randall, Nucl. Phys. B 570 (2000) 455, arXiv:hep-ph/9906527.
[20] T. Gherghetta, G.F. Giudice, J.D. Wells, Nucl. Phys. B 559 (1999) 27, arXiv:hep-ph/9904378.
[21] M. Ibe, R. Kitano, H. Murayama, Phys. Rev. D 71 (2005) 075003, arXiv:hep-ph/0412200.
[22] M. Ibe, T.T. Yanagida, Phys. Lett. B 709 (2012) 374, arXiv:1112.2462 [hep-ph]; M. Ibe, S. Matsumoto, T.T. Yanagida, Phys. Rev. D 85 (2012) 095011, arXiv:1202.2253 [hep-ph].
[23] M. Endo, F. Takahashi, Phys. Rev. D 74 (2006) 063502, arXiv:hep-ph/0606075.
[24] M. Fujii, K. Hamaguchi, Phys. Lett. B 525 (2002) 143, arXiv:hep-ph/0110072; M. Fujii, K. Hamaguchi, Phys. Rev. D 66 (2002) 083501, arXiv:hep-ph/0205044.
[25] F. Takayama, M. Yamaguchi, Phys. Lett. B 485 (2000) 388, arXiv:hep-ph/0005214.
[26] W. Buchmuller, L. Covi, K. Hamaguchi, A. Ibarra, T. Yanagida, J. High Energy Phys. 0703 (2007) 037, arXiv:hep-ph/0702184.
[27] M. Endo, K. Hamaguchi, S. Iwamoto, J. Cosmol. Astropart. Phys. 1002 (2010) 032, arXiv:0912.0585 [hep-ph].

[28] T. Moroi, H. Murayama, M. Yamaguchi, Phys. Lett. B 303 (1993) 289.
[29] M. Bolz, A. Brandenburg, W. Buchmuller, Nucl. Phys. B 606 (2001) 518;
M. Bolz, A. Brandenburg, W. Buchmuller, Nucl. Phys. B 790 (2008) 336, arXiv:hep-ph/0012052.
[30] J. Pradler, F.D. Steffen, Phys. Rev. D 75 (2007) 023509, arXiv:hep-ph/0608344;
J. Pradler, F.D. Steffen, Phys. Lett. B 648 (2007) 224, arXiv:hep-ph/0612291.
[31] M. Fukugita, T. Yanagida, Phys. Lett. B 174 (1986) 45.
[32] G.F. Giudice, A. Notari, M. Raidal, A. Riotto, A. Strumia, Nucl. Phys. B 685 (2004) 89, arXiv:hep-ph/0310123.
[33] W. Buchmuller, P. Di Bari, M. Plumacher, Ann. Phys. 315 (2005) 305, arXiv:hep-ph/0401240.
[34] T. Asaka, K. Hamaguchi, M. Kawasaki, T. Yanagida, Phys. Lett. B 464 (1999) 12, arXiv:hep-ph/9906366;
T. Asaka, K. Hamaguchi, M. Kawasaki, T. Yanagida, Phys. Rev. D 61 (2000) 083512, arXiv:hep-ph/9907559.
[35] P.A.R. Ade, et al., Planck Collaboration, arXiv:1502.01589 [astro-ph.CO].
[36] N. Padmanabhan, D.P. Finkbeiner, Phys. Rev. D 72 (2005) 023508, arXiv:astro-ph/0503486;
T.R. Slatyer, N. Padmanabhan, D.P. Finkbeiner, Phys. Rev. D 80 (2009) 043526, arXiv:0906.1197 [astro-ph.CO];
T. Kanzaki, M. Kawasaki, K. Nakayama, Prog. Theor. Phys. 123 (2010) 853, arXiv:0907.3985 [astro-ph.CO];
D.P. Finkbeiner, S. Galli, T. Lin, T.R. Slatyer, Phys. Rev. D 85 (2012) 043522, arXiv:1109.6322 [astro-ph.CO].
[37] K. Jedamzik, Phys. Rev. D 70 (2004) 083510, arXiv:astro-ph/0405583.
[38] J. Hisano, M. Kawasaki, K. Kohri, T. Moroi, K. Nakayama, Phys. Rev. D 79 (2009) 083522, arXiv:0901.3582 [hep-ph];
J. Hisano, M. Kawasaki, K. Kohri, T. Moroi, K. Nakayama, T. Sekiguchi, Phys. Rev. D 83 (2011) 123511, arXiv:1102.4658 [hep-ph].
[39] O. Adriani, et al., PAMELA Collaboration, Phys. Rev. Lett. 111 (2013) 081102, arXiv:1308.0133 [astro-ph.HE].
[40] M. Aguilar, et al., Phys. Rev. Lett. 110 (2013) 141102.
[41] M. Ackermann, et al., Fermi-LAT Collaboration, arXiv:1503.02641 [astro-ph.HE].
[42] G. Bertone, W. Buchmuller, L. Covi, A. Ibarra, J. Cosmol. Astropart. Phys. 0711 (2007) 003, arXiv:0709.2299 [astro-ph].
[43] K. Ishiwata, S. Matsumoto, T. Moroi, Phys. Lett. B 679 (2009) 1, arXiv:0905.4593 [astro-ph.CO].
[44] S. Ando, K. Ishiwata, arXiv:1502.02007 [astro-ph.CO].
[45] A. Abramowski, et al., HESS Collaboration, Phys. Rev. Lett. 110 (2013) 041301, arXiv:1301.1173 [astro-ph.HE].
[46] M. Baumgart, I.Z. Rothstein, V. Vaidya, arXiv:1412.8698 [hep-ph].
[47] B. Bhattacherjee, M. Ibe, K. Ichikawa, S. Matsumoto, K. Nishiyama, J. High Energy Phys. 1407 (2014) 080, arXiv:1405.4914 [hep-ph].
[48] L. Bergstrom, G. Bertone, J. Conrad, C. Farnier, C. Weniger, J. Cosmol. Astropart. Phys. 1211 (2012) 025, arXiv:1207.6773 [hep-ph].
[49] T. Cohen, M. Lisanti, A. Pierce, T.R. Slatyer, J. Cosmol. Astropart. Phys. 1310 (2013) 061, arXiv:1307.4082.
[50] M. Ibe, S. Matsumoto, S. Shirai, T.T. Yanagida, arXiv:1504.05554 [hep-ph].

Physics Letters B 745 (2015) 112–117

Contents lists available at ScienceDirect

Physics Letters B

www.elsevier.com/locate/physletb

Gravitational waves from Higgs domain walls

Naoya Kitajima [a,*], Fuminobu Takahashi [a,b]

[a] Department of Physics, Tohoku University, Sendai 980-8578, Japan
[b] Kavli IPMU, TODIAS, University of Tokyo, Kashiwa 277-8583, Japan

ARTICLE INFO

Article history:
Received 24 February 2015
Received in revised form 3 April 2015
Accepted 20 April 2015
Available online 22 April 2015
Editor: G.F. Giudice

ABSTRACT

The effective potential for the Standard Model Higgs field allows two quasi-degenerate vacua; one is our vacuum at the electroweak scale, while the other is at a much higher scale. The latter minimum may be at a scale much smaller than the Planck scale, if the potential is lifted by new physics. This gives rise to a possibility of domain wall formation after inflation. If the high-scale minimum is a local minimum, domain walls are unstable and disappear through violent annihilation processes, producing a significant amount of gravitational waves. We estimate the amount of gravitational waves produced from unstable domain walls in the Higgs potential and discuss detectability with future experiments.

© 2015 Published by Elsevier B.V. This is an open access article under the CC BY license (http://creativecommons.org/licenses/by/4.0/). Funded by SCOAP[3].

1. Introduction

The Standard Model (SM) of particle physics has been extremely successful, and the Higgs boson with a mass of 125 GeV discovered at the LHC [1,2] completed the last missing piece of the SM. So far there is no experimental hint for physics beyond the SM, and it may be that the Standard Model is valid up to very high energy scales beyond the reach of the current collider experiments.

In the SM framework, the measured values of the Higgs boson mass and top quark mass imply that the electroweak (EW) vacuum is likely metastable. This is because the Higgs self coupling becomes negative at some high energy scale as a result of the fact that its RGE (renormalization group equation) evolution is dominated by the top Yukawa coupling [3,4]. While such effective potential is acceptable as long as our vacuum is sufficiently long-lived, it may signal that new physics appears around that scale and lift the potential.[1] For example, higher dimensional operators may lift the effective potential so as to make these two vacua degenerate in energy, or even make the EW vacuum stable.

The existence of two quasi-degenerate minima in the Higgs potential has interesting cosmological implications. During inflation, either of the two vacua is randomly selected in each patch of the Universe, if the Higgs field acquires quantum fluctuations large enough to overcome the potential barrier between the two minima. Then, domain walls are formed after inflation. Domain walls are a sheet-like topological defect [5], and they are stable if the two vacua are exactly degenerate. Stable domain walls, however, are a cosmological catastrophe as they eventually dominate the Universe, generating unacceptably large inhomogeneities.[2] If there is an energy difference (bias) between the two vacua, domain walls are unstable and they eventually annihilate [11–14]. The EW vacua is realized in the whole Universe if it is energetically preferred. Interestingly, a significant amount of gravitational waves is emitted in the violent annihilation processes [15–18]. As we shall see shortly, such gravitational waves are within the sensitivity reach of future experiments such as advanced-LIGO [19], KAGRA [20,21], ET [22], LISA [23] and DECIGO [24], if the domain walls are sufficiently long-lived. Thus, gravitational waves can be a probe of another vacuum far beyond the EW scale.[3]

In this letter, we study the gravitational waves generated by collapsing domain walls in the Higgs potential with the quasi-degenerate vacua. In Section 2, we introduce the Higgs potential having the false vacuum at high energy scales and discuss the possibility of the domain wall formation. In Section 3, we calculate the gravitational wave abundance and discuss its detectability

* Corresponding author.
E-mail addresses: kitajima@tuhep.phys.tohoku.ac.jp (N. Kitajima), fumi@tuhep.phys.tohoku.ac.jp (F. Takahashi).

[1] The scale sensitively depends on the top quark mass, and it will be around or beyond the Planck scale for the top quark mass about 171 GeV, the lower side of the experimental range [3,4].

[2] If the high-scale minimum is around or beyond the Planck scale, an eternal topological Higgs inflation may take place avoiding the cosmological disaster [6]. See Refs. [7,8] for the original works of topological inflation. The topological Higgs inflation may provide a dynamical explanation for the multiple-point criticality principle [9]. See also Ref. [10] for the related topics.

[3] The gravitational waves from domain wall annihilation can also be a probe of the SUSY breaking scale [25] or a thermal inflation scenario [26].

http://dx.doi.org/10.1016/j.physletb.2015.04.040
0370-2693/© 2015 Published by Elsevier B.V. This is an open access article under the CC BY license (http://creativecommons.org/licenses/by/4.0/). Funded by SCOAP[3].

with future experiments. Section 4 is devoted to discussion and conclusions.

2. False vacuum in Higgs potential

Let us consider the following Higgs potential lifted by new physics at some high energy scale,

$$V_H = \frac{1}{4}\lambda(\varphi)\varphi^4 + \frac{\varphi^6}{\Lambda^2}, \tag{1}$$

where φ is the Standard Model Higgs scalar field, $\lambda(\varphi)$ is a scale-dependent self coupling constant and Λ is a cutoff scale for the dimension six operator. We have neglected the quadratic term of order the electroweak scale as we are interested in the behavior of the Higgs potential at high energy. Here we simply substitute the Higgs field value for the renormalization scale, $\lambda(\mu) = \lambda(\varphi)$.

The renormalization-group-improved effective potential including one-loop and two-loop corrections in Landau gauge is given in [3], and the gauge-dependence of the effective potential was examined in [4]. More recently, a treatment for higher dimensional operators in the Higgs potential was studied in [27]. For our order of magnitude estimate, however, the following crude approximation is sufficient. We leave further refinement of our analysis for future work, but we believe our main results will not be qualitatively changed.

The scale dependence of the Higgs self coupling $\lambda(\mu)$ is governed by the RGE,

$$(4\pi)^2 \frac{d\lambda}{dt} = \beta_\lambda, \tag{2}$$

where $t = \ln(\mu/M_t)$ and

$$\beta_\lambda = 24\lambda^2 + 12\lambda y_t^2 - 6y_t^4 - 3\lambda(g'^2 + 3g^2) + \frac{3}{8}[2g^4 + (g'^2 + g^2)^2] \tag{3}$$

up to one loop order. Here y_t is the top Yukawa coupling, M_t is the top quark mass, g' and g are respectively the $U(1)_Y$ and the $SU(2)_L$ gauge coupling constants. The top Yukawa coupling gives a dominant contribution to the RGE up to a very high energy scale where the $U(1)_Y$ gauge coupling becomes large. As a result, the Higgs self coupling turns to negative, and the effective potential becomes negative at an intermediate scale in the absence of higher dimensional operators.

The effective potential can be lifted by higher dimensional operators such as the last term in the right-hand-side in Eq. (1).[4] In this case there are two potential minima; one is at the EW scale $\varphi = v_{EW}$, and the other at a much higher scale $\varphi = \varphi_f$. Depending on the size of the higher dimensional operator, the high-scale minimum can be a local or global minimum. In particular, our main interest lies in the case when the two minima are quasi-degenerate and the EW vacuum is slightly energetically preferred:

$$V_H(v_{EW}) \approx V_H(\varphi_f) \approx 0, \tag{4}$$

$$V_H(v_{EW}) < V_H(\varphi_f). \tag{5}$$

If the Higgs field acquires a sufficiently large quantum fluctuations during inflation, both vacua may be populated in different patches of the Universe, leading to domain wall formation after inflation. In a later Universe, the EW vacuum will be selected after domain wall annihilation.

[4] Alternatively, one may lift the potential by introducing e.g. an additional singlet scalar field which gives a positive contribution to the beta function (3) [28–30]. Our results hold in this case too, without significant modifications.

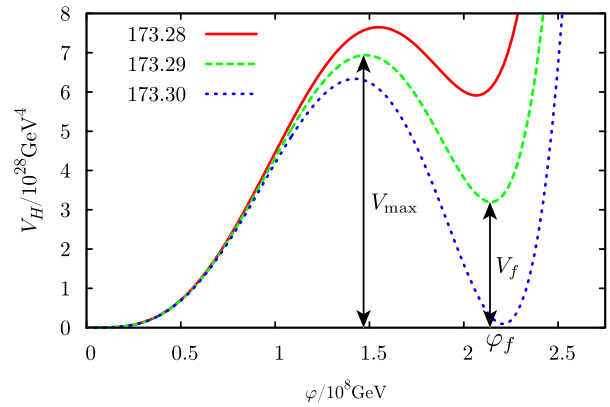

Fig. 1. The effective potential for the Higgs field, $V_H(\varphi)$. We have taken $M_t = 173.28$ (solid red), 173.29 (dashed green) and 173.30 GeV (dotted blue), $m_H = 125.6$ GeV, and $\Lambda = 10^{10}$ GeV. Note that the values of Λ and φ_f are for illustration purposes only. See the text for details.

In Fig. 1 we show the Higgs potential calculated in the present set-up for illustration purposes. We have taken the Higgs boson mass $m_H = 125.6$ GeV, $M_t = 173.28$ (solid (red)), 173.29 (dashed (green)), 173.30 GeV (dotted (blue)) and $\Lambda = 10^{10}$ GeV. One can see that the position of the high-scale minimum, $\varphi = \varphi_f$, is comparable to, but parametrically smaller than Λ because of the loop suppression factor in the RGE. The cut-off scale as well as φ_f increase for smaller values of M_t. For notational simplicity, let V_f and $V_{\max}$ denote the potential energy at the false vacuum and the local maximum, respectively, as shown in the figure for the middle line.

Note that the precise value of Λ obtained in Ref. [4] is about two orders of magnitude larger and it is about 10^{12} GeV for $M_t = 173.3$ GeV. Accordingly, φ_f will be larger by a similar amount. We emphasize here that our analysis in the next section does not depend on the detailed RGE evolution, because we express all the relevant quantities in terms of φ_f, $V_{\max}$ and V_f. One should simply use the result of e.g. Ref. [4] when one relates the value of φ_f to the top quark mass and the Higgs boson mass.

3. Gravitational waves from collapsing domain walls

As we have seen in the previous section, the Higgs potential allows two quasi-degenerate minima, especially if the potential is lifted by higher dimensional operators. This gives rise to a possibility of domain wall formation after inflation. A domain wall is characterized by its tension, σ, which is roughly estimated to be

$$\sigma \sim \left(\frac{\varphi_f^2}{w^2} + V_{\max}\right) w \sim V_{\max}^{1/2}\varphi_f, \tag{6}$$

where $V_{\max}$ is the height of the potential barrier between two minima, $w \sim \varphi_f/V_{\max}^{1/2}$ is the width of the domain wall, and we fix it to minimize the tension in the second equality. In order to avoid the cosmological domain wall problem, the energy bias between the two vacua is necessary to make domain walls unstable. In the presence of the bias, domain walls start to collapse when the energy density of the domain walls become comparable to the bias energy density. As is confirmed by numerical simulations, the evolution of the domain wall network exhibits a scaling behavior [31–34] and the energy density of the domain wall is roughly given by

$$\rho_{dw} \sim \sigma H. \tag{7}$$

Then, the Hubble parameter at the domain wall decay is

$$H_{\rm dec} \sim \frac{V_f}{\sigma} \sim \frac{V_f}{V_{\rm max}^{1/2}\varphi_f}. \tag{8}$$

In order not to generate unacceptably large inhomogeneities, domain walls must decay before they dominate the Universe, which places a lower bound on the energy bias;

$$H_{\rm dec} > H_{\rm dom} \quad \Longleftrightarrow \quad \frac{V_f}{V_{\rm max}} > \left(\frac{\varphi_f}{M_P}\right)^2, \tag{9}$$

where $M_P \simeq 2.4 \times 10^{18}\,\text{GeV}$ is the reduced Planck mass, and $H_{\rm dom} \sim \sigma/M_P^2$ is the Hubble parameter when domain walls would start to dominate the energy density of the Universe if there were not for the bias.

The domain wall collapse is a violent processes, and some part of the energy stored in the domain walls is converted to gravitational waves. The spectrum of the gravitational waves is expected to be peaked at a frequency corresponding to the Hubble scale at the decay, as it is the typical curvature scale of the domain wall system. This was confirmed by detailed numerical calculations [18], and the density parameter of the gravitational waves at the peak frequency at the time of domain wall collapse is given by

$$\Omega_{\rm GW}(t_{\rm dec})|_{\rm peak} = \frac{8\pi\tilde{\epsilon}_{\rm gw}G^2\mathcal{A}^2\sigma^2}{3H_{\rm dec}^2} = \frac{\tilde{\epsilon}_{\rm gw}\mathcal{A}^2}{24\pi}\left(\frac{V_{\rm max}}{V_f}\right)^2\left(\frac{\varphi_f}{M_P}\right)^4, \tag{10}$$

where G is the Newton's gravitational constant and $\tilde{\epsilon}_{\rm gw}$ and $\mathcal{A}$ are numerical factors characterizing respectively the efficiency of the gravitational wave emission and the area of the domain walls. They are determined by the numerical calculations to be $\tilde{\epsilon}_{\rm gw} \simeq 0.7$ and $\mathcal{A} \simeq 0.8$ [18]. Then, the present time density parameter of the gravitational waves at the peak frequency is obtained as

$$\Omega_{\rm GW}h^2|_{\rm peak} \simeq 1.3 \times 10^{-5}\gamma\left(\frac{106.75}{g_*}\right)^{1/3}\Omega_{\rm GW}(t_{\rm dec})|_{\rm peak} \tag{11}$$

where g_* is the relativistic degrees of freedom at the domain wall decay and γ is the dilution factor after the domain wall decay, and it is given by

$$\gamma \simeq \begin{cases} 1 & \text{for } H_{\rm dec} < H_R \\ (H_R/H_{\rm dec})^{2/3} & \text{for } H_{\rm dec} > H_R \end{cases}. \tag{12}$$

Here H_R is the Hubble parameter at the reheating. The peak frequency corresponds to the Hubble parameter at domain wall decay, which is red-shifted by the cosmic expansion until today,

$$f_{\rm peak} = \frac{a(t_{\rm dec})}{a(t_0)}H_{\rm dec} \simeq 160\,\text{Hz}\,\gamma^{-1/2}\left(\frac{g_*}{106.75}\right)^{1/6}\left(\frac{T_X}{10^9\,\text{GeV}}\right) \tag{13}$$

where

$$T_X \simeq \begin{cases} T_{\rm dec} & \text{for } H_{\rm dec} < H_R \\ T_R & \text{for } H_{\rm dec} > H_R \end{cases}, \tag{14}$$

and $T_{\rm dec}$ and T_R are the cosmic temperature at $H = H_{\rm dec}$ and H_R, respectively.

Now let us turn to the domain walls in the SM Higgs potential lifted by new physics. We focus on the case in which the high-scale minimum is a false vacuum and it is quasi-degenerate with the EW vacuum. The position of the false vacuum is at intermediate energy scales, $10^8\ \text{GeV} \lesssim \varphi_f \lesssim 10^{12}\ \text{GeV}$, depending on the values of the top quark mass, the strong gauge coupling, and the Higgs boson mass [3,4]. The height of the potential barrier is determined by solving the RGE, which is roughly $V_{\rm max} \sim 10^{-4}\varphi_f^4$. The bias energy density is treated as a free parameter which is adjusted by tuning Λ.

In the case of the Higgs domain walls, there are generically finite temperature corrections to the Higgs potential, which give an extra contribution to the (time-dependent) energy bias. In the following we derive a condition for thermal effects to have a negligible impact on the domain wall dynamics. The condition can be relaxed in certain situations, and we shall give concrete examples later.

Throughout this letter, we focus on the case in which the position of the false vacuum is always much larger than the cosmic temperature, $\varphi_f \gg T$. Then the thermal mass correction to the effective potential is negligibly small at $\varphi = \varphi_f$. Even for $\varphi \gg T$, however, there is a logarithmic correction arising from the free energy of thermal plasma, the so-called *thermal log* potential [35], which is roughly given by

$$V_T(\varphi) = aT^4 \ln\left(\frac{\varphi}{T}\right), \tag{15}$$

where a is a numerical constant of $O(0.1)$. In addition, there are background thermal plasma in the EW vacuum, while many of the SM particles are non-relativistic in the false vacuum because of $\varphi_f \gg T$. These thermal effects are considered to generate an extra energy bias of order T^4.

After reheating, the thermal energy bias $\sim T^4$ decreases faster than the energy density of domain walls in the scaling regime. Before reheating, both evolve in the same way since the dilute plasma energy density evolves as $T^4 \sim T_R^2 H M_P \propto \rho_{\rm dw}$ (see Eq. (7)) in the case of usual perturbative decay of the inflaton. Thermal effects do not induce the domain wall annihilation if $\rho_{\rm dw} \sim \sigma H \gtrsim T^4$. For a given reheating temperature, this gives a lower bound on the field value at the false vacuum:

$$T_R \lesssim 3 \times 10^8\ \text{GeV}\left(\frac{\varphi_f}{10^{12}\ \text{GeV}}\right)^{3/2} \lesssim V_f^{\frac{1}{4}}, \tag{16}$$

where the second inequality represents the condition for avoiding the domain wall domination (9). The condition (16) implies that the domain walls must annihilate before the reheating.

For the reheating temperature satisfying the condition (16), the thermal plasma energy is always much smaller than $V_{\rm max}$, and so, the use of the tension given in Eq. (6) is justified.[5] If the condition (16) is violated, domain walls will disappear soon after inflation and the resultant gravitational wave signal will be too weak to be detected by future experiments. Also the peak frequency tends to be extremely high.

We would like to emphasize that the bound (16) should be taken with care, because the thermal history after inflation is unknown. Indeed, it is possible to consider some complicated (and contrived) thermal history where thermal effects on the domain wall dynamics are negligible even if (16) is not satisfied. For instance, the inflaton may dominantly decay into hidden sector particles, and the SM sector is reheated when the coupling between the SM and hidden sectors freezes-in well after the domain wall annihilation.[6] We shall return to this issue in Section 4.

[5] The evolution of the domain wall network might deviate from the scaling regime in the presence of background plasma. The existence of plasma could also change the effective area of domain walls $\mathcal{A}$, which results in a shift of the peak frequency for the fixed tension and energy bias. We however expect that such thermal effect on the domain wall dynamics is small as long as thermal energy is much smaller than the energy stored in the domain walls, as we assume in the text.

[6] Our estimate (10) remains unchanged in this case.

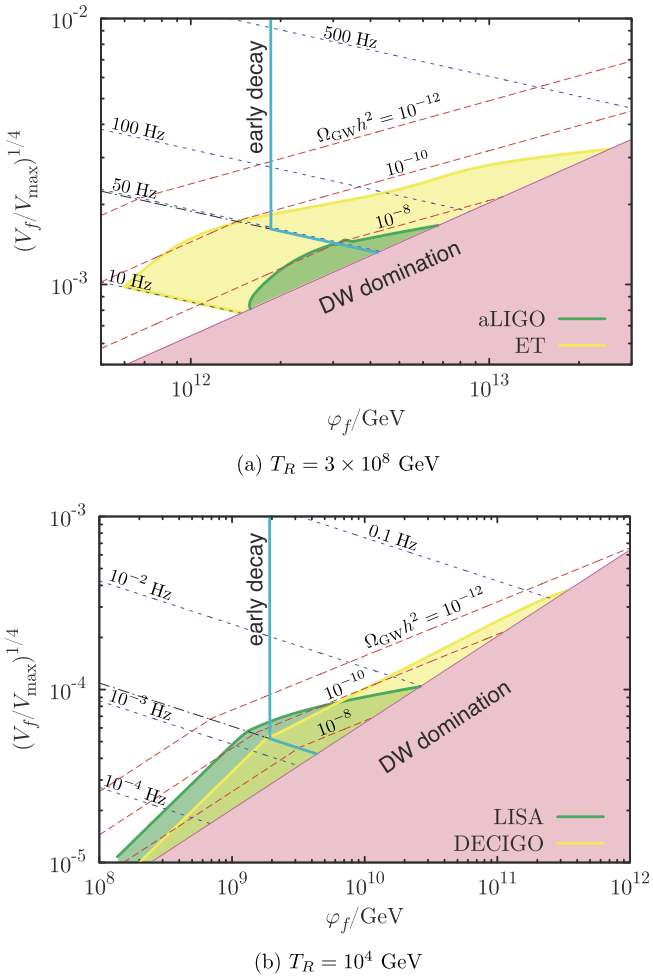

Fig. 2. The contours of $\Omega_{GW}h^2|_{peak}$ (dashed red) and f_{peak} (dotted blue) in the plane of φ_f–$(V_f/V_{max})^{1/4}$. We have set $T_R = 3 \times 10^8$ GeV and $T_R = 10^4$ GeV in the upper and lower panel, respectively. The dash-dotted black line represents the border above (below) which the reheating takes place after (before) the wall decay (16). The lower right shaded (magenta) region is excluded by the domain wall domination (9) and the solid cyan line corresponds to the lower bound on φ_f due to the early domain wall decay by the thermal effect. The thick green and yellow lines represent the sensitivity curves for advanced-LIGO (LISA) and ET (DECIGO) respectively in the upper (lower) panel and the shaded region below the curves will be probed by each experiment.

In Fig. 2, we show the contours of the gravitational wave density parameter at the peak frequency, $\Omega_{GW}h^2|_{peak}$ (dashed (red) lines), as well as the peak frequency, f_{peak} (dotted (blue) lines), in the plane of $(\varphi_f, (V_f/V_{max})^{1/4})$. We have set $T_R = 3 \times 10^8$ GeV in Fig. 2(a) and $T_R = 10^4$ GeV in Fig. 2(b). The shaded (magenta) lower-right triangle region is excluded by the domain wall domination (cf. Eq. (9)) and the solid cyan line is the lower bound on φ_f to avoid the early domain wall decay due to the thermal effects (cf. Eq. (16)). As mentioned earlier, thermal effects are negligible in the region right to the solid cyan line, but it does not necessarily preclude the region left to the solid cyan line because of large uncertainties of thermal history. The thick green and yellow lines represent the sensitivity curves of advanced-LIGO and ET respectively in Fig. 2(a), and LISA and DECIGO in Fig. 2(b), and the shaded region below the curves will be probed by each experiments. The sensitivity curve of KAGRA is expected to be similar to that of advanced-LIGO. Note that it is difficult to generate gravitational waves within the reach of pulsar timing observations such as IPTA [36] and SKA [37] which are sensitive to much lower frequencies ($\sim 10^{-9}$ Hz). It would require the tension of the domain

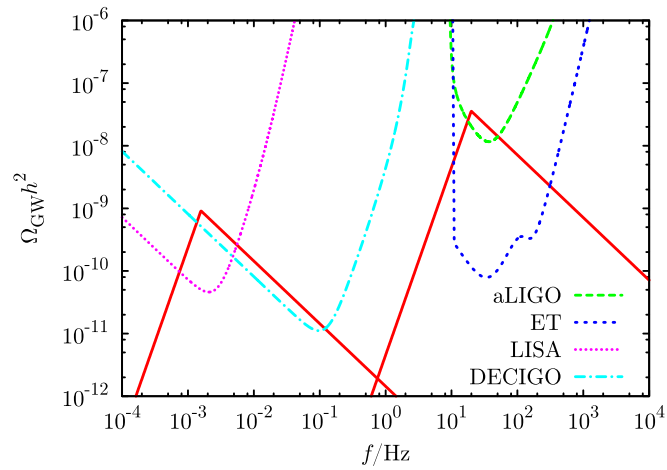

Fig. 3. The typical spectrum of the gravitational waves is shown by the solid (red) lines. We have taken $\varphi_f = 2 \times 10^9$ GeV and $(V_f/V_{max})^{1/4} = 5 \times 10^{-5}$ for the left line and $\varphi_f = 2 \times 10^{12}$ GeV and $(V_f/V_{max})^{1/4} = 10^{-3}$ for the right line.

walls to be close to $(10^5\,\text{GeV})^3$, which cannot be realized within the SM framework.

We show in Fig. 3 the gravitational wave spectrum for certain parameters ($\varphi_f = 2 \times 10^9$ GeV and $(V_f/V_{max})^{1/4} = 5 \times 10^{-5}$ for the left line and $\varphi_f = 2 \times 10^{12}$ GeV and $(V_f/V_{max})^{1/4} = 10^{-3}$ for the right line). According to the precise numerical calculations [18], the gravitational wave spectrum scales as $(f/f_{peak})^3$ for $f < f_{peak}$ and $(f/f_{peak})^{-1}$ for $f > f_{peak}$.

4. Discussion and conclusions

In the previous section we have mentioned that the condition (16) can be relaxed in certain situations. Here we give concrete examples that relax the condition (16) so as to make the wider parameter available. As we shall see below, this requires a more involved thermal history of the Universe.

Suppose that the inflaton dominantly decays into a hidden sector, which is decoupled from the SM sector. This significantly suppresses thermal corrections to the Higgs potential, and the lower bound on φ_f (16) is no longer applied.[7] The SM particles can be thermally populated through various processes much later than the domain wall annihilation. For instance, the hidden sector may contain a U(1) gauge group, which has a small kinetic mixing with the SM $U(1)_Y$. For a sufficiently small kinetic mixing, the SM particles are thermalized through the kinetic mixing well after the domain wall annihilation but before nucleosynthesis, unless the hidden photon is extremely light. If the hidden photon is massless, we need to introduce hidden matter fields (e.g. a Dirac fermion) charged under the hidden U(1) gauge symmetry. The hidden matter fields behave as mini-charged particles, connecting the hidden sector and the SM sector. In this case, the massless hidden photon contributes to the effective neutrino species, N_{eff}, whose precise value depends on the mass of the hidden matter fields [38]. Similarly, if one introduces a gauge singlet scalar field, the SM sector can be produced from the hidden sector through the Higgs portal coupling. In this case, the thermalization of the SM sector can be delayed for a sufficiently small Higgs portal coupling. It is worth noting that there is no

[7] Some amount of the SM plasma is necessarily generated by the Higgs domain walls, because they continuously annihilate in the scaling regime. We have numerically confirmed that the energy density of the SM plasma induced by the Higgs domain walls in the scaling regime is always smaller than that of domain walls, and therefore, it does not induce the domain wall annihilation.

entropy production when the SM sector is thermalized, and our analysis in the previous section can be applied without any modification even in the parameter space left to the solid cyan line in Fig. 2.

Alternatively, the SM sector can be reheated, if one introduces another field (e.g. a modulus field) which dominates the Universe for a short period and decays into the SM particles after the inflaton decay. In this case one has to take account of its thermal effects, the shift of the peak frequency, as well as an extra dilution due to the modified thermal history.

In the SM framework, the Higgs self coupling turns to negative, and the effective potential becomes negative at a high energy scale, based on the perturbative RGE analysis. The scale sensitively depends on the values of the top quark mass, but it is at an intermediate scale for the top quark mass, $M_t \simeq 173\,\text{GeV}$. In such a case, the EW vacuum is metastable, which is acceptable as long as it is sufficiently long-lived. On the other hand, the negative effective potential may signal that new physics appears around that scale and lift the potential, creating a local minimum at an intermediate scale. In a limiting case, the two vacua, one at the EW scale and the other at an intermediate scale, are quasi-degenerate in energy. This requires a certain amount of fine-tuning of the parameters. Once the fine-tuning of the parameters is realized, it gives rise to a possibility of domain wall formation.

For domain walls to be formed after inflation, both vacua must be populated with more or less equal probability during inflation. Domain walls are not formed if one of the two vacua is preferred over the other. This is the case if the Higgs potential is significantly modified through its non-minimal coupling to gravity, or if the quantum fluctuations of the Higgs field is too small to overcome the barrier separating the two vacua. We have assumed that the Higgs field is minimally coupled to gravity as well as the inflaton sector so that the potential is not significantly modified, and that the quantum fluctuations of the Higgs field is sufficiently large to overcome the barrier between the two vacua.

The energy of domain walls is partially converted to gravitational waves through the violent annihilation processes. The gravitational waves are expected to be peaked at a frequency corresponding to the Hubble horizon size at the domain-wall annihilation. The gravitational-wave spectrum looks like that from a phase transition. In the latter case, the gravitational wave spectrum has a peak corresponding to the typical size of bubbles, a few orders of magnitude smaller than the Hubble horizon at the phase transition.

In order to generate gravitational waves within the reach of future experiments, the bias energy density must be so small that domain walls annihilate when they are about to dominate the Universe. While there is no compelling reason for the quasi-degeneracy of the two vacua, it may be due to the multiple-point principle [9] or an important cosmological role (e.g. dark matter, baryogenesis) of the decay products of domain walls. The violent domain wall annihilation processes produce not only gravitational waves but also a large amount of the SM Higgs bosons which soon decay into quarks, leptons and gauge bosons. If the SM Higgs boson is coupled to some heavy degrees of freedom such as right-handed neutrinos, a B–L Higgs field, and a singlet scalar, those heavy particles can be produced through non-perturbative processes, and they may contribute to dark matter, or baryogenesis, etc. [39].

In this letter we have investigated the domain wall formation in the Standard Model Higgs potential lifted by new physics and gravitational wave production due to the domain wall decay. We have shown that the gravitational waves can be within the reach of the future experiments such as advanced LIGO, KAGRA, ET, LISA and DECIGO, if the domain walls decay when their energy density is sizable. In this way, the direct detection experiments of the gravitational wave can be a powerful probe of another vacuum far beyond the EW scale.

Acknowledgements

This work was supported by JSPS Grant-in-Aid for Young Scientists (B) (No. 24740135 [FT]), Scientific Research (A) (No. 26247042 [FT]), Scientific Research (B) (No. 26287039 [FT]), the Grant-in-Aid for Scientific Research on Innovative Areas (No. 23104008 [NK, FT]), and Inoue Foundation for Science [FT]. This work was also supported by World Premier International Center Initiative (WPI Program), MEXT, Japan [FT].

References

[1] G. Aad, et al., ATLAS Collaboration, Phys. Lett. B 716 (2012) 1, arXiv:1207.7214 [hep-ex].
[2] S. Chatrchyan, et al., CMS Collaboration, Phys. Lett. B 716 (2012) 30, arXiv:1207.7235 [hep-ex].
[3] D. Buttazzo, G. Degrassi, P.P. Giardino, G.F. Giudice, F. Sala, A. Salvio, A. Strumia, J. High Energy Phys. 1312 (2013) 089, arXiv:1307.3536 [hep-ph].
[4] A. Andreassen, W. Frost, M.D. Schwartz, Phys. Rev. Lett. 113 (24) (2014) 241801, arXiv:1408.0292 [hep-ph].
[5] A. Vilenkin, E. Shellard, Cosmic Strings and Other Topological Defects, Cambridge Monogr. Math. Phys., Cambridge University Press, 2000.
[6] Y. Hamada, K.y. Oda, F. Takahashi, Phys. Rev. D 90 (9) (2014) 097301, arXiv:1408.5556 [hep-ph].
[7] A.D. Linde, Phys. Lett. B 327 (1994) 208, arXiv:astro-ph/9402031.
[8] A. Vilenkin, Phys. Rev. Lett. 72 (1994) 3137, arXiv:hep-th/9402085.
[9] C.D. Froggatt, H.B. Nielsen, Phys. Lett. B 368 (1996) 96, arXiv:hep-ph/9511371.
[10] Y. Hamada, H. Kawai, K.y. Oda, arXiv:1501.04455 [hep-ph].
[11] A. Vilenkin, Phys. Rev. D 23 (1981) 852.
[12] G.B. Gelmini, M. Gleiser, E.W. Kolb, Phys. Rev. D 39 (1989) 1558.
[13] D. Coulson, Z. Lalak, B.A. Ovrut, Phys. Rev. D 53 (1996) 4237.
[14] S.E. Larsson, S. Sarkar, P.L. White, Phys. Rev. D 55 (1997) 5129, arXiv:hep-ph/9608319.
[15] M. Gleiser, R. Roberts, Phys. Rev. Lett. 81 (1998) 5497, arXiv:astro-ph/9807260.
[16] T. Hiramatsu, M. Kawasaki, K. Saikawa, J. Cosmol. Astropart. Phys. 1005 (2010) 032, arXiv:1002.1555 [astro-ph.CO].
[17] M. Kawasaki, K. Saikawa, J. Cosmol. Astropart. Phys. 1109 (2011) 008, arXiv:1102.5628 [astro-ph.CO].
[18] T. Hiramatsu, M. Kawasaki, K. Saikawa, J. Cosmol. Astropart. Phys. 1402 (2014) 031, arXiv:1309.5001 [astro-ph.CO].
[19] A. Abramovici, W.E. Althouse, R.W.P. Drever, Y. Gursel, S. Kawamura, F.J. Raab, D. Shoemaker, L. Sievers, et al., Science 256 (1992) 325.
[20] K. Somiya, KAGRA Collaboration, Class. Quantum Gravity 29 (2012) 124007, arXiv:1111.7185 [gr-qc].
[21] Y. Aso, et al., KAGRA Collaboration, Phys. Rev. D 88 (4) (2013) 043007, arXiv:1306.6747 [gr-qc].
[22] B. Sathyaprakash, M. Abernathy, F. Acernese, P. Ajith, B. Allen, P. Amaro-Seoane, N. Andersson, S. Aoudia, et al., Class. Quantum Gravity 29 (2012) 124013, arXiv:1206.0331 [gr-qc];
B. Sathyaprakash, M. Abernathy, F. Acernese, P. Ajith, B. Allen, P. Amaro-Seoane, N. Andersson, S. Aoudia, et al., Class. Quantum Gravity 30 (2013) 079501 (Erratum).
[23] P. Amaro-Seoane, S. Aoudia, S. Babak, P. Binetruy, E. Berti, A. Bohe, C. Caprini, M. Colpi, et al., GW Notes 6 (2013) 4, arXiv:1201.3621 [astro-ph.CO].
[24] S. Kawamura, T. Nakamura, M. Ando, N. Seto, K. Tsubono, K. Numata, R. Takahashi, S. Nagano, et al., Class. Quantum Gravity 23 (2006) S125.
[25] F. Takahashi, T.T. Yanagida, K. Yonekura, Phys. Lett. B 664 (2008) 194, arXiv:0802.4335 [hep-ph].
[26] T. Moroi, K. Nakayama, Phys. Lett. B 703 (2011) 160, arXiv:1105.6216 [hep-ph].
[27] A. Eichhorn, H. Gies, J. Jaeckel, T. Plehn, M.M. Scherer, R. Sondenheimer, arXiv:1501.02812 [hep-ph].
[28] N. Haba, K. Kaneta, R. Takahashi, J. High Energy Phys. 1404 (2014) 029, arXiv:1312.2089 [hep-ph].
[29] N. Khan, S. Rakshit, Phys. Rev. D 90 (11) (2014) 113008, arXiv:1407.6015 [hep-ph].
[30] K. Kawana, arXiv:1411.2097 [hep-ph].
[31] W.H. Press, B.S. Ryden, D.N. Spergel, Astrophys. J. 347 (1989) 590.
[32] M. Hindmarsh, Phys. Rev. Lett. 77 (1996) 4495, arXiv:hep-ph/9605332.
[33] T. Garagounis, M. Hindmarsh, Phys. Rev. D 68 (2003) 103506, arXiv:hep-ph/0212359.
[34] A.M.M. Leite, C.J.A.P. Martins, Phys. Rev. D 84 (2011) 103523, arXiv:1110.3486 [hep-ph].

[35] A. Anisimov, M. Dine, Nucl. Phys. B 619 (2001) 729, arXiv:hep-ph/0008058.
[36] R.N. Manchester, Class. Quantum Gravity 30 (2013) 224010.
[37] M. Kramer, arXiv:astro-ph/0409020.
[38] H. Vogel, J. Redondo, J. Cosmol. Astropart. Phys. 1402 (2014) 029, arXiv:1311.2600 [hep-ph].
[39] R. Daido, N. Kitajima, F. Takahashi, in preparation.

計画研究 B02 班

課題名「テラスケール物理がもたらす新しい時空像」

研究組織

(1) 研究代表者

細谷　裕（HOSOTANI, Yutaka）
大阪大学・大学院理学研究科・教授
研究者番号：50324744

(2) 研究分担者

林　青司（LIM, C.S.）
東京女子大学・現代教養学部・教授
研究者番号：80201870

(3) 研究分担者

尾田欣也（ODA, Kin-ya）
大阪大学・大学院理学研究科・准教授
研究者番号：60442943

交付決定額

計画研究 B02 班に配分された交付額を表 1 に示す。

表 1. 交付決定額（配分額）　（金額単位：円）

年度	直接経費	間接経費	合計
平成 23 年度	5,400,000	1,620,000	7,020,000
平成 24 年度	7,000,000	2,100,000	9,100,000
平成 25 年度	7,100,000	2,130,000	9,230,000
平成 26 年度	6,700,000	2,010,000	8,710,000
平成 27 年度	6,700,000	2,010,000	8,710,000
総計	32,900,000	9,870,000	42,770,000

研究成果

1．研究開始当初の背景

標準模型は幾多の実験的テストに耐え、大きな成功を収めていたが、要のヒッグス粒子は未発見であった。その質量を電弱スケール(100 GeV)に保つためには理論のパラメターの不自然な微調整が必要であるという階層性問題や、クォーク・レプトンの質量や世代間混合を司る湯川結合が任意で、理論に多くの不定パラメターが存在するといった問題点を抱えている。この原因はヒッグス相互作用を制御する対称性原理の欠如にある。

ヒッグス相互作用を制御する方法として、余剰次元におけるゲージ・ヒッ グス統合を考える。これは、もともと代表者の細谷が 1983 年に提出したゲージ場とヒッグス場を 5 次元ゲージ理論のなかで統一し、量子効果により対称性を破るという細谷機構に基づいている。 我々の時空は 4 次元ではなく、 5 次元目， 6 次元目の余剰次元があり、余剰次元でのゲージ相互作用が、ヒッグス相互作用としてあらわれると考えるのである。分担者の林は 1998 年このゲージ・ヒッグス統合で階層性問題が解決できることを見いだし、電弱相互作用でのゲージ・ヒッグス統合理論の突破口を開いた。

余剰次元の歴史は古い。1920 年代に Kaluza と Klein は重力と電磁相互作用を 5 次元時空で統一することを提唱した。だが、それを確かめる術はなかった。1970 年ごろより、素粒子の基本相互作用は非可換ゲージ理論の形で統一されることになる。そして 1983 年、細谷は統一理論の柱となる対称性の自発的破れが 5 次元時空のゲージ相互作用の結果、 自然に起ることを発見した。更に、左右非対称でカイラルな弱い相互作用が、オービフォルドの余剰次元で自然に実現できることが見いだされ、電弱相互作用を記述する現実的な余剰次元理論、ゲージ・ヒッグス統合理論が構成されるに至った。

2．研究の目的

余剰次元が存在するという新しい時空描像のもと、ゲージ・ヒッグス統合理論を中心とする余剰次元理論から帰結されるテラスケールの物理を予言し、LHC や暗黒物質探索などの実験観測に直接結びつけ、検証することで新しい時空像を確立していく。

3．研究の方法

余剰次元と実験観測との接点をヒッグスボゾン、KK 励起粒子、暗黒物質、ブラックホール生成等に見極め、テラスケール加速器実験と観測で直接検証する形で時空描像を塗り替える。細谷が 28 年前明らかにした細谷機構を基礎とし、林が 13 年前に整備したゲージ・ヒッグス統合が、ようやく電弱相互作用を記述する現実的な理論となり、実験観測による検証が可能となる。1920 年代に始まった余剰次元による統一のシナリオが、単なる理論的可能性としてではなく、自然科学として実現できる。相対論の出現で時間と空間が融合し、量子論の出現でミクロの世界の基本原理が塗り替えられた。余剰次元の存在は、ミクロの彼方に潜む時空概念の大変革を意味し、我々は、新しい自然観の世界に突入する。

4．研究成果

(1) ゲージ・ヒッグス統合理論の構築

細谷は SO(5)xU(1) ゲージ・ヒッグス統合理論を Randall-Sundrum ワープ空間で構成した。このモデルは、低エネルギー領域では、標準模型とほぼ同じ結果を与える。ヒッグスボゾンがゲージ場の 5 次元目の成分として出現し、量子効果により、電弱対称性が自発的に破れる。ヒッグスボゾンの質量は有限に予言される。階層性問題が自動的に解決される。クォーク・レプトンはカイラルな相互作用を持つ零モードとして現れる。

ヒッグスボゾンは、5 次元目の空間でのアハロノフ・ボーム位相となる。ゲージ不変性により保証された位相として性質から、ヒッグスボゾンの相互作用係数は有限となる。

(2) ゲージ・ヒッグス統合理論の整合性

SO(5)xU(1) ゲージ・ヒッグス統合理論は驚くべき性質を持っていることが判明した。高次元で定義された理論では、各粒子に付随して 5 次元方向への励起モード（KK モード）が無限個出現する。2012 年に発見されたヒッグスボゾンは、例えば、2 光子に崩壊する。この崩壊過程には、無限個の KK モードの寄与があり、総和は発散してしまう危険性がある。ゲージ・ヒッグス統合理論では各モードの寄与の間に相殺が起こり、総和は有限で、かつ非常に小さいことが示された。

その後の実験結果と整合し、ゲージ・ヒッグス統合理論では、5 次元目の空間でのアハロノフ・ボーム位相がある程度小さい限り（つまり、0.1 より小さいかぎり）全てのヒッグスボゾンの崩壊モードのレートの標準模型からのずれは 1%以下になることが示された。

(3) ゲージ・ヒッグス統合理論の予言

SO(5)xU(1) ゲージ・ヒッグス統合理論はいくつか自由にとれるパラメータがある。にもかかわらず、多くの観測可能な物理量は、理論の詳細によらず、アハロノフ・ボーム位相の値でほぼ決まることが示された。この性質はユニバーサリティ（普遍性）と呼ばれる。何故、ユニバーサリティが成立するのかはまだ理解されていない。

例えば、光子や Z ボゾン、クォークの KK 励起モードの質量、クォーク・レプトンの湯川結合の大きさ、ヒッグスボゾンの 3 点、4 点自己相互作用の大きさなどは、すべてアハロノフ・ボーム位相の値でほぼ決まる。位相が 0.1 より小さいと、湯川結合の標準模型からのずれを実験的に観測するのは難しい。LHC 実験で探索可能なのは、光子や Z ボゾンの KK 励起モード（Z'と呼ばれる）で、その質量は 6 TeV から 8 TeV の領域に予言される。これが発見されれば、アハロノフ・ボーム位相の値が決まり、他の物理量（ヒッグスボゾンの 3 点、4 点自己相互作用の大きさなど）に対する予言となる。Z' 事象の発見は、余剰次元探索の要である。

(4) 暗黒物質

理論の詳細に依存するが、SO(5)xU(1) ゲージ・ヒッグス統合理論は暗黒物質の存在を予言する。現在 CMB（宇宙背景マイクロ波）等の観測データから決められた暗黒物質の残存量を説明し、かつ、暗黒物質直接探索の制限を満たすためには、アハロノフ・ボーム位相の値は 0.07 から 0.1 で、暗黒物質候補となる粒子の質量は 2 TeV から 3 TeV の領域に予言される。現在稼働中の、あるいは次期にプランされている暗黒物質直接探索実験で見つかる可能性がある。

(5) ゲージ・ヒッグス統合の理論的精密化

ゲージ・ヒッグス統合は新しい可能性として理論的にも更なる精密化が必要である。林は、ゲージ・ヒッグス統合理論におけるフレーバ混合の仕組みを明らかにした。世代間での FCNC を自然に抑制ための方法が開発された。また、SU(3)モデルで、125 GeV というヒッグス質量を古典レベルで再現することが可能であることも示した。

(6) 新分野の創造

ゲージ・ヒッグス統合理論の基礎となるのが細谷機構による対称性の自発的破れである。通常のヒッグス機構とは異なり、純粋なゲージ相互作用の枠内で、力学的に量子論的に、ゲージ対称性が自発的に破れる。このメカニズムは、これまで、摂動論的に確かめられ、ゲージ・ヒッグス統合理論に応用されてきた。

細谷は、この細谷メカニズムによるゲージ対称性の力学的破れを格子ゲージ理論による数値シミュレーションで非摂動論的に検証できることを示した。格子ゲージ理論の専門家との共同事業である。格子 QCD 理論の技術を応用し、スーパーコンピュータを使い、随伴表現のフェルミオンを含む 4 次元の SU(3)ゲージ理論で、温度やフェルミオン質量が変化させ、Polyakov ループの固有値分布を見ることで、SU(3)ゲージ対称性が SU(2)xU(1) や、U(1)xU(1) 対称性に破れることを示してみせた。

非摂動論的にゲージ対称性の自発的破れを示したことは、将来の物理学に大きな影響を及ぼすものと期待される。また、計算機科学の新しい分野を切り開いたことも貴重である。

(7) インフレーション

標準模型の枠内で、ヒッグス場と重力の間に新しい結合があれば、プランクスケール近傍でインフレーションが起こりえることを尾田は示した。さらに、超弦理論において、ヒッグス場を弦の無質量モードと同定すると、場の値が大きな領域においては、ヒッグス・ポテンシャルは逃避真空に繋がっていることを示した。その結果、ヒッグス場が永遠のインフレーションの起源となっていることを示した。ヒッグス場の物理がプランクスケールの物理に繋がる事を示したのは非常に興味深い。

５．主な発表論文等

〔雑誌論文〕（計３２件）

(1) Y. Hosotani and N. Yamatsu, Gauge-Higgs grand unification, Prog. Theor. Exp. Phys.2015 (2015) 111B01, 1-9. DOI: 10.1093/ptep/ptv153

(2) S. Funatsu, H. Hatanaka and Y. Hosotani, H to Z,gamma in the gauge-Higgs unification, Phys. Rev. D 92 (2015) 115003, 1-20. DOI: 10.1103/PhysRevD.92.115003

(3) Y. Hamada, H. Kawai and K. Oda, Eternal Higgs inflation and the cosmological constant problem, Phys. Rev. D 92 (2015) 045009, 1-30. DOI: 10.1103/PhysRevD.92.045009

(4) C.S. Lim, N. Maru and T. Miura, Is the 126 GeV Higgs boson mass calculable in gauge-Higgs unification?, Prog. Theor. Exp. Phys. 2015 (2015) 043B02, 1-23. DOI: 10.1093/ptep/ptv030

(5) Y. Hamada, H. Kawai, K. Oda and S.C. Park, Higgs inflation from standard model

criticality, Phys. Rev. D 91 (2015) 053008, 1-17. DOI: 10.1103/PhysRevD.91.053008

(6) G. Cossu, H. Hatanaka, Y. Hosotani and J. Noaki, Polyakov loops and the Hosotani mechanism on the lattice, Phys. Rev. D 89 (2014) 094509, 1-22. DOI: 10.1103/PhysRevD.89.0945009

(7) S. Funatsu, H. Hatanaka, Y. Hosotani, Y. Orikasa and T. Shimotani, LHC signals of the SO(5)xU(1) gauge-Higgs unification, Phys. Rev. D 89 (2014) 095019, 1-18. DOI: 10.1103/PhysRevD.89.095019

(8) S. Funatsu, H. Hatanaka, Y. Hosotani, Y. Orikasa and T. Shimotani,Dark matter in the SO(5)xU(1) gauge-Higgs unification, Prog. Theor. Exp. Phys., 2014 (2014) 113B01, 1-40. DOI: 10.1093/ptep/ptu146

(9) C.S. Lim, The Higgs particle and higher-dimensional theories, Prog. Theor. Exp. Phys. 2014 (2014) 02A101, 1-21. DOI: 10.1093/ptep/ptt083

(10) Y. Hamada, H. Kawai and K. Oda, Minimal Higgs inflation, Prog. Theor. Exp. Phys. 2014 (2014) 023B02. DOI: 10.1093/ptep/ptt116

(11) S. Funatsu, H.Hatanaka,Y. Hosotani, Y. Orikasa and T. Shimotani, Novel universality and Higgs decay H to gamma gamma, g g in the SO(5)xU(1) gauge-Higgs unification, Phys. Lett. B 722 (2013) 94-99. DOI: 10.1016/j.physletb.2013.03.040

(12) H. Hatanaka and Y. Hosotani, SUSY breaking scales in the gauge-Higgs unification, Phys. Lett. B 713 (2012) 481-484. DOI: 10.1016/j.physletb.2012.06.039

(13) Y. Hosotani, M. Tanaka and N. Uekusa, Collider signatures of the SO(5)xU(1) gauge-Higgs unification, Phys. Rev. D 84 (2011) 075014, 1-22.

〔学会発表〕（計５７件）

(1) Y. Hosotani, Gauge-Higgs grand unification, PLANCK2015, Ioannia, Greece, 25 – 29 May 2015.

(2) Y. Hosotani, Gauge-Higgs unification from EW to GUT, Scalars 2015, Warsaw, Poland, 3-7 December 2015.

(3) K.Oda, Eternal Higgs inflation, 15th Hellenic School and Workshops on Elementary Particle Physics and Gravity, Corfu, Greece, 13-19 September 2015.

(4) Y. Hosotani, Hosotani mechanism and gauge symmetry breaking on the lattice, Summer Institute 2014, 富士吉田, 山梨, 2014 年 8 月 21 日-28 日

(5) C.S. Lim, Higgs mass and anomalous Higgs interactions in gauge-Higgs unification, PLANCK 2014, Paris, France, 26-30 May 2014

(6) Y. Hosotani, SO(5)xU(1) gauge-Higgs unification, Scalars 2013, Warsaw, Poland, 12-16 September 2013

(7) Y. Hosotani, 126 GeV Higgs boson and universality relations in the SO(5)xU(1) gauge-Higgs unification, Toyama International Workshop on “Higgs as a Probe of New Physics 2013”, 富山, 2013 年 2 月 13 日-16 日

(8) Y. Hosotani, Hosotani mechanism on the lattice, Summer Institute 2012, Sun Moon Lake, Taiwan, 18 - 24 August 2012.

(9) Y. Hosotani, Collider signatures of gauge-Higgs unification, Scalars 2011, Warsaw, Poland, 26 August 2011

主要論文別刷

(2) S. Funatsu, H. Hatanaka and Y. Hosotani, “H to Z,gamma in the gauge-Higgs unification”, Phys. Rev. D 92 (2015) 115003, 1-20. DOI: 10.1103/PhysRevD.92.115003

(7) S. Funatsu, H. Hatanaka, Y. Hosotani, Y. Orikasa and T. Shimotani, “LHC signals of the SO(5)xU(1) gauge-Higgs unification”, Phys. Rev. D 89 (2014) 095019, 1-18.
DOI: 10.1103/PhysRevD.89.095019

(9) C.S. Lim, “The Higgs particle and higher-dimensional theories”, Prog. Theor. Exp. Phys. 2014 (2014) 02A101, 1-21. DOI: 10.1093/ptep/ptt083

(10) Y. Hamada, H. Kawai and K. Oda, “Minimal Higgs inflation”, Prog. Theor. Exp. Phys. 2014 (2014) 023B02. DOI: 10.1093/ptep/ptt116

(11) S. Funatsu, H.Hatanaka,Y. Hosotani, Y. Orikasa and T. Shimotani, “Novel universality and Higgs decay H to gamma gamma, g g in the SO(5)xU(1) gauge-Higgs unification”, Phys. Lett. B 722 (2013) 94-99. DOI: 10.1016/j.physletb.2013.03.040

PHYSICAL REVIEW D **92,** 115003 (2015)

$H \to Z\gamma$ in the gauge-Higgs unification

Shuichiro Funatsu,[1] Hisaki Hatanaka,[2] and Yutaka Hosotani[1]

[1]*Department of Physics, Osaka University, Toyonaka, Osaka 560-0043, Japan*

[2]*Quantum Universe Center, Korea Institute for Advanced Study, Seoul 130-722, Republic of Korea*

(Received 23 October 2015; published 2 December 2015)

The decay rate of the Higgs decay $H \to Z\gamma$ is evaluated at the one-loop level in the $SO(5) \times U(1)$ gauge-Higgs unification. Although an infinite number of loops with Kaluza-Klein states contribute to the decay amplitude, there appears the cancellation among the loops, and the decay rate is found to be finite and nonzero. It is found that the decay rate is well approximated by the decay rate in the standard model multiplied by $\cos^2\theta_H$, where θ_H is the Aharonov-Bohm phase induced by the vacuum expectation value of an extra-dimensional component of the gauge field.

DOI: 10.1103/PhysRevD.92.115003 PACS numbers: 12.60.-i, 11.10.Kk, 11.15.-q, 12.10.-g

I. INTRODUCTION

The Higgs boson of a mass about 125 GeV has been found at LHC [1,2]. The signal strength of each decay mode of the Higgs boson has been consistent with the standard model (SM) [3,4]. Though the decay mode $H \to Z\gamma$ has not been observed so far, it is expected to be seen in the Run 2 at LHC. The decay rate $\Gamma(H \to Z\gamma)$ has been evaluated in the SM, [5] the two Higgs doublet model, [6] the minimal supersymmetric standard model, [6] and the universal extra dimension model [7], and the type-II seesaw model [8].

The gauge-Higgs unification (GHU) is one of the scenarios beyond the SM [9–17]. In GHU the 4D Higgs boson appears as part of the extra-dimensional component of the gauge potentials. When the extra-dimensional space is not simply connected, it is identified with the 4D fluctuation mode of the Aharonov-Bohm (AB) phase θ_H along the extra-dimensional space. The gauge invariance protects the Higgs boson from acquiring divergent mass corrections. The Higgs boson mass is generated at the quantum level, being finite and independent of the cutoff scales in the theory. Especially the $SO(5) \times U(1)$ GHU in the Randall-Sundrum (RS) space-time is phenomenologically successful [18–22]. The Higgs doublet appears in the $SO(5)/SO(4)$ part of the fifth dimensional component of the vector potentials with the custodial symmetry. The model is consistent with the LHC results for $\theta_H < 0.1$. The deviation of the decay rate $\Gamma(H \to \gamma\gamma)$ from the SM, for instance, is less than 1% [23], despite the fact that an infinite number of Kaluza-Klein (KK) mode of the W boson and top quark contribute. Z' events are expected as the excitation of the first KK modes of γ, Z and the lowest mode of Z_R, the neutral $SU(2)_R$ gauge boson. Their masses are almost degenerate, and are estimated to be in the range 4 to 8.5 TeV for $\theta_H = 0.15 \sim 0.07$ [24]. There also exists a dark matter candidate in the model, the lowest KK mode of $SO(5)$-spinor fermion called dark fermions [25]. Its mass is in the range of 2.3–3.1 TeV and the spin-independent scattering cross section per nucleon is $\sigma_N \simeq O(10^{-44})$ cm^2. It may be detected in the 300 live days run of the LUX experiment.

In this paper we focus on the decay mode $H \to Z\gamma$ in the $SO(5) \times U(1)$ GHU. The decay width of $H \to Z\gamma$ has been evaluated in the $SU(3)$ GHU model on flat $M^4 \times (S^1/Z_2)$ by Maru and Okada [26]. They found that it vanishes at the one loop level, due to the group structure of the $SU(3)$ model. In the $SO(5) \times U(1)$ GHU in RS, on the other hand, it is known that the gauge couplings of the SM particles are almost the same as in the SM so that one expects that the process $H \to Z\gamma$ occurs. Furthermore, as in the case of $H \to \gamma\gamma$, one needs to worry about the contributions coming from an infinite number of KK modes running in the loops. The situation in the case of $H \to Z\gamma$ is more involved than that in the case of $H \to \gamma\gamma$. In $H \to \gamma\gamma$, the KK number of virtual particles running the inside loop is conserved. In contrast, in the case of $H \to Z\gamma$, the KK number of virtual particles may change, as both H and Z have off-diagonal couplings in RS. This gives rise to an interesting question whether or not the sum of all these contributions converges. It seems to require more subtle cancellation mechanism to have a finite result than in the case of $H \to \gamma\gamma$. We demonstrate in this paper by direct evaluation that miraculous cancellation takes place among KK-number-conserving and KK-number-violating loops. After all, the deviation of the decay width from that in the SM is $O(1)\%$.

The paper is organized as follows. In Sec. II, the model of the $SO(5) \times U(1)$ GHU is explained. In Sec. III, we review the decay rate of the $H \to \gamma\gamma$ and evaluate the decay rate of the $H \to Z\gamma$ process in the $SO(5) \times U(1)$ GHU. In Sec. IV, the conclusion and discussions are given. In the appendix, we summarize Z and H couplings of various fields which are necessary in calculating the $H \to Z\gamma$ decay rate.

II. MODEL

We consider the $SO(5) \times U(1)$ gauge-Higgs unification in the Randall-Sundrum (RS) warped space [27], whose metric is given by $ds^2 = G_{MN}dx^M dx^N = e^{-2\sigma(y)}\eta_{\mu\nu}dx^\mu dx^\nu + dy^2$,

 © 2015 American Physical Society

where $\eta_{\mu\nu}=\mathrm{diag}(-1,1,1,1)$, $\sigma(y)=\sigma(y+2L)=\sigma(-y)$, and $\sigma(y)=k|y|$ for $|y|\le L$. The Planck and TeV branes are located at $y=0$ and $y=L$, respectively. The bulk region $0<y<L$ is anti-de Sitter (AdS) spacetime with a cosmological constant $\Lambda=-6k^2$. The warp factor is $z_L\equiv e^{kL}\gg 1$, and the Kaluza-Klein mass scale is given by $m_{\mathrm{KK}}=\pi k/(z_L-1)\sim \pi k z_L^{-1}$. The model consists of $SO(5)\times U(1)_X$ gauge fields (A_M,B_M), quark-lepton multiplets Ψ_a, $SO(5)$-spinor fermions (dark fermions) Ψ_{F_i}, brane fermions $\hat{\chi}_{\alpha R}$, and brane scalar $\hat{\Phi}$ [22,23]. The model has been specified in Refs. [24,25]. The bulk part of the action is given by

$$S_{\mathrm{bulk}}=\int d^5x\sqrt{-G}\Big[-\mathrm{tr}\Big(\frac{1}{4}F^{(A)MN}F^{(A)}_{MN}+\frac{1}{2\xi}(f^{(A)}_{\mathrm{gf}})^2+\mathcal{L}^{(A)}_{\mathrm{gh}}\Big)-\Big(\frac{1}{4}F^{(B)MN}F^{(B)}_{MN}+\frac{1}{2\xi}(f^{(B)}_{\mathrm{gf}})^2+\mathcal{L}^{(B)}_{\mathrm{gh}}\Big)$$
$$+\sum_a\bar{\Psi}_a\mathcal{D}(c_a)\Psi_a+\sum_{i=1}^{n_F}\bar{\Psi}_{F_i}\mathcal{D}(c_{F_i})\Psi_{F_i}\Big],$$
$$\mathcal{D}(c)=\Gamma^A e_A{}^M\Big(\partial_M+\frac{1}{8}\omega_{\mathrm{MBC}}[\Gamma^B,\Gamma^C]-ig_A A_M-ig_B Q_X B_M\Big)-c\sigma'(y). \tag{2.1}$$

The gauge fixing and ghost terms are denoted as functionals with subscripts gf and gh, respectively. $F^{(A)}_{MN}=\partial_M A_N-\partial_N A_M-ig_A[A_M,A_N]$, and $F^{(B)}_{MN}=\partial_M B_N-\partial_N B_M$. The color $SU(3)_C$ gluon fields and their interactions have been suppressed. The $SO(5)$ gauge fields A_M are decomposed as

$$A_M=\sum_{a_L=1}^{3}A_M^{a_L}T^{a_L}+\sum_{a_R=1}^{3}A_M^{a_R}T^{a_R}+\sum_{\hat{a}=1}^{4}A_M^{\hat{a}}T^{\hat{a}}, \tag{2.2}$$

where $T^{a_L,a_R}(a_L,a_R=1,2,3)$ and $T^{\hat{a}}(\hat{a}=1,2,3,4)$ are the generators of $SO(4)\simeq SU(2)_L\times SU(2)_R$ and $SO(5)/SO(4)$, respectively. The quark-lepton multiplets Ψ_a are introduced in the vector representation of $SO(5)$, whereas n_F dark fermions Ψ_{F_i} in the spinor representation with $Q_X=\frac{1}{2}$. The dimensionless parameter c, which gives a bulk kink mass, plays an important role in controlling profiles of fermion wave functions. $\bar{\Psi}=i\Psi^\dagger\Gamma^0$.

The orbifold boundary conditions at $y_0=0$ and $y_1=L$ are given by

$$\begin{pmatrix}A_\mu\\A_y\end{pmatrix}(x,y_j-y)=P_{\mathrm{vec}}\begin{pmatrix}A_\mu\\-A_y\end{pmatrix}(x,y_j+y)P_{\mathrm{vec}}^{-1},$$
$$\begin{pmatrix}B_\mu\\B_y\end{pmatrix}(x,y_j-y)=\begin{pmatrix}B_\mu\\-B_y\end{pmatrix}(x,y_j+y),$$
$$\Psi_a(x,y_j-y)=P_{\mathrm{vec}}\Gamma^5\Psi_a(x,y_j+y),$$
$$\Psi_{F_i}(x,y_j-y)=\eta_{F_i}(-1)^jP_{\mathrm{sp}}\Gamma^5\Psi_{F_i}(x,y_j+y),\quad \eta_{F_i}=\pm1,$$
$$P_{\mathrm{vec}}=\mathrm{diag}(-1,-1,-1,-1,+1),$$
$$P_{\mathrm{sp}}=\mathrm{diag}(+1,+1,-1,-1), \tag{2.3}$$

which reduce the $SO(5)\times U(1)_X$ symmetry to $SO(4)\times U(1)_X\simeq SU(2)_L\times SU(2)_R\times U(1)_X$. $SO(4)\times U(1)_X$ symmetry is spontaneously broken to $SU(2)_L\times U(1)_Y$ by the brane scalar $\hat{\Phi}$.

The 4D Higgs field appears as a zero mode in the $SO(5)/SO(4)$ part of the fifth dimensional component of the vector potential $A_y^{\hat{a}}(x,y)$ with custodial symmetry. Without loss of generality one can set $\langle A_y^{\hat{a}}\rangle\propto\delta^{a4}$ when the electroweak symmetry is spontaneously broken. The 4D neutral Higgs field $H(x)$ is a fluctuation mode of the Wilson line phase θ_H which is an Aharonov-Bohm phase in the fifth dimension;

$$A_y^{\hat{4}}(x,y)=\{\theta_H f_H+H(x)\}u_H(y)+\cdots,$$
$$\exp\Big\{\frac{i}{2}\theta_H\cdot 2\sqrt{2}T^{\hat{4}}\Big\}=\exp\Big\{ig_A\int_0^L dy\langle A_y\rangle\Big\},$$
$$f_H=\frac{2}{g_A}\sqrt{\frac{k}{z_L^2-1}}=\frac{2}{g_w}\sqrt{\frac{k}{L(z_L^2-1)}}. \tag{2.4}$$

Here the wave function of the 4D Higgs boson is given by $u_H(y)=[2k/(z_L^2-1)]^{1/2}e^{2ky}$ for $0\le y\le L$ and $u_H(-y)=u_H(y)=u_H(y+2L)$. $g_w=g_A/\sqrt{L}$ is the dimensionless 4D $SU(2)_L$ coupling.

III. $H\to Z\gamma$

The Higgs decay processes $H\to\gamma\gamma$ and $H\to Z\gamma$ are absent at the tree level and occur at the one loop level. In the $SO(5)\times U(1)$ GHU not only the W boson, quarks and leptons in SM but also their KK modes and additional gauge bosons and dark fermions contribute to the processes. We show that these corrections are finite and small in the $SO(5)\times U(1)$ GHU, thanks to the cancellation among them.

A. $\Gamma(H\to\gamma\gamma)$

We shortly review the decay process $H\to\gamma\gamma$ in the $SO(5)\times U(1)$ GHU model. [23] We follow the notation of Ref. [6]. The decay rate in the SM is given by

$$\Gamma(H \to \gamma\gamma)_{\rm SM} = \frac{\alpha^2 g_w^2}{1024\pi^3}\frac{m_H^3}{m_W^2}\left|\sum_i N_{ci} e_i^2 F_i(\tau_i)\right|^2,$$
$$\tau_i = \frac{4m_i^2}{m_H^2}, \tag{3.1}$$

where N_{ci} is the number of the color degrees of freedom and e_i is the electromagnetic charge in units of e. Functions $F_1(\tau)$ and $F_{1/2}(\tau)$ are assigned for gauge bosons and fermions, respectively, and defined by

$$F_1(\tau) = 2 + 3\tau + 3\tau(2-\tau)f(\tau),$$
$$F_{1/2}(\tau) = -2\tau[1 + (1-\tau)f(\tau)],$$
$$f(\tau) = \begin{cases} [\sin^{-1}(\sqrt{1/\tau})]^2 & \text{for } \tau \geq 1, \\ -\frac{1}{4}\left[\ln\frac{1+\sqrt{1-\tau}}{1-\sqrt{1-\tau}} - i\pi\right]^2 & \text{for } \tau < 1. \end{cases} \tag{3.2}$$

In the large τ limit $F_{1/2} \to -\frac{4}{3}$ and $F_1 \to 7$.

In the $SO(5)\times U(1)$ GHU model, KK numbers are conserved by the electromagnetic interactions. The decay rate in the GHU becomes

$$\Gamma(H \to \gamma\gamma) = \frac{\alpha^2 g_w^2}{1024\pi^3}\frac{m_H^3}{m_W^2}\left|\mathcal{F}_W + \frac{4}{3}\mathcal{F}_t + n_F\mathcal{F}_F\right|^2, \tag{3.3}$$

where

$$\mathcal{F}_W = \sum_{n=0}^{\infty}\frac{g_{HW^{(n)}W^{(n)}}}{g_w m_W}\frac{m_W^2}{m_{W^{(n)}}^2}F_1(\tau_{W^{(n)}}) = \sum_{n=0}^{\infty} I_{W^{(n)}}\frac{m_W}{m_{W^{(n)}}}\cos\theta_H F_1(\tau_{W^{(n)}}),$$
$$\mathcal{F}_t = \sum_{n=0}^{\infty}\frac{y_{Ht^{(n)}t^{(n)}}}{y_t^{\rm SM}}\frac{m_t}{m_{t^{(n)}}}F_{1/2}(\tau_{t^{(n)}}) = \sum_{n=0}^{\infty} I_{t^{(n)}}\frac{m_t}{m_{t^{(n)}}}\cos\theta_H F_{1/2}(\tau_{t^{(n)}}),$$
$$\mathcal{F}_F = \sum_{n=1}^{\infty}\frac{y_{HF^{(n)}F^{(n)}}}{y_t^{\rm SM}}\frac{m_t}{m_{F^{(n)}}}F_{1/2}(\tau_{F^{(n)}}) = \sum_{n=1}^{\infty} I_{F^{(n)}}\frac{m_t}{m_{F^{(n)}}}\sin\frac{\theta_H}{2}F_{1/2}(\tau_{F^{(n)}}). \tag{3.4}$$

Here $I_{W^{(n)}}$, $I_{t^{(n)}}$, and $I_{F^{(n)}}$ are defined as $I_{W^{(n)}} = g_{HW^{(n)}W^{(n)}}/g_w m_{W^{(0)}}\cos\theta_H$, $I_{t^{(n)}} = y_{Ht^{(n)}t^{(n)}}/y_t^{\rm SM}\cos\theta_H$, and $I_{F^{(n)}} = y_{HF^{(n)}F^{(n)}}/y_t^{\rm SM}\sin\frac{\theta_H}{2}$. Contributions from light quarks and leptons and their KK modes are negligible.

In Fig. 1, the values of $I_{W^{(n)}}$, $I_{t^{(n)}}$, and $I_{F^{(n)}}$ by the numerical calculation in the $N_F = 4$ and $\theta_H = 0.1153$ case are shown. They approximately behave as

$$I_{W^{(n)}} \simeq (-1)^n\{0.0759 - 0.0065\ln n + 0.0022(\ln n)^2\},$$
$$I_{t^{(n)}} \simeq (-1)^n\{0.2304 - 0.0108\ln n + 0.0017(\ln n)^2\},$$
$$I_{F^{(n)}} \simeq (-1)^n\{1.0341 - 0.0457\ln n + 0.0108(\ln n)^2\} \tag{3.5}$$

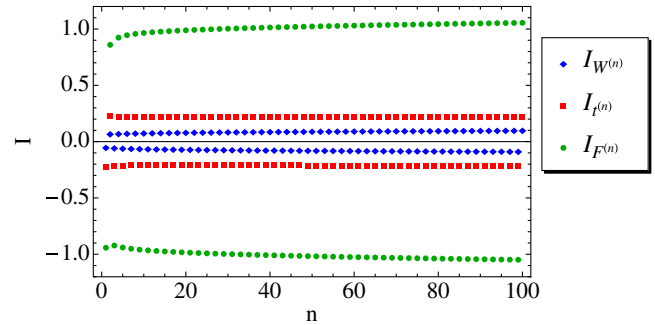

FIG. 1 (color online). Behaviors of $I_{W^{(n)}} = g_{HW^{(n)}W^{(n)}}/g_w m_{W^{(n)}}\cos\theta_H$, $I_{t^{(n)}} = y_{Ht^{(n)}t^{(n)}}/y_t^{\rm SM}\cos\theta_H$ and $I_{F^{(n)}} = y_{HF^{(n)}F^{(n)}}/y_t^{\rm SM}\sin\frac{\theta_H}{2}$ in the case of $n_F = 4$, $z_L = 10^5$ for which $\theta_H = 0.1153$.

for $50 \leq n \leq 200$. Note that the sign alternates in n. As the masses of the KK modes of the W boson, top quark and dark fermion are $m_n \simeq n\cdot m_{\rm KK}/2$, the sum in each $\mathcal{F}$ behaves as $\sum(-1)^n(\ln n)^\alpha/n$ ($\alpha = 0, 1, 2$) and converges. Moreover, the contributions from $n \geq 1$ are suppressed by the ratio of the electroweak scale to the KK scale. Hence the ratio of $\mathcal{F}$ to the zero-mode contribution becomes

$$\frac{\mathcal{F}_W}{\mathcal{F}_{W^{(0)}\rm only}} = 0.9997,$$
$$\frac{\mathcal{F}_t}{\mathcal{F}_{t^{(0)}\rm only}} = 0.9983,$$
$$\frac{\mathcal{F}_F}{\mathcal{F}_{t^{(0)}\rm only}} = -0.0032, \tag{3.6}$$

for $\theta_H = 0.114$ and $n_F = 4$. The ratio of the amplitude to that with only zero modes is

$$\frac{\mathcal{F}_W + \frac{4}{3}\mathcal{F}_t + 4\mathcal{F}_F}{\mathcal{F}_{W^{(0)}\rm only} + \frac{4}{3}\mathcal{F}_{t^{(0)}\rm only}} = 1.0027. \tag{3.7}$$

It is found that the contributions of the KK modes are less than 1% and negligible. The couplings of the zero modes are approximately given by $g_{HWW} \simeq g_{HWW}^{\rm SM}\cos\theta_H = g_w m_W\cos\theta_H$ and $y_t \simeq y_t^{\rm SM}\cos\theta_H$. Therefore the decay rate in the GHU is approximately $\cos^2\theta_H$ times that in the standard model. The deviation from the standard model amounts only 1% for $\theta_H \sim 0.1$.

B. Gauge boson loops

The decay process $H \to Z\gamma$ is more involved than $H \to \gamma\gamma$. The KK number need not be conserved at the Z and H vertices, and $W_R^{(n)}$ also participates. The gauge boson loop processes for $H \to Z\gamma$ are shown in Fig. 2. We note that $HW_R^{(m)}W_R^{(n)}$ couplings vanish. The amplitude of W boson loop Figs. 2(a)–(c) is given in the unitary gauge by

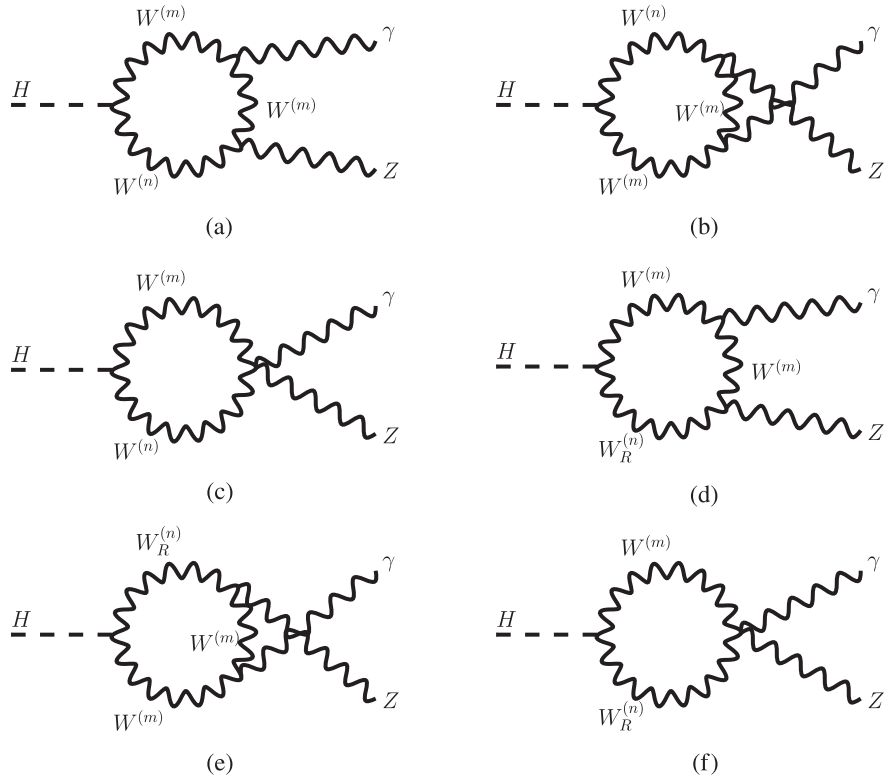

FIG. 2. The gauge boson loop processes for $H \to Z\gamma$ in the $SO(5) \times U(1)$ gauge-Higgs unification. W_R is the $SU(2)_R$ gauge boson and has no zero mode. Since $HW_R^{(m)}W_R^{(n)}$ couplings vanish, there are no diagrams involving two or more W_R' s.

$$
\begin{aligned}
i\mathcal{M}^{(a)}_{W^{(m)},W^{(n)}} + i\mathcal{M}^{(b)}_{W^{(m)},W^{(n)}} + i\mathcal{M}^{(c)}_{W^{(m)},W^{(n)}} &= e g_{HW^{(m)}W^{(n)}} g_{ZW^{(m)}W^{(n)}} \epsilon^*_\mu(k_1)\epsilon^*_\nu(k_2) \int \frac{d^4p}{(2\pi)^4} D_{\tau\alpha}(p, m_{W^{(m)}}) D_\sigma{}^\tau(p-k_1-k_2, m_{W^{(n)}}) \\
&\quad \times [2D_{\beta\rho}(p-k_1, m_{W^{(m)}})\{2\eta^{\alpha\beta}p^\mu - \eta^{\beta\mu}(p-2k_1)^\alpha - \eta^{\alpha\mu}(p+k_1)^\beta\} \\
&\quad \times \{2\eta^{\rho\sigma}(p-k_1)^\nu - \eta^{\sigma\nu}(p-k_1-2k_2)^\rho - \eta^{\rho\nu}(p-k_1+k_2)^\sigma\} \\
&\quad - (2\eta^{\mu\nu}\eta^{\alpha\sigma} - \eta^{\mu\alpha}\eta^{\nu\sigma} - \eta^{\mu\sigma}\eta^{\nu\alpha})], \\
D_{\mu\nu}(p,m) &= \left(\eta_{\mu\nu} - \frac{p_\mu p_\nu}{m^2}\right)\frac{1}{p^2 - m^2 + i\epsilon},
\end{aligned}
\tag{3.8}
$$

where k_1 and k_2 are the photon and the Z boson momenta, respectively. The amplitude (3.8) itself is divergent. However, by adding the $m \leftrightarrow n$ diagrams and using $g_{HW^{(m)}W^{(n)}} = g_{HW^{(n)}W^{(m)}}$ and $g_{ZW^{(m)}W^{(n)}} = g_{ZW^{(n)}W^{(m)}}$, the amplitude becomes

$$
\begin{aligned}
&i\{\mathcal{M}^{(a)}_{W^{(m)},W^{(n)}} + \mathcal{M}^{(b)}_{W^{(m)},W^{(n)}} + \mathcal{M}^{(c)}_{W^{(m)},W^{(n)}} + (m \longleftrightarrow n)\} \\
&\quad = e g_{HW^{(m)}W^{(n)}} g_{ZW^{(m)}W^{(n)}} \epsilon^*_\mu(k_1)\epsilon^*_\nu(k_2)\left(\eta^{\mu\nu} - \frac{k_2^\mu k_1^\nu}{k_1\cdot k_2}\right)\frac{i}{16\pi^2}\frac{1}{m^2_{W^{(m)}}m^2_{W^{(n)}}}\{(m^4_{W^{(m)}} + m^4_{W^{(n)}} + 10m^2_{W^{(m)}}m^2_{W^{(n)}})E_+(m_{W^{(m)}}, m_{W^{(n)}}) \\
&\qquad + ((m^2_{W^{(m)}} + m^2_{W^{(n)}})(m_H^2 - m_Z^2) - m_H^2 m_Z^2)E_-(m_{W^{(m)}}, m_{W^{(n)}}) - (4m^2_{W^{(m)}}m^2_{W^{(n)}}(m_H^2 - m_Z^2) + 2m_Z^4(m^2_{W^{(m)}} + m^2_{W^{(n)}})) \\
&\qquad \times (C_0(m_{W^{(m)}}, m_{W^{(n)}}) + C_0(m_{W^{(n)}}, m_{W^{(m)}}))\}
\end{aligned}
\tag{3.9}
$$

where

$$
\begin{aligned}
C_0(m_1^2, m_2^2) &\equiv C_0(0, m_H^2, m_Z^2, m_1^2, m_1^2, m_2^2), \\
E_\pm(m_1, m_2) &\equiv 1 + \frac{m_Z^2}{m_H^2 - m_Z^2}\{B_0(m_H^2, m_1^2, m_2^2) - B_0(m_Z^2, m_1^2, m_2^2)\} \pm \{m_1^2 C_0(m_1^2, m_2^2) + m_2^2 C_0(m_2^2, m_1^2)\},
\end{aligned}
\tag{3.10}
$$

TABLE I. $J_{W^{(m)}W^{(n)}}$ defined in (3.12) is shown for $0 \le m, n \le 7$ and for $101 \le m, n \le 108$ in the $N_F = 4$, $z_L = 10^5$ case. Only the values larger than that of $O(10^{-4})$ are shown with three significant figures.

	0	1	2	3	4	5	6	7
0	1.00	$O(10^{-4})$	$O(10^{-9})$	$O(10^{-6})$	$O(10^{-11})$	$O(10^{-8})$	$O(10^{-12})$	$O(10^{-9})$
1	$O(10^{-4})$	−0.0580	0.0595	$O(10^{-6})$	$O(10^{-5})$	$O(10^{-10})$	$O(10^{-7})$	$O(10^{-9})$
2	$O(10^{-9})$	0.0595	0.0218	−0.0413	$O(10^{-8})$	$O(10^{-5})$	$O(10^{-9})$	$O(10^{-5})$
3	$O(10^{-6})$	$O(10^{-6})$	−0.0413	−0.0625	0.0637	$O(10^{-6})$	$O(10^{-5})$	$O(10^{-10})$
4	$O(10^{-11})$	$O(10^{-5})$	$O(10^{-8})$	0.0637	0.0226	−0.0432	$O(10^{-7})$	$O(10^{-5})$
5	$O(10^{-8})$	$O(10^{-10})$	$O(10^{-5})$	$O(10^{-6})$	−0.0432	−0.0652	0.0648	$O(10^{-6})$
6	$O(10^{-12})$	$O(10^{-7})$	$O(10^{-9})$	$O(10^{-5})$	$O(10^{-7})$	0.0648	0.0233	−0.0434
7	$O(10^{-9})$	$O(10^{-9})$	$O(10^{-5})$	$O(10^{-10})$	$O(10^{-5})$	$O(10^{-6})$	−0.0434	−0.0673

	101	102	103	104	105	106	107	108
101	−0.0932	0.0705	$O(10^{-6})$	$O(10^{-4})$	$O(10^{-12})$	$O(10^{-5})$	$O(10^{-8})$	$O(10^{-6})$
102	0.0705	0.0328	−0.0406	$O(10^{-6})$	$O(10^{-4})$	$O(10^{-12})$	$O(10^{-5})$	$O(10^{-9})$
103	$O(10^{-6})$	−0.0406	−0.0934	0.0706	$O(10^{-6})$	$O(10^{-4})$	$O(10^{-12})$	$O(10^{-5})$
104	$O(10^{-4})$	$O(10^{-6})$	0.0706	0.0329	−0.0405	$O(10^{-6})$	$O(10^{-4})$	$O(10^{-12})$
105	$O(10^{-12})$	$O(10^{-4})$	$O(10^{-6})$	−0.0405	−0.0937	0.0706	$O(10^{-6})$	$O(10^{-4})$
106	$O(10^{-5})$	$O(10^{-12})$	$O(10^{-4})$	$O(10^{-6})$	0.0706	0.0330	−0.0405	$O(10^{-6})$
107	$O(10^{-8})$	$O(10^{-5})$	$O(10^{-12})$	$O(10^{-4})$	$O(10^{-6})$	−0.0405	−0.0940	0.0707
108	$O(10^{-6})$	$O(10^{-9})$	$O(10^{-5})$	$O(10^{-12})$	$O(10^{-4})$	$O(10^{-6})$	0.0707	0.0331

with the Passarino-Veltman functions [28,29] defined by

$$B_0(k^2, m_1^2, m_2^2) \equiv \frac{(2\pi)^{4-D}}{i\pi^2} \int d^D q \frac{1}{(q^2 - m_1^2)\{(q+k)^2 - m_2^2\}},$$
$$C_0(k_1^2, (k_1 - k_2)^2, k_2^2, m_1^2, m_2^2, m_3^2) \equiv \frac{1}{i\pi^2} \int d^D q \frac{1}{(q^2 - m_1^2)\{(q+k_1)^2 - m_2^2\}\{(q+k_2)^2 - m_3^2\}}. \tag{3.11}$$

For all C_0 and $E_\pm$, the $D \to 4$ limit has been safely taken, so that the amplitude (3.9) is finite.

To obtain the amplitude quantitatively, the numerical values of the couplings $g_{HW^{(m)}W^{(n)}}$ and $g_{ZW^{(m)}W^{(n)}}$ have to be evaluated. The details of evaluation and results are summarized in Appendix. It is convenient to define the dimensionless coupling $J_{W^{(m)}W^{(n)}}$ by

$$J_{W^{(m)}W^{(n)}} \equiv \frac{g_{HW^{(m)}W^{(n)}} g_{ZW^{(m)}W^{(n)}}}{g_w^2 \cos\theta_W \cos\theta_H \sqrt{m_{W^{(m)}} m_{W^{(n)}}}}. \tag{3.12}$$

The value of $J_{W^{(m)}W^{(n)}}$ is tabulated in Table I. It is seen that $J_{W^{(m)}W^{(n)}}$ with $|m-n| \ge 2$ is smaller than $J_{W^{(n)}W^{(n)}}$ by a factor 10^{-2}, whereas $J_{W^{(n\pm1)}W^{(n)}}$ and $J_{W^{(n)}W^{(n)}}$ are of the same order. $J_{W^{(n)}W^{(n)}}$ and $J_{W^{(n)}W^{(n+1)}}$ are plotted in Fig. 3 for $1 \le n \le 100$ in the $N_F = 4$, $z_L = 10^5$ case. $J_{W^{(n)}W^{(n+1)}}$ and $J_{W^{(n)}W^{(n)}}$ for $101 \le n \le 200$ are approximately given by

$$J_{W^{(n)}W^{(n)}} \simeq -0.0272 + 0.00320(\ln n) - 0.00083(\ln n)^2 + (-1)^{n-1}(-0.0563 + 0.00654(\ln n) - 0.00173(\ln n)^2),$$
$$J_{W^{(n)}W^{(n+1)}} \simeq 0.0135 - 0.00160(\ln n) + 0.00041(\ln n)^2 + (-1)^{n-1}(0.0567 - 0.00106(\ln n) + 0.00018(\ln n)^2). \tag{3.13}$$

Next we examine the asymptotic behavior of the amplitude for $m, n \gg 1$. The whole amplitude of the W boson loop is

$$i\mathcal{M}_W = \frac{i}{2} \sum_{m,n}^{\infty} \{\mathcal{M}^{(a)}_{W^{(m)},W^{(n)}} + \mathcal{M}^{(b)}_{W^{(m)},W^{(n)}} + \mathcal{M}^{(c)}_{W^{(m)},W^{(n)}} + (n \longleftrightarrow m)\}. \tag{3.14}$$

The diagonal part of the amplitude in (3.14) for $n \gg 1$ is rewritten as

$$
\begin{aligned}
&i\mathcal{M}^{(a)}_{W^{(n)},W^{(n)}} + i\mathcal{M}^{(b)}_{W^{(n)},W^{(n)}} + i\mathcal{M}^{(c)}_{W^{(n)},W^{(n)}} \\
&\quad = eg_w^2 \cos\theta_W \cos\theta_H \epsilon^*_\mu(k_1)\epsilon^*_\nu(k_2)\left(\eta^{\mu\nu} - \frac{k_2^\mu k_1^\nu}{k_1\cdot k_2}\right)\frac{i}{16\pi^2}\frac{J_{W^{(n)}W^{(n)}}}{2m^3_{W^{(n)}}} \\
&\qquad \times\left\{-\frac{m_H^2 - m_Z^2}{2m^2_{W^{(n)}}}(12m^4_{W^{(n)}} + 2m^2_{W^{(n)}}(m_H^2 - m_Z^2) - m_H^2 m_Z^2)I_1(\tau_{W^{(n)}},\lambda_{W^{(n)}})\right. \\
&\qquad \left. + 4(4m^2_{W^{(n)}}(m_H^2 - m_Z^2) - m_H^2 m_Z^2 + m_Z^4)I_2(\tau_{W^{(n)}},\lambda_{W^{(n)}})\right\},
\end{aligned}
\tag{3.15}
$$

where

$$
\begin{aligned}
I_1(a,b) &= \frac{ab}{2(a-b)} + \frac{a^2b^2}{2(a-b)^2}[f(a)-f(b)] + \frac{a^2b}{(a-b)^2}[g(a)-g(b)], \\
I_2(a,b) &= -\frac{ab}{2(a-b)}[f(a)-f(b)], \\
g(\tau) &= \begin{cases} \sqrt{\tau-1}\sin^{-1}(\sqrt{1/\tau}) & \text{for } \tau \geq 1, \\ \frac{1}{2}\sqrt{1-\tau}\left[\ln\frac{1+\sqrt{1-\tau}}{1-\sqrt{1-\tau}} - i\pi\right] & \text{for } \tau < 1. \end{cases}
\end{aligned}
\tag{3.16}
$$

and $\lambda_i \equiv 4m_i^2/m_Z^2$. τ_i and $f(a)$ are defined in (3.1) and (3.2). Here, we have used

$$
\begin{aligned}
\frac{m_Z^2}{m_H^2 - m_Z^2}(B_0(m_H^2, m^2_{W^{(n)}}, m^2_{W^{(n)}}) - B_0(m_Z^2, m^2_{W^{(n)}}, m^2_{W^{(n)}})) &= -1 - \frac{m_H^2 - m_Z^2}{2m^2_{W^{(n)}}}I_1(\tau_{W^{(n)}},\lambda_{W^{(n)}}) + 2I_2(\tau_{W^{(n)}},\lambda_{W^{(n)}}), \\
C_0(0, m_H^2, m_Z^2, m^2_{W^{(n)}}, m^2_{W^{(n)}}, m^2_{W^{(n)}}) &= -\frac{1}{m^2_{W^{(n)}}}I_2(\tau_{W^{(n)}},\lambda_{W^{(n)}}).
\end{aligned}
\tag{3.17}
$$

The functions I_1, I_2 in (3.17) approach constants for $m_{W^{(n)}} \to \infty$. Since $J_{W^{(m)}W^{(n)}}$ for $|m-n| \geq 2$ are negligible comparing to $J_{W^{(m)}W^{(n)}}$ for $|m-n| \leq 1$, only the amplitude for $|m-n| \leq 1$ need to be retained. For $n \gg 1$ $m_{W^{(n\pm1)}} \simeq m_{W^{(n)}}$ so that

$$
\begin{aligned}
&\frac{1}{2}\sum_m (i\mathcal{M}^{(a)}_{W^{(m)},W^{(n)}} + i\mathcal{M}^{(b)}_{W^{(m)},W^{(n)}} + i\mathcal{M}^{(c)}_{W^{(m)},W^{(n)}} + (n \longleftrightarrow m)) \\
&\quad \simeq eg_w^2 \cos\theta_W \cos\theta_H \epsilon^*_\mu(k_1)\epsilon^*_\nu(k_2)\left(\eta^{\mu\nu} - \frac{k_2^\mu k_1^\nu}{k_1\cdot k_2}\right)\frac{i}{16\pi^2}\frac{1}{2m^3_{W^{(n)}}}(J_{W^{(n)}W^{(n)}} + J_{W^{(n+1)}W^{(n)}} + J_{W^{(n-1)}W^{(n)}}) \\
&\qquad \times\left\{-\frac{m_H^2 - m_Z^2}{2m^2_{W^{(n)}}}(12m^4_{W^{(n)}} + 2m^2_{W^{(n)}}(m_H^2 - m_Z^2) - m_H^2 m_Z^2)I_1(\tau_{W^{(n)}},\lambda_{W^{(n)}}) + 4(4m^2_{W^{(n)}}(m_H^2 - m_Z^2)\right. \\
&\qquad \left. - m_H^2 m_Z^2 + m_Z^4)I_2(\tau_{W^{(n)}},\lambda_{W^{(n)}})\right\} \\
&\quad \approx \text{const} \times \frac{1}{n}(J_{W^{(n)}W^{(n)}} + J_{W^{(n+1)}W^{(n)}} + J_{W^{(n-1)}W^{(n)}}).
\end{aligned}
\tag{3.18}
$$

Therefore the large n part of the sum in the whole amplitude of W boson loop is approximated as

$$
i\mathcal{M}_W \approx \sum_n^\infty \text{const} \times \frac{1}{n}(J_{W^{(n)}W^{(n)}} + J_{W^{(n+1)}W^{(n)}} + J_{W^{(n-1)}W^{(n)}}).
\tag{3.19}
$$

Even though the sums $\sum J_{W^{(n)}W^{(n)}}/n$ and $\sum J_{W^{(n\pm1)}W^{(n)}}/n$ diverge individually, the combination $\sum(J_{W^{(n)}W^{(n)}} + J_{W^{(n+1)}W^{(n)}} + J_{W^{(n-1)}W^{(n)}})/n$ converges since

$$
J_{W^{(n)}W^{(n)}} + J_{W^{(n+1)}W^{(n)}} + J_{W^{(n-1)}W^{(n)}} \simeq (-1)^{n-1}\{-0.0563 + 0.00654(\ln n) - 0.00173(\ln n)^2\}.
\tag{3.20}
$$

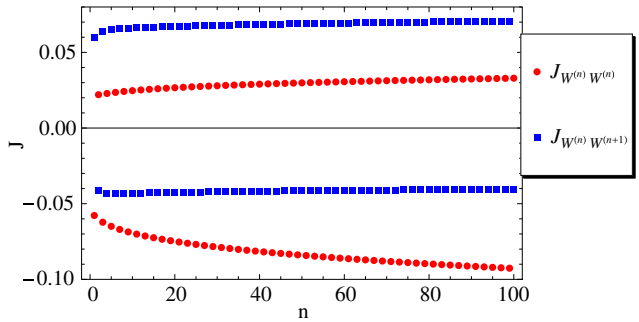

FIG. 3 (color online). $J_{W^{(n)}W^{(n)}}$ and $J_{W^{(n)}W^{(n+1)}}$ are plotted for $1 \le n \le 100$ in the $N_F = 4$, $z_L = 10^5$ case. The red circles and blue squares represent $J_{W^{(n)}W^{(n)}}$ and $J_{W^{(n)}W^{(n+1)}}$, respectively.

Next we consider the amplitudes which contain W_R in the loop. The amplitude $i\mathcal{M}^{(d)}_{W^{(m)},W_R^{(n)}}+i\mathcal{M}^{(e)}_{W^{(m)},W_R^{(n)}}+i\mathcal{M}^{(f)}_{W^{(m)},W_R^{(n)}}$ is obtained from (3.8) by replacing $W^{(n)}$ by $W_R^{(n)}$. The dimensionless coupling $J_{W^{(m)}W_R^{(n)}}$ is also defined as

$$J_{W^{(m)}W_R^{(n)}} \equiv \frac{g_{HW^{(m)}W_R^{(n)}} g_{ZW^{(m)}W_R^{(n)}}}{g_w^2 \cos\theta_W \cos\theta_H \sqrt{m_{W^{(m)}} m_{W_R^{(n)}}}}. \tag{3.21}$$

As is seen in the Table II, $J_{W^{(m)}W_R^{(n)}}$ is appreciable only when $m/2 - n = 0, 1, 2$. Note that $m_{W_R^{(n)}} \simeq n \cdot m_{\rm KK}$ while $m_{W^{(n)}} \simeq n \cdot m_{\rm KK}/2$. For $m/2 - n = 0, 1, 2$, $m_{W^{(m)}} \simeq m_{W^{(n)}} \simeq n \cdot m_{\rm KK}$ is satisfied. Hence the whole amplitude of the $W - W_R$ boson loop is

$$\begin{aligned} i\mathcal{M}_{W_R} &= \sum_{m,n}^{\infty}(i\mathcal{M}^{(d)}_{W^{(m)},W_R^{(n)}} + i\mathcal{M}^{(e)}_{W^{(m)},W_R^{(n)}} + i\mathcal{M}^{(f)}_{W^{(m)},W_R^{(n)}} \\ &\quad + i\mathcal{M}^{(d)}_{W_R^{(n)},W^{(m)}} + i\mathcal{M}^{(e)}_{W_R^{(n)},W^{(m)}} + i\mathcal{M}^{(f)}_{W_R^{(n)},W^{(m)}}) \\ &\approx \sum_{n}^{\infty} \text{const} \times \frac{1}{n}(J_{W^{(n)}W_R^{(n/2)}} + J_{W^{(n)}W_R^{(n/2+1)}} \\ &\quad + J_{W^{(n)}W_R^{(n/2+2)}}). \end{aligned} \tag{3.22}$$

$J_{W^{(n)}W_R^{(n/2)}}$, $J_{W^{(n)}W_R^{(n/2+1)}}$ and $J_{W^{(n)}W_R^{(n/2+2)}}$ are plotted in Fig. 4 for $1 \le n \le 100$ in the $N_F = 4$, $z_L = 10^5$ case. $J_{W^{(n)}W_R^{(n/2)}}$, $J_{W^{(n)}W_R^{(n/2+1)}}$, $J_{W^{(n)}W_R^{(n/2+2)}}$ are approximated in this range by

$$\begin{aligned} J_{W^{(n)}W_R^{(n/2)}} &\simeq -0.0425 - 0.00268(\ln n) + 0.00023(\ln n)^2 \\ J_{W^{(n)}W_R^{(n/2+1)}} &\simeq 0.0411 + 0.00227(\ln n) - 0.00019(\ln n)^2 \\ J_{W^{(n)}W_R^{(n/2+2)}} &\simeq 0.0021 + 0.00017(\ln n) - 0.00001(\ln n)^2. \end{aligned} \tag{3.23}$$

$J_{W^{(n)}W_R^{(n/2)}} + J_{W^{(n)}W_R^{(n/2+1)}} + J_{W^{(n)}W_R^{(n/2+2)}}$ is small, and almost vanishes within numerical errors.

C. Fermion loops

Contributions of fermion loops to $\Gamma(H \to Z\gamma)$ are evaluated similarly. Top quark, charged dark fermions, and their KK excitations give substantial contributions as shown in Fig. 5, whereas contributions from other quarks and leptons are negligible.

The diagrams of fermion loops Fig. 5 (a, b) [or (c,d)], with generic fermions $f^{(m)}$, yield

TABLE II. $J_{W^{(m)}W_R^{(n)}}$ in (3.21) is shown for $0 \le m \le 7$, $1 \le n \le 4$ and for $101 \le m \le 108$, $51 \le n \le 55$ in the $N_F = 4$, $z_L = 10^5$ case. Only values larger than $O(10^{-4})$ are shown explicitly with three significant figures.

		m							
		0	1	2	3	4	5	6	7
n	1	$O(10^{-5})$	$O(10^{-5})$	−0.0118	$O(10^{-7})$	$O(10^{-5})$	$O(10^{-7})$	$O(10^{-4})$	$O(10^{-7})$
	2	$O(10^{-6})$	$O(10^{-6})$	0.0296	$O(10^{-6})$	−0.0299	$O(10^{-6})$	$O(10^{-4})$	$O(10^{-8})$
	3	$O(10^{-8})$	$O(10^{-8})$	0.0014	$O(10^{-6})$	0.0362	$O(10^{-5})$	−0.0373	$O(10^{-6})$
	4	$O(10^{-7})$	$O(10^{-8})$	$O(10^{-5})$	$O(10^{-7})$	0.0018	$O(10^{-6})$	0.0395	$O(10^{-4})$

		m							
		101	102	103	104	105	106	107	108
n	51	$O(10^{-4})$	−0.0499	$O(10^{-6})$	$O(10^{-4})$	$O(10^{-7})$	$O(10^{-4})$	$O(10^{-7})$	$O(10^{-5})$
	52	$O(10^{-5})$	0.0474	$O(10^{-4})$	−0.0499	$O(10^{-6})$	$O(10^{-4})$	$O(10^{-7})$	$O(10^{-4})$
	53	$O(10^{-7})$	0.0026	$O(10^{-5})$	0.0475	$O(10^{-4})$	−0.0499	$O(10^{-6})$	$O(10^{-4})$
	54	$O(10^{-7})$	$O(10^{-4})$	$O(10^{-7})$	0.0026	$O(10^{-5})$	0.0475	$O(10^{-4})$	−0.0499
	55	$O(10^{-8})$	$O(10^{-4})$	$O(10^{-7})$	$O(10^{-4})$	$O(10^{-7})$	0.0026	$O(10^{-5})$	0.0475

$$
\begin{aligned}
i\mathcal{M}^{(a)}_{f^{(m)},f^{(n)}} + i\mathcal{M}^{(b)}_{f^{(m)},f^{(n)}} = & -Q_f e \epsilon^*_\mu(k_1)\epsilon^*_\nu(k_2) \int \frac{d^4p}{(2\pi)^4} \frac{1}{p^2 - m^2_{f^{(m)}}} \frac{1}{(p-k_1)^2 - m^2_{f^{(m)}}} \frac{1}{(p-k_1-k_2)^2 - m^2_{f^{(n)}}} \\
& \times \mathrm{Tr}[(y_{f^{(m)}f^{(n)}} + \hat{y}_{f^{(m)}f^{(n)}}\gamma^5)(\not{p} + m_{f^{(m)}})\gamma^\mu(\not{p} - \not{k}_1 + m_{f^{(m)}})\gamma^\nu(g^V_{Zf^{(m)}f^{(n)}} + g^A_{Zf^{(m)}f^{(n)}}\gamma^5) \\
& \times (\not{p} - \not{k}_1 - \not{k}_2 + m_{f^{(n)}}) + (y_{f^{(m)}f^{(n)}} + \hat{y}_{f^{(n)}f^{(m)}}\gamma^5)(-\not{p} + \not{k}_1 + \not{k}_2 + m_{f^{(n)}})\gamma^\nu \\
& \times (g^V_{Zf^{(m)}f^{(n)}} + g^A_{Zf^{(n)}f^{(m)}}\gamma^5)(-\not{p} + \not{k}_1 + m_{f^{(m)}})\gamma^\mu(-\not{p} + m_{f^{(m)}})]. \qquad (3.24)
\end{aligned}
$$

The Yukawa couplings $y_{f^{(m)}f^{(n)}}$ and $\hat{y}_{f^{(m)}f^{(n)}}$ for $f^{(m)} = t^{(m)}$ and $F^{(m)}$ are given in (A25) and (A31), respectively. The amplitude (3.24) itself involves divergent integrals, but by adding the $m \leftrightarrow n$ diagrams and making use of $y_{f^{(m)}f^{(n)}} = y_{f^{(n)}f^{(m)}}$ and $\hat{y}_{f^{(m)}f^{(n)}} = -\hat{y}_{f^{(n)}f^{(m)}}$, one finds that

$$
\begin{aligned}
i\mathcal{M}^{(a)}_{f^{(m)},f^{(n)}} + i\mathcal{M}^{(b)}_{f^{(m)},f^{(n)}} + (m \leftrightarrow n) = & -\frac{iQ_f e}{4\pi^2}\epsilon^*_\mu(k_1)\epsilon^*_\nu(k_2)\left(\eta^{\mu\nu} - \frac{k_2^\mu k_1^\nu}{k_1 \cdot k_2}\right)\{y_{f^{(m)}f^{(n)}} g^V_{Zf^{(m)}f^{(n)}} G_+(m_{f^{(m)}}, m_{f^{(n)}}) \\
& - \hat{y}_{f^{(m)}f^{(n)}} g^A_{Zf^{(m)}f^{(n)}} G_-(m_{f^{(m)}}, m_{f^{(n)}})\}, \\
G_\pm(m_1, m_2) = & \, 2(m_1 \pm m_2) + \frac{2m_Z^2(m_1 \pm m_2)}{m_H^2 - m_Z^2}(B_0(m_H^2, m_1^2, m_2^2) - B_0(m_Z^2, m_1^2, m_2^2)) \\
& + m_1(2m_1^2 \pm 2m_1 m_2 - m_H^2 + m_Z^2)C_0(0, m_H^2, m_Z^2, m_1^2, m_1^2, m_2^2) \\
& \pm m_2(2m_2^2 \pm 2m_1 m_2 - m_H^2 + m_Z^2)C_0(0, m_H^2, m_Z^2, m_2^2, m_2^2, m_1^2). \qquad (3.25)
\end{aligned}
$$

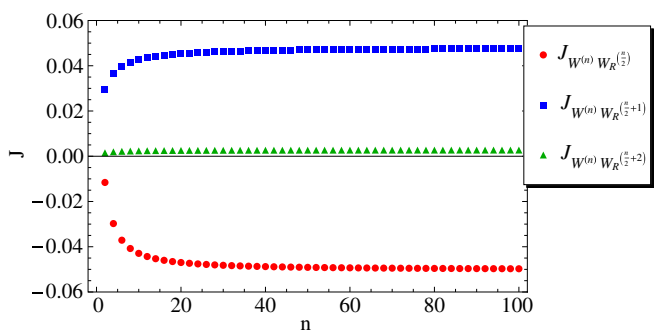

FIG. 4 (color online). $J_{W^{(n)}W_R^{(n/2)}}$, $J_{W^{(n)}W_R^{(n/2+1)}}$ and $J_{W^{(n)}W_R^{(n/2+2)}}$ are plotted for $1 \le n \le 100$ in the $N_F = 4$, $z_L = 10^5$ case. The red circles, blue squares, green triangles represent $J_{W^{(n)}W_R^{(n/2)}}$, $J_{W^{(n)}W_R^{(n/2+1)}}$ and $J_{W^{(n)}W_R^{(n/2+2)}}$, respectively.

In this form the amplitude is finite.

We define $J_{t^{(m)}t^{(n)}}$ and $J_{F^{+(m)}F^{+(n)}}$ by

$$
J_{t^{(m)}t^{(n)}} \equiv \frac{g^V_{Zt^{(m)}t^{(n)}} y_{t^{(m)}t^{(n)}} \cos\theta_W}{g_w y_t \cos\theta_H}, \qquad (3.26)
$$

$$
J_{F^{+(m)}F^{+(n)}} \equiv \frac{g^V_{ZF^{+(m)}F^{+(n)}} y_{F^{(m)}F^{(n)}} \cos\theta_W}{g_w y_t \sin\frac{\theta_H}{2}}. \qquad (3.27)
$$

In the Tables III and IV, $J_{t^{(m)}t^{(n)}}$ and $J_{F^{+(m)}F^{+(n)}}$ by the numerical evaluation are shown. As in the case of $J_{W^{(n)}W^{(n)}}$, $J_{t^{(m)}t^{(n)}}$ and $J_{F^{+(m)}F^{+(n)}}$ for $|m-n| \ge 2$ become negligible for m, $n > 100$. In addition, the terms proportional to

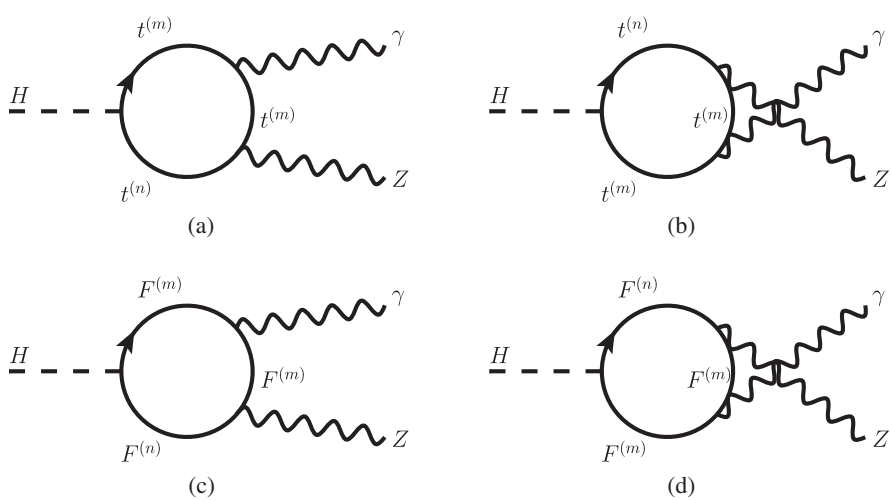

FIG. 5. The fermion loop processes of $H \to Z\gamma$ decay in the $SO(5) \times U(1)$ gauge-Higgs unification. F^+ is the charged dark fermion which does not have a zero mode.

TABLE III. $J_{t^{(m)}t^{(n)}}$ is shown for $0 \le m, n \le 7$ and for $101 \le m, n \le 108$ in the $N_F = 4$, $z_L = 10^5$ case. Only the values larger than $O(10^{-4})$ are shown with three significant figures.

	0	1	2	3	4	5	6	7
0	0.0988	−0.0041	$O(10^{-4})$	$O(10^{-5})$	$O(10^{-7})$	$O(10^{-6})$	$O(10^{-6})$	$O(10^{-7})$
1	−0.0041	−0.0790	0.0638	$O(10^{-5})$	$O(10^{-4})$	$O(10^{-9})$	$O(10^{-10})$	$O(10^{-8})$
2	$O(10^{-4})$	0.0638	−0.0350	−0.0071	$O(10^{-6})$	$O(10^{-6})$	$O(10^{-9})$	$O(10^{-5})$
3	$O(10^{-5})$	$O(10^{-5})$	−0.0071	−0.0763	0.0616	$O(10^{-6})$	$O(10^{-4})$	$O(10^{-9})$
4	$O(10^{-7})$	$O(10^{-4})$	$O(10^{-6})$	0.0616	−0.0338	−0.0071	$O(10^{-6})$	$O(10^{-6})$
5	$O(10^{-6})$	$O(10^{-9})$	$O(10^{-6})$	$O(10^{-6})$	−0.0071	−0.0754	0.0609	$O(10^{-6})$
6	$O(10^{-6})$	$O(10^{-10})$	$O(10^{-9})$	$O(10^{-4})$	$O(10^{-6})$	0.0609	−0.0334	−0.0070
7	$O(10^{-7})$	$O(10^{-8})$	$O(10^{-5})$	$O(10^{-9})$	$O(10^{-6})$	$O(10^{-6})$	−0.0070	−0.0751

	101	102	103	104	105	106	107	108
101	−0.0761	0.0610	$O(10^{-6})$	$O(10^{-4})$	$O(10^{-13})$	$O(10^{-7})$	$O(10^{-8})$	$O(10^{-6})$
102	0.0610	−0.0337	−0.0068	$O(10^{-6})$	$O(10^{-6})$	$O(10^{-13})$	$O(10^{-5})$	$O(10^{-9})$
103	$O(10^{-6})$	−0.0068	−0.0761	0.0610	$O(10^{-6})$	$O(10^{-4})$	$O(10^{-13})$	$O(10^{-7})$
104	$O(10^{-4})$	$O(10^{-6})$	0.0610	−0.0337	−0.0068	$O(10^{-6})$	$O(10^{-6})$	$O(10^{-13})$
105	$O(10^{-13})$	$O(10^{-6})$	$O(10^{-6})$	−0.0068	−0.0761	0.0610	$O(10^{-6})$	$O(10^{-4})$
106	$O(10^{-7})$	$O(10^{-13})$	$O(10^{-4})$	$O(10^{-6})$	0.0610	−0.0337	−0.0068	$O(10^{-6})$
107	$O(10^{-8})$	$O(10^{-5})$	$O(10^{-13})$	$O(10^{-6})$	$O(10^{-6})$	−0.0068	−0.0762	0.0610
108	$O(10^{-6})$	$O(10^{-9})$	$O(10^{-7})$	$O(10^{-13})$	$O(10^{-4})$	$O(10^{-6})$	0.0610	−0.0337

$\hat{y}_{f^{(m)}f^{(n)}} g^A_{Zf^{(m)}f^{(n)}}$ are negligible around $m, n = 100$. The ratio $(\hat{y}_{f^{(m)}f^{(n)}}/y_{f^{(m)}f^{(n)}}) \cdot (g^A_{Zf^{(m)}f^{(n)}}/g^V_{Zf^{(m)}f^{(n)}})$ is smaller than 10^{-4}, and the $\hat{y}_{f^{(m)}f^{(n)}} g^A_{Zf^{(m)}f^{(n)}}$ term in (3.25) may be dropped.

For the asymptotic behavior of the amplitude for m, $n \gg 1$ only the $|m-n| \le 1$ terms are relevant. For $|m-n| \le 1$, $m_{f^{(n\pm1)}} \simeq m_{f^{(n)}}$ and the amplitudes are evaluated as

TABLE IV. $J_{F^{+(m)}F^{+(n)}}$ is shown for $0 \le m, n \le 7$ and for $101 \le m, n \le 108$ in the $N_F = 4$, $z_L = 10^5$ case. Only the values larger than $O(10^{-4})$ are shown with three significant figures.

	1	2	3	4	5	6	7
1	0.2256	−0.0272	$O(10^{-5})$	−0.0040	$O(10^{-8})$	$O(10^{-5})$	$O(10^{-7})$
2	−0.0272	0.2378	0.0824	$O(10^{-6})$	$O(10^{-5})$	$O(10^{-8})$	$O(10^{-5})$
3	$O(10^{-5})$	0.0824	0.2204	−0.3188	$O(10^{-6})$	0.0036	$O(10^{-8})$
4	−0.0040	$O(10^{-6})$	−0.3188	0.2554	0.0866	$O(10^{-6})$	$O(10^{-5})$
5	$O(10^{-8})$	$O(10^{-5})$	$O(10^{-6})$	0.0866	0.2245	−0.3263	$O(10^{-6})$
6	$O(10^{-5})$	$O(10^{-8})$	−0.0036	$O(10^{-6})$	−0.3263	0.2612	0.0874
7	$O(10^{-7})$	$O(10^{-5})$	$O(10^{-8})$	$O(10^{-5})$	$O(10^{-6})$	0.0874	0.2271

	101	102	103	104	105	106	107	108
101	0.2505	−0.3528	$O(10^{-6})$	−0.0033	$O(10^{-11})$	$O(10^{-5})$	$O(10^{-8})$	$O(10^{-5})$
102	−0.3528	0.2918	0.0848	$O(10^{-5})$	$O(10^{-5})$	$O(10^{-12})$	$O(10^{-5})$	$O(10^{-8})$
103	$O(10^{-6})$	0.0848	0.2508	−0.3531	$O(10^{-6})$	−0.0033	$O(10^{-11})$	$O(10^{-5})$
104	−0.0033	$O(10^{-5})$	−0.3530	0.2921	0.0848	$O(10^{-5})$	$O(10^{-5})$	$O(10^{-12})$
105	$O(10^{-11})$	$O(10^{-5})$	$O(10^{-6})$	0.0848	0.2510	−0.3533	$O(10^{-6})$	−0.0033
106	$O(10^{-5})$	$O(10^{-12})$	−0.0033	$O(10^{-5})$	−0.3533	0.2924	0.0847	$O(10^{-5})$
107	$O(10^{-8})$	$O(10^{-5})$	$O(10^{-11})$	$O(10^{-5})$	$O(10^{-6})$	0.0847	0.2512	−0.3535
108	$O(10^{-5})$	$O(10^{-8})$	$O(10^{-5})$	$O(10^{-12})$	−0.0033	$O(10^{-5})$	−0.3535	0.2927

$$
\begin{aligned}
i\mathcal{M}_{\text{fermion}} &\equiv \frac{1}{2}\sum_{m,n}^{\infty}\{i\mathcal{M}^{(a)}_{t^{(m)},t^{(n)}} + i\mathcal{M}^{(b)}_{t^{(m)},t^{(n)}} + i\mathcal{M}^{(c)}_{F^{+(m)},F^{+(n)}} + i\mathcal{M}^{(d)}_{F^{+(m)},F^{+(n)}} + (m \leftrightarrow n)\} \\
&\approx \sum_{n}^{\infty}\frac{i}{4\pi^2}\epsilon^*_\mu(k_1)\epsilon^*_\nu(k_2)\left(\eta^{\mu\nu} - \frac{k_2^\mu k_1^\nu}{k_1\cdot k_2}\right)\frac{e g_w y_t \cos\theta_H}{\cos\theta_W}(m_H^2 - m_Z^2) \\
&\quad\times\left\{\frac{2}{3m_{t^{(n)}}}(J_{t^{(n)}t^{(n)}} + J_{t^{(n+1)}t^{(n)}} + J_{t^{(n-1)}t^{(n)}})[I_1(\tau_{t^{(n)}},\lambda_{t^{(n)}}) - I_2(\tau_{t^{(n)}},\lambda_{t^{(n)}})]\right. \\
&\quad\left. + \frac{1}{m_{F^{+(n)}}}(J_{F^{+(n)}F^{+(n)}} + J_{F^{+(n+1)}F^{+(n)}} + J_{F^{+(n-1)}F^{+(n)}})[I_1(\tau_{F^{+(n)}},\lambda_{F^{+(n)}}) - I_2(\tau_{F^{+(n)}},\lambda_{F^{+(n)}})]\right\}. \qquad (3.28)
\end{aligned}
$$

$J_{t^{(n)}t^{(m)}}$ and $J_{F^{+(n)}F^{+(m)}}$ $(m = n, n+1)$ are plotted in Figs. 6 and 7. They are approximately given, for $101 \le n \le 200$, by

$$
\begin{aligned}
J_{t^{(n)}t^{(n)}} &\simeq -0.0597 + 0.00323(\ln n) - 0.00047(\ln n)^2 + (-1)^{n-1}\{-0.0230 + 0.00122(\ln n) - 0.00018(\ln n)^2\}, \\
J_{t^{(n)}t^{(n+1)}} &\simeq 0.0296 - 0.00162(\ln n) + 0.00024(\ln n)^2 + (-1)^{n-1}\{0.0362 - 0.00143(\ln n) + 0.00020(\ln n)^2\}, \qquad (3.29)
\end{aligned}
$$

$$
\begin{aligned}
J_{F^{+(n)}F^{+(n)}} &\simeq 0.280 - 0.0172(\ln n) + 0.00331(\ln n)^2 + (-1)^{n-1}\{-0.0212 + 0.00131(\ln n) - 0.00026(\ln n)^2\}, \\
J_{F^{+(n)}F^{+(n+1)}} &\simeq -0.138 + 0.0084(\ln n) - 0.00163(\ln n)^2 + (-1)^{n-1}\{-0.2218 + 0.00558(\ln n) - 0.00107(\ln n)^2\}. \qquad (3.30)
\end{aligned}
$$

Adding them, one finds, within numerical errors, that

$$
\begin{aligned}
J_{t^{(n)}t^{(n)}} + J_{t^{(n+1)}t^{(n)}} + J_{t^{(n-1)}t^{(n)}} &\approx (-1)^{n-1}\{-0.0230 + 0.00122(\ln n) - 0.00018(\ln n)^2\}, \\
J_{F^{+(n)}F^{+(n)}} + J_{F^{+(n+1)}F^{+(n)}} + J_{F^{+(n-1)}F^{+(n)}} &\approx (-1)^{n-1}\{-0.0212 + 0.00131(\ln n) - 0.00026(\ln n)^2\}. \qquad (3.31)
\end{aligned}
$$

Since $i\mathcal{M}_f \propto \sum_n (J_{f^{(n)}f^{(n)}} + J_{f^{(n+1)}f^{(n)}} + J_{f^{(n-1)}f^{(n)}})/n$ for large n, the sum converges as in the case of the gauge boson loops.

D. Total amplitude

The ratio of the sum of the all boson contributions to the W boson contribution and that of all the fermion contributions to the top quark contribution are given by

$$
\frac{\mathcal{M}_{\text{boson}}}{\mathcal{M}_{W^{(0)}\text{only}}} = 0.9994, \qquad \frac{\mathcal{M}_{\text{fermion}}}{\mathcal{M}_{t^{(0)}\text{only}}} = 1.0023, \qquad (3.32)
$$

for $z_L = 10^5$, $n_F = 4$, and $\theta_H = 0.1153$, respectively where $\mathcal{M}_{\text{boson}} \equiv \mathcal{M}_W + \mathcal{M}_{W_R}$. The ratio of the whole amplitude to the W boson and top quark contributions is

$$
\frac{\mathcal{M}_{\text{boson}} + \mathcal{M}_{\text{fermion}}}{\mathcal{M}_{W^{(0)}\text{only}} + \mathcal{M}_{t^{(0)}\text{only}}} = 0.9993. \qquad (3.33)
$$

One finds that the KK mode contributions are negligible. As $g_{HW^{(0)}W^{(0)}} \simeq g_w \cos\theta_H$ and $y_{t^{(0)}} \simeq y_{t\text{SM}} \cos\theta_H$, the decay width is approximated by

$$
\Gamma(H \to Z\gamma)_{\text{GHU}} \simeq \Gamma(H \to Z\gamma)_{\text{SM}} \times \cos^2\theta_H. \qquad (3.34)
$$

In the gauge-Higgs unification, the decay width of $H \to WW$, $H \to ZZ$, $H \to bb$ and $H \to \tau\tau$ are suppressed

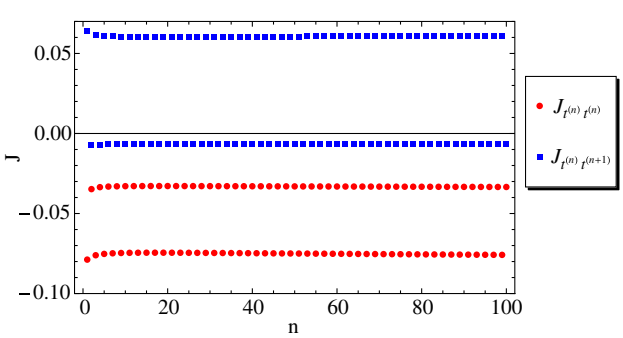

FIG. 6 (color online). $J_{t^{(n)}t^{(n)}}$ and $J_{t^{(n)}t^{(n+1)}}$ are plotted for $1 \le n \le 100$ in the $N_F = 4$, $z_L = 10^5$ case. The red circles and blue squares express $J_{t^{(n)}t^{(n)}}$ and $J_{t^{(n)}t^{(n+1)}}$, respectively.

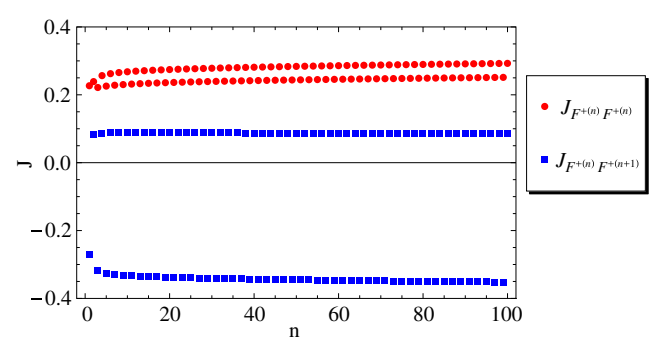

FIG. 7 (color online). $J_{F^{+(n)}F^{+(n)}}$ and $J_{F^{+(n)}F^{+(n+1)}}$ are plotted for $1 \le n \le 100$ in the $N_F = 4$, $z_L = 10^5$ case. The red circles and blue squares express $J_{F^{+(n)}F^{+(n)}}$ and $J_{F^{+(n)}F^{+(n+1)}}$, respectively.

by $\cos^2\theta_H$ at the tree level. The decay width of the $H \to \gamma\gamma$ and $H \to Z\gamma$ are also suppressed by $\cos^2\theta_H$. Therefore the branching ratios of the Higgs decay modes in this model are almost the same as in the SM. The dominant process in the Higgs boson production is $gg \to H$, and the production cross section is also suppressed by $\cos^2\theta_H$. Therefore the signal strength, $\sigma(gg\to H)B(H\to Z\gamma)/[\sigma(gg\to H)B(H\to Z\gamma)]_{\rm SM}$, is approximately $\cos^2\theta_H$ as in the other decay modes. For $\theta_H \sim 0.1$, the deviation from the SM amounts only 1%.

We stress the finiteness of $\Gamma(H \to Z\gamma)$ in the gauge-Higgs unification which results from nontrivial cancellation among contributions of the KK modes. One might wonder why such cancellation takes place and what underlies the finiteness of the amplitude $\mathcal{M}(H \to Z\gamma)$ in the gauge-Higgs unification. We argue that it is guaranteed by the gauge invariance and by the fact that the 4D Higgs field H is the fluctuation mode of the AB phase θ_H. In the effective action the 4D Higgs field $H(x)$ and AB phase θ_H appear in the combination of $\theta_H + H(x)/f_H$ so that $\mathcal{M}(H \to Z\gamma)$ is related to $(\partial/\partial\theta_H)\Pi_{Z\gamma}(\theta_H)$ where $\Pi_{Z\gamma}(\theta_H)$ is the $Z\gamma$ vacuum polarization. The 5D gauge invariance guarantees that $\Pi_{Z\gamma}(\theta_H)$ is periodic in θ_H, and can be expanded in a Fourier series $\Pi_{Z\gamma}(\theta_H) = \sum_n \alpha_n e^{in\theta_H}$. The θ_H-dependence of the Z couplings of the fields running the inside loops is known to be very weak. At the one loop level the dominant θ_H-dependence of $\Pi_{Z\gamma}(\theta_H)$ comes from the propagators inside the loop. Hence the divergence degree is lowered by differentiating $\Pi_{Z\gamma}(\theta_H)$ with respect to θ_H. There should exist a positive integer q such that $\partial^q\Pi_{Z\gamma}/\partial\theta_H^q = \sum_{n\neq 0}(in)^q\alpha_n e^{in\theta_H}$ is finite. This in turn implies that $\Pi_{Z\gamma}(\theta_H) - \alpha_0$ is finite, from which the finiteness of $\mathcal{M}(H \to Z\gamma)$ at the one loop level follows. A similar argument has been employed to prove the finiteness of the effective potential $V_{\rm eff}(\theta_H)$ at the one loop level [30].

IV. CONCLUSION AND DISCUSSIONS

In this paper we have evaluated the decay rate $\Gamma(H \to Z\gamma)$ in the $SO(5) \times U(1)$ gauge-Higgs unification. The processes $H \to \gamma\gamma$ and $H \to Z\gamma$ do not occur at the tree level. They do proceed at the one loop level, where an infinite number of the KK modes of gauge bosons and fermions give loop corrections. Contrary to the naive expectation that the sum of an infinite number of the KK mode contributions may yield substantial corrections to the decay rates in the SM, it has been known that the correction to $\Gamma(H \to \gamma\gamma)$ coming from KK modes turns out very tiny, thanks to the cancellation among the KK mode corrections.

We have examined the process $H \to Z\gamma$ in detail, for which the KK number need not be conserved inside the loop. We have shown, by direct evaluation, that there appears miraculous cancellation among the loop diagrams in which the KK number is conserved in the loop and those in which the KK number is not conserved. As a result the amplitude for $H \to Z\gamma$ becomes finite. We also showed that the correction due to various KK modes is very small. $\Gamma(H \to Z\gamma)$ in the gauge-Higgs unification is approximately $\cos^2\theta_H$ times that in the SM. The deviation from the SM is very small for $\theta_H < 0.1$.

The result is very promising. The $SO(5) \times U(1)$ gauge-Higgs unification yields almost the same phenomenology as the SM at low energies. At higher energy scale it predicts KK excitation modes as Z' and W' events and a dark matter candidate, which awaits confirmation at 14 TeV LHC and by DM direct-detection experiments. Small deviations of HWW and HZZ couplings from the SM will be checked in future colliders [31]. In addition to deriving more predictions for collider experiments, the scenario of the gauge-Higgs unification has to be refined. The scenario of the gauge-Higgs grand unification has been proposed [32]. An attempt has been made to dynamically determine orbifold boundary conditions [33]. The Hosotani mechanism, essential for the electroweak gauge symmetry breaking in the gauge-Higgs unification, has been investigated nonperturbatively on the lattice [34]. The gauge-Higgs unification is one of the keys to investigate the extra dimension.

ACKNOWLEDGMENTS

This work was supported in part by Japan Society for the Promotion of Science, Grants-in-Aid for Scientific Research, No. 23104009 (Y. H.), No. 21244036 (Y. H.), and National Research Foundation of Korea 2012R1A2A1A01006053 (H. H.).

APPENDIX: COUPLINGS OF KK MODES TO Z AND H

We summarize the Z and H couplings of the KK modes relevant for $H \to Z\gamma$.

1. Base functions

Mode functions for KK towers of various fields in the RS spacetime are expressed in terms of Bessel functions. For gauge fields we define

$$\begin{aligned} C(z;\lambda) &= \frac{\pi}{2}\lambda z z_L F_{1,0}(\lambda z, \lambda z_L), \\ C'(z;\lambda) &= \frac{\pi}{2}\lambda^2 z z_L F_{0,0}(\lambda z, \lambda z_L), \\ S(z;\lambda) &= -\frac{\pi}{2}\lambda z F_{1,1}(\lambda z, \lambda z_L), \\ S'(z;\lambda) &= -\frac{\pi}{2}\lambda^2 z F_{0,1}(\lambda z, \lambda z_L), \\ \hat{S}(z;\lambda) &= \frac{C(1;\lambda)}{S(1;\lambda)} S(z;\lambda), \end{aligned} \tag{A1}$$

where $F_{\alpha,\beta}(u,v) = J_\alpha(u)Y_\beta(v) - Y_\alpha(u)J_\beta(v)$. They satisfy

$$\begin{aligned} &C(z_L;\lambda) = z_L, \qquad C'(z_L;\lambda) = 0, \qquad S(z_L;\lambda) = 0, \\ &S'(z_L;\lambda) = \lambda, \qquad CS' - SC' = \lambda z. \end{aligned} \tag{A2}$$

For fermions with a bulk mass parameter c we define

$$\begin{pmatrix} C_L \\ S_L \end{pmatrix}(z;\lambda,c) = \pm\frac{\pi}{2}\lambda\sqrt{zz_L}F_{c+\frac{1}{2},c\mp\frac{1}{2}}(\lambda z,\lambda z_L),$$
$$\begin{pmatrix} C_R \\ S_R \end{pmatrix}(z;\lambda,c) = \mp\frac{\pi}{2}\lambda\sqrt{zz_L}F_{c-\frac{1}{2},c\pm\frac{1}{2}}(\lambda z,\lambda z_L). \tag{A3}$$

They satisfy

$$D_+(c)\begin{pmatrix} C_L \\ S_L \end{pmatrix} = \lambda\begin{pmatrix} S_R \\ C_R \end{pmatrix}, \qquad D_-(c)\begin{pmatrix} C_R \\ S_R \end{pmatrix} = \lambda\begin{pmatrix} S_L \\ C_L \end{pmatrix},$$
$$D_\pm(c) = \pm\frac{d}{dz} + \frac{c}{z},$$
$$C_R = C_L = 1, \qquad S_R = S_L = 0, \quad \text{at } z = z_L,$$
$$C_L C_R - S_L S_R = 1. \tag{A4}$$

In the following we evaluate various couplings by inserting the formulas for the KK expansions. Basic formulas for the KK expansions of gauge fields and quark fields are summarized in Ref. [24], whereas those for dark fermions are given in Ref. [25]. We adopt the same notation as in those references. The numerical values for the various couplings are given for the parameter set

$$z_L = 10^5, \qquad \theta_H = 0.1153,$$
$$m_{\rm KK} = 7.405\ \text{TeV}, \qquad k = 2.357\times 10^8\ \text{GeV},$$
$$c_t = 0.2270, \qquad c_F = 0.3321. \tag{A5}$$

2. $ZW^{(m)}W^{(n)}$ coupling

The $ZW^{(m)}W^{(n)}$ coupling is contained in

$$\begin{aligned}\int_1^{z_L}\frac{dz}{kz}\left(-\frac{1}{4}\right)\mathrm{Tr}[F_{\mu\nu}F_{\rho\sigma}]\eta^{\mu\rho}\eta^{\nu\sigma} &\supset ig_A\int_1^{z_L}\frac{dz}{kz}\mathrm{Tr}[(\partial_\mu\hat{Z}_\nu - \partial_\nu\hat{Z}_\mu)[\hat{W}^+_\rho,\hat{W}^-_\sigma] \\ &\quad + (\partial_\mu\hat{W}^-_\nu - \partial_\nu\hat{W}^-_\mu)[\hat{Z}_\rho,\hat{W}^+_\sigma] + (\partial_\mu\hat{W}^+_\nu - \partial_\nu\hat{W}^+_\mu)[\hat{Z}_\rho,\hat{W}^-_\sigma]]\eta^{\mu\rho}\eta^{\nu\sigma} \\ &\supset i\sum_{m,n} g_{ZW^{(m)}W^{(n)}}\eta^{\mu\rho}\eta^{\nu\sigma}\{(\partial_\mu Z_\nu - \partial_\nu Z_\mu)W^{+(m)}_\rho W^{-(n)}_\sigma \\ &\quad - (\partial_\mu W^{+(m)}_\nu - \partial_\nu W^{+(m)}_\mu)Z_\rho W^{-(n)}_\sigma + (\partial_\mu W^{-(n)}_\nu - \partial_\nu W^{-(n)}_\mu)Z_\rho W^{+(m)}_\sigma\}\end{aligned} \tag{A6}$$

so that one finds that

$$\begin{aligned} g_{ZW^{(m)}W^{(n)}} &= g_w\sqrt{L}\int_1^{z_L}\frac{dz}{kz}\left\{h^L_Z\left(h^L_{W^{(m)}}h^L_{W^{(n)}} + \frac{\hat{h}_{W^{(m)}}\hat{h}_{W^{(n)}}}{2}\right) + h^R_Z\left(h^R_{W^{(m)}}h^R_{W^{(n)}} + \frac{\hat{h}_{W^{(m)}}\hat{h}_{W^{(n)}}}{2}\right)\right. \\ &\quad \left. + \hat{h}_Z\left(\frac{h^L_{W^{(m)}}\hat{h}_{W^{(n)}} + h^R_{W^{(m)}}\hat{h}_{W^{(n)}} + \hat{h}_{W^{(m)}}h^L_{W^{(n)}} + \hat{h}_{W^{(m)}}h^R_{W^{(n)}}}{2}\right)\right\} \\ &= g_w\cos\theta_W\frac{\sqrt{L}}{\sqrt{r_Z r_{W^{(m)}} r_{W^{(n)}}}}\int_1^{z_L}\frac{dz}{kz}\frac{1}{\sqrt{2}}\left[2C_Z((1+\cos^2\theta_H)C_{W^{(m)}}C_{W^{(n)}} + \sin^2\theta_H\hat{S}_{W^{(m)}}\hat{S}_{W^{(n)}})\right. \\ &\quad \left. + \frac{\sin^2\theta_H}{\cos^2\theta_W}\{-C_Z(C_{W^{(m)}}C_{W^{(n)}} + \hat{S}_{W^{(m)}}\hat{S}_{W^{(n)}}) + \hat{S}_Z(C_{W^{(m)}}\hat{S}_{W^{(n)}} + \hat{S}_{W^{(m)}}C_{W^{(n)}})\}\right]. \end{aligned} \tag{A7}$$

Here $C_{W^{(m)}} = C(z;\lambda_{W^{(m)}})$ etc. Numerical values of $g_{ZW^{(m)}W^{(n)}}$ are given in Table V.

TABLE V. $g_{ZW^{(m)}W^{(n)}}/g_w\cos\theta_W$. Only the values larger than $O(10^{-3})$ are shown and written by three significant figures.

	0	1	2	3	4	5	6	7
0	1.	$O(10^{-4})$	$O(10^{-7})$	$O(10^{-5})$	$O(10^{-7})$	$O(10^{-6})$	$O(10^{-8})$	$O(10^{-6})$
1	$O(10^{-4})$	0.996	0.032	$O(10^{-5})$	$O(10^{-4})$	$O(10^{-6})$	$O(10^{-5})$	$O(10^{-6})$
2	$O(10^{-7})$	0.032	0.350	−0.022	$O(10^{-7})$	$O(10^{-4})$	$O(10^{-6})$	$O(10^{-4})$
3	$O(10^{-5})$	$O(10^{-5})$	−0.022	0.996	0.032	$O(10^{-5})$	$O(10^{-4})$	$O(10^{-6})$
4	$O(10^{-7})$	$O(10^{-4})$	$O(10^{-7})$	0.032	0.350	−0.023	$O(10^{-5})$	$O(10^{-4})$
5	$O(10^{-6})$	$O(10^{-6})$	$O(10^{-4})$	$O(10^{-5})$	−0.023	0.996	0.032	$O(10^{-5})$
6	$O(10^{-8})$	$O(10^{-5})$	$O(10^{-6})$	$O(10^{-4})$	$O(10^{-5})$	0.032	0.350	−0.023
7	$O(10^{-6})$	$O(10^{-6})$	$O(10^{-4})$	$O(10^{-6})$	$O(10^{-4})$	$O(10^{-5})$	−0.023	0.996

3. $\gamma Z W^{(m)} W^{(n)}$ coupling

Similarly $\gamma Z W^{(m)} W^{(n)}$ coupling is contained in

$$(g_A)^2 \int_1^{z_L} \frac{dz}{kz} \mathrm{Tr}[[\hat{A}_\mu^{\gamma(A)}, \hat{W}_\nu^+]([\hat{Z}_\rho, \hat{W}_\sigma^-] - [\hat{Z}_\sigma, \hat{W}_\rho^-]) + [\hat{A}_\mu^{\gamma(A)}, \hat{W}_\nu^-]([\hat{Z}_\rho, \hat{W}_\sigma^+] - [\hat{Z}_\sigma, \hat{W}_\rho^+])]\eta^{\mu\rho}\eta^{\nu\sigma}$$
$$\supset \sum_{m,n} g_{\gamma Z W^{(m)} W^{(n)}} \eta^{\mu\rho}\eta^{\nu\sigma}\{A_\mu^\gamma W_\nu^{+(m)}(Z_\rho W_\sigma^{-(n)} - Z_\sigma W_\rho^{-(n)}) + A_\mu^\gamma W_\nu^{-(n)}(Z_\rho W_\sigma^{+(m)} - Z_\sigma W_\rho^{+(m)})\} \tag{A8}$$

so that

$$g_{\gamma Z W^{(m)} W^{(n)}} = -g_w^2 L \int_1^{z_L} \frac{dz}{kz} \left\{ h_\gamma^L h_{W^{(m)}}^L \left(h_Z^L h_{W^{(n)}}^L + \frac{\hat{h}_Z \hat{h}_{W^{(n)}}}{2} \right) + h_\gamma^R h_{W^{(m)}}^R \left(h_Z^R h_{W^{(n)}}^R + \frac{\hat{h}_Z \hat{h}_{W^{(n)}}}{2} \right) \right.$$
$$\left. + \frac{h_\gamma^L + h_\gamma^R}{2} \hat{h}_{W^{(m)}} \left(\frac{h_Z^L \hat{h}_{W^{(n)}} + h_Z^R \hat{h}_{W^{(n)}} + \hat{h}_Z h_{W^{(n)}}^L + \hat{h}_Z h_{W^{(n)}}^R}{2} \right) \right\}$$
$$= -e g_{Z W^{(m)} W^{(n)}}. \tag{A9}$$

The relation $g_{\gamma Z W^{(m)} W^{(n)}} = -e g_{Z W^{(m)} W^{(n)}}$ follows from the gauge invariance as well.

4. $H W^{(m)} W^{(n)}$ coupling

The Higgs coupling $H W^{(m)} W^{(n)}$ is contained in the $\mathrm{Tr} F_{\mu z} F^{\mu z}$ term

$$-i g_A k^2 \int_1^{z_L} \frac{dz}{kz} \mathrm{Tr}(\partial_z \hat{W}_\mu^- [\hat{W}_\nu^+, \hat{H}] + \partial_z \hat{W}_\mu^+ [\hat{W}_\nu^-, \hat{H}]) \eta^{\mu\nu} \supset -\sum_{m,n} g_{H W^{(m)} W^{(n)}} H W_\mu^{+(m)} W_\nu^{-(n)} \eta^{\mu\nu} \tag{A10}$$

so that

$$g_{H W^{(m)} W^{(n)}} = i g_A k^2 \int_1^{z_L} \frac{dz}{kz} \frac{i}{2} u_H(z) [-(\partial_z \hat{h}_{W^{(m)}})(h_{W^{(n)}}^L - h_{W^{(n)}}^R) + \partial_z (h_{W^{(m)}}^L - h_{W^{(m)}}^R) \hat{h}_{W^{(n)}} + (m \longleftrightarrow n)]$$
$$= -g_w \sqrt{\frac{kL}{z_L^2 - 1}} \frac{1}{\sqrt{r_{W^{(m)}} r_{W^{(n)}}}} \sin\theta_H \cos\theta_H \int_1^{z_L} dz \{(\partial_z \hat{S}_{W^{(m)}}) C_{W^{(n)}} - (\partial_z C_{W^{(m)}}) \hat{S}_{W^{(n)}} + (m \longleftrightarrow n)\}. \tag{A11}$$

Numerical values of $g_{H W^{(m)} W^{(n)}}$ are given in Table VI.

TABLE VI. $g_{H W^{(m)} W^{(n)}} / g_w \cos\theta_H$ in the unit of GeV written by three significant figures. The values smaller than $O(10)$ are abbreviated.

	0	1	2	3	4	5	6	7
0	80.0	2.55×10^2	$O(1)$	45.4	$O(10^{-1})$	20.7	$O(10^{-1})$	10.4
1	2.55	-3.50×10^2	1.39×10^4	-1.96×10^2	1.40×10^3	$O(1)$	2.28×10^2	-24.1
2	$O(1)$	1.39×10^4	5.62×10^2	2.06×10^4	2.87×10^2	3.04×10^3	$O(1)$	1.66×10^3
3	45.4	-1.96×10^2	2.06×10^4	-8.40×10^2	2.94×10^4	-4.17×10^2	3.54×10^3	$O(1)$
4	$O(10^{-1})$	1.40×10^3	2.87×10^2	2.93×10^4	1.07×10^3	3.49×10^4	5.11×10^2	4.51×10^3
5	20.7	$O(1)$	3.04×10^3	-4.17×10^2	3.49×10^4	-1.36×10^3	4.46×10^4	-6.40×10^2
6	$O(10^{-1})$	2.28×10^2	$O(1)$	3.54×10^3	5.11×10^2	4.46×10^4	1.60×10^3	4.88×10^4
7	10.4	-24.1	1.66×10^3	$O(1)$	4.51×10^3	-6.40×10^2	4.88×10^4	-1.90×10^3

TABLE VII. $g_{ZW^{(m)}W_R^{(n)}}/g_w \cos\theta_W$. Only the value larger than $O(10^{-3})$ are shown and written by two significant figures.

		m							
		0	1	2	3	4	5	6	7
	1	$O(10^{-4})$	0.003	−0.021	$O(10^{-4})$	0.009	$O(10^{-4})$	−0.008	$O(10^{-4})$
n	2	$O(10^{-5})$	$O(10^{-4})$	0.018	0.003	−0.026	$O(10^{-4})$	0.007	$O(10^{-4})$
	3	$O(10^{-6})$	$O(10^{-5})$	0.004	$O(10^{-4})$	0.020	0.004	−0.028	$O(10^{-4})$
	4	$O(10^{-6})$	$O(10^{-5})$	$O(10^{-4})$	$O(10^{-4})$	0.005	$O(10^{-4})$	0.020	0.004

5. $ZW^{(m)}W_R^{(n)}$ coupling

The $ZW^{(m)}W_R^{(n)}$ coupling in

$$i\sum_{m,n} g_{ZW^{(m)}W_R^{(n)}}\eta^{\mu\rho}\eta^{\nu\sigma}\{(\partial_\mu Z_\nu - \partial_\nu Z_\mu)(W_\rho^{+(m)}W_{R\sigma}^{-(n)} + W_\rho^{-(m)}W_{R\sigma}^{+(n)}) + (\partial_\mu W_\nu^{-(m)} - \partial_\nu W_\mu^{-(m)})Z_\rho W_{R\sigma}^{+(n)} - (\partial_\mu W_\nu^{+(m)} - \partial_\nu W_\mu^{+(m)})Z_\rho W_{R\sigma}^{-(n)} + (\partial_\mu W_{R\nu}^{-(n)} - \partial_\nu W_{R\mu}^{-(n)})Z_\rho W_\sigma^{+(m)} - (\partial_\mu W_{R\nu}^{+(n)} - \partial_\nu W_{R\mu}^{+(n)})Z_\rho W_\sigma^{-(m)}\} \tag{A12}$$

is given by

$$\begin{aligned} g_{ZW^{(m)}W_R^{(n)}} &= g_w\sqrt{L}\int_1^{z_L}\frac{dz}{kz}\left\{h_Z^L h_{W^{(m)}}^L h_{W_R^{(n)}}^L + h_Z^R h_{W^{(m)}}^R h_{W_R^{(n)}}^R + \hat{h}_Z\hat{h}_{W^{(m)}}\frac{h_{W_R^{(n)}}^L + h_{W_R^{(n)}}^R}{2}\right\} \\ &= g_w\cos\theta_W\frac{\sqrt{L}}{\sqrt{r_Z r_{W^{(m)}} r_{W_R^{(n)}}}}\int_1^{z_L}\frac{dz}{kz}\frac{1}{\sqrt{2}}\frac{\sin^2\theta_H}{\cos^2\theta_W}\frac{\cos\theta_H}{\sqrt{1+\cos^2\theta_H}}\{C_Z C_{W^{(m)}} C_{W_R^{(n)}} - \hat{S}_Z\hat{S}_{W^{(m)}}C_{W_R^{(n)}}\}. \end{aligned} \tag{A13}$$

Numerical values of $g_{ZW^{(m)}W_R^{(n)}}$ are given in Table VII.

6. $\gamma ZW^{(m)}W_R^{(n)}$ coupling

Similarly $\gamma ZW^{(m)}W_R^{(n)}$ coupling is contained in

$$\begin{aligned} &(g_A)^2\int_1^{z_L}\frac{dz}{kz}\eta^{\mu\rho}\eta^{\nu\sigma}\mathrm{Tr}[[\hat{A}_\mu^{\gamma(A)},\hat{W}_\nu^+]([\hat{Z}_\rho,\hat{W}_{R\sigma}^-] - [\hat{Z}_\sigma,\hat{W}_{R\rho}^-]) + [\hat{A}_\mu^{\gamma(A)},\hat{W}_\nu^-]([\hat{Z}_\rho,\hat{W}_{R\sigma}^+] - [\hat{Z}_\sigma,\hat{W}_{R\rho}^+]) \\ &\quad\times[\hat{A}_\mu^{\gamma(A)},\hat{W}_{R\nu}^-]([\hat{Z}_\rho,\hat{W}_{R\sigma}^+] - [\hat{Z}_\sigma,\hat{W}_\rho^+]) + [\hat{A}_\mu^{\gamma(A)},\hat{W}_{R\nu}^-]([\hat{Z}_\rho,\hat{W}_{R\sigma}^+] - [\hat{Z}_\sigma,\hat{W}_\rho^+])] \\ &\supset \sum_{m,n} g_{\gamma ZW^{(m)}W_R^{(n)}}\eta^{\mu\rho}\eta^{\nu\sigma}\{A_\mu^\gamma W_\nu^{+(m)}(Z_\rho W_{R\sigma}^{-(n)} - Z_\sigma W_{R\rho}^{-(n)}) + A_\mu^\gamma W_\nu^{-(n)}(Z_\rho W_{R\sigma}^{+(m)} - Z_\sigma W_{R\rho}^{+(m)}) \\ &\quad + A_\mu^\gamma W_{R\nu}^{+(m)}(Z_\rho W_\sigma^{-(n)} - Z_\sigma W_\rho^{-(n)}) + A_\mu^\gamma W_{R\nu}^{-(n)}(Z_\rho W_\sigma^{+(m)} - Z_\sigma W_\rho^{+(m)})\} \end{aligned} \tag{A14}$$

so that

$$\begin{aligned} g_{\gamma ZW^{(m)}W_R^{(n)}} &= -g_w^2\sqrt{L}\int_1^{z_L}\frac{dz}{kz}\left\{h_{\gamma^{(0)}}^L h_{W^{(m)}}^L h_Z^L h_{W_R^{(n)}}^L + h_{\gamma^{(0)}}^R h_{W^{(m)}}^R h_Z^R h_{W_R^{(n)}}^R + \frac{1}{2}(h_{\gamma^{(0)}}^L + h_{\gamma^{(0)}}^R)\hat{h}_{W^{(m)}}\frac{1}{2}\hat{h}_Z(h_{W_R^{(n)}}^L + h_{W_R^{(n)}}^R)\right\} \\ &= -eg_w g_{ZW^{(m)}W_R^{(n)}}. \end{aligned} \tag{A15}$$

The relation $g_{\gamma ZW^{(m)}W_R^{(n)}} = -eg_{ZW^{(m)}W_R^{(n)}}$ follows from the gauge invariance as well.

7. $HW^{(m)}W_R^{(n)}$ and $HW_R^{(m)}W_R^{(n)}$ coupling

Similarly the $HW^{(m)}W_R^{(n)}$ coupling contained in

$$-ig_A k^2\int_1^{z_L}\frac{dz}{kz}\mathrm{Tr}(\partial_z\hat{W}_{R\mu}^-[\hat{W}_\nu^+,\hat{H}] + \partial_z\hat{W}_\mu^+[\hat{W}_{R\nu}^-,\hat{H}])\eta^{\mu\nu} \supset -\sum_{m,n} g_{HW^{(m)}W_R^{(n)}}HW_\mu^{+(m)}W_{R\nu}^{-(n)}\eta^{\mu\nu} \tag{A16}$$

TABLE VIII. $g_{HW^{(m)}W_R^{(n)}}/g_w \cos\theta_H$ in the unit of GeV written by three significant figures. The values smaller than $O(10)$ are abbreviated.

		m							
		0	1	2	3	4	5	6	7
	1	112	−60.7	3.47×10^3	$O(1)$	−55.8	$O(1)$	161	$O(1)$
n	2	80.9	−118	1.72×10^4	−278	1.62×10^4	−70.2	391	$O(1)$
	3	$O(1)$	$O(1)$	4.83×10^3	−260	3.32×10^4	−527	2.93×10^4	−140
	4	30.4	−19.4	1.13×10^3	−17.3	7.96×10^3	−412	4.94×10^4	−789

is given by

$$\begin{aligned} g_{HW^{(m)}W_R^{(n)}} &= i g_A k^2 \int_1^{z_L} \frac{dz}{kz}\frac{i}{2} u_H(z)[\partial_z(h^L_{W_R^{(n)}} - h^R_{W_R^{(n)}})\hat{h}_{W^{(m)}} - (\partial_z \hat{h}_{W^{(m)}})(h^L_{W_R^{(n)}} - h^R_{W_R^{(n)}})] \\ &= -g_w \sqrt{\frac{kL}{z_L^2 - 1}} \frac{1}{\sqrt{r_{W^{(m)}} r_{W_R^{(n)}}}} (-\sin\theta_H \cos\theta_H) \int_1^{z_L} dz[(\partial_z C_{W_R^{(n)}})\hat{S}_{W^{(m)}} - (\partial_z \hat{S}_{W^{(m)}}) C_{W_R^{(n)}}]. \end{aligned} \tag{A17}$$

Numerical values of $g_{HW^{(m)}W_R^{(n)}}$ are given in Table VIII. The $HW_R^{(m)}W_R^{(n)}$ couplings vanish for all m, n as a result of the Lie algebra.

8. $Zt^{(m)}t^{(n)}$ coupling

The Z couplings of the top quark tower are found from

$$\begin{aligned} &\sum_{a=1}^{2} \int_1^{z_L} dz \sqrt{G} \bar{\Psi}_a (-i g_A A_\mu - i g_B Q_{X_a} B_\mu) z \gamma^\mu \Psi_a \supset -i g_w Z_\mu \sqrt{L} \int_1^{z_L} \frac{dz}{k} \\ &\quad \times \left\{ \frac{h_Z^L}{2} (\bar{\tilde{U}}\gamma^\mu \tilde{U} - \bar{\tilde{B}}\gamma^\mu \tilde{B} + \bar{\tilde{t}}\gamma^\mu \tilde{t}) + \frac{h_Z^R}{2} (\bar{\tilde{U}}\gamma^\mu \tilde{U} + \bar{\tilde{B}}\gamma^\mu \tilde{B} - \bar{\tilde{t}}\gamma^\mu \tilde{t}) + \frac{\hat{h}_Z}{2} (\bar{\tilde{B}}\gamma^\mu \tilde{t}' + \bar{\tilde{t}}\gamma^\mu \tilde{t}' + \bar{\tilde{t}'}\gamma^\mu \tilde{B} + \bar{\tilde{t}'}\gamma^\mu \tilde{t}) \right. \\ &\quad \left. + Q_{X_1} t_\phi h_Z^B (\bar{\tilde{B}}\gamma^\mu \tilde{B} + \bar{\tilde{t}}\gamma^\mu \tilde{t} + \bar{\tilde{t}'}\gamma^\mu \tilde{t}') + Q_{X_2} t_\phi h_Z^B \bar{\tilde{U}}\gamma^\mu \tilde{U} \right\}. \end{aligned} \tag{A18}$$

The $Zt^{(m)}t^{(n)}$ couplings are found to be

$$\begin{aligned} &- i \frac{g_w}{\cos\theta_W} \sum_{m,n} Z_\mu (-i) \bar{t}_L^{(m)} \gamma^\mu t_L^{(n)} \frac{\sqrt{L}}{\sqrt{2 r_Z}} \int_1^{z_L} dz \left\{ C_Z f_{U_L}^{(m)} f_{U_L}^{(n)} + \cos\theta_H C_Z (-f_{B_L}^{(m)} f_{B_L}^{(n)} + f_{t_L}^{(m)} f_{t_L}^{(n)}) \right. \\ &\quad + \frac{-\sqrt{2}\sin\theta_H}{2} \hat{S}_Z (f_{B_L}^{(m)} f_{t'_L}^{(n)} + f_{t_L}^{(m)} f_{t'_L}^{(n)} + f_{t'_L}^{(m)} f_{B_L}^{(n)} + f_{t'_L}^{(m)} f_{t_L}^{(n)}) \\ &\quad \left. - 2\sin^2\theta_W C_Z Q_{X_1} (f_{U_L}^{(m)} f_{U_L}^{(n)} + f_{B_L}^{(m)} f_{B_L}^{(n)} + f_{t_L}^{(m)} f_{t_L}^{(n)} + f_{t'_L}^{(m)} f_{t'_L}^{(n)}) \right\} \end{aligned} \tag{A19}$$

for the left-handed component $t_L^{(n)}$ and a similar expression for $t_R^{(n)}$. Noting that $Q_{X_1} = \frac{2}{3}$ and $Q_{X_2} = -\frac{1}{3}$, one finds that

$$Z_\mu \sum_{m,n} \{ g_{Zt_L^{(m)}t_L^{(n)}} \bar{t}_L^{(m)} \gamma^\mu t_L^{(n)} + g_{Zt_R^{(m)}t_R^{(n)}} \bar{t}_R^{(m)} \gamma^\mu t_R^{(n)} \} \tag{A20}$$

TABLE IX. $g^V_{Zt^{(m)}t^{(n)}} = \frac{1}{2}\{g_{Zt_L^{(m)}t_L^{(n)}} + g_{Zt_R^{(m)}t_R^{(n)}}\}$ in the unit of $g/\cos\theta_W$. The values larger than $O(10^{-3})$ are shown. $g^A_{Zt^{(m)}t^{(n)}} = \frac{1}{2}\{g_{Zt_L^{(m)}t_L^{(n)}} - g_{Zt_R^{(m)}t_R^{(n)}}\}$ in the unit of $g/\cos\theta_W$ is smaller than $O(10^{-3})$ in the range of m, $n \leq 10$, except for $g^A_{Zt^{(0)}t^{(0)}} = -0.2501$.

	0	1	2	3	4	5	6	7
0	0.095	−0.008	0.001	$O(10^{-4})$	$O(10^{-5})$	$O(10^{-4})$	$O(10^{-5})$	$O(10^{-5})$
1	−0.008	0.337	0.059	$O(10^{-4})$	0.002	$O(10^{-5})$	$O(10^{-6})$	$O(10^{-6})$
2	0.001	0.059	−0.149	−0.010	$O(10^{-5})$	$O(10^{-4})$	$O(10^{-5})$	$O(10^{-4})$
3	$O(10^{-4})$	$O(10^{-4})$	−0.010	0.338	0.056	$O(10^{-5})$	0.002	$O(10^{-6})$
4	$O(10^{-5})$	0.002	$O(10^{-5})$	0.056	−0.149	−0.010	$O(10^{-5})$	$O(10^{-4})$
5	$O(10^{-4})$	$O(10^{-5})$	$O(10^{-4})$	$O(10^{-5})$	−0.010	0.338	0.056	$O(10^{-4})$
6	$O(10^{-5})$	$O(10^{-6})$	$O(10^{-5})$	0.002	$O(10^{-5})$	0.056	−0.150	−0.010
7	$O(10^{-5})$	$O(10^{-6})$	$O(10^{-4})$	$O(10^{-6})$	$O(10^{-4})$	$O(10^{-4})$	−0.010	0.338

where

$$
\begin{aligned}
g_{Zt_L^{(m)}t_L^{(n)}} &= \frac{g_w}{\cos\theta_W}\frac{\sqrt{2L}}{\sqrt{r_Z r_{t^{(m)}} r_{t^{(n)}}}}\int_1^{z_L} dz\Bigg[\left(\frac{\tilde{\mu}^2}{\mu_2^2}+c_H^2\right)C_L^{(m)}C_L^{(n)}C_Z + \frac{s_H^2}{2}\left(C_L^{(m)}\frac{C_L^{(n)}(1)}{S_L^{(n)}(1)}S_L^{(n)} + \frac{C_L^{(m)}(1)}{S_L^{(m)}(1)}S_L^{(m)}C_L^{(m)}\right)\hat{S}_Z \\
&\quad -\frac{2}{3}\sin^2\theta_W\left\{\left(2\frac{\tilde{\mu}^2}{\mu_2{}^2}+c_H^2+1\right)C_L^{(m)}C_L^{(n)} + s_H^2\frac{C_L^{(m)}(1)}{S_L^{(m)}(1)}S_L^{(m)}\frac{C_L^{(n)}(1)}{S_L^{(n)}(1)}S_L^{(n)}\right\}C_Z\Bigg], \\
g_{Zt_R^{(m)}t_R^{(n)}} &= \frac{g_w}{\cos\theta_W}\frac{\sqrt{2}\sqrt{L}}{\sqrt{r_Z r_{t^{(m)}} r_{t^{(n)}}}}\int_1^{z_L} dz\Bigg[\left(\frac{\tilde{\mu}^2}{\mu_2^2}+c_H^2\right)S_R^{(m)}S_R^{(n)}C_Z + \frac{s_H^2}{2}\left(S_R^{(m)}\frac{C_L^{(n)}(1)}{S_L^{(n)}(1)}C_R^{(n)} + \frac{C_L^{(m)}(1)}{S_L^{(m)}(1)}C_R^{(m)}S_R^{(m)}\right)\hat{S}_Z \\
&\quad -\frac{2}{3}\sin^2\theta_W\left\{\left(2\frac{\tilde{\mu}^2}{\mu_2{}^2}+c_H^2+1\right)S_R^{(m)}S_R^{(n)} + s_H^2\frac{C_L^{(m)}(1)}{S_L^{(m)}(1)}C_R^{(m)}\frac{C_L^{(n)}(1)}{S_L^{(n)}(1)}C_R^{(n)}\right\}C_Z\Bigg].
\end{aligned}
\tag{A21}
$$

Therefore the vector and axial vector coupling are written by

$$
g^V_{Zt^{(m)}t^{(n)}} = \frac{g_{Zt_L^{(m)}t_L^{(n)}} + g_{Zt_R^{(m)}t_R^{(n)}}}{2}, \qquad g^A_{Zt^{(m)}t^{(n)}} = \frac{g_{Zt_L^{(m)}t_L^{(n)}} - g_{Zt_R^{(m)}t_R^{(n)}}}{2}
\tag{A22}
$$

Numerical values of $g^V_{Zt^{(m)}t^{(n)}}$ are given in Table IX.

9. $Ht^{(m)}t^{(n)}$ coupling

The Higgs couplings of the top quark tower are contained in

$$
\begin{aligned}
\int_1^{z_L} dz\sqrt{G}\bar{\Psi}_1(-ig_A kzA_z)\gamma^5\Psi_1 &\supset -ig_w\sqrt{L}H\int_1^{z_L} dz u_H(z)\frac{i}{2}(\bar{B}\gamma^5 t' - \bar{t}\gamma^5 t' - \bar{t}'\gamma^5 B + \bar{t}'\gamma^5 t) \\
&= \frac{g_w k\sqrt{L}}{2}\sum_{m,n} H i t_L^{(m)\dagger} t_R^{(n)}\int_1^{\infty} z_L dz u_H(z)(f_{B_L}^{(m)}f_{t'_R}^{(n)} - f_{t_L}^{(m)}f_{t'_R}^{(n)} - f_{t'_L}^{(m)}f_{B_R}^{(n)} + f_{t'_L}^{(m)}f_{t_R}^{(n)}) + (L\leftrightarrow R) \\
&= i\sum_{m,n} H(g_{Ht_L^{(m)\dagger}t_R^{(n)}} t_L^{(m)\dagger}t_R^{(n)} - g_{Ht_R^{(m)\dagger}t_L^{(n)}} t_R^{(m)\dagger}t_L^{(n)}).
\end{aligned}
\tag{A23}
$$

One finds that

$$
\begin{aligned}
g_{Ht_R^{(m)\dagger}t_L^{(n)}} = g_{Ht_L^{(n)\dagger}t_R^{(m)}} &= -\frac{g_w k\sqrt{L}}{2}\int_1^{z_L} dz u_H(z)(f_{B_R}^{(m)}f_{t'_L}^{(n)} - f_{t_R}^{(m)}f_{t'_L}^{(n)} - f_{t'_R}^{(m)}f_{B_L}^{(n)} + f_{t'_R}^{(m)}f_{t_L}^{(n)}) \\
&= -\frac{g_w\sqrt{kL}}{2}\frac{\sqrt{2}}{\sqrt{(z_L^2-1)r_{t^{(m)}}r_{t^{(n)}}}}\int_1^{z_L} dz z\left\{-\sqrt{2}c_H S_R^{(m)}s_H\frac{C_L^{(n)}(1)}{S_L^{(n)}(1)}S_L^{(n)} + \sqrt{2}s_H\frac{C_L^{(m)}(1)}{S_L^{(m)}(1)}C_R^{(m)}c_H C_L^{(n)}\right\}.
\end{aligned}
\tag{A24}
$$

We denote

$$y_{t^{(m)}t^{(n)}} = \frac{g_{Ht_L^{(m)\dagger}t_R^{(n)}} + g_{Ht_R^{(m)\dagger}t_L^{(n)}}}{2}, \qquad \hat{y}_{t^{(m)}t^{(n)}} = \frac{-g_{Ht_L^{(m)\dagger}t_R^{(n)}} + g_{Ht_R^{(m)\dagger}t_L^{(n)}}}{2}. \tag{A25}$$

For $m = n$

$$y_{t^{(m)}t^{(m)}} = -\frac{g_w k\sqrt{kL}}{2}\frac{\sqrt{z_L^2 - 1}}{r_{t^{(n)}}} s_H c_H \frac{C_L^{(m)}(1)}{S_L^{(m)}(1)}, \qquad \hat{y}_{t^{(m)}t^{(m)}} = 0. \tag{A26}$$

Numerical values of $y_{t^{(m)}t^{(n)}}$ and $\hat{y}_{t^{(m)}t^{(n)}}$ are given in Tables X and XI, respectively.

10. $ZF^{(m)}F^{(n)}$ coupling

The Z couplings of the dark fermion tower are given by

$$\begin{aligned}
&\int_1^{z_L} dz\sqrt{G}\bar{\Psi}_F(-ig_A A_\mu - ig_B Q_{X_F} B_\mu) z\gamma^\mu \Psi_F \\
&= -iZ_\mu \frac{g_w}{\cos\theta_W}\frac{\sqrt{L}}{\sqrt{2}\sqrt{r_Z}}\int_1^{z_L} dz \sum_{m,n}[\{(1+\cos\theta_H)C(z) f_{lL}^{*(m)} f_{lL}^{(n)} + (1-\cos\theta_H)C(z) f_{rL}^{*(m)} f_{rL}^{(n)} \\
&\quad - \sin\theta_H \hat{S}(z)(i f_{lL}^{*(m)} f_{rL}^{(n)} - i f_{rL}^{*(m)} f_{lL}^{(n)})\}\bar{F}_L^{(m)}\gamma^\mu I_3 F_L^{(n)} - 2\sin^2\theta_W (f_{lL}^{*(m)} f_{lL}^{(n)} + f_{rL}^{*(m)} f_{rL}^{(n)}) \\
&\quad \times \bar{F}_L^{(m)}\gamma^\mu (I_3 + Q_{X_F}) F_L^{(n)} + (L \to R)] \\
&= -iZ_\mu \sum_{m,n}\{g_{ZF_L^{+(m)}F_L^{+(n)}}\bar{F}_L^{+(m)}\gamma^\mu F_L^{+(n)} + g_{ZF_R^{+(m)}F_R^{+(n)}}\bar{F}_R^{+(m)}\gamma^\mu F_R^{+(n)} + g_{ZF_L^{0(m)}F_L^{0(n)}}\bar{F}_L^{0(m)}\gamma^\mu F_L^{0(n)} \\
&\quad + g_{ZF_R^{0(m)}F_R^{0(n)}}\bar{F}_R^{0(m)}\gamma^\mu F_R^{0(n)}\},
\end{aligned} \tag{A27}$$

where $F_L^{(n)}$ is a abbreviation of the doublet $(F_L^{+(n)}, F_L^{0(n)})^T$ and I_3 is a isospin operator. For $Q_{X_F} = 1/2$ one finds that

TABLE X. $y_{t^{(m)}t^{(n)}}$ in the unit of $y_t \cos\theta_H$. Only the values larger than $O(10^{-3})$ are shown and written by three significant figures.

	0	1	2	3	4	5	6	7
0	1.00	0.517	0.188	0.049	−0.010	0.044	0.025	0.013
1	0.517	−0.225	1.04	−0.090	0.234	$O(10^{-4})$	$O(10^{-4})$	−0.010
2	0.188	1.04	0.226	0.674	0.088	0.034	$O(10^{-4})$	0.057
3	0.049	−0.090	0.694	−0.217	1.05	−0.087	0.244	$O(10^{-4})$
4	−0.010	0.234	0.088	1.05	0.217	0.670	0.087	0.028
5	0.044	$O(10^{-4})$	0.034	−0.087	0.670	−0.214	1.05	−0.087
6	0.025	$O(10^{-4})$	$O(10^{-4})$	0.244	0.087	1.05	0.215	0.667
7	0.013	−0.010	0.057	$O(10^{-4})$	0.028	−0.087	0.667	−0.213

TABLE XI. $\hat{y}_{t^{(m)}t^{(n)}}$ in the unit of $y_t \cos\theta_H$. Only the values larger than $O(10^{-3})$ are shown and written by three significant figures.

	0	1	2	3	4	5	6	7
0	0	−0.529	0.091	−0.043	−0.015	−0.049	0.015	−0.011
1	0.529	0	−0.040	0.014	−0.005	$O(10^{-4})$	$O(10^{-5})$	0.002
2	−0.091	0.040	0	−0.119	−0.012	−0.011	$O(10^{-4})$	−0.026
3	0.043	0.012	0.119	0	−0.024	0.008	−0.014	$O(10^{-4})$
4	0.015	$O(10^{-3})$	0.012	0.024	0	−0.060	−0.007	−0.005
5	0.049	$O(10^{-4})$	0.011	−0.008	0.062	0	−0.017	0.006
6	−0.015	$O(10^{-4})$	$O(10^{-4})$	0.014	0.007	0.017	0	−0.040
7	0.011	$O(10^{-3})$	0.026	$O(10^{-4})$	0.005	0.006	0.040	0

TABLE XII. $g^V_{ZF^{+(m)}F^{+(n)}} = \frac{1}{2}\{g_{ZF_L^{+(m)}F_L^{+(n)}} + g_{ZF_R^{+(m)}F_R^{+(n)}}\}$ in the unit of $g/\cos\theta_W$. Only the value larger than $O(10^{-3})$ are shown and written by three significant figures.

	1	2	3	4	5	6	7
1	−0.230	0.021	$O(10^{-5})$	−0.001	$O(10^{-6})$	$O(10^{-4})$	$O(10^{-6})$
2	0.021	0.267	0.009	$O(10^{-6})$	$O(10^{-5})$	$O(10^{-6})$	$O(10^{-5})$
3	$O(10^{-5})$	0.009	−0.230	0.024	$O(10^{-6})$	−0.001	$O(10^{-6})$
4	−0.001	$O(10^{-6})$	0.024	0.267	0.009	$O(10^{-6})$	$O(10^{-4})$
5	$O(10^{-6})$	$O(10^{-5})$	$O(10^{-6})$	0.009	−0.229	0.025	$O(10^{-6})$
6	$O(10^{-4})$	$O(10^{-6})$	−0.001	$O(10^{-6})$	0.025	0.267	0.009
7	$O(10^{-6})$	$O(10^{-5})$	$O(10^{-6})$	$O(10^{-4})$	$O(10^{-6})$	0.009	−0.229

$$
\begin{aligned}
g_{ZF_L^{+(m)}F_L^{+(n)}} &= \frac{g_w}{\cos\theta_W}\frac{\sqrt{L}}{2\sqrt{2}}\frac{1}{\sqrt{r_Z}}\int_1^{z_L} dz \frac{1}{\sqrt{r_{F^{(m)}}r_{F^{(n)}}}}\Big\{(1+\cos\theta_H - 4\sin^2\theta_W)C_Z(z)\sin^2\frac{\theta_H}{2}S_L^{(m)}(1)C_L^{(m)}(z)S_L^{(n)}(1)C_L^{(n)}(z) \\
&\quad + (1-\cos\theta_H - 4\sin^2\theta_W)C_Z(z)\cos^2\frac{\theta_H}{2}C_L^{(m)}(1)S_L^{(m)}(z)C_L^{(n)}(1)S_L^{(n)}(z) - \sin\theta_H\hat{S}(z)\sin\frac{\theta_H}{2}\cos\frac{\theta_H}{2} \\
&\quad \times (S_L^{(m)}(1)C_L^{(m)}(z)C_L^{(n)}(1)S_L^{(n)}(z) + C_L^{(m)}(1)S_L^{(m)}(z)S_L^{(n)}(1)C_L^{(n)}(z))\Big\}, \\
g_{ZF_L^{0(m)}F_L^{0(n)}} &= -\frac{g_w}{\cos\theta_W}\frac{\sqrt{L}}{2\sqrt{2}}\frac{1}{\sqrt{r_Z}}\int_1^{z_L} dz \frac{1}{\sqrt{r_{F^{(m)}}r_{F^{(n)}}}}\Big\{(1+\cos\theta_H)C_Z(z)\sin^2\frac{\theta_H}{2}S_L^{(m)}(1)C_L^{(m)}(z)S_L^{(n)}(1)C_L^{(n)}(z) \\
&\quad + (1-\cos\theta_H)C_Z(z)\cos^2\frac{\theta_H}{2}C_L^{(m)}(1)S_L^{(m)}(z)C_L^{(n)}(1)S_L^{(n)}(z) - \sin\theta_H\hat{S}(z)\sin\frac{\theta_H}{2}\cos\frac{\theta_H}{2} \\
&\quad \times (S_L^{(m)}(1)C_L^{(m)}(z)C_L^{(n)}(1)S_L^{(n)}(z) + C_L^{(m)}(1)S_L^{(m)}(z)S_L^{(n)}(1)C_L^{(n)}(z))\Big\}.
\end{aligned}
\tag{A28}
$$

$g_{ZF_R^{+(m)}F_R^{+(n)}}$ and $g_{ZF_R^{0(m)}F_R^{0(n)}}$ are obtained from the formulas for $g_{ZF_L^{+(m)}F_L^{+(n)}}$ and $g_{ZF_L^{0(m)}F_L^{0(n)}}$ by replacing $C_L(z)$ to $S_R(z)$ and $S_L(z)$ to $C_R(z)$, respectively. Numerical values of $g^V_{ZF^{+(m)}F^{+(n)}}$ and $g^V_{ZF^{0(m)}F^{0(n)}}$ are given in Tables XII and XIII, respectively.

11. $HF^{(m)}F^{(n)}$ coupling

The Higgs couplings of the dark fermion tower are given by

$$
\begin{aligned}
&\int_1^{z_L} dz\sqrt{G}\bar{\Psi}_F(-ig_A A_z)\gamma^5\Psi_F \supset -ig_A k\int_1^{z_L} dz\frac{1}{2\sqrt{2}}\sum_{m,n} Hu_H(f_{lL}^{*(m)}\bar{F}_L^{(m)}\gamma^5 f_{rR}^{(n)}F_R^{(n)} + f_{rL}^{*(m)}\bar{F}_L^{(m)}\gamma^5 f_{lR}^{(n)}F_R^{(n)}) + (L\longleftrightarrow R) \\
&= -ig_A k\frac{1}{\sqrt{r_{F^{(m)}}r_{F^{(n)}}}}\int_1^{z_L} dz\frac{1}{2\sqrt{2}}\sin\frac{\theta_H}{2}\cos\frac{\theta_H}{2}\sum_{m,n} Hu_H\{(-S_L^{(m)}(1)C_L^{(m)}(z)C_L^{(n)}(1)C_R^{(n)}(z) \\
&\quad + C_L^{(m)}(1)S_L^{(m)}(z)S_L^{(n)}(1)S_R^{(n)}(z))F_L^{(m)\dagger}F_R^{(n)} + (-S_L^{(m)}(1)S_R^{(m)}(z)C_L^{(n)}(1)S_L^{(n)}(z) + C_L^{(m)}(1)C_R^{(m)}(z)S_L^{(n)}(1)C_L^{(n)}(z))F_R^{(m)\dagger}F_L^{(n)}\} \\
&= iH\sum_{m,n}(g_{HF_L^{(m)\dagger}F_R^{(n)}}F_L^{(m)\dagger}F_R^{(n)} - g_{HF_R^{(m)\dagger}F_L^{(n)}}F_R^{(m)\dagger}F_L^{(n)}),
\end{aligned}
\tag{A29}
$$

TABLE XIII. $g^V_{ZF^{0(m)}F^{0(n)}} = \frac{1}{2}\{g_{ZF_L^{0(m)}F_L^{0(n)}} + g_{ZF_R^{0(m)}F_R^{0(n)}}\}$ in the unit of $g/\cos\theta_W$. Only the values larger than $O(10^{-3})$ are shown and written by three significant figures.

	1	2	3	4	5	6	7
1	−0.002	−0.021	$O(10^{-5})$	0.001	$O(10^{-6})$	$O(10^{-4})$	$O(10^{-6})$
2	−0.021	−0.498	−0.009	$O(10^{-5})$	$O(10^{-5})$	$O(10^{-6})$	$O(10^{-5})$
3	$O(10^{-5})$	−0.009	−0.002	−0.024	$O(10^{-5})$	0.001	$O(10^{-6})$
4	0.001	$O(10^{-5})$	−0.024	−0.498	−0.009	$O(10^{-5})$	$O(10^{-4})$
5	$O(10^{-6})$	$O(10^{-5})$	$O(10^{-5})$	−0.009	−0.002	−0.025	$O(10^{-5})$
6	$O(10^{-4})$	$O(10^{-6})$	0.001	$O(10^{-5})$	−0.025	−0.498	−0.009
7	$O(10^{-6})$	$O(10^{-5})$	$O(10^{-6})$	$O(10^{-4})$	$O(10^{-6})$	−0.009	−0.002

TABLE XIV. $y_{F^{(m)}F^{(n)}}$ in the unit of $y_t \sin\frac{\theta_H}{2}$. The values are written by three significant figures.

	1	2	3	4	5	6	7
1	−0.944	−12.6	0.328	2.85	−0.006	−0.485	0.038
2	−12.6	0.856	8.73	−0.357	−0.174	0.003	0.394
3	0.328	8.73	−0.924	−12.7	0.369	2.65	−0.002
4	2.85	−0.357	−12.7	0.920	9.05	−0.376	−0.277
5	−0.006	−0.174	0.369	9.05	−0.942	−12.7	0.380
6	−0.485	0.003	2.65	−0.376	−12.7	0.941	9.13
7	0.038	0.394	−0.002	−0.277	0.380	9.13	−0.953

TABLE XV. $\hat{y}_{F^{(m)}F^{(n)}}$ in the unit of $y_t \sin\frac{\theta_H}{2}$. Only the values larger than $O(10^{-3})$ are shown and written by three significant figures.

	1	2	3	4	5	6	7
1	0	−6.54	0.117	1.35	−0.017	−0.654	0.013
2	6.54	0	1.62	−0.094	0.168	0.005	0.106
3	−0.117	−1.62	0	−1.26	0.066	0.627	−0.002
4	−1.35	0.094	1.26	0	0.934	−0.057	0.027
5	0.017	−0.168	−0.066	−0.934	0	−0.668	0.044
6	0.654	0.005	−0.627	0.057	0.668	0	0.648
7	−0.013	−0.106	0.002	−0.027	−0.044	−0.648	0

where

$$g_{HF_L^{(m)\dagger}F_R^{(n)}} = g_w \frac{\sqrt{kL}}{\sqrt{r_{F^{(m)}} r_{F^{(n)}}}} \sin\frac{\theta_H}{2}\cos\frac{\theta_H}{2}\int_1^{z_L} dz \frac{1}{2}\frac{1}{\sqrt{z_L^2-1}} z(S_L^{(m)}(1)C_L^{(m)}(z)C_L^{(n)}(1)C_R^{(n)}(z) - C_L^{(m)}(1)S_L^{(m)}(z)S_L^{(n)}(1)S_R^{(n)}(z)),$$

$$g_{HF_R^{(m)\dagger}F_L^{(n)}} = g_w \frac{\sqrt{kL}}{\sqrt{r_{F^{(m)}} r_{F^{(n)}}}} \sin\frac{\theta_H}{2}\cos\frac{\theta_H}{2}\int_1^{z_L} dz \frac{1}{2}\frac{1}{\sqrt{z_L^2-1}} z(-S_L^{(m)}(1)S_R^{(m)}(z)C_L^{(n)}(1)S_L^{(n)}(z) + C_L^{(m)}(1)C_R^{(m)}(z)S_L^{(n)}(1)C_L^{(n)}(z)). \tag{A30}$$

One can show that $g^*_{HF_R^{(m)\dagger}F_L^{(n)}} = g_{HF_R^{(m)\dagger}F_L^{(n)}} = g_{HF_L^{(n)\dagger}F_R^{(m)}}$. We define

$$y_{F^{(m)}F^{(n)}} = \frac{g_{HF_L^{(m)\dagger}F_R^{(n)}} + g_{HF_R^{(m)\dagger}F_L^{(n)}}}{2}, \qquad \hat{y}_{F^{(m)}F^{(n)}} = \frac{-g_{HF_L^{(m)\dagger}F_R^{(n)}} + g_{HF_R^{(m)\dagger}F_L^{(n)}}}{2}. \tag{A31}$$

In particular

$$y_{F^{(n)}F^{(n)}} = g_w \frac{\sqrt{kL}}{\sqrt{r_{F^{(m)}} r_{F^{(n)}}}} \sin\frac{\theta_H}{2}\cos\frac{\theta_H}{2}\frac{1}{4}\sqrt{z_L^2-1} S_L^{(n)}(1)C_L^{(n)}(1). \tag{A32}$$

Numerical values of $y_{F^{(m)}F^{(n)}}$ and $\hat{y}_{F^{(m)}F^{(n)}}$ are given in Tables XIV and XV, respectively.

[1] G. Aad *et al.* (ATLAS Collaboration), Observation of a new particle in the search for the Standard Model Higgs boson with the ATLAS detector at the LHC, Phys. Lett. B **716**, 1 (2012).

[2] S. Chatrchyan *et al.* (CMS Collaboration), Observation of a new boson at a mass of 125 GeV with the CMS experiment at the LHC, Phys. Lett. B **716**, 30 (2012).

[3] G. Aad *et al.* (ATLAS Collaboration), Measurements of Higgs boson production and couplings in diboson final states with the ATLAS detector at the LHC, Phys. Lett. B **726**, 88 (2013).

[4] CMS Collaboration, Report No. CMS-PAS-HIG-13-005.

[5] L. Bergstrom and G. Hulth, Induced Higgs couplings to neutral bosons in e^+e^- collisions, Nucl. Phys. **B259**, 137 (1985).

[6] J. F. Gunion, H. E. Haber, G. L. Kane, and S. Dawson, The Higgs hunter's guide, Front. Phys. **80**, 1 (2000).
[7] F. J. Petriello, Kaluza-Klein effects on Higgs physics in universal extra dimensions, J. High Energy Phys. 05 (2002) 003.
[8] P. S. Bhupal Dev, D. K. Ghosh, N. Okada, and I. Saha, 125 GeV Higgs boson and the type-II seesaw model, J. High Energy Phys. 03 (2013) 150; 05 (2013) 049.
[9] Y. Hosotani, Dynamical mass generation by compact extra dimensions, Phys. Lett. **126B**, 309 (1983).
[10] Y. Hosotani, Dynamics of nonintegrable phases and gauge symmetry breaking, Ann. Phys. (N.Y.) **190**, 233 (1989).
[11] A. Davies and A. McLachlan, Gauge group breaking by Wilson loops, Phys. Lett. B **200**, 305 (1988).
[12] A. Davies and A. McLachlan, Congruency class effects in the Hosotani model, Nucl. Phys. **B317**, 237 (1989).
[13] H. Hatanaka, T. Inami, and C. S. Lim, The gauge hierarchy problem and higher dimensional gauge theories, Mod. Phys. Lett. A **13**, 2601 (1998).
[14] G. Burdman and Y. Nomura, Unification of Higgs and gauge fields in five-dimensions, Nucl. Phys. **B656**, 3 (2003).
[15] C. Csaki, C. Grojean, and H. Murayama, Standard model Higgs from higher dimensional gauge fields, Phys. Rev. D **67**, 085012 (2003).
[16] Y. Matsumoto and Y. Sakamura, 6D gauge-Higgs unification on T^2/Z_N with custodial symmetry, J. High Energy Phys. 08 (2014) 175.
[17] C. S. Lim, N. Maru, and T. Miura, Is the 126 GeV Higgs boson mass calculable in gauge-Higgs unification?, Prog. Theor. Exp. Phys. **2015**, 043B02 (2015).
[18] K. Agashe, R. Contino, and A. Pomarol, The Minimal composite Higgs model, Nucl. Phys. **B719**, 165 (2005).
[19] A. D. Medina, N. R. Shah, and C. E. M. Wagner, Gauge-Higgs unification and radiative electroweak symmetry breaking in warped extra dimensions, Phys. Rev. D **76**, 095010 (2007).
[20] Y. Hosotani and Y. Sakamura, Anomalous Higgs couplings in the $SO(5) \times U(1)_{B-L}$ gauge-Higgs unification in warped spacetime, Prog. Theor. Phys. **118**, 935 (2007).
[21] Y. Hosotani, K. Oda, T. Ohnuma, and Y. Sakamura, Dynamical electroweak symmetry breaking in $SO(5) \times U(1)$ gauge-Higgs unification with top and bottom quarks, Phys. Rev. D **78**, 096002 (2008).
[22] Y. Hosotani, S. Noda, and N. Uekusa, The electroweak gauge couplings in $SO(5) \times U(1)$ gauge-Higgs unification, Prog. Theor. Phys. **123**, 757 (2010).
[23] S. Funatsu, H. Hatanaka, Y. Hosotani, Y. Orikasa, and T. Shimotani, Novel universality and Higgs decay $H \to \gamma\gamma, gg$ in the $SO(5) \times U(1)$ gauge-Higgs unification, Phys. Lett. B **722**, 94 (2013).
[24] S. Funatsu, H. Hatanaka, Y. Hosotani, Y. Orikasa, and T. Shimotani, LHC signals of the $SO(5) \times U(1)$ gauge-Higgs unification, Phys. Rev. D **89**, 095019 (2014).
[25] S. Funatsu, H. Hatanaka, Y. Hosotani, Y. Orikasa, and T. Shimotani, Dark matter in the $SO(5) \times U(1)$ gauge-Higgs unification, Prog. Theor. Exp. Phys. **2014**, 113B01 (2014).
[26] N. Maru and N. Okada, $H \to Z\gamma$ in gauge-Higgs unification, Phys. Rev. D **88**, 037701 (2013).
[27] L. Randall and R. Sundrum, A Large Mass Hierarchy from a Small Extra Dimension, Phys. Rev. Lett. **83**, 3370 (1999).
[28] G. Passarino and M. Veltman, One loop corrections for e^+e^- annihilation into $\mu^+\mu^-$ in the Weinberg model, Nucl. Phys. **B160**, 151 (1979).
[29] A. Denner, Techniques for calculation of electroweak radiative corrections at the one loop level and results for W physics at LEP-200, Fortschr. Phys. **41**, 307 (1993).
[30] Y. Hosotani, Dynamical gauge symmetry breaking by Wilson Lines in the electroweak theory, arXiv:hep-ph/0504272.
[31] D. M. Asner *et al.*, ILC Higgs white paper, arXiv:1310.0763.
[32] Y. Hosotani and N. Yamatsu, Gauge-Higgs grand unification, Prog. Theor. Exp. Phys. **2015**, 111B01 (2015).
[33] K. Yamamoto, The formulation of gauge-Higgs unification with dynamical boundary conditions, Nucl. Phys. **B883**, 45 (2014).
[34] G. Cossu, H. Hatanaka, Y. Hosotani, and J.-I. Noaki, Polyakov loops and the Hosotani mechanism on the lattice, Phys. Rev. D **89**, 094509 (2014).

PHYSICAL REVIEW D **89,** 095019 (2014)

LHC signals of the SO(5) × U(1) gauge-Higgs unification

Shuichiro Funatsu,[1] Hisaki Hatanaka,[2] Yutaka Hosotani,[1] Yuta Orikasa,[1] and Takuya Shimotani[1]

[1]*Department of Physics, Osaka University, Toyonaka, Osaka 560-0043, Japan*

[2]*School of Physics, KIAS, Seoul 130-722, Republic of Korea*

(Received 14 April 2014; published 21 May 2014)

Signatures of the SO(5) × U(1) gauge-Higgs unification at LHC and future colliders are explored. The Kaluza-Klein (KK) mass spectra of γ, Z, Z_R and the Higgs self-couplings obey universality relations with the Aharonov-Bohm phase θ_H in the fifth dimension. The current data at low energies and at LHC indicate $\theta_H < 0.2$. Couplings of quarks and leptons to KK gauge bosons are determined. Three neutral gauge bosons, the first KK modes $Z_R^{(1)}$, $Z^{(1)}$, and $\gamma^{(1)}$, appear as Z' bosons in dilepton events at LHC. For $\theta_H = 0.114$, the mass and decay width of $Z_R^{(1)}$, $Z^{(1)}$, and $\gamma^{(1)}$ are (5.73, 482), (6.07, 342), and (6.08 TeV, 886 GeV), respectively. For $\theta_H = 0.073$ their masses are $8.00 \sim 8.61$ TeV. An excess of events in the dilepton invariant mass should be observed in the Z' search at the upgraded LHC at 14 TeV.

DOI: 10.1103/PhysRevD.89.095019 PACS numbers: 12.60.-i, 11.10.Kk, 11.15.-q, 14.80.Rt

I. INTRODUCTION

The discovery of the Higgs boson of a mass around 126 GeV [1,2] supports the scenario of unification of forces and symmetry breaking envisioned in the standard model (SM) of electroweak interactions. Experimental data so far are consistent with what the SM describes, but more data are necessary to pin down whether or not the discovered boson is definitively the Higgs boson in the SM. Other scenarios such as supersymmetric models [3,4], little Higgs models [5–8], composite Higgs models [9–16], warped extra-dimension models [17–19], and UED models [20–26] have been proposed in anticipation of physics beyond the SM. It is urgent to derive and predict new phenomena which can be observed and checked in the experiments at the upgraded 14 TeV LHC.

The gauge-Higgs unification is formulated in higher-dimensional gauge theory [27–32]. The four-dimensional Higgs boson appears as a part of the extra-dimensional component of gauge fields, being unified with four-dimensional gauge fields such as W, Z, and γ. Dynamics of the Higgs boson are governed by the gauge principle. Most viable is the $SO(5) \times U(1)$ gauge-Higgs unification in the Randall-Sundrum warped space [9,33–37]. At low energies it yields almost the same physics as the SM, being consistent with LHC data and others. Higgs couplings to gauge bosons, quarks, and leptons at the tree level are suppressed by a common factor $\cos\theta_H$, where θ_H is the Aharonov-Bohm phase in the extra dimension [38]. All of the precision measurements [9,39], the tree-unitary constraint [40], and the Z' search [41–43] indicate $\theta_H < 0.2$. Branching fractions of various decay modes of the Higgs boson remain nearly the same as in the SM, and the signal strengths of the Higgs decay modes relative to the SM are $\sim \cos^2\theta_H$ [37]. We note that though the gauge-Higgs unification model has similarity to the composite Higgs models, it is more restrictive and has more predictive power.

To distinguish the gauge-Higgs unification from the SM we examine the prediction of new particles. It has been pointed out that the first Kaluza-Klein (KK) modes of Z and γ, denoted as $Z^{(1)}$ and $\gamma^{(1)}$, must appear around 6 TeV for $\theta_H \sim 0.1$. In this paper we give detailed analysis of production of $Z_R^{(1)}$, $Z^{(1)}$ and $\gamma^{(1)}$ at the upgraded LHC. Here Z_R is the gauge boson associated with $SU(2)_R$, which does not have a zero mode. It will be shown that $Z_R^{(1)}$, $Z^{(1)}$ and $\gamma^{(1)}$ have large widths and can be seen as e^+e^- or $\mu^+\mu^-$ signals. Once their masses are determined, the value of θ_H is fixed from the universality relations, which leads to further prediction of the Higgs self-couplings, etc. Many other signals of gauge-Higgs unification have been discussed in the literature [44–67].

In Sec. II the action of the model is given. In addition to quark-lepton multiplets in the vector representation of $SO(5)$, fermion multiplets in the spinor representation of $SO(5)$ are introduced to realize the observed unstable Higgs boson. In Sec. III the effective potential $V_{\rm eff}(\theta_H)$ is evaluated and relevant parameters of the model are determined. It is shown that there appear universality relations among θ_H, the KK mass scale $m_{\rm KK}$, $m_{Z_R^{(1)}}$, $m_{Z^{(1)}}$, $m_{\gamma^{(1)}}$, and Higgs cubic and quartic couplings. In Sec. IV dilepton ($e^+e^-, \mu^+\mu^-$) signals at LHC in the so-called Z' search are examined. In the SO(5) × U(1) gauge-Higgs unification $Z_R^{(1)}$, $Z^{(1)}$ and $\gamma^{(1)}$ appear as Z' bosons. Their masses are around 6 TeV (8 TeV) for $\theta_H = 0.114$ (0.073), and they have large decay widths. We show that they must be found in the upgraded LHC at 14 TeV. Section V is devoted to conclusions. In the Appendixes we summarize KK mass spectra, wave functions and gauge couplings of gauge fields, quark-leptons, and $SO(5)$-spinor fermions.

II. MODEL

The model is defined in the Randall-Sundrum warped spacetime [17] with the metric

 © 2014 American Physical Society

$$ds^2 = G_{MN}dx^M dx^N = e^{-2\sigma(y)}\eta_{\mu\nu}dx^\mu dx^\nu + dy^2, \quad (2.1)$$

where $\eta_{\mu\nu} = \mathrm{diag}(-1,1,1,1)$, $\sigma(-y) = \sigma(y)$, $\sigma(y+2L) = \sigma(y)$ and $\sigma(y) = k|y|$ for $|y| \le L$. The Planck brane and TeV brane are located at $y = 0$ and $y = L$, respectively. In the bulk region, $0 < y < L$, the cosmological constant is given by $\Lambda = -6k^2$. The warp factor $z_L = e^{kL}$ is large; $z_L \gg 1$. The KK mass scale is given by $m_{\mathrm{KK}} = \pi k/(z_L - 1) \sim \pi k z_L^{-1}$. In the fundamental region $0 \le y \le L$ the metric can be written, in terms of the conformal coordinate $z = e^{ky}$, as

$$ds^2 = \frac{1}{z^2}\left(\eta_{\mu\nu}dx^\mu dx^\nu + \frac{dz^2}{k^2}\right). \quad (2.2)$$

The gauge symmetry in the bulk region is given by $SO(5)\times U(1)_X \times SU(3)_C$ with the corresponding gauge fields A_M, B_M and G_M and gauge couplings g_A, g_B and g_C. Quark-lepton multiplets Ψ_a are introduced in the vector representation **5** of $SO(5)$, whereas additional fermions Ψ_{F_i} are introduced in the spinor representation **4** of $SO(5)$ [34,36,37]. The $SO(5)$ gauge symmetry is partially broken to $SO(4) \simeq SU(2)_L \times SU(2)_R$ by orbifold boundary conditions. On the Planck brane at $y = 0$ ($z = 1$) there live right-handed brane fermions $\hat{\chi}_{\alpha R}$ and brane scalar $\hat{\Phi}$, which are $(\mathbf{2},\mathbf{1})$ and $(\mathbf{1},\mathbf{2})$ representation of $SU(2)_L \times SU(2)_R$, respectively. The brane interactions are manifestly gauge-invariant under $SO(4)\times U(1)_X \times SU(3)_C$. The brane scalar $\hat{\Phi}$ spontaneously breaks $SU(2)_R \times U(1)_X$ to $U(1)_Y$ by $\langle\hat{\Phi}\rangle \gg m_{\mathrm{KK}}$, which, in turn, induces mixing among Ψ_a and $\hat{\chi}_{\alpha R}$ and makes all exotic fermions acquire masses of $O(m_{\mathrm{KK}})$. The resultant theory at low energies (< 1 TeV) has the SM gauge symmetry $SU(2)_L \times U(1)_Y \times SU(3)_C$ with the SM matter content. All $SO(4)\times U(1)_X$ anomalies are cancelled. Finally the $SU(2)_L \times U(1)_Y$ gauge symmetry is dynamically broken to $U(1)_{\mathrm{EM}}$ by the Hosotani mechanism.

The bulk part of the action is given by

$$\begin{aligned} S_{\mathrm{bulk}} = \int d^5x\sqrt{-G}\Bigg[&-\mathrm{tr}\left(\frac{1}{4}F^{(A)MN}F^{(A)}_{MN} + \frac{1}{2\xi_A}(f^{(A)}_{\mathrm{gf}})^2 + \mathcal{L}^{(A)}_{\mathrm{gh}}\right) \\ &- \left(\frac{1}{4}F^{(B)MN}F^{(B)}_{MN} + \frac{1}{2\xi_B}(f^{(B)}_{\mathrm{gf}})^2 + \mathcal{L}^{(B)}_{\mathrm{gh}}\right) \\ &- \mathrm{tr}\left(\frac{1}{2}F^{(G)MN}F^{(G)}_{MN} + \frac{1}{\xi_C}(f^{(G)}_{\mathrm{gf}})^2 + \mathcal{L}^{(G)}_{\mathrm{gh}}\right) \\ &+ \sum_a \bar{\Psi}_a\mathcal{D}(c_a)\Psi_a + \sum_{i=1}^{n_F}\bar{\Psi}_{F_i}\mathcal{D}(c_{F_i})\Psi_{F_i}\Bigg], \\ \mathcal{D}(c) = \Gamma^A e_A{}^M\Bigg(&\partial_M + \frac{1}{8}\omega_{MBC}[\Gamma^B,\Gamma^C] \\ &- ig_A A_M - ig_B Q_X B_M - ig_C Q^{\mathrm{color}} G_M)\Bigg) - c\sigma'(y). \end{aligned} \quad (2.3)$$

The gauge fixing and ghost terms are denoted as functionals with subscripts gf and gh, respectively. $F^{(A)}_{MN} = \partial_M A_N - \partial_N A_M - ig_A[A_M, A_N]$, $F^{(B)}_{MN} = \partial_M B_N - \partial_N B_M$, and $F^{(G)}_{MN} = \partial_M G_N - \partial_N G_M - ig_C[G_M, G_N]$. The gauge fixing function is taken as $f^{(A)}_{\mathrm{gf}} = z^2\{\eta^{\mu\nu}\mathcal{D}_\mu A_\nu + \xi_A k^2 z\mathcal{D}^c_z(A^q_z/z)\}$ with a background field A^c_z ($A_z = A^c_z + A^q_z$), $B^c_z = G^c_z = 0$. $Q^{\mathrm{color}} = 1$ for quark-multiplets and $Q^{\mathrm{color}} = 0$ otherwise. The $SO(5)$ gauge fields A_M are decomposed as

$$A_M = \sum_{a_L=1}^{3} A^{a_L}_M T^{a_L} + \sum_{a_R=1}^{3} A^{a_R}_M T^{a_R} + \sum_{\hat{a}=1}^{4} A^{\hat{a}}_M T^{\hat{a}}, \quad (2.4)$$

where $T^{a_L,a_R}(a_L, a_R = 1,2,3)$ and $T^{\hat{a}}(\hat{a} = 1,2,3,4)$ are the generators of $SO(4) \simeq SU(2)_L \times SU(2)_R$ and $SO(5)/SO(4)$, respectively. The electric charge is given by

$$Q_{\mathrm{EM}} = T^{3_L} + T^{3_R} + Q_X. \quad (2.5)$$

In the fermion part $\bar{\Psi} = i\Psi^\dagger\Gamma^0$ and Γ^M matrices are given by

$$\Gamma^\mu = \begin{pmatrix} & \sigma^\mu \\ \bar{\sigma}^\mu & \end{pmatrix}, \qquad \Gamma^5 = \begin{pmatrix} 1 & \\ & -1 \end{pmatrix},$$
$$\sigma^\mu = (1,\vec{\sigma}), \qquad \bar{\sigma}^\mu = (-1,\vec{\sigma}). \quad (2.6)$$

The $c\sigma'(y)$ term in the action (2.3) gives a bulk kink mass. The dimensionless parameter c plays an important role in controlling profiles of fermion wave functions.

The orbifold boundary conditions at $y_0 = 0$ and $y_1 = L$ are given by

$$\begin{aligned} \begin{pmatrix} A_\mu \\ A_y \end{pmatrix}(x, y_j - y) &= P_{\mathrm{vec}}\begin{pmatrix} A_\mu \\ -A_y \end{pmatrix}(x, y_j + y)P^{-1}_{\mathrm{vec}}, \\ \begin{pmatrix} B_\mu \\ B_y \end{pmatrix}(x, y_j - y) &= \begin{pmatrix} B_\mu \\ -B_y \end{pmatrix}(x, y_j + y), \\ \begin{pmatrix} G_\mu \\ G_y \end{pmatrix}(x, y_j - y) &= \begin{pmatrix} G_\mu \\ -G_y \end{pmatrix}(x, y_j + y), \\ \Psi_a(x, y_j - y) &= P_{\mathrm{vec}}\Gamma^5\Psi_a(x, y_j + y), \\ \Psi_{F_i}(x, y_j - y) &= (-1)^j P_{\mathrm{sp}}\Gamma^5\Psi_{F_i}(x, y_j + y), \\ P_{\mathrm{vec}} &= \mathrm{diag}(-1,-1,-1,-1,+1), \\ P_{\mathrm{sp}} &= \mathrm{diag}(+1,+1,-1,-1). \end{aligned} \quad (2.7)$$

The $SO(5)$ symmetry is reduced to $SO(4) \simeq SU(2)_L \times SU(2)_R$ by the orbifold boundary conditions. At this stage the four-dimensional components of the five-dimensional gauge fields have zero modes in $SO(4)\times U(1)_X \times SU(3)_C$, whereas the extra-dimensional components have zero modes in $SO(5)/SO(4)$, $A^{\hat{a}}_y$ or $A^{\hat{a}}_z$ ($a = 1,\ldots,4$). The latter contains the four-dimensional Higgs field, which is a

doublet both in $SU(2)_L$ and in $SU(2)_R$. Without loss of generality one can set $\langle A_y^{\hat{a}}\rangle \propto \delta^{a4}$ when the EW symmetry is spontaneously broken by the Hosotani mechanism. The zero modes of $A_y^{\hat{a}}$ ($a = 1, 2, 3$) are absorbed by W and Z bosons. The four-dimensional neutral Higgs field $H(x)$ is a fluctuation mode of the Wilson line phase θ_H,

$$A_y^{\hat{4}}(x,y) = \{\theta_H f_H + H(x)\}\tilde{u}_H(y) + \cdots,$$
$$\exp\left\{\frac{i}{2}\theta_H \cdot 2\sqrt{2}T^{\hat{4}}\right\} = \exp\left\{ig_A\int_0^L dy\langle A_y\rangle\right\},$$
$$f_H = \frac{2}{g_A}\sqrt{\frac{k}{z_L^2-1}} = \frac{2}{g_w}\sqrt{\frac{k}{L(z_L^2-1)}}. \tag{2.8}$$

Here the wave function of the four-dimensional Higgs boson is given by $\tilde{u}_H(y) = [2k/(z_L^2-1)]^{1/2}e^{2ky}$ for $0 \le y \le L$ and $\tilde{u}_H(-y) = \tilde{u}_H(y) = \tilde{u}_H(y+2L)$. $g_w = g_A/\sqrt{L}$ is the dimensionless four-dimensional $SU(2)_L$ coupling.

Quark-lepton multiplets Ψ_a are in the vector representation of $SO(5)$. They are decomposed into $SO(4)$ vectors and singlets. One $SO(4)$ vector multiplet contains two $SU(2)_L$ doublets. In each generation

$$\Psi_1 = \left[\begin{pmatrix} T \\ B \end{pmatrix}, \begin{pmatrix} t \\ b \end{pmatrix}, t'\right]_{2/3},$$
$$\Psi_2 = \left[\begin{pmatrix} U \\ D \end{pmatrix}, \begin{pmatrix} X \\ Y \end{pmatrix}, b'\right]_{-1/3},$$
$$\Psi_3 = \left[\begin{pmatrix} \nu_\tau \\ \tau \end{pmatrix}, \begin{pmatrix} L_{1X} \\ L_{1Y} \end{pmatrix}, \tau'\right]_{-1},$$
$$\Psi_4 = \left[\begin{pmatrix} L_{2X} \\ L_{2Y} \end{pmatrix}, \begin{pmatrix} L_{3X} \\ L_{3Y} \end{pmatrix}, \nu'_\tau\right]_{0}, \tag{2.9}$$

where the subscripts denote Q_X. We choose the bulk mass parameters such that $c_1 = c_2$ and $c_3 = c_4$ in each generation. With the boundary condition in (2.7), zero modes appear in

$$\left[Q_{1L} = \begin{pmatrix} T_L \\ B_L \end{pmatrix}, q_L = \begin{pmatrix} t_L \\ b_L \end{pmatrix}, t'_R\right],$$
$$\left[Q_{2L} = \begin{pmatrix} U_L \\ D_L \end{pmatrix}, Q_{3L} = \begin{pmatrix} X_L \\ Y_L \end{pmatrix}, b'_R\right],$$
$$\left[\ell_L = \begin{pmatrix} \nu_{\tau L} \\ \tau_L \end{pmatrix}, L_{1L} = \begin{pmatrix} L_{1XL} \\ L_{1YL} \end{pmatrix}, \tau'_R\right],$$
$$\left[L_{2L} = \begin{pmatrix} L_{2XL} \\ L_{2YL} \end{pmatrix}, L_{3L} = \begin{pmatrix} L_{3XL} \\ L_{3YL} \end{pmatrix}, \nu'_{\tau R}\right]. \tag{2.10}$$

On the Planck brane there exist the brane scalar $\hat{\Phi}$ in $(\mathbf{1},\mathbf{2})$ representation of $SU(2)_L \times SU(2)_R$ with $Q_X = \frac{1}{2}$ and the brane fermions in $(\mathbf{2},\mathbf{1})$ representation of $SU(2)_L \times SU(2)_R$.

$$\hat{\chi}_{1R}^q = \begin{pmatrix} \hat{T}_R \\ \hat{B}_R \end{pmatrix}_{7/6}, \qquad \hat{\chi}_{2R}^q = \begin{pmatrix} \hat{U}_R \\ \hat{D}_R \end{pmatrix}_{1/6},$$
$$\hat{\chi}_{3R}^q = \begin{pmatrix} \hat{X}_R \\ \hat{Y}_R \end{pmatrix}_{-5/6}, \qquad \hat{\chi}_{1R}^l = \begin{pmatrix} \hat{L}_{1XR} \\ \hat{L}_{1YR} \end{pmatrix}_{-3/2},$$
$$\hat{\chi}_{2R}^l = \begin{pmatrix} \hat{L}_{2XR} \\ \hat{L}_{2YR} \end{pmatrix}_{1/2}, \qquad \hat{\chi}_{3R}^l = \begin{pmatrix} \hat{L}_{3XR} \\ \hat{L}_{3YR} \end{pmatrix}_{-1/2}, \tag{2.11}$$

where the subscripts denote Q_X. $\hat{\chi}_{\alpha R}^q$'s are $SU(3)_C$ triplets. With these brane fermions all four-dimensional anomalies in $SO(4) \times U(1)_X$ are cancelled [36].

The brane part of the action is given by

$$\begin{aligned} S_{\text{brane}} = \int d^5x\sqrt{-G}\delta(y)\Big\{ & -(D_\mu\hat{\Phi})^\dagger D^\mu\hat{\Phi} - \lambda_{\hat{\Phi}}(\hat{\Phi}^\dagger\hat{\Phi} - w^2)^2 \\ & + \sum_{\alpha=1}^{3}(\hat{\chi}_{\alpha R}^{q\dagger} i\bar{\sigma}^\mu D_\mu \hat{\chi}_{\alpha R}^q + \hat{\chi}_{\alpha R}^{l\dagger} i\bar{\sigma}^\mu D_\mu \hat{\chi}_{\alpha R}^l) \\ & - i[\kappa_1^q \hat{\chi}_{1R}^{q\dagger}\check{\Psi}_{1L}\tilde{\hat{\Phi}} + \tilde{\kappa}^q\hat{\chi}_{2R}^{q\dagger}\check{\Psi}_{1L}\hat{\Phi} + \kappa_2^q\hat{\chi}_{2R}^{q\dagger}\check{\Psi}_{2L}\tilde{\hat{\Phi}} \\ & + \kappa_3^q\hat{\chi}_{3R}^{q\dagger}\check{\Psi}_{2L}\hat{\Phi} - (\text{H.c.})] \\ & - i[\tilde{\kappa}^l\hat{\chi}_{3R}^{l\dagger}\check{\Psi}_{3L}\tilde{\hat{\Phi}} + \kappa_1^l\hat{\chi}_{1R}^{l\dagger}\check{\Psi}_{3L}\hat{\Phi} + \kappa_2^l\hat{\chi}_{2R}^{l\dagger}\check{\Psi}_{4L}\tilde{\hat{\Phi}} \\ & + \kappa_3^l\hat{\chi}_{3R}^{l\dagger}\check{\Psi}_{4L}\hat{\Phi} - (\text{H.c.})]\Big\}, \end{aligned}$$
$$D_\mu\hat{\Phi} = \left(\partial_\mu - ig_A\sum_{a_R=1}^{3}A_\mu^{a_R}T^{a_R} - iQ_X g_B B_\mu\right)\hat{\Phi},$$
$$\begin{aligned} D_\mu\hat{\chi}_{\alpha R} = \Big(\partial_\mu - ig_A & \sum_{a_L=1}^{3}A_\mu^{a_L}T^{a_L} \\ & - iQ_X g_B B_\mu - ig_C Q^{\text{color}}G_\mu\Big)\hat{\chi}_{\alpha R}, \end{aligned}$$
$$\check{\Psi}_{1L} = \begin{pmatrix} T_L & t_L \\ B_L & b_L \end{pmatrix}\text{etc.}, \qquad \tilde{\hat{\Phi}} = i\sigma_2\hat{\Phi}^*. \tag{2.12}$$

$\langle\hat{\Phi}\rangle = (0, w)^t \neq 0$ breaks $SU(2)_R \times U(1)_X$ to $U(1)_Y$. It also induces mass mixing on the brane,

$$\begin{aligned} S_{\text{brane}}^{\text{mass}} = \int d^5x\sqrt{-G}\delta(y)\Big\{ & -\sum_{\alpha=1}^{3} i\mu_\alpha^q(\hat{\chi}_{\alpha R}^{q\dagger}Q_{\alpha L} - Q_{\alpha L}^\dagger\hat{\chi}_{\alpha R}^q) \\ & - i\tilde{\mu}^q(\hat{\chi}_{2R}^{q\dagger}q_L - q_L^\dagger\hat{\chi}_{2R}^q) \\ & - \sum_{\alpha=1}^{3} i\mu_\alpha^l(\hat{\chi}_{\alpha R}^{l\dagger}L_{\alpha L} - L_{\alpha L}^\dagger\hat{\chi}_{\alpha R}^l) \\ & - i\tilde{\mu}^l(\hat{\chi}_{3R}^{l\dagger}\ell_L - \ell_L^\dagger\hat{\chi}_{3R}^l)\Big\}, \end{aligned}$$
$$\frac{\mu_\alpha^q}{\kappa_\alpha^q} = \frac{\tilde{\mu}^l}{\tilde{\kappa}^q} = \frac{\mu_\alpha^l}{\kappa_\alpha^l} = \frac{\tilde{\mu}^l}{\tilde{\kappa}^l} = w, \tag{2.13}$$

where $\mu_\alpha, \tilde{\mu}$ define brane mass parameters. In the present paper we assume that the brane interactions are diagonal in

the generation of quarks and leptons. In this case all of $\mu_\alpha, \tilde{\mu}$ and w can be taken to be real and positive without loss of generality. As far as $\mu_\alpha, \tilde{\mu} \gg m_{\rm KK}$, only $\tilde{\mu}^q/\mu_2^q$ and $\tilde{\mu}^l/\mu_3^l$ become relevant at low energies.

As shown in Sec. III, the effective potential $V_{\rm eff}(\theta_H)$ is minimized at $\theta_H \neq 0$, thereby the electroweak symmetry breaking taking place. The gauge fields are expanded in KK towers. In particular, four-dimensional components of the $SO(5) \times U(1)_X$ gauge fields are expanded, in the twisted gauge, as

$$A_\mu(x,z) + \frac{g_B}{g_A} B_\mu(x,z) T_B = \hat{W}^-_\mu + \hat{W}^+_\mu + \hat{Z}_\mu + \hat{A}^\gamma_\mu + \hat{W}^-_{R\mu} + \hat{W}^+_{R\mu} + \hat{Z}_{R\mu} + \hat{A}^{\hat{4}}_\mu. \tag{2.14}$$

Here we have introduced T_B such that ${\rm Tr}{T_B}^2 = 1$, ${\rm Tr}T_B T^\alpha = 0$ and ${\rm Tr}T^\alpha T^\beta = \delta^{\alpha\beta}$ where T^α's are generators of $SO(5)$ in the tensorial representation. The $\hat{W}^\pm, \hat{Z}$ and $\hat{A}^\gamma$ towers contain $W^\pm, Z$ and γ. The other towers do not contain light modes. Each of the $\hat{W}^+, \hat{W}^-, \hat{Z}$ towers splits into two KK towers at $\theta_H = 0$. In all, (2.14) contains 11 KK towers. Details of wave functions of each KK tower are tabulated in Appendix B.

The fermion Ψ_{F_i} are introduced in the spinor representation of $SO(5)$ unlike other fields in the bulk which are in the vector or adjoint representations [37]. As explained in the next section, the existence of Ψ_{F_i} in addition to the other bulk fields leads to nontrivial dependence of the effective potential $V_{\rm eff}(\theta_H)$ on θ_H and to the instability of the four-dimensional Higgs boson. The boundary condition $\Psi_{F_i}(x, y_j - y) = (-1)^j P_{\rm sp}\Gamma^5 \Psi_{F_i}(x, y_j + y)$ in (2.7) implies that there is no zero mode for $\theta_H = 0$ and that the lowest KK modes of $\Psi_{F_i}(x,z)$ dominantly couple to the $SU(2)_R$ gauge bosons. If the boundary condition $\Psi_{F_i}(x, y_j - y) = (-1)^{j+1} P_{\rm sp}\Gamma^5 \Psi_{F_i}(x, y_j + y)$ were taken, then the lowest KK modes of $\Psi_{F_i}(x,z)$ would dominantly couple to the $SU(2)_L$ gauge bosons. The lowest, neutral component of Ψ_{F_i} turns out stable and becomes the dark matter of the Universe, as will be explained in a separate paper [67]. For this reason the $SO(5)$-spinor fermion Ψ_{F_i} is called a dark fermion.

III. HIGGS BOSON AND THE UNIVERSALITY

As explained in (2.8), the extra-dimensional component $A_z = (kz)^{-1} A_y$ contains the four-dimensional Higgs field,

$$A^{\hat{4}}_z(x,z) = \{\theta_H f_H + H(x)\} u_H(z) + \cdots,$$
$$u_H(z) = \sqrt{\frac{2}{k(z_L^2 - 1)}}\, z \quad \text{for } 1 \le z \le z_L. \tag{3.1}$$

The value of θ_H is determined by the location of the global minimum of the effective potential $V_{\rm eff}(\theta_H)$. The Higgs boson mass is given by

$$m_H^2 = \frac{1}{f_H^2} \frac{d^2 V_{\rm eff}}{d\theta_H^2}\bigg|_{\rm min}. \tag{3.2}$$

In this section we explain how the parameters of the model are determined, and show that universality relations appear among θ_H, the KK mass $m_{\rm KK}$, the masses of $Z^{(1)}$ and $\gamma^{(1)}$, and the Higgs self-couplings [37].

A. $V_{\rm eff}(\theta_H)$

Let us first consider the case in which all $SO(5)$-spinor fermions (dark fermions) Ψ_{F_i} are degenerate at the tree level, i.e., $c_{F_i} = c_F$ $(i = 1, \ldots, n_F)$. At the one-loop level only the KK towers whose mass spectra depend on θ_H contribute to the effective potential $V_{\rm eff}(\theta_H)$. Those spectra are given by (B6) for the W tower, (B8) for the Z tower, (B22) for the D tower, (C4) for the top quark tower, (C7) for the bottom quark tower, and (C9) for the F tower or the dark fermions. Contributions of other quarks and leptons turn out exponentially suppressed and negligible.

The relevant parameters of the model are $k, z_L, g_A, g_B, c_t, \tilde{\mu}/\mu_2$, c_F and n_F, from which $V_{\rm eff}(\theta_H)$ is determined. Other brane mass parameters are irrelevant so long as $\mu_\alpha, \tilde{\mu}, w \gg m_{\rm KK}$. These eight parameters are chosen such that m_Z, α_w, $\sin^2\theta_W$, m_t, m_b, and m_H take the observed values [68]. (To be precise, $\sin^2\theta_W$ is determined by global fit.) This procedure leaves two parameters, say z_L and n_F, free. The procedure is highly involved as everything must be determined at the global minimum of $V_{\rm eff}(\theta_H)$, which, however, is to be found after all parameters are specified. In other words, all parameters must be determined self-consistently.

First we note that with those given parameters, the one-loop effective potential is given by

$$\begin{aligned}
V_{\rm eff}(\theta_H, c_t, r_t, c_F, n_F, k, z_L, \theta_W; \xi) &= 2(3-\xi^2) I[Q_W] + (3-\xi^2) I[Q_Z] + 3\xi^2 I[Q_D] \\
&\quad - 12\{I[Q_{\rm top}] + I[Q_{\rm bottom}]\} - 8 n_F I[Q_F], \\
I[Q(q;\theta_H)] &= \frac{(kz_L^{-1})^4}{(4\pi)^2} \int_0^\infty dq q^3 \ln\{1 + Q(q;\theta_H)\}, \\
Q_W = \cos^2\theta_W Q_Z &= \frac{1}{2} Q_D = \frac{1}{2} Q_0\left[q; \frac{1}{2}\right] \sin^2\theta_H, \\
Q_{\rm top} &= \frac{Q_{\rm bottom}}{r_t} = \frac{Q_0[q; c_t]}{2(1+r_t)} \sin^2\theta_H, \\
Q_F &= Q_0[q; c_F] \cos^2\frac{1}{2}\theta_H, \\
Q_0[q; c] &= \frac{z_L}{q^2 \hat{F}_{c-\frac{1}{2}, c-\frac{1}{2}}(q z_L^{-1}, q) \hat{F}_{c+\frac{1}{2}, c+\frac{1}{2}}(q z_L^{-1}, q)}, \\
\hat{F}_{\alpha,\beta}(u,v) &= I_\alpha(u) K_\beta(v) - e^{-i(\alpha-\beta)\pi} K_\alpha(u) I_\beta(v),
\end{aligned} \tag{3.3}$$

where $r_t = (\tilde{\mu}/\mu_2)^2$ and K_α and I_α are modified Bessel functions. In the following we take the 't Hooft–Feynman gauge $\xi = 1$.

TABLE I. Parameters and masses in the case of degenerate dark fermions with $n_F = 5$. All masses and k are given in units of TeV.

z_L	θ_H	$m_{\rm KK}$	k	c_t	c_F	$m_{F^{(1)}}$	$m_{Z_R^{(1)}}$	$m_{Z^{(1)}}$	$m_{\gamma^{(1)}}$
10^9	0.473	2.50	7.97×10^8	0.376	0.459	0.353	1.92	1.97	1.98
10^8	0.351	3.13	9.97×10^7	0.357	0.445	0.502	2.40	2.48	2.48
10^7	0.251	4.06	1.29×10^7	0.330	0.430	0.735	3.11	3.24	3.24
10^6	0.172	5.45	1.74×10^6	0.292	0.410	1.11	4.17	4.37	4.38
10^5	0.114	7.49	2.38×10^5	0.227	0.382	1.75	5.73	6.07	6.08
10^4	0.0730	10.5	3.33×10^4	0.0366	0.333	2.91	8.00	8.61	8.61

We adopt the following algorithm to find consistent solutions. We fix the two parameters z_L and n_F.

(1) Suppose that the minimum of $V_{\rm eff}$ is located at $\theta_H = \theta_1$. Equation (B8) and $\sin^2\theta_W$ determine $\lambda_{Z^{(0)}}$, which fixes k by the Z boson mass $m_Z = \lambda_{Z^{(0)}} k$.

(2) c_t and r_t are determined from (C4) and (C7) such that the observed masses of the top and bottom quarks are reproduced.

(3) Now $V_{\rm eff}(\theta_H)$ in (3.3) is evaluated with c_F being a parameter. c_F is determined by the condition

$$\left.\frac{dV_{\rm eff}}{d\theta_H}\right|_{\theta_1} = 0, \tag{3.4}$$

which assures that the minimum of $V_{\rm eff}(\theta_H)$ is located at θ_1.

(4) With these parameters the Higgs boson mass m_H is evaluated from (3.2). This gives $m_H(\theta_1)$, which, in general, differs from the observed value $m_H = 126$ GeV.

(5) We vary the value θ_1 and repeat the procedure from step 1 until we get $m_H(\theta_1) = 126$ GeV.

In this manner the value $\theta_H = \theta_1$ at the minimum is determined as $\theta_H(z_L, n_F)$. All other quantities such as the mass specta of all KK towers, gauge couplings of all particles, and Yukawa couplings of all fermions are determined as functions of z_L, n_F. Determined values for θ_H, $m_{\rm KK}$, $m_{Z^{(1)}}$, etc. are tabulated in Table I in the case of $n_F = 5$.

TABLE II. Parameters and masses in the case of nondegenerate dark fermions with $(n_F^h, n_F^l) = (3, 2)$ and $c_F^l - c_F^h = 0.03$. Masses are given in units of TeV. The values of $m_{\rm KK}$, k, c_t, $m_{Z^{(1)}}$, $m_{Z_R^{(1)}}$, and $m_{\gamma^{(1)}}$ are the same in three digits as those in Table I in the degenerate case.

z_L	θ_H	c_F^h	$m_{F_h^{(1)}}$	$m_{F_l^{(1)}}$
10^9	0.473	0.447	0.384	0.304
10^8	0.351	0.434	0.540	0.444
10^7	0.251	0.418	0.781	0.663
10^6	0.172	0.398	1.17	1.02
10^5	0.114	0.370	1.83	1.64
10^4	0.0730	0.321	3.01	2.77

Smaller c_t and c_F correspond to heavier masses of the top quark and dark fermions $F^{+(1)}$ and $F^{0(1)}$ and give larger contributions to $V_{\rm eff}(\theta_H)$. As n_F gets larger, c_F ($m_{F^{(1)}}$) becomes larger (smaller) with fixed m_H, as the contribution from each dark fermion to $V_{\rm eff}$ becomes small. Given n_F, only a limited region for z_L is allowed. For $n_F = 1, 2, 3$ one cannot reproduce the Higgs mass 126 GeV when z_L becomes too small. When $n_F \geq 4$, one cannot reproduce the top quark mass for $z_L < 10^4$.

Dark fermions may not be degenerate. Suppose that n_F^h multiplets have the bulk mass $c_{F_i} = c_F^h$, and n_F^l multiplets have $c_{F_i} = c_F^l$. Small difference between c_F^h and c_F^l can yield a substantial difference in masses, whereas $V_{\rm eff}(\theta_H)$ is almost unaffected. For instance, when $n_F = n_F^h + n_F^l = 5$, a difference $c_F^l - c_F^h = 0.01(0.03)$ leads to $m_{F_h} - m_{F_l} =$ 30 to 80 GeV (80 to 240 GeV). The dark fermion masses $m_{F_h^{(1)}}$ and $m_{F_l^{(1)}}$ in the case of $(n_F^h, n_F^l) = (3, 2)$ and $c_F^l - c_F^h = 0.03$ are tabulated in Table II. It is found that the numerical values of $m_{\rm KK}$, k, c_t, $m_{Z_R^{(1)}}$, $m_{Z^{(1)}}$, and $m_{\gamma^{(1)}}$ are the same as those in Table I to the accuracy of three digits.

B. The universality

As described above, various quantities such as θ_H, $m_{\rm KK}$, the mass spectra, Higgs cubic and quartic self-couplings λ_3, λ_4, and Yukawa couplings are determined as functions of z_L and n_F in the case of degenerate dark fermions. In other words they depend not only on z_L, but also on how dark fermions are introduced, which could spoil the predictability of the model. Surprisingly it has been found

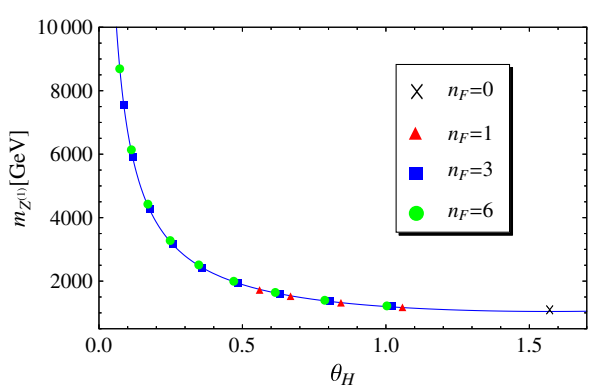

FIG. 1 (color online). θ_H vs $m_{Z^{(1)}}$ for $m_H = 126$ GeV with n_F degenerate dark fermions.

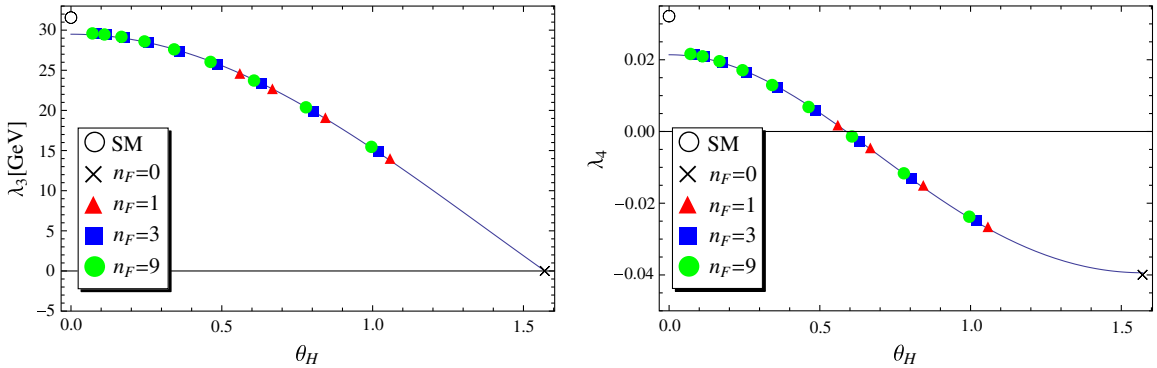

FIG. 2 (color online). θ_H vs λ_3^H and λ_4^H for $m_H = 126$ GeV with n_F degenerate dark fermions. In the SM $\lambda_3^{\rm SM} = 31.5$ GeV and $\lambda_4^{\rm SM} = 0.0320$. The fitting curves are given by (3.6).

in Ref. [37] that universal relations are held among θ_H, $m_{\rm KK}$, $m_{Z_R^{(1)}}$, $m_{Z^{(1)}}$, $m_{\gamma^{(1)}}$, λ_3, and λ_4 irrespective of n_F. This property is called the universality. It implies that once one of these quantities is determined from experiments, then other quantities are predicted, irrespective of the details of the dark fermion sector. The mass spectrum of dark fermions, $m_{F^{(1)}}$, on the other hand, sensitively depends on n_F.

It is most enlightening to express these universal relations as functions of θ_H. The masses $m_{\rm KK}$, $m_{Z_R^{(1)}}$, $m_{Z^{(1)}}$, $m_{\gamma^{(1)}}$ are expressed in the form of

$$m_{\rm KK} \sim \frac{1352\ \text{GeV}}{(\sin\theta_H)^{0.786}}, \qquad m_{Z_R^{(1)}} \sim \frac{1038\ \text{GeV}}{(\sin\theta_H)^{0.784}},$$
$$m_{Z^{(1)}} \sim \frac{1044\ \text{GeV}}{(\sin\theta_H)^{0.808}}, \qquad m_{\gamma^{(1)}} \sim \frac{1056\ \text{GeV}}{(\sin\theta_H)^{0.804}}. \tag{3.5}$$

The relation between θ_H and $m_{Z^{(1)}}$ is plotted in Fig. 1 for $n_F = 0, 1, 3, 6$. One can see that the curve is universal, independent of n_F. (The case of $n_F = 0$ corresponds to $\theta_H = \frac{1}{2}\pi$ and the stable Higgs boson.)

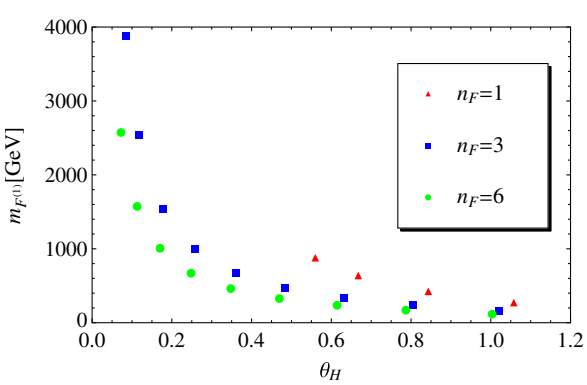

FIG. 3 (color online). θ_H vs m_F for $m_H = 126$ GeV with n_F degenerate dark fermions.

Similarly the Higgs cubic and quartic self-couplings, λ_3 and λ_4 are plotted against θ_H for $n_F = 0, 1, 3, 9$ in Fig. 2. The fitting curves are given by

$$\lambda_3/\text{GeV} = 26.7\cos\theta_H + 1.42(1 + \cos 2\theta_H),$$
$$\lambda_4 = -0.0106 + 0.0304\cos 2\theta_H + 0.00159\cos 4\theta_H. \tag{3.6}$$

These numbers should be compared with $\lambda_3^{\rm SM} = 31.5$ GeV and $\lambda_4^{\rm SM} = 0.0320$ in the SM. We note that the effective potential $V_{\rm eff}(\theta_H)$ is bounded from below so that the negative λ_4 for $\theta_H > 0.6$ does not cause the instability. In the gauge-Higgs unification there is no instability problem in the Higgs couplings.

It should be noted that no universality is found in the mass spectrum of the dark fermions. The mass $m_{F^{(1)}}$ is plotted in Fig. 3 for various n_F.

The universality relations are determined with the fixed Higgs boson mass m_H. If m_H were smaller or larger than the observed value, the universality relations would slightly change. The KK mass scale $m_{\rm KK}$ increases as m_H. The fitting curve is parmetrized as $m_{\rm KK} = \alpha/|\sin\theta_H|^\beta$ with given m_H. The values of α and β for various m_H are tabulated in Table III. We plotted $m_{\rm KK}(\theta_H)$ for $m_H = 110$, 126, 140 GeV in Fig. 4.

We stress that the universality leads to powerful predictions. Once the value of θ_H is determined from, say, $m_{Z^{(1)}}$, many other quantities are predicted for experimental confirmation. The gauge-Higgs unification scenario is very predictive.

TABLE III. Universality relation $m_{\rm KK} = \alpha/|\sin\theta_H|^\beta$ with various value of m_H.

m_H(GeV)	α(TeV)	β
110	1.20	0.733
120	1.30	0.766
126	1.35	0.786
130	1.39	0.800
140	1.49	0.820

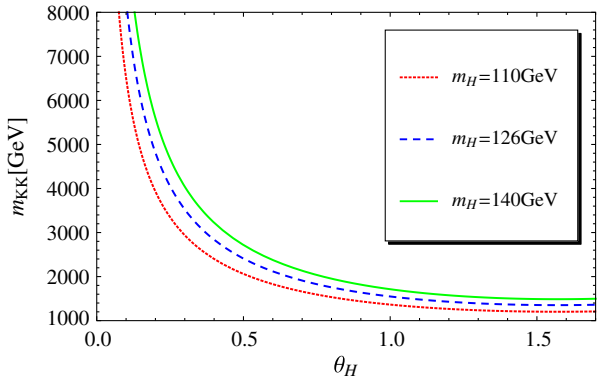

FIG. 4 (color online). θ_H vs m_{KK} with various values of m_H.

IV. e^+e^-, $\mu^+\mu^-$ EVENTS IN THE Z' SEARCH

One of the distinctive predictions of the $SO(5) \times U(1)$ gauge-Higgs unification is the existence of the KK excited modes of Z and γ. Independent of the details of the dark fermion sector the universality predicts that $m_{Z^{(1)}}, m_{\gamma^{(1)}} \sim$ 6 TeV (3 TeV) for $\theta_H = 0.1$ (0.2) as depicted in Fig. 1. $Z^{(1)}$ and $\gamma^{(1)}$ partially decay to e^+e^- or $\mu^+\mu^-$, which should appear as clear signals in the Z' search at LHC [69–74]. We evaluate the production and decay rates of those particles.

In our model there are four kinds of neutral gauge bosons at the TeV scale. [See Eq. (2.14)]. They are the first KK mode of Z boson, $Z^{(1)}$, the first KK mode of photon, $\gamma^{(1)}$, the $Z_R^{(1)}$ boson and the $A^{\hat{4}}$ boson. Among them the $A^{\hat{4}}$ boson does not couple to SM particles so that it escapes from detection in the Z' search. $Z^{(1)}$, $\gamma^{(1)}$, and $Z_R^{(1)}$ are the candidates for Z' bosons.

A. Couplings and decay widths

To evaluate the production and decay rates of Z' bosons we need to know the four-dimensional Z' couplings of quarks and leptons. They are obtained from the five-dimensional gauge interaction terms by inserting wave functions of gauge bosons and quarks or leptons and integrating over the fifth-dimensional coordinate. The couplings of the photon, Z boson and $Z_R^{(1)}$ boson towers can be written as

$$\begin{aligned}\mathcal{L} \supset & \sum_{n,i} A_\mu^{\gamma(n)} [g_{u^iL}^{\gamma^{(n)}} \bar{u}^i_L \gamma^\mu u^i_L + g_{u^iR}^{\gamma^{(n)}} \bar{u}^i_R \gamma^\mu u^i_R + g_{d^iL}^{\gamma^{(n)}} \bar{d}^i_L \gamma^\mu d^i_L + g_{d^iR}^{\gamma^{(n)}} \bar{d}^i_R \gamma^\mu d^i_R + g_{e^iL}^{\gamma^{(n)}} \bar{e}^i_L \gamma^\mu e^i_L + g_{e^iR}^{\gamma^{(n)}} \bar{e}^i_R \gamma^\mu e^i_R] \\ & + \sum_{n,i} Z_\mu^{(n)} [g_{u^iL}^{Z^{(n)}} \bar{u}^i_L \gamma^\mu u^i_L + g_{u^iR}^{Z^{(n)}} \bar{u}^i_R \gamma^\mu u^i_R + g_{d^iL}^{Z^{(n)}} \bar{d}^i_L \gamma^\mu d^i_L + g_{d^iR}^{Z^{(n)}} \bar{d}^i_R \gamma^\mu d^i_R + g_{\nu^iL}^{Z^{(n)}} \bar{\nu}^i_L \gamma^\mu \nu^i_L + g_{\nu^iR}^{Z^{(n)}} \bar{\nu}^i_R \gamma^\mu \nu^i_R \\ & + g_{e^iL}^{Z^{(n)}} \bar{e}^i_L \gamma^\mu e^i_L + g_{e^iR}^{Z^{(n)}} \bar{e}^i_R \gamma^\mu e^i_R] + \sum_{n,i} Z_{R\mu}^{(n)} [g_{u^iL}^{Z_R^{(n)}} \bar{u}^i_L \gamma^\mu u^i_L + g_{u^iR}^{Z_R^{(n)}} \bar{u}^i_R \gamma^\mu u^i_R + g_{d^iL}^{Z_R^{(n)}} \bar{d}^i_L \gamma^\mu d^i_L \\ & + g_{d^iR}^{Z_R^{(n)}} \bar{d}^i_R \gamma^\mu d^i_R + g_{\nu^iL}^{Z_R^{(n)}} \bar{\nu}^i_L \gamma^\mu \nu^i_L + g_{\nu^iR}^{Z_R^{(n)}} \bar{\nu}^i_R \gamma^\mu \nu^i_R + g_{e^iL}^{Z_R^{(n)}} \bar{e}^i_L \gamma^\mu e^i_L + g_{e^iR}^{Z_R^{(n)}} \bar{e}^i_R \gamma^\mu e^i_R], \end{aligned} \tag{4.1}$$

where the superscript i denotes the generation, i.e., $(u^1, u^2, u^3) = (u, c, t)$, etc. Explicit formulas for the gauge couplings are given in Appendix D. The relevant couplings of the Z' bosons are tabulated in Table IV and Table V.

The decay width of the Z' boson is given by

$$\Gamma_{Z'} = \sum_i \frac{m_{Z'}}{12\pi} \left(\frac{(g_{iL}^{Z'})^2 + (g_{iR}^{Z'})^2}{2} + 2 g_{iL}^{Z'} g_{iR}^{Z'} \frac{m_i^2}{m_{Z'}^2} \right) \sqrt{1 - \frac{4m_i^2}{m_{Z'}^2}}. \tag{4.2}$$

Here i runs over all fermions including SM fermions and dark fermions. The contribution of its decay to W^+W^- is very small and can be neglected [59]. The evaluated $\Gamma_{Z'}$ for $\theta_H = 0.114$ is summarized in Table IV. It is seen that all of $Z_R^{(1)}$, $Z^{(1)}$, and $\gamma^{(1)}$ have large decay widths ($300 \sim 900$ GeV) in quite contrast to the narrow width of the Z boson. It is mainly due to the large couplings of right-handed quarks and leptons.

B. Production at LHC

In our study, we calculate the dilepton production cross sections through the Z' boson exchange together with the SM processes mediated by the Z boson and photon. The

TABLE IV. Masses, total decay widths and couplings of the Z' bosons to SM particles in the first generation for $\theta_H = 0.114$. Couplings to μ are approximately the same as those to e.

Z'	m(TeV)	Γ(GeV)	$g_{uL}^{Z'}$	$g_{dL}^{Z'}$	$g_{eL}^{Z'}$	$g_{uR}^{Z'}$	$g_{dR}^{Z'}$	$g_{eR}^{Z'}$
Z	0.0912	2.44	0.257	−0.314	−0.200	−0.115	0.0573	0.172
$Z_R^{(1)}$	5.73	482	0	0	0	0.641	−0.321	−0.978
$Z^{(1)}$	6.07	342	−0.0887	0.108	0.0690	−0.466	0.233	0.711
$\gamma^{(1)}$	6.08	886	−0.0724	0.0362	0.109	0.846	−0.423	−1.29
$Z^{(2)}$	9.14	1.29	−0.00727	0.00889	0.00565	−0.00548	0.00274	0.00856

TABLE V. Masses, total decay widths and couplings of the Z' bosons to SM particles in the first generation for $\theta_H = 0.073$.

Z'	m(TeV)	Γ(GeV)	$g^{Z'}_{uL}$	$g^{Z'}_{dL}$	$g^{Z'}_{eL}$	$g^{Z'}_{uR}$	$g^{Z'}_{dR}$	$g^{Z'}_{eR}$
$Z^{(1)}_R$	8.00	553	0	0	0	0.588	−0.294	−0.896
$Z^{(1)}$	8.61	494	−0.100	0.123	0.0780	−0.426	0.213	0.650
$\gamma^{(1)}$	8.61	1.04×10^3	−0.0817	0.0408	0.123	0.775	−0.388	−1.18

dependence of the cross section on the final state dilepton invariant mass $M_{\ell\ell}$ is described as

$$\frac{d\sigma(pp\to\ell^+\ell^-X)}{dM_{\ell\ell}} = \sum_q \int_{-1}^{1} d\cos\theta \int_{\frac{M^2_{\ell\ell}}{E^2_{\rm CMS}}}^{1} dx_1 \frac{2M_{\ell\ell}}{x_1 E^2_{\rm CMS}} \times f_q(x_1, M^2_{\ell\ell}) f_{\bar q}\left(\frac{M^2_{\ell\ell}}{x_1 E^2_{\rm CMS}}, M^2_{\ell\ell}\right) \frac{d\sigma(\bar q q\to\ell^+\ell^-)}{d\cos\theta}, \tag{4.3}$$

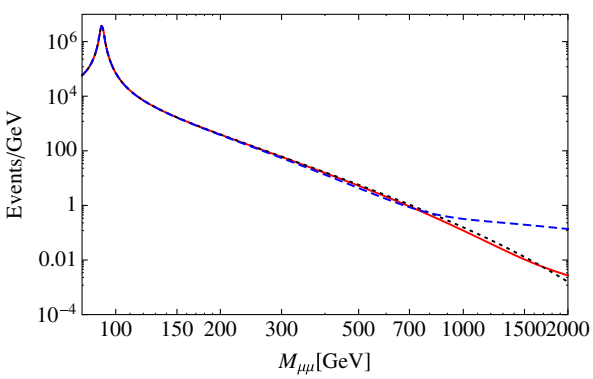

FIG. 5 (color online). The differential cross section multiplied by an integrated luminosity of 20.6 fb^{-1} for $pp\to\mu^+\mu^-X$ at the 8 TeV LHC for $\theta_H = 0.114$ (red solid curve) and for $\theta_H = 0.251$ (blue dashed curve). The black dashed line represents the SM background.

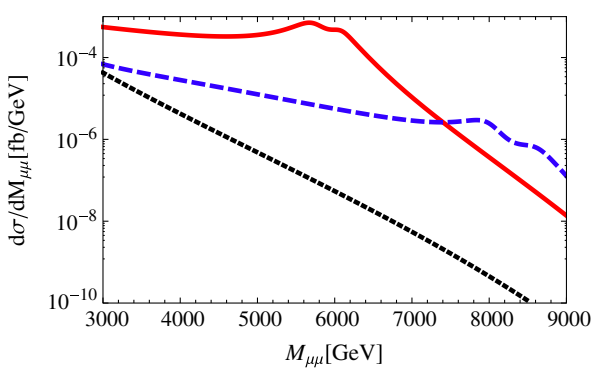

FIG. 6 (color online). The differential cross section for $pp\to\mu^+\mu^-X$ at the 14 TeV LHC for $\theta_H = 0.114$ (red solid curve) and for $\theta_H = 0.073$ (blue dashed curve) . The nearly straight line represents the SM background.

where $E_{\rm CMS}$ is the center-of-mass energy of the LHC and f_q's are the parton distribution functions(PDFs) for q quark. In our numerical analysis, we employ CTEQ5M [75] for the PDFs. Formulas to calculate $d\sigma(\bar q q\to\ell^+\ell^-)/d\cos\theta$ are listed in Appendix E.

Figure 5 shows the differential cross section for $pp\to\mu^+\mu^-$ together with the SM cross section mediated by the Z boson and photon for $\theta_H = 0.114$ ($n_F = 5$, $z_L = 10^5$). The deviation from the SM is very small below 3 TeV because the couplings of the Z boson or photon to SM fermions are almost the same as in the SM. For this reason it is difficult to see the signals of the gauge-Higgs unification at 8 TeV LHC experiments. In the case of $\theta_H = 0.251$ ($n_F = 5$, $z_L = 10^7$), the deviation from the SM is large. The Z' masses are around 3 TeV (See Table 1.) and the decay widths of $Z^{(1)}_R$,$Z^{(1)}$ and $\gamma^{(1)}$ are 341, 221 and 629 GeV. The masses of Z' bosons are heavier than the plot range of Fig. 5. However the decay widths of Z' bosons are very wide and the deviation from the SM is large. Therefore the $\theta_H = 0.251$ case is excluded by the 8 TeV LHC experiments.

On the other hand, at 14 TeV LHC experiments, we expect the signals. Figure 6 shows the differential cross section $d\sigma/dM_{\mu\mu}$ in the range 3 TeV $< M_{\mu\mu} <$ 9 TeV for $\theta_H = 0.114$ and 0.073. The contributions from $Z^{(2)}$ boson and higher KK modes are negligible because the couplings are very small and the widths are very narrow (see Table IV). One sees a very large deviation from the SM, which can be detected at the upgraded LHC.

V. CONCLUSIONS

In the present paper we have explored LHC signals of the $SO(5)\times U(1)$ gauge-Higgs unification, particularly dilepton events associated with the production and decay of the Z' bosons at 14 TeV LHC. In the $SO(5)\times U(1)$ gauge-Higgs unification the four-dimensional Higgs boson appears as a part of the extra-dimensional component of the $SO(5)$ gauge fields, and the quark or lepton multiplets are introduced in the vector representation of $SO(5)$. In addition, dark fermions are introduced in the spinor representation of $SO(5)$, which are vital to realize the observed unstable Higgs boson.

The four-dimensional Higgs boson is the fluctuation mode of the Aharonov-Bohm phase θ_H in the fifth dimension. The phase θ_H, determined by the location of the global minimum of the effective potential $V_{\rm eff}(\theta_H)$,

plays an important role in determining the couplings among gauge boson, quarks and leptons, and the Higgs boson. It has been known that the value $\theta_H < 0.2$ is consistent with the data at low energies.

The shape of $V_{\rm eff}(\theta_H)$, and therefore the location of global minimum θ_H, sensitively depends on the details of the dark fermion sector, which could spoil the predictability of the gauge-Higgs unification scenario. On the contrary, we have shown that there holds the universality in the relations among $m_{\rm KK}$, $m_{Z^{(1)}}$, $m_{\gamma^{(1)}}$, $m_{Z_R^{(1)}}$, λ_3, λ_4 and θ_H, irrespective of the details of the dark fermion sector. For instance, one finds that $m_{Z^{(1)}}(\theta_H) \sim 1044\text{GeV}/(\sin\theta_H)^{0.804}$. The universality implies that once the value of, say, $m_{Z^{(1)}}$ is determined from experiments, then other quantities such as λ_3 and λ_4 are predicted to be tested.

In the $SO(5) \times U(1)$ gauge-Higgs unification the three gauge bosons, $Z_R^{(1)}$, $Z^{(1)}$, and $\gamma^{(1)}$, appear as Z' bosons in dilepton events at LHC. It is interesting that the masses of these bosons turn out around 6 (8 TeV) for $\theta_H = 0.114$ (0.073), which is exactly in the region explored at the 14 TeV LHC. As right-handed quarks and leptons have large couplings to those Z' bosons, the widths of those bosons become large; the decay widths of $Z_R^{(1)}$, $Z^{(1)}$ and $\gamma^{(1)}$ are 482, 342 and 886 GeV (553, 494 GeV and 1.04 TeV) for $\theta_H = 0.114$ (0.073). Notice the relatively large ratio of width/mass $= 0.06 \sim 0.15$ in contrast to that of the Z boson. As the difference in masses of $Z^{(1)}$ and $\gamma^{(1)}$ is small, there should appear two peaks in dilepton events. Due to the large widths the excess of events over those expected in the SM should be seen in much wider range of energies. For $\theta_H = 0.114$, for instance, an excess due to the broad widths of the Z' resonances should be observed above 3 TeV in the dilepton invariant mass. The discovery of the Z' bosons in the 3–9 TeV range would give strong support for the gauge-Higgs unification, signaling the existence of extra dimensions.

In the present paper we have focused on the LHC signals classified in the universality class, specifically on the Z' events. There are other collider signals [76–81] such as the forward-backward asymmetry (at Tevatron) and the charge asymmetry (at LHC) in $t\bar{t}$ pair production and QCD parity violation at LHC [82–86]. We hope to report on these issues in the near future.

ACKNOWLEDGMENTS

This work was supported in part by JSPS KAKENHI Grants No. 23104009 (Y. H. and Y. O.), No. 21244036 (Y. H.) and No. 2518610 (T. S.). H. H. is supported by NRF Research Grant No. 2012R1A2A1A01006053 (HH) of the Republic of Korea.

APPENDIX A: BASE FUNCTIONS

Mode functions for KK towers are expressed in terms of Bessel functions. For gauge fields we define

$$C(z;\lambda) = \frac{\pi}{2}\lambda z z_L F_{1,0}(\lambda z, \lambda z_L), \qquad C'(z;\lambda) = \frac{\pi}{2}\lambda^2 z z_L F_{0,0}(\lambda z, \lambda z_L), \qquad S(z;\lambda) = -\frac{\pi}{2}\lambda z F_{1,1}(\lambda z, \lambda z_L),$$
$$S'(z;\lambda) = -\frac{\pi}{2}\lambda^2 z F_{0,1}(\lambda z, \lambda z_L), \qquad \hat{S}(z;\lambda) = \frac{C(1;\lambda)}{S(1;\lambda)} S(z;\lambda), \qquad F_{\alpha,\beta}(u,v) = J_\alpha(u) Y_\beta(v) - Y_\alpha(u) J_\beta(v). \tag{A1}$$

These functions satisfy

$$C(z_L;\lambda) = z_L, \qquad C'(z_L;\lambda) = 0, \qquad S(z_L;\lambda) = 0, \qquad S'(z_L;\lambda) = \lambda, \qquad CS' - SC' = \lambda z. \tag{A2}$$

For fermions with a bulk mass parameter c, we define

$$\begin{pmatrix} C_L \\ S_L \end{pmatrix}(z;\lambda,c) = \pm\frac{\pi}{2}\lambda\sqrt{z z_L} F_{c+\frac{1}{2},c\mp\frac{1}{2}}(\lambda z, \lambda z_L), \qquad \begin{pmatrix} C_R \\ S_R \end{pmatrix}(z;\lambda,c) = \mp\frac{\pi}{2}\lambda\sqrt{z z_L} F_{c-\frac{1}{2},c\pm\frac{1}{2}}(\lambda z, \lambda z_L). \tag{A3}$$

They satisfy

$$D_+(c)\begin{pmatrix} C_L \\ S_L \end{pmatrix} = \lambda\begin{pmatrix} S_R \\ C_R \end{pmatrix}, \qquad D_-(c)\begin{pmatrix} C_R \\ S_R \end{pmatrix} = \lambda\begin{pmatrix} S_L \\ C_L \end{pmatrix}, \qquad D_\pm(c) = \pm\frac{d}{dz} + \frac{c}{z}, \tag{A4}$$

and

$$C_R = C_L = 1, \qquad S_R = S_L = 0 \quad \text{for } z = z_L, \qquad C_L C_R - S_L S_R = 1, \qquad S_L(z;\lambda,-c) = -S_R(z;\lambda,c). \tag{A5}$$

APPENDIX B: KK TOWERS OF BOSONIC FIELDS

1. Twisted gauge

To find the spectrum and wave function of each KK mode for $\theta_H \neq 0$, it is convenient to move to the twisted gauge in which $\langle \tilde{A}_z \rangle = 0$. This is achieved by a gauge transformation $\tilde{A}_M = \Omega A_M \Omega^{-1} + 1/g_A \Omega \partial_M \Omega^{-1}$ with $\partial_z \Omega = -i g_A \Omega \langle A_z \rangle$;

$$\Omega = \exp\left\{ i g_A \theta_H f_H T^{\hat{4}} \int_y^L dy u_H(y) \right\} = \exp\left\{ i\theta_H \frac{z_L^2 - z^2}{z_L^2 - 1} \sqrt{2} T^{\hat{4}} \right\} \quad \text{for } 1 \leq z \leq z_L. \tag{B1}$$

The orbifold boundary condition matrices P_j at $y = y_j$ $[(y_0, y_1) = (0, L)]$ change from P_j to $\tilde{P}_j = \Omega(y_j - y) P_0 \Omega(y_j + y)^{-1}$. Ω in (B1) has been chosen such that $\Omega|_{y=L} = 1$ and the orbifold boundary condition at the TeV brane remains unchanged. On the other hand, the orbifold boundary condition matrix P_0 changes to $\tilde{P}_0 = \Omega(-y) P_0 \Omega(y)^{-1}$,

$$\tilde{P}_0^{\text{vec}} = \begin{pmatrix} -1 & & & & \\ & -1 & & & \\ & & -1 & & \\ & & & -\cos 2\theta_H & \sin 2\theta_H \\ & & & \sin 2\theta_H & \cos 2\theta_H \end{pmatrix},$$
$$\tilde{P}_0^{\text{sp}} = \begin{pmatrix} \cos\theta_H & -i\sin\theta_H \\ i\sin\theta_H & -\cos\theta_H \end{pmatrix} \otimes I_2. \tag{B2}$$

In the twisted gauge the fields satisfy free equations at the tree level, but obey the θ_H-dependent boundary condition specified by (B2). Wave functions of the four-dimensional components of the gauge fields are expressed in terms of either $C(z;\lambda)$ or $S(z;\lambda)$ in (A1), depending on the boundary condition (Neumann or Dirichelet) at the TeV brane. Wave functions of the fifth-dimensional components of the gauge fields, on the other hand, are expressed in terms of either $C'(z;\lambda)$ or $S'(z;\lambda)$. The boundary condition at the Planck brane at $z = 1$ mixes fields through (B2) and determines eigenvalues $\{\lambda_n\}$ in each KK tower.

2. KK towers of A_μ and B_μ

$A_\mu(x,z)$ and $B_\mu^X(x,z)$ are expanded in KK towers.

$$\tilde{A}_\mu(x,z) + \frac{g_B}{g_A} B_\mu(x,z) T_B = \hat{W}_\mu^- + \hat{W}_\mu^+ + \hat{Z}_\mu + \hat{A}_\mu^\gamma + \hat{W}_{R\mu}^- + \hat{W}_{R\mu}^+ + \hat{Z}_{R\mu} + \hat{A}_\mu^{\hat{4}}, \tag{B3}$$

where

$$\begin{aligned}
\hat{W}_\mu^\mp &= \sum_n W_\mu^{(n)\mp}(x) \left\{ h^L_{W^{(n)}} \frac{T^{1_L} \mp i T^{2_L}}{\sqrt{2}} + h^R_{W^{(n)}} \frac{T^{1_R} \mp i T^{2_R}}{\sqrt{2}} + \hat{h}_{W^{(n)}} \frac{T^{\hat{1}} \mp i T^{\hat{2}}}{\sqrt{2}} \right\}, \\
\hat{Z}_\mu &= \sum_n Z_\mu^{(n)}(x) \left\{ h^L_{Z^{(n)}} T^{3_L} + h^R_{Z^{(n)}} T^{3_R} + \hat{h}_{Z^{(n)}} T^{\hat{3}} + \frac{g_B}{g_A} h^B_{Z^{(n)}} T_B \right\}, \\
\hat{A}_\mu^\gamma &= \sum_n A_\mu^{\gamma(n)}(x) \left\{ h^L_{\gamma^{(n)}} T^{3_L} + h^R_{\gamma^{(n)}} T^{3_R} + \frac{g_B}{g_A} h^B_{\gamma^{(n)}} T_B \right\}, \\
\hat{W}_{R\mu}^\mp &= \sum_n W_{R\mu}^{(n)\mp}(x) \left\{ h^L_{W_R^{(n)}} \frac{T^{1_L} \mp i T^{2_L}}{\sqrt{2}} + h^R_{W_R^{(n)}} \frac{T^{1_R} \mp i T^{2_R}}{\sqrt{2}} \right\}, \\
\hat{Z}_{R\mu} &= \sum_n Z_{R\mu}^{(n)}(x) \left\{ h^L_{Z_R^{(n)}} T^{3_L} + h^R_{Z_R^{(n)}} T^{3_R} + \frac{g_B}{g_A} h^B_{Z_R^{(n)}} T_B \right\}, \quad \hat{A}_\mu^{\hat{4}} = \sum_n A_\mu^{\hat{4}(n)}(x) \hat{h}_{A^{\hat{4}(n)}} T^{\hat{4}}, \\
\hat{W}^\pm &= \frac{\hat{W}^1 \mp i \hat{W}^2}{\sqrt{2}}, \qquad \hat{W}_R^\pm = \frac{\hat{W}_R^1 \mp i \hat{W}_R^2}{\sqrt{2}}.
\end{aligned} \tag{B4}$$

The two gauge coupling constants are related to the weak mixing angle θ_W by

$$c_\phi = \frac{g_A}{\sqrt{g_A^2 + g_B^2}}, \qquad s_\phi = \frac{g_B}{\sqrt{g_A^2 + g_B^2}}, \qquad \cos\theta_W = \frac{1}{\sqrt{1 + s_\phi^2}}. \tag{B5}$$

The KK spectrum and corresponding wave functions for each tower are summarized as follows.

a. W tower

The spectrum of the W tower is given by

$$2S(1;\lambda_{W^{(n)}})C'(1;\lambda_{W^{(n)}}) + \lambda_{W^{(n)}}\sin^2\theta_H = 0, \tag{B6}$$

which includes the W boson as the lowest mode $W = W^{(0)}$. The mode functions are

$$\begin{pmatrix} h^L_{W^{(n)}}(z) \\ h^R_{W^{(n)}}(z) \\ \hat{h}_{W^{(n)}}(z) \end{pmatrix} = \frac{1}{\sqrt{2r_{W^{(n)}}}} \begin{pmatrix} (1+\cos\theta_H)C(z;\lambda_{W^{(n)}}) \\ (1-\cos\theta_H)C(z;\lambda_{W^{(n)}}) \\ -\sqrt{2}\sin\theta_H \hat{S}(z;\lambda_{W^{(n)}}) \end{pmatrix},$$

$$r_{W^{(n)}} = \int_1^{z_L} \frac{dz}{kz}\{(1+\cos^2\theta_H)C(z;\lambda_{W^{(n)}})^2 + \sin^2\theta_H \hat{S}(z;\lambda_{W^{(n)}})^2\}. \tag{B7}$$

b. Z tower

KK spectrum of the Z tower is given by

$$2S(1;\lambda_{Z^{(n)}})C'(1;\lambda_{Z^{(n)}}) + (1+s_\phi^2)\lambda_{Z^{(n)}}\sin^2\theta_H = 0, \tag{B8}$$

which includes the Z boson $Z = Z^{(0)}$. The mode functions of the Z tower are

$$\begin{pmatrix} h^L_{Z^{(n)}}(z) \\ h^R_{Z^{(n)}}(z) \\ \hat{h}_{Z^{(n)}}(z) \\ h^B_{Z^{(n)}} \end{pmatrix} = \frac{1}{\sqrt{1+s_\phi^2}} \frac{1}{\sqrt{2r_{Z^{(n)}}}} \times \begin{pmatrix} \{(1+s_\phi^2)(1+\cos\theta_H) - 2s_\phi^2\}C(z;\lambda_{Z^{(n)}}) \\ \{(1+s_\phi^2)(1-\cos\theta_H) - 2s_\phi^2\}C(z;\lambda_{Z^{(n)}}) \\ -\sqrt{2}(1+s_\phi^2)\sin\theta_H \hat{S}(z;\lambda_{Z^{(n)}}) \\ -2s_\phi c_\phi C(z;\lambda_{Z^{(n)}}) \end{pmatrix},$$

$$r_{Z^{(n)}} = \int_1^{z_L} \frac{dz}{kz}\{c_\phi^2 C(z;\lambda_{Z^{(n)}})^2 + (1+s_\phi^2)[\cos^2\theta_H C(z;\lambda_{Z^{(n)}})^2 + \sin^2\theta_H \hat{S}(z;\lambda_{Z^{(n)}})^2\}. \tag{B9}$$

c. Photon tower

The spectrum of the photon tower is given by

$$C'(1;\lambda_{\gamma^{(n)}}) = 0, \tag{B10}$$

which includes a massless photon $\lambda_{\gamma^{(0)}} = 0$. The mode functions are

$$\begin{pmatrix} h^L_{\gamma^{(n)}}(z) \\ h^R_{\gamma^{(n)}}(z) \\ h^B_{\gamma^{(n)}} \end{pmatrix} = \frac{1}{\sqrt{1+s_\phi^2}} \frac{1}{\sqrt{r_{\gamma^{(n)}}}} \begin{pmatrix} s_\phi C(z;\lambda_{\gamma^{(n)}}) \\ s_\phi C(z;\lambda_{\gamma^{(n)}}) \\ c_\phi \end{pmatrix} C(z;\lambda_{\gamma^{(n)}}),$$

$$r_{\gamma^{(n)}} = \int_1^{z_L} \frac{dz}{kz} C(z;\lambda_{\gamma^{(n)}})^2. \tag{B11}$$

In particular for the photon $\gamma = \gamma^{(0)}$,

$$\begin{pmatrix} h^L_\gamma(z) \\ h^R_\gamma(z) \\ h^B_\gamma \end{pmatrix} = \frac{1}{\sqrt{(1+s_\phi^2)L}} \begin{pmatrix} s_\phi \\ s_\phi \\ c_\phi \end{pmatrix}. \tag{B12}$$

d. W_R tower

The spectrum of the W_R tower is given by

$$C(1;\lambda_{W_R^{(n)}}) = 0. \tag{B13}$$

The corresponding mode functions are

$$\begin{pmatrix} h^L_{W_R^{(n)}}(z) \\ h^R_{W_R^{(n)}}(z) \end{pmatrix} = \frac{1}{\sqrt{2r_{W_R^{(n)}}}} \begin{pmatrix} +1-\cos\theta_H \\ -1-\cos\theta_H \end{pmatrix} C(z;\lambda_{W_R^{(n)}}),$$

$$r_{W_R^{(n)}} = \int_1^{z_L} \frac{dz}{kz} C(z;\lambda_{W_R^{(n)}})^2. \tag{B14}$$

e. Z_R tower

The spectrum of the Z_R tower is given by

$$C(1;\lambda_{Z_R^{(n)}}) = 0, \tag{B15}$$

turning out identical to the W_R tower spectrum, $\lambda_{Z_R^{(n)}} = \lambda_{W_R^{(n)}}$. The corresponding mode functions are

$$\begin{pmatrix} h^L_{Z_R^{(n)}}(z) \\ h^R_{Z_R^{(n)}}(z) \\ h^B_{Z_R^{(n)}} \end{pmatrix} = \frac{1}{\sqrt{1+(1+2t_\phi^2)\cos^2\theta_H}\sqrt{2r_{Z_R^{(n)}}}} \times \begin{pmatrix} -\cos\theta_H - 1 \\ -\cos\theta_H + 1 \\ 2t_\phi\cos\theta_H \end{pmatrix} C(z;\lambda_{Z_R^{(n)}}),$$

$$r_{Z_R^{(n)}} = \int_1^{z_L} \frac{dz}{kz} C(z;\lambda_{Z_R^{(n)}})^2 = r_{W_R^{(n)}}, \qquad t_\phi \equiv \frac{s_\phi}{c_\phi}. \tag{B16}$$

f. $A^{\hat{4}}$ tower

The spectrum and wave functions of $A^{\hat{4}}$ tower are

$$S(1;\lambda_{A^{\hat{4}(n)}}) = 0, \tag{B17}$$

$$h_{A^{\hat{4}(n)}}(z) = \frac{1}{\sqrt{r_{A^{\hat{4}(n)}}}} S(z;\lambda_{A^{\hat{4}(n)}}),$$
$$r_{A^{\hat{4}(n)}} = \int_1^{z_L} \frac{dz}{kz} S(z;\lambda_{A^{\hat{4}(n)}})^2. \tag{B18}$$

3. KK towers of A_z and B_z

$A_z(x,z)$ and $B_z(x,z)$ are expanded in KK towers as

$$\begin{aligned}
\tilde{A}_z(x,z) &= \sum_{a=1}^{3} \hat{G}^a + \sum_{a=1}^{3} \hat{D}^a + \hat{H},\\
\hat{G}^a &= \sum_n G^{a(n)}(x)\{u^L_{G^{(n)}} T^{a_L} + u^R_{G^{(n)}} T^{a_R}\},\\
\hat{D}^a &= \sum_n D^{a(n)}(x)\{u^L_{D^{(n)}} T^{a_L} + u^R_{D^{(n)}} T^{a_R} + \hat{u}_{D^{(n)}} T^{\hat{a}}\},\\
\hat{H} &= \sum_n H^{(n)}(x) u_{H^{(n)}} T^{\hat{4}},\\
B_z(x,z) &= \sum_n B^{(n)}(x) u_{B^{(n)}} T_B.
\end{aligned} \tag{B19}$$

a. G tower

The G tower spectrum and corresponding mode functions are given by

$$C'(1;\lambda_{G^{(n)}}) = 0, \qquad \lambda_{G^{(n)}} \neq 0. \tag{B20}$$

$$u^L_{G^{(n)}} = u^R_{G^{(n)}} = \frac{1}{\sqrt{2}} \frac{1}{\sqrt{r_{G^{(n)}}}} C'(z;\lambda_{G^{(n)}}),$$
$$r_{G^{(n)}} = \int_1^{z_L} \frac{kdz}{z} C'(z;\lambda_{G^{(n)}})^2. \tag{B21}$$

b. D tower

The spectrum of the D tower is given by

$$\begin{aligned}
&S(1;\lambda_{D^{(n)}})C'(1;\lambda_{D^{(n)}}) + \lambda_{D^{(n)}}\sin^2\theta_H\\
&\quad = C(1;\lambda_{D^{(n)}})S'(1;\lambda_{D^{(n)}}) - \lambda_{D^{(n)}}\cos^2\theta_H = 0.
\end{aligned} \tag{B22}$$

Corresponding mode functions are given by

$$\begin{pmatrix} h^L_{D^{(n)}}(z) \\ h^R_{D^{(n)}}(z) \\ \hat{h}_{D^{(n)}}(z) \end{pmatrix} = \frac{1}{\sqrt{2r_{D^{(n)}}}} \begin{pmatrix} \cos\theta_H C'(z;\lambda_{D^{(n)}}) \\ -\cos\theta_H C'(z;\lambda_{D^{(n)}}) \\ -\sqrt{2}\sin\theta_H \hat{S}'(z;\lambda_{D^{(n)}}) \end{pmatrix},$$
$$\hat{S}'(z;\lambda) = \frac{C(1;\lambda)}{S(1;\lambda)} S'(z;\lambda),$$
$$r_{D^{(n)}} = \int_1^{z_L} \frac{kdz}{z} \{\cos^2\theta_H C'(z;\lambda_{D^{(n)}})^2 + \sin^2\theta_H \hat{S}'(z;\lambda_{D^{(n)}})^2\}. \tag{B23}$$

c. Higgs (H) tower

The spectrum of the Higgs tower is determined by

$$\lambda_{H^{(n)}} S(1;\lambda_{H^{(n)}}) = 0, \tag{B24}$$

which includes the zero mode $\lambda_{H^{(0)}} = 0$ for the four-dimensional Higgs boson $H = H^{(0)}$. The mode functions are

$$u_{H^{(0)}}(z) = u_H(z) = \sqrt{\frac{2}{k(z_L^2 - 1)}} z, \tag{B25}$$

for the four-dimensional Higgs boson, and

$$u_{H^{(n)}}(z) = \frac{1}{\sqrt{r_{H^{(n)}}}} S'(z;\lambda_{H^{(n)}}),$$
$$r_{H^{(n)}} = \int_1^{z_L} \frac{kdz}{z} S'(z;\lambda_{H^{(n)}})^2 \tag{B26}$$

for KK-excited states ($n \geq 1$).

d. B tower

The B tower spectrum and corresponding mode functions are given by

$$C'(1;\lambda_{B^{(n)}}) = 0, \qquad \lambda_{B^{(n)}} \neq 0. \tag{B27}$$

$$u_{B^{(n)}} = \frac{1}{\sqrt{r_{B^{(n)}}}} C'(z;\lambda_{B^{(n)}}),$$
$$r_{B^{(n)}} = \int_1^{z_L} \frac{kdz}{z} C'(z;\lambda_{B^{(n)}})^2. \tag{B28}$$

APPENDIX C: WAVE FUNCTIONS OF FERMIONS

Wave functions of KK towers of fermions are expressed in terms of $C_L(z;\lambda,c)$ and $S_L(z;\lambda,c)$ in (A3) for left-handed components and $C_R(z;\lambda,c)$ and $S_R(z;\lambda,c)$ for right-handed components.

1. Quark-lepton towers

Wave functions for the KK tower of an up-type quark t (top) are given by

$$\begin{pmatrix} U_L(x,z) \\ B_L(x,z) \\ t_L(x,z) \\ t'_L(x,z) \end{pmatrix} \supset \frac{\sqrt{k}z^2}{\sqrt{r_{t^{(n)}}}} \begin{pmatrix} a_U^{(n)} C_L^{(2)}(z,\lambda_{t^{(n)}}) \\ a_B^{(n)} C_L^{(1)}(z,\lambda_{t^{(n)}}) \\ a_t^{(n)} C_L^{(1)}(z,\lambda_{t^{(n)}}) \\ a_{t'}^{(n)} S_L^{(1)}(z,\lambda_{t^{(n)}}) \end{pmatrix} t_L^{(n)}(x) \equiv \sqrt{k}z^2 \begin{pmatrix} f_{U_L}^{(n)}(z) \\ f_{B_L}^{(n)}(z) \\ f_{t_L}^{(n)}(z) \\ f_{t'_L}^{(n)}(z) \end{pmatrix} t_L^{(n)}(x),$$

$$\begin{pmatrix} U_R(x,z) \\ B_R(x,z) \\ t_R(x,z) \\ t'_R(x,z) \end{pmatrix} \supset \frac{\sqrt{k}z^2}{\sqrt{r_{t^{(n)}}}} \begin{pmatrix} a_U^{(n)} S_R^{(2)}(z,\lambda_{t^{(n)}}) \\ a_B^{(n)} S_R^{(1)}(z,\lambda_{t^{(n)}}) \\ a_t^{(n)} S_R^{(1)}(z,\lambda_{t^{(n)}}) \\ a_{t'}^{(n)} C_R^{(1)}(z,\lambda_{t^{(n)}}) \end{pmatrix} t_R^{(n)}(x) \equiv \sqrt{k}z^2 \begin{pmatrix} f_{U_R}^{(n)}(z) \\ f_{B_R}^{(n)}(z) \\ f_{t_R}^{(n)}(z) \\ f_{t'_R}^{(n)}(z) \end{pmatrix} t_R^{(n)}(x),$$

$$\begin{aligned} r_{t^{(n)}} &= \int_1^{z_L} dz \{ a_U^{(n)2} C_L^{(2)}(z,\lambda_{t^{(n)}})^2 + (a_B^{(n)2} + a_t^{(n)2}) C_L^{(1)}(z,\lambda_{t^{(n)}})^2 + a_{t'}^{(n)2} S_L^{(1)}(z,\lambda_{t^{(n)}})^2 \} \\ &= \int_1^{z_L} dz \{ a_U^{(n)2} S_R^{(2)}(z,\lambda_{t^{(n)}})^2 + (a_B^{(n)2} + a_t^{(n)2}) S_R^{(1)}(z,\lambda_{t^{(n)}})^2 + a_{t'}^{(n)2} C_R^{(1)}(z,\lambda_{t^{(n)}})^2 \}. \end{aligned} \tag{C1}$$

Here $C_L^{(i)}(z,\lambda_{t^{(n)}}) = C_L(z;\lambda_{t^{(n)}},c_i)$, $S_R^{(i)}(z,\lambda_{b^{(n)}}) = S_R(z;\lambda_{b^{(n)}},c_i)$, etc., and other towers of $Q_{\rm EM} = \frac{2}{3}e$ fermions have been suppressed. The common factors are given by

$$\begin{pmatrix} a_U^{(n)} \\ a_B^{(n)} \\ a_t^{(n)} \\ a_{t'}^{(n)} \end{pmatrix} = \begin{pmatrix} -\sqrt{2}\tilde{\mu}^q C_L^{(1)}/\mu_2^q C_L^{(2)} \\ (1-\cos\theta_H)/\sqrt{2} \\ (1+\cos\theta_H)/\sqrt{2} \\ -\sin\theta_H C_L^{(1)}/S_L^{(1)} \end{pmatrix}, \quad C_L^{(i)} \equiv C_L(1;\lambda_{t^{(n)}},c_i), \qquad S_L^{(i)} \equiv S_L(1;\lambda_{t^{(n)}},c_i), \tag{C2}$$

where $\lambda_{t^{(n)}}$ satisfies

$$(\mu_2^q)^2 C_L(1;\lambda_{t^{(n)}},c_2)\left\{ S_R(1;\lambda_{t^{(n)}},c_1) + \frac{\sin^2\theta_H}{2S_L(1;\lambda_{t^{(n)}},c_1)} \right\} + (\tilde{\mu}^q)^2 C_L(1;\lambda_{t^{(n)}},c_1) S_R(1;\lambda_{t^{(n)}},c_2) = 0, \tag{C3}$$

or for $c_1 = c_2 \equiv c_t$

$$2\left\{ 1 + \left(\frac{\mu_2^q}{\tilde{\mu}^q}\right)^2 \right\} S_L(1;\lambda_{t^{(n)}},c_t) S_R(1;\lambda_{t^{(n)}},c_t) + \left(\frac{\mu_2^q}{\tilde{\mu}^q}\right)^2 \sin^2\theta_H = 0. \tag{C4}$$

For a down-type quark b (bottom), we have

$$\begin{pmatrix} b_L(x,z) \\ X_L(x,z) \\ D_L(x,z) \\ b'_L(x,z) \end{pmatrix} \supset \frac{\sqrt{k}z^2}{\sqrt{r_{b^{(n)}}}} \begin{pmatrix} a_b^{(n)} C_L^{(1)}(z,\lambda_{b^{(n)}}) \\ a_X^{(n)} C_L^{(2)}(z,\lambda_{b^{(n)}}) \\ a_D^{(n)} C_L^{(2)}(z,\lambda_{b^{(n)}}) \\ a_{b'}^{(n)} S_L^{(2)}(z,\lambda_{b^{(n)}}) \end{pmatrix} b_L^{(n)}(x) \equiv \sqrt{k}z^2 \begin{pmatrix} f_{b_L}^{(n)}(z) \\ f_{X_L}^{(n)}(z) \\ f_{D_L}^{(n)}(z) \\ f_{b'_L}^{(n)}(z) \end{pmatrix} b_L^{(n)}(x),$$

$$\begin{pmatrix} b_R(x,z) \\ X_R(x,z) \\ D_R(x,z) \\ b'_R(x,z) \end{pmatrix} \supset \frac{\sqrt{k}z^2}{\sqrt{r_{b^{(n)}}}} \begin{pmatrix} a_b^{(n)} S_R^{(1)}(z,\lambda_{b^{(n)}}) \\ a_X^{(n)} S_R^{(2)}(z,\lambda_{b^{(n)}}) \\ a_D^{(n)} S_R^{(2)}(z,\lambda_{b^{(n)}}) \\ a_{b'}^{(n)} C_R^{(2)}(z,\lambda_{b^{(n)}}) \end{pmatrix} b_R^{(n)}(x) \equiv \sqrt{k}z^2 \begin{pmatrix} f_{b_R}^{(n)}(z) \\ f_{X_R}^{(n)}(z) \\ f_{D_R}^{(n)}(z) \\ f_{b'_R}^{(n)}(z) \end{pmatrix} b_R^{(n)}(x),$$

$$\begin{pmatrix} a_b^{(n)} \\ a_X^{(n)} \\ a_D^{(n)} \\ a_{b'}^{(n)} \end{pmatrix} = \begin{pmatrix} -\sqrt{2}\mu_2^q C_L^{(2)}/\tilde{\mu}^q C_L^{(1)} \\ (1-\cos\theta_H)/\sqrt{2} \\ (1+\cos\theta_H)/\sqrt{2} \\ \sin\theta_H C_L^{(2)}/S_L^{(2)} \end{pmatrix}, \quad C_L^{(i)} \equiv C_L(1;\lambda_{b^{(n)}},c_i), \qquad S_L^{(i)} \equiv S_L(1;\lambda_{b^{(n)}},c_i),$$

$$\begin{aligned} r_{b^{(n)}} &= \int_1^{z_L} dz\{a_b^{(n)2} C_L^{(1)}(z,\lambda_{b^{(n)}})^2 + (a_X^{(n)2} + a_D^{(n)2}) C_L^{(2)}(z,\lambda_{b^{(n)}})^2 + a_{b'}^{(n)2} S_L^{(2)}(z,\lambda_{b^{(n)}})^2\} \\ &= \int_1^{z_L} dz\{a_b^{(n)2} S_R^{(1)}(z,\lambda_{b^{(n)}})^2 + (a_X^{(n)2} + a_D^{(n)2}) S_R^{(2)}(z,\lambda_{b^{(n)}})^2 + a_{b'}^{(n)2} C_R^{(2)}(z,\lambda_{b^{(n)}})^2\}. \end{aligned} \tag{C5}$$

The spectrum is determined by

$$(\tilde{\mu}^q)^2 C_L(1;\lambda_{b^{(n)}},c_1)\left[S_R(1;\lambda_{b^{(n)}},c_2) + \frac{\sin^2\theta_H}{2S_L(1;\lambda_{b^{(n)}},c_2)}\right] + (\mu_2^q)^2 C_L(1;\lambda_{b^{(n)}},c_2) S_R(1;\lambda_{b^{(n)}},c_1) = 0, \tag{C6}$$

or for $c_1 = c_2 = c_t$

$$2\left\{1 + \left(\frac{\mu_2^q}{\tilde{\mu}^q}\right)^2\right\} S_L(1;\lambda_{b^{(n)}},c_t) S_R(1;\lambda_{b^{(n)}},c_t) + \sin^2\theta_H = 0. \tag{C7}$$

For a lepton mupltiplet (ν_τ, τ), the wave functions are given by the following replacement rules:

$$\begin{pmatrix} U \\ B \\ t \\ t' \end{pmatrix} \to \begin{pmatrix} \nu_\tau \\ L_{2Y} \\ L_{3X} \\ \nu'_\tau \end{pmatrix}, \qquad \begin{pmatrix} b \\ D \\ X \\ b' \end{pmatrix} \to \begin{pmatrix} L_{3Y} \\ \tau \\ L_{1Y} \\ \tau' \end{pmatrix}, \quad (\tilde{\mu}^q, \mu_2^q) \to (\mu_3^\ell, \tilde{\mu}^\ell), \qquad (\mu_3^q, \mu_1^q) \to (\mu_1^\ell, \mu_2^\ell), \quad (c_1, c_2) \to (c_4, c_3). \tag{C8}$$

2. Dark fermions ($SO(5)$-spinor fermions)

The spectrum of the KK tower of the dark fermion Ψ_{F_i} is determined by

$$C_L(1;\lambda_{i,n},c_{F_i}) C_R(1;\lambda_{i,n},c_{F_i}) - \sin^2\frac{\theta_H}{2} = 0. \tag{C9}$$

Its KK expansion is given by

$$\Psi_{F_i,R}(x,z) = \sqrt{k}z^2 \sum_{n=1}^{\infty} \left\{ \begin{pmatrix} f_{i,lR}^{(n)}(z) \\ 0 \\ f_{i,rR}^{(n)}(z) \\ 0 \end{pmatrix} F_{i,R}^{+(n)}(x) + \begin{pmatrix} 0 \\ f_{i,lR}^{(n)}(z) \\ 0 \\ f_{i,rR}^{(n)}(z) \end{pmatrix} F_{i,R}^{0(n)}(x) \right\},$$

$$\Psi_{F_i,L}(x,z) = \sqrt{k}z^2 \sum_{n=1}^{\infty} \left\{ \begin{pmatrix} f_{i,lL}^{(n)}(z) \\ 0 \\ f_{i,rL}^{(n)}(z) \\ 0 \end{pmatrix} F_{i,L}^{+(n)}(x) + \begin{pmatrix} 0 \\ f_{i,lL}^{(n)}(z) \\ 0 \\ f_{i,rL}^{(n)}(z) \end{pmatrix} F_{i,L}^{0(n)}(x) \right\}, \tag{C10}$$

where

$$\begin{pmatrix} f_{i,lL}^{(n)}(z) \\ f_{i,lR}^{(n)}(z) \end{pmatrix} = \frac{i\sin\frac{1}{2}\theta_H S_L(1)}{\sqrt{r_i}} \begin{pmatrix} C_L(z) \\ S_R(z) \end{pmatrix} = \frac{\cos\frac{1}{2}\theta_H C_R(1)}{\sqrt{r_i'}} \begin{pmatrix} C_L(z) \\ S_R(z) \end{pmatrix},$$

$$\begin{pmatrix} f_{i,rL}^{(n)}(z) \\ f_{i,rR}^{(n)}(z) \end{pmatrix} = \frac{\cos\frac{1}{2}\theta_H C_L(1)}{\sqrt{r_i}} \begin{pmatrix} S_L(z) \\ C_R(z) \end{pmatrix} = \frac{i\sin\frac{1}{2}\theta_H S_R(1)}{\sqrt{r_i'}} \begin{pmatrix} S_L(z) \\ C_R(z) \end{pmatrix},$$

$$\begin{aligned} r_i &= \int_1^{z_L} dz \left\{ \sin^2\frac{1}{2}\theta_H S_L(1)^2 C_L(z)^2 + \cos^2\frac{1}{2}\theta_H C_L(1)^2 S_L(z)^2 \right\} \\ &= \int_1^{z_L} dz \left\{ \sin^2\frac{1}{2}\theta_H S_L(1)^2 S_R(z)^2 + \cos^2\frac{1}{2}\theta_H C_L(1)^2 C_R(z)^2 \right\}, \\ r_i' &= \int_1^{z_L} dz \left\{ \cos^2\frac{1}{2}\theta_H C_R(1)^2 C_L(z)^2 + \sin^2\frac{1}{2}\theta_H S_R(1)^2 S_L(z)^2 \right\} \\ &= \int_1^{z_L} dz \left\{ \cos^2\frac{1}{2}\theta_H C_R(1)^2 S_R(z)^2 + \sin^2\frac{1}{2}\theta_H S_R(1)^2 C_R(z)^2 \right\}. \end{aligned} \tag{C11}$$

Here $C_L(z) = C_L(z;\lambda_{i,n}, c_{F_i})$, $S_R(z) = S_R(z;\lambda_{i,n}, c_{F_i})$, etc.

APPENDIX D: GAUGE COUPLINGS

In this appendix we summarize the couplings of quarks and leptons to the gauge bosons and their KK excited states, which are necessary in evaluating dilepton events associated with the production of the Z' bosons in Sec. IV. All four-dimensional gauge couplings of quarks and leptons are obtained from

$$\int_1^{z_L} dz \sqrt{G} e_m{}^{\mu} \sum_a \bar{\tilde{\Psi}}_a \Gamma^m (g_A \tilde{A}_\mu + g_B B_\mu Q_X) \tilde{\Psi}_a \tag{D1}$$

by inserting the wave functions of gauge bosons (B4) and those of fermions in Appendix C. Contributions coming from the interactions of the brane fermions are negligibly small, and can be dropped below.

1. $\gamma\bar{f}f$ couplings

The couplings between the nth KK photon and quarks are given by

$$
\begin{aligned}
&A_\mu^{\gamma(n)}(x)\int_1^{z_L} dz g_A \sum_{i=1,2}\bar{\Psi}_i\left\{h^L_{\gamma^{(n)}}T^{3_L}+h^R_{\gamma^{(n)}}T^{3_R}+\frac{g_B}{g_A}h^B_{\gamma^{(n)}}Q_X\right\}\gamma^\mu\Psi_i\\
&\quad\supset A_\mu^{\gamma(n)}(x)g_w\sqrt{L}\int_1^{z_L}dz\left[\bar{t}_L\gamma^\mu t_L(x)\left\{\frac{1}{2}h^L_{\gamma^{(n)}}(f_{t_L}f_{t_L}+f_{U_L}f_{U_L}-f_{B_L}f_{B_L})+\frac{1}{2}h^R_{\gamma^{(n)}}(f_{B_L}f_{B_L}+f_{U_L}f_{U_L}-f_{t_L}f_{t_L})\right.\right.\\
&\qquad\left.+\frac{g_B}{3g_A}h^B_{\gamma^{(n)}}(2f_{B_L}f_{B_L}+2f_{t_L}f_{t_L}+2f_{t'_L}f_{t'_L}-f_{U_L}f_{U_L})\right\}+\bar{b}_L\gamma^\mu b_L(x)\left\{\frac{1}{2}h^L_{\gamma^{(n)}}(f_{X_L}f_{X_L}-f_{b_L}f_{b_L}-f_{D_L}f_{D_L})\right.\\
&\qquad\left.\left.+\frac{1}{2}h^R_{\gamma^{(n)}}(f_{D_L}f_{D_L}-f_{X_L}f_{X_L}-f_{b_L}f_{b_L})+\frac{g_B}{3g_A}h^B_{\gamma^{(n)}}(2f_{b_L}f_{b_L}-f_{D_L}f_{D_L}-f_{b'_L}f_{b'_L}-f_{X_L}f_{X_L})\right\}\right]+(L\to R).
\end{aligned}
\tag{D2}
$$

$(L\to R)$ means that the wave functions of the left-handed fermions (f_{iL}) are changed to those of the right-handed fermions (f_{iR}). The couplings between the photon ($n=0$) and fermions are the same as those in the SM. Similarly the couplings between the nth KK photon and leptons are given by

$$
\begin{aligned}
&A_\mu^{\gamma(n)}(x)g_w\sqrt{L}\int_1^{z_L}dz\left[\bar{\nu}_{\tau L}\gamma^\mu\nu_{\tau L}(x)\left\{\frac{1}{2}h^L_{\gamma^{(n)}}(f_{\nu_{\tau L}}f_{\nu_{\tau L}}+f_{L_{3X,L}}f_{L_{3X,L}}-f_{L_{2Y,L}}f_{L_{2Y,L}})+\frac{1}{2}h^R_{\gamma^{(n)}}(f_{\nu_{\tau L}}f_{\nu_{\tau L}}+f_{L_{2Y,L}}f_{L_{2Y,L}}-f_{L_{3X,L}}f_{L_{3X,L}})\right.\right.\\
&\quad\left.-\frac{g_B}{g_A}h^B_{\gamma^{(n)}}f_{\nu_{\tau L}}f_{\nu_{\tau L}}\right\}+\bar{\tau}_L\gamma^\mu\tau_L(x)\left\{\frac{1}{2}h^L_{\gamma^{(n)}}(f_{L_{1X,L}}f_{L_{1X,L}}-f_{L_{3Y,L}}f_{L_{3Y,L}}-f_{\tau_L}f_{\tau_L})+\frac{1}{2}h^R_{\gamma^{(n)}}(f_{\tau_L}f_{\tau_L}-f_{L_{1X,L}}f_{L_{1X,L}}-f_{L_{3Y,L}}f_{L_{3Y,L}})\right.\\
&\quad\left.\left.-\frac{g_B}{g_A}h^B_{\gamma^{(n)}}(f_{\tau_L}f_{\tau_L}+f_{\tau'_L}f_{\tau'_L}+f_{L_{1X,L}}f_{L_{1X,L}})\right\}\right]+(L\to R)\\
&=A_\mu^{\gamma(n)}(x)g_w\sqrt{L}\int_1^{z_L}dz\bar{\tau}_L\gamma^\mu\tau_L(x)\left\{\frac{1}{2}h^L_{\gamma^{(n)}}(f_{L_{1X,L}}f_{L_{1X,L}}-f_{L_{3Y,L}}f_{L_{3Y,L}}-f_{\tau_L}f_{\tau_L})\right.\\
&\quad\left.+\frac{1}{2}h^R_{\gamma^{(n)}}(f_{\tau_L}f_{\tau_L}-f_{L_{1X,L}}f_{L_{1X,L}}-f_{L_{3Y,L}}f_{L_{3Y,L}})-\frac{g_B}{g_A}h^B_{\gamma^{(n)}}(f_{\tau_L}f_{\tau_L}+f_{\tau'_L}f_{\tau'_L}+f_{L_{1X,L}}f_{L_{1X,L}})\right\}+(L\to R).
\end{aligned}
\tag{D3}
$$

In the last equality, the use of the explicit form of the wave functions ν_τ and the coupling relation (B5) has been made. Neutrinos do not couple to $\gamma^{(n)}$ as expected.

2. $Z\bar{f}f$ couplings

The couplings between $Z^{(n)}$ and quarks are given by

$$
\begin{aligned}
&Z_\mu^{(n)}(x)g_w\sqrt{L}\int_1^{z_L}dz\left[\bar{t}_L\gamma^\mu t_L(x)\left\{\frac{1}{2}h^L_{Z^{(n)}}(f_{t_L}f_{t_L}+f_{U_L}f_{U_L}-f_{B_L}f_{B_L})+\frac{1}{2}h^R_{Z^{(n)}}(f_{B_L}f_{B_L}+f_{U_L}f_{U_L}-f_{t_L}f_{t_L})\right.\right.\\
&\quad\left.+\hat{h}_{Z^{(n)}}(f_{B_L}f_{t'_L}+f_{t_L}f_{t'_L})+\frac{g_B}{3g_A}h^B_{Z^{(n)}}(2f_{B_L}f_{B_L}+2f_{t_L}f_{t_L}+2f_{t'_L}f_{t'_L}-f_{U_L}f_{U_L})\right\}\\
&\quad+\bar{b}_L\gamma^\mu b_L(x)\left\{\frac{1}{2}h^L_{Z^{(n)}}(f_{X_L}f_{X_L}-f_{b_L}f_{b_L}-f_{D_L}f_{D_L})+\frac{1}{2}h^R_{Z^{(n)}}(f_{D_L}f_{D_L}-f_{X_L}f_{X_L}-f_{b_L}f_{b_L})+\hat{h}_{Z^{(n)}}(f_{D_L}f_{b'_L}-f_{X_L}f_{b'_L})\right.\\
&\quad\left.\left.+\frac{g_B}{3g_A}h^B_{Z^{(n)}}(2f_{b_L}f_{b_L}-2f_{D_L}f_{D_L}-2f_{b'_L}f_{b'_L}-f_{X_L}f_{X_L})\right\}\right]+(L\to R).
\end{aligned}
\tag{D4}
$$

Similarly the couplings between $Z^{(n)}$ and leptons are given by

$$Z_\mu^{(n)}(x) g_w \sqrt{L} \int_1^{z_L} dz \Big[\bar{\nu}_{\tau L} \gamma^\mu \nu_{\tau L}(x) \Big\{ \frac{1}{2} h^L_{Z^{(n)}} (f_{\nu_{\tau L}} f_{\nu_{\tau L}} + f_{L_{3X,L}} f_{L_{3X,L}} - f_{L_{2Y,L}} f_{L_{2Y,L}}) + \frac{1}{2} h^R_{Z^{(n)}} (f_{\nu_{\tau L}} f_{\nu_{\tau L}} - f_{L_{3X,L}} f_{L_{3X,L}} + f_{L_{2Y,L}} f_{L_{2Y,L}}) + \hat{h}_{Z^{(n)}} (f_{L_{2Y,L}} f_{\nu'_{\tau L}} + f_{L_{3X,L}} f_{\nu'_{\tau L}}) - \frac{g_B}{g_A} h^B_{Z^{(n)}} f_{\nu_{\tau L}} f_{\nu_{\tau L}} \Big\} + \bar{\tau}_L \gamma^\mu \tau_L(x) \Big\{ \frac{1}{2} h^L_{Z^{(n)}} (f_{L_{1X,L}} f_{L_{1X,L}} - f_{\tau_L} f_{\tau_L} - f_{L_{3Y,L}} f_{L_{3Y,L}}) + \frac{1}{2} h^R_{Z^{(n)}} (f_{\tau_L} f_{\tau_L} - f_{L_{1X,L}} f_{L_{1X,L}} - f_{L_{3Y,L}} f_{L_{3Y,L}}) + \hat{h}_{Z^{(n)}} (f_{\tau_L} f_{\tau'_L} + f_{L_{1X,L}} f_{\tau'_L}) - \frac{g_B}{g_A} h^B_{Z^{(n)}} (f_{\tau_L} f_{\tau_L} + f_{L_{1X,L}} f_{L_{1X,L}} + f_{\tau'_L} f_{\tau'_L}) \Big\} \Big] + (L \to R). \tag{D5}$$

3. $Z_R \bar{f} f$ couplings

The couplings between $Z_R^{(n)}$ and quarks are given by

$$Z_{R\mu}^{(n)}(x) g_w \sqrt{L} \int_1^{z_L} dz \Big[\bar{t}_L \gamma^\mu t_L(x) \Big\{ \frac{1}{2} h^L_{Z_R^{(n)}} (f_{t_L} f_{t_L} + f_{U_L} f_{U_L} - f_{B_L} f_{B_L}) + \frac{1}{2} h^R_{Z_R^{(n)}} (f_{B_L} f_{B_L} + f_{U_L} f_{U_L} - f_{t_L} f_{t_L}) + \frac{g_B}{3 g_A} h^B_{Z_R^{(n)}} (2 f_{B_L} f_{B_L} + 2 f_{t_L} f_{t_L} + 2 f_{t'_L} f_{t'_L} - f_{U_L} f_{U_L}) \Big\} + \bar{b}_L \gamma^\mu b_L(x) \Big\{ \frac{1}{2} h^L_{Z_R^{(n)}} (f_{X_L} f_{X_L} - f_{b_L} f_{b_L} - f_{D_L} f_{D_L}) + \frac{1}{2} h^R_{Z_R^{(n)}} (f_{D_L} f_{D_L} - f_{X_L} f_{X_L} - f_{b_L} f_{b_L}) + \frac{g_B}{3 g_A} h^B_{Z_R^{(n)}} (2 f_{b_L} f_{b_L} - f_{D_L} f_{D_L} - f_{b'_L} f_{b'_L} - f_{X_L} f_{X_L}) \Big\} \Big] + (L \to R). \tag{D6}$$

The couplings between $Z_R^{(n)}$ and leptons are

$$Z_{R\mu}^{(n)}(x) g_w \sqrt{L} \int_1^{z_L} dz \Big[\bar{\nu}_{\tau L} \gamma^\mu \nu_{\tau L}(x) \Big\{ \frac{1}{2} h^L_{Z^{(n)}} (f_{\nu_{\tau L}} f_{\nu_{\tau L}} + f_{L_{3X,L}} f_{L_{3X,L}} - f_{L_{2Y,L}} f_{L_{2Y,L}}) + \frac{1}{2} h^R_{Z^{(n)}} (f_{\nu_{\tau L}} f_{\nu_{\tau L}} - f_{L_{3X,L}} f_{L_{3X,L}} + f_{L_{2Y,L}} f_{L_{2Y,L}}) + \hat{h}_{Z^{(n)}} (f_{L_{2Y,L}} f_{\nu'_{\tau L}} + f_{L_{3X,L}} f_{\nu'_{\tau L}}) - \frac{g_B}{g_A} h^B_{Z^{(n)}} f_{\nu_{\tau L}} f_{\nu_{\tau L}} \Big\} + \bar{\tau}_L \gamma^\mu \tau_L(x) \Big\{ \frac{1}{2} h^L_{Z^{(n)}} (f_{L_{1X,L}} f_{L_{1X,L}} - f_{\tau_L} f_{\tau_L} - f_{L_{3Y,L}} f_{L_{3Y,L}}) + \frac{1}{2} h^R_{Z^{(n)}} (f_{\tau_L} f_{\tau_L} - f_{L_{1X,L}} f_{L_{1X,L}} - f_{L_{3Y,L}} f_{L_{3Y,L}}) + \hat{h}_{Z^{(n)}} (f_{\tau_L} f_{\tau'_L} + f_{L_{1X,L}} f_{\tau'_L}) - \frac{g_B}{g_A} h^B_{Z^{(n)}} (f_{\tau_L} f_{\tau_L} + f_{L_{1X,L}} f_{L_{1X,L}} + f_{\tau'_L} f_{\tau'_L}) \Big\} \Big] + (L \to R). \tag{D7}$$

4. $A^{\hat{4}} \bar{f} f$ couplings

All couplings of quarks and leptons to $A^{\hat{4}(n)}$ vanish.

5. $W \bar{f} f$ couplings

The coupling of quarks and leptons to $W^{(n)-}$ are given by

$$W_\mu^{(n)-}(x) \frac{g_w \sqrt{L}}{\sqrt{2}} \int_1^{z_L} dz [\bar{b}_L \gamma^\mu t_L(x) \{ h^L_{W^{(n)}} (f_{b_L} f_{t_L} + f_{D_L} f_{U_L}) + h^R_{W^{(n)}} (f_{b_L} f_{B_L} + f_{U_L} f_{X_L}) + \hat{h}_{W^{(n)}} (f_{b_L} f_{t'_L} - f_{b'_L} f_{U_L}) \} \bar{\tau}_L \gamma^\mu \nu_{\tau L}(x) \{ h^L_{W^{(n)}} (f_{\tau_L} f_{\nu_{\tau L}} + f_{L_{3X,L}} f_{L_{3Y,L}}) + h^R_{W^{(n)}} (f_{L_{1X,L}} f_{\nu_{\tau L}} + f_{L_{2Y,L}} f_{L_{3Y,L}}) + \hat{h}_{W^{(n)}} (f_{L_{3Y,L}} f_{\nu'_{\tau L}} - f_{\tau'_L} f_{\nu_{\tau L}}) \}] + (L \to R). \tag{D8}$$

The couplings of $W^{(n)+}$ are given by the Hermitian conjugate of (D8).

6. $W_R\bar{f}f$ couplings

The couplings between $W_R^{(n)-}$ and quarks are given by

$$W_{R\mu}^{(n)-}(x)\frac{g_w\sqrt{L}}{\sqrt{2}}\int_1^{z_L}dz\bar{b}_L\gamma^\mu t_L(x)\{h^L_{W_R^{(n)}}(f_{b_L}f_{t_L}+f_{D_L}f_{U_L})+h^R_{W_R^{(n)}}(f_{b_L}f_{B_L}+f_{U_L}f_{X_L})\}+(L\to R)=0. \quad \text{(D9)}$$

In the last equality the use of the explicit form for wave functions has been made. Similarly, for leptons the couplings are

$$W_{R\mu}^{(n)-}(x)\frac{g_w\sqrt{L}}{\sqrt{2}}\int_1^{z_L}dz\bar{\tau}_L\gamma^\mu\nu_{\tau L}(x)\{h^L_{W_R^{(n)}}(f_{\tau_L}f_{\nu_{\tau L}}+f_{L_{3X,L}}f_{L_{3Y,L}})+h^R_{W_R^{(n)}}(f_{\nu_{\tau L}}f_{L_{1X,L}}+f_{L_{2Y,L}}f_{L_{3Y,L}})\}+(L\to R)=0. \quad \text{(D10)}$$

In other words, the couplings between $W_R^{(n)}$ and quarks or leptons vanish.

APPENDIX E: HELICITY AMPLITUDES

Here we provide formulas useful for calculations of cross sections discussed in this paper. We begin with the following interaction between a massive gauge boson (A_μ) with mass m_A and a pair of the SM fermions,

$$\mathcal{L}_{\rm int}=J^\mu A_\mu=\bar{f}\gamma^\mu(g^A_{f_L}P_L+g^A_{f_R}P_R)fA_\mu. \quad \text{(E1)}$$

A helicity amplitude for the process $f(\alpha)\bar{f}(\beta)\to F(\delta)\bar{F}(\gamma)$ is given by

$$\mathcal{M}(\alpha,\beta;\gamma,\delta)=\frac{g_{\mu\nu}}{s-m_A^2+im_A\Gamma_A}J^\mu_{\rm in}(\alpha,\beta)J^\nu_{\rm out}(\gamma,\delta), \quad \text{(E2)}$$

where α,β (γ,δ) denote initial (final) spin states for fermion and antifermion, respectively, and Γ_A is the total decay width of the A boson. We have used the 't Hooft–Feynman gauge for the gauge boson propagator and there is no contribution from Nambu-Goldstone modes in the process with the massless initial states.

The currents for initial and final states are explicitly given by

$$J^\mu_{\rm in}(+,-)=-\sqrt{s}g^A_{f_R}(0,1,i,0),$$
$$J^\mu_{\rm in}(-,+)=-\sqrt{s}g^A_{f_L}(0,1,-i,0), \quad \text{(E3)}$$

and

$$J^\mu_{\rm out}(+,-)=-\sqrt{s}g^A_{F_R}(0,\cos\theta,-i,-\sin\theta),$$
$$J^\mu_{\rm out}(-,+)=\sqrt{s}g^A_{F_L}(0,-\cos\theta,-i,\sin\theta), \quad \text{(E4)}$$

where θ is the scattering angle and $f(F)$ denotes a flavor of the initial (final) state of fermions.

[1] ATLAS Collaboration, Phys. Lett. B **716**, 1 (2012).
[2] CMS Collaboration, Phys. Lett. B **716**, 30 (2012).
[3] H. E. Haber, "Supersymmetry part I (theory)", in the 2013 web edition of the Review of Particle Physics, http://pdg.lbl.gov.
[4] A. Djouadi and J. Quevillon, J. High Energy Phys. 10 (2013), 028.
[5] N. Arkani-Hamed, A. G. Cohen, and H. Georgi, Phys. Lett. B, **513**, 232 (2001).
[6] D. E. Kaplan and M. Schmaltz, J. High Energy Phys. 10 (2003) 039.
[7] M. Schmaltz and D. Tucker-Smith, Annu. Rev. Nucl. Part. Sci. **55**, 229 (2005).
[8] P. Kalyniak, T. Martin, and K. Moats, arXiv:1310.5130.
[9] K. Agashe, R. Contino, and A. Pomarol, Nucl. Phys. **B719**, 165 (2005).
[10] G. F. Giudice, C. Grojean, A. Pomarol, and R. Rattazzi, J. High Energy Phys. 06 (2007) 045.
[11] C. Anastasiou, E. Furlan, and J. Santiago, Phys. Rev. D **79**, 075003 (2009).
[12] B. Gripaios, A. Pomarol, F. Riva, and J. Serra, J. High Energy Phys. 04 (2009) 070.
[13] G. Panico, M. Safari, and M. Serone, J. High Energy Phys. 02 (2011) 103.
[14] B. Bellazzini, C. Csaki, and J. Serra, arXiv:1401.2457.
[15] G. Cacciapaglia and F. Sannino, arXiv:1402.0233.
[16] M. Carena, L. Da Rold, and E. Ponton, arXiv:1402.2987.
[17] L. Randall and R. Sundrum, Phys. Rev. Lett. **83**, 3370 (1999).
[18] K. Agashe, H. Davoudiasl, S. Gopalakrishna, T. Han, G.-Y. Huang, G. Perez, Z.-G. Si, and A. Soni, Phys. Rev. D, **76**, 115015 (2007).
[19] K. Agashe, A. Azatov, T. Han, Y. Li, Z.-G. Si, and L. Zhu, Phys. Rev. D, **81**, 096002 (2010).
[20] T. Appelquist, H.-C. Cheng, and B. A. Dobrescu, Phys. Rev. D **64**, 035002 (2001).

[21] S. Matsumoto, J. Sato, M. Senami, and M. Yamanaka, Phys. Rev. D **80**, 056006 (2009)
[22] K. Nishiwaki, K.-y. Oda, N. Okuda, and R. Watanabe, Phys. Lett. B **707**, 506 (2012).
[23] G. Cacciapaglia, A. Deandrea, J. Ellis, J. Marrouche, and L. Panizzi, Phys. Rev. D **87**, 075006 (2013).
[24] L. Edelhauser, T. Flacke, and M. Kramer, J. High Energy Phys. 08 (2013) 091.
[25] A. Datta, A. Raychaudhuri, and A. Shaw, Phys. Lett. B **730**, 42 (2014).
[26] G. Servant, arXiv:1401.4176.
[27] Y. Hosotani, Phys. Lett. **126B**, 309 (1983); Ann. Phys. (N.Y.) **190**, 233 (1989).
[28] A. T. Davies and A. McLachlan, Phys. Lett. B **200**, 305 (1988); Nucl. Phys. **B317**, 237 (1989).
[29] H. Hatanaka, T. Inami and C. S. Lim, Mod. Phys. Lett. A **13**, 2601 (1998).
[30] G. Burdman and Y. Nomura, Nucl. Phys. **B656**, 3 (2003).
[31] C. Csaki, C. Grojean, and H. Murayama, Phys. Rev. D **67**, 085012 (2003).
[32] C. S. Lim, Prog. Theor. Exp. Phys. **2014**, 02A101 (2014).
[33] A. D. Medina, N. R. Shah, and C. E. M. Wagner, Phys. Rev. D **76**, 095010 (2007).
[34] Y. Hosotani, K. Oda, T. Ohnuma, and Y. Sakamura, Phys. Rev. D **78**, 096002 (2008); **79**, 079902(E) (2009).
[35] M. Serone, New J. Phys. **12**, 075013 (2010).
[36] Y. Hosotani, S. Noda, and N. Uekusa, Prog. Theor. Phys. **123**, 757 (2010).
[37] S. Funatsu, H. Hatanaka, Y. Hosotani, Y. Orikasa, and T. Shimotani, Phys. Lett. B **722**, 94 (2013).
[38] Y. Hosotani and Y. Sakamura, Prog. Theor. Phys. **118**, 935 (2007).
[39] K. Agashe and R. Contino, Nucl. Phys. **B742**, 59 (2006).
[40] N. Haba, Y. Sakamura and T. Yamashita, J. High Energy Phys. 03 (2010) 069.
[41] J. Alcaraz *et al.* (ALEPH and DELPHI and L3 and OPAL and LEP Electroweak Working Group Collaborations), arXiv:hep-ex/0612034.
[42] ATLAS Collaboration, Report no ATLAS-CONF-2013-017.
[43] CMS Collaboration, Report No CMS-PAS-EXO-12-061.
[44] Y. Adachi, C. S. Lim, and N. Maru, Phys. Rev. D **76**, 075009 (2007); Phys. Rev. D **79**, 075018 (2009).
[45] M. Carena, A. D. Medina, B. Panes, N. R. Shah, and C. E. M. Wagner, Phys. Rev. D **77**, 076003 (2008).
[46] Y. Hosotani and Y. Kobayashi, Phys. Lett. B **674**, 192 (2009).
[47] M. Carena, A. D. Medina, N. R. Shah and C. E. M. Wagner, Phys. Rev. D **79**, 096010 (2009).
[48] N. Haba, Y. Sakamura, and T. Yamashita, J. High Energy Phys. 07 (2009) 020.
[49] Y. Hosotani, P. Ko, and M. Tanaka, Phys. Lett. B **680** 179 (2009).
[50] N. Haba, S. Matsumoto, N. Okada, and T. Yamashita, J. High Energy Phys. 03 (2010) 064.
[51] Y. Adachi, C. S. Lim, and N. Maru, Phys. Rev. D **80**, 055025 (2009).
[52] K. Agashe, A. Azatov, T. Han, Y. Li, Z. G. Si, and L. Zhu, Phys. Rev. D **81**, 096002 (2010).
[53] N. Uekusa, arXiv:0912.1218.
[54] K. Cheung and J. Song, Phys. Rev. D **81**, 097703 (2010); **81**, 119905(E) (2010).
[55] Y. Adachi, N. Kurahashi, C. S. Lim, and N. Maru, J. High Energy Phys. 11 (2010) 150.
[56] K. Kojima, K. Takenaga, and T. Yamashita, Phys. Rev. D **84**, 051701 (2011).
[57] T. Yamashita, Phys. Rev. D **84**, 115016 (2011).
[58] Y. Hosotani, M. Tanaka, and N. Uekusa, Phys. Rev. D **82**, 115024 (2010).
[59] Y. Hosotani, M. Tanaka, and N. Uekusa, Phys. Rev. D **84**, 075014 (2011).
[60] H. Hatanaka and Y. Hosotani, Phys. Lett. B **713**, 481 (2012).
[61] J. Park and S. K. Kang, J. High Energy Phys. 04 (2012) 101.
[62] Y. Adachi, N. Kurahashi, N. Maru, and K. Tanabe, Phys. Rev. D **85**, 096001 (2012); arXiv:1201.2290
[63] K. Hasegawa, N. Kurahashi, C. S. Lim, and K. Tanabe, Phys. Rev. D **87**, 016011 (2013).
[64] N. Maru and N. Okada, Phys. Rev. D **87**, 095019 (2013); **88**037701 (2013); arXiv:1310.3348.
[65] M. Kakizaki, S. Kanemura, H. Taniguchi, and T. Yamashita, Phys. Rev. D **89**, 075013 (2014).
[66] F. J. de Anda, arXiv:1403.4902.
[67] S. Funatsu, H. Hatanaka, Y. Hosotani, Y. Orikasa, and T. Shimotani (to be published)
[68] J. Beringer *et al.* (Particle Data Group Collaboration), Phys. Rev. D **86**, 010001 (2012).
[69] L. Basso, A. Belyaev, S. Moretti, G. M. Pruna, and C. H. Shepherd-Themistocleous, Eur. Phys. J. C **71**, 1613 (2011).
[70] S. Iso, N. Okada and Y. Orikasa, Phys. Rev. D **80**, 115007 (2009).
[71] J. L. Hewett and T. G. Rizzo, Phys. Rep. **183**, 193 (1989).
[72] A. Leike, Phys. Rep. **317**, 143 (1999).
[73] P. Langacker, Rev. Mod. Phys. **81**, 1199 (2009).
[74] E. Accomando, A. Belyaev, L. Fedeli, S. F. King, and C. Shepherd-Themistocleous, Phys. Rev. D **83**, 075012 (2011).
[75] J. Pumplin, D. R. Stump, J. Huston, H. L. Lai, P. Nadolsky, and W. K. Tung, J. High Energy Phys. 07 (2002) 012.
[76] T. Aaltonen *et al.* (CDF Collaboration), Phys. Rev. Lett. **101**, 202001 (2008).
[77] T. Aaltonen *et al.* (CDF Collaboration), Phys. Rev. D **87**, 092002 (2013).
[78] V. M. Abazov *et al.* (D0 Collaboration), Phys. Rev. D **88**, 112002 (2013).
[79] V. M. Abazov *et al.* (D0 Collaboration), arXiv:1403.1294.
[80] CMS Collaboration, Phys. Lett. B **717**, 129 (2012).
[81] ATLAS Collaboration, J. High Energy Phys. 02 (2014) 107.
[82] O. Antuñano, J. H. Kühn, and G. Rodrigo, Phys. Rev. D **77**, 014003 (2008).
[83] G. Marques Tavares, and M. Schmaltz, Phys. Rev. D **84**, 054008 (2011).
[84] M. Dittmar, Phys. Rev. D **55**, 161 (1997).
[85] M. Dittmar, A.-S. Nicollerat, and A. Djouadi, Phys. Lett. B **583**, 111 (2004).
[86] N. Haba, K. Kaneta, and S. Tsuno, Phys. Rev. D **87**, 095002 (2013).

PTEP

Prog. Theor. Exp. Phys. **2014**, 02A101 (21 pages)
DOI: 10.1093/ptep/ptt083

The Higgs particle and higher-dimensional theories

C. S. Lim*

Department of Mathematics, Tokyo Woman's Christian University, Tokyo 167-8585, Japan
*E-mail: lim@lab.twcu.ac.jp

Received August 3, 2013; Accepted August 24, 2013; Published February 10, 2014

In spite of the great success of LHC experiments, we do not know whether the discovered "standard model-like" Higgs particle is really what the standard model predicts, or a particle that some new physics has in its low-energy effective theory. Also, the long-standing problems concerning the property of the Higgs and its interactions are still there, and we still do not have any conclusive argument on the origin of the Higgs itself. In this article we focus on higher-dimensional theories as new physics. First we give a brief review of their representative scenarios and closely related 4D scenarios. Among them, we mainly discuss two interesting possibilities of the origin of the Higgs: the Higgs as a gauge boson and the Higgs as a (pseudo) Nambu–Goldstone boson. Next, we argue that theories of new physics are divided into two categories, i.e., theories with normal Higgs interactions and those with anomalous Higgs interactions. Interestingly, both the candidates for the origin of the Higgs mentioned above predict characteristic "anomalous" Higgs interactions, such as the deviation of the Yukawa couplings from the standard model predictions. Such deviations can hopefully be investigated by precision tests of Higgs interactions at the planned ILC experiment. Also discussed is the main decay mode of the Higgs, $H \to \gamma\gamma$. Again, theories belonging to different categories are known to predict remarkably different new physics contributions to this important process.

Subject Index B40, B43

1. Introduction

1.1. What the discovery of the standard model-like Higgs particle means

We have heard of the very impressive results from LHC experiments that a new particle with a mass of 126 (GeV), which behaves like the Higgs particle of the standard model (SM), has been discovered at CERN. So far, the properties of the particle seem to be consistent with the Higgs of the SM, but it would be premature to conclude whether it is really the Higgs of the SM or a standard model-like Higgs particle predicted by some theory of new physics (physics beyond the standard model). In this article we discuss what the discovery of this particle means in the context of higher-dimensional theories with extra dimensions.

1.2. New physics and its "decoupling limit"

Although we are interested in the possibility that the standard model-like Higgs is some particle predicted by new physics, it is at the same time a clear fact that the SM is a very successful theory at low energies ($E \leq M_W$). We thus expect that any theory of new physics reduces into the SM at low energies. To be more precise, we can think of a "decoupling limit" in new physics theories. The limit is achieved by sending the typical mass (energy) scale of new physics, say M, to infinity: $M \to \infty$. In that limit, various new particles predicted to exist in the new physics with masses of

© The Author(s) 2014. Published by Oxford University Press on behalf of the Physical Society of Japan.
This is an Open Access article distributed under the terms of the Creative Commons Attribution License (http://creativecommons.org/licenses/by/3.0/), which permits unrestricted use, distribution, and reproduction in any medium, provided the original work is properly cited.
Funded by SCOAP[3]

Downloaded from http://ptep.oxfordjournals.org/ at Osaka Daigaku Ningen on January 18, 2017

$\mathcal{O}(M)$ are expected to "decouple" from the low-energy sector [1], and the theories are expected to reduce into the SM. From a field theoretical point of view, the effects of new particles at low energies are described by operators with mass dimension higher than 4 (from the viewpoint of 4D space-time), "irrelevant operators" whose Wilson coefficients are suppressed by the inverse powers of M ($1/M^2$ in the case of operators with mass dimension 6). Thus the effects of new heavy particles are suppressed and they "decouple" from the low-energy effective Lagrangian.

Let us note that, according to the argument based on dimensional analysis, marginal or relevant operators with mass dimensions equal to or less than 4 may be affected by the presence of heavy new particles. The argument of Ref. [1] is that such effects only affect the renormalization procedure and can be absorbed into the bare parameters in the process of renormalization. Let us note, however, that the hierarchy problem—to be more precise, the problem of quadratically divergent quantum correction to the Higgs mass—exactly concerns the relation between the observed Higgs mass and the corresponding bare mass(-squared) parameter. Thus, when we consider the hierarchy problem, the contributions of new heavy particles should be seriously taken into account. This is why super-partners in supersymmetry (SUSY) theory can play an important role in the solution to the hierarchy problem. Also, in a type of higher-dimensional gauge theory, "gauge–Higgs unification (GHU)" [2–7], discussed later, the summation over the contributions of all Kaluza–Klein (KK) modes makes the quantum correction to the Higgs mass-squared finite, thus solving the hierarchy problem [8].

For instance, in the MSSM (minimal supersymmetric standard model), two Higgs doubles H_u, H_d are introduced to preserve SUSY. The lighter CP-even neutral scalar particle denoted as a linear combination, $\sqrt{2}[\cos\alpha(\mathrm{Re}H_u^0 - \frac{v_u}{\sqrt{2}}) - \sin\alpha(\mathrm{Re}H_d^0 - \frac{v_d}{\sqrt{2}})]$, is identified with the SM-like Higgs. The angle α is fixed by the parameters in the Higgs potential and $v_{u,d}$ are the VEVs of the two Higgs doublets. The couplings of the SM-like Higgs with matter fermions and gauge bosons generally contain the parameters α and β, where β represents the ratio of the VEVs, $\tan\beta \equiv v_u/v_d$. The decoupling limit of the MSSM is achieved by sending the SUSY breaking mass scale M_{SUSY} to infinity. In this limit, it turns out that just a linear combination of two Higgs doublets that alone develops the VEV $v = \sqrt{v_u^2 + v_d^2}$ becomes the lighter scalar and is identified with the SM-like Higgs, as we naturally expect. Correspondingly, in this limit, $\alpha \to \beta - \frac{\pi}{2}$ and all interactions are known to reduce to those we expect in the SM, as is anticipated from the decoupling theorem [1]. We therefore conclude that the decoupling limit of the MSSM is just the SM, although, in the MSSM, in contrast to the case of the SM, the Higgs mass is "calculable", since the quartic coupling of the Higgs potential receives a contribution only from the "D-term" and the Higgs mass at the tree level is more or less equivalent to the weak gauge boson masses.

Now let us turn to the case of higher-dimensional theories. Because of the presence of the extra dimension, we now get an infinite tower of KK modes with higher extra space momenta and therefore higher 4D masses. The non-zero KK modes are new heavy particles. Hence in higher-dimensional theories the decoupling limit is achieved by

$$M_c = \frac{1}{R} \to \infty, \tag{1.1}$$

where R is a generic size of the extra dimension, being the radius when the extra space is just a circle S^1, and M_c is the corresponding "compactification" mass scale. In this limit, all (non-zero) KK modes, having masses of the order of M_c, are expected to decouple from the low-energy effective Lagrangian.

As a new feature of higher-dimensional gauge theory, it is basically possible to construct a theory in which the Higgs-like particle does not exist in the decoupling limit, i.e. the higgsless model [9]. In this

Downloaded from http://ptep.oxfordjournals.org/ at Osaka Daigaku Ningen on January 18, 2017

type of theory the KK zero-mode with vanishing extra space momentum is excluded by imposing a Dirichlet-type boundary condition for the Higgs field along an interval, as the 1D extra space. Thus all KK modes of the Higgs field have masses of $\mathcal{O}(M_c)$, while the violation of the unitarity of the scattering amplitude of the (longitudinal components of) weak gauge bosons is remedied at higher energies by the presence of a tower of massive non-zero KK modes of the gauge bosons. The decoupling limit of the higgsless theory does not contain SM-like Higgs.

Now we know that at least an SM-like Higgs has been discovered; the higgsless scenario thus seems to be excluded unless a theory with lower M_c is possible without contradicting various experimental data.

Also ruled out is the theory where, even though the decoupling limit is the SM, the modification of the Higgs sector (Higgs interaction) is so huge that it already contradicts reality. The GHU model with H-parity [10,11] is probably such a theory. H-parity is a discrete symmetry under which, among SM fields, only the Higgs field has odd parity while the other fields have even parities. This symmetry exists only when the weak scale and the compactification scale are comparable:

$$x \equiv \frac{g_4}{2}\pi R v = \pi \frac{M_W}{M_c} = \frac{\pi}{2}, \tag{1.2}$$

where g_4 is the 4D gauge coupling constant. Note that, even though M_c is near the weak scale, the masses of non-zero KK modes can be sufficiently large due to the presence of the warp factor when the theory is formulated on the Randall–Sundrum space-time [12–17]. Just as the R-parity implies in the MSSM, the H-parity implies that a single Higgs particle cannot decay into ordinary SM particles, thus making the Higgs stable. As the recently discovered SM-like Higgs particle decays into 2 photons, this interesting scenario seems to be inconsistent with the data.

There still remain other interesting higher-dimensional scenarios. It should be noticed that some of these scenarios are not only consistent with the data, having the SM at their decoupling limits, but they also predict some characteristic deviations from the SM predictions, as we will see below.

Even though the properties of the SM-like Higgs particle seem to be consistent with that of the SM Higgs, we still have a strong motivation to investigate further the properties of the Higgs. Namely, in the SM, in clear contrast to the sector of gauge interaction, the Higgs sector is mysterious, having several long-standing problems, such as the hierarchy problem, as already mentioned, and the problem of many arbitrary parameters in the sector of Higgs interactions, such as Yukawa couplings. We still do not understand the origin of the generation-dependent hierarchical fermion masses and generation (flavor) mixings. These problems all come from the fact that, in contrast to the case of the gauge interactions, there is no guiding principle (symmetry?) to restrict the interactions of the Higgs. Let us note that, even though many of the new physics theories have been proposed mainly in order to solve the hierarchy problem, not all of them have mechanisms to restrict the Yukawa coupling. For instance, in the MSSM there is no principle to restrict the couplings (except for gauge invariance) and the Yukawa couplings are free parameters to start with.

These problems suggest that we have not (fully) understood the origin of the Higgs itself. From such points of view, it will be of crucial importance to study how new physics theories predict the Higgs interactions and to perform precision tests of those interactions. As mentioned above, some higher-dimensional theories and also some closely related 4D theories make very specific predictions concerning the Higgs interactions, i.e. "anomalous Higgs interactions".

Such precision tests will not be easy to perform at the LHC experiment and are expected to be done at the planned ILC experiment.

Downloaded from http://ptep.oxfordjournals.org/ at Osaka Daigaku Ningen on January 18, 2017

2. Brief review of higher-dimensional theories

We now summarize very briefly some of the representative scenarios of new physics based on higher-dimensional theories. Also discussed are 4D scenarios closely related to higher-dimensional gauge theory, i.e. the scenarios in which Higgs is a (pseudo) Nambu–Goldstone (NG) boson due to some global symmetries. Since solving the hierarchy problem has been the main motivation for many new physics theories, we categorize the scenarios depending on their attitudes concerning the hierarchy problem.

2.1. Theory without a solution to the hierarchy problem

The representative and popular scenario of this type is the so-called "universal extra dimension (UED)". It is a straightforward extension of the SM to its higher-dimensional version [18]. All SM particles are allowed to propagate universally in the higher-dimensional bulk space. The extra dimension is assumed to be an orbifold torus divided by its discrete symmetry, such as S^1/Z_2 or T^2/Z_4, in order to realize a chiral (left–right asymmetric) theory needed to incorporate the SM. The theory has a discrete symmetry called KK-parity, under which particles of even (odd) KK numbers have even (odd) KK-parities. Thus the lightest first KK mode, having odd KK-parity, cannot decay into ordinary SM particles with even KK-parities and thus becomes stable, just like the LSP in the MSSM with R-parity; it therefore is a candidate for the dark matter. This KK-parity makes the production of a single first KK excited state impossible at ILC. On the other hand, the production of a second KK excited state with even KK-parity is possible through the KK-number violating processes induced by the quantum loop effects [19].

2.2. Theories with a mechanism to solve the hierarchy problem not invoking any symmetry

We now discuss the scenarios formulated in higher-dimensional space-time that aim to solve the hierarchy problem, namely, to explain naturally the hierarchy between the Planck scale $M_{\rm pl}$ and M_W. The scenarios we discuss are the ADD model with large extra dimension [20] and the Randall–Sundrum model with warped extra dimension [21]. In both scenarios, the SM particles live in a 4D space-time (a brane), not an extra dimension, and only gravity propagates in the bulk. This property leads to new types of solutions to the hierarchy problem, not seen in the theories in ordinary 4D space-time. The mechanism to solve the hierarchy problem does not invoke any symmetry.

Let us first discuss the ADD model. When Einstein proposed his unified theory of gravity and electromagnetism along the idea of Kaluza and Klein, the extra dimension was assumed to be small, i.e. $M_c \simeq M_{\rm pl}$: a "small extra dimension". The basic reason for this is that, in the unified field theory, electromagnetic interaction originates from gravity interaction. Thus the electric charge e is inevitably proportional to the (square root of) the Newton constant G_N. On the other hand, the source of the gravity is the energy-momentum and the electric charge should also be proportional to the extra-dimensional momentum of the order of M_c. In this way, we obtain the relation

$$e = \frac{4\sqrt{\pi G_N}}{R} \to R = \frac{4\sqrt{\pi G_N}}{e} \simeq 4 \times 10^{-32}\ (\text{cm}). \tag{2.1}$$

In the ADD model, all the SM particles, including the photon, are assumed to live in the brane, and the size of the extra dimension is free from the constraint coming from the value of the electric charge. In this scenario, the original higher-dimensional Planck scale $M_{\rm pl}^{(0)}$ is of the order of the weak scale $M_{\rm pl}^{(0)} \sim M_W$, and, to begin with, there is no hierarchy between the Planck scale and the weak scale. Too small a Planck scale may lead to an unacceptably strong gravitational force. This potential

Downloaded from http://ptep.oxfordjournals.org/ at Osaka Daigaku Ningen on January 18, 2017

difficulty is solved by assuming a large extra dimension. Namely, the "gravitational flux" is spread toward the direction of the large extra dimension, thus recovering ordinary very weak 4D gravity. Assuming the presence of an n-dimensional extra dimension, the 4D Planck scale $M_{\rm pl}$ is given as

$$M_{\rm pl}^2 \sim M_{\rm pl}^{(0)2+n} \cdot R^n. \tag{2.2}$$

Assuming that $M_{\rm pl}^{(0)} \sim 1$ (TeV), we get $R \sim 0.1$ (mm) for $n = 2$ (for $n = 1$ the obtained R is unacceptably large). This is the scenario of the "large extra dimension".

While the gravity at distances larger than the compactification size reduces to ordinary Newtonian gravity, at shorter distances, the gravity recovers the original higher-dimensional one whose mass scale is not $M_{\rm pl}$ but $M_{\rm pl}^{(0)} \sim M_W$. Thus the most stringent bound for the ADD model comes from the data from LHC. A search for the anomalous jet + missing E_T events at CMS has put a bound $M_{\rm pl}^{(0)} > 3.0$–5.0 (TeV) for $n = 2$–6 (for higher n the bound is less stringent) [22].

This scenario, however, faces its own new hierarchy problem: the size of the extra dimension 0.1 (mm) for $n = 2$ means $M_c = 2 \times 10^{-2}$ (eV), which implies a new hierarchy $M_c/M_W \sim 10^{-13}$!

Randall and Sundrum pointed out that the new hierarchy problem in the ADD model can be solved once we allow that the bulk space-time is a curved one [21]. They assume that 5D space-time is anti-de Sitter with a negative cosmological constant, while the extra space is compactified on an orbifold S^1/Z_2. The solution to the Einstein equation has a "warp factor":

$$g_{MN} = \begin{pmatrix} e^{-2\kappa|y|} \cdot \eta_{\mu\nu} & 0 \\ 0 & 1 \end{pmatrix}, \tag{2.3}$$

where, in the warp factor $e^{-2\kappa|y|}$, κ is a parameter of the theory of $\mathcal{O}(M_{\rm pl})$ and y is the extra space coordinate. The warp factor may be understood as the factor of "space-like inflation". In fact it mimics the factor e^{Ht} (H: Hubble constant) in the inflationary universe caused by a positive cosmological constant. The sign difference of the cosmological constant may be attributed to the sign difference of the time and space components of the metric tensor. The absolute value $|y|$ in the warp factor is due to the orbifolding of the extra space S^1/Z_2.

Assuming that the SM particles all live in the 4D brane at $y = \pi R$ ("visible brane"), the hierarchy between the Planck scale and the weak scale is naturally realized by the warp factor without any hierarchy between the input parameters of the theory:

$$\frac{M_W}{M_{\rm pl}} \sim e^{-\kappa\pi r_c} \tag{2.4}$$

where r_c is the radius of the circle.

The theory predicts the presence of graviton non-zero KK modes, whose masses are spaced by $\mathcal{O}$ (TeV) and whose gravity couplings are suppressed not by $M_{\rm pl}$ but by $\mathcal{O}$ (TeV). Therefore, such new KK gravitons can be searched for at LHC as the resonance states in the l^+l^- and $\gamma\gamma$ final states. The current lower bound on the KK graviton mass ranges from 0.9 (TeV) to 2.1 (TeV) depending on the parameter of the theory [23,24].

Incidentally, how can this Randall–Sundrum model solve the hierarchy problem at the quantum level, i.e. the problem of quadratic divergence in the quantum correction to the Higgs mass, without relying on some symmetry? Though an explicit argument cannot be found in the literature, the quadratic divergence will also be accompanied by the warp factor after the renormalization of the Higgs field as $\Lambda^2 e^{-2\kappa\pi r_c}$ and the divergence will be harmless.

Downloaded from http://ptep.oxfordjournals.org/ at Osaka Daigaku Ningen on January 18, 2017

2.3. Theories with a mechanism to solve the hierarchy problem invoking some symmetry

The hierarchy problem concerns a very small number. The smallness of the physical observable can be "naturally" preserved under its quantum correction provided that some symmetry is enhanced in the action of the theory when that observable is switched off. This is because, in the case in which the condition is met, even if the observable is induced at quantum level, it should be inevitably proportional to that small number, such that the correction goes away at the limit of exact symmetry.

We now discuss a few representative scenarios of this sort in the context of higher-dimensional theories. Some of them can actually be formulated in 4D space-time, but are closely related to a kind of higher-dimensional gauge theory.

2.3.1. Gauge–Higgs unification. We first discuss the scenario of "gauge–Higgs unification (GHU)". Einstein attempted to unify the gravity and electromagnetic interactions known at that time mediated by bosons with spin $s = 2, 1$ in the framework of 5D gravity theory. We now know that there is also Higgs interaction. So it is natural to expect that gauge and Higgs interactions mediated by $s = 1, 0$ bosons are unified in the framework of higher-dimensional gauge theories. For instance, in the simplest 5D U(1) gauge theory, the gauge field A_M is decomposed into

$$A_M = (A_\mu, A_y) \tag{2.5}$$

where A_μ corresponds to the 4D gauge field (and its non-zero KK partners), while the extra space component A_y—to be more precise, its KK zero mode, behaving as a 4D scalar—is identified with the (SM-like) Higgs field. This is the GHU scenario, the idea of which is not new [2–7]. In particular, Hosotani proposed a mechanism of dynamical spontaneous gauge symmetry breaking due to the VEV of A_y for the non-Abelian case, the "Hosotani mechanism" [5–7].

One pleasing aspect of this scenario is that it provides a new avenue for the solution to the hierarchy problem by virtue of higher-dimensional local gauge symmetry under which A_y transforms inhomogeneously: $A_y \to A_y + \partial_y \lambda$, λ being a y-dependent gauge parameter [8]. We know that a photon never acquires mass, even at the quantum level, since the local mass-squared operator $m_A^2 A_\mu A^\mu$ is forbidden by local gauge symmetry. In the same way, the Higgs (the zero-mode of A_y) never has a local mass-squared operator, thus eliminating the quadratic divergence. What was stressed in Ref. [8] was the importance of the summation over all KK modes at the quantum correction of the Higgs mass. It is frequently argued that, when we consider low-energy effective theories, only KK zero-modes should be taken into account, probably relying on the wisdom of the decoupling theorem [1]. However, as has already been pointed out in the introduction, when we consider the hierarchy problem, heavy new particles play important roles. Also, we should note that a momentum cutoff spoils local gauge invariance. If we truncate the KK modes at some level, it is equivalent to the cutoff of the extra-dimensional momentum. This is why the summation over all KK modes is crucial to get the finite quantum correction to the Higgs mass.

Actually, the Higgs acquires a finite mass at the quantum level. This is because the zero-mode of A_y, i.e. the Higgs, has a physical interpretation as an Aharonov–Bohm (AB) phase or the phase of a Wilson loop. Let us note that the VEV of the Higgs in this scenario is nothing but a constant gauge field, which gives a vanishing field strength and therefore seems to be just a pure gauge configuration. However, in the case in which the extra dimension is a non-simply-connected space like a circle S^1, the constant gauge field can be interpreted as a component of the vector potential generated by the magnetic flux, penetrating inside the circle. Thus the Higgs field is not a pure gauge but has a physical meaning as the AB phase or the phase of the Wilson loop W. At the quantum level, the

Downloaded from http://ptep.oxfordjournals.org/ at Osaka Daigaku Ningen on January 18, 2017

Higgs potential is induced as (the real part of) the polynomial of W. Note that $W = \mathrm{P}(e^{i\frac{g}{2}\oint A_y dy})$ is of course a gauge invariant but global (not local) operator, which has nothing to do with UV divergence. This is why we get a finite but non-vanishing Higgs mass in GHU, which disappears at the "decompactification limit $R \to \infty$", where the Wilson loop is trivial. The situation is very similar to the case of finite temperature field theory. At finite temperature the Coulomb potential of a photon is known to have a mass of $\mathcal{O}(T)$ (T: temperature). The mass disappears as $T \to 0$, corresponding to the decompactification limit.

Another pleasing aspect of GHU is that it may shed some light on the problem of arbitrary Yukawa couplings, for instance. In this scenario the Higgs is originally a gauge field. Therefore Yukawa coupling is gauge coupling to start with and, if we succeed in constructing a realistic model, the Yukawa couplings are expected to be constrained by the gauge principle. On the other hand, it is a non-trivial question how the hierarchical fermion masses are realized starting from the gauge coupling, which is universal for all generations. Fortunately, as a new feature of higher-dimensional gauge theories, when orbifold S^1/Z_2 is adopted as the extra dimension, the so-called Z_2-odd bulk mass term of the form

$$-\epsilon(y)M\bar{\psi}\psi \tag{2.6}$$

is allowed. Here $\epsilon(y)$ is a sign function (± 1 depending on the sign of y), which mimics the kink-like configuration of some scalar field and causes the localization of Weyl fermions at two different fixed points of the orbifold depending on its chirality: the mode functions of the KK zero-mode of right- and left-handed fermions behave as $\propto e^{-M|y|}$, $\propto e^{-M|y-\pi R|}$ (R is the radius of S^1). Since the Yukawa coupling is the overlap integral of these mode functions of different chiralities, we eventually get the exponentially suppressed fermion masses behaving as (M_i being flavor-dependent bulk masses)

$$\sim M_W(\pi R M_i)e^{-\pi R M_i}(R: \text{ the radius of } S^1) \tag{2.7}$$

for lighter (1st and 2nd) generations. We thus have a mechanism to realize the hierarchical fermion masses without any hierarchical structure of the parameters M_i. It is interesting to note that, if we plot the logarithm of observed quark masses as a function of generation number, they align along a straight line, roughly speaking. If we take this seriously, this suggests that the quark masses were all equal before the exponential suppression, which is exactly what GHU implies starting from the universal Yukawa couplings. A study pursuing this line of argument is now ongoing.

For the scenario of GHU to be viable, we need to construct a minimal model based on this scenario, just as the MSSM in the case of SUSY. In this attempt, one non-trivial feature arises. In the case of the MSSM, the SM was just made supersymmetric with the same gauge group SU(2) $\times$ U(1) for the electroweak sector. In the case of GHU, however, this gauge group should be inevitably extended. This is because in this scenario the Higgs is originally a gauge field and therefore belongs to an adjoint representation of the gauge group, while, as is well known, the Higgs in the SM is an SU(2) doublet, i.e. a fundamental representation of SU(2). The breakthrough of this problem is to extend the gauge group a little. The simplest choice is to adopt SU(3) as the electroweak sector. A minimal SU(3) GHU (electroweak) model has been discussed [25,26].

The minimal model is formulated in 5D space-time with an orbifold S^1/Z_2 as its extra dimension. The orbifold is defined by the identification of two points on the circle connected by Z_2 transformation,

$$Z_2 : y \to -y, \tag{2.8}$$

Downloaded from http://ptep.oxfordjournals.org/ at Osaka Daigaku Ningen on January 18, 2017

where y is the coordinate along S^1. We have two fixed points, $y = 0, \pi R$, which are invariant under the transformation. The main motive for adopting the orbifold, not just a manifold like S^1, is the realization of chiral theory by "orbifolding". By identification under Z_2, the degree of freedom of the extra space points becomes one half and, correspondingly, either the right or left Weyl fermion survives as the fermion zero mode.

Another merit of adopting the orbifold is that, by assigning different Z_2-parities for each element of the irreducible representation of SU(3), the gauge symmetry can be explicitly broken by the orbifolding [27], as is explained now.

To realize the mechanism, we assign the Z_2-parities for the elements of the SU(3) triplet representation as follows:

$$\Psi(-y) = -\mathcal{P}\gamma^5\Psi(y) \qquad \left(\mathcal{P} = \begin{pmatrix} 1 & 0 & 0 \\ 0 & 1 & 0 \\ 0 & 0 & -1 \end{pmatrix}\right), \tag{2.9}$$

where the triplet ψ contains the quark fields

$$\psi = \begin{pmatrix} u_L \\ d_L \\ d_R \end{pmatrix}. \tag{2.10}$$

The matrix $\mathcal{P}$ represents the Z_2-parities of the elements of the triplet. Let us note that, as is seen in (2.9), Z_2 has an aspect of chiral transformation for fermions. Thus the zero-mode, having even Z_2-parity, of the upper two elements of ψ is a left-handed fermion, while the zero-mode of the lowest element is right-handed. Thus a chiral theory needed to accommodate the SM is realized. Now it is clear that an ordinary bulk mass term of the form $M\bar{\psi}\psi$ is not allowed, since Z_2 contains a chiral transformation. This is why the Z_2-odd bulk mass term (2.6) is introduced to be consistent with the orbifolding.

The KK zero-mode of the 4D gauge boson sector is given as

$$A_\mu^{(0)} = \frac{1}{2}\begin{pmatrix} W_\mu^3 + \frac{B_\mu}{\sqrt{3}} & \sqrt{2}W_\mu^+ & 0 \\ \sqrt{2}W_\mu^- & -W_\mu^3 + \frac{B_\mu}{\sqrt{3}} & 0 \\ 0 & 0 & -\frac{2}{\sqrt{3}}B_\mu \end{pmatrix}. \tag{2.11}$$

Namely, only the gauge bosons connecting the elements of ψ with the same Z_2-parities have even Z_2-parity and therefore the zero-modes. It is now clear that the zero-mode sector of the gauge bosons is exactly what we need in the SM. In this way, SU(3) gauge symmetry is broken into SU(2) $\times$ U(1) by the orbifolding [27].

The zero-mode sector of the 4D scalar is given as

$$A_y^{(0)} = \frac{1}{\sqrt{2}}\begin{pmatrix} 0 & 0 & \phi^+ \\ 0 & 0 & \phi^0 \\ \phi^- & \phi^{0*} & 0 \end{pmatrix}. \tag{2.12}$$

We find that, this time, only the "broken generator" part G/H ($G = \mathrm{SU}(3)$, $H = \mathrm{SU}(2) \times \mathrm{U}(1)$) has zero-modes. This is because A_μ and A_y should have opposite Z_2-parities, just as x^μ and y have. The "off-diagonal" elements of (2.12) just correspond to the SU(2) doublet of the Higgs field in the SM.

Downloaded from http://ptep.oxfordjournals.org/ at Osaka Daigaku Ningen on January 18, 2017

Thus by orbifolding we just get both the necessary gauge fields and the Higgs doublet of the SM, and nothing else. This seems to suggest that the adjoint representation of SU(3) has been prepared in order to accommodate the gauge–Higgs sector of the SM: $8 \to 3 + 1 + 2 \times 2$.

2.3.2. Higgs as a pseudo Nambu–Goldstone boson. So far, we have discussed supersymmetry and gauge symmetry (the Higgs as a gauge boson in the case of GHU) as possible symmetries for solving the hierarchy problem. There remains a third possibility, i.e. global symmetry: the Higgs as a (pseudo) Nambu–Goldstone (NG) boson. A representative scenario based on this idea is the "little Higgs (LH)".

Quite interestingly, there seems to be a close relation between the GHU and LH scenarios, although the LH is a theory in 4D space-time.

There are a few pieces of "circumstantial evidence" to imply such a close relation:

(a) In both scenarios, the gauge group of the SM is enlarged to some larger group G, which is broken to some subgroup H, and the Higgs is identified with the NG boson of G/H in the case of LH, and A_y of G/H in GHU, as we have seen.
(b) The coupling of A_y to fermions in 5D GHU takes the form $g\bar{\psi}(i\gamma_5)\psi \cdot A_y$, which mimics the pseudo scalar coupling of NG bosons, such as pions.
(c) Both have shift symmetries,

$$A_y \to A_y + \partial_y \lambda \text{ (for GHU)}, \;\; G \to G + \text{const. (for LH)}, \tag{2.13}$$

where the former transformation is a higher-dimensional local gauge transformation and the latter is the transformation of some global symmetry.

Actually, the LH scenario was inspired by the so-called "dimensional deconstruction" scenario, which may be regarded as a "latticized" GHU, as we will see below. So, once we make the scenario of dimensional deconstruction into the bridge between GHU and LH, their mutual relation becomes more solid.

One may wonder how global and local symmetries can be "closely related". The point is that in the LH and also in dimensional deconstruction there is a repetition of a global symmetry, $\mathrm{SU}(m) \times \mathrm{SU}(m) \times \cdots \times \mathrm{SU}(m) = (\mathrm{SU}(m))^N$ with gauge parameters λ_i $(i = 1, 2, \ldots N)$. On the other hand, in the GHU, higher-dimensional local gauge symmetry is described by a gauge parameter $\lambda(y)$. If we treat the integer i of λ_i as a "discretized extra space coordinate", it can be identified. This argument suggests that dimensional deconstruction (and also LH) may be understood, roughly speaking, as a sort of "latticized" GHU.

Dimensional deconstruction

Before going into the LH scenario, we briefly discuss the scenario of dimensional deconstruction [28,29], and its close relationship with the GHU.

The scenario has the following remarkable features:

(a) The Higgs is a pseudo NG boson, a bound state of fermions, just as pions in QCD.
(b) There is a repetition of gauge symmetries: $(G \times G_s)^N$ $(G = \mathrm{SU}(m), G_s = \mathrm{SU}(n))$.
(c) The quantum correction to the Higgs mass is finite (for $N \geq 3$) without relying on SUSY.

The model has N pairs of (say, left-handed) Weyl fermions as matter fields with the bi-fundamental representations of

$$\begin{aligned} &(m, \bar{n}), \;\; (\mathrm{SU}_i(m), \mathrm{SU}_i(n)) \\ &(\bar{m}, n) \; (\mathrm{SU}_{i+1}(m), \mathrm{SU}_i(n)) \; (i = 1 - N), \end{aligned} \tag{2.14}$$

Downloaded from http://ptep.oxfordjournals.org/ at Osaka Daigaku Ningen on January 18, 2017

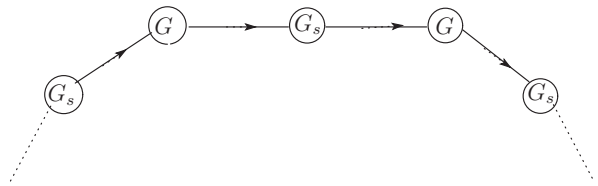

Fig. 1. The moose diagram.

where periodic boundary conditions $\mathrm{SU}_{N+1}(m) = \mathrm{SU}_1(m)$ etc. are imposed. The structure of the theory is represented by a so-called "moose diagram", shown in Fig. 1, where each oriented line corresponds to a Weyl fermion with either the $(m, \bar{n})$ or $(\bar{m}, n)$ representation, depending on whether the blob denoting the gauge group G_s is to the right or left of the line.

Both $\mathrm{SU}(m)$ and $\mathrm{SU}(n)$ have asymptotically free gauge symmetry with typical mass scales Λ, Λ_s. Assuming $\Lambda \ll \Lambda_s$, the $\mathrm{SU}(n)$ interaction becomes strong at higher energy, thus forming a bound state of these Weyl fermions just like the hadrons in QCD. At lower energies, $E \leq \Lambda_s$, the effective low-energy theory is described by pseudo scalars, à la the pion π_i, as (pseudo) NG bosons due to the spontaneous breaking of the chiral symmetry $\mathrm{SU}_i(m) \times \mathrm{SU}_{i+1}(m)$:

$$U_i = \exp^{i\frac{\pi_i^a T_a}{f}} \ (T_a : \text{generators of SU}(m)), \tag{2.15}$$

where f corresponds to the pion decay constant. The non-linear realization U_i behaves as a bi-fundamental representation of the chiral symmetry, i.e. $(m, \bar{m})$ under $(\mathrm{SU}_i(m), \mathrm{SU}_{i+1}(m))$.

Actually, $\mathrm{SU}(m)$ has been gauged and the effective action is a gauged non-linear sigma model:

$$S = \int d^4x \left(-\frac{1}{2g^2} \sum_{j=1}^{N} tr(F_j^{\mu\nu})^2 + f^2 \sum_{j=1}^{N} tr[(D_\mu U_j)^\dagger (D^\mu U_j)] \right), \tag{2.16}$$

with the covariant derivative

$$D_\mu U_j = \partial_\mu U_j - i A_\mu^j U_j + i U_j A_\mu^{j+1}. \tag{2.17}$$

Here A_μ^j are gauge bosons of $\mathrm{SU}(m)$ and $F_j^{\mu\nu}$ are their field strengths.

This is nothing but 5D $\mathrm{SU}(m)$ pure non-Abelian gauge theory, with extra space being latticized: U_j may be regarded as the link variable (the "Wilson line" along the extra dimension). Indeed, in the simplified Abelian case

$$D_\mu U_j \to i[\partial_\mu \pi - gf(A_\mu^{j+1} - A_\mu^j)]U_j, \tag{2.18}$$

and identifying the lattice spacing a of the extra dimension as

$$a = \frac{1}{gf}, \tag{2.19}$$

$D_\mu U_j$ just corresponds to the field strength $F_{\mu y}$ in the GHU:

$$D^\mu U_j \to \partial_\mu A_y - \partial_y A_\mu = F_{\mu y} \ (\pi \equiv A_y). \tag{2.20}$$

Thus, the extra dimension has been constructed by the dynamics in 4D space-time. It should be noticed that above Λ_s the theory recovers to original renormalizable theory, in clear contrast to the non-renormalizable higher-dimensional gauge theory, which the GHU is formulated on.

Downloaded from http://ptep.oxfordjournals.org/ at Osaka Daigaku Ningen on January 18, 2017

The theory has gauge symmetry $(\mathrm{SU(m)})^N$ that is spontaneously broken into a single SU(m):

$$\langle U_i \rangle = 1 \to g_i \langle U_i \rangle g_{i+1}^\dagger = \langle U_i \rangle, \text{ only when } g_i = g_{i+1}, \tag{2.21}$$

where g_i is an element of $\mathrm{SU}_i(m)$. Thus, among U_i $(i = 1, 2, \ldots, N)$, $N - 1$ pieces are "eaten" by the Higgs mechanism, and there remains only one physical (pseudo) NG boson, which is identified as the Higgs. The remaining Higgs,

$$\mathrm{Tr}(U_1 U_2 \cdots U_N), \tag{2.22}$$

is invariant under the gauge transformation, $U_1 U_2 \cdots U_N \to g_1 (U_1 U_2 \cdots U_N) g_1^\dagger$ $(g_{N+1} = g_1)$, and therefore cannot be "gauged away" by taking the unitary gauge.

In the Abelian case, $U_1 U_2 \ldots U_N = e^{\frac{i}{f}(\pi_1 + \cdots \pi_N)}$ $(\phi = \frac{\pi_1 + \pi_2 + \cdots \pi_N}{\sqrt{N}})$, and the field ϕ just corresponds to the zero-mode of A_y, or the phase of the Wilson loop, in GHU: $W = e^{i\frac{g}{2}\oint A_y dy}$.

The field ϕ is a pseudo NG boson. In fact, at the quantum level, its potential is induced:

$$V(\phi) = -\frac{9}{4\pi^2} g^4 f^4 \sum_1^\infty \frac{\cos\left(\frac{2n\sqrt{N}\phi}{f}\right)}{n(n^2N^2 - 1)(n^2N^2 - 4)} + \text{constant}. \tag{2.23}$$

This potential is known to be finite for $N \geq 3$, which can be easily shown by using relations such as $\sum_n \cos(\frac{2\pi}{N} n) = 0$ $(-\frac{N}{2} < n \leq \frac{N}{2})$. Let us note that such summation over all possible n just corresponds to the summation over all KK modes in the GHU, which led to the finite Higgs mass [8]. Thus we may also understand that the scenario of dimensional deconstruction provides a very reasonable regularization scheme for the KK mode sum: we do not have to take the sum over an infinite number of KK modes; instead, just a few modes are enough to guarantee the finiteness of the Higgs mass.

The potential reduces to that in GHU [5–8,25,26] in the limit $N \to \infty$:

$$V(A_y) = \frac{9}{4\pi^2} \frac{1}{(2\pi R)^4} \sum_{n=1}^\infty \frac{\cos(n g A_y 2\pi R)}{n^5}. \tag{2.24}$$

Little Higgs

The purpose of the little Higgs (LH) scenario is to construct a 4D theory including SM, where the Higgs is a pseudo NG boson, while the quadratic divergence of the quantum correction to the Higgs mass cancels out without relying on SUSY. Though LH is a scenario inspired by dimensional deconstruction, in this approach the NG boson need not be a bound state of fermions. So the remnant of the higher-dimensional theory is not apparent. Nevertheless, there still remains some close relation between the LH and GHU scenarios, as has already been mentioned in this subsection. (The correspondence may be rigorously argued once we utilize AdS–CFT correspondence.)

There are various versions of LH models. but here we discuss "the simplest little Higgs" [30] in order to understand the key ingredient of the scenario, "collective breaking".

Interestingly, in the LH the gauge symmetry should also be enlarged. This is basically because the scenario needs a global symmetry that is larger than $SU(2) \times U(1)$, so that even after the Higgs mechanism physical NG bosons remain. Thus, let us consider the simplest SU(3) model with triplet

Downloaded from http://ptep.oxfordjournals.org/ at Osaka Daigaku Ningen on January 18, 2017

scalar ϕ. (The model is eventually extended to that with additional $\mathrm{U}(1)_X$. However, for simplicity, here we ignore it.) The VEV

$$\langle\phi\rangle = \begin{pmatrix} 0 \\ 0 \\ f \end{pmatrix} \tag{2.25}$$

causes a spontaneous breaking of global symmetry SU(3) $\to$ SU(2), and the resultant NG bosons are written as

$$\pi = \begin{pmatrix} -\frac{\eta}{2} & 0 & \phi^+ \\ 0 & -\frac{\eta}{2} & \phi^0 \\ \phi^- & \phi^{0*} & \eta \end{pmatrix}, \tag{2.26}$$

where $h = (\phi^+,\ \phi^0)^t$ is identified with the Higgs doublet. In this model, however, h and η are all absorbed by massive gauge bosons by the Higgs mechanism in the process of spontaneous breakdown of SU(3) $\to$ SU(2), and no physical Higgs remains.

Then we enlarge the model a little and introduce two copies of triplet scalars ϕ_1 and ϕ_2, and introduce covariant derivatives D_μ with the same SU(3) gauge bosons A_μ for both:

$$\mathcal{L} = |D_\mu\phi_1|^2 + |D_\mu\phi_2|^2 \ (D_\mu = \partial_\mu - igA_\mu) \tag{2.27}$$

where two triplet scalars are non-linearly realized:

$$\phi_1 = \exp^{i\frac{\pi_1}{f}}\begin{pmatrix} 0 \\ f \end{pmatrix}, \quad \phi_2 = \exp^{i\frac{\pi_2}{f}}\begin{pmatrix} 0 \\ f \end{pmatrix}. \tag{2.28}$$

For simplicity the decay constants of $\phi_{1,2}$ are taken to be the same: f.

Each sector of the two scalars $\phi_{1,2}$ has its own global SU(3) symmetry. But, once gauge interaction is switched on, the global symmetry is explicitly broken to the "diagonal" $SU(3)$: When each of ϕ_1 and ϕ_2 transforms as

$$\phi_1 \to U_1\phi_1,\ \phi_2 \to U_2\phi_2, \tag{2.29}$$

the gauge fields should transform as

$$A_\mu \to U_1 A_\mu U_1^\dagger, \quad A_\mu \to U_2 A_\mu U_2^\dagger. \tag{2.30}$$

Since one gauge field A_μ couples with both triplets, for consistency it is necessary that $U_1 = U_2$.

The NG boson corresponding to this diagonal SU(3) remains exactly massless, but is "eaten" by the Higgs mechanism. The orthogonal one, in particular its doublet component h, is identified with the Higgs and acquires a mass, since the relevant global symmetry is explicitly broken by the presence of the gauge interaction.

Let us note that, to break the global symmetry explicitly by the gauge interaction, $\mathrm{SU}(3)^2 \to$ SU(3), gauge couplings of A_μ to both U_1 and U_2 are necessary, Namely, the gauge couplings with both triplets collectively break the global symmetry. This is what "collective breaking" means. The physically remaining Higgs is not a real NG boson but a pseudo NG boson, acquiring a mass due to the breaking of the global symmetry. The collective breaking in turn means that, even if the Higgs acquires a mass at quantum level, it should be induced by Feynman diagrams where the gauge interactions with both triplets are included. Thus the diagram leading to the quadratic divergence of the Higgs mass is not allowed (at least at the one-loop level) and the Higgs does not suffer from the

Downloaded from http://ptep.oxfordjournals.org/ at Osaka Daigaku Ningen on January 18, 2017

quadratically divergent quantum correction to the Higgs mass. This is the mechanism of collective breaking in order to remove the quadratic divergence.

Let us note that, in order for the collective breaking to work, the repetition of fields is essential, which seems to correspond to the presence of KK modes in GHU. Also, the quadratic divergence of the Higgs mass disappears as a result of the repetition of fields in the LH model, just as in the case of GHU, where the sum over all KK modes provides a finite Higgs mass [8].

2.4. Close relation between GHU and superstring theory

The GHU also has a very close relation to the superstring theory. In fact, the (bosonic part of the) point particle limit of open superstring theory, i.e. 10D SUSY Yang–Mills theory, may be understood as a sort of GHU.

Pure SUSY Yang–Mills theory with a gauge multiplet alone is possible only for specific space-time dimensionality $D = 3, 4, 6$, and 10, just because the matching of physical degrees of freedom of the gauge boson and the gauge fermion is realized in these dimensions:

$$D - 2 = r\, 2^{[\frac{D-2}{2}]}\ (r = \frac{1}{2} \text{ for Majorana–Weyl}). \tag{2.31}$$

This means that the 10D SUSY Yang–Mills theory (with $r = \frac{1}{2}$) is formulated as a pure SUSY Yang–Mills theory without any need to introduce an additional matter field. Therefore, the only possible origin of the Higgs field is the gauge field, or to be more precise the extra-dimensional component of the 10D gauge field. This is nothing but GHU.

Although it is usually argued that, in supersymmetric theory, the hierarchy problem of quadratic divergence is solved by SUSY, if the theory is regarded as that inspired by superstring, the hierarchy problem may be solved by the mechanism in the GHU as well. In fact, if the mode sum over all KK modes is performed, the quantum correction to the Higgs mass is finite even after the SUSY breaking.

3. Normal vs. anomalous Higgs interactions

Now that a new particle, which behaves like the Higgs particle in the standard model (SM), has been discovered at CERN, only the theory with the SM as its decoupling limit should be acceptable as the theory of new physics. In order to determine which type of theory we should pursue among the remaining candidates, a precision test of the Higgs interaction is quite important. This may not be easy at LHC and we hope that it can be performed at the planned ILC experiment.

Interestingly, representative new physics theories show some sort of deviation of Higgs interactions from those predicted by the SM. For instance, in the MSSM, the couplings of the Higgs interactions generally depend on the parameters β and α. For instance, the ratios of the Yukawa coupling of the SM-like Higgs to that of the SM for the third generation are given as

$$\frac{f_t^{(\mathrm{MSSM})}}{f_t^{(\mathrm{SM})}} = \frac{\cos\alpha}{\sin\beta}, \tag{3.1}$$

$$\frac{f_b^{(\mathrm{MSSM})}}{f_b^{(\mathrm{SM})}} = \frac{f_\tau^{(\mathrm{MSSM})}}{f_\tau^{(\mathrm{SM})}} = -\frac{\sin\alpha}{\cos\beta}. \tag{3.2}$$

Although the Yukawa couplings generally deviate from the predictions of the SM, the deviation is universal for all generations. This is an important prediction of the MSSM. It should also be noted that, at the decoupling limit $\alpha \to \beta - \frac{\pi}{2}$, the deviations just go away, as we anticipated.

Downloaded from http://ptep.oxfordjournals.org/ at Osaka Daigaku Ningen on January 18, 2017

Let us now discuss higher-dimensional theories. We will see that in the gauge–Higgs unification (GHU) and also in the related theories (dimensional deconstruction, little Higgs (LH) and probably superstring) we expect really "anomalous" Higgs interactions, qualitatively different from those in the SM and MSSM, coming from the very fact that the Higgs is not a scalar particle, but is originally a gauge field or a pseudo NG boson.

From the viewpoint of the precision test of the Higgs interactions, it seems to be quite interesting that new physics theories are divided into two categories concerning the Higgs interactions, i.e. theories with normal Higgs interactions and theories with anomalous Higgs interactions. We discuss these two categories separately below.

3.1. Theory with normal Higgs interactions

The higher-dimensional new physics theory of this type that we discuss here is the scenario of the universal extra dimension (UED) [18]. This theory is obtained by simply making the SM higher-dimensional, although to get a chiral theory the extra dimension is assumed to be orbifold, not just a circle or sphere. In particular, its Higgs sector is just as in the SM: no additional Higgs doublet is introduced, in contrast to the case of the MSSM, and the Higgs is just an elementary scalar field even in the bulk, in clear contrast to the case of GHU or LH. Thus the KK zero mode of the Higgs field has just the same Yukawa couplings as those in the SM.

3.2. Theories with anomalous Higgs interactions

GHU

We first discuss gauge–Higgs unification (GHU), as a typical example of the new physics theory with anomalous Higgs interactions. In GHU (we work in 5D space-time), the SM-like Higgs H is the zero-mode of A_y, $A_y^{(0)}$, and has a physical meaning as the Wilson loop phase (the AB phase), coming from the fact that the circle is a non-simply-connected space, as was discussed in the previous section:

$$W = e^{i\frac{g}{2}\oint A_y dy} = e^{ig_4\pi R A_y^{(0)}} \quad \text{(for the Abelian case)}, \tag{3.3}$$

where R is the radius of the circle and, in the line integral along the circle, only the zero mode contribution remains.

The fact that the Higgs should be regarded as an AB phase (or Wilson loop phase) as seen in (3.3) leads to the anomalous Higgs interactions.

To see this, we start from a general argument on the fermion masses and Yukawa couplings that, in any gauge theories with spontaneous gauge symmetry breaking, the fermion mass term is written as

$$m(v)\bar{\psi}\psi, \tag{3.4}$$

where $m(v)$ is a function, say the "mass function", of the VEV $v = \langle H \rangle$. The interaction of the physical Higgs field h with the fermion is expected to be provided by a replacement $v \to v + h$, since the Higgs is the field to denote the shift of H from its VEV. Thus, Yukawa coupling f of h with the (KK zero mode of the) fermion is expected to be given by

$$f = \frac{dm(v)}{dv}. \tag{3.5}$$

This prescription works perfectly in the case of the SM, where $m(v)$ is a linear function of v, $m(v) = fv$. In the case of GHU, the story is a little more complicated. Even if we consider only one flavor,

Downloaded from http://ptep.oxfordjournals.org/ at Osaka Daigaku Ningen on January 18, 2017

the fermion still has an infinite number of KK modes. Thus the mass term and Yukawa couplings are written in the form of matrices in the base of KK modes. Provided that the VEV v is fixed, each KK mode should be given as an eigenvector of the mass matrix determined by v. Thus in the base of KK modes the mass matrix (the matrix form of the mass terms) is diagonalized. The unusual thing, however, is that the matrix denoting the Yukawa couplings is generally non-diagonal even in the base of the mass eigenstates [31]. This characteristic feature of the GHU is closely related to the fact that the mass function $m(v)$ of KK zero mode, for instance, can be a non-linear function, such as trigonometric function, in general reflecting that the Higgs is a phase, as we will see below. Thus, to be precise, the prescription given in (3.5) is only for the diagonal elements of the Yukawa coupling matrix (valid for all KK modes, incidentally).

Since in the GHU the Higgs should be understood as a phase (AB phase), we expect that all physical observables have periodicity in the Higgs field H:

$$v \to v + \frac{2}{g_4 R} \ (g_4 : \text{4D gauge coupling}). \tag{3.6}$$

In fact, we find for the zero mode quarks of light (1st and 2nd) generations (together with the b quark), the quark masses are exponentially suppressed as in (2.7), but in addition, their dependence on the VEV v is approximately a trigonometric function:

$$m(v) \propto \sin\left(\frac{g_4}{2}\pi R v\right), \tag{3.7}$$

which is non-linear in v. Then, the prescription (3.5) yields

$$f \propto \cos\left(\frac{g_4}{2}\pi R v\right). \tag{3.8}$$

It is a remarkable fact that the Yukawa coupling even vanishes for a specific value of the VEV,

$$x \equiv \frac{g_4}{2}\pi R v = \frac{\pi}{2}, \tag{3.9}$$

as was first claimed by Hosotani et al. [10,11].

Although such a drastic case does not seem to be consistent with the recent data from the LHC experiments, it is still possible that GHU predicts anomalous Yukawa couplings for light quarks for a general value of x. In fact, the ratio of the Yukawa coupling predicted by GHU to that predicted by the SM for light quarks is known to be very well approximated by an analytic formula [31],

$$\frac{f_{\text{GHU}}}{f_{\text{SM}}} \simeq x \cot x. \tag{3.10}$$

Note that, at the "decoupling limit",

$$x = \frac{g_4}{2} v \pi R \ll 1 \leftrightarrow M_W \ll \frac{1}{R}, \tag{3.11}$$

the SM prediction is recovered, as is easily seen in (3.10).

Actually, when the bulk mass M_i is switched off, the mass function $m(v)$ becomes a linear function of x, as is seen in Fig. 2(a), just as in the SM, so the Yukawa coupling does not deviate from the SM prediction for $x < \frac{\pi}{2}$. In this case, the periodicity of the mass eigenvalue is realized by a level crossing of the zero mode with the first KK mode at $x = \frac{\pi}{2}$ (see Fig. 2(a)). Namely, at $x = \frac{\pi}{2}$, the zero mode is replaced by the first KK mode whose mass eigenvalue decreases as x increases. For $M_i = 0$, however, mixing between these two modes will not appear because of the conservation of the (absolute value of the) extra space component of the momentum. If we switch on the bulk mass M_i, the translational

Downloaded from http://ptep.oxfordjournals.org/ at Osaka Daigaku Ningen on January 18, 2017

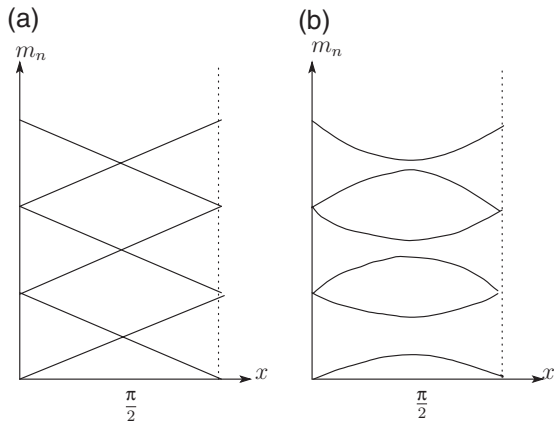

Fig. 2. The mass eigenvalues of KK modes for vanishing bulk mass (Fig. 2(a)) and non-vanishing bulk mass (Fig. 2(b)).

invariance along the extra space is violated by the presence of the bulk mass term (2.6), thus causing mixing between the two modes. Due to the mixing, the degeneracy of the two mass eigenvalues at the level crossing is lifted and a deviation of the mass function from the linearity appears, leading to the trigonometric function for sufficiently large bulk mass M_i, as is seen in Fig. 2(b).

Thus, even though the original seed of the anomalous Higgs interaction is the periodicity characteristic of GHU, more directly it may be attributed to the violation of translational invariance in the extra dimension. From this point of view, it may be worth noting that on the Randall–Sundrum background, the translational invariance is *always* (universally) violated by the presence of the warp factor $e^{-\kappa|y|}$. This should be the reason why, on the Randall–Sundrum background, the Higgs interactions with massive gauge bosons, W and Z, are also anomalous [32,33], while on the flat space-time it is "almost normal" (normal for $x < \frac{\pi}{2}$), as in the gauge–Higgs sector there is no parameter violating translational invariance in the case of flat space-time [31].

From a field theoretical point of view, the reason why we get such non-linearity in the mass function like (3.7) is that, due to the non-diagonal Yukawa couplings mentioned earlier, there appear mixings between the zero mode and non-zero modes, which leads to higher-mass-dimensional operators at tree level of the form $h^{2n+1}\bar{\psi}\psi$ $(n = 1, 2, \ldots)$ (just like the dimension 5 operator in the see-saw mechanism). The coefficients of these higher-mass-dimensional operators are suppressed by the inverse powers of $M_c = \frac{1}{R}$, and as we have already seen, the effects of such "irrelevant" operators disappear at the decoupling limit $M_c \to \infty$.

3.3. *Dimensional deconstruction*

As we have seen in the previous section, though it is formulated on the ordinary 4D space-time, the scenario of dimensional deconstruction may be understood as a "latticized" GHU. We thus expect that the anomalous Higgs interaction is also expected in this scenario. To be more specific, in this case, even if we adopt just periodic boundary conditions for fields like $A_\mu^{N+1} = A_\mu^1$, corresponding to the choice of a circle, not an orbifold, as the extra dimension in GHU, still the latticizing itself breaks the (continuous) translational invariance, which should lead to anomalous Higgs interactions. In fact, the mass eigenvalues in this scenario generally behave as trigonometric functions:

$$m_n(v) = \frac{2}{a}\sin\left(\frac{n\pi}{N} + \frac{g_4 a v}{4}\right) \quad (a : \text{lattice spacing}), \tag{3.12}$$

Downloaded from http://ptep.oxfordjournals.org/ at Osaka Daigaku Ningen on January 18, 2017

which are basically the same as the eigenfrequencies of a system of springs and balls. As can easily be seen, (3.12) reduces to linear functions of v in the continuum limit $a \to 0$, $N \to \infty$, keeping the circumference of the circle $L \equiv Na$ a constant; $m_n(v) \to \frac{2\pi}{L}n + \frac{g_4 v}{2}$. Work on the anomalous interactions in dimensional deconstruction pursuing this line of argument is now in progress (N. Kurahashi et al., work in progress).

3.4. *Little Higgs*

We have also argued that the scenario of little Higgs (LH) has a close relationship with GHU. Just as in the case of GHU, the Higgs is non-linearly realized,

$$U = \exp^{i\frac{H}{v}}, \tag{3.13}$$

and therefore periodicity and non-linearity concerning the Higgs field seem to arise very naturally. Thus we again expect anomalous Higgs interactions in the scenario of LH, though more complete analyses are clearly desirable in this case.

4. $H \to \gamma\gamma$

$H \to \gamma\gamma$ is the clean decay mode of the Higgs, important for the identification of the Higgs particle. This di-photonic decay is induced at the quantum level since the photon is a massless particle, and is a very good testing ground for new physics. It is also sensitive to the Higgs interactions with fermions and gauge bosons running inside the loop diagrams, thus providing useful information on the properties of Higgs interactions, whether they are normal or anomalous, as was discussed in some detail in the previous section. The gluon fusion process $gg \to H$, a main process of Higgs production, is also induced at the quantum level and has some similarity to the photonic Higgs decay, though gauge bosons do not contribute in this case.

In this section we focus on two higher-dimensional new physics scenarios with considerably different properties, as we have already seen in the previous sections: UED and GHU. We will pay a great deal of attention to the differences in the predictions these two scenarios make about the photonic decay.

Recently, there has been an interesting claim that the contribution of the non-zero KK modes of the top quark to the decay amplitude of $H \to \gamma\gamma$ has an opposite sign to that of the top quark in the SM and to that of the KK modes of the top quark in UED [34]. The origin of such a qualitative difference may be rather easily understood once we rely on the operator analysis. Let us assume $M_c = 1/R \gg v$. At first glance, the relevant operator for the photonic decay seems to be $hF_{\mu\nu}F^{\mu\nu}$, with $F_{\mu\nu}$ being the field strength of the photon. If this is the case, the coefficient should be divergent in the process of the KK mode sum, since the mass dimension of the operator is 5. But this operator is not gauge invariant under $\mathrm{SU}(2)_L \times \mathrm{U}(1)_Y$. So, actually the decay amplitude is dominated by a gauge invariant operator of mass dimension 6 written in terms of the Higgs doublet ϕ:

$$\phi^\dagger \phi F_{\mu\nu}F^{\mu\nu}. \tag{4.1}$$

Note that, when one of the Higgs doublets is replaced by its VEV, this yields the dimension 5 operator mentioned above. Now the coefficient of the operator (4.1) is finite, at least for 5D space-time.

Also note that the operator in (4.1) comes from the diagram shown in Fig. 3, obtained by inserting the Higgs doublet ϕ twice to the self-energy diagram of the photon, that is responsible for the, quantum correction to the operator $F_{\mu\nu}F^{\mu\nu}$. So, by utilizing the background field method, the Wilson coefficient of the operator (4.1) is obtainable just by calculating the self-energy diagram with the

Downloaded from http://ptep.oxfordjournals.org/ at Osaka Daigaku Ningen on January 18, 2017

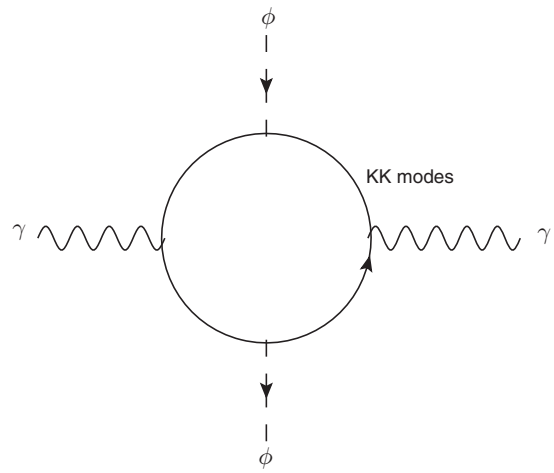

Fig. 3. A diagram contributing to the operator that describes the Higgs decay.

top quark (or its KK modes) inside the loop, having masses given by the VEV v, and finally taking the second derivative with respect to v. Since the coefficient of the self-energy diagram depends logarithmically on the mass of the virtual state, the coefficient of (4.1) is given as

$$C \propto \frac{d^2}{dv^2} \log m_n^2|_{v=0}, \tag{4.2}$$

where m_n are the mass eigenvalues of the nth KK mode.

Now we are ready to discuss the differences between the predictions of UED and GHU. In each scenario, the mass eigenvalue of a fermion is given as follows:

$$m_n = \begin{cases} \sqrt{\left(\frac{n}{R}\right)^2 + (fv)^2} & \text{for UED} \\ \frac{n}{R} + fv & \text{for GHU} \end{cases}. \tag{4.3}$$

Here, for brevity, we have ignored the possible bulk mass, and f is the Yukawa coupling for the zero mode fermion. Then the procedure of (4.2) gives results that are just opposite in sign for the two scenarios:

$$C \propto \begin{cases} 2\frac{f^2}{(\frac{n}{R})^2} & \text{for UED} \\ -2\frac{f^2}{(\frac{n}{R})^2} & \text{for GHU} \end{cases}. \tag{4.4}$$

There is a claim that the new physics contributions of the theories with a mechanism to solve the hierarchy problem invoking some symmetry tend to reduce, e.g., the amplitude of the gluon fusion process. Intuitively, the reason might be the following. In the case of gluon fusion, the field strength in (4.1) is that of the gluon field. Since the QCD sector has no direct connection with the Higgs sector, even if we take off the gluonic field the operator is still gauge invariant and it just becomes the mass-squared operator for the Higgs field. On the other hand, any theories that aim to solve the problem of quadratic divergence of the Higgs mass should have a mechanism to reduce the quantum correction to the Higgs mass-squared by introducing, e.g. super-partners, KK modes, etc. Thus it will be natural to expect some destructive contributions from new heavy particles in this type of theory.

Downloaded from http://ptep.oxfordjournals.org/ at Osaka Daigaku Ningen on January 18, 2017

Let us also note that the operator (4.1) is easily generalized by replacing $\phi^\dagger\phi$ by its arbitrary function $V(\phi)$: i.e. $V(\phi)F^{\mu\nu}F_{\mu\nu}$. If we take off $F^{\mu\nu}F_{\mu\nu}$ again, we just get a Higgs potential $V(\phi)$. On the other hand, in the GHU the potential is completely finite [5–8]. Maru thus claims that the decay amplitude of $H \to \gamma\gamma$ is finite irrespective of the space-time dimension [37].

For a more recent detailed analysis concerning the di-photonic decay in GHU, refer to Ref. [35]. For a recent argument on the contribution of the non-zero KK modes of the top quark in the SO(5) x U(1) GHU on the Randall–Sundrum background, refer to Ref. [36].

Usually, the contributions of lighter generations (1st and 2nd generations) to the photonic Higgs decay are more or less negligible, since their Yukawa couplings are strongly suppressed by very small quark masses. This is why only the contribution of the top quark is seriously taken into account. In the GHU, however, the story is not so simple. Namely, the contribution of each non-zero KK mode of lighter generations of quarks is not strongly suppressed by the corresponding small quark masses. This is because only the mode function of the zero mode exhibits localization at a fixed point and the Yukawa couplings of non-zero KK modes are not exponentially suppressed, being of the order of gauge coupling. So we naturally expect possible significant contributions to the photonic decay from lighter generations as well.

Fortunately or unfortunately, it turns out that, although each KK mode makes a significant contribution to the decay amplitude, as we expected, after the summation over the contributions of all KK modes, the factor suppressed by $1/M_c^2 = 1/(1/R)^2$ (which we expect from the decoupling theorem) just goes away, and the remaining contribution is exponentially suppressed as $e^{-M_i R}$ (M_i : bulkmass) (K. Hasegawa et al., manuscript in preparation).

We recall that a similar exponential suppression factor due to a relatively large bulk mass was found in the process of the calculation of the quantum correction to the Higgs mass-squared [8]. This may not be so surprising, since, as we have argued above, the operator relevant to the photonic decay has some similarity to that of the Higgs potential. We may also notice that the exponential factor mimics the Boltzmann factor in the case of finite-temperature field theory. This factor goes away at the decompactification limit $R \to \infty$, thus suggesting that it comes from a non-local gauge invariant operator due to the Wilson loop. In fact, this should be the reason why we find a finite decay amplitude in GHU irrespective of the dimensionality of the space-time, as was demonstrated in Ref. [37]. We may also understand that the factor is the contribution from the sector with non-zero winding numbers at the Poisson re-summation, which clearly shows the contributions of distances larger than R and is thus suppressed by the exponential factor $e^{-M_i R}$, present in the Yukawa potential.

5. Summary

In spite of the great success of the LHC experiments in discovering a particle consistent with the Higgs of the SM, it is still premature to conclude that the particle *is* the Higgs of the SM. It may be some SM-like Higgs particle predicted by some new physics theory. Also, the Higgs sector of the SM is still mysterious, having a few important long-standing problems, such as the hierarchy problem and the problem of too many arbitrary parameters present in the sector. Thus we should continue to ask what the origin of the Higgs is.

In this article, we have focused on higher-dimensional new physics theories. Also discussed were 4D theories, such as little Higgs (LH) and dimensional deconstruction, which possess some close relationship with the higher-dimensional theory, especially with the gauge–Higgs unification (GHU). Some important common features shared by these scenarios are the presence of the "shift symmetry",

Downloaded from http://ptep.oxfordjournals.org/ at Osaka Daigaku Ningen on January 18, 2017

which guarantees the finiteness of the Higgs mass at the quantum level, and the periodicity: physical observables are periodic in the Higgs field. In GHU the origin of the Higgs field is a gauge field and in the LH and dimensional deconstruction the origin is a (pseudo) Nambu–Goldstone boson.

In order to investigate the origin of the Higgs, precision tests of Higgs interactions will be of crucial importance. We have discussed that new physics theories are divided into two categories: theories with normal Higgs interactions, and theories with anomalous Higgs interactions.

From this point of view, we have demonstrated that, in the scenario of GHU and the related LH and dimensional deconstruction scenarios, the periodicity mentioned above (together with the breakdown of translational invariance along the extra dimension) leads to very characteristic anomalous Higgs interactions, which are never shared by the SM. This should be a very important observation in the attempt to deeply understand the origin of the Higgs particle.

The difference, i.e. normal (as in the case of UED) or anomalous Higgs interactions, also makes the new physics contribution to the main decay mode of the Higgs, $H \to \gamma\gamma$, qualitatively different.

Such crucial precision tests of the Higgs interactions may not be easy at the LHC experiment, but we hope that they will be performed at the planned ILC experiment.

Acknowledgements

The author would like to thank Y. Hosotani, N. Maru, and Y. Sakamura for very useful discussions and explanations of their work, which is relevant to this article. This work was supported in part by the Grant-in-Aid for Scientific Research of the Ministry of Education, Science and Culture, No. 21244036, No. 23654090, No. 23104009.

Funding

Open Access funding: SCOAP[3].

References

[1] T. Appelquist and J. Carazzone, Phys. Rev. D **11**, 2856 (1975).
[2] N. S. Manton, Nucl. Phys. B **158**, 141 (1979).
[3] D. B. Fairlie, Phys. Lett. B **82**, 97 (1979).
[4] D. B. Fairlie, J. Phys. G: Nucl. Part. Phys. **5**, L55 (1979).
[5] Y. Hosotani, Phys. Lett. B **126**, 309 (1983).
[6] Y. Hosotani, Phys. Lett. B **129**, 193 (1983).
[7] Y. Hosotani, Annals Phys. **190**, 233 (1989).
[8] H. Hatanaka, T. Inami, and C. S. Lim, Mod. Phys. Lett. A **13**, 2601 (1998).
[9] C. Csaki, C. Grojean, H. Murayama, L. Pilo, and J. Terning, Phys. Rev. D **69**, 055006 (2004).
[10] Y. Hosotani, K. Oda, T. Ohnuma, and Y. Sakamura, Phys. Rev. D **78**, 096002 (2008).
[11] Y. Hosotani and Y. Kobayashi, Phys. Lett. B **674**, 192 (2009).
[12] K. Agashe, R. Contino, and A. Pomarol, Nucl. Phys. B **719**, 165 (2005).
[13] A. D. Medina, N. R. Shah, and C. E. M. Wagner, Phys. Rev. D **76**, 095010 (2007).
[14] Y. Hosotani, K. Oda, T. Ohnuma, and Y. Sakamura, Phys. Rev. D **78**, 096002 (2008).
[15] Y. Hosotani, K. Oda, T. Ohnuma, and Y. Sakamura, Phys. Rev. D **79**, 079902 (2009).
[16] Y. Hosotani, S. Noda, and N. Uekusa, Prog. Theor. Phys. **123**, 757 (2010).
[17] S. Funatsu, H. Hatanaka, Y. Hosotani, Y. Orikasa, and T. Shimotani, Phys. Lett. B **722** 94 (2013).
[18] T. Appelquist, H.-C. Cheng, and B. A. Dobtescu, Phys. Rev. D **64**, 035002 (2001).
[19] H.-C. Cheng, K. T. Matchev, and M. Schmaltz, Phys. Rev. D **66**, 056006 (2002).
[20] N. Arkani-Hamed, S. Dimopoulos, and G. R. Dvali, Phys. Lett. B **429**, 263 (1998).
[21] L. Randall and R. Sundrum, Phys. Rev. Lett. **83**, 3370 (1999).
[22] CMS collaboration, Physics Analysis Summary CMS PAS EXO-12-048.
[23] CMS collaboration, Physics Analysis Summary CMS PAS EXO-12-06.
[24] G. Aad et al. [ATLAS collaboration], ATLAS-CONF-2013-017.

Downloaded from http://ptep.oxfordjournals.org/ at Osaka Daigaku Ningen on January 18, 2017

[25] M. Kubo, C. S. Lim, and H. Yamashita, Mod. Phys. Lett. A **17**, 2249 (2002).
[26] C. A. Scrucca, M. Serone, and L. Silvestrini, Nucl. Phys. B **669**, 128 (2003).
[27] Y. Kawamura, Prog. Theor. Phys. **103**, 613 (2000).
[28] N. Arkani-Hamed, A. G. Cohen, and H. Georgi, Phys. Rev. Lett. **86**, 4757 (2001).
[29] N. Arkani-Hamed, A. G. Cohen, and H. Georgi, Phys. Lett. B **513**, 232 (2001).
[30] M. Schmaltz, J. High Energy Phys. **0408**, 056 (2004).
[31] K. Hasegawa, N. Kurahashi, C. S. Lim, and K. Tanabe, Phys. Rev. D **87**, 016011 (2013).
[32] Y. Hosotani and Y. Sakamura, Prog. Theor. Phys. **118**, 935 (2007).
[33] Y. Hosotani, K. Oda, T. Ohnuma, and Y. Sakamura, Phys. Rev. D **78**, 096002 (2008).
[34] N. Maru and N. Okada, Phys. Rev. D **77**, 055010 (2008).
[35] N. Maru and N. Okada, Phys. Rev. D **87**, 095019 (2013).
[36] S. Funatsu, H. Hatanaka, Y. Hosotani, Y. Orikasa, and T. Shimotani, Phys. Lett. B **722**, 94 (2013).
[37] N. Maru, Mod. Phys. Lett. A **23**, 2737 (2008).

Downloaded from http://ptep.oxfordjournals.org/ at Osaka Daigaku Ningen on January 18, 2017

PTEP

Prog. Theor. Exp. Phys. **2014**, 023B02 (23 pages)
DOI: 10.1093/ptep/ptt116

Minimal Higgs inflation

Yuta Hamada[1,*], Hikaru Kawai[1,*], and Kin-ya Oda[2,*]

[1] *Department of Physics, Kyoto University, Kyoto 606-8502, Japan*
[2] *Department of Physics, Osaka University, Osaka 560-0043, Japan*
*E-mail: hamada@gauge.scphys.kyoto-u.ac.jp, hkawai@gauge.scphys.kyoto-u.ac.jp, odakin@phys.sci.osaka-u.ac.jp

Received October 4, 2013; Accepted December 8, 2013; Published January 29, 2014

We consider a possibility that the Higgs field in the Standard Model (SM) serves as an inflaton when its value is around the Planck scale. We assume that the SM is valid up to an ultraviolet cutoff scale Λ, which is slightly below the Planck scale, and that the Higgs potential becomes almost flat above Λ. Contrary to the ordinary Higgs inflation scenario, we do not assume the huge non-minimal coupling, of $O(10^4)$, of the Higgs field to the Ricci scalar. We find that Λ must be less than 5×10^{17} GeV in order to explain the observed fluctuation of the cosmic microwave background, no matter how we extrapolate the Higgs potential above Λ. The scale 10^{17} GeV coincides with the perturbative string scale, which suggests that the SM is directly connected with string theory. For this to be true, the top quark mass is restricted to around 171 GeV, with which Λ can exceed 10^{17} GeV. As a concrete example of the potential above Λ, we propose a simple log-type potential. The predictions of this specific model for the e-foldings $N_* = 50$–60 are consistent with the current observation, namely, the scalar spectral index is $n_s = 0.977$–0.983 and the tensor to scalar ratio $0 < r < 0.012$–0.010. Other parameters, $\mathrm{d}n_s/\mathrm{d}\ln k$, n_t, and their derivatives, are also consistent.

Subject Index B53, B57, B72

1. Introduction

It is more and more plausible that the particle discovered at the CERN Large Hadron Collider (LHC) [1,2] around 126 GeV is the Standard Model (SM) Higgs boson. Its couplings to the W and Z gauge bosons, to the top and bottom quarks, and to the tau lepton are all consistent to those in the SM within one standard deviation, even though their values vary by two orders of magnitude; see, e.g., Ref. [3]. No hint of new physics beyond the SM has been found so far at the LHC up to 1 TeV. It is important to examine up to what scale the SM can be a valid effective description of nature.

The determination of the Higgs mass finally fixes all the parameters in the SM. We can now obtain the *bare* parameters at the ultraviolet cutoff scale Λ. These parameters are important. If an ultraviolet (UV) theory such as string theory fails to fit them, it is killed.

The parameters in the SM are dimensionless except for the Higgs mass (or equivalently its vacuum expectation value [VEV]). The dimensionless bare coupling constants can be approximated by the running ones at Λ; see, e.g., the appendix of Ref. [4]. Once the low-energy inputs are given, we can evaluate the running couplings through the renormalization group equations (RGEs) of the SM. Detailed RGE study of the SM tells us that both the Higgs quartic coupling and its beta function

© The Author(s) 2014. Published by Oxford University Press on behalf of the Physical Society of Japan.
This is an Open Access article distributed under the terms of the Creative Commons Attribution License (http://creativecommons.org/licenses/by/3.0/), which permits unrestricted use, distribution, and reproduction in any medium, provided the original work is properly cited.
Funded by SCOAP[3]

Downloaded from http://ptep.oxfordjournals.org/ at Osaka Daigaku Ningen on January 18, 2017

become tiny at the same scale, $\sim 10^{17}$ GeV, for the input value of the Higgs mass around 126 GeV; see, e.g., Refs. [4–11] for the latest analyses.

After fixing all the dimensionless bare couplings, the last remaining parameter in the SM is the bare Higgs mass. The quadratically divergent bare Higgs mass is found to be suppressed too when the UV cutoff is $\Lambda \gtrsim 10^{17}$ GeV [4]; see also Refs. [10,12–14], and Refs. [15–19]. The absence of the bare mass at Λ, along with the vanishing quartic coupling and its beta function, implies that the Higgs potential is approximately flat there and that its height is suppressed compared to (the fourth power of) the cutoff scale.

Following the evidence of the top quark with mass $174 \pm 10^{+13}_{-12}$ GeV [20] in 1994, Froggatt and Nielsen have predicted [21] that the top and Higgs masses are 173 ± 5 GeV and 135 ± 9 GeV, respectively. This prediction is based on the multiple point principle (MPP) that the SM Higgs potential must have another minimum at the Planck scale and that its height is (order-of-magnitude-wise [22,23]) degenerate to the SM one. This assumption is equivalent to the vanishing Higgs quartic coupling and its beta function at the Planck scale. The success of this prediction indicates that at least the top–Higgs sector of the SM remains unaltered up to a very high UV cutoff scale Λ.[1]

In the MPP, it is assumed that there are two vacua that are separated by a potential barrier, as illustrated in the lowermost (green) solid and dashed lines in Fig. 2. In this paper, we consider the case where there is no potential barrier, as illustrated in the middle (blue) and uppermost (red) lines in Fig. 2, so that the Higgs potential can be used for an inflation. In order to have an inflation consistent with the current observational data, we assume that the low-energy SM Higgs potential, depicted by the solid lines, is smoothly connected to an almost flat potential, depicted by the dot-dashed lines, around the UV cutoff scale Λ.[2]

Some of the concrete examples of the flat potential above the cutoff are the following: In the gauge–Higgs unification scenario, the potential for $\langle A_5 \rangle$ is almost flat for large field values $\langle A_5 \rangle \gg R^{-1}$ because of the gauge invariance and is bounded from above by $O(R^{-4})$ [28]; a similar mechanism can be expected in string compactification [29,30]; see also Refs. [31–35]. Another example is the Coleman–Weinberg potential [36] with an explicit momentum cutoff Λ. For a field value beyond Λ, we get a log potential, as we explain in Appendix B. (This possibility is pursued in Sect. 4.2.)

The latest cosmological data [37] constrains the scalar fluctuation amplitude A_s, the spectral index n_s, and the tensor-to-scalar ratio r; see also Ref. [38] for a recent review. By assuming the slow-roll inflation, these values are completely fixed by the potential height $\mathcal{V}_*$ and its derivatives $\mathcal{V}'_*$ and $\mathcal{V}''_*$ at a field value φ_* corresponding to a given e-folding $N_* \simeq 60$. If we allow an arbitrary shape for the Higgs potential in the whole range beyond the electroweak scale, we can trivially satisfy these constraints. In our case, however, the SM potential in the range $\varphi < \Lambda$ is fixed by the known SM parameters. In order to avoid the graceful exit problem [39–41], the potential must be monotonically increasing in the entire region, both below and above Λ. In particular, the value of the SM potential at the cutoff must satisfy $\mathcal{V}_{\rm SM}(\varphi = \Lambda) < \mathcal{V}_*$. As a result, we get an upper bound: $\Lambda \lesssim 10^{17}$ GeV,

[1] As a possible modification, the classically conformal $B - L$ model is considered in [24–26]. This model can realize the "flat" potential at the Planck scale and solve the hierarchy problem [27].

[2] In the original argument of the MPP [21], the partition function was maximized as a function of the bare Higgs mass. In the more recent Ref. [23], Nielsen has generalized their argument and considered several possibilities of the function to be maximized. In the context of Ref. [23], our approach could be regarded as the maximization of the entropy of the universe by requiring the occurrence of the inflation.

Downloaded from http://ptep.oxfordjournals.org/ at Osaka Daigaku Ningen on January 18, 2017

when the top quark mass is $M_t \lesssim 171$ GeV, irrespectively of the extrapolation of the potential above the cutoff $\varphi > \Lambda$.

As stated above, we propose a possible extrapolation of the potential beyond Λ, log plus constant, motivated by the Coleman–Weinberg potential with the cutoff Λ. We show predictions of the spectral indices, their derivatives, etc. of the cosmic microwave background (CMB) in this model.

Our scenario differs from the conventional Higgs inflation scenario [42–47], which achieves the flatness of the Higgs potential by the huge Higgs coupling to the Ricci scalar: $\xi\,|\phi|^2\,\mathcal{R}$ with $\xi \sim 10^4$. The idea of the Higgs inflation is attractive, but it would be even better if we can realize it without such a coupling to gravity. See also Ref. [48,49] for the unitarity issue of the conventional Higgs inflation, which necessitates new particles above M_P/ξ.[3]

This paper is organized as follows. In Sect. 2, we review the constraints from the cosmological observations including the latest results from the Planck experiment. In Sect. 3, we present the RGE running of the dimensionless couplings in the SM in the modified minimal subtraction ($\overline{\text{MS}}$) scheme; we also show the bare Higgs mass-squared parameter at Λ. Then we show that the SM Higgs potential can become flat around 10^{17} GeV. In Sect. 4, we examine a necessary condition that the Higgs field in the SM can serve as an inflaton assuming arbitrary shape of the potential above Λ. In the last section, we summarize our results.

2. Constraints on inflation models

We briefly review and summarize our notation on the cosmological constraints from the CMB data observed at the Planck experiment, basically following Ref. [37]. The curvature and tensor power spectra are expanded around a pivot scale k_* as

$$\mathcal{P}_{\mathcal{R}} = A_s \left(\frac{k}{k_*}\right)^{n_s - 1 + \frac{1}{2}\frac{\mathrm{d}n_s}{\mathrm{d}\ln k}\ln\frac{k}{k_*} + \frac{1}{3!}\frac{\mathrm{d}^2 n_s}{\mathrm{d}\ln k^2}\left(\ln\frac{k}{k_*}\right)^2 + \cdots}, \quad \mathcal{P}_t = A_t \left(\frac{k}{k_*}\right)^{n_t + \frac{1}{2}\frac{\mathrm{d}n_t}{\mathrm{d}\ln k}\ln\frac{k}{k_*} + \cdots}. \tag{1}$$

We take the slow-roll approximation hereafter. The slow-roll parameters at a given position φ of the inflaton potential $\mathcal{V}$ are defined as

$$\epsilon_V = \frac{M_P^2}{2}\frac{\mathcal{V}_\varphi^2}{\mathcal{V}^2}, \quad \eta_V = M_P^2\frac{\mathcal{V}_{\varphi\varphi}}{\mathcal{V}}, \quad \xi_V^2 = M_P^4\frac{\mathcal{V}_\varphi \mathcal{V}_{\varphi\varphi\varphi}}{\mathcal{V}^2}, \quad \varpi_V^3 = M_P^6\frac{\mathcal{V}_\varphi^2\,\mathcal{V}_{\varphi\varphi\varphi\varphi}}{\mathcal{V}^3}. \tag{2}$$

The number of e-folding before the end of inflation t_{end} from a time t_* becomes

$$N_* = \int_{t_*}^{t_{\text{end}}} \mathrm{d}t\, H = \int_{\varphi_*}^{\varphi_{\text{end}}} \frac{\mathrm{d}\varphi}{\dot\varphi} H = \frac{1}{M_P^2}\int_{\varphi_{\text{end}}}^{\varphi_*} \frac{\mathcal{V}}{\mathcal{V}_\varphi}\mathrm{d}\varphi = \frac{1}{M_P}\int_{\varphi_{\text{end}}}^{\varphi_*} \frac{\mathrm{d}\varphi}{\sqrt{2\epsilon_V}}, \tag{3}$$

where we have taken $\mathcal{V}_\varphi > 0$ in the last step. The end of inflation is defined by the field value φ_{end} below which the slow roll condition is violated:

$$\max\left\{\epsilon_V(\varphi_{\text{end}}),\ \left|\eta_V(\varphi_{\text{end}})\right|\right\} = 1. \tag{4}$$

For most reasonable inflation models, the scale that we are observing from the CMB data corresponds to the e-folding in the range [37]

$$50 < N_* < 60. \tag{5}$$

In the following, we evaluate the slow-roll parameters at φ_* that satisfies Eq. (5). (We will also consider the range $40 < N_* < 50$ in Sect. 4.2 for comparison.)

[3] The authors of Refs. [50,51] have proposed a Higgs inflation model in which the Higgs kinetic term is modified; the unitarity issue of this scenario, which involves higher derivatives of the Higgs field, would also be interesting to study.

Downloaded from http://ptep.oxfordjournals.org/ at Osaka Daigaku Ningen on January 18, 2017

The cosmological parameters are given by[4]

$$A_s = \frac{\mathcal{V}}{24\pi^2 M_P^4 \epsilon_V}, \quad A_t = \frac{2\mathcal{V}}{3\pi^2 M_P^4}, \quad r = \frac{A_t}{A_s} = 16\epsilon_V, \tag{6}$$

$$n_s = 1 + 2\eta_V - 6\epsilon_V, \quad n_t = -2\epsilon_V,$$

$$\frac{\mathrm{d}n_s}{\mathrm{d}\ln k} = 16\epsilon_V\eta_V - 24\epsilon_V^2 - 2\xi_V^2, \quad \frac{\mathrm{d}n_t}{\mathrm{d}\ln k} = -4\epsilon_V\eta_V + 8\epsilon_V^2,$$

$$\frac{\mathrm{d}^2 n_s}{\mathrm{d}\ln k^2} = -192\epsilon_V^3 + 192\epsilon_V^2\eta_V - 32\epsilon_V\eta_V^2 - 24\epsilon_V\xi_V^2 + 2\eta_V\xi_V^2 + 2\varpi_V^3, \tag{7}$$

where the quantities are evaluated at the field value φ_*.

At the pivot scale $k_* = 0.05\,\mathrm{Mpc}^{-1}$, the scalar amplitude A_s and the spectral index n_s are constrained by the Planck+WMAP data as [37]

$$A_s = \left(2.196^{+0.051}_{-0.060}\right) \times 10^{-9}, \tag{8}$$

$$n_s = 0.9603 \pm 0.0073, \tag{9}$$

assuming $\mathrm{d}n_s/\mathrm{d}\ln k = \mathrm{d}^2 n_s/\mathrm{d}\ln k^2 = r = 0$.

If we include the tensor-to-scalar ratio r as an extra parameter, the Planck+WMAP+high-ℓ data [37] at the pivot scale $k_* = 0.002\,\mathrm{Mpc}^{-1}$ give the 1σ range for n_s and the 95% CL limit on r as

$$n_s = 0.9600 \pm 0.0071, \quad r < 0.11. \tag{10}$$

On the other hand, if we include $\mathrm{d}n_s/\mathrm{d}\ln k$ as an extra parameter, we obtain the constraint at the pivot scale $k_* = 0.05\,\mathrm{Mpc}^{-1}$ [37]

$$n_s = 0.9561 \pm 0.0080, \quad \frac{\mathrm{d}n_s}{\mathrm{d}\ln k} = -0.0134 \pm 0.0090. \tag{11}$$

One may vary both r and $\mathrm{d}n_s/\mathrm{d}\ln k$ to fit the Planck + WMAP data at the pivot scale $k_* = 0.05\,\mathrm{Mpc}^{-1}$, obtaining [37]

$$n_s = 0.9583 \pm 0.0081, \quad r < 0.25, \quad \frac{\mathrm{d}n_s}{\mathrm{d}\ln k} = 0.021 \pm 0.012, \tag{12}$$

where the constraint on r is given at 95% CL.[5]

We note that the upper bound on r gives that of the inflaton energy scale [37]

$$\mathcal{V}_{\max} = \frac{3\pi^2 A_s}{2} r_{\max} M_P^4 = 1.3 \times 10^{65}\mathrm{GeV}^4 \times \left(\frac{r_{\max}}{0.11}\right). \tag{13}$$

[4] Eq. (17) of Ref. [37] contains a typo (an overall wrong sign for $\mathrm{d}n_s/\mathrm{d}\ln k$). Also note that in the case of $\Lambda\mathrm{CDM} + r + \mathrm{d}n_s/\mathrm{d}\ln k$ in Table 5 of Ref. [37], there is a minus sign missing from the front of the mean value of $\mathrm{d}n_s/\mathrm{d}\ln k$ for Planck + WP and Planck + WP + lensing. We thank the referee for bringing this point to our attention, and Finelli Fabio for his kind clarification.

[5] In terms of the slow-roll parameters, these conditions become

$$\epsilon_V < 0.015, \quad \eta_V = -0.014^{+0.015}_{-0.011}, \quad \left|\xi_V^2\right| = 0.009 \pm 0.006,$$

where the constraint on ϵ_V is given at 95% CL.

Downloaded from http://ptep.oxfordjournals.org/ at Osaka Daigaku Ningen on January 18, 2017

3. SM Higgs potential

The SM Higgs potential much above the electroweak scale but below the cutoff scale Λ is governed by the RGE running of the Higgs quartic coupling λ, which highly depends on the top Yukawa coupling y_t. Therefore we first review how y_t is determined; then we show the numerical results of the RGEs; finally we present the resultant Higgs potential around Λ.

3.1. Coupling constants at the electroweak scale

The most precise determination of the top quark mass is given by a combination of the Tevatron data for the invariant mass of the top quark decay products [52]:

$$M_t^{\rm inv} = 173.20 \pm 0.87\,{\rm GeV}. \tag{14}$$

The problem of the Tevatron determination (14) is that the invariant mass, which is reconstructed from the color singlet final states, cannot be the pole mass of the colored top quark [8]. Instead, the authors of Ref. [8] proposed to get the top mass by fitting the $t\bar{t} + X$ inclusive cross section, and obtained the pole mass:[6]

$$M_t = 173.3 \pm 2.8\,{\rm GeV}. \tag{15}$$

The numerical value of the $\overline{\rm MS}$ Yukawa coupling at the top mass scale can be read off from Ref. [7] as

$$\begin{aligned} y_t(M_t) = {} & 0.93669 + 0.01560\left(\frac{M_t - 173.3\,{\rm GeV}}{2.8\,{\rm GeV}}\right) - 0.00041\left(\frac{\alpha_s(M_Z) - 0.1184}{0.0007}\right) \\ & - 0.00001\left(\frac{M_H - 125.6\,{\rm GeV}}{0.4\,{\rm GeV}}\right) \pm 0.00200_{\rm th}, \end{aligned} \tag{16}$$

where we have employed a combined Higgs mass $M_H = 125.6 \pm 0.4\,{\rm GeV}$. The electroweak gauge couplings at the Z mass scale are [59]

$$g_Y(M_Z) = 0.357418(35), \quad g_2(M_Z) = 0.65184(18). \tag{17}$$

The $\overline{\rm MS}$ strong and quartic couplings at the top mass scale are [7]

$$g_s(M_t) = 1.1644 + 0.0031\left(\frac{\alpha_s(M_Z) - 0.1184}{0.0007}\right) - 0.0013\left(\frac{M_t - 173.3\,{\rm GeV}}{2.8\,{\rm GeV}}\right), \tag{18}$$

$$\lambda(M_t) = 0.12699 + 0.00082\left(\frac{M_H - 125.6\,{\rm GeV}}{0.4\,{\rm GeV}}\right) - 0.00012\left(\frac{M_t - 173.3\,{\rm GeV}}{2.8\,{\rm GeV}}\right) \pm 0.00140_{\rm th}. \tag{19}$$

3.2. Numerical results of SM RGEs

We use the two-loop RGEs in the SM which are summarized in Ref. [4].

[6] As clarified in Refs. [53,54], currently there are two ways to define the $\overline{\rm MS}$ running top mass for a given $\overline{\rm MS}$ running Yukawa $y_t(\mu)$. The $\overline{\rm MS}$ mass used in QCD [8,55,56], which we call $m_t^{\rm QCD}(\mu)$, can be approximately written as $m_t^{\rm QCD}(\mu) \simeq y_t(\mu)V/\sqrt{2}$ with $V = 246.22\,{\rm GeV}$, up to electroweak corrections less than 1%. In Refs. [57,58], $\overline{\rm MS}$ mass is defined as $m_t(\mu) := y_t(\mu)v(\mu)/\sqrt{2}$, where $v(\mu)$ is given by the relation $-m^2(\mu) = \lambda(\mu)\,v^2(\mu)$, with $m^2(\mu)$ being the running mass parameter in the tree potential in the $\overline{\rm MS}$ scheme: $\mathcal{V} = m^2(\mu)\,\phi^\dagger\phi + \lambda(\mu)\,(\phi^\dagger\phi)^2$. There is $\sim 7\%$ difference between $m_t^{\rm QCD}(M_t)$ and $m_t(M_t)$ [58], which is mainly due to the tadpole contribution from the top quark. Though the bound on the pole mass (15) has been derived from that on $m_t^{\rm QCD}(M_t) = 163.3 \pm 2.7\,{\rm GeV}$ [8], it is consistent to use Eq. (15) in obtaining the Yukawa coupling (16) since the pole mass M_t should be the same in both schemes.

Downloaded from http://ptep.oxfordjournals.org/ at Osaka Daigaku Ningen on January 18, 2017

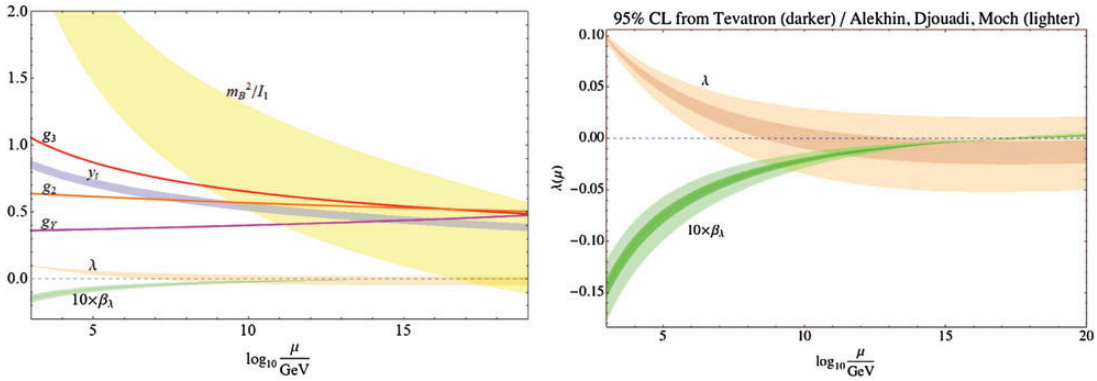

Fig. 1. Left: $\overline{\mathrm{MS}}$ running couplings. The 95% confidence intervals are given for m_B^2/I_1, $y_t(\mu)$, $\lambda(\mu)$, and $10\beta_\lambda(\mu)$; see text for more details. The intervals for the gauge couplings g_Y, g_2, and g_3 are too small to be seen. Right: Enlarged view around the horizontal axis of the graph to the left. Darker bands are the 95% confidence intervals under the (theoretically unjustified) assumption that the Tevatron mass (14) can be identified with the top pole mass M_t.

We show our result of running $\overline{\mathrm{MS}}$ couplings in Fig. 1. The gauge couplings g_Y, g_2, g_3 are drawn by thick lines. The thickness of the curves for y_t, λ, and β_λ comes from the 1.96σ variation of M_t (15), where $\alpha_s(M_z)$ and M_H are fixed to their central values. Similarly, we plot the bare Higgs mass-squared m_B^2, divided by the quadratically divergent integral $I_1 = \Lambda^2/16\pi^2$, as a function of Λ [4,53]. Note that the bare mass m_B^2 is *not* the running mass.

We see that the Higgs quartic coupling λ has a minimum around 10^{17} GeV. This is due to the fact that the beta function of λ receives less negative contribution from the top loop since y_t becomes smaller at high scales.

We can fit the parameters at the reduced Planck scale[7] $M_P := 1/\sqrt{8\pi G} = 2.4 \times 10^{18}$ GeV as

$$\lambda(M_P) = -0.015 - 0.019\left(\frac{M_t - 173.3\,\mathrm{GeV}}{2.8\,\mathrm{GeV}}\right) + 0.002\left(\frac{\alpha_s(M_Z) - 0.1184}{0.0007}\right) + 0.001\left(\frac{M_H - 125.6\,\mathrm{GeV}}{0.4\,\mathrm{GeV}}\right), \tag{20}$$

$$\frac{m_B^2}{M_P^2/16\pi^2} = 0.26 + 0.18\left(\frac{M_t - 173.3\,\mathrm{GeV}}{2.8\,\mathrm{GeV}}\right) - 0.02\left(\frac{\alpha_s(M_Z) - 0.1184}{0.0007}\right) - 0.01\left(\frac{M_H - 125.6\,\mathrm{GeV}}{0.4\,\mathrm{GeV}}\right), \tag{21}$$

$$\beta_\lambda = 0.000103 + 0.000069\left(\frac{M_t - 173.3\,\mathrm{GeV}}{2.8\,\mathrm{GeV}}\right) + 0.000028\left(\frac{M_t - 173.3\,\mathrm{GeV}}{2.8\,\mathrm{GeV}}\right)^2 - 0.000013\left(\frac{M_H - 125.6\,\mathrm{GeV}}{0.4\,\mathrm{GeV}}\right), \tag{22}$$

where the dependence of β_λ on $\alpha_s(M_Z)$ is of $O(10^{-7})$ and is not shown.

[7] In this definition, the graviton fluctuation $h_{\mu\nu}$ around the flat Minkowski spacetime $g_{\mu\nu} = \eta_{\mu\nu} + 2M_P^{-1}h_{\mu\nu}$ becomes canonically normalized.

Downloaded from http://ptep.oxfordjournals.org/ at Osaka Daigaku Ningen on January 18, 2017

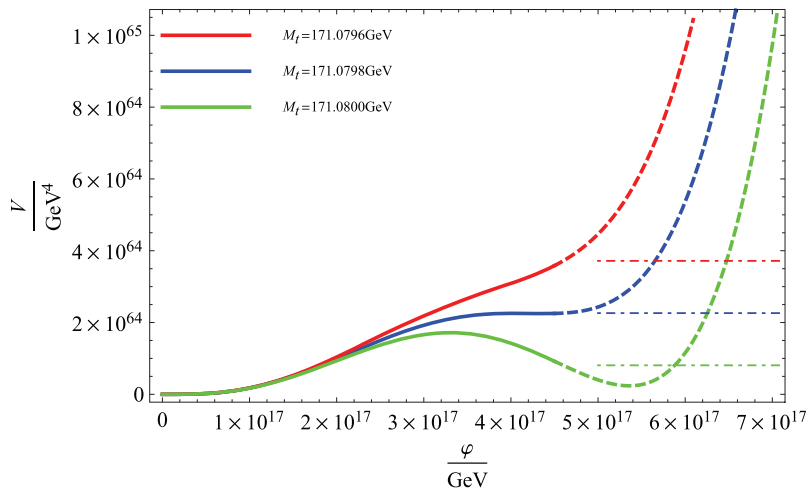

Fig. 2. RGE improved Higgs potential (23), with $M_H = 125.6\,\mathrm{GeV}$ and $\alpha_s = 0.1184$. The solid and dashed lines are the SM Higgs potential (23). Beyond the UV cutoff Λ, which we have taken in this figure to be $4.5 \times 10^{17}\,\mathrm{GeV}$ as an illustration, we assume that the potential becomes flat as depicted by the dot-dashed lines.

3.3. Higgs inflation?

We have seen in Fig. 1 that both the Higgs self coupling λ and its beta function β_λ become very small at high scales $\mu \gtrsim 10^{17}\,\mathrm{GeV}$. This fact suggests that the SM Higgs field could be identified as an inflaton. In the following, we show that the SM Higgs potential becomes flat around $10^{17}\,\mathrm{GeV}$ if we tune the top quark mass. However, we will see that it is difficult to reconcile this potential with the cosmological observation [23,60].

For a field value $V = 246.22\,\mathrm{GeV} \ll \varphi < \Lambda$, the Higgs potential becomes, with RGE improvement,

$$\mathcal{V}_{\mathrm{SM}}(\varphi) = \frac{\lambda(\varphi)}{4}\varphi^4. \tag{23}$$

Around the scale $10^{17}\,\mathrm{GeV}$, this potential strongly depends on the top quark mass, which we show by the solid and dashed lines in Fig. 2. The dot-dashed lines are irrelevant to the argument of this subsection.

If we fine-tune the top mass, we can have a saddle point in the Higgs potential: $\mathcal{V}_\varphi(\varphi) = \mathcal{V}_{\varphi\varphi}(\varphi) = 0$, as indicated by the middle (blue) line in Fig. 2. When we slightly lower the top mass, the saddle point disappears and the potential becomes monotonically increasing, as the upper (red) line. On the contrary, when we slightly raise the top mass, there appears another minimum at a high scale, as the lower (green) line [61,62].

The middle (blue) line case, $M_t = 171.0798\,\mathrm{GeV}$, gives the potential

$$\mathcal{V}_c = 6.0 \times 10^{-10} M_P^4 \sim \left(10^{16}\,\mathrm{GeV}\right)^4 \tag{24}$$

at the saddle point $\varphi_c = 4.2 \times 10^{17}\,\mathrm{GeV}$. One might think of using this saddle point for a Higgs inflation, but it is impossible due to the following reasons: With Eq. (8), this height of potential necessitates $\epsilon_V \sim 10^{-3}$. However, the point of $N_* \gtrsim 50$ becomes too close to the saddle point and gives $\epsilon_V \ll 10^{-3}$.

Downloaded from http://ptep.oxfordjournals.org/ at Osaka Daigaku Ningen on January 18, 2017

In order to avoid this problem, one might try lowering the top mass slightly to reproduce the value of $\epsilon_V \sim 10^{-3}$ at the inflection point $\mathcal{V}_{\varphi\varphi} = 0$. This still does not work because we cannot have enough e-foldings, $N_* \gtrsim 50$, at the inflection point.

As the third trial, one might choose ϵ_V freely at the inflection point so that one can have enough e-folding in passing the inflection point. In this case, one tries to reproduce $\epsilon_V \sim 10^{-3}$ at the higher point with $N_* \sim 50$. However, η_V at this point turns out to be too large to satisfy the slow-roll condition.

We present more detailed discussion in Appendix A.

Note that the precise value of M_t to give the saddle point in Fig. 2 depends on M_H, the details of the RGEs, etc.; the digits of M_t should not be taken literally, but be regarded as an indication of how finely M_t must be tuned to yield a saddle point in the SM. Also, the height of the potential at the saddle point varies when we change, e.g., M_H within the 95% CL, $M_H = (124.8 - 126.4)$ GeV, as

$$\mathcal{V}_c = (1.5\text{–}32.) \times 10^{-10} M_P^4. \tag{25}$$

Therefore the value (24) should be taken as an indication of the order of magnitude.

4. Minimal Higgs inflation

We pursue the possibility that the Higgs potential above Λ becomes sufficiently flat to realize a viable inflation, as the dot-dashed lines in Fig. 2. The inflaton potential is bounded from above as in Eq. (8). In order to avoid the graceful exit problem, the Higgs potential must be monotonically increasing in all the range below and above Λ. Therefore, even if we allow an arbitrary modification above Λ, we still can get a bound: $\Lambda < 5 \times 10^{17}$ GeV. As a concrete example of the modification above Λ, we propose a log-type potential and study its cosmological implications.

4.1. Constraint on top mass from minimal Higgs inflation

We have seen that the scale 10^{17} GeV gives the vanishing beta function β_λ. This scale is close to the string scale in the conventional perturbative superstring theory. Above the string scale, a conventional local field theory is altered. We have shown that the bare Higgs mass becomes very small around this scale [4]. This fact strongly suggests that the Higgs boson is a zero mass state of string theory. If it is the case, after integrating out all the massive stringy states, we get the effective potential, which is meaningful for field values beyond the string scale. The resultant potential beyond the string scale would be greatly modified from that in the SM.[8]

As we discussed in Sect. 1, it is plausible that the effective potential for the field value beyond Λ becomes almost flat. This opens up a possibility that this flat potential can be used for the inflation. In this subsection we first consider a necessary condition for the SM potential at $\varphi < \Lambda$ to allow such a modification in the region $\varphi > \Lambda$.

[8] On the contrary, if the Higgs boson had a string-scale bare mass, it would come from a string massive mode. Then considering the effective potential would become meaningless, as it would become one of the fields to be integrated out.

Downloaded from http://ptep.oxfordjournals.org/ at Osaka Daigaku Ningen on January 18, 2017

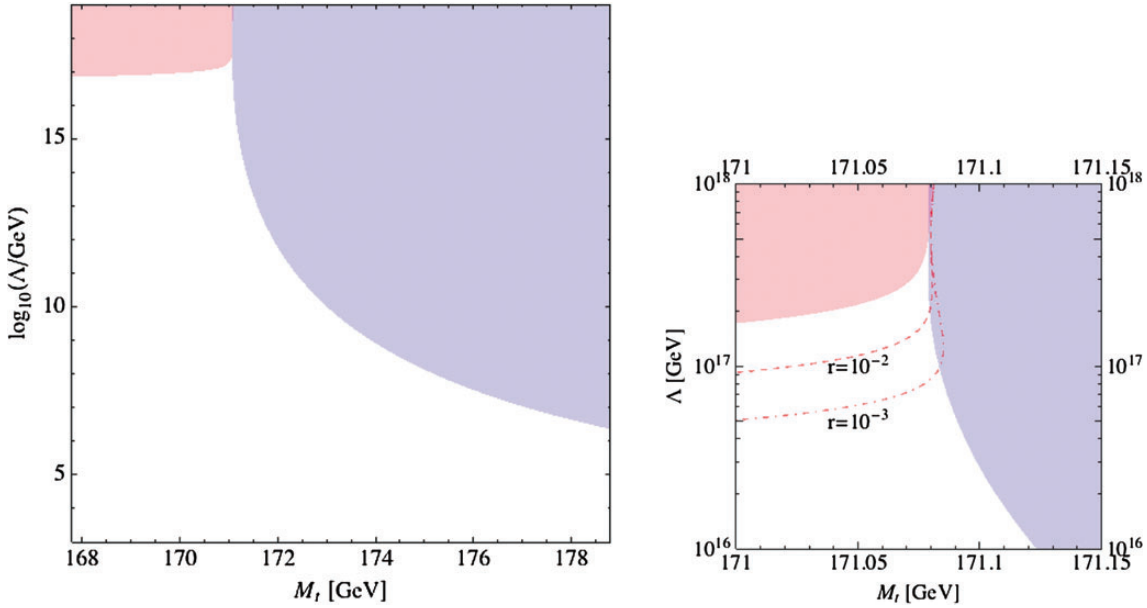

Fig. 3. Left: Regions excluded by Eq. (27) (red, left) and by Eq. (26) (blue, right) in the $\log_{10}(\Lambda/\mathrm{GeV})$ vs M_t plane. Right: Enlarged view for Λ vs M_t. Expected future exclusion limits within 95% CL of $r < 10^{-2}$ and 10^{-3} are also presented by dashed and dot-dashed lines, respectively.

To avoid the graceful exit problem [39–41], the Higgs potential must be a monotonically increasing function of φ in all the range below and above Λ.[9] Therefore, we have

$$\frac{\mathrm{d}\mathcal{V}_{\mathrm{SM}}}{\mathrm{d}\varphi} = \frac{1}{4}\left(\beta_\lambda + 4\lambda\right)\varphi^3 > 0, \tag{26}$$

for all the scales below the cutoff: $\varphi < \Lambda$, and the upper bound (13) leads to

$$\mathcal{V}_{\mathrm{SM}}(\Lambda) < \mathcal{V}_{\mathrm{max}}. \tag{27}$$

We show excluded regions on the Λ–M_t plane from the above two constraints in the left panel of Fig. 3. The left (red) region is excluded by the condition (27) within 95% CL, and the right (blue) region is forbidden by Eq. (26). The right panel is an enlarged view. The dashed and dot-dashed lines correspond to the exclusion limits at the 95% CL, $r < 10^{-2}$ and 10^{-3}, that are expected from the future experiments EPIC [63] and COrE [64], respectively.

We see that the top quark mass needs to be $M_t \lesssim 171$ GeV if we want to have the cutoff scale to be at the string scale $\Lambda \sim 10^{17}$ GeV. If the top quark mass turns out to be heavier, say $M_t \gtrsim 173$ GeV, then this minimal scenario breaks down. However, it is possible that there exists an extra gauge-singlet scalar X that couples to the SM Higgs boson, e.g. as

$$\mathcal{L} = -\frac{\rho}{4!}X^4 - \frac{\kappa}{2}\phi^\dagger\phi X^2, \tag{28}$$

[9] If there is a potential barrier, then the phase transition becomes first order. This is problematic: the false vacuum decays only through the tunneling. The bubbles of true vacuum expand with the speed of light in the exponentially expanding medium of the false vacuum. They can hardly collide with each other. See also Ref. [9] for a possible false vacuum inflation assuming a lowered Planck scale, which we do not employ in this paper.

Downloaded from http://ptep.oxfordjournals.org/ at Osaka Daigaku Ningen on January 18, 2017

where ρ and κ are coupling constants. Then X contributes to the running of λ positively, and the vacuum stability condition becomes milder. Such a scalar naturally arises in the Higgs portal dark matter scenario; see, e.g., Refs. [65–69].[10]

4.2. *Log-type potential*

So far we have not specified anything about the potential shape above Λ. In the following, let us examine the log-type potential:

$$\mathcal{V}(\varphi) = \mathcal{V}_1 \left(C + \ln \frac{\varphi}{M_P} \right). \tag{29}$$

We note that the Coleman–Weinberg potential with an explicit momentum cutoff Λ leads to a log-type potential; see Appendix B.[11] The potential (29) leads to the slow-roll parameters

$$\begin{aligned} \epsilon_V &= \frac{1}{2}\left(\frac{M_P}{\varphi}\right)^2 \left(\frac{1}{C + \ln \frac{\varphi}{M_P}}\right)^2, \quad \eta_V = -\left(\frac{M_P}{\varphi}\right)^2 \frac{1}{C + \ln \frac{\varphi}{M_P}}, \\ \xi_V^2 &= 2\left(\frac{M_P}{\varphi}\right)^4 \left(\frac{1}{C + \ln \frac{\varphi}{M_P}}\right)^2, \quad \varpi_V^3 = -6\left(\frac{M_P}{\varphi}\right)^6 \left(\frac{1}{C + \ln \frac{\varphi}{M_P}}\right)^3. \end{aligned} \tag{30}$$

The end point of the inflation is determined from Eq. (4) for a given constant C:

$$\varphi_{\rm end} = \begin{cases} \dfrac{M_P}{\sqrt{2}\, W\left(\mathrm{e}^C/\sqrt{2}\right)} & \text{for } 0 < C < 0.153, \\ \sqrt{\dfrac{2}{W\left(2\mathrm{e}^{2C}\right)}}\, M_P & \text{for } C > 0.153, \end{cases} \tag{31}$$

where W is the Lambert function defined by $z = W(z)\mathrm{e}^{W(z)}$. Equivalently, the constant C is fixed as a function of $\varphi_{\rm end}$:

$$C = \begin{cases} \dfrac{M_P}{\sqrt{2}\varphi_{\rm end}} - \ln \dfrac{\varphi_{\rm end}}{M_P} & \text{for } \varphi_{\rm end} \geq \sqrt{2} M_P, \\ \left(\dfrac{M_P}{\varphi_{\rm end}}\right)^2 - \ln \dfrac{\varphi_{\rm end}}{M_P} & \text{for } \varphi_{\rm end} \leq \sqrt{2} M_P. \end{cases} \tag{32}$$

The e-folding becomes

$$\begin{aligned} N_* &= \frac{2C-1}{4} \frac{\varphi_*^2 - \varphi_{\rm end}^2}{M_P^2} + \frac{\varphi_*^2}{2M_P^2} \ln \frac{\varphi_*}{M_P} - \frac{\varphi_{\rm end}^2}{2M_P^2} \ln \frac{\varphi_{\rm end}}{M_P} \\ &= \frac{\varphi_*^2}{2M_P^2} \ln \frac{\varphi_*}{\varphi_{\rm end}} - \frac{\varphi_*^2 - \varphi_{\rm end}^2}{4M_P^2} \times \begin{cases} \left(1 - \sqrt{2} M_P/\varphi_{\rm end}\right) & \text{for } \varphi_{\rm end} \geq \sqrt{2} M_P, \\ \left(1 - 2M_P^2/\varphi_{\rm end}^2\right) & \text{for } \varphi_{\rm end} \leq \sqrt{2} M_P. \end{cases} \end{aligned} \tag{33}$$

To summarize: For a given $\varphi_{\rm end}$, we fix the constant C by Eq. (32). Then we can obtain the slow-roll parameters from Eq. (30) at any field value φ. The field value φ_* corresponding to a relevant e-folding N_* is determined from Eq. (33).

[10] Whether X is included or not, our scenario is not altered by the right-handed neutrinos if their Dirac Yukawa couplings are $\lesssim 0.1$.

[11] In terms of the parameters given there, $C = \frac{\mathcal{V}_0}{\mathcal{V}_1} + \ln \frac{M_P}{\Lambda}$.

Downloaded from http://ptep.oxfordjournals.org/ at Osaka Daigaku Ningen on January 18, 2017

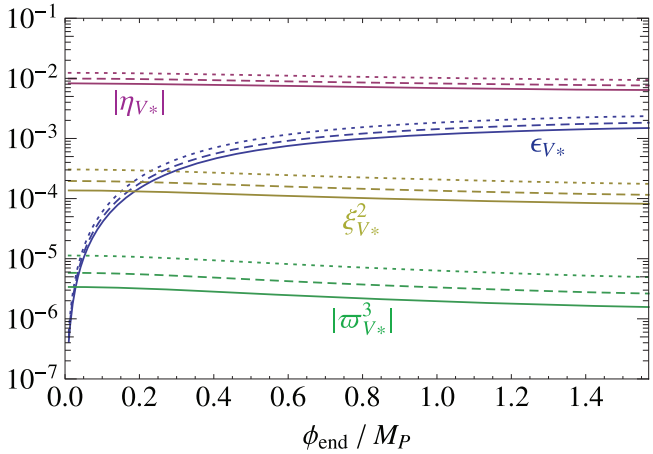

Fig. 4. Slow-roll parameters ϵ_{V*}, η_{V*}, ξ^2_{V*}, and ϖ^3_{V*} as functions of $\varphi_{\rm end}/M_P$ within the range $0.01 < \varphi_{\rm end}/M_P < 1.57$. The dotted, dashed, and solid lines correspond to $N_* = 40$, 50, and 60, respectively.

In this way the slow-roll parameters (30) at a given N_* are completely fixed. Note that they are independent of $\mathcal{V}_1$, the overall normalization of the potential. In Fig. 4, we plot the slow-roll parameters ϵ_V, η_V, ξ^2_V, and ϖ^3_V at the field value φ_* as functions of $\varphi_{\rm end}/M_P$. The dotted, dashed, and solid lines correspond to the values $N_* = 40$, 50, and 60, respectively.[12]

Once the slow-roll parameters are given, the spectral indices, their running, and their running of running are completely fixed. In Fig. 5, we plot them as functions of $\varphi_{\rm end}$. The solid (dotted) lines represent the values for N_* from 50 to 60 (40 to 49). The values for N_* below 50 are just for reference; e.g., late-time thermal inflation [70] can reduce the corresponding N_* to the observed value of k_*; see Ref. [71] for related discussions. When we vary N_* and $\varphi_{\rm end}$ within the ranges $50 \le N_* \le 60$ and $0 < \varphi_{\rm end} < 1.57 M_P$, we get

$$\begin{aligned}
&0.980\text{–}0.984 > n_s > 0.974\text{–}0.979, \quad 0 < r < 0.029\text{–}0.024,\\
&-(4.0\text{–}2.7)\times 10^{-4} > \frac{{\rm d}n_s}{{\rm d}\ln k} > -(5.3\text{–}3.7)\times 10^{-4}, \quad 0 > n_t > -(3.7\text{–}3.0)\times 10^{-3},\\
&-(1.6\text{–}0.9)\times 10^{-5} > \frac{{\rm d}^2 n_s}{{\rm d}\ln k^2} > -(2.2\text{–}1.2)\times 10^{-5}, \quad 0 < \frac{{\rm d}n_t}{{\rm d}\ln k} < (8.2\text{–}5.6)\times 10^{-5},
\end{aligned} \tag{34}$$

where the order of the inequality corresponds to that of $0 < \varphi_{\rm end} < 1.57 M_P$; the range of numbers denoted by the en-dash "–" corresponds to the range $N_* = 50$–60.

So far we have not considered $\mathcal{V}_1$, since it is sufficient to fix C to determine the slow-roll parameters. Now we determine $\mathcal{V}_1$ by the magnitude of the density perturbation (6):

$$\mathcal{V}_1 = 12\pi^2 A_s M_P^4 \left(\frac{M_P}{\varphi_*}\right)^2 \left(\frac{1}{C + \ln\frac{\varphi_*}{M_P}}\right)^3. \tag{35}$$

Then the potential and its derivatives at an e-folding N_* are completely fixed. In Fig. 6, we plot φ_*, $\mathcal{V}_{\rm end}$, and $\mathcal{V}_*$ as functions of $\varphi_{\rm end}$. We indicate N_* as in Fig. 5.

[12] We have chosen the highest end point of the horizontal axis of Fig. 4 to be $\varphi_{\rm end}/M_P = {\rm e}^{W(1/\sqrt{2})} = 1.57$ at which $C = 0$ and $\mathcal{V}(\Lambda) = 0$. In this case, we cannot connect the potential $\mathcal{V}$ to $\mathcal{V}_{\rm SM}$, even if the latter were zero at Λ.

Downloaded from http://ptep.oxfordjournals.org/ at Osaka Daigaku Ningen on January 18, 2017

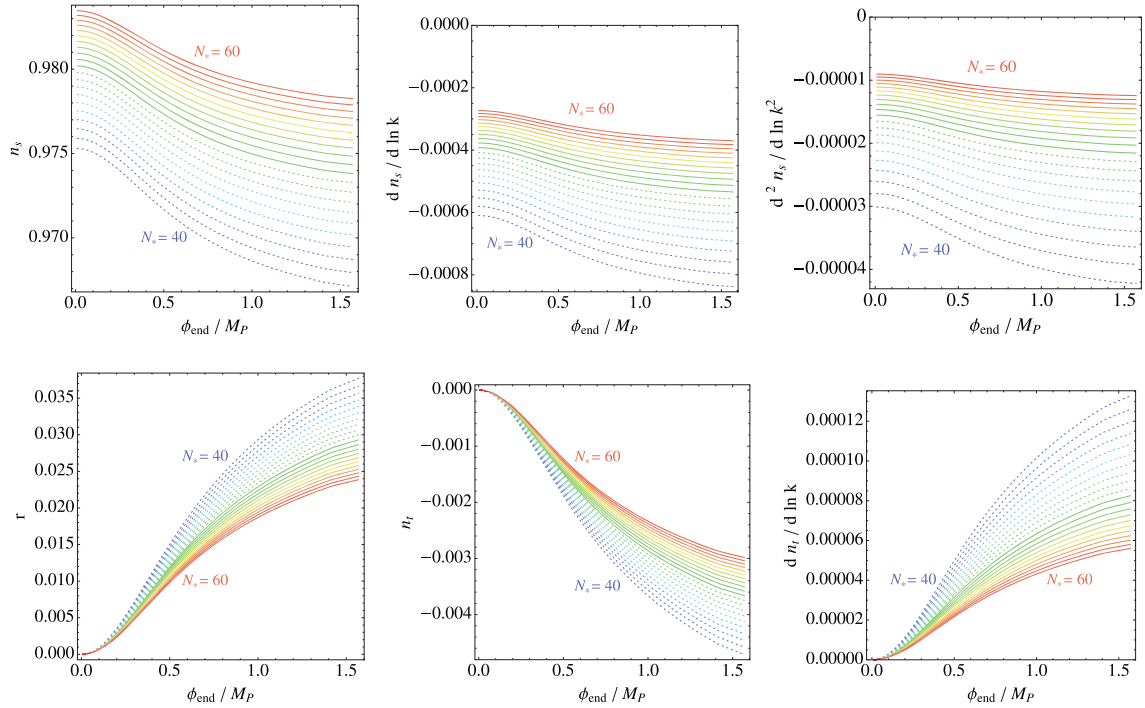

Fig. 5. n_s, $\frac{\mathrm{d}n_s}{\mathrm{d}\ln k}$, $\frac{\mathrm{d}^2 n_s}{\mathrm{d}\ln k^2}$, r, n_t, and $\frac{\mathrm{d}n_t}{\mathrm{d}\ln k}$ as functions of $\varphi_{\mathrm{end}}/M_P$.

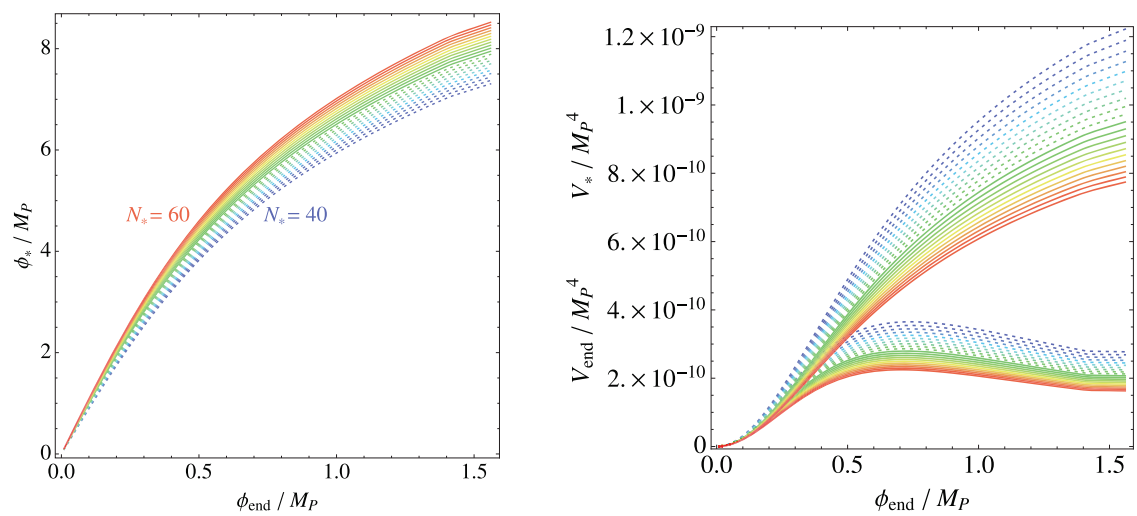

Fig. 6. Left: φ_*/M_P as a function of $\varphi_{\mathrm{end}}/M_P$. Right: Potential values, $\mathcal{V}_* = \mathcal{V}(\varphi_*)$ and $\mathcal{V}_{\mathrm{end}} = \mathcal{V}(\varphi_{\mathrm{end}})$, as functions of $\varphi_{\mathrm{end}}/M_P$. The larger (smaller) values correspond to $\mathcal{V}_*/M_P^4$ ($\mathcal{V}_{\mathrm{end}}/M_P^4$). We indicate N_* as in Fig. 5.

For a given φ_{end} we have obtained the constants $\mathcal{V}_1$ and C. If we demand that the high scale potential (B1), fixed by these values, is directly connected with the SM potential at Λ, then we can fix Λ by

$$\mathcal{V}_1 \left(C + \ln \frac{\Lambda}{M_P} \right) = \mathcal{V}_{\mathrm{SM}}(\Lambda). \tag{36}$$

In Fig. 7 we present the left- and right-hand sides of Eq. (36) for $N_* = 50$ and $M_t = 170.5\,\mathrm{GeV}$ to illustrate the situation. We see that the low-energy SM potential can be directly connected to the

Downloaded from http://ptep.oxfordjournals.org/ at Osaka Daigaku Ningen on January 18, 2017

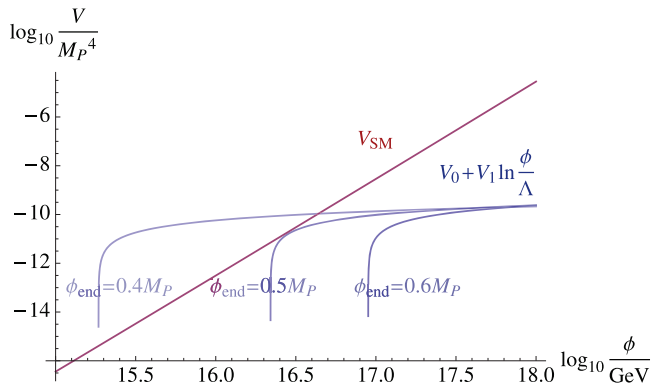

Fig. 7. High-energy potential (B1) for $\varphi_{\rm end} = 0.4M_P$, $0.5M_P$, and $0.6M_P$ with $N_* = 50$ (three blue curves). The red line is the SM potential (23) with the top quark mass $M_t = 170.5\,\text{GeV}$.

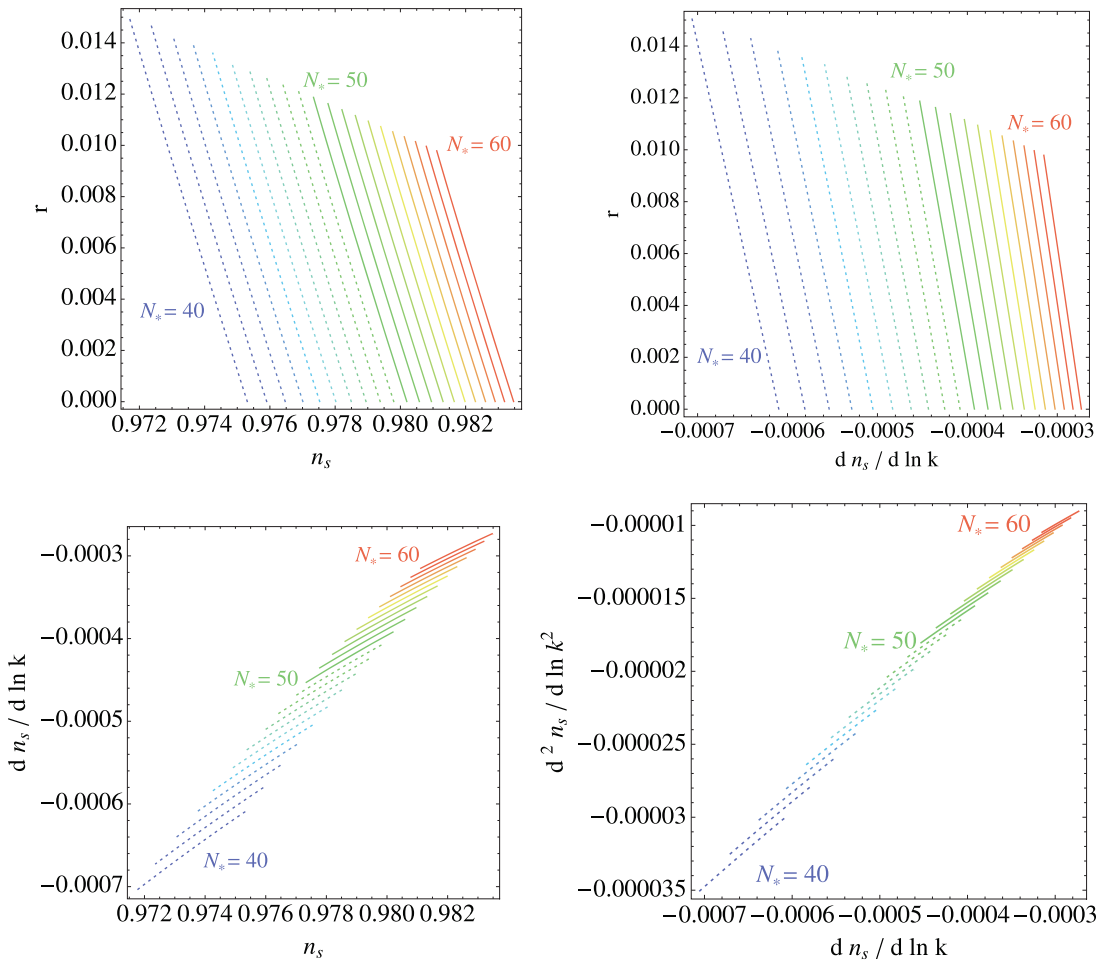

Fig. 8. At the upper-left, upper-right, lower-left, and lower-right, respectively, we have plotted r vs n_s, r vs $\frac{\mathrm{d}n_s}{\mathrm{d}\ln k}$, $\frac{\mathrm{d}n_s}{\mathrm{d}\ln k}$ vs n_s, and $\frac{\mathrm{d}^2n_s}{\mathrm{d}\ln k^2}$ vs $\frac{\mathrm{d}n_s}{\mathrm{d}\ln k}$ for the potential (B1) with $0 < \varphi_{\rm end} < 0.5M_P$.

high-energy one when and only when $\varphi_{\rm end} \lesssim 0.5M_P$. This critical value of $\varphi_{\rm end}$ is not sensitive to the choice of N_* and M_t.

Then we plot r vs n_s, r vs $\frac{\mathrm{d}n_s}{\mathrm{d}\ln k}$, $\frac{\mathrm{d}n_s}{\mathrm{d}\ln k}$ vs n_s, and $\frac{\mathrm{d}^2n_s}{\mathrm{d}\ln k^2}$ vs $\frac{\mathrm{d}n_s}{\mathrm{d}\ln k}$ for $0 < \varphi_{\rm end} < 0.5M_P$ in Fig. 8, which can be compared with Figs. 1–5 in Ref. [37]. When we vary N_* and $\varphi_{\rm end}$ within the ranges

Downloaded from http://ptep.oxfordjournals.org/ at Osaka Daigaku Ningen on January 18, 2017

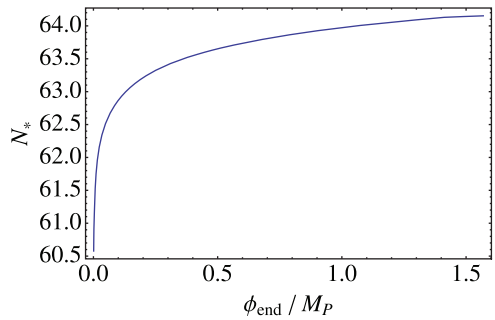

Fig. 9. The e-foldings N_* as a function of $\varphi_{\rm end}/M_P$ corresponding to the pivot scale $k_* = 0.002\,{\rm Mpc}^{-1}$ in the instantaneous decay approximation; see text.

$N_* = 50$–60 and $0 < \varphi_{\rm end} < 0.5M_P$, we get

$$\begin{aligned} &0.980\text{–}0.983 > n_s > 0.977\text{–}0.981, \quad 0 < r < 0.012\text{–}0.010, \\ &-(3.9\text{–}2.7)\times 10^{-4} > \frac{{\rm d}n_s}{{\rm d}\ln k} > -(4.5\text{–}3.1)\times 10^{-4}, \quad 0 > n_t > -(1.5\text{–}1.2)\times 10^{-3}, \\ &-(1.6\text{–}0.9)\times 10^{-5} > \frac{{\rm d}^2 n_s}{{\rm d}\ln k^2} > -(1.8\text{–}1.0)\times 10^{-5}, \quad 0 < \frac{{\rm d}n_t}{{\rm d}\ln k} < (3.1\text{–}2.2)\times 10^{-5}, \end{aligned} \tag{37}$$

where the order of the inequality corresponds to that of $0 < \varphi_{\rm end} < 0.5M_P$; see Eq. (34).

From Fig. 5, we see that we need rather small $N_* \sim 40$ for $0 < \varphi_{\rm end} < 0.5M_P$ in order to account for the observed value of n_s in Eq. (10).

We note that a large field inflation with scale $\gtrsim 10^{17}$ GeV tends to require a relatively high value of N_*, barring the late-time thermal inflation mentioned above. When we approximate that the Higgs field decays into the SM modes instantaneously after the inflation [42], the reheating temperature is given by[13]

$$\frac{\pi^2}{30} g_* T_{\rm reh}^4 = \mathcal{V}_{\rm end}, \tag{38}$$

where $g_* \simeq 106.75$ is the effective number of degrees of freedom in the SM; the resultant reheating temperature is $T_{\rm reh} \simeq 4\times 10^{15}$ GeV for $\varphi_{\rm end} = 0.5M_P$. Then the e-folding number, corresponding to the pivot scale $k_* = 0.002\,{\rm Mpc}^{-1}$ and the Hubble parameter $H_0 = 67.3\,{\rm km\,s^{-1}Mpc^{-1}}$, is given by [37]:

$$N_* \simeq 69 + \frac{1}{4}\ln\frac{\mathcal{V}_*}{M_P^4} + \frac{1}{4}\ln\frac{\mathcal{V}_*}{\mathcal{V}_{\rm end}}. \tag{39}$$

Using the values of $\mathcal{V}_*$ and $\mathcal{V}_{\rm end}$ as depicted in Fig. 6, we get the e-folding number as a function of $\varphi_{\rm end}$, which is plotted in Fig. 9. This indicates that the large field inflation requires $N_* \gtrsim 60$.

On the other hand, as we have seen around Eq. (36) and Eq. (37), we need a small value of $N_* \sim 40$ if we want to directly connect the log potential with the SM one. To do so, $\varphi_{\rm end}$ needs to be relatively small, $\varphi_{\rm end} < 0.5M_P$, and N_* should be around 40 in order to obtain a realistic value of n_s.

[13] We note that the scale $\varphi_{\rm end}$ is beyond Λ, which is the UV cutoff scale of the SM. Generically one expects that, above Λ, extra degrees of freedom appear besides the SM modes. In general, these modes, say excited string modes in string theory, decay with the rate of the order of Λ times a coupling constant, and we assume that these modes in the decay chain do not affect the result very much.

Downloaded from http://ptep.oxfordjournals.org/ at Osaka Daigaku Ningen on January 18, 2017

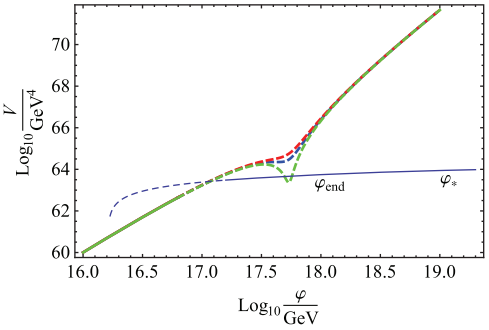

Fig. 10. Log potential (29) plus the correction (40) as a function of φ is drawn in the log-log plot as the solid line to the right, which is the modification of the line for $\varphi_{\mathrm{end}} = 0.5M_P$ in Fig. 7; φ_* and φ_{end} are also indicated. The SM lines are as in Fig. 2, but the SM cutoff is taken to be slightly smaller: $\Lambda \simeq 10^{17}$ GeV.

There are two ways to solve this apparent inconsistency. One is to note that indeed we do not have to connect the log potential to $\mathcal{V}_{\mathrm{SM}}$ so strictly, as it is unclear what happens around $\varphi \sim \Lambda$.[14] All we need is that the end-point value of the inflaton potential is larger than the SM potential at its UV cutoff scale: $\mathcal{V}_{\mathrm{end}} > \mathcal{V}_{\mathrm{SM}}(\Lambda)$ for $\varphi_{\mathrm{end}} > \Lambda$. Then we can take larger φ_{end} to obtain smaller values of n_s.

The other is adding a small correction to the log potential:

$$\Delta\mathcal{V} = \mathcal{V}_1 \left(c_1 \frac{\varphi}{M_P} + c_2 \frac{\varphi^2}{M_P^2} + \cdots \right). \tag{40}$$

For example, if we choose $\mathcal{V}_1 = 4 \times 10^{-11} M_P^4$, $C = 5$, $c_1 = 0.1$, $c_2 = -0.01$, and $c_n = 0$ for $n \geq 3$, then we get $\varphi_{\mathrm{end}} = 0.48\, M_P$, $\varphi_* = 4.7 M_P$, $N_* = 64$, $r = 0.008$, and $n_s = 0.978$. The resultant potential is illustrated in Fig. 10.

5. Summary and discussions

The Higgs potential in the Standard Model (SM) can have a saddle point around 10^{17} GeV, and its height is suppressed because the Higgs quartic coupling becomes small. These facts suggest that the SM Higgs field may serve as an inflaton, without assuming the very large coupling to the Ricci scalar of order 10^4 which is necessary in the ordinary Higgs inflation scenario. In this paper, we have pursued the possibility that the Higgs potential becomes almost flat above the UV cutoff Λ.

Since a first-order phase transition at the end of the inflation leads to the graceful exit problem, the Higgs potential must be monotonically increasing in the whole range below and above Λ. From this condition, we get an upper bound on Λ of the order of 10^{17} GeV.

We have briefly sketched the possible log-type potential above Λ. We present the motivation for this shape in Appendix B, that is, the Coleman–Weinberg one-loop effective potential becomes of this type above Λ when the momentum integral is cut off by Λ. The predictions on the parameters of the cosmic microwave background at the e-foldings $N_* = 50$–60 are: the scalar spectral index, 0.980–$0.983 > n_s > 0.977$–0.981; the tensor to scalar ratio, $0 < r < 0.012$–0.010; the running scalar index, $-(4.5$–$3.1) \times 10^{-4} < \mathrm{d}n_s/\mathrm{d}\ln k < -(3.9$–$2.7) \times 10^{-4}$; the running of running

[14] For example, the Coleman–Weinberg potential that has an explicit momentum cutoff Λ turns into the log-type potential only at large field values $\varphi \gg \Lambda$, as shown in Appendix B.

Downloaded from http://ptep.oxfordjournals.org/ at Osaka Daigaku Ningen on January 18, 2017

scalar index, $-(1.6\text{–}0.9)\times 10^{-5} > \mathrm{d}^2 n_s/\mathrm{d}\ln k^2 > -(1.8\text{–}1.0)\times 10^{-5}$; the tensor spectral index, $0 > n_t > -(1.5\text{–}1.2)\times 10^{-3}$; and the running tensor index, $0 < \mathrm{d}n_t/\mathrm{d}\ln k < (3.1\text{–}2.2)\times 10^{-5}$.

In this paper we have pursued the bottom-up approach from the latest Higgs data, without assuming any other structure than the SM below Λ. We have shown in Fig. 3 that even if we allow arbitrary potential above Λ, still the restriction is rather severe to achieve this minimal Higgs inflation scenario.

It is curious that the upper bound on Λ from the minimal Higgs inflation coincides with the scale where the quartic coupling λ and its beta function (and possibly the bare Higgs mass) vanish. This coincident scale $\sim 10^{17}$ GeV is close to the string scale in the conventional perturbative superstring scenario.[15] This fact may suggest that the physics of the SM, string theory, and the universe are all directly connected.

There are possibilities that realize the flatness from the gauge symmetry as in the gauge–Higgs unification scenario [31–35]—see also Refs. [29,30] for other stringy attempts. Furthermore, Refs. [72,73] derive the log potential of the type (B1). It would be interesting to construct a realistic string model that breaks the supersymmetry at string scale[16] and realizes the flat Higgs potential above Λ consistent with the cosmological observations. One can even go beyond the symmetry argument of the ordinary quantum field theory/string theory to realize the flat potential, such as with the MPP [21–23], the classical conformality around Λ [24–27,77], the multiverse [78], the anthropic principle [79], etc.

Acknowledgements

We thank Tetsutaro Higaki for a useful comment. We also thank Finelli Fabio for his kind explanation about Ref. [37]. This work is in part supported by the Grant-in-Aid for Scientific Research Nos. 22540277 (HK), 23104009, 20244028, and 23740192 (KO), and by the Global COE program "The Next Generation of Physics, Spun from Universality and Emergence." The work of Y. H. was supported by a Grant-in-Aid from the Japan Society for the Promotion of Science (JSPS) Fellows No. 25.1107.

Appendix A. SM Higgs as inflaton

To see more explicitly the argument shown in Sect. 3.3 for the difficulty in directly using the SM Higgs field as an inflaton, we first show how to make a saddle point. Let us expand the potential around the point φ_0 ($\sim 10^{17}$ GeV) of vanishing beta function $\beta_\lambda = 0$:

$$\mathcal{V}|_{\varphi\sim\varphi_0} = \frac{\varphi^4}{4}\left[\lambda_0 + b_2\left(\ln\frac{\varphi}{\varphi_0}\right)^2 + b_3\left(\ln\frac{\varphi}{\varphi_0}\right)^3 + \cdots\right], \tag{A1}$$

where b_i are given by

$$b_2 = \frac{1}{2}\frac{\mathrm{d}^2\lambda}{\mathrm{d}\ln\mu^2} = \frac{1}{2}\sum_i \beta_i\frac{\partial\beta_\lambda}{\partial\lambda_i}, \quad b_n = \frac{1}{n!}\frac{\mathrm{d}^n\lambda}{\mathrm{d}\ln\mu^n} = O\left(\left(16\pi^2\right)^{-n}\right), \tag{A2}$$

with λ_i representing [4] the Yukawa coupling squared, y_t^2 etc., the gauge coupling squared, g_Y^2, g_2^2, g_3^2, and the quartic coupling λ. Note that each $\beta_i = \mathrm{d}\lambda_i/\mathrm{d}\ln\mu$ has a loop suppression factor $1/16\pi^2$. We see that the SM Higgs potential can always have a saddle point by choosing a particular value of λ_0 by adjusting the top quark mass. For example, when we approximate $b_3 = 0$, the saddle point is

[15] See, e.g., Refs. [29,30] for trials to explain the smallness of the quartic coupling in the string theory context.

[16] Generally, the number of superstring vacua that break supersymmetry at string scale is much larger than those that preserves supersymmetry [74–76].

Downloaded from http://ptep.oxfordjournals.org/ at Osaka Daigaku Ningen on January 18, 2017

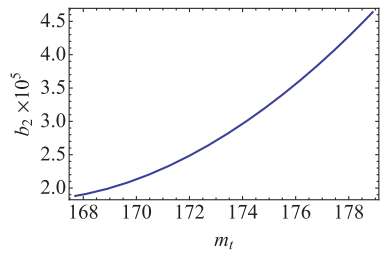

Fig. A1. Running of the beta function b_2 at the scale Λ_0 of vanishing beta function as a function of top pole mass M_t.

realized at $\varphi = \mathrm{e}^{-1/4}\varphi_0$ by choosing $\lambda_0 = b_2/16$. In the SM, b_2 takes values $b_2 \simeq (1.9\text{–}4.6) \times 10^{-5}$ for the 95% confidence interval from the top quark mass (15)—see Fig. A1.

In order to show the difficulty of the inflection point inflation with the SM Higgs potential, it suffices to expand the potential around its inflection point φ_c that satisfies $\mathcal{V}_c'' := \mathcal{V}_{\varphi\varphi}(\varphi_c) = 0$:

$$\mathcal{V}(\varphi) = \mathcal{V}_c + \mathcal{V}_c'(\varphi - \varphi_c) + \frac{\mathcal{V}_c'''}{3!}(\varphi - \varphi_c)^3 + \cdots, \tag{A3}$$

where $\mathcal{V}_c''' := \mathcal{V}_{\varphi\varphi\varphi}(\varphi_c)$ and we tune the top quark mass in order to make $\mathcal{V}_c' := \mathcal{V}_\varphi(\varphi_c)$ very small. The e-folding from $\varphi_c + \delta\varphi_*$ to $\varphi_c - \delta\varphi_{\rm end}$ becomes

$$N_* = \sqrt{\frac{2}{\mathcal{V}_c'\mathcal{V}_c'''}}\frac{\mathcal{V}_c}{M_P^2}\left[\arctan\left(\sqrt{\frac{\mathcal{V}_c'''}{2\mathcal{V}_c'}}\delta\varphi_{\rm end}\right) + \arctan\left(\sqrt{\frac{\mathcal{V}_c'''}{2\mathcal{V}_c'}}\delta\varphi_*\right)\right] + \frac{2\mathcal{V}_c'}{3M_P^2\mathcal{V}_c'''}\ln\frac{2\mathcal{V}_c' + \mathcal{V}_c'''\delta\varphi_*^2}{2\mathcal{V}_c' + \mathcal{V}_c'''\delta\varphi_{\rm end}^2} + \frac{\delta\varphi_*^2 - \delta\varphi_{\rm end}^2}{6M_P^2}. \tag{A4}$$

In the following, we discuss in detail the three cases that are sketched in the text:

- The first possibility is to put $\mathcal{V}_c' = 0$ and earn the e-folding near the saddle point. The e-folding (A4) for $\delta\varphi_{\rm end} > 0$ and $\delta\varphi_* < 0$ becomes

$$N_* = \frac{2\mathcal{V}_c}{M_P^2\mathcal{V}_c'''}\left(\frac{1}{|\delta\varphi_*|} - \frac{1}{\delta\varphi_{\rm end}}\right) - \frac{\delta\varphi_{\rm end}^2 - \delta\varphi_*^2}{6M_P^2} \simeq \frac{2\mathcal{V}_c}{M_P^2\mathcal{V}_c'''\,|\delta\varphi_*|}. \tag{A5}$$

  Close to the saddle point, we have

$$\epsilon_V = \frac{M_P^2\left(\mathcal{V}_c'''\right)^2}{8\mathcal{V}_c^2}\delta\varphi_*^4 + O\left(\delta\varphi_*^7\right). \tag{A6}$$

  Putting Eq. (A5) into Eq. (A6), the slow-roll parameter reads

$$\epsilon_V = \frac{2\mathcal{V}_c^2}{N_*^4 M_P^6\left(\mathcal{V}_c'''\right)^2}, \tag{A7}$$

  and hence the scalar perturbation becomes

$$A_s = \frac{N_*^4 M_P^2\left(\mathcal{V}_c'''\right)^2}{48\pi^2\mathcal{V}_c}. \tag{A8}$$

  From Eq. (A1), we can compute the values in the SM:

$$\mathcal{V}_c''' \sim 10^{-5}\varphi_c \sim 10^{-6}M_P, \tag{A9}$$

  which results in $A_s \gg 1$, far larger than the allowed value (8).

Downloaded from http://ptep.oxfordjournals.org/ at Osaka Daigaku Ningen on January 18, 2017

- As a second possibility, one might introduce small $\mathcal{V}_c' \sim 10^{-11} M_P^3$ at φ_c, in order to realize the value of the correct density perturbation at φ_c. For the SM values $\mathcal{V}_c \sim 10^{-9} M_P^4$ and $\mathcal{V}_c''' = 10^{-6} M_P$, we obtain from Eq. (A4) the e-folding

$$N_* \sim 1. \tag{A10}$$

  This does not work.
- Finally, one may take very tiny $\mathcal{V}_c'$ at φ_c to earn enough e-folding, in order to realize the inflection point inflation scenario [80–89], while obtaining the necessary amount of ϵ_V at a point above the inflection point: $\varphi_c + \delta\varphi_*$ with $\delta\varphi_* > 0$. In passing through the inflection point φ_c from φ_* ($> \varphi_c$) to $\varphi_{\rm end}$ ($< \varphi_c$), we earn the e-folding

$$N_* = \sqrt{\frac{2\pi^2 \mathcal{V}_c^2}{M_P^4 \mathcal{V}_c' \mathcal{V}_c'''}} + O\left(\left(\mathcal{V}_c'\right)^0\right), \tag{A11}$$

  and hence we can have as large an e-folding as we want by tuning $\mathcal{V}_c'$ small. More concretely, we need

$$\mathcal{V}_c' \sim 10^{-15} M_P^3 \tag{A12}$$

  to get $N_* \sim 50$ with Eq. (A9). However, to keep the slow-roll parameter

$$\eta_V = \frac{M_P^2 \mathcal{V}_c'''}{\mathcal{V}_c} \delta\varphi_* + O\left(\delta\varphi_*^2\right) \tag{A13}$$

  sufficiently small, we need to be close to the inflection point:

$$\delta\varphi_* \ll \frac{\mathcal{V}_c}{M_P^2 \mathcal{V}_c'''}. \tag{A14}$$

  Within this range, we get

$$\epsilon_V = \frac{\mathcal{V}_c^2 \eta_V^4}{8 M_P^6 \left(\mathcal{V}_c'''\right)^2} \ll \frac{\mathcal{V}_c^2}{8 M_P^6 \left(\mathcal{V}_c'''\right)^2}. \tag{A15}$$

- When $\delta\varphi_*^2 \gg 2\mathcal{V}_c'/\mathcal{V}_c'''$, we have the same expression as Eq. (A6). From Eq. (A15), we get

$$A_s = \frac{\mathcal{V}_c}{24\pi^2 M_P^4 \epsilon_V} \gg \frac{M_P^2 \left(\mathcal{V}_c'''\right)^2}{3\pi^2 \mathcal{V}_c}. \tag{A16}$$

  Using the SM values, this results in $A_s \gg 10^{-5}$, which is far larger than the observation (8).
- On the contrary, when $\delta\varphi_*^2 \ll 2\mathcal{V}_c'/\mathcal{V}_c'''$, we get $\epsilon_V = M_P^2 \left(\mathcal{V}_c'\right)^2 / 2\mathcal{V}_c^2$ and hence

$$A_s = \frac{\mathcal{V}_c^3}{12\pi^2 M_P^6 \left(\mathcal{V}_c'\right)^2} \sim 1, \tag{A17}$$

  where we have used Eq. (A12). We see that this is too large again.

Downloaded from http://ptep.oxfordjournals.org/ at Osaka Daigaku Ningen on January 18, 2017

Appendix B. Motivating the log-type toy model

We present a motivation for the toy model with the log-type potential at $\varphi > \Lambda$:

$$\mathcal{V} = \mathcal{V}_0 + \mathcal{V}_1 \ln \frac{\varphi}{\Lambda} =: \widetilde{\mathcal{V}}_0 + \mathcal{V}_1 \ln \frac{\varphi}{M_P}. \tag{B1}$$

In the bare perturbation theory (see, e.g., Ref. [4]), the one-loop effective potential for the Higgs field φ is given by

$$\mathcal{V}_{\rm eff}(\varphi) = \frac{m_B^2}{2}\varphi^2 + \frac{\lambda_B}{4}\varphi^4 + \sum_i \frac{N_i}{2}\int \frac{{\rm d}^4 p}{(2\pi)^4} \ln \frac{p^2 + c_i\varphi^2}{p^2}, \tag{B2}$$

where the integration is performed over Euclidean four-momentum.[17] Since we are interested in the behavior of the potential at a field value φ very much larger than the electroweak scale $\varphi \gg V = 246.22\,{\rm GeV}$, we work in the symmetric phase by setting the Higgs VEV to be zero: $V = 0$. The number of degrees of freedom, N_i, and the coupling to the Higgs, c_i, are summarized in Table B1 for species i that have non-negligible coupling to the Higgs. h and χ are the physical and Nambu–Goldstone modes of the Higgs around the field value φ, respectively.[18] Assuming the existence of an underlying gauge-invariant regularization, such as string theory, let us cut off the integral by $|p| < \Lambda$:

$$\frac{{\rm d}\mathcal{V}_{\rm eff}}{{\rm d}\varphi^2} = \frac{1}{2}\left[m_B^2 + \lambda_B\varphi^2 + \sum_i \frac{N_i c_i}{16\pi^2}\left(\Lambda^2 - c_i\varphi^2 \ln \frac{\Lambda^2 + c_i\varphi^2}{c_i\varphi^2}\right)\right]. \tag{B3}$$

The bare Higgs mass m_B^2 is tuned to yield the desired value of the low-energy mass-squared parameter,

$$m_R^2 := 2\left.\frac{{\rm d}\mathcal{V}_{\rm eff}}{{\rm d}\varphi^2}\right|_{\varphi^2\to 0}, \tag{B4}$$

to be zero: $m_R^2 = 0$; see, e.g., Ref. [4].[19] Then we get

$$m_B^2 = -\frac{\Lambda^2}{16\pi^2}\sum_i N_i c_i. \tag{B5}$$

To summarize, we generally have

$$\frac{{\rm d}\mathcal{V}_{\rm eff}}{{\rm d}\varphi^2} = \frac{\varphi^2}{2}\left[\lambda_B - \sum_i \frac{N_i c_i^2}{16\pi^2}\ln \frac{\Lambda^2 + c_i\varphi^2}{c_i\varphi^2}\right]. \tag{B6}$$

We see that the bare mass drops out of the effective potential, as it should. The form (B6) corresponds to the one-loop correction to λ_B. As a side remark, we comment that the condition $m_B^2 = 0$ at this one-loop order, namely $\sum_i N_i c_i = 0$, is the celebrated Veltman condition [4,90].

Rigorously speaking, the effective potential (B2) or (B6) can be trusted only when the field-dependent mass in the loop integral is sufficiently small: $c_i\varphi^2 \ll \Lambda^2$. Nonetheless, let us venture to assume that the expression (B2) or (B6) is still valid even for field values much larger than the

[17] In Eq. (B2), we have tuned the cosmological constant so that we get $\mathcal{V}_{\rm eff} \to 0$ as $\varphi \to 0$.

[18] Though we show our results in the Landau gauge, we can explicitly show that in the R_ξ gauge, depending on the external field φ, the one-loop result (B2) is independent of the gauge parameter ξ if we expand it by $c_i\varphi^2 \ll \Lambda^2$.

[19] Recall that we are working in the symmetric phase.

Downloaded from http://ptep.oxfordjournals.org/ at Osaka Daigaku Ningen on January 18, 2017

Table B1. Constants given in Eq. (B2) for species i providing large c_i.

i	h	χ	W	Z	t
N_i	1	3	6	3	$-4N_c$
c_i	$3\lambda_B$	λ_B	$g_{2B}^2/4$	$(g_{2B}^2+g_{YB}^2)/4$	$y_{tB}^2/2$

cutoff Λ.[20] When we can take $c_j\varphi^2 \gg \Lambda^2$ for some species j, say $j = W, Z, t$, and $c_i\varphi^2 \ll \Lambda^2$ for others i, then

$$\frac{\mathrm{d}\mathcal{V}_{\mathrm{eff}}}{\mathrm{d}\varphi^2} \to \frac{1}{2}\left[m_B^2 + \lambda_B^2\varphi^2 + \frac{\Lambda^4}{16\pi^2\varphi^2}\sum_{j:c_j\varphi^2\gg\Lambda^2}\frac{N_j}{2}\right]. \tag{B7}$$

We note that the bare mass reappears in this limit. As one can see from Fig. 1, both the bare coupling λ_B, approximated by the $\overline{\mathrm{MS}}$ one $\lambda(\Lambda)$, and the bare mass m_B^2 are very close to zero for $\Lambda \gtrsim 10^{17}$ GeV. If the UV theory somehow chooses the bare mass to be zero, as is proposed by Veltman, and also $\lambda_B = 0$, then the effective potential becomes

$$\mathcal{V}_{\mathrm{eff}} \to \mathcal{V}_0 + \frac{\Lambda^4}{16\pi^2}\ln\frac{\varphi}{\Lambda}\sum_{j:c_j\varphi^2\gg\Lambda^2}\frac{N_j}{2} \tag{B8}$$

at $c_j\varphi^2 \gg \Lambda^2$, where $\mathcal{V}_0$ is an integration constant. We see that the potential at very high scales takes the form of Eq. (B1).

We can read off the coefficient $\mathcal{V}_1$ in Eq. (B1) from Eq. (B8):

$$\mathcal{V}_1 = -\frac{3}{32\pi^2}\Lambda^4 \tag{B9}$$

when we put $j = W, Z, t$. We see that we need to add extra scalar fields coupling to the Higgs to make $\mathcal{V}_1$ positive at high scales, as in the Higgs portal dark matter scenario. As an illustration, we assume hereafter that the Higgs potential is not modified up to the cutoff Λ and is connected to Eq. (B1) directly at Λ with arbitrary constants $\mathcal{V}_0$ and $\mathcal{V}_1$, though generally the RGE itself can be changed by the inclusion of the extra scalar fields.

Appendix C. Limiting behavior

We show the limiting behavior of the high-energy potential Eq. (B1).

- In the limit $\mathcal{V}_1 \ll \widetilde{\mathcal{V}}_0$, we get $\widetilde{\mathcal{V}}_0 \to \mathcal{V}_0$,

$$\epsilon_V \to \frac{1}{2}\left(\frac{M_P}{\varphi}\right)^2\left(\frac{\mathcal{V}_1}{\mathcal{V}_0}\right)^2, \quad \eta_V \to -\left(\frac{M_P}{\varphi}\right)^2\frac{\mathcal{V}_1}{\mathcal{V}_0},$$
$$\xi_V^2 \to 2\left(\frac{M_P}{\varphi}\right)^4\left(\frac{\mathcal{V}_1}{\mathcal{V}_0}\right)^2, \quad \varpi_V^3 \to -6\left(\frac{M_P}{\varphi}\right)^6\left(\frac{\mathcal{V}_1}{\mathcal{V}_0}\right)^3, \tag{C1}$$

  and hence

$$\frac{\varphi_{\mathrm{end}}}{M_P} \to \sqrt{\frac{\mathcal{V}_1}{\mathcal{V}_0}} \ll 1, \quad N_* \to \frac{\mathcal{V}_0}{2\mathcal{V}_1}\left(\frac{\varphi_*}{M_P}\right)^2, \quad n_s \to 1 - \frac{1}{N_*}, \quad r \to \frac{4\mathcal{V}_1}{N_*\mathcal{V}_0}. \tag{C2}$$

[20] As is suggested in Ref. [91], the number of effective degrees of freedom may be greatly reduced above the string scale. If this is the case, the naive cutoff removing the modes $|p| > \Lambda$ might be a good illustration of the correct picture.

Downloaded from http://ptep.oxfordjournals.org/ at Osaka Daigaku Ningen on January 18, 2017

For an observed value of A_s, we get

$$\frac{\mathcal{V}_0}{M_P^4} = \sqrt{\frac{6\pi^2 A_s \mathcal{V}_1}{N_* M_P^4}}. \tag{C3}$$

Or if we remove $\mathcal{V}_1 = \mathcal{V}_0 \varphi_*^2 / 2N_* M_P^2$,

$$\frac{\mathcal{V}_0}{M_P^4} = \frac{3\pi^2 A_s}{N_*^2} \frac{\varphi_*^2}{M_P^2}. \tag{C4}$$

Or else, we can rewrite $\mathcal{V}_1 = \left(\frac{\varphi_{\rm end}}{M_P}\right)^2 \mathcal{V}_0$ to yield

$$\mathcal{V}_0 = \frac{6\pi^2 A_s}{N_*} \varphi_{\rm end}^2 M_P^2, \quad \mathcal{V}_1 = \frac{6\pi^2 A_s}{N_*} \varphi_{\rm end}^4, \quad \varphi_* = \sqrt{2N_*}\, \varphi_{\rm end}. \tag{C5}$$

○ In the opposite limit $\widetilde{\mathcal{V}}_0 \ll \mathcal{V}_1$, we get

$$\epsilon_V \to \frac{1}{2}\left(\frac{M_P}{\varphi}\right)^2 \left(\frac{1}{\ln \frac{\varphi}{M_P}}\right)^2, \quad \eta_V = -\left(\frac{M_P}{\varphi}\right)^2 \frac{1}{\ln \frac{\varphi}{M_P}},$$
$$\xi_V^2 = 2\left(\frac{M_P}{\varphi}\right)^4 \left(\frac{1}{\ln \frac{\varphi}{M_P}}\right)^2, \quad \varpi_V^3 = -6\left(\frac{M_P}{\varphi}\right)^6 \left(\frac{1}{\ln \frac{\varphi}{M_P}}\right)^3. \tag{C6}$$

We define the end point of the inflation by the condition: $\max\{\epsilon_V, |\eta_V|\} = \epsilon_V = 1$, to get:

$$\varphi_{\rm end} = {\rm e}^{W(1/\sqrt{2})} M_P = 1.57 M_P. \tag{C7}$$

Then the e-folding number becomes

$$N_* \to -\frac{\varphi_*^2 - \varphi_{\rm end}^2}{M_P^2} + \frac{\varphi_*^2}{2M_P^2} \ln \frac{\varphi_*}{M_P} - \frac{\varphi_{\rm end}^2}{2M_P^2} \ln \frac{\varphi_{\rm end}}{M_P}, \tag{C8}$$

which gives $\varphi_* = 8.54 M_P$ $(7.96 M_P)$ for $N_* = 60$ (50), and hence

$$n_s \to 0.994 \ \ (0.993), \quad r \to 6.2 \times 10^{-3} \ \ (7.2 \times 10^{-3}). \tag{C9}$$

This limit $\widetilde{\mathcal{V}}_0 \ll \mathcal{V}_1$ gives the log-only potential. Note that

$$\mathcal{V}_{\rm end} = W(1/\sqrt{2})\, \mathcal{V}_1 = 0.45\, \mathcal{V}_1. \tag{C10}$$

We also get

$$\mathcal{V}_* = \mathcal{V}_1 \ln \frac{\varphi_*}{M_P} = 24\pi^2 A_s \epsilon_V M_P^4, \tag{C11}$$

which gives $\mathcal{V}_1 = 1.23 \times 10^{-9} M_P^4$ $(1.46 \times 10^{-9} M_P^4)$ and $\mathcal{V}_{\rm end} = 3.23 \times 10^{-9} M_P^4$ $(3.75 \times 10^{-9} M_P^4)$ for $N_* = 60$ (50).

Funding

Open Access funding: SCOAP[3].

Downloaded from http://ptep.oxfordjournals.org/ at Osaka Daigaku Ningen on January 18, 2017

References

[1] G. Aad et al. [ATLAS Collaboration], Phys. Lett. B **716**, 1 (2012) [arXiv:1207.7214].
[2] S. Chatrchyan et al. [CMS Collaboration], Phys. Lett. B **716**, 30 (2012) [arXiv:1207.7235].
[3] P. P. Giardino, K. Kannike, I. Masina, M. Raidal, and A. Strumia, arXiv:1303.3570.
[4] Y. Hamada, H. Kawai, and K.-y. Oda, Phys. Rev. D **87**, 053009 (2013) [arXiv:1210.2538].
[5] M. Holthausen, K. S. Lim, and M. Lindner, J. High Energy Physics **1202**, 037 (2012) [arXiv:1112.2415].
[6] F. Bezrukov, M. Y. Kalmykov, B. A. Kniehl, and M. Shaposhnikov, J. High Energy Physics **1210**, 140 (2012) [arXiv:1205.2893].
[7] G. Degrassi, et al., J. High Energy Physics **1208**, 098 (2012) [arXiv:1205.6497].
[8] S. Alekhin, A. Djouadi, and S. Moch, Phys. Lett. B **716**, 214 (2012) [arXiv:1207.0980].
[9] I. Masina, Phys. Rev. D **87**, 053001 (2013) [arXiv:1209.0393].
[10] F. Jegerlehner, arXiv:1304.7813.
[11] D. Buttazzo, et al., arXiv:1307.3536.
[12] F. Jegerlehner, arXiv:1305.6652.
[13] J. Sola, arXiv:1306.1527.
[14] I. Masina and M. Quiros, arXiv:1308.1242.
[15] M. Al-sarhi, I. Jack, and D. Jones, Z. Phys. C **55**, 283 (1992).
[16] M. Einhorn and D. Jones, Phys. Rev. D **46**, 5206 (1992).
[17] C. F. Kolda and H. Murayama, J. High Energy Physics **0007**, 035 (2000) [arXiv:hep-ph/0003170].
[18] J. Casas, J. Espinosa, and I. Hidalgo, J. High Energy Physics **0411**, 057 (2004) [arXiv:hep-ph/0410298].
[19] D. Jones, Phys. Rev. D **88**, 098301 (2013) [arXiv:1309.7335].
[20] F. Abe et al. [CDF Collaboration], Phys. Rev. Lett. **73**, 225 (1994) [arXiv:hep-ex/9405005].
[21] C. Froggatt and H. B. Nielsen, Phys. Lett. B **368**, 96 (1996) [arXiv:hep-ph/9511371].
[22] C. Froggatt, H. B. Nielsen, and Y. Takanishi, Phys. Rev. D **64**, 113014 (2001) [hep-ph/0104161].
[23] H. B. Nielsen, arXiv:1212.5716.
[24] S. Iso, N. Okada, and Y. Orikasa, Phys. Lett. B **676**, 81 (2009) [arXiv:0902.4050].
[25] S. Iso, N. Okada, and Y. Orikasa, Phys. Rev. D **80**, 115007 (2009) [arXiv:0909.0128].
[26] M. Holthausen, M. Lindner, and M. A. Schmidt, Phys. Rev. D **82**, 055002 (2010) [arXiv:0911.0710].
[27] S. Iso and Y. Orikasa, Prog. Theor. Exp. Phys. **2013**, 023B08 (2013) [arXiv:1210.2848].
[28] Y. Hosotani, Phys. Lett. B **126**, 309 (1983).
[29] A. Hebecker, A. K. Knochel, and T. Weigand, J. High Energy Physics **1206**, 093 (2012) [arXiv:1204.2551].
[30] A. Hebecker, A. K. Knochel, and T. Weigand, Nucl. Phys. **B874**, 1 (2013) [arXiv:1304.2767].
[31] N. Haba, S. Matsumoto, N. Okada, and T. Yamashita, J. High Energy Physics **0602**, 073 (2006) [hep-ph/0511046].
[32] N. Haba, S. Matsumoto, N. Okada, and T. Yamashita, Prog. Theor. Phys. **120**, 77 (2008) [arXiv:0802.3431].
[33] N. Maru and N. Okada, Phys. Rev. D **87**, 095019 (2013) [arXiv:1303.5810].
[34] N. Maru and N. Okada, Phys. Rev. D **88**, 037701 (2013) [arXiv:1307.0291].
[35] N. Maru and N. Okada, arXiv:1307.8181.
[36] S. R. Coleman and E. J. Weinberg, Phys. Rev. D **7**, 1888 (1973).
[37] P. Ade et al. [Planck Collaboration], arXiv:1303.5082.
[38] J. Martin, C. Ringeval, and V. Vennin, arXiv:1303.3787.
[39] A. D. Linde, Phys. Lett. B **108**, 389 (1982).
[40] S. Hawking, I. Moss, and J. Stewart, Phys. Rev. D **26**, 2681 (1982).
[41] A. H. Guth and E. J. Weinberg, Nucl. Phys. B **212**, 321 (1983).
[42] F. Bezrukov and M. Shaposhnikov, Phys. Lett. B **659**, 703 (2008) [arXiv:0710.3755].
[43] F. Bezrukov and M. Shaposhnikov, J. High Energy Physics **0907**, 089 (2009) [arXiv:0904.1537].
[44] F. Bezrukov, A. Magnin, M. Shaposhnikov, and S. Sibiryakov, J. High Energy Physics **1101**, 016 (2011) [arXiv:1008.5157].
[45] A. Salvio, arXiv:1308.2244.
[46] J. Cervantes-Cota and H. Dehnen, Phys. Rev. D **51**, 395 (1995) [arXiv:astro-ph/9412032].
[47] J. Cervantes-Cota and H. Dehnen, Nucl. Phys. B **442**, 391 (1995) [arXiv:astro-ph/9505069].
[48] G. F. Giudice and H. M. Lee, Phys. Lett. B **694**, 294 (2011) [arXiv:1010.1417].

Downloaded from http://ptep.oxfordjournals.org/ at Osaka Daigaku Ningen on January 18, 2017

[49] H. M. Lee, Phys. Lett. B **722**, 198 (2013) [arXiv:1301.1787].
[50] K. Kamada, T. Kobayashi, M. Yamaguchi, and J. Yokoyama, Phys. Rev. D **83**, 083515 (2011) [arXiv:1012.4238].
[51] K. Kamada, T. Kobayashi, T. Takahashi, M. Yamaguchi, and J. Yokoyama, Phys. Rev. D **86**, 023504 (2012) [arXiv:1203.4059].
[52] Tevatron Electroweak Working Group, D0 Collaborations, CDF, arXiv:1305.3929.
[53] Y. Hamada, H. Kawai, and K.-y. Oda, arXiv:1305.7055.
[54] F. Jegerlehner, M. Y. Kalmykov, and B. A. Kniehl, arXiv:1307.4226.
[55] V. M. Abazov et al. [D0 Collaboration], Phys. Lett. B **703**, 422 (2011) [arXiv:1104.2887].
[56] M. Aldaya, K. Lipka, and S. Naumann-Emme [CMS Collaboration], EPJ Web Conf. **28**, 12044 (2012) [arXiv:1201.5336].
[57] R. Hempfling and B. A. Kniehl, Phys. Rev. D **51**, 1386 (1995) [arXiv:hep-ph/9408313].
[58] F. Jegerlehner, M. Y. Kalmykov, and B. A. Kniehl, Phys. Lett. B **722**, 123 (2013) [arXiv:1212.4319].
[59] J. Beringer et al. [Particle Data Group], Phys. Rev. D **86**, 010001 (2012).
[60] G. Isidori, V. S. Rychkov, A. Strumia, and N. Tetradis, Phys. Rev. D **77**, 025034 (2008) [arXiv:0712.0242].
[61] G. Isidori, G. Ridolfi, and A. Strumia, Nucl. Phys. B **609**, 387 (2001) [arXiv:hep-ph/0104016].
[62] V. Branchina and E. Messina, arXiv:1307.5193.
[63] J. Bock et al. [EPIC Collaboration], arXiv:0906.1188.
[64] F. Bouchet et al. [COrE Collaboration], arXiv:1102.2181.
[65] V. Silveira and A. Zee, Phys. Lett. B **161**, 136 (1985).
[66] J. McDonald, Phys. Rev. D **50**, 3637 (1994) [hep-ph/0702143].
[67] C. Burgess, M. Pospelov, and T. ter Veldhuis, Nucl. Phys. B **619**, 709 (2001) [arXiv:hep-ph/0011335].
[68] H. Davoudiasl, R. Kitano, T. Li, and H. Murayama, Phys. Lett. B **609**, 117 (2005) [hep-ph/0405097].
[69] B. Patt and F. Wilczek, arXiv:hep-ph/0605188.
[70] D. H. Lyth and E. D. Stewart, Phys. Rev. D **53**, 1784 (1996) [arXiv:hep-ph/9510204].
[71] A. R. Liddle and S. M. Leach, Phys. Rev. D **68**, 103503 (2003) [astro-ph/0305263].
[72] A. Hebecker, S. C. Kraus, D. Lust, S. Steinfurt, and T. Weigand, Nucl. Phys. B **854**, 509 (2012) [arXiv:1104.5016].
[73] A. Hebecker, S. C. Kraus, M. Kuntzler, D. Lust, and T. Weigand, J. High Energy Physics **1301**, 095 (2013) [arXiv:1207.2766].
[74] H. Kawai, D. Lewellen, and S. Tye, Nucl. Phys. B **269**, 1 (1986).
[75] W. Lerche, D. Lust, and A. Schellekens, Nucl. Phys. B **287**, 477 (1987).
[76] I. Antoniadis, C. Bachas, and C. Kounnas, Nucl. Phys. B **289**, 87 (1987).
[77] K. A. Meissner and H. Nicolai, Phys. Lett. B **648**, 312 (2007) [arXiv:hep-th/0612165].
[78] H. Kawai and T. Okada, Prog. Theor. Phys. **127**, 689 (2012) [arXiv:1110.2303].
[79] L. J. Hall and Y. Nomura, J. High Energy Physics **1003**, 076 (2010) [arXiv:0910.2235].
[80] N. Itzhaki and E. D. Kovetz, J. High Energy Physics **0710**, 054 (2007) [arXiv:0708.2798].
[81] R. Allahverdi, B. Dutta, and A. Mazumdar, Phys. Rev. D **78**, 063507 (2008) [arXiv:0806.4557].
[82] M. Badziak and M. Olechowski, J. Cosmology Astropart. Phys. **0902**, 010 (2009) [arXiv:0810.4251].
[83] K. Enqvist, A. Mazumdar, and P. Stephens, J. Cosmology Astropart. Phys. **1006**, 020 (2010) [arXiv:1004.3724].
[84] S. Hotchkiss, A. Mazumdar, and S. Nadathur, J. Cosmology Astropart. Phys. **1106**, 002 (2011) [arXiv:1101.6046].
[85] S. Hotchkiss, A. Mazumdar, and S. Nadathur, J. Cosmology Astropart. Phys. **1202**, 008 (2012) [arXiv:1110.5389].
[86] A. Chatterjee and A. Mazumdar, J. Cosmology Astropart. Phys. **1109**, 009 (2011) [arXiv:1103.5758].
[87] S. Choudhury and A. Mazumdar, arXiv:1306.4496.
[88] L. Wang, E. Pukartas, and A. Mazumdar, J. Cosmology Astropart. Phys. **1307**, 019 (2013) [arXiv:1303.5351].
[89] S. Choudhury, A. Mazumdar, and S. Pal, J. Cosmology Astropart. Phys. **07**, 041 (2013) [arXiv:1305.6398].
[90] M. Veltman, Acta Phys. Pol. B **12**, 437 (1981).
[91] J. J. Atick and E. Witten, Nucl. Phys. B **310**, 291 (1988).

Downloaded from http://ptep.oxfordjournals.org/ at Osaka Daigaku Ningen on January 18, 2017

Physics Letters B 722 (2013) 94–99

Contents lists available at SciVerse ScienceDirect

Physics Letters B

www.elsevier.com/locate/physletb

Novel universality and Higgs decay $H \to \gamma\gamma, gg$ in the $SO(5) \times U(1)$ gauge-Higgs unification

Shuichiro Funatsu, Hisaki Hatanaka, Yutaka Hosotani, Yuta Orikasa, Takuya Shimotani *

Department of Physics, Osaka University, Toyonaka, Osaka 560-0043, Japan

ARTICLE INFO

Article history:
Received 10 January 2013
Received in revised form 19 March 2013
Accepted 26 March 2013
Available online 28 March 2013
Editor: A. Ringwald

ABSTRACT

The $SO(5) \times U(1)$ gauge-Higgs unification in the Randall–Sundrum warped space with the Higgs boson mass $m_H = 126$ GeV is constructed. A universal relation is found between the Kaluza–Klein (KK) mass scale $m_{\rm KK}$ and the Aharonov–Bohm (AB) phase θ_H in the fifth dimension; $m_{\rm KK} \sim 1350\ {\rm GeV}/(\sin\theta_H)^{0.787}$. The cubic and quartic self-couplings of the Higgs boson become smaller than those in the standard model (SM), having universal dependence on θ_H. The decay rates $H \to \gamma\gamma, gg$ are evaluated by summing contributions from KK towers. Corrections coming from KK excited states are finite and about 0.2% (2%) for $\theta_H = 0.12$ (0.36), branching fractions of various decay modes of the Higgs boson remaining nearly the same as in the SM. The signal strengths of the Higgs decay modes relative to the SM are $\sim \cos^2\theta_H$. The mass of the first KK Z is predicted to be 5.9 (2.4) TeV for $\theta_H = 0.12$ (0.36). We also point out the possible enhancement of $\Gamma(H \to \gamma\gamma)$ due to the large $U(1)_X$ charge of new fermion multiplets.

© 2013 Elsevier B.V. All rights reserved.

With the discovery of a Higgs-like boson at LHC [1,2] it is emergent to pin down its properties to see if it is the Higgs boson in the standard model (SM). The mechanism of electroweak (EW) symmetry breaking is at issue. It is not clear if the EW symmetry is spontaneously broken in a way described in the SM. The mass of the discovered boson is about 126 GeV. Its couplings to other fields, however, may or may not be the same as in the SM. The excess in the decay mode $H \to \gamma\gamma$ has been reported, though more data are necessary for the issue to be settled [3,4].

Many alternative mechanisms for the EW symmetry breaking have been proposed with new physics beyond the SM. Supersymmetry with a light Higgs boson has been a popular scenario in the past, though no evidence has been found so far. It has been discussed that the value $m_H = 126$ GeV can lead to the direct connection to physics at the Planck scale through the vacuum stability of the SM or conformality [5–7]. Many scenarios have been proposed to account for the apparent excess rate for the Higgs decay to two photons at LHC [8–16].

The gauge-Higgs unification scenario is one of the models with new physics at the TeV scale, in which the 4D Higgs boson is identified with the zero mode of the extra-dimensional component of the gauge fields [17–19]. In this Letter we show that the value of the Higgs boson mass $m_H = 126$ GeV has profound implications in the gauge-Higgs unification. We evaluate the decay rates $H \to \gamma\gamma, gg$ by summing contributions from all Kaluza–Klein (KK) excited states of the W boson and fermions in the internal loops. Surprisingly there arises no divergence associated with the infinite sum, thanks to destructive interference in the amplitude. The corrections to the decay rates $H \to \gamma\gamma, gg$ are finite and small, being independent of a cutoff scale. With $m_H = 126$ GeV as an input, the deviation of the branching fractions of the H decay from the values in the SM is found to be 2% or less.

In the $SO(5) \times U(1)$ gauge-Higgs unification model [20] the 4D neutral Higgs field appears as 4D fluctuations of the AB, or Wilson line, phase θ_H along the fifth dimension in the Randall–Sundrum (RS) warped space–time. In the minimal model with quark and lepton multiplets in the vector representation of $SO(5)$ [21,22] the effective potential $V_{\rm eff}(\theta_H)$ is minimized at $\theta_H = \pm\frac{1}{2}\pi$, where the Higgs boson becomes absolutely stable [23]. This is due to the emergence of the H parity invariance [24]. To have an unstable Higgs boson with a mass $m_H = 126$ GeV the model need to be modified by breaking the H parity. Further in the minimal model the consistency with the electroweak precision measurements requires a large warp factor z_L, which typically leads to a larger value $m_H \sim 135$ GeV [25]. The Higgs mass can be made smaller in the supersymmetric version of the model [26].

To solve these problems we introduce n_F fermion multiplets, Ψ_F, in the spinor representation of $SO(5)$ in the model specified in Ref. [22]. The metric of the RS is given by $ds^2 = e^{-2\sigma(y)}\eta_{\mu\nu}\,dx^\mu\,dx^\nu + dy^2$ where $\sigma(y) = k|y|$ for $|y| \leqslant L$ and

* Corresponding author.
E-mail address: shimon@hetmail.phys.sci.osaka-u.ac.jp (T. Shimotani).

0370-2693/$ – see front matter © 2013 Elsevier B.V. All rights reserved.
http://dx.doi.org/10.1016/j.physletb.2013.03.040

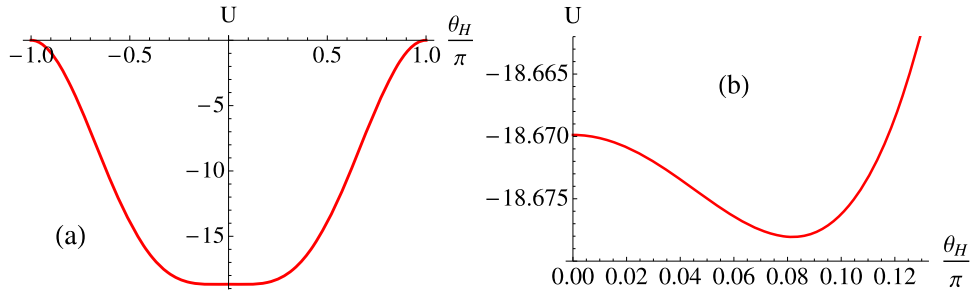

Fig. 1. $V_{\rm eff}(\theta_H)$ for $n_F = 3$, $c_F = 0.353$, $z_L = 10^7$ and $\xi = 1$. $U = (4\pi)^2(kz_L^{-1})^{-4}V_{\rm eff}$ is plotted. The minimum is located at $\theta_H = \pm 0.082\pi = \pm 0.258$. (a): $-\pi \leqslant \theta_H \leqslant \pi$, (b): $0 \leqslant \theta_H \leqslant 0.13\pi$.

Table 1
Values of the various quantities determined from $m_H = 126$ GeV with given z_L for $n_F = 3$. Universal relations among θ_H, $m_{\rm KK}$ and $m_{Z^{(1)}}$, independent of n_F, are observed. See the text.

z_L	θ_H	$m_{\rm KK}$ (TeV)	k (GeV)	c_t	c_F	$m_{F^{(1)}}$ (TeV)	$m_{Z^{(1)}}$ (TeV)
10^{12}	1.02	1.54	4.90×10^{14}	0.413	0.476	0.155	1.19
10^{11}	0.805	1.75	5.56×10^{13}	0.403	0.454	0.232	1.36
10^{10}	0.632	2.03	6.47×10^{12}	0.391	0.433	0.329	1.59
10^{9}	0.485	2.45	7.79×10^{11}	0.376	0.411	0.465	1.93
10^{8}	0.360	3.05	9.72×10^{10}	0.357	0.385	0.668	2.41
10^{7}	0.258	3.95	1.26×10^{10}	0.330	0.353	0.993	3.15
10^{6}	0.177	5.30	1.69×10^{9}	0.296	0.309	1.54	4.25
10^{5}	0.117	7.29	2.32×10^{8}	0.227	0.235	2.53	5.91
2×10^{4}	0.086	9.21	5.87×10^{7}	0.137	0.127	3.88	7.54

$\sigma(y+2L) = \sigma(y)$. The warp factor is $z_L = e^{kL} \gg 1$. Ψ_F satisfies the boundary conditions $\Psi_F(x,-y) = \gamma_5 P\Psi_F(x,y)$ and $\Psi_F(x,L-y) = -\gamma_5 P\Psi_F(x,L+y)$ where $P = \mathrm{diag}(1,1,-1,-1)$ acts on $SO(5)$ spinor indices. Then the mass spectrum $m_n = k\lambda_n$ of the KK tower of Ψ_F is determined by $S_L(1;\lambda_n,c_F)S_R(1;\lambda_n,c_F) + \cos^2\frac{1}{2}\theta_H = 0$. Here $S_{L,R}(z;\lambda,c) = \mp\frac{1}{2}\pi\lambda\sqrt{zz_L}F_{c\pm(1/2),c\pm(1/2)}(\lambda z,\lambda z_L)$, where the upper (bottom) sign refers to L (R). $F_{\alpha,\beta}(u,v) = J_\alpha(u)Y_\beta(v) - Y_\alpha(u)J_\beta(v)$ where J_α, Y_α are Bessel functions. It has been shown that all 4D anomalies in the model of Ref. [22] cancel. This property is not spoiled by the addition of Ψ_F multiplets, as 4D fermions of Ψ_F are vectorlike.

The effective potential $V_{\rm eff}(\theta_H)$ is cast in a simple form of an integral. The relevant part of $V_{\rm eff}(\theta_H)$ is given by

$$\begin{aligned}
&V_{\rm eff}(\theta_H;\xi,c_t,c_F,n_F,k,z_L)\\
&\quad= 2\big(3-\xi^2\big)I[Q_W] + \big(3-\xi^2\big)I[Q_Z] + 3\xi^2 I[Q_S]\\
&\qquad - 12\big\{I[Q_{\rm top}] + I[Q_{\rm bottom}]\big\} - 8n_F I[Q_F],\\
&I\big[Q(q;\theta_H)\big] = \frac{(kz_L^{-1})^4}{(4\pi)^2}\int_0^\infty dq\, q^3 \ln\big\{1 + Q(q;\theta_H)\big\},\\
&Q_W = \cos^2\theta_W\, Q_Z = \frac{1}{2}Q_S = \frac{1}{2}Q_0\left[q;\frac{1}{2}\right]\sin^2\theta_H,\\
&Q_{\rm top} = \frac{Q_{\rm bottom}}{r_t} = \frac{Q_0[q;c_t]}{2(1+r_t)}\sin^2\theta_H,\\
&Q_F = Q_0[q;c_F]\cos^2\frac{1}{2}\theta_H,\\
&Q_0[q;c] = \frac{z_L}{q^2\hat{F}_{c-\frac{1}{2},c-\frac{1}{2}}(qz_L^{-1},q)\hat{F}_{c+\frac{1}{2},c+\frac{1}{2}}(qz_L^{-1},q)}.
\end{aligned} \tag{1}$$

Here $\hat{F}_{\alpha,\beta}(u,v) = I_\alpha(u)K_\beta(v) - e^{-i(\alpha-\beta)\pi}K_\alpha(u)I_\beta(v)$, where I_α, K_α are modified Bessel functions. ξ is a gauge parameter in the generalized R_ξ gauge introduced in Ref. [22]. The formula for $V_{\rm eff}$ in the $\xi = 1$ gauge without the $I[Q_F]$ term has been given in Refs. [21] and [23]. c_t and c_F are the bulk mass parameters for the top-bottom multiplets and Ψ_F, respectively. $r_t \sim (m_b/m_t)^2$ where m_b and m_t are the masses of the bottom and top quark. $V_{\rm eff}(-\theta_H) = V_{\rm eff}(\theta_H)$. Further in the absence of $I[Q_F]$, $V_{\rm eff}$ has symmetry $V_{\rm eff}(\frac{1}{2}\pi + \theta_H) = V_{\rm eff}(\frac{1}{2}\pi - \theta_H)$, representing the H parity invariance. The $I[Q_F]$ term breaks this symmetry. The contributions from light quarks and leptons are negligible.

In the pure gauge theory without fermions $V_{\rm eff}$ is minimized at $\theta_H = 0, \pi$ where the EW symmetry remains unbroken. The top quark contribution has minima at $\theta_H = \pm\frac{1}{2}\pi$, dominating over the gauge field contribution. The fermion Ψ_F shifts the minima toward $\theta_H = 0$. The minimum at $0 < |\theta_H| < \frac{1}{2}\pi$ gives desired phenomenology. The number of the fermion multiplets Ψ_F, n_F, affects the shape of $V_{\rm eff}$ significantly. It will be shown below that the resulting physics, however, is almost independent of n_F. The mass of the Higgs boson, m_H, is given by

$$m_H^2 = \frac{1}{f_H^2}\frac{d^2V_{\rm eff}}{d\theta_H^2}\bigg|_{\rm min}, \qquad f_H = \frac{2}{g_w}\sqrt{\frac{k}{L(z_L^2-1)}} \tag{2}$$

where the second derivative of $V_{\rm eff}$ is evaluated at the minimum of $V_{\rm eff}$, and g_w is the 4D weak $SU(2)_L$ coupling. The experimental data dictate $m_H \sim 126$ GeV.

The parameters of the model are specified in the following manner. Pick values for n_F and z_L. The parameters, k, two gauge coupling constants associated with $SO(5)\times U(1)$, c_t, r_t, and c_F are self-consistently determined such that at the minimum θ_H of $V_{\rm eff}$, m_Z, $\sin^2\theta_W$, $\alpha(m_Z)$, m_t, m_b and $m_H = 126$ GeV are reproduced. We note that all of k, c_t, r_t and c_F implicitly depend on θ_H as well. The KK mass scale is given by $m_{\rm KK} = \pi k z_L^{-1}$. Hence $m_{\rm KK}$ and θ_H, for instance, are determined as functions of n_F and z_L. $V_{\rm eff}(\theta_H)$ for $n_F = 3$ and $z_L = 10^7$ is displayed in Fig. 1.

The AB phase θ_H is the key parameter in gauge-Higgs unification, which controls the couplings of the Higgs boson to other fields. In Table 1 the values for z_L, θ_H, $m_{\rm KK}$, k, c_t, c_F, $m_{F^{(1)}}$ and

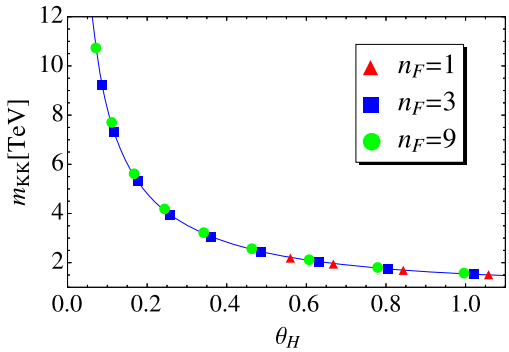

Fig. 2. The relation between θ_H and m_{KK} for $\xi = 1$. Triangles, squares, and circles are for $n_F = 1, 3$ and 9, respectively. The solid curve represents the universal relation (3).

$m_{Z^{(1)}}$ are summarized for $n_F = 3$, where $m_{F^{(1)}}$ is the mass of the lowest mode in the KK tower of Ψ_F and $m_{Z^{(1)}}$ is the mass of the first KK Z boson. As z_L is decreased, θ_H becomes smaller whereas m_{KK} becomes larger. There appears a critical value for z_L below which $m_H = 126$ GeV cannot be realized.

Both θ_H and m_{KK} are physical quantities. They are functions of n_F and z_L. The relation between them are plotted in Fig. 2 for various values of n_F and z_L. As the number of the extra fermions n_F is increased, the location of the minimum of $V_{\rm eff}$ is shifted toward the origin. Nevertheless the relation between θ_H and m_{KK} remains universal. It is approximately given by

$$m_{KK} \sim \frac{1350\ \text{GeV}}{(\sin\theta_H)^{0.787}}, \tag{3}$$

irrespective of n_F and z_L. We note that $m_Z \sim m_{KK}|\sin\theta_H|/(\pi\cos\theta_W\sqrt{kL})$, in which θ_H and $kL = \ln z_L$ are not independent, once m_H is fixed. There must be an underlying reason for the universality relation (3), which remains as a mystery and is left for future investigation. The relation between θ_H and m_{KK}, with $m_{KK} > 3$ TeV for the consistency with low energy data, implies that $\theta_H < 0.3$, which also satisfies the S parameter constraint [20] and the tree-level unitarity constraint [27]. For $\theta_H = 0.1 \sim 0.3$, m_{KK} is predicted to be around $3 \sim 7$ TeV, in a region which can be explored at LHC in the coming years. We have also checked that the m_{KK}–θ_H relation in the $\xi = 0$ gauge is almost the same as in the $\xi = 1$ gauge.

The gauge-Higgs unification model has one parameter, θ_H, to be determined from experiments. With θ_H fixed, all physical quantities are evaluated. By expanding $V_{\rm eff}(\theta_H + (H/f_H))$ in a power series in H around the minimum, one finds $\lambda_n H^n$ couplings. These couplings λ_3 and λ_4 are plotted in Fig. 3 for $n_F = 1, 3$ and 9. The couplings are smaller than those in the SM. For large $\theta_H > 0.55$, λ_4 becomes negative though $V_{\rm eff}$ is bounded from below. It is seen that the relations $\lambda_3(\theta_H)$ and $\lambda_4(\theta_H)$ are also universal and independent of n_F, once $m_H = 126$ GeV is fixed.

The Higgs couplings to W, Z, quarks/leptons and their KK excited states are determined. All of the 3 point couplings of SM particles to H at the tree level are suppressed by a common factor $\cos\theta_H$ [28–31]. It is necessary to find these 3 point couplings of KK states for evaluating the 1-loop processes such as $gg \to H$ and $H \to \gamma\gamma, gg$.

Let us first consider the process $H \to \gamma\gamma$. It proceeds through one-loop diagrams. All charged particles with non-vanishing Higgs couplings contribute. The dominant contributions come from the W boson, top quark, and their KK towers. The extra fermion Ψ_F also contributes. The decay rate is given by [32–34]

$$\begin{aligned}
&\Gamma(H \to \gamma\gamma) \\
&\quad = \frac{\alpha^2 g_w^2}{1024\pi^3}\frac{m_H^3}{m_W^2}\left|\mathcal{F}_W + \frac{4}{3}\mathcal{F}_{\rm top} + \left(2\left(Q_X^{(F)}\right)^2 + \frac{1}{2}\right)n_F\mathcal{F}_F\right|^2, \\
&\mathcal{F}_W = \sum_{n=0}^{\infty}\frac{g_{HW^{(n)}W^{(n)}}}{g_w m_W}\frac{m_W^2}{m_{W^{(n)}}^2}F_1(\tau_{W^{(n)}}), \\
&\mathcal{F}_{\rm top} = \sum_{n=0}^{\infty}\frac{y_{t^{(n)}}}{y_t^{\rm SM}}\frac{m_t}{m_{t^{(n)}}}F_{1/2}(\tau_{t^{(n)}}), \\
&\mathcal{F}_F = \sum_{n=1}^{\infty}\frac{y_{F^{(n)}}}{y_t^{\rm SM}}\frac{m_t}{m_{F^{(n)}}}F_{1/2}(\tau_{F^{(n)}}),
\end{aligned} \tag{4}$$

where $W^{(0)} = W$, $t^{(0)} = t$, $\tau_a = 4m_a^2/m_H^2$ and the functions $F_1(\tau)$ and $F_{1/2}(\tau)$ are defined in Ref. [34]. $Q_X^{(F)}$ is the $U(1)_X$ charge of Ψ_F. $y_t^{\rm SM}$ denotes the top Yukawa coupling in the SM. Note that $F_1(\tau) \to 7$ and $F_{1/2}(\tau) \to -\frac{4}{3}$ for $\tau \to \infty$. The extra fermion multiplet Ψ_F contains particles with electric charges $(Q_X^{(F)} \pm \frac{1}{2})e$. It will be seen below that the contribution $\mathcal{F}_F$ is small for $\theta_H < 0.5$. The $HW^{(n)}W^{(n)\dagger}$ coupling $g_{HW^{(n)}W^{(n)}}$ and the Yukawa couplings $y_{t^{(n)}}$ and $y_{F^{(n)}}$ are unambiguously determined in the gauge-Higgs unification. The infinite sums in (4) turn out finite. The expression for $\mathcal{F}_W$ corresponds to the amplitude in the unitary gauge. It has been shown in Ref. [35] that the correct amplitude is reproduced in the unitary gauge in the SM.

In the gauge-Higgs unification the $HW^{(n)}W^{(n)\dagger}$ and Yukawa couplings result from the $\mathrm{tr}\, F_{\mu 5}F^{\mu 5}$ term and $\overline{\Psi}\Gamma^5 A_5\Psi$ terms in the action, where the vector potential A_5 contains the 4D Higgs field. To good approximation $g_{HWW} \sim g_{HWW}^{\rm SM}\cos\theta_H = g_w m_W\cos\theta_H$ and $y_t \sim y_t^{\rm SM}\cos\theta_H$.

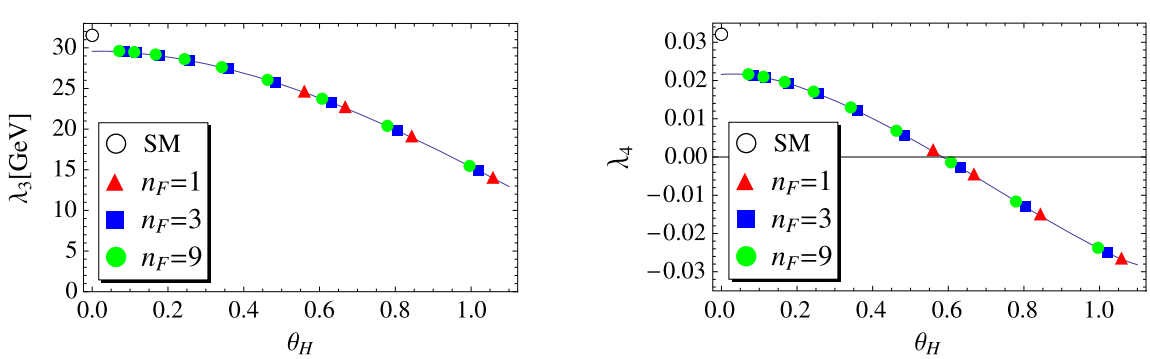

Fig. 3. The cubic coupling λ_3 and quartic coupling λ_4 of the Higgs boson are plotted against θ_H for $n_F = 1, 3$ and 9. The universal relations between (λ_3, λ_4) and θ_H, independent of n_F, are seen. The fitting curves for λ_3 and λ_4 are given by $\lambda_3 = 5.28 + 21.1\cos\theta_H + 3.20\cos 2\theta_H$ and $\lambda_4 = 0.0256 - 0.0537\cos\theta_H + 0.0495\cos 2\theta_H$, respectively. The SM values are $\lambda_3 = 31.5$ GeV and $\lambda_4 = 0.0320$ [6].

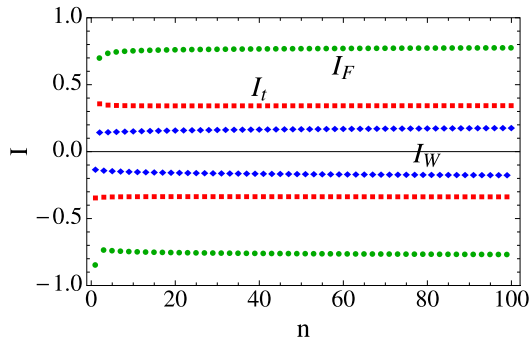

Fig. 4. The ratios $I_{W^{(n)}} = g_{HW^{(n)}W^{(n)}}/g_w m_{W^{(n)}} \cos\theta_H$ in (5), $I_{t^{(n)}} = y_{t^{(n)}}/y_t^{\rm SM}\cos\theta_H$ in (6) and $I_{F^{(n)}} = y_{F^{(n)}}/y_t^{\rm SM}\sin\frac{1}{2}\theta_H$ in (7) are plotted for $n_F = 3$ and $\theta_H = 0.360$ ($z_L = 10^8$) in the range $1 \leqslant n \leqslant 100$. (□: the top quark tower, ◇: the W tower, ○: the Ψ_F tower) $I_{W^{(0)}} = 1.004$ and $I_{t^{(0)}} = 1.012$. The sign of $g_{HW^{(n)}W^{(n)}}$, $y_{t^{(n)}}$ and $y_{F^{(n)}}$ alternates as n increases. $I_{W^{(1)}}, I_{t^{(1)}}, I_{F^{(1)}} < 0$.

One finds that

$$I_{W^{(n)}} = \frac{g_{HW^{(n)}W^{(n)}}}{g_w m_{W^{(n)}}\cos\theta_H} = -\sqrt{kL(z_L^2-1)}\,\frac{\sin\theta_H}{N_{W^{(n)}}}\,\frac{C(1;\lambda_{W^{(n)}})}{S(1;\lambda_{W^{(n)}})},$$

$$N_{W^{(n)}} = \int_1^{z_L}\frac{dz}{z}\left\{\left(1+\cos^2\theta_H\right)C(z;\lambda_{W^{(n)}})^2 + \sin^2\theta_H\,\hat{S}(z;\lambda_{W^{(n)}})^2\right\},$$

$$C(z;\lambda) = \frac{\pi}{2}\lambda z z_L F_{1,0}(\lambda z,\lambda z_L),$$

$$S(z;\lambda) = -\frac{\pi}{2}\lambda z F_{1,1}(\lambda z,\lambda z_L), \qquad \hat{S}(z;\lambda) = \frac{C(1;\lambda)}{S(1;\lambda)}S(z;\lambda). \quad (5)$$

We note that $S(1;\lambda_{W^{(n)}}) = 0$ at $\theta_H = 0$. The values $I_{W^{(n)}}$ are plotted in Fig. 4 for $n_F = 3$ and $\theta_H = 0.360$ ($z_L = 10^8$). One sees that the sign of $I_{W^{(n)}}$ alternates as n increases, and its magnitude is almost constant; $I_{W^{(n)}} \sim (-1)^n\{0.14 + 0.0025\ln n + 0.0011(\ln n)^2\}$ in the range $50 < n < 200$. Note that $|g_{HW^{(n)}W^{(n)}}|$ itself increases with $m_{W^{(n)}}$, in sharp contrast to the behavior in the UED models [8].

Similar behavior is observed for the Yukawa couplings of the top tower. One finds that

$$I_{t^{(n)}} = \frac{y_{t^{(n)}}}{y_t^{\rm SM}\cos\theta_H} = -\frac{g_w}{2y_t^{\rm SM}}\sqrt{kL(z_L^2-1)}\,\frac{\sin\theta_H}{N_{t^{(n)}}}\,\frac{C_L(1;\lambda_{t^{(n)}},c_t)}{S_L(1;\lambda_{t^{(n)}},c_t)},$$

$$N_{t^{(n)}} = \int_1^{z_L} dz\left\{\left(1+\cos^2\theta_H + 2r_t\right)C_L(z;\lambda_{t^{(n)}},c_t)^2 + \sin^2\theta_H\,\hat{S}_L(z;\lambda_{t^{(n)}},c_t)^2\right\},$$

$$C_L(z;\lambda,c) = \frac{\pi}{2}\lambda\sqrt{zz_L}F_{c+(1/2),c-(1/2)}(\lambda z,\lambda z_L),$$

$$\hat{S}_L(z;\lambda,c) = \frac{C_L(1;\lambda,c)}{S_L(1;\lambda,c)}S_L(z;\lambda,c). \quad (6)$$

The values $I_{t^{(n)}}$ are plotted in Fig. 4. The value of $I_{t^{(n)}}$ alternates in sign as n increases, and the magnitude of $y_{t^{(n)}}$ are almost constant for large n.

The behavior of the $y_{F^{(n)}}$ of the extra fermion is slightly different. In contrast to quarks and leptons, the lowest mode $F^{(1)}$ in the KK tower of Ψ_F is massive at $\theta_H = 0$; its mass is approximately given by $m_{F^{(1)}}(\theta_H) \propto \cos\frac{1}{2}\theta_H$. Its Yukawa coupling is, therefore, expected to be $y_{F^{(1)}} \propto \sin\frac{1}{2}\theta_H$, becoming small for small θ_H. Indeed one finds

$$I_{F^{(n)}} = \frac{y_{F^{(n)}}}{y_t^{\rm SM}\sin\frac{1}{2}\theta_H} = -\frac{g_w}{4y_t^{\rm SM}}\sqrt{kL(z_L^2-1)}\,\frac{\cos\frac{1}{2}\theta_H}{N_{F^{(n)}}}\,\frac{C_R(1;\lambda_{F^{(n)}},c_F)}{S_R(1;\lambda_{F^{(n)}},c_F)},$$

$$N_{F^{(n)}} = \int_1^{z_L} dz\left\{\sin^2\frac{\theta_H}{2}C_R(z;\lambda_{F^{(n)}},c_F)^2 + \cos^2\frac{\theta_H}{2}\hat{S}_R(z;\lambda_{F^{(n)}},c_F)^2\right\},$$

$$\hat{S}_R(z;\lambda,c) = \frac{C_R(1;\lambda,c)}{S_R(1;\lambda,c)}S_R(z;\lambda,c). \quad (7)$$

$I_{F^{(n)}}$ is plotted in Fig. 4. Again the value of $y_{F^{(n)}}$ alternates in sign as n increases. For large n, $y_{F^{(n)}}/y_t^{\rm SM} \sim (-1)^n 0.14$ for $(n_F, z_L) = (3, 10^8)$.

With all these Higgs couplings at hand, one can evaluate the rate $\Gamma(H\to\gamma\gamma)$ in (4). As all KK masses increase as $m_n \sim \frac{1}{2}nm_{\rm KK}$ for large n and $F_1, F_{1/2}$ approach constant, the infinite sums rapidly converge as $\sum(-1)^n n^{-1}$ or $\sum(-1)^n n^{-1}(\ln n)^q$ ($q = 1, 2, \ldots$). We have found that the sums saturate with about 50 terms. The behavior of the alternating sign in the Higgs couplings of KK states has been previously noticed in Refs. [36] and [37]. Let $\mathcal{F}_{W\,\rm only}$ ($\mathcal{F}_{\rm top\,only}$) be the contribution of $W = W^{(0)}$ ($t = t^{(0)}$) to $\mathcal{F}_W$ ($\mathcal{F}_{\rm top}$) in (4). For $n_F = 3$ and $z_L = 10^8$ (10^5), which yields $\theta_H = 0.360$ (0.117), one finds that $\mathcal{F}_{W\,\rm only} = 7.873$ (8.330), $\mathcal{F}_{\rm top\,only} = -1.305$ (-1.372), $\mathcal{F}_W/\mathcal{F}_{W\,\rm only} = 0.998$ (0.9996), $\mathcal{F}_{\rm top}/\mathcal{F}_{\rm top\,only} = 0.990$ (0.998) and $\mathcal{F}_F/\mathcal{F}_{\rm top\,only} = -0.033$ (-0.0034).

Let us suppose $Q_X^{(F)} = 0$. In this case we obtain $\mathcal{F}_W + \frac{4}{3}\mathcal{F}_{\rm top} + \frac{3}{2}\mathcal{F}_F = 6.199$ (6.508). Its ratio to $\mathcal{F}_{W\,\rm only} + \frac{4}{3}\mathcal{F}_{\rm top\,only}$ is 1.011 (1.001). In other words, the contributions from KK states and Ψ_F amount to only 1% (0.1%). The dominant effect for the decay rates comes from the $\cos\theta_H$ suppression factor in the amplitudes. Compared to the value in the SM, $\Gamma[H\to\gamma\gamma]$ is suppressed by 10% (1%) for $\theta_H = 0.360$ (0.117). The decay rate to two gluons is [38–40]

$$\Gamma(H\to gg) = \frac{\alpha_s^2 g_w^2 m_H^3}{128\pi^3 m_W^2}|\mathcal{F}_{\rm top}|^2, \quad (8)$$

if Ψ_F is a color singlet. If Ψ_F is a color triplet, $\mathcal{F}_{\rm top}$ is replaced by $\mathcal{F}_{\rm top} + \frac{2}{3}n_F\mathcal{F}_F$ in the above formula. The correction due to KK excited states is small.

In the gauge-Higgs unification all decay rates for $H\to WW$, $ZZ, c\bar{c}, b\bar{b}, \tau\bar{\tau}$ are suppressed by a common factor $\cos^2\theta_H$ at the tree level. We have found that loop corrections due to KK excited states are very small. Consequently the correction to the branching fraction of $H\to\gamma\gamma$ turns out very small, about 2% (0.2%) in the gauge-Higgs unification for $\theta_H = 0.360$ (0.117). The observed event rate for $H\to\gamma\gamma$, for instance, is determined by the product of the Higgs production rate and the branching fraction, $\sigma_H^{\rm prod}\cdot B(H\to\gamma\gamma)$. The production rate is suppressed, compared to the SM, by $\cos^2\theta_H$, but the branching fractions remain nearly the same as in the SM. The gauge-Higgs unification predicts that the signal strength relative to the SM is $\sim\cos^2\theta_H$. For $\theta_H = 0.1$ (0.3), it is about 0.99 (0.91). This is in sharp contrast to other models. In the UED models the contributions of KK states to $\mathcal{F}_{\rm top}$ add up in the same sign and may become sizable [8]. In the gauge-Higgs unification the contributions alternate in sign in the amplitudes, resulting in the destructive interference and giving very small correction.

The rate $\Gamma(H\to\gamma\gamma)$ in Eq. (4) can be enhanced through the factor $2(Q_X^{(F)})^2 + \frac{1}{2}$ for sufficiently large $Q_X^{(F)}$. For example, for $Q_X^{(F)} = 4$ and $n_F = 3$, we obtain the enhancement by a factor 2.22 (1.13) compared with the SM.

The fact $m_H \sim 126$ GeV leads to important consequences in the gauge-Higgs unification. We have found the universal relations among $m_{\rm KK}, \lambda_3, \lambda_4$ and θ_H, which are independent of how many

extra fermions are introduced. The low energy data, the S parameter constraint, and the tree-level unitarity constraint indicate small $\theta_H < 0.3$. The KK mass scale m_{KK} is predicted to be $3 \sim 7$ TeV for $\theta_H = 0.1 \sim 0.3$. The existence of new charged heavy particles can affect the production and decay rates of the Higgs boson through loop diagrams. There are many proposals of models which employ such a mechanism to predict the enhancement of the $H \to \gamma\gamma$ mode over other decay channels [8–16]. In the gauge-Higgs unification there are new charged heavy particles, namely KK excited states of W and top quark. However, we have shown that their couplings to the Higgs boson alternate in sign in each KK tower so that the correction to the decay and production rates becomes very small. The gauge-Higgs unification gives phenomenology at low energies very close to that of the SM so long as $Q_X^{(F)}$ is moderately small.

Nevertheless new rich structure is predicted to emerge. We have seen above that the cubic and quartic self-couplings of the Higgs boson significantly deviate from the SM. The most clear signal for the gauge-Higgs unification would be the production of the first KK states of the Z boson and photon at LHC. Their masses are predicted, for $\theta_H = 0.117$ (0.360), to be $m_{Z^{(1)}} = 5.910$ (2.414) TeV and $m_{\gamma^{(1)}} = 5.913$ (2.421) TeV. The current data [41–44] indicate $m_{Z^{(1)}} > 2.5$ TeV. We have checked that there is a universal relation between θ_H and $m_{Z^{(1)}}$, independent of n_F. The data therefore imply that $\theta_H < 0.35$. Another robust signal would be the production of a pair of the first KK state of the extra fermion, $F^{(1)}\bar{F}^{(1)}$, which become stable. So far no new exotic stable charged fermion has been observed at LHC [45]. Its current limit puts a constraint $m_{F^{(1)}} > 0.5$ TeV. The value of $m_{F^{(1)}}$ depends on both θ_H and n_F so that no universal relation between $m_{F^{(1)}}$ and θ_H is found. $m_{F^{(1)}}$ becomes smaller as n_F increases with θ_H fixed. $m_{F^{(1)}} > 0.5$ TeV implies $\theta_H < 0.45$ for $n_F = 3$. We will come back to these issues with more details separately.

Acknowledgements

This work was supported in part by scientific grants from the Ministry of Education and Science, Grants No. 20244028, No. 23104009 and No. 21244036.

References

[1] ATLAS Collaboration, Phys. Lett. B 716 (2012) 1.
[2] CMS Collaboration, Phys. Lett. B 716 (2012) 30.
[3] ATLAS Collaboration, Coupling properties of the new Higgs-like boson observed with the ATLAS detector at the LHC, ATLAS-CONF-2012-127.
[4] CMS Collaboration, Combination of standard model Higgs boson searches and measurements of the properties of the new boson with a mass near 125 GeV, CMS-PAS-HIG-12-04.
[5] M. Holthausen, K.S. Lim, M. Lindner, JHEP 1202 (2012) 0377;
F. Bezrukov, M.Y. Kalmykov, B.A. Kniehl, M. Shaposhnikov, JHEP 1210 (2012) 140;
I. Masina, The Higgs boson and top quark masses as tests of electroweak vacuum stability, arXiv:1209.0393 [hep-ph];
S. Alekhin, A. Djouadi, S. Moch, Phys. Lett. B 716 (2012) 214;
Y. Hamada, H. Kawai, K. Oda, Bare Higgs mass at Planck scale, arXiv:1210.2538 [hep-ph].
[6] G. Degrassi, S. Di Vita, J. Elias-Miro, J.R. Espinosa, G.F. Giudice, G. Isidori, A. Strumia, JHEP 1208 (2012) 098.
[7] S. Iso, Y. Orikasa, TeV scale B–L model with a flat Higgs potential at the Planck scale – in view of the hierarchy problem, arXiv:1210.2848 [hep-ph].
[8] K. Nishiwaki, K.-y. Oda, N. Okuda, R. Watanabe, Phys. Rev. D 85 (2012) 035026;
G. Belanger, A. Belyaev, M. Brown, M. Kakizaki, A. Pukhov, Testing minimal universal extra dimensions using Higgs boson searches at the LHC, arXiv:1207.0798 [hep-ph].
[9] M. Carena, S. Casagrande, F. Goertz, U. Haisch, M. Neubert, JHEP 1208 (2012) 156.
[10] T. Han, H.E. Logan, B. McElrath, L.-T. Wang, Phys. Lett. B 563 (2003) 191;
T. Han, H.E. Logan, B. McElrath, L.-T. Wang, Phys. Lett. B 603 (2004) 257 (Erratum);
L. Wang, J.M. Yang, Phys. Rev. D 84 (2011) 075024;
J. Reuter, M. Tonini, Can the 125 GeV Higgs be the little Higgs?, arXiv:1212.5930 [hep-ph].
[11] I. Low, A. Vichi, Phys. Rev. D 84 (2011) 045019;
A. Azatov, J. Galloway, Phys. Rev. D 85 (2012) 055013;
A. Azatov, R. Contino, J. Galloway, JHEP 1204 (2012) 127;
M. Gillioz, R. Grober, C. Grojean, M. Muhlleitner, E. Salvioni, JHEP 1210 (2012) 004.
[12] J. Cao, Z. Heng, T. Liu, J.M. Yang, Phys. Lett. B 703 (2011) 462;
J. Cao, Z. Heng, T. Liu, J.M. Yang, JHEP 1203 (2012) 086;
M. Carena, S. Gori, N.R. Shah, C.E.M. Wagner, JHEP 1203 (2012) 014;
M. Carena, S. Gori, N.R. Shah, C.E.M. Wagner, L.-T. Wang, JHEP 1207 (2012) 175;
N.D. Christensen, T. Han, S. Su, Phys. Rev. D 85 (2012) 115018;
V. Barger, M. Ishida, W.-Y. Keung, Flavor-tuned 125 GeV SUSY Higgs boson at the LHC: MSSM and NATURAL SUSY TESTS, arXiv:1207.0779 [hep-ph];
K. Hagiwara, J.S. Lee, J. Nakamura, JHEP 1210 (2012) 002;
B. Bellazzini, C. Petersson, R. Torre, Phys. Rev. D 86 (2012) 033016;
R. Benbrik, M. Gomez Bock, S. Heinemeyer, O. Stal, G. Weiglein, L. Zeune, Eur. Phys. J. C 72 (2012) 2171;
M.R. Buckley, D. Hooper, Phys. Rev. D 86 (2012) 075008;
H. An, T. Liu, L.-T. Wang, Phys. Rev. D 86 (2012) 075030;
N. Haba, K. Kaneta, Y. Mimura, R. Takahashi, Enhancement of Higgs to diphoton decay width in non-perturbative Higgs model, arXiv:1207.5102 [hep-ph];
A. Delgado, G. Nardini, M. Quiros, Large diphoton Higgs rates from supersymmetric triplets, arXiv:1207.6596 [hep-ph];
J.R. Espinosa, C. Grojean, V. Sanz, M. Trott, NSUSY fits, arXiv:1207.7355 [hep-ph];
K. Schmidt-Hoberg, F. Staub, JHEP 1210 (2012) 195;
R. Sato, K. Tobioka, N. Yokozaki, Phys. Lett. B 716 (2012) 441;
H. Davoudiasl, H.-S. Lee, W.J. Marciano, Phys. Rev. D 86 (2012) 095009;
T. Kitahara, JHEP 1211 (2012) 021;
K.J. Bae, T.H. Jung, H.D. Kim, 125 GeV Higgs as a pseudo-Goldstone boson in supersymmetry with vector-like matters, arXiv:1208.3748 [hep-ph].
[13] S. Matsuzaki, K. Yamawaki, Holographic techni-dilaton at 125 GeV, arXiv:1209.2017 [hep-ph];
T. Abe, R. Kitano, Y. Konishi, K. Oda, J. Sato, S. Sugiyama, Minimal dilaton model, arXiv:1209.4544 [hep-ph].
[14] V. Ilisie, A. Pich, Phys. Rev. D 86 (2012) 033001;
K. Kumar, R. Vega-Morales, F. Yu, Phys. Rev. D 86 (2012) 113002;
S. Dawson, E. Furlan, Phys. Rev. D 86 (2012) 015021;
M. Carena, I. Low, C.E.M. Wagner, JHEP 1208 (2012) 060;
L. Wang, X.-F. Han, Phys. Rev. D 86 (2012) 095007;
A. Joglekar, P. Schwaller, C.E.M. Wagner, JHEP 1212 (2012) 064;
N. Arkani-Hamed, K. Blum, R.T. D'Agnolo, J. Fan, 2:1 for naturalness at the LHC?, arXiv:1207.4482 [hep-ph];
L.G. Almeida, E. Bertuzzo, P.A.N. Machado, R.Z. Funchal, JHEP 1211 (2012) 085;
B. Batell, D. McKeen, M. Pospelov, JHEP 1210 (2012) 104;
J. Kearney, A. Pierce, N. Weiner, Vectorlike fermions and Higgs couplings, arXiv:1207.7062 [hep-ph].
[15] P. Draper, D. McKeen, Phys. Rev. D 85 (2012) 115023;
W.-F. Chang, J.N. Ng, J.M.S. Wu, Phys. Rev. D 86 (2012) 033003;
G.D. Kribs, A. Martin, Phys. Rev. D 86 (2012) 095023;
I. Dorsner, S. Fajfer, A. Greljo, J.F. Kamenik, JHEP 1211 (2012) 130.
[16] A. Alves, E. Ramirez Barreto, A.G. Dias, C.A. de S.Pires, F.S. Queiroz, P.S. Rodrigues da Silva, Phys. Rev. D 84 (2011) 115004;
B. Batell, S. Gori, L.-T. Wang, JHEP 1206 (2012) 172;
A.G. Akeroyd, S. Moretti, Phys. Rev. D 86 (2012) 035015;
C.-W. Chiang, K. Yagyu, Higgs boson decays to $\gamma\gamma$ and $Z\gamma$ in models with Higgs extensions, arXiv:1207.1065 [hep-ph].
[17] Y. Hosotani, Phys. Lett. B 126 (1983) 309;
Y. Hosotani, Ann. Phys. (N. Y.) 190 (1989) 233.
[18] A.T. Davies, A. McLachlan, Phys. Lett. B 200 (1988) 305;
A.T. Davies, A. McLachlan, Nucl. Phys. B 317 (1989) 237.
[19] H. Hatanaka, T. Inami, C.S. Lim, Mod. Phys. Lett. A 13 (1998) 2601.
[20] K. Agashe, R. Contino, A. Pomarol, Nucl. Phys. B 719 (2005) 165.
[21] Y. Hosotani, K. Oda, T. Ohnuma, Y. Sakamura, Phys. Rev. D 78 (2008) 096002;
Y. Hosotani, K. Oda, T. Ohnuma, Y. Sakamura, Phys. Rev. D 79 (2009) 079902 (Erratum).
[22] Y. Hosotani, S. Noda, N. Uekusa, Prog. Theoret. Phys. 123 (2010) 757.
[23] Y. Hosotani, M. Tanaka, N. Uekusa, Phys. Rev. D 82 (2011) 115024.
[24] Y. Hosotani, P. Ko, M. Tanaka, Phys. Lett. B 680 (2009) 179.
[25] Y. Hosotani, M. Tanaka, N. Uekusa, Phys. Rev. D 84 (2011) 075014.
[26] H. Hatanaka, Y. Hosotani, Phys. Lett. B 713 (2012) 481.
[27] N. Haba, Y. Sakamura, T. Yamashita, JHEP 1003 (2010) 069.
[28] Y. Hosotani, Y. Sakamura, Prog. Theoret. Phys. 118 (2007) 935.
[29] Y. Sakamura, Phys. Rev. D 76 (2007) 065002.
[30] Y. Hosotani, Y. Kobayashi, Phys. Lett. B 674 (2009) 192.
[31] K. Hasegawa, N. Kurahashi, C.S. Lim, K. Tanabe, Anomalous Higgs interactions in gauge-Higgs unification, arXiv:1201.5001 [hep-ph].

[32] J.R. Ellis, M.K. Gaillard, D.V. Nanopoulos, Nucl. Phys. B 106 (1976) 292.
[33] M.A. Shifman, A.I. Vainshtein, M.B. Voloshin, V.I. Zakharov, Sov. J. Nucl. Phys. 30 (1979) 711.
[34] J.F. Gunion, H.E. Haber, G.L. Kane, S. Dawson, Front. Phys. 80 (2000) 1.
[35] W.J. Marciano, C. Zhang, S. Willenbrock, Phys. Rev. D 85 (2012) 013002.
[36] N. Maru, N. Okada, Phys. Rev. D 77 (2008) 055010.
[37] A. Falkowski, Phys. Rev. D 77 (2008) 055018.
[38] H.M. Georgi, S.L. Glashow, M.E. Machacek, D.V. Nanopoulos, Phys. Rev. Lett. 40 (1978) 692.
[39] S. Dawson, Nucl. Phys. B 359 (1991) 283.
[40] M. Spira, A. Djouadi, D. Graudenz, P.M. Zerwas, Nucl. Phys. B 453 (1995) 17.
[41] ATLAS Collaboration, Search for high-mass dilepton resonances in 6.1/fb of pp collisions at sqrt(s) = 8 TeV with the ATLAS experimen, ATLAS-CONF-2012-129.
[42] ATLAS Collaboration, A search for high-mass resonances decaying to $\tau^+\tau^-$ in pp collisions at $\sqrt{s} = 7$ TeV with the ATLAS detector, arXiv:1210.6604 [hep-ex].
[43] CMS Collaboration, Search for resonances in dilepton mass spectra in pp collisions at $\sqrt{s} = 8$ TeV, CMS-PAS-EXO-12-015.
[44] CMS Collaboration, Search for narrow resonances in dilepton mass spectra in pp collisions at $\sqrt{s} = 8$ TeV, CMS-PAS-EXO-12-016.
[45] CMS Collaboration, Search for multi-charged heavy stable charged particles, CMS-PAS-EXO-11-090.

計画研究 B03 班

課題名「 テラスケールの物理から超弦理論への展開 」

研究組織

(1)研究代表者
渡利　泰山（WATARI, Taizan）
東京大学 ・カブリ数物連携宇宙研究機構・特任准教授
研究者番号：40451819

(4) 研究協力者：　科研費補助事業期間を通して、常時４－５人で推移した。
（多少の入れ替わりあり）

大河内　豊（OOKOUCHI,Yutaka）
九州大学・基幹教育院 自然科学理論系部門 ・准教授
研究者番号　40599990

高柳　匡（TAKAYANAGI,Tadashi）
京都大学, 基礎物理学研究所, 教授
研究者番号　10432353

Yu-Chieh Chung
現所属・不明
研究者番号　40624135

John Kehayias,
Vanderbilt 大学・物理天文学科・特任研究員
研究者番号　30624142

西尾 亮一 (NISHIO, Ryoichi)
SmartNews, Inc.・社員

研究者番号　なし

Dong-Min Gang,
東京大学・カブリ数物連携宇宙研究機構・特任研究員
研究者番号　50748853

Matthias Weissenbacher
東京大学・カブリ数物連携宇宙研究機構・特任研究員
研究者番号　80775677

交付決定額

計画研究 B03 班に配分された交付額を表 1 に示す。

表 1. 交付決定額（配分額）　（金額単位：円）

年度	直接経費	間接経費	合計
平成 23 年度	5,400,000	1,620,000	7,020,000
平成 24 年度	6,800,000	2,040,000	8,840,000
平成 25 年度	6,900,000	2,070,000	8,970,000
平成 26 年度	6,500,000	1,950,000	8,450,000
平成 27 年度	6,500,000	1,950,000	8,450,000
総計	32,100,000	9,630,000	41,730,000

研究成果

１．研究開始当初の背景

素粒子物理のフロンティアを前進させることができるのは究極的には実験である。その中でも加速器実験は重要な位置を占める。一方で、加速器実験でエネルギーの一段高い世界に踏み込んでいくには、非常に長い時間を要する。ゆえに、実験から直接的に分かることだけでなく、その意味するところを十二分に引き出す理論的試みが重要な意味を持つことになる。

そのような理論的試みの中で、実験にもっとも近いところに寄り添うアプローチは、現象論とか模型構築とか呼ばれている。そのアプローチの基本言語は、低エネルギー有効局所場の理論である。そして、このアプローチの限界は２つある。１つは、局所場の理論が許す自由度があまりに大きく、標準模型を超える模型を構築するにあたって、理論的に許される自由度が大きすぎるのである。そしてもう一つは、加速器実験で解析できる事象が、場の理論の摂動的取扱が可能なものに限られていることである。クォークやグルーオンなどの大角度高エネルギー散乱は摂動計算扱えるが、終状態としてハドロンを含むような過程は、摂動計算では扱えない。

超弦理論は、低エネルギー有効局所場の理論を超える理論的枠組みである。であるから、上記の２つの低エネルギー有効局所場の理論の限界を弦理論を用いて乗り越えようとするアプローチが試みられてきた。

(1) 模型構築のアプローチの限界を超えようとする試みとして、超弦理論のコンパクト化が１９８０年代半ばから研究されてきた。しかし、９０年代半ばに起きた超弦理論の理解の飛躍的進歩により、８０年代からの蓄積は大幅なバージョンアップが必要になった。そのバージョンアップが００年代半ばに始まり、理論的基礎での不明な部分が大方片付いたのが、当該科研費補助事業の「研究開始当時」の状況である。

しかし、超弦理論のコンパクト化の現象論のための理論的基礎の理解が固まることと、それを用いて低エネルギーの物理に有用な洞察をもたらすことの間にはまだ相当の距離があった。

(2) 加速器実験での事象の解析を局所場の理論の摂動計算に依拠する、という限界を超えようとする試みとしては、AdS/CFT 対応の応用の研究がなされてきた。

９０年代末から００年代にかけては、AdS 空間上の重力理論を用いて、ハドロンの質量や結合定数、形状因子を計算する手法が開発された。これは、AdS/CFT 対応のハドロン物理への応用において基礎中の基礎になる事項である。

一方、質量や形状因子は、ハドロンの静的、もしくはそれに準ずる低エネルギー領域での性質である。ハドロンの純高エネルギー散乱では、パートンの描像がよい近似になることが知られており、また、散乱の重心系エネルギーが大きいけれども運動量移行が小さい場合(Regge 領域と呼ばれる)には、ハドロン描像とパートン描像の中間・折衷的な性質をもった理論が必要であることが知られている。ゆえに、さらなる理論開発が必要なのである。

２００２年の Polchinski Strassler, および ２００６年の Brower Polchinski Strassler Tan (BPST) の論文は、この方面において突破口を開くものであった。AdS/CFT の枠組みの中でどのようにパートンを扱うべきか、そして Regge 領域の散乱を取り出すには、超弦理論のどのような近似計算を行うべきか、の指針を明らかにしたのである。ただし、06 年の BPST 論文は、２つのハドロンの間の弾性散乱のみを扱う理論的枠組みの提示にとどまった。多種多彩なハドロンの高エネルギー散乱現象を理解するための理論的枠組みとして使えるようになるには、まだ相当の理論の開発が必要、というのが、「研究開始当時」の状況である。

２．研究の目的

新学術領域「テラスケール」の B03 班では、上記 (1), (2) の試みを追及していくことを目的とした。

３．研究の方法

(1) 当該科研費補助事業の開始時点で懸案であったのは、「コンパクト化に導入可能な位相的フラックスを、特異点を持つ多様体においてどう記述するか」という技術的問題である。位相的フラックスは低エネルギー有効理論の物質場の世代数も決定するし、コンパクト化多様体の形状も決定する、ひいては低エネルギー有効理論の結合定数を決定する、というものであるから、まずはここを攻略せねばならない。我々は、05 年の Aspinwall Kallosh 論文、11 年の Esole Yau 論文を徹底的に読み込むことから開始した。

そこから得られた理解を基に、次は、03 年の Ashok Douglas, 04 年の Denef Douglas 論文にお

ける弦理論の解の統計分析を拡張一般化し、統計分析の手法を F-理論コンパクト化にも適用できるようにした。

これらの段階を乗り越えたうえで、F-理論のフラックスコンパクト化で得られる低エネルギー有効理論の統計を調べ、その結果を、ゲージ群、世代数、結合定数など低エネルギーで観測可能な物理量の関数求めるところまで持ち込んだ。結果は次の項で記す。

この超弦理論の真空の統計分布を調べることが可能になることによって、模型構築のアプローチにおいて通常用いられる「自然さ」という考え方に対して、科学的基礎づけを与えることが可能になる。超対称統一理論におけるフレーバー構造の起源についても、この統計に基づいた洞察を超弦理論から引き出せるようになる。

(2) まずは、02 年 Polchinski Strassler 論文、そして 06 年 BPST 論文を精読し消化するところから我々は研究を開始した。

この両論文のあいまいな個所、論理の不備などに修正を加える一方で、我々は この手法を深部仮想的コンプトン散乱過程と呼ばれる高エネルギーハドロン散乱過程に適用した。必要は発明の母である。具体的な物理過程を対象とすることにより、理論的枠組みのどこが拡張再構築を必要としているかが明らかになるので、一石二鳥の狙いである。

深部仮想的コンプトン散乱過程の記述は、摂動計算と一般化されたパートン分布関数(GPD)と呼ばれる 3 変数非摂動関数の組み合わせによってなされるのだが、弦理論(AdS/CFT)に基づいた手法の強みは、[理論的枠組みがきちんと整備拡張された場合に]この非摂動関数の部分について定性的な予言を出すことができることである。この非摂動関数部分は、摂動計算の過程で複雑な畳み込み積分に使われるため、実験データから直接フィットするわけにはいかない。フィットの前に、理論に基づく媒介変数表示を与える必要があるので、この弦理論に基づくアプローチは、その面での進歩をもたらしうる。

4．研究成果

(1) まずは、フラックスコンパクト化による多様体の形状の安定化機構は、本質的に代数幾何におけるネーター・レフシェッツ問題と等価であるという観察に基づき、まずは F-理論の K3xK3 コンパクト化のフラックス存在下での安定解を調べた。K3 多様体の場合にはネーター・レフシェッツ問題を具体的に手で取り扱うことができる。一方でこの同じ設定に対して、Douglas Ashok Denef の統計的手法を F-理論用に一般化した解析を行うことにより、ネーター・レフシェッツ問

題を扱う手法と、統計的手法が同じ結果を与えることを確認した。かくして、汎用性が高い（と目される）Douglas らの手法を、F-理論の一般的なコンパクト化にも用いてよいことが示された。

なお、この過程で、ヘテロ弦理論と F-理論の間の 8 次元での双対性対応が、離散モジュラー群のとり方まで含めて成立していることを(ついでに)厳密に示した。

Douglas らの統計的手法を F-理論の一般のコンパクト化に用いる場合、4 次コホモロジー群を縦成分、横成分、その他成分に分割し、それぞれの成分の次元を求める必要があることも明らかにした。我々は、この各成分の次元を求める数学公式をも導いた。これにより、低エネルギー有効理論の物理量に対して、F-理論のフラックスコンパクト化解の数がどのような統計分布をを示すかを計算できるようになった。

一般的な結果として、次のことが分かった。
まず、有効理論の物質場の世代数に関しては、ガウス分布であり、分散は O(1)程度。これは、現実世界の 3 世代という値と大きな乖離はない。次に、ゲージ群のとり方に関しては、
乱暴に言って、統一理論のようなゲージ群を持つ解は、全くゲージ群がない解に比べて、１０のマイナス１０００乗程度、もしくはもっと、という信じがたい小さな比率であることが分かった。

宇宙定数の値が現在の宇宙での値ほどに小さい確率は、１０のマイナス１００乗程度、という問題がよく知られているが、この問題の発見のインパクトはその上を行くものである。この結果のインパクトから、MIT の研究者は多様体の 4 次コホモロジーの横成分の次元の計算を多くの例について調べ、３０万次元ほどの大きさの横成分があるものを発見した。このことは、上記の比率が、10 のマイナス１０００乗などでは全く済まないことを示している。

この大きな問題をわきにおけば(人間原理という解がないわけではないので)、この統計分布を用いて、現実世界のフレーバー構造の起源のいくつかの仮説について、優劣の判定をつけることができる。ある仮説については、
１万分の１の真空で成り立つのに対し、別の仮説は、１０のマイナス１万乗の比率の真空でしか成り立たないということを示した。

(2)02 年 Polchinski Strassler 論文および 06 年 BPST 論文を精読し、改良を加えた。その結果、パートン分布関数を 2 変数関数に拡張したもの（縦方向運動量 x とローレンツ不変運動量移行 t)について、クロスオーバー転移が存在することを指摘した。

また、06 年 BPST 論文の弾性散乱用に開発された手法を一般化して、２体から２体への散乱な

がら、始状態と終状態で質量が違いうる場合にも適用できるように拡張した。この結果、深部仮想コンプトン散乱にこの AdS/CFT を用いた手法が適用可能になった。

その手法を用いて、3 変数(x, t そしてよじれ具合 eta)に依存する非摂動関数、一般化されたパートン分布関数を求めて、そのいろいろな性質を導いた。

５．主な発表論文等

（研究代表者、研究分担者及び連携研究者には下線）

〔雑誌論文〕（計　１９件）
以下、すべて査読あり。

また、これらの論文はすべて、
http://inspirehep.net/
で入手可能である。　発表順。

① R. Nishio and T. Watari "Heigh-energy Photon-Hadron Scattering in Holographic QCD," Phys.Rev. D84 (2011)075025.

② R. Nishio and T. Watari "Investigating Generalized Parton Distribution in Gravity Dual," Phys.Lett. B707 (2012) 362—368.

③ H. Hayashi, T. Kawano and T. Watari "Constraints on GUT 7-brane Topology in F-theory," Phys.Lett. B708 (2012) 191-194.

④ T. Kawano, Y. Tsuchiya and T. Watari "A Note on Kahler Potential of Charged Matter in F-theory," Phys.Lett. B709 (2012) 254-259.

⑤ R. Nishio, T. Watari, T. Yanagida and K. Yonekura, "Naïve Dimensional Analysis in Holography," Phys.Rev. D86 (2012) 016010.

⑥ A. Braun and T. Watari "On Singular Fibres in F-theory," JHEP 1307 (2013) 031.

⑦ A. Braun, Y. Kimura and T. Watari "The Noether-Lefschetz problem and gauge group resolved landscapes: F-theory on K3 x K3 as a test case," JHEP 1404 (2014) 050.

⑧ A. Braun and T. Watari "Distribution of the Number of Generations in Flux Compactifications," Phys.Rev. D90 (2014) 121901.

⑨ Y. Chung and C. Lin "Topological Inflation with Large Tensor-to-scalar Ratio," JCAP 1407

(2014) 020.

⑩ A. Braun and T. Watari "The Vertical, the Horizontal and the rest: anatomy of the middle cohomology of Calabi-Yau fourfolds and F-theory applications,"JHEP 1501 (2015) 047.

⑪ R. Nishio and T. Watari "Skewness Dependence of generalized parton distributions, conformal OPE and the AdS/CFT correspondence," Phys.Rev. D90 (2014) 125001.

⑫ B. Henning, J. Kehayias, H. Murayama, D. Pinner and T. Yanagida, "A kev string axion from high-scale supersymmetry," Phys.Rev.D90 (2015), 4, 045036.

⑬ S. Hellerman, J. Kehayias and T. Yanagida, "Chaotic inflation from non-linear sigma models in supergravity," Phys. Lett. B742 (2015) 390-393.

⑭ T. Watari "Statistics of F-theory flux vacua for particle physics," JHEP 1511 (2015) 065.

〔学会発表〕（計　１３件）

① 国際会議 String Phenomenology 2011. 11 年 8/22-8/26, 米国ウイスコンシン州マディソン、ウイスコンシン大学にて。"Studying GPD in holographic QCD" Taizan Watari

② 国際会議 Elastic and Diffractive Scattering. 11 年 12/16—12/20, ベトナム、Qui Nhon 市。"Studying GPD in Gravity Dual" Taizan Watari

③ 国際研究集会 CERN Theory Institute 2012 on String Phenomenology. 12 年 7/9—7/20。スイス、ジュネーブ、CERN 研究所にて。 "Note on Kahler Potential of Charged Matter in F-theory" Taizan Watari

④ 国際研究集会 "Relation of string theory to gauge theories and moduli problems of branes." 12 年 9/10—9/14。 ロシア、モスクワ、ステクロフ数学研究所にて。"Particle Physics and Geometric Data for String Compactifications" Taizan Watari

⑤ 国際研究集会 "New Challenges for String Phenomenology" 12 年 9/26—9/28。スペイン、マドリード、マドリード自治大学にて。"Challenges for Stringphenomenology after String Revolution," Taizan Watari

⑥ 国際会議 “Geometry and physics of F-theory” 14 年 2/24—2/27。ドイツ、ハイデルベルグ、ハイデルベルグ大にて。 “Noether-Lefschetz problem and gauge group resolved landscape” Taizan Watari

⑦ 国際研究集会 “Fine-tuning, Anthropics and String Lanscape”14 年 10/8—10/10 スペイン、マドリード、マドリード自治大にて。”Statistics of Gauge groups and Number of generations,” Taizan Watari

⑧ 国際研究集会 “Rikkyo MathPhysics 2015”15 年 1/10—1/12 東京、立教大学にて。
“Geometry of elliptic K3, elliptic Calabi-Yau fourfolds and F-theory” Taizan Watari

⑨ 国際会議 “Physics and Geometry of F-theory” 15 年 2/23-2/26。ドイツ、ミュンヘン、マックスプランク研究所にて。”Geometry of elliptic K3 and Heterotic-F-theory Duality” Taizan Watari

⑩ 国際研究集会 “String/M-theory compactification and moduli stabilization” 15 年 3/4—3/7。米国、ミシガン州アナーバー、ミシガン大学にて。”Some thoughts on Complex Structure Moduli Inflation” Taizan Watari

⑪ 国際会議 “String Phenomenology 2015”15 年 6/8—6/12。スペイン、マドリード、マドリード自治大学にて。”Statistics of Effective Theories in F-theory Flux Compactifications,” Taizan Watari

⑫ 国際研究集会 “Spinfest 2015” 15 年 7/22。茨城県、東海村、KEK 東海事業所。”Skewness dependence of GPD in AdS/QCD” Taizan Watari

⑬ 国際会議 “F-theory at 20”16 年 2/22-2/26。米国カリフォルニア州パサデナ、カリフォルニア工科大にて。”Heterotic string soliton and degeneration of K3 surface”Taizan Watari

国内研究会は集計に含めず。

〔その他〕

研究会開催

“Holography and QCD---Recent Progress and Challenges” 2013 9/24—9/28, 東大柏キャンパス

にて。他財源と共催。参加者は内外から５９名。研究会 web page は、
http://indico.ipmu.jp/indico/conferenceDisplay.py?confId=9

アウトリーチ
一般向け： IPMU News Letter に寄稿
「ニュートリノ振動大角度混合の衝撃」

理数系教養以上向け：雑誌「数理科学」寄稿
2012 年 12 月号、「F-理論の数理」

物理学会会員向け：日本物理学会誌解説記事、2016 年 6 月号 「超弦理論のコンパクト化 After Thirty Years」

主要論文別刷

⑦ A. Braun, Y. Kimura and T. Watari "The Noether-Lefschetz problem and gauge group resolved landscapes: F-theory on K3 x K3 as a test case," JHEP 1404 (2014) 050.

⑧ A. Braun and T. Watari "Distribution of the Number of Generations in Flux Compactifications," Phys.Rev. D90 (2014) 121901.

⑩ A. Braun and T. Watari "The Vertical, the Horizontal and the rest: anatomy of the middle cohomology of Calabi-Yau fourfolds and F-theory applications,"JHEP 1501 (2015) 047.

⑪ R. Nishio and T. Watari "Skewness Dependence of generalized parton distributions, conformal OPE and the AdS/CFT correspondence," Phys.Rev. D90 (2014) 125001.

⑭ T. Watari "Statistics of F-theory flux vacua for particle physics," JHEP 1511 (2015) 065.

Published for SISSA by Springer

Received: February 16, 2014
Accepted: March 3, 2014
Published: April 7, 2014

The Noether-Lefschetz problem and gauge-group-resolved landscapes: F-theory on K3 × K3 as a test case

A.P. Braun,[a] Y. Kimura[b] and T. Watari[c]

[a] *Department of Mathematics, King's College, London WC2R 2LS, U.K.*

[b] *Yukawa Institute for Theoretical Physics, Kyoto University, Kyoto 606-8502, Japan*

[c] *Kavli Institute for the Physics and Mathematics of the Universe, University of Tokyo, Kashiwano-ha 5-1-5, 277-8583, Japan*

E-mail: andreas.braun@kcl.ac.uk, kimura@yukawa.kyoto-u.ac.jp, taizan.watari@ipmu.jp

Abstract: Four-form flux in F-theory compactifications not only stabilizes moduli, but gives rise to ensembles of string vacua, providing a scientific basis for a stringy notion of naturalness. Of particular interest in this context is the ability to keep track of algebraic information (such as the gauge group) associated with individual vacua while dealing with statistics. In the present work, we aim to clarify conceptual issues and sharpen methods for this purpose, using compactification on K3 × K3 as a test case. Our first approach exploits the connection between the stabilization of complex structure moduli and the Noether-Lefschetz problem. Compactification data for F-theory, however, involve not only a four-fold (with a given complex structure) Y_4 and a flux on it, but also an elliptic fibration morphism $Y_4 \longrightarrow B_3$, which makes this problem complicated. The heterotic-F-theory duality indicates that elliptic fibration morphisms should be identified modulo isomorphism. Based on this principle, we explain how to count F-theory vacua on K3 × K3 while keeping the gauge group information. Mathematical results reviewed/developed in our companion paper are exploited heavily. With applications to more general four-folds in mind, we also clarify how to use Ashok-Denef-Douglas' theory of the distribution of flux vacua in order to deal with statistics of sub-ensembles tagged by a given set of algebraic/topological information. As a side remark, we extend the heterotic/F-theory duality dictionary on flux quanta and elaborate on its connection to the semistable degeneration of a K3 surface.

Keywords: Flux compactifications, F-Theory, Superstring Vacua

ArXiv ePrint: 1401.5908

Open Access, © The Authors.
Article funded by SCOAP[3].

doi:10.1007/JHEP04(2014)050

JHEP04(2014)050

Contents

1 Introduction **1**

2 Four-form flux in M/F-theory on K3 × K3 **4**
- 2.1 Review of known results 4
- 2.2 Extending the list 9

3 F-theory classification of elliptic fibrations on a K3 surface **12**
- 3.1 On the Torelli theorem for K3 surfaces 13
- 3.2 When are two elliptic fibrations considered "different" in F-theory? 17

4 A miniature landscape: F-theory on K3 × K3 with $G_0 = 0$ **20**
- 4.1 $\mathcal{J}_1(X)$ and $\mathcal{J}_2(X)$ classification 20
  - 4.1.1 Frame lattice, Mordell-Weil group and U(1) charges 22
- 4.2 Moduli space of F-theory with flux 27
  - 4.2.1 Subspace of K3 moduli space with a given Picard number 27
  - 4.2.2 Moduli space in the presence of flux 28
  - 4.2.3 How to carry out the vacuum counting for F-theory on K3 × K3 in practice 30
- 4.3 Sample statistics 32
  - 4.3.1 Statistics on 7-brane gauge groups and CP violation 32
  - 4.3.2 Stable degeneration "limit" 36

5 Landscapes of F-theory on K3 × K3 with $G_0 \neq 0$ flux **41**
- 5.1 General remarks 42
  - 5.1.1 Primitivity 42
  - 5.1.2 Integrality 43
  - 5.1.3 $\langle W_{\mathrm{GVW}} \rangle = 0$ 45
- 5.2 A landscape of vacua with a rank-16 7-brane gauge group 45
- 5.3 U(1) flux, heterotic-F-theory duality, and GUT 7-brane flux 51
  - 5.3.1 U(1) flux/Mordell-Weil flux 51
  - 5.3.2 GUT 7-brane flux/singular fibre flux 57
- 5.4 Vacuum distribution based on continuous approximation 58

A A note on heterotic string Narain moduli **68**

B Heterotic Cartan flux and semistable degeneration **70**
- B.1 Set-up 70
- B.2 Mordell-Weil group and narrow Mordell-Weil group 72
- B.3 Semistable degeneration 74

C Ashok-Denef-Douglas formula for F-theory **76**

JHEP04(2014)050

1 Introduction

Flux compactifications of type IIB string theory / F-theory can generate large supersymmetric masses for moduli, so that the moduli particles decay well before the period of big-bang nucleosynthesis. In addition to this phenomenological advantage, the discretum of vacua in this class of compactifications provides an ensemble of vacua (or landscape), which gives rise to a scientific/stringy basis for a notion of naturalness [1, 2]. Certainly the (geometric phase) Calabi-Yau compactifications of type IIB / F-theory are not more than a small subset of all possible vacua in string theory. However, one can still think of some use in such a restricted ensemble of vacua because supersymmetric extensions of the Standard Model and grand unification can be naturally accommodated in this framework.

Given a topological configuration of three-form fluxes in type IIB string theory compactified on a Calabi-Yau threefold M_3, the dilaton and complex structure moduli of M_3 are stabilized and their vacuum expectation values (vevs) are determined. By this mechanism, however, not only the moduli vevs (= the coupling constants of the low-energy effective theories), but also a configuration of D7-branes (= (a part of) the gauge group of the effective theories) is determined.

Low-energy effective theories in particle physics are usually crudely classified by such information as gauge groups, matter representations, types of non-vanishing interactions and matter multiplicity, and then the effective theories sharing this information are distinguished by the values of coupling constants. In order to fit this natural framework of thought, ensembles of string flux vacua should also be crudely classified by algebraic and topological information. After this, statistics should be presented in the form of distributions over the moduli space of compactifications sharing the same set of algebraic and topological information. With the statistics of flux vacua presented in this way, we begin to be able to ask such naturalness-related questions as the ratio of the number of vacua having various algebraic and/or topological data or the distribution of various coupling constants (moduli parameters) in a class of theories having a give set of algebraic/topological data. This article aims at taking one step further in this program. The distribution of gauge groups in effective four-dimensional theories derived from string compactifications has been studied from several perspectives in the literature, see [3–6] for examples.

Stabilization / determination of D7-brane configurations can be understood purely in type IIB language in terms of calibration conditions [7, 8]. Another option is to use F-theory, where the 7-brane configuration, dilaton vev and complex structure moduli of M_3 are all treated as part of the complex structure moduli of a Calabi-Yau fourfold Y_4. In F-theory language, there are two ways to understand the mechanism of determination of the moduli vevs. One is to specify the four-form flux on an elliptic fibred Calabi-Yau fourfold Y topologically,[1]

$$[G^{(4)}] \in H^4(Y;\mathbb{Z})\,. \tag{1.1}$$

[1]The four-form flux should be in the Abelian group $\left[H^4(Y;\mathbb{Z}) + \frac{1}{2}[c_2(TY)]\right] \cap H^{2,2}(Y;\mathbb{R})$ [9], with a possibly half-integral shift $(1/2)[c_2(TY)]$. When Y is a smooth Weierstrass model, however, $c_2(TY)$ is always even, and the four-form flux takes its value in (1.3) [10, 11]. In the present case, where we work with $\mathrm{K3}\times\mathrm{K3}$, $c_2(TY)$ is manifestly even and no such issue arises. Hence we ignore this point from now on.

JHEP04(2014)050

The Gukov-Vafa-Witten superpotential

$$W_{\rm GVW} \propto \int_Y \Omega_Y \wedge G^{(4)} \tag{1.2}$$

gives rise to an F-term scalar potential that depends on the complex structure moduli of Y. The minimization of this potential determines the vevs of those moduli. Once the moduli vevs arrive at the minimum of the potential (and if the cosmological constant happens to vanish), the four-form flux $G^{(4)}$ is guaranteed to only have a $(2,2)$ component in the Hodge decomposition under the complex structure corresponding to the vevs [12, 13]. In the presence of the four-form flux, the moduli fields slide down the potential to find a vacuum complex structure, so that $[G^{(4)}]$ only has the $(2,2)$ component. If we are to allow large vacuum expectation values of $W_{\rm GVW}$ $[G^{(4)}]$ may also have $(4,0)$ and $(0,4)$ components.

An alternative way to characterize the vacuum choice of the complex structure of Y is available by focussing on the finitely generated Abelian group

$$H^4(Y;\mathbb{Z}) \cap H^{2,2}(Y;\mathbb{R}) \qquad \left(\text{or } H^4(Y;\mathbb{Z}) \cap H^{2,2}(Y;\mathbb{R}) \oplus [H^{4,0}(Y;\mathbb{C}) + \text{h.c}]\right) . \tag{1.3}$$

The rank of this Abelian group remains constant almost everywhere on the moduli space of the complex structure of Y, but it jumps at special loci. In mathematics, this problem — at which loci in the moduli space the rank of this Abelian group jumps, and how it changes there — is known as the Noether-Lefschetz problem. Once we find a point in the Noether-Lefschetz locus and insert four-form flux in the enhanced part of the Abelian group (1.3), we can no longer go away continuously from the Noether-Lefschetz loci in the moduli space while keeping the flux purely of type $(2,2)$. The higher the codimension of a Noether-Lefschetz locus is in the complex structure moduli space, the more moduli are given masses and stabilized. Therefore, the problem of determination of vacuum complex structure is equivalent to the Noether-Lefschetz problem (e.g., [14]).[2]

This article begins, in sections 2.2, 4.1, 4.3 and 5.2 in particular, with exploiting this equivalence[3] to see how the Noether-Lefschetz problem in F-theory determines statistics of such things as gauge group, discrete symmetry and moduli vevs. We focus our attention on $K3 \times K3$ compactifications of F-theory, as in [15, 16, 18, 21–25]. This compactification cannot be considered realistic enough for an immediate use in particle physics (e.g. there are no matter curves), but a sufficient complexity is involved in this toy model of landscape to make it suitable for the purpose of clarifying various concepts as well as sharpening technical tools.

In the process of deriving statistics, one cannot avoid asking about the modular group (e.g., [17]). In other words, we have to understand when a pair of seemingly different compactification data actually correspond to the same vacuum in physics. In F-theory we have to introduce some equivalence relation among the space of elliptic fibrations that are

[2] We can also draw an analogy with the attractor mechanism [14], although the analogy is particularly good in the case with $G_1 \neq 0$ and $G_0 = 0$ in (2.15), (2.16).

[3] This is an obvious continuation of a program initiated a decade earlier. This idea is already evident in pioneering works such as [14–18], to name a few, and has also been reflected in recent articles such as [19, 20].

JHEP04(2014)050

admitted by Y_4, so that the quotient space corresponds to the set of physically distinct vacua. In section 3.2, we use the duality between heterotic string theory and F-theory, and find that the modulo-isomorphism classification of elliptic fibrations should be adopted. This observation yields two problems. One is purely mathematical: how can we work out the modulo-isomorphism classification of elliptic fibration for a given Y_4? A companion paper by the present authors [26] is dedicated to this problem, with a Calabi-Yau fourfold Y_4 replaced by a K3 surface, and the results in [26] are reviewed mainly in section 4.1 in this article. The other problem is how to use such results in mathematics to carry out vacuum counting in physics. We take on this issue in section 4.2.

Sample statistics, which give us some feeling of what string landscapes can do to answer statistical/naturalness questions in particle physics, are obtained in sections 4.3 and 5.2.

At the same time, though, the study running up to section 5.2 in this article along with [26] also hints that it may not be easy to pursue the Noether-Lefschetz problem approach for Calabi-Yau fourfolds which are not as simple as K3 $\times$ K3 or K3-fibration over some complex surface. One may of course always use the strategy of computing periods, as done e.g. in [27] in the present context. Of course, this approach has its own technical challenges.

The theory of [2, 28, 29] is a promising direction to go beyond a case-by-case study for different choices of fourfolds Y. Therefore, the second theme begins to dominate in section 5.4 toward the end of this article. Since articles as [29] and [17] seemed to have had applications in Type IIB orientifold compactifications in mind primarily, we clarify how to use the Ashok-Denef-Douglas theory to study statistics of flux vacua in F-theory, with the total ensemble resolved into sub-ensembles according to their algebraic and/or topological data such as gauge groups and matter multiplicity. The presentation in [17] sits in the middle between our discussion up to section 5.2 and that of [28, 29], and makes it easier to understand how the conceptual issues discussed in the sections up to 5.3 fit into the Ashok-Denef-Douglas theory. Although the presentation in section 5.4 and appendix C uses $K3 \times K3$ compactification as an example, we tried to phrase it in a way ready for generalization at least to cases with K3-fibred Calabi-Yau fourfolds, and possibly to general F-theory compactifications.

There is also the third theme behind sections 4.3.2, 5.3 and appendix B in this article. In the duality between heterotic string theory and F-theory, the dictionary of flux data has been mostly phrased by using the stable degeneration limit of [30, 31]. This was for good reasons, because [32–34] focused on fluxes in F-theory that are directly responsible for the chirality of non-Abelian (GUT gauge group) charged matter fields on the matter curves. There is an extra algebraic curve in the singular fibre over the matter curve in the F-theory geometry, and a flux can be introduced in this algebraic cycle [33, 34]. For more general flux configurations, however, it is not a priori clear to what extent we can use the $dP_9 \cup dP_9$ limit in the duality dictionary, because $dP_9 \cup dP_9$ is quite different from a K3 surface when it comes to whether two-cycles are algebraic or not. There is the work of [20], indicating that U(1) flux associated with an elliptically fibred geometry with an extra section stabilizes some complex structure moduli. Furthermore, the spectral cover description of vector bundles in heterotic string theory [30] did not rule out twisting

JHEP04(2014)050

information γ which is more general than (5.26) for special choices of complex structure. Section 5.3 and the appendix B provide a comprehensive understanding of this material, generalizing the duality dictionary of the flux data in the literature without relying on the $dP_9 \cup dP_9$ limit. Appendix B also makes a trial attempt of studying how much information of such fluxes can be captured by the $dP_9 \cup dP_9$ limit.

A similar theme has already been studied extensively in the series of papers [35–40]. It will be interesting to clarify the relation between the logical construction given there and the presentation in this article, but this task is beyond the scope of this present article.

All $K3$ surfaces which appear as solutions in this article have Picard number 20, which fixes the rank of the total gauge group to be 18 (this is the 'geometric' gauge group, which can still be further broken by fluxes). Whenever the non-abelian part of the gauge group has rank less than 18, there are U(1) factors which are geometrically realized as extra sections of the elliptic fibration. The explicit construction of extra section has been an active research program in recent years. As discussed in [20, 41, 42], sections can be realized by demanding appropriate factorization conditions in the Weierstrass model. A study of fluxes in (a resolution of) the scenario of [41] appeared in [43]. As already discussed in [41], extra sections can equivalently be obtained by realizing the elliptic fibre as a hypersurface in ambient spaces with more than a single toric divisor. This strategy is systematically exploited in [44–47]. Using toric techniques, in particular the classification of tops, models with I_5 fibres and extra sections were constructed in [48–51]. Given a specific embedding of the fibre, one can also use a similar approach as [52], i.e. use Tate's algorithm, to find all possible degenerations leading to a prescribed gauge group [53]. F-theory compactifications with U(1) symmetries also give rise to an interesting interplay between geometry and anomalies of the effective field theory, see [54–57] for some recent works in this direction.

We regret that we use some mathematical jargon and notations, which are non-standard in the physics literature, without explanations. Sections 2–4 of the mathematical companion paper of the present article [26] should contain the necessary background.

2 Four-form flux in M/F-theory on K3 × K3

2.1 Review of known results

Compactification of F-theory on $Y = \mathrm{K3} \times \mathrm{K3}$ has been studied from various perspectives in the literature. To start off, we begin this section with a review of a result in [18].[4] Their results are immediate for M-theory compactification down to 2+1-dimensions, but it is clear that we can build a study of F-theory compactification down to 3+1-dimensions by adding extra structure and imposing conditions on top of the discussion for M-theory [18].

When the Calabi-Yau fourfold Y is a product of two K3 surfaces, S_1 and S_2, the complex structure moduli space of Y, $\mathcal{M}_{\mathrm{cpx}}(Y)$, is the product of the complex structure moduli space of S_1 and S_2, $\mathcal{M}_{\mathrm{cpx}}(S_1) \times \mathcal{M}_{\mathrm{cpx}}(S_2)$. A discussion of the modular group is postponed to later sections. Over the moduli space of $[h^{3,1}(Y) = h^{1,1}(S_1) + h^{1,1}(S_2) = 40]$

[4] See also sections 2.2, 5.1 and 5.2 in this article, where the material reviewed in this section is extended.

JHEP04(2014)050

dimensions, the Hodge decomposition of $H^4(Y;\mathbb{C})$ varies, because the decompositions of $H^2(S_1;\mathbb{C})$ and $H^2(S_2;\mathbb{C})$ vary on the moduli spaces of the two K3 surfaces.[5]

$$H^{2,2}(Y;\mathbb{R}) = H^{1,1}(S_1;\mathbb{R}) \otimes H^{1,1}(S_2;\mathbb{R}) + [H^{2,0}(S_1;\mathbb{C}) \otimes H^{0,2}(S_2;\mathbb{C}) + \text{h.c.}]\,, \tag{2.1}$$

$$[H^{4,0}(Y;\mathbb{C}) + \text{h.c.}] = [H^{2,0}(S_1;\mathbb{C}) \otimes H^{2,0}(S_2;\mathbb{C}) + \text{h.c.}]\,, \tag{2.2}$$

where $[V + \text{h.c.}]$ for a complex vector space V with $\dim_{\mathbb{C}} V = 1$ denotes the corresponding 2-dimensional vector space over $\mathbb{R}$. The Hodge components $[H^{4,0}(Y;\mathbb{C}) + \text{h.c}]$ are also included here for now, partly because the four-form flux with non-vanishing $(4,0)$ and $(0,4)$ components still preserves AdS supersymmetry. The overlap between $H^2(S_1;\mathbb{Z}) \otimes H^2(S_2;\mathbb{Z}) \subset H^4(Y;\mathbb{Z})$ and $H^{2,2} \oplus [H^{4,0} + \text{h.c.}]$ has the maximal rank, 404, when

$$\text{rank}\left[H^2(S_1;\mathbb{Z}) \cap H^{1,1}(S_1;\mathbb{R})\right] = 20, \qquad \text{rank}\left[H^2(S_2;\mathbb{Z}) \cap H^{1,1}(S_2;\mathbb{R})\right] = 20\,. \tag{2.3}$$

The loci satisfying these conditions have complex codimension 40 in the moduli space $\mathcal{M}_{\text{cpx}}(S_1) \times \mathcal{M}_{\text{cpx}}(S_2)$, and hence are isolated points. Once plenty of fluxes are introduced in this rank 404 free Abelian group, all the complex structure moduli are stabilized.

The Abelian group

$$S_X = \left[H^{1,1}(X;\mathbb{R}) \cap H^2(X;\mathbb{Z})\right] \subset H^2(X;\mathbb{Z}) \tag{2.4}$$

for a K3 surface X is called Neron-Severi lattice (or group), and the rank of S_X — denoted by ρ_X or $\rho(X)$ — is called the Picard number of X. S_X is empty for X with a generic complex structure, but its rank can be as large as 20, which is possible only in points of $\mathcal{M}_{\text{cpx}}(X)$. K3 surfaces with $\rho_X = 20$ are called *attractive K3 surfaces* in [58, 59].[6] Thus, the ensemble of flux vacua of M-theory/F-theory compactifications on $Y = \text{K3} \times \text{K3}$ are mapped into a subset of $\mathcal{M}_{\text{cpx}}(S_1) \times \mathcal{M}_{\text{cpx}}(S_2)$ where both S_1 and S_2 are attractive K3 surfaces.

It is convenient for the classification of K3 surfaces with large Picard number to use the transcendental lattice. For a K3 surface X, it is defined as the orthogonal complement of S_X under the intersection form in $H^2(X;\mathbb{Z})$:

$$T_X := \left[(S_X)^\perp \subset H^2(X;\mathbb{Z})\right]. \tag{2.5}$$

[5] The $H^4(S_1;\mathbb{Z}) \otimes H^0(S_2;\mathbb{Z}) \oplus H^4(S_1;\mathbb{Z}) \otimes H^4(S_2;\mathbb{Z})$ components in $H^4(Y;\mathbb{Z})$ (and their $\mathbb{R}$-coefficient versions) are ignored here, because fluxes in these components do not preserve the $\text{SO}(3,1)$ symmetry in the application to F-theory compactifications. This extra assumption is made implicitly everywhere in this article.

[6] In the mathematics literature, a K3 surface with $\rho_X = 20$ is sometimes called a *singular K3 surface*, although the word "singular" only means "very special" in this case, and does not imply that the surface has a singularity. Ref. [58, 59] introduced the term *attractive K3 surface* for K3 surfaces satisfying the same condition, which allows us to avoid confusing terminology. This terminology is a natural choice: just like the complex structure of Calabi-Yau threefolds for type IIB compactifications is attracted towards special loci in $\mathcal{M}_{\text{cpx}}$ near the horizon of a BPS black hole in 4D $\mathcal{N} = 2$ effective theory of IIB/CY_3 in the attractor mechanism [60], the complex structure of fourfold for F-theory/M-theory should be driven towards special loci in $\mathcal{M}_{\text{cpx}}$ in a cosmological evolution in the presence of (G_1-type) flux due to the F-term potential from (1.2). In both cases, special loci are characterized by the condition that some topological flux falls into some particular Hodge component. [58, 59]. In this article, we follow [58, 59] and use the word attractive K3 surface.

JHEP04(2014)050

For a K3 surface with Picard number ρ_X, $\mathrm{rank}(T_X) = 22 - \rho_X$. K3 surfaces with a given transcendental lattice form a $(20-\rho_X)$-dimensional subspace of $\mathcal{M}_{\mathrm{cpx}}(\mathrm{K3})$, and in particular, attractive K3 surfaces are in one-to-one correspondence[7] with rank-2 transcendental lattices (modulo orientation-preserving basis change).

For an attractive K3 surface X, its rank-2 transcendental lattice has to be even and positive definite. This is equivalent to the condition that, for a set of generators $\{p, q\}$ of T_X, the intersection from is given by[8]

$$\begin{bmatrix} (p,p) & (p,q) \\ (q,p) & (q,q) \end{bmatrix} = \begin{bmatrix} 2a & b \\ b & 2c \end{bmatrix}, \tag{2.7}$$

where a, b, c are all integers, $Q := 4ac - b^2$ is positive, and $a, c > 0$. The 2-dimensional vector space $T_X \otimes \mathbb{C}$ over $\mathbb{C}$ (resp. $T_X \otimes \mathbb{R}$ over $\mathbb{R}$) agrees precisely with the vector space $H^{2,0}(X;\mathbb{C}) \oplus H^{0,2}(X;\mathbb{C})$ (resp. $[H^{2,0}(X;\mathbb{C}) + \text{h.c.}]$), and the complex vector subspace $H^{2,0}(X;\mathbb{C}) \subset T_X \otimes \mathbb{C}$ is identified with $\mathbb{C} \cdot \Omega_X \subset T_X \otimes \mathbb{C}$, where

$$T_X \otimes \mathbb{C} \ni \Omega_X := p + \tau q, \qquad \tau := \frac{-b + i\sqrt{Q}}{2c}. \tag{2.8}$$

With orientation-preserving basis changes of T_X, one can always choose the integers a, b, c such that

$$0 \le |b| \le c \le a \qquad (\text{but} \quad 0 \le b \quad \text{if } c = a) \qquad \text{and } Q > 0\,. \tag{2.9}$$

An attractive K3 surface characterized by integers a, b, c in the way explained above is denoted by $X_{[a\ b\ c]}$ in this article.

For a pair of attractive K3 surfaces S_1 and S_2, let $\{q_1, p_1\}$ and $\{q_2, p_2\}$ be the oriented basis of T_{S_1} and T_{S_2}, respectively. The intersection form in this basis is denoted by

$$\begin{bmatrix} (p_1,p_1) & (p_1,q_1) \\ (q_1,p_1) & (q_1,q_1) \end{bmatrix} = \begin{bmatrix} 2a & b \\ b & 2c \end{bmatrix}, \qquad \begin{bmatrix} (p_2,p_2) & (p_2,q_2) \\ (q_2,p_2) & (q_2,q_2) \end{bmatrix} = \begin{bmatrix} 2d & e \\ e & 2f \end{bmatrix}, \tag{2.10}$$

where a, b, c, d, e and f are all integers. The positive definiteness implies that

$$0 \le |b| \le c \le a, \qquad (\text{but } 0 \le b \text{ if } c = a), \qquad Q_1 := 4ac - b^2 > 0, \tag{2.11}$$

$$0 \le |e| \le f \le d, \qquad (\text{but } 0 \le e \text{ if } f = d), \qquad Q_2 := 4df - c^2 > 0, \tag{2.12}$$

[7] A pair of K3 surfaces X and X' are regarded equivalent iff there is a holomorphic bijection between them.

[8] A set of generators $\{q, p\}$ of T_X with the ordering between q and q specified is called an *oriented basis* of an attractive K3 surface X, if $\mathrm{Im}[\langle \Omega_X, q\rangle / \langle \Omega_X, p\rangle] > 0$. Choosing $\mathrm{Im}(\tau) > 0$ as in (2.8), $\{q, p\}$ is indeed an oriented basis. We follow the convention of [18], and present and parametrize the intersection form of T_X as in (2.7) in this article. But it looks more common in math literatures (such as [61]) and also in [58, 59] to parametrize the intersection form in this way:

$$\begin{bmatrix} (q,q) & (q,p) \\ (p,q) & (p,p) \end{bmatrix} = \begin{bmatrix} 2a & b \\ b & 2c \end{bmatrix}. \tag{2.6}$$

Thus, $[a\ b\ c]$ here (and in [18]) correspond to $[c\ b\ a]$ in [61].

JHEP04(2014)050

where all $a, \cdots, f$ are integers. The holomorphic (2,0)-forms on the K3 surfaces $S_1 = X_{[a\ b\ c]}$ and $S_2 = X_{[d\ e\ f]}$ can then be written as

$$\Omega_{S_1} = p_1 + \tau_1 q_1, \quad \tau_1 = \frac{-b + i\sqrt{Q_1}}{2c}, \qquad \Omega_{S_2} = p_2 + \tau_2 q_2, \quad \tau_2 = \frac{-e + i\sqrt{Q_2}}{2f}. \tag{2.13}$$

Note that $\tau_1 \in \mathbb{Q}[\sqrt{Q_1}]$ and $\tau_2 \in \mathbb{Q}[\sqrt{Q_2}]$. Both $\mathbb{Q}[\sqrt{Q_1}]$ and $\mathbb{Q}[\sqrt{Q_2}]$ are degree 2 ($\mathcal{D} = 2$) algebraic extensions of $\mathbb{Q}$ (see refs. [58, 59]).

In physics applications, we would rather like to impose one more condition. The M2/D3-brane tadpole cancellation is equivalent to

$$\frac{1}{2}\int_Y (G \wedge G) + N_{M2/D3} = \frac{\chi(Y)}{24} = 24\,, \tag{2.14}$$

where $N_{M2/D3}$ is the number of M2/D3-branes minus anti-M2/D3-branes (that are point like) in Y. When we exclude anti M2/D3-branes on Y, $N_{M2/D3} \geq 0$, and thus not all the pairs of attractive K3 surfaces in $\mathcal{M}_{\rm cpx}(S_1) \times \mathcal{M}_{\rm cpx}(S_2)$ qualify for the landscape of flux vacua of M-theory compactified on $Y = \text{K3} \times \text{K3}$.

Aspinwall and Kallosh carried out an explicit study of which pairs of attractive K3 surfaces can satisfy the condition (2.14), within a couple of constraints that make the analysis easier [18]. In order to state one of the constraints introduced in [18], we need the following definition. Let us focus on a pair of attractive K3 surfaces S_1 and S_2. Any $G^{(4)}$ in (1.3) on $Y = S_1 \times S_2$ can be decomposed, under the Hodge structure of Y, into $[G] = [G_1] + [G_0]$, where

$$[G_0] \in \left[H^{1,1}(S_1;\mathbb{R}) \otimes H^{1,1}(S_2;\mathbb{R})\right] = S_{S_1} \otimes S_{S_2} \otimes \mathbb{R}, \tag{2.15}$$

$$[G_1] \in \left[H^{2,0}(S_1;\mathbb{C}) \otimes H^{0,2}(S_2;\mathbb{C}) + \text{h.c.}\right], \tag{2.16}$$

$$\left(\text{or} \quad \in \left[H^{2,0}(S_1;\mathbb{C}) + \text{h.c.}\right] \otimes \left[H^{2,0}(S_2;\mathbb{C}) + \text{h.c.}\right] = T_{S_1} \otimes T_{S_2} \otimes \mathbb{R}\right). \tag{2.17}$$

The explicit study in ref. [18] assumes that

$$[G_0] = 0, \tag{2.18}$$

and[9] $[G_1] \neq 0$ is that of (2.16) rather than (2.17), so that $G^{(4)} = G_1$ is purely of $(2,2)$ type in the Hodge structure of $Y = S_1 \times S_2$, and the vev of $W_{\rm GVW}$ vanishes. Another assumption is to set

$$N_{M2/D3} = 0\,, \tag{2.19}$$

so that

$$\frac{1}{2}[G_1] \cdot [G_1] = 24\,. \tag{2.20}$$

Under these constraints, $[G_1]$ has to be an integral element of $T_{S_1} \otimes T_{S_2}$:

$$[G_1] \in [H^{2,0}(S_1;\mathbb{C}) \otimes H^{0,2}(S_2;\mathbb{C}) + \text{h.c.}] \cap (T_{S_1} \otimes T_{S_2}). \tag{2.21}$$

[9] If the $[G_1]$ component were to vanish, then there would be no interaction in the effective theory violating $\mathcal{N} = 2$ supersymmetry in 3+1 dimensions [15, 22]. Moduli mass terms purely from the $[G_0]$ component are consistent with $\mathcal{N} = 2$ supersymmetry.

JHEP04(2014)050

[a b c]	[d e f]	γ
[8 8 8]	[1 1 1]	$\gamma^{(6)}$
[6 0 3]	[2 0 1]	$\pm i/\sqrt{2}$
[6 0 2]	[1 1 1]	$\gamma^{(6)}$
[4 4 4]	[2 2 2]	$\gamma^{(6)}$
[3 0 3]	[1 0 1]	$(1+i)\gamma^{(4)}$
[3 0 1]	[2 2 2]	$\gamma^{(6)}$
[2 0 1]	[2 0 1]	$\pm 1 \pm i/\sqrt{2}$

[a b c]	[d e f]	γ
[6 0 6]	[1 0 1]	$\gamma^{(4)}$
[6 0 2]	[3 0 1]	$\pm i/\sqrt{3}$
[6 0 1]	[6 0 1]	$\pm i/\sqrt{6}$
[3 0 3]	[2 0 2]	$\gamma^{(4)}$
[3 0 2]	[3 0 2]	$\pm i\sqrt{2/3}$
[2 2 2]	[1 1 1]	$2 \times \gamma^{(6)}$

Table 1. Table 1 of ref. [18] is reproduced here (with minor modifications) for the convenience of the reader. Intersection forms (2.10) of T_{S_1} and T_{S_2} are simply denoted by [a b c] and [d e f] in this table. All the possible choices of $\gamma \in \mathbb{C}$ are listed; $\gamma^{(6)} := \{\pm 2i/\sqrt{3}, \pm 1 \pm i/\sqrt{3}\} = 2i/\sqrt{3} \times \{e^{2\pi i k/6} | k = 0,1,2,3,4,5\}$, $\gamma^{(4)} := \{\pm 1, \pm i\} = \{e^{2\pi i k/4} | k = 0,1,2,3\}$.

It is not always guaranteed for any pair of attractive K3 surfaces S_1 and S_2 that there can be $[G_1] \neq 0$. The Abelian group on the right hand side of (2.21) can be empty. Writing down $[G_1]$ as

$$[G_1] = \mathrm{Re}\left(\gamma \Omega_{S_1} \wedge \overline{\Omega}_{S_2}\right) \tag{2.22}$$

for some $\gamma \in \mathbb{C}$ and expanding this in the integral basis $\{p_1 \otimes p_2,\ q_1 \otimes p_2,\ p_1 \otimes q_2,\ q_1 \otimes q_2\}$ of $T_{S_1} \otimes T_{S_2}$, Aspinwall and Kallosh found that (2.21) is non-empty if and only if

$$^{\exists} m \in \mathbb{Z} \quad \text{s.t.} \quad Q_1 Q_2 = m^2 \,. \tag{2.23}$$

This implies that the two algebraic number fields $\mathbb{Q}[\sqrt{Q_1}]$ and $\mathbb{Q}[\sqrt{Q_2}]$ are the same. All the period integrals of the holomorphic (4,0) form $\Omega_Y = \Omega_{S_1} \wedge \Omega_{S_2}$ take values in the common degree-2 ($\mathcal{D} = 2$) algebraic extension field $\mathbb{Q}[\sqrt{Q_1}]$ of $\mathbb{Q}$ (cf. [17]).

Imposing the condition (2.20) on $[G_1]$ in (2.21), [18] worked out the complete list of pairs of attractive K3 surfaces where there exists a flux $G^{(4)}$ satisfying (2.18), (2.21), (2.20). The result are 13 pairs of attractive K3 surfaces [18], which are listed in table 1 along with all possible values of $\gamma \in \mathbb{C}$.

Two remarks are in order here. First note that for a supersymmetric compactification of M-theory on $Y = S_1 \times S_2$ with a four-form flux $G^{(4)} = G_1$, we could think of a compactification on $\overline{Y} = \overline{S_1} \times \overline{S}_2$ obtained by simply declaring that the holomorphic local coordinates on Y are anti-holomorphic coordinates on $\overline{Y}$, keeping the underlying real-8-dimensional manifold the same. The flux $[G_1] \in H^4(Y;\mathbb{Z})$ remains the same. This new compactification, however, should not be regarded as a vacuum physically different from the original one, only the role of the superpotential and its hermitian conjugate, and that of chiral multiplets and anti-chiral multiplets in the low-energy effective theory, are exchanged. The physics remains the same.

The transcendental lattice of the K3 surface $S_1' = \overline{S}_1$ can be regarded as $T_{S_1'} \cong \mathrm{Span}_{\mathbb{Z}}\{p_1', q_1'\} := \mathrm{Span}_{\mathbb{Z}}\{p_1, -q_1\}$, where the symmetric pairing is described by [a' b' c'] =

JHEP04(2014)050

[a -b c]. The holomorphic $(2,0)$-form is given by[10]

$$\Omega_{S_1'} = p_1' + \tau_1' q_1' := p_1 + \bar{\tau}_1 q_1 = \overline{\Omega}_{S_1}. \tag{2.24}$$

Thus, the four-form flux $G_1 = \mathrm{Re}[\gamma \Omega_{S_1} \wedge \overline{\Omega}_{S_2}]$ is rewritten in terms of $S_1' \times S_2' = \overline{S}_1 \times \overline{S}_2$ as $G_1 = \mathrm{Re}[\gamma^* \Omega_{S_1'} \wedge \overline{\Omega}_{S_2'}]$. Thus, $Y = S_1 \times S_2$ compactification with [a b c], [d e f] and γ and another compactification with [a -b c] and [d -e f] and γ^* are completely equivalent, and should not be regarded as different compactifications (or different vacua). For this reason, only one of each such pairs is shown in table 1.

Secondly, as for M-theory compactification, $Y = S_1 \times S_2$ with $G_1 = \mathrm{Re}(\gamma \Omega_{S_1} \wedge \overline{\Omega}_{S_2})$ and $Y = S_2 \times S_1$ with $G_1 = \mathrm{Re}(\gamma^* \Omega_{S_2} \wedge \overline{\Omega}_{S_1})$ should also be regarded equivalent. Thus, table 1 only shows cases where $a \geq d$, and furthermore, in cases with $a = d$, we impose $c \geq f$.

2.2 Extending the list

Before proceeding to the next section, it is worthwhile to extend the list so that the condition (2.20) is relaxed to

$$\frac{1}{2}[G_1] \cdot [G_1] \leq 24. \tag{2.25}$$

Certainly for any compactification of M-theory over $Y = S_1 \times S_2$ with a four-form flux $[G_1]$ in (2.21) satisfying the inequality above, at least we can introduce an appropriate number of M2-branes to satisfy the tadpole condition (2.14). One might even be able to find a flux $[G_0] \in (S_{S_1} \otimes S_{S_2})$ to satisfy (2.14). See section 5 for more about the case with $[G_0] \neq 0$, however.

Straightforward analysis allows us to extend table 1, so that it contains all pairs of attractive K3 surfaces S_1 and S_2 and a choice of $\gamma \in \mathbb{C}$ satisfying (2.18), (2.21) and (2.25), rather than (2.18), (2.21) and (2.20). The result of our analysis is presented in table 2.

flux	[a b c]	[d e f]	γ	M	F
24	[8 8 8]	[1 1 1]	$\gamma^{(6)}$	6	6
	[6 0 6]	[1 0 1]	$\gamma^{(4)}$	3	3
	[6 0 3]	[2 0 1]	$\pm i/\sqrt{2}$	1	1
	[6 0 2]	[3 0 1]	$\pm i/\sqrt{3}$	1	1
	[6 0 2]	[1 1 1]	$\gamma^{(6)}$	6	6
	[6 0 1]	[6 0 1]	$\pm i/\sqrt{6}$	1	1
	[4 4 4]	[2 2 2]	$\gamma^{(6)}$	6	6
	[3 0 3]	[2 0 2]	$\gamma^{(4)}$	3	3
	[3 0 3]	[1 0 1]	$(1+i)\gamma^{(4)}$	2	2
	[3 0 2]	[3 0 2]	$\pm i\sqrt{2/3}$	1	1
	[3 0 1]	[2 2 2]	$\gamma^{(6)}$	6	6

Table 2. *continued on next page...*

[10] Here, $\{q_1', p_1'\}$ is still an oriented basis of $T_{S_1'}$.

JHEP04(2014)050

Table 2. *. . . continued from previous page*

flux	[a b c]	[d e f]	γ	M	F
	[2 2 2]	[1 1 1]	$2\gamma^{(6)}$	6	6
	[2 0 1]	[2 0 1]	$\pm 1 \pm i/\sqrt{2}$	2	2
23	[6 1 1]	[6 1 1]	$\pm 2i/\sqrt{23}$	1	2
	[3 1 2]	[3 1 2]	$\pm 4i/\sqrt{23}$	1	2
22	[6 2 2]	[3 1 1]	$\pm 2i/\sqrt{11}$	2	2
21	[7 7 7]	[1 1 1]	$\gamma^{(6)}$	6	6
	[6 3 3]	[2 1 1]	$\pm 2i/\sqrt{7}$	2	2
	[1 1 1]	[1 1 1]	$(2 \pm \sqrt{3}i)\gamma^{(6)}$	6	12
20	[5 0 5]	[1 0 1]	$\gamma^{(4)}$	3	3
	[5 0 1]	[5 0 1]	$\pm i/\sqrt{5}$	1	1
	[3 2 2]	[3 2 2]	$\pm 2i/\sqrt{5}$	1	2
	[1 0 1]	[1 0 1]	$(1 \pm 2i)\gamma^{(4)}$	4	4
19	[5 1 1]	[5 1 1]	$\pm 2i/\sqrt{19}$	1	2
18	[6 6 6]	[1 1 1]	$\gamma^{(6)}$	6	6
	[3 3 3]	[2 2 2]	$\gamma^{(6)}$	6	6
	[2 2 2]	[1 1 1]	$2\gamma^{(6)}$	6	6
17					
16	[4 0 4]	[1 0 1]	$\gamma^{(4)}$	3	3
	[4 0 2]	[2 0 1]	$\pm i/\sqrt{2}$	1	1
	[4 0 1]	[4 0 1]	$\pm i/2$	1	1
	[4 0 1]	[1 0 1]	$\gamma^{(4)}$	3	3
	[2 0 2]	[2 0 2]	$\gamma^{(4)}$	3	3
	[2 0 2]	[1 0 1]	$(1+i)\gamma^{(4)}$	2	2
	[2 0 1]	[2 0 1]	± 1	2	2
	[1 0 1]	[1 0 1]	$2\gamma^{(4)}$	3	3
15	[5 5 5]	[1 1 1]	$\gamma^{(6)}$	6	6
	[4 1 1]	[4 1 1]	$\pm 2i/\sqrt{15}$	1	2
	[2 1 2]	[2 1 2]	$\pm 4i/\sqrt{15}$	1	2
14	[4 2 2]	[2 1 1]	$\pm 2i/\sqrt{7}$	2	2
	[2 1 1]	[2 1 1]	$\pm 1 \pm i/\sqrt{7}$	*2	4
13					
12	[4 4 4]	[1 1 1]	$\gamma^{(6)}$	6	6
	[3 0 3]	[1 0 1]	$\gamma^{(4)}$	3	3
	[3 0 1]	[3 0 1]	$\pm i/\sqrt{3}$	1	1
	[3 0 1]	[1 1 1]	$\gamma^{(6)}$	6	6
	[2 2 2]	[2 2 2]	$\gamma^{(6)}$	3	6

Table 2. *continued on next page. . .*

JHEP04(2014)050

Table 2. *. . . continued from previous page*

flux	[a b c]	[d e f]	γ	M	F
	[1 1 1]	[1 1 1]	$2\gamma^{(6)}$	3	6
11	[3 1 1]	[3 1 1]	$\pm 2i/\sqrt{11}$	1	2
10					
9	[3 3 3]	[1 1 1]	$\gamma^{(6)}$	6	6
	[1 1 1]	[1 1 1]	$\sqrt{3}i\gamma^{(6)}$	3	6
8	[2 0 2]	[1 0 1]	$\gamma^{(4)}$	3	3
	[2 0 1]	[2 0 1]	$\pm i/\sqrt{2}$	1	1
	[1 0 1]	[1 0 1]	$(1+i)\gamma^{(4)}$	2	2
7	[2 1 1]	[2 1 1]	$\pm 2i/\sqrt{7}$	1	2
6	[2 2 2]	[1 1 1]	$\gamma^{(6)}$	6	6
5					
4	[1 0 1]	[1 0 1]	$\gamma^{(4)}$	3	3
3	[1 1 1]	[1 1 1]	$\gamma^{(6)}$	3	6
23	[6 -1 1]	[6 1 1]	$\pm 2i/\sqrt{23}$	2	2
22	[3 -1 1]	[6 2 2]	$\pm 2i\sqrt{11}$	2	2
21	[2 -1 1]	[6 3 3]	$\pm 2i/\sqrt{7}$	2	2
20	[3 -2 2]	[3 2 2]	$\pm 2i/\sqrt{5}$	2	2
19	[5 -1 1]	[5 1 1]	$\pm 2i/\sqrt{19}$	2	2
15	[4 -1 1]	[4 1 1]	$\pm 2i/\sqrt{15}$	2	2
14	[2 -1 1]	[2 1 1]	$\pm 1 \pm i/\sqrt{7}$	*4	4
	[2 -1 1]	[4 2 2]	$\pm 2i/\sqrt{7}$	2	2
11	[3 -1 1]	[3 1 1]	$\pm 2i/\sqrt{11}$	2	2
7	[2 -1 1]	[2 1 1]	$\pm 2i/\sqrt{7}$	2	2

Table 2. This table reproduces all the 13 cases with the total flux of G_1 type being 24 in [18]. The first 5/6 of this table covers the cases with $be \geq 0$; see comments at the end of section 2.1. The last 1/6 of this table is the list of cases with $(be) < 0$; this table only shows cases with $b < 0$ (so $e > 0$), in order to reduce the redundant information associated with $S_2 \longleftrightarrow S_1$ and $\gamma \longleftrightarrow \gamma^*$. See section 4.2 for the meaning of the last two columns.

Out of the 66 entries in table 2, some pairs of K3 surfaces appear more than once. In these cases, there are different possible choices of γ which give rise to different contributions to the tadpole that are less than 24. For the pairs $S_1 \times S_2 = X_{[1\ 0\ 1]} \times X_{[1\ 0\ 1]}$ and $X_{[1\ 1\ 1]} \times X_{[1\ 1\ 1]}$, all the possible values of $\gamma \in \mathbb{C}$ (and the corresponding $[G_1] \cdot [G_1]/2$ contribution to the M2/D3 tadpole) are shown in figure 1. They form a lattice within $\mathbb{C}$, and so do $[G_1]$ in (2.21) [58, 59]. In fact, one can show that that the possible values for γ form a lattice for any pair of K3 surfaces satisfying (2.23). The upper bound (2.25), however, allows only finitely many choices of $G^{(4)} = G_1$ for a given pair of attractive K3 surfaces satisfying (2.23).

JHEP04(2014)050

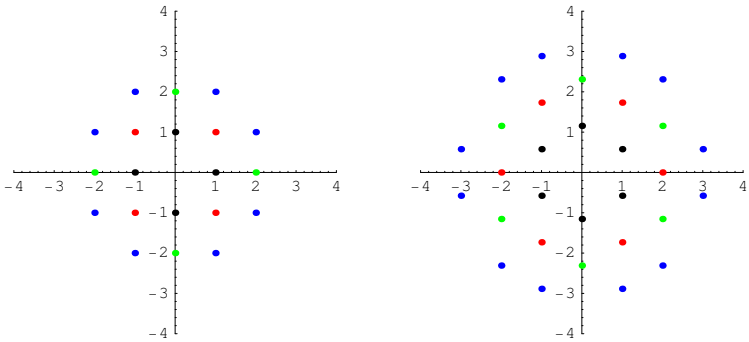

(a) for $X_{[1\ 0\ 1]} \times X_{[1\ 0\ 1]}$ (b) for $X_{[1\ 1\ 1]} \times X_{[1\ 1\ 1]}$

Figure 1. Possible values of $\gamma \in \mathbb{C}$ appearing in table 2 for $X_{[1\ 0\ 1]} \times X_{[1\ 0\ 1]}$ and $X_{[1\ 1\ 1]} \times X_{[1\ 1\ 1]}$, respectively. In (a), black, red, green and blue points (from inside to outside) correspond to $[G_1] \cdot [G_1]/2 = 4, 8, 16$ and 20, respectively, while in (b), the black, red, green and blue points give rise to the contributions $3, 9, 12$ and 21, respectively.

3 F-theory classification of elliptic fibrations on a K3 surface

The study reviewed in the previous section implies that a pair of K3 surfaces S_1 and S_2 corresponding to a pair of transcendental lattices $T_{S_1} = \begin{bmatrix} 2a & b \\ b & 2c \end{bmatrix}$ and $T_{S_2} = \begin{bmatrix} 2d & e \\ e & 2f \end{bmatrix}$ in tables 1 and 2 is realized in the landscape of flux compactifications of M-theory on $Y = S_1 \times S_2$ down to 2+1-dimensions, with all the 40 complex structure moduli stabilised. In order to translate this result to the landscape of F-theory compactifications to 3+1-dimensions, however, we have to impose a couple of extra conditions [18].

One of the conditions to be imposed, of course, is that either one of the K3 surfaces S_1 or S_2 admits an elliptic fibration with a section (in its vacuum complex structure), and the vev of the Kähler moduli should be such that the volume of the elliptic fibre vanishes. Let X be this elliptic fibred K3 surface,[11] and the other one of S_1 and S_2 be denoted by S;

$$Y = X \times S, \qquad \pi_X : X \to \mathbb{P}^1, \qquad \sigma : \mathbb{P}^1 \to X. \tag{3.1}$$

The authors of [18] pointed out that S_1 (resp. S_2) can be identified with a K3 surface of the form $X = T^4/\mathbb{Z}_2$, if and only if all of a, b and c (resp. d, e and f) in table 1 are even (the same rule applies also to table 2), based on a known fact on Kummer surfaces (see [61–63]). Projecting down to $T^2/\mathbb{Z}_2 \simeq \mathbb{P}^1$, we obtain an elliptic fibration with four singular fibres of type I_0^* (namely, $D_4 = \mathrm{SO}(8)$ gauge groups on 7-branes); this is the F-theory/Type IIB orientifold model in [64].

This class of F-theory vacua, which admits a type IIB orientifold interpretation without any approximation or ambiguity, is only a subset of all possible vacua of F-theory, however. In fact, it is known that any K3 surface with $\rho \geq 13$ admits an elliptic fibration with a section (Lemma 12.22 of [65]). Hence all the K3 surfaces in tables 1 and 2 admit an elliptic fibration with a section, so that they all have an interpretation in terms of F-theory if the

[11] In this article, we always imply by "elliptic fibration" that it is accompanied by a section.

JHEP04(2014)050

vev of the Kähler moduli is chosen appropriately. It should be noted, however, that there can be more than one elliptic fibration morphism $\pi_X : X \longrightarrow \mathbb{P}^1$ for a given K3 surface X, and furthermore, the type of singular fibres (type = collection of some of I_n, I_n^*, II, III, IV*, III* and II*) will in general be different for each of the fibrations. We are thus facing at least two questions:

- How do we find out the list of all possible elliptic fibrations, when the transcendental lattice $T_X \subset H^2(X;\mathbb{Z})$ of a K3 surface X is given?
- Suppose that there are two elliptic fibrations $\pi_X : X \longrightarrow \mathbb{P}^1$ and $\pi'_X : X \longrightarrow \mathbb{P}^1$ available; how do we find out whether the two fibrations correspond to the same vacuum in physics or not?

The former question is purely mathematical in nature, while the latter is a question in physics. Our companion paper [26] is dedicated to a study of the first question, while the latter question is addressed in this section. The primary conclusion in this section is (3.23) and the discussion that follows immediately after.[12] We begin by reviewing Torelli theorem for K3 surface in section 3.1, as it plays a crucial role in our discussion in section 3.2.

3.1 On the Torelli theorem for K3 surfaces

In this we discuss the relation between the moduli space of complex structures of K3 surfaces and periods of the holomorphic $(2,0)$ form. Statements of this type are generally referred to as 'Torelli theorems'. For K3 surfaces, there exist several powerful versions, which are closely related to each other, yet shed light on the subject from slightly different angles. Those Torelli theorems combined allow many questions on K3 moduli to be reformulated in terms of lattice theory. The following review on Torelli theorems for K3 surfaces is designed to serve as preparation for section 3.2. This review together with section 2 of [26] is designed to be self-contained, all the jargon and notation without definition or explanation in this section should be explained in section 2 of [26]. See also [63, 66] for a concise mathematical exposition.

We begin with defining such words as "(moduli space of) marked K3 surface" and "period domain", and proceed to explain the period map. A *marked K3 surface* is a K3 surface X for which we have fixed a set of generators for $H^2(X;\mathbb{Z})$, i.e. we consider a pair (X,φ) which consists of the K3 surface X and an isometry between lattices $\varphi : H_2(X;\mathbb{Z}) \longrightarrow \Lambda_{\mathrm{K3}}$, where

$$\Lambda_{\mathrm{K3}} = U \oplus U \oplus U \oplus E_8 \oplus E_8 \,. \tag{3.2}$$

The map φ is called the *marking*. Note that we use conventions in which the A–D–E lattices have a negative definite inner product, as is natural in the present context.

Two marked K3 surfaces (X,φ) and (X',φ') are said to be *equivalent*, if and only if there is an isomorphism $f : X \to X'$ such that $\varphi' \cdot f_* = \varphi$ as an isometry from $H_2(X;\mathbb{Z})$

[12] It is an option to skip this section and proceed to the next section, if one is happy to accept this statement.

JHEP04(2014)050

to $\Lambda_{\rm K3}$. Each point of the *moduli space of marked K3 surface* N corresponds to such an equivalence class of marked K3 surfaces.

The *period domain* D, on the other hand, is a subspace of $\mathbb{P}[\Lambda_{\rm K3}\otimes\mathbb{C}]$ given by

$$D := \{[\omega]\in\mathbb{P}[\Lambda_{\rm K3}\otimes\mathbb{C}] \mid \omega\cdot\omega=0,\ \omega\cdot\overline{\omega}>0\ \}\subset\mathbb{P}[\Lambda_{\rm K3}\otimes\mathbb{C}]\,. \tag{3.3}$$

The global structure of D is given by

$$D\cong O(\Lambda_{\rm K3}\otimes\mathbb{R})/{\rm SO}(2)\times O(1,19)={\rm Gr}^{\rm po}(2;\Lambda_{\rm K3}\otimes\mathbb{R})\,, \tag{3.4}$$

where the superscript "po" stands for "positive and oriented", in the sense that we consider the Grassmannian of oriented 2-dimensional subspaces in $\Lambda_{\rm K3}\otimes\mathbb{R}$ with signature $(2,0)$.[13]

Using the holomorphic $(2,0)$-form $\Omega_X\in H_2(X;\mathbb{C})$ and the intersection form on $H_2(X;\mathbb{C})$, we may map a point in the moduli space of marked K3 surface N to a point in the period domain D:

$$\mathcal{P}: N\ni[(X,\varphi)]\longmapsto\varphi([\Omega_X])\in D\subset\mathbb{P}[\Lambda_{\rm K3}\otimes\mathbb{C}]\,. \tag{3.5}$$

$\mathcal{P}$ is called the *period map*. Here, $[\Omega_X]$ stands for both the complex line $\mathbb{C}\Omega_X\subset H_2(X;\mathbb{C})$ as well as its image in $\mathbb{P}[H_2(X;\mathbb{C})]$; the same notation has already been used in (3.3).

The classic **local Torelli theorem** for K3 surface states that the period map is locally an isomorphism between N and D. For any point in N and its image under the period map in D, we can always take an appropriate open set in N and D so that the period map becomes an isomorphism between the two open sets. Thus, locally in the moduli space(s), K3 surfaces are uniquely determined by their periods.

In the following, we will turn to global aspects of the moduli spaces N and D, and the period map $\mathcal{P}$ between them. While it turns out that complex deformations can be used to introduce local coordinates on N, and to give it the structure of a complex manifold, the moduli space N fails to be Hausdorff. The way the period maps glue globally is expressed by the

> **Global Torelli Theorem, version 1** (see e.g. [66]): the moduli space of marked K3 surfaces N consists of two connected components N^o and $N^{o'}$, and the period map $\mathcal{P}$ maps each one of them surjectively, and also generically injectively to the period domain D.

To elaborate more on this, note first that the group of all the isometries of the lattice $\Lambda_{\rm K3}$ — ${\rm Isom}(\Lambda_{\rm K3})$ — acts naturally on D (from the left), and it also acts on N through the marking; $g\in{\rm Isom}(\Lambda_{\rm K3})$ maps $[(X,\varphi)]\in N$ to $[(X,g\cdot\varphi)]\in N$. The action of this symmetry group on N and D commutes with the period map $\mathcal{P}:N\longrightarrow D$. This isometry group has a structure ${\rm Isom}(\Lambda_{\rm K3})\cong\{\pm{\rm id.}\}\times{\rm Isom}^+(\Lambda_{\rm K3})$. The ${\rm Isom}^+(\Lambda_{\rm K3})$ subgroup is such that the orientation of the 3-dimensional positive definite subspace of $\Lambda_{\rm K3}\otimes\mathbb{R}$ is preserved.

[13] By forgetting the orientation, a twofold cover $D={\rm Gr}^{\rm po}(2;\Lambda_{\rm K3}\otimes\mathbb{R})\to{\rm Gr}^{\rm p}(2;\Lambda_{\rm K3}\otimes\mathbb{R})$ can be constructed; ${\rm Gr}^{\rm p}(2;\Lambda_{\rm K3}\otimes\mathbb{R})\cong O(\Lambda_{\rm K3}\otimes\mathbb{R})/O(2)\times O(1,19)$.

JHEP04(2014)050

A pair of elements $[(X,\varphi)]$ and $[(X,-\varphi)]$ are different points in N because automorphisms of X cannot induce $(-\text{id.})$ on $H_2(X;\mathbb{C})$. The period map $\mathcal{P}: N \longrightarrow D$ sends these two elements to the same point in D, $[\varphi(\Omega_X)] = [-\varphi(\Omega_X)] \in \mathbb{P}[\Lambda_{\text{K3}} \otimes \mathbb{C}]$. In the Torelli theorem above, such a pair of points in N corresponds to two inverse images[14] of a given point in D; one is in N^o, and the other is in the other connected component N'^o. The action of $(-\text{id.}) \in \text{Isom}(\Lambda_{\text{K3}})$ maps these two elements in N to each other, and hence the subgroup $\{\pm\text{id.}\}$ of $\text{Isom}(\Lambda_{\text{K3}})$ acts trivially on D, while it exchanges the two connected components of N.

Next we discuss the classical form of the global Torelli theorem. First, the homomorphism $\text{Aut}(X) \longrightarrow \text{Isom}(H_2(X;\mathbb{Z}))$ is injective (Prop. 2 of section 2 in [62]), where $\text{Aut}(X)$ is the group of automorphisms of a K3 surface X, and $\text{Isom}(H_2(X;\mathbb{Z}))$ is the isometry group of $H_2(X;\mathbb{Z})$ endowed with a symmetric pairing from intersection number. Note that this means that there cannot be any non-trivial automorphism which acts as the identity on $H_2(X;\mathbb{Z})$. Furthermore,

> **Global Torelli Theorem, version 2**: (Prop. of section 7 and Thm. 1 of section 6 in [62]) the image of $\text{Aut}(X)$ under the injective homomorphism is $\text{Isom}(H_2(X;\mathbb{Z}))^{(\text{Hodge eff})}$, the group of isometries that are both Hodge and effective. This means that for a given $\varphi \in \text{Isom}(H_2(X;\mathbb{Z}))^{(\text{Hodge eff})}$, there exists a unique automorphism $f \in \text{Aut}(X)$ such that $\varphi = f_*$. Furthermore, the subgroup $\text{Isom}(H_2(X;\mathbb{Z}))^{(\text{Hodge eff.})} \cong \text{Aut}(X)$ sits inside the group of Hodge isometries, which have the form
>
> $$\text{Isom}\,(H_2(X;\mathbb{Z}))^{(\text{Hodge})} \cong \{\pm\text{id.}\} \times \left[W^{(2)}(S_X) \rtimes \text{Aut}(X)\right]. \tag{3.6}$$
>
> For K3 surfaces X and X' there is an isomorphism of surfaces $f: X \longrightarrow X'$ if and only if there is a Hodge and effective isometry $\varphi: H_2(X;\mathbb{Z}) \longrightarrow H_2(X';\mathbb{Z})$. In this case, $f_* = \varphi$.

See the mathematics literature (such as [62]) or [26] for the definition of Hodge and effective isometries. $W^{(2)}(S_X)$ is the group generated by reflections associated with algebraic curves of self-intersection (-2) in the Neron-Severi lattice S_X. Section 2.2 of [26] explains the structure of the group (3.6) in more detail. Another version of the theorem, which is equivalent to version 2, is also useful:

> **Global Torelli Theorem, version 3** (e.g., Chapt. 10 of [66]): For a pair of K3 surface X and X', there is an automorphism $f: X \longrightarrow X'$, if and only if there is a Hodge isometry $\varphi: H_2(X;\mathbb{Z}) \longrightarrow H_2(X';\mathbb{Z})$. Furthermore, in this case, $\varphi^{-1} \cdot f_* \in \text{Isom}(H_2(X;\mathbb{Z}))^{(\text{Hodge})}$. When it is known that φ maps Pos^+_X to $\text{Pos}^+_{X'}$, then $\varphi^{-1} \cdot f_* \in \text{Isom}^+(H_2(X;\mathbb{Z}))^{(\text{Hodge})}$, the index 2 subgroup of $\text{Isom}(H_2(X;\mathbb{Z}))^{(\text{Hodge})}$ obtained by dropping $\{\pm\text{id.}\}$ from (3.6).

[14] In this version of the Torelli theorem, we included a statement that there are just *two* and not more than two connected components in the moduli space of marked K3 surfaces N. This statement comes from the fact that the full $\text{Isom}^+(H_2(X;\mathbb{Z}))$ subgroup of $\text{Isom}(H_2(X;\mathbb{Z}))$ is realized as the monodromy group on $H_2(X;\mathbb{Z})$ for a given K3 surface X through continuous complex structure deformations [67–69]. See [66] Chapt.10 for more detailed list of references.

JHEP04(2014)050

Having seen these three versions of the Torelli theorem, we may now use the perspective of version 3 of the global Torelli theorem to elucidate the meaning of the expression 'generically injective' used in version 1. Suppose that the period map $\mathcal{P} : N^o \longrightarrow D$ restricted to one of the two connected components maps two points $[(X, \varphi)]$ and $[(X', \varphi')]$ in N^o to one and the same point $[\omega] \in D$. That is, both $[(X, \varphi)]$ and $[(X', \varphi')]$ are contained in $\mathcal{P}^{-1}([\omega]) \cap N^o$. It then follows from version 3 of the global Torelli theorem that there exists an isomorphism of surfaces $f : X \longrightarrow X'$, because $\varphi'^{-1} \cdot \varphi : H_2(X; \mathbb{Z}) \longrightarrow \Lambda_{\mathrm{K3}} \longrightarrow H_2(X'; \mathbb{Z})$ is a Hodge isometry. This means that a marked K3 surface $(X, \varphi' \cdot f)$ is equivalent to the marked K3 surface $[(X', \varphi')]$ in N^o. Thus, if $\mathcal{P} : [(X_0, \varphi_0)] \longmapsto [\omega_0] = \varphi_0([\Omega_X])$, then all elements of $\mathcal{P}^{-1}([\omega_0]) \cap N^o$ can be written in the form of $[(X_0, \varphi)]$ with some marking φ.

Deviation from the injectiveness of the period map $\mathcal{P}|_{N^o}$ therefore corresponds to the variety of marking φ allowed for $\mathcal{P}^{-1}([\omega_0]) \cap N^o$. The remaining variety for φ can also be read out from the version 3 of the global Torelli theorem. Since $[(X, \varphi)]$ belongs to the same connected component as $[(X, \varphi_0)]$, $\varphi_0^{-1} \cdot \varphi \in W^{(2)}(S_X) \rtimes \mathrm{Aut}(X)$, and conversely, any φ satisfying this condition gives rise to $[(X, \varphi)] \in \mathcal{P}^{-1}([\omega_0]) \cap N^o$. Therefore, reminding ourselves of the definition of the equivalence relation between (X, φ) and (X, φ_0) in the moduli space N, we see that

$$\mathcal{P}^{-1}([\omega_0]) \cap N^o = \left\{ [(X, \varphi)] \;\middle|\; \varphi \in \varphi_0 \cdot \left[W^{(2)}(S_X) \rtimes \mathrm{Aut}(X) \right] / \mathrm{Aut}(X) \right\}. \tag{3.7}$$

For a general (non algebraic) complex K3 surface X, the Neron-Severi lattice S_X is trivial, $\rho_X = 0$, so that $W^{(2)}(S_X)$ is the trivial group. In this case, there is only one element $[(X, \varphi)] \in N^o$ that is mapped to a given point $[\omega] \in D$, that is, the period map $\mathcal{P} : N^o \longrightarrow D$ is injective there. Since only a measure-zero subspace of N is occupied by algebraic K3 surfaces, the period map is indeed generically injective. For an algebraic K3 surface X, however, the group $W^{(2)}(S_X)$ can be non-trivial, and there can be multiple points in the inverse image of the period map, as in (3.7). Since our interest in this article is primarily in K3 surfaces X with large Picard number, $\rho_X = \mathrm{rank}(S_X)$, this non-injective behaviour of the period map is of particular importance.

Although we have seen above that any two points in N that are mapped to the same point in D are represented by a common K3 surface X, there are more points in N that share the same K3 surface X. To see this, remember that the $\mathrm{Isom}^+(\Lambda_{\mathrm{K3}})$ subgroup of $\mathrm{Isom}(\Lambda_{\mathrm{K3}})$ acts on individual connected components of N, that is, N^o and $N^{o'}$, as well as on the period domain D. If there is an isometry $g \in \mathrm{Isom}^+(\Lambda_{\mathrm{K3}})$ mapping $[\omega] \in D$ to $[\omega'] \in D$, then it also maps $\mathcal{P}^{-1}([\omega]) \cap N^o$ to $\mathcal{P}^{-1}([\omega']) \cap N^o$. For any element in these inverse images, $[(X, \varphi)] \in \mathcal{P}^{-1}([\omega]) \cap N^o$ and $[(X', \varphi')] \in \mathcal{P}^{-1}([\omega']) \cap N^o$, $\varphi'^{-1} \cdot g \cdot \varphi : H_2(X; \mathbb{Z}) \longrightarrow H_2(X'; \mathbb{Z})$ is a Hodge isometry, and hence the version 3 of the global Torelli theorem implies that there is an isomorphism of surfaces $f : X \longrightarrow X'$. Thus, for all the points $[\omega] \in D$ in a given orbit of $\mathrm{Isom}(\Lambda_{\mathrm{K3}})$, all the points in N mapped to this orbit can be represented by a common K3 surface X and some markings. Conversely, if two points $[X, \varphi]$ and $[(X, \varphi')]$ in N share the same K3 surface, then $\varphi' \cdot \varphi^{-1}$ is an isometry of Λ_{K3} mapping the image of $[(X, \varphi)]$ to that of $[(X, \varphi')]$. Therefore, the $\mathrm{Isom}(\Lambda_{\mathrm{K3}})$-orbit decomposition of the period domain,

JHEP04(2014)050

$\mathrm{Isom}^+(\Lambda_{\mathrm{K3}})\backslash D$ is equivalent to the classification of K3 surfaces modulo isomorphism of surfaces.

Finally, let us take a closer look at how the $\mathrm{Isom}(\Lambda_{\mathrm{K3}})$ symmetry group acts on the moduli space N or N^o. Its action on D is quite simple, but its action on N^o has a more interesting structure, and we will need that in section 3.2. When an element $g \in \mathrm{Isom}^+(\Lambda_{\mathrm{K3}})$ maps $[\omega] \in D$ to another element $[\omega'] \neq [\omega]$, the fibres of those two points under the period map can be described by $\{[(X,\varphi)] \mid \varphi \in \varphi_0 \cdot [W^{(2)}(S_X) \rtimes \mathrm{Aut}(X)]/\mathrm{Aut}(X)\}$ and $\{[(X,\varphi')] \mid \varphi' \in \varphi_0' \cdot [W^{(2)}(S_X) \rtimes \mathrm{Aut}(X)]/\mathrm{Aut}(X)\}$ for some φ_0 and φ_0', respectively.[15] The action of g establishes a one-to-one correspondence between the two fibres by setting $\varphi' = g \cdot \varphi$.

The stabilizer subgroup of $[\omega] \in D$ in $\mathrm{Isom}^+(\Lambda_{\mathrm{K3}})$ is

$$G_{[\omega]} = \varphi_0 \cdot \left[W^{(2)}(S_X) \rtimes \mathrm{Aut}(X)\right] \cdot \varphi_0^{-1} \subset \mathrm{Isom}^+(\Lambda_{\mathrm{K3}}). \tag{3.8}$$

This stabiliser group acts naturally on the inverse image of $[\omega]$, given in (3.7).

3.2 When are two elliptic fibrations considered "different" in F-theory?

In the description of complex structure moduli of K3 surfaces, one can think of several different moduli spaces in mathematics, such as N (or N^o) (the moduli space of marked K3 surfaces), D (the period domain) and $\mathrm{Isom}^+(\Lambda_{\mathrm{K3}})\backslash D$ (the moduli space of K3 surfaces modulo automorphism). These different moduli spaces contain different information and are mutually related in the way we have reviewed above. When we refer to "the moduli space" in string theory applications, however, we want it to parametrize vacua (hopefully with less redundancy in the parametrization, and at least with information on the redundancy), and use it as the target space of a non-linear sigma model to describe light degrees of freedom.

It is considered that, in M-theory compactification on $Y = S_1 \times S_2$ with both S_1 and S_2 being K3 surfaces, the moduli space (in the absence of four-form flux) is given by[16]

$$\left[\mathrm{Isom}^+(\Lambda_{\mathrm{K3}}^{(S_1)}) \times \mathrm{Isom}^+(\Lambda_{\mathrm{K3}}^{(S_2)})\right] \backslash \left[D^{(S_1)} \times D^{(S_2)}\right]. \tag{3.9}$$

It makes perfect sense to take a quotient by the symmetry group $\mathrm{Isom}^+(\Lambda_{\mathrm{K3}})$, because two marked K3 surfaces $[(X,\varphi)]$ and $[(X,\varphi')]$ in N^o which differ only in the markings φ and φ' should not be considered as different compactifications in 11-dimensional supergravity.[17]

[15] Here, $\varphi_0' \notin \varphi_0 \cdot [W^{(2)}(S_X) \rtimes \mathrm{Aut}(X)]$.

[16] We postpone a slightly more refined argument for the choice of the quotient group to section 4.2.2, for M-theory moduli space as well as for F-theory. The essence of the argument in this section remains valid after section 4.2.2.

[17] Homogeneous coordinates can be introduced to the period domain D by taking a basis $\{\Sigma_I\}_{I=1,\cdots,22}$ in the lattice Λ_{K3}. The period integrals $\Pi_I := \int_{\Sigma_I} \omega$ can be used as the coordinates. With these coordinates, the Kähler potential (obtained by dimensional reduction) is given by

$$K \propto -\ln\left[\int_Y (\Omega_{S_1} \wedge \Omega_{S_2}) \wedge (\overline{\Omega}_{S_1} \wedge \overline{\Omega}_{S_2})\right] = -\ln\left[\Pi_I^{(S_1)} C^{IJ} \overline{\Pi}_J^{(S_1)}\right] - \ln\left[\Pi_I^{(S_2)} C^{IJ} \overline{\Pi}_J^{(S_2)}\right], \tag{3.10}$$

where C^{IJ} is the inverse of the intersection form of Λ_{K3} in the basis $\{\Sigma_I\}_{I=1,\cdots,22}$. The action of the $\mathrm{Isom}^+(\Lambda_{\mathrm{K3}}^{(S_1)}) \times \mathrm{Isom}^+(\Lambda_{\mathrm{K3}}^{(S_2)})$ group on the $\Pi_I^{(S_{1,2})}$ leaves the Kähler potential unchanged, because it preserves the intersection form.

JHEP04(2014)050

Since F-theory compactification on an elliptic-fibred Calabi-Yau fourfold is regarded as a special case of M-theory compactification on a Calabi-Yau fourfold, this moduli space can be regarded as a reliable place to start for F-theory as well.

The moduli space of F-theory compactification on a K3 surface X (where we require that there is an elliptic fibration $\pi_X : X \longrightarrow \mathbb{P}^1$ and a section $\sigma : \mathbb{P}^1 \longrightarrow X$) without any flux is given by

$$\mathcal{M}^{\text{cpx}}_{F;\text{K3}} := \left[\text{Isom}^+(\Lambda_{\text{K3}})\right] \setminus \left\{(\phi_U, [\omega]) \mid [\omega]|_{\phi_U(U)} = 0\right\} / \left\{\pm\text{id}._U\right\} , \tag{3.11}$$

where $[\omega] \in D$ as before, and $\phi_U : U \hookrightarrow \Lambda_{\text{K3}}$ is an embedding of the hyperbolic plane lattice U. It is a popular way to make sure that there is an elliptic fibration by specifying a sublattice (which is isomorphic to U) generated by algebraic cycles corresponding to the elliptic fibre and the section (e.g. [26, 70]). A remaining subtlety can arise in the choice of the quotient group. The group $\text{Isom}^+(\Lambda_{\text{K3}})$ acts on D and embeddings of U (while preserving $[\omega]|_{\phi_U(U)} = 0$), while $\{\pm\text{id}._U\}$ is a subgroup of $\text{Isom}(U) \cong \mathbb{Z}_2 \times \mathbb{Z}_2$ (see section 2 of [26]), and acts on embeddings $\phi_U : U \hookrightarrow \Lambda_{\text{K3}}$ from the right by changing ϕ_U to $\pm\phi_U$. We will see shortly that this is the right choice of the quotient group. Once this statement is accepted, then it wouldn't be difficult to accept the following: the moduli space of F-theory compactification on $Y = X \times S$ (where X has an elliptic fibration as before) is given by

$$\mathcal{M}^{\text{cpx}}_{F;\text{K3}} \times \left(\text{Isom}^+(\Lambda^{(S)}_{\text{K3}}) \backslash D^{(S)}\right) . \tag{3.12}$$

Now, in order to justify the statement (3.11), we need to understand the space $\mathcal{M}^{\text{cpx}}_{F;\text{K3}}$ better. It is often a good strategy in understanding a space M to construct a map $f : M \longrightarrow B$ to some simple space B, and study how the "fibres" $f^{-1}(b) \subset M$ change with $b \in B$. First consider a projection

$$\text{fgt}_{[\omega]} : \mathcal{M}^{\text{cpx}}_{F;\text{K3}} \longrightarrow \text{Isom}^+(\Lambda_{\text{K3}}) \backslash \left\{\phi_U : U \hookrightarrow \Lambda_{\text{K3}}\right\} / \left\{\pm\text{id}._U\right\} \tag{3.13}$$

by throwing away the information of $[\omega]$ from $\mathcal{M}^{\text{cpx}}_{F;\text{K3}}$. The base of this forgetful map, "B", consists of only one point: due to the uniqueness (modulo isometry) of even unimodular lattices of signature $(n, n+16)$, there always exists an isometry $\varphi \in \text{Isom}^+(\Lambda_{\text{K3}})$ such that either $\phi'_U = \varphi \cdot \phi_U$ or $-\phi'_U = \varphi \cdot \phi_U$ holds for any two embeddings ϕ_U and ϕ'_U of the hyperbolic plane lattice U. Thus, the whole set $\mathcal{M}^{\text{cpx}}_{F;\text{K3}}$ can be studied by looking at the fibre over just one point in the base; that is, we can take an arbitrary embedding $\phi_{U0} : U \hookrightarrow \Lambda_{\text{K3}}$, and just study the fibre $\text{fgt}^{-1}_{[\omega]}([\phi_{U0}])$. The fibre over this one point is

$$\text{Isom}(U^{\oplus 2} \oplus E_8^{\oplus 2}) \backslash \left\{[\omega] \in D_{U^\perp}\right\} , \tag{3.14}$$

$$D_{U^\perp} := \left\{[\omega] \in \mathbb{P}[(\phi_{U0}(U))^\perp \subset \Lambda_{\text{K3}}] \mid \omega \cdot \omega = 0,\ \omega \cdot \overline{\omega} > 0\right\} . \tag{3.15}$$

Therefore, the set $\mathcal{M}^{\text{cpx}}_{F;\text{K3}}$ is equivalent to (3.14), the global structure of which is

$$\text{Isom}(U^{\oplus 2} \oplus E_8^{\oplus 2}) \backslash \text{Gr}^{\text{po}}(2; (U^{\oplus 2} \oplus E_8^{\oplus 2}) \otimes \mathbb{R}) \cong \text{Isom}(U^{\oplus 2} \oplus E_8^{\oplus 2}) \backslash \text{O}(2, 18; \mathbb{R}) / \text{SO}(2) \times \text{O}(18) . \tag{3.16}$$

JHEP04(2014)050

This is a double cover over what we know as the moduli space of heterotic string compactifications on T^2 [71] (see e.g., also section 5 of [72]),

$$\mathrm{Isom}(U^{\oplus 2}\oplus E_8^{\oplus 2})\backslash \mathrm{Gr}^{\mathrm{p}}(2;(U^{\oplus 2}\oplus E_8^{\oplus 2})\otimes\mathbb{R}) \cong \mathrm{Isom}(U^{\oplus 2}\oplus E_8^{\oplus 2})\backslash \mathrm{O}(2,18;\mathbb{R})/\,\mathrm{O}(2)\times\mathrm{O}(18). \tag{3.17}$$

This argument almost proves[18] that we can take $\mathcal{M}^{\mathrm{cpx}}_{F;\mathrm{K3}}$ in (3.11) as the classification scheme of F-theory vacua when an elliptic fibred K3 surface is involved as part of the compactification data.

We understand that the remaining subtlety — double cover — corresponds, in F-theory language, to a pair of (elliptic fibred) K3 surfaces X and $X' = \overline{X}$ where $H^{2,0}(X;\mathbb{C})$ and $H^{0,2}(X;\mathbb{C})$ in the Hodge decomposition of $H^2(X;\mathbb{C})$ are identified with $H^{0,2}(X';\mathbb{C})$ and $H^{2,0}(X';\mathbb{C})$. X and X' are a mutually complex conjugate pair. The difference between them is only in declaring a complex coordinate as holomorphic or anti-holomorphic, and that should not make a difference in physics in 7+1-dimensions. Thus, even in F-theory, the moduli space of K3 compactification to 7+1-dimensions should be (3.17), rather than (3.16). As we proceed to consider compactifications of F-theory on $Y = X\times S$ along with a four-form flux on Y, it *does* make a difference in low-energy physics in 3+1-dimensions to take complex conjugation of X, while keeping the complex structure of S and the flux. We therefore take (3.12) as the classification scheme for K3 × K3 compactification of F-theory for now; the $\mathbb{Z}_2$ quotient associated with unphysical holomorphic-anti-holomorphic distinction will be implemented in section 4.2 after introducing fluxes.

Let us now start from $\mathcal{M}^{\mathrm{cpx}}_{F;\mathrm{K3}}$ in (3.11) again, and derive a useful way to look at it in order to address the second one of the two questions raised at the beginning of this section. Consider a projection

$$\mathrm{fgt}_{\phi_U}\,:\,\mathcal{M}^{\mathrm{cpx}}_{F;\mathrm{K3}} \longrightarrow \mathrm{Isom}^+(\Lambda_{\mathrm{K3}})\backslash D\,, \tag{3.18}$$

This time, we throw away the information on the embedding ϕ_U from $\mathcal{M}^{\mathrm{cpx}}_{F;\mathrm{K3}}$. As we have seen in section 3.1, the "base" space of this projection, $\mathrm{Isom}^+(\Lambda_{\mathrm{K3}})\backslash D$, corresponds to the classification of K3 surfaces modulo surface isomorphism. Thus, by studying the "fibre" of this projection, we can find the variety of F-theory vacua that (the surface-isomorphism class of) a K3 surface admits.

We begin this study by looking at the fibration structure of the following projection map instead:

$$\mathrm{fgt}_{\phi_U}\,:\,\big\{(\phi_U,[\omega])\,|\,[\omega]\in D,\,[\omega]|_{\phi_U(U)}=0\big\}\,/\,\{\pm\mathrm{id}_U\} \longrightarrow \{[\omega]\,|\,[\omega]\in D\} = D\,. \tag{3.19}$$

Before and after the projection, we are not taking a quotient by the symmetry group $\mathrm{Isom}^+(\Lambda_{\mathrm{K3}})$ action here, which makes the problem easier to get started. For a given $[\omega]\in D$, and for any ϕ_U satisfying the condition $[\omega]|_{\phi_U(U)}=0$, ϕ_U embeds the hyperbolic plane lattice U into $S_{[\omega]} := \big[[\omega]^\perp\subset\Lambda_{\mathrm{K3}}\big]$. That is,

$$\mathrm{fgt}^{-1}_{\phi_U}([\omega]) = \big\{\phi_U : U\hookrightarrow S_{[\omega]}\big\}\,/\,\{\pm\mathrm{id}_U\}\,. \tag{3.20}$$

[18] Without microscopic foundation of F-theory, it is hard to make any precise statement about F-theory physics directly. Here, this problem is overcome by relying on heterotic-F-theory duality.

JHEP04(2014)050

This means geometrically that for any one of the inverse images $[(X_{[\omega]}, \varphi_{[\omega]})] \in \mathcal{P}^{-1}([\omega]) \cap N^o$ under the period map, an embedding of the hyperbolic plane lattice into the Neron-Severi lattice of the K3 surface $X_{[\omega]}$, $S_{X_{[\omega]}}$, is defined:

$$\varphi_{[\omega]}^{-1} \cdot \phi_U : \; U \hookrightarrow S_{X_{[\omega]}} \subset H^2(X_{[\omega]}; \mathbb{Z}) \,. \tag{3.21}$$

The inverse image $\mathcal{P}^{-1}([\omega]) \cap N^o$ of any given element $[\omega] \in D$ is described in (3.7); we can choose an appropriate φ in (3.7) so that either $\varphi^{-1} \cdot \phi_U$ or $\varphi^{-1} \cdot (-\phi_U)$ defines a *canonical embedding* of hyperbolic plane lattice into $S_{X_{[\omega]}}$. This is a sufficient condition to construct an elliptic fibration $\pi_X : X \longrightarrow \mathbb{P}^1$ along with a zero section $\sigma : \mathbb{P}^1 \longrightarrow X$, see section 3.1 of [26] for a more detailed explanation. Each element ϕ_U in $\mathrm{fgt}_{\phi_U}^{-1}([\omega])$ in (3.20) therefore defines an elliptic fibration on X.

Let us now go back to the study of the fibre of the projection (3.18), bringing back the quotient by $\mathrm{Isom}^+(\Lambda_{\mathrm{K3}})$. First of all, when an element $g \in \mathrm{Isom}^+(\Lambda_{\mathrm{K3}})$ maps $[\omega] \in D$ to $[\omega'] := g \cdot [\omega] \neq [\omega]$, taking a quotient does not change the fibre of the projection map. It only establishes a one-to-one identification between the elements in the fibre $\mathrm{fgt}_{\phi_U}^{-1}([\omega])$ and $\mathrm{fgt}_{\phi_U}^{-1}([\omega'])$. The stabilizer subgroup $G_{[\omega]}$ of $\mathrm{Isom}^+(\Lambda_{\mathrm{K3}})$ for $[\omega] \in D$, however, can be non-trivial, as we have seen in (3.8). We have to take a quotient of (3.20) by the stabilizer group $G_{[\omega]}$ in order to obtain the fibre of the projection map in (3.18) at $[[\omega]] \in \mathrm{Isom}^+(\Lambda_{\mathrm{K3}}) \backslash D$. Therefore, we conclude that

$$\begin{aligned}
\mathrm{fgt}_{\phi_U}^{-1}([[\omega]]) &= \Big[W^{(2)}(S_{[\omega]}) \rtimes \varphi_0(\mathrm{Aut}(X_{[\omega]}))\Big] \backslash \left\{\phi_U : U \hookrightarrow S_{[\omega]} \subset \Lambda_{\mathrm{K3}}\right\} / \{\pm \mathrm{id}_U\} \qquad (3.22)\\
&= \Big[W^{(2)}(S_{X_{[\omega]}}) \rtimes \mathrm{Aut}(X_{[\omega]})\Big] \backslash \Big\{\varphi_0^{-1} \cdot \phi_U : U \hookrightarrow S_{X_{[\omega]}} \subset H^2(X_{[\omega]}; \mathbb{Z})\Big\} / \{\pm \mathrm{id}_U\}\\
&= \Big[W^{(2)}(S_{X_{[\omega]}}) \rtimes \mathrm{Isom}(S_{X_{[\omega]}})^{(\text{Amp Hodge})}\Big] \backslash \Big\{\varphi_0^{-1} \cdot \phi_U : U \hookrightarrow S_{X_{[\omega]}}\Big\} / \{\pm \mathrm{id}_U\}\\
&= \mathcal{J}_1(X_{[\omega]}) \,. \qquad (3.23)
\end{aligned}$$

As we have explained in section 3 of [26], this $\mathcal{J}_1(X_{[\omega]})$ corresponds to the classification of elliptic fibrations (π_X, σ) for a K3 surface X ($\pi_X : X \longrightarrow \mathbb{P}^1$ along with $\sigma : \mathbb{P}^1 \longrightarrow X$ so that $\pi_X \cdot \sigma = \mathrm{id}_{\mathbb{P}^1}$) modulo $\mathrm{Aut}(X) \times \mathrm{Aut}(\mathbb{P}^1) = \mathrm{Aut}(X) \times PGL(2; \mathbb{C})$. Therefore, the projection map fgt_{ϕ_U} in (3.18) enables us to apprehend the moduli space (vacuum classification scheme) of F-theory compactifications on K3 surface $\mathcal{M}_{F;\mathrm{K3}}^{\mathrm{cpx}}$ as a fibration over $\mathrm{Isom}^+(\Lambda_{\mathrm{K3}}) \backslash D$ (i.e., complex structure moduli space of K3 surface modulo surface isomorphism), with the fibre given by the $\mathcal{J}_1$ classification (i.e., modulo automorphism) of elliptic fibrations.

4 A miniature landscape: F-theory on K3 × K3 with $G_0 = 0$

4.1 $\mathcal{J}_1(X)$ and $\mathcal{J}_2(X)$ classification

When we classify low-energy effective theories, we normally group together theories with the same gauge groups and matter representations first, and then pay attention to the values of various coupling constants. Although two elliptic fibrations (π_X, σ) and (π'_X, σ') for a K3 surface X are not regarded as the same vacuum (or the same low-energy effective

JHEP04(2014)050

theory) in the absence of an appropriate automorphism in $\mathrm{Aut}(X)\times PGL(2;\mathbb{C})$, they might still have the same gauge groups and matter presentations.

Corresponding to the coarse classification in terms of gauge groups and matter representations is the $\mathcal{J}_2(X)$ classification of elliptic fibrations on a K3 surface X. This is close to the classification of singular fibre types, but slightly different and more suited for physicists' needs. As reviewed in detail in [26],

$$\begin{aligned}\mathcal{J}_1(X) &= \left[W^{(2)}(S_X)\rtimes \mathrm{Isom}(S_X)^{(\text{Amp Hodge})}\right]\backslash\{U\hookrightarrow S_X\}\,/\,\{\pm\mathrm{id}_{\cdot U}\}\,,\\ \mathcal{J}_2(X) &= \left[W^{(2)}(S_X)\rtimes \mathrm{Isom}(S_X)^{(\text{Amp})}\right]\backslash\{U\hookrightarrow S_X\}\,/\,\{\pm\mathrm{id}_{\cdot U}\}\,.\end{aligned} \tag{4.1}$$

Here, the group $\mathrm{Isom}(S_X)^{(\text{Amp Hodge})}$ is a subgroup of $\mathrm{Isom}(S_X)^{(\text{Amp})}$, and hence the $\mathcal{J}_2(X)$ classification is obviously more coarse than the $\mathcal{J}_1(X)$ classification.[19] The $\mathcal{J}_2(X)$ classification is equivalent to the classification of frame lattices of elliptic fibrations modulo isometry. For an elliptic fibration $\pi : X \longrightarrow \mathbb{P}^1$ with a fibre class $[F]\in S_X$, the frame lattice is given by

$$W_{\text{frame}} = \left[[F]^{\perp}\subset S_X\right]\,/\,\langle[F]\rangle\,. \tag{4.2}$$

Readers are referred to [26] for more mathematical aspects of this discussion. The frame lattice W_{frame} (modulo isometry) contains all the information of 7-brane gauge groups and representations of charged matters. Individual equivalence classes in $\mathcal{J}_2(X)$ are referred to as *types*, and those in $\mathcal{J}_1(X)$ as *isomorphism classes*.

There is a systematic procedure to study the $\mathcal{J}_2(X)$ classification for a given K3 surface X with large Picard number ρ_X (see [73] or section 4 of [26]). The $\mathcal{J}_2(X)$ classification of elliptic fibrations has already been studied for some K3 surfaces (i.e., for some particular choices of complex structures of K3 surface). For most generic Kummer surfaces[20] $X = \mathrm{Km}(A)$, for example, there are 25 different types in the $\mathcal{J}_2(X)$ classification [74]. Roughly speaking, this means that the compactifications of F-theory on $Y = X\times S$ with $X = \mathrm{Km}(A)$ admits 25 different choices of 7-brane gauge groups and matter representations. A slightly more special class (2-parameter family) of Kummer surfaces, $X = \mathrm{Km}(E\times F)$, admits 11 different types of elliptic fibrations in the $\mathcal{J}_2(X)$ classification. Reference [73] worked out the $\mathcal{J}_2(X)$ classification for four attractive K3 surfaces, $X_{[1\ 0\ 1]}$, $X_{[1\ 1\ 1]}$, $X_{[2\ 0\ 2]}$ and $X_{[2\ 2\ 2]}$ among others, and found that there are $\mathcal{O}(10\sim 100)$ inequivalent types of elliptic fibrations in the $\mathcal{J}_2(X)$ classification (table 3 in this article contains detailed information of the $\mathcal{J}_2(X)$ classification of $X_{[1\ 1\ 1]}$). We also worked out the $\mathcal{J}_2(X)$ classification partially for another attractive K3 surface $X_{[3\ 0\ 2]}$ (see section4.4 of [26]) and found that there are at least 54 inequivalent types in $\mathcal{J}_2(X)$. Based on such an experience, it may not be too far off the mark to guess that the attractive K3 surfaces in table 2 have $\mathcal{O}(10\sim 100)$ inequivalent types of elliptic fibrations in the $\mathcal{J}_2(X)$ classification.[21]

[19] The quotient group $[W^{(2)}(S_X)\rtimes\mathrm{Isom}(S_X)^{(\text{Amp})}]$ for the $\mathcal{J}_2(X)$ classification is equivalent to $\mathrm{Isom}^+(S_X)$ (an index 2 subgroup of the entire isometry group of the Neron-Severi lattice).

[20] The Picard number of this family is $\rho_X = 17$, so that there are 3 complex structure parameters.

[21] A brute force calculation (or automatized/computerized calculation) following the procedure reviewed in section4 of [26] should be able to verify or correct this statement, but this task is beyond the scope of this article and [26].

JHEP04(2014)050

Let us now focus on a given type of elliptic fibration in $\mathcal{J}_2(X)$ (i.e., we focus on a particular choice of 7-brane gauge group and matter representation) for some K3 surface X. There can be more than one isomorphism class of elliptic fibrations in the $\mathcal{J}_1(X)$ classification (fine classification) that corresponds to the same type. The number of such mutually non-isomorphic elliptic fibrations is referred to as the "number of isomorphism classes", or simply "multiplicity" of that type in this article. Reference [75] worked out the multiplicity for each one of the types in $\mathcal{J}_2(X)$ for $X = \mathrm{Km}(E \times F)$. There is no theory known (at least to the authors) that computes multiplicities for any K3 surface, and the authors of this article made an attempt at generalizing the study of [75] so the multiplicities are estimated, if not computed, for a broader class of K3 surfaces with large Picard number. The primary goal of section 5 of [26] is to develop a theory for this purpose.

One of the solid results obtained in [26] is that the multiplicities are at most 16 for any type and for any one of the 34 attractive K3 surfaces that appear in table 2. For individual attractive K3 surfaces (or for individual types of elliptic fibrations of a given attractive K3 surface), stronger upper bounds on the multiplicity are obtained. For example, the multiplicity is at most 2 for all types of 20 out of the 34 attractive K3 surfaces in table 2, and furthermore, the multiplicity is 1 — any two elliptic fibrations of a given type must be mutually isomorphic — for 10 attractive K3 surfaces among them.[22] See Corollary D in [26] for more information.

There are two remarks to be made: first, it is not guaranteed that $\mathrm{Isom}(S_X)^{(\text{Amp Hodge})}$ is always a normal subgroup of $\mathrm{Isom}(S_X)^{(\text{Amp})}$. If it is, then the map from $\mathcal{J}_1(X)$ to $\mathcal{J}_2(X)$ is regarded as the quotient map under the action of the quotient group $\mathrm{Isom}(S_X)^{(\text{Amp Hodge})}\backslash\mathrm{Isom}(S_X)^{(\text{Amp})}$. The multiplicity of a given type is the number of elements of the orbit under this group. When the quotient group is not a normal subgroup, however, mutually non-isomorphic elliptic fibres do not necessarily form an orbit of a group action.

There seems to be a correlation between the multiplicity of a given type and the Picard number, at least among the examples that have been looked at in [26]. The multiplicities for various types range in $\mathcal{O}(10)$–$\mathcal{O}(100)$ for a 3-parameter family of K3 surfaces $X = \mathrm{Km}(A)$ (where $\rho_X = 17$), while they range in a few-10 for a 2-parameter family of K3 surfaces $X = \mathrm{Km}(E \times F)$ (where $\rho_X = 18$), and the multiplicities often become a few or even less for many attractive K3 surfaces ($\rho_X = 20$) appearing in table 2. This is far from a rigorous mathematical statement, and in particular, it is conceivable that the physics-motivated condition (2.25) has extracted biased samples from all the attractive K3 surfaces. For a study of supersymmetric landscapes, however, it is mandatory to set upper bounds like (2.25) on the flux quanta. The 34 attractive K3 surfaces are then our sample of interest (see also section 5 for a related discussion), and this bias is not a problem at all.

4.1.1 Frame lattice, Mordell-Weil group and U(1) charges

Before proceeding to section 4.2, we take a moment to give a detailed account of how physics information is read out from the frame lattice (4.2). This is largely a well-known

[22] They are $X_{[1\ 0\ 1]}$, $X_{[1\ 1\ 1]}$, $X_{[2\ 0\ 1]}$, $X_{[2\ 1\ 1]}$, $X_{[3\ 0\ 1]}$, $X_{[3\ 1\ 1]}$, $X_{[4\ 0\ 1]}$, $X_{[5\ 1\ 1]}$, $X_{[6\ 1\ 1]}$ and $X_{[3\ 1\ 2]}$.

JHEP04(2014)050

subject, and this section is primarily meant to be a review or reading guide for section 4 of [26]. The details of the following presentation are not directly relevant to the rest of this article. However, this section also contains a generalization of the discussion in [76] in a way applicable to K3 surfaces away from the stable degeneration limit.

The Cartan (maximal torus) part of 7-brane gauge fields in F-theory originates from the three-form field of 11-dimensional supergravity. These fields correspond to fluctuations of the three-form field in the form of $A^a \wedge \omega^a$, where A^a is a vector field in the low-energy effective theory, and ω^a is chosen from

$$F^1/F^0 \cong H^1(B_3; R^1\pi_{Y*}\mathbb{Z})\,; \tag{4.3}$$

$H^2(Y;\mathbb{Z})$ for an elliptic fibred Calabi-Yau fourfold Y with $\pi_Y : Y \longrightarrow B_3$ has a filtration

$$H^2(Y;\mathbb{R}) = F^2 \supset F^1 \supset F^0 \tag{4.4}$$

and

$$F^2/F^1 \cong H^0(B_3; R^2\pi_{Y*}\mathbb{R}) = H^0(B_3;\mathbb{R}), \tag{4.5}$$

$$F^1/F^0 \cong H^1(B_3; R^1\pi_{Y*}\mathbb{R}), \tag{4.6}$$

$$F^0 \cong H^2(B_3; R^0\pi_{Y*}\mathbb{R}) = H^2(B_3;\mathbb{R}). \tag{4.7}$$

This — choosing ω from F^1/F^0 — is because two-forms purely in the base, F^0, correspond to scalars (or two-forms) in the effective theory in 3+1-dimensions, and those containing two-forms in the elliptic fibre, F^2/F^1, to a part of metric in 3+1-dimensions [15]. The total rank of the 7-brane gauge group in the effective theory is therefore $h^2(Y) - h^2(B_3) - 1$ [31]. In the case of $\pi_Y : Y = \mathrm{K3} \times \mathrm{K3} \longrightarrow \mathbb{P}^1 \times \mathrm{K3}$, the rank is $44 - 23 - 1 = 20$.

In the case of $Y = X \times S$ with an elliptic K3 surface X, F^1/F^0 can simply be identified with

$$F^1/F^0 \cong H^1(\mathbb{P}^1; R^1\pi_{X*}\mathbb{R})\,. \tag{4.8}$$

The condition that ω^a be within $F^1 \subset F^2 = H^2(X;\mathbb{R})$ corresponds to $\omega^a \in [[F]^\perp \subset H^2(X;\mathbb{R})]$. One can see that $(F^1/F^0) \cong (T_X \oplus W_{\mathrm{frame}}) \otimes \mathbb{R}$, because i) $H^2(X;\mathbb{R}) = (T_X \oplus S_X) \otimes \mathbb{R}$, and ii) the generator of $F^0 \cong H^2(\mathbb{P}^1;\mathbb{R}) = \mathbb{R}$ is Poincaré dual to the fibre class $[F]$ of the elliptic K3 surface X, and iii) also because of the definition of the frame lattice (4.2). For a K3 surface X with $\rho_X = 20$, rank-2 U(1) gauge fields are associated with $T_X \otimes \mathbb{R}$, while the remaining 18 Cartan U(1)'s are related to $W_{\mathrm{frame}} \otimes \mathbb{R}$.

In the presence of four-form flux purely of G_1 type, the two U(1) vector fields associated with $T_X \otimes \mathbb{R}$ become massive by a Stückelberg mechanism. At the level of analysis in this article (where non-perturbative effects are not considered, and stabilization of Kähler moduli is also ignored), those two U(1) symmetries remain in the effective theory as global symmetries.

The frame lattice is negative definite. As we always assume that the elliptic fibration $\pi_X : X \longrightarrow \mathbb{P}^1$ has a section $\sigma : \mathbb{P}^1 \longrightarrow X$, we can identify a sublattice of S_X isomorphic to W_{frame} in the case of K3 surface X; it is characterized as

$$W_{\mathrm{frame}*} := \Big[(\mathrm{Span}_{\mathbb{Z}}\{[F],[\sigma]\} \cong U)^\perp \subset S_X\Big]\,, \tag{4.9}$$

JHEP04(2014)050

the orthogonal complement of a sublattice generated by the fibre class $[F]$ and the section $[\sigma]$, and we call this sublattice $W_{\text{frame}*}$ the canonical frame lattice of a given elliptic fibration $(\pi_X, \sigma; X, \mathbb{P}^1)$.

The non-Abelian part of the gauge group in F-theory is associated with the (Poincaré dual of the) irreducible (-2) curves in the singular fibres of X that do not meet the zero section $[\sigma]$. They are contained in $W_{\text{frame}*}$ and are linearly independent. The sublattice generated by these (-2)-curves is contained in

$$W_{\text{root}} := \text{Span}_{\mathbb{Z}} \left\{ D \in W_{\text{frame}*} \mid D^2 = -2 \right\} , \tag{4.10}$$

the sublattice generated by norm-(-2) elements of the canonical frame lattice. But this W_{root} — called the root lattice of $W_{\text{frame}*}$ — is also known to be the same as the sublattice generated by the (-2)-curves (not meeting the section) in the singular fibres of X.[23] Therefore, once an elliptic fibration is specified in the form of an embedding of the lattice U into S_X, the non-Abelian part of the gauge group can be read out by calculating the W_{root} lattice from W_{frame} without dealing with defining equations (or the fibration map) of the K3 surface.

When the rank of the frame lattice $W_{\text{frame}*} \cong W_{\text{frame}}$ is larger than W_{root}, there is a massless U(1) vector field in the effective theory (if there is only G_1 component of the flux). Since "W-bosons" in the non-Abelian gauge groups should not be charged under such a U(1) symmetry, the two-form ω^a for such a U(1) vector field should be in the sublattice

$$W_{\text{U}(1)} := \left[W_{\text{root}}^{\perp} \subset W_{\text{frame}} \right] . \tag{4.11}$$

This is equivalent to an object known as the *essential lattice* of an elliptic surface X in the mathematics literature [65, 77], and may also be denoted by $L(X)$. Let $\{\omega^a\}$ be an independent set of generators of $W_{\text{U}(1)} = L(X)$. The massless U(1) vector fields in the effective theory are obtained from

$$C^{(3)} = \sum_{a=1}^{\rho_X - 2 - \text{rk}(W_{\text{root}})} A^a \omega^a , \tag{4.12}$$

where $\rho_X - 2 = \text{rk}(W_{\text{frame}*})$.[24] Theorem 1.3 in [77] states that the relation between the Mordell-Weil group $MW(X)$ and W_{frame} of an elliptically fibred surface is as follows:

$$\text{MW}(X) \cong \text{NS}(X)/[U \oplus W_{\text{root}}] \cong W_{\text{frame}}/W_{\text{root}} . \tag{4.13}$$

Thus, the rank of Mordell-Weil lattice is the same as $\text{rank}(W_{\text{U}(1)})$, the number of massless U(1) vector fields in the effective theory (when $G_1 \neq 0$, and $G_0 = 0$), and serves the

[23] To see this, suppose that D is a generator of W_{root}, i.e., $D \in W$ and $D^2 = -2$. Then either D or $-D$ corresponds to a class containing an effective divisor (curve) due to the Riemann-Roch theorem (Lemma 2.2 in section 1 of [62]), and secondly, it should be mapped down to a point in the base space $\mathbb{P}^1$ of the elliptic fibration, because the effective divisor in $W_{\text{frame}*}$ does not intersect with the fibre class. Therefore, it has to be contained in some singular fibres. The W_{root} lattice is attributed purely to singular fibres, not to any other sort of non-trivial sections of the elliptic fibration.

[24] The ω^a are not necessarily Poincaré dual to effective curves. This does not pose a problem as we only have to carry out a dimensional reduction to obtain their physics properties.

JHEP04(2014)050

purpose of counting degrees of freedom [31]. It should be remembered, though, that the U(1) vector fields are directly associated with two-forms in F^1, and hence in $W_{\rm frame}$, in physics. The connection with the Mordell-Weil group is only through an extra theorem in mathematics [65, 77].[25] To go beyond the degree-of-freedom counting in [31], and extract more physics information, $W_{\rm U(1)}$ lattice is the right object to deal with, as will be clear in the following discussion.

A preceding attempt of extracting more physics data, matter representations in F-theory compactifications on K3 surfaces in particular, has been made in [76]. The discussion in [76] leaves room for further sophistication in that

- only the stable degeneration limit of K3 surface was considered and, instead of a K3 surface, rational elliptic surfaces (X =dP$_9$) were used for the analysis. This means that that $H^2(X;\mathbb{Z}) = S_X$, and the transcendental lattice is trivial. That is now different for a K3 surface.

- The primary interest in [76] was to keep track of matter representations under the non-Abelian part of the gauge group. But one may also be interested in classifying matter representations using not just non-Abelian charges but also massless (as well as global) U(1) charges. As we will see in section 4.3, it is not rare among attractive K3 surfaces that $W_{\rm U(1)}$ is non-empty.

Thus, a revised version of the discussion in [76] is provided in the following, using the lattice-theory language that has already been explaining in this section.

Obviously we can think of (not necessarily light) matter fields originating from "somehow quantizing" an M2-brane wrapped on a cycle in $U^{\oplus 2} \oplus E_8^{\oplus 2} \cong [U_*^\perp \subset H_2(X;\mathbb{Z})]$. Their representations under the massless gauge group associated with two-forms $W_{\rm gauge} := W_{\rm root} \oplus W_{\rm U(1)}$ (resp. under the symmetry group associated with $W_{\rm gauge} \oplus T_X$) should be specified by their weights, elements in the dual space $W^*_{\rm gauge} := {\rm Hom}(W_{\rm gauge}, \mathbb{Z})$ (resp. $W^*_{\rm gauge} \oplus T^*_X$). Any quantized states arising from an M2-brane wrapped on a two-cycle in $[U_*^\perp \subset H_2(X;\mathbb{Z})] \cong U^{\oplus 2} \oplus E_8^{\oplus 2}$ are in the same weight, and the weight is determined by the pairing between the divisors in $W_{\rm gauge}$ (resp. $W_{\rm gauge} \oplus T_X$) and the two-cycle. The collection of weights realized in this way forms a sublattice of the weight lattice $W^*_{\rm gauge}$ (resp. $W^*_{\rm gauge} \oplus T^*_X$). Let $G_{\rm matter}$ (resp. $\widetilde{G}_{\rm matter}$) be the image of this sublattice in the quotient space $G_{W_{\rm gauge}} = W^*_{\rm gauge}/W_{\rm gauge}$ (resp. $(W^*_{\rm gauge}/W_{\rm gauge}) \times G_{T_X}$). $G_{\rm matter}$ (resp. $\widetilde{G}_{\rm matter}$) is referred to as the N-ality of a given effective theory. Remembering that the unimodular lattice $U^{\oplus 2} \oplus E_8^{\oplus 2}$ is an overlattice of $W_{{\rm frame}*} \oplus T_X$, and that $W_{\rm gauge} \subset W_{{\rm frame}*} \subset W^*_{{\rm frame}*} \subset W_{\rm gauge}$, one finds an exact sequence

$$0 \longrightarrow (W_{{\rm frame}*}/W_{\rm gauge}) \longrightarrow \widetilde{G}_{\rm matter} \longrightarrow \Delta \longrightarrow 0\,, \tag{4.14}$$

[25] If we are to exploit this connection, the narrow Mordell-Weil lattice $MW(X)^0$ will be a more appropriate object than $MW(X)$. $MW(X)^0$ is defined as the subgroup of $MW(X)$ that consists of sections of an elliptic fibration $(\pi_X, \sigma; X, \mathbb{P}^1)$ that cross singular fibres only through the (-2) curves meeting the zero section σ, rather than through (-2) curves generating A–D–E root lattices in $W_{\rm root}$. Theorem 8.9 in [77] states that the narrow Mordell-Weil lattice is isomorphic to $W_{\rm U(1)} = L(X)$ as an Abelian group, and the height pairing of $MW(X)^0$ (positive definite) is precisely the intersection form of $L(X)$ (negative definite) times (-1).

JHEP04(2014)050

where Δ is the diagonal subgroup of $G_{S_X} \times G_{T_X} \cong G_{W_{\text{frame}*}} \times G_{T_X}$. This characterizes the N-ality of matter representations $\widetilde{G}_{\text{matter}}$ under the symmetry group. For definitions of lattice theory jargon as well as reviews on background material, see e.g., [26]. If we are to ignore the U(1) symmetry charges associated with the vector fields from T_x (which are not massless in the presence of G_1 type flux), then the N-ality is given by

$$0 \longrightarrow (W_{\text{frame}*}/W_{\text{gauge}}) \longrightarrow G_{\text{matter}} \longrightarrow [(W^*_{\text{frame}*}/W_{\text{frame}*}) \cong G_{S_X}] \longrightarrow 0\,. \tag{4.15}$$

The matter fields in $W_{\text{frame}*}/W_{\text{gauge}}$ form a subgroup in G_{matter}, which means that interactions among these fields must be closed within themselves. Techniques to calculate $W_{\text{frame}*}/W_{\text{gauge}}$ as well as $G_{S_X} \cong \Delta$ are presented in [26], section 4. Note that $W^*_{\text{frame}*} \subset W^*_{\text{gauge}}$ is now regarded as the kernel of

$$[W^*_{\text{gauge}} = \text{Ext}^0(W_{\text{gauge}}, \mathbb{Z})] \longrightarrow [\text{Ext}^1(W_{\text{frame}*}/W_{\text{gauge}}, \mathbb{Z}) = W^*_{\text{gauge}}/W^*_{\text{frame}*}]\,, \tag{4.16}$$

rather than the kernel of

$$[W^*_{\text{root}} = \text{Ext}^0(W_{\text{root}}, \mathbb{Z})] \longrightarrow [\text{Ext}^1(W_{\text{frame}*}/W_{\text{gauge}}, \mathbb{Z}) \cong \text{Tor}(MW(X))] \tag{4.17}$$

as presented in [76]. This difference from [76] is due to the generalization from the stable degeneration limit (rational elliptic surface) to K3 surfaces and the inclusion of information on Abelian charges of the matter fields. It is thus best for physics purposes to extract the information of an elliptic fibration in the form of the sublattice W_{gauge} and the quotient $W_{\text{frame}*}/W_{\text{gauge}}$. Consequently. computation results in [26] are presented in this way.

Explicit examples will help understand the abstract theory above. In this article, we only show table 3, more examples are found in [26]. For an attractive K3 surface $X = X_{[1\ 1\ 1]}$ (often denoted also by X_3), which has 6 different types of elliptic fibrations, the Mordell-Weil group has been computed for any one of these types (see table 1.1 of [73]). It is certainly well-motivated to study Mordell-Weil groups of elliptic fibrations in mathematics, to begin with, and decompose them into their free part and torsion part. However, more suitable for physicists' needs is to extract information from $W_{\text{frame}*}$ in the form of W_{gauge}, $(W_{\text{frame}*}/W_{\text{gauge}})$ and G_{matter}. The subtle differences between them should be visible in the examples in table 3.

When we employ the expansion in the form of (4.12), the gauge kinetic term of the vector fields on $S \times \mathbb{R}^{3,1}$ is given by

$$\propto -\int_{\mathbb{R}^{3,1}} d^4x \int_S d^4y \sqrt{g(y)}\; M_*^4 \left(T_R^{-1} \text{tr}_R \left[F_{mn}F^{mn}\right] - 2(\omega_a, \omega_b) F^a_{mn} F^b_{mn} \right)\,; \tag{4.18}$$

the normalization of the second term is set relatively to that of the first term, so that the maximal torus part of the non-Abelian components also have the same normalization[26] as

[26] When the maximal torus part of a non-Abelian A_{n-1} component is expanded as $C^{(3)} = \sum_{a=1}^{n-1} C_a A^a$, with A^a being $\mathbb{R}$-valued vector fields, then this corresponds to $\text{diag}(-A^1, A^1 - A^2, \cdots, A^{n-2} - A^{n-1}, A^{n-1})$ in the fundamental (n-dimensional) representation of SU(n), since an M2-brane wrapped on C_b — usually assigned to the $(b, b+1)$ entry of the $n \times n$ matrix representation — should have a covariant derivative involving $A^{b-1} - 2A^b + A^{b+1}$. Then $T_n^{-1}\,\text{tr}_n\left[(\text{diag}(-F^1, F^1 - F^2, \cdots, F^{n-1}))^2\right] = 4[(F^1)^2 + \cdots + (F^{n-1})^2] - 4[F^1F^2 + \cdots + F^{n-2}F^{n-1}] = -2(C_a, C_b)F^a_{mn}F^b_{mn}$.

JHEP04(2014)050

W_{gauge}	MW $G_{W_{\text{gauge}}} := W^*_{\text{gauge}}/W_{\text{gauge}}$	$W_{\text{frame}*}/W_{\text{gauge}}$ $G_{\text{matter}} := W^*_{\text{frane}*}/W_{\text{gauge}}$
$A_2E_8E_8$	$\{1\}$ $\mathbb{Z}_3\langle a_3\rangle$	$\{1\}$ $\mathbb{Z}_3\langle a_3\rangle$
A_2D_{16}	$\mathbb{Z}_2\langle \mathbf{sp}\rangle$ $\mathbb{Z}_3\langle a_3\rangle \times \mathbb{Z}_2\langle \mathbf{sp}\rangle \times \mathbb{Z}_2\langle \overline{\mathbf{sp}}\rangle$	$\mathbb{Z}_2\langle \mathbf{sp}\rangle$ $\mathbb{Z}_3\langle a_3\rangle \times \mathbb{Z}_2\langle \mathbf{sp}\rangle$
$D_{10}E_7(-6)$	$\mathbb{Z}\langle(\mathbf{sp},0,\mathbf{56})\rangle \times \mathbb{Z}_2\langle(\overline{\mathbf{sp}},\mathbf{56},0)\rangle$ $(\mathbb{Z}_2\langle \mathbf{sp}\rangle \times \mathbb{Z}_2\langle \overline{\mathbf{sp}}\rangle) \times \mathbb{Z}_2\langle \mathbf{56}\rangle \times \mathbb{Z}_6\langle \mathbf{56}/3\rangle$	$\mathbb{Z}_2\langle(\mathbf{sp},0,\mathbf{56})\rangle \times \mathbb{Z}_2\langle(\overline{\mathbf{sp}},\mathbf{56},0)\rangle$ $\mathbb{Z}_2\langle(\overline{\mathbf{sp}},\mathbf{56},0)\rangle \times \mathbb{Z}_6\langle(\mathbf{sp},0,\mathbf{56}/3)\rangle$
$A_{17}(-6)$	$\mathbb{Z}\langle(3a_{18},\mathbf{56})\rangle \times \mathbb{Z}_3\langle(0,2\cdot\mathbf{56})\rangle$ $\mathbb{Z}_{18}\langle a_{18}\rangle \times \mathbb{Z}_6\langle \mathbf{56}/3\rangle$	$\mathbb{Z}_6\langle(3a_{18},\mathbf{56})\rangle$ $\mathbb{Z}_3\langle(6,0)\rangle \times \mathbb{Z}_3\langle(0,2)\rangle \times \mathbb{Z}_2\langle(9,3)\rangle$
$E_6E_6E_6$	$\mathbb{Z}_3\langle(1,1,1)\rangle$ $\mathbb{Z}_3\langle \mathbf{27}\rangle \times \mathbb{Z}_3\langle \mathbf{27}\rangle \times \mathbb{Z}_3\langle \mathbf{27}\rangle$	$\mathbb{Z}_3\langle(1,1,1)\rangle$ $\mathbb{Z}_3\langle(1,1,1)\rangle \times \mathbb{Z}_3\langle(0,2,1)\rangle$
$A_{11}D_7$	$\mathbb{Z}_4\langle(3a_{12},\mathbf{sp})\rangle$ $\mathbb{Z}_{12}\langle a_{12}\rangle \times \mathbb{Z}_4\langle \mathbf{sp}\rangle$	$\mathbb{Z}_4\langle(3a_{12},\mathbf{sp})\rangle$ $\mathbb{Z}_4\langle(3a_{12},\mathbf{sp})\rangle \times \mathbb{Z}_3\langle(4a_{12},0)\rangle$

Table 3. The N-ality $G_{\text{matter}} \subset G_{W_{\text{gauge}}}$ of the six different types of elliptic fibrations in $\mathcal{J}_2(X)$ for an attractive K3 surface $X = X_3$. In this table, one can confirm that i) $(W_{\text{frame}}/W_{\text{gauge}}) \subset G_{\text{matter}} \subset G_{W_{\text{gauge}}}$, ii) $MW \cong W_{\text{frame}*}/W_{\text{root}} \longrightarrow (W_{\text{frame}*}/W_{\text{gauge}})$ is a quotient, and iii) the quotient of $(W_{\text{frame}*}/W_{\text{gauge}}) \hookrightarrow G_{\text{matter}}$ is always $G_{T_X} \cong \mathbb{Z}_3$ of the attractive K3 surface X_3. In the 3rd and 4th entries, the generators of the rank-1 lattice (-6) are denoted by $2\cdot\mathbf{56}$, because the generator is that of the weight $2\cdot\mathbf{56}$ in E_7^*, when this rank-1 lattice is regarded as $[E_6^\perp \subset E_7]$.

the Abelian components given by the intersection form on the K3 surface X. $T_R^{-1}\,\mathrm{tr}_R[\cdots]$ is the ordinary convention adopted for non-Abelian gauge theories. The gauge coupling constant[27] of the massless U(1) vector fields is given by the opposite of the intersection form on the essential lattice $L(X) = W_{\mathrm{U}(1)}$, $-(\omega_a,\omega_b) = -\int_X \omega_a \wedge \omega_b$, which is equivalent to the (positive definite) height pairing of the narrow Mordell-Weil lattice $MW(X)^0$.

4.2 Moduli space of F-theory with flux

4.2.1 Subspace of K3 moduli space with a given Picard number

The discussion in sections 2.1 and 2.2 centres on (pairs of) attractive ($\rho = 20$) K3 surfaces, while that of sections 3 and 4.1 is applicable for K3 surfaces with any Picard number ρ. Thus all the statements in sections 3 and 4.1 are applicable to the special cases treated in sections 2.1 and 2.2. As a warming up for the discussion in section 4.2.2 and later, however, let us first elaborate a little more about the relation between the characterization of attractive K3 surfaces in terms of (2.7), (2.8), (2.9) and the complex structure moduli space $\mathrm{Isom}^+(\Lambda_{\mathrm{K3}})\backslash D$. This is only to repeat material presented in [18, 58, 59, 78], apart from the purpose of setting up notations that we need later.

[27] Note that this kinetic term most likely corresponds to the one renormalized at the Kaluza-Klein scale, since this is obtained from a simple dimensional reduction (truncation) of 11-dimensional supergravity on a flat spacetime, whose infrared physics (especially when it comes to renormalization) is quite different from what we are really interested in.

JHEP04(2014)050

Let us first define a pair of sublattices $(T_{[\omega]}, S_{[\omega]})$ for $[\omega] \in D$ as

$$S_{[\omega]} := \left[\omega^\perp \subset \Lambda_{\rm K3}\right], \qquad T_{[\omega]} := \left[S_{[\omega]}^\perp \subset \Lambda_{\rm K3}\right]. \tag{4.19}$$

These two sublattices are mutually orthogonal complements in $\Lambda_{\rm K3}$ (which also means that they are primitive sublattices of $\Lambda_{\rm K3}$). Thus, one can define a map

$$D \ni [\omega] \mapsto (T_{[\omega]}, S_{[\omega]}) \in \{(T,S)|\text{ mutually orthog. sublattices of } \Lambda_{\rm K3}\} =: \mathcal{C}\,. \tag{4.20}$$

$\mathcal{C}$ is further decomposed into $\mathcal{C}_\rho$ with $\rho = 0, 1, \cdots, 20$ where $T_{[\omega]}$ and $S_{[\omega]}$ have signature $(2, 20-\rho)$ and $(1, \rho-1)$, respectively, and others which we are not interested in.[28] D is also decomposed into D_ρ with $\rho = 0, \cdots, 20$, where D_ρ is the fibres over $\mathcal{C}_\rho$. Each irreducible component of the fibres is of complex dimension $20-\rho$. The group $\mathrm{Isom}^+(\Lambda_{\rm K3})$ acts also on the $\mathcal{C}_\rho$, and the action on D_ρ and $\mathcal{C}_\rho$ commutes with the map introduced above.

The Theorem 2.10 of [78] states that there is a map that is both injective and surjective between $\mathrm{Isom}^+(\Lambda_{\rm K3})\backslash\mathcal{C}_\rho$ and the classification of even lattice T of signature $(2, 20-\rho)$ modulo isometry, if $\rho \geq 12$ (which comes from a condition $\mathrm{rank}(T) \leq \mathrm{rank}(S) - 2$). In the case of $\rho = 20$, $\mathrm{Isom}^+(\Lambda_{\rm K3})\backslash D_{\rho=20} \longrightarrow \mathrm{Isom}^+(\Lambda_{\rm K3})\backslash\mathcal{C}_{\rho=20}$ (or, equivalently, $D_{\rho=20} \longrightarrow \mathcal{C}_{\rho=20}$) is surjective[29] and the fibre consists of 2 elements; they correspond to the two different choices of an orientation in $T_{[\omega]} \otimes \mathbb{R}$ that turns it into a complex line $[\omega] \in \Lambda_{\rm K3} \otimes \mathbb{C}$. Thus, the scan over even lattices of signature $(2,0)$ with orientation in the basis — the scanning in [18] and in sections 2.1 and 2.2 — is in one-to-one correspondence with $\mathrm{Isom}^+(\Lambda_{\rm K3})\backslash D_{\rho=20}$ [18]. Therefore, the entries in table 2 are regarded as a subset of

$$\left[\mathrm{Isom}^+(\Lambda_{\rm K3}^{(X)})\backslash D_{\rho=20}^{(X)}\right] \times \left[\mathrm{Isom}^+(\Lambda_{\rm K3}^{(S)})\backslash D_{\rho=20}^{(S)}\right], \tag{4.21}$$

specified by the condition (2.25).

4.2.2 Moduli space in the presence of flux

Moduli spaces such as (3.9), (3.11), (3.12) arise from compactifications of M/F-theory without flux. Let us now move on formulate the moduli spaces for compactifications including fluxes, paying close attention to the choice of the quotient group which should tell us when a pair of vacua should be regarded the same in physics and when as distinct.

To get started, let us return to M-theory compactification on $Y = S_1 \times S_2$ down to 2+1-dimensions. Remembering that the moduli space was (3.9) because we take a quotient by $\mathrm{Isom}^+(\Lambda_{\rm K3}^{(S_1)}) \times \mathrm{Isom}^+(\Lambda_{\rm K3}^{(S_2)})$ in order to reduce the unphysical difference in the choice of marking, we claim that the complex structure moduli space[30] of compactifications on

[28] Either $T_{[\omega]}$ or $S_{[\omega]}$ contains all three positive directions in such cases. They are not in the image of D, however.

[29] The original proof of surjectivity of the map from $\mathrm{Isom}^+(\Lambda_{\rm K3})\backslash D_{\rho=20}$ to the set of even lattices of signature $(2,0)$ with orientation in [61] was to show that, for any even $(2,0)$ lattice with orientation, $T^{\rm or}$, a K3 surface can be constructed whose transcendental lattice with an oriented basis becomes the even $(2,0)$ lattice $T^{\rm or}$.

[30] There is nothing wrong to introduce the flux $G^{(4)}$ also in $H^4(S_1;\mathbb{Z}) \otimes H^0(S_2;\mathbb{Z}) \oplus H^0(S_1;\mathbb{Z}) \otimes H^4(S_2;\mathbb{Z})$ in M-theory compactifications down to 2+1-dimensions, where we do not have to preserve SO(3,1) Lorentz symmetry. Strictly speaking, $H^{2,2}(Y;\mathbb{R})$ in this equation should be replaced by its image under the marking. We do not try to be precise beyond our need.

JHEP04(2014)050

$Y = S_1 \times S_2$ in the presence of 4-from flux should be given by the quotient space of

$$\left\{ \left([\omega_1], [\omega_2], G^{(4)}\right) \;\middle|\; [\omega_i] \in D^{(S_i)},\ [G^{(4)}] \in \left(\Lambda_{\rm K3}^{(S_1)} \otimes \Lambda_{\rm K3}^{(S_2)}\right) \cap H^{2,2}(Y;\mathbb{R}) \right\} \tag{4.22}$$

by[31,32]

$$\Gamma = \mathbb{Z}_2 \langle \text{c.c.} \rangle \times \mathbb{Z}_2 \langle \text{exch}_{12} \rangle \ltimes \left[\text{Isom}^+(\Lambda_{\rm K3}^{(S_1)}) \times \text{Isom}^+(\Lambda_{\rm K3}^{(S_2)}) \right] , \tag{4.23}$$

where exch_{12} exchanges S_1 and S_2, and c.c. denotes complex conjugation of the entire $Y = S_1 \times S_2$. As stated at the end of section 2.1, a pair of descriptions related by $\mathbb{Z}_2 \langle \text{c.c.} \rangle \times \mathbb{Z}_2 \langle \text{exch}_{12} \rangle$ should not be regarded distinct vacua in physics.

This moduli space has a number of disconnected components corresponding to topological choices of the four-form flux. For non-trivial fluxes, some moduli have masses, and such connected components of the moduli space have reduced dimensions. Thus, this moduli space should be that of effective theories below the mass scale of stabilized moduli,[33] and can be used at least for the purpose of parametrizing/counting vacua.[34]

It is instructive to use the landscape of vacua already shown in table 2, where $G_0 = 0$, to see what the isolated (completely stabilized) components of this moduli is like. Already the table serves as the list of quotient of $D^{(S_1)}_{\rho=20} \times D^{(S_2)}_{\rho=20}$ by the group (4.23). The rest is to work out the number of different choices of fluxes $G^{(4)} = G_1$ (or equivalently the number of different choices of γ) modulo the action of the residual symmetry in the group (4.23). Written in the second to last column of table 2 is the number of different γ modulo the residual symmetry in $\mathbb{Z}_2 \langle \text{c.c.} \rangle \times \mathbb{Z}_2 \langle \text{exch}_{12} \rangle$. Assuming further that all of the $\text{Isom}(T_{S_1})^{(\text{Hodge})} \times \text{Isom}(T_{S_2})^{(\text{Hodge})} \cong \mathbb{Z}_{m_1} \times \mathbb{Z}_{m_2}$ $(m_{1,2} = 2, 4, 6)$ symmetries of the transcendental lattices T_{S_1} and T_{S_2} can be lifted to isometries of the entire lattice $\Lambda_{\rm K3}$, however,[35] all the γ's are equivalent for all the entries, except in two entries marked by $*$ in the table, where there are two inequivalent values of γ. Thus, we conclude — under this assumption — that the landscape of M-theory compactification on $Y = S_1 \times S_2$ with a four-form flux purely of type G_1 and completely stabilized complex structure moduli consists $1 \times 64 + 2 \times 2 = 68$ vacua.

Let us now turn to F-theory and try to figure out the moduli space for F-theory compactifications on elliptically fibred $X \times S$, with a four-form flux preserving $\text{SO}(3,1)$ symmetry. From the experience so far, it is natural to consider that the moduli space is

[31] Note that $\mathbb{Z}_2 \langle \text{exch}_{12} \rangle$ in the modular group Γ also acts on the Kähler moduli.

[32] To be more precise, we only know that the true modular group should contain this Γ in (4.23) as a subgroup. To draw an analogy, $T^2 \times T^2 \times \cdots$ compactifications of type II string theory has a larger duality group than just $\text{SL}(2;\mathbb{Z}) \times \text{SL}(2;\mathbb{Z}) \times \cdots$. The same comment applies also to the choice of modular group (4.26) for F-theory.

[33] In the case of type IIB/F-theory compactifications, the mass scale is typically $M_{\rm KK}^3/M_{\rm str}^2$ [13].

[34] In order to use this as the target space of a non-linear sigma model below the mass scale of the stabilized moduli, one has to study corrections to the metric (Kähler potential) on moduli space. Note that the classification of matter representations in section 4.1.1 includes information on stringy states, and hence is not a classification of effective field theories below the scale of moduli masses. Note also that the restricted moduli space $\mathcal{M}_*$ to be introduced in section 5.4 should be regarded more as a mathematical (rather than physical) object on which the $\rho_{\rm ind}$ distribution is presented.

[35] This assumption is satisfied, if $p_S : \text{Isom}(S_{S_{1,2}}) \longrightarrow \text{Isom}(q_{1,2})$ is surjective. It is known that this is the case for some K3 surfaces with large Picard number. See [26] for more information.

JHEP04(2014)050

given by

$$\Gamma\backslash\left\{\left([\omega_X],[\omega_S],G^{(4)},\phi_U\right)\,\middle|\;\; G^{(4)}\in L,\;\right\}/\{\pm\mathrm{id}._U\}\,, \tag{4.24}$$

where $([\omega_X],[\omega_S])\in D^{(X)}\times D^{(S)}$, $\phi_U : U\hookrightarrow\left[[\omega_X]^\perp\subset\Lambda_{\mathrm{K3}}\right]$, and the four-form flux $G^{(4)}$ is in

$$\begin{aligned} L := \left(\left[\phi_U(U)^\perp\subset\Lambda_{\mathrm{K3}}^{(X)}\right]\otimes\Lambda_{\mathrm{K3}}^{(S)}\right)\cap \\ \left[\varphi_{[\omega_X]}(H^{2,0}(X_{[\omega_X]};\mathbb{C}))\otimes\varphi_{[\omega_S]}(H^{0,2}(S_{[\omega_S]};\mathbb{C}))+\text{h.c.}\right. \\ \left.+\varphi_{[\omega_X]}(H^{1,1}(X_{[\omega_X]};\mathbb{R}))\otimes\varphi_{[\omega_S]}(H^{1,1}(S_{[\omega_S]};\mathbb{R}))\right]\,, \end{aligned} \tag{4.25}$$

where $(X_{[\omega_X]},\varphi_{[\omega_X]})$ and $(S_{[\omega_S]},\varphi_{[\omega_S]})$ are either one of two inverse images of $[\omega_X]$ and $[\omega_S]$, respectively, under the period map. When only flux of G_1 type is introduced, the last line in L is dropped. The quotient group is given by

$$\Gamma=\mathbb{Z}_2\,\langle\text{c.c.}\rangle\times\mathrm{Isom}^+(\Lambda_{\mathrm{K3}}^{(X)})\times\mathrm{Isom}^+(\Lambda_{\mathrm{K3}}^{(S)})\,. \tag{4.26}$$

The $\mathbb{Z}_2\,\langle\mathrm{exch}_{12}\rangle$ is gone at this point, because we have already set up a convention that it is X, rather than S, whose vev of the volume of elliptic fibre goes to zero. If we are to focus on vacua with $\rho_X=\rho_S=20$, then simply the condition that $([\omega_X],[\omega_S])\in D^{(X)}\times D^{(S)}$ is replaced by $([\omega_X],[\omega_S])\in D^{(X)}_{\rho=20}\times D^{(S)}_{\rho=20}$.

4.2.3 How to carry out the vacuum counting for F-theory on K3×K3 in practice

As long as we consider compactifications on $Y=\mathrm{K3}\times\mathrm{K3}=X\times S$, with the elliptic fibration implemented as $\pi_X : X\longrightarrow\mathbb{P}^1$, all the 7-branes are in the form $\{\text{point}\}\times S$; in particular, there are no matter curves. Thus, all algebraic information (such as gauge groups and matter representations) of low-energy effective theories is captured by the frame lattice $W_{\mathrm{frame}}(X)$ and T_X. This means that

$$\amalg_{[a\ b\ c]}\;\;\mathcal{J}_2(X_{[a\ b\ c]}) \tag{4.27}$$

serves as the classification of effective theories by their algebraic information.[36] Here, $[a\ b\ c]$ runs over the thirty-four choices of the three integers characterizing the transcendental lattice of either S_1 or S_2 in table 2.

Let us take $X_{[1\ 0\ 1]}$ (also denoted by X_4 in the mathematics literature) as the first example. There are 13 different types of elliptic fibrations for this K3 surface [73], i.e., $\#[\mathcal{J}_2(X_{[1\ 0\ 1]})]=13$. When this K3 surface $X_{[1\ 0\ 1]}$ is to be used for the X of $Y=X\times S$ in (3.1), one can use table 2 to see that the other K3 surface S can be $X_{[6\ 0\ 6]}$ or $X_{[3\ 0\ 3]}$ (when $N_{D3}=0$), $X_{[5\ 0\ 5]}$ or $X_{[1\ 0\ 1]}$ (when $N_{D3}=4$), $X_{[4\ 0\ 4]}$, $X_{[4\ 0\ 1]}$, $X_{[2\ 0\ 2]}$ and $X_{[1\ 0\ 1]}$ (when $N_{D3}=8$), $X_{[3\ 0\ 3]}$ (when $N_{D3}=12$), $X_{[2\ 0\ 2]}$, $X_{[1\ 0\ 1]}$ (when $N_{D3}=16$) and finally $X_{[1\ 0\ 1]}$ (when $N_{D3}=20$). There are 12 options for the choice of (S,N_{D3}). For any one of

[36] It may be possible that the difference between a pair of non-equivalent embedding of $T_X\oplus W_{\mathrm{frame}}\oplus U$ into $H_2(X;\mathbb{Z})$ is absorbed by rescaling of U(1) charges, only to result in different gauge coupling constants (gauge kinetic terms). We are not paying attention at this level of detail in this article, however.

JHEP04(2014)050

these 12 choices of $(Y = X_{[1\ 0\ 1]} \times S, N_{D3})$, the stabilizer subgroup of Γ (i.e., the residual modular group) is

$$\mathbb{Z}_2 \langle \text{c.c.} \rangle \times \left[W^{(2)}(S_X) \rtimes \text{Aut}(X) \right] \times \left[W^{(2)}(S_S) \rtimes \text{Aut}(S) \right] , \tag{4.28}$$

which acts on the possible choices of elliptic fibrations $(\phi_U : U \hookrightarrow S_X)$ and flux of G_1 type (γ in table 2). This is quite a complicated problem to work out. If we are to first exploit this remaining symmetry in Γ in (4.26) to eliminate a redundant description of elliptic fibrations, we can use the Corollary D of [26]), which states that any one of the 13 types of elliptic fibrations of $X_{[1\ 0\ 1]}$ consists of a unique isomorphism class. There is no extra multiplicity coming from the difference between the $\mathcal{J}_1(X)$ and the $\mathcal{J}_2(X)$ classifications. The $\mathbb{Z}_2 \langle \text{c.c.} \rangle$ action in Γ is not necessary in eliminating redundant descriptions of elliptic fibrations on $X_{[1\ 0\ 1]}$, and we can exploit this to see that the number of inequivalent choices of the flux $G^{(4)} = G_1$ is not more than the numbers presented in the last column of table 2. Furthermore, in the cases $S = X_{[1\ 0\ 1]}$ or $X_{[2\ 0\ 2]}$, we can also see that the combined choice of flux and elliptic fibration is unique under the action of the whole group Γ because $\text{Isom}(T_S)^{(\text{Hodge})} \cong \mathbb{Z}_4$ and the generator of this group can be extended[37] to an isometry of $H_2(S;\mathbb{Z})$ for $S = X_{[1\ 0\ 1]}$ and $X_{[2\ 0\ 2]}$. For other S, the number of non-equivalent choices of flux and elliptic fibration combined cannot be determined without more information. We thus conclude that for any one of the 13 types of elliptic fibrations in $\mathcal{J}_2(X_{[1\ 0\ 1]})$, the total number of inequivalent choices of $(S, N_{D3}, \gamma, \phi_U)$, and hence the number of inequivalent choices of vacua, is somewhere in between 12 and 23.

The attractive K3 surface $X_{[2\ 1\ 1]}$ is another example for which there is a unique isomorphism class in each type of elliptic fibration (see Corollary D of [26] or footnote 22 in this article). Thus, for theories in the classification of $\mathcal{J}_2(X_{[2\ 1\ 1]})$ in (4.27), the counting of inequivalent vacua arises only from the choice of fluxes (γ), not in the isomorphism classes of elliptic fibrations. Thus, for any type of elliptic fibration in $\mathcal{J}_2(X_{[2\ 1\ 1]})$, the number of inequivalent vacua lies somewhere in between 9 and 18. These statistics originate from (S, N_{D3}) being $(X_{[4\ 2\ 2]}, 10)$, $(X_{[2\ 1\ 1]}, 10)$, $(X_{[2\ 1\ 1]}, 17)$, $(X_{[6\ -3\ 3]}, 3)$, $(X_{[4\ -2\ 2]}, 10)$, $(X_{[2\ -1\ 1]}, 10)$, $(X_{[2\ -1\ 1]}, 17)$ in table 2. Note that we have exploited $\mathbb{Z}_2 \langle \text{c.c.} \rangle$ to set $X = X_{[2\ 1\ 1]}$ rather than $X_{[2\ -1\ 1]}$.

As an example of attractive K3 surfaces where there can be multiple isomorphism classes of elliptic fibrations of the same type, let us first consider $X = X_{[2\ 2\ 2]}$. This K3 surface admits 30 different types of elliptic fibrations, $\#\left[\mathcal{J}_2(X_{[2\ 2\ 2]})\right] = 30$ [73]. The number of isomorphism classes of each type can be either one or two, and it turns out (Example J of [26]) that there is a unique isomorphism class in at least 15 out of the 30 different types. The number of remaining inequivalent choices of flux $G_1 \propto \gamma$ can be estimated as above, and it falls within 7–22, using the information in the last column of table 2. Thus, in conclusion, at least 15 classes of effective theories in $\mathcal{J}_2(X_{[2\ 0\ 2]})$ consist of 7–22 inequivalent vacua individually, and there may be 2× (7–22) inequivalent effective theories of a given algebraic information corresponding to any one of the remaining 15 types in $\mathcal{J}_2(X_{[2\ 0\ 2]})$.

[37] This is because $p_S : \text{Isom}(S_S) \longrightarrow \text{Isom}(q)$ is known to be surjective for $S = X_{[1\ 0\ 1]}$ and $X_{[2\ 0\ 2]}$.

JHEP04(2014)050

Finally, let us take a look at the cases $X = X_{[6\ 0\ 6]}$ and $X = X_{[6\ 6\ 6]}$. For these two attractive K3 surfaces, there is only one possible choice of (S, N_{D3}); $(S, N_{D3}) = (X_{[1\ 0\ 1]}, 0)$ and $(X_{[1\ 1\ 1]}, 6)$, respectively. All the choices of the flux $G_1 \propto \gamma$ turn out to be equivalent under the residual $W^{(2)}(S_S) \rtimes \mathrm{Aut}(S) \subset \mathrm{Isom}^+(\Lambda_{\mathrm{K3}}^{(S)})$ symmetry in Γ, because of the surjectiveness of $p_S : \mathrm{Isom}^+(S_S) \longrightarrow \mathrm{Isom}(q)$ for $S = X_{[1\ 0\ 1]}$ and $X_{[1\ 1\ 1]}$. The number of distinct isomorphism classes of elliptic fibrations is not more than 16 and 12 for $X = X_{[6\ 0\ 6]}$ and $X = X_{[6\ 6\ 6]}$, respectively, for any types in $\mathcal{J}_2(X)$ (Corollary D of [26]). Thus, for these two attractive K3 surfaces chosen as X, the number of inequivalent vacua is bounded from above by 16 and 12, respectively.

4.3 Sample statistics

The example-based study in section 4.2.3 indicates that each class of theories in (4.27) consists of $\mathcal{O}(10)$ vacua inequivalent under the modular group Γ in (4.26). Although the study only covers five attractive K3 surfaces $X_{[a\ b\ c]}$ out of thirty-four, small as well as large a, c are covered in the five examples. We expect that an estimate of the vacuum counting would not be different so much for the other twenty-nine attractive K3 surfaces.

This fact — the numbers of vacua in individual classes of effective theories in (4.27) are much the same — allows us to take a short-cut approach in studying statistical distributions of more inclusive classifications of effective theories. By more inclusive classifications, we mean classifications of low-energy effective theories coarser than in (4.27). One might be interested, for example, in the number of effective theories that contain a certain gauge group G (such as $\mathrm{SU}(3)_C \times \mathrm{SU}(2)_L \times \mathrm{U}(1)_Y$, SU(5) or SO(10)), and compare the numbers for various choices of G. When we ask this question, we have to include all the vacua from (4.27) containing the specified gauge group, regardless of the gauge groups in the hidden sector. Given the fact that the number of vacua in each class of theories in (4.27) are much the same, we can simply count the number of classes of effective theories contained in inclusive classes of theories, because more or less "the same" multiplicity $\mathcal{O}(10)$ factors out in the ratio. In this section, we take this short-cut approach in order to address three questions of interest.

4.3.1 Statistics on 7-brane gauge groups and CP violation

7-brane Gauge Groups. It is one of the most important questions we can address by using a toy/miniature supersymmetric landscape whether or not there are more vacua with an SU(5) unified gauge group than those with $\mathrm{SU}(3)_C \times \mathrm{SU}(2)_L \times \mathrm{U}(1)_Y$ gauge group that just happens to satisfy gauge coupling unification "by accident". As is well-known, it makes sense in the context of unified theories to focus on vacua of string theory realized as compactifications for which the volume of internal space is parametrically larger than the string length. This is because in SU(5) unified gauge theories, for example, the doublet-triplet splitting problem will be too difficult to solve within string theory[38] in a form other than implementing a non-trivial line bundle (flat or non-flat) in the hypercharge direction. The Kaluza-Klein scale has to be set at the scale of gauge coupling unification then. If it

[38] Imagine implementing the missing partner mechanism in string theory, for example.

JHEP04(2014)050

group (non-Abelian)	rk 0	rk 1	rk 2	rk 3	tot.
E_8+ any other	5	2	3	0	10
E_7+ any other	3	5	2	0	10
E_6+ any other	3	5	5	0	13

Table 4. This table shows the number of different types of elliptic fibrations in $X_{[1\ 0\ 1]}$, $X_{[1\ 1\ 1]}$, $X_{[2\ 0\ 2]}$ and $X_{[2\ 2\ 2]}$ that contain one of IV*, III* and II* type singular fibres, and have Mordell-Weil lattice of a given rank. One type, where $W_{\text{frame}} = E_8 \oplus E_6 \oplus D_4$ for $X_{[2\ 2\ 2]}$, is counted twice in this table.

turns out, however, that there are more vacua with the $\mathrm{SU}(3)_C \times \mathrm{SU}(2)_L \times \mathrm{U}(1)_Y$ gauge group and accidental gauge coupling unification than those with SU(5) gauge group in the landscape obtained by assuming geometric compactification, then there must be much more $\mathrm{SU}(3)_C \times \mathrm{SU}(2)_L \times \mathrm{U}(1)_Y$ vacua when we include string vacua with non-geometric (just CFT-based) "internal space". Therefore, it is a necessary condition that there are more SU(5) vacua than $\mathrm{SU}(3)_C \times \mathrm{SU}(2)_L \times \mathrm{U}(1)_Y$ vacua in landscapes based on geometric compactification for the study of SU(5) unification in string compactification. It is this necessary condition that we intend to test below.

Instead of carrying out this test itself, we consider a similar (and a little easier) test in this article. Instead of studying the ratio of vacua with SU(5) × (any non-Abelian) and those with SU(3) × SU(2) × U(1) × (any non-Abelian), we study the ratio[39] of vacua with $E_n \times \mathrm{U}(1)^r \times$ (any non-Abelian) and those with $E_{n-1} \times \mathrm{U}(1)^{r+1} \times$ (any non-Abelian) $(n = 6, 7, 8)$.

The $\mathcal{J}_2(X)$ classification has been worked out completely for four attractive K3 surfaces, $X = X_{[1\ 0\ 1]}$, $X_{[1\ 1\ 1]}$, $X_{[2\ 0\ 2]}$ and $X_{[2\ 2\ 2]}$ [73]. Let us first use these statistics — a subset of (4.27) — and further use the short-cut approach we explained above to see the ratio of vacua with a $E_{6,7,8}$ gauge group on 7-branes along with how many U(1) vector fields they are accompanied. There are 112 different types of elliptic fibrations in $\mathcal{J}_2(X)$ for the four K3 surfaces combined, and 32 among them contain one of $E_{6,7,8}$ as a part of the 7-brane gauge group.[40] Using the information in table 1.1–1.4 of [73], the statistics turns out to be the following (table 4).

In addition to the four attractive K3 surfaces, the authors have partially carried out the $\mathcal{J}_2(X)$ classification for another attractive K3 surface[41] $X_{[3\ 0\ 2]}$ in [26], so that the same statistics as above can be extracted. There are 43 different types of elliptic fibrations on $X_{[3\ 0\ 2]}$ which contain either one of the IV*, III* or II* type singular fibres. The distribution of the rank of the Mordell-Weil lattice turns out be the following (table 5).

[39] It must be a reasonable assumption that such gauge groups originate from 7-branes rather than D3-branes; D3-branes (rather than fractional 3-branes) only give rise to $\mathcal{N} = 4$ super Yang-Mills theory, and furthermore, their gauge couplings are parametrically larger than those of 7-branes because of the volume of four-cycles that the 7-branes are wrapped.

[40] Here, 23/112 is the fraction of the types of elliptic fibration containing IV*, III* or II* type singular fibres in $X_{[1\ 0\ 1]}$, $X_{[1\ 1\ 1]}$, $X_{[2\ 0\ 2]}$ and $X_{[2\ 2\ 2]}$. Such a fraction for an attractive K3 surface $X_{[a\ b\ c]}$ may, however, have some correlation with whether a, c are large or small.

[41] There is no particular reason to choose this attractive K3 surface (rather than thirty-three others) from the perspective of physics.

JHEP04(2014)050

group (non-Abelian)	rk 0	rk 1	rk 2	rk 3	tot.
E_8+ any other	2	5	2	0	9
E_7+ any other	2	9	7	0	18
E_6+ any other	0	8	8	3	19

Table 5. The number of different types of elliptic fibrations of $\mathcal{J}_2(X_{[3\ 0\ 2]})$ containing either one of IV*, III* or II* type singular fibres and having Mordell-Weil lattice with various ranks. Three types with $W_{\rm root} = A_2E_7E_8$, $A_1E_7E_8$ and $A_3E_6E_7$ contribute twice in this table, so that the total number is summed up to 46, rather than 43.

When we compare the numbers in the two tables (tables 4 and 5) for E_n with rank$(MW) = r$ ($E_n \times \mathrm{U}(1)^r \times$ (any non Abelian) massless gauge fields on 7-branes) and for E_{n-1} with rank$(MW) = r+1$ ($E_{n-1} \times \mathrm{U}(1)^{r+1} \times$ (any non Abelian) massless gauge fields on 7-branes), we cannot observe a clear tendency. There are as many $E_n \times \mathrm{U}(1)^r$ (i.e., more unified) vacua as $E_{n-1} \times \mathrm{U}(1)^{r+1}$ (i.e., less unified) vacua in this sample. Although we cannot hope to extract too many lessons from this study based on a miniature landscape, it may not be too outrageous to say that this statistics does not indicate that it is nonsense to study unified theories in compactifications.

CP Violation. Just like in earlier work such as [17], the miniature landscape in this section can also be used to study the fraction of vacua preserving CP symmetry. To be more specific, we study the fraction of CP preserving vacua in the class of effective theories containing $E_8 \times E_8$ gauge group from 7-branes. Such a formulation of the problem is meaningful, because we would eventually like to ask the fraction of CP-preserving/violating vacua in effective theories with the Standard Model gauge group. The choice of the gauge group — $E_8 \times E_8$ — is entirely for a technical reason. For most other choices of the gauge group, we would have to work out the $\mathcal{J}_2(X)$ classification for all the 34 attractive K3 surfaces appearing in table 2. It is known, however, (see [16, 26, 58, 59] or Footnote 49 for an explanation) that any attractive K3 surface admits an elliptic fibration whose frame lattice contains the $E_8 \oplus E_8$ lattice, so that there must be two fibres of type II^*.

In table 2, there are 66 pairs of attractive K3 surfaces $Y = S_1 \times S_2$ for M-theory compactifications. From these, one can find 98 choices of $Y = X \times S = X_{[a\ b\ c]} \times X_{[a'\ b'\ c']}$ for F-theory compactifications, where elliptic fibrations (with the vanishing volume of the fibre) are implemented in $X_{[a\ b\ c]}$. Exploiting the $\mathbb{Z}_2$ ⟨c.c.⟩ in the modular group Γ in (4.26), we can always take $b \geq 0$. We take these 98 different choices as the denominator (whole ensemble) of the statistics (see the cautionary remark at the end of this CP study).

In order to see when the low-energy effective theory possesses CP symmetry, let us write down the Gukov-Vafa-Witten superpotential (1.2), (2.22) explicitly in terms of local coordinates of the moduli space $\mathcal{M}_{K3}^{(S_1)} \times \mathcal{M}_{K3}^{(S_2)}$. Let $\Omega_{S_i}^{\rm tot}$ for $i = 1, 2$ be the total holomorphic $(2,0)$-form on the K3 surface S_i for $i = 1, 2$, including both the vacuum value and fluctuation around it:

$$\Omega_{S_i}^{\rm tot} = \langle \Omega_{S_i} \rangle + \delta\Omega_{S_i} = p_i + q_i(\tau_i + \widetilde{\Pi}_i) + C_I^{(i)} \delta\Pi_I^{(i)}, \qquad i = 1, 2\,. \tag{4.29}$$

JHEP04(2014)050

The Ω_{S_i} which appeared in section 2.1 corresponds to the vacuum value $\langle\Omega_{S_i}\rangle$ here, and $\{C_I^{(i)}\}_{I=1,\cdots,20}$ is a basis of the Neron-Severi lattice S_{S_i}. $\delta\Pi_I^{(i)}$ for $i=1,2$ and $I=1,\cdots,20$ combined are the independent local coordinates of $\mathcal{M}_{K3}^{(S_1)}\times\mathcal{M}_{K3}^{(S_2)}$, and $\widetilde{\Pi}_i$ are determined by the condition $(\Omega_{S_i}+\delta\Omega_{S_i})^2=0$. In practice,

$$\tau_1+\widetilde{\Pi}_1=\frac{-b+i\sqrt{Q_1+2c(\delta\Pi^{(1)})^2}}{2c}=\tau_1+\frac{i\sqrt{Q_1}}{2c}\left(\frac{c(\delta\Pi^{(1)})^2}{Q_1}-\frac{1}{2}\left(\frac{c(\delta\Pi^{(1)})^2}{Q_1}\right)^2+\cdots\right), \tag{4.30}$$

$$\tau_2+\widetilde{\Pi}_2=\frac{-e+i\sqrt{Q_2+2f(\delta\Pi^{(2)})^2}}{2f}=\tau_2+\frac{i\sqrt{Q_2}}{2f}\left(\frac{f(\delta\Pi^{(2)})^2}{Q_2}-\frac{1}{2}\left(\frac{f(\delta\Pi^{(2)})^2}{Q_2}\right)^2+\cdots\right), \tag{4.31}$$

where $(\delta\Pi^{(i)})^2$ is the norm of $C_I^{(i)}\delta\Pi_I^{(i)}$ under the symmetric pairing of the Neron-Severi lattices S_{S_i}. Substituting (4.29) into (1.2), (2.22), we obtain

$$W\propto\left(G_1,(\Omega_{S_1}^{\rm tot}\otimes\Omega_{S_2}^{\rm tot})\right) \tag{4.32}$$

$$\begin{aligned}&=\sqrt{Q_1Q_2}\Big[\mathrm{Re}(\gamma\tau_1\bar{\tau}_2)+\mathrm{Re}(\gamma)(\tau_1+\widetilde{\Pi}_1)(\tau_2+\widetilde{\Pi}_2)\\&\qquad-\mathrm{Re}(\gamma\bar{\tau}_2)(\tau_1+\widetilde{\Pi}_1)-\mathrm{Re}(\gamma\tau_1)(\tau_2+\widetilde{\Pi}_2)\Big],\end{aligned} \tag{4.33}$$

This potential contains mass terms of all the fluctuations,[42] as expected (moduli stabilization), and furthermore quartic and higher order interactions, as is known very well [16, 18, 22, 24].

Note first the vacuum expectation value of this superpotential vanishes. One can see this by expanding (4.33) in a power series of $(\delta\Pi^{(i)})^2$ and evaluating the zero-th order term. The vanishing vev of $W_{\rm GVW}$, however, is a straightforward consequence of choosing the four-form flux to be purely of $(2,2)$ type in the Hodge decomposition. It will be difficult to find a symmetry reason for this vanishing vev of $W_{\rm GVW}$ covering all the 66 pairs of $S_1\times S_2$ for M-theory compactification, or all the 98 choices of $X\times S$ for F-theory. It seems more appropriate to consider that the $\mathcal{D}=2$ condition (2.23) is essential, see the discussion right after (2.23) and (5.11), and also [17]. The integral structure of the flux quanta plays an essential role in determining the moduli vev through $W_{\rm GVW}$. Hence it is not appropriate to apply naive naturalness arguments of bottom up phenomenology.

In a subset of vacua where $b=e=0$ for M-theory ($b=b'=0$ for F-theory), both τ_1 and τ_2 are purely imaginary and the GVW superpotential becomes CP invariant when

[42] Chiral multiplets in the adjoint representation of the non-Abelian 7-brane gauge groups (in $W_{\rm root}$), i.e., transverse fluctuations of the 7-branes, also become massive because of this. This mass term, due to the G_1 type four-form flux, has nothing to do with the level-2 differential

$$d_2:[E_2^{0,1}=H^0(S;K_S)]\to[E_2^{2,0}=H^2(S;\mathcal{O}_S)] \tag{4.34}$$

that we encounter in the spectral sequence calculation in heterotic language [34, 79]. It is only the kernel of this d_2 that remains massless (in the absence of the G_1 type flux), but this d_2 is always trivial for the case of our interest, for reasons that are explained in [80].

JHEP04(2014)050

we choose γ to be either purely real or pure imaginary. In the first case, the two terms in the second line of (4.33) vanish, and all the terms in the superpotential have real valued coefficients. In the latter case, the two terms in the first line of (4.33) vanish, and all the remaining terms — those in the second line — have purely imaginary coefficients. With an appropriate phase redefinition of fermion fields (R-symmetry transformation), those coefficients can be made real valued. Thus, for these two case, all of the coefficients in the effective superpotential can be made real valued (by field redefinitions, if necessary), and CP symmetry is preserved. Following [17], we understand that the CP invariance in the former case is due to the compactification data $([a\ b\ c],[d\ e\ f],\gamma)$ invariant under the $\mathbb{Z}_2\,\langle\text{c.c.}\rangle$ subgroup of the modular group Γ, and is due, in the latter case, to the compactification data being invariant under the combination of the c.c. operation followed by a non-modular group symmetry operation (that somehow becomes an R-symmetry transformation).

Among the 66 pairs of attractive K3 surfaces in table 2, there are 20 pairs where $b = e = 0$ and γ is either purely real or purely imaginary. To turn this statistics into that of F-theory compactifications, note that among the 98 different ways of identifying the 66 pairs with $X \times S$ for F-theory, 30 different ways correspond to $b = b' = 0$ and a purely real/imaginary choice of γ. Although such precise values as 30/98 do not have much importance,[43,44] it will not be too outrageous to conclude that a non-negligible fraction of vacua possesses CP symmetry in the landscape of K3 × K3 compactifications of F-theory with all the 40 complex structure moduli stabilized by the G_1 type four-form flux. See also related discussion in section 5.

4.3.2 Stable degeneration "limit"

F-theory compactifications on $Y = \text{K3}\times\text{K3} = X\times S$ (without a four-form background) are dual to heterotic string compactifications on $Z = T^2\times\text{K3}$ [30, 31, 52, 71, 79, 81–83]. From the heterotic string picture, one would naively expect that the Kaluza-Klein reduction of metric and B-field on T^2 gives rise to 4 massless U(1) vector fields in 7+1-dimensions, in addition to the at most rank-16 gauge group from either $E_8 \times E_8$ or SO(32). Since F-theory compactifications on an attractive K3 surface X have rank 20 gauge groups on 7-branes (two U(1)'s from T_X and rank 18 from W_{frame}), there is no mismatch in the rank of the gauge groups. It often happens in the miniature landscape we studied, however, that there are not more than four U(1) factors in the 7-brane gauge group. In tables 4

[43] It should be noted that we ignore the possibility that an attractive K3 surface may admit more than one type of elliptic fibration where $E_8 \times E_8 \subset W_{\text{root}} \subset W_{\text{frame}}$. In fact, one can find an example of this in section4.4 of [26]: the attractive K3 surface $X_{[3\ 0\ 2]}$ admits a pair of elliptic fibrations where W_{root} are the same, but their W_{frame} are not isometric. We also ignore multiple inequivalent choices of γ (G_1 type flux) and the number of isomorphism classes of elliptic fibrations. These factors should, in principle, be treated as a non-trivial weight on the 98 different choices in the main text. Thus, the precise value of the fraction of CP-invariant vacua does not have much importance.

[44] Complex conjugation $\mathbb{Z}_2\,\langle\text{c.c.}\rangle$ of the M-theory real 8-dimensional manifold is included as a part of the modular group (4.23), (4.26) in this article, while it is not in [17]. This subtle differences, however, only leads to at most a factor of 2 difference in the fraction of CP-preserving vacua. Given the other factors that we did not try to bring under control, this issue would not be particularly important from practical perspectives.

JHEP04(2014)050

and 5, for example, the rank of Mordell-Weil lattice is less than two (meaning that the number of U(1) gauge group is less than four) in a large fraction of the types of elliptic fibrations. By looking at the tables in [73], one can confirm that this phenomenon is not an artefact of requiring either one of E_6, E_7 or E_8 in the 7-brane gauge group. An appropriate interpretation of this phenomenon should be that the large fraction of attractive K3 surfaces in $\mathrm{Isom}^+(\Lambda_{\mathrm{K3}})\backslash D^{(X)}_{\rho=20}$ satisfying both the D3-tadpole condition (2.25) and the pure G_1-type assumption (2.18) does not correspond to the large $\mathrm{vol}(T^2)/\ell_s^2$ region of the heterotic string moduli space. In this case, the supergravity approximation is not valid and some of the non-Abelian 7-brane gauge groups should be understood as stringy effects in heterotic language.

Corresponding to the supergravity (large $\mathrm{vol}(T^2)/\ell_s^2$) "limit" in heterotic string theory is the stable degeneration "limit" of a K3 surface in F-theory [30, 31]. In this section, we discuss a couple of issues associated with this supergravity/stable degeneration "limit", based on the statistics in the miniature landscape. In this article, we mean by large/small "limit" of a moduli parameter xxx the region of moduli space where xxx is parametrically large/small, i.e., xxx $\gg 1$ or xxx $\ll 1$. However, we still assume xxx to be different from literally being ∞ or 0.

Let us begin with reminding ourselves of the following. Suppose that the elliptic fibration of a K3 surface $\pi_X : X \longrightarrow \mathbb{P}^1$ is given by the generalized Weierstrass form (or Tate form)

$$\begin{aligned} y^2 = {} & x^3 + x f_0 z^4 + g_0 z^6 \\ & + \epsilon_\eta (a^{\mathrm{v}}_{0*} z^5 + \epsilon_K^2 a^{\mathrm{v}}_{2*} x z^3 + \epsilon_K^3 a^{\mathrm{v}}_{3*} y z^2 + \epsilon_K^4 a^{\mathrm{v}}_{4*} x^2 z + \cdots) \\ & + \epsilon_\eta (a^{\mathrm{h}}_{0*} z^7 + \epsilon_K^2 a^{\mathrm{h}}_{2*} x z^5 + \epsilon_K^3 a^{\mathrm{h}}_{3*} y z^4 + \cdots), \end{aligned} \tag{4.35}$$

where (x, y) are the coordinates of the elliptic fibre, z the inhomogeneous coordinate of the base $\mathbb{P}^1$, and f_0, g_0, a^{v}_{r*}'s $(r = 0, 2, \cdots)$ and a^{h}_{r*}'s are complex numbers of order unity. In the heterotic dual, $\mathrm{vol}(T^2)/\ell_s^2$ is parametrically large when[45] $|\epsilon_\eta| \ll 1$, $|\epsilon_K| \lesssim \mathcal{O}(1)$. K3 surfaces with an elliptic fibration with small ϵ_η are said to be in the stable degeneration "limit" [30, 31].[46]

[45] The Wilson lines on T^2 are small, so the 8D field theory approximation is valid when one more condition, $|\epsilon_K| \ll 1$, is also satisfied.

[46] A family of K3 surfaces $\pi' : \mathcal{X}' \longrightarrow D$ was introduced in [31], where $D := \{t \in \mathbb{C} \mid |t| \leq 1\}$ is the unit disc, $\mathcal{X}'$ is given by $y^2 = x^3 + f_0 x z^4 + (g_0 z^6 + \epsilon_\eta a^{\mathrm{v}} z^5 + \epsilon_\eta a^{\mathrm{h}} z^7)$ defined as a subspace of (y, x, z, ϵ_η) for some complex valued parameters f_0, g_0, a^{v} and a^{h}. The morphism π' is defined by $\pi' : (y, x, z, \epsilon_\eta) \mapsto t = \epsilon_\eta$. Instead of this family of K3 surfaces, one can also consider another family $\pi : \mathcal{X} \longrightarrow D$ given by $\mathcal{X} := \{(\eta, \xi, u, v, t) \in \mathbb{C}^5 \mid \eta^2 = \xi^3 + f_0 \xi + (g_0 + a^{\mathrm{v}} u + a^{\mathrm{h}} v),\ uv = t\}$ (to be more precise, (η, ξ) and (u, t) are affine coordinates of projective space). The original family $\pi' : \mathcal{X}' \longmapsto D$ is regarded as the base change of order 2 of the second family $\pi : \mathcal{X} \longmapsto D$, $D \ni \epsilon_\eta \mapsto \epsilon_\eta^2 = t \in D$. Other coordinates are mapped by $(u, v) = (\epsilon_\eta/z, \epsilon_\eta z)$, $\eta = y/z^3$ and $\xi = x/z^2$. The second family shows a semistable degeneration, in that i) the threefold $\mathcal{X}$ is non-singular, and ii) the central fibre $X_0 := \pi^{-1}(t = 0)$ consists of two rational elliptic surfaces (a.k.a "dP_9") crossing normally along an elliptic curve at $u = v = 0$. See [84] for more information. Provided that f_0, g_0, a^{v} and a^{h} are generic, $X_t := \pi^{-1}(t)$ for any $t \in D$ has $\mathrm{II}^* + \mathrm{II}^*$-type singular fibre in the non-singular model at $(u, v) = (\infty, 0)$ and $= (0, \infty)$. The Weierstrass model version of this family has two ordinary $E_8 + E_8$ singularities.

JHEP04(2014)050

When $|\epsilon_\eta| \ll 1$, and the heterotic dual (in the supergravity approximation) corresponds to $E_8^{\rm v} \times E_8^{\rm h}$ theory with the structure group $G_{\rm str}^{\rm v} \times G_{\rm str}^{\rm h} \subset E_8^{\rm v} \times E_8^{\rm h}$, so that the unbroken symmetry group in the visible and hidden sector are $H^{\rm v} \times H^{\rm h}$, the non-$U_*$ part of the cohomology group of K3 surface X,

$$[U_*^\perp \subset H_2(X;\mathbb{Z})] \cong [U^{\oplus 2} \oplus E_8^{\oplus 2}] = \mathrm{II}_{2,18}\,, \tag{4.36}$$

contains $H^{\rm v} + G_{\rm str}^{\rm v} + U + U + G_{\rm str}^{\rm h} + H^{\rm h}$. The moduli spaces on both sides of the duality are identified by identifying the right-moving momenta (see appendix A for conventions on the description of T^2 compactification of heterotic string theory)

$$\mathcal{Z}^R := \sqrt{\frac{\alpha'}{2}}(k_8^R + i k_9^R) \in \mathrm{Hom}(\mathrm{II}_{2,18}, \mathbb{C}) \tag{4.37}$$

in heterotic string theory with the period integral $\Omega^{\rm norm.} \in [U_*^\perp \subset \Lambda_{\rm K3}]^* \otimes \mathbb{C}$ satisfying the normalization[47]

$$(\mathcal{Z}^R, \overline{\mathcal{Z}^R}) = 2 \leftrightarrow (\Omega^{\rm norm.}, \overline{\Omega^{\rm norm.}}) = 2\,. \tag{4.38}$$

Parametrically large volume $\mathrm{vol}(T^2)/\ell_s^2$ with $\ell_s^2 := (2\pi)^2\alpha'$ in heterotic string theory corresponds to the behaviour

$$\mathcal{Z}^R|_{U\oplus U} \sim \frac{1}{\sqrt{2}}\left(\frac{\sqrt{\alpha'}}{R_8}, -\frac{R_8}{\sqrt{\alpha'}}, i\frac{\sqrt{\alpha'}}{R_9}, -i\frac{R_9}{\sqrt{\alpha'}}\right), \qquad \mathcal{Z}^R|_{G_{\rm str}^{\rm v}\oplus G_{\rm str}^{\rm h}} \sim \frac{\sqrt{\alpha'}}{R}\,, \tag{4.39}$$

while the period integral becomes

$$\Omega^{\rm norm.}|_{U\oplus U} \sim \frac{1}{\sqrt{2}}\left(\frac{1}{\sqrt{\ln(1/\epsilon_\eta)}}, \sqrt{\ln(1/\epsilon_\eta)}, \frac{1}{\sqrt{\ln(1/\epsilon_\eta)}}, \sqrt{\ln(1/\epsilon_\eta)}\right)\,. \tag{4.40}$$

for small ϵ_η in F-theory. Hence the relation is $\mathrm{vol}(T^2)/\ell_s^2 \sim (R_8 R_9)/\alpha' \sim \ln(1/\epsilon_\eta)$ (see e.g. appendix B of [85]).[48]

Let us now study the distribution of vacua in the miniature landscape, focusing on whether the vacua are close to the stable degeneration "limit" of a K3 surface, or to the large large $\mathrm{vol}(T^2)/\ell_s^2$ "limit" in heterotic language. For this purpose, the volume in heterotic string theory can be defined easily and unambiguously by using the Narain moduli (see below), and we use this $[\mathrm{vol}(T^2)/\ell_s^2]_{\rm Het}$ as the parameter of distribution.

It is then more direct and convenient to deal with the F-theory data in terms of period integrals, rather than the defining equation(s) of K3, since we use the heterotic-F-theory

[47] For the period integral Ω, we can always take $\Omega^{\rm norm.} = \sqrt{2/(\Omega,\overline{\Omega})} \times \Omega$.

[48] In physics, it is an interesting question whether or not the $t = 0$ point should be included in the string-theory moduli space. Along a one-dimensional subspace parametrized by ϵ_η, the distance from a point with finite ϵ_η to the $\epsilon_\eta \longrightarrow 0$ limit diverges, when the metric from the Kähler potential $K = -\ln[\int \Omega \wedge \overline{\Omega}]$ is used (section 5 [72]). It is also impossible to stay within the period domain D while setting $\epsilon_\eta = 0$ (see (4.40)). Note also, however, that ϵ_η can always be absorbed by redefinition of the coordinates (y, x, z) in a special locus $a_0^{\rm h} = a_2^{\rm h} = \cdots = 0$. In this special locus, the K3 surface has a bad singularity in the fibre over the $z = \infty$ point in the base $\mathbb{P}^1$. Although this singularity can be removed by a birational transformation, the new geometry is a rational elliptic surface (where $c_1 \neq 0$), rather than a K3 surface. Physics implications of this mathematical facts should be considered separately.

JHEP04(2014)050

duality. Let us follow [16, 58, 59] and consider (for simplicity and concreteness) only the case in which the gauge groups in the visible and hidden sector E_8 both remain unbroken. For any attractive K3 surface $X = X_{[a\ b\ c]}$ with $T_X = \begin{bmatrix} 2a & b \\ b & 2c \end{bmatrix}$ there always exists such an elliptic fibration.[49] $T_X \oplus T_X[-1]$ forms a sublattice of $U \oplus U$, and $W_{\text{frame}} = E_8 \oplus E_8 \oplus T_X[-1]$. To be more explicit, let the oriented basis of T_X be $\{q, p\}$ and $T_X[-1] = \text{Span}_{\mathbb{Z}}\{Q, P\}$. Then we can embed T_X and $T_X[-1]$ primitively into $U \oplus U = \text{Span}_{\mathbb{Z}}\{v, V\} \oplus \text{Span}_{\mathbb{Z}}\{v', V'\}$ as[50]

$$(p, q, P, Q) = (v, V, v', V') \begin{pmatrix} 1 & & -1 & \\ a & b & a & \\ & 1 & & -1 \\ & c & b & c \end{pmatrix} . \tag{4.41}$$

The period vector $\langle \Omega_X \rangle = (p + \tau_X q, \bullet)$ (with τ_X and Q_X given by τ in (2.8)) is written as

$$\langle \Omega_X \rangle |_{U \oplus U} = (v + (a + b\tau_X)V + \tau_X v' + c\tau_X V', \bullet) \Longrightarrow \langle \Omega_X^{\text{norm.}} \rangle = \sqrt{\frac{2c}{Q_X}}((a + b\tau_X), 1, c\tau_X, \tau_X) \tag{4.42}$$

in the component description of $[U \oplus U]^* \otimes \mathbb{C}$. This moduli data for F-theory is to be identified with

$$Z : \begin{pmatrix} n_1 \\ -w^1 \\ n_2 \\ -w^2 \end{pmatrix} \longrightarrow \frac{i}{\sqrt{2(\text{Im}\tau_H)(\text{Im}\rho_H)}}(-\tau_H, -\rho_H, 1, -\rho_H\tau_H) \begin{pmatrix} n_1 \\ -w^1 \\ n_2 \\ -w^2 \end{pmatrix} \tag{4.43}$$

modulo $\text{Isom}(U \oplus U)$. Here τ_H is the complex structure modulus of T^2 for heterotic string compactification and $\rho_H = (B + iJ)/\ell_s^2$ is the complexified Kähler modulus of T^2. With the condition (2.11), the best identification is [58, 59]

$$\tau_H \leftrightarrow \tau_X , \qquad \rho_H \leftrightarrow c\tau_X , \qquad \tau_H\rho_H \leftrightarrow -(a + b\tau_X) . \tag{4.44}$$

From this, we can read off that

$$\left[\frac{\text{vol}(T^2)}{\ell_s^2} = \text{Im}(\rho_H) \right]_{\text{Het}} = \left[\frac{\sqrt{Q_X}}{2} = \frac{\sqrt{4ac - b^2}}{2} \right]_F , \qquad |\rho_H| = \sqrt{ac} . \tag{4.45}$$

Vacua parametrically close to the stable degeneration limit (i.e., parametrically large $\text{vol}(T^2)/\ell_s^2$ for heterotic string theory) are realized when the attractive K3 surface is characterized by large ac or Q_X. There is an upper limit on the value of a and c, which comes from the D3-brane tadpole condition (2.25). For moderate choices of a, b and c, neither

[49] Indeed, we can always embed T_0 into one of the Niemeier lattices, $T_0 \hookrightarrow E_8 \subset E_8 + E_8 + E_8$, precisely in the same way T_0 is obtained, $T_0 := [T_X[-1]^\perp \subset E_8]$. The frame lattice then becomes simply $T_X[-1] + E_8 + E_8$. See [73] or section 4 of [26] for a more detailed explanation. No special condition on T_X needs to be satisfied for this fibration to exist in the $\mathcal{J}_2(X)$ classification.

[50] The symmetric pairing is given by $(v, V) = (v', V') = 1$, zero otherwise.

JHEP04(2014)050

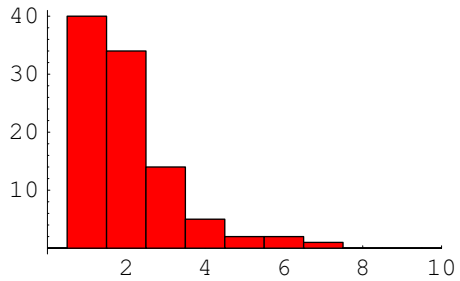

Figure 2. Distribution of $\sqrt{Q}/2 = [\mathrm{vol}(T^2)/\ell_s^2]_{\mathrm{Het}}$ in the miniature landscape (conditions (2.18), (2.25)) from F-theory on K3 × K3.

$|(a+b\tau)|$ nor $|c|$ are large, and hence the F-theory flux vacua are not attracted towards the region where the heterotic dual has a good supergravity approximation.

The distribution of $[\mathrm{vol}(T^2)/\ell_s^2]_{\mathrm{Het}}$, and hence of $\sqrt{Q_X}/2$ in F-theory, is determined and presented in figure 2, using the 98 different identifications of $S_1 \times S_2$ for M-theory in table 2 with $X \times S = X_{[a\ b\ c]} \times X_{[a'\ b'\ c']}$ for F-theory. It is clear that only a small fraction of vacua in the tail of the distribution in figure 2 are in the moduli space of K3 surfaces X in the stable degeneration "limit", or in the large $\mathrm{vol}(T^2)/\ell_s^2$ region of heterotic $E_8 \times E_8$ compactification.

This distribution can be regarded as that of an ensemble of effective theories containing $E_8 \times E_8$ 7-brane gauge groups (which are left unbroken), but it can also be regarded as that of theories with SO(32) 7-brane gauge group.[51]

For moderate choices of a, b and c, we should not expect that ϵ_K is small, either. In other words, all the period integrals in such a K3 surface either vanish or are of order unity. This means that there is no extra singular fibre located closely to a singular fibre supporting 7-brane non-Abelian gauge groups, like H^{v} and H^{h} in the visible and hidden sector. Correspondingly, the appropriate field theory local model is to take H^{v} and H^{h} as the gauge group everywhere[52] on the other K3 surface S.

Let us now turn our attention back to the defining equation (4.35) of the K3 surface. Certainly it is a better and more direct approach for a systematic search for the Noether-Lefschetz locus of Y to parametrize the moduli space by period integrals and deal with the lattices T_X, S_X etc., but it is also nice if we can figure out what kind of defining equations such vacua correspond to. Precisely the same problem has been addressed by [74, 86] for a specific class of K3 surfaces. In the following, we provide a simplified summary of their results so it fits to the context in this article.

[51] See footnote 49, and replace the lattice $L^{(\gamma)} = E_8 \oplus E_8 \oplus E_8$ with $L^{(\beta)} = E_8 \oplus D_{16}; \mathbb{Z}_2$. See [26] for more explanations.

[52] When Y is a non-trivial K3 fibration over some surface S, then there will usually be matter curves and possibly Yukawa points. That is where "singular fibres collide" and the field theory local model should be such that the rank of the gauge group is higher than that of H^{v} or H^{h} by (at least) 1 or 2, respectively [33, 87–89]. In the class of models studied in this article, however, such loci are absent because of the direct product structure $X \times S$.

JHEP04(2014)050

Consider an attractive K3 surface $X_{[2A\ 2B\ 2C]}$ (i.e., special case $a = 2A$, $b = 2B$ and $c = 2C$). Such a K3 surface corresponds to $\mathrm{Km}(E_{\rho_1} \times E_{\rho_2}) = (E_{\rho_1} \times E_{\rho_2})/\mathbb{Z}_2$ with

$$\rho_1 = \frac{-B + i\sqrt{4AC - B^2}}{2C}, \qquad \rho_2 = \frac{-B + i\sqrt{4AC - B^2}}{2} = C\rho_1 \,. \tag{4.46}$$

E_{ρ_i} $(i = 1, 2)$ is an elliptic curve with the complex structure ρ_i, and we let its defining equation[53] be $y^2 = x(x-1)(x-\lambda_i)$. Kummer surfaces associated with a product type Abelian surface, which have $\rho_X = 18$, are known to have at least 11 different types of elliptic fibrations [75]. One of them (type 3 in [75]) has $2\mathrm{IV}^* + 8I_1$ type singular fibres (including two "E_6-type" fibres) in the Kodaira classification. Let us take this type of elliptic fibration as an example. Ref. [86] found that the Weierstrass model for this type of fibration (Inose's pencil) is given by

$$Y^2 = (X{+}4u^2)(X{+}4u^2(\lambda_1{+}\lambda_2))(X{+}4u^2\lambda_1\lambda_2) + \frac{(4u^2)^3}{4}\left\{\frac{\lambda_2(\lambda_2{-}1)}{u} + \lambda_1(\lambda_1{-}1)u\right\}^2, \tag{4.48}$$

where u is the inhomogeneous coordinate on the base $\mathbb{P}^1$, or equivalently,

$$\tilde{Y}\left\{\tilde{Y} - (2u)^3\left(\frac{\lambda_2(\lambda_2{-}1)}{u} + \lambda_1(\lambda_1{-}1)u\right)\right\} = (X{+}4u^2)(X{+}4u^2(\lambda_1{+}\lambda_2))(X{+}4u^2\lambda_1\lambda_2)\,. \tag{4.49}$$

Tate's condition for a IV^* fibre is satisfied at $u = 0$ and $u = \infty$. To turn this $\rho_X = 18$ K3 surface into an attractive K3 surface ($\rho_X = 20$), we only have to make a specific choice of ρ_1 and ρ_2 (and hence $\lambda_{1,2}$) in terms of integers A, B and C as in (4.46). The second equation above is already in the form of the generalized Weierstrass form (Tate form, (4.35)), apart from a shift in X that does not play an essential role.[54] The defining equation of the spectral surface can be read off from the Tate form: $a_0^{\mathrm{v}} = a_2^{\mathrm{v}} = 0$, and $a_3^{\mathrm{v}} y = 0$. Thus, in the language of the supergravity approximation of heterotic string theory, the $\rho_X = 20$ vacua of F-theory are realized due to spectral surfaces (gauge field configurations) which are far from generic and imply an intricate conspiracy among f_0, g_0, a_3^{v} and a_3^{h}. We will come back to this issue in section 5.3 and appendix B.

5 Landscapes of F-theory on K3 × K3 with $G_0 \neq 0$ flux

The study in the previous section is for a landscape with a limited choice of four-form flux; the condition (2.18) has been imposed. Consequently, the number of vacua is limited and the level of complexity of the analysis remains (barely) manageable. One can maintain full control of details, if one wishes, which enables us to understand various subtleties

[53] From the definition given in the main text, it follows that

$$\frac{2^{11}(\lambda_i^2 - \lambda_i + 1)^3}{(\lambda_i - 1)^2\lambda_i^2} = j(\rho_i) = q_i^{-1} + 744 + \mathcal{O}(q_i), \qquad q_i = \exp(2\pi i\rho_i)\,. \tag{4.47}$$

Thus, for large $\mathrm{Im}(\rho_i)$, small $|q_i|$ and large λ_i, $2^{11}\lambda_i^2 \sim e^{-2\pi i\rho_i}$.

[54] The stable degeneration "limit" corresponds to large A and C, and hence to large $\mathrm{Im}(\rho_2)$ and large $|\lambda_2|$. With the coordinate redefinition $\tilde{Y} \to \lambda_2^{9/2}\tilde{Y}'$, $X \to \lambda_2^3 X'$ and $u \to \lambda_2 u'$, one finds that $\epsilon_\eta \sim 1/\sqrt{\lambda_2}$, and hence $t = \epsilon_\eta^2 = 1/\lambda_2$.

JHEP04(2014)050

associated with multiplicity counting and the role played by the modular group. The $G_0 = 0$ assumption on the flux, however, has much to do with this advantage.

Suppose that $Y = X \times S$ for F-theory compactification is given by a pair of attractive K3 surfaces X and S, as in section 2.1. The G_0 type flux is then in $S_X \otimes S_S \otimes \mathbb{R}$ and can be written in the form

$$[G_0] = \sum_{I=1}^{18} C_I \otimes F_I \,, \tag{5.1}$$

where $\{C_I\}_{I=1,\cdots,18}$ is chosen as a basis of $W_{\text{root}} \oplus W_{\text{U}(1)} \subset W_{\text{frame}} \subset S_X$ and $F_I \in S_S \otimes \mathbb{Q} \subset H^{1,1}(S;\mathbb{R})$. The gauge bosons corresponding to the Cartan part of the 7-brane gauge fields remain massless for a rank-rk_7 group when the $\{F_I\}$s span an $(18 - rk_7)$-dimensional subspace of $H^{1,1}(S;\mathbb{R})$. The rest of the Cartan gauge fields become massive through the Stückelberg mechanism. There will be $(18-rk_7)$ global U(1) symmetries left in the effective theory. Non-perturbative corrections break these symmetries, but they may still look like approximate symmetries if the non-perturbative corrections break them only weakly.

Therefore it is not a complete nonsense to focus on a sub-ensemble of vacua of F-theory on K3 $\times$ K3 with $G_{\text{tot}} = G_1 + G_0$ flux of a given value of $(18 - rk_7)$ and to study the statistics of this sub-ensemble, as those compactifications share a common property of the resulting effective theories. In this context, the statistical results of the $G_0 = 0$ landscape in section 4.3 are also of some value. They are regarded as the statistics in the sub-ensemble characterized by the rank $rk_7 = 18$ massless gauge group on 7-branes and $\mathcal{N} = 1$ supersymmetry.

There is hence a physical motivation to study the statistics of the sub-landscape characterized by some properties of the G_0 flux, such as rk_7 (see sections 5.3 and 5.4 for more), and also to compare the numbers of vacua that have G_0 with different properties. These are the kind of problems we address in this section.

5.1 General remarks

5.1.1 Primitivity

Let us begin with a brief remark on the Kähler moduli. For supersymmetric compactifications, $G_{\text{tot}} = G_1 + G_0$ not only has to be purely of Hodge type $(2,2)$, but also primitive:

$$J_Y \wedge G_{\text{tot}} = J_Y \wedge G_0 = 0 \,. \tag{5.2}$$

The Kähler form J_Y on $Y = X \times S$ has the shape

$$J_Y = t_X [F_X] + J_S \,, \tag{5.3}$$

where $t_X \in \mathbb{R}_{0<}$, $[F_X]$ is the fibre class (elliptic divisor) associated with $\pi_X : X \to \mathbb{P}^1$, and J_S a Kähler form on S in the positive cone of S_S (i.e., $J_S \in S_S \otimes \mathbb{R}$, and $J_S^2 > 0$). The primitivity condition (5.2) implies that all of the F_I $(I = 1, \cdots, 18)$ are orthogonal to J_S in the inner product in $S_S \otimes \mathbb{R} \cong H^{1,1}(S;\mathbb{R})$. For a given Kähler form J_S, the G_0 type flux

JHEP04(2014)050

in $W_{\text{frame}*} \otimes [J_S^\perp \subset (S_S \otimes \mathbb{R})]$ always gives rise to a positive contribution — $1/2[G_0] \cdot [G_0]$ — to the D3-tadpole, since both W_{frame} and $[J_S^\perp \subset S_S \otimes \mathbb{R}]$ are negative definite.[55]

Because of the primitivity condition of the four-form flux, the complex structure moduli and Kähler moduli talk to each other. There are two equivalent ways to see how they "talk". One way is, to think of the Kähler moduli (t_X, J_S) as being given first, after which the F_I describing G_0 are forced to be in the subspace $[J_S^\perp \subset S_S \otimes \mathbb{Q}]$, as above. If the ratio of components of J_S are in $\mathbb{Q}$ — this situation is denoted by $[J_S] \in \mathbb{QP}[S_S]$ in this article — then $[J_S^\perp \subset S_S \otimes \mathbb{Q}]$ is of dimension [20-1=19]. If the ratio is not just in $\mathbb{Q}$, but in an extension field of $\mathbb{Q}$, then the dimension of the space for G_0 is smaller than 19. In the rest of this article, we assume that $J_S \in \mathbb{QP}[S_S]$. The other way is to think of the F_I as being given first. In this case, J_S is forced to be in the subspace of $S_S \otimes \mathbb{R}$ orthogonal to all of the F_I due to the D-term potential (e.g., [13, 22]). When the F_I span a $(18 - rk_7)$-dimensional subspace of $S_S \otimes \mathbb{Q}$, the remaining moduli space of J_S is of $(2 + rk_7)$-dimensions (in $\mathbb{R}$).[56,57] Eventually one has to think of stabilization of both complex structure moduli and Kähler moduli, so that these two perspectives are equivalent. Common to these two is the idea that the stabilization of the two groups of moduli can be dealt with separately, which is true as long as there is a separation of scales between those two stabilization mechanisms, such as in the KKLT scenario [90].

In this article, we focus on aspects of complex structure moduli stabilization in flux compactifications, using K3 × K3 as an example. This article is not committed to a particular mechanism of Kähler moduli stabilization available on K3 × K3, except that we implicitly assume this separation of scales. It is thus impossible to determine the full landscape distribution of completely discrete vacua in the product of complex structure and Kähler moduli spaces $\mathcal{M}_{\text{cpx}} \times \mathcal{M}_{\text{Kahler}}$ for K3 × K3, or projections of these distributions to $\mathcal{M}_{\text{cpx}}$, without introducing extra assumptions (on Kähler moduli stabilization). Our statements in the rest of this article are often presented in the form of distributions of flux vacua on $\mathcal{M}_{\text{cpx}}$ for a fixed choice of Kähler moduli.

5.1.2 Integrality

Let us now switch the subject, and discuss the "integrality condition" on $[G_1]$ and $[G_0]$. When both $[G_1]$ and $[G_0]$ are non-zero, each one of them does not have to be integral by itself; only the total flux $[G_{\text{tot}}] = [G_1] + [G_0]$ needs to be integral, i.e. an element of $H^4(Y; \mathbb{Z})$. Once we find that $[G_1]$ does not have to be integral — an element of $T_X \otimes T_S$ —

[55] It is not impossible to think of a case with some F_I not orthogonal to $J_S^\perp$. Such an F_I associated with C_I in W_{root} corresponds to non-anti-self-dual flux on a 7-brane wrapped on a K3 surface S, and is known to lead to a de-Sitter vacuum (if Kähler moduli is stabilized properly). If this negative contribution to the D3-brane tadpole — virtually the presence of an anti-D3-brane — coexists with a positive N_{D3}, we expect D3–D7 hybrid inflation to occur [91].

[56] $t_X \in \mathbb{R}_{0<}$ also remains unconstrained under the primitivity condition.

[57] As long as we keep the flux in the form of $G_0 = \sum_I C_I \otimes F_I$, a perturbation $\delta J = t_b[\sigma_X]$ of the Kähler form does not violate the primitivity condition. Thus, there is no mass given to this degree of freedom either. This mode, however, corresponds to a part of the metric, g_{33}, of the effective field theory on $\mathbb{R}^{3,1}$. Phenomenologically, we are interested in cases where the vacuum value of t_b is zero (the small elliptic fibre volume limit of M-theory), yet the fluctuation in that direction — g_{33} remains massless. Thus, there is no problem at all that the fluctuation t_b does not have a mass.

JHEP04(2014)050

on its own, the condition (2.21) is too restrictive. Contributions to the D3-brane tadpole, $[G_1]\cdot[G_1]/2$ and $[G_0]\cdot[G_0]/2$, are not necessarily integers separately either, though their sum is always integral, when $G_{\rm tot}$ is integral. This means that the search for pairs of attractive K3 surface in sections 2.1 and 2.2 needs to be carried out once again for cases with $G_0 \neq 0$. How large is the impact of this generalization?

In cases where both X and S are attractive K3 surfaces, we can decompose the 22×22-dimensional vector space $H^2(X,\mathbb{R})\times H^2(S,\mathbb{R})$ into

$$[(T_X\otimes T_S)\otimes\mathbb{R}]\oplus[(T_X\otimes S_S)\otimes\mathbb{R}]\oplus[(S_X\otimes T_S)\otimes\mathbb{R}]\oplus[(S_X\otimes S_S)\otimes\mathbb{R}]. \tag{5.4}$$

Such a decomposition is not necessarily possible with integer coefficients, not all of the elements of $H^2(X;\mathbb{Z})$ (resp. $H^2(S;\mathbb{Z})$) can be written in the form of a sum of integral elements in T_X and S_X (resp. T_S and S_S), and not all the elements in $H^2(X,\mathbb{Z})\times H^2(S,\mathbb{Z})$ can be written as a sum of integral elements in

$$[(T_X\otimes T_S)]\oplus[(T_X\otimes S_S)]\oplus[(S_X\otimes T_S)]\oplus[(S_X\otimes S_S)]. \tag{5.5}$$

The integrality of the total flux $[G]=[G_1]+[G_0]$, however, implies that for all the generators of $T_X\otimes T_S$ and $S_X\otimes S_S$, which are all integral four-cycles, the flux quanta evaluated on these cycles are integers. Hence $[G_1]$ and $[G_0]$ are contained within $(T_X\otimes T_S)^*=(T_X^*\otimes T_S^*)\subset(T_X\otimes T_S)\otimes\mathbb{Q}$ and $(S_X\otimes S_S)^*=(S_X^*\otimes S_S^*)\subset(S_X\otimes S_S)\otimes\mathbb{Q}$, respectively.[58] In particular, it follows that $[G_1]$ should be within $T_X^*\otimes T_S^*$, but may not necessarily be within $T_X\otimes T_S$.

In fact, there is a stronger necessary condition than this; although the projection of $H^2(S;\mathbb{Z})\subset T_S^*\oplus S_S^*$ to T_S^* for an attractive K3 surface is always surjective, the projection image of

$$(H^2(S_1;\mathbb{Z})\otimes H^2(S_2;\mathbb{Z}))\cap[H^{4,0}(Y;\mathbb{C})\oplus H^{2,2}(Y;\mathbb{R})\oplus H^{0,4}(Y;\mathbb{C})] \tag{5.6}$$

to $(T_{S_1}\otimes T_{S_2})^*$, for $Y=S_1\times S_2$ with a pair of attractive K3 surfaces S_1 and S_2, is not. In order to state a condition on the image of this projection, note that, for a pair of attractive K3 surfaces S_1 and S_2, the transcendental lattices, Neron-Severi lattices and their dual lattices have the following properties: as Abelian groups,

$$T_{S_i}^*/T_{S_i}\cong\mathbb{Z}_{m_i}\times\mathbb{Z}_{n_i},\qquad S_{S_i}^*/S_{S_i}\cong\mathbb{Z}_{m_i}\times\mathbb{Z}_{n_i},\qquad {}^{\exists}\gamma_i: T_{S_i}^*/T_{S_i}\cong S_{S_i}^*/S_{S_i}\qquad (i=1,2) \tag{5.7}$$

for some positive integers m_i, n_i. It then follows that

$$(T_{S_1}\otimes T_{S_2})^*/(T_{S_1}\otimes T_{S_2})\cong\mathbb{Z}_{m_1m_2}\times\mathbb{Z}_{m_1n_2}\times\mathbb{Z}_{n_1m_1}\times\mathbb{Z}_{n_1n_2}\,. \tag{5.8}$$

One can prove[59] that the image of the integral four-cycles in (5.6) has to be within the subgroup of $(T_{S_1}\otimes T_{S_2})^*$ characterized by

$$\mathrm{LCD}(m_1,m_2)\mathbb{Z}_{m_1m_2}\times\cdots\times\mathrm{LCD}(n_1,n_2)\mathbb{Z}_{n_1n_2}\subset\mathbb{Z}_{m_1m_2}\times\cdots\times\mathbb{Z}_{n_1n_2}\,. \tag{5.9}$$

[58] $T_X\otimes T_S$, $T_X\otimes S_S$, $S_X\otimes T_S$ and $S_X\otimes S_S$ form sublattices of the lattice $H^2(X;\mathbb{Z})\otimes H^2(S;\mathbb{Z})$.

[59] We are not presenting the proof here because it is just technical, and is not particularly illuminating. After all, this is not a sufficient condition. It is not guaranteed that an appropriate $G_0\in W_{\rm frame}\otimes[J_S^\perp\subset S_S]\otimes\mathbb{Q}$ exists and $G_1+G_0=G_{\rm tot}$ becomes integral, even when G_1 satisfies this criterion.

JHEP04(2014)050

Because of this necessary condition on $[G_1]$, one can see that $[G_1]$ still has to be an integral element of $T_X \otimes T_S$ if all the four pairs (m_1, m_2), (m_1, n_2), (n_1, m_2) and (n_1, n_2) are mutually coprime. In this case, all the possible forms of the $[G_1]$ component on a pair of attractive K3 surfaces $X \times S = S_1 \times S_2$ remain the same as in sections 2.1 and 2.2. When the four pairs of integers are not coprime, however, there are more chances for the $[G_1]$ component available in the (sublattice of) the $(T_X \otimes T_S)^*$ lattice than in the $T_X \otimes T_S$ lattice. That makes it easier to pass the D3-tadpole constraint (2.25), even for a pair of attractive K3 surfaces with relatively large values of a, c and d, f. Section 5.2 is devoted to an explicit enumerative study in order to see more of the consequences of this possibility of non-integral choice of G_1.

5.1.3 $\langle W_{\rm GVW} \rangle = 0$

When we write the $[G_1]$ component as $G_1 = \mathrm{Re}[\gamma \Omega_{S_1} \wedge \overline{\Omega}_{S_2}]$, as in [18] or in (2.22), it manifestly has only a $(2,2)$ Hodge component, without $(4,0)$ or $(0,4)$ component. However, we may also ask what is the statistical cost of requiring the absence of the $(4,0)+(0,4)$ components, or equivalently, a vanishingly small cosmological constant. For this purpose, the G_0 component is irrelevant and $[G_1] \in (T_{S_1} \otimes T_{S_2}) \otimes \mathbb{Q}$, which we can write as:

$$[G_1] = k_1(p_1 \otimes p_2) + k_2(p_1 \otimes q_2) + k_3(q_1 \otimes p_2) + k_4(q_1 \otimes q_2)\,, \tag{5.10}$$

where $k_1, k_2, k_3, k_4 \in \mathbb{Q}$ are not necessarily integers. The $(4,0)$ and $(0,4)$ Hodge components of $[G_1]$ are

$$\frac{\bar{\tau}_1\bar{\tau}_2 k_1 - \bar{\tau}_1 k_2 - \bar{\tau}_2 k_3 + k_4}{(\bar{\tau}_1 - \tau_1)(\bar{\tau}_2 - \tau_2)}\, \Omega_{S_1} \wedge \Omega_{S_2} + \frac{\tau_1\tau_2 k_1 - \tau_1 k_2 - \tau_2 k_3 + k_4}{(\bar{\tau}_1 - \tau_1)(\bar{\tau}_2 - \tau_2)}\, \overline{\Omega}_{S_1} \wedge \overline{\Omega}_{S_2}\,. \tag{5.11}$$

Thus, the absence of the $(4,0)+(0,4)$ component is equivalent to the condition that either $(\tau_1\tau_2)$, τ_1, τ_2 and 1 are not linear independent over the field $\mathbb{Q}$, or all of $k_{1,2,3,4}$ vanish (and $G_1 = 0$). For an arbitrary pair of attractive K3 surfaces S_1 and S_2, the period integrals take their values in $\mathbb{Q}[\tau_1, \tau_2]$, which is a degree $\mathcal{D} = 4$ algebraic extension field over $\mathbb{Q}$. The condition for this pair S_1 and S_2 to admit a flux with vanishing cosmological constant[60] (while $G_1 \neq 0$), however, has turned out to be that τ_2 is already contained in $\mathbb{Q}[\tau_1]$, and $\mathbb{Q}[\tau_1, \tau_2]$ is a degree $\mathcal{D} = 2$ extension field of $\mathbb{Q}$. The condition (2.23) is for $\langle W \rangle = 0$, for a general non-vanishing $[G_1]$ in $(T_X \otimes T_S) \otimes \mathbb{Q}$, rather than just for an integral $[G_1] \in (T_X \otimes T_S)$.

5.2 A landscape of vacua with a rank-16 7-brane gauge group

Just like the $G_0 = 0$ landscape in section 4.3, which is interpreted as the ensemble of vacua with rank-18 massless gauge fields on 7-branes, let us also consider the ensemble of F-theory compactifications on K3 × K3 with rank-16 massless gauge fields on 7-branes. This is realized by allowing a $G_0 \neq 0$ with only two terms non-zero in the expansion (5.1). With this study, we hope to elucidate various aspects of the landscape involving $G_0 \neq 0$. In

[60] A closely resembling phenomenon is found in section 4.2.3 of [17]. The extension degree changes from $\mathcal{D} = 4$ to $\mathcal{D} = 2$ for $W = 0$ vacua.

JHEP04(2014)050

the context of F-theory, there is not particular importance to the specific choice of having just two terms in (5.1), or equivalently $rk_7 = 16$. However, this choice makes it easier to link the present discussion to earlier results on type IIB orientifold landscapes, as discussed in section 5.4.

Suppose that $G_0 \neq 0$ flux is introduced by using some $C_{I=1}$ and $C_{I=2}$ in (5.1), where $C_{I=1,2}$ are elements of the frame lattice $W_{\text{frame}}(X_{[a\ b\ c]})$ of some attractive K3 surface $X_{[a\ b\ c]}$. Then the gauge fields along the direction of $C_{I=1,2}$ become massive, and only the gauge fields within $[\{C_{I=1,2}\}^{\perp} \subset W_{\text{frame}}]$ remain massless. Since it is motivated from the perspective of physics to collect vacua with a given unbroken gauge group, it will be interesting to consider, for a given rank-16 $= rk_7$ lattice W_{unbroken}, the vacuum ensemble associated with

$$\Big\{(W_{\text{frame}}, \{C_{I=1,2}\}) \mid W_{\text{frame}} \in \amalg_{X_{[a\ b\ c]} \in \text{Isom}(\Lambda_{\text{K3}})\backslash D_{\rho=20}} \mathcal{J}_2(X_{[a\ b\ c]}), \\ C_{I=1,2} \in W_{\text{frame}},\ [\{C_{1,2}\}^{\perp} \subset W_{\text{frame}}] = W_{\text{unbroken}}\Big\}\,. \tag{5.12}$$

For this reason, it also makes sense to use the notation W_{noscan} instead of W_{unbroken}. These two are used interchangeably in section 5.2, but they are distinguished in section 5.4.

If we are to take the rank-16 lattice to be e.g. $W_{\text{unbroken}} = E_8 \oplus E_8$ or $D_{16}; \mathbb{Z}_2\,\langle \mathbf{sp} \rangle$, then for all the attractive K3 surfaces X, there is an embedding[61] of the transcendental lattice T_X, the hyperbolic plane lattice $U_* \cong \text{Span}_{\mathbb{Z}}\{[F_X], \sigma\}$ associated with elliptic fibration, and W_{unbroken} (which is an even unimodular lattice of signature $(0, 16)$) into the cohomology lattice $\Lambda_{\text{K3}}^{(X)}$:

$$U_* \oplus (T_X \oplus T_X[-1]) \oplus W_{\text{unbroken}} \hookrightarrow U_* \oplus (U \oplus U) \oplus W_{\text{unbroken}} \cong \Lambda_{\text{K3}}^{(X)}\,. \tag{5.13}$$

The Neron-Severi lattice is $S_X \cong U_* \oplus T_X[-1] \oplus W_{\text{unbroken}}$, and the frame lattice is $W_{\text{frame}} \cong T_X[-1] \oplus W_{\text{unbroken}}$. Hence we choose the generators of the rank-2 lattice $T_X[-1] = [W_{\text{unbroken}}^{\perp} \subset W_{\text{frame}}]$ as $\{C_{I=1,2}\}$ [16, 24].

As another example of W_{unbroken}, one can also think of $(D_4 \oplus D_4 \oplus D_4 \oplus D_4); (\mathbb{Z}_2 \times \mathbb{Z}_2)$, in which case a type IIB orientifold interpretation is given. It is known that there is an embedding[62]

$$(U[2] \oplus U[2]) \oplus (U_* \oplus W_{\text{unbroken}}) \hookrightarrow \Lambda_{\text{K3}}^{(X)}\,. \tag{5.14}$$

Furthermore, it is known that for attractive K3 surfaces $X_{[a\ b\ c]}$ with a, b, c even, there is an embedding $T_X \oplus T_X[-1] \hookrightarrow U[2] \oplus U[2]$ ([18, 61–63]). Thus, $W_{\text{frame}} \cong T_X[-1] \oplus W_{\text{unbroken}}$, and the generators of the rank-2 lattice $T_X[-1] = [W_{\text{unbroken}}^{\perp} \subset W_{\text{frame}}]$ are chosen as $\{C_{I=1,2}\}$s. [16, 24] Hence all the attractive K3 surfaces with even a, b, c contribute to the ensemble of vacua characterized by $W_{\text{unbroken}} \cong (D_4^{\oplus 4}); (\mathbb{Z}_2 \times \mathbb{Z}_2)$.

[61] For an embedding of T_X into $U \oplus U$, $[T_X^{\perp} \subset U \oplus U]$ is not necessarily the same as $T_X[-1]$. For two even rank-2 lattices T_1 (positive definite) and T_2 (negative definite) with an isometric discriminant group, $U \oplus U$ can be constructed as an overlattice of $T_1 \oplus T_2$ [92].

[62] For Kummer surfaces associated with product type Abelian surfaces ($\rho_X = 18$), $X = \text{Km}(E_\rho \times E_{\rho'}) = (E_\rho \times E_{\rho'})/\mathbb{Z}_2$, the Neron-Severi lattice is $S_X^{\rho=18} \cong U_* \oplus (D_4^{\oplus 4}); (\mathbb{Z}_2 \times \mathbb{Z}_2)$ and the transcendental lattice is $T_X^{\rho=18} \cong U[2] \oplus U[2]$.

JHEP04(2014)050

Let T_S be the transcendental lattice of the attractive K3 surface S. Modulo $\mathrm{Isom}(\Lambda_{\mathrm{K3}}^{(S)})$, it is always possible to embed T_S into $\Lambda_{\mathrm{K3}}^{(S)}$ as

$$T_S \hookrightarrow (T_S \oplus T_S[-1]) \hookrightarrow (U \oplus U) \oplus U \oplus E_8 \oplus E_8 \cong \Lambda_{\mathrm{K3}}^{(S)} . \tag{5.15}$$

This is not only always possible, but also unique in that any embedding to $\Lambda_{\mathrm{K3}}^{(S)} \cong \mathrm{II}_{3,19}$ (not to $\mathrm{II}_{2,18}$) can be brought in the form above modulo $\mathrm{Isom}(\Lambda_{\mathrm{K3}}^{(S)})$ [78]. Thus, $S_S \cong T_S[-1] \oplus U \oplus E_8 \oplus E_8$. Therefore, the flux $G_{\mathrm{tot}} = G_1 + G_0$ is introduced to the space[63]

$$[(T_X \otimes T_S)^* \oplus (T_X[-1] \otimes (T_S[-1] \oplus U \oplus E_8 \oplus E_8))^*] \cap H^2(X;\mathbb{Z}) \otimes H^2(S;\mathbb{Z}) . \tag{5.16}$$

Now, let us take the case $W_{\mathrm{unbroken}} = E_8 \oplus E_8$ as an example, and work out the details. In order to avoid inessential complexity, we restrict our attention to $Y = X \times S$ of the form $X_{[a\ b\ c]} \times X_{[a'\ b'\ c']}$ with $b = b' = 0$. Embeddings of (5.13), (5.15) are given by[64]

$$(p_1, P_1, q_1, Q_1) = (v_1, V_1, v_1', V_1') \begin{pmatrix} 1 & -1 & & \\ a & a & & \\ & & 1 & -1 \\ & & c & c \end{pmatrix} , \tag{5.17}$$

$$(p_2, P_2, q_2, Q_2) = (v_2, V_2, v_2', V_2') \begin{pmatrix} 1 & -1 & & \\ a' & a' & & \\ & & 1 & -1 \\ & & c' & c' \end{pmatrix} , \tag{5.18}$$

where $\{p_1, q_1\}$ (resp. $\{p_2, q_2\}$) are generators of T_X (resp. T_S), and $\{P_1, Q_1\}$ (resp. $\{P_2, Q_2\}$) are generators of $T_X[-1]$ (resp. $T_S[-1]$). The $(U \oplus U)$ sublattice of $\Lambda_{\mathrm{K3}}^{(X)}$ is generated by $\{v_1, V_1\}$ and $\{v_1', V_1'\}$, and that of $\Lambda_{\mathrm{K3}}^{(S)}$ by $\{v_2, V_2\}$ and $\{v_2', V_2'\}$. The intersection forms on the Us are given by $(v, v) = (V, V) = 0$ and $(v, V) = (V, v) = 1$.

It is now straightforward to enumerate the flux $G_{\mathrm{tot}} = G_1 + G_0$ in (5.16), using the basis give above:

$$\begin{aligned} G_1 = & \frac{n_{11}\mathrm{GCD}(a,a') + m_{11}}{2\mathrm{GCD}(a,a')}(p_1 \otimes p_2) + \frac{n_{22}\mathrm{GCD}(c,c') + m_{22}}{2\mathrm{GCD}(c,c')}(q_1 \otimes q_2) \\ & + \frac{n_{12}\mathrm{GCD}(a,c') + m_{12}}{2\mathrm{GCD}(a,c')}(p_1 \otimes q_2) + \frac{n_{21}\mathrm{GCD}(c,a') + m_{21}}{2\mathrm{GCD}(c,a')}(q_1 \otimes p_2), \end{aligned} \tag{5.19}$$

$$\begin{aligned} G_0 = & \frac{n_{11}\mathrm{GCD}(a,a') - m_{11}}{2\mathrm{GCD}(a,a')}(P_1 \otimes P_2) + \frac{n_{22}\mathrm{GCD}(c,c') - m_{22}}{2\mathrm{GCD}(c,c')}(Q_1 \otimes Q_2) \\ & + (P_1 \otimes F_P) + (Q_1 \otimes F_Q) \\ & + \frac{n_{12}\mathrm{GCD}(a,c') - m_{12}}{2\mathrm{GCD}(a,c')}(P_1 \otimes Q_2) + \frac{n_{21}\mathrm{GCD}(c,a') - m_{21}}{2\mathrm{GCD}(c,a')}(Q_1 \otimes P_2), \end{aligned} \tag{5.20}$$

[63] The $T_X[-1]$ part is meant to be $[W_{\mathrm{unbroken}}^{\perp} \subset W_{\mathrm{frame}}]$, which is the same as $T_X[-1]$ for all the three choices of W_{unbroken} mentioned in the text.

[64] This embedding can be used also for the case $W_{\mathrm{unbroken}} \cong D_{16}; \mathbb{Z}_2$, another even unimodular lattice of signature $(0, 16)$. For the case $W_{\mathrm{unbroken}} \cong (D_4^{\oplus 4}); (\mathbb{Z}_2 \times \mathbb{Z}_2)$, the embedding of $T_X = \mathrm{diag}[4A, 4C]$ and $T_X[-1]$ to $U[2] \oplus U[2]$ is given by the same expression, except that a and c are replaced by A and C.

JHEP04(2014)050

$$G_{\rm tot} = n_{11}(v_1 \otimes v_2 + aa' V_1 \otimes V_2) + m_{11} \frac{a' v_1 \otimes V_2 + a V_1 \otimes v_2}{\mathrm{GCD}(a, a')} + \cdots$$
$$+ (P_1 \otimes F_P) + (Q_1 \otimes F_Q)\,. \tag{5.21}$$

Here, $n_{11}, m_{11}, \cdots, n_{22}, m_{22}$ are integers and $F_P, F_Q \in U \oplus E_8 \oplus E_8 \subset \Lambda_{\rm K3}^{(S)}$. The denominators $\mathrm{GCD}(2a, 2a')$, $\mathrm{GCD}(2c, 2c')$ etc. in (5.19), (5.20) correspond to our earlier discussion around (5.9). G_1 and G_0 are not necessarily integral separately, but $G_{\rm tot}$ is. At this moment, it is not guaranteed that the $(4,0)+(0,4)$ Hodge components vanish. After imposing the $\langle W \rangle = 0$ condition, one is left with the following cases

i) $\mathcal{D} := \dim_{\mathbb{Q}} \mathbb{Q}[\tau_1, \tau_2] = 2$, i.e., the condition (2.23) is satisfied when $G_1 \neq 0$ and there are $(8-\mathcal{D}) = 6$ independent integers out of $\{n_{11}, \cdots, m_{22}\}$, in addition to F_P, F_Q. In this case there are $\mathcal{D} = 2$ less scanning integers just like in sections 2.1), (2.2 and [18].

ii) $\mathcal{D} = 4$, when $G_1 = 0$, and there are $(8 - \mathcal{D}) = 4$ independent integers as well as F_P, F_Q (the "second branch" in section 5 of [22]).

The latter ii) cases leave 16 moduli of X and 18 of S unstabilized, and we restrict our attention only to the cases i) ,as [18] did, in the following.

Note, however, that the Kähler form and the primitivity condition on the flux has been ignored completely in the argument above. The Kähler form J_S on S needs to be introduced in the positive definite part of $[T_S^{\perp} \subset \Lambda_{\rm K3}] \otimes \mathbb{R}$, and the flux G_0 component has to be orthogonal to this J_S. We provide the following presentation for a fixed choice of J_S (rather than scanning over all possible J_S), and in particular, we choose

$$J_S = t_S(v_2'' + V_2'')\,, \tag{5.22}$$

where v_2'' and V_2'' are the generators of the third copy of the hyperbolic plane lattice U in $\Lambda_{\rm K3}^{(S)}$ in (5.15), so that the computation becomes as easy as possible. This means that the primitivity condition does not impose a constraint on the integers $\{n_{11}, \cdots, m_{22}\}$, and F_P, F_Q are chosen from the negative definite lattice $(-2) \oplus E_8 \oplus E_8$. Here, (-2) is the lattice generated by $(v_2'' - V_2'')$, where $(v_2'' - V_2'')^2 = -2$.

Assuming that $W_{\rm unbroken} = E_8 \oplus E_8$ (or $D_{16}; \mathbb{Z}_2 \langle \mathbf{sp} \rangle$), we scan all possible pairs of attractive K3 surfaces of the form $X_{[a\ 0\ c]} \times X_{[a'\ 0\ c']}$ and list up all the possible fluxes (5.19), (5.20) satisfying (i) the condition that $\langle W \rangle = 0$, (ii) the primitivity condition with respect to the Kähler form (5.22) and (iii) the D3-tadpole condition

$$\frac{1}{2} G_{\rm tot} \cdot G_{\rm tot} \leq \frac{\chi(X \times S)}{24} = 24\,; \tag{5.23}$$

the remaining D3-brane charge is supplied by placing an appropriate number of D3-branes.

Scanning within the range of $0 < c \leq a \leq 50$ and $0 < c' \leq a' \leq 50$ for $Y = X \times S = X_{[a\ 0\ c]} \times X_{[a'\ 0\ c']}$, we found that there are 313 different choices of $X \times S$ admitting the flux satisfying all the three conditions above. The distribution of the value of a in these 313 choices are shown in figure 3. If both G_1 and G_0 were required to be integral, there would only be 28 different choices,[65] and the largest possible value of a would be 6.

[65] There are 8 pairs of $[a\ 0\ c]$ and $[d\ 0\ f]$ where $a = d$ and $c = f$ in table 2, and there are 10 pairs where either $a \neq d$ or $c \neq f$. Thus, there are $28 = 8 + 2 \times 10$ different choices of $([a\ 0\ c], [a'\ 0\ c'])$.

JHEP04(2014)050

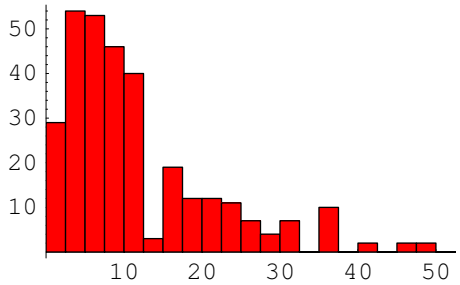

Figure 3. Variety in the choice of pairs of attractive K3 surfaces, $X \times S = X_{[a\ 0\ c]} \times X_{[a'\ 0\ c']}$ is shown in the form of histograms of $a \leq 50$. This distribution is not weighted by the number of flux choices available.

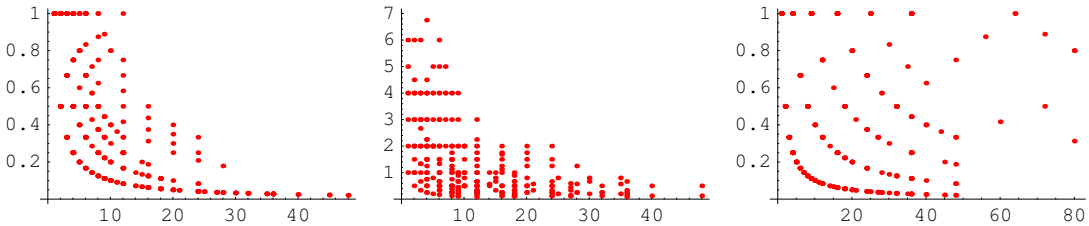

(i) a vs c/a (ii) a vs a'/a (iii) ac vs c/a

Figure 4. Scatter plots showing correlation between various modulus parameters X (horizontal axis) vs Y (vertical axis) for the 313 pairs of attractive K3 surfaces $X \times S = X_{[a\ 0\ c]} \times X_{[a'\ 0\ c']}$. No weight proportional to the number of flux choices is included. (the blank region in the lower right corner of (iii) is an artefact of cutting the scan at $a, a' \leq 50$).

Figure 4 shows the correlation among moduli parameters for the 313 pairs of attractive K3 surfaces admitting a flux satisfying all the three conditions above. For the first two scatter plots (i) and (ii) of figure 4, we can see clear correlations. When a is very large, there is presumably not much freedom to choose a' other than setting it to be comparable to a itself (see (ii)), so that $\mathrm{GCD}(a, a')$ is large, and the D3-tadpole contribution remains below the bound. On the other hand, there is no clear correlation to be read out from the plot (iii), we will have a comment on this in section 5.4.

There is a tremendous amount of combined choices of $X \times S = X_{[a\ 0\ c]} \times X_{[a'\ 0\ c']}$ and the fluxes on it. We found about 795×10^{15} choices satisfying all the three conditions on the flux by naively scanning $\{n_{ij}, m_{ij}, F_P, F_Q\}$ (apart from identification $\{n_{ij}, m_{ij}, F_P, F_Q\} \longleftrightarrow (-1) \times \{n_{ij}, m_{ij}, F_P, F_Q\}$). This large ensemble is dominated by the flux choices on a very small group of possibilities of $X_{[a\ 0\ c]} \times X_{[a'\ 0\ c']}$. There are about 777×10^{15} choices of flux for $X_{[1\ 0\ 1]} \times X_{[1\ 0\ 1]}$, 98% of the ensemble. Almost 99.6% of the ensemble is accounted for when we combine all the flux choices on $X_{[1\ 0\ 1]} \times X_{[1\ 0\ 1]}$, $X_{[2\ 0\ 1]} \times X_{[2\ 0\ 1]}$, $X_{[2\ 0\ 2]} \times X_{[1\ 0\ 1]}$, $X_{[1\ 0\ 1]} \times X_{[2\ 0\ 2]}$ and $X_{[2\ 0\ 2]} \times X_{[2\ 0\ 2]}$.

It is a fluke, though, that the statistics is dominated by a small number of pairs of attractive K3 surfaces. The large number of flux choices for $X_{[a\ 0\ c]} \times X_{[a'\ 0\ c']}$ with small

JHEP04(2014)050

values of a, c, a', c' is primarily due to[66] F_P, F_Q in $(-2) \oplus E_8 \oplus E_8 \subset \Lambda_{\rm K3}^{(S)}$. It is possible for such pairs of K3 surfaces to find a flux $(G_1 + G_0)$ on $(T_X \oplus T_X[-1]) \otimes (T_S \oplus T_S[-1])$ so that the contribution to the D3-tadpole is much smaller than 24. There is a lot of room left in the tadpole condition for an extra G_0-type flux in $T_X[-1] \otimes ((-2) \oplus E_8 \oplus E_8)$. It should be remembered that we should take a quotient of flux configurations on $X \times S = X_{[a\ 0\ c]} \times X_{[a'\ 0\ c']}$ (and elliptic fibration morphisms) by the subgroup of Γ that fixes the embeddings of $U_* \oplus T_X$ and T_S in (5.13), (5.15) and J_S in (5.22). Included in this stabilizer subgroup is $W_{E_8} \times W_{E_8}$, the Weyl group of $E_8 \oplus E_8 \subset \Lambda_{\rm K3}^{(S)}$.

The Weyl group W_{E_8} acts on the 240 roots transitively. We have also confirmed that the norm (-4), (-6), (-10) and (-12) points form single orbits of W_{E_8} on their own. There are at most two W_{E_8} orbits in the norm (-8) points, norm (-14) points and also in the norm (-16) points.[67] Thus, it is not a particularly bad estimate (for the counting of inequivalent flux vacuum) to assume that all the norm $(-2m)$ points in the E_8 root lattice form a single orbit of W_{E_8} for relatively small m such as $m \leq 12$, which is the range that matters under the tadpole condition (5.23). With this crude approximation of the modular group Γ action on fluxes, the total number of "inequivalent" choices of $X \times S = X_{[a\ 0\ c]} \times X_{[a'\ 0\ c']}$ and fluxes $G_{\rm tot}$ combined is reduced to about 7×10^6. About 80% of this ensemble of "inequivalent" vacua still come from fluxes on $X \times S = X_{[1\ 0\ 1]} \times X_{[1\ 0\ 1]}$, and the totality of the flux choices on the five $X \times S$ mentioned above (those with small a, c, a', c') account for 92%. Although the precise percentage values should not be taken too seriously because of the crude estimate of the modular group action (and artificial choice of J_S), it is trustable at the qualitative level that the vacuum statistics of K3 × K3 compactifications of F-theory with a $rk_7 = 16$ 7-brane gauge group $W_{\rm unbroken}$ is dominated by a small number of $X \times S = X_{[a\ b\ c]} \times X_{[a'\ b'\ c']}$ which have small values of a, c, a', c' so that the minimum possible value of $G_{\rm tot}^2/2$ is small. Consequently, the distribution of any observables/moduli parameters (such as $\mathrm{Im}(\rho_H) = \sqrt{ac}$) is determined simply by that of $X \times S = X_{[1\ 0\ 1]} \times X_{[1\ 0\ 1]}$ and a few others.

Before closing this section, it is worthwhile to mention that non-zero flux $G_{\rm tot} = G_1 + G_0$ does not imply that all the 18 + 20 complex structure moduli in $\mathcal{M}_{{\rm K3};F}^{(X)} \times \mathcal{M}_{\rm K3}^{(S)}$ are stabilized. The mass matrix (quadratic part of the superpotential) can be written in the form of

$$\propto \frac{1}{2}\left(\delta\Pi^{(1)}, \delta\Pi^{(2)}\right) \begin{pmatrix} -\mathrm{Im}(\tau_2)\sqrt{Q_2}\gamma & C_I) \otimes (F_I \\ F_I) \otimes (C_I & -\mathrm{Im}(\tau_1)\sqrt{Q_1}\overline{\gamma} \end{pmatrix} \begin{pmatrix} \delta\Pi^{(1)} \\ \delta\Pi^{(2)} \end{pmatrix}, \tag{5.24}$$

where $\delta\Pi^{(X)}$ has 18 components on $W_{\rm frame}$ and $\delta\Pi^{(S)}$ 20 components on S_S. Mass terms in the diagonal block are from (4.33), while the off-diagonal block is due to the G_0 type flux. All the moduli would have non-zero masses if $G_1 \neq 0$ and G_0 were absent (and similarly, full rank G_0 type flux with $rk_7 = 0$ and vanishing G_1 would stabilize all but two complex structure moduli). When both are present, however, the diagonal masses from G_1 and

[66] The 240 roots of E_8 are the norm (-2) points on the E_8 root lattice; there are 2160 points of norm (-4) in the E_8 lattice, and the number of norm $(-2m)$ points scale as m^3 There are 490560 points of norm (-24) in the E_8 lattice [93]. These numbers were used in obtaining the flux choices of order 795×10^{15}.

[67] This is done by computing the $\mathrm{diag}(H_4, H_4)$ action on W_{D_8} orbits, see [93] for more information.

JHEP04(2014)050

off-diagonal masses from G_0 interfere and there may be a zero mass-eigenvalue (and an unstabilized direction of the moduli space) in principle.

One example is to choose $n_{ij} = 0$, $m_{11} = m_{12} = m_{22} = -m_{21} = 1$ and $F_P = F_Q = 0$ in (5.19), (5.20) for a series of infinite pairs of attractive K3 surfaces $X \times S = X_{[k\ 0\ k]} \times X_{[k\ 0\ k]}$ (where $k = 1, 2 \cdots, \infty$). Under this choice of the flux, a one parameter (k) deformation of the complex structure $\Omega_X \wedge \Omega_S = [(v_1 + kV_1) + i(v_1' + kV_1')] \otimes [(v_2 + kV_2) + i(v_2' + kV_2')]$ remains a flat direction, and all the $\rho_X = \rho_S = 20$ points $X_{[k\ 0\ k]} \times X_{[k\ 0\ k]}$ just sit in this flat direction.

Such flux vacua with an unstabilized direction have been removed from the vacuum ensemble studied in this section. To be more precise, our numerical code examined the 4×4 mass matrix on $P_1 \delta\Pi^{(1)}_{P_1} + Q_1 \delta\Pi^{(1)}_{Q_1}$ and $P_2 \delta\Pi^{(2)}_{P_2} + Q_2 \delta\Pi^{(2)}_{Q_2}$, and threw away all the flux configurations for which there is a zero eigenvalue in this mass matrix. Certainly, one should examine the eigenvalues of a $(18 + 20) \times (18 + 20)$ mass matrix for each flux configuration,[68] but we believe that our short-cut approach does not qualitatively distort the distribution of observables in the landscape.

5.3 U(1) flux, heterotic-F-theory duality, and GUT 7-brane flux

The unbroken symmetry W_{unbroken} of interest for a sub-ensemble of vacua can be chosen at one's will. We can choose it to be rank-18 as in sections 2.1, 2.2 and 4.3, or to be rank-16 as in section 5.2, but other choices such as $W_{\text{unbroken}} \cong A_4$, a $\text{SU}(5)_{\text{GUT}}$ landscape, are just as appropriate.

Studies such as the one in section 5.2 are dedicated to a landscape of vacua of individual choices of W_{unbroken}, which we call the W_{unbroken} landscape. Beyond such an analysis, however, it is natural to ask such questions as how properties of the algebraic information W_{unbroken} generally characterize distributions within the W_{unbroken}-landscape, or how the number of vacua in the W_{unbroken}-landscape depends on W_{unbroken}. As a preparation for such a discussion in section 5.4, we make a few remarks in this section.

When we write down the G_0 type flux in the form (5.1), we can take the generators $\{C_I\}_{I=1,\cdots,18}$ of $W_{\text{frame}*}$ to be such that some are from $W_{\text{U}(1)}$, and others from W_{root}. We call the G_0 flux with C_I from $W_{\text{U}(1)}$ a U(1) flux or Mordell-Weil flux, and that with C_I from W_{root} a GUT-brane flux or singular fibre flux. The GUT 7-brane flux corresponds to the line bundles introduced on GUT 7-branes in F-theory (such as those in [94]), or line bundles on a stack of multiple D7-branes in type IIB Calabi-Yau orientifolds. The U(1) flux requires [20] a special choice of complex structure so that there is a non-vertical *algebraic* cycle, meaning that the Mordell-Weil group is non-trivial; the unavoidable tuning of complex structure is an expression equivalent to moduli stabilization.

5.3.1 U(1) flux/Mordell-Weil flux

Let us first ask what the U(1) flux looks like in the light of the duality between F-theory and heterotic string theory. As discussed in the literature (such as [32–34]), there must be

[68] In the case of $rk_7 = 16$, this problem is reduced to that of a $(2 + 20) \times (2 + 20)$ matrix, since the mass matrix of the moduli $\delta\Pi^{(1)}$ in W_{unbroken} does not interfere with the rest.

JHEP04(2014)050

a component of four-form U(1) flux in F-theory whose origin in heterotic string is a flux on the spectral surface. Suppose that $\pi_Z : Z = T^2 \times S \longrightarrow S$ is the elliptically fibred Calabi-Yau threefold for the dual heterotic string compactification, and $(C, \mathcal{N})$ the spectral data describing the vector bundle on Z. The spectral surface C is a subspace of $Z = \mathrm{Jac}(T^2) \times S$ characterized by the zero points of the elliptic functions

$$a_0^{\mathrm{v}} + a_2^{\mathrm{v}} x + a_3^{\mathrm{v}} y + \cdots = 0, \qquad a_0^{\mathrm{h}} + a_2^{\mathrm{h}} x + \cdots = 0 \tag{5.25}$$

on T^2, and $\mathcal{N} = \mathcal{O}_C(\gamma)$ is a line bundle on C specified by a divisor γ on C. *For any complex structure* of Z, S and C [30], one can always find a divisor

$$\gamma_{\mathrm{FMW}} \propto (n\sigma - \pi_C^*(nK_S + \eta)) \,, \tag{5.26}$$

where $\pi_C = \pi_Z|_C$, η is a divisor on S, K_S the canonical divisor of S, and we assume $\mathrm{SU}(n) \subset E_8^{\mathrm{vis}}$ is the structure group of the vector bundle. None of the U(1) fluxes we talk about here, however, should correspond to this Friedman-Morgan-Witten flux in the heterotic "dual". If this flux were to be dual to the U(1) flux in F-theory, we would run into a contradiction immediately: an arbitrary complex structure is allowed on the heterotic side, while it has to be tuned in F-theory. In fact, the generic Friedman-Morgan-Witten flux (5.26) always vanishes, $\gamma = 0$, when the dual F-theory is a K3 $\times$ K3 compactification.

For finely tuned complex structure of the heterotic string compactification data, (Z, S, C), however, there is more variety in the choice of γ on the spectral surface [30]. Suppose that the base K3 surface S is not the general complex analytic one, but has Picard number $\rho_S \geq 2$. This means that we might be able to find a set of $\{F_A\} \subset [J_S^{\perp} \subset S_S]$ generating a rank-k sublattice of S_S. We only consider vector bundles with the structure group contained in $G_{\mathrm{str}}^{\mathrm{v}} \times G_{\mathrm{str}}^{\mathrm{h}} = \mathrm{SU}(N_v) \times \mathrm{SU}(N_h)$. It then appears that we can think of a vector bundle for compactification,

$$V = \oplus_{i=1}^{N_v+N_h} \mathcal{O}_S(D_i) \otimes \mathcal{O}_{T^2}(p_i - e), \qquad D_i = \sum_A n_{(i)}^A F_A \,, \tag{5.27}$$

where the $\{p_i\}$ and e are the zeros and the pole, respectively, of the elliptic functions (5.25). The spectral surface is of the form $C = \cup_i C_{p_i}$ with $C_{p_i} \simeq S$'s corresponding to $p_i \in \mathrm{Jac}(T^2)$, and $\gamma|_{C_{p_i}} = D_i$. This vector bundle is poly-stable with respect to the Kähler form $J_Z = J_{T^2} + J_S$. The unbroken symmetry should be $E_{9-N_v}^{\mathrm{v}} \times E_{9-N_h}^{\mathrm{h}}$ within $E_8 \times E_8$. Moduli parameters include ρ_H and τ_H of T^2, and $(N_v - 1) + (N_h - 1)$ parameters of the flat bundles in (5.25), and hence,in addition to those from the base S, there are $N_v + N_h$ of them.

Dual to this heterotic string compactification should be F-theory on $Y = X \times S$ where the elliptically fibred K3 surface X has the following Neron-Severi and transcendental lattices:[69]

$$\Lambda_{\mathrm{K3}}^{(X)} \supset S_X \oplus T_X = [U_* \oplus E_{9-N_v} \oplus E_{9-N_h}] \oplus [U \oplus U \oplus A_{N_v-1} \oplus A_{N_h-1}] \,. \tag{5.28}$$

K3 surfaces X of this form have Picard number $\rho_X = (20 - N_v - N_h)$, so that the moduli space has dimension $(N_v + N_h)$, which agrees with the counting above. If we are to find

[69] A detailed description of the transcendental lattice is found in [85] for the case of $N_v = 3$.

JHEP04(2014)050

a four-form flux in F-theory dual to γ, that dual flux must be associated with non-U_* cycles that are orthogonal to the unbroken symmetry part $E_{9-N_v} \oplus E_{9-N_h}$. This means that the flux is not in an algebraic cycle, and such a configuration is not stable. The complex structure moduli dynamically tune themselves (due to the GVW potential) so that the associated cycle becomes algebraic. In order to introduce k independent U(1) fluxes in (5.1), the number of unstabilized directions in the moduli space should be reduced by k, and the moduli space becomes $(N_v + N_h - k)$-dimensional [20].[70]

This reduction of the moduli space should also be understandable in the heterotic string description. Certainly V in (5.27) is a holomorphic vector bundle and satisfies the condition $\int J \wedge J \wedge F = 0$ as well as the Bianchi identity of the B-field,

$$0 = \operatorname*{tr}_{\mathfrak{so}(6)} \left[\left(\frac{R}{2\pi} \right)^2 \right] - T_R^{-1} \operatorname{tr}_R \left[\left(\frac{F}{2\pi} \right)^2 \right] + 4\delta^{(4)}_{M5} = 4 \left(-c_2(TZ) - \mathrm{ch}_2(V) + \delta^{(4)}_{M5} \right) , \quad (5.29)$$

where $\delta^{(4)}_{M5}$ is the delta-function valued four-form associated with individual M5-branes wrapped on holomorphic curves in $Z = T^2 \times S$, and $\mathrm{ch}_2(V)$ is the second Chern character of the rank $(N_v + N_h)$ vector bundle V (with the structure group $\mathrm{SU}(N_v) \times \mathrm{SU}(N_h)$). There is a condition that is stronger than (5.29), however:

$$0 = H := dB + \frac{\alpha'}{4} \left(\operatorname{tr} \left[\omega d\omega + \frac{2}{3} \omega\omega\omega \right] - T_R^{-1} \operatorname{tr}_R \left[AdA - i\frac{2}{3} AAA \right] \right) + (\text{source})_{M5} , \quad (5.30)$$

if we are to stick to the framework of heterotic string compactification on a Kähler manifold and constant dilation configuration (Chap.16, [95]). This constraint may also be understood as a combination of the F-term condition of

$$W_{\mathrm{Het}} \propto \int_Z \Omega_Z \wedge H + (2\pi)^2 \alpha' \int_{\Gamma(M5)} \Omega_Z \quad (5.31)$$

with respect to the complex structure moduli of Z and $\langle W_{\mathrm{Het}} \rangle = 0$ for vanishing cosmological constant.[71] $\Gamma(M5)$ is a real 3-chain in $Z = T^2 \times \mathrm{K3}$ whose boundary contains the curves on which M5-branes are wrapped [96]. The exterior derivative of this condition (5.30) reproduces (5.29).

The B-field Bianchi identity, (5.29), can be satisfied by wrapping an appropriate number (N_{M5}) of heterotic NS5-branes (M5-branes in heterotic M-theory) on the fibre T^2. As is well-known in the literature,

$$c_2(TZ) = (24\ \mathrm{pt}_{K3}) \otimes 1_{T^2}, \qquad \mathrm{ch}_2(V) = \frac{1}{2} \sum_{i=1}^{N_v+N_h} (D_i)^2 , \quad (5.32)$$

and the only non-trivial part, which is a four-form on S and scalar on T^2, of the condition (5.29) gives rise to

$$\frac{1}{2} (G_H^{(4)})^2 + N_{M5} = 24 . \quad (5.33)$$

[70] On top of this, G_1 type flux is introduced to fix the remaining moduli. But in the context of heterotic-F-theory duality, we take the G_1 component out of the picture (or assume that it is absent).

[71] Flux of Friedman-Morgan-Witten type γ (5.26) does not vanish in the case of a general Calabi-Yau threefold Z with elliptic fibration (although it vanishes in the present case). This type of flux, however, does not restrict complex structure moduli because it induces a vanishing Chern-Simons term.

JHEP04(2014)050

Here, $G_H^{(4)}$ takes values in the lattice[72] $(A_{N_v-1} \oplus A_{N_h-1}) \otimes [J_S^\perp \subset S_S]$, and is given by

$$G_H^{(4)} = \sum_{I=1}^{N_v-1} C_I \otimes D_I + \sum_{I=1}^{N_h-1} C_I \otimes D_I, \qquad D_I = -(D_{i=1} + \cdots + D_{i=I})\,. \tag{5.34}$$

The condition (5.30) in the two-form component on S and one-form on T^2, however, contains information that is not captured by the Bianchi identity (5.29). In the presence of U(1) flux $\mathcal{O}_S(D_i)$ on S and a flat bundle $\mathcal{O}_{T^2}(p_i - e)$ (i.e., Wilson line) on T^2, there is no contribution to the Chern character, but the Chern-Simons form can be non-zero. Keeping in mind that M5-branes wrapped on T^2 as well as gravitational Chern-Simons form only contribute to (5.30) in the component purely three-form on S, we see that

$$\left(dB - \frac{\alpha'}{4} T_R^{-1}\, \mathrm{tr}_R\, [AdA]\right)\Big|_{\text{2-form on } S,\ \text{1-form on } T^2} = 0\,, \tag{5.35}$$

where the A^3 term in the Chern-Simons form has also been dropped for the Cartan flux configuration. Since the Polyakov action remains invariant by changing the B-field background by $(2\pi)^2\alpha'$ times an integral two-form on the target space, it is possible that the B-field background configuration expanded by using the same set of F_A as in (5.27)

$$B = \sum_A b_A F_A (2\pi)^2 \alpha' \tag{5.36}$$

may have scalars b_A varying topologically on T^2, so that $db_A = \check{\alpha} n_A^8 + \check{\beta} n_A^9$ for some integers n_A^8 and n_A^9 and a basis $\{\check{\alpha}, \check{\beta}\}$ of $H^1(T^2; \mathbb{Z})$. When k independent F_A's in $[J_S^\perp \subset S_S]$ are involved, we find the k independent conditions on the Wilson lines $A = A_I C_I$, $A_I = (2\pi)(\check{\alpha} a_I^8 + \check{\beta} a_I^9)$:

$$\left[db_A + \frac{A_I}{2\pi}\,(C_I, C_J)\, n_A^{(J)}\right] \otimes F_A = 0, \qquad 2n_A^8 - a_I^8 q_A^I = 0, \quad 2n_A^9 - a_I^9 q_A^I = 0, \tag{5.37}$$

where $n_A^{(J)} := -(n_{(i=1)}^A + \cdots + n_{(i=J)}^A)$ and $q_A^I := -(C_{IJ}) n_A^{(J)}$. Hence k combinations of the Wilson lines A_I are required to be torsion points of $\mathrm{Jac}(T^2)$ (equivalent to the origin of $\mathrm{Jac}(T^2)$ when multiplied by some non-zero integer).[73] This is equivalent to k conditions imposed on the spectral surface data ($a^{\mathrm{v}}_{0,2,3,\ldots}$ and $a^{\mathrm{h}}_{0,2,\ldots}$) and f_0 and g_0 (equivalently τ_H).

Let us now translate this interplay among the Cartan flux, B-field topological configuration and the reduction (stabilization) of the moduli space in the language of Narain moduli. The Narain moduli covers not just the region with parametrically large $[\mathrm{vol}(T^2)/\ell_s^2]$ (where supergravity approximation is good), but also the stringy region. When there is a Cartan flux and corresponding topological dB configuration, our observation above —

[72] Note that we define the A–D–E lattice to have negative definite symmetric pairing in this article, and that D_i's are also negative definite, because of the signature $(1, \rho_S - 1)$ of S_S.

[73] It is no longer surprising that $a_3^{\mathrm{v}} y = 0$ and $a_3^{\mathrm{h}} y = 0$ are the spectral surface equation read out from (4.48). These equations mean that the $N_v = 3$-fold spectral cover (also $N_h = 3$) consists of three irreducible pieces sitting at the three 2-torsion points of $\mathrm{Jac}(T^2)$.

JHEP04(2014)050

some combinations of A_I's are forced to be torsions of $\mathrm{Jac}(T^2)$ — is translated into the existence of k vectors[74][75]

$$n_A := (2n_A^8, 0, 2n_A^9, 0, q_A^I)^T \in \mathrm{II}_{2,18}\,, \tag{5.38}$$

satisfying[76]

$$\langle \mathcal{Z}^R, n_A\rangle = 0, \qquad \mathcal{Z}^R \propto \left(-\tau_H,\ -\tilde{\rho}_H,\ 1,\ -\tau_H\tilde{\rho}_H - (a)^2/2,\ a_I\right); \tag{5.39}$$

see appendix A for background material on Narain moduli in heterotic string theory. This mechanism is precisely the same, mathematically, as how algebraic cycles emerge for special choice of complex structure on the other side of the duality.

It must be be obvious that one should define a lattice element

$$\widetilde{G}_H^{(4)} := \sum_A n_A \otimes F_A \in [U \oplus U \oplus A_{N_v-1} \oplus A_{N_h-1}] \otimes [J_S^{\perp} \subset S_S] \tag{5.40}$$

in heterotic string language in order to formulate the Cartan flux and topological dB configuration combined. Within the framework that we have assumed in this section so far,[77] where $Z = T^2 \times S$ is Kähler, $\langle\phi\rangle_{\mathrm{Het}} = \mathrm{const}$ and $\langle H\rangle = 0$ on the heterotic side, the duality map of the flux is given by

$$\widetilde{G}_H^{(4)} = G_0 = G_{\mathrm{tot}}\,. \tag{5.41}$$

Within this class of Cartan flux, the norm of $\widetilde{G}_H^{(4)}$ remains the same as that of $G_H^{(4)}$, because with $w^8 = w^9 = 0$, only n_8^A and n_9^A are allowed to be non-zero. Therefore, the Bianchi identity (5.33) becomes dual to the D3-tadpole condition (5.23).

The duality dictionary above is a generalization and refinement of the preceding discussion in [30, 32–34, 97, 98], in that we can deal with a more general class of fluxes on the heterotic spectral surface (by allowing non-trivial $\langle dB\rangle$), keep track also of flux quanta in the $U \oplus U$ components in the form of $\widetilde{G}_H^{(4)} = G_{\mathrm{tot}}$ or n_A, maintain a clear distinction between algebraic and transcendental cycles on the F-theory side and are able to understand how the dimension of moduli space is reduced.

The conventional dictionary using the stable degeneration limit of K3 surfaces is understood in the following way from the present perspective. Within the framework we have

[74] It is worth drawing attention to the fact that such vectors cannot always be brought into the $[A_{N_v-1} \oplus A_{N_h-1}]$ part of $[U \oplus U \oplus A_{N_v-1} \oplus A_{N_h-1}]$. The flux vectors that can be brought purely into $E_8 \oplus E_8$ may be associated with the flux on a trivial spectral surface in heterotic language, and are dual to the singular fibre flux (GUT brane flux) in F-theory.

[75] We wonder if we have made an error causing the factor of 2?

[76] This condition in heterotic string theory means that there is a class of states (vertex operators) with $(k^R, k^L) \in \mathbb{R}^{2,18}$ satisfying $(\alpha'/4)(k^R)^2 = 0$ and $(\alpha'/4)(k^L)^2 = -(n_A)^2/2 = -(q_A)^2/2$. As we are considering U(1)/Mordell-Weil fluxes here, rather than a GUT 7-brane/singular fibre flux, n_A should belong to $W_{\mathrm{frame}}\backslash W_{\mathrm{root}}$, meaning that $-(n_A)^2 \geq 4$. Thus, none of vertex operators for physical states with this (k^R, k^L) appear in the massless spectrum.

[77] Obviously this is not the most general form of G_{tot}, in particular when $G_1 = 0$. For a fully general choice of G_{tot} on the F-theory side, it is considered that we have to turn on $\langle H\rangle \neq 0$, a non-constant dilaton configuration and non-Kähler metric on the Heterotic string side [23].

JHEP04(2014)050

considered so far, the moduli space of $\mathcal{Z}^R$ ($\propto \Omega_X$) still maintains a free choice of at least τ_H and $\tilde{\rho}_H$, even after maximally possible Cartan fluxes (rank $= N_v + N_h - 2$) are introduced in the $\mathrm{SU}(N_v) \times \mathrm{SU}(N_h)$ structure group (no G_1 component yet, in particular). Thus, from this moduli space we can extract a family of K3 surfaces parametrized by $\tilde{\rho}_H$. This family $\pi : \mathcal{X} \longrightarrow D$ is defined on a disc $D \subset \mathbb{C}$ with $t = 1/\tilde{\rho}_H$ as the coordinate, just like the discussion in footnote 46 for the family defined by (4.35). Mathematically, this family may be augmented by providing the degeneration limit corresponding to $t = 1/\tilde{\rho}_H = 0 \in D$, which is called the central fibre. Each fibre (K3 surface) $\pi^{-1}(\tilde{\rho}_H)$ for some $1/\tilde{\rho}_H \in D$ contains an algebraic cycle (curve) corresponding to n_A in (5.38), (5.39), and those algebraic cycles (curves) for various $\tilde{\rho}_H$ are collectively regarded as an algebraic family of curves, or equivalently as a divisor in $\mathcal{X}$. The intersection of this divisor with the central fibre, $\pi^{-1}(0) = dP_9 \cup dP_9$, determines an algebraic cycle in $dP_9 \cup dP_9$. In this way, the stable degeneration limit of n_A is obtained.

Appendix B describes the behaviour of a semistable degeneration of a K3 surface and its algebraic cycles using a concrete example given by (4.48). We will see there how the semistable degeneration limit of an algebraic cycle can have an image in only one of the two dP_9's (only in visible/hidden sector dP_9).

Just like in the heterotic string picture of F-terms (5.31) leading to the stabilization of Wilson line moduli $\langle A \rangle_I$, we can also understand[78] the stabilization of the D7-brane positions in the dual type IIB theory on the orientifold $K3 \times T^2/\mathbb{Z}_2$. The type IIB version of the superpotential (5.31) is

$$W_{\mathrm{IIB}} \propto \int_M \Omega_M \wedge G^{(3)} + \int_S i_{X*}\Omega_M \wedge F = \int_M \Omega_M \wedge G^{(3)} + \int_S \Omega_{M;ijk}\, \mathrm{tr}\left[X^i F_{lm}\right] , \quad (5.42)$$

where X^i is the fluctuation of D7-brane in the transverse direction. Let us assume that we give a vev D_i to the gauge field strength for the i-th D7-brane. Its contribution can also be described by rewriting the last term above as $W = \int_{\Gamma(D7)} \Omega_M$. Here, $\Gamma(D7)$ is a 3-chain whose boundary consists of a two-cycle Poincaré dual (in S) to D_i and a reference two-cycle D_0. We can expand $D_i = n_i^A F_A$. Furthermore, we can introduce a three-form flux $G^{(3)} = F^{(3)} - \phi H^{(3)}$. Here ϕ is the type IIB axiodilaton and $F^{(3)}$ and $H^{(3)}$ are the type IIB R-R and NS-NS fluxes, respectively. We also expand $G^{(3)} = F^{(3)} - \phi H^{(3)} = (m_F^A - \tau m_H^A) F_A$ for a basis of two-cycles F_A of the $K3$ surface S and some $m_F^A, m_H^A \in H^1(T^2; \mathbb{Z})$. Using that $\Omega_M = \Omega_S \wedge dz$, we can evaluate the superpotential to be

$$W_{\mathrm{IIB}} \propto \sum_A \int_S \Omega_S \wedge F_A \sum_i \left(m_F^A - \phi m_H^A + \int_0^{X_i} n_A^i \, dz \right) . \quad (5.43)$$

The orientifold involution demands that we supply an image D7-brane at $\hat{X}_i = -X^i$ for any D7-brane at X^i. The U(1) gauge field surviving the orientifold involution is $\hat{A}^i - A^i$, so that the image brane also carries a flux $\hat{D}^i = -D^i$ and the two signs cancel in (5.43). The orientifold involution also sends $G^{(3)} \mapsto -G^{(3)}$, so that the only modes that survive are

[78] A closely related discussion is found in section7.3 of [22], see also [21, 23]. The presentation here, however, is for $\langle H \rangle = 0$ and Kähler metric in the heterotic description.

JHEP04(2014)050

those expanded into odd three-forms. All three-forms used for the expansion of $G^{(3)}$ are odd, so that this is already taken care of. We can hence capture the effect of orientifolding by only considering 16 branes at X^i with fluxes D_i on their worldvolume and putting a factor of two in front of the last term in (5.43). The conditions for supersymmetry coming from the superpotential are then written as

$$\sum_i \left(m_F^A - \phi m_H^A + 2 \int_0^{X_i} n_A^i \, dz \right) = 0 \,. \tag{5.44}$$

Just as for the Wilson lines, the positions of the branes should add up to a torsion point of T^2, so that the above can be cancelled by an appropriate choice of F_3. Note that $\phi \to i\infty$ in the weak coupling limit, so that (assuming n_A^i is finite) we cannot use H_3 for the same purpose. This is as expected, as the three-form dB, which took part in the same mechanism on the heterotic side, is turned into $F_3 = dC_2$ under the duality map.

The need to put (some of) the D7-branes at special loci on $T^2/\mathbb{Z}_2$ in order to have supersymmetric world-volume flux and the connection to the existence of algebraic cycles in the F-theory K3 has also been discussed in [20].

A lesson to be learnt from this is that instead of considering G_3 alone, the combination of $G^{(3)}$ and the contribution from D7-branes we see above should be of type $(2,1)$ [24]. This is just like the corresponding condition in heterotic string theory, where the vanishing of H including both dB and the Chern-Simons terms is required. Even for three-form fluxes $H^{(3)}$ and $F^{(3)}$ that cannot be made purely type $(2,1)$ and primitive for any choice of $\langle\phi\rangle$ and complex structure of M, there may be supersymmetric configurations for an appropriate choice of D7/O7-brane configuration. Turning this argument around, one can also see that once a $G^{(3)}$ configuration is found so that the supersymmetric conditions are satisfied for a D7/O7-brane configuration, then all the supersymmetric configurations consist of a sum of this special combination of flux plus any primitive pure $(2,1)$ form.

5.3.2 GUT 7-brane flux/singular fibre flux

Let us also make a brief remark on the GUT 7-brane flux (singular fibre flux), before moving on to the next section. Suppose that a flux (5.1) is introduced for C_I (i.e., the corresponding F_I does not vanish) in an irreducible component R of $W_{\rm root}$. Although there is a gauge theory on 7-brane ($\simeq S \times \mathbb{R}^{3,1}$) with the gauge group R, the flux turns on a non-trivial line bundle on the 7-brane and the symmetry of R is broken down to $[C_I^\perp \subset R]$ in the effective theory below the Kaluza-Klein scale.

The field contents in the effective theory can be described in terms of irreducible representations of the unbroken symmetry group $[C_I^\perp \subset R]$. Let α be a root of R that does not belong to $[C_I^\perp \subset R]$, and $D_\alpha = \sum_I (\alpha, C_I) F_I$ a divisor on S. Since we have assumed from the outset that $F_I \in [J_S^\perp \subset S_S]$, we have that $H^0(S; \mathcal{O}_S(D_{\pm\alpha})) = 0$, as long as the Kähler form J_S is in Amp_S (defined as an open set). If $H^0(S; \mathcal{O}_S(D_\alpha))$ or $H^0(S; \mathcal{O}_S(D_{-\alpha}))$ were non-trivial, then either D_α or $D_{-\alpha}$ is a divisor class represented by an effective curve, which should have a positive intersection number with any other divisor (including J_S) in the ample cone Amp_S. If, however, we allow some (-2)-curves to have zero volume under J_S (i.e., $J_S \in \overline{\mathrm{Amp}}_S \backslash \mathrm{Amp}_S$), some effective divisors may have zero volume and

JHEP04(2014)050

$H^0(S;\mathcal{O}_S(D_{\pm\alpha})) \neq \phi$ is not ruled out mathematically. This is also true when we cannot rely entirely on the local field theory approximation. Just like in toroidal orbifold examples where symmetry may sometimes be restored even in the presence of symmetry-breaking orbifold twists, stringy effects at zero-volume cycles may bring about consequences beyond the local field theory/supergravity approximation. Keeping in mind that

$$\begin{aligned} h^0(S;\mathcal{O}_S(D_\alpha)) + h^0(S;\mathcal{O}_S(D_{-\alpha})) &= h^0(S;\mathcal{O}_S(D_\alpha)) + h^2(S;\mathcal{O}_S(D_\alpha)), \\ &\geq \chi(S;\mathcal{O}_S(D_\alpha)) = 2 + \frac{(D_\alpha)^2}{2} \end{aligned} \tag{5.45}$$

on a K3 surface S, there is always such a zero-volume (-2) curve for a flux such that $(D_\alpha)^2 = -2$. For fluxes where $(D_\alpha)^2 \leq -4$, however, there is no such immediate consequence.

As long as we stay within the field theory approximation (which means that $J_S \in \mathrm{Amp}_S$, or at least $h^0(S;\mathcal{O}_S(D_\alpha)) = 0$), the number of chiral multiplets in the irreducible component containing the root $\pm\alpha$ is given by

$$h^1(S;\mathcal{O}_S(D_{\pm\alpha})) = -\chi(S;\mathcal{O}_S(D_{\pm\alpha})) = -\frac{(D_\alpha)^2}{2} - 2. \tag{5.46}$$

Note that there is no net chirality because of $(D_\alpha, K_S) = 0$.

5.4 Vacuum distribution based on continuous approximation

There have been attempts, most notably in [2, 17, 28, 29], of going beyond a case-by-case analysis of flux configuration counting. We initiate an effort of generalizing their approach by implementing various concepts that we have already developed in this section, so that we can ask statistical questions that are of interest in the context of particle physics, not just in cosmology. To do so, we use what we call the *restricted complex structure moduli space*, which is the space of complex structure deformations leaving a chosen set of divisors algebraic. For a K3 surface (or K3 × K3), we denote this by $\mathcal{M}_*(J_S, W_{\text{noscan}})$. It is the moduli space of complex structures for which the (fixed) Kähler form J_S stays purely of type $(1,1)$ and the divisors spanning W_{noscan} remain algebraic. This means that we only consider complex structures such that $\Omega \cdot W_{\text{noscan}} = 0$.[79] For more general fourfolds (where $H^{2,0} = 0$) the first condition, J_Y being of type $(1,1)$, is automatically satisfied, so that we simply use the notation $\mathcal{M}_*(W_{\text{noscan}})$ here.

I. An approach of [28, 29] is to replace the sum over all the flux configurations taking their value in a lattice by continuous integration. In a theory where there are flux quanta N specified by K integers, the vacuum index density $d\mu_I$ is defined on $\mathcal{M}_*(J_S, W_{\text{noscan}})$ (of complex dimension m) by

$$d\mu_I = d^{2m}z \sum_N \Theta(L_* - L)\delta^{2m}(D_a W, \overline{D_b W}) \det \begin{pmatrix} D_c D_d W & \partial_c \overline{D_d W} \\ \bar\partial_{\bar c} D_d W & \overline{D_c D_d W} \end{pmatrix}_{2m\times 2m} \tag{5.47}$$

$$\approx d^{2m}z \int_N d^K N\, \Theta(L_* - L)\delta^{2m}(D_a W, \overline{D_b W}) \det \begin{pmatrix} D_c D_d W & \partial_c \overline{D_d W} \\ \bar\partial_{\bar c} D_d W & \overline{D_c D_d W} \end{pmatrix}_{2m\times 2m} \tag{5.48}$$

[79] K3 surfaces with this kind of constraint are called *lattice polarized* in the mathematics literature.

JHEP04(2014)050

Here, the z^a are complex local coordinates on $\mathcal{M}_*$. The definition of this index density $d\mu_I$ is independent of the choice of local coordinates on $\mathcal{M}_*$ and becomes an (m,m)-form on $\mathcal{M}_*/\Gamma_*$, where Γ_* is the modular group. The vacuum index density can be used to set a lower bound in the number of vacua (without the condition $\langle W_{\rm GVW}\rangle = 0$).

In type IIB compactification on a Calabi-Yau threefold M_3 with an orientifold projection yielding n irreducible O7-planes, for example, $\mathcal{M}_*(D_4^{\oplus n})$ is the same as the moduli space of complex structures of M_3 together with the axi-dilaton. We only consider configuration of 7-branes such that they appear in the combination of SO(8) 7-brane gauge groups, i.e. we out four D7-branes on each O7-plane. Then the restricted moduli space $\mathcal{M}_*$ has complex dimension $m = (h^{2,1}_{-,\text{prim.}}(M_3)+1)$ and there are $K = 4(h^{2,1}_{-,\text{prim.}}(M_3)+1)$ integers for type IIB three-form quanta satisfying the primitiveness condition $G^{(3)}\wedge J_M = 0$. The delta functions (F-term conditions) reduce the flux space to be integrated from real K dimensions to $K-2m$ dimensions. The remaining integral in the flux space (at each point in the moduli space $\mathcal{M}_*/\Gamma_*$) is over primitive and (2,1) or (0,3)-type (i.e., imaginary self-dual) three-form fluxes $G^{(3)}$ in type IIB Calabi-Yau orientifold. It is bounded in region, because the contribution of such flux to the D3-tadpole

$$\frac{1}{2}G^{(4)}_{\rm tot}\cdot G^{(4)}_{\rm tot} \longrightarrow \frac{i}{2}\frac{G^{(3)}\wedge\overline{G^{(3)}}}{\mathrm{Im}(\phi)} = H^{(3)}\wedge F^{(3)} \tag{5.49}$$

is positive definite and is bounded from above by L_*, the total O3 plane charge in M_3. The vacuum index density thus becomes a finite-valued distribution (m,m)-form on the moduli space $\mathcal{M}_*/\Gamma_*$.

By following the argument of [28, 29], it is not hard to realize that the integral over the finite $(K-2m)$-dimensional region within the flux space d^KN yield a factor $L_*^{(K-2m)/2}$ for $z\in\mathcal{M}_*$. The Jacobian between the moduli space coordinates z_a and the remaining real $2m$ coordinates of the continuous flux space d^KN gives rise to another factor $(L_*)^{2m/2}$. Hence the vacuum index density of the landscape is given by

$$d\mu_I = \frac{1}{(K/2)!}(2\pi L_*)^{K/2}\times\rho_{\text{ind.}}, \tag{5.50}$$

where $\rho_{\text{ind.}}$ is an (m,m)-form on $\mathcal{M}_*/\Gamma_*$. Note that K and m are distinguished intentionally; although the relation $K=4m$ holds in type IIB Calabi-Yau orientifolds, it does not necessarily hold when one pays attention to a restricted subset of the full complex structure moduli space of M_3 (e.g., $K=3$ and $m=1/2$ model for $M_3=T^6$ in [17]), or in applications to F-theory. The (m,m)-form $\rho_{\text{ind.}}$ in (5.50) does not depend on L_* primarily.[80] For this reason, the factor $(L_*)^{K/2}/(K/2)!$ roughly determines the overall number of flux vacua in the landscape on $\mathcal{M}_*/\Gamma_*$ and the distribution within the moduli space $\mathcal{M}_*/\Gamma_*$ is controlled by $\rho_{\text{ind.}}$.

[80] It frequently happens, though, that the integral of $\rho_{\text{ind.}}$ over $\mathcal{M}_*/\Gamma_*$ is not finite, and/or the continuous approximation of the flux quanta (from (5.47) to (5.48)) in some regions of $\mathcal{M}_*/\Gamma_*$ becomes bad, and/or some regions of $\mathcal{M}_*/\Gamma_*$ correspond to decompactification "limits" in dual theories. Because the cut-off for the region in $\mathcal{M}_*/\Gamma_*$ for the continuous approximation depends on the value of L_*, the integral of $\rho_{\text{ind.}}$ with cut-off may depend on L_*. See [17] for such an example.

JHEP04(2014)050

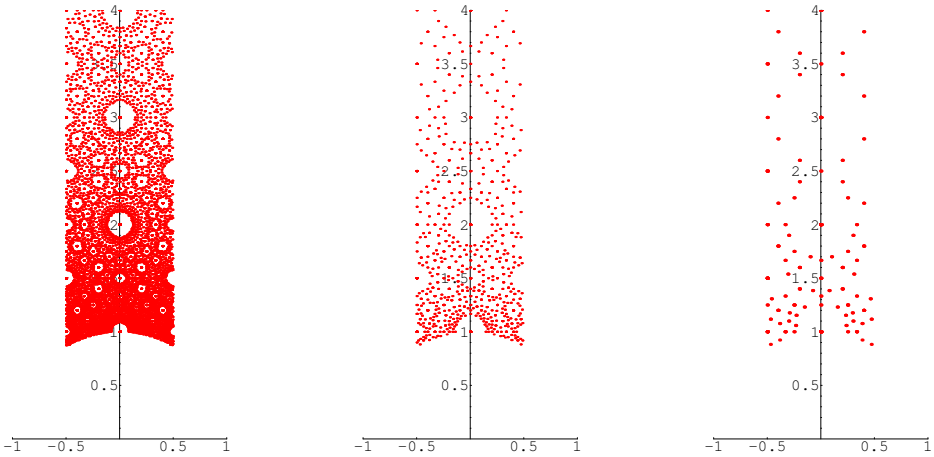

Figure 5. Vacuum distribution in the rigid Calabi-Yau model of [17, 28, 29] shown in the fundamental domain of the axi-dilaton moduli space. Depending on the value of L_*, D3-tadpole, the distribution of vacua in the moduli space can be either almost continuous or genuinely discrete.

Whether the continuous approximation is good or bad crucially depends on the value of L_*. To take an example, let us consider the rigid Calabi-Yau threefold model studied in [17, 28, 29], where $h^{2,1}(M_3) = 0$ and the moduli space $\mathcal{M}$ is that of the axi-dilaton of type IIB string theory. The distribution of flux vacua is presented in figure 5 without making the continuous approximation for three different values of L_*. For the one with $L_* = 150$, which is also found in [29], the continuous approximation looks reasonably good. For cases with small value of L_*, however, the continuous approximation is not very good, as in figure 5 with $L_* = 20$.

When the continuous approximation is not good, it is more appropriate to i) specify the set of points in $\mathcal{M}_*/\Gamma_*$ that admit integral fluxes, and ii) describe how many choices of such integral flux configurations are available at such points [17]. Suppose the dilaton vev $\langle\phi\rangle$ takes its value in an algebraic extension field $\mathcal{F}$ over $\mathbb{Q}$ with $\mathcal{D} := \dim_{\mathbb{Q}}\mathcal{F} = 2$, and the complex structure moduli of M_3 are such that $[\Omega_{M_3}] \in \mathcal{F}\mathbb{P}[H^3(M_3)]$ and $[D_i\Omega_{M_3}] \in \mathcal{F}\mathbb{P}[H^3(M_3)]$ for $i = 1, \cdots, h^{2,1}(M_3)$. Then the number of flux quanta at our disposal (while preserving the F-term conditions) is

$$\kappa = 4(h^{2,1}(M)_{-,\text{prim.}} + 1) - (\mathcal{D} = 2) \times (h^{2,1}(M)_{-,\text{prim.}} + 1), \tag{5.51}$$

which is reduced to

$$\kappa' = 4(h^{2,1}(M)_{-,\text{prim.}} + 1) - (\mathcal{D} = 2) \times (h^{2,1}(M)_{-,\text{prim.}} + 1) - (\mathcal{D} = 2) \tag{5.52}$$

when $\langle W_{\text{GVW}}\rangle = 0$ is required. Consequently, the number of flux configuration scales for a given complex structure $(\langle\phi\rangle, \langle z^a\rangle)$ as $(L_*)^{\kappa/2}$ or $(L_*)^{\kappa'/2}$, respectively [17]. The overall number of flux vacua, estimated to be $(L_*)^{2(h^{2,1}(M)_{-,\text{prim.}}+1)}$, should be reproduced partially from $(L_*)^{\kappa/2}$ times the number of such $\mathcal{D} = 2$ vacua in the fundamental domain

JHEP04(2014)050

of the moduli space, and the rest must come from similar contributions from vacua with different value of the extension degree $\mathcal{D}$.

The $rk_7 = 16$ landscapes of F-theory on K3 $\times$ K3 in section 5.2 fits very well with this discrete picture in two different ways. First, L_* in the type IIB language comes from $\chi(Y_4)/24$ in F-theory, which remains small for $Y_4 = \text{K3}\times\text{K3}$. This is visible most clearly in figure 1, or in the relatively short list of vacuum points (there are 66) in the moduli space in table 2 or merely 170 pairs found in the analysis of section 5.2. These results definitely look closer to the $L_* = 20$ picture in figure 5 than the one with $L_* = 150$.

The second reason is that the number of scanning flux quanta κ available at each isolated point in $\mathcal{M}_*(J_S, W_{\text{noscan}})$ remains the same for all the W_{noscan}-landscapes for F-theory on K3 $\times$ K3 with $rk_7 = \text{rank}(W_{\text{noscan}}) = 16$. This is obvious in the case of the $W_{\text{noscan}} = (D_4^{\oplus 4}); (\mathbb{Z}_2 \times \mathbb{Z}_2)$-landscape, because this is the type IIB orientifold compactification on $M_3 = T^2 \times K3$ with all the O7-planes accompanied by four D7-branes on top of them. But, even for other choices with $\text{rank}(W_{\text{noscan}}) = 16$, the number of scanning flux quanta κ, and hence the estimate of the number of $\mathcal{D} = 2$ vacua should remain much the same, even if W_{noscan} contains $E_{6,7,8}$ type gauge group. The number of flux quanta freely scanned over for a given Kähler form (5.3) and a rank-16 W_{noscan} was

$$\kappa = 8 + 2 \times 17, \qquad \kappa' = 6 + 2 \times 17 \tag{5.53}$$

in the study in section 5.2, which agrees with the type IIB orientifold value (5.51), (5.52) for $h^{2,1}(T^2 \times \text{K3})_{-,\text{prim.}} = 1 + 19$.

The action of the modular group Γ_* is implemented in the continuous approximation of [28, 29] by simply restricting the complex m-dimensional restricted moduli space $\mathcal{M}_*$ to its fundamental region. If L_* is small and one is in a situation of maintaining the discrete approach, one can still restrict the space $\mathcal{M}_*$ to its fundamental region under the action of the modular group Γ_*. Furthermore, one has to take a quotient of integral flux configurations admitted for a given point $[z] \in \mathcal{M}_*/\Gamma_*$ by the residual modular group $\Gamma_*(z)$, the stabilizer subgroup of a representative point $z \in \mathcal{M}_*$ [17]. In the example of type IIB on a rigid Calabi-Yau threefold [17, 28, 29], the first few axi-dilaton vevs for small flux contribution to the D3-tadpole sit at a special point in the axi-dilaton moduli space, $\langle\phi\rangle = i$, where the stabilizer subgroup of the moduli space $\Gamma_* = \text{SL}(2;\mathbb{Z})$ is non-trivial. Flux configurations for $\langle\phi\rangle = i$ have to be modded out by the non-trivial residual modular group.

Exactly the same phenomenon takes place in the case of compactification of F-theory on K3 $\times$ K3. For any point (ω_X, ω_S) in the moduli space $D^{(X)} \times D^{(S)}$, the stabilizer subgroup of Γ in (4.26) contains

$$\left(\left[W^{(2)}(S_X) \rtimes \text{Aut}(X)\right] \times \left[W^{(2)}(S_S) \rtimes \text{Aut}(S)\right]\right) . \tag{5.54}$$

$\mathcal{M}_*(J_S, W_{\text{noscan}})$, however, further specifies an embedding of $[J_S] \in S_S \otimes \mathbb{R}/\mathbb{R}_{\geq 0}$ and $(U_* \oplus W_{\text{noscan}}) \subset S_X$. Thus, only the subgroup of (5.54) preserving this embedding remains as the residual modular group Γ_* acting on the flux configuration. None of the reflection subgroup $W^{(2)}(S_S)$ will be left in the residual modular group as long as J_S is in the interior of the cone $\overline{\text{Amp}}_S$. In our numerical study in section 5.2 J_S is sitting on a boundary of

JHEP04(2014)050

$\overline{\mathrm{Amp}}_S$, so that the $W_{E_8} \times W_{E_8}$ Weyl group in $W^{(2)}(S_S)$ is in the residual modular group Γ_*. Similarly, most of $W^{(2)}(S_X)$ is also gone from the residual modular group because of the embedding of $U_* \oplus W_{\mathrm{noscan}}$. At a point $\omega_X \in D^{(X)}$ where an extra non-Abelian factor of W_{root} emerges outside of W_{noscan}, however, its Weyl group is still a part of Γ_*. The automorphisms in $\mathrm{Aut}(X) \cap \Gamma_*$ at least preserve the elliptic fibration morphism and the zero-section, so this is a small subgroup of $\mathrm{Aut}(X)$. We should also remark that our vacuum counting in section 4.2 exploited all possible $\mathrm{Aut}(S)$ to take a quotient of the set of G_1-type fluxes. Since the argument there does not refer to the choice of J_S, one either has to count varieties in J_S or use only the subgroup of $\mathrm{Aut}(S)$ preserving $J_S \in \overline{\mathrm{Amp}}_S$ when taking a quotient of the flux configurations.

In landscapes where L_* is small, there is a pronounced void structure in the vacuum distribution on $\mathcal{M}_*/\Gamma_*$, and a significant fraction of vacua are accumulated at the special points at the centre of the voids [17, 29]. Sample statistics in section 4.3 and, in particular, section 5.2 must have been strongly influenced by this effect. Especially when it comes to the fraction of symmetric vacua in the statistics (such as the fraction of CP preserving vacua in section 4.3), the small value of L_* from $\chi(Y_4)/24 = 24$ must have a strong impact. Keeping this in mind, one should not view the high fraction of CP symmetric vacua as a generic prediction of F-theory.

II. From the perspective of F-theory, there is no reason to focus our attention only to W_{noscan}-landscapes with $rk_7 = \mathrm{rank}(W_{\mathrm{noscan}}) = 16$. It is thus natural to discuss flux vacuum distribution on the restricted moduli space $\mathcal{M}_*(J_S, W_{\mathrm{noscan}})$. In the rest of this section, we treat $\chi(Y_4)/24$ (or L_*) as if it were a free parameter. By doing so, we can get a feeling for how the vacuum distribution depends on such parameters as rk_7 — the rank of fixed 7-brane gauge groups — in F-theory compactification on general elliptic Calabi-Yau fourfolds (not necessarily K3 × K3). With this in mind, we use the continuous approximation to the space of flux quanta [17, 28, 29].

For K3 × K3, the restricted moduli space $\mathcal{M}_*(J_S, W_{\mathrm{noscan}})$ is of complex dimension $m = (18 - rk_7) + 19$. The vacuum index density (5.48) of [28, 29] in this set-up becomes an (m, m)-form on $\mathcal{M}_*$. Summation over the flux configuration is replaced by an integral, $d^K N$, and the delta functions (F-term condition) remove the integral over the $(3,1)+(1,3)$ Hodge components of the flux. Since we restrict the flux to be orthogonal to W_{noscan}, there are only complex $m = (20-2-rk_7)+(20-1)$ dimensions of such $(3,1)$ components to begin with, and hence all the integrals of the $(3,1)+(1,3)$ components are removed from $\int d^K N$ in (5.48). There are still remaining integrals over real $K - 2m = 2 \times 2 + (18 - rk_7) \times 19$ dimensions of the space of flux configuration; contribution to the D3-brane tadpole is positive definite in this space. This argument will lead to the vacuum index distribution that is an (m, m)-form $\rho_{\mathrm{ind.}}$ on $\mathcal{M}_*(J_S, W_{\mathrm{noscan}})/\Gamma_*$ multiplied by a factor $(L_*)^{K/2}$ with $K = [(20 - rk_7) \times 21]$. By requiring that $\langle W_{\mathrm{GVW}} \rangle = 0$, K is replaced by $K' = K - 2$. Therefore, the number of vacua in the ensemble of a given W_{noscan} and J_S roughly scales as $(L_*)^{-(21/2)\times rk_7}$ as a function of rk_7.

In order to study the ratio of the number of SO(10) vacua to SU(5) vacua in F-theory on K3 × K3 flux vacua, one should also address Kähler moduli stabilization, and

JHEP04(2014)050

the vacuum counting on the choice of J_S need to be used as the weight multiplied on top of the distribution on $\mathcal{M}_*(J_S, W_{\text{noscan}})/\Gamma_*$. It will be arguable whether the K3 × K3 compactification of F-theory is phenomenologically interesting enough to motivate such a laborious study. Unless the weight factor from Kähler moduli stabilization contains very strong rk_7-dependence, it seems very difficult to overturn the statistical ratio of $(L_*)^{-10.5}$ of SO(10) vacua to SU(5) vacua simply coming from the flux statistics for fixed J_S.

In such cases as $W_{\text{noscan}} = A_4$ or D_5 in $Y = X \times S = \text{K3} \times \text{K3}$ compactification of F-theory, there exists a primitive embedding $\phi : U \oplus W_{\text{noscan}} \hookrightarrow \Lambda_{\text{K3}}^{(X)} \cong H_2(X;\mathbb{Z})$. Furthermore, such an embedding is unique modulo $\text{Isom}^+(\Lambda_{\text{K3}}^{(X)})$ due to Theorem 1.14.4 of [99] and Theorem 2.8 of [78] (which is also quoted as Thm. ϵ in [26]). Thus, the restricted moduli space $\mathcal{M}_*$ can be constructed out of a single piece[81] of the restricted period domain

$$\mathbb{P}\left[\left\{\Omega_X \in (\Lambda_{\text{K3}}^{(X)})^* \otimes \mathbb{C} \;\middle|\; \Omega_X \wedge \Omega_X = 0,\ \langle \Omega_X, \phi(U \oplus W_{\text{noscan}})\rangle = 0,\ \Omega_X \wedge \overline{\Omega}_X > 0\right\}\right]. \tag{5.55}$$

If an attractive K3 surface $X = X_{[a\ b\ c]}$ admits an elliptic fibration whose W_{frame} contains a W_{noscan} as above, its Ω_X (equivalently a primitive embedding of its T_X into $[\phi(U \oplus W_{\text{noscan}})^\perp \subset \Lambda_{\text{K3}}^{(X)}]$) should be found in this single piece of restricted period domain. Such an embedding of T_X, however, is no longer unique under the subgroup of $\text{Isom}^+(\Lambda_{\text{K3}})$ preserving the embedding $\phi : (U \oplus W_{\text{noscan}}) \hookrightarrow \Lambda_{\text{K3}}^{(X)}$. In sections 4.1 and 4.2.3, we discussed multiplicities of elliptic fibration on a given attractive K3 surface X and a given isometry class of frame lattice. This multiplicity appears as a part of the non-uniqueness of the embedding of T_X into $[\phi(U \oplus W_{\text{noscan}})^\perp \subset \Lambda_{\text{K3}}^{(X)}]$ modulo the remaining subgroup of $\text{Isom}^+(\Lambda_{\text{K3}})$.

III. Having seen how the vacuum statistics depend on the rank of gauge groups, the next question of interest will be how it depends on the number of generations of matter fields. Since it is impossible to generate a non-zero net chirality on non-Abelian 7-branes in the K3 × K3 set-up, we content ourselves with studying the dependence on the number of vector-like pairs on a non-Abelian 7-brane. As we have seen in section 5.3, the singular fibre fluxes generate some vector-like pairs of matter fields, while reducing the symmetry group on the non-Abelian 7-brane associated with the singular fibre. Thus, we set the problem as follows. For some choice of J_S and $W_{\text{noscan}} \subset W_{\text{frame}}$ as before, let us specify

$$G_{\text{fix}} = \sum_A (C_A \otimes F_A), \qquad C_A \in W_{\text{noscan}} \cap W_{\text{root}}, \qquad F_A \in [J_S^\perp \subset S_S]. \tag{5.56}$$

An ensemble of flux vacua is generated, by allowing the four-form flux $G^{(4)}$ to be $G_{\text{scan}} + G_{\text{fix}}$ for any G_{scan} orthogonal to J_S and W_{noscan}. The vacuum index density distribution of such a landscape is obtained as an (m, m) form over the restricted moduli space $\mathcal{M}_*(J_S, W_{\text{noscan}})/\Gamma_*$. Landscapes with different G_{fix} share the same restricted moduli space as long as W_{noscan} and J_S remain the same. When we take W_{noscan} to be E_7, E_6 or D_5, for

[81] In principle, it is possible that primitive embeddings of $(U \oplus W_{\text{noscan}})$ into $\Lambda_{\text{K3}}^{(X)}$ are not unique modulo $\text{Isom}^+(\Lambda_{\text{K3}}^{(X)})$, depending on what W_{noscan} is. In such cases, the restricted moduli space $\mathcal{M}_*/\Gamma_*$ consists of multiple connected components.

JHEP04(2014)050

example, and $G_{\rm fix} = (C_A \otimes F_A)$ so that the unbroken symmetry becomes E_6, D_5 or A_4, the singular fibre flux $G_{\rm fix}$ determines the number of vector-like pairs in the $\mathbf{27} + \overline{\mathbf{27}}$, $\mathbf{16} + \overline{\mathbf{16}}$ and $\mathbf{10} + \overline{\mathbf{10}}$ representations, respectively, through (5.46). By comparing the numbers of vacua of the ensembles of $(J_S, W_{\rm noscan}; G_{\rm fix})$ with the common $(J_S, W_{\rm noscan})$ and different $G_{\rm fix}$, we can determine the statistical cost of leaving vector-like pairs of matter fields in certain classes of representations in the effective theory.[82]

The result is simple. Our estimate of the number of vacua in such an ensemble is given by

$$(L_{*,\rm eff.})^{K'/2}; \qquad L_{*,\rm eff.} = \frac{\chi(X \times S)}{24} - \frac{1}{2}(G_{\rm fix})^2, \tag{5.57}$$

replacing $L_* = \chi(Y)/24$ by the remaining D3-tadpole $L_{*,\rm eff.}$ to be cancelled by the flux other than $G_{\rm fix}$. The more the number of vector-like pairs, the less the effective value $L_{*,\rm eff.}$. If $L_* = \chi(Y)/24$ were fairly large (and $K'/2$ is not particularly large), then requiring one or two vector-like pairs of the matter field does not reduce the number of vacua too much, relatively. If L_* is not particularly large, then the number of vacua with a few more vector-like pairs of matter fields becomes much smaller. Clearly, this effect is further enhanced when $K'/2$ is large.

IV. Finally, let us study the (m,m)-form distribution $\rho_{\rm ind.}$ over $\mathcal{M}_*/\Gamma_*$ in the context of F-theory compactification, not just the overall number of flux vacua. We begin with a review of what is known about $\rho_{\rm ind}$ in [2, 28, 29].

The most robust result on $\rho_{\rm ind}$ states that, for F-theory compactification without much restriction on the space of scanning four-form fluxes $G^{(4)}_{\rm scan}$, $\rho_{\rm ind}$ is written in the form of the Euler class $e(\nabla)$ on $\mathcal{M}_*$ (which means that it is a differential $2m$-form) associated with a connection ∇ on a real vector bundle with rank $2m$ [2]. The formula [28, 29]

$$\rho_{\rm ind} = \det\left(-\frac{R}{2\pi i} + \frac{\omega}{2\pi}\mathbf{1}\right)_{m\times m} = e(T\mathcal{M}_* \otimes \mathcal{L}^{-1}) = c_n(T\mathcal{M}_* \otimes \mathcal{L}^{-1}), \tag{5.58}$$

is a special case of the more robust result $\rho_{\rm ind} = e(\nabla)$ [2]. Here, ω is the Kähler form and R the curvature $(1,1)$ form of the holomorphic vector bundle $T\mathcal{M}_*$, $\mathcal{L}$ is the line bundle whose first Chern class is $-\omega/(2\pi)$ and $c = \det(-kR/(2\pi i) + \mathbf{1}) = \sum_k c_k t^k$ defines the Chern classes. It takes an extra effort to find for which real vector bundle $\rho_{\rm ind} = e(\nabla)$ for general cases.

It is known that the formula (5.58) can be used at least for two categories of landscapes.

A : type IIB on a Calabi-Yau orientifold M_3 with full scanning of three-form fluxes $G^{(3)}_{\rm scan}$ and with all the D7-branes appearing as an SO(8) configuration [29], i.e. four D7-branes on each O7-plane.

B : F-theory compactification on a Calabi-Yau fourfold Y_4 with the four-form flux scanning in a sufficiently large space.

[82] The net chirality would be proportional to the first power of the four-form flux, while the number of vector-like pairs scales as a square of the flux. This difference should be kept in mind. Note also that the number of vector-like pairs of matter fields may also depend on the representation, even for a given non-Abelian gauge group. Thus, it is dangerous to extract too many lessons out of this result.

JHEP04(2014)050

An example of category B is given by [2]:

$$G^{(4)}_{\text{scan}} \in \left[H^{4,0}(Y;\mathbb{C}) + \text{h.c.}\right] \oplus \left[H^{3,1}(Y;\mathbb{C})_{\text{prim.}} + \text{h.c.}\right] \oplus \left[\left(H^{2,2}(Y;\mathbb{R})_V\right)^{\perp} \subset H^{2,2}(Y;\mathbb{R})\right]. \tag{5.59}$$

Here, $H^{(2,2)}(Y;\mathbb{R})_V$ is the subspace of $H^{2,2}(Y;\mathbb{R})$ spanned by the intersection of any pair of divisors of Y (this naive definition is made more precise shortly).

Let us explain what we mean by a "sufficiently large space" when we introduced category B. Let $V \subset H^4(Y;\mathbb{R})$ be the subspace in which the four-form is scanned to generate a landscape, and let $\{\psi_{I=1,2,\cdots}\}$ be a basis of V. The assumption made (implicitly) in [2] is that the vector space V is large enough that one can make a replacement

$$\left(\int_Y \psi_I \wedge \varphi\right)(A^{-1})^{IJ}\left(\int_Y \psi_J \wedge \chi\right) \Longrightarrow \int_Y \varphi \wedge \chi, \qquad A_{IJ} := \int_Y \psi_I \wedge \psi_J \tag{5.60}$$

for arbitrary differential forms ψ and χ that belong to the vector space[83]

$$G^{(4)}_{\text{scan}} \in \left[H^{4,0}(Y_z;\mathbb{C}) + H^{0,4}(Y_z;\mathbb{C})\right] \oplus \left[H^{3,1}(Y_z;\mathbb{C})_* + H^{1,3}(Y_z;\mathbb{C})_*\right] \oplus H^{2,2}(Y_z;\mathbb{R})_{H*}. \tag{5.61}$$

The quantities $[H^{3,1}(Y_z;\mathbb{C})_*$ and $H^{2,2}(Y_z;\mathbb{R})_{H*}$ are defined in the next paragraph and (5.63).

It is a natural generalization of the category B landscapes above to require extra divisors corresponding to extra 7-brane gauge groups, i.e. introduce a W_{noscan} as done earlier in this section. The moduli space $\mathcal{M}_*(J_Y, W_{\text{noscan}})$ is then reduced in dimensions from the full space of complex structure moduli of Y compatible with a Kähler form J_Y. The $H^{3,1} + H^{1,3}$ components of the flux is then not only required to be primitive, $G^{(4)}_{\text{scan}} \wedge J_Y = 0$, but the same condition is required with regard to the divisors in W_{noscan}. Let $[H^{3,1}(Y_z;\mathbb{C})_* + H^{1,3}(Y_z;\mathbb{C})_*]$ denote the resulting smaller subspace. The $(H^{2,2}_V)^{\perp}$ component of the flux space is also reduced, because $H^{2,2}(Y_z;\mathbb{R})_V$ is larger in dimensions. This new $H^{2,2}(Y_z;\mathbb{R})_V$ is denoted by $H^{2,2}(Y_z;\mathbb{R})_{V*}$. We then have an ensemble of vacua with the four-form flux scanning over the vector space

$$G^{(4)}_{\text{scan}} \in \left[H^{4,0}(Y;\mathbb{C}) + \text{h.c.}\right] \oplus \left[H^{3,1}(Y;\mathbb{C})_* + \text{h.c.}\right] \oplus \left[\left(H^{2,2}(Y;\mathbb{R})_{V*}\right)^{\perp} \subset H^{2,2}(Y;\mathbb{R})\right]; \tag{5.62}$$

Let us refer to these landscapes as category B'.

In order to state the relation between the category A landscapes and category B' landscapes, we need to prepare the following language. Consider a family of Calabi-Yau fourfolds $\pi : \mathcal{Y} \longrightarrow \mathcal{M}_*$, where $Y_z := \pi^{-1}(z)$ is the Calabi-Yau fourfold corresponding to $z \in \mathcal{M}_*$. We have in mind a restricted moduli space $\mathcal{M}_*$ for a specific choice of Kähler form J_Y and some set of divisors W_{noscan} corresponding to the 7-brane gauge groups. The $H^{2,2}(Y_z;\mathbb{R})$ vector space over $\mathbb{R}$ for each $z \in \mathcal{M}_*$ is decomposed as follows. First, $H^{2,2}(Y_z;\mathbb{R})_{V*}$ is defined[84] as the subspace spanned by intersection of Y_z with any pair of

[83] See equations (6.16) and (6.17) and compare with (6.33) and (6.34) in [2].

[84] This (more precise) definition of $H^{2,2}(Y_z;\mathbb{R})_V$ is not the same as the naive "definition" right after (5.59), when $z \in \mathcal{M}_*$ is in a special locus of $\mathcal{M}_*$ so that there are more divisors in Y_z than in generic points of $\mathcal{M}_*$. Contributions from such extra divisors are not included in $H^{2,2}(Y_z;\mathbb{R})_V$ in the precise definition.

JHEP04(2014)050

divisors of $\mathcal{Y}$. Secondly, another subspace $H^{2,2}(Y_z;\mathbb{R})_{H*} \subset H^{2,2}(Y_z;\mathbb{R})$ is defined as

$$\mathrm{Span}_{\mathbb{C}}\left\{(D_aD_b\Omega_Y), \overline{(D_cD_d\Omega_Y)}\right\}|_{a,b,c,d\in 1,\cdots,m} \cap H^{2,2}(Y_z;\mathbb{R})\,, \qquad m = \dim \mathcal{M}_*\,. \tag{5.63}$$

It is known that [2]

i) the vector space of (2,2) Hodge components is divided into $H^{2,2}_{\ell=0} \oplus H^{2,2}_{\ell=1} \oplus H^{2,2}_{\ell=2}$

ii) the intersection form is positive definite on $H^{2,2}_{\ell=0} \oplus H^{2,2}_{\ell=2}$ and negative definite on $H^{2,2}_{\ell=1}$

iii) $H^{2,2}_{\ell=1} \oplus H^{2,2}_{\ell=2}$ is contained in $H^{2,2}(Y_z;\mathbb{R})_{V*}$

The differential forms in the first component, $H^{2,2}_{\ell=0}$ are the primitive $(2,2)$ forms. Thus, the intersection form is positive definite on the orthogonal complement $[(H^{2,2}(Y_z;\mathbb{R})_{V*})^{\perp} \subset H^{2,2}(Y_z;\mathbb{R})]$, and there is a well-defined orthogonal decomposition of the $H^{2,2}(Y_z;\mathbb{R})$ vector space:

$$H^{2,2}(Y_z;\mathbb{R}) = H^{2,2}(Y_z;\mathbb{R})_{H*} \oplus H^{2,2}(Y_z;\mathbb{R})_{RM} \oplus H^{2,2}(Y_z;\mathbb{R})_{V*}. \tag{5.64}$$

Note that the remnant subspace $H^{2,2}(Y_z;\mathbb{R})_{RM}$ is not empty in general [100]. In particular, as explained in detail in appendix C, this happens already in the case of $Y = \mathrm{K3} \times \mathrm{K3}$. As discussed in appendix C, the landscape of category A (roughly speaking, type IIB orientifolds with three-form scanning (C.11)) corresponds to scanning the four-form in the $H^{2,2}(Y;\mathbb{R})_{H*}$ subspace in addition to the first two components of (5.59), i.e., the space (C.5). This is a smaller subspace than (5.62), in principle, in the sense that $H^{2,2}(Y;\mathbb{R})_{RM}$ can be non-empty. This indicates that the scanning space of the flux can be sufficiently large, for the condition (5.60) to hold (and the formula (5.58) also holds consequently), even when the scanning space is smaller than (5.62).

As discussed in appendix C, the four-form scanning we have introduced in this section also corresponds to the vector space (C.5). It is thus reasonable to think of one more category of landscapes in F-theory which contains both the category A landscapes and the ones on $Y = \mathrm{K3} \times \mathrm{K3}$ with arbitrary rk_7 we have considered. Let us call category A' any landscapes generated by scanning four-form flux in the vector space (C.5) for an elliptic fibred Calabi-Yau fourfold[85] $\pi_Y : Y \to B_3$. This is to be contrasted with those in category B' where the four-form flux is scanned in (5.62).

It must now be obvious that the formula (5.58) holds, not just for the landscapes in category B', but also for the landscapes in category A'. Since the condition (5.60) requires that $\psi_I(A^{-1})^{IJ}\psi_J$ be an insertion of a complete system only for φ, χ in (C.5), it is equivalent to say that the entire vector space (C.5) is contained in the space of four-form scanning (or not). Appendix C also provides an alternative (more down to earth) derivation of the formula (5.58) following the line of argument in one of the original articles [29]), rather than the refined version of [2], with an assumption (C.15) and a little more concrete consequence (C.29). We understand that the argument here is enough to justify the formula (5.58) for landscapes in category A'.

[85] A more appropriate way to phrase this is a family of elliptically fibred Calabi-Yau fourfolds $\pi : \mathcal{Y} \longrightarrow \mathcal{M}_*$ for which a generic fibre is not necessarily in the form of K3 × K3 or a K3-fibration.

JHEP04(2014)050

There is an immediate consequence of this observation. Any landscape (an ensemble of vacua) in category B' is decomposed into multiple landscapes (ensembles of vacua) in category A' labelled by $G^{(4)}_{\rm fix}$ in $H^{2,2}(Y;\mathbb{R})_{\rm RM}$. Since all of these landscapes in category A' share the same restricted moduli space $\mathcal{M}_*$, and since the formula (5.58) determines $\rho_{\rm ind}$ only in terms of geometry of $\mathcal{M}_*$, the vacuum index distribution $d\mu_I$ for these landscapes in category A' are the same apart form the $G^{(4)}_{\rm fix}$-dependent overall normalization (5.57).

Let us use (5.58) to derive an explicit result on the distribution of moduli parameters. Consider a landscape of F-theory compactification on $Y = X\times S = {\rm K3}\times{\rm K3}$ with some rank-16 $W_{\rm noscan}$ and $G^{(4)}_{\rm fix}$. Then the restricted moduli space is of the form $\mathcal{M}_* = \mathcal{M}_{\rho_1}\times\mathcal{M}_{\rho_2}\times\mathcal{M}_{\rm K3}(S;J_S)$. This is because the lattice $[(U_*\oplus W_{\rm noscan})^\perp\subset H^2(X;\mathbb{Z})]$ is always signature $(2,2)$, and the intersection form can be made $U\oplus U$ for some $\mathbb{R}$-coefficient basis of the vector space obtained by tensoring $\mathbb{R}$ with the signature $(2,2)$ lattice above. The Kähler forms of the moduli spaces $\mathcal{M}_{\rho_1}$ and $\mathcal{M}_{\rho_2}$ are $K^{(\rho_1)} = -\ln[(\rho_1-\bar\rho_1)/i]$ and $K^{(\rho_2)} = -\ln[(\rho_2-\bar\rho_2)/i]$, respectively. The modulus ρ_1 is interpreted as the axi-dilaton of type IIB orientifold in the case of $W_{\rm noscan} = D_4^{\oplus 4};(\mathbb{Z}_2\times\mathbb{Z}_2)$. By closely following the computation of section 3.1.2 in [29], we obtain

$$\rho_{\rm ind} = \left(-\frac{R^{(\rho_1)}}{2\pi i}+\frac{\omega^{(S)}}{2\pi}+\frac{\omega^{(\rho_1)}}{2\pi}+\frac{\omega^{(\rho_2)}}{2\pi}\right)\wedge\left(-\frac{R^{(\rho_2)}}{2\pi i}+\frac{\omega^{(S)}}{2\pi}+\frac{\omega^{(\rho_1)}}{2\pi}+\frac{\omega^{(\rho_2)}}{2\pi}\right)\wedge \det\left(-\frac{R^{(S)}}{2\pi i}+\left(\frac{\omega^{(S)}}{2\pi}+\frac{\omega^{(\rho_1)}}{2\pi}+\frac{\omega^{(\rho_2)}}{2\pi}\right)\mathbf{1}\right), \tag{5.65}$$

$$= 2\frac{\omega^{(\rho_1)}}{2\pi}\wedge\frac{\omega^{(\rho_2)}}{2\pi}\wedge\left\{c^{(S)}_{m-2}+\left(\frac{\omega^{(S)}}{2\pi}\right)^2\wedge c^{(S)}_{m-4}\right\}, \tag{5.66}$$

where $\omega^{(\rho_1)}$, $\omega^{(\rho_2)}$ and $\omega^{(S)}$ are the Kähler forms on the moduli spaces $\mathcal{M}_{\rho_1}$, $\mathcal{M}_{\rho_2}$ and $\mathcal{M}_{\rm K3}(S;J_S)$, respectively, and $R^{(S)}$, $R^{(\rho_2)}$ and $R^{(\rho_1)}$ the curvature $(1,1)$-forms of the tangent bundles of those moduli spaces.[86] $c^{(S)}_r$'s are the r-th Chern class of the holomorphic rank-$(m-2)$ vector bundle $T\mathcal{M}_{\rm K3}(S;J_S)\otimes(\mathcal{L}^{(S)})^{-1}$, where $\mathcal{L}^{(S)}$ is the line bundle whose first Chern class is $-\omega^{(S)}/2\pi$. Thus, in these set-ups the vacuum index density distribution $\rho_{\rm ind.}$ is factorized for the three pieces of the moduli space. If one is interested only in the distribution of any one among ρ_1, ρ_2 and moduli of the K3 surface S, but not altogether, then the distribution $\rho_{\rm ind}$ can be integrated over the irrelevant coordinates first. For the moduli ρ_1 and ρ_2, in particular,

$$\rho_{\rm ind.}(\rho_1)\propto d[{\rm Re}\rho_1]d[{\rm Im}\rho_1]\frac{1}{({\rm Im}(\rho_1))^2},\qquad \rho_{\rm ind.}(\rho_2)\propto d[{\rm Re}\rho_2]d[{\rm Im}\rho_2]\frac{1}{({\rm Im}(\rho_2))^2}. \tag{5.67}$$

Applying this result to the $W_{\rm noscan} = E_8\oplus E_8$-landscape, in particular, the prediction in the continuous approximation (5.67) for ρ_2 can also be read as that of $[{\rm vol}(T^2)/\ell_s^2]_{\rm Het}$. Our numerical results (not relying on continuous approximation) in section 5.2 agree with this prediction based on the continuous approximation qualitatively in that large ${\rm Im}(\tilde\rho_H) =$

[86] They satisfy $R^{(\rho_i)} = 2i\omega^{(\rho_i)}$.

JHEP04(2014)050

$[\mathrm{vol}(T^2)/\ell_s^2]_{\mathrm{Het}}$ is statistically disfavoured. Note that this happens although we should not expect the continuous approximation to be very good because $\chi(Y)/24 = 24$ is not particularly large.

The result (5.67) also indicates that there is no correlation between the distribution of ρ_1, ρ_2 and the moduli of K3 surface S, if we ignore the difference between the vacuum distribution and the vacuum index distribution. Figure 4 (iii) in section 5.2 may be regarded as a manifestation of the absence of any correlation between ρ_1 and ρ_2.

It is an interesting question how ρ_{ind} depends on $\mathrm{Im}(\tilde{\rho}_H)$ for different values of rk_7. ρ_{ind} is not expected to have a factorized form as (5.67), but it will be in the form of

$$\rho_{\mathrm{ind}} = c^{(X)}_{18-rk_7} c^{(S)}_{19} + \omega^{(X)}\omega^{(S)} c^{(X)}_{17-rk_7} c^{(S)}_{18} + (\omega^{(X)}\omega^{(S)})^2 c^{(X)}_{16-rk_7} c^{(S)}_{17} + \cdots , \tag{5.68}$$

where $c^{(X)}_r$'s are the r-th Chern class of the rank-$(18 - rk_7)$ holomorphic vector bundle $T\mathcal{M}_{\mathrm{K3}}(X; U_* \oplus W_{\mathrm{noscan}}) \otimes \mathcal{L}^{-1}_{(X)}$. It must still be possible to extract the leading power-law behaviour in $\mathrm{Im}(\tilde{\rho}_H)$ in the large $\mathrm{Im}(\tilde{\rho}_H)$ region of the moduli space, using the parametrization (A.6). We leave this as an open problem in this article.

Acknowledgments

We thank Kazuo Hosomichi for useful comments, and Tetsuji Shioda for giving a lecture on Mordell-Weil lattice on K3 surface, in January 2010 at IPMU, Tokyo. A. P. B. likes to thank the IPMU Tokyo for kind hospitality during his visit in summer of 2012, which initiated this collaboration. The work of A. P. B. was supported by a JSPS postdoctoral fellowship under grant PE 12530, and by the STFC under grant ST/J002798/1 and that of T. W. by WPI Initiative, MEXT, Japan and a Grant-in-Aid for Scientific Research on Innovative Areas 2303.

A A note on heterotic string Narain moduli

Although Narain compactificaiton of heterotic string theory is a well-known subject, we leave a brief note here for summary of conventions used in the main text of this article.

A compactification of heterotic string theory on T^2 is specified by embedding an even self-dual lattice $\mathrm{II}_{2,18}$ in a space

$$\mathbb{R}^{2,18} = \left\{ \sqrt{\frac{\alpha'}{2}} (k^R_8, k^R_9, k^L_8, k^L_9, k_{i=11,\cdots,26})^T \right\} \tag{A.1}$$

where the metric on $\mathbb{R}^{2,18}$ is $\mathrm{diag}(\mathbf{1}_{2\times 2}, \mathbf{1}_{18\times 18})$. Let $\{e_{K8}, e_{\bar{w}8}, e_{K9}, e_{\bar{w}9}, e_{I=11,\cdots,26}\}$ be a set of generators of $\mathrm{II}_{2,18}$ (as well as its image in $\mathbb{R}^{2,18}$) where $U = \mathrm{Span}_Z\{e_{K8}, e_{\bar{w}8}\}$, $U = \mathrm{Span}_{\mathbb{Z}}\{e_{K9}, e_{\bar{w}9}\}$, and $E_8 \oplus E_8$ is generated by the rest, $\{e_{I=11,\cdots,26}\}$. Thus, the data

JHEP04(2014)050

of this compactification is written in the form of a $(2+18)\times(2+2+16)$ matrix,

$$\mathcal{Z}=[e_{K8},e_{\bar{w}8},e_{K9},e_{\bar{w}9},e_{I=11},\cdots,e_{I=26}]\,,\quad \mathcal{Z}^T\cdot\begin{pmatrix}\mathbf{1}_{2\times2} & \\ & -\mathbf{1}_{18\times18}\end{pmatrix}\cdot\mathcal{Z}=\begin{pmatrix}U & & & \\ & U & & \\ & & C_{E_8} & \\ & & & C_{E_8}\end{pmatrix}, \tag{A.2}$$

where the U in (A.2) denotes the matrix $\begin{bmatrix} & 1\\ 1 & \end{bmatrix}$ and C_{E_8} the negative of the Cartan matrix of E_8, which is also the (negative definite) intersection form of the E_8 root lattice. General elements of $\mathrm{II}_{2,18}$ are written in the form of $n_8e_{K8}+(-w^8)e_{\bar{w}8}+n_9e_{K9}+(-w^9)e_{\bar{w}9}+\sum_I q^Ie_I$, which is also denoted by $(n_8,-w^8,n_9,(-w^9),q^I)^T$ in the component description. The generators $e_{K8,K9}$ correspond to states with elementary Kaluza-Klein excitation in T^2, and $e_{\bar{w}8,\bar{w}9}$ to states winding T^2 once.

The first two rows of the matrix $\mathcal{Z}$ are denoted by $\mathcal{Z}^R_m$ with $m=8,9$. Introducing $\mathcal{Z}^R:=\mathcal{Z}^R_8+i\mathcal{Z}^R_9$, it follows from relation (A.2) that

$$\mathcal{Z}^R\cdot\begin{pmatrix}U^{-1} & & & \\ & U^{-1} & & \\ & & (C_{E_8})^{-1} & \\ & & & (C_{E_8})^{-1}\end{pmatrix}\cdot\left(\mathcal{Z}^R\right)^T=0\,. \tag{A.3}$$

Because $\mathcal{Z}^R$ can be regarded as an element of $\mathrm{Hom}(\mathrm{II}_{2,18},\mathbb{C})$,

$$\begin{aligned}&\mathcal{Z}^R:(n_8,-w^8,n_9,-w^9,q^I)^T\\ &\quad\longmapsto\sqrt{\frac{\alpha'}{2}}(k^R_8+ik^R_9)\text{ component of }\left(e_{K8}n^8+e_{\bar{w}8}(-w^8)+\cdots+\sum_I e_Iq^I\right),\end{aligned}$$

we see that the relation above can also be written as $(\mathcal{Z}^R,\mathcal{Z}^R)=0$ using the symmetric pairing of the dual lattice $\mathrm{II}^*_{2,18}$ naturally extended bilinearly to $\mathrm{II}^*_{2,18}\otimes\mathbb{C}$. With the same notation, it also follows that

$$\left(\mathcal{Z}^R,\overline{\mathcal{Z}^R}\right)=+2. \tag{A.4}$$

The moduli space of this Narain compactification is parametrized by 18 complex numbers. With a parametrization that is understood intuitively in the supergravity approximation of heterotic $E_8\times E_8$ string theory, $k^R_{m=8,9}$ in $\mathcal{Z}^R$ are written as follows [101]:

$$k^R_m=\frac{n_m}{R_m}-\frac{R_mw^m}{\alpha'}-\sum_I q^IA_{I,m}+\frac{1}{2}\sum_{I,J}A_{I,m}C^{IJ}\left(\sum_n w^nR_nA_{J,n}\right);\quad\text{(no summation in }m) \tag{A.5}$$

$A_{I,m}$'s ($m=8,9$ and $I=11,\cdots,26$) are the Wilson lines on T^2 for the simple roots of $E_8\times E_8$, and $R_{m=8,9}$ the radii of the two directions of T^2. Together with two more $\mathbb{R}$-valued parameters that we have omitted here ($\langle B\rangle=0$, and T^2 is rectangular, just for better readability), there are 2×18 parameters in total. C^{IJ} is the inverse of the

JHEP04(2014)050

matrix $C_{E_8\times E_8}$. Therefore, $\mathcal{Z}^R$ is parametrized by 18 complex numbers. In the component description of $[U\oplus U\oplus E_8\oplus E_8]^*\otimes\mathbb{C}$, it is given by

$$\mathcal{Z}^R=\frac{i}{\sqrt{2\mathrm{Im}(\tau_H)\mathrm{Im}(\tilde{\rho}_H)+\mathrm{Im}(a_P)C^{PQ}\mathrm{Im}(a_Q)}}(-\tau_H,\ -\tilde{\rho}_H,\ 1,\ -\tau_H\tilde{\rho}_H-a_KC^{KL}a_L/2,\ a_I), \tag{A.6}$$

where (under the condition that $\langle B\rangle=0$ and T^2 is rectangular)

$$\tau_H=i\frac{R_9}{R_8},\quad \rho_H=i\frac{R_8R_9}{\alpha'},\quad a_I=iR_9(A_{I,8}+iA_{I,9})=\sqrt{\alpha'\tau_H\rho_H}(A_{I,8}+iA_{I,9}), \tag{A.7}$$

and

$$\tilde{\rho}_H=\rho_H-\frac{a_IC^{IJ}(a-\bar{a})_J}{4i\,\mathrm{Im}(\tau_H)}. \tag{A.8}$$

B Heterotic Cartan flux and semistable degeneration

B.1 Set-up

In this appendix, the discussion on heterotic-F-theory duality of Cartan/Mordell-Weil flux of section 5.3 is made explicit by using the two-parameter family of K3 surfaces (4.48), (4.49) for F-theory (and its heterotic dual) as an example.

If we are to require a pair of IV* singular fibres, this specifies a family of $\rho_X=12+2=14$ K3 surfaces, whose moduli space has dimension 6. Let

$$T_X^{\rho=14}=U\oplus U\oplus A_2\oplus A_2,\qquad W_{\text{frame}}^{\rho=14}=E_6\oplus E_6. \tag{B.1}$$

The two parameter family of K3 surfaces, $X=\mathrm{Km}(E_{\rho_1}\times E_{\rho_2})$, has four more independent algebraic cycles, $\rho_X=18$, and the transcendental lattice is only of rank 4, $T_X^{\rho=18}=U[2]\oplus U[2]$. Such a special family of K3 surfaces can be identified by an embedding $T_X^{\rho=18}\longrightarrow T_X^{\rho=14}$:

$$(\overline{C}_{32},\overline{C}_{14},\overline{C}_{12},\overline{C}_{43})\longmapsto(v,V,v',V',\alpha_1^{\mathrm{v}},\alpha_2^{\mathrm{v}},\alpha_1^{\mathrm{h}},\alpha_2^{\mathrm{h}})\left[\begin{array}{cc|cc}1&1&&\\&2&&\\\hline&&1&1\\&&&2\\\hline&1&&\\&&&1\\\hline&-1&&\\&&&1\end{array}\right], \tag{B.2}$$

where $\overline{C}_{32,14,12,43}$ are generators of $T_X^{\rho=18}=U[2]\oplus U[2]$, $\{v,V,v',V'\}$ those of $U\oplus U\subset T_X^{\rho=14}$, and $\{\alpha_{1,2}^{\mathrm{v}}\}$ and $\{\alpha_{1,2}^{\mathrm{h}}\}$ those of the structure group $A_2=\mathrm{SU}(3)$ in the visible and hidden sectors, respectively.

In this two parameter family of K3 surfaces (Kummer surfaces), the four extra independent algebraic cycles are the generators of the orthogonal complement of the image of

JHEP04(2014)050

$T_X^{\rho=18}$ within $T_X^{\rho=14}$. This lattice is also regarded as the orthogonal complement of the $E_6 \oplus E_6$ lattice within the frame lattice $W^{\rho=18}$ for $\rho = 18$. Hence this is also the essential lattice $L(X) = W_{\mathrm{U}(1)}$ of this elliptic fibration. $L(X) = W_{\mathrm{U}(1)}$ is generated by

$$(P, Q, P', Q') = (v, V, v', V', \alpha_1^{\mathrm{v}}, \alpha_2^{\mathrm{v}}, \alpha_1^{\mathrm{h}}, \alpha_2^{\mathrm{h}}) \left[\begin{array}{cc|cc} & 2 & & -1 \\ \hline -1 & & 2 & \\ \hline 1 & 1 & & \\ & & 1 & 1 \\ \hline 1 & -1 & & \\ & & 1 & -1 \end{array}\right]. \tag{B.3}$$

The period integral is therefore in the form of

$$\mathcal{Z}^R \propto \Omega_X = \left(-\tau_H, -\tilde{\rho}_H; 1, -\tau_H\tilde{\rho}_H + \frac{\tau_H^2+1}{2}; \tau_H + \frac{1}{2}, -\left(\frac{\tau_H}{2}+1\right), 0^6; -\left(\tau_H - \frac{1}{2}\right), \frac{\tau_H}{2} - 1, 0^6\right) \tag{B.4}$$

in the component description of $[U \oplus U \oplus E_8 \oplus E_8]^* \otimes \mathbb{C}$. In the component description using $(T_X^{\rho=18})^* \otimes \mathbb{C}$ (and irrelevant $(W_{\mathrm{U}(1)} \oplus E_6 \oplus E_6)^* \otimes \mathbb{C}$), this becomes

$$(-\tau_H, -(2\tilde{\rho}_H - \tau_H), 1, -\tau_H(2\tilde{\rho}_H - \tau_H)). \tag{B.5}$$

Thus, in the parametrization of Ω_X in terms of τ_H and $\tilde{\rho}_H$, the K3 surface $X = \mathrm{Km}(E_{\rho_1} \times E_{\rho_2})$ varies as

$$\rho_1 = \tau_H, \qquad \rho_2 = 2\tilde{\rho}_H - \tau_H. \tag{B.6}$$

Obviously the parametrization (B.4) follows the convention of Narain moduli for heterotic string compactification, and the correspondence (B.6) should be read as the duality map between the coordinates of the heterotic and F-theory moduli spaces.

In the heterotic string language, the component description of $\mathcal{Z}^R$ in (B.4) is a manifest consequence of the condition (5.39), with the flux data n_A's in (5.38) given by the $k = 4$ column vectors in (B.3). The Wilson lines are constrained to be torsion points in $\mathrm{Jac}(T^2)$ of the heterotic compactification:

$$\mathrm{diag}\left(\frac{\tau_H}{2}, -\frac{\tau_H+1}{2}, \frac{1}{2}\right) \subset \mathfrak{su}(3)^{\mathrm{vis.}}, \qquad \mathrm{diag}\left(-\frac{\tau_H}{2}, \frac{\tau_H-1}{2}, \frac{1}{2}\right) \subset \mathfrak{su}(3)^{\mathrm{hid.}}. \tag{B.7}$$

Wilson lines in the dimension-3 representations of the structure group $\mathrm{SU}(3)^{\mathrm{vis.}} \times \mathrm{SU}(3)^{\mathrm{hid.}}$ take values in 2-torsion points in this case, which is also the direct consequence of the spectral surface equations $a_3^{\mathrm{v}} y = 0$ for the visible sector and $a_3^{\mathrm{h}} y = 0$ for the hidden sector.

JHEP04(2014)050

B.2 Mordell-Weil group and narrow Mordell-Weil group

In the two parameter family of K3 surfaces $X = \mathrm{Km}(E_{\rho_1} \times E_{\rho_2})$ with an elliptic fibration of type $2\mathrm{IV}^* + 8I_1$, the essential lattice is

$$L(X) = W_{\mathrm{U}(1)} \cong A_2[2] \oplus A_2[2] \cong \mathrm{Span}_{\mathbb{Z}}\{P, P'\} \oplus \mathrm{Span}_{\mathbb{Z}}\{Q, Q'\}. \tag{B.8}$$

$E_6 \oplus E_6$ forms the root lattice W_{root} of the frame lattice W_{frame} for generic ρ_1 and ρ_2, and the frame lattice is obtained by adding, to $W_{\mathrm{root}} \oplus W_{\mathrm{U}(1)}$, such glue vectors as

$$\frac{2P + P'}{3} + \omega^{\mathrm{v}}_{\mathbf{27}} + \omega^{\mathrm{h}}_{\mathbf{27}}, \qquad \frac{P + 2P'}{3} + \omega^{\mathrm{v}}_{\mathbf{27}} + \omega^{\mathrm{h}}_{\mathbf{27}} \tag{B.9}$$

$$\frac{2Q + Q'}{3} + \omega^{\mathrm{v}}_{\mathbf{27}} + \omega^{\mathrm{h}}_{\overline{\mathbf{27}}}, \qquad \frac{Q + 2Q'}{3} + \omega^{\mathrm{v}}_{\overline{\mathbf{27}}} + \omega^{\mathrm{h}}_{\mathbf{27}}, \tag{B.10}$$

where $\omega^{\mathrm{v,h}}_{\mathbf{27}}$ [resp. $\omega^{\mathrm{v,h}}_{\overline{\mathbf{27}}}$] are the weights of the $\mathbf{27}$ [resp. $\overline{\mathbf{27}}$] representation of the visible/hidden sector E_6 symmetry. The quotient space $W_{\mathrm{frame}}/W_{\mathrm{root}} \cong MW(X) \cong \mathbb{Z}^{\oplus 4}$ is generated by those four elements and the height pairing of the Mordell-Weil lattice is $A_2^*[-2] \oplus A_2^*[-2]$ in this basis (as is well-known in the literature).

Reference [86] provides explicitly expressions of four generators of $MW(X) \cong \mathbb{Z}^{\oplus 4}$ for the $2\mathrm{IV}^* + 8I_1$-type elliptic fibration on $X = \mathrm{Km}(E_{\rho_1} \times E_{\rho_2})$. The Weierstrass model of X given by (4.48) has four independent non-zero sections, two of which — denoted by $\bar{P}_4$ and $\bar{P}_8$ — are given by

$$(X_4, Y_4) = (-4\lambda_1\lambda_2 z^2, -4z^2(\lambda_1(\lambda_1 - 1)z^2 + \lambda_2(\lambda_2 - 1))), \tag{B.11}$$

$$(X_8, Y_8) = (-4z^2, 4z^2(\lambda_1(\lambda_1 - 1)z^2 + \lambda_2(\lambda_2 - 1))). \tag{B.12}$$

Readers interested in the expressions for the two other sections $\bar{P}_7$ or $\bar{P}_5$ are referred to [86]. We follow [65] and denote rational points of the elliptic curve, as well as the corresponding divisors and elements of the Neron-Severi lattice or the Mordell-Weil group, by P and the corresponding curves by $\bar{P}$.

Modulo $U_* = \mathrm{Span}_{\mathbb{Z}}\{[F], [\sigma + F]\}$ and W_{root}, these four sections generate the Mordell-Weil group $MW(X)$, P_4 and P_8 for one $A_2^*[-2]$, and P_7 and P_5 for the other $A_2^*[-2]$. All four of those sections, however, meet the E_6 singularities at $z = 0$, $(X, Y) = (0, 0)$ and at $z = \infty$, $(X/z^4, Y/z^6) = (0, 0)$. Hence they are not contained within the narrow Mordell-Weil group, $MW(X)^0$, which is consistent with the fact that the generators (B.10) contain weights of non-singlet representations of E_6^{vis} and $E_6^{\mathrm{hid.}}$.

Just like the generators of the essential lattice $L(X) \cong W_{\mathrm{U}(1)}$, $\{P, P', Q, Q'\}$, are obtained as $\mathbb{Z}$-linear combinations of the generators in (B.10), the corresponding sections for the generators of the narrow Mordell-Weil lattice $MW(X)^0$ should also be obtained through the group-law sum of the sections $\bar{P}_{4,8}$ and $\bar{P}_{7,5}$. Sections corresponding to $(2P_4 - P_8) \in MW(X)$ and $(2P_8 - P_4) \in MW(X)$ are given — by using the ordinary group law sum on

JHEP04(2014)050

elliptic curves — by

$$X_{2P_4-P_8} = \frac{4\{\lambda_2^2(\lambda_2-1)^2 + z^2(\lambda_2^2(\lambda_1^2-1)-\lambda_1^2) + z^4\lambda_1^2(\lambda_1-1)^2\}}{(\lambda_1+\lambda_2-\lambda_1\lambda_2)^2}, \tag{B.13}$$

$$Y_{2P_4-P_8} = \frac{4\left\{\begin{array}{l} 2\lambda_2^3(\lambda_2-1)^3 \ +z^2(\lambda_2^5(\lambda_1-1)^2(\lambda_1+1)+O(\lambda_2^4)) \\ +2z^6\lambda_1^3(\lambda_1-1)^3 \ +z^4(\lambda_2^3(\lambda_1-1)^3\lambda_1(\lambda_1+1)+O(\lambda_2^2)) \end{array}\right\}}{(\lambda_1+\lambda_2-\lambda_1\lambda_2)^3}, \tag{B.14}$$

$$X_{2P_8-P_4} = \frac{4\{\lambda_2^2(\lambda_2-1)^2 - z^2\lambda_1\lambda_2(\lambda_2^2+\lambda_1^2-1) + z^4\lambda_1^2(\lambda_1-1)^2\}}{(1-\lambda_1-\lambda_2)^2}, \tag{B.15}$$

$$Y_{2P_8-P_4} = \frac{4\left\{\begin{array}{l} 2\lambda_2^3(\lambda_2-1)^3 \ -z^2(\lambda_2^5(2\lambda_1-1)+O(\lambda_2^4)) \\ +2z^6\lambda_1^3(\lambda_1-1)^3 \ -z^4(\lambda_2^3\lambda_1(\lambda_1-1)(2\lambda_1-1)+O(\lambda_2^2)) \end{array}\right\}}{(1-\lambda_1-\lambda_2)^3}. \tag{B.16}$$

They belong to the narrow Mordell-Weil group $MW(X)^0$. Indeed,

$$(X_{2P_4-P_8}, Y_{2P_4-P_8})|_{z=0} = \left(\left(\frac{2\lambda_2(\lambda_2-1)}{\lambda_1+\lambda_2-\lambda_1\lambda_2}\right)^2, \left(\frac{2\lambda_2(\lambda_2-1)}{\lambda_1+\lambda_2-\lambda_1\lambda_2}\right)^3\right) \neq (0,0), \tag{B.17}$$

$$\left(\frac{X_{2P_4-P_8}}{z^4}, \frac{Y_{2P_4-P_8}}{z^6}\right)\Big|_{z=\infty} = \left(\left(\frac{2\lambda_1(\lambda_1-1)}{(\lambda_1+\lambda_2-\lambda_1\lambda_2)^2}\right)^2, \left(\frac{2\lambda_1(\lambda_1-1)}{(\lambda_1+\lambda_2-\lambda_1\lambda_2)^2}\right)^3\right) \neq (0,0), \tag{B.18}$$

and a similar calculation proves that the section $(2P_8 - P_4)$ also stays away from the two E_6 singularities at $z = 0$ and $z = \infty$. The height pairing is $A_2[-2]$ on the basis of $\{2P_4 - P_8, 2P_8 - P_4\}$, the opposite of $A_2[2] \subset L(X) = W_{\mathrm{U}(1)}$, as expected.

Similarly, we can construct section contained in the narrow Mordell-Weil group from the sections $\bar{P}_7$ and $\bar{P}_5$. We have computed the sections corresponding to $(2P_7 - P_5)$ and $-(P_7 + P_5)$ in $MW(X)$ and confirmed that they indeed belong in $MW(X)^0$. The height pairing on the basis $\{2P_7 - P_5, -(P_7 + P_5)\}$ is $A_2[-2]$. Since we use the explicit expressions of these sections later, we leave them here as a record:

$$X_{2P_7-P_5} = \frac{4\{\lambda_2^2(\lambda_2-1)^2 - z^2\lambda_1(\lambda_2^2(\lambda_1^2-1)+1) + z^4\lambda_1^2(\lambda_1-1)^2\}}{(\lambda_2-\lambda_1\lambda_2-1)^2}, \tag{B.19}$$

$$Y_{2P_7-P_5} = \frac{4\left\{\begin{array}{l} 2\lambda_2^3(\lambda_2-1)^3 \ -z^2(\lambda_2^5\lambda_1^2(\lambda_1-2)+O(\lambda_2^4)) \\ +2z^6\lambda_1^3(\lambda_1-1)^3 \ +z^4(\lambda_2^3\lambda_1^3(\lambda_1-1)(\lambda_1-2)+O(\lambda_2^2)) \end{array}\right\}}{(\lambda_2-\lambda_1\lambda_2-1)^3}, \tag{B.20}$$

$$X_{-(P_7+P_5)} = \frac{4\{\lambda_2^2(\lambda_2-1)^2 - z^2(\lambda_2^3\lambda_1+O(\lambda_2^2)) + z^4\lambda_1^2(\lambda_1-1)^2\}}{(\lambda_1-\lambda_2)^2}, \tag{B.21}$$

$$Y_{-(P_7+P_5)} = \frac{4\left\{\begin{array}{l} 2\lambda_2^3(\lambda_2-1)^3 \ +z^2(\lambda_2^5(2\lambda_1-1)+O(\lambda_2^4)) \\ -2z^6\lambda_1^3(\lambda_1-1)^3 \ -z^4(\lambda_2^3(2\lambda_1-1)\lambda_1(1-\lambda_1)+O(\lambda_2^2)) \end{array}\right\}}{(\lambda_1-\lambda_2)^3}. \tag{B.22}$$

None of the four sections corresponding to $(2P_4 - P_8)$, $(2P_8 - P_4)$, $(2P_7 - P_5)$ and $-(P_7 + P_5)$ in $MW(X)^0$ meet the zero section, σ, of the Weierstrass model given by (4.48).

JHEP04(2014)050

Therefore, $\overline{(2P_4 - P_8)} - \sigma$ and $\overline{(2P_8 - P_4)} - \sigma$ generate $A_2[2] \subset W_{\mathrm{U}(1)}$, and $\overline{(2P_7 - P_5)} - \sigma$ and $\overline{-(P_7 + P_5)} - \sigma$ generate the other $A_2[2] \subset W_{\mathrm{U}(1)}$. Dual to the rank-$k = 4$ Cartan flux in the heterotic string $\mathrm{SU}(N_v = 3) \times \mathrm{SU}(N_h = 3)$ bundle compactification should be four-form fluxes involving the Poincaré dual of these algebraic cycles in X.

B.3 Semistable degeneration

In the large $\mathrm{Im}(\tilde{\rho}_H)$ region of moduli space, where the supergravity description is a good approximation of heterotic string theory, it is more intuitive to choose $\{P + Q, P' + Q'\}$ and $\{P - Q, P' - Q'\}$ as the basis of the rank-$k = 4$ lattice of Cartan flux quanta. The first two generate the $A_2[4]$ sublattice for the visible sector $\mathrm{SU}(N_v = 3)$ structure group and the last two another $A_2[4]$ sublattice for the hidden sector $\mathrm{SU}(N_h = 3)$. In F-theory language, the Poincaré dual of the algebraic cycles $\{P + Q, P' + Q'\}$ and $\{P - Q, P' - Q'\}$ should thus be interpreted as those for the visible and hidden sectors, respectively.

Let us take one step further and identify the equivalent of the visible and hidden sector basis $\{P \pm Q, P' \pm Q'\}$ not just in terms of the heterotic string, or in algebraic (lattice) language for F-theory, but also in terms of the geometry of the K3 surface of F-theory. We have identified four independent algebraic cycles in $W_{\mathrm{U}(1)}$, which are also in one-to-one correspondence with elements in $MW(X)^0$. $\{(2P_4 - P_8), (2P_8 - P_4), (2P_7 - P_5), -(P_7 + P_5)\} \subset MW(X)^0$ are generators of $W_{\mathrm{U}(1)} \cong A_2[2] \oplus A_2[2]$ and are equivalent to $\{P, P', Q, Q'\}$. We claim that the visible and hidden sector basis is given by

$$\text{(visible sect.)} \qquad \overline{(2P_4 - P_8)} - \overline{-(2P_7 - P_5)}, \qquad \overline{(2P_8 - P_4)} - \overline{(P_7 + P_5)}, \tag{B.23}$$

$$\text{(hidden sect.)} \qquad \overline{(2P_4 - P_8)} - \overline{(2P_7 - P_5)}, \qquad \overline{(2P_8 - P_4)} - \overline{-(P_7 + P_5)}. \tag{B.24}$$

This idea comes from the following observations in geometry.

As we have already made clear, the coordinate rescaling in footnote 54 and the coordinate redefinition in footnote 46 allow us to see (4.49) as a family of elliptic K3 surface showing semistable degeneration. In one of the affine patches, the set of equations

$$\begin{cases} \tilde{\eta}^2 = \left(\xi + \frac{4}{\lambda_2}\right)\left(\xi + 4\left(1 + \frac{\lambda_1}{\lambda_2}\right)\right)(\xi + 4\lambda_1) + 2^3\left((1 - 1/\lambda_2)u + \lambda_1(\lambda_1 - 1)v\right)\tilde{\eta}, \\ uv = 1/\lambda_2 \end{cases} \tag{B.25}$$

defines a family of K3 surfaces elliptically fibred over a curve $\{uv = t | (u, v) \in \mathbb{C}^2\}$ parametrized by $t := 1/\lambda_2 \in D \subset \mathbb{C}$. In the large λ_2 limit, $t = 0$, the base curve splits into two irreducible pieces, and the K3 surface also splits into two rational elliptic surfaces (a.k.a dP_9) glued together at one common fibre elliptic curve.

$$\tilde{\eta}^2 = \xi\,(\xi + 4)\,(\xi + 4\lambda_1) + 2^3 u\,\tilde{\eta}\,, \qquad v = 0\,, \tag{B.26}$$

$$\tilde{\eta}^2 = \xi\,(\xi + 4)\,(\xi + 4\lambda_1) + 2^3\lambda_1(\lambda_1 - 1)v\,\tilde{\eta}\,, \qquad u = 0\,, \tag{B.27}$$

are the visible and hidden sector dP_9's, respectively. The E_6 singularities are at $u = \infty$ in the visible sector dP_9 and at $v = \infty$ in the hidden sector dP_9. The common fibre at $u = v = 0$ is given by

$$\tilde{\eta}^2 = \xi(\xi + 4)(\xi + 4\lambda_1)\,. \tag{B.28}$$

JHEP04(2014)050

The two dP_9's (rational elliptic surfaces) should be "type No.27" in the classification in [102].

The sections $\overline{(2P_4 - P_8)}$, $\overline{(2P_8 - P_4)}$, $\overline{(2P_7 - P_5)}$ and $\overline{-(P_7 + P_5)}$, as well as the sections corresponding to their inverse elements in $MW(X)^0$, such as $\overline{(P_7 + P_5)}$, define divisors in the threefold given by (B.25). Intersection of those divisors with the $t = 1/\lambda_2 = 0$ divisor — $dP_9 \cup dP_9$ — defines their semistable degeneration limits mathematically (whatever this means in physics). Working this out explicitly, we found that the limit of both sections $\overline{(2P_4 - P_8)}$ and $\overline{(2P_7 - P_5)}$ are precisely the same in the visible sector dP_9,

$$\xi = \left(\frac{2}{1-\lambda_1}\right)^2 u^2, \qquad \tilde{\eta} = \left(\frac{2}{1-\lambda_1}\right)^3 \left\{u^3 + \frac{1}{2}(\lambda_1 - 1)^2(\lambda_1 + 1)u\right\}. \tag{B.29}$$

This common limit in the visible sector passes through one of the 2-torsion point $(\xi, \tilde{\eta}) = (0, 0)$ in the common elliptic fibre. The semistable degeneration limit of the two sections, however, remain different in the hidden sector dP_9. In the fibre in $v = \infty$, for example,

$$\left(\frac{\xi}{v^2}, \frac{\tilde{\eta}}{v^3}\right) \to \left((-2\lambda_1)^2, (-2\lambda_1)^3\right) \qquad \text{v.s.} \qquad \to \left((2\lambda_1)^2, (2\lambda_1)^3\right) \tag{B.30}$$

for $\overline{(2P_4 - P_8)}$ and $\overline{(2P_7 - P_5)}$, respectively. They are inverse elements under the group law of the elliptic curve. This is why the algebraic cycle $\overline{(2P_4 - P_8)} - \overline{(2P_7 - P_5)}$ is considered to be purely in the hidden sector dP_9. It must also be easy to see that the algebraic cycle $\overline{(2P_4 - P_8)} - \overline{-(2P_7 - P_5)}$ is purely in the visible sector dP_9. A similar story holds also for the pair of sections $\overline{(2P_8 - P_4)}$ and $\overline{-(P_7 + P_5)}$. We do not present details here, except noting that those sections pass through another 2-torsion point in the common elliptic fibre: $(\xi, \tilde{\eta}) = (-4\lambda_1, 0)$.

Back in the regime of finite $|\lambda_2|$, the two sections $\overline{(2P_4 - P_8)}$ and $\overline{(2P_7 - P_5)}$ both cover the entire base $\mathbb{P}^1$, from the visible sector 7-brane at $z = 0$ to the hidden sector 7-brane at $z = \infty$. These two sections are distinct, but they remain very close in the small z region (near the visible sector), with the difference scaling as $1/\lambda_2 \sim e^{2\pi i \tilde{\rho}_H}$. It is thus reasonable to understand this as a stringy effect. When we ignore differences of order $\mathcal{O}(1/\lambda_2)$ to restore the supergravity approximation, the geometric picture described above (using $dP_9 \cup dP_9$) is a reasonably good approximation for large $|\lambda_2|$ and fits perfectly with our intuitive understanding of Cartan fluxes in the visible as well as hidden sector structure group. This is how we were led to the claim (B.23), (B.24), and it is this interesting behaviour of sections under the semistable degeneration of K3 surfaces that reconciles the notion of having Cartan flux purely in the visible/hidden sector with considering sections of the elliptic K3 surface.

Before closing this section, let us try to place the observations based on the example characterized by (B.1) and (B.2) (or equivalently by (B.1) and (B.3)). It is more natural from the perspective of heterotic string theory to take (B.3) as input data for compactification because they are flux data of the gauge fields and B-field. In F-theory language, the essential lattice $L(X) = W_{\mathrm{U}(1)}$ of an elliptic fibration is specified by (B.3), while the embedding (B.2) determines the transcendental lattice of a $\rho = 18$ (two parameter) family of K3 surfaces. When we replace (B.2), (B.3) by some other choice, this means we

JHEP04(2014)050

take different flux quanta for the rank-$k = 4$ Cartan flux in the SU(3) × SU(3) bundle compactification of heterotic string theory, or to use a $\rho = 18$ family of K3 surfaces different from $X = \mathrm{Km}(E_{\rho_1} \times E_{\rho_2})$. There is nothing wrong in doing so. For all different choices of (B.2), (B.3), one can construct a two parameter family of K3 surfaces with four independent sections in the narrow Mordell-Weil group.

Since we are not interested in literally taking $\mathrm{Im}(\rho_H) = [\mathrm{vol}(T^2)/\ell_s^2]_{\mathrm{Het}}$ to infinity for practical applications, we do not need to study the semistable degeneration limit of K3 surfaces, but rather want to consider $\mathrm{Im}(\rho_H)$ very large, but finite.

Given the fact that literature referring to the heterotic-F-theory duality dictionary on the flux has often relied on the stable degeneration limit, however, it is not uninteresting to ask whether the $dP_9 \cup dP_9$ picture loses some information. When compactification data is given in terms of a one parameter family of $dP_9 \cup dP_9$ both in the "type No.27" of [102], along with $G_H^{(4)}$ in (5.34), one has to make sure that the sections pass through some torsion points in the common elliptic fibre. Using these torsion points and the Cartan flux quanta $G_H^{(4)}$, the B-field flux quanta on T^2 must be reproduced at least to some extent. Thus, apart from how far one should go back from the semistable degeneration limit (e.g., the value of λ_2), a great deal of information may be recovered from the description using ($dP_9 \cup dP_9$, $G_H^{(4)}$) by paying attention to such subtleties. We remain inconclusive about this question, however.

C Ashok-Denef-Douglas formula for F-theory

In this section, we begin with a review of the derivation of the vacuum index density distribution (5.58) in [28, 29] for type IIB Calabi-Yau orientifolds, and then generalize its derivation for more general landscapes based on F-theory compactifications, where the four-form fluxes are scanned within the subspace $H^{2,2}(Y_z;\mathbb{R})_H$. We largely follow the presentation in [29], which maintains more intuitive control over what is being done than the sophisticated and polished-up style of [2]. Along the way, we will see that the three-form scanning in type IIB orientifolds and the four-form scanning considered in section 5.4 correspond to scanning only in $H^{2,2}(Y_z;\mathbb{R})_H$ rather than the entire orthogonal complement $[(H^{2,2}(Y_z;\mathbb{R})_V)^\perp \subset H^{2,2}(Y_z;\mathbb{R})] = H^{2,2}(Y_z)_H \oplus H^{2,2}(Y_z)_{RM}$.

The vacuum index density for F-theory flux vacua is defined by [28, 29][87]

$$d\mu_I = d^{2m}z \sum_N \Theta(L_* - L)\delta^{2m}(D_aW, \overline{D_aW})\det\begin{pmatrix} D_aD_bW & \partial_a\overline{D_dW} \\ \bar{\partial}_{\bar{c}}D_bW & \overline{D_cD_dW} \end{pmatrix}_{2m\times 2m}, \quad \text{(C.1)}$$

where $a, b, c, d \in \{1, \cdots, m\}$ label m local complex coordinates of some restricted moduli space $\mathcal{M}_*$ (see section 5.4 for various $\mathcal{M}_*$ of interest). In dealing with such integrals, we

[87] It is worth noting that the diagonal blocks D_aD_bW and $\overline{D_cD_dW}$ are the same as the fermion mass matrix of the low energy effective field theory below the Kaluza-Klein scale or below the moduli mass scale $M_{KK}^3/M_{\mathrm{Str}}^2$. Fluctuations in the directions tangential to $\mathcal{M}_*$ are just as heavy as those in the directions normal to the restricted moduli space generically. The determinant of the $2m$ x $2m$ matrix just makes sure that each topological flux N contributes to $\int d\mu_I$ by 1 (TW thanks T. Eguchi and Y. Tachikawa for discussion).

JHEP04(2014)050

have adopted the conventions of [101], where $\int d^2z\delta^2(z,\bar{z}) = 1$. The tadpole L and the superpotential are given by

$$W \propto \int_Y G^{(4)}_{\rm scan} \wedge \Omega_Y, \qquad L = \frac{1}{2}\int_Y G^{(4)}_{\rm scan} \wedge G^{(4)}_{\rm scan}\,. \tag{C.2}$$

This $d\mu_I$ is a distribution function over the space $\mathcal{M}_*$ and captures all the flux vacua for which the D3-tadpole from the flux configuration L is not more than L_*. The sum over flux quanta $\sum_N$ is replaced by its continuous approximation $\int d^K N$. This expression can be rewritten as [28]

$$d\mu_I \;=\; \frac{(\alpha_0 L_*)^{K/2}}{(K/2)!}\rho_{\rm ind}(\alpha_0), \tag{C.3}$$

$$\rho_{\rm ind}(\alpha_0) := d^{2m}z \int d^K N e^{-\alpha_0 L}\delta^{2m}(D_aW, \overline{D_aW}) \det\begin{pmatrix} D_aD_bW & \partial_a\overline{D_dW} \\ \bar{\partial}_{\bar{c}}D_bW & \overline{D_cD_dW}\end{pmatrix}; \tag{C.4}$$

since $\rho_{\rm ind}(\alpha_0)$ scales as $(\alpha_0)^{-K/2}$, the vacuum index density $d\mu_I$ does not depend on the choice of α_0. By setting $\alpha_0 = L_*^{-1}$, one can see where (and how) the L_* dependence arises in the expression of $\rho_{\rm ind}(L_*^{-1})$. In contrast, by setting $\alpha_0 = 2\pi$, the L_*-dependence of the overall number of vacua in this landscape is seen clearly. We take $\alpha_0 = 2\pi$ throughout this article (as in [28, 29]), and $\rho_{\rm ind}(\alpha_0 = 2\pi)$ is simply denoted by $\rho_{\rm ind}$. The distribution $\rho_{\rm ind}$ can be rewritten in a more useful form in some cases, and that is the subject of the following.

The formulation in [29] accommodates scanning four-form fluxes in

$$G^{(4)}_{\rm scan} \in \left[H^{4,0}(Y_z;\mathbb{C}) + H^{0,4}(Y_z;\mathbb{C})\right] \oplus \left[H^{3,1}(Y_z;\mathbb{C})_* + H^{1,3}(Y_z;\mathbb{C})_*\right] \oplus H^{2,2}(Y_z;\mathbb{R})_{H*}, \tag{C.5}$$

where $H^{3,1}(Y_z;\mathbb{C})_*$ has been introduced in p. 65, and $H^{2,2}(Y_z;\mathbb{R})_{H*}$ was defined in (5.63). The first two components of $G^{(4)}_{\rm scan}$ is parametrized as follows, by $1+m$ complex numbers $\{N_X, N_Y^a\}|_{a=1,\cdots,m}$ ($m = \dim_{\mathbb{C}}\mathcal{M}_*$):

$$\Delta G^{(4)}_{\rm scan} = \left[N_X\Omega_Y + \bar{N}_X\overline{\Omega}_Y\right] + \left[N_Y^a(D_a\Omega_Y) + \bar{N}_Y^{\bar{b}}(\bar{D}_{\bar{b}}\overline{\Omega}_Y)\right], \tag{C.6}$$

using Ω_Y and $\{(D_a\Omega_Y)\}_{a=1,\cdots,m}$ as the basis of $H^{4,0}(Y_z;\mathbb{C})$ and $H^{3,1}(Y_z;\mathbb{C})_*$, respectively. Here,

$$D_a\Omega_Y = \partial_a\Omega_Y + K_a\Omega_Y, \qquad D_aD_b\Omega_Y = (\partial_a + K_a)D_b\Omega_Y - \Gamma^c_{ba}D_c\Omega_Y \tag{C.7}$$

$$K = -\ln\left[\int_Y \Omega_Y \wedge \overline{\Omega}_Y\right], \qquad K_a := \partial_a K. \tag{C.8}$$

The last component, $H^{2,2}(Y_z;\mathbb{R})_{H*}$, is parametrized by

$$\Delta G_{\rm scan} = \sum_{I=1}^{\widetilde{K}} \tilde{N}_I\Omega_I^{(2,2)}, \qquad A_{IJ} := \int_Y \Omega_I^{(2,2)} \wedge \Omega_J^{(2,2)}, \tag{C.9}$$

JHEP04(2014)050

by using a basis $\{\Omega_I^{(2,2)}\}|_{I=1,\cdots,\widetilde{K}}$ of the vector space $H^{2,2}(Y_z;\mathbb{R})_{H*}$ over $\mathbb{R}$; the generators $(D_aD_b\Omega_Y)$ and $\overline{(D_cD_d\Omega_Y)}$ of $H^{2,2}(Y_z;\mathbb{R})_{H*}$ are not necessarily linearly independent. Thus, the continuous approximation $\int d^K N$ of the flux configuration $\sum_N$ is given by

$$\int dN_X d\bar{N}_X e^{-K} \int \prod_{a=1}^{m} [dN_Y^a d\bar{N}_Y^{\bar{a}}] e^{-mK} \det(K_{c\bar{d}})_{m\times m} \int d^{\widetilde{K}} \tilde{N} \sqrt{A_{IJ}}. \tag{C.10}$$

We expect very little confusion to arise from the fact that we use A_{IJ} as the intersection form on the vector space $H^{2,2}(Y_z;\mathbb{R})_{H*}$ here, while it is the intersection form on $H^4(Y_z;\mathbb{R})$ in (5.60).

In the case of a landscape based on a type IIB orientifold using a Calabi-Yau threefold M_3 with 7-branes in the SO(8) configuration and scanning three-form fluxes $F^{(3)}_{\text{scan}}$ and $H^{(3)}_{\text{scan}}$, the four-form is given by

$$G^{(4)}_{\text{scan}} = \frac{1}{\phi-\bar{\phi}} \left[\overline{G^{(3)}}_{\text{scan}} \wedge \Omega_{T^2} - G^{(3)}_{\text{scan}} \wedge \overline{\Omega}_{T^2} \right], \qquad G^{(3)}_{\text{scan}} := F^{(3)}_{\text{scan}} - \phi H^{(3)}_{\text{scan}}, \tag{C.11}$$

we can take [29]

$$N_Z^{\phi i}(D_\phi D_i \Omega_Y) + \text{h.c.} \qquad \left(i = 1, \cdots, m-1 = h^{2,1}_{-,\text{prim.}}(M_3)\right) \tag{C.12}$$

with $N_Z^{\phi i} \in \mathbb{C}$ as a non-redundant parametrization of $H^{2,2}(Y_z;\mathbb{R})_{H*}$. This is due to a relation

$$(D_jD_k\Omega_M) \wedge \Omega_{T^2} = -\mathcal{F}_{ljk}\mathcal{F}_\phi K^{\bar{l}l} K^{\bar{\phi}\phi} e^K \overline{(D_iD_\phi(\Omega_M \wedge \Omega_{T^2}))} \tag{C.13}$$

that follows from[88]

$$D_\phi \Omega_{T^2} = i\mathcal{F}_\phi e^{K^{(T^2)}} \overline{\Omega}_{T^2}, \qquad D_aD_b\Omega_M = i\mathcal{F}_{dab} K^{\bar{c}d} e^{K^{(M)}} \overline{D_c\Omega_M}. \tag{C.14}$$

Let us now consider a more general cases of F-theory compactifications where the moduli space $\mathcal{M}_*$ is not necessarily in the form of $\mathcal{M}_{\text{cpx}}(M_3) \times \mathcal{M}_\phi$, or 7-branes are not necessarily in an SO(8) configuration. We consider a class of landscapes where the restricted moduli space $\mathcal{M}_*$ of a Calabi-Yau fourfold Y is specified by divisors J_Y and W_{noscan} such that there is a relation [103][89] among differential forms[90]

$$(D_aD_b\Omega_Y) = \mathcal{F}_{abcd}\tilde{B}^{cd,\bar{e}\bar{f}} e^K \overline{(D_eD_f\Omega_Y)}, \qquad \overline{(D_aD_b\Omega_Y)} = \overline{\mathcal{F}}_{\bar{a}\bar{b}\bar{c}\bar{d}} \tilde{B}^{cd,\bar{c}\bar{d}} e^K (D_cD_d\Omega_Y) \tag{C.15}$$

for some $^\exists \tilde{B}^{cd,\bar{e}\bar{f}}$ over the moduli space $\mathcal{M}_*$ $(a,b,c,d,e,f \in \{1,\cdots,m\})$.

[88] For T^2, $\mathcal{F}_\phi := \int_{T^2} \Omega_{T^2} \wedge (D_\phi \Omega_{T^2})$. For a Calabi-Yau threefold M, $\mathcal{F}_{ijk} := \int_M \Omega_M \wedge (D_iD_jD_k\Omega_M)$. For T^2, there is the relation $K_{\phi\bar{\phi}} = |\mathcal{F}_\phi|^2 e^{2K^{(T^2)}}$. When we choose the normalization $\Omega_{T^2} = dx + \phi dy$, we have that $\mathcal{F} = 1$.

[89] $\bar{D}_{\bar{g}}(D_aD_b\Omega_Y)$ has only $(3,1)$ Hodge components [103], although $\overline{D_g(D_eD_f\Omega_Y)}$ may also have $(2,2)$ components in addition. In this sense, $\mathcal{F}_{abcd}\tilde{B}^{cd,\bar{e}\bar{f}}$ plays the role of $S^{(2)}$ in eq. (2.20) of [103]. $\tilde{B}^{cd,\bar{e}\bar{f}}e^K$ in this article corresponds to $B^{cd,\bar{e}\bar{f}}$ in [103].

[90] For a Calabi-Yau fourfold Y, $\mathcal{F}_{abcd} := \int_Y \Omega_Y \wedge (D_aD_bD_cD_d\Omega_Y)$. Similarly, for a K3 surface X, $\mathcal{F}_{\alpha\beta} := \int_X \Omega_X \wedge (D_\alpha D_\beta \Omega_X)$.

JHEP04(2014)050

Obviously this is a generalization of (C.13). It is not hard also to see that $Y = X \times S = \mathrm{K3} \times \mathrm{K3}$ also has this property. Using the relation

$$D_\alpha \Omega_X = \mathcal{F}^{(X)}_{\alpha\beta} K^{\bar\gamma\beta} e^{K^{(X)}} \overline{D_\gamma \Omega_X} \tag{C.16}$$

for a K3 surface X and the fact that $\mathcal{F}_{\alpha\beta\kappa\lambda} = \mathcal{F}^{(X)}_{\alpha\beta}\mathcal{F}^{(S)}_{\kappa\lambda}$, one can see that $\tilde{B}^{\beta\lambda,\bar\gamma\bar\mu} = K^{\bar\gamma\beta}_{(X)} K^{\bar\mu\lambda}_{(S)}$ do the job. We will comment on $\tilde{B}^{\alpha\beta,\bar\kappa\bar\lambda}$ later.

Under the condition that $\tilde{B}^{cd,\bar c\bar d}$ exists, one can choose $(D_a D_b \Omega_Y)$'s or $\overline{(D_c D_d \Omega_Y)}$'s as a (still possibly redundant) set of $\mathbb{C}$-coefficient generators of $H^{2,2}(Y_z;\mathbb{R})_{H*}$. Thus, the $H^{2,2}(Y_z;\mathbb{R})$ component (C.9) may be written as

$$\Delta G^{(4)}_{\mathrm{scan}} = N^{ab}_Z (D_a D_b \Omega_Y) = \bar N^{\bar c\bar d}_Z \overline{(D_c D_d \Omega_Y)} \tag{C.17}$$

for some complex valued N^{ab}_Z or their complex conjugates $\bar N^{\bar a\bar b}_Z$. The following reality condition must be satisfied by the (in-principle) complex valued N^{ab}_Z, so that the two expressions agree:

$$\bar N^{\bar c\bar d}_Z = N^{ab}_Z \mathcal{F}_{abcd} \tilde{B}^{cd,\bar c\bar d} e^K, \qquad N^{cd}_Z = \bar N^{\bar a\bar b}_Z \overline{\mathcal{F}}_{\bar a\bar b\bar c\bar d} \tilde{B}^{cd,\bar c\bar d} e^K. \tag{C.18}$$

In the following, we closely follow the presentation in [29], and see that the formula (5.58) holds also in this case. The integration measure (C.10) is used as it is. The D3-tadpole contribution from the flux is written as[91]

$$L = e^{-K}\left(|N_X|^2 - K_{a\bar b} N^a_Y \bar N^{\bar b}_Y + \frac{1}{2} e^{2K} \tilde{B}^{ef,\bar e\bar f} \mathcal{F}_{abef} \overline{\mathcal{F}}_{\bar a\bar b\bar e\bar f} N^{ab}_Z \bar N^{\bar c\bar d}_Z\right); \tag{C.20}$$

the last term is of type $(2,2)$ and hence is positive definite. The F-term conditions (delta-functions)

$$\delta^{2m}(D_a W, \overline{D_b W}) = \delta^{2m}(N_Y, \bar N_Y)\ \left(e^{-mK}\ \det(K_{a\bar b})\right)^{-2} \tag{C.21}$$

eliminate the flux space integral over the $(3,1)+(1,3)$ components from the measure (C.10), and all the remaining directions in the flux space have positive definite contributions to the D3-tadpole [29].

The parametrization of the $(2,2)$ flux component in terms of the N^{ab}_Z satisfying (C.18) may be redundant in general ($Y = \mathrm{K3} \times \mathrm{K3}$ is an example; see the discussion later). Thus, a set of independent flux space coordinates $\tilde N_I \in \mathbb{R}$ $(I = 1, \cdots, \tilde K)$ is introduced and we parametrize

$$N^{ab}_Z = \sum_I Z^{ab}_I \tilde N_I, \qquad \bar N^{\bar a\bar b}_Z = \sum_I \bar Z^{\bar a\bar b}_I \tilde N_I \tag{C.22}$$

without redundancy. The integration measure (C.10) is still used, but now there is an alternative expression for A_{IJ}:

$$\begin{aligned} A_{IJ} &= Z^{ab}_I \int_Y (D_a D_b \Omega_Y) \wedge \overline{(D_a D_b \Omega_Y)} \bar Z^{\bar a\bar b}_J = Z^{ab}_I e^K \tilde{B}^{cd,\bar c\bar d} \mathcal{F}_{abcd} \overline{\mathcal{F}}_{\bar a\bar b\bar c\bar d} \bar Z^{\bar a\bar b}_J, \\ &= \bar Z^{\bar c\bar d}_I \overline{\mathcal{F}}_{\bar a\bar b\bar c\bar d} \bar Z^{\bar a\bar b}_J = Z^{ab}_I \mathcal{F}_{abcd} Z^{cd}_J. \end{aligned} \tag{C.23}$$

The last term in the D3-tadpole contribution is also written as $\Delta L = \tilde N_I \tilde N_J A_{IJ}/2$.

[91] The following relation is used [103, 104]:

$$\int (D_a D_b \Omega_Y) \wedge \overline{(D_c D_d \Omega_Y)} = -e^{-K}\left[R_{a\bar c b\bar d} - K_{a\bar c} K_{b\bar d} - K_{a\bar d} K_{b\bar c}\right] = e^K \tilde{B}^{ef,\bar e\bar f} \mathcal{F}_{abef} \overline{\mathcal{F}}_{\bar c\bar d\bar e\bar f}. \tag{C.19}$$

JHEP04(2014)050

In this case, we case, we can write the determinant in (C.1) as follows:

$$(-1)^m \det \begin{pmatrix} D_a D_b W & \partial_a \overline{D_d W} \\ \bar{\partial}_{\bar{c}}(D_b W) & \overline{D_c D_d W} \end{pmatrix} = \int d^m\theta d^m\bar{\theta} d^m\psi d^m\bar{\psi} \tag{C.24}$$
$$\exp\Big[\quad \theta^a\psi^b \mathcal{F}_{abdf} Z_I^{ef} \tilde{N}_I + \bar{\theta}^{\bar{c}}\bar{\psi}^{\bar{d}} \overline{\mathcal{F}}_{\bar{c}\bar{d}\bar{a}\bar{b}} \bar{Z}_J^{\bar{a}\bar{b}} \tilde{N}_I$$
$$+\theta^a\bar{\psi}^{\bar{d}} N_X e^{-K} K_{a\bar{d}} + \bar{\theta}^{\bar{c}}\psi^b \bar{N}_X e^{-K} K_{b\bar{c}}\Big].$$

Carrying out Gaussian integrals over the complex N_X and real $\tilde{N}_I$ coordinates, we obtain the following formula:

$$\rho_{\text{ind}} = (-1)^m \frac{d^{2m}z}{(2\pi)^m} e^{mK} [\det(K_{a\bar{b}})]^{-1} \int d^m\theta d^m\bar{\theta} d^m\psi d^m\bar{\psi} \tag{C.25}$$
$$\exp\Big[\quad e^{-K}(\theta^a\bar{\psi}^{\bar{d}} K_{a\bar{d}})(\bar{\theta}^{\bar{c}}\psi^b K_{b\bar{c}})$$
$$+ \left(\theta^a\psi^b \mathcal{F}_{abcd} Z_I^{cd} + \bar{Z}_I^{\bar{a}\bar{b}} \overline{\mathcal{F}}_{\bar{a}\bar{b}\bar{c}\bar{d}} \bar{\theta}^{\bar{c}}\bar{\psi}^{\bar{d}}\right) \frac{(A^{-1})^{IJ}}{2} \left(\theta^p\psi^q \mathcal{F}_{pqrs} Z_J^{rs} + \bar{Z}_J^{\bar{p}\bar{q}} \overline{\mathcal{F}}_{\bar{p}\bar{q}\bar{r}\bar{s}} \bar{\theta}^{\bar{r}}\bar{\psi}^{\bar{s}}\right)\Big].$$

In fact, his expression can be further simplified to (5.58). To see this, note that possibly redundant set of generators $\{(D_a D_b \Omega_Y)\}$ or $\{\overline{(D_c D_d \Omega_Y)}\}$ can be written as

$$(D_a D_b \Omega_Y) = e_{ab}^{\ I} \Omega_I^{(2,2)}, \qquad \overline{(D_c D_d \Omega_Y)} = \bar{e}_{\bar{c}\bar{d}}^{\ I} \Omega_I^{(2,2)}, \tag{C.26}$$

using a basis $\{\Omega_I^{(2,2)}\}_{I=1,\cdots,\tilde{K}}$ of the vector space $H^{2,2}(Y_z;\mathbb{R})_{H*}$ over $\mathbb{R}$. The complex valued coefficients $e_{ab}^{\ I}$ and $\bar{e}_{\bar{c}\bar{d}}^{\ I}$ should satisfy

$$Z_I^{\ ab} e_{ab}^{\ J} = \delta_I^{\ J}, \qquad \bar{Z}_I^{\bar{a}\bar{b}} \bar{e}_{\bar{a}\bar{b}}^{\ J} = \delta_I^{\ J}. \tag{C.27}$$

From this, we obtain $\mathcal{F}_{abcd} = e_{ab}^{\ I} Z_I^{\ ef} \mathcal{F}_{efcd}$.

Using this relation, the $\theta^2\psi^2$ term in the exponent of (C.25) can be rewritten as

$$\frac{1}{2}(\theta^a\psi^b e_{ab}^{\ I})(A_{IK})(A^{-1})^{KL}(A_{LJ})(\theta^p\psi^q e_{pq}^{\ J}) = \frac{1}{2}(\theta^a\psi^b e_{ab}^{\ I})(A_{IJ})(\theta^p\psi^q e_{pq}^{\ J}) = \frac{1}{2}\theta^a\psi^b \mathcal{F}_{abpq}\theta^p\psi^q.$$

This vanishes because of the totally symmetric nature of $\mathcal{F}_{abpq}$ and Grassmann nature of the $\theta^a\theta^p$. The $\theta\bar{\theta}\psi\bar{\psi}$ terms in the exponent, on the other hand, become

$$(\theta^a\psi^b e_{ab}^{\ I})(A_{IK})(A^{-1})^{KL}(A_{LJ})(\bar{\theta}^{\bar{p}}\bar{\psi}^{\bar{q}}\bar{e}_{\bar{p}\bar{q}}^{\ J}) = (\theta^a\psi^b e_{ab}^{\ I}) A_{IJ} (\bar{\theta}^{\bar{p}}\bar{\psi}^{\bar{q}}\bar{e}_{\bar{p}\bar{q}}^{\ J})$$
$$= \theta^a\psi^b \mathcal{F}_{abef} \tilde{B}^{ef,\bar{e}\bar{f}} e^K \overline{\mathcal{F}}_{\bar{c}\bar{d}\bar{e}\bar{f}} \bar{\theta}^{\bar{c}}\bar{\psi}^{\bar{d}}.$$

Using all these relations above, one arrives at the expression

$$\rho_{\text{ind.}}$$
$$= (-1)^{\frac{3m^2-m}{2}} [\det(K_{a\bar{b}})]^{-1} \int d^m\theta d^m\bar{\theta} \exp\left[\theta^a\bar{\theta}^{\bar{b}}\left(K_{a\bar{d}}K_{c\bar{b}} - e^{2K}\mathcal{F}_{acef}\tilde{B}^{ef,\bar{e}\bar{f}}\overline{\mathcal{F}}_{\bar{b}\bar{d}\bar{e}\bar{f}}\right)\frac{dz^c \wedge d\bar{z}^{\bar{d}}}{2\pi i}\right]$$
$$= \det\left(-\frac{R^b_{\ a}}{2\pi i} + \frac{\omega}{2\pi}\delta_a^b\right), \tag{C.28}$$

JHEP04(2014)050

Here

$$-R_{\bar{b}ac\bar{d}} = R_{a\bar{b}c\bar{d}} = K_{a\bar{d}}K_{c\bar{d}} + K_{a\bar{b}}K_{c\bar{d}} - e^{2K}\mathcal{F}_{acef}\tilde{B}^{ef,\bar{e}\bar{f}}\overline{\mathcal{F}}_{\bar{b}\bar{d}\bar{e}\bar{f}}\,, \tag{C.29}$$

$$R^b{}_a = R^b{}_{ac\bar{d}}\; dz^c \wedge dz^{\bar{d}}\,, \qquad R^b{}_{ac\bar{d}} = K^{\bar{b}b}R_{\bar{b}ac\bar{d}}\,. \tag{C.30}$$

$R^b{}_a$ is the curvature $(1,1)$ form of the holomorphic tangent bundle $T\mathcal{M}_*$ and $\omega = iK_{c\bar{d}}\; dz^c \wedge dz^{\bar{d}}$ the Kähler form on $\mathcal{M}_*$. The determinant in (C.28) is computed with respect to the a, b indices, so that the result is a $2m$-form on moduli space.

Finally, let us work out detailed descriptions of the vector space $H^{2,2}(Y;\mathbb{R})_{H*}$ as well as the decomposition (5.64) in the case of $Y = X \times S$. There are $K = (20 - rk_7) \times 21$ scanning (real-valued) flux quanta of $G^{(4)}_{\text{scan}}$ introduced in the discussion of 5.4. Among them, two correspond to the $(4,0)+(0,4)$ components $N_X(\Omega_X \otimes \Omega_S) + \text{h.c}$, and $2m$ to the $(3,1)+(1,3)$ component

$$N^\alpha_Y\,[(D_\alpha\Omega_X)\otimes\Omega_S] + N^\kappa_Y\,[\Omega_X\otimes(D_\kappa\Omega_S)] + \text{h.c.} \tag{C.31}$$

in (C.6), where $\alpha = 1, \cdots, (18 - rk_7)$ and $\kappa = 1, \cdots, 19$. The remaining $2 + (18 - rk_7) \times 19$ real-valued flux quanta correspond to the coefficients of these differential forms:

$$\Omega_X \otimes \overline{\Omega}_S, \qquad \overline{\Omega}_X \otimes \Omega_S, \qquad (D_\alpha\Omega_X)\otimes(D_\kappa\Omega_S). \tag{C.32}$$

Noting that there is a relation $(D_\alpha D_\beta \Omega_X) = \mathcal{F}_{\alpha\beta}e^{K^{(X)}}\overline{\Omega}_X$ for a K3 surface X, one finds that i) all of $(D_\alpha D_\beta\Omega_X)\otimes\Omega_S$ for $\alpha, \beta = 1, \cdots, (18 - rk_7)$ are the same as differential forms on $Y = X \times S$ up to normalization, at each given point in the moduli space $\mathcal{M}_*$, ii) all of the $2\times(18 - rk_7)\times 19$ differential forms above belong to $H^{2,2}(Y;\mathbb{R})_{H*}$, and are furthermore linearly independent; iii) this is even a basis of $H^{2,2}(Y;\mathbb{R})_{H*}$, because all the differential forms in the form of $D_aD_b(\Omega_X\otimes\Omega_S)$ have already been exploited, given the relation (C.16). All of these observations combined indicate that the vector space of scanning four-form flux considered in section 5.4 corresponds precisely to the space (C.5).

In the case of $Y = X \times S = \text{K3} \times \text{K3}$, another vector subspace $H^{2,2}(Y;\mathbb{R})_{V*} \subset H^{2,2}(Y;\mathbb{R})$ is generated, on the other hand, by

$$H^4(X;\mathbb{R})\otimes 1_S, \qquad 1_X \otimes H^4(S;\mathbb{R}), \qquad (U_* \oplus W_{\text{noscan}})\otimes J_S \otimes \mathbb{R}. \tag{C.33}$$

Thus, the remaining component, consisting of cycles which are neither "horizontal" or "vertical", is given by

$$H^{2,2}(Y_z;\mathbb{R})_{RM} \cong (U_*\oplus W_{\text{noscan}})\otimes\Big[J_S^\perp \subset H^{1,1}(S;\mathbb{R})\Big]\oplus\Big[(U_*\oplus W_{\text{noscan}})^\perp \subset H^{1,1}(X;\mathbb{R})\Big]\otimes[J_S]. \tag{C.34}$$

This is not empty, and in fact, the first component is where the singular fibre flux (GUT 7-brane flux) $G^{(4)}_{\text{fix}}$ in section 5.3-II and 5.4-III is introduced.

For $\text{K3}\times\text{K3} = X \times S$, the Riemann curvature tensor should become block-diagonal, which is verified as in

$$\begin{aligned} R_{\alpha\bar{\beta}\kappa\bar{\lambda}} &= K^{(X)}_{\alpha\bar{\beta}}K^{(S)}_{\kappa\bar{\lambda}} - \mathcal{F}^{(X)}_{\alpha\gamma}\mathcal{F}^{(S)}_{\kappa\mu}\; K^{\bar{\delta}\gamma}_{(X)}K^{\bar{\nu}\mu}_{(S)}\; e^{2(K^{(X)}+K^{(S)})}\;\overline{\mathcal{F}}^{(X)}_{\bar{\beta}\bar{\delta}}\overline{\mathcal{F}}^{(S)}_{\bar{\lambda}\bar{\nu}} \\ &= K^{(X)}_{\alpha\bar{\beta}}K^{(S)}_{\kappa\bar{\lambda}} - K^{(X)}_{\alpha\bar{\beta}}K^{(S)}_{\kappa\bar{\lambda}} = 0. \end{aligned} \tag{C.35}$$

JHEP04(2014)050

Diagonal blocks are given by

$$R_{\alpha\bar{\beta}\gamma\bar{\delta}} = K^{(X)}_{\alpha\bar{\beta}} K^{(X)}_{\gamma\bar{\delta}} + K^{(X)}_{\alpha\bar{\delta}} K^{(X)}_{\gamma\bar{\beta}} - e^{2K^{(X)}} \mathcal{F}^{(X)}_{\alpha\gamma} \overline{\mathcal{F}}^{(X)}_{\bar{\beta}\bar{\delta}}, \tag{C.36}$$

where we used

$$\tilde{B}^{\alpha\beta,\bar{\alpha}\bar{\beta}} = \frac{K^{\bar{\alpha}\alpha}_{(X)} K^{\bar{\beta}\beta}_{(X)}}{\dim_{\mathbb{C}} \mathcal{M}_{\text{cpx}}(X; U_* \oplus W_{\text{noscan}})}, \qquad \tilde{B}^{\alpha\beta,\bar{\kappa}\bar{\lambda}} = \tilde{B}^{\kappa\lambda,\bar{\alpha}\bar{\beta}} = 0. \tag{C.37}$$

Open Access. This article is distributed under the terms of the Creative Commons Attribution License (CC-BY 4.0), which permits any use, distribution and reproduction in any medium, provided the original author(s) and source are credited.

References

[1] F. Denef, M.R. Douglas and S. Kachru, *Physics of String Flux Compactifications*, *Ann. Rev. Nucl. Part. Sci.* **57** (2007) 119 [hep-th/0701050] [INSPIRE].

[2] F. Denef, *Les Houches Lectures on Constructing String Vacua*, arXiv:0803.1194 [INSPIRE].

[3] J. Kumar and J.D. Wells, *Landscape cartography: A Coarse survey of gauge group rank and stabilization of the proton*, *Phys. Rev.* **D 71** (2005) 026009 [hep-th/0409218] [INSPIRE].

[4] R. Blumenhagen, F. Gmeiner, G. Honecker, D. Lüst and T. Weigand, *The Statistics of supersymmetric D-brane models*, *Nucl. Phys.* **B 713** (2005) 83 [hep-th/0411173] [INSPIRE].

[5] K.R. Dienes, *Statistics on the heterotic landscape: Gauge groups and cosmological constants of four-dimensional heterotic strings*, *Phys. Rev.* **D 73** (2006) 106010 [hep-th/0602286] [INSPIRE].

[6] L.B. Anderson, Y.-H. He and A. Lukas, *Monad Bundles in Heterotic String Compactifications*, *JHEP* **07** (2008) 104 [arXiv:0805.2875] [INSPIRE].

[7] J.F.G. Cascales and A.M. Uranga, *Branes on generalized calibrated submanifolds*, *JHEP* **11** (2004) 083 [hep-th/0407132] [INSPIRE].

[8] J. Gomis, F. Marchesano and D. Mateos, *An Open string landscape*, *JHEP* **11** (2005) 021 [hep-th/0506179] [INSPIRE].

[9] E. Witten, *On flux quantization in M-theory and the effective action*, *J. Geom. Phys.* **22** (1997) 1 [hep-th/9609122] [INSPIRE].

[10] A. Collinucci and R. Savelli, *On Flux Quantization in F-theory*, *JHEP* **02** (2012) 015 [arXiv:1011.6388] [INSPIRE].

[11] A. Collinucci and R. Savelli, *On Flux Quantization in F-theory II: Unitary and Symplectic Gauge Groups*, *JHEP* **08** (2012) 094 [arXiv:1203.4542] [INSPIRE].

[12] S.B. Giddings, S. Kachru and J. Polchinski, *Hierarchies from fluxes in string compactifications*, *Phys. Rev.* **D 66** (2002) 106006 [hep-th/0105097] [INSPIRE].

[13] S. Kachru, M.B. Schulz and S. Trivedi, *Moduli stabilization from fluxes in a simple IIB orientifold*, *JHEP* **10** (2003) 007 [hep-th/0201028] [INSPIRE].

[14] G.W. Moore, *Les Houches lectures on strings and arithmetic*, hep-th/0401049 [INSPIRE].

[15] K. Dasgupta, G. Rajesh and S. Sethi, *M theory, orientifolds and G - flux*, *JHEP* **08** (1999) 023 [hep-th/9908088] [INSPIRE].

JHEP04(2014)050

[16] L. Görlich, S. Kachru, P.K. Tripathy and S.P. Trivedi, *Gaugino condensation and nonperturbative superpotentials in flux compactifications*, *JHEP* **12** (2004) 074 [hep-th/0407130] [INSPIRE].

[17] O. DeWolfe, A. Giryavets, S. Kachru and W. Taylor, *Enumerating flux vacua with enhanced symmetries*, *JHEP* **02** (2005) 037 [hep-th/0411061] [INSPIRE].

[18] P.S. Aspinwall and R. Kallosh, *Fixing all moduli for M-theory on $K3 \times K3$*, *JHEP* **10** (2005) 001 [hep-th/0506014] [INSPIRE].

[19] R. Donagi and M. Wijnholt, *Higgs Bundles and UV Completion in F-theory*, *Commun. Math. Phys.* **326** (2014) 287 [arXiv:0904.1218] [INSPIRE].

[20] A.P. Braun, A. Collinucci and R. Valandro, *G-flux in F-theory and algebraic cycles*, *Nucl. Phys.* **B 856** (2012) 129 [arXiv:1107.5337] [INSPIRE].

[21] K. Becker and K. Dasgupta, *Heterotic strings with torsion*, *JHEP* **11** (2002) 006 [hep-th/0209077] [INSPIRE].

[22] P.K. Tripathy and S.P. Trivedi, *Compactification with flux on $K3$ and tori*, *JHEP* **03** (2003) 028 [hep-th/0301139] [INSPIRE].

[23] K. Becker, M. Becker, K. Dasgupta and P.S. Green, *Compactifications of heterotic theory on nonKähler complex manifolds. 1.*, *JHEP* **04** (2003) 007 [hep-th/0301161] [INSPIRE].

[24] D. Lüst, P. Mayr, S. Reffert and S. Stieberger, *F-theory flux, destabilization of orientifolds and soft terms on D7-branes*, *Nucl. Phys.* **B 732** (2006) 243 [hep-th/0501139] [INSPIRE].

[25] A.P. Braun, A. Hebecker, C. Lüdeling and R. Valandro, *Fixing D7 Brane Positions by F-theory Fluxes*, *Nucl. Phys.* **B 815** (2009) 256 [arXiv:0811.2416] [INSPIRE].

[26] A.P. Braun, Y. Kimura and T. Watari, *On the Classification of Elliptic Fibrations modulo Isomorphism on $K3$ Surfaces with large Picard Number*, arXiv:1312.4421 [INSPIRE].

[27] T.W. Grimm, T.-W. Ha, A. Klemm and D. Klevers, *Computing Brane and Flux Superpotentials in F-theory Compactifications*, *JHEP* **04** (2010) 015 [arXiv:0909.2025] [INSPIRE].

[28] S. Ashok and M.R. Douglas, *Counting flux vacua*, *JHEP* **01** (2004) 060 [hep-th/0307049] [INSPIRE].

[29] F. Denef and M.R. Douglas, *Distributions of flux vacua*, *JHEP* **05** (2004) 072 [hep-th/0404116] [INSPIRE].

[30] R. Friedman, J. Morgan and E. Witten, *Vector bundles and F-theory*, *Commun. Math. Phys.* **187** (1997) 679 [hep-th/9701162] [INSPIRE].

[31] D.R. Morrison and C. Vafa, *Compactifications of F-theory on Calabi-Yau threefolds. 2*, *Nucl. Phys.* **B 476** (1996) 437 [hep-th/9603161] [INSPIRE].

[32] G. Curio and R.Y. Donagi, *Moduli in $N = 1$ heterotic/F theory duality*, *Nucl. Phys.* **B 518** (1998) 603 [hep-th/9801057] [INSPIRE].

[33] R. Donagi and M. Wijnholt, *Model Building with F-theory*, *Adv. Theor. Math. Phys.* **15** (2011) 1237 [arXiv:0802.2969] [INSPIRE].

[34] H. Hayashi, R. Tatar, Y. Toda, T. Watari and M. Yamazaki, *New Aspects of Heterotic–F Theory Duality*, *Nucl. Phys.* **B 806** (2009) 224 [arXiv:0805.1057] [INSPIRE].

JHEP04(2014)050

[35] J. Marsano, N. Saulina and S. Schäfer-Nameki, *Monodromies, Fluxes and Compact Three-Generation F-theory GUTs*, *JHEP* **08** (2009) 046 [arXiv:0906.4672] [INSPIRE].

[36] J. Marsano, N. Saulina and S. Schäfer-Nameki, *Compact F-theory GUTs with U(1) (PQ)*, *JHEP* **04** (2010) 095 [arXiv:0912.0272] [INSPIRE].

[37] J. Marsano, N. Saulina and S. Schäfer-Nameki, *A Note on G-fluxes for F-theory Model Building*, *JHEP* **11** (2010) 088 [arXiv:1006.0483] [INSPIRE].

[38] M.J. Dolan, J. Marsano, N. Saulina and S. Schäfer-Nameki, *F-theory GUTs with U(1) Symmetries: Generalities and Survey*, *Phys. Rev.* **D 84** (2011) 066008 [arXiv:1102.0290] [INSPIRE].

[39] J. Marsano, N. Saulina and S. Schäfer-Nameki, *On G-flux, M5 instantons and U(1)s in F-theory*, arXiv:1107.1718 [INSPIRE].

[40] J. Marsano, N. Saulina and S. Schäfer-Nameki, *Global Gluing and G-flux*, *JHEP* **08** (2013) 001 [arXiv:1211.1097] [INSPIRE].

[41] T.W. Grimm and T. Weigand, *On Abelian Gauge Symmetries and Proton Decay in Global F-theory GUTs*, *Phys. Rev.* **D 82** (2010) 086009 [arXiv:1006.0226] [INSPIRE].

[42] C. Mayrhofer, E. Palti and T. Weigand, *U(1) symmetries in F-theory GUTs with multiple sections*, *JHEP* **03** (2013) 098 [arXiv:1211.6742] [INSPIRE].

[43] S. Krause, C. Mayrhofer and T. Weigand, *G_4 flux, chiral matter and singularity resolution in F-theory compactifications*, *Nucl. Phys.* **B 858** (2012) 1 [arXiv:1109.3454] [INSPIRE].

[44] M. Cvetič, D. Klevers and H. Piragua, *F-Theory Compactifications with Multiple U(1)-Factors: Constructing Elliptic Fibrations with Rational Sections*, *JHEP* **06** (2013) 067 [arXiv:1303.6970] [INSPIRE].

[45] M. Cvetič, A. Grassi, D. Klevers and H. Piragua, *Chiral Four-Dimensional F-theory Compactifications With* SU(5) *and Multiple U(1)-Factors*, arXiv:1306.3987 [INSPIRE].

[46] M. Cvetič, D. Klevers and H. Piragua, *F-Theory Compactifications with Multiple U(1)-Factors: Addendum*, *JHEP* **12** (2013) 056 [arXiv:1307.6425] [INSPIRE].

[47] M. Cvetič, D. Klevers, H. Piragua and P. Song, *Elliptic fibrations with rank three Mordell-Weil group: F-theory with* $\mathrm{U}(1) \times \mathrm{U}(1) \times \mathrm{U}(1)$ *gauge symmetry*, *JHEP* **03** (2014) 021 [arXiv:1310.0463] [INSPIRE].

[48] V. Braun, T.W. Grimm and J. Keitel, *New Global F-theory GUTs with U(1) symmetries*, *JHEP* **09** (2013) 154 [arXiv:1302.1854] [INSPIRE].

[49] J. Borchmann, C. Mayrhofer, E. Palti and T. Weigand, *Elliptic fibrations for* $\mathrm{SU}(5) \times \mathrm{U}(1) \times \mathrm{U}(1)$ *F-theory vacua*, *Phys. Rev.* **D 88** (2013) 046005 [arXiv:1303.5054] [INSPIRE].

[50] V. Braun, T.W. Grimm and J. Keitel, *Geometric Engineering in Toric F-theory and GUTs with U(1) Gauge Factors*, *JHEP* **12** (2013) 069 [arXiv:1306.0577] [INSPIRE].

[51] J. Borchmann, C. Mayrhofer, E. Palti and T. Weigand, SU(5) *Tops with Multiple U(1)s in F-theory*, arXiv:1307.2902 [INSPIRE].

[52] M. Bershadsky, K.A. Intriligator, S. Kachru, D.R. Morrison, V. Sadov and C. Vafa, *Geometric singularities and enhanced gauge symmetries*, *Nucl. Phys.* **B 481** (1996) 215 [hep-th/9605200] [INSPIRE].

JHEP04(2014)050

[53] M. Kuentzler, C. Lawrie and S. Schafer-Nameki, *Tate's algorithm for SU(5) models with extra sections*, to appear.

[54] D.S. Park, *Anomaly Equations and Intersection Theory*, *JHEP* **01** (2012) 093 [arXiv:1111.2351] [INSPIRE].

[55] D.R. Morrison and D.S. Park, *F-Theory and the Mordell-Weil Group of Elliptically-Fibered Calabi-Yau Threefolds*, *JHEP* **10** (2012) 128 [arXiv:1208.2695] [INSPIRE].

[56] M. Cvetič, T.W. Grimm and D. Klevers, *Anomaly Cancellation And Abelian Gauge Symmetries In F-theory*, *JHEP* **02** (2013) 101 [arXiv:1210.6034] [INSPIRE].

[57] T.W. Grimm, A. Kapfer and J. Keitel, *Effective action of* 6*D F-theory with U(1) factors: Rational sections make Chern-Simons terms jump*, *JHEP* **07** (2013) 115 [arXiv:1305.1929] [INSPIRE].

[58] G.W. Moore, *Arithmetic and attractors*, hep-th/9807087 [INSPIRE].

[59] G.W. Moore, *Attractors and arithmetic*, hep-th/9807056 [INSPIRE].

[60] S. Ferrara, R. Kallosh and A. Strominger, *N=2 extremal black holes*, *Phys. Rev.* **D 52** (1995) 5412 [hep-th/9508072] [INSPIRE].

[61] T. Shioda and H. Inose, *On Singular K3 surfaces*, in W.L. Baily Jr. and T. Shioda eds., *Complex analysis and algebraic geometry*, Iwanami Shoten, Tokyo (1977), pg. 119–136.

[62] I.I. Piatetski-Shapiro and I.R. Shafarevich, *Torelli's theorem for algebraic surfaces of type* K3, *Izv. Akad. Nauk SSSR Ser. Mat.* **35** (1971) 530.

[63] W. Barth, K. Hulek, C. Peters and A. Van de Ven, *Compact complex surfaces*, second edition, Springer-Verlag, Berlin (2004).

[64] A. Sen, *F theory and orientifolds*, *Nucl. Phys.* **B 475** (1996) 562 [hep-th/9605150] [INSPIRE].

[65] M. Schütt and T. Shioda, *Elliptic Surfaces*, in *Algebraic geometry in East Asia (Seoul 2008)*, *Adv. Stu. P. M.* **60** (2010) 51 arXiv:0907.0298.

[66] D. Huybrechts, *Lectures on K3 surfaces*, http://www.math.uni-bonn.de/people/huybrech/K3Global.pdf.

[67] T. Matumoto, *On Diffeomorphisms of a K3 Surface*, in M. Nagata et al. eds., *Algebraic and Topological Theories — to the memory of Dr. Takehiko Miyaka*, Kinukuniya, Tokyo (1985), pg. 616–621.

[68] C. Borcea, *Diffeomorphisms of a K3 surface*, *Math. Ann.* **275** (1986) 1.

[69] S.K. Donaldson, *Polynomial invariants for smooth manifolds*, *Topology* **29** (1990) 257 [INSPIRE].

[70] P.S. Aspinwall, *K3 surfaces and string duality*, hep-th/9611137 [INSPIRE].

[71] C. Vafa, *Evidence for F-theory*, *Nucl. Phys.* **B 469** (1996) 403 [hep-th/9602022] [INSPIRE].

[72] M. Bershadsky, T. Pantev and V. Sadov, *F theory with quantized fluxes*, *Adv. Theor. Math. Phys.* **3** (1999) 727 [hep-th/9805056] [INSPIRE].

[73] K.-I. Nishiyama, *The Jacobian fibrations on some K3 surfaces and their Mordell-Weil groups*, *Japan. J. Math.* **22** (1996) 293.

[74] A. Kumar, *Elliptic fibrations on a generic Jacobian Kummer surface*, arXiv:1105.1715.

JHEP04(2014)050

[75] K. Oguiso, *On Jacobian fibrations on the Kummer surfaces of the product of non-isogenous elliptic curves*, *J. Math. Soc. Japan* **41** (1989) 651.

[76] P.S. Aspinwall and D.R. Morrison, *Nonsimply connected gauge groups and rational points on elliptic curves*, *JHEP* **07** (1998) 012 [hep-th/9805206] [INSPIRE].

[77] T. Shioda, *On the Mordell–Weil Lattices*, *Comment. Math. Univ. St. Pauli* **39** (1990) 211.

[78] D.R. Morrison, *On K3 surfaces with large Picard number*, *Invent. Math.* **75** (1984) 105.

[79] M. Bershadsky, A. Johansen, T. Pantev and V. Sadov, *On four-dimensional compactifications of F-theory*, *Nucl. Phys.* **B 505** (1997) 165 [hep-th/9701165] [INSPIRE].

[80] S.H. Katz and E. Sharpe, *D-branes, open string vertex operators and Ext groups*, *Adv. Theor. Math. Phys.* **6** (2003) 979 [hep-th/0208104] [INSPIRE].

[81] S. Kachru and C. Vafa, *Exact results for $N = 2$ compactifications of heterotic strings*, *Nucl. Phys.* **B 450** (1995) 69 [hep-th/9505105] [INSPIRE].

[82] G. Aldazabal, A. Font, L.E. Ibáñez and F. Quevedo, *Chains of $N = 2$, $D = 4$ heterotic type-II duals*, *Nucl. Phys.* **B 461** (1996) 85 [hep-th/9510093] [INSPIRE].

[83] D.R. Morrison and C. Vafa, *Compactifications of F-theory on Calabi-Yau threefolds. 1*, *Nucl. Phys.* **B 473** (1996) 74 [hep-th/9602114] [INSPIRE].

[84] R. Friedman and D. Morrison, *The Birational Geometry of Degenerations: an Overview*, in R. Friedman and D. Morrison eds., *The Birational Geometry of Degenerations*, Birkhäuser, Boston, Basel, Stuttgart (1983).

[85] H. Hayashi, T. Kawano, Y. Tsuchiya and T. Watari, *More on Dimension-4 Proton Decay Problem in F-theory – Spectral Surface, Discriminant Locus and Monodromy*, *Nucl. Phys.* **B 840** (2010) 304 [arXiv:1004.3870] [INSPIRE].

[86] M. Kuwata and T. Shioda, *Elliptic parameters and defining equations for elliptic fibrations on a Kummer surface*, in *Algebraic geometry in East Asia (Hanoi 2005)*, *Adv. Stud. Pure Math.* **50** (2008) 177 math/0609473.

[87] S.H. Katz and C. Vafa, *Matter from geometry*, *Nucl. Phys.* **B 497** (1997) 146 [hep-th/9606086] [INSPIRE].

[88] C. Beasley, J.J. Heckman and C. Vafa, *GUTs and Exceptional Branes in F-theory - I*, *JHEP* **01** (2009) 058 [arXiv:0802.3391] [INSPIRE].

[89] H. Hayashi, T. Kawano, R. Tatar and T. Watari, *Codimension-3 Singularities and Yukawa Couplings in F-theory*, *Nucl. Phys.* **B 823** (2009) 47 [arXiv:0901.4941] [INSPIRE].

[90] S. Kachru, R. Kallosh, A.D. Linde and S.P. Trivedi, *de Sitter vacua in string theory*, *Phys. Rev.* **D 68** (2003) 046005 [hep-th/0301240] [INSPIRE].

[91] K. Dasgupta, C. Herdeiro, S. Hirano and R. Kallosh, *D3/D7 inflationary model and M-theory*, *Phys. Rev.* **D 65** (2002) 126002 [hep-th/0203019] [INSPIRE].

[92] S. Hosono, B.H. Lian, K. Oguiso and S.-T. Yau, *Classification of $c = 2$ rational conformal field theories via the Gauss product*, *Commun. Math. Phys.* **241** (2003) 245 [hep-th/0211230] [INSPIRE].

[93] J. Conway and N. Sloane, *Sphere Packings, Lattices and Groups*, Springer-Verlag (1988).

[94] C. Beasley, J.J. Heckman and C. Vafa, *GUTs and Exceptional Branes in F-theory - II: Experimental Predictions*, *JHEP* **01** (2009) 059 [arXiv:0806.0102] [INSPIRE].

JHEP04(2014)050

[95] M. Green, J. Schwarz and E. Witten, *Superstring Theory*, volume 2, Cambridge University Press, Cambridge, U.K. (1987).

[96] E. Witten, *Branes and the dynamics of QCD*, *Nucl. Phys.* **B 507** (1997) 658 [hep-th/9706109] [INSPIRE].

[97] B. Andreas and G. Curio, *Three-branes and five-branes in $N = 1$ dual string pairs*, *Phys. Lett.* **B 417** (1998) 41 [hep-th/9706093] [INSPIRE].

[98] B. Andreas and G. Curio, *On discrete twist and four flux in $N = 1$ heterotic/F theory compactifications*, *Adv. Theor. Math. Phys.* **3** (1999) 1325 [hep-th/9908193] [INSPIRE].

[99] V.V. Nikulin, *Integral symmetric bilinear forms and some of their applications*, *Math. USSR Izv.* **14** (1980) 103 [English translation of *Izv. Akad. Nauk SSSR Ser. Mat.* **43** (1979) 111].

[100] David R. Morrison, private communication.

[101] J. Polchinski, *String Theory*, Cambridge University Press, Cambridge, U.K. (1998).

[102] K. Oguiso and T. Shioda, *The Mordell–Weil Lattice of a Rational Elliptic Surface*, *Comm. Math. Univ. Sancti Pauli* **40** (1991) 83.

[103] B.R. Greene, D.R. Morrison and M.R. Plesser, *Mirror manifolds in higher dimension*, *Commun. Math. Phys.* **173** (1995) 559 [hep-th/9402119] [INSPIRE].

[104] A. Strominger, *Special geometry*, *Commun. Math. Phys.* **133** (1990) 163 [INSPIRE].

JHEP04(2014)050

PHYSICAL REVIEW D **90,** 121901(R) (2014)

Distribution of the number of generations in flux compactifications

Andreas P. Braun[1] and Taizan Watari[2]

[1]*Department of Mathematics, King's College, London WC2R 2LS, United Kingdom*
[2]*Kavli Institute for the Physics and Mathematics of the Universe, the University of Tokyo, Tokyo 277-8583, Japan*

(Received 24 September 2014; published 30 December 2014)

Flux compactification of string theory generates an ensemble with a large number of vacua, called the landscape. By using the statistics of various properties of low-energy effective theories in the string landscape, one can therefore hope to provide a scientific foundation to the notion of naturalness. This article discusses how to answer such questions of practical interest by using flux compactification of F-theory. It is found that the distribution is approximately in a factorized form given by distribution on the choice of 7-brane gauge group, that on the number of generations $N_{\rm gen}$ and that on effective coupling constants. The distribution on $N_{\rm gen}$ is approximately Gaussian for the range $|N_{\rm gen}| \lesssim 10$. The statistical cost of higher-rank gauge group is also discussed.

DOI: 10.1103/PhysRevD.90.121901 PACS numbers: 11.25.Wx, 11.25.Mj, 12.10.Dm

I. INTRODUCTION

String theory with compactified extra dimensions gives rise to a large number of vacua. The diversity of vacua originates from the choice of topology of compact internal space and flux configurations on it [1]. String theory as understood in this way today therefore does not predict a unique low-energy effective theory. Despite this lack of prediction, there are still many ways in which we can take advantage of such an ensemble of string vacua for a better understanding of particle physics in the real world. Such an ensemble containing a large number of vacua provided by a fundamental theory is referred to as a landscape of vacua, or landscape for short.

At least two ideas have been proposed so far in how to take advantage of such landscape of string theory. One is in the context of understanding the nonvanishing (yet extremely small) dark energy. It has been realized that the very small value was predicted to be "natural" under the combination of three ansatzes, (i) that the universe is occupied with many distinct areas facilitating effective theories with different values of the cosmological constant [2], (ii) that the statistical distribution of dark energy is taken as a principle of arguing naturalness, and (iii) that the observational factor (anthropics) is taken into account in the statistical distribution [3]. The string landscape indeed give rise to such an ensemble of low-energy effective theories with different values of the cosmological constant [4], and eternal inflation has this ensemble of string vacua realized in the universe [5]. Thus the string landscape provides a theoretical foundation for the attempt of understanding dark energy along the lines of (i), (ii), and (iii).

The string landscape can also provide a scientific foundation for a notion of naturalness for various kinds of parameters of the standard model, not just for the value of dark energy. Naturalness has been exploited for decades as a guiding principle in the quest of models beyond the standard model. Arguments relying on naturalness, however, tend to depend on the class of vacua (an ensemble) one has in mind. Since string theory is able to provide a well-motivated ensemble of vacua on which naturalness arguments can be built, this is hence another place where string theory can contribute to progress of theoretical particle physics.

This article aims at making progress in the second direction above. It is known that flux compactification of Type IIB string theory/F-theory stabilizes not only complex structure moduli but also the brane configuration. This means that both gauge groups and coupling constants of the effective theory are determined once a topological flux configuration is given. Exploiting all of the theoretically possible topological flux configurations, an ensemble of low-energy effective theories with various gauge groups and coupling constants is generated in this framework, in principle. To get this done in practice, however, a clever approach is necessary. Low-energy effective theories are usually classified in terms of their algebraic information (such as gauge groups, matter representations and presence/absence of certain types of interactions) first, and then in terms of topological information (such as the number of generations of matter fields in a given representation). Effective theories with the same algebraic and topological information are then specified by the values of coupling constants. The string landscape will be of some use only when the statistical distribution of low-energy observables are presented and studied in compatibility with such a hierarchical classification of effective theories.

This can be done along the line described in [6], which is built on top of pioneering works [7,8]. The study of [6], however, used $\mathrm{K3} \times \mathrm{K3}$ compactification of F-theory, where analysis is a little easier, but we cannot even hope to obtain a semirealistic model of low-energy physics. This article applies the method to more general Calabi–Yau fourfolds for F-theory compactification, derives answers to

 © 2014 American Physical Society

questions of practical interest, and exemplifies the potential power of the method.

Section II is devoted to a review of the method in [6–8] along with new observations in [9]. The method is then applied to a class of compactifications that lead to semi-realistic supersymmetric grand unification (GUT) models in Sec. III. We derive distribution of the number of generations in flux vacua of SU(5) GUT models, and also study how the number of flux vacua scales when we require SO(10), SU(5) or no unification group on 7-branes, respectively. We find that the distribution is in a factorized form to a good approximation, independently of topological choice of geometry. Details and explanations omitted in this article are found in [9].

II. THE METHOD

A family of geometries over a restricted moduli space, $\pi\colon \mathcal{Y} \to \mathcal{M}_*$, is a useful concept when one wants to focus on flux vacua with a given algebraic information. A restricted family and its moduli space, $\pi\colon \mathcal{Y} \to \mathcal{M}_*^{A4}$ (resp. $\mathcal{M}_*^{D5}$), is specified for a topological choice of $(B_3, [S])$, where $[S]$ is a divisor class in B_3. Each member of the family, $\pi^{-1}(p) = Y_p$ for $p \in \mathcal{M}_*^{A4}$ (resp. $\mathcal{M}_*^{D5}$), is a smooth elliptically fibred Calabi–Yau fourfold $\pi_{Y_p}\colon Y_p \to B_3$ with a section, and the discriminant locus of the fibration π_{Y_p} contains an irreducible component in $[S]$ and the generic fiber over it is I_5 (resp. I_1^*) in the Kodaira classification. Any one of such fourfolds in the family over $\mathcal{M}_*^{A4}$ (resp. $\mathcal{M}_*^{D5}$) can be used for F-theory compactification that results in a vacuum with an $R = \mathrm{SU}(5)$ [resp. $R = \mathrm{SO}(10)$] unification group on 7-branes. $\mathcal{M}_*^{A4}$ or $\mathcal{M}_*^{D5}$ parametrizes the complex structure of such geometries.[1] Higher rank 7-brane gauge group implies a larger number of independent divisors

$$[\hat{C}_i] \in [H^2(Y_p;\mathbb{Z}) \cap H^{1,1}(Y_p;\mathbb{R})], \quad i = 1, \ldots, \mathrm{rank}(R), \tag{1}$$

for a generic geometry $\pi^{-1}(p) = Y_p$ in $p \in \mathcal{M}_*$.

An ensemble of F-theory flux vacua with a given algebraic and topological information is specified by a pair $(H_{\mathrm{scan}}, G_{\mathrm{fix}}^{(4)})$, where

$$H_{\mathrm{scan}} \subset [H^4(Y;\mathbb{Z})]_{\mathrm{ker}}, \qquad G_{\mathrm{fix}}^{(4)} \in [H^4(Y;\text{‘}\mathbb{Z}\text{’}]_{\mathrm{prim}}; \tag{2}$$

the subscript "prim" implies $J \wedge G = 0 \in H^6(Y;\mathbb{R})$ (the D-term condition), and "ker" both $J \wedge G = 0$ and $i_{\hat{C}_i}^*(G) = 0 \in H^4(\hat{C}_i;\mathbb{Q})$. The last condition is to make sure that fluxes in H_{scan} do not introduce gauge symmetry breaking (cf. [9]). An ensemble of 4-form flux

$$\{G_{\mathrm{tot}}^{(4)} = G_{\mathrm{scan}}^{(4)} + G_{\mathrm{fix}}^{(4)} | G_{\mathrm{scan}}^{(4)} \in H_{\mathrm{scan}}\} \tag{3}$$

determines an ensemble of vacua of complex structure through the superpotential $W \propto \int_{Y_p} \Omega_{Y_p} \wedge G_{\mathrm{tot}}^{(4)}$.

Statistics of such an ensemble of vacua can be presented as a distribution over the restricted moduli space $\mathcal{M}_*$. The distribution was worked out analytically in a very robust way [7] for the vacuum index density $d\mu_I$,

$$d^{2m}z \sum_{G_{\mathrm{scan}}^{(4)}} \delta^{2m}(DW, \overline{DW}) \det \begin{bmatrix} D^2W & \bar{D}DW \\ D\overline{DW} & \overline{D^2W} \end{bmatrix}, \tag{4}$$

to which each flux vacuum on $\mathcal{M}_*$ contributes by a delta function with coefficient ± 1. Here, $m := \dim_{\mathbb{C}} \mathcal{M}_* = h^{3,1}(Y)$, and the dz's are local holomorphic coordinates on $\mathcal{M}_*$. Derivatives in DW, $\overline{DW}$ etc. are with respect to the fields corresponding to the complex structure moduli tangent to $\mathcal{M}_*$.

Making a continuous approximation [7] of the sum over flux configurations $\sum_{G_{\mathrm{scan}}^{(4)}}$ in (4), the vacuum index density is cast into the following form

$$d\mu_I = \frac{(2\pi L_*)^{K/2}}{(K/2)!} \rho_I, \qquad K := \dim_{\mathbb{R}}(H_{\mathrm{scan}} \otimes \mathbb{R}). \tag{5}$$

Here, L_* is the maximal D3-brane charge available. Although ρ_I depends on the choice of H_{scan}, it is given by

$$c_m(T\mathcal{M}_* \otimes \mathcal{L}) = \det\left(-\frac{R}{2\pi i} + \frac{\omega}{2\pi} \mathbf{1}_{m\times m}\right) \tag{6}$$

for the Kähler form ω on $\mathcal{M}_*$ whenever $(H_{\mathrm{scan}} \otimes \mathbb{R})$ contains the real primary horizontal subspace $H_{H*}^4(Y;\mathbb{R}) \subset H^4(Y;\mathbb{R})$ [6–8]. $H_{H*}^4(Y;\mathbb{R})$ is the real part of the primary horizontal subspace in [10],

$$\mathrm{Span}_{\mathbb{C}}\{\Omega_{Y_p}, D\Omega_{Y_p}, D^2\Omega_{Y_p}, \ldots\} \subset H^4(Y;\mathbb{C}), \tag{7}$$

which does not depend on the choice of $p \in \mathcal{M}_*$.

In order to see how H_{scan} should be chosen to achieve the goal we have set in this article, note that the vector space $H^4(Y;\mathbb{R})$ is decomposed as follows:

$$H_{H*}^4(Y;\mathbb{R}) \oplus H_{RM*}^{2,2}(Y;\mathbb{R}) \oplus H_{V*}^{2,2}(Y;\mathbb{R}); \tag{8}$$

the vertical component $H_{V*}^{2,2}(Y;\mathbb{R})$ is the subspace generated by the wedge products of integral (1,1)-forms on Y_p, which defines a subspace of $H^4(Y;\mathbb{R})$ independent of $p \in \mathcal{M}_*$. The remaining component $H_{RM*}^{2,2}(Y;\mathbb{R})$, thus, should not depend on $p \in \mathcal{M}_*$.

[1] As in [6] and literatures therein, we only consider flux vacua for $(B_3, [S])$ of a given topology and for a given choice of Kähler form J on Y_p that is in $H^2(Y_p;\mathbb{Q}) \cap H^{1,1}(Y_p;\mathbb{R})$ modulo multiplication of $\mathbb{R}^\times$. The (restricted) moduli space $\mathcal{M}$ or $\mathcal{M}_*$ therefore refers only to that of complex structure. It is beyond the scope of this article or [9] to include the scanning over $(B_3, [S])$'s of different topology or their Kähler moduli spaces.

We choose $H_{\rm scan} \otimes \mathbb{R}$ to be $H^4_{H*}(Y;\mathbb{R})$ in this article. As discussed in more detail in [9], $H^4_{H*}(Y;\mathbb{R})$ is contained in $[H^4(Y;\mathbb{R})]_{\rm ker}$. Thus, for this choice of $H_{\rm scan}$, all the vacua share the same symmetry group from 7-branes in the effective theories below the Kaluza–Klein scale. This argument does not exclude the option to take $H_{\rm scan} \otimes \mathbb{R}$ larger that $H^4_{H*}(Y;\mathbb{R})$, but we should not take it to be as large as $[H^{2,2}_{V*}(Y;\mathbb{R})]^\perp$. It is not hard to find families $\pi\colon \mathcal{Y} \to \mathcal{M}_*$ with $h^{2,0}(Y_p) = 0$ where there are algebraic four-forms in $H^{2,2}_{RM*}(Y;\mathbb{R}) \cap H^4(Y;\mathbb{Z})$ that break the symmetry of the 7-brane gauge group [9]. A similar phenomenon has also been observed in [6], where $Y = \mathrm{K3} \times \mathrm{K3}$, and the fourform in $H^{2,2}_{RM*}(Y;\mathbb{R})$ is not dual to an algebraic cycle.

III. THE RESULTS

Let us apply the method described in the previous section to derive statistical distributions of observables of practical interest. The study in [6] used a family of $\mathrm{K3} \times \mathrm{K3}$ for compactification of F-theory, where all the 7-branes are parallel, and there is no light matter fields except those in the adjoint representation of the 7-brane gauge groups. Ensembles of flux vacua in such a setup do not include low-energy effective theories that look close to the (supersymmetric extensions of the) Standard Model. In this article, we therefore use a few other families of elliptically fibred Calabi–Yau fourfolds, for which the low-energy effective theories are at least semirealistic. These effective theories have SU(5) [resp. SO(10)] unification, and $N_{\rm gen}$ generations of matter fields in the $\mathbf{10} + \bar{\mathbf{5}}$ (resp. 16) representations. The task is to determine the value of L_* and K for such families and to study how those values depend on the choice of the unification group or the number of generations $N_{\rm gen}$.

A. Number of generations

We focus on a few choices of $(B_3, [S])$ for which the restricted moduli spaces and families for SU(5) unification are constructed in the way stated at the beginning of the previous section as examples. We choose

$$B_3 = \mathbb{P}[\mathcal{O}_{\mathbb{P}^2} \oplus \mathcal{O}_{\mathbb{P}^2}(n)], \qquad -3 \le n \le 3, \tag{9}$$

which is a $\mathbb{P}^1$-fibration over $\mathbb{P}^2$, and let $[S]$ be the "north-pole section" of the $\mathbb{P}^1$-fibration corresponding to the zero of a section of $\mathcal{O}_{\mathbb{P}^2}$. The range of n is set so that the 7-brane unification group at the S can be as small as SU(5), while the gauge group at the hidden sector [corresponding to the zero of a section of $\mathcal{O}_{\mathbb{P}^2}(n)$] can be completely Higgsed away.

We set $(H_{\rm scan} \otimes \mathbb{R}) = H^4_{H*}(Y;\mathbb{R})$, and choose $G^{(4)}_{\rm fix}$ to be the F-theory dual of the chirality-generating bundle twist in [11], parametrized by $\lambda_{FMW} \in 1/2 + \mathbb{Z}$. This flux gives rise to the net chirality of the matter fields in the 10 vs $\overline{\mathbf{10}}$ (also $\bar{\mathbf{5}}$ vs 5) representation of the SU(5) unification group; $N_{\rm gen} = -(18-n)(3-n)\lambda_{FMW}$ [12]. Since the vanishing cycles for the chiral matter belong to $H^{2,2}_{V*}(Y;\mathbb{Q})$, any flux vacua in the ensemble (3) have the same $N_{\rm gen}$ [9]. In this way, we obtain an ensemble of F-theory flux vacua that share the same algebraic and topological ($N_{\rm gen}$) information. The F-theory dual description of $G^{(4)}_{\rm fix}$ has been determined in [13].

$L_* = \chi(Y)/24 - (G^{(4)}_{\rm fix})^2/2$ is the upper bound on the net D3-brane charges from $G^{(4)}_{\rm scan}$. It depends on $N_{\rm gen}$ through $G^{(4)}_{\rm fix}$ [6] and a straightforward computation reveals that [9,13]

$$L_* = \frac{2163}{4} + \frac{125}{8}n(n+7) - \frac{5N^2_{\rm gen}}{2(18-n)(3-n)}. \tag{10}$$

The maximal values of $L^{\max}_*$ range within ~300 to 800 for the families with $-3 \le n \le 3$ (Table I); details of the calculation are found in [9]. L_* is always an upper convex quadratic function of $N_{\rm gen}$ in F-theory, not just for the choice in (9).

The other number we need to use in (5) is $K = \dim_{\mathbb{R}} H^4_{H*}(Y;\mathbb{R})$. This task boils down to the determination of the dimension of the horizontal component $H^{2,2}_{H*}(Y_p;\mathbb{R})$, since $K = 2 + 2m + \dim_{\mathbb{R}}[H^{2,2}_{H*}(Y_p;\mathbb{R})]$. A general recipe is to use mirror symmetry and determine the dimension of the vertical component of the mirror manifold of Y. The authors derived in [9] the formula for $h^{2,2}_V$, $h^{2,2}_H$ and $h^{2,2}_{RM}$ that is valid for any Calabi–Yau hypersurface of a toric 5-dimensional ambient space.

We carried out the computation of $h^{2,2}_{V*}(Y)$, $h^{2,2}_{H*}(Y)$ and K; for the families for SU(5) unification with B_3 in (9), it turns out that $h^{2,2}_{RM} = 0$. Details of the computation are found in [9], and only the results are recorded in Table I. Certainly the results on $L^{\max}_*$ and K in this table are only for a limited number of choices of B_3 and do not tell us whether they are typical among the results for all other choices of B_3 from 3-dimensional Fano varieties, or how much the values of $L^{\max}_*$ and K can vary for different B_3. But the table at least provides the first example of such calculations.

With this preparation, we can derive the distribution of the number of generations $N_{\rm gen}$ almost immediately. We

TABLE I. Various topological data of the families $\mathcal{Y} \to \mathcal{M}^{A4}_*$ of Calabi–Yau fourfolds for SU(5) unification, with B_3 given in (9). For $n = 3$, $L^{\max}_* = \chi(Y)/24$, as $G^{(4)}_{\rm fix} = N_{\rm gen} = 0$.

n	−3	−2	−1	0	1	2	3
$h^{3,1}_*$	1249	1423	1723	2148	2698	3373	4173
$h^{2,2}_{H*}$	5057	5755	6955	8655	10855	13555	16756
$h^{2,2}_{V*}$	9	9	9	9	9	9	8
$L^{\max}_*$	237	297	387	507	657	837	[1047]
K	7557	8603	10403	12953	16253	20303	25104

have constructed ensembles of flux vacua that are labeled by $\lambda_{FMW} \in 1/2 + \mathbb{Z}$. Each one of those ensembles consists of vacua that lead to effective theories with common algebraic information [SU(5) GUT with chiral matter in the $\mathbf{10} + \bar{\mathbf{5}}$ representation], but their topological information $N_{\rm gen} \propto \lambda_{FMW}$ varies from one ensemble to another. To compare the number of vacua that the individual ensembles contain, one simply needs to integrate ρ_I over $\mathcal{M}_*$, which is to ignore the difference in the value of the effective coupling constants of the vacua in a given ensemble. Since the integral of ρ_I over $\mathcal{M}_*$ usually yields a number of order unity (some region of $\mathcal{M}_*$ may have to be excluded; cf the discussion of D-limits in [7]), we simply make an approximation $\int_{\mathcal{M}_*} \rho_I \approx 1$. Only the prefactor $(2\pi L_*)^{K/2}/[(K/2)!]$ in (5) is then used as an estimate of the number of vacua in a given ensemble. We can use the value of K in Table I, and the $N_{\rm gen}$-dependence of L_* has already been discussed in this article. The number of vacua depends on $N_{\rm gen}$ in a way the volume of a K-dimensional sphere changes as the radius-square L_* decreases quadratically in $N_{\rm gen}$. There is an absolute upper limit on $N_{\rm gen}$ for a given family $\pi\colon \mathcal{Y} \to \mathcal{M}_*^{A4}$ due to the D3-tadpole constraint $L_* \geq 0$.

In the examples of $(B_3, [S])$ we have chosen at the beginning of this section, however, we have $L_* \ll K$ (see Table I). The continuous approximation [7] is not particularly good for such families, and should be replaced by $e^{L_* \ln(\sqrt{2\pi}K/L_*)}$, see [9] for a more detailed discussion.

In fact, it is commonplace to find $L_* \ll K$, not just in the families considered in this section, but in a broader class of families $\pi\colon \mathcal{Y} \to \mathcal{M}_*^R$ of interest. For B_3 with $h^{1,1}(B_3) \approx \mathcal{O}(1)$, for example, $h^{1,1}(Y)$ still remains $\mathcal{O}(1)$, while $h^{3,1}$ is much larger, due to the degrees of freedom for the complex structure of fibration. It is then a quite natural consequence that $h_V^{2,2}$ and $h_{RM}^{2,2}$ are not as large as $h_H^{2,2}$. From this, we find that $K \approx \chi(Y) \approx 24 L_*^{\max} \approx 8\pi L_*^{\max} \gg L_*$. The number of flux vacua for a family $\mathcal{Y} \to \mathcal{M}_*^R$ is then estimated by

$$e^{L_* \ln(\sqrt{2\pi}K/L_*)} \approx e^{K/6} e^{-5cN_{\rm gen}^2}, \tag{11}$$

where c is the coefficient of $N_{\rm gen}^2$ in (10), which remains of order unity. The expansion in $N_{\rm gen}^2$ in the exponent is valid for $N_{\rm gen} \lesssim 10$, since $\chi(Y)/24$ is often around 100–1000. The first factor of (11) depends on the choice of the 7-brane symmetry R [and on $(B_3, [S])$], while the second factor is a Gaussian distribution on $N_{\rm gen}$ for robust choice of $(B_3, [S])$. Algebraic and topological data of effective theories have a factorized distribution. One may further bring the distribution ρ_I on the effective coupling constants back to (11), without integrating it over $\mathcal{M}_*^R$.

TABLE II. Data for families over $\mathcal{M}$, $\mathcal{M}_*^{A4}$ and $\mathcal{M}_*^{D5}$.

	$h^{1,1}$	$h^{3,1}$	$h_{V*}^{2,2}$	$h_{H*}^{2,2}$	$\chi(Y)$	K
no gauge group	3	3277	4	13160	19728	19716
SU(5) model	7	2148	9	8655	12978	12953
SO(10) model	8	2138	10	8618	12924	12896

B. Cost of higher-rank gauge groups

The distribution (5), (6), (11) can be used to derive the statistical cost of requiring a higher rank gauge group on 7-branes. This idea was pursued already in [6], using $Y = \mathrm{K3} \times \mathrm{K3}$ for F-theory compactification; more examples are obtained in this article to estimate the systematics. The choices of $(B_3, [S])$ here are also more realistic than that of $\mathrm{K3} \times \mathrm{K3}$.

The SO(10) version of the family, $\pi\colon \mathcal{Y} \to \mathcal{M}_*^{D5}$, can also be constructed for the choice of $(B_3, [S])$ in (9) using toric geometry. Various topological data for the families over $\mathcal{M}_*^{D5}$, $\mathcal{M}_*^{A4}$ and $\mathcal{M}$ (where no 7-brane gauge symmetry is required) can be computed and the results are recorded in Table II for the $n = 0$ case. For more details of computations, see [9].

One can see from (11) that the difference in the value of K for different choices of 7-brane symmetry R determines the relative number of the corresponding flux quanta (vacua). Ensembles with higher rank 7-brane gauge group have smaller dimension K (Table II), confirming the same observation in [6] based on the family $Y = \mathrm{K3} \times \mathrm{K3}$. This leads to the observation that the rank-4 gauge group on 7-branes is *not* as statistically "natural" as vacua without a gauge group on 7-branes. In the choice of $(B_3, [S])$ in (9) with $n = 0$, for example, vacua with the rank-4 SU(5) unification constitutes only the fraction $e^{-\Delta K/6} \approx e^{-3000}$ of the entire flux vacua (smaller than the fraction 10^{-120} for the cosmological constant). The authors do not provide their interpretations for this inconvenient prediction; a popular attitude will be to hint at poor understanding of string theory, to count on cosmological factors that we did not study here, and/or to resort to anthropics.

IV. OUTLOOK

This article only deals with the easiest applications of the method explained in Sec. II. Various ideas of using (11) and ρ_I to address questions of practical interest are described in detail in [9].

ACKNOWLEDGEMENTS

This work is supported in part by Science and Technology Facilities Council, UK under Grant NO. ST/J002798/1 (APB), and WPI program and Grant-in-Aid for Innovative Areas 2303 from MEXT, Japan (TW).

[1] M. R. Douglas and S. Kachru, Rev. Mod. Phys. **79**, 733 (2007); F. Denef, M. R. Douglas, and S. Kachru, Annu. Rev. Nucl. Part. Sci. **57**, 119 (2007).
[2] S. W. Hawking, Phys. Lett. **134B**, 403 (1984).
[3] S. Weinberg, Phys. Rev. Lett. **59**, 2607 (1987); H. Martel, P. Shapiro, and S. Weinberg, Astrophys. J. **492**, 29 (1998).
[4] R. Bousso and J. Polchinski, J. High Energy Phys. 06 (2000) 006.
[5] A. H. Guth, J. Phys. A **40**, 6811 (2007).
[6] A. P. Braun, Y. Kimura, and T. Watari, J. High Energy Phys. 04 (2014) 050.
[7] S. Ashok and M. R. Douglas, J. High Energy Phys. 01 (2004) 060; F. Denef and M. R. Douglas, J. High Energy Phys. 05 (2004) 072.
[8] F. Denef, arXiv:0803.1194.
[9] A. Braun and T. Watari, Report No. KCL-mth-14-15, Report No. IPMU14-0267.
[10] A. Strominger, Commun. Math. Phys. **133**, 163 (1990); B. R. Greene, D. R. Morrison, and M. R. Plesser, Commun. Math. Phys. **173**, 559 (1995).
[11] R. Friedman, J. Morgan, and E. Witten, Commun. Math. Phys. **187**, 679 (1997).
[12] G. Curio, Phys. Lett. B **435**, 39 (1998); D.-E. Diaconescu and G. Ionesei, J. High Energy Phys. 12 (1998) 001.
[13] J. Marsano and S. Schafer-Nameki, J. High Energy Phys. 11 (2011) 098; T. Grimm and H. Hayashi, J. High Energy Phys. 03 (2012) 027.

Published for SISSA by Springer

Received: September 21, 2014
Accepted: December 16, 2014
Published: January 12, 2015

The vertical, the horizontal and the rest: anatomy of the middle cohomology of Calabi-Yau fourfolds and F-theory applications

A.P. Braun[a] **and T. Watari**[b]

[a] *Department of Mathematics, King's College, London WC2R 2LS, U.K.*

[b] *Kavli Institute for the Physics and Mathematics of the Universe, University of Tokyo, Kashiwano-ha 5-1-5, 277-8583, Japan*

E-mail: andreas.braun@kcl.ac.uk, taizan.watari@ipmu.jp

Abstract: The four-form field strength in F-theory compactifications on Calabi-Yau fourfolds takes its value in the middle cohomology group H^4. The middle cohomology is decomposed into a vertical, a horizontal and a remaining component, all three of which are present in general. We argue that a flux along the remaining or vertical component may break some symmetry, while a purely horizontal flux does not influence the unbroken part of the gauge group or the net chirality of charged matter fields. This makes the decomposition crucial to the counting of flux vacua in the context of F-theory GUTs. We use mirror symmetry to derive a combinatorial formula for the dimensions of these components applicable to any toric Calabi-Yau hypersurface, and also make a partial attempt at providing a geometric characterization of the four-cycles Poincaré dual to the remaining component of H^4. It is also found in general elliptic Calabi-Yau fourfolds supporting SU(5) gauge symmetry that a remaining component can be present, for example, in a form crucial to the symmetry breaking $\mathrm{SU}(5) \longrightarrow \mathrm{SU}(3)_C \times \mathrm{SU}(2)_L \times \mathrm{U}(1)_Y$. The dimension of the horizontal component is used to derive an estimate of the statistical distribution of the number of generations and the rank of 7-brane gauge groups in the landscape of F-theory flux vacua.

Keywords: Flux compactifications, F-Theory, Differential and Algebraic Geometry

ArXiv ePrint: 1408.6167

Open Access, © The Authors.
Article funded by SCOAP[3].

doi:10.1007/JHEP01(2015)047

JHEP01(2015)047

Contents

1 Introduction **1**

2 Ensembles of F-theory flux vacua and the primary horizontal subspace **4**

3 $H^{2,2}$ of a Calabi-Yau fourfold hypersurface of a toric variety **10**

3.1 General setup and known results 11

3.1.1 Triangulations, smoothness and projectivity 12

3.2 Computing $h^{2,2}$ via decomposition 15

3.3 Stratification and geometry of divisors 16

3.4 Combinatorial formula for $h^{2,2}[H^4_{(c)}(Y)] = [h^{n-3,n-3}[H^{2n-6}_c(Y)]]_{n=5}$ 17

3.4.1 Computation of $h^{1,1}(\hat{Y}_i) = h^{n-3,n-3}(\hat{Y}_i)$ for $n \geq 5$ cases 19

3.4.2 The result 22

3.5 Combinatorial formula for $h^{2,2}[H^4_c(Z_\Delta)] = [h^{n-3,2}[H^{n-1}_c(Z_\Delta)]]_{n=5}$ 23

3.6 Vertical, horizontal and the remaining components 24

3.6.1 The vertical component 25

3.6.2 Horizontal and remaining components 31

3.6.3 Triangulation (resolution) independence 35

4 Examples **36**

4.1 The sextic and its mirror 37

4.1.1 Geometry of the sextic: mixed Hodge structure of its subvarieties 37

4.1.2 Geometry of the mirror-sextic: toric stratification 42

4.1.3 Evaluation of $h^{2,2}_V$, $h^{2,2}_H$ and $h^{2,2}_{RM}$ 43

4.2 Computations in practice 44

4.3 Correction terms at work 45

4.4 Elliptic fourfolds 50

4.4.1 SU(5) along $\mathbb{P}^2$ 51

4.4.2 SO(10) along $\mathbb{P}^2$ 52

5 Fourfolds which are not hypersurfaces of toric varieties **52**

5.1 The dimension of $h^{1,1}(\hat{Y}_i)$'s 54

5.2 Determination of $H^4(Y)$ 56

5.3 The vertical components in $H_4(Y)$ 57

5.4 The remaining component 58

6 Distribution of rank of unification group and number of generations **59**

7 Outlook **63**

JHEP01(2015)047

A Geometry of elliptic-fibred Calabi-Yau fourfold for general F-theory SU(5) models **65**
A.1 Construction 65
A.2 Degeneration of singular fibres in higher codimension 68
A.3 Computation of Hodge numbers of the exceptional divisors $\hat{Y}_i = \hat{E}_i|_{\hat{Z}}$ 70
A.4 More on the geometry of the Cartan divisors $\hat{Y}_{1,2,3,4}$ 71

B Dependence of Hodge numbers on the rank of 7-brane symmetry **73**

C Flux controlling the net chirality **76**

1 Introduction

Work in string theory has traditionally focussed on the study of Calabi-Yau threefolds, as they are relevant to compactification of strings theories to four dimensions. From a mathematical point of view, it is very natural to ask about the properties of Calabi-Yau manifolds in (complex) dimensions other than three. Besides the omnipresent torus, two- and four-dimensional Calabi-Yau manifolds have subsequently acquired a central position within string theory.[1]

Two-dimensional Calabi-Yau manifolds, more commonly called K3 surfaces, form a single connected family and have a long history in mathematics (see e.g. the classic [2]). As the simplest non-trivial Calabi-Yau manifolds, they also have long been used to compactify string and supergravity theories. Their full relevance to string theory has only been appreciated with the advent of string dualities [3]. Besides appearing in relation to mirror symmetry [4], it was also in the context of string dualities, and in particular compactifications of F- and M-theory, that Calabi-Yau fourfolds became an intense object of interest. Refs. [5–12] form a partial list of early papers on the subject.

What is common to all Calabi-Yau n-folds is that their Kähler and complex structures are measured by integrating two special harmonic differential forms, the Kähler form $J \in H^{1,1}$ and the holomorphic top-form $\Omega \in H^{n,0}$, over appropriate cycles. However, we may already point out a crucial difference between Calabi-Yau threefolds on one side and K3 surfaces and Calabi-Yau fourfolds on the other side: whereas (powers of) J and $\Omega^{3,0}$ live in different cohomology groups in the case of Calabi-Yau manifolds of odd complex dimensions, $\Omega^{n,0}$ and $J^{n/2}$ share the middle cohomology for Calabi-Yau manifolds of even complex dimensions. For K3 surfaces this observation is tightly connected with the concept of polarization, where both J and $\Omega^{2,0}$ are confined to lie in mutually orthogonal subspaces of H^2. The Torelli theorem for lattice-polarized K3 surfaces states that the complex structure of a K3 surface with a lattice $W \subset H^2$ generated by algebraic cycles is parametrized by the period domain $\mathcal{M}_* = \mathbb{P}\left[\left\{\Omega \in [W^\perp \subset H^2 \otimes \mathbb{C}] \mid \Omega \wedge \Omega = 0, \Omega \wedge \overline{\Omega} > 0\right\}\right]$.

[1] See [1] for a discussion of M-theory compactifications on Calabi-Yau fivefolds.

JHEP01(2015)047

For Calabi-Yau fourfolds, however, there is no such convenient Torelli theorem. Consider a family of Calabi-Yau fourfolds $\pi : \mathcal{Z} \longrightarrow \mathcal{M}_*$ (i.e., $\hat{Z}_p := \pi^{-1}(p)$ for $p \in \mathcal{M}_*$ is a Calabi-Yau fourfold); $\mathrm{Pic}(\hat{Z}_p)$ for a generic choice of $p \in \mathcal{M}_*$ plays a role similar to the lattice polarization in the case of K3 surfaces. For any two classes in $\mathrm{Pic}(\hat{Z}_p)$ with representatives η_1 and η_2, we may form a *vertical cycle* $\eta_1 \wedge \eta_2$, which defines a class in $H^{2,2}(\hat{Z}_p;\mathbb{R}) \cap H^4(\hat{Z};\mathbb{Z})$. The subspace generated by such cycles (for p not in any one of the Noether-Lefschetz loci within $\mathcal{M}_*$) is called the *primary vertical component* of $H^{2,2}$, and is denoted by $H^{2,2}_V(\hat{Z}_p)$. It is identified within $H^4(\hat{Z};\mathbb{Z})$ defined in *topology*, independently of the choice of the "generic" $p \in \mathcal{M}_*$. The period integral $\int \Omega_{\hat{Z}_p}$ takes its value in $H^4(\hat{Z};\mathbb{C})$ and satisfies the obvious constraints $\Omega \wedge \Omega = 0$ and $\Omega \wedge \overline{\Omega} > 0$–(*), but the image of the period map does NOT occupy all of the complement of the primary vertical component. That is, the period domain satisfying (*) may be contained in a space much smaller than

$$\left[(H^{2,2}_V \otimes \mathbb{C})^{\perp} \subset H^4(\hat{Z};\mathbb{C})\right]. \tag{1.1}$$

References [4, 13] introduced another subspace $H^4_H(\hat{Z};\mathbb{C}) \subset H^4(\hat{Z};\mathbb{C})$ called the *primary horizontal* component (see section 2 for a brief review). The period map is locally injective for Calabi-Yau fourfolds and maps $\mathcal{M}_*$ into an $m := h^{3,1}(\hat{Z}_p) = \dim_{\mathbb{C}}\mathcal{M}_*$-dimensional subvariety of $\mathbb{P}[H^4(\hat{Z};\mathbb{C})]$; as we will elaborate on in the next section, $\mathcal{M}_*$ is in fact mapped into the projectivization of the horizontal component, $\mathbb{P}\left[H^4_H(\hat{Z};\mathbb{C})\right]$. The middle cohomology $H^4(\hat{Z};\mathbb{C})$ of a Calabi-Yau fourfold is then decomposed into

$$H^4(\hat{Z};\mathbb{C}) = H^4_H(\hat{Z};\mathbb{C}) \oplus H^{2,2}_{RM}(\hat{Z};\mathbb{C}) \oplus H^{2,2}_V(\hat{Z};\mathbb{C}), \tag{1.2}$$

where the decomposition is orthogonal under the intersection pairing. Unless the $H^4_{RM}(\hat{Z};\mathbb{C})$ component vanishes, the primary horizontal subspace $H^4_H(\hat{Z};\mathbb{C})$ is smaller in dimension than the non-vertical subspace (1.1).

There is another context — flux compactification of F-theory — where one is interested in the decomposition (1.2) of the middle cohomology above. An ensemble of flux vacua is specified by specifying a subspace of

$$\left[H^4(\hat{Z};\mathbb{Z})\right]_{\text{shift}} := H^4(\hat{Z};\mathbb{Z}) + \frac{c_2(T\hat{Z})}{2}; \tag{1.3}$$

when this subspace is affine, the vacuum index distribution over the moduli space $\mathcal{M}_*$ is given by a concise analytic formula [14, 15]. As discussed already in [16], and refined further in section 2 in this article, we can see that any pair of topological four-form fluxes whose difference belongs to the real part of the primary horizontal subspace $H^4_H(\hat{Z};\mathbb{R})$ shares the same symmetry group from 7-branes in their effective theories below the Kaluza-Klein scale. This motivates us to choose the affine subspace as some form of shift of $H^4_H(\hat{Z};\mathbb{R})$. Because the analytic formula of vacuum index density involves the dimension of the affine subspace, it is of interest in physics application of F-theory to know the dimension of $H^4_H(\hat{Z};\mathbb{R})$. Another question of interest is concerns how the space $H^{2,2}_{RM}(\hat{Z};\mathbb{R})$ arises geometrically, and which role it plays in phenomenology applications.

JHEP01(2015)047

Mirror symmetry indicates that [4, 13]

$$\left[H^4_H(\hat{Z};\mathbb{C}) \cap H^{2,2}(\hat{Z}_p;\mathbb{C})\right] =: H^{2,2}_H(\hat{Z}_p;\mathbb{C}) \quad \text{and} \quad H^{2,2}_V(\hat{Z}_{\mathrm{m}};\mathbb{C}) \tag{1.4}$$

have the same dimensions for a mirror pair $(\hat{Z}, \hat{Z}_m)$. This article shares the idea of using the dimension $h^{2,2}_V$ of the mirror $\hat{Z}_m$ to find the dimension $h^{2,2}_H$ of the original geometry $\hat{Z}$ with [17, 18]. References [17, 18] used the intersection ring of the vertical subspace of the mirror $\hat{Z}_m$ not just to determine the dimension $h^{2,2}_H(\hat{Z}) = h^{2,2}_V(\hat{Z}_m)$, but also to compute period integrals of $\hat{Z}$.

We combine this intersection ring in the mirror $\hat{Z}_m$ with a stratification of $\hat{Z}_m$ and a long exact sequence of morphisms of mixed Hodge structure, a combination of techniques that ref. [19] used in order to derive the formula for $h^{1,1}$ and $h^{k-1,1}$ of a toric-hypersurface Calabi-Yau k-fold. With this approach, we are not only able to determine the dimensions $h^{2,2}_V(\hat{Z}_m) = h^{2,2}_H(\hat{Z})$, $h^{2,2}_V(\hat{Z}) = h^{2,2}_H(\hat{Z}_m)$ and $h^{2,2}_{RM}(\hat{Z}) = h^{2,2}_{RM}(\hat{Z}_m)$, but also to construct the cycles representing the remaining component, study their geometry, and discuss their different roles in physics applications.

We start with an introductory discussion in section 2, which motivates the study of the space of non-vertical four-cycles (primary horizontal cycles in particular) in the context of the landscape of flux vacua in F-theory compactifications. Using mirror symmetry, we derive a combinatorial formula for $h^{2,2}_V$, $h^{2,2}_H$, and $h^{2,2}_{RM}$, the dimensions of the space of vertical, horizontal and remaining (i.e. non-vertical and non-horizontal) cycles for Calabi-Yau fourfolds obtained as hypersurfaces of toric varieties in section 3. Already in this simple class of Calabi-Yau fourfolds, the remaining component is found to be non-zero in general. We provide several examples in section 4.

A non-zero $H^{2,2}_{RM}(\hat{Z};\mathbb{C})$ already occurs for the family of Calabi-Yau fourfolds $\hat{Z} = \mathrm{K3} \times \mathrm{K3} = S_1 \times S_2$ with a lattice polarization $W_1 \subset H^2(S_1;\mathbb{Z})$ and $W_2 \subset H^2(S_2;\mathbb{Z})$. Here,

$$h^{2,2}_V = \rho_1\rho_2 + 2, \quad h^{2,2}_{RM} = \rho_1(22-\rho_2) + (22-\rho_1)\rho_2, \quad 2 + 2h^{3,1} + h^{2,2}_H = (22-\rho_1)(22-\rho_2), \tag{1.5}$$

where $\rho_i = \mathrm{rank}(W_i)$ [16]. In this example, the Poincaré duals of $H^{2,2}_{RM}(\hat{Z})$ are not represented by algebraic four-cycles.

Section 5 shows another example of a family $\pi : \mathcal{Z} \longrightarrow \mathcal{M}_*$ where $h^{2,2}_{RM} \neq 0$ and provides some more intuition for the geometry relevant to cycles in $h^{2,2}_{RM}$. This family is a simple example within the class of Calabi-Yau fourfolds motivated by [20, 21] for F-theory compactification where SU(5) unification symmetry is broken down to that of the Standard Model $\mathrm{SU}(3)_c \times \mathrm{SU}(2)_L \times \mathrm{U}(1)_Y$ without the hypercharge $\mathrm{U}(1)_Y$ vector field becoming massive. The remaining component $H^{2,2}_{RM}(\hat{Z})$ in this family contains forms that are Poincaré dual to four-cycles which are non-vertical, but still algebraic over generic points in moduli space. This observation plays an important role in the discussion of section 2, which discusses the relevance of the real primary horizontal subspace $H^4_R(\hat{Z};\mathbb{R}) \subset H^4(\hat{Z};\mathbb{R})$ in the context of the landscape of flux vacua in F-theory compactification.

In section 6, we discuss how the abundance of flux vacua depends on the unification group, and the number of generations. Under rather general assumptions, the dependence on the number of generations is found to factor from the distribution and to be given by a

JHEP01(2015)047

Gaussian quite generically for any choice of base manifold. We also develop an estimate for the dependence of the number of flux vacua on the gauge (unification) group, generalizing earlier attempts in [16]. We estimate that the abundance of flux vacua with e.g. gauge group SU(5) is suppressed by a factor of roughly $e^{\mathcal{O}(1000)}$ when compared to models with no non-abelian gauge group. One can think of this surpression as a fine-tuning wildly surpassing the fine-tuning of 10^{-120} needed to explain the smallness of the cosmological constant. Appendix B contains a further elaboration of how such estimates may be obtained. Finally, we discuss several open problems reserved for future investigation in section 7.

The appendices A and C mostly contain supplementary material and applications. Appendix A reviews details of the geometry of F-theory GUTs with gauge group SU(5) relevant for section 5. Appendix A.3 explains how to compute the Hodge diamond of exceptional divisors in such a geometry by using stratification. Appendix C reviews the construction of chirality-inducing four-form flux, and computation of the D3-tadpole from the geometry and this flux. The numerical results in the appendices B and C are used as input for the discussion in section 6.

A letter [22] by the same authors is focused on a subset of the subjects discussed in this article, and is addressed to a broader spectrum of readers. It covers the subjects of sections 2 and 6 and uses the results of section 4.4.1 and the appendices B and C, while omitting the (mostly technical) material of sections 3 and 5.

2 Ensembles of F-theory flux vacua and the primary horizontal subspace

Supersymmetric compactification of F-theory to 3+1-dimensions is specified by a set of data $(X, B_3, J, G^{(4)})$, where $\pi_X : X \longrightarrow B_3$ is an elliptic fibration with a section, $J \in H^{1,1}(B_3;\mathbb{R})$ a Kähler form on B_3 and a G_4 a four-form flux in $[H^4(X;\mathbb{Z})]_{\text{shift}}$. Once $G^{(4)}$ is given topologically, the superpotential $W \propto \int_X \Omega_X \wedge G^{(4)}$ determines the vacuum expectation value of the complex structure of X, B_3, π_X etc. For an ensemble of fluxes in $[H^4(X;\mathbb{Z})]_{\text{shift}}$, therefore, we obtain an ensemble of low-energy effective theories in 3+1-dimensions, called a landscape.

Flux compactification not only determines the values of low-energy coupling constants, but also the gauge group. Once the complex structure of the elliptic fibration $\pi_X : X \longrightarrow B_3$ is determined by the mechanism above, we know the configuration of 7-branes (i.e. the discriminant locus of π_X). Now, remember that we usually classify low-energy effective theories in their algebraic information such as gauge group, matter representations and unbroken symmetry first, in their topological information such as the number of generations next, and then finally in their values of the coupling constants. It is thus desirable to be able to classify flux vacua in a landscape also in the same way, sorting out first in the algebraic information, secondly in the topological data and finally in the moduli data [16]. This requires to work out what kind of topological flux $G^{(4)}$ results in an effective theory with a given algebraic and topological information.

In order to address this problem, it is useful to consider a family of elliptically fibred Calabi-Yau fourfolds characterized as follows [16]. First, let us choose $(B_3, [S])$ and an algebra R. We specify only the topology of an algebraic three-fold B_3, and let $[S]$ be a

JHEP01(2015)047

divisor class in $\mathrm{Pic}(B_3)$. R is an algebra in the A-D-E series, to be used for a unification group of one's interest. The family $\pi : \mathcal{X} \longrightarrow \mathcal{M}_*^R$ is that of *smooth* Calabi-Yau fourfolds X with an elliptic fibration $\pi_X : X \longrightarrow B_3$ with a section, so that there is a locus of singular fibres of type[2] R along a divisor S of B_3 that belongs to the class $[S]$. The restricted moduli space $\mathcal{M}_*^R$ parametrizes the complex structure of such fourfolds X. For a generic point $p \in \mathcal{M}_*^R$, the corresponding fourfold $X_p := \pi^{-1}(p)$ has the property that $\left[H^{1,1}(X_p;\mathbb{Q}) \cap H^2(X;\mathbb{Q})\right]$ is generated by divisors in the base, the zero-section σ, and $\{\hat{\mathcal{C}}_i\}_{i=1,\cdots,\mathrm{rank}(R)}$ called Cartan divisors. Such a family over the restricted moduli space $\mathcal{M}_*^R$ is a useful notion to express the flux vacua distribution, as we see in eqs. (2.8), (2.9).

There are a couple of physical conditions to be imposed on the fluxes. First of all, the flux preserves the $\mathrm{SO}(3,1)$ symmetry in the effective theory on 3+1-dimensions if and only if the flux $G^{(4)}$ does not have a component that has either "two legs in the T^2 fibre" or "no legs in the T^2 fibre" [23]. This condition is best paraphrased as

$$\sigma \wedge \eta \wedge G^{(4)} = 0, \qquad \eta_1 \wedge \eta_2 \wedge G^{(4)} = 0, \tag{2.1}$$

where σ is (the differential form Poincaré dual to) the zero section, and η, $\eta_{1,2}$ are divisors on B_3, see [24–28]. The D-term condition (equivalently $\mathcal{N} = 1$ supersymmetry condition, primitiveness condition) is that

$$J \wedge G^{(4)} = 0 \in H^6(X;\mathbb{R}). \tag{2.2}$$

The subspace of $[H^4(X;\mathbb{Z})]_{\mathrm{shift}}$ satisfying the two conditions above, (2.1), (2.2), is denoted by $[H^4(X;\mathbb{Z})]_{\mathrm{shift}}^{\mathrm{Lor.prim.}}$. The subspace of $H^4(X;\mathbb{Z})$ without the shift by $c_2(TX)/2$ satisfying the condition (2.1), (2.2) is denoted by $[H^4(X;\mathbb{Z})]^{\mathrm{Lor.prim.}}$.

For a pair of fluxes $G_1^{(4)}$ and $G_2^{(4)}$ in $[H^4(X;\mathbb{Z})]_{\mathrm{shift}}^{\mathrm{Lor.prim.}}$ to preserve the same symmetry group within the 7-brane gauge group R, their difference needs to satisfy

$$i_{\hat{\mathcal{C}}_i}^* \left(G_1^{(4)} - G_2^{(4)}\right) = 0 \in H^4(\hat{\mathcal{C}}_i;\mathbb{Z}), \tag{2.3}$$

where $i_{\hat{\mathcal{C}}_i} : \hat{\mathcal{C}}_i \hookrightarrow X$ is the embedding of the Cartan divisors (generators) $\{\hat{\mathcal{C}}_i\}_{i=1,\cdots,\mathrm{rank}(R)}$. Thus, we formulate an ensemble of fluxes leading to effective theories with a common unbroken symmetry group as

$$\left\{G_{\mathrm{tot}}^{(4)} = G_{\mathrm{scan}}^{(4)} + G_{\mathrm{fix}}^{(4)} \mid G_{\mathrm{scan}}^{(4)} \in H_{\mathrm{scan}}\right\}; \tag{2.4}$$

we choose $G_{\mathrm{fix}}^{(4)}$ and H_{scan} such that $G_{\mathrm{scan}}^{(4)} = 0$ is contained in H_{scan}. $G_{\mathrm{fix}}^{(4)}$ must be in $[H^4(X;\mathbb{Z})]_{\mathrm{shift}}^{\mathrm{Lor.prim.}}$, while H_{scan} needs to be a sub-*set* of the cohomology group $H^4(X;\mathbb{Z})$ satisfying all the conditions (2.1), (2.2), (2.3). Because all of these conditions[3] are linear in $G^{(4)}$, we always take H_{scan} to be a sub-*group* of $H^4(X;\mathbb{Z})$.

We now argue that the real primary horizontal subspace $H_H^4(X;\mathbb{R}) \subset H^4(X;\mathbb{R})$ satisfies all of the conditions (2.1), (2.2), (2.3) modulo $\otimes\mathbb{R}$, and we can hence take H_{scan} to

[2] Here, 'type R' singular fibre means that at a generic point in S, the dual graph of the fibre is given by the extended Dynkin diagram of R.

[3] The condition from D3-brane tadpole is treated separately from the conditions discussed above.

JHEP01(2015)047

contain all of $H^4_H(X;\mathbb{R}) \cap H^4(X;\mathbb{Z})$. To see this, we take a little moment to provide a brief review on the definition of $H^4(X;\mathbb{C})$, and to make clear what we mean by the *real* primary horizontal subspace. For any point $p \in \mathcal{M}^R_*$, we can define a subspace

$$\begin{aligned}&\mathrm{Span}_{\mathbb{C}}\left\{\Omega_{X_p}, D\Omega_{X_p}, D^2\Omega_{X_p}, D^3\Omega_{X_p}, D^4\Omega_{X_p}\right\} \\ &= H^{4,0}(X_p,\mathbb{C}) \oplus H^{3,1}(X_p;\mathbb{C}) \oplus H^{2,2}_H(X_p;\mathbb{C}) \oplus H^{1,3}(X_p;\mathbb{C}) \oplus H^{0,4}(X_p;\mathbb{C}) \subset H^4(X;\mathbb{C}).\end{aligned} \tag{2.5}$$

The cohomology group $H^4(X;\mathbb{C}) = \mathbb{C} \otimes H^4(X;\mathbb{Z})$ is topological; there is a canonical identification between $H^4(X_p;\mathbb{C})$ and $H^4(X_{p'};\mathbb{C})$ for p, p' in a small neighbourhood in $\mathcal{M}_*$ — called flat structure — and the reference to $p \in \mathcal{M}_*$ is suppressed in the expression above. The (p,q)-Hodge components with the canonical identification relative to $H^4(X;\mathbb{C})$, however, vary over $p \in \mathcal{M}^R_*$. The fact that the Picard-Fuchs equations on the period integral are closed in the subspace specified above, however, implies that the space (2.5) remains the same in $H^4(X;\mathbb{C})$ for every $p \in \mathcal{M}_*$ (at least locally) under the canonical identification (flat structure). A reference to $p \in \mathcal{M}^R_*$ is hence suppressed and the invariant subspace is called the primary horizontal subspace $H^4_H(X;\mathbb{C})$. The remaining component in the decomposition (1.2), $H^{2,2}(X_p;\mathbb{C})$, should therefore be independent of $p \in \mathcal{M}_*$ under the canonical identification. This is why reference to $p \in \mathcal{M}_*$ is completely dropped in (1.2); the decomposition (1.2) is topological.

The four-form flux in M-theory/F-theory compactification is real-valued, while the primary horizontal subspace $H^4_H(X;\mathbb{C})$ is complex-valued. Noting, however, that the complex conjugation operation is compatible with the canonical identification (topological tracking) of $H^4(X_p;\mathbb{C})$ for $p \in \mathcal{M}_*$, we also have a decomposition of the real part $H^4(X;\mathbb{R})$:

$$H^4(X;\mathbb{R}) = H^4_H(X;\mathbb{R}) \oplus H^{2,2}_{RM}(X;\mathbb{R}) \oplus H^{2,2}_V(X;\mathbb{R}), \tag{2.6}$$

just like in (1.2). The "primary horizontal subspace" component of $H^4(X;\mathbb{R})$ is what we call the real primary horizontal subspace $H^4_H(X;\mathbb{R})$.

Now, let us see that the four-forms in the real primary horizontal subspace $H^4_R(X;\mathbb{R})$ satisfy all the conditions (2.1), (2.2), (2.3) modulo $\otimes\mathbb{R}$. First, noting that $\sigma \cdot \eta$ and $\eta_1 \cdot \eta_2$ in (2.1) form only a subset of generators of the vertical four-cycles, and that all of the elements of the horizontal component are orthogonal to those in the vertical component in (1.2), it is straightforward to see that the four-forms in $H^4_H(X;\mathbb{R})$ satisfy (2.1).

In order to verify the primitiveness condition, consider the $(h^{3,1}+1) = (m+1)$-dimensional variety occupied by the complex line $\mathbb{C}[\Omega_{X_p}]$ (this is a $\mathbb{C}^\times$-cone over the period domain). Any four-form G in this variety satisfies the condition (2.2), because G is a $(4,0)$-form for some choice $p \in \mathcal{M}_*$ of complex structure on X, and $J \wedge G$ would have become a $(5,1)$-form under that complex structure, if it were non-zero. The absence of such a Hodge component in a Calabi-Yau fourfold X implies that $J \wedge G = 0$. Since all kinds of four-forms in $H^4_H(X;\mathbb{C})$ are obtained by taking derivatives of such G with respect to the local coordinates in $\mathcal{M}_*$, we find that all the four-forms in the (real) horizontal primary subspace satisfy the primitiveness condition (2.2).

Finally, we can make a similar argument to show that the four-forms in $H^4_H(X;\mathbb{R})$ satisfy the condition (2.3). Consider again the set of four-forms realized in the form of Ω_{X_p}

JHEP01(2015)047

for some $p \in \mathcal{M}_*$. Its pull-back to any one of Cartan divisors $\hat{\mathcal{C}}_i$ must be a $(4,0)$-form on a complex *three*-fold $\hat{\mathcal{C}}_i$ under the complex structure of $p \in \mathcal{M}_*$ induced on $\hat{\mathcal{C}}_i \subset X_p$. Thus, the pull-back of such a four-form vanishes in $H^4(\hat{\mathcal{C}}_i;\mathbb{C})$. Taking derivatives with respect to the local coordinates of $\mathcal{M}_*$, we find that the four-forms in $H^4_H(X;\mathbb{R})$ satisfy the condition (2.3).

References [14, 15, 29] studied how the flux vacua are distributed in the complex structure moduli space for ensembles of fluxes of the form (2.4). One of the two key ideas is to replace the vacuum distribution by the vacuum index distribution

$$d\mu_I := d^{2m}z \sum_{G^{(4)}_{\rm scan}\in H_{\rm scan}} \delta^{2m}(DW,\overline{DW})\det\begin{bmatrix} DDW & D\overline{DW} \\ \overline{D}DW & \overline{DDW}\end{bmatrix}_{2m\times 2m} \Theta\left(L_* - \frac{1}{2}(G^{(4)}_{\rm tot})^2\right), \tag{2.7}$$

so that the problem becomes easier. $(z,\bar{z})$ are local coordinates of $\mathcal{M}_*$, $W \propto \int_X \Omega_{X_p}\wedge G^{(4)}$ and L_* is the upper bound of the D3-brane charge allowed for the fluxes $G^{(4)}_{\rm tot}$. The other idea is to make a continuous approximation to $H_{\rm scan}$, which is to treat the subgroup $H_{\rm scan} \subset H^4(X;\mathbb{Z})$ as a vector space $H_{\rm scan}\otimes\mathbb{R}$, and to replace the sum by an integral over the vector space $H_{\rm scan}\otimes\mathbb{R}$. Under the continuous approximation, the vacuum index density $d\mu_I$ is of the form [14, 15] ($L_* \gg K$)

$$d\mu_I \simeq \frac{(2\pi L_*)^{K/2}}{\Gamma(K/2)}\,\rho_I, \qquad K := \dim_{\mathbb{R}}\left(H_{\rm scan}\otimes\mathbb{R}\right), \tag{2.8}$$

where ρ_I is an (m,m) form on $\mathcal{M}_*$. It is given as the Euler class of some real $\mathrm{rank}_{\mathbb{R}} = 2m$ vector bundle on $\mathcal{M}_*$ [29], and can be put in the explicit form

$$\rho_I = c_m(T\mathcal{M}_*\otimes\mathcal{L}^{-1}) = \det\left[-\frac{R}{2\pi i} + \frac{\omega}{2\pi}\mathbf{1}_{m\times m}\right], \tag{2.9}$$

where ω is the Kähler form on $\mathcal{M}_*$ derived from $K = -\ln[\int\Omega\wedge\overline{\Omega}]$, and $\mathcal{L}$ a line bundle satisfying $c_1(\mathcal{L}^{-1}) = \omega/(2\pi)$, whenever the vector space $H_{\rm scan}\otimes\mathbb{R}$ contains the real primary horizontal subspace $H^4_H(X;\mathbb{R})$ [14–16, 29].

Having reminded ourselves of how $H_{\rm scan}$ is used, let us return to the question of how we should take $G^{(4)}_{\rm fix}$ and $H_{\rm scan}$. The problem we set in this article (and also in [16, 22]) is to classify the fluxes in $[H^4(X;\mathbb{Z})]^{\rm Lor.prim.}_{\rm shift}$ into sub-ensembles of the form (2.4) so that each subensemble corresponds to the ensemble of low-energy effective theories with a given set of algebraic (or algebraic and topological) information. $G^{(4)}_{\rm fix}$ is used as a tag of the subensemble. Apart from [16], the $H^{2,2}_{RM}(X;\mathbb{R})$ component has not been carefully discussed (at least from the perspective of the geometry of Calabi-Yau fourfolds) in the context of F-theory phenomenology to our knowledge. In order to address this problem, therefore, it is necessary to reopen the case and understand carefully how the low-energy effective theories are controlled by the fluxes in each one of the components of the decomposition (2.6).

First of all, it is already known that $h^{2,2}_{RM}$ can be non-zero in a family of $X = \mathrm{K3}\times\mathrm{K3}$ [16], as we have already reviewed in the introduction. We will prove in section 5 that the class of families of elliptic fibred Calabi-Yau fourfolds for F-theory compactification with SU(5) unification results in $h^{2,2}_{RM} \neq 0$ precisely in the cases that are well-motivated

JHEP01(2015)047

for a mechanism of SU(5) symmetry breaking in [20, 21]. Despite the presence of the $H^{2,2}_{RM}(X;\mathbb{R})$ component in the middle cohomology, however, we have confirmed (see also the detailed discussion in the appendix A.4 of this article) that the matter surfaces for $\mathbf{10}+\overline{\mathbf{10}}$ representations and also $\bar{\mathbf{5}}+\mathbf{5}$ representations of SU(5) belong to topological classes of $H^{2,2}_{V}(X;\mathbb{Q})$, confirming [25]. This means that the net chirality of these representations is controlled by the flux in the $H^{2,2}_{V}(X;\mathbb{R})$ component.

It has also been indicated that fluxes in $H^{2,2}_{RM}(X;\mathbb{R})$ may break the symmetry of the 7-brane gauge group R based on the family $X = \mathrm{K3}\times\mathrm{K3}$ [16]. Certainly this family is not suitable for realistic compactifications of F-theory in that all the matter fields in the relatively light spectrum are in the adjoint representation of R; this family may also be somehow special in that $h^{2,0}(X) \neq 0$. However, we have confirmed that the flux in the $H^{2,2}_{RM}(X;\mathbb{R})$ component may indeed break the symmetry R; the hypercharge flux of [20, 21] turns out to be precisely in this category.

Given all the observations above we conclude that $H_{\mathrm{scan}}\otimes\mathbb{R}$ should be chosen such that it contains all of the horizontal component $H^4_H(X;\mathbb{R})$ and possibly a part of $H^{2,2}_{RM}(X;\mathbb{R})$. Clearly, $H_{\mathrm{scan}}\otimes\mathbb{R}$ should not contain the entire $H^{2,2}_{RM}(X;\mathbb{R})$ for sub-ensemble of fluxes (2.4) to correspond to an ensemble of effective theories with a given set of algebraic and topological information. An example of the family of $X = \mathrm{K3}\times\mathrm{K3}$ suggests strongly that we should choose $(H_{\mathrm{scan}}\otimes\mathbb{R})$ to be precisely the horizontal component, because any flux in $H^{2,2}_{RM}(X;\mathbb{R})$ breaks some of the 7-brane gauge group and Higgses away vector bosons from the low-energy spectrum in this example. We remain inconclusive about the case of families for realistic F-theory compactification with $(B_3,[S],R)$ (with $R = A_4, D_5$ etc.), however, because the discussion in sections 3 and 5 provides only a partial understanding of the geometry of the $H^{2,2}_{RM}(X;\mathbb{R})$ component. This material is enough, however, to conclude that the formula (2.8), (2.9) of [14, 15] can be used for the ensemble of effective theories with a given algebraic and topological information. In the examples of elliptic fourfolds for F-theory compactification studied in section 4.4 of this paper, the remaining component $H^{2,2}_{RM}(X;\mathbb{R})$ is absent, so that the horizontal component can be identified with $H_{\mathrm{scan}}\otimes\mathbb{R}$.

We have so far assumed that smooth Calabi-Yau fourfolds X with flat elliptic fibration are used for F-theory compactifications with fluxes; it should be rememebered, however, that it is a belief rather than a fact that such smooth models X should be used instead of the Weierstrass models X_s, which are singular for compactifications leading to effective theories with unbroken non-Abelian gauge groups. There may be alternative and/or equivalent formulations of fluxes that lead to the same physics end results. Even when we pursue the direction of using smooth models X, there can be more than one choice of such a smooth model X. All of those different resolutions, however, should describe the low-energy physics of the same vacuum with an unbroken unified symmetry. Thus, no matter how fluxes in F-theory are formulated, all the observable physics consequences should not depend on the choice of resolutions. The dimension of the primary horizontal component ($(H_{\mathrm{scan}}\otimes\mathbb{R})$ to be more precise) should be regarded as one of such physical consequences of F-theory, and hence $K = \dim_{\mathbb{R}}[H^4_H(X;\mathbb{R})]$ must not depend on the choice of the smooth model X for a singular X_s.

JHEP01(2015)047

There is a general argument that is good enough to make us consider that the dimensions of $h^{2,2}_V(X;\mathbb{R})$, $h^{2,2}_H(X;\mathbb{R})$ and $h^{2,2}_{RM}(X;\mathbb{R})$ are resolution independent. It seems reasonable to assume that, for a singular Calabi-Yau fourfold (X_s), any crepant resolution (X) gives rise to the same complex structure moduli space. If this holds, the dimension of the space of primary horizontal (2, 2) cycles, $h^{2,2}_H(X;\mathbb{R})$, as well as $h^{3,1}(X)$ cannot depend on the resolution. By mirror symmetry, the same statement must be true also for the space of primary vertical (2, 2) cycles $h^{2,2}_V(X;\mathbb{R}) = h^{2,2}_H(X_m;\mathbb{R})$, and $h^{1,1}(X) = h^{3,1}(X_m)$, where we assume that all the different resolutions X for X_s share some mirror geometries X_m with a common complex structure moduli space. If furthermore the Euler characteristic is invariant under which resolution is used, it follows that also $h^{2,2}$ cannot be resolution dependent. This is because $h^{2,2}$ is not an independent Hodge number but related to all others by (3.62). From the independence of $h^{2,2}_H(X;\mathbb{R})$ and $h^{2,2}_V(X;\mathbb{R})$ on which resolution is used, it then follows that also $h^{2,2}_{RM}(X;\mathbb{R})$ is independent of the resolution.

The two assumptions we have made are obvious for a Calabi-Yau manifold X given as a hypersurface (or, more generally, complete intersection) in a toric ambient space: for a fixed singular Calabi-Yau manifold, different crepant resolutions correspond to different triangulations of the N-lattice polytope whereas all Hodge numbers, and, in particular the complex structure moduli space depend on the combinatorics of the N- and M-lattice polytopes, but not on triangulations. We will give a more specific proof of this for the expressions we derive in the hypersurface case in section 3.6.3.

More generally, our assumptions follow if different resolutions correspond to different cones in the extended Kähler moduli space, so that they are connected by flop transitions, which are known to leave both the complex structure moduli space and the Euler characteristic invariant. This state of affairs is realized in the geometries which are the main motivation for the present work: F-theory on Calabi-Yau fourfolds supporting non-abelian gauge groups [30–35].

Let us leave a few remarks at the end of this section in order to clarify what the vacuum index density distribution $d\mu_I$ is for, as well as what it is not (yet) for. These are more or less known things, and we include this discussion in this article only as reminder.

The first remark is that a family $\pi : \mathcal{X} \longrightarrow \mathcal{M}^R_*$ for some choice of symmetry R and topology of $(B_3, [S])$ is used to describe the distribution of a subensemble of flux vacua that is *inclusive* in nature. Even though the scanning component of the flux, $G^{(4)}_{\text{scan}}$, is chosen from the real primary *horizontal* component $H^4_H(\hat{Z};\mathbb{R}) \subset H^4(\hat{Z};\mathbb{R})$, it may eventually end up with the Poincaré dual of a algebraic cycle as a result of dynamical relaxation of the complex structure moduli due to the superpotential $W \propto \int \Omega \wedge G^{(4)}$. The delta function $\delta^{2m}(DW, \overline{DW})$ for a given $G^{(4)}_{\text{scan}}$ eventually has a support on a point p in a Noether-Lefschetz locus of $\mathcal{M}^R_*$; see [16, 18, 24] and references therein. For some choice of $G^{(4)}_{\text{scan}}$ (and its corresponding $p \in \mathcal{M}^R_*$) not only the rank of $H^{2,2}(X_p;\mathbb{R}) \cap H^4(X_p;\mathbb{Z})$, but even the rank of $H^{1,1}(X_p;\mathbb{R}) \cap H^2(X_p;\mathbb{Z})$ may be enhanced.[4] For the effective theory corresponding

[4]Depending on what conditions to impose mathematically on behaviour of the family $\mathcal{X} \longrightarrow \mathcal{M}^R_*$ at special loci, the enhancement of the rank of $\text{Pic}(X_p)$ may be phrased differently. The mathematical conditions to impose should ultimately be determined by the (yet unknown) microscopic formulation of F-theory.

JHEP01(2015)047

to such a choice of $G^{(4)}_{\rm scan}$, this can result in an enhanced gauge symmetry forming a hidden sector in addition to the gauge group R, or the symmetry R is enhanced to another R' containing R. Such a subensemble of fluxes with $(H_{\rm scan}\otimes\mathbb{R}) = H^4_H(X;\mathbb{R})$ for $(B_3,[S],R)$ therefore contains not just effective theories with the 7-brane gauge group being precisely R, but also those with an extra factor of gauge group, or those with the 7-brane gauge group larger than R. In this sense, the subensemble (and the distribution $d\mu_I$) captured on the moduli space $\mathcal{M}^R_*$ is an *inclusive* ensemble. With the expectation that only a very small fraction of such an inclusive ensemble has a hidden sector or enhanced symmetry, however, we will refer to vacua in such an ensemble as those with symmetry R; the fraction of such vacua can be estimated by using the discussion in section 6 and the appendix B, and we see the fraction is exponentially small indeed.

Secondly, let us record our understanding of the issue of potential instabilities. Given a topological flux $G^{(4)}_{\rm tot} = G^{(4)}_{\rm scan} + G^{(4)}_{\rm fix}$, we may not be able to find a solution to $DW = 0$ within the restricted moduli space $\mathcal{M}^R_*$. Such a flux, if there is any, has been removed automatically from the ensemble by the time the continuous approximation $H_{\rm scan} \longrightarrow H_{\rm scan}\otimes\mathbb{R}$ is introduced and the distribution $d\mu_I$ is cast into the form of (2.8). When the flux space integral is carried out, the delta-function picks up contributions only from fluxes that satisfy $DW = 0$ somewhere in $\mathcal{M}^R_*$. This argument may be, however, only about the instability issue associated with $DW = 0$ for moduli along $\mathcal{M}^R_*$, i.e., R-singlet moduli. Instability associated with physical "moduli" transverse to $\mathcal{M}^R_*$ may be captured by the effective superpotential $W = \int_S {\rm tr}[\varphi\wedge F]$ of [36, 37].

Thirdly and finally, the Kähler moduli have been (and will be) treated in this work as if they were given by hand, but their stabilization of course also has to be studied separately. The distribution (2.8), (2.9) on the moduli space of complex structure $\mathcal{M}_*$ needs to be convoluted with other data, including stabilization of Kähler moduli and dynamical evolution of cosmology in the early universe. There is nothing to add in this article to this well-known zoom-out picture, aside from reminding ourselves that it may make sense to study the distribution over the complex structure moduli space separately from Kähler moduli stabilization when there is a separation of scales between the stabilization of two distinct sets of moduli. In this case the two problems can be treated separately and then be combined, rather than facing the mixed problem.

3 $H^{2,2}$ of a Calabi-Yau fourfold hypersurface of a toric variety

Suppose that $\hat{Z}$ is a smooth variety and $\{\hat{Y}_i\}$ a set of its divisors. We can introduce the following stratification to $\hat{Z}$:

$$\hat{Z} = (\hat{Z}\setminus\cup_i\hat{Y}_i)\amalg\Big(\cup_i\hat{Y}_i\setminus(\cup_{kj}\hat{Y}_k\cap\hat{Y}_j)\Big)\amalg\cdots\,. \tag{3.1}$$

The first stratum, $Z := \hat{Z}\setminus\cup_i\hat{Y}_i$, is the only one that has the same dimension as $\hat{Z}$; we call it the primary stratum. For the pair $\hat{Z}$ and $Y := \hat{Z}\setminus Z$, there is the long exact sequence (3.11). It was with this exact sequence in combination with the mixed Hodge structure on these cohomology groups that ref. [19] derived a formula of $h^{1,1}(\hat{Z})$ and $h^{n-2,1}(\hat{Z})$ for a Calabi-Yau $(n-1)$-fold hypersurface of a toric n-fold and showed the beautiful mirror correspondence.

JHEP01(2015)047

We find that the same combination of methods — stratification (3.1) and mixed Hodge structure — is also very useful in studying various properties of algebraic cycles in $\hat{Z}$ even when $\hat{Z}$ is not necessarily realized as a hypersurface of a toric variety. Section 5 of this article uses this combination to study the space of vertical cycles of general fourfolds $\hat{Z}$, whereas we can derive stronger results in the case $\hat{Z}$ is a Calabi-Yau $(n-1)$-fold hypersurface of a toric n-fold. In the latter case, which is discussed in the present section, the Hodge-Deligne numbers of the cohomology of the primary stratum can be easily computed by following [38].

By carefully examining the contributions to $H^{2,2}(\hat{Z})$ and using mirror symmetry, we are able to isolate the pieces $h^{2,2}_V(\hat{Z}) = h^{2,2}_H(\hat{Z}_m)$, $h^{2,2}_H(\hat{Z}) = h^{2,2}_V(\hat{Z}_m)$ and $h^{2,2}_{RM}(\hat{Z}) = h^{2,2}_{RM}(\hat{Z}_m)$. The results are given in section 3.6.

3.1 General setup and known results

Let us start by fixing our notation and reviewing some helpful facts; subtleties associated with singularity resolution are summarized in section 3.1.1. Helpful reviews on toric geometry may be found in [39, 40].

A toric variety $\mathbb{P}^n_\Sigma$ can be constructed from a fan Σ, which is composed of strictly convex polyhedral cones in $\mathbb{R}^n$ for a lattice $N := \mathbb{Z}^{\oplus n}$. The dual lattice is denoted by $M = \mathbb{Z}^{\oplus n}$ and the pairing between them for $\nu \in N$ and $\tilde{\nu} \in M$ is denoted by $\langle \nu, \tilde{\nu} \rangle \in \mathbb{Z}$. We also use the notation $N_\mathbb{R} := N \otimes \mathbb{R}$ and $M_\mathbb{R} := M \otimes \mathbb{R}$. For a given fan Σ, $\Sigma(k)$ stands for the collection of all the k-dimensional cones. $\Sigma(0) = \{\vec{0} \in N\}$. We denote the k-skeleton $\cup_{i=0}^k \Sigma(i)$ by $\Sigma[k]$.

By definition, an n-dimensional toric variety contains an open algebraic torus $(\mathbb{C}^*)^n = \mathbb{T}^n$. From this perspective, a fan Σ gives information on how $\mathbb{T}^n$ is compactified. In particular, the fan determines a stratification into algebraic tori of lower dimension: simplicial cones of Σ are in one-to-one correspondence with strata of $\mathbb{P}^n_\Sigma$ such that a k-dimensional cone $\sigma \in \Sigma(k)$ corresponds to a stratum of $\mathbb{P}^n_\Sigma$ isomorphic to $(\mathbb{T})^{n-k}$. For cone σ, we denote the corresponding stratum by $\mathbb{T}_\sigma$.

A lattice polytope is the convex hull in $N_\mathbb{R}$ (or $M_\mathbb{R}$) of a number of lattice points of the lattice N (or M). For a lattice polytope Δ in M the polar (or dual) polytope $\widetilde{\Delta}$ (in N) is defined as

$$\widetilde{\Delta} := \{v \in N_\mathbb{R} | \langle v, w \rangle \geq -1 \quad \forall w \in \Delta\}\,. \tag{3.2}$$

If $\widetilde{\Delta}$ is a lattice polytope as well, it follows that Δ is also the polar of $\widetilde{\Delta}$ and the two are called a reflexive pair. An elementary property which follows from reflexivity is that the origin is the only integral point which is internal to the polytope. Faces of an n-dimensional polytope Δ are denoted by their dimensions[5] as $\Theta^{[n-k]}$. For a pair of reflexive polytopes Δ in $M_\mathbb{R}$ and $\widetilde{\Delta}$ in $N_\mathbb{R}$, there is a one-to-one correspondence between faces $\Theta^{[n-k]}$ of Δ and faces $\widetilde{\Theta}^{[k-1]}$ of $\widetilde{\Delta}$. We frequently use $(\widetilde{\Theta}^{[n-k]}, \Theta^{[k-1]})$ to indicate such a pair of dual faces. Note that an n-dimensional polytope can be considered as its own n-dimensional face. We indicate that a face Θ_a is on a face Θ_b by writing $\Theta_a \leq \Theta_b$. We let $\ell(\Theta)$ stand for the

[5] Faces of a polytope Δ are often referred to in the literature by their codimensions. Codimension-1 faces of Δ are called facets, for example. So, we reserve a notation $\Theta^{(k)} = \Theta^{[n-k]}$ for codimension-k faces, although we are not using this notation in the present article.

JHEP01(2015)047

number of integral points on a face Θ and $\ell^*(\Theta)$ for the number of integral points interior to Θ. The p-skeleton of Δ, i.e. the union of all faces of Δ which have dimension p or less is denoted by $\Delta_{\leq p}$.

Given a reflexive polytope $\widetilde{\Delta}$ we can easily construct a fan Σ by forming the cones over all faces of $\widetilde{\Delta}$. The one-to-one correspondence between $(k-1)$-dimensional faces $\{\widetilde{\Theta}^{[k-1]}\}$ and k-dimensional cones $\Sigma(k)$ in $N_{\mathbb{R}}$ (resp. between $\{\Theta^{[k-1]}\}$ and $\widetilde{\Sigma}(k)$ in $M_{\mathbb{R}}$) is described in the form of a map $\sigma : \{\widetilde{\Theta}^{[k-1]}\} \longrightarrow \Sigma(k)$ (resp. $\tilde{\sigma} : \{\Theta^{[k-1]}\} \longrightarrow \widetilde{\Sigma}(k)$).

Well-known formulae [19, 41, 42] for the Hodge numbers of a Calabi-Yau $(n-1)$-fold hypersurface $\hat{Z}$ are recorded here in the notation adopted above:

$$h^{1,1}(\hat{Z}) = \ell(\widetilde{\Delta}) - (n+1) - \sum_{\widetilde{\Theta}^{[n-1]}} \ell^*(\widetilde{\Theta}^{[1]}) + \sum_{(\widetilde{\Theta}^{[n-2]},\Theta^{[1]})} \ell^*(\widetilde{\Theta}^{[n-2]})\ell^*(\Theta^{[1]})\,, \tag{3.3}$$

$$h^{n-2,1}(\hat{Z}) = \ell(\Delta) - (n+1) - \sum_{\Theta^{[n-1]}} \ell^*(\Theta^{[n-1]}) + \sum_{(\Theta^{[n-2]},\widetilde{\Theta}^{[1]})} \ell^*(\Theta^{[n-2]})\ell^*(\widetilde{\Theta}^{[1]})\,, \tag{3.4}$$

$$h^{m,1}(\hat{Z}) = \sum_{(\widetilde{\Theta}^{[n-m-1]},\Theta^{[m]})} \ell^*(\widetilde{\Theta}^{[n-m-1]})\ell^*(\Theta^{[m]}) \quad \text{for} \quad n-2 > m > 1. \tag{3.5}$$

3.1.1 Triangulations, smoothness and projectivity

The polytope Δ in $M_{\mathbb{R}}$ is regarded as the Newton polyhedron of the defining equation of a Calabi-Yau hypersurface Z_s in $\mathbb{P}^n_{\Sigma}$. Because Z_s is not smooth, in general, we are interested in its projective crepant resolution; $\hat{Z}$ in (3.3)–(3.5) stands for such a resolution. Such resolutions may always be constructed from the data of the polytope for $n \leq 4$ [19]. For Calabi-Yau hypersurfaces of complex dimension 4 (or dimensions larger than that), this is not the case, so that we need to explicitly check in each example.

Constructing a fan Σ over the faces of a polytope $\widetilde{\Delta}$, the resulting cones may be non-simplicial or have (lattice-) volume[6] greater than one. Consequently, the toric variety $\mathbb{P}^n_{\Sigma}$ has singularities. We may, however, subdivide the fan Σ to cure such singularities. We denote the corresponding map between fans by $\phi : \Sigma' \longrightarrow \Sigma$. For $\sigma' \in \Sigma'$, $\phi(\sigma')$ is given by the σ'-containing cone $\sigma \in \Sigma$ with the smallest dimension. The map ϕ (resp. $\tilde{\phi}$) induces a toric morphism $\mathbb{P}^n_{\Sigma'} \longrightarrow \mathbb{P}^n_{\Sigma}$ of (partial) singularity resolution.

Such a morphism will preserve the Calabi-Yau condition of a hypersurface if all of the one-dimensional cones introduced are generated by points on the polytope $\widetilde{\Delta}$ (remember that the origin is the only internal point for a reflexive polytope). A (partial) crepant desingularization of Z_s is hence equivalent to finding a triangulation of the polytope $\widetilde{\Delta}$ in which every n-simplex contains the origin. This is called a star triangulation and the origin is the star point. A maximal desingularization of $\mathbb{P}^n_{\Sigma}$ keeping Z_s Calabi-Yau is found by using all points[7] on $\widetilde{\Delta}$. A triangulation using all points of a polytope is called a fine triangulation.

[6] The "lattice volume" of a cone in $\partial\Delta$ is defined by multiplying $k!$ to the volume of a k-dimensional cone cut-off at $\partial\Delta$. The smallest lattice k-simplex has the lattice volume 1.

[7] In fact, it makes sense to relax this requirement, as points which lie in the interior of facets of $\widetilde{\Delta}$ do not lead to divisors intersecting a Calabi-Yau hypersurface. This can be seen as follows: for any facet F we can find a normal vector n_F such that $< n_F, \nu_i > = 1$ for all vectors ν_i on F. This means that the intersection

JHEP01(2015)047

When subdividing cones in Σ, we want the ambient space $\mathbb{P}^n_{\Sigma'}$ to be a projective variety (i.e. it should be a Kähler manifold), which implies projectivity of the Calabi-Yau hypersurface; the Kählerian nature combined with the trivial canonical bundle implies Ricci-flatness. For an n-dimensional toric variety $\mathbb{P}^n_\Sigma$ given in terms of a fan Σ, a Weil divisor $D = \sum_i a_i D_i$ is also Cartier iff we can find a support function ψ_D with the following properties:

- ψ_D is linear on each cone
- For a given cone of maximal dimension, $\sigma \in \Sigma(n)$, ψ_D can be described by an element m_σ of M satisfying
$$\psi_D|_\sigma = < m_\sigma, \nu_i > = -a_i \tag{3.9}$$
for all one-dimensional cones (determined by the primitive vectors ν_i) in σ.

In this language, the cone of ample curves (or, equivalently, the Kähler cone) is described as the set of divisors for which ψ_D is strongly convex. This means that $\psi_D|_\sigma > -a_j$ for all one-dimensional cones *not* in σ and implies that $m_\sigma \neq m_{\sigma'}$ for two different cones σ and σ' in $\Sigma(n)$. If this cone of ample curves is non-empty, we can find a line bundle which is very ample, i.e. it defines an embedding of the toric variety $\mathbb{P}^n_\Sigma$ into $\mathbb{P}^m$ for some m. Conversely, if no strongly convex support function exists, the corresponding toric variety cannot be projective.

A strongly convex support function ψ_D defines a 'lift' of $\tilde{\Delta}$ into $\mathbb{R}^{n+1}$ by assigning the value of ψ_D to each point on $\tilde{\Delta}$. The triangulation can then be seen as the upper facets of the resulting polyhedron in $\mathbb{R}^{n+1}$. Note that strong convexity means that no $n+2$ points of $\tilde{\Delta}$ are mapped to a hyperplane in $\mathbb{R}^{n+1}$, i.e. faces of $\tilde{\Delta}$ which are subdivided into more than one simplex by a triangulation are not coplanar after this lift. Conversely, any triangulation which descends from a triangulation of a lift of $\tilde{\Delta}$ (with the property that no $n+2$ points are on a common non-vertical plane) to $\mathbb{R}^{n+1}$ can be used to construct a projective toric variety. Triangulations with this property are called regular triangulations.

---

ring contains a linear relation of the form
$$\sum_{\nu_i \in F} D_i + \sum_{j \text{ not} \in F} a_j D_j = 0\,, \tag{3.6}$$
with includes some contribution of divisors whose corresponding primitive vectors ν_j are not in F but lie on other facets. Let us now assume we have refined Σ such that there is a point ν_p interior to the facet F. The associated divisor D_p can only have a non-zero intersection with divisors D_k for which ν_k also lies in F, as all others necessarily lie in different cones of the fan Σ. This means that the above relation implies
$$D_p \cdot \sum_{\nu_i \in F} D_i = 0\,, \tag{3.7}$$
where we sum over all toric divisors coming from points on F. The Calabi-Yau hypersurface is given as the zero-locus of a section of $-K_{\mathbb{P}^n_\Sigma} = \sum_j D_j$, where we sum over all toric divisors. We now find
$$D_p \cdot \sum_j D_j = D_p \cdot \sum_{\nu_i \in F} D_i = 0\,, \tag{3.8}$$
by using the same argument again. Hence D_p does not meet a generic Calabi-Yau hypersurface. Correspondingly, a refinement of Σ introducing ν_p does not have any influence.

JHEP01(2015)047

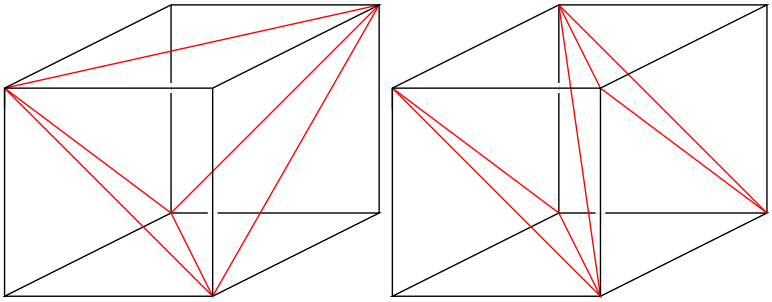

Figure 1. Two fine regular triangulations of a three-dimensional cube. The 'central' 3-simplex of the triangulation on the left has lattice volume 2. As there are no extra lattice points, this triangulation cannot be further refined to become unimodular. Of course the cube shown above does have a unimodular triangulation, as shown on the right. It may happen, however, that the central simplex of the triangulation shown on the left arises as a face of a polytope, in which case no unimodular triangulation can exist.

A maximal projective crepant desingularization (referred to as an *MPCP* of Z_s in [19]) is hence achieved by finding a fine regular star triangulation of $\widetilde{\Delta}$. If all cones of such a triangulation have lattice volume unity the ambient space, and hence the Calabi-Yau hypersurface, become completely smooth and the map $\phi : \Sigma' \to \Sigma$ can rightfully be called a resolution. Triangulations of this type are called unimodular. We will also call simplices of volume unity and cones over such simplices unimodular.

It turns out that unimodular triangulations do not necessarily exist for polytopes of dimension $n \geq 4$. This is only relevant for Calabi-Yau manifolds of dimension ≥ 4 though, as one may always find a triangulation which is 'good enough' in the case of Calabi-Yau threefolds [19]. While any fine triangulation is also unimodular in two dimensions, a simplex can fail to be unimodular in three dimensions or more, even if it does not contain any points besides its vertices. A standard example for this is given in figure 1. For a star triangulation of a reflexive polytope, the lattice volume[8] of any simplex is given by the volume of its 'outward' face, i.e. the face which lies on a facet of $\tilde{\Delta}$. For a polytope of dimension three or less, the facets are at most two-dimensional, so that any fine triangulation is automatically unimodular and the ambient space is smooth. For a Calabi-Yau threefold, the facets of $\tilde{\Delta}$ are three-dimensional. Hence even for a fine triangulation we are not guaranteed a smooth ambient space, as there might be a simplex S with volume greater than unity. However, the singularities which are induced by such cones are point-like: they are located at the intersection of the four divisors spanning S. These points do not meet a generic hypersurface, so that a fine triangulation is still enough to ensure smoothness for Calabi-Yau threefolds. In the case of Calabi-Yau fourfolds, there can be singularities along curves of $\mathbb{P}^n_{\Sigma'}$ which are induced by faces which are not unimodular in a fine triangulation. These generically meet a hypersurface in points, so that smoothness is no longer automatic. For Calabi-Yau fourfolds, we thus need to check explicitly if a triangulation giving a resolution exists.

[8] This is commonly expressed by saying that facets of reflexive polyhedra are at lattice distance one from the origin.

JHEP01(2015)047

In the following, we will assume that we have found a fine regular star triangulation which makes $\mathbb{P}^n_{\Sigma'}$ a smooth projective toric variety and leads to a smooth Calabi-Yau fourfold hypersurface $\hat{Z}$. This means we fix a fan Σ' and a map $\phi : \Sigma' \to \Sigma$. We will come back to the issues discussed in this section, when we look at examples in section 4.

3.2 Computing $h^{2,2}$ via decomposition

Let $\hat{Z}$ be a non-singular compact Calabi-Yau $(n-1)$-fold defined as a hypersurface of a smooth toric ambient space $\mathbb{P}^n_{\Sigma'}$. Let $\{\nu_i\}_{i=1,\cdots,|\Sigma'(1)|}$ be the primitive vectors for all the 1-dimensional cones of the toric fan Σ'. For each one of them, there is a toric divisor D_i given by $\{X_i = 0\} \subset \mathbb{P}^n_{\Sigma'}$. The restriction of D_i to the hypersurface $\hat{Z}$ is denoted by $\hat{Y}_i$. This set of toric divisors $\left\{\hat{Y}_i\right\}$ is used to introduce a stratification (3.1). The primary stratum can be regarded as a hypersurface of $\mathbb{T}^n$,

$$Z := \hat{Z} \backslash Y = \hat{Z} \cap (\mathbb{P}^n_{\Sigma} \backslash \cup_i D_i) = \hat{Z} \cap (\mathbb{T}^n \subset \mathbb{P}^n_{\Sigma'}) \,, \tag{3.10}$$

and its complement is denoted by $Y := \cup_i \hat{Y}_i$.

For a compact non-singular irreducible algebraic variety $\hat{Z}$ and a divisor Y with normal crossings in $\hat{Z}$ (such that $Z = \hat{Z} \backslash Y$ is non-singular), we can write a long exact sequence

$$\begin{tikzcd} \cdots \arrow[r] & H_c^{k-1}(Z) \arrow[r] & H_c^{k-1}(\hat{Z}) \arrow[r] & H_c^{k-1}(Y) \arrow[dll, rounded corners] \\ & H_c^{k}(Z) \arrow[r] & H_c^{k}(\hat{Z}) \arrow[r] & H_c^{k}(Y) \arrow[r] & \cdots \end{tikzcd} \tag{3.11}$$

for the cohomology groups with compact support. Since $\hat{Z}$ and Y are both compact, $H^k(\hat{Z})$ and $H^k(Y)$ are the same as $H_c^k(\hat{Z})$ and $H_c^k(Y)$. All the morphisms in this exact sequence are morphisms of mixed Hodge structure[9] of type $(0,0)$.

In order to use the exact sequence (3.11), we first note [38] that $H_c^i(Z)$ vanishes for $i = 0, \cdots, n-2$, and

$$\begin{aligned} h^{p,q}\left[H_c^{k>(n-1)}(Z)\right] &= h^{p+1,q+1}\left[H_c^{k+2}(\mathbb{T}^n)\right] = \begin{cases} \binom{n}{k+2-n} & p = q = k+1-n \,, \\ 0 & \text{otherwise} \end{cases} \,. \\ h^{p,q}\left[H_c^{n-1}(Z)\right] &= 0 \quad \text{if } p+q > n-1 \,. \end{aligned} \tag{3.12}$$

More information about the non-vanishing parts of $H_c^{n-1}(Z)$ will be provided later.

The main focus in this article is to study $H^4(\hat{Z})$ for a Calabi-Yau fourfold $\hat{Z}$ in a toric ambient space of dimension $n = 5$. In this case, only the weight-4 components of $H_c^4(Z)$, $H_c^4(\hat{Z})$ and $H_c^4(Y)$ are relevant to determining $H^4(\hat{Z})$, and we learn from (3.11) that they satisfy

$$0 \longrightarrow \left[H_c^4(Z)\right]^{4,0} \longrightarrow \left[H_c^4(\hat{Z})\right]^{4,0} \longrightarrow 0, \tag{3.13}$$

[9] For mixed Hodge structure and Hodge-Deligne numbers, see [43] or an easy example discussed in [44]. For an algorithm of computing the Hodge-Deligne numbers, see [38]. We do not intend to provide a systematic exposition on this (well-understood) issue; we just focus on deriving new results such as (3.50) and (3.61). The example presented in section 4.1, however, is best suited to getting accustomed to such concepts.

JHEP01(2015)047

$$0 \longrightarrow \left[H^4_c(Z)\right]^{3,1} \longrightarrow \left[H^4_c(\hat{Z})\right]^{3,1} \longrightarrow \left[H^4_c(Y)\right]^{3,1} \longrightarrow 0, \tag{3.14}$$

$$0 \longrightarrow \left[H^4_c(Z)\right]^{2,2} \longrightarrow \left[H^4_c(\hat{Z})\right]^{2,2} \longrightarrow \left[H^4_c(Y)\right]^{2,2} \longrightarrow 0, \,. \tag{3.15}$$

Let us first focus on $\left(H^4_c(Y)\right)$. Y is not necessarily non-singular, but it can be written as $Y = \cup_i \hat{Y}_i$ where each $\hat{Y}_i$ is a non-singular divisor of $\hat{Z}$. Note that each $\hat{Y}_i$ is not necessarily irreducible. This can happen when ν_i is in a codimension-2 face of $\widetilde{\Delta}$. The (co)homology groups of such geometries can be computed by using the Mayer-Vietoris spectral sequence, and one finds that

$$H^4(Y) = \text{Kernel}\left(\left[\oplus_i H^4(\hat{Y}_i)\right] \longrightarrow \left[\oplus_{i<j} H^4(\hat{Y}_i \cap \hat{Y}_j)\right]\right). \tag{3.16}$$

As each $\hat{Y}_i$ is a smooth hypersurface of a toric variety, its $h^{1,0} = h^{3,1}$ vanishes (see e.g. [38]). Hence $H^4(Y)$ contributes only to the $(H^4_c(\hat{Z}))^{2,2}$ component in (3.13)–(3.15). Furthermore, keeping in mind that all divisors of $\hat{Z}$ occur as components of toric divisors, it is obvious from (3.16) that all vertical $(2,2)$-forms of $\hat{Z}$ are contained in the $H^4(Y)$ quotient of $H^4(\hat{Z})$.

We will discuss later how to compute $h^{2,2}(\hat{Y}_i) = h^{1,1}(\hat{Y}_i)$ and $h^{2,2}(\hat{Y}_i \cap \hat{Y}_j) = h^{0,0}(\hat{Y}_i \cap \hat{Y}_j)$ by using toric data. In order to determine $h^4(Y) = h^{2,2}[H^4(Y)]$ from (3.16), we further need to know the dimension of the cokernel of the homomorphisms in (3.16). We claim that the homomorphism in (3.16) has a cokernel of dimension $n(n-1)/2$.

In order to verify the claim, one needs to note that the kernel of (3.16) is $E^{0,4}_\infty = E^{0,4}_2 = \text{Ker}[d^{0,4}_1 : E^{0,4}_1 \longrightarrow E^{1,4}_1]$ in the Mayer-Vietoris sequence calculation of $H^\bullet(Y)$. The cokernel of the same homomorphism therefore corresponds to

$$\text{Coker}[d^{0,4}_1 : E^{0,4}_1 \longrightarrow E^{1,4}_1] = E^{1,4}_2 = E^{1,4}_\infty, \tag{3.17}$$

which gives rise to the $[H^5(Y)]^{2,2}$ component. It can be determined by exploiting other parts of the long exact sequence (3.11). Focusing on the weight-4 components, we find that the following is exact:

$$0 \longrightarrow \left[H^5_{(c)}(Y)\right]^{2,2} \longrightarrow \left[H^6_c(Z)\right]^{2,2} \longrightarrow 0. \tag{3.18}$$

Using (3.12), $h^{2,2}[H^{n+1}_c(Z)] = h^{n-3,n-3}[H^{n-3}(Z)] = n(n-1)/2$, so we find that

$$\dim\left(\text{Coker}\left[\oplus_i H^4(\hat{Y}_i) \longrightarrow \oplus_{i<j} H^4(\hat{Y}_i \cap \hat{Y}_j)\right]\right) = h^{2,2}\left[H^5_{(c)}(Y)\right] = \frac{n(n-1)}{2}. \tag{3.19}$$

as stated before.

3.3 Stratification and geometry of divisors

For the purpose of capturing $H^4_c(Y)$ and $H^4(Z)$ in terms of combinatorial data of the toric ambient space, we take a moment to digress. To start off, we describe stratifications of Calabi-Yau hypersurfaces $\hat{Z}$ of a toric ambient space $\mathbb{P}^n_{\Sigma'}$. There are two distinct stratifications to which we pay attention: one is associated with the toric fan Σ, and the other with its refinement[10] Σ'.

[10] Remember that by assumption, Σ' is determined by a regular star triangulation turning $\hat{Z}$ into a smooth hypersurface, whereas Σ is a fan over faces of the polytope $\widetilde{\Delta}$.

JHEP01(2015)047

The stratification induced by Σ' is easier to describe, it descends from that on $\mathbb{P}^n_{\Sigma'}$ straightforwardly: each stratum of $\hat{Z}$ is of the form $Z_\sigma = \hat{Z} \cap \mathbb{T}_\sigma$ for $\sigma \in \Sigma'$.

The stratification corresponding to Σ is

$$\hat{Z} = (Z_\Delta) \amalg \left(\amalg_{\Theta^{[n-1]} \leq \Delta} Z_{\Theta^{[n-1]}}\right) \amalg \amalg_{2 \leq k \leq n-1} \left(\amalg_{(\widetilde{\Theta}^{[k-1]}, \Theta^{[n-k]})} [E_{\widetilde{\Theta}^{[k-1]}} \times Z_{\Theta^{[n-k]}}]\right); \quad (3.20)$$

here, the strata are labelled by the faces of Δ, namely, Δ itself, codimension-1 faces $\Theta^{[n-1]}$'s, and all other faces $\Theta^{[n-k]}$'s of codimension $2 \leq k \leq n-1$. It is understood in the expression above, and also in expressions later, that $(\widetilde{\Theta}^{[k-1]}, \Theta^{[n-k]})$ is a dual pair of faces. Due to the one-to-one correspondence between faces of Δ, the faces of $\widetilde{\Delta}$ and the cones in Σ, the strata in (3.20) are in one-to-one correspondence with the cones of the fan Σ. The primary stratum, Z_Δ, corresponds to the 0-dimensional cone $\vec{0} \in \Sigma$, and the $Z_{\Theta^{[n-1]}}$ to the individual 1-dimensional cones in $\Sigma(1)$.

The geometry of $E_{\widetilde{\Theta}^{[k-1]}}$ can be read out from the $(k-1)$-dimensional face $\widetilde{\Theta}^{[k-1]}$ of $\widetilde{\Delta}$. $E_{\widetilde{\Theta}^{[k-1]}}$ has a stratification associated with the maximal simplicial subdivision Σ',

$$E_{\widetilde{\Theta}^{[k-1]}} = \left[(\mathbb{T}^{k-1}\text{'s}) \amalg (\mathbb{T}^{k-2}\text{'s}) \amalg \cdots \amalg \text{points}\right], \quad (3.21)$$

where the number of $\mathbb{T}^{k-1-p}$ in this decomposition is equal to the number of p-simplices in $\widetilde{\Theta}^{[k-1]}$ which are not contained in the boundary of $\widetilde{\Theta}^{[k-1]}$.

The geometries of Z_Δ $(k=0)$ and all the other of $Z_{\Theta^{[n-k]}}$ are given by hypersurfaces of $\mathbb{T}^{\dim_{\mathbb{C}}(\Theta)=(n-k)}$. For each one of the Z_Θ, only the terms in the Newton (Laurent) polynomial corresponding to $\Theta^{[n-k]} \cap M$ are relevant in determining $Z_{\Theta^{[n-k]}} \subset \mathbb{T}^{n-k}$ (which also means all terms originating from $\Delta \cap M$ are relevant in determining $Z_\Delta \subset \mathbb{T}^n$). Obviously the primary stratum Z_Δ is the same as $Z := \hat{Z} \backslash Y$ introduce before.

The stratification for the fan Σ', $\hat{Z} = \amalg_{\sigma \in \Sigma'} Z_\sigma$, is therefore obtained by decomposing the stratification (3.20) under (3.21). Put differently,

$$\left[E_{\widetilde{\Theta}^{[k-1]}} \times Z_{\Theta^{[n-k]}}\right] = \amalg_{\sigma' \in \phi^{-1} \cdot \sigma(\widetilde{\Theta}^{[k-1]})} Z_{\sigma'}, \quad (3.22)$$

where $\phi : \Sigma' \longrightarrow \Sigma$ is the map of toric fans (mapping cones to cones) associated with the subdivision refining Σ to Σ' and $\sigma(\widetilde{\Theta}^{[k-1]})$ is the map identifying a cone of Σ with a face $\widetilde{\Theta}^{[k-1]}$ of $\widetilde{\Delta}$. One can think of $E_{\widetilde{\Theta}^{[k-1]}}$ as the exceptional geometry appearing in a resolution of singularities of $\mathbb{P}^n_\Sigma$ associated with the k-dimensional cone $\sigma(\widetilde{\Theta}^{[k-1]})$.

3.4 Combinatorial formula for $h^{2,2}[H^4_{(c)}(Y)] = [h^{n-3,n-3}[H^{2n-6}_c(Y)]]_{n=5}$

Just like various Hodge numbers of a Calabi-Yau toric hypersurface $\hat{Z}$ are computed by using the stratification and the Hodge-Deligne numbers of the strata [19, 38], Hodge numbers of divisors $\hat{Y}_i$'s of a Calabi-Yau toric hypersurface $\hat{Z}$ can also be computed essentially with the same technique. Once $h^{2,2}(\hat{Y}_i)$'s are computed, it is almost straightforward (as already explained) to determine $h^{2,2}[H^4_c(Y)]$.

The 'Euler characteristics' of Hodge-Deligne numbers of compact support cohomology groups (for some geometry X) are

$$e^{p,q}_c(X) := \sum_k (-)^k h^{p,q}[H^k_c(X)]. \quad (3.23)$$

JHEP01(2015)047

These numbers have the following three nice properties, which were exploited heavily in [19, 38], and will also be in the following.

The first two are additivity,

$$e_c^{p,q}(X_1 \amalg X_2) = e_c^{p,q}(X_1) + e_c^{p,q}(X_2), \tag{3.24}$$

and multiplicativity,

$$e_c^{p,q}(E \times Z) = \sum_{p'+p''=p} \sum_{q'+q''=q} e_c^{p',q'}(E) e_c^{p'',q''}(Z). \tag{3.25}$$

Finally, when an algebraic variety X (of complex dimension $n-1$) is compact and smooth, i.e the mixed Hodge structure on cohomology groups is pure,

$$e_c^{p,q}(X) = (-)^{p+q} h_c^{p,q}(X) = (-)^{p+q} h^{p,q}(X) = (-)^{p+q} h^{n-1-p,n-1-q}(X) \tag{3.26}$$

In a slight abuse of language, we will frequently refer to the $e^{p,q}$ as Hodge-Deligne numbers in the text.

Each divisor component $\hat{Y}_i$ (corresponding to $\rho_i \in \Sigma'(1)$) of a Calabi-Yau $(n-1)$-fold $\hat{Z}$ is compact and smooth, and hence $h^{n-3,n-3}(\hat{Y}_i) = h^{1,1}(\hat{Y}_i)$ is the same as[11] $e_c^{n-3,n-3}(\hat{Y}_i)$. The compact geometry $\hat{Y}_i$ has a stratification associated with Σ', or to be more specific,

$$\hat{Y}_i = \left(\amalg_{\rho_i \leq \sigma \in \Sigma'} Z_\sigma\right) \subset \hat{Z}. \tag{3.27}$$

Because of additivity, $e_c^{n-3,n-3}(\hat{Y}_i)$ is obtained by summing up $e_c^{n-3,n-3}(Z_\sigma)$ $(\sigma \geq \rho_i)$. Using multiplicativity, this calculation is further boiled down to the computation of $e_c^{p,q}(Z_\Theta)$ of various faces $\Theta \leq \Delta$, for which the algorithm of [38] (in combination with (3.12)) can be used.

Here, we record a few crucial formulas from [38] for Hodge-Deligne numbers of the strata Z_Θ. For a face of dimension f there is the 'sum rule'

$$(-1)^{f-1} \sum_q e^{p,q}(Z_\Theta) = (-1)^p \binom{f}{p+1} + \varphi_{f-p}(\Theta)\,, \tag{3.28}$$

where f is the dimension of the face Θ. Here, the functions φ_k are defined as

$$\varphi_k(\Theta) := \sum_{j \geq 1} (-1)^{k-j} \binom{f+1}{k-j} \ell^*(j\Theta)\,, \tag{3.29}$$

where $j\Theta$ stands for the polytope which is obtained by scaling all vertices of the face Θ by j and then taking the convex hull. We introduce the notation

$$\bar{e}_c^{p,q}(Z_\Theta) := e_c^{p,q}(Z_\Theta) - \delta_{p,q}(-1)^{f-1-p} \binom{f}{p+1}\,, \tag{3.30}$$

[11] A completely parallel story holds for any cone $\rho \in \Sigma'(\ell)$ (not in the interior of a facet of $\widetilde{\Delta}$), and for any one of its Hodge numbers.

JHEP01(2015)047

in this article. $bare_c^{p,q}(Z_\Theta)$ is equal to $(-1)^{f-1}h^{p,q}[H^{f-1}(Z_\Theta)]$ except when $(p,q)=(0,0)$. Obviously the sum rule (3.28) can be written as

$$\sum_q \bar{e}_c^{p,q}(Z_\Theta) = (-1)^{f-1}\varphi_{f-p}(\Theta). \tag{3.31}$$

Furthermore, the Hodge numbers obey [38]

$$e^{p,0}(Z_\Theta) = (-1)^f \sum_{\Gamma\leq\Theta,\dim\Gamma=p+1} \ell^*(\Gamma)\,, \tag{3.32}$$

for any $p>0$. For a face of dimension $f\geq 4$ we also have that

$$e^{f-2,1}(Z_\Theta) = (-1)^{f-1}\left(\varphi_2(\Theta) - \sum_{\Gamma\leq\Theta,\dim\Gamma=f-1}\varphi_1(\Gamma)\right). \tag{3.33}$$

3.4.1 Computation of $h^{1,1}(\hat{Y}_i) = h^{n-3,n-3}(\hat{Y}_i)$ for $n\geq 5$ cases

We are primarily interested in $h^{2,2}(\hat{Y}_i)$, where $\hat{Y}_i$ is of $(n-2)=3$-dimensions in a Calabi-Yau $(n-1)=4$-fold $\hat{Z}$, embedded in a toric ambient space $\mathbb{P}^{n=5}_{\Sigma'}$. This can be regarded, however, as a special case of the more general problem of determining $h^{n-3,n-3}(\hat{Y}_i)$ of a divisor $\hat{Y}_i$ of a Calabi-Yau $(n-1)$-fold embedded in a toric ambient space $\mathbb{P}^n_{\Sigma'}$. We shall study the more general version of the problem for $n\geq 5$.

For any 1-dimensional cone ρ_i generated by a primitive vector ν_i in the lattice N, there is a divisor $\hat{Y}_i$ of $\hat{Z}$. Depending on which face contains ν_i in its interior, the computation $h^{n-3,n-3}(\hat{Y}_i)$ has to be treated separately. The divisor $\hat{Y}_i$ is empty if ν_i is interior to an $n-1$-dimensional face of $\widetilde{\Delta}$. Let $\phi(\rho_i)\in\Sigma(k_0)$, i.e., ν_i is an interior point of a (k_0-1)-dimensional face $\widetilde{\Theta}_i^{[k_0-1]}\leq\widetilde{\Delta}$. The cases we have to study are then

- $k_0=1$: i.e., ν_i is one of vertices of $\widetilde{\Delta}$.
- $1<k_0<n-3$: (this case is absent if $n=5$.)
- $k_0=n-3$: i.e., ν_i is an interior point of a codimension-4 face (an edge, if $n=5$).
- $k_0=n-2$: i.e., ν_i is an interior point of a codimension-3 face (a 2dim face, if $n=5$).
- $k_0=n-1$: i.e., ν_i is an interior point of a codimension-2 face. (a 3dim face, if $n=5$)

We work on those five cases one-by-one from now.

The case $k_0=1$. Here, $\nu_i=\widetilde{\Theta}_i^{[0]}$ is a vertex of $\widetilde{\Delta}$. $\hat{Y}_i$ is composed of the following strata:

$$\begin{aligned} Z_{\Theta_i^{[n-1]}}, \quad & [\mathrm{pt}\times Z_{\Theta^{[n-2]}}]_{(\widetilde{\Theta}^{[1]},\Theta^{[n-2]})}, \quad [(\mathbb{T}\text{'s}+\mathrm{pts})\times Z_{\Theta^{[n-3]}}]_{(\widetilde{\Theta}^{[2]},\Theta^{[n-3]})}\,, \\ & \cdots\cdots, \quad \left[\left(\mathbb{T}^{n-3}\text{'s}\sim\mathrm{points}\right)\times Z_{\Theta^{[1]}}\right]_{(\widetilde{\Theta}^{[n-2]},\Theta^{[1]})}. \end{aligned} \tag{3.34}$$

Note that a stratum $Z_\sigma\subset[E_{\widetilde{\Theta}^{[k-1]}}\times Z_{\Theta^{[n-k]}}]$ contributes to $\hat{Y}_i$ only when $\widetilde{\Theta}^{[k-1]}$ contains the vertex ν_i, i.e. $\widetilde{\Theta}^{[k-1]}\geq\widetilde{\Theta}_i^{[0]}$ (equivalently $\Theta^{[n-k]}\leq\Theta_i^{[n-1]}$). Furthermore, $\mathbb{T}^{k-1-p}\subset E_{\widetilde{\Theta}^{[k-1]}}$

JHEP01(2015)047

only contributes when the corresponding p-simplex in $\widetilde{\Theta}^{[k-1]}$ contains ν_i as one of its faces. This is why, for example, only one point $\mathbb{T}^0$ (one 1-simplex) from $E_{\widetilde{\Theta}^{[1]}}$ of a given dual pair $(\widetilde{\Theta}^{[1]}, \Theta^{[n-2]})$ contributes to $\hat{Y}_i$. Such strata combined are denoted by $[E_{\widetilde{\Theta}^{[k-1]}} \times Z_{\Theta^{[n-k]}}]^{\rho_i \leq}$ in this article.

From the first stratum,

$$e_c^{n-3,n-3}(Z_{\Theta_i^{[n-1]}}) = -\binom{n-1}{n-2} = -(n-1) \tag{3.35}$$

picking up the contribution from $h^{n-3,n-3}[H_c^{2n-3}(Z_{\Theta_i^{[n-1]}})]$.

From the k-th group of strata ($k = 2, \cdots, (n-2)$), each pair $(\widetilde{\Theta}^{[k-1]}, \Theta^{[n-k]})$ gives rise to

$$\begin{aligned} e_c^{n-3,n-3}\left([E_{\widetilde{\Theta}^{[k-1]}} \times Z_{\Theta^{[n-k]}}]^{\rho_i \leq}\right) &= \left[{}_{\nu_i}\ell_1^*(\widetilde{\Theta}^{[k-1]}) \times e_c^{k-2,k-2}(\mathbb{T}^{k-2})\right] \times [e_c^{n-k-1,n-k-1}(Z_{\Theta^{[n-k]}})] \\ &= {}_{\nu_i}\ell_1^*(\widetilde{\Theta}^{[k-1]})\,. \end{aligned} \tag{3.36}$$

Here, we have introduce the notation ${}_{\nu_i}\ell_1^*(\widetilde{\Theta})$ for the number of internal 1-simplices in the face $\widetilde{\Theta}$ which end on ν_i or, in other words, have ν_i as a face. In the language of cones

$${}_{\nu_i}\ell_1^*(\widetilde{\Theta}) := \left|\left\{\sigma \in \Sigma'(2) \cap \phi^{-1} \cdot \sigma(\widetilde{\Theta}) \mid \rho_i \leq \sigma\right\}\right| \tag{3.37}$$

We also introduce ${}_{\nu_i}\ell_1(\widetilde{\Delta}_{\leq p})$ for the number of 1-simplices (again containing ν_i as a face) contained in the p-skeleton (faces of dimension p or less) of $\widetilde{\Delta}$.

The contribution from the last group of strata, $k = n-1$, is the same as above, except that $e_c^{n-k-1,n-k-1}(Z_{\Theta^{[n-k]}})$ is not necessarily 1. $Z_{\Theta^{[1]}}$ consists of

$$e_c^{n-k-1,n-k-1}(Z_{\Theta^{[n-k]}}) = e_c^{0,0} = 1 + \ell^*(\Theta^{[1]}), \tag{3.38}$$

points, which is not necessarily 1. Hence the contribution to $e_c^{n-3,n-3}$ is $e_c^{0,0}(Z_{\Theta^{[1]}})$ times larger than that of (3.36). We thus finally obtain

$$h^{1,1}(\hat{Y}_i)|_{\text{if } k_0=1} = {}_{\nu_i}\ell_1(\widetilde{\Delta}_{\leq n-2}) - (n-1) + \sum_{(\widetilde{\Theta}^{[n-2]},\Theta^{[1]})} {}_{\nu_i}\ell_1^*(\widetilde{\Theta}^{[n-2]}) \times \ell^*(\Theta^{[1]}). \tag{3.39}$$

This formula for the divisors $\hat{Y}_i$ of $\hat{Z}$ is quite like that of $\hat{Z}$ in (3.3). The first two terms originate from toric divisors (divisors of the ambient space $\mathbb{P}^n_{\Sigma'}$ of $\hat{Z}$ and the linear equivalence restricted to $\hat{Y}_i$). The correction term at the end of (3.39) also looks quite similar to the last term of (3.3); we will come back in section 3.6 to discuss the geometric interpretation of this term in more detail.

The three cases $1 < k_0 < (n-3)$, $k_0 = (n-3)$ and $k_0 = (n-2)$. The stratification of $\hat{Y}_i$ is described schematically by

$$[E_{\widetilde{\Theta}_i^{[k_0-1]}} \times Z_{\Theta_i^{[n-k_0]}}]^{\rho_i \leq}, \quad \cdots, \left[E_{\widetilde{\Theta}^{[k-1]}} \times Z_{\Theta^{[n-k]}}\right]^{\rho_i \leq}, \cdots, \left[E_{\widetilde{\Theta}^{[n-2]}} \times Z_{\Theta^{[1]}}\right]^{\rho_i \leq}. \tag{3.40}$$

In all the three cases, the contributions to $e_c^{n-3,n-3}$ from all but the first group of strata remain the same as in the $k_0 = 1$ case. The first group of strata gives rise to

$$e_c^{n-3,n-3}([E_{\widetilde{\Theta}_i^{[k_0-1]}} \times Z_{\Theta_i^{[n-k_0]}}]^{\geq \rho_i}) = e_c^{k_0-1,k_0-1}(E^{\geq \rho_i}_{\widetilde{\Theta}_i^{[k_0-1]}}) e_c^{n-k_0-2,n-k_0-2}(Z_{\Theta_i^{[n-k_0]}})$$

JHEP01(2015)047

$$+e_c^{k_0-2,k_0-2}(E^{\geq\rho_i}_{\widetilde{\Theta}_i^{[k_0-1]}})e_c^{n-k_0-1,n-k_0-1}(Z_{\Theta_i^{[n-k_0]}}). \quad (3.41)$$

In all the three cases, $1 < k_0 < n-3$, $k_0 = n-3$ and $k_0 = n-2$, we have that

- $e_c^{k_0-1,k_0-1}(E^{\geq\rho_i}_{\widetilde{\Theta}_i^{[k_0-1]}}) = 1$, because the only contribution comes from $\mathbb{T}^{k_0-1}$ corresponding to the 0-plex ν_i itself
- $e_c^{n-k_0-1,n-k_0-1}(Z_{\Theta_i^{[n-k_0]}}) = 1$
- $e_c^{k_0-2,k_0-2}(E^{\geq\rho_i}_{\widetilde{\Theta}_i^{[k_0-1]}}) = -(k_0-1) + {}_{\nu_i}\ell_1^*(\widetilde{\Theta}^{[k_0-1]})$

The expression for the factor $e_c^{n-k_0-2,n-k_0-2}(Z_{\Theta^{[n-k_0]}})$, however, is different in all the three cases. If $1 < k_0 < n-3$, then $2(n-k_0-2) > (n-k_0-1)$, so that

$$e_c^{n-k_0-2,n-k_0-2}(Z_{\Theta_i^{[n-k_0]}}) = -\binom{n-k_0}{n-k_0-1} = -(n-k_0). \quad (3.42)$$

For the two other cases, $k_0 = (n-3)$ and $k_0 = (n-2)$, however, there is an extra term in $e_c^{n-k_0-2,n-k_0-2}(Z_{\Theta^{[n-k_0]}})$, which we denote by $\bar{e}_c^{n-k_0-2,n-k_0-2}(Z_{\Theta^{[n-k_0]}})$ hereafter.

Therefore, it turns out that $h^{1,1}(\hat{Y}_i)$ remains the same as in (3.39) for $\hat{Y}_i$ with $1 < k_0 < (n-3)$, while

$$\begin{aligned} h^{1,1}(\hat{Y}_i)|_{\text{if } k_0=(n-3),(n-2)} &= {}_{\nu_i}\ell_1(\widetilde{\Delta}_{\leq n-2}) - (n-1) + \sum_{(\widetilde{\Theta}^{[n-2]},\Theta^{[1]})} {}_{\nu_i}\ell_1^*(\widetilde{\Theta}^{[n-2]}) \times \ell^*(\Theta^{[1]}) \\ &\quad + \bar{e}_c^{n-k_0-2,n-k_0-2}(Z_{\Theta_i^{[n-k_0]}}). \end{aligned} \quad (3.43)$$

The correction term in the last line of (3.43) is determined by using the sum rule in [38], (3.28). In the case $k_0 = n-3$, $Z_{\Theta_i^{[n-k_0=3]}}$ is a surface given by a Laurent polynomial in $\mathbb{T}^3$. Therefore,

$$\bar{e}_c^{n-k_0-2,n-k_0-2}(Z_{\Theta_i^{[n-k_0]}}) = \bar{e}_c^{1,1}(Z_{\Theta_i^{[3]}}) = \varphi_2(\Theta_i^{[3]}) - \sum_{\Theta^{[2]}\leq\Theta_i^{[3]}} \varphi_1(\Theta^{[2]}), \quad (3.44)$$

$$= \ell^*(2\Theta_i^{[3]}) - 4\ell^*(\Theta_i^{[3]}) - \sum_{\Theta^{[2]}\leq\Theta_i^{[3]}} \ell^*(\Theta^{[2]}). \quad (3.45)$$

In the case $k_0 = n-2$, $Z_{\Theta_i^{[n-k_0]}}$ is a curve given by a Laurent polynomial in $\mathbb{T}^2$. Thus,

$$\bar{e}_c^{n-k_0-2,n-k_0-2}(Z_{\Theta_i^{[n-k_0]}}) = \bar{e}_c^{0,0}(Z_{\Theta_i^{[2]}}) = -\varphi_2(\Theta_i^{[2]}) + \varphi_1(\Theta_i^{[2]}), \quad (3.46)$$

$$= -\ell^*(2\Theta_i^{[2]}) + 4\ell^*(\Theta_i^{[2]}). \quad (3.47)$$

Again, the first two lines of (3.43) are understood as toric divisors of $\hat{Z}$ restricted on $\hat{Y}_i$. The $(n-1)$-dimensional redundancy among them is simply given by the number of toric linear equivalences. The geometric interpretation of the correction term $\bar{e}_c^{n-k_0-3,n-k_0-3}(Z_{\Theta^{[n-k_0]}})$ is discussed in detail in section 3.6.

JHEP01(2015)047

The cases $k_0 = n-1$. Finally, let us work out $h^{1,1}(\hat{Y}_i)$ for $k_0 = n-1$, where ν_i is in the interior of an codimension-2 face $\widetilde{\Theta}_i^{[n-2]}$ of $\widetilde{\Delta}$. The dual face of Δ is of dimension 1 and denoted by $\Theta_i^{[1]}$. The divisor $\hat{Y}_i$ of the Calabi-Yau $(n-1)$-fold $\hat{Z}$ consists of $e_c^{0,0}(Z_{\Theta_i^{[1]}}) = [1+\ell^*(\Theta_i^{[1]})]$ irreducible components, each of which is a toric variety $E^{\geq\rho_i}_{\widetilde{\Theta}_i^{[n-2]}}$ given by p-simplices $\widetilde{\Theta}_i^{[n-2]}$ containing ν_i as a face. Therefore,

$$e_c^{n-3,n-3}(E^{\geq\rho_i}_{\widetilde{\Theta}_i^{[n-2]}}) = {}_{\nu_i}\ell_1^*(\widetilde{\Theta}^{[n-2]}) - (n-2)\,. \tag{3.48}$$

Note that the "number of linear equivalences" is different from that in all the other cases where $k_0 < (n-1)$: it is now $n-2$ instead of $n-1$. Finally, $h^{1,1}(\hat{Y}_i) = h^{n-3,n-3}(\hat{Y}_i)$ is obtained by multiplying the above expression with $e_c^{0,0}(Z_{\Theta_i^{[1]}}) = [1+\ell^*(\Theta_i^{[1]})]$.

3.4.2 The result

Combining the results of (3.34), (3.43), (3.45), (3.47), (3.48), $h^{n-3,n-3}[H_c^{2n-6}(Y)] = h^{2,2}[H_c^4(Y)]$ is determined. As we have already explained,

$$\begin{aligned} h^{n-3,n-3}[H_c^{2n-6}(Y)] = &\sum_i h^{n-3,n-3}(\hat{Y}_i) \\ &- \left[\sum_{i<j}\left|\left\{\text{irr. nonempty components of } \hat{Y}_i\cap\hat{Y}_j\right\}\right| - \frac{n(n-1)}{2}\right]. \end{aligned} \tag{3.49}$$

Noting that all one-simplices on the $n-3$-skeleton of $\widetilde{\Delta}$ contribute twice in the first line of (3.49) and by (-1) in the second line, and that all one-simplices internal to a $n-2$-dimensional face of $\widetilde{\Delta}$ do so by a factor of $[2+(-1)]\times[1+\ell^*(\Theta^{[1]})]$, we find that

$$\begin{aligned} h^{n-3,n-3}[H_c^{2n-6}(Y)] = &\ \ell_1(\widetilde{\Delta}_{\leq n-2}) + \frac{n(n-1)}{2} \\ &-(n-1)\left[\ell(\widetilde{\Delta}) - \sum_{\widetilde{\Theta}^{[n-1]}\leq\widetilde{\Delta}}\ell^*(\widetilde{\Theta}^{[n-1]}) - \sum_{\widetilde{\Theta}^{[n-2]}\leq\widetilde{\Delta}}\ell^*(\widetilde{\Theta}^{[n-2]}) - 1\right] \\ &-(n-2)\sum_{(\widetilde{\Theta}^{[n-2]},\Theta^{[1]})}\ell^*(\widetilde{\Theta}^{[n-2]})\left[1+\ell^*(\Theta^{[1]})\right], \\ &+\sum_{(\widetilde{\Theta}^{[n-2]},\Theta^{[1]})}\ell_1^*(\widetilde{\Theta}^{[n-2]})\times\ell^*(\Theta^{[1]}), \\ &-\sum_{(\widetilde{\Theta}^{[n-3]},\Theta^{[2]})}\ell^*(\widetilde{\Theta}^{[n-3]})\times\left\{\ell^*(2\Theta^{[2]}) - 4\ell^*(\Theta^{[2]})\right\}. \\ &+\sum_{(\widetilde{\Theta}^{[n-4]},\Theta^{[3]})}\ell^*(\widetilde{\Theta}^{[n-4]})\times\left\{\ell^*(2\Theta^{[3]}) - 4\ell^*(\Theta^{[3]}) - \sum_{\Theta^{[2]}\leq\Theta^{[3]}}\ell^*(\Theta^{[2]})\right\}. \end{aligned} \tag{3.50}$$

Here, $\ell_1(\widetilde{\Delta}_{\leq p})$ denotes the number of 1-simplices on the p-skeleton of $\widetilde{\Delta}$ and $\ell_1^*(\widetilde{\Theta})$ the number of internal 1-simplices on a face $\widetilde{\Theta}$.

JHEP01(2015)047

3.5 Combinatorial formula for $h^{2,2}[H_c^4(Z_\Delta)] = [h^{n-3,2}[H_c^{n-1}(Z_\Delta)]]_{n=5}$

Using the sum rule (3.31) of [38] we immediately find that,

$$\sum_{q=0}^{2} h^{n-3,q}\left[H_c^{n-1}(Z_\Delta)\right] = \varphi_3(\Delta), \tag{3.51}$$

$$\sum_{q=0}^{1} h^{n-3,q}\left[H_c^{n-2}(Z_{\Theta^{[n-1]}})\right] = \varphi_2(\Theta^{[n-1]}), \tag{3.52}$$

$$h^{n-3,0}\left[H_c^{n-3}(Z_{\Theta^{[n-2]}})\right] = \varphi_1(\Theta^{[n-2]}). \tag{3.53}$$

There are six unknowns in the left-hand sides, so that we need three more conditions in order to determine $h^{n-3,2}[H_c^{n-1}(Z)]$, i.e. $h^{2,2}[H_c^4(Z)]$ ($n=5$). They come from the fact that all of the Hodge numbers of components where neither $p=q$, nor $p+q=n-1$ are tightly constrained for a compact smooth hypersurface of a toric variety. For $p=0$ (or $q=0$) such Hodge numbers even vanish. Thus, for the closure of $Z_{\Theta^{[n-1]}}$ (satisfying the condition above), it follows that

$$-h^{n-3,0}[H_c^{n-2}(Z_{\Theta^{[n-1]}})] + \sum_{\Theta^{[n-2]}\leq\Theta^{[n-1]}} h^{n-3,0}[H_c^{n-3}(Z_{\Theta^{[n-2]}})] = 0 \tag{3.54}$$

for any facets $\Theta^{[n-1]}$ of Δ. Similarly for the closure of $Z_\Delta = \hat{Z}$, we obtain

$$\begin{aligned} 0 &= h^{n-3,0}(\hat{Z}) \\ &= h^{n-3,0}[H_c^{n-1}(Z_\Delta)] - \sum_{\Theta^{[n-1]}\leq\Delta} h^{n-3,0}[H_c^{n-2}(Z_{\Theta^{[n-1]}})] + \sum_{\Theta^{[n-2]}\leq\Delta} h^{n-3,0}[H_c^{n-3}(Z_{\Theta^{[n-2]}})]\times 1, \end{aligned} \tag{3.55}$$

where the factor 1 is due to $e^{0,0}(E_{\widetilde{\Theta}^{[2]}}) = (-)^{2+1}[\chi(\text{2d ball}) - \chi(S_1)] = 1$ (see e.g., [38]).

The $(n-3,1)$ component (i.e. $h^{2,1}$ for the case $n=5$) does not vanish, but is given by the formula (3.5) (see [41], with a correction in [9, 12]):

$$\begin{aligned} (-)\sum_{(\widetilde{\Theta}^{[2]},\Theta^{[n-3]})} \ell^*(\widetilde{\Theta}^{[2]})\times\ell^*(\Theta^{[n-3]}) &= (-)^{n-1}e_c^{n-2,2}(\hat{Z}) = (-)^{n-1}e_c^{n-3,1}(\hat{Z}) \\ &= h^{n-3,1}[H_c^{n-1}(Z_\Delta)] - \sum_{\Theta^{[n-1]}\leq\Delta} h^{n-3,1}[H_c^{n-2}(Z_{\Theta^{[n-1]}})] \\ &\quad + \sum_{(\widetilde{\Theta}^{[1]},\Theta^{[n-2]})} h^{n-4,0}[H_c^{n-3}(Z_{\Theta^{[n-2]}})]\times e_c^{1,1}(E_{\widetilde{\Theta}^{[1]}}) \\ &\quad - \sum_{(\widetilde{\Theta}^{[2]},\Theta^{[n-3]})} h^{n-4,0}[H_c^{n-4}(Z_{\Theta^{[n-3]}})]\times e_c^{1,1}(E_{\widetilde{\Theta}^{[2]}}). \end{aligned} \tag{3.56}$$

On the right hand side, $e_c^{1,1}(E_{\widetilde{\Theta}^{[1]}}) = \ell^*(\widetilde{\Theta}^{[1]})$, and $e_c^{1,1}(E_{\widetilde{\Theta}^{[2]}})$ is given by $-2\ell^*(\widetilde{\Theta}^{[2]}) + \ell_1^*(\widetilde{\Theta}^{[2]})$.

In order to solve the six unknowns by using the six conditions above, we need to determine $h^{n-4,0}[H_c^{n-3}(Z_{\Theta^{[n-2]}})]$ and $h^{n-4,0}[H_c^{n-4}(Z_{\Theta^{[n-3]}})]$ appearing in the last condition.

JHEP01(2015)047

As for $h^{n-4,0}[H_c^{n-3}(Z_{\Theta^{[n-2]}})]$, using a similar condition for the closure of $Z_{\Theta^{[n-2]}}$,

$$h^{n-4,0}[H_c^{n-3}(Z_{\Theta^{[n-2]}})] = \sum_{\Theta^{[n-3]}\leq\Theta^{[n-2]}} h^{n-4,0}[H_c^{n-4}(Z_{\Theta^{[n-3]}})] = \sum_{\Theta^{[n-3]}\leq\Theta^{[n-2]}} \varphi_1(\Theta^{[n-3]}). \tag{3.57}$$

For $h^{n-4,0}[H_c^{n-4}(Z_{\Theta^{[n-3]}})]$, we can simply use $h^{n-4,0}[H_c^{n-4}(Z_{\Theta^{[n-3]}})] = \varphi_1(\Theta^{[n-3]})$.

Now we can solve (3.51):

$$h^{n-3,0}[H_c^{n-2}(Z_{\Theta^{[n-1]}})] = \sum_{\Theta^{[n-2]}\leq\Theta^{[n-1]}} \varphi_1(\Theta^{[n-2]}), \tag{3.58}$$

$$h^{n-3,0}[H_c^{n-1}(Z_\Delta)] = \sum_{\Theta^{[n-1]}\leq\Delta}\sum_{\Theta^{[n-2]}\leq\Theta^{[n-1]}} \varphi_1(\Theta^{[n-2]}) - \sum_{\Theta^{[n-2]}\leq\Delta}\varphi_1(\Theta^{[n-2]}) = \sum_{\Theta^{[n-2]}\leq\Delta}\varphi_1(\Theta^{[n-2]}), \tag{3.59}$$

where we used the fact that any $\Theta^{[n-2]}$ is codimension-1 in the boundary of Δ, so that it is shared by precisely two faces $\Theta^{[n-1]}$; those two results (3.58), (3.59) are examples of (3.32).[12] Let us continue with

$$\begin{aligned} h^{n-3,1}[H_c^{n-1}(Z_\Delta)] = &\sum_{\Theta^{[n-1]}\leq\Delta}\varphi_2(\Theta^{[n-1]}) - \sum_{\Theta^{[n-1]}\leq\Delta}\sum_{\Theta^{[n-2]}\leq\Theta^{[n-1]}}\varphi_1(\Theta^{[n-2]}) \\ &- \sum_{(\widetilde{\Theta}^{[1]},\Theta^{[n-2]})}\ell^*(\widetilde{\Theta}^{[1]}) \times \sum_{\Theta^{[n-3]}\leq\Theta^{[n-2]}}\ell^*(\Theta^{[n-3]}), \\ &+ \sum_{(\widetilde{\Theta}^{[2]},\Theta^{[n-3]})}\left(-2\ell^*(\widetilde{\Theta}^{[2]}) + \ell_1^*(\widetilde{\Theta}^{[2]})\right)\times\ell^*(\Theta^{[n-3]}) \\ &- \sum_{(\widetilde{\Theta}^{[2]},\Theta^{[n-3]})}\ell^*(\widetilde{\Theta}^{[2]})\ell^*(\Theta^{[n-3]}). \end{aligned} \tag{3.60}$$

Therefore, we arrive at a the formula

$$\begin{aligned} h^{n-3,2}[H_c^{n-1}(Z_\Delta)] = \varphi_3(\Delta) &- \sum_{\Theta^{[n-1]}\leq\Delta}\varphi_2(\Theta^{[n-1]}) + \sum_{\Theta^{[n-2]}\leq\Delta}\varphi_1(\Theta^{[n-2]}) \\ &+ \sum_{(\widetilde{\Theta}^{[1]},\Theta^{[n-2]})}\ell^*(\widetilde{\Theta}^{[1]}) \times \sum_{\Theta^{[n-3]}\leq\Theta^{[n-2]}}\ell^*(\Theta^{[n-3]}) \\ &+ \sum_{(\widetilde{\Theta}^{[2]},\Theta^{[n-3]})}\left(3\ell^*(\widetilde{\Theta}^{[2]}) - \ell_1^*(\widetilde{\Theta}^{[2]})\right)\times\ell^*(\Theta^{[n-3]}). \end{aligned} \tag{3.61}$$

3.6 Vertical, horizontal and the remaining components

Due to the exact sequence (3.15), we can now compute $h^{2,2}(\hat{Z})$ by summing $h^{2,2}[H^4(Y)]$ in (3.50) and $h^{2,2}(\hat{Z})$ in (3.61). In fact, this is how ref. [19] derived the formula (3.3), (3.4) for $h^{1,1}$ and $h^{3,1}$ of a Calabi-Yau hypersurface fourfold $\hat{Z}$, and it is a straightforward generalization to use (3.15) to determine $h^{2,2}(\hat{Z})$ in this way. The dimension of the $H^{2,2}$

[12] Prop. 5.8 of [38] obtained the formula (3.32) by using the algorithm reviewed here.

JHEP01(2015)047

component, however, does not have to be determined in this way: for a smooth fourfold $\hat{Z}$, the formula [9, 12]

$$h^{2,2}(\hat{Z}) = 44 + 4\left(h^{1,1}(\hat{Z}) + h^{3,1}(\hat{Z})\right) - 2h^{2,1}(\hat{Z})\,. \tag{3.62}$$

makes it possible to determine $h^{2,2}(\hat{Z})$ from the three other Hodge numbers that are already determined through (3.3)–(3.5).

The exact sequence (3.15) is still very useful for the purpose of studying the decomposition (1.2). This is because all the independent divisors of a hypersurface Calabi-Yau fourfold $\hat{Z} \subset \mathbb{P}^5_{\Sigma'}$ appear in the form of irreducible components of toric divisors $\hat{Y}_i$ of $\hat{Z}$. We can therefore take a set of generators of the vertical component $H^{2,2}_V(\hat{Z})$ within $[H^4(Y)]^{2,2}$. Homological equivalence among the generators has already been taken care of in the study of $[H^4(Y)]^{2,2}$ in section 3.4. In this section, we start off with identifying which subspace of $[H^4(Y)]^{2,2}$ corresponds to the vertical component $H^{2,2}_V(\hat{Z})$. Mirror symmetry is then used to identify the horizontal component $H^{2,2}_H(\hat{Z};\mathbb{C}) := H^4_H(\hat{Z};\mathbb{C}) \cap H^{2,2}(\hat{Z};\mathbb{C})$. We will comment on the geometry associated with the remaining component $H^{2,2}_{RM}(\hat{Z};\mathbb{C})$ at the end.

3.6.1 The vertical component

Let us discuss which subspace of $H^{1,1}(\hat{Y}_i)$ is generated by vertical cycles for the cases with $k_0 = 1$, $n-3 = 2$, $n-2 = 3$ and $n-1 = 4$. We begin with a divisor $\hat{Y}_i$ corresponding to a vertex ν_i of $\widetilde{\Delta}$ (i.e., $k_0 = 1$). The formula (3.39) can be rewritten as

$$h^{1,1}(\hat{Y}_i) = {}_{\nu_i}\ell_1(\widetilde{\Delta}_{\leq n-2}) - (n-1) + \sum_{(\widetilde{\Theta}^{[n-2]},\Theta^{[1]})} \left[{}_{\nu_i}\ell_1^{*\circ}(\widetilde{\Theta}^{[n-2]}) + {}_{\nu_i}\ell_1^{*\bullet}(\widetilde{\Theta}^{[n-2]})\right] \times \ell^*(\Theta^{[1]}), \tag{3.63}$$

where ${}_{\nu_i}\ell_1^{*\circ}(\widetilde{\Theta}^{[n-2]})$ is the number of 1-simplices whose endpoints are ν_i and one of the interior points of a face $\widetilde{\Theta}^{[n-2]}$, and ${}_{\nu_i}\ell_1^{*\bullet}(\widetilde{\Theta}^{[n-2]})$ is the number of 1-simplices which run through the interior of $\widetilde{\Theta}^{[n-2]}$, but have both end points on the boundary of $\widetilde{\Theta}^{[n-2]}$. The first two terms account for the dimension of the space of algebraic cycles obtained as the intersection of $\hat{Y}_i$ with another toric divisor (i.e., a divisor of $\hat{Z}$ that descends from the toric ambient space $\mathbb{P}^{n=5}_{\Sigma'}$). When the intersection of a pair of toric divisors of the form $\hat{Y}_i \cap \hat{Y}_j$ corresponds to a 1-simplex counted in ${}_{\nu_i}\ell_1^{*\circ}(\widetilde{\Theta}^{[n-2]})$, however, the toric divisor $\hat{Y}_j$ corresponding to an interior point of a codimension-two face of $\widetilde{\Delta}$ consists of $\ell^*(\Theta^{[1]}) + 1$ irreducible components, each one of which are independent in $H^{1,1}(\hat{Z})$. Therefore each one of $\hat{Y}_i \cap [\hat{Y}_j]_{\rm irr}$'s can be taken as an independent generator of the vertical algebraic cycles. The term ${}_{\nu_i}\ell_1^{*\circ}(\widetilde{\Theta}^{[n-2]})\ell^*(\Theta^{[1]})$ should therefore be counted as a part of the vertical component $H^{2,2}(\hat{Z})$.

1-simplices counted in ${}_{\nu_i}\ell_1^{*\bullet}(\widetilde{\Theta}^{[n-2]})$, however, correspond to algebraic cycles of the form $\hat{Y}_i \cap \hat{Y}_j$, with $\hat{Y}_j$ corresponding to a point in a face of codimension-three or higher. In such cases, $\hat{Y}_i \cap \hat{Y}_j$ consists of $\ell^*(\Theta^{[1]}) + 1$ irreducible components, but only one linear combination of those irreducible components, $\hat{Y}_i \cap \hat{Y}_j$, should be regarded as a vertical cycle. Thus, there are algebraic but non-vertical cycles left over in $h^{1,1}(\hat{Y}_i)$ if and only if

$${}_{\nu_i}\ell_1^{*\bullet}(\widetilde{\Theta}^{[n-2]})\ell^*(\Theta^{[1]}) \neq 0. \tag{3.64}$$

JHEP01(2015)047

Let us move on to $H^{1,1}(\hat{Y}_i)$ for a toric divisor $\hat{Y}_i$ corresponding to an interior point of $\widetilde{\Theta}^{[1]}$ (i.e., $k_0 = n-3 = 2$). The first line of (3.43) is rewritten just like in (3.63), and the same interpretation applies also in this case. The remaining correction term $\bar{e}_c^{1,1}(Z_{\Theta^{[3]}})$ in (3.43) in the $k_0 = n-3$ case is not regarded as part of the vertical component either. To see this, let us use a long exact sequence like (3.11), decomposing $\hat{Y}_i$ into the primary stratum $Z_{\rho_i} = \mathbb{T}^{k_0-1} \times Z_{\Theta_i^{[3]}}$ and the rest $\hat{Y}_i \backslash Z_{\rho_i} = \amalg_{\rho_i < \sigma \in \Sigma'} Z_\sigma$.

$$\begin{tikzcd}
\cdots \arrow[r] & H_c^{2n-6}(Z_{\rho_i}) \arrow[r] & H_c^{2n-6}(\hat{Y}_i) \arrow[r] & H_c^{2n-6}(\hat{Y}_i \backslash Z_{\rho_i}) \arrow[dll, rounded corners] \\
& H_c^{2n-5}(Z_{\rho_i}) \arrow[r] & H_c^{2n-5}(\hat{Y}_i) \arrow[r] & H_c^{2n-5}(\hat{Y}_i \backslash Z_{\rho_i}) \arrow[r] & \cdots .
\end{tikzcd} \tag{3.65}$$

We focus on the $(n-3, n-3)$ components in this sequence in order to study $h^{n-3,n-3}[H_c^{2n-6}(\hat{Y}_i)]$. The cohomology groups $H_c^k(Z_{\rho_i})$ for $k = 2n-6$ and $2n-5$ are determined by

$$[H_c^{2n-6}(\mathbb{T}^{n-4} \times Z_{\Theta_i^{[3]}})]^{n-3,n-3} = [H_c^{2n-8}(\mathbb{T}^{n-4})]^{n-4,n-4} \otimes [H_c^2(Z_{\Theta_i^{[3]}})]^{1,1}, \tag{3.66}$$

$$\begin{aligned}
[H_c^{2n-5}(\mathbb{T}^{n-4} \times Z_{\Theta_i^{[3]}})]^{n-3,n-3} &= [H_c^{2n-9}(\mathbb{T}^{n-4})]^{n-5,n-5} \otimes [H_c^4(Z_{\Theta_i^{[3]}})]^{2,2} \\
&\quad \oplus [H_c^{2n-8}(\mathbb{T}^{n-4})]^{n-4,n-4} \otimes [H_c^3(Z_{\Theta_i^{[3]}})]^{1,1} ,
\end{aligned} \tag{3.67}$$

and (3.12). Thus we find

$$h^{n-3,n-3}[H_c^{2n-6}(Z_{\rho_i})] = \bar{e}_c^{1,1}(Z_{\Theta_i^{[3]}}) , \qquad h^{n-3,n-3}[H_c^{2n-5}(Z_{\rho_i})] = (n-4)+3 . \tag{3.68}$$

As for $H_c^{2n-6}(\hat{Y}_i \backslash Z_{\rho_i})$, it is enough to note that all of the irreducible components (strata) in $\hat{Y}_i \backslash Z_{\rho_i}$ are at most of complex dimension $(n-3)$, so that it suffices to count the number of such irreducible components, which is in turn determined by ${}_{\nu_i}\ell_1(\widetilde{\Delta}_{\leq n-3}) + \sum {}_{\nu_i}\ell_1(\widetilde{\Theta}^{[n-2]}) \left(\ell(\Theta^{[1]})+1\right)$. Therefore, the kernel of $[H_c^{2n-6}(\hat{Y}_i \backslash Z_{\rho_i})]^{n-3,n-3} \longrightarrow [H_c^{2n-5}(Z_{\rho_i})]^{n-3,n-3}$ accounts for the first line of (3.43). The correction term — the second line of (3.43) — comes from $[H^{2n-6}(Z_{\rho_i})]^{n-3,n-3}$. All the vertical components in $[H_c^{2n-6}(\hat{Y}_i)]^{n-3,n-3}$ are contained within $[H_c^{2n-6}(\hat{Y}_i \backslash Z_{\rho_i})]^{n-3,n-3}$, and hence the correction term $\bar{e}_c^{1,1}(Z_\Theta^{[3]})$ does not belong to the vertical component.

In the case $k_0 = n-2$, ν_i is an interior point of a two-dimensional face. The vertical component in $H^{1,1}(\hat{Y}_i)$ is identified in the same way as far as the first line of (3.43) is concerned; the term ${}_{\nu_i}\ell_1^{*\bullet}(\widetilde{\Theta}^{[3]})\ell^*(\Theta^{[1]})$ corresponds to cycles that are algebraic, but not vertical. The interpretation of the correction term $\bar{e}_c^{0,0}(Z_{\Theta_i^{[2]}})$ in (3.43), on the other hand, is quite different from the one in the $k_0 = n-3$ case.

Note first that in this case, $\hat{Y}_i$ is an $(n-2)$-fold which can be regarded as a flat family of toric $(n-3) = (k_0-1)$-dimensional varieties over a curve $\Sigma_{\Theta_i^{[2]}}$, which is the closure of $Z_{\Theta_i^{[2]}} \subset \mathbb{T}^2$. The fibre over any point in $Z_{\Theta_i^{[2]}}$ is given by toric data (ν_i-containing simplices within the face $\widetilde{\Theta}^{[k_0-1]}$). The second thing to note is that $Z_{\Theta_i^{[2]}}$ is a Riemann surface (of

JHEP01(2015)047

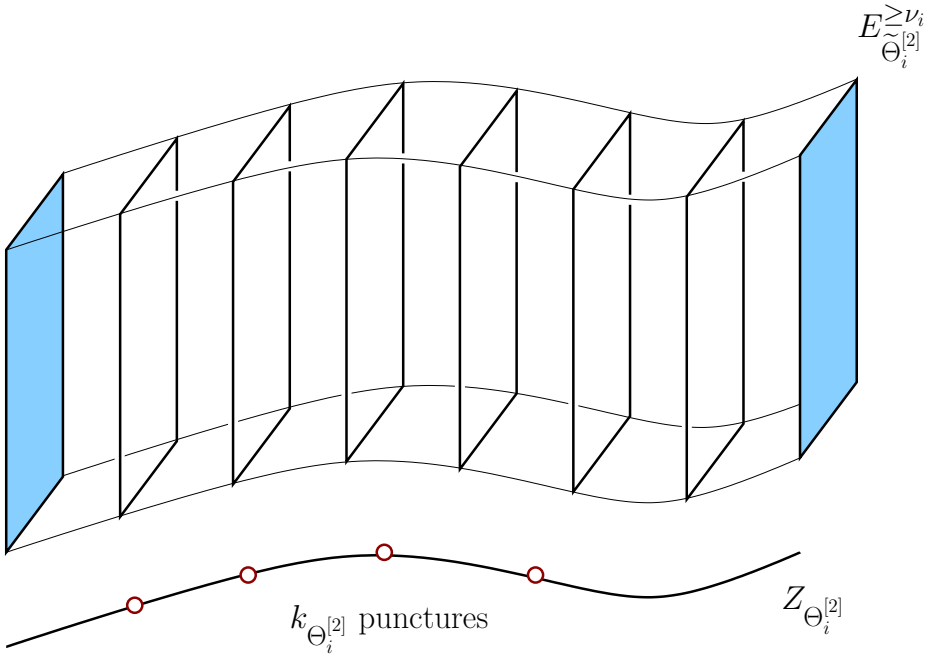

Figure 2. $\hat{Y}_i$ as a fibration of $E^{\geq \nu_i}_{\widetilde{\Theta}_i^{[2]}}$ over the curve $Z_{\Theta_i^{[2]}}$ with $k_{\Theta_i^{[2]}}$ punctures. Divisors of a generic fibre correspond to divisors of $\hat{Y}_i$ by sweeping them over the whole base.

genus $\ell^*(\Theta_i^{[2]})$) with a finite number of punctures. The number of punctures (denoted by $k_{\Theta_i^{[2]}}$) is given by

$$k_{\Theta_i^{[2]}} - 1 = [H_c^1(Z_{\Theta_i^{[2]}})]^{0,0} = 2 - \bar{e}_c^{0,0}(Z_{\Theta_i^{[2]}})\,. \tag{3.69}$$

The compact Riemann surface $\Sigma_{\Theta_i^{[2]}}$ is obtained by filling these $k_{\Theta_i^{[2]}}$ punctures in $Z_{\Theta_i^{[2]}}$. Any one of those punctures is assigned to one of the 1-dimensional faces $\Theta^{[1]} \leq \Theta_i^{[2]}$ (see also footnote 14), and the toric $k_0 - 1$-dimensional fibre geometry is determined by the ν_i-containing simplices in the face $\widetilde{\Theta}^{[k_0]} \geq \widetilde{\Theta}_i^{[k_0-1]}$ dual to $\Theta^{[1]}$. From this point of view, the first line of (3.43), with $-(n-1)$ replaced by $-(k_0-1)$, accounts for the number of irreducible divisors of $\hat{Y}_i$ modulo the toric linear equivalence acting in the fibre direction (see figure 2). The remaining contribution to (3.43) is precisely $\bar{e}_c^{0,0}(Z_{\Theta_i^{[2]}}) - (n - k_0) = 1 - k_{\Theta_i^{[2]}}$. This correction term is now understood as counting only the generic fibre class for an independent divisor in $\hat{Y}_i$, while removing the total fibre class at each one of the $k_{\Theta_i^{[2]}}$ points in $\Sigma_{\Theta_i^{[2]}}$ from the formula of $h^{1,1}(\hat{Y}_i)$. This subtraction is necessary because the total fibre class over any point in $\Sigma_{\Theta_i^{[2]}}$ is algebraically equivalent (see figure 3).

The correction term $\bar{e}_c^{0,0}(Z_{\Theta_i^{[2]}}) = 3 - k_{\Theta_i^{[2]}}$ should always be negative, because this term accounts for the algebraic equivalence relations among the generators of $H_c^{2,2}(\hat{Y}_i)$. It is not hard to see this. For a dual pair of faces $(\widetilde{\Theta}_i^{[2]}, \Theta_i^{[2]})$ and an interior point ν_i of $\widetilde{\Theta}_i^{[2]}$, list up all the dual pairs of faces $\{(\widetilde{\Theta}_a^{[3]}, \Theta_a^{[1]}) \mid a \in A_i\}$ labelled by $a \in A_i$ such that

$$\widetilde{\Theta}_a^{[3]} \geq \widetilde{\Theta}_i^{[2]} \qquad \text{and} \qquad \Theta_a^{[1]} \leq \Theta_i^{[2]}.$$

JHEP01(2015)047

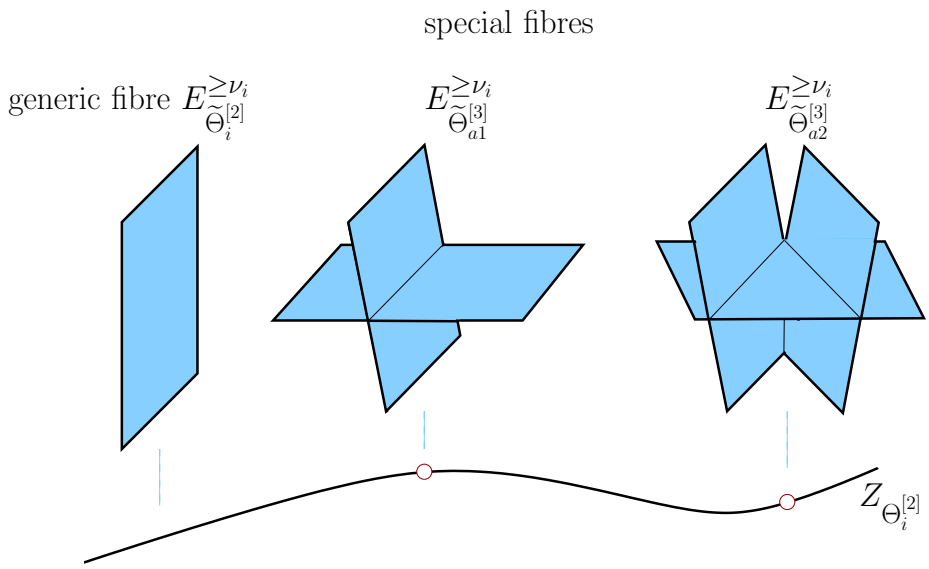

Figure 3. Over specific points, the fibre degenerates and becomes reducible. All fibres are algebraically (and hence homologically) equivalent, however.

Each one of those pairs leaves $\ell(\Theta^{[1]}_a) = [1 + \ell^*(\Theta^{[1]}_a)]$ points in $\Sigma_{\Theta^{[2]}_i}$ for which the fibre of $\hat{Y}_i \longrightarrow \Sigma_{\Theta^{[2]}_i}$ is a (not necessarily irreducible) complex surface $E^{\geq \nu_i}_{\widetilde{\Theta}^{[3]}_a}$ rather than the generic fibre $E^{\geq \nu_i}_{\widetilde{\Theta}^{[2]}_i}$. Therefore

$$\bar{e}^{0,0}_c(Z_{\Theta^{[2]}_i}) = 3 - k_{\Theta^{[2]}_i} = 3 - \sum_{\Theta^{[1]}_a \leq \Theta^{[2]}_i} [1 + \ell^*(\Theta^{[1]}_a)] = 3 - \#\{\Theta^{[1]}_a \leq \Theta^{[2]}_i\} - \sum_{\Theta^{[1]}_a \leq \Theta^{[2]}_i} \ell^*(\Theta^{[1]}_a). \tag{3.70}$$

The last term is obviously negative as the number of edges of a two-dimensional face $\Theta^{[2]}$ is always greater than or equal to 3. Thus, $\bar{e}^{0,0}_c(Z_{\Theta^{[2]}_i}) \leq 0$.

The algebraic equivalence relations encoded in $\bar{e}^{0,0}_c(Z_{\Theta^{[2]}_i})$ are sometimes among algebraic cycles in the vertical component, and sometimes among cycles in the non-vertical component. Figure 4 is a schematic picture of the singular fibres of $\hat{Y}_i \longrightarrow \Sigma_{\Theta^{[2]}_i}$ at the $\ell^*(\Theta^{[1]}_a) + 1$ punctures associated with a given face $\Theta^{[1]}_a \leq \Theta^{[2]}_i$. There is always at least one combination of the total fibre classes that is in the vertical component; such a combination of the total fibre classes is in fact even in the space of vertical cycles generated by toric divisors. Such a fibre class is algebraically equivalent to the generic fibre class of $\hat{Y}_i \longrightarrow \Sigma_{\Theta^{[2]}}$, and is subtracted by the algebraic equivalence on $\Sigma_{\Theta^{[2]}_i}$ corresponding to the $(3 - \#\{\Theta^{[1]}_a \leq \Theta^{[2]}_i\})$ term in $\bar{e}^{0,0}_c(Z_{\Theta^{[2]}_i})$ above.

Suppose that the dual face pair $(\widetilde{\Theta}^{[3]}_a, \Theta^{[1]}_a)$ for an $a \in A_i$ is such that *all* the 1-simplices counted in ${}_{\nu_i}\ell^*_1(\widetilde{\Theta}^{[3]}_a)$ end at interior points of $\widetilde{\Theta}^{[3]}_a$. This means that all the $[1 + \ell^*(\Theta^{[1]}_a)]$ total fibre classes of $\hat{Y}_i \longrightarrow \Sigma_{\Theta^{[2]}_i}$ belong to the space of vertical cycles (see figure 4). Let $A\mathrm{v}_i$ be the subset of the labels $a \in A_i$ satisfying the condition above, and $(\widetilde{\Theta}^{[3]}_{\mathrm{v}}, \Theta^{[1]}_{\mathrm{v}})$ be such a

JHEP01(2015)047

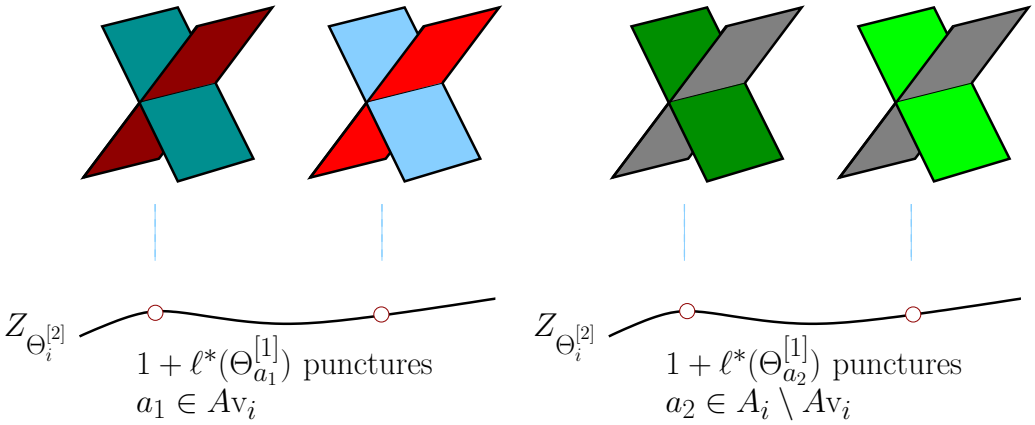

Figure 4. (colour online) Fibre components corresponding to points ν_i contributing to $\Theta_v^{[3]}$ (left hand side) and $\Theta_{nv}^{[3]}$ (right hand side). The fibre components drawn in red, blue and green correspond to fibre components which are obtained by intersecting appropriate divisors. These components arise from one-simplices connecting ν_i to an interior point of the face $\widetilde{\Theta}_a^{[3]}$. When there is a one-simplex connecting ν_i to a point on the boundary of $\widetilde{\Theta}_a^{[3]}$, only the sum of several components of different fibres, drawn in grey, arises from an intersection of divisors (so that it should be considered vertical). Again, the two degenerate fibres on the left hand side are algebraically equivalent, as are the two degenerate fibres on the right hand side.

dual pair of faces. The space of vertical but non-toric cycles originating from $H^{1,1}(\hat{Y}_i)$ is reduced by $-\sum_{\Theta_{\rm v}^{[1]}\leq\Theta^{[2]}}\ell^*(\Theta_{\rm v}^{[1]})$ due to the algebraic equivalence.

A dual pair of faces $(\widetilde{\Theta}_a^{[3]},\Theta_a^{[1]})$ otherwise (i.e., $a\in A_i\setminus Av_i$) has at least one 1-simplex counted in ${}_{\nu_i}\ell_1^*(\widetilde{\Theta}_a^{[3]})$ whose boundary other than ν_i is not in the interior of $\widetilde{\Theta}^{[3]}$. Such pairs of faces are denoted by $(\widetilde{\Theta}_{\rm nv}^{[3]},\Theta_{\rm nv}^{[1]})$. The remaining $-\sum_{\Theta_{\rm nv}^{[1]}\leq\Theta_i^{[2]}}\ell^*(\Theta_{\rm nv}^{[1]})$ independent algebraic equivalences reduce the dimension of the space of algebraic, but non-vertical four-cycles. To summarize,

$$\begin{aligned}
V^{\rm alg}(\hat{Z}) &= \sum_{(\widetilde{\Theta}^{[2]},\Theta^{[2]})}\ell^*(\widetilde{\Theta}^{[2]})\left\{-\ell^*(2\Theta^{[2]})+4\ell^*(\Theta^{[2]})\right\},\\
&= \sum_{(\widetilde{\Theta}^{[2]},\Theta^{[2]})}\ell^*(\widetilde{\Theta}^{[2]})(3-k_{\Theta^{[2]}}) = V^{\rm alg}_{\rm tor}(\hat{Z})+V^{\rm alg}_{\rm cor}(\hat{Z})+V^{\rm alg}_{\rm rm}(\hat{Z}); \qquad (3.71)\\
V^{\rm alg}_{\rm tor}(\hat{Z}) &:= \sum_{(\widetilde{\Theta}^{[2]},\Theta^{[2]})}\ell^*(\widetilde{\Theta}^{[2]})\left(3-\#\{\Theta^{[1]}\leq\Theta^{[2]}\}\right),\\
V^{\rm alg}_{\rm cor}(\hat{Z}) &:= -\sum_{(\widetilde{\Theta}^{[2]},\Theta^{[2]})}\ell^*(\widetilde{\Theta}^{[2]})\sum_{\Theta_{\rm v}^{[1]}\leq\Theta^{[2]}}\ell^*(\Theta_{\rm v}^{[1]}),\\
V^{\rm alg}_{\rm rm}(\hat{Z}) &:= -\sum_{(\widetilde{\Theta}^{[2]},\Theta^{[2]})}\ell^*(\widetilde{\Theta}^{[2]})\sum_{\Theta_{\rm nv}^{[1]}\leq\Theta^{[2]}}\ell^*(\Theta_{\rm nv}^{[1]}). \qquad (3.72)
\end{aligned}$$

All the three terms are negative.

Finally, in the cases of $k_0=n-1$, it is easy to see that all of the generators of the space $\oplus_{\rm irr}H_c^{2,2}([\hat{Y}_i]_{\rm irr})$ are vertical cycles. The space of vertical cycles generated by

JHEP01(2015)047

the toric divisors, however, has a dimension given by (3.48) without being multiplied by $e_c^{0,0}(Z_{\Theta_i^{[1]}}) = [1 + \ell^*(\Theta_i^{[1]})]$.

Having seen which subspace of $H_c^{2,2}(\hat{Y}_i)$ is identified with a part of the vertical component $H^{2,2}(\hat{Z})$, we are now ready to determine the dimension of the vertical component in $H_V^{2,2}(\hat{Z})$. Setting aside the components in $[H^4(Y)]^{2,2}$ that have turned out to be non-vertical, we have

$$h^{2,2}[H^4(Y)] = h_V^{2,2}(\hat{Z}) + \left[RM_a(\hat{Z}) + V_{\rm rm}^{\rm alg}(\hat{Z})\right] + NV_1(\hat{Z}), \tag{3.73}$$

$$h_V^{2,2}(\hat{Z}) = \left[V_{\rm tor}(\hat{Z}) + V_{\rm tor}^{\rm alg}(\hat{Z})\right] + \left[V_{\rm cor}(\hat{Z}) + V_{\rm cor}^{\rm alg}(\hat{Z})\right], \tag{3.74}$$

where

$$\begin{aligned}
V_{\rm tor}(\hat{Z}) &:= \ell_1(\widetilde{\Delta}_{\leq n-2}) + \frac{n(n-1)}{2} \\
&\quad -(n-1)\left[\ell(\widetilde{\Delta}) - \sum_{\widetilde{\Theta}^{[n-1]}\leq\widetilde{\Delta}} \ell^*(\widetilde{\Theta}^{[n-1]}) - \sum_{\widetilde{\Theta}^{[n-2]}\leq\widetilde{\Delta}} \ell^*(\widetilde{\Theta}^{[n-2]}) - 1\right] \\
&\quad -(n-2)\sum_{\widetilde{\Theta}^{[n-2]}} \ell^*(\widetilde{\Theta}^{[n-2]}) \\
V_{\rm cor}(\hat{Z}) &:= \sum_{(\widetilde{\Theta}^{[3]},\Theta^{[1]})} \left[\ell_1^{*\circ}(\widetilde{\Theta}^{[3]}) - 3\ell^*(\widetilde{\Theta}^{[3]})\right] \times \ell^*(\Theta^{[1]}), \\
RM_a(\hat{Z}) &= \sum_{(\widetilde{\Theta}^{[3]},\Theta^{[1]})} \ell_1^{*\bullet}(\widetilde{\Theta}^{[3]})\ell^*(\Theta^{[1]}), \\
NV_1(\hat{Z}) &:= \sum_{(\widetilde{\Theta}^{[1]},\Theta^{[3]})} \ell^*(\widetilde{\Theta}^{[1]}) \times \left(\ell^*(2\Theta^{[3]}) - 4\ell^*(\Theta^{[3]}) - \sum_{\Theta^{[2]}\leq\Theta^{[3]}} \ell^*(\Theta^{[2]})\right).
\end{aligned} \tag{3.75}$$

Here, $\ell_1^{*\circ}(\widetilde{\Theta}^{[3]})$ is the number of 1-simplices that run through the interior of a face $\widetilde{\Theta}^{[3]}$ and have at least one boundary point in the interior of $\widetilde{\Theta}^{[3]}$. $\ell_1^{*\bullet}(\widetilde{\Theta}^{[3]})$ is the number of all other 1-simplices that run through the interior of the face $\widetilde{\Theta}^{[3]}$; it only counts those one-simplices which start and end on the boundary of the face $\widetilde{\Theta}^{[3]}$.

The Chow group $Ch^2(\hat{Z})$ is obtained by taking a quotient of the space of algebraic (complex)-two-cycles by rational equivalence, whereas we have also exploited algebraic equivalence in studying the cohomology group $H^{2,2}(\hat{Z})$. The Deligne cohomology $H_D^4(\hat{Z};\mathbb{Z}(2))$ and the closely related Chow group $Ch^2(\hat{Z})$ not only contain information on the flux field strength $G^{(4)}$ for F-theory, but also on the three-form potential $C^{(3)}$. Truly of interest in the context of physics application, though, will be $H_D^4(\hat{Z}_p;\mathbb{Z}(2))$ for $\hat{Z}_p$ corresponding to a point $p \in \mathcal{M}_*$ in some Noether-Lefschetz locus, rather than that of $\hat{Z}_p$ at a generic point $p \in \mathcal{M}_*$. Fluxes which are in the primary horizontal subspace may also become algebraic in a Noether-Lefschetz locus, where we are expected to end up from the superpotential $W \propto \int_{\hat{Z}} G^{(4)} \wedge \Omega$. Ignoring the original context of physics applications, however, let us leave an interesting observation on $Ch^2(\hat{Z})$ for $\hat{Z}$ corresponding to a generic point $p \in \mathcal{M}_*$. The relevance of the refined data contained in $Ch^2(\hat{Z})$ (compared with

JHEP01(2015)047

homology) to F-theory fluxes has recently been discussed in [45] (see also the literatures therein).

For $\hat{Z}_p$ at a generic point in complex structure moduli space $p \in \mathcal{M}_*$, algebraic cycles generate a subspace of $H^{2,2}(\hat{Z})$ with a dimension no less than

$$V_{\rm tor}(\hat{Z}) + V_{\rm cor}(\hat{Z}) + RM_a(\hat{Z}) + V^{\rm alg}(\hat{Z}),$$

and possibly larger than this by at most $NV_1(\hat{Z})$. Only the first term descends from algebraic cycles of the toric ambient space. Apart from the last term, all the equivalence relations that have been exploited are linear (rational) equivalence. The last term, $V^{\rm alg}(\hat{Z})$, introduces algebraic equivalence relations among those cycles as we have already seen. They are associated with divisors $\hat{Y}_i$ of $\hat{Z}$ corresponding to interior points ν_i of two-dimensional faces $\widetilde{\Theta}^{[2]} \leq \widetilde{\Delta}$. The threefolds $\hat{Y}_i$ can be seen as flat fibrations of surfaces over curves $\Sigma_{\Theta^{[2]}}$ with genus $g = \ell^*(\Theta^{[2]})$. The fibre classes over any two points in $\Sigma_{\Theta^{[2]}}$ are mutually algebraically equivalent, and they are identified in the cohomology group. Under rational equivalence, however, they form a family of *inequivalent* classes parametrized by $g = \ell^*(\Theta^{[2]})$ complex parameters. This is analogous to divisors (points) on the curve $\Sigma_{\Theta^{[2]}}$, which are classified under linear equivalence by $\mathrm{Pic}(\Sigma_{\Theta^{[2]}})$, which has $g = \dim_{\mathbb{C}}[\mathrm{Pic}^0(\Sigma^{[2]}_{\Theta})]$ complex parameters more than the discrete data (the first Chern class) counted in $H^{1,1}(\Sigma_{\Theta^{[2]}})$. Noting that

$$h^{2,1}(\hat{Z}) = \sum_{(\widetilde{\Theta}^{[2]},\Theta^{[2]})} \ell^*(\widetilde{\Theta}^{[2]})\ell^*(\Theta^{[2]}) = \sum_{(\widetilde{\Theta}^{[2]},\Theta^{[2]})} \ell^*(\widetilde{\Theta}^{[2]})g(\Sigma_{\Theta^{[2]}}), \tag{3.76}$$

we see that the $Ch^2(\hat{Z})$ group contains $h^{2,1}(\hat{Z})$ more complex parameters than the cohomology group, and that this difference comes from divisors $\hat{Y}_i$ of $\hat{Z}$ that are regarded as flat surface fibration over curves with $g > 0$.

3.6.2 Horizontal and remaining components

Since the vertical component $H^{2,2}_V(\hat{Z})$ has been identified within $[H^4(Y)]^{2,2}$, the horizontal and the remaining components in the decomposition (1.2) should live in $[H^4(Z_\Delta)]^{2,2}$ and the remaining space within $[H^4(Y)]^{2,2}$. We are going to use mirror symmetry to identify the horizontal component $H^{2,2}_H(\hat{Z})$ in $[H^4_c(Z_\Delta)]^{2,2}$.

To this end, it is convenient to verify a couple of relations among the combinatorial data first. Let us introduce the following decomposition in order to facilitate the discussion:

$$h^{2,2}[H^4(Z_\Delta)] := H_{\rm mon}(\hat{Z}) + H^{\rm red}(\hat{Z}) + NV_3(\hat{Z}), \tag{3.77}$$

where

$$\begin{aligned} H_{\rm mon}(\hat{Z}) &:= \varphi_3(\Delta) - \sum_{\Theta^{[4]}} \varphi_2(\Theta^{[4]}) + \sum_{\Theta^{[3]}} \varphi_1(\Theta^{[3]}), \\ H^{\rm red}(\hat{Z}) &:= \sum_{(\widetilde{\Theta}^{[2]},\Theta^{[2]})} \Big(3\ell^*(\widetilde{\Theta}^{[2]}) - \ell^*_1(\widetilde{\Theta}^{[2]})\Big) \times \ell^*(\Theta^{[2]}), \end{aligned}$$

JHEP01(2015)047

$$NV_3(\hat{Z}) := \sum_{(\widetilde{\Theta}^{[1]},\Theta^{[3]})} \sum_{\Theta^{[2]}\leq\Theta^{[3]}} \ell^*(\widetilde{\Theta}^{[1]}) \times \ell^*(\Theta^{[2]}) \,. \tag{3.78}$$

We claim that

$$H_{\rm mon}(\hat{Z}) = V_{\rm tor}(\hat{Z}_m), \quad H^{\rm red}(\hat{Z}) = V^{\rm alg}(\hat{Z}_m), \quad NV_1(\hat{Z}) + NV_3(\hat{Z}) = V_{\rm cor}(\hat{Z}_m) + RM_a(\hat{Z}_m). \tag{3.79}$$

This also means that the following relation holds:

$$h^{2,2}[H^4_c(Z_\Delta)] + NV_1(\hat{Z}) = V_{\rm tor}(\hat{Z}_m) + V_{\rm cor}(\hat{Z}_m) + RM_a(\hat{Z}_m) + V^{\rm alg}(\hat{Z}_m). \tag{3.80}$$

Let us verify the relations (3.79) one by one. As for the first one, note that

$$\begin{aligned}
&H_{\rm mon}(\hat{Z}) \\
&= [\ell(2\Delta) - (n+1)\ell(\Delta) + \frac{n(n+1)}{2}] \qquad (3.81)\\
&\quad - \sum_{\Theta^{[n-1]}\leq\Delta} [\ell^*(2\Theta^{[n-1]}) - n\ell^*(\Theta^{[n-1]})] + \sum_{\Theta^{[n-2]}\leq\Delta} \ell^*(\Theta^{[n-2]}), \\
&= [\ell(2\Delta) - \ell(\Delta) - \sum_{\Theta^{[n-1]}} \ell^*(2\Theta^{[n-1]})] \qquad (3.82)\\
&\quad -n[\ell(\Delta) - \sum_{\Theta^{[n-1]}} \ell^*(\Theta^{[n-1]})] + \frac{n(n+1)}{2} + \sum_{\Theta^{[n-2]}\leq\Delta} \ell^*(\Theta^{[n-2]}), \\
&= [\ell(2\Delta) - \ell(\Delta) - \sum_{\Theta^{[n-1]}} \ell^*(2\Theta^{[n-1]})] - [\ell(\Delta) - 1 - \sum_{\Theta^{[n-1]}} \ell^*(\Theta^{[n-1]})], \qquad (3.83)\\
&\quad + \left[-n + \frac{n(n+1)}{2}\right], \\
&\quad - \left[(n-1)\left[\ell(\Delta) - 1 - \sum_{\Theta^{[n-1]}} \ell^*(\Theta^{[n-1]}) - \sum_{\Theta^{[n-2]}} \ell^*(\Theta^{[n-2]})\right] + (n-2)\sum_{\Theta^{[n-2]}} \ell^*(\Theta^{[2]}),\right].
\end{aligned}$$

Obviously one only needs to verify that (3.83) is equal to $\ell_1(\Delta_{\leq n-2})$ in order to prove that $H_{\rm mon}(\hat{Z}) = V_{\rm tor}(\hat{Z}_m)$. Secondly, we see that the first term in (3.83) counts the number of lattice points in M at the "lattice-distance-2" that are not in the interior of n-dimensional cones, while the second term in (3.83) counts lattice points at the "lattice distance 1". Now remember that we assume existence of a fine unimodular triangulation of the polytope Δ (so that both $\hat{Z}_m$ and the ambient toric variety $\mathbb{P}^n_\Sigma$ are smooth). For a cone whose base at the lattice-distance 1 is a minimum volume k-simplex, lattice points at the distance 1 are the $k+1$ vertices of the k-simplex, while those at the distance 2 consist of $\binom{k+1}{1} + \binom{k+1}{2} = \binom{k+2}{2} =: N_{k,2}$ points corresponding to the vertices and 1-simplices on the k-simplex (see figure 5).[13] Because any cone of the fan $\widetilde{\Sigma}$ can be decomposed into such cones of the fan $\widetilde{\Sigma}'$,

$$\ell(2\Theta) = \ell(\Theta) + \ell_1(\Theta) \tag{3.84}$$

[13] The slice of such a cone at the distance h becomes a k-dimensional pyramid of height h (see footnote 16). The number of interior points of such a pyramid is $N_{k,h-k-1} = (h-k)_k/k!$, which becomes positive only when $h > k$. That is, a lattice point corresponding to a k-simplex is found only at the lattice distance $h > k$. At the distance 2, $\partial(2\widetilde{\Delta})$, the lattice points correspond only to vertices or 1-simplices on $\partial\widetilde{\Delta}$.

JHEP01(2015)047

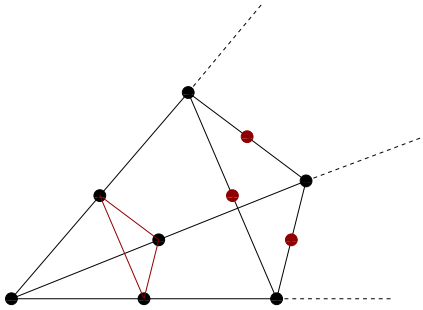

Figure 5. (colour online) The lattice points at the distance-2 layer are in one-to-one correspondence with the lattice points and 1-simplices at the distance-1 layer.

for any faces $\Theta < \Delta$. Using recursion with respect to the faces of Θ, similar relations can be derived for the number of internal one-simplices, $\ell_1^*(\Theta)$. This proves the equality between $\ell_1(\Delta_{\leq n-2})$ and (3.83) and also the first relation $H_{\rm mon}(\hat{Z}) = V_{\rm tor}(\hat{Z}_m)$ in (3.79).

The second one of the relations (3.79) $H^{\rm red}(\hat{Z}) = V^{\rm alg}(\hat{Z}_m)$ can be verified for each one of dual pairs, $(\widetilde{\Theta}^{[2]}, \Theta^{[2]})$. Using the relation (3.84) for the 2-dimensional face $\widetilde{\Theta}^{[2]} < \widetilde{\Delta}$, we find that[14]

$$\bar{e}_c^{0,0}(Z_{\widetilde{\Theta}^{[2]}}) = -\ell^*(2\widetilde{\Theta}^{[2]}) + 4\ell^*(\widetilde{\Theta}^{[2]}) = \left(3\ell^*(\widetilde{\Theta}^{[2]}) - \ell_1^*(\widetilde{\Theta}^{[2]})\right). \tag{3.89}$$

The third relation in (3.79) is equivalent to

$$\ell^*(2\Theta^{[3]}) - 4\ell^*(\Theta^{[3]}) = \ell_1^*(\Theta^{[3]}) - 3\ell^*(\Theta^{[3]}) \tag{3.90}$$

for each one of the faces $\Theta^{[3]} < \Delta$. This relation also follows from (3.84).

Toric divisors on $\hat{Z}_m$ are mirror to monomial deformations of the defining equation of the hypersurface $\hat{Z}$. It is thus reasonable to consider that the space spanned by mutual intersections of toric divisors — a $V_{\rm tor}(\hat{Z}_m)$-dimensional subspace of the primary vertical subspace of $\oplus_p H^{p,p}(\hat{Z}_m)$ — is mirror to second order monomial deformations of $\hat{Z}$, which must be a subspace of the primary horizontal subspace of $\oplus_p H^{p,n-1-p}(\hat{Z})$. This subspace

[14]The relation (3.69), (3.70) between $\bar{e}_c^{0,0}(Z_{\widetilde{\Theta}^{[2]}}) = -\ell^*(2\widetilde{\Theta}^{[2]}) + 4\ell^*(\widetilde{\Theta}^{[2]})$ and the number of punctures $k_{\widetilde{\Theta}^{[2]}}$ can also be derived purely combinatorially, without looking at the geometry of the curve and punctures on it. To see this, note first that $k_{\widetilde{\Theta}^{[2]}} = V_B$, where V_B is the number of lattice points appearing on the boundary of a two-dimensional simplicial complex $\widetilde{\Theta}^{[2]}$. Now, let T be the number of 2-simplices in $\widetilde{\Theta}^{[2]}$, E_I and E_B the number of 1-simplices in the interior and boundary of $\widetilde{\Theta}^{[2]}$, and V_I and V_B the number of points in the interior and boundary of $\widetilde{\Theta}^{[2]}$. The topology of $\widetilde{\Theta}^{[2]}$ and $\partial\widetilde{\Theta}^{[2]}$ indicates that

$$0 = V_B - E_B, \tag{3.85}$$

$$1 = (V_B + V_I) - (E_B + E_I) + T, \tag{3.86}$$

$$3T = 2E_I + E_B. \tag{3.87}$$

From this, we find that

$$3V_I - E_I = 3 - V_B = 3 - k_{\Theta^{[2]}}. \tag{3.88}$$

The left-hand side is precisely the right-hand side of (3.89), and is hence equal to $\bar{e}_c^{0,0}(Z_{\widetilde{\Theta}^{[2]}})$ combinatorially. This completes a combinatorial proof of the relation (3.69), (3.70), which also follows from the geometry of the curve $Z_{\widetilde{\Theta}^{[2]}}$).

JHEP01(2015)047

should have a dimension $H_{\rm mon}(\hat{Z}) = V_{\rm tor}(\hat{Z}_m)$ because of mirror symmetry. This reasoning seems to work very well: the first line of the expression (3.83) of $H_{\rm mon}(\hat{Z})$ counts the number of lattice points $2\Delta \cap M$ of the form $\tilde{\nu}_\alpha + \tilde{\nu}_\beta$ where $\tilde{\nu}_\alpha$ and $\tilde{\nu}_\beta$ have corresponding monomial deformations $D_\alpha \Omega_{\hat{Z}}$ and $D_\beta \Omega_{\hat{Z}}$, and there is a 1-simplex joining the lattice points $\tilde{\nu}_\alpha$ and $\tilde{\nu}_\beta$. It is quite reasonable to identify the point $\tilde{\nu}_\alpha + \tilde{\nu}_\beta$ in $2\Delta \cap M$ with the quadratic complex structure deformation $D_\alpha D_\beta \Omega_{\hat{Z}}$ (or $(\Omega^{-1} D_\alpha \Omega) \cdot (\Omega^{-1} D_\beta \Omega)$ in $H^2(\hat{Z}; \wedge^2 T\hat{Z})$ of [4]).

According to mirror symmetry, the subspace of non-vertical components with the dimension $NV_1(\hat{Z}) + NV_3(\hat{Z})$ must be decomposed into

$$\begin{aligned} H_{\rm cor}(\hat{Z}) &:= V_{\rm cor}(\hat{Z}_m) = \sum_{(\widetilde{\Theta}^{[1]}, \Theta^{[3]})} \ell^*(\widetilde{\Theta}^{[1]}) \times \left[\ell_1^{*\circ}(\Theta^{[3]}) - 3\ell^*(\Theta^{[3]}) \right], \\ RM_a^m(\hat{Z}) &:= RM_a(\hat{Z}_m) = \sum_{(\widetilde{\Theta}^{[1]}, \Theta^{[3]})} \ell^*(\widetilde{\Theta}^{[1]}) \ell_1^{*\bullet}(\Theta^{[3]}) . \end{aligned} \tag{3.91}$$

The space generated by $H_{\rm cor}$ generators must also be part of the primary horizontal subspace. The $H_{\rm cor}$-dimensional subspace of the primary horizontal component must correspond to $D^2 \Omega_{\hat{Z}}$ which involve at least one deformation that is not represented by a monomial, i.e. the last term of (3.4). It is reasonable that the expression of $H_{\rm cor}(\hat{Z})$ above vanishes when there is no pair of dual faces where $\ell^*(\widetilde{\Theta}^{[1]}) \ell^*(\Theta^{[3]}) \neq 0$, because there should be no non-monomial deformation of complex structure in that case.

The correction term $H^{\rm red}(\hat{Z})$ in (3.77) is mirror to the $V^{\rm alg}(\hat{Z}_m)$ algebraic equivalences, and hence will represent some redundancy in the description of the quadratic deformations of complex structure by $H_{\rm mon}(\hat{Z}) + H_{\rm cor}(\hat{Z})$ generators and $RM_a^m(\hat{Z})$ for the non-horizontal non-vertical components. $H^{\rm red}(\hat{Z})$ can be split into three, just like we did for $V^{\rm alg}(\hat{Z})$. The dimensions of those three pieces are denoted by $H^{\rm red}_{\rm mon}(\hat{Z})$, $H^{\rm red}_{\rm cor}(\hat{Z})$ and $H^{\rm red}_{\rm rm}(\hat{Z})$.

By using mirror symmetry, we finally arrive at the following formula for the vertical, horizontal and remaining components of $H^{2,2}(\hat{Z})$ of a Calabi-Yau fourfold $\hat{Z}$ obtained as a hypersurface of a toric variety $\mathbb{P}^5_{\Sigma'}$.

$$h^{2,2}(\hat{Z}) = h^{2,2}_V(\hat{Z}) + h^{2,2}_{RM}(\hat{Z}) + h^{2,2}_H(\hat{Z}), \tag{3.92}$$

$$h^{2,2}_H(\hat{Z}) = \left[H_{\rm mon}(\hat{Z}) + H^{\rm red}_{\rm mon}(\hat{Z}) \right] + \left[H_{\rm cor}(\hat{Z}) + H^{\rm red}_{\rm cor}(\hat{Z}) \right], \tag{3.93}$$

$$h^{2,2}_{RM}(\hat{Z}) = \left[RM_a(\hat{Z}) + V^{\rm alg}_{\rm rm}(\hat{Z}) \right] + \left[RM_a^m(\hat{Z}) + H^{\rm red}_{\rm rm}(\hat{Z}) \right]. \tag{3.94}$$

This result shows under which circumstances the remaining component is present. It is quite reasonable from the perspective of mirror symmetry, though, that the remaining component $H^{2,2}_{RM}(\hat{Z})$ has a dimension that is symmetric under the exchange of Δ and $\widetilde{\Delta}$.

The term $RM_a(\hat{Z})$ describes the space of algebraic cycles on divisors $\hat{Y}_i$ of $\hat{Z}$ that are not obtained by restriction of divisors of $\hat{Z}$; that is, they come from

$$\text{Coker} \left[i^*_{\hat{Y}_i \hookrightarrow \hat{Z}} : NS(\hat{Z}) \longrightarrow NS(\hat{Y}_i) \right]. \tag{3.95}$$

We do not have a robust theory on the component with the dimension $RM_a^m(\hat{Z})$ at this moment. Some of this component come from $NV_1(\hat{Z})$-dimensional subspace of $[H^4(Y)]^{2,2}$,

JHEP01(2015)047

but some may also come from the $NV_3(\hat{Z})$-dimensional subspace of $[H^4_c(Z_\Delta)]^{2,2}$. There are some examples where (a part of) the $RM^m_a(\hat{Z})$-dimensional space also represents algebraic but non-vertical cycles characterized by (3.95), as we will see in section 4.3. Not all of the components in this $RM^m_a(\hat{Z})$-dimensional space may be of this form for general choices of Δ and $\widetilde{\Delta}$, however. We just simply do not know at this moment.

3.6.3 Triangulation (resolution) independence

As we have already explained in section 2, formulating F-theory compactification on resolved fourfolds only makes sense if the dimensions of the vertical, horizontal and the remaining components (i.e., $h^{2,2}_V$, $h^{2,2}_H$ and $h^{2,2}_{RM}$) of a Calabi-Yau fourfold $\hat{Z}$ are independent of the choice of crepant resolution of singularities of Z_s (fine regular unimodular triangulation of $\widetilde{\Delta}$).[15] As we have discussed, this follows from the independence of the complex structure moduli space on which resolution is chosen.

In this section we supplement this general argument with a more specific discussion of triangulation independence for the construction discussed in this section, i.e. for resolutions $\hat{Z}$ of Z_s obtained by fine unimodular triangulations of the polytope $\widetilde{\Delta}$.

It is easy to see, first, that $H_{\rm mon}(\hat{Z})$ and $V^{\rm alg}_{\rm tor}(\hat{Z})$ do not depend on the triangulation of Δ (or $\widetilde{\Delta}$), because their expressions only involve the numbers of lattice points in polytopes. Since $V_{\rm tor}(\hat{Z})$ and $H^{\rm red}_{\rm mon}(\hat{Z})$ are mirror to $H_{\rm mon}(\hat{Z}_m)$ and $V^{\rm alg}_{\rm tor}(\hat{Z}_m)$, they are also independent of the triangulation of $\widetilde{\Delta}$ (or Δ); although the expression of $V_{\rm tor}(\hat{Z})$ involves a number of 1-simplices explicitly, we have seen by using (3.84) that $V_{\rm tor}(\hat{Z})$ is equal to $H_{\rm mon}(\hat{Z}_m)$, and the number of 1-simplices used in $V_{\rm tor}(\hat{Z})$ does not depend on the choice of triangulation. This means that both

$$\left[V_{\rm tor}(\hat{Z}) + V^{\rm alg}_{\rm tor}(\hat{Z})\right] \quad \text{and} \quad \left[H_{\rm mon}(\hat{Z}) + H^{\rm red}_{\rm mon}(\hat{Z})\right]$$

are independent of triangulations.

The dimensions of other components such as $V_{\rm cor}(\hat{Z})$, $V^{\rm alg}_{\rm cor}(\hat{Z})$, $RM_a(\hat{Z})$, etc., however, involve counting the number of 1-simplices with much more specific restrictions, and it is not obvious at first sight how we see triangulation-independence. Let us look at (3.94), however, where four terms are grouped into two. The first two terms do not depend on the triangulation of Δ, but they may depend on the triangulation of $\widetilde{\Delta}$; the last two terms, on the other hand, do not depend on the triangulation of $\widetilde{\Delta}$, but they may depend on the triangulation of Δ. The dimension of $h^{2,2}_{RM}(\hat{Z})$, however, has no chance of depending on the choice of triangulation of Δ by construction. This means that the last two terms of (3.94) combined — $[RM^m_a(\hat{Z}) + H^{\rm red}_{\rm rm}(\hat{Z})]$ — should not depend on the choice of a triangulation of Δ, and not just on the triangulation of $\widetilde{\Delta}$. Taking its mirror, we see that the combination

[15] To be more precise, the formulation of F-theory suggests this resolution independence only for Calabi-Yau fourfolds where Z_s is given by a Weierstrass-model elliptic fibration over B_3, and $\hat{Z}$ is a crepant resolution of Z_s such that $\hat{Z} \longrightarrow B_3$ remains a flat fibration. Thus, the statement here is stretching the "suggestion" a bit too far by not demanding a flat elliptic fibration, and also restricting the range of validity by focusing on $\hat{Z}$ which are obtained as hypersurfaces of toric fivefolds. Thus, an attempt of formulating flux in F-theory using resolved models $\hat{Z}$ will still survive, even when the dimensions $h^{2,2}_V$, $h^{2,2}_H$ and $h^{2,2}_{RM}$ may turn out to depend on resolutions for some Calabi-Yau fourfolds Z_s which do not admit elliptic fibrations.

JHEP01(2015)047

of the first two terms,

$$[RM_a(\hat{Z}) + V^{\rm alg}_{\rm rm}(\hat{Z})],$$

also does not depend on the triangulation of $\widetilde{\Delta}$. This proves that $h^{2,2}_{RM}(\hat{Z})$ is independent of which (fine, regular, unimodular) triangulation is chosen.

In order to prove that $h^{2,2}_{V}(\hat{Z})$ is also independent of the triangulation of $\widetilde{\Delta}$, note that $V^{\rm alg}(\hat{Z})$ and $NV_1(\hat{Z}_m) + NV_3(\hat{Z}_m)$ are independent of triangulation; they depend only on numbers of lattice points, not on 1-simplices. This means that the combination $V^{\rm alg}_{\rm cor}(\hat{Z}) + V^{\rm alg}_{\rm rm}(\hat{Z})$ is also independent of triangulation, because $V^{\rm alg}_{\rm tor}(\hat{Z})$ is, and so is the combination $[V_{\rm cor}(\hat{Z}) + RM_a(\hat{Z})]$ because of the relation (3.79). From all above, we see that the combination

$$\left[V_{\rm cor}(\hat{Z}) + V^{\rm alg}_{\rm cor}(\hat{Z})\right],$$

the second group of terms in (3.74), is also independent of triangulation. Obviously the independence of $[H_{\rm cor}(\hat{Z}) + H^{\rm red}_{\rm cor}(\hat{Z})]$ also follows from mirror symmetry.

We have therefore seen that the six groups of terms in (3.74), (3.93), (3.94) are separately independent of the choice of triangulations of $\widetilde{\Delta}$ and Δ in a toric-*hypersurface* realization of a smooth $\hat{Z}$ and singular Z_s. This statement is almost the same as the similar statement in section 2, although the argument in section 2 is about arbitrary crepant resolutions $\hat{Z}$ of Z_s, i.e. $\hat{Z}$ does not have to be a toric hypersurface. When a Calabi-Yau fourfold hypersurface $\hat{Z}$ of a toric fivefold is also realized as a complete intersection in an ambient space of higher dimensions, the separation between $[V_{\rm tor} + V^{\rm alg}_{\rm tor}]$ and $[V_{\rm cor} + V^{\rm alg}_{\rm cor}]$ may not remain the same, in general. One can also see that the argument for triangulation-independence given here exploits some combinatorics of toric data, (3.84), but still relies partially on mirror symmetry. This means that there must be some triangulation independent relations involving such numbers as $\ell^{*\bullet}_1(\Theta^{[3]})$, $\ell^{*}_1(\widetilde{\Theta}^{[1]})$ etc.

4 Examples

A couple of examples of toric-hypersurface Calabi-Yau fourfolds are presented in this section. We begin with the pair of sextic $(6) \subset \mathbb{P}^5$ and its mirror in section 4.1, where the geometry is so simple that we can compute everything by hand. It serves well for the purpose of digesting such notions as stratification and mixed Hodge structure. We will see how things work together nicely so that the long exact sequence (3.11) holds. For more complicated toric-hypersurface Calabi-Yau fourfolds, however, we need to use the computer packages `TOPCOM` [46] and `sage` [47] partially in the computation (see section 4.2). Examples in section 4.3 bring the formulae (3.74), (3.93), (3.94) and (3.72), (3.75), (3.78), (3.91) to life. We chose examples where various terms have non-zero contributions, so that we can test our geometric interpretation developed in the previous section. In section 4.4, we work on examples to be used in F-theory compactification for unified theories, and compute $h^{2,2}_V$, $h^{2,2}_H$ and $h^{2,2}_{RM}$. The results in this section are used as an input in section 6, along with additional results from appendices C and B, to study how the number of flux vacua depends on the number of generations $N_{\rm gen}$ or on the choice of the unification group of low-energy effective theories.

JHEP01(2015)047

4.1 The sextic and its mirror

As a first canonical example, let us discuss the sextic fourfold $\hat{Z}_6$, a degree-six hypersurface of $\mathbb{P}^5$, and its mirror manifold denoted by $\hat{Z}_{6,m}$. With this definition, it is easy to find (using index theorems and the Lefschetz hyperplane theorem) that the Hodge numbers of $\hat{Z}_6$ are

$$h^{p,q}(\hat{Z}_6) = \begin{array}{|ccccc} 1 & & & & 1 \\ & 426 & 0 & 1 & \\ & 0 & 1752 & 0 & \\ & 1 & 0 & 426 & \\ 1 & & & & 1 \\ \hline \end{array} . \tag{4.1}$$

In this presentation of the Hodge numbers, p starts from 0 and increases to the right, while q begins with 0 and increases upward. We will use the same presentation style in this article, when we write down the numbers $e_c^{p,q}$. For the sextic, $h^{1,1}(\hat{Z}_6) = 1$ is generated by $H|_{\hat{Z}_6}$, restriction of the hyperplane class of $\mathbb{P}^5$. The vertical component $H_V^{2,2}(\hat{Z})$ is generated by $H^2|_{\hat{Z}_6}$, and we expect $h_V^{2,2}(\hat{Z}) = 1$. Mirror symmetry also indicates that $h_H^{2,2}(\hat{Z}_{6,m}) = 1$. We compute $h_H^{2,2}(\hat{Z}_6) = h_V^{2,2}(\hat{Z}_{6,m})$ and $h_{RM}^{2,2}(\hat{Z}_6) = h_{RM}^{2,2}(\hat{Z}_{6,m})$ in section 4.1.3. Sections 4.1.1 and 4.1.2 are only meant to be warming up exercise for readers unfamiliar with such notions as mixed Hodge structure or toric stratification.

As a toric variety, $\mathbb{P}^5$ can be described by a fan over the faces of a polytope $\tilde{P}_6$, whose six vertices in $\mathbb{Z}^{\oplus 5}$ are given by

$$\begin{pmatrix} -1 & 0 & 0 & 0 & 0 & 1 \\ -1 & 0 & 0 & 0 & 1 & 0 \\ -1 & 0 & 0 & 1 & 0 & 0 \\ -1 & 0 & 1 & 0 & 0 & 0 \\ -1 & 1 & 0 & 0 & 0 & 0 \end{pmatrix} . \tag{4.2}$$

The dual polytope P_6 has six vertices in $\mathbb{Z}^{\oplus 5}$:

$$\begin{pmatrix} -1 & -1 & -1 & -1 & -1 & 5 \\ -1 & -1 & -1 & -1 & 5 & -1 \\ -1 & -1 & -1 & 5 & -1 & -1 \\ -1 & -1 & 5 & -1 & -1 & -1 \\ -1 & 5 & -1 & -1 & -1 & -1 \end{pmatrix} , \tag{4.3}$$

and one quickly recognizes that the fan Σ over the faces of P_6 gives rise to an orbifold of $\mathbb{P}^5$.

4.1.1 Geometry of the sextic: mixed Hodge structure of its subvarieties

The sextic $\hat{Z}_6$ has six toric divisors $\hat{Y}_i$, $i = 1, \cdots, 6$, corresponding to the six vertices of $\tilde{P}_6$. These toric divisors $\hat{Y}_i$ are all $(6) \subset \mathbb{P}^4$. Similarly, $\hat{Y}_i \cap \hat{Y}_j$ are surfaces $(6) \subset \mathbb{P}^3$, while $\hat{Y}_i \cap \hat{Y}_j \cap \hat{Y}_k$ are curves $(6) \subset \mathbb{P}^2$ and $\hat{Y}_i \cap \hat{Y}_j \cap \hat{Y}_k \cap \hat{Y}_l$ are six points in $\mathbb{P}^1$. These

JHEP01(2015)047

facts can be read out from the fact that the k-dimensional faces $\Theta^{[k]}$ of the polytope P_6 are k-dimensional pyramids of height-6 (7 points in one edge),[16] which are regarded as the complete linear system of the divisor $6H$ of $\mathbb{P}^k$. Exploiting e.g. index theorems in combination with the Picard-Lefschetz hyperplane theorem one easily finds that

$$
h^{p,q}(\hat{Y}_i) = \left|\begin{array}{cccc} 5 & & & 1 \\ & 255 & 1 & \\ & 1 & 255 & \\ 1 & & & 5 \end{array}\right. \qquad h^{p,q}(\hat{Y}_i \cap \hat{Y}_j) = \left|\begin{array}{ccc} 10 & & 1 \\ & 86 & \\ 1 & & 10 \end{array}\right.
$$

$$
h^{p,q}(\hat{Y}_i \cap \hat{Y}_j \cap \hat{Y}_k) = \left|\begin{array}{cc} 10 & 1 \\ 1 & 10 \end{array}\right. \qquad h^{p,q}(\hat{Y}_i \cap \hat{Y}_j \cap \hat{Y}_k \cap \hat{Y}_l) = \left|\begin{array}{c} 6 \end{array}\right. . \tag{4.4}
$$

We begin with the direct computation of $H^k(Y)$ using the explicit results (4.4) and the Mayer-Vietoris spectral sequence, where $Y = \cup_i \hat{Y}_i$ is the complement of the primary stratum Z_{P_6} in $\hat{Z}_6$. The compact support cohomology groups of Z_{P_6}, on the other hand, are obtained by following the algorithm of [38] (which we have reviewed partially in the previous section). Those computations allow us to see that the long exact sequence (3.11) nicely reproduces the Hodge diamond (4.1); see (4.12).

It is important in the sum rule (3.28), (3.31) and the algorithm of [38] that they can be applied to polytopes that do not necessarily correspond to the complete linear system defining a family of Calabi-Yau hypersurfaces; the sum rule (3.31) has been used in (3.52), (3.53), for example. Thus, we will compute $e_c^{p,q}(Z_{\Theta^{[k]}})$ from the Hodge diamonds of the subvarieties (4.4), and confirm that the sum rule (3.28), (3.31) is indeed satisfied at the end of this section.

The cohomology group of the compact (but singular) geometry $Y = \cup_i \hat{Y}_i$ is computed by the Mayer-Vietoris spectral sequence. At the stage of $d_1^{pq} : E_1^{p,q} \longrightarrow E_1^{p+1,q}$, we have

$$
\begin{array}{|c|cc|cc|cc}
\begin{array}{c} 6\times(1) \\ 0 \end{array} & & & & & & \\ \hline
\begin{array}{c} 6\times(0,1,0) \\ 6\times(5,255,255,5) \end{array} & \begin{array}{c}\longrightarrow \\ \longrightarrow\end{array} & \begin{array}{c} 15\times(1) \\ 0 \end{array} & & & & \\ \hline
\begin{array}{c} 6\times(0,1,0) \\ 0 \end{array} & \begin{array}{c}\longrightarrow \\ \longrightarrow\end{array} & \begin{array}{c} 15\times(10,86,10) \\ 0 \end{array} & \begin{array}{c}\longrightarrow \\ \longrightarrow\end{array} & \begin{array}{c} 20\times(1) \\ 20\times(10,10) \end{array} & & \\ \hline
6\times(1) & \longrightarrow & 15\times(1) & \longrightarrow & 20\times(1) & \longrightarrow & 15\times(6)
\end{array} , \tag{4.5}
$$

where $\dim(E_1^{p,q})$ is shown in the $(p+1)$-th column from the left and the $(q+1)$-th row from the bottom, in a form maintaining the information of the Hodge filtration. To proceed to the stage $E_2^{p,q}$ in the spectral sequence calculation, we need to know the morphisms

[16] A k-dimensional pyramid of height-h is (anything lattice-isomorphic to) the minimal k-dimensional simplex in a lattice $\mathbb{Z}^{\oplus k}$ enlarged by a positive integer h. The number of lattice points on such a pyramid is $N_{k,h} := [(h+1)(h+2)\cdots(h+k)]/k!$, while the number of interior points is given by $N_{k,h-k-1}$.

JHEP01(2015)047

$d_1^{pq} : E_1^{p,q} \longrightarrow E_1^{p+1,q}$. In the case of the sextic, the morphism $d_1 : E_1^{0,q} \longrightarrow E_1^{1,q}$ has a 5-dimensional image for $q = 0, 2, 4$, while $d_1 : E_1^{1,q} \longrightarrow E_1^{2,q}$ has a 10-dimensional image for $q = 0, 2$. The morphism $d_1 : E_1^{2,0} \longrightarrow E_1^{3,0}$ has a 10-dimensional image. Combining all of the above, we have that

$$\dim(E_2^{p,q}) = \begin{array}{|c|c|c|c|} \hline (6) & & & \\ \hline (0,1,0) & (10) & & \\ (30,1530,1530,30) & & & \\ \hline (0,1,0) & (150,1275,150) & (10) & \\ & & (200,200) & \\ \hline (1) & (0) & (0) & (80) \\ \hline \end{array} . \tag{4.6}$$

We conclude from this that

$$h^{3,3}[H^6(Y)] = 6, \quad h^{2,2}[H^5(Y)] = 10, \quad h^{0,0}[H^0(Y)] = 1, \quad h^{1,1}[H^2(Y)] = 1, \tag{4.7}$$

and all other Hodge-Deligne numbers of the cohomology groups $H^k(Y)$ with $k = 0, 1, 2, 5, 6$ vanish. As for $H^k(Y)$ with $k = 3, 4$,

$$h^{p,q}[H^3(Y)] = \begin{array}{|cccc} 30 & & & \\ 150 & 1530 & & \\ 200 & 1275 & 1530 & \\ 80 & 200 & 150 & 30 \end{array} , \qquad h^{p,q}[H^4(Y)] = \begin{array}{|ccc} 0 & & \\ 0 & 1 & \\ 10 & 0 & 0 \end{array} . \tag{4.8}$$

Let us now move on to the computation the Hodge-Deligne numbers of the cohomology group of the top (primary) stratum $Z_6 = \hat{Z}_6 \setminus Y = Z_{P_6}$. They are determined by the algorithm of §5 in [38], which is precisely the one we adopted in section 3.5. We only need the values of the functions φ_i for the polytope P_6,

$$\varphi_1(P_6) = 1, \quad \varphi_2(P_6) = 456, \quad \varphi_3(P_6) = 3431, \quad \varphi_4(P_6) = 3431, \quad \varphi_5(P_6) = 456, \tag{4.9}$$

in order to use the algorithm.[17] It turns out that

$$h^{p,q}[H_c^4(Z_{P_6})] = \begin{array}{|ccccc} 1 & & & & \\ 30 & 426 & & & \\ 150 & 1530 & 1751 & & \\ 200 & 1275 & 1530 & 426 & \\ 80 & 200 & 150 & 30 & 1 \end{array} . \tag{4.10}$$

[17] This task has already been carried out partially in section 3.5. $h^{2,1}$ of $H_c^4(Z_{P_6})$ is given by (3.60), while (3.61) determines $h^{2,2}$. The formulae (3.32), (3.58), (3.59) can be used to determine $h^{p,q}$'s of $H_c^4(Z_{P_6})$ with $p = 1, 2, 3, 4$, while $h^{3,1}$ is determined by (3.33), (3.4). The sum rule (3.28), (3.31) still has to be used along with (4.9), however, to determine two more Hodge-Deligne numbers $h^{1,1}$ and $h^{0,0}$ of $H_c^4(Z_{P_6})$.

JHEP01(2015)047

Using the Hodge-Deligne numbers of other cohomology groups $H_c^k(Z_{P_6})$ given in (3.12), we also see that

$$e_c^{p,q}(Z_{P_6}) = \begin{array}{|ccccc} 1 & & & & 1 \\ 30 & 426 & & -5 & \\ 150 & 1530 & 1761 & & \\ 200 & 1265 & 1530 & 426 & \\ 80 & 200 & 150 & 30 & 1 \end{array} . \tag{4.11}$$

With all the Hodge-Deligne numbers of the cohomology groups $H_c^k(Z_{P_6})$ and $H^k(Y)$ determined, we are now ready to see that the long exact sequence (3.11) reproduces the Hodge diamond of the sextic (4.1):

$$\begin{array}{ccccccccc} [H_c^4(Z_{P_6})] & \to & [H^4(\hat{Z})] & \to & [H^4(Y)] & \to & [H_c^5(Z_{P_6})] & \to & [H^5(\hat{Z})] \\ h^{2,2}=1751 & \to & h^{2,2}=1752 & \to & h^{2,2}=1 & \to & 0 & & \\ h^{3,1}=426 & \to & h^{3,1}=426 & \to & h^{3,1}=0 & & & & \\ h^{4,0}=1 & \to & h^{4,0}=1 & \to & h^{4,0}=0 & & & & \\ & & 0 & \to & h^{1,1}=10 & \to & h^{1,1}=10 & \to & 0 \end{array} ; \tag{4.12}$$

$h^{p,q}[H_c^4(Z_{P_6})]$ for (p,q) with $p+q<4$ are irrelevant here, because $h^{p,q}[H^3(Y)] = h^{p,q}[H_c^4(Z_{P_6})]$ for $p+q<4$, as one can see from (4.8) and (4.10).

The study above used the Mayer-Vietoris spectral sequence and the Hodge numbers of subvarieties (4.4) to determine the Hodge-Deligne numbers of $H^k(Y)$. This is doable by hand only for such a simple geometry as the sextic, however. The Hodge-Deligne numbers of $H^k(Y)$ in more complicated geometries are dealt with much more systematically under the approach using the toric stratification (3.1) and the algorithm and sum rule of [38]. We therefore confirm from here, toward the end of this section, that the sum rule (3.28) is satisfied indeed by $e_c^{p,q}(Z_{\Theta^{[k]}})$'s of various faces $\Theta^{[k]}$ of the polytope P_6.

The polytope P_6 has six vertices $\Theta^{[0]}$ in (4.3), $\binom{6}{2}=15$ faces $\Theta^{[1]}$ of dimension-1, $\binom{6}{3}=20$ faces $\Theta^{[2]}$ of dimension-2, $\binom{6}{4}=15$ faces $\Theta^{[3]}$ of dimension-3, and $\binom{6}{5}=6$ facets $\Theta^{[4]}$. All the faces of a given dimension k are lattice-isomorphic, thanks to the high symmetry of the sextic-mirror-sextic. Each one of the k-dimensional faces has $\binom{k+1}{1}$ facets $\Theta^{[k-1]}$ of dimension-$(k-1)$, $\binom{k+1}{2}$ faces $\Theta^{[k-2]}$ of dimension-$(k-2)$, etc., all the way to $\binom{k+1}{k}=(k+1)$ faces $\Theta^{[0]}$, i.e., vertices.

Let us begin with the face $\Theta^{[1]}$. The hypersurface $Z_{\Theta^{[1]}} \subset \mathbb{T}^1$ consists of six points, just like in the last entry of (4.4). This means that $e_c^{0,0}(Z_{\Theta^{[1]}})=6$, and $\bar{e}_c^{0,0}(Z_{\Theta^{[1]}})=5$. Because $\Theta^{[1]}$ is a 1-dimensional pyramid of height 6, $\ell^*(\Theta^{[1]})=N_{1,6-2}=5$ (see footnote 16), the sum rule (3.31) — which states that $\bar{e}_c^{0,0}(Z_{\Theta^{[1]}})=\varphi_1(\Theta^{[1]})=\ell^*(\Theta^{[1]})=5$ in this case — is satisfied indeed.

The next step is to verify the sum rule for $Z_{\Theta^{[2]}}$. It is a degree-6 curve of $\mathbb{P}^2=\mathbb{P}^2_{\Theta^{[2]}}$ (i.e., $g=10$ curve, $\hat{Y}_i \cap \hat{Y}_j \cap \hat{Y}_k$ in (4.4)), with 3 set of six points (i.e., $Z_{\Theta^{[1]}}$) removed. Using

JHEP01(2015)047

the additivity of $e_c^{p,q}$'s, we find that

$$e_c^{p,q}(Z_{\Theta^{[2]}}) = \begin{vmatrix} -10 & 1 \\ 1 & -10 \end{vmatrix} - 3 \begin{vmatrix} \\ 6 \end{vmatrix} = \begin{vmatrix} -10 & 1 \\ -17 & -10 \end{vmatrix}, \qquad \bar{e}_c^{p,q}(Z_{\Theta^{[2]}}) = \begin{vmatrix} -10 & \\ -15 & -10 \end{vmatrix}. \tag{4.13}$$

The sum $\sum_q \bar{e}_c^{p,q}$ is indeed equal to $-\varphi_{2-p}(\Theta^{[2]})$ given by $\varphi_1(\Theta^{[2]}) = \ell^*(\Theta^{[2]}) = N_{2,6-3} = 10$ and $\varphi_2(\Theta^{[2]}) = \ell^*(2\Theta^{[2]}) - 3\ell^*(\Theta^{[2]}) = N_{2,12-3} - 3 \cdot N_{2,6-3} = 25$.

A similar computation for $\Theta^{[3]}$ and $\Theta^{[4]}$ proceeds as follows:

$$e_c^{p,q}(Z_{\Theta^{[3]}}) = \begin{vmatrix} 10 & & 1 \\ & 86 & \\ 1 & & 10 \end{vmatrix} - 4 \begin{vmatrix} -10 & 1 \\ -17 & -10 \end{vmatrix} - 6 \begin{vmatrix} \\ 6 \end{vmatrix} = \begin{vmatrix} 10 & & 1 \\ 40 & 82 & \\ 33 & 40 & 10 \end{vmatrix}, \tag{4.14}$$

$$e_c^{p,q}(Z_{\Theta^{[4]}}) = \begin{vmatrix} -5 & & & 1 \\ & -255 & 1 & \\ & 1 & -255 & \\ 1 & & & -5 \end{vmatrix} - 5 \begin{vmatrix} 10 & & 1 \\ 40 & 82 & \\ 33 & 40 & 10 \end{vmatrix} - 10 \begin{vmatrix} -10 & 1 \\ -17 & -10 \end{vmatrix} - 10 \begin{vmatrix} \\ 6 \end{vmatrix}. \tag{4.15}$$

We thus find that

$$\bar{e}_c^{p,q}(Z_{\Theta^{[3]}}) = \begin{vmatrix} 10 & & \\ 40 & 85 & \\ 30 & 40 & 10 \end{vmatrix}, \qquad \bar{e}_c^{p,q}(Z_{\Theta^{[4]}}) = -\begin{vmatrix} 5 & & & \\ 50 & 255 & & \\ 100 & 425 & 255 & \\ 50 & 100 & 50 & 5 \end{vmatrix}, \tag{4.16}$$

which are consistent with the sum rule on $\sum_q \bar{e}_c^{p,q}(\Theta^{[k]})$ using the value of $\varphi_{k-p}(\Theta^{[k]})$ given by

$$\varphi_1(\Theta^{[3]}) = 10, \qquad \varphi_2(\Theta^{[3]}) = 125, \qquad \varphi_3(\Theta^{[3]}) = 80, \tag{4.17}$$

$$\varphi_1(\Theta^{[4]}) = 5, \qquad \varphi_2(\Theta^{[4]}) = 305, \qquad \varphi_3(\Theta^{[4]}) = 780, \qquad \varphi_4(\Theta^{[4]}) = 205. \tag{4.18}$$

As a final consistency check, one can compute $e_c^{p,q}(Y)$ by using the additivity of $e_c^{p,q}$ and the stratification of Y into non-compact and smooth subsets:

$$\begin{aligned} e_c^{p,q}(Y) &= \binom{6}{2} e_c^{p,q}(Z_{\Theta^{[1]}}) + \binom{6}{3} e_c^{p,q}(Z_{\Theta^{[2]}}) + \binom{6}{4} e_c^{p,q}(Z_{\Theta^{[3]}}) + \binom{6}{5} e_c^{p,q}(Z_{\Theta^{[4]}}) \\ &= \begin{vmatrix} -30 & & & 6 \\ -150 & -1530 & -9 & \\ -200 & -1264 & -1530 & \\ -79 & -200 & -150 & -30 \end{vmatrix}. \end{aligned} \tag{4.19}$$

One can see that this result is consistent with $e_c^{p,q}(Y)$ given directly from the Hodge-Deligne numbers of $H^k(Y)$ in (4.7), (4.8). Also, $e_c^{p,q}(Z_{P_6}) + e_c^{p,q}(Y)$ reproduces the Hodge diamond (4.1), as it should be.

JHEP01(2015)047

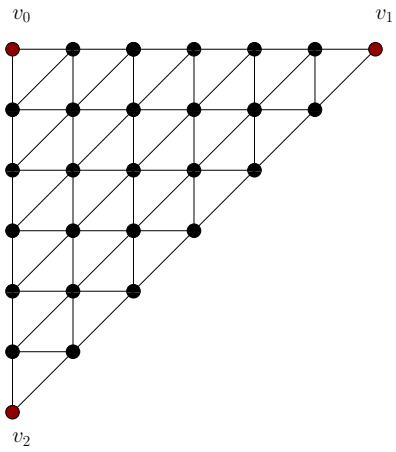

Figure 6. A 2-dimensional face of P_6, $\Theta^{[2]}$. We have shown vertices, integral points, and a simple triangulation.

4.1.2 Geometry of the mirror-sextic: toric stratification

Let us now use the mirror-to-sextic $\hat{Z}_{6,m}$ fourfold to have a close look at the stratification associated with the toric divisors $\left\{\hat{Y}_i\right\}$. The stratification of $\hat{Z}_6$ was very simple — $Z_6 + \binom{6}{1} Z_{\Theta^{[4]}} + \binom{6}{2} Z_{\Theta^{[3]}} + \cdots + \binom{6}{4} Z_{\Theta^{[1]}}$ — because all the faces $\widetilde{\Theta}^{[k]}$ of the polytope $\tilde{P}_6$ are lattice-isomorphic to the minimal simplex of k-dimension, so that any one of $E_{\widetilde{\Theta}^{[k]}}$'s consists of a single point. The faces $\Theta^{[k]}$ $(k < n = 5)$ of the polytope P_6 are not, however.

To the primary stratum of $\hat{Z}_{6,m}$, $\binom{6}{1} \times Z_{\widetilde{\Theta}^{[4]}}$ is added first. Each one of the $Z_{\widetilde{\Theta}^{[4]}}$'s is a $\mathbb{P}^3$ with five hyperplanes removed.

Coming next are the strata $\binom{6}{2} \times E_{\Theta^{[1]}} \times Z_{\widetilde{\Theta}^{[3]}}$. The geometry of $Z_{\Theta^{[3]}}$ is a $\mathbb{P}^2$ with four hyperplanes removed, while $E_{\Theta^{[1]}}$ is the exceptional locus of an A_4 singularity resolution. This exceptional locus $E_{\Theta^{[1]}}$ has a stratification that consists of five $\mathbb{T}^1$'s and six points, because $\ell^*(\Theta^{[1]}) = 5$ and $\ell_1^*(\Theta^{[1]}) = 6$.

Similarly, there are strata $\binom{6}{3} \times E_{\Theta^{[2]}} \times Z_{\widetilde{\Theta}^{[2]}}$. Each one of $Z_{\widetilde{\Theta}^{[2]}}$ is $\mathbb{P}^1$ with three points removed, while $E_{\Theta^{[2]}}$ has a stratification comprised of ten $\mathbb{T}^2$'s, $3 \times 15 = 45$ $\mathbb{T}^1$'s and thirty-six points. If a polytope $\Theta^{[2]}$ is given the triangulation shown in figure 6, then $E_{\Theta^{[2]}}$ contains ten compact complex surfaces isomorphic to dP_3.

The only remaining strata are $\binom{6}{4} \times Z_{\widetilde{\Theta}^{[1]}} \times E_{\Theta^{[3]}}$; each $Z_{\widetilde{\Theta}^{[1]}}$ consists of a single point. It is not too difficult to find a unimodular fine triangulation of $\Theta^{[3]}$ by hand. For this triangulation, it turns out that $\ell_1^*(\Theta^{[3]}) = 155$. This number satisfies $\ell^*(2\Theta^{[3]}) - \ell^*(\Theta^{[3]}) = N_{3,8} - N_{3,2} = 155 = \ell_1^*(\Theta^{[3]})$, a special case of (3.84). Because of this relation, $\ell_1^*(\Theta^{[3]})$ does not depend on the triangulation we choose.

For the mirror sectic, we can also compute the numbers $e_c^{p,q}$'s for $E_{\Theta^{[k]}}$ and $Z_{\widetilde{\Theta}^{[4-k]}}$ as well the primary stratum, and we can then use their multiplicativity and additivity to compute $e^{p,q}(Y)$, just as we did for the case of the sextic. All these details, however, are not recorded here.

JHEP01(2015)047

4.1.3 Evaluation of $h_V^{2,2}$, $h_H^{2,2}$ and $h_{RM}^{2,2}$

Let us now evaluate the dimension of the vertical, horizontal and the remaining components in $H^{2,2}$ given by (3.74), (3.93), (3.94), respectively; we do this both for the sextic $\hat{Z}_6$ and its mirror $\hat{Z}_{6,m}$.

Let us begin with the vertical component $H_V^{2,2}$ of the sextic $\hat{Z}_6$. Because all the faces of the polytope $\widetilde{P}_6$ do not have an interior point (except $\widetilde{P}_6$ itself), both $V_{\rm cor}(\hat{Z}_6)$ and $V^{\rm alg}(\hat{Z}_6)$ vanish. Therefore the vertical component comes purely from intersections of toric divisors,

$$h_V^{2,2}(\hat{Z}_6) = V_{\rm tor}(\hat{Z}_6) = \binom{6}{2} + 10 - 4\cdot 6 = 1\,, \tag{4.20}$$

where we have used (3.75). The vertical component $H_V^{2,2}(\hat{Z})$ is generated by $H^2|_{\hat{Z}_6}$, as we discussed already at the beginning of this section.

The same formula (3.74) can be used also to determine the dimension of the vertical (2,2)-forms on the mirror fourfold $\hat{Z}_{6,m}$, $h_V^{2,2}(\hat{Z}_{6,m})$. We first note that $V_{\rm cor}(\hat{Z}_{6,m})$ and $V^{\rm alg}(\hat{Z}_{6,m})$ vanish, as there are no interior points in $\widetilde{\Theta}^{[1]}$, $\widetilde{\Theta}^{[2]}$ and $2\widetilde{\Theta}^{[2]}$. In order to evaluate $V_{\rm tor}(\hat{Z}_{6,m})$, we need to count the number of 1-simplices in the polytope P_6. We find that

$$\ell_1((P_6)_{\leq 3}) = \binom{6}{4}\cdot \ell_1(\Theta^{[3]}) + \binom{6}{3}\cdot \ell_1^*(\Theta^{[2]}) + \binom{6}{2}\cdot \ell_1(\Theta^{[1]}) = 3315, \tag{4.21}$$

using the 1-simplex counting presented in section 4.1.2. To determine the dimensions subtracted due to the toric rational equivalence, the second and third line of $V_{\rm tor}(\hat{Z}_{6,m})$, we also need $\sum_{\Theta^{[4]}\leq P_6} \ell^*(\Theta^{[4]}) = \binom{6}{5}\cdot N_{4,1} = 30$ and $\sum_{\Theta^{[3]}\leq P_6} \ell^*(\Theta^{[3]}) = \binom{6}{4}\cdot N_{3,2} = 150$. Hence

$$h_V^{2,2}(\hat{Z}_{6,m}) = V_{\rm tor}(\hat{Z}_{6,m}) = 3315 + 10 - 4(462 - 30 - 150 - 1) - 3\cdot 150 = 1751. \tag{4.22}$$

This result already indicates that $h_V^{2,2}(\hat{Z}_{6,m}) = 1751$ and $h_H^{2,2}(\hat{Z}_{6,m}) = h_V^{2,2}(\hat{Z}_6) = 1$ add up to yield all of $h^{2,2}(\hat{Z}_{6,m}) = 1752$. Thus, the remaining component should be absent in $\hat{Z}_{6,m}$ as well as in $\hat{Z}_6$. It is not difficult to see this directly. First, $RM_a(\hat{Z}_6) = RM_a^m(\hat{Z}_{6,m})$ vanishes because all the faces $\widetilde{\Theta}^{[3]}$ of $\widetilde{P}_6$ are minimal three-dimensional simplices and no 1-simplices are introduced upon triangulation; $\ell_1^{*\bullet}(\widetilde{\Theta}^{[3]}) = 0$. Secondly, $RM_a^m(\hat{Z}_6) = RM_a(\hat{Z}_{6,m})$ also vanishes because all of the one-dimensional faces $\widetilde{\Theta}^{[1]}$ of $\widetilde{P}_6$ do not have an interior point.

Similarly, one can evaluate the dimension of the horizontal component $h_H^{2,2}(\hat{Z}_6)$ and $h_H^{2,2}(\hat{Z}_{6,m})$ directly from the formulae in the previous section, although we already know their results. As in the discussion for the vertical component above, one can see that both $H^{\rm red}$ and $H_{\rm cor}$ vanish for both $\hat{Z}_6$ and $\hat{Z}_{6,m}$. Thus, the horizontal component only comes from the monomial deformation $H_{\rm mon}$; the results are

$$h_H^{2,2}(\hat{Z}_6) = H_{\rm mon}(\hat{Z}_6) = 3431 - 6\cdot 305 + 15\cdot 10 = 1751\,, \tag{4.23}$$

and

$$h_H^{2,2}(\hat{Z}_{6,m}) = H_{\rm mon}(\hat{Z}_6) = 1 - 0 + 0 = 1 \tag{4.24}$$

by using $\varphi_3(\widetilde{P}_6) = 1$.

JHEP01(2015)047

4.2 Computations in practice

For practical applications to fourfolds more complicated than the sextic, we clearly do not want to evaluate (3.74), (3.93), (3.94) by hand. What is even worse, it is a non-trivial task to find an appropriate triangulation of $\widetilde{\Delta}$. Certainly the value of $h_V^{2,2}$, $h_H^{2,2}$ and $h_{RM}^{2,2}$ do not depend on the choice of triangulation, as we have seen at the end of section 3.6, but at least we have to make sure that there is at least one triangulation that is fine, regular and unimodular (see section 3.1.1), or otherwise the formulae in the previous section cannot be applied.

In this section we hence explain how to evaluate (3.74), (3.93), (3.94) in practice using existing computer software. The computation of Hodge numbers is most efficiently carried out using the package PALP [48] (described in some more detail in [49]). In the present context, PALP is also useful to construct a reflexive polytope from a combined weight system.

In order to obtain triangulation we use the package `TOPCOM` [46]. It is able to perform fine regular triangulations, which are, however, not necessarily star. Furthermore, as we have explained in section 3.1.1, a fine triangulation does not always give rise to a smooth Calabi-Yau hypersurface, let alone a smooth ambient space.

Even though a fine star triangulation is naturally related to a maximally subdivided fan, we may also use a fine regular triangulation of $\widetilde{\Delta}$ which is not star for practical purposes. Let us hence assume we have found a regular, fine (non-star) triangulation of $\widetilde{\Delta}$. This clearly gives rise to triangulations of all faces of $\widetilde{\Delta}$ which are mutually consistent, i.e. the triangulations of any two neighbouring faces induce the same triangulation on their intersection. We may then construct a fan Σ' (or, if we like a star triangulation) over all simplices on $\partial\widetilde{\Delta}$ obtained this way. As discussed e.g. in [19] (see also [50]), regularity of the original triangulation implies existence of a strongly convex support function on the simplices on $\partial\widetilde{\Delta}$, which in turn can be lifted to a strongly convex support function on the cones of Σ'.

We hence feed the configuration of integral points on $\partial\widetilde{\Delta}$ into `TOPCOM` to generate a fine regular triangulation, given in terms of five-simplices. As explained above, this can be cast into the data of a fan Σ', or, equivalently, a star triangulation. Such manipulations can be conveniently carried out using the computer algebra system `sage` [47]. In particular, `sage` already contains many routines to construct and analyse lattice polytopes.

Having obtained a regular star triangulation, we only need to check unimodularity. Again, this can be easily done by checking that the lattice volumes of all five-dimensional cones are unity.

With a smooth ambient space at hand, we are ready to evaluate the formulae (3.74), (3.93), (3.94). This can again efficiently be done using `sage`. The computation of the whole procedure outlined above (without any optimization) can be done in a few hours (for polytopes $\widetilde{\Delta}$ with $\mathcal{O}(100)$ points such as the mirror sextic) to a few days (for polytopes with several 1000 points such as the mirrors of the cases discussed in section 4.4) using an off-the-shelf PC at the time of writing.

Note that a straightforward evaluation of eqs. (3.74), (3.93), (3.94) requires a triangulation of both $\widetilde{\Delta}$ and Δ, even though we expect the final result to be independent of any triangulation.

JHEP01(2015)047

4.3 Correction terms at work

The sextic and its mirror are clearly very degenerate examples for the evaluation of (3.74), (3.93), (3.94), as the polytope $\widetilde{P}_6$ for $\mathbb{P}^5$ does not have any interior points of any of its faces and furthermore does not require triangulation. In this section 4.3, we present some examples for which various correction terms in (3.74), (3.93), (3.94) give a non-zero contribution.

Our first example is given by the following pair of reflexive polytopes

$$\widetilde{P}_B = \begin{pmatrix} -2 & -2 & 0 & 0 & 0 & 0 & 0 & 0 & 0 & 0 & 0 & 0 & 0 & 0 & 2 & 2 \\ -2 & 0 & -2 & -2 & 0 & 0 & 0 & 0 & 0 & 0 & 0 & 0 & 2 & 2 & 0 & 2 \\ 0 & 0 & -2 & 0 & -2 & -2 & 0 & 0 & 0 & 0 & 2 & 2 & 0 & 2 & 0 & 0 \\ 0 & 0 & 0 & 0 & -2 & 0 & -2 & 0 & 0 & 2 & 0 & 2 & 0 & 0 & 0 & 0 \\ 1 & 1 & 1 & 1 & 1 & 1 & 1 & -1 & 1 & -1 & -1 & -1 & -1 & -1 & -1 & -1 \end{pmatrix}, \tag{4.25}$$

and

$$P_B = \begin{pmatrix} -1 & -1 & -1 & 0 & 0 & 0 & 0 & 0 & 0 & 0 & 0 & 0 & 0 & 1 & 1 & 1 \\ 0 & 0 & 0 & -1 & -1 & 0 & 0 & 0 & 0 & 0 & 0 & 1 & 1 & 0 & 0 & 0 \\ -1 & 0 & 0 & 0 & 0 & -1 & 0 & 0 & 0 & 0 & 1 & 0 & 0 & 0 & 0 & 1 \\ 0 & -1 & 0 & -1 & 0 & 0 & -1 & 0 & 0 & 1 & 0 & 0 & 1 & 0 & 1 & 0 \\ -1 & -1 & -1 & -1 & -1 & -1 & -1 & -1 & 1 & 1 & 1 & 1 & 1 & 1 & 1 & 1 \end{pmatrix}. \tag{4.26}$$

As before, we have simply given the polytopes in terms of a matrix containing their vertices. We have confirmed, however, that there is a fine unimodular regular triangulation for both of the polytopes $\widetilde{P}_B$ and P_B, following the procedure described in section 4.2. The Calabi-Yau fourfold $\hat{Z}_B \subset \mathbb{P}^5_{\Sigma'_B}$ has the Hodge numbers

$$h^{p,q}(\hat{Z}_B) = \begin{array}{|ccccc} 1 & & & & 1 \\ & 11 & 0 & 97 & \\ & 0 & 476 & 0 & \\ & 97 & 0 & 11 & \\ 1 & & & & 1 \\ \hline \end{array}. \tag{4.27}$$

The Hodge diamond of the mirror $\hat{Z}_{B,m} \subset \mathbb{P}^5_{\widetilde{\Sigma}'_B}$ is the left-right (or top-bottom) flip of the Hodge diamond above.

Evaluation of (3.74), (3.93), (3.94) gives that $h^{2,2}(\hat{Z}_B) = h^{2,2}(\hat{Z}_{B,m})$ should be decomposed as $h^{2,2}_V(\hat{Z}_B) = 440$, $h^{2,2}_H(\hat{Z}_B) = 32$ and $h^{2,2}_{RM}(\hat{Z}_B) = 4$. In particular

	$V_{\text{tor}} + V^{\text{alg}}_{\text{tor}}$	$V_{\text{cor}} + V^{\text{alg}}_{\text{cor}}$	$RM_a + V^{\text{alg}}_{\text{rm}}$	$RM^m_a + H^{\text{red}}_{\text{rm}}$	$H_{\text{cor}} + H^{\text{re}}_{\text{cor}}$	$H_{\text{mon}} + H^{\text{red}}_{\text{mon}}$
$\hat{Z}_B$	$442-2$	$0-0$	$0-0$	$4-0$	$0-0$	$32-0$
$\hat{Z}_{B,m}$	$32-0$	$0-0$	$4-0$	$0-0$	$0-0$	$442-2$

. (4.28)

JHEP01(2015)047

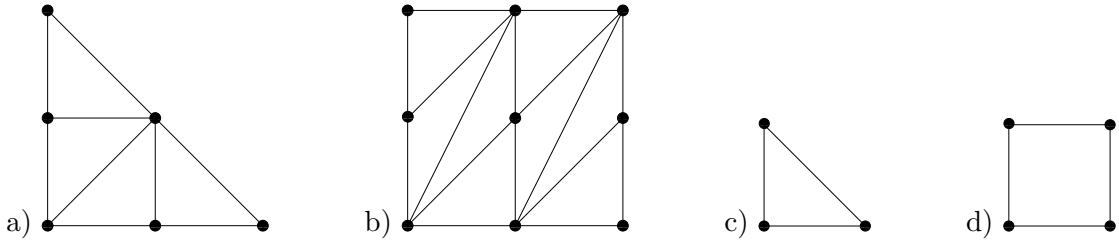

Figure 7. The two isomorphism classes of 2-dimensional faces of the polytope $\widetilde{P}_B$, $\widetilde{\Theta}^{[2]}_T$ and $\widetilde{\Theta}^{[2]}_S$ are shown in (a) and (b), whereas those of the polytope P_B, $\Theta^{[2]}_t$ and $\Theta^{[2]}_s$ are in (c) and (d), respectively. A specific fine unimodular triangulation of those faces is also shown in (a) and (b).

As can already be seen from the lists of vertices above, we find $\ell^*(\widetilde{\Theta}^{[1]}) = 1$ for all 1-dimensional faces of $\widetilde{P}_B$ and $\ell^*(\Theta^{[1]}) = 0$ for all 1-dimensional faces of P_B. This already explains why $[V_{\rm cor}(\hat{Z}_B) + RM_a(\hat{Z}_B)] = 0$, $[NV_1(\hat{Z}_{B,m}) + NV_3(\hat{Z}_{B,m})] = 0$. Furthermore, none of the 2-dimensional faces of P_B has any interior points (there are 80 triangles $\Theta^{[2]}_t$ and 18 squares $\Theta^{[2]}_s$ with 3, resp. 4 integral points; see figure 7 (c,d)), so that also $V^{\rm alg}(\hat{Z}_{B,m}) = 0$, $H^{\rm red}(\hat{Z}_B) = 0$ and $NV_3(\hat{Z}_B) = 0$ follows.

The correction term $V^{\rm alg}(\hat{Z}_B) = -2$ is understood as follows. There are 98 dual pairs of faces $(\widetilde{\Theta}^{[2]}, \Theta^{[2]})$ in the pair of polytopes $(\widetilde{P}_B, P_B)$; among them, 64 are of the type $(\widetilde{\Theta}^{[2]}_T, \Theta^{[2]}_t)$, 16 are of the type $(\widetilde{\Theta}^{[2]}_T, \Theta^{[2]}_s)$, 16 are of the type $(\widetilde{\Theta}^{[2]}_S, \Theta^{[2]}_t)$ and 2 are of the type $(\widetilde{\Theta}^{[2]}_S, \Theta^{[2]}_s)$, modulo lattice-isomorphism; see figure 7 (a–d) for the notation of $\widetilde{\Theta}^{[2]}_{T,S}$ and $\Theta^{[2]}_{t,s}$. The correction term $V^{\rm alg}(\hat{Z}_B) = -2$ originates from the 2 dual pairs $(\widetilde{\Theta}^{[2]}_S, \Theta^{[2]}_s)$. There is a divisor $\hat{Y}_i$ of $\hat{Z}_B$ for each pair, which is regarded as a surface fibration over a curve $\Sigma_{\Theta^{[2]}_s}$. The generic fibre is a surface, which is $\mathbb{P}^1 \times \mathbb{P}^1 \subset E_{\widetilde{\Theta}^{[2]}_S}$ in the case the triangulation of $\widetilde{\Theta}^{[2]}_S$ is the one in figure 7 (b). The base $\Sigma_{\Theta^{[2]}_s}$ is a curve of genus $g = \ell^*(\Theta^{[2]}_s) = 0$, because $\Theta^{[2]}_s$ corresponds to the complete linear system of $H_1 + H_2$ of $\mathbb{P}^1 \times \mathbb{P}^1$. he fibre may degenerate at $k_{\Theta^{[2]}_s} = 4$ points $\Sigma_{\Theta^{[2]}_s} \setminus Z_{\Theta^{[2]}_s}$. A naive toric calculation counts the fibre class $k_{\Theta^{[2]}_s} - 2$ times, and the correction term $\Delta V^{\rm alg}(\hat{Z}_B) = \bar{e}^{0,0}_c(\Theta^{[2]}_s) = -1$ removes the overcounting of the fibre class; $k_{\Theta^{[2]}_s} - 2 + \bar{e}^{0,0}_c = 1$ because of (3.69). Because all the four faces $\Theta^{[1]}$ of $\Theta^{[2]}_s$ do not have an interior point (see figure 7 (d)), this contributes to $V^{\rm alg}_{\rm tor}(\hat{Z}_B)$ and not to $V^{\rm alg}_{\rm cor+rm}$.

Although we do not have a particular geometric interpretation for the correction term $H^{\rm red}(\hat{Z}_{B,m})$, certainly the contribution $H^{\rm red}(\hat{Z}_{B,m}) = -2$ comes from the same two dual pairs of the faces isomorphic to $(\widetilde{\Theta}^{[2]}_S, \Theta^{[2]}_s)$.

The correction term $RM_a(\hat{Z}_{B,m}) = 4$ is understood as follows. The 64 dual pairs of faces $(\widetilde{\Theta}^{[1]}, \Theta^{[3]})$ are classified (modulo lattice isomorphisms) into four types. All the $\widetilde{\Theta}^{[1]}$'s are isomorphic, and $\Theta^{[3]}$'s have one of the four shapes, a tetrahedron, a pyramid with a rectangular base, a 3-dimensional prism, and a diamond, shown in figure 8. The correction term $RM_a(\hat{Z}_{B,m})$ comes from the pairs $(\widetilde{\Theta}^{[1]}, \Theta^{[3]}_{\rm dia})$. The one-simplex in $\Theta^{[3]}_{\rm dia}$ in figure 8 is surrounded by four triangles and four tetrahedra, realizing a geometry $\mathbb{T}^1 \times \mathbb{P}^1 \times \mathbb{P}^1$ in the toric ambient space $\mathbb{P}^5_{\widetilde{\Sigma}'_B} = \mathbb{P}^5_{\widetilde{P}_B}$ for $\hat{Z}_{B,m}$. The hypersurface equation selects $[1 + \ell^*(\widetilde{\Theta}^{[1]})] = \ell(\widetilde{\Theta}^{[1]}) - 1 = 2$ points out of $\mathbb{T}^1$. Thus, this one-simplex does not represent

JHEP01(2015)047

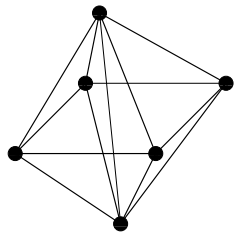

Figure 8. The 64 faces of 3-dimensions in P_B form four lattice-isomorphism classes. One of them looks like the one in this figure, and is denoted by $\Theta^{[3]}_{\rm dia}$. Four out of 64 belong to this class. The face $\Theta^{[3]}_{\rm dia}$ contains a single internal one-simplex (also shown in the figure) after triangulation. One example of such a face has $(-1,\,0,\,-1,\,0,\,-1)$, $(-1,\,0,\,0,\,-1,\,-1)$, $(-1,\,0,\,0,\,0,\,-1)$, $(0,\,0,\,0,\,0,\,1)$, $(0,\,0,\,0,\,1,\,1)$, and $(0,\,0,\,1,\,0,\,1)$ as its vertices.

a single irreducible algebraic cycle, but consists of two irreducible ones, each of which is isomorphic to $\mathbb{P}^1\times\mathbb{P}^1$. These two irreducible algebraic cycles combined are vertical and can be obtained as the intersection of divisors corresponding to the two boundary points of the 1-simplex in $\Theta^{[3]}_{\rm dia}\leq P_B$. This piece is counted as part of $V_{\rm tor}(\hat{Z}_{B,m})$. The other $\ell^*(\widetilde{\Theta}^{[1]})=1$ combination of the irreducible algebraic cycles, however, is not realized as a vertical cycle, and is counted as a part of $RM_a(\hat{Z}_{B,m})$. There are four such dual pairs of faces $(\widetilde{\Theta}^{[1]},\Theta^{[3]}_{\rm dia})$, and this is how $RM_a(\hat{Z}_{B,m})=4$ is obtained.

Finally, we obtain $RM^m_a(\hat{Z}_B)=4$ in the following way. It comes from the same four dual pairs of type $(\widetilde{\Theta}^{[1]},\Theta^{[3]}_{\rm dia})$. As noted already, $\ell^*(\widetilde{\Theta}^{[1]})=1$ for all 1-dimensional faces of the polytope $\widetilde{P}_B$, and the 1-simplex in figure 8 contributes to $\ell^{*\bullet}_1(\Theta^{[3]}_{\rm dia})$ *combinatorially*; each pair of dual faces $(\widetilde{\Theta}^{[1]},\Theta^{[3]}_{\rm dia})$ gives rise to a 1×1 contribution to $RM^m_a(\hat{Z}_B)$, and there are four such pairs. The *geometric* interpretation of this component, however, is not as directly related to the 1-simplex in $\Theta^{[3]}_{\rm dia}$ as the interpretation of $RM_a(\hat{Z}_{B,m})$ is. Remember that $NV_3(\hat{Z}_B)=0$, and note that $V_{\rm cor}(\hat{Z}_{B,m})=H_{\rm cor}(\hat{Z}_B)$ vanishes in this example. The face $\Theta^{[3]}_{\rm dia}$ does not have an interior point or 1-simplex ending on such an interior point. This means that $RM^m_a(\hat{Z}_B)$ originates purely from $NV_1(\hat{Z}_B)$ in this example. Let us now focus on one of the four pairs of $(\widetilde{\Theta}^{[1]},\Theta^{[3]}_{\rm dia})$, and let ν_i and $\hat{Y}_i$ be the interior point of $\widetilde{\Theta}^{[1]}$ and the corresponding divisor of $\hat{Z}_B$, respectively. This divisor $\hat{Y}_i$ contains a group of strata forming a $\mathbb{P}^1$ fibration over a surface $Z_{\Theta^{[3]}_{\rm dia}}$. This surface has $\bar{e}^{1,1}_c(Z_{\Theta^{[3]}_{\rm dia}})=1$, which is the origin of $RM^m_a(\hat{Z}_B)\neq0$. The Hodge diamond of this divisor $\hat{Y}_i$ is reconstructed by collecting $e^{p,q}_c$ of all the relevant strata (see (3.27)), and we found that it is

$$h^{p,q}(\hat{Y}_i)=\begin{array}{|ccccc}
 & & & & 1\\
 & & & 11 & \\
 & & 11 & & \\
 & 1 & & & \\
1 & & & &
\end{array}\;; \tag{4.29}$$

$h^{2,0}(\hat{Y}_i)$ vanishes because $\ell^*(\Theta^{[3]}_{\rm dia})=0$. All of the components in $H^{1,1}_c(\hat{Y}_i)$ and $H^{2,2}_c(\hat{Y}_i)$ are therefore algebraic, but the exact sequence (3.65) shows that only a 10-dimensional subspace of the $h^{2,2}_c(\hat{Y}_i)=11$-dimensional space of algebraic cycles is realized in the form

JHEP01(2015)047

of vertical cycles. The remaining $\bar{e}_c^{1,1} = 1$-dimensional contribution to $H_c^{2,2}(\hat{Y}_i)$ is regarded as part of the $RM_a^m(\hat{Z}_B)$ component, which is algebraic (and hence non-horizontal), but not vertical. In this example, we see that the $RM_a^m(\hat{Z}_B)$-component is also characterized by (3.95), not just the elements in $RM_a(\hat{Z})$ are.

In this example, the correction terms for $H^{1,1}(\hat{Z}_B)$ and $H^{1,1}(\hat{Z}_{B,m})$, i.e. the last term in (3.3), vanish and all divisor classes are generated by toric divisors for both fourfolds. This means we can easily compute the dimensions of $H_V^{2,2}(\hat{Z}_B)$ and $H_V^{2,2}(\hat{Z}_{B,m})$ by using the intersection ring of the ambient toric space restricted to $\hat{Z}_B$ and $\hat{Z}_{B,m}$. This computation reproduces the dimensions of the vertical components in (4.28), $h_V^{2,2}(\hat{Z}_B) = 440$ and $h_V^{2,2}(\hat{Z}_{B,m}) = 32$. Using mirror symmetry, we can then also recover the dimensions of the horizontal components. From $h^{2,2} = 476$ it follows again that the remaining component must be 4-dimensional.

A second example is defined by the dual pair of polyhedra

$$\widetilde{P}_S = \begin{pmatrix} -1 & 0 & 0 & 0 & 0 & 1 \\ -1 & 0 & 0 & 0 & 1 & 0 \\ -15 & -1 & 5 & 11 & 0 & 0 \\ -3 & 1 & 1 & 1 & 0 & 0 \\ -9 & -1 & 5 & 5 & 0 & 0 \end{pmatrix}, \; P_S = \begin{pmatrix} -1 & -1 & -1 & -1 & -1 & 5 \\ -1 & -1 & -1 & -1 & 5 & -1 \\ -1 & 0 & 0 & 1 & 0 & 0 \\ 0 & -1 & 4 & -1 & -1 & -1 \\ 2 & 0 & -1 & -1 & 0 & 0 \end{pmatrix}, \tag{4.30}$$

where we have displayed the vertices in the form of a matrix. It turns out that these two polyhedra are equivalent, so that they define the same Calabi-Yau fourfold, which is hence self-mirror. We have found fine regular and unimodular triangulations for both $\widetilde{P}_S$ and P_S, which are used for the computations below. The hodge numbers are

$$h^{p,q}(\hat{Z}_S) = \begin{array}{|cccc} 1 & & & 1 \\ & 30 & 101 & 30 \\ & 101 & 82 & 101 \\ & 30 & 101 & 30 \\ 1 & & & 1 \end{array} . \tag{4.31}$$

and we find

	$V_{\text{tor}} + V_{\text{tor}}^{\text{alg}}$	$V_{\text{cor}} + V_{\text{cor}}^{\text{alg}}$	$RM_a + V_{\text{rm}}^{\text{alg}}$	$RM_a^m + H_{\text{rm}}^{\text{red}}$	$H_{\text{cor}} + H_{\text{cor}}^{\text{re}}$	$H_{\text{mon}} + H_{\text{mon}}^{\text{red}}$
$\hat{Z}_S$	$41 - 0$	$0 - 0$	$150 - 150$	$150 - 150$	$0 - 0$	$41 - 0$

. (4.32)

As expected for a self-mirror fourfold with $h_{RM}^{2,2} = 0$, the result is $h_V^{2,2} = \frac{1}{2}h^{2,2}$.

Let us comment on the computation of $NV_3(\widetilde{P}_S)$, which was zero in the example before. There are three 1-dimensional faces with $\ell^*(\widetilde{\Theta}^{[1]}) = 5$. In $\widetilde{P}_S$ they have vertices at $\{(0,0,-1,1,-1),(0,0,5,1,5)\}$, $\{(0,0,-1,1,-1),(0,0,11,1,5)\}$ and $\{(0,0,5,1,5),(0,0,11,1,5)\}$. They are dual to 3-dimensional faces each of which contains 10 points interior to their 2-dimensional faces. As all other 1-dimensional faces have $\ell^* = 0$, we hence find $NV_3(\widetilde{P}_S) = 150$.

JHEP01(2015)047

Just like in the example P_B, the correction term for $H^{1,1}(\hat{Z}_S)$ vanishes and we can independently verify that $h^{2,2}_V(\hat{Z}_S) = h^{2,2}_V(\hat{Z}_{S,m}) = 41$ by using the intersection ring of the ambient space.

We now discuss an example for which $h^{2,2}_{RM} \neq 0$ and not all toric divisors are irreducible. The vertices of the polytopes defining this example and its mirror are

$$\widetilde{P}_3 = \begin{pmatrix} -1 & 0 & 0 & 0 & 0 & 0 & 0 & 0 & 0 & 0 & 0 & 0 & 1 \\ -3 & -2 & -2 & -1 & -1 & 0 & 0 & 0 & 2 & 2 & 4 & 4 & 0 \\ -5 & -3 & -2 & -2 & -2 & 0 & 0 & 4 & 1 & 1 & 3 & 4 & 0 \\ -8 & -5 & -4 & -3 & -2 & 0 & 2 & 2 & 0 & 1 & 1 & 2 & 0 \\ -7 & -5 & -5 & -2 & -2 & 1 & 1 & -3 & 1 & 1 & 1 & 1 & 0 \end{pmatrix} \tag{4.33}$$

and

$$P_3 = \begin{pmatrix} -1 & -1 & -1 & -1 & -1 & -1 & -1 & -1 & 0 & 1 & 1 & 8 & 10 \\ -1 & -1 & -1 & 0 & 1 & 1 & 3 & 4 & -1 & -1 & 4 & 0 & 1 \\ 1 & 1 & 2 & 0 & -2 & -1 & 0 & -1 & 1 & 2 & -1 & 0 & -1 \\ -1 & 0 & 0 & 0 & 2 & 0 & 0 & 0 & -1 & 0 & 0 & 0 & 0 \\ 1 & 0 & -1 & -1 & -1 & -1 & -1 & -1 & 1 & -1 & -1 & -1 & -1 \end{pmatrix}. \tag{4.34}$$

We have found a fine, regular and unimodular triangulation for both polytopes. The hodge numbers are

$$h^{p,q}(\hat{Z}_3) = \begin{array}{|ccccc} 1 & & & & 1 \\ & 76 & 11 & 67 & \\ & 11 & 594 & 11 & \\ & 67 & 11 & 76 & \\ 1 & & & & 1 \end{array}. \tag{4.35}$$

Evaluation of (3.74), (3.93) and (3.94) gives

	$V_{\text{tor}} + V^{\text{alg}}_{\text{tor}}$	$V_{\text{cor}} + V^{\text{alg}}_{\text{cor}}$	$RM_a + V^{\text{alg}}_{\text{rm}}$	$RM^m_a + H^{\text{red}}_{\text{rm}}$	$H_{\text{cor}} + H^{\text{re}}_{\text{cor}}$	$H_{\text{mon}} + H^{\text{red}}_{\text{mon}}$
$\hat{Z}_3$	$212 - 6$	$0 - 0$	$177 - 74$	$118 - 61$	$29 - 0$	$199 - 0$
$\hat{Z}_{3,m}$	$199 - 0$	$29 - 0$	$118 - 61$	$177 - 74$	$0 - 0$	$212 - 6$

, (4.36)

so that

$$h^{2,2}_V(\hat{Z}_3) = 206 \qquad h^{2,2}_{RM}(\hat{Z}_3) = 160 \qquad h^{2,2}_H(\hat{Z}_3) = 228 \tag{4.37}$$

In this example, the correction term to $h^{1,1}(\hat{Z}_{3,m})$ is equal to 10 and some of the toric divisors are reducible, giving rise to a non-zero contribution to $V_{\text{cor}}(\hat{Z}_{3,m})$. One can check that the intersection ring of the ambient toric space restricted to $\hat{Z}_{3,m}$ gives rise to 199 four-cycles in this case, as expected from $V_{\text{tor}}(\hat{Z}_{3,m}) + V^{\text{alg}}_{\text{tor}}(\hat{Z}_{3,m}) = 199$. For $V_{\text{cor}}(\hat{Z}_3)$, the correction term to $h^{1,1}$ vanishes and all 206 vertical four-cycles are obtained by the restriction of intersections of toric divisors.

JHEP01(2015)047

4.4 Elliptic fourfolds

In this section we come to our objects of interest, which are elliptic fourfolds. With the machinery to treat toric hypersurfaces in place, let us discuss elliptic fibrations over toric base manifolds. A smooth elliptic fourfold over a toric base B_3 not supporting any gauge group can be obtained by taking a generic Calabi-Yau hypersurface in an appropriate fibration of $\mathbb{P}^2_{123}$ over B_3. The elliptic fibration morphism π then descends from the toric morphism projecting down to B_3. Torically, we may realize such a situation by setting up a polytope $\widetilde{\Delta}^{\pi}_{B_3}$ with vertices

$$\begin{pmatrix} -1 \\ 0 \\ 0 \end{pmatrix}, \begin{pmatrix} 0 \\ -1 \\ 0 \end{pmatrix}, \begin{pmatrix} 3 \\ 2 \\ 0 \end{pmatrix}, \begin{pmatrix} 3 \\ 2 \\ \vec{v}_1 \end{pmatrix}, \cdots, \begin{pmatrix} 3 \\ 2 \\ \vec{v}_n \end{pmatrix}. \tag{4.38}$$

Here, the $\vec{v}_i$ are the generators of the 1-dimensional cones in the fan of the toric variety B_3. The above assignment ensures that X_1 (the coordinate associated with $(-1,0,0,0,0)$) is a section of $-3K_{B_3}$ and X_2 (the coordinate associated with $(0,-1,0,0,0)$) is a section of $-2K_{B_3}$.

For appropriate base manifolds B_3, a generic hypersurface $\hat{Z}^{\pi}_{B_3}$ in the toric variety defined by a fan over faces of the polytope $\widetilde{\Delta}^{\pi}_{B_3}$ is a smooth elliptic Calabi-Yau manifold with $h^{1,1}(\hat{Z}^{\pi}_{B_3}) = h^{1,1}(B_3)+1$. A compactification of F-theory on such a manifold will not give rise to any gauge symmetry in the low energy effective action.

The (combinatorially) simplest example is $B_3 = \mathbb{P}^3$, where we choose

$$\vec{v}_1 = \begin{pmatrix} 1 \\ 0 \\ 0 \end{pmatrix}, \vec{v}_2 = \begin{pmatrix} 0 \\ 1 \\ 0 \end{pmatrix}, \vec{v}_3 = \begin{pmatrix} 0 \\ 0 \\ 1 \end{pmatrix}, \vec{v}_4 = \begin{pmatrix} -1 \\ -1 \\ -1 \end{pmatrix}. \tag{4.39}$$

Another class of examples we will discuss in the following is given by taking a toric base defined by

$$\vec{v}_1 = \begin{pmatrix} 1 \\ 0 \\ 0 \end{pmatrix}, \vec{v}_2 = \begin{pmatrix} -1 \\ 0 \\ 0 \end{pmatrix}, \vec{v}_3 = \begin{pmatrix} n \\ 1 \\ 1 \end{pmatrix}, \vec{v}_4 = \begin{pmatrix} 0 \\ -1 \\ 0 \end{pmatrix}, \vec{v}_5 = \begin{pmatrix} 0 \\ 0 \\ -1 \end{pmatrix}. \tag{4.40}$$

Let us denote the resulting threefolds by $B_3^{(n)}$. We can also characterize them as $\mathbb{P}\left[\mathcal{O}_{\mathbb{P}^2} \oplus \mathcal{O}_{\mathbb{P}^2}(n)\right]$, i.e. they are themselves fibrations of $\mathbb{P}^1$ over $\mathbb{P}^2$. Hence the resulting fourfolds are K3 fibred and for F-theory compactifications there is a heterotic dual. One may think of $[z_1 : z_2]$ as coordinates on the $\mathbb{P}^1$ fibre (they also define two sections of the $\mathbb{P}^1$ fibration) and $[z_3 : z_4 : z_5]$ as coordinates on the $\mathbb{P}^2$ base.

Using the methods described earlier in this paper, we may now easily compute the Hodge numbers and the dimension of $H^{2,2}_V$, $H^{2,2}_H$ and $H^{2,2}_{RM}$ for these examples. The results are given in table 1.

JHEP01(2015)047

B_3	$\mathbb{P}^3$	$B_3^{(-3)}$	$B_3^{(-2)}$	$B_3^{(-1)}$	$B_3^{(0)}$	$B_3^{(1)}$	$B_3^{(2)}$	$B_3^{(3)}$
$h^{1,1}$	2	3	3	3	3	3	3	3
$h^{2,1}$	0	1	0	0	0	0	0	1
$h^{3,1}$	3878	4358	3757	3397	3277	3397	3757	4358
$h^{2,2}$	15564	17486	15084	13644	13164	13644	15084	17486
$h^{2,2}_V$	2	4	4	4	4	4	4	4
$h^{2,2}_H$	15562	17482	15080	13640	13160	13640	15080	17482
$h^{2,2}_{RM}$	0	0	0	0	0	0	0	0
K	23320	26200	22596	20436	19716	20436	22596	26200

Table 1. Hodge numbers and $h^{2,2}_V$, $h^{2,2}_H$ and $h^{2,2}_{RM}$ for generic elliptic fibrations, based on the polytopes with vertices (4.38), over base spaces $\mathbb{P}^3$, and $B_3^{(n)}$.

For a fourfold given by toric data such as (4.38), we may engineer models with a prescribed gauge group G over a divisor S in the base by choosing the monomials appearing in the defining equation of the hypersurface $\hat{Z}^{\pi}_{B_3}$ appropriately. If S is given by a toric divisor of the ambient space, this is equivalent to deleting points from the dual polytope $\Delta^{\pi}_{B_3,G}$ in the M-lattice. If this process results in another reflexive polytope $\Delta^{\pi}_{B_3,G}$, we may construct the dual $\widetilde{\Delta}^{\pi}_{B_3,G}$, which contains more points than $\widetilde{\Delta}^{\pi}_{B_3}$. If the resulting hypersurface $\hat{Z}_G$ is smooth, these extra points can be interpreted as the exceptional divisors of a resolution.

We may also reverse this process and define our models with an appropriate $\widetilde{\Delta}^{\pi}_{B_3}$, which is what we will do in the following. This anticipates the resolution process (which is another way to find the new vertices to add) and only allows those monomials in Δ leading to the desired fibre structure. This approach is similar to the one used in [51] and the tops of [52–54]. Equivalently, the polytopes used may also be constructed from the combined weight systems of appropriately resolved fourfolds.

In the following we will present a few examples for gauge groups SU(5) and SO(10).

4.4.1 SU(5) along $\mathbb{P}^2$

For a fourfold given as a hypersurface in a toric ambient space via a reflexive polytope such as (4.38), we may engineer fibres of type I_5 in Kodaira's classification along a divisor $[z_k]$ in the base (leading to SU(5) gauge symmetry in a compactification of F-theory) by adding the vertices:[18]

$$\vec{v}_{e_1} = \begin{pmatrix} 2 \\ 1 \\ \vec{v}_k \end{pmatrix}, \vec{v}_{e_2} = \begin{pmatrix} 1 \\ 0 \\ \vec{v}_k \end{pmatrix}, \vec{v}_{e_3} = \begin{pmatrix} 0 \\ 0 \\ \vec{v}_k \end{pmatrix}, \vec{v}_{e_4} = \begin{pmatrix} 1 \\ 1 \\ \vec{v}_k \end{pmatrix} \tag{4.41}$$

[18]To be more precise, we take the convex hull of these points and the polytope (4.38). In the resulting polytope, $\vec{v}_{e_1}$ is not a vertex, but lies on an edge between $\vec{v}_k$ and $\vec{v}_{e_2}$.

JHEP01(2015)047

B_3	$\mathbb{P}^3$	$B_3^{(-3)}$	$B_3^{(-2)}$	$B_3^{(-1)}$	$B_3^{(0)}$	$B_3^{(1)}$	$B_3^{(2)}$	$B_3^{(3)}$
$h^{1,1}$	6	7	7	7	7	7	7	7
$h^{2,1}$	0	1	0	0	0	0	0	0
$h^{3,1}$	2204	1249	1423	1723	2148	2698	3373	4173
$h^{2,2}$	8884	5066	5764	6964	8664	10864	13564	16764
$h^{2,2}_V$	7	9	9	9	9	9	9	8
$h^{2,2}_H$	8877	5057	5755	6955	8655	10855	13555	16756
$h^{2,2}_{RM}$	0	0	0	0	0	0	0	0
K	13287	7557	8603	10403	12953	16253	20303	25104

Table 2. Hodge numbers, decomposition of $H^{2,2}$ and K for Calabi-Yau fourfolds with SU(5) gauge group based on the reflexive polytopes $\widetilde{\Delta}^{\pi}_{\mathbb{P}^3,\,\mathrm{SU}(5)}$ and $\widetilde{\Delta}^{\pi}_{B_3^{(n)},\,\mathrm{SU}(5)}$.

to the polytope (4.38). For the examples of B_3 discussed in the last section, this leads to reflexive polytopes $\widetilde{\Delta}^{\pi}_{\mathbb{P}^3,\,\mathrm{SU}(5)}$ and $\widetilde{\Delta}^{\pi}_{B_3^{(n)},\,\mathrm{SU}(5)}$ (for $n = -3\cdots 3$). For the bases $B_3^{(n)}$, we place S along the divisor $[z_1]$ (the divisor corresponding to $\vec{v}_1$ in (4.40)). This means that S is a $\mathbb{P}^2$ in the base of the elliptic fibration.

Evaluating (3.74), (3.93) and (3.94) gives the results in table 2.

Note that in each case, $h^{1,1}$ has increased by four, corresponding to the exceptional divisors. The value of $h^{2,2}_V(\hat{Z}^{\pi}_{B_3^{(0)},\,\mathrm{SU}(5)}) = 9$ has already been independently computed in [27]. In the last case, $h^{2,2}_V(\hat{Z}^{\pi}_{B_3^{(3)},\,\mathrm{SU}(5)}) = 8$ because the **10** matter curve is absent there.

4.4.2 SO(10) along $\mathbb{P}^2$

In a similar fashion as done in the last section we may construct the polytopes $\widetilde{\Delta}^{\pi}_{B_3,\,\mathrm{SO}(10)}$. As (generic) models with gauge group SO(10) can be obtained by a further degeneration of SU(5) models, the polytope $\widetilde{\Delta}^{\pi}_{B_3,\,\mathrm{SO}(10)}$ contains $\widetilde{\Delta}^{\pi}_{B_3,\,\mathrm{SU}(5)}$. The vertices which have to be added to $\widetilde{\Delta}^{\pi}_{B_3,\,\mathrm{SU}(5)}$ to achieve gauge group SO(10) along z_1 are:

$$\vec{v}_{e_5} = \begin{pmatrix} 2 \\ 1 \\ 2\vec{v}_k \end{pmatrix}, \; \vec{v}_{e_6} = \begin{pmatrix} 3 \\ 2 \\ 2\vec{v}_k \end{pmatrix}. \tag{4.42}$$

For these cases we find the hodge numbers given in table 3.

5 Fourfolds which are not hypersurfaces of toric varieties

In the last section, we have shown how $H^{2,2}(\hat{Z},\mathbb{Q})$ is decomposed into vertical cycles, horizontal cycles and the remaining part $H^{2,2}_{RM}(\hat{Z},\mathbb{Q})$ for the case of hypersurfaces in toric varieties. As we have seen, the remaining part can be non-zero when divisors of $\hat{Z}$ have algebraic cycles which are not obtained by intersection with other divisors, cf. (3.95).

JHEP01(2015)047

B_3	$\mathbb{P}^3$	$B_3^{(-3)}$	$B_3^{(-2)}$	$B_3^{(-1)}$	$B_3^{(0)}$	$B_3^{(1)}$	$B_3^{(2)}$	$B_3^{(3)}$
$h^{1,1}$	7	8	8	8	8	8	8	8
$h^{2,1}$	0	0	0	0	0	0	0	0
$h^{3,1}$	2189	1221	1402	1708	2138	2692	3370	4172
$h^{2,2}$	8828	4958	5684	6908	8628	10844	13556	16764
$h^{2,2}_V$	8	10	10	10	10	10	10	10
$h^{2,2}_H$	8820	4948	5674	6898	8618	10834	13546	16754
$h^{2,2}_{RM}$	0	0	0	0	0	0	0	0
K	13200	7392	8480	10316	12896	16220	20288	25100

Table 3. Hodge numbers, decomposition of $H^{2,2}$ and K for Calabi-Yau fourfolds with SU(5) gauge group based on the reflexive polytopes $\widetilde{\Delta}^{\pi}_{\mathbb{P}^3,\,\mathrm{SO}(10)}$ and $\widetilde{\Delta}^{\pi}_{B_3^{(n)},\,\mathrm{SO}(10)}$.

In this section we discuss another class of Calabi-Yau fourfolds which can have a non-vanishing remaining part and are motivated in the study of F-theory compactifications: elliptic fibrations with singular fibres of type I_5 along a divisor S.

Let B_3 be a smooth Fano threefold, and let Z_s be a fourfold given by imposing a Weierstrass equation in the ambient space $\mathbb{P}[\mathcal{O}_{B_3}\oplus\mathcal{O}_{B_3}(-2K_{B_2})\oplus\mathcal{O}_{B_3}(-3K_{B_3})]$. We may choose the Weierstrass equation to be

$$X_1^2 = X_2^3 + a_5X_1X_2X_3 + a_4X_2^2X_3^2s + a_3X_1X_3^3s^2 + a_2X_2X_3^4s^3 + a_0X_3^6s^5, \tag{5.1}$$

where $X_{3,2,1}$ are the homogeneous coordinates of an ambient space containing the fibre $\mathbb{P}[\mathcal{O}\oplus\mathcal{O}(-2K_{B_3})\oplus\mathcal{O}(-3K_{B_3})]$. A morphism $\bar{\pi}: Z_s \longrightarrow B_3$ defining an elliptic fibration naturally follows from this. Let $[S]$ be some divisor class of B_3 and s a global section of $\mathcal{O}_{B_3}(S)$, so that the zero locus of s is S. $a_{r=5,4,3,2,0}$'s are global sections of appropriate line bundles $\mathcal{O}_{B_3}(-(6-r)K_{B_3}-(5-r)S)$ making (5.1) a Calabi-Yau manifold. These conditions leave moduli for s and the $a_{r=5,4,3,2,0}$, and we assume that they are chosen generic (in the sense that they are not in a Noether-Lefschetz locus). Fourfolds Z_s obtained in this way have an A_4 singularity along the subvariety $s = X_2 = X_1 = 0$. A compact and non-singular fourfold $\hat{Z}$ can be obtained by carrying out the canonical resolution of the A_4 singularity in Z_s first, and then going through a small resolution. The elliptic fibration $\pi: \hat{Z} \longrightarrow B_3$ remains a flat morphism [30]. Some more details about this resolution procedure are reviewed in appendices A.1 and A.2 so that there is no ambiguity in the notation used in this article.

This class of geometries generalizes the examples discussed in section 4.4, where $\hat{Z}$ is realized as a hypersurface of a toric variety. As a canonical example, we can think of $B_3 = \mathbb{P}^3$, and S a quadratic or cubic (or possibly degree $d = 4$) hypersurface of B_3. It is known that $S = \mathbb{P}^1\times\mathbb{P}^1$ in the $d = 2$ case, $S = dP_6$ when $d = 3$, and $S = \mathrm{K3}$ for $d = 4$. In these cases, $i^*: H^{1,1}(B_3;\mathbb{C}) \longrightarrow H^{1,1}(S;\mathbb{C})$ is not surjective, which is a welcome feature in F-theory compactifications [20, 21].

In this section we study the difference between the algebraic and vertical components in $H^{2,2}(\hat{Z};\mathbb{Q})$ for this class of geometries. This is done by dividing $\hat{Z}$ into a collection of

JHEP01(2015)047

(transversally intersecting) divisors $Y = \cup_i \hat{Y}_i \subset \hat{Z}$ and its complement $Z := \hat{Z} \backslash Y$, just like we did in section 3 when studying the case where $\hat{Z}$ is a toric hypersurface. Here, we choose a collection of divisors $Y = \cup_i \hat{Y}_i$ exploiting the fibration structure: the first five $\hat{Y}_i$, $i = 0, 1, 2, 3, 4$, are reserved for the five irreducible components of the family of I_5 Kodaira fibres over the divisor S in B_3. Apart from those, the collection $\cup_i \hat{Y}_i$ consists of the zero section σ of the elliptic fibration $\pi : \hat{Z} \longrightarrow B_3$ and the divisors $\pi^*(D_i)$'s, where $\{D_i\}$ is some basis of $\mathrm{Pic}(B_3)$.

We use the long exact sequence (3.11) with the separation $\hat{Z} = Y \amalg Z$ described above. The $H^4_c(Y)$-based algebraic cycles are studied by looking at

$$\mathrm{Ker}\left[[H^4_c(Y)]^{2,2} \longrightarrow [H^5_c(Z)]^{2,2}\right]. \tag{5.2}$$

There are two things to be worked out: the first is to determine the (dimension of the) algebraic components in $[H^4_c(Y)]^{2,2}$ for cases where $\hat{Z}$ is not necessarily a hypersurface of a toric variety, and the second is to determine $h^{2,2}[H^5_c(Z)] = h^{2,2}[H^3(Z)]$. It is known that $h^{2,2}[H^5_c(\hat{Z})] = 0$ when $\hat{Z}$ is a hypersurface of a toric variety, but this is not necessarily true for more general cases (note that $2 + 2 \geq 3$, and Z is smooth and non-compact).

Let us now work out $[H^4_c(Y)]^{2,2}$. It is determined by the Mayer-Vietoris spectral sequence, and by (3.16), in particular. This task consists of determining $H^4(\hat{Y}_i)$, $H^4(\hat{Y}_i \cap \hat{Y}_j)$ and the morphism between them.

5.1 The dimension of $h^{1,1}(\hat{Y}_i)$'s

We begin by computing the dimension of $h^2(\hat{Y}_i) = h^4(\hat{Y}_i)$ for the compact and generically smooth divisors $\hat{Y}_i \in \left\{\sigma, \pi^*(D_i), \hat{Y}_{0,1,2,3,4}\right\}$.

For $\hat{Y}_i = \sigma \simeq B_3$, $H^{2,2}_c(B_3) = H^{1,1}(B_3) = NS(B_3)$.

For $\hat{Y}_i = \pi^*(D_i)$ for one of the basis elements of $NS(B_3)$, $H^{1,1}(\pi^*(D))$ is generated by restrictions of the divisors σ, $\hat{Y}_{0,1,2,3,4}$ and divisors of B_3, where we assume that $D_i \cdot S$ is not empty in B_3 for now. To verify this, the Hodge diamond of the threefold $\pi^*(D) \subset \hat{Z}$ can be determined by decomposing $\hat{Z}$ into strata first, and then by collecting strata that belong to $\pi^*(D)$. It is convenient to start from the following stratification of the threefold $\pi^*(D)$: the surface $D \subset B_3$ is decomposed into $D \backslash (D \cap S)$, $D \cap (S \backslash (\Sigma_{(\mathbf{10})} \cup \Sigma_{(\mathbf{5})}))$ and $D \cap \Sigma_{(\mathbf{10})}$ and $D \cap \Sigma_{(\mathbf{5})}$, and the elliptically fibred threefold $\pi^*(D) \subset \hat{Z}$ is also decomposed accordingly to the stratification in the base. The Hodge number of the compact and smooth geometry $\pi^*(D)$ is obtained by summing up the Hodge-Deligne numbers of the strata. To $h^{1,1}(\pi^*(D)) = h^{2,2}(\pi^*(D))$, only the first two strata contribute.

$$\begin{aligned} h^{2,2}(\pi^*(D)) &= \left[e^{0,0}_c(T^2) e^{2,2}_c(D \backslash (D \cap S)) + e^{1,1}_c(T^2) e^{1,1}_c(D \backslash (D \cap S))\right] \\ &\quad + e^{1,1}_c(I_5) e^{1,1}_c(D \cap S) \\ &= 1 + [h^{1,1}_{\mathrm{alg}}(D \subset B_3) - 1] + 5 = 1 + h^{1,1}_{\mathrm{alg}}(D) + 4. \end{aligned} \tag{5.3}$$

The claim is now verified.[19] If $D_i \cdot S = 0$ in B_3, however, $H^{1,1}(\pi^*(D_i))$ is generated by $\pi^*(D_j|_{D_i})$ for D_j's in $NS(B_3)$ and $\sigma|_{\pi^*(D_i)}$.

[19] To be more precise, the term $e^{1,1}_c(T^2) e^{1,1}_c(D \backslash (D \cap S))$ should be decomposed into the region where the fibre is a smooth T^2 and type II fibre. However, $e^{1,1}_c = 1$ for the type II fibre, so that there is no difference after all.

JHEP01(2015)047

We assume that a basis $\{D_i\}$ of $NS(B_3)$ is chosen such that the number of D_i's with $D_i \cdot S \neq \phi$ is the same as the dimension $\tilde{\rho}_B$ of the image of

$$i^* : H^{1,1}(B_3) \longrightarrow H^{1,1}(S). \tag{5.4}$$

In order to determine the Hodge numbers of the five other divisors $\hat{Y}_{0,1,2,3,4}$ comprising the I_5 fibre over the divisor $S \subset B_3$, we introduce the following stratification of S:

$$S = S^\circ \amalg \Sigma^\circ_{(\mathbf{10})} \amalg \widetilde{\Sigma}^\circ_{(\mathbf{5})} \amalg P_{E6} \amalg P_{D6}\,. \tag{5.5}$$

Here, $\Sigma_{(\mathbf{10})}$ is the curve in S given by $a_5|_S = 0$, and $\Sigma_{(\mathbf{5})}$ the curve in S given by $(a_0 a_5^2 - a_2 a_5 a_3 + a_4 a_3^2)|_S = 0$. Those two curves intersect in S, and P_{E6} and P_{D6} denote the collection of such intersection points of two different kinds; P_{E6} are the points where $a_5 = a_4 = 0$, and P_{D6} where $a_5 = a_3 = 0$. $\Sigma^\circ_{(\mathbf{10})}$ is defined as $\Sigma_{(\mathbf{10})} \backslash (P_{E6} \cup P_{D6})$. The curve $\Sigma_{(\mathbf{5})}$ forms a double point singularity at each one of the points in P_{D6}; $\widetilde{\Sigma}^\circ_{(\mathbf{5})}$ is obtained by resolving the double point singularities (to obtain a curve $\widetilde{\Sigma}_{(\mathbf{5})}$), and then removing the lift of the points of P_{E6} and P_{D6}. Finally, $S^\circ := S \backslash (\Sigma_{(\mathbf{10})} \cup \Sigma_{(\mathbf{5})})$ (see [55, 56]).

The Hodge numbers of the five divisors can be calculated by using the stratification of the geometry of S as described above, and the additivity and multiplicativity of the Euler characteristics of the Hodge-Deligne numbers $e^{p,q}$. Appendix A.3 explains how to carry out the computation in practice, taking the Hodge numbers of $\hat{Y}_4$ as an example. The result is

$$e_c^{p,q}(\hat{Y}_4) = \begin{vmatrix} 0 & h^{2,0}(S) & 0 & 1 \\ h^{2,0}(S) & -2g_{10} & [h^{1,1}(S)+3] & 0 \\ 0 & [h^{1,1}(S)+3] & -2g_{10} & h^{2,0}(S) \\ 1 & 0 & h^{2,0}(S) & 0 \end{vmatrix} = (-)^{p+q} h^{3-p,3-q}(\hat{Y}_4)\,, \tag{5.6}$$

where the Hodge numbers are given in terms of $h^{2,0}(S)$ and $h^{1,1}(S)$ and the genera g_{10} and $\tilde{g}_5$ of the (resolved) matter curves; we assume that $h^{1,0}(S) = 0$ here. The appendix A contains more information on the generators of $H^{1,1}(\hat{Y}_4)$.

Similar computations can be carried out for the four other divisors in the I_5 fibre. The results are:

$$e_c^{p,q}(\hat{Y}_0) = e_c^{p,q}(\hat{Y}_1) = \begin{vmatrix} 0 & h^{2,0}(S) & 0 & 1 \\ h^{2,0}(S) & 0 & [h^{1,1}(S)+1] & 0 \\ 0 & [h^{1,1}(S)+1] & 0 & h^{2,0}(S) \\ 1 & 0 & h^{2,0}(S) & 0 \end{vmatrix}, \tag{5.7}$$

$$e_c^{p,q}(\hat{Y}_2) = \begin{vmatrix} 0 & h^{2,0}(S) & 0 & 1 \\ h^{2,0}(S) & -g_{10} & [h^{1,1}(S)+2] & 0 \\ 0 & [h^{1,1}(S)+2] & -g_{10} & h^{2,0}(S) \\ 1 & 0 & h^{2,0}(S) & 0 \end{vmatrix}, \tag{5.8}$$

JHEP01(2015)047

$$e_c^{p,q}(\hat{Y}_3) = \begin{vmatrix} 0 & h^{2,0}(S) & 0 & 1 \\ h^{2,0}(S) & -\tilde{g}_5 & [h^{1,1}(S)+2] & 0 \\ 0 & [h^{1,1}(S)+2] & -\tilde{g}_5 & h^{2,0}(S) \\ 1 & 0 & h^{2,0}(S) & 0 \end{vmatrix} . \tag{5.9}$$

5.2 Determination of $H^4(Y)$

Next, $H^4(Y)$ is determined as the kernel of (3.16). Since we have chosen all of the $\hat{Y}_i$'s to be irreducible, $h^4(\hat{Y}_i \cdot \hat{Y}_j) = 1$ for any pair of those divisors $(i \neq j)$ with a non-empty intersection $\hat{Y}_i \cdot \hat{Y}_j$. We switch to the dual (homology group) language in this subsection and the next. $H_4(Y)$ is the cokernel of the morphism

$$d^1 : \quad \left[\oplus_{i<j} H_4(\hat{Y}_i \cdot \hat{Y}_j)\right] = E^1_{1,4} \longrightarrow E^1_{0,4} = \left[\oplus_i H_4(\hat{Y}_i)\right], \tag{5.10}$$

and the contribution to $H_4(\hat{Z})$ from $H_4(Y)$ is characterized as the cokernel of the boundary map

$$\delta : \left[H_5^{\rm BM}(Z) = H_5(\hat{Z}, Y)\right] \longrightarrow H_4(Y). \tag{5.11}$$

We have already learned that

$$\begin{aligned} \dim[H_4(\sigma \simeq B_3)] &= \rho_B, \\ \dim[H_4(\pi^*(D_i)] &= h^{1,1}(D_i) + 1, && (\text{if } D_i \cdot S = \phi) \\ \dim[H_4(\pi^*(D_i)] &= h^{1,1}(D_i) + 1 + 4, && (\text{if } D_i \cdot S \neq \phi) \\ \dim[H_4(\hat{Y}_0)] &= \rho_S + 1, \\ \dim[H_4(\hat{Y}_1)] &= \rho_S + 1, \\ \dim[H_4(\hat{Y}_2)] &= \rho_S + 2, \\ \dim[H_4(\hat{Y}_3)] &= \rho_S + 2, \\ \dim[H_4(\hat{Y}_4)] &= \rho_S + 3, \end{aligned} \tag{5.12}$$

where $\rho_S := h^{1,1}(S)$ and $\rho_B = h^{1,1}(B_3)$. On the other hand,

$$\dim\left[\oplus_{i<j} H_4(\hat{Y}_i \cap \hat{Y}_j)\right] = \rho_B + \frac{\rho_B(\rho_B - 1)}{2} + 5\tilde{\rho}_B + 8\,, \tag{5.13}$$

and $\oplus_{i<j} H_4(\hat{Y}_i \cap \hat{Y}_j)$ is generated by four-cycles of the form

i) $\sigma \cdot \pi^*(D_i)$

ii) $\pi^*(D_i \cdot D_j)$ with $i \neq j \leq \rho_B$

iii) $\pi^*(D_i) \cdot \hat{Y}_{0,1,2,3,4}$ for $D_i \cdot S \neq \phi$

iv) intersections among $\hat{Y}_{0,1,2,3,4}$, neglecting self-intersections

There are ρ_B four-cycles in the group i) above. In $[\oplus_i H_4(\hat{Y}_i)]$, a given cycle of the form $(\hat{Y}_i \cdot \hat{Y}_j) = \sigma \cdot D_i$ appears once in $H_4(\sigma)$ and once in $H_4(\pi^*(D_i))$. Thus, there are ρ_B independent four-cycles $[\sigma \cdot D_i]$ in $H_4(Y)$ remaining in the Cokernel of the morphism (5.10).

JHEP01(2015)047

The second group ii) of four-cycles above are mapped into $\oplus_i H_4(\pi^*(D_i))$, and also leave a cokernel of dimension ρ_B. These cycles are represented by $\pi^*(\text{curves} \subset B_3)$.

A given four-cycle of the form $\pi^*(D_i) \cdot \hat{Y}_{1,2,3,4}$ (with $D_i \cdot S \neq \phi$) among the group iii) of four-cycles appears once in $H_4(\hat{Y}_{1,2,3,4})$ and once in $H_4(\pi^*(D_i))$. Thus, all of the $4\rho_S$ generators of $H_4(\hat{Y}_{1,2,3,4})$ are in the cokernel. The remaining four-cycles in the third group are of the form $\pi^*(D_i) \cdot \hat{Y}_S$. As only a $\tilde{\rho}_B$-dimensional subspace of $H^{1,1}(S)$ descends from $H^{1,1}(B_3)$, the images of these cycles in $H_4(\pi^*(D_i))$ are mapped to a $\tilde{\rho}_B$-dimensional subspace of $H_4(\hat{Y}_S)$, so that their contribution to the cokernel is $\rho_S - \tilde{\rho}_B$-dimensional.

So far, we have identified $2\rho_B + 4\rho_S + \rho_S - \tilde{\rho}_B$ independent generators of the cokernel of (5.10) in $H_4(Y)$. Besides the summands already covered in the discussion above, there are $(1 + 1 + 2 + 2 + 3) = 9$-dimensions remaining in $\oplus_i H_4(\hat{Y}_i)$, and eight dimensions remaining in $\oplus_{i<j} H_4(\hat{Y}_i \cdot \hat{Y}_j)$. We choose $\hat{Y}_2 \cdot \hat{Y}_4$ as the remaining representative of thecokernel and may conclude that

$$\dim[H_4(Y)] = 2\rho_B + 5\rho_S - \tilde{\rho}_B + 1. \tag{5.14}$$

5.3 The vertical components in $H_4(Y)$

The $(2\rho_B+1)$-dimensional subspace of $H_4(Y)$ which may be represented by $\sigma \cdot D_i$ and $D_i \cdot D_j$ is clearly composed of vertical four-cycles. However, not all of $H_4(Y)$ arises in this way.

The remaining $4\rho_S + (\rho_S - \tilde{\rho}_B)$-dimensional subspace of $H_4(Y)$ is generated by four-cycles of the form $\hat{Y}_{1,2,3,4} \cdot \pi^*(\omega)$ or $\hat{Y}_S \cdot \pi^*(\omega)$ for some $\omega \in H^{1,1}(S)$ (Poincaré duality is implicit everywhere). If ω is in the image of (5.4), then such a four-cycle is vertical. Thus, at least a subspace of dimension $4\tilde{\rho}_B$ is also vertical.

Intersections of the form $\hat{Y}_i \cdot \hat{Y}_j$ for $i, j \in \{0, 1, 2, 3, 4\}$ and $i \neq j$ are all vertical four-cycles as well. They are already contained in the $(2\rho_B + 1)$-dimensional subspace of $H_4(Y)$ referred to at the beginning of this subsection, however.

The last remaining group of vertical four-cycles are of the form $\hat{Y}_i \cdot \hat{Y}_i$ for $i = 0, 1, 2, 3, 4$. Such self-intersections can be computed by using such relations as

$$\hat{Y}_1 \cdot \hat{Y}_1 \sim \hat{Y}_1 \cdot \left[\nu^*_{\text{tot}}(D_S) - \hat{Y}_0 - \hat{Y}_2 - \hat{Y}_3 - \hat{Y}_4\right]. \tag{5.15}$$

Noting that both $c_1(N_{S|B_3})$ and $c_1(B_3)|_S$ are in the image of (5.4), and using the relations (A.46)–(A.47), one finds that these vertical four-cycles are not independent from those that we have discussed already. Therefore, we conclude that the vertical four-cycles form a subspace of dimension

$$2\rho_B + 4\tilde{\rho}_B + 1 \tag{5.16}$$

in $H_4(Y)$.

The remaining $5(\rho_S - \tilde{\rho}_B)$-dimensional subspace of $H_4(Y)$ cannot be represented by vertical four-cycles. This subspace has a clear geometric interpretation: for any cycle in S which does not descend from B_3, we can form five vertical four-cycles by taking the fibre components of the I_5 fibre over S.

JHEP01(2015)047

5.4 The remaining component

A four-cycle in $H_4(Y)$ represents a topological four-cycle in $\hat{Z}$ only if it is in the cokernel of the boundary map,

$$\text{Coker}\left[H_5(\hat{Z},Y) \longrightarrow H_4(Y)\right] \subset H_4(\hat{Z}). \tag{5.17}$$

For the general class of geometries $\hat{Z}$ described at the beginning of this section, we do not have a clear method of computation for $H_5(\hat{Z},Y)$. Although it is difficult to find *all* the generators of $H_5(\hat{Z},Y)$ and their images in $H_4(Y)$, it is easier to identify *some* generators of $H_5(\hat{Z},Y)$ and study their images in $H_4(Y)$. This way, we can at least establish an upper bound on the cokernel.

For every two-cycle Σ in $H_2(S)$ whose Poincaré dual is in the cokernel of (5.4), there exists a three-chain γ in B_3 with $\Sigma = \partial\gamma$. This three-chain γ and the boundary morphism $H_3(B_3,S) \longrightarrow H_2(S)$ are lifted under the elliptic fibration. Clearly, $\pi^{-1}(\gamma)$ is in $H_5(\hat{Z},Y)$ and its boundary in $H_5(\hat{Z},Y) \longrightarrow H_4(Y)$ is represented by $\pi^{-1}_{\hat{Y}_0}(\Sigma)+\pi^{-1}_{\hat{Y}_1}(\Sigma)+\cdots+\pi^{-1}_{\hat{Y}_4}(\Sigma)$; there are $(\rho_S-\tilde{\rho}_B)$ independent choices of Σ and consequently $(\rho_S-\tilde{\rho}_B)$ independent choices of $\pi^{-1}(\gamma)$. This means that only $4(\rho_S-\tilde{\rho}_B)$ out of the $5(\rho_S-\tilde{\rho}_B)$ non-vertical cycles in $H_4(Y)$ can become non-trivial four-cycles in $H_4(\hat{Z})$. If there are more cycles in $H_5(\hat{Z},Y)$ than the ones considered, this number may decrease.

As the five-chains $\pi^{-1}(\gamma)$ constructed above map only to non-vertical cycles in $H_4(Y)$ under the boundary map (5.17), we find that there is at most a $(2\rho_B+4\tilde{\rho}_B+1)$-dimensional subspace of $H_4(\hat{Z})$ that is represented by vertical four-cycles. If there are more five-chains in $H_5(\hat{Z},Y)$ than those we discussed above, this subspace may be smaller. Since all the independent divisors are included in the collection $\cup_i\hat{Y}_i$, all the vertical four-cycles have already been listed up.

The case $(\rho_S-\tilde{\rho}_B)>0$ is not without phenomenological motivation [20, 21]. The non-vertical cycles spanning at most $4(\rho_S-\tilde{\rho}_B)$-dimensions in $H_4(\hat{Z})$, are precisely the Poincaré duals of four-forms that can break SU(5) unification symmetry down to the gauge group of the Standard Model, while keeping the vector field of $\mathrm{U}(1)_Y$ massless. In this scenario, those four-cycles of $H_4(Y)$ need to represent topologically non-trivial four-cycles in $H_4(\hat{Z})$. If $h^{2,0}(S)=0$, those four-cycles are automatically algebraic, so they are not horizontal either. The four-forms (four-cycles) of this type in the class of geometries studied in this section are another class of examples of the remaining component $H^{2,2}_{RM}(\hat{Z})$, and they are also characterized by the property (3.95). See [57] for an explicit construction of such cycles.

Certainly, all of the components of $H^{2,2}_V(\hat{Z})$ are contained in (5.17), and some cycles from $H^{2,2}_{RM}(\hat{Z})$ also are, but we cannot say we have exhausted all the components of $H^{2,2}_{RM}(\hat{Z})$. Therefore we should use mirror symmetry, $h^{2,2}_H(\hat{Z})=h^{2,2}_V(\hat{Z}_m)$, in order to determine $h^{2,2}_H(\hat{Z})$. That will be doable once we can construct a smooth model $\hat{Z}$ as a complete intersection Calabi-Yau of a toric ambient space [58, 59]. Such an analysis will be a generalization of what we have done in section 3. A crucial step in constructing such a smooth model is to carry out the resolution of the singularities in the Weierstrass model Z_s in toric language. This process was to add the points (4.41) in section 4.4.1. The essence of this procedure lies in the fact that the divisor S, the component of the discriminant locus for an

JHEP01(2015)047

I_5 fibre, is a toric divisor of B_3 (represented by a vertex in the polytope). This procedure works not just in the case when B_3 itself is toric (as in section 4.4.1), but also in cases where B_3 is regarded as a complete intersection in a toric ambient space $\mathbb{P}^k_{\Sigma'_*}$, as long as this property — S is regarded as a toric divisor of $P^k_{\Sigma'_*}$ restricted on B_3 — is maintained, as discussed in [51].[20] It is an extra step to verify that a further small resolution exists, which is equivalent to finding an appropriate triangulation of the polytope; a smooth model $\hat{Z}$ needs to come out as a complete intersection Calabi-Yau, while satisfying the flat-fibration condition [30]. It is beyond the scope of this article, however, to study all of these issues.

The examples discussed in section 4.4 indeed satisfy (5.16). In section 4.4, we furthermore found that $H^{2,2}_{RM} = 0$ for all examples. This of course fits with the facts that S was a toric divisor of the (toric) bases B_3 of the elliptic fibrations in all cases, so that all of $H^{1,1}(S)$ is obtained by restricting divisors of the base; at least there is no component in $H^{2,2}_{RM}$ that is characterized by (5.17) because of $\rho_S = \tilde{\rho}_B$.

6 Distribution of rank of unification group and number of generations

There is mounting evidence that the decomposition of $H^4(\hat{Z};\mathbb{R})$ of a Calabi-Yau fourfold $\hat{Z}$ in a family $\pi : \mathcal{Z} \longrightarrow \mathcal{M}_*$ has a non-trivial $H^{2,2}_{RM}(\hat{Z};\mathbb{R})$ component. In addition to the families of $\hat{Z} = \mathrm{K3} \times \mathrm{K3}$ in [16] (see also (1.5)), we have seen in sections 3–5 that the four-forms in $H^{2,2}_{RM}(\hat{Z};\mathbb{R})$ are often Poincaré dual to topologically non-trivial cycles on divisors. Flux in such a four-cycle violates the condition (2.3), and hence we are led to take $H_{\mathrm{scan}} \otimes \mathbb{R}$ to be the primary horizontal subspace $H^4_H(\hat{Z};\mathbb{R})$ of a family $\mathcal{Z} \longrightarrow \mathcal{M}_*$ specified by $(B_3, [S], R)$, for an ensemble with the same unbroken symmetry in the effective theories (as stated already in section 2).

The vacuum index density distribution $d\mu_I$ of such a subensemble of F-theory flux vacua becomes a product of a prefactor and a distribution ρ_I (top-dimensional differential form) on $\mathcal{M}_*$, as in (2.8), (2.9). Since the integral of ρ_I over the fundamental domain of $\mathcal{M}_*$ often returns a number of order unity (see [14]; so called "D-limit" regions may have to be removed from $\mathcal{M}_*$), the prefactor therefore gives an estimate of the number of flux vacua with a given set of gauge group, matter representations, multiplicities and choice of $(B_3, [S])$. The distribution of the value of coupling constants of such a class of low-energy effective theories is given by the distribution ρ_I on $\mathcal{M}_*$ without being integrated. In this article and ref. [22], we only discuss the physics consequences coming from the prefactor. We

[20] In case B_3 is a complete intersection of a toric ambient space $\mathbb{P}^k_{\Sigma'_*}$ and S is given by $s|_{B_3} = 0$ of some section $s \in \Gamma(\mathbb{P}^k_{\Sigma'_*}; \mathcal{O}(D_S))$ on the toric ambient space, (D_S is a Cartier divisor of the fine unimodular Σ'_*) it is possible to embed the original toric ambient space $\mathbb{P}^k_{\Sigma'_*}$ into another toric variety, the total space of $\mathcal{O}(D_S)$, by s, and so are B_3 and S. B_3 is still a complete intersection of the new toric ambient space, and now S is also regarded as a toric divisor, satisfying the condition in the main text. This case, however, lacks generality, in that the divisor class of S needs to be in the image of $i^* : \mathrm{Pic}(\mathbb{P}^k_{\Sigma'_*}) \longrightarrow \mathrm{Pic}(B_3)$. Such a situation can be improved by choosing a different embedding in many cases. An alternative approach exists in the case the divisor S of B_3 is very ample. One can use the projective embedding of B_3 using the complete linear system of S; the divisor S is regarded as the hyperplane divisor of the new ambient space $\mathbb{P}^{\dim|S|-1}$ restricted on the image of B_3, one of the conditions assumed in the main text. We do not know, however, what kind of conditions have to be imposed on B_3 so that the image of B_3 in $\mathbb{P}^{\dim|S|-1}$ is regarded as a complete intersection.

JHEP01(2015)047

learn how the number of vacua depends on the choice of the algebraic information (7-brane gauge group = unification group R) and topological information (number of generations $N_{\rm gen}$) of the low-energy effective theories, starting with concrete examples and extracting the essence later on.

Let us begin with the choice $R = \mathrm{SU}(5)$ for the unification group and use the $(B_3, [S])$ we studied explicitly already in section 4.4.1 (except the one with $B_3 = \mathbb{P}^3$). At the beginning, we pay attention to the sub-ensembles for individual $N_{\rm gen}$, the net chirality in the $\mathbf{10}+\bar{\mathbf{5}}$ vs $\overline{\mathbf{10}}+\mathbf{5}$ representations of SU(5). This is done by taking $H_{\rm scan}\otimes\mathbb{R}$ to be that of the real primary horizontal subspace of the families in section 4.4.1, and $G^{(4)}_{\rm fix}$ to be the flux generating chirality. As this class of F-theory compactifications has a dual description in Heterotic string theory, it is well-known how chirality is generated. For the Heterotic string compactified on an elliptically fibred Calabi-Yau threefold with the base $B_2 = S = \mathbb{P}^2$, $\pi_{\rm Het} : Z_{\rm Het} \longrightarrow B_2 = S$. Reference [60] introduced the origin of chirality in the form of

$$\gamma_{FMW} = \lambda_{FMW}\left[5j_*(\Sigma_{(\mathbf{10})}) - (\pi_{\rm Het}\cdot i_C)^*(\Sigma_{(\mathbf{10})})\right], \qquad \lambda_{FMW} \in \frac{1}{2}+\mathbb{Z}, \tag{6.1}$$

where γ is a divisor with (possibly half) integral coefficient on a spectral surface $C \subset Z_{\rm Het}$, $i_C : C \hookrightarrow Z_{\rm Het}$ and $j : \Sigma_{(\mathbf{10})} \hookrightarrow C$ are the embedding maps. It is known from [61, 62] that

$$N_{\rm gen} = -(18-n)(3-n)\lambda_{FMW}. \tag{6.2}$$

The F-theory dual description of γ_{FMW} has also been known in the literature [25]; necessary details are reviewed briefly in the appendix C; see (C.2) for the explicit form of the flux. The maximum contribution to the D3-brane charges from $G^{(4)}_{\rm scan}$, L_*, is given by (C.1), where $G^{(4)}_{\rm fix}$ is assumed to be orthogonal to the scanning space $H_{\rm scan}$.

The flux scanning space $H_{\rm scan}\otimes\mathbb{R}$ is chosen to be the real primary horizontal subspace $H^4_H(\hat{Z};\mathbb{R})$, for the reason discussed in section 2. The dimension of this subspace, K, and the value of L_* above, are computed in section 4.4.1 and appendix C, respectively. These numbers can be fed into the prefactor $(2\pi L_*)^{K/2}/[(K/2)!]$ in (2.8).

We should note by looking at the values of L_* and K summarized in table 6, however, that the condition $K \ll L_*$ is not satisfied. It is thus expected that the formula (2.8) is not going to be very precise. In fact, it is not surprising that $L_* \ll K$ holds in the examples of our interest, rather than $L_* \gg K$. As we have considered base spaces with only small $h^{1,1}$, the resulting fourfolds $\hat{Z}$ also only have a rather small number of divisors whereas $h^{3,1}(\hat{Z})$ is rather large. More generally, one could try to argue that taking B_3 to be Fano leads to $h^{3,1}(\hat{Z}) \gg h^{1,1}(\hat{Z})$. In any case, $h^{2,2}_H \gg h^{2,2}_V$ in table 2 should be regarded as a natural consequence of $h^{3,1} \gg h^{1,1}$. Although we do not have a general feeling about when $h^{2,2}_{RM}$ becomes large or small relatively to $h^{2,2}_H$ or $h^{2,2}_V$ for general Calabi-Yau fourfolds, at least the remaining component is much smaller than the horizontal component in dimension, $h^{2,2}_{RM} \ll h^{2,2}_H$, in table 2. It seems reasonable to even make a guess from this experience and the result (1.5) that $h^{2,2}_{RM} \ll \max[h^{2,2}_H, h^{2,2}_V]$ whenever $h^{3,1} \gg h^{1,1}$ or $h^{3,1} \ll h^{1,1}$.

In cases where

$$h^{3,1} \gg h^{1,1}, \qquad h^{2,2}_H \gg h^{2,2}_V, \qquad h^{2,2}_H \gg h^{2,2}_{RM}, \quad \text{and} \quad h^{2,1} \approx \mathcal{O}(1), \tag{6.3}$$

JHEP01(2015)047

we find a relation

$$\chi(\hat{Z}) \approx K, \qquad L_*|_{G^{(4)}_{\text{fix}}=0} \sim \frac{\chi(\hat{Z})}{24} \sim \frac{K}{24}, \tag{6.4}$$

which implies $L_* \ll K$. In such cases, one can even use (3.62) to derive a relation

$$K \approx 6h^{3,1} + \text{const.}, \tag{6.5}$$

where the constant term comes from "44" in (3.62); the relation (3.62) implies that $h^{2,2}_H$ does not increase quadratically in $h^{3,1}$, but only linearly.

Let us now try to find a better estimate for the number of vacua when $L_* \ll K$ holds. The reason (2.8) predicts essentially no vacua in this case is that it approximates the number of lattice points at a specific distance L_* from the origin in a K dimensional lattice by the surface area of a sphere. We hence count the number of lattice points at 'generic' positions on such a sphere. If we increase the dimension K while holding L_* fixed it is hence no surprise that no such points remain. This does not mean, however, that there are no more solutions; this is easily seen by restricting the flux quanta to an n-dimensional subspace. Applying (2.8), we then count the points at generic positions of an n-dimensional sphere.

Following this logic, we may approximate the number of flux vacua in the case $L_* \ll K$ by[21]

$$\sum_{n=1}^{L_*} \binom{K}{n} \frac{(2\pi L_*)^{n/2}}{(n/2)!} \,. \tag{6.6}$$

The reason we only sum contributions up to $n = L_*$ is that we expect no more solutions with $n > L_*$ non-zero flux quanta switched on. We may further approximate the above sum by only taking the dominant contribution, corresponding to the last term with $n = L_*$. This gives the estimate

$$\binom{K}{L_*} \frac{(2\pi L_*)^{L_*/2}}{(L_*/2)!} \approx e^{L_* \ln\left(\sqrt{2\pi} K/L_*\right)} \tag{6.7}$$

for the number of flux vacua in the case $L_* \ll K$.

L_* is always an upper convex quadratic function of N_{gen},

$$L_* = L_*|_{G^{(4)}_{\text{fix}}=0} - cN^2_{\text{gen}} \tag{6.8}$$

for some $c > 0$ as in (C.6), and we can expand the exponent in terms of N_{gen} for relatively small number of generations. Retaining only the next-to-leading term and using (6.4) we obtain

$$\exp[L_*|_{G^{(4)}_{\text{fix}}=0} \ln(K/L_*|_{G^{(4)}_{\text{fix}}=0}) - cN^2_{\text{gen}}(1 + \ln(K/L_*|_{G^{(4)}_{\text{fix}}=0}))] \tag{6.9}$$

$$\simeq \; e^{K/6} \exp\left[-5cN^2_{\text{gen}}\right] . \tag{6.10}$$

for the distribution of vacua as a function of N_{gen}.

It is interesting to note that the distribution function (6.10) has a factorized form. The first factor $e^{K/6}$ depends on the algebraic information such as R as well as $(B_3, [S])$,

[21] A similar approach to tackle cases with $L_* \ll K$ is proposed in [14].

JHEP01(2015)047

but it does not depend on $N_{\rm gen}$. The second factor contains the $N_{\rm gen}$-dependence. The distribution function on the value of coupling constants of the low-energy effective theories, ρ_I, can be multiplied to (6.10), as it was in (2.8), if one wishes. One should not expect that the formula (2.9) remains to be a very good approximation at the quantitative level because the condition $K \ll L_*$ does not hold, but still it is not terribly bad to expect that ρ_I still retains qualitative aspects of the distribution of the coupling constants after smearing over local regions in the moduli space $\mathcal{M}_*$.

The distribution of the number of generations in the low-energy effective theories is given by the second factor, which is the Gaussian distribution with the variance $1/(10c)$, for relatively small $N_{\rm gen}$. This should be regarded as a very robust prediction of landscapes based on F-theory flux compactification, as long as the condition (6.3) is satisfied in the relevant family of fourfolds $\pi : \mathcal{Z} \longrightarrow \mathcal{M}_*^R$. As for the coefficient c in (6.8), we can read it out from (C.6),

$$c = \frac{5}{(18-n)(3-n)}, \tag{6.11}$$

for the examples we studied in section 4.4.1. Also for many other choices of $(B_3, [S])$, the coefficient c is determined by the intersection ring associated with only a few divisors in $\hat{Z}$, and is expected to be more or less of order unity, as in (6.11). Of course the Gaussian distribution is not a good approximation for $N_{\rm gen}^2$ large enough to be comparable to the absolute limit $\chi(\hat{Z})/24$; the distribution absolutely vanishes, since it is impossible to satisfy the D3-tadpole condition without supersymmetry breaking. Since the value of $\chi(\hat{Z})/24$ often comes at the order of hundreds to thousands [9, 12, 63], however, the distribution of $N_{\rm gen}$ is approximately Gaussian at least for the range $N_{\rm gen} \lesssim 10$. The distribution for this range (covering $N_{\rm gen} = 3$) will be sufficient information for our practical interest. The variance $\langle N_{\rm gen}^2 \rangle$ is of order $1/(10c) \sim 10^{-1}$.

Let us now focus on the first factor of the distribution function (6.10), $e^{K/6}$, from which we learn the statistical cost of unified symmetry (7-brane gauge group) R with higher rank. For the purpose of taking ratios of the number of vacua with different unified symmetries R_1 and R_2, the ratio $e^{(K_1-K_2)/6}$ may be studied instead by $e^{h_1^{3,1}-h_2^{3,1}}$, when the condition (6.3) is satisfied. This makes things much easier, since it is much easier to compute/estimate $h^{3,1}$ than $h_H^{2,2}$. Appendix B exploits this $\Delta K \approx 6\Delta h^{3,1}$ relation and develops the discussion further. In the rest of this section, however, we stick to the dimension K of the primary horizontal space. It is also worth mentioning that $e^{K/6}$ is regarded as a refinement of the popular "10^{500}", a crude estimate of the number of flux vacua of Type IIB Calabi-Yau orientifold compactifications.

It has been widely accepted at the intuitive level that more general flux leads to geometry stabilized at more general values of the complex structure, and hence with less unbroken symmetry (fewer independent divisors). This intuition has been made quantitative by the factor $e^{K/6}$; ref. [16] used a family of Calabi-Yau fourfolds that are topologically $\hat{Z} = \mathrm{K3} \times \mathrm{K3}$, and the computation of K for other families in this article adds more examples. The results in the family $\hat{Z} = \mathrm{K3} \times \mathrm{K3}$ and in the cases in section 4.4 remain similar, though there is difference in detail. In the family of $\hat{Z} = \mathrm{K3} \times \mathrm{K3}$, K is linear in the rank of 7-brane gauge group, and $K = 21 \times (20 - \mathrm{rank}_7)$ (where vanishing cosmological constant is not required;

JHEP01(2015)047

B_3	$\mathbb{P}^3$	$B_3^{(-3)}$	$B_3^{(-2)}$	$B_3^{(-1)}$	$B_3^{(0)}$	$B_3^{(1)}$	$B_3^{(2)}$	$B_3^{(3)}$	$\mathbb{P}^1 \times \mathrm{K3}$
$K_{R=\phi}$	23320	26200	22596	20436	19716	20436	22596	26200	
$K_{R=A4}$	13287	7557	8603	10403	12953	16253	20303	25104	
$K_{R=D5}$	13200	7392	8480	10316	12896	16220	20288	25100	
$\Delta K_{0\text{-}4}$	10033	18663	13993	10033	7123	4183	2293	1096	84
$\Delta K_{4\text{-}5}$	87	165	123	87	57	33	15	4	21

Table 4. The value of $K_{R=\phi}$, $K_{R=A4}$ and $K_{R=D5}$ in the first three rows are extracted from tables 1, 2 and 3, respectively. In the case $B_3 = \mathbb{P}^1 \times \mathrm{K3}$, the value of $\Delta K_{0\text{-}4} = K_{R=\phi} - K_{R=A4}$ and $\Delta K_{4\text{-}5} = K_{R=A4} - K_{R=D5}$ is determined by using $21 \times \Delta\mathrm{rank}_7$.

see [16] for more). The value of K becomes smaller for a subensemble with higher-rank unification group R. This remains true in the cases we studied in section 4.4 (see table 4).

At the quantitative level, the difference in the dimension of the flux scanning space K for SU(5) unification and SO(10) unification, $K_{R=A4} - K_{R=D5}$, remains more or less around order $\mathcal{O}(10)$ for all the geometries listed in table 4, and the ratio of the number of vacua with a stack of SU(5) 7-branes to that with a stack of SO(10) 7-branes remains of order $e^{\mathcal{O}(10)}$. The fraction of vacua with a stack of SU(5) 7-branes in $[S]$ in all the flux vacua on B_3 is given by $e^{-\Delta K_{0\text{-}4}/2}$; the value of $\Delta K_{0\text{-}4} = K_{R=\phi} - K_{R=A4}$ can be 1000–10000 for $B_3 = \mathbb{P}^3$ and $B_3^{(n)}$ studied in section 4.4, as opposed to the value $\Delta K_{0\text{-}4} \sim 100$ in the family $\hat{Z} = \mathrm{K3} \times \mathrm{K3}$. As we have discussed, we may estimate $\Delta K_{R_1 R_2}$ by (six times) the number of complex structure moduli which are fixed when enhancing R_1 to R_2. The result for $\hat{Z} = \mathrm{K3} \times \mathrm{K3}$ is certainly very special. For more general fourfolds, where the number of moduli is much larger, it seems plausible that the number of complex structure moduli we need to fix to achieve a gauge group of rank 4 or 5 is typically $\mathcal{O}(100)$ to $\mathcal{O}(1000)$, irrespective of the specific $(B_3, [S])$ used. Besides our concrete results (summarized in table 4), such numbers are typical for the dimensions of the middle cohomology of Calabi-Yau fourfolds.

Note that we have assumed a fixed choice of $[S]$ so far. This way of thinking is perfectly reasonable when comparing the statistical cost of enhancing a group of low rank, which we assume is given on $[S]$, to a group of higher rank. When we want to tackle the physically more interesting question of comparing the abundance of models with no gauge group to a model with gauge group R for *some* $[S]$, we need to be able to sum over various choices of $[S]$. While we do not expect this to make a relevant contribution in cases where $h^{1,1}(B_3)$ is small, an exhaustive discussion is beyond the scope of the present work.

7 Outlook

Let us leave a few remarks on open problems at the end of the main text. We start off with an obvious open problem of mathematical flavour. The study we carried out in section 3 for toric-hypersurface Calabi-Yau fourfolds has a clear generalization to Calabi-Yau fourfolds obtained as complete intersection in toric ambient spaces [58, 59]. This makes it possible to determine the dimension of the primary horizontal subspace $H^4_H(\hat{Z};\mathbb{R})$ and

JHEP01(2015)047

also to elucidate the geometric origin of the cycles in the remaining component $H^{2,2}_{RM}(\hat{Z})$ for more general cases. We stopped at the level of finding evidence that $H^{2,2}_{RM}(\hat{Z})$ is non-empty in geometries that are motivated for phenomenological applications, and provided their geometric characterization (3.95) for the cycles we identified; not all of the cycles in the remaining component may have been found, however. More detail will be learned about this geometry by this generalization, as we already stated at the end of section 5.

One can come up with various physics applications of the idea developed in [14–16, 64] and this article. For example, it is an interesting question whether SU(5) unification due to the presence of a stack of SU(5) 7-brane is more "natural" than accidental gauge coupling unification in supersymmetric Standard Models with stacks of U(3), U(2) and U(1) D7-branes wrapped on different topological cycles, with one U(1) remaining anomaly free. At least by comparing the number of flux vacua in those two categories, we will have a partial information that is needed in answer to this "naturalness" question. Although a very crude baby-version study was carried out in [16], this question deserves much more serious study.

This article did not try to include the symmetry breaking $\mathrm{SU}(5)_{\mathrm{GUT}} \longrightarrow \mathrm{SU}(3)_C \times \mathrm{SU}(2)_L \times \mathrm{U}(1)_Y$. If one is to use the geometry with non-surjective $H^{1,1}(B_3) \longrightarrow H^{1,1}(S)$ as motivated in [20, 21], the flux $G^{(4)}_{\mathrm{fix}}$ needs to have non-zero component both in $H^{2,2}_V(\hat{Z})$ for $N_{\mathrm{gen}} \neq 0$, and in $H^{2,2}_{RM}(\hat{Z})$ for the $\mathrm{SU}(5)_{\mathrm{GUT}}$ symmetry breaking. One then needs to think more carefully about the integral structure (flux quantization) of the space $H^{2,2}_V(\hat{Z}) \oplus H^{2,2}_{RM}(\hat{Z}) \oplus H^{2,2}_H(\hat{Z})$; a study of the integral structure in the H_{mon} component is found in [17, 18]. Note also that if we set $G^{(4)}_{\mathrm{fix}}$ so that $G^{(4)}_{\mathrm{scan}} = 0$ is contained in H_{scan}, then $G^{(4)}_{\mathrm{fix}}$ may not always be orthogonal to the elements of H_{scan}.

The statistical cost of requiring an extra global U(1) symmetry can also be studied by computing the dimension $K = \dim_{\mathbb{R}}[H_{\mathrm{scan}} \otimes \mathbb{R}]$. One needs to be careful in how we take the scanning space of the flux H_{scan}. The U(1) vector field does not have to remain in the massless spectrum (indeed, we do not want it to be), but its symmetry should not be broken spontaneously (possibly apart from non-perturbative symmetry breaking exponentially suppressed to the level harmless in phenomenology). Eventually this statistical cost needs to be compared against the cost of alternatives. In the application to the dimension-4 proton decay problem, an alternative will be a discrete symmetry, while in the application to the "approximately rank-1" problem of Yukawa matrices (cf. [65, 66]), the alternative is to tune a moduli parameter. See also [18].

Obviously one can also exploit the distribution ρ_I in (2.9) to study distribution of the values of the coupling constants in a low-energy effective theory. Certainly the formula[22] (2.9) is not expected to be very precise, because we expect $L_* \ll K$ in many cases. Experience in explicit numerical studies suggests (see [15] and also figure 5 of [16]) that qualitative aspects of the actual distribution are still captured by the distribution function ρ_I even in cases where $L_* \ll K$.

[22]See [18] and references therein for the period integral computation to be used in formula (2.9). In the presence of corrections to the Kähler potential $-\ln[\int_{\hat{Z}} \Omega \wedge \overline{\Omega}]$, ρ_I may not be given simply by the formula (2.9) with the Weil-Peterson metric of $\mathcal{M}_*$. The authors thank Y. Nakayama and Y. Sumitomo for raising this issue.

JHEP01(2015)047

It should also be noted that the scanning component of the flux, $G^{(4)}_{\rm scan}$, may play another role in addition to determining the coupling constants of the low-energy effective theories. All the fluxes in the form of $G^{(4)}_{\rm fix} + G^{(4)}_{\rm scan}$ with $G^{(4)}_{\rm scan} \in H^4_H(\hat{Z};\mathbb{R})$ give rise to effective theories with the same $N_{\rm gen}$, but the number of extra vector-like pairs of matter in the $\mathrm{SU}(5)_{\rm GUT}$ $\bar{\mathbf{5}}+\mathbf{5}$ representations may vary among such an ensemble of vacua. It has been known widely since the work of [67] that there tend to be many vector-like pairs that do not seem to be present in supersymmetric Standard Models that work phenomenologically well. It took an enormous effort to find a topological choice that leads to small number of vector like pairs. Such studies as [65, 67], however, are equivalent to only use the flux $G^{(4)}_{\rm fix}$ in the form of (C.2), or γ_{FMW} in (6.1), and set $G^{(4)}_{\rm scan} = 0$. With the freedom for $G^{(4)}_{\rm scan}$, however, there may be a new insight on the issue of the number of vector like pairs.

As already mentioned in section 3.6.1, specifying fluxes in F-theory (or, more generally M-theory) backgrounds via a four-form G_4 in (co)homology is not sufficient information to properly characterize all degrees of freedom [68, 69]. In particular, we need to specify the three form C_3. It is an open problem how to include this data in the vacuum counting problem, i.e. the setup of [14, 15].

Acknowledgments

We thank Andrés Collinucci, Roberto Valandro, Ryuichiro Kitano and Sakura Schäfer-Nameki for discussions. The work of A. P. B. was supported by the STFC under grant ST/J002798/1 and that of T. W. by WPI Initiative, MEXT, Japan and a Grant-in-Aid for Scientific Research on Innovative Areas 2303.

A Geometry of elliptic-fibred Calabi-Yau fourfold for general F-theory SU(5) models

A.1 Construction

The geometry considered in section 5, smooth elliptically fibred Calabi-Yau fourfolds for general F-theory SU(5) models, has been studied in [25, 30, 70], see also [51, 71]. We briefly review the construction of the geometry here, so that no ambiguity remains in the notation used.

The construction begins with an ambient space

$$A_0 := \mathbb{P}\left[\mathcal{O}_{B_3} \oplus \mathcal{O}_{B_3}(-2K_{B_3}) \oplus \mathcal{O}_{B_3}(-3K_{B_3})\right], \tag{A.1}$$

where B_3 is a complex 3-dimensional (Fano) variety. A fourfold Z_s is defined as a hypersurface of A_0 by the equation (5.1). The projection $\pi_{A_0} : A_0 \longrightarrow B_3$ defines an elliptic fibration morphism $\pi_{Z_s} : Z_s \longrightarrow B_3$.

Let X_3, X_2 and X_3 be the homogeneous coordinates corresponding to the $W\mathbb{P}^2_{1:2:3}$ fibre of the ambient space $\pi_{A_0} : A_0 \longrightarrow B_3$, and σ be the zero section defined by $X_3 = 0$. D_{X_1}, D_{X_2} and D_{X_3} denotes the zero locus of X_1, X_2 and X_3 in A_0, respectively. It follows that

$$D_{X_1} \sim 3\left(\sigma + c_1(B_3)\right), \qquad D_{X_2} \sim 2\left(\sigma + c_1(B_3)\right). \tag{A.2}$$

JHEP01(2015)047

Consider a line bundle on B_3, and let s be a global holomorphic section of this line bundle. The divisor defined by the zero locus of s is denoted by S, i.e. $s \in \Gamma(B_3; \mathcal{O}_{B_3}(S))$. The section s is used in the hypersurface equation of Z_s in (5.1), which implements the condition for an I_5 Kodaira fibre over S [72]. The divisor $\pi^*_{A_0}(S)$ in A_0 is denoted by D_S.

First blow-up. The fourfold Z_s has A_4 singularity along a subvariety of A_0 given by

$$Y_1 := D_S \cdot D_{X_1} \cdot D_{X_2}. \tag{A.3}$$

Thus, we blow up at this locus and let $A_1 := \mathrm{Bl}_{Y_1} A_0$. The blow-up morphism is denoted by $\nu_1 : A_1 \longrightarrow A_0$, and the exceptional divisor by $\mathcal{E}_1$. The center of the blowup Y_1 is contained in Z_s, and Z_s is of multiplicity $k = 2$ along Y_1. Thus,

$$\nu_1^*(Z_s) = Z_s^{(1)} + 2\mathcal{E}_1, \tag{A.4}$$

where $Z_s^{(1)}$ is the proper transform of Z_s. The proper transforms of D_S, D_{X_1} and D_{X_2} are denoted by $D_S^{(1)}$, $D_{X_1}^{(1)}$ and $D_{X_2}^{(1)}$, respectively.

Second blow-up. The fourfold $Z_s^{(1)}$ still has a singularity of type A_2 along the subvariety

$$Y_2 := \mathcal{E}_1 \cdot D_{X_1}^{(1)} \cdot D_{X_2}^{(1)} \tag{A.5}$$

in A_1. Thus, let $A_2 := \mathrm{Bl}_{Y_2} A_1$. The blow-up morphism is denoted by $\nu_2 : A_2 \longrightarrow A_1$, and the exceptional divisor $\mathcal{E}_2$. The hypersurface $Z_s^{(1)}$ of A_1 contains Y_2 with the multiplicity 2, and hence

$$\nu_2^*(Z_s^{(1)}) = Z_s^{(2)} + 2\mathcal{E}_2, \tag{A.6}$$

where $Z_s^{(2)}$ is the proper transform of $Z_s^{(1)}$ under this blow-up morphism. The proper transforms of $\mathcal{E}_1$, $D_{X_1}^{(1)}$ and $D_{X_2}^{(1)}$ are denoted by $\mathcal{E}_1^{(2)}$, $D_{X_1}^{(2)}$ and $D_{X_2}^{(2)}$, respectively. $\nu_2^*(D_S^{(1)})$ is denoted by $D_S^{(2)}$.

Small resolution. The fourfold $Z_s^{(2)}$ still has singularities at loci with codimension higher than two. These singularities can be resolved while the proper transform of $Z_s^{(2)}$ remains a flat family of curves over B_3 [30]. We provide a description of two such small resolutions in the following. The two small resolutions correspond, when B_3 and $[S]$ are the ones studied in section 4.4.1, to having $\langle \vec{v}_{e_1}, \vec{v}_{e_3} \rangle$ in the SR ideal, or having $\langle \vec{v}_{e_2}, \vec{v}_{e_4} \rangle$ in the SR ideal. We only describe the first resolution in detail and then add a brief comment concerning the second type.

Small resolution [a]. Let $Y_3^{[a]} := \mathcal{E}_1^{(2)} \cdot D_{X_1}^{(2)}$, and $A_3^{[a]} := \mathrm{Bl}_{Y_3^{[a]}} A_2$. The blow-up morphism is $\nu_3^{[a]} : A_3^{[a]} \longrightarrow A_2$, and the exceptional divisor is $\mathcal{E}_3^{[a]}$. The hypersurface $Z_s^{(2)}$ of A_2 contains $Y_3^{[3]}$ with multiplicity 1, and hence

$$(\nu_3^{[a]})^*(Z_s^{(2)}) = Z_s^{(3)[a]} + \mathcal{E}_3^{[a]}, \tag{A.7}$$

where $Z_s^{(3)[a]}$ is the proper transform of $Z_s^{(2)}$ under the morphism $\nu_3^{[a]}$. Proper transforms of other divisors in A_2 are denoted by

$$(\nu_3^{[a]})^*(\mathcal{E}_1^{(2)}) = \mathcal{E}_1^{(3)[a]} + \mathcal{E}_3^{[a]}, \quad (\nu_3^{[a]})^*(D_{X_1}^{(2)}) = D_{X_1}^{(3)[a]} + \mathcal{E}_3^{[a]} \tag{A.8}$$

JHEP01(2015)047

for divisors involved in the blow-up, and $D_{X_2}^{(3)[a]} := (\nu_3^{[a]})^*(D_{X_2}^{(2)})$, $D_S^{(3)[a]} := (\nu_3^{[a]})^*(D_S^{(2)})$ and $\mathcal{E}_2^{(3)[a]} := (\nu_3^{[a]})^*(\mathcal{E}_2)$ for the others.

The fourfold $Z_s^{(3)[a]}$ only becomes non-singular after one more step of blow-up in the ambient space. Let us take $Y_4^{[a]} := \mathcal{E}_2^{(3)[a]} \cdot D_{X_1}^{(3)[a]}$ as the centre of the blow-up; $A_4^{[a]} := \mathrm{Bl}_{Y_4^{[a]}} A_3^{[a]}$. The blow-up morphism is denoted by $\nu_4^{[a]} : A_4^{[a]} \longrightarrow A_3^{[a]}$, and the exceptional divisor by $\mathcal{E}_4^{[a]}$. The hypersurface $Z_s^{(3)[a]}$ of $A_3^{[a]}$ contains $Y_4^{[a]}$ with the multiplicity 1, and hence

$$(\nu_4^{[a]})^*(Z_s^{(3)[a]}) = \hat{Z}^{[a]} + \mathcal{E}_4^{[a]}. \tag{A.9}$$

The proper transforms of other divisors of A_3 are

$$(\nu_4^{[a]})^*(\mathcal{E}_2^{(3)[a]}) = \mathcal{E}_2^{(4)[a]} + \mathcal{E}_4^{(4)[a]}, \qquad (\nu_4^{[a]})^*(D_{X_1}^{(3)[a]}) = \hat{D}_{X_1}^{[a]} + \mathcal{E}_4^{(4)[a]}, \tag{A.10}$$

and

$$(\nu_4^{[a]})^*(D_{X_2}^{(3)[a]}) = \hat{D}_{X_2}^{[a]}, \qquad (\nu_4^{[a]})^*(D_S^{(3)[a]}) = \hat{D}_S^{[a]}, \tag{A.11}$$

$$(\nu_4^{[a]})^*(\mathcal{E}_1^{(3)[a]}) = \mathcal{E}_1^{(4)[a]}, \qquad (\nu_4^{[a]})^*(\mathcal{E}_3^{[a]}) = \mathcal{E}_3^{(4)[a]}. \tag{A.12}$$

In order to simplify the notation, we now relabel the exceptional divisors according to their intersections. Over a generic point on S, the four exceptional divisors $\mathcal{E}_{1,2,3,4}^{(4)[a]}$ together with $D_S^{(4)[a]}$ meet according to the extended Dynkin diagram of A_4 (see the first picture in figure 10). Namely,

$$D_S^{(4)[a]} \equiv \hat{E}_0 \tag{A.13}$$

$$\mathcal{E}_1^{(4)[a]} \equiv \hat{E}_1 \qquad \mathcal{E}_2^{(4)[a]} \equiv \hat{E}_2 \tag{A.14}$$

$$\mathcal{E}_3^{(4)[a]} \equiv \hat{E}_4 \qquad \mathcal{E}_4^{(4)[a]} \equiv \hat{E}_3\,. \tag{A.15}$$

As a consequence of four successive morphisms, $(\nu_{\mathrm{tot}}^{[a]} := \nu_1 \cdot \nu_2 \cdot \nu_3^{[a]} \cdot \nu_4^{[a]}) : A_4 \longrightarrow A_0$,

$$\nu_{\mathrm{tot}}^*(Z_s) = \hat{Z}^{[a]} + 2\hat{E}_1 + 4\hat{E}_2 + 5\hat{E}_3 + 3\hat{E}_4. \tag{A.16}$$

One also finds that

$$\nu_{\mathrm{tot}}^*(D_S) = \hat{D}_S + \hat{E}_1 + \hat{E}_2 + \hat{E}_3 + \hat{E}_4, \tag{A.17}$$

$$\nu_{\mathrm{tot}}^*(D_{X_2}) = \hat{D}_{X_2}^{[a]} + \hat{E}_1 + 2\hat{E}_2 + 2\hat{E}_3 + \hat{E}_4, \tag{A.18}$$

$$\nu_{\mathrm{tot}}^*(D_{X_1}) = \hat{D}_{X_1}^{[a]} + \hat{E}_1 + 2\hat{E}_2 + 3\hat{E}_3 + 2\hat{E}_4. \tag{A.19}$$

A simple way to represent intersections among divisors of the ambient space is by a diagram such as figure 9. It organizes the information in the same way as a fan over faces of a polytope does in the context of toric geometry. In fact, figure 9 is a two-dimensional projection of a A_4 'top' with a triangulation corresponding to the resolution $[a]$.

The divisors $\hat{D}_{X_1}$, $\hat{D}_{X_2}$, $\hat{E}_{1,2,3,4}$ and $\hat{E}_0$ of $A_4^{[a]}$ define divisors of $\hat{Z}^{[a]}$. They are denoted by $\hat{Y}_{X_1}$, $\hat{Y}_{X_2}$, $\hat{Y}_{1,2,3,4}$ and $\hat{Y}_0$, respectively.

JHEP01(2015)047

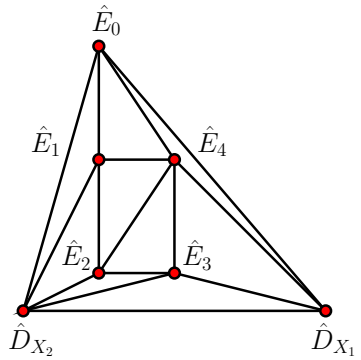

Figure 9. A schematic diagram showing how (some of) the divisors of the ambient space $A_4^{[a]}$ intersect; if a set of points in this diagram does not share a simplex, the corresponding divisors has empty intersection. This diagram shows the history of successive blow-ups starting from the original ambient space A_0. This diagram for $A_4^{[b]}$ is such that the 1-simplex joining $\hat{E}_2$ and $\hat{E}_4$ is replaced by another joining $\hat{E}_1$ and $\hat{E}_3$. In the examples we used in section 4.4.1, this diagram appears in the form of 2-dimensional faces of the polytope $\widetilde{\Delta}$.

Small resolution [b]. In an alternative small resolution, one can take $Y_3^{[b]} := \mathcal{E}_2 \cdot D_{X_1}^{(2)}$ in A_2, so that $A_3^{[b]} := \mathrm{Bl}_{Y_3^{[b]}} A_2$. In the next step, the subvariety $Y_4^{[b]} := \mathcal{E}_1^{(3)[b]} \cdot D_{X_1}^{(3)[b]}$ of $A_3^{[b]}$ is chosen as the centre of the blow-up; it will be clear what the divisors $\mathcal{E}_1^{(3)[b]}$ and $D_{X_1}^{(3)[b]}$ stand for. The resulting non-singular fourfold is denoted by $\hat{Z}^{[b]}$.

Note that in the small resolution [b] $\mathcal{E}_4^{[b]}$ corresponds to the fourth fibre component and $\mathcal{E}_3^{(4)[b]}$ to the third, instead of the other way around. By computing which intersections between the exceptional divisors vanish, one finds that this resolution furthermore corresponds to a triangulation where the line connection between $\hat{E}_2$ and $\hat{E}_4$ has been replaced by a line from $\hat{E}_1$ to $\hat{E}_3$

It is obvious from this property of the intersection ring that $\hat{Z}^{[a]}$ and $\hat{Z}^{[b]}$ are not the same geometries. In fact, we can turn $\hat{Z}^{[a]}$ into $\hat{Z}^{[b]}$ by a flop transition, which can already be anticipated from the fact that they only differ by a small resolution. The rich net of phases connected by flop transitions in F-theory compactifications with non-abelian gauge groups and the connection to group- and gauge theory has been explored in [30–35].

Any physics consequences in an SU(5) symmetric vacuum should remain the same whether the resolution [a] or [b] is used in formulating the flux background, as we have remarked in section 2. It is quite likely (see section 2) that $h_V^{2,2}$, $h_H^{2,2}$ and $h_{RM}^{2,2}$ will indeed turn out to be the same for both [a] and [b]. For this reason, we pay attention only to the small resolution [a] described above, and use in section 5 in the main text, as well as in the rest of this appendix. The superscript [a] will hence be dropped completely in the following.

A.2 Degeneration of singular fibres in higher codimension

An elliptic fibration $\pi_{\hat{Z}} : \hat{Z} \longrightarrow B_3$ is obtained by restricting $(\pi_{A_4} := \pi_{A_0} \cdot \nu_{\mathrm{tot}}) : A_4 \longrightarrow B_3$ on $\hat{Z} \subset A_4$. In this notation, the total fibre class over $S \subset B_3$ is $\pi_{\hat{Z}}^*(S) = \hat{Y}_0 + \hat{Y}_1 + \hat{Y}_2 + \hat{Y}_3 + \hat{Y}_4$. Over a generic point in S, the fibres of this projection become curves

JHEP01(2015)047

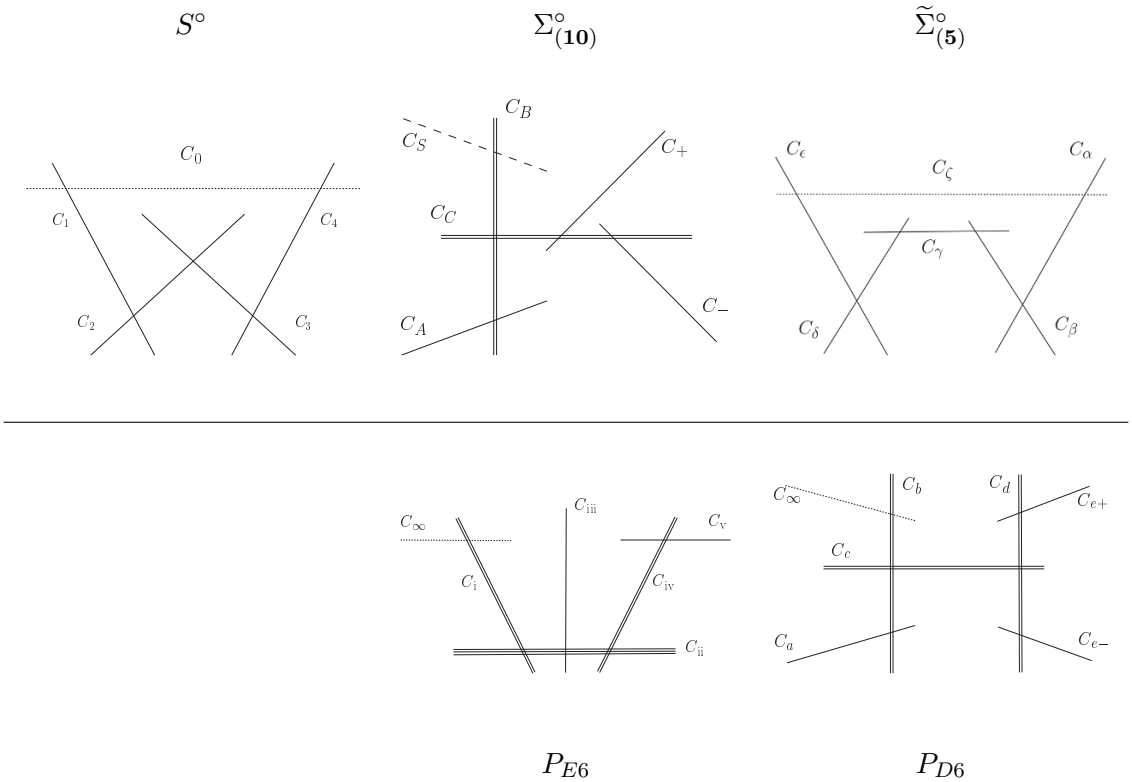

Figure 10. Schematic picture of how irreducible curves in singular fibre share points. This information is used in computing the Hodge diagrams of the divisors $\hat{Y}_{0,1,2,3,4}$ in section A.3.

$C_0+C_1+C_2+C_3+C_4$, which are all $\mathbb{P}^1$'s. A further restriction is given by only considering the divisors $\hat{Y}_i$, $\pi_{\hat{Y}_i} : \hat{Y}_i \longrightarrow S$.

Let us record known results on degeneration of singular fibre components, as we need them in the computation in the appendix A.3. The degeneration over the matter curve $\Sigma_{(\mathbf{10})} \subset S$ is:

$$\begin{aligned} &\pi^*_{\hat{Y}_0}(\Sigma_{(\mathbf{10})}) = S_\infty, \qquad \pi^*_{\hat{Y}_1}(\Sigma_{(\mathbf{10})}) = S_B, \qquad \pi^*_{\hat{Y}_2}(\Sigma_{(\mathbf{10})}) = S_C + S_+, \\ &\pi^*_{\hat{Y}_3}(\Sigma_{(\mathbf{10})}) = S_-, \qquad \pi^*_{\hat{Y}_4}(\Sigma_{(\mathbf{10})}) = S_A + S_B + S_C. \end{aligned} \tag{A.20}$$

Within $\hat{Z}$, $\hat{Y}_1 \cdot \hat{Y}_4 = S_B$, and $\hat{Y}_2 \cdot \hat{Y}_4 = S_C$. At a generic point in $\Sigma_{(\mathbf{10})}$, the fibre becomes a collection of curves, $C_S + C_A + 2C_B + 2C_C + C_+ + C_-$, all $\mathbb{P}^1$'s.

The degeneration over the matter curve $\Sigma_{(\mathbf{5})}$ is:

$$\begin{aligned} &\pi^*_{\hat{Y}_0}(\Sigma_{(\mathbf{5})}) = S_\zeta, \qquad \pi^*_{\hat{Y}_1}(\Sigma_{(\mathbf{5})}) = S_\epsilon, \qquad \pi^*_{\hat{Y}_2}(\Sigma_{(\mathbf{5})}) = S_\delta, \\ &\pi^*_{\hat{Y}_3}(\Sigma_{(\mathbf{5})}) = S_\gamma + S_\beta, \qquad \pi^*_{\hat{Y}_4}(\Sigma_{(\mathbf{5})}) = S_\alpha, \end{aligned} \tag{A.21}$$

Over a generic point in $\Sigma_{(\mathbf{5})}$ these surfaces become curves that are denoted by $C_{\alpha,\beta,\gamma,\delta,\epsilon}$ and C_ζ, respectively.

At any one of E_6 points,

$$C_0 \longrightarrow C_\infty, \qquad C_1 \longrightarrow C_{\mathrm{i}}, \qquad C_2 \longrightarrow C_{\mathrm{ii}} + C_{\mathrm{iii}},$$

JHEP01(2015)047

$$C_3 \longrightarrow C_{\rm iv} + C_{\rm v}, \qquad C_4 \longrightarrow C_{\rm i} + 2C_{\rm ii} + C_{\rm iv}, \tag{A.22}$$

At any one of D_6 points,

$$\begin{aligned} &C_0 \longrightarrow C_\infty, && C_1 \longrightarrow C_b, && C_2 \longrightarrow C_c + C_d, \\ &C_3 \longrightarrow C_d + C_{e+} + C_{e-}, && C_4 \longrightarrow C_a + C_b + C_c \end{aligned} \tag{A.23}$$

A.3 Computation of Hodge numbers of the exceptional divisors $\hat{Y}_i = \hat{E}_i|_{\hat{Z}}$

Using the result reviewed in the appendix A.2 and the stratification described in section 5.1, we compute the Hodge numbers of the divisors $\hat{Y}_{0,1,2,3,4}$ in $\hat{Z}$. The computation of $\chi(\hat{Z})$ in [55] is similar in spirit.

Let us first work out the Hodge-Deligne numbers of the various strata of the surface $S \subset B_3$. Using the divisor $\eta := c_1(N_{S|B_3}) + 6c_1(S)$ on S the number of E_6 and D_6 points is given by

$$N_E := (5K_S + \eta) \cdot (4K_S + \eta), \qquad N_D := (5K_S + \eta) \cdot (3K_S + \eta). \tag{A.24}$$

Thus the only non-vanishing $e_c^{p,q}$ of P_{E6} and P_{D6} are

$$e_c^{0,0}(P_{E6}) = N_E, \qquad e_c^{0,0}(P_{D6}) = N_D\,. \tag{A.25}$$

The genus g_{10} of the matter curve $\Sigma_{(\mathbf{10})}$ is determined by

$$2g_{10} - 2 = (5K_S + \eta) \cdot (6K_S + \eta). \tag{A.26}$$

The complement of P_{E6} and P_{D6} in $\Sigma_{(\mathbf{10})}$, denoted by $\Sigma^\circ_{(\mathbf{10})}$, has the following Hodge-Deligne numbers:

$$e_c^{p,q}(\Sigma^\circ_{(\mathbf{10})}) = \begin{vmatrix} -g_{10} & 1 \\ (1 - N_E - N_D) & -g_{10} \end{vmatrix}. \tag{A.27}$$

The genus g_5 of the matter curve $\Sigma_{(\mathbf{5})}$ is formally given by

$$2g_5 - 2 = (10K_S + 3\eta) \cdot (11K_S + 3\eta)\,. \tag{A.28}$$

However, there is a double point singularity at each of the points in P_{D6}. The resolved curve $\widetilde{\Sigma}_{(\mathbf{5})}$ has the genus

$$\tilde{g}_5 = g_5 - N_D. \tag{A.29}$$

The curve $\widetilde{\Sigma}^\circ_{(\mathbf{5})}$ is obtained by removing the points P_{E6} and the lift of the points P_{D6} from $\widetilde{\Sigma}_{(\mathbf{5})}$. Thus we find that

$$e_c^{p,q}(\widetilde{\Sigma}^\circ_{(\mathbf{5})}) = \begin{vmatrix} -\tilde{g}_5 & 1 \\ (1 - N_E - 2N_D) & -\tilde{g}_5 \end{vmatrix}. \tag{A.30}$$

Finally, the Hodge-Deligne numbers of $S^\circ := S \backslash (\Sigma_{(\mathbf{10})} \cup \Sigma_{(\mathbf{5})})$ are obtained by using the additivity of $e_c^{p,q}$. Assuming that $h^{1,0}(S) = 0$, we find that

$$e_c^{p,q}(S^\circ) = (-)^{p+q} h^{p,q}(S) - e_c^{p,q}(\Sigma^\circ_{(\mathbf{10})}) - e_c^{p,q}(\widetilde{\Sigma}^\circ_{(\mathbf{5})}) - e_c^{p,q}(P_{E6}) - e_c^{p,q}(P_{D6})$$

JHEP01(2015)047

$$= \begin{vmatrix} h^{2,0}(S) & 0 & 1 \\ (g_{10}+\tilde{g}_5) & (h^{1,1}(S)-2) & 0 \\ (-1+N_E+2N_D) & (g_{10}+\tilde{g}_5) & h^{2,0}(S) \end{vmatrix} . \tag{A.31}$$

We are now ready to compute the Hodge numbers of the exceptional divisors $\hat{Y}_{0,1,2,3,4} = \hat{E}_{0,1,2,3,4}|_{\hat{Z}}$. Let us take $\hat{Y}_4$ as an example; the Hodge numbers of the other $\hat{Y}_i$ are determined analogously. The stratification of $\hat{Y}_4$ is:

$$\begin{aligned} \hat{Y}_4 = [C_4 \times S^\circ] \ \amalg \ \left[(C_A + C_B + C_C) \times \Sigma^\circ_{(\mathbf{10})}\right] \ \amalg \ \left[C_\alpha \times \widetilde{\Sigma}^\circ_{(\mathbf{5})}\right] \\ \amalg \ [(C_{\rm i} + C_{\rm ii} + C_{\rm iv}) \times P_{E6}] \ \amalg \ [(C_a + C_b + C_c) \times P_{D6}] \,. \end{aligned} \tag{A.32}$$

Using the multiplicativity and additivity of $e_c^{p,q}$, we find that

$$\begin{aligned} e_c^{2,2}(\hat{Y}_4) &= e_c^{1,1}(C_4)e_c^{1,1}(S^\circ) + e_c^{0,0}(C_4)e_c^{2,2}(S^\circ) \\ &\quad + e_c^{1,1}(C_A+C_B+C_C)e_c^{1,1}(\Sigma^\circ_{(\mathbf{10})}) + e_c^{1,1}(C_\alpha)e_c^{1,1}(\widetilde{\Sigma}^\circ_{(\mathbf{5})}) \\ &= (h^{1,1}(S)-2)+1+3+1 = h^{1,1}(S)+3, \end{aligned} \tag{A.33}$$

$$\begin{aligned} e_c^{2,1}(\hat{Y}_4) &= e_c^{1,1}(C_4)e_c^{1,0}(S^\circ) + e_c^{0,0}(C_4)e_c^{2,1}(S^\circ) \\ &\quad + e_c^{1,1}(C_A+C_B+C_C)e_c^{1,0}(\Sigma^\circ_{(\mathbf{10})}) + e_c^{1,1}(C_\alpha)e_c^{1,0}(\widetilde{\Sigma}^\circ_{(\mathbf{5})}) \\ &= (g_{10}+\tilde{g}_5)+0-3g_{10}-\tilde{g}_5 = -2g_{10}. \end{aligned} \tag{A.34}$$

$h^{2,2}(\hat{Y}_4) = h^{1,1}(\hat{Y}_4)$ is given by $e_c^{2,2}(\hat{Y}_4)$, and $h^{2,1}(\hat{Y}_4)$ by $-e_c^{2,1}(\hat{Y}_4)$.

A.4 More on the geometry of the Cartan divisors $\hat{Y}_{1,2,3,4}$

$H^{1,1}(\hat{Y}_0)$ is generated by $\pi^*_{\hat{Y}_0}(H^{1,1}(S))$ and $\hat{Y}_1|_{\hat{Y}_0}$. Although σ defines a divisor on $\hat{Y}_0$ as well, it can be written in terms of the generators above. To see this, note that

$$\nu^*_{\rm tot}[-c_1(B_3)] = \sigma + \nu^*_{\rm tot}(D_{X_1} - 2D_{X_2}) = \sigma + \hat{D}_{X_1} - 2\hat{D}_{X_2} - \hat{E}_1 - 2\hat{E}_2 - \hat{E}_3. \tag{A.35}$$

From this, we obtain

$$0 = \left[\sigma - \hat{E}_1 + \nu^*_{\rm tot}(c_1(B_3))\right]|_{\hat{E}_0}, \tag{A.36}$$

because $\hat{E}_0 \cdot \hat{E}_2 = \hat{E}_0 \cdot \hat{E}_3 = 0$ in the ambient space A_4 (see figure 9). Using the relations $\hat{Z} \sim (3\hat{D}_{X_2} + \hat{E}_1 + 2\hat{E}_2 + \hat{E}_3) \sim (2\hat{D}_{X_1} + \hat{E}_3 + \hat{E}_4)$ and the intersection ring information of the ambient space A_4 in figure 9, it also follows that $(\hat{Y}_1 - \hat{Y}_4)|_{\hat{Y}_0} = (\hat{E}_1 - \hat{E}_4) \cdot \hat{E}_0 \cdot \hat{Z} \sim 0$.

$H^{1,1}(\hat{Y}_1)$ is generated by $\pi^*_{\hat{Y}_1}(H^{1,1}(S))$ and $\hat{Y}_2|_{\hat{Y}_1}$. A few more comments are in order here. First,

$$\left(\hat{Y}_0 - \hat{Y}_2\right)\Big|_{\hat{Y}_1} \sim (\nu^*_{\rm tot}(D_S) - \nu^*_{\rm tot}(D_{X_2}))|_{\hat{Y}_1} \sim \pi^*_{\hat{Y}_1}\left[c_1(N_{S|B_3}) - 2c_1(B_3)|_S\right]. \tag{A.37}$$

That is, both $\hat{Y}_0|_{\hat{Y}_1}$ and $\hat{Y}_2|_{\hat{Y}_1}$ are sections of the flat fibration $\pi_{\hat{Y}_1} : \hat{Y}_1 \longrightarrow S$, but they are different only modulo $\pi^*_{\hat{Y}_1}(H^{1,1}(S))$. In the derivation above, we have used

$$\hat{D}_{X_2}|_{\hat{Y}_1} = \hat{D}_{X_2} \cdot \hat{E}_1 \cdot \hat{Z} \sim \hat{D}_{X_2} \cdot \hat{E}_1 \cdot (2\hat{D}_{X_1} + \hat{E}_3 + \hat{E}_4) = 0\,, \tag{A.38}$$

JHEP01(2015)047

because none of $\hat{D}_{X_1}$, $\hat{E}_3$ and $\hat{E}_4$ share a face together with both $\hat{D}_{X_2}$ and $\hat{E}_1$. This is a generalization of the toric statement that the 1-simplex $\langle \hat{D}_{X_2}, \hat{E}_1 \rangle$ ($\langle \nu_2, \nu_9 \rangle$ in the notation of [27]) is inside a facet of the polytope and hence does not give rise to a non-trivial divisor in $\hat{Y}_1$. Finally, one can see that $\hat{Y}_1 \cdot \hat{Y}_4 = S_B$ is the total fibre component over the matter curve $\Sigma_{(\mathbf{10})}$ in $\pi_{\hat{Y}_1} : \hat{Y}_1 \longrightarrow S$, by observing that

$$\nu^*_{\text{tot}}(D_{X_1} - D_{X_2})|_{\hat{Y}_1} = \left[\hat{D}_{X_1} - \hat{D}_{X_2} + \hat{E}_3 + \hat{E}_4\right]|_{\hat{Y}_1} = \hat{E}_4|_{\hat{Y}_1}, \tag{A.39}$$

$$\nu^*_{\text{tot}}(\sigma + c_1(B_3))|_{\hat{Y}_1} = \nu^*_{\text{tot}}(c_1(B_3)) = \pi^*_{\hat{Y}_1}(c_1(B_3)|_S)\,. \tag{A.40}$$

The matter curve $\Sigma_{(\mathbf{10})}$ is in the class $[5K_S + \eta] = c_1(N_{S|B_3}) + c_1(S) = c_1(B_3)|_S$.

$H^{1,1}(\hat{Y}_2)$ is generated by $\pi^*_{\hat{Y}_2}(H^{1,1}(S))$, $\hat{Y}_3|_{\hat{Y}_2}$ and $\hat{Y}_4|_{\hat{Y}_2}$. Both $\hat{Y}_1|_{\hat{Y}_2}$ and $\hat{Y}_3|_{\hat{Y}_2}$ are sections of the flat fibration $\pi_{\hat{Y}_2} : \hat{Y}_2 \longrightarrow S$, but they are different only by the pullback of $H^{1,1}(S)$:

$$\left(\hat{Y}_1 - \hat{Y}_3\right)\Big|_{\hat{Y}_2} = \nu^*_{\text{tot}}\left(2D_S - D_{X_1}\right)|_{\hat{Y}_2} \sim \pi^*_{\hat{Y}_2}(2c_1(N_{S|B_3}) - 3c_1(B_3)|_S)\,. \tag{A.41}$$

The other generator $\hat{Y}_4|_{\hat{Y}_2} = S_C$ is one of the two singular fibre components in the flat family $\pi_{\hat{Y}_2} : \hat{Y}_2 \longrightarrow S$ along with the matter curve $\Sigma_{(\mathbf{10})}$. This four-cycle can be chosen as the matter surface for the hypermultiplets in the SU(5)-($\mathbf{10} + \overline{\mathbf{10}}$) representations.

$H^{1,1}(\hat{Y}_3)$ is generated by $\pi^*_{\hat{Y}_3}(H^{1,1}(S))$ and two other independent generators, which can be chosen as $\hat{Y}_4|_{\hat{Y}_3}$ and $\hat{Y}_2|_{\hat{Y}_3}$. $\hat{Y}_3$ is also regarded as a flat family of curves over S, $\pi_{\hat{Y}_3} : \hat{Y}_3 \longrightarrow S$, of which both $\hat{Y}_2|_{\hat{Y}_3}$ and $\hat{Y}_4|_{\hat{Y}_3}$ define a section. Divisors $\hat{D}_{X_1}|_{\hat{Y}_3}$ and $\hat{D}_{X_2}|_{\hat{Y}_3}$ are linearly equivalent to the generators above; using

$$\nu^*_{\text{tot}}(D_{X_2} - 2D_S) = \hat{D}_{X_2} - 2\hat{D}_S - \hat{E}_1 - \hat{E}_4, \tag{A.42}$$

for example, one obtains a relation

$$\hat{Y}_4|_{\hat{Y}_3} \sim \hat{D}_{X_2}|_{\hat{Y}_3} + \pi^*_{\hat{Y}_3}(2K_S). \tag{A.43}$$

Also, by using $\nu^*_{\text{tot}}(D_{X_1} - 3D_S)$ instead of $\nu^*_{\text{tot}}(D_{X_2} - 2D_S)$, we find that

$$\hat{D}_{X_1}|_{\hat{Y}_3} \sim \hat{Y}_4|_{\hat{Y}_3} + \hat{Y}_2|_{\hat{Y}_3} - \pi^*_{hatY_3}(3K_S)\,. \tag{A.44}$$

The matter surface for the SU(5)-($\bar{\mathbf{5}} + \mathbf{5}$)-representations is given by a difference between the two divisors on $\hat{Y}_3$: $\text{div}(a_3 X_{\hat{E}_4} + a_5 X_{\hat{D}_2})|_{\hat{Y}_3} - \hat{E}_2|_{\hat{Y}_3}$, where $X_{\hat{E}_4}$ and $X_{\hat{D}_{X_2}}$ are the homogeneous coordinates of $A_4^{[a]}$ corresponding to the divisors $\hat{E}_4$ and $\hat{D}_{X_2}$, respectively. The divisor $\{a_3 X_{\hat{E}_4} + a_5 X_{\hat{D}_{X_2}} = 0\}$ on $\hat{Y}_3$ consists of two irreducible components. One component is $\hat{E}_2|_{\hat{Y}_3}$, to be subtracted away, and the other one is an irreducible component of the singular fibre over the matter curve $\Sigma_{(\mathbf{5})}$, the matter surface S_γ. Thus, it is in the divisor class $[\hat{E}_4 + \nu^*_{\text{tot}}(c_1(N_{S|B_3}) + 3c_1(B_3)|_S)] - \hat{E}_2$ on $\hat{Y}_3$. From this, we can conclude that the matter surface for the ($\bar{\mathbf{5}} + \mathbf{5}$) representations also belongs to the class of a vertical cycles.

$H^{1,1}(\hat{Y}_4)$ is generated by $\pi^*_{\hat{Y}_4}(H^{1,1}(S))$ and three more divisors $\hat{Y}_3|_{\hat{Y}_4}$, $\hat{Y}_1|_{\hat{Y}_4} = S_B$ and $\hat{Y}_2|_{\hat{Y}_4} = S_C$. The last two of these form two out of the three singular fibre components

JHEP01(2015)047

over the matter curve $\Sigma_{(\mathbf{10})}$. Although $\hat{Y}_0|_{\hat{Y}_4}$ also defines a section of the flat fibration $\pi_{\hat{Y}_4} : \hat{Y}_4 \longrightarrow S$, there is a relation

$$\begin{aligned}\left(\hat{Y}_3 - \hat{Y}_0\right)\Big|_{\hat{Y}_4} &= \nu^*_{\text{tot}}(D_{X_2} - D_S)|_{\hat{Y}_4} - (\hat{E}_2 + \hat{D}_{X_2})|_{\hat{Y}_4} \\ &= -\hat{Y}_2|_{\hat{Y}_4} + \pi^*_{\hat{Y}_4}(2c_1(B_3)|_S - c_1(N_{S|B_3}))\,. \end{aligned} \tag{A.45}$$

Using all the relations above, one can derive the following rational equivalence relations:

$$\begin{aligned}
\hat{Y}_0 \cdot \hat{Y}_1 &\sim \pi^*(D_S) \cdot \sigma + c_1(B_3) \cdot \hat{Y}_0, \\
\hat{Y}_1 \cdot \hat{Y}_2 &\sim \pi^*(D_S) \cdot \sigma + c_1(B_3) \cdot (\hat{Y}_0 + 2\hat{Y}_1) - c_1(N_{S|B_3}) \cdot \hat{Y}_1, \\
\hat{Y}_2 \cdot \hat{Y}_3 &\sim \pi^*(D_S) \cdot \sigma + c_1(B_3) \cdot (\hat{Y}_0 + 2\hat{Y}_1 + 3\hat{Y}_2) - c_1(N_{S|B_3}) \cdot (\hat{Y}_1 + 2\hat{Y}_2), \\
\hat{Y}_3 \cdot \hat{Y}_4 &\sim \pi^*(D_S) \cdot \sigma - (\hat{Y}_2 \cdot \hat{Y}_4) + c_1(B_3) \cdot (\hat{Y}_0 + 2\hat{Y}_4) - c_1(N_{S|B_3}) \cdot \hat{Y}_4, \\
\hat{Y}_4 \cdot \hat{Y}_0 &\sim \pi^*(D_S) \cdot \sigma + c_1(B_3) \cdot \hat{Y}_0,
\end{aligned} \tag{A.46}$$

and

$$\hat{Y}_1 \cdot \hat{Y}_4 \sim c_1(B_3) \cdot \hat{Y}_1. \tag{A.47}$$

The matter surfaces for the $\mathbf{10}$ and $\bar{\mathbf{5}}$ representations are different under rational equivalence only by

$$\begin{aligned}[S_\gamma] - [-S_C] &\sim \left[\hat{Y}_3 \cdot \left\{\hat{Y}_4 + c_1(N) + 3c_1(B_3) - \hat{Y}_2\right\}\right] - \left[-\hat{Y}_2 \cdot \hat{Y}_4\right] \\ &\sim c_1(B_3) \cdot (-2\hat{Y}_1 - 3\hat{Y}_2 + 3\hat{Y}_3 + 2\hat{Y}_4) + c_1(N_{S|B_3}) \cdot (\hat{Y}_1 + 2\hat{Y}_2 + \hat{Y}_3 - \hat{Y}_4).\end{aligned} \tag{A.48}$$

If we turn on a flux which does not break SU(5) gauge invariance, this guarantees that the chirality in the $\mathbf{10}$ representation is the same as that in $\bar{\mathbf{5}}$ representation, as also observed in [25].

B Dependence of Hodge numbers on the rank of 7-brane symmetry

The number of flux vacua that have a stack of 7-branes with symmetry R scales as $e^{K/6}$, $K = \dim[H^4_H(X;\mathbb{R})]$, as we have seen in section 6. In this appendix, we use the approximate relation (6.5), which holds in the cases satisfying the condition (6.3), to study the statistics of the unification symmetry R. Instead of studying how the dimension of the primary horizontal subspace K depends on the symmetry R, we will estimate how $h^{3,1}$ changes for different choices of R.

Let us start from a family for $(B_3, [S], R_1)$, and suppose that the enhancement of the 7-brane symmetry R_1 to R_2 occurs when a section $f \in \Gamma(B_3; \mathcal{O}(D))$ of some line bundle $\mathcal{O}_{B_3}(D)$ vanishes along S; the section f is used in a defining equation of the Weierstrass model, and the geometry gets more singular for $f|_S = 0$. The line bundle $\mathcal{O}_{B_3}(D)$ here is determined by Tate's algorithm, as we will discuss more explicitly later on. Requiring f to vanish along S, the number of independent complex structure moduli is reduced roughly by

$$\Delta h^{3,1} = h^0(B_3; \mathcal{O}_{B_3}(D)) - h^0(B_3; \mathcal{O}_{B_3}(D - S)). \tag{B.1}$$

JHEP01(2015)047

One can then use the exact sequence

$$0 \longrightarrow \mathcal{O}_{B_3}(D-S) \longrightarrow \mathcal{O}_{B_3}(D) \longrightarrow i_*\left[\mathcal{O}_S(D|_S)\right] \longrightarrow 0 \tag{B.2}$$

to set an upper bound

$$\Delta h^{3,1} \leq h^0(S;\mathcal{O}_S(D|_S)). \tag{B.3}$$

This inequality is saturated when $h^1(B_3;\mathcal{O}_{B_3}(D-S))$ vanishes. From this, we can derive the crude estimate

$$e^{h^0(S;\mathcal{O}_S(D|_S))} \tag{B.4}$$

on the statistical cost of unification symmetry R_2 relatively to R_1.

Let us use the examples we studied in section 4.4 to see how this works in practice. We focus on the case $B_3^{(n)} = \mathbb{P}[\mathcal{O}_{\mathbb{P}^2} \oplus \mathcal{O}_{\mathbb{P}^2}(n)]$ and study the enhancement from $R_1 = A_4$ to $R_2 = D_5$ along $S = \mathbb{P}^2$. The condition for this $A_4 \to D_5$ enhancement is $(f = a_5)|_S = 0$; note also that $a_5 \in \Gamma(B_3;\mathcal{O}_{B_3}(-K_{B_3}))$ and hence $D|_S = S - K_S = (3-n)H_{\mathbb{P}^2}$. The estimated upper bound on $\Delta h^{3,1}$ therefore becomes

$$h^0\left(S;\mathcal{O}_S(D|_S)\right) = h^0\left(\mathbb{P}^2;\mathcal{O}_{\mathbb{P}^2}((3-n)H)\right) = \frac{(5-n)(4-n)}{2}. \tag{B.5}$$

The value of $\Delta K_{4\text{-}5}$ in table 4 is estimated reasonably well by $6 \times h^0(S;\mathcal{O}_S(D|_S)) = 3(5-n)(4-n)$ indeed.[23]

Let us now use this argument to study how the statistical cost varies for different enhancement of symmetries $R_1 \to R_2$. Suppose that the Weierstrass model Z_s is parametrized by the generalized Weierstrass equation (Tate's form),

$$y^2 + b_1 xy + b_3 y = x^3 + x^2 b_2 + x b_4 + b_6\,. \tag{B.6}$$

When b_i vanishes along S with the order of vanishing n_i, let $b_i = s^{n_i} b_{i|n_i}$. The dictionary between the order of vanishing n_i's and the 7-brane symmetry R is known [72], and the necessary information is recorded in table 5.

An immediate generalization of the $A_4 \to D_5$ enhancement is the enhancement $A_m \to D_{m+1}$, $m \in 2\mathbb{N}$. In these cases, $f = b_{1|0}$ and $D = -K_{B_3}$ for any $m \in 2\mathbb{N}$, not just for $m = 4$. Thus, the same value $h^0(S;\mathcal{O}_S(-K_{B_3}|_S)) = h^0(S;\mathcal{O}_S(S-K_S))$ provides an approximate upper bound on $\Delta h^{3,1}$ for any $m \in 2\mathbb{N}$.

One can also think of two separate chains of symmetry enhancement, $A_m \to A_{m+1} \to A_{m+2}$ and $D_{m+1} \to D_{m+2} \to D_{m+3}$. The statistical cost increases at the same pace in these two chains; as the rank increases by two from A_m to A_{m+2}, or from D_{m+1} to D_{m+3}, we need to set the sections $b_{3|m/2}|_S$, $b_{4|m/2+1}|_S$, $b_{6|m+1}|_S$ and $b_{6|m+2}|_S$ to zero in any one of those two chains (see table 5). This is consistent with the result above that the statistical

[23] It is a little misleading to use these examples to emphasize that this estimate is good. The $\mathbb{P}^1$-fibration structure over S in $B_3^{(n)}$ defines a normal coordinate of S that remains well-defined globally on $B_3^{(n)}$. We do not intend to claim that $6h^0(S;\mathcal{O}_S(D|_S))$ is a good estimate of ΔK rather than a good estimate of the upper bound on ΔK.

JHEP01(2015)047

		b_1	b_3	b_4	b_6
A_m	I^s_{m+1}	0	$m/2$	$m/2+1$	$m+1$
A_{m+1}	I^s_{m+2}	0	$m/2+1$	$m/2+1$	$m+2$
A_{m+2}	I^s_{m+3}	0	$m/2+1$	$m/2+2$	$m+3$
D_{m+1}	I^{*s}_{m-3}	1	$m/2$	$m/2+1$	$m+1$
D_{m+2}	I^{*s}_{m-2}	1	$m/2+1$	$m/2+1$	$m+1$
D_{m+3}	I^{*s}_{m-1}	1	$m/2+1$	$m/2+2$	$m+3$

		b_1	b_2	b_3	b_4	b_6
A_4	I^s_5	0	1	2	3	5
D_5	I^{*s}_1	1	1	2	3	5
E_6	IV^{*s}	1	2	2	3	5
E_7	III^*	1	2	3	3	5
E_8	II^*	1	2	3	4	5

Table 5. Order of vanishing n_i of b_i's required for various types of singular fibre (7-brane gauge group); information relevant to the discussion in this section is extracted from a table in [72]. $m \in 2\mathbb{N}$ is assumed in this table. The order of vanishing for b_2 is 1 for any one in the I^s_k and I^{*s}_k series.

cost for the enhancement $A_m \to D_{m+1}$ remains much the same for any $m \in 2\mathbb{N}$. Noting that $b_{i|n_i} \in \Gamma(B_3; \mathcal{O}_{B_3}(-iK_{B_3} - n_i S))$, and hence

$$b_{3|m/2}|_S \in \Gamma(S; \mathcal{O}_S(-3K_{B_3}|_S - m/2S)), \qquad b_{6|m+1}|_S \in \Gamma(S; \mathcal{O}_S(-6K_{B_3}|_S - (m+1)S)),$$
$$b_{4|m/2+1}|_S \in \Gamma\Big(S; \mathcal{O}_S(-4K_{B_3}|_S - \frac{m+2}{2}S)\Big), \quad b_{6|m+2}|_S \in \Gamma(S; \mathcal{O}_S(-6K_{B_3}|_S - (m+2)S)), \tag{B.7}$$

one finds that the statistical cost for enhancement by rank-one, measured by $\Delta K/\Delta m \approx 6\Delta h^{3,1}/\Delta m$, becomes larger for higher rank m in the case $c_1(N_{S|B_3}) < 0$; if $c_1(N_{S|B_3}) > 0$, on the other hand, the cost for one-rank enhancement decreases for higher rank m, because $\Delta h^{3,1}$ is bounded from above by smaller value. One should be careful in interpreting this phenomenon for $c_1(N_{S|B_3}) > 0$; it looks as if higher rank gauge groups become just as "natural" as lower rank gauge groups at first sight, but it may also be that the choice of complex structure for such a high rank enhancement has already become impossible.

Let us finally look at the chain of symmetry enhancements $E_m \to E_{m+1}$; $A_4 \to D_5$ is also regarded as a part of this chain. In this chain, we need to set the section

$$\big[a_{9-m|0} \propto b_{m-3|m-4}\big]\big|_S \in \Gamma(S; \mathcal{O}_S(S - (m-3)K_S)) \tag{B.8}$$

to zero for the enhancement $E_m \to E_{m+1}$. Thus, the statistical cost for one-rank enhancement, $\Delta K/\Delta m$, becomes increasingly large in higher rank (larger m), if $K_S < 0$. [Note that there are chiral multiplets in the adjoint representation of E_m in the spectrum below the Kaluza-Klein scale, if $K_S > 0$ instead.][24] Interestingly, the behaviour of $\Delta K/\Delta m$ is controlled by the normal bundle $N_{S|B_3}$ in the (IIB-like) A_m type and D_m type chains of symmetry enhancement, and by the canonical bundle K_S in the E_m type chain available in F-theory.

[24] In the case of $\hat{Z} = \mathrm{K3} \times \mathrm{K3}$ [16], the dimension of the primary horizontal subspace, K, and $h^{3,1}$ are linear in the rank of the 7-brane gauge group rank_7, and $\Delta K/\Delta\mathrm{rank}_7$ remains constant, in particular. This simple result for $\mathrm{K3} \times \mathrm{K3}$ compactifications of F-theory should be understood as an artefact of trivial bundles K_S and $N_{S|B_3}$.

JHEP01(2015)047

C Flux controlling the net chirality

In order to consider an ensemble of fluxes leading to effective theories with a given number of generations (net chirality) $N_{\rm gen}$, $G^{(4)}_{\rm fix}$ needs to be chosen so that it generates the net chirality $N_{\rm gen}$. If we take the scanning space $H_{\rm scan}$ to be the real primary horizontal subspace $H^4_H(X;\mathbb{R})$, then all the flux vacua end up with effective theories with one and the same value of $N_{\rm gen}$ in such an ensemble. This appendix begins with writing down the four-form flux generating the net chirality, which is already a well-understood subject in the literature. We then move on to compute the D3-tadpole bound

$$\frac{\chi(\hat{Z})}{24} - \frac{1}{2}(G^{(4)}_{\rm fix})^2 = L_* \geq \frac{1}{2}(G^{(4)}_{\rm scan})^2. \tag{C.1}$$

We implicitly used that $G^{(4)}_{\rm fix} \wedge G^{(4)}_{\rm scan} = 0$, which follows because the chirality generating flux $G^{(4)}_{\rm fix}$ is chosen within the vertical component $H^{2,2}_V(\hat{Z};\mathbb{R})$ (because the matter surface belongs to the space of vertical cycles), and the primary horizontal subspace is orthogonal to the vertical component.

The choice of $(B_3,[S])$ in section 4.4.1 is a simple generalization of [27]; $B_3 = \mathbb{P}[\mathcal{O}_{\mathbb{P}^2} \oplus \mathcal{O}_{\mathbb{P}^2}(n)]$ instead of $B_3 = \mathbb{P}[\mathcal{O}_{\mathbb{P}^2} \oplus \mathcal{O}_{\mathbb{P}^2}] = \mathbb{P}^1 \times \mathbb{P}^2$. In order to determine the flux $G^{(4)}_{\rm fix}$ generating the chirality of SU(5) unification models, the conditions for Lorentz SO(3,1) symmetry (2.1) and unbroken SU(5) symmetry (2.3) were imposed on the space of vertical four-forms $H^{2,2}_V(\hat{Z};\mathbb{R})$. As we can think of the Kähler form as being expanded in a basis consisting of divisors of the base, the section, the generic fibre class and the exceptional fibre components, these constraints also automatically make the D-term (2.2) vanish. It is legitimate, as we stated above, to search the chirality generating flux $G^{(4)}_{\rm fix}$ from $H^{2,2}_V(\hat{Z};\mathbb{R})$, because the matter surface belongs to the space of vertical four-cycles. We have seen in section 4.4.1 that the space $H^{2,2}_V(\hat{Z};\mathbb{R})$ has nine dimensions, while the conditions of unbroken SO(3,1) Lorentz and SU(5) unified symmetries result in eight independent constraints. This is true for all the cases with $-3 \leq n \leq 2$, not just the case $n = 0$ in [27]. After a straightforward computation, it turns out that

$$G^{(4)}_{\rm fix} = \lambda\left(5\hat{Y}_4 \cdot \hat{Y}_2 + (2S + (3+n)H_{\mathbb{P}^2}) \cdot (2\hat{Y}_1 - 2\hat{Y}_4 - \hat{Y}_2 + \hat{Y}_3)\right), \tag{C.2}$$

where $\lambda \in \mathbb{R}$ and $H_{\mathbb{P}^2}$ is the hyperplane divisor of the base $\mathbb{P}^2$. We have confirmed that this flux is equivalent to the one given in [25] and, in the case of $n = 0$, to the choice of [27] with $\lambda = -3\beta$, exploiting rational equivalence. The net chirality for the SU(5) $\mathbf{10}$-$\overline{\mathbf{10}}$ representations is given by

$$N_{\rm gen} = \chi_{\mathbf{10}} = -\lambda(18-n)(3-n). \tag{C.3}$$

The choice of such chirality generating flux is quantized due to the condition $G^{(4)}_{\rm fix} \in [H^4(\hat{Z};\mathbb{Z})]_{\rm shift}$. It is not an easy task, to say the least, to determine the integral basis of $[H^4(\hat{Z};\mathbb{Z})]_{\rm shift} \cap H^{2,2}_V(\hat{Z};\mathbb{Q})$, but fortunately this task can be detoured in the cases we are dealing with. Here, a dual description in Heterotic string theory exists, and it is known

JHEP01(2015)047

n	-3	-2	-1	0	1	2
$\chi(\hat{Z})/24$	$1263/4$	$719/2$	$869/2$	$2163/4$	$2713/4$	847
$\frac{1}{2}(G_{\text{fix}}^{(4)})^2$	$315/4$	$125/2$	$95/2$	$135/4$	$85/4$	10
$L_*^{\max}$	237	297	387	507	657	837
K	7557	8603	10403	12953	16253	20303

Table 6. The value of $\chi(\hat{Z})/24$ as well as $(G_{\text{fix}}^{(4)})^2/2$ and L_* for $\lambda = \pm 1/2$, when L_* becomes maximal for a given n. The result of $K := \dim_{\mathbb{R}}[H_H^4(\hat{Z};\mathbb{R})]$ is copied from table 2.

that (6.1) gives rise to the net chirality (6.2). We should thus identify $\lambda_{FMW} = \lambda$, and the quantization

$$\lambda = \frac{1}{2}(1+2a), \qquad a \in \mathbb{Z} \tag{C.4}$$

follows from that of that of λ_{FMW} [25]. As discussed in [25], $G_{\text{fix}}^{(4)}$ with this quantization condition satisfies $G_{\text{fix}}^{(4)} \in [H^4(\hat{Z};\mathbb{Z})]_{\text{shift}}$.

Now that $G_{\text{fix}}^{(4)}$ is given explicitly, we are ready to compute the D3-tadpole upper bound L_*. The standard computation techniques of toric geometry allow us to compute $\int_{\hat{Z}} G_{\text{fix}}^{(4)} \wedge G_{\text{fix}}^{(4)}$. We find that

$$L_* = \frac{2163}{4} + \frac{125}{8}n(n+7) - \frac{5(18-n)(3-n)}{2}\lambda^2 \tag{C.5}$$

$$= \frac{2163}{4} + \frac{125}{8}n(n+7) - \frac{5N_{\text{gen}}^2}{2(18-n)(3-n)}. \tag{C.6}$$

It is not obvious from the above equation whether L_* becomes integer or not, but L_* is indeed; see table 6. The computation here is essentially that of [55], although a K3-fibre is used instead of the stable degeneration limit $dP_9 \cup dP_9$, and a specific resolution of singularity is employed. The value of the D3-tadpole upper bound L_* depends on the number of generation N_{gen}. This result is used in section 6 (and also [22]) to derive the distribution of N_{gen} in the landscape of F-theory flux vacua.

Open Access. This article is distributed under the terms of the Creative Commons Attribution License (CC-BY 4.0), which permits any use, distribution and reproduction in any medium, provided the original author(s) and source are credited.

References

[1] A.S. Haupt, A. Lukas and K.S. Stelle, *M-theory on Calabi-Yau five-folds*, *JHEP* **05** (2009) 069 [arXiv:0810.2685] [INSPIRE].

[2] R. Hudson, *Kummer's quartic surface*, Cambridge University Press, Cambridge U.K. (1905).

[3] P.S. Aspinwall, *K3 surfaces and string duality*, hep-th/9611137 [INSPIRE].

[4] B.R. Greene, D.R. Morrison and M.R. Plesser, *Mirror manifolds in higher dimension*, *Commun. Math. Phys.* **173** (1995) 559 [hep-th/9402119] [INSPIRE].

JHEP01(2015)047

[5] K. Becker and M. Becker, *M theory on eight manifolds*, *Nucl. Phys.* **B 477** (1996) 155 [hep-th/9605053] [INSPIRE].

[6] S. Sethi, C. Vafa and E. Witten, *Constraints on low dimensional string compactifications*, *Nucl. Phys.* **B 480** (1996) 213 [hep-th/9606122] [INSPIRE].

[7] I. Brunner and R. Schimmrigk, *F-theory on Calabi-Yau fourfolds*, *Phys. Lett.* **B 387** (1996) 750 [hep-th/9606148] [INSPIRE].

[8] P. Mayr, *Mirror symmetry, $N = 1$ superpotentials and tensionless strings on Calabi-Yau four folds*, *Nucl. Phys.* **B 494** (1997) 489 [hep-th/9610162] [INSPIRE].

[9] A. Klemm, B. Lian, S.S. Roan and S.-T. Yau, *Calabi-Yau fourfolds for M-theory and F-theory compactifications*, *Nucl. Phys.* **B 518** (1998) 515 [hep-th/9701023] [INSPIRE].

[10] K. Mohri, *F-theory vacua in four-dimensions and toric threefolds*, *Int. J. Mod. Phys.* **A 14** (1999) 845 [hep-th/9701147] [INSPIRE].

[11] M. Bershadsky, A. Johansen, T. Pantev and V. Sadov, *On four-dimensional compactifications of F-theory*, *Nucl. Phys.* **B 505** (1997) 165 [hep-th/9701165] [INSPIRE].

[12] M. Kreuzer and H. Skarke, *Calabi-Yau four folds and toric fibrations*, *J. Geom. Phys.* **26** (1998) 272 [hep-th/9701175] [INSPIRE].

[13] A. Strominger, *Special geometry*, *Commun. Math. Phys.* **133** (1990) 163 [INSPIRE].

[14] S. Ashok and M.R. Douglas, *Counting flux vacua*, *JHEP* **01** (2004) 060 [hep-th/0307049] [INSPIRE].

[15] F. Denef and M.R. Douglas, *Distributions of flux vacua*, *JHEP* **05** (2004) 072 [hep-th/0404116] [INSPIRE].

[16] A.P. Braun, Y. Kimura and T. Watari, *The Noether-Lefschetz problem and gauge-group-resolved landscapes: F-theory on $K3 \times K3$ as a test case*, *JHEP* **04** (2014) 050 [arXiv:1401.5908] [INSPIRE].

[17] T.W. Grimm, T.-W. Ha, A. Klemm and D. Klevers, *Computing brane and flux superpotentials in F-theory compactifications*, *JHEP* **04** (2010) 015 [arXiv:0909.2025] [INSPIRE].

[18] N.C. Bizet, A. Klemm and D.V. Lopes, *Landscaping with fluxes and the E_8 Yukawa point in F-theory*, arXiv:1404.7645 [INSPIRE].

[19] V.V. Batyrev, *Dual polyhedra and mirror symmetry for Calabi-Yau hypersurfaces in toric varieties*, *J. Alg. Geom.* **3** (1994) 493 [alg-geom/9310003] [INSPIRE].

[20] M. Buican, D. Malyshev, D.R. Morrison, H. Verlinde and M. Wijnholt, *D-branes at singularities, compactification and hypercharge*, *JHEP* **01** (2007) 107 [hep-th/0610007] [INSPIRE].

[21] C. Beasley, J.J. Heckman and C. Vafa, *GUTs and exceptional branes in F-theory — II: experimental predictions*, *JHEP* **01** (2009) 059 [arXiv:0806.0102] [INSPIRE].

[22] A.P. Braun and T. Watari, *Distribution of number of generations in flux compactifications*, to appear.

[23] K. Dasgupta, G. Rajesh and S. Sethi, *M theory, orientifolds and G-flux*, *JHEP* **08** (1999) 023 [hep-th/9908088] [INSPIRE].

JHEP01(2015)047

[24] A.P. Braun, A. Collinucci and R. Valandro, *G-flux in F-theory and algebraic cycles*, *Nucl. Phys.* **B 856** (2012) 129 [arXiv:1107.5337] [INSPIRE].

[25] J. Marsano and S. Schäfer-Nameki, *Yukawas, G-flux and spectral covers from resolved Calabi-Yau's*, *JHEP* **11** (2011) 098 [arXiv:1108.1794] [INSPIRE].

[26] T.W. Grimm and R. Savelli, *Gravitational instantons and fluxes from M/F-theory on Calabi-Yau fourfolds*, *Phys. Rev.* **D 85** (2012) 026003 [arXiv:1109.3191] [INSPIRE].

[27] T.W. Grimm and H. Hayashi, *F-theory fluxes, chirality and Chern-Simons theories*, *JHEP* **03** (2012) 027 [arXiv:1111.1232] [INSPIRE].

[28] M. Cvetič, A. Grassi, D. Klevers and H. Piragua, *Chiral four-dimensional F-theory compactifications with* SU(5) *and multiple* U(1)*-factors*, *JHEP* **04** (2014) 010 [arXiv:1306.3987] [INSPIRE].

[29] F. Denef, *Les Houches lectures on constructing string vacua*, arXiv:0803.1194 [INSPIRE].

[30] M. Esole and S.-T. Yau, *Small resolutions of* SU(5)*-models in F-theory*, *Adv. Theor. Math. Phys.* **17** (2013) 1195 [arXiv:1107.0733] [INSPIRE].

[31] H. Hayashi, C. Lawrie and S. Schäfer-Nameki, *Phases, flops and F-theory:* SU(5) *gauge theories*, *JHEP* **10** (2013) 046 [arXiv:1304.1678] [INSPIRE].

[32] H. Hayashi, C. Lawrie, D.R. Morrison and S. Schäfer-Nameki, *Box graphs and singular fibers*, *JHEP* **05** (2014) 048 [arXiv:1402.2653] [INSPIRE].

[33] M. Esole, S.-H. Shao and S.-T. Yau, *Singularities and gauge theory phases*, arXiv:1402.6331 [INSPIRE].

[34] M. Esole, S.-H. Shao and S.-T. Yau, *Singularities and gauge theory phases II*, arXiv:1407.1867 [INSPIRE].

[35] A.P. Braun and S. Schäfer-Nameki, *Box graphs and resolutions I*, arXiv:1407.3520 [INSPIRE].

[36] R. Donagi and M. Wijnholt, *Model building with F-theory*, *Adv. Theor. Math. Phys.* **15** (2011) 1237 [arXiv:0802.2969] [INSPIRE].

[37] C. Beasley, J.J. Heckman and C. Vafa, *GUTs and exceptional branes in F-theory — I*, *JHEP* **01** (2009) 058 [arXiv:0802.3391] [INSPIRE].

[38] V.I. Danilov and A.G. Khovanskii, *Newton polyhedra and an algorithm for computing Hodge-Deligne numbers*, *Math. USSR Izv.* **29** (1987) 279.

[39] V.I. Danilov, *The geometry of toric varieties*, *Russ. Math. Surv.* **33** (1978) 97.

[40] W. Fulton, *Introduction to toric varieties*, Princeton University Press, Princeton U.S.A. (1993).

[41] V.V. Batyrev and D.I. Dais, *Strong McKay correspondence, string theoretic Hodge numbers and mirror symmetry*, *Topology* **35** (1996) 901 [alg-geom/9410001] [INSPIRE].

[42] V.V. Batyrev and L.A. Borisov, *Mirror duality and string theoretic Hodge numbers*, *Invent. Math.* **126** (1996) 183 [alg-geom/9509009] [INSPIRE].

[43] C. Peters and J. Steenbrink, *Mixed Hodge structures*, Ergebnisse der Mathematik und ihrer Grenzgebiete. 3. Folge/A Series of Modern Surveys in Mathematics, Springer, Berlin Heidelberg Germany (2008).

JHEP01(2015)047

[44] *Hodge structure wikipedia webpage*, http://en.wikipedia.org/wiki/Hodge_structure #Example_of_curves, accessed August 12 2014.

[45] M. Bies, C. Mayrhofer, C. Pehle and T. Weigand, *Chow groups, Deligne cohomology and massless matter in F-theory*, arXiv:1402.5144 [INSPIRE].

[46] J. Rambau, *TOPCOM: triangulations of point configurations and oriented matroids*, in *Mathematical software — ICMS* 2002, A.M. Cohen, X.-S. Gao and N. Takayama eds., World Scientific, Singapore (2002), pg. 330.

[47] Sage Development Team collaboration, W. Stein et al., *Sage mathematics software (version* 6.1.1*)*, http://www.sagemath.org/, (2014).

[48] M. Kreuzer and H. Skarke, *PALP: a package for analyzing lattice polytopes with applications to toric geometry*, *Comput. Phys. Commun.* **157** (2004) 87 [math/0204356] [INSPIRE].

[49] A.P. Braun, J. Knapp, E. Scheidegger, H. Skarke and N.-O. Walliser, *PALP — a user manual*, arXiv:1205.4147 [INSPIRE].

[50] J. De Loera, J. Rambau and F. Santos, *Kummer's quartic surface*, Springer, Berlin Heidelberg Germany (2010).

[51] R. Blumenhagen, T.W. Grimm, B. Jurke and T. Weigand, *Global F-theory GUTs*, *Nucl. Phys.* **B 829** (2010) 325 [arXiv:0908.1784] [INSPIRE].

[52] P. Candelas and A. Font, *Duality between the webs of heterotic and type-II vacua*, *Nucl. Phys.* **B 511** (1998) 295 [hep-th/9603170] [INSPIRE].

[53] P. Candelas, E. Perevalov and G. Rajesh, *Toric geometry and enhanced gauge symmetry of F-theory/heterotic vacua*, *Nucl. Phys.* **B 507** (1997) 445 [hep-th/9704097] [INSPIRE].

[54] E. Perevalov and H. Skarke, *Enhanced gauged symmetry in type-II and F-theory compactifications: Dynkin diagrams from polyhedra*, *Nucl. Phys.* **B 505** (1997) 679 [hep-th/9704129] [INSPIRE].

[55] B. Andreas and G. Curio, *On discrete twist and four flux in $N = 1$ heterotic/F-theory compactifications*, *Adv. Theor. Math. Phys.* **3** (1999) 1325 [hep-th/9908193] [INSPIRE].

[56] H. Hayashi, R. Tatar, Y. Toda, T. Watari and M. Yamazaki, *New aspects of heterotic F-theory duality*, *Nucl. Phys.* **B 806** (2009) 224 [arXiv:0805.1057] [INSPIRE].

[57] A.P. Braun, A. Collinucci and R. Valandro, *Hypercharge flux in F-theory and the stable Sen limit*, *JHEP* **07** (2014) 121 [arXiv:1402.4096] [INSPIRE].

[58] L. Borisov, *Towards the mirror symmetry for Calabi-Yau complete intersections in Gorenstein toric Fano varieties*, alg-geom/9310001.

[59] V.V. Batyrev and L.A. Borisov, *On Calabi-Yau complete intersections in toric varieties*, alg-geom/9412017 [INSPIRE].

[60] R. Friedman, J. Morgan and E. Witten, *Vector bundles and F-theory*, *Commun. Math. Phys.* **187** (1997) 679 [hep-th/9701162] [INSPIRE].

[61] G. Curio, *Chiral matter and transitions in heterotic string models*, *Phys. Lett.* **B 435** (1998) 39 [hep-th/9803224] [INSPIRE].

[62] D.-E. Diaconescu and G. Ionesei, *Spectral covers, charged matter and bundle cohomology*, *JHEP* **12** (1998) 001 [hep-th/9811129] [INSPIRE].

JHEP01(2015)047

[63] J. Gray, A.S. Haupt and A. Lukas, *All complete intersection Calabi-Yau four-folds*, *JHEP* **07** (2013) 070 [arXiv:1303.1832] [INSPIRE].

[64] O. DeWolfe, A. Giryavets, S. Kachru and W. Taylor, *Enumerating flux vacua with enhanced symmetries*, *JHEP* **02** (2005) 037 [hep-th/0411061] [INSPIRE].

[65] H. Hayashi, T. Kawano, Y. Tsuchiya and T. Watari, *Flavor structure in F-theory compactifications*, *JHEP* **08** (2010) 036 [arXiv:0910.2762] [INSPIRE].

[66] C. Cordova, *Decoupling gravity in F-theory*, *Adv. Theor. Math. Phys.* **15** (2011) 689 [arXiv:0910.2955] [INSPIRE].

[67] R. Donagi, Y.-H. He, B.A. Ovrut and R. Reinbacher, *The particle spectrum of heterotic compactifications*, *JHEP* **12** (2004) 054 [hep-th/0405014] [INSPIRE].

[68] G. Curio and R.Y. Donagi, *Moduli in $N = 1$ heterotic/F-theory duality*, *Nucl. Phys.* **B 518** (1998) 603 [hep-th/9801057] [INSPIRE].

[69] E. Diaconescu, G.W. Moore and D.S. Freed, *The M-theory three form and E_8 gauge theory*, hep-th/0312069 [INSPIRE].

[70] S. Krause, C. Mayrhofer and T. Weigand, *G_4 flux, chiral matter and singularity resolution in F-theory compactifications*, *Nucl. Phys.* **B 858** (2012) 1 [arXiv:1109.3454] [INSPIRE].

[71] T.W. Grimm, S. Krause and T. Weigand, *F-theory GUT vacua on compact Calabi-Yau fourfolds*, *JHEP* **07** (2010) 037 [arXiv:0912.3524] [INSPIRE].

[72] M. Bershadsky et al., *Geometric singularities and enhanced gauge symmetries*, *Nucl. Phys.* **B 481** (1996) 215 [hep-th/9605200] [INSPIRE].

JHEP01(2015)047

PHYSICAL REVIEW D **90,** 125001 (2014)

Skewness dependence of generalized parton distributions, conformal OPE, and the AdS/CFT correspondence

Ryoichi Nishio[1,2,*] and Taizan Watari[2]

[1]*Department of Physics, University of Tokyo, Tokyo 113-0033, Japan*
[2]*Kavli Institute for the Physics and Mathematics of the Universe, University of Tokyo, Kashiwa-no-ha 5-1-5, 277-8583, Japan*

(Received 2 September 2014; published 1 December 2014)

The traditional idea of the Pomeron/Reggeon description for hadron scattering is now being given theoretical foundation in gravity dual descriptions, where Pomeron corresponds to an exchange of spin-$j \in 2\mathbb{Z}$ states in the graviton trajectory. Deeply virtual Compton scattering (DVCS) is essentially a two-to-two scattering process of a hadron and a photon, and hence one should be able to study nonperturbative aspects (the generalized parton distribution [GPD]) of this process by the Pomeron/Reggeon process in gravity dual. We find, however, that even one of the most developed formulations of gravity dual, Pomeron [Brower-Polchinski-Strassler-Tan (BPST), 2006], is not able to capture skewness dependence of GPD properly. Therefore, we compute Reggeon wave functions on AdS_5 so that the formalism of BPST can be generalized. These wave functions are used to determine the DVCS amplitude, bring it to the form of conformal operator product expansion/collinear factorization, and extract a holographic model of GPD, which naturally fits into the framework known as "dual parametrization," or the "(conformal) collinear factorization approach."

DOI: 10.1103/PhysRevD.90.125001 PACS numbers: 12.38.Aw, 11.25.Tq, 13.85.-t

I. INTRODUCTION

Scattering processes of hadrons involve nonperturbative information of QCD. When it comes to scattering with the center of mass energy higher than the QCD scale, lattice computation will not have enough computation power in a near future, yet perturbative QCD is able to say something only about the hard components involved in the scattering. This is where holographic descriptions of strongly coupled gauge theories may find a role to play. Although we cannot expect gravitational "dual" descriptions to be both calculable and perfectly equivalent to the QCD of the real world at the same time, we still hope to be able to learn nonperturbative aspects of hadrons at the qualitative level, using calculable holographic dual descriptions of nearly conformal strongly coupled gauge theories.

String theory started out as the dual resonance model describing scattering amplitudes of hadrons. One of its major problems as a theory of hadrons was a "prediction" that the amplitude of the elastic scattering of two hadrons falls off exponentially, e^{Bt} in the momentum transfer squared t for some $B > 0$, although the amplitude is known in reality to fall off in a power law in $|-t|$ for hard scattering. The prediction, however, is now understood as that of string theory with a flat background metric; the amplitude of elastic scattering turns into such a power law indeed when the target space of string theory has a warped metric. At the qualitative level, string theory on a warped spacetime—holographic (gravitational dual) descriptions—can be a viable theory of hadron scattering [1–3].

The holographic technique can be used to study not just amplitudes of hadron scattering as a whole, but also to extract the information of partons within hadrons [2]. Parton distribution functions (PDFs) are defined by the inverse Mellin transformation of hadron matrix elements of gauge singlet parton-bilinear operators in QCD, and gravity dual descriptions can be used to determine matrix elements of the gauge singlet operators. The PDF extracted in this way satisfies Dokshitzer-Gribov-Lipatov-Altarelli-Parisi [(DGLAP), q^2-evolution] and Balitsky-Fadin-Kuraev-Lipatov [(BFKL), $\ln(1/x)$-evolution] equations (e.g., [4–7]); just like in perturbative QCD [8], these two evolution equations follow from how the saddle point j^* moves in the complex angular momentum j-plane integral (the inverse Mellin transform). The holographic description for the PDF and the generalized parton distribution (GPD) also shows crossover transition between this DGLAP/BFKL behavior and the Regge behavior [3] (see also [7]). Thus, the parton information studied in this way may be used to understand nonperturbative issues associated with partons in a hadron at qualitative level.

In this article, we study two-body–two-body scattering between a hadron and a photon (that is possibly virtual) in gravitational dual descriptions; $\gamma^*(q_1) + h(p_1) \to \gamma^{(*)}(q_2) + h(p_2)$. A special case of this scattering—the forward scattering with $q_1 = q_2$ and $p_1 = p_2$—has been studied extensively in the literature (e.g., [2,4–7]) for the study of deep inelastic scattering (DIS) and PDF, and some references also cover the case of nonforward elastic scattering

*Present address: SmartNews, Inc.

 © 2014 American Physical Society

$[(q_1)^2 = (q_2)^2,\ (q_1 - q_2)^2 \neq 0]$. This article extends the analysis so that all kinds of skewed ($q_1^2 \neq q_2^2$) cases are covered. In hadron physics, therefore, the kinematics needed for deeply virtual Compton scattering, hard exclusive vector meson production and timelike Compton scattering processes [9] is covered in this analysis. With the full skewness dependence included in this analysis, it is also possible to use the result of this study to bridge a gap between data in such scattering processes at nonzero skewness [10] and the transverse profile of partons in a hadron, which is encoded by GPD at zero skewness [11].

From a theoretical perspective, the task of this article is to generalize the formalism of [2,3] (see also [4,6,7]) so that it can be used for two-body-to-two-body scattering that is not necessarily elastic. Pomeron/Reggeon propagators have been treated as if they were for a scalar field in [2,3,7], but they correspond to an exchange of stringy states with nonzero (arbitrarily high) spins; for the study of scattering with nonzero skewness, the polarization of a higher spin state propagator should also be treated with care (see also the approach in [12,13]).

It is a notoriously difficult problem to compute scattering of strings on a curved background geometry. We do not pretend that the generalization of the formalism in this article is something derived from string theory without a flaw. This is rather an attempt at capturing an approximately correct picture of nonperturbative aspects in hadron scattering that string theory would predict in the distant future. We are forced to rely sometimes on physics intuition —and to ignore subtleties or corrections that are not under our control—when we face situations where not enough techniques have been developed in string theory at the moment.

This article is organized as follows. We begin in Sec. II A with a review of parametrization of GPD in terms of conformal OPE (operator product expansion) because the expansion in a series of conformal primary operators becomes the key concept in using AdS/CFT correspondence (cf. [5]). After plainly stating what needs to be done in the gravity dual approach in Sec. II B, we proceed to explain our basic gravity dual setting and an idea of how to construct a scattering amplitude of our interest by using string field theory in Secs. III and IV. Section V shows the results of computing wave functions of spin-j fields on AdS_5, while a more detailed account of the derivation of wave functions is given in Appendix A. Classification of eigenmodes that turn out to be relevant for the "twist-2" operators in later sections is given in Sec. V A, and wave functions are presented as analytic functions of the complex spin (angular momentum) variable j in Sec. V B. These wave functions are organized into irreducible representations of conformal algebra in Sec. V C; the representation for spin-j primary operators contain more eigenmode components than those treated by the Pomeron exchange amplitude in the formalism of [3], indicating that more contributions are needed in the scattering amplitude with nonvanishing skewness than in the formalism of [3]. These wave functions (and propagators) are used in Sec. VI in organizing scattering amplitude on AdS_5. The amplitude obtained in this way can be cast into the form of conformal OPE, from which one can also extract GPD as a function of kinematical variables. We are not committed to a particular form of implementing confining effects in the holographic description, as discussed in Sec. V D. Some qualitative aspects of the GPD profile are examined in Sec. VII. This paper in Phys. Rev. D is based on the preprints [14].

Not surprisingly, holographic models of GPD so obtained provide a special subclass of GPD models that have been called dual parametrization or (conformal) collinear factorization approach in the QCD/hadron community [15–18]. After all, it is the combination of the dual resonance model and the AdS/CFT correspondence that are being used.

We found that interesting preprints [12,13] cover a subject that is closely related to our study in Secs. V and VI and in Appendix A. References [12,13] mainly deal with correlation functions of CFTs as functions of spacetime coordinates, whereas we deal with them in this article as functions of incoming/outgoing momenta, and confinement effects are also implemented, so that we can study hadron scattering processes.

II. OUR APPROACH: CONFORMAL OPE AND GRAVITY DUAL

A. Review: Conformal OPE of DVCS amplitude

1. Notation and conventions

Deeply virtual Compton scattering (DVCS) $\gamma^* + h \to h + \gamma$, hard exclusive vector meson production (VMP) $e + h \to e + h + V$ and timelike Compton scattering (TCS) processes $e + h \to e + h + e^+e^-$ are shown in Figs. 1(a), 1(c), and 1(d), respectively. As a part of all these processes, the photon-hadron two-body-to-two-body scattering amplitude,

$$\mathcal{M}(\gamma^* h \to \gamma^{(*)} h) = (\epsilon_1^\mu) T_{\mu\nu} (\epsilon_2^\nu)^*, \tag{1}$$

is involved.[1] This two-body-to-two-body scattering amplitude with this exclusive choice of the final states (Fig. 2) is truly nonperturbative information, and this is the subject of this article. Because the "final state" photon is required to be on-shell $q_2^2 = 0$ in DVCS and timelike[2] $q_2^2 < 0$ in VMP

[1]There are two contributions from (a) the $\gamma^* + h \to \gamma + h$ virtual Compton scattering and (b) the Bethe-Heitler process in the leptoproduction process of a photon on a target hadron h: $\ell + h \to \ell + \gamma + h$, and they interfere. They can be separated experimentally, however, by exploiting kinematical dependence and polarization [19]. It thus makes sense to focus only on the amplitude (a).

[2]We use the $(-,+++)$ metric throughout this paper.

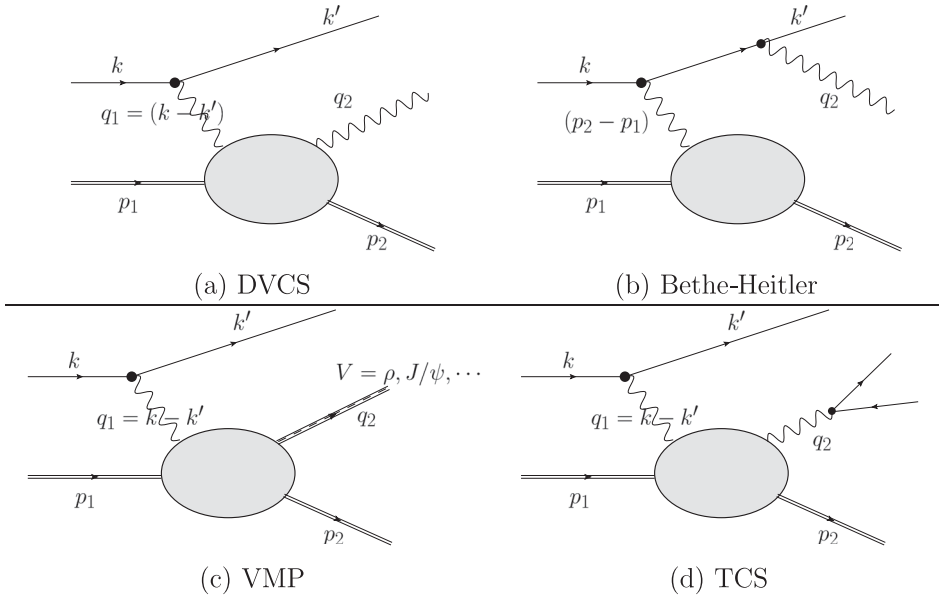

FIG. 1. Panels (a),(b) are diagrams contributing to the leptoproduction process of photon on a hadron, $\ell + h \to \ell + \gamma + h$, (c) is the exclusive vector meson production process, and, finally, (d) is the timelike Compton scattering process.

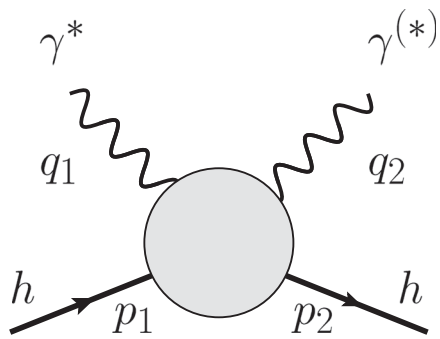

FIG. 2. Photon-hadron two-body-to-two-body scattering amplitude.

and TCS, we are interested in developing a theoretical framework to calculate this nonperturbative amplitude in the case where q_2^2 is different from spacelike $q_1^2 > 0$.

Just like in the QCD/hadron literature, we use the following notation for Lorentz invariant kinematical variables:

$$p^\mu = \frac{1}{2}(p_1^\mu + p_2^\mu), \qquad q^\mu = \frac{1}{2}(q_1^\mu + q_2^\mu),$$
$$\Delta^\mu = p_2^\mu - p_1^\mu = q_1^\mu - q_2^\mu, \tag{2}$$

$$x = \frac{-q^2}{2p\cdot q}, \qquad \eta = \frac{-\Delta\cdot q}{2p\cdot q},$$
$$s = W^2 = -(p+q)^2, \qquad t = -\Delta^2. \tag{3}$$

η is called skewness; in the scattering process of our interest, $q_1^2 = q^2 + \Delta^2/4 + q\cdot\Delta$ and $q_2^2 = q^2 + \Delta^2/4 - q\cdot\Delta$ are not the same; hence, the skewness does not vanish.

We will focus on high-energy scattering; for a typical energy scale of hadron masses/confinement scale Λ, we assume that

$$\Lambda^2 \ll q_1^2, W^2, \quad \text{while } |t| \lesssim \mathcal{O}(\Lambda). \tag{4}$$

The photon-hadron scattering amplitude (Fig. 2) in the real-world QCD (where all charged partons are fermions), the Compton tensor is given by the hadron matrix element with the insertion of two QED currents J^μ,

$$T^{\mu\nu} = i\int d^4x e^{-iq\cdot x}\langle h(p_2)|T\{J^\nu(x/2)J^\mu(-x/2)\}|h(p_1)\rangle. \tag{5}$$

For simplicity, we assume that the target hadron is a scalar and further pay attention only to the structure function V_1 appearing in the gauge-invariant decomposition[3] of the Compton tensor:

$$\begin{aligned} T^{\mu\nu} = {} & V_1 P[q_1]^{\mu\rho} P[q_2]^\nu_\rho + V_2(p\cdot P[q_1])^\mu (p\cdot P[q_2])^\nu \\ & + V_3(q_2\cdot P[q_1])^\mu (q_1\cdot P[q_2])^\nu \\ & + V_4(p\cdot P[q_1])^\mu (q_1\cdot P[q_2])^\nu \\ & + V_5(q_2\cdot P[q_1])^\mu (p\cdot P[q_2])^\nu + A\epsilon^{\mu\nu\rho\sigma} q_{1\rho} q_{2\sigma}. \end{aligned} \tag{7}$$

[3]Here, we introduced a convenient notation:

$$P[q]_{\mu\nu} = \left[\eta_{\mu\nu} - \frac{q_\mu q_\nu}{q^2}\right]. \tag{6}$$

These structure functions, $V_{1,2,3,4,5}(x,\eta,t,q^2)$, should be expressed in terms of the kinematical variables x,η, and t, and one of the primary purposes of this article is to study how the structure functions depend on the skewness η.

2. Light-cone operator product expansion

The light-cone OPE can be applied to the product of currents $T\{J^\nu J^\mu\}$ before evaluating it as a hadron matrix element. Let the expansion be

$$i\int d^4x e^{-iq\cdot x}T\{J^\nu(x/2)J^\mu(-x/2)\} = \sum_I \mathcal{C}^{\mu\nu}_{I\rho_1\cdots\rho_{j_I}}(q)\mathcal{O}_I^{\rho_1\cdots\rho_{j_I}}(0;q^2) \tag{8}$$

for some basis of local operators $\mathcal{O}_I^{\rho_1\cdots\rho_{j_I}}$ renormalized at $\mu^2=q^2$. $C^{\mu\nu}_{I\rho_1\cdots\rho_{j_I}}$'s are the corresponding Wilson coefficients renormalized at $\mu^2=q^2$. If we were to evaluate these local operators on the right-hand side with the same state for both bra and ket, $\langle h(p_2)|$ and $|h(p_1)\rangle$, with $p_2^\mu=p_1^\mu$, then the Compton tensor and its structure functions do not receive nonzero contributions from local operators that are given by the total derivative of some other local operators. In the case of our interest, however, such operators do contribute.

Let us take a series of operators in QCD that are called twist-2 operators in the weak coupling limit. The twist-2 operators in the flavor-nonsinglet sector are labeled by two integers, j,l,

$$\mathcal{O}^\alpha_{j,l} := [(-i)^{j+l-1}\partial^{\mu_{j+1}}\cdots\partial^{\mu_{j+l}}\overline{\Psi}_a\gamma^{\mu_1}(\overleftrightarrow{D})^{\mu_2}\cdots(\overleftrightarrow{D})^{\mu_j}\lambda^\alpha_{ab}\Psi_b]_{\text{t.s.t.l.}}(0;q^2), \tag{9}$$

with an $N_F\times N_F$ flavor matrix $(\lambda^\alpha)_{ab}$. Similarly, in the flavor-singlet sector, there are two series of twist-2 operators with the label j,l, given by quark bilinear and gluon bilinear. Here, these operators are made totally symmetric and traceless (t.s.t.l) in the $j+l$ Lorentz indices so that they transform in irreducible representations of the Lorentz group SO(3, 1), $\overleftrightarrow{D}:=\vec{D}-\overleftarrow{D}$.

Suppose that the hadron matrix element of the operator $\mathcal{O}^\alpha_{j,l}$ is given by

$$\langle h(p_2)|\mathcal{O}^\alpha_{j,l}|h(p_1)\rangle = \sum_{k=0}^{j}[\Delta^{\mu_1}\cdots\Delta^{\mu_{k+l}}p^{\mu_{k+l+1}}\cdots p^{\mu_{j+l}}]_{\text{t.s.t.l.}}A_{j,k}(t;q^2)(-2)^{j-k}; \tag{10}$$

the reduced matrix element $A^\alpha_{j,k}(t)$ is nonperturbative information and cannot be determined by perturbative QCD. If we pay attention only to Wilson coefficients $C^{\mu\nu}_{j,l,\alpha;\mu_1\cdots\mu_{j+l}}$ that are proportional to $\eta^{\mu\nu}$ and are to write them as[4]

$$\eta^{\mu\nu}\mathcal{C}^\alpha_{j,l}\frac{q_{\rho_1}\cdots q_{\rho_{j+l}}}{(q^2)^{j+l}}, \tag{11}$$

then the twist-2 flavor-nonsinglet contribution to the structure function V_1 becomes

$$V_1 \simeq \sum_{j,l}\mathcal{C}^\alpha_{j,l}\frac{1}{x^{j+l}}\sum_{k=1}^{j}A^\alpha_{j,k}(t;q^2)\eta^{k+l} =: \sum_j \mathcal{C}^\alpha_j(\vartheta)\frac{1}{x^j}A^\alpha_j(\eta,t;q^2), \tag{12}$$

where $\vartheta:=(\eta/x)$, $\mathcal{C}^\alpha_j(\vartheta):=\sum_{l=0}^\infty\mathcal{C}^\alpha_{j,l}\vartheta^l$, and $A^\alpha_j(\eta,t):=\sum_{k=0}^j\eta^kA^\alpha_{j,k}(t)$. If the structure function V_1 receives contributions only from even $j\in\mathbb{Z}$, then this j summation is rewritten as

$$V_1(x,\eta,t;q^2)\simeq-\int\frac{dj}{4i}\frac{1+e^{-\pi ij}}{\sin(\pi j)}\mathcal{C}^\alpha_j(\vartheta)\frac{1}{x^j}A^\alpha_j(\eta,t;q^2) \tag{13}$$

in the form of inverse Mellin transformation; here, $\mathcal{C}^\alpha_j(\vartheta;q^2)$ and $A^\alpha_j(\eta,t;q^2)$ are now meant to be holomorphic functions on j (possibly with some poles and cuts) that coincide with the original ones at $j\in 2\mathbb{Z}$. Precisely the same story also holds true for the flavor-singlet sector.

Because the structure function is given by the inverse Mellin transform of a product of three factors, namely, (a) the signature factor $\mp[1\pm e^{-\pi ij}]/\sin(\pi j)$, (b) the Wilson coefficients $\mathcal{C}^\alpha_j$, and (c) the hadron matrix elements A^α_j, it can be regarded as a convolution of inverse Mellin transforms of those three factors. The inverse Mellin transform of the signature factor becomes

$$\int\frac{dj}{2\pi i}\frac{1}{x^j}\frac{\pi}{2}\frac{\mp[1\pm e^{-\pi ij}]}{\sin(\pi j)}=\frac{-1}{2}\left[\frac{1}{1-x+i\epsilon}\pm\frac{1}{1+x}\right], \tag{14}$$

which corresponds to propagation of the parton in a perturbative calculation [20], and the inverse Mellin transform of the matrix element is called the generalized parton distribution:

$$H^\alpha(x,\eta,t;\mu^2=q^2)=\int\frac{dj}{2\pi i}\frac{1}{x^j}A^\alpha_j(\eta,t;\mu^2=q^2). \tag{15}$$

GPD $H^\alpha(x,\eta,t;\mu^2)$ of a hadron h is nonperturbative information, just like the ordinary PDF, which is obtained

[4]In the leading order of QCD perturbation, $\mathcal{C}^\alpha_{j,0}=-[1+(-1)^j]$ for $j=2,4,\ldots$ and $(\lambda^\alpha)_{ab}=[\text{diag}(4/9,1/9,1/9)]_{\text{t.l.}}$.

by simply setting $\eta = 0$ and $t = 0$. For a phenomenological fit of the experimental data of DVCS and VMP, some function form of the GPD needs to be assumed because of the convolution involved in the scattering amplitude [10]. Setting up a model (and assuming a function form) for the nonperturbative information in terms of $A_j(\eta, t; q^2)$ rather than the GPD itself $[H(x, \eta, t; q^2)]$ is called dual parametrization [15–18], and some phenomenological Ansätze have been proposed. In this article, we aim at deriving a qualitative form of $A_j(\eta, t)$ by using a gravitational dual (that is analytic in j), instead of assuming the form of $A_j(\eta, t)$ by hand.

3. Renormalization and OPE in dilatation eigenbasis

Remembering that the distinction between the $\gamma^* + h \to \gamma + h$ scattering amplitude and GPD originates from the factorization into the Wilson coefficients and local operators (and their matrix elements), one will notice that the GPD defined in this way should depend on the choice of the basis of local operators. Although the choice of operators $\mathcal{O}^\alpha_{j,l}$, with $j \geq 1$ and $l \geq 0$, in (9) appears to be the most natural (and intuitive) one for the twist-2 operators in the flavor-nonsinglet sector, there is nothing wrong with taking different linear combinations of these operators as a basis when the corresponding Wilson coefficients also become linear combinations of what they are for $\mathcal{O}^\alpha_{j,l}$. Given the fact that the operators $\mathcal{O}^\alpha_{j,l}$ mix with one another under renormalization, it should not be compulsory for us to stick to the basis $\mathcal{O}^\alpha_{j,l}$.

Under the perturbation of QCD, the flavor-nonsinglet twist-2 operators are renormalized under

$$\mu \frac{\partial}{\partial \mu} [\mathcal{O}_{j-m,m}(0; \mu^2)] = -[\gamma^{(j)}]_{mm'} [\mathcal{O}_{j-m',m'}(0; \mu^2)]; \tag{16}$$

because operators can mix only with those with the same number of Lorentz indices, the anomalous dimension matrix $[\gamma]$ is block diagonal in the basis of $\mathcal{O}^\alpha_{j,l}$. The $j \times j$ matrix for the operators $\mathcal{O}^\alpha_{j-m,m}$ $(m = 0, \ldots, j-1)$ is denoted by $[\gamma^{(j)}]$. This matrix is upper triangular in this basis, and the diagonal entries are given by the anomalous dimensions of the twist-2 spin-j operators without a total derivative:

$$[\gamma^{(j)}]_{mm} = \gamma(j - m). \tag{17}$$

Therefore, the eigenvalue of the anomalous dimension matrix is $\{\gamma(j-m)\}_{m=0,\ldots,j-1}$ in this diagonal block, and the corresponding operator $\overline{\mathcal{O}}^\alpha_{j-m-1,m}$ is a linear combination of operators $\mathcal{O}_{j-m',m'}$, with $m' = m, \ldots, j-1$ [21]. The corresponding Wilson coefficient $\overline{\mathcal{C}}^\alpha_{j-m-1,m}$ for such an operator is a linear combination of $\mathcal{C}^\alpha_{j-m',m'}$, with $m' = m, \ldots, 0$. In this operator basis, matrix elements and Wilson coefficients renormalize multiplicatively, without mixing.[5]

In this new basis of local operators, the structure function becomes

$$\begin{aligned} V_1 &\simeq \sum_{n,K} \overline{\mathcal{C}}^\alpha_{n,K} \frac{1}{x^{n+1+K}} \sum_k \overline{A}^\alpha_{n+1,k}(t; \mu^2) \eta^{K+k} \\ &=: \sum_n \overline{C}^\alpha_n(\vartheta) \frac{1}{x^{n+1}} \overline{A}^\alpha_{n+1}(\eta, t; \mu^2), \end{aligned} \tag{18}$$

where

$$\overline{C}^\alpha_n(\vartheta) = \sum_{K=0}^{\infty} \overline{\mathcal{C}}^\alpha_{n,K} \vartheta^K, \tag{19}$$

and $\overline{A}^\alpha_{n+1,k}(t; \mu^2)$ is the reduced matrix element of the operator[6] $\overline{\mathcal{O}}^\alpha_{n,0}(0; \mu^2)$. The structure function is therefore written as yet another inverse Mellin transform,

$$V_1 \simeq -\int \frac{dj}{4i} \frac{1 + e^{-\pi i j}}{\sin(\pi j)} \overline{C}^\alpha_{j-1}(\vartheta) \frac{1}{x^j} \overline{A}^\alpha_j(\eta, t; \mu^2). \tag{20}$$

Yet another GPD can also be defined by using $\overline{A}^\alpha$ instead of $A^\alpha_j(\eta, t; q^2)$:

$$\overline{H}^\alpha(x, \eta, t; \mu^2) = \int \frac{dj}{2\pi i} \frac{1}{x^j} \overline{A}^\alpha_j(\eta, t; \mu^2). \tag{21}$$

When it comes to the description of the $\gamma^* + h \to \gamma + h$ scattering amplitude as a whole, it does not matter which operator basis is used. In order to talk about the distribution of partons in the transverse directions in a hadron, we only need GPD at $\eta = 0$. The newly defined GPD $\overline{H}$ does just as good a job as the H defined in (15); they are the same at $\eta = 0$.

Even within the dual parametrization approach, it has been advantageous to use this operator basis because it becomes much easier to implement a phenomenological assumption (a function form) of $\overline{A}^\alpha_j(\eta, t; \mu^2)$ that is consistent with renormalization group flow [15].

[5]In reality, the anomalous dimension matrix depends on the coupling constant α_s, and α_s changes over the scale. Thus, the eigenoperator of the renormalization/dilatation also changes over the scale. In scale invariant theories (and in theories with only slow running in α_s), however, this multiplicative renormalization is exact or a good approximation (cf. [22]).

[6]Just like $\mathcal{O}_{j,l} = (-i\partial)^l \mathcal{O}_{j,0}$, there is a relation $\bar{\mathcal{O}}_{n,K} = (-i\partial)^K \bar{\mathcal{O}}_{n,0}$ in the new basis. This is why all the hadron matrix elements of $\bar{\mathcal{O}}_{n,K}$ can be parametrized by $\bar{A}_{n+1,k}$, just like those of $\mathcal{O}_{j,l}$ are by $A_{j,k}$. Here, n corresponds to the conformal spin, which is sometimes denoted by j in the literature. In this article, however, we maintain $j = n + 1$.

4. Conformal OPE

Although the hadron matrix element is essentially nonperturbative and is not calculable within perturbative QCD, more discussion has been made of the Wilson coefficients $\overline{C}^{\alpha}_{n,K}$. They still have to be calculated order by order in perturbation theory, if one is interested strictly in the QCD of the real world. If one is interested in gauge theories that are more or less "similar" to QCD, however, stronger statements can be made for a system with higher symmetry: conformal symmetry. One can think of $\mathcal{N}=4$ super Yang-Mills theory or $\mathcal{N}=1$ supersymmetric $\mathrm{SU}(N)\times\mathrm{SU}(N)$ gauge theory of [23] as an example of theories with exact (super)conformal symmetry. The QED probe in the real-world QCD can be replaced by gauging global symmetries [such as (a part of) SU(4) R symmetry of $\mathcal{N}=4$ super Yang-Mills theory and $\mathrm{SU}(2)\times\mathrm{SU}(2)\times\mathrm{U}(1)$ symmetry of [23]]. By applying the conformal symmetry, one can derive stronger statements on the Wilson coefficients of primary operators appearing in the OPE.

Suppose that we are interested in the OPE of two primary operators, A and B, that are both scalar under SO(3,1). If we take the basis of local operators for the expansion to be primary operators $\overline{\mathcal{O}}_n$ (with j_n Lorentz indices and an l_n scaling dimension) and their descendants $\partial^K\overline{\mathcal{O}}_n$ (with j_n+K Lorentz indices), then in the OPE,

$$T\{A(x)B(0)\}=\sum_n\left(\frac{1}{x^2}\right)^{\frac{1}{2}(l_A+l_B-l_n+j_n)}\sum_{K=0}^{\infty}c_{n,K}\frac{x^{\rho_1}\cdots x^{\rho_{j_n+K}}}{(x^2)^{j_n+K}}\times[\partial^K\overline{\mathcal{O}}_n(0)]_{\rho_1\cdots\rho_{j_n+K}}. \tag{22}$$

The conformal symmetry determines all the coefficients of the descendants $c_{n,K}$ ($K\geq 1$) in terms of that of the primary operator, $c_{n,0}=:c_n$. Ignoring the mixture of nontraceless contributions, one finds that [24]

$$T\{A(x)B(0)\}\simeq\sum_n\left(\frac{1}{x^2}\right)^{\frac{1}{2}(l_A+l_B-l_n+j_n)}x^{\rho_1}\cdots x^{\rho_{j_n}}c_n\times{}_1F_1\left(\frac{l_A-l_B+l_n+j_n}{2},l_n+j_n;x\cdot\partial\right)\times[\overline{\mathcal{O}}_n(0)]_{\rho_1\cdots\rho_{j_n}}. \tag{23}$$

A question of real interest to us is the OPE of conserved currents J^ν and J^μ. They are not scalars of SO(3,1), but the same logic as in [24] can be used also to show that, in the terms with Wilson coefficients proportional to $\eta^{\mu\nu}$,

$$T\{J^\nu(x)J^\mu(0)\}\simeq\eta^{\mu\nu}\sum_n\left(\frac{1}{x^2}\right)^{3-\frac{\tau_n}{2}}x^{\rho_1}\cdots x^{\rho_{j_n}}c_n\times{}_1F_1\left(\frac{l_n+j_n}{2},l_n+j_n;x\cdot\partial\right)\times[\overline{\mathcal{O}}_n(0)]_{\rho_1\cdots\rho_{j_n}}+\cdots, \tag{24}$$

where $\tau_n:=l_n-j_n$ is the twist, a mixture of the nontraceless (and hence higher twist) contributions is ignored, and terms with Wilson coefficients without $\eta^{\mu\nu}$ are all omitted here. The scaling dimension of conserved currents $l_A=l_B=3$ has been used. The momentum space version of the OPE is [25]

$$i\int d^4x\,e^{-iq_2\cdot x}T\{J^\nu(x)J^\mu(0)\}\simeq\eta^{\mu\nu}\sum_n\frac{(2\pi)^2\Gamma(\frac{l_n+j_n-2}{2})}{4^{2-\frac{\tau_n}{2}}\Gamma(3-\frac{\tau_n}{2})}c_n\frac{(-2i)^{j_n}q_2^{\rho_1}\cdots q_2^{\rho_{j_n}}}{(q_2^2)^{\frac{\tau_n}{2}-1}(q_2^2)^{j_n}}\times{}_2F_1\left(\frac{l_n+j_n}{2},\frac{l_n+j_n}{2}-1,l_n+j_n;\frac{-2iq_2\cdot\partial}{q_2^2}\right)\overline{\mathcal{O}}_n(0)+\cdots, \tag{25}$$

or, equivalently [18],

$$i\int d^4(x-y)e^{-iq\cdot(x-y)}T\{J^\nu(x)J^\mu(y)\}\simeq\eta^{\mu\nu}\sum_n\frac{(2\pi)^2\Gamma(\frac{l_n+j_n-2}{2})}{4^{2-\frac{\tau_n}{2}}\Gamma(3-\frac{\tau_n}{2})}c_n\frac{(-2i)^{j_n}q^{\rho_1}\cdots q^{\rho_{j_n}}}{(q^2)^{\frac{\tau_n}{2}-1}(q^2)^{j_n}}\times{}_2F_1\left(\frac{l_n+j_n-2}{4},\frac{l_n+j_n}{4},\frac{l_n+j_n}{2};\left(\frac{iq\cdot\partial}{q^2}\right)^2\right)\overline{\mathcal{O}}_n\left(\frac{x+y}{2}\right)+\cdots. \tag{26}$$

Either in the form of (25) or (26), the primary operators $\overline{\mathcal{O}}_n$ and the corresponding coefficients c_n are renormalized multiplicatively.

B. AdS/CFT approach

In AdS/CFT correspondence, type IIB string theory on $\mathrm{AdS}_5\times W$ with a five-dimensional Einstein manifold W corresponds to a gauge theory on $\mathbb{R}^{3,1}$ with an exact conformal symmetry; theories with an exact conformal symmetry, however, are qualitatively different from the QCD in the real world. But the type IIB string on a geometry that is close to $\mathrm{AdS}_5\times W$, except with the confining end in the infrared, may be used to extract a qualitative lesson on strongly coupled gauge theories with confinement, which are not qualitatively different from the QCD.

In a dual pair of a conformal field theory (CFT) and a string theory on a background $\mathrm{AdS}_5 \times W$, primary operators of the CFT are in one-to-one correspondence with string states on AdS_5, and their correlation functions can be calculated by using the wave functions of the string states on AdS_5. When the background geometry is changed from $\mathrm{AdS}_5 \times W$ to some warped geometry that is nearly AdS_5 with an end in the infrared, then the wave functions might be used to calculate matrix elements of the corresponding "primary" operators in an almost conformal theory. The correspondence between the operators and string states can be made precise, because they are both classified in terms of the representation of the conformal algebra, which is shared by both of the dual theories.

In order to determine GPD $\overline{H}$ in gravitational dual descriptions, it is therefore sufficient to determine wave functions of string states corresponding to the primary operators of interest. Although there is plenty of literature discussing the correspondence between the (superconformal) primary operators and string states at the supergravity level, it is known that the flavor-singlet twist-2 operators (labeled by the spin j) correspond to the stringy excitations with arbitrary high spin j that are in the same trajectory as the graviton [3,26]. Our task is, therefore, to determine the wave functions of such string states. Needless to say, one has to fix all of the gauge degrees of freedom associated with string component fields (not just the general coordinate invariance associated with the graviton) before working out the mode decomposition. Furthermore, wave functions need to be grouped together properly so that they form an irreducible representation of the conformal group in order to establish correspondence with a primary operator of the gauge theory side, which also forms an irreducible representation of the conformal group, along with its descendants.

It will be clear by the end of this article that all such technical work is necessary and essential for the purpose of extracting skewness dependence of GPD.

There are two different (but equivalent) ways to study the DVCS $\gamma^* + h \to \gamma^{(*)} + h$ amplitude and GPD in gravitational dual descriptions. One is to determine the hadron matrix elements of spin-j primary operators by using appropriate wave functions; GPD $\overline{H}$ is obtained by the inverse Mellin transform of the matrix elements. Using the Wilson coefficients that are governed by the conformal symmetry [see (26)], the DVCS amplitude will also be obtained. Conversely, the other way is to calculate disc/sphere amplitude directly, with the vertex operators given (approximately) by using the wave functions associated with the target hadron (see Secs. III and IV). We will identify the structure of conformal OPE in the expression for the $\gamma^* + h \to \gamma^{(*)} + h$ scattering amplitude in gravity dual [see (160), (163), (178)], with the Wilson coefficient for the twist-2 operators precisely as predicted by conformal symmetry (26). That also makes it possible to read out hadron matrix elements, and to extract the GPD. In these approaches, one can hope to work also for higher twist contributions, in principle, but we are not ambitious enough to do that in this article. In this article, we will proceed with the latter approach.

III. GRAVITY DUAL SETTINGS

A number of warped solutions to the type IIB string theory have been constructed, and they are believed to be dual to some strongly coupled gauge theories. When the geometry is close to $\mathrm{AdS}_5 \times W$ with some five-dimensional Einstein manifold W, with weak running of the anti–de Sitter (AdS) radius along the holographic radius, the corresponding gauge theory will also have approximate conformal symmetry, and the gauge coupling constant runs slowly. If the $\mathrm{AdS}_5 \times W$ geometry has a smooth end at the infrared as in [27], then the dual gauge theory will end up with confinement. Gravitational backgrounds in the type IIB string theory with the properties we stated above all provide a decent framework for studying qualitative aspects of nonperturbative information associated with gluons/Yang-Mills theory on $3+1$ dimensions.

In studying the $h + \gamma^* \to h + \gamma$ scattering process in a gravitational dual, we need a global symmetry to be gauged weakly, just like QED for QCD. In type IIB D-brane constructions of gauge theories that have a gravity dual, U(1) subgroups of an R symmetry or a flavor symmetry on D7-branes can be used as the models of the electromagnetic U(1) symmetry. Therefore, we have in mind gravity dual models on a background that is approximately $\mathrm{AdS}_5 \times W$ with a nontrivial isometry group on W, or with a D7-brane configuration on it, as in [2].

Our interest, however, is not so much in writing down an exact mathematical expression based on a particular gravity dual model that is equivalent to a particular strongly coupled gauge theory, but more in extracting qualitative information of partons in hadrons of confining gauge theories in general. It is, therefore, more suitable for this purpose to use a simplified setup that carries common (and essential) features of the type IIB models that we described above. Throughout this article, we assume a pure $\mathrm{AdS}_5 \times W$ metric background,

$$ds^2 = G_{MN} dx^M dx^N = g_{mn} dx^m dx^n + R^2 (g_W)_{ab} d\theta^a d\theta^b, \tag{27}$$

$$g_{mn} dx^m dx^n = e^{2A(z)} (\eta_{\mu\nu} dx^\mu dx^\nu + dz^2), \quad e^{2A(z)} = \frac{R^2}{z^2}; \tag{28}$$

that is, we ignore the running effect, and we do not specify the five-dimensional manifold W. The dilaton vacuum expectation value is simply assumed to be constant, $e^\phi = g_s$. A confining effect—the infrared end of this

geometry—can be introduced, for example, by sharply cutting off the AdS_5 space at $z = \Lambda^{-1}$ (hard wall models), or by similar alternatives (soft wall models). We are not committed to a particular implementation of the infrared cutoff in this article (see the discussion in Sec. V D), except in a couple of places where we write down some concrete expressions for illustrative purposes (Secs. VII A and VII D). The energy scale Λ associated with (any form of implementation of) the infrared cutoff corresponds to the confining energy scale in the dual gauge theories. When we consider (a simplified version of the) models with D7-branes for flavor, we assume that the D7-brane world volume wraps on a three-cycle on W and extends all the way down to the infrared end of the holographic radius z; i.e., all of $0 \le z \le \Lambda^{-1}$. This corresponds to assuming massless quarks. In this article, we will not pay attention to physics where spontaneous chiral symmetry breaking is essential.

As we stated earlier, we would like to work out the $h + \gamma^* \to h + \gamma^{(*)}$ scattering amplitude by using the gravity dual models. This is done by summing up sphere/disc amplitudes, along with those with higher genus world sheets. We will restrict our attention to kinematical regions where saturation is not important (i.e., large q^2 and/or not too small x, and large N_c). That allows us to focus only on sphere/disc amplitudes, with the insertion of four vertex operators corresponding to the incoming and outgoing hadron h and (possibly virtual) photon γ.

As a string-based model of the target hadron h [that is SO(3,1) scalar], we have in mind either a scalar "glueball"[7] that has nontrivial R-charge, or a scalar meson made of matter fields. The former corresponds to a vertex operator [in the $(-1,-1)$ picture]

$$V(p) = :e^{ip_\mu \cdot X^{\hat{\mu}}} \psi^m \tilde{\psi}^n g_{mn} \Phi(Z; m_n) Y(\Theta):, \qquad (29)$$

where $Y(\Theta)$ is a "spherical harmonics" on W, and the latter to

$$V(p) = :e^{ip_\mu \cdot X^{\hat{\mu}}} \psi \Phi(Z; m_n):, \qquad (30)$$

where ψ corresponds to the D7-brane fluctuations in its transverse directions. $\Phi(Z)$ is the wave function on AdS_5, with the argument promoted to the field on the world sheet [3]. The vertex operators above are approximate expressions in the $(\alpha'/R^2) \sim 1/\sqrt{\lambda}$ expansion (e.g., [28]) in a theory formulated with a nonlinear σ model given by (27). If we are to employ the hard wall implementation of the infrared boundary, with the AdS_5 metric in the bulk without modification, then the wave function $\Phi(Z; m_n)$ is of the form

$$\sqrt{t_h}\Phi(z; m_n) = 2\Lambda z^2 \frac{J_{\ell_\phi - 2}(j_{\ell_\phi - 2,n}\Lambda z)}{|J'_{\ell_\phi - 2}(j_{\ell_\phi - 2,n})|}. \qquad (31)$$

[7]By glueball, we only mean a bound state of fields in super Yang-Mills theory.

This wave function is that of the nth lightest hadron corresponding to some scalar operator with conformal dimension ℓ_ϕ; the hadron mass $m_n = j_{\ell_\phi - 2,n}\Lambda$ is given by the nth zero of the Bessel function $J_{\ell_\phi - 2}$. We will comment on the normalization factor $\sqrt{t_h}$ in later sections, though it disappears from the expression for physical observables.

The "photon" current in the correlation function/matrix element $T^{\nu\mu}$ in the gauge theory description corresponds to the insertion of vertex operators associated with non-normalizable wave functions, rather than with the normalizable wave functions (31) for the target hadron state. If we are to employ an R-symmetry current as the string-based model of the QED current, then the corresponding closed string vertex operator is

$$V(q) = :e^{iq_\mu \cdot X^{\hat{\mu}}} v_a(\Theta) A_m(Z; q)(\psi^a \tilde{\psi}^m + \psi^m \tilde{\psi}^a):, \qquad (32)$$

with some Killing vector $v_a \partial/\partial\theta^a$ on W. The vertex operator in the case of a D7-brane U(1) current is

$$V(q) = :e^{iq_\mu \cdot X^{\hat{\mu}}} A_m(Z; q)\psi^m:. \qquad (33)$$

The wave function $A_m(Z; q)$ on AdS_5 is of the form

$$A_\mu(z; q) = \left[\delta_\mu^{\hat{\kappa}} - \frac{q_\mu q^{\hat{\kappa}}}{q^2}\right]\epsilon_\kappa(q)(qz)K_1(qz) + q_\mu \frac{q^{\hat{\kappa}}\epsilon_\kappa(q)}{2q^2}(qz)^2 K_2(qz), \qquad (34)$$

$$A_z(z; q) = -i\partial_z \frac{q^{\hat{\kappa}}\epsilon_\kappa(q)}{2q^2}(qz)^2 K_2(qz). \qquad (35)$$

Here, q stands for $\sqrt{q^2}$, although it sometimes imply four-momentum q^μ, depending on the local context in this article. The rationale for our choice of the terms proportional to $(q \cdot \epsilon)$ will be explained later on in Appendix A.4, but those terms should not be relevant in the final result because of the gauge invariance of $T^{\nu\mu}$. When the infrared boundary is implemented by the hard wall, $K_1(qz)$ should be replaced by $K_1(qz) + [K_0(q/\Lambda)/I_0(q/\Lambda)]I_1(qz)$, and $K_2(qz)$ by an arbitrary linear combination of $K_2(qz)$ and $I_2(qz)$.

It is not as easy to calculate the sphere/disc amplitudes in practice, however. It has been considered that the parton contributions to $\gamma^* + h \to \gamma^{(*)} + h$ scattering are given by an amplitude with states in the leading trajectory with arbitrary high spin being exchanged [3]. These fields are not scalar on AdS_5 but come with multiple degrees of freedom associated with polarizations. Such polarization of higher spin fields propagating on AdS_5 needs to be treated properly—including such issues as covariant derivatives and kinetic mixing among different polarizations (diagonalization of the Virasoro generator L_0)—in gravity dual

descriptions in order to be able to discuss the skewness dependence of the GPD/DVCS amplitude. The direct impact of the curved background geometry can be implemented through the nonlinear σ model on the world sheet, but one has to define the vertex operators as a composite operator properly in such an interacting theory. The Ramond-Ramond background is an essential ingredient in making the warped background metric stable, yet a nonzero Ramond-Ramond background cannot be implemented in the Neveu-Schwarz-Ramond (NSR) formalism.

Instead of using a world-sheet calculation in the NSR formalism when implementing the effect of a curved background (27), we use string field theory action on flat space in this article and make it covariant. Because the gravity dual setup of our interest is in type IIB string theory, we are thus supposed to use superstring field theory for closed string and open string modes. In order to avoid technical complications associated with the interacting superstring field theories, however, we employ a sort of toy-model approach by using the cubic string field theory for bosonic string theory.

In our toy-mode approach, we deal with the cubic string field theory on AdS_5 ($\times$ some internal compact manifold), and ignore instability of the background geometry. The probe photon in this toy-model gravity dual setup will be the massless vector state of bosonic string theory with the wave function (34), (35). The target hadron can be any scalar states, (say, the tachyon) with the wave function (31). We are to construct a toy-model amplitude of the $h+\gamma^* \to h+\gamma^{(*)}$ scattering by using the two-to-two scattering of the massless photon and some scalar in bosonic string theory on the AdS_5 background. In short, this is to maintain the spirit of the setup in [2,3] and use the bosonic cubic string field theory to compute and obtain something concrete, from which qualitative lessons are to be extracted for the setup of our interest.

One of the costs of this approach (without the technical complexity of interacting superstring field theory) is that we have to restrict our attention to the Reggeon exchange (flavor-nonsinglet) amplitude because the cubic bosonic string field theory deals with open strings, not the closed (i.e., flavor neutral) string. The amplitude constructed in this way is certainly not faithful to the equations of type IIB string theory, either. Since our motivation is not in constructing yet another exact solution to superstring theory, however, we still expect that this (flavor-nonsinglet) toy-mode amplitude in bosonic string still maintains some fragrance of hadron scattering amplitude to be calculated in superstring theory. This discussion continues in Sec. VII C.

IV. CUBIC STRING FIELD THEORY

Section IV A summarizes the technical details of cubic string field theory that we will need in later sections. We then proceed in Sec. IV B to explain an idea of how to reproduce disc amplitude only from string field theory t-channel amplitude, using photon-tachyon scattering on a flat spacetime background as an example. This idea of constructing amplitude is generalized in Sec. VI for scattering on a warped spacetime, and we will see that this construction of the amplitude allows us to cast the amplitude almost immediately into the form of conformal OPE (25), (26).

A. Action of the cubic SFT on a flat spacetime

The action of the cubic string field theory (SFT) is given by [29]

$$S = -\frac{1}{2\alpha'}\int\left(\Phi * Q_B\Phi + \frac{2}{3}g_o\Phi*\Phi*\Phi\right), \quad (36)$$

$$= -\frac{1}{2\alpha'}\left(\Phi\cdot Q_B\Phi + \frac{2g_o}{3}\Phi\cdot\Phi*\Phi\right), \quad (37)$$

where g_o is a coupling constant of mass dimension $(1-D/2)$, where $D=26$ is the spacetime dimensions of bosonic string theory.[8] Q_B is the Becchi-Rouet-Stora-Tyutin (BRST) operator, and $*$ and $\cdot$ are the star product and inner product of the string fields, respectively; all of the technical details we need for this article are summarized below in this section, but more information is found, e.g., in [29,30]. The string field Φ is, as a ket state, expanded in terms of the Fock states as in

$$\Phi = |\Phi\rangle = \phi(x)|\downarrow\rangle + (A_M(x)\alpha^M_{-1} + C(x)b_{-1} + \overline{C}(x)c_{-1})|\downarrow\rangle + \left(f_{MN}(x)\frac{1}{\sqrt{2}}\alpha^M_{-1}\alpha^N_{-1} + ig_M(x)\frac{1}{\sqrt{2}}\alpha^M_{-2} + h(x)b_{-1}c_{-1} + \cdots\right)|\downarrow\rangle, \quad (38)$$

with component fields $\phi, A_M, C, \overline{C}, f_{MN}, g_M, h, \ldots$; we have already chosen the Feynman-Siegel gauge here. We will eventually be interested only in the states with a vanishing ghost number, $N_{\rm gh}=0$, because states with a nonzero ghost number do not appear in the t-channel/s-channel exchange for the disc amplitude.

The Hilbert space of one string state is spanned by the Fock states given (in this gauge) by

$$\prod_{a=1}^{h_a}\alpha^{M_a}_{-n_a}\prod_{b=1}^{h_b}b_{-l_b}\prod_{c=1}^{h_c}c_{-m_c}|\downarrow\rangle, \quad (39)$$

with $1\le n_1\le n_2\le\cdots\le n_{h_a}$, $1\le l_1<l_2<\cdots<l_{h_b}$, and $1\le m_1<m_2<\cdots<m_{h_c}$. Let us use $Y := \{\{n_a\}\text{'s}, \{l_b\}\text{'s}, \{m_c\}'s\}$ as the label distinguishing

[8]The sign of the interaction term is just a matter of convention, because field redefinition for all of the component fields $\Phi\to-\Phi$ is always possible. Under this redefinition, however, the covariant derivative can be either $\partial_m - i\rho(A_\mu)$ or $\partial_m + i\rho(A_m)$. The sign convention above is for $\partial_m - i\rho(A_m)$, following the convention of Sec. 6.5 of Polchinski's textbook.

different Fock states of string on a flat spacetime. The mass of these Fock states is determined by

$$\alpha' k^2 + (N^{(Y)} - 1) = 0, \quad N^{(Y)} = \sum_{a=1}^{h_a} n_a + \sum_{b=1}^{h_b} l_b + \sum_{c=1}^{h_c} m_c. \tag{40}$$

A component field corresponding to a Fock state may be further decomposed into a multiple irreducible representation of the Lorentz group, but at least the rank-h_a totally symmetric traceless tensor representation is always contained. The Fock states of particular interest to us are the ones in the leading trajectory: $Y = \{1^N, 0, 0\}$, so that all the n_a's are 1, $h_b = h_c = 0$, and $N^{(Y)} = h_a$. The totally symmetric traceless tensor component field of these states is denoted by $(N!)^{-1/2} A^{(Y)}_{M_1 \cdots M_{h_a}}$.

The kinetic term—the first term of (36), (37)—is written down in terms of the component fields as follows:

$$-\frac{1}{2\alpha'}\Phi \cdot Q_B \Phi = \frac{1}{2}\int d^{26}x \, \mathrm{tr}\Big[\phi(x)\Big(\partial^2 + \frac{1}{\alpha'}\Big)\phi(x) + A_M(x)\partial^2 A^M(x) + f_{MN}(x)\Big(\partial^2 - \frac{1}{\alpha'}\Big)f^{MN}(x) + g_M(x)\Big(\partial^2 - \frac{1}{\alpha'}\Big)g^M(x) - h(x)\Big(\partial^2 - \frac{1}{\alpha'}\Big)h(x) + \cdots\Big]. \tag{41}$$

The totally symmetric tensor component field of the Fock states in the leading trajectory $Y = \{1^N, 0, 0\}$ has a kinetic term

$$\frac{1}{2}\int d^{26}x \, \mathrm{tr}\Big[A^{M_1 \ldots M_j}\Big(\partial^2 - \frac{N-1}{\alpha'}\Big)A_{M_1 \ldots M_j}\Big]. \tag{42}$$

The cubic string field theory action in the Feynman-Siegel gauge has two nice properties: First, the kinetic terms of those Fock states do not mix in the flat spacetime background, and second, the second derivative operators are simply given by the d'Alembertian operator, without complicated restrictions or mixing among various polarizations in the component fields.

The second term of the action (36), (37) gives rise to interactions involving three component fields. Interactions involving Fock states with small excitation level N are [30]

$$\begin{aligned} -\frac{1}{2\alpha'}\frac{2g_o}{3}\Phi \cdot \Phi * \Phi &= -\int d^{26}x \frac{g_o \lambda_{\mathrm{sft}}}{3\alpha'}\hat{E}(\mathrm{tr}[\phi^3(x)] \\ &\quad + \sqrt{\frac{8\alpha'}{3}}\mathrm{tr}\Big[(-iA_M)(\phi \overleftrightarrow{\partial}^M \phi)\Big] \\ &\quad - \frac{8\alpha'}{9\sqrt{2}}\mathrm{tr}[f_{MN}(\phi \overleftrightarrow{\partial}^M \overleftrightarrow{\partial}^N \phi)] - \frac{5}{9\sqrt{2}}\mathrm{tr}[f^M_M \phi^2] \\ &\quad + \frac{2\sqrt{\alpha'}}{3}\mathrm{tr}[(\partial_M g^M)\phi^2] - \frac{11}{9}\mathrm{tr}[h\phi^2]) + \cdots, \end{aligned} \tag{43}$$

where $\lambda_{\mathrm{sft}} = 3^{9/2}/2^6$ [31], $\overleftrightarrow{\partial}^M = (\overleftarrow{\partial^M} - \overrightarrow{\partial^M})$, and

$$\hat{E} = \exp\Big[-2\alpha' \ln\Big(\frac{2}{3^{3/4}}\Big)(\partial^2_{(1)} + \partial^2_{(2)} + \partial^2_{(3)})\Big]. \tag{44}$$

The $\partial^2_{(1,2,3)}$ designates the taking of derivatives of the first, second, and third fields.[9]

Interactions involving totally symmetric leading trajectory states are also of interest to us. The tachyon-tachyon–$Y = \{1^N, 0, 0\}$ cubic coupling with N derivatives is given by

$$-\frac{g_o \lambda_{\mathrm{sft}}}{\alpha'}\int d^{26}x \, \hat{E} \, \mathrm{tr}\Big[A^{(Y)}_{M_1 \cdots M_N}(\phi(-i\overleftrightarrow{\partial}^{M_1}) \cdots (-i\overleftrightarrow{\partial}^{M_N})\phi)\Big]\Big(\frac{8\alpha'}{27}\Big)^{\frac{N}{2}}\frac{1}{\sqrt{N!}} \tag{45}$$

in the interaction part of the action. The photon (level-1 state)-photon–$Y = \{1^N, 0, 0\}$ coupling in the cubic string field theory includes

$$-\frac{g_o \lambda_{\mathrm{sft}}}{\alpha'}\int d^{26}x \, \hat{E} \, \mathrm{tr}\Big[A^{(N)}_{M_1 \cdots M_N}(A_L(-i\overleftrightarrow{\partial}^{M_1}) \cdots (-i\overleftrightarrow{\partial}^{M_N})A_K)\Big(\frac{8\alpha'}{27}\Big)^{\frac{N}{2}}\eta^{KL}\frac{\frac{16}{27}}{\sqrt{N!}} + \cdots\Big], \tag{46}$$

where we kept only the terms that have N derivatives and are proportional to η^{KL}, as they are necessary in deriving (61).

[9]Concretely,

$$\hat{E}A(x)B(x)C(x) = \Big[\Big(\frac{27}{16}\Big)^{\frac{\alpha'}{2}\partial^2}A(x)\Big]\Big[\Big(\frac{27}{16}\Big)^{\frac{\alpha'}{2}\partial^2}B(x)\Big]\Big[\Big(\frac{27}{16}\Big)^{\frac{\alpha'}{2}\partial^2}C(x)\Big].$$

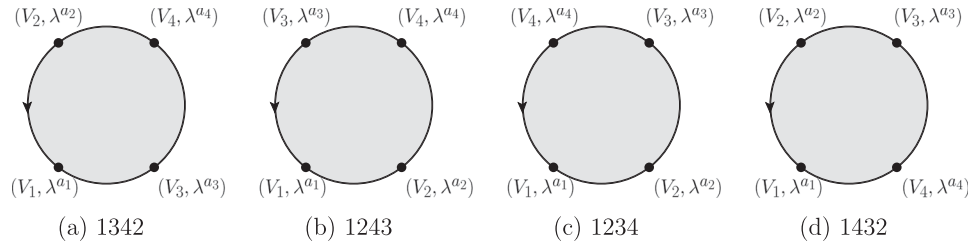

FIG. 3. Disc amplitudes with two photon vertex operators (V_1 and V_2) and two tachyon vertex operators (V_3 and V_4) inserted. Kinematical amplitudes given by the disc amplitudes above are multiplied by the Chan-Paton factors $\mathrm{tr}[\lambda^{a_1}\lambda^{a_3}\lambda^{a_4}\lambda^{a_2}]$ in (a), $\mathrm{tr}[\lambda^{a_1}\lambda^{a_2}\lambda^{a_4}\lambda^{a_3}]$ in (b), $\mathrm{tr}[\lambda^{a_1}\lambda^{a_2}\lambda^{a_3}\lambda^{a_4}]$ in (c) and $\mathrm{tr}[\lambda^{a_1}\lambda^{a_4}\lambda^{a_3}\lambda^{a_2}]$ in (d), respectively. The two disc amplitudes (a),(b) become $\mathcal{M}_{\mathrm{Ven}}(s,t)$, while (c),(d) become $\mathcal{M}_{\mathrm{Ven}}(u,t)$.

B. Cubic SFT scattering amplitude and *t*-channel expansion

Before proceeding to study the $h+\gamma^* \to h+\gamma^{(*)}$ scattering amplitude by using the cubic string field theory on the warped spacetime background, let us remind ourselves how to obtain t-channel operator product expansion from the amplitude calculation based on string field theory, by using tachyon-photon scattering on the flat spacetime as an example.

Let us consider the disc amplitude of tachyon-photon scattering. The vertex operators labeled by $i=1,2$, $V_i = :\epsilon^i_M \partial X^M e^{ik_i\cdot X}:$ are for photon incoming ($i=1$) and outgoing ($i=2$) states, which come with Chan-Paton matrices λ^{a_i}. Tachyon incoming ($i=3$) and outgoing ($i=4$) states correspond to vertex operators $V_i = :e^{ik_i\cdot X}:$ with Chan-Paton matrices λ^{a_i}. The photon-tachyon scattering amplitude $A+\phi \to A+\phi$ in bosonic open string theory (Veneziano amplitude) is given by[10]

$$\mathcal{M}_{\mathrm{Ven}}(s,t) = -\left(\frac{g_o^2}{\alpha'}\right)\frac{\Gamma(-\alpha' t-1)\Gamma(-\alpha' s-1)}{\Gamma(-\alpha'(s+t)-1)}\epsilon_M(k_2)\epsilon_N(k_1)\left\{\left[\eta^{MN}-\frac{k_1^M k_2^N}{k_1\cdot k_2}\right](\alpha' s+1)\right.$$
$$\left.+2\alpha'\left(\left[p^M - k_1^M\frac{k_2\cdot p}{k_1\cdot k_2}\right]-\frac{k_2^M}{2}\right)\left(\left[p^N - k_2^N\frac{k_1\cdot p}{k_2\cdot k_1}\right]-\frac{k_1^N}{2}\right)(\alpha' t+1)\right\}, \tag{47}$$

which is to be multiplied by the Chan-Paton factor $\mathrm{Tr}[\lambda^{a_2}\lambda^{a_4}\lambda^{a_3}\lambda^{a_1}+\lambda^{a_4}\lambda^{a_2}\lambda^{a_1}\lambda^{a_3}]$ [see Figs. 3(a) and 3(b)]. If the Chan-Paton matrices of a pair of incoming and outgoing vertex operators, λ^{a_1} and λ^{a_2}, commute with each other,[11] then the Chan-Paton factors from Figs. 3(c) and 3(d) are the same, and the total kinematical part of the amplitude for this Chan-Paton factor becomes $\mathcal{M}_{\mathrm{Ven}}(s,t)+\mathcal{M}_{\mathrm{Ven}}(u,t)$.

Let us stay focused on $\mathcal{M}_{\mathrm{Ven}}(s,t)$ alone for now. The amplitude proportional to η^{MN} can be expanded, as is well known, as a sum only of t-channel poles[12]:

$$\frac{g_o^2}{\alpha'}\frac{\Gamma(-\alpha' t-1)\Gamma(-\alpha' s)}{\Gamma(-\alpha'(s+t)-1)} = \frac{g_o^2}{\alpha'}\int_0^1 dx\, x^{-\alpha' t-2}(1-x)^{-\alpha' s-1}, \tag{48}$$

$$= \frac{g_o^2}{\alpha'}\sum_{N=0}^{\infty}\frac{-1}{\alpha' t-(N-1)}\frac{(\alpha' s+1)\cdots(\alpha' s+N)}{N!}. \tag{49}$$

The Veneziano amplitude (47) can also be obtained in cubic string field theory [32]. In the cubic SFT, the scattering amplitude consists of two pieces, a collection of t-channel exchange diagrams and s-channel diagrams (Fig. 4):

$$\mathcal{M}_{\mathrm{Ven}}(s,t) = \sum_Y \mathcal{M}_Y^{(t)}(s,t) + \sum_Y \mathcal{M}_Y^{(s)}(s,t). \tag{50}$$

Infinitely many one string states (39) with zero ghost number ($h_b = h_c$)—labeled by Y—can be exchanged in the t channel or the s channel, and the corresponding contributions are in the form of

$$\mathcal{M}_Y^{(t)} = \frac{f_Y^{(t)}(s,t)}{-\alpha' t-1+N^{(Y)}}, \qquad \mathcal{M}_Y^{(s)} = \frac{f_Y^{(s)}(t,s)}{-\alpha' s-1+N^{(Y)}}, \tag{51}$$

[10]Here, $p := (k_3-k_4)/2$, the averaged momentum of the tachyon before and after the scattering, just like in (2).

[11]Just like in the case where both λ^{a_1} and λ^{a_2} are an $N_F\times N_F$ matrix $\mathrm{diag}(2/3,-1/3,-1/3)$.

[12]It is also possible to expand this as a sum of s-channel poles only; that is the celebrated s-t duality of the Veneziano amplitude.

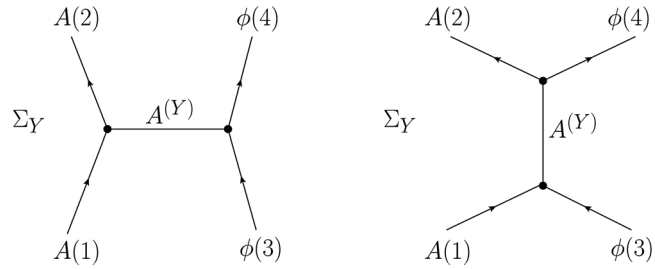

FIG. 4. Two types of diagrams contribute to the photon-tachyon scattering amplitude $\mathcal{M}_{\rm Ven}(s,t)$ in cubic string field theory: the t-channel exchange of one string states labeled by Y (left panel) and the s-channel exchange (right panel).

where $f_Y^{(t)}$ and $f_Y^{(s)}$ are regular functions at finite s and t; $N^{(Y)}$ is the excitation level (40) of a component field $A^{(Y)}$.

Because both the world-sheet calculation (47), (49) and the cubic SFT calculation (50), (51) are the same thing, $\mathcal{M}_{\rm Ven}(s,t)$ in both approaches should be exactly the same functions of (s,t). Therefore, for an arbitrary given value of s, the residue of all the poles in the complex t plane should be the same. We also know that the Veneziano amplitude can be expanded purely in the infinite sum of t-channel poles with t-independent residues. This means that the full Veneziano amplitude (47) can be reproduced just from the t-channel cubic SFT amplitude[13] $\sum_Y \mathcal{M}_Y^{(t)}(s,t)$ through the following procedure:

$$\sum_Y \frac{f_Y^{(t)}(s,t)}{-\alpha' t - 1 + N^{(Y)}} \to \sum_Y \frac{f_Y^{(t)}(s,(N^{(Y)}-1)/\alpha')}{-\alpha' t - 1 + N^{(Y)}} = \mathcal{M}_{\rm Ven}(s,t). \tag{52}$$

To see that this prescription really works, let us take a look at the amplitudes of t-channel exchange of one string states with small excitation level $N^{(Y)} = 0, 1, 2$. Focusing on the amplitude of $A + \phi \to A + \phi$ proportional to η^{MN}, we find that the tachyon exchange in the t channel [Fig. 5(a)] gives rise to the amplitude [33]

$$\mathcal{M}_\phi^{(t)}(s,t) = \left(\frac{g_o \lambda_{\rm sft}}{\alpha'}\right)^2 \left(\frac{2}{3^{3/4}}\right)^{-2\alpha' t - 2\alpha' t + 4} \frac{-1}{t + 1/\alpha'} = \frac{g_o^2}{\alpha'}\left(\frac{27}{16}\right)^{\alpha' t + 1} \frac{-1}{\alpha' t + 1}, \tag{53}$$

which is obtained simply by using the ϕ-ϕ-ϕ vertex rule (43) and the A-A-ϕ vertex rule (45). The prescription (52) turns this amplitude into

[13]The t-channel and s-channel amplitudes of the cubic SFT, $\sum_Y \mathcal{M}_Y^{(t)}$ and $\sum_Y \mathcal{M}_Y^{(s)}$, correspond to the integration over $[0, 1/2]$ and $[1/2, 1]$, respectively, in (48) [32]. Thus, $\sum_Y \mathcal{M}_Y^{(s)}$ does not contain a pole in t.

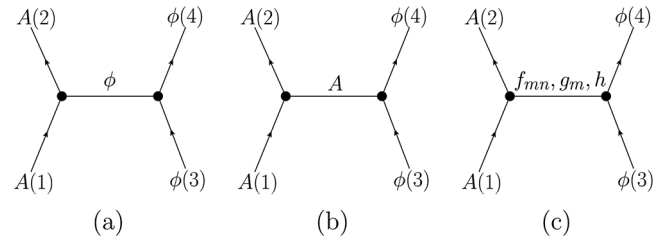

FIG. 5. t-channel exchange diagrams for $A + \phi \to A + \phi$ scattering in cubic string field theory. The tachyon ($N = 0$), photon ($N = 1$), and level-2 states are exchanged in diagrams (a), (b), and (c), respectively.

$$\to \mathcal{M}_\phi(s,t) = \frac{g_o^2}{\alpha'} \frac{-1}{\alpha' t + 1}, \tag{54}$$

which reproduces the $N = 0$ term of (49).

The t-channel exchange of level $N^{(Y)} = 1$ excited states can also be calculated in the cubic string field theory [Fig. 5(b)]. The amplitude proportional to η^{MN} is

$$\mathcal{M}_A^{(t)}(s,t) = \frac{g_o^2}{\alpha'}\left(\frac{27}{16}\right)^{\alpha' t} \frac{-1}{\alpha' t}\left[\frac{\alpha'(s-u)}{2}\right], \tag{55}$$

where $(s-u) = (k_{(1)} - k_{(2)}) \cdot (k_{(4)} - k_{(3)})$. Using the relation $\alpha'(s+t+u) = -2$ in the tachyon-photon scattering to eliminate u in favor of s and t, and following the prescription (52)—which is to exploit $\alpha' t = 0$ in the numerator—this amplitude is replaced by [33]

$$\longrightarrow \mathcal{M}_A(s,t) = \frac{g_o^2}{\alpha'} \frac{-(\alpha' s + 1)}{\alpha' t}. \tag{56}$$

Once again, this reproduces the level $N = 1$ contribution to the Veneziano amplitude (49).

A similar calculation for level-2 state exchange can be carried out [Fig. 5(c)]. Using the vertex rule in (43) for the level-2–ϕ-ϕ couplings, and also the interactions among level-2–A-A couplings in the literature, the cubic SFT t-channel amplitude is given by [33]

$$\mathcal{M}_f^{(t)}(s,t) = \frac{g_o^2}{\alpha'}\left(\frac{27}{16}\right)^{\alpha' t - 1} \frac{-1}{\alpha' t - 1} \times \left[\frac{(\alpha'(s-u))^2}{8} - \frac{5(\alpha' t + 2)}{16 \cdot 2} + \frac{490}{16^2 \cdot 2}\right], \tag{57}$$

$$\mathcal{M}_g^{(t)}(s,t) = \frac{g_o^2}{\alpha'}\left(\frac{27}{16}\right)^{\alpha' t - 1} \frac{-1}{\alpha' t - 1}\left[-\frac{36\alpha' t}{16^2}\right], \tag{58}$$

$$\mathcal{M}_h^{(t)}(s,t) = \frac{g_o^2}{\alpha'}\left(\frac{27}{16}\right)^{\alpha' t - 1} \frac{-1}{\alpha' t - 1}\left[-\frac{11^2}{16^2}\right]. \tag{59}$$

After using $\alpha' u = -\alpha'(s+t) - 2$ to eliminate u in favor of s and t, and further following the prescription (52) ($\alpha' t \to 1$

in the numerator), one will see that the level $N^{(Y)} = 2$ amplitude turns into

$$\to (\mathcal{M}_f + \mathcal{M}_g + \mathcal{M}_h)(s,t) = \frac{g_o^2}{\alpha'}\frac{-1}{\alpha' t - 1}\left[\frac{(\alpha' s)^2 + 3(\alpha' s) + 2}{2}\right]. \tag{60}$$

Once again, this is precisely the same as the $N = 2$ contribution to the Veneziano amplitude (49).

Contributions from the t-channel exchange of states in the leading trajectory can also be examined systematically. Using the vertex rule (45), (46) involving the states in the leading trajectory ($Y = \{1^N, 0, 0\}$), one finds that the amplitude proportional to η^{MN} is

$$\mathcal{M}^{(t)}_{\{1^N,0,0\}} \simeq \frac{g_o^2}{\alpha'}\left(\frac{27}{16}\right)^{\alpha' t-(N-1)}\frac{-1}{\alpha' t-(N-1)}\frac{(\alpha'(s-u)/2)^N}{N!}, \tag{61}$$

where we maintained only the terms with the highest power of either s or u. After using the kinematical relation $\alpha'(s+t+u)+2=0$ to eliminate u in favor of s and t, and following the prescription (52) [$\alpha' t \to (N-1)$ in the numerator], we obtain the large-(α's) leading power contribution to the Nth term of (49) with the correct coefficient.

We have, therefore, seen that the prescription (52) allows us to use the t-channel exchange amplitude in the cubic string field theory to construct the full disc scattering amplitude. In Sec. VI, this prescription is extended for the disc scattering amplitudes on a spacetime with a curved background metric, which is the situation of real interest in the context of hadron scattering.

V. MODE DECOMPOSITION ON AdS_5

Let us now proceed to work out mode decomposition of the totally symmetric (traceless) component field on the warped spacetime. The correspondence between the primary operators of the conformal field theory on the (UV) boundary and wave functions on AdS_5 is made clear in this section. The Pomeron/Reggeon wave functions are obtained as a *holomorphic* function of the spin variable j since we need to do so for the further inverse Mellin transformation. The wave functions will then also be used to construct the scattering amplitude of $h + \gamma^* \to h + \gamma^{(*)}$ and GPD in Secs. VI and VII.

Let the bilinear (free) part of the (bulk) action of a rank-j tensor field on AdS_5 be[14]

$$S_{\text{eff kin}} = -\frac{1}{2}\frac{t_{Ay}}{R^3}\int d^4x \int dz\sqrt{-g(z)}g^{m_1n_1}\cdots g^{m_jn_j} \times \left[g^{m_0n_0}(\nabla_{m_0}A^{(y)}_{m_1\cdots m_j})(\nabla_{n_0}A^{(y)}_{n_1\cdots n_j}) + \left(\frac{c_y}{R^2} + \frac{N^{(y)}_{\text{eff}}}{\alpha'}\right)A^{(y)}_{m_1\cdots m_j}A^{(y)}_{n_1\cdots n_j}\right], \tag{62}$$

where we assume that kinetic mixing between different fields is either absent or sufficiently small. Here, the dimensionless parameter $N^{(y)}_{\text{eff}}$ is $N^{(Y)} - 1$ for an $N^{(Y)} \in \mathbf{Z}_{\geq 0}$ for bosonic open string ($j \leq N^{(Y)}$), which would be $4(N^{(Y)} - 1)$ for an $N^{(Y)} \in \mathbf{Z}_{\geq 1}$ for closed string ($j \leq 2N^{(Y)}$). This field is regarded as a reduction of some field with spherical harmonics on the internal manifold,[15] and hence $j \leq h_a$, in general. Another dimensionless coefficient c_y may contain a contribution from the "mass" associated with the spherical harmonics over the internal manifold and may also include the ambiguity (which is presumably of order unity) associated with making d'Alembertian of the flat metric background covariant.[16] The combination $(c_y/R^2 + N^{(y)}_{\text{eff}}/\alpha')$ is denoted by M^2_{eff}.

The equation of motion (in the bulk part)[17] then becomes

$$g^{m_1m_2}(\nabla_{m_1}\nabla_{m_2}A^{(y)}_{n_1\cdots n_j}) - \left(\frac{c_y}{R^2} + \frac{N^{(y)}_{\text{eff}}}{\alpha'}\right)A^{(y)}_{n_1\cdots n_j} = 0. \tag{64}$$

Solutions to this equation of motion can be obtained from solutions of the following eigenmode equation,[18]

$$\nabla^2 A_{m_1\cdots m_j} = -\frac{\mathcal{E}}{R^2}A_{m_1\cdots m_j}, \tag{65}$$

[14]The dimensionless constant t_{Ay} is something like N_c^2 for a mode obtained by a reduction of closed string component fields in higher dimensions. More comments on t_{Ay} for open string states is found in footnote 27.

[15]The internal manifold would be a five-dimensional one, W, for closed string modes in type IIB, and a three-cycle one for open string states on the flavor D7-branes. For sufficiently small x, however, amplitudes of exchanging modes with nontrivial spherical harmonics on these internal manifolds are relatively suppressed, and we are not interested very much.

[16]The ambiguity in c_y/R^2 includes insertion of the curvature tensor,

$$([\nabla_M, \nabla_N])^{Q'}_{Q} = -\Gamma^{Q'}_{QN,M} + \Gamma^{Q'}_{QM,N} + \Gamma^{L}_{QM}\Gamma^{Q'}_{LN} - \Gamma^{L}_{QN}\Gamma^{Q'}_{LM} = \frac{\delta^{Q'}_M g_{QN} - \delta^{Q'}_N g_{QM}}{R^2}, \tag{63}$$

which vanishes in flat space. Depending on details of how it is inserted, the value of c_y may not be the same for all the individual irreducible components of SO(4,1) in a rank-j tensor field $A_{m_1\cdots m_j}$.

[17]There is also an IR boundary part of the equation motion. We will come back to this issue in Sec. V D.

[18]The differential operator $\nabla^2 := g^{mn}\nabla_m\nabla_n$ is Hermitian under the measure $d^4x dz\sqrt{-g(z)}g^{m_1n_1}\cdots g^{m_jn_j}$.

by imposing the on-shell condition

$$\frac{(\mathcal{E}+c_y)}{\sqrt{\lambda}}+N_{\rm eff}^{(y)}=0 \qquad (\text{i.e.,}\quad \mathcal{E}+R^2M_{\rm eff}^2=0). \tag{66}$$

We will work out the eigenmode decomposition for rank-j tensor fields in the following, where we have to work only for a separate j, without referring to the mass parameter.[19]

The eigenmode wave functions are used not just for a construction of solutions to the equation of motions, but also in constructing the Reggeon exchange contributions to the $h+\gamma^*\to h+\gamma^{(*)}$ scattering amplitude. The propagator is proportional to

$$\frac{-i}{\frac{\mathcal{E}+c_y}{\sqrt{\lambda}}+N_{\rm eff}^{(y)}-i\epsilon}\frac{\alpha' R^3}{t_{Ay}}. \tag{67}$$

The mode equation for a rank-j tensor field $A_{m_1\cdots m_j}$ on AdS_5 is further decomposed into those of irreducible representations of SO(4,1). For simplicity of argument, we deal only with the mode equations for the totally symmetric (and traceless) rank-j tensor fields. Namely,

$$A_{m_1\cdots m_j}=A_{m_{\sigma(1)}\cdots m_{\sigma(j)}} \quad \text{for } {}^\forall\sigma\in\mathfrak{S}_j. \tag{68}$$

We call them spin-j fields.

The eigenmode equation (65) for a totally symmetric spin-j field can be decomposed into $j+1$ pieces, labeled by $k=0,\ldots,j$:

$$\begin{aligned}&((R^2\Delta_j)-[(2k+1)j-2k^2+3k])A_{z^k\mu_1\cdots\mu_{j-k}}\\&\quad+2zk\partial^{\hat\rho}A_{z^{k-1}\rho\mu_1\cdots\mu_{j-k}}+k(k-1)A^{\hat\rho}_{z^{k-2}\rho\mu_1\cdots\mu_{j-k}}\\&\quad-2z(D[A_{z^{k+1}\ldots}])_{\mu_1\cdots\mu_{j-k}}+(E[A_{z^{k+2}\ldots}])_{\mu_1\cdots\mu_{j-k}}\\&=-\mathcal{E}A_{z^k\mu_1\cdots\mu_{j-k}}.\end{aligned} \tag{69}$$

Here,

$$A_{z^k\mu_1\cdots\mu_{j-k}}:=A_{\underbrace{z\cdots z}_{k}\mu_1\cdots\mu_{j-k}} \tag{70}$$

and can be regarded as a rank-$(j-k)$ totally symmetric tensor of the SO(3,1) Lorentz group. The SO(3,1) indices with $\hat{}$ in the superscript, such as $\hat\rho$ in $\partial^{\hat\rho}$, are raised by the four-dimensional (4D) Minkowski metric $\eta^{\rho\sigma}$ from a subscript σ, not by the five-dimensional (5D) warped metric g^{mn}. $D[a]$ and $E[a]$ are operations creating totally symmetric rank-$(r+1)$ and rank-$(r+2)$ tensors of SO(3,1), respectively, from a totally symmetric rank-r tensor of SO(3,1), a:

$$(D[a])_{\mu_1\cdots\mu_{r+1}}:=\sum_{i=1}^{r+1}\partial_{\mu_i}a_{\mu_1\cdots\check{\mu_i}\cdots\mu_{r+1}}, \tag{71}$$

$$(E[a])_{\mu_1\cdots\mu_{r+2}}:=2\sum_{p<q}\eta_{\mu_p\mu_q}a_{\mu_1\cdots\check{\mu_p}\cdots\check{\mu_q}\cdots\mu_{r+2}}. \tag{72}$$

The differential operator Δ_j in the first term is defined, as in [3], by

$$\begin{aligned}R^2\Delta_j&:=R^2z^{-j}\left[\left(\frac{z}{R}\right)^5\partial_z\left[\left(\frac{R}{z}\right)^3\partial_z\right]\right]z^j+R^2\left(\frac{z}{R}\right)^2\partial^2,\\&=z^2\partial_z^2+(2j-3)z\partial_z+j(j-4)+z^2\partial^2.\end{aligned} \tag{73}$$

The eigenmode equation (65), (69) is a generalization of the "Schrödinger equation" of [3] determining the Pomeron wave function. As we will see, the single-component Pomeron wave function discussed in [3], etc. corresponds to (93)—that of the $(n,l,m)=(0,0,0)$ eigenmode in our language, and the Schrödinger equation to (90), (A10); there are other eigenmodes, whose wave functions are to be determined in the following.

In the following sections, V A and V B, we simply state the results of the eigenmode decomposition of (65), (69) for spin-j fields. A more detailed account is given in Appendix A.

A. Eigenvalues and eigenmodes for $\Delta^\mu=0$

Because of the $(3+1)$-dimensional translational symmetry in ∇^2, solutions to the eigenmode equations can be classified by the eigenvalues of the generators of translation, $(-i\partial_\mu)$. Until the end of Sec. V B, we will focus on eigenmodes in the form of

$$A_{m_1\cdots m_j}(x,z)=e^{i\Delta\cdot x}A_{m_1\cdots m_j}(z;\Delta) \tag{74}$$

and study the eigenmode equation (65) separately for different eigenvalues Δ^μ.

The eigenmode equation for $\Delta^\mu=0$ and that for $\Delta^\mu\neq 0$ are qualitatively different and need separate study. The eigenmodes for $\Delta^\mu\neq 0$ will be presented in Sec. V B (and Appendix A.2); we begin in Sec. V A (and Appendix A.1) with the eigenmode equation for $\Delta^\mu=0$, which is also regarded as an approximation of the eigenmode equation for $\Delta^\mu\neq 0$ in the asymptotic UV boundary region (at the least, $\Delta z\ll 1$ and z may be as small as R).

For now, we relax the traceless condition on the spin-j field $A_{m_1\cdots m_j}$ ($m_i=0,1,\ldots,3,z$), and we just assume that the rank-j tensor field $A_{m_1\cdots m_j}$ is totally symmetric.[20]

[19] There are many states with the same value of j, but with different c_y and $N_{\rm eff}^{(y)}$.

[20] This only makes the following presentation more far-reaching; in the end, it is quite easy to identify which eigenmodes fall into the traceless part within $A_{m_1\cdots m_j}$. See (82)–(84) at the end of Sec. V A.

Consider the following decomposition of the space of z-dependent field configuration $A_{m_1\cdots m_j}(z;\Delta=0)$:

$$A_{z^k\mu_1\cdots\mu_{j-k}}(z;\Delta^\mu=0)=\sum_{N=0}^{[(j-k)/2]}(E^N[a^{(k,N)}])_{\mu_1\cdots\mu_{j-k}};\qquad(75)$$

here, $(a^{(k,N)}(z;\Delta^\mu=0))_{\mu_1\cdots\mu_{j-k-2N}}$ is a rank-$(j-k-2N)$ totally symmetric tensor of SO(3,1), and it satisfies the 4D-traceless condition

$$\eta^{\hat{\mu}_1\hat{\mu}_2}a^{(k,N)}_{\mu_1\cdots\mu_{j-k-2N}}=0.\qquad(76)$$

Thus, the field configuration can be described by $a^{(k,N)}$'s with $0\le k\le j$, $0\le N\le[(j-k)/2]$. These components form groups labeled by $n=0,\ldots,j$, where the nth group consists of $a^{(k,N)}$'s, with $k+2N=n$; they are all rank-$(j-n)$ totally symmetric tensors of SO(3,1); let us call the subspace spanned by the components in this nth group the nth subspace. The eigenmode equation for $\Delta^\mu=0$ becomes block diagonal under the decomposition into these subspaces labeled by $n=0,\ldots,j$ [see (A3) in the appendix]. Therefore, the eigenmode equation for $\Delta^\mu=0$ can be studied separately for the individual diagonal blocks.

The nth diagonal block contains $[n/2]+1$ components, and hence there are $[n/2]+1$ eigenmodes. Let $\mathcal{E}_{n,l}$ $(l=0,\ldots,[n/2])$ be the eigenvalues in the nth diagonal block. The corresponding eigenmode wave function is of the form

$$(a^{(k,N)}(z;\Delta^\mu=0))_{\mu_1\cdots\mu_{j-n}}=c_{k,l,n}(\epsilon^{(n,l)})_{\mu_1\cdots\mu_{j-n}}z^{2-j-i\nu},\qquad(77)$$

where $\epsilon^{(n,l)}$ is a z-independent, k-independent rank-$(j-n)$ tensor of SO(3,1) ($c_{k,l,n}\in\mathbb{R}$). In the eigenmode equation for $\Delta^\mu=0$, the eigenmode wave functions are all in a simple power of z, and the power is parametrized by $i\nu$ ($\nu\in\mathbb{R}$). The eigenvalues $\mathcal{E}_{n,l}$ are functions of ν; once the mass-shell condition (66) is imposed, the eigenmodes turn into solutions of the equation of motion and $i\nu$ is determined by the mass parameter.

The eigenmodes with smaller (n,l) are as follows:

$$\mathcal{E}_{0,0}=(j+4+\nu^2),\quad a^{(0,0)}(z)_{\mu_1\cdots\mu_j}=\epsilon^{(0,0)}_{\mu_1\cdots\mu_j}z^{2-j-i\nu},\qquad(78)$$

$$\mathcal{E}_{1,0}=(3j+5+\nu^2),\qquad a^{(1,0)}(z)_{\mu_1\cdots\mu_{j-1}}=\epsilon^{(1,0)}_{\mu_1\cdots\mu_{j-1}}z^{2-j-i\nu},\qquad(79)$$

$$\mathcal{E}_{2,0}=(5j+4+\nu^2),$$
$$\begin{pmatrix}a^{(0,1)}(z)_{\mu_1\cdots\mu_{j-2}}\\ a^{(2,0)}(z)_{\mu_1\cdots\mu_{j-2}}\end{pmatrix}=\begin{pmatrix}1\\-4j\end{pmatrix}\epsilon^{(2,0)}_{\mu_1\cdots\mu_{j-2}}z^{2-j-i\nu},\qquad(80)$$

$$\mathcal{E}_{2,1}=(j+2+\nu^2),$$
$$\begin{pmatrix}a^{(0,1)}(z)_{\mu_1\cdots\mu_{j-2}}\\ a^{(2,0)}(z)_{\mu_1\cdots\mu_{j-2}}\end{pmatrix}=\begin{pmatrix}1\\2\end{pmatrix}\epsilon^{(2,1)}_{\mu_1\cdots\mu_{j-2}}z^{2-j-i\nu}.\qquad(81)$$

Empirically, the j dependence of the eigenvalues in the nth diagonal block appears to be $\mathcal{E}_{n,l}=((2n+1-4l)j+\nu^2+O(1))$ $(l=0,\ldots,[n/2])$ [see (A12)–(A27) in the Appendix for more samples of the eigenvalues], and we promote this j dependence as a rule of the labeling of the eigenmodes with l.

The eigenmode with $l=0$ is found in any one of the diagonal blocks ($n=0,\ldots,j$). Its eigenvalue is

$$\mathcal{E}_{n,0}=(2n+1)j+2n-n^2+4+\nu^2,\qquad(82)$$

and

$$c_{2\bar{k},0,2\bar{n}}=(-)^{\bar{k}}4^{\bar{k}}\frac{\bar{n}!}{(\bar{n}-\bar{k})!}\frac{(j-\bar{n}+1)!}{(j-\bar{n}-\bar{k}+1)!},\quad(n=2\bar{n},\bar{k}=0,\ldots,\bar{n}),\qquad(83)$$

$$c_{2\bar{k}+1,0,2\bar{n}+1}=(-)^{\bar{k}}4^{\bar{k}}\frac{\bar{n}!}{(\bar{n}-\bar{k})!}\frac{(j-\bar{n})!}{(j-\bar{n}-\bar{k})!},\quad(n=2\bar{n}+1,\bar{k}=0,\ldots,\bar{n}).\qquad(84)$$

These $(n,l)=(n,0)$ eigenmodes are characterized by the 5D-traceless condition

$$g^{m_1m_2}A_{m_1\cdots m_j}=0.$$

Thus, the eigenmodes within the 5D-traceless (and totally symmetric) component—the spin-j field—for $\Delta^\mu=0$ are labeled simply by $n=0,\ldots,j$.

B. Mode decomposition for nonzero Δ_μ

1. Diagonal block decomposition for the $\Delta^\mu\neq 0$ case

The eigenmode equation (65), (69) is much more complicated in the case of $\Delta^\mu\neq 0$ because of the second and fourth terms in (69). The eigenmode equation is still made block diagonal for an appropriate decomposition of the space of field $A_{m_1\cdots m_j}(z;\Delta^\mu)$.

Consider a decomposition

$$A_{z^k\mu_1\cdots\mu_{j-k}}(z;\Delta^\mu)=\sum_{s=0}^{j-k}\sum_{N=0}^{[s/2]}(\tilde{E}^N D^{s-2N}[a^{(k,s,N)}])_{\mu_1\cdots\mu_{j-k}},\qquad(85)$$

where a new operation $a\mapsto\tilde{E}[a]$ on a totally symmetric SO(3,1) tensor a,

$$(\tilde{E}[a])_{\mu_1\cdots\mu_{r+2}} := 2\sum_{p<q}\left(\eta_{\mu_p\mu_q} - \frac{\partial_{\mu_p}\partial_{\mu_q}}{\partial^2}\right)a_{\mu_1\cdots\check{\mu_p}\cdots\check{\mu_q}\cdots\mu_{r+2}}, \tag{86}$$

is used. $a^{(k,s,N)}$'s are totally symmetric, 4D-traceless [i.e., (76)] rank-$(j-k-s)$ tensor fields of SO(3,1) that satisfy an additional condition, the 4D-transverse condition:

$$\partial^{\hat{\rho}}(a^{(k,s,N)})_{\rho\mu_2\cdots\mu_{j-k-s}} = i\Delta^{\hat{\rho}}(a^{(k,s,N)})_{\rho\mu_2\cdots\mu_{j-k-s}} = 0. \tag{87}$$

The space of field configuration $A_{m_1\cdots m_j}(z;\Delta^\mu)$ is now decomposed into $a^{(k,s,N)}$'s, with $0 \le k \le j$, $0 \le s \le j-k$, $0 \le N \le [s/2]$; these components form groups labeled by $m = 0,\ldots,j$, where the mth group consists of $a^{(k,s,N)}$'s, with $k+s=m$; they are all rank-$(j-m)$, totally symmetric 4D-traceless and 4D-transverse tensors of SO(3,1); let us call the subspace spanned by the components in this mth group the mth subspace. The eigenmode equation for $\Delta^\mu \neq 0$ becomes block diagonal under the decomposition into these subspaces labeled by $m = 0,\ldots,j$. The eigenmode equation for the mth sector is given by (A39) in Appendix A.2. The mth subspace should have

$$\sum_{s=0}^{m}([s/2]+1) \tag{88}$$

eigenmodes.

Eigenvalues $\mathcal{E}$ are determined in terms of the characteristic exponent in the expansion of the solution in the power series of z. Let the first term in the expansion be $z^{2-j-i\nu}$; the eigenvalues are functions of ν then. Because the indicial equation at the regular singular point $z \simeq 0$ allows us to determine the eigenvalues in terms of ν, the eigenvalues in the case of $\Delta^\mu \neq 0$ cannot be different from the ones we have already known in the $\Delta^\mu = 0$ case. In the mth diagonal block, the eigenvalues consist of $\mathcal{E}_{n,l}$, with $0 \le n \le m$, $0 \le l \le [n/2]$.

To summarize, the eigenmodes in the totally symmetric rank-j tensor field of SO(4,1) are labeled by (n,l,m) and Δ^μ and ν. Their eigenvalues $\mathcal{E}_{n,l}$ depend only on n and l (with $0 \le n \le j$ and $0 \le l \le [n/2]$) and ν. Corresponding eigenmodes are denoted by

$$\begin{aligned} A(x,z)^{n,l,m;\Delta,\nu}_{z^k\mu_1\cdots\mu_{j-k}} &= e^{i\Delta\cdot x}A^{n,l,m}_{z^k\mu_1\cdots\mu_{j-k}}(z;\Delta^\mu,\nu) \\ &= e^{i\Delta\cdot x}\sum_{N=0}^{[s/2]}\tilde{E}^N D^{s-2N}[\epsilon^{(n,l,m)}]\frac{b^{(j-m)}_{s,N}}{\Delta^{s-2N}}\Psi^{(j);s,N}_{i\nu;n,l,m}(-\Delta^2,z). \end{aligned} \tag{89}$$

$\epsilon^{(n,l,m)}$ is a (z-independent) totally symmetric 4D-traceless 4D-transverse rank-$(j-m)$ tensor of SO(3,1), and all the s's appearing in the expression above are understood as $s = m-k$. $b^{(r)}_{s,N}$ is a constant whose definition is given in (A38) in the Appendix.

2. Single-component Pomeron wave function

The Pomeron wave function that has been discussed in the literature (e.g., [3]) does not look as awful as (89). To our knowledge, the Pomeron wave function in the literature in the context of hadron high-energy scattering has been a single component one, $\Psi_{i\nu}(t,z)$. How is $A^{n,l,m}_{m_1\cdots m_j}(z;\Delta^\mu,\nu)$ related to $\Psi_{i\nu}(-\Delta^2;z)$?

In the block diagonal decomposition of the eigenmode equation, there is only one subspace where the diagonal block is 1×1. That is the $m=0$ subspace, which consists only of $a^{(0,0,0)}$. The eigenmode equation is

$$\left[\Delta_j - \frac{j}{R^2}\right]a^{(0,0,0)}(z;\Delta^\mu) = -\frac{\mathcal{E}}{R^2}a^{(0,0,0)}(z;\Delta^\mu). \tag{90}$$

This equation, as well as (A10) in the $\Delta^\mu = 0$ case, corresponds to the Schrödinger equation in [3] determining the Pomeron wave function. It should be noted, however, that we consider that ∇^2 is the operator relevant to the eigenmode decomposition[21] rather than Δ_j; furthermore, the operator ∇^2 and Δ_j has a simple relation $\nabla^2 = \Delta_j - j/R^2$ only on this $m=0$th subspace of a totally symmetric rank-j tensor field of SO(4,1).

The eigenvalue is

$$\mathcal{E}_{0,0} = (j+4+\nu^2), \tag{91}$$

when we define the first term in the power series expansion of z to be $z^{2-j-i\nu}$. The eigenmode wave function is

$$a^{(0,0,0)}(z;\Delta^\mu)_{\mu_1\cdots\mu_j} = \epsilon^{(0,0,0)}_{\mu_1\cdots\mu_j}\Psi^{(j)}_{i\nu}(-\Delta^2,z), \tag{92}$$

$$\Psi^{(j)}_{i\nu}(-\Delta^2,z) := \frac{2}{\pi}\sqrt{\frac{\nu\sinh(\pi\nu)}{2R}}e^{(j-2)A}K_{i\nu}(\Delta z), \tag{93}$$

where $e^{2A(z)} = (R/z)^2$ is the warp factor introduced in (28). The normalization factor is determined [3][22] so that it satisfies the normalization condition[23]

[21] Thus, the propagator (67) uses the eigenvalue of ∇^2, rather than that of Δ_j. The eigenvalue $\mathcal{E}$ of ∇^2 in the $m=0$th subspace is $(j+4+\nu^2)$ as in (91), instead of $(4+\nu^2)$. Reference [3] uses a mode $h_{mn} \propto z^{-2}(\eta_{\mu\nu},\delta_{zz})$ of the spin-2 field to fix the details of (65), (66) and (90). This $h_{mn} \propto z^{-2}(\eta_{\mu\nu},\delta_{zz})$ mode, however, corresponds to the $(n,l) = (2,1)$ mode of the spin-$j=2$ field in (A17), rather than the 5D-traceless 5D-transverse mode $(n,l) = (0,0)$. The eigenvalue $\mathcal{E}_{2,1} = (2+j+\nu^2)$ with $j=2$ becomes $(4+\nu^2)$, though.

[22] The Pomeron wave function in [7] was of the form (124), which becomes (93) in the limit of $\Lambda \to 0$, while we keep z and Δ^μ fixed.

[23] The normalization condition is generalized to (99) later on.

$$\int d^4x \int dz \sqrt{-g(z)} e^{-2jA} [e^{i\Delta\cdot x} \Psi^{(j)}_{i\nu}(-\Delta^2, z)] \times [\Psi^{(j)}_{i\nu'}(-\Delta'^2, z) e^{-i\Delta'\cdot x}] = (2\pi)^4 \delta^4(\Delta - \Delta')\delta(\nu - \nu'). \tag{94}$$

The single component Pomeron/Reggeon wave function $\Psi^{(j)}_{i\nu}(-\Delta^2, z)$ is now understood as $\Psi^{(j);0,0}_{i\nu;0,0,0}(-\Delta^2, z)$.

3. 5D-traceless 5D-transverse Modes

The eigenmode equation (65) for a totally symmetric rank-j tensor field of SO(4,1) should be closed within its 5D-traceless component. The subspace of 5D-traceless component is characterized by the 5D-traceless condition

$$g^{m_1 m_2} A_{m_1 \cdots m_j}(z; \Delta^\mu) = 0. \tag{95}$$

The fact that the Hermitian operator ∇^2 maps this subspace to itself implies that the eigenmode equation of ∇^2 is block diagonal, when the space of (not-necessarily-5D-traceless) $A_{m_1 \cdots m_j}$ is decomposed into the sum of the 5D-traceless subspace and its orthogonal complement. The collection of the eigenmodes with $l = 0$ corresponds to the subspace of 5D-traceless field configuration.

Similarly, one can think of a subspace of field configuration satisfying both the 5D-traceless condition (95) and the 5D-transverse condition

$$g^{nm_1} \nabla_n A_{m_1 m_2 \cdots m_j} = 0. \tag{96}$$

Obviously this is a subspace of the subspace of the 5D-traceless modes we discussed above. Since the Hermitian operator ∇^2 on AdS_5 maps this new subspace also to itself, the eigenmode equation of ∇^2 should also become block diagonal when the subspace of 5D-traceless modes is decomposed into this new subspace and its orthogonal complement.

As we will see in Appendix A.3, there is only one such mode satisfying this set of conditions (95), (96) in each one of the mth diagonal block. Thus, the combination of the 5D-traceless and 5D-transverse conditions allows us to determine an eigenmode completely. This mode turns out to be $(n, l, m) = (0, 0, m)$ (for $0 \le m \le j$). Put differently, the eigenmodes with the eigenvalue $\mathcal{E}_{n,l} = \mathcal{E}_{0,0} = (j + 4 + \nu^2)$ are characterized by the traceless and transverse conditions on AdS_5.

The eigenmode wave functions of the 5D-traceless transverse modes $(n, l, m) = (0, 0, m)$ are (see Appendix A.3)

$$\Psi^{(j);s,N}_{i\nu;0,0,m}(-\Delta^2, z) = \sum_{a=0}^{N} (-)^a {}_N C_a \left(\frac{z^3 \partial_z z^{-3}}{\Delta}\right)^{s-2a} [(z\Delta)^m \Psi^{(j);0,0}_{i\nu;0,0,0}(-\Delta^2, z)] \times N_{j,m}. \tag{97}$$

$N_{j,m}$ is a dimensionless normalization constant. We choose it to be[24]

$$N^{-2}_{j,m} = {}_j C_m \frac{\Gamma(j + 1 - i\nu)}{\Gamma(j + 1 - m - i\nu)} \frac{\Gamma(j + 1 + i\nu)}{\Gamma(j + 1 - m + i\nu)} \frac{\Gamma(3/2 + j - m)}{2^m \Gamma(3/2 + j)} \frac{\Gamma(2 + 2j)}{\Gamma(2 + 2j - m)}, \tag{98}$$

so that the eigenmode wave functions are normalized as in

$$\int d^4x \int_0 dz \sqrt{-g(z)} g^{m_1 n_1} \cdots g^{m_j n_j} A^{n,l,m;\Delta,\nu}_{m_1 \cdots m_j}(x, z) A^{n',l',m';\Delta',\nu'}_{n_1 \cdots n_j}(x, z) = (2\pi)^4 \delta^4(\Delta + \Delta')\delta(\nu - \nu')\delta_{n,n'}\delta_{l,l'}\delta_{m,m'} [\epsilon^{(n,l,m)}(\Delta)] \cdot [\epsilon^{(n',l',m')}(\Delta')]. \tag{99}$$

Here, $[\epsilon^{(n,l,m)}] \cdot [\epsilon'^{(n,l,m)}] := \epsilon^{(n,l,m)}_{\mu_1 \cdots \mu_{j-m}} \epsilon'^{(n,l,m)}_{\nu_1 \cdots \nu_{j-m}} \eta^{\hat{\mu}_1 \hat{\nu}_1} \cdots \eta^{\hat{\mu}_{j-m} \hat{\nu}_{j-m}}$.

4. Propagator

The propagator of the totally symmetric rank-j tensor field (respectively, the spin-j field) on AdS_5 is given by summing up propagators of the (n, l, m) modes [respectively, the (n, l, m) modes with $l = 0$]. For the purpose of writing down the propagator of a given (n, l, m) eigenmode, it is convenient to introduce the following notation:

$$A^{n,l,m;\Delta,\nu}_{m_1 \cdots m_j}(x, z) = [A^{n,l,m;\Delta,\nu}_{m_1 \cdots m_j}(x, z)]^{\hat{\kappa}_1 \cdots \hat{\kappa}_{j-m}} \epsilon^{(n,l,m)}_{\kappa_1 \cdots \kappa_{j-m}} = e^{i\Delta\cdot x} [A^{n,l,m}_{m_1 \cdots m_j}(z; \Delta^\mu, \nu)]^{\hat{\kappa}_1 \cdots \hat{\kappa}_{j-m}} \epsilon^{(n,l,m)}_{\kappa_1 \cdots \kappa_{j-m}}. \tag{100}$$

With this notation, the propagator of the (n, l, m) mode is given by

[24] Note that $N_{j,m} = 1$, if $m = 0$.

$$G(x,z;x',z')^{(n,l,m)}_{m_1\cdots m_j;n_1\cdots n_j} = \int \frac{d^4\Delta}{(2\pi)^4}\int_0^\infty d\nu \frac{-iP^{(j-m)}_{\rho_1\cdots\rho_{j-m};\sigma_1\cdots\sigma_{j-m}}}{\frac{\mathcal{E}_{n,l+c}}{\sqrt{\lambda}}+N_{\rm eff}-i\epsilon}\frac{\alpha' R^3}{t_y} \times [A^{n,l,m;\Delta,\nu}_{m_1\cdots m_j}(x,z)]^{\hat\rho_1\cdots\hat\rho_{j-m}}[A^{n,l,m;-\Delta,\nu}_{n_1\cdots n_j}(x',z')]^{\hat\sigma_1\cdots\hat\sigma_{j-m}}. \tag{101}$$

Here, $P^{(j-m)}_{\rho_1\cdots\rho_{j-m};\sigma_1\cdots\sigma_{j-m}}$ is a polarization tensor generalizing $\eta_{\rho\sigma}-\partial_\rho\partial_\sigma/\partial^2$; when an orthogonal basis $\epsilon_a(q)\cdot\epsilon_b(-q)=\delta_{a,b}D_a$ of rank-r 4D-traceless 4D-transverse tensors is given,

$$P^{(r)}_{\mu_1\cdots\mu_r;\nu_1\cdots\nu_r} := \sum_a \frac{1}{D_a}\epsilon(q)_{a;\mu_1\cdots\mu_r}\epsilon(-q)_{a;\nu_1\cdots\nu_r}. \tag{102}$$

An alternative characterization of this $P^{(r)}_{\mu_1\cdots\mu_r;\nu_1\cdots\nu_r}$ is given by a combination of the following two conditions: one is

$$P^{(r)}_{\mu_1\cdots\mu_r;\nu_1\cdots\nu_r}\epsilon_a^{\hat\nu_1\cdots\hat\nu_r} = \epsilon_{a;\mu_1\cdots\mu_r}, \tag{103}$$

and the other is that $P^{(r)}_{\mu_1\cdots\mu_r;\nu_1\cdots\nu_r}$ also be a totally symmetric 4D-transverse 4D-traceless tensor with respect to $(\mu_1\cdots\mu_r)$ for any choice of $(\nu_1\cdots\nu_r)$. Its explicit form (A74), given in the Appendix, is useful for practical computations.

C. Representation in the dilatation eigenbasis

It is an essential process in the application of the AdS/CFT correspondence to classify solutions to the equation of motions on the gravity dual background (AdS_5) into irreducible representations of the conformal group SO(4,2) (or possibly its supersymmetric extension). In the CFT description, primary operators are in one-to-one correspondence with (highest weight) irreducible representations of the conformal group, and it is believed that one can establish a one-to-one correspondence between (i) a primary operator in the CFT description and (ii) a group of solutions to the equation of motion forming an irreducible representation in the gravity dual description. Once this correspondence is given, hadron matrix elements of the primary operators in a (nearly conformal) field theory can be calculated by using the corresponding solutions to the equations of motion (the wave functions) on AdS_5. Note that the hadron matrix elements of the primary operators are all that remain unknown in the formulation of conformal operator product expansion (26).

Let P_μ, K_μ, $L_{\mu\nu}$, and D denote the generators of the unitary operators of the conformal group transformation on the Hilbert space. They satisfy the following commutation relations:

$$[D,P_\mu]=iP_\mu,\qquad [P_\rho,L_{\mu\nu}]=i(\eta_{\rho\mu}P_\nu-\eta_{\rho\nu}P_\mu), \tag{104}$$

$$[D,K_\mu]=-iK_\mu,\quad [K_\rho,L_{\mu\nu}]=i(\eta_{\rho\mu}K_\nu-\eta_{\rho\nu}K_\mu), \tag{105}$$

$$[P_\mu,K_\nu]=-2i(\eta_{\mu\nu}D+L_{\mu\nu}), \tag{106}$$

$$[L_{\mu\nu},L_{\rho\sigma}]=i(\eta_{\nu\rho}L_{\mu\sigma}-\eta_{\nu\sigma}L_{\mu\rho}-\eta_{\mu\rho}L_{\nu\sigma}+\eta_{\mu\sigma}L_{\nu\rho}). \tag{107}$$

When such a conformal symmetry exists in a conformal field theory in $3+1$ dimensions, these generators have a representation as differential operators on fields on $\mathbb{R}^{3,1}$; these differential operators are denoted by $\mathcal{P}_\mu$, $\mathcal{K}_\mu$, $\mathcal{L}_{\mu\nu}$, and $\mathcal{D}$. The generators and the differential operators on a CFT are in the following relation:

$$[\mathcal{O}(x),P_\mu]=\mathcal{P}_\mu\mathcal{O}(x),\qquad [\mathcal{O}(x),K_\mu]=\mathcal{K}_\mu\mathcal{O}(x),$$
$$[\mathcal{O}(x),D]=\mathcal{D}\mathcal{O}(x),\ldots, \tag{108}$$

and these differential operators acts on primary operators as follows:

$$\mathcal{D}\overline{\mathcal{O}}_n(x)=-i(x\cdot\partial+l_n)\overline{\mathcal{O}}_n(x), \tag{109}$$

$$\mathcal{L}_{\mu\nu}\overline{\mathcal{O}}_n(x)=(i(x_\mu\partial_\nu-x_\nu\partial_\mu)+[S_{\mu\nu}])\overline{\mathcal{O}}_n(x), \tag{110}$$

$$\mathcal{P}_\mu\overline{\mathcal{O}}_n(x)=-i\partial_\mu\overline{\mathcal{O}}_n(x), \tag{111}$$

$$\mathcal{K}_\mu\overline{\mathcal{O}}_n(x)=(-i(2x_\mu x\cdot\partial-x^2\partial_\mu)-i2l_nx_\mu-x^\nu[S_{\mu\nu}])\overline{\mathcal{O}}_n(x), \tag{112}$$

where l_n is the scaling dimension of the operator $\overline{\mathcal{O}}_n$ and $[S_{\mu\nu}]$ a finite dimensional representation of SO(3,1) generators satisfying the same commutation relation as $L_{\mu\nu}$'s. Thus, for a primary operator $\overline{\mathcal{O}}_n(x)$, $\overline{\mathcal{O}}_n(x=0)$ plays the role of the highest weight state

$$[\overline{\mathcal{O}}_n(0),K_\mu]=0,\qquad [\overline{\mathcal{O}}_n(0),D]=-il_n\overline{\mathcal{O}}_n(0); \tag{113}$$

all other states in the highest weight state representation—descendants—are generated by applying $[\bullet,P_\mu]$ multiple times; the whole representation, therefore, is spanned by a collection of

$$\{\overline{\mathcal{O}}_n(0),\partial_\mu\overline{\mathcal{O}}_n(0),\partial_\mu\partial_\nu\overline{\mathcal{O}}_n(0),\ldots\}; \tag{114}$$

it is also equivalent to a collection of $\overline{\mathcal{O}}(x=x_0)$, with arbitrary $x_0\in\mathbb{R}^{3,1}$.

In the preceding sections, we have worked on solutions to the eigenmode equation on AdS_5; once the mass-shell condition (66) is imposed, they become solutions to the equation of motion. They are obtained as an eigenmode of the spacetime translation in $3+1$ dimensions, $(-i\partial^\mu)=\Delta^\mu$. Under the conformal group SO(4,2), which contains Lorentz SO(3,1) symmetry, however, an irreducible representation has to include solutions with all kinds of eigenvalues Δ^μ.

In the case of a scalar field on AdS_5, one can think of the following linear combination $G(x,z;x_0;R_0)$ (for some $R_0\ll\Delta^{-1}$):

$$G(x,z;x_0) = \frac{i}{\pi^2}\frac{\Gamma(l_n)}{\Gamma(l_n-2)}R_0^{l_n-4}\left(\frac{z}{z^2+(x-x_0)^2}\right)^{l_n} = \int\frac{d^4\Delta}{(2\pi)^4}e^{i\Delta\cdot(x-x_0)}\frac{(\Delta z)^2K_{l_n-2}(\Delta z)}{(\Delta R_0)^2K_{l_n-2}(\Delta R_0)}. \quad (115)$$

The factor $[e^{i\Delta\cdot x}(\Delta z)^2K_{l_n-2}(\Delta z)]$ in the integrand on the right-hand side is a solution to the equation of motion of a scalar field on AdS_5 whose mass square M_{eff}^2 is given by $l_n - 2 = i\nu = \sqrt{4+M_{\mathrm{eff}}^2R^2}$. The coefficient of the linear combination, $e^{-i\Delta\cdot x_0}[(\Delta R_0)^2K_{l_n-2}(\Delta R_0)]^{-1}$, is chosen so that the integrand behaves as

$$e^{i\Delta\cdot(x-x_0)}\left(\frac{z}{R_0}\right)^{4-l_n} \quad (116)$$

at $0 \le z \ll \Delta^{-1}$. The space of solutions to the equation of motion $G(x,z;x_0)$ parametrized by $x_0 \in \mathbb{R}^{3,1}$ is alternatively spanned by derivatives of $G(x,z;x_0)$ with respect to x_0^μ at $x_0^\mu = 0$. It is easy to see that this basis,

$$\{G(x,z;0), \partial_\mu^{(x_0)}G(x,z;0), \partial_\mu^{(x_0)}\partial_\nu^{(x_0)}G(x,z;0), \ldots\}, \quad (117)$$

is an eigenbasis under the action of dilatation, $\mathcal{D} := i(z\partial_z + x\cdot\partial)$, and their weights are $-il_n, -i(l_n+1), -i(l_n+2), \ldots$, respectively. Correspondence between scalar field wave functions on AdS_5 and scalar primary operators of the dual CFT is established in this way [34].

Let us now generalize the discussion above slightly to construct an analogue of $G(x,z;x_0)$ for a spin-j field $A_{m_1\cdots m_j}$ on AdS_5, from which the dilatation eigenbasis is constructed. To this end, note that all of the $(0,0,m)$ modes $(m = 0,\ldots,j)$ have the leading $z^{2-j-i\nu}$ term in the power series expansion only in the $A_{z^0\mu_1\cdots\mu_j}$ component, not in any other $A_{z^k\mu_1\cdots\mu_{j-k}}$ components[25] with $k > 0$. It is possible to choose $\epsilon^{(0,0,m)}(\Delta^\mu)$ properly so that

$$\sum_{m=0}^{j}[A^{0,0,m;\Delta,\nu}_{\mu_1\cdots\mu_j}(x,z)]^{\hat\kappa_1\cdots\hat\kappa_{j-m}}\epsilon^{(0,0,m)}_{\kappa_1\cdots\kappa_{j-m}}e^{-i\Delta\cdot x_0} \simeq e^{i\Delta\cdot(x-x_0)}\left(\frac{z}{R_0}\right)^{2-j-i\nu}\epsilon_{\mu_1\cdots\mu_j} \quad (118)$$

in the region near the UV boundary $z \ll \Delta^{-1}$, where $\epsilon_{\mu_1\cdots\mu_j}$ is a Δ^μ-independent 4D-traceless totally symmetric rank-j tensor of SO(3,1); the condition on $\epsilon^{(0,0,m)}(\Delta^\mu)$ is

$$\epsilon_{\mu_1\cdots\mu_j} = \left(\frac{R_0}{R}\right)^{2-j}K_{i\nu}(\Delta R_0)\frac{2}{\pi}\sqrt{\frac{\nu\sinh(\pi\nu)}{2R}} \times\sum_{m=0}^{j}\frac{N_{j,m}\Gamma(m-j-i\nu)}{\Gamma(-j-i\nu)} \times\sum_{N=0}^{[m/2]}\frac{b^{(j-m)}_{m,N}}{\Delta^{m-2N}}(\tilde E^N D^{m-2N}[\epsilon^{(0,0,m)}])_{\mu_1\cdots\mu_j}. \quad (119)$$

[25]Use (97).

It is possible to invert this relation by using (A37) and writing down $\epsilon^{(0,0,m)}(\Delta^\mu)$ in terms of $\epsilon_{\mu_1\cdots\mu_j}$, though we will not present the result here. What really matters to us is that $\epsilon^{(0,0,m)}(\lambda\Delta) = \epsilon^{(0,0,m)}(\Delta)\lambda^{i\nu}$. With $\epsilon^{(0,0,m)}$'s satisfying the condition above, one can see that the following linear combination of solutions to the equation of motion,

$$G_{m_1\cdots m_j}(x,z;x_0) := \int\frac{d^4\Delta}{(2\pi)^4}\sum_{m=0}^{j}[A^{0,0,m;\Delta,\nu}_{m_1\cdots m_j}(x,z)]^{\hat\kappa_1\cdots\hat\kappa_{j-m}}\epsilon^{(0,0,m)} \times(\Delta)_{\kappa_1\cdots\kappa_{j-m}}e^{-i\Delta\cdot x_0}, \quad (120)$$

has a property

$$G_{m_1\cdots m_j}(\lambda x,\lambda z;\lambda x_0) = \lambda^{-(2+j+i\nu)}G_{m_1\cdots m_j}(x,z;x_0). \quad (121)$$

$i\nu$ is determined by the mass parameter on AdS_5 once the mass-shell condition (66) is imposed. Therefore, $G_{m_1\cdots m_j}(x,z;0)$ is an eigenstate of dilatation, and so are the derivatives of $G_{m_1\cdots m_j}(x,z;x_0)$ with respect to x_0^μ at $x_0^\mu = 0$. All of the derivatives combined forms of a dilatation eigenbasis in the space of solutions with the equation of motion of a spin-j field.

It is now clear that the eigenmodes with $(n,l,m) = (0,0,m)$ $(0 \le m \le j)$ and arbitrary Δ^μ as a whole—modes that satisfy the 5D-traceless and 5D-transverse conditions (95), (96)—form an irreducible representation of the conformal group. If one is interested purely in the matrix element of a spin-j primary operator $\overline{\mathcal{O}}_n(x_0 = 0)$ of an approximately conformal gauge theory, then the matrix element can be calculated by using the wave function $G_{m_1\cdots m_j}(x,z;0)$. Note that the $m = 0$ mode alone—where the Pomeron/Reggeon wave function has a single component, as in [3]—cannot reproduce all of the matrix elements associated with matrix elements of spin-j primary operators.

D. Confinement effect

1. Top-down approach

QCD in the real world is not a conformal gauge theory, but it has a mass gap in the hadron spectrum due to confinement. Confinement of a nearly conformal strongly coupled gauge theory is realized in its gravitational dual description in the form of a nearly AdS geometry with a minimum value in the warp factor.

Klebanov-Strassler geometry of type IIB string theory [27] will be one of the most popular background geometries of this kind. The Klebanov-Strassler geometry is not dual to a confining gauge theory that is asymptotically free, however; it is dual to a gauge theory that is confining in the infrared, but its 't Hooft couplings become stronger and stronger toward ultraviolet. Such geometries as Klebanov-Strassler are not truly dual to the QCD of the real world, but

one will still be able to learn a lot from studying the mode decomposition on such geometries.

Mode decomposition can be carried out once we know the background configuration and the action of the bilinear fluctuations around the background; we do not need interactions of stringy fields. Thus, it will be a doable task, at least at the supergravity level. Reduction over the $W_5 = T^{1,1}$ geometry has been worked out in the literature, and one is left to translate the smoothness condition of mode functions at the tip of the deformed warped conifold into the language of boundary conditions on a warped $(4+1)$-dimensional spacetime.[26] The authors do not find a reason not to work on it, except that it will take extra time to do so.

In this article, however, we set a higher priority in getting a broader perspective on the subject ranging from string theory to hadron physics, and we avoid taking too much time to solve technical problems in string theory. Instead, we discuss, in the following, two temporary approaches of implementing the confinement effects; one is an effective-theory model building approach and the other is a phenomenological approach. We will proceed with the phenomenological approach in the following sections, although we understand that the topdown approach above will eventually replace/back up/verify the phenomenological approach to be adopted in this article. The following "effective theory model building approach" is not used in this article, but we present it here because it helps us understand the physical meaning (the hidden assumptions) of the phenomenological approach.

2. Effective theory model building approach

The hard wall model and its variations are introduced in order to mimic the presence of a minimum value of the warped factor, mass gap, and nearly AdS background geometry. It remains simple enough so that analytic results are obtained in a relatively short amount of time, though we cannot discuss the stability of the geometry or the theoretical consistency of string theory.

With this philosophy in mind, one could think of implementing the confining effect in the form of

$$S = \int d^4x \int_0^{1/\Lambda} dz \sqrt{-g(z)}\mathcal{L}_{\rm bulk} + \int d^4x \sqrt{-g}|_{z=1/\Lambda}\mathcal{L}_{\rm bdry}, \tag{122}$$

where the background geometry remains AdS_5 and the holographic radius z is cut off at $z = \Lambda^{-1}$. Note that different choices of $\mathcal{L}_{\rm bdry}$ lead to a different physics; to be more precise, different choices of $(\mathcal{L}_{\rm bulk}, \mathcal{L}_{\rm bdry})$ modulo partial integration should be regarded as different models. It is reasonable to have such freedom in the choice of effective-theory models because we know that there is more than one holographic background of type IIB string theory that is dual to confining gauge theories. Such constraints as SO(3,1) symmetry unbroken global symmetry of a strongly coupled gauge theory, however, are very weak in constraining $\mathcal{L}_{\rm bdry}$.

Once a model is fixed, the Euler-Lagrange equation of this theory includes not only the equation of motion in the bulk (64)=(65), (66), but also the boundary conditions at $z = 1/\Lambda$. Different models (i.e., different $\mathcal{L}_{\rm bdry}$) predict different Pomeron/Reggeon wave functions.

We require that SO(3,1) symmetry is preserved even in $\mathcal{L}_{\rm bdry}$. Boundary conditions might introduce mixing between the eigenmode decomposition determined in the bulk, in principle, but the unbroken SO(3,1) symmetry excludes mixing between SO(3,1)-irreducible tensors of different ranks. This observation still does not exclude mixing among (n, l, m) modes of a spin-j totally symmetric field on AdS_5 with a common m, but different (n, l)'s.

3. Phenomenological approach

As an alternative approach, one can think of a phenomenological approach, which is to start from a small number of parameters and let the physical consequences constrain those parameters. When one finds that reasonable physical consequences cannot be available under a given set of parameters, then a few more parameters will be introduced so that more freedom is available.

As one of the simplest trial parametrizations of the confining effect, we make the following changes in the mode functions $\Psi^{(j);0,0}_{i\nu;0,0,m}(\Delta, z)$:

$$K_{i\nu}(\Delta z) \to \left[K_{i\nu}(\Delta z) + \frac{\pi}{2}\frac{c^{(j)}_{i\nu;0,0,m}}{\sin(\pi i\nu)} I_{i\nu}(\Delta z)\right] =: \text{“}K_{i\nu}(\Delta z)\text{”}. \tag{123}$$

$c^{(j)}_{i\nu;0,0,m}$'s, which may depend on Δ^2 and Λ, are the parameters we introduce. An implicit assumption here is that the confining effect does not introduce mixing among modes with different (n, l, m)'s. Under this assumption, however, the parametrization above does not lose any generality; once the ratio between the $K_{i\nu}(\Delta z)$ wave and $I_{i\nu}(\Delta z)$ is given for $\Psi^{(j);0,0}_{i\nu;0,0,m}(-\Delta^2, z)$, there is no freedom left for the other $\Psi^{(j);s,N}_{i\nu;0,0,m}(-\Delta^2, z)$ functions ($(s, N) \neq (0, 0)$) of the same $(n, l, m) = (0, 0, m)$ mode because the relation among them is completely fixed by the equation of motion in the bulk. In Sec. VII A, we will carry out a test of whether this simple parametrization works well or not.

When the infrared boundary is introduced in the holographic background geometry, the normalization of the

[26] Such geometries typically are in the form of $\mathbb{R}^{3,1} \times W'_n$, which nearly remains constant around the tip of the throat $r = 0$, and a shrinking $(5-n)$ cycle with the metric $ds^2 = dr^2 + r^2(d\Omega_{5-n})^2$. For simplicity, let $n = 4$ and $d\Omega_1 = d\theta$. A scalar field $\phi(r, \theta)$ with smooth configuration in the coordinate $(r\cos\theta, r\sin\theta)$ is decomposed into $\sum_k e^{ik\theta}\phi_k(r)$ when the mode $\phi_k(r)$ needs to be in the form of $r^k \times \mathrm{fcn}(r^2)$. Thus, $\partial_r[r^{-k}\phi_k(r)] = 0$ at $r = 0$.

Pomeron/Reggeon wave function also needs to be changed. In the case of the $(n,l,m)=(0,0,0)$ mode, with the Dirichlet boundary condition at the IR boundary $z=1/\Lambda$, for example, the wave function $\Psi^{(j);0,0}_{i\nu;0,0,0}=\Psi^{(j)}_{i\nu}(-\Delta^2,z)$ was given the following normalization [3,7]:

$$\Psi^{(j)}_{i\nu}(-\Delta^2,z)=e^{(j-2)A}\frac{2}{\pi}\sqrt{\frac{\nu\sinh(\pi\nu)}{2R}}\sqrt{\frac{I_{i\nu}(x_0)}{I_{-i\nu}(x_0)}}\times\left[K_{i\nu}(\Delta z)-\frac{K_{i\nu}(x_0)}{I_{i\nu}(x_0)}I_{i\nu}(\Delta z)\right], \tag{124}$$

with an extra factor $\sqrt{I_{i\nu}(x_0)/I_{-i\nu}(x_0)}$, where $x_0 \coloneqq \Delta/\Lambda$. This result is generalized as follows. By repeating the same argument as in Appendix A.3.a, one finds that the normalization factor $N_{j,m}$ should be replaced by

$$N_{j,m}\to N_{j,m}\times\frac{1}{\sqrt{1-c^{(j)}_{i\nu;0,0,m}}}. \tag{125}$$

The Dirichlet boundary condition for the $m=0$ mode above corresponds to $(1-c^{(j)}_{i\nu;0,0,0})=[I_{-i\nu}(x_0)/I_{i\nu}(x_0)]$; the modified normalization (124) is a special case of (125). The mode functions are defined, so far, for $\nu\geq\mathbb{R}$ since the eigenvalue $\mathcal{E}_{0,0}=4+j+\nu^2$ depends only on ν^2. When the mode function is analytically continued to the $\nu<0$ region, the mode function for $-\nu$ should be the same as $+\nu$. From this observation, it follows that

$$(1-c^{(j)}_{-i\nu;0,0,m})=(1-c^{(j)}_{i\nu;0,0,m})^{-1}. \tag{126}$$

VI. ORGANIZING THE SCATTERING AMPLITUDE ON AdS_5

A. "Effective" string field action on AdS_5

If we are to start from type IIB string theory in ten dimensions with a background that is approximately $\mathrm{AdS}_5\times W_5$ (except near the infrared boundary), one can think of an effective theory on AdS_5 after carrying out spherical harmonics mode decomposition on W_5. As we have already discussed in Sec. V how to construct propagators in such an effective theory, we would now like to construct the scattering amplitude.

For this purpose, we need interaction among string fields, and we turn to cubic string field theory, which we reviewed already in Sec. IV. This allows us to write down a concrete expression for the scattering amplitude. Clearly the biggest drawback of this approach is in the fact that no stable background geometry $\mathrm{AdS}_5\times W_{21}$ is known in bosonic string theory for a 21-dimensional internal manifold W_{21}. In the following, we will construct an effective action on AdS_5 by carrying out dimensional reduction of the cubic string field theory action, as if there exists an $\mathrm{AdS}_5\times W_{21}$ solution to bosonic string theory. This is not meant to claim that we obtain such an action as an effective theory of bosonic string theory, but to use it as a starting point in constructing a toy-model scattering amplitude of a hadron and a (virtual) photon that may still carry some fragrance of interaction structure in superstring theory.

Let us start off by clarifying the relation between the normalization of string component fields in (38), (41), (42) and that of the component fields in (62). All of the component fields in (38) are normalized so that they have canonically normalized kinetic terms in the action in the 26-dimensional spacetime. Now, we make them dimensionless by the redefinition $\phi\to g_o^{-1}\phi$, $A_M\to g_o^{-1}A_M$, etc. All of the terms in the cubic string field theory—both the kinetic terms and the interactions—will then have $(1/g_o^2)$ as an overall factor. When a mode decomposition of the following form is assumed for the component in this new normalization,

$$\phi(x,z,\theta)=\sum_y\phi^{(y)}(x,z)Y_y(\theta),$$
$$A_M(x,z,\theta)=\begin{cases}\sum_y A^{(y)}_m(x,z)Y_y(\theta) & M=m=0,\ldots,3,z\\ 0 & M=5,\ldots,25.\end{cases} \tag{127}$$

Similarly decomposition holds for spin-h_a fields $A_{M_1\cdots M_{h_a}}(x,z,\theta)$; we take spherical harmonics $Y_y(\theta)$ (labeled by y) to be dimensionless, so that the component fields on AdS_5 such as $\phi^{(y)}(x,z)$, $A^{(y)}_m(x,z)$, $A^{(y)}_{m_1\cdots m_{h_a}}(x,z)$ are also dimensionless.

The overall coefficient of the effective action on AdS_5 then becomes a dimension-$(+3)$ parameter

$$\frac{\mathrm{vol}(W_{21})}{2(g_o)^2}\times\mathcal{O}(1), \tag{128}$$

which is to be identified with the overall coefficient $t_y/(2R^3)$ in (62). Reduction of interaction terms (43), (45), (46) also yields the same overall factor (128), apart from possibly one order factor coming from the overlap integration of spherical harmonics over the internal manifold. Because the amplitudes from exchanging states with higher spherical harmonics are suppressed in small-x DIS and DVCS (e.g., [7]), we will be interested only in the interactions involving $\phi^{(y)}$-$\phi^{(y)}$–(intermediate states) and $A^{(y)}_m$-$A^{(y)}_m$–(intermediate states) cubic couplings, with the intermediate states having spherical harmonics $Y(\theta)=1$. The overall factor of the cubic interactions then becomes precisely the same as that of the kinetic terms of $\phi^{(y)}$ and $A^{(y)}_m$.

For this reason, we write down the following interaction terms for the effective action on AdS_5:

$$S_{\text{eff int}} = -\frac{t_{\phi y}\lambda_{\text{sft}}}{3\alpha' R^3}\int d^4x dz\sqrt{-g(z)}\hat{E} \times \left(3\,\text{tr}[\phi_y^2\phi] + \sqrt{\frac{8\alpha'}{3}}\text{tr}[(-iA_m)(\phi_y\overleftrightarrow{\nabla}^m\phi_y)] - \frac{8\alpha'}{9\sqrt{2}}\text{tr}[f_{mn}(\phi_y\overleftrightarrow{\nabla}^m\overleftrightarrow{\nabla}^n\phi_y)] - \frac{5}{9\sqrt{2}}\text{tr}[f_m^m\phi_y^2] + \frac{2\sqrt{\alpha'}}{3}\text{tr}[(\nabla_m g^m)\phi_y^2] - \frac{11}{9}\text{tr}[h\phi_y^2]\right) + \cdots. \tag{129}$$

Fields without a label y are to be used for the intermediate states exchanged in the t channel (in the sense that we explained in Sec. IV B); ϕ_y are for the incoming and outgoing states. Partial derivatives have been replaced by covariant derivatives on AdS_5. Similarly, all other interactions, such as (45), (46) in 26 dimensions, also give rise to their corresponding cubic interactions on AdS_5. Certainly such a choice of effective action on AdS_5 will be one of the most likely (and simple) setups that may still maintain some aspects of scattering amplitude in string theory, although top-down justification is not given.

We will only sum t-channel amplitudes where $Y_y(\theta) = 1$ modes of the stringy states in the leading Reggeon/Pomeron trajectory are exchanged, because that constitutes the dominant contribution in small-x scattering. Thus, three-point interactions of such modes with incoming and outgoing tachyon states are necessary, which we write down as follows,

$$\Delta S_{\text{eff int}} = -\frac{t_h\lambda_{\text{sft}}}{R^3\alpha'}\int d^4x dz\sqrt{-g(z)}\hat{E} \times \text{tr}[A^{(Y)}_{m_1\cdots m_N}(\phi\overleftrightarrow{\nabla}^{m_1}\cdots\overleftrightarrow{\nabla}^{m_N}\phi)]\left(\frac{8\alpha'}{27}\right)^{\frac{N}{2}}\frac{(-i)^N}{\sqrt{N!}}, \tag{130}$$

by keeping only the $Y_y(\theta) = 1$ modes and replacing the derivatives in (45) by covariant derivatives. The normalization constant $t_{\phi y}$ for the target hadron kinetic term is now simply written as t_h, as we will have to pay attention only to the individual choices of target hadrons [the individual choices of $Y_y(\theta)$] in the external states. Similarly, we also need interaction of the same group of modes with the incoming and outgoing photon states, which we write down as follows:

$$\Delta S_{\text{eff int}} = -\frac{t_\gamma\lambda_{\text{sft}}}{R^3\alpha'}\int d^4x dz\sqrt{-g(z)}\hat{E} \times \text{Tr}\left[A^{(N)}_{m_1\cdots m_N}(A_l(-i\overleftrightarrow{\nabla}^{m_1})\cdots(-i\overleftrightarrow{\nabla}^{m_N})A_k)\left(\frac{8\alpha'}{27}\right)^{\frac{N}{2}}\frac{g^{kl}\frac{16}{27}}{\sqrt{N!}} + \cdots\right], \tag{131}$$

following the same procedure by starting from (46). We have retained only the terms that have N derivatives and are proportional to η^{kl}, as they are necessary in determining the twist-2 contributions to the structure function V_1. Since we need the normalization constant t_{Ay} of the kinetic term of the external state only for the spherical harmonics $Y(\theta) = 1$, we no longer need to refer to the choice of spherical harmonics; t_{Ay} is therefore rewritten as t_γ.

B. External states wave function

The vertex operator insertions in the world-sheet calculation are replaced by appropriate external state wave functions in amplitude calculations based on string field theories.

First, the insertions of a vertex operator of the form (33) for the U(1) currents on flavor D7-branes are replaced by wave functions for the massless vector field in bosonic string theory. We use the wave functions for the incoming state $\gamma^*(q_1)$ and the outgoing state $\gamma^{(*)}(q_2)$:

$$A^{\text{in}}_m(x_\gamma, z_\gamma) = R\int\frac{d^4q_1}{(2\pi)^4}e^{iq_1\cdot(x_\gamma-(\bar{x}-(\Delta x)/2)}A_m(z_\gamma; q_1), \tag{132}$$

$$A^{\text{out}}_m(x_\gamma, z_\gamma) = R\int\frac{d^4q_2}{(2\pi)^4}e^{-iq_2\cdot(x_\gamma-(\bar{x}+(\Delta x)/2))}A_m(z_\gamma; q_2), \tag{133}$$

where $A_m(z; q)$ on the right-hand sides are the wave functions given in (35). A factor R is inserted here because we adopted a normalization convention, so that $A^{(\text{in/out})}_m(x, z)$ on AdS_5 is dimensionless.[27] The arguments of the electromagnetic current insertions $T\{J^\nu(x)J^\mu(y)\}$—coordinates in boundary theory x and $y \in \mathbb{R}^{3,1}$—are now denoted by $\bar{x} + (\Delta x)/2$ and $\bar{x} - (\Delta x)/2$, respectively.

[27] $A_m(x, z)$ is often normalized so that it has mass dimension $(+1)$, and hence this factor R is not then necessary. In a case in which the gauging of a global symmetry of a strongly coupled gauge theory is realized in the form of a flavor D7-brane, the natural reduction of the 7-brane action on a three-cycle leads to the form of

$$S_{\text{eff}} \sim -\frac{N_c}{R}\int d^4x dz\sqrt{-g(z)}F_{mn}F^{mn}; \tag{134}$$

the external state wave function (132), (133) without the factor R can be used in such cases. In the presentation adopted in this section, where a bosonic string is used and the gauge field is assigned zero mass dimension (like other higher spin fields), the factor R is included in (132), (133) and the kinetic term of $F_{mn}F^{mn}$ has the coefficient t_γ/R^3 instead. Thus, we can think of t_γ as something like N_c.

The vertex operators (30) for the target hadron are replaced by wave functions of the form

$$\phi^{\rm in}(x_h, z_h) = e^{ip_1\cdot x_h}\Phi(z_h; m_n),$$
$$\phi^{\rm out}(x_h, z_h) = e^{-ip_2\cdot x_h}\Phi(z_h; m_n), \tag{135}$$

where $\Phi(z;m)$'s on the right-hand sides are the wave function given by (31). The first one is for the incoming state and the second for the outgoing hadron.

C. Leading trajectory contribution to the Compton tensor

When the target hadron is to be identified with some Kaluza-Klein state of the tachyon of bosonic string theory, then $\ell_\phi - 2 = \sqrt{4 + M_{\rm eff}^2 R^2} = \sqrt{4 + c - \sqrt{\lambda}}$ is not real valued for $\lambda \gg 1$. We treat this $\ell_\phi - 2$ as if it were real valued, until the last moment. Since our true interest is in the scattering amplitude in type IIB string theory, or in hadron scattering in the real world, this problem is absent in such situations, and we do not bother about this issue.

Let us combine all the pieces together to organize an amplitude of photon-tachyon scattering given by a t-channel exchange of a leading trajectory spin-j state reduced to AdS_5, with $Y_y(\theta) = 1$. Such an amplitude—denoted by $i\mathcal{M}^{(t)}_{(N_{\rm eff}=j,j)}$—consists of a t-channel exchange of all the eigenmodes labeled by (n, l, m). We will further focus on contributions from $(n, l, m) = (0, 0, m)$. It is given by

$$\begin{aligned} i\mathcal{M}^{(t)}_{(j,j);(0,0,m)} \simeq{}& \frac{-it_\gamma}{R^3\alpha'}\int d^4x_\gamma dz_\gamma \sqrt{-g(z_\gamma)}J^{\gamma\gamma}_{k_1\cdots k_j;pq} g^{pq}(g^{k_1r_1}\cdots g^{k_jr_j})(z_\gamma)\left(\frac{\alpha'}{2}\right)^{j/2} e^{-2A(z_\gamma)} \\ &\times \frac{-it_h}{R^3\alpha'}\int d^4x_h dz_h \sqrt{-g(z_h)}J^{hh}_{l_1\cdots l_j}(g^{l_1s_1}\cdots g^{l_js_j})(z_h)\left(\frac{\alpha'}{2}\right)^{j/2} e^{-2A(z_h)} \\ &\times \frac{1}{j!}\left(\frac{27}{16}\right)^{\alpha' t-(j-1)}[e^{2A(z_\gamma)}e^{2A(z_h)}G^{(0,0,m)}(x_\gamma, z_\gamma; x_h, z_h)_{r_1\cdots r_j;s_1\cdots s_j}]; \end{aligned} \tag{136}$$

just like in the amplitude calculation in Sec. IV B, this amplitude is meant to be the coefficient of $\mathrm{Tr}[\lambda^{\gamma 2}\lambda^{\gamma 1}\lambda^{h1}\lambda^{h2}]$. $J^{\gamma\gamma}$ and J^{hh} (above) are given by the external state wave functions as follows:

$$J^{\gamma\gamma}_{k_1\cdots k_j;pq}(x_\gamma, z_\gamma) = (-i)^j[A^{\rm out}_p \overleftrightarrow{\nabla}_{k_1}\cdots\overleftrightarrow{\nabla}_{k_j}A^{\rm in}_q](x_\gamma, z_\gamma), \tag{137}$$

$$J^{hh}_{l_1\cdots l_j}(x_h, z_h) = (-i)^j[\phi^{\rm in}\overleftrightarrow{\nabla}_{l_1}\cdots\overleftrightarrow{\nabla}_{l_j}\phi^{\rm out}](x_h, z_h). \tag{138}$$

Here, $\phi^{\rm in/out}(x_h, z_h)$ are both of mass dimension (-1), and $A^{\rm in/out}_m(x_\gamma, z_\gamma)$ is of mass dimension $(+3) + \dim[\epsilon_\mu]$. From this expression, one can see that the first line has mass dimension $(+6) + 2\times\dim[\epsilon_\mu]$, the second line (-2), and the last line 0. Thus, $i\mathcal{M}^{(t)}_{(j,j);(0,0,m)}$ is a function of p_1^κ, p_2^κ, $\overline{x}^\kappa$ and Δx^κ of mass dimension $4 + 2\times\dim[\epsilon_\mu]$. This is precisely the property expected for

$$(i)^2\langle h(p_2)|T\{J^\nu(\overline{x}+(\Delta x)/2)J^\mu(\overline{x}-(\Delta x)/2)\}|h(p_1)\rangle\epsilon^1_\mu\epsilon^{2*}_\nu. \tag{139}$$

Its Fourier transform with respect to $(\Delta x)^\mu$ becomes $(iT^{\mu\nu})\times e^{-i\overline{x}\cdot(p_2-p_1)}$.

If we carry out an integration over d^4x_γ, d^4x_h, and $d^4(\Delta x)$ first, then the three integration variables Δ^μ in (101) and $q_{1,2}$ in (132), (133) are determined in terms of the input $p^\mu_{1,2}$ and q^μ; we have $\Delta^\mu := (p_2 - p_1)^\mu$, $q^\mu_2 = (q - \Delta/2)^\mu$ and $q_1 := (q + \Delta/2)^\mu$. As a result, it follows that

$$\begin{aligned} [T^{\mu\nu}\epsilon^1_\mu\epsilon^{2*}_\nu]^{(t)} ={}& \int d^4(\Delta x)e^{-iq\cdot(\Delta x)}\mathcal{M}^{(t)}_{(j,j);(0,0,m)}|_{\overline{x}=0} \\ \simeq{}& \frac{t_\gamma}{R^3\alpha'}\int dz_\gamma\sqrt{-g(z_\gamma)}\overline{J}^{\gamma\gamma}_{k_1\cdots k_j;pq}R^2 g^{pq}(g^{k_1r_1}\cdots g^{k_jr_j})\left(\frac{\alpha'}{2}\right)^{j/2}\frac{t_h}{R^3\alpha'}\int dz_h\sqrt{-g(z_h)}\overline{J}^{hh}_{l_1\cdots l_j}(g^{l_1s_1}\cdots g^{l_js_j})\left(\frac{\alpha'}{2}\right)^{j/2} \\ &\times\frac{1}{j!}\left(\frac{27}{16}\right)^{\alpha' t-(j-1)}\frac{R^3\alpha'}{t_{(j,j,1)}}\int_0^\infty d\nu\,\frac{P^{(j-m)}_{\rho_1\cdots\rho_{j-m};\sigma_1\cdots\sigma_{j-m}}}{\frac{\mathcal{E}_{0,0}+c_y}{\sqrt{\lambda}}+N_{\rm eff}-i\epsilon}[A^{0,0,m}_{r_1\cdots r_j}(z_\gamma;-\Delta,\nu)]^{\hat\rho_1\cdots\hat\rho_{j-m}}[A^{0,0,m}_{s_1\cdots s_j}(z_h;\Delta,\nu)]^{\hat\sigma_1\cdots\hat\sigma_{j-m}}, \end{aligned} \tag{140}$$

where

$$\overline{J}^{\gamma\gamma}_{k_1\cdots k_j;pq}(z_\gamma) = (-i)^j[A_p(z_\gamma;-q_2)\overleftrightarrow{\nabla}_{k_1}\cdots\overleftrightarrow{\nabla}_{k_j}A_q(z_\gamma;q_1)], \tag{141}$$

$$\overline{J}^{hh}_{l_1\cdots l_j}(z_h) = (-i)^j[\Phi(z_h;p_1)\overleftrightarrow{\nabla}_{l_1}\cdots\overleftrightarrow{\nabla}_{l_j}\Phi(z_h;-p_2)]. \tag{142}$$

Although momentum vectors are used in the second arguments of the external state wave functions A and Φ here, instead of their Lorentz-invariant momentum square, this is only to remind ourselves of the sign when ∇'s act on the wave functions.

The expression (140) is meant to be a part of the t-channel contribution to the Compton tensor $[T^{\mu\nu}\epsilon^1_\mu\epsilon^{2*}_\nu]^{(t)}$, and we should obtain the full contribution to the Compton tensor $[T^{\mu\nu}\epsilon^1_\mu\epsilon^{2*}_\nu]$ after employing the prescription (52). At least this prescription tells us to set the factor $(27/16)^{[\alpha' t-(j-1)]}$ in the fourth line to $(27/16)^{\mathcal{O}(1/\sqrt{\lambda})}\simeq 1$. Now, we claim that this is the only necessary change under this prescription, so far as the amplitude of $(0,0,m)$-mode exchange is concerned.

To see this, remember that, prior to applying the prescription (52), we need to rewrite the residues of the t-channel poles in terms only of the Mandelstam variables s and t, not of u. Let us take the expression $[\Phi_h\overleftrightarrow{\nabla}_m\Phi_h]g^{mn}[A_\gamma\overleftrightarrow{\nabla}_n A_\gamma]$ as an example which captures the feature of contraction of SO(4,1) indices in (140). In the scattering $\phi(P_1)+A(Q_1)\to\phi(P_2)+A(Q_2)$, with $P_{1,2}$ and $Q_{1,2}$ "momenta" $\sim$ derivatives in five dimensions, $(s-u)\sim(P_1+P_2)\cdot(Q_1+Q_2)$ is converted to $(2s+t)$ in the following steps:

$$\begin{aligned}(P_1+P_2)\cdot(Q_1+Q_2) &= (2P_1+(P_2-P_1))\cdot(Q_1+Q_2),\\ &= (2P_1)\cdot(Q_1+Q_2)+(Q_1-Q_2)\cdot(Q_1+Q_2) = (2P_1)\cdot(2Q_1+(Q_2-Q_1))+(Q_1)^2-(Q_2)^2,\\ &= (2P_1)\cdot(2Q_1+(P_1-P_2))+(Q_1)^2-(Q_2)^2 = (4P_1\cdot Q_1)+(-2P_1\cdot P_2)+2(P_1)^2+(Q_1)^2-(Q_2)^2;\end{aligned}$$

each one of the steps above is regarded as either one of partial integration in $dx_\gamma dz_\gamma$, one in $dx_h dz_h$, or a rewriting of (P_2-P_1) by (Q_1-Q_2) or vice versa. The last procedure is to pass a derivative on one side of the propagator to the other. Because of the 5D-transverse condition characterizing the $(0,0,m)$ modes, such terms proportional to ∇ drop out from the amplitudes exchanging the $(0,0,m)$ modes. Noting that the prescription (52) modifies the $-2(P_1\cdot P_2)\sim t$ term above into the propagator mass, and that this term appeared only after passing a derivative ∇ through the propagator, we see that the term which would have been affected by the prescription (52) has indeed already dropped out.

1. Casting the amplitude into the form of OPE

So far, the (virtual) photon and the target hadron have been treated equally in the scattering amplitude. We are interested, however, in the $h+\gamma^*\to h+\gamma^{(*)}$ scattering in the regime of generalized Bjorken scaling, where

$$|(q^2)|,(q\cdot p),|(q_1\cdot\Delta)|,|(q_2\cdot p)|\gg|\Delta^2|,m_h^2,\Lambda^2, \tag{143}$$

while the ratio among $(q\cdot p)$, (q^2), and $(q\cdot\Delta)$—namely, x and η—is kept finite. It is, thus, desirable to rewrite the scattering amplitude (the structure functions) in a form that fits to the conformal OPE. To do this, we follow a prescription that has been used in the study of DIS in holographic models.

Let us focus on the following factors that appear in the third and fourth lines of (140):

$$\int_0^\infty d\nu[A^{0,0,m}_{r_1\cdots r_j}(z_\gamma;-\Delta,\nu)]^{\hat\rho_1\cdots\hat\rho_{j-m}} \times[A^{0,0,m}_{s_1\cdots s_j}(z_h;\Delta,\nu)]^{\hat\sigma_1\cdots\hat\sigma_{j-m}}\times[\cdots]. \tag{144}$$

The last factor $[\cdots]$ denotes the remaining ν dependence (denominator) in the integrand; we need to remember only that $\mathcal{E}_{0,0}=(4+j+\nu^2)$, and hence it is even under the change $\nu\to-\nu$.

We begin with the case $m=0$. The expression (144) for the $m=0$ case becomes

$$\begin{aligned}&\int_0^\infty d\nu[\Psi^{(j);0,0}_{i\nu;0,0,0}(-\Delta^2;z_\gamma)][\Psi^{(j);0,0}_{i\nu;0,0,0}(-\Delta^2;z_h)]\times[\cdots],\\ &=\frac{2}{\pi^2R}\int_0^\infty d\nu\frac{\nu\sinh(\pi\nu)}{(1-c^{(j)}_{i\nu;0,0,0})}[e^{(j-2)A(z_\gamma)}\text{“}K_{i\nu}(\Delta z_\gamma)\text{”}]\\ &\quad\times[e^{(j-2)A(z_h)}\text{“}K_{i\nu}(\Delta z_h)\text{”}]\times[\cdots]\end{aligned} \tag{145}$$

multiplied by a factor $[\delta^{\hat\rho_1}_{r_1}\cdots\delta^{\hat\rho_j}_{r_j}\delta^{\hat\sigma_1}_{s_1}\cdots\delta^{\hat\sigma_j}_{s_j}]$. Using the fact that $K_{i\nu}(x)=i\pi/2\times(I_{i\nu}(x)-I_{-i\nu}(x))/[\sinh(\pi\nu)]$, the ν integral above can be rewritten as

$$\frac{1}{\pi R}\int_{-\infty}^{+\infty}d\nu i\nu[e^{(j-2)A(z_\gamma)}I_{i\nu}(\Delta z_\gamma)][\text{“}K_{i\nu}(\Delta z_h)\text{”}e^{(j-2)A(z_h)}]\times[\cdots], \tag{146}$$

where we used the relation (126). This expression is more convenient than (145); this is because (i) the z_γ integration is dominated in the region $qz_\gamma\lesssim 1$ because of the photon external state wave functions containing $K_1(q_{1,2}z)$, (ii) $I_{i\nu}(\Delta z_\gamma)$ decreases rapidly toward positive $i\nu$ for $qz_\gamma\lesssim 1$ and $q\gg\Delta$ [a generalized Bjorken scaling (143)], and (iii) the rapidly decreasing $I_{i\nu}(\Delta z_\gamma)$ in the lower half of the

complex ν plane allows us to close the ν integration contour through the large-radius lower half complex ν plane (see [7] and the literature therein).

It is straightforward to generalize this treatment for all other $m \neq 0$ modes. Note that the Pomeron/Reggeon wave function $[A^{0,0,m}_{m_1\cdots m_j}(z;\Delta,\nu)]^{\hat\rho_1\cdots\hat\rho_{j-m}}$ for $m \neq 0$ is obtained from that of $m = 0$ by multiplying $(\Delta z)^m$ and $N_{j,m}$ (which is even in ν), applying differential operators in z and manipulating Lorentz indices. Obviously the order of such manipulations on the wave function and the procedure from (145) to (146) can be exchanged.

Therefore, the contribution to the Compton tensor from the leading trajectory spin-j state $(0,0,m)$ mode is

$$\begin{aligned}(T^{\mu\nu}\epsilon^1_\mu\epsilon^{2*}_\nu)_{(j,j);(0,0,m)} \simeq{}& \frac{1}{j!}\frac{t_\gamma\sqrt{\lambda}}{t_y\pi}\left(\frac{\alpha'}{2}\right)^j\int_{-\infty}^{+\infty}d\nu\frac{P^{(j-m)}_{\rho_1\cdots\rho_{j-m};\sigma_1\cdots\sigma_{j-m}}}{\frac{\mathcal{E}_{0,0}+c_y}{\sqrt{\lambda}}+N_{\rm eff}-i\epsilon}i\nu\\ &\times\frac{R^2}{R^3}\int dz_\gamma\sqrt{-g(z_\gamma)}\overline{J}^{\gamma\gamma}_{k_1\cdots k_j;pq}g^{pq}(g^{k_1r_1}\cdots g^{k_jr_j})[\overline{\overline{A}}^{0,0,m}_{r_1\cdots r_j}(z_\gamma;-\Delta,\nu)]^{\hat\rho_1\cdots\hat\rho_{j-m}}\\ &\times\frac{t_h}{R^3}\int dz_h\sqrt{-g(z_h)}\overline{J}^{hh}_{l_1\cdots l_j}(g^{l_1s_1}\cdots g^{l_js_j})[\overline{A}^{0,0,m}_{s_1\cdots s_j}(z_h;\Delta,\nu)]^{\hat\sigma_1\cdots\hat\sigma_{j-m}},\end{aligned}\tag{147}$$

where $\overline{A}$ and $\overline{\overline{A}}$ are obtained from A by removing the factor $(2/\pi)\sqrt{[\nu\sinh(\pi\nu)/2R]}$ in (93) first, then replacing $K_{i\nu}(\Delta z_h)$ by "$K_{i\nu}(\Delta z_h)$" in $\overline{A}(z_h)$, while replacing $K_{i\nu}(\Delta z_\gamma)$ by $I_{i\nu}(\Delta z_\gamma)$ in $\overline{\overline{A}}(z_\gamma)$. Short distance (stringy) parameters such as AdS radius R and string length $\sqrt{\alpha'}$ can be eliminated from this expression of the Compton tensor so that it is written purely in terms of parameters of strongly coupled gauge theory/hadron physics;

$$\begin{aligned}(T^{\mu\nu}\epsilon^1_\mu\epsilon^{2*}_\nu)_{(j,j);(0,0,m)} \simeq{}& \frac{1}{j!}\frac{t_\gamma\sqrt{\lambda}}{t_y\pi}\left(\frac{1}{2\sqrt{\lambda}}\right)^j\int_{-\infty}^{+\infty}d\nu\frac{P^{(j-m)}_{\rho_1\cdots\rho_{j-m};\sigma_1\cdots\sigma_{j-m}}}{\frac{\mathcal{E}_{0,0}+c_y}{\sqrt{\lambda}}+N_{\rm eff}-i\epsilon}i\nu\\ &\times\int_0\frac{dz_\gamma}{z_\gamma}[A_p(z_\gamma;q_2)(-i\overleftrightarrow{\nabla})^j_{k_1\cdots k_j}A_q(z_\gamma;q_1)]\delta^{\hat p\hat q}z^j[\delta^{\hat k_1\hat r_1}\cdots\delta^{\hat k_j\hat r_j}][e^{(2-j)A}\overline{\overline{A}}^{0,0,m}_{r_1\cdots r_j}(z_\gamma;-\Delta,\nu)]^{\hat\rho's}\\ &\times t_h\int_0\frac{dz_h}{z_h^3}[\Phi(-i\overleftrightarrow{\nabla})^j_{l_1\cdots l_j}\Phi]z^j[\delta^{\hat l_1\hat s_1}\cdots\delta^{\hat l_j\hat s_j}][e^{(2-j)A}\overline{A}^{0,0,m}_{s_1\cdots s_j}(z_h;\Delta,\nu)]^{\hat\sigma's}.\end{aligned}\tag{148}$$

Each line of this expression has zero mass dimension, hence $T^{\mu\nu}$ is also of zero mass dimension, as expected from the Fourier transform of the matrix element (139).

The leading twist contribution to the Compton tensor $T^{\mu\nu}$ should be obtained by summing up the amplitudes of exchanging the spin-j field in the leading trajectory, with $m = 0,\ldots,j$ also being summed. It is known in the literature that, for each spin j, the second line of (149) becomes something close to the Wilson coefficient of the OPE, and the third line of (149) something close to the operator matrix element. We will elaborate more on it, with a particular emphasis on the role played by the summation over m. For now, we define

$$\begin{aligned}C^{0,0,m} :={}& \int_0\frac{dz}{z}\left[A_p(z;-q_2)(-i\overleftrightarrow{\nabla})^j_{k_1\cdots k_j}A_q(z;q_1)\right]\times\left[\frac{(2\Lambda)^{i\nu-j}}{\Delta^{i\nu}}\Gamma(i\nu+1)\right]\\ &\times\delta^{\hat p\hat q}z^j\left[\delta^{\hat k_1\hat r_1}\cdots\delta^{\hat k_j\hat r_j}\right]\left[e^{(2-j)A}\overline{\overline{A}}^{0,0,m}_{r_1\cdots r_j}(z;-\Delta,\nu)\right]^{\hat\rho_1\cdots\hat\rho_{j-m}}\epsilon^{(0,0,m)}_{\rho_1\cdots\rho_{j-m}}\end{aligned}$$

and

$$\Gamma^{0,0,m} := t_h\int_0^{1/\Lambda}\frac{dz}{z^3}\left[\Phi(-i\overleftrightarrow{\nabla})^j_{l_1\cdots l_j}\Phi\right]z^j\times\left[\left(\frac{\Delta}{2\Lambda}\right)^{i\nu}\frac{\Lambda^j}{\Gamma(i\nu)}\right]\times\left[\delta^{\hat l_1\hat s_1}\cdots\delta^{\hat l_j\hat s_j}\right]\left[e^{(2-j)A}\overline{A}^{0,0,m}_{s_1\cdots s_j}(z;\Delta,\nu)\right]^{\hat\sigma_1\cdots\hat\sigma_{j-m}}\epsilon^{(0,0,m)}_{\sigma_1\cdots\sigma_{j-m}}\tag{149}$$

separately. The factor $[\Gamma(i\nu+1)(2\Lambda)^{i\nu-j}/\Delta^{i\nu}]$ in $C^{0,0,m}$ and a similar factor in $\Gamma^{0,0,m}$ are introduced so that $C^{0,0,m}$ and $\Gamma^{0,0,m}$ correspond to the OPE Wilson coefficients and hadron matrix elements, respectively, renormalized at $\mu_F \sim \Lambda$, as we will see later.

We will focus on the spin-even contribution to a flavor-nonsinglet component of the structure function V_1 in (7). The V_1 structure function is picked up here, only because it is computed a little more easily than other structure functions. We will not touch flavor-singlet components in this article, apart from a brief discussion in Sec. VII C; this is because the cubic SFT with a Chan-Paton factor in Sec. IV is not an adequate tool to study the singlet components. The coefficient $C^{0,0,m}$ above is decomposed, just like $T^{\mu\nu}\epsilon^1_\mu\epsilon^{2*}_\nu$ is; the spin-j (with $j \in 2\mathbb{Z}$) contribution to the structure function $V_1^{+,\alpha}$—spin even (+) and flavor nonsinglet (α)—is denoted by $C^{0,0,m}_{V_1;+,\alpha}$.

2. Amplitude of the ($m = 0$)-mode exchange

We first study $V_1^{+,\alpha}$ from the $m = 0$-mode exchange. With the Reggeon wave function given by $\Psi^{(j);0,0}_{i\nu;0,0,0}(t,z) = \Psi^{(j)}_{i\nu}(t,z)$ in (93), this $m = 0$ contribution is expected to be the closest to what has been studied in the literature (such as [3,4,6,7]). Indeed, we reproduce the expression known in the literature, but with a little refinement, in (163).

Note first that the Reggeon wave functions $\overline{\overline{A}}^{0,0,m=0}_{r_1\cdots r_j}$ and $\overline{A}^{0,0,m=0}_{s_1\cdots s_j}$ are nonzero only when all the r_i's and s_i's are in the $3+1$ Minkowski directions $(r_1\cdots r_j) = (\rho_1\cdots\rho_j)$ and $(s_1\cdots s_j) = (\sigma_1\cdots\sigma_j)$; furthermore, the wave function is 4D-transverse and 4D-traceless totally symmetric tensors of SO(3,1).

This makes it much easier to evaluate the matrix element $\Gamma^{0,0,m=0}$. Because

$$(\nabla^k\Phi)_{\sigma_1\cdots\sigma_k} = \partial_{\sigma_1}\cdots\partial_{\sigma_k}\Phi + [\text{terms proportional to}\,\eta_{\sigma_a\sigma_b}], \tag{150}$$

only

$$\begin{aligned}[\Phi(z;p_1)(-i\overleftrightarrow{\nabla})^j\Phi(z;-p_2)]_{\sigma_1\cdots\sigma_j} &:= \sum_{k=0}^{j} {}_jC_k[(i\nabla)^{j-k}\Phi(z;p_1)]_{\sigma_{k+1}\cdots\sigma_j}[(-i\nabla)^k\Phi(z,-p_2)]_{\sigma_1\cdots\sigma_k}\\ &\to (-1)^j(p_1+p_1)_{\sigma_1}\cdots(p_1+p_2)_{\sigma_j}\Phi(z;p_1)\Phi(z;-p_2)\end{aligned} \tag{151}$$

contributes to $\Gamma^{0,0,m=0}$:

$$\Gamma^{0,0,m=0} = \left[\epsilon^{(0,0,0)}_{\sigma_1\cdots\sigma_j}(-1)^j(p_1+p_2)^{\hat\sigma_1}\cdots(p_1+p_2)^{\hat\sigma_j}\right]\overline{g}^{0,0,0}(j,i\nu,\Delta), \tag{152}$$

$$\overline{g}^{0,0,0}(j,i\nu,\Delta) := \int_0^{1/\Lambda}\frac{dz}{z^3}(\Lambda z)^j t_h(\Phi(z;m_h))^2\frac{\{\text{“}K_{i\nu}(\Delta z)\text{”}\}}{[(\frac{\Delta}{2\Lambda})^{-i\nu}\Gamma(i\nu)]}; \tag{153}$$

note here that the confinement effect has been included in the form of (i) introducing a cut in the holographic radius $z_h \le 1/\Lambda$ and (ii) $K_{i\nu}(\Delta z_h)$ is modified to $K_{i\nu}(\Delta z_h)$ in (123). The expression of $\overline{g}^{0,0,0}$ here, or that of $\Gamma^{0,0,m}$ in (149), implicitly ignores the possibility of $\mathcal{L}_{\text{bdry}} \neq 0$. For practical purposes, though, this may not be a big deal, since Ref. [6] reports that such confinement effects do not play a significant role quantitatively for most of the kinematical region.

Let us also evaluate the Wilson coefficient $C^{0,0,m=0}$. The expression

$$[A_p(z;-q_2)(-i\overleftrightarrow{\nabla})^jA_q(z;q_1)_q]_{\rho_1\cdots\rho_j}\delta^{\hat p\,\hat q} := \sum_{k=0}^{j}{}_jC_k[(i\nabla)^{j-k}A(z;-q_2)]_{\rho_{k+1}\cdots\rho_j p}[(-i\nabla)^kA(z;q_1)]_{\rho_1\cdots\rho_k q}\delta^{\hat p\,\hat q} \tag{154}$$

appearing in $C^{0,0,m=0}$ can be evaluated by using the fact that

$$(\nabla^kA)_{\rho_1\cdots\rho_k\kappa} \equiv (\partial_{\rho_1}\cdots\partial_{\rho_k}A_\kappa) - \sum_{a=1}^{k}\frac{\eta_{\mu_a\kappa}}{z}(\partial_{\rho_1}\cdots\check\partial_{\rho_a}\cdots\partial_{\rho_k}A_z) - \sum_{1\le a<b\le k}\frac{\eta_{\rho_a\kappa}}{z^2}(\partial_{\rho_1}\cdots\check\partial_{\rho_a}\cdots\check\partial_{\rho_b}\cdots\partial_{\rho_k}A_{\rho_b}), \tag{155}$$

$$(\nabla^kA)_{\rho_1\cdots\rho_k z} \equiv (\partial_{\rho_1}\cdots\partial_{\rho_k}A_z) + \frac{1}{z}\sum_{a=1}^{k}(\partial_{\rho_1}\cdots\check\partial_{\rho_a}\cdots\partial_{\rho_k}A_{\rho_a}) \tag{156}$$

modulo terms proportional to $\eta_{\rho_c\rho_d}$. As we will focus only on the structure function $V_1^{+,\alpha}$, we can further drop the terms with A_z in (155), (156). Then the expression above becomes

$$\begin{aligned}&[\eta^{\mu\nu}\epsilon^1_\mu\epsilon^{2*}_\nu](q_1+q_2)_{\rho_1}\cdots(q_1+q_2)_{\rho_j}\\ &+\frac{2}{z^2}\sum_{a\neq b}\epsilon(-q_2)_{\rho_a}\epsilon(q_1)_{\rho_b}(q_1+q_2)_{\rho_1}\cdots_{\check\rho_a\check\rho_b}\cdots(q_1+q_2)_{\rho_j}\end{aligned} \tag{157}$$

multiplied by $[(q_1z)K_1(q_1z)][(q_2z)K_1(q_2z)]$.

There are two remaining tasks in evaluating the $(m=0)$-mode contribution to the $V_1^{+,\alpha}$ structure function: (a) one is to carry out the z_γ integral and (b) the other is to sum $C^{0,0,0}\Gamma^{0,0,0}$ for different polarizations of $\epsilon^{(0,0,0)}$. As for the z_γ integral, the integrand sharply falls off[28] at $z_\gamma \approx q^{-1}$ because of the photon wave functions of the form $[(q_i z)K_{i\nu}(q_i z)]$. The z_γ integral in $C^{0,0,m}$ over the holographic radius $z_\gamma \in [0,\Lambda^{-1}]$ therefore comes mainly from a very small fraction of it, $\Lambda/q \ll 1$, in the regime of generalized Bjorken scaling (143). It is then all right to make an approximation that

$$I_{i\nu}(\Delta z_\gamma) \approx \frac{1}{\Gamma(i\nu+1)}\left(\frac{\Delta z_\gamma}{2}\right)^{i\nu}[1+\mathcal{O}(\Delta/q)] \quad \text{when } (\Delta z_\gamma) \lesssim \Delta/q \ll 1, \tag{158}$$

and also to replace the range of integral $z_\gamma \in [0,\Lambda^{-1}]$ to $[0,+\infty)$, as in the literature; the error caused by this approximation is only in the higher order in (Δ/q), and the twist-$(2+\gamma(j))$ contribution is still obtained properly. The integral is then cast into the form of (B1) with $\delta = j+i\nu$ for the first line of (157) [respectively $\delta = j+i\nu-2$ for the second line of (157)] and $\vartheta = \eta/x$; thus we can use the analytic expression (B3), (B5) in the Appendix.

The other task, (b) tensor computations, is carried out in Appendix A.6. Using the results of (A77) and (A81), one finds that the contribution to $(C^{0,0,0}_{V_1;+,\alpha})_{m=0}$ from the second line of (157) is roughly

$$\frac{q^2\Delta^2}{(q\cdot\Delta)(p\cdot q)} \ll 1 \tag{159}$$

times smaller than the contribution from the first line of (157) in the generalized Bjorken scaling regime (143), and hence it is ignored, when only the twist-$[2+\gamma(j)]$ contributions are retained.

Combining all of the above, the spin-$j \in 2\mathbb{Z}$ contribution is

$$(V_1^{+,\alpha})_{j,m=0} \approx \frac{\sqrt{\lambda}}{\Gamma(j+1)\pi}\frac{t_\gamma}{t_y}\int_{-\infty}^{+\infty} d\nu \frac{1}{\frac{4+j+\nu^2+c_j}{\sqrt{\lambda}}+j-1-i\epsilon} \times C_1(j+i\nu,\vartheta)\left(\frac{\Lambda}{q}\right)^{i\nu-j} \times \left(\frac{1}{\sqrt{\lambda}x}\right)^j \overline{g}^{0,0,0}(j,i\nu,\Delta)\hat{d}_j([\eta]), \tag{160}$$

where C_1 is given in (B5) and $\hat{d}_j$ is a polynomial of degree j in the argument

$$[\eta] := \eta \times \sqrt{\frac{-4p^2}{\Delta^2}} = \eta\sqrt{\frac{4m_h^2+\Delta^2}{\Delta^2}} \tag{161}$$

and is given in terms of Legendre polynomial, as in (A79).

Now that all of the factors of the spin-j contribution to $V_1^{+,\alpha}$ are given as analytic functions of j, it is possible to convert the sum over the (spin-$j \in 2\mathbb{N}$) string states in the leading trajectory to a contour integral in the complex angular momentum plane:

$$(V_1^{+,\alpha})_{m=0} = -\int \frac{dj}{4i}\frac{1+e^{\pi i j}}{\sin(\pi j)}(V_1^{+,\alpha})_{j,m=0}, \tag{162}$$

with the contour in the j plane moving just below the real positive axis toward the left, and then just above the real positive axis toward the right. The integration contour in the ν plane is deformed so that it picks up the residue of the pole in the lower complex ν plane coming from the t-channel propagation of strings. Thus,

$$(V_1^{+,\alpha})_{m=0} \approx -\int \frac{dj}{4i}\frac{1+e^{\pi i j}}{\sin(\pi j)}\frac{t_\gamma/t_y}{\Gamma(j+1)}\frac{\lambda}{i\nu_j} \times C_1\left(j+i\nu_j,\frac{\eta}{x}\right)\left(\frac{\Lambda}{q}\right)^{\gamma(j)} \times \left(\frac{1}{\sqrt{\lambda}x}\right)^j \overline{g}^{0,0,0}(j,i\nu_j,\Delta)\hat{d}_j([\eta]), \tag{163}$$

where $\gamma(j) = i\nu_j - j$ and $i\nu_j \geq 0$ is a function of j determined by the on-shell condition

$$j-1+\frac{4+j+\nu^2+c_j}{\sqrt{\lambda}} = 0. \tag{164}$$

This is the result known in [2–7], etc.; under an assumption that $\overline{g}^{0,0,0}(j,i\nu_j,\Delta)$ does not grow too rapidly for a large $\mathrm{Re}(j)$ to cancel the large factor $\Gamma(j+1)$ in the denominator, the integration contour in the j plane can be deformed toward the left in the j plane, as in the classical Watson-Sommerfeld transformation; this is how the non-converging $j \in 2\mathbb{N}$ sum of the OPE is rendered well defined for physical kinematics $x<1$. The integrand forms a saddle point due to the two factors $(1/x)^j$ and $(\Lambda/q)^{\gamma(j)}$;

[28] In DVCS, VMP, and TCS, the incoming photon has spacelike momentum q_1, although the outgoing photon may be either on shell or timelike. The sharp cutoff in the z_γ integral comes from the wave function of the incoming photon. Since the wave function of the outgoing photon remains a Hankel function even for VMP and TCS, rather than $I_{i\nu}(qz_\gamma)$, the approximation of replacing the integration interval $z_\gamma \in [0,\Lambda^{-1}]$ by $z_\gamma \in [0,\infty)$ remains valid. In such applications, $\vartheta > 1$, and the expressions (B1) and (B5) should be understood through analytic continuation. The authors thank the Physical Review D referee for bringing this issue to our attention.

let j_* in the complex j plane be where the saddle point is.[29] The integrand also has poles in the j plane. The hadron matrix element $\overline{g}^{0,0,0}$ contains $c^{(j)}_{i\nu_j;0,0,0}$ in its definition, and $c^{(j)}_{i\nu;0,0,0}$ may have a pole in the j plane [3].[30] The saddle point value j_* has a larger real part than any one of the poles, where $\ln(q/\Lambda)$ is large relatively to $\ln(1/x)$; the j integral is well approximated by the saddle point value of the integrand and yields the DGLAP regime. When $\ln(1/x)$ is large relatively to $\ln(q/\Lambda)$, however, one of the poles may have a real part larger than $\mathrm{Re}(j_*)$. Then the integral is approximated by the residue at such a leading pole. In this way, the string-theory result $(V_1^{+,\alpha})_{m=0}$ goes back and forth between the DGLAP phase and Regge phase, depending on the kinematical variables x, (q^2/Λ^2) and $t=-\Delta^2$ [3,7].

The derivation of (163) was not just a review of preceding works, however. First, the integration over z_γ yields a function $C_1(j+i\nu_j,\eta/x)$, which has precisely the same form as the one expected from the conformal OPE; comparing (25), (26) and (B3), (B5), one finds that they agree, under the identification

$$[(l_n+j_n-2)=2j_n+(\tau_n-2)]\Leftrightarrow[(j+i\nu_j)=2j+\gamma(j)]. \tag{165}$$

The expression (163) is indeed regarded as conformal OPE contributions from twist-$\tau_n=(2+\gamma(j))$ operators.

Second, the η dependence of the $m=0$ contribution is now worked out. As we will see later in Sec. VII, it comes in a form that fits very well with what has been known as dual parametrization of GPD [15]. One will also notice that the argument of the degree-j polynomial $\hat{d}_j([\eta])$ is $[\eta]$ in (161), rather than η. This means that the coefficients of the η^2 term and higher diverge in the $t=-\Delta^2\to 0$ limit. This indicates that it is essential to sum the $m\neq 0$ modes to obtain results that are physically sensible. We will address this issue in Sec. VII A.

We have considered amplitudes from a t-channel exchange of states that (a) are in the leading trajectory and (b) have 5D-traceless and 5D-transverse polarizations, and that have used the prescription (52), so that we obtained the contributions that correspond to the twist-$[2+\gamma(j)]$ operators in the conformal OPE. When the amplitudes with a t-channel exchange of other modes are included, cancellation due to BRST symmetry is at work among some of them, but other physical contributions remain. Computation of those contributions will shed a light on the higher twist contributions to the DVCS amplitudes. To do this, however, we need wave functions of modes other than the $(n,l,m)=(0,0,m)$ modes, and detailed knowledge on the interaction terms in the string field theory more than (130), (131); furthermore, the prescription (52)—the process carried out just before Sec. VI C 1—becomes more complicated for modes other than the $(0,0,m)$ modes. After all of this, one then has to work out which operators in QCD correspond to which group of modes in the t-channel exchange in the gravity dual calculation. Although this is an interesting question, we do not address that problem in this article.

3. Preparation

Let us move on to the amplitudes of $m\geq 1$-mode exchange. We begin with deriving a few general properties of those amplitudes, which makes the subsequent computations less tedious.

First, we observe that the hadron matrix element $\Gamma^{0,0,m}$ vanishes for any odd value of m. To see that this statement is true, we use the following property of $J^{hh}_{l_1\cdots l_j}$:

$$\begin{aligned}&\Phi(z,p_1)\overleftrightarrow{\nabla}_{\{l_1}\cdots\overleftrightarrow{\nabla}_{l_j\}}\Phi(z,-p_2)\\&\quad=(-1)^j\Phi(z,-p_2)\overleftrightarrow{\nabla}_{\{l_1}\cdots\overleftrightarrow{\nabla}_{l_j\}}\Phi(z,p_1);\end{aligned} \tag{166}$$

this is true in a process where the initial state hadron $h(p_1)$ continues to be the same hadron $h(p_2)$ in the final state, so that $-(p_1)^2=-(p_2)^2=m_h^2$. This property is used below to study when $J^{hh}_{z^k\lambda_{k+1}\cdots\lambda_j}\overline{A}^{z^k\lambda_{k+1}\cdots\lambda_j}$ vanishes for various $k=0,\ldots,m$.

For an even j, the SO(3,1) indices of $J^{hh}_{z^k\lambda_{k+1}\cdots\lambda_j}$ are provided by an even number of $(p_1+p_2)_\lambda$'s and even (respectively odd) number of Δ_λ's when k is even (respectively odd). The hadron matrix element $\Gamma^{0,0,m}$ receives a nonvanishing contribution from $J^{hh}_{z^k\lambda_{k+1}\cdots\lambda_j}\overline{A}^{z^k\hat{\lambda}_{k+1}\cdots\hat{\lambda}_j}$ (no sum in k) only when the D operator (71) is used for an even (respectively odd) number of times in the Reggeon wave function (89). This means that s is even (respectively odd), and hence $\Gamma^{0,0,m}$ can be nonzero only when $m=k+s$ is even.

For an odd j, the SO(3,1) indices of $J^{hh}_{z^k\lambda_{k+1}\cdots\lambda_j}$ are provided by an odd number of $(p_1+p_2)_\lambda$'s and an even (respectively odd) number of Δ_λ's when k is even (respectively odd). Thus, the matrix element $\Gamma^{0,0,m}$ receives a nonzero contribution only when an even (respectively odd) number of the D operator is used in (89). This means, once again, that s is even (respectively odd), and hence $\Gamma^{0,0,m}$ can be nonzero only when $m=k+s$ is even. This statement for an odd j is not more than a side remark, though, since we focus on the spin-even contribution $\propto[1+e^{-\pi ij}]/\sin(\pi j)$ in this article.

[29]The saddle point value j_* is determined by $\frac{\partial\gamma(j)}{\partial j}\big|_{j=j_*}=\frac{\ln(1/x)}{\ln(q/\Lambda)}$.

[30]For example, imagine a case $(1-c^{(j)}_{i\nu;0,0,0})=[I_{-i\nu}(\Delta/\Lambda)/I_{i\nu}(\Delta/\Lambda)])$; the factor $c^{(j)}_{i\nu_j;0,0,0}$ has poles $j=\alpha_{\mathbb{R},n}(t)$ $(n=1,2,\ldots)$ in the j plane given by the condition $j_{i\nu_j,n}=\sqrt{t}/\Lambda$; $j_{\mu,n}$'s are the nth zero of the Bessel function J_μ.

Second, $\Gamma^{0,0,m}$ can always be written in the form of

$$\Gamma^{0,0,m} = [(-2)^{j-m}(p^{\hat{\sigma}_1}\cdots p^{\hat{\sigma}_{j-m}})\cdot \epsilon^{(0,0,m)}_{\sigma_1\cdots\sigma_{j-m}}] \times \overline{g}^{0,0,m}(j, i\nu, \Delta^2), \tag{167}$$

and $\overline{g}^{0,0,m}$ is an SO(3,1) scalar of mass dimension m; we have encountered a special case of this statement in (152), (153). This statement itself is understood as follows. When we write down the covariant derivatives in $\overline{J}^{hh}_{z^k\lambda_1\cdots\lambda_{j-k}}$ explicitly, the SO(3,1) indices—there are $(j-k)$ of them—are one of either p_λ, Δ_λ, and $\eta_{\lambda\lambda'}$; $\eta_{\lambda\lambda'}$ can be further rewritten as $\eta_{\lambda\lambda'} - \Delta_\lambda\Delta_{\lambda'}/\Delta^2$ and $\Delta_\lambda\Delta_{\lambda'}$. Suppose that there are N_p of the SO(3,1) indices from $\{p_\lambda\}$'s, N_Δ indices from $\{\Delta_\lambda\}$'s, and $N_{\tilde{\eta}}$ from $\tilde{\eta}_{\lambda\lambda'}$'s in a given term; $N_p + N_\Delta + 2N_{\tilde{\eta}} = (j-k)$. When such an SO(3,1) tensor is contracted with $\sum_N^{[(m-k)/2]} \tilde{E}^N D^{m-k-2N}[\epsilon^{(0,0,m)}]$ in the Reggeon wave function $\overline{A}^{0,0,m}_{z^k\lambda_1\cdots\lambda_{j-k}}$, it remains nonzero only when $(m-k-2N) = N_\Delta$ and $N \geq N_{\tilde{\eta}}$ because of the relation (A37). It is not hard now to see that all of the remaining terms are proportional to the prefactor of $\overline{g}^{0,0,m}$ in (167); the mass dimension of the remaining scalar factor (the reduced matrix element) $\overline{g}^{0,0,m}$ follows from the fact that $\Gamma^{0,0,m}$ is defined to be of mass dimension j.

Finally, we note that the twist-$[2+\gamma(j)]$ contribution to the coefficient $C^{0,0,m}$ arises only from the contraction $\overline{J}^{\gamma\gamma}_{z^k\kappa_{k+1}\cdots\kappa_j}\overline{\overline{A}}^{z^k\hat{\kappa}_{k+1}\cdots\hat{\kappa}_j}$, with $k=0$. We have already seen an example of this in the $m=0$ amplitude; the first term of (157) contributes to (163), while the second term does not because of (159), and the first term came from the $k=0$ contraction.

In order to verify the claim above, note first that both an extra ∂_z and an extra power of $1/z$ virtually change the integral of $C^{0,0,m}$ by about an extra power of $q \sim q_1 \sim q_2 \gg \Lambda, \Delta$. Explicitly writing down covariant derivatives in $\overline{J}^{\gamma\gamma}_{z^k\kappa_1\cdots\kappa_{j-k}}$ and evaluating the integrals only by the order of magnitudes, one can see that

$$(C^{0,0,m}_{V_1;+,\alpha})_k \sim \sum_M^{[\frac{j-k}{2}]} \left(\frac{\Lambda}{q}\right)^{i\nu-j} \frac{q^{k+2M}}{(q^2)^j}\left[\overbrace{(q_\kappa\cdots q_\kappa)}^{j-k-2M}(\eta_{\kappa\kappa}q^2)^M\right] \cdot \sum_N^{[\frac{s}{2}]} \frac{1}{\Delta^{s-2N}}\tilde{E}^N D^{s-2N}[\epsilon^{(0,0,m)}]. \tag{168}$$

The $M=0$ contribution above is further evaluated by using the definition of $\tilde{E}$ and D operators. Details of computation are found partially in (A82); we find that

$$(C^{0,0,m}_{V_1;+,\alpha})_{k,M=0} \sim \left(\frac{\Lambda}{q}\right)^{i\nu-j} \frac{\overbrace{(q_\kappa\cdots q_\kappa)}^{j-m}\epsilon^{(0,0,m)}}{(q^2)^j}\left(\frac{(q\cdot\Delta)}{\Delta}\right)^s q^k. \tag{169}$$

Keeping the relation $m = k+s$ and also the result (167) in mind, we obtain

$$C^{0,0,m}_{k,M=0}\cdot\Gamma^{0,0,m} \sim \left(\frac{\Lambda}{q}\right)^{i\nu-j}\frac{(q\cdot p)^{j-m}}{(q^2)^j}\left(\frac{(q\cdot\Delta)}{\Delta}\right)^s q^k \times \overline{g}^{0,0,m} \sim \left(\frac{\Lambda}{q}\right)^{i\nu-j}\left(\frac{1}{x}\right)^j \eta^{m-k}\left(\frac{(q^2)(\Delta^2)}{(q\cdot p)^2}\right)^{\frac{k}{2}}\frac{\overline{g}^{0,0,m}}{\Delta^m}. \tag{170}$$

Therefore, this is regarded as a twist-$[2+\gamma(j)+k/2]$ contribution in the generalized Bjorken scaling regime. Thus, only the $k=0$ term remains a twist-$[2+\gamma(j)]$ contribution, and the terms with $k>0$ are irrelevant to GPD.

The analysis becomes a little more complicated when $M>0$ terms are also included, but not in an essential way. Contributions with some (k,M) correspond to twist-$(2+\gamma+M+k/2)$, and only the $k=M=0$ terms contribute to GPD. This means that $C^{0,0,m}$ can be evaluated under the following approximation:

$$[A_p(z;-q_2)(-i\overleftrightarrow{\nabla})^j A_q(z;q_1)]^{\hat{m}_1\cdots\hat{m}_j}\delta^{\hat{p}\,\hat{q}}\overline{\overline{A}}_{m_1\cdots m_j} \to [A_\mu(z;-q_2)(-i\overleftrightarrow{\partial})^j A_\nu(z;q_1)]^{\hat{\kappa}_1\cdots\hat{\kappa}_j}\eta^{\mu\nu}\overline{\overline{A}}_{\kappa_1\cdots\kappa_j}. \tag{171}$$

4. Wilson coefficients, conformal OPE and hadron matrix elements

The twist-$[2+\gamma(j)]$ contribution to $C^{0,0,m}_{V_1;+,\alpha}$ can be determined completely, using the approximations above.

$$C^{0,0,m}_{V_1;+,\alpha} \simeq \left(\frac{2\Lambda}{\Delta}\right)^{i\nu}\frac{\Gamma(i\nu+1)}{(2\Lambda)^j}\int\frac{dz}{z}[(q_1z)K_1(q_1z)][(q_2z)K_1(q_2z)]z^j \times \sum_{N=0}^{[\frac{m}{2}]}[2^j(q^{\hat{\rho}_1}\cdots q^{\hat{\rho}_j})\cdot\tilde{E}^N D^{m-2N}[\epsilon^{(0,0,m)}]_{\rho_1\cdots\rho_j}]\frac{b^{(j-m)}_{m,N}}{\Delta^{m-2N}}[e^{(2-j)A}\overline{\overline{\Psi}}^{(j);m,N}_{i\nu;0,0,m}]. \tag{172}$$

The product of rank-j SO(3,1) tensors in the second line is reduced to a product of rank-$(j-m)$ tensors by the computation in (A82). The Reggeon wave function $\overline{\overline{\Psi}}$ is also rewritten by using the small $(\Delta z_\gamma) \lesssim (\Delta/q)$ approximation (158):

$$[e^{(2-j)A}\overline{\overline{\Psi}}^{(j);m,N}_{i\nu;0,0,m}] \simeq \sum_{a=0}^{N}(-1)^a {}_N C_a(\zeta^{j+1}\partial_\zeta^{m-2a}[\zeta^{-1-j+m}(\zeta/2)^{i\nu}])_{\zeta\to(\Delta z)}\frac{N_{j,m}}{\Gamma(i\nu+1)}. \tag{173}$$

The $a=0$ term in this expression has the lowest dimension in $\zeta = \Delta z_\gamma \lesssim (\Delta/q)$, and hence we only need to retain the $a=0$ term for a given N for the twist-$[2+\gamma(j)]$ contribution. Thus,

$$[e^{(2-j)A}\overline{\overline{\Psi}}^{(j);m,N}_{i\nu;0,0,m}] \simeq 2^{-i\nu}\frac{(-1)^m\Gamma(j+1-i\nu)}{\Gamma(j+1-i\nu-m)}(\Delta z_\gamma)^{i\nu}\frac{N_{j,m}}{\Gamma(i\nu+1)}. \tag{174}$$

Using this expression and (A82) in (172), we obtain

$$\begin{aligned} C^{0,0,m}_{V_1;+,\alpha} &\simeq \frac{\Lambda^{i\nu-j}}{q^{i\nu+j}}\frac{j!}{(j-m)!}\sum_{N=0}^{[m/2]}\left[\frac{(q\cdot\Delta)^2}{\Delta^2}\right]^N(-i)^m\frac{(q\cdot\Delta)^{m-2N}}{\Delta^{m-2N}}b^{(j-m)}_{m,N}[(q_{\mu_1}\cdots q_{\mu_{j-m}})\cdot\epsilon^{(0,0,m)}] \\ &\quad\times\int\frac{dz}{z}[(q_1z)K_1(q_1z)][(q_2z)K_1(q_2z)](qz)^{j+i\nu}\frac{(-1)^m\Gamma(j+1-i\nu)}{\Gamma(j+1-i\nu-m)}N_{j,m}, \end{aligned} \tag{175}$$

$$\begin{aligned} &= \left(\frac{\Lambda}{q}\right)^{i\nu-j}\frac{[(q_{\mu_1}\cdots q_{\mu_{j-m}})\cdot\epsilon^{(0,0,m)}]}{(q^2)^j}\frac{(q\cdot\Delta)^m}{\Delta^m}C_1\left(j+i\nu,\frac{\eta}{x}\right) \\ &\quad\times i^m\frac{j!}{(j-m)!}N_{j,m}\frac{\Gamma(j+1-i\nu)}{\Gamma(j+1-i\nu-m)}\left(\sum_{N=0}^{[m/2]}b^{(j-m)}_{m,N}\right), \end{aligned} \tag{176}$$

$$\begin{aligned} &= \left(\frac{\Lambda}{q}\right)^{i\nu-j}\frac{[(q_{\mu_1}\cdots q_{\mu_{j-m}})\cdot\epsilon^{(0,0,m)}]}{(q^2)^j}\frac{(q\cdot\Delta)^m}{\Delta^m}C_1\left(j+i\nu,\frac{\eta}{x}\right) \\ &\quad\times i^m\frac{\Gamma(j+1+i\nu-m)}{N_{j,m}\Gamma(j+1+i\nu)}, \end{aligned} \tag{177}$$

where (B1), (B5) is used for the equality in the middle, while (A67) is used for the last one.

Repeating the same argument as in Sec. VI C 2, we thus arrive at

$$\begin{aligned} (V_1^{+,\alpha})_m &\simeq -\int\frac{dj}{4i}\frac{1+e^{-\pi ij}}{\sin(\pi j)}\frac{t_\gamma/t_y}{\Gamma(j+1)}\frac{\lambda}{i\nu_j}C_1(j+i\nu_j)\left(\frac{\Lambda}{q}\right)^{\gamma(j)} \\ &\quad\times\left(\frac{1}{\sqrt{\lambda}x}\right)^j\eta^m\hat{d}_{j-m}([\eta])\frac{\overline{g}^{0,0,m}}{\Delta^m}\frac{i^m}{N_{j,m}} \\ &\quad\times\frac{\Gamma(j+1+i\nu-m)}{\Gamma(j+1+i\nu)}; \end{aligned} \tag{178}$$

the computation in (A77), (A79) for an even j and m was used once again. Similar to the case of the $m=0$ amplitude, this expression is in the form of the conformal OPE and inverse Mellin transformation in (20). It should be noted that the integrand can be defined as a holomorphic function of j (apart from poles and cuts), using the definition of C_1 in (B1) and that of $\hat{d}_{j-m}$ in (A79), not just for an integer-valued j; at the same time, $\eta^m\hat{d}_{j-m}([\eta])$ becomes a polynomial of η of degree j for $j\in 2\mathbb{N}$, which is one of the important properties expected for the hadron matrix element [9].

The integration contour of (178) is chosen so that it circles around the pole at $j=m$ after running just below the real positive axis in the j plane and before running just above the real positive axis. Only spin-j stringy states with $m\le j$ contribute then. It is not obvious whether the contour can be deformed so that it encircles $j=0,2,\ldots,m$ without changing $(V_1^{+,\alpha})_m$, and we leave it an open question. $\hat{d}_{j-m}$ in (178) is given by a Legendre polynomial of degree $(j-m)$ when $j-m$ is an even positive integer, but otherwise it is defined by the hypergeometric function, as in (A79), and it may or may not have a zero at negative even integer $(j-m)$ so that the pole from $\sin(\pi j)$ is canceled. Similarly, $\overline{g}^{0,0,m}(j,i\nu_j,\Delta)/N_{j,m}$ may or may not have a zero at negative integer $(j-m)$. The authors have not found a reason to believe that they have a zero, but we may be wrong.

The twist-$[2+\gamma(j)]$ contribution to the structure function $V_1^{+,\alpha}$ is obtained by summing $(V_1^{+,\alpha})_m$ from the $(n,l,m)=(0,0,m)$ modes with $m=0,2,\ldots$:

$$V_1^{+,\alpha} = \sum_{m=0,2,\ldots}^{\infty}(V_1^{+,\alpha})_m. \tag{179}$$

Combining (163), (178) with (179), a holographic version of (20) is obtained. It is not obvious, though, whether or not the integration variable j in (178) for all the different m's should be identified. If we are to define $j' \coloneqq (j-m)$ and use it as a new variable of integration, then the integration contour of (178) would be the same for all different m's; the cost of doing so, however, is this:

$$C_1(j+i\nu_j,\vartheta)\left(\frac{\Lambda}{q}\right)^{\gamma(j)}\frac{1}{x^j}\eta^m\hat{d}_{j-m} = [C_1(j'+m+i\nu_{j'+m},\vartheta)\times\vartheta^m]\left(\frac{\Lambda}{q}\right)^{\gamma(j'+m)}\frac{1}{x^{j'}}\hat{d}_{j'}. \tag{180}$$

Certainly $\hat{d}_{j'}$ still remains to be a polynomial of degree at most j', but the expression no longer fits into the form of conformal OPE. For this reason, we identify the integration variable j in (178) for all $m=0,2,\ldots$ with that (complex angular momentum) of the inverse Mellin transformation (20). This implies that the reduced hadron matrix element of the spin-j primary operator is given a holographic expression

$$\overline{A}_j^{+,\alpha}(\eta,t) \propto \sum_{m=0}^{j}\frac{(-1)^{m/2}}{\sqrt{\lambda}^j\Gamma(j+1)}\frac{\overline{g}^{0,0,m}(j,i\nu_j,\Delta^2)}{N_{j,m}\Delta^m} \times\frac{\Gamma(j+1+i\nu_j-m)}{\Gamma(j+1+i\nu_j)}\times\eta^m\hat{d}_{j-m}([\eta]). \tag{181}$$

5. The $(m=2)$-mode hadron matrix element

Most aspects of the expression (178) are dictated by basic principles of field theory, such as (conformal) OPE. Additional information from the holographic setup is found primarily in the hadron matrix element $\overline{g}^{0,0,m}(j,i\nu,\Delta)$, apart from the anomalous dimension $\gamma(j)=i\nu_j-j$ of the twist-$[2+\gamma(j)]$ operators. Now we have seen that $\overline{g}^{0,0,0}(j,i\nu_j,\Delta)$ is not the only hadron matrix element contributing to the nonperturbative information of $h+\gamma^*\to h+\gamma^{(*)}$; let us take a moment here to have a closer look at one of the new hadron matrix elements we encounter, $\overline{g}^{0,0,2}(j,i\nu,\Delta)$.

The hadron matrix element $\Gamma^{0,0,m}$ receives contributions from $\overline{J}^{hh}_{z^k\lambda_{k+1}\cdots\lambda_j}\overline{A}^{\hat{z}^k\hat{\lambda}_{k+1}\cdots\hat{\lambda}_j}$'s, with $k=0,1,\ldots,m$. The contribution from each k can be written in the form of (167), and hence $(\overline{g}^{0,0,m}(j,i\nu,\Delta))_k$ is defined ($k\le m$). We compute $(\overline{g}^{0,0,2})_k$ explicitly for $k=0,1,2$.

For this purpose, we need the following technical results:

$$(\nabla^l\Phi)_{\lambda_1\cdots\lambda_l} \equiv (\partial_{\lambda_1}\cdots\partial_{\lambda_l}\Phi) - \sum_{1\le a<b\le l}\frac{\eta_{\lambda_a\lambda_b}}{z}\left(\partial_{\lambda_1}\cdots\underset{\tilde{\lambda}_a\tilde{\lambda}_b}{\cdots}\cdots\partial_{\lambda_l}\left(\partial_z+\frac{l-a-1}{z}\right)\Phi\right) \tag{182}$$

modulo terms proportional to $\eta_{\lambda_a\lambda_b}\eta_{\lambda_c\lambda_d}$ instead of (150), and

$$(\nabla^l\Phi)_{\lambda_1\cdots z\cdots\lambda_l} \equiv \left(\partial_z+\frac{l-1}{z}\right)\partial_{\lambda_1}\cdots\underset{\tilde{\lambda}_a}{\cdots}\cdots\partial_{\lambda_l}\Phi,$$
$$(\nabla^l\Phi)_{\lambda_1\cdots z\cdots z\cdots\lambda_l} \equiv \left[\left(\partial_z+\frac{l-1}{z}\right)\left(\partial_z+\frac{l-2}{z}\right)+\frac{a-1}{z^2}\right] \times\partial_{\lambda_1}\cdots\underset{\tilde{\lambda}_a\tilde{\lambda}_b}{\cdots}\cdots\partial_{\lambda_l}\Phi, \tag{183}$$

modulo terms proportional to $\eta_{\lambda_c\lambda_d}$.

It is now a straightforward computation to use the relations above as well as the explicit Reggeon wave functions $\overline{A}$ determined in Sec. V to derive the following:

$$\begin{aligned}
\frac{\overline{g}^{0,0,2}_{k=2}}{N_{j,2}\Delta^2} &= \frac{j(j-1)}{2}\int_0^{1/\Lambda}\frac{dz}{z^3}(\Lambda z)^j\frac{\{z^2\text{“}K_{i\nu}(\Delta z)\text{”}\}}{[(\frac{\Delta}{2\Lambda})^{-i\nu}\Gamma(i\nu)]}t_h\left[2\{-\Phi(\partial_z^2\Phi)+(\partial_z\Phi)^2\}-\frac{2}{z}\Phi(\partial_z\Phi)-\frac{4(j-2)}{3z^2}\Phi^2\right],\\
\frac{\overline{g}^{0,0,2}_{k=1}}{N_{j,2}\Delta^2} &= \frac{j(j-1)}{2}\int_0^{1/\Lambda}\frac{dz}{z^3}(\Lambda z)^j\frac{\{z^{j+1}\partial_z(z^{1-j}\text{“}K_{i\nu}(\Delta z)\text{”})\}}{[(\frac{\Delta}{2\Lambda})^{-i\nu}\Gamma(i\nu)]}\left[\frac{-2t_h}{z}\Phi^2\right],\\
\frac{\overline{g}^{0,0,2}_{k=0}}{N_{j,2}\Delta^2} &= j(j-1)\int_0^{1/\Lambda}\frac{dz}{z^3}(\Lambda z)^j\left(\frac{\{[z^{j+1}\partial_z^2z^{1-j}-(z\Delta)^2]\text{“}K_{i\nu}(\Delta z)\text{”}\}}{[(\frac{\Delta}{2\Lambda})^{-i\nu}\Gamma(i\nu)]}\times\left[\frac{p^2}{(j-\frac{1}{2})\Delta^2}t_h\Phi^2\right]\right.\\
&\quad\left.+\frac{\{-z^2\text{“}K_{i\nu}(\Delta z)\text{”}\}}{[(\frac{\Delta}{2\Lambda})^{-i\nu}\Gamma(i\nu)]}\times t_h\left[\frac{1}{z}\Phi(\partial_z\Phi)+\frac{j-2}{3z^2}\Phi^2\right]\right).
\end{aligned} \tag{184}$$

These results are used in the study below.

VII. A HOLOGRAPHIC MODEL OF GPD

The differential cross section of the DVCS process involves an integral of GPD; GPD needs to be parametrized first, and then the parameters are determined by fitting the data [10]. The idea of dual parametrization of GPD [15]—also known as collinear factorization approach [17,18]—is to expand the reduced hadron matrix element $\overline{A}_j^{+,\alpha}(\eta,t)$ as

$$\overline{A}_j^{+,\alpha}(\eta,t)=\sum_{m=0}^{j}\overline{\Gamma}_m^{+,\alpha}(j,t)\eta^m\times[\eta^{j-m}d_{j-m}(1/\eta)], \tag{185}$$

where $d_\ell(\cos\theta)$'s are polynomials of degree ℓ in the argument $(\cos\theta)$; Legendre polynomials, Gegenbauer polynomials, or Jacobi polynomials are used, depending on the helicity change of the target hadron h in the scattering process [9]. When the target hadron is a scalar, as in the study of this article, a Legendre polynomial is chosen for d_ℓ [15]. With no ambiguity introduced in the polynomials $d_{j-m}(x)$, $\overline{\Gamma}_m^{+,\alpha}(j,t)$'s are the fully general, yet nonredundant parametrization for the reduced hadron matrix element for GPD.

At the end of the study in the preceding sections, we arrived at a holographic model of GPD, with the reduced hadron matrix element given by (181) for the flavor-nonsinglet sector. String theory—the descendant of the dual resonance model—yields a result that fits straightforwardly with the format of the dual parametrization (185); this should not be a surprise, but rather must be something the authors of [15] have anticipated. With the string-theory implementation provided, one can now move forward; now

$$\overline{\Gamma}_m^{+,\alpha}(j,t)\sim(-1)^{m/2}\frac{\overline{g}^{0,0,m}(j,i\nu_j,\Delta)}{N_{j,m}\Delta^m} \tag{186}$$

can be computed using holographic backgrounds, independently from experimental data. Certainly the matrix elements $[\overline{g}^{0,0,m}/\Delta^m]$ will depend on holographic backgrounds to be used for computation, and predictions from individual holographic backgrounds should not be taken seriously at the quantitative level. But it is still worth looking closely into qualitative features of the holographic hadron matrix elements $\overline{g}^{0,0,m}/\Delta^m$ to learn nonperturbative aspects of $\overline{\Gamma}_m^{+,\alpha}(j,t)$.

A. $\Delta^2\to 0$ limit

As we have already remarked earlier in this article, the holographic result (181) is not precisely in the same form of parametrization as in (185); the argument of the polynomial $\hat{d}_{j-m}$ is $[\eta]$ as defined in (161), rather than η. This difference itself does not raise an issue immediately; $[\eta]$ is the same as η in the hard scattering regime, $\Delta^2\gg m_h^2$.

Let us study how the hadron matrix element behaves in the $t=-\Delta^2\to 0$ limit, however. The matrix element $\overline{g}^{0,0,0}(j,i\nu_j,\Delta)$ has already been studied in the literature and is known not to diverge or vanish in the $\Delta^2\to 0$ limit. The polynomial $\hat{d}_j([\eta])$ to be multiplied with this $\overline{g}^{0,0,0}(j,i\nu_j,\Delta)$, however, has diverging coefficients in all of the terms $\eta^2,\eta^4,\ldots$ except the η^0 term. Therefore, the $m=0$ contribution (163) alone does not have a physically reasonable behavior in the $\Delta^2\to 0$ limit. A natural expectation will be that the hadron matrix element $\overline{A}_j^{+,\alpha}(\eta,t)$ still has a reasonable behavior after summing up $m=0,2,\ldots,j$.

To get started, we focus on the η^2 term. It is generated from the $(m=0)$-mode exchange, and also from the $(m=2)$-mode exchange. There is a $(p^2)/\Delta^2$ factor both in $\overline{g}^{0,0,0}\times\hat{d}_j([\eta])|_{\eta^2}$ and $\overline{g}^{0,0,2}/\Delta^2\times\eta^2$, and hence both diverge in the $\Delta^2\to 0$ limit. When they are summed, however, the divergence may cancel, as we see in the following. Let us study the coefficient of the η^2 term

$$-\int\frac{dj}{4i}\frac{1+e^{-\pi ij}}{\sin(\pi j)}\left(\frac{\Lambda}{q}\right)^{i\nu-j}\left(\frac{1}{\sqrt{\lambda}x}\right)^{j}C_1\left(j+i\nu,\frac{\eta}{x}\right)\times\frac{\lambda}{i\nu_j}\frac{t_\gamma/t_y}{\Gamma(j+1)}\times\eta^2 \tag{187}$$

in the $\Delta^2\to 0$ limit, picking up a contribution to the integral $\overline{g}^{0,0,0}$ and $\overline{g}^{0,0,2}$ from the $I_{-i\nu}(\Delta z_h)$ component in $K_{i\nu}(\Delta z_h)$ first.[31] Then in that limit, the coefficient of the expression (187) becomes

$$\frac{p^2}{\Delta^2}\lim_{\Delta^2\to 0}\left[\overline{g}^{0,0,0}(j,i\nu_j,\Delta)\frac{j(j-1)}{(j-\frac{1}{2})}-\frac{\overline{g}^{0,0,2}(j,i\nu_j,\Delta)/(p^2)}{(j-1+i\nu_j)(j+i\nu_j)N_{j,2}}\right]+\mathcal{O}(\Delta^0). \tag{189}$$

The two terms in $\lim_{\Delta^2\to 0}[\cdots]$ cancel each other, as one can see by using the approximation in footnote 31. Thus, the η^2 term in $\overline{A}_j^{+,\alpha}(\eta,t)$ also has a finite limit value in the $\Delta^2\to 0$ limit.

It is quite likely, however, that the $I_{i\nu}(\Delta z)$ component in $K_{i\nu}(\Delta z)$ has just as important a contribution as the $I_{-i\nu}(\Delta z)$ component does in the $\Delta^2\to 0$ limit to the hadron matrix elements $\overline{g}^{0,0,0}$ and $\overline{g}^{0,0,2}$; the coefficient $(1-c^{(j)}_{i\nu;0,0,m})$ may behave as $(\Delta/\Lambda)^{-2i\nu}$ in the $\Delta^2\to 0$ limit. Because we have seen above that the divergence (p^2/Δ^2) cancels when only the $I_{-i\nu}(\Delta z)$ component is taken into account, the contributions from the $I_{i\nu}(\Delta z)$ should also have some cancellation mechanism. Using an approximation for the $I_{i\nu}(\Delta z)$ components in $K_{i\nu}(\Delta z)$ similar to the one in footnote 31, one finds that the (p^2/Δ^2) divergence cancels in the η^2 coefficient, if and only if

[31]The leading divergence in the $\Delta^2\to 0$ limit comes from

$$K_{i\nu}(\Delta z)\sim\left(\frac{\pi}{2}\right)\frac{I_{-i\nu}(\Delta z)}{\sin(\pi i\nu)}\simeq\left(\frac{\pi}{2}\right)\frac{(\Delta z/2)^{-i\nu}}{\sin(\pi i\nu)\Gamma(-i\nu+1)}=\frac{\Gamma(i\nu)}{2}(\Delta z/2)^{-i\nu}. \tag{188}$$

$$\lim_{\Delta^2/\Lambda^2\to 0}\left[\left(\frac{\Delta}{2\Lambda}\right)^{2i\nu}\left\{(1-c^{(j)}_{i\nu_j;0,0,0})-(1-c^{(j)}_{i\nu_j;0,0,2})\times\frac{(j-1-i\nu_j)(j-i\nu_j)}{(j-1+i\nu_j)(j+i\nu_j)}\right\}\right]=0. \tag{190}$$

The coefficients $c^{(j)}_{i\nu;0,0,m}$ are functions of Δ/Λ, rather than complex numbers. The discussion above shows that physically sensible implementations of the confining effect require one of the conditions above between the two functions $c^{(j)}_{i\nu;0,0,0}$ and $c^{(j)}_{i\nu;0,0,2}$.

The η^{2M} term with $M=2,\ldots,$ instead of the η^2 term in (187), also receives divergent contributions from amplitudes of the $(m=0,2,\ldots,2M)$-mode exchange. There will be an apparent divergence of order $(p^2/\Delta^2)^M$, $(p^2/\Delta^2)^{M-1},\ldots,(p^2/\Delta^2)$. The cancellation of divergence in the $\Delta^2\to 0$ limit will set M conditions on the $\Delta^2/\Lambda^2\to 0$ limit of $(1-c^{(j)}_{i\nu_j;0,0,2M})$.

In a phenomenological approach of implementing the confining effect, that is all we can say for now. With a little more of a model building mind-set, however, we can find some solutions to the conditions above. It is not hard to verify that the combination of

$$[\partial_z(\Psi^{(j);0,0}_{i\nu;0,0,0}(t,z))]|_{z\Lambda=1}=0,$$
$$[\partial_z(\Psi^{(j);2,0}_{i\nu;0,0,2}(t,z))]|_{z\Lambda=1}=0 \tag{191}$$

results in $c^{(j)}_{i\nu;0,0,0}$ and $c^{(j)}_{i\nu;0,0,2}$ satisfying the condition (190). It is tempting to generalize this and impose the boundary condition $\partial_z[\Psi^{(j);2M,0}_{i\nu;0,0,2M}]=0$ to determine $c^{(j)}_{i\nu;0,0,2M}$, though we do not know whether all of the m_h^2/Δ^2 divergences above are removed under this boundary condition. The top-down approach is much more authentic and well motivated than such a hand-waving and wishful approach, and we do not try to speculate beyond that; we use this implementation of the confining effect, (191), only to "get the feeling" in the numerical presentation in Sec. VII D.

B. Large Δ^2 behavior

Certainly the holographic model of GPD yields a result of the reduced hadron matrix element that fits perfectly with the dual parametrization. The holographic result, however, turns out to be a little more complicated than the models that have often been explored for the purpose of phenomenological fit of the DVCS data. An example of a model for phenomenological fit (see, e.g., [18]) was to introduce an ansatz that

$$\overline{\Gamma}^{+,\alpha}_m(j,t)=f_{j,m}\Sigma_{j-m}(t), \tag{192}$$

where only one $(t=-\Delta^2)$-dependent *function* is involved in the form of a "form factor" $\Sigma_{j-m}(t)$ for some spin $(j-m)$, and all the remaining nonperturbative information is reduced to some *numbers* $f_{j,m}\in\mathbb{R}$. The function $\Sigma_J(t)$ may also be parametrized by an ansatz like

$$\Sigma_J(t)=\frac{1}{J-\alpha_0-\alpha'_{\rm eff}t}\frac{1}{[1-\frac{t}{m^2(J)}]^p}, \tag{193}$$

in order to implement both the Regge behavior and the power-law form factor in the hard regime $1\ll -t/\Lambda^2$. To fit the data in practice, it is certainly unavoidable to reduce the unknown information into a finite set of real numbers.

A theoretical picture based on the holographic model, on the other hand, suggests that the $t=-\Delta^2$ dependence is more complicated than this. If we strictly stick to the expansion (185), then individual $\overline{\Gamma}^{+,\alpha}_m(j,t)$'s may diverge at $t=-\Delta^2=0$, as we have seen above, and are not like form factors. The $\overline{\Gamma}^{+,\alpha}_m(j,t)$ would not depend only on the difference $(j-m)$, as in (192), either; we have already seen that $\overline{\Gamma}^{+,\alpha}_{m=2}(j,t)\propto\overline{g}^{0,0,m=2}/\Delta^2$ diverges at $t=-\Delta^2\to 0$ for an arbitrary j, but there is no such divergence in $\overline{\Gamma}^{+,\alpha}_{m=0}(j,t)\propto\overline{g}^{0,0,0}$, for example. Therefore, holographic models of GPD might be used as a theoretical guide to think of parametrization (for fitting) that is different from (192).

The holographic model provided by the calculation in the previous section involves infinitely many spin-dependent form factors, $\overline{g}^{0,0,m}(j,i\nu_j,\Delta)/\Delta^m$. We can still find that they share a common behavior at large $\Delta^2=-t$. To see this, note that $K_{i\nu}(\Delta z_h)$ in the Reggeon wave function effectively cuts off the integral over the holographic radius z_h at $z_h\lesssim 1/\Delta$ in the regime

$$\Lambda^2, m_h^2\ll\Delta^2\ll|q^2|,(p\cdot q),|(q\cdot\Delta)|. \tag{194}$$

The explicit form of $\Psi^{(j);s,N}_{i\nu;0,0,m}(z;\Delta)$ in (97) is not more than a modification of $K_{i\nu}(\Delta z)$ by a function of Δz_h, and hence they still play just the role of cutting off the integral at $z_h\Delta\lesssim 1$. The "current" $\overline{J}^{hh}_{z^k\lambda_{k+1}\cdots\lambda_j}$ provides extra mth powers of either $1/z$ or ∂_z and $(j-m)$-momenta p_λ, in addition to $[\Phi]^2$, which behaves like

$$[\Phi]\sim z(\Lambda z)^{\ell_\phi-1} \tag{195}$$

in the region $z\lesssim 1/\Delta\ll 1/\Lambda$; ℓ_ϕ is the conformal dimension of an operator in a strongly coupled gauge theory dual to the holographic model, which is a property of the target hadron h. The $\tilde{E}^N D^{s-2N}[\epsilon]/\Delta^{2-2N}$ operation on the SO(3,1) tensor in (89) does not introduce any power of (Δ/Λ) or (Λz). Therefore, we find in the hard scattering regime (194) that

$$\frac{\overline{g}^{0,0,m}}{\Delta^m} \sim \left(\frac{\Delta}{\Lambda}\right)^{i\nu} \times (\Lambda/\Delta)^{j+2(\ell_\phi-1)} \times \Delta^m/\Delta^m \sim \frac{1}{(\Delta/\Lambda)^{2\ell_\phi-2-\gamma(j)}}. \tag{196}$$

Interestingly, the reduced hadron matrix elements $\overline{g}^{0,0,m}/\Delta^m$ for (j,m) have the large Δ^2 power-law behavior that is independent of m; $2\Delta_\phi$ reflects a property of the target hadron h, and $-(2+\gamma(j)) = -\tau_n$ is j dependent, but the power does not depend on m.[32] Holographic models suggest this j-dependent $p = \text{const} - \gamma(j)/2$ scaling behavior as an alternative to the fixed-power $p = \text{const.}$ scaling of (193).

We have chosen a factorization into the Wilson coefficient and the matrix element that corresponds to renormalization at $\mu = \Lambda$; this choice was made implicitly when we chose a factor $[\Delta^{i\nu}/\Lambda^{i\nu-j}]^{\pm 1}$ at the time the amplitude was factorized into $C^{0,0,m}$ and $\Gamma^{0,0,m}$ in (149). When we keep the renormalization scale μ arbitrary (e.g., taking μ higher than Δ when $\Delta \gg \Lambda$), the Wilson coefficient contains a factor $(\mu/q)^{\gamma(j)}$ instead of $(\Lambda/q)^{\gamma(j)}$, and the reduced matrix element also has the following large Δ^2 behavior,

$$\frac{\overline{g}^{0,0,m}}{\Delta^m} \sim \frac{1}{(\Delta/\Lambda)^{2\ell_\phi-2}} \times \frac{1}{(\mu/\Delta)^{\gamma(j)}}. \tag{197}$$

C. Pomeron and superstring

We have so far talked about Reggeon and the flavor-nonsinglet sector in Secs. VI and VII, instead of Pomeron. Since the flavor-singlet sector ($\approx$ gluon) dominates in small-x physics, that was not a desired choice.

This is due to technical limitations in string theory at this moment. In order to deal with the propagation of string states on a curved spacetime, vertex operators and L_0 (the Virasoro generator) need to be defined properly as composite operators; the nonlinear σ model for $\mathrm{AdS}_5 \times W_5$ on the world sheet becomes conformal and the renormalization of the composite operators well defined, however, only after the Ramond-Ramond background is also implemented (e.g., [35]). Presumably an option in the future will be to implement the Klebanov-Strassler model and its variations in the Green-Schwarz formalism. One then computes the spectrum of stringy excited states, and further works out the world-sheet OPE, in the form of

$$V^{(q_1)}(z)V^{(-q_2)}(-z) \sim \sum_I C_I(z)\mathcal{O}_I(0), \tag{198}$$

using operators $\mathcal{O}_I(0)$ at the middle point, where $V^{(q_1)}$ and $V^{(-q_2)}$ are the vertex operators corresponding to the incoming and outgoing photons (32). In this way, we would not have to use string field theory.

It may also be possible to use bosonic string field theory for closed string theory, instead of the bosonic open string field theory we used in Sec. IV of this article. Bosonic closed string field theory is also well understood already [36]. Certainly the bosonic closed string field theory is not for type IIB superstring theory, but it will still allow us to get the feeling of how much open string (flavor-nonsinglet sector) and closed string (flavor-singlet sector) theories are different, from theoretical perspectives, as well as in phenomenological consequences. At least it is known that the Virasoro-Shapiro amplitude is generated, not just by the one string exchange in the t channel, the s channel, and the u channel, but also a four-point contact interaction vertex in string field theory [37]. The Virasoro-Shapiro amplitude does not have a simple s-t duality of the Veneziano amplitude, either. Certainly it is possible to write it down in the form of "t-channel" expansion only (cf. [3] and [7]), but we also need to be aware that the discussion in these two references did not use the OPE at the middle point as in (198), but instead used an OPE of the form $V(z)V(0) \sim \sum_I C_I(z)\mathcal{O}_I(0)$. To get the skewness dependence right, this difference really matters. Thus, an analogue of the prescription (52) needs to be worked out separately for the closed string amplitude.

Orthodox approaches such as those above are way beyond the scope of this article. One can hardly overestimate the importance of such a solid approach, but at the same time, very few would find the following guess terribly wrong. For practical purposes, therefore, one can live with that for the time being. First of all, the on-shell relation for the bosonic open string in (164) will be replaced by

$$\frac{j}{2} - 1 + \frac{4 + j + \nu^2 + c_j}{4\sqrt{\lambda}} = 0, \tag{199}$$

with the constraint $c_{j=1} = -4$ for the bosonic open string replaced by $c_{j=2} = -2$. Interaction vertices should also be different; looking at the difference between the Veneziano amplitude and the Virasoro-Shapiro amplitude, one finds that the following replacements should be made:

$$\frac{t_\gamma/t_y}{\Gamma(j+1)} \to \frac{t_\gamma/t_y}{[\Gamma(j/2)]^2}, \qquad \left(\frac{1}{\sqrt{\lambda}x}\right)^j \to \left(\frac{1}{4\sqrt{\lambda}x}\right)^j. \tag{200}$$

The overall normalization t_γ/t_y is like $N_c/N_c^{-2} \sim N_c^{-1}$ now, when the Pomeron (closed string) contribution is used in the t channel, and the source field for the "QED current" is implemented in the form of the D7-brane gauge field; the $1/N_c$ scaling (see footnotes 14 and 27) is also the natural expectation in the large N_c argument.

[32] This scaling was known already for $\bar{g}^{0,0,0}$ [7].

D. Numerical results

At the end of this article, we leave a few plots of numerical evaluation of various results that have been obtained. We do not intend to provide a quantitative (precise) prediction from holography, as we have repeatedly emphasized our perspective on this issue in this article; the holographic approach to GPD will provide at best a qualitatively new way to think of how to parametrize the matrix elements for GPD. Having said that, it is still desirable to grasp various expressions in a more intuitive form and bring them down to more practical situations. This section serves this purpose.

There are a couple of parameters that need to be specified in order to obtain numerical outputs in a few summary plots. We used the on-shell relation (164), which means that we should understand the numerical results to be that of the Reggeon contribution. We adopted $c_j + 4 = 0$ for all j, although there is no rationale to specify the j dependence in this way (see [12,38] and the literature therein for how to work out the j dependence of c_j). The confining effect was implemented in the form of the boundary condition (191) for the Reggeon wave function. As for the target hadron, we set the mass term of the scalar field to be $5/R^2$ (i.e., $c_y = 5$), just like the lowest nontrivial spherical harmonics on $W_5 = S^5$ for the type IIB dilaton field [39]. The operator dimension in the dual CFT becomes $\ell_\phi = 2 + \sqrt{4 + R^2 M_{\rm eff}^2} = 2 + \sqrt{4 + c_y} = 5$.

Figure 6 shows the reduced matrix element $\overline{g}^{0,0,0}(j, i\nu_j, \Delta)$ for the $(m = 0)$-mode exchange; the results for different values of spin $j = 1$, 1.5, 2, 2.5 are shown in the figure. Lattice computation can be used to determine matrix elements at integer-valued spins, but the analytic expression (153) allows us to determine the matrix element even for noninteger spin, so that the inverse Mellin transformation is possible, and we can also talk of the matrix elements evaluated at the saddle point value of spin $j = j^*$. Panel (b) in Fig. 6 is essentially the same as that of Fig. 5 in [7], while panel (a) shows $\overline{g}^{0,0,0}$ without normalizing the matrix element by its value at $t = -\Delta^2 = 0$. Since they are not the matrix element of a "conserved current" for $j \neq 1$, the matrix element does not necessarily approach 1 in the $\Delta^2 \to 0$ limit. Panel (b) has a property such that $\overline{g}^{0,0,0}$ is soft ($\overline{g}^{0,0,0}$ gets smaller slowly in Δ^2) for a larger j; this is consistent with the observation in (196) because $\partial\gamma(j)/\partial j > 0$.

A numerical result for the η^2 term in $\overline{A}_j^{+,\alpha}$, which is proportional to

$$\overline{g}^{0,0,0}(j, i\nu_j, \Delta) \times \left[\frac{p^2}{\Delta^2}\frac{j(j-1)}{j-\frac{1}{2}}\right] + \frac{\overline{g}^{0,0,2}(j, i\nu_j, \Delta)}{N_{j,2}\Delta^2} \times \frac{-1}{(j + i\nu_j)(j - 1 + i\nu_j)}, \tag{201}$$

is shown in Fig. 7, using $j = 2$. The first and second terms of (201) both diverge at the $\Delta^2 \to 0$ limit, as we saw in Sec. VII A, but their sum has a finite value at $\Delta^2 = 0$, as one can see in the figure. It is worth mentioning that this finite limit value ≈ -700 is much larger than that of $\overline{g}^{0,0,0}$. This is likely due, at least partially, to the hadron mass m_h value in this case; for the value of parameters we chose, $m_h = j_{\ell_\phi - 2,1}\Lambda$, $j_{3,1} \simeq 6.4$, and $m_h^2/\Lambda^2 \approx 40$. An extra derivative ∂_z in the matrix elements $\overline{g}_k^{0,0,2}$ is more like m_h than Λ, and hence the second term can be larger than the first term by about $(m_h/\Lambda)^2$. The factor $(m_h/\Lambda)^2 \approx 40$ does not explain all of the moderately large value -700, however. The $t = -\Lambda^2$ dependence of the η^0 term [i.e., $\overline{g}^{0,0,0}(j, i\nu_j, \Delta)$] is quite different from that of the coefficient of the η^2, at least at small Δ^2.

In the DGLAP phase, a crude approximation of the GPD is given by

$$\overline{H}^{+,\alpha}(x, \eta, t; q^2) \approx \left(\frac{1}{x}\right)^{j_*} \left(\frac{\Lambda}{q}\right)^{\gamma(j_*)} \overline{A}_{j*}^{+,\alpha}(\eta, t), \tag{202}$$

where j^* is the saddle point value of j depending primarily on $\ln(1/x)$, $\ln(q/\Lambda)$, and $t = -\Lambda^2$. Apart from applications

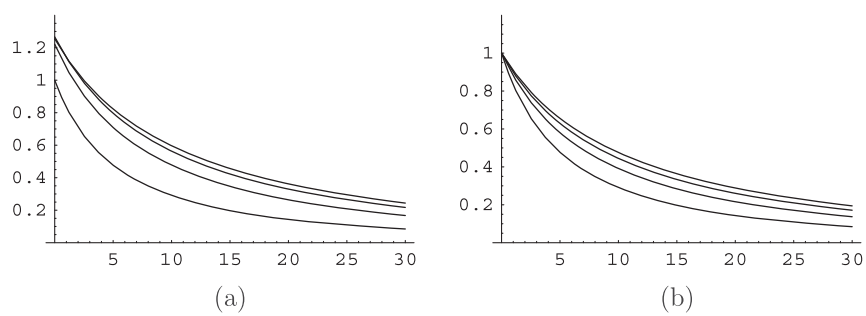

FIG. 6. Panel (a) shows $\overline{g}^{0,0,0}(j, i\nu_j, \Delta)$ as a function of Δ^2/Λ^2. The curve at the bottom is for $j = 1$, while the one at the top is for $j = 2.5$; the two in the middle correspond to $j = 1.5$ and $j = 2$. Panel (b) shows $\overline{g}^{0,0,0}(\Delta)/\overline{g}^{0,0,0}(\Delta = 0)$, i.e., $\overline{g}^{0,0,0}(j, i\nu_j, \Delta)$ normalized at the value of $\Delta^2 = 0$. The curve at the bottom is for $j = 1$, and the curve goes up for $j = 1.5$, 2, and 2.5; this softer behavior for larger j is consistent with (196).

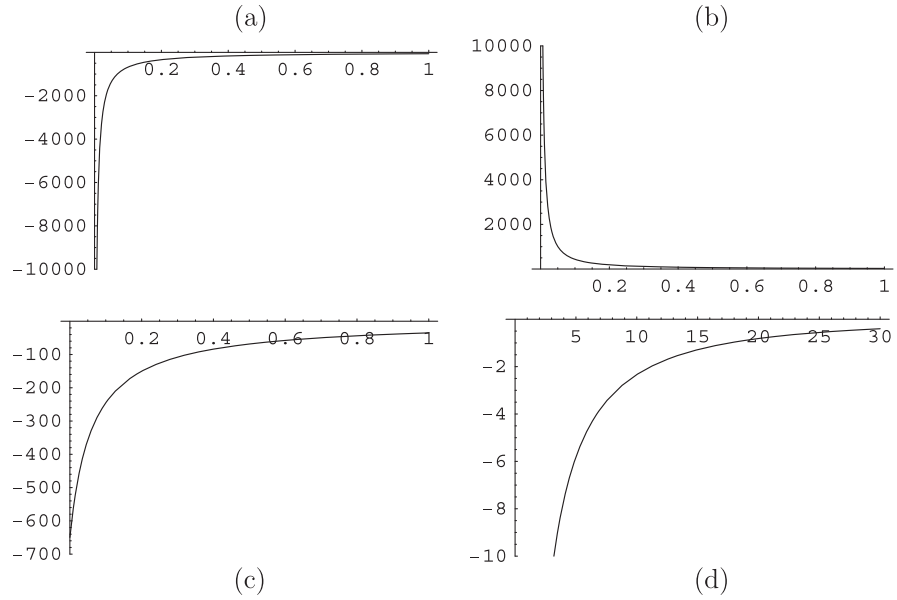

FIG. 7. The first and second term of (201) are plotted in (a) and (b), respectively, as functions of Δ^2/Λ^2; parameters are set to the values described in the text, and we used $j = 2$ in these figures. Although both (a) and (b) diverge at $\Delta^2 \to 0$, they add up to be (c), where the $\Delta \to 0$ limit is finite. The large Δ^2 behavior is seen better in panel (d).

to the timelike Compton scattering with very large (positive) lepton invariant mass square, the relevant range of $|\eta|$ is not much more than x in such processes as TCS, DVCS, and VMP. Suppose, in the power series expansion of $\overline{A}^{+,\alpha}_{j*}$ in η, that all of the terms with a different power of η have a (t-dependent) coefficient at most of $\mathcal{O}(1)$. Then the GPD [or $\overline{A}^{+,\alpha}_{j*}(\eta, t)$] in the small-$x$ regime would not have skewness dependence very much in the range of interest, $|\eta| \lesssim x$, because η^2 and higher-order terms are small relative to the η^0 term. The coefficient of the η^2 term, however, turns out to be of $\mathcal{O}(-700)$ for $\Delta^2 \approx 0$, which at least contains a factor m_h^2/Λ^2. Thus, for the range of moderately small x's, such as $x \sim 10^{-1}$ and $|\eta| \lesssim x$, the η^2 term in $\overline{A}^{+,\alpha}_{j*}(\eta, t)$ can be just as important as the η^0 term for small Δ^2. Consequently the prediction/fit of the slope parameter

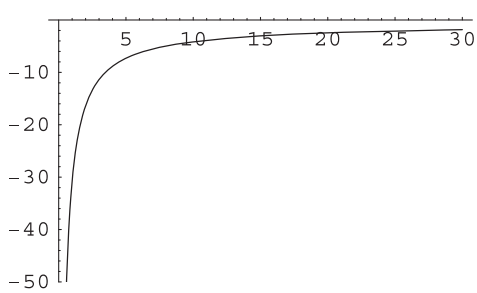

FIG. 8. The ratio of the coefficient of the η^2 term of $\bar{A}^{+,\alpha}_{j}(\eta, t)$ to that of the η^0 term, as a function of $-t/\Lambda^2 = \Delta^2/\Lambda^2$. We used $j = 2$ and other parameters described in the text. This is the ratio of Fig. 7(d) to Fig. 6(a).

(the t dependence) may also be affected since the η^2 term with a steeper t dependence is involved. Toward higher Δ^2, however, the ratio of the coefficient of the η^2 term to that of the η^0 term changes as in a numerical computation shown in Fig. 8. Since the η^2-term coefficient becomes not more than 10 times the η^0 term for $5\Lambda^2 \lesssim (\Delta^2 = -t)$ at $j = 2$ in this numerical computation, the η^0 term alone will become a good enough approximation in this range of t, even for the moderately small $|\eta| \lesssim x \approx \mathcal{O}(10^{-1})$; for an even smaller x, the η^2 term can be negligible for a broader range of $t = -\Lambda^2$. We have nothing more to say about the η^4 term and higher at this moment, or whether this moderately large value ≈ 700 is an artifact of a specific implementation of confining effects we adopted for the numerical presentation in this section. If this relatively large coefficient of the η^2 term (and also higher-order terms) turns out to be a robust consequence of holographic models, that may be regarded as an unexpected lesson from holography to phenomenology.

ACKNOWLEDGMENTS

We thank Wen Yin, with whom we worked at an earlier stage of this project, for the discussion and Simeon Hellerman and Teruhiko Kawano for their useful comments. This work is supported in part by the JSPS Research Fellowships for Young Scientists (R. N.), the WPI Initiative, and a Grant-in-Aid for Scientific Research on Innovative Areas 2303 from MEXT, Japan (R. N. and T. W.).

APPENDIX A: MORE ON THE MODE DECOMPOSITION ON AdS_5

For convenience, let us copy here the eigenmode equation (65) for a totally symmetric rank-j tensor field on AdS_5; the equation consists of the following equations labeled by $k = 0, \ldots, j$:

$$\begin{aligned}&((R^2\Delta_j) - [(2k+1)j - 2k^2 + 3k])A_{z^k\mu_1\cdots\mu_{j-k}} \\ &\quad + 2zk\partial^{\hat\rho}A_{z^{k-1}\rho\mu_1\cdots\mu_{j-k}} + k(k-1)A^{\hat\rho}_{z^{k-2}\rho\mu_1\cdots\mu_{j-k}} \\ &\quad - 2z(D[A_{z^{k+1}\ldots}])_{\mu_1\cdots\mu_{j-k}} + (E[A_{z^{k+2}\ldots}])_{\mu_1\cdots\mu_{j-k}} \\ &= -\mathcal{E}A_{z^k\mu_1\cdots\mu_{j-k}}. \end{aligned} \tag{A1}$$

1. Eigenvalues and eigenmodes for $\Delta^\mu = 0$

a. Block diagonal decomposition

In the main text, we considered a decomposition of the rank-j totally symmetric tensor field with $(-i\partial_\mu) = \Delta_\mu = 0$ in the form of

$$A_{z^k\mu_1\cdots\mu_{j-k}}(z;\Delta^\mu = 0) = \sum_{N=0}^{[(j-k)/2]} (E^N[a^{(k,N)}])_{\mu_1\cdots\mu_{j-k}},$$

where $a^{(k,N)}$'s are z-dependent rank-$(j-k-2N)$ totally symmetric tensor fields of SO(3, 1), satisfying the 4D-traceless condition (76). This is indeed a decomposition, in that all of the degrees of freedom in $A_{z^k\mu_1\cdots\mu_{j-k}}(z;\Delta^\mu = 0)$ are described by $a^{(k,N)}(z)_{\mu_1\cdots\mu_{j-k-2N}}$, with $0 \le N \le [(j-k)/2]$ without redundancy. To see this, one needs only to note that there is a relation[33] that, for a totally symmetric 4D-traceless rank-r SO(3, 1) tensor a,

$$\eta^{\hat\rho\hat\sigma}E^N[a]_{\rho\sigma\mu_1\cdots\mu_{r+2N-2}} = 4N(r+N+1)E^{N-1}[a]_{\mu_1\cdots\mu_{r+2N-2}}. \tag{A2}$$

Using this relation, $a^{(k,N)}_{\mu_1\cdots\mu_{j-k-2N}}$ can be retrieved from $A_{z^k\mu_1\cdots\mu_{j-k}}$, progressing from ones with a larger N to ones with a smaller N.

Let us now see that the eigenmode equation (65), (69), (A1) can be made block diagonal by using this decomposition. The eigenmode equation (A1) with the label k for $\Delta^\mu = 0$ can be rewritten by using this relation (A2) as follows:

$$\begin{aligned}&\sum_N [(R^2\Delta_j - [(2k+1)j - 2k^2 + 3k] + \mathcal{E})E^N[a^{(k,N)}] \\ &\quad + k(k-1)[4(N+1)(j-k-N+2)]E^N[a^{(k-2,N+1)}] \\ &\quad + E^N[a^{(k+2,N-1)}]] = 0. \end{aligned}$$

[33]This relation can be verified recursively in N.

Although this equation has to hold only after the summation in N, it actually has to be satisfied separately for different N's. To see this, let us first multiply $\eta^{\hat\rho\hat\sigma}$ for $[(j-k)/2]$ times and contract indices just like in (A2); we obtain an equation that involves only $a^{(k,[(j-k)/2])}$, $a^{(k-2,[(j-k)/2]+1)}$, and $a^{(k+2,[(j-k)/2]-1)}$. Next, multiply $\eta^{\hat\rho\hat\sigma}$ for $[(j-k)/2]-1$ times to obtain another equation involving $a^{(k,[(j-k)/2]-1)}$, $a^{(k-2,[(j-k)/2])}$, and $a^{(k+2,[(j-k)/2]-2)}$. In this way, we obtain

$$\begin{aligned}&(R^2\Delta_j - [(2k+1)j - 2k^2 + 3k] + \mathcal{E})a^{(k,N)} \\ &\quad + k(k-1)[4(N+1)(j-k-N+2)]a^{(k-2,N+1)} \\ &\quad + a^{(k+2,N-1)} = 0 \quad (\text{for } {}^\forall k, N). \end{aligned} \tag{A3}$$

Fields $a^{(k,N)}$'s with the same $k + 2N = n$ form a system of coupled equations, but those with different $n = k + 2N$ do not mix. Thus, the eigenmode equation for $\Delta^\mu = 0$ is decomposed into sectors labeled by n. The nth sector consists of z-dependent fields that are all in the $(j-n) = (j-k-2N)$ totally symmetric tensor of SO(3, 1).

b. Classification of eigenmodes for $\Delta^\mu = 0$

Let us now study the eigenmode equations in more detail for the separate diagonal blocks we have seen. Simultaneous treatment is possible for all of the nth sectors with an even n and for all of the sectors with an odd n.

Let us first look at the nth sector of the eigenmode problem for an $n = 2\bar n \le j$. In the eigenmode equation of $\Delta^\mu = 0$, we can assume[34] the same z dependence for all of the fields in this diagonal block:

$$a^{(k,N)}(z)_{\mu_1\cdots\mu_{j-n}} = \bar a^{(k,N)}_{\mu_1\cdots\mu_{j-n}} z^{2-j-i\nu}, \qquad k + 2N = n, \tag{A4}$$

where $\bar a^{(k,N)}$'s are (x,z)-independent 4D-traceless rank-$(j-n)$ tensors of SO(3, 1). The eigenmode equations with the label $(k,N) = (2\bar k, \bar n - \bar k)$, with $\bar k = 0, \ldots, \bar n$, are relevant to the $n = 2\bar n$ sector and are now written in a matrix form:

$$\sum_{\bar k'=0}^{\bar n} \mathcal{D}_{2\bar k,2\bar k'}\bar a^{(2\bar k',\bar n-\bar k')} = ((4+\nu^2) - \mathcal{E})\bar a^{(2\bar k,\bar n-\bar k)}, \tag{A5}$$

where

(i) diagonal $(k,k') = (2\bar k, 2\bar k)$ entry: $\mathcal{D}_{2\bar k,2\bar k} = -[(2k+1)j - 2k^2 + 3k]$,
(ii) diagonal$^+$; $(k,k') = (2\bar k, 2\bar k + 2)$ entry: $\mathcal{D}_{2\bar k,2\bar k+2} = 1$,
(iii) diagonal$^-$; $(k,k') = (2\bar k, 2\bar k - 2)$ entry: $\mathcal{D}_{2\bar k,2\bar k-2} = k(k-1) \times 4(\bar n - \bar k + 1)(j - \bar n - \bar k + 2)$.

[34]This is because, in the absence of $z^2\partial^2$ term, the operator Δ_j becomes a constant multiplication when it acts on a simple power of z. Upon $z^{2-j-i\nu}$, for example, $R^2\Delta_j$ returns $-(4+\nu^2)$.

There must be $(\overline{n}+1)$ independent eigenmodes in this $(\overline{n}+1)\times(\overline{n}+1)$ matrix equation. Let $\mathcal{E}_{n,l}$ denote the collection of eigenvalues in this $n=2\overline{n}$th diagonal block, and $l=0,\ldots,\overline{n}=n/2$ label distinct eigenmodes. The corresponding eigenmode wave function for the $(n=2\overline{n},l)$ mode is in the form of

$$a^{(k,N)}(z;\Delta^\mu=0)=a^{(2\overline{k},\overline{n}-\overline{k})}=c_{2\overline{k},l,n}\epsilon^{(n,l)}z^{2-j-i\nu}, \tag{A6}$$

where $\epsilon^{(n,l)}$ is an (x,z)-independent 4D-traceless totally symmetric rank-$(j-n)=(j-2\overline{n})$ tensor of SO(3, 1), and $c_{2\overline{k},l,n}$ are (x,z)-independent constants determined as the eigenvector corresponding to the eigenvalue $\mathcal{E}_{n,l}$.

Similarly, in the $n=2\overline{n}+1\leq j$th sector of the eigenmode problem, with an odd n, we can assume a simple power law for all of the component fields involved in this sector;

$$a^{(k,N)}(z)_{\mu_1\cdots\mu_{j-n}}=\overline{a}^{(k,N)}_{\mu_1\cdots\mu_{j-n}}z^{2-j-i\nu},\qquad k+2N=n, \tag{A7}$$

where $\overline{a}^{(k,N)}$ are (x,z)-independent 4D-traceless totally symmetric tensors of SO(3, 1). The eigenmode equation with the label $(k,N)=(2\overline{k}+1,\overline{n}-\overline{k})$, with $\overline{k}=0,\ldots,\overline{n}$, are relevant to this sector, and in the matrix form, the eigenmode equation now looks like

$$\sum_{\overline{k}'=0}^{\overline{n}}\mathcal{D}_{2\overline{k}+1,2\overline{k}'+1}\overline{a}^{(2\overline{k}'+1,\overline{n}-\overline{k})}=((4+\nu^2)-\mathcal{E})\overline{a}^{(2\overline{k}+1,\overline{n}-\overline{k})}, \tag{A8}$$

where

(i) diagonal $(k,k')=(2\overline{k}+1,2\overline{k}+1)$ entry: $\mathcal{D}_{2\overline{k}+1,2\overline{k}+1}=-[(2k+1)j+(-2k^2+3k)]$,
(ii) diagonal$^+$ $(k,k')=(2\overline{k}+1,2\overline{k}+3)$ entry: $\mathcal{D}_{2\overline{k}+1,2\overline{k}+3}=1$,
(iii) diagonal$^-$ $(k,k')=(2\overline{k}+1,2\overline{k}-1)$ entry: $\mathcal{D}_{2\overline{k}+1,2\overline{k}-1}=k(k-1)\times 4(\overline{n}-\overline{k}+1)(j-\overline{n}-\overline{k}+1)$.

From here, $\overline{n}+1$ independent modes arise; their eigenvalues are denoted by $\mathcal{E}_{n,l}$, and $l=\{0,\ldots,\overline{n}\}$ is the label distinguishing different modes. The eigenmode labeled by $(n=2\overline{n}+1,l)$ has a wave function

$$a^{(k,N)}(z;\Delta^\mu=0)=a^{(2\overline{k}+1,\overline{n}-\overline{k})}=c_{2\overline{k}+1,l,n}\epsilon^{(n,l)}z^{2-j-i\nu}, \tag{A9}$$

where $\epsilon^{(n,l)}$ is an (x,z)-independent 4D-traceless rank-$(j-n)$ totally symmetric tensor of SO(3, 1), and $c_{2\overline{k}+1,l,n}$ is the eigenvector for the (n,l) eigenmode determined in the matrix equation above.

c. Explicit examples

Let us take a moment to see how the general theory above works in practice.

The easiest of all is the $n=0$ sector, which contains only one rank-j 4D-traceless field, $a^{(0,0)}$. The eigenmode equation is

$$\left[\Delta_j-\frac{[(2k+1)j-2k^2+3k]_{k=0}}{R^2}\right]a^{(0,0)}=\left[\Delta_j-\frac{j}{R^2}\right]a^{(0,0)}=-\frac{\mathcal{E}_{0,0}}{R^2}a^{(0,0)}. \tag{A10}$$

The eigenmode wave function has the form

$$a^{(0,0)}(z)_{\mu_1\cdots\mu_j}=\epsilon^{(0,0)}_{\mu_1\cdots\mu_j}z^{2-j-i\nu}, \tag{A11}$$

and the eigenvalue $\mathcal{E}_{n,l}$ is

$$\mathcal{E}_{0,0}=(j+4+\nu^2). \tag{A12}$$

Also to the $n=1$ sector, only one rank-$(j-1)$ 4D-traceless tensor field contributes. That is $a^{(1,0)}$. The eigenmode equation becomes

$$[R^2\Delta_j-[(2k+1)j-2k^2+3k]|_{k=1}]a^{(1,0)}=[R^2\Delta_j-(3j+1)]a^{(1,0)}=-\mathcal{E}_{1,0}a^{(1,0)}. \tag{A13}$$

The solution is

$$a^{(1,0)}(z)_{\mu_1\cdots\mu_{j-1}}=\epsilon^{(1,0)}_{\mu_1\cdots\mu_{j-1}}z^{2-j-i\nu},\qquad \mathcal{E}_{1,0}=(3j+5+\nu^2). \tag{A14}$$

In the $n=2$ sector, two rank-$(j-2)$ 4D-traceless fields are involved. They are $a^{(0,1)}$ and $a^{(2,0)}$. After introducing the z dependence $\propto z^{2-j-i\nu}$, the eigenmode equation (A5) in the $n=2$ sector becomes

$$\begin{bmatrix}-j & 1\\ 8j & -(5j-2)\end{bmatrix}\begin{pmatrix}\overline{a}^{(0,1)}\\ \overline{a}^{(2,0)}\end{pmatrix}=((4+\nu^2)-\mathcal{E})\begin{pmatrix}\overline{a}^{(0,1)}\\ \overline{a}^{(2,0)}\end{pmatrix}. \tag{A15}$$

One of the two eigenmodes is

$$\mathcal{E}_{2,0}=(4+5j+\nu^2),\ \begin{pmatrix}a^{(0,1)}(z)_{\mu_1\cdots\mu_{j-2}}\\ a^{(2,0)}(z)_{\mu_1\cdots\mu_{j-2}}\end{pmatrix}=\begin{pmatrix}1\\ -4j\end{pmatrix}\epsilon^{(2,0)}_{\mu_1\cdots\mu_{j-2}}z^{2-j-i\nu}, \tag{A16}$$

and the other is

$$\mathcal{E}_{2,1} = (2 + j + \nu^2), \begin{pmatrix} a^{(0,1)}(z)_{\mu_1\cdots\mu_{j-2}} \\ a^{(2,0)}(z)_{\mu_1\cdots\mu_{j-2}} \end{pmatrix} = \begin{pmatrix} 1 \\ 2 \end{pmatrix} \epsilon^{(2,1)}_{\mu_1\cdots\mu_{j-2}} z^{2-j-i\nu}. \tag{A17}$$

In the $n = 3$ sector, two rank-$(j-3)$ 4D-traceless tensor fields are involved: $a^{(1,1)}$ and $a^{(3,0)}$. The eigenmode equations (A8) become

$$\begin{bmatrix} -(3j+1) & 1 \\ 24(j-1) & -(7j-9) \end{bmatrix} \begin{pmatrix} \overline{a}^{(1,1)} \\ \overline{a}^{(3,0)} \end{pmatrix} = ((4+\nu^2) - \mathcal{E}) \begin{pmatrix} \overline{a}^{(1,1)} \\ \overline{a}^{(3,0)} \end{pmatrix}. \tag{A18}$$

So, one of the two eigenmodes is

$$\mathcal{E}_{3,0} = (7j + 1 + \nu^2), \begin{pmatrix} a^{(1,1)}(z)_{\mu_1\cdots\mu_{j-3}} \\ a^{(3,0)}(z)_{\mu_1\cdots\mu_{j-3}} \end{pmatrix} = \begin{pmatrix} 1 \\ -4(j-1) \end{pmatrix} \epsilon^{(3,0)}_{\mu_1\cdots\mu_{j-3}} z^{2-j-i\nu}, \tag{A19}$$

and the other one is

$$\mathcal{E}_{3,1} = (3j - 1 + \nu^2), \begin{pmatrix} a^{(1,1)}(z)_{\mu_1\cdots\mu_{j-3}} \\ a^{(3,0)}(z)_{\mu_1\cdots\mu_{j-3}} \end{pmatrix} = \begin{pmatrix} 1 \\ 6 \end{pmatrix} \epsilon^{(3,1)}_{\mu_1\cdots\mu_{j-3}} z^{2-j-i\nu}. \tag{A20}$$

Finally, in the $n = 4$ sector, the eigenmode equation (A5) is given by

$$\begin{bmatrix} -j & 1 & 0 \\ 16(j-1) & -(5j-2) & 1 \\ 0 & 48(j-2) & -(9j-20) \end{bmatrix} \begin{pmatrix} \overline{a}^{(0,2)} \\ \overline{a}^{(2,1)} \\ \overline{a}^{(4,0)} \end{pmatrix} = ((4+\nu^2) - \mathcal{E}) \begin{pmatrix} \overline{a}^{(0,2)} \\ \overline{a}^{(2,1)} \\ \overline{a}^{(4,0)} \end{pmatrix}. \tag{A21}$$

There are three solutions. First,

$$\mathcal{E}_{4,0} = (9j - 4 + \nu^2), \tag{A22}$$

$$(a^{(0,2)}, a^{(2,1)}, a^{(4,0)}) = (1, -8(j-1), 32(j-1)(j-2))\epsilon^{(4,0)} z^{2-j-i\nu}, \tag{A23}$$

second,

$$\mathcal{E}_{4,1} = (5j - 6 + \nu^2), \tag{A24}$$

$$(a^{(0,2)}, a^{(2,1)}, a^{(4,0)}) = (1, -(4j-10), -48(j-2))\epsilon^{(4,1)} z^{2-j-i\nu}, \tag{A25}$$

and, finally,

$$\mathcal{E}_{4,2} = (j + \nu^2), \tag{A26}$$

$$(a^{(0,2)}, a^{(2,1)}, a^{(4,0)}) = (1, 4, 24)\epsilon^{(4,2)} z^{2-j-i\nu}. \tag{A27}$$

An empirical relation is observed in the j dependence of the eigenvalues we have worked out so far. The eigenvalues in the nth sector are in the form of $\mathcal{E}_{n,l} = \nu^2 + (2n + 1 - 4l)j + \mathcal{O}(1)$ for $0 \le l \le [n/2]$.

d. 5D-traceless modes: the $l = 0$ modes

Although the precise expressions for the eigenvalues $\mathcal{E}_{n,l}$ and the eigenvectors $c_{k,l,n}$ are not given for all of the eigenmodes, there is a class of eigenmodes whose eigenvalues and eigenvectors (wave functions) are fully understood.

As we discussed in Sec. V B 3, it is possible to require both that a field is an eigenmode and that it satisfies the 5D-traceless condition (95) at the same time. In the $n = (k + 2N)$th sector, the 5D-traceless condition becomes

$$\begin{aligned} 0 &= (E^N[a^{(k,N)}])^{\hat{\rho}}_{\rho\mu_3\cdots\mu_{j-n}} + (E^{N-1}[a^{(k+2,N-1)}])_{\mu_3\cdots\mu_{j-n}}, \\ &= E^{N-1}[4N(j-n+N+1)a^{(k,N)} + a^{(k+2,N-1)}] \\ &\quad \times \begin{cases} k = 0, 2, \ldots, 2(\overline{n}-1) & (\text{even } n), \\ k = 1, 3, \ldots, 2\overline{n}-1 & (\text{odd } n). \end{cases} \end{aligned} \tag{A28}$$

Thus, the 5D-traceless condition uniquely determines one eigenmode in each one of the nth sectors.

$$\mathcal{E}_{n,0} = (2n+1)j + 2n - n^2 + 4 + \nu^2 \tag{A29}$$

and

$$\begin{aligned} c_{2\overline{k},0,2\overline{n}} &= (-)^{\overline{k}} 4^{\overline{k}} \frac{\overline{n}!}{(\overline{n}-\overline{k})!} \frac{(j-\overline{n}+1)!}{(j-\overline{n}-\overline{k}+1)!}, \\ c_{2\overline{k}+1,0,2\overline{n}+1} &= (-)^{\overline{k}} 4^{\overline{k}} \frac{\overline{n}!}{(\overline{n}-\overline{k})!} \frac{(j-\overline{n})!}{(j-\overline{n}-\overline{k})!}. \end{aligned} \tag{A30}$$

2. MODE DECOMPOSITION FOR NONZERO Δ_μ

a. Diagonal block decomposition for the $\Delta^\mu \neq 0$ case

Let us now turn our attention to the eigenmode equations (65), (69) with $\Delta^\mu \neq 0$. Because of the second and fourth terms in (69), the eigenmode problem becomes much more complicated. We begin by finding a diagonal block decomposition suitable for the case with $\Delta^\mu \neq 0$.

In the main text, we introduced a decomposition of a totally symmetric rank-j tensor field $A_{m_1\cdots m_j}$ of SO(4, 1) into a collection of totally symmetric 4D-traceless 4D-transverse tensor fields of SO(3, 1). Instead of (75), a new decomposition is given by (85), (A31):

$$A_{z^k\mu_1\cdots\mu_{j-k}}(z;\Delta^\mu) = \sum_{s=0}^{j-k}\sum_{N=0}^{[s/2]}(\tilde{E}^N D^{s-2N}[a^{(k,s,N)}])_{\mu_1\cdots\mu_{j-k}}, \tag{A31}$$

where $a^{(k,s,N)}$ are totally symmetric 4D-traceless 4D-transverse rank-$(j-k-s)$ tensor fields of SO(3, 1). An operation $a \mapsto \tilde{E}[a]$ on a totally symmetric SO(3, 1) tensor a is given by (86).

In order to see that the parametrization of $A_{z^k\mu_1\cdots\mu_{j-k}}$ by $(a^{(k,s,N)})_{\mu_1\cdots\mu_{j-k-s}}$'s above is indeed a decomposition, one needs to see that $a^{(k,s,N)}$'s can be retrieved from $A_{z^k\mu_1\cdots\mu_{j-k}}$ so that the degrees of freedom $a^{(k,s,N)}$ are independent. For this purpose, it is convenient to derive some relations analogous to (A2). First of all, note that $E[D[a]] = D[E[a]]$ and[35] $\tilde{E}[D[a]] = D[\tilde{E}[a]]$ for a totally symmetric SO(3, 1) tensor a. If the rank-r tensor a is also 4D transverse and 4D traceless, one can then derive the following relations:

$$\partial^{\hat\rho}(E^t D^{s-2t}[a])_{\rho\mu_2\cdots\mu_{r+s}} = -\Delta^2(s-2t)E^t D^{s-2t-1}[a] + (2t)E^{t-1}D^{s-2t+1}[a], \tag{A33}$$

$$\eta^{\hat\rho\hat\sigma}(E^t D^{s-2t}[a])_{\rho\sigma\mu_3\cdots\mu_{r+s}} = -\Delta^2(s-2t)(s-2t-1)E^t D^{s-2t-2}[a] + 4t(r+s-t+1)E^{t-1}D^{s-2t}[a], \tag{A34}$$

$$\partial^{\hat\rho}(\tilde{E}^N D^{s-2N}[a])_{\rho\mu_2\cdots\mu_{r+s}} = -(s-2N)\Delta^2\tilde{E}^N D^{s-2N-1}[a], \tag{A35}$$

$$\left(\eta^{\hat\rho\hat\sigma} - \frac{\partial^{\hat\rho}\partial^{\hat\sigma}}{\partial^2}\right)(\tilde{E}^N D^{s-2N}[a])_{\rho\sigma\mu_3\cdots\mu_{r+s}} = 4N(r+N+1/2)\tilde{E}^{N-1}D^{s-2N}[a]. \tag{A36}$$

With the relations above, it is now possible to compute

$$\left(\eta^{\hat\mu_1\hat\mu_2} - \frac{\partial^{\hat\mu_1}\partial^{\hat\mu_2}}{\partial^2}\right)\cdots\left(\eta^{\hat\mu_{2p-1}\hat\mu_{2p}} - \frac{\partial^{\hat\mu_{2p-1}}\partial^{\hat\mu_{2p}}}{\partial^2}\right)\frac{\partial^{\hat\mu_{2p+1}}}{\partial^2}\cdots\frac{\partial^{\hat\mu_{2p+q}}}{\partial^2}(\tilde{E}^N D^{s-2N}[a])_{\mu_1\cdots\mu_{r+s}} = \begin{cases} \frac{b^{(r)}_{s-2p-q,N-p}}{b^{(r)}_{s,N}}(\tilde{E}^{N-p}D^{s-2N-q}[a])_{\mu_{2p+q+1}\cdots\mu_{r+s}} & \text{if } p \le N \quad \text{and} \quad q \le s-2N, \\ 0 & \text{otherwise,} \end{cases} \tag{A37}$$

where we assume that a is a totally symmetric 4D-traceless 4D-transverse rank-r tensor of SO(3, 1). In the last line,

$$b^{(r)}_{s,N} := \frac{1}{4^N N!(s-2N)!}\frac{\Gamma(r+3/2)}{\Gamma(r+N+3/2)}. \tag{A38}$$

It is now clear how to retrieve $a^{(k,s,N)}$ from the $A_{z^k\mu_1\cdots\mu_{j-k}}$ given by (85), (A31). First, one has to multiply $\eta^{\hat\rho\hat\sigma} - \partial^{\hat\rho}\partial^{\hat\sigma}/\partial^2$ and $\partial^{\hat\sigma}/\partial^2$ by $A_{z^k\mu_1\cdots\mu_{j-k}}$ as many times as possible in order to obtain $a^{(k,s,N)}$ with a larger N and $(s-2N)$. Then $a^{(k,s,N)}$'s with smaller N or $(s-2N)$ can be determined by multiplying $\eta^{\hat\rho\hat\sigma} - \partial^{\hat\rho}\partial^{\hat\sigma}/\partial^2$ and $\partial^{\hat\sigma}/\partial^2$ fewer times.

Let us now return to the eigenmode equation for the cases with $\Delta^\mu \neq 0$. Following precisely the same argument as in Sec. A. 1, one can see that the eigenmode equation can be separated into the following independent equations labeled by k, s, and N:

$$\begin{aligned}&[R^2\Delta_j - [(2k+1)j - 2k^2 + 3k] + \mathcal{E}]a^{(k,s,N)} + 2zk(s+1-2N)(\partial^2)a^{(k-1,s+1,N)} \\ &\quad + k(k-1)(s+2-2N)(s+1-2N)(\partial^2)a^{(k-2,s+2,N)} + 4k(k-1)(N+1)(j-m+N+3/2)a^{(k-2,s+2,N+1)} \\ &\quad - 2za^{(k+1,s-1,N)} + a^{(k+2,s-2,N-1)} + (\partial^2)^{-1}a^{(k+2,s-2,N)} = 0 \quad \text{for } {}^\forall k, s, N.\end{aligned} \tag{A39}$$

The relations (A33), (A34) were used to evaluate the second–fourth terms of (A1). One can see that $a^{(k,s,N)}$'s with a common value of $m := k+s$ form coupled eigenmode equations, but those with different m's do not. Thus, $a^{(k,s,N)}(z;\Delta^\mu)$'s with $k+s=m$ form the mth subspace of $A_{m_1\cdots m_j}(z;\Delta^\mu)$, and the eigenmode equation becomes block diagonal in the decomposition into the subspaces labeled by $m = 0, \ldots, j$.

[35]

$$E^t D^{s-2t}[a] = \sum \eta_{\mu_{p_1}\mu_{p_2}}\cdots\eta_{\mu_{p_{2t-1}}\mu_{p_{2t}}}\partial_{\mu_{p_{2t+1}}}\cdots\partial_{\mu_{p_s}}[a]_{\mu_1\ldots\ldots\mu_{r+s}}, \tag{A32}$$

where the sum is taken over all possible ordered choices of $p_1, p_2, \ldots, p_s \in \{1, \ldots, j\}$ such that $p_i \neq p_j$ for $i \neq j$.

The eigenmode equation on the mth subspace is given by the equation above, with $0 \le k = (m - s) \le m$ and $0 \le N \le [s/2]$. Thus, the total number of equations is

$$\sum_{s=0}^{m} ([s/2] + 1), \tag{A40}$$

and the same number of eigenvalues should be obtained from the mth sector.

b. Examples

The sector m = 0.—There is only one field $a^{(0,0,0)}$ in this sector, and the eigenmode equation is

$$\left[\Delta_j - \frac{j}{R^2}\right] a^{(0,0,0)}(z;\Delta^\mu) = -\frac{\mathcal{E}}{R^2} a^{(0,0,0)}(z;\Delta^\mu). \tag{A41}$$

Assuming a power series expansion for the solution to this equation, beginning with some power $z^{2-j-i\nu}$, the eigenvalue is determined as a function of $(i\nu)$:

$$\mathcal{E}_{0,0} = (j + 4 + \nu^2),$$

and the wave function can be chosen as

$$a^{(0,0,0)}(z;\Delta^\mu)_{\mu_1\cdots\mu_j} = \epsilon^{(0,0,0)}_{\mu_1\cdots\mu_j} \Psi^{(j)}_{i\nu}(-\Delta^2, z), \tag{A42}$$

$$\Psi^{(j)}_{i\nu}(\Delta^2, z) := \frac{2}{\pi}\sqrt{\frac{\nu \sinh(\pi\nu)}{2R}} e^{(j-2)A} K_{i\nu}(\Delta z). \tag{A43}$$

The sector m = 1.—The eigenmode equation in this sector becomes

$$\begin{bmatrix} R^2\Delta_j - j & -2z \\ -2z\Delta^2 & R^2\Delta_j - (3j+1) \end{bmatrix} \begin{pmatrix} a^{(0,1,0)} \\ a^{(1,0,0)} \end{pmatrix} = -\mathcal{E} \begin{pmatrix} a^{(0,1,0)} \\ a^{(1,0,0)} \end{pmatrix}. \tag{A44}$$

Assuming the power series expansion in z, beginning with $z^{2-j-i\nu}$ terms, we obtain two eigenvalues depending on $i\nu$. They are given by evaluating $R^2\Delta_j - j$ and $R^2\Delta_j - (3j+1)$ on $z^{2-j-i\nu}$:

$$\mathcal{E}_{0,0} = (j + 4 + \nu^2) \quad \text{and} \quad \mathcal{E}_{1,0} = (3j + 5 + \nu^2). \tag{A45}$$

The sector m = 2.—The eigenmode equation becomes

$$\left((R^2\Delta_j + \mathcal{E})\mathbf{1}_{4\times 4} + \begin{bmatrix} -j & & -2z & 1/\partial^2 \\ & -j & & 1 \\ 4z\partial^2 & & -(3j+1) & -2z \\ 4\partial^2 & 8j-4 & 4z\partial^2 & -(5j-2) \end{bmatrix} \right) \begin{pmatrix} a^{(0,2,0)} \\ a^{(0,2,1)} \\ a^{(1,1,0)} \\ a^{(2,0,0)} \end{pmatrix} = 0. \tag{A46}$$

The indicial equation relating the exponent $(2 - j - i\nu)$ at $z = 0$ and the eigenvalues split into two parts; three eigenvalues of this matrix,

$$\begin{pmatrix} -j & & 1 \\ & -j & 1 \\ 4 & (8j-4) & -(5j-2) \end{pmatrix}, \tag{A47}$$

determine $-\mathcal{E} - (4 + \nu^2)$ for the three eigenmodes, and $-(\mathcal{E} - (4 + \nu^2)) = -(3j + 1)$ for the last eigenmode. Therefore, the four eigenvalues in the $m = 2$ sector are

$$\mathcal{E}_{0,0} = (j + 4 + \nu^2), \qquad \mathcal{E}_{1,0} = (3j + 5 + \nu^2),$$
$$\mathcal{E}_{2,0} = (5j + 4 + \nu^2), \qquad \mathcal{E}_{2,1} = (j + 2 + \nu^2). \tag{A48}$$

In all of the examples above, the mth sector consists of eigenmodes with eigenvalues $\mathcal{E}_{n,l}$ for $0 \le n \le m$, $0 \le l \le [n/2]$. The number of eigenmodes is, of course, the same as in (A40).

3. Wave functions of 5D-traceless 5D-transverse modes

As we discussed toward the end of Sec. V B, it is possible to require for a rank-j totally symmetric tensor field configuration $A_{m_1\cdots m_j}(z;\Delta^\mu)$ to be an eigenmode and to be 5D traceless and 5D transverse (95), (96) at the same time. We will see in the following that these two extra conditions (95), (96) leave precisely one eigenmode in each one of the block diagonal sectors labeled by $m = 0, \ldots, j$. We will further determine the wave function profile of such eigenmodes.

Let us first rewrite the 5D-traceless condition (95) in a more convenient form:

$$\eta^{\hat\rho\hat\sigma} A_{z^{k-2}\rho\sigma\mu_1\cdots\mu_{j-k}} + A_{z^k\mu_1\cdots\mu_{j-k}} = 0, \tag{A49}$$

which, in the mth sector, means

$$a^{(k,s,N)} = (s + 2 - 2N)(s + 1 - 2N)\Delta^2 a^{(k-2,s+2,N)} + 4(N+1)(j - m + N + 3/2) a^{(k-2,s+2,N+1)} \tag{A50}$$

for $N = 0, \ldots, [s/2]$; $k + s = m$ is understood. Under the 5D-traceless condition, the 5D-transverse condition

$$(k-1)\eta^{\hat{\rho}\hat{\sigma}} A_{z^{k-2}\rho\sigma\mu_1\cdots\mu_{j-k}} + z\partial^{\hat{\rho}} A_{z^{k-1}\rho\mu_1\cdots\mu_{j-k}} + (z\partial_z + (k-4)) A_{z^k\mu_1\cdots\mu_{j-k}} = 0 \tag{A51}$$

becomes

$$z\partial^{\hat{\rho}} A_{z^{k-1}\rho\mu_1\cdots\mu_{j-k}} + (z\partial_z - 3) A_{z^k\mu_1\cdots\mu_{j-k}} = 0. \tag{A52}$$

In the mth sector ($k + s = m$), therefore,

$$(s + 1 - 2N)\Delta^2 a^{(k-1,s+1,N)} = z^3\partial_z z^{-3} a^{(k,s,N)} \tag{A53}$$

for $N = 0, \ldots, [s/2]$. Hereafter, we use a simplified notation $\mathcal{D} \coloneqq z^3\partial_z z^{-3}$. One can see that all of the $a^{(k,s,N)}$'s with $k + s = m$ and $N \leq [s/2]$ can be determined from $a^{(m,0,0)}$ by using the relations (A50), (A53). This observation already implies that there can be at most one eigenmode in a given mth sector that satisfies both the 5D-traceless and the 5D-transverse conditions.

For now, let us assume that there is one, and proceed to determine the wave function. The wave function—z dependence—of $a^{(m.0.0)}(z;\Delta^\mu)$ can be determined from the eigenmode equation (A39), with $k = m$, $s = N = 0$. Using (A50) and (A53), we can rewrite the equation as

$$[R^2\Delta_j - \{(2m+1)j - m^2 + 2m\} - 2m(z\partial_z - 3) + \mathcal{E}] \times a^{(m,0,0)}(z;\Delta) = 0. \tag{A54}$$

For this equation,

$$(a^{(m,0,0)}(z;\Delta))_{\mu_1\cdots\mu_{j-m}} = \epsilon_{\mu_1\cdots\mu_{j-m}} \left(\frac{z}{R}\right)^{2-j} (\Delta z)^m K_{i\nu}(\Delta z), \qquad \mathcal{E} = (j + 4 + \nu^2), \tag{A55}$$

is a solution, where $\epsilon_{\mu_1\cdots\mu_{j-m}}$ is a z-independent 4D-traceless 4D-transverse totally symmetric rank-$(j-m)$ tensor of SO (3, 1). From the value of the eigenvalue, it turns out that the 5D-traceless 5D-transverse mode in the mth sector corresponds to the $(n, l, m) = (0, 0, m)$ mode. The z dependence we determined above implies that

$$\Psi^{(j);0,0}_{i\nu;0,0,m}(-\Delta^2, z) \propto (\Delta z)^m \Psi^{(j);0,0}_{i\nu;0,0,0}(-\Delta^2, z). \tag{A56}$$

This result corresponds to the $(s, N) = (0, 0)$ case of (97). The normalization constant $N_{j,m}$ is determined later in this section.

Let us now proceed to determine other $\Psi^{(j);s,N}_{i\nu;0,0,m}$, not just for $(s, N) = (0, 0)$. Using the 5D-transverse condition, (A53), $a^{(m-1,1,0)}(z;\Delta)$ can be determined from $a^{(m,0,0)}(z;\Delta)$.

$$a^{(m-1,1,0)} = \frac{\mathcal{D}}{\Delta^2} a^{(m,0,0)}, \qquad \Psi^{(j);1,0}_{i\nu;0,0,m} = \frac{\mathcal{D}}{\Delta}\Psi^{(j);0,0}_{i\nu;0,0,m}. \tag{A57}$$

In order to determine the $s = 2$ components $a^{(m-2,2,N)}$ ($N = 0, 1$) of the $(n, l) = (0, 0)$ mode in the mth sector, one has to use both the 5D-transverse condition and the 5D-traceless condition:

$$2\Delta^2 a^{(m-2,2,0)} = \mathcal{D} a^{(m-1,1,0)}, \tag{A58}$$

$$2\Delta^2 a^{(m-2,2,0)} - 4(j - m + 3/2) a^{(m-2,2,1)} = a^{(m,0,0)}. \tag{A59}$$

Therefore,

$$a^{(m-2,2,0)} = \frac{1}{2\Delta^2}\left(\frac{\mathcal{D}}{\Delta}\right)^2 a^{(m,0,0)},$$
$$a^{(m-2,2,1)} = \frac{1}{4(j-m+3/2)}\left\{\left(\frac{\mathcal{D}}{\Delta}\right)^2 - 1\right\} a^{(m,0,0)}. \tag{A60}$$

After factoring out the normalization factor $(b^{(j-m)}_{s,N}/\Delta^{s-2N})$ and the common 4D-tensor $\epsilon^{(0,0,m)}$, we obtain

$$\Psi^{(j);2,0}_{i\nu;0,0,m} = \left(\frac{\mathcal{D}}{\Delta}\right)^2 \Psi^{(j);0,0}_{i\nu;0,0,m},$$
$$\Psi^{(j);2,1}_{i\nu;0,0,m} = \left\{\left(\frac{\mathcal{D}}{\Delta}\right)^2 - 1\right\} \Psi^{(j);0,0}_{i\nu;0,0,m}. \tag{A61}$$

The 5D-transverse conditions (A53) determine the $s = 3$ components $a^{(m-3,3,N)}(z;\Delta)$ ($N = 0, 1$) from the $s = 2$ components:

$$a^{(m-3,3,0)} = \frac{1}{6\Delta^3}\left(\frac{\mathcal{D}}{\Delta}\right)^3 a^{(m,0,0)},$$
$$a^{(m-3,3,1)} = \frac{1}{4(j-m+3/2)\Delta}\left\{\left(\frac{\mathcal{D}}{\Delta}\right)^3 - \left(\frac{\mathcal{D}}{\Delta}\right)\right\} a^{(m,0,0)}, \tag{A62}$$

and after factoring out the normalization factor $(b^{(j-m)}_{s,N}/\Delta^{s-2N})$ and $\epsilon^{(0,0,m)}$ as before, we obtain

$$\Psi^{(j);3,0}_{i\nu;0,0,m} = \left(\frac{\mathcal{D}}{\Delta}\right)^3 \Psi^{(j);0,0}_{i\nu;0,0,m},$$
$$\Psi^{(j);3,1}_{i\nu;0,0,m} = \left\{\left(\frac{\mathcal{D}}{\Delta}\right)^3 - \left(\frac{\mathcal{D}}{\Delta}\right)\right\} \Psi^{(j);0,0}_{i\nu;0,0,m}. \tag{A63}$$

The $s = 3$ components determined purely by the conditions (A53) satisfy the 5D-traceless condition (A50) with the $s = 1$ component:

$$6\Delta^2 a^{(m-3,3,0)} - 4(j - m + 3/2) a^{(m-3,3,1)} = \frac{\mathcal{D}}{\Delta^2} a^{(m,0,0)} = a^{(m-1,1,0)}. \tag{A64}$$

In this way, the wave functions $\Psi^{(j);s,N}_{i\nu;0,0,m}(-\Delta^2,z)$ for all (s,N) are determined, and the result is

$$\Psi^{(j);s,N}_{i\nu;0,0,m}(-\Delta^2,z) = \sum_{a=0}^{N}(-)^a{}_N C_a\left(\frac{\mathcal{D}}{\Delta}\right)^{s-2a}[(z\Delta)^m\Psi^{(j);0,0}_{i\nu;0,0,0}(-\Delta^2,z)]\times N_{j,m}. \tag{A65}$$

The only remaining concern was that there are more conditions from (A50), (A53) than number of components $a^{(k,s,N)}$ in the mth sector; there can be at most one eigenmode satisfying these 5D-traceless 5D-transverse conditions, as we stated earlier, but there may be no eigenmode left if the conditions are overdetermining. We have confirmed, however, that the wave functions (97), (A65) satisfy all of the relations given by (A50), (A53).

a. Normalization

We have yet to determine the normalization factor $N_{j,m}$; as in the main text, we choose (99) to be the normalization condition. Orthogonal nature among the eigenmodes is guaranteed because of the Hermitian nature of the operator $\alpha'(\nabla^2 - M^2)$. It is thus sufficient to focus only on the divergent part of the integral in the normalization condition in order to determine $N_{j,m}$.

The divergent part of the integral in (99) comes only from terms with $s=m$, $k=0$, $(0\le N\le[m/2])$, and $a=0$. For a given m,

$$\begin{aligned}[\epsilon\cdot\epsilon']\delta(\nu-\nu') \sim N_{j,m}^2\int_0 dz\sqrt{-g(z)}e^{-2jA} &\times\left(\sum_{N=0}^{[m/2]}\tilde{E}^N D^{m-2N}[\epsilon^{(0,0,m)}]\frac{b^{(j-m)}_{m,N}}{\Delta^{m-2N}}\frac{z^3\partial_z^m z^{-3}}{\Delta^m}(z\Delta)^m\Psi^{(j);0,0}_{i\nu;0,0,m}(-\Delta^2,z)\right)_{\mu_1\cdots\mu_j}\\ &\times\left(\sum_{M=0}^{[m/2]}\tilde{E}^M D^{m-2M}[\epsilon^{(0,0,m)}]\frac{b^{(j-m)}_{m,M}}{\Delta^{m-2M}}\frac{z^3\partial_z^m z^{-3}}{\Delta^m}(z\Delta)^m\Psi^{(j);0,0}_{i\nu;0,0,m}(-\Delta^2,z)\right)^{\hat{\mu}_1\cdots\hat{\mu}_j}.\end{aligned} \tag{A66}$$

The divergent part of the integral in this expression comes from

$$\begin{aligned}&\left(\frac{2}{\pi}\right)^2\frac{\nu\sinh(\pi\nu)}{2}\int dx x^{2j-5}[x^3\partial_x^m x^{-1-j+m}K_{i\nu}(x)][x^3\partial_x^m x^{-1-j+m}K_{i\nu'}(x)]\\ &\simeq\prod_{p=1}^{m}[(j-p+1)^2+\nu^2]\delta(\nu-\nu') = \frac{\Gamma(j+1-i\nu)\Gamma(j+1+i\nu)}{\Gamma(j+1-m-i\nu)\Gamma(j+1-m+i\nu)}\delta(\nu-\nu').\end{aligned}$$

Noting that

$$\begin{aligned}&\left(\sum_{N=0}^{[m/2]}\tilde{E}^N D^{m-2N}[\epsilon^{(0,0,m)}]\frac{b^{(j-m)}_{m,N}}{\Delta^{m-2N}}\right)\left(\sum_{M=0}^{[m/2]}\tilde{E}^M D^{m-2M}[\epsilon'^{(0,0,m)}]\frac{b^{(j-m)}_{m,M}}{\Delta^{m-2M}}\right),\\ &= \frac{j!}{(j-m)!}\left(\sum_{N=0}^{[m/2]}b^{(j-m)}_{m,N}\right)\epsilon^{(0,0,m)}_{\mu_1\cdots\mu_{j-m}}\cdot\epsilon'^{(0,0,m)\hat{\mu}_1\cdots\hat{\mu}_{j-m}},\end{aligned}$$

we find that (A66) implies

$$\begin{aligned}N_{j,m}^{-2} &= \frac{\Gamma(j+1-i\nu)\Gamma(j+1+i\nu)}{\Gamma(j+1-m-i\nu)\Gamma(j+1-m+i\nu)}\frac{j!}{(j-m)!}\left(\sum_{N=0}^{[m/2]}b^{(j-m)}_{m,N}\right),\\ &= \frac{\Gamma(j+1-i\nu)}{\Gamma(j+1-m-i\nu)}\frac{\Gamma(j+1+i\nu)}{\Gamma(j+1-m+i\nu)}{}_jC_m\frac{\Gamma(3/2+j-m)}{2^m\Gamma(3/2+j)}\frac{\Gamma(2+2j)}{\Gamma(2+2j-m)}.\end{aligned} \tag{A67}$$

4. A note on the wave function of the massless vector field

For a rank-1 tensor (vector) field on AdS_5, we can determine the wave function of the $(n,l,m)=(1,0,1)$ eigenmode, not just for the $(n,l,m)=(0,0,m)$ modes with $m=0,1$. With the eigenvalue $\mathcal{E}_{1,0}=(3j+5+\nu^2)|_{j=1}$,

$$a^{(0,1,0)} = \epsilon^{(1,0,1)} z^2 K_{i\nu}(\Delta z),$$
$$a^{(1,0,0)} = \epsilon^{(1,0,1)} \partial_z (z^2 K_{i\nu}(\Delta z)) \tag{A68}$$

is the eigenvector solution to (A44).

The $(n,l,m) = (0,0,1)$ mode and the $(n,l,m) = (1,0,1)$ mode are independent, even after the mass-shell condition (66) for generic vector fields in bosonic string theory. However, for the massless vector field A_m obtained by the simple dimensional reduction of the massless vector field $A_M^{(Y)}$ with $Y = \{1,0,0\}$, these two modes become degenerate. To see this, note that $c_y = -4$ for this mode, so that the mass-shell condition (66) implies,

$$(j + 4 + \nu^2 + c_y)|_{j=1} = 0 \ (0,0,1) \text{ mode},$$
$$(3j + 5 + \nu^2 + c_y)|_{j=1} = 0 \ (1,0,1) \text{ mode}, \tag{A69}$$

or, equivalently, $i\nu = 1$ and $i\nu = 2$, respectively, for these two modes. It is now obvious that the terms proportional to $(\epsilon \cdot q)$ in (35) are in the form of this $(n,l,m) = (1,0,1)$ mode. With the relations $x^3 \partial_x [x^{-3+2} K_1(x)] = -x^3 [x^{-1} K_2(x)]$ and $\partial_x [x^2 K_2(x)] = -x^2 K_1(x)$, one can also see that the wave function for the $(n,l,m) = (0,0,1)$ mode is also proportional to the form given in (35) when the on-shell condition is imposed.

5. Projection operator of SO(3, 1) tensors

Note first that

$$a = \sum_{s=0}^{r} \sum_{N=0}^{[s/2]} \tilde{E}^N D_\Delta^{s-2N} [a^{(s,N)}] \tag{A70}$$

is an *orthogonal* decomposition of a totally symmetric SO(3, 1) tensor a of rank r into totally symmetric 4D-traceless 4D-transverse SO(3, 1) tensors $a^{(s,N)}$ of rank $(r-s)$. Here, the metric is given by

$$[b_{(-\Delta)}] \cdot [a_{(\Delta)}] := [b_{(-\Delta)}]_{\rho_1 \cdots \rho_r} [a_{(+\Delta)}]_{\sigma_1 \cdots \sigma_r} \eta^{\hat{\rho}_1 \hat{\sigma}_1} \cdots \eta^{\hat{\rho}_r \hat{\sigma}_r}, \tag{A71}$$

as in the main text. To see that the decomposition is orthogonal under this metric, one needs to use only (A37) to verify that

$$[\tilde{E}^M D_{-\Delta}^{t-2M} [b^{(t,M)}]] \cdot [\tilde{E}^N D_\Delta^{s-2N} [a^{(s,N)}]]$$
$$= \delta_{M,N} \delta_{t-2M,s-2N} \frac{\Delta^{2(s-2N)}}{b_{s,N}^{(r-s)}} [b^{(t,M)}] \cdot [a^{(s,N)}]. \tag{A72}$$

Using the fact that (A70) is an orthogonal decomposition, let us construct projection operators $\overline{P}^{(r;s,N)}$ that extract various components $a^{(s,N)}$ from a totally symmetric SO(3, 1) tensor a of rank r. We introduced an operator $P^{(r)}$ in (102) which acts on rank-r SO(3, 1) tensors. From what we have seen above, it can be used to extract the $a^{(s,N)=(0,0)}$ component from a rank-r tensor a. That is, $\overline{P}^{(r;0,0)} = P^{(r)}$. It is straightforward to see that the projection operator for other components $a^{(s,N)}$ with general (s,N) is given by

$$\overline{P}^{(r;s,N)} := \sum_a \frac{b_{s,N}^{(r-s)}}{\Delta^{2(s-2N)}} \frac{1}{D_a} (\tilde{E}^N D_\Delta^{s-2N} [\epsilon_a])_{\rho_1 \cdots \rho_r}$$
$$\times (\tilde{E}^N D_{-\Delta}^{s-2N} [\epsilon_a])_{\sigma_1 \cdots \sigma_r}, \tag{A73}$$

where ϵ_a's are an orthogonal basis of totally symmetric 4D-traceless 4D-transverse SO(3, 1) tensors of rank $(r-s)$.

It is also useful to have a concrete form of the projection operator $P^{(r)}$, not just its abstract definition in (102). We find that it is given by

$$P^{(r)} \cdot a = \sum_{M=0}^{[\frac{j}{2}]} \frac{(-1)^M \Gamma(r + \frac{1}{2} - M)}{4^M M! \Gamma(r + \frac{1}{2})}$$
$$\times \sum_{k=0}^{r-2M} \frac{(-1)^k}{k!} [\tilde{E}^M D^k OP_{(p,q)=(M,k)}] \cdot a, \tag{A74}$$

where $OP_{(p,q)}$ is the operator given in (A37). A totally symmetric rank-r tensor a is converted once into rank-$(r - 2M - k)$ tensors, and then they are converted back to a rank-r tensor under the operator $P^{(r)}$. To see that all of the $\tilde{E}^N D^{s-2N} [a^{(s,N)}]$ components are projected out by $P^{(r)}$, one needs to use only the following formula [40]:

$$\sum_{M=0}^{N} (-1)^M {}_N C_M \frac{\Gamma(r - N + \frac{3}{2})}{\Gamma(r - N + \frac{3}{2} - M)} \frac{\Gamma(r + \frac{1}{2} - M)}{\Gamma(r + \frac{1}{2})}$$
$$= \frac{\Gamma(\frac{1}{2} - r)}{\Gamma(\frac{1}{2} - r + N) \Gamma(1 - N)}, \tag{A75}$$

which vanishes for an integer $N \geq 0$.

6. Some tensor computations

Let us derive a more concrete expression for the product $(q^{\mu_1} \ldots q^{\mu_r}) \cdot [P^{(r)}]^{\nu_1 \ldots \nu_r}_{\mu_1 \ldots \mu_r} \cdot (p_{\nu_1} \ldots p_{\nu_r})$ by using the explicit expression for the projection operator $P^{(r)}$ to the SO(3, 1)-transverse SO(3, 1)-traceless rank-r tensor:

$$(q^{\mu_1} \ldots q^{\mu_r}) \cdot [P^{(r)}]^{\nu_1 \ldots \nu_r}_{\mu_1 \ldots \mu_r} \cdot (p_{\nu_1} \ldots p_{\nu_r})$$
$$= \sum_{M=0}^{[r/2]} \frac{(-1)^M \Gamma(j + \frac{1}{2} - M)}{4^M M! \Gamma(j + \frac{1}{2})} \frac{r!}{(r - 2M)!}$$
$$\times \left[q^2 - \frac{(q \cdot \Delta)^2}{\Delta^2} \right]^M (p^2)^M (q \cdot p)^{r-2M}, \tag{A76}$$

where we made $p \cdot \Delta = 0$. Within the regime of $q^2, (p \cdot q), (q \cdot \Delta) \gg \Lambda^2, \Delta^2, p^2$ that we have been interested in this article, $(q \cdot \Delta)^2 / \Delta^2 \gg q^2$. Thus, after ignoring q^2,

$$(q^{\mu_1}\dots q^{\mu_r})\cdot[P^{(r)}]^{\nu_1\dots\nu_r}_{\mu_1\dots\mu_r}\cdot(p_{\nu_1}\dots p_{\nu_r})$$
$$\approx (p\cdot q)^r\sum_{M=0}^{[r/2]}\frac{\Gamma(r+\frac{1}{2}-M)}{4^M M!\Gamma(r+\frac{1}{2})}\frac{r!}{(r-2M)!}\left[\left(\frac{q\cdot\Delta}{q\cdot p}\right)^2\frac{p^2}{\Delta^2}\right]^M$$
$$=: (p\cdot q)^r\times\hat{d}_r(\eta,\Delta^2). \tag{A77}$$

This introduces $\hat{d}_r$, which is a polynomial of skewness $(q\cdot\Delta)/(p\cdot q)=-2\eta$ of degree $2[r/2]$.

When r is even, this polynomial of η can also be rewritten by using a Legendre polynomial, $P_\ell(x)$, which is defined by ([41], page 82)

$$P_\ell(x) = {}_2F_1\left(-\ell,\ell+1,1;\frac{1-x}{2}\right)$$
$$= \frac{(2\ell-1)!!}{\ell!}x^\ell\,{}_2F_1\left(-\frac{\ell}{2},\frac{1-\ell}{2},\frac{1}{2}-\ell;\frac{1}{x^2}\right). \tag{A78}$$

For an even r,

$$\hat{d}_r(\eta,\Delta^2)=\sum_{M=0}^{r/2}\frac{(-\frac{r}{2})_M(\frac{1-r}{2})_M}{M!(\frac{1}{2}-r)_M}\left(-\frac{4p^2}{\Delta^2}\eta^2\right)^M={}_2F_1\left(-\frac{r}{2},\frac{1-r}{2},\frac{1}{2}-r;\frac{(4m_h^2+\Delta^2)\eta^2}{\Delta^2}\right)$$
$$=\frac{r!}{(2r-1)!!}\left[\sqrt{\frac{4m_h^2+\Delta^2}{\Delta^2}}\eta\right]^r P_r\left(\sqrt{\frac{\Delta^2}{4m_h^2+\Delta^2}}\frac{1}{\eta}\right)=:\hat{d}_r([\eta]), \tag{A79}$$

where we used the kinematical relation $4p^2=-(4m_h^2+\Delta^2)$.

Similarly, it is also necessary to compute the following expression in order to study the $m=0$ exchange amplitude in Sec. VI C 2:

$$\left[\sum_{a\neq b}\epsilon^{2*}_{\rho_a}\epsilon^1_{\rho_b}q_{\rho_1}\cdots{}_{\check{\rho_a}\check{\rho_b}}\cdots q_{\rho_j}\right]\cdot[P^{(j)}]^{\hat{\rho}_1\cdots\hat{\rho}_j}_{\sigma_1\cdots\sigma_j}\cdot[p^{\hat{\sigma}_1}\cdots p^{\hat{\sigma}_j}], \tag{A80}$$

which is also evaluated as above. The term proportional to $\eta^{\hat{\mu}\hat{\nu}}\epsilon^{2*}_\nu\epsilon^1_\mu$ (the contribution to the structure function V_1) is

$$2^2\sum_{M=1}^{[j/2]}\frac{(-1)^M\Gamma(j+\frac{1}{2}-M)}{4^M M!\Gamma(j+\frac{1}{2})}\frac{j!}{(j-2M)!2!}\left[q^2-\frac{(q\cdot\Delta)^2}{\Delta^2}\right]^{M-1}(p^2)^M(q\cdot p)^{j-2M}$$
$$\approx -2\frac{\Delta^2}{(q\cdot\Delta)^2}\times(q\cdot p)^j\sum_{M=1}^{[j/2]}\frac{\Gamma(j+\frac{1}{2}-M)}{4^M M!\Gamma(j+\frac{1}{2})}\frac{j!}{(j-2M)!}\left[\left(\frac{q\cdot\Delta}{q\cdot p}\right)^2\frac{p^2}{\Delta^2}\right]^M. \tag{A81}$$

This expression is once again a polynomial of η of degree $2[j/2]-2$ and is roughly of order $\Delta^2/(q\cdot p)^2$ times the expression (A77).

We will also need the following computation in Secs. VI C 3 and VI C 4:

$$(q_{\mu_1}\cdots q_{\mu_{j-k}})\cdot(\tilde{E}^N D^{s-2N}_{-\Delta}[\epsilon^{(0,0,m)}])^{\hat{\mu}_1\cdots\hat{\mu}_{j-k}}=\frac{(j-k)!}{(j-m)!}\left[q^2-\frac{(q\cdot\Delta)^2}{\Delta^2}\right]^N(-iq\cdot\Delta)^{s-2N}[(q_{\mu_1}\cdots q_{\mu_{j-m}})\cdot\epsilon^{(0,0,m)}]. \tag{A82}$$

APPENDIX B: CONFORMAL OPE COEFFICIENTS FROM AdS INTEGRALS

Let us introduce an integral,

$$C_1(\delta,\vartheta):=(1-\vartheta^2)^{1/2}\int_0^\infty dy y^{1+\delta}K_1(y\sqrt{1+\vartheta})K_1(y\sqrt{1-\vartheta}), \tag{B1}$$

which we encounter as the photon-photon– Pomeron/Reggeon vertex on AdS_5. $\vartheta=\eta/x$ and $\delta=j+i\nu$ in that context.

It is known ([42], page 101), if $\mathrm{Re}(\alpha+\beta)>0$ and $\mathrm{Re}(1\pm\nu\pm\mu-\rho)>0$, that

$$\int_0^\infty dt t^{-\rho}K_\mu(\alpha t)K_\nu(\beta t) = 2^{-\rho-2}\alpha^{\rho-\nu-1}\beta^\nu[\Gamma(1-\rho)]^{-1} \times\Gamma\left(\frac{1+\nu+\mu-\rho}{2}\right)\Gamma\left(\frac{1+\nu-\mu-\rho}{2}\right)\Gamma\left(\frac{1-\nu+\mu-\rho}{2}\right)\Gamma\left(\frac{1-\nu-\mu-\rho}{2}\right) \times {}_2F_1\left(\frac{1+\nu+\mu-\rho}{2},\frac{1+\nu-\mu-\rho}{2};1-\rho;1-\frac{\beta^2}{\alpha^2}\right). \tag{B2}$$

Substituting in $\rho=-1-\delta$, $\mu=1$, $\nu=-1$, $\alpha=\sqrt{1-\vartheta}$, and $\beta=\sqrt{1+\vartheta}$, we obtain

$$C_1(\delta,\vartheta)=\frac{\Gamma(\frac{\delta}{2})(\Gamma(\frac{\delta}{2}+1))^2\Gamma(\frac{\delta}{2}+2)}{\Gamma(\delta+2)}2^{\delta-1}(1-\vartheta)^{-\frac{\delta}{2}}{}_2F_1\left(\frac{\delta}{2},\frac{\delta+2}{2};\delta+2;\frac{2\vartheta}{\vartheta-1}\right). \tag{B3}$$

An equivalent, but slightly different expression is also obtained by using the following relation ([41], page 60):

$${}_2F_1(\alpha,\beta,2\beta;2z)=(1-z)^{-\alpha}{}_2F_1\left(\frac{\alpha}{2},\frac{\alpha+1}{2},\beta+\frac{1}{2};\left(\frac{z}{1-z}\right)^2\right); \tag{B4}$$

namely,

$$C_1(\delta,\vartheta)=2^{\delta-1}\frac{\delta+2}{\delta}\frac{(\Gamma(\frac{\delta}{2}+1))^4}{\Gamma(\delta+2)}{}_2F_1\left(\frac{\delta}{4},\frac{\delta}{4}+\frac{1}{2};\frac{\delta}{2}+\frac{3}{2};\vartheta^2\right). \tag{B5}$$

As a function of $\vartheta=\eta/x$, (B3) and (B5) are precisely of the form (25) and (26), respectively, required in the conformal OPE coefficients.

[1] J. Polchinski and M. J. Strassler, Phys. Rev. Lett. **88**, 031601 (2002).
[2] J. Polchinski and M. J. Strassler, J. High Energy Phys. 05 (2003) 012.
[3] R. C. Brower, J. Polchinski, M. J. Strassler, and C.-I. Tan, J. High Energy Phys. 12 (2007) 005.
[4] Y. Hatta, E. Iancu, and A. H. Mueller, J. High Energy Phys. 01 (2008) 026.
[5] L. Cornalba and M. S. Costa, Phys. Rev. D **78**, 096010 (2008); L. Cornalba, M. S. Costa, and J. Penedones, J. High Energy Phys. 03 (2010) 133; Phys. Rev. Lett. **105**, 072003 (2010).
[6] R. C. Brower, M. Djuric, I. Sarcevic, and C.-I Tan, J. High Energy Phys. 11 (2010) 051.
[7] R. Nishio and T. Watari, Phys. Lett. B **707**, 362 (2012); Phys. Rev. D **84**, 075025 (2011).
[8] For example, see G. Altarelli, R. D. Ball, and S. Forte, in *Proceedings of 17th Autumn School, QCD: Perturbative or Nonperturbative?, Lisbon, Portugal, 1999*, edited by L. S. Ferreira *et al.* (World Scientific, Singapore, 2001).
[9] M. Diehl, Phys. Rep. **388**, 41 (2003); A. V. Belitsky and A. V. Radyushkin, Phys. Rep. **418**, 1 (2005).
[10] O. V. Teryaev, arXiv:hep-ph/0510031; I. V. Anikin and O. V. Teryaev, Phys. Rev. D **76**, 056007 (2007); M. Diehl and D. Y. Ivanov, Eur. Phys. J. C **52**, 919 (2007); M. V. Polyakov, Phys. Lett. B **659**, 542 (2008).
[11] M. Burkardt, Phys. Rev. D **62**, 071503 (2000); **66**, 119903 (E) (2002); J. P. Ralston and B. Pire, Phys. Rev. D **66**, 111501 (2002); M. Diehl, Eur. Phys. J. C **25**, 223 (2002); **31**, 277(E) (2003); M. Burkardt, Int. J. Mod. Phys. A **18**, 173 (2003).
[12] M. S. Costa, V. Goncalves, and J. Penedones, J. High Energy Phys. 12 (2012) 091.
[13] M. S. Costa, J. Drummond, V. Goncalves, and J. Penedones, J. High Energy Phys. 04 (2014) 094; M. S. Costa, V. Goncalves, and J. Penedones, J. High Energy Phys. 09 (2014) 064.
[14] R. Nishio and T. Watari, arXiv:1212.3322; arXiv:1408.6365.
[15] A. V. Belitsky, B. Geyer, D. Mueller, and A. Schafer, Phys. Lett. B **421**, 312 (1998); M. V. Polyakov, Nucl. Phys. **B555**, 231 (1999); M. V. Polyakov and A. G. Shuvaev, arXiv:hep-ph/0207153.
[16] V. Guzey and M. V. Polyakov, Eur. Phys. J. C **46**, 151 (2006); V. Guzey and T. Teckentrup, Phys. Rev. D **74**, 054027 (2006).
[17] D. Mueller and A. Schafer, Nucl. Phys. **B739**, 1 (2006).

[18] K. Kumericki, D. Mueller, and K. Passek-Kumericki, Nucl. Phys. **B794**, 244 (2008).
[19] M. Vanderhaeghen, P. A. M. Guichon, and M. Guidal, Phys. Rev. Lett. **80**, 5064 (1998); Phys. Rev. D **60**, 094017 (1999); A. V. Belitsky, D. Mueller, and A. Kirchner, Nucl. Phys. **B629**, 323 (2002); M. Diehl and S. Sapeta, Eur. Phys. J. C **41**, 515 (2005).
[20] X.-D. Ji, Phys. Rev. D **55**, 7114 (1997).
[21] A. V. Efremov and A. V. Radyushkin, Teor. Mat. Fiz. **42**, 147 (1980) [Theor. Math. Phys. **42**, 97 (1980)].
[22] A. V. Belitsky and D. Mueller, Nucl. Phys. **B527**, 207 (1998).
[23] I. R. Klebanov and E. Witten, Nucl. Phys. **B536**, 199 (1998).
[24] S. Ferrara, R. Gatto, and A. F. Grillo, Nucl. Phys. **B34**, 349 (1971).
[25] D. Mueller, Phys. Rev. D **58**, 054005 (1998).
[26] S. S. Gubser, I. R. Klebanov, and A. M. Polyakov, Nucl. Phys. **B636**, 99 (2002).
[27] I. R. Klebanov and M. J. Strassler, J. High Energy Phys. 08 (2000) 052.
[28] R. Rohm and E. Witten, Ann. Phys. (N.Y.) **170**, 454 (1986).
[29] E. Witten, Nucl. Phys. **B268**, 253 (1986).
[30] E. Cremmer, A. Schwimmer, and C. B. Thorn, Phys. Lett. B **179**, 57 (1986); D. J. Gross and A. Jevicki, Nucl. Phys. **B283**, 1 (1987); **B287**, 225 (1987); W. Taylor, Nucl. Phys. **B585**, 171 (2000).
[31] H. Hata, "String theory and string field theory" (in Japanese).
[32] S. B. Giddings, Nucl. Phys. **B278**, 242 (1986).
[33] C. B. Thorn, Nucl. Phys. **B287**, 61 (1987).
[34] O. Aharony, S. S. Gubser, J. M. Maldacena, H. Ooguri, and Y. Oz, Phys. Rep. **323**, 183 (2000).
[35] R. R. Metsaev and A. A. Tseytlin, Phys. Lett. B **436**, 281 (1998).
[36] B. Zwiebach, Nucl. Phys. **B390**, 33 (1993).
[37] M. Saadi and B. Zwiebach, Ann. Phys. (N.Y.) **192**, 213 (1989).
[38] L. Cornalba, arXiv:0710.5480.
[39] H. J. Kim, L. J. Romans, and P. van Nieuwenhuizen, Phys. Rev. D **32**, 389 (1985).
[40] Mathematica, Wolfram Research.
[41] S. Moriguchi, K. Udagawa, and S. Hitotsumatsu, *Suu-Gaku Koushiki Shu (Math Formulas) III* (Iwanami Shoten, Tokyo, 1987).
[42] W. Magnus, F. Oberhettinger, and R. Soni, *Formulas and Theorems for the Special Functions in Mathematical Physics* (Springer-Verlag, Berlin, 1966).

Published for SISSA by Springer

Received: July 12, 2015
Revised: September 30, 2015
Accepted: October 25, 2015
Published: November 10, 2015

Statistics of F-theory flux vacua for particle physics

Taizan Watari

Kavli Institute for the Physics and Mathematics of the Universe, University of Tokyo, Kashiwa-no-ha 5-1-5, 277-8583, Japan

E-mail: taizan.watari@ipmu.jp

Abstract: Supersymmetric flux compactification of F-theory in the geometric phase yields numerous vacua, and provides an ensemble of low-energy effective theories with a variety of symmetry, matter multiplicity and Lagrangian parameters. Theoretical tools have already been developed so that we can study how the statistics of those flux vacua depend on the choice of symmetry and some of the Lagrangian parameters. In this article, we estimate the fraction of i) vacua that have a U(1) symmetry for spontaneous R-parity violation, and ii) those that realise ideas which achieve hierarchical eigenvalues of the Yukawa matrices. We also learn a lesson that the number of flux vacua is reduced very much when the unbroken $U(1)_Y$ symmetry is obtained from a non-trivial Mordell-Weil group, while it is not, when $U(1)_Y$ is in SU(5) unification. It also turns out to be likely that vacua with an approximate U(1) symmetry form a locus of accumulation points of the flux vacua distribution.

Keywords: Flux compactifications, F-Theory, Differential and Algebraic Geometry, GUT

ArXiv ePrint: 1506.08433

Open Access, © The Authors.
Article funded by SCOAP^3.

doi:10.1007/JHEP11(2015)065

JHEP11(2015)065

Contents

1 Introduction **1**

2 A quick review of the formulation **3**

3 Fraction of flux vacua with enhanced symmetries **4**
- 3.1 Statistical cost of spontaneous R-parity violation 4
- 3.2 GUT's and SU(3) × SU(2) × U(1) 10

4 Distribution of Lagrangian parameters **13**
- 4.1 Symmetry breaking scale of an approximate U(1) symmetry 13
- 4.2 Statistical cost of Yukawa hierarchical structure problem 16
  - 4.2.1 Split matter curve under a U(1) symmetry 18
  - 4.2.2 Gaussian wavefunction due to large complex structure 19

A Fourfolds for SU(5) × U(1) symmetry **22**
- A.1 $\mathrm{Bl}_{[1:0:0]}WP_{[1:2:3]}$-fibred ambient space 23
- A.2 F_1-fibred ambient space 26

B SU(6) 7-branes for up-type Yukawa coupling **29**

C Monodromy around the U(1)-enhancement limit **32**
- C.1 $6g-3$ topological four-cycles 32
- C.2 Monodromy 34

1 Introduction

Flux compactification of F-theory/Type IIB string theory generates a discretum of vacua in the complex structure parameter space, making it possible to *count* vacua and argue statistics of some of observables in the low-energy effective theories [1, 2]. It is virtually impossible to work out the vacuum for each one of individual flux configurations in practice, but this difficulty can be overcome in an approximate treatment of this problem introduced by Ashok-Denef-Douglas [3, 4]. Their treatment becomes a very powerful tool, when used for F-theory compactifications [2, 5], since one can estimate the number of flux vacua that lead to low-energy effective theories with a given set of 7-brane gauge groups and the number of generations of matter fields. It turns out [6, 7] that the number of flux vacua is reduced in the order of $10^{-O(100)}$ generically as we require the rank of 7-brane gauge group to be higher by one. Focusing on an ensemble of flux vacua with a given 7-brane gauge group, one further finds that the number of flux vacua follows the Gaussian distribution on the number of generations $N_{\rm gen}$, with the variance $\langle N_{\rm gen}^2 \rangle$ not more than O(1).

JHEP11(2015)065

Obviously the analysis method above can be applied also to more refined and practical problems. It often happens in model building that more than one theoretically and phenomenologically consistent idea (model) has been proposed for a given phenomenon, and one cannot say which is better within the framework of low-energy effective field theory. By counting the number of flux vacua that realise various ideas and comparing the numbers, however, one can introduce a measure of naturalness on those consistent ideas. Such attempts have been made often in Type IIB compactifications so far; we are returning to this program by using F-theory compactifications so that we can address questions involving non-Abelian/Abelian gauge groups in the low-energy effective theories.

There are two kinds of naturalness/statistics questions. Note first that a low-energy effective theory is specified by providing a set of model data; a set of data consists of algebraic data (e.g. symmetry), topological data (e.g., matter multiplicity) and moduli data (i.e. coupling constants, symmetry breaking scale, etc.). Since a choice of algebraic and topological data is discrete in nature, we ask such questions as how much fraction of flux vacua survives when a certain symmetry is imposed. Section 3 is devoted to this category of problems. Moduli data, on the other hand, show up as continuous parameters in effective theories, and the flux vacua statistics need to be presented as a continuous distribution on the parameter space. This second category of questions is addressed by using F-theory compactifications in section 4.

Sections 3.1 and 3.2 deal with

- dimension-4 proton decay: spontaneous R-parity violation (v.s. $\mathbb{Z}_2$ symmetry),
- SU(5) unification v.s. SU(3) $\times$ SU(2) $\times$ U(1) without unification,

respectively. We do not get our hands on discrete symmetries in this article; we just estimate statistical cost of introducing an extra U(1) symmetry, which is relevant to both of the physics questions above. Section 4 begins with a recap of [53, 55]; observations made in these articles — originally in Type IIB context — hold readily in F-theory compactifications. We then discuss

- distribution of symmetry breaking scale of an approximate U(1) symmetry,
- two solutions to the hierarchical structure problem of Yukawa matrices,

in sections 4.1 and 4.2, respectively. The first and last of the four subjects above are found in the list of "possible applications" in [6, 7], and we just carry out the analysis in this article. Discussions in sections 3.2 and 4.1, on the other hand, are more like thought provoking ideas than solid analysis. The appendix A is a brief review note on two constructions of fourfold geometry for F-theory compactifications with a U(1) symmetry; the appendix B provides a little more details about SU(6) unification models with up-type Yukawa coupling in F-theory than in the literature. Monodromy of four-cycles in a fourfold is studied in the appendix C.2, as we need the result in section 4.1.

JHEP11(2015)065

2 A quick review of the formulation

Suppose that one is interested in estimating the number of flux vacua which have a given set of algebraic and topological properties in the effective theory below the Kaluza-Klein scale. Once we specify topology of the base threefold B_3 and of the divisor class $S \subset B_3$ supporting unification gauge group (7-brane),[1] we can think of a family of non-singular Calabi-Yau fourfolds $\hat{Y}_4$ with elliptic fibration over B_3 consistent with the set of algebraic properties one is interested in. Let $\mathcal{M}_*$ be the space of complex structure parameters for this family.[2] Statistics of flux vacua should turn out as a scatter plot on this parameter space $\mathcal{M}_*$. When the ensemble of topological flux configurations is replaced by its continuous approximation [3, 4], the scatter plot of vacua turns into a vacuum distribution function (an (m,m)-form on $\mathcal{M}_*$; $m := \dim_{\mathbb{C}}\mathcal{M}_*$). Ashok-Douglas [3] introduced vacuum index density $d\mu_I$, to which individual flux vacua contribute by ± 1 (rather than by $+1$). It is also an (m,m)-form on $\mathcal{M}_*$ under the continuous approximation, and is much easier to compute [3, 4]. For this practical reason, we also use the vacuum index density $d\mu_I$ in this article, instead of the vacuum density.

The vacuum index density turns out to have the following expression [2–5]:[3]

$$d\mu_I \sim \left\{ \begin{array}{ll} \dfrac{(2\pi L_*)^{K/2}}{(K/2)!} & \text{if } K \ll L_* \\ \dfrac{K^{L_*}}{L_*!} & \text{if } L_* \ll K \end{array} \right\} \times \rho_I, \qquad \rho_I = \det{}_{m\times m}\left(-\frac{R}{2\pi i} + \frac{\omega}{2\pi}\mathbf{1}_{m\times m}\right). \tag{2.1}$$

Here, R is the curvature two-form of $T\mathcal{M}_*$ and ω the Kähler form on $\mathcal{M}_*$. K is the dimension of an Affine subspace

$$\{G_{\text{fix}} + \Delta G \mid \Delta G \in H_{\text{scan}}\} \subset H^4(\hat{Y}_4;\mathbb{R}) \tag{2.2}$$

in which the four-form flux is scanned freely; H_{scan} is a vector subspace of $H^4(\hat{Y}_4;\mathbb{R})$, and $K := \dim_{\mathbb{R}} H_{\text{scan}}$. L_* is the upper bound on the 3-brane charge that the scanning component of the four-form flux ΔG contributes to. See [6, 7] for more detailed explanations. For the ensemble of fluxes above to correspond to an inclusive enough ensemble of effective theories with a given set of algebraic and topological data, H_{scan} needs to contain the primary horizontal component

$$\left[H^{4,0}(\hat{Y}_4;\mathbb{C}) + \text{h.c.}\right] \oplus \left[H^{3,1}(\hat{Y}_4;\mathbb{C}) + \text{h.c.}\right] \oplus H^{2,2}_H(\hat{Y}_4;\mathbb{R}). \tag{2.3}$$

[1] In this article, except in section 3.2, we use the two expressions *unification group* and *non-Abelian 7-brane gauge group* interchangeably, because gauge coupling unification is guaranteed when a flux on S breaks the non-Abelian gauge group symmetry on S to its subgroup $G_1 \times G_2 \times \cdots$.

[2] We avoid using the term "moduli space" for this meaning for the most part in this article. The space $\mathcal{M}_*$ is introduced and used in the present context just as a mathematical construct on which the result (vacuum index density $d\mu_I$) is presented, not as the non-linear sigma model target space in some approximation scheme of low-energy effective theory; once flux is introduced, these two notions are not the same. We hope to make this distinction clear by avoiding the word "moduli space" for the former, although it is perfectly correct to refer to the former as a moduli space in math context.

[3] The prefactor for $L_* \ll K$ was discussed in [3], but was corrected in [2, 6, 7].

JHEP11(2015)065

This condition on the minimum inclusiveness of flux ensemble is also known to be a necessary and sufficient condition for the formula of ρ_I in (2.1) to hold in F-theory compactifications [2, 5]. This means that

$$K \geq K_0 := 2(1 + h^{3,1}) + h^{2,2}_H. \tag{2.4}$$

Specific physics questions of one's interest determine how inclusive an ensemble of effective theories one wants to pay attention to, and how large a subspace of $H^{2,2}_V(\hat{Y}_4;\mathbb{R}) \oplus H^{2,2}_{RM}(\hat{Y}_4;\mathbb{R})$ should be included in $H_{\rm scan}$; the choice of $K - K_0$ is discussed in an application to the spontaneous R-parity violation scenario in section 3.1; see also [5–7].

As the integral $\int \rho_I$ over a fundamental domain of $\mathcal{M}_*$ usually turns out to have a value of order unity, we can just use the prefactor in (2.1) as an estimate of the number of flux vacua that have a set of algebraic and topological data specified at the beginning; we just use this prefactor for the study in section 3. The distribution ρ_I can be used to study statistical distribution of coupling constants / Lagrangian parameters within a class of low-energy effective theories with a given set of algebraic and topological properties; this ρ_I is used for the study in section 4.

One needs to keep in mind that the distribution as well as the estimate of the number of flux vacua here does not require that the vacuum expectation value (vev) of superpotential is much smaller than the Planck-scale-cubed; a large fraction of vacua has AdS supersymmetry. Stabilisation of Kähler moduli is not studied either. For these reasons and for other reasons stated elsewhere in this article, the formula (2.1) should be regarded only as partial information of statistical distribution of observables in string landscapes.

3 Fraction of flux vacua with enhanced symmetries

3.1 Statistical cost of spontaneous R-parity violation

Dimension-4 proton decay problem in supersymmetric Standard Models can be avoided, for example, by either imposing a $\mathbb{Z}_2$-symmetry (matter/R-parity) or assuming spontaneous breakdown of a U(1) symmetry triggered by a non-zero Fayet-Iliopoulos parameter (spontaneous R-parity violation).[4] When we assume that the $\mathbb{Z}_2$ symmetry originates from a $\mathbb{Z}_2$ symmetry of a geometry for compactification, complex structure parameters of the geometry need to be in a special sub-locus for enhancement of the $\mathbb{Z}_2$ symmetry [8, 9], and the flux vacua that end up in such a sub-locus will constitute small fraction of all the flux vacua [10, 11] (see also a remark at the end of this section 3.1). The spontaneous R-parity violation scenario (see [12–14] for its string implementation) also requires tuning, because we need a U(1) symmetry. This tuning should be translated into restriction on flux configuration. In this section 3.1, we estimate the fraction of flux configurations that have an extra U(1) symmetry. Comparing the fraction of flux vacua for the spontaneous R-parity

[4] For right-handed neutrinos to be able to have large Majorana masses, it is better that the U(1) symmetry is broken at high energy. Despite the spontaneous breaking, the SUSY-zero mechanism [15] remain at work in getting rid of dangerous proton decay operators at least for some UV constructions (see [13] for discussion).

JHEP11(2015)065

violation and that for matter/R-parity, one could argue which solution to the dimension-4 proton decay problem is more "natural" in terms of flux vacua statistics.

There are two different ways to implement an extra U(1) symmetry in F-theory compactifications. One is to assume a 7-brane locus $S \times \mathbb{R}^{3,1}$ with an SU(6) or SO(10) gauge group, and introduce a U(1) flux on the complex surface S, so that the symmetry is broken[5] from SU(6) or SO(10) to $\mathrm{SU}(3)_C \times \mathrm{SU}(2)_L \times \mathrm{U}(1)_Y \times \mathrm{U}(1)$ [12, 14].[6] The other [20–23] is to get an extra U(1) symmetry by assuming a Calabi-Yau fourfold with a non-trivial Mordell-Weil group [24]. In the latter implementation, more variety is available in the choice of U(1) charge assignment than those that follow from Heterotic string geometric (supergravity) compactification [25–28].

To get started, let us first take a moment to consider how one should choose $H_{\rm scan}$ for this problem. We address this question by working on a few concrete examples. First of all, the base threefold is set to be $B_3 = \mathbb{P}^1 \times \mathbb{P}^2$, and we require SU(5) 7-branes along a divisor $S = H_{\mathbb{P}^1} = \mathrm{pt} \times \mathbb{P}^2$ in B_3. There is a wide variety in constructing families of Calabi-Yau fourfolds with a non-trivial Mordell-Weil group[7] [27, 28], but we just pick up only two of them to work on; in both of the two constructions, a Calabi-Yau fourfold Y_4 is obtained as a hypersurface of an ambient space that has a toric surface fibration over the base manifold B_3; the fibre surface is a blow-up of $WP^2_{[1:2:3]}$ in one of the two, and it is $F_1 = dP_1$ in the other. The appendix A provides a brief summary note on the facts about the two constructions.

In the first construction (see the appendix A.1), where $\mathrm{Bl}_{[1:0:0]}WP^2_{[1:2:3]}$ is the fibre of the ambient space, the vertical component of $H^{2,2}$, namely, $H^{2,2}_V(\hat{Y}_4;\mathbb{Q})$, is of 11 dimensions. Four among them are generated by

$$\sigma_0 \cdot H_{\mathbb{P}^1}, \qquad \sigma_0 \cdot H_{\mathbb{P}^2}, \qquad H_{\mathbb{P}^1} \cdot H_{\mathbb{P}^2}, \qquad H_{\mathbb{P}^2} \cdot H_{\mathbb{P}^2}, \tag{3.1}$$

where σ_0 is a zero section of $\pi : \hat{Y}_4 \longrightarrow B_3$ and $H_{\mathbb{P}^2}$ the hyperplane divisor of $\mathbb{P}^2$. Four other generators are the vanishing two-cycles of rank-4 SU(5) symmetry fibred over $H_{\mathbb{P}^2}|_S$:

$$E_a \cdot H_{\mathbb{P}^2} \qquad\qquad (a = 1, 2, 3, 4), \tag{3.2}$$

where E_a's are the Cartan divisors of SU(5). All the three remaining generators are vanishing cycles associated with charged matter fields; two are for the $\bar{\mathbf{5}}_{-2}$ and $\bar{\mathbf{5}}_{+3}$ representations of the $\mathrm{SU}(5) \times \mathrm{U}(1)$ symmetry, and the last one for the $\mathbf{1}_5$ representation. The dimension

[5] The F-theory implementation of spontaneous R-parity violation scenario is always an example of "T-brane" [16]. The D-term condition $\sum_i q_i|\phi_i|^2 - \xi = 0$ in the 4D effective theory corresponds [17, 18] to a (D-term) BPS condition $[\varphi, \overline{\varphi}] + \omega \wedge F = 0$ in the effective field theory on $S \times \mathbb{R}^{3,1}$ (Katz-Vafa type field theory [19]). The off-diagonal components of the Higgs field vev $\langle\varphi\rangle$ is therefore essential in the spontaneous R-parity violation scenario [12, 14].

[6] We maintain the discussion simple here, by assuming SU(5) unification. Once the "tempting argument" in page 8 is verified, however, it will be obvious what to conclude about the statistical cost of various implementations of the spontaneous R-parity violation scenario even in the absence of SU(5) unification.

[7] We do not work on the $H_{\rm scan}$-determination problem for the SU(6) or SO(10) realisation of the spontaneous R-parity violation in this article. That will be a doable problem. As we see later, however, precise determination of $H_{\rm scan}$ is not much of importance when $h^{3,1} \gg h^{1,1}$.

JHEP11(2015)065

of the remaining (i.e., non-horizontal non-vertical) component is determined by using the formula of [6, 7]; it turns out that $h^{2,2}_{RM} = 0$.

How should we choose $H_{\rm scan}$, then? First of all, the four-form ΔG needs to stay away from the 8 four-cycles listed in (3.1), (3.2) in order not to break the SO(3,1) and SU(5) unification symmetry.[8] Secondly, the net chirality "$N_{\rm gen}$" of $\bar{\mathbf{5}}_{-2}$ and $\bar{\mathbf{5}}_{+3}$ need to be fixed, which means that the integral of a four-form over these two cycles need to have values designated by a phenomenology (low-energy) model of interest. Therefore, there should not be scanning of ΔG in the 8+2 dimensions of $H^{2,2}_{RM}(\hat{Y};\mathbb{R}) \oplus H^{2,2}_{V}(\hat{Y}_4;\mathbb{R})$. The net chirality of the $\mathbf{1}_5$ field, however, may be chosen arbitrarily, as they do not appear in the low-energy spectrum in the spontaneous R-parity violation scenario.[9] Thus, this means that the four-form flux quanta can be scanned also in a one dimensional subspace of $H^{2,2}_{RM}(\hat{Y};\mathbb{R}) \oplus H^{2,2}_{V}(\hat{Y}_4;\mathbb{R})$ for the question we are facing. This brings us to

$$K = K_0 + 1. \tag{3.3}$$

Let us also work on one more construction of a Calabi-Yau fourfold with a non-trivial Mordell-Weil group, where the ambient space of $\hat{Y}_4$ has F_1 fibre (see a review in the appendix A.2). The construction comes with a topological choice of two divisors κ^1 and κ^2 on B_3; we stick to the same choice of $(B_3, [S])$ as before for now. The choice of the divisor classes κ^1, κ^2 changes the topological class of various matter curves, but the U(1) charge assignment is not affected. When the two divisors are parameterised by

$$\kappa^1 = a_1 H_{\mathbb{P}^1} + a_2 H_{\mathbb{P}^2}, \qquad \kappa^2 = b_1 H_{\mathbb{P}^1} + b_2 H_{\mathbb{P}^2}, \tag{3.4}$$

we focus our attention to the choices satisfying the conditions

$$b_1 = 0, \quad a_1 = 1, 2, \quad 0 \le a_2, b_2, \quad 0 \le 6 + a_2 - 2b_2, \quad 0 \le 6 - 2a_2 + b_2, \tag{3.5}$$

since some of the coefficients $A_{0,1}$, $A_{1,0}$, $B_{-1,1}$, $B_{0,0}$, $b_{1,-1|2}$, $C_{-2,1}$, $c_{-1,0|1}$, $c_{0,1|3}$ and $c_{1,-2|5}$ in the defining equation of $\hat{Y}_4$ (A.7), (A.8), (A.15) would vanish identically otherwise.[10] We further focus on cases with $a_2 = 0$, when the non-singular fourfold $\hat{Y}_4$ remains a flat fibration over B_3, and the low-energy spectrum is guaranteed to be free from tensionless string (cf [29–31]). This means that $0 \le b_2 \le 3$.

We studied geometry associated with $H^{2,2}(\hat{Y}_4)$ carefully for $a_1 = 1$ and $0 < b_2 < 3$. The non-vertical and non-horizontal component $H^{2,2}_{RM}(\hat{Y}_4)$ turns out to be trivial, which follows from the formula in [6, 7]. The vertical component $H^{2,2}_{V}(\hat{Y}_4;\mathbb{R})$ has 13 independent generators. The five independent generators other than those in (3.1), (3.2) all correspond to the vanishing cycles associated with charged matter fields. Three correspond to $\bar{\mathbf{5}}_0$, $\bar{\mathbf{5}}_1$

[8] We ignore SU(5) symmetry breaking to the Standard Model gauge group in this article, in order not to be distracted by unessential details.

[9] This argument is a little simplified too much for phenomenology, but we keep the story simple in this article (see [13] for more). After all, small changes in the argument in these paragraphs do not severely affect the qualitative conclusion we draw later in this section.

[10] This constraint is not from physical reasons; when one of those conditions is not satisfied, it often happens that analysis of geometry is done better by using an ambient space that has a fibre other than $F_1 = dP_1$.

JHEP11(2015)065

and $\bar{\mathbf{5}}_{-1}$, and two others to $\mathbf{1}_1$ and $\mathbf{1}_2$. Repeating the same argument as in the case of the first construction, we find that $H_{\rm scan}$ has a dimension

$$K = K_0 + 2. \tag{3.6}$$

Spontaneous R-parity violation, or the SUSY-zero mechanism more generally, is a little special in that the U(1) symmetry exerts some controlling power on types of interactions in the low-energy effective theory even after it is broken spontaneously at high-energy (primarily for dimension-4 operators, not necessarily on non-renormalisable operators; see [13] for discussion). Chirality is not well-defined any more, however, for SU(5)-neutral U(1)-charged matter fields after the spontaneous breaking of the U(1). Without the chirality protection, they do not survive in the low-energy spectrum.[11] For this reason, when we count the number of flux vacua that realise the spontaneous R-parity violation scenario, it is appropriate that the flux quanta changing the net chirality of SU(5)-neutral U(1)-charged fields should be scanned, as we have discussed above in detail. Some part of the vertical component of $H^{2,2}(\hat{Y}_4)$ therefore contributes to the dimension K of the scanning space of flux $H_{\rm scan}$, and $K > K_0$.

Let us now study the statistical cost of an extra U(1) symmetry. An easiest way to do that is to compute L_* and K for some concrete choices of $(B_3, [S])$, and work out the prefactor of (2.1). Comparing the prefactor for the case with an SU(5)×U(1) symmetry with the one for the case with just SU(5) unification, we can estimate the tuning cost of the spontaneous R-parity violation scenario. We will take this experimental approach first, by using $B_3 = \mathbb{P}^1 \times \mathbb{P}^2$ and $S = H_{\mathbb{P}^1}$ as before, and then discuss later how the tuning cost depends on the choice of $(B_3, [S])$.

It takes extra efforts to compute the dimension of the horizontal component $h^{2,2}_H$ (by using the formula in [6, 7]) and $\chi(\hat{Y}_4)$ (which are used for L_* in (2.1)), but there is a short-cut for such choices as $B_3 = \mathbb{P}^1 \times \mathbb{P}^2$. So long as $h^{3,1}(\hat{Y}_4) \gg h^{1,1}(\hat{Y}_4)$, which is the case for the topology of $(B_3, [S])$ we chose above, $H^{2,2}(\hat{Y}_4)$ is dominated by the horizontal component, i.e.,

$$h^{2,2}(\hat{Y}_4) \sim h^{2,2}_H(\hat{Y}_4) \gg h^{2,2}_V(\hat{Y}_4), \quad h^{2,2}_{RM}(\hat{Y}_4), \tag{3.7}$$

as experience in [6, 7] shows. This is enough to see that [2, 6, 7]

$$L_* \sim \frac{\chi(\hat{Y}_4)}{24} \sim \frac{b_4}{24} \sim \frac{K}{24}, \qquad \frac{K^{L_*}}{(L_*)!} \sim \exp\left[\frac{b_4(\hat{Y}_4)}{24}\ln(24)\right]. \tag{3.8}$$

Furthermore, if one is interested only in the ratio of two prefactors $K^{L*}/(L_*)!$ (relative tuning cost) in geometries with $h^{3,1} \gg h^{1,1}$, a relation [32–34]

$$h^{2,2} = 4(h^{3,1} + h^{1,1}) + 44 - 2h^{2,1} \tag{3.9}$$

[11] By "low-energy" and "high-energy", we mean $\mathcal{O}(1\text{–}1000)$ TeV and $\mathcal{O}(10^{13-16})$ GeV in this paragraph, whereas we also use the term low-energy (effective theory) in the sense that an intended energy scale is below the Kaluza-Klein scale. It will not be difficult to figure out from the context in which meaning "low-energy" is used at each place in this article.

JHEP11(2015)065

implies that $\Delta h^{2,2} \sim 4\Delta h^{3,1}$, and $\Delta b_4 \sim 6\Delta h^{3,1}$. All these combined allows us to estimate the relative tuning cost by [6, 7]

$$\exp\left[\frac{\ln(24)}{4} \times (\Delta h^{3,1})\right]. \tag{3.10}$$

Numerically,[12] $[\ln(24)]/4 \simeq 0.8$. The fraction of flux vacua with an enhanced symmetry is determined in this expression by the number of complex structure parameters to be tuned.

Now we only need to compute $h^{3,1}$'s and compare.

$$WP_{[1:2:3]}\text{-fibred, no gauge group} \qquad h^{3,1} = 3277, \tag{3.11}$$

$$WP_{[1:2:3]}\text{-fibred, SU(5) gauge group} \qquad h^{3,1} = 2148, \tag{3.12}$$

which are the reference values of $h^{3,1}$ for $(B_3, [S])$ we have chosen. In the spontaneous R-parity violation scenario realised in a rank-5 unification,

$$WP_{[1:2:3]}\text{-fibred, SO(10) gauge group} \qquad h^{3,1} = 2138, \tag{3.13}$$

$$WP_{[1:2:3]}\text{ fibred, SU(6) gauge group} \qquad h^{3,1} \sim 1900. \tag{3.14}$$

The values of $h^{3,1}$ are taken from [6, 7] for SU(5) and SO(10), and the value for SU(6) is computed in the appendix B. Among the Mordell-Weil implementations of the extra U(1), we have also computed $h^{3,1}$ for the two constructions referred to earlier (and reviewed in the appendix A); Batyrev's formula for toric hypersurface Calabi-Yau's is used for these results:

$$\mathrm{Bl}_{[1:0:0]}WP^2_{[1:2:3]}\text{-fibred} \qquad h^{3,1} = 932, \tag{3.15}$$

$$F_1\text{-fibred, no.2} \qquad h^{3,1} = 7(b_2)^2 - 12b_2 + 372, \quad (a_1 = 1, \quad 0 < b_2 < 3). \tag{3.16}$$

It turns out, for $(B_3, [S])$ we chose, that the cost of the Mordell-Weil implementations of the spontaneous R-parity violation comes at the order of e^{-1000}, relatively to generic SU(5) unification; the number of flux vacua is reduced that much by requiring an extra U(1) symmetry through the existence of a non-trivial section. In the other group of implementations, namely rank-5 unifications with U(1) flux, the cost comes out as something like e^{-10} for SO(10) and e^{-200} for SU(6). All these cost estimates have been read out by comparing $h^{3,1}$ in (3.13)–(3.16) with that in (3.12).

It is tempting to argue, based on the numerical experiment for a single choice of $(B_3, [S])$ though, that the Mordell-Weil implementations of an extra U(1) tend to be much more costly than those through unification with one rank higher.[13] Plausible explanation

[12] This numerical value should not be taken at face value. The underlying cohomology lattice of the flux scanning space H_{scan} is not necessarily unimodular, whereas the derivation of the prefactor $K^{L_*}/L_*!$ is stated in [2, 6, 7] in its simplest form, where the underlying lattice is unimodular. The relative tuning cost in (3.10) should be read only as $\exp[\mathcal{O}(1) \times (\Delta h^{3,1})]$.

[13] It is naive just to compare the tuning cost of those different implementations. The SO(10) and SU(6) implementations predict SO(10)-like and SU(6)-like flavour structure automatically, and the tuning cost for appropriate flavour structure in SU(5) unification is not the same as those in SU(6) or SO(10) unification. This tuning cost for flavour is significant in SO(10) unification, because both quark doublets and lepton doublets live on the same matter curve. The tuning cost for flavour in SU(6) unification will vary for its particle identifications; see discussion in the appendix B.

JHEP11(2015)065

will be that the Mordell-Weil implementations require more parameters to be tuned, because existence of an extra section restrains geometry over the entire base manifold B_3; the implementations through rank-5 unification, on the other hand, require higher order of vanishing of some sections along a divisor in B_3, which is a condition only on semi-local geometry. It is desirable, however, that this argument is either confirmed (or refuted instead) by $h^{3,1}$ computation for other constructions of Calabi-Yau's with a non-trivial Mordell-Weil group, and for other choices of $(B_3, [S])$.

Studies show [35–37] that Calabi-Yau fourfolds eligible for supersymmetric compactification of F-theory are distributed almost evenly in the $h^{3,1} \gg h^{1,1}$ corner and $h^{3,1} \ll h^{1,1}$ corner of the $h^{3,1}$–$h^{1,1}$ plane; this fits very well with an observation that a morphism of elliptic fibration to some threefold is allowed for large fraction of Calabi-Yau fourfolds with various topology [38, 39]. Such a choice as $B_3 = \mathbb{P}^1 \times \mathbb{P}^2$, which we used for the numerical experiment above, ends up in the corner of $h^{3,1} \gg h^{1,1}$, and hence the estimates of the fraction of flux vacua with an extra U(1) symmetry is hardly typical values for all the possible topological choices of $(B_3, [S])$.

It is not hard to find out how things go in the $h^{3,1}$–$h^{1,1}$ plane for various choices of $(B_3, [S])$, if we maintain K close to K_0. Along an $h^{3,1} + h^{1,1} = \text{const}$ line in the $h^{3,1}$–$h^{1,1}$ plane, the Euler number $\chi \sim 2(h^{3,1} + h^{1,1}) + h^{2,2} \sim 6(h^{3,1} + h^{1,1})$ and the value of $L_* \sim \chi/24$ do not change much, but the value of $K_0 \sim 2[1 + h^{3,1}] + h^{2,2}_H$ increases toward the $h^{3,1} \gg h^{1,1}$ corner. The prefactor in (2.1) is an increasing function of K for a given L_*, regardless of whether $L_* \ll K$ or $L_* \gg K$. The more Fano-like B_3 is, the *ample*r sections are available to $(-K_B)^{\otimes \text{positive}}$, the larger $h^{3,1}$ is, and the larger the number of flux vacua is, after all. When a stack of SU(5) 7-branes is required along $S \subset B_3$, more sections (and hence $h^{3,1}$, and the flux vacua) are lost when B_3 is more Fano like; the loss is severer, if $c_1(N_{S|B_3})$ is "positive". The relative tuning cost is higher for Fano-like B_3, with positive $c_1(N_{S|B_3})$. Experience in [6, 7] also shows, however, that the number of remaining flux vacua (i.e., those with an SU(5) symmetry) tends to be larger in Fano-like B_3 and positive $c_1(N_{S|B_3})$, despite the severer tuning cost for the SU(5) 7-branes. The same story will hold, even when SU(5) × U(1) symmetry is required instead.

Let us note that the qualitative argument above is naive in various respects. First, we set $K = K_0$ above for simplicity, but there is a large room for $K - K_0$, when B_3 is far from being Fano, and $c_1(N_{S|B_3})$ far from being "positive". Such a set-up is possible in F-theory compactifications [35–37, 40, 41], and it is known in such cases that there can be many other 7-branes with non-Abelian gauge groups, and $h^{1,1} \gg h^{3,1}$ for the fourfolds. It is then expected from experience in [6, 7] that $h^{2,2}_V \gg h^{2,2}_H$. One then needs to ask how much four-form flux can be introduced in the vertical component $H^{2,2}_V(\hat{Y}_4; \mathbb{Q})$ without breaking SO(3,1) symmetry and supersymmetry (if one wishes); based on an answer to this technical question, one can then wonder how inclusive an ensemble of low-energy effective theory one is interested in, and how large $(K - K_0)$ is. Secondly, particle physics with SU(5) unification is not all we need in this universe. Some source of supersymmetry breaking needs to be present. While anti-D3 branes may be able to play some role, dynamical supersymmetry breaking in a non-Abelian gauge theory (e.g. the 3-2 model in [42]) might also be at work. The tuning-cost-free non-Abelian gauge group in the non-Higgsable cluster

JHEP11(2015)065

may have something to do with dynamical supersymmetry breaking. Thirdly, the Kähler moduli need to be stabilised without a tachyon. U(1) fluxes change the effective number of Kähler moduli to be stabilised non-perturbatively, through the Fayet-Iliopoulos D-term potential (primitiveness condition of the flux). Finally, inflation or cosmological evolution in general may introduce some preference in the choice of $(B_3, [S])$. All these issues are beyond the scope of this article.

This article does not try to estimate the fraction of flux vacua with an unbroken matter/R-parity symmetry. If one is to argue which one of R-parity and spontaneous R-parity violation is more natural solution to the dimension-4 proton decay problem in terms of flux vacua statistics, we also need an estimate for the R-parity scenario. Although there are earlier works on this issue in the context of Type IIB orientifold compactifications (e.g. [10, 11]), further study in F-theory is desirable. It is worth reminding ourselves that the fact that $L_* \ll K$ in cases of $h^{3,1} \gg h^{1,1}$ may have an important implication to this issue. Continuous approximation to the space of fluxes in [3, 4] is fairly good when $K \ll L_*$; intuitively, as in [43], that is when the radius-square (L_*) of a K-dimensional "sphere"[14] is much larger than the number of dimensions K. In the case with $L_* \ll K$ (which is the case at least when $h^{1,1} \ll h^{3,1}$), however, much larger fraction of flux configurations may end up with special points in the complex structure parameter space (sometimes with an accidental discrete symmetry) than expected in the continuous approximation [4, 44].

3.2 GUT's and SU(3) × SU(2) × U(1)

Pursuit of supersymmetric SU(5) unification is a primary motivation to study F-theory compactification. The doublet-triplet splitting problem motivates compactification in the geometric phase (supergravity regime), rather than stringy regime, because it is solved in a simple way by topology (hypercharge line bundle or Wilson line) on an internal space [45, 46]; the up-type Yukawa coupling of the form $\mathbf{10}^{ij}\mathbf{10}^{kl}\mathbf{5}^{m}\epsilon_{ijklm}$ hints at algebra of the exceptional Lie groups $E_{6,7,8}$ [12]. There is no direct experimental evidence (such as proton decay) so far for unification, however; certainly renormalisation group of the minimal supersymmetric Standard Model (MSSM) is consistent with gauge coupling unification, but we do not know for sure what the particle spectrum is like at energy scale higher than TeV. If one does not take SU(5) unification seriously, then string vacua based on CFT's with a non-geometric target space are perfectly qualified for the description of the real world; we do not have to require that $E_{6,7,8}$ algebra be relevant for "compactification" either.

With this perspective in mind, it makes sense to ask a question which is more popular in the ensemble of supersymmetric vacua of F-theory compactification in the geometric phase, SU(5) unification or MSSM without unification. If there are more MSSM vacua without unification than vacua with SU(5) unification within the landscape of F-theory, the MSSM vacua will surely outnumber vacua with unification in the entire string landscape, which includes string vacua based on non-geometric CFT's, and those without a dual

[14] In reality, the lattice $H^4(\hat{Y};\mathbb{Z})$ is not positive definite. It still seems, however, that this "intuition" holds at least to some extent, because the Bousso-Polchinski like prefactor of (2.1) was obtained in [3, 4] without assuming that the lattice is positive definite.

JHEP11(2015)065

description in F-theory. Democracy, or simple majority rule, may not be the ultimate vacuum selection principle of string theory, but this question will still be of interest for those who are concerned about particle physics.

It is necessary, before answering the question above, to think what *unification* means. The motivation of unified theories at the very beginning [47] was to explain quantisation of hypercharges. This charge quantisation is achieved in any realisation of the Standard Model in F-theory/Type IIB string theory, however. Even when the U(1) hypercharge is not embedded into a larger non-Abelian group, charges of (p, q) strings (or M2-branes) are determined by algebraic topology, and the charges turn out to be quantised. Charge quantisation is therefore not a distinction criterion of, or motivation for, unification from the perspective of string theory.

Let us list up a couple of criteria for unified theories:

- $\mathrm{SU}(3)_C \times \mathrm{SU}(2)_L \times \mathrm{U}(1)_Y$ originates from a single stack of branes,
- all of $\mathrm{SU}(3)_C$, $\mathrm{SU}(2)_L$ and $\mathrm{U}(1)_Y$ are understood in a semi-simple brane configuration
- gauge coupling unification is explained automatically,
- matter fields in some of the five irreducible representations of the Standard Model, $(\mathbf{3}, \mathbf{2})_{1/6}$, $(\bar{\mathbf{3}}, \mathbf{1})_{-2/3}$, $(\bar{\mathbf{3}}, \mathbf{1})_{+1/3}$, $(\mathbf{1}, \mathbf{2})_{-1/2}$ and $(\mathbf{1}, \mathbf{1})_{+1}$, are localised in the same locus in the internal space.

SU(5) GUT models discussed in section 3.1 satisfy all of those criteria. On the other hand, none of those criteria is satisfied, if $\mathrm{SU}(3)_C$ and $\mathrm{SU}(2)_L$ come from 7-branes on topologically different divisors S_3 and S_2, respectively, and $\mathrm{U}(1)_Y$ from a non-trivial section in the Mordell-Weil group. There will be constructions that satisfy some of the criteria, but not all, but we will foucus on the two extreme cases in this article, to keep the story simple.

Let us use $B_3 = \mathbb{P}^1 \times \mathbb{P}^2$, as before, and quantify the number of flux vacua of those different implementations of the Standard Model, so that we can compare. Here, we do not pay attention to the dimension-4 proton decay problem or any other phenomenological requirements. For SU(5) unification, we already have a result,

$$h^{3,1} = 3277 \longrightarrow h^{3,1} = 2148, \qquad \Delta h^{3,1} = -1129 \qquad \text{for SU(5) on} \quad S = H_{\mathbb{P}^1}. \tag{3.17}$$

If we deform this Calabi-Yau fourfold further so that only $\mathrm{SU}(3) \times \mathrm{SU}(2)$ remains unbroken, the two gauge group factors are localised on divisors S_3 and S_2 both of which belong to the same divisor class as $S = H_{\mathbb{P}^2}$.

$$h^{3,1} = 3277 \longrightarrow h^{3,1} = 2149, \qquad \Delta h^{3,1} = -1128 \qquad S_3 \sim S_2 \sim H_{\mathbb{P}^1}. \tag{3.18}$$

We can go back to the family of fourfolds for SU(5) unification by suppressing one deformation parameter corresponding to $H^0(S; N_{S|B_3}) = H^0(\mathbb{P}^2; \mathcal{O})$ in this case. Therefore, the tuning cost for the unbroken U(1) hypercharge symmetry is obtained by $-\Delta h^{3,1} = 1$ in (3.10) in the case of SU(5) unification.

JHEP11(2015)065

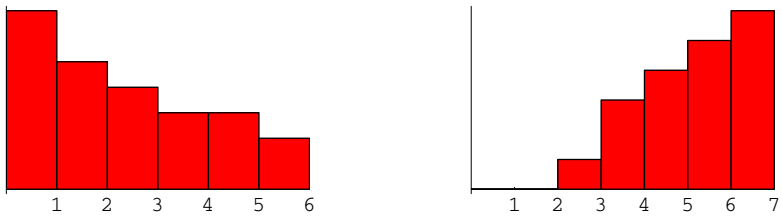

(a) $c_1(N_{S|B}) > 0$ (A_n, D_n) (b) $c_1(N_{S|B}) < 0$ (A_n, D_n)

Figure 1. Extra tuning cost $-(\Delta L_*)/(\Delta\text{rank})$ decreases or increases for higher rank, depending on whether $c_1(N_{S|B_3})$ is positive or negative, as one goes down the A_n or D_n chain. $c_1(N_{S|B})$ is replaced by K_S in the case of E_n series.

In case we require SU(3) and SU(2) 7-branes on two divisors, S_3 and S_2, respectively, in different divisor classes in B_3, back of the envelope calculation[15] reveals that

$$h^{3,1} = 3277 \longrightarrow h^{3,1} = 2130,\ \Delta h^{3,1} = -1147, \qquad S_3 = H_{\mathbb{P}^1}, \quad S_2 = H_{\mathbb{P}^2}; \tag{3.21}$$

$$h^{3,1} = 3277 \longrightarrow h^{3,1} = 2087,\ \Delta h^{3,1} = -1190, \qquad S_3 = H_{\mathbb{P}^2}, \quad S_2 = H_{\mathbb{P}^1}. \tag{3.22}$$

Comparing these $\Delta h^{3,1}$'s with that in (3.18), we see that the topological configuration of $\mathrm{SU}(3)\times\mathrm{SU}(2)$ 7-branes does not make much difference in the fraction of flux vacua. If the hypercharge symmetry is obtained as a Mordell-Weil U(1) in addition to such $\mathrm{SU}(3)\times\mathrm{SU}(2)$ 7-brane configurations (cf [48]), $h^{3,1}$ will be reduced further by 1000 or so, as we have experienced in section 3.1. The number of flux vacua does not depend very much on topological configuration of 7-branes for $\mathrm{SU}(3)_C \times \mathrm{SU}(2)_L$, but it does very much on how we obtain $\mathrm{U}(1)_Y$.

The original motivation for unification — explaining quantisation of hypercharge — is no longer persuasive in string construction of particle physics, because it is explained without relying on unification. Unification may still have advantage in F-theory compactification in the geometric phase, in that the tuning cost for having an unbroken U(1) hypercharge in addition to $\mathrm{SU}(3)_C \times \mathrm{SU}(2)_L$ is small, in terms of flux vacua counting.

We should leave a cautionary remark on the B_3-dependence of this argument, however. Extra tuning cost for one extra rank of 7-brane gauge group has a behaviour shown in figure 1, where the behaviour is qualitatively different for cases with "positive" $c_1(N_{S|B_3})$ and "negative" $c_1(N_{S|B_3})$, when one goes down the chain of $A_n = \mathrm{SU}(n+1)$ series and $D_n = \mathrm{SO}(2n)$ series [6, 7]. When a divisor $c_1(N_{S|B_3})$ on S is negative, in particular, it may happen sometimes that $\Delta L_*/\Delta\text{rank} = 0$ for a choice of 7-brane gauge group with a

[15] Reasoning behind the values of $h^{3,1}$'s are

$$[2 + 3N_{3,2} + 4N_{5,2} + 6N_{8,2} + 7N_{11,2} + 10N_{16,2}] - [1 + 4 + 2N_{2,2} + 4N_{5,2} + 5N_{8,2}] - 6 = 2130, \tag{3.19}$$

$$[2 + 3N_{3,2} + 4N_{5,2} + 6N_{8,2} + 8N_{10,2} + 11N_{15,2}] - [1 + 4 + 2N_{2,2} + 4N_{5,2} + 6N_{7,2}] - 6 = 2087, \tag{3.20}$$

where $N_{h,2} = (h+1)(h+2)/2$ is the number of lattice points on a 2-dimensional pyramid of height h. We do not think that these values of $h^{3,1}$ are necessarily correct, but will not be off so much as to lose credibility in the estimate $\Delta h^{3,1} \approx -1000$. Because discusion in the main text is not affected by 10% change in the estimate of $\Delta h^{3,1}$, we do not need to compute $\Delta h^{3,1}$ at a precision better than that.

JHEP11(2015)065

small rank; the rank of 7-brane gauge group can be large to some extent without losing the number of flux vacua. This is the phenomenon called non-Higgsable cluster [24, 40, 41]. When either $SU(3)_C$ or $SU(2)_L$ or both are identified with 7-brane gauge groups in a non-Higgsable cluster [49], the tuning cost argument above is affected inevitably. In a family of fourfolds where the Mordell-Weil group is non-trivial everywhere on its complex structure parameter space [50–52], we cannot talk of relative statistical cost of requiring an extra U(1) symmetry; in such a case, we need to discuss relative tuning cost of U(1) through some transitions connecting such a family to another where the fourfolds have different topology, or to use the prefactor in (2.1) directly to estimate the number of flux vacua.

4 Distribution of Lagrangian parameters

While the prefactor in the formula (2.1) can be used to estimate the number of flux vacua with a given set of algebraic and topological properties (i.e., symmetry, matter multiplicity etc.), the (m, m)-form ρ_I in (2.1) can be used to "derive" distribution of Lagrangian parameters in such an ensemble of vacua. This is a source of rich information, as is evident already in its applications to Type IIB compactifications [53, 54]. In this section, we will discuss its F-theory applications in the context of particle physics.

It should be remembered, though, that the expression for ρ_I was derived by assuming that the continuous approximation of the K-dimensional flux space is good, while the approximation is not good in the case of $K \gg L_*$. It may be that the distribution ρ_I remains to have reasonable level of predictability, while the problem of bad approximation is mitigated, when the complex structure parameter space $\mathcal{M}_*$ is binned very coarsely, and ρ_I is used only by being integrated over such a large bin. Justification is not given even to this hope, however. When one is interested in the choice of $(B_3, [S])$ where $K \gg L_*$, one should keep this remark in mind.

4.1 Symmetry breaking scale of an approximate U(1) symmetry

We discuss applications of the distribution ρ_I in both sections 4.1 and 4.2. The set-up for the application in section 4.1 is chosen so that it suits best for exploring creative ways to use the distribution ρ_I; the physics problems discussed in section 4.1 should be interesting on their own, but we are focused more in finding out creative ways to use ρ_I, rather than in carrying out solid analysis of the physics problems being discussed. Section 4.2, on the other hand, is devoted to a more problem-oriented application.

While it is not theoretically impossible to compute period integrals and evaluate ρ_I, it is not practical to do so, when there are O(1000) complex structure parameters. Fortunately, it is possible to learn essential features of the distribution ρ_I without carrying out such computations, as experience in Type IIB applications indicates [53, 55]. First, the parameter space of complex structure $\mathcal{M}_*$ has a natural set of coordinates; in a case a Calabi-Yau n-fold is given by a toric hypersurface, for example, we can use, for the coordinates of $\mathcal{M}_*$, various products of monomial coefficients that are invariant under rescaling [56]. The distribution ρ_I will show more or less uninteresting behaviour on these coordinates in $\mathcal{M}_*$, except at special loci in $\mathcal{M}_*$. ρ_I exhibits singular behaviour in these

JHEP11(2015)065

coordinates, when the period integrals involve logarithm of those coordinates; only derivatives of logarithm introduce poles. Logarithm of such coordinates indicates that there is a non-trivial monodromy of cycles [55]. All the arguments above hold true for applications to Calabi-Yau fourfolds.[16]

Consider a family of Calabi-Yau fourfolds $Y_{n=4}$ obtained as a hypersurface of an ambient space given by $WP_{[1:2:3]}$-fibration over some B_3;

$$X^3 + Y^2 + XYZA_1 + X^2Z^2A_2 + YZ^3A_3 + XZ^4A_4 + Z^6A_6 = 0, \tag{4.1}$$

with $A_k \in \Gamma(B_{n-1=3}; \mathcal{O}_B(-kK_B))$. Let $\mathcal{M}_*$ be its parameter space of complex structure. Sitting within this family is a family of Calabi-Yau fourfolds with the ambient space replaced by $\mathrm{Bl}_{[1:0:0]}W\mathbb{P}_{[1:2:3]}$-fibration over B_3; the last term Z^6A_6 is simply dropped (followed by small resolution) to get to the sub-family given by (A.2), where there is a non-trivial section in Y_4, and hence a U(1) symmetry in the low-energy effective theory. Let $\mathcal{M}_*^{\mathrm{U}(1)} \subset \mathcal{M}_*$ be the locus of this sub-family. We study the behaviour of ρ_I on $\mathcal{M}_*$ near the locus of this sub-family.

In the $A_6 \longrightarrow 0$ limit, Y_4 has a curve of codimension-three conifold singularity, $X = Y = A_3 = A_4 = 0$ [23]; this curve in B_3 is denoted by Σ. The conifold transition in such a limit was studied extensively in [57]. The genus of this curve is determined by

$$2g(\Sigma) - 2 = (-3K_B) \cdot (-4K_B) \cdot (-6K_B) = 72(c_1(TB_3))^3. \tag{4.2}$$

Incidentally, the parameter space $\mathcal{M}_*^{\mathrm{U}(1)}$ for this $A_6 \longrightarrow 0$ limit is of complex codimension-$(-\Delta h^{3,1})$ in $\mathcal{M}_*$, where

$$(-\Delta h^{3,1}) = h^0(B_3; \mathcal{O}_B(-6K_B)) - h^0(B_3; \mathcal{O}_B(-3K_B)) - h^0(B_3; \mathcal{O}_B(-2K_B)); \tag{4.3}$$

the first term is obviously the degree of freedom in A_6. The last two terms are there because only the ϵ_1-term in the automorphism of the form

$$\delta Y = XZ\epsilon_1 + Z^3\epsilon_3, \qquad \delta X = Z^2\epsilon_2, \qquad \epsilon_k \in \Gamma(B_3; \mathcal{O}_B(-kK_B)) \tag{4.4}$$

survives for Y_4 in the sub-family over $\mathcal{M}_*^{\mathrm{U}(1)}$. One can see that $(-\Delta h^{3,1}) = g$, at least when B_3 is a Fano variety. Indeed, because the divisor $(-K_B)$ is ample, Kodaira's vanishing theorem implies that

$$h^q(B_3; \mathcal{O}_B(-nK_B)) = 0 \qquad \text{for } q > 0, \quad n \geq 0. \tag{4.5}$$

Combining this theorem and the expression for $(-\Delta h^{3,1})$, we find that

$$(-\Delta h^{3,1}) = 36(c_1(TB_3))^3 + 1 = g. \tag{4.6}$$

[16] Certainly there is small difference between threefolds and fourfolds; the number of cycles $b_3 \sim 2h^{2,1}$ for period integrals is not much different from $2h^{2,1}$ period integrals forming special coordinates for Calabi-Yau threefolds, there are much larger number of four-cycles $b_4 \sim 2h^{3,1} + h^{2,2} \sim 6h^{3,1} + \text{const}$ than the number of independent period integrals for fourfolds. We do not see this difference as a serious obstacle in recycling the Type IIB lesson in the main text for the application to F-theory.

JHEP11(2015)065

This agreement always holds at local level, but $(-\Delta h^{3,1}) = g - \tilde{h}^{2,1} \leq g$ at global level [57]; the argument above shows that $\tilde{h}^{2,1} = 0$ at least when B_3 is a Fano variety.

$6g-3$ topological four-cycles are identified in the local geometry of Y_4 [57], and all of them are lifted to topological cycles in the global geometry of Y_4 at least when B_3 is a Fano variety. Period integrals on these $6g-3$ four-cycles vanish when all the g transverse coordinates of $\mathcal{M}_*^{\mathrm{U}(1)} \hookrightarrow \mathcal{M}_*$ are set to zero; see [57] and the appendix C. We found, in the appendix C.2, that there are at least g independent generators of unipotent monodromy[17] acting on these topological four-cycles, and the period integrals are of the form,

$$\Pi_{\widetilde{A}_k} \sim z_k, \qquad \Pi_{\widetilde{C}^k} \sim c^{kl} z_l \ln(z's); \tag{4.7}$$

the $A_6 \longrightarrow 0$ limit corresponds to $z_1 = z_2 = \cdots z_g = 0$. It is then quite likely, as in [53, 55], that the (m,m)-form distribution ρ_I on $\mathcal{M}_*$ has an asymptotic behaviour

$$\rho_I \approx \rho_I^{\mathrm{U}(1)} \wedge \rho_I^{\perp}, \qquad \rho_I^{\perp} := \prod_{k=1}^{g} \frac{dz_k \wedge d\bar{z}_k}{|z_k|^2 (\ln(|z|^2))^2} \sim \prod_{k=1}^{g} d[\arg(z_k)] \wedge \frac{d\ln(1/|z_k|^2)}{[\ln(1/|z_k|^2)]^2} \tag{4.8}$$

near $\mathcal{M}_*^{\mathrm{U}(1)}$. While derivation of the asymptotic form above is not as rigorous as it is desired to be, let us explore what this behaviour implies, assuming that it is correct.

The most important consequence is that the fraction of flux vacua with hierarchically small value of $\mathrm{U}(1)$ symmetry breaking parameter $|z_k|$ is not hierarchically small, but is only suppressed by some power of the logarithm of the hierarchy, $\ln(1/|z_k|^2)$. That makes it much more *natural* to think of approximate $\mathrm{U}(1)$ symmetry in bottom-up model building. Secondly, though, it is likely that the $\mathrm{U}(1)$ symmetry is preserved approximately only if all the $|z_k|$'s are hierarchically small; that is, what really matters will be a fraction of flux vacua satisfying, say, $|z_k|^2 < \delta$ for $^\forall k = 1, \cdots, g$ for some small δ. This then implies that only the fraction

$$\int_{\mathcal{M}_*^{\mathrm{local}};\leq\delta} \rho_I^{\perp} = \prod_k \left[\int_{\ln(1/\delta)}^{+\infty} \frac{d\ln(1/|z_k|^2)}{[\ln(1/|z_k|^2)} \right] = \frac{1}{[\ln(1/\delta)]^g} \tag{4.9}$$

of flux vacua in $\mathcal{M}_*$ has such an approximate $\mathrm{U}(1)$ symmetry in the effective theory Lagrangian, with the symmetry breaking not more than δ. The value of $g(\Sigma)$ is often quite large; when $B_3 = \mathbb{P}^3$, for example, $g = 36 \times 4^3 + 1$. Thus, the fraction of flux vacua decreases very quickly, when we require the approximate $\mathrm{U}(1)$ symmetry to be preserved for very hierarchically small δ.

Let us take one more step and ask the following question. Although ρ_I or (2.1) is presented in the form of a continuous distribution, it is originally a scatter plot on $\mathcal{M}_*$ of isolated flux vacua. What is the smallest value $\delta_{\min}$ of the approximately preserved $\mathrm{U}(1)$ symmetry in $\mathcal{M}_* \setminus \mathcal{M}_*^{\mathrm{U}(1)}$? This is a prototype of such questions as what the minimum symmetry breaking scale is for supersymmetry and flavour symmetry in string landscape.

A wild speculation will be to think as follows. When we set δ small enough, the fraction of flux vacua (4.9) becomes so small that it reaches the fraction of flux vacua on $\mathcal{M}_*^{\mathrm{U}(1)}$

[17] Unipotent monodromy means, here, that a monodromy matrix is a sum of a nilpotent matrix and the identity matrix.

JHEP11(2015)065

among those on $\mathcal{M}_*$. The integral of $\rho_I^\perp$ over the normal coordinates of $\mathcal{M}_*^{\mathrm{U}(1)} \hookrightarrow \mathcal{M}_*$ in such a small region as $|z_k|^2 < \delta$ may correspond to flux vacua that sit right on top of the $\mathcal{M}_*^{\mathrm{U}(1)}$ locus. This thought leads to a relation

$$\left[\frac{1}{\ln(1/\delta_{\min})}\right]^g = \exp\left[\frac{\ln(24)}{4}(\Delta h^{3,1})\right], \tag{4.10}$$

where (3.10) — valid for cases with $h^{3,1} \gg h^{1,1}$ — was used in the right hand side. Geometry dependence through $g = -\Delta h^{3,1}$ drops out from this relation then, and we find that

$$\delta_{\min} \sim \exp\left[-e^{\frac{\ln(24)}{4}}\right]. \tag{4.11}$$

This "prediction", however, is not as powerful as it looks. We have to keep in mind the limited reliability in the value of "ln(24)/4", as remarked in footnote 12. It will not be still too bad to conclude that $\delta_{\min}$ will not be much smaller than

$$\exp[-e^{(\text{a few})}] \approx \exp[-10] \approx 10^{-(3\text{-}4)}, \tag{4.12}$$

provided all the speculative arguments leading to this conclusion are not wrong.[18]

4.2 Statistical cost of Yukawa hierarchical structure problem

In section 4.2, we discuss the fraction of flux vacua that realise solutions to the hierarchical structure problem of Yukawa matrices. Each one of codimension-three singularity (matter-curve intersection) points in F-theory compactifications for SU(5) unification gives rise to an approximately rank-1 Yukawa matrix, provided complex structure is generic [58–61], but the up-type [resp. down-type and charged lepton] Yukawa matrix in the low-energy effective theory below the Kaluza-Klein scale receives contributions from all the "E_6"-type points [resp. D_6 type] on $S \subset B_3$. The number of "E_6"-type and D_6-type points are determined by topological intersection numbers, and are generically not equal to one [61, 62]. The approximately rank-1 nature of the Yukawa matrices at short distance in F-theory is therefore lost at energy scale below the Kaluza-Klein scale, at least in a

[18] Here is a recap of the major caveats. First, as remaked already just before section 4.1, very little is known about the validity of the continuous approximation in the flux scanning space for cases with $K \gg L_*$; there is a related discussion in [4, 44], but we need to go beyond. The relevant question here is whether ρ_I can still be used after coarse binning. Secondly, monodromy analysis leading to (4.7) neither study all the generators of the monodromy group nor period integrals of all the $(6g-3)$ topological four-cycles; the asymptotic behaviour of ρ in (4.8) is derived by looking at partial contributions, while ignoring other terms; thus it is worth doing reanalysis of (4.7), (4.8) for those who prefer solid and rigorous analysis. Thirdly, we assumed that the U(1) symmetry breaking parameter δ in the low-energy effective theory will be tied with max($|z_k|^2$'s), rather than with min($|z_k|^2$'s) or anything else. This assumption, however, relies only on intuition of the author, without any justification. Finally, the "wild guess" leading to (4.10) is nothing more than a guess at this moment. As remarked at the beginning, the primary purpose of the discussion of this section 4.1 is in illustrating possible scope of particle physics applications of ρ_I, rather than in having a final word on the physics problems in question. A lot more work needs to be done, as we have discussed in this footnote, in order to establish the various claims and guesses made in this section 4.1, and those tasks are beyond the scope of this article.

JHEP11(2015)065

generic flux vacuum. There have been proposed a few ideas,[19] however, how to exploit the approximate rank-1 nature at short distance. We pick up two among them[20] for the study in this section 4.2.

One of the two ideas is to tune parameters so that only a single "E_6"-type point contributes to the up-type Yukawa matrix in the effective theory below the Kaluza-Klein scale (and just one D_6-type point to the down-type Yukawa matrix); this idea was proposed originally in [59, 65] and the Yukawa matrices in this scenario have been studied carefully in [60, 66–71]. In order to make sure that the low-energy Yukawa matrix receives contribution only from just one "E_6"-type point, it is safe to consider that splitting of matter curves is controlled by a U(1) symmetry [14, 22, 23].

It is true that, for the CKM mixing angles to be small, the single "E_6"-type point and the single D_6-type point should be at the same point in S, or at least be close enough [72]; this property does not follow from a U(1) symmetry (and the matter curve factorisation). If one is happy to ignore this aspect in the mixing angle and to focus on the hierarchical structure of the Yukawa eigenvalues for now,[21] then the study in section 3.1 as well as section 4.1 can be used to study statistical aspects of this idea of tuning. We will be brief in section 4.2.1 for this reason.

The other idea whose tuning we discuss in section 4.2.2 is a string-theory implementation of the idea of [76, 77]. Sections of a line bundle on a torus T^2 (a term "magnetised torus" is sometimes used for this) are given by Theta functions, which become approximately Gaussian for large complex structure of T^2; the exponentially small tail of the Gaussian wavefunctions is used to create hierarchical structure among three copies of $(Q, \bar{U}, \bar{E}) = \mathbf{10}$, which leads to realistic mixing angles and hierarchy in Yukawa eigenvalues [73–75, 78–80]. See [61, 81] for more detailed account of the string implementation of this idea. In this idea, therefore, one assumes that the matter curve for SU(5)-$\mathbf{10}$ representation has a large complex structure parameter.[22] We estimate how much fraction of flux vacua we lose by requiring this tuning in the complex structure parameter of the matter curve, by exploiting the "distribution" ρ_I.

[19] In Heterotic string compactification with SU(5) unification, at least some neighbourhoods of orbifold limits of the parameter space must be included as a part of the semi-realistic corners of string landscape [63]. Also, when a Calabi-Yau threefold for Heterotic string compactification has an elliptic fibration, one can translate the solutions in F-theory to Heterotic language. The whole picture of the landscape of Heterotic string parameter space remains to be far from clear, however. When it comes to G_2-holonomy compactification of M-theory, the author is unaware of any idea in the literature to get around the difficulty in the up-type Yukawa matrix when SU(5) unification is assumed [12] (Reference [64] arrived at the same observation independently).

[20] In this article, we do not study the statistics of the idea of alignment among Yukawa matrices due to a discrete symmetry [61].

[21] It is understood in phenomenology community, by now, that mixing angles will carry more fundamental information than the hierarchical Yukawa eigenvalues (see, e.g., [73–75]). This is because the CKM mixing angles reflect properties only of three quark doublets $(\mathbf{3}, \mathbf{2})_{+1/6} \subset \mathbf{10}$, and the lepton mixing angles those of just the three lepton doublets $(\mathbf{1}, \mathbf{2})_{-1/2} \subset \bar{\mathbf{5}}$, whereas the down-type/charged lepton Yukawa eigenvalues reflect the properties of both $(\bar{D}, L) = \bar{\mathbf{5}}$ and $(Q, \bar{E}) \subset \mathbf{10}$.

[22] Before making this assumption on the complex structure parameter, we make another assumption (a discrete choice in topology) that this matter curve has $g = 1$. Generalisation of this idea to higher genus cases has not been studied very much, apart from partial attempt in [61].

JHEP11(2015)065

4.2.1 Split matter curve under a U(1) symmetry

Suppose that the matter curves $\Sigma_{(\mathbf{10})}$ and $\Sigma_{(\bar{\mathbf{5}})}$ for the $\mathbf{10}$ and $\bar{\mathbf{5}}$ representations of Georgi-Glashow SU(5) unification are split into irreducible pieces, due to an extra unbroken U(1) symmetry originating from a non-trivial section. Let $\Sigma_{(\mathbf{10})} = \cup_a \Sigma_{(\mathbf{10});a}$ and $\Sigma_{(\bar{\mathbf{5}})} = \cup_b \Sigma_{(\bar{\mathbf{5}});b}$ be the irreducible decomposition protected by the U(1) symmetry. The idea of [59, 65] assumes, among other things, that there is a pair $\Sigma_{(\mathbf{10});a0}$ and $\Sigma_{(\bar{\mathbf{5}});b0}$ such that they intersect transversely (i.e., "E_6"-type) just once in the SU(5) 7-brane locus S; the matter $\mathbf{10} = (Q, \bar{U}, \bar{E})$ are localised in $\Sigma_{(\mathbf{10});a0}$ and H_u in $\Sigma_{(\bar{\mathbf{5}});b0}$, respectively, so that the single transverse intersection point gives rise to the approximately rank-1 up-type Yukawa matrix at low-energy. It is an interesting question whether there are such Calabi-Yau fourfold geometries. The two constructions of fourfolds with a non-trivial Mordell-Weil group which we reviewed in the appendix A do not have enough freedom to accommodate such configuration of matter curves, but this is far from being a no-go. Given the variety of constructions for fourfolds with a non-trivial Mordell-Weil group [27, 28], it may not be too bad to assume that there are constructions satisfying the assumption above. The rest of this section 4.2.1 is based on that assumption.

We have already estimated in section 3.1 the fraction of flux vacua that have an unbroken U(1) symmetry from a non-trivial Mordell-Weil group; factorisation of matter curves just follows as a consequence of the U(1) symmetry. Given the fact that the faction of such vacua depends on the choice of a construction of fourfolds with a non-trivial Mordell-Weil group, as well as on the choice of topology of $(B_3, [S])$, we do not find it meaningful to estimate the cost at precision higher than in section 3.1. By using the results there, we conclude right away that the cost of an extra U(1) symmetry to split the matter curves is something like

$$e^{-1000} \sim 10^{-\mathcal{O}(100)} \qquad \text{for } (B_3, [S]) = (\mathbb{P}^1 \times \mathbb{P}^2, H_{\mathbb{P}^1}). \tag{4.13}$$

The tuning cost estimated above should be compared against the naive estimate of the non-triviality of flavour structure of the Standard Model, first of all. Suppose that individual Yukawa eigenvalues are tuned to be small enough, one by one, by tuning the complex structure parameters by hand, and that these tunings for individual eigenvalues can be carried out independently from each other. Then the total tuning cost of the hierarchical eigenvalues of the Standard Model by this naive individual tuning is estimated by[23]

$$\left(\frac{\lambda_c}{\lambda_t}\frac{\lambda_u}{\lambda_t}\right)\left(\frac{\lambda_e}{\lambda_\tau}\frac{\lambda_\mu}{\lambda_\tau}\right) \approx \left(10^{-2}\cdot 10^{-4.5}\right) \times \left(10^{-1}\cdot 10^{-3.5}\right) = 10^{-11}. \tag{4.14}$$

[23] As we assume SU(5) unification, the hierarchical eigenvalues either in the down-type quark sector or charged lepton sector should be taken into account in this naive estimate of the tuning, not both. Also, only the ratio of the eigenvalues is used in this estimate, because the value of $(\tan\beta)$ is not known yet. On top of the naive estimate in the main text, one should multiply the tuning for the small mixing angles in the quark sector, $\theta_{us}\cdot\theta_{ub}\cdot\theta_{cb} \sim 10^{-4.5}$, in principle. We did not include this, however, because the idea of matter-curve splitting under a U(1) symmetry does not attempt to reproduce the small CKM mixing angles.

JHEP11(2015)065

It is much easier,[24] therefore, to obtain the semi-realistic hierarchical structure of Yukawa eigenvalues by just an accidental tuning, by chance of 10^{-11}, than by matter-curve splitting under a Mordell-Weil U(1) symmetry, at least for choices of $(B_3, [S])$ with $h^{3,1} \gg h^{1,1}$.

In fact, we may not have to require that the U(1) symmetry for matter-curve splitting is exact. Higher precision is required for a U(1) symmetry in the application to the dimension-4 proton decay problem, but that is not the case in the application to the flavour structure; the level of precision required for flavour physics is not more than $m_e/(174\ \text{GeV}) \sim 10^{-5.6}$. This motivates us to pay attention also to flux vacua with an approximate U(1) symmetry, where the matter curves $\Sigma_{(\mathbf{10})}$ and $\Sigma_{(\bar{\mathbf{5}})}$ are near the factorisation limit. Qualitative aspects of flux vacua distribution with an approximate U(1) symmetry in section 4.1 will remain the same, even after requiring an extra SU(5) symmetry on $S \subset B_3$, because the geometry of U(1) symmetry breaking (i.e., conifold transition) in SU(5) models remains qualitatively the same as in the case without SU(5) unification, at least away from the GUT divisor $S \subset B_3$; the $A_4 = A_3 = 0$ curve in B_3 — Σ — in the SU(5) models has a component given by $a_2 = a_3 = 0$, where $A_4 = s^3 a_2$ and $A_3 = s^2 a_3$. An approximate U(1) symmetry is realised in much larger number of flux vacua than an exact U(1) symmetry is, and therefore the tuning problem for the hierarchical structure may be alleviated in this way.

It remains to be seen, however, to what extent the idea of [59, 65] works successfully even in the presence of a small symmetry breaking in the approximate U(1) symmetry. The question we asked at the end of section 4.1 — the minimum symmetry breaking scale δ_{min} — may also become relevant in this context.

4.2.2 Gaussian wavefunction due to large complex structure

The second solution to the hierarchical structure problem of low-energy Yukawa matrices also requires tuning in one of the complex structure parameters. We use the distribution ρ_I in (2.1) in order to estimate the fraction of flux vacua for this solution.

As we have reminded ourselves at the beginning of section 4.1, the two important things in using ρ_I are i) to identify the natural coordinates of the parameter space $\mathcal{M}_*$, and ii) to find out the locus of $\mathcal{M}_*$ where there is a unipotent monodromy on the four-cycles of $\hat{Y}_4$. Although we also need dictionary between the coordinates on $\mathcal{M}_*$ and parameters of the low-energy Lagrangian (Yukawa couplings in particular), this part has already been worked out in the literature at the level we need in the present context [17, 18, 58, 61].[25]

The dictionary we use is the following. Let us use the base $B_3 = \mathbb{P}^1 \times \mathbb{P}^2$, and the SU(5) 7-brane locus $S = \text{pt} \times \mathbb{P}^2 \subset B_3$ for concreteness. With a generic choice of complex structure of a fourfold $\hat{Y}_4$ for SU(5) unification, the matter curve $\Sigma_{(\mathbf{10})}$ is an irreducible curve[26] of genus 1, so that we can use the second solution. Let τ be the complex structure parameter of the genus one curve $\Sigma_{(\mathbf{10})}$. The j-invariant of an elliptic curve has an expansion

$$j \simeq e^{-2\pi i\tau} + 744 + \mathcal{O}(e^{2\pi i\tau}) \tag{4.15}$$

[24] There is no proof, however, that such an accidental tuning for individual Yukawa eigenvalues are possible, or impossible, in string theory moduli space.

[25] Except one caveat: see footnote 27.

[26] When the base manifold is $B_3 = \mathbb{P}[\mathcal{O}_{\mathbb{P}^2} \oplus \mathcal{O}_{\mathbb{P}^2}(nH_{\mathbb{P}^2})]$, the genus of this matter curve is determined by $2g(\Sigma_{(\mathbf{10})}) - 2 = (3-n)(-n)$. We chose $n = 0$ in this article so that $2g - 2 = 0$.

JHEP11(2015)065

which is convenient for large $\mathrm{Im}(\tau)$. Hierarchical Yukawa eigenvalues as well as small mixing angles in the CKM matrix follow, if $\mathrm{Im}(\tau)$ is parametrically large, or equivalently, the value of $|j(\Sigma_{(\mathbf{10})})|$ is exponentially large. This j-invariant of the genus one curve should be some modular function over the $m = h^{3,1} = 2148$-dimensional space $\mathcal{M}_*$ of complex structure of this compactification for SU(5) unification.

The first task in this section 4.2.2 is to identify the natural coordinates on $\mathcal{M}_*$ and to find out how $j(\Sigma_{(\mathbf{10})})$ depends on these coordinates. The Calabi-Yau fourfold $\hat{Y}_4$ in question — for the choice of $(B_3, [S])$ — is given as a hypersurface of a toric variety:

$$\begin{aligned} y^2 + x^3 &+ (a_{5|0} + s a_{5|1} + s^2 a_{5|2}) xy + (s a_{4|1} + s^2 a_{4|2} + \cdots) x^2 \\ &+ (s^2 a_{3|2} + s^3 a_{3|3} + \cdots) y + (s^3 a_{2|3} + \cdots) x + (s^5 a_{0|5} + \cdots) = 0, \end{aligned} \tag{4.16}$$

where s is the inhomogeneous coordinate of $\mathbb{P}^1$, and is regarded as the normal coordinate of $S \subset B_3$. We understand here that all the terms corresponding to interior lattice points of facets of the dual polytope are set to zero in this defining equation; the automorphism group action on the monomial coefficients is now gauge-fixed for the most part, and only the coordinate rescaling $(\mathbb{C}^\times)^4$ acts on the coefficients. As a part of standard story in the toric hypersurface construction of Calabi-Yau manifolds, the complex structure parameter space $\mathcal{M}_*$ is given a natural set of coordinates; each one of them is in the form of

$$z_a := \prod_{\tilde{\nu}_\alpha} (a_\alpha)^{\tilde{\ell}^a_\alpha}, \tag{4.17}$$

where α runs over the monomials in the defining equation, and a labels linear relations $\sum_\alpha \tilde{\ell}^a_\alpha \tilde{\nu}_\alpha = 0$ in the dual lattice M of the toric data (e.g. [56]). In the case of $\hat{Y}_4$ we consider, there are 2148 such independent coordinates.

The matter curve $\Sigma_{(\mathbf{10})}$ is given by $a_{5|0} = 0$, and $a_{5|0}$ is a cubic homogeneous function on $S \cong \mathbb{P}^2$:

$$a_{5|0} = a^{5|0}_{300} T^3 + a^{5|0}_{210} T^2 U + a^{5|0}_{201} T^2 V + \cdots + a^{5|0}_{003} V^3, \tag{4.18}$$

where $[T : U : V]$ are the homogeneous coordinates of $\mathbb{P}^2 \cong S$. None of the ten terms in this cubic form corresponds to an interior point of a facet of the dual polytope, and hence we should retain all of them. Using the ten coefficients $a^{5|0}_{300}, \cdots, a^{5|0}_{003}$, seven independent rescaling invariants (i.e., the coordinates of the form (4.17)) can be constructed. The j-invariant of $\Sigma_{(\mathbf{10})}$ should depend on the seven coordinates out of[27] the 2148 coordinates of $\mathcal{M}_*$.

Before talking of how the j-invariant of a generic cubic curve of $\mathbb{P}^2$ depends on its monomial coefficients, let us have a look at the result for easier ones. When an elliptic

[27] An idea that large $\mathrm{Im}(\tau)$ of the matter curve $\Sigma_{(\mathbf{10})}$ results in Gaussian profile of wavefunctions along $\Sigma_{(\mathbf{10})}$ and consequently to hierarchical Yukawa eigenvalues is spelled out [61] in the language of Katz-Vafa type field theory (field theory local model) on $S \times \mathbb{R}^{3,1}$. Very little discussion is found in the literature, however, over to what extent we can rely on this field theory picture for generic choice of complex structure parameters. Put differently, is it really true that only the coefficients $a^{5|0}_{***}$'s are relevant to the hierarchical structure?

JHEP11(2015)065

curve is given in the Weierstrass form or Hesse form, the j-invariant is given in this way:

$$y^2 = x^3 + fx + g: \qquad j = 4^4 \times 27 \frac{f^3}{4f^3 + 27g^2}, \tag{4.19}$$

$$a_1 X^3 + a_2 Y^3 + a_3 Z^3 + a_0 XYZ = 0: \qquad j = -\frac{z(z-216)^3}{27(z+27)}, \quad z := \left(\frac{a_0^3}{a_1 a_2 a_3}\right). \tag{4.20}$$

The condition $\mathrm{Im}(\tau) \gg 1$ corresponds to the vanishing locus of the denominator, $4f^3 + 27g^2 \simeq 0$ or $z + 27 \simeq 0$, or the discriminant locus, to put differently. When the defining equation is in the Jacobi form,

$$w^2 = c_0 u^4 - c_1 u^3 + c_2 u^2 - c_3 u + c_4, \tag{4.21}$$

the discriminant locus is given by

$$\begin{aligned} &6912 c_0^3 c_4^3 - 3456 c_0^2 c_2^2 c_4^2 + 432 c_0 c_2^4 c_4 - 5184 c_0^2 c_1 c_3 c_4^2 \\ &- 2160 c_0 c_1 c_2^2 c_3 c_4 - 162 c_0 c_1^2 c_3^2 c_4 + 27 c_1^2 c_2^2 c_3^2 - 108 c_1^3 c_3^3 \\ &- 729 c_1^4 c_4^2 + 3888 c_0 c_1^2 c_2 c_4^2 - 108 c_1^2 c_2^3 c_4 + 486 c_1^3 c_2 c_3 c_4 \\ &\quad - 729 c_0^2 c_3^4 + 3888 c_0^2 c_2 c_3^2 c_4 - 108 c_0 c_2^3 c_3^2 + 486 c_0 c_1 c_2 c_3^3 = 0. \end{aligned} \tag{4.22}$$

For the j-invariant of those curves to be exponentially large, which is what we want for phenomenology, then the discriminant needs to be exponentially small; that seems to be a general lesson from elliptic curves given by those different forms of defining equations.

The matter curve $\Sigma_{(\mathbf{10})}$ is given by a generic cubic (4.18) in $\mathbb{P}^2$, but this is not much different from all the elliptic curves above. Any generic cubic can be cast into the Jacobi form (4.21) (e.g., [82]; recent appearance in physics literature includes [83]). Using the discriminant locus of the Jacobi form (4.22), one can then detect the discriminant locus in the coefficients of the general cubic form, and hence in the complex structure parameter space $\mathcal{M}_*$ of F-theory compactification. This procedure is easier when such a point as $[T : U : V] = [0 : 0 : 1] \in \mathbb{P}^2$ is in the curve $a_{5|0} = 0$ (i.e., $a_{003}^{5|0} = 0$); the left-hand side of (4.22) — a homogeneous function of $c_{0,1,2,3,4}$ of degree 6 — becomes a homogeneous function of $a_{***}^{5|0}$'s ($a_{003}^{5|0} = 0$) of degree 12. The most general case, where $a_{003}^{5|0}$ does not necessarily vanish, can be reduced to the $a_{003}^{5|0} = 0$ case above, by redefinition of the coordinates, $T \to T + solV$, $a_{300}^{5|0} sol^3 + a_{201}^{5|0} sol^2 + a_{102}^{5|0} sol + a_{003}^{5|0} = 0$. It appears, then, that the expression (4.22) would involve a cubic root of a function of the coefficients $a_{***}^{5|0}$'s, but those terms cancel, and the expression of the discriminant turns into a form

$$\propto \text{polynomial}_1 \sqrt{\text{polynomial}_3} + \text{polynomial}_2. \tag{4.23}$$

The discriminant locus of the general cubic form should be the zero locus of an expression proportional to $(\text{polynomial}_1)^2 \text{polynomial}_3 - (\text{polynomial}_2)^2$. This polynomial in the ten coefficients $a_{***}^{5|0}$ can be rewritten as a rational function of the seven coordinates z_a's of $\mathcal{M}_*$ modulo an overall factor that is not relevant in the present context. Once again, this rational function of z_a's needs to be exponentially small, in order for the solution to the hierarchical structure problem to work.

JHEP11(2015)065

The complex structure parameter space $\mathcal{M}_*$ has a codimension-1 locus of $\mathrm{Im}(\tau) = \infty$, or equivalently $j(\Sigma_{(\mathbf{10})}) = \infty$. Unless there is unipotent monodromy around this locus (an issue we come back to shortly), the distribution of ρ_I will remain featureless around this locus, and the fraction of vacua for the phenomenological solution is estimated by how finely the normal coordinate has to be tuned for phenomenology.[28] Hierarchically small Yukawa eigenvalues require that the value of the normal coordinate (the rational function in z_a's) be hierarchically small. Because a single tuning of $1/j(\Sigma_{(\mathbf{10})})$ already does the job (including the CKM mixing angles), however, the total tuning cost in this solution will not be as severe as 10^{-11} (or $10^{-11} \times 10^{-4.5}$) estimate for the naive individual tunings in (4.14).

It is worth noting that the idea of [76, 77] was to translate the hierarchically small values of Yukawa eigenvalues into a moderately large (but not hierarchically large) parameter in the exponent (like $\mathrm{Im}(\tau)$). In the F-theory implementation [61, 78–80] of this idea, however, the value of $\mathrm{Im}(\tau)$ is likely not to be the right measure of required fine-tuning, but the value of $1/j(\Sigma_{(\mathbf{10})}) \sim e^{2\pi i\tau}$ is, in the statistics of F-theory flux vacua, according to the argument above.

Let us briefly have a look at whether the distribution ρ_I on $\mathcal{M}_*$ has singularity at the $j(\Sigma_{(\mathbf{10})}) = \infty$ locus; if it does, then the right measure of fine-tuning will not be $e^{2\pi i\tau}$ but $1/\mathrm{Im}(\tau)$. Certainly the $\mathrm{Im}(\tau) = i\infty$ point is the locus of unipotent monodromy of one-cycles on $\Sigma_{(\mathbf{10})}$. There may also be some unipotent monodromy among three-cycles in the matter surface for SU(5)-**10** representation, because of the monodromy of one-cycles. The matter surface — a four-cycle — remains invariant in this limit, however. The author does not have a positive or negative evidence for non-trivial monodromy of horizontal four-cycles at the $j(\Sigma_{(\mathbf{10})}) = \infty$ locus of the complex structure moduli space $\mathcal{M}_*$; positive evidence is necessary in order to avoid the conclusion in the previous paragraph.

Acknowledgments

The author thanks Andreas Braun, James Halverson, Bert Schellekens, Yuji Tachikawa, Tsutomu Yanagida and Timo Weigand for discussions and communications. He also owes a lot to the organisers and participants of workshops "Physics and Geometry of F-theory" at Max Planck Institute, Munich and "Stringphenomenology 2015" at IFT, Madrid. This work is supported in part by WPI Initiative and a Grant-in-Aid for Scientific Research on Innovative Areas 2303, MEXT, Japan.

A Fourfolds for SU(5) × U(1) symmetry

This appendix is a brief summary note on Calabi-Yau fourfold geometry to be used for F-theory compactification when one wants to have SU(5) × U(1) symmetry in the effective theory below the Kaluza-Klein scale. There may be a few statements in the following that have not been written down in the literature, but those results can be derived by using procedure that has become almost standard these days. For this reason, only the results are stated, without detailed explanation.

[28] The distribution ρ_I for F-theory compactification has been used in this way for phenomenology already in [84].

JHEP11(2015)065

divisor	toric vectors in N_F
D'_X	$\nu'_X = (-1, 0)$
D'_Y	$\nu'_Y = (0, -1)$
D'_Z	$\nu'_Z = (2, 3)$
D'_W	$\nu'_W = (-1, -1)$

(a) $\mathrm{Bl}_{[1:0:0]}WP_{[1:2:3]}$

divisor	toric vectors in N_F
D'_0	$\nu'_0 = (0, 1)$
D'_∞	$\nu'_\infty = (0, -1)$
D'_1	$\nu'_1 = (1, 0)$
D'_2	$\nu'_2 = (-1, 1)$

(b) F_1

Table 1. Toric vectors in $N_F = \mathbb{Z} \oplus \mathbb{Z}$ for $\mathrm{Bl}_{[1:0:0]}WP_{[1:2:3]}$ (weighted projective space $WP^2_{[1:2:3]}$ blown up at one point) and a Hirzebruch surface $F_1 = dP_1$. The two neighbouring lattice points of the polytope for ν'_Z in (a) [resp. ν'_0 in (b)] are $(1, 2)$ and $(1, 1)$ [resp. ν'_1 and ν'_2], which sum up to be ν'_Z [resp. ν'_0]; this means that D'_Z [resp. D'_0] can be used as a section. Those two neighbouring points are both vertices of the polytope in (b), while they are not in (a); this makes it impossible to introduce the twisting by $\mathcal{O}_{B_{n-1}}(\kappa^{1,2})$ in the case (a) without introducing an unintended non-Abelian symmetry $\mathrm{SU}(3) \times \mathrm{SU}(2)$.

In this article, we only consider elliptic fibration with a section for F-theory compactification; let $\hat{Y}_n$ be a non-singular Calabi-Yau n-fold, $\pi : \hat{Y}_n \longrightarrow B_{n-1}$ an elliptic fibration morphism, and we assume that there is a divisor σ_0 of $\hat{Y}_n$ which is one-to-one with the base B_{n-1} under π, except in complex codimension-two loci in B_{n-1}. Low-energy effective theory has a U(1) symmetry, if the elliptic fibration $\pi : \hat{Y}_n \longrightarrow B_{n-1}$ has more sections than just a single section σ_0 [24].

We restrict our attention to cases where toric surfaces are used to construct the elliptic curve E in the fibre. It is best to use a toric surface such as $WP_{[1:2:3]}$ and $F_1 = dP_1$ (Hirzebruch surface), where the polytope $\widetilde{\Delta}_F \subset (\mathbb{Z} \oplus \mathbb{Z}) \otimes \mathbb{R} =: N_F \otimes \mathbb{R}$ contains a vertex ν'_v whose two neighbouring lattice points on $\widetilde{\Delta}_F$, denoted by ν'_a and ν'_b, satisfy $\nu'_a + \nu'_b = \nu'_v$ [85]; the divisor corresponding to ν'_v then defines one point in E. In such toric surfaces as $\mathrm{Bl}_{[1:0:0]}WP_{[1:2:3]}$ and F_1 (whose toric data are shown in table 1), there is one more independent divisor which can be chosen to be degree-1 on E; this divisor defines another point in E. When such a toric surface is fibred over some base B_{n-1} to be an ambient space for $\hat{Y}_n$, those two points in E become sections of the elliptic fibration. The rest of this note deals only with the two toric surfaces above. See [26] for other choices of toric surfaces to be fibred.

A.1 $\mathrm{Bl}_{[1:0:0]}WP_{[1:2:3]}$-fibred ambient space

A Calabi-Yau n-fold Y_n is constructed as a hypersurface of an ambient space

$$\mathbb{P}\left\{\begin{matrix} (-1 & 0 & 1 & 1) \\ (0 & 1 & 2 & 3) \end{matrix}\right\}[\mathcal{O}_B \oplus K_B \oplus \mathcal{O}_B \oplus \mathcal{O}_B]\,. \tag{A.1}$$

Here, the rank-4 fibre of the bundle over the base B_{n-1} is made projective[29] under the $\mathbb{C}^\times \times \mathbb{C}^\times$ action; one can choose two independent relations among the toric vectors in

[29] In order not to leave any ambiguity in the notation, we remark that the ordinary $WP_{[1:2:3]}$-fibred ambient space for a Calabi-Yau with elliptic fibration and a holomorphic section is denoted by $\mathbb{P}_{(1\,2\,3)}[\mathcal{O} \oplus \mathcal{O}_B(-2K_B) \oplus \mathcal{O}_B(-3K_B)] = \mathbb{P}_{(1\,2\,3)}[K_B \oplus \mathcal{O}_B \oplus \mathcal{O}_B]$.

JHEP11(2015)065

the form of $\sum_i \ell_i \nu'_i = 0 \in N_F = \mathbb{Z} \oplus \mathbb{Z}$, such as $-\nu'_W + \nu'_X + \nu'_Y = 0$ and $\nu'_Z + 2\nu'_X + 3\nu'_Y = 0$, and define the corresponding $\mathbb{C}^\times$ actions as $(\lambda \in \mathbb{C}^\times) : X_i \longrightarrow X_i \times \lambda^{\ell_i}$ for homogeneous coordinates X_i corresponding to the toric divisors D'_i. This ambient space is a $\mathrm{Bl}_{[1:0:0]} WP^2_{[1:2:3]}$-fibration over B_{n-1}.

A hypersurface Y_n of this ambient space is given by an equation

$$X^3W^2 + Y^2W + XYZWA_1 + X^2Z^2WA_2 + YZ^3A_3 + XZ^4A_4 = 0, \tag{A.2}$$

where $A_n \in \Gamma(B_{n-1}; \mathcal{O}_B(-nK_B))$ determines the complex structure of an elliptic fibred manifold Y_n. X, Y, Z and W are the homogeneous coordinates associated with divisors D_X, D_Y, D_Z and D_W, respectively, which are the D'_X, D'_Y D'_Z and D'_W divisors on the fibre, all over the base B_{n-1}. A section $D_Z|_{Y_n}$ is chosen as the zero section σ_0. Another section $\sigma_1 = D_W|_{Y_n} = \{W = 0\}|_{Y_n}$ does not intersect with the zero section σ_0. When the ambient space is blown down to the $WP_{[1:2:3]}$-fibred one, D_W is mapped to $(x, y) := (XW/Z^2, YW/Z^3) = (0, 0)$.

The n-fold Y_n develops a complex codimension-two locus of A_4 singularity (when the fibre of the ambient space is blown down to $WP_{[1:2:3]}$), when we require

$$A_n = s^{n-1} a_{6-n}, \qquad a_{n-1} \in \Gamma(B_{n-1}; \mathcal{O}_B(-nK_B - (n-1)S)) \tag{A.3}$$

for $n = 1, \cdots, 4$. S is a divisor of B_{n-1}, and s is a section of $\mathcal{O}_B(S)$ such that $S = \{s = 0\}$. A non-singular $\hat{Y}_n$ is constructed by a standard process of A_4 singularity resolution, followed by small resolutions associated with loci of charged matter fields; figure 2 (a) describes this process diagrammatically.[30] Let this blow-up morphism be $\nu : \hat{Y}_n \longrightarrow Y_n$; we also use the same ν for the morphism between the corresponding ambient spaces.

The zero section of $(\pi \cdot \nu) : \hat{Y}_n \longrightarrow B_{n-1}$ is given by $\sigma_0 := \nu^*(D_Z)|_{\hat{Y}_n}$; we will drop "$\nu^*$" or "$|_{\hat{Y}_n}$" in the following for simpler notations, however, unless subtleties are involved. Another section $\sigma_1 \sim D_W$ for $\pi : Y_n \longrightarrow B_{n-1}$ defines a section in $\hat{Y}_n$ except subtleties in the fibre of $S \subset B_{n-1}$. When we set

$$\sigma''_1 \sim \bar{D}_W - D_Z + K_B + (2E_1 + 4E_2 + 6E_3 + 3E_4)/5, \tag{A.4}$$

where $\bar{D}_W$ is the proper transform of D_W under $\nu : \hat{Y}_n \longrightarrow Y_n$, and $E_{1,2,3,4}$ the four exceptional divisors of $\nu : \hat{Y}_n \longrightarrow Y_n$, all of $\sigma''_1 \cdot \sigma_0$ and $\sigma''_1 \cdot E_{1,2,3,4}$ are mapped to the trivial divisor class in B_{n-1} under $(\pi \cdot \nu)_*$. References for the statements up to this point include [23, 87, 88].

There are three distinct groups of SU(5)-charged matter fields in this case [22], as summarised in table 2. The U(1)-charge of these SU(5)-charged matter fields can be determined by using the topological class of σ''_1 in (A.4); the results — shown in table 2 — indicates that the U(1) symmetry generated by σ''_1 shows up as the U(1) part of the $\mathrm{U}(3) \subset E_7$ structure group of the Higgs bundle in the field theory local model (Katz-Vafa type field theory) on $S \times \mathbb{R}^{3,1}$ (cf [22, 23]). The 6D anomaly cancellation condition

[30] $\nu'_{E1} = \nu'_S + \nu'_X + \nu'_Y$, $\nu'_{E2} = \nu'_{E1} + \nu'_X + \nu'_Y$, $\nu'_{E4} = \nu'_{E1} + \nu'_Y$, $\nu'_{E3} = \nu'_{E2} + \nu'_Y$. Then add ν'_W. A 1-simplex (2-dim cone) $< \nu'_W \nu'_{E3} >$ bisecting the cone $< \nu'_{E3} \nu'_X \nu'_Y >$ provides a small resolution of the conifold singularity over the $a_2 = a_3 = 0$ locus in B_{n-1}.

JHEP11(2015)065

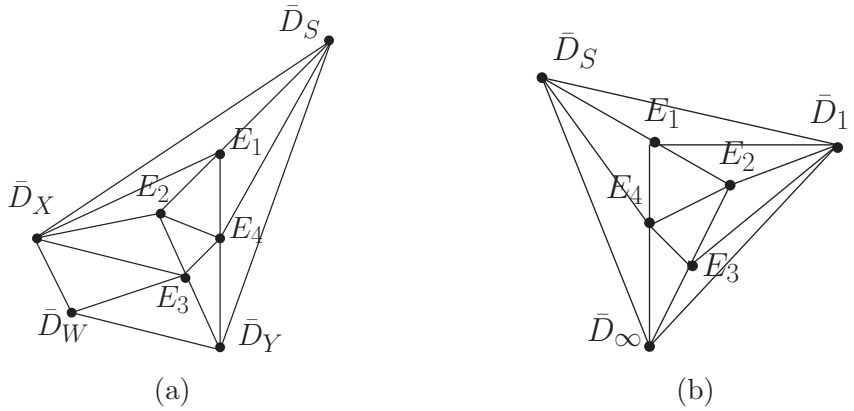

Figure 2. Blow-up procedure shown diagrammatically. Subdivision of a triangle using its centre of mass corresponds to a blow-up of the ambient space centred at a codimension-three locus, and a subdivision of an edge using its centre of mass to a blow-up of the ambient space centred at a codimension-two locus. These graphs can be seen as triangulation of cones, if the base B_{n-1} is also toric, and the divisor S a toric divisor, although we do not assume that B_{n-1} is toric in this summary note. The diagram (a) is for the $\mathrm{Bl}_{[1:0:0]}WP^2_{[1:2:3]}$-fibred ambient space and (b) for the F_1-fibred ambient space. Note in (a) that the triangulation of $\bar{D}_X$-E_3-$\bar{D}_Y$-$\bar{D}_W$ resolves the conifold singularity associated with the U(1)-charge ± 5 matter field; the graph (b) is the same as the blow-up procedure in [86].

bdle	repr.	curve def. eq.	curve div. class	vanishing cycle
$\mathbf{3}$	$\mathbf{10}_{-1}$	$a_5\vert_S = 0$	$(-K_B)\vert_S$	$(-E_2 \cdot E_4)\vert_{\hat{Y}_n}$
$\wedge^2\mathbf{3}$	$\bar{\mathbf{5}}_{-2}$	$(a_4a_3 - a_2a_5)\vert_S = 0$	$(-3S - 5K_B)\vert_S$	$\left(-(\bar{D}_Y - K_B - E_4) \cdot E_3\right)\vert_{\hat{Y}_n}$
$\wedge^3\bar{\mathbf{3}}$	$\bar{\mathbf{5}}_{+3}$	$a_3\vert_S = 0$	$(-2S - 3K_B)\vert_S$	$(\bar{D}_X \cdot E_3)\vert_{\hat{Y}_n}$

Table 2. Summary of geometry associated with the SU(5)-charged matter fields in the case of $\mathrm{Bl}_{[1:0:0]}WP^2_{[1:2:3]}$-fibred ambient space. The matter locus — codimension-1 in S — is given by the defining equation in the third column; this matter locus belongs to the divisor class on S shown in the fourth column. The last column shows the corresponding class of vanishing cycle (complex codimension-two in $\hat{Y}_n$). The first column shows the representation of the U(3) structure group of the Higgs bundle on S.

indicates that an SU(5)-neutral hypermultiplet with U(1)-charge ± 5 is localised in the fibre of a codimension-two $a_2 = a_3 = 0$ locus in B_{n-1}, and that they are all the matter fields charged under the SU(5) $\times$ U(1) symmetry (see [23, 89]).

This construction can be used for spontaneous R-parity violation. The hierarchical structure problem of Yukawa eigenvalues, however, cannot be solved by using this construction (without further symmetry or tuning of parameters), because all the "E_6"-type points on S contribute to the up-type Yukawa matrix in the low-energy effective theory. See figure 3 (a) for the configuration of matter curves.

JHEP11(2015)065

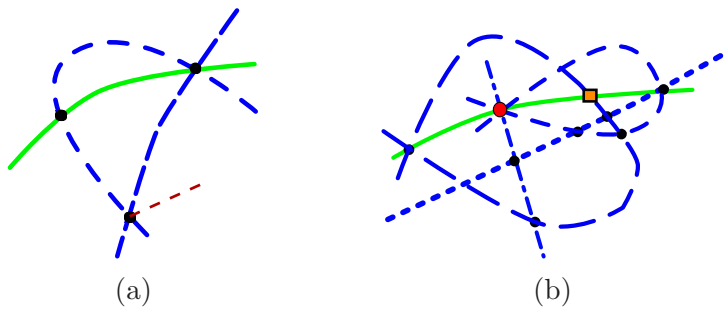

Figure 3. (colour online) Configuration of matter curves and interaction points on the SU(5) 7-brane S shown schematically. The picture (a) is for the case of $\mathrm{Bl}_{[1:0:0]}WP^2_{[1:2:3]}$-fibred ambient space, and (b) for the case of F_1-fibred ambient space with the no.2 choice of the order of vanishing. Solid curve (green) is the matter curve for SU(5)-**10** representation in both (a) and (b). In the picture (a), the long dashed and dashed curves (both blue) are the matter curves for $\bar{\mathbf{5}}_3$ and $\bar{\mathbf{5}}_{-2}$, respectively. The dotted curve (red) is where SU(5)-neutral U(1)-charged fields are localised in B_3, "projected" on to S. In the picture (b), the long dashed, dashed, dotted and dash-dotted curves (all in blue) are the matter curves for $\bar{\mathbf{5}}_0$, $\bar{\mathbf{5}}_{-1}$, $\bar{\mathbf{5}}_1$ and $\bar{\mathbf{5}}_2$ representations, respectively. The "E_6"-type point for up-type Yukawa is indicated by a square (orange), while the point with F_1-fibre by a large circle (red).

A.2 F_1-fibred ambient space

$F_1 = dP_1$ can be used as fibre of the ambient space, instead of $\mathrm{Bl}_{[1:0:0]}WP^2_{[1:2:3]}$, in constructing a Calabi-Yau n-fold with a non-trivial Mordell-Weil group. We then use an ambient space

$$\mathbb{P}^{\left\{\begin{matrix}(1\ 1\ 0\ 0)\\(0\ 1\ 1\ 1)\end{matrix}\right\}}\left[K_B \oplus \mathcal{O}_B \oplus \mathcal{O}_B(\kappa^1) \oplus \mathcal{O}_B(\kappa^2)\right], \tag{A.5}$$

where the fibre can be twisted by introducing two divisors κ^1 and κ^2 of the base B_{n-1} [90]. The fibre is F_1; the four line bundles above correspond to the toric vectors ν'_0, ν'_∞, ν'_1 and ν'_2 in table 1 (b), respectively. The zero locus of the line bundles are the divisors denoted by $D_{0,\infty,1,2}$, and the corresponding homogeneous coordinates are denoted by $X_{0,\infty,1,2}$. There are linear equivalence relations

$$D_1 - \kappa^1 \sim D_2 - \kappa^2, \qquad D_\infty \sim D_0 - K_B + D_2 - \kappa^2. \tag{A.6}$$

An elliptic fibred Calabi-Yau n-fold Y_n is given as a hypersurface of this ambient space by[31]

$$\begin{aligned} &X_\infty^2(A_{0,1}X_1 + A_{1,0}X_2) + X_\infty X_0(B_{-1,1}X_1^2 + B_{0,0}X_1X_2 + B_{1,-1}X_2^2) \\ &+ X_0^2(C_{-2,1}X_1^3 + C_{-1,0}X_1^2X_2 + C_{0,-1}X_1X_2^2 + C_{1,-2}X_2^3) = 0. \end{aligned} \tag{A.7}$$

[31] This equation can also be written down by using Affine charts for the fibre. In the chart corresponding to a cone $\langle \nu'_0, \nu'_1\rangle$ [resp. $\langle \nu'_0, \nu'_2\rangle$], Affine coordinates are $(u,\omega) = (X_1/X_2, X_2X_0/X_\infty)$ [resp. $(v,\omega') = (X_2/X_1, X_1X_0/X_\infty)$]. In the chart for the cone $\langle \nu'_\infty, \nu'_1\rangle$ [resp. $\langle \nu'_\infty, \nu'_2\rangle$], the Affine coordinates are $(u,w) = (X_1/X_2, X_\infty/(X_0X_2))$ [resp. $(v,w') = (X_2/X_1, X_\infty/(X_0X_1))$].

JHEP11(2015)065

Complex structure of Y_n is encoded in the choice of

$$\begin{aligned} A_{n_1,n_2} &\in \Gamma(B_{n-1}; \mathcal{O}(n_1\kappa^1 + n_2\kappa^2)), \\ B_{n_1,n_2} &\in \Gamma(B_{n-1}; \mathcal{O}(n_1\kappa^1 + n_2\kappa^2 - K_B)), \\ C_{n_1,n_2} &\in \Gamma(B_{n-1}; \mathcal{O}(n_1\kappa^1 + n_2\kappa^2 - 2K_B)). \end{aligned} \tag{A.8}$$

We take D_0 ($X_0 = 0$ locus) as the zero section[32] σ_0 of the elliptic fibration $\pi_Y : Y_n \longrightarrow B_{n-1}$. There is also a section corresponding to the degree-1 divisor $(D'_1 - D'_0)|_E$ of the fibre, which is denote by σ_1. It is geometrically given by

$$[X_\infty(B_{-1,1}X_1^2 + \cdots + B_{1,-1}X_2^2) + X_0(C_{-2,1}X_1^3 + \cdots + C_{1,-2}X_2^3) = 0] - 2[X_\infty = 0], \tag{A.9}$$

and belongs to the divisor class $(D_1 - D_0 + \kappa^2)$. Since

$$\pi_{Y*}(\sigma_1 \cdot \sigma_0) = [B_{\rm sym} = 0], \tag{A.10}$$

$$B_{\rm sym} := B_{1,-1}A_{0,1}^2 - B_{0,0}A_{0,1}A_{1,0} + B_{-1,1}A_{1,0}^2 \in \Gamma\left(B_{n-1}; \mathcal{O}(\kappa^1 + \kappa^2 - K_B)\right), \tag{A.11}$$

we take

$$\sigma_1'' := \sigma_1 - [B_{\rm sym} = 0] - \sigma_0 + K_B \sim (D_1 - \kappa^1 - 2D_0 + 2K_B) \tag{A.12}$$

as the generator of a U(1) symmetry in the low-energy effective theory.

The charge-± 2 matter fields under this U(1) symmetry are localised in the codimension-two locus of B_{n-1} given by[33]

$$\begin{aligned} B_{\rm sym} &= C_{\rm sym} = 0, \\ C_{\rm sym} &:= C_{1,-2}A_{0,1}^3 - C_{0,-1}A_{0,1}^2A_{1,0} + C_{-1,0}A_{0,1}A_{1,0}^2 - C_{-2,1}A_{1,0}^3 \\ &\qquad \in \Gamma\left(B_{n-1}; \mathcal{O}(\kappa^1 + \kappa^2 - 2K_B)\right). \end{aligned} \tag{A.13}$$

Matter fields with charge ± 1 are localised in a class $4(\kappa^1 + \kappa^2 - 2K_B) \cdot (-\kappa^1 - \kappa^2 - 2K_B)$. All that has been stated so far is the same as (or obvious generalisation of) [25, 88].

Let us consider a case where an n-fold Y_n develops A_4 singularity at the $X_\infty = X_1 = 0$ point in the F_1 fibre over a divisor $S \subset B_{n-1}$, so that there is a stack of 7-branes for an SU(5) gauge theory along $S \subset B_{n-1}$. The sections A_{n_1,n_2}, B_{n_1,n_2} and C_{n_1,n_2}'s defining the complex structure of the n-fold Y_n need to have certain order of vanishing along the divisor $S \subset B_{n-1}$ then. There are a couple of different choices, as shown in table 3, at least in a study of local geometry. The no.3 choice of the order of vanishing, however, may have a problem, when a global geometry is studied; at least in a few examples using compact toric ambient spaces, we found that the singular fibre over S in a resolved n-fold $\hat{Y}_n$ becomes I_6

[32] It is a rational section, but not a holomorphic one, when $\kappa^1 \cdot \kappa^2$ is non-empty.

[33] Consider the case X_n is a threefold. In the I_2 fibre of a such a codimension-2 point in the base B_2, σ_0 is a point in one of the two $\mathbb{P}^1$'s, and σ_1 wraps that $\mathbb{P}^1$. In the I_2 fibre over a $A_{1,0} = A_{0,1} = 0$ point, however, σ_0 wraps one of the two $\mathbb{P}^1$'s (being a rational section when $\kappa^1 \cdot \kappa^2$ is non-empty), while σ_1 wraps the other $\mathbb{P}^1$.

JHEP11(2015)065

choice	$A_{0,1}$	$A_{1,0}$	$B_{-1,1}$	$B_{0,0}$	$B_{1,-1}$	$C_{-2,1}$	$C_{-1,0}$	$C_{0,-1}$	$C_{1,-2}$
no.1	0	0	0	0	1	2	3	4	5
no.2	0	0	0	0	2	0	1	3	5
no.3	0	1	0	0	3	0	0	2	5
no.4	0	3	0	0	4	0	0	1	5

Table 3. The order of vanishing required for A_4 singularity.

	matter curve def. eq. ($\|_S = 0$)	curve divisor class ($\|_S$)	vanishing cycle ($\|_{\hat{Y}_n}$)
$\mathbf{10}_0$	$B_{0,0}$	$-K_B$	$-E_2 \cdot E_4$
$\bar{\mathbf{5}}_0$	$(c_{1,-2\|5}B_{0,0}^2 - c_{0,-1\|3}B_{0,0}b_{1,-1\|2} + c_{-1,0\|1}b_{1,-1\|2}^2)$	$\kappa^1 - 2\kappa^2 - 4K_B - 5S$	$E_3 \cdot (\bar{D}_1 - E_2 - K_B)$
$\bar{\mathbf{5}}_{-1}$	$A_{0,1}B_{0,0}^2 - A_{1,0}B_{-1,1}B_{0,0} + C_{-2,1}A_{1,0}^2$	$\kappa^2 - 2K_B$	$-\bar{D}_S \cdot (D_0 - E_1 - K_B)$
$\bar{\mathbf{5}}_1$	$C_{-2,1}$	$-2\kappa^1 + \kappa^2 - 2K_B$	$\bar{D}_S \cdot \bar{D}_\infty$
$\bar{\mathbf{5}}_2$	$A_{1,0}$	κ^1	$\bar{D}_S \cdot (\kappa^1 - \bar{D}_1)$

Table 4. Summary of geometry associated with SU(5)-charged matter fields in the case of F_1-fibred ambient space, and the no.2 choice of the order of vanishing. See caption of table 2.

type of Kodaira classification unintentionally. The rest of this summary note focuses on the no.2 choice of the order of vanishing. It is not clear whether the choice of toric vectors in section 3 of [25] corresponds to any one of the order of vanishing in table 3.

Under the no.2 choice of the order of vanishing, singular Y_n can be made non-singular (denoted by $\hat{Y}_n$) by successive blow-ups of the ambient space; the same blow-up procedure as in [91], shown in figure 3 (b), does the job in this case. The proper transforms of the divisor D_1, D_∞ and $D_S = \pi_Y^*(S)$ are denoted by $\bar{D}_1$, $\bar{D}_\infty$ and $\bar{D}_S$, respectively.

$$\begin{aligned} D_S &= \bar{D}_S + E_1 + E_2 + E_3 + E_4, \\ D_1 &= \bar{D}_1 + E_1 + 2E_2 + 2E_3 + E_4, \\ D_\infty &= \bar{D}_\infty + E_1 + 2E_2 + 3E_3 + 2E_4. \end{aligned}$$

When we choose

$$\sigma_1'' \sim (D_2 - \kappa^2 - 2D_0 + 2K_B) \tag{A.14}$$

as a U(1) generator, the conditions $(\pi_Y \cdot \nu)_*(\sigma_0 \cdot \sigma_1'') = (\pi_Y \cdot \nu)_*(E_{1,2,3,4} \cdot \sigma_1'') = 0 \in \mathrm{Pic}(B_{n-1})$ are satisfied.

SU(5)-charged matter fields are localised in five distinct codimension-1 loci in S, as summarised in table 4. There, we used the following notations, as in [65, 92]:

$$B_{1,-1} =: sb_{1,-1|1}, \quad C_{-1,0} =: sc_{-1,0|1}, \quad C_{0,-1} =: s^3 c_{0,-1|3}, \quad C_{1,-2} =: s^5 c_{1,-2|5}. \tag{A.15}$$

The divisor classes of $\bar{\mathbf{5}}$-representation matter fields sum up to be $(-8K_B - 5S)|_S$, which is vital to the 6D box anomaly cancellation. There are also SU(5)-neutral, but U(1)-charged

JHEP11(2015)065

matter fields. Their location — codimension-two in B_{n-1} — is inferred by using the 6D anomaly cancellation conditions; we are led to the following solution:

$$\text{charge } \pm 2 \quad (\kappa^1 + \kappa^2 - K_B) \cdot (\kappa^1 + \kappa^2 - 2K_B) - 5S \cdot \kappa^1 \subset B_{n-1}, \tag{A.16}$$

$$\text{charge } \pm 1 \quad 16K_B^2 - 4(\kappa^1 + \kappa^2)^2 - 10S \cdot (-\kappa^1 + \kappa^2 - 2K_B) \subset B_{n-1}. \tag{A.17}$$

A part of the $B_{\text{sym}} = C_{\text{sym}} = 0$ locus for the charge-± 2 fields — $5S \cdot \kappa^1$ — has been subtracted, which is reasonable because the $B_{\text{sym}} = C_{\text{sym}} = 0$ conditions are satisfied automatically at $A_{1,0} = s = 0$.

When F-theory is compactified to 3+1-dimensions in this way, by using a Calabi-Yau fourfold $\hat{Y}_{n=4}$, geometric configuration of the matter curves on S is schematically like figure 3 (b). Most of the intersection points of the matter curves in S are one of the "E_6"-type, D_6 type and A_6-type, but none of those local descriptions apply to the intersection points where matter curves for $\mathbf{10}_0$, $\bar{\mathbf{5}}_2$ and $\bar{\mathbf{5}}_{-1}$-representations meet. The fibre of $(\pi_Y \cdot \nu) : \hat{Y}_4 \longrightarrow B_3$ is a surface F_1 at such points in B_3. Tensionless strings may show up in the effective theory on 3+1-dimensions in this case [29–31]. For phenomenological purposes, it is thus safe to restrict our attention to cases where the divisor class $\kappa^1|_S$ is trivial (so that $A_{1,0}|_S$ remains non-zero on S).

This $\kappa^1|_S = 0$ condition implies, first of all, that the $\bar{\mathbf{5}}_2$–$\mathbf{5}_{-2}$ matter fields do not appear in the low-energy spectrum. When this set-up with a U(1) symmetry is used for spontaneous R-parity violation scenario, matter identification should be the following. First, the up-type Higgs needs to be identified with the doublet part of $\mathbf{5}_0$ so that the up-type Yukawa couplings are generated. Secondly, for the charged lepton Yukawa couplings to be generated, L and H_d need to originate from $\bar{\mathbf{5}}_1$ and $\bar{\mathbf{5}}_{-1}$ or vice versa. $\bar{D}$'s of the supersymmetric Standard Models need to be on the same matter curve as L's in order for the down-type Yukawa couplings to be generated.

The $\kappa^1|_S = 0$ condition also implies that the splitting of the matter curve of $\bar{\mathbf{5}}$ representation in this set-up cannot be used for the hierarchical structure problem of the up-type Yukawa matrix. In the absence of the matter curve of $\bar{\mathbf{5}}_2$ matter field and of the interaction points indicated by a large circle (red) in figure 3 (b), all the "E_6" type points arise in the form of $\mathbf{10}_0$–$\mathbf{10}_0$–$\bar{\mathbf{5}}_0$ interaction points at $c_{-1,0|1} = B_{0,0} = 0$. Therefore, the result of [61, 62] that the number of "E_6"-type points is even still holds true.

B SU(6) 7-branes for up-type Yukawa coupling

Reference [12] introduced a class of F-theory compactifications with a stack of SU(6) 7-branes at the divisor S in the base B_3, which accommodates SU(5) unification and generates its up-type Yukawa couplings. Some details of the construction of this class of compactifications were missing in [12], however. Thanks to the development in the study of F-theory since then, we can fill the missing details now.

Let us first note that the class of F-theory compactification with an SU(6) 7-brane locus above is somewhat different from general F-theory compactification characterised by the Tate condition for the I_6-type singular fibre. To see this, remember that the Tate

JHEP11(2015)065

condition for the I_6-type singular fibre in a non-singular elliptic fibration $\pi : \hat{Y}_n \longrightarrow B_{n-1}$ corresponds to the following set of the order of vanishing of the coefficients in the generalised Weierstrass form [92]:

$$0 = y^2 + x^3 + A_1 xy + A_2 x^2 + A_3 y + A_4 x + A_6, \tag{B.1}$$

$$A_1 \sim s^0, \quad A_2 \sim s^1, \quad A_3 \sim s^3, \quad A_4 \sim s^3, \quad A_6 \sim s^6; \tag{B.2}$$

here, $s \in \Gamma(B; \mathcal{O}_B(S))$, and the $\{s = 0\}$ locus corresponds to the divisor S. It is thus convenient to write the Weierstrass equation in the following form:

$$y^2 + x^3 + a_5 xy + a_4 s x^2 + a_3 s^3 y + a_2 s^3 x + a_0 s^6 = 0. \tag{B.3}$$

where $a_{0,2,3,4,5}$ are holomorphic sections of appropriate line bundles on B_{n-1}.

When we consider F-theory compactification of this type to 3+1-dimensions, using a Calabi-Yau fourfold, straightforward analysis reveals that the matter curves in S are given by

$$\Sigma_{(\wedge^2 \mathbf{6})} : \quad a_5|_S = 0, \qquad \Sigma_{(\mathbf{6})} : \quad (a_2^2 - a_2 a_5 a_3 + a_0 a_5^2)|_S = 0; \tag{B.4}$$

Katz-Vafa type field theory for these matter fields are SO(12) (D_6) and SU(7) (A_6) gauge theories, respectively. These two matter curves intersect at points $a_5|_S = a_2|_S = 0$; physics around these points (including Yukawa couplings) is captured by a field theory with SO(14) (D_7) gauge group. We cannot expect an up-type Yukawa coupling of the form $\Delta W \sim \mathbf{10}^{\cdot\cdot}\mathbf{10}^{\cdot\cdot}\mathbf{5}^{\cdot}\epsilon_{\cdot\cdot\cdot\cdot\cdot}$ in such a class of F-theory compactifications [12, 93].

An idea of ref. [12] is to use Heterotic compactification, and to translate and generalise it in the language of F-theory compactification. To be more explicit, imagine a Heterotic string compactification on an elliptic fibred Calabi-Yau threefold (Z, S, π), where $\pi : Z \longrightarrow S$, with a vector bundle $V_3 \oplus V_2$ whose structure group is $\mathrm{SU}(3) \times \mathrm{SU}(2) \subset E_8$. V_3 and V_2 are given by the Fourier-Mukai transform of spectral data $(C_3, \mathcal{N}_3)$ and $(C_2, \mathcal{N}_2)$, where C_3 and C_2 are divisors of Z that are 3-fold and 2-fold covering over S, respectively, and $\mathcal{N}_3$ and $\mathcal{N}_2$ are line bundles on C_3 and C_2, respectively. For generic complex structure of Z, the spectral surfaces C_3 and C_2 are given by

$$c_0 + c_2 x + c_3 y = 0, \qquad d_0 + d_2 x = 0, \tag{B.5}$$

respectively, where

$$c_k \in \Gamma(S; \mathcal{O}_S(kK_S + \eta_3)), \qquad d_k \in \Gamma(S; \mathcal{O}_S(kK_S + \eta_2)) \tag{B.6}$$

for some divisors $\eta_{2,3}$ of S. The F-theory dual of this compactification should be given by (Y_4, B_3), where the base threefold $B_3 = \mathbb{P}\left[\mathcal{O}_S(6K_S + \eta_3 + \eta_2) \oplus \mathcal{O}_S\right]$ is a $\mathbb{P}^1$-fibration over S, and the elliptic fibre of $\pi : Y_4 \longrightarrow B_3$ is given by [17, 58, 94–96]

$$y^2 = x^3 + f_0 x s^4 + g_0 s^6 + (c_0 s^3 + c_2 s x + c_3 y)(d_0 s^2 + d_2 x), \tag{B.7}$$

where s is an inhomogeneous coordinate of the $\mathbb{P}^1$-fibre in $B_3 \longrightarrow S$.

JHEP11(2015)065

Now, we generalise it to general B_3 and its effective divisor S, and define $\pi : Y_4 \longrightarrow B_3$ by the same equation as above; the coefficients f_0, g_0, c_k's and d_k's, however, are promoted to holomorphic sections on B_3 as follows:

$$c_k \in \Gamma(B_3; \mathcal{O}_B((k-4)K_B + a + (k-3)S)), \qquad f_0 \in \Gamma(B_3; \mathcal{O}_B(-4K_B - 4S), \tag{B.8}$$

$$d_k \in \Gamma(B_3; \mathcal{O}_B(-a + (k-2)(K_B + S))), \qquad g_0 \in \Gamma(B_3; \mathcal{O}_B(-6K_B - 6S), \tag{B.9}$$

where a is some divisor on B_3; this is a generalisation, in that the translation from Heterotic string compactification is reproduced by setting $(2K_S + \eta_2) = -a|_S$ and $(6K_S + \eta_2 + \eta_3) = S|_S = c_1(N_{S|B_3})$.

One can read out from the discriminant and singularity of this generalised Weierstrass form that there are three distinct matter curves,[34]

$$\Sigma_{(\wedge^3\mathbf{6})} : \; d_2|_S = 0, \tag{B.10}$$

$$\Sigma_{(\wedge^2\mathbf{6})} : \; c_3|_S = 0, \tag{B.11}$$

$$\Sigma_{(\mathbf{6})} : \; (c_3^2 d_0^3 + c_2^2 d_0^2 d_2 - 2c_0 c_2 d_0 d_2^2 + c_0^2 d_2^3 + c_3^2 d_0 d_2^2 f_0 - c_3^2 d_2^3 g_0)|_S = 0. \tag{B.12}$$

Those three curves intersect at $c_3|_S = d_2|_S = 0$ points in S. We can choose the gauge group of the Katz-Vafa type field theory (field theory local model) around these matter curves to be E_6, D_6, A_6; physics around a $c_3|_S = d_2|_S = 0$ point is described by an E_7 gauge theory; a non-trivial Higgs bundle background with the structure group $\mathrm{SU}(2) \times \mathrm{U}(1) \subset E_7$ breaks the E_7 symmetry down to SU(6); Yukawa coupling $\Delta W = \mathbf{6} \cdot \wedge^2\mathbf{6} \cdot \wedge^3\mathbf{6}$ is generated at each one of those $c_3|_S = d_2|_S = 0$ points.

Such an SU(6) 7-brane configuration in F-theory can be used for SU(5) unification by turning on a line bundle on S, so that the symmetry is reduced to SU(5); further breaking to the Standard Model gauge group is not impossible, although we stay away from such details. There are two possible particle identifications. The first possibility is to identify SU(5)-**10** matter fields with the $\wedge^3\mathbf{6}$ representation of SU(6), and $H(\mathbf{5})$ within **adj**. of SU(6) [12]; the other possibility is to find the **10** matter field in $\wedge^2\mathbf{6}$ of SU(6), when the $H(\mathbf{5})$ field also has to come from the same $\wedge^2\mathbf{6}$ representation of SU(6); the latter possibility was overlooked in [12]. In any one of those two possibilities, Yukawa couplings are generated along the entire matter curve ($\Sigma_{(\wedge^3\mathbf{6})}$ or $\Sigma_{(\wedge^2\mathbf{6})}$), not only at isolated points in the 7-brane S (cf [18]). This makes it impossible to exploit the approximately codimension-1 nature of Yukawa matrices from isolated Yukawa points [58–60]. The idea of [78–80] (or something similar to the one in [61]) may still be implemented in the latter identification with a tuning $j(\Sigma_{(\wedge^2\mathbf{6})}) \gg 1$; it is desirable to have a separate study to see if that is the case, however.

Before closing this section, we compute $h^{3,1}$ for Calabi-Yau fourfolds with such an SU(6) unification. We choose $(B_3, [S])$ to be $B_3 = \mathbb{P}^1 \times \mathbb{P}^2$ and $[S] = \mathrm{pt} \times \mathbb{P}^2$, so the result can be compared with $h^{3,1}$ for other classes of compactifications with a rank-5 symmetry

[34] The linearised analysis [97] is able to determine the defining equation of the spectral cover for associated bundles such as $(V_3 \otimes V_2)$ approximately. All the terms except those involving f_0 or g_0 in the defining equation of $\Sigma_{(\mathbf{6})}$ can be obtained in that way.

JHEP11(2015)065

$(3K_{\mathbb{P}^2}+\eta_2)$	-2	-1	0	1	2
$(3K_{\mathbb{P}^2}+\eta_3)$	2	1	0	-1	-2
$h^{3,1}$	1917	1908	1904	1905	1911

Table 5. $h^{3,1}$ of Calabi-Yau fourfolds for SU(6) unification, provided $B_3 = \mathbb{P}^1 \times \mathbb{P}^2$ and $[S] = \mathrm{pt} \times \mathbb{P}^2$.

(SO(10) and SU(5) × U(1)) in the main text. The choice of $(B_3, [S])$ above introduces a constraint[35] in the Heterotic string language: $(3K_S + \eta_2) + (3K_S + \eta_3) = 0$. See table 5 for the results.[36]

C Monodromy around the U(1)-enhancement limit

C.1 $6g - 3$ topological four-cycles

This appendix C begins with a brief review. We came to be interested in section 4.1 in a compact Calabi-Yau fourfold Y_4 with its complex structure parameter in $\mathcal{M}_*$ close to the $\mathcal{M}_*^{\mathrm{U}(1)}$ locus; Y_4 contains a local geometry of deformed conifold along a curve Σ, and this local geometry of Y_4 is modelled by a geometry Y_{local}, which is explained shortly. Four-cycles in Y_{local} as well as their lift to the global geometry Y_4 was studied in [57]; results of [57] that we need in section 4.1 are reviewed here. The review is followed by analysis of monodromy of those cycles and period integrals.

The local geometry model Y_{local}, which is denoted by $\widetilde{X}^\flat$ in [57], is realised as a hypersurface of the total space of a rank-4 vector bundle over a Riemann surface Σ,

$$\mathcal{L}^{\otimes 3} \oplus \mathcal{L}^{\otimes 3} \oplus \mathcal{L}^{\otimes 2} \oplus \mathcal{L}^{\otimes 4} \longrightarrow \Sigma, \tag{C.1}$$

where the Riemann surface Σ satisfies $6|(2g(\Sigma)-2)$, and $\mathcal{L}^{\otimes 6} = K_\Sigma$. The defining equation of Y_{local} in this ambient space is

$$YA_3 = XA_4 + A_6; \tag{C.2}$$

Y, A_3, X and A_4 are the coordinates of the rank-4 fibre of the bundle in (C.1), and

$$A_6 \in \Gamma(\Sigma; K_\Sigma) \cong \mathbb{C}^g =: \mathcal{M}_*^{\mathrm{local}} \tag{C.3}$$

[35] Intuitively, this constraint means that the instanton number is distributed equally into the hidden and visible sectors; $(6K_S + \eta_0) = 0 = -(6K_S + \eta_\infty)$.

[36] Computation was done by partially using a reasoning available in the Heterotic dual supergravity regime. An elliptic fibred Calabi-Yau threefold over base $\mathbb{P}^2$ for Heterotic string compactification has 273 moduli (272 for complex structure and 1 for the volume of T^2-fibre), first of all. Automorphism of the Calabi-Yau three-fold has already been exploited. The hidden sector E_8 vector bundle comes with 1502 moduli, which is verified easily in F-theory language. We counted the vector bundle moduli of SU(2)×SU(3) in the visible sector by counting the degree of freedom in the spectral surfae:

$$\mathrm{SU}(2): \quad \frac{(n_2+11)(n_2+10)}{2} + \frac{(n_2+5)(n_2+4)}{2} - 1, \tag{B.13}$$

$$\mathrm{SU}(3): \quad \frac{(n_3+11)(n_3+10)}{2} + \frac{(n_3+5)(n_3+4)}{2} + \frac{(n_3+2)(n_3+1)}{2} - 1, \tag{B.14}$$

where n_2 and n_3 parametrise the distribution of instanton numbers in the SU(2), SU(3) vector bundles through $\eta_2 = n_2 H_{\mathbb{P}^2}$, $\eta_3 = n_3 H_{\mathbb{P}^2}$.

JHEP11(2015)065

governs the complex structure of this local geometry; this $A_6 \in \Gamma(\Sigma; K_\Sigma)$ descends from $A_6 \in \Gamma(B_3; \mathcal{O}_B(-6K_B))$ on the compact set-up by simple restriction on $\Sigma \subset B_3$. $\mathcal{L}^{\otimes 6} := \mathcal{O}_\Sigma(-6K_B|_\Sigma)$ is the same as K_Σ, because of the adjunction formula for $\Sigma := \{A_3 = A_4 = 0\} \subset B_3$. The g-dimensional space $\mathcal{M}_*^{\text{local}}$ is regarded as the g directions normal to $\mathcal{M}_*^{\text{U}(1)}$ in $\mathcal{M}_*$, at least when B_3 is a Fano variety.

Reference [57] identified $6g-3$ four-cycles in this local fourfold geometry Y_{local}. Let $Z := \partial\overline{Y_{\text{local}}}$ be the boundary, which is a seven dimensional manifold over $\mathbb{R}$. Using a long exact sequence

$$0 \longrightarrow H_4(Z;\mathbb{Z}) \longrightarrow H_4(Y_{\text{local}};\mathbb{Z}) \longrightarrow H_4^{BM}(Y_{\text{local}};\mathbb{Z}) \longrightarrow H_3(Z;\mathbb{Z}) \longrightarrow 0, \tag{C.4}$$

it turns out that both $H_4(Y_{\text{local}};\mathbb{Q})$ and $H_4^{BM}(Y_{\text{local}};\mathbb{Q})$ are of dimension $4g-3$; kernels and cokernels of the homomorphisms in the exact sequence above introduces a filtration structure

$$H_4(Y_{\text{local}};\mathbb{Q}) \supset (H_4(Y_{\text{local}};\mathbb{Q}))^0 =: \text{Span}_{\mathbb{Q}}\left\{\widetilde{A}_{i=1,\cdots,g}, \widetilde{A}'^{j=1,\cdots,g}\right\}, \tag{C.5}$$

$$H_4(Y_{\text{local}};\mathbb{Q}) \;/\; (H_4(Y_{\text{local}};\mathbb{Q}))^0 =: \text{Span}_{\mathbb{Q}}\left\{[\widetilde{B}_\ell] \mid \ell = 1,\cdots,2g-3\right\}, \tag{C.6}$$

and

$$H_4^{BM}(Y_{\text{local}};\mathbb{Q}) \supset \left(H_4^{BM}(Y_{\text{local}};\mathbb{Q})\right)^0 =: \text{Span}_{\mathbb{Q}}\left\{\widetilde{B}'_\ell \mid \ell = 1,\cdots,2g-3\right\}, \tag{C.7}$$

$$H_4^{BM}(Y_{\text{local}};\mathbb{Q}) \;/\; \left(H_4^{BM}(Y_{\text{local}};\mathbb{Q})\right)^0 =: \text{Span}_{\mathbb{Q}}\left\{[\widetilde{C}]^{i=1,\cdots,g},\ [\widetilde{C}']_{j=1,\cdots,g}\right\}; \tag{C.8}$$

Overall, $2g + (2g-3) + 2g$ four-cycles, $\widetilde{A}$'s, $\widetilde{B}$'s and $\widetilde{C}$'s are identified in either $H_4(Y_{\text{local}})$ or $H_4^{BM}(Y_{\text{local}})$. The intersection pairing $H_4(Y_{\text{local}};\mathbb{Q}) \times H_4^{BM}(Y_{\text{local}};\mathbb{Q}) \longrightarrow \mathbb{Q}$ vanishes on $(H_4(Y_{\text{local}};\mathbb{Q}))^0 \times \left(H_4^{BM}(Y_{\text{local}};\mathbb{Q})\right)^0$.

The four-cycles $\tilde{A}_i$'s and $\widetilde{A}'^j$'s are the nearly vanishing S_3 cycle (often referred to as the A-cycle) of deformed conifold fibred over the one-cycles α_i's and β^j of the genus g curve Σ. Four-cycles $\widetilde{B}_\ell$'s ($\ell = 1,\cdots,2g-3$), on the other hand, are topologically S_4, and arise in the form of S_3 fibred over intervals I_ℓ on Σ; the interval I_ℓ ($\ell = 1,\cdots,2g-3$) is stretched between a pair of points $p_0, p_\ell \in \Sigma$, where $\{p_0, p_{\ell=1,\cdots,2g-3}\} \subset \Sigma$ are the zeros of the section $A_6 \in \Gamma(\Sigma; K_\Sigma)$. Choice of the interval I_ℓ (between p_0 and p_ℓ) comes with freedom of $+H_1(\Sigma;\mathbb{Z})$; this is how the filtration structure arises in $H_4(Y_{\text{local}};\mathbb{Z})$; by choosing an interval I_ℓ, a representative four-cycle $\widetilde{B}_\ell$ is chosen for a quotient class $[\widetilde{B}_\ell]$. Geometric description of the four-cycles $\widetilde{C}$'s is given later in this appendix.

Period integral is defined for all of these $6g-3$ four-cycles in Y_{local}; their period integrals should depend on the g independent moduli of $\mathcal{M}_*^{\text{local}}$. Let $\{\lambda^i\}_{i=1,\cdots,g}$ be the 1-forms of Σ normalised so that $\int_{\alpha_i}\lambda^j = \delta_i^{\ j}$. By parameterising A_6 on Σ (and parameterising also $\mathcal{M}_*^{\text{local}}$) as

$$A_6 = \sum_i z_i \lambda^i, \tag{C.9}$$

we can write down the period integrals for the four-cycles $\widetilde{A}$'s as

$$\Pi_{\widetilde{A}_i} = z_i, \qquad \Pi_{\widetilde{A}'^j} = \tau^{jk} z_k, \tag{C.10}$$

JHEP11(2015)065

where $\tau^{jk} := \int_{\beta^j} \lambda^k$ is the period matrix of the curve Σ. The period integrals for the four-cycles $\widetilde{B}_\ell$'s are given by

$$\Pi_{\widetilde{B}_\ell} = \tilde{\mu}(p_\ell)^i z_i, \tag{C.11}$$

using the lift of Abel-Jacobi map

$$\tilde{\mu} : \Sigma \ni q \longmapsto \left(\int_{p_0}^q \lambda^1, \int_{p_0}^q \lambda^2, \cdots, \int_{p_0}^q \lambda^g \right) \in \mathbb{C}^g; \tag{C.12}$$

although the Abel-Jacobi map itself depends only on the parameters in $\mathcal{M}_*^{\mathrm{U}(1)}$, dependence on the $\mathcal{M}_*^{\mathrm{local}}$ parameters in $\Pi_{\widetilde{B}_\ell}$ comes in through p_ℓ's as well as z_i's. When the interval I_ℓ from p_0 to p_ℓ is changed by $H_1(\Sigma;\mathbb{Z})$, the period integral $\Pi_{\widetilde{B}_\ell}$ changes by $n^i \Pi_{\widetilde{A}_i} + m_j \Pi_{\widetilde{A}'^j}$ for some $n^i, m_j \in \mathbb{Z}$. This transformation constitutes a part of the modular group [57].

Some of the four-cycles $\widetilde{A}$'s in $H_4(Y_{\mathrm{local}})$ in the local geometry may not be regarded as topological cycles $H_4(Y_4)$ in the global geometry; all the $\widetilde{A}$'s can be deformed to be topological cycles in $Z = \partial\overline{Y_{\mathrm{local}}}$, and such a four-cycle may, in principle, be obtained as a boundary of a five-cycle in $Y_4 \backslash Y_{\mathrm{local}}$. The relation $(-\Delta h^{3,1}) = g$ for the global geometry Y_4 (which holds at least when B_3 is a Fano), and its consequence $\tilde{h}^{2,1} = 0$, in particular, implies that all of the $2g$ four-cycles $\widetilde{A}$'s remain to be topological four-cycles of the global geometry Y_4. Similarly, the four-cycles $\widetilde{C}$'s in $H_4^{BM}(Y_{\mathrm{local}})$ can be regarded as topological cycles of Y_4, only when their boundaries in $H_3(\partial\overline{Y_{\mathrm{local}}})$ are obtained also as boundaries of some cycles in $H_4^{BM}(Y_4 \backslash \overline{Y_{\mathrm{local}}})$. The Poincare duality indicates, however, that all of these $2g$ four-cycles $\widetilde{C}$'s are also lifted to those in the global geometry Y_4, at least when B_3 is Fano. In the conifold transition at the $A_6 \longrightarrow 0$ limit, those $2g + (2g-3) + 2g$ topological four-cycles shrink, and one four-cycle ($\mathbb{P}^1$ for small resolution over the curve Σ) emerges in the global geometry Y_4; $-\Delta h^{3,1} = -\Delta h^{1,3} = g$, and $-\Delta h^{2,2} = (4g-3) - 1 = 4(-\Delta h^{3,1} - \Delta h^{1,1})$. See [57] for more information.

C.2 Monodromy

In order to study monodromy of those four-cycles in the local geometry Y_{local}, we assume that Σ is a hyperelliptic curve in this appendix C.2:

$$t^2 = P(s); \qquad P(s) = -\prod_{i=1}^{2g+2} (s - s_i); \tag{C.13}$$

we further assume that all the s_i's are real valued, and

$$0 < s_1 < s_2 \ll s_3 < s_4 \ll \cdots \ll s_{2g-1} < s_{2g} \ll s_{2g+1} < s_{2g+2}. \tag{C.14}$$

although a higher genus curve Σ is not always in the form of a hyperelliptic curve, complex structure of Σ can be continuously deformed from the one chosen above; since we are interested primarily in questions of topological nature, it is enough to study for Σ given above.

Before getting into the study of monodromy, we first need to have a concrete construction of the cycles $\widetilde{C}^i$'s ($i = 1, \cdots, g$), whose monodromy we are interested in. Math

JHEP11(2015)065

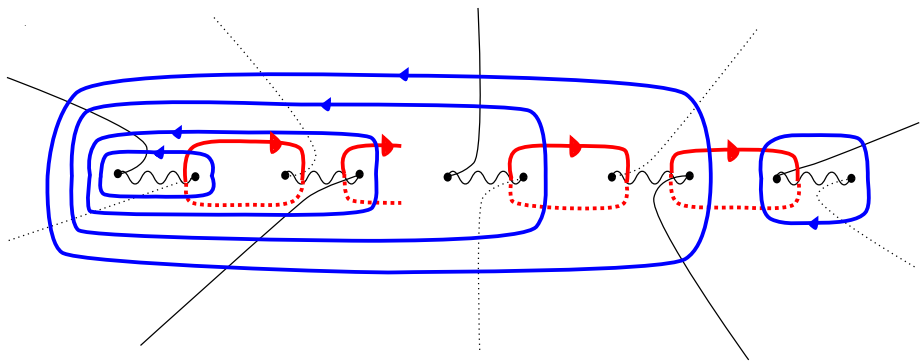

Figure 4. (colour online) A hyperelliptic curve Σ is obtained by gluing together two sheets of this s-plane ($\mathbb{C} \cup \{\infty\}$) along the branch cuts (wavy lines) between s_1–s_2, s_3–s_4, $\cdots$, s_{2g+1}–s_{2g+2}; this picture is drawn for the case with $g = 4$. Description of line bundles $\mathcal{L}^{\otimes k}$ requires branch cuts in the $U^{(s)}$ patch; the cuts for this purpose are drawn in thin (solid or dotted) lines in this figure. Thick grey (red) loops, from left to right, are the cycles α_1, α_2 (drawn partially), α_{g-1} and α_g. Thick dark (blue) loops, from left to right, are β^1, β^2, β^{g-1} and β^g; one more remaining loop in the thick dark (blue) line at the right end of this picture is β'^g; β^g and β'^g are isomorphic in Σ, but they are not within the $U^{(s)}$ patch.

preparation is thus in order here. The line bundle $K_\Sigma = \mathcal{L}^{\otimes 6}$ can be described by three Zariski open patches of Σ.

$$U^{(s)}: \quad t \neq 0, \infty; \qquad U^{(t)}: \quad P'(s) \neq 0,\ s \neq \infty; \qquad U^{(\infty)}: \quad s \neq 0, s_i. \tag{C.15}$$

Sections of K_Σ are written down in the form of $A = a^{(s)}ds$, $A^{(t)}dt$ and $A^{(\infty)}d(1/s)$ in the $U^{(s)}$, $U^{(t)}$ and $U^{(\infty)}$ patch, respectively; these trivialisation descriptions are identified by using transition functions:

$$a^{(t)} = \frac{2t}{P'(s)} a^{(s)}, \qquad a^{(\infty)} = (-s^2) a^{(s)}. \tag{C.16}$$

$H^0(\Sigma; K_\Sigma)$ is of g dimensions, and are of the form[37]

$$A_6^{(s)} ds = \frac{c_0 + c_1 s + \cdots + c_{g-1} s^{g-1}}{t} ds = \frac{c_0 (1/s)^{g-1} + \cdots c_{g-1}}{(t/s^{g+1})} d(1/s) = A_6^{(\infty)} d(1/s). \tag{C.17}$$

The fibre coordinates Y of $\mathcal{L}^{\otimes 3}$ and X of $\mathcal{L}^{\otimes 2}$, for example, become $Y^{(s)}$, $Y^{(t)}$ and $Y^{(\infty)}$, and $X^{(s)}$, $X^{(t)}$ and $X^{(\infty)}$, respectively, in the trivialisation patches, and are identified between the overlapping patches as in

$$Y^{(t)} = \left(\frac{2t}{P'(s)}\right)^{3/6} Y^{(s)}, \qquad X^{(t)} = \left(\frac{2t}{P'(s)}\right)^{2/6} X^{(s)}. \tag{C.18}$$

Branch cuts are introduced in these $U^{(s)}$, $U^{(t)}$ and $U^{(\infty)}$; see figure 4 for the branch cuts in the $U^{(s)}$ patch; the coordinates $Y^{(s)}$ and $X^{(s)}$ at one point in $U^{(s)} \subset \Sigma$ and the coordinates

[37] There must be a linear relation between $\{c_0, c_1, \cdots, c_{g-1}\}$ and z_i's ($i = 1, \cdots, g$) in (C.9), but we do not need to know it in detail.

JHEP11(2015)065

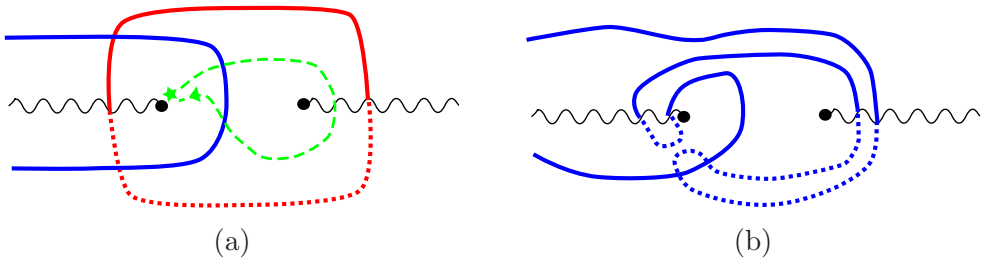

Figure 5. (colour online) (a) A loop γ_k ($k = 1, \cdots, g-1$) in the $\mathcal{M}_*^{\rm local} \cong \mathbb{C}^g$ parameter space is given by continuously changing the parameter a_k in the s-plane, starting from $s = s_{2k}$, going around $s = s_{2k+1}$ and returning to $s = s_{2k}$, as shown by a dashed (green) arrow line in this picture. At the end of this deformation procedure, the loop β^k has been deformed in the way shown in (b) by a thick solid (blue) line.

$Y^{(s)\prime}$ and $X^{(s)\prime}$ at the same point that we reach after circling around a branch point (where $t = 0$) by phase $+2\pi$ are identified through

$$Y^{(s)\prime} = Y^{(s)} \times \zeta_6^{-3}, \qquad X^{(s)\prime} = X^{(s)} \times \zeta_6^{-2}; \qquad \zeta_6 := e^{\frac{2\pi i}{6}}. \tag{C.19}$$

Fibre coordinates need to be identified through similar relations also across the branch cuts in $U^{(t)}$ and $U^{(\infty)}$. Equations (C.18) are made well-defined in this way. The same holds true also for the fibre coordinates A_3 and A_4.

Let us take a point $q \in U^{(s)} \subset \Sigma$. The local fourfold geometry $Y_{\rm local}$ has a three-dimensional fibre

$$Y^{(s)} A_3^{(s)} = X^{(s)} A_4^{(s)} + A_6^{(s)}; \tag{C.20}$$

$Y^{(s)}$, $A_3^{(s)}$, $X^{(s)}$ and $A_4^{(s)}$ are coordinates, while $A_6^{(s)}$ is a parameter. This is a deformed conifold, and there is a canonical choice of compact three-cycle and a semi-canonical choice of non-compact three-cycle intersecting at one point; they are referred to as A-cycle and B-cycle; the choice of the B-cycle is not canonical, in that the B-cycle is deformed to be $B+A$ topologically, when the complex phase of the parameter $A_6^{(s)}$ changes as $A_6^{(s)} \longrightarrow A_6^{(s)} \times e^{i\alpha}$, $\alpha \in [0, 2\pi]$, as well-known in deformed conifold.

Now, we are ready to provide description of the $2g$ remaining four-cycles, $\widetilde{C}^{i=1,\cdots,g}$ and $\widetilde{C}'_{j=1,\cdots,g}$ in $Y_{\rm local}$. Since this task is topological in nature, we can choose the parameter $A_6 \in \mathcal{M}_*^{\rm local}$ arbitrarily; we choose it to be

$$A_6 = A_6^* := \epsilon \frac{(s - s_*)^{g-1}}{t} ds, \qquad s_{2g+2} \ll s_* \in \mathbb{R} \tag{C.21}$$

for now. First of all, the cycles $\widetilde{A}_{i=1,\cdots,g}$ and $\widetilde{A}'^{j=1,\cdots,g}$ are the A-cycle fibred over the one-cycles $\alpha_{i=1,\cdots,g}$ and $\beta^{j=1,\cdots,g}$ in Σ, as in the appendix C.1; see figure 4 for how to choose the basis of $H_1(\Sigma;\mathbb{Z})$. Secondly, for this choice of A_6^*, the cycles $\widetilde{B}_{\ell=1,\cdots,2g-3}$ are all located in the $s \sim s_* \gg s_{2g+2}$ region; we see after constructing $\widetilde{C}$'s that $\widetilde{B}_\ell$'s and $\widetilde{A}$–$\widetilde{C}$'s are mutually orthogonal in the intersection form. Finally, we claim that the B-cycle of the deformed conifold comes back to itself, not to $B + mA$ with $m \neq 0$, after a point $q \in \Sigma$ moves along any one of $\{\alpha_i, \beta^j\}$. To verify this claim, first note that the loop β^k crosses

JHEP11(2015)065

the branch cut in $U^{(s)}$ for k-times in the counter-clockwise direction; this means that the fibre coordinate of $\mathcal{L}^{\otimes a}$ at the end of a loop along β^k is $\zeta_6^{-a\times k} = e^{-2\pi i\times\frac{a\cdot k}{6}}$ times the one at the beginning of the loop. The parameter $(A_6^*)^{(s)}$, on the other hand, changes its phase by $e^{-2\pi ik}$ due to the factor $1/t$. Those two phases on both sides of (C.20) cancel, and there is no net change in the phase of the deformation parameter (not even a multiple of 2π) along the loop β^k. Thus, the B-cycle comes back to itself. The B-cycle fibred over β^k $(k = 1, \cdots, g)$ forms a four-cycle $\widetilde{C}^k$. Similarly, we note that the loop α_k crosse the branch cuts in $U^{(s)}$ for (-1) times in the counter-clockwise direction. The parameter $(A_6^*)^{(s)}$ changes its phase by $e^{+2\pi i}$ due to the factor $1/t$, on the other hand. Those two effects cancel, and there is no net change in the phase. Thus, the B-cycle comes back to itself at the end of the loop α_k. This is how a four-cycle $\widetilde{C}'_k$ is obtained $(k = 1, \cdots, g)$. By construction, $\widetilde{A}_i \cdot \widetilde{C}^j = \delta_i^{\ j}$, $\widetilde{A}'^k \cdot \widetilde{C}'_h = \delta^k_{\ h}$, and the intersection number vanishes for all other combinations of $\widetilde{A}$'s and $\widetilde{C}$'s.

Finally, we study monodromy of those four-cycles in Y_{local}. Monodromy is studied for loops departing and returning to a reference point in $\mathcal{M}_*^{\text{local}} = \mathbb{C}^g$, and we choose

$$A_6 = A_6^{**} := \epsilon\frac{(s-s_2)(s-s_4)\cdots(s-s_{2(g-1)})}{t}ds \tag{C.22}$$

as the reference point.[38,39] At this reference point, let $\widetilde{A}_k$ and $\widetilde{A}'^k$ $(k = 1, \cdots, g)$ be the four-cycle given by the A-cycle along α_k and β^k, respectively. $g-1$ more four-cycles $\widetilde{C}^k$ $(k = 1, \cdots, g-1)$ are the B-cycle fibred over $\beta^k + k\alpha_k$ in Σ; this loop in Σ crosses $+k$ times along β^k and $k\times(-1)$ times along $k\alpha_k$, and there is no net change in the phase of A_6^{**} along the loop. One more four-cycle, $\widetilde{C}^g$, is the B-cycle fibred over a one-cycle $\beta'^g \sim \beta^g$ on Σ shown in figure 4. We will focus on monodromy associated with those $3g$ four-cycles.

It is convenient to adopt the following parameterisation of $\mathcal{M}_*^{\text{local}} \cong H^0(\Sigma; K_\Sigma)$:

$$A_6 = \epsilon\frac{(s-a_1)(s-a_2)\cdots(s-a_{g-1})}{t}ds, \qquad \{(\epsilon, a_1, \cdots, a_{g-1})\} \in \mathbb{C}^g. \tag{C.23}$$

The reference point A_6^{**} corresponds to choosing $a_k = s_{2k}$ for $k = 1, \cdots, g-1$. Loops γ_k for $k = 1, \cdots, g-1$ in $\mathcal{M}_*^{\text{local}}$ are such that a_k is changed continuously in the s-plane in the way designated in figure 5 (a), while the value of ϵ and all other a_m's $(m = 1, \cdots, g-1$ but $m \neq k)$ are held fixed. One can keep track of topology of the four-cycles $\widetilde{A}$'s and $\widetilde{C}$'s along the loop γ_k in $\mathcal{M}_*^{\text{local}}$, by deforming the one-cycles $\beta^m + m\alpha_m$ $(m = 1, \cdots, g-1)$ and β'^g so that the zero of $A_6^{(s)}$ is avoided. This is enough to conclude that all the $3g$ four-cycles, namely, $\widetilde{A}$'s, $\widetilde{A}'$'s and $\widetilde{C}$'s, remain the same at the end of a loop γ_k except $\widetilde{C}^k$. Furthermore, because the one-cycle β^k needs to be deformed as in figure 5 (b) at the end

[38]The point A_6^* in $\mathcal{M}_*^{\text{local}}$ is useful in that all the $6g-3$ four-cycles can be constructed systematically. The point A_6^{**} is more convenient as the reference point of the monodromy study. This is just a matter of convenience.

[39]The degree $2g-2$ divisor corresponding to this choice of $A_6 = A_6^{**}$ is a collection of the $g-1$ points $\{(s,t) = (s_{2i}, 0) \mid i = 1, \cdots, g-1\} \subset \Sigma$ with multiplicity 2 for all of them. They are the $2g-2$ points $\{p_0, \cdots, p_{2g-3}\}$ used in construction of the four-cycles $\widetilde{B}_\ell$'s [57].

JHEP11(2015)065

of the loop γ_k, there is a non-trivial monodromy

$$\gamma_k : \left(\widetilde{A}_k, \widetilde{C}^k\right) \to \left(\widetilde{A}_k, \widetilde{C}^k\right) \begin{pmatrix} 1 & 1 \\ & 1 \end{pmatrix}, \qquad \left(\widetilde{A}_{m\neq k}, \widetilde{A}'^j, \widetilde{C}^{m\neq k}\right) \to \left(\widetilde{A}_{m\neq k}, \widetilde{A}'^j, \widetilde{C}^{m\neq k}\right). \tag{C.24}$$

We study monodromy along one more loop γ_ϵ in $\mathcal{M}_*^{\text{local}}$, which is to change the phase of the parameter ϵ by 2π, while all the a_m's with $m = 1, \cdots, g-1$ are held fixed. Topological cycles $\widetilde{A}_k$'s for $k = 1, \cdots, g$ remain the same under the complex structure deformation along γ_ϵ. Topological cycles $\widetilde{C}^k$'s are not, however. These cycles are all in the form of the B-cycle fibred over some one-cycle in Σ; after complex structure deformation along γ_ϵ, the original B-cycle comes back as $B + A$-cycle. This means that

$$\gamma_\epsilon : \widetilde{C}^{k\neq g} \longmapsto \widetilde{C}^k + k\widetilde{A}_k + \widetilde{A}'^k, \qquad \widetilde{C}^g \longmapsto \widetilde{C}^g + \widetilde{A}'^g. \tag{C.25}$$

This is enough to conclude that the period integrals depend on ϵ as

$$\Pi_{\widetilde{A}_k}, \quad \Pi_{\widetilde{A}'^k} \sim \epsilon, \qquad \Pi_{\widetilde{C}^{k\neq g}} \sim \left(\tau^{km} z_m + k z_k\right) \ln(\epsilon), \qquad \Pi_{\widetilde{C}^g} \sim (\tau^{gm} z_m) \ln(\epsilon). \tag{C.26}$$

It is a much more involved problem to determine the full monodromy group repreesnted on the space of $6g-3$ four-cycles, and also the period integrals. We do not do so in this article, since we do not need such a thorough analysis for the sketchy argument in the main text.

Open Access. This article is distributed under the terms of the Creative Commons Attribution License (CC-BY 4.0), which permits any use, distribution and reproduction in any medium, provided the original author(s) and source are credited.

References

[1] M.R. Douglas and S. Kachru, *Flux compactification*, *Rev. Mod. Phys.* **79** (2007) 733 [hep-th/0610102] [INSPIRE].

[2] F. Denef, *Les Houches lectures on constructing string vacua*, arXiv:0803.1194 [INSPIRE].

[3] S. Ashok and M.R. Douglas, *Counting flux vacua*, *JHEP* **01** (2004) 060 [hep-th/0307049] [INSPIRE].

[4] F. Denef and M.R. Douglas, *Distributions of flux vacua*, *JHEP* **05** (2004) 072 [hep-th/0404116] [INSPIRE].

[5] A.P. Braun, Y. Kimura and T. Watari, *The Noether-Lefschetz problem and gauge-group-resolved landscapes: F-theory on $K3 \times K3$ as a test case*, *JHEP* **04** (2014) 050 [arXiv:1401.5908] [INSPIRE].

[6] A.P. Braun and T. Watari, *Distribution of the number of generations in flux compactifications*, *Phys. Rev.* **D 90** (2014) 121901 [arXiv:1408.6156] [INSPIRE].

[7] A.P. Braun and T. Watari, *The vertical, the horizontal and the rest: anatomy of the middle cohomology of Calabi-Yau fourfolds and F-theory applications*, *JHEP* **01** (2015) 047 [arXiv:1408.6167] [INSPIRE].

[8] S. Weinberg, *Supersymmetry at ordinary energies. 1. Masses and conservation laws*, *Phys. Rev.* **D 26** (1982) 287 [INSPIRE].

JHEP11(2015)065

[9] A.E. Faraggi, *Proton stability in superstring derived models*, *Nucl. Phys.* **B 428** (1994) 111 [hep-ph/9403312] [INSPIRE].

[10] M. Dine and Z. Sun, *R symmetries in the landscape*, *JHEP* **01** (2006) 129 [hep-th/0506246] [INSPIRE].

[11] M. Dine, *Naturalness under stress*, *Ann. Rev. Nucl. Part. Sci.* **65** (2015) 13 [arXiv:1501.01035] [INSPIRE].

[12] R. Tatar and T. Watari, *Proton decay, Yukawa couplings and underlying gauge symmetry in string theory*, *Nucl. Phys.* **B 747** (2006) 212 [hep-th/0602238] [INSPIRE].

[13] M. Kuriyama, H. Nakajima and T. Watari, *Theoretical framework for R-parity violation*, *Phys. Rev.* **D 79** (2009) 075002 [arXiv:0802.2584] [INSPIRE].

[14] R. Tatar, Y. Tsuchiya and T. Watari, *Right-handed neutrinos in F-theory compactifications*, *Nucl. Phys.* **B 823** (2009) 1 [arXiv:0905.2289] [INSPIRE].

[15] Y. Nir and N. Seiberg, *Should squarks be degenerate?*, *Phys. Lett.* **B 309** (1993) 337 [hep-ph/9304307] [INSPIRE].

[16] S. Cecotti, C. Cordova, J.J. Heckman and C. Vafa, *T-branes and monodromy*, *JHEP* **07** (2011) 030 [arXiv:1010.5780] [INSPIRE].

[17] R. Donagi and M. Wijnholt, *Model building with F-theory*, *Adv. Theor. Math. Phys.* **15** (2011) 1237 [arXiv:0802.2969] [INSPIRE].

[18] C. Beasley, J.J. Heckman and C. Vafa, *GUTs and exceptional branes in F-theory — I*, *JHEP* **01** (2009) 058 [arXiv:0802.3391] [INSPIRE].

[19] S.H. Katz and C. Vafa, *Matter from geometry*, *Nucl. Phys.* **B 497** (1997) 146 [hep-th/9606086] [INSPIRE].

[20] J. Marsano, N. Saulina and S. Schäfer-Nameki, *Monodromies, fluxes and compact three-generation F-theory GUTs*, *JHEP* **08** (2009) 046 [arXiv:0906.4672] [INSPIRE].

[21] J. Marsano, N. Saulina and S. Schäfer-Nameki, *Compact F-theory GUTs with* U(1)(PQ), *JHEP* **04** (2010) 095 [arXiv:0912.0272] [INSPIRE].

[22] H. Hayashi, T. Kawano, Y. Tsuchiya and T. Watari, *More on dimension-4 proton decay problem in F-theory — Spectral surface, discriminant locus and monodromy*, *Nucl. Phys.* **B 840** (2010) 304 [arXiv:1004.3870] [INSPIRE].

[23] T.W. Grimm and T. Weigand, *On abelian gauge symmetries and proton decay in global F-theory GUTs*, *Phys. Rev.* **D 82** (2010) 086009 [arXiv:1006.0226] [INSPIRE].

[24] D.R. Morrison and C. Vafa, *Compactifications of F-theory on Calabi-Yau threefolds. 2*, *Nucl. Phys.* **B 476** (1996) 437 [hep-th/9603161] [INSPIRE].

[25] V. Braun, T.W. Grimm and J. Keitel, *New global F-theory GUTs with* U(1) *symmetries*, *JHEP* **09** (2013) 154 [arXiv:1302.1854] [INSPIRE].

[26] V. Braun, T.W. Grimm and J. Keitel, *Geometric engineering in toric F-theory and GUTs with* U(1) *gauge factors*, *JHEP* **12** (2013) 069 [arXiv:1306.0577] [INSPIRE].

[27] D. Klevers, D.K. Mayorga Pena, P.-K. Oehlmann, H. Piragua and J. Reuter, *F-theory on all toric hypersurface fibrations and its Higgs branches*, *JHEP* **01** (2015) 142 [arXiv:1408.4808] [INSPIRE].

[28] C. Lawrie, S. Schäfer-Nameki and J.-M. Wong, *F-theory and all things rational: surveying* U(1) *symmetries with rational sections*, *JHEP* **09** (2015) 144 [arXiv:1504.05593] [INSPIRE].

[29] E. Witten, *Phase transitions in M-theory and F-theory*, *Nucl. Phys.* **B 471** (1996) 195 [hep-th/9603150] [INSPIRE].

JHEP11(2015)065

[30] P. Mayr, *Mirror symmetry, $N = 1$ superpotentials and tensionless strings on Calabi-Yau four folds*, *Nucl. Phys.* **B 494** (1997) 489 [hep-th/9610162] [INSPIRE].

[31] P. Candelas, D.-E. Diaconescu, B. Florea, D.R. Morrison and G. Rajesh, *Codimension three bundle singularities in F-theory*, *JHEP* **06** (2002) 014 [hep-th/0009228] [INSPIRE].

[32] S. Sethi, C. Vafa and E. Witten, *Constraints on low dimensional string compactifications*, *Nucl. Phys.* **B 480** (1996) 213 [hep-th/9606122] [INSPIRE].

[33] A. Klemm, B. Lian, S.S. Roan and S.-T. Yau, *Calabi-Yau fourfolds for M-theory and F-theory compactifications*, *Nucl. Phys.* **B 518** (1998) 515 [hep-th/9701023] [INSPIRE].

[34] M. Kreuzer and H. Skarke, *Calabi-Yau four folds and toric fibrations*, *J. Geom. Phys.* **26** (1998) 272 [hep-th/9701175] [INSPIRE].

[35] W. Taylor, *On the Hodge structure of elliptically fibered Calabi-Yau threefolds*, *JHEP* **08** (2012) 032 [arXiv:1205.0952] [INSPIRE].

[36] L.B. Anderson and W. Taylor, *Geometric constraints in dual F-theory and heterotic string compactifications*, *JHEP* **08** (2014) 025 [arXiv:1405.2074] [INSPIRE].

[37] J. Halverson and W. Taylor, *P^1-bundle bases and the prevalence of non-Higgsable structure in 4D F-theory models*, *JHEP* **09** (2015) 086 [arXiv:1506.03204] [INSPIRE].

[38] J. Gray, A.S. Haupt and A. Lukas, *All complete intersection Calabi-Yau four-folds*, *JHEP* **07** (2013) 070 [arXiv:1303.1832] [INSPIRE].

[39] J. Gray, A.S. Haupt and A. Lukas, *Topological invariants and fibration structure of complete intersection Calabi-Yau four-folds*, *JHEP* **09** (2014) 093 [arXiv:1405.2073] [INSPIRE].

[40] D.R. Morrison and W. Taylor, *Classifying bases for 6D F-theory models*, *Central Eur. J. Phys.* **10** (2012) 1072 [arXiv:1201.1943] [INSPIRE].

[41] D.R. Morrison and W. Taylor, *Non-Higgsable clusters for 4D F-theory models*, *JHEP* **05** (2015) 080 [arXiv:1412.6112] [INSPIRE].

[42] I. Affleck, M. Dine and N. Seiberg, *Dynamical supersymmetry breaking in four-dimensions and its phenomenological implications*, *Nucl. Phys.* **B 256** (1985) 557 [INSPIRE].

[43] R. Bousso and J. Polchinski, *Quantization of four form fluxes and dynamical neutralization of the cosmological constant*, *JHEP* **06** (2000) 006 [hep-th/0004134] [INSPIRE].

[44] O. DeWolfe, A. Giryavets, S. Kachru and W. Taylor, *Enumerating flux vacua with enhanced symmetries*, *JHEP* **02** (2005) 037 [hep-th/0411061] [INSPIRE].

[45] E. Witten, *Symmetry breaking patterns in superstring models*, *Nucl. Phys.* **B 258** (1985) 75 [INSPIRE].

[46] E. Witten, *New issues in manifolds of* SU(3) *holonomy*, *Nucl. Phys.* **B 268** (1986) 79 [INSPIRE].

[47] H. Georgi and S.L. Glashow, *Unity of all elementary particle forces*, *Phys. Rev. Lett.* **32** (1974) 438 [INSPIRE].

[48] L. Lin and T. Weigand, *Towards the standard model in F-theory*, *Fortsch. Phys.* **63** (2015) 55 [arXiv:1406.6071] [INSPIRE].

[49] A. Grassi, J. Halverson, J. Shaneson and W. Taylor, *Non-Higgsable QCD and the standard model spectrum in F-theory*, *JHEP* **01** (2015) 086 [arXiv:1409.8295] [INSPIRE].

[50] M.R. Douglas, D.S. Park and C. Schnell, *The Cremmer-Scherk mechanism in F-theory compactifications on $K3$ manifolds*, *JHEP* **05** (2014) 135 [arXiv:1403.1595] [INSPIRE].

[51] D.R. Morrison and W. Taylor, *Sections, multisections and* U(1) *fields in F-theory*, arXiv:1404.1527 [INSPIRE].

JHEP11(2015)065

[52] G. Martini and W. Taylor, *6D F-theory models and elliptically fibered Calabi-Yau threefolds over semi-toric base surfaces*, *JHEP* **06** (2015) 061 [arXiv:1404.6300] [INSPIRE].

[53] A. Giryavets, S. Kachru and P.K. Tripathy, *On the taxonomy of flux vacua*, *JHEP* **08** (2004) 002 [hep-th/0404243] [INSPIRE].

[54] J.P. Conlon and F. Quevedo, *On the explicit construction and statistics of Calabi-Yau flux vacua*, *JHEP* **10** (2004) 039 [hep-th/0409215] [INSPIRE].

[55] T. Eguchi and Y. Tachikawa, *Distribution of flux vacua around singular points in Calabi-Yau moduli space*, *JHEP* **01** (2006) 100 [hep-th/0510061] [INSPIRE].

[56] D. Cox and S. Katz, *Mirror symmetry and algebraic geometry*, American Mathematical Society, U.S.A. (1999).

[57] K. Intriligator, H. Jockers, P. Mayr, D.R. Morrison and M.R. Plesser, *Conifold transitions in M-theory on Calabi-Yau fourfolds with background fluxes*, *Adv. Theor. Math. Phys.* **17** (2013) 601 [arXiv:1203.6662] [INSPIRE].

[58] H. Hayashi, T. Kawano, R. Tatar and T. Watari, *Codimension-3 singularities and Yukawa couplings in F-theory*, *Nucl. Phys.* **B 823** (2009) 47 [arXiv:0901.4941] [INSPIRE].

[59] J.J. Heckman and C. Vafa, *Flavor Hierarchy from F-theory*, *Nucl. Phys.* **B 837** (2010) 137 [arXiv:0811.2417] [INSPIRE].

[60] S. Cecotti, M.C.N. Cheng, J.J. Heckman and C. Vafa, *Yukawa couplings in F-theory and non-commutative geometry*, arXiv:0910.0477 [INSPIRE].

[61] H. Hayashi, T. Kawano, Y. Tsuchiya and T. Watari, *Flavor structure in F-theory compactifications*, *JHEP* **08** (2010) 036 [arXiv:0910.2762] [INSPIRE].

[62] C. Cordova, *Decoupling gravity in F-theory*, *Adv. Theor. Math. Phys.* **15** (2011) 689 [arXiv:0910.2955] [INSPIRE].

[63] W. Buchmüller, K. Hamaguchi, O. Lebedev and M. Ratz, *Supersymmetric standard model from the heterotic string (II)*, *Nucl. Phys.* **B 785** (2007) 149 [hep-th/0606187] [INSPIRE].

[64] J.L. Bourjaily, *Local models in F-theory and M-theory with three generations*, arXiv:0901.3785 [INSPIRE].

[65] J. Marsano, N. Saulina and S. Schäfer-Nameki, *F-theory compactifications for supersymmetric GUTs*, *JHEP* **08** (2009) 030 [arXiv:0904.3932] [INSPIRE].

[66] J.P. Conlon and E. Palti, *Aspects of flavour and supersymmetry in F-theory GUTs*, *JHEP* **01** (2010) 029 [arXiv:0910.2413] [INSPIRE].

[67] F. Marchesano and L. Martucci, *Non-perturbative effects on seven-brane Yukawa couplings*, *Phys. Rev. Lett.* **104** (2010) 231601 [arXiv:0910.5496] [INSPIRE].

[68] C.-C. Chiou, A.E. Faraggi, R. Tatar and W. Walters, *T-branes and Yukawa couplings*, *JHEP* **05** (2011) 023 [arXiv:1101.2455] [INSPIRE].

[69] A. Font, L.E. Ibáñez, F. Marchesano and D. Regalado, *Non-perturbative effects and Yukawa hierarchies in F-theory* SU(5) *unification*, *JHEP* **03** (2013) 140 [*Erratum ibid.* **1307** (2013) 036] [arXiv:1211.6529] [INSPIRE].

[70] L. Aparicio, A. Font, L.E. Ibáñez and F. Marchesano, *Flux and instanton effects in local F-theory models and hierarchical fermion masses*, *JHEP* **08** (2011) 152 [arXiv:1104.2609] [INSPIRE].

[71] A. Font, F. Marchesano, D. Regalado and G. Zoccarato, *Up-type quark masses in* SU(5) *F-theory models*, *JHEP* **11** (2013) 125 [arXiv:1307.8089] [INSPIRE].

JHEP11(2015)065

[72] L. Randall and D. Simmons-Duffin, *Quark and lepton flavor physics from F-theory*, arXiv:0904.1584 [INSPIRE].

[73] L.J. Hall, H. Murayama and N. Weiner, *Neutrino mass anarchy*, *Phys. Rev. Lett.* **84** (2000) 2572 [hep-ph/9911341] [INSPIRE].

[74] N. Haba and H. Murayama, *Anarchy and hierarchy*, *Phys. Rev.* **D 63** (2001) 053010 [hep-ph/0009174] [INSPIRE].

[75] T. Yanagida, a remark at a workshop *Neutrino*, ICRR, University of Tokyo, Japan (2001).

[76] N. Arkani-Hamed and S. Dimopoulos, *New origin for approximate symmetries from distant breaking in extra dimensions*, *Phys. Rev.* **D 65** (2002) 052003 [hep-ph/9811353] [INSPIRE].

[77] N. Arkani-Hamed and M. Schmaltz, *Hierarchies without symmetries from extra dimensions*, *Phys. Rev.* **D 61** (2000) 033005 [hep-ph/9903417] [INSPIRE].

[78] L.J. Hall, M.P. Salem and T. Watari, *Quark and lepton masses from gaussian landscapes*, *Phys. Rev. Lett.* **100** (2008) 141801 [arXiv:0707.3444] [INSPIRE].

[79] L.J. Hall, M.P. Salem and T. Watari, *Statistical understanding of quark and lepton masses in gaussian landscapes*, *Phys. Rev.* **D 76** (2007) 093001 [arXiv:0707.3446] [INSPIRE].

[80] L.J. Hall, M.P. Salem and T. Watari, *Neutrino mixing and mass hierarchy in Gaussian landscapes*, *Phys. Rev.* **D 79** (2009) 025010 [arXiv:0810.2561] [INSPIRE].

[81] D. Cremades, L.E. Ibáñez and F. Marchesano, *Computing Yukawa couplings from magnetized extra dimensions*, *JHEP* **05** (2004) 079 [hep-th/0404229] [INSPIRE].

[82] I. Shafarevich, *Basic algebraic geometry*, Springer (1988), see Chapter I, section 1.4.

[83] M. Cvetič, D. Klevers and H. Piragua, *F-theory compactifications with multiple* U(1)*-factors: constructing elliptic fibrations with rational sections*, *JHEP* **06** (2013) 067 [arXiv:1303.6970] [INSPIRE].

[84] A. Hebecker, P. Mangat, F. Rompineve and L.T. Witkowski, *Tuning and backreaction in F-term axion monodromy inflation*, *Nucl. Phys.* **B 894** (2015) 456 [arXiv:1411.2032] [INSPIRE].

[85] A. Grassi and V. Perduca, *Weierstrass models of elliptic toric* $K3$ *hypersurfaces and symplectic cuts*, *Adv. Theor. Math. Phys.* **17** (2013) 741 [arXiv:1201.0930] [INSPIRE].

[86] T.W. Grimm and H. Hayashi, *F-theory fluxes, chirality and Chern-Simons theories*, *JHEP* **03** (2012) 027 [arXiv:1111.1232] [INSPIRE].

[87] M. Bershadsky, T. Pantev and V. Sadov, *F theory with quantized fluxes*, *Adv. Theor. Math. Phys.* **3** (1999) 727 [hep-th/9805056] [INSPIRE].

[88] D.R. Morrison and D.S. Park, *F-theory and the Mordell-Weil group of elliptically-fibered Calabi-Yau threefolds*, *JHEP* **10** (2012) 128 [arXiv:1208.2695] [INSPIRE].

[89] D.S. Park and W. Taylor, *Constraints on* $6D$ *supergravity theories with abelian gauge symmetry*, *JHEP* **01** (2012) 141 [arXiv:1110.5916] [INSPIRE].

[90] P. Candelas and A. Font, *Duality between the webs of heterotic and type-II vacua*, *Nucl. Phys.* **B 511** (1998) 295 [hep-th/9603170] [INSPIRE].

[91] M. Esole and S.-T. Yau, *Small resolutions of* SU(5)*-models in F-theory*, *Adv. Theor. Math. Phys.* **17** (2013) 1195 [arXiv:1107.0733] [INSPIRE].

[92] M. Bershadsky et al., *Geometric singularities and enhanced gauge symmetries*, *Nucl. Phys.* **B 481** (1996) 215 [hep-th/9605200] [INSPIRE].

[93] D. Berenstein, *Branes versus GUTS: challenges for string inspired phenomenology*, hep-th/0603103 [INSPIRE].

JHEP11(2015)065

[94] S. Katz, P. Mayr and C. Vafa, *Mirror symmetry and exact solution of* $4D$ $N = 2$ *gauge theories: 1*, *Adv. Theor. Math. Phys.* **1** (1998) 53 [hep-th/9706110] [INSPIRE].

[95] P. Berglund and P. Mayr, *Heterotic string/F theory duality from mirror symmetry*, *Adv. Theor. Math. Phys.* **2** (1999) 1307 [hep-th/9811217] [INSPIRE].

[96] H. Hayashi, R. Tatar, Y. Toda, T. Watari and M. Yamazaki, *New aspects of heterotic-F theory duality*, *Nucl. Phys.* **B 806** (2009) 224 [arXiv:0805.1057] [INSPIRE].

[97] R. Donagi and M. Wijnholt, *Higgs bundles and UV completion in F-theory*, *Commun. Math. Phys.* **326** (2014) 287 [arXiv:0904.1218] [INSPIRE].

JHEP11(2015)065

計画研究 B04 班

課題名「テラスケール物理における世代構造の研究」

研究組織

(1) 研究代表者

久野純治（HISANO, Junji）
名古屋大学・基礎理論研究センター・教授
研究者番号：60300670

(2) 研究分担者

前川展祐（MAEKAWA, Nobuhiro）
名古屋大学・基礎理論研究センター・准教授
研究者番号：40273429

進藤哲央（SHINDOU, Tetsuo）
工学院大学・基礎・教養教育部門・准教授
研究者番号：60553039

(3) 連携研究者

棚橋誠治（TANABASHI, Masaharu）
名古屋大学・理学研究科・教授
研究者番号：00270398

戸部和弘(TOBE, Kazuhiro)
名古屋大学・理学研究科・准教授
研究者番号：20451510

(4) 協力研究者

津村浩二（TSUMURA, Koji）
大村裕司（OMURA, Yuji）
阿部智広（ABE, Tomohiro）
F. Beye
永田夏海（NAGATA, Natumi）
村松祐（MURAMATSU, Yu）
榎本成志（ENOMOTO, Seishi）
冬頭かおり（FUYUTO, Kaori）
他、名古屋大学学生、ポスドクなど。

交付決定額

計画研究 B04 班に配分された交付額を表 1 に示す。

表 1. 交付決定額（配分額）　（金額単位：円）

年度	直接経費	間接経費	合計
平成 23 年度	3,300,000	990,000	4,290,000
平成 24 年度	7,600,000	2,280,000	9,880,000
平成 25 年度	7,700,000	2,310,000	10,010,000
平成 26 年度	7,300,000	2,190,000	9,490,000
平成 27 年度	7,300,000	2,190,000	9,490,000
総計	33,200,000	9,960,000	43,160,000

研究成果

1．研究開始当初の背景

クォーク・レプトンの持つ世代の階層構造の存在は、素粒子標準模型における大きな謎の 1 つである。この謎を解決するにはクォーク・レプトンがいかにして質量を獲得したのかを

理解する必要が゛あるとともに、素粒子模型の入れ物となる時空の構造の解明が゛不可欠で゛ある。素粒子質量の起源を司るヒッグ゛ス粒子、そして時空構造から予言される超対称粒子やカルザ゛ー・ク ライン粒子が゛ LHC 実験で゛発見されれば゛、世代構造の理解に向けて大きな一歩となる。

レプ゜トンやハド゛ロンの低エネルギ゛ーで゛の精密測定実験に加え、LHC 実験によって新粒子の質量や相互作用の測定が゛なされれば゛テラスケール物理の全貌が゛明らかになり、世代の理解が゛さらに深まる。新粒子が゛世代に依存した相互作用を持つかもしれないからだ゛。特にその存在が゛有望視されている超対称性や余剰次元はクォーク・レプ゜トンのパ゜ートナーの粒子の存在を予言し、それらの相互作用や質量に新たな世代構造が゛現れる。クォーク・レプ゜トンの質量の階層構造は余剰次元におけるクォーク・レプ゜トンの配位から導かれるという指摘が゛なされている。大統一理論の痕跡が゛世代に依存して超対称粒子の相互作用に現れることが゛議論されている。テラスケール物理は豊富な世代の情報を持っており、その理解を通してテラスケール物理の背後にある物理を探ることが゛で゛きる。

テラスケール物理における世代構造の理解は宇宙の物質・反物質非対称性の起源の理解につなが゛る。三世代を予言した小林・益川理論は観測されている素粒子過程の物質・反物質非対 称性(CP 非対称性)をよく説明する一方で゛、宇宙の物質・反物質非対称性を説明するには不十分で゛ある。LHC 実験で゛複数のヒッグ゛ス粒子やクォーク・レプ゜トンのパ゜ートナーの粒子が゛発見されれば゛、新たな CP 非対称性の起源の可能性が゛出てくる。新粒子の性質、特にその粒子が゛導く CP 非対称性を研究することにより、テラスケール物理による宇宙の物質(バ゛リオン数)生成の可能 性や、ニュートリノ質量起源と密接な関係のあるシーソー機構によるレプ゜トジ゛ェネシス(宇宙のレプ゜トン数生成)の理解が゛大きく進むと期待される。

２．研究の目的

クォーク・レプ゜トンの持つ世代の階層構造の存在は、素粒子物理学の大きな謎の 1 つで゛ある。素粒子模型の入れ物で゛ある時空の構造が゛ LHC 実験により明らかになれば゛世代構造の理解に向けて大きな一歩となる。本研究計画は、テラスケール物理における世代構造の解明、テラスケールを超える新しい素粒子像の構築、そして宇宙の物質・反物質非対称性の起源の解明を目指す。

レプ゜トンやハド゛ロンの低エネルギ゛ーで゛の精密測定結果に加え、LHC 実験によって新粒子の質量 や相互作用の測定結果を用いることで゛、テラスケール物理のもつ世代構造の全貌を明らかにする。時空構造と関係のある超対称性や余剰次元が゛クォーク・レプ゜トンのパ゜ートナーの粒子の存在を予言し、テラスケール物理は標準模型よりも遙かに豊かな世代構造を持つ。その構造を明らかにすることで゛、さらにテラスケール物理の背後にある物理を探る。力と物質の統一の大統 一理論の構築、余剰次元空間内で゛のクォーク・レプ゜トンの配位による世代構造の出現、ニュートリノ質量の起源を解明する。これによりテラスケール物理を超えた、新しい素粒

子像の構築を行う。

テラスケール物理における世代構造の理解は宇宙の物質・反物質非対称性の起源の解明に繋が゛る。新粒子の性質、特にその粒子の持つ物質・反物質非対称性を研究することにより、テラスケール物理による宇宙の物質(バ゛リオン数)生成の可能性を明らかにし、また、ニュートリノ質量起源と密接な関係のあるシーソー機構によるレプ゜トジ゛ェネシス(宇宙のレプ゜トン数生成)の解明を行う。

3．研究の方法

(1) レプ゜トン、ハト゛ロンの電気双極子能率や希過程の探索から超対称模型や余剰次元模型の構造、期待される質量スペ゜クトラム、そして LHC 実験で゛の事象のパ゜ターンを明らかにする。

(2) 代表的なテラスケールの模型において宇宙のバ゛リオン数生成が゛可能で゛あるかど゛うかを明らかにし、そこから LHC 実験や低エネルギ゛ー実験においてど゛の様なシグ゛ナルが゛で゛るのかを明らかにする。

(3) 中性子やミューオン(g-2)など゛テラスケール物理に 感度ある観測量を際評価し、そのテラスケール物理の予言をする際の不定性を明らかにする。

(4) LHC 実験において超対称粒子やカルザ゛ー・クライン粒子が゛発見された際には、新粒子のスペ゜クトラムをもとに模型を選別し、残された可能性をさらに絞り込むための研究を行う。

(5) 超対称粒子が゛発見された際には、そこから期待されるよりニュートリノ質量の起源、レプ゜トジ゛ェネシス、大統一理論に向けてより基本的な理論 の構築を行い、陽子崩壊、レプ゜トンやハト゛ロンの電気双極子能率や希過程など゛低エネルギ゛ー実験によるその検証の可能性を検討する。

(6) 新しいテラススケール物理が゛発見されなかった場合 今日まで゛の素粒子物理学の考察から考えて、テラスケールを大きく超えてまで゛新しい物理が゛存在しないことは考えにくい。新しい物理のスケールを探るべ゛く、低エネルギ゛ー実験、LHC 実験と矛盾のない理論を再検討し、より高いエネルギ゛ースケールを間接的ならも探ることので゛きるレプ゜トンやハト゛ロンの電気双極子能率や希過程で゛その理論が゛その兆候が゛検出可能かど゛うか を明らかにする。

4．研究成果

(1) フレーバーの物理

標準模型を超える理論に電気双極子能率(EDM)は感度がある。久野は、クォークの EDM、カラーEDM の中性子 EDM への寄与を QCD 和則、次元 6 までの CP 対称性を破る相互作用のウィルソン係数のくりこみ群の方程式の導出など、中性子の EDM の系統的な評価のための研究を行

った。また標準模型を超える理論として、観測されたヒッグス粒子の質量から期待される超対称性の破れが 100TeV 程度の MSSM、電弱バリオン数生成を導く四世代模型やヒッグス拡張模型などの模型における EDM を評価し、模型に制限を与えるとともに、将来実験での検証の可能性の議論をした。

久野は、超対称性の破れが 100TeV 程度の模型の可能性として新たな物質場やゲージ場の導入が考えられ、その MSSM とは異なるフレーバーの物理の予言が有ることを示した。また、進藤は、超対称性シーソー模型におけるレプトンフレーバーを破る過程の研究を行った。LHC で測定された 125GeV のヒッグス質量をインプットとしてあつかった場合に，$\mu \to e\gamma$ や $\tau \to \mu\gamma$ などのプロセスに対し，どのような予言が得られるかを明らかにした。また、進藤はニュートリノ質量が TeV である可能性を探り、模型の構築を行った。

(2) ヒッグスセクターの物理

久野は、SU(2)二重項のヒッグス場以外で ρ パラメータを自然に 1 する可能性として SU(2)七重項がある。SU(2)七重項を含む現実的な模型を構築し、その現象論的予言を明らかにした。

また、久野はヒッグス場と電弱相互作用をする暗黒物質との有効理論を構築し、そこから期待される現象の整理を行った。

進藤は、ヒッグスセクターの拡張により、ニュートリノ質量が量子補正によって生じる模型を構築し、その現象論的研究を行った。LHC 等の実験によって模型が検証可能であることを示した。また，電弱バリオン数生成に必要な強い 1 次相転移が可能であることをあきらかにした。また、別の拡張ヒッグス模型において久野は電弱バリオン数生成により宇宙のバリオン数生成の説明が可能かを明らかにした。

(3) 大統一模型の研究

X ボゾンによる陽子崩壊は大統一理論の検証において非常に重要である。久野はその予言の信頼度を上げるため、超対称模型の枠組みで GUT スケールでの量子効果、陽子崩壊の演算子への 2 ループでの量子補正を評価し予言に取り込んだ。また、観測されたヒッグス粒子の質量を説明する可能性として、新たな物質場を導入や大きな超対称性の破れの導入がある。これらの模型における陽子崩壊の予言を明らかにし、将来実験との関係を明らかにした。また、前川は物質場が大統一の場にどのように埋め込まれているかを陽子崩壊の様々なモードの分岐比の研究から明らかにできることを示した。

世代対称性を持つ E6 大統一理論は自発的に CP 対称性を破るとクォークセクターは小林-益川位相の起源を説明しつつ超対称 CP 問題を解く等多くの利点が知られていたがニュートリノは現実と合わないと思われていたが、前川はニュートリノに関しても現実を再現するだけで無く後に確認された Ue3 に対 する予言も通常の E6 大統一理論と同様になっていることを示した。またこの模型における宇宙のレプトン数生成の可能性を明らかにした。

５．主な発表論文等

（研究代表者、研究分担者及び連携研究者には下線）

〔雑誌論文〕（計 44 件）

[1] Kari Fuyuto, Junji Hisano, Eibun Senaha, “Toward verification of electroweak baryogenesis by electric dipole moments”, Phys. Lett. (査読有) B755 (2016)491-497, 10.1016/j.physletb.2016.02.053.

[2] Takuya Ishihara, Nobuhiro Maekawa, Mao Takegawa, Masato Yamanaka, “Leptogenesis in E_6*U(1)$_A$ SUSY GUT model”, JHEP (査読有) 1602 (2016) 108, 10.1007/JHEP02(2016)108.

[3] Junji Hisano, Daiki Kobayashi, Wataru Kuramoto, Takumi Kuwahara, “Nucleon Electric Dipole Moments in High-Scale Supersymmetric Models”, JHEP (査読有) 1511 (2015) 085, 10.1007/JHEP11(2015)085.

[4] Shinya Kanemura, Tetsuo Shindou, Hiroaki Sugiyama, “R-Parity Conserving Supersymmetric Extension of the Zee Model”, Phys. Rev.(査読有) D92 (2015) no.11,115001,10.1103/PhysRevD.92.115001.

[5] Toru Goto, Yasuhiro Okada, Tetsuo Shindou, Minoru Tanaka, Ryoutaro Watanabe,“Lepton flavor violation in the supersymmetric seesaw model after the LHC 8 TeV run”,Phys.Rev.(査読有) D91 (2015) no.3, 033007,10.1103/PhysRevD.91.033007.

[6] Shinya Kanemura, Kunio Kaneta, Naoki Machida, Tetsuo Shindou,“New resonance scale and fingerprint identification in minimal composite Higgs models”, Phys.Rev.(査読有) D91 (2015) 115016,10.1103/PhysRevD.91.115016.

[7] Junji Hisano, Natsumi Nagata, Yuji Omura,“Interpretations of the ATLAS Diboson Resonances”, Phys.Rev. (査読有) D92 (2015) no.5, 055001, 10.1103/PhysRevD.92.055001.

[8] Junji Hisano, Koji Ishiwata, Natsumi Nagata,“QCD Effects on Direct Detection of Wino Dark Matter”, JHEP (査読有) 1506 (2015) 097, 10.1007/JHEP06(2015)097.

[9] Junji Hisano, Takumi Kuwahara, Yuji Omura,“Threshold Corrections to Baryon Number Violating Operators in Supersymmetric SU(5) GUTs”, Nucl.Phys. (査読有) B898 (2015) 1-29, 10.1016/j.nuclphysb.2015.06.022.

[10] Junji Hisano, Yu Muramatsu, Yuji Omura, Masato Yamanaka,“Flavor violating Z' from SO(10) SUSY GUT in High-Scale SUSY”,Phys.Lett. (査読有) B744 (2015) 395-400, 10.1016/j.physletb.2015.04.020.

[11] Junji Hisano, Ryo Nagai, Natsumi Nagata.“Effective Theories for Dark Matter Nucleon Scattering”, JHEP (査読有) 1505 (2015) 037, 10.1007/JHEP05(2015)037.

[12] Junji Hisano, Daiki Kobayashi, Naoya Mori, Eibun Senaha,“Effective Interaction of Electroweak-Interacting Dark Matter with Higgs Boson and Its Phenomenology” Phys.Lett.

(査読有) B742 (2015) 80-85, 10.1016/j.physletb.2015.01.012.
[13] Nobuhiro Maekawa, Yu Muramatsu, Yoshihiro Shigekami,"Sizable D-term contribution as a signature of E_6*SU(2)$_F$*U(1)$_A$ SUSY GUT model",PTEP（査読有）2014 (2014) no.11, 113B02.10.1093/ptep/ptu151.
[14] Seishi Enomoto, Nobuhiro Maekawa, Tomohiro Matsuda, "Preheating with higher dimensional interaction",Phys.Rev.（査読有）D91 (2015) no.10, 103504,10.1103/PhysRevD.91.103504.
[15] Nobuhiro Maekawa, Kenichi Takayama,"The heavy graviton, naturalness, and sizable anomaly mediation",PTEP (査読有) 2014 (2014) 093B04,10.1093/ptep/ptu118.
[16] Nobuhiro Maekawa, Yu Muramatsu. "Nucleon decay via dimension-6 operators in E_6*SU(2)$_F$*U(1)$_A$ SUSY GUT model",PTEP（査読有）2014 (2014) no.11, 113B03, 10.1093/ptep/ptu150.
[17] Tomohiro Abe, Junji Hisano, Teppei Kitahara, Kohsaku Tobioka,"Gauge invariant Barr-Zee type contributions to fermionic EDMs in the two-Higgs doublet models",JHEP (査読有) 1401 (2014) 106,
10.1007/JHEP01(2014)106.
[18] Seishi Enomoto, Satoshi Iida, Nobuhiro Maekawa, Tomohiro Matsuda,"Beauty is more attractive: particle production and moduli trapping with higher dimensional interaction", JHEP (査読有) 1401 (2014) 141,10.1007/JHEP01(2014)141.
[19] Shinya Kanemura, Naoki Machida, Tetsuo Shindou, "Radiative neutrino mass, dark matter and electroweak baryogengesis from the supersymmetric gauge theory with confinement",Phys.Lett.(査読有) B738 (2014)178-186,10.1016/j.physletb.2014.09.013.
[20] Shinya Kanemura, Naoki Machida, Tetsuo Shindou, Toshifumi Yamada,"A UV complete model for radiative seesaw scenarios and electroweak baryogengesis based on the supersymmetric gauge theory",Phys.Rev.（査読有）D89 (2014) no.1, 013005,10.1103/PhysRevD.89.013005.
[21] Shinya Kanemura, Eibun Senaha, Tetsuo Shindou, Toshifumi Yamada, "Electroweak phase transition and Higgs boson couplings in the model based on supersymmetric strong dynamics",JHEP(査読有) 1305 (2013) 066,10.1007/JHEP05(2013)066.
[22] Kaori Fuyuto, Junji Hisano, Natsumi Nagata, Koji Tsumura,"QCD Corrections to Quark (Chromo)Electric Dipole Moments in High-scale Supersymmetry", JHEP (査読有) 1312 (2013) 010, 10.1007/JHEP12(2013)010.
[23] Nobuhiro Maekawa, Yu Muramatsu. "Nucleon decay via dimension-6 operators in anomalous U(1)_A supersymmetric GUT", Phys.Rev.（査読有）D88 (2013) no.9, 095008, 10.1103/PhysRevD.88.095008.

[24] Junji Hisano, Daiki Kobayashi, Takumi Kuwahara, Natsumi Nagata, "Decoupling Can Revive Minimal Supersymmetric SU(5)", JHEP（査読有）1307 (2013) 038, 10.1007/JHEP07(2013)038.
[25] Junji Hisano, Takumi Kuwahara, Natsumi Nagata,"Grand Unification in High-scale Supersymmetry",Phys.Lett. (査読有) B723 (2013) 324-329,10.1016/j.physletb.2013.05.017.
[26] Junji Hisano, Daiki Kobayashi, Yu Muramatsu, Natsumi Nagata, " Two-loop Renormalization Factors of Dimension-six Proton Decay Operators in the Supersymmetric Standard Models",Phys.Lett. (査読有) B724 (2013) 283-287,10.1016/j.physletb.2013.06.030.
[27] Junji Hisano, Koji Tsumura, " Higgs boson mixes with an SU(2) septet representation",Phys.Rev. (査読有) D87 (2013) 053004,10.1103/PhysRevD.87.053004.
[28] Kaori Fuyuto, Junji Hisano, Natsumi Nagata,"Neutron electric dipole moment induced by strangeness revisited",
Phys.Rev. (査読有) D87 (2013) no.5, 054018, 10.1103/PhysRevD.87.054018.
[29] Junji Hisano, Koji Ishiwata, Natsumi Nagata,"Direct Search of Dark Matter in High-Scale Supersymmetry",Phys.Rev. (査読有) D87 (2013) 035020,10.1103/PhysRevD.87.035020.
[30] Junji Hisano, Koji Tsumura, Masaki J.S. Yang,"QCD Corrections to Neutron Electric Dipole Moment from Dimension-six Four-Quark Operators",Phys.Lett. (査読有) B713 (2012) 473-480, 10.1016/j.physletb.2012.06.038.
[31] Paolo Gondolo, Junji Hisano, Kenji Kadota."The Effect of quark interactions on dark matter kinetic decoupling and the mass of the smallest dark halos", Phys.Rev. (査読有) D86 (2012) 083523,10.1103/PhysRevD.86.083523.
[32] Junji Hisano, Daiki Kobayashi, Natsumi Nagata,"Enhancement of Proton Decay Rates in Supersymmetric SU(5) Grand Unified Models",Phys.Lett.（査読有）B716 (2012) 406-412, 10.1016/j.physletb.2012.08.037.
[33] Junji Hisano, Jeong Yong Lee, Natsumi Nagata, Yasuhiro Shimizu,"Reevaluation of Neutron Electric Dipole Moment with QCD Sum Rules",Phys.Rev.（査読有）D85 (2012) 114044,10.1103/PhysRevD.85.114044.
[34] Nobuhiro Maekawa, Kenichi Takayama,
"Neutrino properties in E_6 x $SU(2)_F$ SUSY GUT with spontaneous CP violation",Phys.Rev. (査読有) D85 (2012) 095015,10.1103/PhysRevD.85.095015.
[35] Yasuhiro Kurata, Nobuhiro Maekawa,"Averaged Number of the Lightest Supersymmetric Particles in Decay of Superheavy Particle with Long Lifetime",Prog.Theor.Phys. (査読有) 127 (2012) 657-664,10.1143/PTP.127.657.
[36] Shinya Kanemura, Tetsuo Shindou, Toshifumi Yamada,"A light Higgs scenario based on the TeV-scale supersymmetric strong dynamics",Phys.Rev.(査読有) D86 (2012) 055023,

10.1103/PhysRevD.86.055023.
[37] By Shinya Kanemura, Eibun Senaha, Tetsuo Shindou,"First-order electroweak phase transition powered by additional F-term loop effects in an extended supersymmetric Higgs sector",Phys.Lett.(査読有) B706 (2011) 40-45,10.1016/j.physletb.2011.10.046.
[38] Mayumi Aoki, Shinya Kanemura, Tetsuo Shindou, Kei Yagyu,"Decoupling property of the supersymmetric Higgs sector with four doublets",JHEP(査読有) 1111 (2011) 038,10.1007/JHEP11(2011)038.
[39] Junji Hisano, Koji Ishiwata, Natsumi Nagata, "Direct Detection of Dark Matter Degenerate with Colored Particles in Mass",Phys.Lett.(査読有) B706 (2011) 208-212,10.1016/j.physletb.2011.11.017.
[40] Junji Hisano, Wei-Shu Hou, Fanrong Xu, "Updating the neutron electric dipole moment in a fourth generation standard model",Phys.Rev.(査読有) D84 (2011) 093005,10.1103/PhysRevD.84.093005.
[41] Seishi Enomoto, Nobuhiro Maekawa, "Baryogengesis by B-L generation due to superheavy particle decay", Phys.Rev. (査読有) D84 (2011) 096007, 10.1103/PhysRevD.84.096007.
[42] Motoharu Ito, Shogo Kuwakino, Nobuhiro Maekawa, Sanefumi Moriyama, Keijiro Takahashi, Kazuaki Takei, Shunsuke Teraguchi, Toshifumi Yamashita,"Heterotic E_6 GUTs and Partition Functions",JHEP (査読有) 1112 (2011) 100,10.1007/JHEP12(2011)100.
[43] Junji Hisano, Koji Ishiwata, Natsumi Nagata, Tomohiro Takesako,"Direct Detection of Electroweak-Interacting Dark Matter",JHEP (査読有) 1107 (2011) 005, 10.1007/JHEP07(2011)005.
[44] Junji Hisano, Masahiro Kawasaki, Kazunori Kohri, Takeo Moroi, Kazunori Nakayama, Toyokazu Sekiguchi,"Cosmological constraints on dark matter models with velocity-dependent annihilation cross section", Phys.Rev.(査読有) D83 (2011) 123511,10.1103/PhysRevD.83.123511.

〔学会発表〕(計 59 件)

[1] Junji Hisano, "QCD Effects on Direct Detection of Wino Dark Matter", Particle Phenomenology From the Early Universe to High Energy Colliders (招待講演), 2015 年 4 月 9 日, Portoroz, Slovenia
[2] Junji Hisano, "Probing the TeV scale and beyond with EDMs", Symposium: New Generation Quantum Theory -Particle Physics, Cosmology, and Chemistry- (招待講演), 2015 年 10 月 27 日, 京都大学
[3] Junji Hisano, "How to study SUSY standard model(s) at O(100) TeV", the 5th KEK Flavor

Factory Workshop (KEK-FF2015) (招待講演), 2015 年 10 月 27 日, Waterras Common in the center of Tokyo

[4] 進藤哲央,“素粒子標準模型を超える理論の探求”, 第 2 回先進工学イノベーションフォーラム, 2015 年 11 月 2 日, 工学院大学

[5] Nobuhiro Maekawa, "Neutrino masses and mixings as an evidence of GUT, and the impact to nucleon decay and leptogenesis”, the Next generation Nucleon decay and Neutrino detector (NNN15) workshop (招待講演), 2015 年 10 月 16 日-2015 年 10 月 31 日, Stony Brook, New York, USA

[6]Nobuhiro Maekawa,"GUT with neutrinos”,the Workshop for Neutrino Programs with facilities in Japan（招待講演）, 2015 年 8 月 4 日、JPARC

[7] T. Shindou,“Lepton flavour violation in the SUSY seesaw model after the LHC 8TeV run”, 2nd KIAS-NTCS Joint Workshop (招待講演), 2014 年 12 月 26 日, National Taiwan University, Taiwan

[8] 進藤哲央, “Constraint on NP models by Higgs”, 第一回 ATLAS+Belle II 研究会(招待講演), 2014 年 11 月 25 日, 東京大学

[9] T. Shindou, “BSM interpretation of LHCb results and future prospects”, Rencontres du Vietnam 2014: Physics at LHC and beyond (招待講演), 2014 年 8 月 16 日, Qui-nhyon, Vietnam

[10] N. Maekawa, "Heavy gravitino, naturalness and sizable anomaly mediation ”, PASCOS2014, 2014 年 6 月 22-27 日、Warsaw, Poland

[11] 前川展祐、“Neutrino properties in E_6*$SU(2)_F$ SUSY GUT with spontaneous CP violation”, 次世代の加速器ニュートリノ実験ワークショップ (招待講演)、2014 年 6 月 21 日、京都大

[12] 久野純治, “Probing the TeV scale and beyond with EDMs”, Workshop "Flavors of New Physics”（招待講演)、2015 年 3 月, 原子力研究機構

[13] 久野純治, “Probing the TeV scale and beyond with EDMs”, Workshop “Probing the TeV scale and beyond” （招待講演), 2014 年 7 月, University in Mainz.

[14] 久野純治, “Probing the TeV scale and beyond”, 4th KIAS Workshop on particle physics and cosmology （招待講演), 2014 年 10 月, KIAS

[15] N.Maekawa, “Vacuum selection and inflation via particle production in anomalous U(1) model”, PASCOS2013, 2013 年 11 月 20 日-2013 年 11 月 26 日、台北、台湾

[16] J.Hisano, “Proton Decay in SUSY GUTs revisited”. Third workshop on Flavor Symmetry (FLASY13), 2013 年 7 月 1 日～2013 年 7 月 5 日、新潟大学

[17] T. Shindou, “Introduction to Flavour Physics in Models Beyond the Standard Model”, KEK-PH2013(招待講演), 2013 年 03 月 06 日~2013 年 03 月 07 日, KEK

[18] T. Shindou, “Extended SUSY Higgs Sector and EW Baryogenesis”, SUSY2012, 2012 年 10 月 16 日, Peking University

[19] J.Hisano, “Lepton-Flavor Violation and Physics beyond the Standard Model”, 2th International Workshop on Tau Lepton Physics (TAU 2012)(招待講演), 2012 年 09 月 28 日, Nagoya univ.

[20] J.Hisano, “eevaluation of Neutron Electric Dipole Moment with QCD Sum Rules”, Quark Confinement and the Hadron Spectrum X(招待講演), 2012 年 09 月 17 日, TUM, Germany

[21] J.Hisano, “Lepton-Flavor Violation and Physics beyond the Standard Model”, 7th Workshop on the CKM Unitarity Triangle (CKM 2012)(招待講演), 2012 年 09 月 28 日, University of Cincinnati

[22] N. Maekawa,“Cosmology in Natural GUT”,COSMO11, 2011 年 8 月 25 日, ポルトガル

[23] T. Shindou, “ Extended SUSY Higgs sector and first-order electroweak phase transition”,KEKPH2012, 2012 年 2 月 29 日, KEK

主要論文別刷

[1] “Reevaluation of Neutron Electric Dipole Moment with QCD Sum Rules”,
Junji Hisano, Jeong Yong Lee, Natsumi Nagata, Yasuhiro Shimizu,
Published in Phys.Rev. D85 (2012) 114044

[2] “Decoupling Can Revive Minimal Supersymmetric SU(5)”,
Junji Hisano, Daiki Kobayashi, Takumi Kuwahara, Natsumi Nagata,
Published in JHEP 1307 (2013) 038

[3] “Higgs boson mixes with an SU(2) septet representation”,
Junji Hisano, Koji Tsumura,
Published in Phys.Rev. D87 (2013) 053004

[4] “Gauge invariant Barr-Zee type contributions to fermionic EDMs in the two-Higgs doublet models”,
Tomohiro Abe, Junji Hisano, Teppei Kitahara, Kohsaku Tobioka,
Published in JHEP 1401 (2014) 106, Erratum: JHEP 1604 (2016) 161

[5] “Toward verification of electroweak baryogenesis by electric dipole moments”,
Kaori Fuyuto, Junji Hisano, Eibun Senaha,
Published in Phys.Lett. B755 (2016) 491-497

PHYSICAL REVIEW D **85,** 114044 (2012)

Reevaluation of neutron electric dipole moment with QCD sum rules

Junji Hisano,[1,2] Jeong Yong Lee,[1] Natsumi Nagata,[1,3] and Yasuhiro Shimizu[4,5]

[1]*Department of Physics, Nagoya University, Nagoya 464-8602, Japan*
[2]*IPMU, TODIAS, University of Tokyo, Kashiwa 277-8568, Japan*
[3]*Department of Physics, University of Tokyo, Tokyo 113-0033, Japan*
[4]*Department of Physics, Tohoku University, Sendai, 980-8578 Japan*
[5]*IIAIR, Tohoku University, Sendai, 980-8578 Japan*

(Received 18 April 2012; published 26 June 2012)

We study the neutron electric dipole moment in the presence of the *CP*-violating operators up to dimension five in terms of the QCD sum rules. It is found that the operator product expansion calculation is robust when exploiting a particular interpolating field for a neutron, while there exist some uncertainties on the phenomenological side. By using input parameters obtained from the lattice calculation, we derive a conservative limit for the contributions of the *CP*-violating operators. We also show the detail of the derivation of the sum rules.

DOI: 10.1103/PhysRevD.85.114044 PACS numbers: 14.20.Dh, 11.55.Hx, 13.40.Em

I. INTRODUCTION

A variety of experimental efforts [1] has precisely determined the elements of the Cabibbo-Kobayashi-Maskawa (CKM) matrix [2,3], which is a source of *CP* violation in the standard model (SM). All of *CP*-violating processes ever observed are well-explained in terms of the single physical phase in the CKM matrix. The SM, which is based on the $SU(3)_C \times SU(2)_L \times U(1)_Y$ gauge symmetry, allows another *CP*-violating interaction: the θ term in the QCD sector. The *CP*-violating phenomena caused by the interaction are, however, quite different from those induced by the CKM phase; the QCD θ term gives rise to the *CP* violation in the flavor-conserving processes, while the CKM phase induces the *CP* violation in the flavor-changing ones. Furthermore, TeV-scale physics beyond the SM, such as the minimal supersymmetric standard model, often provides other *CP*-violating sources. In fact, additional *CP*-violating interactions are necessary from the cosmological point of view, since the observed baryon asymmetry in the Universe is not explained within the SM interactions.

The electric dipole moment (EDM) of the neutron is one of the physical quantities that are quite sensitive to the *CP* violation in the flavor-conserving interaction. Since there has been no experimental evidence for its existence so far, a severe constraint is imposed on the *CP*-violating interactions. The currently most stringent limit for the neutron EDM is given by the Institut Laue-Langevin experiment [4]:

$$|d_n| < 2.9 \times 10^{-26}\ e\,\mathrm{cm} \qquad (90\%\ \mathrm{C.L.}). \tag{1}$$

Moreover, several experimental projects which use ultracold neutrons are now under development and expected to have much improved sensitivities. For example, the nEDM Collaboration at the Paul Scherrer Institute [5] plans to deliver a sensitivity of $\sim 5 \times 10^{-27}\ e\,\mathrm{cm}$ and eventually to reach into the regime of $10^{-28}\ e\,\mathrm{cm}$. Similar sensitivities are expected to be achieved by the nEDM Collaboration at the Spallation Neutron Source at the U.S. Oak Ridge National Laboratory [6], the CryoEDM experiment [7], the NOP Collaboration at J-PARC [8], and the experiment at KEK-RCNP-TRIUMF [9]. Such high sensitivities provide an opportunity to probe the flavor-conserving *CP*-violating interactions in the TeV-scale physics beyond the SM. Furthermore, we may probe the flavor violation in the new physics indirectly. Even if the new flavor-violating interactions are introduced in the new physics, the relative *CP* phase between them and the CKM matrix may contribute to the EDM [10].

In order to translate the experimental limits for the neutron EDM into constraints on the *CP* violation on the Lagrangian at the parton level, one needs to obtain a relation between these two quantities. There are some attempts to derive the relation based on the naive dimensional analysis, the chiral perturbation theory, and the QCD sum rules, though they are considered to have large uncertainties. It is ultimately desired that the lattice QCD simulation would evaluate it in the future. There has been discussion of evaluation of the neutron EDM with lattice simulation [11].

In this work, we evaluate the neutron EDM with the QCD sum rules [12], including the *CP*-violating operators up to dimension five. It is considered that the QCD sum rules allow us to derive the relation more systematically than the naive dimensional analysis and the chiral perturbation theory [13]. Similar attempts have been already made in the previous works, e.g., in a series of papers by Pospelov and Ritz [14,15], and references therein. We also derive the sum rules for the neutron EDM, while we use the lattice QCD simulation result for the low-energy constant in the numerical evaluation of the neutron EDM. It is found that this gives a more conservative estimate than carrying out all of the evaluation within the framework of the QCD sum rules. This approach provides a way of eliminating theoretical errors from the calculation, while there still

 © 2012 American Physical Society

remains uncertainty resulting from the QCD sum rule technique itself.

This paper is organized as follows. In Sec. II, we review the CP-violating interactions at the parton level up to dimension five. From Sec. III, the analysis of the neutron EDM with the QCD sum rules starts. In Sec. III, we discuss phenomenological aspects of the correlator of the interpolating field to a neutron and, in Sec. IV, show the properties of the neutron-interpolating field. In Sec. V, the quark propagators are derived on the CP-violating and electromagnetic background. They are used to evaluate the operator product expansion (OPE) for the correlator in Sec. VI. The sum rules for the neutron EDM are derived in Sec. VII. We found that there is a difference between results in Refs. [14,15] and ours. In Sec. VIII, we extract the low-energy constant from the lattice QCD simulation result. In Sec. IX, our numerical results for the neutron EDM are derived. In Sec. X, the neutron EDM is discussed assuming that the Peccei-Quinn symmetry solves the strong CP problem [16]. Section XI is devoted to conclusion and discussion.

In the appendix, we show some useful formulas to derive the quark condensates in the CP-violating background. In Appendix A 1, we estimate the effect of the CP-violating interactions on the generic quark bilinear condensate $\langle 0|\bar{q}\Gamma q|0\rangle$, with Γ a 4×4 constant matrix, as well as on the quark and gluon background fields. In Appendix A 2, validity of the usage of the classical equations of motion of quarks in evaluation of the quark condensates is discussed. In Appendix A 3, the Wilson-line operators for the quark fields are discussed in the Fock-Schwinger gauge.

II. EFFECTIVE LAGRANGIAN

Let us first express the flavor-conserving CP-violating terms in the low-energy effective Lagrangian for the system consisting of light quarks and a gluon. We include all of the CP-violating operators up to dimension five:

$$\mathcal{L}_{\not{C}P} = -\sum_{q=u,d,s} m_q \bar{q} i\theta_q \gamma_5 q + \theta_G \frac{\alpha_s}{8\pi} G^A_{\mu\nu}\tilde{G}^{A\mu\nu} - \frac{i}{2}\sum_{q=u,d,s} d_q \bar{q}(F\cdot\sigma)\gamma_5 q - \frac{i}{2}\sum_{q=u,d,s}\tilde{d}_q \bar{q} g_s (G\cdot\sigma)\gamma_5 q. \tag{2}$$

Here, m_q represents the quark masses, $F_{\mu\nu}$ and $G^A_{\mu\nu}$ are the electromagnetic and gluon field strength tensors, respectively, g_s is the strong coupling constant ($\alpha_s = g_s^2/4\pi$), $F\cdot\sigma \equiv F_{\mu\nu}\sigma^{\mu\nu}$, $G\cdot\sigma \equiv G^A_{\mu\nu}\sigma^{\mu\nu}T^A$, and $\tilde{G}^A_{\mu\nu} \equiv \frac{1}{2}\epsilon_{\mu\nu\rho\sigma}G^{A\rho\sigma}$ with $\epsilon^{0123} = +1$. T^A denotes the generators in the $SU(3)_C$ algebra. The second, third, and fourth terms in Eq. (2) are called the effective QCD θ term and the electric and chromoelectric dipole moments (CEDMs) for quarks, respectively. The EDMs and CEDMs for quarks are dimension-five operators, and they are sensitive to the TeV-scale physics beyond the SM. The coefficients of the CP-violating operators (θ_q, θ_G, d_q, and $\tilde{d}_q$) are all assumed to be quite small, and we keep only the terms up to the first order of these parameters.

The first two terms in Eq. (2) are mutually related by the chiral rotation. Consider the following infinitesimal chiral rotation:

$$q \to q' = (1 - i\epsilon\rho_q\gamma_5)q, \tag{3}$$

where ϵ is an infinitesimal real constant and ρ_q are certain parameters for each quark. The Noether current associated with the transformation is given as

$$J_{5\mu} = \sum_{q=u,d,s}\rho_q \bar{q}\gamma_\mu\gamma_5 q. \tag{4}$$

The divergence of this current does not vanish. Instead,

$$\partial^\mu J_{5\mu} = \frac{\alpha_s}{4\pi}\Big(\sum_q \rho_q\Big) G^A_{\mu\nu}\tilde{G}^{A\mu\nu} + \sum_q 2im_q\rho_q\bar{q}\gamma_5(1+i\theta_q\gamma_5)q - \sum_q \rho_q[d_q\bar{q}(F\cdot\sigma)q + \tilde{d}_q\bar{q}g_s(G\cdot\sigma)q]. \tag{5}$$

Hereafter we choose ρ_q as

$$\rho_q = \theta_q/\theta_Q, \qquad \theta_Q \equiv \sum_{q=u,d,s}\theta_q. \tag{6}$$

Then, if we take the infinitesimal parameter in Eq. (3) as $\epsilon = \theta_Q/2$, the Lagrangian in Eq. (2) varies by

$$\delta\mathcal{L} = \partial^\mu J_{5\mu}\cdot\frac{\theta_Q}{2} = \sum_q m_q\bar{q}i\theta_q\gamma_5 q + \theta_Q\frac{\alpha_s}{8\pi}G^a_{\mu\nu}\tilde{G}^{a\mu\nu}, \tag{7}$$

which implies that

$$\mathcal{L}_{\not{C}P} \to \mathcal{L}'_{\not{C}P} = \bar{\theta}\frac{\alpha_s}{8\pi}G^A_{\mu\nu}\tilde{G}^{A\mu\nu} - \frac{i}{2}\sum_{q=u,d,s} d_q\bar{q}(F\cdot\sigma)\gamma_5 q - \frac{i}{2}\sum_{q=u,d,s}\tilde{d}_q\bar{q}g_s(G\cdot\sigma)\gamma_5 q, \tag{8}$$

where $\bar{\theta} = \theta_G + \theta_Q$.

Therefore, it is found that the γ_5-mass terms are always reduced to the ordinary ones, and it is $\bar{\theta}$ that is regarded as a physical parameter. Of course, one may in turn rotate out the θ term into the imaginary mass term through an appropriate chiral rotation.

In addition, there remains still some arbitrariness in the quark mass phases θ_q, since they are redefined into another through an $SU(3)$ chiral rotation. In this paper, we choose an appropriate set of θ_q so that the choice significantly reduces the CP-violating contribution to the vacuum expectation values of the quark bilinear. We take the condition in Ref. [17] to determine θ_q; that is, after the θ term

rotated into the γ_5-mass term, the following relation should be satisfied:

$$\langle \Omega_{\not{C}P} | \mathcal{L}_{\not{C}P} | M^A \rangle = 0 \qquad (M^A = \pi, K, \eta). \tag{9}$$

The above condition is evaluated by using the partially conserved axial-vector current (PCAC) relations. In the current case, it is sufficient to examine the conditions for π^0 and η^0. By using the PCAC relations, one may readily deduce the conditions for the CP-violating parameters from Eq. (9):

$$\bar{\theta}(m_u\rho_u - m_d\rho_d) = \tfrac{1}{2}m_0^2(\tilde{d}_u - \tilde{d}_d),$$
$$\bar{\theta}(m_u\rho_u + m_d\rho_d - 2m_s\rho_s) = \tfrac{1}{2}m_0^2(\tilde{d}_u + \tilde{d}_d - 2\tilde{d}_s). \tag{10}$$

In the calculation we parametrize the condensate $\langle \bar{q} g_s (G\cdot\sigma) q\rangle$ as [18]

$$\langle \bar{q} g_s (G\cdot\sigma) q\rangle = -m_0^2 \langle \bar{q} q\rangle. \tag{11}$$

With the relation $\sum_q \rho_q = 1$, we then determine the quark mass phases as follows:

$$\rho_u = \frac{m_*}{m_u}\left[1 + \frac{m_0^2}{2\bar{\theta}}\left\{\frac{\tilde{d}_u - \tilde{d}_d}{m_d} + \frac{\tilde{d}_u - \tilde{d}_s}{m_s}\right\}\right],$$
$$\rho_d = \frac{m_*}{m_d}\left[1 + \frac{m_0^2}{2\bar{\theta}}\left\{\frac{\tilde{d}_d - \tilde{d}_u}{m_u} + \frac{\tilde{d}_d - \tilde{d}_s}{m_s}\right\}\right], \tag{12}$$
$$\rho_s = \frac{m_*}{m_s}\left[1 + \frac{m_0^2}{2\bar{\theta}}\left\{\frac{\tilde{d}_s - \tilde{d}_u}{m_u} + \frac{\tilde{d}_s - \tilde{d}_d}{m_d}\right\}\right],$$

where

$$m_* \equiv \frac{m_u m_d m_s}{m_u m_d + m_d m_s + m_u m_s}. \tag{13}$$

III. PHENOMENOLOGICAL BEHAVIOR OF THE CORRELATOR

The QCD sum rules are based on an analysis of the correlator of interpolating fields.[1] In the method, OPE allows one to consistently separate the long- and short-distance contributions to the correlator, and the long-distance contributions are evaluated by condensations of quarks and a gluon. By comparing the evaluated correlator with the phenomenological model, the properties for the low-lying parts of the hadronic spectrum are derived. The Borel transformation is applied to the correlator there. In this section, we first discuss the phenomenological model for the correlator.

In the present case, the interpolating field must have the same quantum numbers as those of the neutron, and it is denoted by $\eta_n(x)$ hereafter. On a background with CP-violating sources, the matrix element of the interpolating field between the vacuum and the one-particle neutron state is given as

$$\langle \Omega_{\not{C}P} | \eta_n(x) | N_{\not{C}P}(\boldsymbol{p}, s)\rangle = Z^{(1/2)}_{n,\not{C}P} \cdot u_{n,CP}(\boldsymbol{p}, s) e^{-ip\cdot x}, \tag{14}$$

where $|\Omega_{\not{C}P}\rangle$ and $|N_{\not{C}P}(\boldsymbol{p}, s)\rangle$ indicate the vacuum and the one-particle neutron state on the CP-violating background, respectively. The spinor $u_{n,\not{C}P}(\boldsymbol{p}, s)$ is the on-shell neutron wave function which satisfies the Dirac equation:

$$(\not{p} - m_{n,\not{C}P} \cdot e^{-i\alpha_n\gamma_5}) u_{n,\not{C}P}(\boldsymbol{p}, s) = 0. \tag{15}$$

Here we include a phase factor $e^{-i\alpha_n\gamma_5}$ into the mass term, which in general might appear as CP is broken in the vacuum. Since $Z^{(1/2)}_{n,\not{C}P}$ and $m_{n,\not{C}P}$ are both even in terms of the CP-violating parameters [11], up to the first order of them,

$$Z^{(1/2)}_{n,\not{C}P} = Z^{(1/2)}_n, \qquad m_{n,\not{C}P} = m_n, \tag{16}$$

where m_n is the mass of the neutron and $\lambda_n \equiv Z^{(1/2)}_n$ is the coupling between the physical neutron state and the interpolating field without CP-violating sources. Then the solution of Eq. (15) turns out to be

$$u_{n,\not{C}P}(\boldsymbol{p}, s) = e^{(i/2)\alpha_n\gamma_5} u_n(\boldsymbol{p}, s), \tag{17}$$

with $u_n(\boldsymbol{p}, s)$ an ordinary spinor wave function which satisfies $(\not{p} - m_n) u_n(\boldsymbol{p}, s) = 0$. As a result, Eq. (14) leads to

$$\langle \Omega_{\not{C}P} | \eta_n(x) | N_{\not{C}P}(\boldsymbol{p}, s)\rangle = \lambda_n e^{(i/2)\alpha_n\gamma_5} u_n(\boldsymbol{p}, s) e^{-ip\cdot x}. \tag{18}$$

The low-energy constant λ_n is to be determined later.

Now we analyze the correlator of the interpolating fields from the phenomenological viewpoint. It is defined as

$$\Pi(q) \equiv i \int d^4x e^{iq\cdot x} \langle \Omega_{\not{C}P} | T\{\eta_n(x)\bar{\eta}_n(0)\} | \Omega_{\not{C}P}\rangle_F, \tag{19}$$

where the subscript F implies that the correlator is evaluated on an electromagnetic field background. Our goal is to extract the EDM of the neutron from the correlator. The phase factor in Eq. (18), however, causes a mixture between electric and magnetic dipole moment structures and makes it difficult to pick out only the EDM from the QCD sum rules. So we first examine the Lorentz structures of the correlator and select a term independent of the phase α_n, i.e., chiral-invariant. As discussed in Ref. [14], up to the leading order on the background electromagnetic field, the correlator $\Pi(q)$ is estimated by inserting an effective vertex such as

$$\mathcal{L}_n = -\frac{i}{2} d_n \bar{N}(F\cdot\sigma)\gamma_5 N = \frac{d_n}{2}\bar{N}\tilde{F}\cdot\sigma N. \tag{20}$$

Here, N [$\equiv N(x)$] denotes the renormalized neutron field which is approximately equivalent to $\lambda_n^{-1} e^{-i\alpha_n\gamma_5/2}\eta_n(x)$, and d_n is the EDM of the neutron. A similar procedure to those in Ref. [14] shows that terms with an odd number of Dirac matrices are independent of the phase factor α_n, and furthermore, those proportional to $\{\tilde{F}\cdot\sigma, \not{q}\}$ are the unique choice in this case. Therefore we focus only on such terms

[1] There are many review articles about the QCD sum rules. For example, see Ref. [19].

in the following calculation. Then, the phenomenological expression of the correlator is found to be[2]

$$\Pi^{(\mathrm{phen})}(q) = \tfrac{1}{2} f(q^2)\{\tilde{F}\cdot\sigma, \not{q}\} + \cdots, \tag{21}$$

where dots indicate terms with other Lorentz structures and

$$f(q^2) = \left(\frac{\lambda_n^2 d_n m_n}{(q^2 - m_n^2)^2} + \frac{A(q^2)}{q^2 - m_n^2} + B(q^2)\right) \tag{22}$$

with $A(q^2)$ and $B(q^2)$ functions which have no pole at $q^2 = m_n^2$. As noted in Ref. [14], since we are effectively dealing with a three-point function, it might be inconsistent to parametrize the continuum contribution in terms of a usual ansatz for the spectral function with a certain threshold in the QCD sum rules. We just neglect the contribution with expecting its significance to be small enough. Furthermore, we assume that the function $A(q^2)$ has little dependence on q^2 and regard it as a constant when we conduct the Borel transformation.

IV. NEUTRON-INTERPOLATING FIELD

In this section, we give a discussion on the choice of the neutron-interpolating field which we use for the QCD sum rule calculation. The field must have the same quantum numbers as the neutron. The most general interpolator for the neutron on the ordinary CP-even background is parametrized as

$$\eta_n(x) = j_1(x) + \beta j_2(x), \tag{23}$$

where

$$j_1(x) = 2\epsilon_{abc}(d_a^T(x)C\gamma_5 u_b(x))d_c(x) \tag{24}$$

and

$$j_2(x) = 2\epsilon_{abc}(d_a^T(x)Cu_b(x))\gamma_5 d_c(x). \tag{25}$$

Here the subscripts a, b, and c denote the color indices, and C is the charge conjugation matrix. The interpolator $j_1(x)$ is often used in lattice simulations. While $j_2(x)$ vanishes in the nonrelativistic limit, it should be included to the whole interpolating field since we deal with light quarks. The unphysical parameter β is to be fixed later so that the calculation is transparent.

When the calculation is carried out on the CP-violating background, however, the interpolating fields include additional components. This point is easily understood when one considers the chiral rotation discussed in Sec. II. As we have seen in Sec. II, the chiral rotation (3) transforms the Lagrangian $\mathcal{L}$ into another. The same transformation, in turn, changes the interpolators $j_1(x)$ and $j_2(x)$ into other ones as

$$\begin{aligned} j_1(x) &\to j_1(x) - i\epsilon[(\rho_u + \rho_d)i_1(x) + \rho_d i_2(x)], \\ j_2(x) &\to j_2(x) - i\epsilon[(\rho_u + \rho_d)i_2(x) + \rho_d i_1(x)], \end{aligned} \tag{26}$$

where

$$\begin{aligned} i_1(x) &= 2\epsilon_{abc}(d_a^T(x)Cu_b(x))d_c(x), \\ i_2(x) &= 2\epsilon_{abc}(d_a^T(x)C\gamma_5 u_b(x))\gamma_5 d_c(x). \end{aligned} \tag{27}$$

Therefore, with generic CP-violating terms as in Eq. (2), the interpolators acquire mixing terms as

$$\begin{aligned} \tilde{j}_1(x) &= j_1(x) + i\epsilon i_1(x) + i\delta i_2(x), \\ \tilde{j}_2(x) &= j_2(x) + i\epsilon i_2(x) + i\delta i_1(x), \\ \tilde{i}_1(x) &= i_1(x) + i\epsilon j_1(x) + i\delta j_2(x), \\ \tilde{i}_2(x) &= i_2(x) + i\epsilon j_2(x) + i\delta j_1(x), \end{aligned} \tag{28}$$

with ϵ and δ the small constants which are suppressed by the CP-violating parameters. Furthermore, the above expressions are rewritten as

$$\begin{aligned} \tilde{j}_1(x) &= (1 + i\delta\gamma_5)[j_1(x) + i\epsilon i_1(x)], \\ \tilde{j}_2(x) &= (1 + i\delta\gamma_5)[j_2(x) + i\epsilon i_2(x)], \\ \tilde{i}_1(x) &= (1 + i\delta\gamma_5)[i_1(x) + i\epsilon j_1(x)], \\ \tilde{i}_2(x) &= (1 + i\delta\gamma_5)[i_2(x) + i\epsilon j_2(x)], \end{aligned} \tag{29}$$

because

$$i_1(x) = \gamma_5 j_2(x), \qquad i_2(x) = \gamma_5 j_1(x). \tag{30}$$

Now that we concentrate on the chiral-invariant structure in the correlator of the neutron-interpolating field as discussed in Sec. III, the infinitesimal chiral rotation factor $(1 + i\delta\gamma_5)$ is ignorable. After all, the neutron-interpolating field which we deal with has the following structure:

$$\eta_n(x) = j_1(x) + \beta j_2(x) + i\epsilon[i_1(x) + \beta i_2(x)]. \tag{31}$$

The small constant ϵ is determined by the condition that the interpolating field $\eta_n(x)$ has a vanishing correlator with the current $\xi_n(x)$ defined as follows:

$$\xi_n(x) = i_1(x) + \beta i_2(x) + i\epsilon[j_1(x) + \beta j_2(x)]. \tag{32}$$

In what follows, however, we sweep away the contribution of the mixture terms in the interpolating field by choosing an appropriate value for the parameter β. In the subsequent sections, we calculate the correlator of $\eta_n(x)$ by using the OPE method. The correlator is expressed by the sum of the correlators for each component interpolator as

$$\begin{aligned} &\langle\Omega_{\not{C}P}|T\{\eta_n(x)\bar{\eta}_n(0)\}|\Omega_{\not{C}P}\rangle_F \\ &\quad = \langle j_1, \bar{j}_1\rangle + \beta[\langle j_1, \bar{j}_2\rangle + \langle j_2, \bar{j}_1\rangle] + \beta^2\langle j_2, \bar{j}_2\rangle \\ &\qquad + i\epsilon[\gamma_5\langle j_2, \bar{j}_1\rangle + \langle j_1, \bar{j}_2\rangle\gamma_5] + i\epsilon\beta[\{\langle j_1, \bar{j}_1\rangle, \gamma_5\} \\ &\qquad + \{\langle j_2, \bar{j}_2\rangle, \gamma_5\}] + i\epsilon\beta^2[\gamma_5\langle j_1, \bar{j}_2\rangle + \langle j_2, \bar{j}_1\rangle\gamma_5], \end{aligned} \tag{33}$$

[2]In the published versions of Refs. [14,15], the coefficient of the double pole in Eq. (22) is different from ours by a factor of 2, while that in the revised arXiv versions is consistent with ours.

where

$$\langle a, \bar{b}\rangle \equiv \langle \Omega_{\not{C}P}|T\{a(x)\bar{b}(0)\}|\Omega_{\not{C}P}\rangle_F. \tag{34}$$

As discussed in Sec. III, we focus on parts of the correlators which have the Lorentz structures with an odd number of gamma matrices. Such terms anticommute with γ_5. Thus, in this case, the above expression leads to

$$\begin{aligned}&\langle \Omega_{\not{C}P}|T\{\eta_n(x)\bar{\eta}_n(0)\}|\Omega_{\not{C}P}\rangle_F|_{\gamma\,\mathrm{odd}}\\ &= \langle j_1, \bar{j}_1\rangle + \beta[\langle j_1, \bar{j}_2\rangle + \langle j_2, \bar{j}_1\rangle] + \beta^2\langle j_2, \bar{j}_2\rangle\\ &\quad + i\epsilon(1-\beta^2)[\langle j_1, \bar{j}_2\rangle - \langle j_2, \bar{j}_1\rangle]\gamma_5.\end{aligned} \tag{35}$$

This equation shows that the mixing terms in the interpolating field do not affect the correlator if one sets β to be ± 1. As we will see later, for our calculation, $\beta = +1$ is an appropriate choice, since this choice eliminates the subleading terms with an infrared logarithm, which yields ambiguity due to the infrared cutoff.[3] With this choice, one may simultaneously exclude the contribution of the mixing terms. Thus, we will not calculate such mixing contributions with keeping in mind that we will finally take $\beta = +1$ when we derive the QCD sum rules.[4] That is to say, we deal with the correlator

$$\begin{aligned}&\langle \Omega_{\not{C}P}|T\{\eta_n(x)\bar{\eta}_n(0)\}|\Omega_{\not{C}P}\rangle_F\\ &= \langle j_1, \bar{j}_1\rangle + \beta[\langle j_1, \bar{j}_2\rangle + \langle j_2, \bar{j}_1\rangle] + \beta^2\langle j_2, \bar{j}_2\rangle,\end{aligned} \tag{37}$$

and after the computation, we set $\beta = +1$.

V. QUARK PROPAGATORS ON THE *CP*-VIOLATING BACKGROUND

When evaluating the correlator (19) in the OPE, we need to obtain the quark propagators on the CP-violating background with an electromagnetic background field F. They are defined as follows:

$$[S^q_{ab}(x)]_{\alpha\beta} \equiv \langle \Omega_{\not{C}P}|T[q_{a\alpha}(x)\bar{q}_{b\beta}(0)]|\Omega_{\not{C}P}\rangle_F, \tag{38}$$

where α and β denote spinor indices. Expanding the propagators as

$$\begin{aligned}[S^q_{ab}(x)]_{\alpha\beta} &= [S^{q(0)}_{ab}(x)]_{\alpha\beta} + \chi^q_{a\alpha}(x)\bar{\chi}^q_{b\beta}(0)\\ &\quad + [S^q_{ab}(x)]_{\alpha\beta}|_{1\mathrm{photon}} + [S^q_{ab}(x)]_{\alpha\beta}|_{1\mathrm{gluon}} + \cdots,\end{aligned} \tag{39}$$

we evaluate each term in x space. The first term is the free propagator, and the second term describes the correlator of the quark background fields, with $\chi^q_{a\alpha}(x)$ a classical Grassmann field which indicates the quark background field. The third and fourth terms represent the propagators including one photon and gluon, respectively. In the derivation of the quark propagators we use the classical equations of motion for quark fields given as

$$\begin{aligned}i\not{D}q &= m_q(1 + i\theta_q\gamma_5)q + \frac{i}{2}\sum_{q=u,d,s} d_q(F\cdot\sigma)\gamma_5 q\\ &\quad + \frac{i}{2}\sum_{q=u,d,s}\tilde{d}_q g_s(G\cdot\sigma)\gamma_5 q,\\ -i\bar{q}\overleftarrow{\not{D}} &= m_q\bar{q}(1 + i\theta_q\gamma_5) + \frac{i}{2}\sum_{q=u,d,s} d_q\bar{q}(F\cdot\sigma)\gamma_5\\ &\quad + \frac{i}{2}\sum_{q=u,d,s}\tilde{d}_q g_s\bar{q}(G\cdot\sigma)\gamma_5,\end{aligned} \tag{40}$$

where $D_\mu = \partial_\mu - ie_qA_\mu - ig_sG^A_\mu T^A$ and $\bar{q}\overleftarrow{\not{D}} = \partial_\mu\bar{q}\gamma^\mu + ie_q\bar{q}\not{A} + ig_s\bar{q}\not{G}^AT^A$. The electromagnetic and gluon fields are denoted as A_μ and G^A_μ, respectively, with e_q the quark charge.

The first term in Eq. (39), $[S^{q(0)}_{ab}(x)]_{\alpha\beta}$, is readily evaluated by using the equations of motion without electromagnetic and gluon background fields. The result is

$$S^{q(0)}_{ab}(x) = \frac{i\delta_{ab}}{2\pi^2}\frac{\not{x}}{(x^2)^2} - \frac{m_q\delta_{ab}}{4\pi^2x^2}(1 - i\theta_q\gamma_5), \tag{41}$$

where we keep the terms up to the first order of the quark mass m_q.

Next, we evaluate the third and fourth terms in Eq. (39). These terms again are obtained from the equations of motion (40). In this calculation, it is convenient to use the Fock-Schwinger gauge [21] for both the electromagnetic and the gluon fields:

$$x^\mu A_\mu(x) = x^\mu G^A_\mu(x) = 0. \tag{42}$$

In this gauge, the fields are expanded by their field strength, such as

$$\begin{aligned}A_\mu(x) &= \frac{1}{2\cdot 0!}x^\nu F_{\nu\mu}(0) + \frac{1}{3\cdot 1!}x^\alpha x^\nu(D_\alpha F_{\nu\mu}(0))\\ &\quad + \frac{1}{4\cdot 2!}x^\alpha x^\beta x^\nu(D_\alpha D_\beta F_{\nu\mu}(0)) + \cdots.\end{aligned} \tag{43}$$

By using the expression, the gauge covariant form of the propagators is obtained as follows:

$$\begin{aligned}S^q_{ab}(x)|_{1\mathrm{photon}} &= -\frac{ie_q}{32\pi^2}\delta_{ab}\Big[\frac{1}{x^2}\{\not{x}, F\cdot\sigma\}\\ &\quad - im_q(1 - i\theta_q\gamma_5)F\cdot\sigma\log(-\Lambda^2_{\mathrm{IR}}x^2)\Big]\\ &\quad - \frac{d_q}{8\pi^2}\delta_{ab}\Big[\frac{\not{x}\tilde{F}\cdot\sigma\not{x}}{(x^2)^2} + \frac{m_q}{2x^2}\{\not{x}, \tilde{F}\cdot\sigma\}\Big],\end{aligned} \tag{44}$$

[3]The choice of β for the sum rules including only the QCD θ term is discussed in Ref. [20]. They argue that the optimal choice of β is $-1 \le \beta \le 0$ rather than 1, which is consistent with the conventional choices favored from a viewpoint of evaluation of λ_n. The discussion is, however, not applicable to the present case, since our sum rules contain several unknown parameters.

[4]The neutron-interpolating field for $\beta = +1$ is simply expressed as

$$\eta_n(x) = \tfrac{1}{2}\epsilon^{abc}(d^T_a C\sigma_{\mu\nu}d_b)\sigma^{\mu\nu}\gamma_5 u_c. \tag{36}$$

$$S^q_{ab}(x)|_{1\text{gluon}} = -\frac{ig_s}{32\pi^2}\Big[\frac{1}{x^2}\{\not{x}, G_{ab}\cdot\sigma\} - im_q(1-i\theta_q\gamma_5)G_{ab}\cdot\sigma\log(-\Lambda^2_{\rm IR}x^2)\Big] - \frac{\tilde{d}_q g_s}{8\pi^2}\Big[\frac{\not{x}\tilde{G}_{ab}\cdot\sigma\not{x}}{(x^2)^2} + \frac{m_q}{2x^2}\{\not{x}, \tilde{G}_{ab}\cdot\sigma\}\Big], \quad (45)$$

with $G^{\mu\nu}_{ab} = G^{A\mu\nu}T^A_{ab}$. Here, a certain infrared (IR) cutoff $\Lambda_{\rm IR}$ is introduced in logarithmic terms. It was replaced to the quark masses when deriving the propagator from the equation motions. However, the contribution to the OPE with small quark momenta around the quark masses should not be included so that the IR cutoff is introduced.

Finally, we translate the quark and gluon background fields into their condensates. Here we just give resultant expressions for the relations between them. The details of the derivation is presented in Appendix A 1.

A single quark line, $\chi^q_{a\alpha}(x)\bar{\chi}^q_{b\beta}(0)$, is related with the quark condensate as

$$\chi^q_{a\alpha}(x)\bar{\chi}^q_{b\beta}(0) = \langle\Omega_{\not{C}P}|q_{a\alpha}(x)\bar{q}_{b\beta}(0)|\Omega_{\not{C}P}\rangle_F, \quad (46)$$

and it is to be expressed in terms of $\langle\bar{q}q\rangle$ as follows:

$$\chi^q_{a\alpha}(x)\bar{\chi}^q_{b\beta}(0) = -\frac{\delta_{ab}}{12}(1+i\theta_G\rho_q\gamma_5)_{\alpha\beta}\langle\bar{q}q\rangle + \frac{i}{48}\delta_{ab}\not{x}m_q\langle\bar{q}q\rangle - \frac{i}{96}\delta_{ab}\Big[\bar{\theta}m_q\rho_q e_q\chi + d_q + \Big(\kappa - \frac{1}{2}\xi\Big)e_q\tilde{d}_q\Big] \times\{\tilde{F}\cdot\sigma, \not{x}\}_{\alpha\beta}\langle\bar{q}q\rangle + \frac{i}{96}m_q e_q\chi\delta_{ab}\{F\cdot\sigma, \not{x}\}_{\alpha\beta}\langle\bar{q}q\rangle - \frac{i}{24}e_q\chi\delta_{ab}(\tilde{F}\cdot\sigma\gamma_5[1+i\rho_q\theta_G\gamma_5])_{\alpha\beta}\langle\bar{q}q\rangle. \quad (47)$$

Here, χ, κ, and ξ are the parameters for the quark condensates defined as [22]

$$\langle\bar{q}\sigma_{\mu\nu}q\rangle_F = e_q\chi F_{\mu\nu}\langle\bar{q}q\rangle, \quad (48)$$

$$g_s\langle\bar{q}G^A_{\mu\nu}T^A q\rangle_F = e_q\kappa F_{\mu\nu}\langle\bar{q}q\rangle, \quad (49)$$

$$2g_s\langle\bar{q}\gamma_5\tilde{G}^A_{\mu\nu}T^A q\rangle_F = ie_q\xi F_{\mu\nu}\langle\bar{q}q\rangle. \quad (50)$$

Also, in our calculation, we need the interaction part of the quark and gluon background fields,

$$g_s\chi^q_{a\alpha}(x)\bar{\chi}^q_{b\beta}(0)[G_{\mu\nu}]_{cd} = \langle g_s q_{a\alpha}(x)[G_{\mu\nu}]_{cd}\bar{q}_{b\beta}(0)\rangle_{F,\not{C}P}, \quad (51)$$

and it leads to the following equation:

$$g_s\chi^q_{a\alpha}(x)\bar{\chi}^q_{b\beta}(0)[G_{\mu\nu}]_{cd} = -\frac{1}{32}\Big(\delta_{ad}\delta_{bc} - \frac{1}{3}\delta_{ab}\delta_{cd}\Big)\langle\bar{q}q\rangle\Big[e_q\Big(\kappa F_{\mu\nu} - \frac{i}{2}\xi\tilde{F}_{\mu\nu}\gamma_5\Big)(1+i\theta_G\rho_q\gamma_5) - \frac{i}{4}m_q e_q\not{x}\Big(\kappa F_{\mu\nu} + \frac{1}{2}\bar{\theta}\rho_q\xi\tilde{F}_{\mu\nu}\Big) - \frac{i}{24}m_q m_0^2\epsilon_{\mu\nu\rho\sigma}x^\rho\gamma^\sigma\gamma_5 - \frac{i}{24}\bar{\theta}m_q\rho_q m_0^2(x_\mu\gamma_\nu\gamma_5 - x_\nu\gamma_\mu\gamma_5) - \frac{1}{12}m_0^2\sigma_{\mu\nu} - \frac{i}{12}m_0^2\theta_G\rho_q\sigma_{\mu\nu}\gamma_5\Big]_{\alpha\beta}. \quad (52)$$

VI. OPE ANALYSIS OF THE CORRELATOR

A. Leading order

Now we calculate the correlation function of the interpolating fields $\eta_n(x)$ in terms of the OPE. First, we carry out the leading-order calculation for the correlator

$$\Pi(x) = \langle\Omega_{\not{C}P}|T\{\eta_n(x)\bar{\eta}_n(0)\}|\Omega_{\not{C}P}\rangle_F. \quad (53)$$

As in Eq. (37), this correlator is decomposed into four correlators. We deal with them inclusively by using the following notation:

$$\Pi_{kl}(x) = \langle\Omega_{\not{C}P}|T\{j_k(x)\bar{j}_l(0)\}|\Omega_{\not{C}P}\rangle_F \qquad (k, l = 1, 2). \quad (54)$$

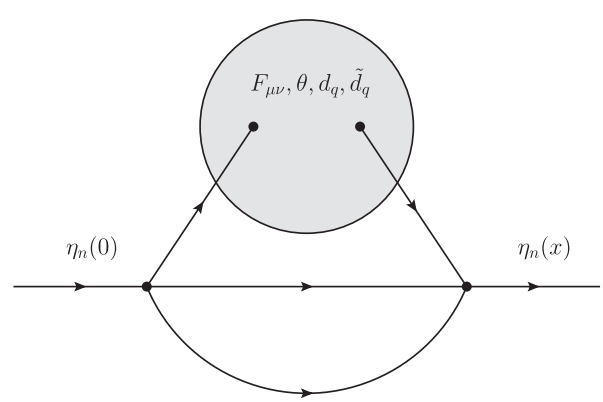

FIG. 1. Diagram which yields the leading contribution without emitting either a gluon or a photon.

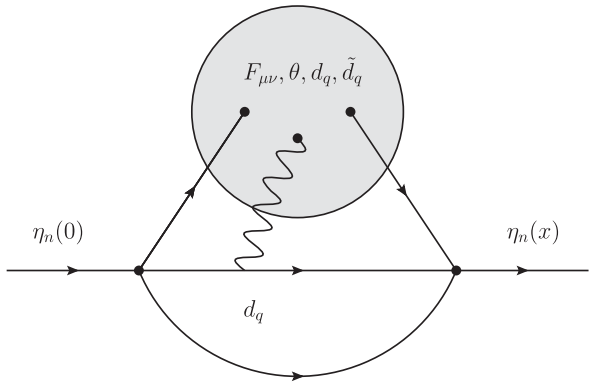

FIG. 2. Diagram which yields the leading and the next-to-leading-order contributions with emitting a photon. Those contributions vanish when $\beta = +1$.

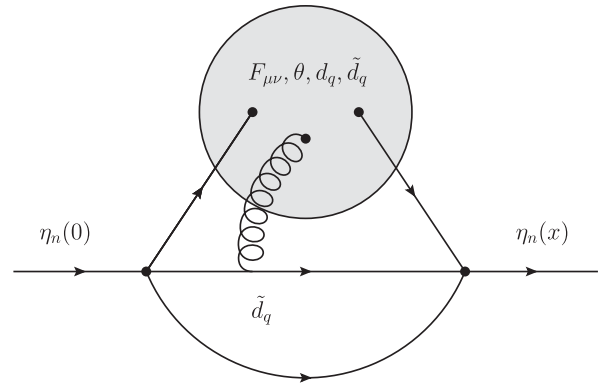

FIG. 3. Diagram which yields the leading and the next-to-leading-order contributions with emitting a gluon. Those contributions vanish when $\beta = +1$.

In Figs. 1–3, the diagrams which contribute to the correlators are illustrated. We denote each contribution to the correlators by the upper indices, i.e., $\Pi^{(I)}(x)$ or $\Pi^{(I)}_{kl}(x)$ with $I = 1, 2, 3$. From now on, we use the following abbreviation:

$$\bar{S}^{q}(x) \equiv C S^{qT}(x) C^{\dagger}, \tag{55}$$

with C the charge conjugation matrix.

Let us begin with evaluating $\Pi^{(1)}_{kl}(x)$. Each $\Pi^{(1)}_{kl}(x)$ is expressed in terms of the propagators $S^{q}_{ab}(x)$ as

$$\begin{aligned}
\Pi^{(1)}_{11}(x) &= 4\epsilon_{abc}\epsilon_{a'b'c'}\{-\mathrm{Tr}[\gamma_5 S^{u}_{ba'}(x)\gamma_5 \bar{S}^{d}_{ab'}(x)]S^{d}_{cc'}(x) + S^{d}_{cb'}(x)\gamma_5 \bar{S}^{u}_{ba'}(x)\gamma_5 S^{d}_{ac'}(x)\},\\
\Pi^{(1)}_{12}(x) &= 4\epsilon_{abc}\epsilon_{a'b'c'}\{-\mathrm{Tr}[\gamma_5 S^{u}_{ba'}(x)\bar{S}^{d}_{ab'}(x)]S^{d}_{cc'}(x)\gamma_5 + S^{d}_{cb'}(x)\bar{S}^{u}_{ba'}(x)\gamma_5 S^{d}_{ac'}(x)\gamma_5\},\\
\Pi^{(1)}_{21}(x) &= 4\epsilon_{abc}\epsilon_{a'b'c'}\{-\mathrm{Tr}[S^{u}_{ba'}(x)\gamma_5 \bar{S}^{d}_{ab'}(x)]\gamma_5 S^{d}_{cc'}(x) + \gamma_5 S^{d}_{cb'}(x)\gamma_5 \bar{S}^{u}_{ba'}(x) S^{d}_{ac'}(x)\},\\
\Pi^{(1)}_{22}(x) &= 4\epsilon_{abc}\epsilon_{a'b'c'}\{-\mathrm{Tr}[S^{u}_{ba'}(x)\bar{S}^{d}_{ab'}(x)]\gamma_5 S^{d}_{cc'}(x)\gamma_5 + \gamma_5 S^{d}_{cb'}(x)\bar{S}^{u}_{ba'}(x) S^{d}_{ac'}(x)\gamma_5\}.
\end{aligned} \tag{56}$$

When the propagators include neither a photon- nor gluon-emitting term, the expressions reduce to

$$\begin{aligned}
\Pi^{(1)}_{11}(x) &= 24\{\mathrm{Tr}[\gamma_5 S^{u}(x)\gamma_5 \bar{S}^{d}(x)]S^{d}(x) + S^{d}(x)\gamma_5 \bar{S}^{u}(x)\gamma_5 S^{d}(x)\},\\
\Pi^{(1)}_{12}(x) &= 24\{\mathrm{Tr}[\gamma_5 S^{u}(x)\bar{S}^{d}(x)]S^{d}(x)\gamma_5 + S^{d}(x)\bar{S}^{u}(x)\gamma_5 S^{d}(x)\gamma_5\},\\
\Pi^{(1)}_{21}(x) &= 24\{\mathrm{Tr}[S^{u}(x)\gamma_5 \bar{S}^{d}(x)]\gamma_5 S^{d}(x) + \gamma_5 S^{d}(x)\gamma_5 \bar{S}^{u}(x) S^{d}(x)\},\\
\Pi^{(1)}_{22}(x) &= 24\{\mathrm{Tr}[S^{u}(x)\bar{S}^{d}(x)]\gamma_5 S^{d}(x)\gamma_5 + \gamma_5 S^{d}(x)\bar{S}^{u}(x) S^{d}(x)\gamma_5\},
\end{aligned} \tag{57}$$

where

$$S^{q}_{ab}(x) = \delta_{ab} S^{q}(x). \tag{58}$$

As discussed in Sec. III, we focus on the terms proportional to $\{\tilde{F}\cdot\sigma, \not{q}\}$. For this reason we extract only the terms including $\{\tilde{F}\cdot\sigma, \not{x}\}$. They are found to be

$$\begin{aligned}
\Pi^{(1)}_{11}(x) &= \frac{i}{16\pi^4}\langle\bar{q}q\rangle\frac{1}{(x^2)^3}\{\tilde{F}\cdot\sigma, \not{x}\}\Big[(4e_d m_d\rho_d - e_u m_u\rho_u)\chi\bar{\theta} + \chi\{(e_d m_u\rho_u - e_u m_d\rho_d)\theta_Q + (e_u m_d\rho_u - e_d m_u\rho_d)\theta_G\}\\
&\quad + (6d_d - d_u) + \Big(\kappa - \frac{1}{2}\xi\Big)(6e_d\tilde{d}_d - e_u\tilde{d}_u)\Big],\\
\Pi^{(1)}_{12}(x) &= \Pi^{(1)}_{21}(x) = \frac{i}{16\pi^4}\langle\bar{q}q\rangle\frac{1}{(x^2)^3}\{\tilde{F}\cdot\sigma, \not{x}\}\Big[(4e_d m_d\rho_d - e_u m_u\rho_u)\chi\bar{\theta} + (2d_d - d_u) + \Big(\kappa - \frac{1}{2}\xi\Big)(2e_d\tilde{d}_d - e_u\tilde{d}_u)\Big],\\
\Pi^{(1)}_{22}(x) &= \frac{i}{16\pi^4}\langle\bar{q}q\rangle\frac{1}{(x^2)^3}\{\tilde{F}\cdot\sigma, \not{x}\}\Big[(4e_d m_d\rho_d - e_u m_u\rho_u)\chi\bar{\theta} + \chi\{(e_u m_d\rho_d - e_d m_u\rho_u)\theta_Q + (e_d m_u\rho_d - e_u m_d\rho_u)\theta_G\}\\
&\quad + (6d_d - d_u) + \Big(\kappa - \frac{1}{2}\xi\Big)(6e_d\tilde{d}_d - e_u\tilde{d}_u)\Big].
\end{aligned} \tag{59}$$

Thus, $\Pi^{(1)}(x)$ is given as

$$\Pi^{(1)}(x) = \frac{i}{16\pi^4}\langle\bar{q}q\rangle\frac{1}{(x^2)^3}\{\tilde{F}\cdot\sigma, \not{x}\}\Big[(1+\beta)^2(4e_d m_d\rho_d - e_u m_u\rho_u)\chi\bar{\theta} + (1-\beta^2)\chi\{(e_d m_u\rho_u - e_u m_d\rho_d)\theta_Q + (e_u m_d\rho_u - e_d m_u\rho_d)\theta_G\} + 2(3+2\beta+3\beta^2)d_d - (1+\beta)^2 d_u + \left(\kappa - \frac{1}{2}\xi\right)\{2(3+2\beta+3\beta^2)e_d\tilde{d}_d - (1+\beta)^2 e_u\tilde{d}_u\}\Big], \tag{60}$$

and for $\beta = +1$, the above expression reduces to

$$\Pi^{(1)}(x) = \frac{i}{4\pi^4}\langle\bar{q}q\rangle\frac{1}{(x^2)^3}\{\tilde{F}\cdot\sigma, \not{x}\}\Big[(4e_d m_d\rho_d - e_u m_u\rho_u)\chi\bar{\theta} + (4d_d - d_u) + \left(\kappa - \frac{1}{2}\xi\right)(4e_d\tilde{d}_d - e_u\tilde{d}_u)\Big]. \tag{61}$$

Next, we evaluate $\Pi^{(2)}$. Here, we again use the expressions in Eq. (57), while one of the propagators in each correlator is $S^q(x)|_{1\text{photon}}$ in this case. The result is given as

$$\Pi^{(2)}_{11}(x) = \frac{i}{8\pi^4}(2d_d - d_u)\langle\bar{q}q\rangle\frac{1}{(x^2)^3}\{\tilde{F}\cdot\sigma, \not{x}\}, \qquad \Pi^{(2)}_{12}(x) = \Pi^{(2)}_{21}(x) = -\frac{i}{8\pi^4}d_d\langle\bar{q}q\rangle\frac{1}{(x^2)^3}\{\tilde{F}\cdot\sigma, \not{x}\},$$
$$\Pi^{(2)}_{22}(x) = \frac{i}{8\pi^4}d_u\langle\bar{q}q\rangle\frac{1}{(x^2)^3}\{\tilde{F}\cdot\sigma, \not{x}\}, \tag{62}$$

and they lead to

$$\Pi^{(2)}(x) = \frac{i}{8\pi^4}[2(1-\beta)d_d - (1-\beta^2)d_u]\langle\bar{q}q\rangle\frac{1}{(x^2)^3}\{\tilde{F}\cdot\sigma, \not{x}\}. \tag{63}$$

Therefore, we find that $\Pi^{(2)}$ vanishes when we take $\beta = +1$:

$$\Pi^{(2)}(x) = 0. \tag{64}$$

Finally, we study $\Pi^{(3)}$. In this case, we use the equations in Eq. (56). By using Eq. (52), we find the resultant expressions as

$$\Pi^{(3)}_{11}(x) = \frac{i}{16\pi^4}\left[-e_d\tilde{d}_d\left(\kappa - \frac{1}{2}\xi\right) + (e_d\tilde{d}_u - e_u\tilde{d}_d)\left(\kappa + \frac{1}{2}\xi\right)\right]\langle\bar{q}q\rangle\frac{1}{(x^2)^3}\{\tilde{F}\cdot\sigma, \not{x}\},$$
$$\Pi^{(3)}_{12}(x) = \Pi^{(3)}_{21}(x) = \frac{i}{16\pi^4}e_d\tilde{d}_d\left(\kappa - \frac{1}{2}\xi\right)\langle\bar{q}q\rangle\frac{1}{(x^2)^3}\{\tilde{F}\cdot\sigma, \not{x}\},$$
$$\Pi^{(3)}_{22}(x) = \frac{i}{16\pi^4}\left[-e_d\tilde{d}_d\left(\kappa - \frac{1}{2}\xi\right) - (e_d\tilde{d}_u - e_u\tilde{d}_d)\left(\kappa + \frac{1}{2}\xi\right)\right]\langle\bar{q}q\rangle\frac{1}{(x^2)^3}\{\tilde{F}\cdot\sigma, \not{x}\}. \tag{65}$$

Thus, $\Pi^{(3)}(x)$ is given as

$$\Pi^{(3)}(x) = \frac{i}{16\pi^4}\langle\bar{q}q\rangle\frac{1}{(x^2)^3}\{\tilde{F}\cdot\sigma, \not{x}\}\left[-(1-\beta)^2\left(\kappa - \frac{1}{2}\xi\right)e_d\tilde{d}_d + (1-\beta^2)\left(\kappa + \frac{1}{2}\xi\right)(e_d\tilde{d}_u - e_u\tilde{d}_d)\right]. \tag{66}$$

Again, the correlator turns out to vanish for $\beta = +1$:

$$\Pi^{(3)}(x) = 0. \tag{67}$$

Taking the above discussion into account, we conclude that the correlator $\Pi(x)$ is given as

$$\Pi(x) = \frac{i}{16\pi^4}\langle\bar{q}q\rangle\frac{1}{(x^2)^3}\{\tilde{F}\cdot\sigma, \not{x}\}\Big[(1+\beta)^2(4e_d m_d\rho_d - e_u m_u\rho_u)\chi\bar{\theta} + (1-\beta^2)\chi\{(e_d m_u\rho_u - e_u m_d\rho_d)\theta_Q + (e_u m_d\rho_u - e_d m_u\rho_d)\theta_G\} + (10+6\beta^2)d_d - (3+2\beta-\beta^2)d_u + \tilde{d}_d\Big\{2\Big[(3+2\beta+3\beta^2) - \frac{1}{2}(1-\beta)^2\Big]e_d\left(\kappa - \frac{1}{2}\xi\right) - (1-\beta^2)e_u\left(\kappa + \frac{1}{2}\xi\right)\Big\} + \tilde{d}_u\Big\{(1-\beta^2)e_d\left(\kappa + \frac{1}{2}\xi\right) - (1+\beta)^2 e_u\left(\kappa - \frac{1}{2}\xi\right)\Big\}\Big], \tag{68}$$

and its Fourier transform is

$$\Pi(q) = i\int d^4x e^{iq\cdot x}\Pi(x)$$
$$= \frac{1}{64\pi^2}\langle\bar{q}q\rangle\log\left(\frac{-q^2}{\Lambda^2}\right)\{\tilde{F}\cdot\sigma, \not{q}\}\Big[(1+\beta)^2(4e_d m_d\rho_d - e_u m_u\rho_u)\chi\bar{\theta} + (1-\beta^2)\chi\{(e_d m_u\rho_u - e_u m_d\rho_d)\theta_Q$$
$$+ (e_u m_d\rho_u - e_d m_u\rho_d)\theta_G\} + (10+6\beta^2)d_d - (3+2\beta-\beta^2)d_u + \tilde{d}_d\Big\{2\Big[(3+2\beta+3\beta^2) - \frac{1}{2}(1-\beta)^2\Big]$$
$$\times e_d\left(\kappa - \frac{1}{2}\xi\right) - (1-\beta^2)e_u\left(\kappa + \frac{1}{2}\xi\right)\Big\} + \tilde{d}_u\Big\{(1-\beta^2)e_d\left(\kappa + \frac{1}{2}\xi\right) - (1+\beta)^2 e_u\left(\kappa - \frac{1}{2}\xi\right)\Big\}\Big]. \tag{69}$$

Here, a certain ultraviolet mass scale Λ is introduced, though it is irrelevant to our final result. When one sets $\beta = +1$, this expression reduces to

$$\Pi(q)^{(\mathrm{OPE})} = \frac{1}{16\pi^2}\langle\bar{q}q\rangle\log\left(\frac{-q^2}{\Lambda^2}\right)\{\tilde{F}\cdot\sigma, \not{q}\}\Big[(4e_d m_d\rho_d - e_u m_u\rho_u)\chi\bar{\theta} + (4d_d - d_u) + \left(\kappa - \frac{1}{2}\xi\right)(4e_d\tilde{d}_d - e_u\tilde{d}_u)\Big]. \tag{70}$$

Equation (69) corresponds to Eqs. (9–12) in Ref. [15]. After taking $\beta = +1$, we find that the CEDM contribution, i.e., the last term in Eq. (70), differs from those in the reference by a factor of 4. In addition, the sign in front of ξ is opposite to the one in Ref. [15].

B. Next-to-leading order

Figures 2 and 3 yield the next-to-leading-order (NLO) contributions. By using the propagator given in Eq. (44), we evaluate the contribution by the diagram in Fig. 2 as

$$\Pi^{(2)}_{11}(x)_{\mathrm{NLO}} = \frac{i}{32\pi^4}\langle\bar{q}q\rangle\frac{1}{(x^2)^2}\log(-\Lambda^2_{\mathrm{IR}}x^2)\{\tilde{F}\cdot\sigma, \not{x}\}[e_d m_d\rho_d\bar{\theta} + (e_u m_u\rho_d - e_d m_d\rho_u)\theta_G + (e_d m_d\rho_d - e_u m_u\rho_u)\theta_Q],$$
$$\Pi^{(2)}_{12}(x)_{\mathrm{NLO}} = \Pi^{(2)}_{21}(x)_{\mathrm{NLO}} = -\frac{i}{32\pi^4}\langle\bar{q}q\rangle\frac{1}{(x^2)^2}\log(-\Lambda^2_{\mathrm{IR}}x^2)\{\tilde{F}\cdot\sigma, \not{x}\}e_d m_d\rho_d\bar{\theta},$$
$$\Pi^{(2)}_{22}(x)_{\mathrm{NLO}} = \frac{i}{32\pi^4}\langle\bar{q}q\rangle\frac{1}{(x^2)^2}\log(-\Lambda^2_{\mathrm{IR}}x^2)\{\tilde{F}\cdot\sigma, \not{x}\}[e_d m_d\rho_d\bar{\theta} - (e_u m_u\rho_d - e_d m_d\rho_u)\theta_G - (e_d m_d\rho_d - e_u m_u\rho_u)\theta_Q], \tag{71}$$

and therefore, $\Pi^{(2)}(x)_{\mathrm{NLO}}$ is found to be

$$\Pi^{(2)}(x)_{\mathrm{NLO}} = \frac{i}{32\pi^4}\langle\bar{q}q\rangle\frac{1}{(x^2)^2}\log(-\Lambda^2_{\mathrm{IR}}x^2)\{\tilde{F}\cdot\sigma, \not{x}\}[(1-\beta)^2 e_d m_d\rho_d\bar{\theta} + (1-\beta^2)\{(e_u m_u\rho_d - e_d m_d\rho_u)\theta_G$$
$$+ (e_d m_d\rho_d - e_u m_u\rho_u)\theta_Q\}]. \tag{72}$$

The gluon contribution illustrated in Fig. 3 is also calculated by using the propagator displayed in Eq. (45). The resultant expressions are

$$\Pi^{(3)}_{11}(x)_{\mathrm{NLO}} = -\frac{i}{64\pi^4}\langle\bar{q}q\rangle\frac{1}{(x^2)^2}\log(-\Lambda^2_{\mathrm{IR}}x^2)\{\tilde{F}\cdot\sigma, \not{x}\}\Big[e_d m_d\rho_d\left(\kappa + \frac{1}{2}\xi\right)\bar{\theta} + (e_d m_u\rho_d - e_u m_d\rho_u)\left(\kappa - \frac{1}{2}\xi\right)\theta_G$$
$$+ (e_u m_d\rho_d - e_d m_u\rho_u)\left(\kappa - \frac{1}{2}\xi\right)\theta_Q\Big],$$
$$\Pi^{(3)}_{12}(x)_{\mathrm{NLO}} = \Pi^{(3)}_{21}(x)_{\mathrm{NLO}} = \frac{i}{64\pi^4}\langle\bar{q}q\rangle\frac{1}{(x^2)^2}\log(-\Lambda^2_{\mathrm{IR}}x^2)\{\tilde{F}\cdot\sigma, \not{x}\}\bar{\theta}e_d m_d\rho_d\left(\kappa + \frac{1}{2}\xi\right),$$
$$\Pi^{(3)}_{22}(x)_{\mathrm{NLO}} = -\frac{i}{64\pi^4}\langle\bar{q}q\rangle\frac{1}{(x^2)^2}\log(-\Lambda^2_{\mathrm{IR}}x^2)\{\tilde{F}\cdot\sigma, \not{x}\}\Big[e_d m_d\rho_d\left(\kappa + \frac{1}{2}\xi\right)\bar{\theta} - (e_d m_u\rho_d - e_u m_d\rho_u)\left(\kappa - \frac{1}{2}\xi\right)\theta_G$$
$$- (e_u m_d\rho_d - e_d m_u\rho_u)\left(\kappa - \frac{1}{2}\xi\right)\theta_Q\Big], \tag{73}$$

and then,

$$\Pi^{(3)}(x)_{\rm NLO} = -\frac{i}{64\pi^4}\langle\bar{q}q\rangle\frac{1}{(x^2)^2}\log(-\Lambda_{\rm IR}^2x^2)\{\tilde{F}\cdot\sigma, \not{x}\}\Big[(1-\beta)^2\bar{\theta}e_dm_d\rho_d\Big(\kappa+\frac{1}{2}\xi\Big) + (1-\beta^2)\{(e_dm_u\rho_d - e_um_d\rho_u)\theta_G + (e_um_d\rho_d - e_dm_u\rho_u)\theta_Q\}\Big(\kappa-\frac{1}{2}\xi\Big)\Big]. \tag{74}$$

From the results in Eqs. (72) and (74), it is found that taking $\beta = +1$ makes the NLO contributions vanish, as mentioned before. Thus, we find that the correlator given in Eq. (70) is valid up to the next-to-leading order.

VII. QCD SUM RULES

In order to derive the QCD sum rules for the present case, we first extract the coefficient functions of $\{\tilde{F}\cdot\sigma, \not{q}\}$ from both the phenomenological and the OPE correlators, $\Pi^{(\rm phen)}$ in Eq. (21) and $\Pi^{(\rm OPE)}$ in Eq. (70), respectively:

$$C^{(\rm phen)}(Q^2) \equiv \frac{1}{2}\Big[\frac{\lambda_n^2 d_n m_n}{(Q^2+m_n^2)^2} - \frac{A}{Q^2+m_n^2}\Big], \tag{75}$$

$$C^{(\rm OPE)}(Q^2) \equiv \frac{1}{16\pi^2}\langle\bar{q}q\rangle\Theta\log\Big(\frac{Q^2}{\Lambda^2}\Big), \tag{76}$$

with $Q^2 \equiv -q^2$ and

$$\Theta \equiv (4e_dm_d\rho_d - e_um_u\rho_u)\chi\bar{\theta} + (4d_d - d_u) + (\kappa - \tfrac{1}{2}\xi)(4e_d\tilde{d}_d - e_u\tilde{d}_u). \tag{77}$$

In Eq. (75), we neglect the continuum contribution and think of A as a constant, as discussed above. The QCD sum rules are obtained by equating the coefficient functions after the Borel transformation, i.e.,

$$\mathcal{B}[C^{(\rm phen)}(Q^2)] = \mathcal{B}[C^{(\rm OPE)}(Q^2)], \tag{78}$$

where the Borel transformation of the function $f(Q^2)$ is defined as

$$\mathcal{B}[f(Q^2)] \equiv \lim_{\substack{Q^2,n\to\infty\\ Q^2/n=M^2}} \frac{(Q^2)^{n+1}}{n!}\Big(\frac{-d}{dQ^2}\Big)^n f(Q^2), \tag{79}$$

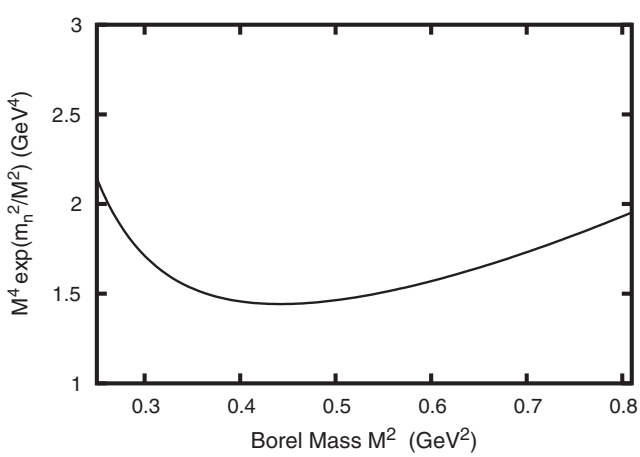

FIG. 4. Dependence of our sum rules on Borel mass M^2. The range of M is set to be 0.5 GeV $\leq M \leq$ 0.9 GeV.

with M so-called the Borel mass. Then, we finally derive the sum rules as follows:

$$\lambda_n^2 d_n m_n - AM^2 = -\Theta\langle\bar{q}q\rangle\frac{M^4}{8\pi^2}e^{(m_n^2/M^2)}. \tag{80}$$

All we have to do is now reduced to determining the Borel mass M and the coupling λ_n, as well as estimating the parameter A.

To illustrate the dependence of the sum rules on the Borel mass, we plot $M^4e^{(m_n^2/M^2)}$, which is included in the right-hand side of Eq. (80), as a function of the Borel mass squared M^2 in Fig. 4. Here, the range of M is set to be 0.5 GeV $\leq M \leq$ 0.9 GeV. From the figure we find that the Borel mass dependence of our sum rule is moderate in the range of 0.6 GeV $\lesssim M \lesssim$ 0.8 GeV.

VIII. DETERMINATION OF λ_n FROM THE LATTICE

The low-energy constant λ_n determines the normalization of the QCD sum rules so that the uncertainties are directly linked to the final result. We extract its numerical value from the lattice QCD calculation presented in Ref. [23], in which the QCD matrix elements for the proton decay rate are evaluated. In fact, they evaluate a similar quantity for proton, though the isospin symmetry allows us to interpret it for the present purpose.

First, we introduce a generic notation for three-quark operators with an arbitrary spin structure:

$$\mathcal{O}^{\Gamma\Gamma'}(\boldsymbol{x},t) \equiv \epsilon_{abc}[d_a^T(\boldsymbol{x},t)C\Gamma u_b(\boldsymbol{x},t)]\Gamma' d_c(\boldsymbol{x},t), \tag{81}$$

with Γ and Γ' arbitrary 4×4 matrices. In the current case, the relevant matrices are $R = P_R \equiv \frac{1}{2}(1+\gamma_5)$ or $L = P_L \equiv \frac{1}{2}(1-\gamma_5)$. Now we define parameters α_1 and α_2 as follows:

$$\langle 0|\mathcal{O}^{RL}|N(\boldsymbol{p},s)\rangle = \alpha_1 P_L u_n(\boldsymbol{p},s),\qquad \langle 0|\mathcal{O}^{LL}|N(\boldsymbol{p},s)\rangle = \alpha_2 P_L u_n(\boldsymbol{p},s). \tag{82}$$

The phase definition is fixed such that α_1 and α_2 are both real and $\alpha_1 < 0$. The parity transformation of the above equations implies that

$$\langle 0|\mathcal{O}^{LR}|N(\boldsymbol{p},s)\rangle = -\alpha_1 P_R u_n(\boldsymbol{p},s),\qquad \langle 0|\mathcal{O}^{RR}|N(\boldsymbol{p},s)\rangle = -\alpha_2 P_R u_n(\boldsymbol{p},s). \tag{83}$$

The interpolating fields j_1 and j_2 are expressed in terms of the operators as

$$j_1(x) = 2(\mathcal{O}^{RL}(x) + \mathcal{O}^{RR}(x) - \mathcal{O}^{LL}(x) - \mathcal{O}^{LR}(x)), \tag{84}$$

$$j_2(x) = 2(\mathcal{O}^{LR}(x) - \mathcal{O}^{LL}(x) + \mathcal{O}^{RR}(x) - \mathcal{O}^{RL}(x)). \tag{85}$$

Thus their matrix elements between the vacuum and one-particle states are given as

$$\langle 0|j_1|N(\boldsymbol{p},s)\rangle = 2(\alpha_1 - \alpha_2)u_n(\boldsymbol{p},s), \tag{86}$$

$$\langle 0|j_2|N(\boldsymbol{p},s)\rangle = -2(\alpha_1 + \alpha_2)u_n(\boldsymbol{p},s), \tag{87}$$

and they lead to

$$\langle 0|\eta_n|N(\boldsymbol{p},s)\rangle = 2[(\alpha_1 - \alpha_2) - \beta(\alpha_1 + \alpha_2)]u_n(\boldsymbol{p},s). \tag{88}$$

From the equation we may relate λ_n with the parameters α_1 and α_2:

$$\lambda_n(\mu) = 2[(\alpha_1 - \alpha_2) - \beta(\alpha_1 + \alpha_2)], \tag{89}$$

with μ the renormalization scale. The parameters α_1 and α_2 at $\mu = 2$ GeV are estimated in Ref. [23] as

$$\alpha_1 = -0.0112 \pm 0.0012_{(\mathrm{stat})} \pm 0.0022_{(\mathrm{syst})}\ \mathrm{GeV}^3, \tag{90}$$

$$\alpha_2 = 0.0120 \pm 0.0013_{(\mathrm{stat})} \pm 0.0023_{(\mathrm{syst})}\ \mathrm{GeV}^3. \tag{91}$$

For $\beta = 1$, $\lambda_n(\mu = 2\ \mathrm{GeV})$ is given as

$$\begin{aligned}\lambda_n &= -4\alpha_2 \\ &= -0.0480 \pm 0.0052_{(\mathrm{stat})} \pm 0.0092_{(\mathrm{syst})}\ \mathrm{GeV}^3.\end{aligned} \tag{92}$$

Since the QCD parameter used here is evaluated at $\mu = 1$ GeV, we need to translate the above value of λ_n into that of $\mu = 1$ GeV. The one-loop correction for λ_n is

$$\lambda_n(\mu = 1\ \mathrm{GeV}) = \left(\frac{\alpha_s(1\ \mathrm{GeV})}{\alpha_s(m_c)}\right)^{-(2/9)}\left(\frac{\alpha_s(m_c)}{\alpha_s(2\ \mathrm{GeV})}\right)^{-(6/25)} \times \lambda_n(\mu = 2\ \mathrm{GeV}), \tag{93}$$

which results in a reduction factor of $\simeq 0.91$. As a result, we obtain

$$\lambda_n = -0.0436 \pm 0.0047_{(\mathrm{stat})} \pm 0.0084_{(\mathrm{syst})}\ \mathrm{GeV}^3 \tag{94}$$

for $\beta = +1$.

Let us compare the value of λ_n obtained here with those used in the previous works. In Ref. [14], for example, they exploit the values for λ_n evaluated in Ref. [24][5] by using the QCD sum rules. Two Dirac-γ structures, $\mathbb{1}$ and $\not{p}$, provide different sum rules. As evaluated in Ref. [24], these two sum rules yield relatively small values for λ_n; the lattice QCD value is several times larger than the values evaluated by using the QCD sum rules. The author in Ref. [24] also estimates the error for these values. It is about 30% for the sum rules result while 20% for the lattice QCD result. The lattice QCD result might have an uncertainty in the chiral extrapolation. Since there is no more guiding principle for judging which estimation is valid, we exploit the lattice QCD result in Eq. (94), because this choice leads to a rather conservative constraint for CP-violating sources.

[5]Note that the notation used in Ref. [24] is different from ours:

$$\lambda_n = 2\lambda_{\mathcal{O}} = \frac{2}{(2\pi)^2}\tilde{\lambda}_{\mathcal{O}}. \tag{95}$$

Also, notice that there is some difference between the results described in Ref. [24] and the corresponding expressions shown in Ref. [14].

IX. RESULTS

Now we estimate the neutron EDM by using the results obtained above. First of all, we rewrite the sum rules in Eq. (80) in a simple form:

$$c_0 + c_1 x = f(x), \tag{96}$$

where $x = M^2$ and

$$f(x) \equiv \frac{x^2}{8\pi^2}\exp\left(\frac{m_n^2}{x}\right), \quad c_0 \equiv \frac{d_n\lambda_n^2 m_n}{-\Theta\langle\bar{q}q\rangle}, \quad c_1 \equiv \frac{-A}{-\Theta\langle\bar{q}q\rangle}. \tag{97}$$

The right-hand side of Eq. (96) describes the behavior of the coefficient function obtained from the OPE calculation, while the left-hand side represents the phenomenological one. The first and second terms in the left-hand side correspond to the double and single pole contributions, i.e., the first and second terms in Eq. (22), respectively. Once given a Borel mass point $x = M^2$, one may readily pick out c_0 and c_1 from the tangent line to the function $f(x)$ at the point. Then, they are expressed as the functions of x as

$$\begin{aligned} c_0(x) &= \frac{1}{8\pi^2}(m_n^2 x - x^2)\exp\left(\frac{m_n^2}{x}\right), \\ c_1(x) &= \frac{1}{8\pi^2}(2x - m_n^2)\exp\left(\frac{m_n^2}{x}\right). \end{aligned} \tag{98}$$

From these expressions, it is found that the single pole contribution vanishes at $x = m_n^2/2$. Since the parameter A is unknown, this choice of x is favorable in order to estimate the double pole contribution. Then, at this point the value of c_0 is

$$c_0 = 1.8 \times 10^{-2} \quad (\text{for } x = m_n^2/2), \tag{99}$$

and, therefore, the neutron EDM d_n is evaluated as

$$d_n = \frac{-c_0\langle\bar{q}q\rangle}{\lambda_n^2 m_n}\Theta = 1.2 \times 10^{-1}\Theta. \tag{100}$$

Here we take $\langle\bar{q}q\rangle = -(0.225\ \mathrm{GeV})^3$.

The choice of the Borel mass, $M^2 = m_n^2/2$, is, however, quite arbitrary, and deviation from the above result due to the different choice of the Borel mass should be taken into account as a theoretical uncertainty. In Fig. 5, we plot the ratio of the single and double pole contributions as a function of M^2. From this figure, we find that the single pole contribution rapidly increases when the Borel mass is varied from $M^2 = m_n^2/2$. We here assume our sum rules to be valid within the region of the Borel mass in which the single pole contribution is less than 30% of the double pole contribution. This assumption leads to $0.36\ \mathrm{GeV}^2 < M^2 < 0.50\ \mathrm{GeV}^2$, and, in this region, d_n takes the following values:

$$d_n = 1.2^{+0.6}_{-0.3} \times 10^{-1}\Theta. \tag{101}$$

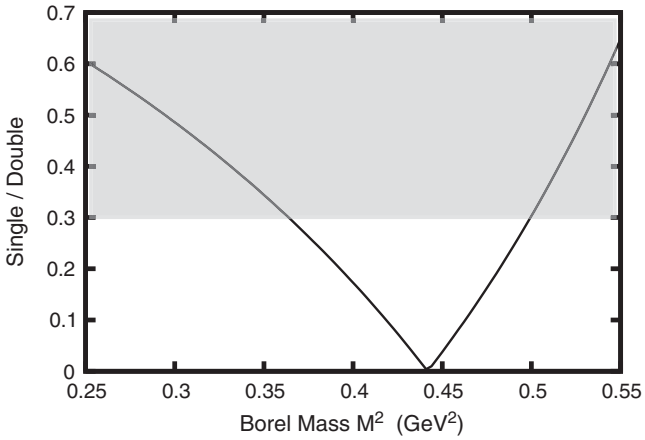

FIG. 5. Ratio of single and double pole contributions as a function of Borel mass M^2. The shaded region illustrates that single pole contribution is more than 30% of double pole contribution.

Here, the lower value corresponds to the upper limit of the Borel mass, and vice versa.

Next, we discuss the uncertainty of the OPE calculation. In this case, the truncation of the OPE leads to the uncertainty. Let us estimate it by evaluating the relative size of the higher-order contributions. Among them, the four-quark condensates such as $\langle \bar{q}q\bar{q}q\rangle$ are expected to yield sizable contributions, since they are free from loop suppression. On the assumption that these contributions vanish when one takes the quark masses to be zero, we expect that they are suppressed by at least a factor of $\langle \bar{q}q\rangle^{(2/3)}/M^2 \simeq 0.1$. Therefore, the uncertainty of the OPE calculation is estimated to be $\mathcal{O}(10)\%$.

Taking the above discussion into account, we finally evaluate the neutron EDM with theoretical uncertainty as follows:

$$d_n = 1.2^{+0.6}_{-0.3} \pm 0.1^{+0.7}_{-0.4} \times 10^{-1}\Theta, \tag{102}$$

where the first uncertainty stems from the phenomenological calculation while the second one comes from the approximation in the OPE. We also include uncertainties originate from those in λ_n [see Eq. (94)], which is indicated by the third error in the above equation.[6] After all, it is found that there is almost an $\mathcal{O}(1)$ factor of uncertainty in our sum rule calculation.

Let us compare the result with those obtained by using the values of λ_n calculated with the QCD sum rules. In Ref. [22], the authors adopt $\lambda_n^2 = 1.05/(2\pi)^4\ \mathrm{GeV}^3$ for $\beta = -1$ from the QCD sum rules derived for the nucleon mass. The λ_n for $\beta = -1$ is equal to that for $\beta = 1$ in the nonrelativistic quark limit. In Ref. [25], it is shown that the neutron EDM prediction in the nonrelativistic quark model with the $SU(6)$ spin-flavor symmetry is derived in the QCD sum rules using the value of λ_n. By substituting the value into Eq. (100), one obtains $d_n = 3.3 \times 10^{-1}\Theta$. The "realistic" value of λ_n evaluated by the QCD sum rules in Ref. [24], $\lambda_n \simeq 0.022\ \mathrm{GeV}^3$, leads to a slightly larger result: $d_n = 4.6 \times 10^{-1}\Theta$. Thus, the overall factors of d_n of these results are several times larger than that of our result.

For convenience, we substitute the numerical values for the QCD parameters in Eq. (101). Here we take $m_0^2 = 0.8\,\mathrm{GeV}^2$, $\chi = -5.7 \pm 0.6\,\mathrm{GeV}^{-2}$, $\xi = -0.74 \pm 0.2$, and $\kappa = -0.34 \pm 0.1$ [18,26]. Then, with those parameters the center values, we find

$$d_n = 4.2 \times 10^{-17}\bar{\theta}[e\ \mathrm{cm}] + 0.47 d_d - 0.12 d_u + e(-0.18\tilde{d}_u + 0.18\tilde{d}_d - 0.008\tilde{d}_s). \tag{103}$$

The contributions from $\bar{\theta}$ and the quark CEDMs to d_n may be changed furthermore by about $\pm 10\%$, mainly due to the theoretical uncertainty of χ.

X. UNDER THE PECCEI-QUINN SYMMETRY

It is known that $O(1)$ $\bar{\theta}$ induces a too large neutron EDM, the strong CP problem. The Peccei-Quinn (PQ) symmetry is one of the solutions for the strong CP problem. If the PQ symmetry is introduced, $\bar{\theta}$ vanishes dynamically. However, if the quark CEDMs are nonvanishing, a linear term is induced to the axion potential [27],

$$V(\bar{\theta}) = K'\bar{\theta} - \tfrac{1}{2}K\bar{\theta}^2, \tag{104}$$

where K is the topological susceptibility

$$K = -i\lim_{k\to 0} i \int d^4x e^{ikx} \left\langle T\left[\frac{\alpha_s}{8\pi} G\tilde{G}(x) \frac{\alpha_s}{8\pi} G\tilde{G}(0)\right]\right\rangle \tag{105}$$

and K' is calculated by

$$K' = -i\lim_{k\to 0} i \int d^4x e^{ikx} \times \left\langle T\left[\frac{\alpha_s}{8\pi} G\tilde{G}(x) \frac{i}{2} \sum_{q=u,d,s} \tilde{d}_q \bar{q} g_s (G\cdot\sigma)\gamma_5 q(0)\right]\right\rangle. \tag{106}$$

Minimizing the axion potential, an effective θ term is induced from the quark CEDM:

$$\bar{\theta}_{\mathrm{ind}} = -\frac{K'}{K} = \frac{m_0^2}{2} \sum_{q=u,d,s} \frac{\tilde{d}_q}{m_q}. \tag{107}$$

Taking the induced θ term into account, the neutron EDM in the presence of the PQ symmetry is estimated as

$$d_n^{\mathrm{PQ}} = 1.2^{+0.6}_{-0.3} \pm 0.1^{+0.7}_{-0.4} \times 10^{-1}\Theta^{\mathrm{PQ}}, \tag{108}$$

where

$$\Theta^{\mathrm{PQ}} = 4d_d - d_u + \left(\frac{m_0^2}{2}\chi + \kappa - \frac{1}{2}\xi\right)(4e_d\tilde{d}_d - e_u\tilde{d}_u). \tag{109}$$

The contributions from the strange quark CEDM are canceled in the presence of the PQ symmetry [15]. Again, we

[6] We approximate the error in λ_n as the rms of the statistical and systematic errors displayed in Eq. (94).

substitute the numerical values for the QCD parameters as presented in the previous section. The result is

$$d_n^{\rm PQ} = 0.47 d_d - 0.12 d_u + e(0.35\tilde{d}_d + 0.17\tilde{d}_u). \quad (110)$$

XI. CONCLUSION AND DISCUSSION

We have studied the neutron EDM induced by the CP-violating interactions up to the dimension-five operators. In order to derive the relation between the CP-violating interactions and the neutron EDM, we have used the QCD sum rule technique. There are several phenomenological parameters to estimate the relation numerically. Pospelov and Ritz also analyzed the neutron EDM by using the QCD sum rules [14,15], and they determined the low-energy constant λ_n within the framework in the QCD sum rules. On the other hand, we have extracted the λ_n parameter from lattice calculations. This approach allows us to reduce a theoretical uncertainty and leads to a conservative constraint on the CP violations. Our result is about 70% smaller compared with the one obtained by Pospelov and Ritz. There still remains a sizable uncertainty resulting from the QCD sum rules itself due to a choice of the Borel mass scale. We have estimated the uncertainty from the Borel mass scale by assuming that the single pole contribution is less than 30% of the double pole contributions. This assumption leads to the theoretical error of about $\mathcal{O}(1)$.

Finally, we briefly comment on the contribution of the CP-violating dimension-six operators. Among the dimension-six operators, the following operator, called the Weinberg operator:

$$\mathcal{L}_{\not{C}P} = \tfrac{1}{3} w f_{ABC} G^A_{\mu\nu} \tilde{G}^{B\nu\lambda} G^{C\mu}_{\lambda},$$

might be comparable to the quark EDM and CEDM contributions, since they suffer from the chiral suppression. The other CP-violating dimension-six operators are effective four-quark operators of light quarks, which are negligible in the neutron EDM in typical high-energy models, since the Wilson coefficients are suppressed by the quark masses.[7] In our QCD sum rule calculation it is found that the contribution from the Weinberg operator is $\mathcal{O}(\langle\bar{q}q\rangle^2)$ and thus subdominant. There are a lot of discussions on the significance of the Weinberg operator [29], though no consensus has been reached yet.

ACKNOWLEDGMENTS

One of the authors (J. H.) appreciates useful discussion with Yasumichi Aoki. This work is supported by Grant-in-Aid for Scientific research from the Ministry of Education, Science, Sports, and Culture (MEXT), Japan, No. 20244037, No. 20540252, No. 22244021, and No. 23104011 (J. H.), and also by World Premier International Research Center Initiative (WPI Initiative), MEXT, Japan. The work of N. N. is supported by the Japan Society for the Promotion of Science for Young Scientists.

[7] If the CP-violating four-quark operators include heavy quarks, the CEDMs for the light quarks and the Weinberg operators are radiatively induced by integration of the heavy quarks as shown in Ref. [28].

APPENDIX

In this appendix, we list some techniques which we use to carry out the calculation.

1. Quark condensates on the CP-violating background

In this section, we discuss the effects of the CP-violating interactions on the quark condensates as well as on the quark and gluon background fields. We begin by estimating it for the generic quark bilinear condensate $\langle 0|\bar{q}\Gamma q|0\rangle$, with Γ a 4×4 constant matrix for which the quark bilinear $\bar{q}\Gamma q$ is an Hermitian operator. Then, by using the results obtained there, we derive the relations between the quark condensates and the background fields.

First, we evaluate the quark bilinear $\bar{q}\Gamma q$ on the CP-violating background. The contribution of the QCD θ term at the leading order is evaluated as [30]

$$\langle 0|\bar{q}\Gamma q|0\rangle_{\theta_G} = i\int d^4x \langle 0|T\{\bar{q}(0)\Gamma q(0)\theta_G \frac{\alpha_s}{8\pi} \times G^a_{\mu\nu}(x)\tilde{G}^{a\mu\nu}(x)\}|0\rangle + \mathcal{O}(\theta^2). \quad (A1)$$

Substituting Eq. (5) into the above expression, we obtain

$$\langle 0|\bar{q}\Gamma q|0\rangle_{\theta_G} = i\int d^4x \langle 0|T\Big\{\bar{q}(0)\Gamma q(0)\frac{\theta_G}{2}\Big[\partial^\mu J_{5\mu}(x) - 2i\sum_{q=u,d,s} m_q\rho_q\bar{q}(x)\gamma_5 q(x)\Big]\Big\}|0\rangle + \mathcal{O}(\theta^2), \quad (A2)$$

with $\rho_q = \theta_q/\theta_Q$. The first term in the equation is calculated with the aid of the integration by parts:

$$\begin{aligned} & i\int d^4x \langle 0|T\Big\{\bar{q}(0)\Gamma q(0)\frac{\theta_G}{2}\partial^\mu J_{5\mu}(x)\Big\}|0\rangle \\ &= -\frac{i\theta_G}{2}\int d^4x \langle 0|[J^0_5(x), \bar{q}(0)\Gamma q(0)]\delta(x^0)|0\rangle \\ &= \frac{i\theta_G}{2}\rho_q\langle 0|\bar{q}\{\gamma_5, \Gamma\}q|0\rangle. \end{aligned} \quad (A3)$$

For the second term, we insert the intermediate states and keep only the contributions of the one-particle states of the pseudo Nambu-Goldstone bosons π^0 and η^0:

$$\begin{aligned} & -i\sum_{q=u,d,s}\int d^4x \langle 0|T\{\bar{q}(0)\Gamma q(0)\theta_G m_q\rho_q\bar{q}(x)i\gamma_5 q(x)\}|0\rangle \\ &= -\frac{\theta_G}{f_\pi m_\pi^2}(m_u\rho_u - m_d\rho_d)\langle\bar{q}q\rangle\langle 0|\bar{q}\Gamma q|\pi^0\rangle \\ &\quad -\frac{\theta_G}{\sqrt{3}f_\pi m_\eta^2}(m_u\rho_u + m_d\rho_d - 2m_s\rho_s)\langle\bar{q}q\rangle\langle 0|\bar{q}\Gamma q|\eta^0\rangle, \end{aligned} \quad (A4)$$

where f_π is the pion decay constant[8] and m_π and m_η denote the masses of π^0 and η^0, respectively.[9] As a result, we obtain

$$\begin{aligned}\langle 0|\bar{q}\Gamma q|0\rangle_{\theta_G} = &\frac{i\theta_G}{2}\rho_q\langle 0|\bar{q}\{\gamma_5,\Gamma\}q|0\rangle \\ &-\frac{\theta_G}{f_\pi m_\pi^2}(m_u\rho_u - m_d\rho_d)\langle\bar{q}q\rangle\langle 0|\bar{q}\Gamma q|\pi^0\rangle \\ &-\frac{\theta_G}{\sqrt{3}f_\pi m_\eta^2}(m_u\rho_u + m_d\rho_d - 2m_s\rho_s) \\ &\times\langle\bar{q}q\rangle\langle 0|\bar{q}\Gamma q|\eta^0\rangle. \end{aligned} \tag{A6}$$

Other contributions also may be evaluated through a similar procedure. For the contribution of the γ_5-mass terms,

$$\begin{aligned}\langle 0|\bar{q}\Gamma q|0\rangle_{\theta_q} = &-\frac{\theta_Q}{f_\pi m_\pi^2}(m_u\rho_u - m_d\rho_d)\langle\bar{q}q\rangle\langle 0|\bar{q}\Gamma q|\pi^0\rangle \\ &-\frac{\theta_Q}{\sqrt{3}f_\pi m_\eta^2}(m_u\rho_u + m_d\rho_d - 2m_s\rho_s) \\ &\times\langle\bar{q}q\rangle\langle 0|\bar{q}\Gamma q|\eta^0\rangle, \end{aligned} \tag{A7}$$

while for the contribution of the quark CEDM terms,

$$\begin{aligned}\langle 0|\bar{q}\Gamma q|0\rangle_{q\mathrm{CEDM}} = &\frac{1}{f_\pi m_\pi^2}\frac{m_0^2}{2}(\tilde{d}_u - \tilde{d}_d)\langle\bar{q}q\rangle\langle 0|\bar{q}\Gamma q|\pi^0\rangle \\ &+\frac{1}{\sqrt{3}f_\pi m_\eta^2}\frac{m_0^2}{2}(\tilde{d}_u + \tilde{d}_d - 2\tilde{d}_s) \\ &\times\langle\bar{q}q\rangle\langle 0|\bar{q}\Gamma q|\eta^0\rangle. \end{aligned} \tag{A8}$$

Furthermore, it is found that the quark EDMs induce no contribution.

Taking all of the contributions into account, we obtain the CP-violating contribution to the quark condensates as

$$\begin{aligned}&\langle 0|\bar{q}\Gamma q|0\rangle_{\not{C}P} \\ &= \frac{i\theta_G}{2}\rho_q\langle 0|\bar{q}\{\gamma_5,\Gamma\}q|0\rangle + \frac{1}{f_\pi m_\pi^2}\Big[\frac{m_0^2}{2}(\tilde{d}_u - \tilde{d}_d) \\ &\quad - \bar{\theta}(m_u\rho_u - m_d\rho_d)\Big]\langle\bar{q}q\rangle\langle 0|\bar{q}\Gamma q|\pi^0\rangle \\ &\quad + \frac{1}{\sqrt{3}f_\pi m_\eta^2}\Big[\frac{m_0^2}{2}(\tilde{d}_u + \tilde{d}_d - 2\tilde{d}_s) \\ &\quad - \bar{\theta}(m_u\rho_u + m_d\rho_d - 2m_s\rho_s)\Big]\langle\bar{q}q\rangle\langle 0|\bar{q}\Gamma q|\eta^0\rangle \\ &= \frac{i\theta_G}{2}\rho_q\langle 0|\bar{q}\{\gamma_5,\Gamma\}q|0\rangle. \end{aligned} \tag{A9}$$

[8]We use the PCAC relation for π^0,

$$\partial_\mu J_A^\mu(x) = -f_\pi m_\pi^2\pi(x), \tag{A5}$$

and a similar relation for η^0.

[9]The effect of the π^0-η^0 mixing is suppressed by a small factor of $(m_u - m_d)/m_s$, and we ignore it for brevity.

Here, the second equality comes from the conditions in Eq. (10). Thus, the choice of the quark mass phases in Eq. (12) reduces the contribution of the CP-violating interactions to the vacuum condensates into a quite simple expression.

Note that the CP-violating contribution to the quark condensates vanishes in the basis where the θ term is completely rotated out into the imaginary mass term. Thus, the choice of this basis, which is often adopted in the chiral Lagrangian approach, simplifies the calculation. In our paper, however, we remain in a general basis in order to display each contribution explicitly.

Next, we discuss the way of translating the quark and gluon background fields into their condensates. To begin with, we consider a single quark line $\chi^q_{a\alpha}(x)\bar{\chi}^q_{b\beta}(0)$. In this case, it is related with the quark condensate as follows:

$$\chi^q_{a\alpha}(x)\bar{\chi}^q_{b\beta}(0) = \langle\Omega_{\not{C}P}|q_{a\alpha}(x)\bar{q}_{b\beta}(0)|\Omega_{\not{C}P}\rangle_F. \tag{A10}$$

Using the Fierz identity, the right-hand side of the expression leads to

$$\begin{aligned}&\langle\Omega_{\not{C}P}|q_{a\alpha}(x)\bar{q}_{b\beta}(0)|\Omega_{\not{C}P}\rangle_F \\ &= -\frac{\delta_{ab}}{12}\Big[\langle\bar{q}(0)q(x)\rangle_{F,\not{C}P} + \gamma_5\langle\bar{q}(0)\gamma_5 q(x)\rangle_{F,\not{C}P} \\ &\quad + \gamma^\mu\langle\bar{q}(0)\gamma_\mu q(x)\rangle_{F,\not{C}P} - \gamma^\mu\gamma_5\langle\bar{q}(0)\gamma_\mu\gamma_5 q(x)\rangle_{F,\not{C}P} \\ &\quad + \frac{1}{2}\sigma^{\mu\nu}\langle\bar{q}(0)\sigma_{\mu\nu}q(x)\rangle_{F,\not{C}P}\Big]_{\alpha\beta}. \end{aligned} \tag{A11}$$

These quark condensate terms are evaluated by conducting the short-distance expansion of the quark field in the Fock-Schwinger gauge as

$$q(x) = q(0) + x^\mu D_\mu q(0) + \cdots. \tag{A12}$$

We note that in this gauge one does not need to care about Wilson-line operators for the quark fields. (See Appendix A 3.)

In the case of CP-even vacuum, the Lorentz and CP invariance of vacuum tell us that

$$\langle\bar{q}\gamma_5 q\rangle = \langle\bar{q}\gamma_\mu q\rangle = \langle\bar{q}\gamma_\mu\gamma_5 q\rangle = 0. \tag{A13}$$

On the other hand, on an electromagnetic background, $\langle\bar{q}\sigma_{\mu\nu}q\rangle$ may have a nonzero vacuum expectation value proportional to the electromagnetic field strength $F_{\mu\nu}$. The electromagnetic field dependence for quark condensates is given as

$$\langle\bar{q}\sigma_{\mu\nu}q\rangle_F = \chi_q F_{\mu\nu}\langle\bar{q}q\rangle, \tag{A14}$$

where χ_q is called the quark condensate magnetic susceptibility [22]. Similar parametrization is used for the condensates including the gluon background field:

$$g_s\langle\bar{q}G^A_{\mu\nu}T^A q\rangle_F = \kappa_q F_{\mu\nu}\langle\bar{q}q\rangle, \tag{A15}$$

$$2g_s\langle\bar{q}\gamma_5\tilde{G}^A_{\mu\nu}T^A q\rangle_F = i\xi_q F_{\mu\nu}\langle\bar{q}q\rangle. \tag{A16}$$

As in Ref. [22], we assume χ_q, κ_q, and ξ_q to be proportional to the quark charge:

$$\chi_q = e_q\chi, \qquad \kappa_q = e_q\kappa, \qquad \xi_q = e_q\xi. \tag{A17}$$

This assumption corresponds to neglecting of the closed-loop contribution with gluon exchange.

Now let us consider the effect of the CP-violating interaction in Eq. (2) to the quark condensates. By using Eq. (A9) and the expansion in Eq. (A12), we evaluate each quark condensate on the CP-violating background as follows (with omitting the subscriptions F and $\not{C}P$ for simplicity as long as it is not confusing):

$$\langle\bar{q}(0)q(x)\rangle = \langle\bar{q}q\rangle, \tag{A18}$$

$$\langle\bar{q}(0)\gamma_5 q(x)\rangle = \langle\bar{q}\gamma_5 q\rangle_{\not{C}P} = i\theta_{G\rho q}\langle\bar{q}q\rangle, \tag{A19}$$

$$\begin{aligned}\langle\bar{q}(0)\gamma_\mu q(x)\rangle &= x^\nu\langle\bar{q}\gamma_\mu D_\nu q\rangle \\ &= \frac{1}{2}x^\nu\langle\bar{q}\{\gamma_\mu D_\nu + \gamma_\nu D_\mu\}q\rangle \\ &\quad + \frac{1}{2}x^\nu\langle\bar{q}\{\gamma_\mu D_\nu - \gamma_\nu D_\mu\}q\rangle \\ &= \frac{1}{4}x^\nu g_{\mu\nu}\langle\bar{q}\not{D}q\rangle + \frac{i}{4}x^\nu\langle\bar{q}\not{D}, \sigma_{\mu\nu}]q\rangle \\ &= -\frac{i}{4}m_q x_\mu\langle\bar{q}q\rangle,\end{aligned} \tag{A20}$$

where we use the classical equations of motion in the quark condensates and move the covariant derivatives with help of total derivative. The validity of this procedure is discussed in Appendix A 2. Furthermore,

$$\begin{aligned}\langle\bar{q}(0)\gamma_\mu\gamma_5 q(x)\rangle &= x^\nu\langle\bar{q}\gamma_\mu D_\nu\gamma_5 q\rangle \\ &= \frac{1}{4}x^\nu g_{\mu\nu}\langle\bar{q}\not{D}\gamma_5 q\rangle + \frac{i}{4}x^\nu\langle\bar{q}[\not{D}, \sigma_{\mu\nu}]\gamma_5 q\rangle \\ &= \frac{i}{2}m_q e_q\chi(\bar{\theta}\rho_q F_{\mu\nu} + \tilde{F}_{\mu\nu})x^\nu\langle\bar{q}q\rangle \\ &\quad + \frac{i}{2}\left(d_q + \left[\kappa - \frac{1}{2}\xi\right]e_q\tilde{d}_q\right)x^\nu F_{\mu\nu}\langle\bar{q}q\rangle,\end{aligned} \tag{A21}$$

and

$$\begin{aligned}\langle\bar{q}(0)\sigma_{\mu\nu}q(x)\rangle &= \langle\bar{q}\sigma_{\mu\nu}q\rangle \\ &= \langle\bar{q}\sigma_{\mu\nu}q\rangle_{CP\,\text{even}} + \langle\bar{q}\sigma_{\mu\nu}q\rangle_{\not{C}P} \\ &= e_q\chi[F_{\mu\nu} - \theta_G\rho_q\tilde{F}_{\mu\nu}]\langle\bar{q}q\rangle.\end{aligned} \tag{A22}$$

Taking the above discussion into account and using the relation

$$F_{\mu\nu}x^\mu\gamma^\nu\gamma_5 = +\tfrac{1}{4}\{\tilde{F}\cdot\sigma, \not{x}\} \tag{A23}$$

and

$$F\cdot\sigma = i\tilde{F}\cdot\sigma\gamma_5, \tag{A24}$$

we finally obtain the expression for the single quark line as follows:

$$\begin{aligned}\chi^q_{a\alpha}(x)\bar{\chi}^q_{b\beta}(0) &= -\frac{\delta_{ab}}{12}(1 + i\theta_G\rho_q\gamma_5)_{\alpha\beta}\langle\bar{q}q\rangle + \frac{i}{48}\delta_{ab}\not{x}_{\alpha\beta}m_q\langle\bar{q}q\rangle - \frac{i}{96}\delta_{ab}\left[\bar{\theta}m_q\rho_q e_q\chi + d_q + \left(\kappa - \frac{1}{2}\xi\right)e_q\tilde{d}_q\right] \\ &\quad \times\{\tilde{F}\cdot\sigma, \not{x}\}_{\alpha\beta}\langle\bar{q}q\rangle + \frac{i}{96}m_q e_q\chi\delta_{ab}\{F\cdot\sigma, \not{x}\}_{\alpha\beta}\langle\bar{q}q\rangle - \frac{i}{24}e_q\chi\delta_{ab}(\tilde{F}\cdot\sigma\gamma_5[1 + i\rho_q\theta_G\gamma_5])_{\alpha\beta}\langle\bar{q}q\rangle.\end{aligned} \tag{A25}$$

Last, we evaluate the interaction part of the quark and gluon background fields:

$$g_s\chi^q_{a\alpha}(x)\chi^{-q}_{b\beta}(0)[G_{\mu\nu}]_{cd} = \langle g_s q_{a\alpha}(x)[G_{\mu\nu}]_{cd}\bar{q}_{b\beta}(0)\rangle_{F,\not{C}P}. \tag{A26}$$

Again, we use the Fierz identity and the short-distance expansion of the quark field, and through a similar calculation, we find the following results:

$$\begin{aligned}g_s\chi^q_{a\alpha}(x)\bar{\chi}^q_{b\beta}(0)[G_{\mu\nu}]_{cd} &= -\frac{1}{32}\left(\delta_{ad}\delta_{bc} - \frac{1}{3}\delta_{ab}\delta_{cd}\right)\langle\bar{q}q\rangle\times\left[e_q\left(\kappa F_{\mu\nu} - \frac{i}{2}\xi\tilde{F}_{\mu\nu}\gamma_5\right)(1 + i\theta_G\rho_q\gamma_5)\right. \\ &\quad - \frac{i}{4}m_q e_q\not{x}\left(\kappa F_{\mu\nu} + \frac{1}{2}\bar{\theta}\rho_q\xi\tilde{F}_{\mu\nu}\right) - \frac{i}{24}m_q m_0^2\epsilon_{\mu\nu\rho\sigma}x^\rho\gamma^\sigma\gamma_5 - \frac{i}{24}\bar{\theta}m_q\rho_q m_0^2(x_\mu\gamma_\nu\gamma_5 - x_\nu\gamma_\mu\gamma_5) \\ &\quad \left. - \frac{1}{12}m_0^2\sigma_{\mu\nu} - \frac{i}{12}m_0^2\theta_G\rho_q\sigma_{\mu\nu}\gamma_5\right]_{\alpha\beta}.\end{aligned} \tag{A27}$$

2. EQUATIONS OF MOTION

Let us discuss the validity of using classical equations of motion for quark condensates. We investigate the following quantity:

$$\langle 0|\bar{q}\Gamma(i\not{D} - m_q)q|0\rangle_\theta, \tag{A28}$$

where Γ is a (c-number) 4×4 matrix. The subscript indicates that this quantity is evaluated in the θ vacuum. One may readily generalize the discussion here for the case with other CP-violating sources. The discussion presented in this section is based on Ref. [31].

First, we define the generating functional $Z[\eta]_\theta$ on the same background:

$$Z[\eta]_\theta \equiv \int \mathcal{D}\bar{q}\mathcal{D}q \exp\left[i\int d^4x\{\mathcal{L} + \eta\bar{q}\Gamma(i\not{D} - m_q)q\}\right]. \tag{A29}$$

Here, the Lagrangian density $\mathcal{L}$ is

$$\mathcal{L} = \bar{q}(i\not{D} - m_q)q. \tag{A30}$$

The functional derivative of the generating function with respect to the function η yields Eq. (A28), that is,

$$\langle 0|\bar{q}\Gamma(i\not{D} - m_q)q|0\rangle_\theta \propto \frac{\delta Z[\eta]_\theta}{\delta\eta(0)}\bigg|_{\eta=0}. \tag{A31}$$

Now we replace the integration variable $\bar{q}$ with a new integration variable $\bar{q}'$ as

$$\bar{q} \to \bar{q}' = \bar{q} - \eta\bar{q}\Gamma. \tag{A32}$$

Since this step does not change the integral, then we obtain

$$Z[\eta] = \int \mathcal{D}\bar{q}\mathcal{D}q\left[\mathrm{Det}\left\{\frac{\delta\bar{q}'}{\delta\bar{q}}\right\}\right]^{-1}\exp\left[i\int d^4x\mathcal{L} + \mathcal{O}(\eta^2)\right], \tag{A33}$$

where the inverse of the Jacobian comes from the transformation of the measure for the fermionic variable.

Next, we evaluate the Jacobian in the expression above. Since we are interested in the first-order derivative of the generating function, we expand the Jacobian in η and keep only terms linear in η:

$$\frac{\delta\bar{q}'_\beta(y)}{\delta\bar{q}_\alpha(x)} = \delta_{\alpha\beta}\delta^4(x-y) - \eta(y)\Gamma_{\alpha\beta}\delta^4(x-y) + \mathcal{O}(\eta^2). \tag{A34}$$

Using the identity

$$\mathrm{Det}\, M = \exp \mathrm{Tr}\ln M, \tag{A35}$$

we readily obtain the Jacobian as

$$\mathrm{Det}\left\{\frac{\delta\bar{q}'}{\delta\bar{q}}\right\} = \exp\left[-\mathrm{Tr}(\Gamma)\int d^4x\eta(x)\delta^4(x-x)\right]. \tag{A36}$$

It is found that if the trace of the matrix Γ is nonzero, the Jacobian yields a singular factor, while if it vanishes, we need careful treatment for evaluating this term. So, in the following discussion, we divide Γ into two types; one is the term proportional to the unit matrix, and the other is the traceless part.

First, we consider the case $\Gamma \propto \mathbb{1}$. Using Eqs. (A31), (A33), and (A36), we obtain the following equation:

$$\langle 0|\bar{q}\Gamma(i\not{D} - m_q)q|0\rangle_\theta = -i\mathrm{Tr}(\Gamma)\delta^4(0). \tag{A37}$$

Once we carry out the normal ordering for the composite operator $\bar{q}\Gamma(i\not{D} - m_q)q$, the singular factor in the right-hand side vanishes. Thus we conclude that, after normal ordering,

$$\langle 0|\bar{q}\Gamma(i\not{D} - m_q)q|0\rangle_\theta = 0, \tag{A38}$$

when $\Gamma \propto \mathbb{1}$. This equation implies that we may use the equations of motion for quark condensates in this case.

Next, we shall turn to the traceless part. In this case, the Jacobian in Eq. (A36) is written in terms of the anomaly function defined as

$$\mathcal{A}(x) \equiv 2\mathrm{Tr}(\Gamma)\delta^4(x-x). \tag{A39}$$

With this function, Eq. (A36) leads to

$$\mathrm{Det}^{-1}\left\{\frac{\delta\bar{q}'}{\delta\bar{q}}\right\} = \exp\left[+\frac{1}{2}\int d^4x\eta(x)\mathcal{A}(x)\right]. \tag{A40}$$

The usual analysis for the chiral anomaly tells us that the function $\mathcal{A}(x)$ in Eq. (A39) does not vanish only for the case $\Gamma = \gamma_5$. Thus, if $\Gamma \neq \gamma_5$, Eq. (A38) is satisfied. When $\Gamma = \gamma_5$, on the other hand, the function $\mathcal{A}(x)$ is evaluated as

$$\mathcal{A}(x) = \frac{\alpha_s}{4\pi}G^A_{\mu\nu}\tilde{G}^{A\mu\nu}. \tag{A41}$$

From Eqs. (A31), (A33), and (A40), we eventually find that

$$\langle 0|\bar{q}\gamma_5(i\not{D} - m_q)q|0\rangle_\theta = -\frac{i\alpha_s}{8\pi}\langle 0|G^A_{\mu\nu}\tilde{G}^{A\mu\nu}|0\rangle_\theta. \tag{A42}$$

This expression is simplified via the axial current anomaly equation:

$$\partial^\mu(\bar{q}\gamma_\mu\gamma_5 q) = 2im_q\bar{q}\gamma_5 q + \frac{\alpha_s}{4\pi}G^A_{\mu\nu}\tilde{G}^{A\mu\nu}. \tag{A43}$$

Then, Eq. (A42) leads to

$$\langle 0|\bar{q}\gamma_5 i\not{D}q|0\rangle_\theta = \frac{1}{2i}\langle 0|\partial^\mu(\bar{q}\gamma_\mu\gamma_5 q)|0\rangle_\theta = 0. \tag{A44}$$

Therefore, we are not able to use the classical equations of motion for quark condensates in this case.

As a result, we find that

$$\langle 0|\bar{q}\Gamma i\not{D}q|0\rangle_\theta = \begin{cases}\langle 0|\bar{q}\Gamma m_q q|0\rangle_\theta & (\text{for } \Gamma = \mathbb{1}, \gamma_\mu, \gamma_\mu\gamma_5, \sigma_{\mu\nu}) \\ 0 & (\text{for } \Gamma = \gamma_5).\end{cases} \tag{A45}$$

Also, its conjugate leads to

$$-\langle 0|\bar{q}i\overleftarrow{\not{D}}\Gamma q|0\rangle_\theta = \begin{cases}\langle 0|\bar{q}m_q\Gamma q|0\rangle_\theta & (\text{for } \Gamma = \mathbb{1}, \gamma_\mu, \gamma_\mu\gamma_5, \sigma_{\mu\nu}) \\ 0 & (\text{for } \Gamma = \gamma_5).\end{cases} \tag{A46}$$

Before concluding the section, we add a comment on the condensate of the total derivative terms. As we have already conducted in Eq. (A44), the Lorentz invariance of vacuum implies that condensates of the divergence of quark bilinear always vanish, i.e.,

$$\langle 0|\partial^\mu(\bar{q}\Gamma_\mu q)|0\rangle = \partial^\mu\langle 0|(\bar{q}\Gamma_\mu q)|0\rangle = 0, \tag{A47}$$

with Γ_μ a constant matrix which transforms as a vector under the Lorentz transformation, such as γ_μ, $\gamma_\mu\gamma_5$, or so

on. On the other hand, the total derivative of the quark bilinear is written as

$$\partial^\mu(\bar{q}\Gamma_\mu q) = (\partial^\mu \bar{q})\Gamma_\mu q + \bar{q}\Gamma_\mu(\partial^\mu q) = \bar{q}\,\overleftarrow{D}^\mu\,\Gamma_\mu q + \bar{q}\Gamma_\mu D^\mu q. \tag{A48}$$

Thus we find

$$\langle 0|\bar{q}\,\overleftarrow{D}^\mu\,\Gamma_\mu q|0\rangle = -\langle \bar{q}\Gamma_\mu D^\mu q|0\rangle. \tag{A49}$$

3. WILSON LINE IN FOCK-SCHWINGER GAUGE

Quark fields $q(x)$ are always accompanied by an appropriate Wilson-line operator in order to compensate the different gauge transformation property of the quark fields at different space-time points. In the Fock-Schwinger gauge, however, one may always choose a particular path which makes the Wilson-line operator equal to identity [32]. We show this statement in the following. The Wilson line is written as

$$U_P(x,0) = P\left\{\exp\left[ig_s\int_0^1 ds\,\frac{dx'^\mu(s)}{ds}G^A_\mu(x'(s))T^A\right]\right\}, \tag{A50}$$

where

$$x'(0) = 0, \qquad x'(1) = x, \tag{A51}$$

and P denotes path ordering. This operator depends on the choice of the integration path. Here we take a path such that

$$x'(s) = sx. \tag{A52}$$

Then,

$$U_P(x,0) = P\left\{\exp\left[ig_s\int_0^1 ds x^\mu G^A_\mu(sx)T^A\right]\right\}. \tag{A53}$$

In the Fock-Schwinger field, the gluon field is expanded as

$$G_\mu(x) = \frac{1}{2\cdot 0!}x^\nu G_{\nu\mu}(0) + \frac{1}{3\cdot 1!}x^\alpha x^\nu(D_\alpha G_{\nu\mu}(0)) + \frac{1}{4\cdot 2!}x^\alpha x^\beta x^\nu(D_\alpha D_\beta G_{\nu\mu}(0)) + \cdots. \tag{A54}$$

Inserting this expression into Eq. (A53), we readily find that all terms in the exponential vanish due to the antisymmetric property of the gluon field strength tensor. Therefore,

$$U_P(x,0) = 1. \tag{A55}$$

[1] K. Nakamura *et al.* (Particle Data Group Collaboration), J. Phys. G **37**, 075021 (2010).
[2] N. Cabibbo, Phys. Rev. Lett. **10**, 531 (1963).
[3] M. Kobayashi and T. Maskawa, Prog. Theor. Phys. **49**, 652 (1973).
[4] C. A. Baker *et al.*, Phys. Rev. Lett. **97**, 131801 (2006).
[5] K. Bodek *et al.*, arXiv:0806.4837.
[6] D. H. Beck *et al.* (nEDM Collaboration), arXiv:1111.1273.
[7] S. N. Balashov *et al.*, arXiv:0709.2428.
[8] Y. Arimoto *et al.* (NOP Collaboration), http://j-parc.jp/researcher/Hadron/en/pac_1001/pdf/KEK_J-PARC-PAC2009-11.pdf.
[9] Y. Masuda, in Proceedings of UCN2010, RCNP, Japan (unpublished).
[10] J. Hisano, M. Nagai, and P. Paradisi, Phys. Lett. B **642**, 510 (2006); Phys. Rev. D **78**, 075019 (2008); **80**, 095014 (2009).
[11] E. Shintani *et al.*, Phys. Rev. D **72**, 014504 (2005); F. Berruto, T. Blum, K. Orginos, and A. Soni, Phys. Rev. D **73**, 054509 (2006); E. Shintani *et al.*, Phys. Rev. D **75**, 034507 (2007); E. Shintani, S. Aoki, and Y. Kuramashi, Phys. Rev. D **78**, 014503 (2008); S. Aoki, R. Horsley, T. Izubuchi, Y. Nakamura, D. Pleiter, P. E. L. Rakow, G. Schierholz, and J. Zanotti, arXiv:0808.1428.
[12] M. A. Shifman, A. I. Vainshtein, and V. I. Zakharov, Nucl. Phys. **B147**, 385 (1979); **B147**, 448 (1979).
[13] A. Pich and E. de Rafael, Nucl. Phys. **B367**, 313 (1991); J. Hisano and Y. Shimizu, Phys. Rev. D **70**, 093001 (2004); K. Ottnad, B. Kubis, U. G. Meissner, and F. K. Guo, Phys. Lett. B **687**, 42 (2010).
[14] M. Pospelov and A. Ritz, Phys. Rev. Lett. **83**, 2526 (1999); Nucl. Phys. **B573**, 177 (2000).
[15] M. Pospelov and A. Ritz, Phys. Rev. D **63**, 073015 (2001).
[16] R. D. Peccei and H. R. Quinn, Phys. Rev. Lett. **38**, 1440 (1977).
[17] R. J. Crewther, P. Di Vecchia, G. Veneziano, and E. Witten, Phys. Lett. **88B**, 123 (1979); **91B**, 487(E) (1980).
[18] V. M. Belyaev and B. L. Ioffe, Zh. Eksp. Teor. Fiz. **83**, 876 (1982) [Sov. Phys. JETP **56**, 493 (1982)].
[19] L. J. Reinders, H. Rubinstein, and S. Yazaki, Phys. Rep. **127**, 1 (1985); S. Narison, Lect. Notes Phys. **26**, 1 (1989); M. A. Shifman, Prog. Theor. Phys. Suppl. **131**, 1 (1998).
[20] S. Narison, Phys. Lett. B **666**, 455 (2008).
[21] V. A. Novikov, M. A. Shifman, A. I. Vainshtein, and V. I. Zakharov, Fortschr. Phys. **32**, 585 (1984).
[22] B. L. Ioffe and A. V. Smilga, Nucl. Phys. **B232**, 109 (1984).
[23] Y. Aoki *et al.* (RBC-UKQCD Collaboration), Phys. Rev. D **78**, 054505 (2008).
[24] D. B. Leinweber, Ann. Phys. (N.Y.) **254**, 328 (1997).
[25] M. Pospelov and A. Ritz, Ann. Phys. (N.Y.) **318**, 119 (2005).
[26] I. I. Kogan and D. Wyler, Phys. Lett. B **274**, 100 (1992).

[27] I. I. Y. Bigi and N. G. Uraltsev, Sov. Phys. JETP **73**, 198 (1991).
[28] J. Hisano, K. Tsumura, and M. J. S. Yang, arXiv:1205.2212.
[29] D. A. Demir, M. Pospelov, and A. Ritz, Phys. Rev. D **67**, 015007 (2003).
[30] M. A. Shifman, A. I. Vainshtein, and V. I. Zakharov, Nucl. Phys. **B166**, 493 (1980).
[31] H. D. Politzer, Nucl. Phys. **B172**, 349 (1980).
[32] S. V. Mikhailov and A. V. Radyushkin, Phys. Rev. D **45**, 1754 (1992).

Published for SISSA by Springer

Received: April 18, 2013
Accepted: June 19, 2013
Published: July 8, 2013

Decoupling can revive minimal supersymmetric SU(5)

Junji Hisano,[a,b] **Daiki Kobayashi,**[a] **Takumi Kuwahara**[a] **and Natsumi Nagata**[a,c]

[a] *Department of Physics, Nagoya University, Nagoya 464-8602, Japan*

[b] *Kavli Institute for the Physics and Mathematics of the Universe (WPI), Todai Institutes for Advanced Study, the University of Tokyo, Kashiwa 277-8568, Japan*

[c] *Department of Physics, University of Tokyo, Tokyo 113-0033, Japan*

E-mail: hisano@eken.phys.nagoya-u.ac.jp, koba@th.phys.nagoya-u.ac.jp, kuwahara@th.phys.nagoya-u.ac.jp, natsumi@eken.phys.nagoya-u.ac.jp

Abstract: We revisit proton decay via the color-triplet Higgs multiplets in the minimal supersymmetric grand unified model with heavy sfermions. Although the model has been believed to be excluded due to the too short lifetime of proton, we have found that it is possible to evade the experimental constraints on the proton decay rate if the supersymmetric particles have masses much heavier than the electroweak scale. With such heavy sfermions, the 126 GeV Higgs boson is naturally explained, while they do not spoil the gauge coupling unification and the existence of dark matter candidates. Since the resultant proton lifetime lies in the regions which may be reached in the future experiments, proton decay searches may give us a chance to verify the scenario as well as the supersymmetric grand unified models.

Keywords: Supersymmetry Phenomenology

ArXiv ePrint: 1304.3651

© SISSA 2013

doi:10.1007/JHEP07(2013)038

JHEP07(2013)038

Contents

1 Introduction **1**

2 High-scale SUSY **3**

3 Proton decay in the minimal SUSY SU(5) GUT **4**

4 Results **8**

5 Conclusions and discussion **12**

A Renormalization factors **13**
A.1 Long-range factors 13
A.2 Short-range factors 14

B Formulae for proton decay rate **18**

1 Introduction

The discovery of the Higgs boson [1, 2] has opened the way for physics beyond the Standard Model (SM). It is certainly a striking hint for understanding the high-energy physics, as elementary scalar particles may play an important role in realizing our complicated world with apparent broken symmetries. The theories with supersymmetry (SUSY) naturally include such scalar particles; the Higgs boson might be a superpartner of chiral fermions, called higgsinos. Besides, there exists a set of scalar particles for each SM fermion, as well as adjoint fermions for the SM gauge bosons. Then, astonishingly enough, we find that with these extra particles the gauge coupling constants of the SM are to be unified at a certain high-energy scale with great accuracy [3–7]. This observation motivates us to study the supersymmetric grand unified theories (SUSY GUTs) [8, 9].

The SUSY GUTs predict an exciting phenomenon: proton decay. It is induced by the exchanges of the color-triplet Higgs multiplets and the X-bosons, and their effects are described in terms of the dimension-five and -six effective operators, respectively. In the minimal SUSY SU(5) GUT [8, 9], which is a simple supersymmetric extension of the original SU(5) GUT [10], the former process yields the dominant decay modes, such as $p \to K^+\bar{\nu}$. The lifetime of the channel is estimated as $\tau(p \to K^+\bar{\nu}) \lesssim 10^{30}$ yrs [11, 12], with the SUSY particles, in particular those of the third generation, assumed to have masses of around the electroweak scale. On the other hand, the Super-Kamiokande experiment gives stringent limits on the channels: $\tau(p \to K^+\bar{\nu}) > 4.0 \times 10^{33}$ yrs [13]. This contradiction makes it widely believed that the minimal SUSY SU(5) GUT has been already excluded and, therefore, needs some extensions in order to suppress the dimension-five proton decay.

JHEP07(2013)038

As is often the case with SUSY models, the SUSY GUTs are usually discussed within the context of the low-scale supersymmetry. Recently, experiments at the Large Hadron Collider (LHC) provide limits on the SUSY models. The ATLAS and CMS Collaborations have been searching for the SUSY particles and imposed severe constraints on their masses, especially those of squarks and gluino [14–16]. The mass bounds have began to exceed 1 TeV and, thus, the low-energy SUSY models are confronted with difficulties. Moreover, the observed mass of the Higgs boson around 126 GeV [1, 2] might also indicate the SUSY scale is considerably higher than the electroweak scale; in the minimal SUSY Standard Model (MSSM), the mass of the lightest Higgs boson is below the Z-boson mass at tree level, so sufficient mass difference between stops and top quark is required in order to raise the Higgs boson mass through the radiative corrections [17–21].

In fact, the SUSY models with heavy SUSY particles have a lot of attractive features [22–28]. First of all, since the flavor changing neutral current (FCNC) processes and/or the electric dipole moments induced by SUSY particles are suppressed by their masses, the SUSY flavor and CP problems [29] are relaxed when the masses are considerably heavy. As mentioned to above, the heavy sfermions yield sufficient radiative corrections to lift the Higgs mass up to 126 GeV [30–33]. They do not spoil the gauge coupling unification since the sfermions form complete SU(5) multiplets. Actually, it turns out that the unification is improved in the sense that the required threshold corrections at the GUT scale tend to be reduced [34]. As for the cosmology, the gravitino problem is avoided because of the high-scale SUSY breaking, and the thermal leptogenesis scenario well works with high reheating temperature [35]. Further, this high-scale SUSY scenario naturally accommodates dark matter (DM) candidates, which might be detected in future dark matter experiments directly [36–39] and indirectly [32, 40, 41]. Thus, with the recent LHC results considered, the high-scale SUSY scenario is even promising from a phenomenological point of view.

Interestingly, this scenario also provides an alternative solution to the problem regarding the dimension-five proton decay in the minimal SUSY GUT. The dimension-five operators generated via the color-triplet Higgs exchange contain squarks and/or sleptons in their external lines. These fields are to be integrated out below the SUSY scale through the wino or higgsino exchanging processes, and then the four-Fermi operators, suppressed by the sfermion masses, are induced. Hence, their effects are expected to be extremely reduced when the SUSY scale is much higher than the electroweak scale.

In this paper, we study such possibilities within the context of the high-scale SUSY scenario. We will find that the minimal SUSY SU(5) GUT actually evades the constraints from the proton decay experiments with the SUSY braking scales which naturally explain the 126 GeV Higgs boson and the existence of dark matter in the Universe. The resultant proton lifetime lies in the regions which may be reached in the future proton decay experiments. Therefore, although the high-scale SUSY scenario is hard to be probed in the collider experiments, the proton decay searches may give us a chance to verify the scenario as well as the existence of supersymmetry and the grand unification.

This paper is organized as follows: In section 2, a high-scale SUSY model which we discuss in this work and its phenomenology are briefly explained. In the next section, we

JHEP07(2013)038

give a set of formulae for evaluating the proton decay rate via the dimension-five operators. Then, we show the resultant proton lifetime in the model, and compare it with current experimental limits in section 4. Section 5 is devoted to conclusions and discussion.

2 High-scale SUSY

To begin with, we describe a high-scale SUSY model which we deal with in the following discussion. Assume that there exists a SUSY breaking hidden sector where the SUSY breaking is triggered by a chiral superfield Z which is not a gauge singlet. Then, with a generic form of Kähler potential, all the scalar bosons except the lightest Higgs boson acquire masses of

$$M_S \sim \frac{F_Z}{M_*}\,, \tag{2.1}$$

with F_Z and M_* the F-component vacuum expectation value (VEV) of the field Z and the mediation scale of the SUSY breaking, respectively.The gravitino mass is $m_{3/2} = F_Z/\sqrt{3}M_{\rm Pl}$, and it is the same order as the scalar masses when M_* is around the Planck scale, $M_{\rm Pl}$. The soft masses for the two doublet Higgses and the μ-term are fine-tuned in order to realize the electroweak symmetry breaking at the proper scale. The gaugino masses, on the other hand, are not generated by the dimension-five operators like

$$\int d^2\theta\ Z{\rm Tr}[W^\alpha W_\alpha]\,, \tag{2.2}$$

since the symmetry under which the superfield Z is charged prohibits such an operator. Here, W_α denotes the gauge field-strength chiral superfield. Instead, they are induced by the anomaly mediation mechanism [42, 43]:

$$M_a = \frac{b_a g_a^2}{16\pi^2} m_{3/2}\,, \tag{2.3}$$

where M_1, M_2, and M_3 are the masses of bino, wino, and gluino, respectively, and b_a are the one-loop beta-function coefficients of the gauge coupling constants g_a ($a = 1,\ 2$, and 3 for $\mathrm{U}(1)_Y$, $\mathrm{SU}(2)_L$, and $\mathrm{SU}(3)_C$, respectively). This expression tells us that the gaugino masses are suppressed by one-loop factors compared with the gravitino mass. Similarly, since we assume that the superfield which breaks supersymmetry is not a gauge-singlet, the A-terms are generated with the suppression by the loop factors. Finally, the higgsino mass, μ_H, is somewhat model-dependent; it might lie around the same order of gaugino masses when some additional symmetries exist, or be as large as gravitino masses if it is generated by the Kähler potential. Thus we regard it as a free parameter in the following discussion.

In this scenario, the lightest SUSY particle (LSP) is either wino, which turns out to be the lightest gaugino, or the lighter higgsino. Then, it is found that in any case the LSP may explain the dark matter in the Universe. Indeed, the thermal relic abundance of wino and higgsino DM with a mass of 2.7–3.0 TeV [44] and 1 TeV [45], respectively, accounts for the observed density of DM. With relatively small masses, the non-thermal production of them also might be consistent with the observation [46, 47]. The wino or higgsino DM in this model implies sfermion masses lie around 10^2–10^3 TeV.

JHEP07(2013)038

From now on, we assume the sfermions are nearly degenerate in mass, and their masses are collectively denoted by M_S. The mass is supposed to be $M_S \simeq 10^2$–10^3 TeV, and either wino or higgsino is assumed to be the LSP. Models with such a mass spectrum and their phenomenology have been enthusiastically studied in the previous literature [48–55].

As mentioned to in the Introduction, the mass spectrum does not spoil the gauge coupling unification [23, 24], since the sfermions are embedded in the complete multiplets of SU(5). In fact, the unification may be improved [34]; a renormalization group analysis reveals that all of the GUT scale particles, especially the color-triplet Higgs multiplets, possibly lie around the GUT scale $\simeq 10^{16}$ GeV, contrary to the case of the low-energy SUSY. It indicates that the threshold corrections to the gauge coupling constants at the GUT scale are reduced in the high-scale SUSY scenario. Thus, the SUSY GUTs are still well-motivated.

3 Proton decay in the minimal SUSY SU(5) GUT

In this section, we review the proton decay in the minimal SUSY SU(5) GUT. In this model, the MSSM matter fields are embedded in a $\bar{\mathbf{5}} \oplus \mathbf{10}$ representation. The $\mathrm{SU}(2)_L$ singlet down-type quarks $\bar{D}$ and doublet leptons L are incorporated into the $\bar{\mathbf{5}}$ fields, Φ, while the $\mathrm{SU}(2)_L$ singlet up-type quarks, $\bar{U}$, doublet quarks, Q, and singlet leptons, $\bar{E}$, are formed into the $\mathbf{10}$ representations, Ψ. Here all the superfields are expressed in terms of the left-handed chiral superfields. The explicit form of the multiplets is

$$\Phi = \begin{pmatrix} \bar{D}_1 \\ \bar{D}_2 \\ \bar{D}_3 \\ E \\ -N \end{pmatrix}, \qquad \Psi = \frac{1}{\sqrt{2}} \begin{pmatrix} 0 & \bar{U}_3 & -\bar{U}_2 & U^1 & D^1 \\ -\bar{U}_3 & 0 & \bar{U}_1 & U^2 & D^2 \\ \bar{U}_2 & -\bar{U}_1 & 0 & U^3 & D^3 \\ -U^1 & -U^2 & -U^3 & 0 & \bar{E} \\ -D^1 & -D^2 & -D^3 & -\bar{E} & 0 \end{pmatrix}, \tag{3.1}$$

with

$$L = \begin{pmatrix} N \\ E \end{pmatrix}, \qquad Q^\alpha = \begin{pmatrix} U^\alpha \\ D^\alpha \end{pmatrix}. \tag{3.2}$$

Here, $\alpha = 1, 2, 3$ denotes the color index. The MSSM Higgs superfields, on the other hand, are embedded into a pair of $\mathbf{5}$ and $\bar{\mathbf{5}}$ superfields accompanied with the new Higgs superfields H_C^α and $\bar{H}_{C\alpha}$ called the color-triplet Higgs multiplets:

$$H = \begin{pmatrix} H_C^1 \\ H_C^2 \\ H_C^3 \\ H_u^+ \\ H_u^0 \end{pmatrix}, \qquad \bar{H} = \begin{pmatrix} \bar{H}_{C1} \\ \bar{H}_{C2} \\ \bar{H}_{C3} \\ H_d^- \\ -H_d^0 \end{pmatrix}, \tag{3.3}$$

where the last two components are corresponding to the MSSM Higgs superfields,

$$H_u = \begin{pmatrix} H_u^+ \\ H_u^0 \end{pmatrix}, \qquad H_d = \begin{pmatrix} H_d^0 \\ H_d^- \end{pmatrix}. \tag{3.4}$$

JHEP07(2013)038

Exchanges of the color-triplet Higgs multiplets induce the baryon-number violating interactions. They are coupled with the ordinary matter fields by the Yukawa coupling terms in the superpotential:[1]

$$W_{\text{Yukawa}} = \frac{1}{4} h^{ij} \epsilon_{abcde} \Psi_i^{ab} \Psi_j^{cd} H^e - \sqrt{2} f^{ij} \Psi_i^{ab} \Phi_{ja} \bar{H}_b \,, \tag{3.5}$$

where $i, j = 1, 2, 3$ and $a, b, c, \ldots = 1$–5 represent the generations and the SU(5) indices, respectively. The Yukawa couplings h^{ij} and f^{ij} in eq. (3.5) have redundant degrees of freedom, most of which are eliminated by the field re-definition of Ψ and Φ [56]. We parametrize the couplings according to ref. [57] as

$$\begin{aligned} h^{ij} &= f_{u_i} e^{i\varphi_i} \delta_{ij} \,, \\ f^{ij} &= V_{ij}^* f_{d_j} \,, \end{aligned} \tag{3.6}$$

with V_{ij} the Cabibbo-Kobayashi-Maskawa (CKM) matrix. The phase factors φ_i are subject to a constraint

$$\varphi_1 + \varphi_2 + \varphi_3 = 0 \,, \tag{3.7}$$

and thus two of them are independent parameters. The Yukawa coupling terms in eq. (3.5) are written with the component fields as follows:

$$\begin{aligned} W_{\text{Yukawa}} = {} & f_{u_i} e^{i\varphi_i} \epsilon_{rs} \overline{U}_{i\alpha} Q_i^{\alpha r} H_u^s - V_{ij}^* f_{d_j} \epsilon_{rs} Q_i^{\alpha r} \overline{D}_{j\alpha} H_d^s - f_{d_j} \epsilon_{rs} V_{ij}^* \overline{E}_i L_j^r H_d^s \\ & - \frac{1}{2} f_{u_i} e^{i\varphi_i} \epsilon_{\alpha\beta\gamma} \epsilon_{rs} Q_i^{\alpha r} Q_i^{\beta s} H_C^\gamma + V_{ij}^* f_{d_j} \epsilon_{rs} Q_i^{\alpha r} L_j^s \overline{H}_{C\alpha} \\ & + f_{u_i} e^{i\varphi_i} \overline{U}_{i\alpha} \overline{E}_i H_C^\alpha - V_{ij}^* f_{d_j} \epsilon^{\alpha\beta\gamma} \overline{U}_{i\alpha} \overline{D}_{j\beta} \overline{H}_{C\gamma} \,. \end{aligned} \tag{3.8}$$

Here, r, s are the $\text{SU}(2)_L$ indices. In the following discussion, we also use the flavor basis for the matter fields. The relations between the flavor and gauge eigenstates are given as

$$\begin{aligned} Q_i &= \begin{pmatrix} U_i' \\ V_{ij} D_j' \end{pmatrix}, & L_i &= \begin{pmatrix} N_i' \\ E_i' \end{pmatrix}, \\ \bar{U}_i &= e^{-i\varphi_i} \bar{U}_i', & \bar{D}_i &= \bar{D}_i', & \bar{E}_i &= V_{ij} \bar{E}_j' \,, \end{aligned} \tag{3.9}$$

where primes represent the flavor eigenstates.

The Yukawa interactions of color-triplet Higgs multiplets give rise to the dimension-five baryon-number violating operators. The processes in which the operators are induced are illustrated by the diagrams in figure 1. After the color-triplet Higgs multiplets are decoupled, we obtain the effective superpotential as

$$\begin{aligned} W_5 = {} & + \frac{1}{2M_{H_C}} f_{u_i} f_{d_l} V_{kl}^* e^{i\varphi_i} \epsilon_{\alpha\beta\gamma} \epsilon_{rs} \epsilon_{tu} Q_i^{\alpha r} Q_i^{\beta s} Q_k^{\gamma t} L_l^u \\ & + \frac{1}{M_{H_C}} f_{u_i} e^{i\varphi_i} f_{d_l} V_{kl}^* \epsilon^{\alpha\beta\gamma} \overline{U}_{i\alpha} \overline{E}_i \overline{U}_{k\beta} \overline{D}_{l\gamma} \,, \end{aligned} \tag{3.10}$$

[1] In this paper we evaluate the proton decay rate with the SU(5) symmetric Yukawa couplings which are evaluated with up-type and down-type quark masses and the Cabibbo-Kobayashi-Maskawa matrix, though the ratios of charged lepton and down-type quark masses are not necessarily consistent with them. We have checked that, even if the lepton masses are used for f_{d_i}, our consequence presented below is not changed significantly.

JHEP07(2013)038

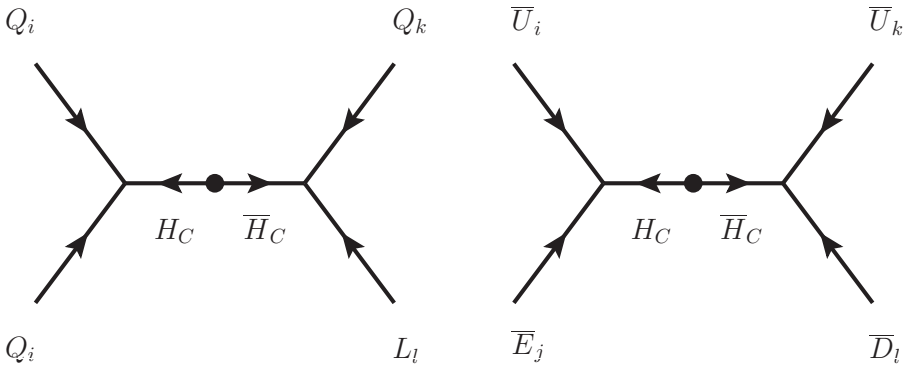

Figure 1. Supergraphs which illustrate color-triplet Higgs exchanging processes where dimension-five effective operators for proton decay are induced. Bullets indicate color-triplet Higgs mass term.

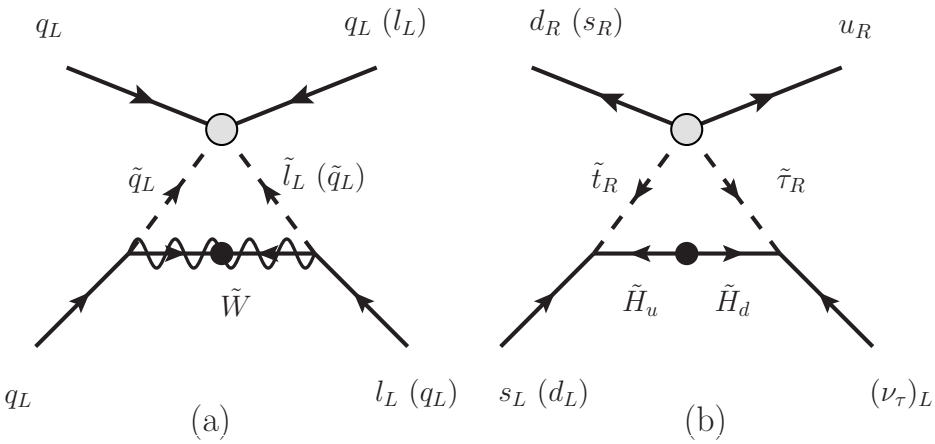

Figure 2. One-loop diagrams which yield the baryon-number violating four-Fermi operators. Diagrams (a) and (b) are generated by charged wino and higgsino exchanging processes, respectively. Gray dots indicate dimension-five effective interactions, while black dots represent wino or higgsino mass terms.

which yields the dimension-five effective operators,

$$\mathcal{L}_5 = \int d^2\theta W_5 \quad + \quad \text{h.c.}\,. \tag{3.11}$$

The effective operators contain sfermions in their external lines. Below the SUSY breaking scale, M_S, these sfermions turn into the SM fermions via the charged wino and higgsino exchanging processes shown in figure 2. In this figure, the gray and black dots indicate the dimension-five effective interactions and the mass terms for wino or higgsino, respectively. The first operator in eq. (3.10) contributes to the diagram (a), while the second one induces the diagram (b). Although the contribution of the diagram (b) is suppressed by the CKM matrix elements as it is generated in the flavor changing process, it is found to be sizable because of the large Yukawa couplings of the third generation fermions [11, 58]. The contributions of flavor-conserving neutral gauginos and higgsino

JHEP07(2013)038

exchange are in general suppressed by the Yukawa couplings of the first generation, thus negligible. Among them, the gluino contribution might be sizable because of the large coupling. It turns out, however, that the gluino contribution vanishes in the limit where squarks are degenerate in mass, and we consider such a case in the following calculation. When sfermion mass matrices have large flavor mixing, the contributions may also be significant, though we do not take into account such a situation for simplicity.

After the electroweak symmetry breaking, the charged wino and higgsino are mixed with each other. In the following calculation, however, we neglect the effect since we mainly consider the case where $M_2, \mu_H \gg m_W$ with m_W the mass of W-boson. When the masses of wino and higgsino are nearly degenerate, the mixing effects might be significant. It is straight-forward to modify the formulae obtained below in such a case.

Evolving the four-Fermi operators from the SUSY breaking scale to the hadron scale ($\sim 1\,\mathrm{GeV}$) according to the renormalization group equations (RGEs), we finally obtain the effective operators for proton decay as

$$\begin{aligned}\mathcal{L}_6 =& \frac{\alpha_2^2}{M_{H_C} m_W^2 \sin 2\beta}\Bigg[2F(M_2, M_S^2) \sum_{i,j=2,3} \overline{m}_{u_i}\overline{m}_{d_j} V_{u_i d} V_{u_i s} V^*_{ud_j} e^{i\varphi_i} \\ &\times A_R^{(i,j)} \epsilon_{\alpha\beta\gamma}\left\{(u_L^\alpha d_L^\beta)(\nu_{Lj} s_L^\gamma) + (u_L^\alpha s_L^\beta)(\nu_{Lj} d_L^\gamma)\right\} \\ &- \frac{\overline{m}_t^2 \overline{m}_\tau V^*_{tb} e^{i\varphi_1}}{m_W^2 \sin 2\beta} F(\mu_H, M_S^2) \overline{A}_R \epsilon_{\alpha\beta\gamma} \\ &\times \left\{\overline{m}_d V_{ud} V_{ts} (u_R^\alpha d_R^\beta)(\nu_\tau s_L^\gamma) + \overline{m}_s V_{us} V_{td} (u_R^\alpha s_R^\beta)(\nu_\tau d_L^\gamma)\right\}\Bigg] \\ &+ \text{h.c.},\end{aligned} \tag{3.12}$$

where we use the two-component spinor notation for the SM fermion fields; all of the quarks are written in the flavor basis though primes are omitted for simplicity; M_S is the mass of sfermions with all the sfermions assumed to be degenerate in mass; $\overline{m}_q$ are the masses of quarks defined in the $\overline{\mathrm{DR}}$ scheme at the scale of $\mu = 2\,\mathrm{GeV}$; u_2, d_2, u_3, and d_3 denote c, s, t, and b quarks, respectively; $\alpha_2 \equiv g_2^2/4\pi$ with g_2 the $\mathrm{SU}(2)_L$ gauge coupling constant at the electroweak scale; $\tan\beta \equiv \langle H_u^0\rangle/\langle H_d^0\rangle$; $A_R^{(i,j)}$ and $\overline{A}_R$ in eq. (3.12) represent the renormalization factors. These factors include the renormalization effects for both the couplings and the effective operators. The estimation of these factors is carried out in appendix A.

The loop function $F(M, M_S^2)$ is given as

$$F(M, M_S^2) = M\left[\frac{1}{M_S^2 - M^2} - \frac{M^2}{(M_S^2 - M^2)^2}\ln\left(\frac{M_S^2}{M^2}\right)\right], \tag{3.13}$$

where M is either the wino mass, M_2, or the higgsino mass, μ_H. In the limit of $M \ll M_S$, the function leads to

$$F(M, M_S^2) \to \frac{M}{M_S^2}, \qquad (M_S \gg M), \tag{3.14}$$

while in the limit of $M \to M_S$, it follows that

$$F(M, M_S^2) \to \frac{1}{2M_S}, \qquad (M \to M_S)\ . \tag{3.15}$$

JHEP07(2013)038

Note that the function is proportional to M, when $M \lesssim M_S$. For this reason, the contribution of the diagrams in figure 2 is enhanced when the masses of the exchanged particles are large. In particular, in the case of $\mu_H \gg M_2$, the higgsino exchange contribution (the diagram (b) in figure 2) dominates the wino exchange one. We also find from the behavior of the loop function that the transition amplitude is considerably suppressed when the sfermions have sufficiently large masses. Thus, we expect that the experimental constraints on the proton decay rate may be avoided in the high-scale SUSY scenario.

The effective operators in eq. (3.12) are written in terms of partons. In order to derive the decay amplitude for proton, we need to obtain the matrix elements of the quarks appearing in the operators between the proton state $|p\rangle$ and the kaon state $|K^+\rangle$. With the matrix elements, we finally obtain the partial decay widths, $\Gamma(p \to K^+\bar{\nu}_\mu)$ and $\Gamma(p \to K^+\bar{\nu}_\tau)$, and the sum of them well approximates the total decay rate of the $p \to K^+\bar{\nu}$ channel. Explicit formulae for the decay widths as well as the determination of the matrix elements are presented in appendix. B.

Before concluding this section, we briefly comment on the proton decay via the SU(5) gauge boson exchange. The SU(5) gauge bosons, called X-bosons, give rise to the dimension-six operators which contribute to proton decay by the $p \to \pi^0 e^+$ channel. In ref. [34], it is pointed out that the GUT scale in the high-scale SUSY tends to be slightly lower than that in the low-energy SUSY. Thus, the proton decay rate in this channel is expected to be enhanced. It turns out, however, that the resultant lifetime is generally long enough [59] to evade the current experimental bound, $\tau(p \to \pi^0 e^+) > 1.29 \times 10^{34}$ yrs [60]. Thus, we ignore the contribution in the following calculation.

4 Results

Now we show numerical results of the proton decay lifetime in the high-scale SUSY scenario. We will see below that the resultant lifetime is well above the current experimental limits in a wide range of parameter region.

First, we consider the case where the higgsino mass is of the order of the sfermion masses, M_S. In this case, the higgsino exchange contribution (the diagram (b) in figure 2) dominates the wino exchange one, as mentioned to in the previous section. For this reason, the lifetime has little dependence on the additional phases, φ_i in eq. (3.6), as well as the wino mass. Thus, it is possible to make a robust prediction for the proton decay lifetime. As the right-handed stop and stau run in the loop in the higgsino exchanging diagram, M_S should be regarded as their masses, which we assume to be degenerate for brevity. For $M_S = \mu_H$, the proton lifetime τ_p is approximately given as[2]

$$\tau_p \simeq 4 \times 10^{35} \times \sin^4 2\beta \left(\frac{0.1}{\overline{A}_R}\right)^2 \left(\frac{M_S}{10^2\ \text{TeV}}\right)^2 \left(\frac{M_{H_C}}{10^{16}\ \text{GeV}}\right)^2 \ \text{yrs}\,, \tag{4.1}$$

and found to be well above the current experimental limits, $\tau(p \to K^+\bar{\nu}) > 4.0 \times 10^{33}$ yrs [13], with the SUSY scale being much higher than the electroweak scale.

[2]The renormalization factor reduces the proton decay rate for larger M_S when $M_S = \mu_H = (10^2$–$10^5)$ TeV, as described in figure 8 in appendix. A.

JHEP07(2013)038

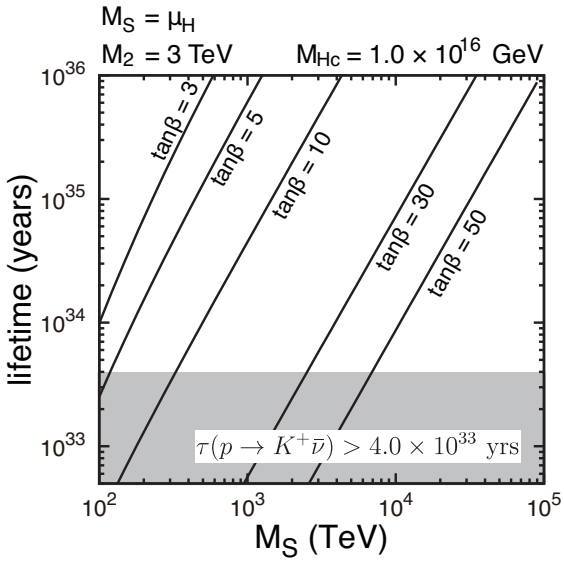

Figure 3. Lifetime of $p \to K^+\bar{\nu}$ mode as functions of $M_S = \mu_H$. Wino mass is set to be 3 TeV and $M_{H_C} = 1.0 \times 10^{16}$ GeV. Solid lines correspond to $\tan\beta = 3, 5, 10, 30$, and 50 from left-top to right-bottom, respectively. Shaded region is excluded by the current experimental bound, $\tau(p \to K^+\bar{\nu}) > 4.0 \times 10^{33}$ yrs [13].

Let us investigate it in detail. To begin with, we consider the mass of the color-triplet Higgs multiplets, M_{H_C}. As mentioned to in section 2, through the RGE analysis discussed in refs. [57, 61] with requiring the gauge coupling unification, one finds that M_{H_C} may be around the GUT scale in the case of high-scale SUSY [34]. The prediction is, however, quite sensitive to the mass spectrum below the GUT scale, especially to the masses of higgsinos and gauginos. Thus, in the following discussion, we just fix M_{H_C} to be around the GUT scale. One easily obtains proton lifetimes corresponding to other values of M_{H_C} by using the power law given in eq. (4.1).

In figure 3, we present the lifetime of the $p \to K^+\bar{\nu}$ mode as functions of $M_S = \mu_H$. Here, the wino mass is set to be 3 TeV, while the result scarcely depends on the mass as long as $M_2 \ll M_S$. The color-triplet Higgs mass is fixed to $M_{H_C} = 1.0 \times 10^{16}$ GeV. The solid lines are for $\tan\beta = 3, 5, 10, 30$, and 50 from left-top to right-bottom, respectively. The shaded region is excluded by the current experimental bound, $\tau(p \to K^+\bar{\nu}) > 4.0 \times 10^{33}$ yrs [13]. The figure illustrates the behavior presented in eq. (4.1). Moreover, it is found that the proton decay lifetime in the high-scale SUSY scenario may evade the experimental constraints, especially for small $\tan\beta$ and high SUSY breaking scales. We also show a similar plot for a relatively small value of M_{H_C} in figure 4, where the mass is taken to be 1.0×10^{15} GeV. The wino mass is again set to be $M_2 = 3$ TeV, and the solid lines correspond to $\tan\beta = 3, 5, 10$, and 30 from left-top to right-bottom, respectively. We see that the relation between the results presented in figures 3 and 4 is well explained by the simple power law in eq. (4.1), though the renormalization factors may also be changed with different values of M_{H_C}. For this reason, we just fix $M_{H_C} = 1.0 \times 10^{16}$ GeV in the following analysis. One easily read other results with different values of M_{H_C} by using the relation given in eq. (4.1).

JHEP07(2013)038

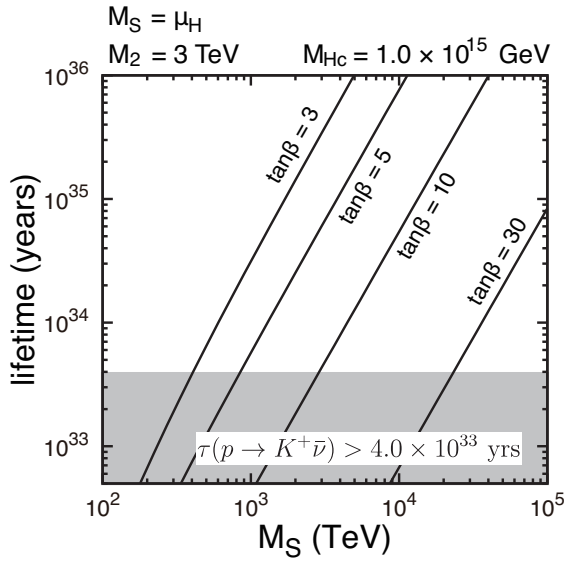

Figure 4. Lifetime of $p \to K^+\bar{\nu}$ mode as functions of $M_S = \mu_H$. Wino mass is set to be 3 TeV and $M_{H_C} = 1.0 \times 10^{15}$ GeV. Solid lines correspond to $\tan\beta = 3, 5, 10$, and 30 from left-top to right-bottom, respectively. Shaded region is excluded by the current experimental bound, $\tau(p \to K^+\bar{\nu}) > 4.0 \times 10^{33}$ yrs [13].

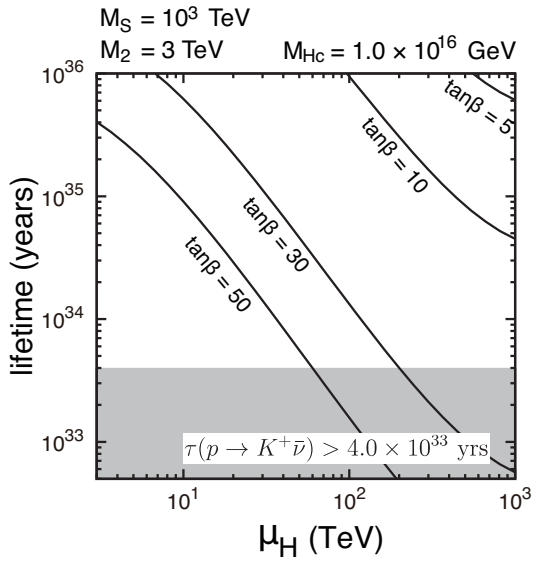

Figure 5. Lifetime of $p \to K^+\bar{\nu}$ mode as functions of μ_H. Wino, sfermion and color-triplet Higgs masses are set to be $M_2 = 3$ TeV, $M_S = 10^3$ TeV, and $M_{H_C} = 1.0 \times 10^{16}$ GeV, respectively. Solid lines correspond to $\tan\beta = 5, 10, 30$, and 50 from right-top to left-bottom, respectively. Shaded region is excluded by the current experimental bound, $\tau(p \to K^+\bar{\nu}) > 4.0 \times 10^{33}$ yrs [13].

Next, we consider the case where the higgsinos are lighter than the sfermions. In this case, the lifetime depends on the new phases appearing in eq. (3.6). Here, we take the phases so that they yield the maximal amplitude for the proton decay rate, i.e., we require that each term in eqs. (B.5) and (B.6) be constructive. This requirement together with

JHEP07(2013)038

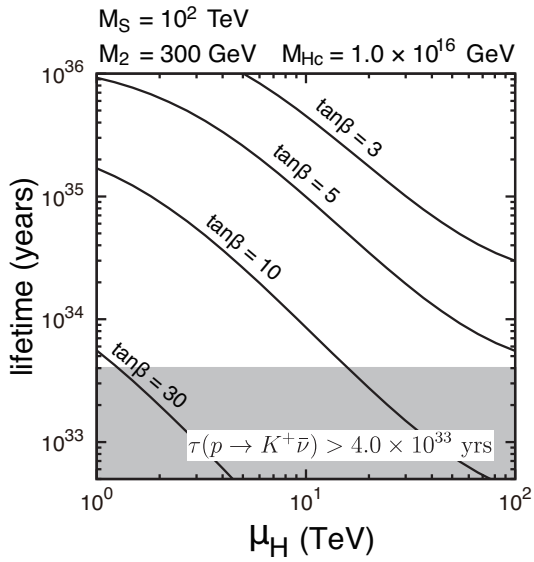

Figure 6. Lifetime of $p \to K^+\bar{\nu}$ mode as functions of μ_H. Wino, sfermion, and color-triplet Higgs masses are set to be $M_2 = 300\,\text{GeV}$, $M_S = 10^2\,\text{TeV}$, and $M_{H_C} = 1.0 \times 10^{16}$ GeV, respectively. Solid lines correspond to $\tan\beta = 3, 5, 10$, and 30 from right-top to left-bottom, respectively. Shaded region is excluded by the current experimental bound, $\tau(p \to K^+\bar{\nu}) > 4.0 \times 10^{33}$ yrs [13].

the constraint (3.7) uniquely determines all of the phases φ_i. Since the choice of phases gives the maximal proton decay rate, we are to obtain the most stringent limit on the parameters. In addition, we assume that both the higgsino and wino mass parameters are real and positive. However, as long as one chooses the phases constructively, the results would not change since it is possible to include the extra phases of the higgsino and wino masses into the redefinition of the phases φ_i.

In figure 5, we plot the proton lifetime as functions of the higgsino mass. Here, the wino, sfermion,[3] and color-triplet Higgs masses are set to be $M_2 = 3\,\text{TeV}$, $M_S = 10^3\,\text{TeV}$, and $M_{H_C} = 1.0 \times 10^{16}$ GeV, respectively. The solid lines correspond to $\tan\beta = 5, 10, 30$, and 50 from right-top to left-bottom, respectively. Again the shaded region is excluded by the current experimental bound, $\tau(p \to K^+\bar{\nu}) > 4.0 \times 10^{33}$ yrs [13]. It is found that the lifetime considerably depends on the mass of higgsino as well as the value of $\tan\beta$. It illustrates that the higgsino contribution is dominant in a wide range of parameter region. Indeed, the contribution gets more significant as the higgsino mass is raised up. We also show a similar plot in the case of $M_2 = 300\,\text{GeV}$ and $M_S = 100\,\text{TeV}$ in figure 6. In this case, large $\tan\beta$ region is excluded even if the higgsino mass is around 1 TeV, while with a rather small value of $\tan\beta$ the proton lifetime easily exceeds the experimental limit. Anyway, we have found that in the high-scale SUSY scenario, the minimal SUSY SU(5) GUT is still alive without any conspiracy of suppressing the dimension-five operators.

[3]To be concrete, we regard M_S as the stop mass, and all of the other sfermion masses are assumed to be degenerate with M_S. Generally speaking, stops are lighter than other sfermions, especially those of the first and second generations. So, even though one relaxes the degeneration assumption, one ends up obtaining a smaller proton decay rate.

JHEP07(2013)038

5 Conclusions and discussion

In this work, we have evaluated the proton decay lifetime via the dimension-five operators in the high-scale SUSY scenario. It is found that the higgsino exchanging diagram gives rise to the dominant contribution in a wide range of parameter region. After all, we have revealed that the proton lifetime may evade the current experimental limit and, thus, the minimal SUSY SU(5) GUT is not excluded in the high-scale SUSY scenario.

In the $\mu_H \simeq M_S$ case, after M_{H_C} being fixed, the proton lifetime depends only on M_S and $\tan\beta$. In fact, these two parameters are also crucial for the prediction of the Higgs boson mass in the high-scale SUSY scenario. Therefore, since now we know that the mass of Higgs boson is 126 GeV, it is possible to relate the M_S and $\tan\beta$ in the present scenario [30–33]. Further, if the mass spectrum is somehow fixed, we are able to constraint M_{H_C} by requiring the gauge coupling unification [34, 57, 61]. Precise analyses in this direction enable us to predict proton decay rate in this scenario, and future experiments may examine the prediction. Such kind of model-dependent study is carried out on another occasion.

While the dimension-five proton decay is suppressed by the heavy sfermion masses, the dimension-six one through the X-boson exchange does not suffer from such a suppression. As referred to above, the GUT scale in the high-scale SUSY is slightly lower than the ordinary one. Since the dimension-six proton decay lifetime scales as $\propto M_X^4$ with M_X the mass of X-boson, it may be significantly enhanced even by a small change in the GUT scale. In such a case, the $p \to \pi^0 e^+$ mode may dominate the $p \to K^+\bar{\nu}$ mode, and both of the modes might be searched in future experiments. For instance, the expected sensitivities of the Hyper-Kamiokande with ten years exposure [13] are 1.3×10^{35} and 2.5×10^{34} years at 90 % confidence level for the $p \to e^+\pi^0$ and $p \to \bar{\nu}K^+$ modes,[4] respectively, which enable us to explore a wide range of parameter region in high-scale SUSY models.

After all, the minimal SUSY SU(5) GUT is still quite promising, and the proton decay experiments may reveal the existence of supersymmetry as well as the grand unification.

Note added: while this work was being finalized, we noticed the authors in refs. [55, 63] discussed the dimension-five proton decay in a similar context. In ref. [55], they have just shown dimensional analysis to constraint the dimension-five operators, while in ref. [63], the proton lifetime is examined in supergravity unified models.

Acknowledgments

We thank Norimi Yokozaki for stimulating us into this work. N.N. is also grateful to Toru Goto for fruitful discussions. The work of N.N. is supported by Research Fellowships of the Japan Society for the Promotion of Science for Young Scientists. The work of J.H. is supported by Grant-in-Aid for Scientific research from the Ministry of Education, Science, Sports, and Culture (MEXT), Japan, No. 20244037, No. 20540252, No. 22244021 and No. 23104011, and also by World Premier International Research Center Initiative (WPI Initiative), MEXT, Japan.

[4] Recent improvements in the analysis of the $K^+ \to \pi^+\pi^0$ decay channel may provide a better sensitivity for the $p \to \bar{\nu}K^+$ mode: 3.2×10^{34} years at 90 % confidence level [62].

JHEP07(2013)038

A Renormalization factors

Here we present the explicit expressions for the renormalization factors defined in eq. (3.12). First, we write the renormalization factors $A_R^{(i,j)}$ and $\overline{A}_R$ as the products of the long- and short-distance renormalization factors:

$$A_R^{(i,j)} \equiv A_L A_S^{(i,j)} \,,$$
$$\overline{A}_R \equiv \overline{A}_L \overline{A}_S \,, \tag{A.1}$$

where A_L and $\overline{A}_L$ represent the long-distance QCD renormalization factors between the electroweak scale ($\mu = m_Z$ with m_Z the Z-boson mass) and the scale of $\mu = 2\,\text{GeV}$, while $A_S^{(i,j)}$ and $\overline{A}_S$ correspond to the short-distance renormalization effects between the electroweak and GUT scales. All of the effects are to be computed at one-loop level.

A.1 Long-range factors

First, we discuss the long-distance renormalization factors. The factors consist of two effects; one is the running of the quark masses from $\mu = 2\,\text{GeV}$ to $\mu = m_Z$, and the other is the renormalization effect of the four-Fermi operators in eq. (3.12) from $\mu = m_Z$ to $\mu = 2\,\text{GeV}$. We neglect the QED corrections since the electromagnetic coupling is much smaller than the strong coupling.

Before analyzing the renormalization effects, we first discuss the input parameters for quark masses. In ref. [64], the values of the light quark masses m_q ($q = u, d, s$) are given in the $\overline{\text{MS}}$ scheme at $\mu \simeq 2\,\text{GeV}$, while those for c- and b-quarks are presented in the $\overline{\text{MS}}$ at $\mu = m_c$ and m_b, respectively. Since we define $\overline{m}_q$ in eq. (3.12) in the $\overline{\text{DR}}$ scheme, we convert the input parameters into those in the $\overline{\text{DR}}$ scheme. We use the one-loop relation [65]:

$$\overline{m}_q(\mu) = m_q(\mu)\left(1 - \frac{\alpha_s(\mu)}{3\pi}\right), \tag{A.2}$$

where $\alpha_s \equiv g_s^2/4\pi$ with g_s the strong coupling constant. For c- and b-quarks, we evolve the masses to $\mu = 2\,\text{GeV}$ by using the RGEs. For top quark, on the other hand, the pole mass is displayed in ref. [64]. The relation between the pole mass and the $\overline{\text{DR}}$ mass is given by [65]

$$m_t = \overline{m}_t(\mu)\left[1 + \frac{\alpha_s(\mu)}{3\pi}\left(6\log\frac{\mu}{\overline{m}_t} + 5\right)\right] . \tag{A.3}$$

Now we consider the QCD renormalization effects. The RGEs for the Wilson coefficients of the effective operators in eq. (3.12) at one-loop [66] are given as[5]

$$\mu\frac{\partial}{\partial\mu}C = -\frac{4g_s^2}{16\pi^2}C \,. \tag{A.4}$$

[5]Two-loop effects are also calculated in ref. [67], though their contribution is found to be small.

JHEP07(2013)038

By using the equation, as well as the RGEs for the quark masses, we readily obtain the long-range renormalization factors A_L and $\overline{A}_L$:

$$A_L = \frac{\overline{m}_{u_i}\overline{m}_{d_i}(m_Z)\cdot C(2\text{ GeV})}{\overline{m}_{u_i}\overline{m}_{d_i}(2\text{ GeV})\cdot C(m_Z)} = \left(\frac{\alpha_s(2\text{ GeV})}{\alpha_s(m_b)}\right)^{-\frac{18}{25}}\left(\frac{\alpha_s(m_b)}{\alpha_s(m_Z)}\right)^{-\frac{18}{23}},$$
$$\overline{A}_L = \frac{\overline{m}_t^2\overline{m}_{d_i}(m_Z)\cdot C(2\text{ GeV})}{\overline{m}_t^2\overline{m}_{d_i}(2\text{ GeV})\cdot C(m_Z)} = \left(\frac{\alpha_s(2\text{ GeV})}{\alpha_s(m_b)}\right)^{-\frac{6}{5}}\left(\frac{\alpha_s(m_b)}{\alpha_s(m_Z)}\right)^{-\frac{30}{23}}. \tag{A.5}$$

Numerically, we have

$$A_L = 0.53, \qquad \overline{A}_L = 0.34, \tag{A.6}$$

at one-loop level.

A.2 Short-range factors

Next, we evaluate the short-distance renormalization factors. They are composed of three factors. First, the effective operators given at the GUT scale receive the renormalization effects as they are taken down to the electroweak scale. Second, the Yukawa couplings in the color-triplet Higgs exchanging process are determined through the running of the couplings from the electroweak scale to the GUT scale. Third, the interaction vertices in the one-loop diagrams in figure 2 are obtained by evolving the $\mathrm{SU}(2)_L$ gauge coupling and the Yukawa couplings according to the RGEs from the electroweak scale to the SUSY breaking scale, $\mu = M_S$.

Let us begin with the running of the Yukawa couplings. Initial values for the Yukawa coupling constants are given by

$$y_{u_i}(m_Z) = \frac{g_2}{\sqrt{2}m_W}\overline{m}_{u_i}(m_Z)\,,$$
$$y_{d_i}(m_Z) = \frac{g_2}{\sqrt{2}m_W}\overline{m}_{d_i}(m_Z)\,,$$
$$y_{e_i}(m_Z) = \frac{g_2}{\sqrt{2}m_W}\overline{m}_{e_i}(m_Z)\,. \tag{A.7}$$

In the SM, the Yukawa couplings flow according to the following RGEs at one-loop level:

$$\mu\frac{\partial}{\partial\mu}y_{u_i} = \frac{1}{16\pi^2}y_{u_i}\left[\frac{3}{2}(y_{u_i}^2 - y_{d_i}^2) + Y_2 - \frac{17}{20}g_1^2 - \frac{9}{4}g_2^2 - 8g_3^2\right],$$
$$\mu\frac{\partial}{\partial\mu}y_{d_i} = \frac{1}{16\pi^2}y_{d_i}\left[\frac{3}{2}(y_{d_i}^2 - y_{u_i}^2) + Y_2 - \frac{1}{4}g_1^2 - \frac{9}{4}g_2^2 - 8g_3^2\right],$$
$$\mu\frac{\partial}{\partial\mu}y_{e_i} = \frac{1}{16\pi^2}y_{e_i}\left[\frac{3}{2}y_{e_i}^2 + Y_2 - \frac{9}{4}g_1^2 - \frac{9}{4}g_2^2\right], \tag{A.8}$$

where Y_2 is given as

$$Y_2 = \sum_i (3y_{u_i}^2 + 3y_{d_i}^2 + y_{e_i}^2)\,, \tag{A.9}$$

and we neglect the off-diagonal components for simplicity. The equations are also applicable when the renormalization scale exceeds the gaugino masses. Above the higgsino mass,

JHEP07(2013)038

eq. (A.8) is valid except that Y_2 is modified to

$$Y_2 = \sum_i (3y_{u_i}^2 + 3y_{d_i}^2 + y_{e_i}^2) + \frac{3}{10}g_1^2 + \frac{3}{2}g_2^2 \ . \tag{A.10}$$

Here we assume the ordinary supersymmetric relation for the gaugino-Higgs-higgsino couplings. The couplings may deviate the relation when the SUSY breaking scale is much higher than the gaugino and higgsino masses, but it is found that the deviation is usually not so significant [23, 24].

At the SUSY breaking scale, the Yukawa couplings y_f are matched with the supersymmetric ones, $\overline{y}_f$, as follows:

$$\begin{aligned}
\overline{y}_{u_i}(M_S) &= \frac{1}{\sin\beta} y_{u_i}(M_S)\,, \\
\overline{y}_{d_i}(M_S) &= \frac{1}{\cos\beta} y_{d_i}(M_S)\,, \\
\overline{y}_{e_i}(M_S) &= \frac{1}{\cos\beta} y_{e_i}(M_S)\ .
\end{aligned} \tag{A.11}$$

Above $\mu = M_S$, the RGEs for the Yukawa couplings are given as

$$\begin{aligned}
\mu\frac{\partial}{\partial\mu}\overline{y}_{u_i} &= \frac{1}{16\pi^2}\overline{y}_{u_i}\left[3\sum_j \overline{y}_{u_j}^2 + 3\overline{y}_{u_i}^2 + \overline{y}_{d_i}^2 - \frac{13}{15}g_1^2 - 3g_2^2 - \frac{16}{3}g_3^2\right], \\
\mu\frac{\partial}{\partial\mu}\overline{y}_{d_i} &= \frac{1}{16\pi^2}\overline{y}_{d_i}\left[\sum_j (3\overline{y}_{d_j}^2 + \overline{y}_{e_j}^2) + 3\overline{y}_{d_i}^2 + \overline{y}_{u_i}^2 - \frac{7}{15}g_1^2 - 3g_2^2 - \frac{16}{3}g_3^2\right], \\
\mu\frac{\partial}{\partial\mu}\overline{y}_{e_i} &= \frac{1}{16\pi^2}\overline{y}_{e_i}\left[\sum_j (3\overline{y}_{d_j}^2 + \overline{y}_{e_j}^2) + 3\overline{y}_{e_i}^2 - \frac{9}{5}g_1^2 - 3g_2^2\right].
\end{aligned} \tag{A.12}$$

Then, at the GUT scale, the Yukawa couplings f_{u_i} and f_{d_i} in eq. (3.6) are defined by

$$\begin{aligned}
f_{u_i} &\equiv \overline{y}_{u_i}(M_{H_C})\,, \\
f_{d_i} &\equiv \overline{y}_{d_i}(M_{H_C})\ .
\end{aligned} \tag{A.13}$$

For the gauge couplings, the one-loop gauge coupling beta function coefficients are given in the SM as

$$b_a = (41/10, -19/6, -7)\,, \tag{A.14}$$

for $\mathrm{U}(1)_Y$, $\mathrm{SU}(2)_L$, and $\mathrm{SU}(3)_C$, respectively. Above the gaugino threshold, the coefficients are converted to[6]

$$b_a = (41/10, -11/6, -5)\,, \tag{A.15}$$

and after the higgsinos showing up, they lead to

$$b_a = (9/2, -7/6, -5)\ . \tag{A.16}$$

[6]When evaluating the renormalization factors, we take the gluino mass equal to wino mass for simplicity.

JHEP07(2013)038

Finally, in the MSSM, they are given as

$$b_a = (33/5, 1, -3) \ . \tag{A.17}$$

The short-distance renormalization factors for the four-Fermi operators in eq. (3.12) are presented in ref. [66]. For the effective operators generated by the wino exchanging diagram, the renormalization factor for the Wilson coefficient is

$$C(\mu) = \left(\frac{\alpha_3(\mu)}{\alpha_3(\mu_0)}\right)^{-\frac{2}{b_3}} \left(\frac{\alpha_2(\mu)}{\alpha_2(\mu_0)}\right)^{-\frac{15}{2b_2}} \left(\frac{\alpha_1(\mu)}{\alpha_1(\mu_0)}\right)^{-\frac{1}{10b_1}} C(\mu_0) \, , \tag{A.18}$$

while for those induced by the higgsino exchange, we have

$$\overline{C}(\mu) = \left(\frac{\alpha_3(\mu)}{\alpha_3(\mu_0)}\right)^{-\frac{2}{b_3}} \left(\frac{\alpha_2(\mu)}{\alpha_2(\mu_0)}\right)^{-\frac{9}{4b_2}} \left(\frac{\alpha_1(\mu)}{\alpha_1(\mu_0)}\right)^{-\frac{11}{20b_1}} \overline{C}(\mu_0) \ . \tag{A.19}$$

In the case of $\mu > M_S$, the theory is to be regarded as supersymmetric, and the renormalization factors are obtained as the product of the wave function renormalizations of the fields in the effective operators [68]. The wino contribution to the effective operators in eq. (3.12) is induced by the effective operators with a form like

$$C_{ij} \int d^2\theta \epsilon_{\alpha\beta\gamma}\epsilon_{rs}\epsilon_{tu} Q_i^{\alpha r} Q_i^{\beta s} Q_1^{rt} L_j^u \, , \tag{A.20}$$

with $i, j = 2, 3$, while the higgsino contribution is generated by

$$\overline{C} \int d^2\theta \epsilon^{\alpha\beta\gamma} \overline{U}_{3\alpha} \overline{E}_3 \overline{U}_{1\beta} \overline{D}_{l\gamma} \, , \tag{A.21}$$

with $l = 1, 2$. Then, the REGs for the Wilson coefficients of the operators are

$$\mu \frac{\partial}{\partial \mu} C_{ij} = \frac{1}{16\pi^2} \left[2(\overline{y}_{u_i}^2 + \overline{y}_{d_i}^2) + \overline{y}_{e_j}^2 - 8g_3^2 - 6g_2^2 - \frac{2}{5} g_1^2 \right] C_{ij} \, , \tag{A.22}$$

and

$$\mu \frac{\partial}{\partial \mu} \overline{C} = \frac{1}{16\pi^2} \left[2(\overline{y}_t^2 + \overline{y}_\tau^2) - 8g_3^2 - \frac{12}{5} g_1^2 \right] \overline{C} \ . \tag{A.23}$$

Note that in this case it is important to take the Yukawa interactions into account since the effective operators contain the third generation chiral superfields.

With the RGEs presented above, we finally compute the short-distance renormalization factors as follows:

$$\begin{aligned} A_S^{(i,j)} &= \frac{m_W^2 \sin 2\beta f_{u_i} f_{d_j}}{4\pi \ \overline{m}_{u_i} \overline{m}_{d_j}(m_Z)} \frac{\alpha_2(M_S)}{\alpha_2^2(m_Z)} \cdot \frac{C(m_Z)}{C(M_S)} \frac{C_{ij}(M_S)}{C_{ij}(M_{H_C})} \, , \\ \overline{A}_S &= \frac{m_W^4 \sin^2 2\beta f_t \overline{y}_t(M_S) \overline{y}_\tau(M_S) f_{d_i}}{(4\pi)^2 \alpha_2^2(m_Z) \overline{m}_t^2 \overline{m}_\tau \overline{m}_{d_i}(m_Z)} \cdot \frac{\overline{C}(m_Z)}{\overline{C}(M_{H_C})} \ . \end{aligned} \tag{A.24}$$

With the results obtained above, we compute the renormalization factors. We present $A_R^{(i,j)}$ and $\overline{A}_R$ in figures 7 and 8, respectively, as functions of M_S. In both figures, we take $M_S = \mu_H$, $M_2 = 3\,\text{TeV}$, and $M_{H_C} = 1.0 \times 10^{16}\,\text{GeV}$. In the left graph in figure 7,

JHEP07(2013)038

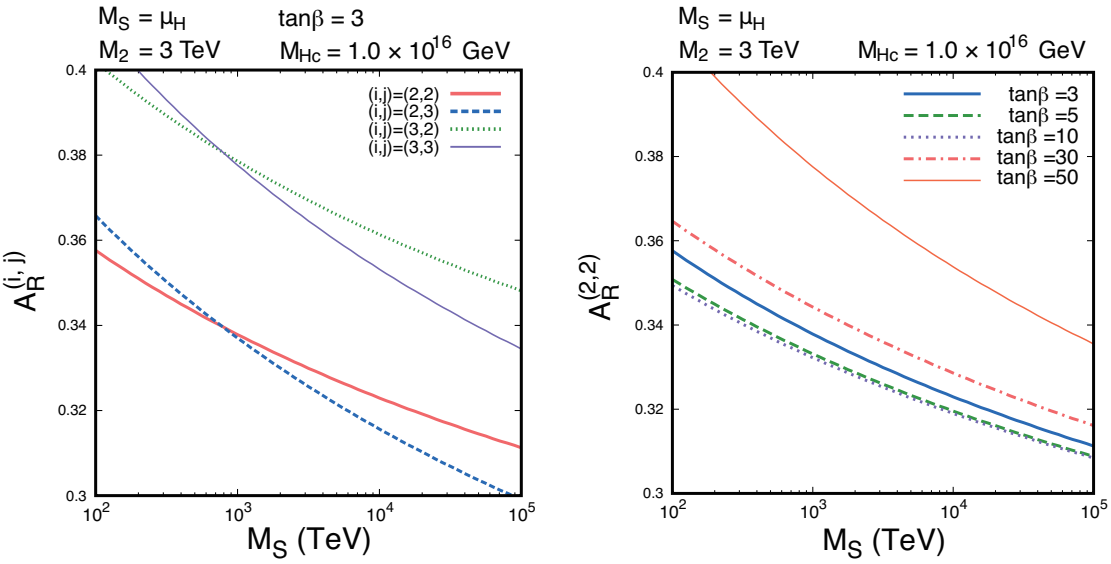

Figure 7. Left: $A_R^{(i,j)}$ with $(i,j) = (2,2),\ (2,3),\ (3,2),\ (3,3)$ as functions of M_S. Here we set $\tan\beta = 3$, $M_S = \mu_H$, $M_2 = 3\,\text{TeV}$, and $M_{H_C} = 1.0 \times 10^{16}\,\text{GeV}$. Right: $A_R^{(2,2)}$ as functions of M_S. Same parameters as in the left graph are used except for $\tan\beta$. Each line corresponds to different values of $\tan\beta$ ($\tan\beta = 3, 5, 10, 30, 50$).

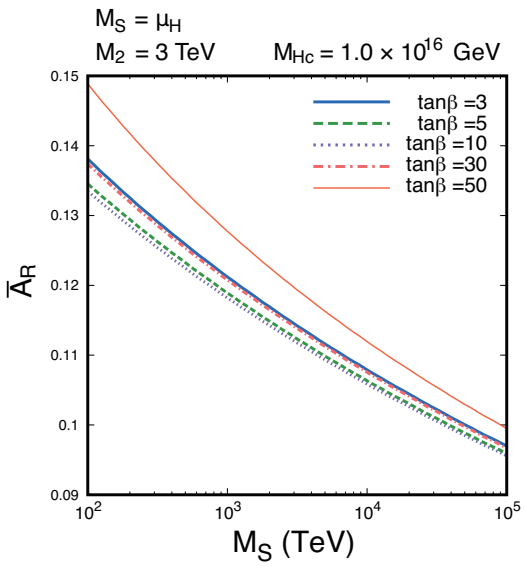

Figure 8. $\overline{A}_R$ as functions of M_S. Here we set $M_S = \mu_H$, $M_2 = 3\,\text{TeV}$, and $M_{H_C} = 1.0 \times 10^{16}\,\text{GeV}$. Each line shows different values of $\tan\beta$.

each $A_R^{(i,j)}$ is presented with $\tan\beta$ fixed to be $\tan\beta = 3$, while in the right graph the behavior of $A_R^{(2,2)}$ is shown for different values of $\tan\beta$ ($\tan\beta = 3, 5, 10, 30, 50$). Similarly, each line in figure 8 corresponds to $\overline{A}_R$ evaluated with various $\tan\beta$'s. It is found that the renormalization factors decrees as the SUSY scale increases, while their dependence on $\tan\beta$ is somewhat complicated. In addition, the left panel in figure 7 illustrates that the effects of the third generation Yukawa couplings are significant.

JHEP07(2013)038

B Formulae for proton decay rate

In this section, we display the formulae for the partial decay widths of $p \to K^+\bar{\nu}$ channels as well as the hadronic matrix elements which we need to evaluate the decay widths. Let us start with the matrix elements. We divide the derivation into two steps.[7] First, we express them in terms of the low-energy constants α_p and β_p by using the chiral perturbation techniques [71–73]:

$$\begin{aligned}
\langle K^+|\epsilon_{\alpha\beta\gamma}(u_L^\alpha d_L^\beta)s_L^\gamma|p\rangle &= \frac{\beta_p}{\sqrt{2}f_\pi}\left(1+\frac{D+3F}{3}\frac{m_p}{M_B}\right)P_L u_p\,,\\
\langle K^+|\epsilon_{\alpha\beta\gamma}(u_L^\alpha s_L^\beta)d_L^\gamma|p\rangle &= \frac{\beta_p}{\sqrt{2}f_\pi}\left(\frac{2D}{3}\frac{m_p}{M_B}\right)P_L u_p\,,\\
\langle K^+|\epsilon_{\alpha\beta\gamma}(u_R^\alpha d_R^\beta)s_L^\gamma|p\rangle &= \frac{\alpha_p}{\sqrt{2}f_\pi}\left(1+\frac{D+3F}{3}\frac{m_p}{M_B}\right)P_L u_p\,,\\
\langle K^+|\epsilon_{\alpha\beta\gamma}(u_R^\alpha s_R^\beta)d_L^\gamma|p\rangle &= \frac{\alpha_p}{\sqrt{2}f_\pi}\left(\frac{2D}{3}\frac{m_p}{M_B}\right)P_L u_p\,,
\end{aligned} \tag{B.1}$$

where $f_\pi \simeq 92.2\,\text{MeV}$ [64] is the pion decay constant and the baryon-meson couplings D and F are given as $D \simeq 0.80$ and $F \simeq 0.47$, respectively. m_p denotes the proton mass, while M_B represents the baryon mass parameter in the chiral Lagrangian, which we choose as $M_B \simeq (m_{\Sigma^0} + m_{\Lambda^0})/2$ with m_{Σ^0} and m_{Λ^0} the masses of Σ^0 and Λ^0, respectively. u_p is the four-component spinor wave function of proton, and P_L is the projection operator defined by $P_L \equiv (1-\gamma_5)/2$. The low-energy constants α_p and β_p are defined as

$$\begin{aligned}
\langle 0|\epsilon_{\alpha\beta\gamma}(u_R^\alpha d_R^\beta)u_L^\gamma|p\rangle &= \alpha_p P_L u_p\,,\\
\langle 0|\epsilon_{\alpha\beta\gamma}(u_L^\alpha d_L^\beta)u_L^\gamma|p\rangle &= \beta_p P_L u_p\,,
\end{aligned} \tag{B.2}$$

with $|0\rangle$ the vacuum state. Second, we determine the constants α_p and β_p. We extract them from the results of lattice simulations [74]:

$$\begin{aligned}
\alpha_p &= -0.0112 \pm 0.0012_{(\text{stat})} \pm 0.0022_{(\text{syst})}\ \text{GeV}^3\,,\\
\beta_p &= 0.0120 \pm 0.0013_{(\text{stat})} \pm 0.0023_{(\text{syst})}\ \text{GeV}^3\,,
\end{aligned} \tag{B.3}$$

where they are evaluated at $\mu = 2\,\text{GeV}$.

With the matrix elements and the effective operators in eq. (3.12), it is straightforward to derive the partial decay widths of the $p \to K^+\bar{\nu}_\mu$ and $p \to K^+\bar{\nu}_\tau$ channels. The result is

$$\Gamma(p \to K^+\bar{\nu}_i) = \frac{m_p \alpha_2^4 |C_i|^2}{64\pi f_\pi^2 M_{H_C}^2 m_W^4 \sin^2 2\beta}\left(1-\frac{m_K^2}{m_p^2}\right)^2, \tag{B.4}$$

[7] Calculation of the matrix elements is also conducted by using the direct method [69], in which the three-point correlation functions relevant for proton decay are directly computed on the lattice. Preliminary for the recent progress is reported in ref. [70].

JHEP07(2013)038

with $(i = \mu, \tau)$ and

$$C_\mu = 2\beta_p F(M_2, M_S^2)\left\{1 + (D+F)\frac{m_p}{M_B}\right\}\overline{m}_s V_{us}^* \sum_{i=2,3} \overline{m}_{u_i} V_{u_i d} V_{u_i s} e^{i\varphi_i} A_R^{(i,2)}\,, \tag{B.5}$$

$$\begin{aligned} C_\tau = {} & 2\beta_p F(M_2, M_S^2)\left\{1 + (D+F)\frac{m_p}{M_B}\right\}\overline{m}_b V_{ub}^* \sum_{i=2,3} \overline{m}_{u_i} V_{u_i d} V_{u_i s} e^{i\varphi_i} A_R^{(i,3)} \\ & - \alpha_p \frac{\overline{m}_t^2 \overline{m}_\tau V_{tb}^* e^{i\varphi_1}}{m_W^2 \sin 2\beta} F(\mu_H, M_S^2)\overline{A}_R \times \\ & \times \left\{\overline{m}_d V_{ud} V_{ts}\left(1 + \frac{D+3F}{3}\frac{m_p}{M_B}\right) + \overline{m}_s V_{us} V_{td} \frac{2D}{3}\frac{m_p}{M_B}\right\}. \end{aligned} \tag{B.6}$$

References

[1] ATLAS collaboration, *Observation of a new particle in the search for the standard model Higgs boson with the ATLAS detector at the LHC*, *Phys. Lett.* **B 716** (2012) 1 [arXiv:1207.7214] [INSPIRE].

[2] CMS collaboration, *Observation of a new boson at a mass of* 125 *GeV with the CMS experiment at the LHC*, *Phys. Lett.* **B 716** (2012) 30 [arXiv:1207.7235] [INSPIRE].

[3] S. Dimopoulos, S. Raby and F. Wilczek, *Supersymmetry and the scale of unification*, *Phys. Rev.* **D 24** (1981) 1681 [INSPIRE].

[4] W.J. Marciano and G. Senjanović, *Predictions of supersymmetric grand unified theories*, *Phys. Rev.* **D 25** (1982) 3092 [INSPIRE].

[5] M. Einhorn and D. Jones, *The weak mixing angle and unification mass in supersymmetric* SU(5), *Nucl. Phys.* **B 196** (1982) 475 [INSPIRE].

[6] U. Amaldi, W. de Boer and H. Furstenau, *Comparison of grand unified theories with electroweak and strong coupling constants measured at LEP*, *Phys. Lett.* **B 260** (1991) 447 [INSPIRE].

[7] P. Langacker and M.-x. Luo, *Implications of precision electroweak experiments for* M_t, ρ_0, $\sin^2\theta_W$ *and grand unification*, *Phys. Rev.* **D 44** (1991) 817 [INSPIRE].

[8] S. Dimopoulos and H. Georgi, *Softly broken supersymmetry and* SU(5), *Nucl. Phys.* **B 193** (1981) 150 [INSPIRE].

[9] N. Sakai, *Naturalness in supersymmetric guts*, *Z. Phys.* **C 11** (1981) 153 [INSPIRE].

[10] H. Georgi and S. Glashow, *Unity of all elementary particle forces*, *Phys. Rev. Lett.* **32** (1974) 438 [INSPIRE].

[11] T. Goto and T. Nihei, *Effect of RRRR dimension five operator on the proton decay in the minimal* SU(5) *SUGRA GUT model*, *Phys. Rev.* **D 59** (1999) 115009 [hep-ph/9808255] [INSPIRE].

[12] H. Murayama and A. Pierce, *Not even decoupling can save minimal supersymmetric* SU(5), *Phys. Rev.* **D 65** (2002) 055009 [hep-ph/0108104] [INSPIRE].

[13] K. Abe et al., *Letter of intent: the hyper-Kamiokande experiment — Detector design and physics potential*, arXiv:1109.3262 [INSPIRE].

JHEP07(2013)038

[14] ATLAS collaboration, *Search for squarks and gluinos with the ATLAS detector in final states with jets and missing transverse momentum using* 4.7 fb^{-1} *of* $\sqrt{s} = 7$ *TeV proton-proton collision data*, *Phys. Rev.* **D 87** (2013) 012008 [arXiv:1208.0949] [INSPIRE].

[15] ATLAS collaboration, *Search for squarks and gluinos with the ATLAS detector using final states with jets and missing transverse momentum and* 5.8 fb^{-1} *of* $\sqrt{s} = 8$ *TeV proton-proton collision data*, ATLAS-CONF-2012-109 (2012).

[16] CMS collaboration, *Search for new physics in the multijet and missing transverse momentum final state in proton-proton collisions at* $\sqrt{s} = 7$ *TeV*, *Phys. Rev. Lett.* **109** (2012) 171803 [arXiv:1207.1898] [INSPIRE].

[17] Y. Okada, M. Yamaguchi and T. Yanagida, *Upper bound of the lightest Higgs boson mass in the minimal supersymmetric standard model*, *Prog. Theor. Phys.* **85** (1991) 1 [INSPIRE].

[18] Y. Okada, M. Yamaguchi and T. Yanagida, *Renormalization group analysis on the Higgs mass in the softly broken supersymmetric standard model*, *Phys. Lett.* **B 262** (1991) 54 [INSPIRE].

[19] H.E. Haber and R. Hempfling, *Can the mass of the lightest Higgs boson of the minimal supersymmetric model be larger than* $m(Z)$*?*, *Phys. Rev. Lett.* **66** (1991) 1815 [INSPIRE].

[20] J.R. Ellis, G. Ridolfi and F. Zwirner, *Radiative corrections to the masses of supersymmetric Higgs bosons*, *Phys. Lett.* **B 257** (1991) 83 [INSPIRE].

[21] J.R. Ellis, G. Ridolfi and F. Zwirner, *On radiative corrections to supersymmetric Higgs boson masses and their implications for LEP searches*, *Phys. Lett.* **B 262** (1991) 477 [INSPIRE].

[22] J.D. Wells, *Implications of supersymmetry breaking with a little hierarchy between gauginos and scalars*, hep-ph/0306127 [INSPIRE].

[23] N. Arkani-Hamed and S. Dimopoulos, *Supersymmetric unification without low energy supersymmetry and signatures for fine-tuning at the LHC*, *JHEP* **06** (2005) 073 [hep-th/0405159] [INSPIRE].

[24] G. Giudice and A. Romanino, *Split supersymmetry*, *Nucl. Phys.* **B 699** (2004) 65 [*Erratum ibid.* **B 706** (2005) 65-89] [hep-ph/0406088] [INSPIRE].

[25] N. Arkani-Hamed, S. Dimopoulos, G. Giudice and A. Romanino, *Aspects of split supersymmetry*, *Nucl. Phys.* **B 709** (2005) 3 [hep-ph/0409232] [INSPIRE].

[26] J.D. Wells, *PeV-scale supersymmetry*, *Phys. Rev.* **D 71** (2005) 015013 [hep-ph/0411041] [INSPIRE].

[27] L.J. Hall and Y. Nomura, *A finely-predicted Higgs boson mass from a finely-tuned weak scale*, *JHEP* **03** (2010) 076 [arXiv:0910.2235] [INSPIRE].

[28] L.J. Hall and Y. Nomura, *Spread supersymmetry*, *JHEP* **01** (2012) 082 [arXiv:1111.4519] [INSPIRE].

[29] F. Gabbiani, E. Gabrielli, A. Masiero and L. Silvestrini, *A complete analysis of FCNC and CP constraints in general SUSY extensions of the standard model*, *Nucl. Phys.* **B 477** (1996) 321 [hep-ph/9604387] [INSPIRE].

[30] G.F. Giudice and A. Strumia, *Probing high-scale and split supersymmetry with Higgs mass measurements*, *Nucl. Phys.* **B 858** (2012) 63 [arXiv:1108.6077] [INSPIRE].

[31] M. Ibe and T.T. Yanagida, *The lightest Higgs boson mass in pure gravity mediation model*, *Phys. Lett.* **B 709** (2012) 374 [arXiv:1112.2462] [INSPIRE].

JHEP07(2013)038

[32] M. Ibe, S. Matsumoto and T.T. Yanagida, *Pure gravity mediation with $m_{3/2} = 10$–100 TeV*, *Phys. Rev.* **D 85** (2012) 095011 [arXiv:1202.2253] [INSPIRE].

[33] L.E. Ibáñez and I. Valenzuela, *The Higgs mass as a signature of heavy SUSY*, *JHEP* **05** (2013) 064 [arXiv:1301.5167] [INSPIRE].

[34] J. Hisano, T. Kuwahara and N. Nagata, *Grand unification in high-scale supersymmetry*, *Phys. Lett.* **B 723** (2013) 324 [arXiv:1304.0343] [INSPIRE].

[35] M. Fukugita and T. Yanagida, *Baryogenesis without grand unification*, *Phys. Lett.* **B 174** (1986) 45 [INSPIRE].

[36] J. Hisano, K. Ishiwata and N. Nagata, *A complete calculation for direct detection of Wino dark matter*, *Phys. Lett.* **B 690** (2010) 311 [arXiv:1004.4090] [INSPIRE].

[37] J. Hisano, K. Ishiwata and N. Nagata, *Gluon contribution to the dark matter direct detection*, *Phys. Rev.* **D 82** (2010) 115007 [arXiv:1007.2601] [INSPIRE].

[38] J. Hisano, K. Ishiwata, N. Nagata and T. Takesako, *Direct detection of electroweak-interacting dark matter*, *JHEP* **07** (2011) 005 [arXiv:1104.0228] [INSPIRE].

[39] J. Hisano, K. Ishiwata and N. Nagata, *Direct search of dark matter in high-scale supersymmetry*, *Phys. Rev.* **D 87** (2013) 035020 [arXiv:1210.5985] [INSPIRE].

[40] J. Hisano, S. Matsumoto and M.M. Nojiri, *Explosive dark matter annihilation*, *Phys. Rev. Lett.* **92** (2004) 031303 [hep-ph/0307216] [INSPIRE].

[41] J. Hisano, S. Matsumoto, M.M. Nojiri and O. Saito, *Non-perturbative effect on dark matter annihilation and gamma ray signature from galactic center*, *Phys. Rev.* **D 71** (2005) 063528 [hep-ph/0412403] [INSPIRE].

[42] L. Randall and R. Sundrum, *Out of this world supersymmetry breaking*, *Nucl. Phys.* **B 557** (1999) 79 [hep-th/9810155] [INSPIRE].

[43] G.F. Giudice, M.A. Luty, H. Murayama and R. Rattazzi, *Gaugino mass without singlets*, *JHEP* **12** (1998) 027 [hep-ph/9810442] [INSPIRE].

[44] J. Hisano, S. Matsumoto, M. Nagai, O. Saito and M. Senami, *Non-perturbative effect on thermal relic abundance of dark matter*, *Phys. Lett.* **B 646** (2007) 34 [hep-ph/0610249] [INSPIRE].

[45] M. Cirelli, A. Strumia and M. Tamburini, *Cosmology and astrophysics of minimal dark matter*, *Nucl. Phys.* **B 787** (2007) 152 [arXiv:0706.4071] [INSPIRE].

[46] T. Gherghetta, G.F. Giudice and J.D. Wells, *Phenomenological consequences of supersymmetry with anomaly induced masses*, *Nucl. Phys.* **B 559** (1999) 27 [hep-ph/9904378] [INSPIRE].

[47] T. Moroi and L. Randall, *Wino cold dark matter from anomaly mediated SUSY breaking*, *Nucl. Phys.* **B 570** (2000) 455 [hep-ph/9906527] [INSPIRE].

[48] K.S. Jeong, M. Shimosuka and M. Yamaguchi, *Light Higgsino in Heavy Gravitino Scenario with Successful Electroweak Symmetry Breaking*, *JHEP* **09** (2012) 050 [arXiv:1112.5293] [INSPIRE].

[49] R. Saito and S. Shirai, *Gravitational wave probe of high supersymmetry breaking scale*, *Phys. Lett.* **B 713** (2012) 237 [arXiv:1201.6589] [INSPIRE].

[50] R. Sato, S. Shirai and K. Tobioka, *Gluino decay as a probe of high scale supersymmetry breaking*, *JHEP* **11** (2012) 041 [arXiv:1207.3608] [INSPIRE].

JHEP07(2013)038

[51] B. Bhattacherjee, B. Feldstein, M. Ibe, S. Matsumoto and T.T. Yanagida, *Pure gravity mediation of supersymmetry breaking at the LHC*, *Phys. Rev.* **D 87** (2013) 015028 [arXiv:1207.5453] [INSPIRE].

[52] L.J. Hall, Y. Nomura and S. Shirai, *Spread supersymmetry with Wino LSP: gluino and dark matter signals*, *JHEP* **01** (2013) 036 [arXiv:1210.2395] [INSPIRE].

[53] N. Arkani-Hamed, A. Gupta, D.E. Kaplan, N. Weiner and T. Zorawski, *Simply unnatural supersymmetry*, arXiv:1212.6971 [INSPIRE].

[54] T. Moroi and M. Nagai, *Probing supersymmetric model with heavy sfermions using leptonic flavor and CP-violations*, *Phys. Lett.* **B 723** (2013) 107 [arXiv:1303.0668] [INSPIRE].

[55] D. McKeen, M. Pospelov and A. Ritz, *EDM signatures of PeV-scale superpartners*, arXiv:1303.1172 [INSPIRE].

[56] J.R. Ellis, M.K. Gaillard and D.V. Nanopoulos, *Baryon number generation in grand unified theories*, *Phys. Lett.* **B 80** (1979) 360 [*Erratum ibid.* **82B** (1979) 464] [INSPIRE].

[57] J. Hisano, H. Murayama and T. Yanagida, *Nucleon decay in the minimal supersymmetric* SU(5) *grand unification*, *Nucl. Phys.* **B 402** (1993) 46 [hep-ph/9207279] [INSPIRE].

[58] V. Lucas and S. Raby, *Nucleon decay in a realistic* SO(10) *SUSY GUT*, *Phys. Rev.* **D 55** (1997) 6986 [hep-ph/9610293] [INSPIRE].

[59] J. Hisano, D. Kobayashi and N. Nagata, *Enhancement of proton decay rates in supersymmetric* SU(5) *grand unified models*, *Phys. Lett.* **B 716** (2012) 406 [arXiv:1204.6274] [INSPIRE].

[60] Super-Kamiokande collaboration, H. Nishino et al., *Search for nucleon decay into charged anti-lepton plus meson in Super-Kamiokande I and II*, *Phys. Rev.* **D 85** (2012) 112001 [arXiv:1203.4030] [INSPIRE].

[61] J. Hisano, H. Murayama and T. Yanagida, *Probing GUT scale mass spectrum through precision measurements on the weak scale parameters*, *Phys. Rev. Lett.* **69** (1992) 1014 [INSPIRE].

[62] M. Miura, *Plans and prospects for the Hyper-Kamiokande detector*, talk given at the *International Workshop on Baryon and Lepton Number Violation (BLV2013)*, April 8–11, Heidelberg, Germany (2013).

[63] M. Liu and P. Nath, *Higgs boson mass, proton decay, naturalness and constraints of LHC and Planck data*, arXiv:1303.7472 [INSPIRE].

[64] Particle Data Group collaboration, J. Beringer et al., *Review of particle physics*, *Phys. Rev.* **D 86** (2012) 010001 [INSPIRE].

[65] Y. Yamada, *Two loop renormalization of gaugino mass in supersymmetric gauge model*, *Phys. Lett.* **B 316** (1993) 109 [hep-ph/9307217] [INSPIRE].

[66] L. Abbott and M.B. Wise, *The effective hamiltonian for nucleon decay*, *Phys. Rev.* **D 22** (1980) 2208 [INSPIRE].

[67] T. Nihei and J. Arafune, *The two loop long range effect on the proton decay effective Lagrangian*, *Prog. Theor. Phys.* **93** (1995) 665 [hep-ph/9412325] [INSPIRE].

[68] M.T. Grisaru, W. Siegel and M. Roček, *Improved methods for supergraphs*, *Nucl. Phys.* **B 159** (1979) 429 [INSPIRE].

JHEP07(2013)038

[69] Y. Aoki, C. Dawson, J. Noaki and A. Soni, *Proton decay matrix elements with domain-wall fermions*, *Phys. Rev.* **D 75** (2007) 014507 [hep-lat/0607002] [INSPIRE].

[70] Y. Aoki, *Proton decay matrix elements from lattice QCD*, talk given at *International Workshop on Grand Unified Theories (GUT2012)*, March 15–17, Kyoto, Japan (2012).

[71] M. Claudson, M.B. Wise and L.J. Hall, *Chiral lagrangian for deep mine physics*, *Nucl. Phys.* **B 195** (1982) 297 [INSPIRE].

[72] S. Chadha and M. Daniel, *Chiral lagrangian calculation of nucleon decay modes induced by $D = 5$ supersymmetric operators*, *Nucl. Phys.* **B 229** (1983) 105 [INSPIRE].

[73] JLQCD collaboration, S. Aoki et al., *Nucleon decay matrix elements from lattice QCD*, *Phys. Rev.* **D 62** (2000) 014506 [hep-lat/9911026] [INSPIRE].

[74] RBC-UKQCD collaboration, Y. Aoki et al., *Proton lifetime bounds from chirally symmetric lattice QCD*, *Phys. Rev.* **D 78** (2008) 054505 [arXiv:0806.1031] [INSPIRE].

JHEP07(2013)038

PHYSICAL REVIEW D **87,** 053004 (2013)

Higgs boson mixes with an $SU(2)$ septet representation

Junji Hisano[1,2,*] and Koji Tsumura[1,†]

[1]*Department of Physics, Nagoya University, Nagoya 464-8602, Japan*
[2]*IPMU, TODIAS, University of Tokyo, Kashiwa 277-8568, Japan*
(Received 28 January 2013; published 12 March 2013)

We study the possibility of the Higgs boson, which consists of an $SU(2)$ doublet and a septet. The vacuum expectation value of a septet with hypercharge $Y = 2$ is known to preserve the electroweak rho parameter unity at the tree level. Therefore, the septet can give a significant contribution to the electroweak symmetry breaking. Because of the mixing with the septet, the gauge coupling of the standard-model-like Higgs boson is larger than that in the standard model. We show the sizable vacuum expectation value of the Higgs septet can be allowed under the constraint from the electroweak precision data. The signal strengths of the Higgs boson for the diphoton and a pair of weak gauge boson decay channels at the LHC are enhanced, while those for the fermionic decay modes are suppressed. The mass of additional neutral Higgs boson is also bounded by the current LHC data for the standard model Higgs boson. We discuss the phenomenology of the multiply charged Higgs bosons, which come from the septet.

DOI: 10.1103/PhysRevD.87.053004 PACS numbers: 12.15.Lk, 12.60.Fr

I. INTRODUCTION

The Higgs boson has been discovered at the LHC [1,2]. However, detailed information such as interaction strengths with each particle has not yet been tested very precisely. The most evident signal excess compared with the background at both experiments (ATLAS [3] and CMS [4]) has been observed in the diphoton decay channel of the Higgs boson. So far, the reported rates of this channel are larger than the value predicted in the standard model (SM). The second best excess was discovered by the $ZZ(\to 4\ell)$ decay mode. We have also seen the small excess in the WW decay channel. The fermionic decay modes of the Higgs boson have not yet been established directly.

The Higgs sector of the SM is still uncertain, which can be extended in various ways. One of the promising extensions is supersymmetry, which is motivated by the stability of the Higgs boson mass under the quantum corrections. In this model, the Higgs sector is required to have an even number of the doublet. Another interesting extension is the Higgs triplet model [5], which consists of the SM Higgs doublet and a Higgs triplet with $Y = 1$. In this model, Majorana neutrino masses are generated from the small vacuum expectation value (VEV) of the triplet. Since there are many extensions of the SM, we need to discriminate them from each other at further precision measurement of the Higgs boson.

The Veltman's rho parameter [6] has been measured very precisely. It would be a good guiding principle to construct beyond the SM. For an arbitrary number of $SU(2)$ scalar multiplets, which have an isospin j_ϕ, a hypercharge Y_ϕ, and a VEV v_ϕ, the rho parameter at tree level is calculated as

$$\rho = \frac{\Sigma_\phi[j_\phi(j_\phi + 1) - Y_\phi^2]v_\phi^2}{\Sigma_\phi 2Y_\phi^2 v_\phi^2}. \tag{1}$$

The precision measurement suggests that ρ is very close to unity. In the SM, the Higgs doublet ($j_\phi = \frac{1}{2}$ and $Y_\phi = \frac{1}{2}$) predicts $\rho = 1$. The multiple doublet extensions of the SM, e.g., the minimal supersymmetric standard model, also predict $\rho = 1$ at tree level. It is known that the next minimal representation, which satisfies $\rho = 1$, is a septet with $Y_\phi = 2$, and the next next minimal one is a 26-plet with $Y_\phi = \frac{15}{2}$. In the usual Higgs representation, the VEV is bounded to be small. For instance, in the Higgs triplet model which consists of a doublet and a triplet Higgs field, the VEV of the triplet is constrained to be less than 3 GeV (2σ level) from $\rho_0 = 1.0004^{+0.0003}_{-0.0004}$ [7], where $\rho_0 = \rho/\rho_{\rm SM}$. If we allow the cancellation among various contributions, the rho parameter can remain unity [8].

In this paper, we construct a framework of the low energy effective theory, which contains a Higgs doublet and a Higgs septet with sizable VEVs. The electroweak sector of the model is extended due to the presence of the septet while keeping the rho parameter unity at tree level. The model is consistent with the electroweak precision data based on the S and T parameter analysis. The gauge coupling of the SM-like Higgs boson can be largely deviated from the SM value due to the mixing with the septet component. The signal strengths of the Higgs boson for the diphoton and for the weak gauge boson pair decays can be enhanced, while those for fermionic decay channels are suppressed. Additional Higgs bosons appear in the weak scale and may be discovered at the LHC. In particular, the singly charged Higgs boson can be produced by the $W^\pm Z$ fusion mechanism.

This paper is organized as follows. In Sec. II, we present a model which consists of a Higgs doublet and a Higgs

*hisano@eken.phys.nagoya-u.ac.jp
†ko2@eken.phys.nagoya-u.ac.jp

 © 2013 American Physical Society

septet. The electroweak precision constraints and the signal strengths of the Higgs bosons at the LHC are studied in Sec. III. The characteristic signatures of the extra (septetlike) Higgs boson are discussed. Conclusions and discussion are given in Sec. IV.

II. THE MODEL

A scalar septet field (χ) with $Y = 2$ is introduced to the SM in addition to the SM Higgs doublet (Φ) with $Y = 1/2$. The Higgs potential is given by

$$\mathcal{V} = -\mu_2^2 \Phi^\dagger \Phi + M_7^2 \chi^\dagger \chi + \lambda (\Phi^\dagger \Phi)^2 - \frac{1}{\Lambda^3}\{(\chi^* \Phi^5 \Phi^*) + \text{H.c.}\} + \sum_{A=1}^{4} \lambda_A (\chi^\dagger \chi \chi^\dagger \chi)_A + \sum_{B=1}^{2} \kappa_B (\Phi^\dagger \Phi \chi^\dagger \chi)_B, \tag{2}$$

where

$$(\Phi^\dagger \Phi \chi^\dagger \chi)_1 = \Phi^{*i} \Phi_i \chi^{*abcdef} \chi_{abcdef}, \tag{3}$$

$$(\Phi^\dagger \Phi \chi^\dagger \chi)_2 = \Phi^{*i} \Phi_j \chi^{*jabcde} \chi_{iabcde}, \tag{4}$$

$$(\chi^\dagger \chi \chi^\dagger \chi)_1 = \chi^{*ijklmn} \chi_{ijklmn} \chi^{*abcdef} \chi_{abcdef}, \tag{5}$$

$$(\chi^\dagger \chi \chi^\dagger \chi)_2 = \chi^{*ijklmn} \chi_{ijklmf} \chi^{*abcdef} \chi_{abcden}, \tag{6}$$

$$(\chi^\dagger \chi \chi^\dagger \chi)_3 = \chi^{*ijklmn} \chi_{ijklef} \chi^{*abcdef} \chi_{abcdmn}, \tag{7}$$

$$(\chi^\dagger \chi \chi^\dagger \chi)_4 = \chi^{*ijklmn} \chi_{ijkdef} \chi^{*abcdef} \chi_{abclmn}, \tag{8}$$

and

$$(\chi^* \Phi^5 \Phi^*) = \chi^{*abcdef} \Phi_a \Phi_b \Phi_c \Phi_d \Phi_e \Phi^{*g} \epsilon_{fg} \tag{9}$$

with $\Phi_1 = \omega_2^+$ and $\Phi_2 = (v_2 + h_2 + i z_2)/\sqrt{2}$. We here introduce the symmetric tensor notation of the septet field as $\chi_{111111} = \chi_3$, $\chi_{111112} = \chi_2/\sqrt{6}$, $\chi_{111122} = \chi_1/\sqrt{15}$, $\chi_{111222} = \chi_0/\sqrt{20}$, $\chi_{112222} = \chi_{-1}/\sqrt{15}$, $\chi_{122222} = \chi_{-2}/\sqrt{6}$, and $\chi_{222222} = \chi_{-3}$ with $\chi_{-2} = (v_7 + h_7 + i z_7)/\sqrt{2}$. Although the Higgs septet can break the electroweak symmetry properly, the Higgs doublet is required for the mass generation of SM fermions. Without a nonrenormalizable term with mass dimension seven, $\chi^* \Phi^5 \Phi^*$, the Higgs potential is conserved under an accidental global $U(1)$ transformations of the doublet and the septet, separately. Therefore, a breaking term of the global symmetry is added in order to avoid an exact massless Nambu-Goldstone boson.

As an example, the dimension-seven operator can be generated from the one-loop contribution given in Fig. 1 by introducing two scalar quintuplets $\Sigma_{I,II}(Y = 1)$ and a scalar triplet $\Delta(Y = 0)$, which are odd under the extra discrete symmetry. The renormalizable Lagrangian related to this one-loop diagram is given by

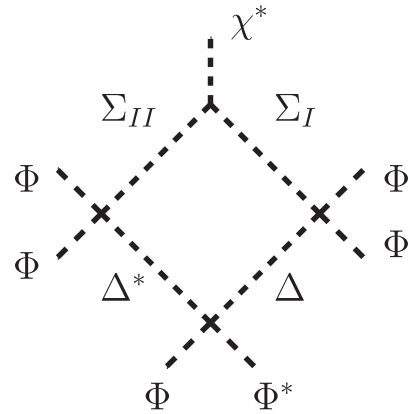

FIG. 1. Radiative generation of dimension-seven operator $\chi^* \Phi^5 \Phi^*$ from the renormalizable UV theory.

$$\mathcal{L}_{\not{U}(1)} = \mu \chi_{abcdef} \Sigma_I^{*abci} \Sigma_{II}^{*defj} \epsilon_{ij} + \Phi_i \Phi_j (c_I \Sigma_I^{*ijkl} + c_{II} \Sigma_{II}^{*ijkl}) \Delta_{kl} + f \Phi_a \Phi^{*b} \Delta^{*ac} \Delta_{bc} + \text{H.c.}, \tag{10}$$

where μ is a soft breaking mass parameter of the global $U(1)$ symmetry and $c_{I,II}$ and f are the coupling constants. In the following discussion, we take into account the dimension-seven operator instead of specifying the UV completion of the model without limiting the generality of the low energy effective theory.[1]

If $M_7^2 < 0$, the Higgs septet and the Higgs doublet develop the VEVs independently. In this case, there are possibilities of the charge-breaking vacua. In addition, the stability of the vacuum is unclear even in the charge-conserving vacuum. In this paper, we consider the case with $M_7^2 > 0$, where the VEV of the Higgs septet is induced through the higher dimensional operator,

$$v_7 \simeq \frac{\sqrt{3}}{24} \frac{v_2^6}{\Lambda^3 M_7^2}. \tag{11}$$

The VEVs of the Higgs doublet and septet are automatically aligned so that the charge-conserving vacuum is realized. Furthermore, we assume that λ_{1-4} and $\kappa_{1,2}$ in the Higgs potential are sufficiently small for simplicity. In this case, we can parametrize the model by only two parameters with the SM-like Higgs boson mass as shown later. Let us remind you that the septet quartic coupling constants generically produce mass splittings among the septetlike scalar bosons, and the latter coupling constants generate mixings between the doublet and the septet. In the following discussion, we mostly neglect the effect of λ_{1-4} and $\kappa_{1,2}$, but a few important implications will be mentioned in the relevant parts.

[1]Phenomenology of the UV theories including dark matter will be studied [9].

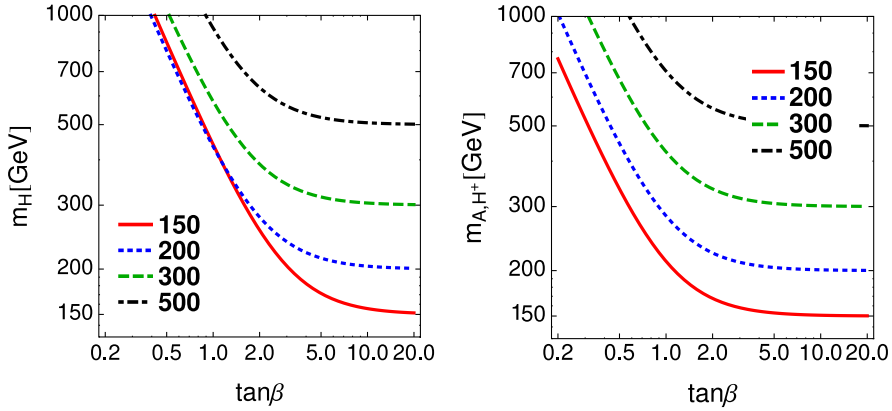

FIG. 2 (color online). Masses for H (left), A, and $H_1^\pm$ (right) are given as functions of $\tan\beta$. The solid, dotted, dashed, and dot-dashed curves correspond to $M_7 = 150$, 200, 300, and 500 GeV, respectively.

The mass matrices for the scalar sector are diagonalized by

$$\begin{pmatrix} h_7 \\ h_2 \end{pmatrix} = \begin{pmatrix} c_\alpha & -s_\alpha \\ s_\alpha & c_\alpha \end{pmatrix} \begin{pmatrix} H \\ h \end{pmatrix}, \tag{12}$$

$$\begin{pmatrix} z_7 \\ z_2 \end{pmatrix} = \begin{pmatrix} c_\beta & -s_\beta \\ s_\beta & c_\beta \end{pmatrix} \begin{pmatrix} z \\ A \end{pmatrix}, \tag{13}$$

$$\begin{pmatrix} \chi_{-1} \\ \chi^*_{-3} \\ \omega_2^+ \end{pmatrix} = \begin{pmatrix} \frac{\sqrt{10}}{4} & \frac{\sqrt{6}}{4} & 0 \\ -\frac{\sqrt{6}}{4} & \frac{\sqrt{10}}{4} & 0 \\ 0 & 0 & 1 \end{pmatrix} \begin{pmatrix} c_\beta & 0 & -s_\beta \\ 0 & 1 & 0 \\ s_\beta & 0 & c_\beta \end{pmatrix} \begin{pmatrix} \omega^+ \\ H_2^+ \\ H_1^+ \end{pmatrix}, \tag{14}$$

where z and $\omega^\pm$ are the electroweak Nambu-Goldstone bosons, the ratio of VEVs is $\tan\beta = v_2/(4v_7)$, and the CP even scalar boson mixing is α. Note that the doublet VEV is dominated in the large $\tan\beta$ limit. Mass eigenvalues are calculated as

$$m_h^2 = \left(1 + \frac{3}{2}\frac{1}{t_\beta t_\alpha}\right) M_7^2, \tag{15}$$

$$m_H^2 = \left(1 - \frac{3}{2}\frac{t_\alpha}{t_\beta}\right) M_7^2, \tag{16}$$

$$m_A^2 = m_{H_1^\pm}^2 = M_7^2/s_\beta^2, \tag{17}$$

$$m_{H_2^\pm}^2 = m_{H^{2\pm}}^2 = m_{H^{3\pm}}^2 = m_{H^{4\pm}}^2 = m_{H^{5\pm}}^2 = M_7^2, \tag{18}$$

where $\chi_3 = H^{5+}$, $\chi_2 = H^{4+}$, $\chi_1 = H^{3+}$, and $\chi_0 = H^{2+}$. There are four input parameters. We here choose $v = (\sqrt{2}G_F)^{-1/2}$, $m_h = 126$ GeV, M_7, and $\tan\beta$. The electroweak interactions of these scalar bosons are determined straightforwardly.

In Fig. 2, masses for H (left), A, and $H_1^\pm$ (right) are shown as functions of $\tan\beta$. The solid, dotted, dashed, and dot-dashed curves denote the cases for $M_7 = 150$, 200, 300, and 500 GeV, respectively. They coincide with the M_7 value at the large $\tan\beta$ region. Mass splittings can be large in the small $\tan\beta$ region, and $m_H > m_A$ is satisfied. We can see from Eq. (11) that the UV completion of the dimension-seven operator spoils rapidly for $\tan\beta \ll 1$. As for the reference, the values of m_H and m_A are listed in Table I.

Let us discuss the modification of the Higgs coupling constant. The correction factors for the gauge interaction of the CP even Higgs bosons are given by

$$C_V^h = s_\beta c_\alpha - 4c_\beta s_\alpha, \tag{19}$$

$$C_V^H = s_\beta s_\alpha + 4c_\beta c_\alpha. \tag{20}$$

The factors are normalized by the SM Higgs boson coupling constant, i.e., $C_V^\phi \equiv \lambda_{\phi VV}/\lambda_{H_{\rm SM}VV}$. Similar correction factors for the Yukawa interaction are also given by

$$C_F^h = c_\alpha/s_\beta, \tag{21}$$

$$C_F^H = s_\alpha/s_\beta. \tag{22}$$

These expressions are the same as in the so-called type-I two Higgs doublet model [10].

In Fig. 3, we show the modification factors C_V^ϕ and C_F^ϕ of the CP even Higgs boson ($\phi = h, H$) for $M_7 = 150$ GeV (top left), $M_7 = 200$ GeV (top right), $M_7 = 300$ GeV

TABLE I. Masses of the heavy CP even and CP odd Higgs bosons are listed for $M_7 = 150$, 200, 300, and 500 GeV.

(m_H, m_A) [GeV]	$\tan\beta = 3$	$\tan\beta = 5$	$\tan\beta = 10$	$\tan\beta = 20$
$M_7 = 150$ GeV	(204., 158.)	(171., 153.)	(156., 151.)	(151., 150.)
$M_7 = 200$ GeV	(238., 211.)	(214., 204.)	(204., 201.)	(202., 200.)
$M_7 = 300$ GeV	(343., 316.)	(316., 306.)	(304., 301.)	(302., 301.)
$M_7 = 500$ GeV	(563., 527.)	(523., 510.)	(506., 502.)	(503., 501.)

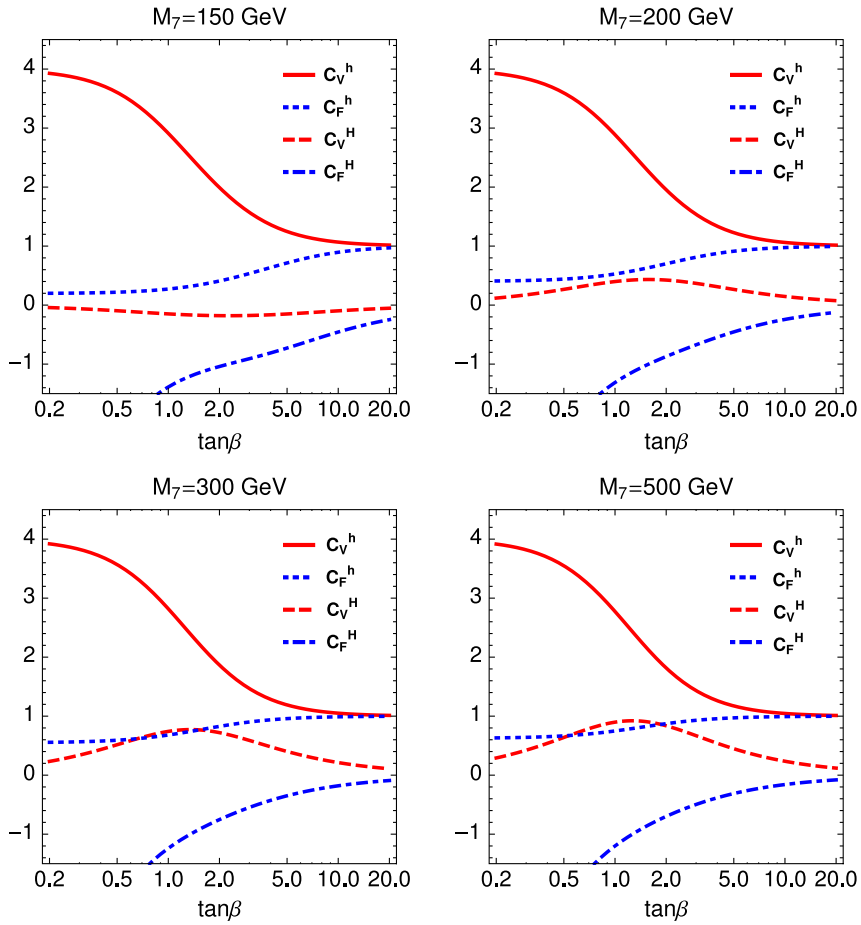

FIG. 3 (color online). Correction factors for the gauge and the Yukawa coupling constants of the CP even Higgs bosons are presented as functions of $\tan\beta$ for $M_7 = 150$ GeV (top left), $M_7 = 200$ GeV (top right), $M_7 = 300$ GeV (bottom left), and $M_7 = 500$ GeV (bottom right). The solid, dotted, dashed, and dot-dashed curves express C_V^h, C_F^h, C_V^H, and C_F^H, respectively.

(bottom left), and $M_7 = 500$ GeV (bottom right). The solid, dotted, dashed, and dot-dashed curves represent C_V^h, C_F^h, C_V^H, and C_F^H, respectively. Since the doublet VEV is dominated in the large $\tan\beta$ region, the coupling strengths of h become SM-like, while those of H vanish. The maximal value of C_V^h is four, which is determined by the hypercharges of the septet and the doublet. The gauge interaction of the SM-like Higgs boson is greater than one for all plots because of the mixing with the septet component. The prediction $C_V^h > 1$ can also be obtained in the Georgi-Machacek model, which has been studied with the Higgs boson signal at the LHC [11,12].

III. PHENOMENOLOGY

In this section, we investigate the current experimental constraint from the electroweak precision data and also from the Higgs boson searches at the LHC. The LHC signatures of the model are also studied.

We begin with the constraint from the electroweak sector. In this model, the oblique corrections [13] from the scalar bosons are calculated as

$$S = \frac{1}{4\pi}[(C_V^h)^2 G^{hZ\prime} + (C_V^H)^2 G^{HZ\prime} + 30 c_\beta^2 G^{H_2^\pm W\prime} + 30 s_\beta^2 F^{H_1^\pm H_2^\pm \prime} - \frac{1}{3}\ln m_{H_1^\pm}^2 - 15 \ln m_{H_2^\pm}^2 + (4 s_\alpha s_\beta - c_\alpha c_\beta) F^{hA\prime} + (4 c_\alpha s_\beta + s_\alpha c_\beta) F^{HA\prime}], \quad (23)$$

$$T = \frac{\sqrt{2} G_F}{\alpha_{\rm EM}(4\pi)^2}[(C_V^h)^2 \Delta G^h + (C_V^H)^2 \Delta G^H - 15 c_\beta^2 \Delta G^{H_2^\pm}], \quad (24)$$

where the loop functions $G^{xy\prime}$, $F^{xy\prime}$, and ΔG^x are given in the Appendix.

In Fig. 4, the deviations of the S parameter (left) and T parameter (right) are plotted for $M_7 = 150$ GeV (solid line), $M_7 = 200$ GeV (dotted line), $M_7 = 300$ GeV (dashed line), and $M_7 = 500$ GeV (dot-dashed line) as functions of $\tan\beta$. The current experimental bounds on oblique parameters are $\Delta S = 0.04 \pm 0.09$ and $\Delta T = 0.07 \pm 0.08$ with the 88% correlation by fixing $\Delta U = 0$ [7]. In the small $\tan\beta$ region, relatively larger negative (positive) contributions to the S (T) parameter are

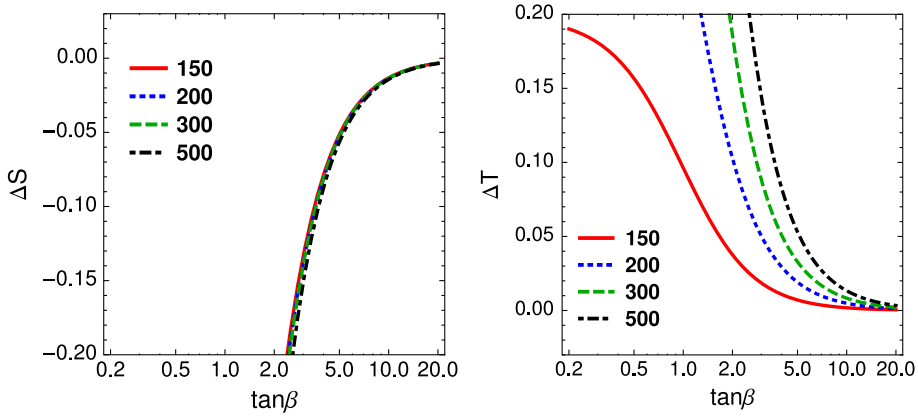

FIG. 4 (color online). Oblique corrections are evaluated as functions of $\tan\beta$. The solid, dotted, dashed, and dot-dashed curves represent the cases for $M_7 = 150$, 200, 300, and 500 GeV, respectively.

found. For $\Delta T = 0$, ΔS is constrained to be larger than $-0.08(-0.11)$ at 68(90)% confidence level. From the S parameter only, $\tan\beta \gtrsim 5$ is obtained. Because we are fixing the value of $\tan\beta$, these effects are nondecoupling for higher M_7. In fact, the largest contribution to the T parameter is seen for $M_7 = 500$ GeV. As for the reference, the values of ΔS and ΔT are listed in Table II.

Let us turn to the LHC phenomenology. At the LHC, we have found the Higgs boson around 126 GeV using $\gamma\gamma$ and $ZZ(\to 4\ell)$ decay channels. Since the coupling constants of the SM-like Higgs boson are corrected, these signal strengths can be changed. Roughly speaking, 90% of the Higgs bosons come from the gluon fusion mechanism at the LHC with $\sqrt{s} = 7$ TeV and/or $\sqrt{s} = 8$ TeV without selection cuts. Assuming the dominance of the gluon fusion production cross section, the signal strengths are evaluated as

$$\mu^h_{VV} \simeq (C^h_F)^2 \frac{1}{(C^h_F)^2(\mathcal{B}_{bb} + \mathcal{B}_{cc} + \mathcal{B}_{\tau\tau} + \mathcal{B}_{gg}) + (C^h_V)^2(\mathcal{B}_{WW} + \mathcal{B}_{ZZ})}(C^h_V)^2, \tag{25}$$

$$\mu^h_{f\bar{f}} \simeq (C^h_F)^2 \frac{1}{(C^h_F)^2(\mathcal{B}_{bb} + \mathcal{B}_{cc} + \mathcal{B}_{\tau\tau} + \mathcal{B}_{gg}) + (C^h_V)^2(\mathcal{B}_{WW} + \mathcal{B}_{ZZ})}(C^h_F)^2, \tag{26}$$

$$\mu^h_{\gamma\gamma} \simeq (C^h_F)^2 \frac{1}{(C^h_F)^2(\mathcal{B}_{bb} + \mathcal{B}_{cc} + \mathcal{B}_{\tau\tau} + \mathcal{B}_{gg}) + (C^h_V)^2(\mathcal{B}_{WW} + \mathcal{B}_{ZZ})} R, \tag{27}$$

where

$$R = \left| \frac{C^h_F N_c Q_t^2 A_{1/2}(\tau_t) + C^h_V A_1(\tau_W)}{N_c Q_t^2 A_{1/2}(\tau_t) + A_1(\tau_W)} \right|^2, \tag{28}$$

$$A_{1/2}(\tau) = 2[\tau + (\tau - 1)f(\tau)]\tau^{-2}, \tag{29}$$

$$A_1(\tau) = -[2\tau^2 + 3\tau + 3(2\tau - 1)f(\tau)]\tau^{-2}, \tag{30}$$

with $\tau_x = m_h^2/(4m_x^2)$ and

$$f(\tau) = \begin{cases} \arcsin^2\sqrt{\tau} & \tau \le 1, \\ -\frac{1}{4}\left[\ln\frac{1+\sqrt{1-\tau^{-1}}}{1-\sqrt{1-\tau^{-1}}} - i\pi\right]^2 & \tau > 1. \end{cases} \tag{31}$$

The recommended values of the branching ratios of the SM Higgs boson are listed in Table III [14]. Because we are neglecting the interactions between the doublet and the septet in the Higgs potential, the (multiply) charged Higgs boson loop contributions are omitted.[2]

In Fig. 5, the signal strengths of the SM-like Higgs boson at the LHC are shown as functions of $\tan\beta$ for $M_7 = 150$ GeV (top left), $M_7 = 200$ GeV (top right), $M_7 = 300$ GeV (bottom left), and $M_7 = 500$ GeV (bottom right). The solid, dotted, and dashed curves denote the signal strengths for $\gamma\gamma$, $VV^*(V = W, Z)$, and $f\bar{f}$ decays, respectively, of the SM-like Higgs boson h. As we have seen in Fig. 3, the production cross section of the Higgs boson via gluon fusion is suppressed by $(C^h_F)^2$. On the other hand, the $b\bar{b}$ decay channel, which is the main decay mode of the SM Higgs boson, is suppressed in the present model. Furthermore, the effective gauge coupling of the SM-like Higgs boson is larger than that of the SM

[2]Detailed studies of the extended scalar sector are beyond the scope of this paper. It will be shown in elsewhere [9].

TABLE II. Oblique corrections to S and T parameters are listed for $M_7 = 150$, 200, 300, and 500 GeV.

$(\Delta S, \Delta T)$	$\tan\beta = 3$	$\tan\beta = 5$	$\tan\beta = 10$	$\tan\beta = 20$
$M_7 = 150$ GeV	$(-0.13, 0.019)$	$(-0.05, 0.007)$	$(-0.013, 0.002)$	$(-0.003, 0.)$
$M_7 = 200$ GeV	$(-0.14, 0.050)$	$(-0.05, 0.019)$	$(-0.014, 0.005)$	$(-0.003, 0.001)$
$M_7 = 300$ GeV	$(-0.14, 0.088)$	$(-0.05, 0.033)$	$(-0.013, 0.008)$	$(-0.003, 0.002)$
$M_7 = 500$ GeV	$(-0.15, 0.14)$	$(-0.06, 0.053)$	$(-0.014, 0.013)$	$(-0.004, 0.003)$

TABLE III. Recommended value for the Higgs boson decay branching ratios for $m_{H_{\rm SM}} = 126$ GeV.

	$\mathcal{B}_{bb}$	$\mathcal{B}_{cc}$	$\mathcal{B}_{\tau\tau}$	$\mathcal{B}_{WW}$	$\mathcal{B}_{ZZ}$	$\mathcal{B}_{gg}$
$m_{H_{\rm SM}} = 126$ GeV	0.56	0.028	0.062	0.23	0.029	0.085

Higgs boson. Therefore, the net contributions to μ^h_{VV} can be enhanced. The diphoton decay mode is more enhanced than the VV mode due to the enhanced gauge interaction and the suppressed Yukawa interaction in the loop. For $M_7 = 150$ GeV, $\mu^h_{\gamma\gamma}$ can be close to 1.2 with $\tan\beta \simeq 5$, which is allowed by electroweak precision data. In this case, μ^h_{VV} is close to unity, which is favored by the current experimental data. For larger M_7, $\mu^h_{\gamma\gamma}$ can be larger than 1.5 in the small $\tan\beta$ region, which is, however, excluded by electroweak precision data.

It is too early to discuss the precise values of the signal strengths. Qualitatively, the larger signal strengths for the bosonic decay modes and the smaller signal strengths for the fermionic decay modes are predicted. You might consider that the enhancement of the diphoton decay rate is not sufficient to explain the observations at the LHC. However, in the Higgs septet there are many multiply charged Higgs

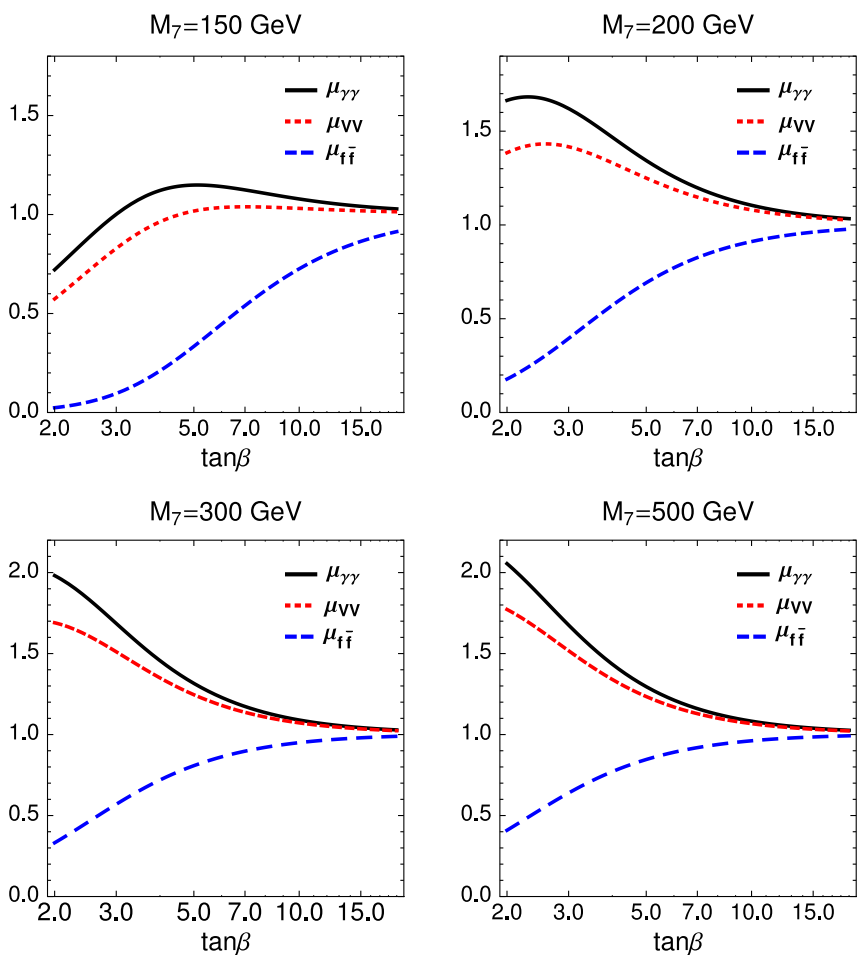

FIG. 5 (color online). Signal strengths for each Higgs boson decay mode at the LHC are shown as functions of $\tan\beta$. The mass scale M_7 is chosen as 150 (top left), 200 (top right), 300 (bottom left), and 500 GeV (bottom right).

TABLE IV. Signal strength for $H \to VV$ decay modes are listed for $M_7 = 150$, 200, 300, and 500 GeV.

$(m_H$ [GeV], $\mu_{VV}^H)$	$\tan\beta = 5$	$\tan\beta = 6$	$\tan\beta = 7$	$\tan\beta = 8$	$\tan\beta = 9$	$\tan\beta = 10$
$M_7 = 150$ GeV	(171., 0.44)	(165., 0.31)	(161., 0.20)	(159., 0.13)	(157., 0.081)	(156., 0.062)
$M_7 = 200$ GeV	(214., 0.21)	(210., 0.15)	(207., 0.11)	(206., 0.089)	(205., 0.071)	(204., 0.059)
$M_7 = 300$ GeV	(316., 0.12)	(311., 0.087)	(308., 0.065)	(306., 0.050)	(305., 0.040)	(304., 0.032)
$M_7 = 500$ GeV	(523., 0.12)	(516., 0.084)	(512., 0.063)	(509., 0.048)	(507., 0.038)	(503., 0.031)

bosons, which may further enhance the diphoton signal if there are interactions between the doublet and the septet.

The current LHC bound for the heavier SM Higgs boson can be rescaled to constrain the mass of H using C_F^H and C_V^H factors. For the heavier CP even Higgs boson, the strongest bound comes from the signal strength of weak gauge boson decay modes. By using the recommended values of the SM Higgs decay branching ratios, the signal strength is evaluated in Table IV, where only the decay modes into the SM particles are included. The decays of $H \to AZ^*$ and $H \to H_1^\pm W^{\mp *}$ give a negligible contribution due to the small mass splittings. From the LHC data [4,15], the signal strength is constrained to be less than 0.1–0.3 for $m_H = 150$–500 GeV. For $M_7 \simeq 200$ GeV, $\tan\beta \gtrsim 5$ is allowed by current experimental data. For smaller M_7, $\tan\beta$ is required to be small in order to avoid the constraint from the nondiscovery of such a boson.

The smoking gun of the septet contribution would be the presence of the $ZW^\mp H^\pm$ vertex. This kind of interaction is prohibited in the multi-Higgs doublet models, which give $\rho = 1$ at tree level. The higher dimensional representation can generate this vertex; however, the size of the coupling strength is suppressed by the small VEV due to the strong constraint from the rho parameter. Since the VEV of the Higgs septet with $Y = 2$ can be sizable, a relatively large $ZW^\mp H^\pm$ vertex is allowed. In this model, we have

$$\mathcal{L}_v = +\frac{\sqrt{15}}{2} g g_Z v c_\beta Z_\mu (H_2^- W^{+\mu} + H_2^+ W^{-\mu}). \quad (32)$$

Note that if the term proportional to κ_i exists in the Higgs potential, $H_1^\pm$ also couples with $ZW^\mp$ via the mixing with $H_2^\pm$. If the charged Higgs boson $H_2^\pm$ is sufficiently light and $\tan\beta \lesssim 10$, $H_2^\pm$ can be produced by $W^\pm Z$ fusion at the LHC [16]. The precision measurement of this coupling is possible at the International Linear Collider by using the recoil method via $e^+e^- \to Z^* \to W^\mp H_2^\pm$ [17].

The presence of the multiply charged Higgs bosons is also an interesting feature of the model. Because of the relatively large VEV of the septet, the doubly charged Higgs boson in this model mostly decays into the same-signed weak gauge bosons and is produced via the $W^\pm W^\pm \to H^{2\pm}$ process. Such a process has been studied [18] in the context of the Higgs triplet model and the Georgi-Machacek model. The multiply charged Higgs boson with an electric charge higher than two has a long decay chain, which provides multiple weak boson final states.

IV. CONCLUSIONS

We have studied the model that consists of the Higgs doublet with $Y = 1/2$ and the Higgs septet with $Y = 2$. The VEVs of the doublet and the septet preserve the electroweak rho parameter unity at tree level without any cancellation. The presence of the Higgs septet can give substantial contributions to the electroweak symmetry breaking. A nonrenormalizable operator is introduced in order to break the accidental global symmetry. A UV completion of the operator is also presented. From the viewpoint of the UV completion, it would be difficult to introduce much higher dimensional representations with a sizable VEV such as a 26-plet with $Y = \frac{15}{2}$. Therefore, the Higgs septet would only be a realistic possibility besides doublets.

In this model, the gauge coupling constant of the SM-like Higgs boson (h) is predicted to be larger than that in the SM. We have shown that the modified electroweak interactions due to the sizable VEV of the Higgs septet are consistent with the electroweak precision data. The signal strengths of the SM-like Higgs boson at the LHC for the diphoton and for the weak boson pair decay modes are enhanced, while those for the fermionic decay channels are suppressed. The mass of the additional CP even neutral Higgs boson (H) is constrained by the current LHC data depending on the ratio of the VEVs. The VEV of the Higgs septet induces a sizable $W^\mp Z H^\pm$ vertex ($H^\pm$ is the charged Higgs boson in the Higgs septet), which is forbidden in the multi-Higgs doublet extension of the SM and is highly suppressed by the VEV, e.g., in the Higgs triplet model. One of the interesting signatures of the model would be the $W^\pm Z$ fusion production of the charged Higgs boson at the LHC.

The electroweak sector of the model has been discussed in this paper. We mention the implications of the model. As we have slightly noted, the diphoton decay rate of the SM-like Higgs boson can be enhanced by the effects of the multiply charged Higgs boson loops. Such an effect generally requires larger coupling constants in the Higgs potential. Therefore, the mass degeneracy among the septetlike scalar bosons would be resolved. These mass splitting may give sizable contributions to the electroweak precision parameters as in the two Higgs doublet models [19]. The potential parameters are further bounded by perturbative unitarity and the vacuum stability. If the singly charged Higgs boson is light, it may be constrained by

flavor data. The Higgs sector with the Higgs septet potentially has rich phenomena. It would be worth investigating further [9].

ACKNOWLEDGMENTS

We thank Masaharu Tanabashi for valuable comments. This work is supported by Grant-in-Aid for Scientific research from the Ministry of Education, Science, Sports, and Culture (MEXT), Japan, Grants No. 20244037, No. 20540252, No. 22244021, and No. 23104011, and also by World Premier International Research Center Initiative (WPI Initiative), MEXT, Japan.

APPENDIX: ONE-LOOP INTEGRALS

The loop functions used in the evaluation of the oblique parameters are listed below:

$$F^{xy} = \frac{m_x^2 + m_y^2}{2} - \frac{m_x^2 m_y^2}{m_x^2 - m_y^2} \ln \frac{m_x^2}{m_y^2}, \tag{A1}$$

$$G^{xV} = F^{xV} + 4m_V^2\left(-1 + \frac{m_x^2 \ln m_x^2 - m_V^2 \ln m_V^2}{m_x^2 - m_V^2}\right), \tag{A2}$$

$$\Delta G^x = G^{xW} - G^{xZ}, \tag{A3}$$

$$F^{xy\prime} = -\frac{1}{3}\left(+\frac{4}{3} - \frac{m_x^2 \ln m_x^2 - m_y^2 \ln m_y^2}{m_x^2 - m_y^2} - \frac{m_x^2 + m_y^2}{(m_x^2 - m_y^2)^2} F^{xy}\right), \tag{A4}$$

$$G^{xV\prime} = F^{xV\prime} + 4m_V^2\left(-\frac{1}{(m_x^2 - m_V^2)^2} F^{xV}\right). \tag{A5}$$

[1] ATLAS Collaboration, Phys. Lett. B **716**, 1 (2012).
[2] CMS Collaboration, Phys. Lett. B **716**, 30 (2012).
[3] ATLAS Collaboration, Report No. ATLAS-CONF-2012-170.
[4] CMS Collaboration, Report No. CMS-PAS-HIG-12-045.
[5] W. Konetschny and W. Kummer, Phys. Lett. **70B**, 433 (1977); M. Magg and C. Wetterich, Phys. Lett. **94B**, 61 (1980); T. P. Cheng and L. F. Li, Phys. Rev. D **22**, 2860 (1980); J. Schechter and J. W. F. Valle, Phys. Rev. D **22**, 2227 (1980).
[6] D. A. Ross and M. J. G. Veltman, Nucl. Phys. **B95**, 135 (1975); M. J. G. Veltman, Nucl. Phys. **B123**, 89 (1977).
[7] Particle Data Group, Phys. Rev. D **86**, 010001 (2012).
[8] H. Georgi and M. Machacek, Nucl. Phys. **B262**, 463 (1985); M. S. Chanowitz and M. Golden, Phys. Lett. **165B**, 105 (1985).
[9] J. Hisano and K. Tsumura (to be published).
[10] J. F. Gunion, H. E. Haber, G. Kane, and S. Dawson, *The Higgs Hunter's Guide*, Frontiers in Physics series (Addison-Wesley, Reading, MA, 1990).
[11] S. Chang, C. A. Newby, N. Raj, and C. Wanotayaroj, Phys. Rev. D **86**, 095015 (2012).
[12] D. Carmi, A. Falkowski, E. Kuflik, T. Volansky, and J. Zupan, J. High Energy Phys. 10 (2012) 196.
[13] M. E. Peskin and T. Takeuchi, Phys. Rev. Lett. **65**, 964 (1990); Phys. Rev. D **46**, 381 (1992).
[14] https://twiki.cern.ch/twiki/bin/view/LHCPhysics/CrossSections.
[15] ATLAS Collaboration, Report No. ATLAS-CONF-2012-169.
[16] E. Asakawa, S. Kanemura, and J. Kanzaki, Phys. Rev. D **75**, 075022 (2007).
[17] S. Kanemura, K. Yagyu, and K. Yanase, Phys. Rev. D **83**, 075018 (2011).
[18] P. F. Perez, T. Han, G.-y. Huang, T. Li, and K. Wang, Phys. Rev. D **78**, 015018 (2008); C.-W. Chiang, T. Nomura, and K. Tsumura, Phys. Rev. D **85**, 095023 (2012).
[19] S. Kanemura, Y. Okada, H. Taniguchi, and K. Tsumura, Phys. Lett. B **704**, 303 (2011).

Published for SISSA by Springer

Received: November 22, 2013
Accepted: December 29, 2013
Published: January 20, 2014

Gauge invariant Barr-Zee type contributions to fermionic EDMs in the two-Higgs doublet models

Tomohiro Abe,[a] **Junji Hisano,**[b,c] **Teppei Kitahara**[d] **and Kohsaku Tobioka**[c,d]

[a] *Theory Group, KEK,*
1-1 Oho, Tsukuba, 305-0801, Japan
[b] *Department of Physics, Nagoya University,*
Furo-cho, Chikusa-ku, Nagoya 464-8602, Japan
[c] *Kavli Institute for the Physics and Mathematics of the Universe (WPI),*
University of Tokyo,
5-1-5 Kashiwanoha, Kashiwa, 277-8583, Japan
[d] *Department of Physics, University of Tokyo,*
7-3-1 Hongo, Bunkyo-ku, 113-0033, Japan

E-mail: abetomo@post.kek.jp, hisano@eken.phys.nagoya-u.ac.jp, kitahara@hep-th.phys.s.u-tokyo.ac.jp, kohsaku.tobioka@ipmu.jp

Abstract: We calculate all gauge invariant Barr-Zee type contributions to fermionic electric dipole moments (EDMs) in the two-Higgs doublet models (2HDM) with softly broken Z_2 symmetry. We start by studying the tensor structure of $h \to VV'$ part in the Barr-Zee diagrams, and we calculate the effective couplings in a gauge invariant way by using the pinch technique. Then we calculate all Barr-Zee diagrams relevant for electron and neutron EDMs. We make bounds on the parameter space in type-I, type-II, type-X, and type-Y 2HDMs. The electron and neutron EDMs are complementary to each other in discrimination of the 2HDMs. Type-II and type-X 2HDMs are strongly constrained by recent ACME experiment's result, and future experiments of electron and neutron EDMs may search $\mathcal{O}(10)$ TeV physics.

Keywords: Beyond Standard Model, CP violation, Electromagnetic Processes and Properties

ArXiv ePrint: 1311.4704

Open Access, © The Authors.
Article funded by SCOAP[3].

doi:10.1007/JHEP01(2014)106

JHEP01(2014)106

Contents

1 Introduction **2**

2 Models **3**

3 Effective vertices **4**
- 3.1 Tensor structure of the effective vertices 4
- 3.2 Effective $h\gamma\gamma$ and $hZ\gamma$ vertices — W boson loop — 6
- 3.3 Effective $h\gamma\gamma$ and $hZ\gamma$ vertices — fermion, $H^{\pm}$ loop — 8
- 3.4 Effective $H^{\mp}W^{\pm}\gamma$ vertices — W, $H^{\pm}$ loop — 9

4 EDM from Barr-Zee diagram **9**

5 Numerical results **12**

6 Conclusions and discussion **19**

A 2HDMs **20**
- A.1 Relations between mass and gauge eigenstates 20
- A.2 Higgs masses in 2HDMs 21
- A.3 Interactions in 2HDMs 22
  - A.3.1 $\bar{f}$-f-V couplings 22
  - A.3.2 Yukawa couplings 23
  - A.3.3 $\mathcal{L}_{\rm WWW}$ 24
  - A.3.4 W^+-W^--h couplings 24
  - A.3.5 V-H^+-H^- couplings 25
  - A.3.6 $W^{\pm}$-$H^{\mp}$-h couplings 25
  - A.3.7 s^+-s^--h couplings 25
  - A.3.8 $W^{\pm}$-$\pi^{\mp}$-h couplings 26
  - A.3.9 V-$W^{\pm}$- $\pi^{\mp}$ couplings 26
  - A.3.10 Some four-point couplings 26

B EDM formula details **26**
- B.1 Fermion loops ($h\gamma\gamma$ and $hZ\gamma$) 26
- B.2 Charged Higgs loops ($h\gamma\gamma$ and $hZ\gamma$) 27
- B.3 W loops ($h\gamma\gamma$ and $hZ\gamma$) 27
- B.4 $H^{\mp}W^{\pm}\gamma$ 28
- B.5 CEDMs 28

C Derivation for effective $H^-W^+\gamma$ vertex **28**

JHEP01(2014)106

1 Introduction

The standard model (SM) has been worked very well for a long time, and its last missing piece, the Higgs boson, was finally discovered by the Large Hadron Collider (LHC) experiment at CERN [1, 2]. This is a triumph of the SM and a great step to understand physics at the electroweak scale. However, there are many unsolved problems within the SM, for example, the observed dark matter particles and baryon asymmetry in the Universe. From theoretical viewpoint, the gauge hierarchy problem is still in question. Hence, there have been many attempts to solve such problems in frameworks beyond the SM.

In a bottom-up approach towards new physics beyond the SM, an attractive option is to study the two-Higgs doublet models (2HDMs). They are simple and may be low-energy effective theories of various new physics models. Since 2HDMs generally have dangerous flavor changing neutral currents (FCNCs), we particularly consider 2HDMs with softly broken Z_2 symmetry which suppresses the FCNCs. If two Higgs fields do not distinguish the generations of quarks and leptons, the models are classified, with respect to the Yukawa interactions, into four types: type-I, type-II, type-X, and type-Y. One of the important feature of 2HDMs is that there is a new CP violation source in the Higgs potential.

In general, the powerful tool to seek new physics including 2HDMs is of course the LHC which may directly probe physics up to a few TeV. Another possibility is provided by low energy precision measurements, such as in flavor physics. The remarkable feature is that these measurements have a potential to investigate new physics beyond the LHC reach by orders of magnitude. In particular, the electric dipole moments (EDMs) are interesting because the EDMs are highly sensitive to CP violation in physics beyond the SM. While the SM predictions of EDMs are much lower than the current experimental bounds, assuming the strong CP problem is solved by some mechanism, such as the Peccei-Quinn symmetry [3, 4], new physics around TeV scale would give large values within the reach of the future EDM measurements [5–7]. In addition, the electroweak baryogenesis (EWBG) [8–11], which needs a new CP violation source, may lead to larger values of EDMs than the SM predictions.

The EDM measurements, therefore, are concrete tests on 2HDMs containing a new CP phase. In the models, the one-loop contributions to the fermionic EDMs are too small to observed since those contributions are proportional to the third power of small Yukawa couplings. Some two-loop diagrams, called the Barr-Zee diagrams [12], which we show in figure 1, may give sizable contributions to the EDMs, since they are suppressed by only one power of small Yukawa couplings. These diagrams contain one-loop effective vertices, $h\gamma\gamma$, $h\gamma Z$, and $H^{\mp}W^{\pm}\gamma$. The Type-II case was evaluated in refs. [13, 14], but the results in the previous works are not gauge invariant. We improve this point by using the pinch technique [15–17] and make the Barr-Zee diagrams gauge invariant. We also study EDMs in the other three types as well as the type-II.

We organize this paper as follows. In section 2, we briefly review the 2HDMs with softly-broken Z_2 symmetry. In section 3, we study the tensor structure of the effective vertices which are needed to evaluate the Barr-Zee diagrams, and show the gauge invariant tensor structure. After that, we calculate the effective vertices explicitly and show that the diagrams which include the gauge bosons are not gauge invariant. This implies that we

JHEP01(2014)106

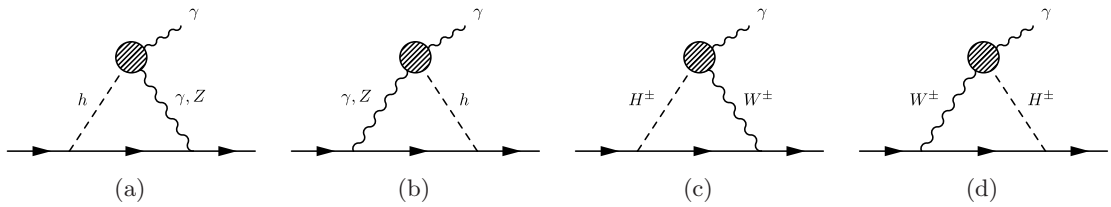

Figure 1. Barr-Zee diagrams, which contribute to fermionic EDMs at two-loop level.

need some non-Barr-Zee diagrams to make the effective vertices gauge invariant. We show it by using the pinch technique. The formulae of the gauge invariant Barr-Zee diagrams are given in section 4, and their numerical evaluation is presented in section 5. There we discuss the complementarity between the electron and neutron EDM measurements in discrimination of 2HDMs, and also prospects of future experiments. Section 6 is devoted to conclusions and discussion. Notations and details of the calculation are given in the appendices.

2 Models

We briefly review the models discussed in this paper. We have two Higgs doublets, H_1 and H_2, and they have the vacuum expectation values (VEVs). The Higgs doublets are parametrized as follows,

$$H_i = \begin{pmatrix} \pi_i^+ \\ \frac{1}{\sqrt{2}}\left(v_i + \sigma_i - i\pi_i^3\right) \end{pmatrix}, \qquad (i = 1, 2)\,. \tag{2.1}$$

In order to avoid the dangerous FCNC problems, we introduce the Z_2 symmetry. The Z_2 symmetry is assumed to be softly broken so that the domain-wall formation in the early universe is suppressed. Under this symmetry, the Higgs doublets are translated into $H_1 \to +H_1$ and $H_2 \to -H_2$, and the Higgs potential is given as

$$\begin{aligned} V = {} & m_1^2 H_1^\dagger H_1 + m_2^2 H_2^\dagger H_2 - \left(\left(\mathrm{Re}m_3^2 + i\mathrm{Im}m_3^2\right) H_1^\dagger H_2 + (h.c.)\right) \\ & + \frac{1}{2}\lambda_1 \left(H_1^\dagger H_1\right)^2 + \frac{1}{2}\lambda_2 \left(H_2^\dagger H_2\right)^2 + \lambda_3 \left(H_1^\dagger H_1\right)\left(H_2^\dagger H_2\right) + \lambda_4 \left(H_1^\dagger H_2\right)\left(H_2^\dagger H_1\right) \\ & + \left(\lambda_5 e^{i2\phi}\left(H_1^\dagger H_2\right)^2 + (h.c.)\right). \end{aligned} \tag{2.2}$$

The third and last terms in this potential contain complex parameters. While one of them can be eliminated by redefinition of Higgs fields, another phase is physical so that CP symmetry is broken. In this paper we take the Higgs VEVs, v_1 and v_2, real using the gauge symmetry and also redefinition of a Higgs field. In this basis, two phases in the potential are related to each others by the stationary condition of the potential, $V' = 0$. In this paper we choose ϕ as an input parameter for CP violation.

We also use the following variables for convenience in this paper,

$$\cos\beta = \frac{v_1}{v}\,, \quad \sin\beta = \frac{v_2}{v}\,, \tag{2.3}$$

$$M^2 \equiv \frac{v_1^2 + v_2^2}{v_1 v_2}\mathrm{Re}m_3^2\,, \tag{2.4}$$

JHEP01(2014)106

Type	I	II	X	Y
u	H_2	H_2	H_2	H_2
d	H_2	H_1	H_2	H_1
ℓ	H_2	H_1	H_1	H_2

Table 1. Summary of the Higgs fields which couple to quarks and leptons in four types.

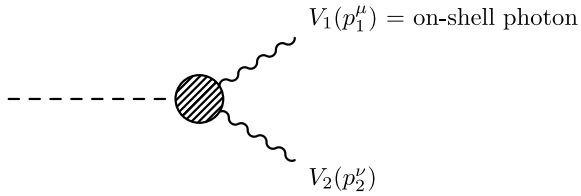

Figure 2. Effective Higgs boson-vector boson-vector boson vertices.

and where

$$v = \sqrt{v_1^2 + v_2^2} = \left(\sqrt{2}G_F\right)^{-1/2} \simeq 246\,\text{GeV}\,. \tag{2.5}$$

G_F is the Fermi constant. It is easy to find the charged Higgs boson mass,

$$m_{H^\pm}^2 = M^2 - \frac{1}{2}v^2(\lambda_4 + \lambda_5\cos(2\phi)). \tag{2.6}$$

On the other hand, since CP symmetry is broken in the Higgs potential, we need to diagonalize a 3 by 3 matrix to find the neutral Higgs masses.

The Yukawa interaction in this model is given by

$$\mathcal{L}_{\text{Yukawa}} = -\overline{q}_L\widetilde{H}_2 y_u u_R - \overline{q}_L H_i y_d d_R - \overline{\ell}_L H_j y_e e_R + h.c.\,, \tag{2.7}$$

where $\widetilde{H}_2 = \epsilon H_2^*$, and $i, j = 1$ or 2, depending on the type of 2HDMs. While up-type quarks couple to only to H_2, leptons and down-type quarks couple to either H_1 or H_2 due to the Z_2 symmetry. We summarize which Higgs fields couple to fermions in table 1.

The detail information of the models, such as mass eigenvalues, mixings, and interactions of the Higgs bosons, are given in appendix A.

3 Effective vertices

In this section we calculate effective vertices relevant for the Barr-Zee diagrams in a gauge invariant way. To make our point clear, we start by exploring the relevant form of the effective vertices shown in figure 2. Then we calculate effective $h\gamma\gamma$, $hZ\gamma$ and $H^\mp W^\pm\gamma$ vertices . We also calculate the pinch terms to make the vertices gauge invariant.

3.1 Tensor structure of the effective vertices

We study the tensor structure of the effective vertices shown in figure 2. This part has two Lorentz indices, and does not contain γ-matrices. Then it is generally written as

$$\Gamma^{\mu\nu} = A_0 g^{\mu\nu} + A_1 p_1^\mu p_1^\nu + A_2 p_2^\mu p_2^\nu + A_{12} p_1^\mu p_2^\nu + A_{21} p_2^\mu p_1^\nu + i\Gamma_5 \epsilon^{\mu\nu\rho\sigma} p_{1\rho} p_{2\sigma}, \tag{3.1}$$

JHEP01(2014)106

where p_1^μ and p_2^ν are the momenta of V_1 and V_2, respectively, and their direction is outgoing. We consider the case that V_1 is on-shell photon, and thus the terms proportional to p_1^μ are dropped. In addition, the gauge symmetry of photon requires $\Gamma^{\mu\nu}p_{1\mu} = 0$. Then, the effective vertex for h-V_1-V_2 in the case that V_1 is on-shell photon is defined with only two form factors as

$$\Gamma^{\mu\nu}(p_1,p_2) = \Gamma(p_1,p_2)\left(-(p_1p_2)g^{\mu\nu} + p_2^\mu p_1^\nu\right) + i\Gamma^5(p_1,p_2)\epsilon^{\mu\nu\rho\sigma}p_{1\rho}p_{2\sigma}\,. \tag{3.2}$$

Note that this tensor structure is led from the gauge symmetry of on-shell photon. Then all the effective vertices must be this form. We emphasize this point because sometimes this point seems overlooked, for example the tensor structure in eq. (9) in ref. [13] is different from eq. (3.2).

However, in the actual calculation, we would find terms proportional to $p_2^\mu p_2^\nu$ and $g^{\mu\nu}$, which should vanish and do not appear in eq. (3.2), namely we would find the effective vertices become

$$\widetilde{\Gamma}^{\mu\nu}(p_1,p_2) = \Gamma^{\mu\nu}(p_1,p_2) + \Gamma^P(p_1,p_2)g^{\mu\nu} + \Gamma^D(p_1,p_2)p_2^\mu p_2^\nu\,, \tag{3.3}$$

where $\Gamma^{\mu\nu}(p_1,p_2)$ is defined in eq. (3.2). These extra terms, Γ^P and Γ^D, are apparently against the gauge invariance, but, nevertheless, they would appear. See, for example, eq. (9) in ref. [13]. As we will see the following sections, we find they disappear *if* we take on-shell conditions for all the external legs. However, we should keep them off-shell except for a single photon because we use the effective vertices to calculate the Barr-Zee diagrams. Hence we need to consider how to deal with these gauge variant terms.

Fortunately, it is found that the $p_2^\mu p_2^\nu$ term does not contribute to the EDMs at two-loop level. If $\Gamma^{\mu\nu}(p_1,p_2)$ contains terms proportional to $p_2^\mu p_2^\nu$, the diagrams shown in figure 1 contain the following structures,

$$\overline{u}(p+q)\not{\ell}\frac{1}{\not{p}+\not{q}-\not{\ell}-m_f}u(p)\,, \tag{3.4}$$

$$\overline{u}(p+q)\frac{1}{\not{p}+\not{\ell}-m_f}\not{\ell}u(p)\,, \tag{3.5}$$

where eq. (3.4) (eq. (3.5)) comes from figures 1(a) and 1(c) (figures 1(b) and 1(d)). If we omit $\mathcal{O}(y_f^2)$ terms, we can ignore the mass term in the fermion propagator and the mass of the external fermions. Then, by using the equation of motion of the external fermions,

$$\overline{u}(p+q)(\not{\ell}-\not{p}-\not{q})\frac{1}{\not{p}+\not{q}-\not{\ell}}u(p)\,, \tag{3.6}$$

$$\overline{u}(p+q)\frac{1}{\not{p}+\not{\ell}}(\not{\ell}+\not{p})u(p)\,. \tag{3.7}$$

Now it is apparent that these terms do not contain $\sigma^{\mu\nu}\gamma^5$ structure because all the γ-matrices are canceled out. Therefore the terms which are proportional to $p_2^\mu p_2^\nu$ in the effective vertices do not contribute to the EDMs. Then we can safely drop the Γ^D term from eq. (3.3).

On the other hand, the Γ^P term in eq. (3.3) remains as long as we take off-shell conditions. This is nothing strange because the gauge invariance is promised for S-matrix, not for effective coupling. Then the gauge invariance will recover once we calculate non-Barr-Zee diagrams as well as the Barr-Zee diagrams, namely a full two-loop order calculation

JHEP01(2014)106

manifestly gives the gauge invariant results. However, it is very tough work to accomplish it. Instead of the full two-loop order calculation, we make the effective vertex gauge invariant by borrowing some terms from non-Barr-Zee diagrams. This technique is known as the pinch technique, and the borrowed terms are called pinch terms [15–17]. As we will see in the fallowing section, we find that Γ^P term in eq. (3.3) is completely compensate with the pinch terms.

Hereafter we calculate both $-(p_1p_2)g^{\mu\nu} + p_2^\mu p_1^\nu$ and $g_{\mu\nu}$ terms, and demonstrate the latter term completely vanishes thanks to the pinch terms.

3.2 Effective $h\gamma\gamma$ and $hZ\gamma$ vertices — W boson loop —

Now we move on to calculate the effective vertices for $h\gamma\gamma$ and $hZ\gamma$, which appear in figures 1(a) and 1(b). In the following, p_1 is the momentum of the external (on-shell) photon where $p_1^2 = 0$, and p_2 is the momentum of the virtual gauge boson in the Barr-Zee diagram. Note that the diagrams which contain both W and $H^\pm$ in the loop are absent in the 2HDM because $g_{\gamma W^\pm H^\mp} = g_{ZW^\pm H^\mp} = 0$, where $H^\pm$ is a physical charged scalar not a NG boson.

In this subsection, we focus on W boson loops of the $h\gamma\gamma$ and $hZ\gamma$ effective vertices because we find these are not gauge invariant as long as we keep off-shell conditions. We work in 't Hooft-Feynman gauge and find the $h\gamma\gamma$ and $hZ\gamma$ effective vertices are given by

$$\begin{aligned}\Gamma^{\mu\nu}_{hG\gamma}(p_1,p_2) = &+\frac{e}{(4\pi)^2}\frac{1}{m_W^2}g_{WWh}g_{WWG}\\ &\times\Bigg[\Gamma^A_{hG\gamma}\left(p_2^\mu p_1^\nu - p_2p_1g^{\mu\nu}\right) + \Gamma^P_{hG\gamma}\left(p_2^2 - m_G^2\right)g^{\mu\nu} + \Gamma^B_{hG\gamma}p_2^\mu p_2^\nu\\ &+\Gamma^C_{hG\gamma}\left[(p_1+p_2)^2 - m_h^2\right]g^{\mu\nu}\Bigg],\end{aligned} \tag{3.8}$$

where

$$\Gamma^A_{hG\gamma} = 4\left(-4J_1(m_W^2) + 6J_2(m_W^2) + \frac{m_G^2}{m_W^2}\left(J_1(m_W^2) - J_2(m_W^2)\right) + \left(1 - \frac{1}{2}\frac{m_G^2}{m_W^2}\right)\frac{m_h^2}{m_W^2}J_2(m_W^2)\right), \tag{3.9}$$

$$\Gamma^P_{hG\gamma} = +3J_1\left(m_W^2\right), \tag{3.10}$$

$$\begin{aligned}\Gamma^B_{hG\gamma} = &-3J_1\left(m_W^2\right) + \frac{m_G^2}{m_W^2}\left(J_1\left(m_W^2\right) - J_2\left(m_W^2\right)\right) + \frac{1}{2}\frac{m_G^2}{p_2^2}\left(1 - 2J_1\left(m_W^2\right)\right)\\ &+\frac{m_G^2}{m_W^2}\frac{(p_1+p_2)^2}{p_2^2}J_2\left(m_W^2\right),\end{aligned} \tag{3.11}$$

$$\Gamma^C_{hG\gamma} = -\left(1 - \frac{m_G^2}{m_W^2}\right)J_1\left(m_W^2\right), \tag{3.12}$$

where G stands for Z or γ, and where

$$J_1\left(m^2\right) = \int_0^1 dx\int_0^{1-x} dy\frac{1}{1 - \frac{p_2^2}{m^2}x(1-x) - \frac{(p_1+p_2)^2 - p_2^2}{m^2}xy}, \tag{3.13}$$

$$J_2\left(m^2\right) = \int_0^1 dx\int_0^{1-x} dy\frac{xy}{1 - \frac{p_2^2}{m^2}x(1-x) - \frac{(p_1+p_2)^2 - p_2^2}{m^2}xy}. \tag{3.14}$$

JHEP01(2014)106

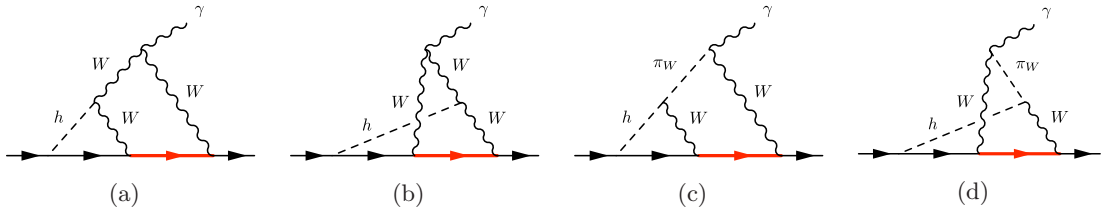

Figure 3. Diagrams containing the pinch terms for the effective $h\gamma\gamma$ and $hZ\gamma$ vertices. We pinch the fermion lines shown with red color. The dashed lines attached to the fermion lines are the physical scalars, and those not attached are would-be NG bosons.

The explicit forms of couplings, such as g_{WWh} and g_{WWG}, are given in appendix A. This result is consistent with previous works, for example in eq. (9) in ref. [13].

Although the gauge invariance requires $\Gamma^P = \Gamma^B = \Gamma^C = 0$ as we discussed in section 3, it is not satisfied in eq. (3.8). So we should consider the gauge invariance for the EDM calculation carefully. As discussed in ref. [13], the Γ^C term does not contribute to the EDMs. Because this term is proportional to inverse of neutral Higgs propagator, it can reduce neutral Higgs propagator in Barr-Zee diagram. Then we can apply the vertex relation[1] $\sum_h g^A_{\ell\ell h} g_{WWh} = 0$, where $g^A_{\ell\ell h}$ is axial-scalar coupling of external fermion ℓ with neutral Higgs bosons h and $\sum_h$ is summation for three neutral Higgs bosons. The Γ^B terms do not contribute to the EDMs neither, because these terms do not keep $\sigma^{\mu\nu}\gamma^5$ structure as we discussed in section 3.1. Then only the Γ^P terms are problematic. Actually the Γ^P terms vanish once we consider the pinch contributions as will be shown.

There are many two-loop diagrams which contribute to the EDMs, as well as the Barr-Zee diagrams. Once we calculate all the diagrams, the result must be gauge invariant. Therefore the gauge variant terms we discussed above should be canceled out by contributions from non-Barr-Zee diagrams. In order to see this cancellation, we do not need to calculate all the diagrams, but only *the pinch contributions*. The gauge invariance of eq. (3.8) would be recovered by borrowing some terms from non-Barr-Zee diagrams.

For this purpose, we calculate the diagrams shown in figure 3. These diagrams contain derivative couplings which are contracted with the gamma matrices by the Lorentz index. Then, these terms cancel out internal fermion propagators. We pick up the terms in which the fermion lines with red color in figure 3 are canceled out, and they are just the pinch contributions which make Barr-Zee contributions gauge invariant. These terms are schematically shown in figure 4. In 't Hooft-Feynman gauge,[2] we find

$$\text{Fig. 3}|_{\text{pinch}} = \sum_h \int_\ell i\tilde{\Gamma}^{\mu\nu}_{hG\gamma}(-q,\ell)\frac{i}{(q-\ell)^2-m_h^2}\frac{-ig_{\nu\rho}}{\ell^2-m_G^2}(-i\gamma^\rho g_{G\ell\ell})\frac{i}{\not{p}+\not{q}-\not{\ell}-m_f}(-ig_{\ell\ell h}), \tag{3.15}$$

where

$$\tilde{\Gamma}^{\mu\nu}_{hG\gamma}(p_1,p_2) = -g^{\mu\nu}3\frac{e}{(4\pi)^2}\frac{g_{WWh}}{m_W^2}g_{WWG}(p_2^2-m_G^2)J_1(m_W^2). \tag{3.16}$$

[1] We show this vertex relation in appendix A.3.4.

[2] In other gauge, we would need other diagrams as well as shown in figure 3.

JHEP01(2014)106

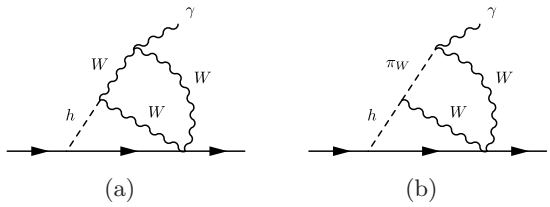

Figure 4. Diagrams (a) and (b) are the diagrams after pinched away the red lines. Figures 3(a) and 3(b) and figures 3(c) and 3(d) become diagrams (a) and (b), respectively.

Here, J_1 is given in eq. (3.13), $g_{G\ell\ell}$ and $g_{\ell\ell h}$ are couplings of external fermion ℓ with gauge and Higgs bosons, respectively, and $\int_\ell = \int d^4\ell/(2\pi)^4$. Since figure 1(a) with effective $hG\gamma$ vertices is calculated as

$$\text{Fig. 1(a)} = \sum_h \int_\ell i\Gamma^{\mu\nu}_{hG\gamma}(-q,\ell)\frac{-ig_{\nu\rho}}{\ell^2-m_G^2}\frac{i}{(\ell-q)^2-m_h^2}\left(-i\gamma^\rho g_{\ell\ell G}\right)\frac{i}{\not p+\not q-\not\ell-m_f}(-ig_{\ell\ell h}), \tag{3.17}$$

we find eq. (3.16) is nothing but parts of the effective vertices by comparing eq. (3.17) to eq. (3.15), and cancels the second term in eq. (3.8) (Γ^P) which is gauge variant term. In other words, the pinch term certainly cancels the gauge variant term and make the effective coupling gauge invariant.

After adding the pinch terms, we finally find the gauge invariant W loop contributions to the effective $h\gamma\gamma$ and $hZ\gamma$ vertices for the Barr-Zee diagrams,

$$\Gamma^{\mu\nu}_{hG\gamma}(p_1,p_2) = \frac{e}{(4\pi)^2}\frac{1}{m_W^2}g_{WWh}g_{WWG}\Gamma^A_{hG\gamma}\left(-(p_1p_2)g^{\mu\nu}+p_2^\mu p_1^\nu\right), \tag{3.18}$$

where $\Gamma^A_{hG\gamma}$ is given in eq. (3.9).

3.3 Effective $h\gamma\gamma$ and $hZ\gamma$ vertices — fermion, $H^\pm$ loop —

For the Barr-Zee diagram calculation, we need other contributions to effective $h\gamma\gamma$ and $hZ\gamma$ vertices. We calculate the fermion loop contribution to the effective $h\gamma\gamma$ and $hZ\gamma$ vertices. We denote the fermion as f. Note that they are independent from the gauge fixing terms. Hence Γ^P and Γ^D in eq. (3.3) are zero. We find Γ and Γ_5 defined in eq. (3.2) are

$$\Gamma_{hG\gamma}(p_1,p_2) = +\frac{N_c}{(4\pi)^2}2eQ_f g^V_{ffh}\left(g^L_{Gff}+g^R_{Gff}\right)\frac{2}{m_f}\left(J_1\left(m_f^2\right)-4J_2\left(m_f^2\right)\right), \tag{3.19}$$

$$\Gamma^5_{hG\gamma}(p_1,p_2) = +\frac{N_c}{(4\pi)^2}2eQ_f\left(ig^A_{ffh}\right)\left(g^L_{Gff}+g^R_{Gff}\right)\frac{2}{m_f}J_1\left(m_f^2\right), \tag{3.20}$$

where N_c is the color factor, for example $N_c = 3$ for the top quark loop, Q_f is the QED charge of the fermion in the loop, for example $Q_f = 2/3$ for the top quark loop.

The diagrams with the charged Higgs boson loop are also independent from the gauge fixing terms. Thus Γ^P and Γ^D in eq. (3.3) are zero. We find Γ and Γ_5 defined in eq. (3.2) are

$$\Gamma_{hG\gamma}(p_1,p_2) = -4\frac{1}{(4\pi)^2}eg_{hH^+H^-}g_{GH^+H^-}\frac{2}{m_H^2}J_2\left(m_H^2\right), \tag{3.21}$$

$$\Gamma^5_{hG\gamma}(p_1,p_2) = 0. \tag{3.22}$$

JHEP01(2014)106

3.4 Effective $H^\mp W^\pm \gamma$ vertices — W, $H^\pm$ loop —

The effective vertices for $H^\mp W^\pm \gamma$, shown in figures 1(c) and 1(d), are also necessary to calculate the all the Barr-Zee diagrams. Note that these Barr-Zee contributions have not been studied in the literature yet, and we first calculate them. To find a gauge invariant set for the Barr-Zee diagrams, we need to take into account for the pinch contributions. Calculations are tedious and long, so the details are given in appendix C. After summing up all terms which are relevant for the EDM calculations, we find the following gauge invariant effective vertex:

$$\Gamma^{\mu\nu}_{H^-W^+\gamma}(p_1,p_2) = +\frac{1}{(4\pi)^2}\left(p_{2\mu}p_{1\nu} - p_2 p_1 g_{\mu\nu}\right) \tag{3.23}$$
$$\times\left(+\sum_h e g_{W^+H^-h} g_{WWh}\int_0^1 dz\int_0^{1-z} dy\,\frac{-2yz-4z+4-\frac{m_H^2-m_h^2}{m_W^2}2yz}{m_W^2(1-z)+m_h^2 z - p_2^2 z(1-z) - 2p_1p_2yz}\right.$$
$$\left.-\sum_h e g_{W^+H^-h} g_{HHh}\int_0^1 dz\int_0^{1-z} dy\,\frac{4yz}{m_H^2(1-z)+m_h^2 z - p_2^2 z(1-z) - 2p_1p_2yz}\right),$$

$$\Gamma^{\mu\nu}_{H^+W^-\gamma}(p_1,p_2) = \left(\Gamma^{\mu\nu}_{H^-W^+\gamma}(p_1,p_2)\right)^*. \tag{3.24}$$

Here we have already omitted the terms which do not contribute to the EDM calculations.[3]

There might also be fermion loops in the effective $H^\mp W^\pm \gamma$ vertices. It is found that the fermion loops in the effective $H^\mp W^\pm \gamma$ vertices do not contribute to the EDMs if we consider only the CP phase in the Higgs potential in 2HDMs. While another CP phase is present in the Cabibbo-Kobayashi-Maskawa (CKM) matrix, the contributions to the EDMs should be much suppressed due to the GIM mechanism. Then, we do not calculate the fermion loop contributions to the effective $H^\mp W^\pm \gamma$ vertices in this paper.

4 EDM from Barr-Zee diagram

In this section we calculate diagrams in figure 1. The EDM, d_ℓ, for fermion ℓ is defined through

$$\mathcal{H}_{\rm eff} = i\frac{d_\ell}{2}\overline{\psi}_\ell \sigma_{\mu\nu}\gamma_5\psi_\ell F^{\mu\nu}, \tag{4.1}$$

where

$$\sigma_{\mu\nu} = \frac{i}{2}[\gamma_\mu,\gamma_\nu]. \tag{4.2}$$

Once we get the gauge invariant effective vertex whose tensor structure is given in eq. (3.2), we find the neutral Higgs boson contributions to d_ℓ as

$$(d_\ell)^{\text{Fig. 1(a)}}_{+\text{Fig. 1(b)}} = \frac{1}{2}\sum_{G=Z,\gamma}\sum_h\left(g^L_{G\ell\ell}+g^R_{G\ell\ell}\right)\int_\ell\left(i g^A_{h\ell\ell}\Gamma_{hG\gamma}(0,\ell)+g^V_{h\ell\ell}\Gamma^5_{hG\gamma}(0,\ell)\right)\frac{1}{\ell^2-m_G^2}\frac{1}{\ell^2-m_h^2}. \tag{4.3}$$

where $g^{L(R)}_{G\ell\ell}$ is for couplings of left(right)-handed fermion ℓ with gauge boson G, and $g^{V(A)}_{\ell\ell h}$ is for (axial) scalar couplings with scalar boson h. Here we keep only the leading term for p and q, and ignore mass term in the fermion propagator, and we have used a relation, $\epsilon^{\mu\nu\alpha\beta}\gamma_\alpha\gamma_\beta = -i\gamma^5[\gamma^\mu,\gamma^\nu]$.

[3] These terms do not contribute to the on-shell $H^- \to W^-\gamma$ process neither.

JHEP01(2014)106

Note that we work in 't Hooft-Feynman gauge in eq. (4.3). If we work in other gauge, gauge boson propagators contain the terms that proportional to ℓ_ν and contract with the effective vertices. Since $\Gamma^{\mu\nu}(-q,\ell)\ell_\nu = 0$, the terms proportional to ℓ_ν in the gauge boson propagators always vanish. Therefore the Barr-Zee diagrams are gauge invariant *as long as* the effective vertices are gauge invariant.

In the similar manner, we find the charged Higgs boson contribution to the leptonic EDMs as

$$(d_\ell)^{\text{Fig. 1(c)}}_{\text{+Fig. 1(d)}} = \frac{1}{2\sqrt{2}}\frac{e}{s_W}\int_\ell \frac{1}{\ell^2 - m_W^2}\frac{1}{\ell^2 - m_H^2} i\text{Im}\left(g^R_{H^+\bar{\nu}e}\Gamma_{H^-W^+\gamma}(0,\ell)\right). \tag{4.4}$$

Here we have used the following relations,

$$g^L_{H^-\bar{e}\nu} = \left(g^R_{H^+\bar{\nu}e}\right)^*, \tag{4.5}$$

$$\Gamma_{H^+W^-\gamma}(0,\ell) = \left(\Gamma_{H^-W^+\gamma}(0,\ell)\right)^*. \tag{4.6}$$

The charged Higgs contributions to the up-type and down-type quark EDMs are derived by replacing $g^R_{H^+\bar{\nu}e}\Gamma_{H^-W^+\gamma}$ in eq. (4.4) by $g^R_{H^-\bar{d}u}\Gamma_{H^+W^-\gamma}$ and $g^R_{H^+\bar{u}d}\Gamma_{H^-W^+\gamma}$, respectively.

The chromo-EDMs (cEDMs) also contribute to the neutron EDM. Its definition is similar to eq. (4.1), replace $F_{\mu\nu}$ by $g_s G_{\mu\nu}$,

$$\mathcal{H}_{\text{eff}} = i\frac{d^c_q}{2}\bar{q}g_s\sigma_{\mu\nu}\gamma_5 G^{\mu\nu}q\,, \tag{4.7}$$

where g_s and $G_{\mu\nu}$ are the QCD coupling and the field strength of the gluon, respectively.

The formulae of EDMs include complicated functions. Here, we show the approximated expressions in the *decoupling limit* for qualitative discussion, while all plots are drawn by using the exact formulae. The exact formula are given in appendix B. In the decoupling limit all the non-SM particles are degenerated, heavier than the electroweak scale, and decoupled from the SM sector. We can take such a limit by $M \to \infty$ where M is defined in eq. (2.4).

Since the results depend on the Yukawa structure, we introduce the following notation to simplify our expressions:

$$\mathcal{G}^A_x = \begin{array}{c} \\ u/c/t \\ d/s/b \\ e/\mu/\tau \end{array} \begin{array}{c} \begin{array}{cccc} \text{Type-I} & \text{Type-II} & \text{Type-X} & \text{Type-Y} \end{array} \\ \begin{pmatrix} 1 & 1 & 1 & 1 \\ -1 & \tan^2\beta & -1 & \tan^2\beta \\ -1 & \tan^2\beta & \tan^2\beta & -1 \end{pmatrix} \end{array}, \tag{4.8}$$

$$\mathcal{S}_x = \begin{array}{c} u/c/t \\ d/s/b \\ e/\mu/\tau \end{array} \begin{pmatrix} -1 \\ 1 \\ 1 \end{pmatrix}, \tag{4.9}$$

where index A represents type of the model, and index x is for flavor.

JHEP01(2014)106

It is found that the EDMs for fermion ℓ in the decoupling limit are approximated to be

$$\left(\frac{d_\ell}{e}\right)_W \simeq -X\mathcal{G}_\ell^A \times \left(e\left(15+2\ln\left(\frac{M}{\mathrm{TeV}}\right)\right)\left(g^L_{\gamma\ell\ell}+g^R_{\gamma\ell\ell}\right) + g_{ZWW}\left(6.5+0.71\ln\left(\frac{M}{\mathrm{TeV}}\right)\right)\left(g^L_{Z\ell\ell}+g^R_{Z\ell\ell}\right)\right), \tag{4.10}$$

$$\left(\frac{d_\ell}{e}\right)_{\mathrm{top}} \simeq +X\times\left(e\left(5.3\mathcal{G}_\ell^A+7.6\right)\left(g^L_{\gamma\ell\ell}+g^R_{\gamma\ell\ell}\right)+e\left(1.4\mathcal{G}_\ell^A+2.0\right)\left(g^L_{Z\ell\ell}+g^R_{Z\ell\ell}\right)\right), \tag{4.11}$$

$$\left(\frac{d_\ell}{e}\right)_{\mathrm{bottom}} \simeq +X\times\left(e\left(0.018\mathcal{G}_\ell^A+0.022\mathcal{G}_b^A\right)\left(g^L_{\gamma\ell\ell}+g^R_{\gamma\ell\ell}\right) +e\left(0.0075\mathcal{G}_\ell^A+0.0087\mathcal{G}_b^A\right)\left(g^L_{Z\ell\ell}+g^R_{Z\ell\ell}\right)\right), \tag{4.12}$$

$$\left(\frac{d_\ell}{e}\right)_{\mathrm{tau}} \simeq +X\times\left(e\left(0.024\mathcal{G}_\ell^A+0.029\mathcal{G}_\tau^A\right)\left(g^L_{\gamma\ell\ell}+g^R_{\gamma\ell\ell}\right) +e\left(0.00034\mathcal{G}_\ell^A+0.00038\mathcal{G}_\tau^A\right)\left(g^L_{Z\ell\ell}+g^R_{Z\ell\ell}\right)\right), \tag{4.13}$$

$$\left(\frac{d_\ell}{e}\right)_{H^\pm} \simeq +X\mathcal{G}_\ell^A\times\left(0.34e\left(g^L_{\gamma\ell\ell}+g^R_{\gamma\ell\ell}\right)+0.34g_{ZH^+H^-}\left(g^L_{Z\ell\ell}+g^R_{Z\ell\ell}\right)\right), \tag{4.14}$$

$$\left(\frac{d_\ell}{e}\right)_{HW\gamma} \simeq -X\mathcal{G}_\ell^A\mathcal{S}_\ell\times\left(0.23+0.20\ln\left(\frac{M}{\mathrm{TeV}}\right)\right), \tag{4.15}$$

$$(d_q^c)_{\mathrm{top}} \simeq +X\times g_s^2\left(4.0\mathcal{G}_q^A+5.7\right), \tag{4.16}$$

$$(d_q^c)_{\mathrm{bottom}} \simeq +X\times g_s^2\left(0.053\mathcal{G}_q^A+0.065\mathcal{G}_b^A\right), \tag{4.17}$$

where

$$X=\frac{1}{(4\pi)^4}\frac{m_\ell}{M^2}\cos^2\beta\lambda_5\sin 2\phi\,, \tag{4.18}$$

and we use $\overline{MS}$ mass of M_Z scale, $m_e = 0.511\,\mathrm{MeV}$, $m_\tau = 1.75\,\mathrm{GeV}$, $m_u = 1.40\,\mathrm{MeV}$, $m_t = 170.9\,\mathrm{GeV}$, $m_d = 2.92\,\mathrm{MeV}$ and $m_b = 2.94\,\mathrm{GeV}$. Notice that the EDMs and cEDMs are proportional to $\lambda_5\sin 2\phi = \mathrm{Im}[\lambda_5\exp(i2\phi)]$, namely the imaginary part of the coupling which is needed for CP violation.

It is found that the W loop contributions are dominant in large parameter region. Among the contributions from fermion loops, only the top quark contributions are relevant in the decoupling limit as long as $\tan\beta \lesssim 10$. In the similar manner, we can make approximation of cEDMs. The diagrams with charged Higgs boson in $h\gamma\gamma$, $hZ\gamma$, and $H^\mp W^\pm\gamma$ couplings are smaller than the other contributions. Note that the contributions from Z boson exchange diagrams are proportional to $\left(g^L_{Z\ell\ell}+g^R_{Z\ell\ell}\right)$. Although this factor is numerically small at electron EDM case, one must not ignore at quark EDM case. Actually, Z boson exchange diagrams occupy $30-50\%$ of all contribution at down quark EDM case.

In the decoupling limit the bottom quark and tau lepton contributions are small because of their small Yukawa couplings. In the non-decoupling region, however, these are not

JHEP01(2014)106

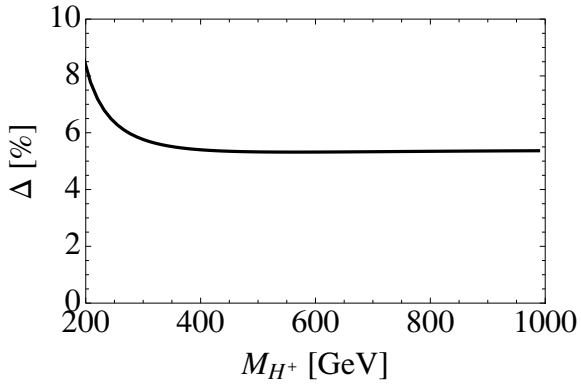

Figure 5. Numerical improvement of electron EDM by the pinch contributions in the type-II 2HDM. We take $\tan\beta = 10$, $\lambda_1 = \lambda_3 = \lambda_4 = \lambda_5 \sin 2\phi = 0.5$ and require the 126 GeV Higgs mass.

necessarily valid. Their leading contributions are given by diagrams in which heavy Higgs propagate, and their values are approximately $\mathcal{O}\left(X\mathcal{G}_\ell^A\mathcal{G}_{b/\tau}^A\left(m_{h_3}^2 - m_{h_2}^2\right)/M^2\right)$, where h_3 and h_2 is the heaviest and the next heaviest Higgs bosons, respectively. These contributions are enhanced by $\tan^2\beta$ when $\tan\beta \gg 1$. Thus, when $\tan\beta$ is large, the contribution may be sizable in the non decoupling region.

5 Numerical results

Now we evaluate the EDMs numerically. At first, in figure 5, we show the numerical improvement by the pinch contributions. Here we consider the electron EDM in the type-II 2HDM. The vertical axis in the figure 5 is difference of the gauge invariant EDM contribution and non-invariant one, Δ, defined as

$$\Delta = \frac{(d_e)_{\text{gauge non-inv.}} - (d_e)_{\text{gauge inv.}}}{(d_e)_{\text{gauge inv.}}}\,, \tag{5.1}$$

where the gauge non-invariant EDM contribution $(d_e)_{\text{gauge non-inv.}}$ is gotten by calculating only Barr-Zee diagrams [13, 14]. The horizontal axis is the mass of charged Higgs boson. We take $\tan\beta = 10$, $\lambda_1 = \lambda_3 = \lambda_4 = \lambda_5 \sin 2\phi = 0.5$ and require the mass of lightest neutral scalar to be 126 GeV, then λ_2 is uniquely determined. We find that the pinch contributions are 5%-8%. This is not big improvement from the numerical point of view. However, we would like to emphasize that our result is now gauge invariant, which must be satisfied when we discuss observables.

Next, we discuss dependence of the electron EDM on the types of 2HDMs. The contributions from each types of diagrams to the electron EDM for type-I and II cases in figures 6 and 7, respectively. Here we take $\tan\beta = 3$ or 50, and $\lambda_1 = \lambda_3 = \lambda_4 = \lambda_5 \sin 2\phi = 0.5$ as a benchmark. We also require the mass of lightest neutral Higgs to be 126 GeV.

It is found that in the type-I case the W boson contribution to $h \to \gamma\gamma$ is dominant and that all contributions to the electron EDM are proportional to $1/\tan^2\beta$ for $\tan\beta \gtrsim 1$. On the other hand, the electron EDM in the type-II case is qualitatively different from the type-I case. Even when $\tan\beta$ is large, the W boson and top quark contributions are

JHEP01(2014)106

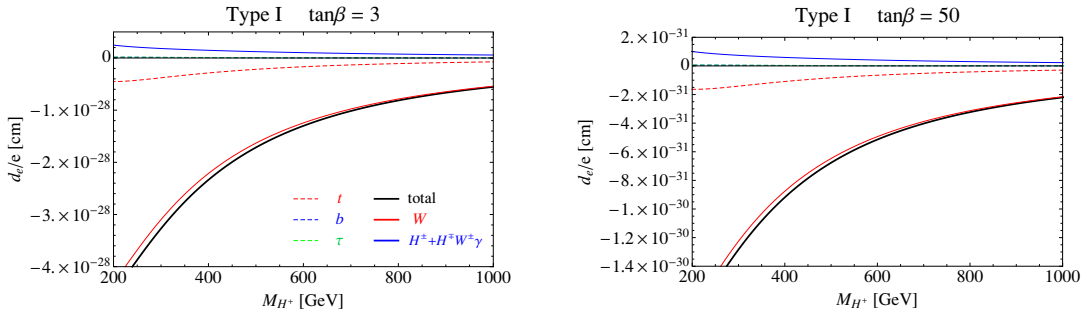

Figure 6. Anatomy of the type-I electron EDM. Various Barr-Zee contributions to the electron EDM are shown as functions of charged Higgs mass M_H^+. We take $\tan\beta = 3$ or 50, and $\lambda_1 = \lambda_3 = \lambda_4 = \lambda_5 \sin 2\phi = 0.5$. The mass of lightest neutral Higgs is 126 GeV. We see that W loop is the dominant contribution. The qualitative feature are independent from $\tan\beta$.

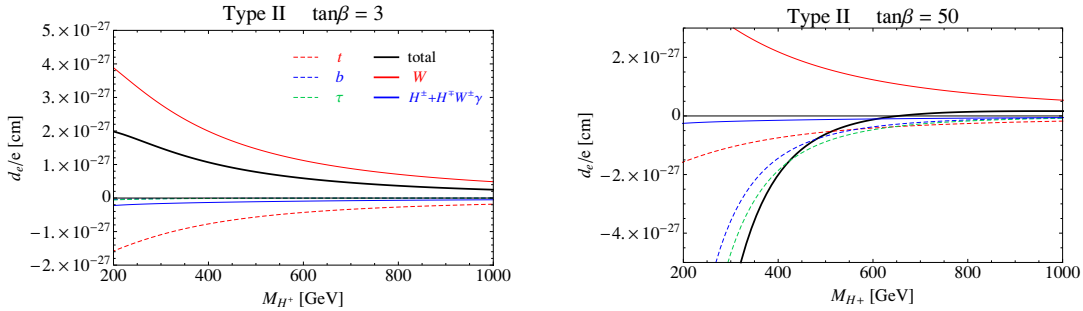

Figure 7. Anatomy of the type-II electron EDM. The input parameters are the same as in figure 6. In contrast of the type-I case, the qualitative feature depends on $\tan\beta$. For large $\tan\beta$, bottom quark and tau lepton contributions are sizable due to the $\tan\beta$ enhancement of their Yukawa couplings.

experiments	sensitivities on d_e
Fr [18]	$1 \times 10^{-29} e$ cm
YbF molecule [19]	$1 \times 10^{-30} e$ cm
WN ion [20]	$1 \times 10^{-30} e$ cm

Table 2. Future prospects on electron EDM.

not suppressed and the bottom quark and tau lepton contributions also become dominant due to the non-decoupling effect. Since the signs of the bottom quark and tau lepton contributions are opposite to that of the W boson, the accidental cancellation occurs in some parameter region. Thus, the $\tan\beta$ dependence is non-trivial in the type-II case.

In figures 8, the electron EDM is shown in four types of 2HDMs as functions of $\tan\beta$ and charged Higgs boson mass. We take $\lambda_1 = \lambda_3 = \lambda_4 = \lambda_5 \sin 2\phi = 0.5$ and $\lambda_2 = 0.25$. The regions filled with red color in the figures show the excluded regions by the latest upper bound on electron EDM, which is derived by the ACME experiment,

$$|d_e| < 8.7 \times 10^{-29} e \text{ cm} \ \ (90\% \text{ CL [3]}) . \tag{5.2}$$

The blue dashed lines are the future prospects given in table 2.

JHEP01(2014)106

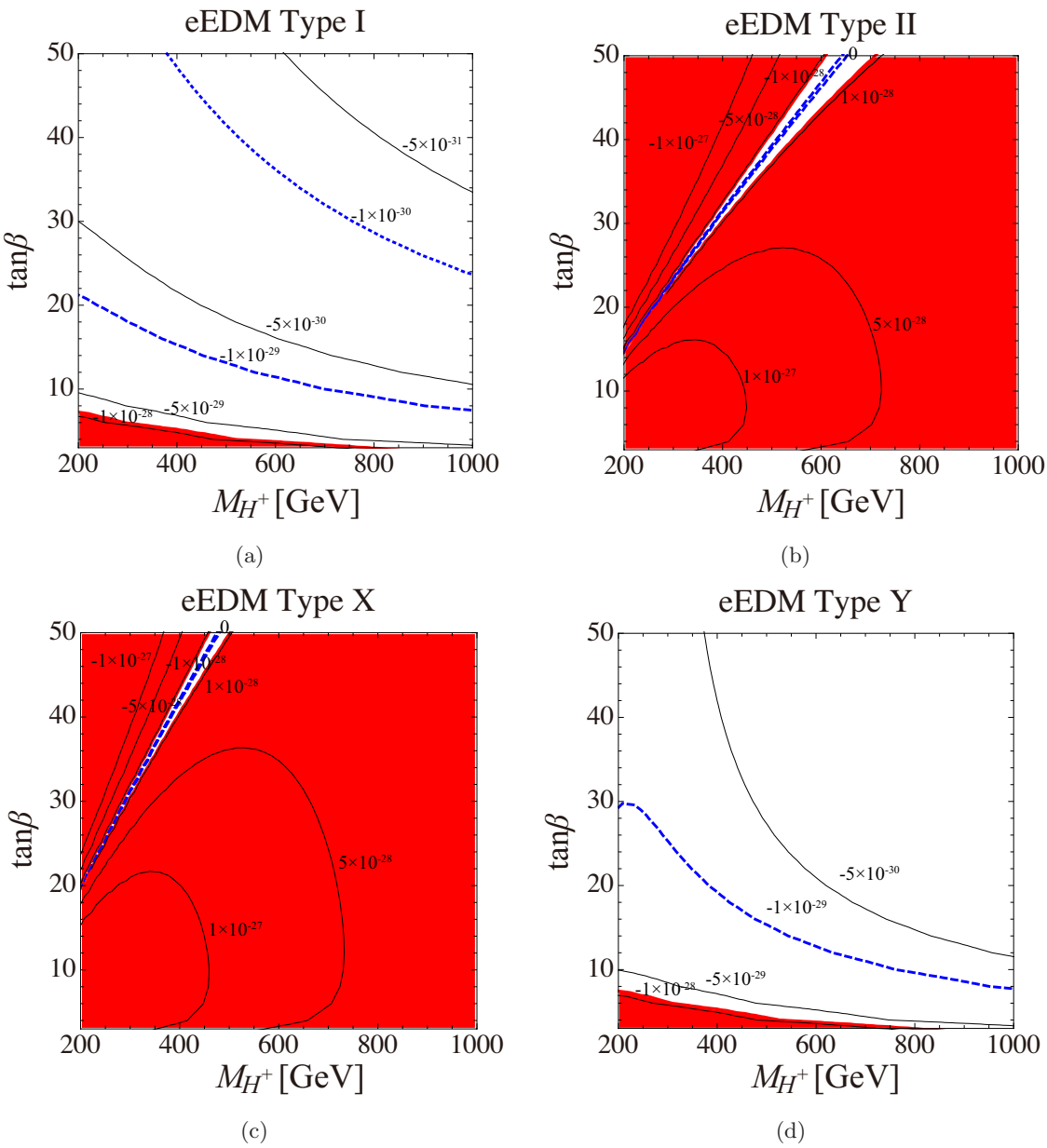

Figure 8. Electron EDM on charged Higgs boson mass and $\tan\beta$ plane in four types of 2HDMs. We take $\lambda_1 = \lambda_3 = \lambda_4 = \lambda_5 \sin 2\phi = 0.5$ and $\lambda_2 = 0.25$. The regions filled with red color show the current bound [3]. The blue dashed lines are the future prospects given in table 2.

The electron EDM in the type-X and Y models has similar behavior to the type-II and I ones, respectively, because leptons couple to H_2 in type-I and Y models, and to H_1 in type-II and X models. We find that type-II and type-X 2HDMs are strongly constrained by the recent ACME experimental result, except for regions where the cancellation among diagrams occurs, as shown in figure 8. Furthermore, the future experiments could cover wide parameter regions with charged Higgs mass smaller than 1 TeV even in type-I and Y cases.

JHEP01(2014)106

experiments	sensitivities on $\lvert d_n \rvert$
cyro EDM [27]	$1.7 \times 10^{-28} e$ cm
PSI (Phase II) [28]	$5 \times 10^{-28} e$ cm

Table 3. Future prospects for neutron EDM.

Next let us consider the neutron EDM. Even when the Peccei-Quinn mechanism [21] is operative, the neutron EDM is generated by higher-dimensional CP-violating operators in QCD, such as quark EDMs and also cEDMs with mass dimension up to 5. The neutron EDM is evaluated from the up and down quarks EDM and cEDM with the QCD sum rules [22–24]. The evaluation still $\mathcal{O}(1)$ uncertainties from the excited state contribution to the correlation function [22], and also from input parameters [23]. In this paper we use the result in ref. [24] since it gives more conservative prediction for the neutron EDM,

$$d_n = 0.79 d_d - 0.20 d_u + e\,(0.59 d_d^c + 0.30 d_u^c)\,. \tag{5.3}$$

Here, the Peccei-Quinn mechanism is assumed.

Before going to evaluate the neutron EDM, we discuss behaviors of the quark EDMs and cEDMs in the 2HDMs. We plot the contributions from each types of diagrams to the down and up quark EDMs and cEDMs in the type-I case in figures 9 and 10. The input parameters are the same as in figure 6. We see that the W boson and top quark contributions give the dominant contributions to the EDMs and cEDMs, respectively, and the $\tan\beta$ dependence is $1/\tan^2\beta$, as expected from eq. (4.18). It is found that the sizes of cEDMs and EDMs are comparable to each others so that both contributions have to be included in evaluation of the neutron EDM.

In figures 11 and 12, the contributions from each types of diagrams to the down and up quark EDMs and cEDMs in the type-II case are also shown. The EDMs and cEDMs have qualitatively different behaviors from the type-I case. We find that the largest contribution to the neutron EDM comes from down quark cEDM. The top quark loop dominates in the down quark cEDM (and also the up quark cEDM) for small $\tan\beta$, while the bottom quark one quickly dominates it when $\tan\beta$ is large. The later comes from the non-decoupling effect. Thus, the neutron EDM would be enhanced when $\tan\beta$ is large. It is also found that the down quark EDM has similar behavior to the electron EDM in the type-II case, though it is smaller than the down quark cEDM in the neutron EDM.

Here, we ignore the QCD corrections to the quark EDMs and cEDMs. The QCD corrections may change them up to $\mathcal{O}(10)\%$ [25, 26], while the neutron EDM evaluation from the quark EDMs and cEDMs may have larger uncertainties. See ref. [26] for evaluation for the QCD corrections to the Barr-Zee diagrams.

Now we show the neutron EDM in four types of 2HDMs in figure 13. The regions filled with red color in figure 13 show the excluded region by the current neutron EDM data,

$$\lvert d_n \rvert < 2.9 \times 10^{-26} e \text{ cm } (90\% \text{ CL [4]}). \tag{5.4}$$

The blue dashed lines are the future prospects given in table 3.

JHEP01(2014)106

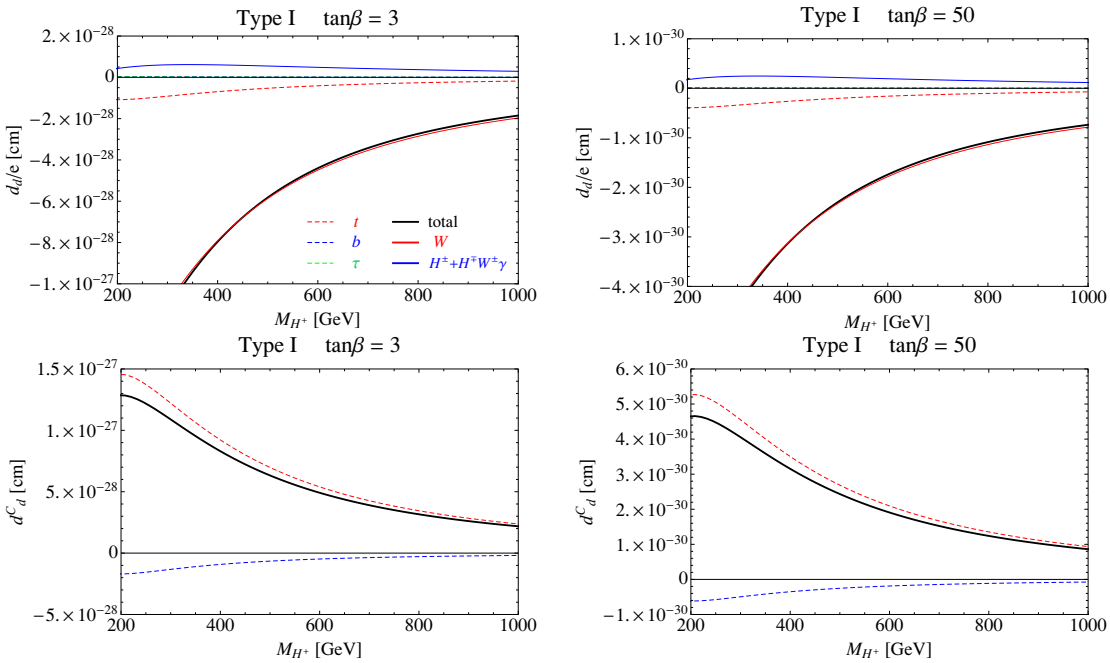

Figure 9. Anatomy of the type-I down quark EDM and cEDM. Various Barr-Zee contributions to the EDM and cEDM are shown as functions of charged Higgs mass M_H^+. We take $\tan\beta = 3$ and 50. Other input parameters are the same as in figure 6. We see that W and top give dominant contributions to EDM and cEDM, respectively.

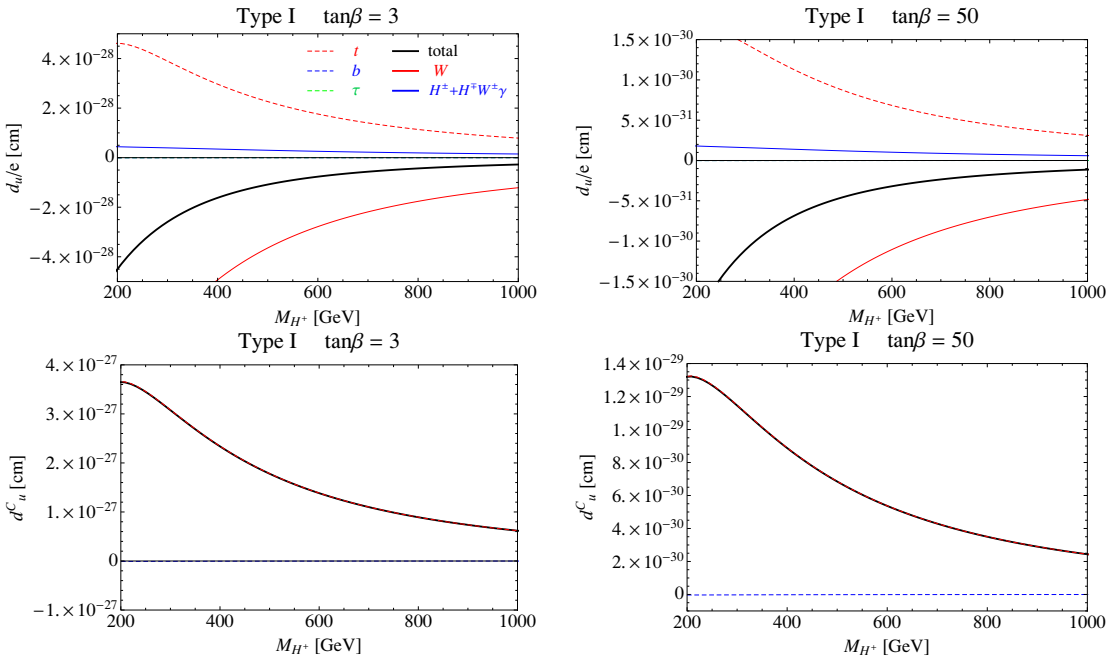

Figure 10. Anatomy of the type-I up quark EDM and cEDM. We taketan $\beta = 3$ and 50. Other input parameters are the same as in figure 6. We see that W and top give dominant contributions.

JHEP01(2014)106

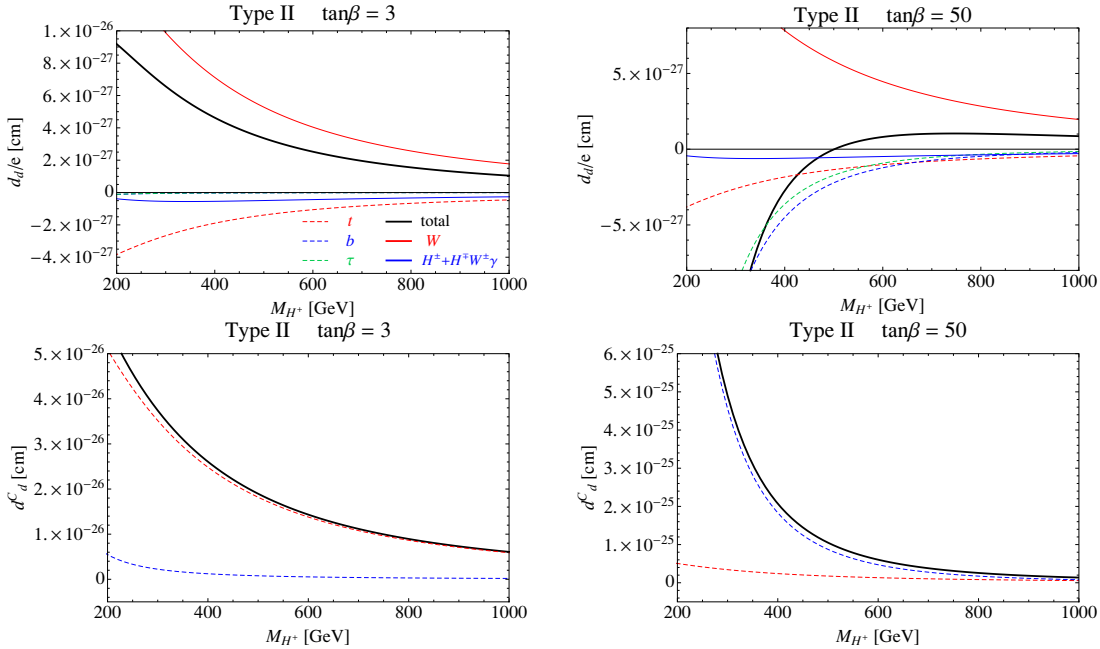

Figure 11. Anatomy of the type-II down quark EDM and cEDM. We take $\tan\beta = 3$ and 50. Other input parameters are the same as in figure 6. In contrast of the type-I case, the qualitative feature depends on $\tan\beta$. For large $\tan\beta$, the bottom quark and tau lepton contributions are sizable due to the $\tan\beta$ enhancement of their Yukawa couplings.

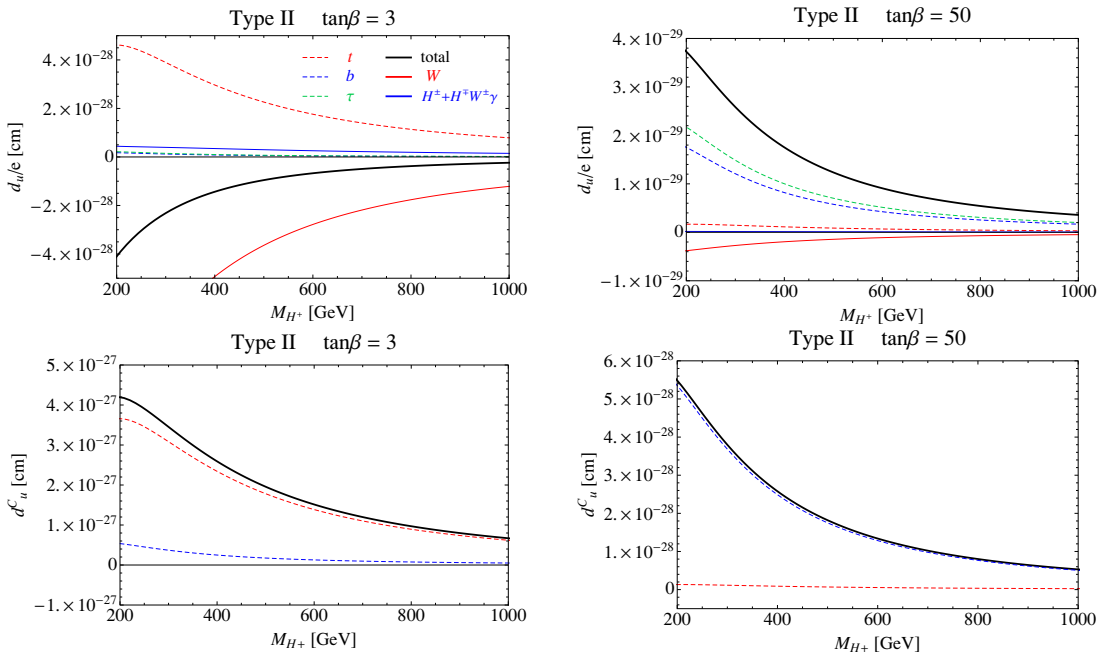

Figure 12. Anatomy of the type-II up quark EDM and cEDM. We take $\tan\beta = 3$ and 50. Other input parameters are the same as in figure 6. In contrast of the type-I case, the qualitative feature depends on $\tan\beta$. For large $\tan\beta$, bottom and tau contributions are sizable due to the $\tan\beta$ enhancement of their Yukawa couplings.

JHEP01(2014)106

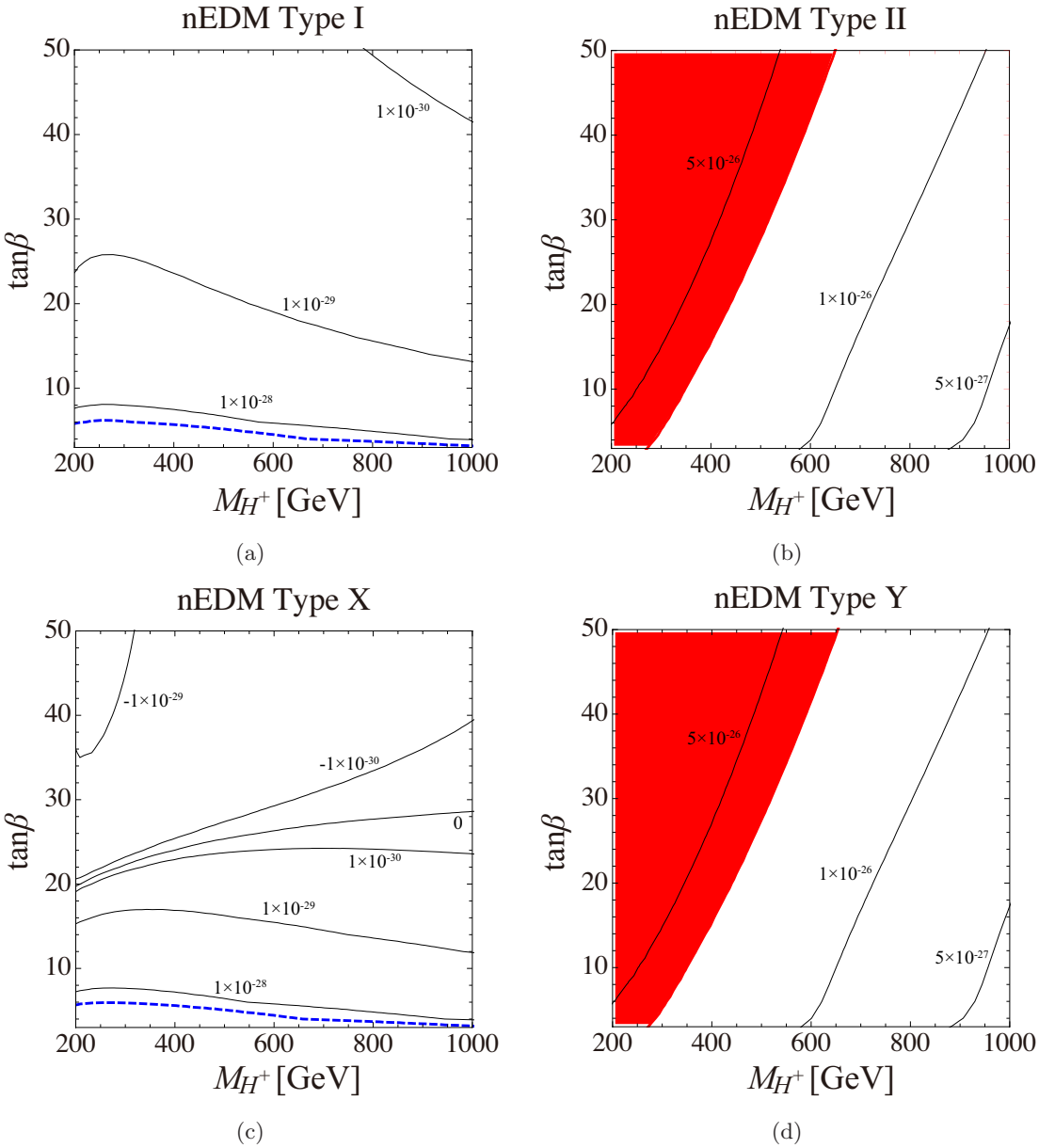

Figure 13. Neutron EDM on charged Higgs boson mass and $\tan\beta$ plane. The input parameters are the same as in figure fig:eEDM. The region filled with red color show the current bound [4]. The blue dashed lines are the future prospects given in table 3.

It is found that the neutron EDM in the type-X case has similar behavior to the type-I in low $\tan\beta$ region because the down quark Yukawa couplings in these two types are the same. The difference in high $\tan\beta$ region between figures 13(a) and 13(c) is due to the large $\tan\beta$ enhancement of the tau lepton Yukawa coupling. The behavior of the neutron EDM in the type-Y case is quite similar to the type-II case. This is because the cEDM contribution is dominant in both cases.

It is found in comparison of figure 8 with figure 13 that both measurements of the electron and neutron EDMs are complementary to each others in order to discriminate the 2HDMs. We may choose one from the four models in future.

JHEP01(2014)106

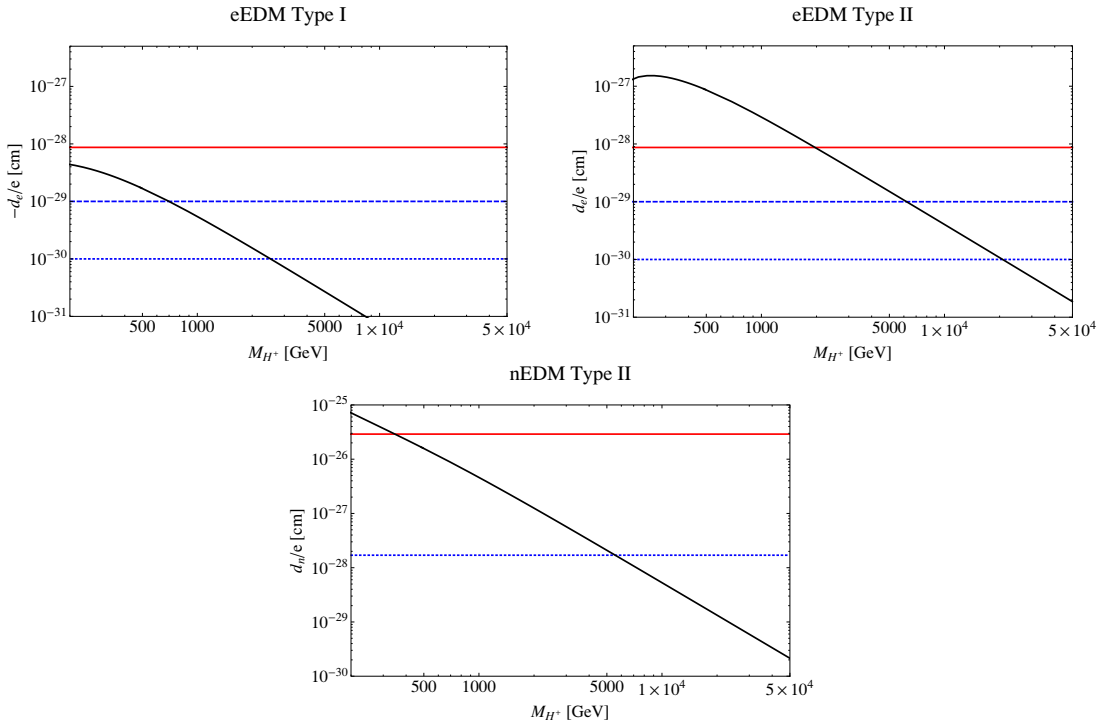

Figure 14. Electron and Neutron EDMs at large $m_H^\pm$ region in the type-II case. We take $\tan\beta = 10$, $\lambda_1 = \lambda_3 = \lambda_4 = \lambda_5 \sin 2\phi = 0.5$ and require the 126 GeV Higgs boson mass. The red and blue lines are current bounds [3, 4] and future prospects given in tables 2 and 3, respectively.

Before closing this section, we would like to give a comment on the constraints on the parameter space. We have shown that some parameter regions are constrained by EDMs in figures 8 and 13. The constrained regions have an overlap with other constraints, such as flavor physics [29, 30] or direct search of heavy Higgs bosons [31]. Note that it is known that the custodial SU(2) symmetry is broken in the Higgs potential in 2HDMs with the CP violation, and ρ parameter might deviate from one at the one loop level [32]. However, if heavy Higgs boson mass scale M is large or if coupling $\lambda_1 - \lambda_5$ are not large, this contribution is small. We checked that this contribution does not conflict with the current bound in all figure of this paper.

6 Conclusions and discussion

In this paper, we evaluated fermionic EDMs in 2HDMs with softly broken Z_2 symmetry. We started by calculating the Barr-Zee diagrams in a gauge invariant way by using the pinch technique. The modification by the gauge invariant calculation is 5%–8% numerically. This does not change the previous result drastically, but important because physical quantities must be calculated in a gauge invariant way. We evaluated the electron and neutron EDMs in all four types in the 2HDMs. We find that type-II and type-X 2HDMs are strongly constrained by the latest ACME experiment bound on the electron EDM. The electron and neutron EDM measurements will improve in the future experiments. They are possible to seek physics at $\mathcal{O}(10)$ TeV scale (figure 14). The electron and neutron EDMs

JHEP01(2014)106

have different sensitivities on the 2HDMs, and they are complementary to each other in discrimination of the type of 2HDMs.

We have not addressed that the contributions from non-Barr-Zee type diagrams in this paper. Although they are naively expected to be smaller than the contributions from the Barr-Zee diagrams, they would become important once experiments find the EDMs and start precise measurements. To evaluate them, we need to calculate all diagrams at two-loop level. This issue may be discussed elsewhere.

It is worth referring to relation between EWBG and EDMs. In the 2HDMs, it is known that EWBG may occur through a strongly first order electroweak phase transition [33–38]. For example, ref. [37] numerically showed that the 2HDMs with softly-broken Z_2 symmetry may accommodate a strongly first order phase transition when the lightest neutral Higgs boson is around 125 GeV. In order to achieve the EWBG, one needs some CP violation phases in Higgs potential. The EDM searches could indirectly constrain parameter space which achieve the EWBG. In this paper, we find that low $\tan\beta$ regions in 2HDMs are disfavored by electron EDM. On the other hand, in fact, a strongly first order phase transition, which is needed for EWBG, prefers low $\tan\beta$ region [37]. Therefore there is a tension between EWBG and current bound on the EDM.

Acknowledgments

The authors thank the Yukawa Institute for Theoretical Physics at Kyoto University, where this work was initiated during the YITP workshop on "LHC vs. Beyond the Standard Model (YITP-W-12-21)", March 19-25, 2013, and also acknowledge the participants of the workshop for very active discussions. They would also like to thank Koji Tsumura, Eibun Senaha, Ryosuke Sato, and Yasuhiro Yamamoto for useful discussions. The work of J.H. is supported by Grant-in-Aid for Scientific research from the Ministry of Education, Science, Sports, and Culture (MEXT), Japan, No. 24340047, No. 23104011 and No. 22244021, and also by World Premier International Research Center Initiative (WPI Initiative), MEXT, Japan. The figures for this paper were drawn using Feynmf [39].

A 2HDMs

In this appendix, we present mass spectrum and also interactions in 2HDMs, which are used in text.

A.1 Relations between mass and gauge eigenstates

While eight scalar fields are present in 2HDMs,

$$\sigma_{1,2}\,, \quad \pi^{\pm}_{1,2}\,, \quad \pi^{3}_{1,2}\,,$$

as in eq. (2.1), those states are not mass eigenstates, namely their mass matrices are not diagonalized. We call them the gauge eigenstates. Corresponding to them, there are eight

mass eigenstates, which we denote them as

$$\begin{aligned} h_{1,2,3} &\quad \text{(neutral Higgs bosons)}, \\ H^{\pm} &\quad \text{(charged Higgs bosons)}, \\ \pi_{Z,W^{\pm}} &\quad \text{(would-be NG bosons)}. \end{aligned}$$

These two-types of states are related with orthogonal or unitary matrices which diagonalize the mass matrices. For the fields which include would-be NG bosons the matrices are given as

$$\begin{aligned} \begin{pmatrix} \pi_Z \\ \pi_A \end{pmatrix} &= \begin{pmatrix} \cos\beta & \sin\beta \\ -\sin\beta & \cos\beta \end{pmatrix} \begin{pmatrix} \pi_1^3 \\ \pi_2^3 \end{pmatrix}, \\ \begin{pmatrix} \pi_{W^{\pm}} \\ H^{\pm} \end{pmatrix} &= \begin{pmatrix} \cos\beta & \sin\beta \\ -\sin\beta & \cos\beta \end{pmatrix} \begin{pmatrix} \pi_1^{\pm} \\ \pi_2^{\pm} \end{pmatrix}. \end{aligned} \tag{A.1}$$

The matrix U for physical neutral Higgs bosons is given by a 3 by 3 matrix as

$$\begin{pmatrix} h_1 \\ h_2 \\ h_3 \end{pmatrix} = U^T \begin{pmatrix} \sigma_1 \\ \sigma_2 \\ \pi_A \end{pmatrix} = \begin{pmatrix} \omega_{h1}^{\sigma_1} & \omega_{h1}^{\sigma_2} & \omega_{h1}^{\pi_A} \\ \omega_{h2}^{\sigma_1} & \omega_{h2}^{\sigma_2} & \omega_{h2}^{\pi_A} \\ \omega_{h3}^{\sigma_1} & \omega_{h3}^{\sigma_2} & \omega_{h3}^{\pi_A} \end{pmatrix} \begin{pmatrix} \sigma_1 \\ \sigma_2 \\ \pi_A \end{pmatrix} \tag{A.2}$$

where

$$\sum_X \omega_i^X \omega_j^X = \delta_{ij}, \quad \sum_i \omega_i^X \omega_i^Y = \delta^{XY}. \tag{A.3}$$

These relations are useful to find relations among some couplings.

A.2 Higgs masses in 2HDMs

The mass terms for the neutral physical Higgs bosons are given by

$$\mathcal{L} \supset \frac{1}{2} \begin{pmatrix} \sigma_1 & \sigma_2 & \pi_A \end{pmatrix} \widetilde{\mathcal{M}}_{\rm N}^2 \begin{pmatrix} \sigma_1 \\ \sigma_2 \\ \pi_A \end{pmatrix}, \tag{A.4}$$

where

$$\begin{aligned} \left(\widetilde{\mathcal{M}}_{\rm N}^2\right)_{11} &= v_1^2 \lambda_1 + M^2 \sin^2\beta\,, \\ \left(\widetilde{\mathcal{M}}_{\rm N}^2\right)_{22} &= v_2^2 \lambda_2 + M^2 \cos^2\beta\,, \\ \left(\widetilde{\mathcal{M}}_{\rm N}^2\right)_{33} &= M^2 - v^2 \lambda_5 \cos(2\phi)\,, \\ \left(\widetilde{\mathcal{M}}_{\rm N}^2\right)_{21} = \left(\widetilde{\mathcal{M}}_{\rm N}^2\right)_{12} &= \left(v^2 \lambda_{345} - M^2\right) \sin\beta\cos\beta\,, \\ \left(\widetilde{\mathcal{M}}_{\rm N}^2\right)_{31} = \left(\widetilde{\mathcal{M}}_{\rm N}^2\right)_{13} &= \frac{1}{2} v^2 \lambda_5 \sin(2\phi) \sin\beta\,, \\ \left(\widetilde{\mathcal{M}}_{\rm N}^2\right)_{32} = \left(\widetilde{\mathcal{M}}_{\rm N}^2\right)_{23} &= \frac{1}{2} v^2 \lambda_5 \sin(2\phi) \cos\beta\,, \end{aligned} \tag{A.5}$$

JHEP01(2014)106

where

$$\lambda_{345} = \lambda_3 + \lambda_4 + \lambda_5 \cos(2\phi)\,, \tag{A.6}$$

and M^2 is defined in eq. (2.4). This mass matrix satisfies

$$\widetilde{\mathcal{M}}^2_{\rm N} = U \begin{pmatrix} m^2_{h_1} & & \\ & m^2_{h_2} & \\ & & m^2_{h_3} \end{pmatrix} U^T. \tag{A.7}$$

In large M limit, we find the following expressions for mass and mixing angles.

$$\begin{aligned}
m^2_{h_1} &= \frac{v_1^4\lambda_1 + v_2^4\lambda_2 + 2v_1^2v_2^2\lambda_{345}}{v^2} + \mathcal{O}\left(M^{-2}\right), \\
m^2_{h_2} &= M^2\left(1 + \mathcal{O}\left(M^{-2}\right)\right), \\
m^2_{h_3} &= M^2\left(1 + \mathcal{O}\left(M^{-2}\right)\right). \\
\begin{pmatrix} \omega^{\sigma_1}_{h_1} \\ \omega^{\sigma_2}_{h_1} \\ \omega^{\pi_A}_{h_1} \end{pmatrix} &= \begin{pmatrix} \cos\beta\left(1 - X\sin^2\beta\right) \\ \sin\beta\left(1 + X\cos^2\beta\right) \\ -\frac{v_1v_2\lambda_5\sin(2\phi)}{M^2} \end{pmatrix} + \mathcal{O}\left(M^{-4}\right), \\
\begin{pmatrix} \omega^{\sigma_1}_{h_2} \\ \omega^{\sigma_2}_{h_2} \\ \omega^{\pi_A}_{h_2} \end{pmatrix} &= \begin{pmatrix} -\sin\beta\sin\theta \\ \cos\beta\sin\theta \\ \cos\theta \end{pmatrix} + \mathcal{O}\left(M^{-2}\right), \\
\begin{pmatrix} \omega^{\sigma_1}_{h_3} \\ \omega^{\sigma_2}_{h_3} \\ \omega^{\pi_A}_{h_3} \end{pmatrix} &= \begin{pmatrix} -\sin\beta\cos\theta \\ \cos\beta\cos\theta \\ -\sin\theta \end{pmatrix} + \mathcal{O}\left(M^{-2}\right),
\end{aligned} \tag{A.8}$$

where

$$\begin{aligned}
\tan(2\theta) &= \frac{\left(\cos^2\beta - \sin^2\beta\right)}{\sin^2\beta\cos^2\beta\left(\lambda_1 + \lambda_2 - 2\lambda_{345}\right) - \lambda_5\cos^2\phi} v^2\lambda_5\sin(2\phi), \\
X &= \frac{v_1^2\lambda_1 - v_2^2\lambda_2 - \left(v_1^2 - v_2^2\right)\lambda_{345}}{M^2}\,.
\end{aligned} \tag{A.9}$$

A.3 Interactions in 2HDMs

Couplings which are relevant to calculation for the gauge invariant Barr-Zee contributions are written in this subsection. Our convention of the sign in covariant derivative is

$$D_\mu = \partial_\mu + igV_\mu\,. \tag{A.10}$$

We denote s and c as sine and cosine of the Weinberg angle, respectively, in the following.

A.3.1 $\bar{f}$-f-V couplings

These couplings are the same as the SM case, but we show them here to establish our conventions. For neutral gauge bosons,

$$\mathcal{L} \supset -\sum_{G=\gamma,Z} \overline{f}\gamma^\mu g_{Gff} f G_\mu\,, \tag{A.11}$$

JHEP01(2014)106

where g_{Gff} contains chirality structure,

$$g_{Gff} = g^L_{Gff} P_L + g^R_{Gff} P_R \,, \tag{A.12}$$

where

$$\begin{aligned} g^L_{\gamma ff} &= eQ \,, \\ g^R_{\gamma ff} &= eQ \,, \\ g^L_{Zff} &= \frac{e}{sc}\left(T^3 - s^2 Q\right), \\ g^R_{Zff} &= \frac{e}{sc}\left(-s^2 Q\right). \end{aligned} \tag{A.13}$$

For W boson,

$$\mathcal{L} \supset -\frac{1}{\sqrt{2}} \overline{u} \gamma^\mu g_{Wud} d W^+_\mu + h.c. \,, \tag{A.14}$$

where

$$g_{Wud} = V_{\rm CKM} \frac{e}{s} P_L \,, \tag{A.15}$$

where $V_{\rm CKM}$ is for the CKM matrix.

A.3.2 Yukawa couplings

The Yukawa interaction terms are described as

$$-\begin{pmatrix} \overline{u} & \overline{d} \end{pmatrix} \begin{pmatrix} m_u^{\rm diag.} + \sum_s g_{uus} s & \sum_s g_{\overline{u}ds^+} s^+ \\ \sum_s g_{\overline{d}us^-} s^- & m_d^{\rm diag.} + \sum_s g_{dds} s \end{pmatrix} \begin{pmatrix} u \\ d \end{pmatrix}, \tag{A.16}$$

where $s = h_1, h_2, h_3, \pi_Z$, and $s^\pm = H^\pm, \pi_{W^\pm}$. We define g^V and g^A as

$$g = g^V + i\gamma^5 g^A. \tag{A.17}$$

Finally we find explicit expressions of the couplings. For the neutral Higgs bosons,

$$\begin{aligned} g^V_{uuh} &= \frac{m_u^{\rm diag.}}{v} \frac{1}{\sin\beta} \omega_h^{\sigma_2}, \\ g^A_{uuh} &= \frac{m_u^{\rm diag.}}{v} \frac{1}{\tan\beta} \omega_h^{\pi_A}, \\ g^V_{ddh} &= \begin{cases} \frac{m_d^{\rm diag.}}{v} \frac{1}{\cos\beta} \omega_h^{\sigma_1} & (i=1) \\ \frac{m_d^{\rm diag.}}{v} \frac{1}{\sin\beta} \omega_h^{\sigma_2} & (i=2) \end{cases}, \\ g^A_{ddh} &= \begin{cases} \frac{m_d^{\rm diag.}}{v} \tan\beta \omega_h^{\pi_A} & (i=1) \\ -\frac{m_d^{\rm diag.}}{v} \frac{1}{\tan\beta} \omega_h^{\pi_A} & (i=2) \end{cases}. \end{aligned} \tag{A.18}$$

Here, i corresponds to the same suffix of H_i which couples to down-type quarks.

JHEP01(2014)106

For the physical charged Higgs boson,

$$
\begin{aligned}
g^V_{\overline{u}dH^+} &= \frac{1}{\sqrt{2}}\left(V_{\rm CKM}\frac{m_d^{\rm diag.}}{v_i}\left(-\delta_{1i}\sin\beta+\delta_{2i}\cos\beta\right)-\frac{m_u^{\rm diag.}}{v_2}V_{\rm CKM}\cos\beta\right),\\
g^A_{\overline{u}dH^+} &= -\frac{i}{\sqrt{2}}\left(V_{\rm CKM}\frac{m_d^{\rm diag.}}{v_i}\left(-\delta_{1i}\sin\beta+\delta_{2i}\cos\beta\right)+\frac{m_u^{\rm diag.}}{v_2}V_{\rm CKM}\cos\beta\right),\\
g^V_{\overline{d}uH^-} &= -\frac{1}{\sqrt{2}}\left(V^\dagger_{\rm CKM}\frac{m_u^{\rm diag.}}{v_2}\cos\beta-\frac{m_d^{\rm diag.}}{v_i}V^\dagger_{\rm CKM}\left(-\delta_{1i}\sin\beta+\delta_{2i}\cos\beta\right)\right),\\
g^A_{\overline{d}uH^-} &= \frac{i}{\sqrt{2}}\left(V^\dagger_{\rm CKM}\frac{m_u^{\rm diag.}}{v_2}\cos\beta+\frac{m_d^{\rm diag.}}{v_i}V^\dagger_{\rm CKM}\left(-\delta_{1i}\sin\beta+\delta_{2i}\cos\beta\right)\right),
\end{aligned}
\tag{A.19}
$$

where i in the suffix is again the same suffix of H_i which couples to down-type quarks. Sometime the followings are useful:

$$
\begin{aligned}
g_{\overline{u}dH^+} &= g^L_{\overline{u}dH^+}P_L+g^R_{\overline{u}dH^+}P_R \qquad\qquad (A.20)\\
&= +\sqrt{2}\left[\left(-\frac{m_u^{\rm diag.}}{v}V_{\rm CKM}\frac{1}{\tan\beta}\right)P_L+\left(V_{\rm CKM}\frac{m_d^{\rm diag.}}{v}\left(-\delta_{1i}\tan\beta+\delta_{2i}\frac{1}{\tan\beta}\right)\right)P_R\right],\\
g_{\overline{d}uH^-} &= g^L_{\overline{d}uH^-}P_L+g^R_{\overline{d}uH^-}P_R\\
&= -\sqrt{2}\left[\left(-\frac{m_d^{\rm diag.}}{v}V^\dagger_{\rm CKM}\left(-\delta_{1i}\tan\beta+\delta_{2i}\frac{1}{\tan\beta}\right)\right)P_L+\left(V^\dagger_{\rm CKM}\frac{m_u^{\rm diag.}}{v}\frac{1}{\tan\beta}\right)P_R\right].
\end{aligned}
$$

A.3.3 $\mathcal{L}_{\rm WWW}$

These couplings are the same as the SM case, but we show them here to establish our conventions.

$$
\begin{aligned}
\mathcal{L}\supset-\sum_{G=\gamma,Z} ig_{WWG}\Big\{&\left(\partial^\alpha W^{+\beta}\right)W^{-\mu}G^\nu(g_{\alpha\mu}g_{\beta\nu}-g_{\alpha\nu}g_{\beta\mu})\\
&+W^{+\beta}(\partial^\alpha W^{-\mu})G^\nu(g_{\alpha\nu}g_{\beta\mu}-g_{\alpha\beta}g_{\mu\nu})\\
&+W^{+\beta}W^{-\mu}(\partial^\alpha G^\nu)(g_{\alpha\beta}g_{\mu\nu}-g_{\alpha\mu}g_{\beta\nu})\Big\},
\end{aligned}
\tag{A.21}
$$

where

$$
\begin{aligned}
g_{WWA} &= e\,,\\
g_{WWZ} &= \frac{e}{s}c\,.
\end{aligned}
\tag{A.22}
$$

A.3.4 W^+-W^--h couplings

$$
\mathcal{L}\supset\sum_h g_{WWh}W^+_\mu W^{-\mu}h+\frac{1}{2}g_{ZZh}Z_\mu Z^{-\mu}h\,,
\tag{A.23}
$$

where

$$
\begin{aligned}
g_{WWh} &= 2\frac{m_W^2}{v}\left[\cos\beta\omega_h^{\sigma_1}+\sin\beta\omega_h^{\sigma_2}\right],\\
g_{ZZh} &= 2\frac{m_Z^2}{v}\left[\cos\beta\omega_h^{\sigma_1}+\sin\beta\omega_h^{\sigma_2}\right].
\end{aligned}
\tag{A.24}
$$

JHEP01(2014)106

By using eq. (A.3), we find that

$$\sum_h g^A_{\ell\ell h} g_{WWh} = 0\,. \tag{A.25}$$

A.3.5 V-H^+-H^- couplings

$$\mathcal{L} \supset +i\left(H^+\partial_\mu H^- - H^-\partial_\mu H^+\right)\left(g_{\gamma H^+H^-}A^\mu + g_{ZH^+H^-}Z^\mu\right), \tag{A.26}$$

where

$$\begin{aligned} g_{\gamma H^+H^-} &= e, \\ g_{ZH^+H^-} &= \frac{1}{2}\frac{e}{sc}\left(c^2 - s^2\right). \end{aligned} \tag{A.27}$$

A.3.6 $W^\pm$-$H^\mp$-h couplings

$$\begin{aligned} \mathcal{L} \supset &+ ig_{hW^-H^+}\left(h\partial_\mu H^+ - H^+\partial_\mu h\right)W^{-\mu} \\ &+ ig_{hW^+H^-}\left(h\partial_\mu H^- - H^-\partial_\mu h\right)W^{+\mu}, \end{aligned} \tag{A.28}$$

where

$$g_{hW^\pm H^\mp} = \pm\frac{1}{2}\frac{e}{s}\left(-\sin\beta\omega_h^{\sigma_1} + \cos\beta\omega_h^{\sigma_2} \mp i\omega_h^{\pi_A}\right). \tag{A.29}$$

By using eq. (A.3), we find that

$$\sum_h g_{hW^+H^-} g_{WWh} = 0\,. \tag{A.30}$$

A.3.7 s^+-s^--h couplings

$$\begin{aligned} \mathcal{L} \supset &+ g_{H^+H^-h}H^+H^-h \\ &+ g_{\pi_{W^+}\pi_{W^-}h}\pi_{W^+}\pi_{W^-}h \\ &+ g_{\pi_{W^+}H^-h}\pi_{W^+}H^-h + g_{H^+\pi_{W^-}h}H^+\pi_{W^-}h \\ &+ \frac{1}{2}g_{\pi_Z\pi_Z h}\pi_Z\pi_Z h, \end{aligned} \tag{A.31}$$

where

$$\begin{aligned} g_{H^+H^-h} &= +\frac{v_1}{v^2}\left(-v_1^2\lambda_3 + v_2^2(-\lambda_1 + \lambda_4 + \lambda_5\cos(2\phi))\right)\omega_h^{\sigma_1} \\ &\quad + \frac{v_2}{v^2}\left(-v_2^2\lambda_3 + v_1^2(-\lambda_2 + \lambda_4 + \lambda_5\cos(2\phi))\right)\omega_h^{\sigma_2} \\ &\quad + \frac{v_1 v_2}{v}\lambda_5\sin(2\phi)\omega_h^{\pi_A}, \\ g_{\pi_{W^+}\pi_{W^-}h} &= -\frac{m_h^2}{2m_W^2}g_{W^+W^-h}\,, \\ g_{\pi_{W^+}H^-h} &= -\frac{m_{H^\pm}^2 - m_h^2}{m_W}g_{hW^+H^-}\,, \\ g_{H^+\pi_{W^-}h} &= +\frac{m_{H^\pm}^2 - m_h^2}{m_W}g_{hW^-H^+}\,, \\ g_{h\pi_Z\pi_Z} &= -\frac{m_h^2}{2m_Z^2}g_{ZZh}\,. \end{aligned} \tag{A.32}$$

JHEP01(2014)106

A.3.8 $W^{\pm}$-$\pi^{\mp}$-h couplings

$$\begin{aligned}\mathcal{L} \supset &+ i g_{hW^-\pi^+} \left(h\partial_\mu \pi^+ - \pi^+ \partial_\mu h\right) W^{-\mu} \\ &+ i g_{hW^+\pi^-} \left(h\partial_\mu \pi^- - \pi^- \partial_\mu h\right) W^{+\mu},\end{aligned} \tag{A.33}$$

where

$$g_{hW^\pm\pi^\mp} = \pm \frac{1}{2m_W} g_{WWh}\,. \tag{A.34}$$

A.3.9 V-$W^{\pm}$- $\pi^{\mp}$ couplings

$$\mathcal{L} \supset + \sum_{V=\gamma,Z} \left(g_{VW^-\pi^+} V_\mu W^{-\mu} \pi^+ + g_{VW^+\pi^-} V_\mu W^{+\mu} \pi^-\right), \tag{A.35}$$

where

$$\begin{aligned} g_{\gamma W^\mp \pi^\pm} &= +e m_W\,, \\ g_{ZW^\mp\pi^\pm} &= -e s_W m_Z\,. \end{aligned} \tag{A.36}$$

A.3.10 Some four-point couplings

$$\begin{aligned}\mathcal{L} \supset &+ g_{H^-\pi_{W^+}\pi_{W^-}\pi_{W^+}} H^- \pi_{W^+}\pi_{W^-}\pi_{W^+} \\ &+ \frac{1}{2} g_{H^-\pi_{W^+}\pi_Z\pi_Z} H^- \pi_{W^+}\pi_Z\pi_Z \\ &+ g_{H^-\pi_{W^+}H^-H^+} H^- \pi_{W^+} H^- H^+\end{aligned} \tag{A.37}$$

where

$$\begin{aligned} g_{H^-\pi_{W^+}\pi_{W^-}\pi_{W^+}} &= \sum_h \frac{1}{m_W} g_{hW^+H^-} g_{\pi_{W^+}\pi_{W^-}h}\,, \\ g_{H^-\pi_{W^+}\pi_Z\pi_Z} &= \sum_h \frac{1}{m_W} g_{hW^+H^-} g_{\pi_Z\pi_Z h}\,, \\ g_{H^-\pi_{W^+}H^-H^+} &= \sum_h \frac{1}{m_W} g_{hW^+H^-} g_{hH^+H^-}\,. \end{aligned} \tag{A.38}$$

B EDM formula details

In this section we present formulae for the Barr-Zee contributions to fermionic EDMs and cEDMs.

B.1 Fermion loops ($h\gamma\gamma$ and $hZ\gamma$)

After substituting eqs. (3.19) and (3.20) for eq. (4.3), we find the fermion loop contributions to the EDMs for fermion ℓ are

$$\begin{aligned}\left(\frac{d_\ell}{e}\right)_{\text{fermion}} = &-\frac{m_\ell}{(4\pi)^4}\sqrt{2}G_F \sum_f \sum_h \sum_{G=\gamma,Z} N_c Q_f \left(g^L_{G\ell\ell} + g^R_{G\ell\ell}\right) \\ &\times \left[\frac{g^A_{h\ell\ell}}{m_\ell/v}\frac{g^V_{hff}}{m_f/v}\mathcal{I}^G_1(m_f,m_h) + \frac{g^V_{h\ell\ell}}{m_\ell/v}\frac{g^A_{hff}}{m_f/v}\mathcal{I}^G_2(m_f,m_h)\right],\end{aligned} \tag{B.1}$$

JHEP01(2014)106

where

$$\mathcal{I}_1^G(m_f, m_h) = \left(g_{Gff}^L + g_{Gff}^R\right) \frac{m_f^2}{m_h^2 - m_G^2} \left(I_1(m_f, m_G) - I_1(m_f, m_h)\right),$$
$$\mathcal{I}_2^G(m_f, m_h) = \left(g_{Gff}^L + g_{Gff}^R\right) \frac{m_f^2}{m_h^2 - m_G^2} \left(I_2(m_f, m_G) - I_2(m_f, m_h)\right), \tag{B.2}$$

and where[4]

$$I_1(m_1, m_2) = \int_0^1 dz \left(1 - 2z(1-z)\right) \frac{m_2^2}{m_1^2 - m_2^2 z(1-z)} \ln \frac{m_2^2 z(1-z)}{m_1^2},$$
$$I_2(m_1, m_2) = \int_0^1 dz \frac{m_2^2}{m_1^2 - m_2^2 z(1-z)} \ln \frac{m_2^2 z(1-z)}{m_1^2}. \tag{B.4}$$

B.2 Charged Higgs loops ($h\gamma\gamma$ and $hZ\gamma$)

By substituting the result in eq. (3.21) into eq. (4.3), we find the charged Higgs contribution to the EDMs,

$$\left(\frac{d_\ell}{e}\right)_{\text{scalar}} = +\frac{m_\ell}{(4\pi)^4} \sqrt{2} G_F \sum_h \sum_{G=\gamma,Z} \left(g_{G\ell\ell}^L + g_{G\ell\ell}^R\right) \frac{g_{h\ell\ell}^A}{m_\ell/v} \frac{g_{hH^+H^-}}{v} \mathcal{I}_3^G(m_H^\pm, m_h) \tag{B.5}$$

where

$$\mathcal{I}_3^G(m_H^\pm, m_h) = -\frac{1}{2} g_{GH^+H^-} \frac{v^2}{m_h^2 - m_G^2} \times \Big[\left(I_1(m_{H^\pm}, m_G) - I_1(m_{H^\pm}, m_h)\right) - \left(I_2(m_{H^\pm}, m_G) - I_2(m_{H^\pm}, m_h)\right) \Big]. \tag{B.6}$$

B.3 W loops ($h\gamma\gamma$ and $hZ\gamma$)

The EDM contributions from W boson loops are

$$\left(\frac{d_\ell}{e}\right)_W = +\frac{m_\ell}{(4\pi)^4} \sqrt{2} G_F \sum_h \sum_{G=\gamma,Z} \left(g_{G\ell\ell}^L + g_{G\ell\ell}^R\right) \frac{g_{h\ell\ell}^A}{m_\ell/v} \frac{g_{WWh}}{2m_W^2/v} \mathcal{I}_W^G(m_h), \tag{B.7}$$

where

$$\mathcal{I}_W^G(m_h) = g_{WWG} \frac{2m_W^2}{m_h^2 - m_G^2} \times \Bigg[-\frac{1}{4} \left\{ \left(6 - \frac{m_G^2}{m_W^2}\right) + \left(1 - \frac{m_G^2}{2m_W^2}\right) \frac{m_h^2}{m_W^2} \right\} \left[I_1(m_W, m_h) - I_1(m_W, m_G)\right] + \left\{ \left(-4 + \frac{m_G^2}{m_W^2}\right) + \frac{1}{4} \left(6 - \frac{m_G}{m_W^2} + \left(1 - \frac{m_G}{2m_W^2}\right) \frac{m_h^2}{m_W^2}\right) \right\} \left[I_2(m_W, m_h) - I_2(m_W, m_G)\right] \Bigg]. \tag{B.8}$$

[4] The functions $f(z)$ and $g(z)$ in refs. [12, 13] are related to I_1 and I_2 as follows:

$$I_1(m_1, m_2) = -2\frac{m_2^2}{m_1^2} f\left(\frac{m_1^2}{m_2^2}\right), \quad I_2(m_1, m_2) = -2\frac{m_2^2}{m_1^2} g\left(\frac{m_1^2}{m_2^2}\right). \tag{B.3}$$

JHEP01(2014)106

B.4 $H^{\mp}W^{\pm}\gamma$

In this paper we first find the EDM contributions from $H^{\mp}W^{\pm}\gamma$ vertices which are generated by W and charged Higgs boson loops. The detail of this derivation is given in appendix C. The contributions to the EDMs are

$$\frac{d_\ell}{e} = -\frac{m_\ell}{(4\pi)^4}\sqrt{2}G_F\mathcal{S}_\ell \sum_h \left(\frac{g^A_{\ell\ell h}}{m_\ell/v}\frac{g_{WWh}}{2m_W^2/v}\frac{e^2}{2s^2}\mathcal{I}_4(m_h^2,m_H^2) + \frac{g^A_{\ell\ell h}}{m_\ell/v}\frac{g_{HHh}}{v}\mathcal{I}_5(m_h^2,m_H^2)\right), \tag{B.9}$$

where

$$\begin{aligned}\mathcal{I}_4\left(m_h^2,m_H^2\right) &= \frac{m_W^2}{m_H^2-m_W^2}\left(I_4\left(m_W^2,m_h^2\right)-I_4\left(m_H^2,m_h^2\right)\right),\\ \mathcal{I}_5\left(m_h^2,m_H^2\right) &= \frac{m_W^2}{m_H^2-m_W^2}\left(I_5\left(m_W^2,m_h^2\right)-I_5\left(m_H^2,m_h^2\right)\right),\end{aligned} \tag{B.10}$$

and where

$$\begin{aligned}I_4\left(m_1^2,m_h^2\right) &= \int_0^1 dz\left(z(1-z)^2-4(1-z)^2+\frac{m_H^2-m_h^2}{m_W^2}z(1-z)^2\right)\\ &\qquad\times\frac{m_1^2}{m_W^2(1-z)+m_h^2z-m_1^2z(1-z)}\ln\left(\frac{m_W^2(1-z)+m_h^2z}{m_1^2z(1-z)}\right),\\ I_5\left(m_1^2,m_h^2\right) &= +2\int_0^1 dz\frac{m_1^2z(1-z)^2}{m_H^2(1-z)+m_h^2z-m_1^2z(1-z)}\ln\left(\frac{m_H^2(1-z)+m_h^2z}{m_1^2z(1-z)}\right),\end{aligned} \tag{B.11}$$

and s is sine of the Weinberg angle. Here we have used the following relations among the coupling,

$$\begin{aligned}\mathrm{Im}\left(\frac{g^R_{H^+\bar{\nu}e}}{\sqrt{2}m_e/v}\frac{g_{W^+H^-h}}{e/(2s_W)}\right) &= \frac{g^A_{eeh}}{m_e/v},\\ \mathrm{Im}\left(\frac{g^R_{H^+\bar{u}d}}{\sqrt{2}m_d/v}\frac{g_{W^+H^-h}}{e/(2s_W)}\right) &= \frac{g^A_{ddh}}{m_d/v},\\ \mathrm{Im}\left(\frac{g^R_{H^-\bar{d}u}}{\sqrt{2}m_u/v}\frac{g_{W^-H^+h}}{e/(2s_W)}\right) &= \frac{g^A_{uuh}}{m_u/v}.\end{aligned} \tag{B.12}$$

B.5 CEDMs

The effective Hamiltonian for the cEDM is defined as eq. (4.7). We find

$$d_q^c = +\frac{m_q}{(4\pi)^4}\sqrt{2}G_F\sum_f\sum_h 2g_s^2\frac{m_f^2}{m_h^2}\left[\frac{g^A_{hqq}}{m_q/v}\frac{g^V_{hff}}{m_f/v}I_1(m_f,m_h)+\frac{g^V_{hqq}}{m_q/v}\frac{g^A_{hff}}{m_f/v}I_2(m_f,m_h)\right]. \tag{B.13}$$

C Derivation for effective $H^-W^+\gamma$ vertex

In this appendix, we present explicit derivation of the effective $H^-W^+\gamma$ vertex, which is generated from bosonic loop diagrams, in 2HDMs.

JHEP01(2014)106

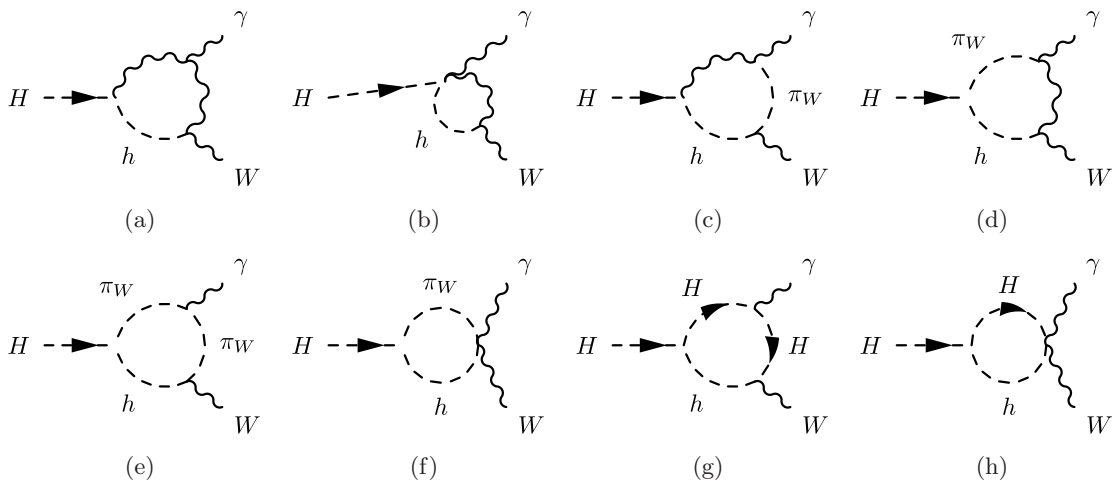

Figure 15. Diagrams for the vertex corrections to $H^-W^+\gamma$. Figures 15(a)–15(f) depend on the gauge fixing parameter ξ, while figures 15(g) and 15(h) are independent of ξ.

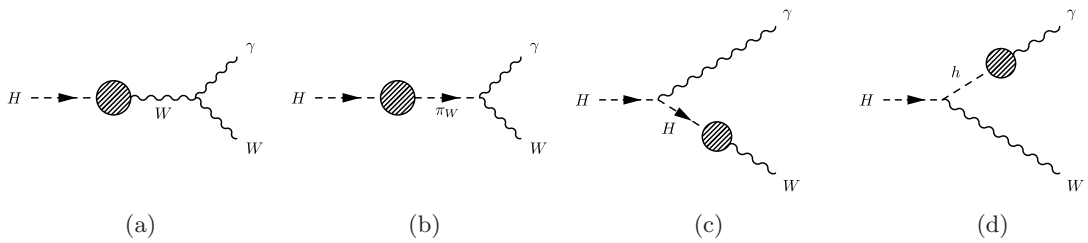

Figure 16. Diagrams of wave function type corrections.

There are two types of loop diagrams; vertex corrections (figure 15) and wave function corrections (figure 16). The diagrams in figure 16(d) give nothing because of C-invariance. The contributions from figure 16(c) is always proportional to p_2^ν. Thus they do not contribute to the on-shell amplitude of $H^\mp \to W^\mp\gamma$ nor the EDM at two-loop level by the same discussion in section 3. Hence what we need to calculate are only the diagrams in figures 15, 16(a), and 16(b). In this section, we calculate these diagrams in 't Hooft-Feynman gauge.

First, let us consider the diagrams in figures 15(a)–15(f). These diagrams depend on

JHEP01(2014)106

the gauge fixing parameter of W boson. We find

$$\begin{aligned}
\sum \text{Figs. 15(a)-15(f)} = &+\frac{i}{(4\pi)^{D/2}}\Gamma(3-D/2)\left(p_{2\mu}p_{1\nu}-p_2p_1g_{\mu\nu}\right)\sum_h eg_{W^+H^-h}g_{WWh} \\
&\times\int_{x+y+z=1}\frac{-2yz-4z+4-\frac{m_H^2-m_h^2}{m_W^2}2yz}{\left[m_W^2(1-z)+m_h^2z-p_2^2z(1-z)-2p_1p_2yz\right]^{3-D/2}} \\
&+\frac{i}{(4\pi)^{D/2}}g_{\mu\nu}\sum_h eg_{W^+H^-h}g_{WWh} \\
&\times\left[\Gamma(2-D/2)\int_0^1 dz\frac{-(1+z)}{\left[m_W^2z+m_h^2(1-z)-p_H^2z(1-z)\right]^{2-D/2}}\right. \\
&-\frac{m_H^2-m_h^2}{m_W^2}\Gamma(2-D/2)\int_0^1 dz\frac{\frac{1}{2}(-1+2z)}{\left[m_W^2z+m_h^2(1-z)-p_H^2z(1-z)\right]^{2-D/2}} \\
&+\left(p_H^2-m_H^2\right)\Gamma(3-D/2) \\
&\left.\times\int_{x+y+z=1}\frac{1}{\left[m_W^2(1-z)+m_h^2z-p_2^2z(1-z)-2p_1p_2yz\right]^{3-D/2}}\right],
\end{aligned} \tag{C.1}$$

where $p_H^2=(p_1+p_2)^2$. We find $g_{\mu\nu}$ terms, which are not gauge invariant. We will show these terms are canceled with other diagrams, that is, the pinch contributions.

The diagrams in figures 15(g) and 15(h) are independent from the gauge fixing parameter.

$$\begin{aligned}
\text{Fig. 15(g)}+\text{Fig. 15(h)} = &-\frac{i}{(4\pi)^{D/2}}\Gamma(3-D/2)\left(p_{2\mu}p_{1\nu}-p_2p_1g_{\mu\nu}\right)\sum_h eg_{W^+H^-h}g_{HHh} \\
&\times\int_{x+y+z=1}\frac{4yz}{\left[m_H^2(1-z)+m_h^2z-p_2^2z(1-z)-2p_1p_2yz\right]^{3-D/2}} \\
&-\frac{i}{(4\pi)^{D/2}}\Gamma(2-D/2)g_{\mu\nu}\sum_h eg_{W^+H^-h}g_{HHh} \\
&\times\int_0^1 dz\frac{-1+2z}{\left[m_H^2z+m_h^2(1-z)-p_H^2z(1-z)\right]^{2-D/2}}.
\end{aligned} \tag{C.2}$$

Next we calculate the diagrams in figures 16(a) and 16(b). First we define the following notation for self-energies.

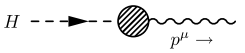

$$= i\Pi^\mu_{H^-W^+}(p) = ip^\mu\Pi_{H^-W^+}\left(p^2\right), \tag{C.3}$$

$$= i\Pi_{H^-\pi_{W^+}}\left(p^2\right). \tag{C.4}$$

The direction of the momentum of Π^μ_{HW} is shown in its figure. Using this notation, we find

$$\begin{aligned}
\text{Fig. 16(a)} + \text{Fig. 16(b)} = &\frac{-ig_{\mu\nu}}{p_H^2-m_W^2}\left(-em_Wi\Pi_{H^-\pi_{W^+}}\left(p_H^2\right)-em_W^2\Pi_{H^-W^+}\left(p_H^2\right)\right) \\
&+\left(p_2^2-m_W^2\right)\frac{-ig_{\mu\nu}}{p_H^2-m_W^2}\left(-e\Pi_{H^-W^+}\left(p_H^2\right)\right).
\end{aligned} \tag{C.5}$$

JHEP01(2014)106

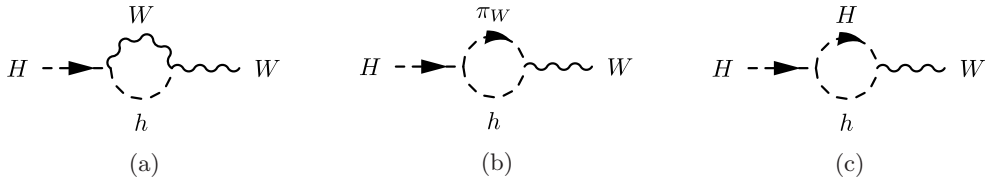

Figure 17. Diagrams for $\Pi_{H^-W^+}$.

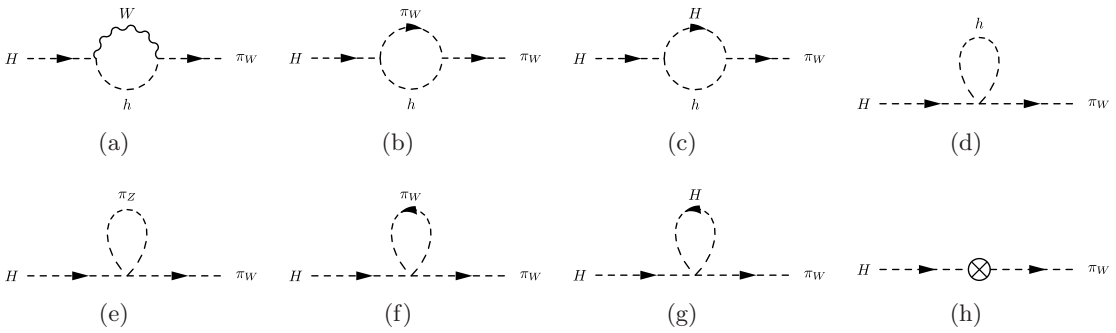

Figure 18. Diagrams for $\Pi_{H^-\pi_{W^+}}$. The last one is for the counter term.

Here we ignored $p_2^\mu p_2^\nu$ terms because they do not contribute to the EDMs as we discussed in section 3. Note that the $\left(p_2^2 - m_W^2\right)$ term does not also contribute to the on-shell amplitudes nor the EDMs at two-loop level. If we calculate the EDMs with this term, we immediately see that q^2 dependence completely canceled out. Thus, we only need the first term in eq. (C.5).

Figure 17 shows the diagrams for $\Pi_{H^-W^+}(p^2)$. We find

$$\begin{aligned} i\Pi_{H^-W^+}(p^2) = &+\frac{i}{(4\pi)^{D/2}}\Gamma(2-D/2)g_{WWh}g_{hW^+H^-}\int_0^1 dx\frac{-(2-x)+\frac{m_H^2-m_h^2}{m_W^2}(x-\frac{1}{2})}{\left[m_W^2(1-x)+m_h^2x-p^2x(1-x)\right]^{2-D/2}} \\ &+\frac{i}{(4\pi)^{D/2}}\Gamma(2-D/2)g_{HHh}g_{hW^+H^-}\int_0^1 dx\frac{1-2x}{\left[m_H^2x+m_h^2(1-x)-p^2x(1-x)\right]^{2-D/2}}. \end{aligned} \tag{C.6}$$

Figure 18 shows the diagrams for $\Pi_{H^-\pi_{W^+}}(p^2)$. We find figures 18(d)–18(g) are canceled by figure 18(h), so we do not calculate them. Figure 18(h) is the counter term for $H - \pi_W$ mixing, and it is also related with the counter terms for the Higgs tadpoles (figure 19(i)),

$$\delta_{H^-\pi_{W^+}} = \sum_h \frac{1}{m_W} g_{hW^+H^-}\delta_h\,, \tag{C.7}$$

where δ's are defined through

$$\mathcal{L} \supset -\delta_{H^-\pi_{W^+}} H^-\pi_{W^+} + \sum_h \delta_h h\,. \tag{C.8}$$

It is easy to find this relation by analyzing the Higgs potential. We take renormalization conditions in which all tadpole diagrams are completely canceled by their counter terms.

JHEP01(2014)106

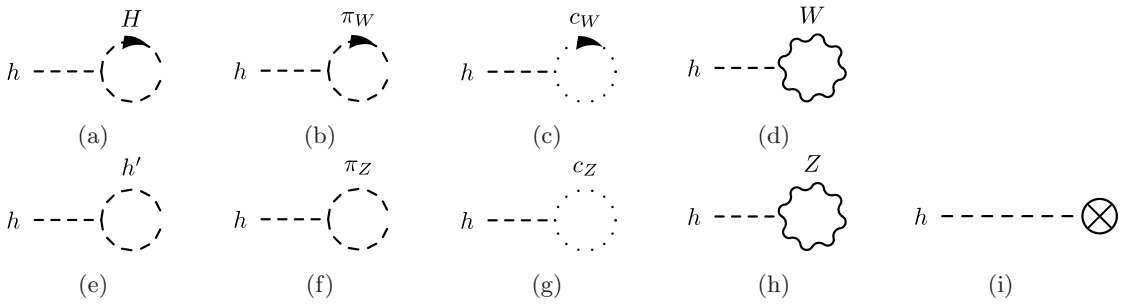

Figure 19. Tadpoles diagrams.

Then $\delta_{H^-\pi_{W^+}}$ is not arbitrary but should be calculated from the tadpole diagrams and eq. (C.8). We show the tadpole diagrams in figure 19. After calculating tadpole diagrams, using eq. (C.7), we find

$$\begin{aligned}
\text{Fig. 18(h)} = &-\left(\text{Fig. 18(d)} + \text{Fig. 18(e)} + \text{Fig. 18(f)} + \text{Fig. 18(g)}\right) \\
&+ i\sum_h \left(\frac{m_H^2 - m_h^2}{2m_W^3} g_{WWh} g_{hW^+H^-} + \frac{g_{HHh} g_{hW^+H^-}}{m_W}\right) \int_\ell \frac{1}{\ell^2 - m_h^2} \\
&- i\sum_h \frac{g_{HHh} g_{hW^+H^-}}{m_W} \int_\ell \frac{1}{\ell^2 - m_H^2} \\
&+ i\sum_h \frac{m_h^2}{2m_W^3} g_{HHh} g_{hW^+H^-} \int_\ell \frac{1}{\ell^2 - m_W^2}.
\end{aligned} \tag{C.9}$$

Now we have calculated all the diagrams shown in figure 18, and we find

$$\begin{aligned}
i\Pi_{H^-\pi_{W^+}} = &+ \frac{\Gamma(2-D/2)}{(4\pi)^{D/2}} \frac{1}{2m_W} g_{WWh} g_{W^+H^-h} \\
&\times \int_0^1 dx \left[\frac{p^2(1+2x) + m_h^2}{\left[m_W^2 x + m_h^2(1-x) - p^2 x(1-x)\right]^{2-D/2}}\right. \\
&\qquad \left. + \frac{m_H^2 - m_h^2}{m_W^2} \frac{m_W^2 - p^2(1-2x)}{\left[m_W^2 x + m_h^2(1-x) - p^2 x(1-x)\right]^{2-D/2}}\right] \\
&- \frac{\Gamma(2-D/2)}{(4\pi)^{D/2}} \frac{1}{m_W} g_{HHh} g_{W^+H^-h} p^2 \int_0^1 dx \frac{1-2x}{\left[m_H^2 x + m_h^2(1-x) - p^2 x(1-x)\right]^{2-D/2}}.
\end{aligned} \tag{C.10}$$

We have finished preparing to calculate figure 16(a) + figure 16(b). Substituting

JHEP01(2014)106

eqs. (C.6) and (C.10) into the first term in eq. (C.5), then we find

$$
\begin{aligned}
\text{Fig. 16(a)} + \text{Fig. 16(b)} = & -ig_{\mu\nu}\frac{1}{(4\pi)^{D/2}}\Gamma(2-D/2)eg_{W^+H^-h} \\
& \times \left[g_{WWh}\int_0^1 dx \frac{-(1+x)+\frac{m_H^2-m_h^2}{2m_W^2}(1-2x)}{\left[m_W^2 x + m_h^2(1-x) - p_H^2 x(1-x)\right]^{2-D/2}} \right. \\
& + g_{WWh}\frac{p_H^2-m_H^2}{2\left(p_H^2-m_W^2\right)}\int_0^1 dx \frac{1}{\left[m_W^2 x + m_h^2(1-x) - p_H^2 x(1-x)\right]^{2-D/2}} \\
& \left. + g_{HHh}\int_0^1 dx \frac{(1-2x)}{\left[m_H^2 x + m_h^2(1-x) - p_H^2 x(1-x)\right]^{2-D/2}} \right] .
\end{aligned}
\tag{C.11}
$$

Here we dropped the $(p_2^2 - m_W^2)g_{\mu\nu}$ term because it does not contribute to what we are interested in. Note that the first term in the bracket in eq. (C.11) is canceled with eq. (C.1), and the second term is canceled with eq. (C.2).

So far we have calculated many diagrams, vertex corrections and wave function corrections. The corrections are not so simple and some of them canceled out, so we give a short summary so far here. After summing up all the correction we have calculated so far, we find

$$
\begin{aligned}
& + \frac{i}{(4\pi)^{D/2}}\Gamma(3-D/2)\left(p_{2\mu}p_{1\nu} - p_2 p_1 g_{\mu\nu}\right) \\
& \quad \times \left(+ \sum_h eg_{W^+H^-h}g_{WWh}\int_{x+y+z=1} \frac{-2yz - 4z + 4 - \frac{m_H^2-m_h^2}{m_W^2}2yz}{\left[m_W^2(1-z) + m_h^2 z - p_2^2 z(1-z) - 2p_1p_2yz\right]^{3-D/2}} \right. \\
& \qquad \left. - \sum_h eg_{W^+H^-h}g_{HHh}\int_{x+y+z=1} \frac{4yz}{\left[m_H^2(1-z) + m_h^2 z - p_2^2 z(1-z) - 2p_1p_2yz\right]^{3-D/2}} \right) \\
& + \frac{i}{(4\pi)^{D/2}}g_{\mu\nu}\left(p_H^2 - m_H^2\right)\sum_h eg_{W^+H^-h}g_{WWh} \\
& \quad \times \left[+\Gamma(3-D/2)\int_{x+y+z=1} \frac{1}{\left[m_W^2(1-z) + m_h^2 z - p_2^2 z(1-z) - 2p_1p_2yz\right]^{3-D/2}} \right. \\
& \qquad \left. -\Gamma(2-D/2)\frac{1}{2\left(p_H^2-m_W^2\right)}\int_0^1 dx \frac{1}{\left[m_W^2 x + m_h^2(1-x) - p_H^2 x(1-x)\right]^{2-D/2}} \right] .
\end{aligned}
\tag{C.12}
$$

Note that the last two terms are not gauge invariant in the sense that we discussed in section 3. Since they are proportional to $p_H^2 - m_H^2$, if we take the charged Higgs boson on-shell, they are dropped and the result becomes gauge invariant. However, now we need to take the charged Higgs boson off shell, so we still need some other terms to cancel them.

To find a gauge invariant set for the Barr-Zee diagrams, we need to take into account for the pinch contributions shown in figure 20. After pinching the fermion propagators with

JHEP01(2014)106

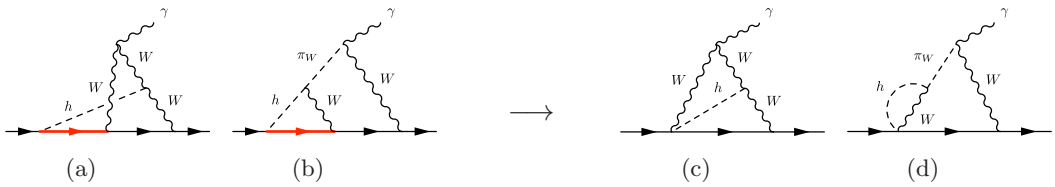

Figure 20. Pinch contributions.

red color in figures 20(a) and 20(b), the pinch contributions for $H^-W^+\gamma$ effective vertex for the Barr-Zee diagrams arise. They are schematically shown in figures 20(c) and 20(d). We denote their contributions as $\Gamma_{\rm P}^{\mu\nu}$ and $i\Pi_{\rm P}$, respectively. Then we find

$$i\Gamma_{\rm P}^{\mu\nu}(p_1,p_2) = -i\frac{\Gamma(3-D/2)}{(4\pi)^{D/2}} e g_{W^+H^-h} g_{WWh} g^{\mu\nu} \times \left(p_H^2 - m_H^2\right) \int_{x+y+z=1} \frac{1}{\left[m_W^2(1-z) + m_h^2 z - p_2^2 z(1-z) - 2p_1p_2yz\right]^{3-D/2}}, \tag{C.13}$$

$$i\Pi_{\rm P}(p_H^2) = +\frac{\Gamma(2-D/2)}{(4\pi)^{2-D/2}} \frac{1}{2m_W} g_{W^+H^-h} g_{WWh} \left(p_H^2 - m_H^2\right) \times \int_0^1 dx \frac{1}{\left[m_W^2 x + m_h^2(1-x) - p_H^2 x(1-x)\right]^{2-D/2}}. \tag{C.14}$$

Using eq. (C.5), we find that $\Gamma_{\rm P}^{\mu\nu}$ and $i\Pi_{\rm P}$ completely cancel the second term in eq. (C.12), namely these pinch contributions really make the effective vertex correction gauge invariant.

Open Access. This article is distributed under the terms of the Creative Commons Attribution License (CC-BY 4.0), which permits any use, distribution and reproduction in any medium, provided the original author(s) and source are credited.

References

[1] ATLAS collaboration, *Observation of a new particle in the search for the Standard Model Higgs boson with the ATLAS detector at the LHC*, *Phys. Lett.* **B 716** (2012) 1 [arXiv:1207.7214] [INSPIRE].

[2] CMS collaboration, *Observation of a new boson at a mass of 125 GeV with the CMS experiment at the LHC*, *Phys. Lett.* **B 716** (2012) 30 [arXiv:1207.7235] [INSPIRE].

[3] ACME collaboration, J. Baron et al., *Order of Magnitude Smaller Limit on the Electric Dipole Moment of the Electron*, *Science* (2013) [arXiv:1310.7534] [INSPIRE].

[4] C. Baker et al., *An Improved experimental limit on the electric dipole moment of the neutron*, *Phys. Rev. Lett.* **97** (2006) 131801 [hep-ex/0602020] [INSPIRE].

[5] M. Pospelov and A. Ritz, *Electric dipole moments as probes of new physics*, *Annals Phys.* **318** (2005) 119 [hep-ph/0504231] [INSPIRE].

[6] M. Raidal et al., *Flavour physics of leptons and dipole moments*, *Eur. Phys. J.* **C 57** (2008) 13 [arXiv:0801.1826] [INSPIRE].

[7] T. Fukuyama, *Searching for New Physics beyond the Standard Model in Electric Dipole Moment*, *Int. J. Mod. Phys.* **A 27** (2012) 1230015 [arXiv:1201.4252] [INSPIRE].

JHEP01(2014)106

[8] V. Kuzmin, V. Rubakov and M. Shaposhnikov, *On the Anomalous Electroweak Baryon Number Nonconservation in the Early Universe*, Phys. Lett. **B 155** (1985) 36 [INSPIRE].

[9] A.G. Cohen, D. Kaplan and A. Nelson, *Progress in electroweak baryogenesis*, Ann. Rev. Nucl. Part. Sci. **43** (1993) 27 [hep-ph/9302210] [INSPIRE].

[10] V. Rubakov and M. Shaposhnikov, *Electroweak baryon number nonconservation in the early universe and in high-energy collisions*, Usp. Fiz. Nauk **166** (1996) 493 [*Phys. Usp.* **39** (1996) 461] [hep-ph/9603208] [INSPIRE].

[11] M. Trodden, *Electroweak baryogenesis*, Rev. Mod. Phys. **71** (1999) 1463 [hep-ph/9803479] [INSPIRE].

[12] S.M. Barr and A. Zee, *Electric Dipole Moment of the Electron and of the Neutron*, Phys. Rev. Lett. **65** (1990) 21 [*Erratum ibid.* **65** (1990) 2920] [INSPIRE].

[13] R. Leigh, S. Paban and R. Xu, *Electric dipole moment of electron*, Nucl. Phys. **B 352** (1991) 45 [INSPIRE].

[14] D. Chang, W.-Y. Keung and T. Yuan, *Two loop bosonic contribution to the electron electric dipole moment*, Phys. Rev. **D 43** (1991) 14 [INSPIRE].

[15] G. Degrassi and A. Sirlin, *Gauge invariant selfenergies and vertex parts of the Standard Model in the pinch technique framework*, Phys. Rev. **D 46** (1992) 3104 [INSPIRE].

[16] G. Degrassi and A. Sirlin, *Gauge dependence of basic electroweak corrections of the standard model*, Nucl. Phys. **B 383** (1992) 73 [INSPIRE].

[17] A. Denner, *Techniques for calculation of electroweak radiative corrections at the one loop level and results for W physics at LEP-200*, Fortsch. Phys. **41** (1993) 307 [arXiv:0709.1075] [INSPIRE].

[18] Y. Sakemi et al., *Search for a permanent EDM using laser cooled radioactive atom*, J. Phys. Conf. Ser. **302** (2011) 012051 [INSPIRE].

[19] D. Kara, I. Smallman, J. Hudson, B. Sauer, M. Tarbutt and E.A. Hinds, *Measurement of the electron's electric dipole moment using YbF molecules: methods and data analysis*, New J. Phys. **14** (2012) 103051 [arXiv:1208.4507] [INSPIRE].

[20] D. Kawall, *Searching for the electron EDM in a storage ring*, J. Phys. Conf. Ser. **295** (2011) 012031 [INSPIRE].

[21] R. Peccei and H.R. Quinn, *CP Conservation in the Presence of Instantons*, Phys. Rev. Lett. **38** (1977) 1440 [INSPIRE].

[22] M. Pospelov and A. Ritz, *Neutron EDM from electric and chromoelectric dipole moments of quarks*, Phys. Rev. **D 63** (2001) 073015 [hep-ph/0010037] [INSPIRE].

[23] J. Hisano, J.Y. Lee, N. Nagata and Y. Shimizu, *Reevaluation of Neutron Electric Dipole Moment with QCD Sum Rules*, Phys. Rev. **D 85** (2012) 114044 [arXiv:1204.2653] [INSPIRE].

[24] K. Fuyuto, J. Hisano, N. Nagata and K. Tsumura, *QCD Corrections to Quark (Chromo)Electric Dipole Moments in High-scale Supersymmetry*, JHEP **12** (2013) 010 [arXiv:1308.6493] [INSPIRE].

[25] G. Degrassi, E. Franco, S. Marchetti and L. Silvestrini, *QCD corrections to the electric dipole moment of the neutron in the MSSM*, JHEP **11** (2005) 044 [hep-ph/0510137] [INSPIRE].

JHEP01(2014)106

[26] J. Hisano, K. Tsumura and M.J. Yang, *QCD Corrections to Neutron Electric Dipole Moment from Dimension-six Four-Quark Operators*, *Phys. Lett.* **B 713** (2012) 473 [arXiv:1205.2212] [INSPIRE].

[27] S. Balashov et al., *A proposal for a cryogenic experiment to measure the neutron electric dipole moment (nEDM)*, arXiv:0709.2428 [INSPIRE].

[28] K. Kirch, http://vmsstreamer1.fnal.gov/Lectures/Colloquium/presentations/130213Kirch.pdf.

[29] U. Haisch, *$\bar{B} \to X_s\gamma$: Standard Model and Beyond*, arXiv:0805.2141 [INSPIRE].

[30] F. Mahmoudi and O. Stal, *Flavor constraints on the two-Higgs-doublet model with general Yukawa couplings*, *Phys. Rev.* **D 81** (2010) 035016 [arXiv:0907.1791] [INSPIRE].

[31] CMS collaboration, *Higgs to tau tau (MSSM) (HCP)*, CMS-PAS-HIG-12-050.

[32] A. Pomarol and R. Vega, *Constraints on CP-violation in the Higgs sector from the rho parameter*, *Nucl. Phys.* **B 413** (1994) 3 [hep-ph/9305272] [INSPIRE].

[33] N. Turok and J. Zadrozny, *Electroweak baryogenesis in the two doublet model*, *Nucl. Phys.* **B 358** (1991) 471 [INSPIRE].

[34] A.G. Cohen, D. Kaplan and A. Nelson, *Spontaneous baryogenesis at the weak phase transition*, *Phys. Lett.* **B 263** (1991) 86 [INSPIRE].

[35] J.M. Cline and P.-A. Lemieux, *Electroweak phase transition in two Higgs doublet models*, *Phys. Rev.* **D 55** (1997) 3873 [hep-ph/9609240] [INSPIRE].

[36] L. Fromme, S.J. Huber and M. Seniuch, *Baryogenesis in the two-Higgs doublet model*, *JHEP* **11** (2006) 038 [hep-ph/0605242] [INSPIRE].

[37] G. Dorsch, S. Huber and J. No, *A strong electroweak phase transition in the 2HDM after LHC8*, *JHEP* **10** (2013) 029 [arXiv:1305.6610] [INSPIRE].

[38] J.M. Cline, K. Kainulainen and M. Trott, *Electroweak Baryogenesis in Two Higgs Doublet Models and B meson anomalies*, *JHEP* **11** (2011) 089 [arXiv:1107.3559] [INSPIRE].

[39] T. Ohl, *Drawing Feynman diagrams with Latex and Metafont*, *Comput. Phys. Commun.* **90** (1995) 340 [hep-ph/9505351] [INSPIRE].

JHEP01(2014)106

Published for SISSA by Springer

Received: April 21, 2016
Accepted: April 22, 2016
Published: April 26, 2016

Erratum: Gauge invariant Barr-Zee type contributions to fermionic EDMs in the two-Higgs doublet models

Tomohiro Abe,[a] **Junji Hisano,**[b,c] **Teppei Kitahara**[d] **and Kohsaku Tobioka**[c,d]

[a] *Theory Group, KEK,*
1-1 Oho, Tsukuba, 305-0801, Japan
[b] *Department of Physics, Nagoya University,*
Furo-cho, Chikusa-ku, Nagoya 464-8602, Japan
[c] *Kavli Institute for the Physics and Mathematics of the Universe (WPI),*
University of Tokyo,
5-1-5 Kashiwanoha, Kashiwa, 277–8583, Japan
[d] *Department of Physics, University of Tokyo,*
7-3-1 Hongo, Bunkyo-ku, 113-0033, Japan

E-mail: abetomo@post.kek.jp, hisano@eken.phys.nagoya-u.ac.jp, kitahara@hep-th.phys.s.u-tokyo.ac.jp, kohsaku.tobioka@ipmu.jp

Erratum to: JHEP01(2014)106

ArXiv ePrint: 1311.4704

Open Access, © The Authors.
Article funded by SCOAP[3].

doi:10.1007/JHEP04(2016)161

JHEP04(2016)161

Here we fix several typographical errors in equations. All numerical results do not change.

- The right hand side of eq. (A.4) has additional minus sign.
- The function of $\tan(2\theta)$ in eq. (A.9) should be replaced by

$$\tan(2\theta) = \frac{-(\cos^2\beta - \sin^2\beta)}{\sin^2\beta\cos^2\beta\,(\lambda_1 + \lambda_2 - 2\lambda_{345}) + \lambda_5\cos 2\phi}\lambda_5\sin(2\phi). \tag{1}$$

- g_{WWA} in eq. (A.22) should be replaced by $g_{WW\gamma}$.
- $Z^{-\mu}$ in eq. (A.23) should be replaced by Z^{μ}.
- In eqs. (B.5) and (B.6), $m_H^{\pm}$ should be replaced by $m_{H^{\pm}}$.
- Equation (B.8) should be replaced by

$$\begin{aligned}
\mathcal{I}_W^G(m_h) = g_{WWG}&\frac{2m_W^2}{m_h^2 - m_G^2} \\
&\times\left[-\frac{1}{4}\left\{\left(6 - \frac{m_G^2}{m_W^2}\right) + \left(1 - \frac{m_G^2}{2m_W^2}\right)\frac{m_h^2}{m_W^2}\right\}\left[I_1(m_W, m_h) - I_1(m_W, m_G)\right]\right. \\
&+\left\{\left(-4 + \frac{m_G^2}{m_W^2}\right) + \frac{1}{4}\left(6 - \frac{m_G^2}{m_W^2} + \left(1 - \frac{m_G^2}{2m_W^2}\right)\frac{m_h^2}{m_W^2}\right)\right\} \\
&\left.\times\left[I_2(m_W, m_h) - I_2(m_W, m_G)\right]\right].
\end{aligned} \tag{2}$$

We thank Motoi Endo for pointing them out.

Open Access. This article is distributed under the terms of the Creative Commons Attribution License (CC-BY 4.0), which permits any use, distribution and reproduction in any medium, provided the original author(s) and source are credited.

JHEP04(2016)161

Physics Letters B 755 (2016) 491–497

Contents lists available at ScienceDirect

Physics Letters B

www.elsevier.com/locate/physletb

Toward verification of electroweak baryogenesis by electric dipole moments

Kaori Fuyuto [a,*], Junji Hisano [b,a,c], Eibun Senaha [d]

[a] Department of Physics, Nagoya University, Nagoya 464-8602, Japan
[b] Kobayashi-Maskawa Institute for the Origin of Particles and the Universe, Nagoya University, Nagoya 464-8602, Japan
[c] Kavli IPMU (WPI), University of Tokyo, Kashiwa, Chiba 277-8584, Japan
[d] Department of Physics and Center for Mathematics and Theoretical Physics, National Central University, Taoyuan, 32001, Taiwan

ARTICLE INFO

Article history:
Received 19 October 2015
Received in revised form 21 January 2016
Accepted 23 February 2016
Available online 2 March 2016
Editor: M. Trodden

ABSTRACT

We study general aspects of the CP-violating effects on the baryon asymmetry of the Universe (BAU) and electric dipole moments (EDMs) in models extended by an extra Higgs doublet and a singlet, together with electroweak-interacting fermions. In particular, the emphasis is on the structure of the CP-violating interactions and dependences of the BAU and EDMs on masses of the relevant particles. In a concrete mode, we investigate a relationship between the BAU and the electron EDM for a typical parameter set. As long as the BAU-related CP violation predominantly exists, the electron EDM has a strong power in probing electroweak baryogenesis. However, once a BAU-unrelated CP violation comes into play, the direct correlation between the BAU and electron EDM can be lost. Even in such a case, we point out that verifiability of the scenario still remains with the help of Higgs physics.

© 2016 The Authors. Published by Elsevier B.V. This is an open access article under the CC BY license (http://creativecommons.org/licenses/by/4.0/). Funded by SCOAP[3].

1. Introduction

The particle content of the standard model (SM) has been completed by the discovery of the 125 GeV Higgs boson at the Large Hadron Collider (LHC) [1]. So far, there is no clear signal beyond the SM in laboratory experiments. Nevertheless, the cosmological problems such as the origin of the baryon asymmetry of the Universe (BAU) and identification of the cold dark matter still remain unsolved within the SM.

One of the mechanisms for generating the BAU is electroweak baryogenesis (EWBG) [2,3]. In this scenario, the BAU arises during the electroweak phase transition (EWPT), and its feasibility depends on properties of models at the GeV/TeV scales. From the viewpoint of the testability, EWBG is the first scenario that is verified or falsified by the ongoing and upcoming experiments, among others. As is well known, the SM has the two drawbacks that prevent it from generating the BAU: absence of both a strong first-order EWPT [4] and a sufficient amount of CP violation [5]. Supersymmetric (SUSY) models may naturally solve those issues simultaneously. For example, in the minimal SUSY SM model (MSSM), a light scalar top (stop) could induce the strong first-order EWPT, and the fermionic superpartners provide the substantial amount of CP violation. However, it turns out that the light stop scenario in the MSSM is not consistent with the LHC Run 1 data such as the Higgs signal strengths and the direct stop searches [6]. In addition, the light stop scenario in more general framework beyond the MSSM is also found to be incompatible with the current LHC data [7]. Given this fact, the colored particles may no longer the candidates for archiving the strong first-order EWPT. Therefore, whatever a UV theory might be, the possibility of EWBG can be investigated in the framework of an effective field theory of non-colored particles after integrating out irrelevant heavy degrees of freedom, *i.e.*,

$$\text{UV theories} \supset \text{multi-Higgs} + \text{EW-interacting fermions}. \tag{1}$$

Experiments that are most sensitive to the CP violation are measurements of the electric dipole moments (EDMs) of electron, neutron and atoms etc. Clarifying relationships between the BAU-related CP violations and the EDMs are indispensable for the test of the EWBG scenario. In some analyses in the literature, the CP-violating effect is incorporated by higher dimensional operators assuming only one Higgs doublet and by which the BAU is evaluated. In such a case, the CP-violating effects peculiar to the finite temperature, such as a resonant enhancement pointed out in Ref. [8],

* Corresponding author.
E-mail addresses: fuyuto@th.phys.nagoya-u.ac.jp (K. Fuyuto), hisano@eken.phys.nagoya-u.ac.jp (J. Hisano), senaha@ncu.edu.tw (E. Senaha).

http://dx.doi.org/10.1016/j.physletb.2016.02.053
0370-2693/© 2016 The Authors. Published by Elsevier B.V. This is an open access article under the CC BY license (http://creativecommons.org/licenses/by/4.0/). Funded by SCOAP[3].

are missing, which drastically changes the correlation between the BAU and EDM.

In this Letter, we clarify similarities and differences between the BAU-related CP violation and the EDM-related one with particular emphasis on the structure of the interactions and the mass dependences of the relevant particles. As an illustration, we consider a framework in which the Higgs sector is augmented by an additional Higgs doublet and a singlet, and in addition, $SU(2)_L$ doublet fermions and singlet fermion are introduced to accommodate CP violation for baryogenesis. In our setup, the structure of the CP-violating interactions are more generic than those in SUSY models. We evaluate the CP-violating source term for the BAU in the closed-time-path formalism and relate it with the electron EDM. The correlation between the two CP-violating quantities is elucidated as functions of the EW-interacting fermion masses.

As a specific example, we consider a next-to-MSSM-like model and work out the relationship between the BAU and electron EDM. It is found that the electron EDM is the useful probe of the baryogenesis favored region as long as the BAU-related CP violation predominately exists in the model. However, there is a case in which a BAU-unrelated CP violation, if it exists, alters the intimate connection between the BAU and EDM, which makes it difficult to test EWBG via the electron EDM experiment only. Nevertheless, such a specific case is possible only in the case that the doublet-singlet Higgs boson mixing exists, which is needed for a tree-potential-driven strong first-order EWPT, and thus still testable in combination with Higgs physics.

2. General aspects of CP-violating effects on the BAU and EDMs

Before going to present our model, we here give a simple but rather generic argument about the relationship between the BAU-related CP violation and EDM. For illustrative purposes, we consider the framework in which two Higgs doublets and two species of EW-interacting fermions (denoted as $\psi_{i,j}$) are present. For definite, ψ_i is assumed to be Dirac fermion and ψ_j Majorana fermion. This setup applies to the bino-driven EWBG in the MSSM [9], the singlino-driven EWBG in the next-to-MSSM [10] and the Z'ino-driven EWBG in the $U(1)'$-MSSM [11] in proper limits. We expect that the following discussion would hold in other cases by making an appropriate translation.

Let us parameterize the relevant interactions as

$$\mathcal{L} = \frac{1}{\sqrt{2}}\bar{\psi}_i\big(c_L v_a P_L + c_R v_b P_R\big)\psi_j + \text{h.c.}, \tag{2}$$

where $v_{a,b}$ $(a,b=1,2)$ denote the Higgs vacuum expectation values (VEVs), and $c_{L,R}$ are the complex parameters. With this Lagrangian, we evaluate the source terms in the diffusion equation of ψ_i in the closed-time-path formalism [8]. The vector current of ψ_i has the form

$$\partial_\mu j^\mu_{\psi_i} = S_{\psi_i}, \tag{3}$$

where only the CP-violating source term is shown on the right-hand side. In a VEV insertion approximation [8], S_{ψ_i} to leading order is induced by the process shown in Fig. 1, which is cast into the form

$$\begin{aligned} S_{\psi_i}(X) &= \kappa_S \cdot 2m_i m_j \mathrm{Im}(c_L c_R^*) v^2(X)\dot{\beta}(X)\mathcal{I}^f_{ji} \\ &\equiv C_{\mathrm{BAU}}\mathrm{Im}(c_L c_R^*), \end{aligned} \tag{4}$$

where $\kappa_S = +1$ for $(a,b)=(2,1)$, $\kappa_S = -1$ for $(a,b)=(1,2)$ and $\kappa_S = 0$ for $(a,b)=(1,1),\ (2,2)$. $m_{i,j}$ are the masses of $\psi_{i,j}$, $\dot{\beta}(X)$ is the time derivative of $\beta(X) = \tan^{-1}(v_2(X)/v_1(X))$, and $\mathcal{I}^f_{ji}$ denotes a thermal function as will be given below. One can see that $S_{\psi_i}(X)$

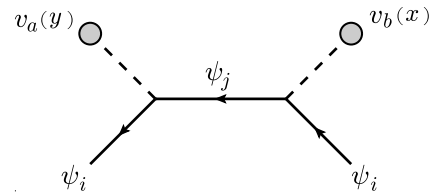

Fig. 1. A representative scattering process of ψ_i with the Higgs bubble walls, which leads to a dominant CP-violating source term for the BAU.

would vanish not only for $\mathrm{Im}(c_L c_R^*) = 0$ but also the cases in which one of the following condition is fulfilled: $v(X) = 0$, $\dot{\beta}(X) = 0$ and $\mathcal{I}^f_{ji} = 0$. Since the EWPT is of first order, the Higgs VEVs depend on a spacetime variable X, and the profiles of which can be determined by static bubble configurations at a nucleation temperature. In most cases, the shapes of $v(X)$ and $\beta(X)$ would be approximated by kink-type configurations, so the $\dot{\beta}(X)$ is proportional to a variation of $\beta(X)$ along the line connecting broken and symmetric phases. In the MSSM, $\dot{\beta}(X)$ roughly scales as $1/m_A^2$ [12], where m_A is the CP-odd Higgs boson mass, which implies that $S_{\psi_i}(X)$ in Eq. (4) would completely disappear if the Higgs sector is composed of only one Higgs doublet, as already indicated in the case of $\kappa_S = 0$. From this argument, it is expected that the presence of the extra Higgs boson with a nonzero VEV may be essential for successful EWBG, regardless of the strong first-order EWPT realization. Here, it should be reminded that there is another type of the source term that is not suppressed in the large m_A limit, which may appear as a higher order correction to the approximation we have made here (see, *e.g.*, Refs. [13,14]). As long as the BAU is explained by a resonant enhancement, which is indeed the case in our analysis, such a source term would not play a central role.[1]

The behavior of the thermal function $\mathcal{I}^f_{ji}$ is somewhat complicated, and in some specific region it is strongly governed by the finite temperature physics. The explicit form of $\mathcal{I}^f_{ji}$ is [8]

$$\begin{aligned} \mathcal{I}^f_{ji} = \int_k \frac{k^2}{\omega_j\omega_i}\Big[&\Big\{\big(1-2\mathrm{Re}(n_i)\big)I_{ji} + (i \leftrightarrow j)\Big\} \\ &- 2\big(\mathrm{Im}(n_j)+\mathrm{Im}(n_i)\big)G_{ji}\Big], \end{aligned} \tag{5}$$

where $\int_k = \int_0^\infty dk/(4\pi^2)$, $n_i = 1/(e^{(\omega_i - i\Gamma_i)/T}+1)$, $\omega_i = \sqrt{k^2+m_i^2}$, with Γ_i being the thermal widths of ψ_i. Here, I_{ij} and G_{ij} are respectively expressed by

$$I_{ij} = \Gamma_+\left[\frac{\omega_+}{(\omega_+^2+\Gamma_+^2)^2} + \frac{\omega_-}{(\omega_-^2+\Gamma_+^2)^2}\right], \tag{6}$$

$$G_{ij} = \frac{1}{2}\left[\frac{\omega_+^2-\Gamma_+^2}{(\omega_+^2+\Gamma_+^2)^2} - \frac{\omega_-^2-\Gamma_+^2}{(\omega_-^2+\Gamma_+^2)^2}\right], \tag{7}$$

where $\omega_\pm = \omega_i \pm \omega_j$ and $\Gamma_+ = \Gamma_i + \Gamma_j$. One can see that $\mathcal{I}^f_{ji}$ vanishes if $\Gamma_i = \Gamma_j = 0$. Since $\Gamma_{i,j} \simeq gT$, where g represents a typical coupling in a model and T a temperature, $S_{\psi_i}(X)$ first emerges to order of $\mathcal{O}(g^4)$ assuming $|c_L| = |c_R| \simeq g$.

[1] As nicely reviewed in Ref. [3] (see also Ref. [15]), it is known that the VEV insertion approximation is vulnerable to theoretical uncertainties and may yield an overestimated BAU compared to an all-order VEV resummation method [13,14,16]. However, it is shown in a scalar toy model that the resonance enhancement is still effective in more consistent treatment of transport equations [17]. Although a practical application to the EWBG remains open, especially for a fermion case, we expect that the VEV insertion method would give a reasonable order-of-magnitude estimate of the BAU.

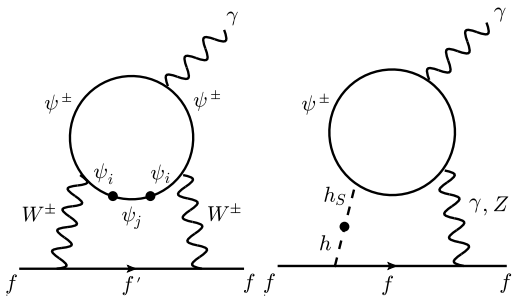

Fig. 2. Two-loop Barr–Zee diagrams induced by the BAU-related CP violation (left) and the BAU-unrelated one (right). The blobs indicate the mass insertions. Here, h and h_S are the Higgs bosons coming from the doublet and singlet, respectively. The size of the h-h_S mixing is intimately related to strength of the strong first-order EWPT in the tree potential driven scenario.

As is well known, S_{ψ_i} has a resonant enhancement at $m_i = m_j$, the behavior of which comes from G_{ij}. Since $\omega_{i,j} \gg \Gamma_{i,j}$, one may approximate G_{ij} as

$$G_{ij} \simeq -\frac{1}{2}\frac{\omega_-^2 - \Gamma_+^2}{(\omega_-^2 + \Gamma_+^2)^2} + \mathcal{O}\left(\frac{1}{\omega_+^2}\right). \tag{8}$$

One can see that G_{ij} has a peak at $\omega_- = 0$, which can yield the dominant source for the BAU.

We now study the impact of $\mathrm{Im}(c_L c_R^*)$ on the EDM. Since the new fermions have the EW charges, the following interactions exist.

$$\mathcal{L} = \frac{g_2}{\sqrt{2}}\left(\overline{\psi^+}\gamma^\mu \psi_i W_\mu^+ + \overline{\psi}_i \gamma^\mu \psi^+ W_\mu^-\right) - e\overline{\psi^+}\gamma^\mu \psi^+ A_\mu, \tag{9}$$

where $\psi^\pm$ denote electrically charged members in the $\mathrm{SU}(2)_L$ multiplet fermion. We assume that ψ_i is the neutral member of the same multiplet. In this case, the WW-mediated Barr–Zee diagram is induced, as shown in Fig. 2.[2] The EDM of a fermion f using the mass insertion method is given by

$$\begin{aligned}\frac{d_f^{WW}}{e} &= \mp\frac{\alpha_{\mathrm{em}}^2}{64\pi^2 s_W^4}\frac{m_f m_{\psi^\pm} m_j v_a v_b}{m_W^4}\mathrm{Im}(c_L c_R^*) F_{WW} \\ &\equiv C_{\mathrm{EDM}}^{WW}\,\mathrm{Im}(c_L c_R^*).\end{aligned} \tag{10}$$

where the negative (positive) sign is the case that f is up-type (down-type) fermion, $F_{WW} = (f_{WW}(r_i, r_+) - f_{WW}(r_j, r_+))/(m_i^2 - m_j^2)$ with $r_i = m_i^2/m_W^2$, $r_j = m_j^2/m_W^2$ and $r_\pm = m_{\psi^\pm}^2/m_W^2$. The explicit form of f_{WW} is given in Ref. [21]. We emphasize that unlike $S_{\psi_i}(X)$ in Eq. (4), Eq. (10) does not vanish for $(a, b) = (1, 1)$ or $(2, 2)$, in addition, d_f^{WW}/e is not enhanced at $m_i = m_j$, which are the prominent differences between the two CP-violating quantities. One may find that $d_f^{WW}/e \propto m_f m_j/m_i^3$ for $m_i \gg m_j$ and $d_f^{WW}/e \propto m_f/(m_i m_j)$ for $m_j \gg m_i$, which signifies another distinct feature of the EDM as discussed below. In what follows, we confine ourself to the cases of $(a, b) = (2, 1)$ and $(1, 2)$.

It is worth making a comment on that the mass insertion method used in Eq. (10) not only makes it easy to see the relationship between the CP-violating source term and the EDM but also gives the numerically good approximation.

[2] Here, we assume that the Higgs sector is CP conserving and extra Higgs bosons are sufficiently heavy. Under this assumption, the charged Higgs W-mediated Barr–Zee contribution induced by the same CP phase would be subdominant and the following discussion would not be altered drastically. The case without this assumption will be given in [18]. For a discussion of the EDMs in the CP-violating MSSM and 2HDM, see, *e.g.*, Refs. [19,20].

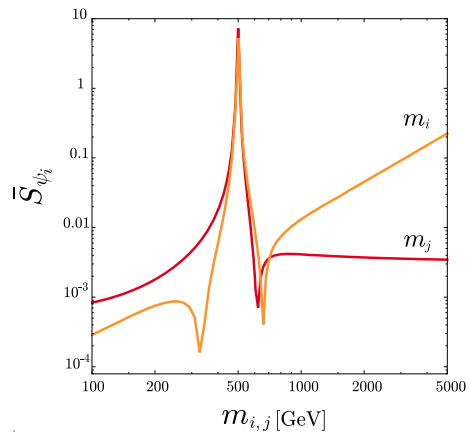

Fig. 3. $\bar{S}_{\psi_i}$ as a function of m_i with a fixed m_j and the other away around. We set $\tan\beta = 1$ and the fixed mass is 500 GeV.

Eliminating $\mathrm{Im}(c_L c_R^*)$ in Eq. (4) using Eq. (10), one finds

$$S_{\psi_i} = \frac{C_{\mathrm{BAU}}}{C_{\mathrm{EDM}}^{WW}}\left(\frac{d_f^{WW}}{e}\right). \tag{11}$$

In order to see the correlation between S_{ψ_i} and d_f^{WW}/e in more detail, we define

$$\bar{S}_{\psi_i} = \frac{C_{\mathrm{BAU}}}{v^2(X)\dot{\beta}(X) C_{\mathrm{EDM}}^{WW}} \cdot \left(\frac{d_f^{WW}}{e}\right)_{\mathrm{EXP}}. \tag{12}$$

In what follows, we consider the electron EDM as the experimental constraint, *i.e.*, $|d_e^{\mathrm{exp}}| = 8.7 \times 10^{-29}\ e \cdot \mathrm{cm}$ [22]. Here, we get rid of $v^2(X)\dot{\beta}(x)$ in C_{BAU} since it is rather model dependent.

In Fig. 3, $\bar{S}_{\psi_i}$ is plotted as a function of m_i with a fixed m_j or the other away around. As an example, we take $\tan\beta = 1$, and the fixed mass is set to 500 GeV. As explained above C_{BAU} has a peak at $m_i = m_j$. However, the decoupling behaviors in the large mass limits are substantially different from each other. For the varying m_j case, $\bar{S}_{\psi_i}$ becomes more or less flat in the large mass region while it grows for the varying m_i case. The latter is due to the rapid suppression of C_{EDM}^{WW} that scales as m_j/m_i^3 as mentioned above. Note that $\mathrm{Im}(c_L c_R^*) \gtrsim 1$ for $m_i \gtrsim 1$ TeV since d_f^{WW}/e is fixed.

Now we move on to discuss a possibility that the aforementioned correlation between the CP-violating source term and the EDM is spoiled by contamination of BAU-unrelated CP violation. As delineated below, such a situation can arise when we address the issue of the strong first-order EWPT.

The SM Higgs sector has to be extended in such a way that the EWPT is of first order. There are two representative cases for achieving this:

- Thermal loop driven case
- Tree potential driven case

For example, the former corresponds to the SM, MSSM and a two Higgs doublet model (2HDM) and so on. In such cases, the cubic-like terms arising from the bosonic thermal loops play an essential role in inducing the first-order EWPT. In the latter case, on the other hand, a specific structure of a tree-level Higgs potential is the dominant source for generating a barrier separating the two degenerate minima at a critical temperature. One of such an example is the EWPT in the SM with a real singlet Higgs boson (rSM) [23,24]. In this case, nonzero doublet-singlet Higgs mixing

terms are responsible for the strong first-order EWPT.[3] Once the singlet Higgs field (S) exists, it is conceivable that the following interactions may give rise to an extra source for CP violation.

$$\mathcal{L} = \overline{\psi^+}(g^S + i\gamma_5 g^P)\psi^+ S. \tag{13}$$

If the doublet-singlet Higgs mixing is present, the Higgs-photon(Z)-mediated Barr–Zee diagrams could be generated, as depicted in Fig. 2. In this case, the EDM is the sum of those diagrams, in addition to d_f^{WW}.

$$\frac{d_f}{e} = \frac{d_f^{WW}}{e} + \frac{d_f^{H\gamma}}{e} + \frac{d_f^{HZ}}{e}. \tag{14}$$

As far as EWBG is concerned, the new CP-violating phase appearing in Eq. (13) is not directly related to baryogenesis. Therefore, the linear correlation between the CP-violating source term and the EDM in Eq. (11) no longer hold. One of the interesting possibilities is that if a cancellation among those contributions becomes effective, it is possible for d_f to be made highly suppressed but with the nonzero d_f^{WW}, so the BAU-related CP violation is not constrained by a single EDM experiment in this case.

Nevertheless, one may probe such a parameter space with Higgs physics since the nonzero doublet-singlet Higgs mixing parameter and $g^{S,P}$ would lead to some deviations in the Higgs signal strengths. We will explicitly demonstrate this possibility in the next section.

So far, we have exclusively focused on the relationship between the CP-violating source term and the EDM. Here, we comment on the dependence of $\mathrm{Im}(c_L c_R^*)$ on the baryon number density (n_B) briefly. Under some mild assumptions, one may have

$$n_B = \kappa_B \frac{S_{\mathrm{CPV}}}{\sqrt{\Gamma_{\mathrm{CPC}}}}, \tag{15}$$

where κ_B is a coefficient. S_{CPV} is a CP-violating term arising from S_{ψ_i} discussed above and Γ_{CPC} a CP-conserving particle changing rate. For the latter, for example, the interactions in Eq. (2) induce

$$\Gamma_{\psi_i}(X) = \frac{1}{T}\Big[\big(|c_L|^2 v_a^2(X) + |c_R|^2 v_b^2(X)\big)\mathcal{F}_{ji} + 2\mathrm{Re}\big(c_L c_R^*\big) v_1(X) v_2(X) m_i m_j \mathcal{R}_{ji}\Big], \tag{16}$$

where $\mathcal{F}_{ji}$ and $\mathcal{R}_{ji}$ are the thermal functions presented in Ref. [11]. As studied in Ref. [27], Γ_{ψ_i} also has the resonant behavior at $m_i = m_j$, rendering n_B smaller. It should be emphasized that a cancellation between the first and second terms in Γ_{ψ_i} can happen depending on the choice of $\mathrm{Arg}(c_L c_R^*)$ and $m_{i,j}$. Therefore, n_B does not necessarily take its maximal value at $\mathrm{Arg}(c_L c_R^*) = \pi/2$ or $-\pi/2$, which may relax the EDM constraint to some extent.

3. A model

Now, we define our model and give basic ingredients for calculating the BAU and the electron EDM (previous studies along the same line can be found in Refs. [15,28]). The particle content of the Higgs and the new EW-interacting fermion sectors in the model is shown in Table 1. The total Lagrangian is given by

$$\mathcal{L} = \mathcal{L}_{2\mathrm{HDM}} + \frac{1}{2}\partial_\mu S \partial^\mu S - V_S - V_{\Phi S} + \mathcal{L}_{\tilde{\Phi}\tilde{S}},$$

[3] In singlet-extended models, there could be a nontrivial minimum on the singlet field axis induced by another phase transition prior to the EWPT. In contrast to this, the EWPT could occur by multi-steps which was first discussed in the 2HDM [25]. For a recent study on the multi-step EWPT, see, *e.g.*, Refs. [15,26].

Table 1
Particle content of the Higgs and the new EW-interacting fermion sectors.

Particles	$\mathrm{SU}(3)_C \times \mathrm{SU}(2)_L \times \mathrm{U}(1)_Y$	Z_2
Φ_1	$(\mathbf{1},\ \mathbf{2},\ 1/2)$	$-$
Φ_2	$(\mathbf{1},\ \mathbf{2},\ 1/2)$	$+$
S	$(\mathbf{1},\ \mathbf{1},\ 0)$	$-$
$\tilde{\Phi}_1$	$(\mathbf{1},\ \mathbf{2},\ -1/2)$	$-$
$\tilde{\Phi}_2$	$(\mathbf{1},\ \mathbf{2},\ 1/2)$	$+$
$\tilde{S}^0$	$(\mathbf{1},\ \mathbf{1},\ 0)$	$-$

$$\begin{aligned}\mathcal{L}_{\tilde{\Phi}\tilde{S}} = &\sum_{i=1,2} \overline{\tilde{\Phi}_i} i\bar{\sigma}^\mu D_\mu \tilde{\Phi}_i + \overline{\tilde{S}^0} i\bar{\sigma}^\mu \partial_\mu \tilde{S}^0 \\ &- \epsilon_{ab}\Big[\sum_{j=1,2}\Big(\tilde{\Phi}_1^a c_{1j}\Phi_j^b + \tilde{\Phi}_2^a c_{2j}(i\tau^2\Phi_j^{b*})\Big)\tilde{S}^0 \\ &\qquad + (\mu + \lambda S)\tilde{\Phi}_1^a\tilde{\Phi}_2^b + \mathrm{h.c.}\Big] \\ &+ \frac{1}{2}(\mu_{\tilde{S}} + \kappa S)\tilde{S}^0\tilde{S}^0 + \mathrm{h.c.},\end{aligned} \tag{17}$$

where $\tilde{\Phi}_{1,2}$ and $\tilde{S}^0$ are the two-component spinors, and $\epsilon_{12} = -\epsilon_{21} = +1$. As is the case in the MSSM, to avoid a lepton flavor violation, we impose a matter parity under which new EW-interacting fermions are odd and the SM fermions are even. Furthermore, as in the ordinary 2HDM, another Z_2 symmetry ($\Phi_1 \to -\Phi_1$ and $\Phi_2 \to \Phi_2$) is enforced to evade tree-level Higgs-mediated flavor-changing-neutral current processes. Depending on Z_2 charge assignments for the fermions, four types of the Yukawa interactions are possible. However, the following analysis does not depend on those types since the top Yukawa coupling is the only relevant that is common to all the types.

The Higgs fields are parametrized as

$$\Phi_{i=1,2}(x) = \begin{pmatrix}\phi_i^+ \\ \phi_i^0\end{pmatrix} = \begin{pmatrix}\phi_i^+ \\ \frac{1}{\sqrt{2}}(v_i + h_i(x) + ia_i(x))\end{pmatrix}, \tag{18}$$

$$S(x) = v_S + h_S(x), \tag{19}$$

where $v_1 = v\cos\beta$, $v_2 = v\sin\beta$ with $v = 246$ GeV.

In the following, we consider a CP-conserving Higgs sector and take a rSM-like limit in which $\sin(\beta - \alpha) = 1$, where α denotes a mixing angle between two CP-even Higgs bosons ($h_{1,2}$). In this case, only one state (defined as h) has the VEV and gives the masses of the gauge bosons and fermions. Since the strong first-order EWPT is assumed to be driven by the tree-Higgs potential, the heavy Higgs bosons do not necessarily have the so-called non-decoupling effect which is needed in the thermal loop driven strong first-order EWPT case [29] (for a recent work, see, *e.g.*, Ref. [30]). The detailed comparison between the two cases will be given elsewhere [18].

Since we have the singlet Higgs boson in this model, h mixes with h_S through a mixing γ as

$$\begin{pmatrix}h \\ h_S\end{pmatrix} = \begin{pmatrix}c_\gamma & -s_\gamma \\ s_\gamma & c_\gamma\end{pmatrix}\begin{pmatrix}H_1 \\ H_2\end{pmatrix}. \tag{20}$$

In our scenario, H_1 is the SM-like Higgs boson whose mass is 125 GeV, and H_2 is the singlet-like Higgs boson which is assumed to be heavier than H_1. Another CP-even Higgs boson originated from the Higgs doublet is denoted as H_3 which is heavier than H_2.

In response to Z_2 charges assignments of $\tilde{\Phi}_{1,2}$ and $\tilde{S}$, there are several types of the interactions among the new EW-interacting fermions and Higgs bosons [18]. Here, we focus on one of them as an example. The Z_2 charge assignment is listed in Table 1.

The relevant interactions among the EW-interacting fermions and Higgs bosons are

$$\mathcal{L}^{\rm int}_{\Phi\tilde{S}} \ni -\sum_{i=1,2} H_i \overline{\tilde{H}^+}\left(g^S_{H_i\tilde{\bar{H}}\tilde{H}} + i\gamma_5 g^P_{H_i\tilde{\bar{H}}\tilde{H}}\right)\tilde{H}^+ + \left[\overline{\tilde{H}^0}\left(c_L^{\tilde{H}^0\tilde{S}}\phi_2^0 P_L + c_R^{\tilde{H}^0\tilde{S}}\phi_1^0 P_R\right)\tilde{S} + \text{h.c.}\right], \tag{21}$$

where the fermions are expressed in terms of the four-component spinors. Each coupling is respectively given by

$$g^S_{H_1\tilde{\bar{H}}\tilde{H}} = |\lambda|\cos\phi_{\lambda\tilde{H}} s_\gamma, \quad g^P_{H_1\tilde{\bar{H}}\tilde{H}} = -|\lambda|\sin\phi_{\lambda\tilde{H}} s_\gamma, \tag{22}$$

$$g^S_{H_2\tilde{\bar{H}}\tilde{H}} = |\lambda|\cos\phi_{\lambda\tilde{H}} c_\gamma, \quad g^P_{H_2\tilde{\bar{H}}\tilde{H}} = -|\lambda|\sin\phi_{\lambda\tilde{H}} c_\gamma, \tag{23}$$

$$c_L^{\tilde{H}^0\tilde{S}} = -c_{12}e^{-i\phi_{\tilde{S}}/2}, \quad c_R^{\tilde{H}^0\tilde{S}} = c_{21}^* e^{i(\phi_{\tilde{H}}+\phi_{\tilde{S}}/2)}, \tag{24}$$

where we have defined $\lambda = |\lambda|e^{i\phi_\lambda}$, $\mu + \lambda v_S = |\mu + \lambda v_S|e^{i\phi_{\tilde{H}}}$, $\mu_{\tilde{S}} = |\mu_{\tilde{S}}|e^{i\phi_{\tilde{S}}}$ and $\phi_{\lambda\tilde{H}} = \phi_\lambda - \phi_{\tilde{H}}$. As discussed in the previous section, the interactions in the second line of Eq. (21) plays an essential role in generating the CP-violating term that fuels the BAU. For notational simplicity, we define $\phi = -(\phi_{\tilde{H}} + \phi_{\tilde{S}})$ hereafter.

4. Numerical analysis

Following a calculation method formulated and developed in Refs. [8,27,31], we estimate n_B by

$$n_B = \frac{-3\Gamma_B^{(s)}}{2D_q\lambda_+}\int_{-\infty}^{0} dz' n_L(z')e^{-\lambda_- z'}, \tag{25}$$

where $\lambda_\pm = \left[v_w \pm \sqrt{v_w^2 + 4\mathcal{R}D_q}\right]/(2D_q)$, $\Gamma_B^{(s)}$ is a baryon number changing rate in the symmetric phase, v_w is a velocity of the bubble wall, D_q is a diffusion constant of the quarks, and $\mathcal{R}$ is a relaxation term, which is $(15/4)\Gamma_B^{(s)}$ in our model. n_L is the total number density of all the left-handed quarks and leptons [27,31,32]. We follow the estimation of n_L performed in [27].

Since the EWPT is reduced to that in the rSM, we adopt S2 scenario investigated in Ref. [24] as a benchmark in which $m_{H_2} = 170$ GeV, $\cos\gamma \simeq 0.94$ and $v_C/T_C = 206.75$ GeV/111.76 GeV. In addition, we take $\tan\beta = 1$, $v_w = 0.4$, $\Gamma_{\tilde{H}} = 0.025T$, $\Gamma_{\tilde{S}} = 0.003T$, and use an approximation, $\dot{\beta} = v_w\Delta\beta/L_w$ taking $\Delta\beta = 0.015$. Under this assumption, n_B does not depend on L_w. Moreover, the constant VEV but $v_C/2$ is used in calculating n_B, which may give a simple approximation of kink-type VEV [18]. For the heavy Higgs boson masses, we set 400 GeV, and for a softly Z_2 broken mass, which is a mixing mass between Φ_1 and Φ_2, 250 GeV is taken. For the other parameters, we refer to the values adopted in Ref. [11]. In the following, the electron EDM is calculated in the mass eigenbasis of the neutral fermions rather than the mass insertion method, although the both are not much numerically different.

We first present the case where the electron EDM is induced by only the WW-mediated Barr–Zee diagram. In Fig. 4, contours of $Y_B/Y_B^{\rm obs}$ and $|d_e|$ are shown in the $(m_{\tilde{H}}, m_{\tilde{S}})$ plane. We take $|c_L^{\tilde{H}^0\tilde{S}}| = |c_R^{\tilde{H}^0\tilde{S}}| = 0.42$, $\phi = 225°$ and $|\lambda| = 0$. Here, ϕ is chosen in such a way that the cancellation in $\Gamma_{\rm CPC}$ is effective. In this figure, the orange region is excluded by the current experimental limit of the electron EDM, $|d_e^{\rm exp}| < 8.7\times10^{-29}$ $e\cdot$cm, and the dashed line corresponds to $|d_e| = 1.0\times10^{-29}$ $e\cdot$cm which is reachable by the future experiments [33]. The black solid (dashed) line indicates $Y_B/Y_B^{\rm obs} = 1$ (0.1). One can see that $|d_e|$ gets rapidly suppressed as $m_{\tilde{H}}$ increases but does not in the large $m_{\tilde{S}}$ case, as discussed in Sec. 2. Furthermore, the BAU is sufficiently generated if $m_{\tilde{H}} \simeq m_{\tilde{S}}$

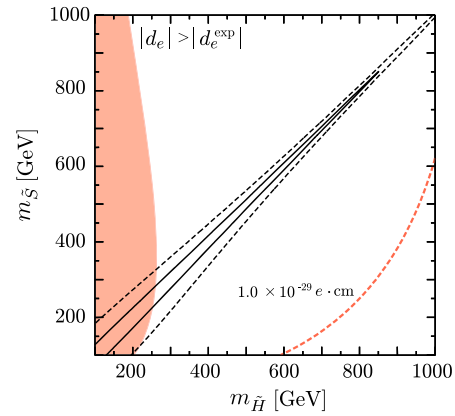

Fig. 4. The contours of $Y_B/Y_B^{\rm obs}$ and $|d_e|$ in the $(m_{\tilde{H}}, m_{\tilde{S}})$ plane. The region colored in orange is excluded by the current experimental limit of the electron EDM, and the orange dashed line corresponds to $|d_e| = 1.0\times10^{-29}$ $e\cdot$cm. The black solid and dashed lines represent $Y_B/Y_B^{\rm obs} = 1$ and 0.1, respectively. We set $|c_L^{\tilde{H}^0\tilde{S}}| = |c_R^{\tilde{H}^0\tilde{S}}| = 0.42$ and $\phi = 225°$. (For interpretation of the references to color in this figure legend, the reader is referred to the web version of this article.)

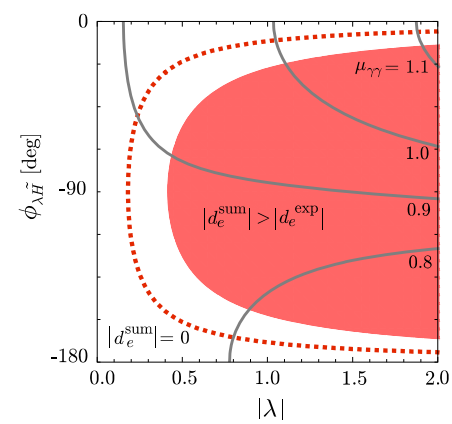

Fig. 5. Impact of BAU-unrelated CP violation on $|d_e|$. The region colored in red is excluded by the current experimental limit of the electron EDM, and the red dashed line corresponds to $|d_e^{\rm sum}| = |d_e^{WW} + d_e^{H\gamma}| = 0$. The gray lines represent $\mu_{\gamma\gamma} = 1.1,\ 1.0,\ 0.9$ and 0.8 from top to bottom. The input parameters are the same as in Fig. 4, but with $m_{\tilde{H}} = 300$ GeV and $m_{\tilde{S}} = 277$ GeV, which gives $Y_B/Y_B^{\rm obs} = 1$. (For interpretation of the references to color in this figure legend, the reader is referred to the web version of this article.)

due to the resonant effect. Our result shows that the successful EWBG region would be entirely verified by the future experiments of the electron EDM even if the BAU calculated here is underestimated by a factor of 10 or even more due to lack of precise knowledge of the bubble profiles etc.

Next, we consider the case in which the BAU-unrelated CP-violating phase $\phi_{\lambda\tilde{H}}$ comes into play. Fig. 5 shows the electron EDM in the $(|\lambda|, \phi_{\lambda\tilde{H}})$ plane. In this figure, we take the same input parameters as in Fig. 4, but with $m_{\tilde{H}} = 300$ GeV and $m_{\tilde{S}} = 277$ GeV, which yields $Y_B/Y_B^{\rm obs} = 1$. Here, we define $d_e^{\rm sum} = d_e^{WW} + d_e^{H\gamma}$. Note that d_e^{HZ} is accidentally suppressed with a factor of $(1/4 - \sin^2\theta_W) \simeq 0.02$ and thus numerically unimportant. While the red region is excluded by the current limit of the electron EDM, the dashed line indicates the exquisite cancellation between d_e^{WW} and $d_e^{H\gamma}$, resulting in $d_e^{\rm sum} = 0$.

In such a case, it is worth while to consider the other EDMs which might be complementary. The naive estimates show that $d_u \sim -1/3(m_u/m_e)d_e^{WW}$ and $d_d \sim 2/3(m_d/m_e)d_e^{WW}$ under the condition of $d_e^{\rm sum} = 0$, which lead to $d_n \sim d_p \sim \mathcal{O}(1)\times10^{-28}$ $e\cdot$cm. Although the current experimental bounds of d_n and d_p are not

strong enough to probe this parameter region, the future experiments might be accessible. For example, it is expected that $|d_n| < 3 \times 10^{-28}$ $e \cdot$cm at the Spallation Neutron Source [34] and $|d_n| < 1 \times 10^{-28}$ $e \cdot$cm at TRIUMF [34], and the future experimental sensitivity of d_p would be 10^{-29} $e \cdot$cm at Brookhaven National Laboratory [35]. Since it seems impossible to have the sufficient BAU with more suppressed d_n and d_p than such experimental sensitivities, the EWBG-viable region in this model would be fully tested. Detailed analysis with extensive numerical work will be conducted in Ref. [18].

Since $d_e^{H\gamma}$ is correlated with the signal strength of the Higgs decay to two gammas (denoted by $\mu_{\gamma\gamma}$, for the explicit formula, see, *e.g.,* Ref. [36]), we also examine it. $\mu_{\gamma\gamma}$ is represented by the gray lines: $\mu_{\gamma\gamma} = 1.1,\ 1.0,\ 0.9,$ and 0.8 from top to bottom. The whole region is still within the 2σ region of the current LHC data, $\mu_{\gamma\gamma} = 1.17 \pm 0.27$ (ATLAS) and $\mu_{\gamma\gamma} = 1.14^{+0.26}_{-0.23}$ (CMS). We remark that the sensitivity of $\mu_{\gamma\gamma}$ is expected to be improved up to $\mathcal{O}(5)\%$, and Higgs coupling to the gauge bosons ($\cos\gamma$ in the current setup) up to $\mathcal{O}(0.1)\%$ at future colliders such as the high-luminosity LHC (HL-LHC) [37], International Linear Collider (ILC) [38] and TLEP [39]. Therefore, the testability of EWBG in this scenario still persists.

Before closing this section, we briefly mention about the differences between our results and those in Refs. [15,28]. In Ref. [28], $d_e^{WW} = 0$ if the two vector-like fermion masses are degenerate, and the dominant contribution in d_e may come from the $d_e^{H\gamma}$-type Barr–Zee diagram. As pointed out in [28,40], this contribution could be canceled by the singlet Higgs boson if exists. This cancellation mechanism is in stark contrast to our case in which $d_e^{H\gamma} \simeq -d_e^{WW} \neq 0$. In Ref. [15], on the other hand, one may obtain $d_e(\simeq d_e^{H\gamma}) = 0$ without relying on any cancellation mechanism while maintaining the BAU, which differs from our case as well. Correspondingly, $\mu_{\gamma\gamma}$ in the most EWBG-viable region in each model can be different.

5. Conclusions

We have studied the relationship between the CP-violating source term for the BAU and the EDMs in the framework where the extra Higgs doublet and the singlet as well as the new EW-interacting fermions ($\psi_{i,j}$) are introduced. We scrutinized the ratio $\bar{S}_{\psi_i}$ (defined by Eq. (12)) as functions of the EW-interacting fermion masses. In the region where new fermions are degenerate, $\bar{S}_{\psi_i}$ is resonantly enhanced due to the thermal effect appearing in the source term. In the large mass limits of the fermions, on the other hand, $\bar{S}_{\psi_i}$ gets milder or larger depending on the fermion species, and the behaviors of which are mostly governed by the property of the loop function of the EDM rather than that of the CP-violating source term for the BAU.

As a concrete example, we considered the next-to-MSSM-like model and investigated the correlation between the BAU and the electron EDM for a typical parameter set. It is found that as long as the BAU-related CP violation predominantly exists, the current electron EDM places some constraints on the EWBG-favored region, and more importantly, it would probe the whole region if it is improved up to 1.0×10^{-29} $e \cdot$cm. However, once the BAU-unrelated CP violation comes into action, the strong connection between the BAU and electron EDM is not guaranteed any more, which makes it challenging to probe the parameter space with the electron EDM only. Nevertheless, even in such a case, the scenario could be probed with the aid of Higgs physics.

Acknowledgements

This work is supported by Grant-in-Aid for Scientific research from the Ministry of Education, Science, Sports, and Culture (MEXT), Japan, No. 23104011 (J.H.). The work of J.H. is also supported by World Premier International Research Center Initiative (WPI Initiative), MEXT, Japan. The work of K.F. is supported by Research Fellowships of the Japan Society for the Promotion of Science for Young Scientists, No. 15J01079. E.S. is supported in part by the Ministry of Science and Technology, Taiwan under Grant No. MOST 104-2811-M-008-011.

References

[1] G. Aad, et al., ATLAS Collaboration, Phys. Lett. B 716 (2012) 1;
S. Chatrchyan, et al., CMS Collaboration, Phys. Lett. B 716 (2012) 30.
[2] V.A. Kuzmin, V.A. Rubakov, M.E. Shaposhnikov, Phys. Lett. B 155 (1985) 36;
For reviews on electroweak baryogenesis, see A.G. Cohen, D.B. Kaplan, A.E. Nelson, Annu. Rev. Nucl. Part. Sci. 43 (1993) 27;
M. Quiros, Helv. Phys. Acta 67 (1994) 451;
V.A. Rubakov, M.E. Shaposhnikov, Usp. Fiz. Nauk 166 (1996) 493;
K. Funakubo, Prog. Theor. Phys. 96 (1996) 475;
M. Trodden, Rev. Mod. Phys. 71 (1999) 1463;
W. Bernreuther, Lect. Notes Phys. 591 (2002) 237;
J.M. Cline, arXiv:hep-ph/0609145;
T. Konstandin, Phys. Usp. 56 (2013) 747, Usp. Fiz. Nauk 183 (2013) 785.
[3] D.E. Morrissey, M.J. Ramsey-Musolf, New J. Phys. 14 (2012) 125003.
[4] K. Kajantie, M. Laine, K. Rummukainen, M.E. Shaposhnikov, Phys. Rev. Lett. 77 (1996) 2887;
K. Rummukainen, M. Tsypin, K. Kajantie, M. Laine, M.E. Shaposhnikov, Nucl. Phys. B 532 (1998) 283;
F. Csikor, Z. Fodor, J. Heitger, Phys. Rev. Lett. 82 (1999) 21;
Y. Aoki, F. Csikor, Z. Fodor, A. Ukawa, Phys. Rev. D 60 (1999) 013001.
[5] M.B. Gavela, P. Hernandez, J. Orloff, O. Pene, Mod. Phys. Lett. A 9 (1994) 795;
M.B. Gavela, P. Hernandez, J. Orloff, O. Pene, C. Quimbay, Nucl. Phys. B 430 (1994) 382;
P. Huet, E. Sather, Phys. Rev. D 51 (1995) 379;
T. Konstandin, T. Prokopec, M.G. Schmidt, Nucl. Phys. B 679 (2004) 246.
[6] T. Cohen, D.E. Morrissey, A. Pierce, Phys. Rev. D 86 (2012) 013009;
D. Curtin, P. Jaiswal, P. Meade, J. High Energy Phys. 1208 (2012) 005;
M. Carena, G. Nardini, M. Quiros, C.E.M. Wagner, J. High Energy Phys. 1302 (2013) 001;
K. Krizka, A. Kumar, D.E. Morrissey, Phys. Rev. D 87 (9) (2013) 095016.
[7] A. Katz, M. Perelstein, M.J. Ramsey-Musolf, P. Winslow, Phys. Rev. D 92 (9) (2015) 095019.
[8] A. Riotto, Nucl. Phys. B 518 (1998) 339;
A. Riotto, Phys. Rev. D 58 (1998) 095009.
[9] Y. Li, S. Profumo, M. Ramsey-Musolf, Phys. Lett. B 673 (2009) 95.
[10] K. Cheung, T.J. Hou, J.S. Lee, E. Senaha, Phys. Lett. B 710 (2012) 188.
[11] E. Senaha, Phys. Rev. D 88 (5) (2013) 055014.
[12] J.M. Moreno, M. Quiros, M. Seco, Nucl. Phys. B 526 (1998) 489.
[13] M. Carena, J.M. Moreno, M. Quiros, M. Seco, C.E.M. Wagner, Nucl. Phys. B 599 (2001) 158.
[14] M. Carena, M. Quiros, M. Seco, C.E.M. Wagner, Nucl. Phys. B 650 (2003) 24.
[15] S. Inoue, G. Ovanesyan, M.J. Ramsey-Musolf, arXiv:1508.05404 [hep-ph].
[16] T. Konstandin, T. Prokopec, M.G. Schmidt, Nucl. Phys. B 716 (2005) 373;
T. Konstandin, T. Prokopec, M.G. Schmidt, M. Seco, Nucl. Phys. B 738 (2006) 1.
[17] V. Cirigliano, C. Lee, M.J. Ramsey-Musolf, S. Tulin, Phys. Rev. D 81 (2010) 103503;
V. Cirigliano, C. Lee, S. Tulin, Phys. Rev. D 84 (2011) 056006.
[18] K. Fuyuto, J. Hisano, E. Senaha, in preparation.
[19] Y. Li, S. Profumo, M. Ramsey-Musolf, Phys. Rev. D 78 (2008) 075009.
[20] T. Abe, J. Hisano, T. Kitahara, K. Tobioka, J. High Energy Phys. 1401 (2014) 106;
S. Inoue, M.J. Ramsey-Musolf, Y. Zhang, Phys. Rev. D 89 (11) (2014) 115023;
K. Cheung, J.S. Lee, E. Senaha, P.Y. Tseng, J. High Energy Phys. 1406 (2014) 149.
[21] J. Ellis, J.S. Lee, A. Pilaftsis, J. High Energy Phys. 1010 (2010) 049.
[22] J. Baron, et al., ACME Collaboration, Science 343 (2014) 269.
[23] J. Choi, R.R. Volkas, Phys. Lett. B 317 (1993) 385;
J.R. Espinosa, M. Quiros, Phys. Lett. B 305 (1993) 98;
K.E.C. Benson, Phys. Rev. D 48 (1993) 2456;
S. Das, P.J. Fox, A. Kumar, N. Weiner, J. High Energy Phys. 1011 (2010) 108;
D.J.H. Chung, A.J. Long, Phys. Rev. D 84 (2011) 103513;
P.H. Damgaard, D. O'Connell, T.C. Petersen, A. Tranberg, Phys. Rev. Lett. 111 (22) (2013) 221804;
S. Profumo, M.J. Ramsey-Musolf, G. Shaughnessy, J. High Energy Phys. 0708 (2007) 010;

S. Profumo, M.J. Ramsey-Musolf, C.L. Wainwright, P. Winslow, Phys. Rev. D 91 (3) (2015) 035018;
J.M. Cline, K. Kainulainen, J. Cosmol. Astropart. Phys. 1301 (2013) 012.
[24] K. Fuyuto, E. Senaha, Phys. Rev. D 90 (1) (2014) 015015.
[25] D. Land, E.D. Carlson, Phys. Lett. B 292 (1992) 107;
A. Hammerschmitt, J. Kripfganz, M.G. Schmidt, Z. Phys. C 64 (1994) 105.
[26] H.H. Patel, M.J. Ramsey-Musolf, Phys. Rev. D 88 (2013) 035013;
N. Blinov, J. Kozaczuk, D.E. Morrissey, C. Tamarit, Phys. Rev. D 92 (3) (2015) 035012.
[27] C. Lee, V. Cirigliano, M.J. Ramsey-Musolf, Phys. Rev. D 71 (2005) 075010.
[28] W. Chao, M.J. Ramsey-Musolf, J. High Energy Phys. 1410 (2014) 180.
[29] K. Funakubo, A. Kakuto, K. Takenaga, Prog. Theor. Phys. 91 (1994) 341;
S. Kanemura, Y. Okada, E. Senaha, Phys. Lett. B 606 (2005) 361.
[30] G.C. Dorsch, S.J. Huber, J.M. No, J. High Energy Phys. 1310 (2013) 029;
G.C. Dorsch, S.J. Huber, K. Mimasu, J.M. No, Phys. Rev. Lett. 113 (21) (2014) 211802;
K. Fuyuto, E. Senaha, Phys. Lett. B 747 (2015) 152.
[31] P. Huet, A.E. Nelson, Phys. Rev. D 53 (1996) 4578.
[32] A.G. Cohen, D.B. Kaplan, A.E. Nelson, Phys. Lett. B 336 (1994) 41.
[33] Y. Sakemi, K. Harada, T. Hayamizu, M. Itoh, H. Kawamura, S. Liu, H.S. Nataraj, A. Oikawa, et al., J. Phys. Conf. Ser. 302 (2011) 012051;
D.M. Kara, I.J. Smallman, J.J. Hudson, B.E. Sauer, M.R. Tarbutt, E.A. Hinds, New J. Phys. 14 (2012) 103051;
D. Kawall, J. Phys. Conf. Ser. 295 (2011) 012031.
[34] J.L. Hewett, et al., arXiv:1205.2671 [hep-ex];
K. Kumar, Z.T. Lu, M.J. Ramsey-Musolf, arXiv:1312.5416 [hep-ph].
[35] V. Anastassopoulos, et al., arXiv:1502.04317 [physics.acc-ph].
[36] C.W. Chiang, E. Senaha, Phys. Lett. B 750 (2015) 147.
[37] ATLAS Collaboration, arXiv:1307.7292 [hep-ex];
CMS Collaboration, arXiv:1307.7135.
[38] H. Baer, T. Barklow, K. Fujii, Y. Gao, A. Hoang, S. Kanemura, J. List, H.E. Logan, et al., arXiv:1306.6352 [hep-ph];
T. Barklow, J. Brau, K. Fujii, J. Gao, J. List, N. Walker, K. Yokoya, arXiv:1506.07830 [hep-ex].
[39] M. Bicer, et al., TLEP Design Study Working Group Collaboration, J. High Energy Phys. 1401 (2014) 164.
[40] D. McKeen, M. Pospelov, A. Ritz, Phys. Rev. D 86 (2012) 113004.

先端加速器 LHC が切り拓くテラスケールの素粒子物理学
～真空と時空への新たな挑戦～
平成 23 年度～平成 27 年度科学研究費助成事業(科学研究費補助金)
（新学術領域研究(研究領域提案型)）

領域ホームページ
http://www.icepp.s.u-tokyo.ac.jp/terascale/